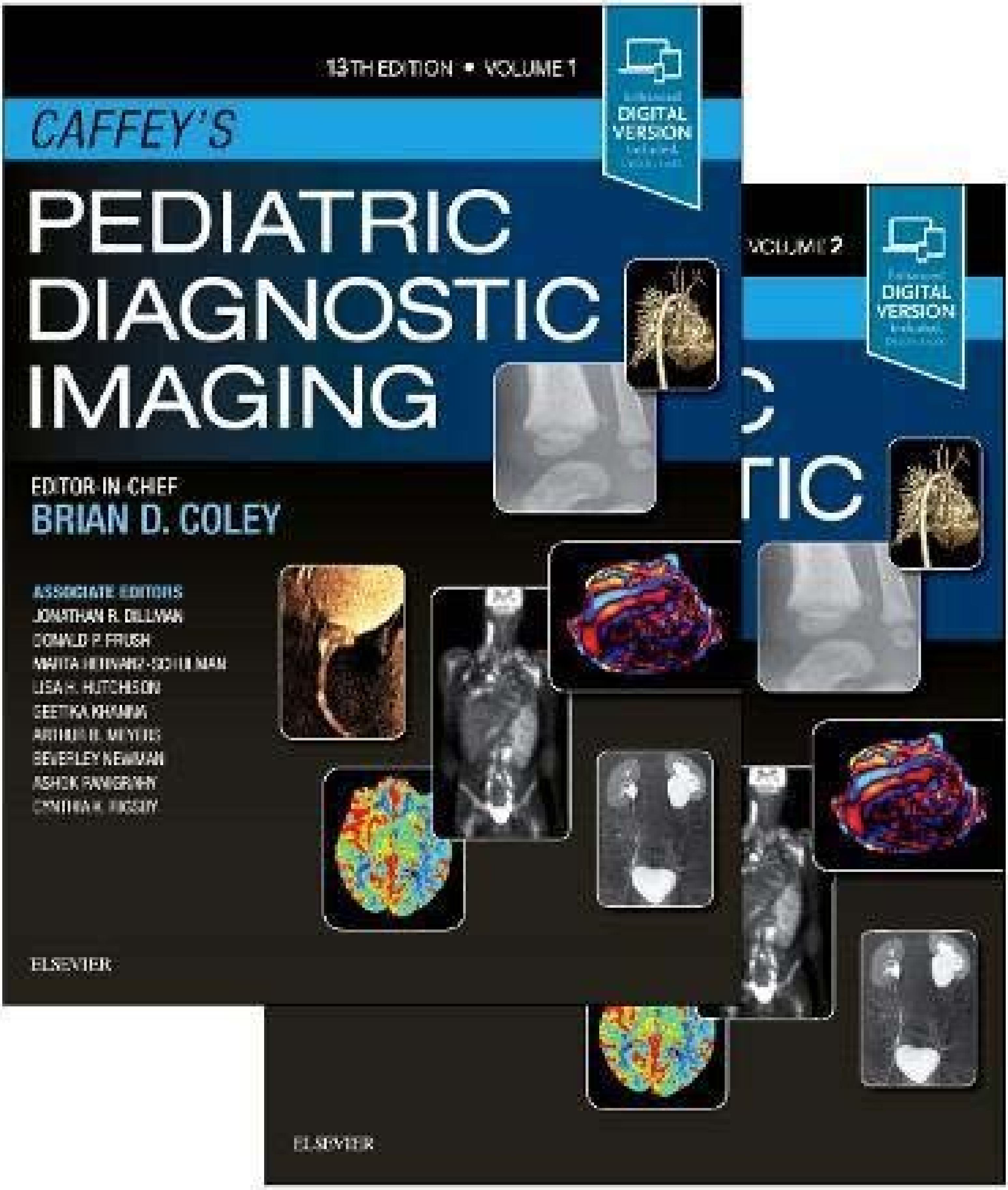

13TH EDITION • VOLUME 1

# CAFFEY'S
# PEDIATRIC DIAGNOSTIC IMAGING

EDITOR-IN-CHIEF
**BRIAN D. COLEY**

ASSOCIATE EDITORS
JONATHAN R. DILLMAN
DONALD P. FRUSH
MARTA HERNANZ-SCHULMAN
LISA H. HUTCHISON
GEETIKA KHANNA
ARTHUR B. MEYERS
BEVERLEY NEWMAN
ASHOK PANIGRAHY
CYNTHIA K. RIGSBY

ELSEVIER

# 2-Volume Set

# *CAFFEY'S*
# PEDIATRIC DIAGNOSTIC IMAGING

# CAFFEY'S

# PEDIATRIC DIAGNOSTIC IMAGING

13TH EDITION

**Editor-in-Chief**

**BRIAN D. COLEY, MD**
Radiologist-in-Chief
The Frederic N. Silverman Chair of Pediatric Radiology
Department of Radiology
Cincinnati Children's Hospital Medical Center
Professor
Departments of Radiology and Pediatrics
University of Cincinnati College of Medicine
Cincinnati, Ohio

ELSEVIER

ELSEVIER

1600 John F. Kennedy Blvd.
Ste 1800
Philadelphia, PA 19103-2899

**Caffey's Pediatric Diagnostic Imaging,** Thirteenth Edition ISBN: 978-0-323-49748-0
**Copyright © 2019 by Elsevier, Inc. All rights reserved.**

No part of this publication may be reproduced or transmitted in any form or by any means, electronic or mechanical, including photocopying, recording, or any information storage and retrieval system, without permission in writing from the publisher. Details on how to seek permission, further information about the Publisher's permissions policies and our arrangements with organizations such as the Copyright Clearance Center and the Copyright Licensing Agency, can be found at our website: www.elsevier.com/permissions.

This book and the individual contributions contained in it are protected under copyright by the Publisher (other than as may be noted herein).

**Notices**

Knowledge and best practice in this field are constantly changing. As new research and experience broaden our understanding, changes in research methods, professional practices, or medical treatment may become necessary.

Practitioners and researchers must always rely on their own experience and knowledge in evaluating and using any information, methods, compounds, or experiments described herein. In using such information or methods they should be mindful of their own safety and the safety of others, including parties for whom they have a professional responsibility.

With respect to any drug or pharmaceutical products identified, readers are advised to check the most current information provided (i) on procedures featured or (ii) by the manufacturer of each product to be administered, to verify the recommended dose or formula, the method and duration of administration, and contraindications. It is the responsibility of practitioners, relying on their own experience and knowledge of their patients, to make diagnoses, to determine dosages and the best treatment for each individual patient, and to take all appropriate safety precautions.

To the fullest extent of the law, neither the Publisher nor the authors, contributors, or editors, assume any liability for any injury and/or damage to persons or property as a matter of products liability, negligence or otherwise, or from any use or operation of any methods, products, instructions, or ideas contained in the material herein.

Previous editions copyright 2013 by Saunders; 2008, 2004, 1993, 1985, 1978, 1972, 1967, 1961, 1956, 1950, 1945 by Mosby; imprints of Elsevier, Inc.

ISBN: 978-0-323-49748-0

Library of Congress Cataloging-in-Publication Data

Names: Coley, Brian D., editor.
Title: Caffey's pediatric diagnostic imaging / editor-in-chief, Brian D. Coley.
Other titles: Pediatric diagnostic imaging
Description: Thirteenth edition. | Philadelphia, PA : Elsevier, [2019] | Includes bibliographical references and index.
Identifiers: LCCN 2017028145 | ISBN 9780323497480 (hardcover : alk. paper)
Subjects: | MESH: Diagnostic Imaging–methods | Child | Infant | Fetal Diseases–diagnosis | Prenatal Diagnosis–methods
Classification: LCC RJ51.R3 | NLM WN 240 | DDC 618.92/007572–dc23 LC record available at https://lccn.loc.gov/2017028145

*Content Strategist:* Robin Carter
*Content Development Specialist:* Ann Anderson
*Publishing Services Manager:* Patricia Tannian
*Project Manager:* Stephanie Turza
*Design Direction:* Renee Duenow

Printed in China

Last digit is the print number: 9 8 7 6 5 4 3 2 1

Working together
to grow libraries in
developing countries

www.elsevier.com • www.bookaid.org

*For our children.*

*And to the memory of Tom Slovis, MD*
*(1941-2018)*
*Former editor of this text, radiologist, clinician,*
*mentor, friend, mensch.*

# Associate Editors

**Jonathan R. Dillman, MD, MSc**
Associate Professor
Associate Chief of Research
Medical Director, Imaging Research Center
Department of Radiology
Cincinnati Children's Hospital Medical Center
University of Cincinnati College of Medicine
Cincinnati, Ohio

**Donald P. Frush, MD, FACR, FAAP**
Professor of Radiology and Pediatrics
Duke University Medical Center
Durham, North Carolina

**Marta Hernanz-Schulman, MD, FAAP, FACR**
Professor of Radiology and Pediatrics
Departments of Radiology and Radiological Sciences
Vanderbilt University Medical Center
Radiology Vice-Chair in Pediatrics
Medical Director, Diagnostic Imaging
Monroe Carell Jr. Children's Hospital at Vanderbilt
Nashville, Tennessee

**Lisa H. Hutchison, MD, FAAP, FACR**
Director, Pediatric Radiology
Alliance Radiology
Overland Park Regional Medical Center
Overland Park, Kansas

**Geetika Khanna, MD, MS**
Professor of Radiology
Mallinckrodt Institute of Radiology
Radiologist-in-Chief
St. Louis Children's Hospital
Washington University School of Medicine
St. Louis, Missouri

**Arthur B. Meyers, MD**
Department of Radiology
Nemours Children's Health System
Nemours Children's Hospital
Associate Professor of Radiology
University of Central Florida College of Medicine
Clinical Associate Professor of Pediatric Radiology
The Florida State College of Medicine
Orlando, Florida

**Beverley Newman, BSc, MB BCh**
Professor of Radiology
Department of Radiology
Lucile Packard Children's Hospital
Stanford University
Stanford, California

**Ashok Panigrahy, MD**
Professor
Radiologist-in-Chief
Children's Hospital of Pittsburgh of UPMC
Vice Chair, Clinical and Translational Imaging Research
Department of Radiology
University of Pittsburgh Medical Center
Pittsburgh, Pennsylvania

**Cynthia K. Rigsby, MD, FACR**
Pediatric Radiologist
Department of Medical Imaging
Ann & Robert H. Lurie Children's Hospital of Chicago
Professor
Departments of Radiology and Pediatrics
Northwestern University Feinberg School of Medicine
Chicago, Illinois

# Contributors

**Wael Abdalla, MD**
Asisstant Professor
Children's Hospital of Pittsburgh of UPMC
Department of Radiology
University of Pittsburgh Medical Center
Pittsburgh, Pennsylvania

**Kalie Adler, DO**
Diagnostic Radiologist
Kansas City, Missouri

**Prachi P. Agarwal, MD**
Clinical Professor
Division of Cardiothoracic Radiology
Department of Radiology
University of Michigan
Ann Arbor, Michigan

**Tahani M. Ahmad, MD**
Staff Pediatric Radiologist and Neuroradiologist
Department of Diagnostic Imaging
IWK Health Center
Assistant Professor
Department of Medical Imaging
Dalhousie University
Halifax, Nova Scotia, Canada

**Evelyn Y. Anthony, MD**
Professor of Radiology and Pediatrics
Department of Radiological Sciences
Wake Forest School of Medicine
Winston-Salem, North Carolina

**Christopher G. Anton, MD**
Associate Professor
Department of Radiology
Cincinnati Children's Hospital Medical Center
Cincinnati, Ohio

**Sudha A. Anupindi, MD**
Director of Pediatric Gastrointestinal & Hepatic Imaging
Associate Professor of Radiology
Division of Body Imaging, Department of Radiology
The Children's Hospital of Philadelphia
University of Pennsylvania Perelman School of Medicine
Philadelphia, Pennsylvania

**Kimberly E. Applegate, MD**
Division Chief of Pediatric Radiology
Department of Radiology
University of Kentucky
Lexington, Kentucky

**Lauren W. Averill, MD**
Nemours Children's Health System
Associate Professor of Radiology and Pediatrics
Sidney Kimmel Medical College of Thomas Jefferson University
Philadelphia, Pennsylvania

**E. Michel Azouz, MD, FRCPC**
Pediatric Radiologist
Department of Medical Imaging
Montreal Children's Hospital
Montreal, Quebec, Canada

**Paul Babyn, MDCM**
Head
Department of Medical Imaging
University of Saskatchewan
Saskatoon, Saskatchewan, Canada

**Patrick N. Bacon, MD**
Pediatric Radiologist
TRA-MINW
Tacoma, Washington

**D. Gregory Bates, MD**
Clinical Professor
Department of Radiology
Ohio State University College of Medicine and Public Health
Pediatric Radiologist
Nationwide Children's Hospital
Columbus, Ohio

**Gerald G. Behr, MD**
Associate Attending Physician
Department of Radiology
Memorial Sloan Kettering Cancer Center
New York, New York

**Ellen Cecilia Benya, MD**
Associate Professor
Department of Radiology
Northwestern University Feinberg School of Medicine
Chicago, Illinois

**Larry A. Binkovitz, MD**
Associate Professor
Department of Diagnostic Radiology
Mayo Clinic
Rochester, Minnesota

**Susan Blaser, MD**
Staff Neuroradiologist
Division of Paediatric Neuroradiology
The Hospital for Sick Children
Toronto, Ontario, Canada

**Stefan Bluml, PhD**
Director, New Imaging Technology Lab
Department of Radiology
Children's Hospital Los Angeles
Associate Professor of Research, Radiology & Biomedical Engineering
University of Southern California
Los Angeles, California

**Timothy N. Booth, MD**
Professor
Department of Radiology and Otolaryngology
Children's Medical Center
University of Texas Southwestern Medical Center
Dallas, Texas

**Brandon P. Brown, MD**
Assistant Professor
Department of Radiology and Imaging Sciences
Riley Hospital for Children at Indiana University Health
Indiana University School of Medicine
Indianapolis, Indiana

**Dorothy Bulas, MD**
Professor of Pediatrics and Radiology
Department of Diagnostic Imaging and Radiology
Children's National Health Systems
Washington, DC

**Angela Byrne, MD**
Department of Radiology
Children's Hospital of British Columbia
Vancouver, British Columbia, Canada

**Joseph A. Camarda, MD**
Pediatric Cardiologist
Ann & Robert H. Lurie Children's Hospital of Chicago
Assistant Professor
Division of Cardiology
Department of Pediatrics
Northwestern University Feinberg School of Medicine
Chicago, Illinois

**Christopher I. Cassady, MD**
EB Singleton Department of Pediatric Radiology
Texas Children's Hospital
Houston, Texas

**Kim M. Cecil, PhD**
Professor and MR Spectroscopist
Radiology and Imaging Research Center
Cincinnati Children's Hospital Medical Center
Cincinnati, Ohio

**Rafael C. Ceschin, PhD**
Assistant Professor
Department of Radiology
Children's Hospital of Pittsburgh of UPMC
Department of Biomedical Informatics
University of Pittsburgh School of Medicine
Pittsburgh, Pennsylvania

**Frandics P. Chan, MD, PhD**
Associate Professor
Department of Radiology
Stanford University Medical Center
Stanford, California

**Teresa Chapman, MD**
Director, Fetal MRI
Department of Radiology
Seattle Children's Hospital
Professor
Department of Radiology
University of Washington School of Medicine
Seattle, Washington

**Govind B. Chavhan, MBBS, MD, DABR, DNB**
Staff Radiologist
Department of Diagnostic Imaging
The Hospital for Sick Children
Associate Professor
Medical Imaging
University of Toronto
Toronto, Ontario, Canada

**Katrina F. Chu, MD**
Clinical Fellow in Radiology
Massachusetts General Hospital
Harvard Medical School
Boston, Massachusetts

**Winnie C. W. Chu, MD**
Professor
Departments of Imaging and Interventional Radiology
The Chinese University of Hong Kong
Hong Kong, China

**Harris L. Cohen, MD**
Professor and Chairman
Department of Radiology
Professor
Departments of Pediatrics and Obstetrics & Gynecology
University of Tennessee Health Science Center
Radiologist-in-Chief
Le Bonheur Children's Hospital
Memphis, Tennessee

**Mougnyan Cox, MD**
Neuroradiology Fellow
Hospital of the University of Pennsylvania
Philadelphia, Pennsylvania

**J. A. Gordon Culham, MD, FRCPC**
Department of Radiology
BC Children's Hospital
Professor
Department of Radiology
University of British Columbia
Vancouver, British Columbia, Canada

**Alan Daneman, BSc, MBBCh, FRCPC, FRANZCR**
Professor
Department of Medical Imaging
University of Toronto
Department of Diagnostic Imaging
The Hospital for Sick Children
Toronto, Ontario, Canada

**Kassa Darge, MD, PhD**
Professor of Radiology and Surgery
Perelman School of Medicine
University of Pennsylvania
Radiologist-in-Chief
William L. Van Alen Endowed Chair
Department of Radiology
Children's Hospital of Philadelphia
Philadelphia, Pennsylvania

**Joseph T. Davis, MD**
Medical Instructor of Radiology
Duke University Medical Center
Durham, North Carolina

**R. Andrew deFreitas, MD**
Division of Pediatric Cardiology
Ann & Robert H. Lurie Children's Hospital of Chicago
Assistant Professor
Department of Pediatrics
Northwestern University Feinberg School of Medicine
Chicago, Illinois

**Katyucia De Macedo Rodrigues, MD**
Research Fellow
Department of Radiology
Boston Children's Hospital
Research Fellow
Department of Radiology
A.A. Martinos Center
Massachusetts General Hospital
Boston, Massachusetts

**Jonathan R. Dillman, MD, MSc**
Associate Professor
Associate Chief of Research
Medical Director, Imaging Research Center
Department of Radiology
Cincinnati Children's Hospital Medical Center
University of Cincinnati College of Medicine
Cincinnati, Ohio

**Lincoln O. Diniz, MD, MPH**
Assistant Professor
Norton Children's Hospital
Louisville, Kentucky

**Laura Dinneen, MD**
Assistant Professor of Pediatric Radiology
University of Missouri–Kansas City School of Medicine
Kansas City, Missouri

**Michael Ditchfield, MBBS, FRANZCR, MD**
Head, Paediatric Imaging
Monash Health
Professor
Diagnostic Imaging
Monash University
Melbourne, Victoria, Australia

**Mary T. Donofrio, MD**
Professor of Pediatrics
George Washington University School of Medicine and Health Sciences
Director, Fetal Heart Program and Critical Care Delivery Program
Children's National Heart Institute
Children's National Health System
Washington, DC

**Adam L. Dorfman, MD**
Clinical Professor
Department of Pediatrics and Communicable Diseases
Department of Radiology
University of Michigan
Ann Arbor, Michigan

**Andrea Schwarz Doria, MD, PhD**
Staff Radiologist/Senior Scientist
Research Director, Department of Diagnostic Imaging
The Hospital for Sick Children
Professor, Associate Vice-Chair of Research (Injury, Repair and Inflammation)
Department of Medical Imaging
University of Toronto
Toronto, Ontario, Canada

**Laura A. Drubach, MD**
Assistant Professor
Department of Radiology
Boston Children's Hospital
Boston, Massachusetts

**Josée Dubois, MD, FRCP, MSc**
Professor
Department of Radiology, Radio-oncology and Nuclear Medicine
University of Montreal
Head, Department of Medical Imaging
CHU Sainte-Justine
Montreal, Quebec, Canada

**Jerry Dwek, MD**
Clinical Adjunct Professor
Department of Radiology
University of California at San Diego
San Diego, California

**Wendy Drew Ellis, MD**
Assistant Professor of Radiology and Radiologic Sciences and Pediatrics
Monroe Carell Jr. Children's Hospital at Vanderbilt
Nashville, Tennessee

**Monica Epelman, MD**
Vice-Chair of Radiology
Nemours Children's Health System
Nemours Children's Hospital
Professor of Radiology
University of Central Florida College of Medicine
Orlando, Florida

**Judy A. Estroff, MD**
Division Chief, Fetal-Neonatal Imaging
Department of Radiology
Boston Children's Hospital
Associate Professor
Department of Radiology
Harvard Medical School
Boston, Massachusetts

**Eric P. Eutsler, MD**
Assistant Professor
Department of Radiology
Mallinckrodt Institute of Radiology
Washington University School of Medicine
St. Louis, Missouri

**Eric Faerber, MD, FACR**
Department of Radiology
St. Christopher's Hospital For Children
Philadelphia, Pennsylvania

**Nancy R. Fefferman, MD**
Associate Professor of Radiology
Vice Chair of Education
Section Chief, Pediatric Radiology
Department of Radiology
NYU School of Medicine
New York, New York

**Mark Ferguson, MD**
Assistant Professor
Seattle Children's Hospital
University of Washington School of Medicine
Department of Radiology
Seattle, Washington

**Tamara Feygin, MD**
Associate Professor of Clinical Radiology
Perelman School of Medicine
University of Pennsylvania
Staff Neuroradiologist
The Children's Hospital of Philadelphia
Philadelphia, Pennsylvania

**Kristin A. Fickenscher, MD**
Associate Professor
Department of Radiology
Children's Mercy Hospital
University of Missouri–Kansas City
Kansas City, Missouri

**A. Michelle Fink, MRCP, FRCR, FRANZCR**
Honorary Consultant Radiologist
Department of Medical Imaging
The Royal Children's Hospital
Melbourne, Victoria, Australia

**Tyson R. Finlinson, DO**
University of Missouri–Kansas City
Kansas City, Missouri

**Donald P. Frush, MD, FACR, FAAP**
Professor of Radiology and Pediatrics
Duke University Medical Center
Durham, North Carolina

**Andre Dietz Furtado, MD**
Assistant Professor
Children's Hospital of Pittsburgh of UPMC
Department of Radiology
University of Pittsburgh Medical Center
Pittsburgh, Pennsylvania

**Asvin M. Ganapathi, MD**
Department of Surgery
Duke University Medical Center
Durham, North Carolina

**Michael S. Gee, MD, PhD**
Chief of Pediatric Radiology
Massachusetts General Hospital
Associate Professor of Radiology
Harvard Medical School
Boston, Massachusetts

**Maryam Ghadimi Mahani, MD**
Clinical Assistant Professor
Divisions of Pediatric and Cardiothoracic Radiology
Department of Radiology
University of Michigan
Ann Arbor, Michigan

**Hyun Woo Goo, MD, PhD**
Department of Radiology and Research Institute of Radiology
Asan Medical Center
University of Ulsan College of Medicine
Seoul, South Korea

**P. Ellen Grant, MD**
Associate Professor
Department of Radiology
Director
Fetal Neonatal Neuroimaging and Developmental Science, Newborn Medicine
Children's Hospital Boston
Boston, Massachusetts

**J. Damien Grattan-Smith, MBBS**
Department of Radiology
Children's Healthcare of Atlanta
Atlanta, Georgia

**S. Bruce Greenberg, MD**
Professor of Radiology and Pediatrics
Department of Radiology
University of Arkansas for Medical Sciences
Little Rock, Arkansas

**Mary-Louise C. Greer, MBBS**
Pediatric Radiologist
Department of Diagnostic Imaging
The Hospital for Sick Children
Assistant Professor
Department of Medical Imaging
University of Toronto
Toronto, Ontario, Canada

**R. Paul Guillerman, MD**
Professor
Department of Radiology
Baylor College of Medicine
Houston, Texas

**Matthew R. Hammer, MD**
Assistant Professor
Department of Pediatric Radiology
Children's Health and UT Southwestern Medical Center
Dallas, Texas

**James René Herlong, MD**
Division Chief, Pediatric Cardiology
Sanger Heart and Vascular Institute
Charlotte, North Carolina

**Marta Hernanz-Schulman, MD, FAAP, FACR**
Professor of Radiology and Pediatrics
Departments of Radiology and Radiological Sciences
Vanderbilt University Medical Center
Radiology Vice-Chair in Pediatrics
Medical Director, Diagnostic Imaging
Monroe Carell Jr. Children's Hospital at Vanderbilt
Nashville, Tennessee

**Melissa A. Hilmes, MD**
Assistant Professor
Division of Pediatric Radiology
Department of Radiology and Radiological Sciences
Monroe Carrell Jr Children's Hospital
Vanderbilt University Medical Center
Vanderbilt University
Nashville, Tennessee

**Ross Holwerda, MD**
Department of Radiology
University of Missouri–Kansas City
Kansas City, Missouri

**Nazia Husain, MBBS, MPH**
Division of Pediatric Cardiology
Ann & Robert H. Lurie Children's Hospital of Chicago
Assistant Professor
Department of Pediatrics
Northwestern University Feinberg School of Medicine
Chicago, Illinois

**Lisa H. Hutchison, MD, FAAP, FACR**
Director, Pediatric Radiology
Alliance Radiology
Overland Park Regional Medical Center
Overland Park, Kansas

**Celso Hygino da Cruz Jr., MD, PhD**
CDPI/DASA, Americas Medical City
Rio de Janeiro, Brazil

**Andrew Johansen, MD**
Department of Radiology
Children's Mercy Hospital
University of Missouri–Kansas City
Kansas City, Missouri

**Joyce T. Johnson, MD**
Assistant Professor
Department of Pediatrics
Ann & Robert H. Lurie Children's Hospital of Chicago
Chicago, Illinois

**J. Herman Kan, MD**
Section Chief, Musculoskeletal Imaging
E.B. Singleton Department of Pediatric Radiology
Texas Children's Hospital
Associate Professor
Baylor College of Medicine
Houston, Texas

**Yassine Kanaan, MD**
Attending Physician
Department of Radiology
Texas Scottish Rite Hospital for Children
Dallas, Texas

**Ronald J. Kanter, MD**
Director, Electrophysiology
Nicklaus Children's Hospital
Miami, Florida

**Boaz Karmazyn, MD**
Professor of Radiology
Department of Radiology and Imaging Sciences
Riley Hospital for Children at Indiana University Health
Indiana University School of Medicine
Indianapolis, Indiana

**Sue Creviston Kaste, DO**
Full Member
Departments of Diagnostic Imaging and Oncology
St. Jude Children's Research Hospital
Full Professor
Department of Radiology
University of Tennessee Health Science Center
Memphis, Tennessee

**Travis H. Kauffman, DO**
Department of Radiology
University of Missouri–Kansas City
Kansas City, Missouri

**Geetika Khanna, MD, MS**
Professor of Radiology
Mallinckrodt Institute of Radiology
Radiologist-in-Chief
St. Louis Children's Hospital
Washington University School of Medicine
St. Louis, Missouri

**Amy B. Kolbe, MD**
Assistant Professor
Department of Radiology
Mayo Clinic
Rochester, Minnesota

**Korgün Koral, MD, MBA**
Professor
Director of Pediatric Neuroradiology and Pediatric MRI
Cohen Children's Medical Center
Donald and Barbara Zucker School of Medicine at Hofstra/Northwell
Hempstead, New York

**Steven Kraus, MD**
Staff Radiologist
Division Chief, Fluoroscopy
Department of Radiology
Cincinnati Children's Hospital Medical Center
Associate Professor of Radiology and Pediatrics
University of Cincinnati College of Medicine
Cincinnati, Ohio

**Rajesh Krishnamurthy, MD**
Radiologist-In-Chief
Nationwide Children's Hospital
Clinical Professor of Radiology
Ohio State University
Columbus, Ohio

**Ramkumar Krishnamurthy, PhD, DABMP-MRI**
MRI Physicist
Department of Radiology
Nationwide Children's Hospital
Columbus, Ohio

**Ralph S. Lachman, MD**
Clinical Professor
Stanford University
Stanford, California;
Professor Emeritus
Associate Director
International Skeletal Dysplasia Registry
UCLA
Los Angeles, California

**Hollie A. Lai, MD**
CHOC Children's
Department of Radiology
Orange, California

**Brooke S. Lampl, DO**
Clinical Assistant Professor of Radiology
Interim Co-Section Director, Pediatric Radiology
Imaging Institute, Cleveland Clinic
Cleveland, Ohio

**Tal Laor, MD**
Professor
Department of Radiology
Boston Children's Hospital
Boston, Massachusetts

**Bernard F. Laya, MD, DO**
Director of Radiology
Institute of Radiology
St. Luke's Medical Center–Global City
Taguig City, Philippines;
Professor of Radiology and Associate Dean
St. Luke's College of Medicine–WHQM
Quezon City, Philippines

**James Leach, MD**
Professor of Radiology
Department of Radiology and Medical Imaging
Cincinnati Children's Hospital Medical Center
University of Cincinnati College of Medicine
Cincinnati, Ohio

**Henrique M. Lederman, MD, PhD**
Senior Professor of Radiology
Department of Diagnostic Imaging
Paulista School of Medicine
Federal University of Sao Paulo (UNIFESP)
Chief, Division of Diagnostic Imaging
Pediatric Oncology Institute, GRAACC
Sao Paulo, Brazil

**Edward Y. Lee, MD**
Chief, Division of Thoracic Imaging
Associate Professor
Departments of Radiology and Medicine
Pulmonary Division
Boston Children's Hospital
Harvard Medical School
Boston, Massachusetts

**Simon Lee, MD**
Assistant Professor
Departments of Pediatrics and Cardiology
Ann & Robert H. Lurie Children's Hospital of Chicago
Chicago, Illinois

**Andrew J. Lodge, MD**
Associate Professor, Surgery
Associate Professor, Pediatrics
Duke University Medical Center
Durham, North Carolina

**Joseph V. Loeb, DO**
Radiology Resident
Department of Radiology
University of Missouri–Kansas City
Kansas City, Missouri

**Jimmy C. Lu, MD**
Clinical Associate Professor
Department of Pediatrics and Communicable Diseases
Department of Radiology
University of Michigan
Ann Arbor, Michigan

**Karen Lyons, MD**
Assistant Professor of Radiology
Arkansas Children's Hospital
Little Rock, Arkansas

**Alexis B. Rothenberg Maddocks, MD**
Assistant Professor of Radiology
Morgan Stanley Children's Hospital
Columbia University Medical Center
New York, New York

**John B. Mawson, MB, ChB**
Director, Department of Radiology
BC Children's Hospital
Assistant Professor
Department of Radiology
University of British Columbia
Vancouver, British Columbia, Canada

**M. Beth McCarville, MD**
Member
Department of Diagnostic Imaging
St. Jude Children's Research Hospital
Memphis, Tennessee

**Amie M. McPherson, MD**
House Officer
Department of Radiological Sciences
Wake Forest Baptist Medical Center
Winston-Salem, North Carolina

**James S. Meyer, MD**
Associate Professor of Radiology
University of Pennsylvania School of Medicine
Associate Radiologist-in-Chief
Department of Radiology
Children's Hospital of Philadelphia
Philadelphia, Pennsylvania

**Arthur B. Meyers, MD**
Department of Radiology
Nemours Children's Health System
Nemours Children's Hospital
Associate Professor of Radiology
University of Central Florida College of Medicine
Clinical Associate Professor of Pediatric Radiology
The Florida State College of Medicine
Orlando, Florida

**Stephen F. Miller, MD**
Department of Radiology
Le Bonheur Children's Hospital
Associate Professor
Department of Radiology
University of Tennessee Health Science Center
Memphis, Tennessee

**Grace S. Mitchell, MD, MBA**
Department of Radiology
Children's Mercy Kansas City
Assistant Professor
University of Missouri–Kansas City
Kansas City, Missouri

**Karen K. Moeller, MD**
Director of Neuroradiology
Norton Children's Hospital
Louisville, Kentucky

**Kevin R. Moore, MD**
Vice Chair of Radiology
Director of MR Imaging
Department of Medical Imaging
Primary Children's Medical Center
Adjunct Associate Professor of Radiology
Department of Radiology
University of Utah
Salt Lake City, Utah

**Srikala Narayanan, MD**
Assistant Professor
Department of Pediatric Radiology
Children's Hospital of Pittsburgh
University of Pittsburgh Medical Center
Pittsburgh, Pennsylvania

**Oscar M. Navarro, MD**
Associate Professor
Department of Medical Imaging
University of Toronto
Fellowship Program Director
Department of Diagnostic Imaging
The Hospital for Sick Children
Toronto, Ontario, Canada

**Josephine M. Ndolo, MBChB, MMed**
Clinical Fellow in Pediatric Radiology
Department of Radiology and Radiological Sciences
Vanderbilt University Medical Center
Monroe Carell Jr. Children's Hospital at Vanderbilt
Nashville, Tennessee

**Marvin D. Nelson Jr., MD**
Chairman, Department of Radiology
Children's Hospital Los Angeles
Professor
Department of Radiology
USC Keck School of Medicine
Los Angeles, California

**Beverley Newman, BSc, MB BCh**
Professor of Radiology
Department of Radiology
Lucile Packard Children's Hospital
Stanford University
Stanford, California

**David B. Nielsen, MD**
Assistant Professor
University of Missouri–Kansas City
Pediatric Radiologist
Children's Mercy Hospital and Clinics
Kansas City, Missouri

**Kay North, DO**
Department of Radiology
Children's Mercy Hospital
Kansas City, Missouri

**Julie Currie O'Donovan, MD**
Pediatric Radiologist
Department of Radiology
Nationwide Children's Hospital
Columbus, Ohio

**Erin K. Opfer, DO**
Pediatric Radiologist
Assistant Professor
Department of Pediatric Radiology
Children's Mercy Hospital and Clinics
Kansas City, Missouri

**Robert C. Orth, MD, MPH, PhD**
Assistant Professor
Department of Pediatric Radiology
Texas Children's Hospital
Houston, Texas

**Randolph Otto, MD**
Associate Professor
Department of Radiology
Seattle Children's Hospital
University of Washington School of Medicine
Seattle, Washington

**Deepa R. Pai, MD, MHSA**
Associated Chief of Critical Care
Department of Radiology
Children's Hospitals and Clinics of Minnesota
Minneapolis, Minnesota

**Harriet J. Paltiel, MD**
Radiologist
Department of Radiology
Boston Children's Hospital
Associate Professor
Department of Radiology
Harvard Medical School
Boston, Massachusetts

**Ashok Panigrahy, MD**
Professor
Radiologist-in-Chief
Children's Hospital of Pittsburgh of UPMC
Vice Chair, Clinical and Translational Imaging Research
Department of Radiology
University of Pittsburgh Medical Center
Pittsburgh, Pennsylvania

**Angira Patel, MD**
Assistant Professor
Department of Pediatrics
Ann & Robert H. Lurie Children's Hospital of Chicago
Chicago, Illinois

**Amanda M. Perak, MD**
Fellow
Department of Preventive Medicine
Northwestern University Feinberg School of Medicine
Instructor
Division of Cardiology
Ann & Robert H. Lurie Children's Hospital of Chicago
Chicago, Illinois

**Daniel J. Podberesky, MD**
Radiologist-in-Chief
Department of Radiology
Nemours Children's Health System
Associate Professor of Radiology
University of Central Florida and Florida State University Colleges of Medicine
Orlando, Florida

**Avrum N. Pollock, MD, FRCPC**
Clinical Professor of Radiology
Department of Radiology
Division of Neuroradiology
The Children's Hospital of Philadelphia
Philadelphia, Pennsylvania

**Andrada R. Popescu, MD**
Physician
Department of Medical Imaging
Ann & Robert H. Lurie Children's Hospital
Assistant Professor
Department of Radiology
Northwestern University Feinberg School of Medicine
Chicago, Illinois

**Tina Young Poussaint, MD**
Attending Neuroradiologist
Department of Radiology
Boston Children's Hospital
Professor of Radiology
Department of Radiology
Harvard Medical School
Boston, Massachusetts

**Sanjay P. Prabhu, MBBS, FRCR**
Director, Advanced Image Analysis Lab
Staff Pediatric Neuroradiologist
Department of Radiology
Boston Children's Hospital
Assistant Professor of Radiology
Harvard Medical School
Boston, Massachusetts

**Sumit Pruthi, MD**
Associate Professor
Departments of Radiology and Pediatrics
Chief, Pediatric Neuroradiology
Monroe Carell Jr. Children's Hospital at Vanderbilt
Nashville, Tennessee

**Anand Dorai Raju, MD**
Assistant Professor
Department of Radiology
Le Bonheur Children's Hospital
University of Tennessee Health Science Center
Memphis, Tennessee

**Brian Reilly, RT(R)**
3D Imaging Specialist
Department of Medical Imaging
Ann & Robert H. Lurie Children's Hospital of Chicago
Chicago, Illinois

**Ricardo Restrepo, MD**
Chief of Interventional Radiology Section
Department of Radiology
Niklaus Children's Hospital
Voluntary Professor
Department of Radiology
Florida International University
Miami, Florida

**John F. Rhodes, MD**
Director
Congenital Heart Center and Pediatric/Adult Congenital Interventional Cardiology
Medical University of South Carolina
Charleston, South Carolina

**Cynthia K. Rigsby, MD, FACR**
Pediatric Radiologist
Department of Medical Imaging
Ann & Robert H. Lurie Children's Hospital of Chicago
Professor
Departments of Radiology and Pediatrics
Northwestern University Feinberg School of Medicine
Chicago, Illinois

**Douglas C. Rivard, DO**
Assistant Professor
Department of Radiology
Children's Mercy Hospital and Clinics
Kansas City, Missouri

**Michael Rivkin, MD**
Co-Director, Stroke and Cerebrovascular Center
Intensive Care Neurology Service
Department of Neurology
Boston Children's Hospital
Associate Professor
Department of Neurology
Harvard Medical School
Boston, Massachusetts

**Ashley James Robinson, MB, ChB, FRCR, FRCPC**
Associate Professor of Clinical Radiology
Department of Radiology
Weill Cornell Medical College
New York, New York;
Vice-Chair, Radiology
Sidra Medical and Research Center
Doha, Qatar

**Joshua D. Robinson, MD**
Pediatric Cardiologist
Ann & Robert H. Lurie Children's Hospital of Chicago
Assistant Professor
Division of Cardiology
Departments of Pediatrics and Radiology
Northwestern University Feinberg School of Medicine
Chicago, Illinois

**Diana P. Rodriguez, MD**
Clinical Assistant Professor
Department of Radiology
School of Medicine and Public Health
The Ohio State University
Department of Radiology
Nationwide Children's Hospital
Columbus, Ohio

**Nancy Rollins, MD**
Medical Director
Department of Radiology
Children's Medical Center
Professor
Department of Radiology
University Texas Southwestern Medical Center
Dallas, Texas

**Arlene A. Rozzelle, MD**
Associate Professor
Department of Surgery
Wayne State University School of Medicine
Chief, Department of Plastic and Reconstructive Surgery
Children's Hospital of Michigan
Director, CHM Cleft/Craniofacial Anomalies
Program Director, CHM Vascular Anomalies Team
Children's Hospital of Michigan
Detroit, Michigan

**Gauravi K. Sabharwal, MD**
Department of Radiology
Henry Ford Hospital
Detroit, Michigan

**Erica K. Schallert, MD**
Assistant Professor
Department of Radiology
Baylor College of Medicine
Pediatric Radiologist
Department of Pediatric Radiology
Texas Children's Hospital
Houston,Texas

**Andrew H. Schapiro, MD**
Assistant Professor
Department of Radiology
Cincinnati Children's Hospital Medical Center
Cincinnati, Ohio

**David N. Schidlow, MD**
Assistant Professor of Pediatrics
George Washington University School of Medicine and Health Sciences
Pediatric and Fetal Cardiology
Children's National Heart Institute
Children's National Health System
Washington, DC

**Vincent J. Schmithorst, PhD**
Assistant Professor
Children's Hospital of Pittsburgh of UPMC
Department of Radiology
University of Pittsburgh Medical Center
Pittsburgh, Pennsylvania

**Erin Simon Schwartz, MD**
Associate Professor
Department of Radiology
Perelman School of Medicine
University of Pennsylvania
Clinical Director
The Lurie Family Foundations' Magnetoencephalography Imaging Center
The Children's Hospital of Philadelphia
Philadelphia, Pennsylvania

**Jayne M. Seekins, MD**
Clinical Assistant Professor
Department of Radiology
Stanford University School of Medicine
Stanford, California

**Sabah Servaes, MD**
Associate Professor
Department of Radiology
Children's Hospital of Philadelphia
Philadelphia, Pennsylvania

**Anuradha S. Shenoy-Bhangle, MD**
Instructor
Harvard Medical School
Staff Radiologist
Department of Abdominal Imaging
Beth Israel Deaconess Medical Center
Boston, Massachusetts

**Elizabeth F. Sheybani, MD**
West County Radiology Group
St. Louis, Missouri

**Anna Shifrin, MD**
Staff Neuroradiologist
Director of Neuroradiology
Department of Radiology
Winchester Hospital
Winchester, Massachusetts

**Richard M. Shore, MD**
Section Head, General Radiology and Nuclear Medicine
Professor of Radiology
Northwestern University Feinberg School of Medicine
Children's Memorial Hospital
Chicago, Illinois

**Sudha P. Singh, MD**
Assistant Professor
Department of Radiology and Radiological Sciences
Vanderbilt University
Nashville, Tennessee

**Carlos J. Sivit, MD**
Senior Vice Chairman
Department of Radiology
University Hospitals of Cleveland
Professor of Radiology and Pediatrics
Case Western Reserve School of Medicine
Cleveland, Ohio

**Thomas L. Slovis, MD**
Emeritus Professor
Departments of Radiology and Pediatrics
Wayne State University School of Medicine
Detroit, Michigan

**Ethan A. Smith, MD**
Associate Professor
Department of Radiology
Cincinnati Children's Hospital Medical Center
University of Cincinnati College of Medicine
Cincinnati, Ohio

**Jordan Smith, DO**
Department of Radiology
University of Missouri–Kansas City
Kansas City, Missouri

**Sally J. Smith, DO**
Pediatric Radiologist
Department of Radiology
Nationwide Children's Hospital
Assistant Professor
Department of Radiology
The Ohio State University Medical Center
Columbus, Ohio

**Susan Sotardi, MD, MS**
Neuroradiology Fellow
Department of Neuroradiology
Massachusetts General Hospital
Boston, Massachusetts

**Vera R. Sperling, MD**
Assistant Professor
Department of Radiology
Children's Hospital of Pittsburgh of UPMC
University of Pittsburgh Medical Center
Pittsburgh, Pennsylvania

**Stephanie E. Spottswood, MD, MSPH**
Professor of Radiology and Pediatrics
Department of Radiology and Radiological Sciences
Vanderbilt University Medical Center
Chief, Pediatric Nuclear Medicine
Monroe Carell Jr. Children's Hospital at Vanderbilt
Nashville, Tennessee

**A. Luana Stanescu, MD**
Assistant Professor
Department of Radiology
Seattle Children's Hospital
University of Washington School of Medicine
Seattle, Washington

**Lisa States, MD**
Associate Professor
Department of Radiology
The Children's Hospital of Philadelphia
Philadelphia, Pennsylvania

**Peter J. Strouse, MD, FACR**
Professor and Director
Section of Pediatric Radiology
Department of Radiology
University of Michigan Health System
Ann Arbor, Michigan

**Subramanian Subramanian, MD**
Assistant Professor
Department of Radiology
Children's Hospital of Pittsburgh
University of Pittsburgh Medical Center
Pittsburgh, Pennsylvania

**Benita Tamrazi, MD**
Assistant Professor
Department of Radiology
Children's Hospital Los Angeles
Los Angeles, California

**George A. Taylor, MD**
Radiologist-in-Chief Emeritus
Department of Radiology
Boston Children's Hospital
John A. Kirkpatrick Emeritus Professor of Radiology (Pediatrics)
Department of Radiology
Harvard Medical School
Boston, Massachusetts

**Mahesh M. Thapa, MD**
Associate Professor
Department of Radiology
Seattle Children's Hospital
Seattle, Washington

**Jean A. Tkach, PhD**
Associate Professor
Department of Radiology
University of Cincinnati
Cincinnati, Ohio

**Jason F. Tobler, MD**
Pediatric Radiologist
Department of Radiology
Children's Mercy Kansas City
Kansas City, Missouri

**Alexander J. Towbin, MD**
Associate Chief, Clinical Operations and Radiology Informatics
Associate Professor
Cincinnati Children's Hospital
Cincinnati, Ohio

**Shreyas Vasanawala, MD, PhD**
Associate Professor
Department of Radiology
Stanford University
Stanford, California

**Arastoo Vossough, MD, PhD**
Associate Professor
Department of Radiology
University of Pennsylvania
Children's Hospital of Philadelphia
Philadelphia, Pennsylvania

**Robert G. Wells, MD**
Pediatric Radiologist
Milwaukee Radiologists Ltd.
Milwaukee, Wisconsin

**Joshua D. Wermers, DO**
Department of Diagnostic Radiology
University of Missouri–Kansas City
Kansas City, Missouri

**Hollie C. West, MD**
Adjunct Assistant Professor
Department of Radiology
Cincinnati Children's Hospital Medical Center
University of Cincinnati College of Medicine
Cincinnati, Ohio

**Sjirk J. Westra, MD**
Pediatric Radiologist
Department of Radiology
Massachusetts General Hospital
Associate Professor of Radiology
Harvard Medical School
Boston, Massachusetts

**Elysa Widjaja, MD, MPH**
Pediatric Neuroradiologist
Department of Diagnostic Imaging
Hospital for Sick Children
Associate Professor
University of Toronto
Toronto, Ontario, Canada

**Peter Winningham, MD**
Children's Mercy Hospital Radiology Fellow
University of Missouri–Kansas City
Kansas City, Missouri

**Jessica L. Wisnowski, PhD**
Assistant Professor
Department of Radiology
Children's Hospital Los Angeles
Keck School of Medicine
University of Southern California
Los Angeles, California

**Ali Yikilmaz, MD**
Chief, Department of Radiology
Goztepe Research and Training Hospital
Istanbul Medeniyet University
Istanbul, Turkey

**Giulio Zuccoli, MD**
Professor
Department of Radiology
Director of Pediatric Neuroradiology
Children's Hospital of Pittsburgh
University of Pittsburgh Medical Center
Pittsburgh, Pennsylvania

**Evan J. Zucker, MD**
Clinical Assistant Professor of Radiology
Department of Radiology
Lucile Packard Children's Hospital
Stanford University School of Medicine
Stanford, California

# Foreword

A book. A book! Such a wonderful thing, and especially, a book on pediatric radiology! In the days of the internet and random access to learning, there is still an important place for a comprehensive text, such as *Caffey's Pediatric Diagnostic Imaging*.

In 1945, John Caffey wrote and edited the first edition of this text, then called *Caffey's Pediatric X-Ray Diagnosis*. Caffey's text ushered the infancy of the specialty of pediatric radiology. It was meticulously illustrated with cases from Caffey's work at Babies Hospital in New York City. The book was carefully referenced. At the time, it was a comprehensive guide to anything that might be diagnosed or evaluated with radiographs in children. Emphasis was placed on normal—normal Roentgen anatomy, normal variants, and normal development. The book was an invaluable aid to anyone interpreting radiographs in children. It helped to establish the specialty of pediatric radiology—we were big time!

Caffey's 1945 1st edition was *not* the first textbook in pediatric radiology. A few decades earlier, in 1910, Morgan Rotch published *Living Anatomy and Pathology: The Diagnosis of Diseases of Early Life By the Roentgen Method*. While undoubtedly useful to radiology practitioners at the time, the limited utility of radiographs at the time is illustrated throughout the text. Other early texts were published in Germany. Caffey himself published a 160-page section on pediatric radiology in *Golden's Looseleaf Radiology* in 1941 entitled "Roentgen Diagnosis in Infants and Children." This effort was clearly a precursor for the much larger, more comprehensive 1st edition of *Caffey's Pediatric X-Ray Diagnosis*. Very few copies of this "pre-Caffey's" exist.

Looking back at the "pre-Caffey's" and the subsequent 1st edition of *Caffey's Pediatric X-Ray Diagnosis*, one gets a sense of the contemporary excitement with the benefits of radiography and careful image interpretation to improving the healthcare of children. Radiology was integral to pediatric medicine. Glaringly, one is struck by the absence of any discussion of child abuse—these books preceded Caffey's seminal article on this subject, published in 1946 in *The American Journal of Roentgenology and Radium Therapy*. Careful perusal of the texts shows nothing related to the topic of child abuse although undoubtedly Caffey's mind was already spinning with the challenge of these cases (the six cases in the 1946 article ranged back to 1933).

Recognizing the rapid advancement of medicine and improvement and ever-increasing utilization of radiography, fluoroscopy, and later other imaging modalities, Caffey, Caffey and colleagues, Caffey protégés, and eventually distant academic descendants (which we all are) have churned out edition after edition of *Caffey's Pediatric X-Ray Diagnosis*, morphing into *Caffey's Pediatric Diagnostic Imaging* with the 10th edition in 2004. With each edition, new information about injury and disease in children was incorporated, better examples of pathologies were illustrated, imaging techniques and photography were updated, and new modalities were introduced. The text grew and grew. With the 6th edition, in 1972, the text expanded to two volumes. With the 11th edition, in 2008, the two volumes totaled 3,195 pages (plus a gargantuan index)—a hefty weight good for muscle building but a challenge for a reader to consume from cover to cover. You didn't lug *Caffey's Pediatric Diagnostic Imaging* around, rather you kept multiple copies handy—in the reading room, in your office, at home.

Nonetheless, the text was a comprehensive reference. If you needed to look up something, it was in the book. If you read the book cover to cover, you didn't miss anything. Writing was by true experts in the subspecialties of pediatric radiology. Many chapters (e.g., the bone marrow chapter by Guillerman, the metabolic bone disease chapters by Shore in the 11th edition) are the best writing that exists on the respective subjects.

With the 12th edition, parts of the book migrated online, including references and some of the "less essential" images. For those of us who love books and reading, this was a troublesome development. Being tethered to a computer and having to log in and find this supplemental information was somewhat burdensome. This change, however, represented a smart compromise between content and size and harkened the coming of age of *Caffey's Pediatric Diagnostic Imaging* in the digital era. The online features have been continued with the 13th edition.

With the 13th edition, Dr. Coley and his team have again reinvigorated the text, building from a solid foundation of the 12th edition and subfoundations from every preceding edition. Again, an awesome array of authors has been assembled, bringing in exciting new blood in the field of pediatric radiology. Of the 187 contributing authors, 72 are new to the 13th edition. Authors are drawn from around the world. Medicine, and specifically pediatric radiology, continues to advance at a breathtaking pace. The new text reflects this—with updated information on new modalities, new techniques, and new perspectives on old diseases. Particular attention has been given to expanding the focus on prenatal imaging. This melds well with discussions of embryology and neonatal conditions. Additional attention to the exploding and varied use of MRI is noted throughout the text. Indeed, imaging is much more complex than in Caffey's day; however, as with all previous editions, the current text maintains an emphasis on radiography, not to be overlooked.

Hearty congratulations go to Dr. Coley and his nine associate editors for a job very well done. Putting together a multi-editor, multi-author comprehensive textbook and keeping it cohesive, consistent, and timely is not an easy task. Thank you!

*Caffey's Pediatric Diagnostic Imaging* remains a comprehensive go-to reference and text on pediatric radiology. If you wish to know more about an entity in pediatric radiology, it is here. If you want to get everything, you can start on page 1 and read it through to the end. You don't know what you don't know. If you want to know it all, use this book.

**Peter J. Strouse, MD, FACR**
*John F. Holt Collegiate Professor of Radiology & Director, Section of Pediatric Radiology, C. S. Mott Children's Hospital, Department of Radiology, University of Michigan Health System*
*President, The Society for Pediatric Radiology*
*Co-Editor (for the Americas),* ***Pediatric Radiology***

# Preface to First Edition

> *Shadows are but dark holes in radiant streams, twisted rifts beyond the substance, meaningless in themselves.*
>
> *He who would comprehend Röntgen's pallid shades need always to know well the solid matrix whence they spring. The physician needs to know intimately each living patient through whom the racing black light darts, and flashing the hidden depths reveals them in a glowing mirage of thin images, each cast delicately in its own halo, but all veiled and blended endlessly.*
>
> *Man—warm, lively, fleshy man—and his story are both root and key to his shadows; shadows cold, silent and empty.*
>
> (JOHN CAFFEY)

Within a few weeks after Röntgen announced his now renowned discovery to the world in December, 1895, the X-ray method of examination was applied to infants and children. The Vienna letter of February 29 (M. Rec. 49:312, 1896) contained a roentgen print of the arm of an infant made of Kreidl in Vienna: this is the second reproduction of a roentgen image in the American literature. Credit for the first recorded roentgen examination of an infant in the United States undoubtedly belongs to Dr. E. P. Davis of New York City, who described the roentgen shadows cast by the trunk of a living infant and the skull of a dead fetus in March, 1896. In his remarkable article (The study of the infant body and the pregnant womb by the roentgen ray, Am. J. M. Sc. 111:263, 1896) Dr. Davis also included three drawings of shadows visualized by means of a skiascope—shadows visualized by means of a skiascope—shadows of the feet, elbows and orbit of a living infant. Feilchenfeld's discussion of spina ventosa in May, 1896, is probably the first roentgen description of morbid anatomy in children (Berlin. Klin. Wchnschr. 33:403, 1896). There were only two roentgen pediatric publications in 1896; the number increased to 14 in 1897.

In 1898, Escherich of Graz had had sufficient experience with pediatric roentgen examinations to write a general exposition on the merits and weaknesses of the method (La valeur diagnostique de la radiographie chez les enfants, Rev. d. mal. de l'enf. 16:233, May 1898). This is a highly interesting and illuminating discussion in which Escherich points out the roentgen examination was already not being used as commonly in young patients as in adults. He states that a roentgen laboratory was established especially for children at Graz in 1897, and it seems probable that this was the first of its kind.

A single film is reproduced—a print of an infantile hand and forearm which shows rachitic changes. The uncertainties of the mediastinal shadows, which still bedevil us, were fully appreciated by Escherich, and he was quite unhappy about this baffling structure "in which so many important infantile lesions lie concealed." He was enthusiastic in regard to the possible estimation of the state of hydration of soft tissues in infantile diarrhea from their roentgen densities.

Reyher's German monograph in 1908 is the earliest review of the world literature of pediatric roentgenology which I have found (Reyher, P.: Die roentgenologische Diagnostik in der Kinderheilkunde, Ergebn. d. inn. Med. U. Kinderh. 2:613, 1908). In it there are 276 references to articles published during the first 12 years following Röntgen's discovery, and these furnish a good key for the study of the early writings in this field. The appendix contains 40 small but clear roentgen prints.

Rotch's The Roentgen Ray in Pediatrics appeared in 1910—the first book in any language devoted exclusively to pediatric X-ray diagnosis and still, I believe, the only one in English. Dr. Thomas Morgan Rotch was Professor of Pediatrics, Harvard University, and an outstanding podiatrist of his time.[*]

In this pioneer treatise he stresses the importance of mastering the shadows of normal structure before attempting the recognition and interpretation of the abnormal, and he carefully correlates the clinical findings with the roentgen findings in the cases illustrated; 42 of 264 figures depict the "normal living anatomy of infants and children." This material was taken largely from the files of the Boston Children's Hospital, and the author's statement that more than 2,300 cases were available for study demonstrates that roentgen examination had long been a commonplace in his clinic. Dr. Rotch's early fostering of roentgen examination of infants and children, his appreciation of the special problems in applying this method to the young, his careful anatomicroroentgen studies and his text, monumental for this time, all mark him as the father of pediatric roentgenology in America.

Two years later—1912—the first German book, Reyher's Das Roentgenverfahren in der Kinderheilkunde, was published. Later and more familiar texts are Gralka's Roentgendiagnostik im Kindesalter (1927), Becker's Roentgendiagnostik und Strahlentherapie in der Kinderheilkunde (1931) and the Handbuch der Roentgendiagnostik und Therapie im Kindesalter by Engel and Schall (1933). As far as I have been able to determine, no book on pediatric roentgen diagnosis has been published in English during the 35 years which have passed since Rotch's unique publication in 1910. The absence of pediatric roentgenology in the flood of medical texts which has streamed from the American and English presses during the last three decades constitutes a dereliction unmatched in other equally important fields of medical diagnosis — a literary developmental hypoplasia which it is hoped *Pediatric X-Ray Diagnosis* will remedy.

This book stems from the roentgen conferences held semimonthly at the Babies Hospital during the last 20 years. The films reproduced herein were all selected from our own roentgen files save those for which credit to others is indicated in the legends. The purpose of the author is two-fold: description of shadows cast by normal and morbid tissues, and clinical appraisal of roentgen findings in pediatric diagnosis. Roentgen physics, technic and therapy have been omitted intentionally. As references and acknowledgments testify, the writer has borrowed freely from the literature and is indebted to many contributors for subject matter and illustrations. To all of them I am sincerely grateful. In the broad and deep field of pediatric diagnosis, selection of the most appropriate material has posed many dilemmas. In the main, data have been chosen which have proved the most useful and instructive in solving the common and important diagnostic problems which have arisen during two decades in a large and busy pediatric hospital and out-patient clinic.

The limitations of space do not permit adequate recognition here of all those to whom credit is due for the making of this book. The roentgen examinations which are its foundation could not have been made without the cooperation of thousands of patients—many weak and painweary; to all of these I am profoundly thankful. Intimate clinical contacts have been maintained and essential collateral examinations have been made possible through the sustained collaboration of my colleagues—attending physicians and surgeons, resident physicians and nurses. I am under deep and solid obligation to Dr. Rustin McIntosh who read the entire manuscript; his discerning criticism and valuable suggestions are responsible for numerous corrections and improvements in the text. The sympathetic reception given to our early endeavors by Dr. Ross Golden will always be remembered gratefully, as well as his continuing wise and friendly counsel. We have benefited much and often from the discipline of the necropsy table—from the instructive dissections of Dr. Martha Wollstein, Dr. Beryl Paige and Dr. Dorothy Anderson.

---

[*] Jacobi, A.: In memoriam Thomas Morgan Rotch, Am. J. Dis. Child. 8:245, 1914.

To none, however do I owe more than to my loyal coworkers in the roentgen department of the Babies Hospital—Edgar Watts, Cecelia Peck, Moira Shannon, Mary Fennell and Mary Jean Cadman—for their gentle handling of patients, unfailing industry and superlative technical skill. Mrs. Cadman typed the manuscript; I am grateful to her for the speedy completion of a thorny chore. The drawings are the work of Alfred Feinberg, and they reflect his rich experience in medical illustration.

The final phase in the preparation of the manuscript was saddened by the death of Mr. H. A. Simons, President of the Year Book Publishers. His stimulating enthusiasm and generosity were indispensable to the completion of the book during these unsettled war years. His passing was a grievous loss. The task of publication has fallen to the capable and patient hands of Mr. Paul Perles and Mrs. Anabel Ireland Janssen.

**John Caffey**
*Babies Hospital*
*New York 32*
*June 10, 1945*

# Preface

A small number of valuable and influential texts have outlived their creators, evolving over years through the efforts of new authors and editors. Sir William Osler's *The Principles and Practice of Medicine* was published from 1892 to 2001; Sir Vincent Zachary Cope's *Early Diagnosis of the Acute Abdomen*, currently in its 22nd edition, first appeared in 1921; other such venerable texts still being published include Harrison's *Principles of Internal Medicine* (1950), Nelson's *Textbook of Pediatrics* (1945), and Goodman & Gilman's *The Pharmacological Basis of Therapeutics* (1941). *Caffey's Pediatric Diagnostic Imaging* (originally *Caffey's Pediatric X-ray Diagnosis* through the first nine editions) is the longest continuously published textbook in the subspecialty, having proven its value over seven decades.

This book began as a labor of love for John Caffey in an era without computers, digital images, or PubMed. Each chapter was meticulously dictated, typed, corrected, and typed again. Each radiograph was carefully selected from Dr. Caffey's own teaching file at Babies Hospital in New York City. Dr. Caffey, initially trained as a pediatrician, was an astute clinician who stressed that the radiographic findings were only one part of the diagnostic evaluation; proper patient care required the integration of the history, physical exam, laboratory data, and imaging. Despite the great effort involved, he was the sole author of the first four editions.

With the 1967 fifth edition, former Caffey fellow Dr. Frederic N. Silverman of Children's Hospital Cincinnati participated in preparation of the text, and continued as a co-editor of the sixth and seventh editions. With the death of Dr. Caffey in 1978, Silverman became sole editor of the eighth edition in 1985. Over time, Dr. Silverman added authors and expanded sections. Dr. Jerald P. Kuhn joined Silverman as co-editor with the 1993 ninth edition, and then succeeded him as editor. For the 2003 tenth edition, Dr. Kuhn added Drs. Jack O. Haller and Thomas L. Slovis as co-editors, two important figures in pediatric radiology education. Dr. Slovis lead the production of the eleventh edition, which was a significant modernization of the text and figures. This addition had eight associate editors overseeing subsections of the text, reflecting the growing complexity and expertise required in delivering pediatric imaging care. The twelfth edition was the first to be available electronically, with expanded image and video content. New associate editors were added to provide the best expertise possible. This has continued with the current thirteenth edition, with updated content reflecting the changes in the field.

Given how we now access information and educational content, it is fair to ask if books like this are still relevant. Clearly, I have a biased viewpoint. The quality of the information retrieved online is often unclear, and much of that content is condensed and truncated, leaving out important details and associations. I believe that well-constructed prose from an author with expert knowledge and practical real-world experience, coupled with illustrative images, remains a powerful and efficient way to transmit information and facilitate learning. Lists of facts and bullet point paragraphs cannot convey more complex concepts and syntheses. No matter what the medium, content counts. And books like this one have tremendously valuable content.

Still, as we learn more about the science of education, what is the best method of presenting information to learners young and old? There is ongoing debate as to the best medium in which to disseminate complex and comprehensive content. Books are simple to use. They are familiar. It is easy to flip from section to section, to go back a few pages without losing your place. You can take notes in the margins. Books can also be heavy and cumbersome. They are costly to manufacture. Electronic formats have their pros and cons as well. A light, portable laptop or tablet may contain thousands of books' worth of information. Images can be manipulated like in actual practice. Video and animations can augment the learning experience. Online texts can be accessed anywhere with an Internet connection. Content length need not be dictated by physical page limitations. However, screen size dictates and somewhat limits the amount and method of information displayed. Moving back and forth between content sections can be awkward.

This thirteenth edition reflects this tension. There is a physical book, but there is also an online and electronic presence. Additional content is available online to supplement the print volume and to allow those who prefer electronic media to take advantage of the material in an alternate way.

I would like to thank the team at Elsevier, beginning with Robin Carter, the acquisition editor who still believes in the importance of works such as this. Ann Anderson is our content development specialist, among whose many tasks included prodding me to actually get my work done. Stephanie Turza is our project manager, who calmly kept the book moving along. Our designer Renee Duenow and our art buyer Nichole Beard helped create the book's look, and multimedia producer Vinod Kothaparamtath made the online content possible. And of course, thank you to the authors and editors who shared their time and expertise to make this edition possible.

**Brian D. Coley, MD**

# Video Contents

## Chapter 14 Prenatal, Congenital, and Neonatal Abnormalities

- Fetal Swallowing
- Normal Fetal Swallowing

## Chapter 55 Neoplasia

- Mucoepidermoid Carcinoma

## Chapter 67 Magnetic Resonance Imaging for Congenital Heart Disease

- Aortic Stenosis, Sagittal and Coronal Time-Resolved
- Aortic Coarctation
- Aortic Stenosis

## Chapter 69 Surgical Considerations for Congenital Heart Disease

- Cardiac MRI in a Patient with Previously Repaired Tetralogy of Fallot, View 1
- Cardiac MRI in a Patient with Previously Repaired Tetralogy of Fallot, View 2

## Chapter 73 Left Heart Lesions

- Marginally Hypoplastic Left Ventricle to Evaluate for a Two-Ventricle Versus Single-Ventricle Repair
- Bicuspid Aortic Valve in a 25-Year-Old with History of Aortic Coarctation
- Bicuspid Aortic Valve in a 25-Year-Old with History of Aortic Coarctation, Showing Upward Ballooning of the Aortic Valve Leaflets and Turbulent Poststenotic Jet
- Systolic Flow Void Beyond the Coarctation Consistent with Turbulent Flow Across the Coarctation

## Chapter 75 Conotruncal Anomalies

- Tetralogy of Fallot, Status Post-Repair, Status Post–Pulmonary Valve Replacement
- Tetralogy of Fallot, Status Post-Repair, Status Post–Transcatheter Pulmonary Valve Replacement
- Markedly Dilated Right Ventricle with Overall Mildly Depressed Systolic Function
- Dilated Right Ventricular Outflow Tract with Dyskinetic Anterior Wall in the Region of the Prior Transannular Patch
- To-and-Fro Flow in the Main Pulmonary Artery
- Hypertrophy of the Right Ventricle with Bowing of the Interventricular Septum into the Lower Pressure Left Ventricle
- Anterior and Leftward Aorta Arising From the Morphologic Right Ventricle
- Dephasing Jet at the Pulmonary Valve

## Chapter 78 Syndromes and Chromosomal Anomalies

- Tortuous Aorta and Iliac Arteries with Multiple Stenoses: Infant with Loeys Dietz Syndrome
- Diffuse Arterial Tortuosity and Multiple Stenoses
- Thickening of the Right and Left Ventricle Myocardium with Small Ventricular Cavities: 6-Month-Old Girl with Features of LEOPARD Syndrome
- Spectrum of Anatomic Abnormalities: 2-Day-Old Female with Cantrell Syndrome (Pentalogy of Cantrell)

## Chapter 79 Myocardial, Endocardial and Pericardial Diseases

- Hypertrophic Cardiomyopathy with Severe Asymmetric Thickening of the Left Ventricular Septal Wall

## Chapter 80 Cardiac and Pericardial Tumors

- Cardiac Fibroma with Gorlin Syndrome

## Chapter 85 Prenatal Gastrointestinal and Hepatobiliary Imaging

- Duodenal Obstruction with Hyperperistalsis

## Chapter 97 Disorders of Swallowing

- Laryngeal Penetration
- Laryngeal Penetration and Tracheal Aspiration

## Chapter 100 Hypertrophic Pyloric Stenosis

- Sonographic Sweep to Find Antropyloric Canal: Sweep Terminating at Normal Pylorus 100-1
- Sonographic Sweep to Find Antropyloric Canal: Sweep Terminating at Abnormal, Hypertrophied Pylorus of HPS
- Transient Appearance of HPS during Normal Peristaltic Activity in a Normal Infant
- Passage of Air Through Abnormal Pyloric Canal
- Changes in the Length and Thickness of the Abnormal Antropyloric Canal in Real Time

## Chapter 102 Congenital and Neonatal Abnormalities

- UGI Evaluation of the Duodenum
- Midgut Volvulus
- Midgut Volvulus
- Chronic Midgut Volvulus

## Chapter 104 Acquired Lesions of the Small Intestines

- Crohn Stricture Causing Partial Small Bowel Obstruction
- Crohn Disease Ileal Stricture

## Chapter 107 Intussusception

- Active Peristalsis in Transient Small Bowel Intussusception
- Air Reduction of Intussusception

## Chapter 112 Prenatal Imaging and Intervention

- Fetal Autosomal Recessive Polycystic Kidney Disease on Ultrasound

## Chapter 130 Prenatal Musculoskeletal Imaging

- Amniotic Band Syndrome

# 1

# Radiation Bioeffects, Risks, and Radiation Protection in Medical Imaging in Children

*Joseph T. Davis and Donald P. Frush*

Diagnostic imaging has evolved from the single technique of radiography discussed in the first edition of *Caffey's Pediatric X-Ray Diagnosis* in 1945 to a specialty with many modalities and techniques. Many of these modalities use ionizing radiation, and some, such as computed tomography (CT) and nuclear imaging, entail relatively high doses of radiation.[1] Therefore the imaging community (and our medical colleagues) must jointly adhere to two of the principles of radiation protection for our patients: justification (i.e., the examination is warranted) and optimization (i.e., the appropriate technique is used). For example, in computed or direct digital radiographic examinations, image processing can accommodate overexposures. The image can be adjusted to appear as if it were obtained using standard techniques, whereas with screen film technology, the film image would be recognized as overexposed (dark) (Fig. 1.1). Without accountability for displaying dose metrics (such as the exposure index available with digital radiography), it is difficult or impossible to account for patient exposures in clinical practice.[2] Additionally, uninformed and potentially irresponsible justification of medical imaging occurs when persons are unfamiliar with the methods of estimating an effective radiation dose during CT examinations in children.[3,4] Increasing accountability is expected from the medical community with regard to the use of imaging modalities that expose children (as well as adults) to ionizing radiation. As such, a basic understanding of radiation biology, including bioeffects, radiation doses of various types of imaging examinations, and risks of radiation, is essential for the pediatric imager. A glossary of terms and dose descriptors is found in the addendum at the end of this chapter.

## TRENDS IN MEDICAL RADIATION EXPOSURE TO CHILDREN

Approximately 4 billion imaging examinations using ionizing radiation (i.e., radiography, fluoroscopy/angiography, CT, and nuclear imaging) are performed annually worldwide.[5] In the United States, medical imaging currently accounts for a significant percentage of the annual radiation exposure to the population.[6] Natural or background sources account for about 50% of the annual radiation exposure in the United States, and diagnostic medical radiation accounts for most of the remainder, an approximately sixfold increase during the past 30 years (Figs. 1.2A and B). CT alone accounts for nearly 25% of all radiation exposure to the US population.[6,7] Many reasons exist for the increased use of diagnostic medical radiation, and much use of such radiation is based on sound medical decision making. However, other factors determine use as well, including defensive medicine.

## PATHOPHYSIOLOGY OF RADIATION EFFECTS

Hall has written an excellent review of radiobiology for the radiologist.[8] The biologic effects of radiation result primarily from damage to deoxyribonucleic acid (DNA). The x-ray particle, the photon, gives up its energy to produce a fast recoil electron, which may damage DNA directly but which also can interact with a molecule of water to produce a free radical (Fig. 1.3). A free radical is a highly reactive atom or molecule with an unpaired electron in the outer shell:

$$H_2O \rightarrow H_2O^+ + e^-$$

$$H_2O^+ + H_2O \rightarrow H_3O^+ + OH^*$$

where the asterisk indicates a free radical.

Two-thirds of x-ray damage occurs via OH radicals, suggesting that someday this component of radiation damage might be reduced through the use of chemical radioprotectants. The topic of radioprotectants was recently well reviewed.[9]

The biologic effects of radiation result primarily from damage to double-stranded DNA as opposed to single-strand injury (see Fig. 1.3). Single-strand breaks of DNA are readily repaired and are presumed to have a negligible effect. Breaks in both DNA strands that are opposite or separated by a few base pairs are much more difficult to repair. These double-strand breaks can cause important biologic effects, including genetic mutations, carcinogenesis, and cell death. Dicentric and fragmented breaks typically result in cell death, whereas nonlethal translocation repairs may cause impaired cellular function, including development of an oncogene.[8]

The biochemical and physiologic damage produced by radiation generally occurs within hours or days, but the impact of these changes, such as the induction of cancer, can take decades to manifest. This carcinogenic process has several steps. Aberrations in chromosomes (e.g., deletions, translocations, or aneuploidy) are produced by DNA damage. Because these damaged cells survive, they become "stable aberrations" (some with neoplastic transformation), the first step to radiation-induced carcinogenesis. The second step is cellular immortality; that is, most cancer cells are descendants of a single cell that originally underwent neoplastic transformation. The third step is tumorgenicity. The radiation exposure induces a cellular genomic instability that is transmitted to progeny, which Little described as "a persistent enhancement in the rate of which genetic changes arise in the descendants of the irradiated cells after many generations of replication…[this process] has been termed a nontargeted effect of radiation as genomic damage occurs in the cells that in themselves receive no direct radiation exposure."[10]

Most childhood tumors occur sporadically, but in 10% to 15% of the cases, a strong family association and genetic basis for radiation sensitivity are present. Persons with certain diseases are uniquely sensitive to radiation-induced cancers, although the exact mechanism is unclear (Box 1.1).

## TYPES OF RADIATION BIOEFFECTS

The two types of biologic effects from radiation are tissue effects (also called *deterministic effects*) and stochastic (random) effects.

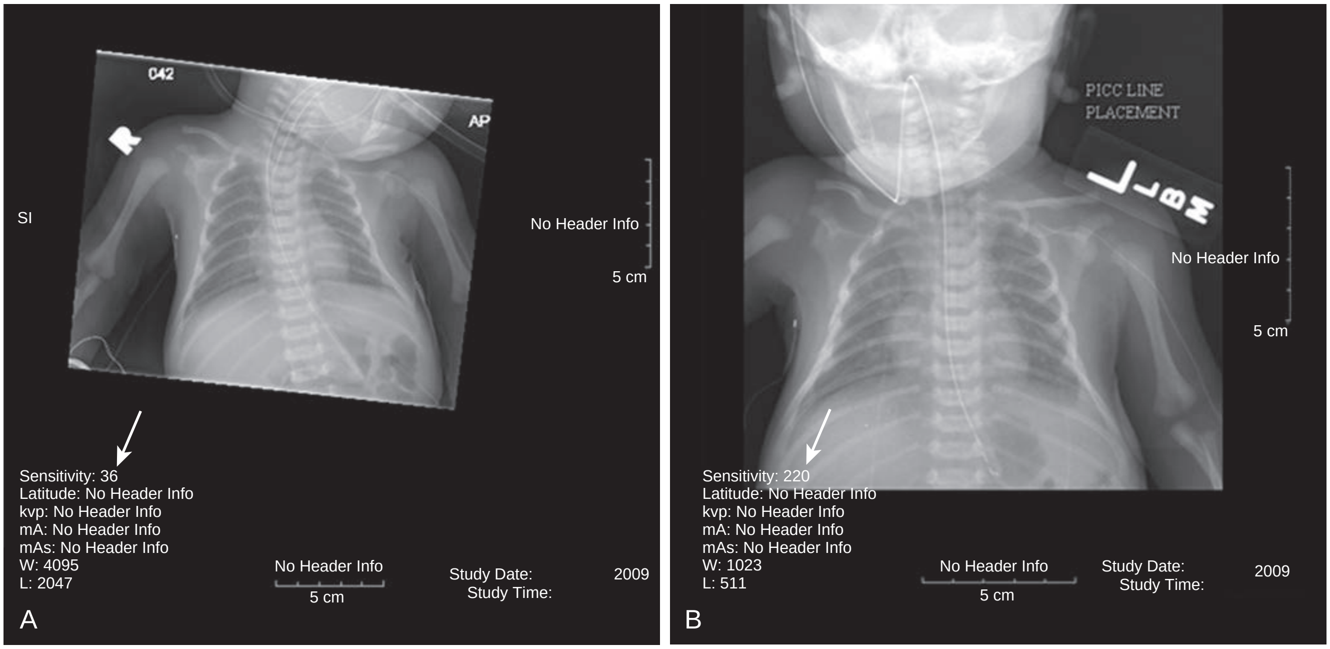

**Figure 1.1.** (A) Neonatal chest radiograph has an exposure index ("S" value 39) *(arrow)* that was very low, indicating a relatively high radiation exposure, which would have rendered this image dark with film screen technology. This radiograph was processed to yield appropriate contrast and brightness. (B) After adjustment to a more appropriate exposure index ("S" value 220) *(arrow)*. The image quality is very similar. The left arm was included because assessment was for percutaneous indwelling central catheter placement. *(From Frush DP. Radiation protection in children undergoing medical imaging. In Daldrup-Link HE, Gooding CA, eds.* Essentials of Pediatric Radiology. *Cambridge: Cambridge University Press; 2010. Used with permission.)*

**BOX 1.1** Inherited Human Syndromes Associated With Sensitivity to X-Rays

- Ataxia-telangiectasia
- Basal cell nevoid syndrome
- Cockayne syndrome
- Down syndrome
- Fanconi anemia
- Gardner syndrome
- Nijmegan breakage syndrome
- Usher syndrome

*From Hall EJ.* Radiobiology for the Radiologist. *5th ed. Philadelphia: Lippincott Williams & Wilkins; 2000.*

**TABLE 1.1** Deterministic Dose Rates

| Skin Injury | Approximate Threshold |
|---|---|
| **Skin** | |
| Transient erythema | 200 rad (2 Gy) |
| Dry desquamation | 1000 rad (10 Gy) |
| Moist desquamation | 1500 rad (15 Gy) |
| Temporary epilation | 200 rad (2 Gy) |
| Permanent epilation | 700 rad (7 Gy) |
| **Late effects on tissue** | **More variable** |

*Modified from Hall EJ.* Radiobiology for the Radiologist. *5th ed. Philadelphia: Lippincott Williams & Wilkins; 2000.*

Tissue bioeffects are characterized by a threshold dose, and the severity of the effect is dose dependent. For example, cataracts occur above a threshold recent data suggest is near 500 mGy.[11] Table 1.1 shows some of the doses for deterministic effects. In general, such effects from diagnostic imaging doses are extremely rare. Exceptions with head perfusion CT scanning in adults have been reported.[12] Deterministic effects such as skin ulcers and burns should never occur from diagnostic imaging, but they are occasionally seen with relatively lengthy interventional procedures.

Stochastic effects are more of a concern because they have the potential to occur at any dose, and the severity of the effect is independent of the dose. No threshold exists with stochastic effects, but the probability of an effect (e.g., cancer) increases with increasing doses.

## FETUSES AND CHILDREN HAVE GREATER RADIATION RISKS

From a public health perspective, all ionizing radiation, including that from medical imaging, is considered to be potentially harmful because we assume that no threshold exists below which radiation is safe (i.e., no harmful effects will occur). This "linear no threshold" model is applied to low-level radiation exposure.[13,14]

The effects of radiation are greatest on rapidly developing tissues and organs—in fetuses, infants, and young children. In pregnancy, the major biologic effects of fetal demise, growth restriction, organ malformations, and cognitive deficits are seen only with doses far in excess of routine diagnostic imaging.[15] The risk of developing cancer from exposure of a fetus to radiation is uncertain; potential effects could be seen with uterine doses that occur as a result of relatively high direct exposures (e.g., a pelvis CT scan for possible appendicitis). No data in humans indicate that genetic effects result from diagnostic levels of radiation.

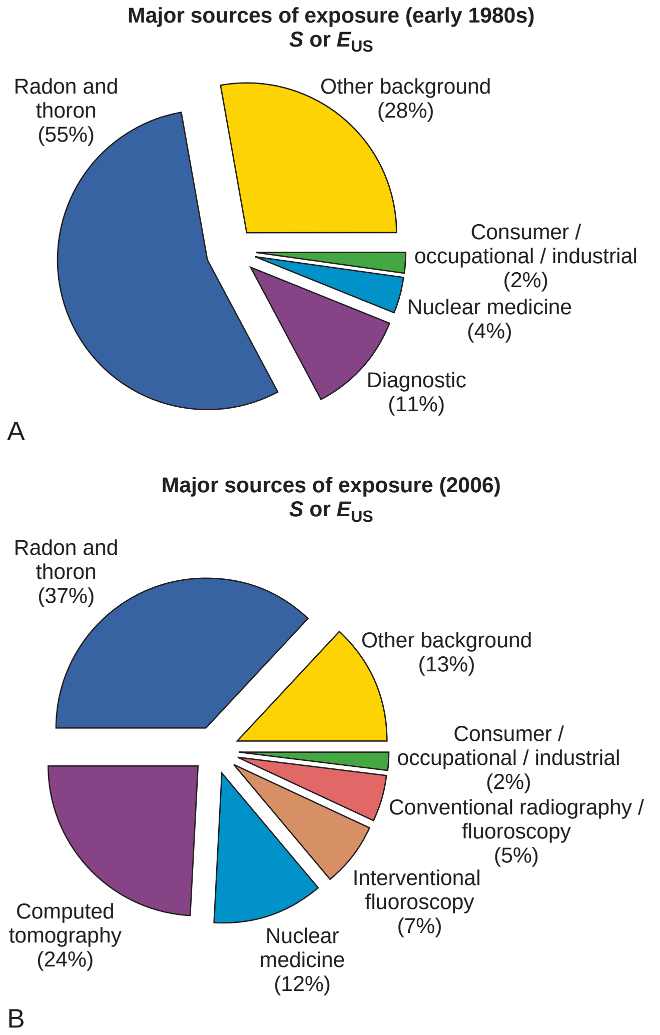

**Figure 1.2.** All exposure categories for the collective effective dose (%), early 1980s (A) and 2006 (B). *(Data from the National Council on Radiation Protection & Measurements.* Ionizing radiation exposure of the population of the United States [NCRP report No. 160]. *Bethesda, MD: National Council on Radiation Protection & Measurements; 2009. Used with permission.)*

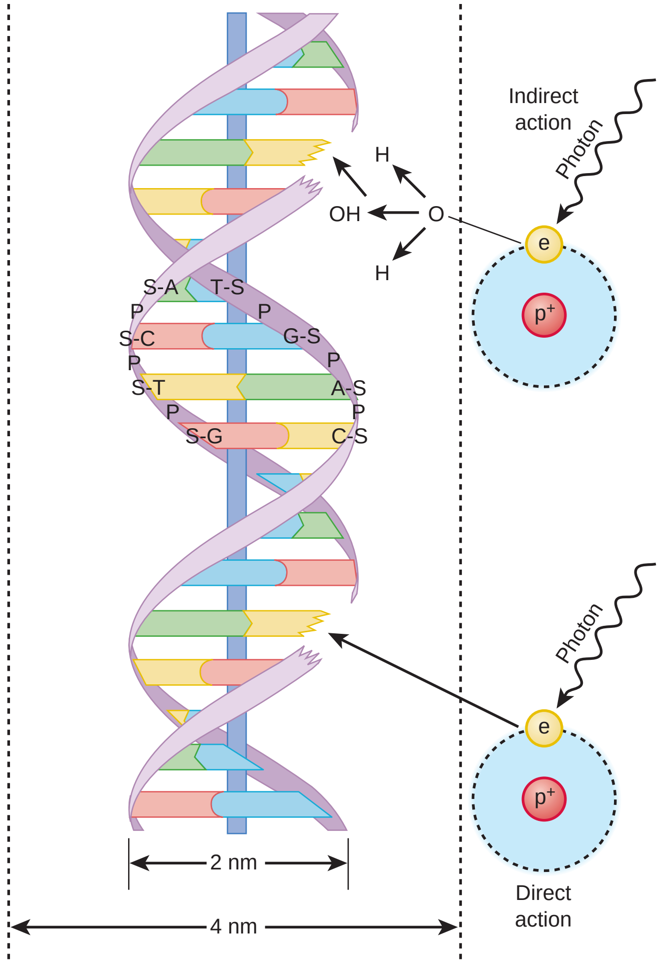

**Figure 1.3. Direct and indirect action.** Indirect action (top part of figure), an electron damages the deoxyribonucleic acid (DNA). In indirect action, the secondary electron interacts with a water molecule to produce a hydroxyl radical that then damages DNA, in this case affecting a single strand. *(From Hall EJ. Radiation biology for pediatric radiologists.* Pediatr Radiol. *2009;39[1]:S57–S64. Used with permission.)*

Compared with middle-aged adults, children are from 2 to 15 times more sensitive to radiation-induced carcinogenesis.[16,17] However, Shuryak et al. recently noted that the cancer induction risk (greater at younger ages) must be balanced with the radiation-induced promotion of premalignant damage (greater in middle age), which may differ for certain types of cancer.[18] Thus cancer risks may be higher in the adult population than traditionally believed.[19]

Low-dose effects have been described by Pierce and Preston, who studied the data from atomic bomb survivors reported by the Radiation Effects Research Foundation.[20] Among persons who had received dosages of 0.005 to 0.2 sievert (500 mrad to 20 rad), 35,000 people survived, and 5000 cases of cancer developed. The authors made the following conclusions: first, the solid cancer risk persists for more than 50 years. Second, there is a 10% increase over the expected cancer rate.[20] Low-dose relative risk factors are shown in Fig. 1.4.

The overall increased risk of excess cancer for the entire population suggested by the International Commission on Radiological Protection is 5% per sievert for low doses and low-dose rate. This value is an average value; for adults in late middle age, the excess risk decreases to only 1% per sievert, whereas for children, the excess risk may be as high as 16% per sievert for girls and 12% per sievert for boys. The female dose is higher because of the greater incidence of breast and thyroid cancers (Fig. 1.5). Radiation risks from diagnostic imaging low-level radiation were reviewed recently.[21] Two excellent reviews also recently were published by Linet et al. (e-Table 1.2).[22,23] We have cautious uncertainty regarding cancer risk and low-level radiation.[24,25] As Hricak et al. state, “In brief, there is reasonable, though not definitive, epidemiologic evidence that organ doses in the range from 5 to 125 mSv result in a very small but statistically significant nonzero increase in cancer risk.”[26]

## RADIATION EXPOSURES FROM VARIOUS IMAGING MODALITIES

When discussing radiation dose, it is important to state clearly whether entrance dose, skin dose, exit dose, or organ (absorbed) dose is considered. For example, a vast difference can exist between skin dose and gonadal dose for the same incident radiation. (The terms for dose and quantitative comparisons are provided in the glossary, and dose metrics are provided in Box 1.2.) “Effective

**e-TABLE 1.2** Risk of Specific and Total Childhood Cancers Associated With Early Life Postnatal Medical Radiation Exposure

| Study | Upper Age Limit (y) | Type/No. of Cases | Type/No. of Controls | Method of Exposure to Assessment | Type of Exposure | Exposure Prevalence in Controls | Estimated Relative Risk |
|---|---|---|---|---|---|---|---|
| **LEUKEMIA** | | | | | | | |
| Stewart et al., UK (1953–1955) | 10 | Deceased (619) | Population (619) | Interview, medical records | Diagnostic | 12.9 | 1.2 |
| | | | | | Therapeutic | 0.2 | 5.0 |
| Polhemus & Koch, US (1950–1957) | NS | Incident (251) | Hospital (251) | Questionnaire | Diagnostic | 41.4 | 2.1* |
| | | | | | Fluoroscopic | 3.2 | 3.5* |
| | | | | | Therapeutic | 3.6 | 3.7* |
| Ager et al., US (1965) | 4 | Deceased (109) | Siblings (102) | Interview, medical records | Any | 16.7 | 1.3 |
| | | | Neighborhood (110) | | | 18.2 | 1.1 |
| Graham et al., US (1966) | 14 | Incident (319) | Population (884) | Medical records | Any | 36.0 | 1.2 |
| | | | | | >1 site | 7.6 | 2.1 |
| Shu et al., China (1974–1986) | 14 | Incident, prevalent (309) | Population (618) | Interview | Any | 27.3 | 0.9 |
| Fajardo-Gutierrez et al., Mexico (1993) | 14 | Incident, prevalent (79) | Population, hospital (148) | Interview | Any | 27.0 | 1.1 |
| **ACUTE LYMPHOCYTIC LEUKEMIA** | | | | | | | |
| Shu, China (1974–1986) | 14 | Incident, prevalent (172) | Population (618) | Interview | Any | 27.3 | 0.9 |
| Magnani et al., Italy (1981–1984) | NS | Incident, prevalent (142) | Hospital (307) | Interview | Diagnostic | 45.9 | 0.7 |
| Shu et al., China (1986–1991) | 14 | Incident (166) | Population (166) | Interview | Any | — | 1.6 |
| Shu, US (1989–1993) | 15 | Incident (1842) | Population (1986) | Interview | Diagnostic | 39 | 1.1 |
| Infante-Rivard, Canada (1980–1998) | 14 | Incident (701) | Population (701) | Interview | Diagnostic, 1 | 19.1 | 1.1 |
| | | | | | Diagnostic, ≥2 | 18.8 | 1.5* |
| **ACUTE MYELOID LEUKEMIA** | | | | | | | |
| Shu et al., China (1974–1986) | 14 | Incident, prevalent (92) | Population (618) | Interview | Any | 27.3 | 1.0 |
| **LYMPHOMA** | | | | | | | |
| Shu et al., China (1981–1991) | 14 | Incident (87) | Population (166) | Interview | Any | — | 1.6* |
| **BRAIN TUMORS** | | | | | | | |
| Howe et al., Canada (1977–1983) | 19 | Incident (74) | Population (138) | Interview | Chest diagnostic | 8.0 | 2.1 |
| | | | | | Skull diagnostic | 4.3 | 6.7* |
| McCredie et al., Australia (1985–1989) | 14 | Incident (82) | Population (164) | Interview | Dental | 9.1 | 0.4 |
| | | | | | Skull diagnostic | 2.4 | 2.3 |
| Shu et al., China (1981–1991) | 14 | Incident (107) | Population (107) | Interview | Any | — | 1.5 |
| Schuz et al., Germany (1993–1997) | 15 | Incident (466) | Population (2458) | Interview | Any | 4.3 | 0.8 |
| **ASTROCYTOMA** | | | | | | | |
| Kuijten et al., US (1980–1986) | 14 | Incident (163) | RDD (163) | Interview | Head or neck | NS | 1.0 |
| | | | | | Dental | NS | 0.9 |
| Bunin et al., US/Canada (1986–1989) | 5 | Incident (155) | RDD (155) | Interview | Head, neck, or dental | 13.5 | 1.2 |
| | | | | | Dental | 9.0 | 1.0 |
| | | | | | Head | 3.2 | 1.1 |
| **PERIPHERAL NEUROEPITHELIOMA** | | | | | | | |
| Bunin et al., US/Canada (1986–1989) | 5 | Incident (166) | RDD (166) | Interview | Head, neck, or dental | 12.0 | 1.1 |
| | | | | | Dental | 8.4 | 0.5 |
| | | | | | Head | 4.2 | 0.9 |
| **NEUROBLASTOMA** | | | | | | | |
| Greenberg et al., US (1972–1981) | 14 | Incident (104) | Hospital (208) | Medical records | Chest | 33.2 | 0.3* |
| | | | Wilms (105) | | | 11.7 | 2.0 |
| | | | | | Cranial | 6.2 | 0.3 |
| | | | | | | 1.3 | 1.6 |
| | | | | | Abdominal | 6.7 | 0.4 |
| | | | | | | 3.9 | 0.8 |

*Continued*

**e-TABLE 1.2** Risk of Specific and Total Childhood Cancers Associated With Early Life Postnatal Medical Radiation Exposure—cont'd

| Study | Upper Age Limit (y) | Type/No. of Cases | Type/No. of Controls | Method of Exposure to Assessment | Type of Exposure | Exposure Prevalence in Controls | Estimated Relative Risk |
|---|---|---|---|---|---|---|---|
| **OSTEOSARCOMA** | | | | | | | |
| Gelberg et al., US (1997) | 24 | Incident (130) | Population (130) | Interview | Medical | NS | 1.0 |
| **EWING SARCOMA** | | | | | | | |
| Daigle et al., US (1975–1981) | 20 | Incident, prevalent (98) | RDD (98) | Interview | Any | NS | 1.0 |
| | | Incident, prevalent (95) | Siblings (95) | | | NS | 1.0 |
| Winn et al., US (1983–1985) | 22 | Incident (204) | RDD (204) | Interview | Diagnostic | 37.7 | 1.6* |
| | | | | | Dental | 50.0 | 1.2 |
| **ALL SITES** | | | | | | | |
| Stewart et al., UK (1953–1955) | 10 | Deceased (1299) | Populaton (1299) | Interview, medical records | Diagnostic | 13.6 | 1.0 |
| | | | | | Therapeutic | 0.2 | 2.7 |
| Hartley et al., UK (1980–1983) | 14 | Incident (535) | General practitioner (1068) | Interview, medical records | Neonatal | 0.3 | 2.0 |
| | | Incident (465) | Hospital (928) | | Diagnostic | 1.0 | 1.1 |
| Shu et al., China (1994) | 14 | Incident (642) | Population (642) | Interview | Any | — | 1.3* |

*NS,* Not specified; *RDD,* random-digit dialing.
*Statistically significant.
*From Linet MS, Slovis TL, Miller DL, et al. Cancer risks associated with external radiation from diagnostic imaging procedures.* CA Cancer J Clin. *2012;62:75–100.*

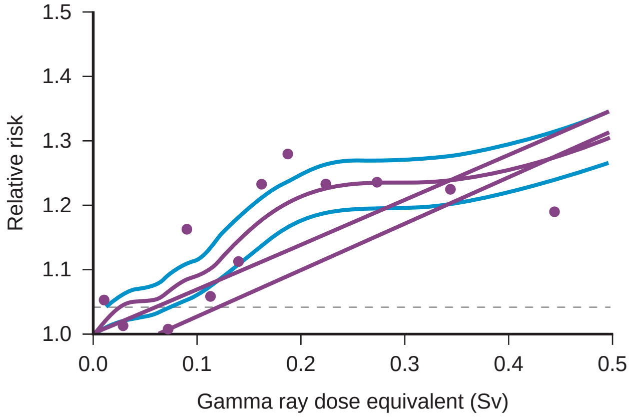

**Figure 1.4. Estimated low-dose risks.** Age-specific cancer rates over the 1958 through 1994 follow-up period relative to the rates for unexposed people averaged over the follow-up for sex and for age at exposure. The dashed line represents ±1 standard deviation error for the smooth purple curve. The upper straight line is the linear risk estimate computed from the range 0 to 2 Sv. The second straight line beginning at 0.06 Sv is the upper 95% confidence limit for such a quantity. *(From Pierce DA, Preston DL. Radiation-related cancer risks at low doses among atomic bomb survivors.* Radiat Res. *2000;154:178–186.)*

**BOX 1.2** Radiation Metrics

**A. ABSORBED DOSE—RADIATION ABSORBED DOSE (rad), GRAY (Gy)**

1 Gy = 100 rad
1 cGy = 1 rad = 1000 mrad
1 mGy = 100 mrad

**B. USE OF ABSORBED DOSE EQUIVALENT—RADIATION-EQUIVALENT—MAN (rem), SIEVERT (Sv)**

1 Sv = 100 rem
10 mSv = 1 rem = 1000 mrem
1 mSv = 100 mrem
Rem = rad × quality factor
Rem = rad × 1
Because the quality factor for x-ray and γ-rays = 1, rad = rem

**C. NUCLEAR MEDICINE**

1. Unit of radioactivity—becquerel (Bq)
   Bq = 1 disintegration/sec
2. Unit of radioactivity—curie (Ci)
   1 Ci = 3.7 × $10^{10}$ Bq (disintegration/sec)
   1 Ci = 2.2 × $10^{12}$ disintegration/min
   10 mCi = 370 mBq

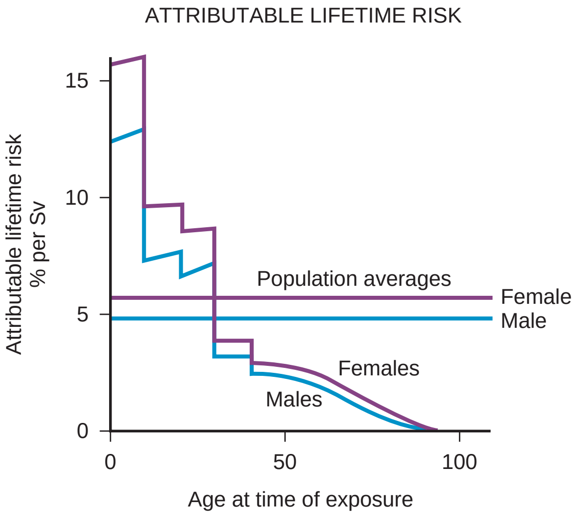

**Figure 1.5. Lifetime risk of excess cancer per sievert (SV) as a function of age at the time of exposure.** Data from atomic bomb survivors. Although the average risk for a population is about 5% per sievert, the risk varies considerably with age; children are much more sensitive than adults. At early ages, girls are more sensitive than boys. *(From Hall EJ. Introduction to session I. helical CT and cancer risk.* Pediatr Radiol. *2002;32:225–227.)*

dose" is one measure of radiation that is widely used in discussions of medical radiation. It is commonly used because it is relatively easily derived and allows gross comparisons of dose estimations between examinations of different regions as well as different modalities. However, the application of effective dose in medical imaging can be problematic.[27,28]

Published estimates for radiation doses in adults and children include those by Fahey et al. and Mettler et al.[29,30] In summary, radiographic dose ranges from a fraction of a millisievert (for extremity evaluation) to somewhat larger doses of more than 1.0 mSv for more extensive examinations, such as a lumbar spine series. Fluoroscopic doses depend on technical parameters, especially fluoroscopy time, filters employed, magnification, and frame rate, and can vary widely from very low–dose cystography to doses in tens of millisieverts for complex interventional procedures. CT can deliver a relatively large dose of ionizing radiation. The number of these examinations has been increasing rapidly, with children up to 15 years old undergoing approximately 11% of all CT examinations.[31] More recent information has shown that the dose (CTDI; see glossary) from CT in adults is less than 1.0 mSv to as much as 40 mSv.[29,30] Typical pediatric CT doses should be less than 10 mSv,[29,32] and with iterative reconstruction technologies, an increasing fraction of body examinations are approaching or being performed in the submillisievert range. Data on radiation doses from select pediatric imaging examinations are found in Tables 1.3 and 1.4.

## STRATEGIES FOR OPTIMIZING RADIATION DOSES FOR CHILDREN

The fundamental principles for protecting children from radiation during imaging include justification and optimization. Justification for a study can be difficult to define, although summary recommendations and appropriateness criteria for medical imaging are available.[33] The possible use of imaging modalities that do not depend on ionizing radiation, especially magnetic resonance imaging and sonography, is fundamental in justification decisions.

When an examination is considered justified, the imaging technique should be optimized. Radiation reduction is not always appropriate because some examinations require multiple and additional projections, greater fluoroscopy time or magnification, or lower image noise (requiring a higher dose) to answer specific clinical questions. Implicit here is the "as low as reasonable achievable" principle, which entails using the amount of radiation necessary for diagnosis and no more (or less).

Patient preparation and examination planning are paramount. Planning includes communicating with the ordering clinician when necessary to clarify examination indications.[34] Communication also is important both before and during fluoroscopic and angiographic examinations to minimize potentially nonuseful fluoroscopy. Use of appropriately trained staff and involvement with qualified medical physicists, along with licensing, certification, and accreditation considerations and routine reviews of equipment function and

**TABLE 1.3** Radiation Dose to Children by Age at Diagnostic Examination

| | Dose (mSv) (by Age at Exposure [y]) | | | | | |
|---|---|---|---|---|---|---|
| **Examination*** | **0** | **1** | **5** | **10** | **15** | **Adult** |
| **RADIOGRAPHY†‡** | | | | | | |
| Skull AP | — | 0.037 | 0.058 | — | — | 0.084 |
| Skull LAT | — | 0.025 | 0.031 | — | — | 0.041 |
| Chest PA | 0.023 | 0.024 | 0.037 | 0.025 | 0.026 | 0.051 |
| Abdomen AP | 0.077 | 0.197 | 0.355 | 0.509 | 0.897 | 2.295 |
| Pelvis AP | 0.085 | 0.121 | 0.230 | 0.309 | 0.556 | 1.783 |
| **DENTAL RADIOGRAPHY†** | | | | | | |
| Intraoral | | | 0.008 | | | 0.011 |
| Panoramic | | | 0.015 | | | 0.015 |
| **DIAGNOSTIC FLUOROSCOPY PROCEDURES†** | | | | | | |
| MCU | 0.807 | 0.763 | 0.688 | 0.640 | 0.677 | 2.789 |
| Barium swallow | 0.645 | 0.589 | 0.303 | 0.760 | 0.581 | 1.632 |
| Barium meal | 2.209 | 2.226 | 1.427 | 2.137 | 2.386 | 5.158 |
| Cardiac ASD occlusion | | | | 3.88 | | 5.158 |
| Cardiac PDA occlusion | | | | .021 | | |
| Cardiac VSD occlusion | | | | 12.1 | | |
| **COMPUTED TOMOGRAPHY§** | | | | | | |
| Brain | 2.3 | 2.2 | 1.9 | 2.0 | 2.2 | 1.9 |
| Facial bone/ sinuses | 1.4 | 0.5 | 0.5 | 0.5 | 0.6 | 0.9 |
| Chest | 1.9 | 2.2 | 2.5 | 3.0 | 3.3 | 5.9 |
| Entire abdomen | 3.6 | 4.8 | 5.4 | 5.8 | 6.7 | 10.4 |
| Spine | 4.4 | 11.4 | 8 | 7.6 | 6.9 | 10.1 |

*AP,* Anteroposterior; *ASD,* atrial septal defect; *LAT,* lateral; *MCU,* micturating cystourethrography; *PA,* posterolateral; *PDA,* patent ductus arteriosus; *VSD,* ventricular septal defect.

*Dosimetric quantities are all effective doses in millisieverts (mSv).

†From Hart D, Hillier MC. *Dose to Patients From Medical X-ray Examinations in the UK–2000 Review*. Chilton, UK: National Radiological Protection Board; 2007.

‡From Hart D, Hillier MC. *Dose to Patients From Medical X-ray Examinations in the UK—2002 Review*. Chilton, UK: National Radiological Protection Board; 2002.

§From Galanski M, Nagel HD, Stamm G. *Paediatric CT Exposure Practice in the Federal Republic of Germany—Results of a Nation-Wide Survey in 2005/2006*. Hannover, Germany: Hannover Medical School; 2006. Radiation doses are based on a German nationwide survey on multislice CT. The radiation dose in each age group category is the dose administered to pediatric patients who are newborn (the 0-year category), those ages >0–1 year (the 1-year category), those ages 2–5 years (the 5-year category), those ages 6–10 years (the 10-year category), and those ages 11–15 years (the 15-year category).

protocols as part of quality control and assessment, are becoming expected components of radiation protection in medicine.[35]

Dose management strategies in pediatric radiographic imaging include collimation, evaluation of the number of projections required, consideration of the source to receptor and patient to receptor distances, shielding when appropriate, use of grids, filtering, consideration of exposure factors, and use of postprocessing techniques. General strategies for protecting patients during radiography can be found in International Atomic Energy Agency educational material.[36]

A number of dose management strategies exist for fluoroscopy and interventional radiology, including those by the International Atomic Energy Agency and Alliance for Radiation Safety in Pediatric Imaging (Image Gently Campaign).[37–39] These strategies include avoiding field overlap and electronic magnification, placement of the image intensifier before fluoroscopic activation, use of appropriate grids and positioning (i.e., source to patient and patient to intensifier distances), collimation, and use of pediatric-specific filters. In addition, last image hold, pulsed fluoroscopy, image store, video capture, and alerts are part of examination optimization for children. Video recording during studies can provide review without use of additional fluoroscopy.

Contemporary strategies and examination optimization for radiation dose management in pediatric CT, including protocol optimization, are available.[40–43] Adjustment in the parameters that are primarily responsible for the dose delivered—tube current (milliamperes), gantry cycle time in seconds, peak kilovoltage, and table speed—should be based on the size of the child, examination indication, prior examinations, and region examined. Additional efforts should include minimizing multiphase examinations, excessive scan length, and overlapping regions of examination. Tube current modulation, organ-based dose modulation (in which the tube current is reduced in an arc to reduce the surface dose to anterior structures such as the breasts when the patient is supine), iterative reconstructive technologies, kVp, rapid table translation, and dual-source/dual-energy technology also have provided real or potential opportunities for dose reduction, improved examination quality, or a combination of both. The use of shielding in the region of scanning, which usually is discussed for breast tissue, is debated.[44,45] A more in-depth discussion of radiation protection in children undergoing diagnostic imaging is available.[46]

## COMMUNICATION OF RADIATION RISK

Given existing information regarding the risk of medical radiation, communication of that risk with patients, their families, and health care providers is important, but fraught. Many clinicians are aware of the study by Pearce et al. demonstrating one excess case each of leukemia and brain tumor for every 10,000 pediatric head CT scans.[47] Methodologic issues limited the conclusions drawn; however, even if this reported risk is accurate, when a CT scan is performed in a setting meeting appropriate clinical criteria, the benefits far outweigh the risks. In fact, *not* performing a clinically indicated CT scan because of radiation risk concerns is more likely to cause harm than the indicated scan itself.[48]

As such, educational efforts are extremely important, particularly given increased scrutiny and concern regarding medical radiation and the risk of cancer. To these ends, the Image Gently Alliance[49,50] has been a successful education and awareness organization for informed use of ionizing radiation in medical imaging in children.

Continued needs include more evidence-based research and decision support to improve utilization,[51] better dose estimations,[6,7] ongoing optimization of diagnostic reference levels for pediatric imaging, alerts and notifications on imaging equipment,[52] and dose monitoring for all modalities as well as dose tracking and relevant imaging providers.[53]

## APPENDIX: GLOSSARY AND DOSE DESCRIPTORS

As we probe more deeply into the effects of radiation, it is important to use precise definitions. Some of the most pertinent terms are provided in this glossary.[8]

**Absolute risk:** The risk of an adverse effect that is independent of other causes of that same health effect.

**Absorbed dose (D):** The energy imparted to matter per unit of mass by ionizing radiation at a specific point. The Systeme Internationale (SI) unit of absorbed dose is joules per kilogram (J/kg); the Gray (Gy). The previously used special unit of absorbed dose, the rad, was defined as being an energy absorption dose of 100 erg/g; 1 Gy = 100 rad.

**ALARA (as low as reasonably achievable):** The principle of limiting the radiation dose administered to exposed individuals to levels as low as are reasonably achievable, taking into account economic and social factors.

**TABLE 1.4** Typical Effective Radiation Dose of Common Radiologic Procedures in Children

| Examination | Typical Effective Dose by Age of Exposure (mSv) | | | | Adult |
|---|---|---|---|---|---|
| | **Newborn** | **1 Year** | **5 Years** | **10 Years** | |
| Chest x-ray | 0.02 | | | | |
| Intraoral dental radiography | 0.005 | | | | |
| Dental orthopantomogram | 0.01 | | | | |
| Cone beam craniofacial dental CT | <1 | | | | |
| Head CT | 6 | 3.7 | 2 | 2.2 | 2 |
| Chest CT | 1.7 | 1.8 | 3 | 3.5 | 7 |
| Abdominal CT | 5.3 | 4.2 | 3.7 | 3.7 | 7 |
| FDG PET CT | 15.3 | | | | |
| Tc-99m bone scan | 6 | | | | |
| Fluoroscopic cystogram | 0.33 | | | | |
| Fluoroscopic pediatric interventional cardiology | 1 to 37 | | | | |

*Adapted from World Health Organization.* Communicating Radiation risks in Paediatric Imaging: Information to support healthcare discussions about benefit and risk. *http://www.who.int/ionizing_radiation/pub_meet/radiation-risks-paediatric-imaging/en/. Accessed March 21, 2017.*

**Background radiation:** The radiation in the natural environment, including cosmic rays and radiation from the naturally radioactive elements, found outside and inside the bodies of humans and animals. Background radiation also is called *natural radiation*. The term also may mean radiation that is unrelated to a specific experiment.

**CTDI:** Computed tomography dose index, a radiation exposure index defined as the average dose of a single CT slice acquisition of a given protocol performed on a standard 100 mm pencil chamber dosimeter within a standard phantom.

**Effective dose:** The radiation dose, accounting for the fact that some types of radiation are more damaging than are others and some parts of the body are more sensitive to radiation than are others. It is defined as the sum, over specified tissues, of the products of the equivalent doses in the exposed tissues and the weighting factors for those tissues.

**Exposure:** Exposure is used more often in its more general sense and not as the specially defined radiation quantity. It is a measure of the quantity of radiation based on its ability to ionize air through which it passes. The previously used special unit of exposure, the roentgen (R), has been replaced with the SI unit of exposure, coulombs per kilogram (C/kg); $1\ \text{R} = 2.58 \times 10^{-4}$ C/kg (exactly). The physical quantity exposure may be replaced by the quantity air kerma in air, especially for calibration of monitoring instruments: 1 R = 10 mGy air kerma.

**Free radical:** A fragment of an atom or molecule that contains an unpaired electron in the outer shell and is very reactive.

**Gamma rays:** High-energy, short-wavelength electromagnetic radiation ($\gamma$). Gamma radiation frequently accompanies $\alpha$ and $\beta$ emissions and always accompanies fission. Gamma rays are very penetrating and are best stopped or shielded against by dense materials, such as lead or depleted uranium. Gamma rays are indistinguishable from x-rays except for their source: gamma rays originate inside the nucleus, and x-rays originate from outside.

**Gray (Gy):** The special name for the SI unit of absorbed dose (kerma) and specific energy imparted equal to 1 J/kg. The previous unit of absorbed dose, the rad, has been replaced by the gray: 1 Gy = 100 rad.

**Hereditary effects of radiation:** Radiation effects that can be transferred from parent to offspring; any changes in the genetic material of sex cells caused by radiation.

**Kerma (kinetic energy released per unit mass):** The sum of the initial kinetic energies of all the charged ionizing particles liberated by uncharged ionizing particles per unit mass of a specified material. Kerma is measured in the same unit as absorbed dose. The SI unit of kerma is joules per kilogram (J/kg), and its special name is the gray (Gy). Kerma can be quoted for any specified material at a point in free space or in an absorbing medium.

**Lifetime risk:** The risk of dying of some particular cause over the entire course of a person's life.

**Linear no threshold (LNT):** The theory based on a linear dose response that no level of radiation exposure can be assumed to be absolutely safe.

**Rad:** The old unit of absorbed dose, equivalent to an energy absorption of 100 erg/g. Superseded by the Gray (see absorbed dose).

**Relative risk:** The situation in which the risk of a disease resulting from some injury is expressed as some percentage increase of the spontaneous rate of occurrence of that disease. Relative risk is in contrast to an absolute risk, in which the risk of a disease resulting from an injury does not depend on the normal rate of occurrence of that disease.

**Rem:** Old unit of equivalent or effective dose. It is the product of absorbed dose (in rads), the radiation weighting factor, and the tissue weighting factor; 1 rem = 0.01 Sv.

**Roentgen (R):** A unit of exposure to ionizing radiation named after Wilhelm Röntgen, the German scientist who discovered x-rays in 1895. It is that amount of $\gamma$ rays or x-rays required to produce ions carrying one electrostatic unit of electric charge (either positive or negative) in 1 $\text{cm}^3$ of dry air under standard conditions.

**Sievert (Sv):** Unit of equivalent dose or effective dose: 1 Sv = 100 rem.

**Stochastic effect:** The effect, the probability of which, rather than its severity, is a function of radiation dose without threshold. More generally, stochastic means random in nature.

**Tissue (deterministic) effect:** An effect with a threshold, the severity of which increases as the dose increases.

## KEY POINTS

- Radiation can have a direct action on DNA or operate indirectly through free radicals.
- In medicine, biologic effects from radiation are primarily a result of double-strand DNA breaks.
- In diagnostic imaging, radiation effects are stochastic effects, primarily cancer induction (vs. deterministic effects such as skin burns seen at much higher doses).
- Fetal and childhood tissues are more susceptible to the stochastic effects of radiation.
- Key principles of protecting persons from diagnostic radiation are justification (only perform indicated examinations) and optimization (use appropriate examination techniques).
- Dose metrics (i.e., exposure or dose estimations) should be part of the examination information for every modality that uses ionizing radiation.

## SUGGESTED READINGS

Fahey FH, Treves ST, Adelstein SJ. Minimizing and communicating radiation risk in pediatric nuclear medicine. *J Nucl Med*. 2011;52:1240–1251.

Frush DP. CT dose and risk estimates in children. *Pediatr Radiol*. 2011;41:483–487.

Hall EJ. Radiation biology for pediatric radiologists. *Pediatr Radiol*. 2009;39(1):S57–S64.

Hricak H, Brenner DJ, Adelstein SJ, et al. Managing radiation use in medical imaging: multifaceted challenge. *Radiology*. 2011;258:889–905.

Linet MS, Slovis TL, Miller DL, et al. Cancer risks associated with external radiation from diagnostic imaging procedures. *CA Cancer J Clin*. 2012;62(2):75–100.

McCollough CH, Schueler BA, Atwell TD, et al. Radiation exposure and pregnancy: when should we be concerned? *Radiographics*. 2007;27:909–917.

## REFERENCES

Full references for this chapter can be found on www.expertconsult.com.

## REFERENCES

1. http://www.acr.org/~/media/ACR/Documents/AppCriteria/RRLInformation/pdf.
2. Don S. Radiosensitivity of children: potential for overexposure in CR and DR and magnitude of doses in ordinary radiographic examinations. *Pediatr Radiol*. 2004;34(3):S167–S172.
3. Strauss K. Radiation safety summit—method to estimate radiation dose to pediatric patients from CT scans. *Pediatr Radiol*. 2011;41:210–211.
4. http://www.aapm.org/pubs/reports/. Accessed March 21, 2017.
5. International Atomic Energy Agency. *Technical Meeting on Review of Radiation Protection Guidance for Medical Workers, Vienna, 17-19 November 2008* (website). http://rpop.iaea.org/RPOP/RPoP/Content/PastEvents/MeetingsRadiationprotectionmedicalworkersnov2008.htm. Accessed March 21, 2017.
6. National Council on Radiation Protection & Measurements. *Ionizing radiation exposure of the population of the United States* (NCRP report No. 160). Bethesda, Md: National Council on Radiation Protection & Measurements; 2009.
7. Larson DB, Johnson LW, Schnell LW, et al. Rising use of CT in child visits to the emergency department in the United States, 1995-2008. *Radiology*. 2011;259(3):793–801.
8. Hall EJ. Radiation biology for pediatric radiologists. *Pediatr Radiol*. 2009;39(1):S57–S64.
9. Mettler FA Jr, Brenner D, Coleman CN, et al. Can radiation risks to patients be reduced without reducing radiation exposure? The status of chemical radioprotectants. *AJR Am J Roentgenol*. 2011;196(3):616–618.
10. Little JB, et al. Ionizing radiation. In: Kufe DW, Pollock RE, Weichselbaum RR, eds. *Holland-Frei Cancer Medicine*. 6th ed. Ontario, BC: Decker; 2003.
11. International Commission on Radiological Protection. *Statement on Tissue Reactions* (website). http://www.icrp.org/docs/ICRP%20Statement%20on%20Tissue%20Reactions.pdf. Accessed March 20, 2017.
12. U.S. Food and Drug Administration. *Safety investigation of CT brain perfusion scans: update 11/9/2010*. http://www.fda.gov/medicaldevices/safety/alertsandnotices/ucm185898.htm. Accessed March 21, 2017.
13. Little MP, Wakeford R, Tawn EJ, et al. Risks associated with low doses and low dose rates of ionizing radiation: why linearity may be (almost) the best we can do. *Radiology*. 2009;251:6–12.
14. Tubiana M, Feinendegen LE, Yang C, et al. The linear no-threshold relationship is inconsistent with radiation biologic and experimental data. *Radiology*. 2009;251:13–22.
15. McCollough CH, Schueler BA, Atwell TD, et al. Radiation exposure and pregnancy: when should we be concerned? *Radiographics*. 2007;7:909–917.
16. Brenner DJ, Elliston CD, Hall EJ, et al. Estimated risks of radiation-induced fatal cancer from pediatric CT. *AJR Am J Roentgenol*. 2001; 176:289–296.
17. Radiological Society of North America. *Categorical course in physics: radiation dose and image quality for pediatric CT: clinical considerations*. Oak Brook, IL: Radiological Society of North America; 2006.
18. Shuryak I, Sachs RK, Brenner DJ. Cancer risks after radiation exposure in middle age. *J Natl Cancer Inst*. 2010;102:1–9.
19. United Nations Scientific Committee on the Effects of Atomic Radiation. *Sources, Effects, and Risks of Ionizing Radiation: UNSCEAR 2012 Report*. http://www.unscear.org/docs/publications/2012/UNSCEAR_2012_Report.pdf. Accessed March 23, 2017.
20. Pierce DA, Preston DL. Radiation-related cancer risks at low doses among atomic bomb survivors. *Radiat Res*. 2000;154:178–186.
21. Frush DP. CT dose and risk estimates in children. *Pediatr Radiol*. 2011;41:483–487.
22. Linet M, Kim K, Rajaraman P. Children's exposure to diagnostic medical radiation and cancer risk: epidemiologic and dosimetric considerations. *Pediatr Radiol*. 2009;39(1):S4–S26.
23. Linet MS, Slovis TL, Miller DL, et al. Cancer risks associated with external radiation from diagnostic imaging procedures. *CA Cancer J Clin*. 2012;62(2):75–100.
24. Mathews J, Forsythe A, Brady Z, et al. Cancer risk in 680,000 people exposed to computed tomography scans in childhood or adolescence: data linkage study of 11 million Australians. *BMJ*. 2013;346:f2360.
25. Boice JD. Radiation epidemiology and recent paediatric computed tomography studies. *Ann ICRP*. 2015;44(1 suppl):236–248.
26. Hricak H, Brenner DJ, Adelstein SJ, et al. Managing radiation use in medical imaging: a multifaceted challenge. *Radiology*. 2011;258:889–905.
27. McCollough CH, Christner JA, Kofler JM. How effective is effective dose as a predictor of radiation risk? *AJR Am J Roentgenol*. 2010;194:890–896.
28. Martin CJ. Effective dose: how should it be applied to medical exposures? *Br J Radiol*. 2007;80:639–647.
29. Fahey FH, Treves ST, Adelstein SJ. Minimizing and communicating radiation risk in pediatric nuclear medicine. *J Nucl Med*. 2011;52:1240–1251.
30. Mettler FA, Huda W, Yoshizumi TT, et al. Effective doses in radiology and diagnostic nuclear medicine: a catalog. *Radiology*. 2008; 248(1):254–256.
31. Frush DP, Applegate K. Computed tomography and radiation: understanding the issues. *J Am Coll Radiol*. 2004;1:113–119.
32. Thomas K, Wang B. Age-specific effective doses for pediatric MSCT examinations at a large children's hospital using DLP conversion coefficients: a simple estimation method. *Pediatr Radiol*. 2008;38:645–656.
33. Hendee WR, Becker GJ, Borgstede JP, et al. Addressing overutilization in medical imaging. *Radiology*. 2010;257:240–245.
34. Malone J, Guleria R, Craven C, et al. Justification of diagnostic medical exposures, some practical issues: report of an International Atomic Energy Agency Consultation. *Br J Radiol*. 2012;85(1013): 523–538.
35. The Joint Commission. *Sentinel Event Alert, Issue 47: Radiation risks of diagnostic imaging* (website). http://www.jointcommission.org/sea_issue_47/. Accessed March 21, 2017.
36. International Atomic Energy Agency. *Be informed about the safe use of ionizing radiation in medicine* (website). http://rpop.iaea.org. Accessed March 21, 2017.
37. Miller D, Balter S, Schueler B, et al. Clinical radiation management for fluoroscopically guided interventional procedures. *Radiology*. 2010;257(2):321–332.
38. Sidhu M, Goske MJ, Connolly B, et al. Image Gently, Step Lightly: promoting radiation safety in pediatric interventional radiology. *AJR Am J Roentgenol*. 2010;195:299–301.
39. The Alliance for Radiation Safety in Pediatric Imaging. *Welcome to Image Gently:a practice quality improvement (PQI) program in computed tomography (CT) scans in children* (website). http://www.imagegently.org/Roles-What-can-I-do/Radiologist/PQI-Program-in-CT. Accessed March 21, 2017.
40. Nievelstein RAJ, van Dam I, van der Molen A. Multidetector CT in children: current concepts and dose reduction strategies. *Pediatr Radiol*. 2010;40:1324–1344.
41. Frush DP. MDCT in children: scan techniques and contrast issues. In: Kalra MK, Saini S, Rubin GD, eds. *MDCT: From Protocols to Practice*. Milan, Italy: Springer; 2008.
42. Singh S, Kalra M, Moore M, et al. Dose reduction and compliance with pediatric CT protocols adapted to patient size, clinical indication, and number of prior studies. *Radiology*. 2009;252(1):200–206.
43. Strauss KJ, Goske MJ, Kaste SC, et al. Image Gently: ten steps you can take to optimize image quality and lower CT dose for pediatric patients. *AJR Am J Roentgenol*. 2010;194:868–873.
44. Kim S, Frush D, Yoshizumi T. Bismuth shielding in CT: support for use in children. *Pediatr Radiol*. 2010;40:1739–1743.
45. Geleijns J, Wang J, McCollough C. The use of breast shielding for dose reduction in pediatric CT: arguments against the proposition. *Pediatr Radiol*. 2010;40(11):1744–1747.
46. Frush DP. Radiation protection in children undergoing medical imaging. In: Daldrup-Link HE, Gooding CA, eds. *Essentials of Pediatric Radiology*. Cambridge: Cambridge University Press; 2010.
47. Pearce MS, Salotti JA, Little MP, et al. Radiation exposure from CT scans in childhood and subsequent risk of leukaemia and brain tumours: a retrospective cohort study. *Lancet*. 2012;380:499–505.
48. Guillerman RP. From 'Image Gently' to image intelligently: a personalized perspective on diagnostic radiation risk. *Pediatr Radiol*. 2014;44(suppl 3):S444–S449.
49. Goske MJ, Applegate KE, Frush DP, et al. The Image Gently campaign: working together to change practice. *AJR Am J Roentgenol*. 2008;190(2):273–274.
50. Goske MJ, Applegate KE, Frush DP, et al. Image Gently: progress and challenges in CT education and advocacy. *Pediatr Radiol*. 2011;41:461–466.
51. Sistrom CL, Dang PA, Weilburg JB, et al. Effect of computerized order entry with integrated decision support on the growth of outpatient procedure volumes: seven-year time series. *Radiology*. 2009;251: 147–155.
52. Hampton T. Radiation oncology organization, FDA announces radiation safety initiatives. *JAMA*. 2010;303(13):1239–1240.
53. Rehani M, Frush DP. Tracking radiation exposure of patients. *Lancet*. 2010;376:754–755.

# 2

# Magnetic Resonance Safety

*Ramkumar Krishnamurthy and Jean A. Tkach*

Magnetic resonance imaging (MRI) has proved to be a powerful diagnostic imaging tool in children and adults. MRI uses low-energy nonionizing radio waves, and as such it is particularly well suited for pediatric and longitudinal imaging studies. MRI exploits a wide variety of intrinsic tissue-specific properties to generate a wide spectrum of tissue contrast, thus providing detailed information about anatomy, physiology, and function. For clinical MRI examinations, the acquisition techniques used and the specific acquisition parameters selected are manipulated to generate the type of image contrast most relevant to the underlying medical question. Unlike MRI, ultrasound is limited by the restriction of air and bony anatomy, and radiography and computed tomography uses ionizing radiation. Compared with other diagnostic imaging modalities, MRI has proved to be superior at imaging soft tissues. In addition, MRI enables images to be obtained in any plane and can provide true volumetric data acquisition.

MRI, when performed following the right conditions and guidelines, presents no apparent safety risks, and millions of MRI examinations are performed each year without incident. However, when not appropriately managed, safety concerns exist from the following: each of the three electromagnetic fields (Table 2.1), external contrast agent (typically gadolinium-based), associated acoustic noise, and other issues (e.g., sedation). Notably, most MR-related injuries and the few fatalities that have occurred primarily were a result of the failure to adhere to MR safety guidelines for the MRI environment, or they occurred because inaccurate or outdated MR safety-related information was used for biomedical implants and devices.[1,2]

To prevent similar adverse MR safety-related incidents from occurring, it is imperative that the potential safety risks intrinsic to the MR environment be understood and respected by users of this powerful imaging technology.

## SAFETY CONSIDERATIONS: ELECTROMAGNETIC FIELDS

### Main Static Magnetic Field

### Biologic Effects of Static Magnetic Fields

The majority of MRI systems in clinical use today operate at main or static magnetic field strengths of 0.2 to 3.0 tesla (T), with 1.5 T and 3.0 T units being used predominantly. The static field of a 1.5 T scanner is approximately 30,000 times stronger than Earth's magnetic field (roughly 0.00005 T). The most recent United States Food and Drug Administration (FDA) guidelines state that, for adults, children, and infants older than 1 month, diagnostic MRI systems that operate at or below 8 T are considered to be a nonsignificant risk. For neonates, the limit is 4 T.[3] In practice, 3 T is the highest field strength in common clinical use. Initially, some concern was expressed that the strong magnetic fields might have irreversible detrimental biologic/health effects in humans, including alterations in cell growth and morphology, cell reproduction and teratogenicity, DNA structure and gene expression, prenatal and postnatal reproduction and development, blood-brain barrier permeability, nerve activity, cognitive function and behavior, cardiovascular dynamics, hematologic indexes, temperature regulation, circadian rhythms, immune responsiveness, and other biologic processes.[4–22] However, a comprehensive review of the literature indicates that short-term exposures (of a duration comparable to an MR examination) to high-static magnetic fields produce no appreciable long-term detrimental biologic effects.[23,24]

Although no lasting adverse effects of short-term exposures to high magnetic field strengths have been reported, several relatively transient reversible biologic effects are known to occur, including electrocardiographic changes and benign sensory effects. These effects have been reported primarily at field strengths greater than 2 T, and the sensory effects appear to occur most often when a person's head is moved rapidly within the static magnetic field. The elevation in electrocardiographic T waves is believed to be due to magnetohydrodynamic phenomena.[25,26] The voltage associated with the magnetohydrodynamic effect is not considered hazardous at the magnetic field strengths approved for clinical use. However, at higher field strengths, the possibility exists that the induced potential might exceed 40 mV (voltage produced across large arteries are on the order of 5 mV/T), which is the threshold for depolarization of cardiac muscle.[27]

Several short-term, relatively benign sensory effects have been reported at higher field strengths, including vertigo, nausea, headaches, flashing lights (also known as magnetophosphenes), a metallic taste, and/or sensation in dental fillings.[28]

### Interaction of the Main Magnetic Field With Ferromagnetic Objects

**Torque and Attractive Forces.** The field associated with an MR scanner can be separated into two spatial regions defined by the types of interaction with ferromagnetic objects that predominate in each region. The first region surrounds the magnet isocenter and is contained within the bore of the MRI scanner. The magnetic field in this region essentially is temporally constant and homogeneous in strength. A magnetic object introduced into this region of the static field is subjected to a torque that acts to align it with the magnetic field, just as magnetic material aligns itself with the poles of a permanent bar magnet or a compass needle aligns itself with the Earth's magnetic field.[29] Hence any nonspherical metallic object that enters the spatially homogenous static region of the field will be subjected to a rotational force or torque such that its long axis will be aligned with that of the main magnetic field. If the metallic implants are not sufficiently anchored by the surrounding tissue (e.g., bone in the case of an orthopedic implant), the resultant rotational motion will cause trauma to the surrounding tissue. The magnitude of these effects depends on the geometry and mass of the object, as well as the characteristics of the MR system's magnetic field.

In the second region (the fringe field), the strong magnetic field strength drops off rapidly as the distance from the magnet increases, producing a large spatial gradient that typically is greatest in regions immediately adjacent to the magnet. Modern day scanners have actively shielded main magnetic fields, which significantly increases the spatial gradient. Metallic objects introduced into this magnetic field gradient experience a translational (attractive) and rotational force. The translation will be in the direction of the higher field strength. The strength of the attractive/translational force will depend on the size of the object and its location within the gradient field and will increase rapidly as the object approaches the magnet. As such, the metallic object will be accelerated along the direction of the spatial gradients in the static field and

## Abstract:

Following MRI safety guidelines is critical in ensuring a successful and safety event-free MRI experience. However, there are unique considerations in adhering to safety guidelines in children compared with as an adult population. The higher use of sedation also makes following MRI safety guidelines challenging.

## Keywords:

Pediatric MRI safety
ACR guidelines

**TABLE 2.1** Principal Mechanisms of Interaction of the Three Main MRI Energy Fields With Tissues and Some Related Effects

| Magnetic Resonance–Related Electromagnetic Field | Mechanism of Interaction | Potential Effects |
|---|---|---|
| Static magnetic field (T) | Polarization/ magnetization | Elevated electrocardiographic T wave and/or transient sensory effects (e.g., vertigo, nausea, phosphenes, and metallic taste) |
| Transient gradient magnetic field (dB/dt) | Induced currents<br>Acoustic noise | Peripheral nerve stimulation<br>Physiologic stress, anxiety, temporary hearing loss |
| Radio frequency field (specific absorption rate) | Thermal heating | Local burns |

*From Bushong SC. Biologic effects of magnetic resonance imaging. In:* MR safety, magnetic resonance imaging: physical and biological principles. *3rd ed. St Louis: Mosby; 2003.*

quickly can become a dangerous projectile. Depending on the size and composition of the metallic object, these attractive/translational effects may begin as soon as the object is introduced into the scan room. Once the object enters the uniform field within the bore of the magnet, acceleration will cease and the object will come to a stop.[25]

The potential hazards associated with the spatial gradients are greatest for high magnetic field strengths and large fringe fields. In general, the forces increase approximately as the square of the field strength but will vary depending on the composition of the object.[30] For example, at 3 T compared with 1.5 T, the force on a paramagnetic material (e.g., a stainless steel scalpel) is 5 times greater, whereas the force on a ferromagnetic object (e.g., a steel wrench) is 2.5 times greater.[30] Finally, even for a given field strength, the magnitude and footprint of the spatial gradients can vary between magnet configurations. For example, it has been reported that short-bore MR systems have significantly higher spatial gradients than long-bore scanners, particularly those operating at 3 T.[31,32] This finding highlights the multiple nuances and factors that must be considered when evaluating and establishing MR safety guidelines and operating procedures for any object before it may be introduced into a specific MRI environment. It is a common misconception that the magnet is only "on" when the images are being acquired. However, the magnet is *always* on, and signage to indicate the "Magnet is ON" should be displayed conspicuously on the door to the MR scan room.

**Missile/Projectile Effect.** The projectile/missile effect, wherein a ferromagnetic object is accelerated toward the isocenter of the magnet, is the most widely recognized and publicized safety hazard associated with MRI. Objects constructed partially or entirely of ferromagnetic materials (e.g., iron, nickel, cobalt, and the rare earth metals chromium, gadolinium, and dysprosium) are strongly attracted to the magnet bore. Steel objects also are highly ferromagnetic, as are some medical grades of stainless steel. Notably, working a metal by machining, molding, and/or bending it, for example, can alter its magnetic properties and, as a result, some forms of nonmagnetic stainless steel can be made magnetic. For this reason, the MR safety of a given metallic object must be evaluated in its final form.[33] If any doubt remains regarding the presence of ferromagnetic material, the object should be checked with a permanent magnet and/or a ferromagnetic wand as a final precautionary measure before it enters the scan room.

Any individual in the path between the object and the center of the magnet (e.g., the patient lying in the magnet bore) can be seriously injured or killed.[34] Numerous instances of MR-related accidents involving objects such as scalpels, scissors, oxygen tanks, intravenous line poles, wheelchairs, transport carts, floor buffers, mop buckets, vacuum cleaners, other medical devices, and even firearms have been documented. Any injuries related to ferromagnetic projectiles must be documented; the necessary forms can be accessed on the FDA website.[35,36] More comprehensive information regarding these online resources is provided in a later section of this chapter.

To prevent potentially devastating MR-related accidents from occurring, it is essential that access to areas that exceed the 5 Gauss line (see next section) must be rigorously restricted and vigilantly supervised at all times. All patients, accompanying family members, and hospital personnel with a demonstrated need to enter the MR environment must be appropriately educated to the potential hazards and rigorously screened for contraindications.

**5 Gauss Line.** Failure to adhere to safe practices within the MR environment has led to most of the MR-related accidents and fatalities. These incidents have involved the inappropriate introduction of metallic objects and/or implanted medical devices into the scan room. Five gauss (G) (1G = 0.0001 T) and below are considered "safe" levels of static magnetic field exposure for the general public.[29] The 5 G line identifies the perimeter around an MR scanner within which the static magnetic fields are higher than 5 G; it is the most commonly recognized MR safety policy.[25] Safety considerations require that this distance from the magnet be determined and that areas with field strength greater than 5 G be identified with appropriate and conspicuous signage. Importantly, the 5 G line extends in three dimensions; thus when the MR area is sited, the extent of the fringe field to the floors above and below the magnet must be considered. Because of the potential hazards, access to this area must be rigorously controlled and supervised.

## Time-Varying Gradient Magnetic Fields

During imaging acquisition, gradient magnetic fields are transiently imposed along the main magnetic field to spatially localize and encode the spins. These gradient magnetic fields (current clinical gradient strengths vary between 30–90 mT/m) are much weaker than the static magnetic field and are generated by gradient coils located inside the magnet bore. Each orthogonal axis (i.e., $x$, $y$, and $z$) has a pair of gradient coils. For a given direction, a linear gradient magnetic field is generated within the main magnetic field by applying electrical current in opposite directions to the coil pair over a short time interval.[27] When this gradient magnetic field is applied, the magnetic field intensity changes rapidly, giving rise to a time-varying magnetic field. The rate of change in a magnetic field (dB) occurs over time (dt) and usually is measured and reported in units of dB/dt expressed in milliteslas per meter per millisecond (mT/m/msec). During the rise time of the magnetic field, an electrical current can be induced in any electrical conductor (e.g., implanted medical device, wire, human body). Notably, the magnitude of the time-varying magnetic field along each of the three spatial directions (i.e., $x$, $y$, and $z$) is zero at the center of the magnet and increases linearly with increasing distance from the isocenter.

Because the human body is a conductor, the rapidly switching magnetic fields can induce electrical fields and current in a patient (as described by Faraday's law of induction) that may lead to the stimulation of muscle and nerve tissues.[27] The mean threshold levels (measured in tesla per second) for various stimulations are 3600 T/sec for the heart, 900 T/sec for the respiratory system, 90 T/sec for pain, and 60 T/sec for the peripheral nerves. However, the exact values differ significantly among individuals.[25] Experience has shown that sufficient dB/dt levels can produce brief muscle twitches and peripheral nerve stimulation (PNS) perceptible as a "tingling" or "tapping" sensation. This sensation can become uncomfortable and/or painful as the gradient magnetic field increases to 50% to 100% above perception thresholds.[37] For these reasons, threshold sensations, when reported, should not be ignored, because they may readily escalate to uncomfortable levels. Although cardiac stimulation is a concern, studies conducted in dogs have shown that the cardiac stimulation threshold for the most sensitive 1% of the population is 20 times, and the mean defibrillation threshold is 500 times, the energy required for PNS.[33] The exceedingly strong and/or rapidly switching gradient magnetic fields necessary to achieve cardiac stimulation threshold levels are more than an order of magnitude greater than those used in commercially available MR systems.[37–39]

In practice, the potential for PNS is greatest for fast imaging (e.g., echo planar imaging [EPI]) acquisitions, particularly when oblique imaging planes are obtained where the combined contributions of gradients from more than one axis result in a higher effective slew and/or when the readout (i.e., frequency encode) lies along the cranio-caudal direction.[25]

Normal imaging sequences (e.g., conventional spin echo and gradient echo) induce currents of a few tens of milliamperes per square meter, a level far below that present in the normal brain and heart tissue. However, as noted previously, PNS is quite possible for the rapid imaging techniques such as EPI and for high-performance gradients. These effects can be controlled by limiting the maximum rate of change in the magnetic field gradients. The current FDA standard is based on the threshold for sensation, rather than a specific numerical value of dB/dt. Specifically, "current FDA guidance limits the time rate of change of magnetic field (dB/dt) to levels which do not result in painful peripheral nerve stimulation."[29] This policy reflects in part the complexity of modeling and calculating the current distribution in the body associated with the pulsed gradient fields. Correspondingly, dB/dt levels below that resulting in painful stimulation are considered a nonsignificant risk by the FDA. It is important to note that dB/dt is a function of the gradient strength and rise time and not of the static field strength. Thus dB/dt is of equal concern for both lower and higher field scanners.

Clinically, two operating modes for the radio frequency (RF) and gradient field levels used for imaging are permissible, normal and first level controlled (Table 2.2). In normal mode, the system output levels are below those that will cause physiologic stress and therefore are appropriate for all subjects. Alternatively, in first level controlled mode, one of the MR system outputs (e.g., dB/dt) may reach a value that may cause physiologic stress and thus may not be appropriate for the most medically compromised patients. Operation in this mode requires authorization by appropriate clinical staff and vigilant medical supervision during the examination. Institutional Review Board approval is required for operation above these levels (second level controlled). In practice, the commercial MR systems monitor dB/dt throughout the examination and generate a warning for the specific protocols for which PNS is likely. For normal operating mode, the dB/dt threshold level is set at 80% of the mean threshold value for PNS stimulation, and it is set at 100% for the first level.[30] In addition, the MR operator should remain in constant verbal contact with the patient and instruct him or her to report any tingling, muscle twitching, or painful sensations that occur during scanning. This contact is not possible for infants and for sedated, noncommunicative, or otherwise compromised patients. Operationally, dB/dt can be reduced by increasing the field of view and/or slice thickness, reducing the matrix size, and decreasing receiver bandwidth.

**TABLE 2.2** International Electrotechnical Commission/Food and Drug Administration Operating Modes for Magnetic Resonance Imaging Diagnostic Equipment

| Operating Mode | Conditions/Qualifications |
|---|---|
| Normal mode | Will not cause stress; suitable for all patients |
| First level controlled mode | May cause stress; requires medical supervision and positive action by operator to enter |
| Second level controlled mode | Institutional Review Board approval required |

*From Center for Devices and Radiological Health, Food and Drug Administration.* FDA guidelines for magnetic resonance equipment safety*: Available at http://www.aapm.org/meetings/02AM/pdf/8356-48054.pdf.*

## Radiofrequency Fields

### Biologic Effects

One of the primary safety concerns in MRI is tissue heating. The conductivity of tissue allows the absorption of RF energy, which is transformed into heat as a result of resistive losses.[40,41] The heating is greatest at the periphery of the body, and thus the skin is the most prone to this effect.[30] When thermally challenged, the body responds by thermoregulatory mechanisms and attempts to dissipate the heat by means of convection, conduction, radiation, and evaporation. If these attempts are not completely successful, the heat accumulates, resulting in a rise in local tissue and/or systemic core temperatures,[40–42] which has the potential to produce physiologic changes.[27] For humans, the typical skin temperature is about 33°C, whereas core temperature is about 37°C. Experience has shown that, when the body is subjected to significant RF power levels, it immediately attempts to dissipate the heat load through vasodilatation of the blood vessels of the skin, with the skin approaching core temperature. This response mechanism allows the body to reduce heat fairly rapidly and typically is evidenced by flushing of the skin, which in itself is not harmful and usually subsides within several hours.

The dose measure used to describe this energy absorption or heat dose is the specific absorption rate (SAR). SAR is defined in the International Electrotechnical Commission standard as the amount of RF power (measured in watts) absorbed per patient mass in kilograms (W/kg). The MR system software calculates an SAR for each imaging sequence and enforces the limits established by the FDA. Because SAR depends on patient weight, it is important that an accurate value be entered during the patient registration procedure. The amount of RF energy absorbed is dependent on the frequency (as determined by the static magnetic field strength), the RF coil used, the volume (size), composition (conductivity), and configuration of the exposed tissue and the duty cycle and type of RF pulses applied, as well as other factors.[40–44] Notably, SAR increases with the square of the frequency (and hence magnetic field strength) and patient size.[30] Consequently, for a given pulse sequence, doubling the field strength (e.g., 1.5 vs. 3 T) results in a factor of four increase in SAR. SAR can be minimized by decreasing the power and/or duty cycle of the RF pulses. In practice, this minimization can be accomplished by increasing the repetition time (TR), reducing the number of slices, and, when feasible, reducing the RF flip angle (because SAR is proportional to the square of the flip angle). A person's ability to respond to the thermal challenge and effectively dissipate the heat is influenced by the rate at which the energy is deposited and the duration of the exposure. Underlying health conditions such as cardiovascular disease, hypertension, diabetes, fever, old age, obesity, or a compromised ability to perspire can impair a person's ability to tolerate the thermal challenge.[45–49] In addition, certain medications such as diuretics, β-blockers, calcium channel blockers, amphetamines, muscle relaxants, and sedatives can alter the body's thermoregulatory responses significantly, with some medications actually having a synergistic effect with respect to tissue heating caused by RF exposure.[2] Finally, the ability of the subject to dissipate heat is also affected by the ambient temperature, relative humidity, and airflow in the MR scan room.

To prevent excessive heat stress and/or local tissue damage, the FDA has established guidelines to limit allowable whole-body SAR levels to those that produce no more than a 1°C increase in tissue and/or core temperature beyond the normal 37°C.[27] As with dB/dt, two levels of clinical operation are possible for SAR. Note, however, that only the whole-body SAR limit is increased, from 2 W/kg to 4 W/kg, in the advancement from normal to first level controlled operation. The SAR limit for normal and first level controlled operating modes for the head is 3.2 W/kg (1°C maximum temperature increase) averaged over head mass and 10 W/kg temperature over any 10 g of tissue for the torso and extremities.[50] These SAR limits correspond to time-averaged values over a 6-minute interval. Exceptions to the specified FDA guidelines include infants and pregnant women, for whom the FDA recommends that the limits be reduced by a factor of two. Similarly, for patients with thermoregulatory compromise (e.g., cardiovascular impairment, cerebral vascular impairment, and diabetes), the FDA recommends a whole-body SAR limit of 1.5 W/kg.[33] In addition, the SAR limits are reduced when the ambient temperature rises above 24°C (75°F) or if the humidity exceeds 60%.

### Interaction With Other Devices

Additional safety concerns associated with RF irradiation exist when objects made from conductive materials that have an elongated shape or are looped, such as electrodes, monitor leads, guidewires, and certain types of catheters (e.g., catheters with thermistors or other conducting components), are present in the magnet bore.[38,51–56] The rapidly changing magnetic field associated with the RF can induce an electromotive force in the conductor and, hence, current flow, which, because of electrical resistance, will lead to heating of the conductor. If the conductor is in contact with the skin, burns can result. Incidents of first-, second-, and third-degree burns have been reported.[2,25] In addition, because the body is a conductor, inadvertent conductive loops can arise in the absence of any external conductors, when, for example, the patient's hands or calves are in contact to form a closed loop. In such cases, heating can occur at the high-resistance skin-to-skin contact point, which can result in local redness and blistering. To minimize the possibility of RF burns, all conductors (e.g., leads and coils) that are not being used should be removed from the magnet bore. In addition, the integrity of all conductors that must remain in the magnet bore should be verified before the MR examination, and these cables, leads, and/or wires should be kept as straight as possible and run down the center of the bore. In addition, the patient should be thermally and/or electrically isolated (e.g., using pads and/or sheets or blankets) from direct contact with all conductors and all RF body transmitters, as well as surface coils, and skin-to-skin contact should be avoided. The MR operator must be extra vigilant to mitigate the potential heating risks for infants and sedated or other noncommunicative patients. Any metallic object in or on the patient may absorb RF energy, resulting in excessive heating that may lead to thermal damage of surrounding tissue; the potential for this effect is greatest at higher field strengths.[27,33]

## ACOUSTIC NOISE

The predominant and most widely recognized source of MRI-related acoustic noise is the time-varying gradient magnetic field applied during MRI. The rapid pulsed currents within the gradient coils in the presence of the static magnetic field create strong Lorentz forces that produce a torque on the coil itself, causing it to move and/or vibrate against its mounting. This movement, analogous to that of the diaphragm of a loudspeaker, creates the loud chirping, tapping, knocking, and banging noises heard by the subject during MRI.[2,27] Sound levels for MRI are measured in A-weighted decibels (dBA), which takes the frequency response of the human auditory system into account. As a reference, normal conversation is approximately 60 dBA (www.osha.gov), and a difference of 6 dBA represents a doubling of sound intensity. Sound pressure levels (SPL) of 81 to 117 dBA are common for standard 1.5 T MRI examinations[57] and can be as high as 130 dBA for high-speed acquisitions such as echo planar imaging (EPI) and techniques that use nontraditional (i.e., non-Cartesian) k-space trajectories, such as propeller, radial, and spiral sequences. Although many factors influence the intensity of the MR-related acoustic noise (e.g., gradient coil design, gradient amplitude and slew rate, size of patient, location of patient in magnet bore), higher field strength systems tend to be louder.

MRI-related acoustic noise may lead to simple annoyance, difficulties in verbal communication, heightened anxiety, and temporary or potentially permanent hearing loss for both the patient and other persons in or near the MR scan room.[58–70] In addition, the noise may cause confusion and/or extreme anxiety in more vulnerable patients such as children and elderly persons and in persons with psychiatric disorders.[58,60,71] MRI-related noise also has been reported to produce alterations in physiologic parameters in neonates, which may be problematic in light of their immature cardiac physiology and cerebrovascular regulation.[62] Furthermore, the acoustic noise levels may cause discomfort to sedated patients, and certain drugs are known to increase hearing sensitivity.[61] Because exposure duration is one of the most influential factors in determining the effect of noise on hearing, it is unlikely that the noise levels experienced during the relatively short MR examinations will have a long-term negative effect on hearing.[72,73] It is the short-term effects of MR-related acoustic noise that are the primary concern.

The FDA indicates that MR-related acoustic noise levels must be below the level of concern established by pertinent federal regulatory or other recognized standard-setting organizations.[74] Guidelines for acceptable acoustic noise levels associated with MRI are based on Occupational Safety and Health Administration (OSHA) guidelines for industrial workers, which recognize that the risk is a function of its intensity and the duration of exposure.[25] OSHA standards stipulate that, to avoid hearing damage, the peak unweighted SPL cannot exceed 140 dB[27] and the A-weighted root mean square SPL cannot exceed 99 dBA, with hearing protection in place. Because the acoustic noise level for many sequences can exceed 99 dBA, the MR manufacturer must recommend that it is necessary for the MR system operator to provide the patient with hearing protection.[2] Hearing protection should also be given to all other persons who will be present in the scan room during the MR exam.

The Noise Reduction Rating (NRR) is the standard for hearing protection devices established by the Environmental Protection Agency. For a given noise attenuator, the NRR value is the mean attenuation value (in dB) for the device minus two standard deviations, corresponding to the minimum noise reduction achieved by 98% of the population. For MR examinations, adequate hearing protection can be most easily and effectively accomplished with earplugs (≈29–32 dBA NRR) and/or headphones (≈29–49 dBA for adults and 7–12 dBA mini muffs for infants). Notably, the NRR reported for earplugs will not be realized if they are improperly inserted or do not fit snugly, as often may be the case for young pediatric patients. Although the combined use of earplugs and headphones do not produce additive effects in hearing protection per se, they can increase the NRR by 5 to 6 dB (equivalent to approximately half the sound intensity) for frequencies less than or equal to 2000 Hz (http://www.biac.duke.edu/research/

safety/tutorial.asp). At frequencies higher than 2000 Hz, hearing protection is limited by bone conduction, and the combined use of headphones and earplugs is less beneficial. Nevertheless, the harmonic response of MR systems for a wide spectrum of imaging protocols contains a significant amount of energy at or below 2000 Hz so that combined use is still advisable (Fig. 2.1). MR manufacturers are actively working to further decrease noise levels by using methods such as quieter MR sequences, active noise cancellation filters, acoustic hoods,[57] and vacuum packing.[71]

## CLAUSTROPHOBIA

Many patients find the confinement of the MRI bore at least somewhat disconcerting. For some patients, this discomfort is extreme and can result in anxiety that may escalate into panic. In these cases, sedation is required to perform the MR examination. Claustrophobic reactions in the scanner typically are characterized by a fear of suffocation and/or a fear that something will happen while they are confined.[75] Operationally, experience suggests that this reaction can be minimized by maintaining frequent verbal contact with the individual throughout the examination and sufficient airflow (e.g., a bore fan) to reduce heat and mitigate the fear of suffocation. In addition, the individual also should be provided with an emergency panic notification device (e.g., a pneumatic squeeze bulb) to allow him or her to summon help at any time throughout the examination. In fact, such a device should be provided to all nonsedated communicative patients as a means of notifying the MR operator immediately upon any sign of discomfort, including local heating or tugging of ferromagnetic objects (e.g., a belt or shoes).

## MEDICAL IMPLANTS, DEVICES, AND OTHER METALLIC POTENTIAL HAZARDS

### Passive and Electrically Active Medical Devices

The MR environment may be unsafe for persons with certain medical implants or devices that are made out of ferromagnetic materials. For passive implants (i.e., any medical device that serves its function without the supply of power, such as aneurysm clips, shunts, or stents) made of ferromagnetic materials, the primary concern is movement and/or dislodgement,[31,32,35,36,52,76–85] although excessive heating of the implant is also possible (Table 2.3). Several incidents have occurred in which metallic implants were mistakenly introduced into the MR environment and were dislodged within or from the body, resulting in blindness or death.[25] For electrically active implants such as deep brain or vagal nerve stimulators and drug pumps, excessive heating at the lead tips and associated tissue damage is the primary safety concern.[54,86–88] Device malfunction, device heating, induced currents, and movement and/or dislodgement also are potential hazards (see Table 2.3).

When it is known that a patient has an implant (passive or active), the implant should be considered a contraindication for MRI until documented proof of its MR compatibility and safety

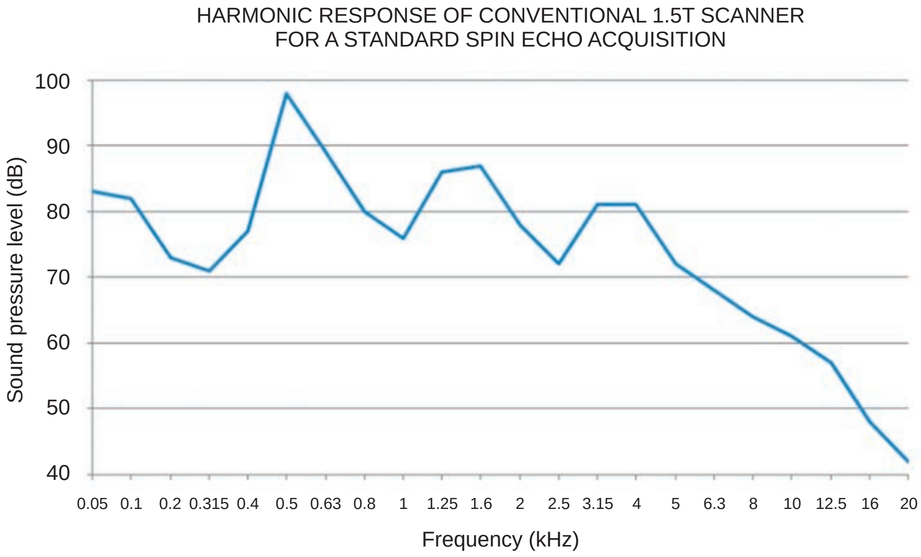

**Figure 2.1.** Harmonic response of a conventional 1.5 T magnetic resonance scanner for a standard spin echo acquisition demonstrating significant energy below 2 kHz. The human auditory range is 20 Hz to 20 kHz.

**TABLE 2.3** Magnetic Resonance Environment Medical Device Concerns

| Component of Magnetic Resonance Environment | Medical Device Concern | Potential Adverse Effect |
|---|---|---|
| Static magnetic field (always on) | Rotational force (torque) on object<br>Translational force on object | Tissue damage as object rotates to align with main field;<br>Tissue trauma as object accelerates toward magnet bore (projectile/missile effect) |
| Gradient magnetic field (pulsed during imaging) | Induced currents due to dB/dt | Device malfunction or failure |
| Radio frequency field (pulsed during imaging) | Radio frequency–induced currents resulting in heating<br>Electromagnetic interference—active | Patient burns (thermal and electrical)<br>Device malfunction, induced noise (monitoring devices) |

*From Food and Drug Administration.* Primer on medical device interactions with magnetic resonance imaging, US Food and Drug Administration (FDA) Systems. *Available at http://www.cognitiveneuro.org/SafetyReadings/FDAExternalDeviceGuidance%201997.pdf.*

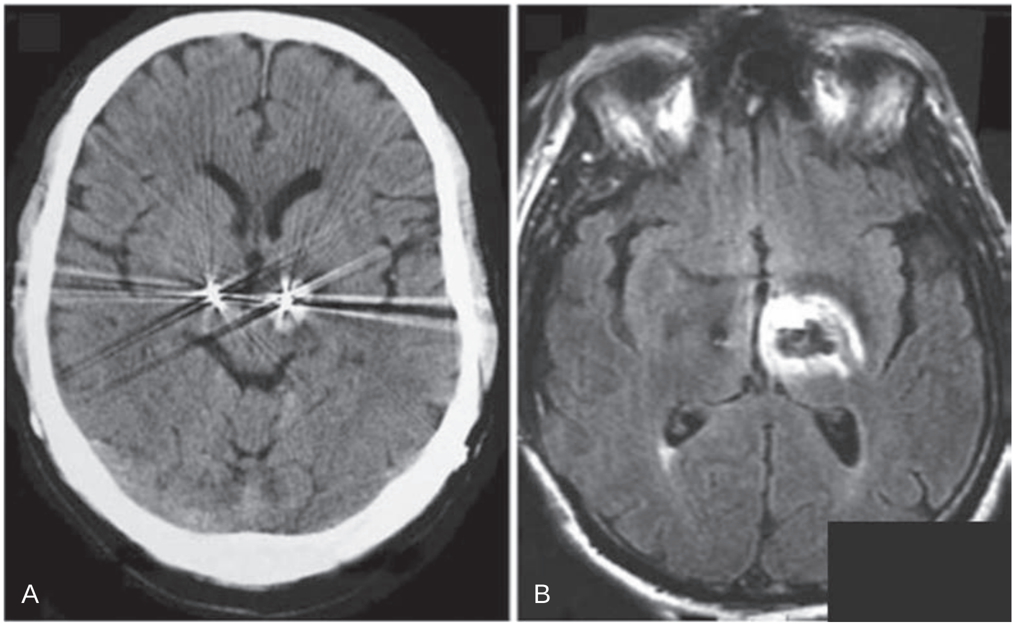

**Figure 2.2. Adverse event due to failure to adhere to medical device product guidelines.** Tissue damage (brain hemorrhage) as a result of radiofrequency heating at the left deep brain stimulator (DBS) lead tip that occurred during a routine MR examination of the lumbar spine. The CT (A) and MRI (B) images of the brain were acquired immediately after a lumbar spine MR scan performed on a 1.0 T MR scanner using the body coil to transmit and a surface coil to receive, and a relatively SAR aggressive imaging protocol. Alternatively, the DBS device manufacturers specified the MR conditions under which MRI can be accomplished safely for patients implanted with this device as a 1.5 T scanner using a transmit receive head coil and head SAR levels at or below 0.1 W/kg. *(From Henderson JM, Tkach JA, Phillips M, et al. Permanent neurological deficit related to magnetic resonance imaging in a patient with implanted deep brain stimulation electrodes for Parkinson's disease: case report.* Neurosurgery. *2005;57:1063.)*

is verified. The documented information must contain the exact model and serial number of the device, which should be recorded in the patient's medical record. If such information is not available, the radiologist or MR technologist should consult the implanting or monitoring physician. Once the device is identified, the associated device documentation typically is available online, posted on the device manufacturer's website. The device labeling should be carefully reviewed for information regarding behavior in the MR environment specific to the exact MR scanner and set of imaging conditions to be used to perform the examination. Salient MR-related information includes system parameters such as field strength(s), magnet types and manufacturers, RF transmit coils, system software versions, and imaging conditions (e.g., RF power levels and gradient slew rates [dB/dt]). In addition, when appropriate, information regarding the configuration of the device itself, such as lead length and routing, that were evaluated and reported in the device labeling must also be considered. Note that the safety information for any implantable medical devices (passive or active) and medical equipment applies only to the magnetic field strengths, MR system configurations, RF coils, and/or imaging conditions evaluated. Safety at 1.5 T does not necessarily imply safety at 3 T, and vice versa. The consequences of failing to strictly adhere to the product information regarding MR safety can be catastrophic to the patient (Fig. 2.2).[86,89]

Several comprehensive reviews of the topic of MR safety and implants have been published,[2,76,90–94] and more than 1,200 objects have been tested for MR safety, with more than 200 evaluated at 3 T or higher.[95] This MR safety information is readily available to the public as published reports, compiled lists online (www.MRIsafety.com), and in the *Reference Manual for Magnetic Resonance Safety, Implants and Devices*, a publication compiled and updated annually.[96]

## Other Metallic Potential Hazards

In addition to implantable devices, it must be documented that the patient has no other form of metal in his or her body, including metal filings, shrapnel, and abandoned leads (e.g., a pacemaker). If the patient indicates that such materials may be present, or if sufficient reason exists to suspect that such materials might be present (e.g., for noncommunicative or pediatric patients), a radiograph must be obtained, and if the presence of such materials is confirmed, the MR examination should not be performed. All of the precautions and considerations previously outlined apply not only to patients but also to any hospital personnel and/or patient family members who may accompany the patient to the MR environment.

Some body piercing jewelry is ferromagnetic, and certain tattoos and permanent cosmetics may contain irregularly shaped iron oxide or other metal-based pigments and therefore may be of concern. In these instances, mild to moderate movement or displacement in the MR environment may occur that, in the case of the tattoos and/or permanent cosmetics, may result in localized swelling and/or irritation. In addition, when the jewelry or pigments are contained within the transmit RF coil, a risk of localized heating also exists. For these reasons, patients and/or individuals should be informed of the potential risks. Body jewelry should be removed before entering the MR environment. If removal is not possible and the individual chooses to proceed, the jewelry should be stabilized (e.g., with application of adhesive tape or a bandage) and, if it is contained within the transmit RF coil, it should be wrapped with gauze or tape to insulate it from underlying skin.[95] Similarly, for tattoos and permanent cosmetics, if any concern exists that heating may occur, an ice pack or cold compress can be applied to the site as a precautionary measure. Adverse events associated with tattoos and/or permanent cosmetics are relatively infrequent, and when they do occur, they are relatively minor and transient.[35,36,95,97] In the opinion of the FDA, "The risks of avoiding an MRI when your doctor has recommended one are likely to be much greater than the risks of complications from an interaction between the MRI and tattoo or permanent makeup. Instead of avoiding an MRI, individuals who have tattoos or permanent makeup should inform the radiologist or technician of this fact in order to take appropriate precautions, avoid complications, and assure the best results."[2,98]

A comprehensive and updated list of reported adverse MR safety-related incidents can be accessed online from the Manufacturer and User Facility Device Experience Database (MAUDE; available at https://www.accessdata.fda.gov/scripts/cdrh/cfdocs/cfmaude/search.cfm)[36] and the Medical Device Report (available at http://www.fda.gov/MedicalDevices/Safety/ReportaProblem/ucm2005291.htm),[35] both of which are compiled and maintained by the FDA Center for Devices and Radiological Health.[95]

## MAGNETIC RESONANCE "SAFETY" LABELING

In response to the severity of the potential hazards of the presence of ferromagnetic objects in the MR environment, the FDA has implemented a well-defined and stringent evaluation and labeling convention. Medical equipment, devices, and/or implants are now classified as "MR safe," "MR unsafe," and "MR conditional."[99,100] These terms replace the previous MR-related evaluation and labeling convention of "MR safe" and "MR compatible."

The replacement of these previous designations and definitions by "MR safe," "MR unsafe," and "MR conditional" was deemed necessary because the earlier designations were confusing and the terms often were used inappropriately. To clarify and prevent misuse, the new set of terms and associated icons was developed (Fig. 2.3).[29,99–101] "MR safe" and/or "MR unsafe" designates an item (e.g., a medical device, equipment, or implant) as unequivocally safe or unsafe in any or all MRI environments (e.g., regardless of field strength, magnet type, and RF coils) and imaging conditions (e.g., RF power levels and gradient slew/switching rates [dB/dt]) and for all configurations of device/object use. "MR safe" objects include nonconducting, nonmetallic, and/or nonmagnetic items such as plastic or gauze tape. "MR unsafe" items include any magnetic object such as a pair of ferromagnetic/metal scissors, scalpel, wrench, or cleaning bucket.[95]

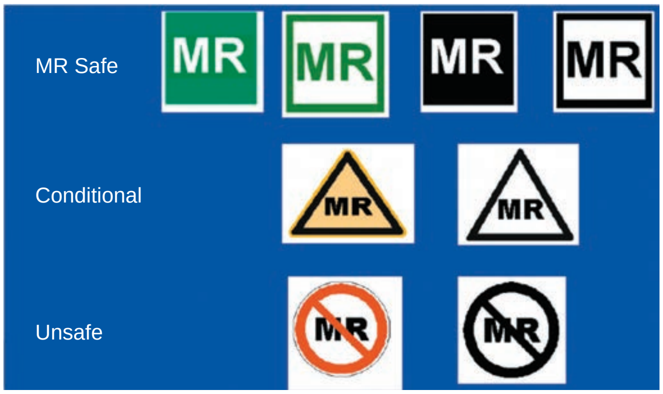

**Figure 2.3. International magnetic resonance safety labeling icons.** US FDA labeling criteria (developed by American Society for Testing and Materials International) for portable objects (e.g., medical devices, implants, medical equipment, oxygen tanks, housekeeping equipment, and tools) that may or may not enter the MR environment. Square/green "MR safe" labels correspond to objects that are totally nonreactive, triangular/yellow labels correspond to objects with "MR conditional" status, and round/red labels identify an object as being "MR unsafe." The use of the new labeling convention has been adopted by the FDA and applied to items prospectively (but not retrospectively), beginning approximately in August 2005. *(From ASTM International.* Standard practice for marking medical devices and other items for safety in the magnetic resonance environment *[designation F203-5], West Conshohocken, PA: ASTM International; 2005.)*

Alternatively, "MR conditional" indicates an item that has no known hazards for very specific combination(s) of MR environment and imaging conditions. When appropriate, additional conditions of use of the item (e.g., routing of leads associated with a neurostimulation system) also are specified. Notably, the use of the new labeling convention has only been applied to items prospectively, beginning approximately as of August 2005.[95] Because it has not been applied by the FDA retrospectively, the labeling for many currently used items may still adhere to the prior definitions of and labeling as "MR safe" and "MR compatible."

## MAGNETIC RESONANCE SAFETY, FACILITY OPERATION, AND PATIENT CARE GUIDELINES

In light of the extreme severity of the potential hazards associated with the improper management of the MR environment, all hospital personnel who may have reason to be in the MR department, patients, and patient family members must be appropriately educated and screened for metallic objects and/or electrically active devices on or within their person well before entering the scan room. The education must include information about the behavior of metallic objects in static magnetic fields and the associated hazards.[95] The importance and necessity of these measures are highlighted by the fact that the majority of adverse MR safety incidents have been due either to deficiencies in and/or failure to enforce screening or MR environment access control procedures and practices, resulting in contraindicated personal items and other potentially problematic objects entering the MR scan room.[35,36]

### Magnetic Resonance Safety Education and Screening

Because of the danger of inappropriately introducing ferromagnetic materials into the MR environment, the following educational and screening procedures have been implemented for facilities and apply to both patient and nonpatient populations. Access to areas that exceed the 5 G line must be vigilantly restricted and supervised at all times.[25] It is important to remind all persons entering the MR facility that the magnet is always "on," even when no examinations are being performed. Screening involves both written documentation and a verbal review. The written screening questionnaire is designed to elicit information about the presence of a medical device, implant, or other ferromagnetic object within or on the individual and/or of the existence of an underlying condition (e.g., pregnancy or disability) that may require special consideration. Once completed, an oral interview is conducted to verify the information reported, and the individual is given the opportunity to express concerns and have any remaining questions about the examination answered before entrance into the MR environment is finally allowed.

The education and screening must be performed by a health care worker specially trained in MR safety who has a comprehensive appreciation and understanding of the potential hazards of the MR environment and procedures and is familiar with the information and implications of the contents of the screening forms for patients and other individuals. Because some of the questions included on the patient screening form may not be relevant for nonpatients, separate screening forms for the patient and nonpatient groups have been compiled. Template screening forms for patients (English and Spanish versions) and a screening form for nonpatient individuals can be downloaded for use at www.MRIsafety.com.[91,92]

The fact that a patient has had a previous MR examination without incident does not ensure the safety of current or future studies. For example, the patient may have undergone a surgical procedure and/or experienced an accident involving a metallic foreign body in the interim that now makes him or her ineligible to enter the MR environment. The exact conditions (e.g., static magnetic field strength of the MR system, RF coil used, orientation of the patient, body part evaluated, or orientation of a metallic implant or object) also can alter the safety profile substantially.[94,102,103] Therefore comprehensive screening must be conducted each time any person prepares to enter the MR environment.

With respect to pregnancy, in 1991, the Safety Committee of the Society for Magnetic Resonance Imaging issued a document entitled "Policies, Guidelines, and Recommendations for MR Imaging Safety and Patient Management,"[2,104] which stated that "MR imaging may be used in pregnant women if other non-ionizing forms of diagnostic imaging are inadequate or if the examination provides important information that would otherwise require exposure to ionizing radiation (e.g., fluoroscopy, CT). Pregnant patients should be informed that, to date, there has been no indication that the use of clinical MR imaging during pregnancy has produced deleterious effects." This policy was adopted by the American College of Radiology (ACR) and remains the current "standard of care"; it is applicable to MR systems operating at static magnetic field strengths up to and including 3 T.[2] Because no deleterious effects of MRI exposure on the fetus have been documented during any stage of development, pregnant women can undergo MRI examinations at any point during their pregnancy, provided that the MRI study is clinically indicated.

## CONTRAST AGENTS

Contrast enhanced MRI (CE-MRI) examinations are widely performed for their ability to provide superior information about the anatomy and physiology. Gadolinium-based contrast agents (GBCA) are widely used for this purpose. It is estimated that around 40% to 50% of all MRIs are performed with GBCAs, and that around 10 million such examinations are performed every year in the United States alone. Contrast agents are never to be used without a physician-prescribed injection in pediatric patients. Qualified MR technologists may start the IV and administer FDA-approved GBCA injections. Certain precautions have to be taken. First, the kidney function of the patient needs to be assessed. The estimate glomerular filtration rate (eGFR) needs to be greater than 30 mL/min/ 1.73 m2. However, precaution should be taken to use the right equation to calculate the eGFR in children. The current accepted equation is the bedside Schwartz equation. Second, the name of the administered contrast agent, the administered dose, and route of administration, as well as any allergic reaction needs to be noted. Third, patients with prior contrast reaction, after careful clinical consideration, can be pretreated with antihistamines and corticosteroids. Also, alternate contrast agent can be considered for repeat studies.

### Magnetic Resonance Facility Operating Procedure Guidelines

In recognition and acknowledgement of the appreciable potential hazards and severe consequences of failure to adhere to safety precautions associated with the MR environment, the ACR formed the Blue Ribbon Panel on MR Safety. First convened in 2001, the panel reviewed and refined the current MR safety practices and guidelines and established new ones when appropriate. The results of this first review were published in 2002[104] and became the de facto industry standards for safe and responsible practice in both clinical and research MR environments. The results of the most recent revisions were published as the "ACR Guidance Document for Safe MR Practices: 2013."[93]

The ACR outlines well-defined methodologies and procedures to ensure and enforce safe and restricted exposure and access to the MR environment most appropriate to the existing state of the MR technology, recognizing that this is continuously evolving. Specifically, in their 2007 publication, the ACR stated that the ACR MR Safe Practice Guidelines document was intended to be used as a template for MR facilities to follow in the development of their own individualized MR safety program.[93] In addition, the ACR recommended that, once established, each site should regularly review, reevaluate, and update its safety program as the field of MR, and MR safety, continues to evolve. The ACR also recommended that each site name an MR medical director whose responsibilities include ensuring that MR safe practice guidelines are established and maintained as current and appropriate for the site.[93]

One of the recommendations is the separation of the general MR facility into four zones of increasing potential MR-related danger.[93] Zone 1 is to include all areas that are freely accessible to the general public, such as outside areas surrounding a freestanding MRI facility or the corridor in an imaging department. Zone 2 is defined as the area controlled and supervised by the MR personnel, such as the reception area and patient preparation area. Zone 3 is the area where there is potential for injury from ferromagnetic objects and equipment. Access to this zone must be vigilantly and strictly controlled and limited by MR personnel. These areas include the operator control room, computer room, and/or any areas immediately adjacent to the MR scan room. Finally, Zone 4 is the MR scan room itself. This zone must be clearly marked with warning signs and notification of high magnetic field strengths within this area, including a sign that the magnet is always on. Access to Zone 4 is strictly limited to persons with a demonstrated need to be there (i.e., patients and medical personnel) and then only after comprehensive education about the MR environment and a rigorous screening.

Also, the 2013 ACR recommendations have listed three pediatric specific guidelines, which are worth studying[93]:

1. Sedation and monitoring issues. Children form the biggest group requiring sedation due to multiple reasons. Sedation protocols, that can be tailored to meet the imaging institution's resources, have to meet the safety guidelines set by the American Academy of Pediatrics, the American Society of Anesthesiologists, and the Joint Commission on Accreditation of Healthcare Organizations.
2. Pediatric screening issues. Children are not reliable historians and have to be screened more vigilantly. It is recommended that older children and teenagers be screened both in the presence of guardians, as well as separately to maximize that possibility of all potential safety issues being disclosed. Extra vigilant screening for hidden MR unsafe objects needs to be performed.
3. MRI safety of accompanying family members. Pediatric patients form the largest group having accompanying family members into Zone 4. These accompanying members are recommended to be limited to one, must be thoroughly screened for safety issues, and given hearing protection.

## CONCLUSION

The potential health hazards associated with MR are directly attributable to the three main electromagnetic fields that make up the MR environment: (1) a strong static magnetic field, including its associated spatial gradient; (2) pulsed gradient magnetic fields; and (3) pulsed RF fields. For a properly operating system, the hazards associated with direct interactions of these fields and the body is negligible. However, it is the interactions of these fields with medical devices and/or ferromagnetic objects inadvertently introduced within the fields that create potential concerns for human safety. To prevent adverse MR safety-related incidents and allow the full benefit of this powerful imaging modality to be realized, it is imperative that the potential safety risks intrinsic to the MR environment be understood and respected by all persons exposed to the MR environment. Comprehensive education and screening to rule out contraindications of both patient and nonpatient groups who enter the MR environment is imperative.

## SUGGESTED READINGS

Bushong SC. *Magnetic Resonance Imaging: Physical and Biological Principles*. 3rd ed. St Louis: Mosby; 2003.

Hornak JP. *The basics of MRI*. Available at: http://www.cis.rit.edu/htbooks/mri/.

Kanal E, Barkovich AJ, Bell C, et al. ACR guidance document for safe MR practices: 2013. *J Magn Reson Imaging*. 2013;37:501–530.

Shellock FG, ed. *Magnetic Resonance Procedures: Health Effects and Safety*. Boca Raton, FL: CRC Press; 2001.

Stafford RJ. *Physics of MRI safety*. Available at: http://www.aapm.org/meetings/amos2/pdf/59-17207-59975-979.pdf.

### Mr Safety Websites

**Danger! Flying objects!** (http://simplyphysics.com/flying_objects.html) is an illustrative gallery from the educative "Simply Physics" site, an MRI portal created by Dr. Moriel NessAiver, PhD. The gallery depicts the dangers resulting from common hospital-based ferromagnetic medical equipment.

**ECRI Institute** (https://www.ecri.org) is an independent, nonprofit organization that researches the best approaches to improving the safety, quality, and cost-effectiveness of patient care. ECRI is designated an Evidence-Based Practice Center by the US Agency for Healthcare Research and Quality and is listed as a federal Patient Safety Organization by the US Department of Health and Human Services.

**MRIsafety** (http://www.mrisafety.com), developed and maintained by Dr. Frank Shellock, provides up-to-date information on MRI safety-related topics. Impressively, the latest information regarding screening patients with implants, materials, and medical devices is provided. A key feature of the site is The List, a searchable database that contains more than 1200 implants and devices, including more than 200 objects tested at 3 T for MRI safety. Moreover, the site includes a summary section that is a presentation of more than 100 peer-reviewed articles on MRI bioeffects and safety. Other features include a downloadable Pre-MRI Screening form and safety information.

**ReviseMRI** (http://www.revisemri.com/questions/safety) is designed principally as a revision aid but also may be used as an educational resource. Contents include a detailed question and answer section, web-based animated tutorials, interactive learning tools, and links to resources for further reading in common textbooks and online for nearly every question and answer posed.

**The Institute for Magnetic Resonance Safety, Education and Research** (http://www.imrser.org) is a multidisciplinary professional organization headed by Director Dr. Frank Shellock. It focuses on information and research on magnetic resonance (MR) safety, while "promoting awareness, understanding, and communication of MR safety issues through education and research," and has useful sections, including MRI Safety Guidelines and MR Safety Papers.

**The US Food and Drug Administration** has a **Center for Devices and Radiological Health,** which is an integral part of the Department of Health & Human Services. Online documents available include "A Primer on Medical Device Interactions with Magnetic Resonance Imaging Systems" at http://www.fda.gov/MedicalDevices/DeviceRegulationandGuidance/GuidanceDocuments/ucm107721.htm and "MRI Safety" at http://www.fda.gov/MedicalDevices/Safety/AlertsandNotices/ucm135362.htm.

Two important **MRI accident databases** derived from the Database of Medical Device Related Accidents and Events are available from Maude Accidents Database (http://www.accessdata.fda.gov/scripts/cdrh/cfdocs/cfMAUDE/search.cfm) and the UK Medical Devices Agency (http://www.mhra.gov.uk/index.htm#page=DynamicListMedicines).

**Medicalphysicsweb** (http://medicalphysicsweb.org) is a unique site for the medical physics community. It provides in-depth analysis and incisive commentary on the fundamental research, emerging technologies, and clinical applications that underpin the dynamic disciplines of medical physics and biomedical engineering.

## REFERENCES

Full references for this chapter can be found on www.expertconsult.com.

## REFERENCES

1. Chaljub G, Kramer LA, Johnson RF 3rd, et al. Projectile cylinder accidents resulting from the presence of ferromagnetic nitrous oxide or oxygen tanks in the MR suite. *AJR Am J Roentgenol*. 2001;177:27–30.
2. Shellock FG, Crues JV. MR procedures: biologic effects, safety, and patient care. *Radiology*. 2004;232:635–652.
3. Center for Devices and Radiologic Health, Food and Drug Administration. *Criteria for significant risk investigations of magnetic resonance diagnostic devices*. Available at: http://www.fda.gov/downloads/MedicalDevices/DeviceRegulationandGuidance/GuidanceDocuments/UCM072688.pdf. Accessed December 15, 2016.
4. Geard CR, Osmak RS, Hall EJ, et al. Magnetic resonance and ionizing radiation: a comparative evaluation in vitro of oncogenic and genotoxic potential. *Radiology*. 1984;152:199–202.
5. Heinrichs WL, Fong P, Flannery M, et al. Midgestational exposure of pregnant BALB/c mice to magnetic resonance imaging conditions. *Magn Reson Imaging*. 1988;6:305–313.
6. Hong CZ, Shellock FG. Short-term exposure to a 1.5 tesla static magnetic field does not affect somato-sensory-evoked potentials in man. *Magn Reson Imaging*. 1990;8:65–69.
7. Schenck JF, Dumoulin CL, Redington RW, et al. Human exposure to 4.0-Tesla magnetic fields in a whole-body scanner. *Med Phys*. 1992;19:1089–1098.
8. Kangarlu A, Burgess RE, Zhu H, et al. Cognitive, cardiac, and physiological safety studies in ultra high field magnetic resonance imaging. *Magn Reson Imaging*. 1999;17:1407–1416.
9. Shellock FG. Biological effects and safety aspects of magnetic resonance imaging. *Magn Reson Q*. 1989;5:243–261.
10. Brody AS, Embury SH, Mentzer WC, et al. Preservation of sickle cell blood-flow patterns during MR imaging: an in vivo study. *AJR Am J Roentgenol*. 1988;151:139–141.
11. Tenforde T, Budinger T. Biological effects and physical safety aspects of NMR imaging and in vivo spectroscopy. In: Thomas S, Dixon R, eds. *NMR in Medicine: Instrumentation and Clinical Applications*. New York: American Association of Physicists in Medicine; 1986.
12. Vogl TJ, Paulus W, Fuchs A, et al. Influence of magnetic resonance imaging on evoked potentials and nerve conduction velocities in humans. *Invest Radiol*. 1991;26:432–437.
13. Weiss J, Herrick RC, Taber KH, et al. Bio-effects of high magnetic fields: a study using a simple animal model. *Magn Reson Imaging*. 1992;10:689–694.
14. Yuh WT, Fisher DJ, Shields RK, et al. Phantom limb pain induced in amputee by strong magnetic fields. *J Magn Reson Imaging*. 1992;2:221–223.
15. Prasad N, Wright DA, Ford JJ, et al. Safety of 4-T MR imaging: study of effects on developing frog embryos. *Radiology*. 1990;174:251–253.
16. Prasad N, Bushong SC, Thornby JI, et al. Effect of nuclear magnetic resonance on chromosomes of mouse bone marrow cells. *Magn Reson Imaging*. 1984;2:37–39.
17. Cooke P, Morris PG. The effects of NMR exposure on living organisms. II. A genetic study of human lymphocytes. *Br J Radiol*. 1981;54:622–625.
18. Schwartz JL, Crooks LE. NMR imaging produces no observable mutations or cytotoxicity in mammalian cells. *AJR Am J Roentgenol*. 1982;139:583–585.
19. Tyndall DA, Sulik KK. Effects of magnetic resonance imaging on eye development in the C57BL/6J mouse. *Teratology*. 1991;43:263–275.
20. McRobbie D, Foster MA. Pulsed magnetic field exposure during pregnancy and implications for NMR foetal imaging: a study with mice. *Magn Reson Imaging*. 1985;3:231–234.
21. Brockway JP, Bream PR Jr. Does memory loss occur after MR imaging? *J Magn Reson Imaging*. 1992;2:721–728.
22. Besson JA, Foreman EI, Eastwood LM, et al. Cognitive evaluation following NMR imaging of the brain. *J Neurol Neurosurg Psychiatry*. 1984;47:314–316.
23. Schenck JF. Health effects and safety of static magnetic fields. In: Shellock FG, ed. *Magnetic Resonance Procedures: Health Effects and Safety*. Boca Raton, Fla: CRC Press; 2001.
24. Schenck JF. Safety of strong, static magnetic fields. *J Magn Reson Imaging*. 2000;12:2–19.
25. Price RR. The AAPM/RSNA physics tutorial for residents. MR imaging safety considerations. Radiological Society of North America. *Radiographics*. 1999;19:1641–1651.
26. Chung SM. Safety issues in magnetic resonance imaging. *J Neuroophthalmol*. 2002;22:35–39.
27. Zhuo J, Gullapalli RP. AAPM/RSNA physics tutorial for residents: MR artifacts, safety, and quality control. *Radiographics*. 2006;26:275–297.
28. Schenck JF. Health and physiological effects of human exposure to whole-body four-tesla magnetic fields during MRI. *Ann N Y Acad Sci*. 1992;649:285–301.
29. Center for Devices and Radiologic Health, Food and Drug Administration. *A primer on medical device interactions with magnetic resonance imaging systems*. Available at: http://www.cognitiveneuro.org/SafetyReadings/FDAExternalDeviceGuidance%201997.pdf. Accessed May 15, 2017.
30. Zaremba L. *FDA guidelines for magnetic resonance equipment safety*. Presented at the Annual Meeting of the American Association of Physicists in Medicine, Montreal, July 16, 2002. Available at: http://www.aapm.org/meetings/02AM/pdf/8356-48054.pdf. Accessed May 15, 2017.
31. Shellock FG, Tkach JA, Ruggieri PM, et al. Aneurysm clips: evaluation of magnetic field interactions and translational attraction by use of "long-bore" and "short-bore" 3.0-T MR imaging systems. *AJNR Am J Neuroradiol*. 2003;24:463–471.
32. Shellock FG, Tkach JA, Ruggieri PM, et al. Cardiac pacemakers, ICDs, and loop recorder: evaluation of translational attraction using conventional ("long-bore") and "short-bore" 1.5- and 3.0-Tesla MR systems. *J Cardiovasc Magn Reson*. 2003;5:387–397.
33. Duke-UNC Brain Imaging and Analysis Center. *MRI safety tutorial* (website): http://www.biac.duke.edu/research/safety/tutorial.asp. Accessed May 15, 2017.
34. ECRI Institute. *Patient death illustrates the importance of adhering to safety precautions in magnetic resonance environments*. Available at: http://www.bic.mni.mcgill.ca/~mferre/fmri.html/hazard_MRI_080601.pdf. Accessed May 15, 2017.
35. Center for Devices and Radiologic Health, Food and Drug Administration. *MDR data files* (website): http://www.fda.gov/MedicalDevices/Safety/ReportaProblem/ucm124073.htm. Accessed May 15, 2017.
36. Center for Devices and Radiologic Health, Food and Drug Administration. *Manufacturer and user facility device experience database (MAUDE)*. Available at: http://www.fda.gov/MedicalDevices/DeviceRegulationandGuidance/PostmarketRequirements/ReportingAdverseEvents/ucm127891.htm. Accessed May 15, 2017.
37. Schaefer DJ, Bourland JD, Nyenhuis JA. Review of patient safety in time-varying gradient fields. *J Magn Reson Imaging*. 2000;12:20–29.
38. Nyenhuis JA, Kildishev AV, Bourland JD, et al. Heating near implanted medical devices by the MRI RF-magnetic field. *IEEE Transact Magn*. 1999;35:4133–4135.
39. Bourland JD, Nyenhuis JA, Schaefer DJ. Physiologic effects of intense MR imaging gradient fields. *Neuroimaging Clin N Am*. 1999;9:363–377.
40. Schaefer DJ. Safety aspects of radiofrequency power deposition in magnetic resonance. *Magn Reson Imaging Clin N Am*. 1998;6:775–789.
41. Shellock FG. Radiofrequency energy-induced heating during MR procedures: a review. *J Magn Reson Imaging*. 2000;12:30–36.
42. Schaefer DJ. Health effects and safety of radiofrequency power deposition associated with magnetic resonance procedures. In: Shellock FG, ed. *Magnetic Resonance Procedures: Health Effects and Safety*. Boca Raton, Fla: CRC Press; 2001.
43. Gordon CJ. Normalizing the thermal effects of radiofrequency radiation: body mass versus total body surface area. *Bioelectromagnetics*. 1987;8:111–118.
44. National Council on Radiation Protection and Measurements. *Biological effects and exposure criteria for radiofrequency electromagnetic fields*. Bethesda, MD: National Council on Radiation Protection and Measurements; 1986.
45. Rowell LB. Cardiovascular aspects of human thermoregulation. *Circ Res*. 1983;52:367–379.
46. Drinkwater BL, Horvath SM. Heat tolerance and aging. *Med Sci Sports*. 1979;11:49–55.
47. Kenney WL. Physiological correlates of heat intolerance. *Sports Med*. 1985;2:279–286.
48. Barany FR. Abnormal vascular reactions in diabetes mellitus; a clinical physiological study. *Acta Med Scand Suppl*. 1955;304:1–129.
49. Buskirk ER, Lundegren H, Magnusson L. Heat acclimatization patterns in obese and lean individuals. *Ann N Y Acad Sci*. 1965;131:637–653.
50. International Electrotechnical Commission. *Medical electrical equipment Part 2-33: Particular requirements for the basic safety and essential performance of magnetic resonance equipment for medical diagnosis*. Geneva: International Electrotechnical Commission; 2010.

51. Smith CD, Nyenhuis JA, Kildishev AV. Health effects of induced electrical currents: implications for implants. In: Shellock FG, ed. *Magnetic Resonance Procedures: Health Effects and Safety*. Boca Raton, FL: CRC Press; 2001.
52. Shellock FG. Magnetic resonance safety update 2002: implants and devices. *J Magn Reson Imaging*. 2002;16:485–496.
53. Chou CK, McDougall JA, Can KW. Absence of radiofrequency heating from auditory implants during magnetic resonance imaging. *Bioelectromagnetics*. 1995;16:307–316.
54. Rezai AR, Finelli D, Nyenhuis JA, et al. Neurostimulation systems for deep brain stimulation: in vitro evaluation of magnetic resonance imaging-related heating at 1.5 tesla. *J Magn Reson Imaging*. 2002;15:241–250.
55. Finelli DA, Rezai AR, Ruggieri PM, et al. MR imaging-related heating of deep brain stimulation electrodes: in vitro study. *AJNR Am J Neuroradiol*. 2002;23:1795–1802.
56. Shellock FG, Hatfield M, Simon BJ, et al. Implantable spinal fusion stimulator: assessment of MR safety and artifacts. *J Magn Reson Imaging*. 2000;12:214–223.
57. Nordell A, Lundh M, Horsch S, et al. The acoustic hood: a patient-independent device improving acoustic noise protection during neonatal magnetic resonance imaging. *Acta Paediatr*. 2009;98:1278–1283.
58. McJury M. Acoustic noise and magnetic resonance procedures. In: Shellock FG, ed. *Magnetic Resonance Procedures: Health Effects and Safety*. Boca Raton, FL: CRC Press; 2001.
59. Brummett RE, Talbot JM, Charuhas P. Potential hearing loss resulting from MR imaging. *Radiology*. 1988;169:539–540.
60. Quirk ME, Letendre AJ, Ciottone RA, et al. Anxiety in patients undergoing MR imaging. *Radiology*. 1989;170:463–466.
61. Laurell GF. Combined effects of noise and cisplatin: short- and long-term follow-up. *Ann Otol Rhinol Laryngol*. 1992;101:969–976.
62. Philbin MK, Taber KH, Hayman LA. Preliminary report: changes in vital signs of term newborns during MR. *AJNR Am J Neuroradiol*. 1996;17:1033–1036.
63. Counter SA, Olofsson A, Borg E, et al. Analysis of magnetic resonance imaging acoustic noise generated by a 4.7 T experimental system. *Acta Otolaryngol*. 2000;120:739–743.
64. Price DL, De Wilde JP, Papadaki AM, et al. Investigation of acoustic noise on 15 MRI scanners from 0.2 T to 3 T. *J Magn Reson Imaging*. 2001;13:288–293.
65. Shellock FG, Ziarati M, Atkinson D, et al. Determination of gradient magnetic field-induced acoustic noise associated with the use of echo planar and three-dimensional, fast spin echo techniques. *J Magn Reson Imaging*. 1998;8:1154–1157.
66. Strainer JC, Ulmer JL, Yetkin FZ, et al. Functional MR of the primary auditory cortex: an analysis of pure tone activation and tone discrimination. *AJNR Am J Neuroradiol*. 1997;18:601–610.
67. Ulmer JL, Biswal BB, Mark LP, et al. Acoustic echoplanar scanner noise and pure tone hearing thresholds: the effects of sequence repetition times and acoustic noise rates. *J Comput Assist Tomogr*. 1998;22:480–486.
68. Bandettini PA, Jesmanowicz A, Van Kylen J, et al. Functional MRI of brain activation induced by scanner acoustic noise. *Magn Reson Med*. 1998;39:410–416.
69. Goldman AM, Gossman WE, Friedlander PC. Reduction of sound levels with antinoise in MR imaging. *Radiology*. 1989;173:549–550.
70. Hurwitz R, Lane SR, Bell RA, et al. Acoustic analysis of gradient-coil noise in MR imaging. *Radiology*. 1989;173:545–548.
71. McJury M, Shellock FG. Auditory noise associated with MR procedures: a review. *J Magn Reson Imaging*. 2000;12:37–45.
72. Miller LE, Keller AM. Regulation of occupational noise. In: Harris CM, ed. *Handbook of Noise Control*. New York: McGraw-Hill; 1979.
73. Melnick W. Hearing loss from noise exposure. In: Harris CM, ed. *Handbook of Noise Control*. New York: McGraw-Hill; 1979.
74. Zaremba LA. FDA guidance for magnetic resonance system safety and patient exposures: current status and future considerations. In: Shellock FG, ed. *Magnetic Resonance Procedures: Health Effects and Safety*. Boca Raton, FL: CRC Press; 2001.
75. Harris LM, Robinson J, Menzies RG. Evidence for fear of restriction and fear of suffocation as components of claustrophobia. *Behav Res Ther*. 1999;37:155–159.
76. Shellock FG. *Magnetic Resonance Procedure: Health Effects and Safety*. Boca Raton, FL: CRC Press; 2001.
77. Shellock FG. Biomedical implants and devices: assessment of magnetic field interactions with a 3.0-Tesla MR system. *J Magn Reson Imaging*. 2002;16:721–732.
78. Kangarlu A, Shellock FG. Aneurysm clips: evaluation of magnetic field interactions with an 8.0 T MR system. *J Magn Reson Imaging*. 2000;12:107–111.
79. Yuh WT, Hanigan MT, Nerad JA, et al. Extrusion of eye socket magnetic implant after MR imaging: potential hazard to patient with eye prosthesis. *J Magn Reson Imaging*. 1991;1:711–713.
80. Fagan LL, Shellock FG, Brenner RJ, et al. Ex vivo evaluation of ferromagnetism, heating, and artifacts of breast tissue expanders exposed to a 1.5-T MR system. *J Magn Reson Imaging*. 1995;5:614–616.
81. Shellock FG. MR imaging and cervical fixation devices: evaluation of ferromagnetism, heating, and artifacts at 1.5 Tesla. *Magn Reson Imaging*. 1996;14:1093–1098.
82. Shellock FG, Shellock VJ. Cardiovascular catheters and accessories: ex vivo testing of ferromagnetism, heating, and artifacts associated with MRI. *J Magn Reson Imaging*. 1998;8:1338–1342.
83. Kanal E, Shellock FG. Aneurysm clips: effects of long-term and multiple exposures to a 1.5-T MR system. *Radiology*. 1999;210:563–565.
84. Kanal E, Shellock FG, Lewin JS. Aneurysm clip testing for ferromagnetic properties: clip variability issues. *Radiology*. 1996;200:576–578.
85. Klucznik RP, Carrier DA, Pyka R, et al. Placement of a ferromagnetic intracerebral aneurysm clip in a magnetic field with a fatal outcome. *Radiology*. 1993;187:855–856.
86. Rezai AR, Finelli D, Rugieri P, et al. Neurostimulators: potential for excessive heating of deep brain stimulation electrodes during magnetic resonance imaging. *J Magn Reson Imaging*. 2001;14:488–489.
87. Shellock FG, Cosendai G, Park SM, et al. Implantable microstimulator: magnetic resonance safety at 1.5 Tesla. *Invest Radiol*. 2004;39:591–599.
88. Baker KB, Nyenhuis JA, Hrdlicka G, et al. Neurostimulation systems: assessment of magnetic field interactions associated with 1.5- and 3-Tesla MR systems. *J Magn Reson Imaging*. 2005;21:72–77.
89. Henderson JM, Tkach J, Phillips M, et al. Permanent neurological deficit related to magnetic resonance imaging in a patient with implanted deep brain stimulation electrodes for Parkinson's disease: case report. *Neurosurgery*. 2005;57:E1063, discussion E1063.
90. Shellock FG. Magnetic resonance bioeffects, safety, and patient management. In: Edelman R, Hesselink J, Zlatkin M, et al, eds. *Clinical Magnetic Resonance Imaging*. Philadelphia: Saunders; 2005.
91. Shellock FG. *Welcome to MRI safety.com*. Available at: http://www.mrisafety.com/. Accessed May 15, 2017.
92. *Institute for Magnetic Resonance Safety, Education, and Research*. Available at: www.IMRSER.org. Accessed May 15, 2017.
93. Kanal E, Barkovich AJ, Bell C, et al. ACR guidance document for safe MR practices: 2013. *J Magn Reson Imaging*. 2013;37:501–530.
94. Sawyer-Glover AM, Shellock FG. Pre-MRI procedure screening: recommendations and safety considerations for biomedical implants and devices. *J Magn Reson Imaging*. 2000;12:510.
95. Shellock FG, Spinazzi A. MRI safety update 2008: part 2, screening patients for MRI. *AJR Am J Roentgenol*. 2008;191:1140–1149.
96. Shellock FG. *Reference Manual for Magnetic Resonance Safety, Implants, and Devices: 2011 ed*. Los Angeles: Biomedical Research Publishing; 2011.
97. Tope WD, Shellock FG. Magnetic resonance imaging and permanent cosmetics (tattoos): survey of complications and adverse events. *J Magn Reson Imaging*. 2002;15:180–184.
98. Food and Drug Administration. *Tattoos and permanent makeup*. Available at: https://www.fda.gov/cosmetics/productsingredients/products/ucm108530.htm. Accessed May 15, 2017.
99. ASTM International. *Standard Practice for Marking Medical Devices and Other Items for Safety in the Magnetic Resonance Environment*. Conshohocken, PA: ASTM International; 2005.
100. Woods TO. Standards for medical devices in MRI: present and future. *J Magn Reson Imaging*. 2007;26:1186–1189.
101. Shellock FG, Woods TO, Crues JV 3rd. MR labeling information for implants and devices: explanation of terminology. *Radiology*. 2009;253:26–30.
102. Sawyer-Glover A, Shellock FG. Pre-magnetic resonance procedure screening. In: Shellock FG, ed. *Magnetic Resonance Procedures*. Boca Raton, FL: CRC Press; 2001.
103. Kanal E, Borgstede JP, Barkovich AJ, et al. American College of Radiology White Paper on MR Safety. *AJR Am J Roentgenol*. 2002;178:1335–1347.
104. Shellock FG, Kanal E. Policies, guidelines, and recommendations for MR imaging safety and patient management, SMRI Safety Committee. *J Magn Reson Imaging*. 1991;1:97–101.

# 3

# Complications of Contrast Media

*Gauravi K. Sabharwal*

## ALLERGIC-LIKE REACTIONS

### Introduction

Contrast media (CM) are an essential aid in diagnostic medical imaging. They are used primarily to enhance the visibility of blood vessels, organs, and pathology in the body. CM are considered pharmacologic agents, and, like any other medication, they are not without adverse effects.

### Incidence

Scant data are available regarding the incidence of contrast reactions in children for at least three reasons: (1) few clinical trials with children as subjects have been performed to obtain federal approval of an agent[1]; (2) assessing symptoms, particularly mild ones in very young children, is difficult; and (3) differentiating true contrast reactions from symptoms is difficult because of sedation, synchronous medications, anxiety, and other preexisting diseases.[2]

In children, use of any intravenous (IV) CM is discriminative and exclusive.[3] Administration of nonionic iodinated contrast is associated with a low incidence of adverse effects.[2] Dillman et al.[4] reported a 0.18% incidence of acute allergic-like reactions to IV administration of nonionic iodinated CM in children, similar to 0.23% reported in the adult population.[5] Most of the contrast reactions are mild in both children[4] and adults.[2,5,6] Of all the reported allergic reactions in children, 15% (<0.03% overall) were severe in degree.[4] Fatal reactions are very rare, suggesting the effectiveness of aggressive preventive measures and advancement in management of these reactions.[2]

Gadolinium-based contrast media (GBCM) demonstrate a better safety profile[7] with a lower incidence of allergic-like reactions of 0.04%.[8]

### Risk Factors

As with adults, children need to be appropriately screened before CM are administered. Screening includes a complete and specific history from the accompanying adults. Attempts should be made to identify any variables that may preclude the use of the CM or potentially increase the eventuality of an adverse reaction. Factors that may increase this risk include the following:

1. Known prior reaction to CM.[9-12]
2. Known allergies to food products or medications; minor allergies do not pose a significant risk, but a prior anaphylactic reaction to any substance should heighten awareness of the possibility of a similar reaction to CM administration.
3. A history of asthma.[9,12]
4. Known renal disease; renal function in such patients can worsen after administration of CM.
5. Known heart disease, sickle cell disease, or diabetes mellitus.

Other disease entities, such as pheochromocytoma, dehydration, heart failure, severe hyperthyroidism, and β-blocker therapy, that are known risk factors in adults have not been studied in the pediatric population (Box 3.1).

### Pathogenesis

The exact pathogenesis of untoward events after the administration of CM remains obscure and poorly understood. Most of the symptoms resemble an allergic or anaphylactoid reaction to a medication or allergen. However, definitive evidence is lacking that these reactions are truly allergic reactions because antibodies and the typical allergic cascade to these agents have not been identified.[12]

### Classification of Allergic-Like Contrast Reactions

Based on severity, contrast reactions can be classified as mild, moderate, or severe. Flushing and a sensation of warmth are considered physiologic responses (Box 3.2).

**Mild reactions** are usually of short duration and resolve without the need for any treatment. However, patients should be carefully observed until the symptoms resolve because the symptoms could progress to more severe reactions.

**Moderate reactions** require some form of treatment. More important, close observation is essential until the symptoms resolve. Vital signs should be monitored and IV access should be secured.

**Severe reactions,** which are rare, can be life threatening. They could present a worsening of mild or moderate reactions. Prompt and aggressive treatment may be required. The assistance of a rapid response or code team often may be necessary.

### Management

In the event of any adverse reaction to CM, the IV contrast injection should be discontinued. All reactions and management of the reactions should be documented in the patient care notes, and notation of a contrast allergy should become part of the patient's permanent medical record. The following protocols closely follow the American College of Radiology (ACR) guidelines for management of acute reactions in children.[2] The specific agents used in the management of an adverse reaction are determined by individual institutional pharmacy formulary and policy. Some institutions require the radiology personnel to call for assistance (e.g., a rapid response team) if they administer IV epinephrine for the management of these adverse reactions (given the rare incidence of these events and hence the lack of uniformity in preparedness for these reactions).[13,14] To be prepared for such reactions, weight-based dosages of the medications used for management should be posted in clearly visible areas where CM are administered to children. Regular review of treatment protocols and practice of contrast reaction scenarios should be performed by radiologists and staff. If at any time a patient does not respond to treatment or the situation seems concerning, it is appropriate to seek additional medical support immediately. This support may be sought from another radiologist in the department or through activation of an institutional rapid response or code team.

### Urticaria

Urticaria, the most common reaction to CM, is limited to skin and subcutaneous tissue. Worsening of symptoms can be caused by the accompanying pruritus. Findings on physical examination include the following:

- Red raised wheals that blanch with pressure
- Patchy, symmetric involvement
- Itching, often intense
- Stable vital signs

Mild urticaria is usually self-limiting and does not require treatment.

**BOX 3.1** Risk Factors for Allergic-Like Contrast Reactions

- Prior reaction to contrast media
- Prior anaphylactic reaction
- Moderate to severe allergies to food products or medications
- History of asthma
- Preexisting renal or heart disease
- Diabetes mellitus or sickle cell disease
- Concomitant use of certain medications

**BOX 3.2** Classification of Allergic-Like Contrast Reaction

**MILD**

- Nausea/vomiting
- Mild urticaria
- Pallor

**MODERATE**

- Severe vomiting
- Significant urticaria
- Mild vasovagal reaction
- Mild bronchospasm
- Dyspnea
- Tachycardia and hypotension

**SEVERE**

- Laryngeal edema
- Pulmonary edema
- Moderate to severe bronchospasm
- Cardiovascular collapse
- Bradycardia and hypotension
- Seizures

Close observation for 30 to 60 minutes, or until resolution, is recommended because urticaria may progress to a moderate reaction. Medications may include $H_1$-receptor blockers (such as diphenhydramine) or α-agonists (such as epinephrine). The accompanying parents/responsible adults should be cautioned about the possibility of drowsiness when diphenhydramine is administered. If urticaria is extensive, pay close attention to the patient's blood pressure and watch for signs and symptoms of hypotension, especially orthostatic hypotension.

## Bronchospasm

The patient may present with varying degrees of cough, wheezing, and/or difficulty breathing. It is most important to ensure the presence of an adequate airway. Administer 6 to 10 L/min of oxygen via a face mask. Vital signs should be monitored. Medications may include β-agonists (i.e., bronchodilators), intramuscular epinephrine for mild symptoms, and IV epinephrine for more acute and severe symptoms.

## Facial or Laryngeal Edema

Swelling of the face may be mild without any significant progression. At this time, only observation may be required. An adequate airway and IV access should be secured. However, if the patient presents with other symptoms such as varying degrees of cough, hoarseness, dysphagia, and/or difficulty breathing, more aggressive measures need to be taken. Medications include intramuscular, intramuscular, or IV epinephrine. The patient should be closely monitored.

## Pulmonary Edema

The patient may present with tachypnea, tachycardia, shortness of breath, diaphoresis, agitation, and/or bibasilar rales. Blood-tinged sputum is a late-presenting sign. The airway must be secured and supplemental oxygen should be administered. Medications may include diuretics. Pulmonary edema is a severe response that usually should involve a rapid response or code team.

## Hypotension With Tachycardia (Anaphylaxis)

Anaphylaxis can be a life-threatening response to CM. Symptoms may include difficulty breathing, chest tightness, a thready pulse, a rapid or irregular heart rate, dizziness, hoarseness, and/or loss of consciousness. The rapid response or code team should be called the moment this adverse effect is suspected. Meanwhile, management should be initiated with Trendelenburg positioning, securing of the airway, rapid fluid resuscitation, and administration of IV epinephrine.

## Hypotension With Bradycardia (Vasovagal Reaction)

Patients may present with pallor, a decreased level of consciousness, diaphoresis, and a decreased heart rate. Management should be initiated with Trendelenburg positioning, securing of the airway, hydration, and administration of atropine if bradycardia persists (Box 3.3).

## Delayed Reactions

Delayed reactions appear to occur more frequently than acute/immediate reactions to administration of CM. The incidence ranges from 2% to 12%.[15,16] No definite data are available on the incidence and symptoms of delayed reactions in children. In adults, rash, itching, and other cutaneous manifestations predominate.[16] Other symptoms include fevers, chills, nausea, vomiting, headaches, abdominal pain, drowsiness, and dizziness.[16] These symptoms can manifest any time from 1 hour to 2 days after administration of the contrast agent and usually resolve spontaneously by 7 days.[15-17]

## Prevention

Before any study requiring administration of IV CM is begun, it is imperative to identify patients who would be at high risk for adverse reactions. If risk factors are identified, the need for the examination should be reassessed with the ordering clinician. Other modalities that may offer the same level of diagnosis but do not require administration of contrast agents should be considered. The possibility of performing the same test without the use of CM also should be entertained.

Ultimately, if the examination is considered absolutely necessary, the patient with known risk factors for adverse reactions should be premedicated with a combination of an antihistamine and corticosteroids. The regimen suggested by the ACR[2] is described in Table 3.1.

## Extravasation

Extravasation is a well-recognized complication of contrast-enhanced imaging that occurs in approximately 0.7% of all noniodinated contrast injections.[18-21] The incidence is much lower in GBCM injections. This is believed also to be due to the smaller volume generally administered and the slower injection flow rates.

### Risk Factors

Extravasation is more prone to occur in patients who are unable to verbalize their symptoms, such as infants, younger children, and severely ill and unconscious patients.[22,23] Increased rates also

### **BOX 3.3** Management of Acute Reactions in Children

**URTICARIA**

- No treatment is needed in most cases. However, if symptomatic consider an $H_1$-receptor blocker such as diphenhydramine (Benadryl), PO/IM or via a slow IV push over 1–2 minutes, 1 mg/kg, up to 50 mg.
- For moderate or severe itching or if the urticaria is widely disseminated, consider an $H_1$-receptor blocker such as diphenhydramine (Benadryl), PO/IM or via a slow IV push over 1–2 minutes, 1 mg/kg, up to 50 mg.

**FACIAL EDEMA**

- Secure the airway and administer $O_2$, 6 to 10 L/min (via mask, face tent, or blow-by stream). Monitor electrocardiogram, $O_2$ saturation (pulse oximeter), and blood pressure.
- Administer an α-agonist such as epinephrine (1 : 10,000), 0.1 mL/kg (0.01 mg/kg) via a slow IV push over 1–2 minutes, up to 1 mg total dose (maximum single dose of 1.0 mL or 0.1 mg). Repeat in 5 to 15 minutes as needed.
- Consider administering an $H_1$-receptor blocker such as diphenhydramine (Benadryl), PO/IM or via a slow IV push over 1–2 minutes, 1 mg/kg, up to 50 mg.
- Note: If facial edema is mild and no reaction progression occurs, observation alone may be appropriate. If the patient is not responsive to therapy, call for assistance.

**BRONCHOSPASM**

- Secure the airway and administer $O_2$, 6 to 10 L/min (via mask, face tent, or blow-by stream). Monitor electrocardiogram, $O_2$ saturation (pulse oximeter), and blood pressure.
- Administer an inhaled β-agonist (e.g., a bronchiolar dilator such as albuterol [Proventil or Ventolin]), 2 puffs (90 mcg/puff for a total of 180 mcg) from an inhaler. Repeat up to 3 times.
- If bronchospasm progresses, administer epinephrine IM (1 : 1000), 0.01 mL/kg (0.01 mg/kg), maximum 0.3 mL (0.3 mg) for a total of up to 1 mL (1 mg) or epinephrine IV (1 : 10,000), 0.1 mL/kg (0.01 mg/kg) via a slow IV push over 1–2 minutes, up to 1 mg total dose (maximum single dose of 1.0 mL or 0.1 mg). Repeat in 5 to 15 minutes as needed. If the patient is not responsive to therapy, call for assistance for severe bronchospasm or if $O_2$ saturation <88% persists.

**LARYNGEAL EDEMA**

- Secure the airway and administer $O_2$, 6 to 10 L/min (via mask, face tent, or blow-by stream). Monitor electrocardiogram, $O_2$ saturation (pulse oximeter), and blood pressure.
- Administer epinephrine (1 : 10,000), 0.1 mL/kg (0.01 mg/kg) via a slow IV push over 1–2 minutes, up to 1 mg total dose (maximum single dose of 1.0 mL or 0.1 mg) or epinephrine IM (1 : 1000), 0.01 mL/kg (0.01 mg/kg), maximum 0.3 mL (0.3 mg) for a total of up to 1 mL (1 mg). Repeat in 5 to 15 minutes as needed. If the patient is not responsive to therapy, call for assistance.

**PULMONARY EDEMA**

- Secure the airway and administer $O_2$, 6 to 10 L/min (via mask, face tent, or blow-by stream). Monitor electrocardiogram, $O_2$ saturation (pulse oximeter), and blood pressure.
- Administer a diuretic: IV furosemide (Lasix), 0.5–1.0 mg/kg over 2 minutes for a maximum dose of 40 mg.

**HYPOTENSION WITH TACHYCARDIA (ANAPHYLACTIC SHOCK)**

- Secure the airway and administer $O_2$, 6 to 10 L/min (via mask). Monitor electrocardiogram, $O_2$ saturation (pulse oximeter), and blood pressure.
- Elevate the legs 60 degrees or more (preferred) or use the Trendelenburg position.
- Keep the patient warm.
- Administer a rapid infusion of IV or IO normal saline solution or Ringer's lactate.
- If severe, administer epinephrine (1 : 10,000), 0.1 mL/kg (0.01 mg/kg) via a slow IV push over 1–2 minutes, up to 1 mg total dose (maximum single dose of 1.0 mL or 0.1 mg) or epinephrine IM (1 : 1000), 0.01 mL/kg (0.01 mg/kg), maximum 0.3 mL (0.3 mg) for a total of up to 1 mL (1 mg). Repeat in 5 to 15 minutes as needed. If the patient is not responsive to therapy, call for assistance (e.g., cardiopulmonary arrest response team or 911).

**HYPOTENSION WITH BRADYCARDIA (VAGAL REACTION)**

- Secure the airway and give $O_2$, 6 to 10 L/min (via mask). Monitor electrocardiogram, $O_2$ saturation (pulse oximeter), and blood pressure.
- Elevate the legs 60 degrees or more (preferred) or use the Trendelenburg position.
- Keep the patient warm.
- Administer a rapid infusion of IV or IO normal saline solution or Ringer's lactate. Caution should be used to avoid hypervolemia in children with myocardial dysfunction.
- Administer atropine IV, 0.2 mL/kg of 0.1 mL solution (0.02 mg/kg) if the patient does not respond quickly to above steps. Use a minimum single dose of 0.1 mg. Maximum single dose of 0.6–1.0 mg. Maximum total dose: 1 mg for infants and children; 2 mg for adolescents. If the patient is not responsive to therapy, call for assistance.

*IM,* Intramuscular; *IO,* intraosseous; *IV,* intravenous; *PO,* by mouth.

*From American College of Radiology.* ACR manual on contrast media. *American College of Radiology, Version 10.3, 2017. Available at: https://www.acr.org/~/media/ACR/Documents/PDF/QualitySafety/Resources/Contrast-Manual/Contrast_Media.*

**TABLE 3.1** Pediatric Premedication Regimen for Prevention of Contrast Reaction

| Medication | Dosage | Timing |
|---|---|---|
| Prednisone | 0.5-0.7 mg/kg PO (up to 50 mg) | 13 hours, 7 hours, and 1 hour before contrast injection |
| Diphenhydramine | 1.25 mg/kg PO (up to 50 mg) | 1 hour before contrast injection |

*PO,* By mouth.

*From American College of Radiology.* ACR manual on contrast media. *American College of Radiology, Version 10.3, 2017. Available at: https://www.acr.org/~/media/ACR/Documents/PDF/QualitySafety/Resources/Contrast-Manual/Contrast_Media.*

are noted in patients receiving chemotherapy, likely because of increased friability of the vein wall.[23-25]

Other risk factors include the site of injection, IV access type, and the method of injection.[23] Although the antecubital fossa is the single most common extravasation site, most of these events occur in patients with venous access elsewhere.[18] Increased incidents have been noted with injections at the dorsum of the hand.[26] Other risk factors also include venous thrombosis, extremity edema, multiple venous access attempts, and use of a tourniquet.[2,22,23] Extravasations are more frequent where preexisting catheters are used as access sites for administration of the CM.[24] At least two studies did not note any significant difference in the incidence of extravasation with the use of power injectors (Box 3.4).[26,27]

**BOX 3.4** Risk Factors for Intravenous Contrast Extravasation

Infants, young children, severely ill patients, and unconscious patients
Patients with friable veins
Presence of venous thrombosis or extremity edema
Injection sites other than antecubital fossa
Large volume of contrast medium
Injection through indwelling catheters
Multiple venous access attempts
Use of a tourniquet

**BOX 3.5** Signs and Symptoms of Contrast Extravasation

Pain, erythema, burning and/or tingling, tightness, swelling at the affected extremity
Blisters, skin ulceration, soft tissue necrosis
Compartment syndrome
Altered tissue perfusion
Paresthesia
Diminished arterial pulses

### Presentation

The immediate symptoms of extravasation can be quite variable. Some patients present with a burning sensation, whereas others remain asymptomatic. Close attention should be paid to young children and unconscious patients because they may not be able to express these sensations. On physical examination, the extravasation site may be red, swollen, and tender.[2]

Most incidents are self-limiting and resolve spontaneously within 1 to 2 days. These incidents usually are restricted to the skin and subcutaneous tissue.[2] The injuries can range from transient tightness of the skin to tissue ulceration and necrosis to acute compartment syndromes. Severe reactions have been observed with both small and large volumes of extravasated contrast. However, the majority of severe reactions have been observed with larger volumes (Box 3.5).[28]

### Management

A definite treatment approach has not been accepted because of a lack of consensus on the appropriate management of extravasation.[22,29,30] Minor symptoms can be treated with elevation of the affected extremity above the level of the heart to help reduce edema by promoting resorption of the fluid.[2,23] Sufficient data are lacking to support either warm or cold compresses over the affected limb.[2] Hyaluronidase injected subcutaneously may help speed resorption, but insufficient evidence exists to suggest routine use. Regardless, close monitoring of the patient is warranted. These events should be documented in the patient's medical records and appropriate directions should be provided to seek medical attention in the event of worsening symptoms.

Severe extravasation injuries require a surgical consultation. Such injuries may present as worsening of pain or swelling, skin blistering, decreased capillary refill, diminished pulses, and a change in sensation of the affected extremity.[2,22] Compartment syndrome can develop even with less than 100 mL of extravasated fluid.[18] Thus it is prudent to conclude that signs and symptoms, rather than the volume extravasated, should be used as a scale for seeking surgical consultation (Box 3.6).

**BOX 3.6** Management of Contrast Extravasation

Elevation of extremity
Cold/warm compresses
Frequent monitoring of capillary refill, arterial pulses
Frequent questioning for progression of symptoms
Surgical consultation

## Contrast-Induced Nephropathy

Limited data are available on the nephrotoxic effects of iodinated CM in children. The ACR recommends following the principles used for adults in the prevention and management of contrast-induced nephropathy (CIN).[2] Risk factors include preexisting renal insufficiency, diabetes mellitus, and multiple CM administrations during the same day.

CIN has been described as either an absolute increase in serum creatinine by at least 0.5 mg/dL within 48 hours of contrast injection[31] or an increase of more than 25% within 72 hours of contrast administration.[32] However, serum creatinine cannot be reliably used as a measure of renal function in this setting in the pediatric population.[2] The estimated glomerular filtration rate (GFR) is used widely for this purpose. The National Kidney Disease Education Program has provided information regarding the measurement of GFR at its website (http://www.nkdep.nih.gov/lab-evaluation/gfr-calculators.shtml) and advocates use of the bedside isotope dilution mass spectrometry–traceable Schwartz GFR calculator for children equation[33]:

$$\begin{aligned}&\text{GFR}\ (\text{mL/min/1.73 m}^2)\\&\quad = (0.41 \times \text{Height [cm]})/\text{Creatinine (mg/dL)}\end{aligned}$$

A GFR of less than 30 mL/min is associated with an increased risk of CIN. Cystatin C, a protein that is produced by all nucleated cells and is exclusively eliminated by glomerular filtration, has been suggested as a better indicator of GFR than serum creatinine.

No significant studies have been conducted to understand the nephrotoxic effects, risk factors, or prevention of CIN in children. Hence when CIN is a concern for a pediatric patient, the clinician ordering the test and the radiologist must carefully consider the need for the study and the potential use of other modalities or unenhanced imaging.

## Nephrogenic Systemic Fibrosis

Nephrogenic systemic fibrosis (NSF) is a disease characterized primarily by skin fibrosis, but it may involve multiple organs. Its association with GBCM was first documented in 2006.[34] Very few cases of NSF have been reported from various data sources.[35] Not enough data exist in the pediatric population to provide guidelines for the prevention of NSF in children. The ACR[2] recommends following adult guidelines for identifying patients at risk and the use of GBCM. Risk factors include decreased renal function with GFR less than 30 mL/min, high doses of administered gadolinium, and postsurgical status.[34,36,37] Discreet use of GBCM in accordance with guidelines by various European and US agencies has resulted in a significant decline in the number of cases encountered. Gadolinium agents should be used with caution in infants and preterm babies because their renal function is immature.[38]

## Gadolinium Deposition and Toxicity

There have been recent reports of intracranial gadolinium deposition (predominantly in the dentate nuclei, but also in globus pallidus and thalamus)[39-41] after multiple injections of GBCM over varying periods in children. The clinical significance of this accumulation remains uncertain. However, until a better understanding of the clinical implications is achieved, clinicians and radiologists should use discretion and caution in administering linear GBCM[39] to children.

## Gadolinium and Serum Calcium Levels

Interference with laboratory test of serum calcium is noted with certain linear nonionic GBCM.[42-44] This transient and pseudo hypocalcemia is also attributed to higher doses of GBCM and to impaired renal function.[42]

### KEY POINTS

- Although allergic-like reactions are rare, they sometimes happen after injection of iodinated contrast media; thus screening for risk factors is important.
- A guide describing management and weight-based doses of the medications should be within reach of every radiologist and should be posted in every room where a contrast injection occurs.
- The GFR should be calculated for all children before the injection of iodinated contrast material.
- All reactions and the management provided should be documented in the medical record.
- Patients with extravasation (any volume) should be closely monitored for worsening of pain and development of other symptoms suggesting compartment syndrome or tissue necrosis.
- Gadolinium should be used with caution in infants because of the immaturity of their renal function.

## SUGGESTED READINGS

American College of Radiology. *ACR manual on contrast media*. American College of Radiology, Version 10.3, 2017. http://www.acr.org/QualitySafety/Resources/Contrast-Manual.

Brockow K. Immediate and delayed reactions to radiocontrast media: is there an allergic mechanism? *Immunol Allergy Clin North Am*. 2009;29(3):453–468.

Mendichovszky IA, Marks SD, Simcock CM, et al. Gadolinium and nephrogenic systemic fibrosis: time to tighten practice. *Pediatr Radiol*. 2008;38:489–496.

Namasivayam S, Kalra MK, Torres WE, et al. Adverse reactions to intravenous iodinated contrast media: a primer for radiologists. *Emerg Radiol*. 2006;12:210–215.

Rudnick MR, Keselheim A, Goldfarb S. Contrast-induced nephropathy: how it develops, how to prevent it. *Cleve Clin J Med*. 2006;73:75–80.

Schaverein MV, Evison D, McCulley SJ. Management of large volume CT contrast medium extravasation injury: technical refinement and literature review. *J Plast Reconstr Aesthet Surg*. 2008;61(5):562–565.

## REFERENCES

Full references for this chapter can be found on www.expertconsult.com.

## REFERENCES

1. Brasch RC. Contrast media toxicity in children. *Pediatr Radiol*. 2008;38:281–284.
2. From American College of Radiology. *ACR manual on contrast media*. American College of Radiology, Version 10.3, 2017. Available at: https://www.acr.org/~/media/ACR/Documents/PDF/QualitySafety/Resources/Contrast-Manual/Contrast_Media.
3. Cohen MD, Smith JA. Intravenous use of ionic and nonionic contrast agents in children. *Radiology*. 1994;191:793–794.
4. Dillman JR, Strouse PJ, Ellis JH, et al. Incidence and severity of acute allergic-like reactions to i.v. nonionic iodinated contrast material in children. *AJR Am J Roentgenol*. 2007;118:1643–1647.
5. Cochran ST, Bomyea K, Sayre JW. Trends in adverse events after IV administration of contrast media. *AJR Am J Roentgenol*. 2001;176:1385–1388.
6. Mortelé KJ, Olivia MR, Ondategui S, et al. Universal use of nonionic iodinated contrast medium for CT: evaluation of safety in a large urban teaching hospital. *AJR Am J Roentgenol*. 2005;184:31–34.
7. Geller J, Kasahara M, Martinez M, et al. Safety and Efficacy of Gadoxetate Disodium–Enhanced Liver MRI in Pediatric Patients aged >2 Months to <18 Years—Results of a Retrospective, Multicenter Study. *Magn Reson Insights*. 2016;9:21–28.
8. Dillman JR, Ellis JH, Cohan RH, et al. Frequency and severity of acute allergic-like reactions to gadolinium-containing IV contrast media in children and adults. *AJR Am J Roentgenol*. 2007;189:1533–1538.
9. Katayama H, Yamaguchi K, Kozuka T, et al. Adverse reactions to ionic and nonionic contrast media: a report from the Japanese Committee on the Safety of Contrast Media. *Radiology*. 1990;175:621–628.
10. Fischer H, Doust V. An evaluation of pretesting in the problem of serious and fatal reactions to excretory urography. *Radiology*. 1992;103:497–501.
11. Witten D. Reactions to urographic contrast media. *JAMA*. 1975;231:974–977.
12. Morcos SK, Thomsen HS. Adverse reactions to iodinated contrast media. *Eur Radiol*. 2003;13:181–184.
13. Chamberlain D, Smith A, Woollard M, et al. Trials of teaching methods in basic life support: comparison of simulated CPR performance after first training and at 6 months, with a note on the value of re-training. *Resuscitation*. 2002;53(2):179–187.
14. Wolfram RW, Warren CM, Doyle CR, et al. Retention of pediatric advanced life support (PALS) course concepts. *J Emerg Med*. 2003;25(4):475–479.
15. Yoshikawa H. Late adverse reactions to nonionic contrast media. *Radiology*. 1992;183:737–740.
16. Christiansen C, Pichler WJ, Skotland T. Delayed allergy-like reactions to X-ray contrast media: mechanistic considerations. *Eur Radiol*. 2000;10:1965–1975.
17. Webb JAW, Stacul F, Thomsen HS, et al. Late adverse reactions to intravascular iodinated contrast media. *Eur Radiol*. 2003;13:181–184.
18. Wang CL, Cohan RH, Ellis JH, et al. Frequency, management, and outcome of extravasation of nonionic iodinated contrast medium in 69,657 intravenous injections. *Radiology*. 2007;243:80–87.
19. Bullard MA, Cohan RH, Ellis JH, et al. Extravasation of intravenous contrast material: incidence, management, outcome. *Acad Radiol*. 1997;4:711–718.
20. Federle MP, Chang PJ, Confer S, et al. Frequency and effects of extravasation of ionic and nonionic CT contrast media during rapid bolus injection. *Radiology*. 1998;206:637–640.
21. Jacobs JE, Birnbaum BA, Langlotz CP. Contrast media reactions and extravasation: relationship to intravenous injection rates. *Radiology*. 1998;209:411–416.
22. Cohan RH, Ellis JH, Garner WL. Extravasation of radiographic contrast material: recognition, prevention and treatment. *Radiology*. 1996;200:593–604.
23. Bellin M, Jakobsen JA, Tomassin I, et al. Contrast medium extravasation injury: guidelines for prevention and management. *Eur Radiol*. 2002;12:2807–2812.
24. Sistrom CL, Gay SB, Peffley L. Extravasation of iopamidol and iohexol during contrast-enhanced CT: report of 28 cases. *Radiology*. 1991;180:707–710.
25. Gault DT. Extravasation injuries. *Br J Plast Surg*. 1993;46:91–96.
26. Amaral JG, Traubici J, BenDavid G, et al. Safety of power injector use in children as measured by incidence of extravasation. *AJR Am J Roentgenol*. 2006;187:580–583.
27. Jacobs JE, Birnbaum BA, Langlotz CP. Contrast media reactions and extravasation: relationship to intravenous injection rates. *Radiology*. 1998;209:411–416.
28. Upton J, Mulliken JB, Murray JE. Major intravenous extravasation injuries. *Am J Surg*. 1979;137:497–506.
29. Park KS, Kim SH, Park JH, et al. Methods for mitigating soft-tissue injury after subcutaneous injection of water-soluble contrast media. *Invest Radiol*. 1993;28:332–334.
30. Yucha CB, Hastings-Tolsma TM, Szeverenyi N. Effects of elevation on intravenous extravasations. *J Intraven Nurs*. 1994;17:231–234.
31. Solomon R, Werner C, Mann D, et al. Effects of saline, mannitol, and furosemide to prevent acute decreases in renal function induced by radiocontrast agents. *N Engl J Med*. 1994;331:1416–1420.
32. Porter GA. Contrast medium-associated nephropathy. Recognition and management. *Invest Radiol*. 1993;28(suppl 4):S11–S18.
33. Schwartz GJ, Muñoz A, Schneider MF, et al. New equations to estimate GFR in children with CKD. *J Am Soc Nephrol*. 2009;20:629–637.
34. Grobner T. Gadolinium—a specific trigger for the development of nephrogenic fibrosing dermopathy and nephrogenic systemic fibrosis? *Nephrol Dial Transplant*. 2006;21:1104–1108.
35. Nardone B, Saddleton E, Laumann AE, et al. Pediatric nephrogenic systemic fibrosis is rarely reported: a RADAR report. *Pediatr Radiol*. 2014;44(2):173–180.
36. Karcaaltincaba M, Oguz B, Haliloglu M. Current status of contrast-induced nephropathy and nephrogenic systemic fibrosis in children. *Pediatr Radiol*. 2009;39:382–384.
37. Perez-Rodriguez J, Lai S, Ehst BD, et al. Nephrogenic systemic fibrosis: incidence, associations, and effect of risk factor assessment—report of 33 cases. *Radiology*. 2009;250:371–377.
38. Penfield JG. Nephrogenic systemic fibrosis and the use of gadolinium-based contrast agent. *Pediatr Nephrol*. 2008;23:2121–2129.
39. Flood TF, Stence NV, Maloney JA, et al. Pediatric brain: repeated exposure to linear gadolinium-based contrast material is associated with increased signal intensity at unenhanced T1-weighted MR imaging. *Radiology*. 2016;28:160356. [Epub ahead of print].
40. Ramalho J, Castillo M, AlObaidy M, et al. High signal intensity in globus pallidus and dentate nucleus on unenhanced T1-weighted MR images: evaluation of two linear gadolinium-based contrast agents. *Radiology*. 2015;276:836–844.
41. Miller JH, Hu HH, Pokorney A, et al. MRI brain signal intensity changes of a child during the course of 35 gadolinium contrast examinations. *Pediatrics*. 2015;136:1637–1640.
42. Prince MR, Erel HE, Lent RW, et al. Gadodiamide administration causes spurious hypocalcemia. *Radiology*. 2003;227:639–646.
43. Baker JF, Kratz LC, Stevens GR, et al. Pharmacokinetics and safety of the MRI contrast agent gadoversetamide injection (Opti-MARK) in healthy pediatric subjects. *Invest Radiol*. 2004;39:334–339.
44. Löwe A, Balzer T, Hirt U. Interference of gadolinium-containing contrast-enhancing agents with colorimetric calcium laboratory testing. *Invest Radiol*. 2005;40:521–525.

## PART 1 Orbit

# 4

# Embryology, Anatomy, Normal Findings, and Imaging Techniques

*Srikala Narayanan, Eric Faerber, and Andre Dietz Furtado*

## EMBRYOLOGY OF THE EYE

Development of the eye originates from neuroectoderm, surface ectoderm, and neural crest cells.[1–3] The neuroectodermal layer gives rise to the retina, iris, and optic nerve; the surface ectoderm gives rise to the lens; the neural crest cells are responsible for vascular structures, sclera, choroid, and mesenchymal tissue from which the adnexal structures, bony orbit, fat, and nerve sheaths arise.[4,5]

The prime regulatory gene for human eye development is *PAX6*, a member of the PAX (paired box) family of transcription factors. This gene initially is expressed in a band contained in the anterior neural ridge of the neural plate before the process of neurulation.[6] A single eye field is present at this stage, which then separates into two primordial optic structures under the direction of sonic hedgehog *(SHH)*, which belongs to a family of vertebrate genes involved with encoding inductive signals during embryogenesis and is part of a vast signaling network that affects development of many tissues and organs.[6]

The earliest sign of embryonic eye development is at day 22 with the appearance of a pair of shallow grooves evaginating on either side of the prosencephalon or forebrain.[6] The grooves form the optic vesicles in contact with surface ectoderm. Invagination of the optic vesicle leads to formation of a double-walled optic cup. This cup has two layers that become the retina, separated by the intraretinal space. The outer layer contains pigment granules that appear during the fifth week of development. The inner layer has two parts. The pars optica retinae occupies the posterior four-fifths and contains cells that ultimately differentiate into the rod and cone cells responsible for light reception. The pars ceca retinae, within the anterior fifth of the inner layer, divides into the pars iridica retinae, which will form the inner layer of the iris, and the pars ciliaris retinae, which will be involved with formation of the ciliary body. The central retinal artery results from the residuum of the embryonic hyaloid artery, which regresses by 4 months of gestation. The lips of the choroid fissure fuse during the seventh week; the mouth of the optic cup becomes the future pupil.

Elongation of surface ectoderm cells in contact with the optic vesicle results in formation of the lens placode, which develops into the lens vesicle. The lens vesicle becomes located in the mouth of the optic cup (Fig. 4.1). Cells located in the posterior wall of the vesicle elongate, forming long fibers that fill the lumen of the vesicle, reaching the anterior wall of the lens vesicle by the seventh week of development. The vascular capsule is a mesenchymal condensation that covers the lens. The hyaloid artery supplies the lens, forming a plexus on its posterior surface.[7]

The primary vitreous develops from mesenchyme within the optic cup, which has an embryonic fissure, known as the *canal of Cloquet*. The hyaloid artery reaches the globe through this canal.

The hyaloid artery and its branches are a transient vascular system that nourishes structures of the eye, subsequently involuting by the 35th week of gestation.[5]

The choroid and sclera are formed from mesenchyme surrounding the optic cup. The ciliary body and ciliary processes are formed from the anterior portion of the choroid.[7]

The optic cup and brain are connected by the optic stalk. The choroid fissure is a groove on the ventral surface of the optic stalk, wherein lie the hyaloid vessels. The fissure closes at 7 weeks' gestation, during which time a narrow tunnel is formed inside the optic stalk. The inner and outer walls of the stalk fuse, becoming the optic nerve. The center contains a portion of the hyaloid artery, the central artery of the retina. The exterior of the optic nerve is covered by a continuation of the choroid and sclera, along with the pia, arachnoid, and dura.[6]

Development of the eye continues into postnatal life. The fovea centralis of the retina becomes differentiated by 4 months after birth. The cones remain poorly developed until 4 months after birth.[8] The infant globe and orbit reach 80% of adult size during the first few years of life, with full size reached by approximately 13 years of age.

## NORMAL ANATOMY OF THE ORBIT AND EYE

The orbits are cone-shaped cavities containing the globes, extraocular muscles, blood vessels, nerves, retrobulbar fat, and lacrimal glands. Each orbit is bounded by the floor of the anterior cranial fossa superiorly, the maxillary sinus inferiorly, the ethmoid sinus medially, and the temporal bone and middle cranial fossae anterolaterally and posterolaterally (Figs. 4.2 and 4.3).

The orbital septum is a thin connective tissue membrane that arises from the peripheral periosteum of the anterior osseous orbit and attaches to the tarsal plates of the eyelids. The septum divides the orbit into an anterior preseptal space and a deeper postseptal space. The postseptal space is divided by the extraocular muscle cone (consisting of the four rectus muscles) into intraconal, conal, and extraconal compartments. The lacrimal gland lies in the superolateral quadrant of the orbit.

The globe occupies about 20% of the orbital cavity. It is divided by the lens into an anterior chamber filled with aqueous humor and a posterior chamber containing vitreous humor found between the lens and retina. The globe contains the retina, uveal layer, and sclera. The sclera is covered anteriorly by the conjunctiva, continuous with the mucous membrane of the eyelid (Fig. 4.4). Tenon fascia separates the globe and extraocular muscle insertions from the orbital fat.

The retrobulbar space extends from the orbital septum anteriorly to the orbital apex posteriorly. The space contains six extraocular muscles (the superior, inferior, lateral, and medial rectus muscles

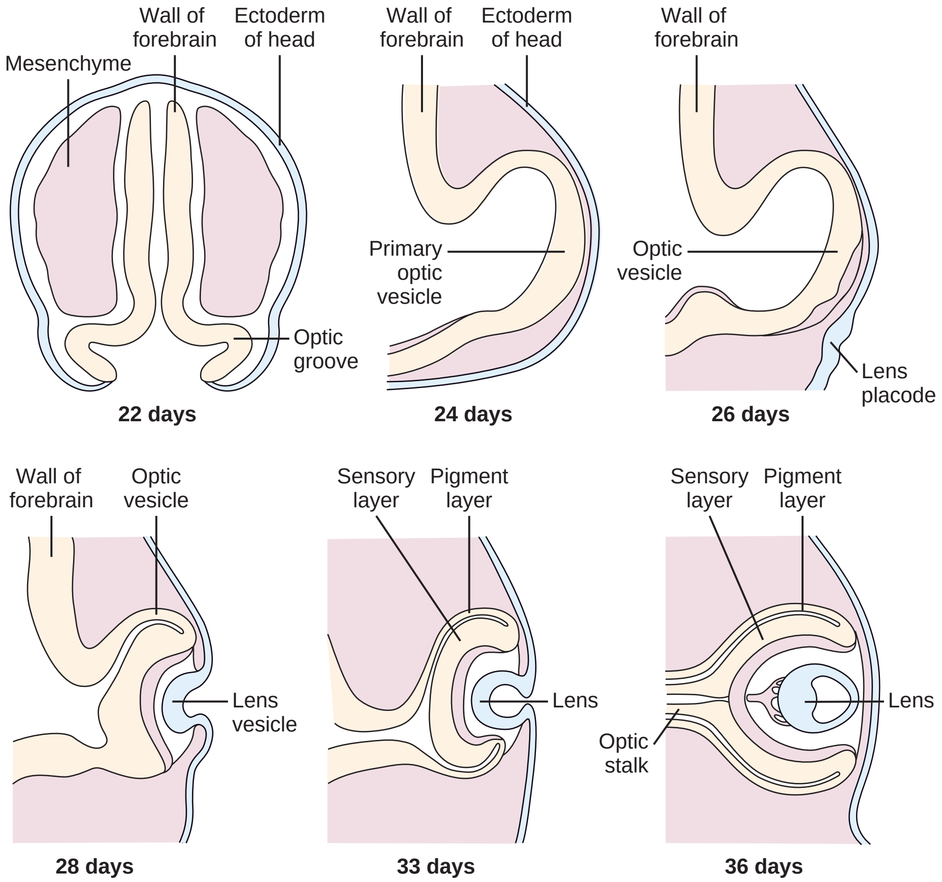

**Figure 4.1. Early development of the human eye.** *(From Carlson BM.* Human Embryology and Developmental Biology*, 2nd ed. St. Louis: Mosby; 1999.)*

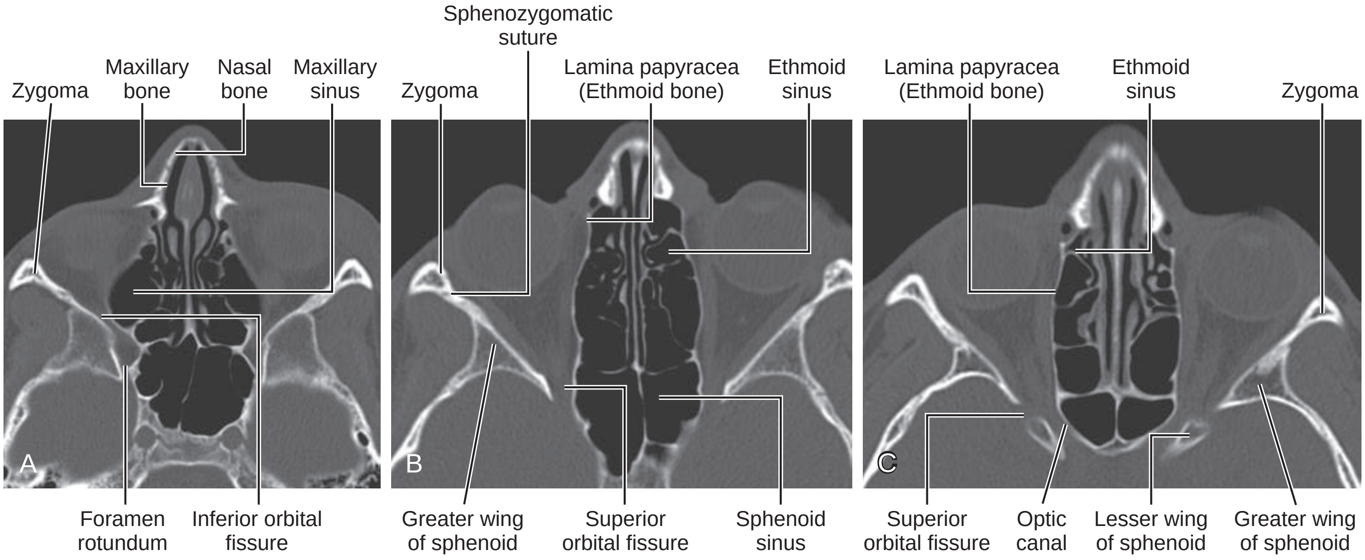

**Figure 4.2. Axial anatomy of the bony orbit.** (A–C) Axial noncontrast computed tomography images from inferior to superior location.

and the inferior and superior oblique muscles), vascular structures, and the optic nerve, surrounded by fat.

The optic nerve is divided into four segments: (1) an intraocular segment penetrating the sclera, (2) an intraorbital segment in the intraconal space, (3) an intracanalicular segment in the optic canal, and (4) an intracranial segment extending from the optic canal to the optic chiasm. It is fully myelinated by 7 months of age. It continues to increase in thickness for the first 8 years of life.

Optic nerve sheath diameter in children as measured on magnetic resonance imaging (MRI) is 3.1 mm in the 0- to 3-year

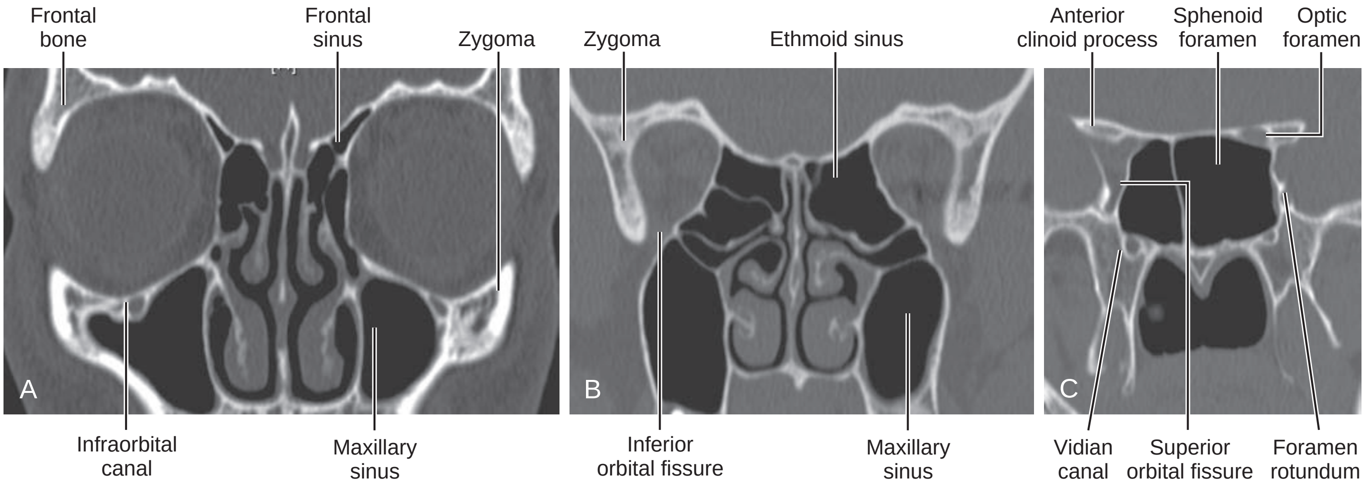

**Figure 4.3. Coronal anatomy of the bony orbit.** (A–C) Coronal noncontrast computed tomography images from anterior to posterior location.

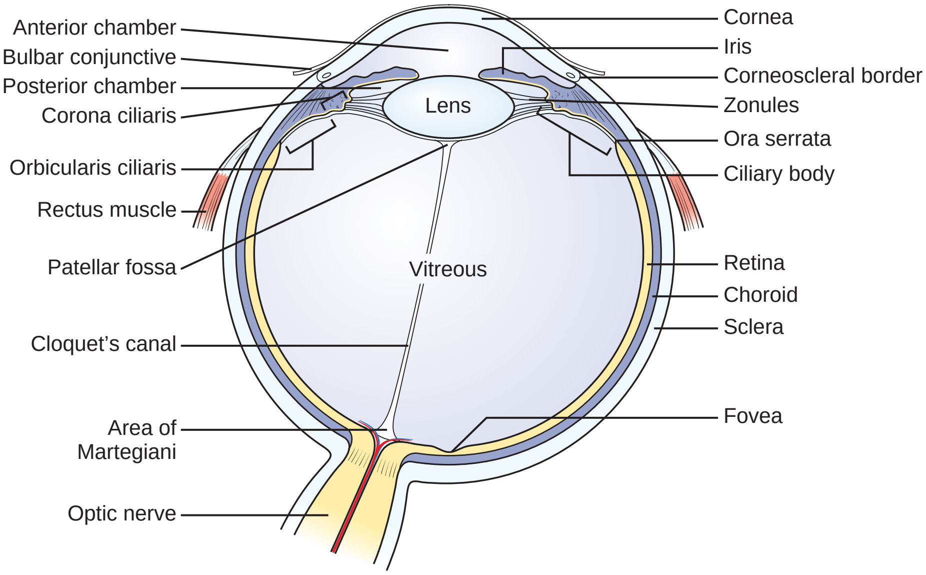

**Figure 4.4. Normal anatomy of the eye.** *(From Jakobiec FA, Ozanics V. General topographic anatomy of the eye. In Jakobiec FA, ed.* Ocular Anatomy, Embryology and Teratology, *New York: Harper & Row; 1982.)*

age group, 3.41 mm between 3 and 6 years, 3.55 mm between 6 and 12 years, and 3.56 mm in the 12- to 18-year age group.[9]

## IMAGING TECHNIQUES

Computed tomography (CT) and MRI are the main imaging modalities for the orbit and optic pathway. Ultrasonography may be useful for specific indications.

### Ultrasound

Ultrasound is extremely beneficial in infants and children because it does not use ionizing radiation, it is widely available, and the need for sedation is rare. The primary indications are disease or conditions of the anterior chamber preventing fundoscopic examination of the remainder of the eye, such as hyphema and trauma, nonneoplastic leukocoria, assessment of vascular integrity of the retina or an underlying lesion, and follow-up of neoplastic causes of leukocoria after treatment.[10] Secondary indications include further elucidation of intraconal and extraconal lesions and assessment of lacrimal masses.[7] Ultrasound is less helpful in showing osseous abnormalities of the orbit.

The procedure is performed with the patient supine. Initially a small amount of gel is placed over the upper eyelid. Images are obtained using a high-resolution (7.0–18.0 MHz) linear-array transducer with color Doppler capability.[10] Power output must be decreased to avoid mechanical or thermal injury. Scanning is usually performed in the axial plane; however, other planes also may be used to evaluate the entire globe (Fig. 4.5A).[10]

Color Doppler imaging is an important component of the ultrasound examination because it permits demonstration of the ophthalmic artery and vein, the central artery of the retina, the retinal vein, ciliary and lacrimal arteries and accompanying veins, and the superior ophthalmic vein (Fig. 4.5B).[10]

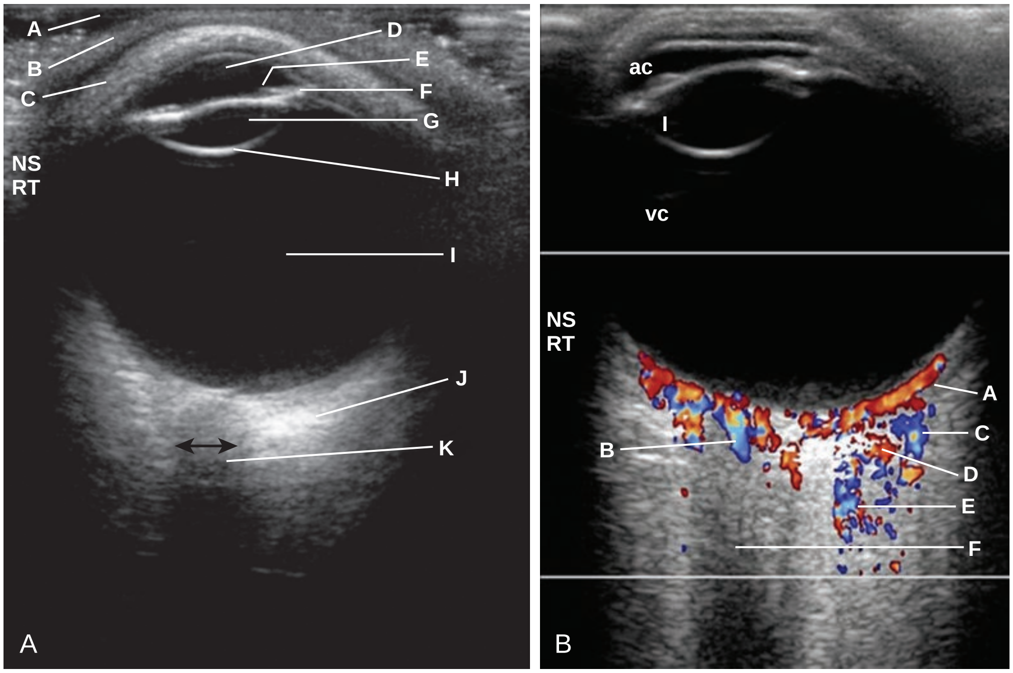

**Figure 4.5. Normal ophthalmic axial ultrasound of a teenager.** (A) Using a broadband, high-resolution linear-array transducer (5–17 MHz extended-frequency range), sterile gel *(A)* is placed on the skin *(B)* over the upper eyelid *(C),* which remains shut throughout the examination. The anechoic anterior chamber *(D),* the iris *(E),* the ciliary apparatus *(F),* the anechoic lens *(G)* with the posterior reflective echo *(H),* the anechoic vitreous chamber *(I),* and the hypoechoic optic nerve *(J)* are demonstrated and the optic nerve width *(double-ended black arrow)* can be measured. (B) Normal color Doppler examination of the eye in the same patient. Color Doppler imaging shows very good flow in the choroidal vessels *(A),* central retinal artery *(B),* lacrimal vein *(C)* and artery *(D),* as well as in the ophthalmic artery *(E)*. The anterior chamber *(ac),* lens *(l),* and vitreous chambers *(vc)* are again noted. Different parts of the eye can be examined by having the patient move the eye as instructed. *(Courtesy Faridali Ramji, MD.)*

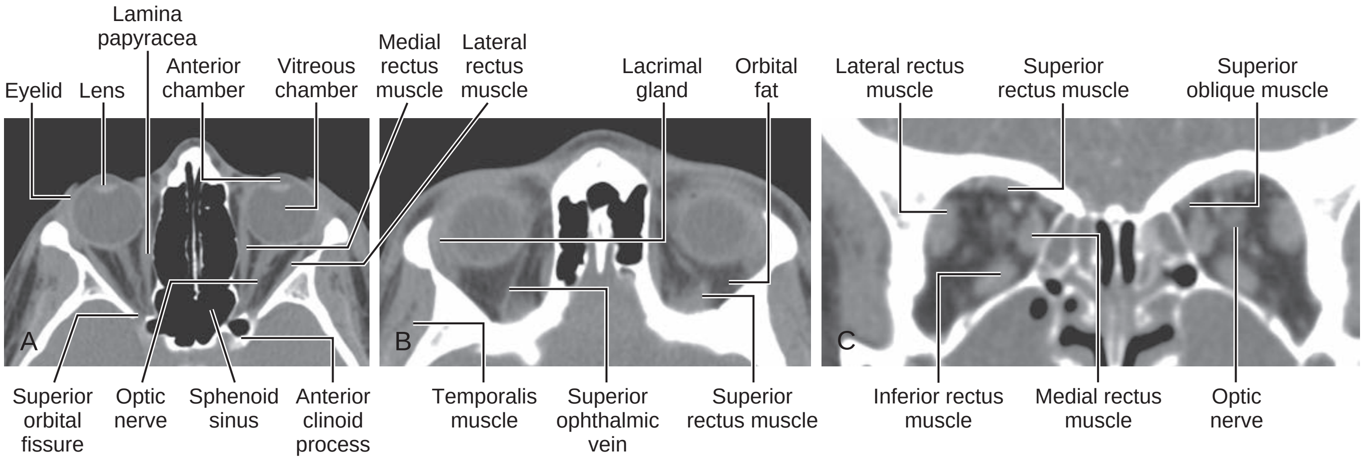

**Figure 4.6. Orbital anatomy on CT.** (A) Axial. (B) Axial more cephalad than A. (C) Coronal (after administration of contrast material).

## Computed Tomography

CT is ideal for showing osseous abnormalities, calcification, and foreign bodies. Excellent anatomic detail is obtained rapidly, with high contrast of orbital tissues. Rapid scan times also decrease the need for sedation in many patients. Common indications include orbital trauma, evaluation of orbital cellulitis, and orbital masses. It is also the imaging modality of choice when intraorbital foreign body is suspected.[11] Disadvantages of CT include use of ionizing radiation, limited imaging planes compared with MRI, beam-hardening artifact, and the potential risk from iodinated contrast media.

High-resolution, thin-section scans with a slice thickness of 2 to 3 mm are obtained in the axial planes with subsequent coronal and sagittal reformatted images, which eliminate further radiation to the patient (Fig. 4.6). The axial plane is usually parallel to the

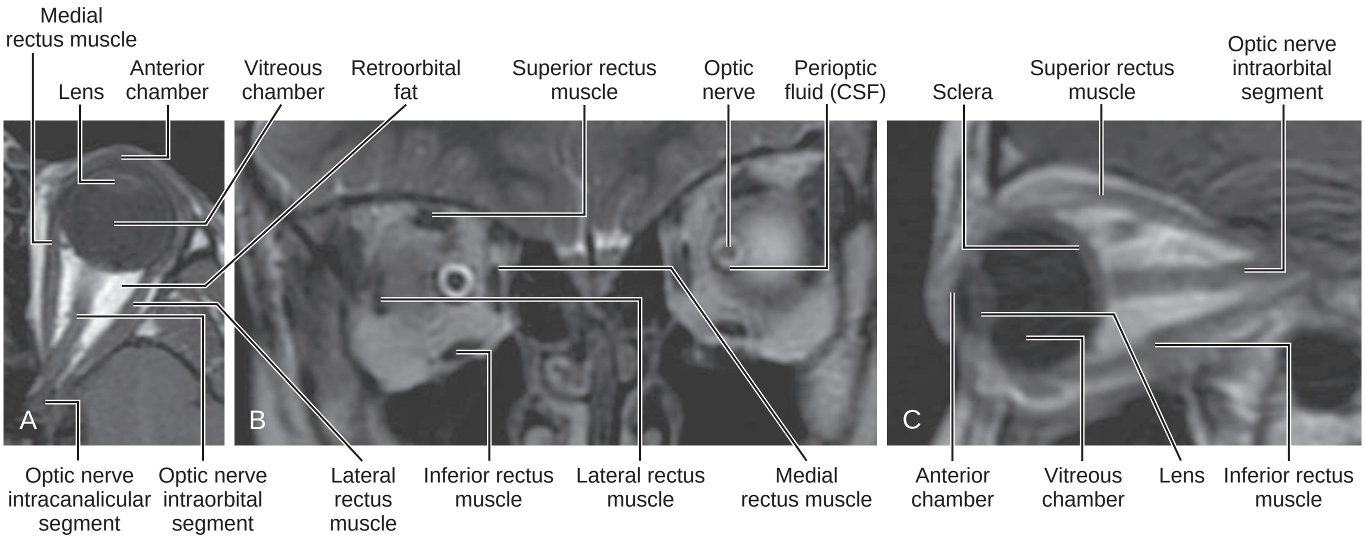

**Figure 4.7. Orbital anatomy on MRI.** (A) Axial T1-weighted image. (B) Coronal T2-weighted image. (C) Sagittal oblique T1-weighted image. *CSF*, Cerebrospinal fluid.

canthomeatal line. Thinner images, especially in the coronal plane, may be obtained when indicated, such as visualization of the orbital floor for a blow-out fracture.

## Magnetic Resonance Imaging

MRI is ideal for imaging the soft tissue abnormalities of the orbit. Orbital MRI involves high-resolution imaging with thin sections (Fig. 4.7); MRI of the brain often is performed concomitantly. Common indications include orbital benign and malignant tumors, infectious or inflammatory etiologies such as optic neuritis, vascular malformations, and congenital anomalies. Although the lack of ionizing radiation is appealing in infants and children, MRI requires a longer scan time than other modalities, and it is less helpful in detecting calcifications, although high-resolution susceptibility weighted imaging could be helpful.

For purely orbital pathology, T1-weighted and fast spin echo (FSE) T2-weighted images with fat saturation or short-tau inversion recovery (STIR) images that suppress the orbital fat are used. Axial and coronal T1-weighted images usually are obtained in an oblique plane parallel to the optic nerve with thin sections with a small field of view (e.g., 20 cm) and a high-resolution matrix (512 × 192). Axial and coronal FSE inversion recovery images are performed through the orbit and chiasm. FIESTA (fast imaging employing steady-state acquisition) and CISS (Constructive Interference Steady State ) are sequences that provides high-resolution images with excellent image contrast and high signal-to- noise ratio. High-resolution 3D FIESTA or CISS images through the orbits can be used to best delineate optic papilla protrusion in cases of increased intracranial pressure. Diffusion weighted imaging (DWI) can help with restricted diffusion seen in epidermoid, tumors with high cellularity, and abscess. Susceptibility weighted images through the orbits can depict retinal hemorrhages in selected cases such as nonaccidental trauma, though gold standard is ophthalmoscopic examination.[12]

Contrast material is administered intravenously for ocular and orbital disease, such as neoplasms, inflammatory and infectious processes, and vascular malformations, with T1-weighted imaging performed with fat saturation in the axial and coronal planes. In some centers, small surface coils are used, which may provide better spatial resolution but are not useful for imaging apical lesions or intracranial disease extension.

Contrast-enhanced MRI of the orbit and brain, using a head coil, is recommended for the evaluation of suspected retinoblastoma, possible subarachnoid seeding of retinoblastoma, and bilateral retinoblastoma. Early detection is made possible for intraocular extension and optic nerve involvement as well as assessment of extraocular and intracranial extension and leptomeningeal spread.[14]

### KEY POINTS

- The globe reaches its full size by 13 years.
- The orbital septum divides the orbit into an anterior preseptal space and a deeper postseptal space.
- CT is used in acute setting for indications such as trauma, orbital cellulitis, and suspected intraorbital foreign body, and provides the best images of the bony orbit.
- MRI is the modality of choice for demonstrating the soft tissues and adjacent intracranial structures.

### SUGGESTED READINGS

Burns NS, Iyer RS, Robinson AJ, et al. Diagnostic imaging of fetal and pediatric orbital abnormalities. *AJR Am J Roentgenol*. 2013;201(6):W797–W808.
Mafee MF, Karimi A, Shah J, et al. Anatomy and pathology of the eye: role of MR imaging and CT. *Neuroimaging Clin N Am*. 2005;15:23–47.
Ramji FG, Slovis TJ, Baker JD. Orbital sonography in children. *Pediatr Radiol*. 1996;26:245–258.

### REFERENCES

Full references for this chapter can be found on www.expertconsult.com.

## REFERENCES

1. Ozanics V, Jakobiec FA. Prenatal development of the eye and its adnexa. In: Jakobiec FA, ed. *Ocular Anatomy, Embryology and Teratology*. Philadelphia: Harper and Row; 1982.
2. Smith CG, Gallie BLK, Morin JD. Normal and abnormal development of the eye. In: Cawford JS, Morin JD, eds. *The Eye in Childhood*. New York: Grune and Stratton; 1983.
3. Torczynski E. Normal development of the eye and orbit before birth: the development of the eye. In: Isenberg SJ, ed. *The Eye in Infancy*. Chicago: Year Book Medical; 1989.
4. Bilaniuk LT, Farber M. Imaging of developmental anomalies of the eye and the orbit. *AJNR Am J Neuroradiol*. 1992;13:793–803.
5. Tortori-Donato P, Rossi A, Biancheri R. The orbit. In: Totori-Donato P, Rossi A, eds. *Pediatric Neuroradiology*. Heidelberg: Springer-Verlag; 2005.
6. Sadler TW. Eye. In: Sadler TW, ed. *Langman's Medical Embryology*. 12th ed. Philadelphia: Lippincott Williams & Wilkins; 2012.
7. Mafee MF. Eye and orbit. In: Mafee MF, Valvassori GE, Becker M, eds. *Imaging of the Head and Neck*. 2nd ed. New York: Thieme; 2005.
8. Hoar RM. Embryology of the eye. *Environ Health Perspect*. 1982;44:31–34.
9. Shofty B, Ben-Sira L, Constantini S, et al. Optic nerve sheath diameter on MR imaging: establishment of norms and comparison of pediatric patients with idiopathic intracranial hypertension with healthy controls. *AJNR Am J Neuroradiol*. 2012;33:366–369.
10. Ramji FG, Slovis TJ, Baker JD. Orbital sonography in children. *Pediatr Radiol*. 1996;26:245–258.
11. Sung EK, Nadgir RN, Fujita A, et al. Injuries of the globe: what can the radiologist offer? *Radiographics*. 2014;34(3):764–776.
12. Kaufman IM, Mafee ME, Song CD. Retinoblastoma and simulations lesion: role of CT, MR imaging, and use of GD-DTPA contrast enhancement. *Radiol Clin North Am*. 1998;36:1101–1117.
13. Zuccoli G, Panigrahy A, Haldipur A, et al. Susceptibility weighted imaging depicts retinal hemorrhages in abusive head trauma. *Neuroradiology*. 2013;55(7):889–893. doi:10.1007/s00234.013-1180-7.
14. Rauschecker AM, Patel CV, Yeom KW, et al. High-resolution MR imaging of the orbit in patients with retinoblastoma. *Radiographics*. 2012;32(5):1307–1326.

# 5

# Prenatal, Congenital, and Neonatal Abnormalities

*Ashley James Robinson, Angela Byrne, and Susan Blaser*

Assessment of the orbits is part of a detailed fetal sonographic or magnetic resonance imaging (MRI) scan, particularly in the setting of suspected central nervous system malformation. When further assessment is performed by fetal MRI, obvious ocular pathologies can be missed, particularly if they are bilateral and symmetric. Diagnoses can be further honed or even altered completely when a coexisting ocular pathology is found.

Ocular evaluation comprises assessment for the presence or absence of eyes, the morphology of the lens and vitreous, and ocular biometry.[1]

## PRESENCE OR ABSENCE OF THE EYES

### Anophthalmia and Microphthalmia

The only way that anophthalmia and microphthalmia truly can be differentiated is pathologically, with anophthalmia being complete absence of the globe but the presence of the ocular adnexa (i.e., eyelids, conjunctiva, and lacrimal apparatus).

#### Primary Anophthalmia

With primary anophthalmia, ocular tissue in the orbit is completely absent because no development of the eyes has occurred. Primary anophthalmia usually is associated with chromosomal abnormalities such as trisomy 13 or genetic syndromes such as CHARGE syndrome, incontinentia pigmenti, Norrie disease, *SOX2*-related eye disorders, Walker-Warburg syndrome, and oculo-auriculo-vertebral spectrum.[2-7]

#### Secondary Anophthalmia

Loss of ocular tissue caused by an insult during development results in secondary anophthalmia. Etiologies include infection (e.g., rubella), a vascular event (e.g., Goldenhar syndrome), or a toxic or metabolic event (e.g., low or high vitamin A levels). The ocular diameter is below the fifth percentile.[8]

Matthew-Wood syndrome (also known as Spear syndrome, PMD, or PDAC syndrome) is composed of pulmonary hypoplasia/agenesis, diaphragmatic hernia/eventration, anophthalmia/microphthalmia, and cardiac defect.[9] In a case of congenital diaphragmatic hernia, associated abnormal orbital morphology and biometry and cardiac anomalies can allow this diagnosis to be made antenatally (e-Fig. 5.1).

Walker-Warburg syndrome, a type of congenital muscular dystrophy, also can be diagnosed antenatally through the association of Dandy-Walker spectrum, along with a Z-shaped brainstem on midline sagittal MRI views, an occipital cephalocele, and ocular asymmetry (Fig. 5.2 and e-Fig. 5.3).

Aicardi syndrome is a rare genetic malformation syndrome that can be diagnosed antenatally by the association of partial or complete absence of the corpus callosum, ocular abnormalities, and a posterior fossa cyst. Aicardi syndrome is thought to be caused by a defect on the X chromosome because it has only been seen in girls and in boys with Klinefelter syndrome (Fig. 5.4 and e-Fig. 5.5).

## MORPHOLOGY OF THE LENS AND VITREOUS

On ultrasound examination, the lens and vitreous are equally hypoechoic; however, the outline of the lens can be seen as a thin hyperechoic ovoid anteriorly within the globe. Typically, however, the only reflection from the lens is from the surfaces perpendicular to the insonating beam, and it can be difficult to see (Fig. 5.6).

On T2-weighted MRI, the entire lens has a low signal compared with the high signal of the vitreous (Fig. 5.7). By endovaginal ultrasound, the lens is visible by 14 weeks as a thin echogenic rim with an anechoic center. The hyaloid artery can be seen as an echogenic line bisecting the vitreous, which, during conversion of the primary vitreous to mature secondary vitreous, gradually becomes beaded as it involutes, a process that should be completed by 30 weeks of menstrual age.[10,11] The remnant channel through the vitreous is known as the Cloquet canal. On MRI, nonspherical globe morphology can be normal up to 29 weeks.[12]

### Persistent Hyperplastic Primary Vitreous

Failure of involution of the hyaloid artery results in a spectrum of abnormalities known as persistent hyperplastic primary vitreous, which is seen frequently with trisomy syndromes and other forms of abnormal brain development.[13,14] It is usually unilateral. Clinically the presentation is variable and includes leukocoria, vitreous hemorrhage, retinal detachment, microphthalmos, and lens opacification.

The diagnosis can be made antenatally or by ultrasound, computed tomography (CT), or MRI postnatally. Ultrasound can detect the hyaloid vessel. A cone-shaped retrolental density is the characteristic finding on CT and MRI. CT findings include a small irregular lens with a shallow anterior chamber; intravitreal densities of variable shape, suggesting the persistence of fetal tissue in the Cloquet canal; and enhancement of abnormal intravitreal tissue after intravenous administration of contrast media. On MRI the appearance is that of low-signal-intensity linear plaques extending from the posterior part of the lens to the optic nerve head. Calcification is unusual (Fig. 5.8 and e-Fig. 5.9).

### Cataracts

Cataracts are seen in a variety of metabolic, infectious, genetic, and chromosomal abnormalities that affect the fetus, including toxoplasmosis; x-irradiation; in vitro fertilization; persistent hyperplastic primary vitreous; PHACE, Nance-Horan, Adams-Oliver, Walker-Warburg, and Neu-Laxova syndromes; rhizomelic chondrodysplasia punctata; trisomy 17 mosaicism; and trisomy 21 (Fig. 5.10).[5,15-26]

### Optic Nerve Hypoplasia

Optic nerve hypoplasia is usually sporadic and difficult to detect prenatally; however, it has a number of associations that potentially can be diagnosed prenatally because of associated structural abnormalities, several of which are discussed in this chapter (Box 5.1 and Fig. 5.11).

Septo-optic dysplasia can be extremely difficult to diagnose antenatally and is usually suspected because of the absence of the cavum septi pellucidi. Associated optic nerve hypoplasia potentially can be detected by measurement of the transverse diameter of the optic chiasm, the normal growth of which has been described by ultrasound[27-29] and can, with some difficulty, be assessed by MRI.[30]

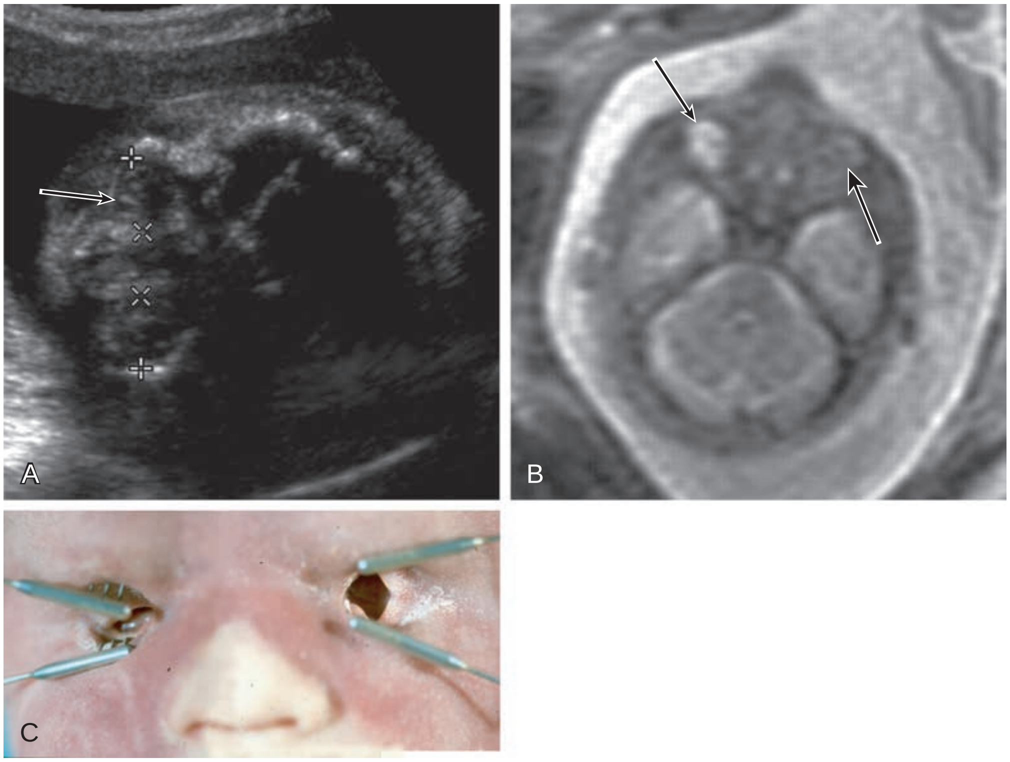

**e-Figure 5.1. Matthew-Wood syndrome.** (A) Fetal ultrasonography showed that biometry was delayed and the lens and globe have an abnormal appearance, appearing echogenic *(arrow).* (B) Fetal MRI shows apparent anophthalmia *(large arrow)* and microphthalmia *(small arrow).* (C) A postmortem examination reveals that the globes are absent. *(From Robinson AJ, Blaser S, Toi A, et al. Magnetic resonance imaging of the fetal eyes—morphologic and biometric assessment for abnormal development with ultrasonographic and clinicopathologic correlation.* Pediatr Radiol. *2008;38:971–981.)*

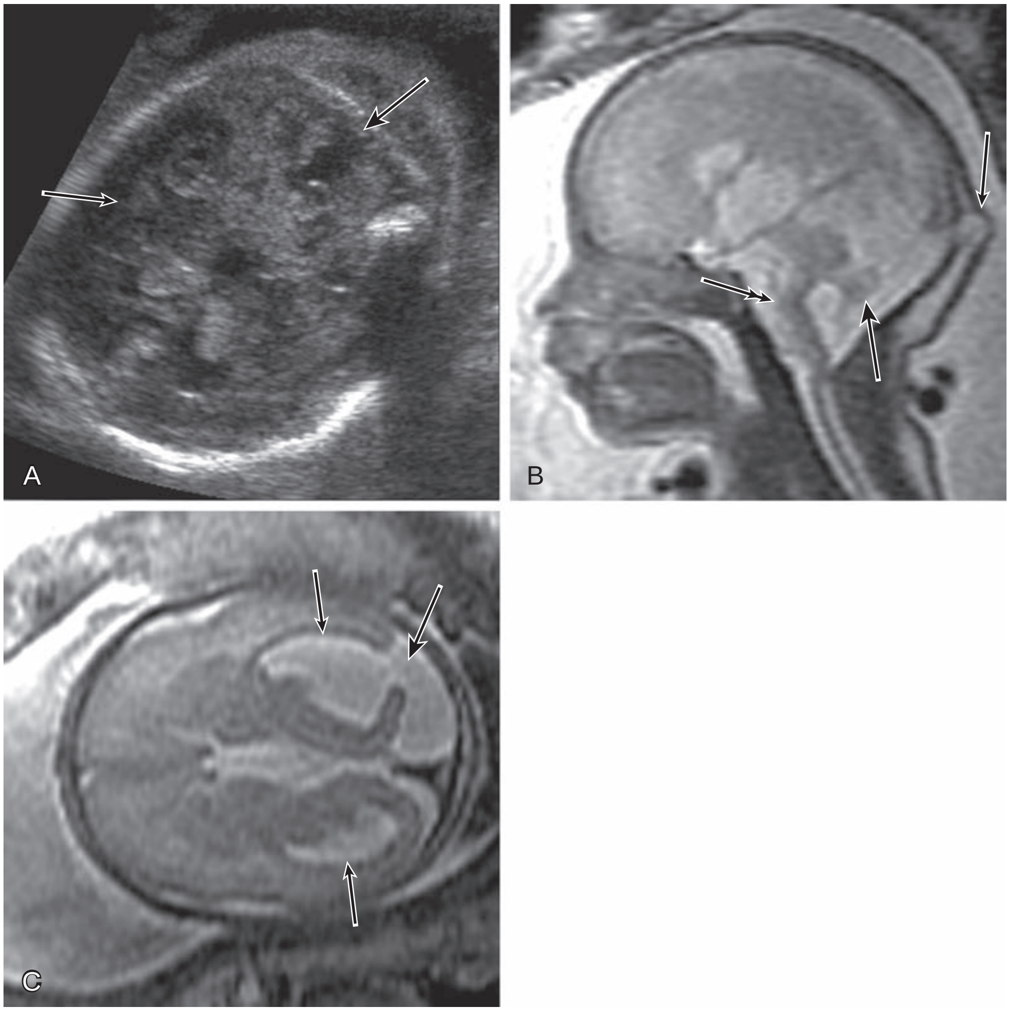

**e-Figure 5.3. Walker-Warburg syndrome.** (A) Prenatal ultrasound shows a defect in the cerebellar vermis *(arrows).* (B) Sagittal fetal MRI shows a Z-shaped brainstem *(double arrow),* a small vermis *(large arrow),* and an occipital cephalocele *(small arrow).* (C) Axial fetal MRI shows asymmetric ventriculomegaly *(small arrows)* plus a cortical defect *(large arrow).*

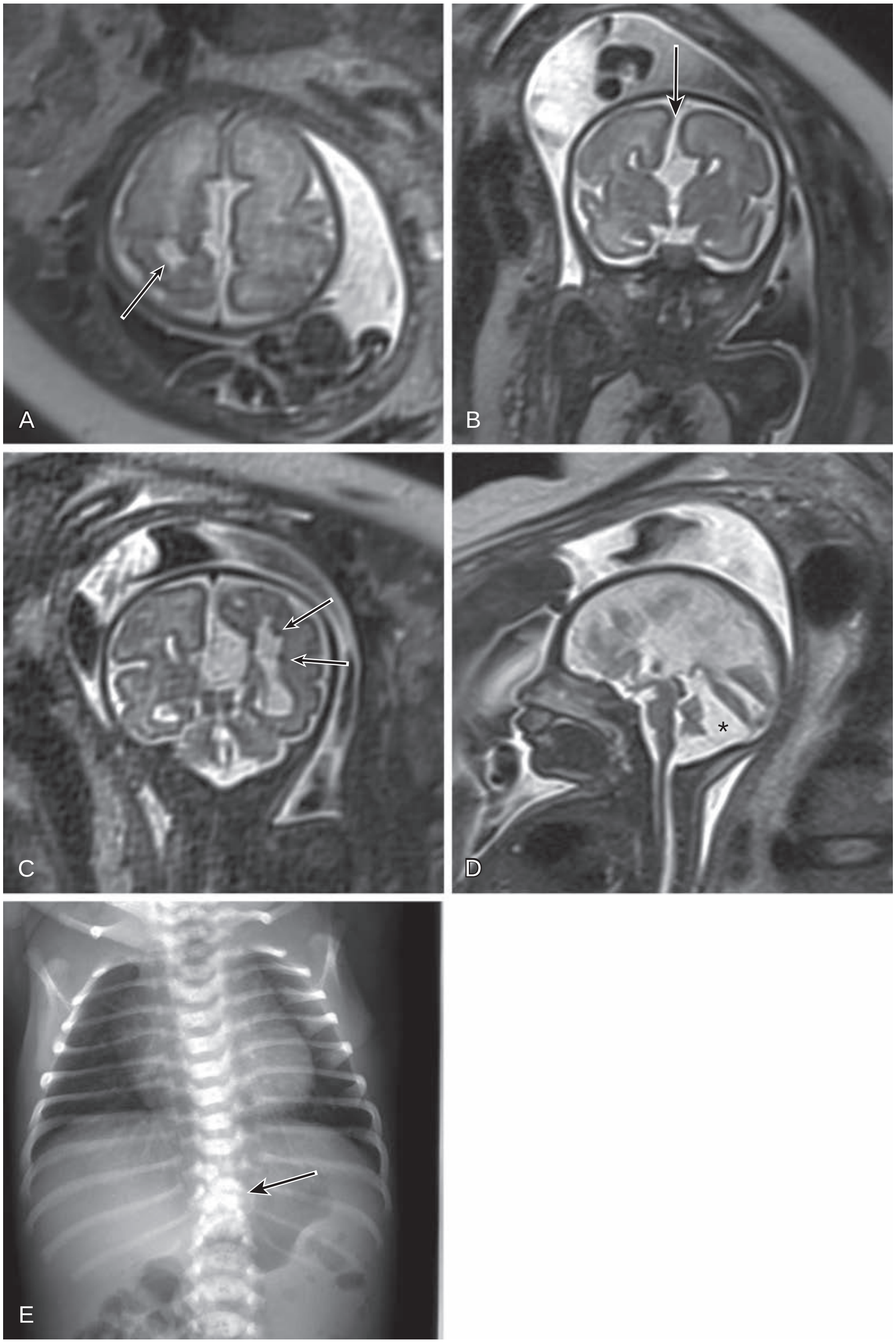

**e-Figure 5.5. Aicardi syndrome.** (A) Axial fetal MRI shows a porencephalic cyst *(arrow).* (B) Coronal fetal MRI shows callosal dysgenesis with a "high-riding" third ventricle continuous with an interhemispheric fissure *(arrow).* (C) Coronal fetal MRI shows subependymal heterotopias *(arrows).* (D) Sagittal fetal MRI shows a posterior fossa cyst with abnormal cerebellar vermis. (E) Neonatal chest radiograph shows vertebral segmentation anomalies *(arrow).*

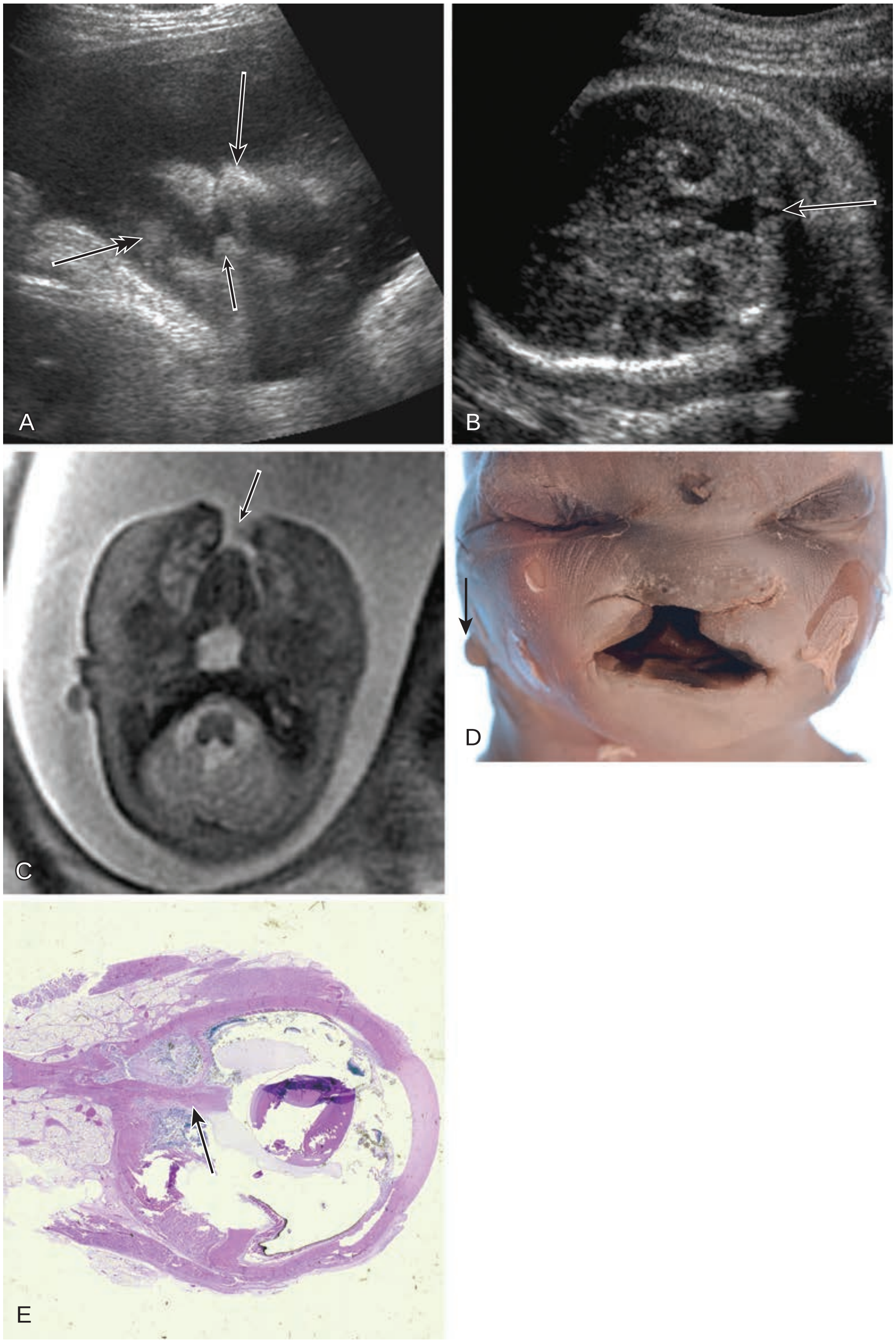

**e-Figure 5.9. Persistent hyperplastic primary vitreous.** (A) Fetal ultrasound shows midline facial clefting including maxillary processes *(small arrow),* the frontonasal process *(large arrow),* and the chin *(double arrow).* (B) Fetal ultrasound shows a vermian defect *(arrow).* (C) Axial fetal MRI confirms midline facial clefting *(arrow).* (D) Gross pathologic specimen demonstrates hypertelorism and additional microtia *(arrow).* (E) Histopathologic specimen confirms persistence of the hyaloid artery *(arrow).* (D, *From Robinson AJ, Blaser S, Toi A, et al. Magnetic resonance imaging of the fetal eyes—morphologic and biometric assessment for abnormal development with ultrasonographic and clinicopathologic correlation.* Pediatr Radiol. *2008;38:971–981.)*

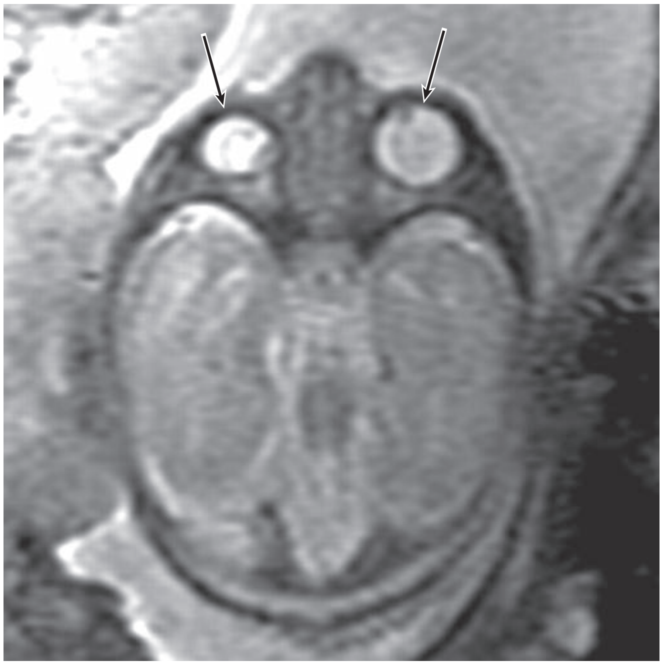

**Figure 5.2. Walker-Warburg syndrome.** Fetal MRI shows asymmetric globes *(arrows). (From Robinson AJ, Blaser S, Toi A, et al. Magnetic resonance imaging of the fetal eyes—morphologic and biometric assessment for abnormal development with ultrasonographic and clinicopathologic correlation.* Pediatr Radiol. *2008;38:971–981.)*

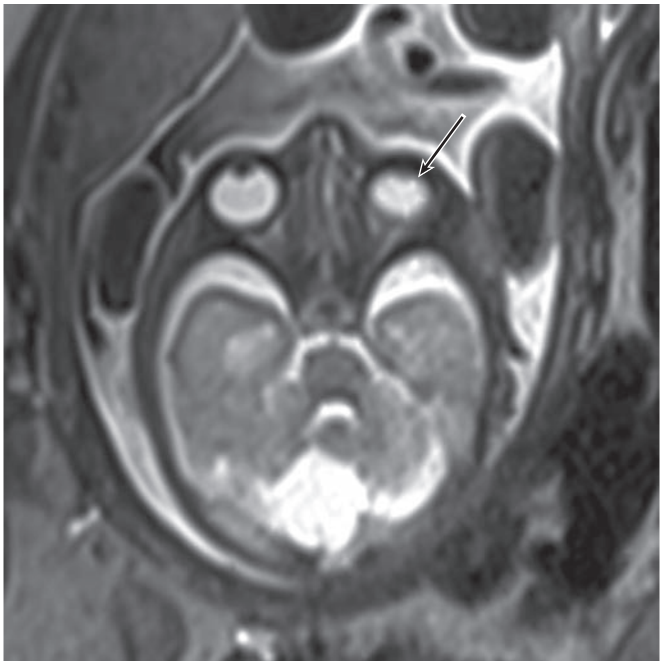

**Figure 5.4. Aicardi syndrome.** Fetal MRI image demonstrates unilateral microphthalmia *(arrow).*

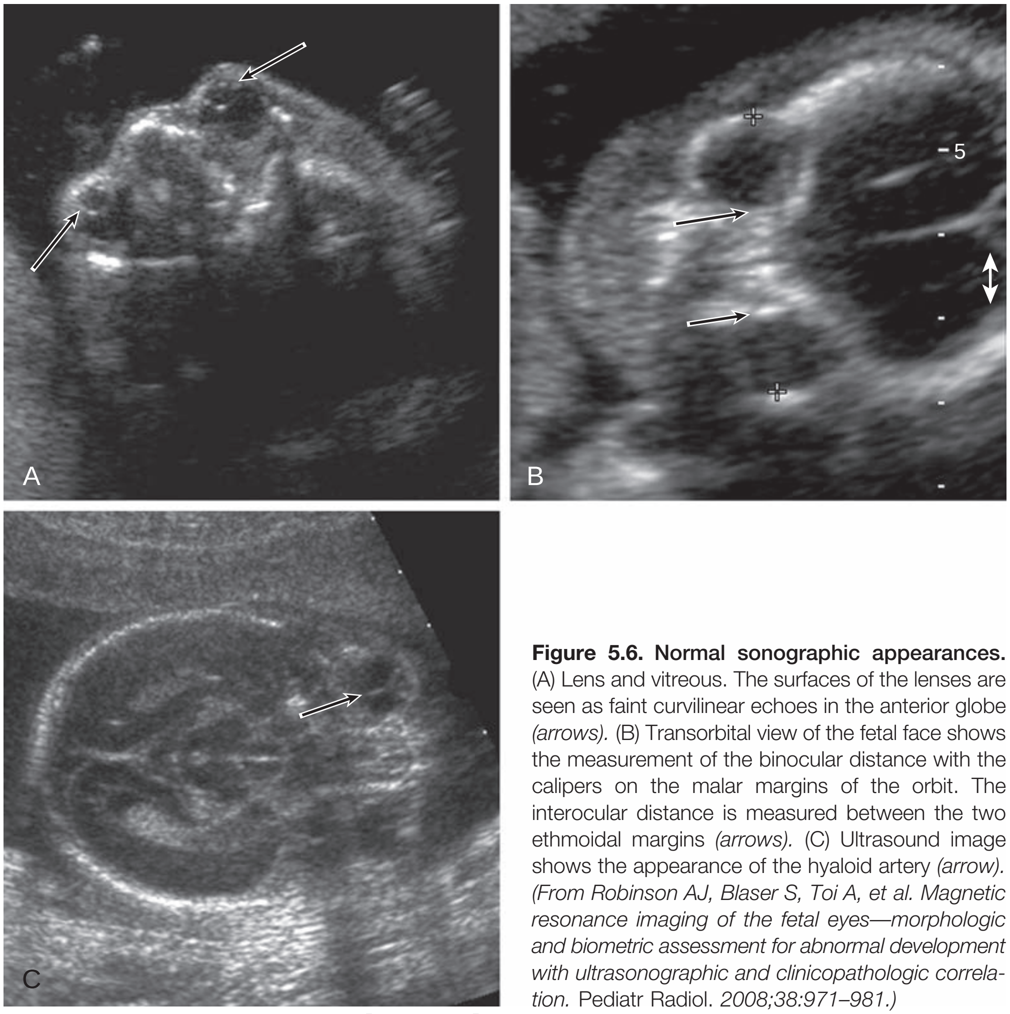

**Figure 5.6. Normal sonographic appearances.** (A) Lens and vitreous. The surfaces of the lenses are seen as faint curvilinear echoes in the anterior globe *(arrows).* (B) Transorbital view of the fetal face shows the measurement of the binocular distance with the calipers on the malar margins of the orbit. The interocular distance is measured between the two ethmoidal margins *(arrows).* (C) Ultrasound image shows the appearance of the hyaloid artery *(arrow). (From Robinson AJ, Blaser S, Toi A, et al. Magnetic resonance imaging of the fetal eyes—morphologic and biometric assessment for abnormal development with ultrasonographic and clinicopathologic correlation.* Pediatr Radiol. *2008;38:971–981.)*

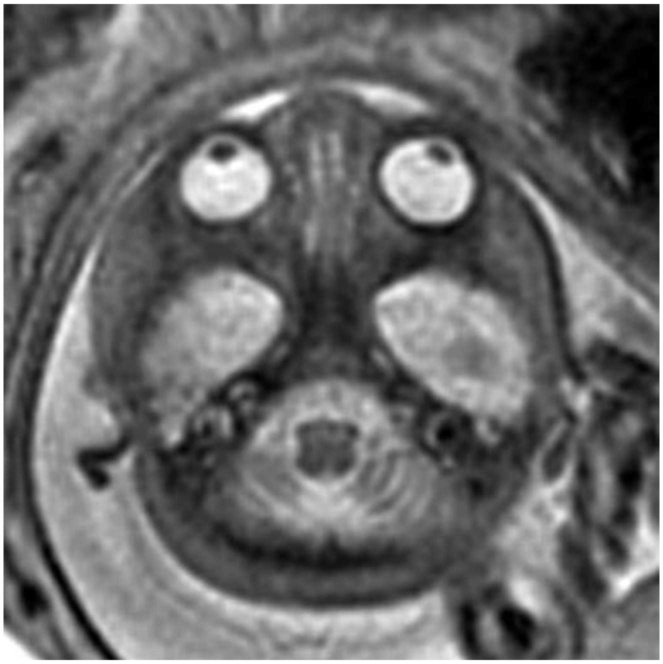

**Figure 5.7. Normal orbits on fetal MRI.** The entire lens has a low signal compared with the high signal of the vitreous. *(From Robinson AJ, Blaser S, Toi A, et al. Magnetic resonance imaging of the fetal eyes—morphologic and biometric assessment for abnormal development with ultrasonographic and clinicopathologic correlation.* Pediatr Radiol. *2008;38:971–981.)*

**BOX 5.1** Associations With Optic Nerve Hypoplasia

Aicardi syndrome
Anticonvulsants
CHARGE association
Chromosome 7(q22–q34) and 7(q32–q34) interstitial duplication
Chromosome 17 interstitial deletion
Congenital muscular dystrophy
Distal 5q deletion syndrome
Dominant inheritance
Duane retraction syndrome
Ethanol toxicity
Frontonasal dysplasia
Goldenhar-Gorlin syndrome
Idiopathic growth hormone deficiency
Isotretinoin toxicity
Jadassohn sebaceous nevus
Maternal diabetes mellitus
Orbital hemangioma
Partial deletion of chromosome 6p
Periventricular leukomalacia
Septo-optic dysplasia
Suprasellar teratoma
Valproic acid toxicity

*Modified from Dutton GN. Congenital disorders of the optic nerve: excavations and hypoplasia.* Eye (Lond). *2004;18:1038–1048.*

## Coloboma, Morning Glory Disc, and Peripapillary Staphyloma

Coloboma, morning glory syndrome, and peripapillary staphyloma are all congenital anomalies that are excavations of the optic disc and can significantly impair visual function.[31]

Coloboma is a unilateral or bilateral congenital condition caused by incomplete closure of the embryonic fissure. Clinical features include visual field defects. On examination, coloboma appears as an enlarged, sharply circumscribed, deeply excavated optic disc, usually occurring inferiorly with increased risk of macular detachment. Other associated ocular findings include microphthalmos with an orbital cyst, a persistent hyaloid artery, and retinal dysplasia. Coloboma also may be part of the CHARGE syndrome (i.e., coloboma, heart defects, choanal atresia, growth retardation, and genital and ear abnormalities), and it may be associated with numerous other syndromes. Coloboma can be detected by fetal MRI (Fig. 5.12).[32]

Morning glory syndrome is a congenital anomaly of the optic disc in which there is a funnel-shaped excavation of the posterior fundus incorporating the optic nerve, surrounded by an elevated annulus of chorioretinal pigment. It is named for the ophthalmoscopic resemblance to the morning glory flower. Morning glory syndrome occurs more frequently in females and presents with poor vision, amblyopia, and strabismus with leukocoria. In the first months of life there is an increased risk of retinal detachment and associated cerebral abnormalities, including moyamoya disease (e-Fig. 5.13).

Staphyloma occurs as a result of weakening of the outer layer of the eye (cornea or sclera) by an inflammatory or degenerative condition and is an abnormal protrusion of uveal tissue caused by sclero-uveal ectasia. It is most commonly unilateral and nonhereditary.

## Coats Disease

Coats disease is a rare, congenital, nonhereditary disorder characterized by retinal telangiectasia resulting in massive intraretinal and subretinal lipid accumulation, exudative retinal detachment, and blindness. It is usually isolated, unilateral, and occurs predominantly in young males, with the onset of symptoms occurring in the first decade of life. It appears as a hyperechoic mass on ultrasound without posterior acoustic shadowing. Vitreous and subretinal hemorrhage may be present. On CT, the globe is hyperdense and enhancement of the subretinal exudate is seen. This exudate is hyperintense on T1- and T2-weighted MRI sequences (Fig. 5.14). It is important to differentiate this entity from retinoblastoma, which usually presents as a calcified mass and may require enucleation of the globe.

## Norrie Disease

Norrie disease is an X-linked recessive disorder caused by mutations in the *NDP* gene that leads to congenital blindness in male infants. The ocular findings are characterized by retinal dysplasia and the development of a white, vascularized, retrolental mass that may lead to phthisis bulbi. Cataracts and leukocoria also may be present. Norrie disease is associated with progressive hearing loss in one-third of patients, and up to 50% of patients have developmental delay, movement disorders, psychotic features, or behavioral problems. CT demonstrates dense vitreous chambers as a result of vitreous or subretinal hemorrhage, microphthalmia, optic nerve atrophy, a retrolental mass, and retinal detachment.

# BIOMETRY

Growth charts for the fetal lens and orbit,[33-35] orbital total axial length (TAL),[36] eye volume,[37] and the measurements of binocular distance (BOD) and interocular distance (IOD) have been determined sonographically.[38-40] The orbits are measured according to the bony landmarks of the medial and lateral orbital walls. The orbital measurements ideally are made in the axial plane, with both orbits of equal and largest possible diameter.[8] The BOD is measured between the two malar margins, and the IOD is measured between the two ethmoidal margins of the bony orbits. These bony landmarks are difficult to see with fetal MRI and therefore standard sonographic growth charts cannot accurately be applied to fetal MRI studies.

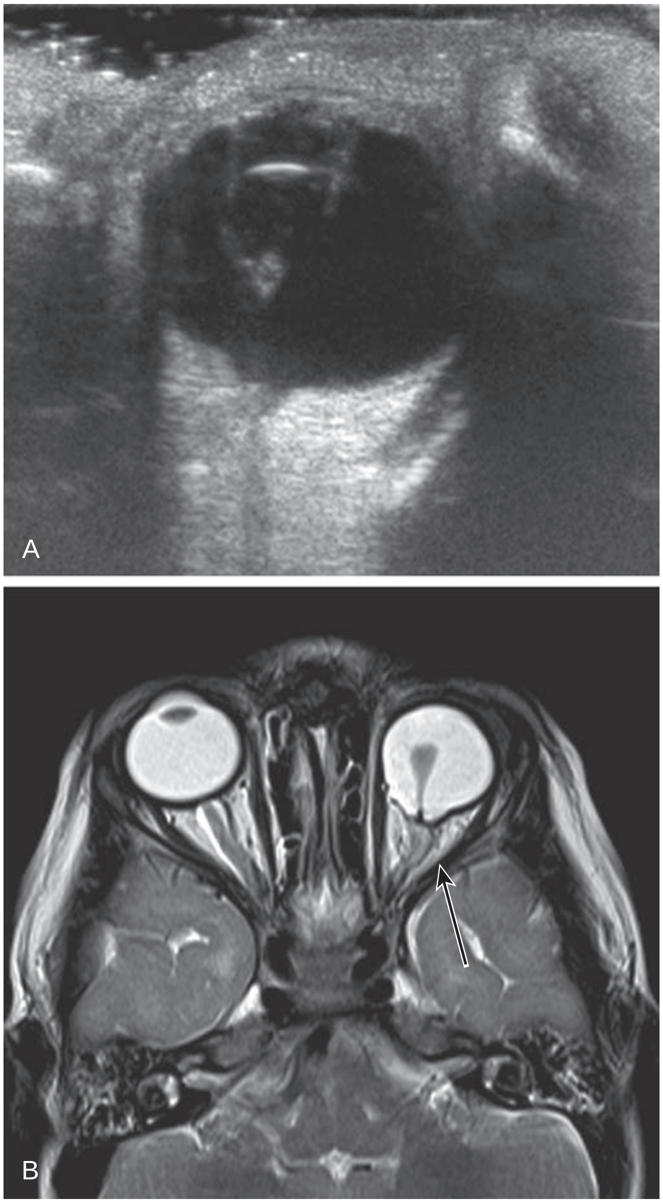

**e-Figure 5.13. Morning glory disc.** (A) Ultrasound of the left eye shows bandlike echogenicity extending to the defect in the retina in a morning glory disc. (B) Axial T2-weighted MRI shows funnel-shaped excavation of the posterior fundus in keeping with a morning glory disc *(arrow).*

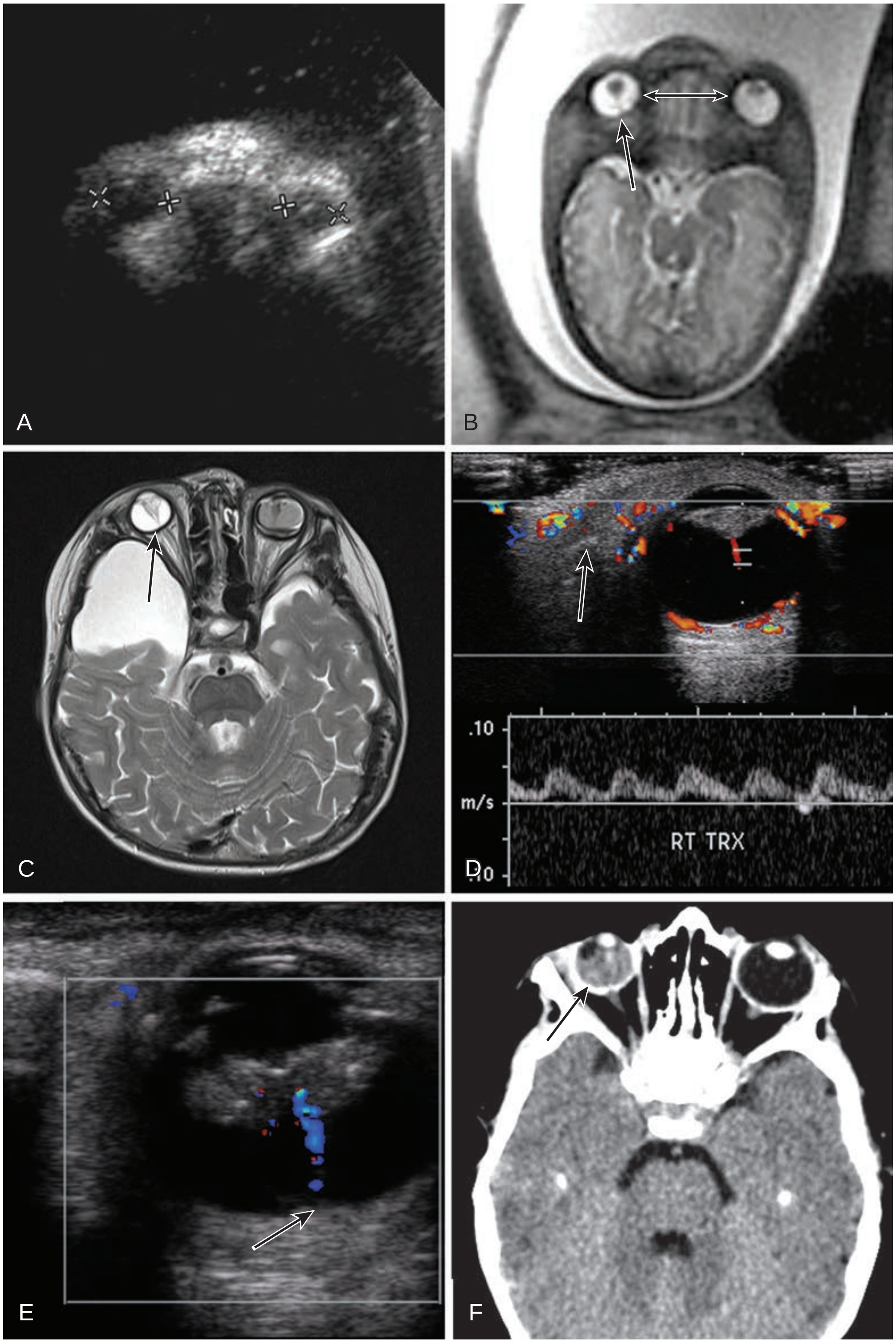

**Figure 5.8. Persistent hyperplastic primary vitreous.** (A) Fetal ultrasonography shows the absence of normal anatomy and ocular hyperechogenicity. (B) Fetal MRI shows hypertelorism *(double-headed arrow)* plus a persistent hyaloid artery *(large arrow)* and a triangular-shaped lens. (C) Postnatal axial T2-weighted MRI demonstrates a low funnel-like signal extending from the right posterior lens to the optic nerve head *(arrow).* A similar low signal is noted on the left with associated vitreous hemorrhage. Note the incidental right middle cranial fossa arachnoid cyst. (D) Doppler ultrasound reveals an arterial waveform within the hyaloid artery *(arrow).* (E) Ultrasound shows thickening of the soft tissues posterior to the lens and a hyaloid vessel *(arrow).* (F) Axial noncontrast CT image shows increased attenuation in the right posterior chamber in keeping with vitreous hemorrhage *(arrow)* with linear high density centrally in persistent hyperplastic primary vitreous.

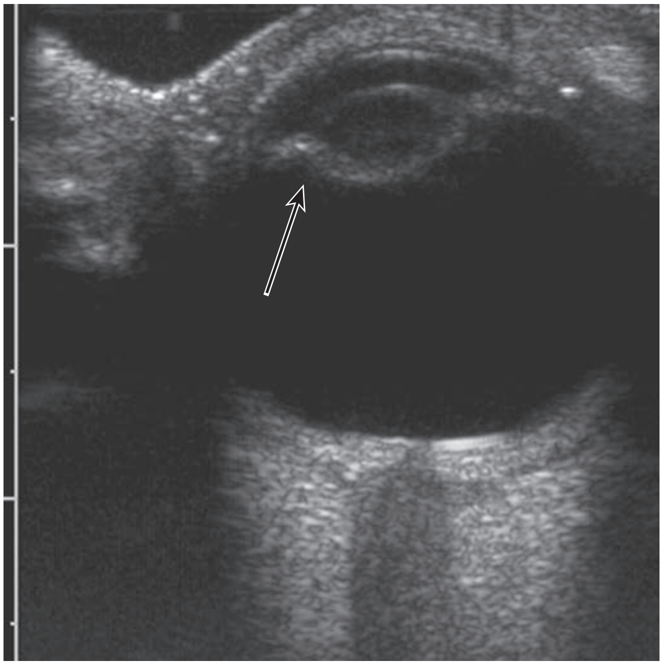

**Figure 5.10. Cataract.** Transverse ultrasound of the left eye shows increased echogenicity of the lens *(arrow)* indicating a cataract.

On MRI the BOD and IOD measurements can be made in any plane from true axial to true coronal, provided both eyes can be seen in the same image and have the most equal and largest possible transverse diameters. The BOD and IOD are respectively measured between the two malar or ethmoidal margins of each vitreous (Fig. 5.15). These measurements can be plotted against gestational age (Table 5.1).[1] Other available nomograms also include orbital volume,[41] measurements of the anteroposterior globe diameter,[42] and the diameter of the lens.[43]

## Hypotelorism

Hypotelorism is defined as an IOD below the fifth percentile.[8]

### Primary

During normal embryologic development, the opening for the eye forms during development of the face, when the paired nasal swellings on either side migrate medially and inferiorly and fuse with the midline frontal swelling to form the nose. Overmigration results in primary hypotelorism; the two halves of the face (and more often than not the underlying halves of the brain) lie too close together ("the face predicts the brain"),[44] and both the BOD and IOD therefore are decreased. This scenario most commonly results in an anomaly within the spectrum of holoprosencephaly,[45] which in around 55% of cases is associated with a variety of chromosomal abnormalities, most commonly trisomy 13 (Fig. 5.16 and e-Fig. 5.17).[38]

### Secondary

Secondary hypotelorism is usually the result of abnormalities of the bony skull, such as microcephaly, plagiocephaly, and metopic synostosis (e-Fig. 5.18).[8]

## Hypertelorism

Hypertelorism is defined as an IOD above the 95th percentile.[8]

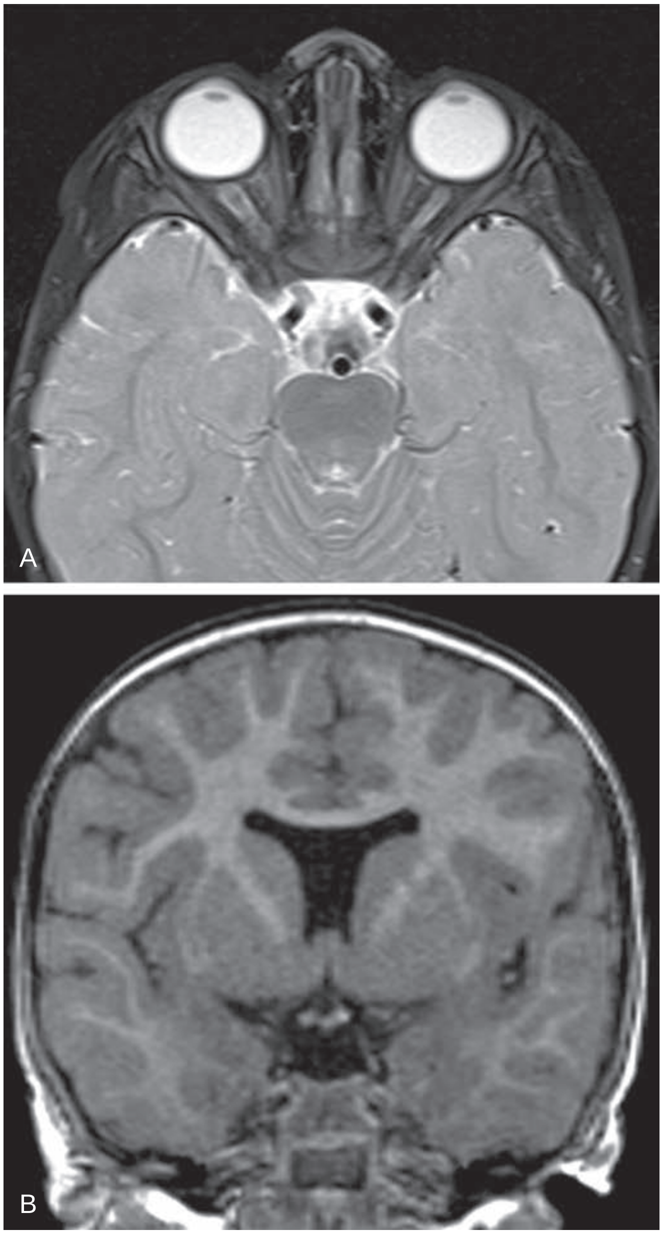

**Figure 5.11. Optic nerve hypoplasia/septo-optic dysplasia.** (A) Axial T2-weighted fat-saturated MRI of the orbits shows bilateral optic nerve hypoplasia. (B) Coronal T1-weighted MRI demonstrates an associated small chiasm and absent cavum septi pellucidi.

### Primary

During fetal development, if the nasal swellings do not migrate medially and inferiorly far enough that they fuse with the midline frontal swelling, the result is primary hypertelorism, in which the two halves of the face (and often the underlying halves of the brain) lie too far apart. Primary hypertelorism can result from many chromosomal anomalies and syndromes,[2] including median facial cleft syndrome, also known as frontonasal dysplasia (Fig. 5.19 and e-Fig. 5.20). This median facial cleft syndrome is composed of hypertelorism, facial clefting, and as a result of the two cerebral hemispheres "being too far apart," callosal agenesis. IOD may be the most reliable means of making the diagnosis of hypertelorism, because by ultrasound this measurement is usually more than 2

*Text continued on p. 36*

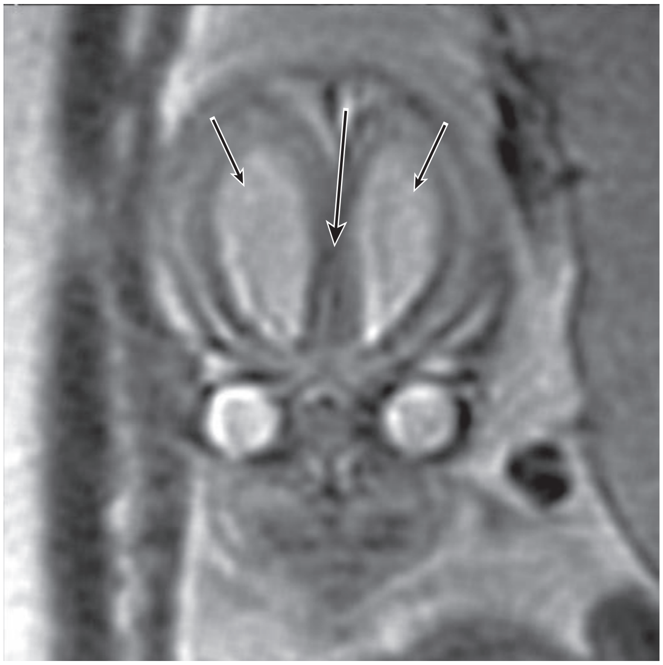

**e-Figure 5.17. Holoprosencephaly.** Coronal fetal MRI shows mild hypotelorism, but not below the 5th percentile. In addition, the cavum septi pellucidi *(large arrow)* and corpus callosum are absent, and ventriculomegaly is present *(small arrows). (From Robinson AJ, Blaser S, Toi A, et al. Magnetic resonance imaging of the fetal eyes—morphologic and biometric assessment for abnormal development with ultrasonographic and clinicopathologic correlation.* Pediatr Radiol. *2008;38:971–981.)*

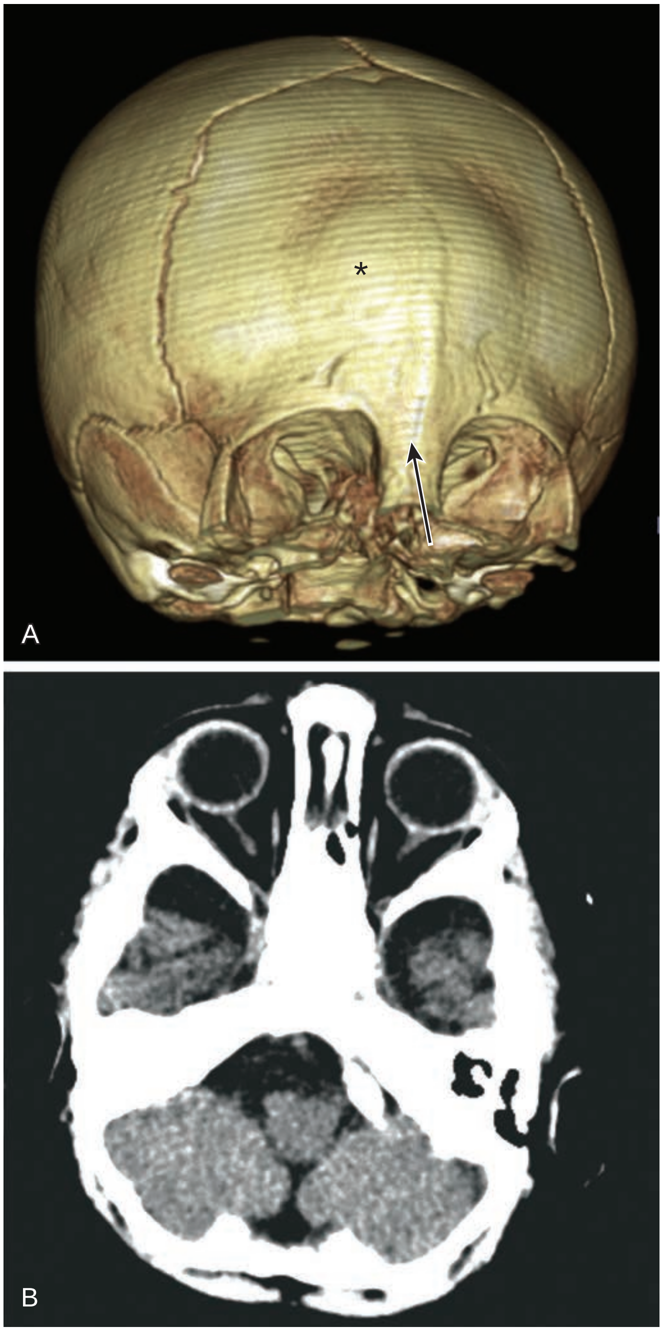

**e-Figure 5.18. Metopic synostosis.** (A) Three-dimensional CT reconstruction of the skull showing metopic synostosis *(arrow)* and associated bowing of the adjacent frontal bone *(asterisk).* (B) Axial CT scan in the same patient shows hypotelorism.

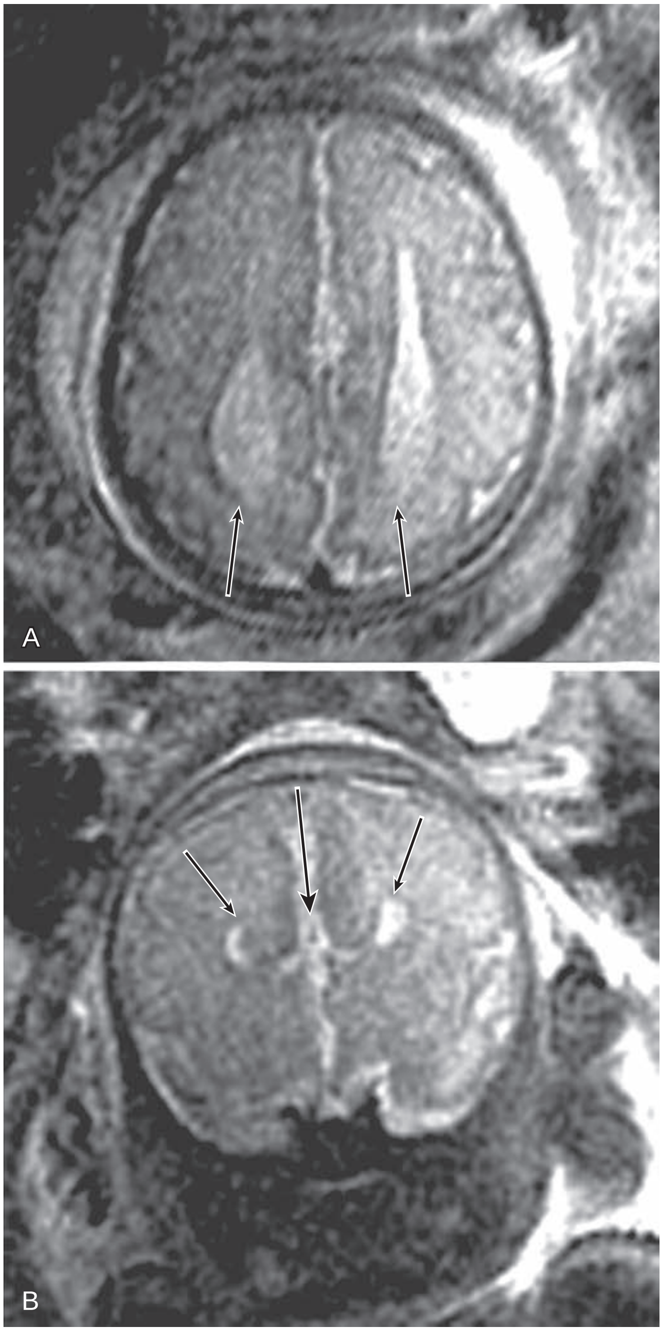

**e-Figure 5.20. Frontonasal dysplasia.** (A) Axial fetal MRI shows colpocephaly *(arrows)*. (B) Coronal fetal MRI shows "longhorn steer" configuration of the lateral ventricles *(small arrows)* and third ventricle continuous with an interhemispheric fissure *(large arrow)*.

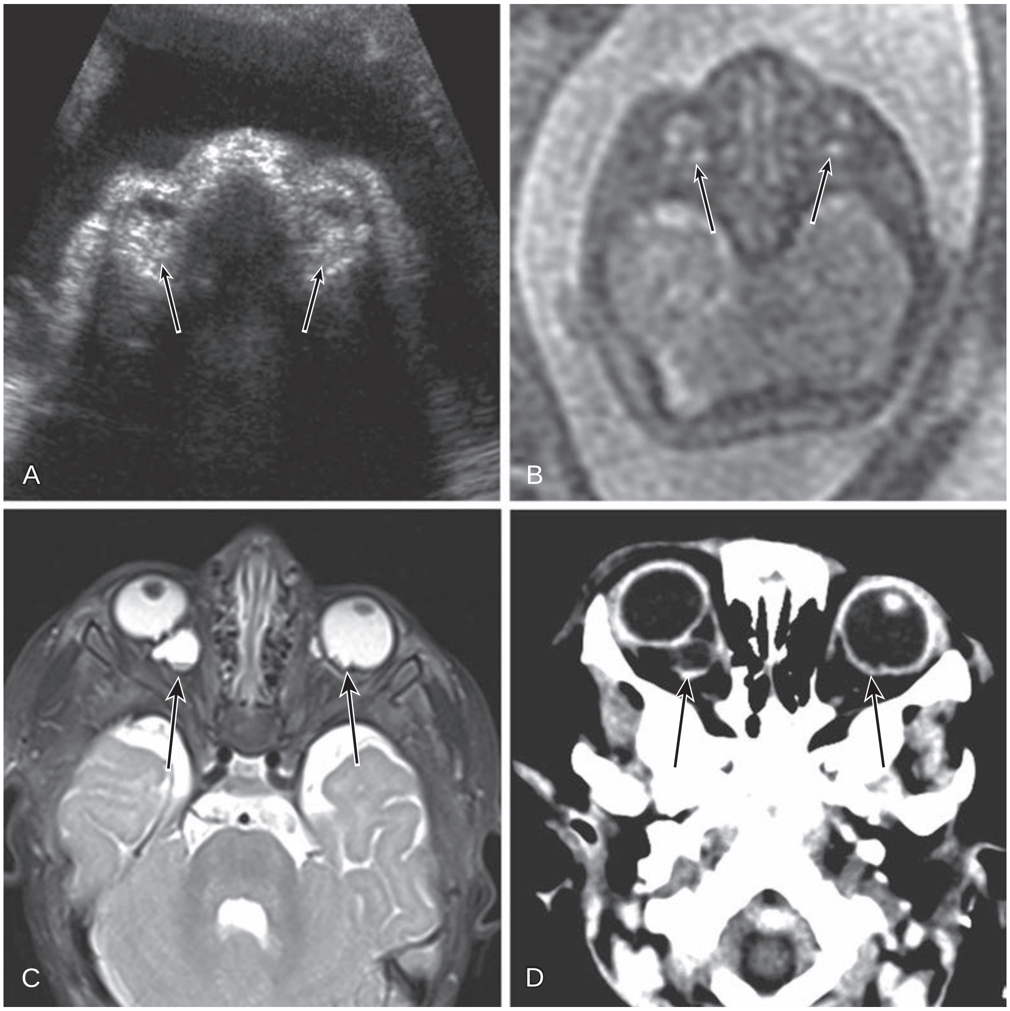

**Figure 5.12. Coloboma.** (A) Prenatal ultrasound image demonstrates abnormal echogenicity of the globes *(arrows),* but the lenses appear relatively normal. (B) Axial fetal MRI shows bilateral, symmetric, abnormal globes with mixed low- and high-signal vitreous *(arrows)* and no definite lens structures. (C) Postnatal axial T2-weighted MRI shows bilateral cystic colobomata *(arrows).* (D) Noncontrast CT image showing cystic coloboma of the posterior right orbit *(arrows). (*B, *From Robinson AJ, Blaser S, Toi A, et al. Magnetic resonance imaging of the fetal eyes—morphologic and biometric assessment for abnormal development with ultrasonographic and clinicopathologic correlation.* Pediatr Radiol. *2008;38:971–981.)*

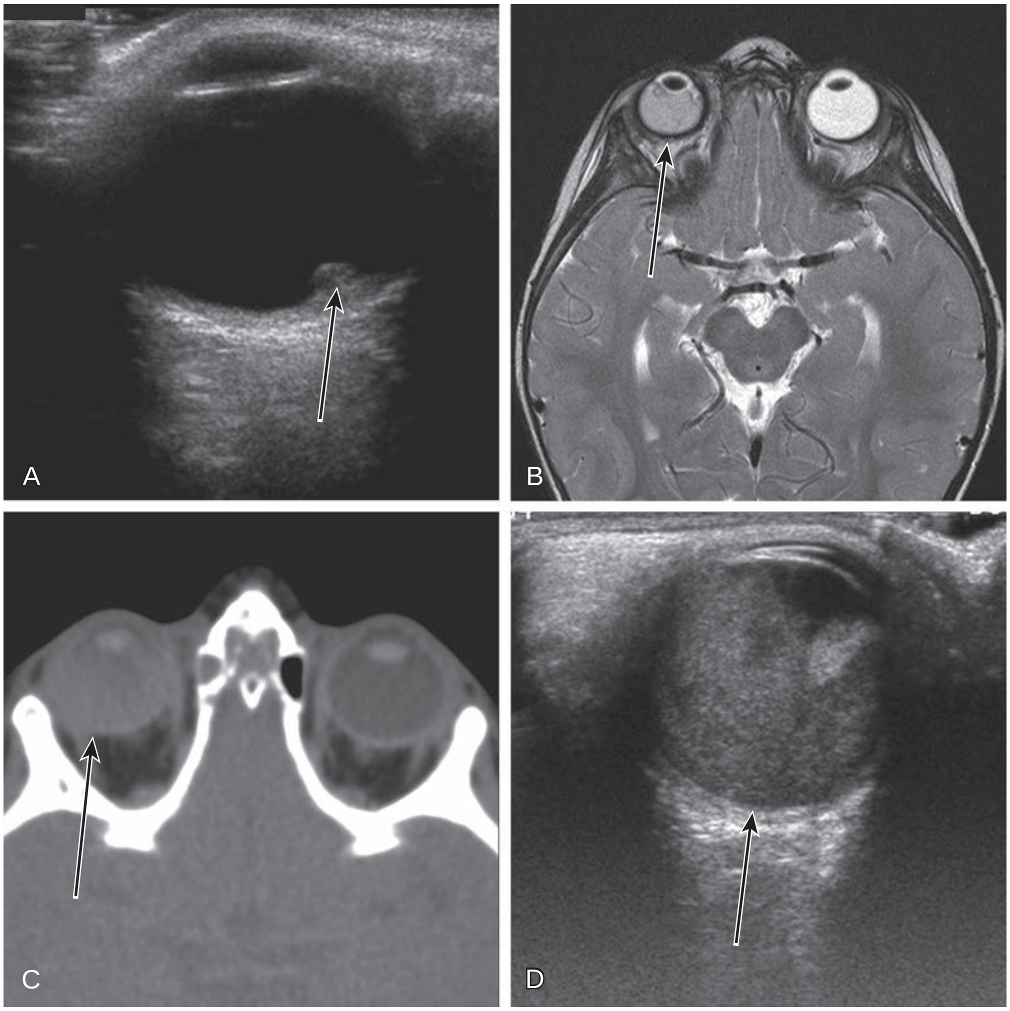

**Figure 5.14. Coats disease.** (A) Ultrasound shows a hyperechoic mass in the posterior vitreous *(arrow)* without posterior acoustic shadowing. (B) Axial T2-weighted MRI shows intermediate signal within the right vitreous *(arrow)* in keeping with proteinaceous exudate. (C) Unenhanced orbital CT demonstrates homogenous hyperattenuation of the right globe *(arrow)* and a normal left globe. (D) Ultrasound of the right eye shows hyperechogenicity within the vitreous *(arrow)* and a more focal area of increased echogenicity anteriorly.

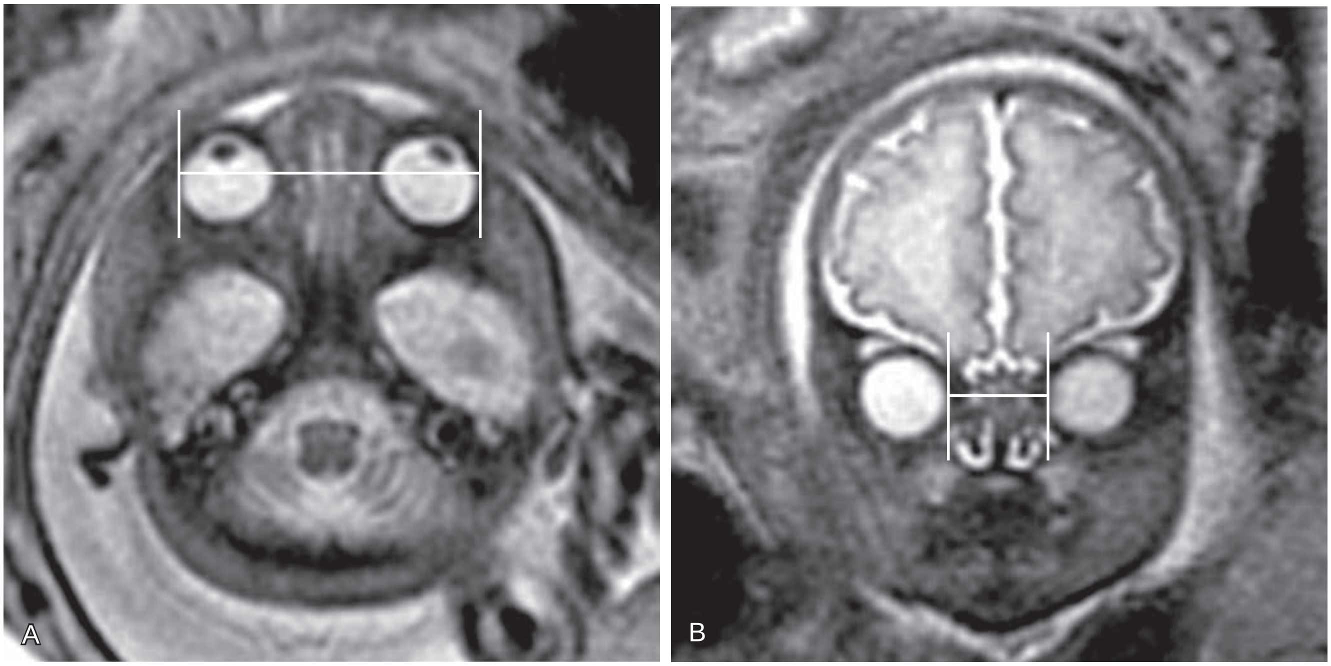

**Figure 5.15. Ocular biometry measurements by MRI.** (A) The binocular distance is measured between the two malar margins of each high-signal vitreous. The measurements can be made in any plane orthogonal to the sagittal plane. (B) The interocular distance is measured in the coronal plane between the two orbital margins of each high-signal vitreous. *(From Robinson AJ, Blaser S, Toi A, et al. Magnetic resonance imaging of the fetal eyes—morphologic and biometric assessment for abnormal development with ultrasonographic and clinicopathologic correlation.* Pediatr Radiol. *2008;38:971–981.)*

**TABLE 5.1** Fetal Magnetic Resonance Imaging Measurements of Binocular Distance, Interocular Distance, and Ocular Diameter in Relation to Gestational Age

| | **BOD** | | | **IOD** | | | **OD** | | |
|---|---|---|---|---|---|---|---|---|---|
| **GA** | **5% CI** | **50% CI** | **95% CI** | **5% CI** | **50% CI** | **95% CI** | **5% CI** | **50% CI** | **95% CI** |
| 15 | 16.6 | 20.8 | 21.4 | 7.4 | 9.8 | 12.3 | 3.4 | 5.5 | 6.4 |
| 16 | 19.0 | 22.8 | 24.0 | 8.2 | 10.6 | 13.3 | 4.2 | 6.1 | 7.1 |
| 17 | 21.3 | 24.8 | 26.5 | 9.0 | 11.4 | 14.3 | 5.0 | 6.7 | 7.9 |
| 18 | 23.4 | 26.8 | 28.9 | 9.7 | 12.1 | 15.2 | 5.7 | 7.3 | 8.5 |
| 19 | 25.4 | 28.7 | 31.1 | 10.4 | 12.9 | 16.1 | 6.4 | 7.9 | 9.2 |
| 20 | 27.3 | 30.5 | 33.2 | 11.1 | 13.6 | 16.9 | 7.0 | 8.5 | 9.8 |
| 21 | 29.1 | 32.3 | 35.2 | 11.7 | 14.3 | 17.6 | 7.6 | 9.0 | 10.4 |
| 22 | 30.8 | 34.1 | 37.1 | 12.3 | 14.9 | 18.4 | 8.2 | 9.6 | 10.9 |
| 23 | 32.4 | 35.8 | 38.9 | 12.8 | 15.6 | 19.1 | 8.8 | 10.1 | 11.4 |
| 24 | 34.0 | 37.4 | 40.7 | 13.4 | 16.2 | 19.8 | 9.3 | 10.6 | 11.9 |
| 25 | 35.5 | 39.0 | 42.4 | 13.9 | 16.8 | 20.4 | 9.8 | 11.1 | 12.4 |
| 26 | 37.0 | 40.6 | 44.0 | 14.4 | 17.4 | 21.0 | 10.3 | 11.6 | 12.9 |
| 27 | 38.4 | 42.1 | 45.5 | 14.9 | 17.9 | 21.6 | 10.8 | 12.0 | 13.3 |
| 28 | 39.7 | 43.5 | 47.0 | 15.3 | 18.5 | 22.2 | 11.3 | 12.5 | 13.8 |
| 29 | 41.0 | 44.9 | 48.5 | 15.8 | 19.0 | 22.8 | 11.7 | 12.9 | 14.2 |
| 30 | 42.3 | 46.3 | 49.9 | 16.2 | 19.5 | 23.3 | 12.1 | 13.4 | 14.6 |
| 31 | 43.5 | 47.6 | 51.2 | 16.6 | 19.9 | 23.8 | 12.5 | 13.8 | 15.0 |
| 32 | 44.6 | 48.8 | 52.5 | 17.0 | 20.4 | 24.3 | 12.9 | 14.2 | 15.4 |
| 33 | 45.8 | 50.0 | 53.8 | 17.4 | 20.8 | 24.8 | 13.3 | 14.6 | 15.7 |
| 34 | 46.9 | 51.2 | 55.0 | 17.8 | 21.2 | 25.3 | 13.7 | 15.0 | 16.1 |
| 35 | 48.0 | 52.3 | 56.2 | 18.2 | 21.5 | 25.7 | 14.1 | 15.3 | 16.4 |
| 36 | 49.0 | 53.3 | 57.3 | 18.5 | 21.9 | 26.2 | 14.4 | 15.7 | 16.7 |
| 37 | 50.0 | 54.4 | 58.5 | 18.9 | 22.2 | 26.6 | 14.8 | 16.0 | 17.1 |
| 38 | 51.0 | 55.3 | 59.6 | 19.2 | 22.5 | 27.0 | 15.1 | 16.3 | 17.4 |
| 39 | 52.0 | 56.2 | 60.6 | 19.5 | 22.7 | 27.4 | 15.4 | 16.6 | 17.7 |
| 40 | 52.9 | 57.1 | 61.7 | 19.9 | 23.0 | 27.8 | 15.8 | 16.9 | 18.0 |

*BOD,* Binocular distance; *CI,* confidence interval; *GA,* gestational age; *IOD,* interocular distance; *OD,* ocular diameter.

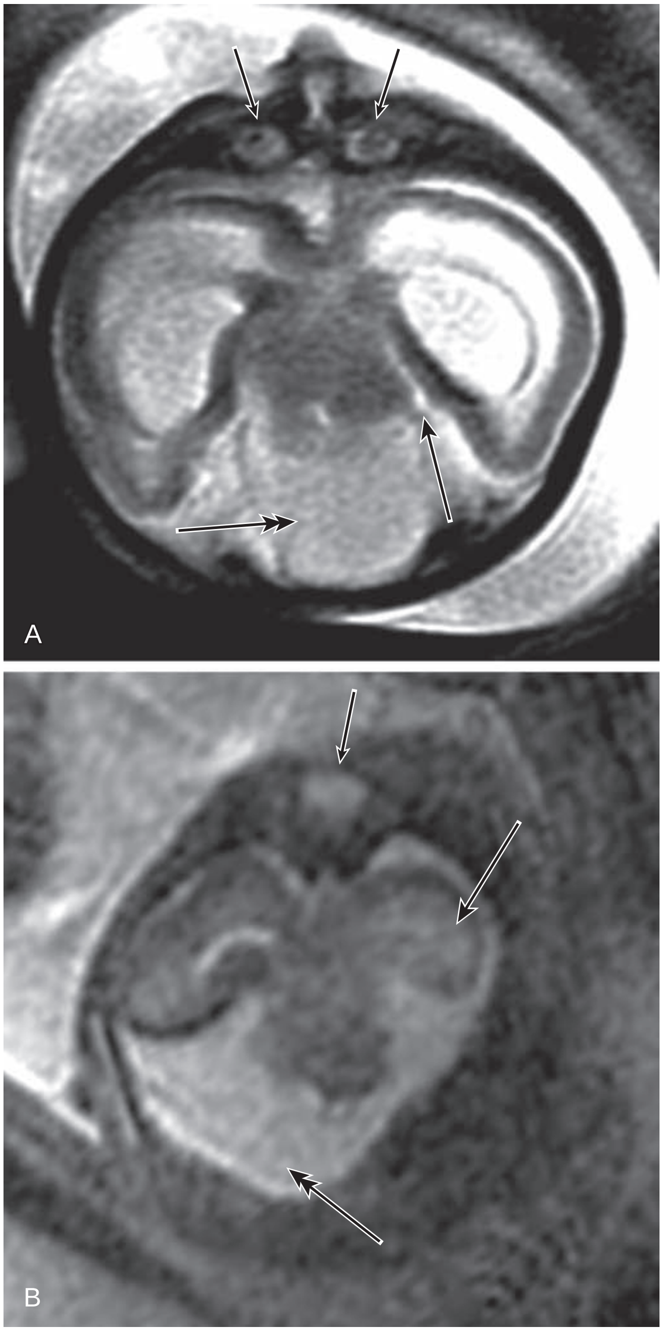

**Figure 5.16. Holoprosencephaly.** (A) Axial fetal MRI shows severe hypotelorism and microphthalmia *(small arrows).* A dorsal interhemispheric cyst is present *(double arrow),* and the hippocampus touches the brainstem at the ambient cistern *(long arrow)* in keeping with lobar holoprosencephaly. (B) Axial fetal MRI shows a single small midline globe *(small arrow).* The hippocampus is not touching the brainstem *(long arrow),* and wide communication of the ambient cistern with the dorsal interhemispheric cyst is present *(double arrow)* in keeping with alobar holoprosencephaly. *(From Robinson AJ, Blaser S, Toi A, et al. Magnetic resonance imaging of the fetal eyes—morphologic and biometric assessment for abnormal development with ultrasonographic and clinicopathologic correlation.* Pediatr Radiol. *2008;38:971–981.)*

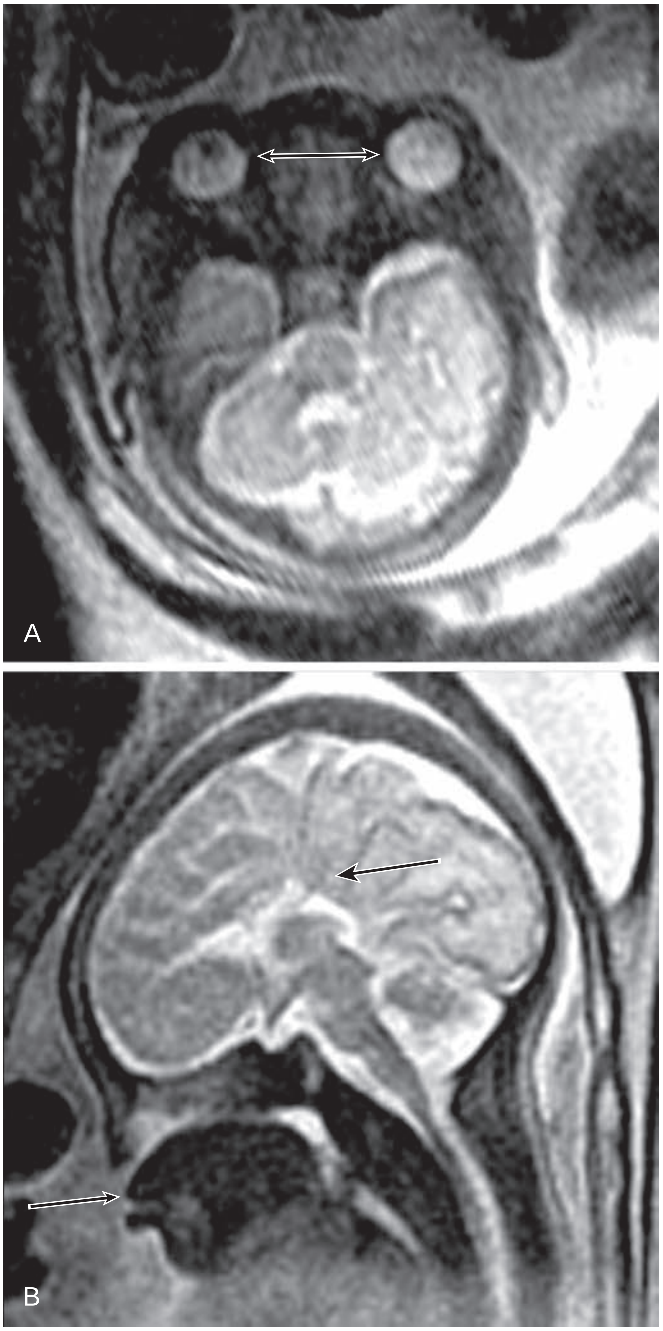

**Figure 5.19. Frontonasal dysplasia.** (A) Axial fetal MRI shows hypertelorism *(double-headed arrow).* The binocular distance and interocular distance were both greater than the 95th percentile for gestational age. (B) Midline sagittal fetal MRI shows absence of the corpus callosum *(large arrow)* and a facial defect with absence of the hard palate separating the nasal and oral cavities, with the tongue protruding through the defect *(small arrow).* (A, *From Robinson AJ, Blaser S, Toi A, et al. Magnetic resonance imaging of the fetal eyes—morphologic and biometric assessment for abnormal development with ultrasonographic and clinicopathologic correlation.* Pediatr Radiol. *2008;38:971–981.)*

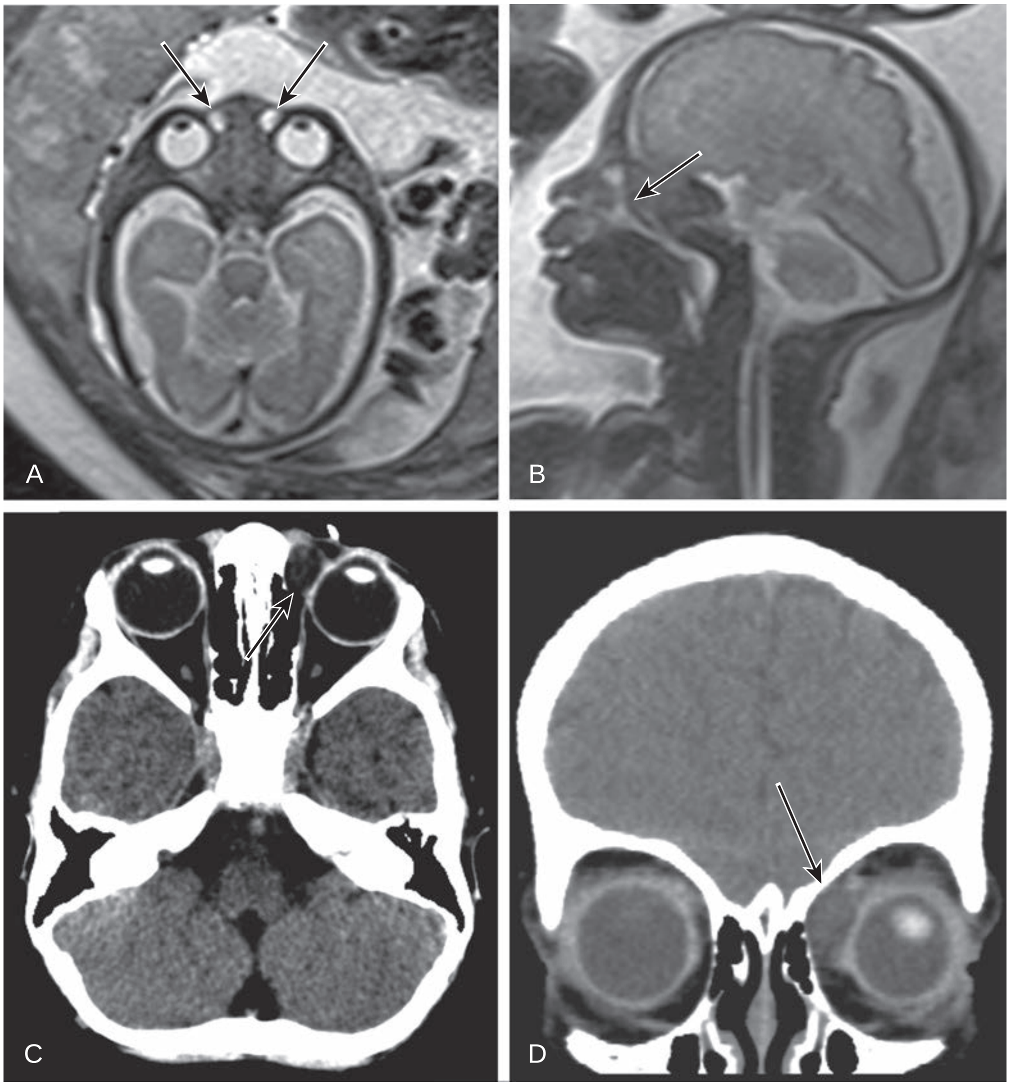

**Figure 5.23. Dacryocystocele.** (A) Axial fetal MRI shows bilateral cysts in the medial canthi *(arrows).* (B) Sagittal fetal MRI showing a dilated nasolacrimal duct *(arrow).* (C) Axial noncontrast CT shows a well-circumscribed low attenuation in the region of the left nasolacrimal duct *(arrow).* (D) Coronal CT shows a left dacryocystocele *(arrow).*

standard deviations from the mean, whereas the BOD remains at the upper limit of normal.[8]

### Secondary

Secondary hypertelorism typically results from abnormalities of the skull, the most common being anterior cephalocele and craniosynostoses (e-Figs. 5.21 and 5.22).[2,45,46]

## OTHER ORBITAL ABNORMALITIES

### Fetal Eye Movements

On ultrasound, fetal eye movements can be seen from 14 weeks. The incidence, pattern, and frequency are increasingly being used in the evaluation of development of the fetal brainstem and functional networks.[47-51]

### Dacryocystocele

Congenital dacryocystocele is a distention of the nasolacrimal duct, usually as a result of obstruction at its distal end at the valve of Hasner. Prenatal ultrasound and MRI can be used to make the diagnosis (Fig. 5.23).[52,53] The incidence on prenatal MRI studies has been reported to be between 0.7% and 2.7%, but only 50% of affected eyes are symptomatic postnatally. Congenital dacryocystocele is not expected to be seen before 24 weeks of gestation because nasolacrimal duct canalization is incomplete, and even normal fluid-filled nasolacrimal ducts can only be seen by MRI after 24 weeks of gestation. Dacryocystoceles also can resolve spontaneously before delivery as a result of rupture of the valve of Hasner.[54,55]

KEY POINTS

- Routine assessment of the orbit should include the presence or absence of the eyes, morphology of the lens and vitreous, and ocular biometry.
- Detection of orbital abnormalities often can be a critical step in diagnosing fetal dysmorphology.
- The existing sonographic growth charts for ocular biometry cannot be directly applied to fetal MRI; dedicated MRI nomograms should be used.

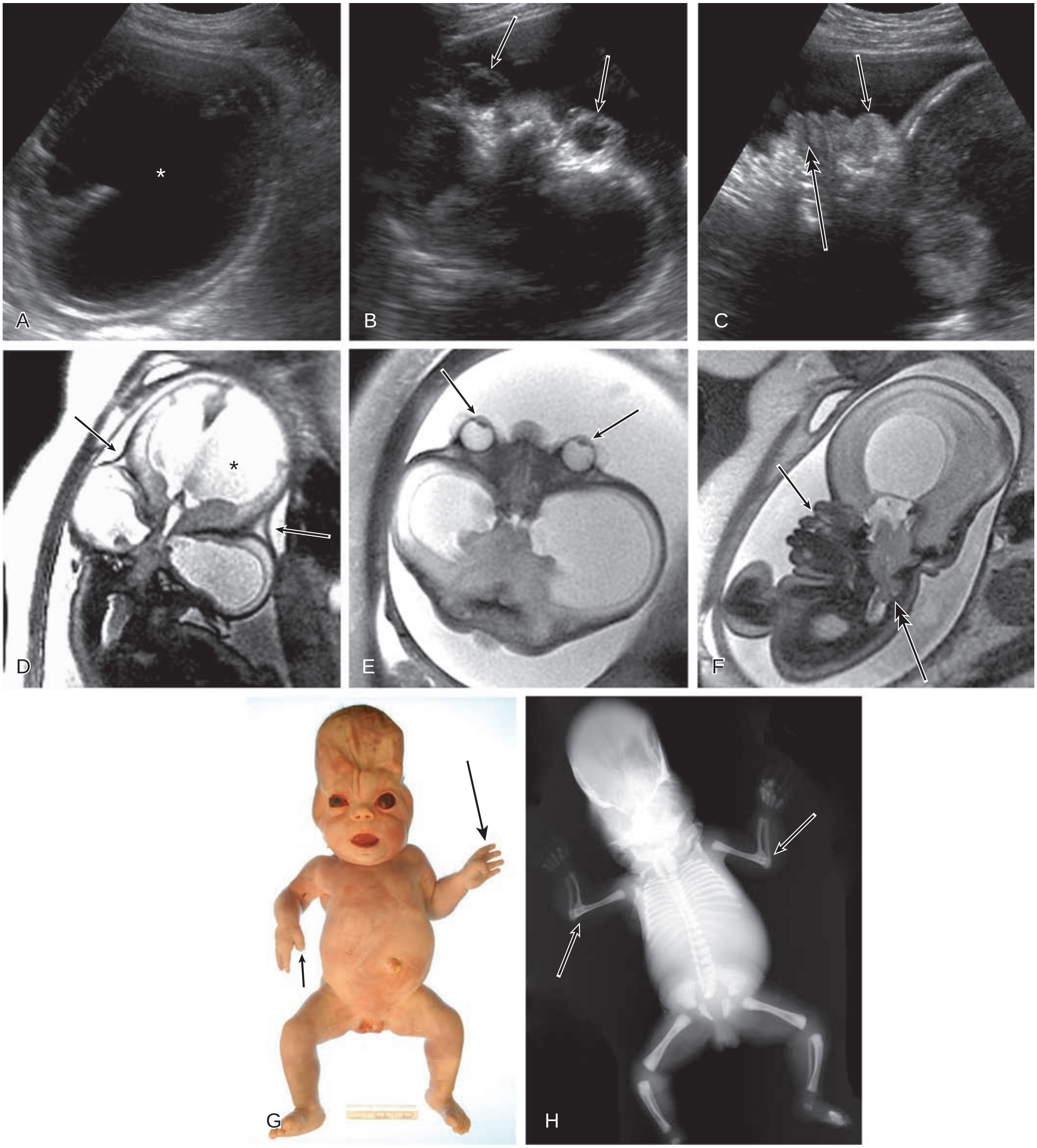

**e-Figure 5.21. Craniosynostosis and hypertelorism.** (A) Fetal ultrasound shows severe ventriculomegaly *(asterisk).* (B) Axial transorbital ultrasound image shows severe hypertelorism and exophthalmos *(arrows).* (C) Sagittal ultrasound shows midface hypoplasia *(small arrow)* and protruding lips *(double arrow).* (D) Coronal fetal MRI shows ventriculomegaly *(asterisk)* and a cloverleaf skull *(arrows).* (E) Axial fetal MRI shows severe ventriculomegaly, exorbitism *(arrows),* and hypertelorism. (F) Sagittal fetal MRI shows midface hypoplasia *(arrow)* and protrusion of posterior fossa contents into the cervical canal *(double arrow).* (G) The gross pathologic specimen shows hypertelorism, broad thumbs *(small arrow),* and syndactyly *(long arrow).* (H) Specimen radiograph showing bilateral elbow ankylosis (*arrows*), characteristic of Pfeiffer syndrome. *(*B, E, *and* G, *From Robinson AJ, Blaser S, Toi A, et al. Magnetic resonance imaging of the fetal eyes—morphologic and biometric assessment for abnormal development with ultrasonographic and clinicopathologic correlation.* Pediatr Radiol. *2008;38:971–981.)*

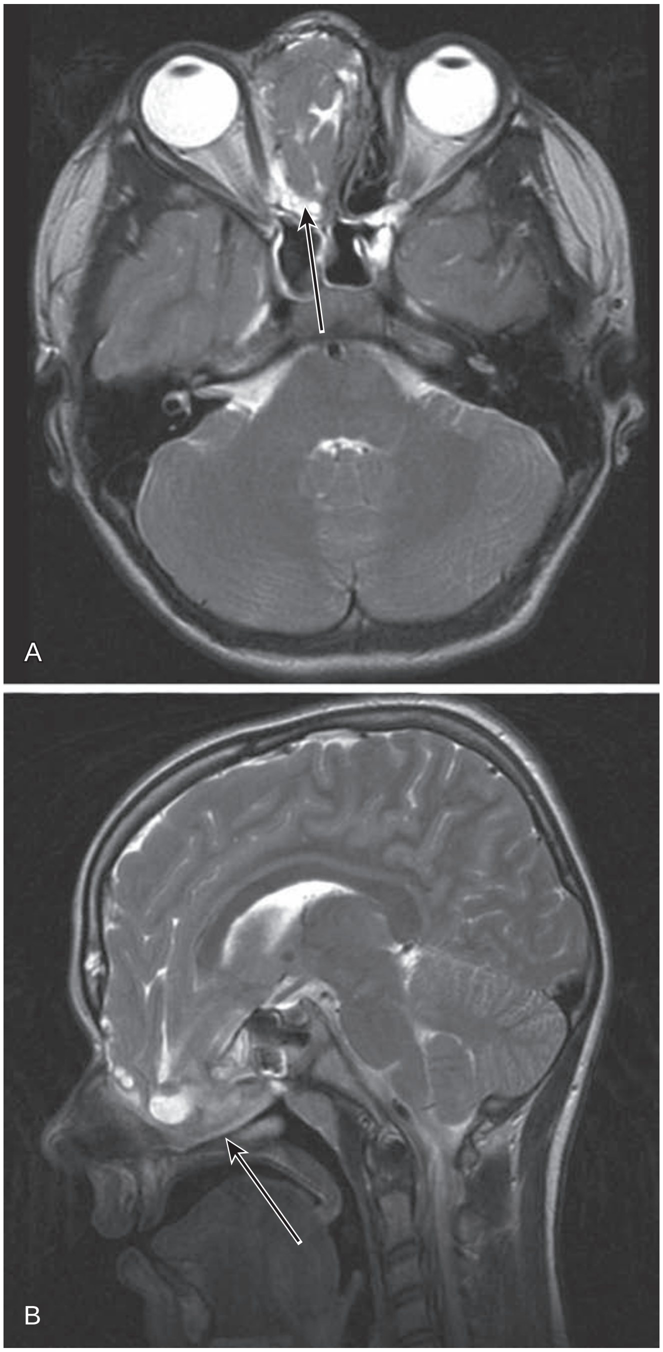

**e-Figure 5.22. Encephalocele and hypertelorism.** (A) Axial T2-weighted MRI demonstrates right inferior frontal lobe herniation *(arrow)* causing hypertelorism. (B) Sagittal T2-weighted MRI shows an anterior nasal encephalocele *(arrow).*

## SUGGESTED READINGS

Bardakjian T, Weiss A, Schneider A. *Anophthalmia/microphthalmia overview*. Available at http://www.ncbi.nlm.nih.gov/books/NBK1378/. Accessed December 24, 2016.

Dutton GN. Congenital disorders of the optic nerve: excavations and hypoplasia. *Eye (Lond)*. 2004;18:1038–1048.

Li XB, Kasprian G, Hodge JC, et al. Fetal ocular measurements by MRI. *Prenat Diagn*. 2010;30:1064–1071.

Paquette LB, Jackson HA, Tavare CJ, et al. In utero eye development documented by fetal MR imaging. *AJNR Am J Neuroradiol*. 2009;30:1787–1791.

Ramji FG, Slovis TL, Baker JD. Orbital sonography in children. *Pediatr Radiol*. 1996;26:245–258.

Robinson AJ. Orbit. In: Kline-Fath B, Bulas DI, Bahado-Singh R, eds. *Fundamental and Advanced Fetal Imaging: Ultrasound and MRI*. Philadelphia: Wolters Kluwer; 2015.

Robinson AJ, Blaser S, Toi A, et al. Magnetic resonance imaging of the fetal eyes—morphologic and biometric assessment for abnormal development with ultrasonographic and clinicopathologic correlation. *Pediatr Radiol*. 2008;38:971–981.

## REFERENCES

Full references for this chapter can be found on www.expertconsult.com.

## REFERENCES

1. Robinson AJ, Blaser S, Toi A, et al. Magnetic resonance imaging of the fetal eyes—morphologic and biometric assessment for abnormal development with ultrasonographic and clinicopathologic correlation. *Pediatr Radiol*. 2008;38:971–981.
2. Robson CD, Barnewolt CE. MR imaging of fetal head and neck anomalies. *Neuroimaging Clin N Am*. 2004;14:273–291.
3. Berg C, Geipel A, Germer U, et al. Prenatal detection of Fraser syndrome without cryptophthalmos: case report and review of the literature. *Ultrasound Obstet Gynecol*. 2001;18:76–80.
4. Fryns JP, van Schoubroeck D, Vandenberghe K, et al. Diagnostic echographic findings in cryptophthalmos syndrome (Fraser syndrome). *Prenat Diagn*. 1997;17:582–584.
5. Bardakjian T, Weiss A, Schneider A. *Anophthalmia/microphthalmia overview*. Available at http://www.ncbi.nlm.nih.gov/books/NBK1378/. Accessed October 19, 2012.
6. Strigini F, Valleriani A, Cecchi M, et al. Prenatal ultrasound and magnetic resonance imaging features in a fetus with Walker-Warburg syndrome. *Ultrasound Obstet Gynecol*. 2009;33(3):363–365.
7. Castori M, Brancati F, Rinaldi R, et al. Antenatal presentation of the oculo-auriculo-vertebral spectrum (OAVS). *Am J Med Genet A*. 2006;140(14):1573–1579.
8. Babcook C. The fetal face and neck. In: Callen P, ed. *Ultrasonography in Obstetrics and Gynecology*. Philadelphia: W.B. Saunders; 2000.
9. Chitayat D, Sroka H, Keating S, et al. The PDAC syndrome (pulmonary hypoplasia/agenesis, diaphragmatic hernia/eventration, anophthalmia/microphthalmia, and cardiac defect) (Spear syndrome, Matthew-Wood syndrome): report of eight cases including a living child and further evidence for autosomal recessive inheritance. *Am J Med Genet A*. 2007;143:1268–1281.
10. Achiron R, Kreiser D, Achiron A. Axial growth of the fetal eye and evaluation of the hyaloid artery: in utero ultrasonographic study. *Prenat Diagn*. 2000;20:894–899.
11. Birnholz JC, Farrell EE. Fetal hyaloid artery: timing of regression with US. *Radiology*. 1988;166:781–783.
12. Whitehead MT, Vezina G. Normal developmental globe morphology on fetal MR imaging. *AJNR Am J Neuroradiol*. 2016;37:1733–1737.
13. Ramji FG, Slovis TL, Baker JD. Orbital sonography in children. *Pediatr Radiol*. 1996;26:245–258.
14. Milic A, Blaser S, Robinson A, et al. Prenatal detection of microtia by MRI in a fetus with trisomy 22. *Pediatr Radiol*. 2006;36:706–710.
15. Reches A, Yaron Y, Burdon K, et al. Prenatal detection of congenital bilateral cataract leading to the diagnosis of Nance-Horan syndrome in the extended family. *Prenat Diagn*. 2007;27:662–664.
16. Fayol L, Garcia P, Denis D, et al. Adams-Oliver syndrome associated with cutis marmorata telangiectatica congenita and congenital cataract: a case report. *Am J Perinatol*. 2006;23:197–200.
17. Başbuğ M, Serin IS, Ozçelik B, et al. Prenatal ultrasonographic diagnosis of rhizomelic chondrodysplasia punctata by detection of rhizomelic shortening and bilateral cataracts. *Fetal Diagn Ther*. 2005;20:171–174.
18. Terhal P, Sakkers R, Hochstenbach R, et al. Cerebellar hypoplasia, zonular cataract, and peripheral neuropathy in trisomy 17 mosaicism. *Am J Med Genet A*. 2004;130:410–414.
19. Vutova K, Peicheva Z, Popova A, et al. Congenital toxoplasmosis: eye manifestations in infants and children. *Ann Trop Paediatr*. 2002;22:213–218.
20. Cengiz B, Baxi L. Congenital cataract in triplet pregnancy after IVF with frozen embryos: prenatal diagnosis and management. *Fetal Diagn Ther*. 2001;16:234–236.
21. Romain M, Awoust J, Dugauquier C, et al. Prenatal ultrasound detection of congenital cataract in trisomy 21. *Prenat Diagn*. 1999;19:780–782.
22. Beinder EJ, Pfeiffer RA, Bornemann A, et al. Second-trimester diagnosis of fetal cataract in a fetus with Walker-Warburg syndrome. *Fetal Diagn Ther*. 1997;12:197–199.
23. Drought A, Wimalasundera R, Holder S. Ultrasound diagnosis of bilateral cataracts in a fetus with possible cerebro-ocular congential muscular dystrophy during the routine second trimester anomaly scan. *Ultrasound*. 2015;23:181–185.
24. Frieden IJ, Reese V, Cohen D. PHACE syndrome. The association of posterior fossa brain malformations, hemangiomas, arterial anomalies, coarctation of the aorta and cardiac defects, and eye abnormalities. *Arch Dermatol*. 1996;132(3):307–311.
25. Shapiro I, Borochowitz Z, Degani S, et al. Neu-Laxova syndrome: prenatal ultrasonographic diagnosis, clinical and pathological studies, and new manifestations. *Am J Med Genet*. 1992;43:602–605.
26. Brent RL. The effects of ionizing radiation, microwaves, and ultrasound on the developing embryo: clinical interpretations and applications of the data. *Curr Probl Pediatr*. 1984;14:1–87.
27. Kusanovic J, Mittal P, Goncalves L, et al. 3D ultrasound evaluation of the fetal optic chiasm: a potential parameter for the differential diagnosis of developmental midline brain anomalies. *Ultrasound Obstet Gynecol*. 2005;26:311.
28. Bault JP. Prognostic value of fetal optic chiasm measurements in foetuses with septal agenesis. *Ultrasound Obstet Gynecol*. 2007;30:367–455.
29. Bault JP, Salomon LJ. Fetal optic chiasm measurements: reference range at 22-36 weeks of gestation. *Ultrasound Obstet Gynecol*. 2007;30:547–653.
30. Whitby E. In utero magnetic resonance imaging of developmental abnormalities of the fetal CNS. In: Griffiths P, Paley M, Whitby E, eds. *Imaging the Central Nervous System of the Fetus and Neonate*. New York: Taylor and Francis; 2006.
31. Dutton GN. Congenital disorders of the optic nerve: excavations and hypoplasia. *Eye (Lond)*. 2004;18:1038–1048.
32. Righini A, Avagliano L, Doneda C, et al. Prenatal magnetic resonance imaging of optic nerve head coloboma. *Prenat Diagn*. 2008;28:242–246.
33. Dilmen G, Köktener A, Turhan NO, et al. Growth of the fetal lens and orbit. *Int J Gynaecol Obstet*. 2002;76:267–271.
34. Goldstein I, Tamir A, Zimmer EZ, et al. Growth of the fetal orbit and lens in normal pregnancies. *Ultrasound Obstet Gynecol*. 1998;12:175–179.
35. Sukonpan K, Phupong V. A biometric study of the fetal orbit and lens in normal pregnancies. *J Clin Ultrasound*. 2009;37(2):69–74.
36. Feldman N, Melcer Y, Levinsohn-Tavor O, et al. Prenatal ultrasound charts of orbital total axial length measurement (TAL): a valuable data for correct fetal eye malformation assessment. *Prenat Diagn*. 2015;35:558–563.
37. Bojikian KD, de Moura CR, Tavares IM, et al. Fetal ocular measurements by three-dimensional ultrasound. *J AAPOS*. 2013;17:276–281.
38. Rosati P, Guariglia L. Early transvaginal fetal orbital measurements: a screening tool for aneuploidy? *J Ultrasound Med*. 2003;22:1201–1205.
39. Trout T, Budorick NE, Pretorius DH, et al. Significance of orbital measurements in the fetus. *J Ultrasound Med*. 1994;13:937–943.
40. Mayden KL, Tortora M, Berkowitz RL, et al. Orbital diameters: a new parameter for prenatal diagnosis and dating. *Am J Obstet Gynecol*. 1982;144:289–297.
41. Velasco-Annis C, Gholipour A, Afacan O, et al. Normative biometrics for fetal ocular growth using volumetric MRI reconstruction. *Prenat Diagn*. 2015;35:400–408.
42. Li XB, Kasprian G, Hodge JC, et al. Fetal ocular measurements by MRI. *Prenat Diagn*. 2010;30:1064–1071.
43. Paquette LB, Jackson HA, Tavare CJ, et al. In utero eye development documented by fetal MR imaging. *AJNR Am J Neuroradiol*. 2009;30:1787–1791.
44. Demyer W, Zeman W, Palmer CG. The face predicts the brain: diagnostic significance of median facial anomalies for holoprosencephaly (arrhinencephaly). *Pediatrics*. 1964;34:256–263.
45. Stroustrup A, Levine D. MR imaging of the fetal skull, face and neck. In: Levine D, ed. *Atlas of Fetal MRI*. Boca Raton, FL: Taylor & Francis; 2005.
46. Cohen MM Jr, Richieri-Costa A, Guion-Almeida ML, et al. Hypertelorism: interorbital growth, measurements, and pathogenetic considerations. *Int J Oral Maxillofac Surg*. 1995;24(6):387–395.
47. Inoue M, Koyanagi T, Nakahara H, et al. Functional development of human eye movement in utero assessed quantitatively with real-time ultrasound. *Am J Obstet Gynecol*. 1986;155:170–174.
48. Horimoto N, Hepper PG, Shahidullah S, et al. Fetal eye movements. *Ultrasound Obstet Gynecol*. 1993;3:362–369.
49. Chuang YM, Guo WY, Ho DM, et al. Skew ocular deviation: a catastrophic sign on MRI of fetal glioblastoma. *Childs Nerv Syst*. 2003;19:371–375.
50. Woitek R, Kasprian G, Lindner C, et al. Fetal eye movements on magnetic resonance imaging. *PLoS ONE*. 2013;8:e77439.
51. Schöpf V, Schlegl T, Jakab A, et al. The relationship between eye movement and vision develops before birth. *Front Hum Neurosci*. 2014;8:775.
52. Goldberg H, Sebire NJ, Holwell D, et al. Prenatal diagnosis of bilateral dacryocystoceles. *Ultrasound Obstet Gynecol*. 2000;15:448–449.
53. Davis WK, Mahony BS, Carroll BA, et al. Prenatal sonographic detection of benign dacryocystoceles (lacrimal duct cysts). *J Ultrasound Med*. 1987;6:461–465.
54. Yazici Z, Kline-Fath BM, Yazici B, et al. Congenital dacryocystocele: prenatal MRI findings. *Pediatr Radiol*. 2010;40:1868–1873.
55. Brugger PC, Weber M, Prayer D. Magnetic resonance imaging of the fetal efferent lacrimal pathways. *Eur Radiol*. 2010;20:1965–1973.

# 6

# Orbit Infection and Inflammation

Benita Tamrazi

A wide variety of disease processes can cause inflammatory changes in the orbit, including infection, idiopathic inflammation, granulomatous disease, thyroid-related disease, optic neuritis, and sickle cell disease. Additionally, metabolic diseases can also affect the optic nerves, leading to vision loss. Many of these disease processes can share a similar imaging appearance, and consequently a good understanding of their pathophysiology and clinical presentation is needed to formulate a useful differential diagnosis.

## PERIORBITAL AND ORBITAL CELLULITIS

***Etiologies, Pathophysiology, and Clinical Presentation.*** Infections of the orbit account for more than half of primary orbital disease processes.[1] An orbital infection is described by its location with respect to the orbital septum, specifically as either preseptal (periorbital) or postseptal (orbital). The orbital septum—the anterior reflection of the periosteum of the orbital wall onto the tarsal plate of the eyelid—divides the orbit into preseptal and postseptal compartments. *Periorbital cellulitis* refers to infection anterior to the orbital septum involving the eyelid and ocular adnexa. *Orbital cellulitis* refers to infection posterior to the orbital septum. This distinction is important because orbital cellulitis carries the risks of abscess, blindness, venous thrombosis, intracranial extension, and death. Defects in the orbital septum, direct extension from sinus infection, and valveless veins provide infection access to the postseptal orbit. Sinusitis is the most common cause (60%–85%), with stye, dacryoadenitis/cystitis, dental abscess, skin breaks, and hematogenous seeding being less common.[2,3] *Staphylococcus aureus*, *S. epidermidis*, and *S. pyogenes* account for ~75% of infections; rates of *Hemophilus influenzae* and streptococcal pneumonia are declining as a result of immunization.[2] Patients present with erythema, swelling, warmth, and tenderness of the eyelid. Although ophthalmoplegia and proptosis predict postseptal involvement and abscess, approximately 50% of patients with an abscess do not have these symptoms. As a result, the guidelines for imaging are unclear and vary: edema preventing a complete examination, signs of central nervous system involvement, deteriorating vision, proptosis, ophthalmoplegia, and/or deterioration after 24 to 48 hours of treatment.[4–6]

***Imaging.*** Periorbital cellulitis presents with eyelid swelling and thickening of the preseptal soft tissues on computed tomography (CT) (Fig. 6.1A) and with T2 hyperintensity on magnetic resonance imaging (MRI).[3,7,8] In orbital cellulitis, similar inflammatory changes of the extraconal and/or intraconal orbital fat are present. The most common complication of orbital cellulitis is subperiosteal abscess, frequently involving the lamina papyracea, and directly extending from ethmoid sinus disease (Fig. 6.1B).

***Treatment.*** Treatment consists of oral antibiotics covering staphylococcus and streptococcus for periorbital cellulitis and admission to the hospital with administration of intravenous (IV) antibiotics for orbital cellulitis. Surgical intervention for drainage of an abscess is required in only 12% of admitted patients,[4] and an orbital abscess can be treated with IV antibiotics if it is small or appears in a young child.[9,10]

## SUPERIOR OPHTHALMIC VEIN THROMBOSIS

Superior ophthalmic vein (SOV) thrombosis is a complication of orbital cellulitis that results from inflammatory thrombophlebitis or direct venous invasion by infection; 33% to 75% of isolated SOV thrombosis leads to cavernous sinus thrombosis, which carries a mortality rate of 20%.[11,12] Imaging with CT or MRI demonstrates an enlarged S-shaped SOV below the superior rectus muscle with a filling defect and peripherally enhancing vasa vasorum on postcontrast images, with thrombus sometimes also seen in the ipsilateral cavernous sinus (Fig. 6.2).[13] Restricted diffusion of the SOV also has been reported, facilitating identification.[14] Treatment consists of aggressive use of antibiotics with or without corticosteroids and anticoagulation, which are not proven therapies.[11,12]

## DACRYOCYSTITIS

Dacryocystitis is inflammation and dilatation of the lacrimal sac, a structure located along the inner canthus.[15] In neonates, dacryocystitis can complicate 33% to 65% of cases of congenital dacryocystocele caused by incomplete canalization of the distal nasolacrimal duct.[16,17] In older children, dacryocystitis can result from other causes of nasolacrimal duct obstruction, including rhinitis/sinusitis, tumor, or trauma/fracture. CT or MRI demonstrates a cystic medial canthus mass with adjacent inflammatory changes (e-Fig. 6.3).[18–20] Treatment typically consists of antibiotics and dacryocystorhinostomy.

## OCULAR TOXOCARIASIS

Ocular toxocariasis refers to infection of the globe by the nematodes *Toxocara canis* or *Toxocara cati* and is most common in the southeastern United States in children 6 to 12 years of age as a result of ingestion of food or soil contaminated by the feces of dogs or cats. It presents with painless unilateral vision loss, strabismus, and leukocoria.[21]

CT and MRI demonstrate an intravitreal enhancing mass with or without adjacent uveoscleral thickening and retinal detachment. A normal-sized globe containing a mass without calcification differentiates toxocariasis from other common causes of leukocoria (e.g., retinoblastoma, persistent hyperplastic primary vitreous, Coats disease, and retinopathy of prematurity).[22,23]

## ORBITAL PSEUDOTUMOR (IDIOPATHIC ORBITAL INFLAMMATION)

***Etiologies, Pathophysiology, and Clinical Presentation.*** Idiopathic orbital inflammatory syndrome, also known as orbital pseudotumor (OP), is an inflammatory, nongranulomatous process with unknown underlying cause. Essentially, this is a diagnosis of exclusion for patients presenting with exophthalmos. Pediatric OP is rare, accounting for only 7% to 16% of cases of OP.[24,25] Children present similarly to adults with pain, proptosis, a mass, swelling, and motility restriction; however, children more frequently demonstrate ptosis and bilateral or intraocular involvement.

***Imaging.*** Both CT and MRI are useful in evaluating OP.[26–28] Lacrimal gland involvement is most common, with enlargement and adjacent inflammatory change. Myositis also occurs frequently, typically with unilateral tubular thickening of extraocular muscles and tendons (compared with Graves orbitopathy, which tends to be bilateral with tendon sparing). OP may involve the uvea and

## Abstract:

Imaging findings of orbital infection and inflammation are provided with a wide differential diagnosis presented for review, including infection, idiopathic inflammation, granulomatous disease, thyroid-related disease, optic neuritis, and sickle cell disease. The imaging findings, clinical presentation, and treatment are reviewed.

## Keywords:

Orbit
MR imaging
inflammation
infection
Graves Orbitopathy
Granulomatous disease
optic neuritis

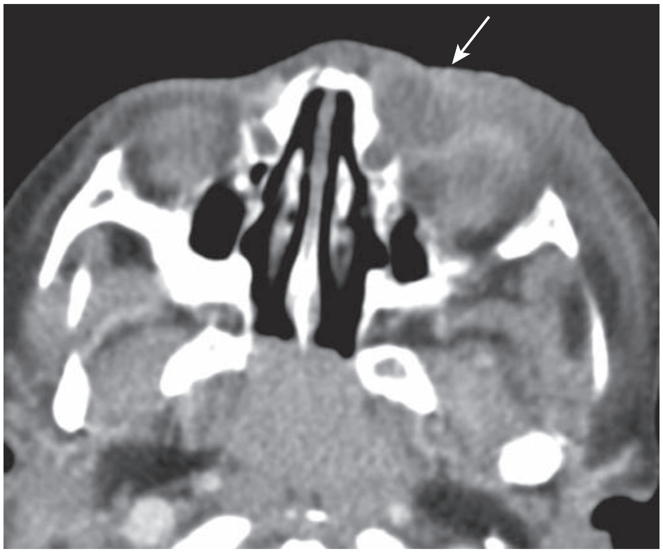

**e-Figure 6.3. Dacryocystitis.** Contrast-enhanced CT image of dacryocystitis causing periorbital cellulitis demonstrates a cystic medial canthus mass *(arrow)* with adjacent inflammatory changes.

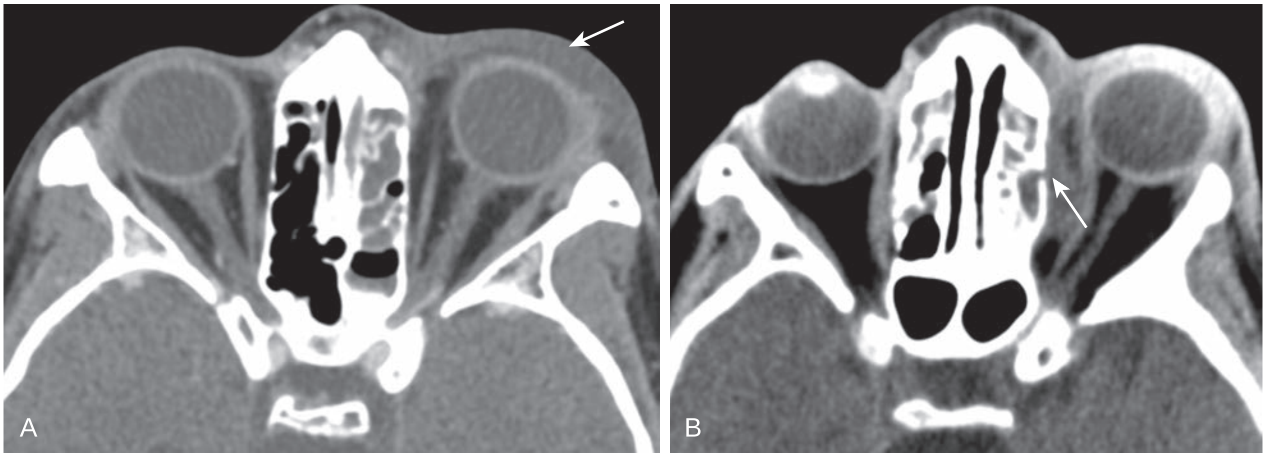

**Figure 6.1. Periorbital and orbital cellulitis.** (A) CT image of periorbital cellulitis from adjacent sinusitis demonstrates preseptal soft tissue swelling *(arrow)*. (B) CT image of orbital cellulitis demonstrates a subperiosteal abscess with cortical dehiscence of the ethmoid wall *(arrow)* and adjacent postseptal inflammatory changes.

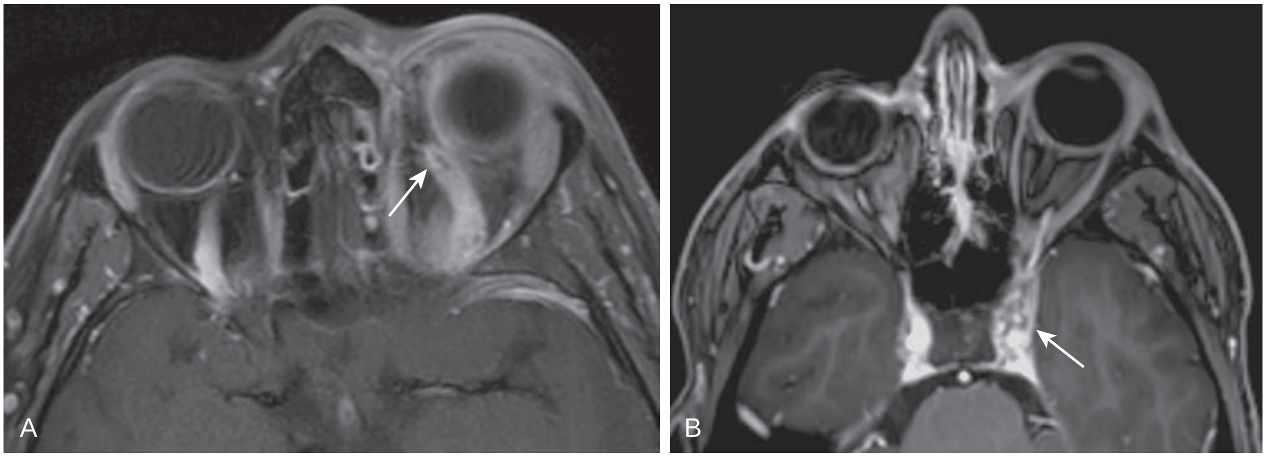

**Figure 6.2. Orbital cellulitis with superior ophthalmic vein and cavernous sinus thrombosis.** (A) Axial T1-weighted postcontrast fat-saturated MR image of the orbit demonstrates a focal filling defect in the superior ophthalmic vein consistent with thrombus in the setting of orbital cellulitis *(arrow)*. (B) Axial T1-weighted post contrast MR image of the brain demonstrates filling defect in the ipsilateral cavernous sinus consistent with thrombus *(arrow)*.

sclera with thickening and enhancement (Fig. 6.4). Perineuritis, which involves the optic nerve sheath, demonstrates “tramline” inflammatory changes and enhancement surrounding the optic nerve (see Fig. 6.4). Inflammation can extend through the orbital fissures and optic canal into the cavernous sinus and middle cranial fossa. The differential diagnosis includes infection, lymphoma, Wegener granulomatosis, sarcoidosis, and Graves orbitopathy. Diffusion-weighted imaging may be helpful in the diagnosis with the intensity of lymphoid lesions > OP > cellulitis on b-value = 1,000 images.[29]

***Treatment.*** Administration of oral corticosteroids often results in a rapid response (within 1–2 days); radiation is used in refractory cases.[25,30] Recurrence after withdrawal of steroids occurs frequently in adults (~50%) but has been reported in only one child.[24,31] Biopsy is reserved for atypical symptoms or poor response. Recently, cases of OP have been identified as part of IgG4-related disease, a systemic inflammatory disease demonstrating excellent response to rituximab and corticosteroids.[32,33]

## GRAVES ORBITOPATHY (THYROID ORBITOPATHY)

***Etiologies, Pathophysiology, and Clinical Presentation.*** Graves orbitopathy is an orbital inflammatory process seen in persons with Graves disease, which is an autoimmune thyroid disease from thyroid-stimulating hormone receptor autoantibodies. Pediatric Graves disease is uncommon, yet children who have the disease experience Graves orbitopathy at similar rates as do adults, in one-third to two-thirds of cases.[34–36] Graves orbitopathy is milder in children than in adults, with mild proptosis and mild eyelid retraction or lag. In children, no cases of compressive optic neuropathy have been reported, and strabismus is rare.

***Imaging and Treatment.*** Imaging demonstrates fusiform enlargement of extraocular muscles (involving muscle bellies and sparing tendons), which is bilateral in 90% of cases and frequently involves the inferior and medial recti (Fig. 6.5). Active disease can be differentiated from fibrotic disease by evaluating the T2 signal intensity and dynamic contrast enhancement of the muscles (T2

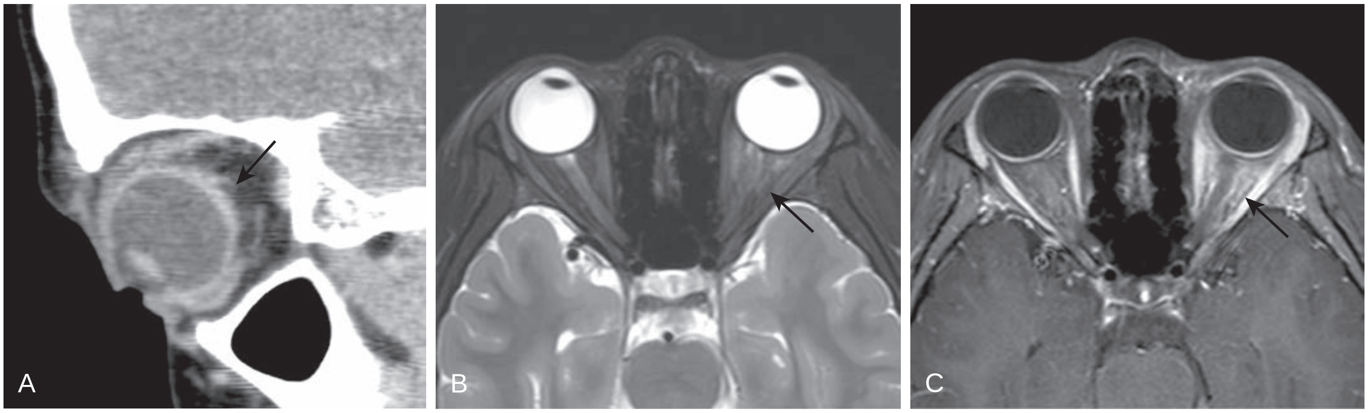

**Figure 6.4. Orbital pseudotumor.** (A) Sagittal contrast-enhanced CT image of scleral involvement by a pseudotumor causing posterior scleritis with subtle thickening of the posterior sclera *(arrow)*. (B) Axial T2-weighted fat-saturated MR image in a different patient with a pseudotumor demonstrating ill-defined T2 hyperintensity of the intraconal fat *(arrow)*. (C) Axial T1-weighted fat-saturated postcontrast MR image demonstrating corresponding "tramline" enhancement of the optic nerve sheath and ill-defined enhancement of the intraconal fat *(arrow)*.

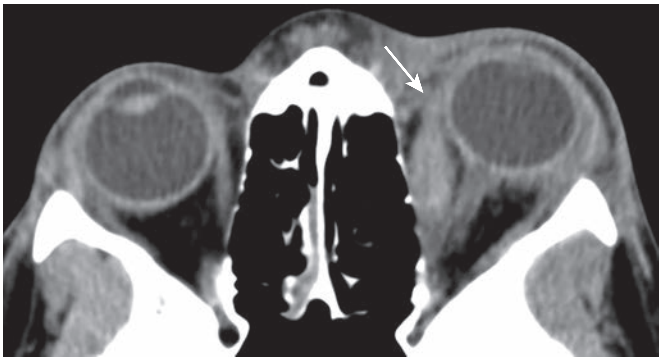

**Figure 6.5. Graves orbitopathy.** Contrast-enhanced CT image demonstrates fusiform enlargement of the medial rectus muscle belly with sparing of the tendons *(arrow)*.

hyperintensity, shorter time to peak, and greater enhancement and washout ratios are found in active disease), an important distinction because medical therapy is not effective in fibrotic disease.[37–39] Most pediatric cases can be controlled with antithyroid medication alone; steroids, radiation therapy, or surgery are not required, as is often the case with adults.[34–36]

## SARCOIDOSIS

Sarcoidosis is a multisystem disease of unclear etiology characterized by noncaseating granulomas. Sarcoidosis is rare in children; however, a unique form appears in children younger than 5 years and presents with rash, uveitis, and arthritis.[40] In older children and adults, ocular involvement is seen in ~25% of cases, most commonly with uveitis.[40–43] Additional orbital structures involved can include the lacrimal gland and sac, eyelid, orbital soft tissues, optic nerve and sheath, and extraocular muscles, with enlargement and enhancement of these structures.[44,45] Involvement can be well circumscribed (in 85% of cases) or diffuse (in 15% of cases). The mainstay of treatment is oral steroids, which generally results in a good response; methotrexate or surgery is used for refractory cases. In patients with isolated orbital involvement (63%), systemic disease develops in 8% within 5 years.[46]

## WEGENER GRANULOMATOSIS

Wegener granulomatosis is a necrotizing granulomatous vasculitis of small- and medium-sized vessels associated with antineutrophil cytoplasmic antibodies. Pediatric Wegener granulomatosis is rare; it presents in adolescence with a female predominance.[47,48] Orbital involvement occurs in approximately 50% of adults (and is the presenting feature in 15%), but it is less common in children.[49,50] Orbital disease may be primary or extend from the sinuses with osseous erosion. The globe (conjunctivitis and scleritis), lacrimal gland, retrobulbar space, optic nerve, and extraocular muscles all can be involved. Imaging demonstrates granulomatous masses with variable enhancement and characteristic T2-weighted hypointensity on MRI, presumably related to fibrocollagenous tissue (e-Fig. 6.6).[51,52] Symmetric lacrimal gland enlargement can also be seen. Treatment in children can vary but typically consists of administration of steroids and cyclophosphamide.

## OPTIC NEURITIS

***Etiologies, Pathophysiology, and Clinical Presentation.*** Optic neuritis (ON) involves inflammation or demyelination of the optic nerve and often presents with unilateral eye pain and visual loss. ON may be idiopathic or related to multiple sclerosis (MS), neuromyelitis optica, or acute disseminated encephalomyelitis. ON behaves differently in children than in adults, likely reflecting different etiologies, with parainfectious ON being common in children (in one-third to two-thirds of cases).[53–57] Compared with adults, ON in children is more often bilateral (in 37% to 66% of cases), less often painful (in 37% of cases), and more often demonstrates disk swelling (in 46%–85% of cases) and profound vision loss. In children, it tends to have better visual recovery and is less often associated with MS.

***Imaging.*** MRI demonstrates contrast enhancement (>90%), T2-weighted hyperintensity, and enlargement of the optic nerves acutely, with mild volume loss developing chronically.[58,59] Intraorbital involvement is most common (Fig. 6.7). Intracanalicular and long segment involvement and persistent signal change over time correlate to worse visual outcomes. Diffusion tensor imaging of optic nerves is difficult to perform clinically yet demonstrates decreased axial diffusivity acutely and increasing radial diffusivity and apparent diffusion coefficient values during recovery, correlating to changes in visual acuity and retinal nerve fiber layer thinning.[60–62] Decreased fractional anisotropy values also can be seen in the optic tracts and radiations, possibly as a result of Wallerian and transsynaptic degeneration.[63–65] Magnetization transfer ratios, which are thought to decrease with demyelination, are more sensitive than T2 spin echo imaging. They progressively decrease in the optic nerve, with a nadir at 240 days, and then mildly increase

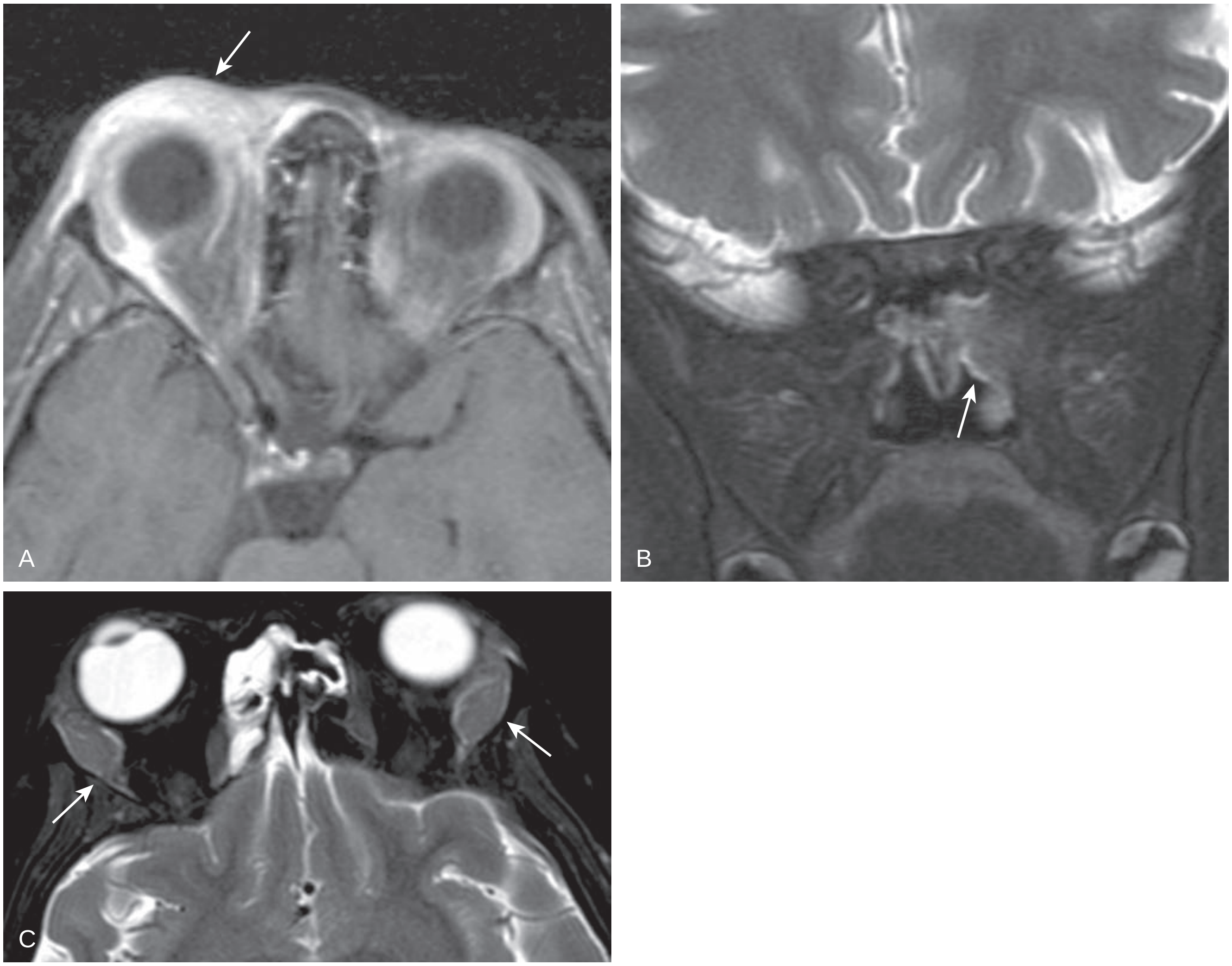

**e-Figure 6.6. Wegener granulomatosis.** (A) Axial T1-weighted fat-saturated postcontrast MR image of the orbit demonstrating inflammatory changes and enhancement adjacent to the lacrimal gland in the preseptal orbit, similar in appearance to periorbital cellulitis *(arrow)*. (B) Coronal T2-weighted fat-saturated MR image demonstrates a mass centered on the sphenopalatine foramen with osseous erosion and extension to the orbital apex with characteristic T2 hypointensity, making it difficult to visualize on MR imaging *(arrow)*. (C) Axial STIR MR image of the orbits in another patient demonstrates diffuse, symmetric enlargement of the lacrimal glands *(arrows)*.

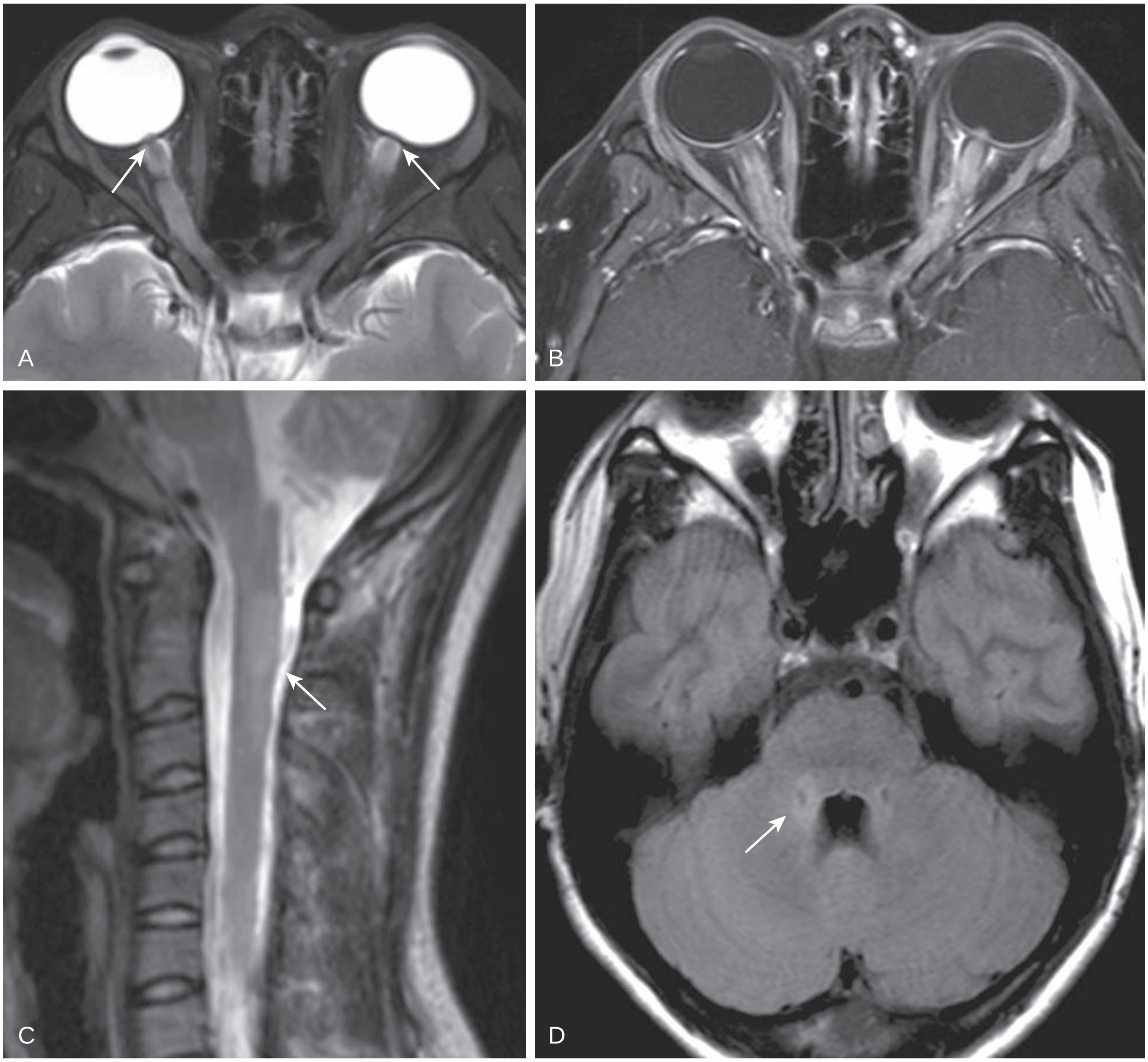

**Figure 6.7. Optic neuritis.** (A) Axial T2-weighted and (B) T1-weighted fat-saturated postcontrast MR images of the orbits demonstrating abnormal T2 hyperintensity and enhancement of the bilateral optic nerves with papilledema *(arrows)*. (C) Sagittal T2-weighted MR image of the cervical spine demonstrates a characteristic central long segment cord lesion in a patient with neuromyelitis optica (NMO) *(arrow)*. (D) Axial T2-weighted fluid attenuated inversion recovery MR image in the same patient with NMO demonstrating subtle hyperintensity adjacent to the fourth ventricle in regions of high aquaporin 4 concentration *(arrow)*.

(possibly from remyelination), also correlating to changes in visual acuity.[66,67]

***Treatment.*** ON in children is usually treated with IV methylprednisolone followed by an oral prednisolone taper.[68] Although no large randomized controlled trials have been performed in children, in adults this therapy accelerates visual recovery and decreases the risk of MS for 2 years.[69]

## Optic Neuritis and Multiple Sclerosis

Most ON research has been conducted with adult subjects, and it has been found that MS develops in 50% of adults with ON within 15 years.[69] In children, the largest series with the longest follow-up demonstrated a 19% conversion to MS (13% in 10 years).[56] As with adults, almost all children in whom MS developed had an abnormal MRI scan at baseline, and MS developed in almost no children who had a normal MRI scan.[53,54] Furthermore, optic disk swelling is associated with a decreased risk of MS in adults and is a common feature of pediatric ON, likely reflecting the often parainfectious nature of ON in children.[53–57]

## Optic Neuritis and Neuromyelitis Optica (Devic Disease)

***Etiologies, Pathophysiology, and Clinical Presentation.*** Neuromyelitis optica (NMO) is an inflammatory demyelinating disease of the optic nerves and spinal cord related to NMO–immunoglobulin G (IgG), a serum autoantibody targeting aquaporin 4, a water channel on astrocytes at the blood-brain barrier.[70,71] The distinction of NMO from MS is important because NMO has a worse prognosis and requires different treatment. Diagnostic criteria for children are similar to those for adults: clinical diagnosis of ON and transverse myelitis with either a cord lesion on MRI or NMO-IgG seropositivity.[72,73] The prognosis is poor: more than 50% of patients have vision loss or lose the ability to ambulate within 5 years. NMO-IgG seropositivity may indicate a worse prognosis with a relapsing course.[74–76] Parainfectious NMO is common in children and typically is NMO-IgG negative and monophasic.[77,78] Accordingly, pediatric NMO has a better prognosis and a longer time before the onset of disability.[79,80]

***Imaging.*** Characteristic cord lesions are centrally located and extend three or more segments in length (Fig. 6.7C). Up to 60% of patients also demonstrate brain lesions, which are part of the new diagnostic criteria.[81] Findings include nonspecific signal changes, MS-like lesions (10%), and T2-weighted hyperintensity in areas of high aquaporin 4 concentration adjacent to the third and fourth ventricles (Fig. 6.7D). Signal changes in the distribution of aquaporin 4 may be specific for NMO and are seen more frequently in children.[81,82]

***Treatment.*** Treatment of persons with NMO consists of immunosuppression (IV methylprednisolone ± plasmapheresis acutely, with oral prednisone and azathioprine for maintenance), compared with immunomodulation for persons with MS.[70,79] NMO-IgG positivity in persons with isolated ON or transverse myelitis may represent a limited form of NMO, requiring more aggressive treatment.[76] Similarly, NMO-IgG negativity in children may predict a parainfectious etiology with a monophasic course not requiring immunosuppressive therapy.[74,75]

### Optic Neuritis and Acute Disseminated Encephalomyelitis

Acute disseminated encephalomyelitis (ADEM) is an autoimmune inflammatory and typically monophasic demyelinating disease of the central nervous system that occurs days to weeks after a viral illness or vaccination. Visual loss is seen in up to one-fourth of patients with ADEM, and ON in persons with ADEM tends to be bilateral with swollen optic discs.[83–85] Although no clear guidelines exist, treatment usually consists of IV steroids with favorable outcomes.[86] The high frequency of parainfectious ON in children (in one-third to two-thirds of cases) likely contributes to the different presentation and more favorable prognosis of ON in children compared with adults.

## PAPILLEDEMA

Papilledema is another cause of optic disc swelling in children. It is the result of elevated intracranial pressure due to intracranial mass/inflammation, hydrocephalus, venous sinus thrombosis, or pseudotumor cerebri. Visual loss may result.[87] MRI demonstrates optic disc elevation, dilated perioptic subarachnoid spaces, and optic nerve tortuosity (see Fig. 6.7A and B).[88,89] Enhancement and restricted diffusion of the optic disc have been described, perhaps as a result of venous congestion and ischemia.[90,91]

## SICKLE CELL DISEASE

***Etiologies, Pathophysiology, and Clinical Presentation.*** Sickle cell disease (SCD) is an inherited autosomal-recessive disease of the sickle beta globin gene that results in chronic hemolytic anemia and recurrent vaso-occlusive crises and infection. A vaso-occlusive crisis can affect any bone with active bone marrow. Orbital wall involvement is seen almost exclusively in children because of a greater volume of marrow space in this location during childhood. Patients present with acute periorbital pain, swelling, proptosis, and restricted extraocular movements. Subperiosteal hemorrhage can be a complication in 36% of cases. Resultant orbital compression syndrome can cause optic nerve compression and vision loss.[92–95]

***Imaging.*** MRI demonstrates bone marrow edema and hemorrhage with or without subperiosteal hemorrhage (Fig. 6.8A). It is important to differentiate bone marrow infarction from osteomyelitis given that both can occur in persons with SCD. On MRI, infarction demonstrates thin peripheral contrast enhancement, whereas infection demonstrates thick peripheral, geographic, or irregular contrast enhancement with or without cortical defects.[96] Areas of high signal intensity on T1-weighted fat-saturated

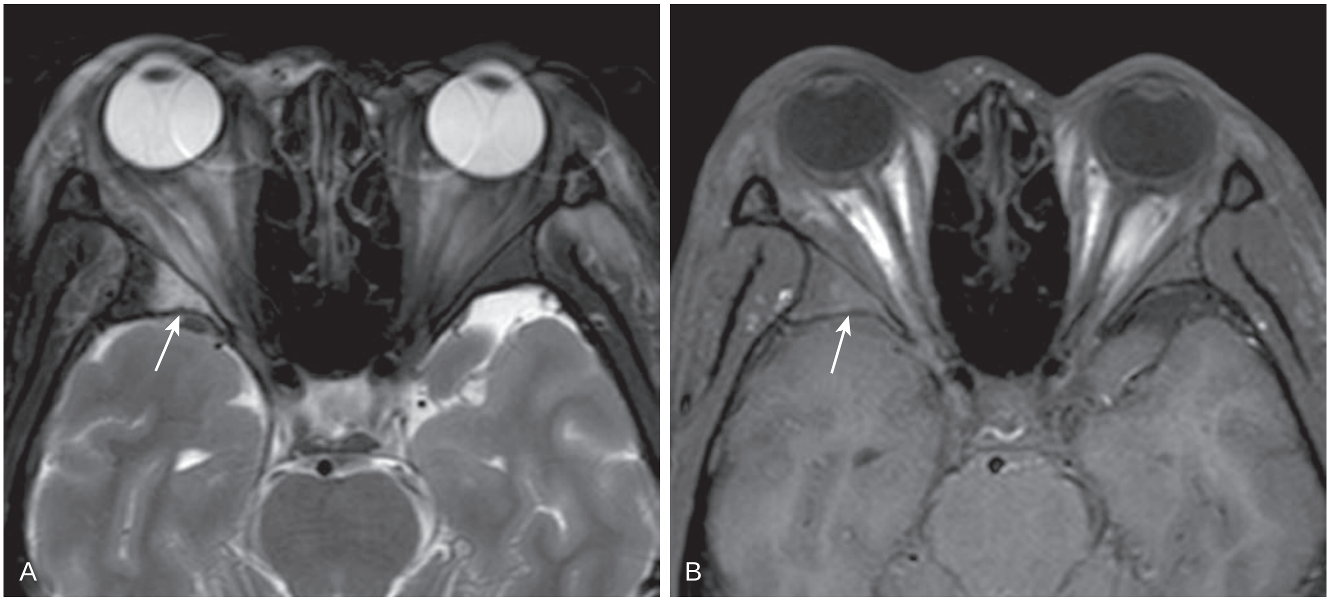

**Figure 6.8. Sickle cell disease.** (A) Axial T2-weighted fat-saturated MR image of the orbits demonstrating bone marrow infarction in a patient with sickle cell disease, with T2 hyperintensity of the bone marrow of the lateral wall of the right orbit and adjacent inflammatory changes of the extraconal fat *(arrow)*. (B) Axial T1-weighted fat-saturated noncontrast MR image of the orbit in the same patient demonstrating subtle T1 hyperintensity of the bone marrow from sequestration of red blood cells *(arrow)*.

noncontrast MRI due to sequestration of red blood cells also has been found to be helpful in detecting areas of infarction and distinguishing them from infection (Fig. 6.8B).[97]

***Treatment.*** Treatment consists of conservative management for SCD crises. In cases of optic nerve compression and vision change, IV steroids and/or surgical drainage of hematomas may be required.

## LEBER HEREDITARY OPTIC NEUROPATHY

***Etiologies, Pathophysiology, and Clinical Presentation.*** Leber hereditary optic neuropathy (LHON) is the most common genetic mitochondrial disease, affecting 1 in 25,000 persons.[98] Deficient adenosine triphosphate production leads to degeneration of retinal ganglion cells. Three mitochondrial deoxyribonucleic acid mutations (G3460A, G11778A, and T14484C) account for more than 90% of cases with incomplete penetrance: 50% in males and 10% in females. Accordingly, LHON is most common in young males, with a median age of 24 years. Painless bilateral clouding of vision, centrocecal scotoma, and impairment of color vision progresses to vision loss and optic nerve atrophy in 6 months. Most patients show no functional improvement, remaining legally blind.

***Imaging.*** Most patients demonstrate no imaging findings, yet acutely, T2 hyperintensity, enlargement, and enhancement of the optic nerves, chiasm, and tracts can be seen. A small portion of patients, particularly females, demonstrate MS-like lesions in the brain preceding or more commonly after optic nerve involvement after an average of 4.3 years.[99,100]

***Treatment.*** No treatment is available that significantly improves visual outcome, but recent trials have focused on Idebenone.[101,102] Patients with LHON and MS-like lesions may need immunosuppressive therapy.

## AUTOSOMAL-DOMINANT OPTIC ATROPHY

Autosomal-dominant optic atrophy (ADOA) is the most common hereditary optic neuropathy related to mutations in the optic atrophy 1 *(OPA1)* gene (encoding a mitochondrial guanosine triphosphatase).[103] Selective retinal ganglion cell loss results in isolated, progressive, and permanent vision loss, typically in the first 2 decades of life. Extraocular neurologic involvement is seen in up to one-sixth of patients, with sensorineural hearing loss being the most common manifestation, likely as a result of *OPA1* expression in the inner ear.[104] Few studies describe the imaging appearance of ADOA, although a decrease in the size of the optic nerves throughout their length can be seen.[105]

## KRABBE DISEASE (GLOBOID CELL LEUKODYSTROPHY)

Krabbe disease is an autosomal-recessive neurodegenerative disorder with a deficiency in galactosylceramide β-galactosidase, a lysosomal enzyme responsible for myelin breakdown and turnover. This deficiency leads to accumulation of neurotoxic psychosine and galactosylceramide, which form globoid cells. Early-, late-, and adult-onset forms are described. Presentation is most common at 3 to 6 months of age, with death by 2 to 3 years of age. Optic nerve enlargement is an uncommon manifestation, perhaps as a result of globoid cell accumulation in optic nerves, as described at autopsy (e-Fig. 6.9).[106–109] The major differential considerations in children with enlarged optic nerves and signal changes in both the white matter and deep grey nuclei are Krabbe disease and neurofibromatosis type 1 with optic pathway gliomas.

### KEY POINTS

- Infection involving the postseptal orbit carries the risks of abscess formation, vision loss, venous thrombosis, intracranial extension, and death, requiring admission for monitoring and IV antibiotics.
- Many disease processes in the orbit can look similar on imaging, with presentation as an ill-defined inflammatory mass: infection, OP, Wegener granulomatosis, sarcoidosis, and lymphoma.
- Causes of optic neuritis in children include an idiopathic cause, MS, NMO, and ADEM.
- Optic neuritis behaves differently in children, which likely is related to its frequent parainfectious nature: it is painless, bilateral, presents with disk edema and profound vision loss, generally results in a good recovery, and infrequently progresses to MS.
- Although uncommon, metabolic disease also should be considered in a child with vision loss and changes to the optic nerves on imaging.

### SUGGESTED READINGS

Gorospe L, Royo A, Berrocal T, et al. Imaging of orbital disorders in pediatric patients. *Eur Radiol*. 2003;13:2012–2026.

Hopper KD, Sherman JL, Boal DK, et al. CT and MR imaging of the pediatric orbit. *Radiographics*. 1992;12:485–503.

Narla LD, Newman B, Spottswood SS, et al. Inflammatory pseudotumor. *Radiographics*. 2003;23:719–729.

Saito N, Nadgir RN, Flower EN, et al. Clinical and radiologic manifestations of sickle cell disease in the head and neck. *Radiographics*. 2010;30:1021–1035.

Smirniotopoulos JG, Bargallo N, Mafee MF. Differential diagnosis of leukokoria: radiologic-pathologic correlation. *Radiographics*. 1994;14:1059–1079.

### REFERENCES

Full references for this chapter can be found on www.expertconsult.com.

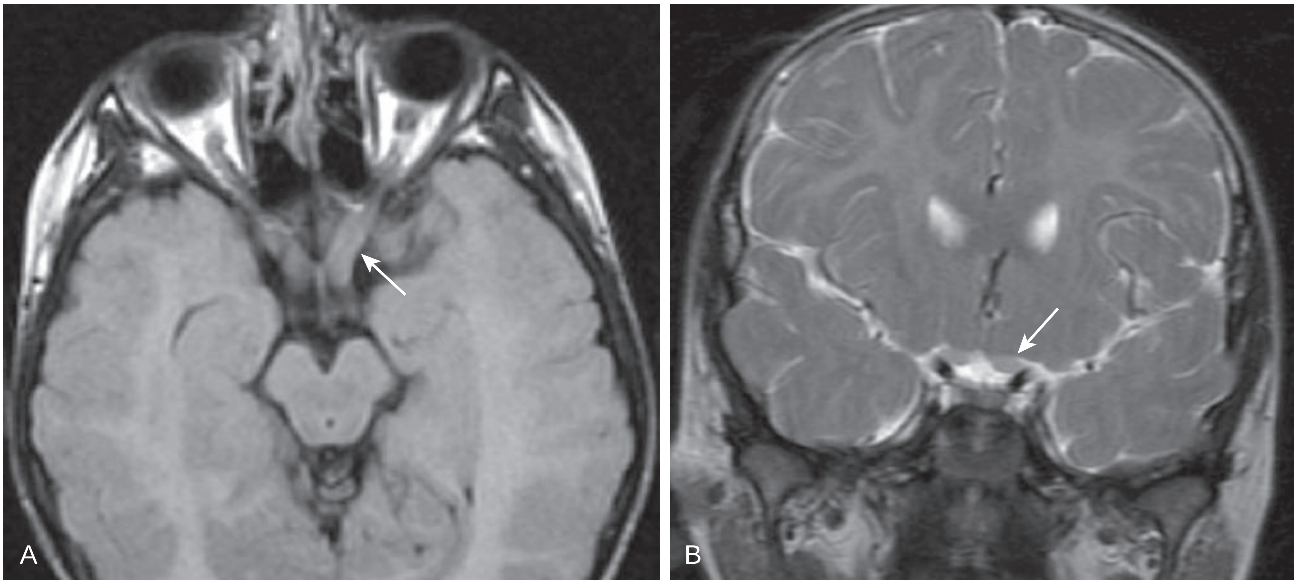

**e-Figure 6.9. Metabolic disease.** (A) Axial T2-weighted fluid attenuated inversion recovery and (B) coronal T2-weighted MR images of an unknown metabolic disease process, possibly late-onset Krabbe disease, demonstrating mild enlargement and hyperintensity of the optic nerves with associated diffuse white matter signal changes *(arrows)*.

## REFERENCES

1. Mafee MF. Orbit: embryology, anatomy, and pathology. In: Som PM, Curtin HD, eds. *Head and Neck Imaging*. 4th ed. St Louis, MO: Mosby; 2003:529–654.
2. Hauser A, Fogarasi S. Periorbital and orbital cellulitis. *Pediatr Rev*. 2010;31:242–249.
3. Reid J. Complications of pediatric paranasal sinusitis. *Pediatr Radiol*. 2004;34:933–942.
4. Mahalingam-Dhingra A, Lander L, Preciado DA, et al. Orbital and periorbital infections: a national perspective. *Arch Otolaryngol Head Neck Surg*. 2011;137(8):769–773.
5. Sobol SE, Marchand J, Tewfik TL, et al. Orbital complications of sinusitis in children. *J Otolaryngol*. 2002;31(3):131–136.
6. Rudloe TF, Harper MB, Prabhu SP, et al. Acute periorbital infections: who needs emergent imaging? *Pediatrics*. 2010;125:e719–e726.
7. Towbin R, Han BK, Kaufman RA, et al. Postseptal cellulitis: CT in diagnosis and management. *Radiology*. 1986;158:735–737.
8. Gorospe L, Royo A, Berrocal T, et al. Imaging of orbital disorders in pediatric patients. *Eur Radiol*. 2003;13:2012–2026.
9. Greenberg MF, Pollard ZF. Medical treatment of pediatric subperiosteal orbital abscess secondary to sinusitis. *J AAPOS*. 1998;2(6):351–355.
10. Yang M, Quah BL, Seah LL, et al. Orbital cellulitis in children-medical treatment versus surgical management. *Orbit*. 2009;28(2–3):124–136.
11. Schmitt NJ, Beatty RL, Kennerdell JS. Superior ophthalmic vein thrombosis in a patient with dacryocystitis-induced orbital cellulitis. *Ophthal Plast Reconstr Surg*. 2005;21(5):387–389.
12. Berenholz L, Kessler A, Shlomkovitz N, et al. Superior ophthalmic vein thrombosis: complication of ethmoidal rhinosinusitis. *Arch Otolaryngol Head Neck Surg*. 1998;124:95–97.
13. Walker JC, Sandhu A, Pietris G. Septic superior ophthalmic vein thrombosis. *Clin Experiment Ophthalmol*. 2002;30:144–146.
14. Parmar H, Gandhi D, Mukherji SK, et al. Restricted diffusion in the superior ophthalmic vein and cavernous sinus in a case of cavernous sinus thrombosis. *J Neuroophthalmol*. 2009;29(1):16–20.
15. Kassel EE, Schatz CJ. Lacrimal apparatus. In: Som PM, Curtin HD, eds. *Head and Neck Imaging*. 4th ed. St. Louis, MO: Mosby; 2003:655–733.
16. Wong RK, VanderVeen DK. Presentation and management of congenital dacryocystocele. *Pediatrics*. 2008;122(5):e1108–e1112.
17. Shekunov J, Griepentrog GJ, Diehl NN, et al. Prevalence and clinical characteristics of congenital dacryocystocele. *J AAPOS*. 2010;14(5):417–420.
18. Rand PK, Ball WS Jr, Kulwin DR. Congenital nasolacrimal mucoceles: CT evaluation. *Radiology*. 1989;173:691–694.
19. Farrer RS, Mohammed TL, Hahn FJ. MRI of childhood dacryocystocele. *Neuroradiology*. 2003;45:259–261.
20. Asheim J, Spickler E. CT demonstration of dacryolithiasis complicated by dacryocystitis. *AJNR Am J Neuroradiol*. 2005;26:2640–2641.
21. Ament CS, Young LH. Ocular manifestations of helminthic infections: onchocerciasis, cysticercosis, toxocariasis, and diffuse unilateral subacute neuroretinitis. *Int Ophthalmol Clin*. 2006;46(2):1–10.
22. Smirniotopoulos JG, Bargallo N, Mafee MF. From the archives of the AFIP: differential diagnosis of leukokoria: radiologic-pathologic correlation. *Radiographics*. 1994;14:1059–1079.
23. Kadom N, Sze RW. Radiological reasoning: leukocoria in a child. *AJR Am J Roentgenol*. 2008;191:s40–s44.
24. Kitei D, DiMario FJ Jr. Childhood orbital pseudotumor: case report and literature review. *J Child Neurol*. 2008;23(4):425–430.
25. Yan J, Qui H, Wu Z, et al. Idiopathic orbital inflammatory pseudotumor in Chinese children. *Orbit*. 2006;25:1–4.
26. Ding ZX, Lip G, Chong V. Idiopathic orbital pseudotumour. *Clin Radiol*. 2011;66:886–892.
27. Narla LD, Newman B, Spottswood SS, et al. Inflammatory pseudotumor. *Radiographics*. 2003;23:719–729.
28. Park SB, Lee JH, Weon YC, et al. Imaging findings of head and neck inflammatory pseudotumor. *AJR Am J Roentgenol*. 2009;193:1180–1186.
29. Kapur R, Sepahdari AR, Mafee MF, et al. MR imaging of orbital inflammatory syndrome, orbital cellulitis, and orbital lymphoid lesions: the role of diffusion-weighted imaging. *AJNR Am J Neuroradiol*. 2009;30:64–70.
30. Guerriero S, Leo ED, Piscitelli D, et al. Orbital pseudotumor in a child: diagnostic implications and treatment strategies. *Clin Exp Med*. 2011;11(1):61–63.
31. Mendenhall WM, Lessner AM. Orbital pseudotumor. *Am J Clin Oncol*. 2010;33:304–306.
32. Carruthers MN, Stone JH, Khosroshahi A. The latest on IgG4-RD: a rapidly emerging disease. *Curr Opin Rheumatol*. 2012;24:60–69.
33. Wallace ZS, Khosroshahi A, Jakobiec FA, et al. IgG4-related systemic disease as a cause of "idiopathic" orbital inflammation, including orbital myositis, and trigeminal nerve involvement. *Surv Ophthalmol*. 2012;57(1):26–33.
34. Eha J, Pitz S, Pohlenz J. Clinical features of pediatric Graves' orbitopathy. *Int Ophthalmol*. 2010;30:717–721.
35. Goldstein SM, Katowitz WR, Moshang T, et al. Pediatric thyroid–associated orbitopathy: the Children's Hospital of Philadelphia experience and literature review. *Thyroid*. 2008;18(9):997–999.
36. Durairaj VD, Bartley GB, Garrity JA. Clinical features and treatment of Graves ophthalmopathy in pediatric patients. *Ophthal Plast Reconstr Surg*. 2006;22(1):7–12.
37. Yokoyama N, Nagataki S, Uetani M, et al. Role of magnetic resonance imaging in the assessment of disease activity in thyroid-associated ophthalmopathy. *Thyroid*. 2002;12(3):223–227.
38. Jiang H, Wang Z, Xian J, et al. Evaluation of rectus extraocular muscles using dynamic contrast-enhanced MR imaging in patients with Graves' ophthalmopathy for assessment of disease activity. *Acta Radiol*. 2012;53(1):87–94.
39. Kirsch EC, Kaim AH, DeOliveira MG, et al. Correlation of signal intensity ratio on orbital MRI-TIRM and clinical activity score as a possible predictor of therapy response in Graves' orbitopathy—a pilot study at 1.5 T. *Neuroradiology*. 2010;52:91–97.
40. Shetty AK, Gedalia A. Childhood sarcoidosis: a rare but fascinating disorder. *Pediatr Rheumatol*. 2008;6:16.
41. El Hansali Z, Oukabli M, Laktaoui A, et al. Childhood sarcoidosis: ophthalmological manifestations and diagnostic difficulties in two cases. *J Fr Ophtalmol*. 2012;35(4):290.e1–290.e5.
42. Miller AK, Khademian Z, Pearl PL. Uveitis and white matter abnormalities in pediatric sarcoidosis. *Arch Ophthalmol*. 2010;67(7):890–891.
43. Prabhakaran VC, Saeed P, Esmaeli B, et al. Orbital and adnexal sarcoidosis. *Arch Ophthalmol*. 2007;125(12):1657–1662.
44. Carmody RF, Mafee MF, Goodwin JA, et al. Orbital and optic pathway sarcoidosis: MR findings. *AJNR Am J Neuroradiol*. 1994;15(4):775–783.
45. Mafee MF, Dorodi S, Pai E. Sarcoidosis of the eye, orbit, and central nervous system. Role of MR imaging. *Radiol Clin North Am*. 1999;37(1):73–87.
46. Demirci H, Christianson MD. Orbital and adnexal involvement in sarcoidosis: analysis of clinical features and systemic disease in 30 cases. *Am J Ophthalmol*. 2011;151(6):1074–1080.
47. Cabral DA, Uribe AG, Benseler S, et al. Classification, presentation, and initial treatment of Wegener's granulomatosis in childhood. *Arthritis Rheum*. 2009;60(11):3413–3424.
48. Akikusa JD, Schneider R, Harvey EA, et al. Clinical features and outcome of pediatric Wegener's granulomatosis. *Arthritis Rheum*. 2007;57(5):837–844.
49. Duffy M. Advances in diagnosis, treatment, and management of orbital and periocular Wegener's granulomatosis. *Curr Opin Ophthalmol*. 1999;10:352–357.
50. Vischio JA, McCrary CT. Orbital Wegener's granulomatosis: a case report and review of the literature. *Clin Rheumatol*. 2008;27:1333–1336.
51. Courcoutsakis NA, Langford CA, Sneller MC, et al. Orbital involvement in Wegener granulomatosis: MR Findings in 12 patients. *J Comput Assist Tomogr*. 1997;21(3):452–458.
52. Provenzale JM, Mukherji S, Allen NB, et al. Orbital involvement by Wegener's granulomatosis: imaging findings. *AJR Am J Roentgenol*. 1996;166:929–934.
53. Bonhomme GR, Waldman AT, Balcer LJ, et al. Pediatric optic neuritis: brain MRI abnormalities and risk of multiple sclerosis. *Neurology*. 2009;72(10):881–885.
54. Wilejto M, Shroff M, Buncic JR, et al. The clinical features, MRI findings, and outcome of optic neuritis in children. *Neurology*. 2006;67(2):258–262.
55. Morales DS, Siatkowski RM, Howard CW, et al. Optic neuritis in children. *J Pediatr Ophthalmol Strabismus*. 2000;37(5):254–259.
56. Lucchinetti CF, Kiers L, O'Duffy A, et al. Risk factors for developing multiple sclerosis after childhood optic neuritis. *Neurology*. 1997;49(5):1413–1418.
57. Lana-Peixoto MA, Cardoso de Andrade G. The clinical profile of childhood optic neuritis. *Arq Neuropsiquiatr*. 2001;59(2–B):311–317.
58. Kupersmith MJ, Alban T, Zeiffer B, et al. Contrast-enhanced MRI in acute optic neuritis: relationship to visual performance. *Brain*. 2002;125:812–822.

59. Hickman SJ, Toosy AT, Jones SJ, et al. A serial MRI study following optic nerve mean area in acute optic neuritis. *Brain*. 2004;127:2498–2505.
60. Naismith RT, Xu J, Tutlam NT, et al. Disability in optic neuritis correlates with diffusion tensor-derived directional diffusivities. *Neurology*. 2009;72:589–594.
61. Naismith RT, Xu J, Tutlam NT, et al. Diffusion tensor imaging in acute optic neuropathies. *Arch Neurol*. 2011;12:e1–e7.
62. Smith SA, Williams ZR, Ratchford JN, et al. Diffusion tensor imaging of the optic nerve in multiple sclerosis: association with retinal damage and visual disability. *AJNR Am J Neuroradiol*. 2011;32(9):1662–1668.
63. Kolbe S, Bajraszewski C, Chapman C, et al. Diffusion tensor imaging of the optic radiations after optic neuritis. *Hum Brain Mapp*. 2001;13:e1–e15.
64. Dasenbrock HH, Smith SA, Ozturk A, et al. Diffusion tensor imaging of the optic tracts in multiple sclerosis: association with retinal thinning and visual disability. *J Neuroimaging*. 2011;21:e41–e49.
65. Reich DS, Smith SA, Gordon-Lipkin EM, et al. Damage to the optic radiation in multiple sclerosis is associated with retinal injury and visual disability. *Arch Neurol*. 2009;66(8):998–1006.
66. Hickman SJ, Toosy AT, Jones SJ, et al. Serial magnetization transfer imaging in acute optic neuritis. *Brain*. 2004;127(3):692–700.
67. Boorstein JM, Moonis G, Boorstein SM, et al. Optic neuritis: imaging with magnetization transfer. *AJR Am J Roentgenol*. 1997;169:1709–1712.
68. Sun MH, Wang HS, Chen KJ, et al. Clinical characteristics of optic neuritis in Taiwanese children. *Eye*. 2011;25(11):1527–1528.
69. Optic Neuritis Study Group. Multiple sclerosis risk after optic neuritis: final optic neuritis treatment trial follow-up. *Arch Neurol*. 2008;65(6):727–732.
70. Lennon VA, Wingerchuk DM, Kryzer TJ, et al. A serum autoantibody marker of neuromyelitis optica: distinction from multiple sclerosis. *Lancet*. 2004;364(9451):2106–2112.
71. Lennon VA, Kryzer TJ, Pittock SJ, et al. IgG marker of optic-spinal multiple sclerosis binds to the aquaporin-4 water channel. *J Exp Med*. 2005;202:473–477.
72. Krupp LB, Banwell B, Tenembaum S, et al. Consensus definitions proposed for pediatric multiple sclerosis and related disorders. *Neurology*. 2007;68:s7–s12.
73. Wingerchuk DM, Lennon VA, Pittock SJ, et al. Revised diagnostic criteria for neuromyelitis optica. *Neurology*. 2006;66(10):1485–1489.
74. Huppke P, Blüthner M, Bauer O, et al. Neuromyelitis optica and NMO-IgG in European pediatric patients. *Neurology*. 2010;75(19):1740–1744.
75. Banwell B, Tenembaum S, Lennon VA, et al. Neuromyelitis optica-IgG in childhood inflammatory demyelinating CNS disorders. *Neurology*. 2008;70(5):344–352.
76. Weinshenker BG, Wingerchuk DM, Vukusic S, et al. Neuromyelitis optica: IgG predicts relapse after longitudinally extensive transverse myelitis. *Ann Neurol*. 2006;59:566–569.
77. Nakamura Y, Ikeda K, Yoshii Y, et al. Influenza-associated monophasic neuromyelitis optica. *Intern Med*. 2011;50:1605–1609.
78. Sellner J, Hemmer B, Mühlau M. The clinical spectrum and immunobiology of parainfectious neuromyelitis optic (Devic) syndromes. *J Autoimmunity*. 2010;34:371–379.
79. Lotze TE, Northrop JL, Hutton GJ, et al. Spectrum of pediatric neuromyelitis optica. *Pediatrics*. 2008;122:e1039–e1047.
80. Collongues N, Marignier R, Zéphir H, et al. Long-term follow-up of neuromyelitis optica with a pediatric onset. *Neurology*. 2010;75(12):1084–1088.
81. Pittock SJ, Lennon VA, Krecke K, et al. Brain abnormalities in neuromyelitis optica. *Arch Neurol*. 2006;63:390–396.
82. Pittock SJ, Weinshenker BG, Lucchinetti CF, et al. Neuromyelitis optica brain lesions localized at sites of high aquaporin 4 expression. *Arch Neurol*. 2006;63:964–968.
83. Toker E, Yenice O, Yilmaz Y. Isolated bilateral optic neuropathy in acute disseminated encephalomyelitis. *J Pediatr Ophthalmol Strabismus*. 2003;40(4):232–235.
84. Bangsgaard R, Larsen VA, Milea D. Isolated bilateral optic neuritis in acute disseminated encephalomyelitis. *Acta Ophthalmol Scand*. 2006;84:815–817.
85. Tenembaum S, Chamoles N, Fejerman N. Acute disseminated encephalomyelitis: a long-term follow-up study of 84 pediatric patients. *Neurology*. 2002;59:1224–1231.
86. Sonnevillea R, Kleinb IF, Wolff M. Update on investigation and management of postinfectious encephalitis. *Curr Opin Neurol*. 2010; 23:300–304.
87. Schirmer CM, Hedges TR. Mechanisms of visual loss in papilledema. *Neurosurg Focus*. 2007;23(5):E5.
88. Jinkins JR, Athale S, Xiong L, et al. MR of optic papilla protrusion in patients with high intracranial pressure. *AJNR Am J Neuroradiol*. 1996;17:665–668.
89. Seitz J, Held P, Strotzer M, et al. Magnetic resonance imaging in patients diagnosed with papilledema: a comparison of 6 different high-resolution T1- and T2(*)-weighted 3-dimensional and 2-dimensional sequences. *J Neuroimag*. 2002;12(2):164–171.
90. Pakzad-Vaezi K, Cochrane D, Sargent M, et al. Conventional and diffusion-weighted magnetic resonance imaging findings in a pediatric patient with a posterior fossa brain tumor and papilledema. *Pediatr Neurosurg*. 2009;45:414–418.
91. Brodsky MC, Glasier CM. Magnetic resonance visualization of the swollen optic disc in papilledema. *J Neuroophtalmol*. 1995;15(2):122–124.
92. Ganesh A, Al-Zuhaibi S, Pathare A, et al. Orbital infarction in sickle cell disease. *Am J Ophthalmol*. 2008;146:595–601.
93. Noble J, Schendel S, Weizblit N, et al. Orbital wall infarction in sickle cell disease. *Can J Ophthalmol*. 2008;43:603–604.
94. Ozkavukcu E, Fitoz S, Yagmurlu B, et al. Orbital wall infarction mimicking periorbital cellulitis in a patient with sickle cell disease. *Pediatr Radiol*. 2007;37:388–390.
95. Saito N, Nadgir RN, Flower EN, et al. Clinical and radiologic manifestations of sickle cell disease in the head and neck. *Radiographics*. 2010;30:1021–1035.
96. Umans H, Haramati N, Flusser G. The diagnostic role of gadolinium enhanced MRI in distinguishing between acute medullary bone infarct and osteomyelitis. *Magn Reson Imaging*. 2000;18:255–262.
97. Jain R, Sawhney S, Rizvi SG. Acute bone crises in sickle cell disease: the T1 fat-saturated sequence in differentiation of acute bone infarcts from acute osteomyelitis. *Clin Radiol*. 2008;63:59–70.
98. Yu-Wai-Man P, Turnbull TM, Chinnery PF. Leber hereditary optic neuropathy. *J Med Genet*. 2002;39:162–169.
99. Perez F, Anne O, Debruxelles S, et al. Leber's optic neuropathy associated with disseminated white matter disease: a case report and review. *Clin Neurol Neurosurg*. 2009;11:83–86.
100. Kuker W, Weir A, Quaghebeur G, et al. White matter changes in Leber's hereditary optic neuropathy: MRI findings. *Eur J Neurol*. 2007;14:591–593.
101. Newman NJ. Treatment of Leber hereditary optic neuropathy. *Brain*. 2011;134:2447–2455.
102. Klopstock T, Yu-Wai-Man P, Dimitriadis K, et al. A randomized placebo-controlled trial of idebenone in Leber's hereditary optic neuropathy. *Brain*. 2011;134:2677–2686.
103. Milea D, Amati-Bonneau P, Reynier P, et al. Genetically determined optic neuropathies. *Curr Opin Neurol*. 2010;23:24–28.
104. Yu-Wai-Man P, Griffiths PG, Gorman GS, et al. Multi-system neurological disease is common in patients with OPA1 mutations. *Brain*. 2010;133:771–786.
105. Votruba M, Leary S, Losseff N, et al. MRI of the intraorbital optic nerve in patients with autosomal dominant optic atrophy. *Neuroradiology*. 2000;42:180–183.
106. Hussain SA, Zimmerman HH, Abdul-Rhaman OA, et al. Optic nerve enlargement in Krabbe disease: a pathophysiologic and clinical perspective. *J Child Neurol*. 2011;26(5):642–644.
107. Patel B, Gimi B, Vachha B, et al. Optic nerve and chiasm enlargement in a case of infantile Krabbe disease: quantitative comparison with 26 age-matched controls. *Pediatr Radiol*. 2008;38:697–699.
108. Jones BV, Barron TF, Towfighi J. Optic nerve enlargement in Krabbe's disease. *AJNR Am J Neuroradiol*. 1999;20(7):1228–1231.
109. Bussiere M, Kotylak T, Naik K, et al. Optic nerve enlargement associated with globoid cell leukodystrophy. *Can J Neurol Sci*. 2006;33:235–236.

# 7 Orbital Neoplasia

Tamara Feygin and Avrum N. Pollock

A wide variety of primary and secondary neoplasms may affect the orbit. Most orbital masses are benign and slow growing, but approximately 20% are malignant. Making the correct diagnosis may be difficult for several reasons. In children, it may be challenging to obtain an accurate history and physical examination. The presenting symptoms (and imaging findings) of different pathologic entities may overlap considerably. Nonneoplastic masses may present with visual loss and destructive changes of the orbit, raising concerns for malignancy. At the same time, some malignant tumors of the orbit may closely resemble inflammatory cellulitis, both clinically and on imaging. Some orbital lesions have a high association with systemic and genetic disorders, and, in these cases, represent just the "tip of the iceberg." Diagnosis of an orbital lesion behooves the interpreter to diligently search for concurrent lesions elsewhere in the body.

A precise and timely diagnosis of an orbital mass can be crucial for successful treatment and prevention of blindness. Imaging plays an integral role, and, at times, more than one imaging modality may be required to allow delineation of the lesion's morphology and extent. Proper utilization of imaging modalities, in particular ultrasonography (US), computed tomography (CT), magnetic resonance imaging (MRI), positron emission tomography (PET), and, in selected cases, conventional angiography, should be thoughtfully considered. Newer advanced imaging technologies contribute to the precise diagnosis of orbital pathology. The radiologist should recommend the best imaging modality to be used in specific clinical scenarios.

US is primarily a tool used by ophthalmologists in the assessment of diseases of the globe and extraocular muscles (EOMs). This modality is especially valuable for the evaluation of young children with leukocoria but may be suboptimal in assessing the full extent of extraocular and intracranial spread of a primary ocular mass.

CT is a very effective tool in the diagnosis of pediatric orbital disease. It is widely available and often may serve as the initial imaging modality for evaluation of acute proptosis, orbital cellulitis, and trauma. CT is excellent at depicting calcifications and evaluating potential bony involvement. Current CT equipment allows for rapid acquisition of high-resolution images in the axial plane, with near real-time additional computed reformation images in the coronal and/or sagittal planes, thus avoiding the need for direct acquisition of images in orthogonal planes. Three-dimensional (3D) reformations are important for surgical planning and better depiction of orbital volumes (e-Fig. 7.1A). The data acquisition is rapid enough to obviate the need for sedation in many cases. Pediatric CT use has declined in recent years due to the continued trepidation regarding potential deleterious effects of radiation.

Many orbital lesions are optimally imaged utilizing MRI, especially since the advent of surface coils and fat suppression (FS) techniques. Protocols for orbital imaging include high-resolution, small field of view (FOV) thin-slice T1-weighted (T1W), T2-weighted (T2W), and postcontrast-enhanced (CE) sequences in the orthogonal planes.

Utilization of FS is essential when imaging the orbit, as it allows better tissue discrimination and distinction from intraorbital fat and better assessment of the bone marrow within the bony orbit. Diffusion-weighted imaging (DWI) plays an important role in further characterizing the tissues within and around tumors. Diffusion sequences based on nonecho planar principles and on parallel imaging produce images of better quality with less geometric distortion. Apparent diffusion coefficient (ADC) mapping may help in the differentiation of benign and malignant lesions and may play a role in the grading of malignancies as poorly differentiated versus well differentiated. DWI/ADC can increase the conspicuity of early bone marrow infiltration (e-Fig. 7.1B). Increased ADC values within a diffusion-restricting mass, after the initiation of therapy, usually indicates a favorable response to therapy. Arterial spin labeling (ASL) is a noninvasive method utilizing magnetized protons/water molecules in arterial blood as a tracer (e-Fig. 7.1C). It allows measurement of tissue perfusion and may be helpful in the delineation of high-flow vascular lesions, benign and malignant, and in the potential assessment of treatment response. Both DWI and ASL imaging may help to pinpoint the most aggressive component of an orbital lesion (with restricted diffusion and increased perfusion) and help to target biopsy sites to allow successful tissue sampling. Constructive interference steady-state (CISS) is a heavily T2W volumetric sequence that allows isotropic image reformations in any plane, and exquisite depiction of minute lesions (e-Fig. 7.1D).

Meticulous attention should be paid for the presence of bone erosion and possible intracranial invasion. Tumor extension through the orbital foramina and fissures is better delineated on MRI, whereas erosive bony changes are better depicted on CT. CT and MRI are complimentary imaging techniques in the evaluation of orbital tumors, and, in some cases, both may be indicated for proper and complete evaluation of complex orbital masses. Most protocols for imaging of orbital tumors include brain imaging in the evaluation of potential intracranial extension or in the search for additional lesions. When planned in advance, CT and MRI may also allow for intraoperative navigation, thereby assisting the surgeon with lesion localization in the operating theater. PET imaging and recently introduced hybrid PET/CT systems may be successfully utilized in assessing malignant orbital lesions. Most malignant orbital masses demonstrate increased uptake of $^{18}$F-fluorodeoxyglucose (FDG) (e-Fig. 7.1E). PET/CT is most often helpful in monitoring therapeutic response, particularly if a residual mass remains on MRI after completion of therapy. Residual or recurrent active disease will continue to exhibit increased uptake of FDG, while masses with inactive, scarred tumor will show no uptake on PET. PET/CT can also identify other areas of involvement remote from the orbit, which can be seen with metastases and lymphoma. Metaiodobenzylguanidine (MIBG) scintigraphy is mainly used for the detection of distant neuroblastoma (NB) metastases (e-Fig. 7.1F). Recently introduced optical coherence tomography (OCT), a noninvasive method based on the utilization of near-infrared light, is remarkable for very good tissue penetration and excellent resolution. OCT has recently been applied in the imaging of optic pathway gliomata and retinal lesions.

A combination of imaging findings, along with clinical signs and symptoms, may narrow the differential diagnosis, although the definitive diagnosis is almost always based on histopathologic findings.

The following discussion of orbital pathology imaging is divided into four categories: (1) ocular lesions, (2) optic nerve sheath lesions, (3) primary orbital lesions, and (4) lesions that secondarily involve the orbit.

## Abstract:

This chapter is dedicated to orbital imaging in children. The common and uncommon imaging features of a variety of benign and malignant orbital lesions are described.

Imaging plays an important role in evaluation of orbital disease. To make the correct diagnosis of orbital lesions in children may be challenging. The presenting symptoms (and imaging findings) of different pathologic entities in the orbits may overlap considerably. Non-neoplastic orbital masses may present in a dramatic fashion with visual loss and destructive changes of the orbit, raising concerns for malignancy. At the same time, some malignant tumors of the orbit may closely resemble inflammatory cellulitis both clinically and on imaging. Some of the orbital lesions have a high association with systemic and genetic disorders and, in these cases, represent just the "tip of the iceberg." Diagnosis of the orbital lesion may prompt diligent search of concurrent lesions elsewhere in the body. New imaging modalities and new applications of existing technologies have been developed and successfully implemented in clinical practice. The radiologist should be familiar with modern orbital imaging modalities and should be able to recommend appropriate testing for the ordering clinician.

## Keywords:

orbital imaging
retinoblastoma
RMS
teratoma
benign orbital lesions
primary orbital malignant tumors
orbital metastases

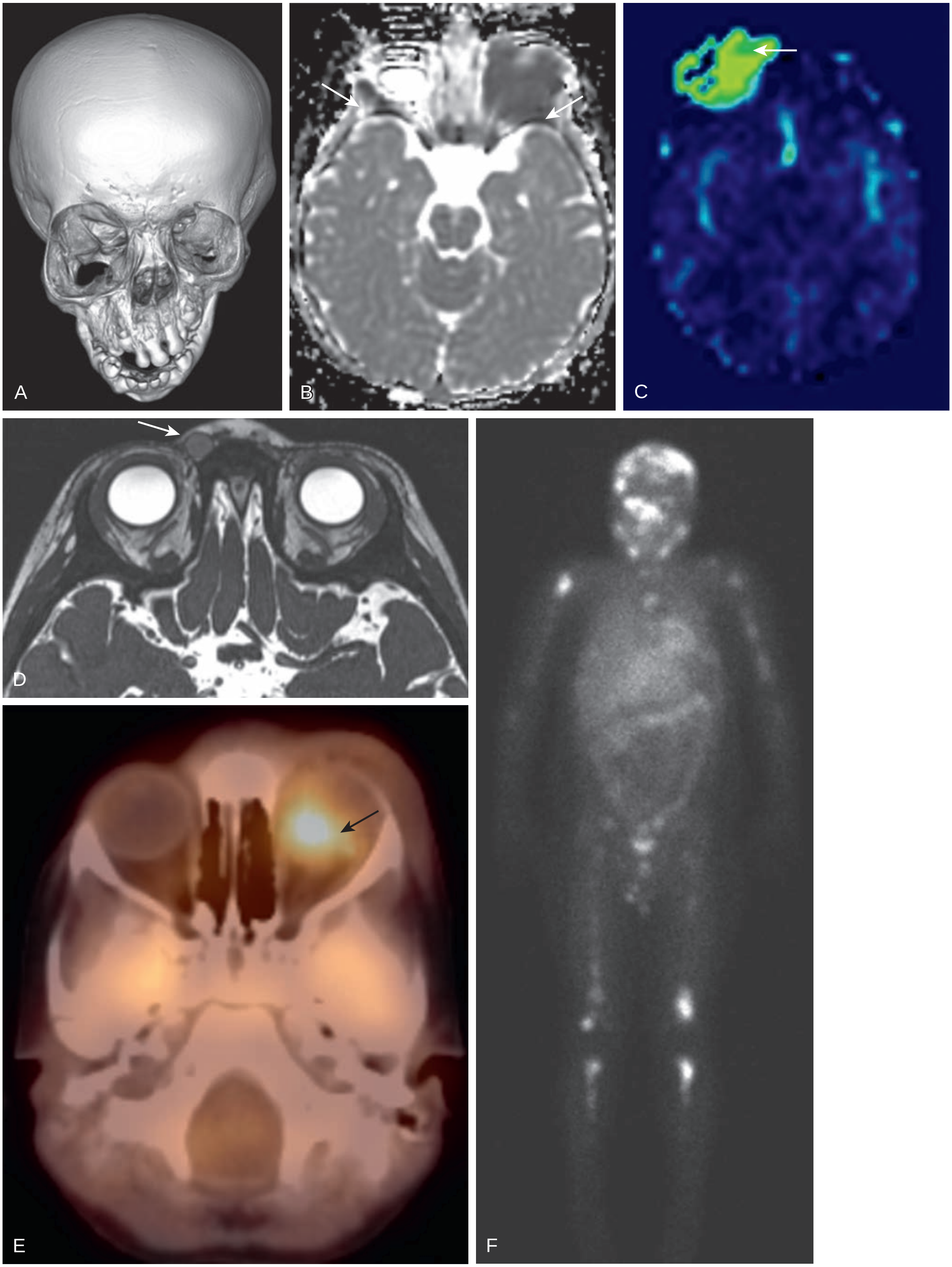

**e-Figure 7.1. Imaging techniques.** (A) Three-dimensional reconstructed orbital noncontrast CT in a patient with NF1 with sphenoid wing dysplasia and marked enlargement of the right bony orbit. (B) Apparent diffusion coefficient (ADC) mapping in patient with leukemia demonstrates restricted diffusivity within the left orbital chloroma and within bone marrow *(arrows),* indicative of leukemic infiltration. (C) Arterial spin labeling (ASL) image demonstrates a highly vascular lesion *(arrow)* of the right orbit (infantile hemangioma). (D) Axial constructive interference steady-state (CISS) image demonstrates a small epidermoid of the right orbit without osseous involvement *(arrow)*. (E) PET/CT images in a patient with a left orbital mass demonstrates increased uptake of $^{18}$F-fluorodeoxyglucose (FDG) *(arrow)* within the lesion (rhabdomyosarcoma). (F) I-123 Metaiodobenzylguanidine (MIBG) scan in a patient with metastatic NB demonstrates multiple foci of increased tracer uptake in the appendicular skeleton and the skull/face, including within the orbits.

## OCULAR LESIONS

### Retinoblastoma

Retinoblastoma (RB) is the most common intraocular pediatric tumor, arising from retinal cone precursor cells. This tumor typically affects children younger than 4 years of age. Even though RB is considered a congenital type of malignant tumor, it is rarely recognized in neonates. Attempts to detect small fetal ocular lesions in utero in high-risk fetuses have, to date, been unsuccessful. Loss or mutation of RB genes (*RB1* gene located on chromosome 13 band q14) causes absence of RB control protein and subsequent uncontrolled cell division and tumor growth. Two forms of RB—germline (familial or sporadic) and somatic sporadic—differ in their clinical presentations and prognoses. Germline RB may be autosomal dominant (familial), but is more likely to result from a new sporadic mutation. Familial RB usually manifests as bilateral multifocal disease, but in 10% to 15% of patients with unilateral involvement, a germline mutation can be found. Familial RB clinically presents at an earlier age (mean age, 6 months). Patients with heritable *RB1* mutations have increased risk (progressive throughout their lifetime) of the development of other malignancies. This risk is tripled in patients who have undergone radiation therapy. Secondary tumors include osteogenic and soft tissue sarcomas, leukemia, and malignant melanoma. Secondary non-ocular tumors are the leading cause of death in these patients, rather than the primary RB itself. Patients with heritable RB are at a 50% risk for the transmission of the disease to their offspring.

Sporadic RB is usually solitary, unilateral, and associated with postzygotic somatic mutation of the *RB1* gene. This type of RB is usually present in older children (the average age at presentation varies from 13–18 months). Genetic testing is indicated in all patients with RB. Patients with sporadic noninvasive intraocular tumors have an excellent prognosis, with a survival rate greater than 90% in countries with resources to provide modern treatment.

Recent advances in RB treatment have resulted in a new approach to tumor classification. The International Retinoblastoma Classification Grouping is based on expected results of modern chemotherapy regimens and predicted salvage of the globe. There are several variants of this classification, which are based on tumor size, location, and associated seeding (Box 7.1). The tumors range from group A (RB less than 3 mm) to group E (massive destructive RB) (Fig. 7.2A). The pathologic TNM system for RB describes important prognostic information about tumor spread through the sclera into the orbit, invasion of the optic nerve, and presence of distant metastases.

RB may present with a variety of symptoms, the most frequent clinical signs being that of leukocoria (Fig. 7.2B) and strabismus. Leukocoria (or white pupillary reflex) is the most common presenting sign of RB and reflects replacement of vitreous by tumor tissue. Retinal hemorrhage may obscure the visibility of the underlying mass on clinical exam; therefore every unexplained retinal hemorrhage in a young child requires mandatory imaging assessment. Strabismus is usually related to a tumor located within the macula. In contrast to leukocoria, tumors presenting with strabismus as their initial sign are associated with a higher survival rate and a higher chance of salvage of the globe.

Clinical presentations may differ depending on patterns of tumor growth. Endophytic tumors, which arise from internal retinal layers, grow anteriorly into the vitreous, with resultant tendency to vitreous seeding. Exophytic tumors, which arise from external retinal layers grow into the subretinal space and tend to have retinal detachment, earlier choroidal involvement, and increased risk of metastatic spread. Most tumors develop mixed patterns. A rare diffuse form of RB occurs in 2% of cases and manifests by diffuse infiltrative growth within the retina, without noticeable nodular mass, and without intralesional calcifications. This diffuse infiltrative type of RB presents at a later age, with the clinical symptoms at times mimicking an inflammatory process such as pseudoinflammatory glaucoma.

Imaging may reliably distinguish RB from a host of other conditions that also may present with leukocoria (persistent hyperplastic primary vitreous [PHPV], retinopathy of prematurity [ROP], congenital cataract, Coats disease, and acquired toxocariasis). In many RB centers, ocular US has replaced orbital CT for initial disease assessment. Three-dimensional high-frequency US is sufficient for assessment of tumor and calcifications but is less suitable for the evaluation of extraocular spread. RB is readily visible on US as an echogenic irregular retinal mass with focal acoustic shadows. CT is an excellent tool for depicting ocular

**BOX 7.1** International Classification of Retinoblastoma

- Group A—Retinoblastoma < 3 mm
- Group B—Retinoblastoma > 3 mm, macular location, or minor subretinal fluid
- Group C—Retinoblastoma with localized seeds
- Group D—Retinoblastoma with diffuse seeds
- Group E—Massive retinoblastoma necessitating enucleation

Notes: This classification is based on tumor size, location, and associated seeding. This new classification system is designed to simplify grouping and assist in predicting treatment outcomes.

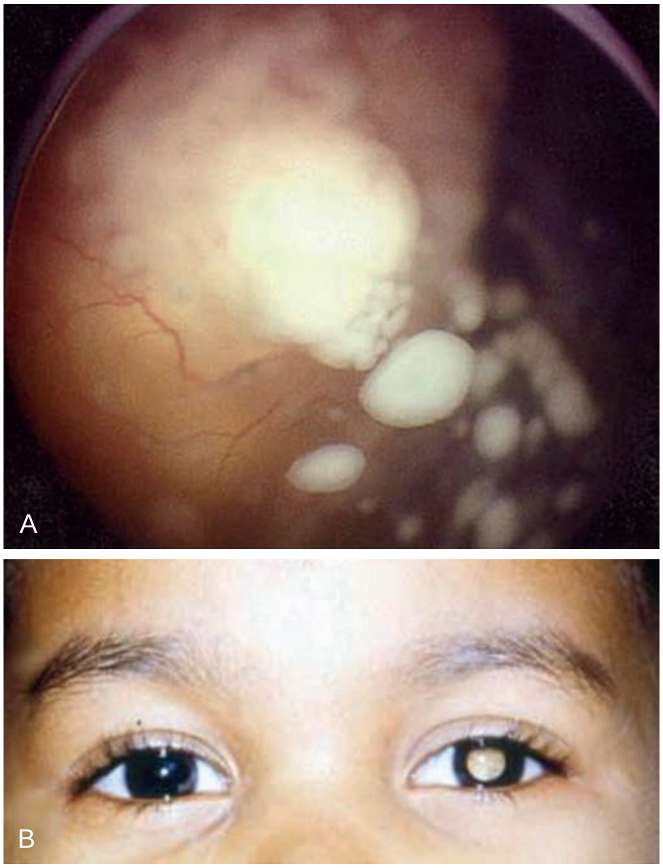

**Figure 7.2. Retinoblastoma (RB).** (A) Ophthalmoscopic examination under anesthesia photo demonstrates multifocal RB (white plaques), indicating group D disease. (B) Clinical photo demonstrates left-sided leukocoria in a patient with RB.

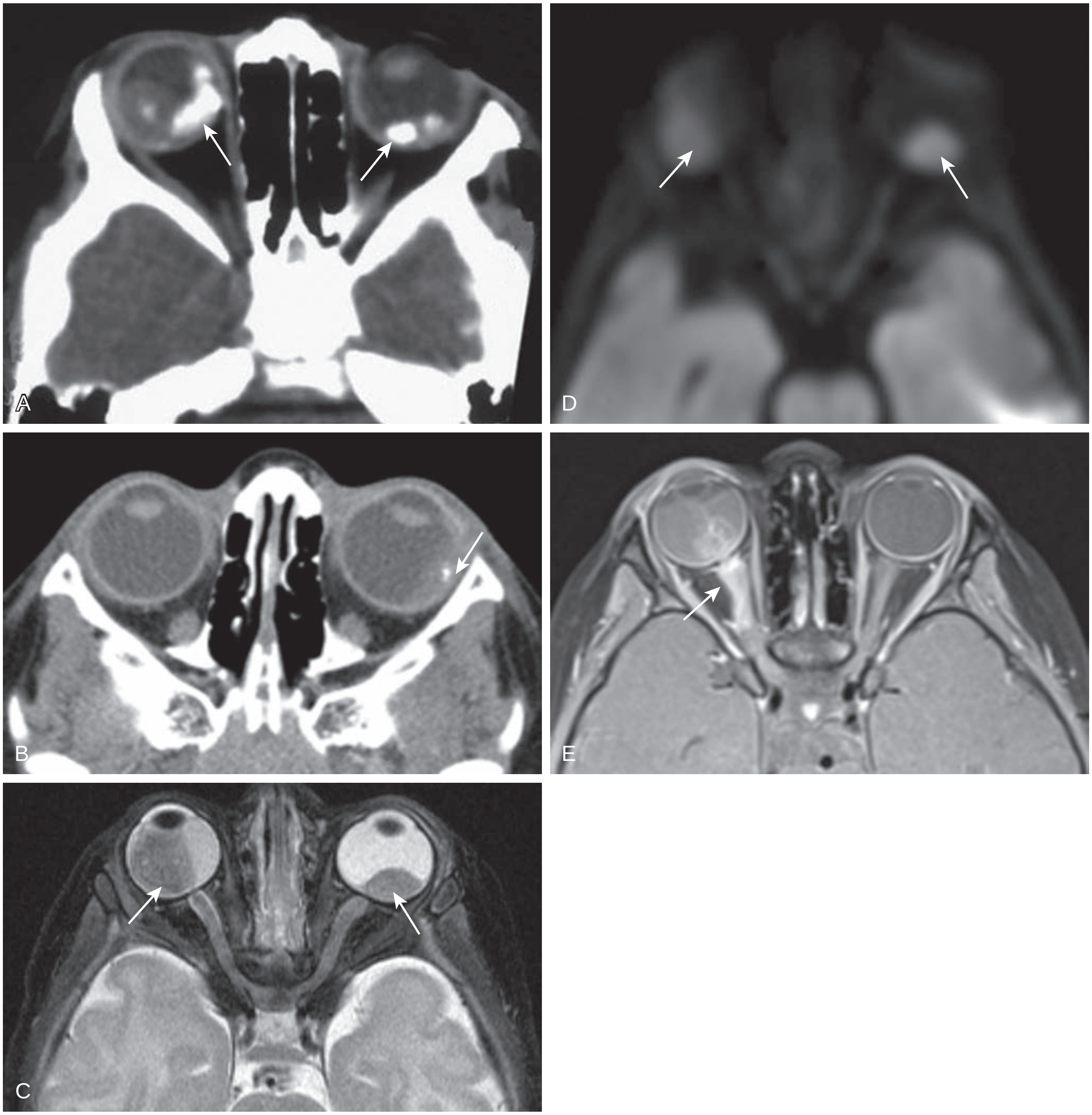

**Figure 7.3. Retinoblastoma in four different patients.** (A) Noncontrast CT image through the orbits demonstrates bilateral, markedly calcified bilateral ocular masses *(arrows)*. (B) Noncontrast CT image in another patient demonstrates a unilateral, left-sided, small calcified mass *(arrow)*. (C) Axial fat-saturated T2-weighted and (D) axial diffusion-weighted imaging (DWI) MR image demonstrate bilateral, lobulated, T2-hypointense, retinal-based masses that exhibit diffusion restriction *(arrows)*. (E) Axial contrast-enhanced fat-saturated T1-weighted MR image demonstrates advanced RB of the right globe involving intraorbital optic nerve *(arrow)*.

calcifications (Figs. 7.3A and B), but its use in RB evaluation has decreased due to concerns of associated radiation risks. MRI has become a relatively quick and convenient modality in the evaluation of RB. A variety of tailored MRI sequences are beneficial in illustrating RB morphology and extension. The malignant, markedly cellular nature of this neoplasm (composed of immature retinoblasts) is confirmed on T2W and DWI sequences (Figs. 7.3C and D), whereas intraocular hemorrhages and calcifications are best depicted on gradient echo (GE) sequences. Essential detection of the aggressive features of advanced disease, such as invasion of the postlaminar optic nerve or anterior chamber, can be best demonstrated on contrast-enhanced sequences, although are best demonstrated histologically on the enucleated specimen. It is essential to thoroughly search for even subtle choroidal thickening, and abnormal uveal or optic nerve enhancement (Fig. 7.3E). At times, retinal detachment and hemorrhage may be indistinct from tumor margin; therefore even the most modern imaging techniques may underestimate the degree of tumor extension.

Advanced disease may present with intraorbital, intracranial tumor extension and/or with distant metastases. Distant osseous metastases from RB can be found in the skull, spine, and long bones, with focal and diffuse involvement of the bones' marrow (e-Figs. 7.4A and B). Leptomeningeal and parenchymal metastases may occur (e-Fig. 7.4C). Whole-body MRI or conventional whole-body bone scan can be performed in the metastatic workup. Orbital or intracranial secondary tumors may often be differentiated from primary advanced metastatic RB lesions by their different imaging features (e-Fig. 7.4D). MRI is a valuable tool for disease monitoring and in the evaluation of treatment response but does not replace an examination under anesthesia by an experienced ophthalmologic oncologist. Vitreous seeding is the leading cause of treatment failure requiring enucleation and is almost below the threshold level of detection of present MRI modern day scanning techniques.

Trilateral (single midline) and quadrilateral (occurrence with a second midline tumor) RB refer to the uncommon association (3%–8%) of bilateral RB (rarely with unilateral RB) with intracranial histologically similar primary intracranial neuroectodermal tumor, most often in the pineal region. Suprasellar location of trilateral tumor has been reported with increased frequency in young patients with the unilateral familial form of RB. These lesions usually present within a year of the initial discovery of the ocular lesions, although, in a minority of cases, may be seen at the time of RB diagnosis (e-Fig. 7.4E). Diligent search for potential associated intracranial tumor should be performed during the first 4 years from the time of diagnosis. The diagnosis of trilateral RB had been associated with a dismal prognosis. However, early detection of intracranial lesions, and aggressive strategies including stem cell transplant, may improve cure rates.

Over the past several decades, standard treatment for RB has evolved from prior methods of surgical enucleation or external radiation. Most RB referral centers are now using alternative therapies that are aimed at eye salvage and avoiding the risks inherent with radiotherapy. These methods include systemic chemotherapy, and intraarterial and intravitreous chemotherapy, along with focal treatments (eye-sparing radiotherapy [local plaque radiation], laser photocoagulation, and cryotherapy) as the primary treatment modality, especially when tumors are small.

## Medulloepithelioma

Medulloepithelioma is another pediatric intraocular tumor that may present with leukocoria. This tumor is histologically distinct from RB and represents a rare embryonal type of neoplasm arising from the nonpigmented epithelial lining of the ciliary body. Some authors consider poorly differentiated medulloepitheliomas to be under the category of primitive neuroectodermal tumor (PNET). Patients are usually diagnosed in the first decade of life (at a mean age of 6 years of age). Clinical signs and imaging features of medulloepithelioma may closely resemble those of an RB. The lesion presents as a nodular enhancing intraocular mass arising from the ciliary body and may reveal internal calcifications (Fig. 7.5) and may restrict on DWI. Retinal detachment is common. Tumors may be benign or malignant, but metastatic disease is uncommon. Medulloepitheliomas have been divided into two types, teratoid and nonteratoid (diktyoma), based on their histology. More complex teratoid medulloepitheliomas are composed of heteroplastic elements, including cartilage, which may have associated calcifications, whereas the nonteratoid diktyoma presents as a well-defined, noncalcified mass, with associated diffuse contrast enhancement.

## Hereditary Ocular Hamartomatosis

Many neurocutaneous disorders (phakomatoses) have typical ocular masses that may or may not be visible with imaging techniques. These lesions represent hereditary hamartomas, which are composed of tissues with limited capacity for proliferation. Examples may be seen in the setting of tuberous sclerosis (TS), neurofibromatosis (NF), as well as Sturge–Weber (SW) and von Hippel–Lindau (VHL) diseases.

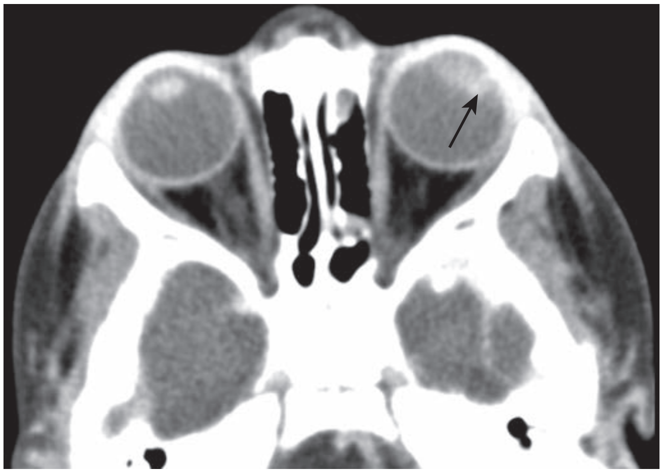

**Figure 7.5. Medulloepithelioma.** Axial contrast-enhanced CT of the orbit in a patient with a known medulloepithelioma demonstrates an amorphous lesion in the anterior chamber of the left globe, with associated punctate calcification, in the region of the ciliary body *(arrow)*.

Ocular manifestations of TS include astrocytic hamartoma of the retina and optic disc. These lesions have a typical appearance on ophthalmologic examination; however, they may calcify as patients age and may resemble drusen when located on the optic disc. On high-resolution T2W imaging, hamartomas of TS are detectable as small hypointense nodules within the globe (e-Fig. 7.6A).

Ocular stigmata of NF may present as macrophthalmosis and neuronal hamartomas of the iris, called Lisch nodules, which only occur with NF type 1 (e-Fig. 7.6B). Lisch nodules can only rarely be visualized with imaging.

Patients with SW syndrome and VHL disease may have ocular vascular hamartomas (e-Fig. 7.6C). Choroidal vascular malformations (formerly known as hemangioma), typical for SW syndrome, may be diffuse or localized, and can simulate melanoma on fundoscopic exam. These lesions may be differentiated from one another on MRI examination. Choroidal vascular hamartoma demonstrates T1W and T2W hyperintensity, which is opposite to the T2W signal characteristics expected with melanoma (hyperintense T1W signal and a hypointense T2W signal). Ocular manifestations of VHL consist of retinal angiomatosis, which may cause severe complications including retinal detachment and ocular destruction, and usually present later in childhood or in early adulthood (second and third decades of life).

## Drusen

Disc drusen are nonhamartomatous subretinal lesions without astrocytic hyperplasia. They consist of intrapapillary, partially calcified hyaline bodies that form concretions of unknown nature. Drusen are likely the most common etiology for congenital bilateral elevation of the optic nerve discs. Drusen may be detected on fundoscopic evaluation or may be seen as an incidental finding on imaging. In both scenarios, it is important to establish the benign nature of disc elevation so as not to confuse drusen with true papilledema. Drusen may be diagnosed by US, which demonstrates foci of increased echogenicity, or these lesions can be seen on CT as punctuate calcifications within the optic nerve heads (e-Fig. 7.7). MRI demonstrates isolated mild protrusion of the optic discs into the vitreous without perioptic CSF space enlargement or other imaging features of papilledema. Clinically,

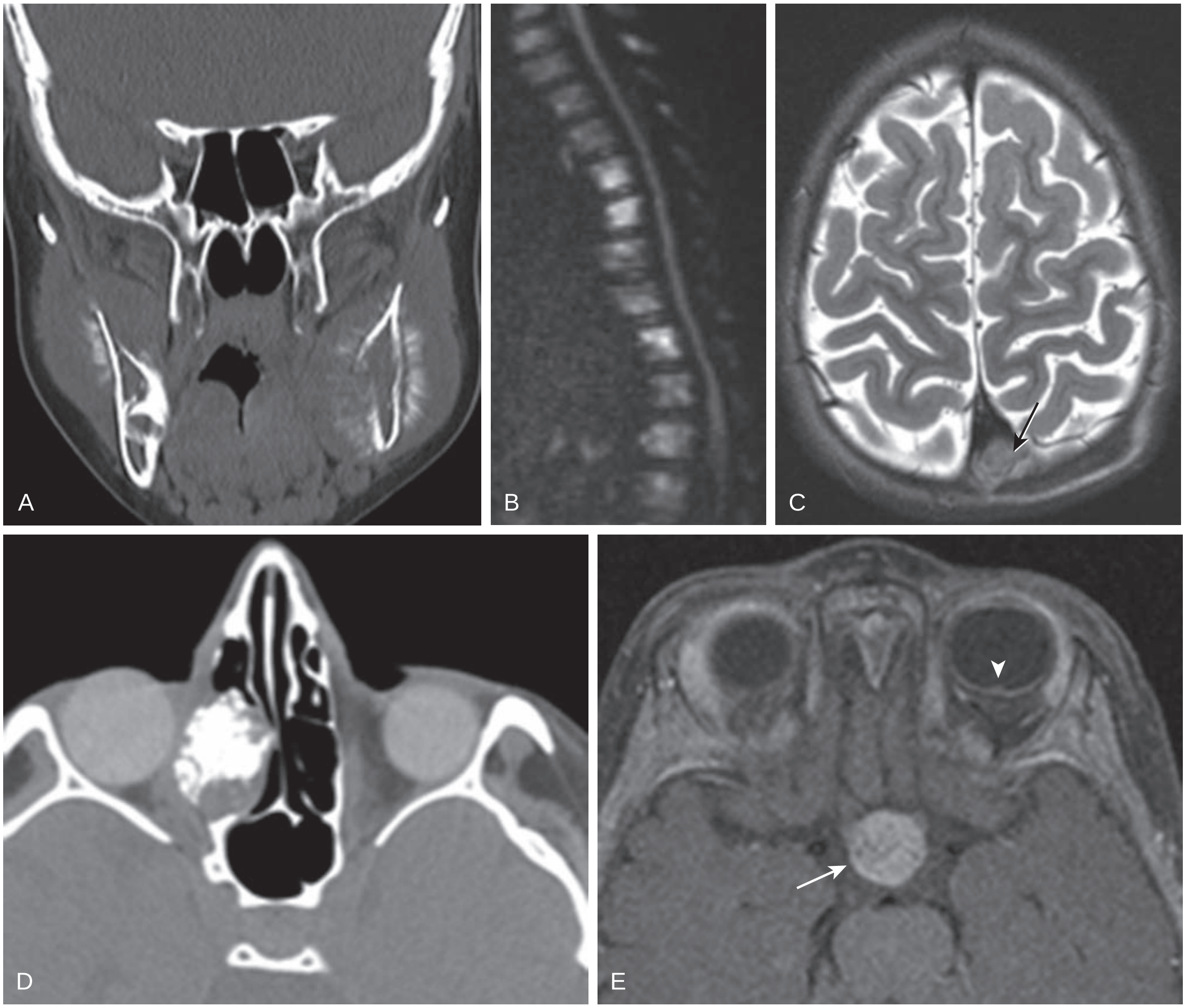

**e-Figure 7.4. Metastatic retinoblastoma (RB) in five different patients.** (A) Coronal noncontrast CT of the face demonstrates bilateral speculated/starburst type of periosteal new bone formation. (B) Sagittal diffusion-weighted imaging (DWI) MR image of the spine demonstrates multifocal vertebral restricted diffusion within the bone marrow. (C) Axial fat-saturated T2-weighted MR image through the vertex demonstrates a mass within the left parietal bone marrow, abutting the posterior aspect of the superior sagittal sinus/dura *(arrow)*. (D) Axial noncontrast CT image through the midorbital level in a patient with bilateral ocular prostheses postbilateral enucleation demonstrates a markedly dense (bony-type matrix) mass in the posterior right ethmoid air cells in keeping with a radiation-induced osteosarcoma. (E) Axial contrast-enhanced fat-saturated T1-weighted MR image at the level of the optic chiasm demonstrates rounded avidly enhancing suprasellar mass *(arrow)* in keeping with a trilateral retinoblastoma (RB). Note the tiny lesion at the 6 o'clock position of the left globe *(arrowhead)* in keeping with RB.

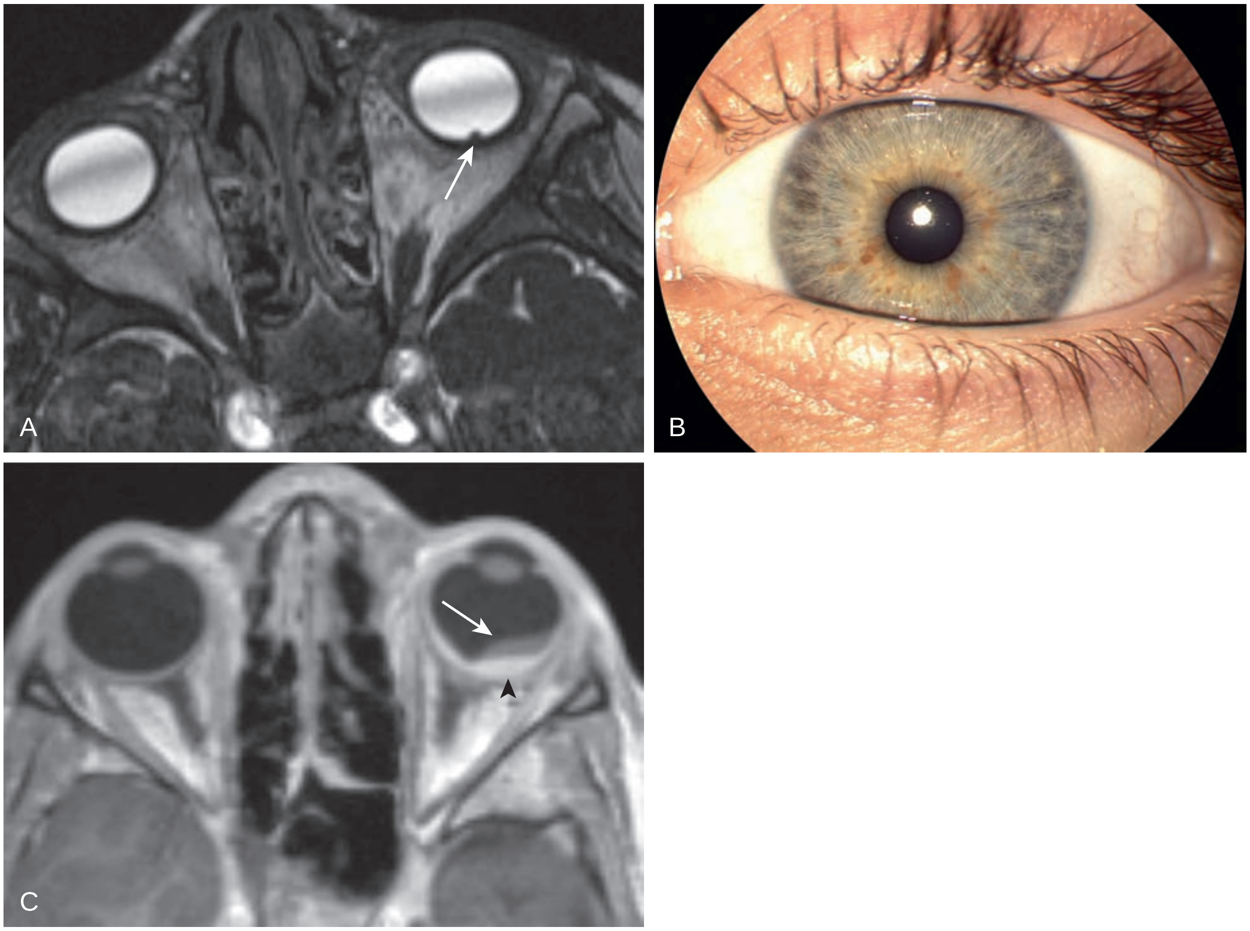

**e-Figure 7.6. Hereditary ocular hamartomatosis in three separate patients.** (A) High-resolution T2-weighted (constructive interference steady-state, CISS) MR image of a patient with tuberous sclerosis (TS) demonstrates a T2 hypointense nodule *(arrow)* at the 5 to 6 o'clock position of the left globe, in keeping with an astrocytic hamartoma of the retina. (B) Clinical photo of the iris of a patient with NF1 demonstrates yellowish-brown areas of discoloration at the 5 and 7 o'clock positions, in keeping with Lisch nodules (neuronal hamartomas of the iris). (C) Axial contrast-enhanced T1-weighted MR image at the mid-orbital level in a patient with von Hippel–Landau (VHL) demonstrates a biconvex enhancing mass extending from the 5 to 7 o'clock positions of the left globe in keeping with a retinal angioma *(black arrowhead)*. There is an associated retinal detachment *(white arrow)*.

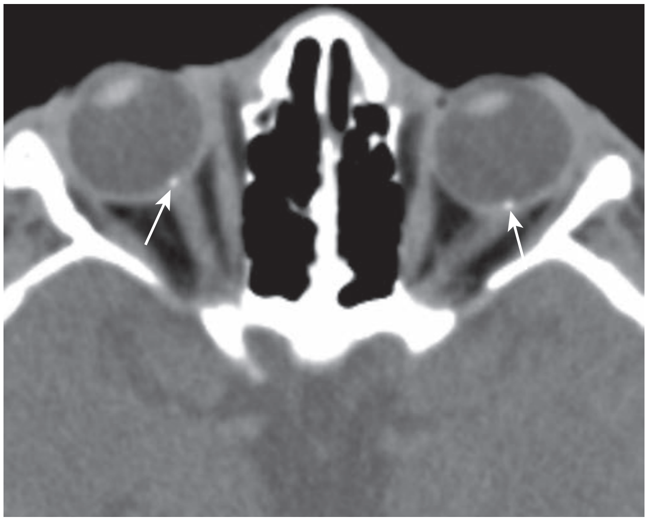

**e-Figure 7.7. Drusen.** Axial noncontrast CT image of the orbit in a patient with pseudopapilledema demonstrates bilateral mineralization of optic nerve discs *(arrows)*.

drusen are usually asymptomatic and only rarely may be associated with slowly progressive visual loss.

## OPTIC NERVE-SHEATH COMPLEX TUMORS

Optic nerve-sheath complex lesions include neoplasms of the optic nerves (gliomata), optic nerve sheaths (meningiomas), or rare cases of intraconal peripheral primitive neuroectodermal tumors (pPNETs).

### Optic Nerve Glioma

Optic nerve glioma (ONG) is the most common primary neoplasm of the optic nerve in children. ONG may be seen in the setting of NF1 (Fig. 7.8A) or may present as an isolated tumor (nonsyndromic) (Fig. 7.8B). ONGs, which are associated with NF1 (also see Chapter 35), are most often bilateral lesions that may involve the optic nerve and surrounding subarachnoid space, and are remarkable for their low-grade nature and favorable prognosis. Nonsyndromic ONGs are usually unilateral and histologically are either pilocytic or fibrillary astrocytomas. The mortality rate for these tumors is approximately 5% when the tumor involves only the optic nerve, but hypothalamic involvement portends a more ominous prognosis. Despite their benign histology, some series report mortality rates approaching 50%.

### Orbital Meningioma

Orbital meningioma is not a common pediatric lesion, but can be seen in patients in the first decade of life. It differs in many ways from adult meningioma. Meningioma of the orbit may be seen more frequently in children than in adults, and tend to grow more rapidly and to a larger size, undergo malignant changes, and have a greater rate of recurrence. Orbital meningioma may be a primary tumor of the perioptic space (pediatric primary optic nerve sheath meningioma [PPONSM]) (e-Figs. 7.9A and B). PPONSM is the most common form seen in children, possibly due to early presentation with visual symptoms, but may be poorly discernable on imaging in its early stages and may present only with slowly progressive optic nerve atrophy (e-Fig. 7.9C). Perioptic meningioma in children is associated with NF2 with greater incidence than in adults. Detection of PPONSM in a child requires a thorough search for NF or rare meningiomatosis. Meningioma may occur in an extraconal location arising from the orbital wall periosteum. Meningioma may also extend into the orbit from a primary intracranial meningioma (e-Fig. 7.9D) arising from the cavernous sinus, falciform ligament, anterior clinoid process, sphenoid wing, etc. On CT, meningioma may appear as a hyperattenuating/isoattenuating mass containing internal stippled calcifications. It is often associated with bony changes, including hyperostosis, enlargement of the optic canal, and occasionally pneumosinus dilatans (e-Fig. 7.9E).

The tram-track sign, which reflects a thickened optic nerve sheath, is a common imaging feature of perioptic meningioma. MRI is the most accurate imaging modality to diagnose and follow patients with meningioma. Most meningiomas demonstrate isointense/hypointense signal on T1W imaging, variable signal on T2W imaging, as well as avid enhancement on contrast-enhanced sequences, as well as restricted diffusion on DWI due to their increased/dense cellularity (e-Fig. 7.9F). Younger patients may have a higher incidence of intracranial extension.

### Peripheral Primitive Neuroectodermal Tumor

Peripheral primitive neuroectodermal tumor (pPNET) is malignant tumor of neuroepithelial origin that arises outside of the central nervous system. An orbital location is extremely rare, but most reported cases do occur in children. It appears that pPNET is the least aggressive subtype of tumor among other similar small cell tumors, with a favorable prognosis seen after complete tumor resection.

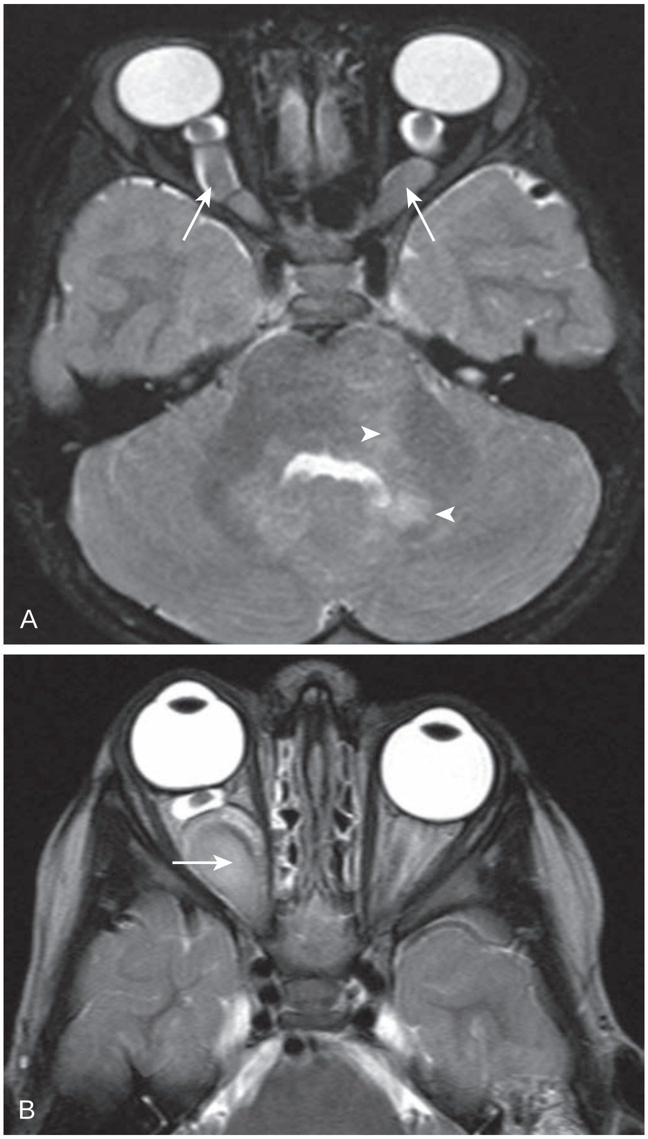

**Figure 7.8. Optic nerve glioma (ONG).** (A) ONG in a patient with neurofibromatosis NF1. Axial fat-saturated T2-weighted MR image of the orbits demonstrates bilaterally symmetrically enlarged and tortuous intracanalicular portions of the optic nerves associated *(arrows)*. Areas of signal abnormality within the cerebellar white matter indicate spongiform changes of NF1 *(arrowheads)*. (B) Isolated right ONG. Axial T2-weighted MR image of the orbits demonstrates an ONG with similar expansion and tortuosity of the optic nerve to the case in A *(arrow)* but with unilateral involvement of the right optic nerve and without additional imaging findings of NF1.

Histopathologically, pPNETs demonstrate small blue round cells, and many authors consider pPNET and extra-osseous Ewing sarcoma at opposite ends of the same spectrum due to their similar histopathologic features and chromosomal rearrangements with translocation (q24; q12). This rare tumor of the orbit presents as an enhancing, T2W hypointense intraconal lesion with restricted diffusion (e-Fig. 7.10). Treatment usually includes globe enucleation, high-dose chemotherapy, and stem cell transplantation. Orbital Ewing sarcoma can also represent metastatic disease from a primary Ewing sarcoma elsewhere in the body.

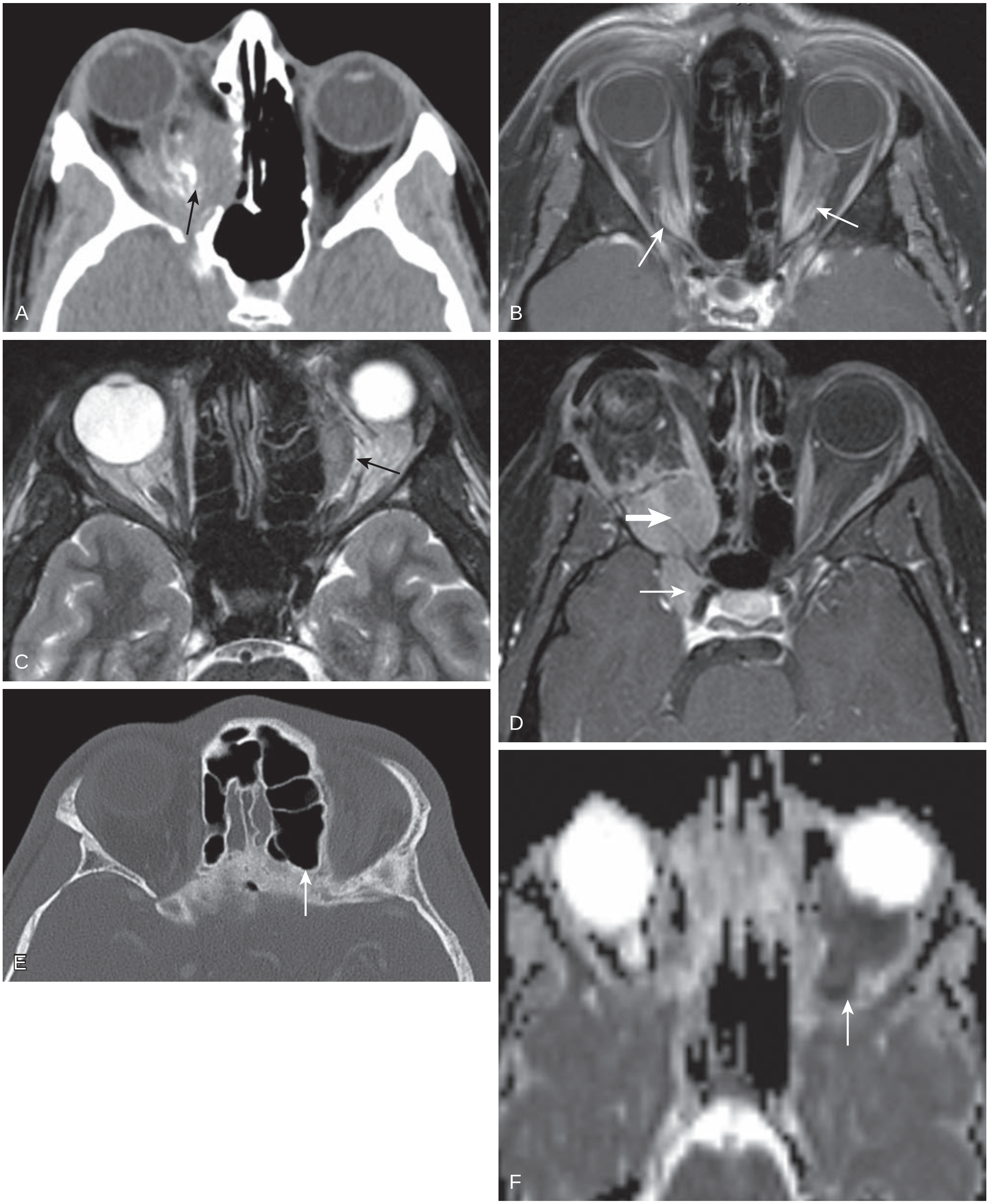

**e-Figure 7.9. Orbital meningioma/pediatric primary optic nerve sheath meningioma (PPONSM) in six different patients.** (A) Axial contrast-enhanced CT image through the orbits demonstrates dural enhancement along the distal intraorbital and intracanalicular segments of the right optic nerve *(arrow)*. (B) Axial contrast-enhanced fat-saturated T1-weighted MR image through the orbits demonstrates dural enhancement along the distal intraorbital and intracanalicular segments of the bilateral optic nerves *(arrows)*. (C) Axial fat-saturated T2-weighted MR image through the orbits demonstrates optic nerve atrophy on the left *(arrow)*. (D) Axial contrast-enhanced fat-saturated T1-weighted MR image through the orbits demonstrates right-sided orbital extension *(thick arrow)* from a primary intracranial meningioma *(thin arrow)* emanating from the region of the ipsilateral cavernous sinus. (E) Axial contrast-enhanced CT image through the orbits demonstrates focal left ethmoid sinus expansion *(arrow),* known as pneumosinus dilatans. (F) Axial apparent diffusion coefficient (ADC) MR image through the orbits demonstrates left-sided diffusion restriction on ADC image *(arrow)*.

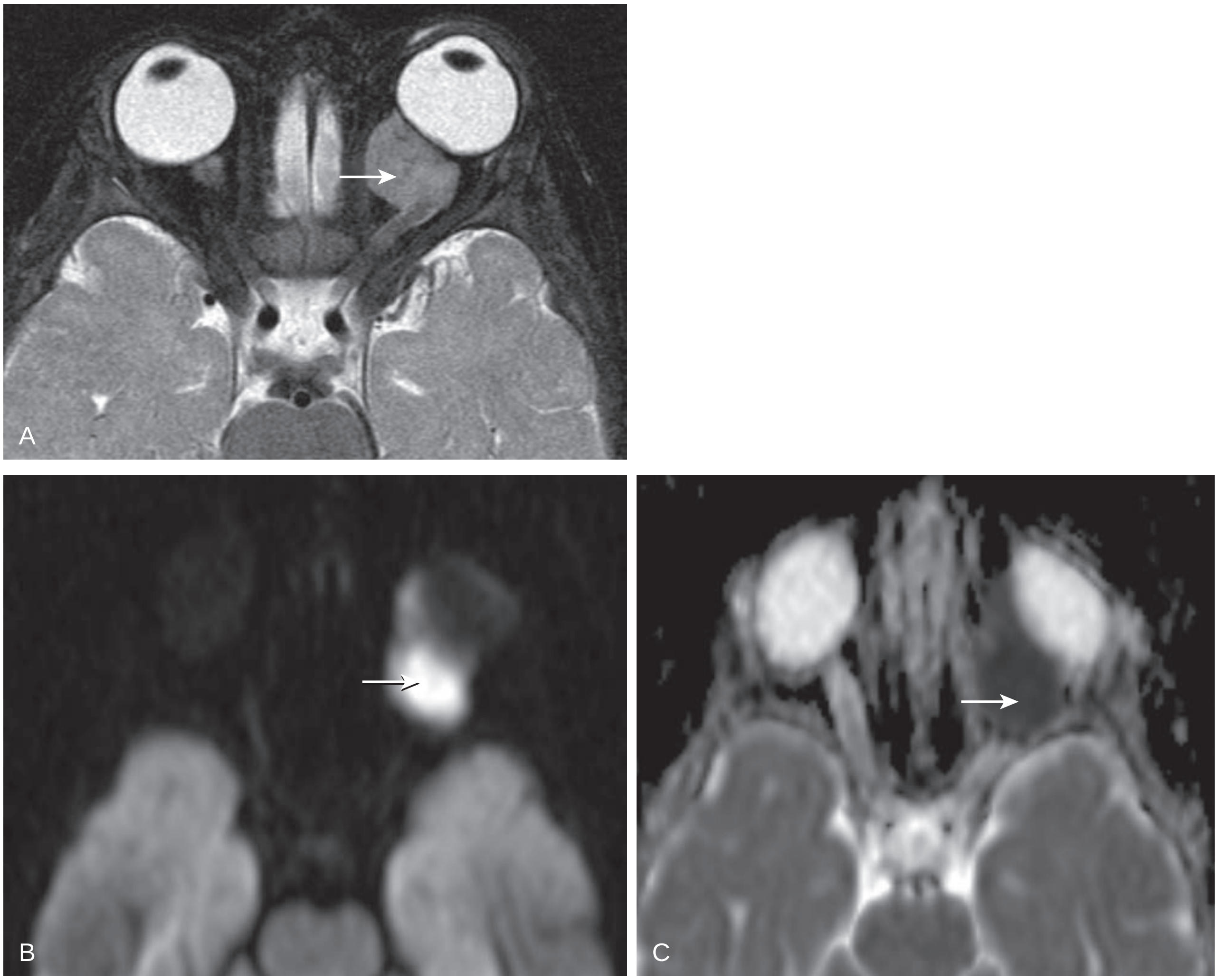

**e-Figure 7.10. Orbital peripheral primitive neuroectodermal tumor (pPNET).** (A) Axial fat-saturated T2-weighted, (B) diffusion-weighted imaging (DWI), and (C) axial apparent diffusion coefficient (ADC) MR images show a left-sided, posteriorly located intraconal T2-hypointense lesion with associated marked restricted diffusion *(arrows)*. The restricted diffusion suggests a densely cellular tumor, a finding almost invariably seen with PNETs.

Primary optic nerve tumors are not the only cause of optic nerve enlargement. Other causes include nonneoplastic conditions such as inflammatory pseudotumor, optic neuritis, and sarcoid granulomata. Enlargement of the optic nerve-sheath complexes/dilated perioptic space may be related to increased intracranial pressure, posttraumatic perineural hematoma, or leukemic infiltration or may represent a normal variant.

## ORBITAL LESIONS

### Vascular Lesions

The Mulliken and Glowacki classification is widely accepted and divides a heterogeneous group of vascular lesions (including orbital vascular pathology) into two types: true neoplasms and nonneoplastic vascular malformations. Vascular malformations are congenital lesions but are often clinically occult at birth and tend to present later in life. However, infantile hemangiomas (IH) become clinically apparent shortly after birth, and some of the rarer orbital vascular tumors may even be diagnosed prenatally.

#### Orbital Hemangioma

Orbital hemangiomas affect 2.5% to 10% of infants and are almost solely benign IH. Orbital IH usually appears shortly after birth, although up to 40% may be visible at birth as only a faint cutaneous mark. IHs are known for their predictable clinical course: proliferation, stabilization, and involution. During the proliferative phase of growth, they will become raised, bulky, and compressible. The most variable stage of involution may occur over a period of years. Some persistent fibro-fatty mass without calcifications or abnormal cutaneous pigmentation may remain even after resolution, mainly leading to cosmetic concerns rather than functional stigmata. Only a small percentage of IH lead to complications, such as ulcerations and bleeding. However, due to their location, early age of presentation, and potential for very rapid growth, orbital IH may cause devastating visual impairment. This complication results from obscuration of light delivery to the eye, especially if the eyelids are involved. Impairment of visual input early in life prevents the formation of the neural pathways necessary for the development of proper vision later in life and can cause deprivation amblyopia ("lazy" eye) and blindness.

IH often appears hyperintense on T2W imaging, avidly takes up gadolinium, and may have multiple flow voids (Figs. 7.11A and B) and increased vascularity seen on perfusion imaging. Although usually nonsyndromic, some hemangiomas are known to occur in conjunction with other systemic abnormalities, such as the PHACES syndrome (**P**osterior fossa malformations, **H**emangiomas, **A**rterial abnormalities, **C**ardiac abnormalities, **E**ye abnormalities, and **S**ternal clefts) (Fig. 7.11C).

The imaging differential diagnosis for hemangioma includes rhabdomyosarcoma (RMS), vascular malformation, infantile fibromatosis, and infantile fibrosarcoma. The vascular features of IH, particularly the flow voids on MRI, help to distinguish IH from these other lesions. RMS may be very vascular and contain flow voids but typically occurs in an older age group and often will demonstrate restricted diffusion on DWI. Most IH are managed conservatively as they tend to resolve on their own. However, tumors that can or do compromise vision are aggressively treated. Therapeutic options include propranolol, systemic or intralesional corticosteroids, interferon, and laser therapy or surgery.

#### Veno-lymphatic Malformation

Veno-lymphatic malformation (VLM) encompasses a group of vascular lesions consisting of vascular channels of varying sizes and histologic types. Some lesions consist primarily of lymphatic vessels and are called lymphatic malformations, whereas others are composed mainly of venous channels and thus are called venous malformations (formerly known as cavernous hemangiomas). Most lesions contain both types of vessels, and their clinical presentation and imaging appearances depend on the prevalence of lymphatic or venous components within the individual lesion. Orbital VLMs are classified into three groups on the basis of anatomic location: superficial, deep, and combined lesions. The superficial lesions mostly contain lymphatic vessels, whereas in contrast, the deep lesions are predominantly or completely venous in nature, reflecting the distribution of vessels within the normal orbit. Superficial lesions may involve the eyelid and/or conjunctiva and tend to present at an early age. Deep lesions in the retrobulbar orbit, although present from birth, may manifest later in life and even in young adulthood. Unlike IH, VLMs grow with the patient and don't involute spontaneously. Clinically, these lesions usually present with progressive or acute painless proptosis, but they may present with restricted movement of the EOMs. Intermittent change in size may occur as a result of recurrent hemorrhage, secondary to fragile vessels within the intervening connective tissue. Imaging features may reflect the dual nature of these vascular malformations, with multicystic lymphatic components often containing blood-fluid levels, while enhancing solid venous components at times will contain phleboliths. Uncomplicated lymphatic components usually do not demonstrate contrast enhancement or at most may show some peripheral enhancement. On US, lymphatic malformations demonstrate cystic spaces filled with blood and fluid, which lack Doppler flow. The CT appearance may be inconclusive, not fully reflecting the internal complexity of the lesion (Fig. 7.12A) at times, with the lesion presenting as a nonspecific soft tissue mass with associated proptosis. MRI fully demonstrates the complex natures of VLMs (Figs. 7.12B and C).

Treatment of orbital vascular lesions remains challenging. In the past, conservative management was preferred if the patient's vision was not jeopardized. Surgical excision is often difficult and associated with numerous complications, in addition to a high rate of recurrence. Intralesional sclerotherapy is an effective method of debulking low-flow malformations, as well as an attractive alternative to surgical resection.

#### Orbital Varix

Primary congenital venous varices (uncommonly affecting children) represent distensible venous malformations in the retrobulbar compartment of the orbit or elsewhere in the orbit (e-Figs. 7.13A and B), which may enlarge with dependent posture. The varix may consist of marked enlargement of a single orbital vein or may present as a tangled multivascular mass. Clinically, these lesions may present with globe displacement that may augment and increase in conspicuity when the Valsalva maneuver is performed. At times, these lesions are collapsed and may be undetectable. There is a high association of orbital varices with intracranial developmental venous (e-Fig. 7.13C). Occasionally, these lesions may lead to spontaneous orbital hemorrhage. Secondary varices may occur in the setting of intracranial dural venous thrombosis or arteriovenous shunting.

## NONVASCULAR ORBITAL MASSES

Orbital masses constitute a mixed group of benign and malignant, primary and secondary tumors, inflammatory masses, and congenital cysts.

#### Orbital Schwannomas

Orbital schwannomas in children are very uncommon and mostly seen in association with NF2. Schwannomas of any nerve in and around the orbit may be observed. These are eccentrically located, T1 isointense-hypointense and T2 hyperintense masses, with avid

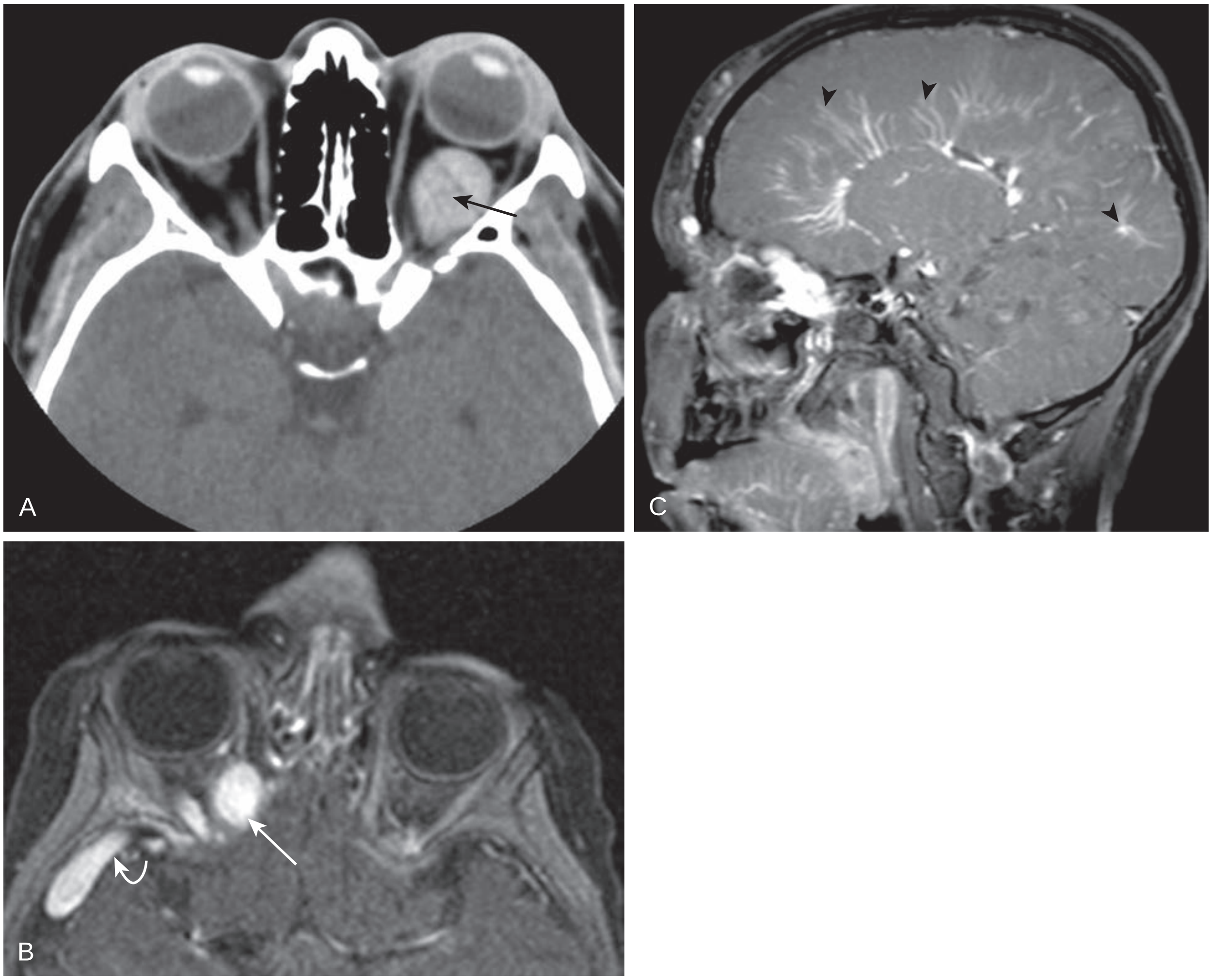

**e-Figure 7.13. Orbital varix.** (A) Axial contrast-enhanced CT of the orbits in a patient with a left-sided venous varix demonstrates tubular enhancement within the posterior half of left orbit *(arrow),* indicating a vascular lesion that is not specific for, but is suggestive of, a venous varix. (B) Axial contrast-enhanced fat-saturated T1-weighted MR image at midorbital level and (C) sagittal midline contrast-enhanced fat-saturated T1-weighted MR image of the brain in a patient with multiple venous abnormalities. Note the posteromedial left orbital venous varix *(straight arrow)* and associated anterolateral right middle cranial fossa varix (*curved arrow* in B). Note the multiple associated intracranial developmental venous anomalies (DVA) (*arrowheads* in C), a known association of orbital varices with DVAs.

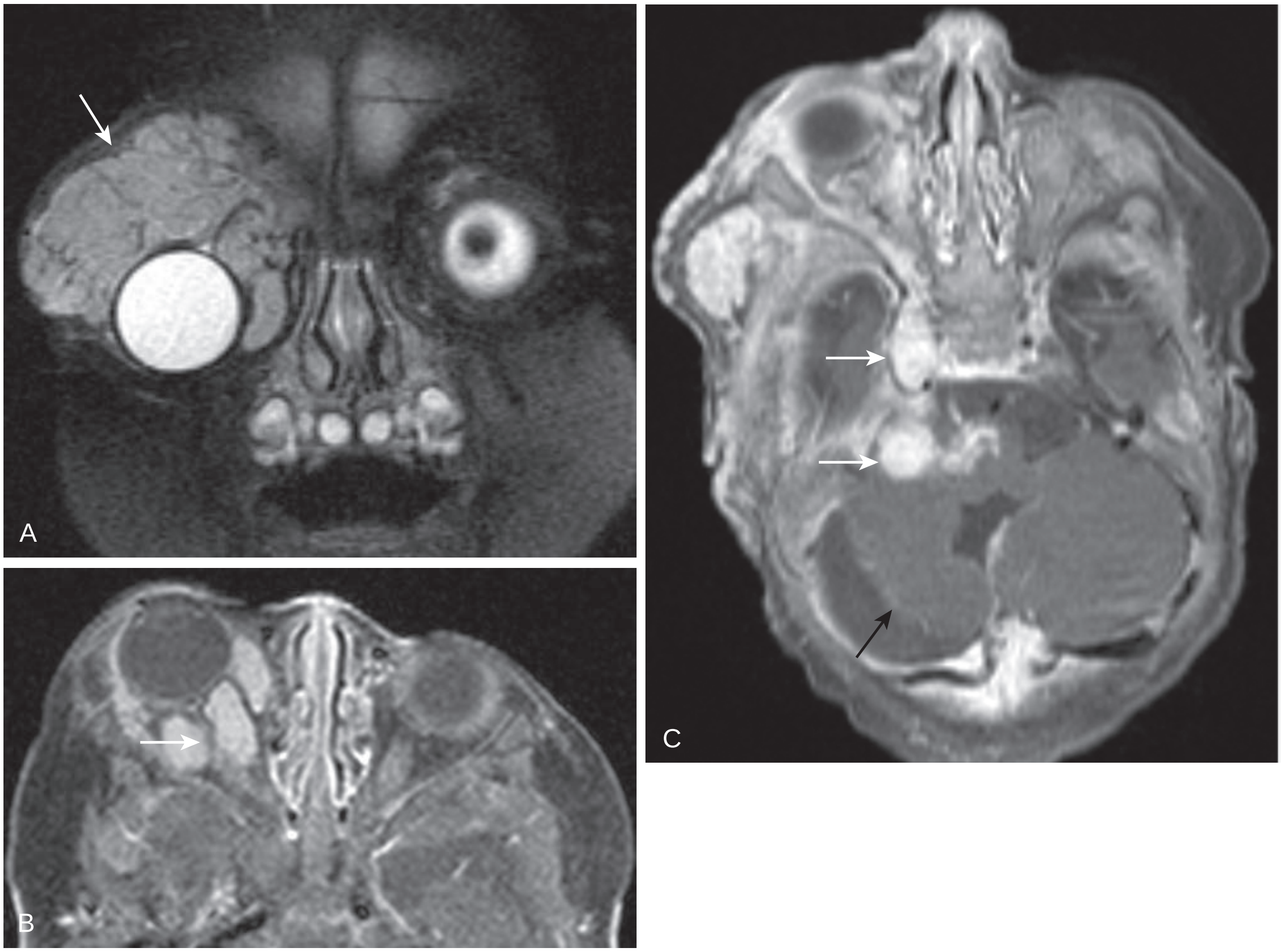

**Figure 7.11. Infantile hemangioma (IH).** (A) Coronal fat-saturated T2-weighted MR image demonstrates a lobulated mass surrounding the right globe in the supraorbital region *(arrow),* with associated flow voids. (B) Axial contrast-enhanced fat-saturated T1-weighted MR image demonstrates intraconal extension of this avidly enhancing lesion *(arrow)*. (C) Axial contrast-enhanced fat-saturated T1-weighted MR image in a patient with PHACES syndrome demonstrates multiple facial and orbital and intracranial IHs *(white arrows)*. In addition, the cerebellum is anomalous *(black arrow),* with diminution of the right cerebellar hemisphere, which is a common association of PHACES.

contrast enhancement (e-Fig. 7.14). These tumors are usually much smaller than plexiform neurofibromas. When schwannomas become large, they can undergo internal cystic degeneration.

**Orbital Teratoma.** Orbital teratoma is a very rare congenital tumor often diagnosed prenatally with US and fetal MRI (e-Fig. 7.15A). These tumors usually contain multiple tissue types, including fat, calcium, and bone. Teratomas of the orbit are most often benign and well differentiated; however, they may lead to significant proptosis when located at the orbital apex (e-Fig. 7.15B). The imaging appearance of a teratoma is quite distinctive; it presents as a very large multicystic mass with enhancing solid component and calcification. Presence of intralesional fat is almost pathognomonic (e-Figs. 7.15C and D).

**Orbital Rhabdomyosarcoma.** RMS is the most common malignant soft tissue tumor in childhood, and the orbits and paranasal sinuses are the second most common site of occurrence. The embryonal type is the most common variety of orbital RMS; the alveolar and pleomorphic varieties occur rarely. The mean age at presentation is 6 years. RMS was previously thought to arise from skeletal muscle but now is generally believed to originate from pluripotential mesenchymal cells that have the capacity to differentiate into skeletal muscle. RMS is an aggressive, fast-growing tumor that most often manifests with rapidly progressive proptosis or globe displacement and should be considered in the differential diagnosis in any child with this clinical presentation. Other common signs and symptoms include conjunctival and palpebral swelling, which may erroneously suggest the clinical diagnosis of orbital cellulitis, and may lead to confusion with respect to patient presentation and imaging appearance.

Most tumors are extraconal in location, but intraconal components may also be present. The most typical location for the common embryonal is in the superonasal quadrant. The less prevalent alveolar form more often affects the inferior orbit. RMS grows rapidly and behaves aggressively, frequently invading the adjacent bones and soft tissues, although advanced disease is less often encountered today due to greater awareness of the diagnosis. Both CT and MRI play important roles in the preoperative evaluation, staging, and follow-up of orbital RMS tumors. On T2W imaging, these lesions may appear as hypointense, isointense, and even hyperintense with respect to EOMs (Figs. 7.16A and B). Due to the high degree of RMS cellularity, the lesions may be predominantly hyperattenuating on CT and exhibit restricted

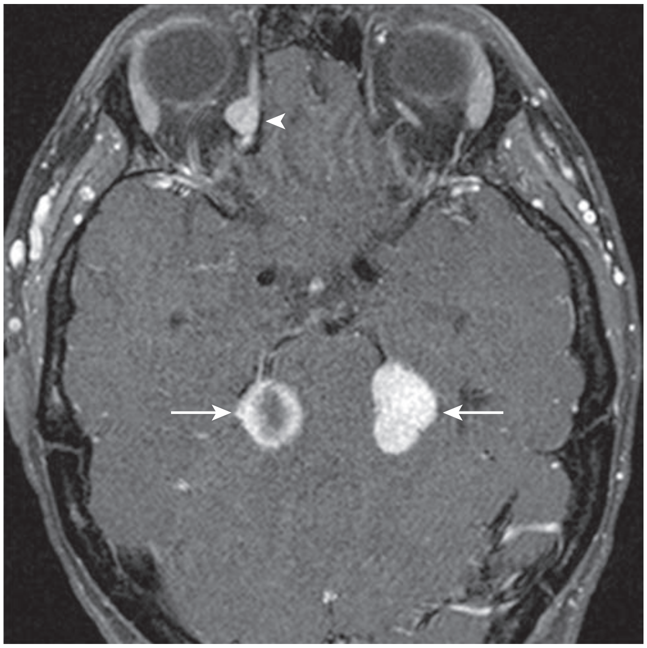

**e-Figure 7.14. Orbital schwannoma.** Axial contrast-enhanced fat-saturated T1-weighted MR image of the orbits in a patient with NF2 and multiple schwannomas. Note the avidly enhancing ovoid mass in the medial left orbit near its roof *(arrowhead),* in keeping with a V1 branch schwannoma of left CN V. Note also the bilateral asymmetric (left greater than right) similar appearing lesions around the lateral margins of the brainstem/cerebral peduncles in keeping with additional intracranial schwannomas.

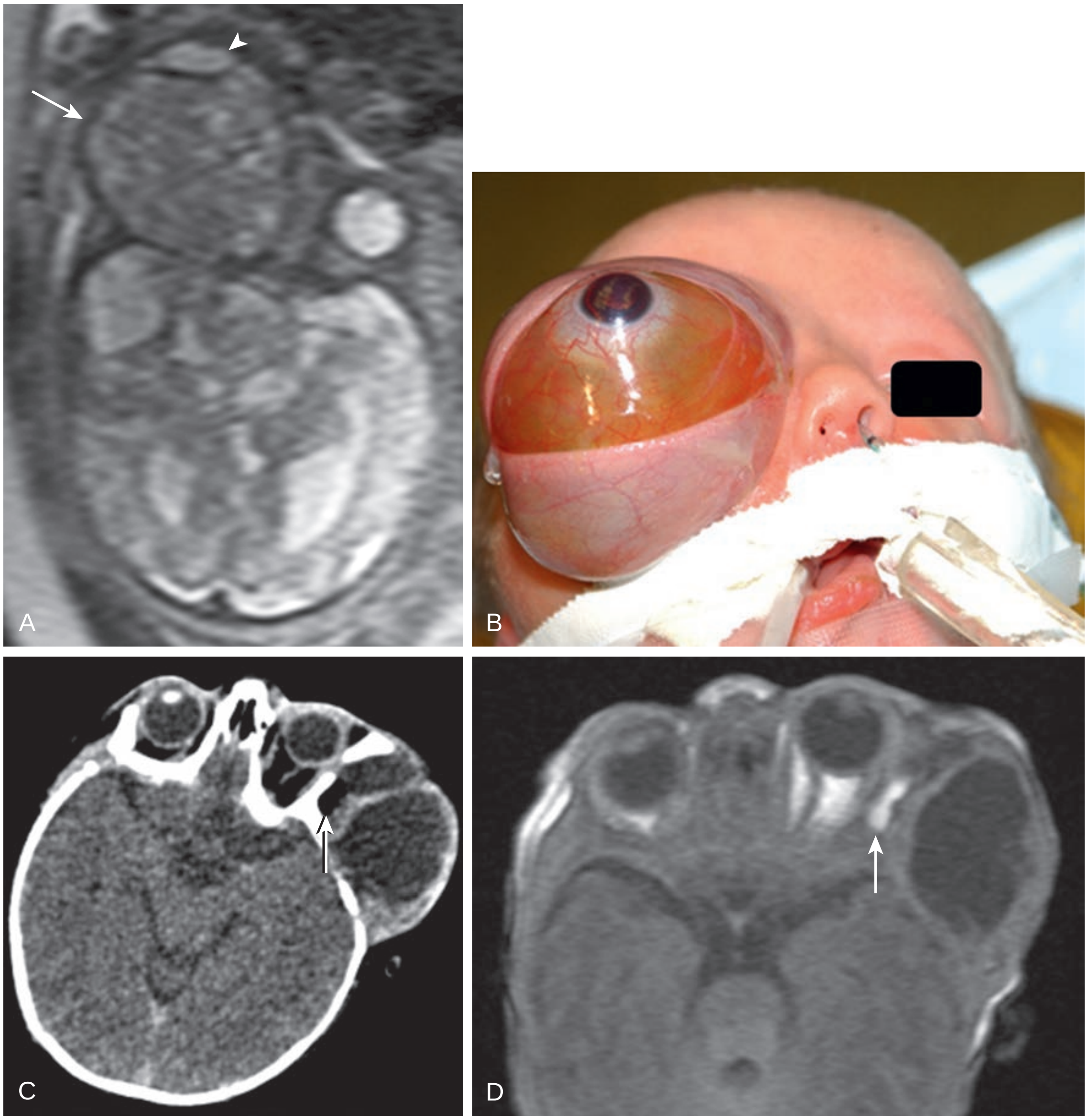

[redacted]

**e-Figure 7.15. Orbital teratoma in two different patients.** (A) Axial HASTE fetal MR image of the orbits demonstrates a very large, slightly T2-hypointense lesion in the region of the left orbit *(arrow),* with associated marked anterior/ventral displacement of the globe *(arrowhead),* in keeping with a teratoma. (B) Clinical photo of the same patient postdelivery demonstrates a markedly enlarged bulbous appearing right globe (buphthalmos). (C) Axial noncontrast CT and D, axial T1-weighted MR images of the orbits in another patient demonstrate a large soft tissue mass lateral to the left orbit with a visible fatty component *(arrow)* (low attenuating on CT and hyperintense on T1W imaging).

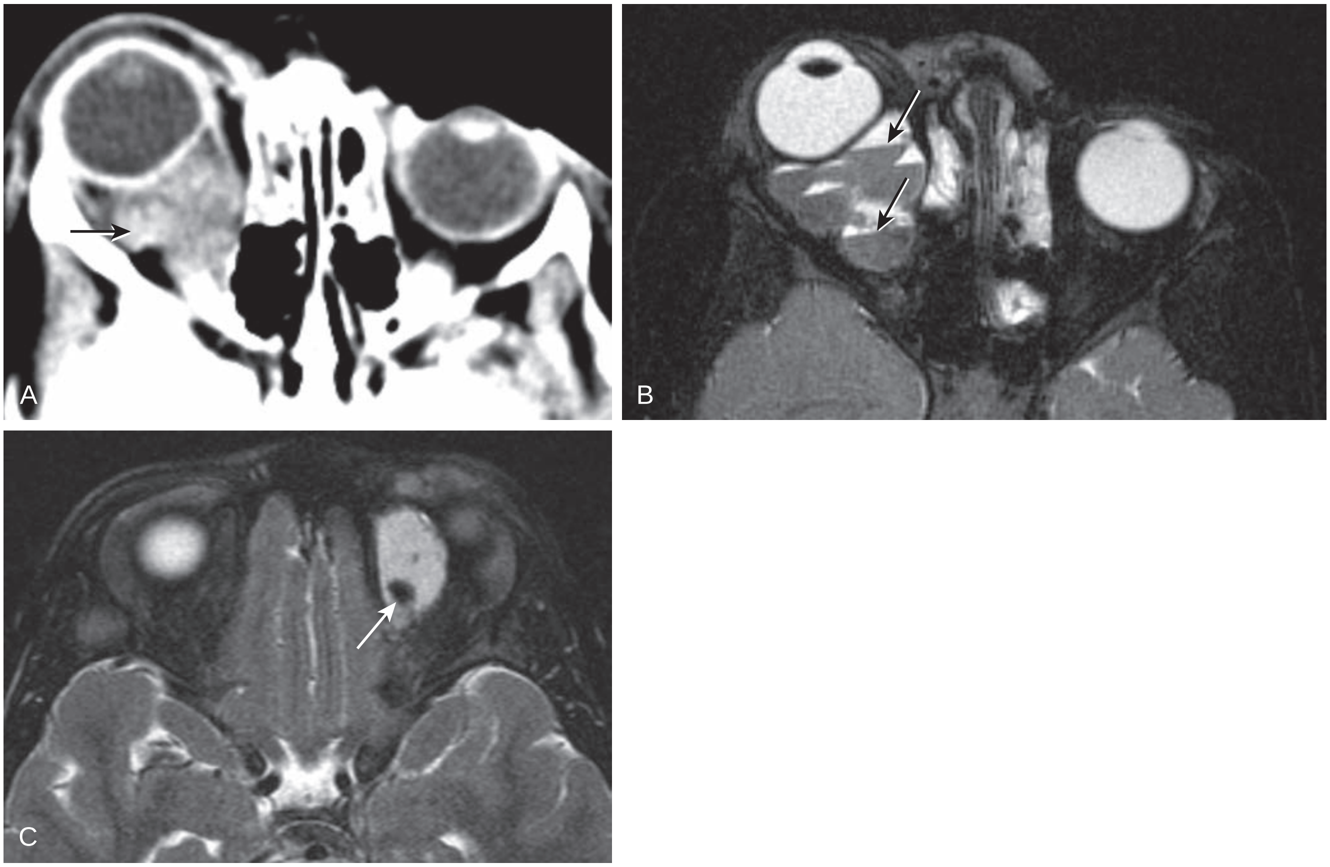

**Figure 7.12. Veno-lymphatic malformation (VLM) in two different patients.** (A) Axial contrast-enhanced CT image and (B) axial fat-saturated T2-weighted MR image of the orbits demonstrates a right-sided intraconal soft tissue mass posterior to the right globe (*arrow* in A), which is associated with anterior displacement of the right globe. Although the finding on CT is nonspecific, the multiple fluid-fluid levels on MRI (*arrows* in B) help to clarify the diagnosis. (C) Axial fat-saturated T2-weighted MR image of the orbits in another patient with a venous predominant VLM demonstrates an ovoid T2 hypointense lesion near the roof of the left orbit secondary to a phlebolith *(arrow)*.

diffusion on DWI. On T1W contrast-enhanced MR images, RMS will have moderate to marked enhancement, and, in some cases, a component of highly vascular internal tissue that may mimic the appearance of a hemangioma (Fig. 7.16C). Meticulous search is required for assessment of local invasion into the paranasal sinuses, as well as for intracranial spread via the orbital fissures, with potential spread into the cavernous sinuses, and, at times, into the middle cranial fossa (Fig. 7.16D). Favorable prognostic factors include lack of distant metastases, a primary site within the orbit, disease confined to the orbit, gross total surgical resection, a patient age younger than 10 years, an embryonal histologic type, and a tumor size of 5 cm or less. The most important prognostic factor is response to therapy, which is assessed with follow-up imaging. Advances in chemotherapy and radiotherapy have improved survival rates of patients with orbital RMS. This improved survival rate has allowed observation of the late effects of radiotherapy on both facial growth (e.g., bony hypoplasia/growth arrest of the orbit and facial asymmetry) and visual function (e.g., cataract, keratopathy, and retinopathy).

## Fibrous Tumors

Solitary fibrous tumor (SFT) is an uncommon spindle cell tumor of mesenchymal origin. This tumor mainly occurs in the visceral cavities; an orbital location is infrequent. Presently, SFT is considered to be in the same spectrum of neoplasms as hemangiopericytoma; it may be benign or more aggressive depending on the number of mitoses present pathologically. Orbital hemangiopericytoma and some cases previously regarded as fibrous histiocytoma, giant cell angiofibroma of the orbit, and SFT, have overlapping morphologic and immunohistochemical features and should be designated as SFT. Orbital SFT demonstrates great variability and may present as a slow-growing, well-circumscribed enhancing mass, or may resemble an inflammatory lesion (e-Fig. 7.17), and hence the imaging features are nonspecific. Painless proptosis is a common clinical sign. Aggressive bony or intracranial invasion is not typical for SFT. The diagnosis mainly relies on immunohistochemistry confirmation.

The spectrum of other orbital fibrous tumors in children may be exemplified by benign fibromatosis and fibrosarcoma. Differentiation of these lesions may be very difficult due to marked overlap of imaging features, and at times, even their histologic appearances. Some authors believe that the only reliable diagnostic criterion for malignancy in infants is the presence of metastasis.

## Rhabdoid Tumors

Rhabdoid tumors of the orbital region occur in young children with a mean age of 15 months at presentation. This lesion can be highly vascular (e-Fig. 7.18 A) and may mimic more benign lesions such as IH. These rare malignant tumors are highly aggressive and lethal, with death occurring within 12 months of presentation.

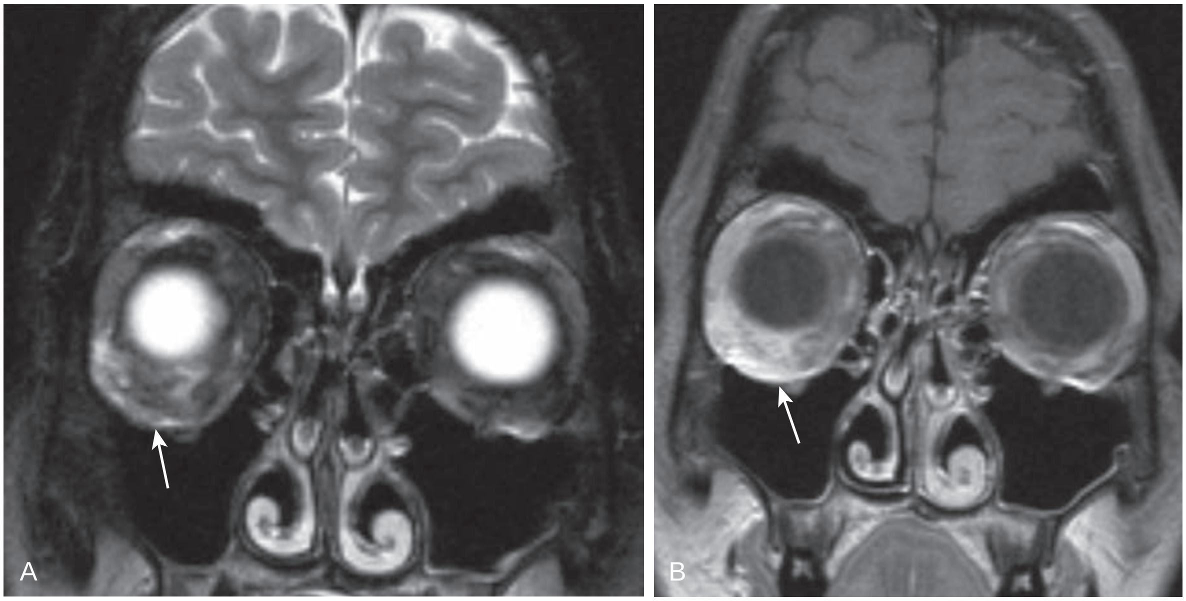

**e-Figure 7.17. Solitary fibrous tumor (SFT).** (A) Coronal fat-saturated T2-weighted and (B) coronal contrast-enhanced fat-saturated T1-weighted MR images demonstrate a fairly T2 dark (suggesting its fibrous nature) and contrast avid lesion in the lower orbital region on the right *(arrows)*.

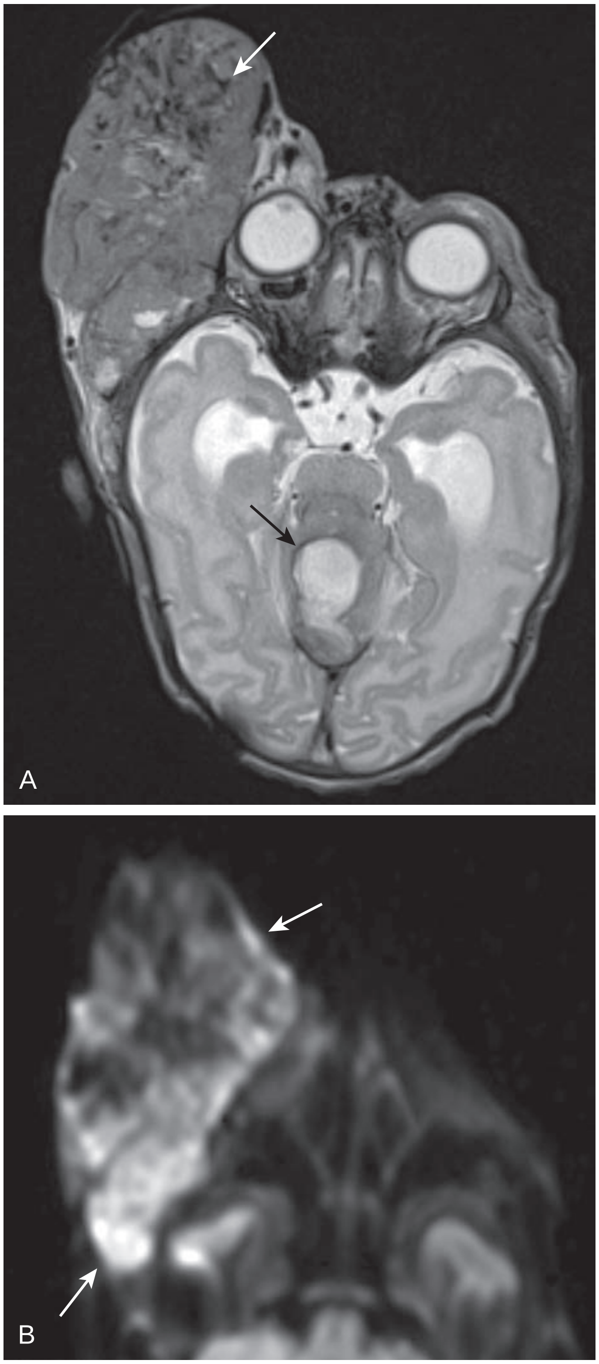

**e-Figure 7.18. Congenital rhabdoid tumor.** (A) Axial fat-saturated T2-weighted and (B) axial diffusion-weighted imaging MR images demonstrate a right-sided lobulated, heterogeneous, extremely vascular mass along the right lateral orbit, with numerous intratumoral flow voids indicating marked vascularity (*white arrow* in A). Note the area of hemorrhage (*black arrow* in A) in the posterior fossa, secondary to Kasabach-Merritt syndrome, due to platelet sequestration by the large orbital vascular mass. In addition, the lesion demonstrates restricted diffusion (*arrows* in B).

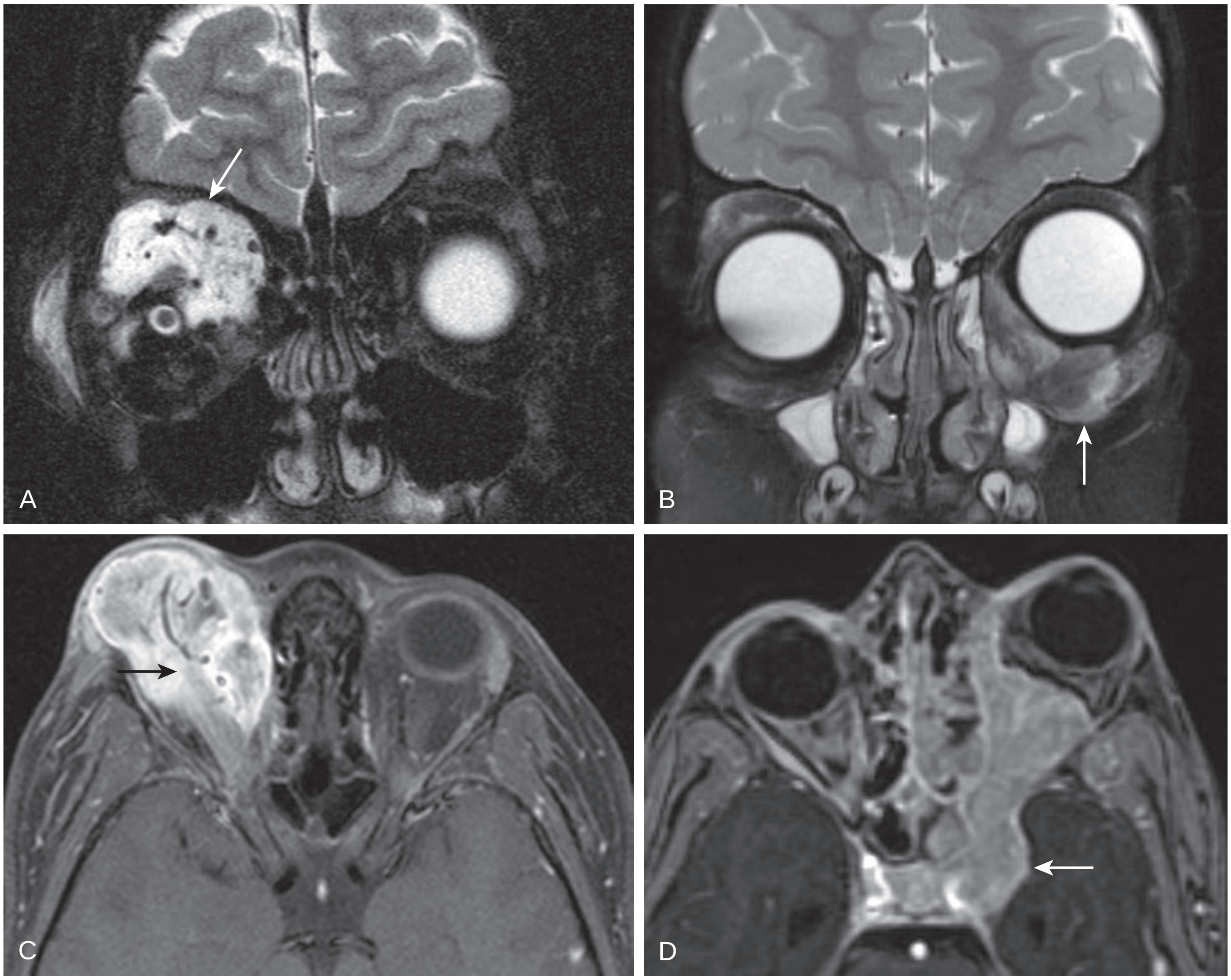

**Figure 7.16. Orbital rhabdomyosarcoma (RMS).** Coronal fat-saturated T2-weighted MR images (A and B) in two separate patients demonstrates the T2 hyperintense nature of these lesions *(arrows),* large, mainly extraconal lesion with flow voids seen in A, and more bland appearing along the lower left orbital region in B. (C) Axial contrast-enhanced fat-saturated T1-weighted MR image of the same patient as in A demonstrates an avidly enhancing tumor, with multiple flow voids *(arrow)* indicative of the highly vascular nature of this lesion. (D) Axial contrast-enhanced fat-saturated T1-weighted MR image in a different patient with left-sided orbital RMS demonstrates posterior intracranial extension of the tumor along the posterior orbital fissures/foramina into the ipsilateral middle cranial fossa, to involve the cavernous sinus *(arrow)*.

Their dense cellularity/cell packing produces restricted diffusion on DWI (e-Fig. 7.18 B).

## Inclusion Cysts (Epidermoid/Dermoid)

Dermoid and epidermoid cysts are congenital developmental ectodermal inclusion cysts, constituting up to 5% of all orbital masses. Inclusion cysts occur commonly around the orbit, especially around the region of sutures (frontozygomatic or frontolacrimal). Epidermoid cysts contain epithelial elements and cholesterol crystals and may be bounded by a thin capsule, whereas dermoid cysts may contain dermal appendages, including hair and sebaceous glands, and are surrounded by a fibrous capsule. Inclusion cysts usually present as a painless subcutaneous nodule, and they mainly cause cosmetic deformity, but later in life they may grow, partially rupture, and become inflamed and symptomatic. Osseous remodeling may occur but without associated periosteal reaction.

These lesions are well-demarcated, cystic-appearing, extraconal masses with differing degrees of fatty content. Uncomplicated superficial dermoid cysts are well depicted as low attenuating on orbital CT, without the need for intravenous contrast, as these lesions (if uninfected) should not enhance (Fig. 7.19A). MRI is superior for more detailed depiction of any possible intracranial connection and for the presence of a potential sinus tract. These lesions are hyperintense on T1W imaging due to their fatty content. Mild rim enhancement may occasionally be seen and is considered normal, whereas the appearance of a more irregular type of enhancement is suggestive of prior rupture with a secondary inflammatory reaction. Epidermoid cysts are hyperintense on T2W imaging (Fig. 7.19B) and fluid attenuated inversion recovery (FLAIR) sequences and exhibit restricted diffusion on DWI (Fig. 7.19C).

## Orbital Pseudotumor (Idiopathic Orbital Inflammation)

Orbital pseudotumor represents a noninfectious infiltration of the orbital structures by lymphocytes and plasma cells, usually without associated osseous involvement. The etiology remains

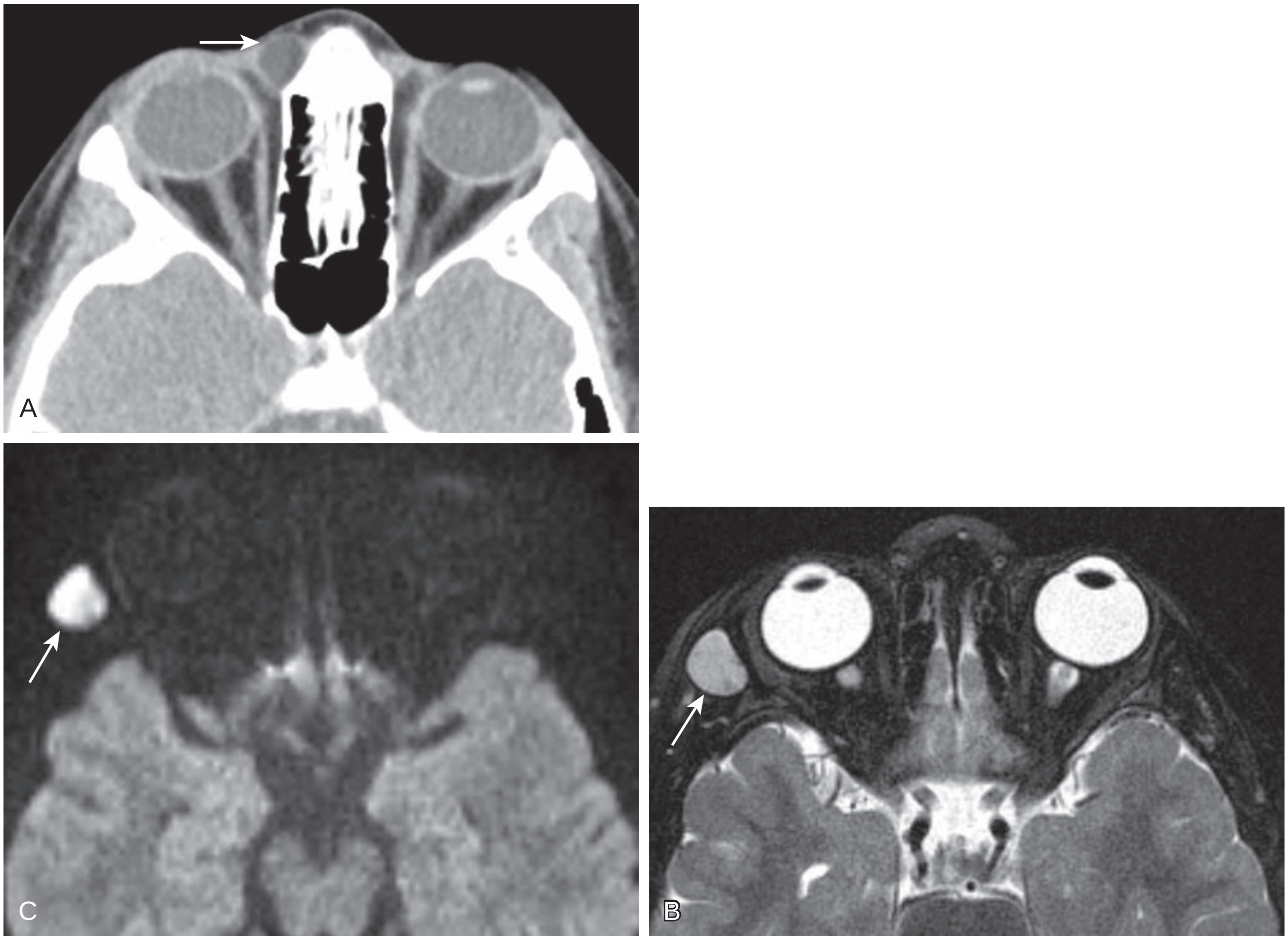

**Figure 7.19. Orbital epidermoid in two different patients.** (A) Axial noncontrast CT of the orbits demonstrates an ovoid area of low-attenuation (fat) within the anterior soft tissues medial to the right globe *(arrow)*. (B) Axial fat-saturated T2-weighted and (C) axial diffusion-weighted imaging MR images demonstrate a similar lesion along the right lateral orbital soft tissues *(arrows),* which is bright on T2-weighted imaging but exhibits restricted diffusion on DWI, as is typically seen with epidermoid cysts.

unclear. The disease may present as unilateral, isolated involvement of the EOMs but may also manifest with a more diffuse pattern involving multiple orbital sites. It can also present with neuritis or an extra bulbar mass. CT and MRI are equally effective in depicting the extent of disease (Figs. 7.20A and B). In children, orbital pseudotumor presents with an acute onset of painful proptosis and painful eye movement. The clinical presentation of orbital pseudotumor may be the best discriminator between this disease process and thyroid-associated orbitopathy (TAO). Orbital myositis usually appears as enlargement of the EOMs with mild surrounding inflammatory changes and anterior extension into the tendinous insertion. The imaging features of orbital myositis may be fairly similar to the early stage of TAO, although the tendinous portion/insertion of the EOMs is spared in patients with TAO. Excellent response to steroid treatment, with cessation of pain, is typical in cases of orbital pseudotumor. In rare cases, a biopsy is necessary to exclude malignancy.

## Thyroid-Associated Orbitopathy

TAO, previously referred to as thyroid ophthalmopathy, is an autoimmune disease that may or may not be contemporaneously associated with acute/active thyroid disease. This disease leads to thickening (usually symmetric) of the EOMs, but with sparing of the anterior musculotendinous junction, resulting in the so-called "coke-bottle"-like appearance (e-Fig. 7.21A). Patients usually present with disturbance of ocular motility, caused by swelling of rectus muscles at insertion sites into the globe, and injection of overlying vessels. Any EOM may be involved, with the inferior and medial rectus muscles being most commonly involved. EOMs may be infiltrated with lymphocytes, and fluid may accumulate in the periorbital tissues. Additionally, there is often increase in volume of the retrobulbar fat, which is associated with exophthalmos/proptosis. This condition is not common among pediatric patients but occasionally may be observed in teenagers (e-Fig. 7.21B). Eye findings in pediatric TAO are usually mild, and TAO-associated optic neuropathy has never been reported.

## Langerhans Cell Histiocytosis

Langerhans cell histiocytosis (LCH) is a granulomatous disease resulting from proliferation and infiltration of abnormal histiocytes within various tissues. Orbital lesions occur mainly in young children, ages 1 to 4 years. Orbital disease may accompany widespread disease, but occasionally it may be the first (and at times, the only) manifestation of LCH. The lesions arise from the orbital bone or bone marrow and spread directly to the orbit. Orbital disease may present clinically with proptosis and rapidly

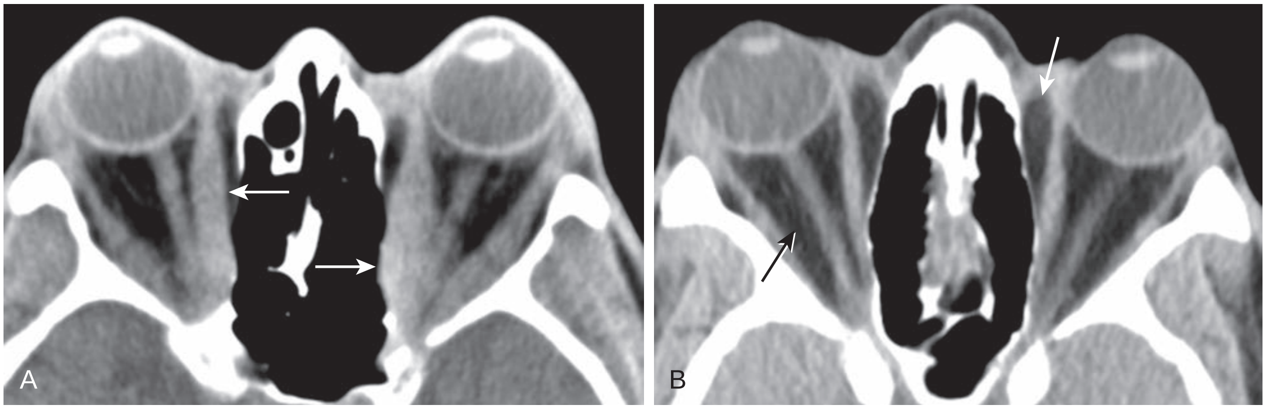

**e-Figure 7.21. Thyroid-associated orbitopathy (TAO) in two different patients.** (A) Axial noncontrast CT of the orbit demonstrates fusiform thickening of the bilateral medial rectus muscles *(arrows)* with anterior tapering at the myotendinous junctions, the so-called "coke-bottle" appearance. (B) Axial noncontrast CT of the orbit demonstrates increase in orbital fat deposition *(arrows),* a known association of TAO.

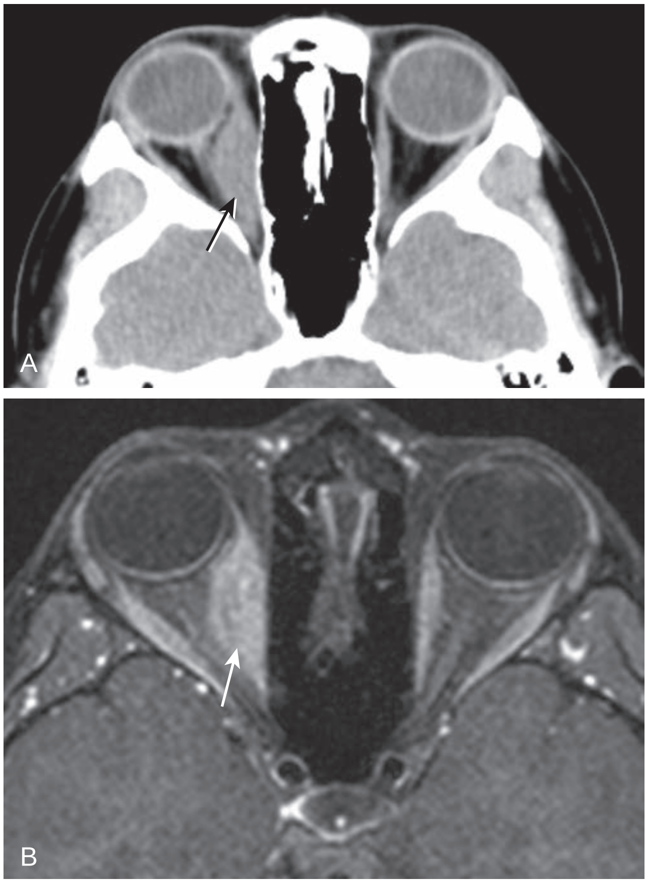

**Figure 7.20. Orbital pseudotumor.** (A) Axial contrast-enhanced CT and (B) axial contrast-enhanced fat-saturated T1-weighted MR images of the orbit in a patient with known right-sided inflammatory orbital pseudotumor. Note the fusiform enhancement and enlargement of the right medial rectus muscle *(arrows),* with extension to the myotendinous junction.

enlarging periorbital masses, or even with visual loss and destructive changes of the orbit.

CT and MRI are complimentary imaging techniques in the evaluation of LCH orbital lesions, and, in some cases, both may be indicated before treatment and when assessing for potential residual or recurrent disease. At times, the imaging features are often so typical for LCH that there is no need for biopsy. CT demonstrates expansile soft tissue masses in the posterolateral orbits, with a predilection for the frontosphenoid sutures. The lesions are usually associated with areas of osseous destruction, which show sharp and nonsclerotic ("punched out") margins typically without significant periosteal reaction (e-Fig. 7.22A). MRI demonstrates periorbital heterogeneous lesions that may contain blood-fluid levels (e-Fig. 7.22B) and foci of restricted diffusion. The masses exhibit diffuse enhancement on CT and MRI. Evaluation for intracranial extension is imperative, especially on contrast-enhanced sequences (e-Fig. 7.22C). Discovery of a solitary orbital LCH lesion necessitates additional imaging in search of other possible sites of involvement. LCH orbital masses may resemble NB metastases by certain imaging features; both lesions may demonstrate restricted diffusion, diffuse enhancement, and intraosseous and extraosseous components. The type of osseous involvement may help to distinguish the "clear-cut" margins of LCH from the permeative pattern and aggressive periosteal reaction of NB. Bone destruction in LCH typically is more pronounced than that seen with RMS.

### Granulomatosis With Polyangiitis and Sarcoidosis

Granulomatosis with polyangiitis (Wegener granulomatosis) is an autoimmune process that, in addition to pulmonary and paranasal involvement, may involve the orbit. Ocular involvement may be seen in 18% to 50% of cases, in which there is a propensity for lacrimal gland involvement (e-Fig. 7.23). The lesions are usually bilateral, with poor or no response to steroid treatment.

Sarcoidosis is an inflammatory, multisystem, granulomatous disease of unknown etiology, which, in addition to pulmonary and vascular involvement, affects the orbit in 25% of all patients. Any part of the orbit may be involved; a mass lesion within the lacrimal gland or the lacrimal sac can be the sole presentation of this disease (e-Fig. 7.24).

### Osteoma and Fibrous Dysplasia

Osteomas are benign, slow-growing, bone-forming tumors. Although osteomas of the facial region are not common, at times they may occur within the region of the paranasal sinuses, and, if allowed to grow large, may break through into the orbit and even intracranially. Osteomas within the orbits demonstrate typical imaging features of a broad-based expansile osseous mass, sometimes with an inner ground-glass lucent area, surrounded by dense compact bone. Osteomas usually do not cause bony destruction, even when these lesions are large. CT is the best imaging modality to delineate the lesion's characteristics and extension. MRI findings may be confusing, as the mature dense bone of the osteoma, representing most of the lesion's volume, may not be distinguishable from the air in the paranasal sinuses, as air and compact bone lack the MRI excitable protons of water molecules. These lesions are very dense, thereby appearing very "white" on CT and very "black" on MRI (e-Fig. 7.25).

Fibrous dysplasia is a systemic osseous disease that often involves the skull. Although usually sclerotic in appearance, with a "ground-glass" appearance, there are phases of this disease in which lysis/lucency may be a predominate feature, thereby mimicking LCH. The MRI features may be confusing, with intermediate signal on T1W and T2W imaging, with an appearance more typical and characteristic on CT (e-Fig. 7.26).

## METASTATIC LESIONS INVOLVING THE ORBITS

Orbital metastases are less common in children than in adults. Primary tumors that may metastasize to the bony orbit are NB, lymphoma and leukemia, and very rarely Wilms tumor and Ewing sarcoma. Ocular choroid metastases, which are quite common in adults, are exceedingly rare in children. However, leukemic deposits may infiltrate the optic nerve, which represents an emergency, as vision may decline precipitously.

### Neuroblastoma

NB is the most common metastatic tumor of young pediatric patients. In 8% of cases, NB first presents with acute orbital symptoms related to tumoral hemorrhage, sudden proptosis, and ecchymosis (so-called "raccoon eyes"). NB metastases are bilateral in 50% of cases and originate in the osseous walls of the orbits. Permeative bony destruction or spiculated thickening with aggressive periosteal reaction of the lateral wall and roof of the orbit are characteristic findings (Fig. 7.27A). Epidural tumor deposits may extend to the sutural margins and cause sutural diastasis (Fig. 7.27B) without elevation of intracranial pressure. Soft tissue masses often contain calcifications. Infiltration of the deep spaces of the face and neck and intracranial extension is often seen. Lesions may be heterogeneous on T1W and T2W images when compared with muscle. Marked heterogeneity of contrast enhancement can be seen due to hemorrhage and necrosis (Fig.

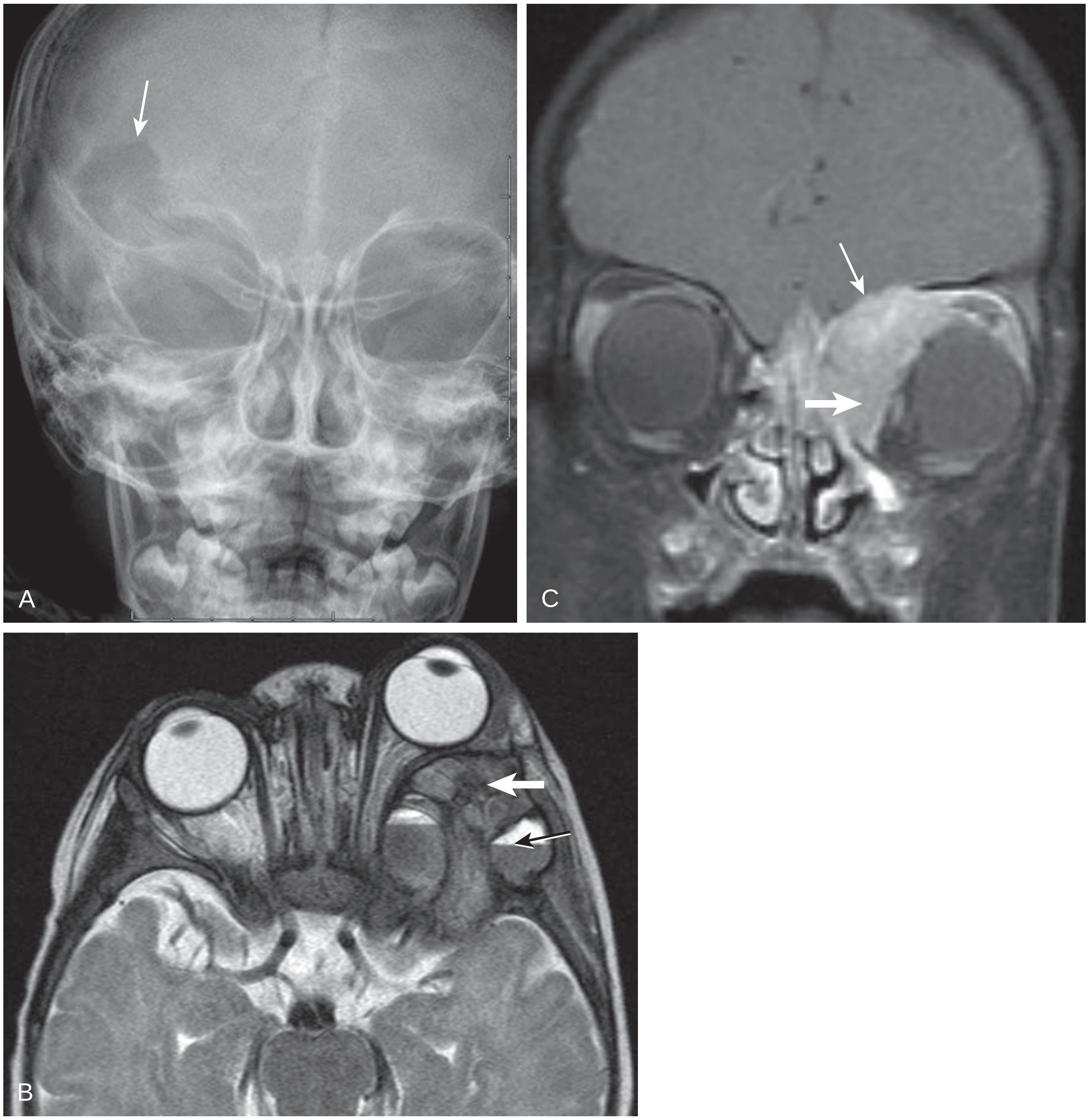

**e-Figure 7.22. Langerhans cell histiocytosis (LCH) in three different patients.** (A) Frontal radiograph of the skull demonstrates a right-sided supraorbital lucent lesion with beveled edges *(arrow),* typical of LCH. (B) Axial T2-weighted MR image demonstrates marked left-sided proptosis, associated with a posterior bony lesion along the greater wing of the sphenoid *(white arrow)* and with associated fluid-fluid levels *(black arrow)*. Although these findings are more commonly seen with aneurysmal bone cysts and telangiectatic osteosarcomas, they also are seen in LCH lesions. (C) Coronal contrast-enhanced fat-saturated T1-weighted MR image demonstrates an avidly enhancing, left-sided medially based LCH lesion *(thick arrow)* with a propensity for invasion of the skull base and thickening and enhancement of the adjacent dura *(thin arrow)*.

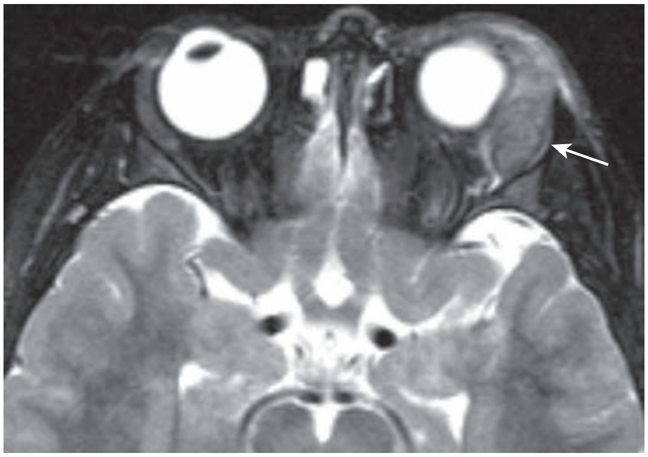

**e-Figure 7.23. Granulomatosis with polyangiitis (Wegener granulomatosis).** Axial fat-saturated T2-weighted MR image demonstrates enlargement of the left lacrimal gland *(arrow)*.

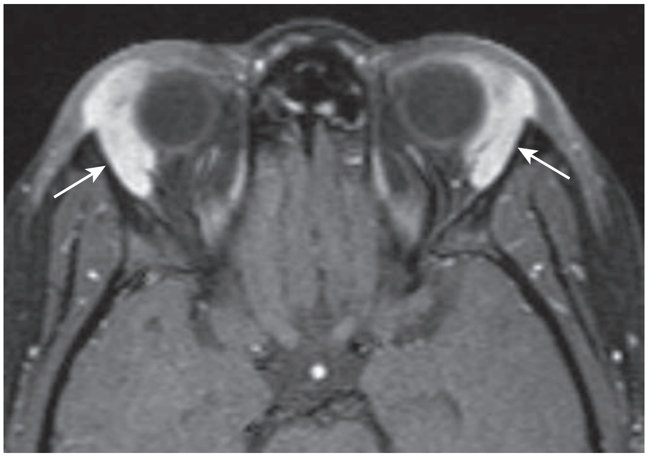

**e-Figure 7.24. Sarcoidosis.** Axial contrast-enhanced fat-saturated T1-weighted MR image demonstrates symmetric, bilaterally enlarged lacrimal glands, with avid contrast enhancement *(arrows)*.

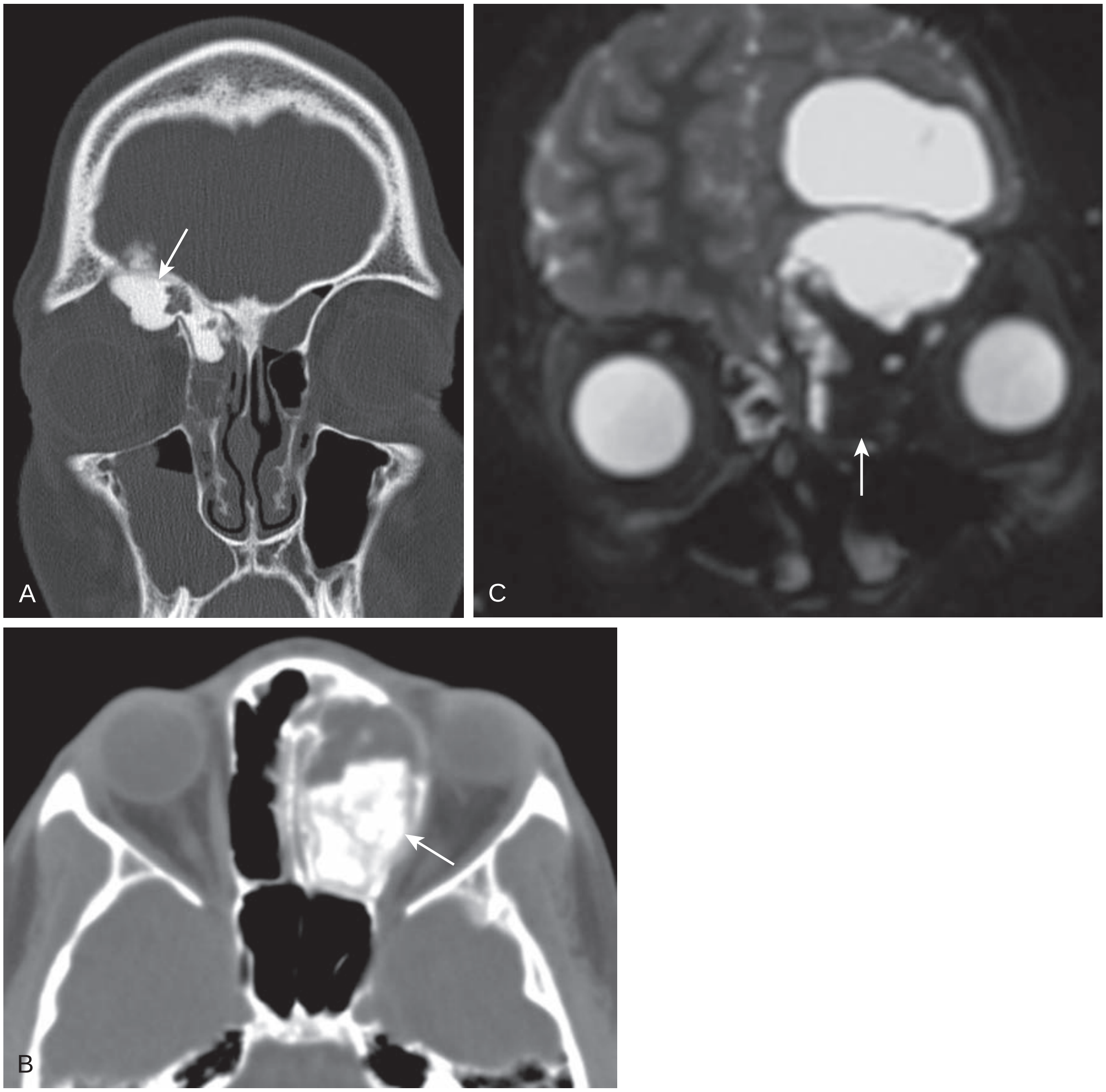

**e-Figure 7.25. Orbital osteoma in two different patients.** (A) Coronal noncontrast CT of the orbit and sinus region in a patient with a known right frontal sinus osteoma demonstrates a markedly dense lesion emanating from the right frontal sinus, similar in attenuation to that of enamel and dense bone *(arrow),* in keeping with a right frontal osteoma, with extension into the right orbit via a breach of the right orbital roof *(arrow)*. (B) Axial noncontrast CT and C, coronal fat-saturated T2-weighted MR images of the orbits demonstrate a markedly CT dense (bone-producing) lesion *(arrows)* with corresponding marked MRI signal loss, in keeping with a left ethmoid sinus region osteoma.

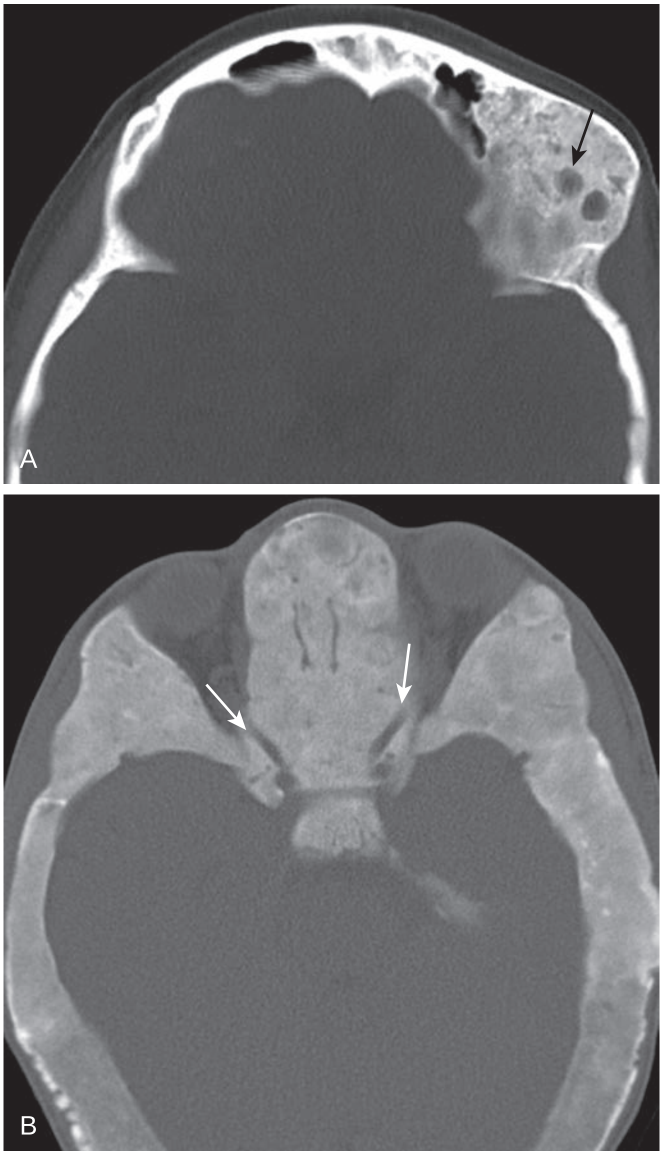

**e-Figure 7.26. Fibrous dysplasia (FD).** (A) Axial noncontrast CT at the level of the supraorbital frontal bone demonstrates ground-glass sclerosis with central areas of cystic lucencies *(arrow),* in keeping with FD. (B) Axial noncontrast CT of the head at the level of the orbits demonstrates diffuse marrow expansion and sclerosis associated with bilateral optic canal narrowing/impingement *(arrows)*.

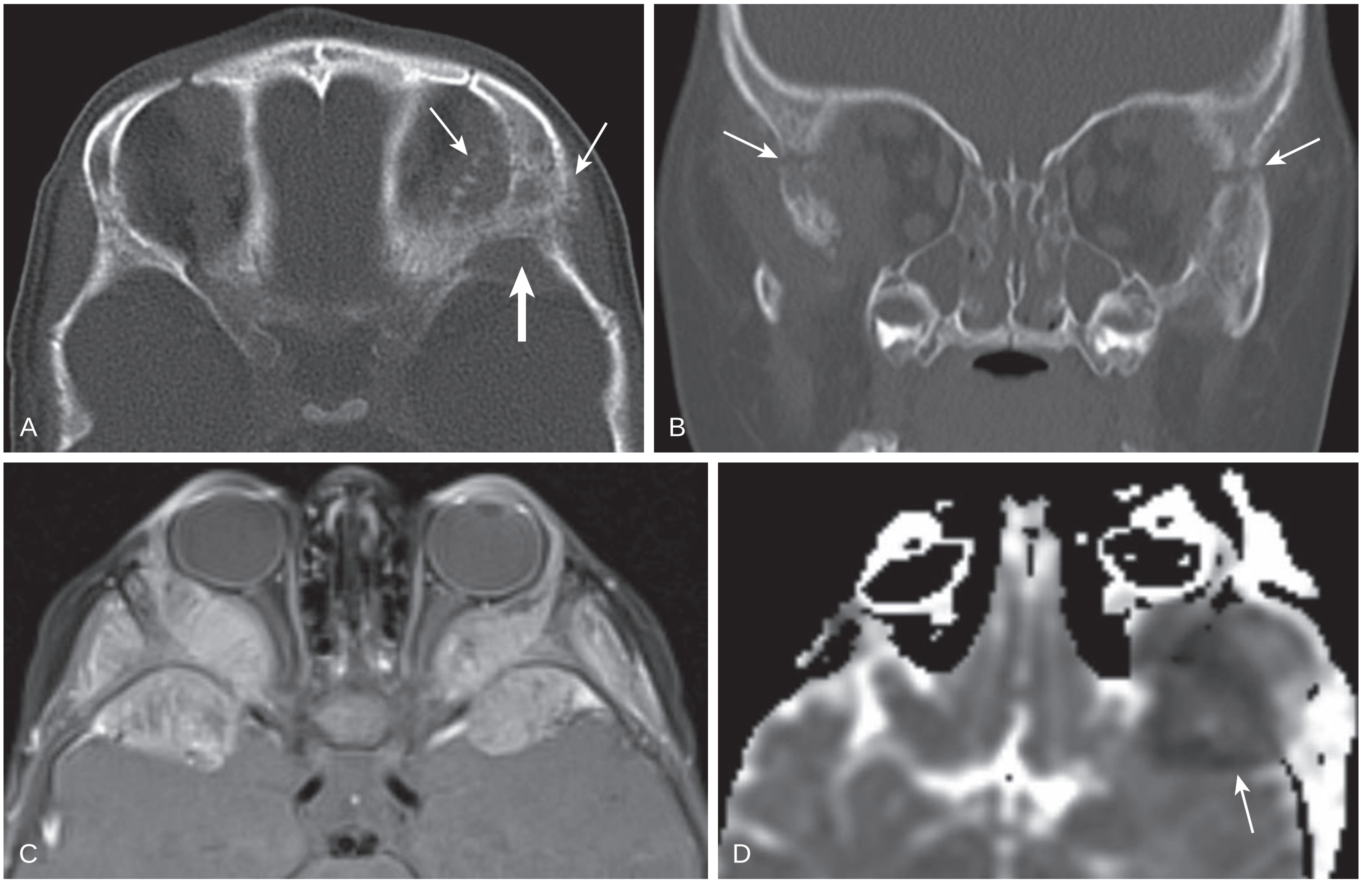

**Figure 7.27. Orbital neuroblastoma (NB) metastases in four different patients.** (A) Axial noncontrast CT image of the orbits demonstrates a moth-eaten, spiculated appearance of the bone surrounding the left orbit, which is a typical appearance of a NB that has metastasized to the orbits/skull base *(arrows)*. (B) Coronal reformatted noncontrast CT image demonstrates bilateral sutural irregularity and widening *(arrows),* highly suggestive of NB metastases (especially in the absence of an intracranial cause for increased intracranial pressure). (C) Axial contrast-enhanced fat-saturated T1-weighted MR image of the orbits demonstrates bilaterally symmetric lobulated enhancing soft tissue masses, around the bony orbit, with a speculated appearance, in the vicinity of cranial sutures, highly suggestive of metastatic NB. (D) Axial ADC MR image demonstrates marked restricted diffusion *(arrow pointing to dark signal)* along the posterolateral aspect of the orbit, with involvement of temporal bone, indicating marked cellularity of the tumor.

7.27C). NB metastases demonstrate restricted diffusion on DWI (Fig. 7.27D).

## Leukemia and Lymphoma

Marrow malignancies, lymphoma and leukemia, account for 10% to 15% of orbital masses. Extramedullary metastases to the orbits are most often associated with acute myelogenous leukemia (AML) in younger children and non-Hodgkin lymphoma (NHL) in older children. In patients with AML, the metastatic focus is referred to as a chloroma (derived from the Greek word *chloros* meaning “green”) due to their green tint.

Rarely, leukemic deposit is the initial presenting sign of AML, although it more commonly occurs in the setting of recurrent disease. The subperiosteal space along the lateral orbital wall is often a location of involvement; however, any location in the orbit may be involved. Imaging features resemble the bony metastases of NB, including invasion of the sutures of the orbital walls as well as periosteal reaction. Bilateral disease is seen in approximately one-third of cases. Invasion of the orbital fat and extension to the eyelid are common. Masses are isoattenuating to hyperattenuating on CT (e-Fig. 7.28A), isointense on T1W and T2W imaging (e-Fig. 7.28B) when compared with muscle, and demonstrate variable degrees of enhancement. Calcification is not a feature of leukemic disease. DWI demonstrates restricted diffusion in the soft tissue masses and the involved bony structures.

Imaging plays a crucial role in the detection of optic nerve involvement (e-Fig. 7.28C) and in guiding therapy to prevent irreversible visual loss. Compressive neuropathy (e-Fig. 7.29A) of the optic nerve is a known complication of orbital chloroma and lymphoma, even without direct infiltration of the optic nerve/sheath complex. Radiation to the optic nerves and intrathecal chemotherapy should be initiated promptly to preserve vision.

NHL (a tumor composed of B cells) often presents with extranodal disease. Most patients with orbital lymphoma also have systemic disease. NHL commonly involves the lacrimal gland and encases the globe. CT may demonstrate a hyperattenuating mass with sharply defined margins. MRI findings include T2W hypointense masses (e-Fig. 7.29B), with restricted diffusion (e-Fig. 7.29C). Orbital lymphoma ranges from very malignant tumors to much less malignant, indolent lesions, such as ocular adnexal Mucosa Associated Lymphoid Tissue (MALT) lymphoma. Imaging features as well as histologic features of different lymphoma types may overlap significantly.

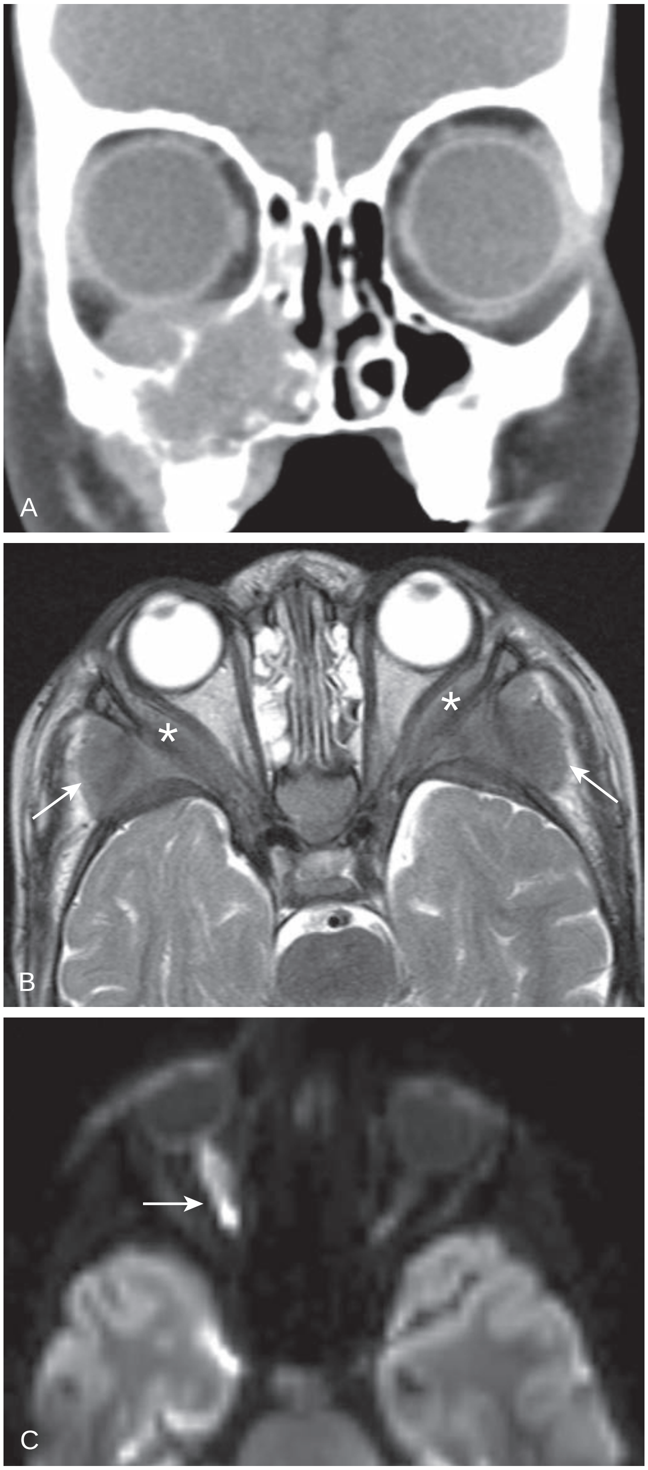

**e-Figure 7.28. Leukemia in three different patients.** (A) Coronal reformatted contrast-enhanced CT in a patient with AML demonstrates soft tissue opacification of the right maxillary sinus with bony breakthrough into the floor of the left orbit and inferolateral wall of the right maxillary sinus. (B) Axial T2-weighted MR image of the orbits in a patient with acute myelogenous leukemia (AML) demonstrates T2 dark soft tissue masses surrounding the posterolateral aspects of both orbits *(arrows),* with soft tissue extending to involve the inner tables of the posterior bony walls of both orbits *(asterisks)*. (C) Axial diffusion-weighted imaging MR image in a leukemic patient with direct optic nerve involvement as evidenced by restricted diffusion *(arrow)*.

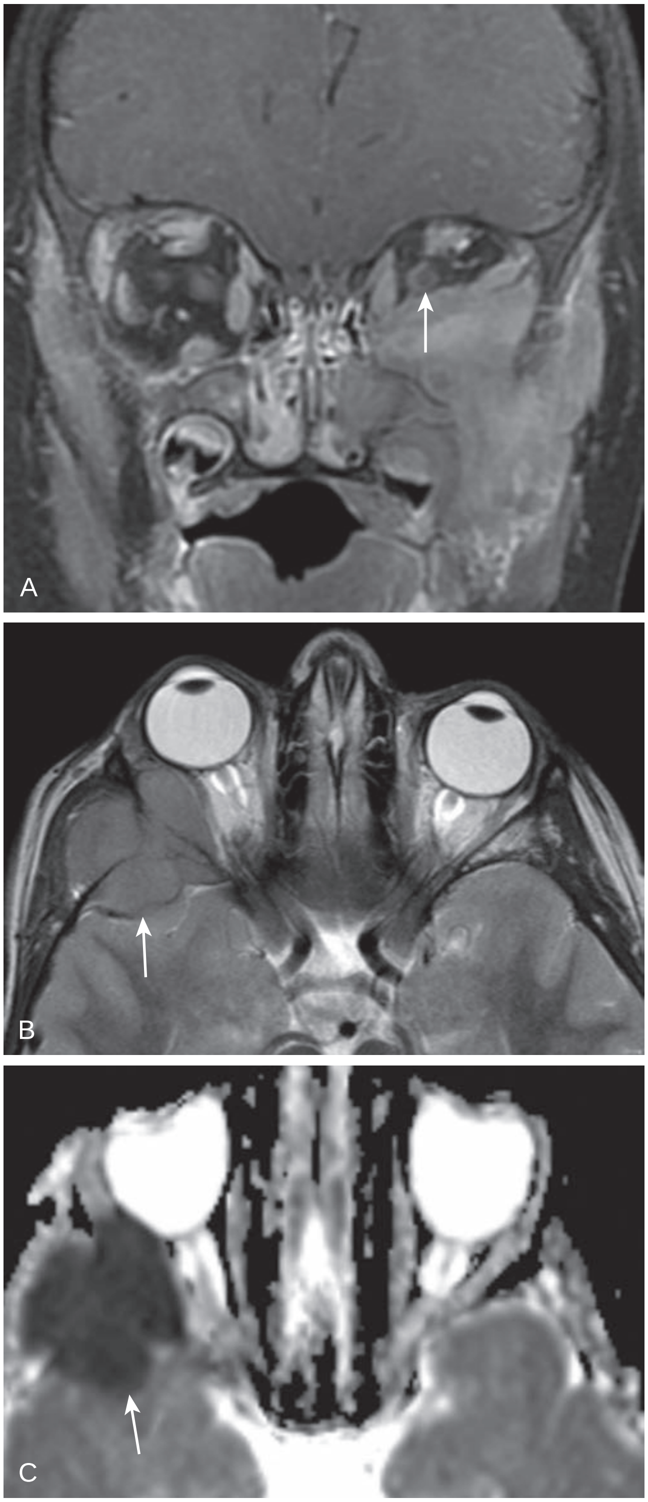

**e-Figure 7.29. Lymphoma.** (A) Coronal contrast-enhanced fat-saturated T1-weighted MR image of the orbit in a patient with lymphoma demonstrating a large enhancing facial mass extending into the orbit, causing upward displacement of the left optic nerve *(arrow)*. (B) Axial T2-weighted and (C) apparent diffusion coefficient (ADC) MR images demonstrate a lobulated T2 isointense mass about the right orbit, on both sides of the greater wing of the sphenoid, associated with diffusion restriction *(arrows)*.

## KEY POINTS

- Retinoblastoma is the most common intraocular pediatric tumor. Leukocoria is the most common presenting clinical sign.
- Optic nerve glioma is the most common pediatric primary neoplasm of the ocular nerve, often associated with NF type I.
- Orbital hemangiomas affect 2.5% to 10% of infants and are almost solely benign IHs.
- Rhabdomyosarcoma is the most common malignant soft tissue tumor in childhood, and the orbits and paranasal sinuses are the second-most common site of occurrence.
- Dermoid and epidermoid cysts are congenital developmental ectodermal inclusion cysts, constituting up to 5% of all orbital masses.
- Orbital metastatic disease may be due to NB, leukemia, or lymphoma.

## SUGGESTED READINGS

Brennan RC, Wilson MW, Kaste S, et al. US and MRI of pediatric ocular masses with histopathological correlation. *Pediatr Radiol*. 2012;42(6):738–749.

Pollock AN, Shekdar K, Feygin T. Benign orbital lesions. *J Pediatr Neuroradiol*. 2015;4:97–115.

Rao AA, Naheedy JH, Chen JY, et al. A clinical update and radiologic review of pediatric orbital and ocular tumors. *J Oncol*. 2013;2013:975908.

## REFERENCES

Full references for this chapter can be found on www.expertconsult.com

## REFERENCES

1. Chung EM, Specht CS, Schroeder JW. From the archives of the AFIP: pediatric orbit tumors and tumor like lesions: neuroepithelial lesions of the ocular globe and optic nerve. *Radiographics*. 2007;27(4):1159–1186.
2. Rao AA, Naheedy JH, Chen JY, et al. A clinical update and radiologic review of pediatric orbital and ocular tumors. *J Oncol*. 2013;2013:975908.
3. Sepahdari AR, Politi LS, Aakalu VK, et al. Diffusion weighted imaging of orbital masses: multi-institutional data support a 2-ADC threshold model to categorize lesions as benign, malignant, or indeterminate. *AJNR Am J Neuroradiol*. 2014;35(1):170–175.
4. Xu XL, Singh HP, Wang L, et al. Rb suppresses human cone-precursor derived retinoblastoma tumours. *Nature*. 2014;514(7522):385–388.
5. Staffieri SE, McGillivray G, Elder JE, et al. Managing fetuses at high risk of retinoblastoma: lesion detection on screening MRI. *Prenat Diagn*. 2015;35(2):174–178.
6. Paquette LB, Miller D, Jackson HA, et al. In utero detection of retinoblastoma with fetal magnetic resonance and ultrasound: initial experience. *AJP Rep*. 2012;2(1):55–62.
7. Smirniotopoulos JG, Bargallo N, Mafee MF. Differential diagnosis of leukokoria: radiologic-pathologic correlation. *Radiographics*. 1994; 14(5):1059–1079.
8. Shields CL, Ghassemi F, Tuncer S, et al. Clinical spectrum of diffuse infiltrating retinoblastoma in 34 consecutive eyes. *Ophthalmology*. 2008;115(12):2253–2258.
9. de Graaf P, van der Valk P, Moll AC, et al. Contrast-enhancement of the anterior eye segment in patients with retinoblastoma: correlation between clinical MR imaging, and histopathologic findings. *AJNR Am J Neuroradiol*. 2010;31(2):237–245.
10. Brisse HJ, Guesmi M, Aerts I, et al. Relevance of CT and MRI in retinoblastoma for the diagnosis of postlaminar invasion with normal-size optic nerve: a retrospective study of 150 patients with histological comparison. *Pediatr Radiol*. 2007;37(7):649–656.
11. Tateishi U, Hasegawa T, Miyakawa K, et al. CT and MRI features of recurrent tumors and second primary neoplasms in pediatric patients with retinoblastoma. *AJR Am J Roentgenol*. 2003;181(3):879–884.
12. Feygin T, Leahey AM. Advanced imaging, Clinical approach. *J Pediatr Neuroradiol*. 2015;4:82–96.
13. Kaliki S, Shields CL, Eagle RC Jr, et al. Ciliary body medulloepithelioma: analysis of 41 cases. *Ophthalmology*. 2013;120(12).
14. Shields JA, Eagle RC Jr, Shields CL, et al. Congenital neoplasms of the nonpigmented ciliary epithelium (medulloepithelioma). *Ophthalmology*. 1996;103.
15. Shields CL, et al. Optical coherence tomography of retinal astrocytic hamartoma in 15 cases. *Ophthalmology*. 2006;113(9):1553–1557.
16. Brennan RC, Wilson MW, Kaste S, et al. US and MRI of pediatric ocular masses with histopathological correlation. *Pediatr Radiol*. 2012;42(6):738–749.
17. Pollock AN, Shekdar K, Feygin T. Benign orbital lesions. *J Pediatr Neuroradiol*. 2015;4:97–115.
18. Kurz-Levin M, Landau K. A comparison of imaging techniques for diagnosing drusen of the optic nerve head. *Arch Opthalmol*. 1999;8:117 1045–117 1049.
19. Alniemi ST, Griepentrog GJ, Diehl N, et al. Rate of amblyopia in periocular infantile hemangiomas. *Arch Ophthalmol*. 2012;130(7):943–944.
20. Bauman NM, McCarter RJ, Guzzetta PC, et al. Propranolol vs prednisolone for symptomatic proliferating infantile hemangiomas: a randomized clinical trial. *JAMA Otolaryngol Head Neck Surg*. 2014;140(4):323–330.
21. Metry DW, Dowd CF, Barkovich AJ, et al. The many faces of PHACE syndrome. *J Pediatr*. 2001;139(1):117–123.
22. Judd CD, Chapman PR, Koch B, et al. Intracranial infantile hemangiomas associated with PHACE syndrome. *AJNR Am J Neuroradiol*. 2007;28(1):25–29.
23. Mishra A, Alsawidi K, Abuhajar R, et al. Orbital venous lymphatic malformation: role of imaging. *Oman J Ophthalmol*. 2009;2(3):141–142.
24. Rootman J. Vascular malformations of the orbit: hemodynamic concepts. *Orbit*. 2003;22(2):103–120.
25. Bisdorff A, Mulliken JB, Carrico J, et al. Intracranial vascular anomalies in patients with periorbital lymphatic and lymphaticovenous malformations. *AJNR Am J Neuroradiol*. 2007;28(2):335–341.
26. Harold Lee HB, Garrity JA, Cameron JD, et al. Primary optic nerve sheath meningioma in children. *Surg Ophthalmol*. 2008;53(6):543–558.
27. Gnanaraj L, Skibell BC, Coret-Simon J, et al. Massive congenital orbital teratoma. *Ophthal Plast Reconstr Surg*. 2005;21(6):445–447.
28. Castillo BV Jr, Kaufman L. Pediatric tumors of the eye and orbit. *Pediatr Clin North Am*. 2003;50(1):149–172.
29. Conneely MF, Mafee MF. Orbital rhabdomyosarcoma and simulating lesions. *Neuroimaging Clin N Am*. 2005;15(1):121–136.
30. Romero R, Castano A, Abelairas J, et al. Peripheral primitive neuroectodermal tumour of the orbit. *Br J Ophthalmol*. 2011;95(7):915–920.
31. Goldsmith JD, van de Rijn M, Syed N. Orbital hemangiopericytoma and solitary fibrous tumor: a morphologic continuum. *Int J Surg Pathol*. 2001;9(4):295–302.
32. Furusato E, Valenzuela IA, Fanburg-Smith JC, et al. Orbital solitary fibrous tumor: encompassing terminology for hemangiopericytoma, giant cell angiofibroma, and fibrous histiocytoma of the orbit: reappraisal of 41 cases. *Hum Pathol*. 2011;42(1):120–128.
33. Ahuja R, Azar NF. Orbital dermoids in children. *Semin Ophthalmol*. 2006;21(3):207–211.
34. Mendenhall WM, Lessner AM. Orbital pseudotumor. *Am J Clin Oncol*. 2010;33(3):304–306.
35. Goldstein SM, Katowitz WR, Moshang T, et al. Pediatric thyroid-associated orbitopathy: the Children's Hospital of Philadelphia experience and literature review. *Thyroid*. 2008;18(9):997–999.
36. Kilborn TN, Teh J, Goodman TR. Paediatric manifestations of Langerhans cell histiocytosis: a review of the clinical and radiological findings. *Clin Radiol*. 2003;58(4):269–278.
37. Provenzale JM, Mukherji S, Allen NB, et al. Orbital involvement by Wegener's granulomatosis: imaging findings. *AJR Am J Roentgenol*. 1996;166(4):929–934.
38. Bidar M, Wilson MW, Laquis SJ, et al. Clinical and imaging characteristics of orbital leukemic tumors. *Ophthal Plast Reconstr Surg*. 2007;23(2):87–93.
39. de Fátima Soares M, Braga FT, da Rocha AJ, et al. Optic nerve infiltration by acute lymphoblastic leukemia: MRI contribution. *Pediatr Radiol*. 2005;35(8):799–802.
40. Jee WH, Choi KH, Choe BY, et al. Fibrous dysplasia: MR imaging characteristics with radiopathologic correlation. *AJR Am J Roentgenol*. 1996;167(6):1523–1527.

# 8

# Nose and Sinonasal Cavities

*Diana P. Rodriguez*

## DEVELOPMENT AND ANATOMY OF THE NOSE AND SINONASAL CAVITIES

The craniofacial structures form from a complex sequence of events dictated by molecular changes during the third to 10th gestational weeks. The nose forms in the fourth gestational week from the frontonasal processes and two nasal placodes that develop dorsal to the stomodeum. The nose derives from ectoderm, mesoderm, and a deep cartilaginous capsule. The posterior nasal septum and the sphenoid and ethmoid bones form from neural crests. The skull base and nose are formed by mesenchymal structures that later fuse and ossify.[1,2] Neural tube closure anomalies of the anterior neuropore (primitive frontonasal region) may result in developmental frontonasal midline masses.[2] A temporary fontanelle, *the fonticulus nasofrontalis*, forms between the nasal bones and inferior frontal bones and later fuses to form the frontonasal suture in the eighth gestational week. The *pre-nasal space* is another transient space located between the posterior aspect of the frontal and nasal bones, and anterior aspect of the nasal cartilage. This space extends from the foramen cecum, a midline opening just anterior to the crista galli of the ethmoid bone, to the osteocartilaginous junction. The dura extends through the foramen cecum and comes in close contact to the skin and later involutes and obliterates, while the nasal process of the frontal bone grows. Failure of regression of these structures may result in midline developmental anomalies such as nasal dermoids, cephaloceles, and nasal neuroglial heterotopia.[3]

The nasal cavity is triangular and separated in the midline by the nasal septum. The nasal cavity is composed of a cartilaginous portion anteriorly and an osseous portion posteriorly, which is formed by the perpendicular plate of the ethmoid posterosuperiorly and the vomer posteroinferiorly. The opening to each nasal cavity is known as the vestibule, which is bounded medially by the columella and nasal septum and laterally by the nasal alae. The cribriform plate is the roof of the nasal cavity, and the floor is the hard and soft palate. Posteriorly, the nasal cavity communicates with the nasopharynx via the choanae, after rupture of the oronasal membrane during the fetal period. From the lateral wall of the nasal cavity, three pairs of turbinates (superior, middle, and inferior) project into the nasal cavity, each with a corresponding meatus below them. The middle turbinate is attached to the cribriform plate via the vertical lamella and to the lamina papyracea via the basal lamella (Fig. 8.1).

### Paranasal Sinuses

The paranasal sinuses form as diverticula from the walls of the nasal cavities and become air-filled extensions in the adjacent bones—maxilla, ethmoid, frontal, and sphenoid. The original openings of the diverticula persist as the ostia of the sinuses that communicate with the nasal cavity (Figs. 8.2A and B).

The mucosal lining of the nasal cavities is contiguous with the paranasal sinuses and consists of pseudostratified, columnar, ciliated epithelium containing mucinous and serous glands,[4] whereas the nasal septum is lined by squamous mucosa.[5] In the human embryo, ethmoidal and maxillary sinus budding can be detected at 11 to 12 gestational weeks and at 14 to 15 gestational weeks, respectively.[6] In general, only rudimentary maxillary and ethmoid sinuses, which continue to expand until puberty or early adulthood, are present at birth.[7] The sinuses also are linked to facial growth and dentition.[7–14]

### Ethmoid Sinuses

The ethmoid sinuses are already developed in number and pneumatized at birth but continue to expand, reaching adult proportions at about 12 years of age (Fig. 8.3).[15] The ethmoid sinuses consist of a paired group of a variable number of cells (3–18) within the lateral masses of the ethmoid bone. The ethmoid bone also consists of the cribriform plate superiorly and the perpendicular plate, which is part of the nasal septum. The ethmoid sinus is bordered medially by the nasal cavity and laterally by the lamina papyracea; its roof is formed by the cribriform plate and fovea ethmoidalis (see Fig. 8.1). The anterior and posterior ethmoid air cells are separated by the basal lamella (see Fig. 8.3C), which is the lateral attachment of the middle turbinate to the lamina papyracea. Drainage of the anterior ethmoid air cells occurs via the ethmoid bulla into the hiatus semilunaris and middle meatus. The posterior ethmoid air cells drain into the superior meatus and then into the sphenoethmoid recess (see Fig. 8.2A).

The anterior ethmoidal artery arises from the ophthalmic artery in the orbit, pierces the lamina papyracea, and exits through the ethmoid roof in the superomedial wall of the orbit, 2 to 3 mm behind the anterior wall of the bulla ethmoidalis. Occasionally, the anterior ethmoidal artery passes within the bony septae of the ethmoid sinuses and is suspended in a mesentery without a bony cover (e-Fig. 8.4).[16]

#### Anatomic Variants

Any asymmetry in the height of the ethmoid roof should be documented by the radiologist due to risk of surgical penetration during endoscopic surgery on the side where the roof is lower.[17,18]

Concha bullosa refers to the pneumatization of the middle turbinate as a result of intramural extension of posterior ethmoid air cells (Fig. 8.5B). A large concha bullosa can eventually cause obstruction of the nasal cavity.

Extramural expansion of ethmoid air cells can result in anatomic variants, including the following: Agger nasi cells (Fig. 8.5A), which are the most anterior and inferior cells involving the lacrimal bone or maxilla; Haller cells, which are middle ethmoid air cells extending into the inferomedial floor of the orbit (Fig. 8.5C); and Onodi cells, which are posterior sphenoethmoid air cells with prominent superolateral pneumatization in close relationship to the optic nerve canal.[16]

### Maxillary Sinuses

The maxillary sinuses are very small and pneumatized at birth and undergo rapid inferolateral expansion during the first years of life, reaching full size between 15 to 18 years of age. The floor of the maxillary sinus is seen usually at the level of the middle

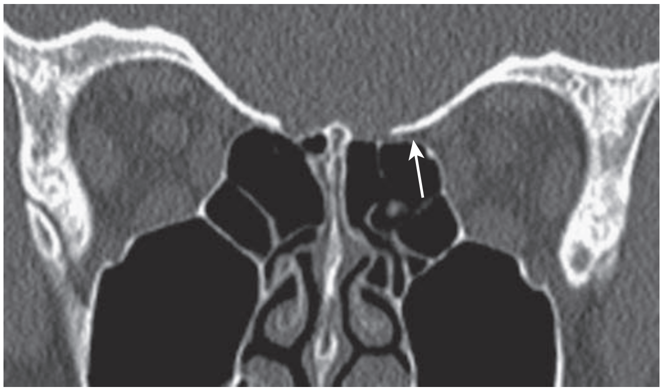

**e-Figure 8.4. Anterior ethmoidal artery canal.** Coronal CT image shows the normal bony canal for the anterior ethmoidal artery on the left side *(arrow)*.

meatus during infancy; it reaches the level of the nasal floor by 8 to 9 years of age, and by age 12 years, it is located at the level of the hard palate.[9] The maxillary floor lies below the level of the nasal floor in 65% of adults (e-Fig. 8.6).[19]

The maxillary sinus is the largest of the sinuses. Its roof is formed by the orbital floor, which carries the bony canal for the infraorbital nerve; the medial wall is formed by the lateral nasal wall. The posterior wall of the maxillary sinus forms the pterygopalatine fossa (Fig. 8.7A). The maxillary sinus drains via the maxillary ostium located superomedially into the infundibulum, the hiatus semilunaris, and the middle meatus (see Fig. 8.2A).

Developmental variations of the maxillary sinus include an accessory ostium, unilateral hypoplasia, and septations that can compartmentalize the sinus cavity. Maxillary molar roots may impinge on the walls of the sinuses.

## Sphenoid Sinus

The sphenoid sinus pneumatizes in a ventrodorsal direction from 7 months to 2 years of age. Significant sinus expansion occurs between 3 and 8 years of age, with complete pneumatization usually present by age 10 years (e-Fig. 8.8).[12] Its superior border is formed by the sella turcica, posteriorly by the clivus, anteriorly by the ethmoid sinus, and inferiorly by the nasopharynx (see Figs. 8.2A and B). This sinus drains anteriorly via the sphenoethmoid recess. Lateral recesses of the sphenoid sinus are formed from pneumatization of the pterygoid process in 44% of people (see Fig. 8.7A). Benign sphenoid marrow variants, which sometimes are mistaken for lesions, can be seen adjacent to the pneumatized sphenoid sinus (e-Fig. 8.9).

Important anatomic relationships of the sphenoid sinus include the optic canal and nerve located superolaterally; the foramen rotundum with the maxillary nerve that courses along the inferolateral margin of the sphenoid sinus; the vidian canal, which usually runs along the floor of the sphenoid sinus; and the cavernous portion of the internal carotid artery, which protrudes laterally into the sinus (see Fig. 8.7B). The sphenoid sinus septum usually is aligned anteriorly with the nasal septum but can deviate posteriorly, forming unequal sphenoid cavities (see Fig. 8.7C). Absent pneumatization in a child older than 9 years is usually abnormal and warrants clinical investigation (see Fig. 8.7D).

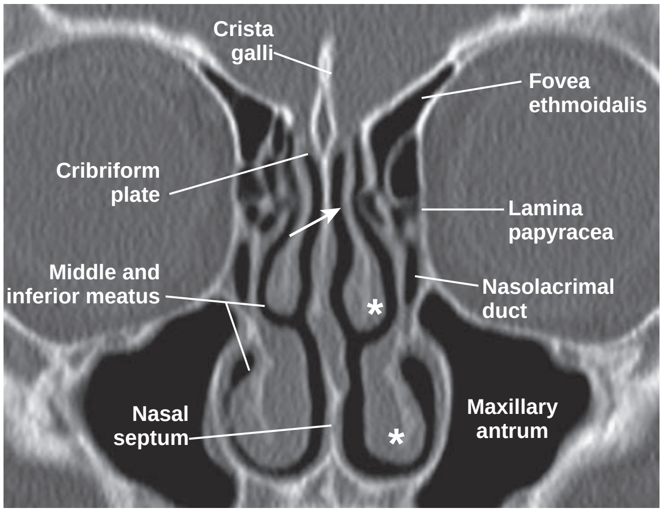

**Figure 8.1. Anatomy of the nasal cavity demonstrated in a 13-year-old.** Coronal CT image shows middle and inferior turbinates *(asterisks)* and vertical lamella of the middle turbinate *(arrow)* attached to the cribriform plate.

## Frontal Sinuses

The frontal sinuses are absent at birth and are the last to develop once bone marrow conversion has occurred. The frontal sinus is considered an extension of the anterior ethmoid air cells, pneumatizes between 2 to 8 years, and continues to expand until the second decade of life.[9,14] The frontal sinuses consist of paired, often asymmetric cells. The anterior wall corresponds to the outer cortical table of the frontal bone, and its posterior wall separates this sinus from the anterior cranial fossa. This sinus drains via the frontal recess, which is an hourglass-like narrowing between the frontal sinus and the anterior middle meatus (see Fig. 8.2A). Hypoplasia and aplasia of the frontal sinus can be seen in 4% and 5% of the population, respectively.

# IMAGING OF THE PARANASAL SINUSES

## Radiography

Although plain radiography is less costly and more widely available than computed tomography (CT), it has significant limitations. Plain radiography often overestimates or underestimates findings, does not localize pathology well, and does not provide important

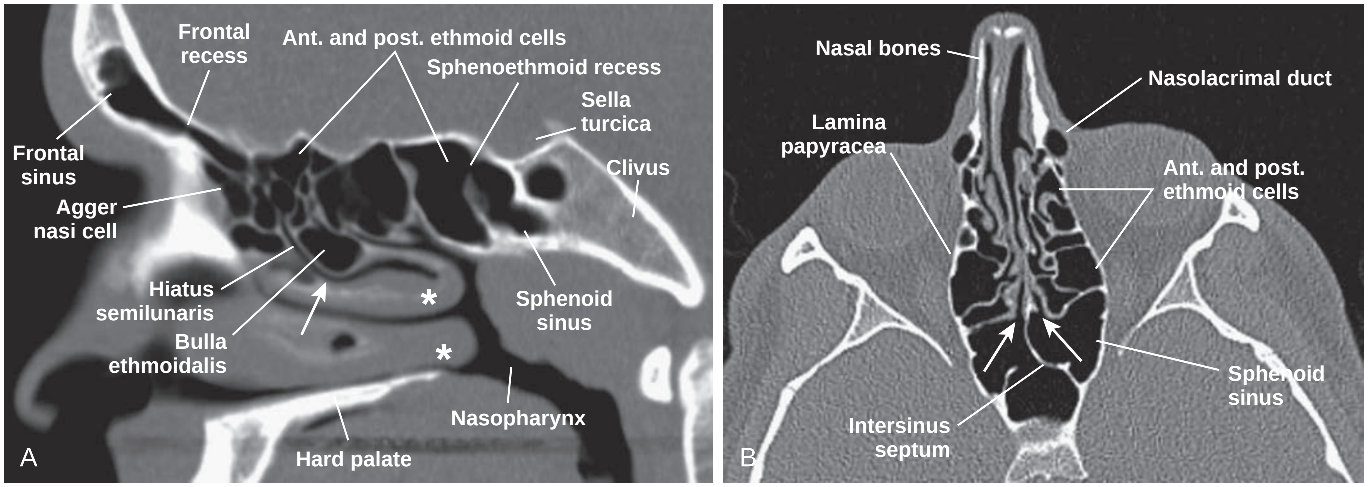

**Figure 8.2. Normal sinus openings.** (A) Sagittal CT image shows frontal recess of the frontal sinus, hiatus semilunaris, middle meatus *(arrow),* sphenoethmoid recess, and middle and inferior turbinates *(asterisks)*. (B) Axial CT image shows sphenoethmoid recesses *(arrows)*.

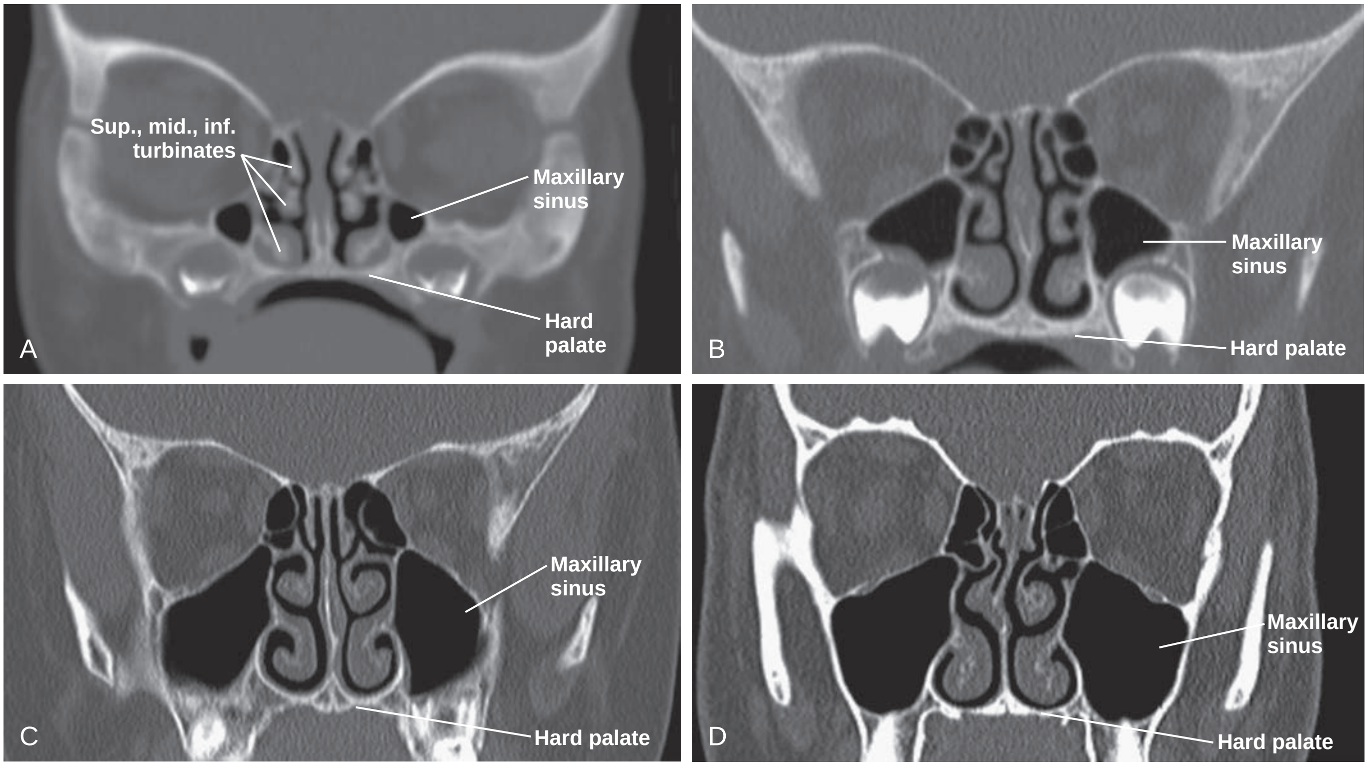

**e-Figure 8.6. Maxillary sinus development.** Coronal CT images show maxillary sinuses at (A) 1 month, (B) 3 years, (C) 7 years, and (D)15 years.

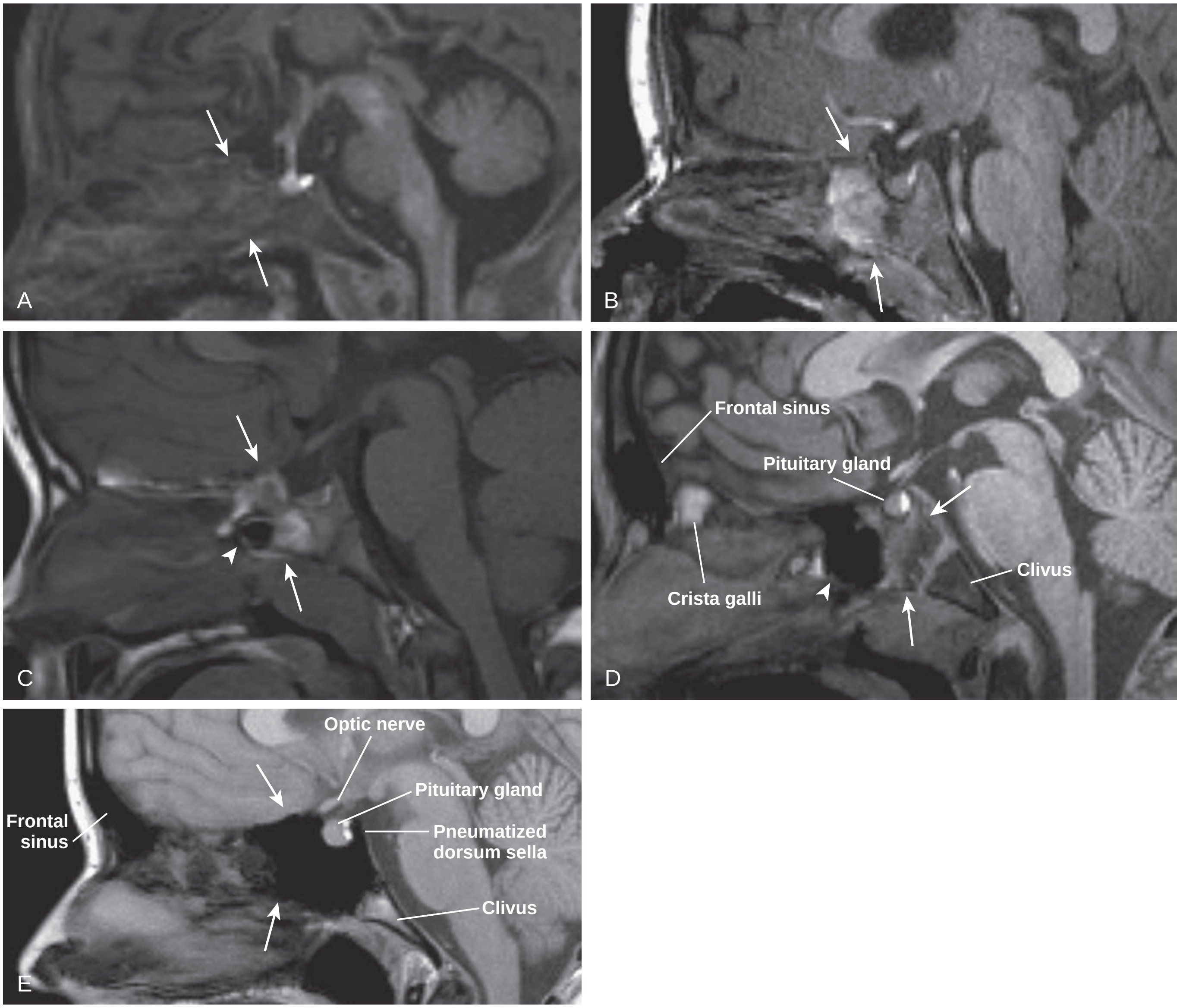

**e-Figure 8.8. Sphenoid sinus development.** Sagittal T1-weighted MR images. (A) Hematopoietic marrow (T1 hypointense) of the sphenoid bone in a newborn *(thin arrows)*. (B) Fatty transformation of the anteroinferior aspect of the sphenoid bone in a 12-month-old *(arrows)*. (C) Pneumatization of the anteroinferior aspect of the sphenoid sinus in a 3-year-old *(arrowhead)* with fatty sphenoid marrow *(arrows)*. (D) Further pneumatization of the sphenoid sinus *(arrowhead)* and fatty transformation of the sphenoid bone *(arrows)*. (E) Fully pneumatized sphenoid sinus *(arrows),* including the dorsum sella in a 14-year-old boy.

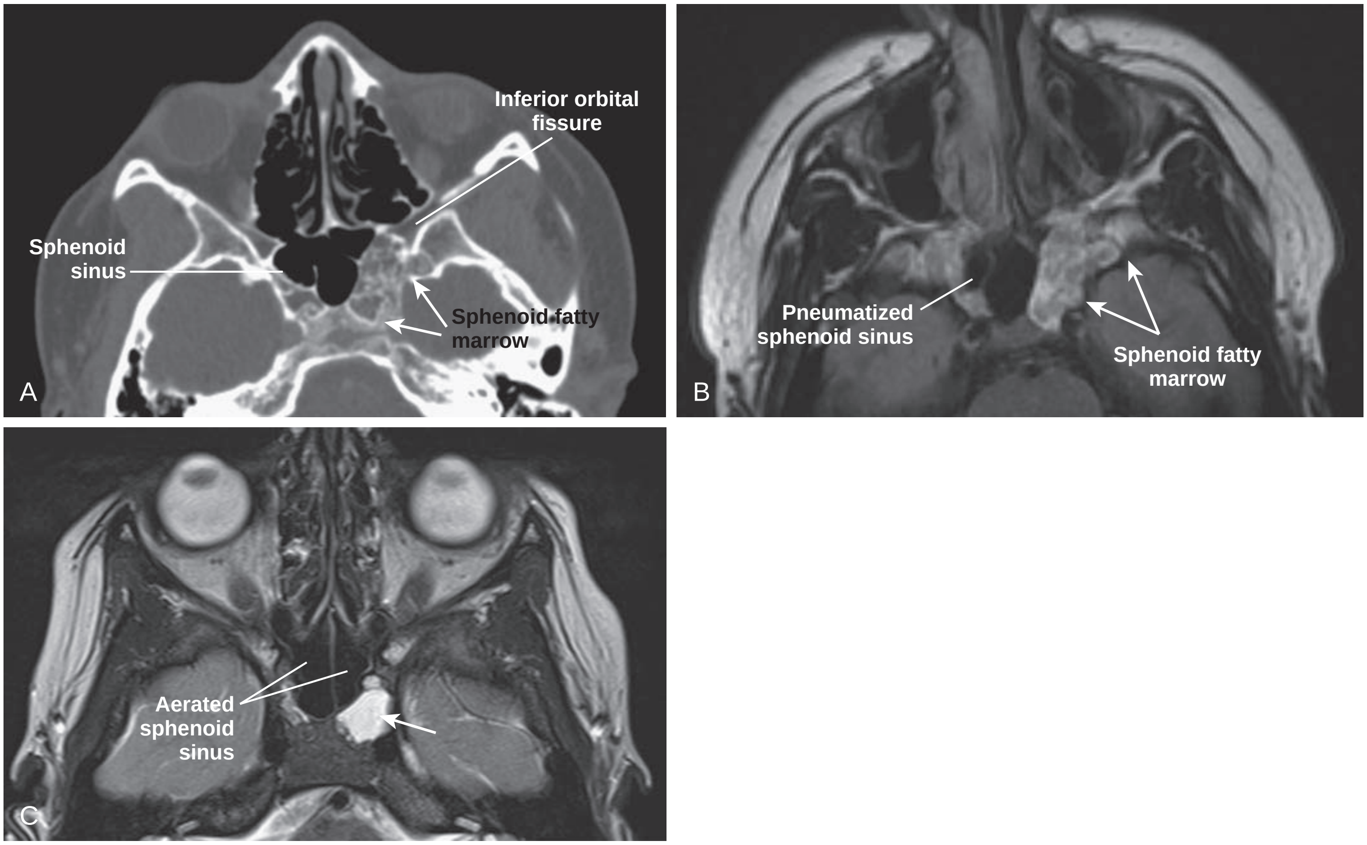

**e-Figure 8.9. Benign sphenoid marrow variants.** (A) Axial CT image shows asymmetric fatty marrow of nonpneumatized sphenoid bone on the left side. (B) Axial T1-weighted MR image shows correlation of T1-hyperintense normal marrow of the sphenoid bone, which can simulate mass (neoplasm/erosion). (C) Axial CT image in another patient shows retained fluid in the left lateral recess of the sphenoid sinus.

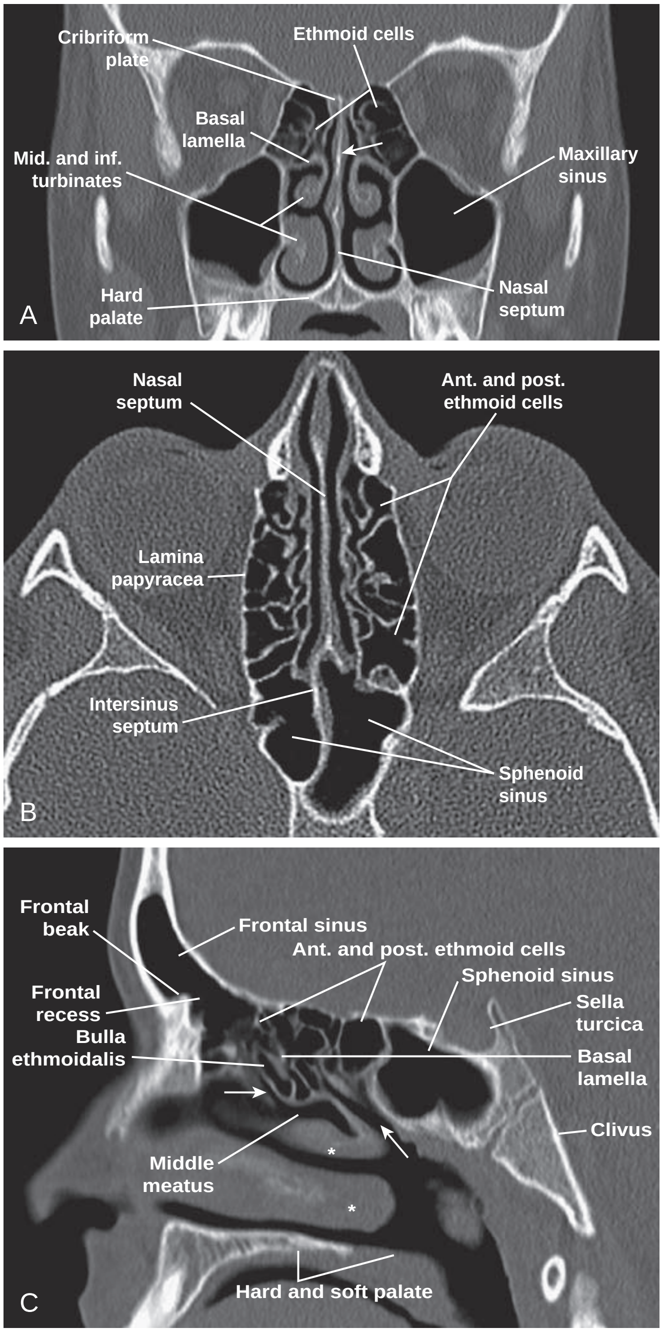

**Figure 8.3. Normal anatomy of the sinuses demonstrated by fully developed sinuses in a 13-year-old boy.** (A) Coronal CT image shows the perpendicular plate of the ethmoid bone *(arrow)*. (B) Axial CT image and (C) sagittal CT image shows hiatus semilunaris *(arrow at left),* drainage passage of posterior ethmoid cells *(arrow at right),* and middle and inferior turbinates *(asterisks)*.

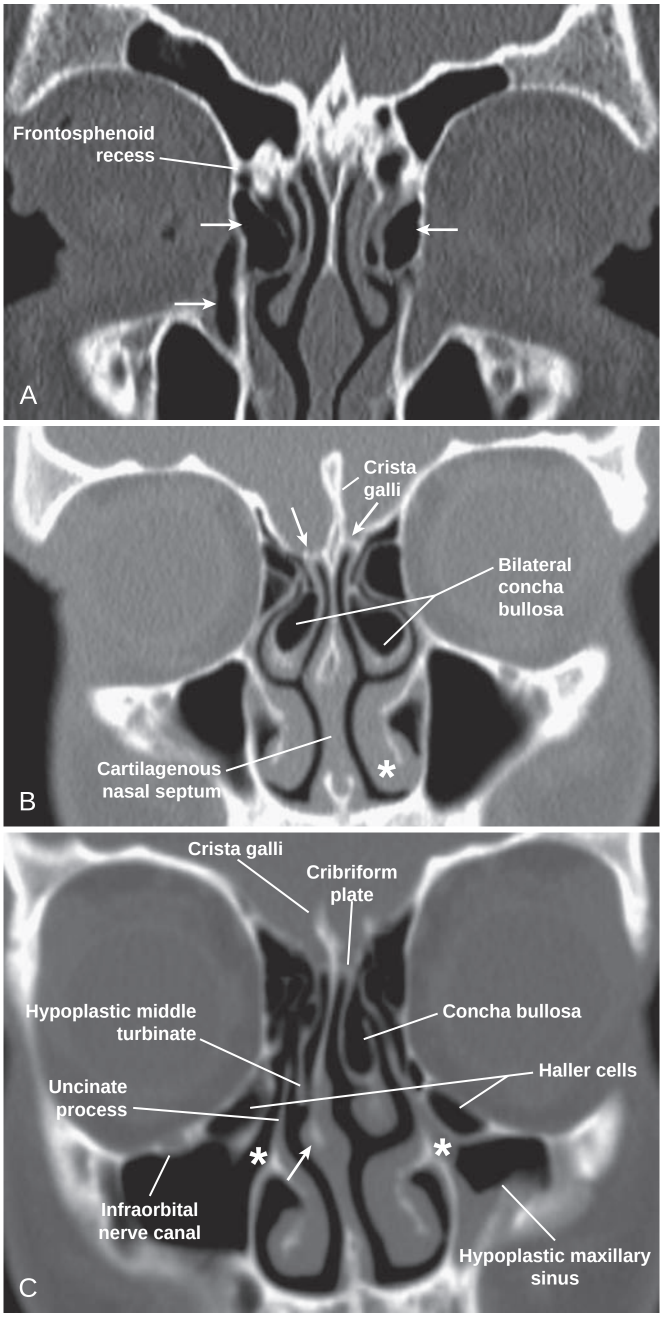

**Figure 8.5. Anatomic variants.** (A) Coronal CT image shows bilateral Agger nasi cells *(top arrows),* the nasolacrimal canal *(bottom arrow),* and the right frontoethmoidal recess. (B) Bilateral concha bullosa, asymmetric height of the ethmoid roofs *(arrows),* and the inferior turbinate *(asterisk)* are shown. (C) A hypoplastic right middle turbinate, rightward nasal septal deviation, Haller cells, and infundibulum *(asterisks)* are shown.

anatomic detail.[20] The paranasal sinus series traditionally consists of four views (Caldwell, Waters, posteroanterior, and lateral) that are technically difficult to perform in children. The Waters view is obtained by angulating the beam in 5-degree increments per year (up to age 6 years) to compensate for the progressive enlargement of the maxillary antra throughout childhood (Fig. 8.10). This approach improves visualization of the maxillary sinuses by projecting them over the petrous pyramids but can create double contours that simulate mucosal thickening. Air fluid levels also can be obscured as a result of beam angulation. Using only the Waters view radiograph has been shown to have 32% false-negative results and 49.2% false-positive results when compared with CT. Abnormalities in the ethmoid and sphenoid sinuses are not detected on a Waters radiograph.[21] Ethmoid disease on the Caldwell projection is limited, and the lateral view for evaluating the sphenoid sinus is of little value in children younger than 4 years.[20,23]

Sinusitis is considered a clinical diagnosis that should not be made on the basis of imaging findings alone.[23] The American

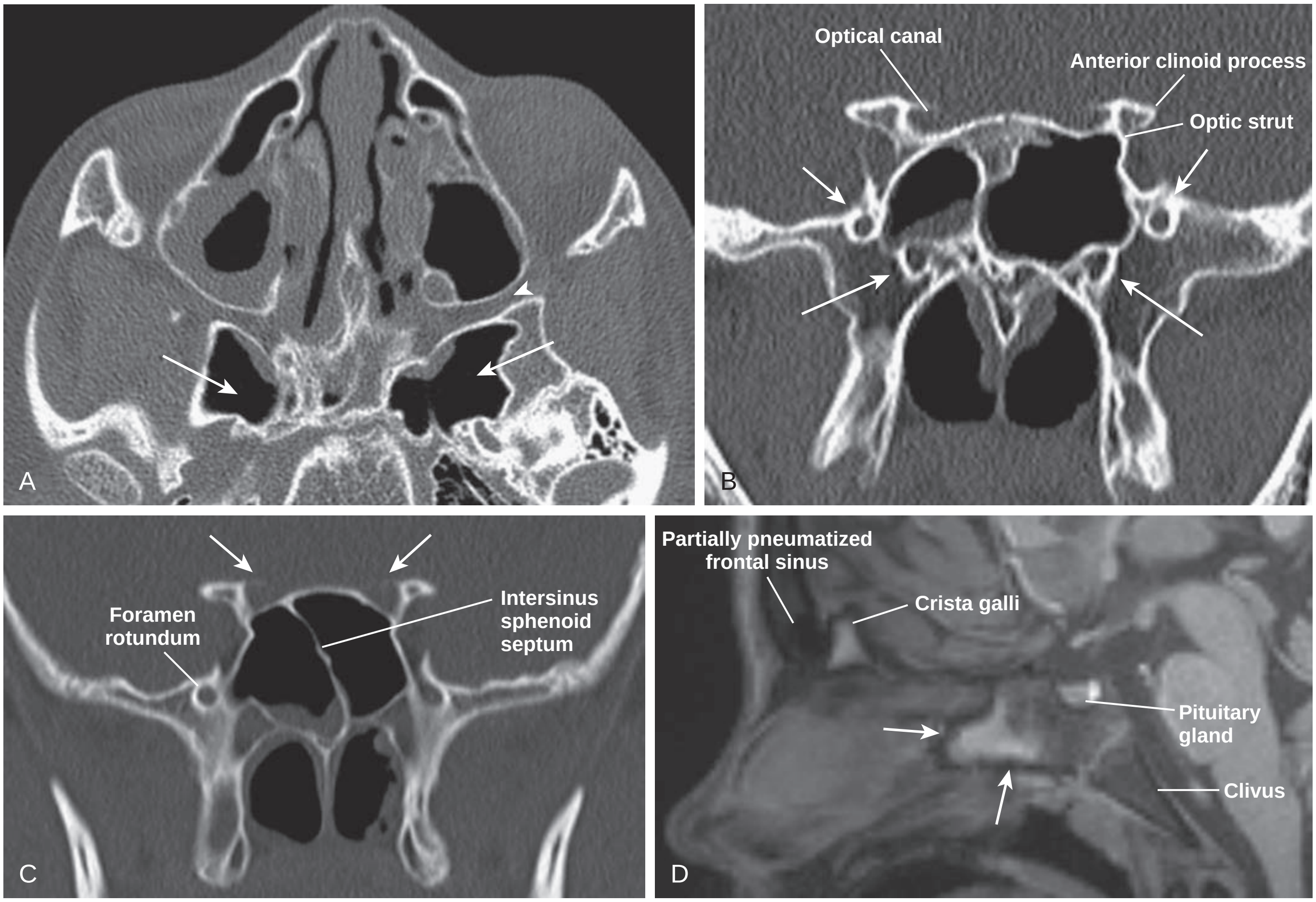

**Figure 8.7. Sphenoid sinus anatomy and variants.** (A) Axial CT image shows hyperpneumatization of the sphenoid sinus involving the pterygoid plates bilaterally *(arrows);* the pterygopalatine fossa *(arrowhead)* also is shown. (B) Coronal CT image shows foramen rotundum *(short arrows)* and the vidian canal *(long arrows)* bilaterally. (C) Coronal CT image shows insertion of the intersinus septum into the right optic canal *(arrows)*. (D) Sagittal T1-weighted MR image demonstrates a nonpneumatized sphenoid sinus in an 11-year-old boy with fatty transformation of its anteroinferior portion *(arrows)*.

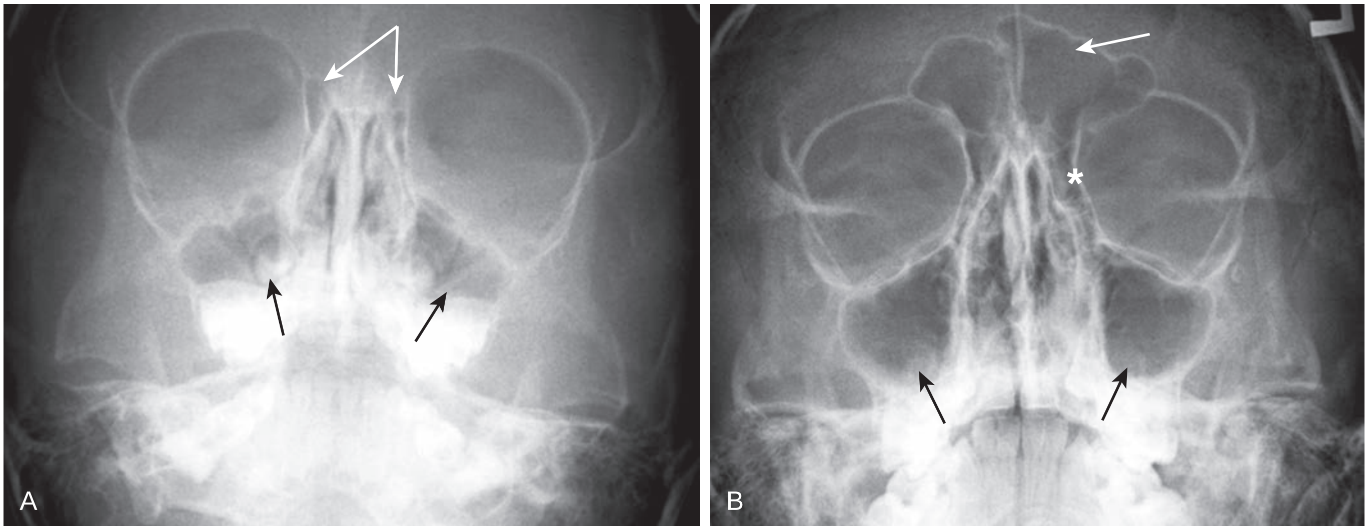

**Figure 8.10. Waters view radiograph.** (A) Maxillary sinuses *(black arrows)* and ethmoid air cells *(white arrows)* in a 3-year-old child. (B) Maxillary sinuses *(black arrows),* frontal sinus *(white arrow),* and ethmoid air cells *(asterisk)* in an 11-year-old child.

College of Radiology does not recommend the use of plain radiography in diagnosing sinusitis in children,[23] and similarly, American Academy of Pediatrics (AAP) guidelines state that plain radiographs are unnecessary for diagnosing sinonasal disease in children younger than 6 years.[7,24] Plain films do not play a role in evaluating sinonasal masses or complications of sinusitis.

## Computed Tomography

CT nicely demonstrates paranasal sinus bony anatomy, soft tissue changes, lesion calcification, and osseous changes. Coronal images best demonstrate the anatomy of the ostiomeatal unit, as well as important anatomic landmarks and variants, effectively providing a road map for functional endoscopic sinus surgery. For these reasons, CT is considered the imaging modality of choice for evaluating inflammatory disease of the paranasal sinuses (i.e., recurrent and chronic sinusitis). CT plays an important role in detecting orbital and intracranial complications of sinusitis. Along with magnetic resonance imaging (MRI), CT is an excellent tool for evaluating sinonasal masses.

Currently, multidetector CT with volume isometric imaging allows axial image acquisition with the patient in a neutral supine position. Images are subsequently reformatted in the coronal and sagittal planes. Slice thickness is usually 2.5 mm, and anatomic coverage extends from the upper teeth to 2 cm above the frontal sinus. If orbital or intracranial complications of sinusitis are suspected clinically, the study should be performed after the intravenous (IV) administration of contrast material, and imaging of the brain should be considered. Images are displayed in both soft tissue and bone algorithms.

Awareness of and concern about the potentially harmful radiation side effects is particularly important in children.[25,26] The practice of the "as low as is reasonably achievable" (ALARA) principle among the radiologic community is critical, with special attention given to CT protocols and parameters.[25,27] In evaluating paranasal sinuses, it is possible to reduce radiation techniques for maxillofacial CT imaging, even to a level comparable to that used for standard radiographic images, without sacrificing diagnostic image quality.[28]

## Magnetic Resonance Imaging

MRI is valuable in evaluating complications of sinusitis (e.g., intracranial extension), as well as inflammatory disease associated with sinus or parasinal neoplasm. Although MRI detects bone marrow involvement, it is less sensitive for bony erosions than CT. Other limitations include its availability, higher costs, and the frequent need for sedation in young children.

The normal nasal cycle of vasodilation and mucosal edema, followed by vasoconstriction and mucosal shrinkage, varies from 50 minutes to 6 hours. The signal intensity during the edematous phase is indistinguishable from that of inflammatory change. As with CT and plain radiographs, sinus MRI typically shows a high incidence of findings in asymptomatic persons (13%–37%) and mucosal thickening of less than 3 mm that is likely insignificant.[5] MRI can differentiate mucosal thickening from sinus secretions (Fig. 8.11).

MRI is very useful in evaluating neoplasms. An estimated 90% to 95% of tumors in the sinuses or nasal cavity exhibit moderately lower signal intensity on T2-weighted images (from hypercellularity) compared with most acute inflammatory diseases (including polyps, mucoceles, and retention cysts), which produce a bright signal on T2-weighted images. However, more mature granulation tissue and fibrosis also have a lower T2 signal, making it difficult to distinguish from tumor. Certain fungal infections, in contrast to other types of acute inflammatory disease, also have a lower T2 signal.

# IMAGING ANATOMY OF THE SINONASAL CAVITIES

## Ostiomeatal Unit

Regarded as an important anatomic region for potential surgical intervention, the ostiomeatal unit is a complex anatomic structure at the crossroads of mucociliary drainage from the frontal, anterior ethmoid, and maxillary sinuses.[29] It includes the uncinate process, infundibulum, ethmoid bulla, hiatus semilunaris, and middle meatus (Fig. 8.12).[16]

The uncinate process arises from the upper medial maxillary wall and defines the wall of the infundibulum.[30] The infundibulum is the channel defined laterally by orbit or Haller cells and medially by the uncinate process. The ethmoid bulla is a dominant middle ethmoid air cell that protrudes inferomedially into the infundibulum and hiatus semilunaris. The hiatus semilunaris is a semilunar region between the tip of the uncinate process and ethmoid bulla.

# CONGENITAL LESIONS OF THE NOSE

## Choanal Atresia

Choanal atresia, the most common congenital abnormality of the nasal cavity, is thought to result from failure of rupture of the oronasal membrane during the sixth week of fetal life. It consists of obstruction of the posterior opening of the nasal cavity, which is mixed bony-membranous in approximately 70% of cases and pure bony atresia in 30% of cases. The existence of a purely membranous atresia is questionable.[31] Choanal atresia can be unilateral (in 50%–60% of cases) or bilateral, and it is twice as common in girls.

***Clinical Presentation.*** Bilateral choanal atresia presents with severe immediate onset of respiratory distress in the newborn, because infants are obligate nasal breathers. Symptoms are aggravated by feeding and relieved by crying. The inability to pass a nasogastric tube in a neonate with well-aerated lungs suggests the diagnosis. Unilateral choanal atresia usually is diagnosed later in childhood and presents with unilateral purulent rhinorrhea.

***Imaging.*** Noncontrast CT is the imaging modality of choice. Nasal secretions should be suctioned before imaging is performed; administration of a nasal topical vasoconstrictor spray helps in reducing mucosal thickening. High-resolution imaging in bone algorithm will aid in delineating the bone margins. Findings consist of narrowing of the posterior choana (<0.34 cm in children <2 years of age) and enlargement and thickening of the vomer (>0.23 cm), which sometimes is fused to the maxilla.[32] Medial bowing and thickening of the posterior aspect of the lateral wall of the nasal cavity also is seen. The nasal cavity often is filled with air, soft tissue, and fluid (Fig. 8.13). CT will identify other causes of bilateral nasal obstruction, such as pyriform aperture stenosis and bilateral nasolacrimal duct (NLD) mucoceles. Bilateral choanal atresia can be associated with other congenital abnormalities in 75% of cases, such as CHARGE syndrome.

***Treatment.*** The oral airway should be secured and surgical correction of bilateral atresia should be performed as soon as possible after diagnosis. Transpalatal or transnasal endoscopic surgical techniques may be used.

## Congenital Nasal Pyriform Aperture Stenosis

Congenital nasal pyriform aperture stenosis is a rare form of nasal obstruction that consists of narrowing of the nasal pyriform aperture as a result of bony overgrowth of the nasal process of the maxilla.[33] It should be suspected in any neonate with upper respiratory obstruction and must be differentiated from choanal atresia and other congenital nasal masses.

***Clinical Presentation.*** Symptoms depend on the severity of the stenosis and are similar to those in patients with choanal

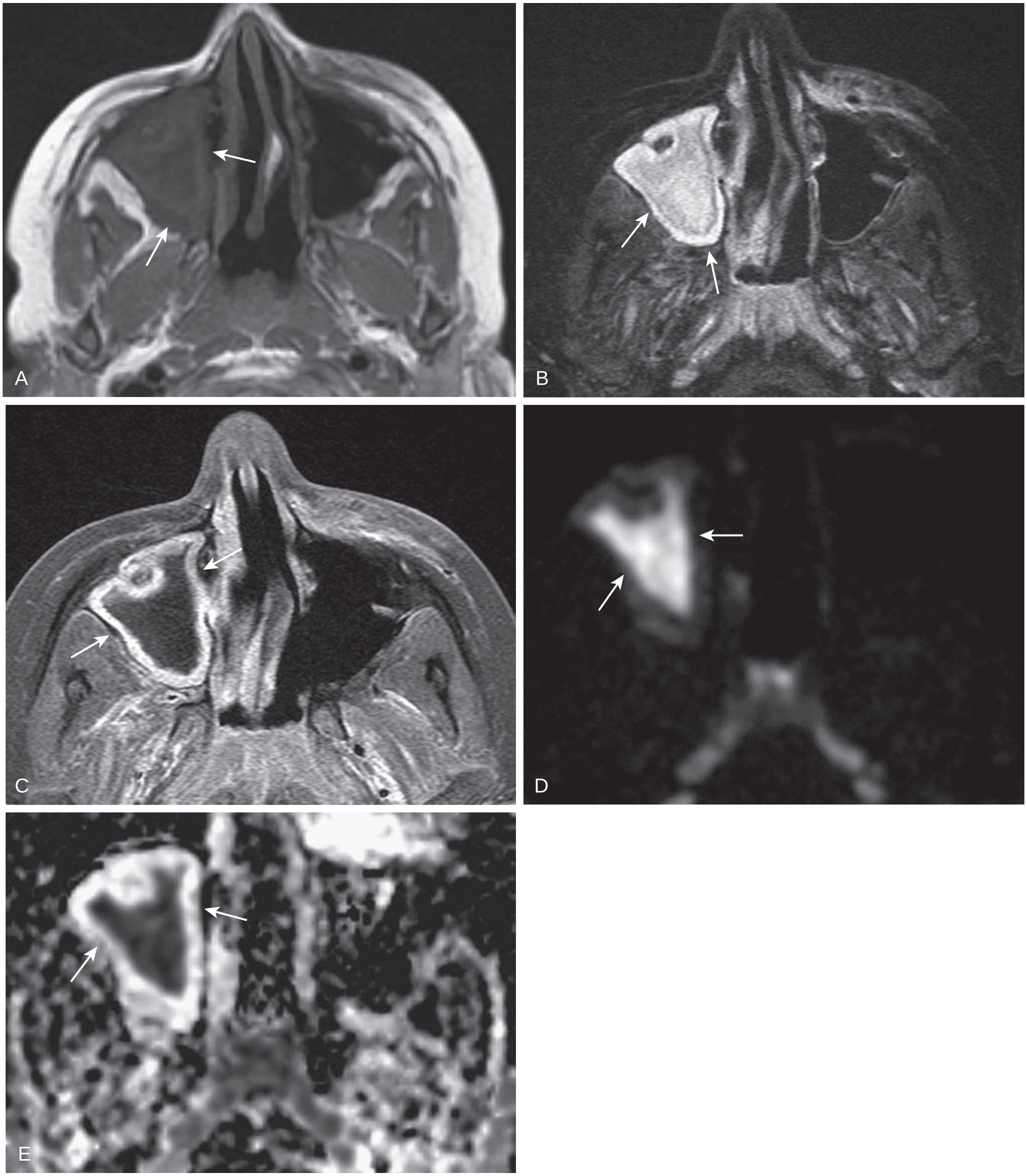

**Figure 8.11. Acute bacterial sinusitis in a 10-year-old boy.** (A) Axial T1-weighted MR image shows hypointense material in the right maxillary sinus *(arrows)*. (B) Axial T2-weighted MR image shows corresponding T2-hyperintense material *(arrows)*. (C) Axial T1-weighted MR image with fat saturation and contrast shows circumferential mucosal enhancementl *(arrows)*. (D and E) Corresponding decreased diffusivity in the right maxillary sinus is shown on diffusion-weighted imaging (D) and apparent diffusion coefficient maps (E) consistent with purulent materiall *(arrows)*.

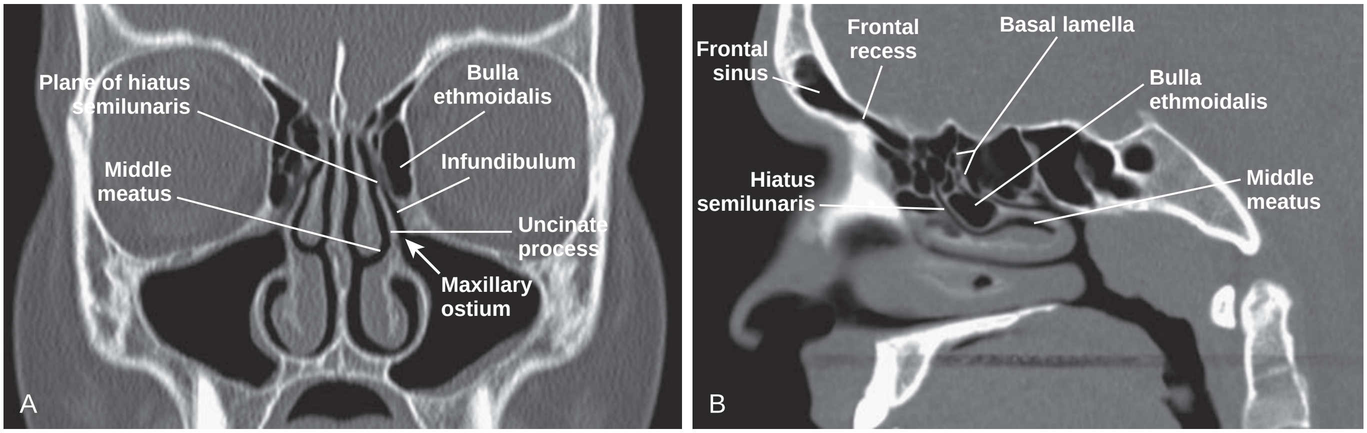

**Figure 8.12. Ostiomeatal unit (OMU).** (A) Coronal CT image shows the OMU components: middle meatus, uncinate process, infundibulum, bulla ethmoidalis, maxillary ostium, and plane of the hiatus semilunaris. (B) Sagittal CT image demonstrates the hiatus semilunaris.

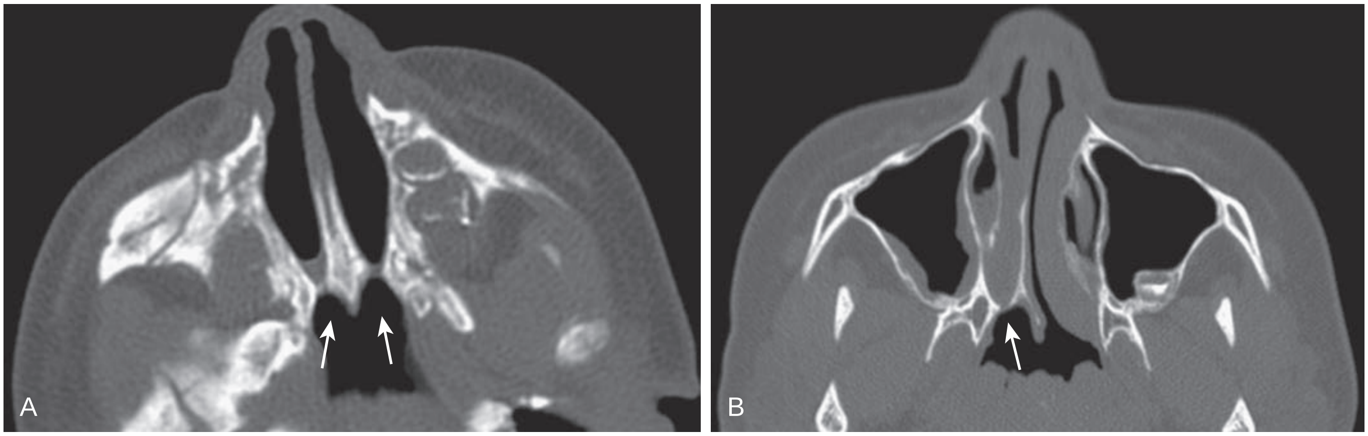

**Figure 8.13. Choanal atresia.** (A) Axial CT image in a 1-day-old neonate with severe respiratory distress shows bilateral bony choanal atresia with retained fluid in the right nasal cavity, medial bowing of the lateral nasal wall, and a thickened vomer *(arrows)*. (B) Axial CT image in a 12-year-old child with chronic nasal obstruction and purulent rhinorrhea shows unilateral (right) bony atresia with fluid in the nasal cavity *(arrow)*.

atresia, including cyanosis in the neonatal period that is exacerbated with feeding and relieved by crying. Congenital nasal pyriform aperture stenosis can present in association with other congenital anomalies such as holoprosencephaly, hypopituitarism, a single mega-incisor, hypotelorism, cleft palate, clinodactyly, or absent olfactory bulbs.[34,35] A central mega-incisor often is associated with intracranial abnormalities, and thus further evaluation with MRI of the brain is indicated in these cases.

***Imaging.*** Congenital nasal pyriform aperture stenosis is confirmed with CT and is characterized by overgrowth of the medial nasal process of the maxilla, resulting in narrowing of the anterior bony nasal cavity, and is usually bilateral. A pyriform aperture of less than 11 mm in a term infant is diagnostic.[33] The choanae are usually normal in caliber, but choanal atresia may coexist.[34] The hard palate is usually hypoplastic and triangular-shaped with the presence of a median maxillary single incisor tooth (mega-incisor) (Fig. 8.14).

***Treatment.*** Treatment consists of securing the airway, with surgical intervention required in severe cases.

## Congenital Nasolacrimal Duct Mucocele

Congenital NLD mucocele consists of a cystic dilatation of the NLD due to obstruction of its distal opening. This results in the classic triad: dacryocystocele (dilated nasolacrimal sac) located in the medial canthus, dilated NLD with expansion of its osseous canal, and an intranasal mass (mucocele). In contrast, a classic dacryocystocele results from proximal obstruction secondary to failure of canalization during the sixth month of fetal life. Congenital NLD mucoceles and classic dacryocystoceles can be unilateral or bilateral.

***Clinical Presentation.*** A dacryocystocele presents clinically as a round, bluish, medial, canthal mass usually identified at birth, and may vary in size from 5 to 10 mm. The classic NLD mucocele triad usually presents in the neonatal period as an intranasal mass causing airway obstruction if it is bilateral. Neonates also can present with difficulty breathing while feeding.

***Imaging.*** CT findings include a well-circumscribed, rounded, unilateral or bilateral hypodense "cystic" lesion in the medial canthus and/or anteroinferior nasal cavity. The cyst can communicate with an enlarged NLD and canal (Fig. 8.15A). Large cysts may cause nasal septal deviation. Association with choanal atresia has been described. Contrast-enhanced CT will show no enhancement or minimal thin wall enhancement. Infected dacryocystoceles present with thick rim enhancement.

MR findings include a T1-weighted hypointense and T2-weighted hyperintense well-circumscribed mass at the medial canthus and/or nasal cavity with no enhancement or minimal wall enhancement

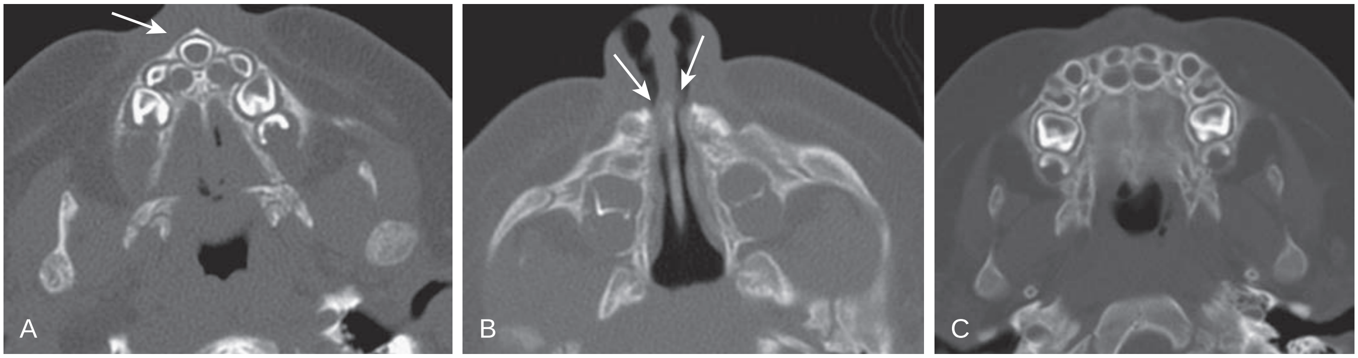

**Figure 8.14. Congenital nasal pyriform aperture stenosis in a 1 1/2-month-old infant with episodes of respiratory distress during breastfeeding.** (A) Axial CT image shows a triangular hard palate and solitary central maxillary mega-incisor *(arrow)*. (B) An axial CT image shows narrowing of the anterior and inferior nasal passages *(arrows)*. (C) Axial CT of a normal infant maxilla for comparison.

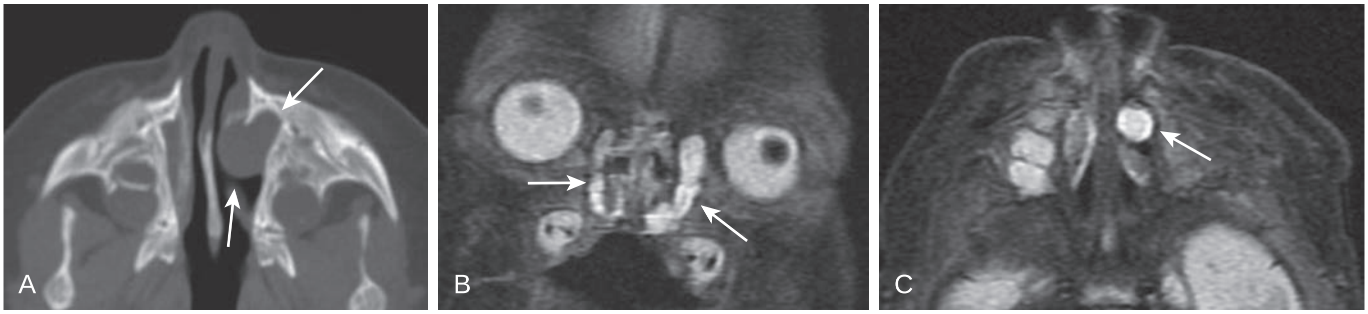

**Figure 8.15. Congenital nasolacrimal duct mucoceles in a 1-day-old neonate.** (A) Axial CT image shows a left nasal round soft tissue mass with enlargement of the ipsilateral nasolacrimal duct and canal *(arrows)*. (B and C) Coronal and axial fast spin-echo inversion recovery MR images show bilateral cystic enlargement of the nasolacrimal sacs and ducts *(arrows)*.

(Figs. 8.15B and C). NLD mucoceles and dacryocystoceles can be diagnosed prenatally with fetal ultrasound or MRI.[36]

***Treatment.*** Congenital dacryocystoceles may resolve with conservative treatment, but many become infected and require treatment; most need surgical intervention.[36]

## OTHER CONGENITAL/DEVELOPMENTAL NASAL MIDLINE MASSES

Frontonasal or intranasal developmental masses that result from anomalies of the anterior neuropore can present similarly and should be in the differential diagnosis. These include anterior cephaloceles, nasal neuroglial heterotopia, and nasal dermoids.

Cephaloceles consist of herniation of intracranial contents (meninges, cerebrospinal fluid [CSF], and brain) through a skull defect that occurs from failure of neural tube closure and are classified by location. Anterior cephaloceles include subtypes such as basal, frontoethmoidal, and nasopharyngeal. Frontoethmoidal (sincipital) cephaloceles present as an external nonenhancing soft tissue mass contiguous with the intracranial brain that extends through a bony defect. The adjacent meninges may enhance. These include frontonasal, nasoethmoidal, and naso-orbital cephaloceles. On the other hand, basal cephaloceles are occult, result from failed ossification of neural crest cells through the osseous defect, and may contain pituitary tissue, optic nerves, or vascular structures (e-Fig. 8.16E). These present with nasal or nasopharyngeal obstruction and include transethmoidal, sphenoethmoidal, and sphenopharyngeal types (e-Fig. 8.16A).

Nasal neuroglial heterotopia is a nonenhancing extranasal (along the nasal dorsum) or intranasal solid soft tissue mass without connection between the mass and intracranial contents. It consists of sequestered dysplastic, nonneoplastic neurogenic brain tissue (e-Figs. 8.16B and C).

Nasal dermoid may present as an enhancing tract or fistula from the tip of the nose to the foramen cecum (intracranially) just anterior to the crista galli with or without a dermoid/epidermoid cysts along its tract (e-Fig. 8.16D). On diffusion-weighted imaging, the cyst can demonstrate restricted diffusion.

## IMAGING OF INFECTIOUS AND INFLAMMATORY SINONASAL DISEASE

### Sinusitis

Rhinosinusitis is characterized by inflammation of the sinonasal mucosa, usually after an upper respiratory infection (URI). Children contract an average of three to eight viral URIs per year that are generally self-limited, with no antimicrobial therapy required.[37] However, acute bacterial sinusitis (ABS) can complicate viral rhinosinusitis in up to 6% to 7% of affected children.[24] Other predisposing conditions for sinusitis are allergic rhinitis, immunoglobulin deficiency, immotile cilia syndrome, cystic fibrosis (CF), and anatomic abnormalities causing obstruction of the drainage pathways. The AAP has defined five categories of bacterial rhinosinusitis: acute, subacute, recurrent acute, ABS superimposed on chronic disease, and chronic sinusitis.[24]

Bacterial sinusitis remains a challenging clinical diagnosis because the signs and symptoms of sinusitis typically seen in adults are noted less frequently in children. Because specific clinical signs in children are generally few, and symptoms overlap between ABS

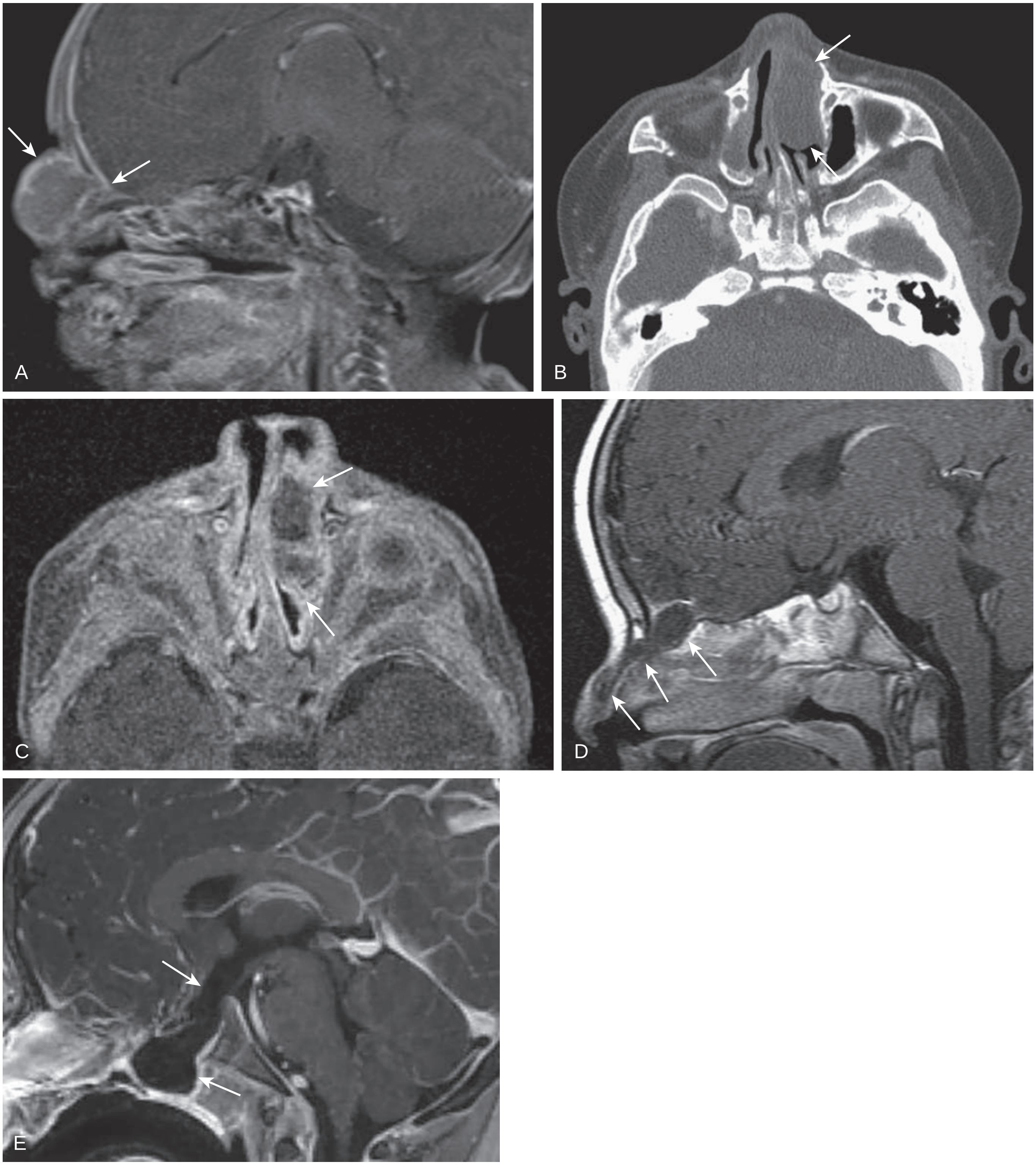

**e-Figure 8.16. Developmental nasal midline masses.** (A) Naso-orbital cephalocele in a newborn. Sagittal contrast-enhanced T1-weighted MR image shows a nonenhancing frontonasal mass with intracranial dural connection *(arrows)*. (B) Nasal glial heterotopia in a neonate *(arrows)*. Axial contrast-enhanced CT image shows a nonenhancing left intranasal mass. (C) Axial contrast-enhanced T1-weighted MR image in the same patient shows a T1-hypointense nonenhancing mass without intracranial connection *(arrows)*. (D) Nasal dermoid cysts in a 3-year-old. Sagittal contrast-enhanced T1-weighted MR image shows a dermal sinus tract with nasal and intracranial dermoid cysts *(arrows)*. (E) Basal cephalocele in a 3-year-old. Sagittal contrast-enhanced T1-weighted MR image shows a large nasopharyngeal CSF-filled mass lesion *(top arrow),* which extends through the sphenoid bone into the nasopharynx with peripheral meningeal enhancement *(bottom arrow)*.

and uncomplicated viral URI, it is often difficult to differentiate these two. A presumptive clinical diagnosis of ABS should be made when a child with an acute URI presents with the following: persistent illness, that is, nasal discharge (of any quality) or daytime cough, or both lasting more than 10 days without improvement; or worsening course, that is, worsening or new onset of nasal discharge, daytime cough, or fever after initial improvement; or severe onset, that is, concurrent fever (temperature ≥39°C/102.2°F) and purulent nasal discharge for at least 3 consecutive days.[24,37]

The gold standard for diagnosis of acute or chronic sinusitis remains aspiration from the sinus cavities with the recovery of bacteria in a high density (>10 colony-forming units/mL).[24] However, this method is impractical, invasive, and time-consuming and is rarely performed.

## Acute Sinusitis

The most common causative microorganisms of ABS are *Streptococcus pneumoniae* (30% of ABS cases), nontypeable *Haemophilus influenzae* (30%), and *Moraxella catarrhalis* (10%). *Staphylococcus aureus* is a rare cause of ABS but is isolated in children with orbital and intracranial complications of ABS.

The updated AAP practice guideline for the diagnosis and management of ABS in children and adolescents contains changes including a clinical presentation designated "worsening course," inclusion of new data on the effectiveness of antibiotics in children with acute sinusitis, and a review of evidence indicating that imaging is not necessary to identify those children who will benefit from antimicrobial therapy.[24]

***Imaging.*** Imaging of the paranasal sinuses in children with uncomplicated ABS is unnecessary because the results will not affect treatment decisions. Imaging cannot differentiate between viral and bacterial sinusitis. Mucosal abnormalities are reported routinely on radiographs, CT, and MRI in asymptomatic patients who undergo imaging for other indications. The incidence of abnormal findings is very high in infants and young children, and soft tissue changes can persist for months on MRI after an acute infection.[23] For these reasons, clinical correlation is vital when evaluating imaging findings in children.

***Treatment.*** A course of antibiotics is recommended to speed resolution of symptoms and to prevent possible complications. In uncomplicated ABS, amoxicillin remains the antimicrobial agent of choice. Amoxicillin-clavulanate is indicated in children with moderate to severe illness or when resistance is suspected, children less than 2 years of age, children that attend child care, or recently treated patients. Reassessment should occur if there is symptom progression worsening or failure to improve within 72 hours of initial management.[24]

## Chronic Sinusitis

The AAP defines chronic sinusitis as episodes of inflammation of the paranasal sinuses lasting more than 90 days. Patients have persistent residual respiratory symptoms such as cough, rhinorrhea, and/or nasal obstruction. Children who experience chronic sinusitis usually are older (at least 4–7 years of age) and often have a history of recurrent ABS. Other associated factors are recurrent viral URIs, allergic and nonallergic rhinitis, CF, immunodeficiency, ciliary dyskinesia, sinus and facial anatomic abnormalities, and gastroesophageal reflux.[38]

Clinical findings are similar to those of acute infection but are characterized mostly by a continuous nasal discharge and congestion with a persistent nighttime cough. Other symptoms include chronic headache, chronic halitosis, intermittent fever, sleep deprivation, and general malaise. In chronic sinusitis, *Staphylococcus aureus*, coagulation negative *Staphylococcus*, anaerobic organisms, gram-negative bacteria, and fungi are the most commonly encountered colonizing organisms.[38]

***Imaging.*** Radiography can show mucosal thickening or sinus opacification, and occasionally, sclerotic, thickened walls. CT findings include peripheral mucosal thickening in a hypoaerated or contracted sinus with sclerotic thickened walls, although these findings are uncommon in children. Calcifications may be seen occasionally, and sinonasal polyposis also may be present. Secretions can be dense depending on their content. MR findings include mucosal thickening that enhances with administration of contrast material. Retained secretions will vary in signal intensity depending on content (see Fig. 8.11). Desiccated secretions are hypointense on T2-weighted imaging.

***Treatment.*** Initial trial therapy includes environmental control, allergic therapy if indicated, antibiotics for 21 days directed to resistant organisms, nasal saline solution irrigation, and topical nasal steroids. Second-line therapy includes oral decongestants and oral steroids. Initial surgical therapies include adenoidectomy, sinus lavage, and, less frequently, balloon catheter dilation and endoscopic sinus surgery (ESS). In the case of failed initial surgical treatment, ESS is performed in most patients (85%) as definitive therapy.[39]

## Complications of Rhinosinusitis

Orbital and intracranial complications of rhinosinusitis can result from delayed diagnosis and treatment, antibiotic-resistant or aggressive organisms, or incomplete treatment. Signs and symptoms of orbital complications include periorbital edema, proptosis, chemosis, decreased visual acuity, and/or limited ocular motility. Potential intracranial complications should be suspected when a patient has a history of acute sinusitis combined with severe intractable headache, an altered level of consciousness, focal neurologic deficits, or signs of meningitis.[40]

Orbital complications usually result from the spread of ethmoid infection that occurs via valveless ethmoid veins that traverse the lamina papyracea. Extension of disease also can arise (in order of frequency) from the sphenoid, frontal, and maxillary sinuses. Complications include orbital cellulitis with inflammatory edema, preseptal cellulitis, postseptal cellulitis, subperiosteal abscess (Fig. 8.17), orbital abscess (e-Fig. 8.18), optic neuritis, and cavernous sinus thrombosis.

Intracranial complications include epidural empyema, subdural empyema, meningitis, cerebritis, and parenchymal abscess (e-Fig. 8.19). Subgaleal involvement, such as with Pott puffy tumor and

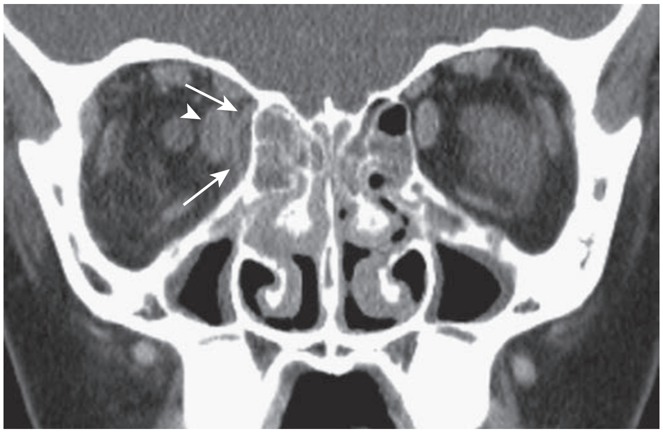

**Figure 8.17. Orbital subperiosteal abscess in a 9-year-old girl.** Coronal contrast-enhanced CT image shows a small, low-attenuation, rim-enhancing fluid collection consistent with an abscess *(arrows)* in the medial aspect of the orbit with mass effect on the medial rectus muscle *(arrowhead),* which is thickened. Bilateral ethmoid sinus disease with infiltration of the right retro-orbital fat is demonstrated.

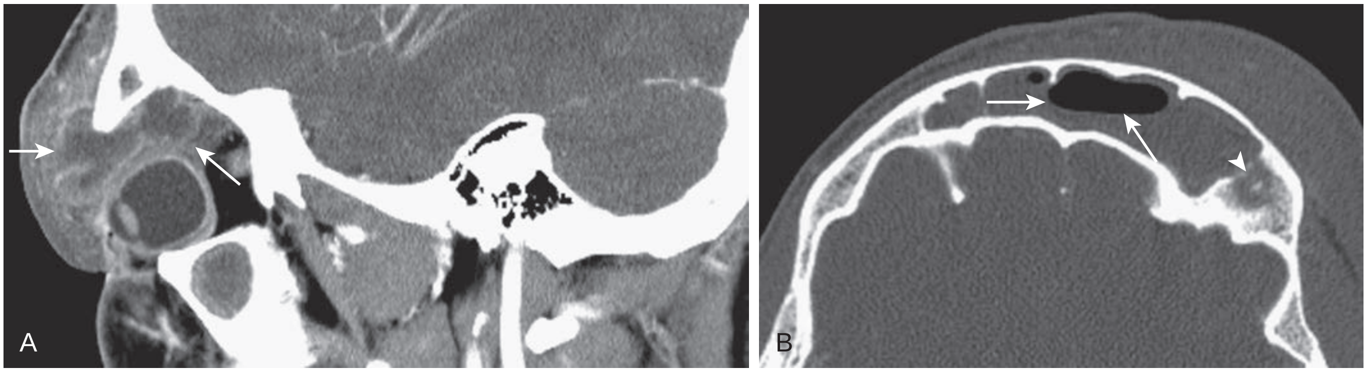

**e-Figure 8.18. Intraorbital abscess and frontal bone osteomyelitis in a 14-year-old boy.** (A) Sagittal reformat contrast-enhanced sagittal CT image shows a large, multiloculated, intraorbital abscess with significant effect of the mass on the globe *(arrows)*. (B) Axial CT image shows an osteolytic lesion in the frontal bone consistent with osteomyelitis *(arrowhead)* and an air-fluid level in the frontal sinus *(small arrows)*.

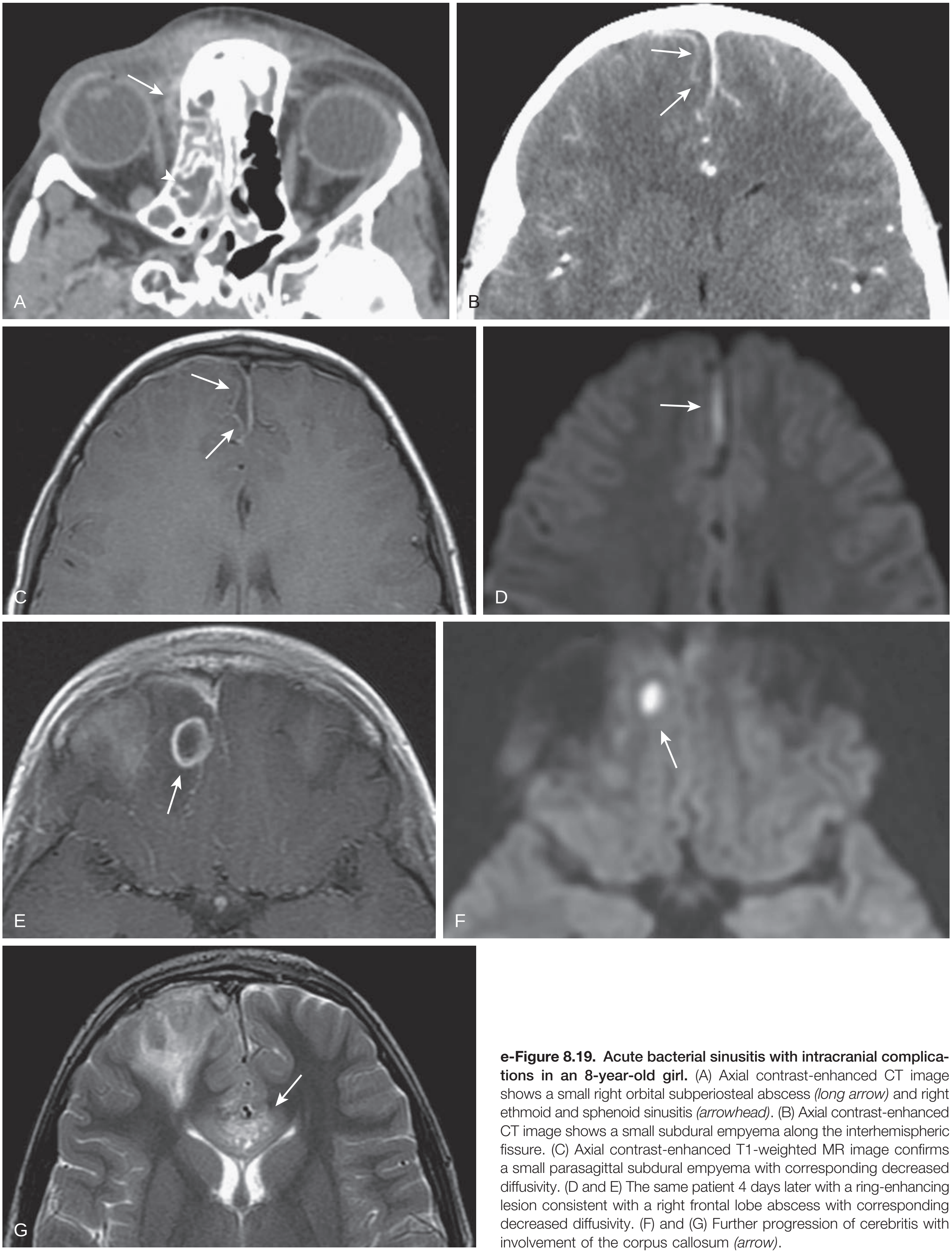

**e-Figure 8.19. Acute bacterial sinusitis with intracranial complications in an 8-year-old girl.** (A) Axial contrast-enhanced CT image shows a small right orbital subperiosteal abscess *(long arrow)* and right ethmoid and sphenoid sinusitis *(arrowhead)*. (B) Axial contrast-enhanced CT image shows a small subdural empyema along the interhemispheric fissure. (C) Axial contrast-enhanced T1-weighted MR image confirms a small parasagittal subdural empyema with corresponding decreased diffusivity. (D and E) The same patient 4 days later with a ring-enhancing lesion consistent with a right frontal lobe abscess with corresponding decreased diffusivity. (F) and (G) Further progression of cerebritis with involvement of the corpus callosum *(arrow)*.

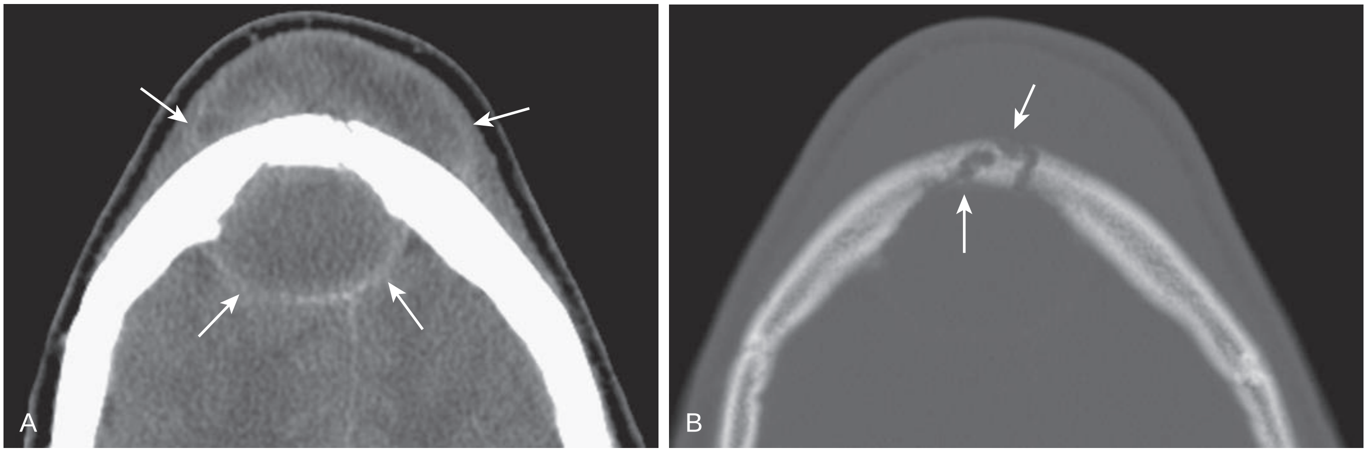

**Figure 8.20. Pott puffy tumor and epidural abscess in a 16-year-old boy.** (A) Contrast-enhanced CT image in a soft tissue window shows a large subperiosteal abscess *(top arrows)* and a large epidural abscess *(bottom arrows)*. (B) Axial CT image in a bone window shows erosion of the frontal bone consistent with osteomyelitis *(arrows)*.

osteomyelitis, also can occur (Fig. 8.20). Vascular complications are infrequent and include mycotic aneurysm, stenosis of the cavernous segment of the internal carotid artery (which, in very rare instances, can result in brain infarction[41]), and venous sinus thrombosis. Superior sagittal thrombosis usually results from frontal sinusitis, whereas sigmoid sinus thrombosis and cavernous sinus thrombosis are associated more often with sphenoid sinusitis.

***Imaging.*** Imaging enables diagnosis and accurate presurgical planning when necessary. For the initial evaluation, contrast-enhanced CT is the imaging modality of choice and should include both the paranasal sinuses and brain. Noncontrast CT should not be performed because it increases the radiation dose without providing any additional diagnostic information. CT can demonstrate fluid collections with rim enhancement consistent with subperiosteal abscesses (see Fig. 8.17) and bone erosion of osteomyelitis as seen with Pott puffy tumor (extracranial subperiosteal abscess from frontal sinusitis) (see Fig. 8.20).[42,43]

MRI is indicated to further assess known or suspected intracranial extension of disease and should include imaging of the brain, sinuses, and orbits. MRI protocols for the brain should include diffusion and contrast-enhanced sequences and should evaluate for venous thrombosis. MRI protocols for the paranasal sinuses and orbits should include high-resolution axial and coronal images before and after administration of gadolinium. MRI is more sensitive than CT in the assessment of leptomeningeal enhancement, small extraaxial fluid collections, and parenchymal abnormalities such as cerebritis and cerebral abscess (see e-Fig. 8.19E–G). MRI also can detect early stages of osteomyelitis by demonstrating bone marrow edema with associated contrast enhancement. Diffusion-weighted imaging will show restricted diffusion of fluid collections with purulent contents (see Fig. 8.11).

Subperiosteal abscesses appear hypointense on T1-weighted imaging and hyperintense on T2-weighted imaging with peripheral contrast enhancement. Signs of cavernous sinus thrombosis include enlargement or heterogeneous enhancement of the cavernous sinus with associated enlargement or thrombosis of the superior ophthalmic vein (Fig. 8.21). Subdural and epidural empyemas appear as T1-hypointense and T2-hyperintense fluid collections with adjacent dural enhancement and central decreased diffusivity as a result of the presence of purulent material (see e-Figs. 8.19B through D). Cerebritis appears as a poorly defined area of T2 prolongation without ring enhancement, whereas a cerebral abscess will present as a ring-enhancing lesion with central decreased diffusivity and perilesional edema (see e-Figs. 8.19E and F).

***Treatment.*** Treatment includes combinations of systemic intravenous antibiotics and surgical interventions such as drainage of the sinuses, functional endoscopic sinus surgery, and craniotomy. Because of the high incidence of seizures associated with intracranial abscess, prophylactic anticonvulsant therapy is recommended.[40]

## Sinonasal Disease in Cystic Fibrosis

CF is caused by a genetic defect in the long arm of chromosome 7, which affects the protein that regulates transmembrane passage of chloride and causes dysfunction of multiple organs and systems.[44] High concentrations of chloride, mucus thickness, and reduction of mucociliary clearance predisposes to inflammation and chronic infection of the respiratory tract. Nearly all persons with CF present clinically with nasal obstruction and chronic rhinosinusitis.[45] The most common colonizing organisms in order of frequency are *Pseudomonas aeruginosa*, *S. aureus*, and *Streptococcus viridans*.[46]

***Imaging.*** CT is the imaging modality of choice for evaluating sinus disease in patients with CF and will nearly always show abnormalities. Findings include mucosal thickening and sinonasal polyposis. The incidence of nasal polyposis in children with CF varies between 10% and 86%.[47–49] High-attenuation material often is present in the sinus cavities, consistent with inspissated secretions (Fig. 8.22). However, superimposed fungal infection has a similar appearance and cannot be excluded by imaging. Bony sclerosis and thickening of the sinuses can be seen in older patients. Frontal sinus hypoplasia or aplasia is a common finding and may be a result of chronic obstruction. The severity of the imaging findings does not necessarily correlate with the severity of symptoms.[45]

***Treatment.*** Medical and surgical treatment depends on symptoms and the overall condition of the patient, including pulmonary status and infection frequency. Not all patients will require surgery.[50] Imaging findings of CF cannot be differentiated from other causes of chronic sinusitis such as allergic sinusitis with polyposis or fungal allergic sinusitis.

## Allergic Sinusitis

It is estimated that allergic rhinosinusitis affects about 10% of the population. In the United States, the most common form is seasonal pollinosis, resulting from an immunoglobulin E reagin–antibody reaction (type I immunologic disorder), which manifests clinically with sneezing, nasal obstruction, and rhinorrhea. This condition can result in hypertrophic, thickened, and redundant

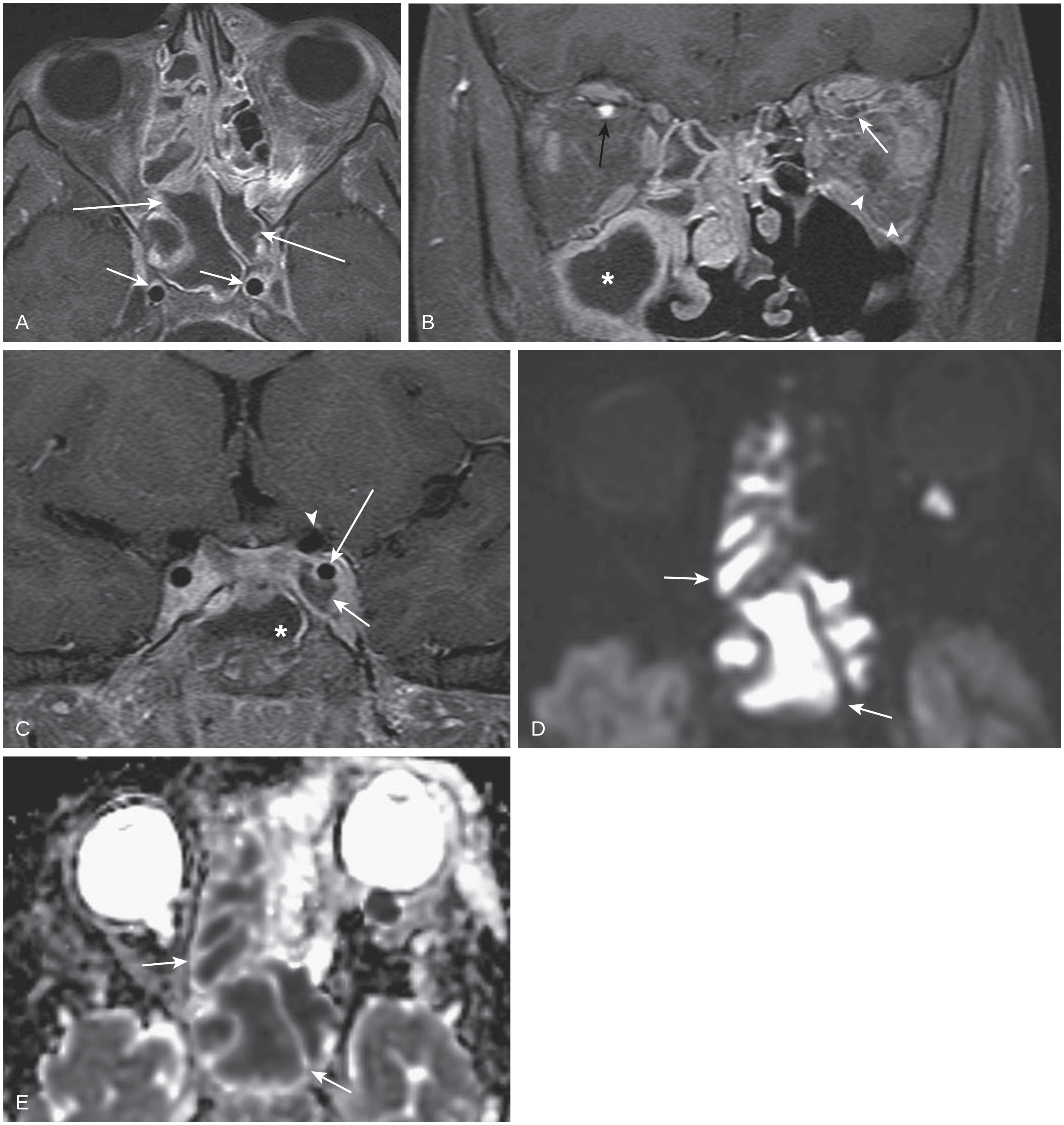

**Figure 8.21. Sinusitis with a left periorbital abscess and cavernous sinus thrombosis in a 10-year-old boy.** (A) Axial contrast-enhanced fat-saturated T1-weighted MR image shows hypointense fluid within the ethmoid and sphenoid sinuses with circumferential mucosal enhancement *(long arrows)* and normal flow voids of the cavernous internal carotid artery (ICA) segments *(short arrows)*. (B) Coronal fat-saturated T1-weighted MR image shows a thrombus in the left superior ophthalmic vein *(white arrow),* normal enhancement of the right superior ophthalmic vein *(black arrow),* and inflammatory changes in the retro-orbital fat *(arrowheads)*. The right maxillary sinus is fluid-filled *(asterisk)*. (C) Coronal fat-saturated T1-weighted MR image shows a thrombus in the left cavernous sinus *(bottom arrow)* and normal flow void of the left ICA cavernous segment *(long arrow)* and left ICA supraclinoid segment *(arrowhead)*. A fluid-filled sphenoid sinus is shown *(asterisk)*. Corresponding restricted diffusion on diffusion-weighted imaging (D) and apparent diffusion coefficient maps (E) are consistent with purulent material *(arrows)*.

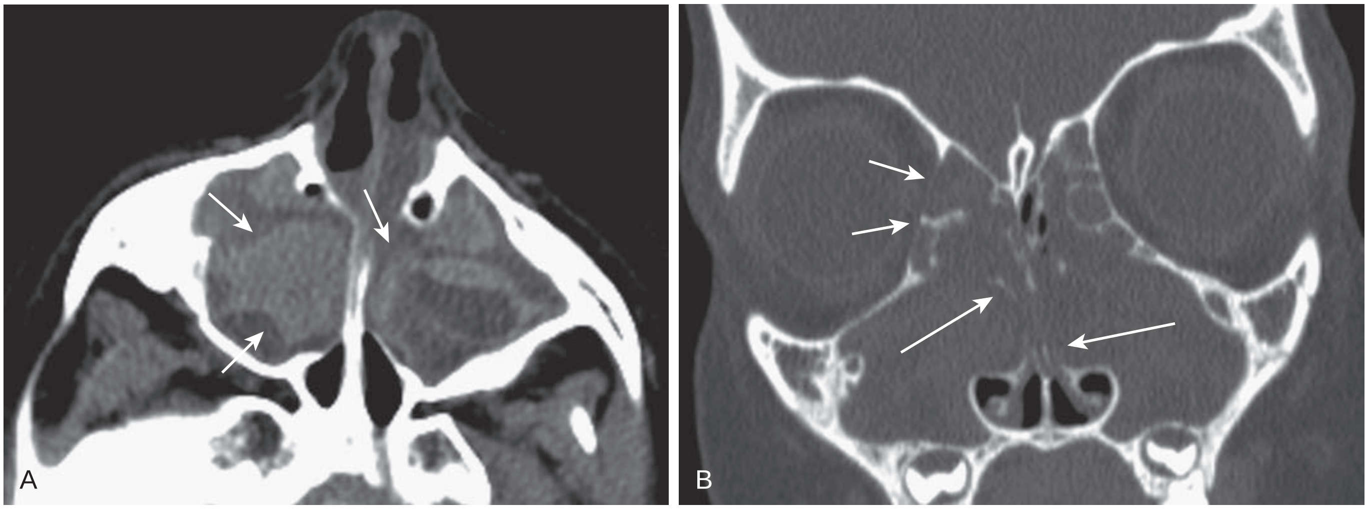

**Figure 8.22. Cystic fibrosis in an 8-year-old child.** (A) Axial CT image shows high attenuation secretions in the maxillary sinuses *(arrows)*. (B) Coronal CT image shows polyps causing expansion of the sinuses *(short arrows)* and nasal cavity with demineralization of septations *(long arrows)*.

mucosa, which is prone to bacterial infection. Allergic sinusitis often coexists with chronic asthma, and 30% of patients will present with polyps. Conversely, up to 80% of patients with polyps have asthma.[51,52] The association of allergic asthma, allergy to aspirin, and aggressive polyposis is known as Samter triad (e-Fig. 8.23). Polyps in this condition can be destructive and invade the anterior cranial fossa.[5]

## Fungal Rhinosinusitis Disorders

Fungal infections can cause both acute and chronic rhinosinusitis. These infections have been classified into four clinicopathologic types that can present as either tissue-invasive disorders (acute invasive fulminant disease and chronic invasive infection) or noninvasive disorders (noninvasive mycotic colonization ["fungus ball" or mycetoma] and allergic fungal [mycotic] sinusitis).[53] All of these entities are rare in children.

Acute invasive fulminant disease occurs in immunosuppressed patients and clinically presents as pale mucosa that can progress to gangrene. Spread through neuronal routes can cause vascular invasion with intracranial spread and parenchymal infarcts. Mucormycosis is a disease caused by several types of fungi and can have an acute and fulminant course. In patients with diabetes, mucormycosis can present more as a chronic tissue-invasive infection and frequently causes periorbital invasion (orbital apex syndrome).[53]

A fungal ball or "mycetoma" consists of fungal hyphae compressed into a thick exudate within a sinus lumen.[53] It is a benign fungal colonization and may occur in patients with previous sinus surgery, oral-sinus fistula, a history of chemotherapy or radiotherapy for cancer, or in those without any known predisposing factor.

Allergic fungal rhinosinusitis should be considered in all adults with chronic sinusitis, but it is rarely seen in young children. Clinical presentation may include a history of allergic sinusitis, chronic rhinosinusitis, nasal polyps, allergic asthma, and immunosuppression, and it can present with proptosis from an inflammatory mass.[38,54] The diagnosis is primarily histopathologic. At surgery, a characteristic inspissated sinonasal inflammatory exudate called allergic mucin is encountered and must be positive for fungal hyphae on fungal staining or cultures. No evidence for mucosal fungal invasion should be present.[54]

***Imaging.*** Radiographically, fungal disease is difficult, if not impossible, to distinguish from bacterial infection. Radiographic signs include sinonasal polyposis with a heterogenous soft tissue inflammatory mass with remodeling or destruction of bone and increased densities in the sinuses, which can represent calcifications. Allergic mucin is largely responsible for the sinus CT hyperattenuation.[54] MRI findings can suggest fungal infection because, in contrast to the high signal intensity on T2-weighted images seen with acute bacterial disease, the presence of calcium, air, or ferromagnetic elements in the fungus causes decreased signal intensity on T1-weighted and T2-weighted images. However, inspissated secretions as seen in patients with CF can have a similar appearance.

# INFLAMMATORY SINONASAL MASSES

## Cysts, Polyps, and Mucoceles

Cysts and polyps are frequent complications of inflammatory rhinosinusitis. A mucous retention cyst results from the obstruction of a submucosal mucinous gland, and the cyst wall is the duct epithelium. These cysts can occur in any sinus but are more frequent in the inferior aspect of the maxillary sinuses. A serous retention cyst results from the accumulation of serous fluid in the submucosal layer of the sinus mucosal lining.[5] These cysts are not inflammatory lesions and appear as dome-shaped, well-defined, homogeneous, nonenhancing structures on CT; they are hypointense on T1-weighted MR images and hyperintense on T2-weighted images (Fig. 8.24A). Cysts also can be found incidentally in 10% to 30% of patients.[55]

Polyps, in contrast, are a manifestation of an allergic or inflammatory process, or both. When they are associated with an allergy, polyps tend to be multiple. These lesions can become large and cause bony distortion with expansion and erosion. Polyps can be difficult to distinguish from mucous retention cysts in some cases and malignancies in others. Polyps have a high T2-weighted MR signal, in contrast to most neoplasms, which helps in the diagnosis.

An antrochoanal polyp (ACP) is a solitary maxillary sinus polyp that fills the sinus, expands the sinus ostium, and prolapses through it into the posterior choana, presenting as a nasal or nasopharyngeal polyp (Figs. 8.24B and C). Rarely, sphenochoanal and ethmochoanal polyps can also occur. In the general population, these polyps represent 4% to 6% of all nasal polyps; however, in children the incidence increases to 28% to 33%.[56] ACPs differ from inflammatory polyps; they tend to be fibrotic with minimal inflammation and are composed of a cystic portion filling the maxillary sinus and a solid dumbbell-shaped portion that emerges into the nasal cavity through the maxillary infundibulum or through an accessory

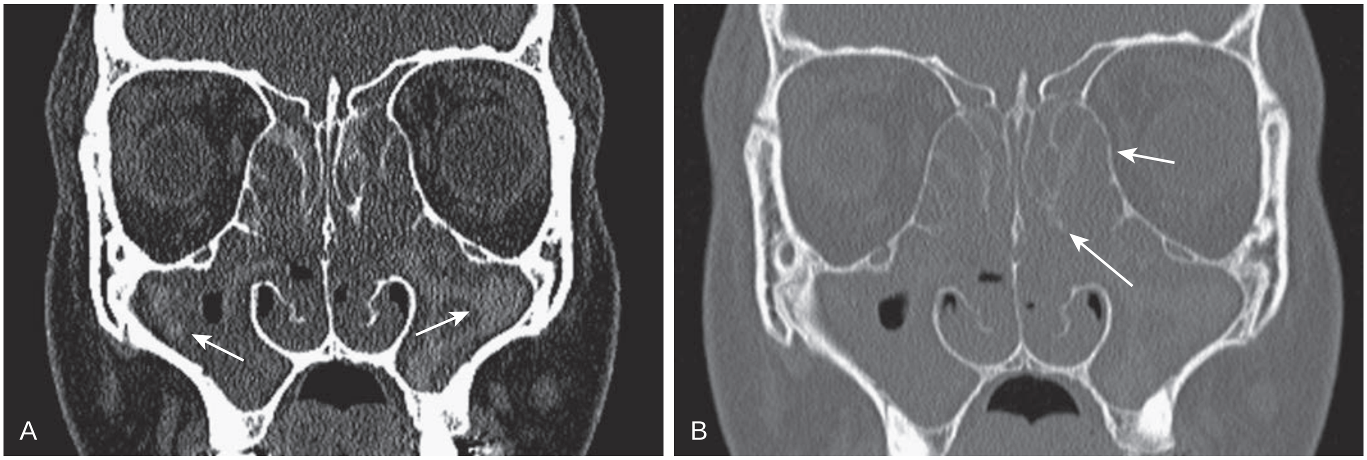

**e-Figure 8.23. Allergic sinusitis (Samter triad) in a 15-year-old boy.** (A) Coronal CT image with soft tissue window shows high attenuation inspissated secretions in the maxillary sinuses *(arrows)*. (B) Coronal CT image with bone window shows expanded sinuses and nasal cavity as a result of extensive polyposis with demineralized osseous structures *(arrows)*.

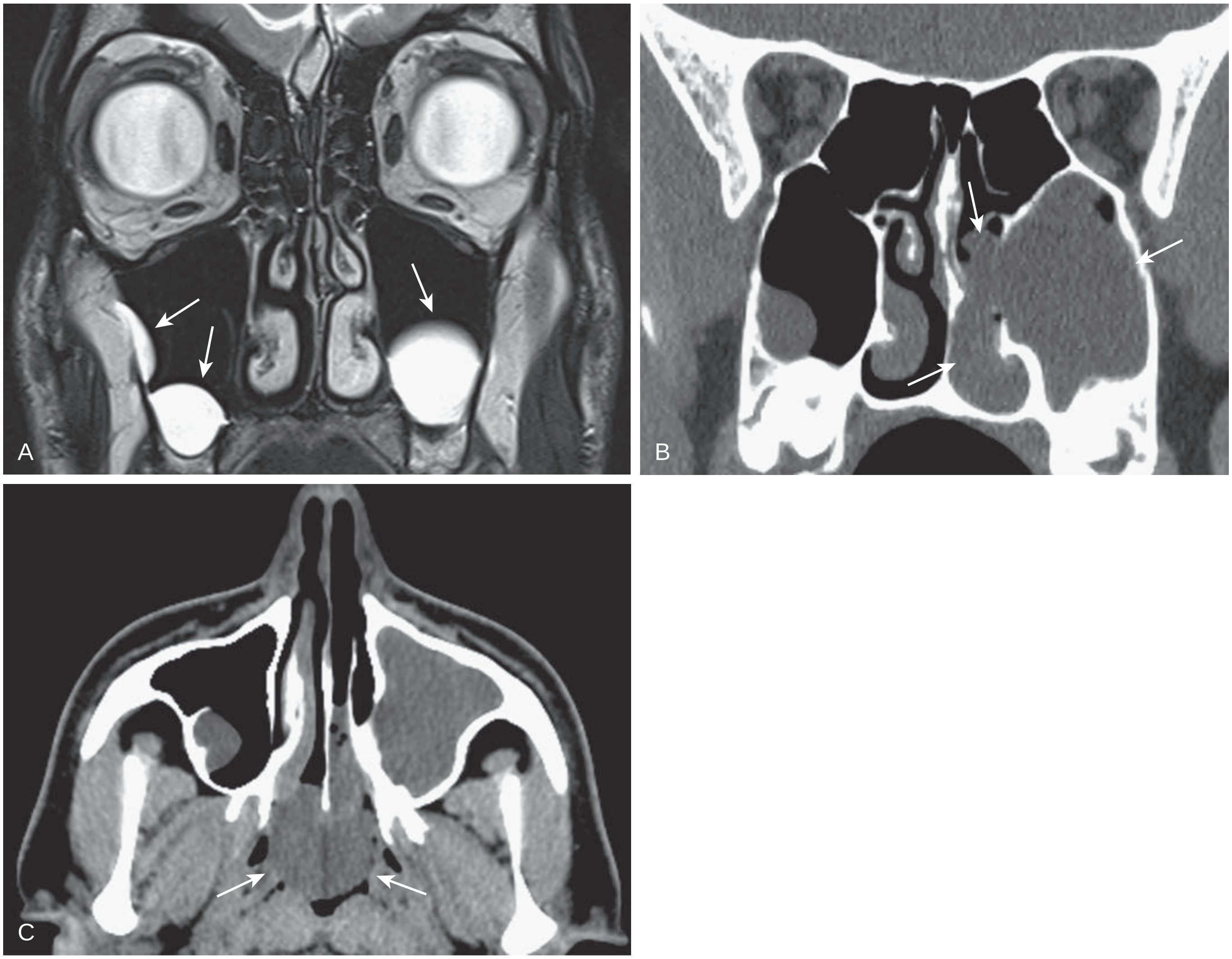

**Figure 8.24. Sinus polyps and retention cysts.** (A) Coronal T2-weighted MR image in a 17-year-old boy shows multiple hyperintense maxillary retention cysts *(arrows)*. (B) Axial coronal CT image in a 16-year-old boy shows a large antrochoanal polyp that fills in the left maxillary antrum extending through the ostium to the nasal cavity *(arrows)*. (C) Coronal CT image shows posterior extension of the polyp to the nasal choana, crossing the midline to the right *(arrows)*.

ostium of the maxillary sinus. These polyps are usually unilateral solitary lesions; however, bilateral ACPs can be seen in 20% to 25% of cases. The clinical presentation is nasal obstruction and discharge, mouth breathing, snoring, and sleep apnea.

On CT, most ACPs have mucoid attenuation and show mucosal surface contrast enhancement without central enhancement. ACPs can appear denser when inspissated secretions are present. On MRI, ACPs are usually hyperintense on T2-weighted images because of their high water content.

Mucoceles, which are most common in the frontal (60%) and ethmoid (30%) sinuses and result from obstruction or sequestration of a portion of the sinus, are cystic lesions lined with respiratory epithelium and filled with mucoid secretions.[57] Mucoceles are rare in the sphenoid[58] and maxillary sinuses. The association of mucoceles and CF is frequent.[59] Clinical symptoms result from the mass effect of the lesion and depend on location; these symptoms may include proptosis, headache, cranial nerve impingement, or nasal obstruction (e-Fig. 8.25).

On CT, mucoceles are low-density, nonenhancing masses that can expand the sinus. Thin rim enhancement can occur; however, if enhancement is thick or nodular, infection should be considered. Calcification in the wall suggests remote infection. The signal varies on MRI, depending on the relative concentrations of water, protein, and mucus.

If the bony wall of the portion of the sinus bordering the brain is disrupted and the rim of the sinus enhances, it is likely that the mucocele is adherent to thickened dura that may lead to complications such as empyema, meningitis, and abscess. A mucocele within the sphenoid sinus before enhancement may mimic the appearance of a pituitary adenoma or chordoma. After administration of IV contrast material, however, these entities should be differentiated easily.

## Neoplasms of the Sinonasal Cavity

Benign neoplasms and tumor-like conditions of the sinonasal cavity in children include fibro-osseous lesions (e.g., fibrous dysplasia and ossifying fibroma), bony tumors (e.g., giant cell tumor and aneurysmal bone cyst) (e-Fig. 8.26A), juvenile nasopharyngeal angiofibroma (Fig. 8.27), nasal pleomorphic adenoma, odontogenic cysts or tumors, and vascular tumors such as hemangiomas and nasal pyogenic granuloma.

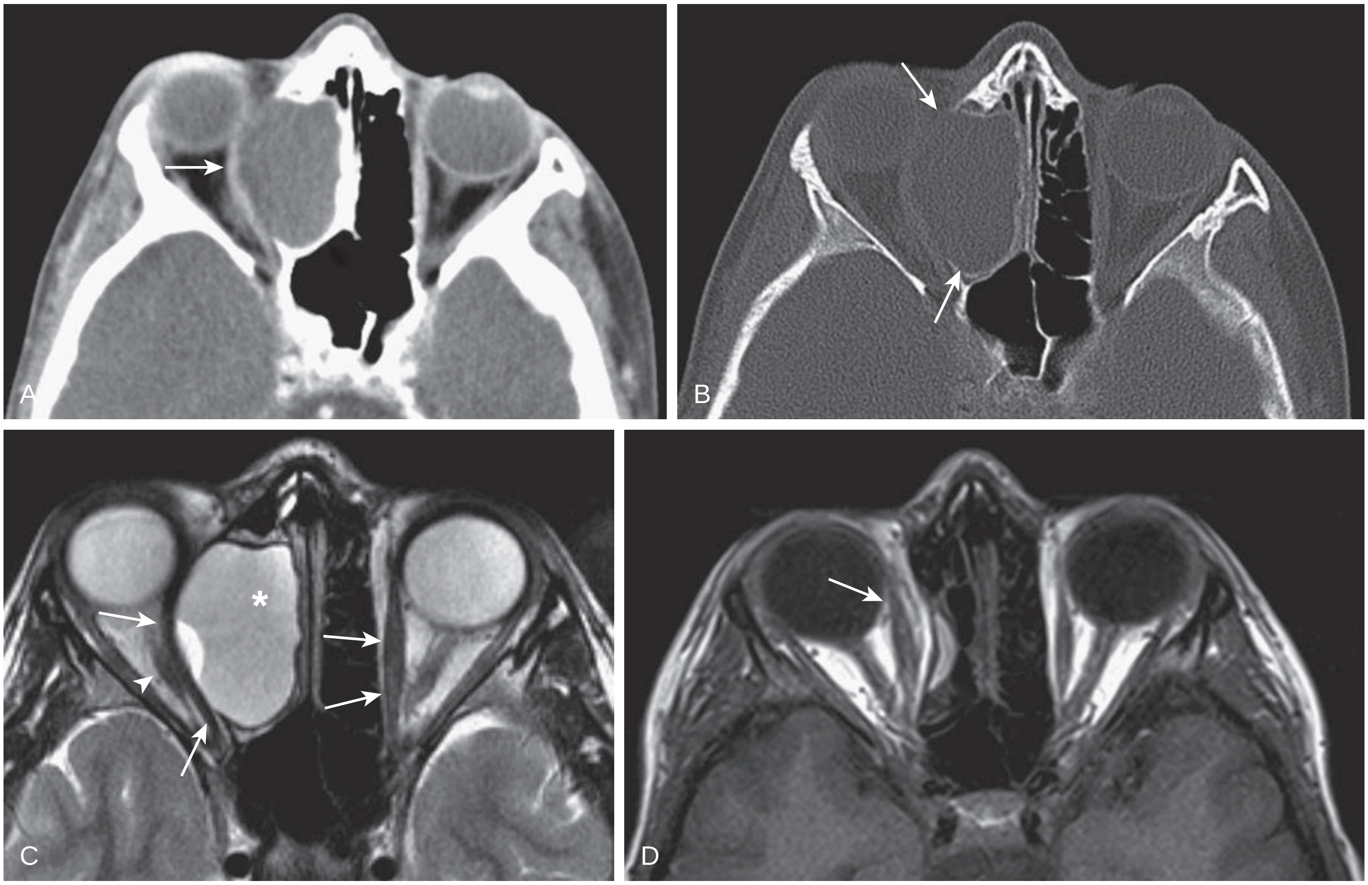

**e-Figure 8.25. Ethmoidal mucocele in a 13-year-old.** (A) Axial contrast-enhanced CT image shows a well-circumscribed, nonenhancing, hypodense, expansile mass centered in the right ethmoid sinus with significant effect of the mass on the right orbit, causing proptosis and lateral deviation of the medial rectus muscle *(arrow)*. (B) Axial CT image shows bone remodeling and septal destruction *(arrows)*. (C) Axial T2-weighted MR image shows a cystic, hyperintense, expansile lesion *(asterisk)* and lateral displacement of the right medial rectus muscle compared with the left *(arrows)*. The optic nerve is laterally displaced *(arrowhead)*. (D) After endoscopic marsupialization, resolution of the ethmoidal expansion and proptosis is seen. Note the normal position of the medial rectus muscle *(arrow)*.

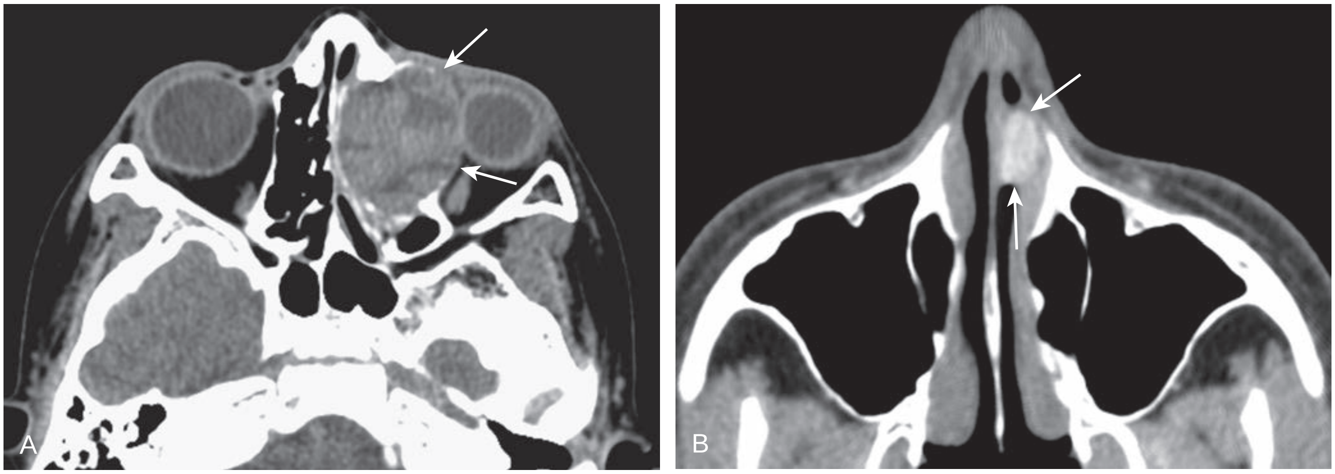

**e-Figure 8.26. Benign nasosinal neoplasms.** (A) Aneurysmal bone cyst in a 7-year-old child. Axial contrast-enhanced computed tomography image shows a left intranasal expansile lesion with intrinsic fluid-fluid levels and effect of the mass on the orbit *(arrows)*. (B) Nasal pyogenic granuloma in a 13-year-old boy. Axial contrast-enhanced CT image shows a well-circumscribed, avidly enhancing oval mass in the anterior left nasal cavity *(arrows)*.

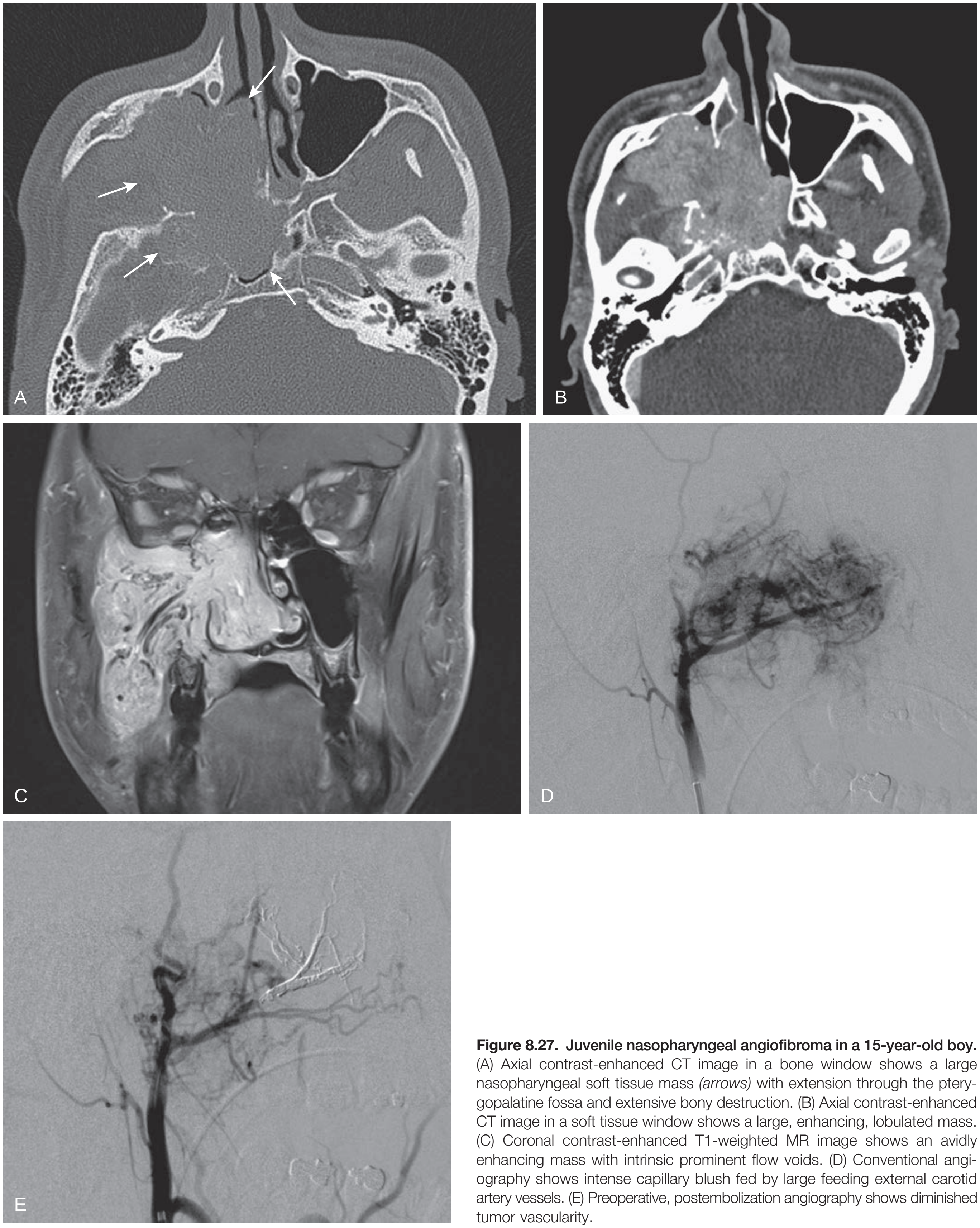

**Figure 8.27. Juvenile nasopharyngeal angiofibroma in a 15-year-old boy.** (A) Axial contrast-enhanced CT image in a bone window shows a large nasopharyngeal soft tissue mass *(arrows)* with extension through the pterygopalatine fossa and extensive bony destruction. (B) Axial contrast-enhanced CT image in a soft tissue window shows a large, enhancing, lobulated mass. (C) Coronal contrast-enhanced T1-weighted MR image shows an avidly enhancing mass with intrinsic prominent flow voids. (D) Conventional angiography shows intense capillary blush fed by large feeding external carotid artery vessels. (E) Preoperative, postembolization angiography shows diminished tumor vascularity.

Hemangiomas are benign vascular tumors that can occur in the face and neck and may also present as a nasal mass. Infantile hemangioma is the most common tumor in infancy and presents on imaging as a well-defined, lobular hypervascular soft tissue mass, with hypointense signal on T1-weighted images and bright signal on T2-weighted images.

Pyogenic granuloma, also known as lobular capillary hemangioma, is a benign vascular tumor of capillary proliferation that can arise from the skin, or from oral or nasal mucosa. The etiology remains unclear; trauma and hormonal changes may play a role, however, it can also present spontaneously without a clear cause. Nasal pyogenic granuloma is rare and can arise from the anterior nasal septum, turbinates, or roof of the nasal cavity. In children, there is a slight male predilection. Clinical presentation is with epistaxis, nasal obstruction, rhinorrhea, and pain. On nonenhanced CT, it appears as a well-circumscribed, hypoattenuating, 1 to 2 cm homogeneous soft tissue mass, without calcification, and can cause bone remodeling. On contrast-enhanced CT, there is intense diffuse enhancement (e-Fig. 8.26B). On MR imaging, it is isointense to cerebral gray matter on T1-weighted imaging and heterogeneously hyperintense on T2-weighted imaging, with marked contrast enhancement and a nonenhancing hypointense rim. The preferred treatment for nasal pyogenic granuloma is surgical excision.

Malignant neoplasms of the sinonasal cavity in children include rhabdomyosarcoma (e-Fig. 8.28), leukemia (e-Figs. 8.29A and B), lymphoma (e-Fig. 8.29C), nasopharyngeal carcinoma (e-Fig. 8.30), metastatic disease (neuroblastoma), and rarely esthesioneuroblastoma.

## FRACTURES OF FACIAL BONES

Nasal fractures, which typically result from direct frontal impact, occur most often in the lower third of the nasal bone. Lateral blows cause more complex fractures and often are associated with other facial fractures. Associated dislocation of the septal cartilage and fracture of the nasal spine also can be seen.

Radiographs may evaluate simple fractures, but CT is the preferred method to evaluate more complex fractures and for preoperative planning.[60] Ultrasound has proven to be a reliable diagnostic tool for the evaluation of nasal fractures, especially in low-grade nasal fractures.[61,62]

After nasal trauma, nasal examination by anterior rhinoscopy is mandatory to exclude septal hematoma. Early diagnosis and treatment, consisting of incision and drainage, are critical to avoid complications such as abscess formation, septal necrosis and perforation, and "saddle-nose" deformity. A septal hematoma most often appears on CT as an isodense to hypodense collection centered in the nasal septum but may also be heterogeneous.

### KEY POINTS

- Maxillary and ethmoid sinuses are present at birth. Sphenoid sinuses develop after fatty marrow transformation of the sphenoid bone. Frontal sinuses appear between 6 and 12 years of age.
- Plain radiographs are extremely limited in the evaluation of the paranasal sinuses and are not indicated in children younger than 2 years.
- With all imaging, a high incidence of mucosal thickening is seen in asymptomatic individuals.
- CT is indicated in patients with complicated acute sinusitis and is the gold standard study that guides management of recurrent or chronic sinusitis and serves as a road map for functional endoscopic sinus surgery.
- MRI is the imaging modality of choice in evaluating intracranial complications of sinusitis.
- CT and MRI are complementary in assessing and mapping neoplasms.

### SUGGESTED READINGS

Karmazyn B, Coley BD, Robertson ME, et al. *Sinusitis—child*. American College of Radiology (ACR) Appropriateness Criteria, 2012. Available at: https://acsearch.acr.org/docs/69442/Narrative.

Mafee MF, Tran BH, Chapa AR. Imaging of rhinosinusitis and its complications: plain film, CT, and MRI. *Clin Rev Allergy Immunol*. 2006;30(3):165–186.

Som PM, Naidich TP. Illustrated review of the embryology and development of the facial region, part 1: early face and lateral nasal cavities. *AJNR Am J Neuroradiol*. 2013;34(12):2233–2240.

Som PM, Naidich TP. Illustrated review of the embryology and development of the facial region, part 2: late development of the fetal face and changes in the face from the newborn to adulthood. *AJNR Am J Neuroradiol*. 2014;35(1):10–18.

Steele RW. Chronic sinusitis in children. *Clin Pediatr (Phila)*. 2005;44(6):465–471.

Ummat S, Riding M, Kirkpatrick D. Development of the ostiomeatal unit in childhood: a radiological study. *J Otolaryngol*. 1992;21(5):307–314.

Wald ER, Applegate KE, Bordley C, et al. Clinical practice guideline for the diagnosis and management of acute bacterial sinusitis in children aged 1 to 18 years. *Pediatrics*. 2013;132(1):e262–e280.

### REFERENCES

Full references for this chapter can be found on www.expertconsult.com.

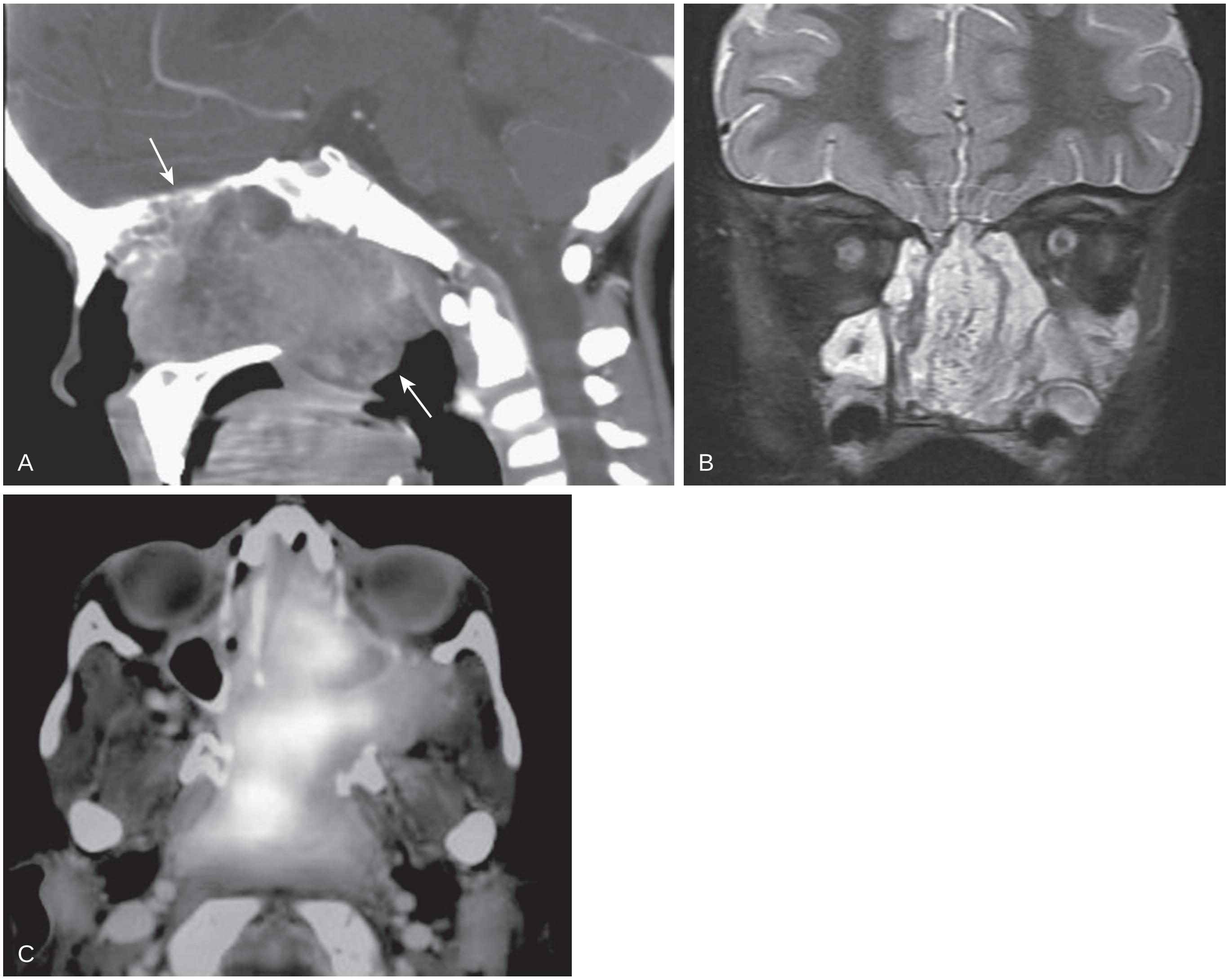

**e-Figure 8.28. Nasopharyngeal rhabdomyosarcoma in a 4-year-old girl.** (A) Sagittal contrast-enhanced CT image shows a large heterogeneous soft tissue mass in the nasopharynx with bony destruction. (B) Coronal fat-saturated T2-weighted MR image shows a large, nasopharyngeal, heterogeneous mass. (C) Axial fluorodeoxyglucose–positron emission tomography image shows a fluorodeoxyglucose-avid mass.

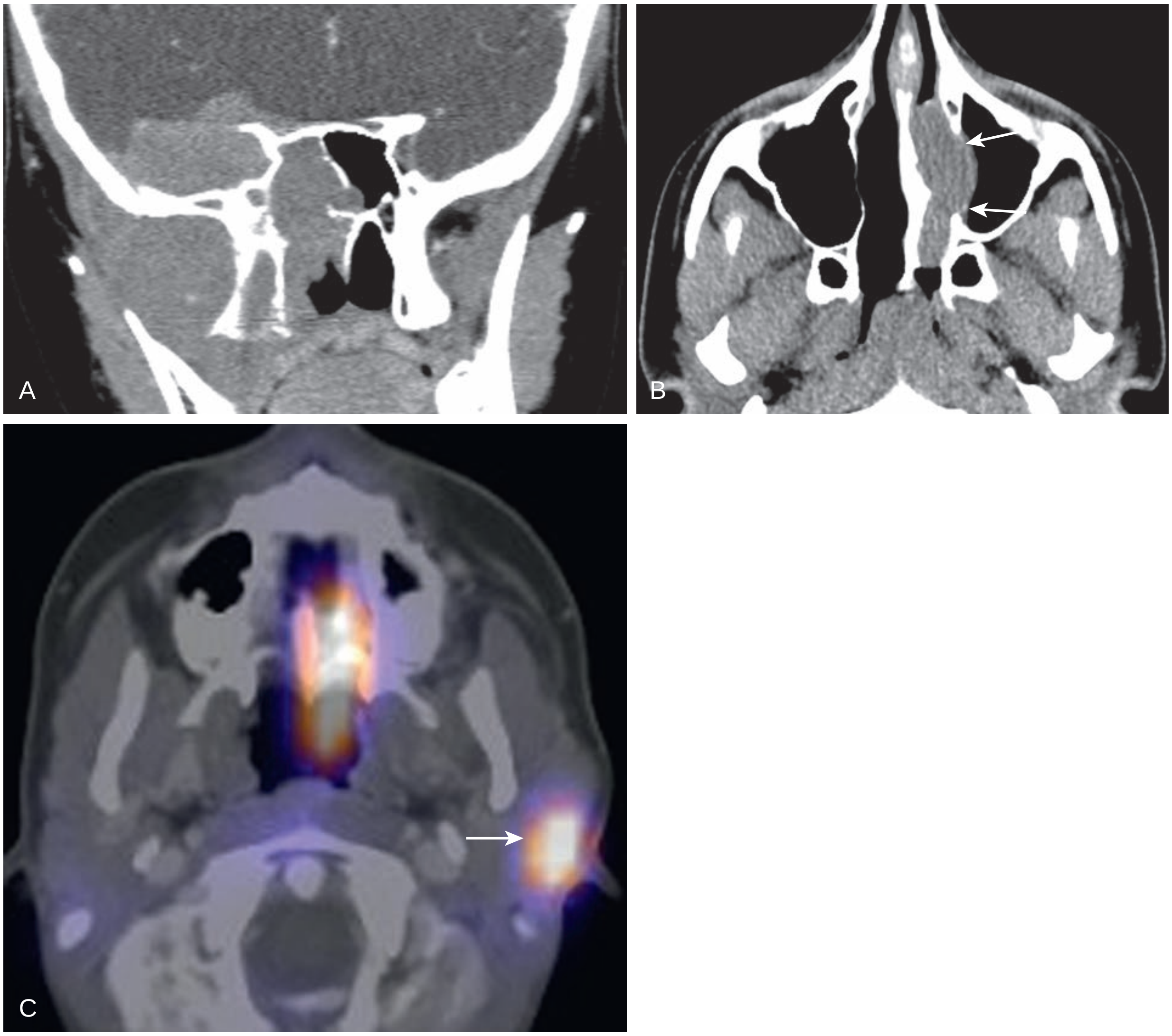

**e-Figure 8.29. Leukemia and lymphoma.** (A) Acute lymphocytic leukemia in a 9-year-old girl. Coronal contrast-enhanced CT image shows a large enhancing soft tissue mass centered in the right infratemporal fossa with extension to the skull base, middle cranial fossa, and sphenoid sinus, with bony remodeling and destruction. (B and C) Nasal T-cell lymphoma in a 10-year-old boy. (B) Axial CT image shows a soft tissue mass, which is isodense to muscle within the left nasal cavity. There is remodeling and/or destruction of the medial wall of the left maxillary sinus *(arrows)*. (C) Axial F-18-FDG- PET/CT image shows FDG avidity of this mass *(arrow)*.

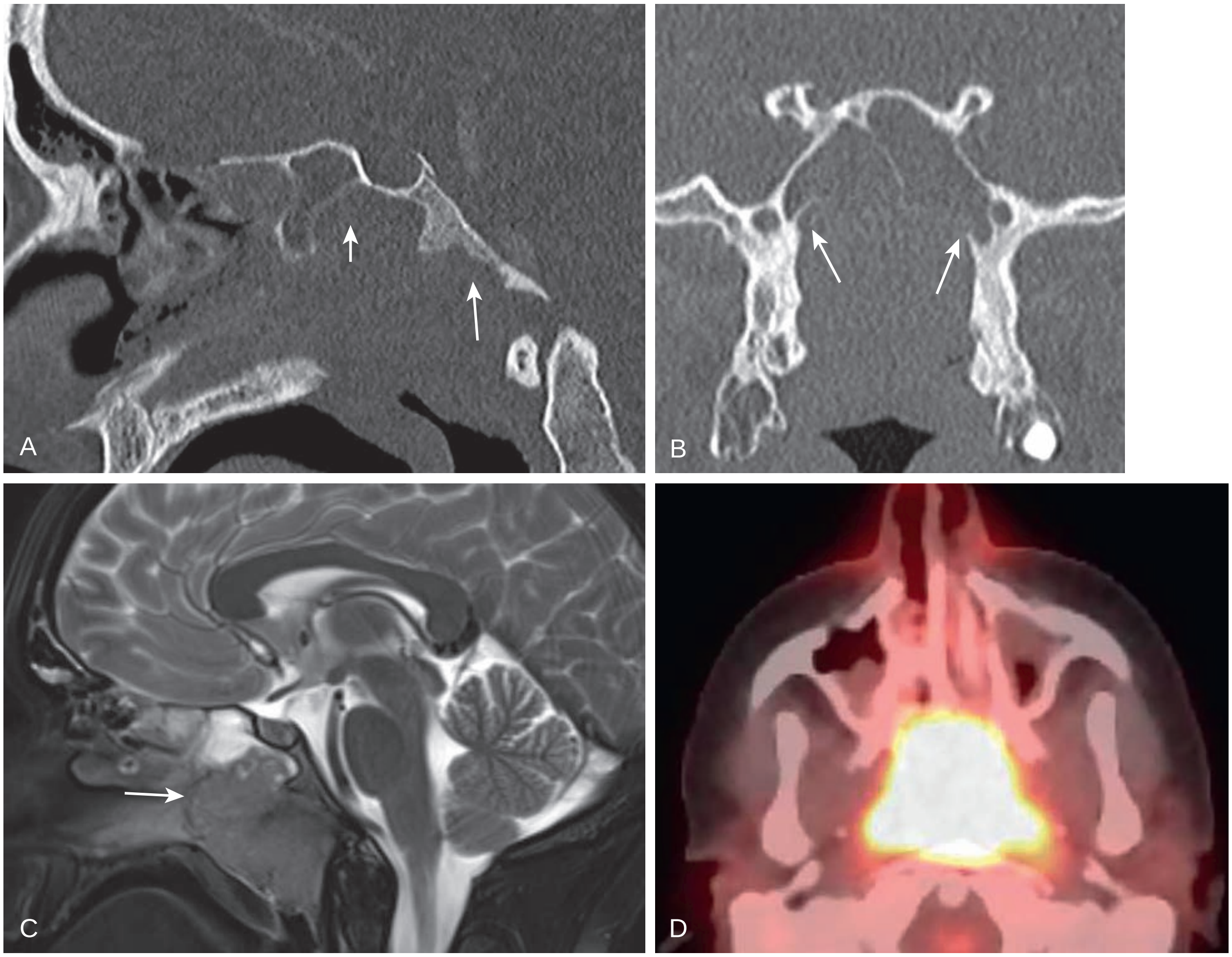

**e-Figure 8.30. Nasopharyngeal carcinoma in a 17-year-old girl.** (A) Sagittal CT image shows a large nasopharyngeal soft tissue mass that extends superiorly into the sphenoid sinus with bony destruction of its floor *(short arrow),* erosion of the clivus *(long arrow),* and extension into the posterior nasal cavity. (B) Coronal CT image shows superior extension of mass into the sphenoid sinus with destruction of the bilateral vidian nerve canals *(arrows)*. (C) Sagittal T2-weighted MR image shows hypointense signal of the nasopharyngeal mass. The sphenoid sinus is occupied by mass and secretions. There is no intracranial extension of mass. (D) Axial F-18-FDG-PET/CT image shows that the mass is hypermetabolic.

## REFERENCES

1. Som PM, Naidich TP. Illustrated review of the embryology and development of the facial region, part 2: late development of the fetal face and changes in the face from the newborn to adulthood. *AJNR Am J Neuroradiol*. 2014;35(1):10–18.
2. Som PM, Naidich TP. Illustrated review of the embryology and development of the facial region, part 1: early face and lateral nasal cavities. *AJNR Am J Neuroradiol*. 2013;34(12):2233–2240.
3. LaPlante JK, Pierson NS, Hedlund GL. Common pediatric head and neck congenital/developmental anomalies. *Radiol Clin North Am*. 2015;53(1):181–196.
4. Antunes MB, Gudis DA, Cohen NA. Epithelium, cilia, and mucus: their importance in chronic rhinosinusitis. *Immunol Allergy Clin North Am*. 2009;29(4):631–643.
5. Som C, ed. *Head and Neck Imaging*. 5th ed. St Louis: Elsevier Mosby; 2011.
6. Wang R, Jiang S, Gu R. The embryonic development of the ostiomeatal complex from 8 to 40 weeks[in Chinese]. *Zhonghua Er Bi Yan Hou Ke Za Zhi*. 1994;29(3):131–133.
7. Adibelli ZH, Songu M, Adibelli H. Paranasal sinus development in children: a magnetic resonance imaging analysis. *Am J Rhinol Allergy*. 2011;25(1):30–35.
8. Weiglein A, Anderhuber W, Wolf G. Radiologic anatomy of the paranasal sinuses in the child. *Surg Radiol Anat*. 1992;14(4):335–339.
9. Shah RK, Dhingra JK, Carter BL, et al. Paranasal sinus development: a radiographic study. *Laryngoscope*. 2003;113(2):205–209.
10. Medina J, Hernandez H, Tom LW, et al. Development of the paranasal sinuses in children. *Am J Rhinol*. 1997;11(3):203–209.
11. Nayak S. Radiologic anatomy of the paranasal air sinuses. *Semin Ultrasound CT MR*. 1999;20(6):354–378.
12. Szolar D, Preidler K, Ranner G, et al. Magnetic resonance assessment of age-related development of the sphenoid sinus. *Br J Radiol*. 1994;67(797):431–435.
13. Aoki S, Dillon WP, Barkovich AJ, et al. Marrow conversion before pneumatization of the sphenoid sinus: assessment with MR imaging. *Radiology*. 1989;172(2):373–375.
14. Barghouth G, Prior JO, Lepori D, et al. Paranasal sinuses in children: size evaluation of maxillary, sphenoid, and frontal sinuses by magnetic resonance imaging and proposal of volume index percentile curves. *Eur Radiol*. 2002;12(6):1451–1458.
15. Wolf G, Anderhuber W, Kuhn F. Development of the paranasal sinuses in children: implications for paranasal sinus surgery. *Ann Otol Rhinol Laryngol*. 1993;102(9):705–711.
16. Vaid S, Vaid N, Rawat S, et al. An imaging checklist for pre-FESS CT: framing a surgically relevant report. *Clin Radiol*. 2011;66(5):459–470.
17. Reiss M, Reiss G. Height of right and left ethmoid roofs: aspects of laterality in 644 patients. *Int J Otolaryngol*. 2011;2011:508907.
18. Lebowitz RA, Terk A, Jacobs JB, et al. Asymmetry of the ethmoid roof: analysis using coronal computed tomography. *Laryngoscope*. 2001;111(12):2122–2124.
19. Alberti PW. Applied surgical anatomy of the maxillary sinus. *Otolaryngol Clin North Am*. 1976;9(1):3–20.
20. McAlister WH, Lusk R, Muntz HR. Comparison of plain radiographs and coronal CT scans in infants and children with recurrent sinusitis. *AJR Am J Roentgenol*. 1989;153(6):1259–1264.
21. Konen E, Faibel M, Kleinbaum Y, et al. The value of the occipitomental (Waters') view in diagnosis of sinusitis: a comparative study with computed tomography. *Clin Radiol*. 2000;55(11):856–860.
22. [deleted in review]
23. Karmazyn B, Coley BD, Dempsey-Robertson ME, et al. *Sinusitis—child. American College of Radiology (ACR) appropriatness criteria*, 2012. Available at: https://acsearch.acr.org/docs/69442/Narrative.
24. Wald ER, Applegate KE, Bordley C, et al. Clinical practice guideline for the diagnosis and management of acute bacterial sinusitis in children aged 1 to 18 years. *Pediatrics*. 2013;132(1):e262–e280.
25. Paterson A, Frush DP. Dose reduction in paediatric MDCT: general principles. *Clin Radiol*. 2007;62(6):507–517.
26. Shah NB, Platt SL. ALARA: Is there a cause for alarm? Reducing radiation risks from computed tomography scanning in children. *Curr Opin Pediatr*. 2008;20(3):243–247.
27. Goske MJ, Applegate KE, Boylan J, et al. The 'Image Gently' campaign: increasing CT radiation dose awareness through a national education and awareness program. *Pediatr Radiol*. 2008;38(3):265–269.
28. Mulkens TH, Broers C, Fieuws S, et al. Comparison of effective doses for low-dose MDCT and radiographic examination of sinuses in children. *AJR Am J Roentgenol*. 2005;184(5):1611–1618.
29. Ummat S, Riding M, Kirkpatrick D. Development of the ostiomeatal unit in childhood: a radiological study. *J Otolaryngol*. 1992;21(5):307–314.
30. Wake M, Takeno S, Hawke M. The uncinate process: a histological and morphological study. *Laryngoscope*. 1994;104(3 Pt 1):364–369.
31. Brown OE, Pownell P, Manning SC. Choanal atresia: a new anatomic classification and clinical management applications. *Laryngoscope*. 1996;106(1 Pt 1):97–101.
32. Slovis TL, Renfro B, Watts FB, et al. Choanal atresia: precise CT evaluation. *Radiology*. 1985;155(2):345–348.
33. Brown OE, Myer CM 3rd, Manning SC. Congenital nasal pyriform aperture stenosis. *Laryngoscope*. 1989;99(1):86–91.
34. Visvanathan V, Wynne DM. Congenital nasal pyriform aperture stenosis: a report of 10 cases and literature review. *Int J Pediatr Otorhinolaryngol*. 2012;76(1):28–30.
35. Van Den Abbeele T, Triglia JM, Francois M, et al. Congenital nasal pyriform aperture stenosis: diagnosis and management of 20 cases. *Ann Otol Rhinol Laryngol*. 2001;110(1):70–75.
36. Wong RK, VanderVeen DK. Presentation and management of congenital dacryocystocele. *Pediatrics*. 2008;122(5):e1108–e1112.
37. Steele RW. Rhinosinusitis in children. *Curr Allergy Asthma Rep*. 2006;6(6):508–512.
38. Steele RW. Chronic sinusitis in children. *Clin Pediatr (Phila)*. 2005;44(6):465–471.
39. Beswick DM, Ramadan H, Baroody FM, et al. Practice patterns in pediatric chronic rhinosinusitis: a survey of the American Rhinologic Society. *Am J Rhinol Allergy*. 2016;30(6):418–423.
40. Hicks CW, Weber JG, Reid JR, et al. Identifying and managing intracranial complications of sinusitis in children: a retrospective series. *Pediatr Infect Dis J*. 2011;30(3):222–226.
41. Perez Barreto M, Sahai S, Ameriso S, et al. Sinusitis and carotid artery stroke. *Ann Otol Rhinol Laryngol*. 2000;109(2):227–230.
42. Tsai BY, Lin KL, Lin TY, et al. Pott's puffy tumor in children. *Childs Nerv Syst*. 2010;26(1):53–60.
43. Blumfield E, Misra M. Pott's puffy tumor, intracranial, and orbital complications as the initial presentation of sinusitis in healthy adolescents, a case series. *Emerg Radiol*. 2011;18(3):203–210.
44. Rommens JM, Iannuzzi MC, Kerem B, et al. Identification of the cystic fibrosis gene: chromosome walking and jumping. *Science*. 1989;245(4922):1059–1065.
45. Sakano E, Ribeiro AF, Barth L, et al. Nasal and paranasal sinus endoscopy, computed tomography and microbiology of upper airways and the correlations with genotype and severity of cystic fibrosis. *Int J Pediatr Otorhinolaryngol*. 2007;71(1):41–50.
46. Godoy JM, Godoy AN, Ribalta G, et al. Bacterial pattern in chronic sinusitis and cystic fibrosis. *Otolaryngol Head Neck Surg*. 2011;145(4):673–676.
47. Weber SA, Ferrari GF. Incidence and evolution of nasal polyps in children and adolescents with cystic fibrosis. *Braz J Otorhinolaryngol*. 2008;74(1):16–20.
48. Yung MW, Gould J, Upton GJ. Nasal polyposis in children with cystic fibrosis: a long-term follow-up study. *Ann Otol Rhinol Laryngol*. 2002;111(12 Pt 1):1081–1086.
49. Kovell LC, Wang J, Ishman SL, et al. Cystic fibrosis and sinusitis in children: outcomes and socioeconomic status. *Otolaryngol Head Neck Surg*. 2011;145(1):146–153.
50. Rickert S, Banuchi VE, Germana JD, et al. Cystic fibrosis and endoscopic sinus surgery: relationship between nasal polyposis and likelihood of revision endoscopic sinus surgery in patients with cystic fibrosis. *Arch Otolaryngol Head Neck Surg*. 2010;136(10):988–992.
51. Marseglia GL, Merli P, Caimmi D, et al. Nasal disease and asthma. *Int J Immunopathol Pharmacol*. 2011;24(suppl 4):7–12.
52. Triglia JM, Nicollas R. Nasal and sinus polyposis in children. *Laryngoscope*. 1997;107(7):963–966.
53. deShazo RD, Chapin K, Swain RE. Fungal sinusitis. *N Engl J Med*. 1997;337(4):254–259.
54. Schubert MS. Allergic fungal sinusitis: pathophysiology, diagnosis and management. *Med Mycol*. 2009;47(suppl 1):S324–S330.
55. Kanagalingam J, Bhatia K, Georgalas C, et al. Maxillary mucosal cyst is not a manifestation of rhinosinusitis: results of a prospective three-dimensional CT study of ophthalmic patients. *Laryngoscope*. 2009;119(1):8–12.

56. Chen JM, Schloss MD, Azouz ME. Antro-choanal polyp: a 10-year retrospective study in the pediatric population with a review of the literature. *J Otolaryngol*. 1989;18(4):168–172.
57. Lund VJ, Milroy CM. Fronto-ethmoidal mucocoeles: a histopathological analysis. *J Laryngol Otol*. 1991;105(11):921–923.
58. Lui YW, Dasari SB, Young RJ. Sphenoid masses in children: radiologic differential diagnosis with pathologic correlation. *AJNR Am J Neuroradiol*. 2011;32(4):617–626.
59. Nicollas R, Facon F, Sudre-Levillain I, et al. Pediatric paranasal sinus mucoceles: etiologic factors, management and outcome. *Int J Pediatr Otorhinolaryngol*. 2006;70(5):905–908.
60. Kim BH, Seo HS, Kim AY, et al. The diagnostic value of the sagittal multiplanar reconstruction CT images for nasal bone fractures. *Clin Radiol*. 2010;65(4):308–314.
61. Lee MH, Cha JG, Hong HS, et al. Comparison of high-resolution ultrasonography and computed tomography in the diagnosis of nasal fractures. *J Ultrasound Med*. 2009;28(6):717–723.
62. Hong HS, Cha JG, Paik SH, et al. High-resolution sonography for nasal fracture in children. *AJR Am J Roentgenol*. 2007;188(1):W86–W92.

# 9

# Embryology, Anatomy, Normal Findings, and Imaging Techniques

Korgün Koral

## EMBRYOLOGY

A detailed study of the development of the ear is beyond the scope of this chapter; only the key embryologic events and their timing are discussed here. It is important to appreciate that the inner ear is derived from the neuroectoderm, whereas the middle ear and the external ear develop from the branchial apparatus, explaining why the abnormalities of the inner ear are generally isolated from the abnormalities of the middle ear/external ear and vice versa. It is also important to remember that the pharyngeal clefts give rise to the ectodermal structures, pouches give rise to the endodermal structures, and intervening arches give rise to the mesodermal structures.

### External Ear

The external auditory meatus (canal) is derived from the first pharyngeal cleft. At the beginning of the third month, the epithelial cells at the bottom of the meatus proliferate and form the meatal plug. The meatal plug dissolves in the seventh month and the epithelial lining of the floor of the meatus participates in the formation of the definitive tympanic membrane. The lateral part of the tympanic membrane arises from the ectoderm, and the medial part of it from the endoderm. There is an intermediate layer of connective tissue in between, called fibrous stratum, derived from the mesoderm.

The pinna (auricle) develops from six mesenchymal proliferations, called hillocks, which are located at the dorsal ends of the first and second pharyngeal arches. They surround the first pharyngeal cleft (future external auditory meatus). These hillocks gradually fuse and form the definitive auricle.[1]

### Middle Ear

The tympanic cavity is derived from the endoderm and develops from the first pharyngeal pouch. This pouch grows laterally until it comes in contact with the floor of the first pharyngeal cleft. The lateral part of the pouch gives rise to the primitive tympanic cavity. The medial part of the pouch is smaller and forms the eustachian tube. The malleus and incus are derived from the cartilage of the first pharyngeal arch, whereas the stapes is derived from the second pharyngeal arch. The ossicles remain embedded in the mesenchyme until the eighth month, when the surrounding tissue dissolves. The tympanic cavity expands dorsally to form the mastoid antrum in late fetal life. Pneumatization of the mastoid process continues after birth.[1]

### Inner Ear

The otic placodes become visible on each side of rhombencephalon on the 22nd day of gestation; they are the first indications of developing ears. The otic placodes invaginate rapidly and form the otic (auditory) vesicles. From the ventral components of the otic placodes, the cochlea and the saccule develop. From the dorsal components of the otic placodes, the utricle, the semicircular canals, and the endolymphatic duct arise. These epithelial structures are collectively named the membranous labyrinth.

Between 6 and 8 weeks of gestation, the cochlear duct, arising from the saccule, penetrates the surrounding mesenchyme and completes the 2½ turns. The ductus reuniens is the thin, residual connection between the cochlea and saccule. At the 10th week, the cartilage surrounding the cochlear duct undergoes vacuolization and two perilymphatic spaces are formed: the scala tympani and the scala vestibuli. The cochlear duct (scala media) is separated from the scala vestibuli by the vestibular membrane and from the scala tympani by the basilar membrane. The lateral wall of the cochlear duct remains attached to the surrounding cartilage by the spiral ligament. Medially, the cochlear duct is attached to the modiolus, which is the axis of the bony cochlea. At the sixth week, semicircular canals appear as outpouchings of the utricular (posterior) component of the otic vesicle.[1]

## ANATOMY AND NORMAL FINDINGS

Learning the anatomy of the temporal bone may appear intimidating initially; however, there are tremendous returns for the relatively small investment of study time. That is because the normal imaging anatomy of the temporal bone is exquisitely displayed on computed tomography (CT) and magnetic resonance imaging (MRI), leaving relatively few gray zones where interpretation is difficult. An exhaustive review of the temporal bone anatomy is beyond the scope of this chapter. What follows is a simple guide for those not previously exposed to temporal bone imaging.

The temporal bone consists of tympanic, squamous, petrous, and mastoid parts, and a styloid process.[2] It may be easier to divide the temporal bone into compartments when studying its anatomy or when reviewing imaging studies. Here, these compartments are presented from lateral to medial.

### Pinna and External Auditory Canal

Abnormalities of the pinna usually coexist with the abnormalities of the external auditory canal (EAC) and middle ear. Mayer et al.[3] reported that ossicular abnormalities were present in 98% of the temporal bones with microtia and EAC abnormality. It may be difficult to detect subtle abnormalities of the pinna, but it is generally possible to identify gross malformations on a temporal bone CT.

The EAC is oval in shape in cross section. Its walls (anterior and posterior; superior and inferior) run parallel throughout the course of the EAC. The EAC consists of two segments: the membranous (fibrocartilaginous) segment makes up the lateral one third of the EAC, and the medial bony segment forms the remainder.[4]

The tympanic membrane separates the EAC from the middle ear cavity and is attached to the tympanic annulus, which is a circumferential bony prominence at the medial-most aspect of the bony EAC. Superiorly, the tympanic membrane attaches

## Abstract:

Understanding the temporal bone anatomy is key to perform clinically relevant examinations and interpretations of the pediatric temporal bone. Having a basic knowledge of the embryology is very useful to conceptualize the congenital malformations of the temporal bone. In this chapter, an introduction to temporal bone embryology and imaging anatomy is provided along with some technical considerations of temporal bone imaging.

## Keywords:

temporal bone
anatomy
children
pediatric
magnetic resonance imaging
computerized tomography

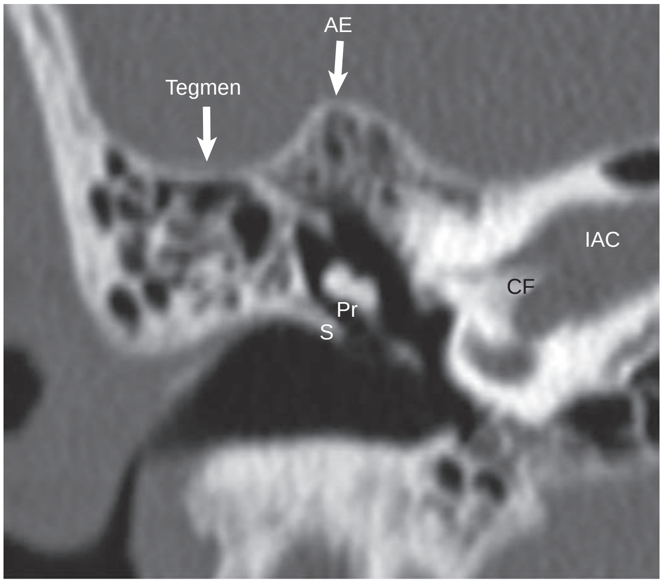

**Figure 9.1.** Reconstructed coronal CT image displays the bony segment of the external auditory canal, middle ear cavity, and mastoid air cells. Tegmen typmani *(Tegmen),* arcuate eminence *(AE),* scutum *(S),* Prussak space *(Pr),* crista falciformis *(CF),* internal auditory canal *(IAC).*

to the scutum (Fig. 9.1), which is an important bony landmark in the diagnosis of cholesteatoma. If not thickened, one needs to use wide window settings on CT to visualize the tympanic membrane.

## Middle Ear Cavity (Cleft)

The middle ear cavity is the normally aerated space, via the eustachian tube, medial to the tympanic membrane. It is arbitrarily divided into three compartments: epitympanum (attic), mesotympanum, and hypotympanum. If lines are drawn parallel to the superior and inferior walls of the bony segment of the EAC in the coronal plane, the part of the middle ear cavity above the upper line is the epitympanum (attic) and is the largest portion and houses most of the ossicular chain. The mesotympanum lies between the two lines. The hypotympanum is below the lower line and is normally nonexistent or very small in children (Fig. 9.2).

### Ossicles

The malleus, incus, and stapes form the ossicular chain, which is responsible for amplification (around 30%) and transmission of the sound waves from the tympanic membrane to the oval window on the vestibule.[5]

The manubrium (handle) and the lateral process of the malleus are embedded in the tympanic membrane. The tympanic membrane has two parts, divided by the lateral process of the malleus: a smaller pars flaccida superiorly, and a larger pars tensa inferiorly.[6] Cranial to the manubrium is the neck of the malleus to which the tendon of the tensor tympani muscle attaches. The tensor tympani muscle is a Meckel cartilage (derived from the first branchial arch) structure and is innervated by the only branch of the trigeminal nerve that has motor fibers: V3 (mandibular branch). The head of the malleus forms the “ice cream” of the familiar “ice cream cone” appearance and articulates with the body of the incus (Fig. 9.3). The malleoincudal joint is a diarthrodial (synovial) articulation, as is the incudostapedial joint (see Figs. 9.3 and 9.4). The incus is the largest of the three middle ear ossicles. Its body articulates with the head of the malleus and forms the “cone” on axial images. The short process of the incus (better seen on axial images) extends from the body dorsally and resides in the fossa incudus to which it is secured by ligaments that are invisible on CT. The long process of the incus extends inferiorly from the body. The lenticular process of the incus joins the long process forming a nearly 90-degree angle. The long and lenticular processes of the incus are very delicate and more prone to erosion from infection and/or inflammation than other parts of the ossicular chain. The lenticular process is cup shaped medially and articulates with the head (capitulum) of the stapes. The head of the stapes is connected to the crura (anterior and posterior), which subsequently join the footplate of the stapes. The opening between the crura of the stapes is called the obturator foramen and is where the stapedial artery resides in fetal life. The stapes footplate

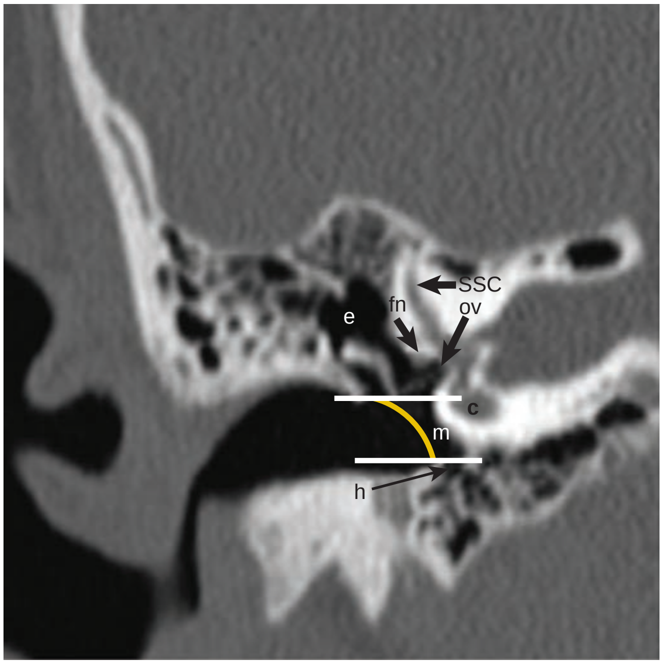

**Figure 9.2.** Reconstructed coronal CT image shows the lines drawn to define epitympanum *(e),* mesotympanum *(m),* and hypotympanum *(h).* The tympanic membrane is outlined by the yellow curvilinear line. Superior semicircular canal *(SSC),* cochlea *(c),* oval window *(ov),* facial nerve *(fn).*

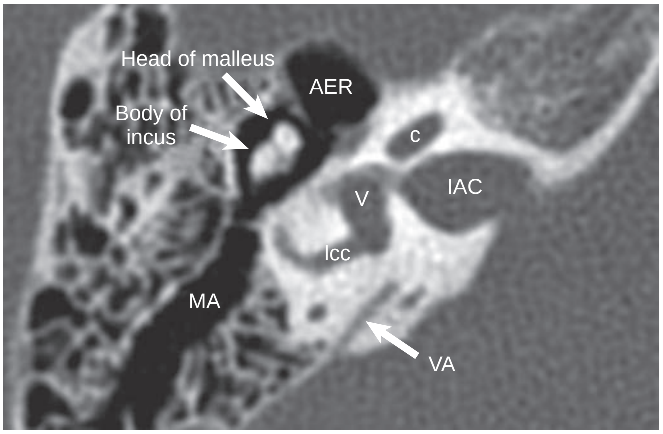

**Figure 9.3.** Axial CT image demonstrates the “ice cream cone” appearance of the head of the malleus and incus. Anterior epitympanic recess *(AER),* cochlea *(c),* vestibule *(V),* mastoid antrum *(MA),* lateral semicircular canal *(lcc),* vestibular aqueduct *(VA),* internal auditory canal *(IAC).*

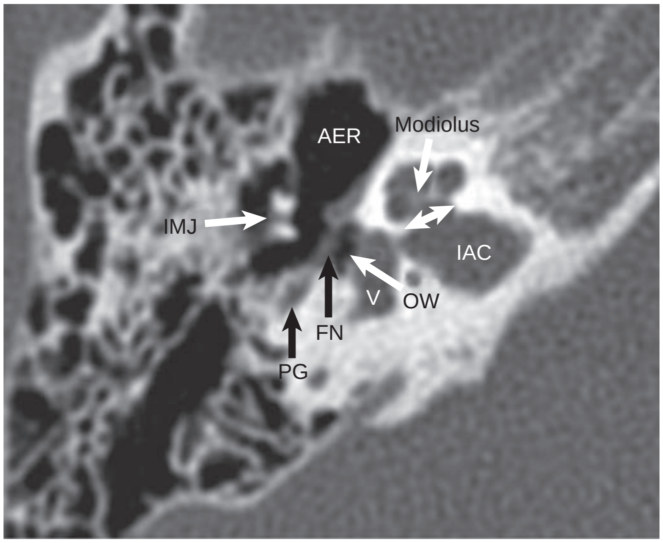

**Figure 9.4.** Axial CT image shows the cochlear aperture *(double-headed arrow)* and *modiolus*. Oval window *(OW),* facial nerve *(FN),* posterior genu of the facial nerve *(PG),* vestibule *(V),* internal auditory canal *(IAC),* anterior epitympanic recess *(AER),* incudomalleolar joint *(IMJ)*.

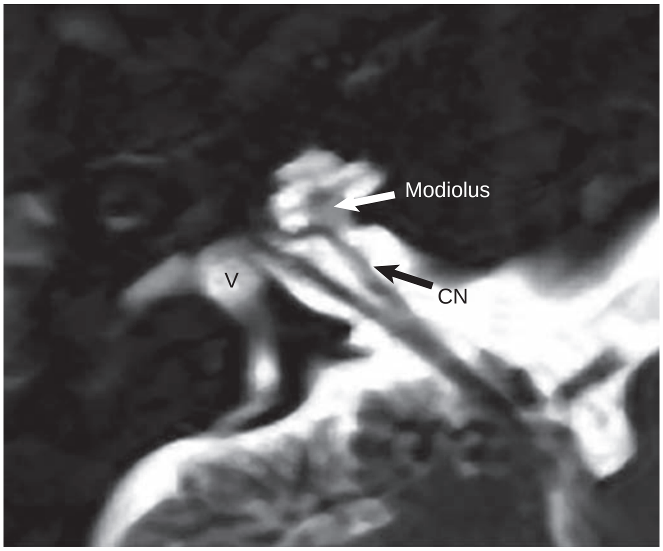

**Figure 9.5.** Axial balanced fast field echo MRI displays the cochlea and *modiolus*. The cochlear nerve *(CN)* enters the cochlea through the cochlear aperture. Vestibule *(V).*

articulates with the oval window forming the syndesmotic (fibrous) stapediovestibular joint.[5]

## Recesses and Ridges of the Middle Ear Cavity

The sinus tympani is the medial and posterior recess of the middle ear cavity. It can occasionally be deep, making the visualization of the soft tissue lesions within it difficult at surgery. Lateral to the sinus tympani is a triangular bony prominence: the pyramidal eminence. The stapedius muscle (innervated by the facial nerve) may occasionally be imaged on CT arising from the pyramidal eminence and extending to the stapes. Lateral to the pyramidal eminence is the facial recess.

The Prussak space is important because soft tissue lesions within it may be hidden from the view of the clinical examiner (see Fig. 9.1). The Prussak space is medial to the scutum and lateral to the malleolar head. The superior malleolar ligament (which is not seen on CT) forms the cranial border of the Prussak space.

The anterior epitympanic recess (see Figs. 9.3 and 9.4) is contiguous with the middle ear cavity through an incomplete septum, termed the *cog*, whose integrity may be lost due to infection or inflammation.[5]

## Mastoid Air Cells

The interconnected, air-filled mastoid air cells communicate with a mastoid antrum, which in turn communicates with the middle ear cavity (see Figs. 9.3 and 9.4). The connection between the middle ear cavity and mastoid antrum is called the aditus ad antrum (opening to antrum). The mastoid air cells are separated by innumerable thin septa. The Koerner septum is the bony thickening that runs obliquely through the mastoid air cells and is an important surgical landmark. The roof of the middle ear cavity is called the tegmen tympani (see Fig. 9.1).

## Facial and Vestibulocochlear Nerves and Internal Auditory Canal

The facial nerve has motor, parasympathetic, and special sensory (taste) fibers. Its nuclei are in the dorsal pons. The motor fibers of the facial nerve swing posterior to the nuclei of the abducens nerve, generating the swellings of the facial colliculi. It is important to remember that the facial nerve has a rather long intraaxial segment extending from the nuclei through the nerve exit zone at the surface of the lateral pons. The cisternal and canalicular segments of the facial nerve are evaluated on high-resolution T2-weighted MRI of the temporal bone. The cisternal segment, the longest segment of the facial nerve, can routinely be identified on high-resolution MRI. The facial nerve enters the internal auditory canal (IAC) through the porus acusticus and is named the canalicular segment thereafter. In the IAC, the facial nerve lies in the anterior-superior quadrant. The lateral-most aspect of the IAC is termed the *fundus*, which is divided by the crista falciformis (see Fig. 9.1) into superior and inferior compartments. The superior compartment is further divided into anterior and posterior parts by a vertical, variably calcified/ossified arachnoid membrane, called the Bill's bar. The cochlear nerve occupies the anterior-inferior quadrant and the vestibular nerve (superior and inferior branches) is seen in the posterior quadrants[7] (Figs. 9.5 and 9.6).

The facial nerve enters the labyrinthine canal where it occupies approximately 95% of its volume. The labyrinthine segment of the facial nerve is particularly susceptible to ischemia because its bony confines do not leave room for swelling during inflammation. The labyrinthine segment synapses at the geniculate ganglion from which the parasympathetic greater superficial petrosal nerve (GSPN) arises. The GSPN recruits some sympathetic fibers and becomes the vidian nerve and provides the parasympathetic innervation of the lacrimal gland. Distal to the geniculate ganglion, the facial nerve makes a dorsal turn and becomes the tympanic segment. The distal labyrinthine segment, geniculate ganglion, and proximal tympanic segment make up the anterior genu. The tympanic segment of the facial nerve lies at the medial wall of the tympanic cavity and immediately inferior to the lateral semicircular canal. The tympanic segment has a thin, inconsistent bony covering and lies just lateral to the oval window. The posterior genu is a nearly 90-degree bend where the tympanic segment meets the mastoid (or descending) segment (see Fig. 9.4). The mastoid segment exits the temporal bone through the stylomastoid foramen. Just proximal to the stylomastoid foramen, the chorda tympani arises from the mastoid segment, extends into the middle ear cavity in its own canal, and traverses the middle ear cavity within the tympanic membrane, between the manubrium of the malleus and incus. The chorda tympani contains the taste sensation fibers from the anterior

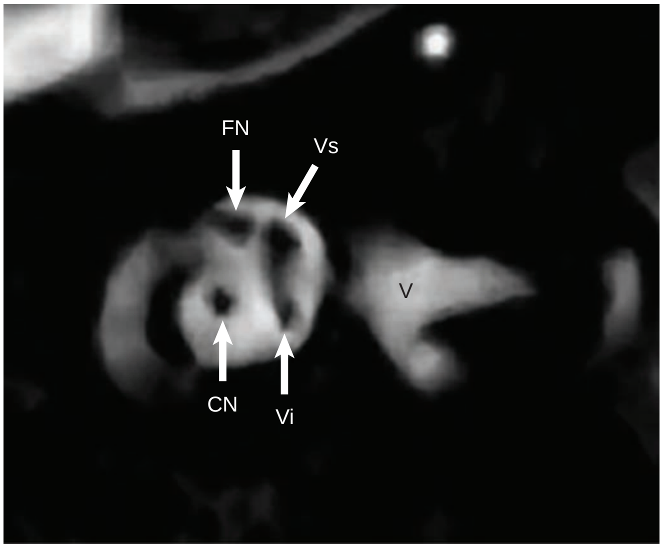

**Figure 9.6.** Oblique sagittal balanced fast field echo MRI through the fundus of the internal auditory canal shows the facial nerve *(FN),* cochlear nerve *(CN),* and superior *(Vs)* and inferior *(Vi)* branches of the vestibular nerves.

two-thirds of the tongue, as well as the parasympathetic fibers to the submandibular and sublingual glands.[2] After exiting the temporal bone, the facial nerve traverses the parotid gland (but does not innervate it) and innervates the facial musculature. The parotid gland is divided by the facial nerve into deep and superficial lobes.

The cochlear nerve is equal in size or slightly larger than the facial nerve, as seen on oblique-sagittal T2-weighted MRI. It enters the cochlea through the cochlear aperture, which can be appreciated on both CT and MRI. Stenosis or atresia of the cochlear aperture is usually associated with deficiency or absence of the cochlear nerve.

### Oval Window/Round Window

The stapes footplate resides on the oval window (see Fig. 9.4). It can easily be appreciated on both the axial and coronal CT images. Abnormalities of the oval window include atresia and stenosis, which are usually associated with abnormalities of ossicles and external ear. The round window is easier to appreciate on coronal images as a fluid-air interface at the inferior aspect of the vestibule.

### Jugular Bulb/Carotid Canal

The right jugular bulb is generally the dominant one. The term *high-riding* is used when the jugular bulb and basal turn of the cochlea are seen on the same axial image. Without bony dehiscence or protrusion of the internal jugular vein into the posterior tympanic cavity, a high-riding jugular bulb is insignificant. The carotid canal should be identified in all temporal bone examinations. The aberrant internal carotid artery running in the tympanic cavity is a very rare but important anomaly.

### Vestibular Aqueduct/Cochlear Aqueduct

The vestibular aqueduct (seen on CT) is the bony housing of the endolymphatic duct and sac (seen on MRI, usually when enlarged) (see Fig. 9.3). The vestibular aqueduct is considered enlarged when it measures greater than 1.0 mm at its midpoint.[8]

Although its enlargement is commonly associated with sensorineural hearing loss (SNHL), this observation does not alter the management if the patient is otherwise a good cochlear implantation candidate.

### Foramen Ovale/Foramen Spinosum

Identification of the foramen spinosum posterolateral to the foramen ovale is important because when it is absent, in about one-third of the cases it is associated with a persistent stapedial artery. The obturator foramen of the stapes should be inspected thoroughly for a soft tissue density when the foramen spinosum is not visualized.

### Temporomandibular Joint and Mandibular Head/Condyle

All temporal bone CT examinations should evaluate the temporomandibular joint because dysplasia is commonly associated with abnormalities of the auricle and ossicles, particularly aural atresia.

## Inner Ear

MRI is the modality of choice in the assessment of the inner ear, but attention should be paid to the bony labyrinth on temporal bone CT examinations because many of the inner ear abnormalities can be seen. The cochlea lies anterior to the IAC and is made up of basal, middle, and apical turns. The basal and middle turns are complete 360-degree turns, whereas the apical turn covers 180 degrees, hence the 2½ turns. On MRI the line representing the osseous spiral lamina is consistently seen throughout the cochlear lumen. The modiolus is the bony axis of the cochlea and has a "star" or "crown" shape and can be seen atop the cochlear aperture (see Figs. 9.4 and 9.5). The vestibule has a delicate, nearly cylindrical shape (see Figs. 9.3 and 9.5). The semicircular canals (superior, posterior, and lateral) are at right angles to each other and connect to the vestibule. Although one expects six openings in the inner surface of the vestibule (two for each semicircular canal), there are five openings because the posterior limb of the superior semicircular canal and the superior limb of the posterior semicircular canal unite to form the common crus, which has its own opening to the vestibule. The lateral semicircular canal is slightly larger than the other two semicircular canals.

### Petromastoid (Subarcuate) Canal

The petromastoid canal (PMC) is almost always visualized on temporal bone CT. It lies underneath the arch of the superior semicircular canal and is closer to its posterior limb. Its size decreases with age. The PMC houses the vascular supply to the tympanic segment of the facial nerve, middle ear cavity, and regional mastoid air cells. It appears as a T2-weighted hyperintense structure that is relatively wider laterally in infants (e-Fig. 9.7).[9]

## IMAGING TECHNIQUES

CT is reserved for conductive hearing loss whereas MRI is used in the evaluation of SNHL. A low-dose technique is employed in volumetric CT acquisition. At our institution the imaging parameters include a kVp of 90 and an mA of 80, resulting in a dose length product of approximately 90 mGy.cm. The lenses should be outside the field of the primary beam. Coronal (and if necessary oblique-sagittal) reformations are generated. The slice thickness is on the order of 0.5 to 0.6 mm.

For high-resolution MRI, three-dimensional acquisition (e.g., T2-weighted or a steady state sequence) of the membranous labyrinth is performed in the axial plane. The reconstructed images yield an effective slice thickness of 0.75 mm. Oblique-sagittal images of the cerebellopontine angles and IACs are acquired. It is prudent to complement the temporal bone MRI with a brain MRI to exclude central causes of hearing loss.

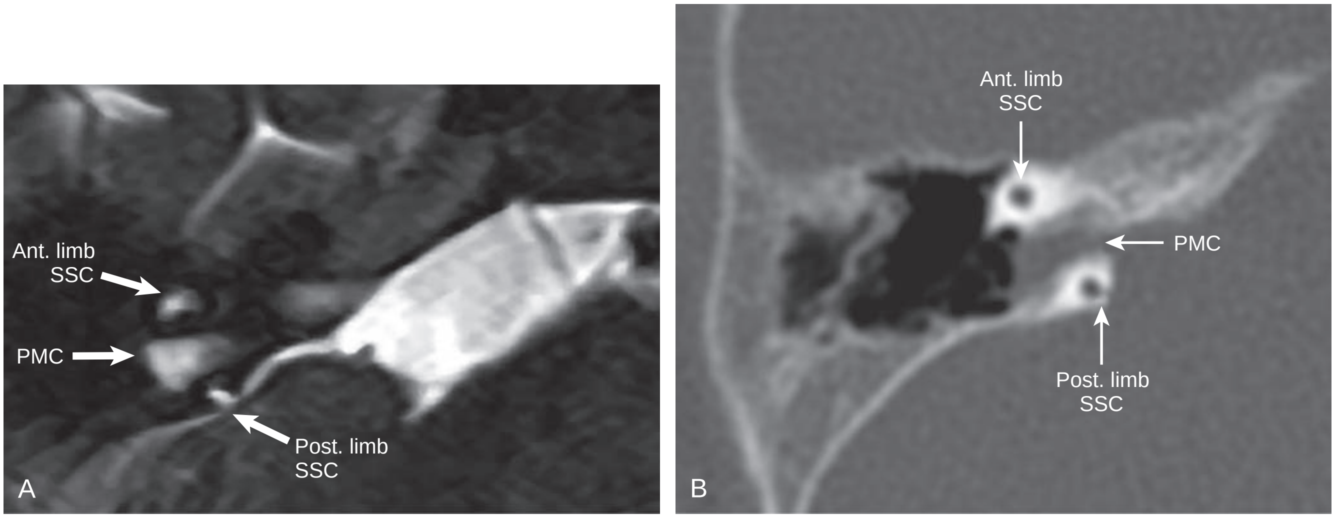

**e-Figure 9.7.** Axial balanced fast field echo MRI (A) and axial CT (B) images cranial to the internal auditory canal in a 6-month-old boy show the petromastoid canal *(PMC)*. Anterior *(Ant. limb SSC)* and posterior *(Post. limb SSC)* limbs of the semircircular canal.

## KEY POINTS

- The developmental abnormalities of the external ear and middle ear generally coexist and are separate from the abnormalities of the inner ear, because the external ear and middle ear are derived from the pharyngeal apparatus whereas the inner ear arises from the neuroectoderm.
- In general, CT is reserved for the evaluation of conductive hearing loss (e.g., aural atresia, cholesteatoma) whereas MRI is used in the workup of sensorineural hearing loss (primarily in the evaluation of cochlear implantation candidacy).
- The lenses should be kept outside the primary beam during CT acquisition.

## SUGGESTED READINGS

Fatterpekar GM, Doshi AH, Dugar M, et al. Role of 3D CT in the evaluation of the temporal bone. *Radiographics*. 2006;26(suppl 1):S117–S132.

Lane JI, Lindell EP, Witte RJ, et al. Middle and inner ear: improved depiction with multiplanar reconstruction of volumetric CT data. *Radiographics*. 2006;26(1):115–124.

Niu Y, Wang Z, Liu Y, et al. Radiation dose to the lens using different temporal bone CT scanning protocols. *AJNR Am J Neuroradiol*. 2010;31(2):226–229.

Shah LM, Wiggins RH 3rd. Imaging of hearing loss. *Neuroimaging Clin N Am*. 2009;19:287–306.

## REFERENCES

Full references for this chapter can be found on www.expertconsult.com.

## REFERENCES

1. Sadler TW. Ear. In: Sadler TW, ed. *Langman's Medical Embryology*. Baltimore: Williams & Wilkins; 1990:328–337.
2. Warwick R, Williams PL. The Temporal Bones. In: Warwick R, Williams PL, eds. *Gray's Anatomy*. 35th British Edition ed. Philadelphia: Longman Group Ltd.; 1973:291–296.
3. Mayer TE, Brueckmann H, Siegert R, et al. High-resolution CT of the temporal bone in dysplasia of the auricle and external auditory canal. *AJNR Am J Neuroradiol*. 1997;18(1):53–65.
4. Castillo M, Valerie LJ, Buchman C. The External Auditory Canal and Pinna. In: Swartz JD, Loevner LA, eds. *Imaging of the Temporal Bone*. 4th ed. New York: Thieme; 2009:25–57.
5. Swartz JD. The Middle Ear and Mastoid. In: Swartz JD, Loevner LA, eds. *Imaging of the Temporal Bone*. 4th ed. New York: Thieme; 2009:58–246.
6. Warwick R, Williams PL. The Auditory and Vestibular Apparatus. In: Warwick R, Williams PL, eds. *Gray's Anatomy*. Philadelphia: Longman Group Ltd.; 1973:1134–1158.
7. Raghavan P, Mukherjee S, Phillips CD. Imaging of the facial nerve. *Neuroimaging Clin N Am*. 2009;19(3):407–425.
8. Vijayasekaran S, Halsted MJ, Boston M, et al. When is the vestibular aqueduct enlarged? A statistical analysis of the normative distribution of vestibular aqueduct size. *AJNR Am J Neuroradiol*. 2007;28(6):1133–1138.
9. Koral K, Vachha B, Gimi B, et al. MRI of the petromastoid canal in children. *J Magn Reson Imaging*. 2014;39(4):966–971.

# 10

# Congenital and Neonatal Abnormalities

*Timothy N. Booth*

The discussion of congenital and neonatal temporal bone abnormalities in this chapter is approached from lateral to medial. External canal atresia and associated middle and inner ear anomalies are discussed initially. Isolated middle ear anomalies with associated branchial arch malformations are then addressed, along with associated anomalous development of the middle ear windows. A classification and description of inner ear malformations is discussed along with potential surgical outcomes. Finally, vascular anomalies involving the temporal bone are briefly discussed.

## EXTERNAL AUDITORY CANAL ATRESIA

***Clinical Presentation and Etiologies.*** The external and middle ear both are derived from the branchial apparatus, in contrast to the inner ear, which is of neuroectodermal origin. As a result, dysplasia of the external auditory canal (EAC) is commonly associated with a malformed auricle and anomalies of the middle ear and the mandible. These children usually present with microtia and conductive hearing loss (CHL). Mild stenosis of the EAC with normal or mildly malformed pinna may also occur.[1] Inner ear anomalies occur in 20% of children with aural atresia and are more likely to involve the vestibular apparatus (usually without profound sensorineural hearing loss ([SNHL]).[2] Atresia of the EAC is more common than inner ear anomalies with an incidence of 1 in 10,000 to 20,000 at birth. It is bilateral in one-third of cases, and appears to be more common in the United States than elsewhere.[3]

***Imaging.*** A spectrum of involvement is seen, with only mild bony stenosis of the EAC present in some children. Canal atresia may be membranous or bony. The severity of middle ear anomalies correlates with the extent of external malformation. Preoperative CT plays an integral role in determining potential candidates for hearing restorative surgery and should be performed shortly before intended surgery.[4] If SNHL is present, magnetic resonance imaging (MRI) may offer additional information that may affect treatment.

Ossicular anomalies are often associated with EAC atresia. The handle of the malleus is commonly fused to the atretic plate (e-Fig. 10.1). The malleus may be fused to the incus, with severe dysplasia usually present. The incudostapedial joint can be involved as well and is demonstrated on axial and coronal images. Patent oval and round windows are essential in achieving a good surgical outcome with oval window atresia seen with syndromic associations (Fig. 10.2). The stapes can be dysplastic, malpositioned, or absent. Significant abnormalities of the stapes often necessitate removal and placement of a total ossicular prosthesis. The size of the middle ear cavity is significant, and the degree of mastoid pneumatization also may affect the surgical approach.[5,6] Rarely, a boomerang-shaped ossicular mass has been reported in more severe cases of EAC atresia with both medial and lateral fixation points (e-Fig. 10.3).[7] Mild stenosis of the EAC with no associated microtia may be seen in children presenting with CHL with computed tomography (CT) showing fusion of the manubrium to the anterior tympanic annulus[1] (e-Fig. 10.4).

Determining the position of the facial nerve position is critical. The most common anomaly involves anterior displacement of the descending segment of the facial nerve, with the stylomastoid foramen lying just posterior to the temporal mandibular joint. The posterior genu usually is more anteriorly positioned immediately posterior to the level of the oval window[8] (Fig. 10.5). Less commonly, the tympanic segment may be positioned into the oval window or more inferiorly over the cochlear promontory. Atresia or stenosis of the oval window is usually associated with this anomalous facial nerve position. The facial nerve can be hypoplastic and difficult to visualize[9] (Box 10.1).

Syndromic EAC atresia usually is associated with more severe middle ear anomalies and a higher incidence of inner ear anomalies. Multiple genetic associations have been found[10,11] (e-Fig. 10.6), (Table 10.1).

***Treatment.*** Grading systems have been developed to assess the probability of surgical success. These systems take into account such findings as middle ear volume, ossicular anomalies, and the status of the oval window.[3,12] Transmastoid and anterior surgical approaches are used, with formation of a new tympanic membrane, mobilization of the ossicles, and possibly placement of an ossicular prosthesis. Active middle ear implants have recently been introduced as a potential treatment with a simplified grading system proposed.[13] The presence of a cholesteatoma also is a potential issue in both the imaging evaluation and surgical management of these patients.

## ISOLATED MIDDLE EAR ANOMALIES

***Clinical Presentation and Etiologies.*** Minor ear anomalies are associated with a normal EAC and are much less common. Minor ear anomalies usually present with a nonprogressive CHL, and a child with unexplained CHL should undergo CT evaluation to search for possible etiology.[14] Ossicular abnormalities may be unilateral or bilateral, with unilateral ossicular abnormalities usually sporadic and isolated. Bilateral anomalies may be associated with autosomal-dominant inheritance, and syndromic associations include Goldenhar and Treacher Collins syndrome. Round window atresia is caused by a deficiency in the development of cartilage during ossification of the otic capsule and typically is associated with CHL. Oval window atresia is likely caused by anomalous development of the second branchial arch and classically is associated with a mixed sensorineural and CHL. Oval window atresia can be seen with the CHARGE association (*C*oloboma of the eye, *H*eart defect, *A*tresia of choanae, *R*etarded growth and development, *G*enital anomalies, and *E*ar defect with deafness).

***Imaging.*** High-resolution CT using both axial and reconstructed coronal planes is the imaging modality of choice in evaluating patients with isolated middle ear anomalies. Anomalies of the stapes include aplasia, partial absence, columnar deformity, fusion of the head to the promontory, and footplate fixation. The incus can be aplastic; it can be fused to the lateral semicircular canal or scutum; it can have a malformed long process; it may be absent; or it may be fixed at the incudostapedial joint (e-Fig. 10.7). Similar anomalies involve the malleus; rarely, a bony bar fixes the malleus to the anterior lateral epitympanic wall[15,16] (Fig. 10.8). These anomalies have been classified into five classes on the basis of their surgical success rate and include (from better to worse):

Class 1: Normal stapes with abnormal incus or malleus
Class 2: Mobile stapes footplate
Class 3: Stapes footplate fixation only
Class 4: Stapes footplate fixation with other anomaly
Class 5: No stapes footplate[17,18]

Congenital stapes deformity or fixation may be associated with a perilymphatic fistula.[19]

## Abstract:

The temporal bone is a complex anatomical region that has varied embryologic origins. This chapter will focus on congenital abnormalities and discuss clinical presentation, appropriate imaging, as well as surgical implications. Normal variants that may mimic disease and affect surgical approach will be reviewed. The reader should have a thorough understanding of congenital pathology and variants that involve the temporal bone and regional structures.

## Keywords:

Temporal bone
congenital
conductive
sensorineural
atresia
syndrome

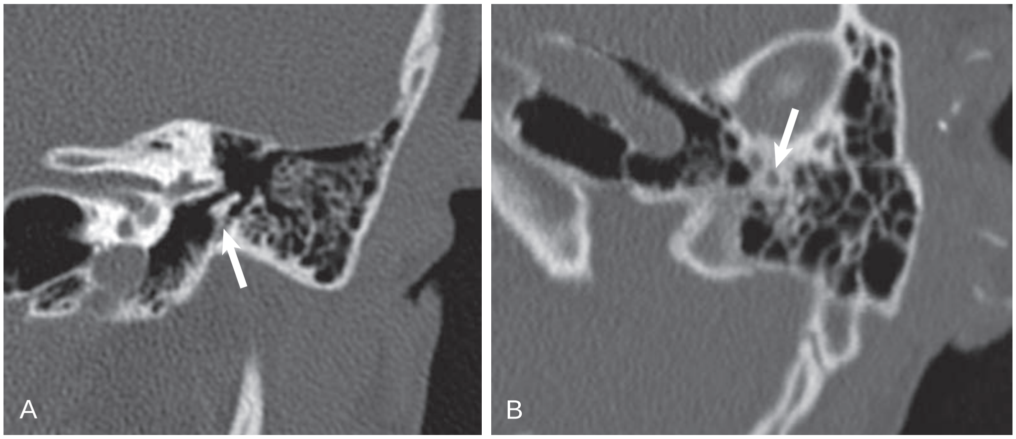

**e-Figure 10.1. Microtia and conductive hearing loss in a 10-year-old.** (A) Coronal high-resolution CT shows bony atresia of the external auditory canal and fusion of the malleus to the atretic plate *(arrow)*. (B) Axial image shows that the stylomastoid foramen is positioned anteriorly *(arrow)*.

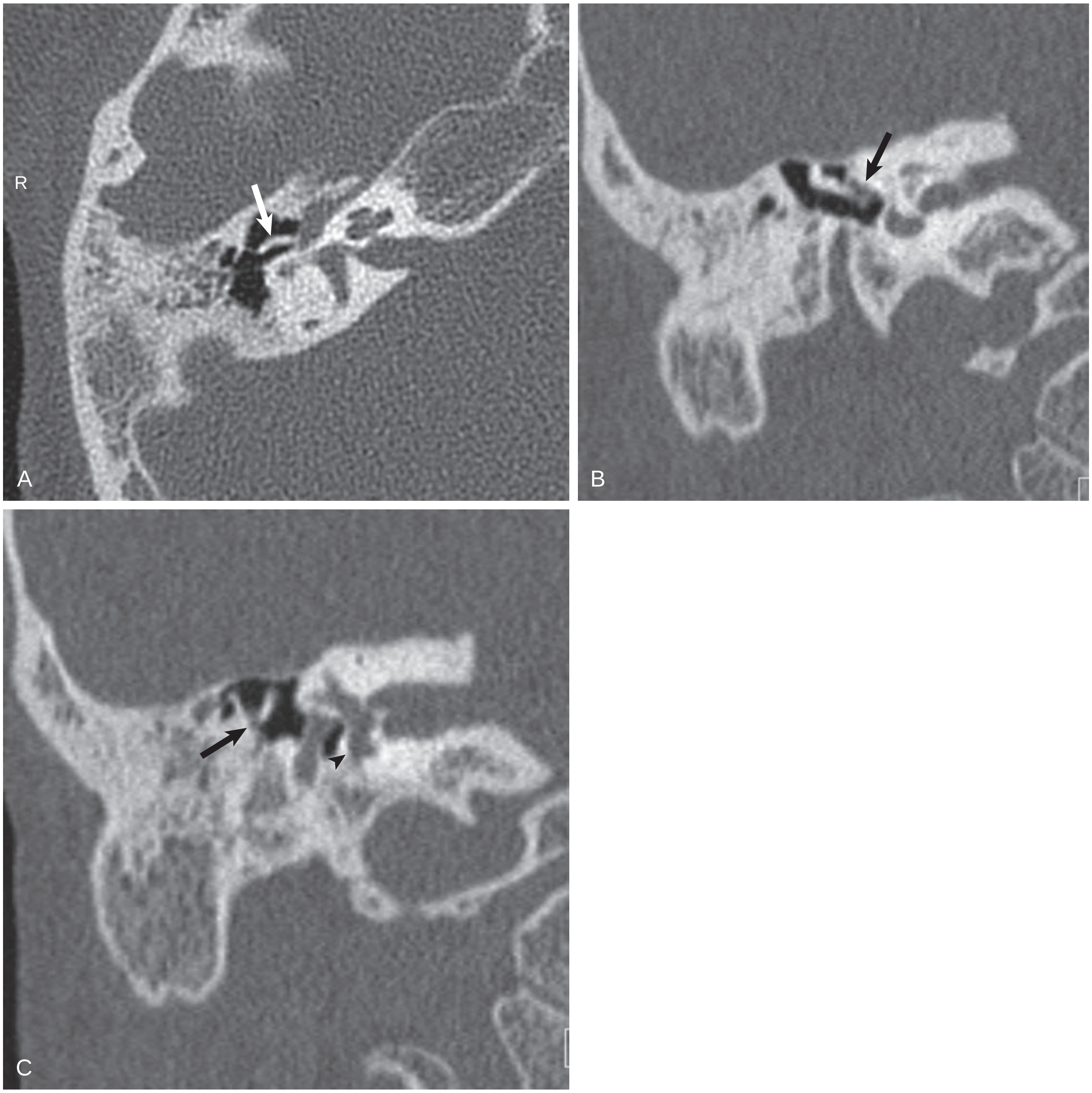

**e-Figure 10.3. Microtia and hearing loss in a 5-year-old.** (A) Axial high-resolution CT image show a boomerang configuration to a fused malleus and incus *(arrow)*. (B and C) Coronal reconstructions demonstrate superior, medial, and lateral fixation points with the medial fixation point at the proximal tympanic facial nerve *(arrows)* with the posterior genu at the level of the oval window *(arrowhead)*.

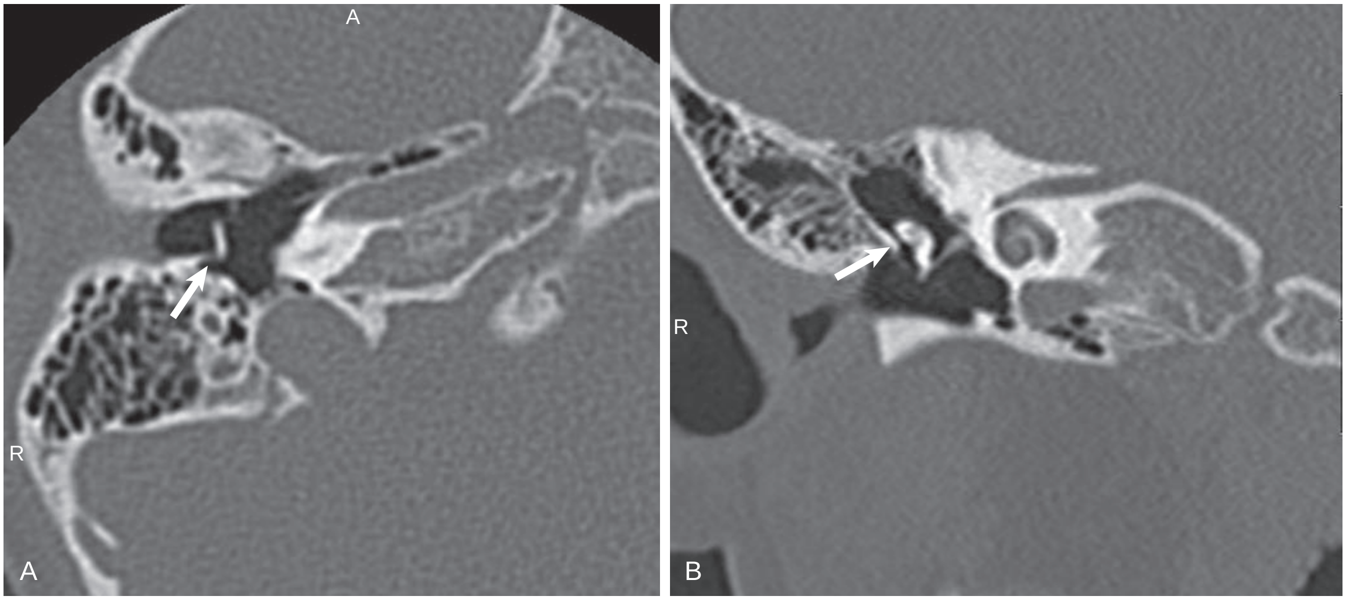

**e-Figure 10.4. Conductive hearing loss and normal pinna in a 4-year-old.** (A) Axial high-resolution CT image shows clockwise rotation of the handle of the malleus, which is fused to the posterior tympanic annulus *(arrow)*. (B) Coronal reconstruction demonstrates narrowing of Prussack space due to lateral ossicular position *(arrow)*.

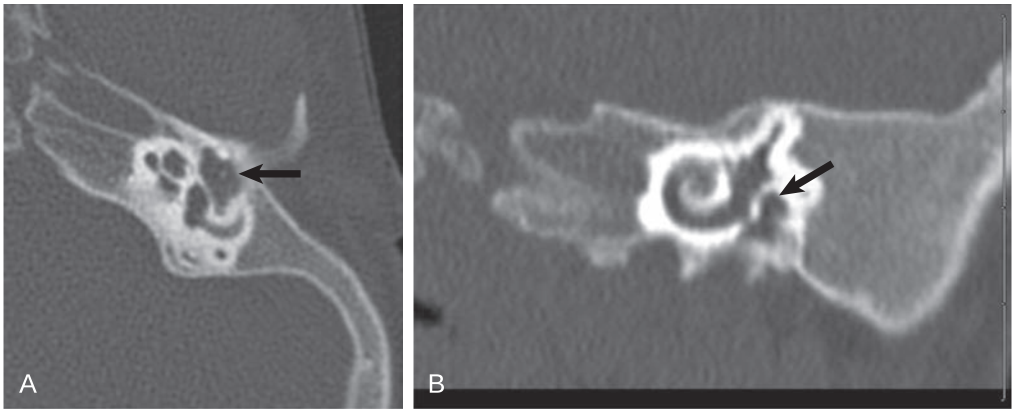

**e-Figure 10.6. Treacher Collins syndrome in a 4-year-old.** (A) Axial and (B) coronal high-resolution CT images show a markedly hypoplastic middle ear cavity with absent ossicles *(arrows)*. The external auditory canal and oval window are atretic.

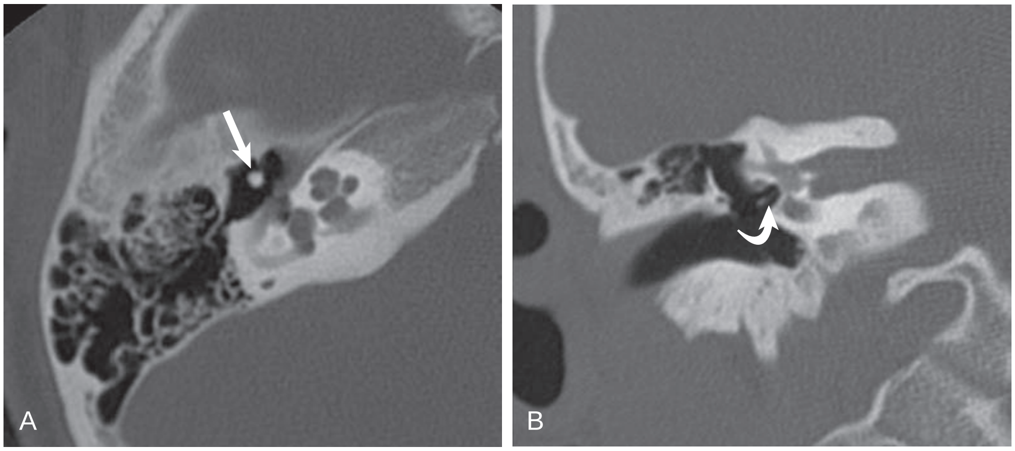

**e-Figure 10.7. Right-sided conductive hearing loss in a 6-year-old with no history of middle ear disease or surgery.** (A) Axial and (B) coronal high-resolution CT images through the middle ear. Congenital absence of the short and long process of the incus is noted. The head of the malleus *(straight arrow)* and lenticular process of the incus *(curved arrow)* are present.

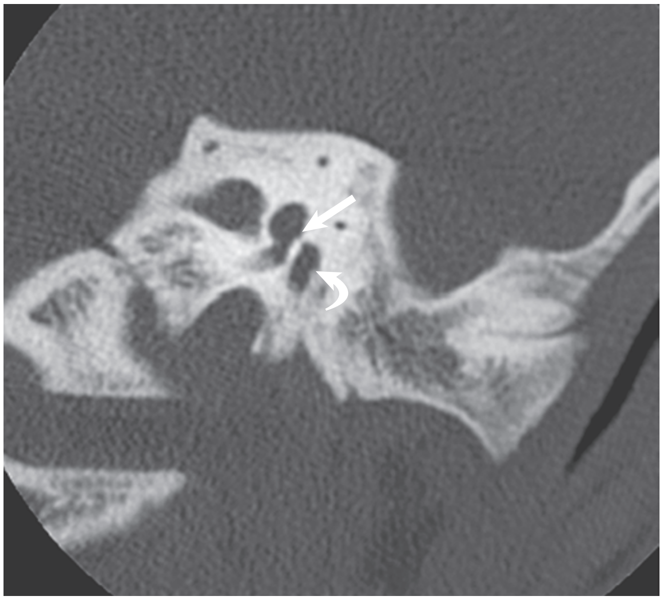

**Figure 10.2. Bilateral microtia and conductive hearing loss in a 5-year-old.** Coronal high-resolution CT image at the expected level of the oval window demonstrates that the middle ear cavity is markedly hypoplastic and opacified *(curved arrow)*. The oval window is atretic and the facial nerve is not well demonstrated *(straight arrow)*. This patient would be a poor surgical candidate for middle ear reconstructive surgery.

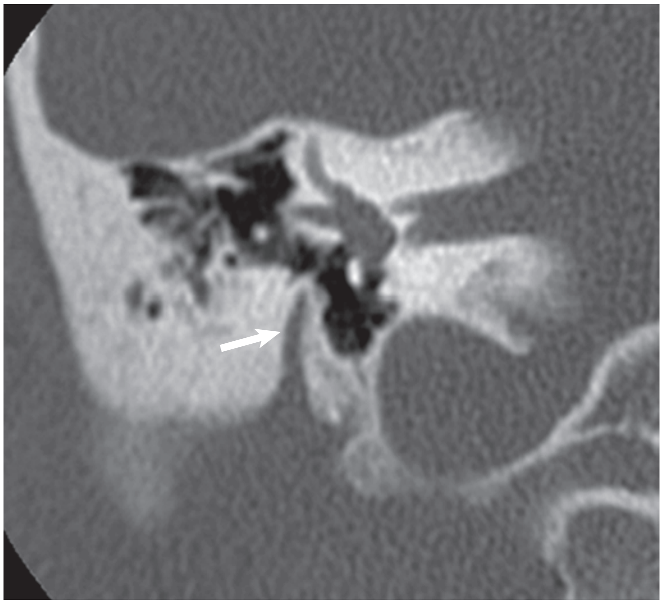

**Figure 10.5. External auditory canal atresia.** Coronal high-resolution CT image shows anterior displacement of the descending facial nerve *(arrow)* with the posterior genu at the level of the oval window.

**BOX 10.1** Preoperative Imaging Evaluation of External Auditory Canal Atresia

- Ossicular chain (presence, position, fixation)
- Middle ear size
- Status of oval and round window
- Position of facial nerve
- Coexisting inner ear malformations

**TABLE 10.1** Syndromes Associated With CHL, Microtia, and EAC Stenosis/Atresia

| Syndrome | Microtia (%) | Gene |
|---|---|---|
| Auriculo-condylar | 100 | *PLCB4*, *GNAI3* |
| Bixler (hypertelorism-microtia-clefting) | 100 | |
| Bosley–Salih–Alorainy | 33 | *HOXA1* |
| Branchio-oculo-facial | 20 severe, >80 mild | *TFAP2A* |
| Branchio-oto-renal/branchio-otic | 30–60/80–90 | *EYA1*, *SIX1*, *SIX5* |
| CHARGE | 80–100 | *CHD7*, *(SEMA3E)* |
| Fraser | 75–85 | *FRAS1*, *FREM2*, *GRIP1* |
| Kabuki | 80–85 | *MLL2*, *KDM6A* |
| Klippel–Feil | 60 | *GDF6* |
| Labyrinthine aplasia, microtia, and microdontia (congenital deafness, inner ear agenesis, microtia, microdontia) | 100 | *FGF3* [a] |
| Lacrimo-auriculo-dento-digital | 70–80 | *FGFR2*, *FGFR3*, *FGF10* |
| Mandibulofacial dysostosis (MFD) | 100 | *HOXD* |
| MFD with microcephaly (MFD Guion–Almeida type) | 98 | *EFTUD2* |
| Meier–Gorlin (Ear-patella-short stature) | 97–100 | *ORC1*, *ORC4*, *ORC6*, *CDT1*, *CDC6* |
| Microtia, hearing impairment, and cleft palate | 100 | *HOXA2* |
| Miller | 100 | *DHODH* |
| Nager | 80 | *SF3B4* |
| Oculo-auricular | 100 | *HMX1* |
| Pallister–Hall | 90 | *GLI3* |
| Townes–Brocks | 88 | *SALL1* |
| Treacher Collins | 60–80 | *TCOF1*, *POL1RC*, *POL1RD* |
| Wildervanck (Cervico-oculo-acoustic) | 25–50 | *FGF13* |

*From Bartel-Friedrich S. Congenital auricular malformations: Description of anomalies and syndromes.* Facial Plast Surg. *2015;31:567–580.*

Round window atresia is not associated with malposition of the facial nerve or ossicular abnormalities, but malposition has been reported in association with oval window atresia.[20,21] A normal EAC is present in isolated atresia of the oval window. The absent oval window often is associated with malposition of the tympanic segment of the facial nerve into or inferior to the atretic oval window. The stapes is malformed and oriented toward the tympanic facial nerve rather than the oval window. The long and lenticular portions of the incus are abnormal. Anomalous development of the second branchial arch is likely the cause, with the facial nerve, incus, and a portion of the stapes arising from this arch[22,23] (Fig. 10.9).

The CHARGE association usually presents with mixed hearing loss and has typical imaging features; oval window atresia is present in nearly all cases (e-Fig. 10.10). Anomalies of the incus and stapes are found along with fixation of the malleus to the anterior tympanic wall. The inner ear is malformed in all cases, and the cochlea is hypoplastic. Vestibular findings include a small vestibule and absent semicircular canals. The facial nerve often is difficult to identify in these patients and may be small and malpositioned.[24,25] A hypoplastic clivus and absent olfactory bulbs are additional findings that may be seen with MRI, which is recommended as these patients commonly have cochlear nerve deficiency.[26,27]

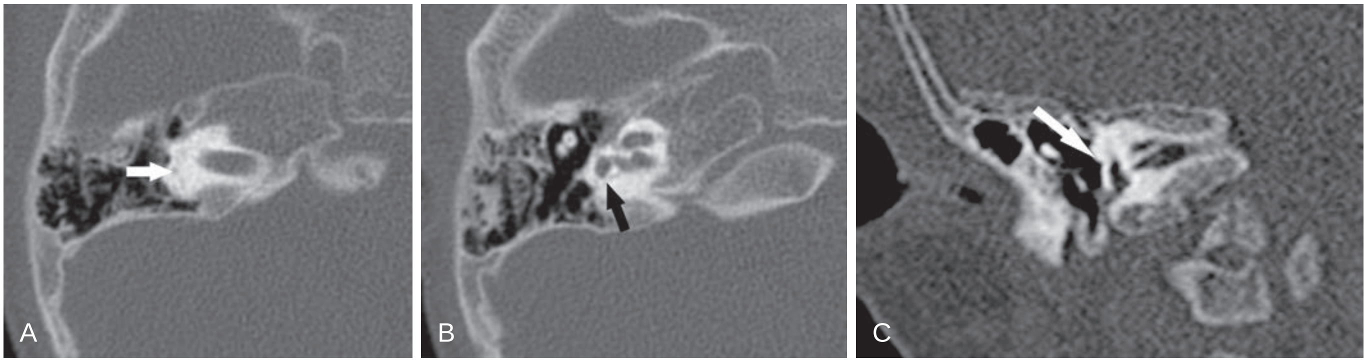

**e-Figure 10.10. A 9-year-old with CHARGE syndrome and oval window atresia.** A and B, Axial high-resolution computed tomography (CT) images demonstrate a very hypoplastic vestibule and absent semicircular canals *(arrows)*. C, A coronal CT image shows absence of the oval window *(arrow)*.

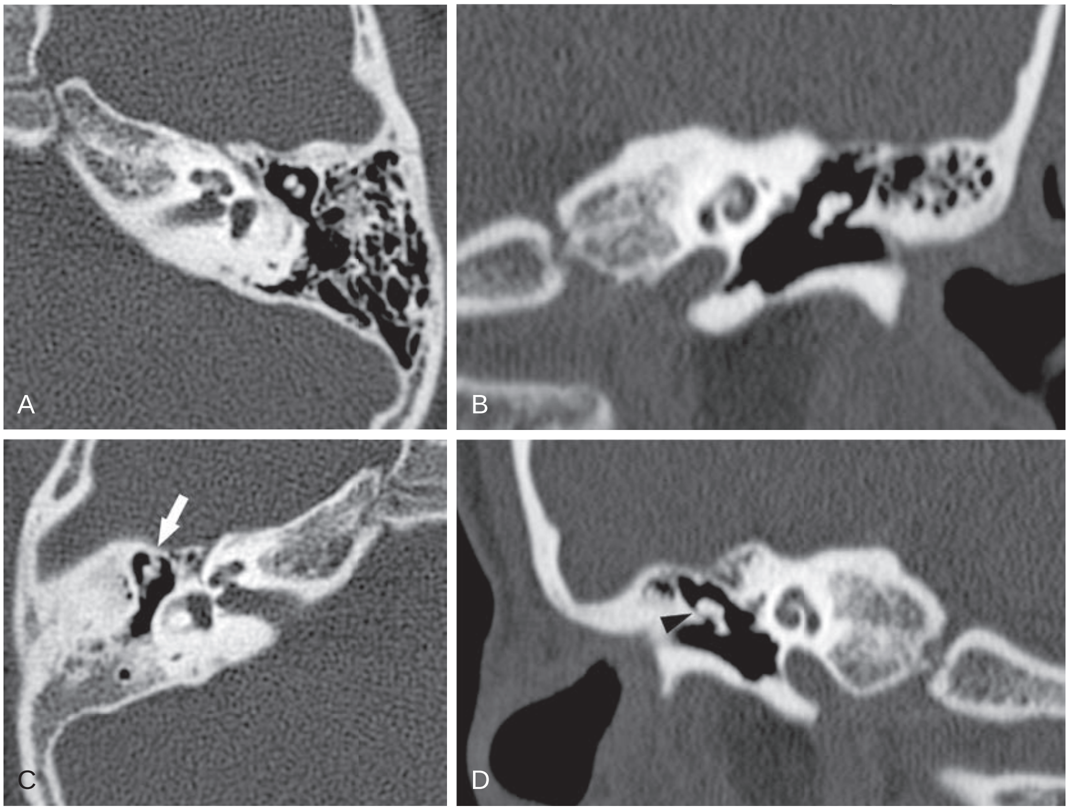

**Figure 10.8. A 10-year-old boy with right-sided conductive hearing loss.** A and B, Axial and coronal high-resolution computed tomography through the normal left middle ear. C and D, Corresponding axial and coronal computed tomography images of the right middle ear shows incomplete separation of the malleolar head from the tegmen *(arrow)* and narrowing of Prussak space *(arrowhead)*. Ossicular fixation was confirmed surgically.

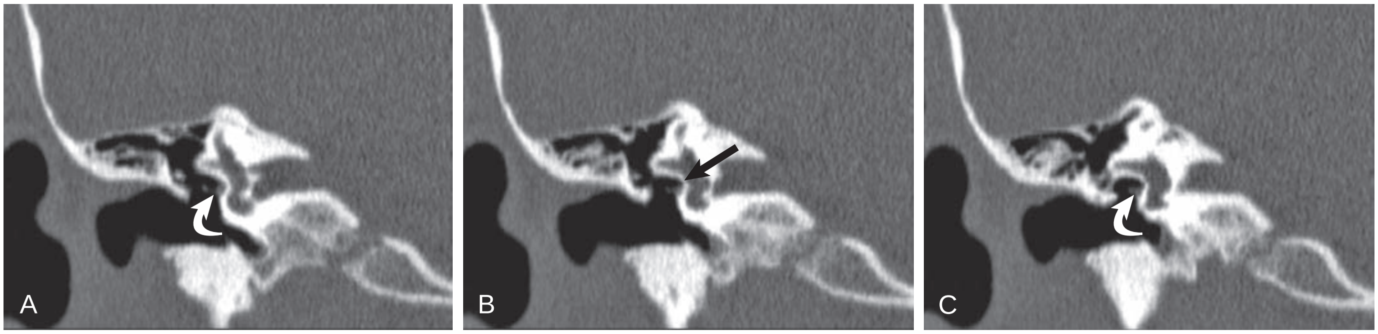

**Figure 10.9. Oval window atresia.** Seven-year-old with mixed hearing loss and a 60-dB threshold. (A–C) Coronal high-resolution CT images from anterior to posterior. The oval window is atretic *(arrow),* with displacement of the facial nerve within and slightly below the structure *(curved arrows)*. The stapes was not visualized, and the lenticular process of the incus appears adherent to the displaced facial nerve.

***Treatment.*** Ossicular chain reconstruction is the mainstay of treatment. Accurate preoperative assessment is essential to plan the appropriate procedure. The status of the oval window is important because atresia imparts a poor surgical prognosis. Determining the facial nerve position is essential.

## INNER EAR ANOMALIES

***Clinical Presentation and Etiologies.*** Study of the genetic defects associated with congenital SNHL is increasing. Nonsyndromic congenital SNHL is not associated with additional medical anomalies and constitutes 70% of cases. Genetic mutations found in persons with nonsyndromic congenital hearing loss are most commonly autosomal recessive, with approximately 50% of nonsyndromic recessive SNHL caused by a mutation in the *GJB2* gene.[28] In this subset of patients with *GJB2* mutation, CT usually demonstrates no or subtle abnormalities with no patient having an enlarged vestibular aqueduct in a recent series.[29]

Children with enlarged endolymphatic ducts have mutations of the *SLC26A4 (PDS)* gene in up to 82% of the hereditary cases and 30% of the sporadic cases.[30] Auditory neuropathy/dyssynchrony may be associated with mutations in the *OTOF* gene, as well as associated brain anomalies. These patients typically have a poor response to hearing aids and may benefit from earlier cochlear implantation.[31,32] The future classification of congenital hearing loss is likely to be based on a combined genetic and morphologic evaluation.

Syndromic congenital SNHL accounts for 30% of cases, with Pendred (enlarged vestibular aqueduct, thyroid dysfunction), Usher, Waardenburg, and branchio-oto-renal syndromes representing a large percentage of the associated syndromes. Characteristic imaging findings may suggest the diagnosis in some patients[28] (Table 10.2) (e-Fig. 10.11). A wide spectrum of syndromes is associated with congenital anomalies of the ear, which include inner ear malformations.[9,33]

Congenital SNHL can be difficult to diagnose clinically in sporadic cases, and perinatal insults can be responsible. Congenital cytomegalovirus infection, hypoxia, ototoxic drugs, kernicterus, and, rarely, tumors should be considered and may be suggested by MRI[34] (Fig. 10.12).

***Imaging.*** Inner ear imaging evaluation for congenital SNHL may be accomplished with high-resolution CT and/or high resolution fluid sensitive MRI. Cochlear and vestibular anomalies, intracranial abnormalities, and deficiency of the cochlear nerve often are found in children with congenital SNHL.[35] MRI is preferred because it provides improved evaluation of the membranous labyrinth and endolymphatic sac, and direct visualization of the cochlear nerve; it also permits a better evaluation of intracranial structures compared with CT.

The wide spectrum of congenital inner ear anomalies previously were all grouped together as "Mondini dysplasia." These anomalies were reclassified into five types, based on the stage of arrested development and appearance of the cochlea.[36] More recently, a revised classification by Sennaroglu has been proposed to better describe the anomalies of the cochlea found in children with SNHL. The sequence of anomalies corresponds to the timing of the potential insult to the developing inner ear, with the more severe anomalies occurring earlier in gestation[37]:

1. Complete labyrinthine aplasia (Michel malformation): All labyrinthine structures are absent (Fig. 10.13).
2. Cochlear aplasia: The cochlea is completely absent and the cochlear promontory is absent on coronal high resolution CT. A normal or malformed vestibule and semicircular canals may be present (e-Fig. 10.14).
3. Common cavity: A single cystic cavity represents the cochlea and vestibule without further differentiation (e-Fig. 10.15). Formed semicircular canals may be present.
4. Incomplete partition type I: The modiolus and cribriform area are absent, resulting in a cystic appearance. The vestibule is abnormally enlarged and cystic but remains a separate structure.
5. Cochlear hypoplasia: The cochlea shows further differentiation with the presence of a small cochlea, with a height less than 4 mm and fewer than two and a half turns (e-Fig. 10.16). A spectrum of severity is present, ranging from a

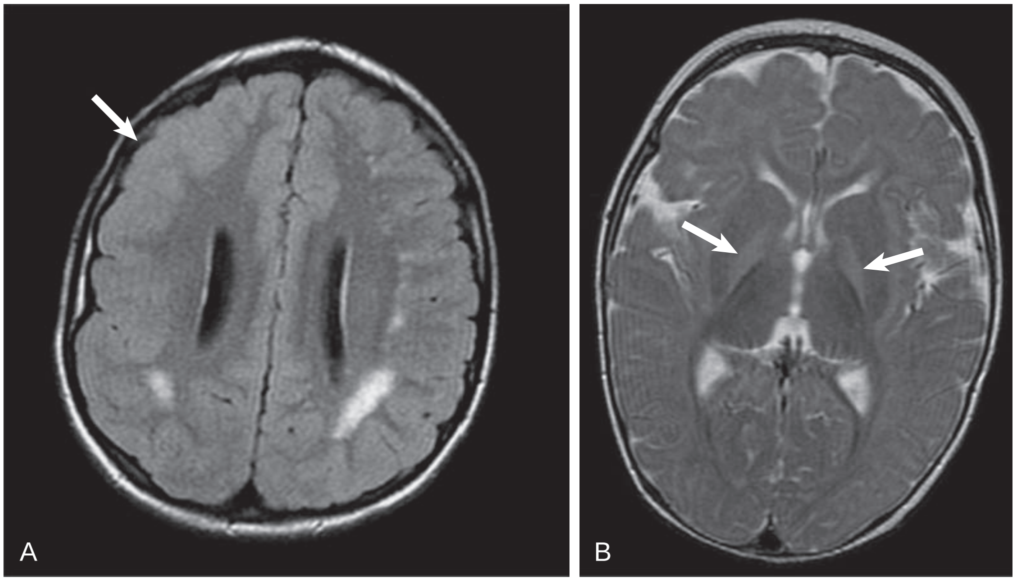

**Figure 10.12. Congenital sensorineural hearing loss.** (A) Axial fluid attenuated inversion recovery MR image shows abnormal increased signal within the supratentorial white matter. Cortical dysplasia is present within the right frontal region *(arrow)*. The findings are consistent with congenital cytomegalovirus infection. (B) Axial T2-weighted MR image through the basal ganglia in a different child with sensorineural hearing loss and a history of prematurity shows an increased T2-weighted signal in the globus pallidus bilaterally *(arrows),* consistent with kernicterus.

**TABLE 10.2** Syndromes Associated With and Characteristic of Inner Cochlear Anomalies

| Syndrome | Cochlea | Other Findings | Gene |
|---|---|---|---|
| Branchio-oto-renal/branchio-otic | Hypoplastic apical turn with "unwound" appearance. | Facial nerve canal medial to cochlea, funnel IAC, patulous Eustachian tube | *EYA1*, *SIX1*, *SIX5* |
| X-linked mixed hearing loss (incomplete partition type III) | Incomplete partition type III. "Corkscrew" appearance of cochlea, absent modiolus | Enlarged facial nerve canal and IAC, associated with gusher | *POU3F4* |
| Pendred syndrome | Incomplete partition type II. "Baseball cap" cochlea with absent lateral notch. Deficient modiolus | Dilated endolymphatic sac/vestibular aqueduct. Dilated vestible | SLC26A4 (PDS) |

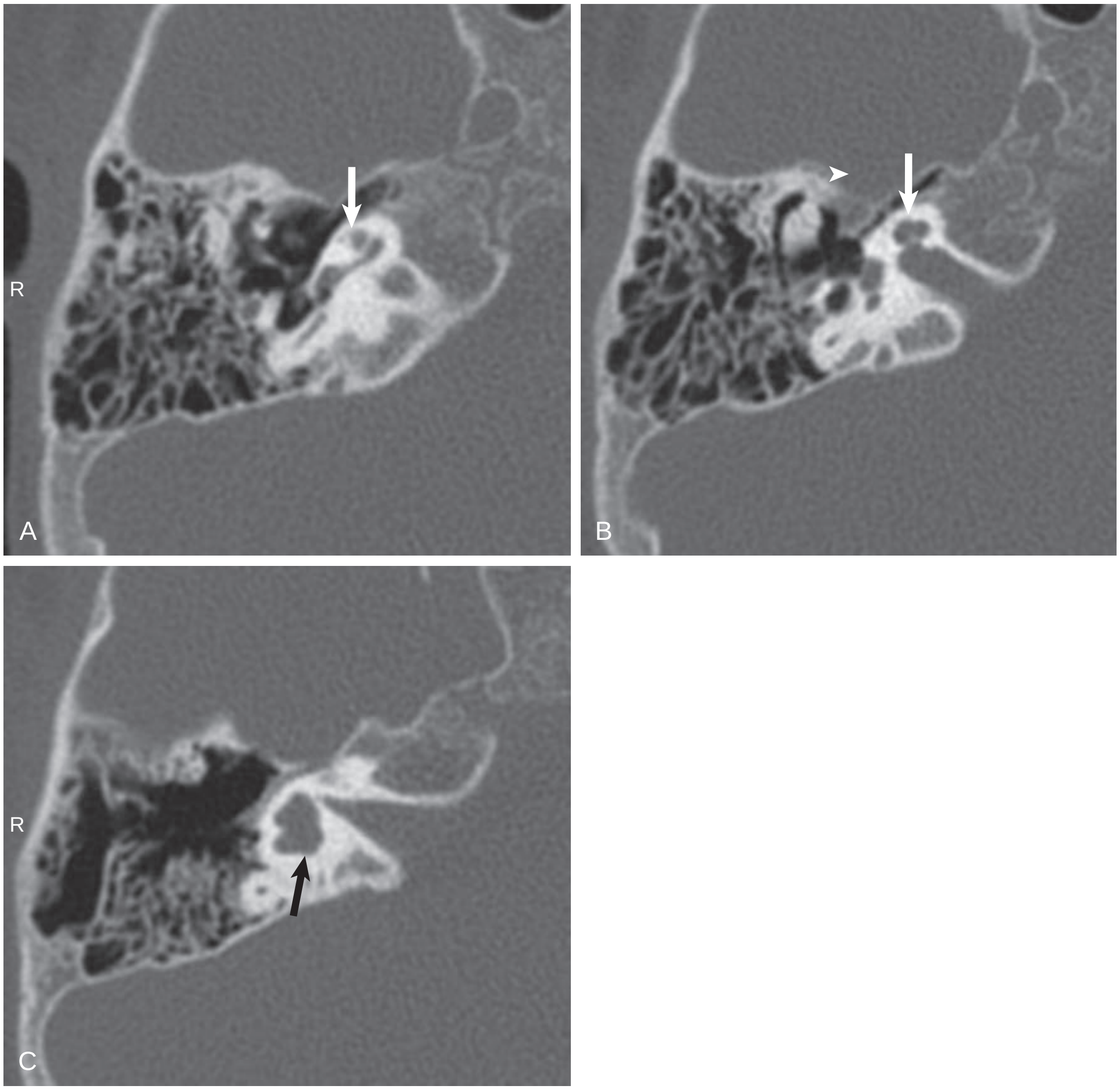

**e-Figure 10.11. Pre-auricular pits and hearing loss in a 5-year-old.** (A–C) Axial high-resolution CT images from inferior to superior. (A and B) There is an "unwound" cochlea with hypoplastic apical and middle turns *(arrows)*. The head of the malleus is also fixed to the anterior superior wall of the middle ear *(arrowhead)*. (C) A dysmorphic vestibule is present *(arrow)*.

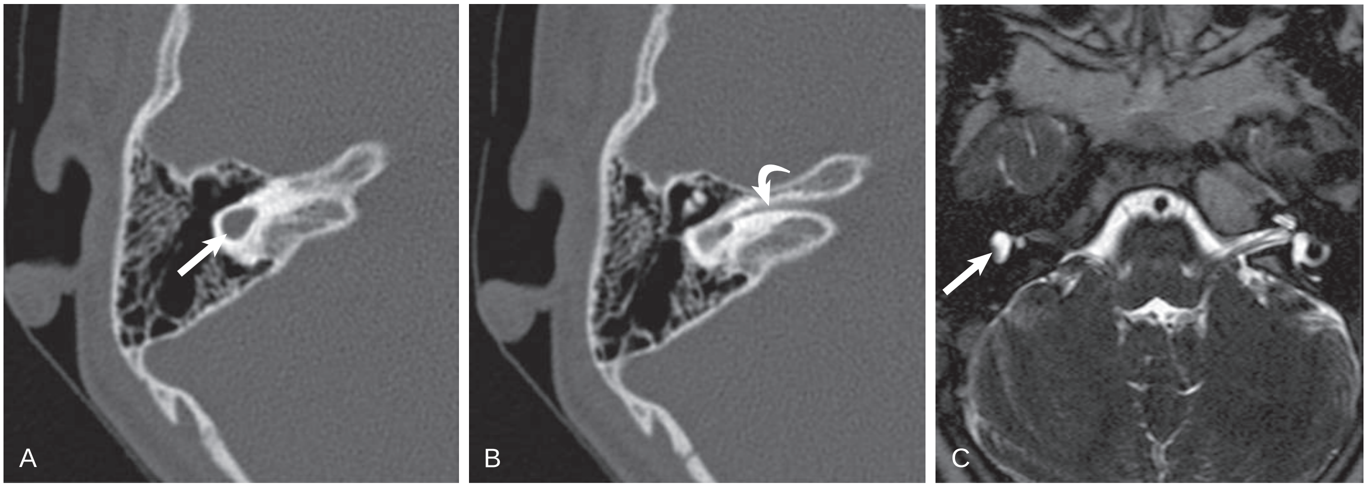

**e-Figure 10.14. Cochlear aplasia.** (A and B) Axial high-resolution CT images in a 6-year-old with profound bilateral SNHL show a single fluid cavity *(straight arrow),* which represents a dysplastic vestibule. The cochlea is absent and the internal auditory canal is small *(curved arrow)*. (C) Axial three-dimensional T2-weighted MR image of a different patient demonstrates cochlear aplasia *(arrow)* on the right with a hypoplastic internal auditory canal and absence of the cochlear nerve *(not shown)*.

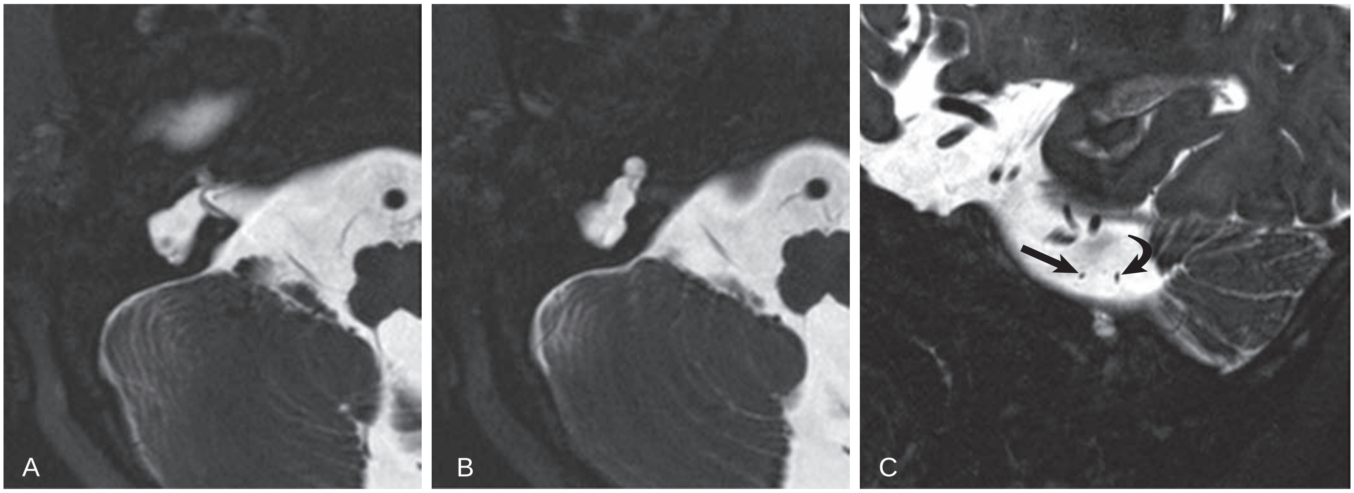

**e-Figure 10.15. Common cavity malformation.** (A and B) Axial 3D T2-weighted MR images in a 1-year-old with profound hearing loss show a large fluid-filled cavity replacing the cochlea and vestibule. The semicircular canals are absent. (C) Oblique sagittal 3D T2-weighted MR image through the cerebellopontine angle demonstrates a facial nerve *(straight arrow)* and a diminutive vestibulocochlear nerve *(curved arrow)*. The cochlear nerve was absent in the more lateral internal auditory canal *(not shown)*.

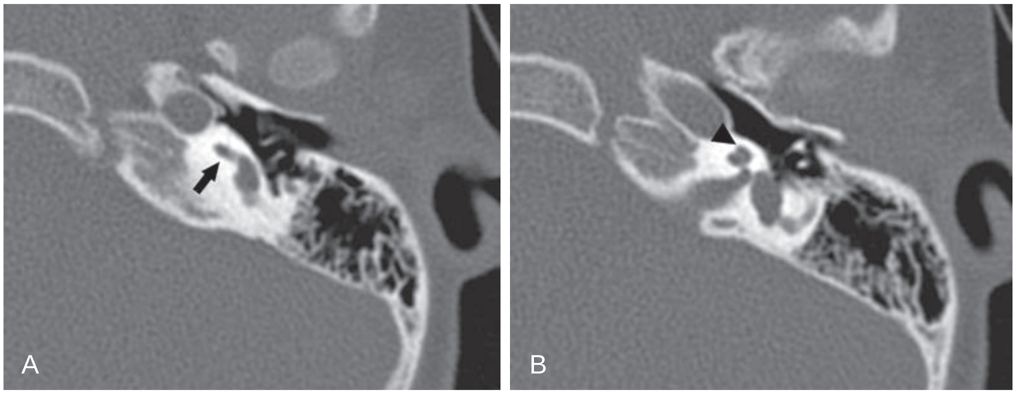

**e-Figure 10.16. A 4-year-old with bilateral sensorineural hearing loss.** A and B, Axial high-resolution computed tomography images show a hypoplastic cochlea with a small basal turn *(arrow)* and rudimentary apical turns *(arrowhead)*.

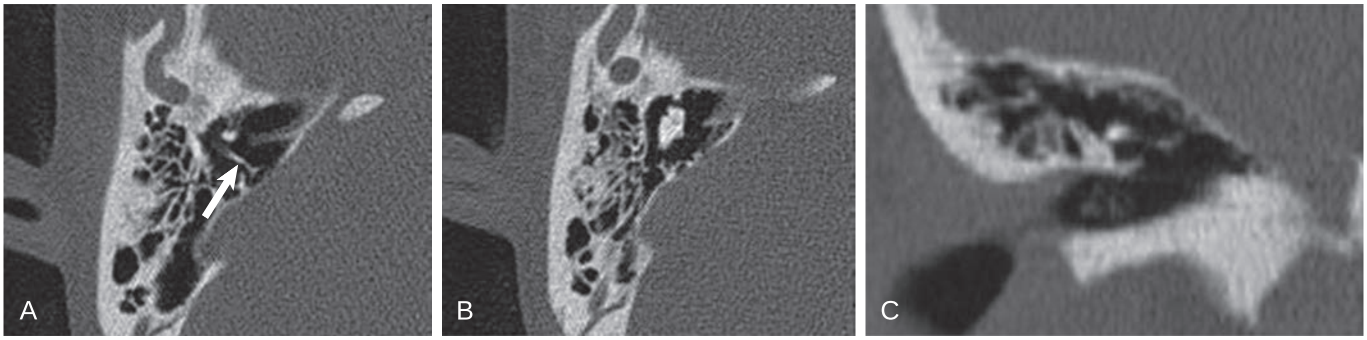

**Figure 10.13. Complete labyrinthine aplasia (Michel malformation).** (A and B) Axial high-resolution CT images and (C) coronal reformatted image of a child with profound hearing loss show complete absence of the membranous labyrinth. Imaging findings are consistent with an early embryologic insult and resultant aplasia (Michel deformity). The ossicles are abnormally oriented *(arrow)*. *(Images courtesy of Nafi Aygun, MD, Johns Hopkins, Baltimore, MD.)*

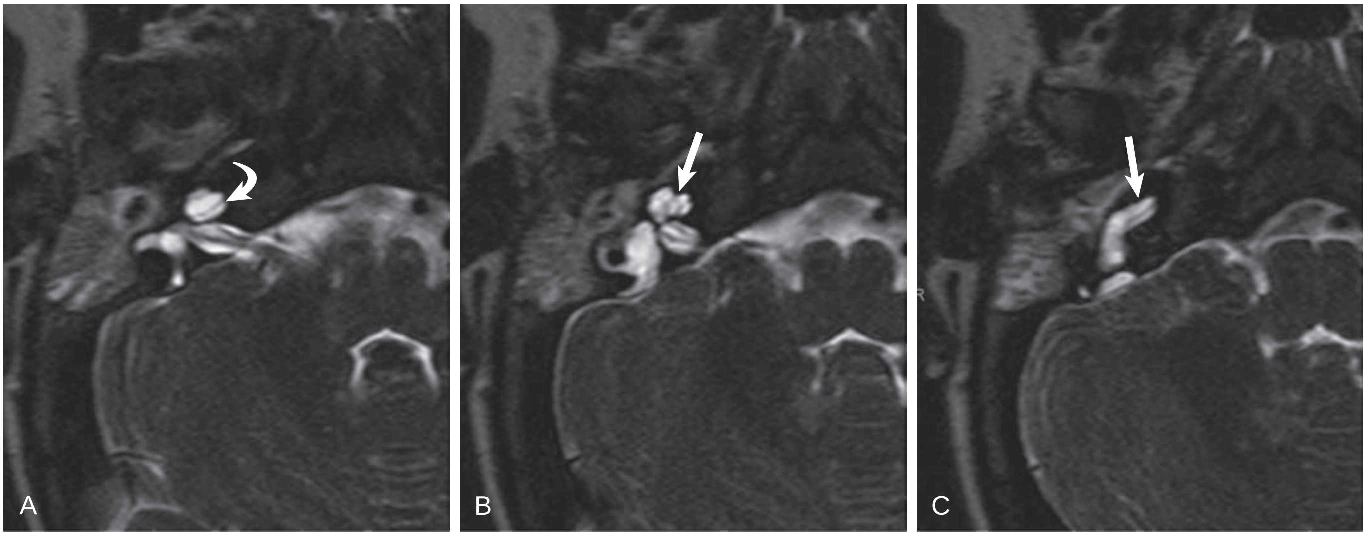

**Figure 10.17. Incomplete partition type II (classic Mondini deformity).** (A–C) Axial 3D T2-weighted MR images in a 9-month-old with bilateral SNHL show a mildly dysplastic basal turn with coalescent apical and middle turns *(straight arrows)*. The intrascalar septum is deficient and scalar asymmetry is present *(curved arrow)*. A dilated endolymphatic duct and enlarged vestibule also are noted. The constellation of findings is typical for incomplete partition type II (Mondini deformity).

small cochlear bud to a well-formed basal turn and small apical and middle turns.

6. Incomplete partition type II (classic Mondini deformity): A normal basal turn of the cochlea is present. The middle and apical structures become a single cystic structure with an incomplete or absent interscalar septum and scalar asymmetry. A dilated vestibule and enlarged vestibular aqueduct/endolymphatic duct often are associated (Fig. 10.17). Numerous syndromes may have an associated Mondini defect, including DiGeorge, Waardenburg, Alagille, Klippel–Feil, Wildervanck, and Pendred syndromes, and chromosomal trisomies.[38]
7. Incomplete partition type III (X-linked mixed hearing loss): There is deficient bone between basal turn of cochlea and internal auditory canal (IAC) as well as the modiolus (corkscrew appearance). The labyrinthine facial, vestibular, and singular canals are enlarged. The patient is at risk for a cerebrospinal fluid (CSF) gusher during surgery (e-Fig. 10.18).[39] A mutation involving *POU3F4* has been suggested as a cause.[40]

It has been suggested that cochlear hypoplasia may be further subcategorized into cochlear bud, basal turn cochlea, and hypoplastic cochlea.[41] MRI has allowed for improved visualization and categorization of the milder forms of cochlear malformation. Modiolar deficiency often is found in children undergoing evaluation for SNHL, with the cochlear modiolus appearing flattened and with a diminished number of bony projections extending into the cochlea (e-Fig. 10.19). In normal ears, the scala vestibuli (anterior) is approximately equal in size to the scala tympani (posterior). Scalar asymmetry is present when the anterior chamber is larger and can be present in children with SNHL (see Fig. 10.17).[42]

Anomalies of the vestibule usually are associated with other inner ear abnormalities and are seldom isolated. The semicircular canals may be partially or completely assimilated into the vestibule. The diameter of the vestibule should normally be equal to the diameter of the bony plug between the vestibule and lateral semicircular canal.[42] The bony island should be 3 mm or larger[43] (e-Fig. 10.20). Although the abnormal vestibule is usually dilated, it can be small. If the vestibule is small, the oval window is frequently stenotic or atretic, and the facial nerve is often malpositioned.

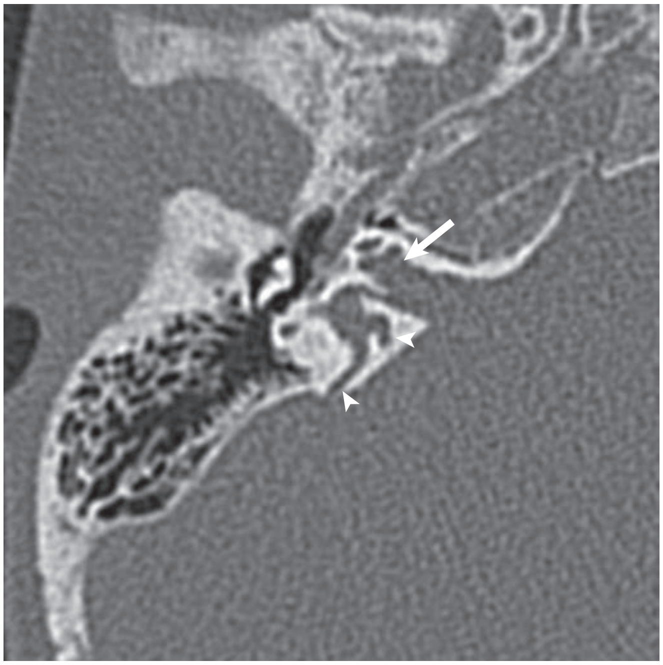

**e-Figure 10.18. Incomplete partition type III (X-linked mixed hearing loss).** Axial high-resolution CT image in an 11-year-old male with bilateral mixed hearing loss demonstrates an absent modiolus and widened cochlear aperture *(arrow)*. The singular canal and malpositioned vestibular aqueduct are enlarged *(arrowheads)*.

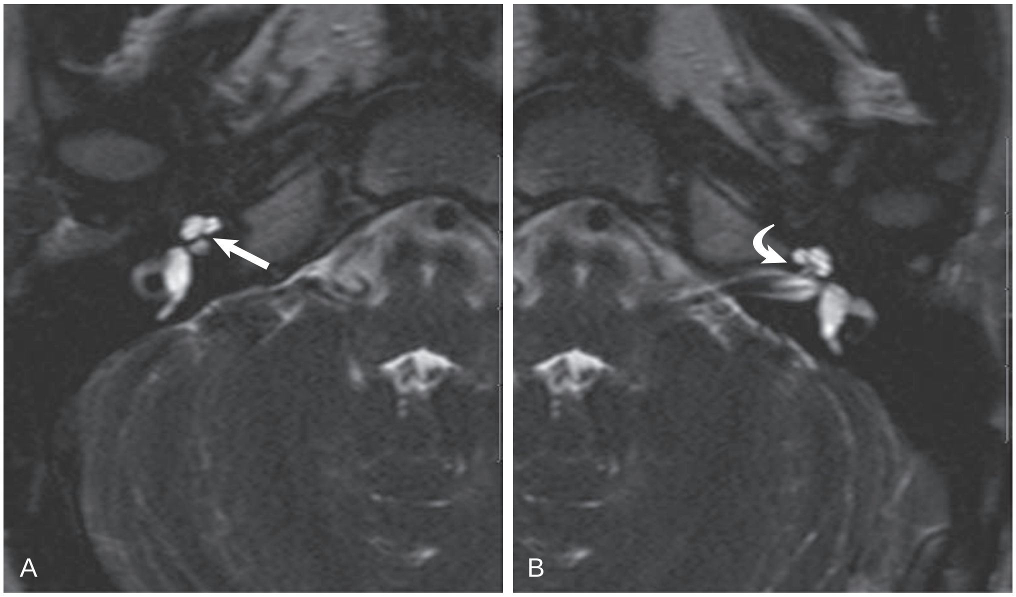

**e-Figure 10.19. Profound right sensorineural hearing loss in a 6-year-old.** Axial 3D T2-weighted MR images show a flattened deficient modiolus *(arrow)* on the right (A) and the normal left for comparison (B, *curved arrow*). The internal auditory canal was small on the right with absence of the right cochlear nerve *(not shown)*.

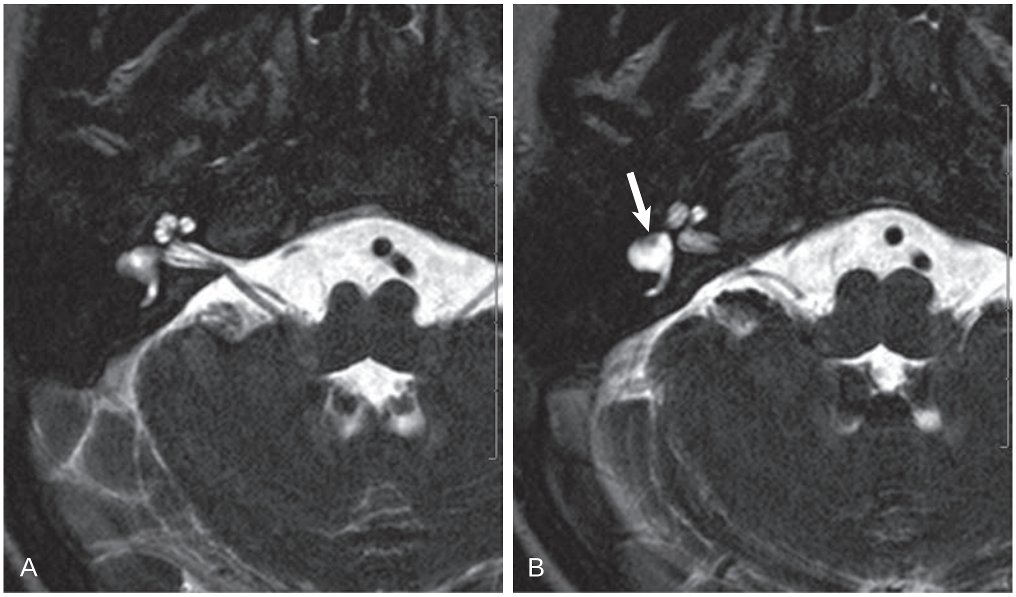

**e-Figure 10.20. Bilateral sensorineural hearing loss in a 3-year-old.** (A and B) Axial 3D T2-weighted MR images show incorporation of the lateral semicircular canal into the vestibule with absence of the normal bony plug or island *(arrow)*. The cochlea is normal.

This constellation of findings are found in the CHARGE association, along with absent semicircular canals.[24] Absent semicircular canals with a large or deformed vestibule can be seen in Waardenburg syndrome associated with *SOX10* mutations. Isolated absence of the posterior semicircular canal is seen in this syndrome and also in Alagille syndrome (e-Fig. 10.21).[44] A small vestibular bone island has been documented in Down syndrome patients along with small IACs and cochlear nerve canals with borderline association of SNHL.[45]

Enlargement of the vestibular aqueduct often is reported as the most common inner ear anomaly to be demonstrated by imaging; however, using 3D fluid-sensitive MRI sequences, milder forms of cochlear dysplasia may be more common.[35] An enlarged vestibular aqueduct is associated with progressive SNHL, complete hearing loss after trauma, as well as CHL due to a third window phenomenon.[46] The aqueduct is enlarged when the midaperture diameter is 1.0 mm or greater and is best demonstrated on axial CT.[43] CT, as compared with MRI, may have a greater yield for enlarged vestibular aqueduct.[47] Although, MRI can directly demonstrate a dilated endolymphatic duct as well as the sac. Dilatation of the sac may be seen as an isolated abnormality in children with SNHL. MRI has demonstrated that a large percentage of these cases have associated anomalies of the membranous labyrinth (84%), which include modiolar deficiencies, scalar asymmetry, an enlarged vestibule, and an enlarged lateral semicircular canal[42] (Box 10.2) (e-Fig. 10.22).

Embryologically, the endolymphatic duct and sac form at the same time as partitioning of the cochlea occurs, which may explain the common association of cochlear dysplasia. Most cases of large vestibular aqueduct are sporadic, but it also has been reported in persons with Pendred syndrome, distal renal tubular acidosis, CHARGE association, and branchio-oto-renal syndrome.[48,49] The presence of heterogeneous signal within the sac on steady-state T2-weighted MR images may correlate with high protein levels, indicating the presence of Pendred syndrome and possibly the development of goiter.[50]

**BOX 10.2** Associations of an Enlarged Endolymphatic Duct

- Modiolar deficiency
- Scalar asymmetry
- An enlarged vestibule and lateral semicircular canal
- Dehiscent semicircular canals
- SLC26A4 (PDS) gene mutation
- Incomplete partition type II (Mondini deformity)

The size and contents of the IAC should be evaluated on MRI in all patients. The IACs are usually symmetric; however, considerable variability is found in shape, size, and orientation. The IAC may be absent or hypoplastic with severe IAC narrowing associated with deficiency or absence of the cochlear nerve. A duplicated IAC represents the facial nerve canal and a hypoplastic IAC with the presence of a deficient or absent cochlear nerve.[51] A duplicated IAC has been reported to be associated with pontine tegmental cap dysplasia and other entities[52] (e-Fig. 10.23).

It is important to note that the size of the IAC correlates with the presence or absence of the cochlear nerve; however, a normal-sized cochlear nerve can be associated with a small IAC, and a deficient or absent cochlear nerve can be seen with a normal IAC.[35] The osseous channel for the cochlear nerve (cochlear aperture) is well demonstrated on CT, with a small or absent channel representing an indirect sign of cochlear nerve deficiency or absence[53] (e-Fig. 10.24). A cutoff value of 1.5 mm has been suggested for the size of the cochlear nerve canal, with a value of equal or lower size suggesting deficiency of the cochlear nerve.[54]

The size and presence of the cochlear nerve is best assessed with direct oblique sagittal MR images through the IAC. The cochlear nerve should be greater or equal in size to the adjacent facial nerve (Fig. 10.25). If the IAC is stenotic and the cochlear nerve is not well seen, the vestibulocochlear nerve complex can be found in the cerebellopontine cistern, with the vestibulocochlear nerve complex normally greater than two times the size of the adjacent facial nerve.[55,56] The IAC may be enlarged in neurofibromatosis type 1 as a result of dural ectasia or in association of translabyrinthine fistulae in children who have severe malformations of the inner ear.[57] PHACES syndrome (*P*osterior fossa malformations, *H*emangiomas, *A*rterial anomalies, *C*ardiac defects, *E*ye abnormalities, *S*ternal cleft) may be associated with a large IAC, possibly relating to an involuted infantile hemangioma.[58]

***Treatment.*** Hearing aids and cochlear implantation are the most common interventions in a child with SNHL. CT and MRI are

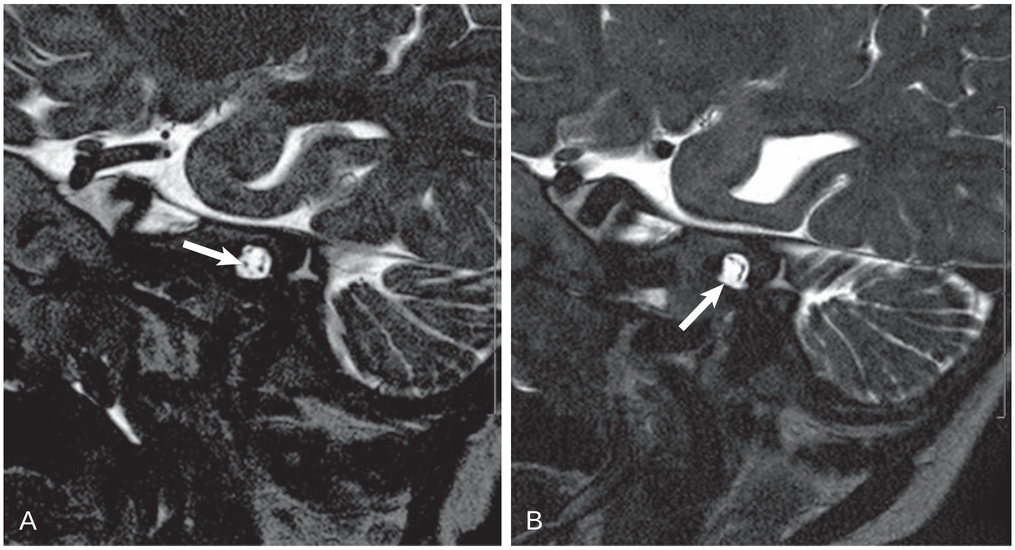

**Figure 10.25. Cochlear nerve aplasia.** One-year-old with profound right sensorineural hearing loss. (A) Left and (B) right oblique sagittal 3D T2-weighted MR images show absence of the right cochlear nerve and a normal left cochlear nerve *(arrows)*.

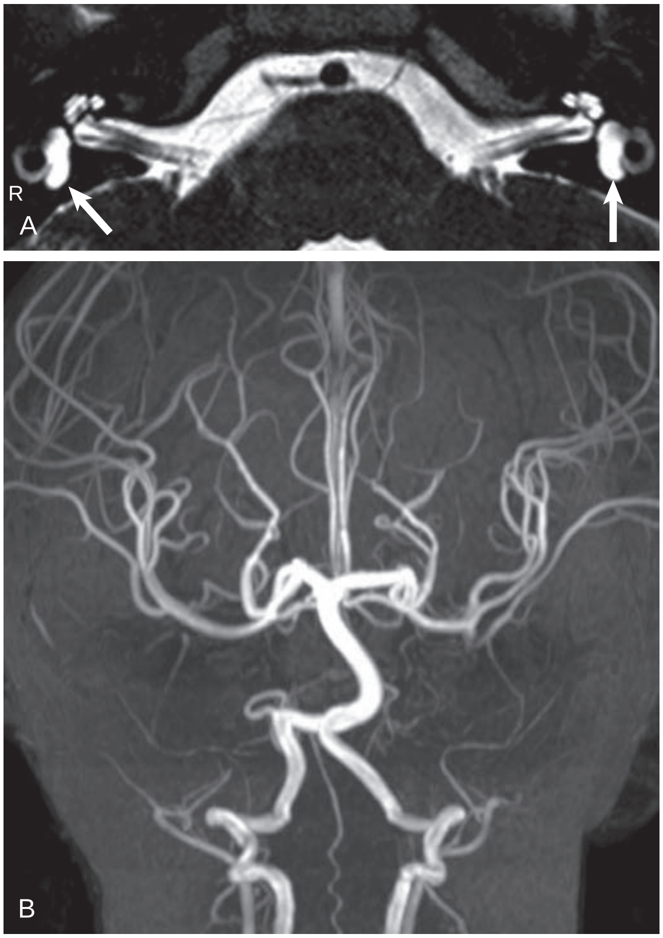

**e-Figure 10.21. Chronic cholestasis and Alagille syndrome in a 4-year-old.** (A) Axial 3D T2-weighted MR image show absent posterior semicircular canals with a rudimentary pouch projecting from the posterior vestibule *(arrows)*. (B) MR arteriogram demonstrates congenital absence of the internal carotid arteries with large vertebral and basilar arteries present.

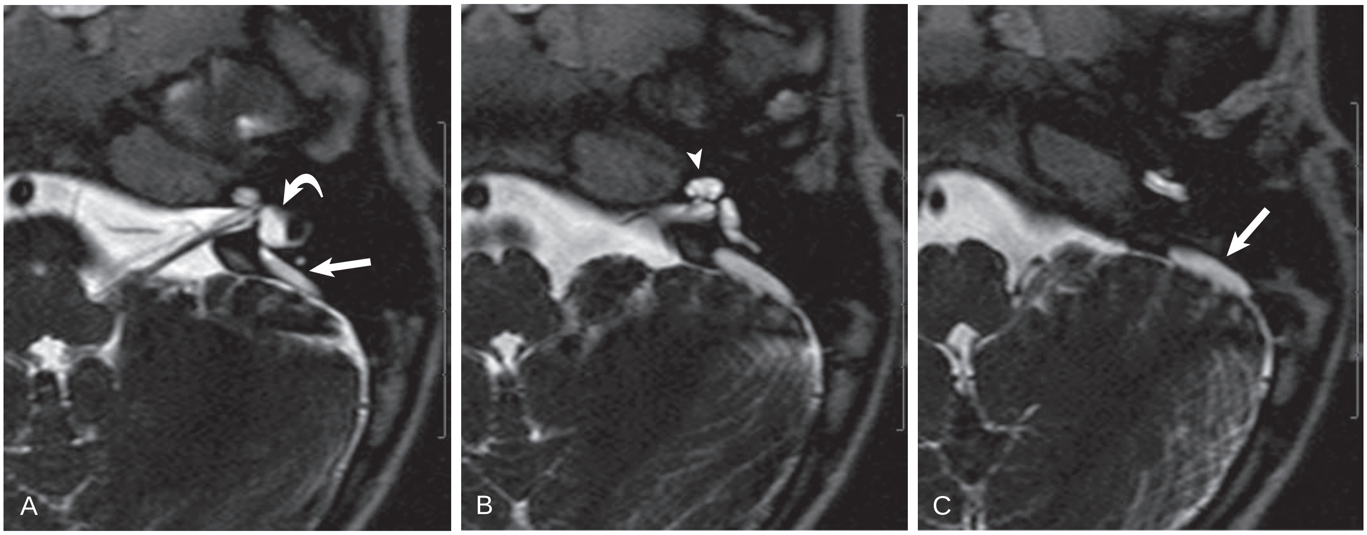

**e-Figure 10.22. Progressive bilateral sensorineural hearing loss in a 5-year-old.** (A–C) Axial 3D T2-weighted MR images demonstrate an enlarged endolymphatic duct and sac *(straight arrows)*. The cochlea is malformed (incomplete partition type II) *(arrowhead)* with a deficient modiolus. The vestibule is abnormally enlarged as well *(curved arrow)*.

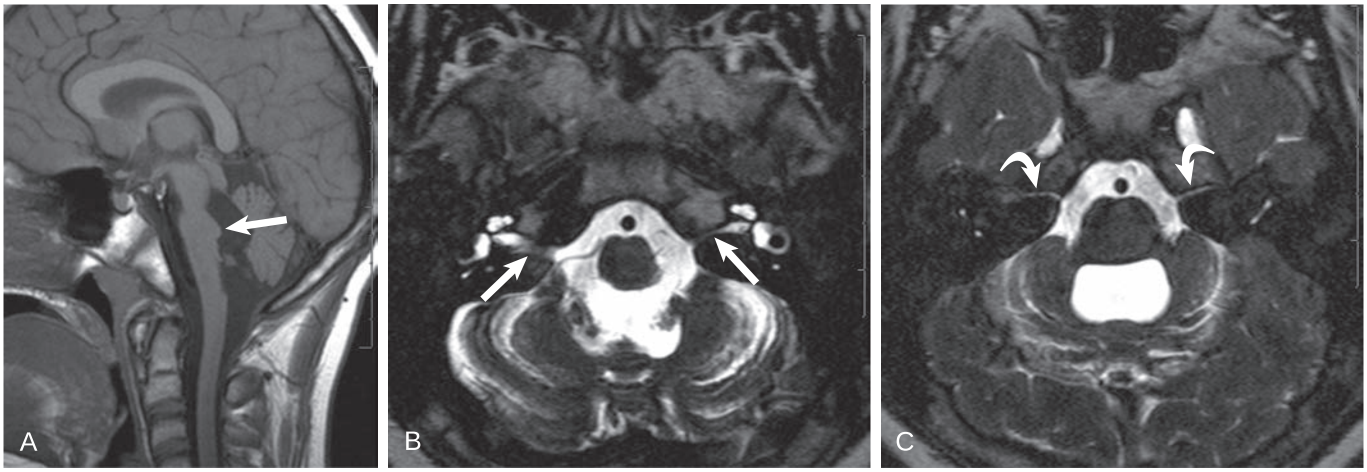

**e-Figure 10.23. Pontine tegmental cap dysplasia in a 14-year-old.** Bilateral sensorineural hearing loss and corneal ulcers (fifth cranial nerve) were present clinically. (A) Midline sagittal T1-weighted MR image shows a markedly dysmorphic brainstem with a typical dorsal protrusion *(arrow)*. (B and C) Axial 3D T2-weighted MR images demonstrate small native internal auditory canals *(straight arrows)* and accessory canals for both facial nerves *(curved arrows)*.

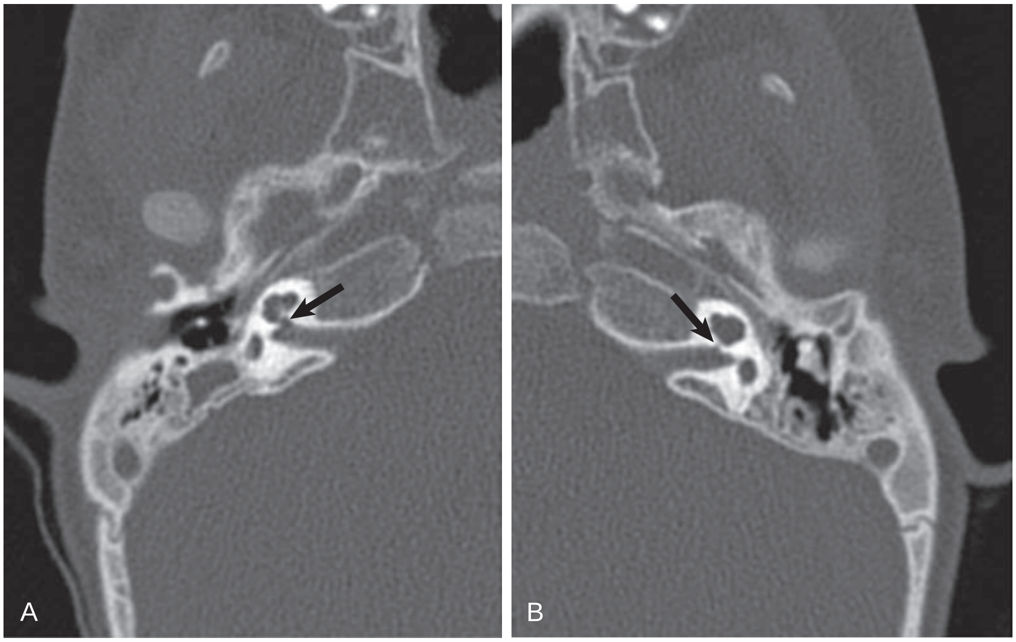

**e-Figure 10.24. Bilateral sensorineural hearing loss in a 2-year-old.** (A and B) Axial high-resolution CT images show a normal cochlear nerve canal on the right and absence of the cochlear nerve on the left *(arrows)*. MRI demonstrated a normal nerve on the right and an absent nerve on the left *(not shown)*. The internal auditory canals are symmetric in size. The left cochlea is malformed (B) with only a cystic fluid collection present (incomplete partition type I).

able to classify the severity of inner ear malformations encountered. MRI is better able to evaluate the intracranial contents and directly visualize the cochlear nerve, which allows the otolaryngologist to better assess the potential success of implantation and potentially directs the side to be implanted. After implantation, CT becomes the mainstay in the evaluation of complications and implant position.

## CEREBROSPINAL FLUID FISTULA, GUSHER, AND RECURRENT MENINGITIS

***Clinical Presentation and Etiologies.*** Recurrent meningitis, perilymphatic fistula, or gusher may be caused by anomalies associated with modiolar deficiency and absent lamina cribrosa, which may be found in severe inner ear anomalies, incomplete partition type I, and X-linked mixed hearing loss. There is a resultant abnormal communication between the subarachnoid space and middle ear. Congenital perilymphatic fistula is a cause of unexplained asymmetric SNHL in children, recurrent meningitis, vertigo, as well as a gusher during stapes surgery. The most common site of a fistula is in the region of the stapes footplate, resulting from malformation of the stapes. Fistulas may occur via a dilated cochlear aqueduct or more commonly via a deficient lamina cribrosa.[57]

***Imaging.*** CT findings include deficient modiolus, lamina cribrosa, and fluid or soft tissue protruding though the oval window. This bulging oval window is well demonstrated on MRI (e-Fig. 10.26). Less commonly, the labyrinthine facial nerve canal may be enlarged, and the IAC has an undulating contour.[59] This anatomy may result in perilymphatic fistula and a gusher during stapedial footplate manipulation or cochlear implantation.[60]

***Treatment.*** Knowledge of the potential perilymphatic fistula is important preoperatively and can obviate the need for a second surgery. A preemptive packing procedure can prevent the development of a significant leak during manipulation of the oval and or round window.

## VASCULAR ABNORMALITIES

***Clinical Presentation and Etiologies.*** Vascular abnormalities often are encountered in the temporal bone. The anomalies can be asymptomatic or result in CHL and may alter potential surgery. A child with a glomus tumor or hemangioma may present with a vascular, bluish mass within the middle ear cavity (Box 10.3).

***Imaging.*** Arterial: The internal carotid artery (ICA) may be congenitally absent on either one or both sides. The entity can be confirmed by documenting absence of the associated carotid canal on CT.

With an aberrant ICA, the cervical portion of the ICA may regress during embryogenesis and is replaced by an anastomosis of the enlarged inferior tympanic and caroticotympanic arteries. The aberrant ICA enters the tympanic cavity, posterior to the course of the normal ICA, through an enlarged tympanic canaliculus. It joins the horizontal carotid canal through a dehiscence in the carotid plate. This abnormality may be unilateral or bilateral. Clinical presentations include tinnitus, vertigo, hearing loss, and ear pain. An aberrant ICA also can be associated with a persistent stapedial artery (e-Fig. 10.27).

The stapedial artery usually regresses during the third month of gestation. The persistent stapedial artery is a rare anomaly that may be unilateral or bilateral and may occur with or without an aberrant ICA. The anomalous artery originates at the genu of the ICA. The artery courses superiorly over the cochlear promontory and through the crura of the stapes into the tympanic segment of the facial nerve canal. The CT appearance includes enlargement of the tympanic segment of the facial nerve and absence of foramen spinosum[61,62] (Fig. 10.28). It is important to know that the foramen spinosum can be absent in 3% of the normal population.[63]

Venous: Variants of the jugular bulb include agenesis, atresia, stenosis, diverticulum, protrusion, and high location. Agenesis of the jugular bulb is extremely rare. Associated agenesis of the sigmoid bulb may be present, with redirection of flow via transmastoid channels into regional scalp veins. Associated dilated venous collaterals should be described because they may affect potential surgery. Jugular atresia and stenosis may be isolated or associated with other disorders such as achondroplasia, Crouzon syndrome, and CHARGE association. MR or CT venography may be used to assess for venous obstruction in these patients[64] (e-Fig. 10.29).

A high jugular bulb is the most common variant, characterized by elevation of the roof of the jugular bulb above the inferior tympanic ring or floor of the IAC. It usually is unilateral but may be bilateral in up to 12% of cases. It is well demonstrated by CT or jugular venography.

Protrusion of the jugular bulb through a dehiscence of the floor of the middle ear into the hypotympanum is a common vascular anomaly of the temporal bone (e-Fig. 10.30). Clinically, the bluish mass behind the tympanic membrane may be mistaken for a vascular mass in the middle ear. Symptoms include hearing loss, usually CHL due to obstruction of the oval window or contact with the ossicles, pulsatile tinnitus, and headaches. The enhancing soft tissue mass in the middle ear and the bony defect above the jugular bulb in the floor of the hypotympanum are demonstrated on CT.[65]

A jugular diverticulum emanates from a jugular bulb that rises superomedially in the petrous pyramid. In contrast to a protruding bulb, it is more medially and posteriorly located in the petrous bone and does not invade the middle ear. The diagnosis is made only by imaging because it is not visible clinically.

***Treatment.*** These lesion abnormalities need to be recognized and qualify them as "don't touch" lesions, with surgery usually being avoided. The presence of a jugular diverticulum may affect surgery involving the IAC and should be commented on in the imaging report.[47,61]

### **BOX 10.3** Vascular Abnormalities of the Middle Ear

- Agenesis ICA
- Aberrant ICA
- Persistent stapedial artery
- Dehiscent-protruding jugular bulb
- Jugular bulb diverticulum
- Venous agenesis—obstruction

### KEY POINTS

- Facial nerve position in EAC atresia is critical.
- Round window atresia usually is associated with CHL.
- Isolated oval window atresia is a second branchial arch anomaly associated with mixed hearing loss. A malformed incus and stapes often is associated with mixed hearing loss, along with a malpositioned facial nerve.
- Imaging findings in persons with CHARGE association include ossicular fixation, a small vestibule, absent semicircular canals, and oval window atresia.
- The cochlear nerve canal should be greater or equal to 1.5 mm.
- Deficiency of the lamina cribrosa or cochlear modiolus can predispose to recurrent meningitis and a CSF gusher during surgery.

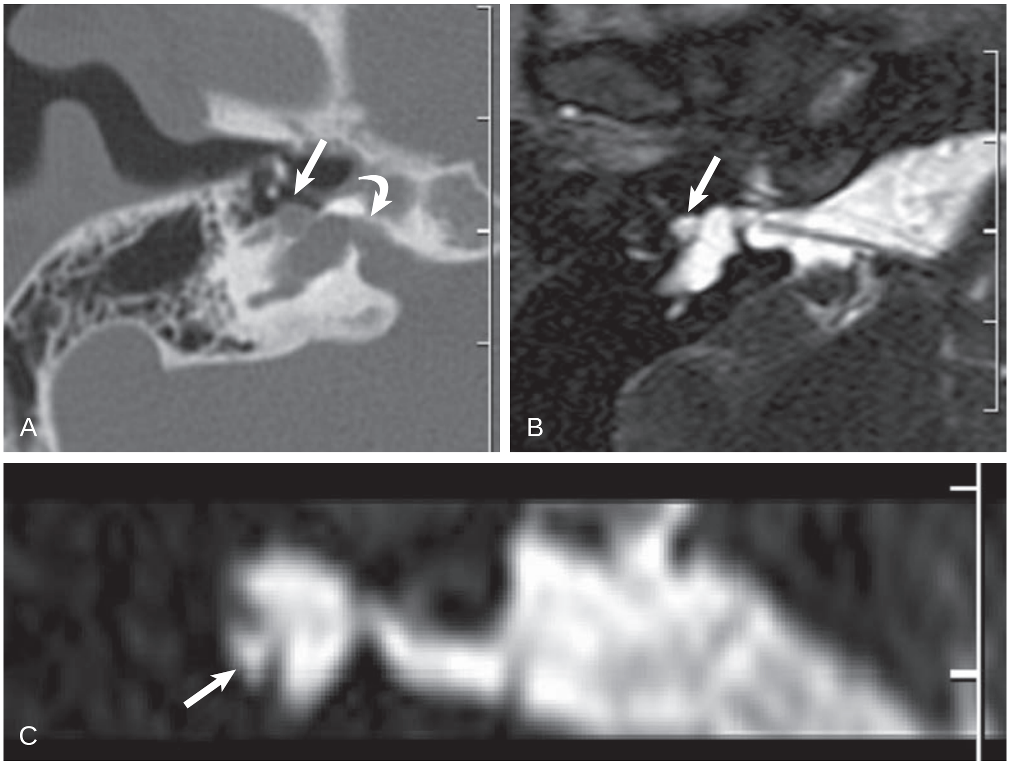

**e-Figure 10.26. Profound hearing loss and recurrent meningitis in an 11-year-old.** (A) Axial CT image shows fluid bulging through the oval window *(straight arrow)* and a deficient lamina cribrosa *(curved arrow)*. (B and C) Axial and coronal reformatted 3D T2-weighted MR images show fluid protruding through the oval window *(arrows)*.

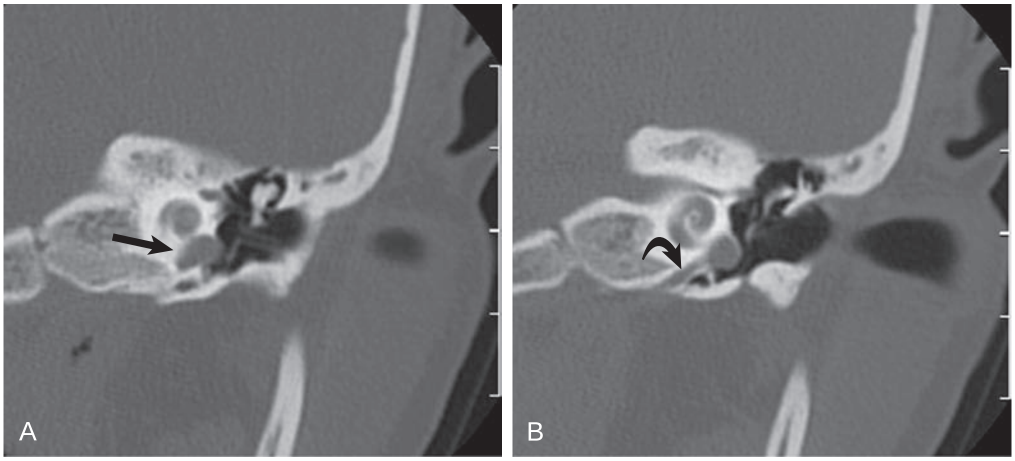

**e-Figure 10.27. Aberrant internal carotid artery.** (A and B) Coronal high-resolution CT images show a vascular structure protruding into the middle ear cavity lateral to the cochlea *(straight arrow)*. The aberrant internal carotid artery enters the temporal bone via the inferior tympanic canaliculus *(curved arrow)*.

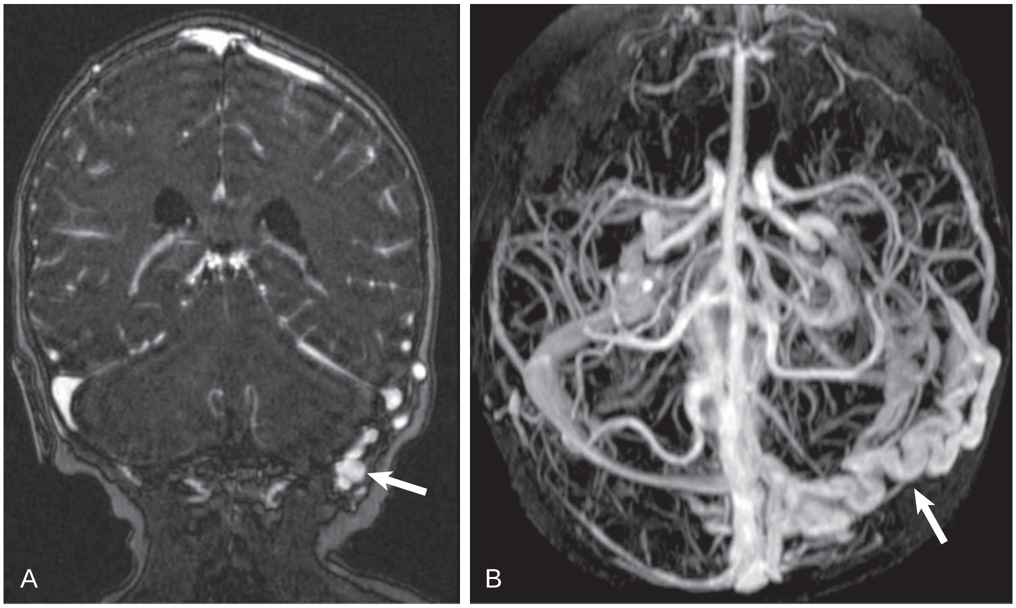

**e-Figure 10.29. Crouzon syndrome and hearing loss.** (A and B) Coronal source and maximum-intensity projection images from a gadolinium-enhanced MR venogram show stenosis of the jugular bulb with extensive extracranial collateral formation *(arrows)*.

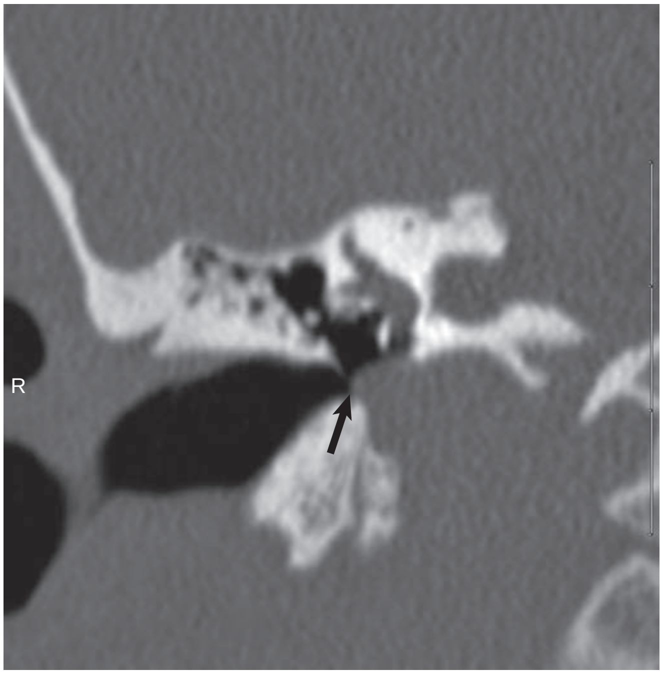

**e-Figure 10.30. High-riding protruding jugular bulb in a child with a clinically suspected middle ear mass.** A coronal reconstructed computed tomography image shows the jugular bulb extending into the middle ear cavity and compromising the round window *(arrow)*.

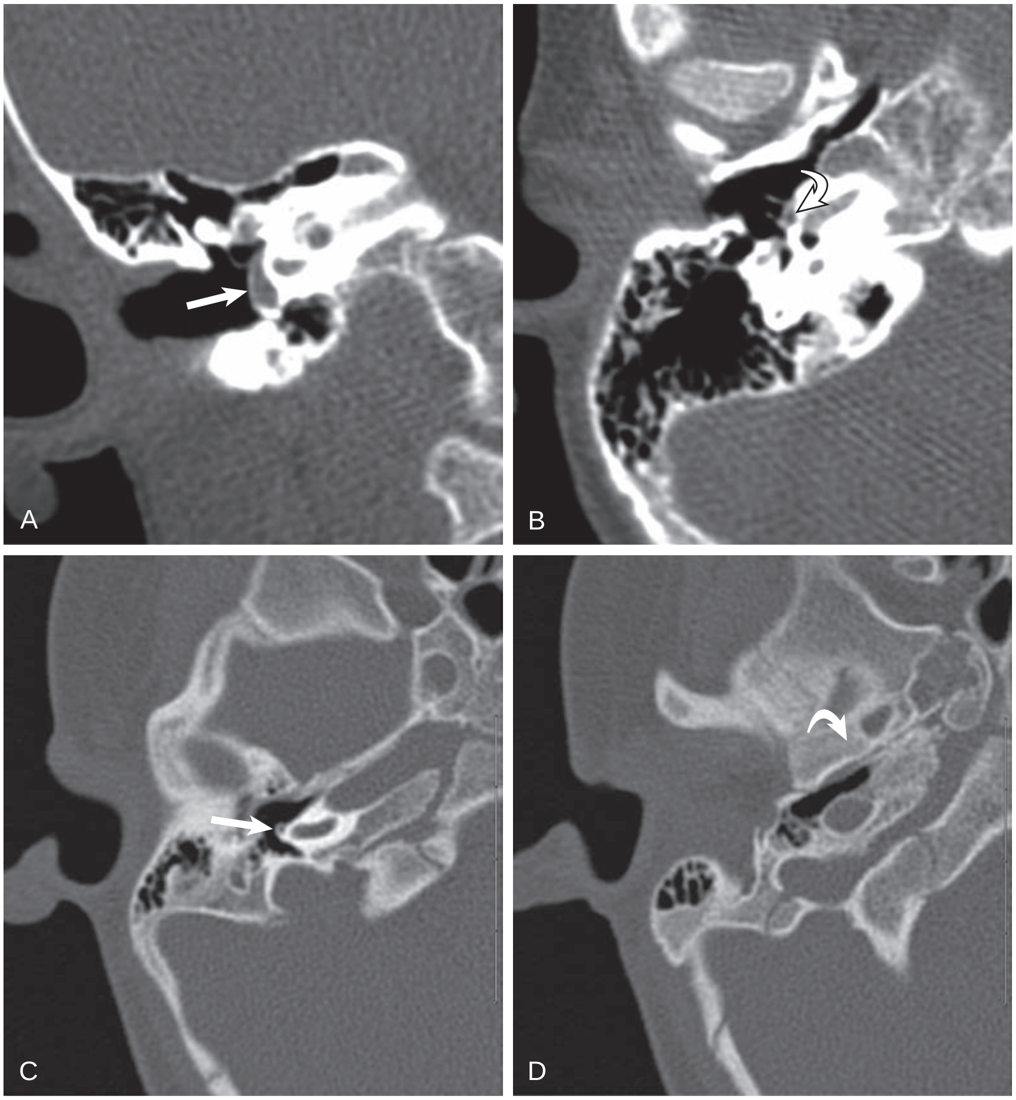

**Figure 10.28. Persistent stapedial artery.** (A) Coronal and (B) axial high-resolution CT images show a vascular structure ascending vertically along the cochlear promontory *(straight arrow)* through the stapedial crura *(curved arrow)*. (C and D) Axial CT images in a different patient demonstrating a bony covered vessel on the cochlear promontory *(straight arrow)* and absence of the foramen spinosum *(curved arrow)*.

## SUGGESTED READINGS

Glastonbury CM, Davidson HC, Harnsberger HR, et al. Imaging findings of cochlear nerve deficiency. *AJNR Am J Neuroradiol*. 2002;23:635–643.

Huang BY, Zdanski C, Castillo M. Pediatric hearing loss, part 1: practical aspects for neuroradiologists. *AJNR Am J Neuroradiol*. 2012;33:211–217.

Huang BY, Zdanski C, Castillo M. Pediatric hearing loss, part 2: syndromic and acquired causes. *AJNR Am J Neuroradiol*. 2012;33:399–406.

Koesling S, Kunkel P, Schul T. Vascular anomalies, sutures and small canals of the temporal bone on axial CT. *Eur J Radiol*. 2005;54:335–343.

McClay JE, Booth TN, Parry DA, et al. Evaluation of pediatric sensorineural hearing loss with magnetic resonance imaging. *Arch Otolaryngol Head Neck Surg*. 2008;134:945–952.

Park K, Choung YH. Isolated congenital ossicular anomalies. *Acta Oto Laryngol*. 2009;129:419–422.

Sennaroglu L, Saatci I. Unpartitioned versus incompletely partitioned cochleae: radiologic differentiation. *Otol Neurotol*. 2004;25:520–529.

## REFERENCES

Full references for this chapter can be found on www.expertconsult.com.

## REFERENCES

1. Jacob R, Gupta S, Isaacson B, et al. High resolution CT findings in children with a normal pinna or grade I microtia and unilateral mild stenosis of the external canal. *AJNR Am J Neuroradiol*. 2015;36:176–180.
2. Vrabec JT, Lin JW. Inner ear anomalies in congenital aural atresia. *Otol Neurotol*. 2010;31:1421–1426.
3. Jahrsdoerfer RA, Yeakley JW, Aguilar EA, et al. Grading system for the selection of patients with congenital aural atresia. *Am J Otol*. 1992;13:6–12.
4. Gassner EM, Mallouhi A, Jaschke WR. Preoperative evaluation of external canal atresia on high-resolution CT. *AJR Am J Roentgenol*. 2004;182:1305–1312.
5. Swartz JD, Wolfson RJ, Mauriello AJ, et al. External auditory canal dysplasia: CT evaluation. *Laryngoscope*. 1985;95:841–845.
6. Swartz JD, Faerber EN. Congenital malformations of the external and middle ear: high resolution CT findings of surgical import. *AJR Am J Roentgenol*. 1985;144:501–506.
7. Mukherjee S, Kesser BW, Raghaven P. The "boomerang" malleus-incus complex in congenital aural atresia. *AJNR Am J Neuroradiol*. 2014;35:2181–2185.
8. Takegoshi H, Kaga K, Kikuchi S, et al. Facial canal anatomy in patients with microtia: evaluation of the temporal bones with thin-section CT. *Radiology*. 2002;225:852–858.
9. Mayer TE, Brueckmann H, Siegert R, et al. High-resolution CT of the temporal bone in dysplasia of the auricle and external canal. *AJNR Am J Neuroradiol*. 1997;18:53–65.
10. Mafee MF, Valvassori GE. Radiology of craniofacial anomalies. *Otolaryngol Clin North Am*. 1981;14:939–988.
11. Batel-Friedrick S. Congenital auricular malformations: description of anomalies and syndromes. *Facial Plast Surg*. 2015;31:567–580.
12. Nguyen VT, Paek G, Hu J, et al. Presurgical CT evaluation of congenital aural atresia. *Neurographics*. 2015;5:231–237.
13. Frenzel H, Sprinzl G, Widmann G, et al. Grading system for selection of patients with congenital aural atresia for active middle ear implants. *Neuroradiology*. 2013;55:895–911.
14. Dougherty W, Kesser BW. Conductive hearing loss in children. *Otolaryngol Clin N Am*. 2015;48:955–974.
15. Romo LV, Casselman JW, Robson CD. Temporal bone: congenital anomalies. In: Som PM, Curtin HD, eds. *Head and Neck Imaging*. 4th ed. St Louis: Mosby; 2003.
16. Kurosaki Y, Tanaka YO, Itai Y. Malleus bar as a rare cause of congenital malleus fixation: CT demonstration. *AJNR Am J Neuroradiol*. 1998;19:1229–1230.
17. Teunissen EB, Cremers WR. Classification of congenital middle ear anomalies. Report on 144 ears. *Ann Otol Rhinol Laryngol*. 1993; 102:606–612.
18. Park K, Choung YH. Isolated congenital ossicular anomalies. *Acta Oto Laryngol*. 2009;129:419–422.
19. Cousins VC, Milton CM. Congenital ossicular anomalies: a review of 68 cases. *Am J Otol*. 1988;9:76–80.
20. Vercruysse JP, Casselman J, De Foer B, et al. Congenital bilateral oval and round window aplasia with a hypoplastic stapes. *Otol Neurotol*. 2006;27:441–442.
21. Linder TE, Ma F, Huber A. Round window atresia and its effect on sound transmission. *Otol Neurotol*. 2003;24:259–263.
22. Booth TN, Vezina LG, Karcher G. Imaging and clinical evaluation of isolated atresia of the oval window. *AJNR Am J Neuroradiol*. 2000;21:171–174.
23. Zeifer B, Sabini P, Sonne J. Congenital absence of the oval window: radiologic diagnosis and associated anomalies. *AJNR Am J Neuroradiol*. 2000;21:322–327.
24. Lemmerling M, Dhooge I, Mollet P, et al. CT of the temporal bone in CHARGE association. *Neuroradiology*. 1998;40:262–265.
25. Satar B, Mukherji SK, Telian SA. Congenital aplasia of the semicircular canals. *Otol Neurotol*. 2003;24:437–446.
26. Fujita K, Aida N, Asakura Y, et al. Abnormal basiocciput development in CHARGE syndrome. *AJNR Am J Neuroradiol*. 2008;30:629–634.
27. Blustajn J, Kirsch C, Panigraphy A, et al. Olfactory anomalies in CHARGE syndrome: imaging findings of a potential major diagnostic criterion. *AJNR Am J Neuroradiol*. 2008;29:1266–1269.
28. Alford RL, Arnos KS, Fox M, et al. American college of medical genetics and genomics guideline for the clinical evaluation and etiologic diagnosis of hearing loss. *Genet Med*. 2014;16:347–355.
29. Kenna MA, Rehm HL, Frangulov A, et al. Temporal bone abnormalities in children with GJB2 mutations. *Laryngoscope*. 2011;121:630–635.
30. Campbell C, Cucci RA, Prasad S, et al. Pendred syndrome, DFNB4, and PDS/SLC26A4 identification of eight novel mutations and possible genotype-phenotype correlations. *Hum Mutat*. 2001;17:403–411.
31. Rodriguez-Ballesteros M, del Castillo FJ, Martin Y, et al. Auditory neuropathy in patients carrying mutations of the otoferlin gene (OTOF). *Hum Mutat*. 2003;22:451–456.
32. Huang BY, Roche JP, Buchman CA, et al. Brain stem and inner ear abnormalities in children with auditory neuropathy spectrum disorder and cochlear nerve deficiency. *AJNR Am J Neuroradiol*. 2010;31:1972–1979.
33. Toriello HV, Reardon W, Gorlin RJ. *Hereditary Hearing Loss and its Syndromes*. 2nd ed. Oxford: Oxford University Press; 2004.
34. Rehm HL. A genetic approach to the child with sensorineural hearing loss. *Semin Perinatol*. 2005;29:173–181.
35. McClay JE, Booth TN, Parry DA, et al. Evaluation of pediatric sensorineural hearing loss with magnetic resonance imaging. *Arch Otolaryngol Head Neck Surg*. 2008;134:945–952.
36. Jackler RK, Luxford WM, House WF. Congenital malformations of the inner ear: a classification based on embryogenesis. *Laryngoscope*. 1987;97:2–14.
37. Sennaroglu L, Saatci I. Unpartitioned versus incompletely partitioned cochleae: radiologic differentiation. *Otol Neurotol*. 2004;25:520–529.
38. Benton C, Bellet PS. Imaging of congenital anomalies of the temporal bone. *Neuroimaging Clin N Am*. 2000;10:35–53.
39. Saylisoy S, Armagan I, Gurbuz MK, et al. Computed tomographic findings of X-linked deafness: a spectrum from child to mother, from young to old, from boy to girl, from mixed to sudden hearing loss. *J Comput Assist Tomogr*. 2014;38:20–24.
40. Choi JW, Min B, Kim A, et al. De novo large genomic deletions involving *POU3F4* in incomplete partition type III inner ear anomaly in east Asian populations and implications for genetic counseling. *Otol Neurotol*. 2015;36:184–190.
41. Giesemann AM, Goetz F, Neuburger J, et al. Appearance of the hypoplastic cochleae in CT and MRI: a new subclassification. *Neuroradiology*. 2011;53:49–61.
42. Davidson HC, Harnsberger HR, Lemmerling MM, et al. MR evaluation of vestibulocochlear anomalies associated with large endolymphatic duct and sac. *AJNR Am J Neuroradiol*. 1999;20:1435–1441.
43. Boston M, Halstead M, Meinzen-Derr J, et al. The large vestibular aqueduct: a new definition based on audiologic and computed tomography correlation. *Otolaryngol Head Neck Surg*. 2007;136:972–977.
44. Elmaleh-Berges M, Baumann C, Noel-Petroff N, et al. Spectrum of temporal bone abnormalities in patients with Waardenburg syndrome and SOX10 mutations. *AJNR Am J Neuroradiol*. 2013;34:1257–1263.
45. Intrapiromkul J, Aygun N, Tunkel DE, et al. Inner ear anomalies seen on CT images in people with Down syndrome. *Pediatr Radiol*. 2012;42:1449–1455.
46. Curtin H. Imaging of conductive hearing loss with a normal tympanic membrane. *AJR*. 2016;206:49–56.
47. Kachniarz B, Chen JX, Gilani S, et al. Diagnostic yield of MRI for pediatric hearing loss: a systematic review. *Otolaryngol Head Neck Surg*. 2015;152:5–22.
48. Berrettini S, Forli F, Bogazzi F, et al. Large vestibular aqueduct syndrome: audiological, radiological, clinical and genetic features. *Am J Otolaryngol*. 2005;26:363–371.
49. Naganawa S, Koshikawa T, Fukatsu H, et al. Enlarged endolymphatic duct and sac syndrome: relationship between MR findings and genotype of mutation in Pendred syndrome gene. *Magn Reson Imaging*. 2004;22:25–30.
50. Oh SH, Choi BY, Son KR, et al. Can magnetic resonance imaging provide clues to the inner ear functional status of enlarged vestibular aqueduct subjects with PDS mutation? *Otol Neurotol*. 2008;29:593–600.
51. Demir OI, Cakmakci H, Erdag T, et al. Narrow duplicated internal auditory canal: radiological findings and review of the literature. *Pediatr Radiol*. 2005;35:1220–1223.
52. Desai NK, Young L, Miranda M, et al. Pontine tegmental cap dysplasia (PTCD): the neurootologic perspective. *Otolaryngol Head Neck Surg*. 2011;145(6):992–998.
53. Fatterpekar GM, Mukherji SK, Alley J, et al. Hypoplasia of the bony canal for the cochlear nerve in patients with congenital sensorineural hearing loss: initial observations. *Radiology*. 2000;215:243–246.
54. Miyasaka M, Nosaka S, Mormoto N, et al. CT and MR imaging for pediatric cochlear implantation: emphasis on the relationship between the cochlear nerve canal and the cochlear nerve. *Pediatr Radiol*. 2010;40:1509–1516.

55. Casselman JW, Offeciers FE, Govaerts PJ, et al. Aplasia and hypoplasia of the vestibulocochlear nerve: diagnosis with MR imaging. *Radiology*. 1997;202:773–781.
56. Glastonbury CM, Davidson HC, Harnsberger HR, et al. Imaging findings of cochlear nerve deficiency. *AJNR Am J Neuroradiol*. 2002;23:635–643.
57. Phelps PD. Congenital cerebrospinal fluid fistulae of the petrous temporal bone. *Clin Otolaryngol Allied Sci*. 1986;11:79–92.
58. Judd CD, Chapman PR, Koch B, et al. Intracranial infantile hemangiomas associated with PHACE syndrome. *AJNR Am J Neuroradiol*. 2007;28:25–29.
59. Ehmer DR, Booth T, Kutz W, et al. Radiographic diagnosis of trans-stapedial cerebrospinal fluid fistula. *Otolaryngol Head Neck Surg*. 2010;142:694–698.
60. Hang AX, Kim GG, Zdanski CJ. Cochlear implantation in unique pediatric populations. *Curr Opin Otolarnyngol Head Neck Surg*. 2012;20:507–517.
61. Koesling S, Kunkel P, Schul T. Vascular anomalies, sutures and small canals of the temporal bone on axial CT. *Eur J Radiol*. 2005;54:335–343.
62. Silbergleit R, Quint DJ, Mehta BA, et al. The persistent stapedial artery. *AJNR Am J Neuroradiol*. 2000;21:572–577.
63. Ginsberg LA, Pruett SW, Chen MY, et al. Skull base foramina of the middle cranial fossa: reassessment of normal variation with high resolution CT. *AJNR Am J Neuroradiol*. 1994;15:283–291.
64. Rollins NK, Booth T, Shapiro K. MR venography in children with complex craniosynostosis. *Pediatr Neurosurg*. 2000;32:308–315.
65. Overton SB, Ritter FN. A high placed jugular bulb in the middle ear: a clinical and temporal bone study. *Laryngoscope*. 1973;83:1986–1991.

# 11

# Infection and Inflammation

Timothy N. Booth

Infectious and inflammatory disorders commonly involving the temporal bone; external, middle, and inner ear; and the facial nerve are discussed in this chapter.

The auricle, the cartilaginous canal, and the external auditory canal (EAC) comprise the external ear, with the tympanic membrane representing the division between the external and middle ear.

The middle ear is predominately composed of the tympanic cavity and its contents. The Eustachian tube connects the middle ear to the nasopharynx and can be a path for the spread of infection. All air spaces are lined with mucosa, which makes them susceptible to the spread of infection and inflammation. The membranous and bony labyrinths make up the inner ear, with potential communication with the subarachnoid space.

## EXTERNAL EAR

### External Otitis

***Clinical Presentation and Etiologies.*** Children present with variable degrees of pain, as well as secretions that can be serous early and progress to frank purulence. External otitis is associated with swimming and can be caused by a number of pathogens, including fungi. Otomycosis is more common in the postsurgical ear and presents in a similar fashion to a bacterial infection.[1]

***Imaging.*** The diagnosis of otitis externa should be made clinically; however, the diagnosis can be made in the evaluation of periauricular inflammation with parotiditis and an infected type 1 branchial cleft cyst also being a consideration.[2] Soft tissue swelling centered within the EAC, is demonstrated on computed tomography (CT) (e-Fig. 11.1). The condition is termed *malignant* or *necrotizing otitis externa* when there is more extensive involvement of regional soft tissues and bone.[3] Langerhans cell histiocytosis can infiltrate the soft tissue of the external canal but is more often associated with extensive bony destruction commonly associated with middle ear and mastoid involvement. Involvement of the petrous apex is encountered more frequently with rhabdomyosarcoma.[4]

***Treatment.*** Usual treatment comprises appropriate antibiotics and antifungal treatment in the postoperative ear. Surgical intervention is typically not necessary.

### Malignant (Necrotizing) Otitis Externa

***Clinical Presentation and Etiologies.*** Usually, the presentation is acute, with associated systemic symptoms of fever and leukocytosis. *Pseudomonas aeruginosa* is the most common cause. Diabetes is a common predisposing condition; however, any condition resulting in immunodeficiency can predispose.[5–7]

***Imaging.*** CT shows extensive inflammation within the EAC and can demonstrate bony destruction. Magnetic resonance imaging (MRI) with gadolinium demonstrates osteomyelitis, with increased signal on fat-suppressed T2-weighted images and abnormal enhancement in the regional bone. MRI is useful in confirming central skull base involvement, especially in the presence of multiple cranial nerve palsies, and in evaluating for intracranial complications.[7] It is important to consider prior surgical history as a transcanal approach can result in irregularity and bony defects in the absence of infection.[8]

Single photon emission CT (SPECT) technetium-99m bone scan is an effective way to confirm or exclude bone involvement in a patient whose condition evokes high clinical suspicion and can be positive in the absence of osseous destruction on CT.[9] In adults, radionuclide antigranulocytic studies have shown promise in diagnosis and follow-up as well.[10]

***Treatment.*** Several weeks of intravenous antibiotics are required. CT helps assess the extent of inflammation and surrounding bony involvement and is used to stratify patients into nonsevere and severe groups, with the latter offered early surgical intervention and debridement.[11] Children are reported to have better outcomes compared with adults.

### Other Lesions Encountered Within the External Auditory Canal

Acquired cholesteatoma may present as debris or a mass within the EAC (e-Fig. 11.2), as can keratosis obturans.[12] Exostoses of the external canal may result from chronic inflammation caused by prolonged exposure to water. Exostoses tend to be bilateral, broad based, and of bony density. Foreign bodies and osteomas can also occur in the external canal, with osteomas appearing pedunculated and very dense (e-Fig. 11.3).[13]

## MASTOID AND MIDDLE EAR

### Acute Infections

#### Otitis Media

***Clinical Presentation and Etiologies.*** Otitis media is the most common childhood infection treated with antibiotics. The otoscopic findings are critical to the diagnosis. Acute otitis media typically presents with fever, ear pain, and a red tympanic membrane.[14] The initial cause of the infection is likely viral and may not require treatment with antibiotics, but it may be bacterial or represent a secondary bacterial infection. Complications may occur in up to 10%, but conservative practice guidelines have not led to an increased incidence of acute mastoiditis.[15]

***Imaging.*** CT and MRI have little place in the evaluation of uncomplicated acute otitis media. It is important to realize that fluid in the middle ear and mastoid is often found in asymptomatic individuals and may have no significance.

#### Mastoiditis

***Clinical Presentation and Etiologies.*** Acute mastoiditis is the most common complication of acute otitis media and usually presents with high fever and elevated systemic inflammatory markers. Bacterial infections are most commonly caused by *Streptococcus pneumoniae* and group A beta-hemolytic streptococci. Nonbacterial causes include tuberculosis and fungal infections. Disease in the very young or infections that are not responsive to antibiotic therapy should raise the suspicion of an atypical infection or possible Langerhans cell histiocytosis (e-Fig. 11.4).[16] Facial nerve paralysis is uncommon in bacterial mastoiditis, usually is temporary, and the presence may suggest atypical etiologies. Complications of acute mastoiditis are common in children, reported in up to 25% of cases.[17–19]

***Imaging.*** Mastoid air fluid levels can be seen in uncomplicated acute mastoiditis; however, the diagnosis remains a clinical diagnosis.

## Abstract:

The temporal bone is a complex region, which is susceptible to both infectious and inflammatory conditions. This chapter will review the most common etiologies and discuss clinical presentation, indication for imaging and findings, as well as potential treatment options. The reader should have a thorough understanding of infectious and inflammatory pathologies that involve the temporal bone and regional structures.

## Keywords:

Temporal bone
Infection
Inflammation
mastoiditis
otomastoiditis
cholesteatoma
labyrinthitis

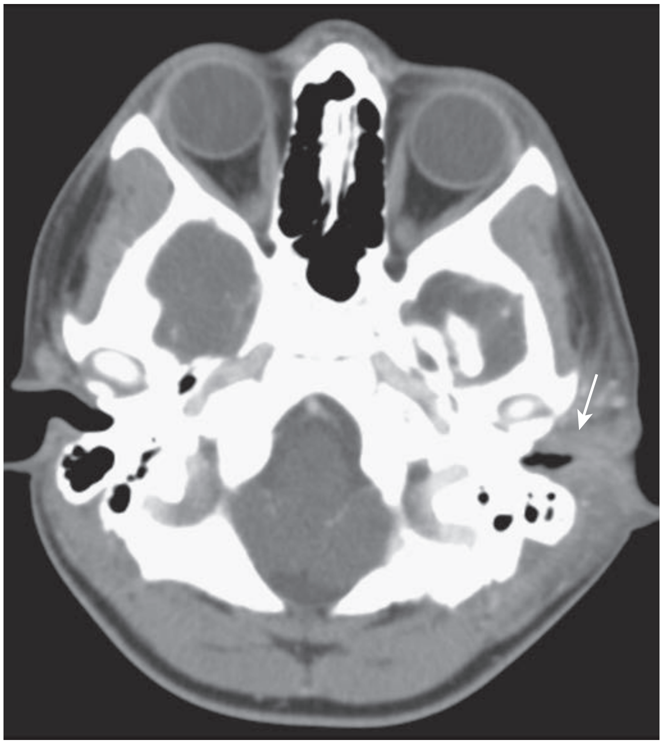

**e-Figure 11.1. Otitis externa in a 13-year-old with ear pain and soft tissue swelling.** Axial postcontrast CT through the level of the external canal shows extensive inflammation surrounding the left external canal *(arrow)* with normal aeration of the adjacent mastoids and a normal parotid gland *(not shown)*.

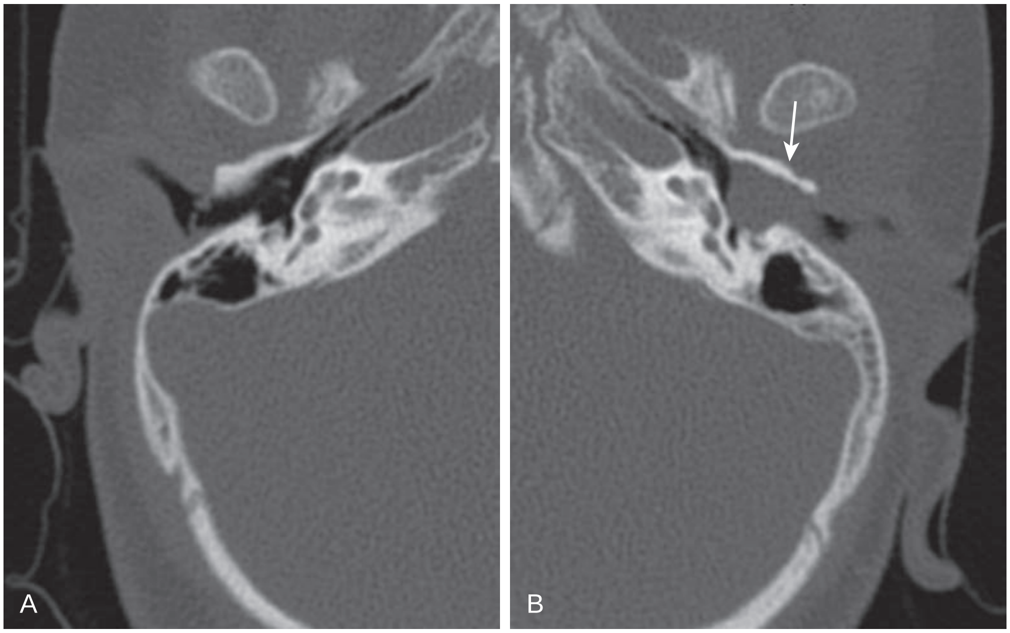

**e-Figure 11.2. Acquired cholesteatoma in a 5-year-old with otorrhea.** (A) Axial CT image through the normal right external canal. (B) Axial CT image through the left external canal. A large soft tissue mass with erosion of the anterior wall *(arrow)* is present. The tympanic membrane bulges medially with findings representing an external canal cholesteatoma.

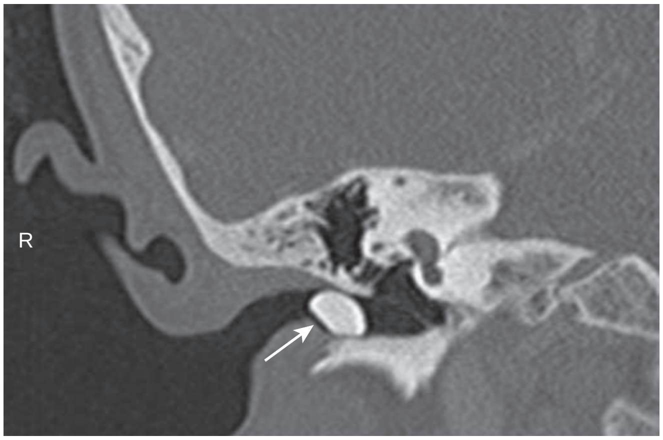

**e-Figure 11.3. Foreign body in an 8-year-old with mass in the external canal.** Axial CT image demonstrates a dense mass in the external canal *(arrow)*. Surgery revealed the mass to represent a foreign body rather than an osteoma, but both should be considered.

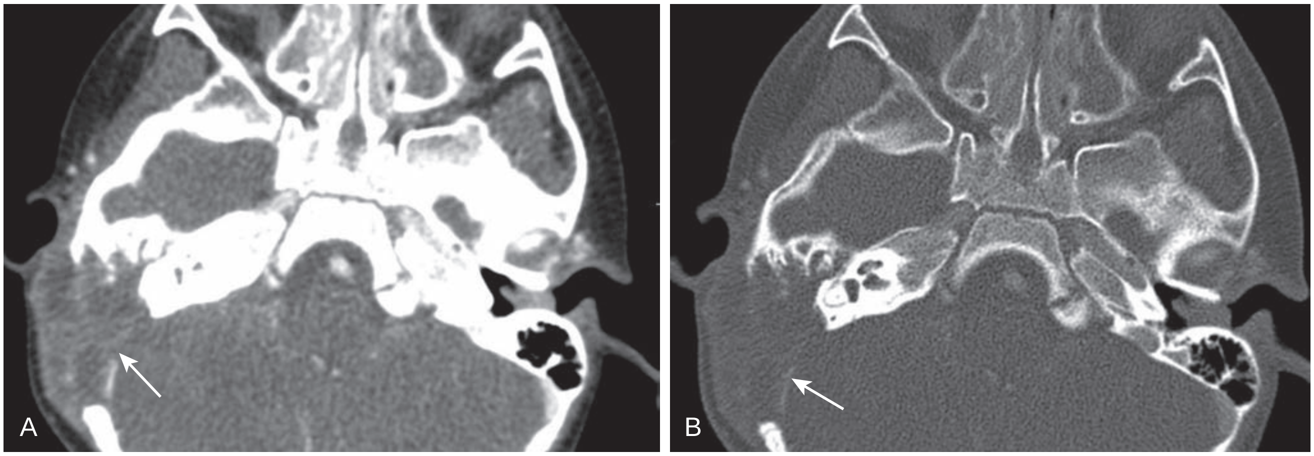

**e-Figure 11.4. Langerhans cell histiocytosis in a 2-year-old with periauricular soft tissue swelling.** (A and B) Axial CT through mastoids, soft tissue (A) and bone windows (B) show a destructive mass centered within the posterior lateral mastoid region *(arrows)*.

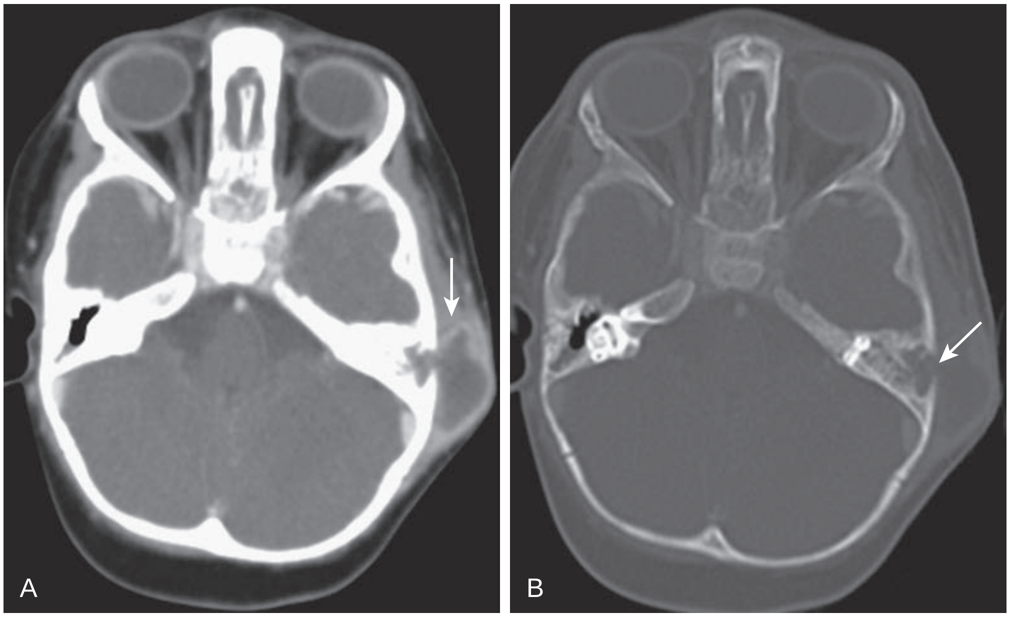

**Figure 11.5. Mastoiditis in a 2-year-old with post auricular swelling.** (A) Axial CT image through the mastoids shows a large subperiosteal abscess *(arrow)*. (B) Axial CT with bone windows demonstrates destruction of the lateral mastoid wall *(arrow)*. No intracranial extension is present with a normally enhancing sigmoid sinus.

Imaging becomes useful in evaluating for possible complications, with CT diagnosing the complications of mastoiditis with a high sensitivity and positive predictive value.[20] MRI and magnetic resonance venography (MRV) are valuable in assessing intracranial involvement and associated dural sinus thrombosis.

The initial CT finding is decreased definition of the mastoid trabeculae caused by inflammatory hyperemia. With the development of bone destruction, the process is termed coalescent mastoiditis.[21] The subsequent development of a subperiosteal abscess is, by far, the most common complication and typically occurs in the postauricular region where bone is thin, termed the Macewen triangle. CT demonstrates a rim-enhancing fluid collection that is adherent to bone; the underlying bone is usually intact but may show focal destruction (Fig. 11.5). The infection may also progress inferiorly through the mastoid tip, resulting in a Bezold abscess (e-Fig. 11.6) or anterior lateral resulting in a Luc abscess beneath the temporalis muscle.[22] The Eustachian tube allows infection to spread into the retropharyngeal space, and children with mastoiditis may present with a retropharyngeal abscess and rarely Grisel syndrome or tortocolis.[23] MRI findings suggestive of mastoiditis over simple effusion include signal intensity hypointense to cerebrospinal fluid (CSF) on T2-weighted images, restricted diffusion, and intense enhancement (e-Fig. 11.7).[24] Routine MR imaging in all cases of acute mastoiditis is likely not necessary and should be reserved for those patients with suspected intracranial complications.[25]

Mastoid infection may extend to the central skull base though the continuous mucosal spaces, resulting in petrous apicitis and osteomyelitis. Petrous apicitis classically presents as the clinical Gradenigo triad of purulent otorrhea, pain in the distribution of the fifth cranial nerve, and ipsilateral sixth cranial nerve palsy.[26] CT demonstrates bony destruction, commonly subtle in children, and associated epidural empyema. MRI demonstrates a peripherally enhancing fluid collection within the apex, and diffusion-weighted images show restricted diffusion with associated empyema or, less commonly, brain abscess (Fig. 11.8).

Pathways that allow infectious intracranial extension include bone erosion, thrombophlebitis, and preformed pathways. The oval and round windows, cochlear and vestibular aqueducts, internal auditory canal, dehiscent tegmen, and patent petrosquamosal suture are preformed pathways that allow early or late intracranial extension. These pathways may lead to the development of suppurative labyrinthitis, as shown by abnormal enhancement of the membranous labyrinth (e-Fig. 11.9). Meningitis can occur via these pathways by spread to the subarachnoid space.[21]

Meningitis, epidural empyema, dural sinus thrombosis, and cerebellar or cerebral abscesses are intracranial complications of mastoiditis. Bony erosion commonly involves the relatively thin sigmoid plate (Trautmann triangle) and may result in an epidural empyema or anterior lateral cerebellar abscess. Usually, significant compression of the adjacent sigmoid sinus occurs, and it may be difficult to distinguish between extrinsic mass effect and thrombosis of the sinus. Nodular thickening surrounding the sigmoid sinus on contrast-enhanced CT has been shown to be associated with empyema and the need for surgical intervention, whereas a smooth halo is not usually associated with an epidural abscess (e-Fig. 11.10).[27] Erosion through the tegmen results in a middle cranial fossa epidural empyema and/or temporal lobe abscess (Fig. 11.11). Veins allow organisms to readily traverse both bone and dura, resulting in thrombophlebitis. The sigmoid sinus is the most common to become thrombosed; however, the lateral, petrosal, and cavernous sinuses may be involved, especially with infection of the petrous apex.[21,28,29] Venous sinus thrombosis may lead to venous infarctions or otitic hydrocephalus caused by impaired venous drainage.[30] Gadolinium-enhanced MRV can be helpful in diagnosing dural sinus thrombosis (e-Fig. 11.12). Diffusion-weighted images show increased signal from purulent material, which may be especially helpful in postoperative imaging (Fig. 11.13 and Box 11.1).[28] Mastoid fluid may be the result rather than the cause of venous thrombosis, and additional findings should be sought for a definitive diagnosis of mastoiditis as the cause of dural sinus thrombosis (e-Fig. 11.14).[31]

***Treatment.*** Subperiosteal abscess and other complications have traditionally been treated with drainage, cortical mastoidectomy, and ventilation tube.[17,18] However, more conservative surgical management has been recently reported. Antibiotic therapy, followed by retroauricular puncture and grommet insertion, has been proven to be an effective alternative to surgical management of

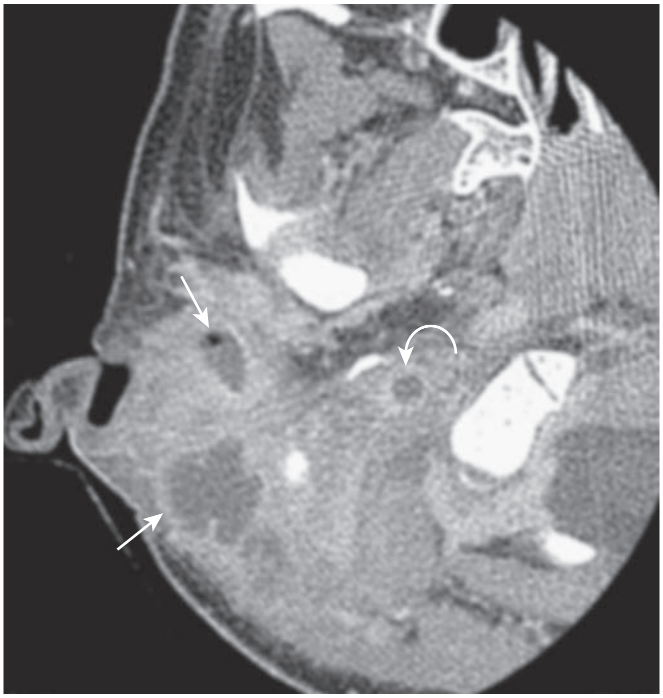

**e-Figure 11.6. Complicated mastoiditis.** Axial postcontrast CT shows a Bezold abscess inferior to the mastoids *(arrows)* with the anterior fluid collection containing air. Thrombosis of the internal jugular vein is also present *(curved arrow)*. *(Case courtesy of L. Gilbert Vezina MD.)*

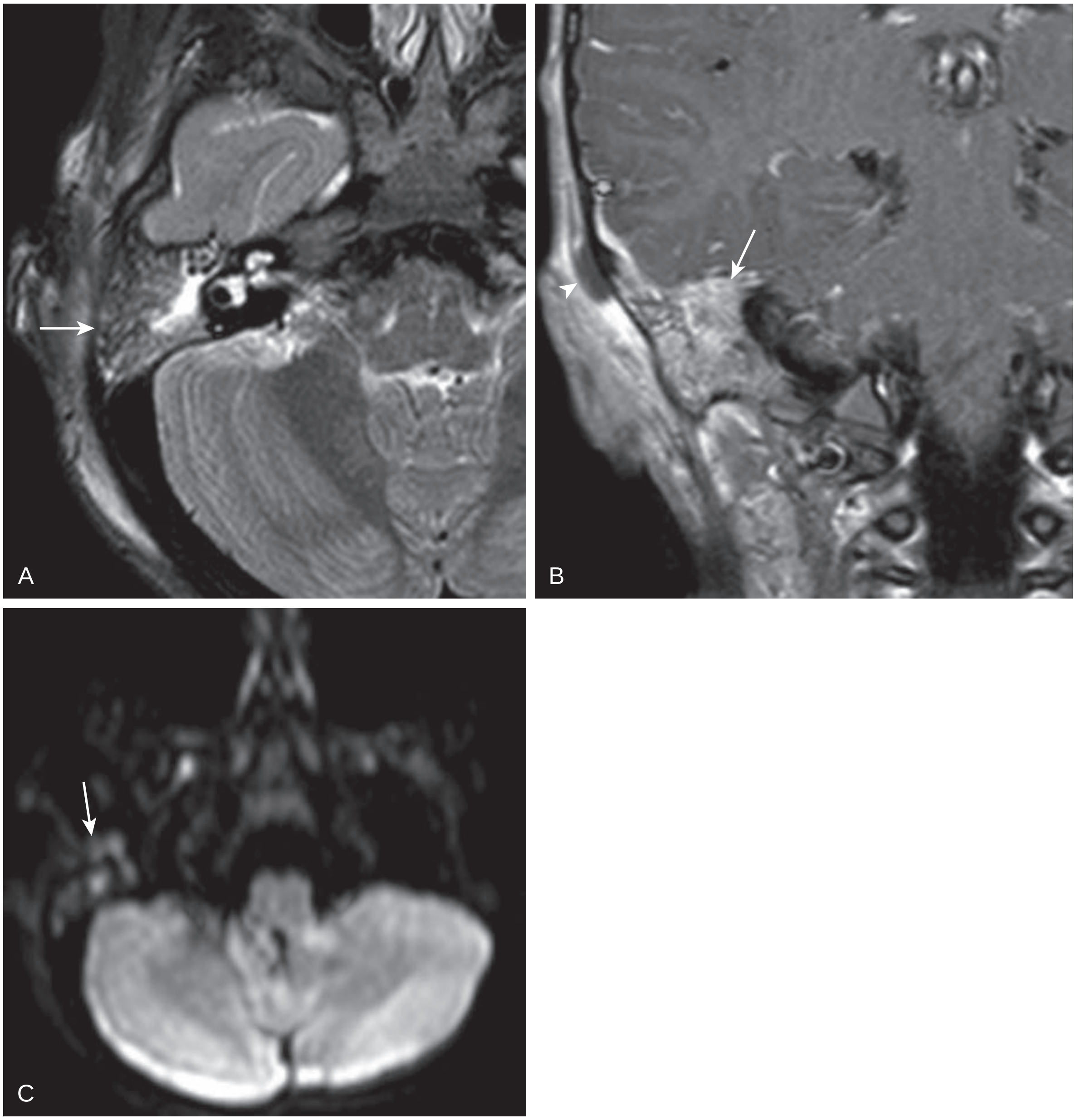

**e-Figure 11.7. Mastoiditis, MRI findings.** (A) Axial T2-weighted MR images show relatively low T2 signal fluid within the right mastoids *(arrow)*. (B) Axial postgadolinium T1-weighted MR images with fat suppression. Extensive enhancement within the right mastoid is present *(arrow),* no enhancement on the left. Dural enhancement is present and a small subperiosteal abscess *(arrowhead)*. (C) Diffusion-weighted MR image shows foci of restricted diffusion *(arrow)*.

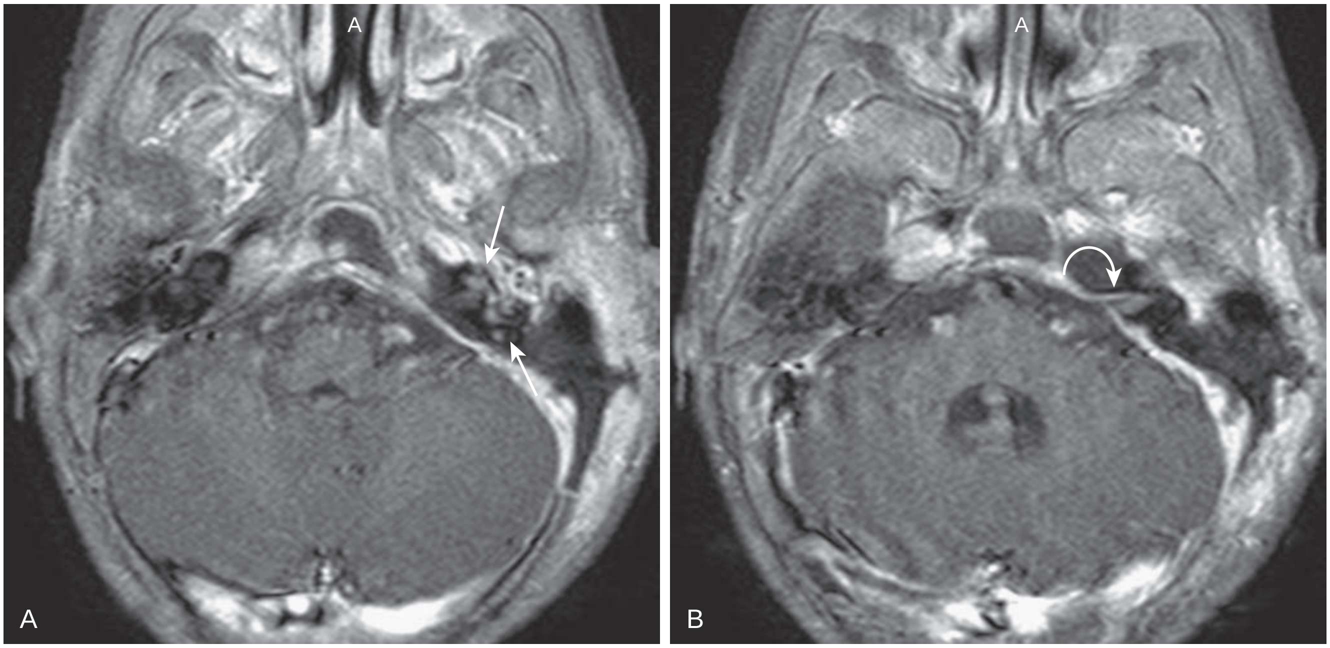

**e-Figure 11.9. Suppurative labyrinthitis in an 18-month-old with mastoiditis.** (A and B) Axial postgadolinium T1-weighted MR images through the membranous labyrinth shows extensive peripheral enhancement throughout the mastoids and extension to the central skull base along with regional dural enhancement. Abnormal enhancement is present within the left internal auditory canal *(curved arrow),* cochlea, and vestibular system *(arrows),* consistent with suppurative labyrinthitis. A left-sided mastoidectomy has been performed.

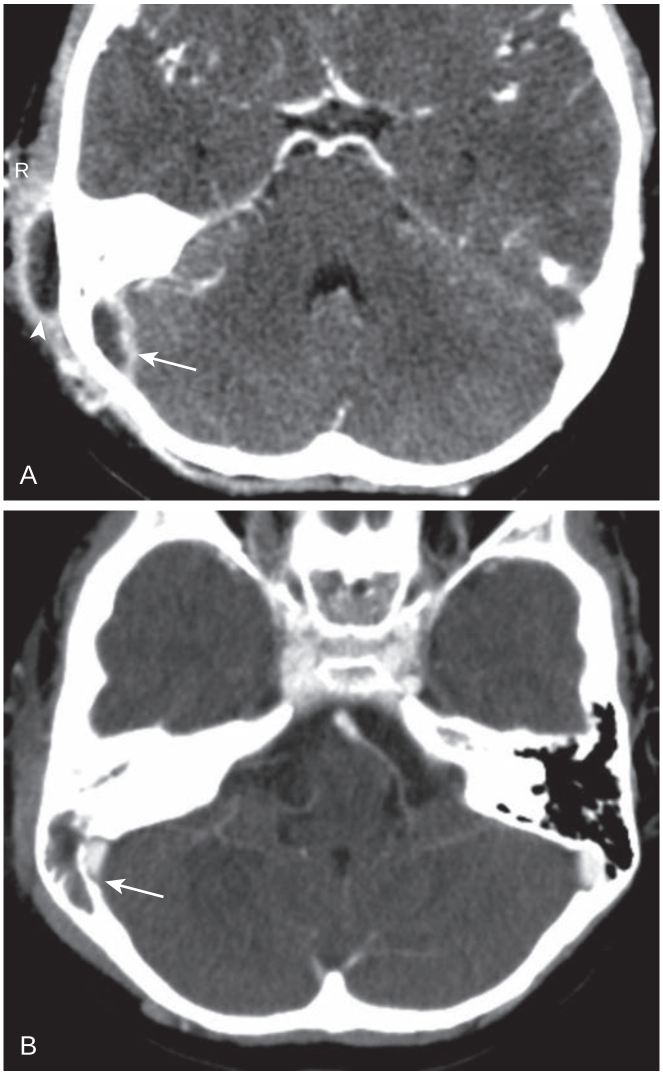

**e-Figure 11.10. Mastoiditis, “halo” sign on CT.** (A and B) Axial postcontrast CT in different patients. (A) Nodular soft tissue thickening along the lateral aspect of the right sigmoid sinus is present *(arrow)* with an epidural empyema confirmed at surgery. A subperiosteal abscess is present as well *(arrowhead)*. (B) A thin “halo” of soft tissue surrounds the right sigmoid sinus *(arrow)* with the patient treated conservatively. The sigmoid sinus is normally in direct contact with the inner table of the skull.

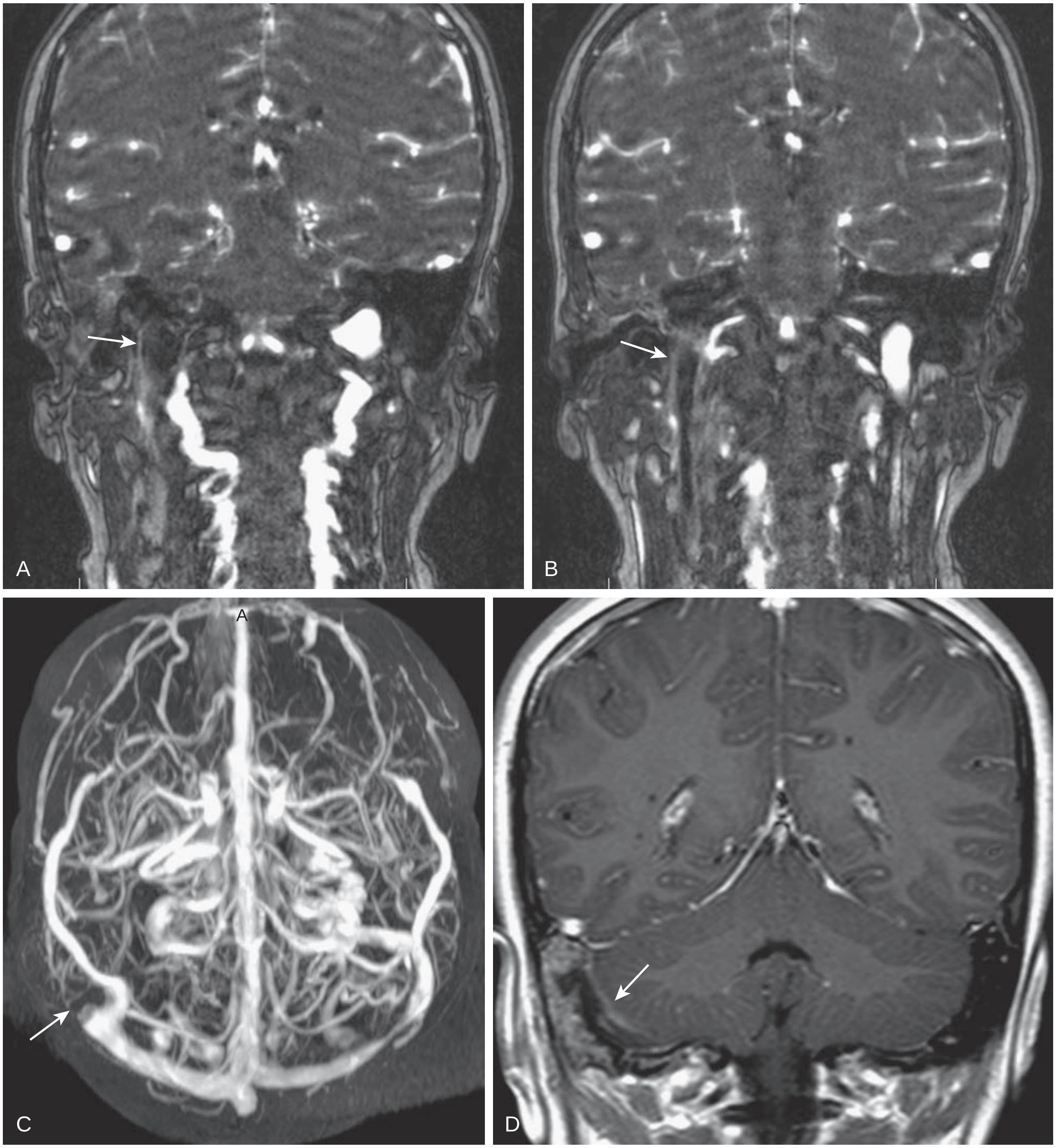

**e-Figure 11.12. Venous thrombosis in a 9-year-old with mastoiditis.** (A and B) Coronal source images from a gadolinium-enhanced MRV show a central filling defect in the jugular bulb and high internal jugular vein *(arrows),* representing venous thrombosis. (C) Maximum-intensity projection shows abrupt occlusion of the distal transverse sinus on the right *(arrow)*. (D) Coronal postgadolinium T1-weighted MR image demonstrates a small coexisting epidural abscess *(arrow)*.

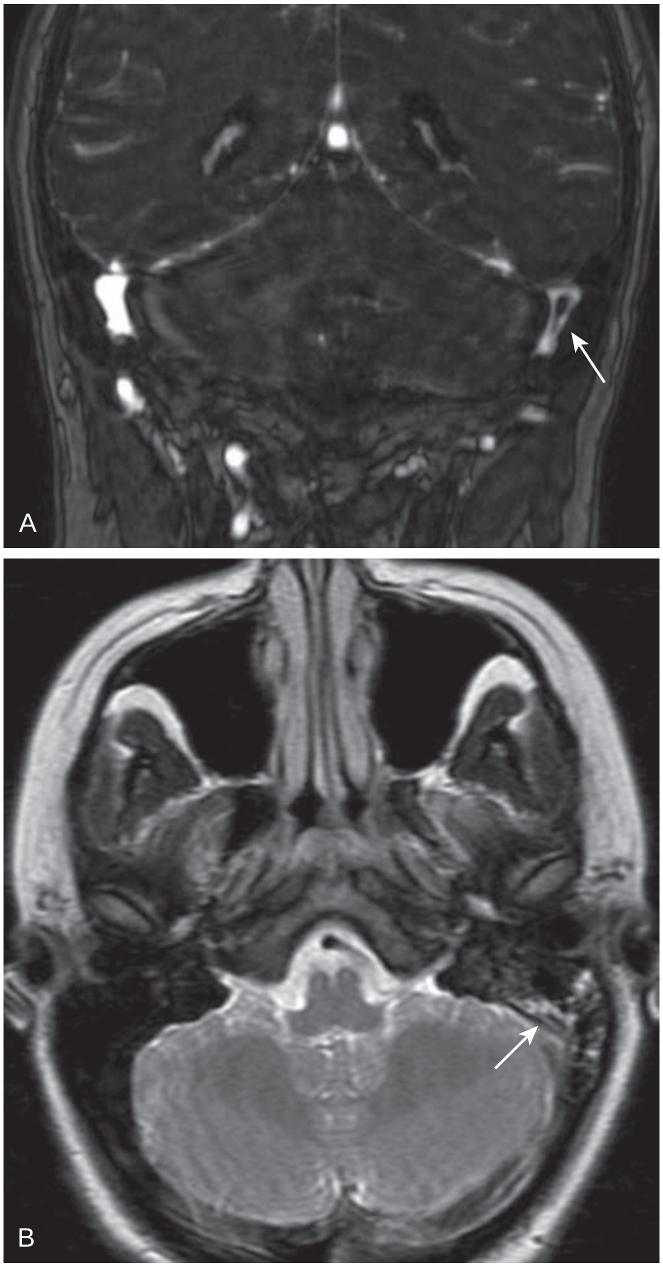

**e-Figure 11.14. Dural sinus thrombosis and mastoid effusion.** (A) Gadolinium-enhanced MRV shows thrombus in the left sigmoid sinus *(arrow)*. (B) Axial T2-weighted MR image shows an ipsilateral mastoid effusion *(arrow)*. No other evidence of mastoiditis is present clinically or by imaging.

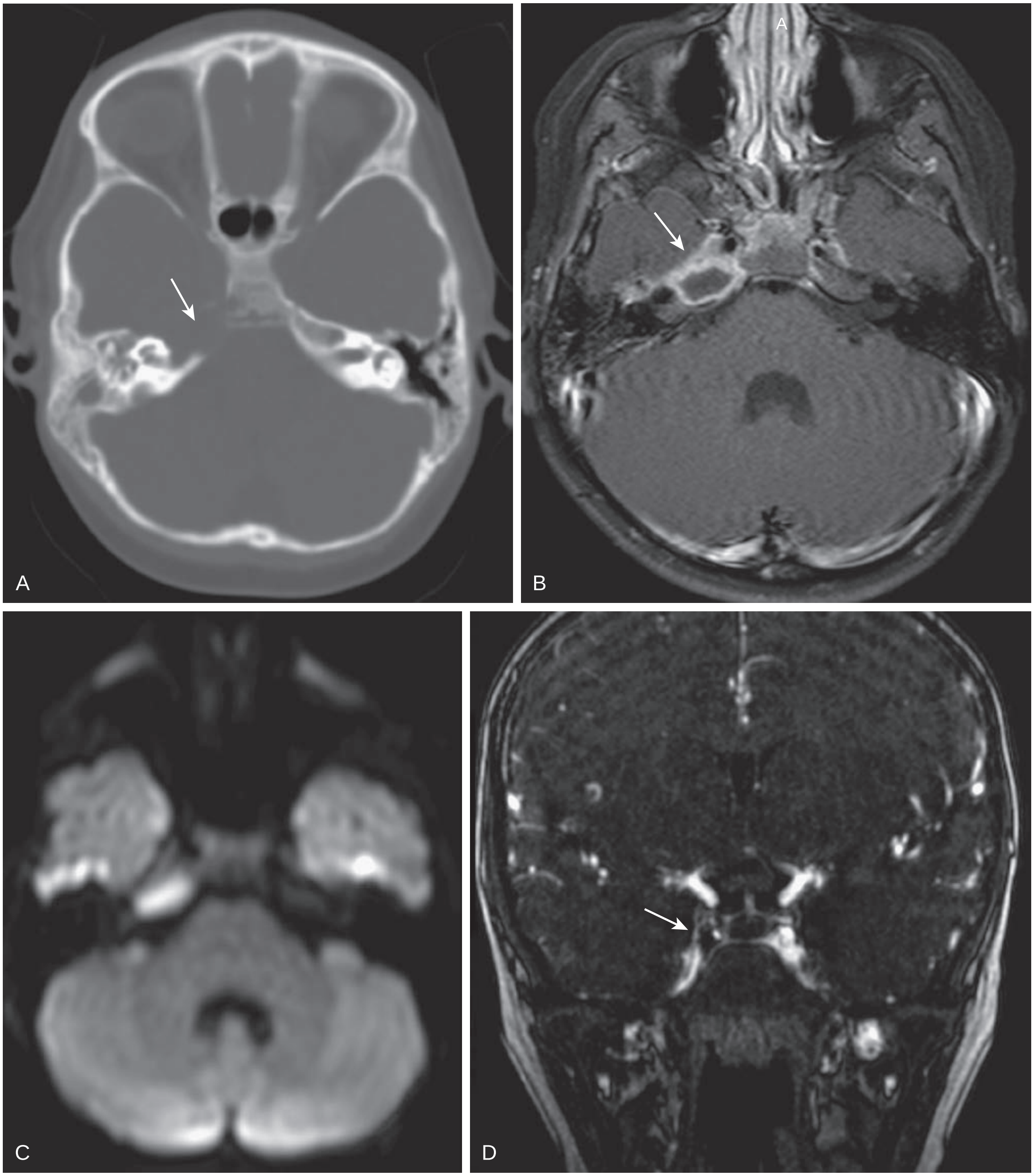

**Figure 11.8. Petrous apicitis in a 6-year-old with headache and right sixth nerve palsy.** (A) Axial CT shows absence of the right petrous apex *(arrow)*. (B) Axial postgadolinium T1-weighted MR image shows a rim-enhancing fluid collection in the right petrous apex with associated dural enhancement *(arrow)*. The left internal carotid artery is narrowed, likely relating to inflammation within the cavernous sinus. (C) Restricted diffusion is present on the axial diffusion-weighted image. (D) Gadolinium-enhanced MRV shows a filling defect in the right cavernous sinus consistent with thrombosis *(arrow)*.

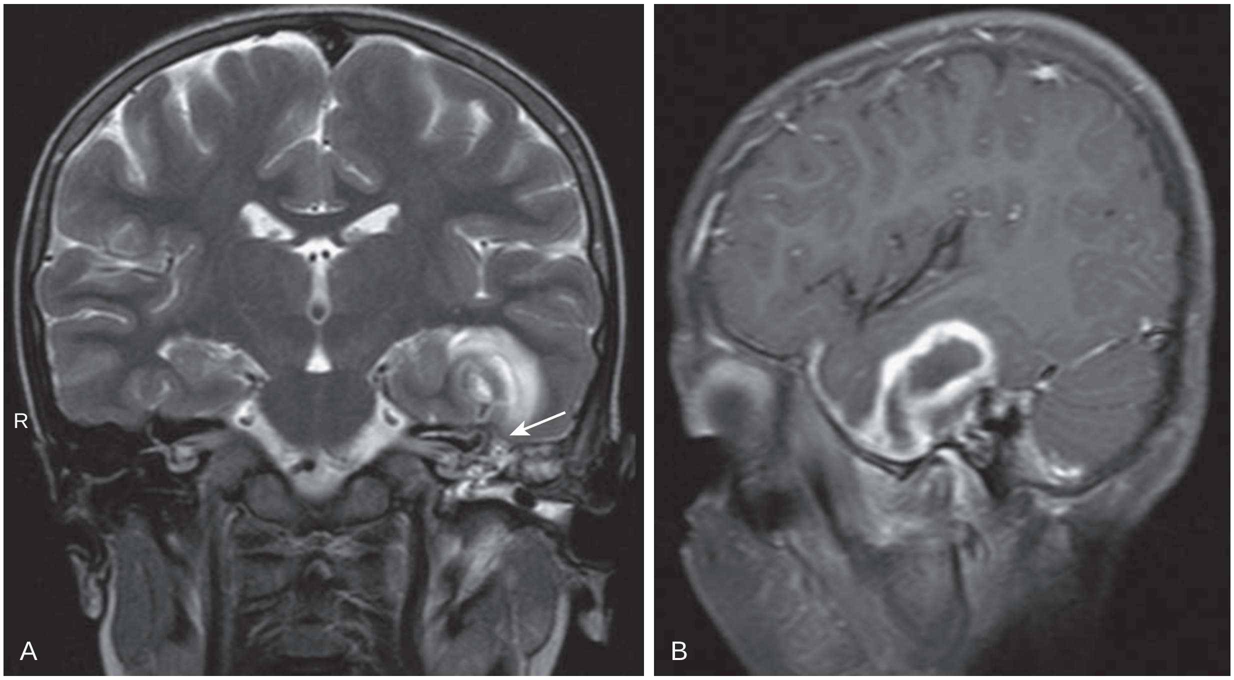

**Figure 11.11. Brain abscess in an 8-year-old with complicated mastoiditis.** (A) Coronal T2-weighted MR image shows fluid in the left mastoid and middle ear. A defect is present within the tegmen *(arrow)* associated with a large temporal intraaxial lesion. (B) Left parasagittal post-gadolinium T1-weighted MR image demonstrates rim enhancement of the temporal mass, consistent with abscess.

**BOX 11.1** Complications of Mastoiditis

Subperiosteal abscess
Central skull base osteomyelitis
Venous thrombosis
Meningitis
Epidural or subdural empyema
Intraparenchymal abscess

complicated mastoiditis.[32,33] Intracranial involvement is treated more aggressively with neurosurgical consultation and drainage of extra-axial empyemas and intraparenchymal abscesses.

## Chronic Infections

### Chronic Otomastoiditis

***Clinical Presentation and Etiologies.*** Persistent retraction of the tympanic membrane and fluid within the middle ear cavity may be associated with chronic otitis media (COM). Tympanic membrane perforations from chronic middle ear infections typically involve the pars tensa. In contrast, retraction and perforation involving the pars flaccida portion of the tympanic membrane are usually caused by Eustachian tube dysfunction. Children often present for imaging because of development of conductive hearing loss. Hearing loss may be from ossicular erosions caused by chronic suppurative otomastoiditis or may be related to ossicular fixation, tympanosclerosis, or both.

***Imaging.*** Ossicular erosions associated with COM frequently involve the distal portion of the long process of the incus and are associated with retraction rather than bulging of the tympanic membrane and lack of mass effect.[34] Tympanosclerosis is caused by the deposition of hyalinized, often calcific, granulation tissue in the middle ear cavity. On CT, tympanosclerosis may appear as multiple middle ear masses with regions of increased density. Isolated involvement of the tympanic membrane may occur or be seen in conjunction with middle ear involvement (Fig. 11.15). Increased thickness of the ossicles may be present on imaging studies, suggesting osteitis.[29,35]

***Treatment.*** Imaging is helpful in determining the extent of ossicular erosion and disease before surgical intervention in COM. High-resolution CT should be used selectively and only if complications are suspected.[36] Surgical outcome is generally poor for tympanosclerosis, but appears to depend on the extent of disease.[37]

### Acquired Cholesteatoma

***Clinical Presentation and Etiologies.*** Cholesteatoma is composed of squamous epithelium and keratin debris, most commonly introduced into the middle ear and mastoid via retractions or perforations in the tympanic membrane. A careful otoscopic examination of the ear is essential in the initial diagnosis of cholesteatoma, and CT is typically used to diagnose the extent of the lesion or associated complications.[38] These can be subdivided into pars flaccida and pars tensa cholesteatoma. Pars flaccida lesions are caused by Eustachian tube dysfunction and begin in the Prussak space before spreading into the epitympanum. Pars tensa lesions are the result of COM and perforations within the more inferior tympanic membrane, with extension of disease medial to the ossicles and into the oval window and region of the tympanic facial nerve.

***Imaging.*** High-resolution CT is the primary imaging modality in children. The differentiation of COM without cholesteatoma from COM with cholesteatoma may be difficult. Cholesteatoma usually is associated with more extensive bony erosions, including short process of the incus, lateral wall of the attic, facial nerve canal, tegmen tympani, and superior margin of the external canal or scutum (e-Fig. 11.16). Mass effect is also a significant suggestive finding, with ossicular displacement and bulging of the tympanic

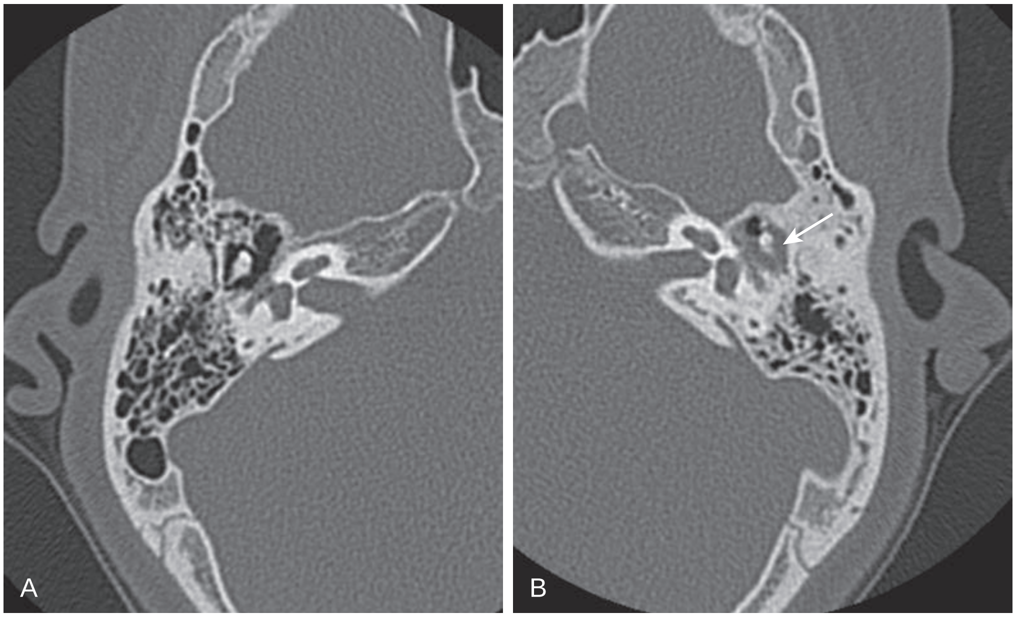

**e-Figure 11.16. Cholesteatoma in a 13-year-old.** (A) Normal axial high resolution CT of the right temporal bone. (B) Axial high-resolution CT of the left temporal bone. Significant erosion of the short process of the incus is present *(arrow),* with subtle medial displacement of the ossicles.

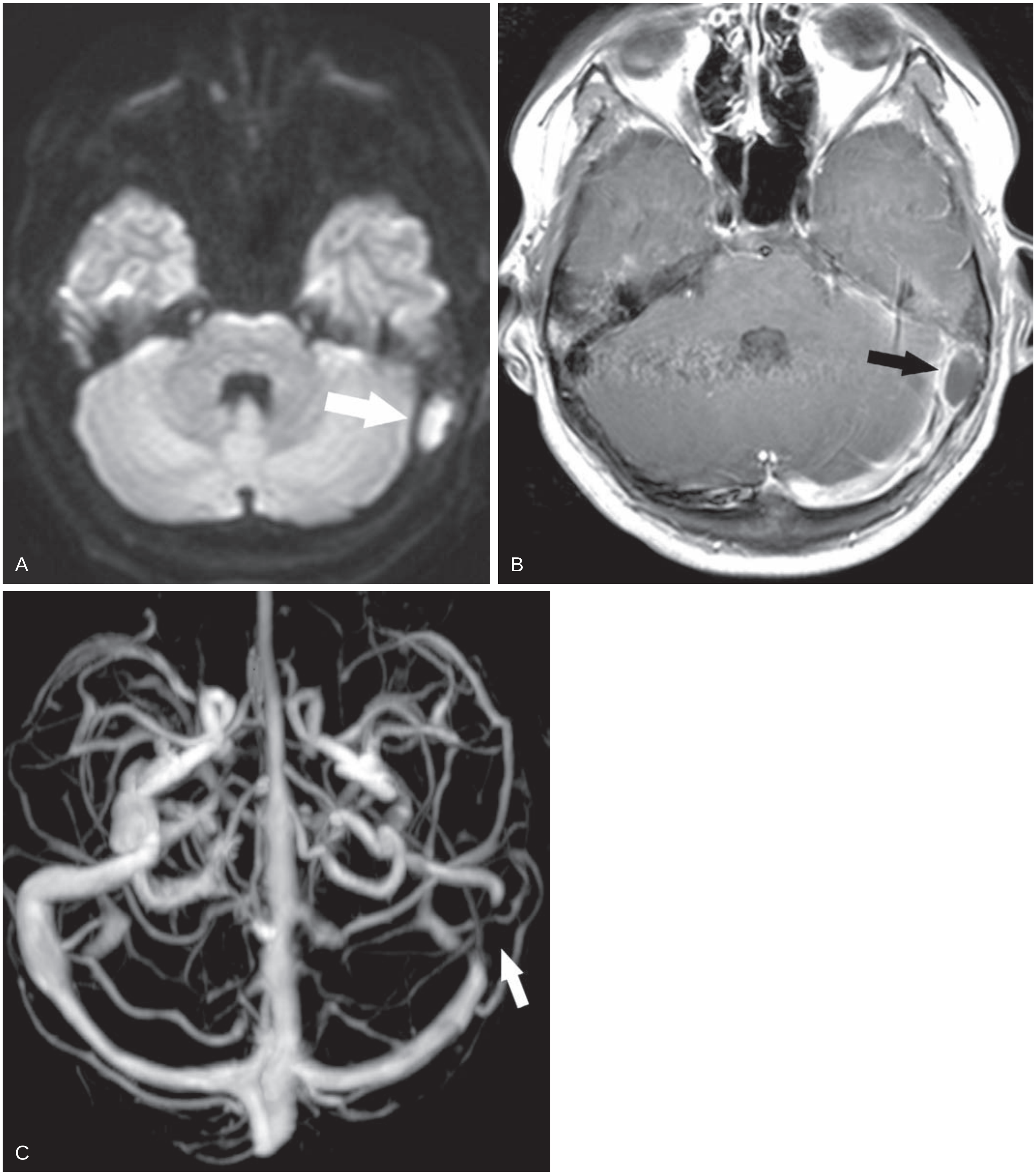

**Figure 11.13. Epidural abscess in an 11-year-old with mastoiditis.** (A and B) Axial diffusion-weighted and postgadolinium T1-weighted MR images shows restricted diffusion in a rim-enhancing fluid collection *(arrows)*. (C) Axial maximum-intensity projection image from a gadolinium-enhanced MRV shows extrinsic mass effect on the sigmoid sinus, with no intrinsic filling defect *(arrow)*. No thrombus was demonstrated after surgical drainage of the epidural abscess.

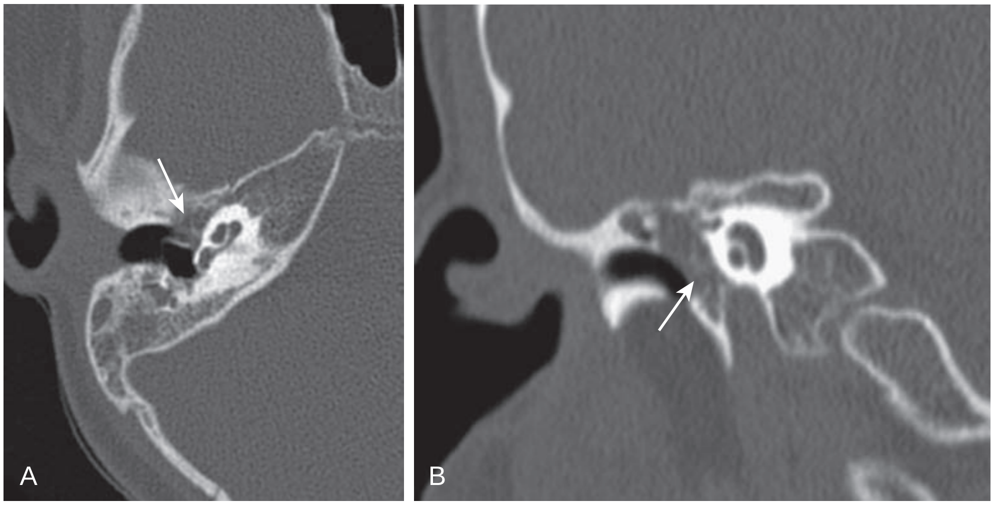

**Figure 11.15. Chronic otitis media and tympanosclerosis in a 9-year-old.** (A and B) Axial and coronal high-resolution CT images though the middle ear show abnormal soft tissue is present throughout the anterior middle ear cavity with lacelike increased density *(arrows)*.

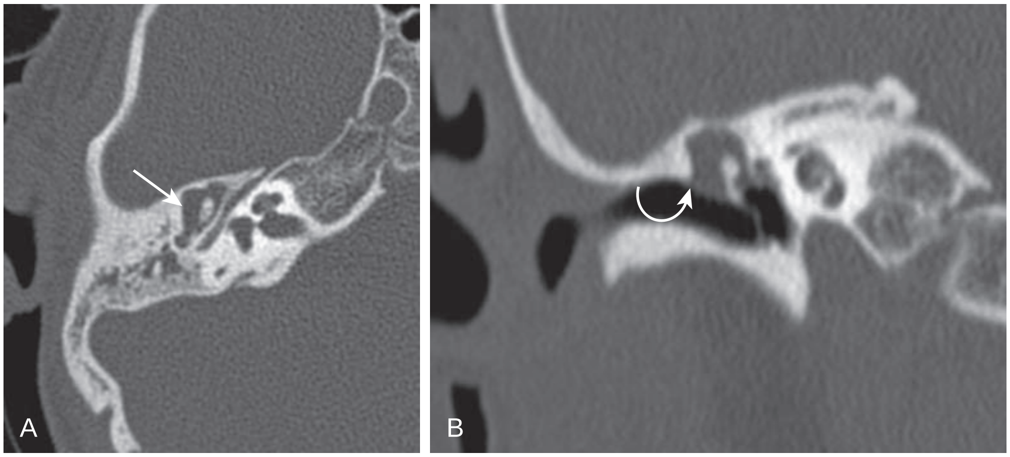

**Figure 11.17. Cholesteatoma in a 5-year-old with chronic ear infections.** (A and B) Axial and coronal high-resolution CT images through the middle ear. The ossicles are displaced medially with abnormal soft tissue in Prussak space and epitympanum *(arrow)*. The scutum is eroded *(curved arrow)*. At surgery, a pars flaccida cholesteatoma was removed.

membrane noted on CT.[34] The ossicular chain typically lies an equal distance from the medial and lateral walls of the middle ear cavity. The position of the ossicles should be evaluated on all imaging studies, with the structures displaced medially with a pars flaccida and laterally with a pars tensa cholesteatoma (Fig. 11.17). Associated erosion of Körner septum in the mastoid antrum may also be seen. Erosion may also involve the bony separation of the middle ear cavity and the cochlea or lateral semicircular canal, resulting in a gusher and complete sensorineural hearing loss (SNHL) during surgery. Cholesteatomas are histologically benign but may be locally aggressive and extend outside the confines of the temporal bone (Box 11.2).[39,40] MRI with nonechoplanar diffusion imaging may help in the diagnosis and determining the extent of disease in the initial evaluation.[41]

CT evaluation of the postoperative ear is quite difficult, and differentiation of fluid from granulation tissue and recurrent cholesteatoma is nearly impossible. Nonechoplanar diffusion MRI sequences have demonstrated cholesteatomas that are less than 5 mm in diameter and have a greater than 90% sensitivity and specificity.[42,43] Increased signal compared with regional fat on diffusion-weighted images is considered consistent with cholesteatoma. Increased signal on T2-weighted images and peripheral enhancement on postgadolinium T1-weighted images can be confirmatory (Fig. 11.18).[44] Delayed imaging can be helpful as well but not as useful in the pediatric population because of sedation issues. Fusing MRI and CT data has been investigated as a potential surgical guidance tool.[45]

**BOX 11.2** Important Structures to Evaluate in the Assessment of Cholesteatoma

Tegmen tympani and tegmen mastoidinium
Facial canal
Bony margin of lateral semicircular canal
Ossicles
Extratemporal extension
Labyrinthine involvement

***Treatment.*** Management in patients with COM and suspected cholesteatoma is usually operative. MRI, specifically diffusion-weighted imaging, has shown promise in evaluation of postoperative

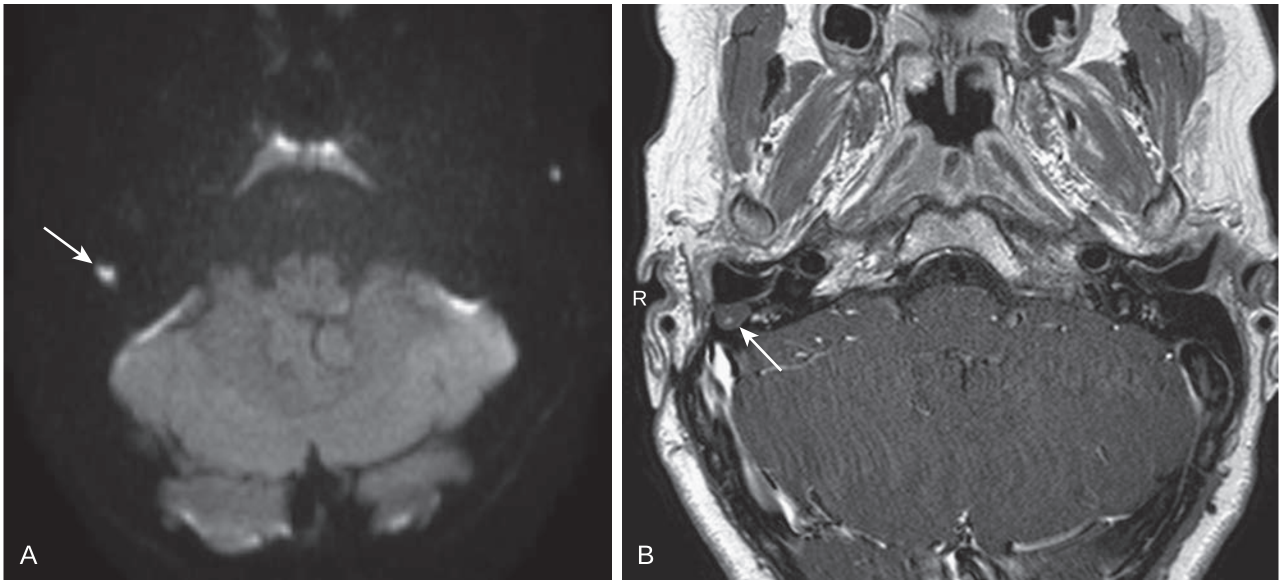

**Figure 11.18. Recurrent cholesteatoma in a 9-year-old after mastoidectomy for cholesteatoma.** (A) Axial diffusion-weighted MR image demonstrates a focus of increased signal within the right mastoid *(arrow)*. (B) Axial postgadolinium T1-weighted MR image shows the lesion to be fluid intensity without enhancement *(arrow)*. Surgery confirmed a 5-mm cholesteatoma.

patients and will likely replace the standard second-look surgery for residual cholesteatoma.[43,44]

## INNER EAR AND PETROUS TEMPORAL BONE

### Labyrinthitis

***Clinical Presentation and Etiologies.*** Bacterial labyrinthitis is most commonly a complication of meningitis but can be caused from extension of infections involving the regional mucosal spaces. Other causes of labyrinthitis include viral, syphilitic, posttraumatic with labyrinthine hemorrhage, and autoimmune disorders.[39] Cholesteatoma with resultant translabyrinthine fistula may also result in labyrinthitis.[40] Sickle cell disease has a known association with SNHL and labyrinthine hemorrhage.[46]

***Imaging.*** Labyrinthine hemorrhage manifests as increased T1-weighted signal MR images. Enhancement within the membranous labyrinth can be demonstrated on postgadolinium T1-weighted and fluid-attenuated inversion-recovery images and is predictive of the development of SNHL (e-Fig. 11.19).[47,48]

### Labyrinthitis Ossificans

***Clinical Presentation and Etiologies.*** Labyrinthitis ossificans is the end result of a labyrinthine infection, hemorrhage, or toxic insult to the membranous labyrinth. Bacterial meningitis is the most common cause and results in profound SNHL, which may occur as early as 2 weeks after the initial infection. Fibrous tissue is initially deposited within the membranous labyrinth, followed by ossification.

***Imaging.*** Acutely, MRI may demonstrate findings of labyrinthitis; however, the normal high T2-weighted signal within the cochlea and vestibular system is preserved. In the subacute fibrous phase of the inflammatory response, MRI shows loss of the normal high T2-weighted signal in the membranous labyrinth. Ossification occurs in the latter stages of labyrinthitis and is well demonstrated on CT (e-Fig. 11.20). High-resolution T2-weighted images are needed to visualize both scalar chambers of the cochlea that should be evaluated in these children, as isolated involvement of the scala tympani is common (e-Fig. 11.21).[49] A short segment of decreased signal within the proximal scala tympani of the inferior basal turn may be the only finding on T2-weighted images (e-Fig. 11.22).[50] CT shows increased density within the labyrinth late in the course of disease, and, at this stage, cochlear implantation is more difficult. Complete ossification of the cochlea must be differentiated from cochlear aplasia, which demonstrates absence of the cochlear promontory.

***Treatment.*** The only treatment available for children with labyrinthitis ossificans is cochlear implantation. The early diagnosis of fibrous cochlear obstruction on MRI caused by labyrinthitis is important because as the process continues, cochlear implantation becomes more difficult.

### Cholesterol Granuloma

***Clinical Presentation and Etiologies.*** Cholesterol granuloma is the result of inflammation and obstruction that initiates repetitive hemorrhage and subsequent formation of granulation tissue. Sites of involvement include the middle ear cavity, petrous apex, and rarely the EAC. Petrous apex cholesterol granuloma are much more common in adults, but may be found incidentally or present with headaches and deficits in cranial nerves VI, VII, IX, X, XI, and XII.[51]

***Imaging.*** The CT appearance is that of an expansile, nonaggressive, and nonenhancing soft tissue mass. The mass is of high signal intensity on both T1- and T2-weighted MRI scans and low signal on diffusion-weighted images, which differentiates the lesion from a cholesteatoma (e-Fig. 11.23). Long term follow up imaging may be of help to differentiate from simple or proteinaceous entrapped fluid.[52,53]

***Treatment.*** Asymptomatic lesions are usually monitored. If cranial nerve palsies are present or symptoms are progressive, surgical drainage may be performed with fenestration or tube placement.

## FACIAL NERVE

### Lyme Disease

***Clinical Presentation and Etiologies.*** Lyme disease is multisystemic and caused by an infection by the tick-borne spirochete

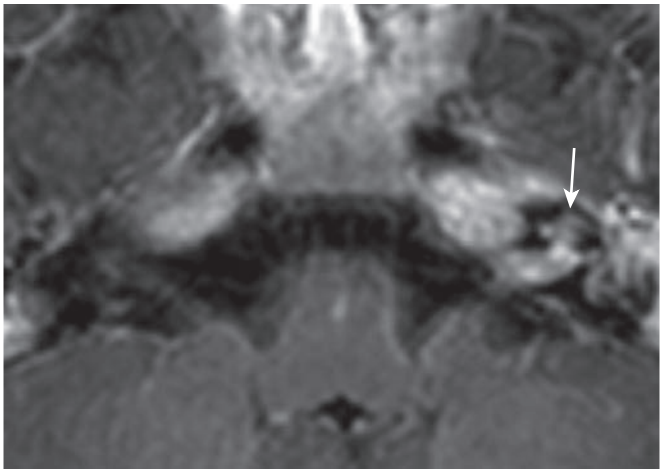

**e-Figure 11.19. Labyrinthitis due to meningitis in an 18-month-old with meningitis being evaluated for empyema.** Axial gadolinium-enhanced T1-weighted MR image through the internal auditory canal shows intense enhancement in the right internal auditory canal as well as the ipsilateral membranous labyrinth *(arrow)*. On follow-up, profound left sensorineural hearing loss was present.

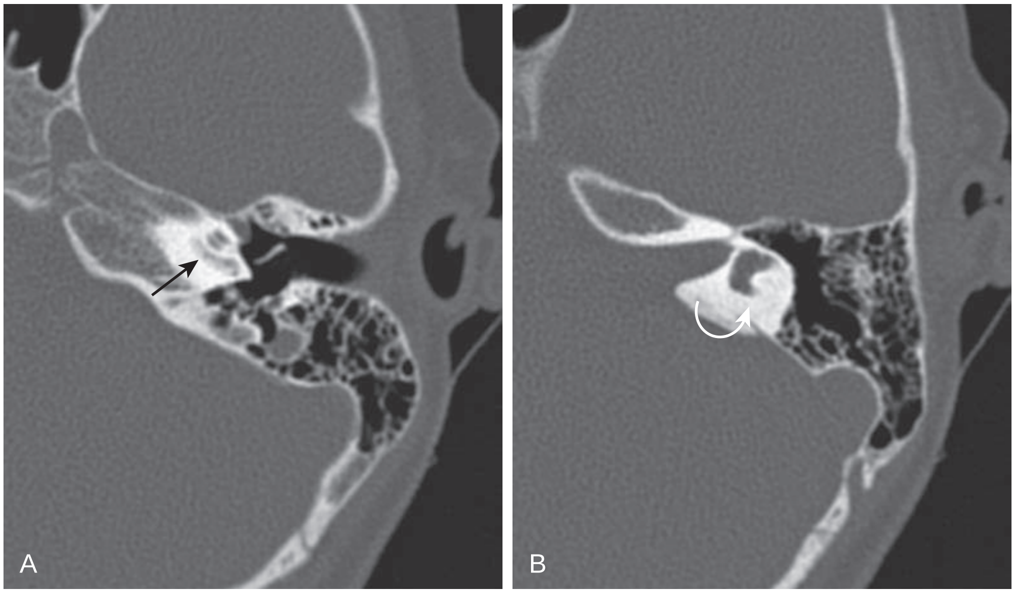

**e-Figure 11.20. Ossifying labyrinthitis in a 6-year-old with sensorineural hearing loss and remote history of prior pneumococcal meningitis.** (A and B) Axial CT images through the cochlea and vestibule, respectively. Abnormal increased density within the cochlea *(straight arrow)* and obliteration of the lateral semicircular canal *(curved arrow)* are seen.

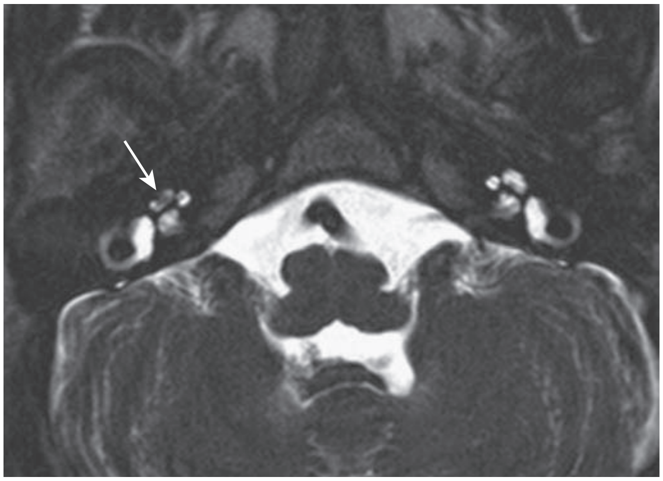

**e-Figure 11.21. Labyrinthitis in a 3-year-old with right sensorineural hearing loss and prior meningitis.** Axial three-dimensional T2-weighted MR image through the cochlea shows low T2-weighted signal intensity within the middle and apical turns of the right cochlea *(arrow),* consistent with fibrous tissue and early labyrinthitis. CT was normal without ossification demonstrated *(not shown)*.

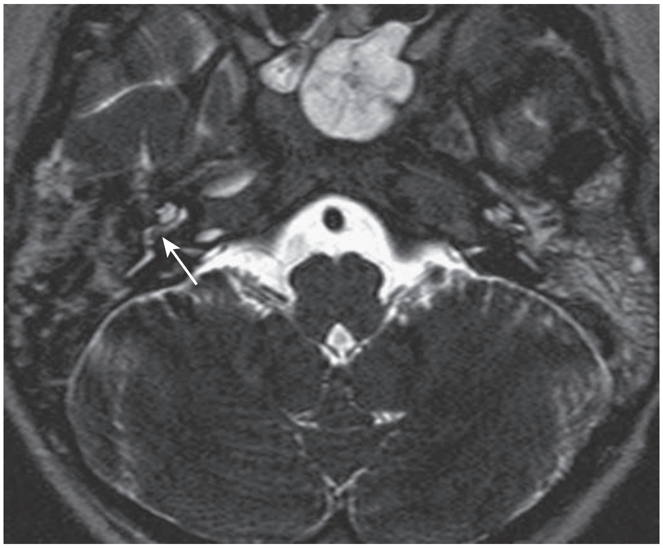

**e-Figure 11.22. Sensorineural hearing loss and meningitis in a 5-year-old.** Axial three-dimensional T2-weighted MR image through the right cochlea shows a hypointense plug at the junction of the scala tympani and vestibule *(arrow),* which was confirmed at cochlear implantation. Sphenoid sinus disease is also present.

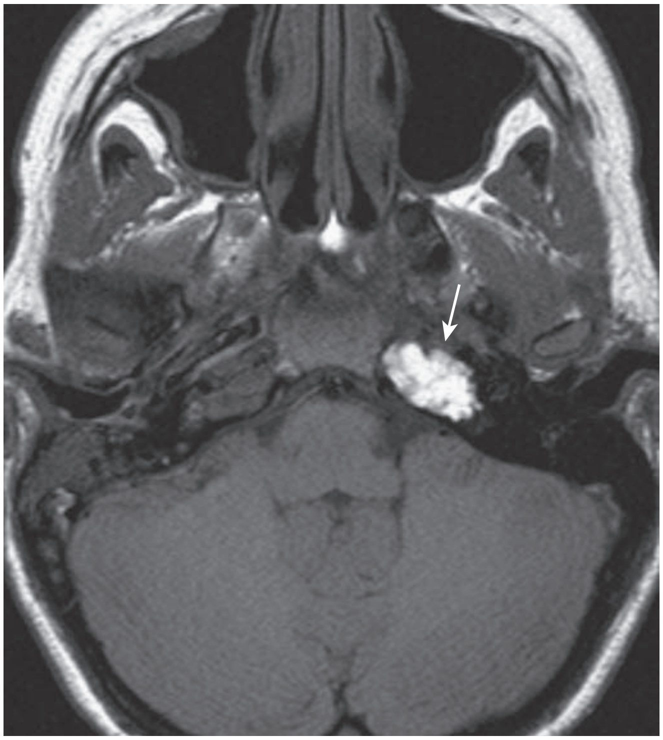

**e-Figure 11.23. Cholesterol granuloma in a 12-year-old with incidental lesion left petrous apex.** Axial T1-weighted MR image at the level of the petrous apex shows an expansile T1-weighted hyperintense lesion on the left *(arrow)*.

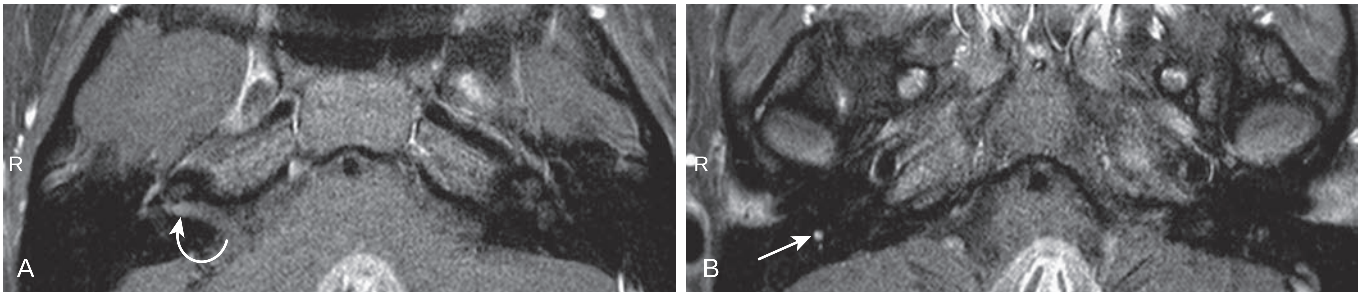

**Figure 11.26. Recurrent left facial paralysis and likely Bell palsy in a 16-year-old female.** (A and B) Axial postgadolinium T1-weighted fat-suppressed MR images show abnormal enhancement of the right intracanalicular facial nerve *(curved arrow)* and asymmetric enhancement of the tympanic and descending facial nerve on the right *(arrow)*. No mass is demonstrated and the right facial palsy eventually resolved.

*Borrelia burgdorferi.* Three stages with influenza-like symptoms exist, with a classic rash occurring in stage 1. In stage 2, cardiac and neurologic symptoms occur. Stage 3 manifests with arthritic and chronic neurologic symptoms, sometimes years later. Clinical central nervous system involvement has been reported to occur in up to 15% of patients. Neurologic symptoms include myelopathies, encephalitis, pain syndromes, cerebellar dysfunction, movement disorders, and cranial nerve palsies.[54,55] Bilateral facial nerve palsy is a common neurologic manifestation of Lyme disease and should suggest the diagnosis.

***Imaging.*** Involvement of the brain may manifest with foci of increased T2-weighted signal, but parenchymal MRI abnormalities in Lyme disease are rare. Small foci of increased T2-weighted signal are quite common, thus making the finding nonspecific.[56,57] Postgadolinium studies may show enhancement within these lesions, increasing the specificity. Meningeal enhancement may occur, but more commonly, abnormal enhancement of the involved cranial nerves is present. The facial and trigeminal nerves are most often involved, with bilateral facial nerve involvement being a classic presentation (e-Fig. 11.24).[58,59] Hearing loss has also been reported, possibly caused by cochlear nerve involvement. The differential diagnosis would include bilateral Lyme disease, autoimmune disease, demyelinating neuropathy (Miller–Fisher syndrome), and neoplastic etiologies (e-Fig. 11.25).

***Treatment.*** Oral antibiotics are the standard treatment for early-stage Lyme disease, usually doxycycline for adults and children older than 8 years. With central neurologic involvement, intravenous antibiotics are required.

## Bell Palsy

***Clinical Presentation and Etiologies.*** Bell palsy is the most common cause of acute lower motor neuron unilateral facial nerve palsy. A viral etiology has been postulated; however, ischemic and possibly autoimmune contributions are likely contributing factors.[60] Bell palsy is a diagnosis of exclusion, and other potential etiologies of facial nerve paralysis in childhood include trauma, infection, neoplasm, and congenital anomalies. Virologic tests have suggested herpes simplex type 1 and varicella-zoster as possible etiologies.

***Imaging.*** With typical Bell palsy, complete recovery usually occurs within 6 to 8 weeks, and imaging is not necessary in the acute phase. If prolonged paralysis or other neurologic signs are present, MRI evaluation is suggested.[61] Imaging of Bell palsy demonstrates abnormal, asymmetric enhancement and mild enlargement of the facial nerve. It is important to realize that the normal facial nerve segments can enhance (geniculate ganglion, tympanic, and mastoid segments). The labyrinthine segment can normally show some mild enhancement. Any enhancement of the facial nerve within the internal auditory canal and strong enhancement of the labyrinthine segment is considered pathologic (Fig. 11.26).[62,63] Mild enhancement of the normal canalicular facial nerve may be noted at 3-Tesla MRI.[64]

Varicella zoster virus infection can also result in the more severe Ramsay Hunt syndrome, manifesting clinically with facial nerve palsy, SNHL, tinnitus, vertigo, ataxia, and a painful vesicular eruption within the region of the auricle.[65] MRI demonstrates not only abnormal enhancement of the facial nerve but also the vestibulocochlear nerve and membranous labyrinth (e-Fig. 11.27).[66]

***Treatment.*** The quantitative intensity of enhancement has been correlated with the outcome for these patients.[67] Antiviral agents and corticosteroids are the preferred treatment in the acute phase; however, antiviral therapy has little effect on prognosis.[68] Surgery to decompress the facial nerve is controversial when performed in patients with complete Bell palsy that has not responded to medical therapy. Imaging can potentially direct the surgeon to the more affected portion of the nerve.[69]

### KEY POINTS

- Carefully inspect the images in patients with mastoiditis for intracranial and venous complications.
- Mastoid fluid may result from dural sinus thrombosis and not be the cause.
- A cholesteatoma demonstrates mass effect and bony erosion, and has increased diffusion-weighted MR signal.
- MRI is more sensitive in demonstrating cochlear obstruction in the fibrous stage of labyrinthitis ossificans.
- Enhancement of the labyrinth is predictive of the development of SNHL in children with meningitis.

### SUGGESTED READINGS

Dobben GD, Raofi B, Mafee MF, et al. Otogenic intracranial inflammation: role of magnetic resonance imaging. *Top Magn Reson Imaging*. 2000;11:76–86.
Huang BY, Zdanski C, Castillo. Pediatric sensorineural hearing loss, part 2: syndromic and acquired causes. *AJNR Am J Neuroradiol*. 2012;33:399–406.
Lemmerling MM, De Foer B, Verbist BM, et al. Imaging of inflammatory and infectious diseases of the temporal bone. *Neuroimaging Clin N Am*. 2009;19:321–337.
Li P, Linos E, Gurgel RK, et al. Evaluating the utility of non-echoplanar diffusion-weighted imaging in the preoperative evaluation of cholesteatoma: a meta-analysis. *Laryngoscope*. 2013;123:1247–1250.
Oestreicher-Kedem Y, Raveh E, Kornreich L. Complications of mastoiditis in children at the onset of the new millennium. *Ann Otol Rhinol Laryngol*. 2005;114:147–152.
Radhakrishnan R, Son HJ, Koch BL. Petrous apex lesions in the pediatric population. *Pediatr Radiol*. 2014;44:325–339.

### REFERENCES

Full references for this chapter can be found on www.expertconsult.com.

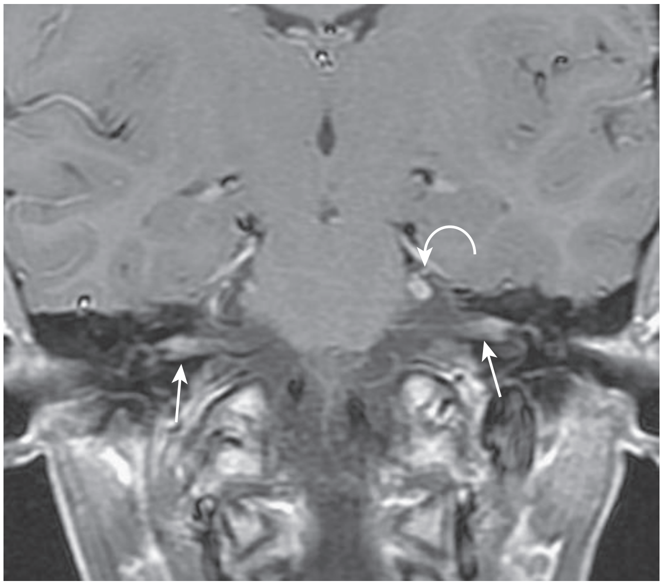

**e-Figure 11.24. Lyme disease and multiple cranial palsies in a 15-year-old.** Coronal postgadolinium T1-weighted MR image shows abnormal enhancement of the facial nerves within the internal auditory canals *(arrows)* and an enlarged, enhancing left trigeminal nerve *(curved arrow)*. *(Case courtesy of L. Gilbert Vezina, MD.)*

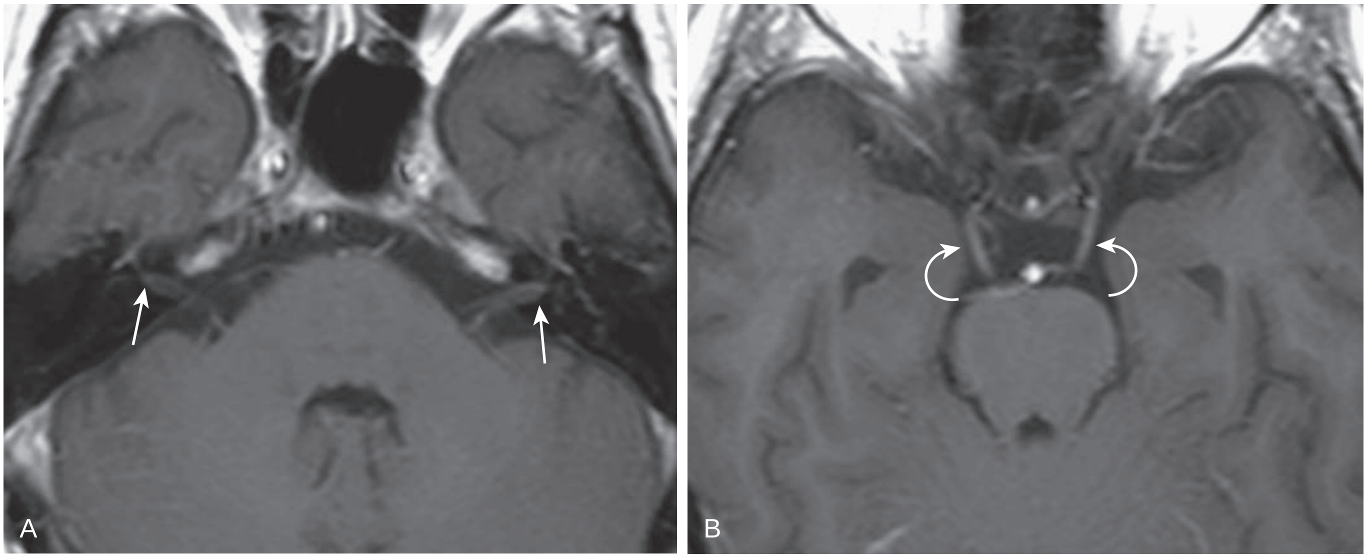

**e-Figure 11.25. Bilateral facial nerve palsy in a 17-year-old.** (A and B) Axial postgadolinium T1-weighted MR images show abnormal enhancement of the intracanalicular facial nerves and labyrinthine segment on the right *(arrows)*. Abnormal enhancement of both third nerves *(curved arrows)* is also present. The child was diagnosed with polyphenotypic leukemia.

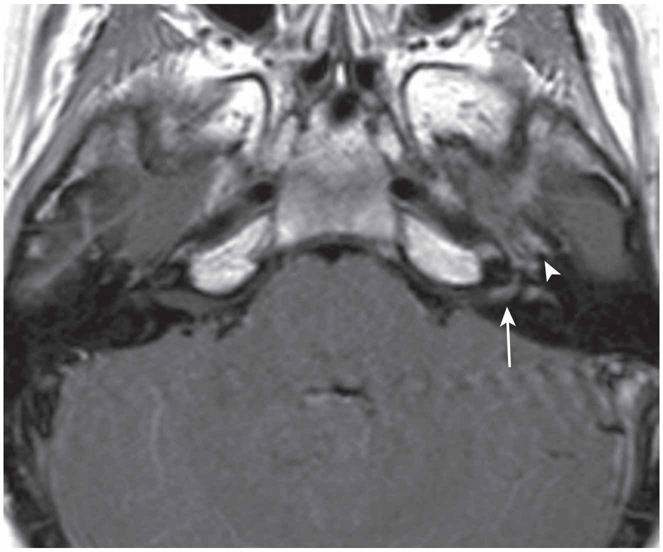

**e-Figure 11.27. Ramsay Hunt syndrome in an 11-year-old with left facial nerve palsy, hearing loss, and vesicular eruption.** Axial post-gadolinium T1-weighted MR image shows abnormal enhancement within the lateral left internal auditory canal *(arrow)* as well as the left vestibule *(arrowhead)*.

## REFERENCES

1. Ho T, Vrabec JT, Yoo D, et al. Otomycosis: clinical features and treatment indications. *Otolaryngol Head Neck Surg*. 2006;135:787–791.
2. Lowe LH, Stokes LS, Johnson JE. Swelling at the angle of the mandible: imaging of the pediatric parotid gland and periparotid region. *Radiographics*. 2001;21:1211–1227.
3. Abramo TJ, Beers SL. Otitis externa review. *Pediatr Emerg Care*. 2004;20:250–253.
4. Chevallier KM, Wiggins RH, Quinn NA, et al. Differentiating pediatric rhabdomyosarcoma and Langerhans cell histiocytosis of the temporal bone by imaging appearance. *AJNR Am J Neuroradiol*. 2016;37:1185–1189.
5. Franco-Vidal V, Blanchet H, Bebear C, et al. Necrotizing external otitis: a report of 46 cases. *Otol Neurotol*. 2007;28:771–773.
6. Berenholz L, Katzenell U, Harell M. Evolving resistant pseudomonas to ciprofloxacin in malignant otitis externa. *Laryngoscope*. 2002;112:1619–1622.
7. Kesser BW, Carfrae MJ. Malignant otitis externa. *Otolaryngol Clin North Am*. 2008;41:537–549.
8. Mingkwansook V, Curtin HD, Kelly HR. CT findings in the external auditory canal after transcanal surgery. *AJNR Am J Neuroradiol*. 2015;36:982–986.
9. Okapala NCE, Siraj QH, Nilssen E, et al. Radiological and radionuclide investigation of malignant otitis externa. *J Laryngol Otol*. 2005;119:71–75.
10. Galletti F, Cammaroto G, Galletti B, et al. Technetium-99m ($^{99m}$Tc)-labelled sulesomab in the management of malignant external otitis: is there any role. *Eur Arch Otorhinolaryngol*. 2015;272:1377–1382.
11. Peleg U, Perez R, Raveh D, et al. Stratification for malignant external otitis. *Otolaryngol Head Neck Surg*. 2007;137:301–305.
12. Yoon YH, Park CH, Kim EH, et al. Clinical characteristics of external canal cholesteatoma in children. *Otolaryngol Head Neck Surg*. 2008;139:661–664.
13. Nemzek WR, Swartz JD. Temporal bone: inflammatory disease. In: Som PM, Curtin HAD, eds. *Head and Neck Imaging*. 4th ed. St. Louis, MO: Mosby; 2003:1173–1244.
14. Morris PS, Leach AJ. Acute and chronic otitis media. *Pediatr Clin North Am*. 2009;56:1383–1399.
15. Kristian A, Hostmark K, Hansen S, et al. Acute mastoiditis in children: a 10-year retrospective and validated multicenter study. *Pediatr Infect Dis J*. 2013;32:436–440.
16. Fernandez-Latorre F, Menor-Serano F, Alonso-Charterine S, et al. Langerhan's cell histiocytosis of the temporal bone in pediatric patients: imaging and follow-up. *AJR Am J Roentgenol*. 2000;174:217–221.
17. Oestreicher-Kedem Y, Raveh E, Kornreich L. Complications of mastoiditis in children at the onset of the new millennium. *Ann Otol Rhinol Laryngol*. 2005;114:147–152.
18. Glikkich RE, Eavey RD, Iannuzzi RA, et al. A contemporary analysis of acute mastoiditis. *Arch Otolaryngol Head Neck Surg*. 1996;122:135–139.
19. Palva T, Virtanen H, Makinen J. Acute and latent mastoiditis in children. *J Laryngol Otol*. 1985;99:127–136.
20. Migirov L. Computed tomographic versus surgical findings in complicated acute otomastoiditis. *Ann Otol Rhinol Laryngol*. 2003;112:675–677.
21. Mafee MF, Singleton EL, Valvassori GE. Acute otomastoiditis and its complications: role of CT. *Radiology*. 1985;155:391–397.
22. Scrafton DK, Qureishi A, Nogueira C, et al. Luc's Abscess as an unlucky complication of mastoiditis. *Ann R Coll Surg Engl*. 2014;96:e28–e30.
23. Coca-Pelaz A, Vicanco-Allende A, Meilan-Martinez A, et al. Grizel's syndrome as a sequela of complicated acute mastoiditis. *Acta Otorrinolaringol Esp*. 2013;64:161–164.
24. Saat R, Mahmood G, Laulajainen-Hongisto A, et al. Comparison of MR imaging findings in paediatric and adult patients with acute mastoiditis and incidental intramastoid bright signal on T2-weighted images. *Eur Radiol*. 2016;26:2632–2639.
25. Marom T, Roth Y, Boaz M, et al. Acute mastoiditis in children: necessity and timing of imaging. *Pediatr Infect Dis J*. 2016;35:30–34.
26. Gradeningo G. Ueber Circumscripte leptomeningitis mit spinalen symptomen. *Arch Ohrenheilk*. 1904;52:60–62.
27. Horowitz G, Fishman G, Brenner A, et al. A novel radiographic sign and new classifying system in mastoiditis-related epidural abscess. *Otol Neurotol*. 2015;36:1378–1382.
28. Dobben GD, Raofi B, Mafee MF, et al. Otogenic intracranial inflammation: role of magnetic resonance imaging. *Top Magn Reson Imaging*. 2000;11:76–86.
29. Robson CD, Robertson RL, Barnes PD. Imaging of pediatric temporal bone abnormalities. *Neuroimaging Clin N Am*. 1999;9:133–155.
30. Kuczkowski J, Dubaniewicz-Wybieralska M, Przewozny T, et al. Otitic hydrocephalus associated with lateral sinus thrombosis and acute mastoiditis in children. *Int J Pediatr Otorhinolaryngol*. 2006;70:1817–1823.
31. Shah LM, Khaleel ZL, Harnsberger HR, et al. Mastoid findings secondary to posterior fossa dural venous thrombosis. *AJR Am J Roentgenol*. 2013;201:406–411.
32. Bakhos D, Trijolet JP, Moniniere S, et al. Conservative management of acute mastoiditis in children. *Arch Otolaryngol Head Neck Surg*. 2011;137:346–350.
33. Zanetti D, Nassif N. Indications for surgery in acute mastoiditis and their complications in children. *Int J Pediatr Otorhinolaryngol*. 2006;70:1175–1182.
34. Mafee MF, Aimi K, Kahen HL, et al. Chronic otomastoiditis: a conceptual understanding of CT findings. *Radiology*. 1986;160:193–200.
35. Palacios E, Valvassori G. Tympanosclerosis. (brief article) (statistical data included). *Ear Nose Throat J*. 2000;79:17.
36. Alzoubi FQ, Odat HA, Al-balas HA, et al. The role of preoperative CT scan in patients with chronic otitis media. *Eur Arch Otorhinolaryngol*. 2009;266:807–809.
37. Yetiser S, Hidir Y, Karatas E, et al. Management of tympanosclerosis with ossicular fixation: review and presentation of long-term results of 30 new cases. *J Otolaryngol*. 2007;36:303–308.
38. Isaacson G. Diagnosis of pediatric cholesteatoma. *Pediatrics*. 2007;120:603–608.
39. Lemmerling MM, De Foer B, Verbist BM, et al. Imaging of inflammatory and infectious diseases of the temporal bone. *Neuroimaging Clin N Am*. 2009;19:321–337.
40. Mafee MF. MRI and CT in the evaluation of acquired and congenital cholesteatomas of the temporal bone. *J Otolaryngol*. 1993;22:239–248.
41. Migirov L, Wolf M, Grrenberg G, et al. Non-EPI DW MRI in planning the surgical approach to primary and recurrent cholesteatoma. *Otol Neurotol*. 2014;35:121–125.
42. De Foer B, Vercruysse JP, Bernaerts A, et al. Middle ear cholesteatoma: non-echo planar diffusion-weighted imaging versus delayed gadolinium-enhanced T1-weighted MR imaging—value in detection. *Radiology*. 2010;255:866–872.
43. Li P, Linos E, Gurgel RK, et al. Evaluating the utility of non-echo-planar diffusion-weighted imaging in the evaluation of cholesteatoma: a meta-analysis. *Laryngoscope*. 2013;123:1247–1250.
44. Schwartz KM, Lane JI, Bolster BD, et al. The utility of diffusion weighted imaging for cholesteatoma evaluation. *AJNR Am J Neuroradiol*. 2011;32:430–436.
45. Yamashita K, Hiwatashi A, Togao O, et al. High-resolution three-dimentional diffusion-weighted MRI/CT image data fusion for cholesteatoma surgical planning: a feasibility study. *Eur Arch Otorhinolaryngol*. 2015;272:3821–3824.
46. Liu BP, Saito N, Wang JJ, et al. Labyrinthitis ossificans in a child with sickle cell disease: CT and MRI findings. *Pediatr Radiol*. 2009;39:999–1001.
47. Hegarty JL, Patel S, Fischbein N, et al. The value of enhanced magnetic resonance imaging in the evaluation of endocochlear disease. *Laryngoscope*. 2002;112:8–17.
48. Kopelovich JC, Germiller JA, Laury AM, et al. Early prediction of postmeningitic hearing loss in children using magnetic resonance imaging. *Arch Otolaryngol Head Neck Surg*. 2011;137:441–447.
49. Isaacson B, Booth T, Kutz JW, et al. Labyrinthitis ossificans: how accurate is MRI in predicting cochlear obstruction? *Otolaryngol Head Neck Surg*. 2009;140:692–696.
50. Booth TN, Roland P, Kutz JW, et al. High-resolution 3-D T2-weighted imaging in the diagnosis of labyrinthitis ossificans: emphasis on subtle cochlear involvement. *Pediatr Radiol*. 2013;43:1584–1590.
51. Miyamoto RC, Miyamoto RT. Pediatric neurotology. *Semin Pediatr Neurol*. 2003;4:298–303.
52. Pisaneschi MJ, Langer B. Congenital cholesteatoma and cholesterol granuloma of the temporal bone: role of magnetic resonance imaging. *Top Magn Reson Imaging*. 2000;11:87–97.
53. Radhakrishnan R, Jung Son H, Koch BL. Perous apex lesions in the pediatric population. *Pediatr Radiol*. 2014;44:325–339.
54. Cryan B, Wright DJ. Lyme disease in paediatrics. *Arch Dis Child*. 1991;66:1359–1363.
55. Logigian EL, Kaplan RF, Steere AC. Chronic neurologic manifestations of Lyme disease. *N Engl J Med*. 1990;323:1438–1444.
56. Fernandez RE, Rothberg M, Ferencz G, et al. Lyme disease of the CNS: MR imaging findings in 14 cases. *AJNR Am J Neuroradiol*. 1990;11:428–431.

57. Belman AL, Coyle PK, Roque C, et al. MRI findings in children infected by *Borrelia burgdorferi*. *Pediatr Neurol*. 1992;8:428–431.
58. Vanzieleghem B, Lemmerling M, Carton D, et al. Lyme disease in a child presenting with bilateral facial nerve palsy: MRI findings and review of the literature. *Neuroradiology*. 1998;40:739–742.
59. Agarwal R, Sze G. Neuro-Lyme disease: MR imaging findings. *Radiology*. 2009;253:167–173.
60. Yanagihara N. Etiology and pathophysiology of Bell's palsy. *Ann Otol Rhinol Laryngol*. 1988;137(suppl):1–27.
61. Alaani A, Hogg R, Saravanappa N, et al. An analysis of diagnostic delay in unilateral facial paralysis. *J Laryngol Otol*. 2005;119:184–188.
62. Tren R, Dillon WP, Jackler RK. Contrast-enhanced MR imaging of the facial nerve in 11 patients with Bell's palsy. *AJNR Am J Neuroradiol*. 1990;11:735–741.
63. Veillon F, Ramos-Taboada L, Abu-Eid M, et al. Imaging of the facial nerve. *Eur J Radiol*. 2010;74:341–348.
64. Hong HS, Yi BH, Cha JG, et al. Enhancement pattern of the normal facial nerve at 3.0 T temporal MRI. *Br J Radiol*. 2010;83:118–121.
65. Cha HE, Baek MK, Yoon BK, et al. Clinical features and management of facial nerve paralysis in children; analysis of 24 cases. *J Laryngol Otol*. 2010;124:402–406.
66. Sartoretti-Schefer S, Wichmann W, Valavanis A. Idiopathic, herpetic, and HIV-associated facial nerve palsies: abnormal enhancement patterns. *AJNR Am J Neuroradiol*. 1994;15:479–485.
67. Kress B, Griesbeck F, Stippich C, et al. Bell palsy: quantitative analysis of MR imaging data as a method of predicting outcome. *Radiology*. 2004;230:504–509.
68. Wolfovitz A, Yehudai N, Luntz M. Prognostic factors for facial nerve palsy in a pediatric population: a retrospective study and review. *Otol Neurotol*. 2016;doi:10.1002/lary.26307.
69. Grogan PM, Gronseth GS. Practice parameter: steroids, acyclovir, and surgery for Bell's palsy (an evidence-based review): report of the Quality Standards Subcommittee of the American Academy of Neurology. *Neurology*. 2001;56:830–836.

# 12

# Neoplasia

*Korgün Koral*

## OVERVIEW

Pediatric neoplasms of the temporal bone are relatively infrequent. However, the imaging specialist has to be familiar with the common malignancies and their imaging appearances. One important task of the radiologist is to define the extent of the lesion both within the temporal bone and, if present, intracranially (Box 12.1).

## RHABDOMYOSARCOMA

Rhabdomyosarcoma is the most common soft tissue sarcoma of childhood, accounting for approximately 60% of all soft tissue sarcomas and 5% to 8% of all childhood cancers.[1] Approximately 40% of all rhabdomyosarcomas are in the head and neck region. Temporal bone rhabdomyosarcomas are relatively rare. In a study of 39 pediatric head and neck rhabdomyosarcoma, there were 6 patients (15%) with temporal bone involvement.[2] Histologically, embryonal rhabdomyosarcomas are the most common type.[3] The most common presentation of rhabdomyosarcoma is chronic otitis media that is not responsive to therapy.[2] Some patients may present with swelling or facial nerve palsy.[3]

The role of computed tomography (CT) is to demonstrate bone erosion and soft tissue mass (Fig. 12.1A). Magnetic resonance imaging (MRI) is indicated for evaluation of intracranial extension and involvement of the vascular structures (internal carotid artery, jugular vein, and dural venous sinuses). MRI generally shows a nonspecific, enhancing, destructive mass (Fig. 12.1B and D).

Treatment regimens combining chemotherapy and radiotherapy, with or without surgery, have improved the once dismal outcomes of patients with temporal bone rhabdomyosarcoma. In a study of 14 patients, a 5-year disease-free survival rate of 82% was reported.[3]

## LANGERHANS CELL HISTIOCYTOSIS

Langerhans cell histiocytosis (LCH) is a histiocytic proliferation of unknown etiology. The diagnosis of LCH is made by demonstration of the characteristic electron microscopic features or CD1a positivity in the involved tissue.[4] In children younger than 15 years, the incidence of LCH is estimated to be 0.5 in 100,000 children per year.[5] The mean age at presentation is 12 years, and there is no sex predilection. The most common form of LCH is a solitary osteolytic lesion of the skull and spine.[6]

Although ear and temporal bone involvement is relatively rare, symptoms of ear infection may be the reason to seek medical attention. The temporal bone may be involved in isolation or as part of polyostotic or systemic disease.[7] Temporal bone involvement may be unilateral or bilateral (30% of cases). Conductive hearing loss is occasionally seen.[8]

On CT, the lesion is characterized by a nonspecific, lytic soft tissue mass. As in the calvarial LCH, there is no periosteal reaction of the residual bone, which has sharp, well-defined margins (Fig. 12.2). The role of MRI is in the evaluation of hypothalamic-pituitary axis, which may be concomitantly involved in systemic LCH. The treatment of temporal bone LCH is generally with chemotherapy.

## LYMPHOMA

Primary lymphoma of the temporal bone is rare.[9] The lesions are generally lytic and may be associated with epidural components (Fig. 12.3).

## ENDOLYMPHATIC SAC TUMOR

Endolymphatic sac tumor (ELST) is a rare neoplasm arising from the epithelium of the endolymphatic sac. This adenomatous neoplasm is typically located at the posterior aspect of the temporal bone. ELST is rare in adults and even rarer in children. Patients with von Hippel–Lindau disease have an increased risk of developing ELST, particularly bilaterally.[10] Characteristic imaging findings show a retrolabyrinthine mass resulting in bone erosion (Fig. 12.4). On MR, despite the tumor's increased vascularity, signal voids are rarely seen.[11] The lesions show intense enhancement with intravenous gadolinium. The treatment is wide surgical resection.

## OSTEOSARCOMA

Primary osteosarcoma of the temporal bone is exceedingly rare.[12] The lesions can be osteoblastic, lytic, or mixed (Fig. 12.5).

## EXOSTOSIS AND OSTEOMA

Exostoses and osteomas are benign bony tumors of the external auditory canal.[11] These tumors are rarely encountered in children. Exostoses generally result from prolonged exposure to cold water and referred to as the "surfer's ear" or "swimmer's ear." Osteomas are rarer than exostoses and may also arise in the middle ear, mastoid, or petrous segments of the temporal bone.

**BOX 12.1**

The imaging report of a temporal mass should include:
- Location (external ear/middle ear and mastoid air cells/inner ear/cerebellopontine angle cistern/internal auditory canal)
- Cranial nerve and vascular involvement
- Intracranial extension

## Abstract:

In this chapter some common and less common neosplasms involving the pediatric temporal bone are discussed. Langherhans cell histiocytosis is by far the most common lesion involving the pediatric temporal bone. Rhabdomyosarcoma is seen less frequently. The role of imaging is critical in assessing the extent of the disease process and evaluating response to therapy.

## Keywords:

temporal bone
pediatric
children
tumor
magnetic resonance imaging
computerized tomography

## SCHWANNOMA

Schwannomas are rare in children, but they are encountered in children with neurofibromatosis type 2 (NF2). For NF2, the best diagnostic clue is bilateral enhancing cerebellopontine angle/internal auditory canal masses (Fig. 12.6). Both the vestibular nerve and facial nerve may be involved in the cerebellopontine angle or internal auditory canal. Treatment is resection with the goal of preservation of hearing. Schwannomas can be seen in the remainder of the cranial nerves. Intracranial and spinal meningiomas and ependymomas may be seen.[13]

## HEMANGIOPERICYTOMA

Hemangiopericytoma is a highly vascular tumor, which is rarely seen in children.[14] In the cerebellopontine angle, the main differential consideration is meningioma (Fig. 12.7). Treatment is resection usually followed with radiotherapy.

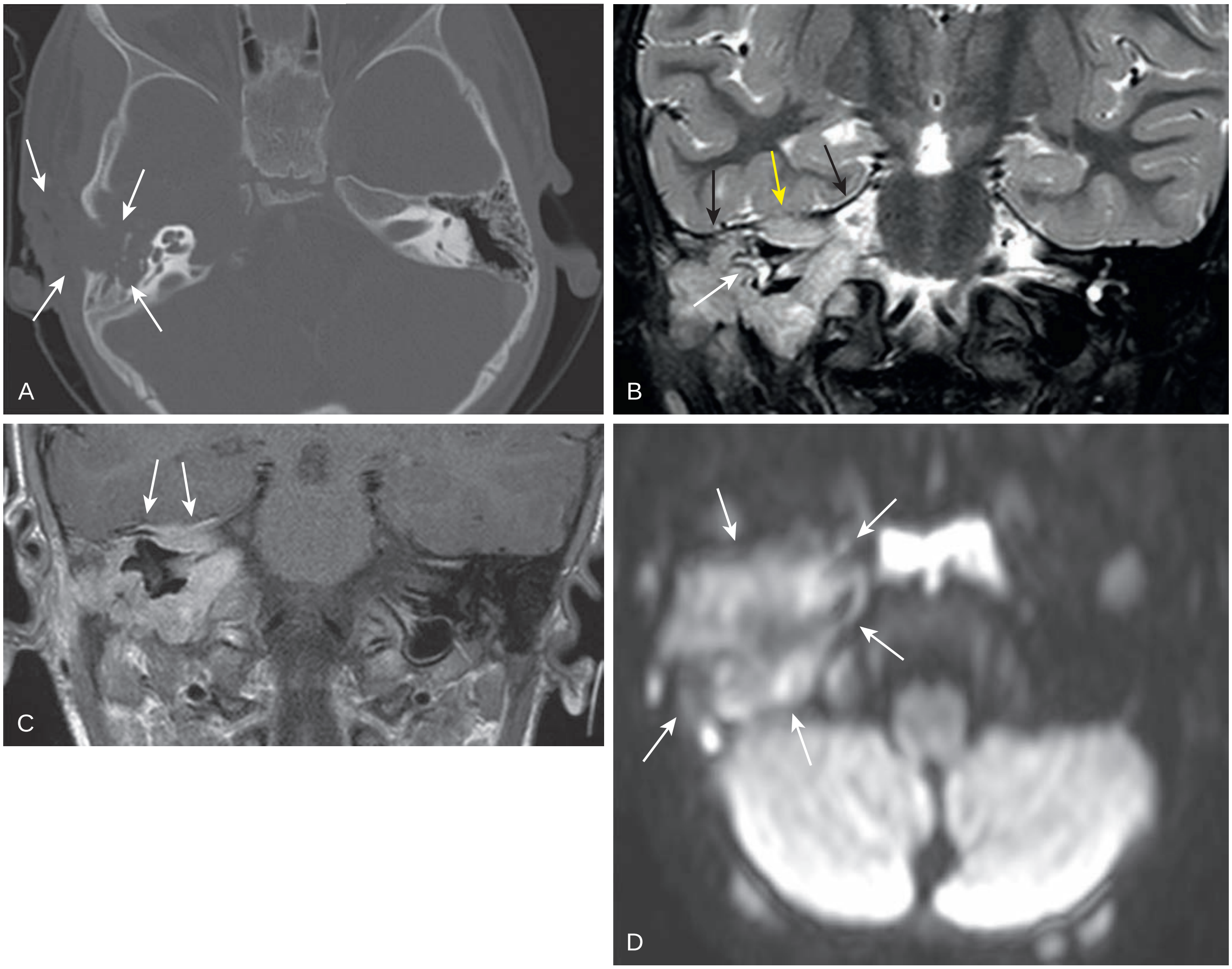

**Figure 12.1. Rhabdomyosarcoma in a 2-year-old boy with hearing loss and right periauricular swelling.** (A) Axial CT shows a large, soft tissue mass of the right temporal bone *(arrows)* with extensive osseous destruction. (B) Coronal STIR MR image shows the hyperintense mass of the right temporal bone. The focal loss of integrity of the floor of right middle cranial fossa *(yellow arrow)* and intact dura *(black arrows)* are shown. Destruction of the bony labyrinth *(white arrow)* by the mass is shown. (C) Coronal fat-suppressed gadolinium-enhanced T1-weighted MR image shows thick enhancement at the floor of the right middle cranial fossa *(arrows),* consistent with parameningeal spread. (D) Axial diffusion weighted MR image shows that the lesion *(arrows)* is predominantly isointense to adjacent brain indicative of hypercellularity.

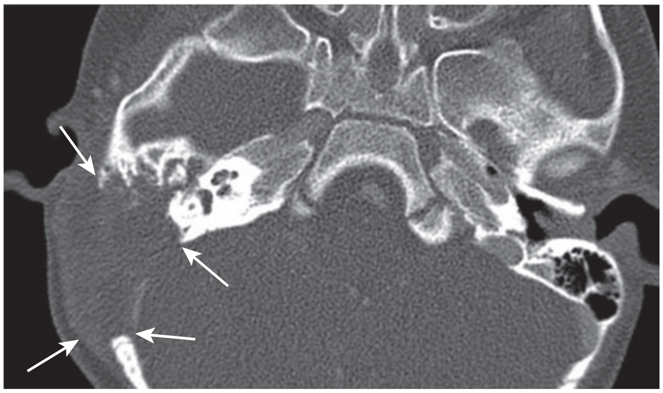

**Figure 12.2. Langerhans cell histiocytosis in 3-year-old boy with retroauricular mass.** Axial CT shows a lytic lesion *(arrows)* involving the mastoid, petrous, and squamous segments of the right temporal bone. The margins of the residual bone are sharp.

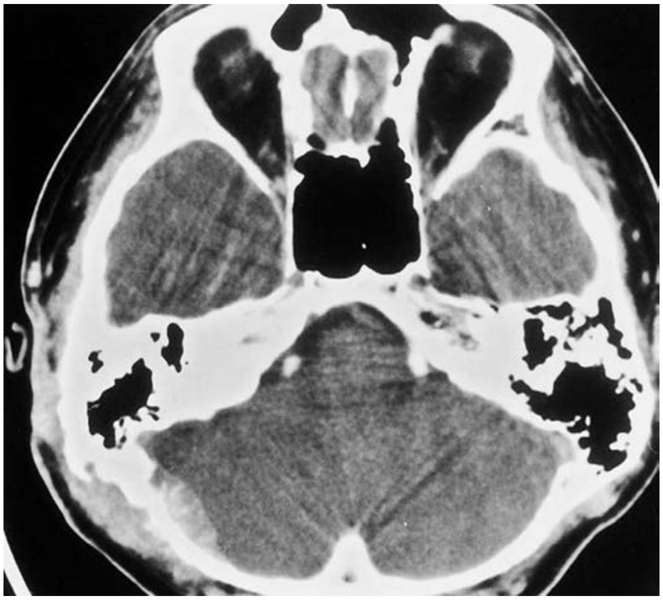

**Figure 12.3. Lymphoma in a 15-year-old boy with a retroauricular mass.** An enhancing mass is seen on CT arising from the mastoid segment of the temporal bone and involving the occipital bone (*Clin. Imaging.* 2003;27:386–388).

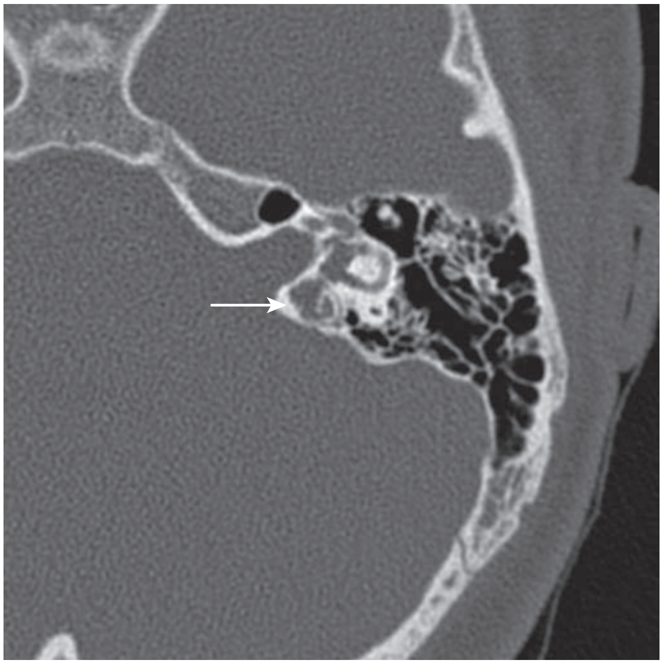

**Figure 12.4. Endolymphatic sac tumor in 14-year-old boy with sensorineural hearing loss.** Axial, noncontrast CT shows a lytic, expansile lesion *(arrow)* posterior to the vestibule, in the expected location of the vestibular aqueduct.

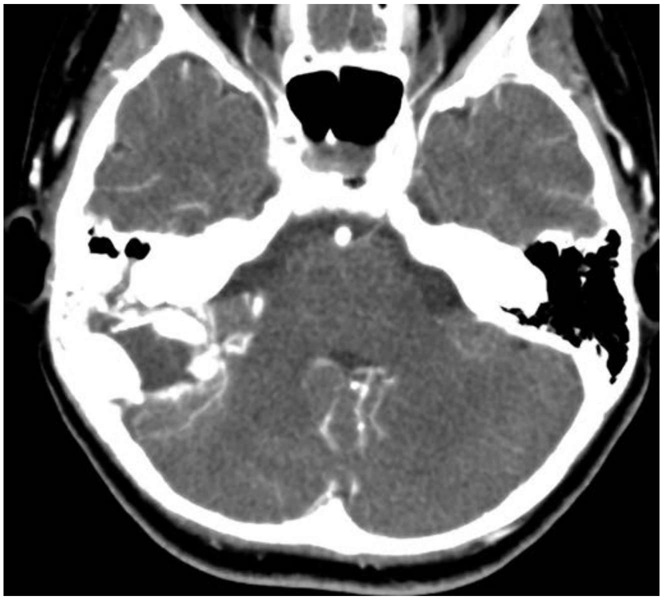

**Figure 12.5. Osteosarcoma in a 9-year-old female, with right facial nerve palsy, who underwent heart transplantation 4 years earlier.** Contrast enhanced axial CT image shows a lytic, vascular mass arising from the mastoid segment of the temporal bone with intracranial extension.

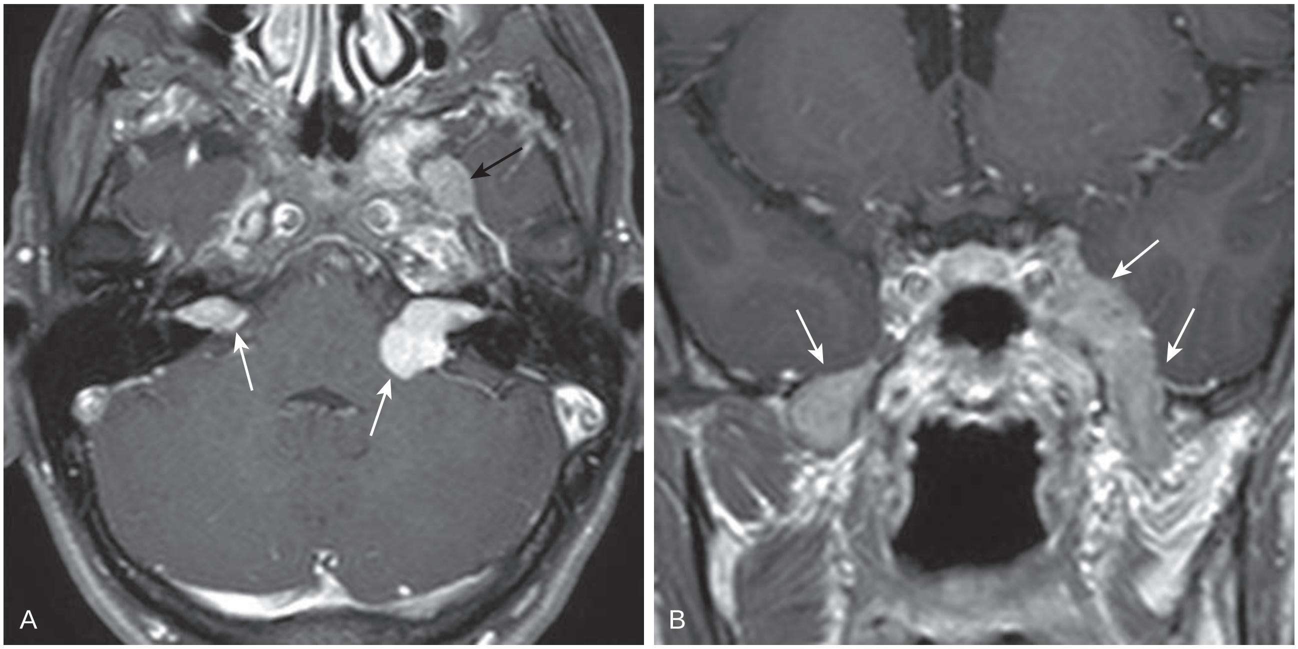

**Figure 12.6. Vestibular schwannomas in a 15-year-old male with neurofibromatosis type 2.** (A) Axial fat-suppressed gadolinium-enhanced T1-weighted MR image shows bilateral internal auditory canal schwannomas *(white arrows)*. An enhancing mass is seen in the left foramen ovale *(black arrow)*. (B) Coronal gadolinium-enhanced T1-weighted MR image shows nerve sheath tumors in the foramina ovale *(arrows)*. There is greater involvement of the left Meckel's cave.

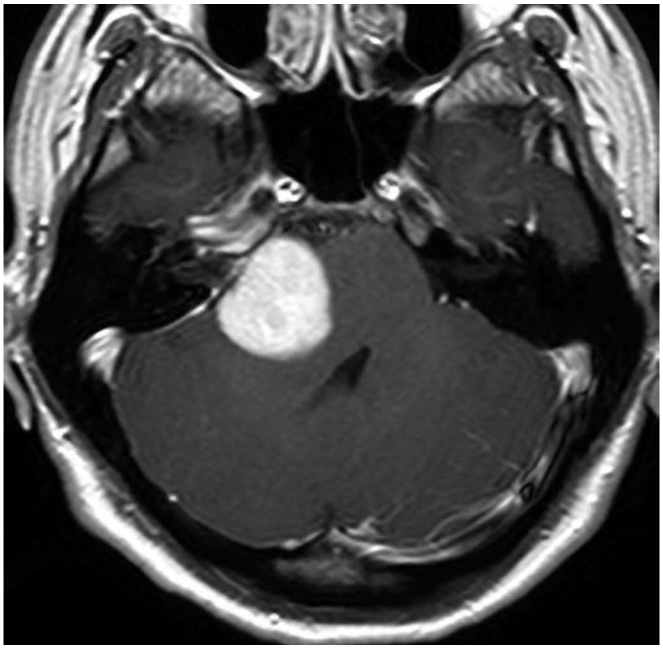

**Figure 12.7. Hemangiopericytoma in a 15-year-old male with an intensely enhancing right cerebellopontine angle mass.** The mass does not extend into the internal auditory canal. The primary differential diagnosis is meningioma.

## KEY POINTS

- Temporal bone tumors are rare in children.
- LCH and rhabdomyosarcoma are the most common neoplasms.
- Bilateral lytic temporal bone masses are almost pathognomonic for LCH.

## SUGGESTED READING

De Foer B, Kenis C, Vercruysse JP, et al. Imaging of temporal bone tumors. *Neuroimaging Clin N Am*. 2009;19(3):339–366.

## REFERENCES

Full references for this chapter can be found on www.expertconsult.com.

## REFERENCES

1. Arndt CAS. Soft Tissue Sarcomas. In: Behrman RE, Kliegman RM, Jenson HB, eds. *Nelson Textbook of Pediatrics*. 17th ed. Philadelphia: Saunders; 2004:1714–1717.
2. Sbeity S, Abella A, Arcand P, et al. Temporal bone rhabdomyosarcoma in children. *Int J Pediatr Otorhinolaryngol*. 2007;71(5):807–814.
3. Durve DV, Kanegaonkar RG, Albert D, et al. Paediatric rhabdomyosarcoma of the ear and temporal bone. *Clin Otolaryngol Allied Sci*. 2004;29(1):32–37.
4. Ladisch S. Histiocytosis Syndromes of Childhood. In: Behrman RE, Kliegman RM, Jenson HB, eds. *Nelson Textbook of Pediatrics*. 17th ed. Philadelphia: Saunders; 2004:1727–1730.
5. Beverley PC, Egeler RM, Arceci RJ, et al. The Nikolas Symposia and histiocytosis. *Nat Rev Cancer*. 2005;5(6):488–494.
6. Paulus W, Perry A. Histiocytic Tumours. In: Louis DN, Ohgaki H, Wiestler OD, et al, eds. *WHO Classification of Tumours of the Central Nervous System*. 4th ed. Lyon: IARC; 2007:193–196.
7. Saliba I, Sidani K, El Fata F, et al. Langerhans' cell histiocytosis of the temporal bone in children. *Int J Pediatr Otorhinolaryngol*. 2008; 72(6):775–786.
8. Surico G, Muggeo P, Muggeo V, et al. Ear involvement in childhood Langerhans' cell histiocytosis. *Head Neck*. 2000;22(1):42–47.
9. Koral K, Curran JG, Thompson A. Primary non-Hodgkin's lymphoma of the temporal bone. CT findings. *Clin Imaging*. 2003;27(6):386–388.
10. Janse van Rensburg P, van der Meer G. Magnetic resonance and computed tomography imaging of a grade IV papillary endolymphatic sac tumour. *J Neurooncol*. 2008;89(2):199–203.
11. De Foer B, Kenis C, Vercruysse JP, et al. Imaging of temporal bone tumors. *Neuroimaging Clin N Am*. 2009;19(3):339–366.
12. Sharma SC, Handa KK, Panda N, et al. Osteogenic sarcoma of the temporal bone. *Am J Otolaryngol*. 1997;18(3):220–223.
13. Akeson P, Holtas S. Radiological investigation of neurofibromatosis type 2. *Neuroradiology*. 1994;36(2):107–110.
14. Tashjian VS, Khanlou N, Vinters HV, et al. Hemangiopericytoma of the cerebellopontine angle: a case report and review of the literature. *Surg Neurol*. 2009;72(3):290–295.

# 13

# Embryology and Anatomy of the Neck

*Wael Abdalla and Vera R. Sperling*

## EMBRYOLOGY OF THE NECK

Accurate diagnosis and successful treatment of congenital anomalies and masses of the neck are dependent on an understanding of the complex embryologic development of this region and the anomalies that result from abnormal development.

This chapter will focus on the embryology of the neck and the oral cavity. The embryology of the orbit, face and sinuses, temporal bone, and ear are addressed in Chapters 4, 8, 9, and 18.

Many of the structures of the head and neck form from an interaction between somitomeres, somites, the mesenchyme, and the branchial apparatus.

### Development of the Mesenchyme

The mesenchyme is derived from three main sources:

1. The lateral plate mesoderm, which forms the laryngeal cartilages and regional connective tissue
2. The neural crest cells, whose migration initiates the formation of the pharyngeal arch skeletal structures and regional bone, cartilage, tendons, and glandular stroma
3. The ectodermal placodes, from which originate the fifth, seventh, ninth, and tenth cranial nerves (CNs)

### Development of the Mesoderm, Somitomeres, and Somites

After neurulation occurs, the mesoderm subdivides into the lateral, intermediate, and paraxial mesoderm. The lateral mesoderm forms most of the throat and larynx. The intermediate mesoderm does not form any part of the head and neck. The paraxial mesoderm forms the 7 somitomeres and 42 to 44 paired somites. The five most rostral somites are involved in the formation of head and neck musculature (Fig. 13.1). The somitomeres and somites form before the development of the branchial apparatus.

The branchial apparatus, that is, the branchial arches, clefts, pouches, and membrane, begin to form late in the third week of gestation. The buccopharyngeal membrane breaks down, and the mesodermal branchial bars begin to form six pairs of branchial arches. The fifth arch is rudimentary and disappears.

The fourth somitomere invades the first branchial arch and generates the formation of the muscles of mastication, that is, the masseter, pterygoid, and temporalis muscles. These muscles are innervated by the trigeminal nerve (CN V).

The seventh somitomere interacts with the third brachial arch to form the stylopharyngeus muscle, which is innervated by the glossopharyngeal nerve (CN IX).

The first four occipital somites invade the fourth and sixth brachial arches and thus stimulate the formation of the extrinsic and intrinsic laryngeal muscles innervated by the vagus nerve (CN X) and the cranial segment of the spinal accessory nerve (CN XI).

The third through seventh somites form the sternocleidomastoid muscle and trapezius and are innervated by the spinal accessory nerve (CN XI).

The intrinsic and extrinsic tongue muscles are likely derived from the second through fourth occipital somites and are innervated by the hypoglossal nerve (CN XII).

The contribution of the somitomeres and somites to the formation of muscles and their distinct innervation is unchanged throughout growth and development. Thus although many muscles migrate in location, their nerve supply is maintained and hence their branchial arch origin can always be identified (see Fig. 13.1).

### Development of the Branchial Apparatus

Formation of the branchial apparatus occurs between the fourth through seventh weeks of development. The pharynx constitutes much of the foregut during the first few weeks of development. Formation of the five branchial arches (I, II, III, IV, and VI) results from the breakdown of the buccopharyngeal membrane and segmentation of the mesoderm. Migration of neural crest cells to this location stimulates growth and development. Each arch has its own outer epithelial lining of ectoderm separated by five clefts and an inner epithelial lining of endoderm with five corresponding pouches and a central cartilaginous core, which is a mesenchymal derivative that participates in the formation of the characteristic skeletal, muscular, ligamentous, vascular, and neural components of each arch.

Shortly after formation of the branchial arches, the first and second arches undergo mesodermal proliferation, thus creating the epicardial ridge, which contains the mesodermal precursor of the sternocleidomastoid, the trapezius, and the infrahyoid and lingual muscles. The nerves of the epicardial ridge are the hypoglossal (CN XII) and spinal accessory (CN XI) nerves. The proliferation of mesenchyme overgrows branchial arches II, III, and IV and narrows branchial clefts II, III, and IV. Subsequently, an ectodermal pit is formed—the cervical sinus of His—which obliterates with further development; failure of obliteration results in formation of branchial sinus, clefts, or cysts of types II, III, or IV.

#### Branchial Apparatus and Its Contribution to the Structures of the Neck

**Branchial Arches.** The first branchial arch (Fig. 13.2) is composed of a dorsal segment known as the maxillary process and a ventral segment known as Meckel cartilage or the mandibular process; both involute. The ossification around Meckel cartilage is the precursor of the mandible and the sphenomandibular cartilage in the neck. The muscle derivatives of the first arch are the muscles of mastication (the masseter, pterygoid, and temporalis muscles), the tensor tympani and tensor veli palatine muscles, the anterior belly of the digastric muscle, and the mylohyoid muscle. The trigeminal nerve (CN V) provides motor and sensory innervation to the first branchial arch.

The second branchial arch is also known as Reichert cartilage. It gives rise to the upper body and lesser cornu of the hyoid bone, the styloid process, and stylohyoid ligament. The muscle derivatives include the platysma, the posterior belly of the digastric, and the stylohyoid. The nerve of the second brachial arch is the facial nerve (CN VII), which is primarily motor. The main sensory component is the chorda tympani branch that is carried with a branch of the trigeminal nerve (CN V3) to supply taste to the anterior two-thirds of the tongue. The artery of the second brachial arch is the stapedial artery, which normally regresses aside from some contributions to the internal and external carotid arteries.

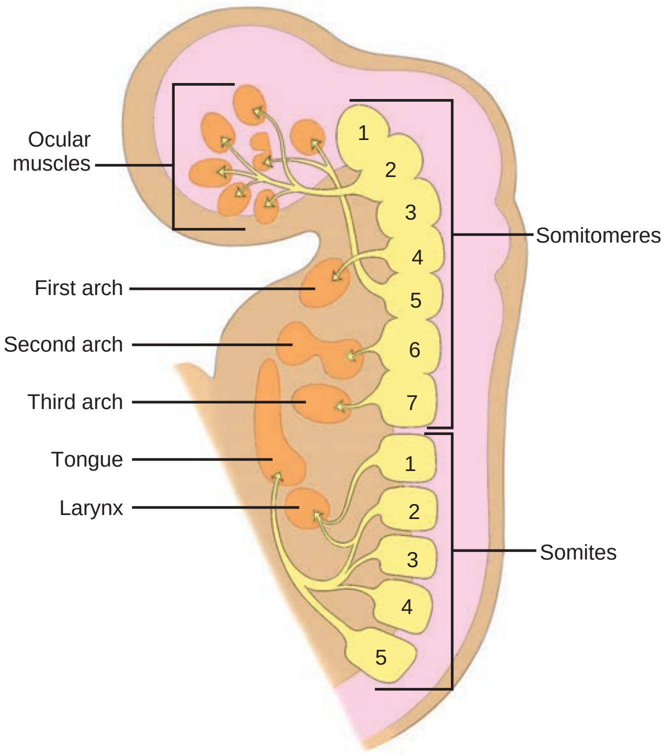

**Figure 13.1. Embryology.** A sagittal section shows the relationship of somitomeres and somites and their corresponding derivatives. *(From Som P, Curtin H.* Head and neck imaging*, 4th ed, Philadelphia, PA: Mosby; 2003.)*

The third branchial arch cartilage derivatives include the greater cornu and inferior body of the hyoid. The muscle derivatives include the stylopharyngeus and superior and middle pharyngeal constrictors. The nerve of the third brachial arch is the glossopharyngeal nerve (CN IX). The neural crest cells of the third branchial arch also form the carotid bodies. The artery of the third branchial arch contributes to the common carotid artery and the internal and external carotid arteries.

The fourth and sixth branchial arch cartilage derivatives fuse to form the larynx and the laryngeal cartilages (the thyroid, cricoid, arytenoid, corniculate, and cuneiform). Muscle derivatives include the cricothyroid muscle, the levator veli palatini, and the inferior pharyngeal constrictors. The muscle derivatives of the sixth arch are the remaining intrinsic muscles of the larynx. The nerve of the fourth arch is the superior laryngeal nerve, and the nerve of the sixth arch is the recurrent laryngeal nerve. Both are branches of the vagus nerve (CN X). The artery of the fourth branchial arch contributes to the aortic arch on the left and the subclavian artery on the right. The artery of the sixth branchial arch becomes the ductus arteriosus and the pulmonary artery. Between the branchial arches lie the paired branchial pouches and clefts.

**Branchial Pouches.** The first branchial pouch does not contribute to the structures of the neck. The second branchial pouch gives rise to the palatine tonsils and tonsillar fossa. The third branchial pouch gives rise to the inferior parathyroids and thymus. The early embryologic connections to the pharynx normally are obliterated. The fourth branchial pouch gives rise to the superior parathyroid glands and the ultimobranchial body, which contains the parafollicular cells (C cells) of the thyroid gland. The fifth branchial pouch degenerates. The branchial clefts do not contribute to any neck structures and are obliterated as development occurs (Tables 13.1 and 13.2).

**TABLE 13.1** Derivatives of the Branchial Arches

| Arch | Nerve | Muscles | Skeletal Structures | Ligaments | Artery |
|---|---|---|---|---|---|
| First (mandibular) | Trigeminal nerve (CN V) (maxillary and mandibular branches only) | Muscles of mastication, mylohyoid,; anterior belly of digastric, tensor tympani, tensor veli palatine | Malleus incus | Anterior ligament of malleus, sphenomandibular ligament | Maxillary artery |
| Second (hyoid) | Facial nerve (CN VII) | Muscles of facial expression, stapedius, stylohyoid, posterior belly of digastric | Stapes, styloid process, lesser cornu and upper body of the hyoid bone | Stylohyoid ligament | Stapedial artery (rarely) |
| Third | Glossopharyngeal nerve (CN IX) | Stylopharyngeus, superior and middle pharyngeal constrictors | Greater cornu and lower part of body of the hyoid bone | | Contributions to the carotid arteries |
| Fourth and sixth | Superior laryngeal branch of vagus nerve (CN X)—fourth arch; recurrent laryngeal branch of vagus nerve (CN X)—sixth arch | Cricothyroid, levator veli palatine, inferior pharyngeal constrictors, intrinsic muscles of larynx, striated muscles of the esophagus | Thyroid, cricoid, arytenoid, corniculate, cuneiform cartilages | | The artery of the fourth arch contributes to the subclavian artery on the right and the aortic arch on the left; the artery of the sixth arch forms the ductus arteriosus and the pulmonary artery |

*CN,* Cranial nerve.
*Adapted from Moore KL, Persaud MG, Torchia MG.* Before we are born*, Philadelphia, PA: Saunders/Elsevier; 2008.*

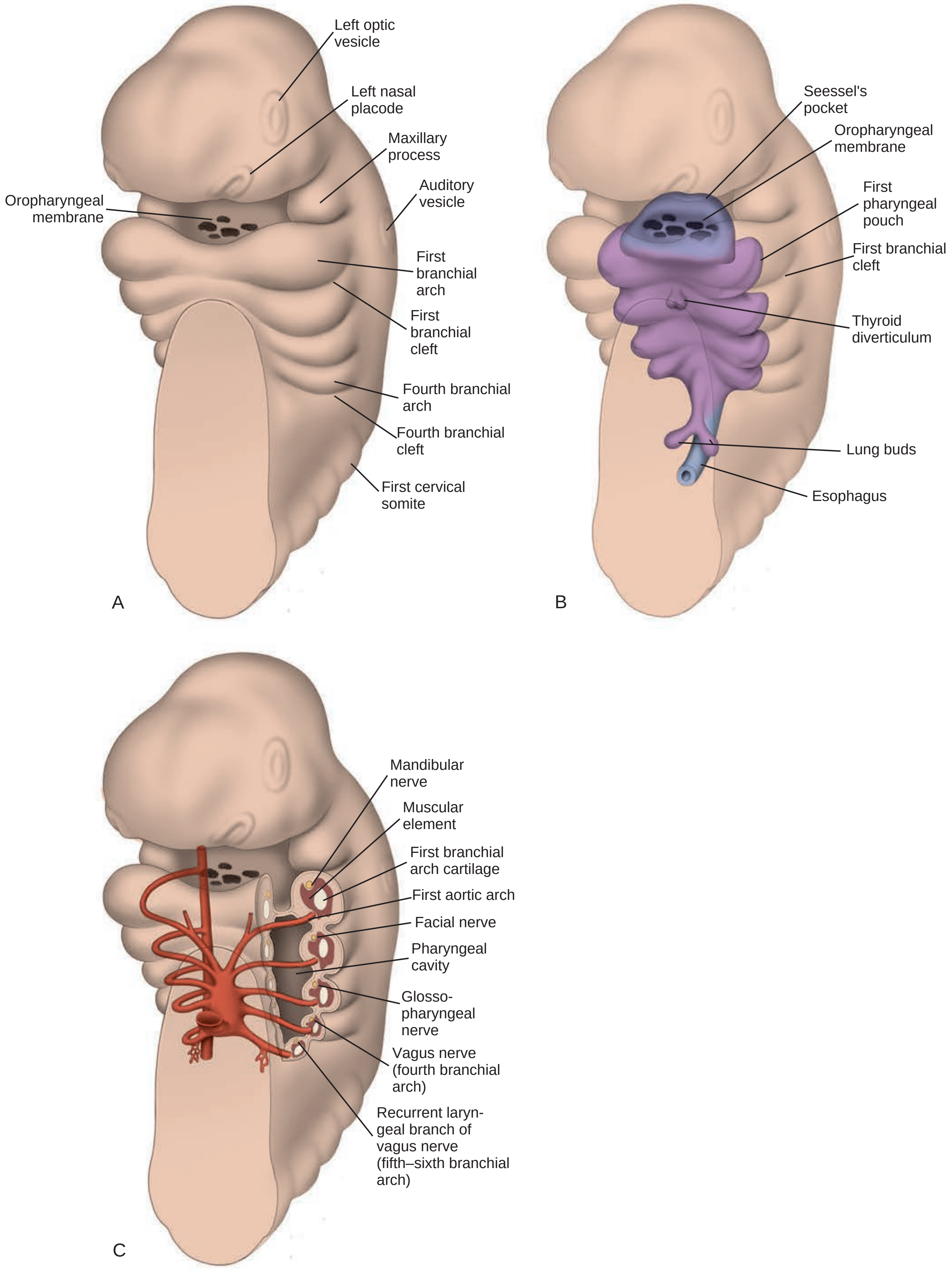

**Figure 13.2. Embryology.** Relationship of (A) branchial arches and (B) clefts and (C) subsequent derivative structures. *(From Som P, Curtin H. Head and neck imaging. 4th ed, Philadelphia, PA: Mosby; 2003.)*

## EMBRYOLOGY OF THE TONGUE

The tongue forms from the first four branchial arches. Two lateral and one central swelling, the tuberculum impar, form from the first branchial arch. A second central swelling, the copula/hypobranchial eminence, forms from the second, third, and fourth branchial arches. A third central swelling from the fourth branchial arch forms the epiglottis. Thus the anterior two-thirds or body of the tongue forms from the first branchial arch, whereas the root of the tongue forms from the second, third, and fourth branchial arches. The groove formed where the anterior and posterior portions of the tongue fuse is called the terminal sulcus.

The hypoglossal nerve (CN XII) innervates all the intrinsic tongue muscles and all extrinsic tongue muscles but the palatoglossus. Sensory innervation is by the lingual branch of CN V3, the chorda tympani branch of CN VII, the lingual branch of CN IX, and the recurrent laryngeal branch of CN X.

## EMBRYOLOGY OF THE THYROID GLAND

The thyroid gland originates from a median endodermal thickening in the floor of the primitive pharynx in the third to fourth week of development. The thyroid primordium develops between the tuberculum impar and the copula of the first and second pouches. The foramen cecum is the remnant of the thyroid primordium in this location, between the anterior two-thirds and the posterior one-third of the tongue. The thyroid gland passes anterior to the hyoid and laryngeal cartilages and descends anterior to the thyrohyoid membrane and the strap muscles. The thyroid gland reaches its final position by the seventh week of development. During its inferior migration, the thyroid anlage is connected to the tongue by the normally transient thyroglossal duct. Innervation of the thyroid gland is primarily by the sympathetic middle cervical ganglion.

**TABLE 13.2** Derivatives of the Branchial Pouches

| Pouch | Derivatives |
|---|---|
| First | Eustachian tube, middle ear, portions of mastoid bone |
| Second | Palatine tonsils, tonsillar fossa |
| Third | Inferior parathyroids, thymus |
| Fourth and sixth | Superior parathyroids, parafollicular cells of thyroid |

*Adapted from Moore KL, Persaud MG, Torchia MG.* Before we are born*, Philadelphia, PA: Saunders/Elsevier; 2008.*

## EMBRYOLOGY OF THE SALIVARY GLANDS

The common pathway for salivary gland development is the ingrowth of surface epithelium (primarily ectoderm, but also endoderm for minor salivary gland formation) into the underlying mesenchyme.

The precursors of the parotid gland appear between the fourth to sixth weeks of gestation, and the submandibular and sublingual glands appear between the sixth to eighth weeks of gestation. The minor salivary glands do not develop until the twelfth week of gestation.

A process of proliferation, division, and canalization occurs. Interaction with and stimulation by the autonomic nervous system is essential for normal salivary gland development and function. The final process of encapsulation occurs in reverse to the order of development and growth. Encapsulation of the parotid gland occurs after formation of the lymphatic system, accounting for the presence of intraparotid lymph nodes.

The parotid gland is innervated by CN IX, the submandibular and sublingual glands are innervated by CN VII, and the minor salivary glands are innervated by CN V.

## ANATOMY OF THE NECK

Clinical evaluation and classic anatomy divides the neck into triangles. The largest are the anterior and posterior triangles, which are defined and separated by the sternocleidomastoid muscles. The anterior triangle is further subdivided into the paired carotid and submandibular triangles (separated by the posterior belly of the digastric muscle) and the single midline submental and infrahyoid muscular triangles. The posterior triangle consists of the paired occipital and subclavian triangles, which are separated by the inferior belly of the omohyoid muscle (Fig. 13.3). The central cavity is divided into the nasopharynx, oropharynx, hypopharynx, and oral cavity.

This approach to neck anatomy does not reflect anatomy as defined by the fascial layers, that is, the superficial and deep cervical fascia of the head and neck. The deep cervical fascia is composed of three layers:

1. The superficial layer of the deep cervical fascia (SL-DCF), also known as the investing fascia, which defines the masticator, parotid, and submandibular spaces; it also contributes to the carotid space

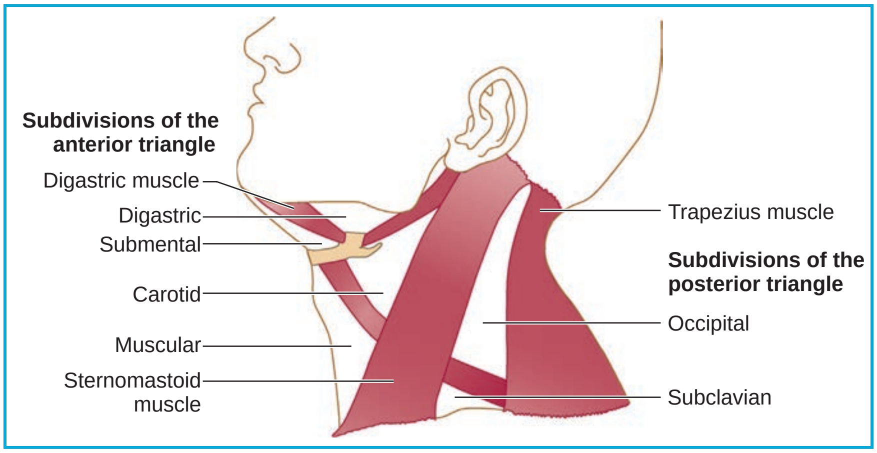

**Figure 13.3.** Traditional triangular division of neck spaces.

2. The middle layer of the deep cervical fascia (ML-DCF), also known as the visceral fascia, which primarily forms the buccopharyngeal and pharyngobasilar fascia and the fascia of the tensor veli palatine; it also contributes to the carotid space
3. The deep layer of the deep cervical fascia (DL-DCF), also known as the prevertebral fascia, which forms the perivertebral space and then is subdivided into the anterior prevertebral and posterior paraspinal compartments; the alar fascia is a small component of the DL-DCF and also contributes to the carotid sheath

The advent of cross-sectional imaging enabled a new approach to neck anatomy defined by the concept of dividing the neck into the suprahyoid and infrahyoid compartments, with further subdivision of each compartment into fascially defined spaces (Figs. 13.4 and 13.5). The resultant refined approach to differential diagnosis, combined with the use of surgically and pathologically defined common terminology and nomenclature, has improved communication between radiologists and clinicians.

The pharyngeal mucosal space, which is located in the suprahyoid neck, is the surface of pharynx. It encompasses the nasopharyngeal, oropharyngeal, and hypopharyngeal mucosa. Centrally located, it is posterior to the retropharyngeal space and lateral to the parapharyngeal space. It is not a true fascially enclosed space because only its deep margin is bound by the ML-DCF.

The parapharyngeal space is located in the suprahyoid neck; it extends from the skull base to the submandibular space. The medial fascial boundary is the visceral/buccopharyngeal fascia. The pterygomandibular raphe and masticator space is its anterior boundary. Laterally and posteriorly, it is bounded by the carotid and retropharyngeal space.

The carotid space, which is located in both the suprahyoid and infrahyoid neck, extends from the skull base to the aortic arch. All three layers of deep cervical fascia form the carotid sheath. The carotid sheath is better defined in the infrahyoid neck and more loosely formed in the suprahyoid neck.

The retropharyngeal space, which is located in both the suprahyoid and infrahyoid neck, extends from the skull base to T3. The ML-DCF constitutes the anterior wall, and the DL-DCF constitutes the posterior wall. The lateral wall is the alar fascia, a small fragment of the DL-DCF. It is posterior to the pharyngeal mucosal space in the suprahyoid neck and the visceral space in the infrahyoid neck, anterior to the danger space posterior, and medial to the carotid space.

The masticator space, which is located in the suprahyoid neck, extends from the superior aspect of suprazygomatic masticator space/temporal fossa at the level of parietal bone to the inferior aspect of the infrazygomatic masticator space/undersurface of the posterior body of the mandible. It is bounded by a sling of the SL-DCF that extends from the inferior mandible to the skull base and zygomatic arch. It is anterior to the parotid space, anterolateral to the parapharyngeal space, and lateral to the pharyngeal mucosal space. Superior to it is the skull base, including the foramina ovale and spinosum.

The parotid space, which is located in the suprahyoid neck, extends superiorly from the external auditory canal and mastoid tip to below angle of mandible. It is enclosed by the SL-DCF.

The perivertebral space, which is located in both the suprahyoid and infrahyoid part of the neck, extends from the skull base to T4 and consists of a prevertebral and a paraspinal component. It is enveloped by the DL-DCF. The perivertebral space is posteromedial to the carotid space and medial to the posterior cervical space.

The visceral space, which is located in the infrahyoid neck, lies anterior to the retropharyngeal space in the midline and is enclosed by the ML-DCF.

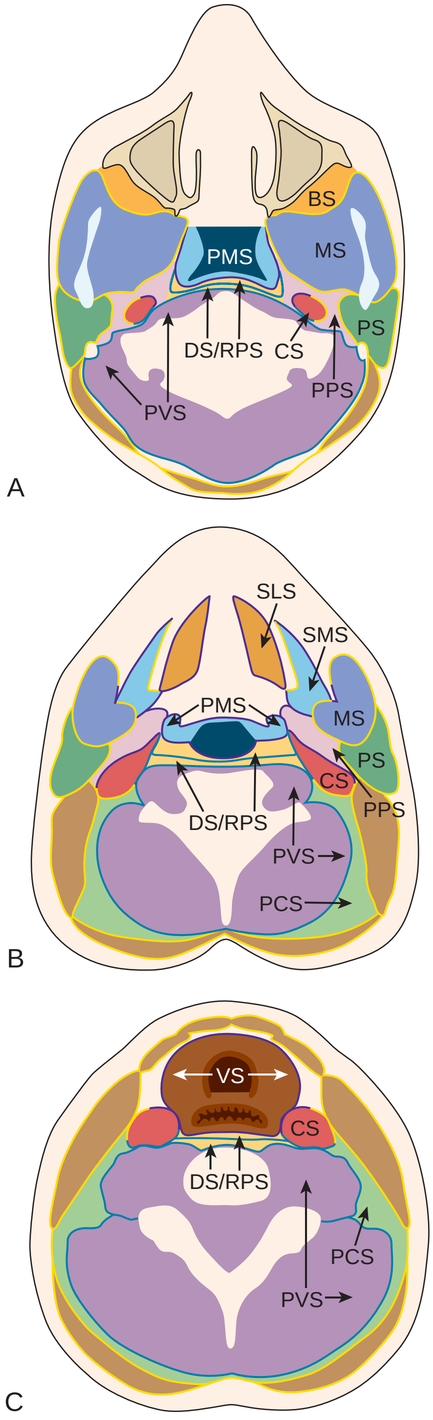

**Figure 13.4. Fascial compartments of the neck.** (A) Spaces and investing fascia of the suprahyoid neck and the level of the nasopharynx. (B) Spaces and investing fascia of the suprahyoid neck at the level of the oropharynx. (C) Spaces and investing fascia of the infrahyoid neck. *BS,* Buccal space; *CS,* carotid space; *DS,* danger space; *MS,* masticator space; *PCS,* posterior cervical space; *PMS,* pharyngeal mucosal space; *PPS,* parapharyngeal space; *PS,* parotid space; *PVS,* perivertebral space; *RPS,* retropharyngeal space; *VS,* visceral space. *(Redrawn from Harnsberger HR, Hudgins P, Wiggins R, et al.* Diagnostic imaging: head and neck, *Salt Lake City, UT: Amirsys Inc; 2004.)*

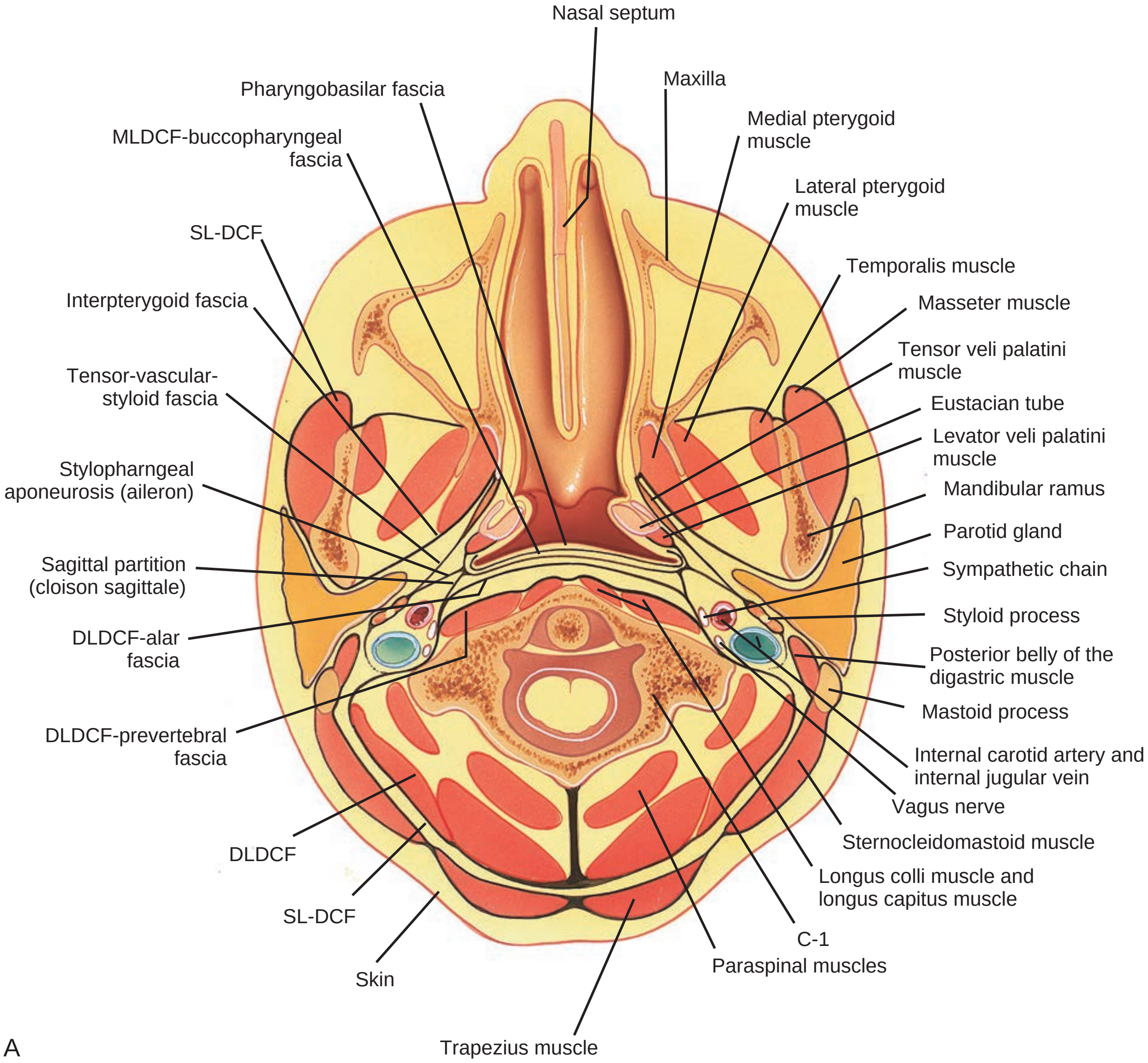
Nasal septum
Pharyngobasilar fascia
Maxilla
Medial pterygoid muscle
MLDCF-buccopharyngeal fascia
Lateral pterygoid muscle
SL-DCF
Temporalis muscle
Interpterygoid fascia
Masseter muscle
Tensor veli palatini muscle
Tensor-vascular-styloid fascia
Eustacian tube
Levator veli palatini muscle
Stylopharngeal aponeurosis (aileron)
Mandibular ramus
Parotid gland
Sagittal partition (cloison sagittale)
Sympathetic chain
Styloid process
DLDCF-alar fascia
Posterior belly of the digastric muscle
Mastoid process
DLDCF-prevertebral fascia
Internal carotid artery and internal jugular vein
Vagus nerve
DLDCF
Sternocleidomastoid muscle
Longus colli muscle and longus capitus muscle
SL-DCF
C-1
Paraspinal muscles
Skin
A
Trapezius muscle

**Figure 13.5. Fascial compartments of the neck.** Axial sections at the level of C4 (A), C7 (B), and T1 (C) show the relationship of the investing fascial layers with anatomic structures. *(From Som P, Curtin H.* Head and neck imaging, *4th ed, St. Louis, MO: Mosby; 2003.)*

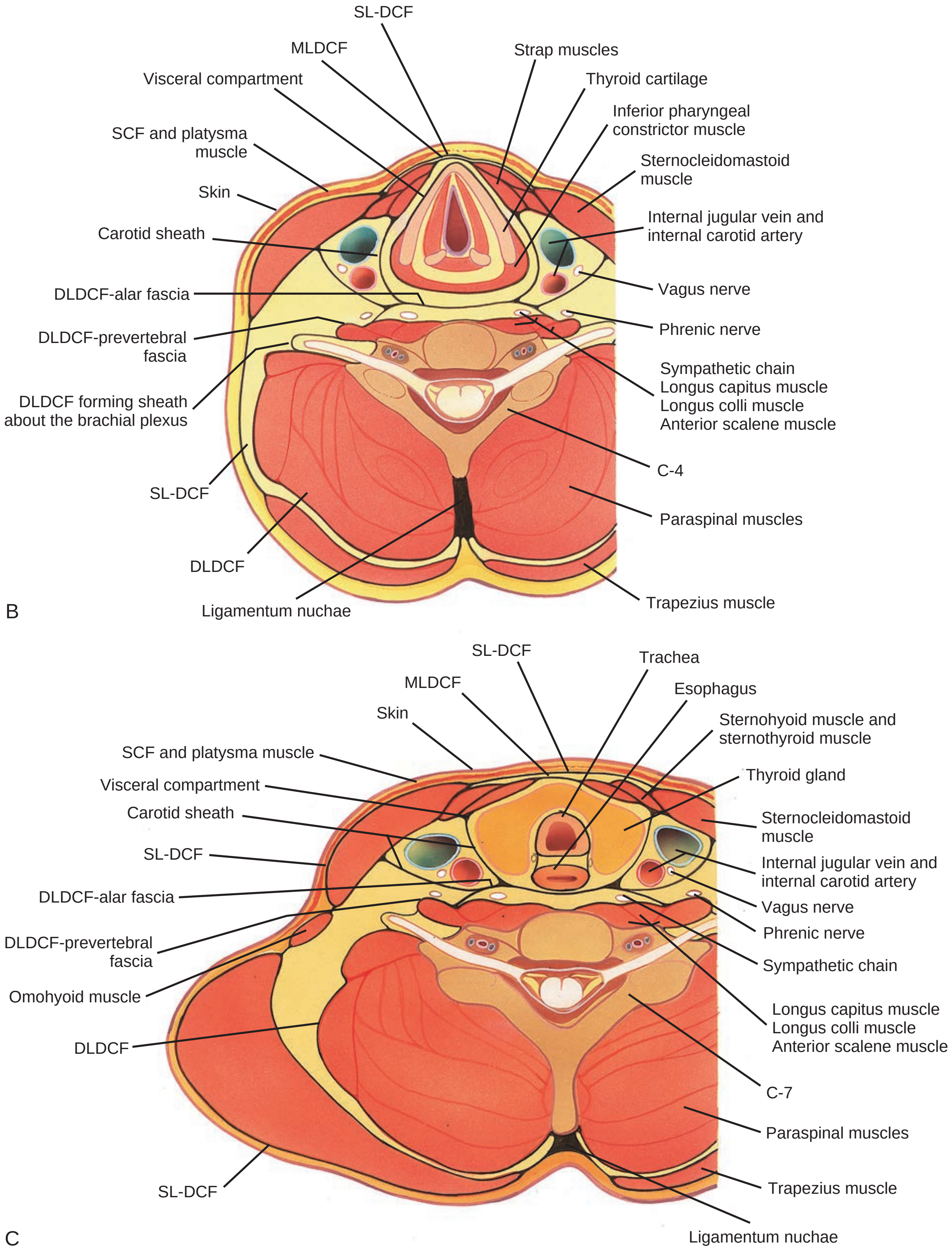

**Figure 13.5, cont'd.**

**TABLE 13.3** Anatomic Spaces of the Suprahyoid Neck

| Space | Contents |
|---|---|
| Pharyngeal mucosal space | Mucosa, minor salivary glands and lymphoid tissue, pharyngobasilar fascia, buccopharyngeal fascia, superior and middle pharyngeal constrictor muscles, levator veli palatini muscle, cartilaginous end of eustachian tube (torus tubarius) |
| Parapharyngeal space (prestyloid parapharyngeal space) | Deep portion of parotid gland, minor salivary glands, pterygoid venous plexus, internal maxillary artery, ascending pharyngeal artery, branches of cranial nerve V3, cervical sympathetic chain and fat |
| Carotid space (retrostyloid parapharyngeal space) | Internal carotid artery, internal jugular vein, cranial nerves IX–XII, sympathetic chain, lymph nodes—deep cervical chain |
| Retropharyngeal space | Fat, lymph nodes—retropharyngeal (medial and lateral) |
| Masticator space | Ramus and posterior body of mandible, muscles of mastication—pterygoid, masseter, and temporalis; mandibular division trigeminal nerve (V3)—inferior alveolar and lingual nerves, inferior alveolar vein and artery, pterygoid venous plexus |
| Parotid space | Parotid gland and duct, cranial nerve VII, external carotid artery, retromandibular vein, lymph nodes—intraparotid and periparotid |
| Perivertebral space | Prevertebral muscles, scalene muscles, vertebral artery and vein, brachial plexus, phrenic nerve<br>Vertebral bodies and discs |

*Adapted from Som PM, Curtin HD.* Head and neck imaging, *4th ed, St Louis, MO: Mosby; 2003.*

**TABLE 13.4** Anatomic Spaces of the Infrahyoid Neck

| Space | Contents |
|---|---|
| Visceral space | Larynx, hypopharynx and cervical esophagus, trachea, thyroid gland, parathyroid glands, lymph nodes, recurrent laryngeal nerve (branch cranial nerve X), third and fourth branchial apparatus and thyroid/parathyroid anlage remnants |
| Retropharyngeal space | Fat, remnants of third branchial apparatus |
| Carotid space | Common and internal carotid arteries, internal jugular vein, cranial nerve X, sympathetic chain, lymph nodes, carotid body, second branchial apparatus remnants |
| Perivertebral space | Prevertebral, scalene, and paraspinal muscles, brachial plexus, phrenic nerve, vertebral artery and vein<br>Vertebral bodies and discs |
| Anterior cervical space | Extension of submandibular space of suprahyoid neck<br>Composed of fat |
| Posterior cervical space | Cranial nerve XI, spinal accessory nodes, preaxillary brachial plexus, fat |

The posterior cervical space extends from the mastoid tip to the level of the clavicle. Its superficial boundary is the SL-DCF, and its deep boundary is the deep cervical DL-DCF. It lies posterior to the carotid sheath, posteromedial to the sternocleidomastoid muscle, and anterolateral to the paraspinal component of the perivertebral space (Tables 13.3 and 13.4).

## ANATOMY OF THE ORAL CAVITY

The oral cavity is located anterior to the oropharynx. It is separated from the oropharynx by the soft palate, anterior tonsillar pillars, and circumvallate papillae. The mylohyoid muscle separates the lower oral cavity into the submandibular and sublingual spaces, and forms the floor of the mouth, arising from the mandible and attaching to the hyoid.

The submandibular space, which is located inferior and lateral to the mylohyoid muscle and superior to the hyoid bone, is enveloped by the SL-DCF. Posteriorly, no fascial separation is found between the submandibular space, the sublingual space, and the inferior parapharyngeal space.

The sublingual space, which is located superior and medial to mylohyoid muscle and lateral to genioglossus-geniohyoid muscle complex, is not enclosed by fascia (Table 13.5).

**TABLE 13.5** Contents of the Submandibular and Sublingual Spaces

| Space | Contents |
|---|---|
| Submandibular | Submandibular gland, submandibular and submental lymph nodes, facial artery and vein, inferior cranial nerve XII, anterior belly of digastric muscle |
| Sublingual | Hyoglossus muscle (anterior margin), lingual nerve (sensory branches of cranial nerve V3 and the chorda tympani branch of cranial nerve VII), distal cranial nerve IX and cranial nerve XII, lingual artery and vein, sublingual gland and duct, deep portion of the submandibular gland and duct |

### KEY POINTS

- Knowledge of embryology and anatomy of the neck is essential in interpreting imaging studies and formulating an effective differential diagnosis.
- Cross-sectional imaging has resulted in replacement of the clinically oriented subdivision of neck structures by fascially based anatomic spaces that more closely correspond to surgical and pathologic landmarks.

### SUGGESTED READINGS

Jinkins JR. *Atlas of Neuroradiologic Embryology, Anatomy, and Variants*. Philadelphia: Lippincott Williams & Wilkins; 2000.

Moore K, Persaud TVN. *Before We Are Born: Essentials of Embryology and Birth Defects*. 7th ed. Philadelphia: Saunders; 2008.

Som PM, Curtin HD. Fascia and spaces of the neck. In: Som PM, Curtin HD, eds. *Head and Neck Imaging*. 4th ed. St. Louis: Mosby; 2003.

Som PM, Smoker WRK, Balboni A, et al. Embryology and anatomy of the neck. In: Som PM, Curtin HD, eds. *Head and Neck Imaging*. 4th ed. St. Louis: Mosby; 2003.

# 14

# Prenatal, Congenital, and Neonatal Abnormalities

*Anna Shifrin and Tamara Feygin*

Congenital lesions of the neck consist of a variety of entities, some of which become apparent at birth or shortly thereafter, whereas others present later in life. This chapter will focus on congenital lesions that can be recognized in the fetus or the newborn. Many congenital cervical lesions may be diagnosed prenatally, making it essential for pediatric radiologists to be familiar with their general patterns on fetal imaging.

Presence of mass lesions in the fetal/neonatal neck may considerably influence other organs and systems because of the complex anatomy of the neck and the proximity of the lesion to vascular, upper gastrointestinal, and especially airway structures. Conditions that may result in potentially life-threatening trachea-laryngeal obstruction include extrinsic causes such as cervical teratomas, vascular malformations, and vascular rings, and intrinsic causes such as congenital high airway obstruction syndrome (CHAOS) and upper airway hemangiomas. Giant fetal neck masses may grow to obstruct the esophagus, causing an accumulation of amniotic fluid (polyhydramnios) and increasing the risk of preterm labor. Accurate depiction and distinction of these entities with imaging facilitate prenatal counseling and delivery planning. Some congenital cervical lesions may be associated with other serious anomalies and may be the first manifestation of a systemic disease or syndrome, potentially requiring further investigation. For accurate diagnosis, it may be necessary to utilize complementary imaging modalities.

## IMAGING MODALITIES

Imaging tools for the fetal neck are ultrasonography (US) and magnetic resonance imaging (MRI). The neonatal neck may be assessed by US, computed tomography (CT), and MRI. Rarely, indeterminate vascular lesions may require evaluation with conventional angiography. Lateral radiography of the neck may still be used in emergent initial evaluation of upper airway pathology but is rarely of value in the workup of congenital lesions.

### Ultrasonography

US supplemented by Doppler (for evaluation of blood flow) is a noninvasive, real-time, high-resolution imaging modality, which provides excellent anatomic images. It is equally useful for primary obstetric imaging and for portable bedside evaluation of a neck mass in the distressed child. Obstetric US includes routine evaluation of the head, face, and neck, as well as an assessment of airway patency and fetal swallowing. The swallowing pattern may be difficult to confirm with US, hence ancillary signs of upper gastrointestinal (GI) tract compromise (a small stomach or polyhydramnios) should be routinely searched for. US nicely demonstrates a lesion's morphology, reliably distinguishes the cystic and solid components, and shows fat and calcifications. Color Doppler depicts the major neck vessels, demonstrates a lesion's vascularity and blood supply, and detects possible arteriovenous shunting. Three-dimensional US clearly depicts the relationship of a cervical mass with adjacent facial and skull base structures (e-Fig. 14.1). Potential shortcomings of fetal US involve cases with poor acoustic windows or abnormal fetal position with unusual flexion and extension of the fetal neck. US imaging of neck lesions in young children is performed with high-resolution transducers and may be sufficient for immediate diagnosis. However, assessment of surrounding tissue invasion may be suboptimal.

### Computed Tomography

CT may serve as the initial imaging modality for evaluation of congenital lesions; it is widely available and offers fast data acquisition. However, suboptimal soft tissue resolution and continued concerns of radiation exposure have resulted in decreasing use in recent years.

### Magnetic Resonance Imaging

MRI is a superb imaging modality for the evaluation of fetal or neonatal neck lesions. Fetal MRI is considered safe to perform in the second and third trimesters, and is approved by the US Food and Drug Administration (FDA) for magnet field strengths up to 3.0 Tesla. Fetal MRI before 17 weeks of gestational age is typically of little value because of the relatively poor image quality in a small fetus and is avoided because of the unknown safety of exposure to magnetic fields during organogenesis. Fetal MRI is usually performed for further assessment of a cervical mass detected by routine obstetric US. The MRI protocol for fetal neck imaging includes the following: (1) half-Fourier acquisition single-shot turbo (HASTE) magnetic resonance (MR) sequence (excellent for imaging of normal anatomic structures and depiction of cervical lesions); (2) spoiled gradient echo T1-weighted sequence (helpful for imaging the thyroid gland and blood flow within the major cervical vessels, as well as for depiction of intralesional blood products and calcification); (3) gradient echo planar imaging (helpful for detection of blood products, calcification, and bony detail); and (4) dynamic steady state or balanced gradient echo sequences (valuable in the assessment of swallowing function in the fetus [see Video 14.2]). The details of fetal swallowing and possible airway compromise should always be carefully examined. Knowledge of airway status may help facilitate delivery planning, including use of the Ex Utero Intrapartum Treatment (EXIT) procedure to allow time to secure the airway while the neonate is still attached to the umbilical cord.

MRI sequences for imaging neonatal neck lesions include high-resolution thin T1- and T2-weighted and postcontrast imaging with fat-suppression in orthogonal planes. Diffusion-weighted imaging is useful for characterization of hypercellular tumors and infected cystic lesions with viscous, purulent content.

## VASCULAR NECK LESIONS

The Mulliken and Glowacki classification of vascular lesions divides pediatric vascular lesions into two major categories: (1) vascular tumors and (2) vascular malformations. These lesions have different treatments and prognoses. The classification, based on pathologic differences as well as the clinical and cellular behavior of vascular lesions, was widely accepted and adopted by the International Society for the Study of Vascular Anomalies in 1996 and was expanded in 2014. Some additional entities have since been identified that are complex and less easily classified by generic headings. Vascular tumors are classified as benign, locally aggressive or borderline, and malignant. Some known genetic

## Abstract:

Congenital lesions of the neck consist of a variety of entities, some of which become apparent at birth or shortly thereafter, whereas others present later in life. This chapter will focus on congenital lesions that can be recognized in the fetus or the newborn. Many congenital cervical lesions may be diagnosed prenatally, making it essential for pediatric radiologists to be familiar with their general patterns on fetal imaging. Presence of mass lesions in the fetal/neonatal neck may considerably influence other organs and systems because of the complex anatomy of the neck and the proximity of the lesion to vascular, upper gastrointestinal, and especially airway structures.

## Keywords:

fetal head and neck imaging
fetal MRI
pediatric MRI
congenital neck lesions
hemangioma
malformation
fibromatosis

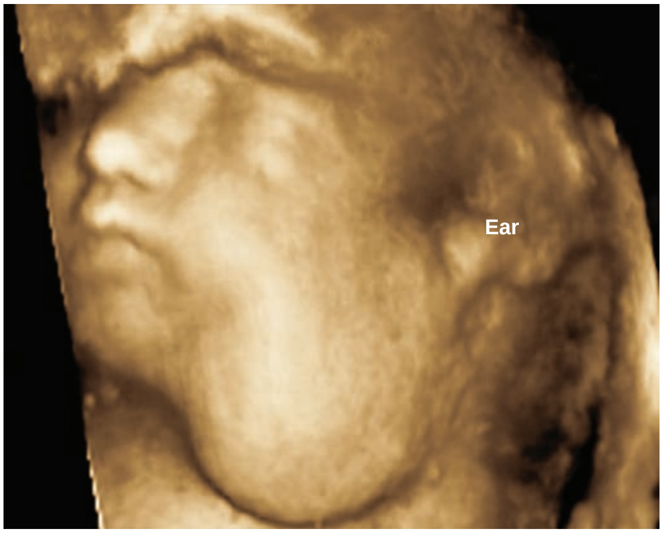

**e-Figure 14.1. Lymphatic malformation.** Three-dimensional prenatal sonogram shows a large mass of the fetal neck extending into the lower face and ear. *(Courtesy Dr. Beverly Coleman.)*

defects underlying vascular anomalies have been discovered. Despite the recent revisions, this classification should not be perceived as a final arrangement. A better understanding of the molecular biology and genetics of vascular anomalies may lead to further refinement of the existing classification system.

## VASCULAR TUMORS

Hemangioma is the most common vascular tumor of infancy. It is a true endothelial tumor with increased mitotic activity during the proliferative phase and eventual involution. Two major types are recognized: (1) congenital (rare) and (2) infantile (common). The previously used categorization of hemangioma types as capillary, juvenile, or cavernous is no longer accepted. All types of hemangiomas have overlapping clinical, imaging, and histopathologic features.

### Infantile Hemangioma

Infantile hemangiomas are benign vascular neoplasms with an increased incidence in premature children with low birth weight. These lesions have a predictable clinical course of growth and involution which progresses through several stages. The nascent phase, with a subtle precursor lesion (macula, multiple telangiectasias, or discoloration), may be observed in the first 2 to 4 weeks of life or may be present at birth. The proliferative phase is remarkable for rapid tumor growth in the first year of life. In the proliferative stage, the hemangioma appears as a bulky, compressible lesion of strawberry-red color and may have cutaneous as well as deep components. On cross-sectional imaging, it appears as a lobulated mass with intense uniform enhancement, usually with presence of intralesional flow voids on MRI (Fig. 14.2). Proliferation may be biphasic. Careful assessment of upper airway status is important because the deep portions of a cervical hemangioma may enlarge at this stage sufficiently to impinge on the airway and cause obstruction. The final involution phase may continue for up to 12 years, as the rate of regression is variable. Involution is never complete as there is residual fibro-fatty tissue, although the residual lesion may not be grossly visible. Infantile hemangiomas are positive for the glucose transporter 1 (GLUT-1) marker at all stages of lesion development. Most infantile hemangiomas do not cause any morbidity or mortality but may create cosmetic inconvenience. On the other hand, a hemangioma of the neck is considered an alarming lesion if it assumes a beard distribution (involvement of the lower face, anterior neck, and submandibular and parotid regions) because of the high risk of airway compromise and an increased incidence of subglottic hemangioma. In addition, cervical and facial infantile hemangiomas have a known association with PHACES syndrome (***P***osterior fossa malformations, ***H***emangiomas, ***A***rterial, ***C***ardiac anomalies, ***E***ye anomalies, ***S***ternal cleft). The arterial anomalies often seen in PHACES syndrome represent a spectrum of congenital arterial lesions ipsilateral to the cutaneous hemangioma. This necessitates careful searching (and monitoring) with imaging for potential vascular abnormalities once a diagnosis of segmental hemangioma is established. Infantile hemangiomas involving the upper airway (Fig. 14.3) become symptomatic in the proliferative phase, causing biphasic stridor, respiratory distress, and potentially life-threatening airway obstruction, which may require emergent intubation. These hemangiomas are often multifocal and occur above and below the vocal cords. Close monitoring with cross-sectional imaging is indicated because laryngoscopy may not accurately depict the degree of invasion. MRI is preferred in the setting of intubation or tracheostomy. In rare cases, mostly in the setting of underlying PHACES syndrome, segmental infantile hemangioma may be associated with central nervous system hemangiomas in intracranial (e-Fig. 14.4) or intraspinal locations. In the past, infantile hemangiomas have been confused with other vascular neoplasms, particularly kaposiform hemangioendothelioma (KHE) and tufted angioma, especially in the setting of consumptive coagulopathy (Kasabach-Merritt phenomenon). It is now generally accepted that infantile hemangiomas are rarely, if ever, responsible for this phenomenon.

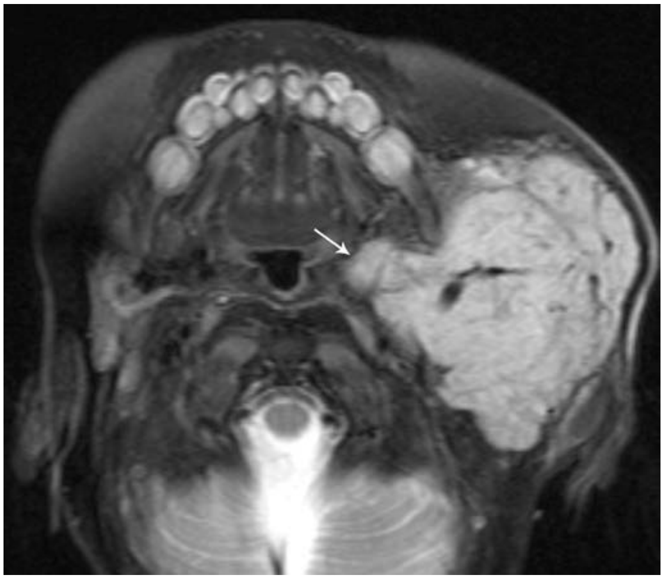

**Figure 14.2. Parotid infantile hemangioma.** Axial T2-weighted fat-saturated MR image shows a well-circumscribed lobular soft tissue mass in the left parotid with intrinsic flow voids and deep extension into the ipsilateral parapharyngeal space *(small arrow)*. The upper airway remains patent.

### Congenital Hemangioma

Congenital hemangiomas are uncommon lesions that are fully developed at birth and do not undergo a proliferative stage in postnatal life. These lesions may be diagnosed in utero as early as 12 weeks of gestational age. Two types of congenital hemangiomas are described: (1) rapidly involuting congenital hemangioma (RICH) and (2) noninvoluting congenital hemangioma (NICH). A partially involuting type (PICH) has also been described. RICH has a predilection for scalp and neck locations. On prenatal imaging, it appears as a large heterogeneous mass, emanating from the posterior neck (e-Fig. 14.5) with increased vascularity, best demonstrated on obstetric Doppler US and MR gradient echo planar imaging. Postnatal imaging features of RICH include large irregular flow voids and arterial aneurysms, direct arteriovenous shunts (seen on angiography), and calcifications. Their imaging appearance may occasionally resemble congenital infantile fibrosarcoma. Large RICH lesions may have a dramatic presentation at birth with high-output congestive heart failure (Fig. 14.6). Rapid involution is usually completed by 14 months of age. Usually, RICH is managed conservatively, although complications may prompt surgical excision. NICH, on the contrary, never involutes and may even grow with the child. It usually has an imaging appearance similar to infantile hemangioma, being more homogeneous with uniform parenchymal enhancement.

### Hemangioma Treatment

Most hemangiomas resolve spontaneously, however, approximately 10% to 20% require treatment, which includes pharmacologic, surgical, or laser intervention. Treatment is indicated in cases when functional or cosmetic complications arise that are worse than the side effects of intervention. Lesion size and location,

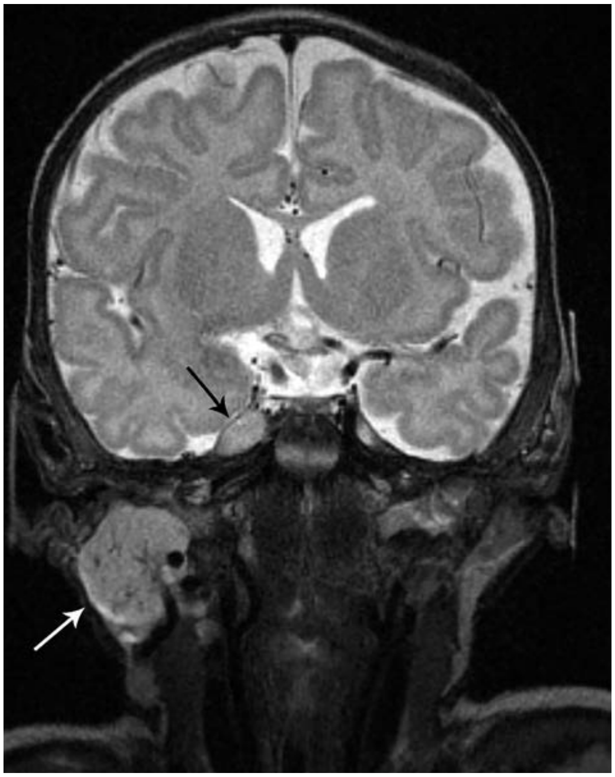

**e-Figure 14.4. Multifocal infantile hemangiomas with intracranial lesions.** Coronal fat-saturated T2-weighted MR image shows cervical *(white arrow)* and Meckel cave *(black arrow)* hemangiomas.

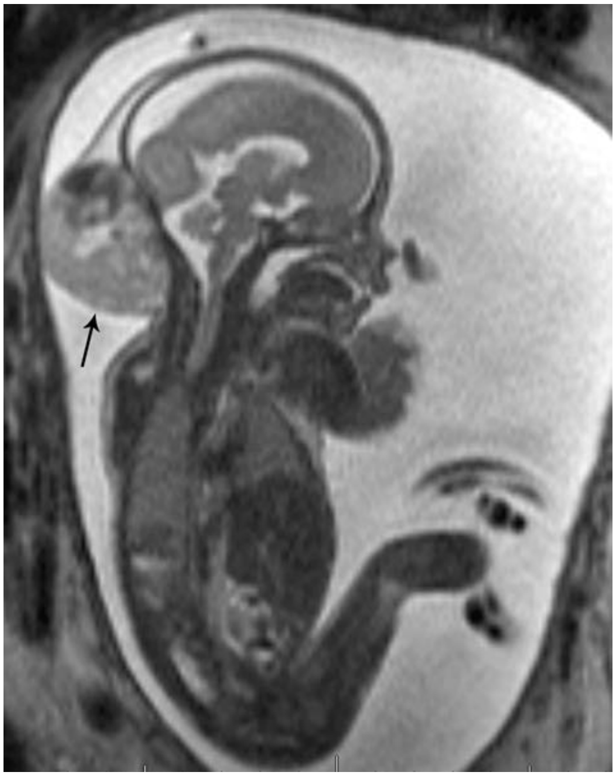

**e-Figure 14.5. Congenital hemangioma.** Sagittal fetal half-Fourier acquisition single-shot turbo (HASTE) MRI image shows a complex soft tissue mass in the posterior neck *(small arrow)* with internal hypointensity, indicative of blood products.

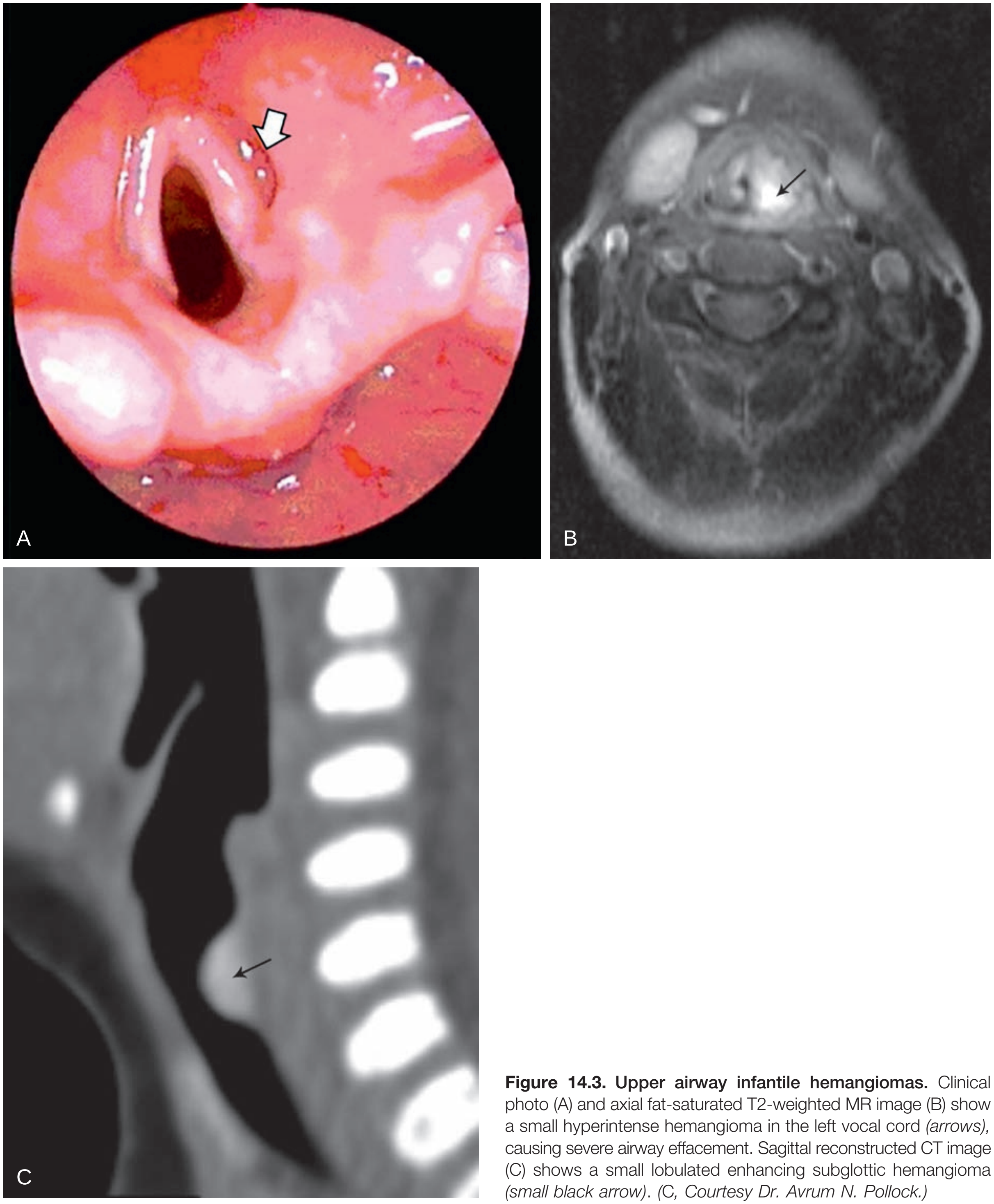

**Figure 14.3. Upper airway infantile hemangiomas.** Clinical photo (A) and axial fat-saturated T2-weighted MR image (B) show a small hyperintense hemangioma in the left vocal cord *(arrows),* causing severe airway effacement. Sagittal reconstructed CT image (C) shows a small lobulated enhancing subglottic hemangioma *(small black arrow)*. *(C, Courtesy Dr. Avrum N. Pollock.)*

patient age, and phase of the lesion (proliferative, involuting, and mature) also influence the method and timing of intervention.

## Kaposiform Hemangioendothelioma and Tufted Angioma

KHE and tufted angioma (TA) are very rare vascular tumors of infancy and early childhood, respectively. KHE and TA may represent parts of the same neoplastic spectrum. Both tumors differ from hemangioma by histopathologic and clinical appearance. KHE is classified as a locally aggressive tumor of intermediate malignancy and presents as an ill-defined vascular mass with stranding in the subcutaneous fat, intralesional calcifications, and prominent feeding and draining vessels (e-Fig. 14.7). It tends to cause bony destruction. The head and neck are uncommon locations. Tufted angioma has benign growth potential and is typically located on the upper back and neck. These vascular tumors may both manifest as Kasabach-Merritt phenomenon, a severe thrombocytopenia with mild to moderate coagulopathy resulting from intralesional platelet trapping. Awareness of these features should

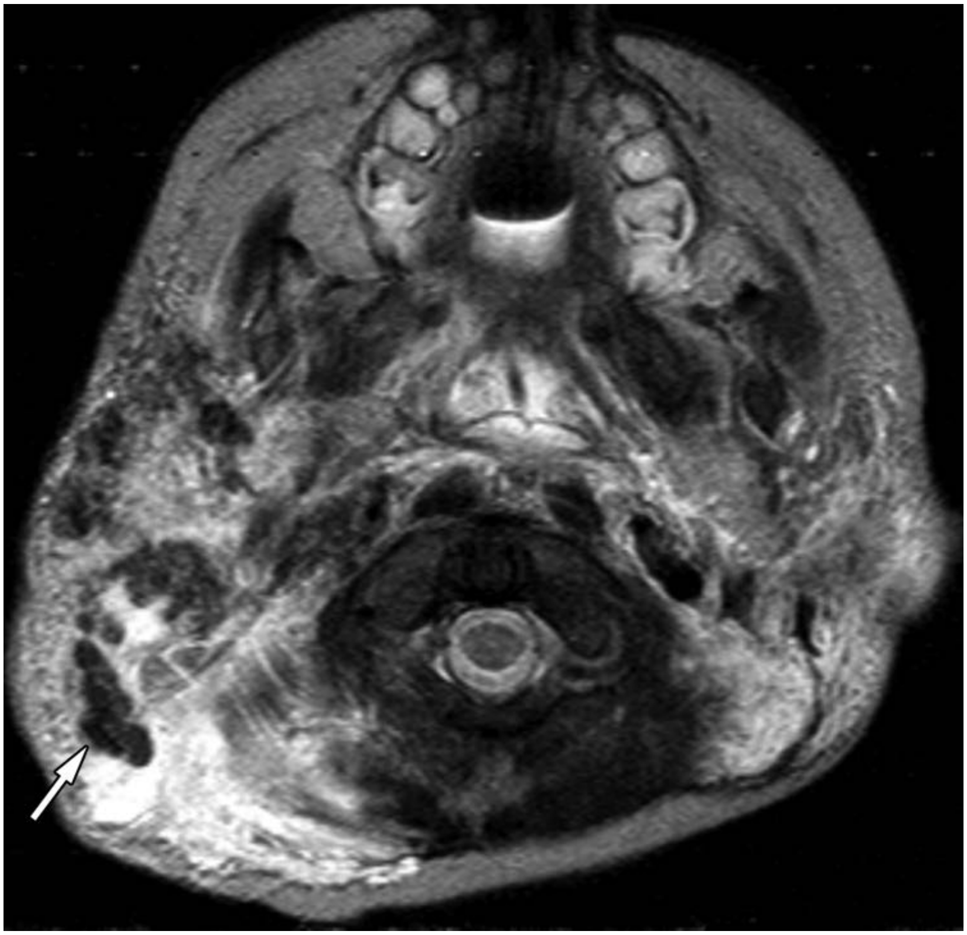

**e-Figure 14.7. Kaposiform hemangioendothelioma.** Axial fat-saturated T2-weighted MR image shows an ill-defined vascular mass with stranding in the subcutaneous fat and intralesional calcifications *(arrow)*.

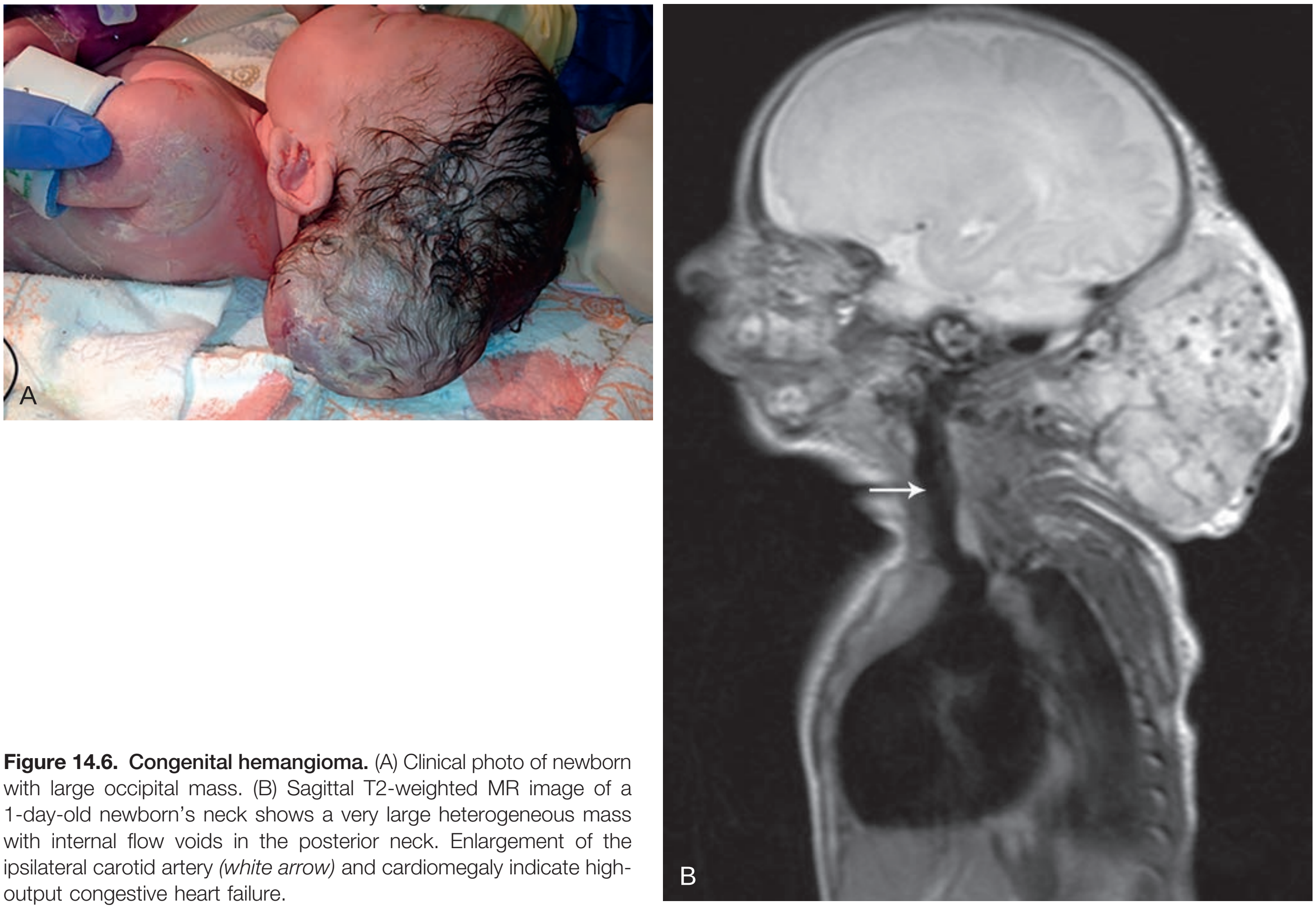

**Figure 14.6. Congenital hemangioma.** (A) Clinical photo of newborn with large occipital mass. (B) Sagittal T2-weighted MR image of a 1-day-old newborn's neck shows a very large heterogeneous mass with internal flow voids in the posterior neck. Enlargement of the ipsilateral carotid artery *(white arrow)* and cardiomegaly indicate high-output congestive heart failure.

prompt radiologists to include KHE/TA in the differential diagnosis for pediatric vascular masses. KHE/TA are GLUT-1 negative, which can be used to distinguish them from infantile hemangioma if the histologic diagnosis is uncertain.

## SPECTRUM OF VASCULAR MALFORMATIONS

Vascular malformations are congenital nonneoplastic lesions further classified according to the type of abnormal vessel comprising the lesion. Additionally, vascular lesions are classified on the basis of their hemodynamics as high-flow and low-flow types. Low-flow lesions consist of any combination of capillary, venous, and lymphatic components, whereas high-flow lesions contain arterial components. Cervical venolymphatic malformations, similar to those located elsewhere in the body, represent a spectrum of entities consisting of a combination of anomalous lymphatic and venous channels. When the lymphatic vascular component is prevalent, lesions are called lymphatic malformations, whereas those with dominant venous components are called venous malformations. The venolymphatic lesions may be further divided into macrocystic and microcystic based on the size of the lesions' cystic components. Four histologic types are identified, but they differ only on the basis of lymphatic channel size and are otherwise pathologically identical.

Vascular malformations grow in proportion to the patient's growth but may exhibit rapid growth or expansion after infection, trauma, or hormonal changes such as during puberty or pregnancy. Vascular malformations do not involute spontaneously.

*Venolymphatic malformations* of the neck may be diagnosed prenatally or may present in the perinatal period. The most pure lymphatic malformation, which seemingly consists of lymphatic channels only, is represented by a fetal nuchal cystic hygroma. A focal nuchal translucency, perceived as a hypoechoic subcutaneous region in the posterior neck, may be identified on obstetric US at 11 to 14 weeks' gestational age; it is considered a normal finding if it measures below a defined threshold and eventually involutes by term.

A pathologic nuchal cystic hygroma develops in cases of failure of appropriate connections between the lymphatic jugular sac and jugular vein. This lesion becomes apparent as a nuchal thickening at 18 to 20 weeks' gestational age. Approximately 60% of nuchal cystic hygromas are associated with some type of chromosome abnormalities (Turner syndrome, trisomy 18 and 21), and multiple other syndromes. Abnormal accumulation of lymph may cause lymphedema and nonimmune hydrops, a condition with a high mortality rate. Cystic hygroma appears on US as translucent nuchal thickening with no identifiable arterial or venous flow by Doppler. MRI reveals focal edema of the posterior fetal neck and, in severe cases, may reveal associated lymphedema, pleural effusions, ascites, and anasarca (e-Fig. 14.8).

*Lymphatic/venolymphatic malformations* of the fetal/neonatal neck may be discovered prenatally, may be seen at birth, or may "silently" grow with a child in the first few years before suddenly becoming symptomatic after spontaneous hemorrhage or infection. These lesions usually present as large, transpatial, multicystic masses with intervening septae and fluid–fluid levels (Fig. 14.9), although a small venolymphatic malformation may occasionally be seen as a unilocular cyst. US demonstrates septated hypoechoic cystic lesions without internal vascularity, although some vascular flow may be seen within the intralesional septae. Lymphatic malformations may have a very complex appearance because of their multicompartmental nature and internal hemorrhages

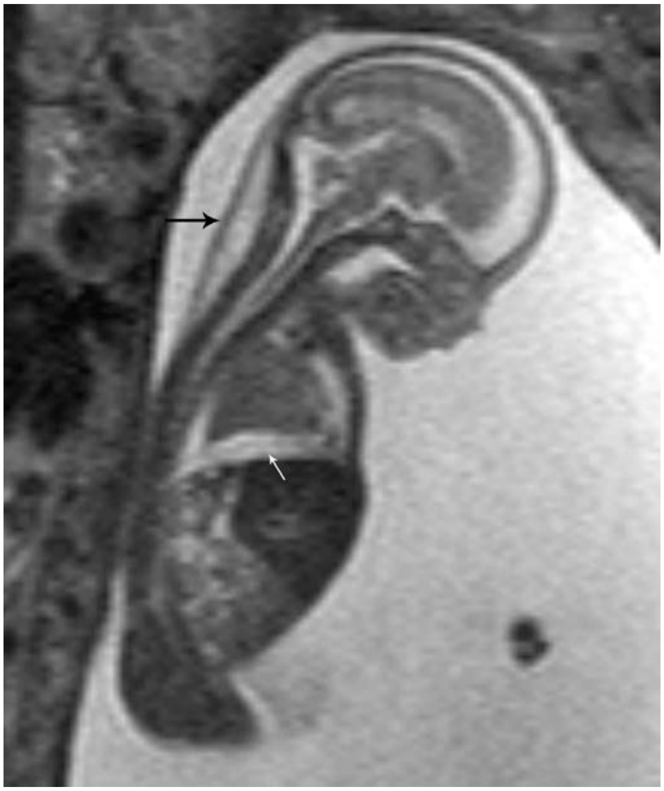

**e-Figure 14.8. Fetal nuchal cystic hygroma.** Sagittal fetal half-Fourier acquisition single-shot turbo (HASTE) MR image of a 19-week-old fetus shows a unilocular cystic mass within the posterior fetal neck *(black arrow)* and moderate pleural effusion *(white arrow),* compressing the lung.

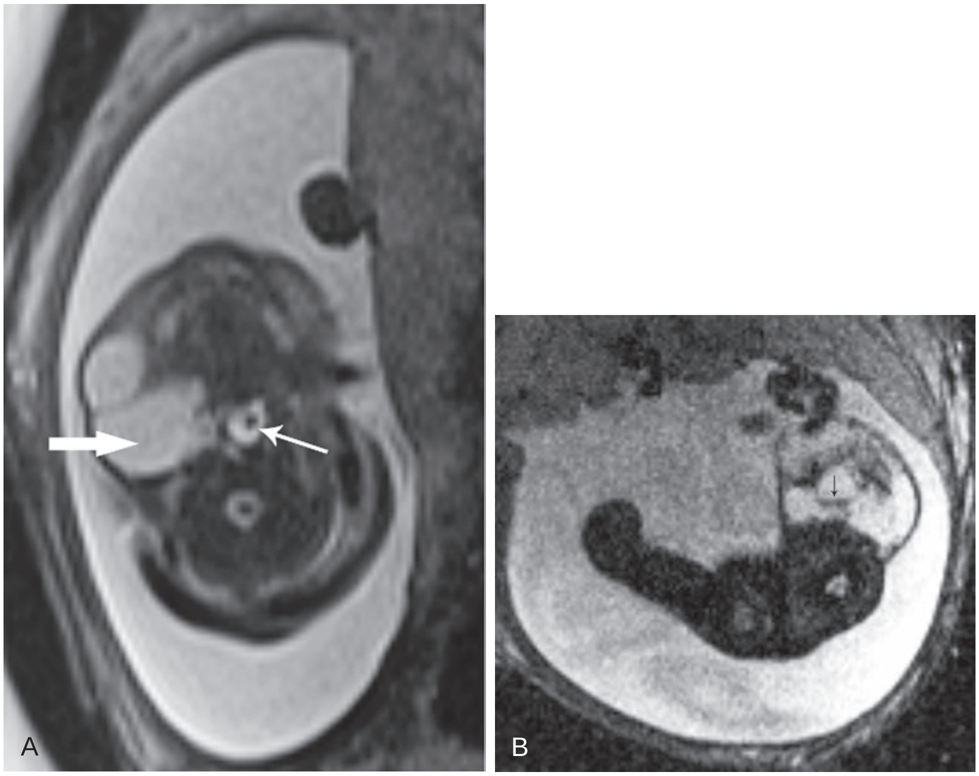

**Figure 14.9. Venolymphatic malformations.** (A) Axial half-Fourier acquisition single-shot turbo spin echo (HASTE) fetal MR image shows a multicystic mass of the lateral neck *(large arrow)*. The fetal airway remains patent *(small white arrow)*. (B) Fetal gradient echo planar MR image shows a blood-fluid level *(arrow)* within the cystic neck mass.

(Fig. 14.10). Relatively thick intralesional septations (e-Fig. 14.11) or foci of chronic hemorrhage may show enhancement and mimic solid portions of a cystic teratoma. Absence of calcifications and relatively mild mass effect onto surrounding structures despite the large size of the lesion are characteristic features. Absence or presence of calcifications is easier to establish on fetal US; blood products and calcifications may be occasionally confused on fetal MRI. The current approach to treatment of venolymphatic malformations is interventional sclerotherapy with doxycycline or other sclerosants, which provides excellent results for large macrocystic head and neck lesions. Therapy for microcystic and mixed lesions continues to be a challenge.

## VENOUS VASCULAR MALFORMATIONS

Venous malformations represent slow-growing lesions that consist of dysplastic venous channels that may have a minor lymphatic component. They are present at birth but usually manifest clinically later in life. On imaging, they appear as well-defined, ovoid, heterogeneous lesions with strong enhancement and occasional intralesional phleboliths (Figs. 14.12A and B). A calcified phlebolith may occasionally simulate a flow void on MRI, leading to an erroneous identification of the lesion as a hemangioma. Many lesions may be successfully treated with sclerotherapy, although larger and infiltrative lesions may be more challenging to treat.

## SYSTEMIC LYMPHATIC MALFORMATIONS

Systemic lymphatic malformations include rare conditions known as lymphangiomatosis and Gorham-Stout disease (vanishing bone disease). These entities are poorly understood and likely represent a spectrum of congenital disorders of lymphatic development.

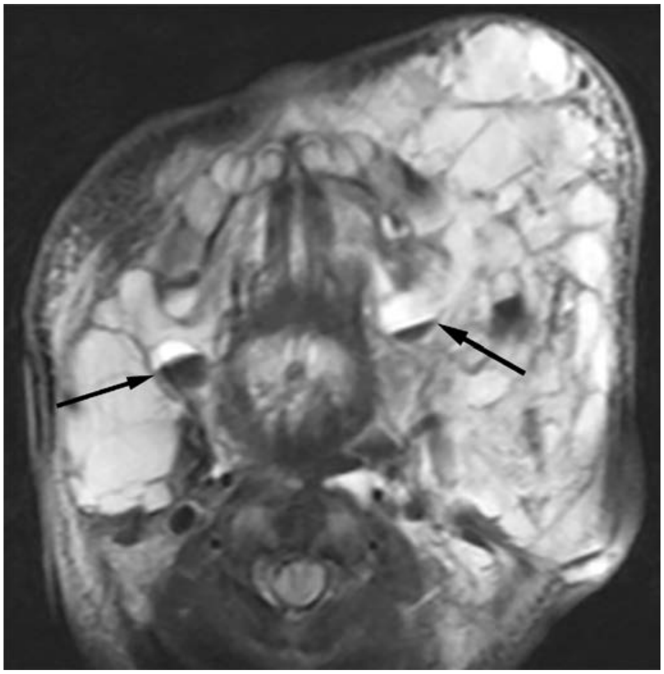

**Figure 14.10. Venolymphatic malformation.** Axial fat-saturated T2-weighted MR image in a neonate demonstrates numerous blood-fluid levels *(arrows)* within the multicompartmental neck mass.

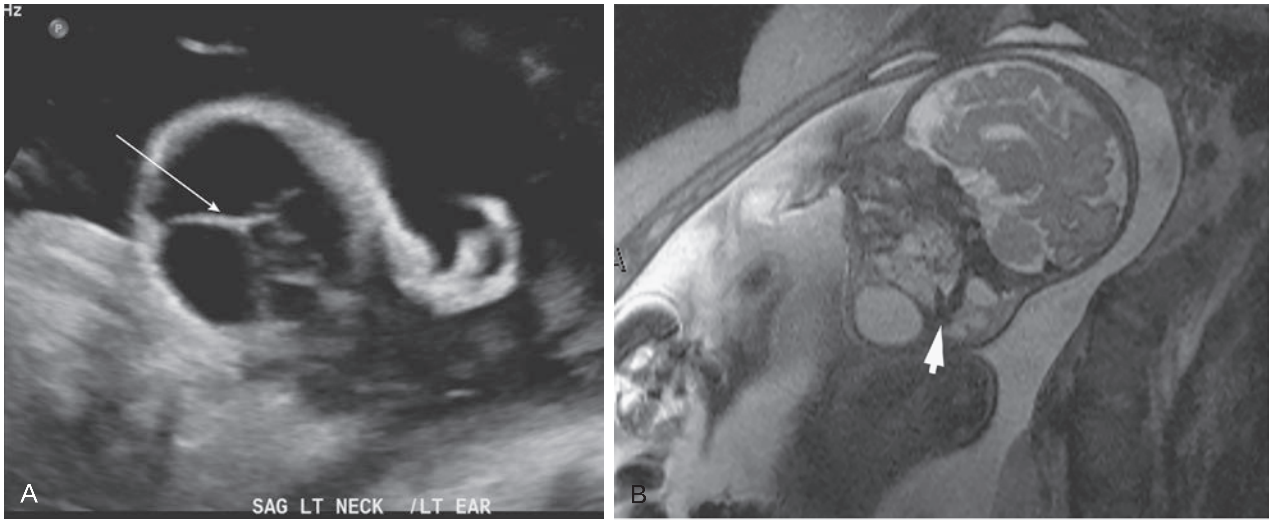

**e-Figure 14.11. Venolymphatic malformation.** (A) Fetal sonogram and (B) fetal MRI half-Fourier acquisition single-shot turbo (HASTE) imaging demonstrates multicystic lesions with thick septations *(arrows)*.

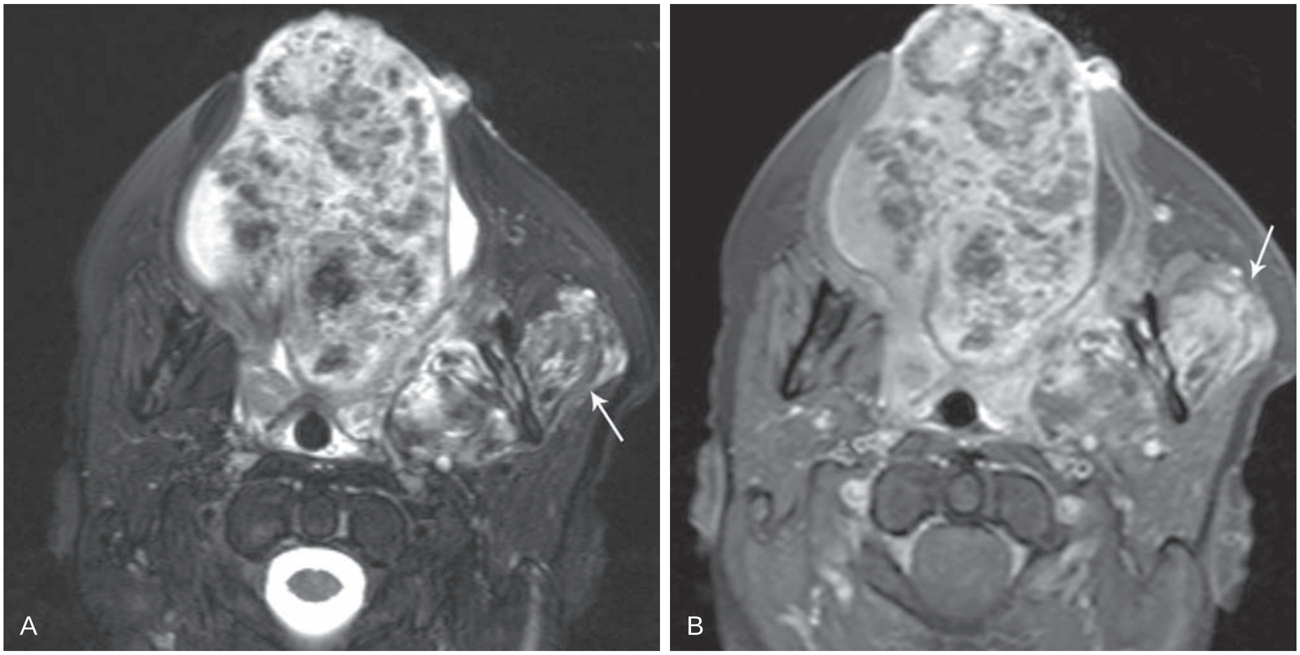

**Figure 14.12. Venous malformation.** (A) Axial fat-saturated T2-weighted and (B) axial fat-saturated postcontrast MR images show an ovoid heterogeneous enhancing lesion with numerous hypointense phleboliths, almost replacing the tongue. Superficial component is indicated by the *arrow*.

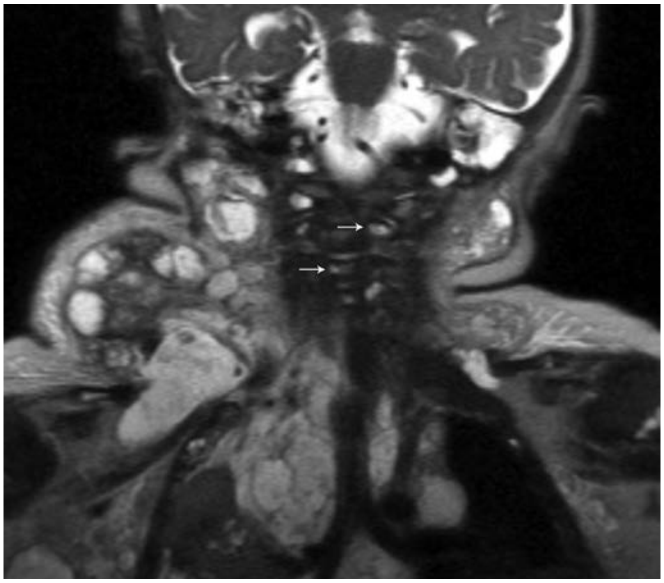

**Figure 14.13. Lymphangiomatosis.** Coronal short TI inversion recovery (STIR) MR image shows a large complex cystic mass in the lateral neck, extending into the thorax, and numerous small cysts *(small white arrows)* involving the vertebra.

They manifest with numerous foci of vascular and lymphatic proliferation, involving multiple organs, including bones and lungs (Fig. 14.13 and e-Fig. 14.14A and B), and often cause serious consequences. Osseous involvement of the face and neck may be observed in both entities; however, spontaneous, progressive osteolysis appears more diffuse and is reported to be more symptomatic in cases of Gorham disease.

Kaposiform lymphangiomatosis is a rare, aggressive, recently described lymphatic disorder with overlapping imaging features with other lymphatic anomalies. Presence of hemorrhagic effusions and moderate thrombocytopenia (50–100,000/µl) favor this diagnosis.

## TERATOMA

Teratoma of the neck accounts for only 5% to 10% of all fetal and neonatal teratomas. Most cervical teratomas are benign, yet it is the most common fetal neck mass with potential to cause fetal demise secondary to airway obstruction. On rare occasions, large vascular teratomas may result in nonimmune fetal hydrops and subsequent fetal death. Teratomas usually originate in the anterolateral neck and may involve the face and cranial base, sometimes extending to the thorax. Interval lesion enlargement in late gestation often causes hyperextension of the neck, which is characteristic of cervical teratoma. The lesion may be intimately associated with the thyroid gland and, in addition to tracheal compression, may cause esophageal compression. Teratomas are composed of all three germ layers with tissue differentiation that infrequently results in the presence of identifiable organs or fetal parts (e-Fig. 14.15). Oropharyngeal teratomas may grow rapidly during gestation. Teratomas are subdivided into mature, immature, and malignant types, each of which differs by histology and hence imaging appearance. Benign mature lesions are mostly cystic, whereas immature lesions tend to be more solid. Malignant teratomas are uncommonly found in the neck and are less aggressive compared with other locations. Most teratomas demonstrate a combination of cystic and solid components (Fig. 14.16). Intratumoral foci of hemorrhage and necrosis are suggestive of malignancy (Fig. 14.17A). Intralesional fat (Fig. 14.17B) and calcifications are nearly pathognomonic findings for teratoma but may not always be discernible on fetal MRI and are better seen on US (e-Fig. 14.18). Cervical teratoma and congenital hemangioma share many MRI and US features, including interval growth in utero. The diagnosis may be quite challenging and both imaging modalities are often necessary for optimal assessment. Postnatal assessment of teratoma may include CT, which is readily available and may demonstrate intralesional fat, calcifications and osseous

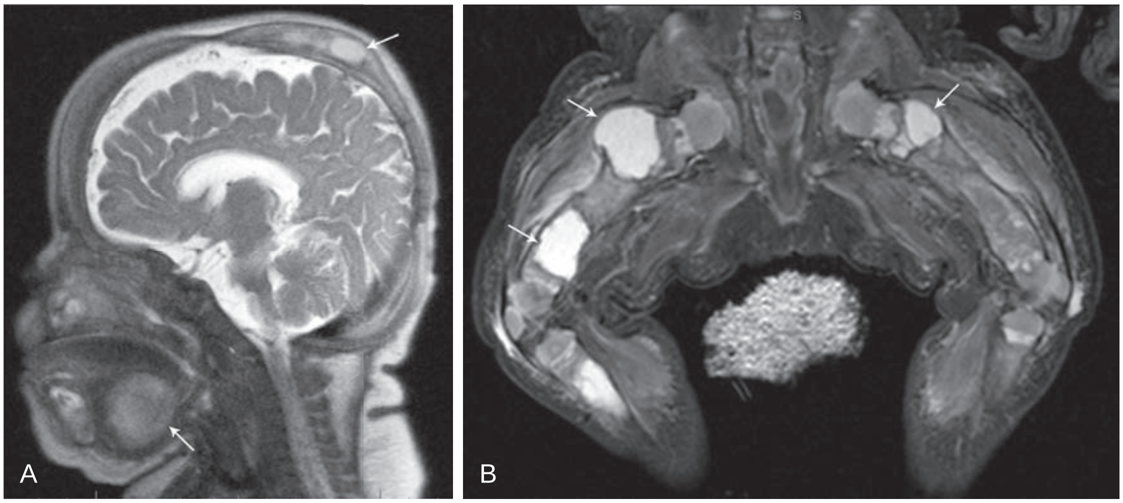

**e-Figure 14.14. Gorham-Stout disease.** (A) Sagittal STIR MR image through the head and (B) coronal STIR MR image through the lower extremities show numerous intraosseous and submandibular neck cystic lymphatic malformations.

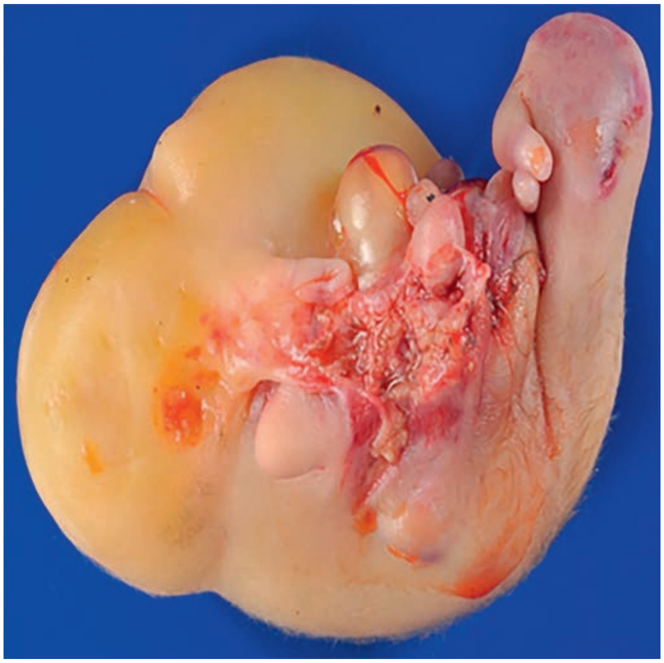

**e-Figure 14.15. Oropharyngeal teratoma.** Clinical photo of pathology specimen shows a fat-containing mass with the inclusion of bony structures and fingers.

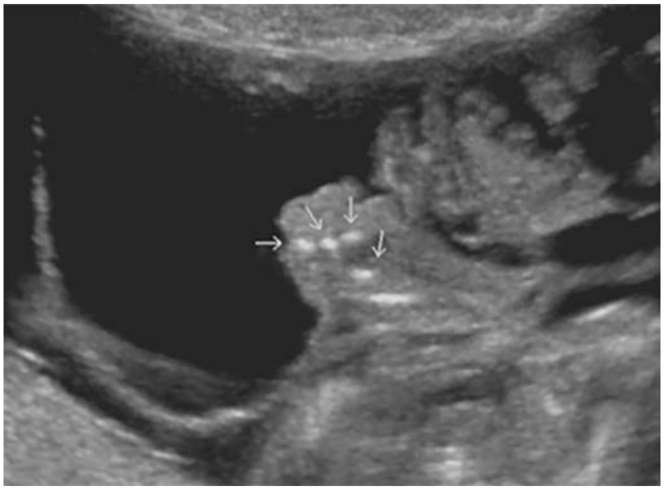

**e-Figure 14.18. Cervical teratoma.** Fetal sonogram shows punctate calcifications within a cervical mass, a typical feature of teratomas.

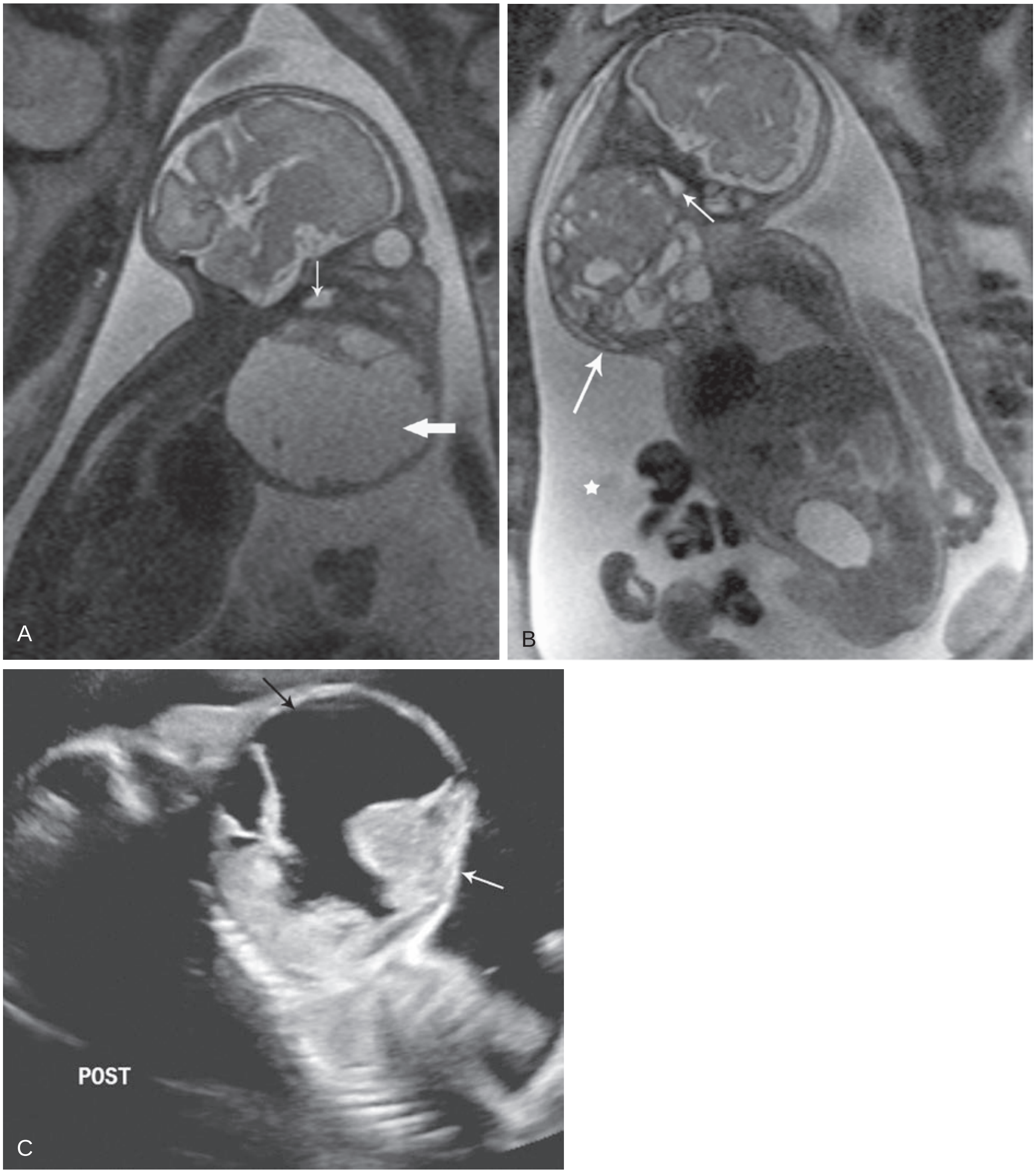

**Figure 14.16. Fetal neck teratomas.** (A) Sagittal fetal half-Fourier acquisition single-shot turbo (HASTE) MR image shows a predominantly cystic teratoma *(large arrow)* with a small solid component in the anterolateral neck. Upper airways are distended, but motion of soft palate *(small arrow)* is preserved. (B) Fetal HASTE MR image shows a mixed, predominantly solid teratoma *(large arrow)* in the anterolateral neck, which severely narrows the fetal nasopharynx *(small arrow)*. (C) Fetal ultrasound shows a mixed teratoma in the fetal neck with cystic *(black arrow)* and solid *(white arrow)* components.

involvement. MRI is, however, superb for precise depiction of lesion morphology and extension. Magnetic resonance angiography may provide crucial information about the vascular supply for surgical planning.

Surgical treatment of teratomas may be curative, although the mortality rate remains high. Persistent disfiguration of facial structure, voice issues, and hypothyroidism are among the common complications.

## CERVICAL CYSTIC MASSES

A variety of unilocular cystic neck lesions may be diagnosed on prenatal imaging or may present in neonates. These lesions are uncommon; they originate from different embryonic structures, and their precise diagnosis may be challenging, especially in fetuses. Perinatal cystic neck lesions include dermoid and epidermoid cysts, laryngoceles, foregut duplication cysts, and thymic cysts.

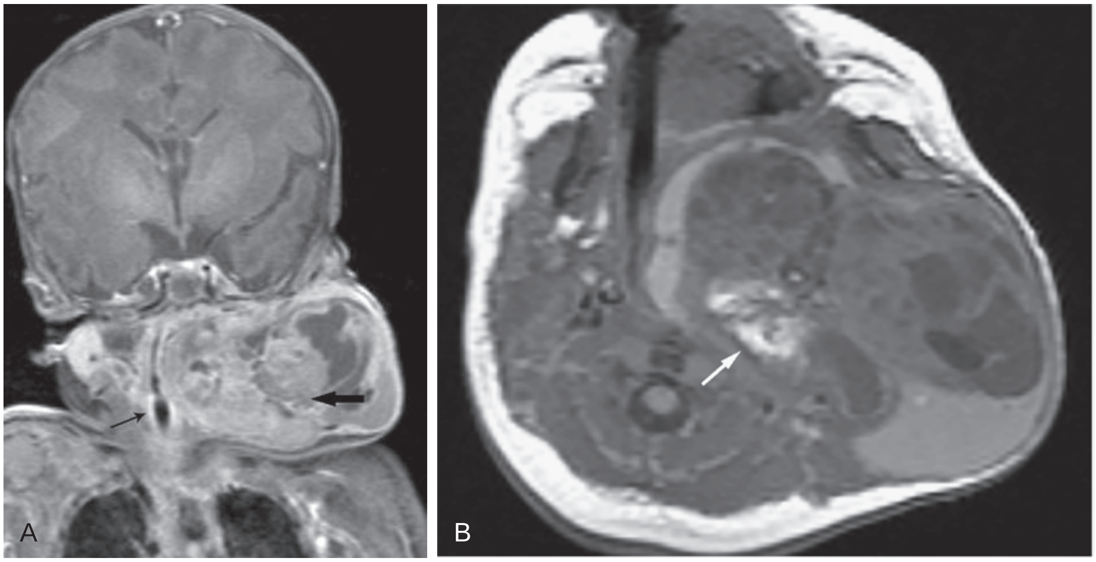

**Figure 14.17. Neonatal malignant teratoma.** (A) Coronal fat-saturated postcontrast MR image shows a large heterogeneous neck mass *(large arrow)* with necrotic areas, which severely narrows and displaces the upper airway *(small arrow)*. (B) Axial T1-weighted MR image shows a large mass of the neck that contains internal fat *(arrow),* a typical feature of teratomas.

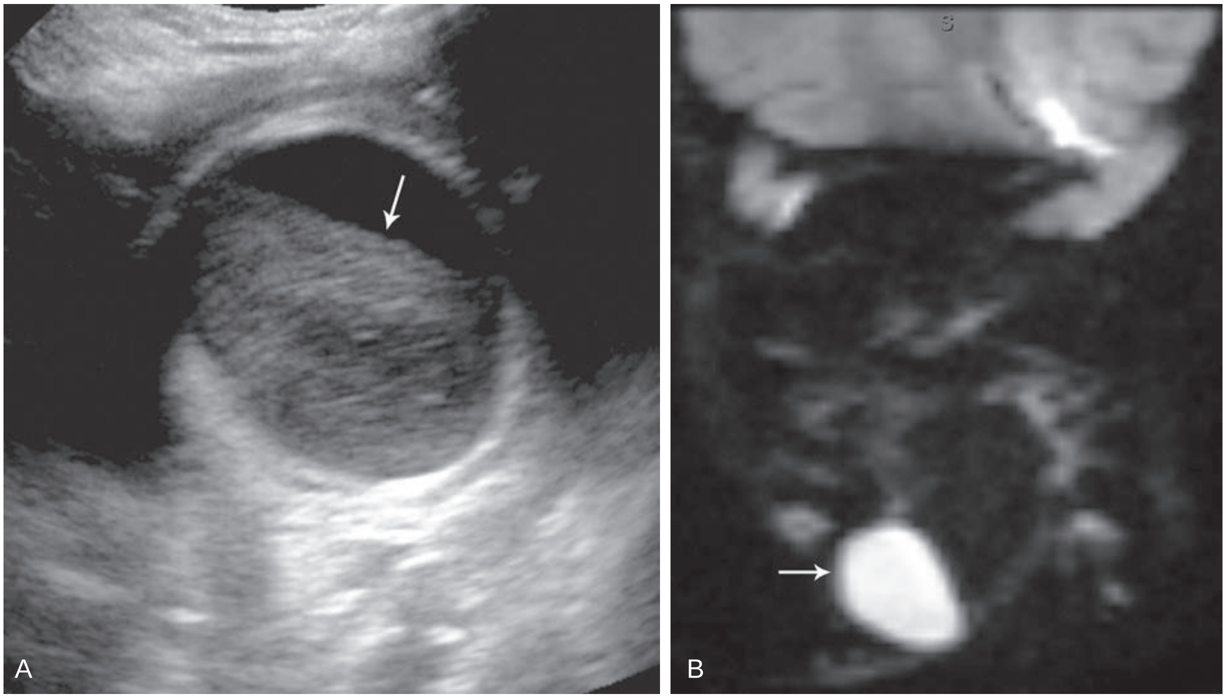

**Figure 14.19. Cervical epidermoid.** (A) Sonogram shows a submandibular unilocular cystic structure, with *arrow* pointing to layering hyperechoic cyst contents. (B) Diffusion-weighted MR image of the cystic submandibular mass, with *arrow* pointing to the restricted diffusion within the lesion.

## Dermoid/Epidermoid Cysts

Dermoid cysts are benign congenital lesions that contain ectodermal elements, including hair follicles and sweat and sebaceous glands. Cervical dermoids are most commonly seen in the floor of the mouth, in the submandibular or sublingual spaces, or at the suprasternal notch. They often demonstrate fatty content with imaging. Epidermoid cysts are rare congenital unilocular lesions, which may closely resemble a thyroglossal duct cyst; however, a characteristic pattern of restricted diffusion typical for epidermoids helps distinguish these entities. Compared with dermoid cysts, epidermoid cysts appear earlier, with most lesions being evident during infancy (Fig. 14.19) or diagnosed prenatally (e-Fig. 14.20). Dermoids and epidermoids have different histology, but it is not always possible to differentiate them on imaging. It is more important to define the lesion position in relation to the oral floor muscles, as it may guide a surgical approach.

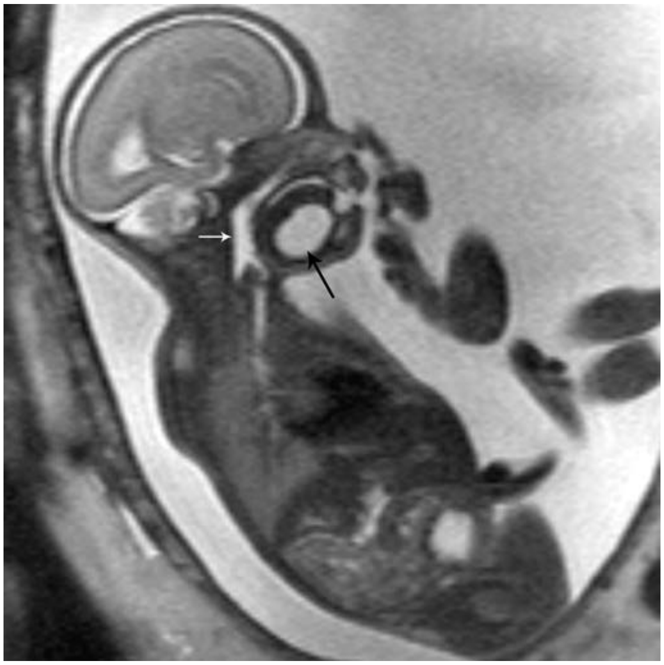

**e-Figure 14.20. Cervical epidermoid.** Fetal sagittal MRI shows unilocular submandibular epidermoid *(black arrow)*. The airways are patent; the hypopharynx is distended *(white arrow)*.

## Laryngocele

Most laryngoceles are acquired lesions, seen in middle-aged persons involved in activities that cause increased supraglottic pressure. Congenital laryngoceles are rare and likely reflect congenital enlargement of the laryngeal saccule. The three types of laryngoceles are internal, external, and combined laryngoceles. The internal laryngocele is found entirely within the larynx, whereas the external or mixed types protrude through the thyrohyoid membrane and may extend into the lateral neck. Clinically, laryngoceles may manifest as fluctuating soft tissue masses causing airway obstruction in young infants, or the masses may be diagnosed prenatally (e-Fig. 14.21). Evaluation of a laryngocele with high-resolution cross-sectional imaging depicts the anatomic boundaries of the lesion and the contents of the cyst, which may be filled with air, fluid, or proteinaceous material.

## Foregut Duplication Cyst

Foregut duplication cysts in the neck may be incidental findings; may present in the neonate with frank respiratory distress secondary to obstruction; or may be diagnosed prenatally as unilocular cystic mass in the anterior compartment of the fetal neck and mediastinum (e-Fig. 14.22). The cyst may or may not communicate with the esophagus; however, a thorough search for this communication should be performed. Detection of abnormal canalization of the gastrointestinal tract confirms the diagnosis of foregut duplication cyst. Preoperative imaging is recommended to differentiate these lesions from other congenital head and neck masses. Surgical excision with complete removal of the mucosal lining is curative.

## Thymic Cyst

Thymic cysts may rarely present within the neck, communicating with pharyngeal structures through the thyrohyoid membrane. Thymic cysts may be found in the midline or anterior to the sternocleidomastoid muscle (e-Figs. 14.23A and B), where they may resemble a branchial arch anomaly.

# CERVICAL SOFT TISSUE MASSES

## Ectopic Thymus

Ectopic thymus is usually discovered incidentally on neck imaging performed for unrelated indications. It may be seen anywhere along the course of the primordial thymopharyngeal duct, from the mandibular angle to the thoracic inlet. This lesion most often can be found along the carotid sheath but may extend to the midline (Fig. 14.24A) or may be bilateral. The imaging features are identical to orthotopic thymus (Fig. 14.24B). Ectopic thymus usually resolves with involution of the intrathoracic orthotopic thymus.

## Fetal/Neonatal Goiter

Goiter is a rare cause of fetal neck mass. It may occur in the setting of maternal thyroid disorders such as Graves disease or Hashimoto thyroiditis, or as a manifestation of primary fetal hypothyroidism/hyperthyroidism. Fetal thyroid function may be assessed by US-guided umbilical cord blood sampling (cordocentesis). The fetal thyroid may be markedly enlarged, causing

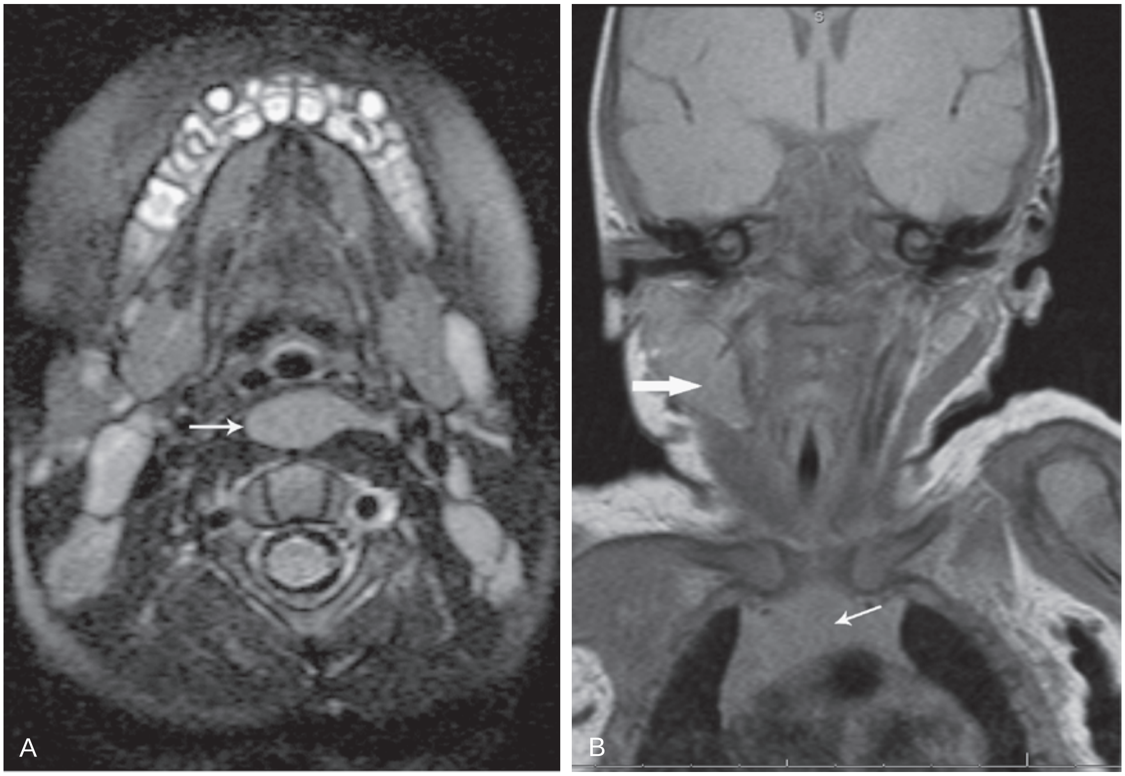

**Figure 14.24. Ectopic thymus.** (A) Axial T2-weighted MR image shows an unusual retropharyngeal location of ectopic thymus *(arrow)*. (B) Ectopic thymus *(large arrow)* in the right lateral neck of a 1-week-old infant has signal characteristics similar to the visualized orthotopic thymus *(small arrow)*. The lesion elicits no significant mass effect.

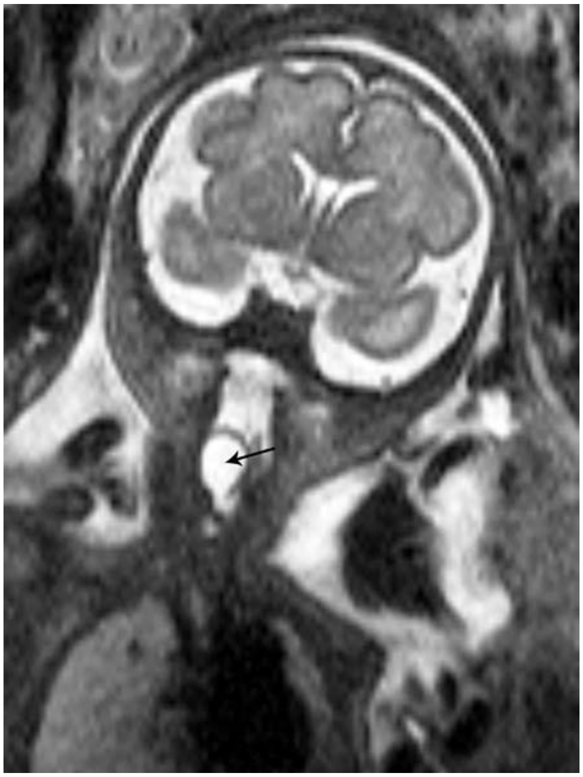

**e-Figure 14.21. Fetal laryngocele.** Coronal fetal half-Fourier acquisition single-shot turbo (HASTE) MR image shows a small cystic lesion *(arrow)* originating from the fetal larynx.

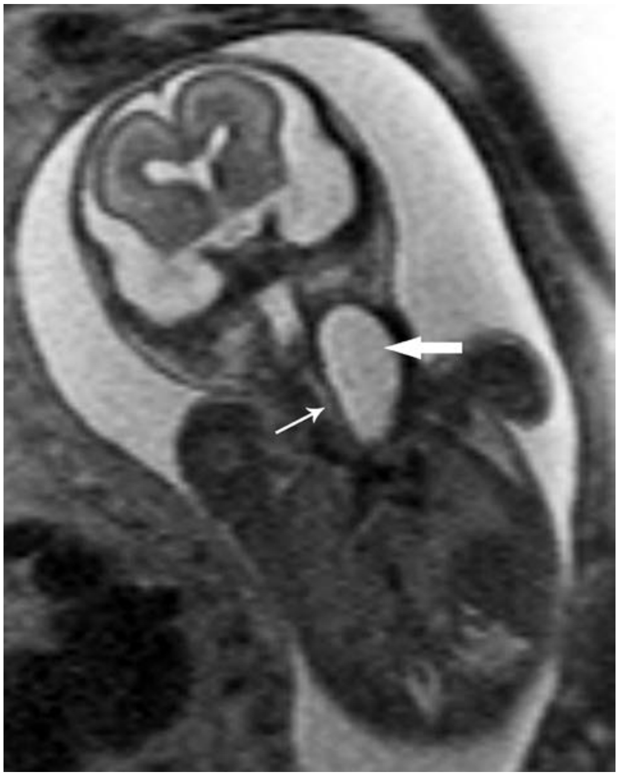

**e-Figure 14.22. Fetal esophageal duplication cyst.** Coronal fetal half-Fourier acquisition single-shot turbo MR image shows a large unilocular cystic structure in the fetal anterolateral neck *(large white arrow),* which continues into the superior mediastinum. The fetal airways appear patent *(small white arrow)*.

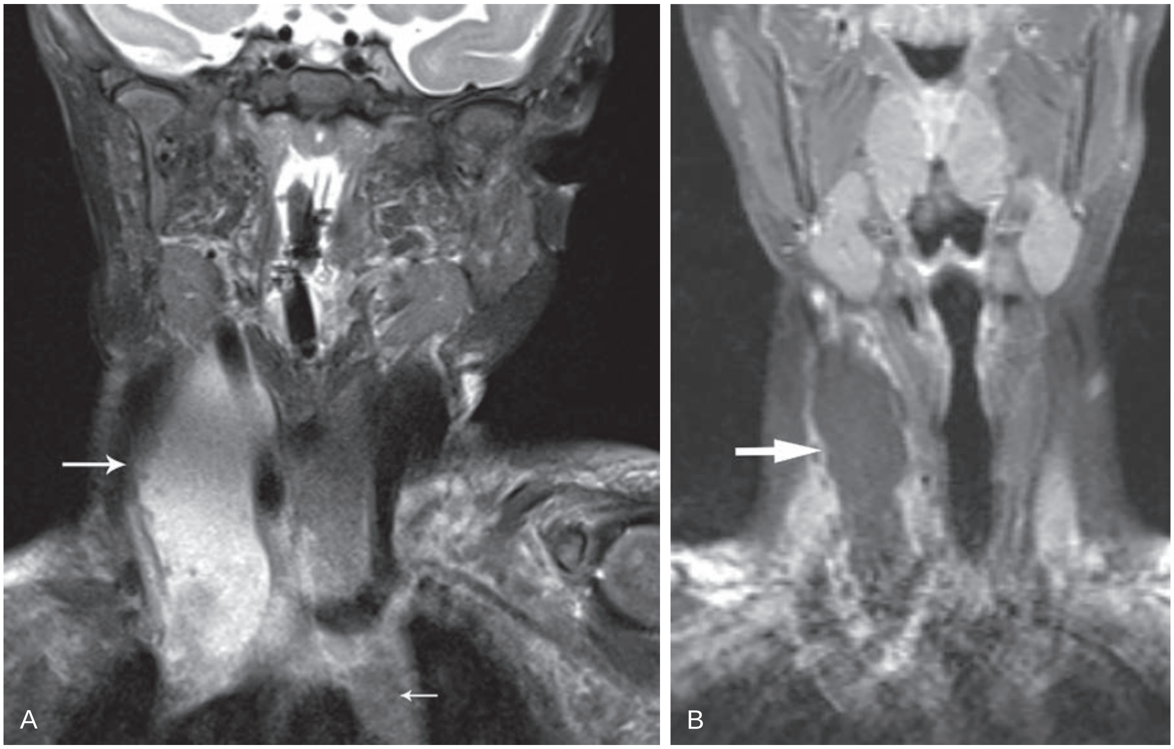

**e-Figure 14.23. Thymic cyst.** (A) Coronal STIR and (B) coronal fat-saturated contrast-enhanced MR images show an elongated cystic structure in the right neck, anterior to the sternocleidomastoid muscle *(arrows)*.

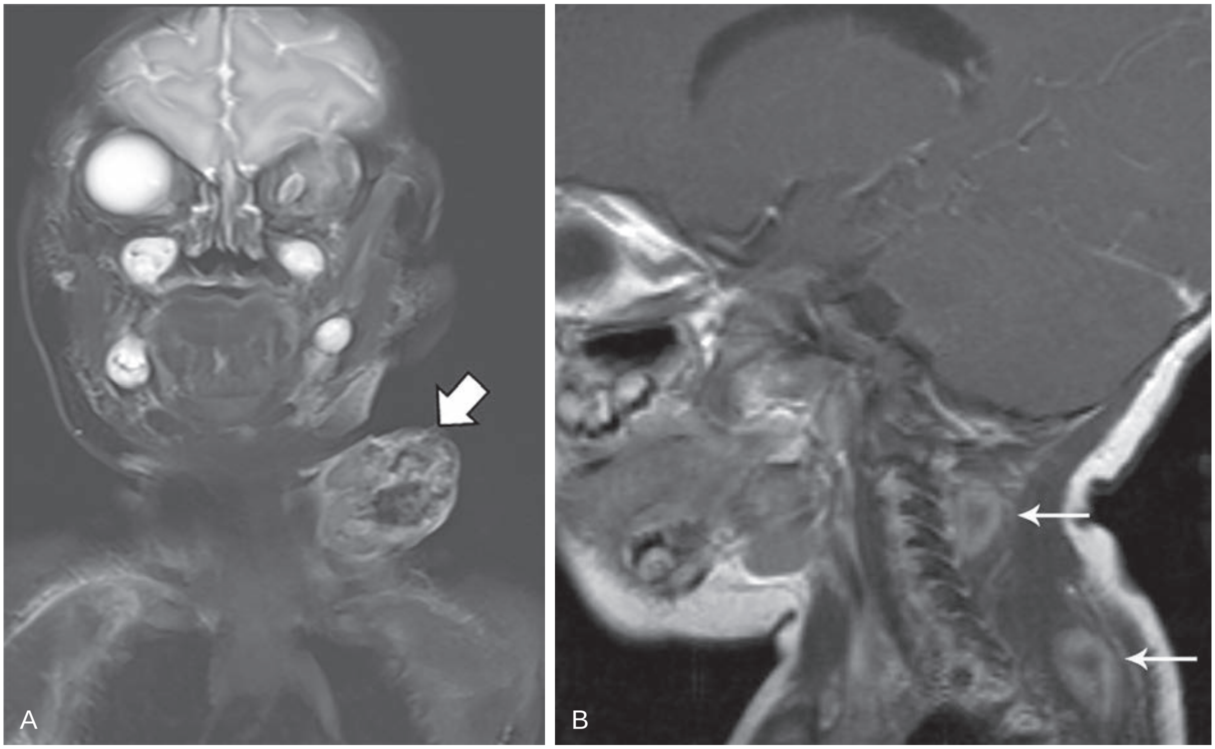

**Figure 14.26. Infantile fibromatoses.** (A) Aggressive infantile fibromatosis in a 3-day-old patient. Coronal STIR MR image shows a large heterogeneous mass in the left neck *(arrow)*. (B) Sagittal contrast-enhanced T1-weighted MR image shows multiple scattered nodular masses *(white arrows)* of the neonatal neck with typical "target" appearance of desmoid type of infantile fibromatosis.

neck hyperextension, airway obstruction, and/or esophageal compression. Fetal goiter may be diagnosed on US as a bilobed echogenic vascular mass in the anterior neck; fetal MRI demonstrates a midline mass with high signal on T1-weighted imaging (e-Fig. 14.25). Treatment of fetal goiter includes intraamniotic thyroxin injection, the main goal being reduction of the goiter's size and prevention of tracheal obstruction. Fetal goiter may be associated with congenital deafness in the setting of Pendred syndrome.

## Infantile Fibromatoses

Infantile fibromatosis represents a spectrum of rare congenital disorders that involve the skeletal and smooth muscle in very young children. It may manifest as a solitary form or as a multicentric form with visceral involvement. Aggressive infantile fibromatosis occurs in the first 2 years of life and may present as a nodular soft tissue mass in the head and neck with an imaging appearance mimicking infantile fibrosarcoma or hemangioma (Fig. 14.26A). A desmoid type of fibromatosis may present as a nodular tumor which often grows along the nerve sheath or vascular bundle and has a tendency to hemorrhage or necrotize in the central portion, producing a target appearance on imaging (Fig. 14.26B). The prognosis is favorable for solitary neck lesions. These lesions usually stop growing or spontaneously regress.

*Fibromatosis colli* is a benign condition that involves the sternocleidomastoid muscle only. It usually affects neonates and manifests as a hard unilateral soft tissue mass associated with ipsilateral torticollis caused by the muscular contraction and rotation of the chin to the opposite side. Imaging with US or MRI may be performed if the clinical presentation is unusual. Both modalities reveal diffuse or focal enlargement of sternocleidomastoid muscle (Fig. 14.27) and no discrete mass or lymphadenopathy. Congenital torticollis usually spontaneously resolves within a few months. A child with cervical lymphadenitis and retropharyngeal abscess may present with a postinflammatory torticollis known as Grisel syndrome; this condition is caused by increased ligamentous laxity.

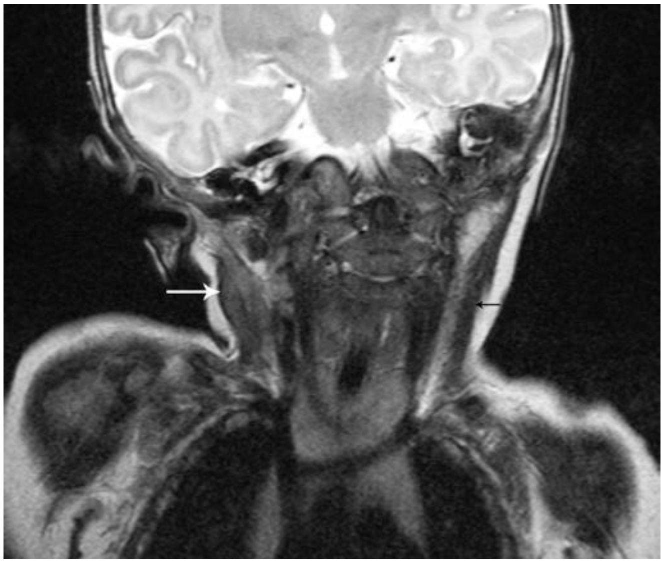

**Figure 14.27. Fibromatosis colli.** Coronal T2-weighted MR image shows diffuse thickening and hyperintensity of the right sternocleidomastoid muscle *(white arrow),* associated with ipsilateral torticollis. The left sternocleidomastoid muscle *(black arrow)* demonstrates normal thickness and signal intensity.

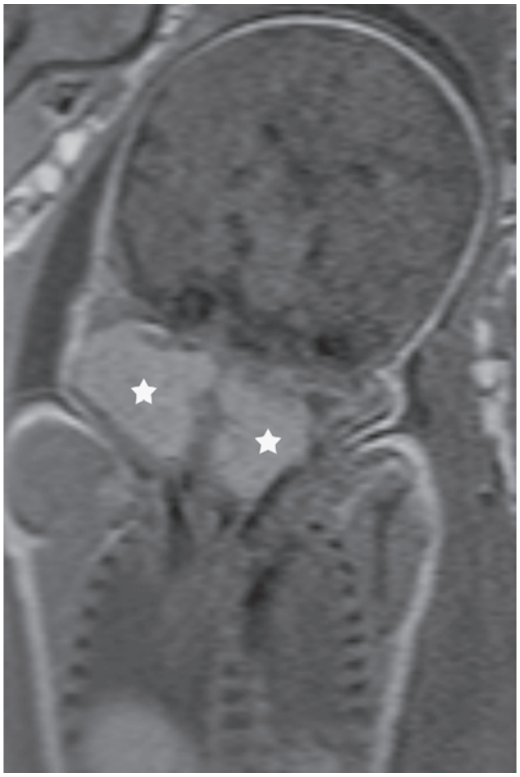

**e-Figure 14.25. Fetal goiter.** Coronal fetal T1-weighted MR image shows the bilobed, uniformly T1-hyperintense lesion *(stars),* indicative of the iodine content of thyroid gland.

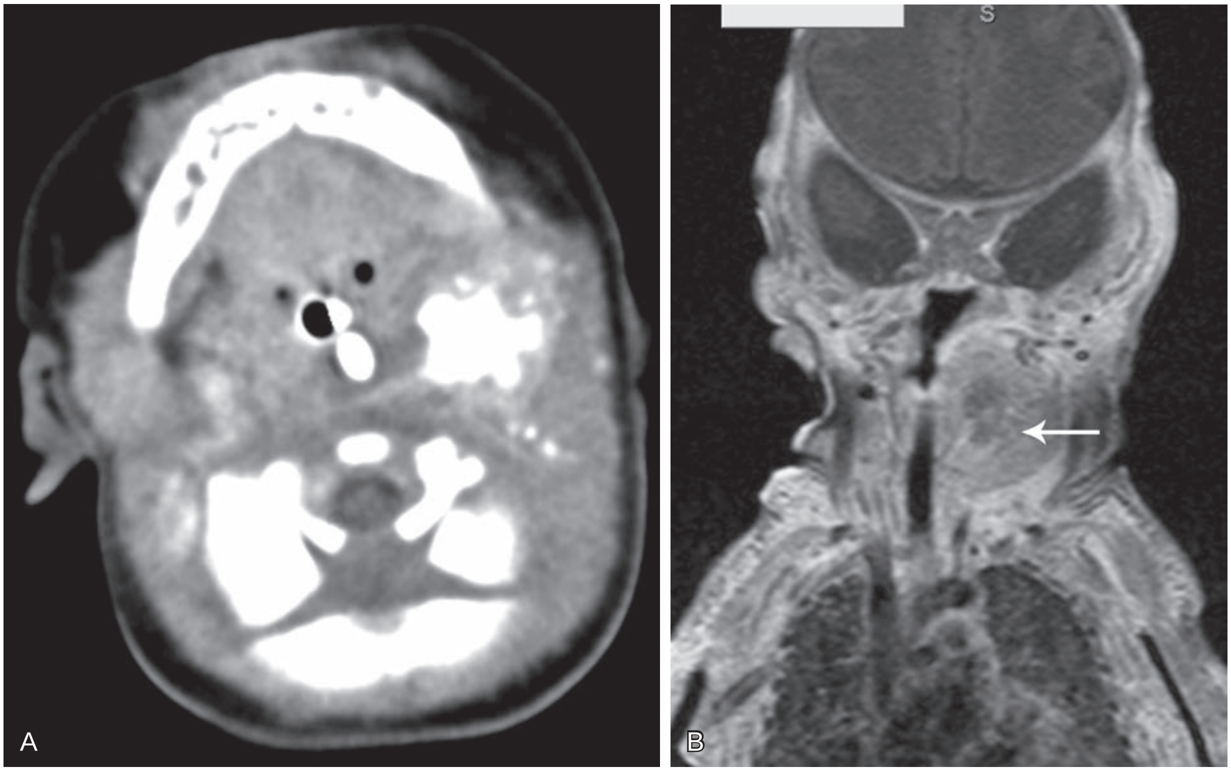

**Figure 14.28. Primary cervical neuroblastoma.** (A) CT and (B) coronal contrast-enhanced fat-saturated T1-weighted MR images show a heterogeneous mass *(small white arrow)* within the left neck, along the presumed course of the sympathetic chain with central lack of enhancement, which proves to be a chunky internal calcification on CT.

## NEONATAL NECK MALIGNANCY

### Neuroblastoma

Neuroblastoma is a common malignant tumor of childhood. Less than 5% occur within the neck as a primary site, arising in the sympathetic ganglia. Cervical location of neuroblastoma is more common in young infants, and it has been reported prenatally. This tumor has a known association with Horner syndrome. Both CT and MRI may depict tumor extension, presence of mineralization, and bony or spinal canal invasion (Fig. 14.28). Restricted diffusion on MRI confirms the hypercellular, malignant nature of this tumor. Intratumoral dystrophic calcifications are observed in 50% of cases. The prognosis and treatment plan depends on tumor genetics. Low- and intermediate-risk *MYCN* negative patients generally have a favorable outcome and usually are treated with surgical resection and chemotherapy, while high-risk *MYCN*-amplified patients require a combined and aggressive treatment with surgery, chemotherapy, radiotherapy, and immunotherapy.

### Congenital Infantile Fibrosarcoma

Congenital infantile fibrosarcoma, a rare tumor of infancy, has a markedly different clinical course and a more favorable prognosis compared with adult fibrosarcoma. It may present at birth or soon after, or may be diagnosed in utero. Infantile fibrosarcoma has unique cytogenetic findings that help to distinguish this tumor from other infantile tumors such as embryonal rhabdomyosarcoma and infantile fibromatosis. The tumor appears as a large solid soft tissue mass of the neck (e-Fig. 14.29), which may be rather homogeneous or have central necrosis and hemorrhage.

KEY POINTS

- The majority of congenital neck lesions are benign.
- Many congenital lesions may be diagnosed prenatally.
- Some congenital lesions may be associated with systemic disorders, potentially requiring further investigation.
- Vascular masses are classified into vascular tumors and vascular malformations.

### SUGGESTED READINGS

Boye E, Jinin M, Olsen BR, et al. Infantile haemangioma: challenges, new insights and therapeutic promise. *Craniofac Surg*. 2009;20(suppl 1):678–684. PMID: 19190505.
LaPlante JK, Pierson NS, Hedlund GL. Common pediatric head and neck congenital/developmental anomalies. *Radiol Clin North Am*. 2015;53(1):181–196. PMID: 25476180.
Merrow AC, Gupta A, Patel MN, et al. 2014 Revised Classification of Vascular Lesions from the International Society for the Study of Vascular Anomalies: Radiologic-Pathologic Update. *Radiographics*. 2016;36(5):1494–1516. PMID: 27517361.
Oliver ER, Coleman BG, DeBari SE, et al. Fetal lymphatic malformations: more variable than we think? *J Ultrasound Med*. 2017;PMID: 28127788.
Robson CD. Imaging of head and neck neoplasms in children. *Pediatr Radiol*. 2010;40(4):499–509. PMID: 20225112.

### REFERENCES

Full references for this chapter can be found on www.expertconsult.com.

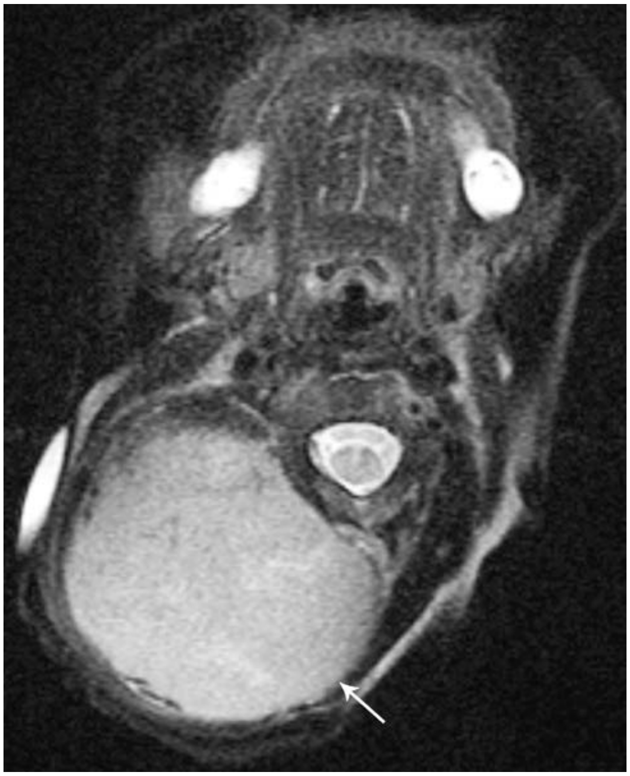

**e-Figure 14.29. Congenital infantile fibrosarcoma.** Axial fat-saturated T2-weighted MR image shows a large solid homogeneous soft tissue mass *(white arrow)* in this neonate's posterolateral neck.

## REFERENCES

1. Dremmen MH, Tekes A, Mueller S, et al. Lumps and bumps of the neck in children-neuroimaging of congenital and acquired lesions. *J Neuroimaging*. 2016;26(6):562–580. PMID: 27510326.
2. Brown RE, Harave S. Diagnostic imaging of benign and malignant neck masses in children—a pictorial review. *Quant Imaging Med Surg*. 2016;6(5):591–604. PMID: 27942480.
3. Friedman ER, John SD. Imaging of pediatric neck masses. *Radiol Clin North Am*. 2011;49(4):617–632. PMID: 21807165.
4. Grassi R, Farina R, Floriani I, et al. Assessment of fetal swallowing with gray-scale and color Doppler sonography. *AJR*. 2005;185(5):1322–1327. PMID: 16247157.
5. Laje P, Johnson MP, Howell LJ, et al. Ex utero intrapartum treatment in the management of giant cervical teratomas. *J Pediatr Surg*. 2012;47(6):1208–1216. PMID: 22703795.
6. Tranvinh E, Yeom KW, Iv M. Imaging neck masses in the neonate and young infant. *Semin Ultrasound CT MR*. 2015;36(2):120–137. PMID: 26001942.
7. LaPlante JK, Pierson NS, Hedlund GL. Common pediatric head and neck congenital/developmental anomalies. *Radiol Clin North Am*. 2015;53(1):181–196. PMID: 25476180.
8. Mulliken JB, Glowacki J. Hemangiomas and vascular malformations in infants and children: a classification based on endothelial characteristics. *Plast Reconstr Surg*. 1982;69(3):412–422. PMID: 7063565.
9. Merrow AC, Gupta A, Patel MN, et al. 2014 Revised classification of vascular lesions from the International Society for the Study of Vascular Anomalies: radiologic-pathologic update. *Radiographics*. 2016;36(5):1494–1516. PMID: 27517361.
10. Dasgupta R, Fishman SJ. ISSVA classification. *Semin Pediatr Surg*. 2014;23(4):158–161. PMID: 25241091.
11. Nozaki T, Matsusako M, Mimura H, et al. Imaging of vascular tumors with an emphasis on ISSVA classification. *Jpn J Radiol*. 2013;31(12):775–785. PMID: 24135879.
12. Mahady K, Thust S, Berkeley R, et al. Vascular anomalies of the head and neck in children. *Quant Imaging Med Surg*. 2015;5(6):886–897. PMID: 26807370.
13. Jahnke MN. Vascular Lesions. *Pediatr Ann*. 2016;45(8):e299–e305. PMID: 27517358.
14. Calvo-Garcia MA, Kline-Fath BM, Adams DM, et al. Imaging evaluation of fetal vascular anomalies. *Pediatr Radiol*. 2015;45(8):1218–1229. PMID: 25492302.
15. Hoff SR, Rastatter JC, Richter GT. Head and neck vascular lesions. *Otolaryngol Clin North Am*. 2015;48(1):29–45. PMID: 25439548.
16. Huoh KC, Rosbe KW. Infantile hemangiomas of the head and neck. *Pediatr Clin North Am*. 2013;60(4):937–949. PMID: 23905829.
17. Rossler L, Rothoeft T, Teig N, et al. Ultrasound and color Doppler in infantile subglottic haemangioma. *Pediatr Radiol*. 2011;41:1421–1428. PMID: 21904830.
18. Restrepo R, Palani R. Hemangiomas revisited: the useful, the unusual and the new. Part 1. *Pediatr Radiol*. 2011;41:895–904. PMID: 21594550.
19. Boye E, Jinin M, Olsen BR, et al. Infantile haemangioma: challenges, new insights and therapeutic promise. *Craniofac Surg*. 2009;20(suppl 1):678–684. PMID: 19190505.
20. Menapace D, Mitkov M, Towbin R, et al. The changing face of complicated infantile hemangioma treatment. *Pediatr Radiol*. 2016;46(11):1494–1506. PMID: 27450406.
21. Cheng CE, Friedlander SF. Infantile hemangiomas, complications and treatments. *Semin Cutan Med Surg*. 2016;35(3):108–116. PMID: 27607318.
22. Luu M, Frieden IJ. Infantile hemangiomas and structural anomalies: PHACE and LUMBAR syndrome. *Semin Cutan Med Surg*. 2016;35(3):117–123. PMID: 27607319.
23. Viswanathan V, Smith ER, Mulliken JB, et al. Infantile hemangiomas involving the neuraxis: clinical and imaging findings. *AJNR Am J Neuroradiol*. 2009;30:1005–1013. PMID: 19213817.
24. Berenguer B, Mulliken JB, Enjolras O, et al. Rapidly involuting congenital hemangioma: clinical and histopathologic features. *Pediatr Development Pathol*. 2003;6:495–510. PMID: 15018449.
25. Konez O, Burrows PE, Mulliken JB, et al. Angiographic features of rapidly involuting congenital hemangioma (RICH). *Pediatr Radiol*. 2003;33:15–19. PMID: 12497230.
26. Keating LJ, Soares GM, Muratore CS. Rapidly involuting congenital hemangioma. *Med Health R I*. 2012;95(5):149–152. PMID: 22808633.
27. Schafer F, Tapia M, Pinto C. Rapidly involuting congenital haemangioma. *Arch Dis Child Fetal Neonatal Ed*. 2014;99(5):F422. PMID: 24225221.
28. Fadell MF 2nd, Jones BV, Adams DM. Prenatal diagnosis and postnatal follow-up of rapidly involuting congenital hemangioma (RICH). *Pediatr Radiol*. 2011;41(8):1057–1060. PMID: 21337126.
29. Lee PW, Frieden IJ, Streicher JL, et al. Characteristics of noninvoluting congenital hemangioma: a retrospective review. *J Am Acad Dermatol*. 2014;70(5):899–903. PMID: 24630000.
30. Ryu YJ, Choi YH, Cheon JE, et al. Imaging findings of Kaposiform hemangioendothelioma in children. *Eur J Radiol*. 2017;86:198–205. PMID: 28027747.
31. Kazlouskaya V, Lytvynenko B, Blochin E. Tufted hemangioma: clinical case and literature review. *Dermatol Pract Concept*. 2014;4(2):33–35. PMID: 24855571.
32. Croteau SE, Gupta D. The clinical spectrum of kaposiform hemangioendothelioma and tufted angioma. *Semin Cutan Med Surg*. 2016;35(3):147–152. PMID: 27607323.
33. Oliver ER, Coleman BG, DeBari SE, et al. Fetal Lymphatic Malformations: More Variable Than We Think? *J Ultrasound Med*. 2017;PMID: 28127788.
34. Peranteau WH, Iyoob SD, Boelig MM, et al. Prenatal growth characteristics of lymphatic malformations. *J Pediatr Surg*. 2017;52(1):65–68. PMID: 27836363.
35. Molina FS, Avgidou K, Kagan KO, et al. Cystic hygromas, nuchal edema, and nuchal translucency at 11–14 weeks of gestation. *Obstet Gynecol*. 2006;107(3):678–683. PMID: 16507941.
36. Hubbard AM, Crombleholme TM, Adzick NS. Prenatal MRI evaluation of giant neck masses in preparation for the fetal exit procedure. *Am J Perinatol*. 1998;15(4):253–257. PMID: 9565224.
37. Herruela-Suffee C, Warin M, Castier-Amouyel M, et al. Whole-body MRI in generalized cystic lymphangiomatosis in the pediatric population: diagnosis, differential diagnoses, and follow-up. *Skeletal Radiol*. 2016;45(2):177–185. PMID: 26545884.
38. Ruggieri P, Montalti M, Angelini A, et al. Gorham-Stout disease: the experience of the Rizzoli Institute and review of the literature. *Skeletal Radiol*. 2011;40(11):1391–1397. PMID: 20972870.
39. Kato H, Ozeki M, Fukao T, et al. Craniofacial CT findings of Gorham-Stout disease and generalized lymphatic anomaly. *Neuroradiology*. 2016;58(8):801–806. PMID: 27126342.
40. Liu Y, Zhong DR, Zhou PR, et al. Gorham-Stout disease: radiological, histological, and clinical features of 12 cases and review of literature. *Clin Rheumatol*. 2016;35(3):813–823. PMID: 25227772.
41. Goyal P, Alomari AI, Kozakewich HP, et al. Imaging features of kaposiform lymphangiomatosis. *Pediatr Radiol*. 2016;46(9):1282–1290. PMID: 27053281.
42. Cahill AM, Nijs E, Ballah D, et al. Percutaneous sclerotherapy in neonatal and infant head and neck lymphatic malformations: a single center experience. *J Pediatr Surg*. 2011;46(11):2083–2095. PMID: 22075337.
43. Tu JH, Do HM, Patel V, et al. Sclerotherapy for lymphatic malformations of the head and neck in the pediatric population. *J Neurointerv Surg*. 2016;PMID: 27707871.
44. White CL, Olivieri B, Restrepo R, et al. Low-flow vascular malformation pitfalls: from clinical examination to practical imaging evaluation–part 1, lymphatic malformation mimickers. *AJR Am J Roentgenol*. 2016;206(5):940–951. PMID: 26999565.
45. Colletti G, Ierardi AM. Understanding venous malformations of the head and neck: a comprehensive insight. *Med Oncol*. 2017;34(3):42. PMID: 28181207.
46. Olivieri B, White CL, Restrepo R, et al. Low-flow vascular malformation pitfalls: from clinical examination to practical imaging evaluation–part 2, venous malformation mimickers. *AJR Am J Roentgenol*. 2016;206(5):952–962. PMID: 26999647.
47. Robson CD. Imaging of head and neck neoplasms in children. *Pediatr Radiol*. 2010;40(4):499–509. PMID: 20225112.
48. Paradis J, Koltai PJ. Pediatric teratoma and dermoid cysts. *Otolaryngol Clin North Am*. 2015;48(1):121–136. PMID: 25439551.
49. Gaddikeri S, Vattoth S, Gaddikeri RS, et al. Congenital cystic neck masses: embryology and imaging appearances, with clinicopathological correlation. *Curr Probl Diagn Radiol*. 2014;43(2):55–67. PMID: 24629659.
50. Koeller KK, Alamo L, Adair CF, et al. Congenital cystic masses of the neck: radiologic-pathologic correlation. *Radiographics*. 1999;19(1):121–146. PMID: 9925396.

51. Ibrahim M, Hammoud K, Maheshwari M, et al. Congenital cystic lesions of the head and neck. *Neuroimaging Clin N Am*. 2011;21(3):621–639. viii. PMID: 21807315.
52. Saha D, Sinha R, Pai RR, et al. Laryngeal cysts in infants and children– a pathologist's perspective (with review of literature). *Int J Pediatr Otorhinolaryngol*. 2013;77(7):1112–1117. PMID: 23684174.
53. Prowse S, Knight L. Congenital cysts of the infant larynx. *Int J Pediatr Otorhinolaryngol*. 2012;76(5):708–711. PMID: 22376997.
54. Edwards RM, Chapman T, Horn DL, et al. Imaging of pediatric floor of mouth lesions. *Pediatr Radiol*. 2013;43(5):523–535. PMID: 23429804.
55. Sturm JJ, Dedhia K, Chi DH. Diagnosis and management of cervical thymic cysts in children. *Cureus*. 2017;9(1):e973. PMID: 28191377.
56. Vlachopapadopoulou EA, Vakaki M, Karachaliou FE, et al. Ectopic intrathyroidal thymus in childhood: a sonographic finding leading to misdiagnosis. *Horm Res Paediatr*. 2016;86(5):325–329. PMID: 27756075.
57. Tanrivermis Sayit A, Elmali M, Hashimov J, et al. Bilateral ectopic cervical thymus presenting as a neck mass: Ultrasound and magnetic resonance imaging. *Pediatr Int*. 2016;58(9):943–945. PMID: 27463062.
58. Ozel A, Akdur PO, Celebi I, et al. Ectopic cervical thymus as a rare cause of pediatric neck mass: the role of ultrasound and MRI in the diagnosis. Case report. *Med Ultrason*. 2015;17(2):248–251. PMID: 26052578.
59. Fujii S, Nagaishi J, Mukuda N, et al. Evaluation of fetal thyroid with 3D gradient echo T1-weighted MR imaging. *Magn Reson Med Sci*. 2016;PMID: 28025468.
60. Léger J. Management of fetal and neonatal Graves' disease. *Horm Res Paediatr*. 2016;PMID: 27978517.
61. Harreld JH, Kilani RK, Lascola CD, et al. MR imaging of fetal goiter. *AJNR Am J Neuroradiol*. 2011;32(8):E160. PMID: 21816913.
62. Nath CA, Oyelese Y, Yeo L, et al. Three-dimensional sonography in the evaluation and management of fetal goiter. *Ultrasound Obstet Gynecol*. 2005;25(3):312–314. PMID: 15736184.
63. Skelton E, Howlett D. Fibromatosis colli: the sternocleidomastoid pseudotumour of infancy. *J Paediatr Child Health*. 2014;50(10):833–835. PMID: 24548127.
64. Haque S, Bilal Shafi BB, Kaleem M. Imaging of torticollis in children. *Radiographics*. 2012;32(2):557–571. PMID: 22411949.
65. Park SH, Park SH, Lee SH. Grisel syndrome: pathophysiological evidence from magnetic resonance imaging findings. *Ann Rehabil Med*. 2013;37(5):713–716. PMID: 24236260.
66. Reichman EF, Shah J. Grisel syndrome: an unusual and often unrecognized cause of torticollis. *Pediatr Emerg Care*. 2015;31(8):577–580. PMID: 26244725.
67. Sargar KM, Sheybani EF, Shenoy A, et al. Pediatric fibroblastic and myofibroblastic tumors: a pictorial review. *Radiographics*. 2016;36(4):1195–1214. PMID: 27399243.
68. Hourani R, Taslakian B, Shabb NS, et al. Fibroblastic and myofibroblastic tumors of the head and neck: comprehensive imaging-based review with pathologic correlation. *Eur J Radiol*. 2015;84(2):250–260. PMID: 25467227.
69. Murphey MD, Ruble CM, Tyszko SM, et al. Musculoskeletal fibromatosis: radiologic-pathologic correlation. *Radiographics*. 2009;29:2143–2183. PMID: 19926768.
70. Güzelmansur I, Aksoy HT, Hakverdi S, et al. Fetal cervical neuroblastoma: prenatal diagnosis. *Case Rep Med*. 2011;2011:529749. PMID: 21826149.
71. Gorincour G, Dugougeat-Pilleul F, Bouvier R, et al. Prenatal presentation of cervical congenital neuroblastoma. *Prenat Diagn*. 2003;23(8):690–693. PMID: 12913877.
72. Csanády M, Vass G, Bartyik K, et al. Multidisciplinary management of cervical neuroblastoma in infants. *Int J Pediatr Otorhinolaryngol*. 2014;78(12):2103–2106. PMID: 25306308.
73. Barrea C, Vigouroux T, Karam J, et al. Horner syndrome in children: a clinical condition with serious underlying disease. *Neuropediatrics*. 2016;47(4):268–272. PMID: 27148776.
74. Zafeiriou DI, Economou M, Koliouskas D, et al. Congenital Horner's syndrome associated with cervical neuroblastoma. *Eur J Paediatr Neurol*. 2006;10(2):90–92. PMID: 16595184.

# 15

# Infection and Inflammation

Tyson R. Finlinson, Grace S. Mitchell, and Lisa H. Hutchison

Primary inflammatory processes in the pediatric neck are common, and contrast-enhanced computed tomography (CT) allows for characterization of the involved spaces, detecting complications, and determining appropriate clinical management.

## PHARYNGOTONSILLITIS AND PERITONSILLAR ABSCESS

***Overview.*** Acute infectious pharyngitis and tonsillitis are common and do not require imaging for diagnosis. However, when a peritonsillar abscess is suspected, imaging is used for diagnosis and to guide management.[1]

***Etiology.*** Most pharyngitis cases are self-limited viral infections. However, up to 30% are bacterial, most often secondary to group A β-hemolytic *Streptococcus* (GAS).[1] These patients present with fever and odynophagia. If symptoms do not improve with antibiotics, the possibility of peritonsillar abscess should be considered.[2]

***Imaging.*** Routine pharyngitis and tonsillitis do not require imaging.[1] However, if complications are suspected, contrast-enhanced CT is performed.[3] Findings of uncomplicated tonsillitis include unilateral or bilateral enlarged, enhancing tonsils with parapharyngeal fat inflammation. A peripherally enhancing, hypodense fluid collection within or adjacent to the tonsil suggests abscess (Fig. 15.1).[3]

***Treatment.*** Viral tonsillitis is self-limiting and treatment is supportive. If GAS infection is confirmed by rapid antigen test or throat culture, the patient will receive antibiotics. Recurrent tonsillitis is treated with tonsillectomy.[4] Focal fluid collections identified by CT may require surgical drainage.

## LEMIERRE SYNDROME

***Overview.*** An uncommon complication of oropharyngeal infection is suppurative thrombophlebitis of the internal jugular vein, also known as Lemierre syndrome. This often occurs in previously healthy teenagers.[5] Rare complications include septic emboli, osteomyelitis, and arterial vasospasm or occlusion leading to infarction.[6]

***Etiology.*** Lemierre syndrome is most commonly caused by *Fusobacterium necrophorum* infection, an anaerobic gram-negative bacterium found in normal oral flora.[6] Recognition is important because of high rates of morbidity and mortality.[5,7] Patients present with sore throat, lateral neck pain, swelling, and fever.[5] Tachypnea, tachycardia, and hypoxia may occur with pulmonary involvement. Infection spreads from the peritonsillar space to the carotid space, causing internal jugular vein thrombosis.[5] Septic embolic may then seed other organs.[7,8] Spread to the retropharyngeal space and osseous structures can cause osteomyelitis.

***Imaging.*** Contrast-enhanced CT findings include inflammatory changes that may involve multiple neck spaces and jugular vein thrombus.[5] Inflammatory findings range from cellulitis with soft tissue enhancement to abscess formation (Figs. 15.2 and 15.3). Color Doppler ultrasound (US) is useful to diagnose and follow thrombophlebitis, but does not reliably evaluate deep neck inflammation.[5,6] Acute neurologic symptoms may be evaluated with cranial CT or magnetic resonance imaging (MRI).[7-9]

***Treatment.*** High-dose intravenous antibiotics are the mainstay for treatment of *Fusobacterium* infection. Anticoagulation therapy is used in up to 27% of patients; however, its use is controversial.[5] The rates of morbidity and mortality are higher than with other head and neck infections, with an estimated mortality rate of 6%.[2,9]

## RETROPHARYNGEAL ABSCESS

***Overview.*** Suppurative lymphadenitis associated with tonsillitis, sinonasal infection, and dental infection are common causes of retropharyngeal abscess. Rarely is abscess secondary to pharyngeal or esophageal perforation.[10,11] The retropharyngeal space is a potential space that extends from the nasopharynx to the superior mediastinum.[10] Morbidity rates increase if an abscess extends below the T4 vertebra into the mediastinum, termed a *danger space* infection. Uncommonly, retropharyngeal tissue thickening may be due to hemorrhage (especially in hemophilia), neuroblastoma, and, rarely, anterior myelomeningocele.

***Etiology.*** Retropharyngeal abscesses are the sequelae of GAS, but *Staphylococcus aureus* and anaerobes have also been reported.[2,10] Symptoms include fever, pain, dysphagia, neck swelling, and sore throat. Cervical lymphadenopathy and torticollis are also common.[11,12]

***Imaging.*** Lateral radiographs may show thickening of the prevertebral tissues (>8 mm at C2) and anterior airway and esophagus displacement (Fig. 15.4). CT is needed to distinguish cellulitis from abscess.[4] Grisel syndrome is an inflammation-induced laxity of the atlantoaxial joint, which results in atlantoaxial rotatory subluxation of C1 and C2 that is self-limiting. Contrast-enhanced CT can evaluate for rim-enhancing abscesses, mediastinal involvement, thrombophlebitis, and osteomyelitis and guide surgical drainage if needed.[4,10]

***Treatment.*** Surgical drainage is often required, as conservative medical management only has a success rate between 18% and 57%.[10]

## CERVICAL LYMPHADENITIS

***Overview.*** Cervical lymphadenitis is common, and acute cases can be caused by viral or bacterial pathogens. Imaging is used when there is no clinical improvement after standard therapy, or if abscess is suspected.[13]

***Etiology.*** Cervical lymphadenitis is secondary to infection from a head and neck source, such as tonsils, pharynx, or teeth. Symptoms include a tender, focal neck mass and fever.[13] Lymph node enlargement is often due to a self-limiting reactive hyperplasia from viral infection.[14] Bacterial causes include *S. aureus* and streptococcal species and may lead to nodal suppuration. Kawasaki disease can also present with acute cervical lymphadenitis, but other features such as rash are also present.[13-15]

***Imaging.*** Involved nodes are enlarged, measuring greater than 1 cm in short axis. Suppurative or necrotic nodes are characterized by central hypoechogenicity or hypodensity on US and CT (Fig. 15.5).[12] Infectious nodes and malignant adenopathy cannot be distinguished by imaging; however, infectious adenopathy is more common.

***Treatment.*** Viral lymphadenitis is usually self-limiting, and acute bacterial lymphadenitis generally responds to antibiotic therapy.[12] Lymphadenopathy unresponsive to medical therapy may require follow-up imaging, surgical intervention, or biopsy to exclude malignancy.[2,14]

## Abstract:

Primary infectious and inflammatory processes in the pediatric neck are common and usually diagnosed clinically. However, imaging is often necessary to evaluate for associated complications and to help guide appropriate management. Some such conditions include pharyngotonsillitis, peritonsillar abscess, Lemierre syndrome, retropharyngeal abscess, cervical lymphadenitis, mycobacterial lymphadenitis, cat scratch disease, infectious mononucleosis, human immunodefiency virus, and sialoadenitis. The ability to distinguish between these conditions can help direct clinical outcomes, as potential treatments can range from supportive care to surgical management. The varied presentations of infectious and inflammatory conditions of the pediatric neck can be evaluated by imaging to determine the extent of disease, assess for potential complications, and direct appropriate treatment.

## Keywords:

Pediatric neck
infection
inflammation
pharyngotonsillitis
peritonsillar abscess
Lemierre syndrome
cervical lymphadenitis
retropharyngeal abscess

## MYCOBACTERIAL LYMPHADENITIS

***Overview.*** Mycobacterial infection is an important cause of chronic cervical lymphadenitis. In the United States, 70% to 95% of cases of mycobacterial lymphadenitis are caused by nontuberculous mycobacteria (NTM).[13] NTM lymphadenitis typically affects children between 1 and 5 years of age.[16] It is important to differentiate tuberculous and nontuberculous causes, as the treatments differ.

***Etiology.*** Cervical mycobacterial lymphadenitis, also known as *scrofula*, may be caused by various species, including *Mycobacterium tuberculosis*, *M. bovis*, and *M. avium-intracellulare*. The illness is often indolent with nodal enlargement that slowly develops over several weeks. A strongly positive tuberculin skin test suggests *M. tuberculosis*, whereas a weakly positive test suggests NTM.[13] The diagnosis is made with aspiration and culture.

***Imaging.*** On CT, *M. tuberculosis* lymphadenitis key features include a nodal mass with central low-attenuation fluid surrounded by a thick rim of enhancement (Fig. 15.6).[17,18] Unlike other nodal infections, atypical TB shows little to no surrounding inflammation. Nodal calcification may be noted. On MRI, the thick enhancing rim demonstrates T1 intermediate signal and T2 hypointensity. The central necrotic areas are T2 hyperintense and T1 intermediate signal.[18] Differential diagnoses include lymphoma and metastatic disease.[18] CT of NTM also shows low-attenuation ring-enhancing nodes. Unlike *M. tuberculosis* lymphadenitis, calcifications are uncommon, although it is often impossible to distinguish between them by imaging alone (Fig. 15.7).[19]

***Treatment.*** Multiantibiotic therapy for 12 to 18 months is the preferred treatment for *M. tuberculosis*,[13] whereas NTM adenitis requires complete excision.[16] Prognosis for both conditions is excellent with appropriate therapy.

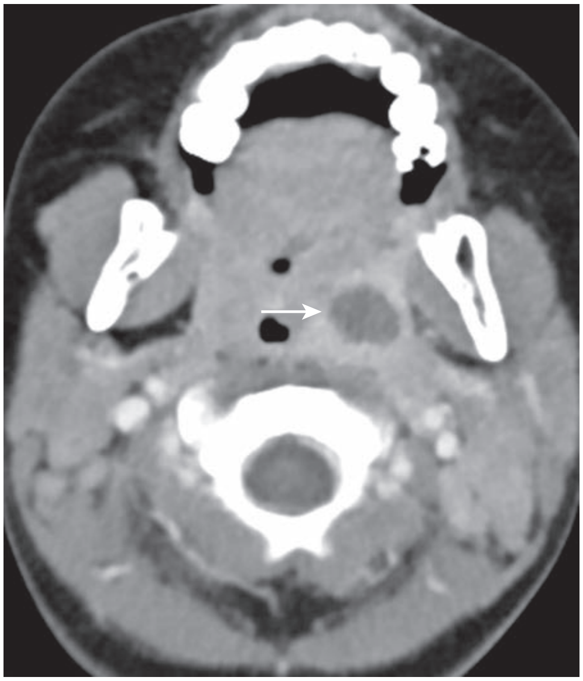

**Figure 15.1. Peritonsillar abscess in a 3-year-old girl with fever, pain, and fussiness.** Axial contrast-enhanced CT of the suprahyoid neck shows a peripherally enhancing low-attenuation fluid collection *(arrow)* lateral to the left tonsil.

## CAT SCRATCH DISEASE

***Overview.*** Cat scratch disease is a self-limiting, granulomatous infection most common in patients under 18 years.[20] Rarely, disseminated disease can cause granulomas in the liver or spleen, osteomyelitis, discitis, encephalitis, meningitis, ophthalmitis, and cranial neuritis.

***Etiology.*** Cat scratch is caused by *Bartonella henselae*, a gram-negative bacillus. The most common presentation is painful lymphadenopathy at the site of inoculation with lack of fever and constitutional symptoms. Disseminated disease can occur in 5% to 10% of cases.[21] The diagnosis is often confirmed with serologic testing.

***Imaging.*** Findings are nonspecific, with US showing enlarged hypoechoic lymph nodes with posterior acoustic enhancement and surrounding soft tissue hyperechogenicity.[21] Hyperemia is seen on Doppler US, and CT reveals enlarged nodes with central hypodensity (e-Fig. 15.8).[22]

***Treatment.*** Most cases resolve without antibiotics, although disseminated disease can be treated with antibiotics.[23]

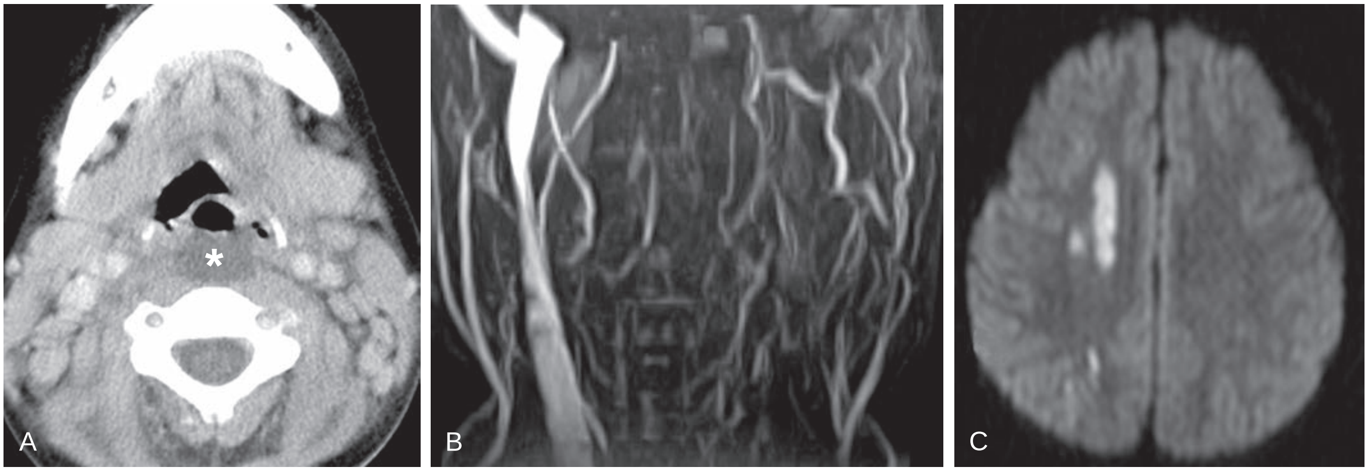

**Figure 15.2. Lemierre syndrome (*Fusobacterium necrophorum* infection) complicated by stroke in a 6-year-old girl with fever, difficulty swallowing, and nuchal rigidity.** (A) Axial contrast-enhanced CT shows low-attenuation retropharyngeal fluid *(asterisk).* (B) Magnetic resonance venogram 2 days later confirms lack of left internal jugular vein patency. (C) Diffusion-weighted MRI of the brain reveals multiple small foci of hyperintensity secondary to emboli.

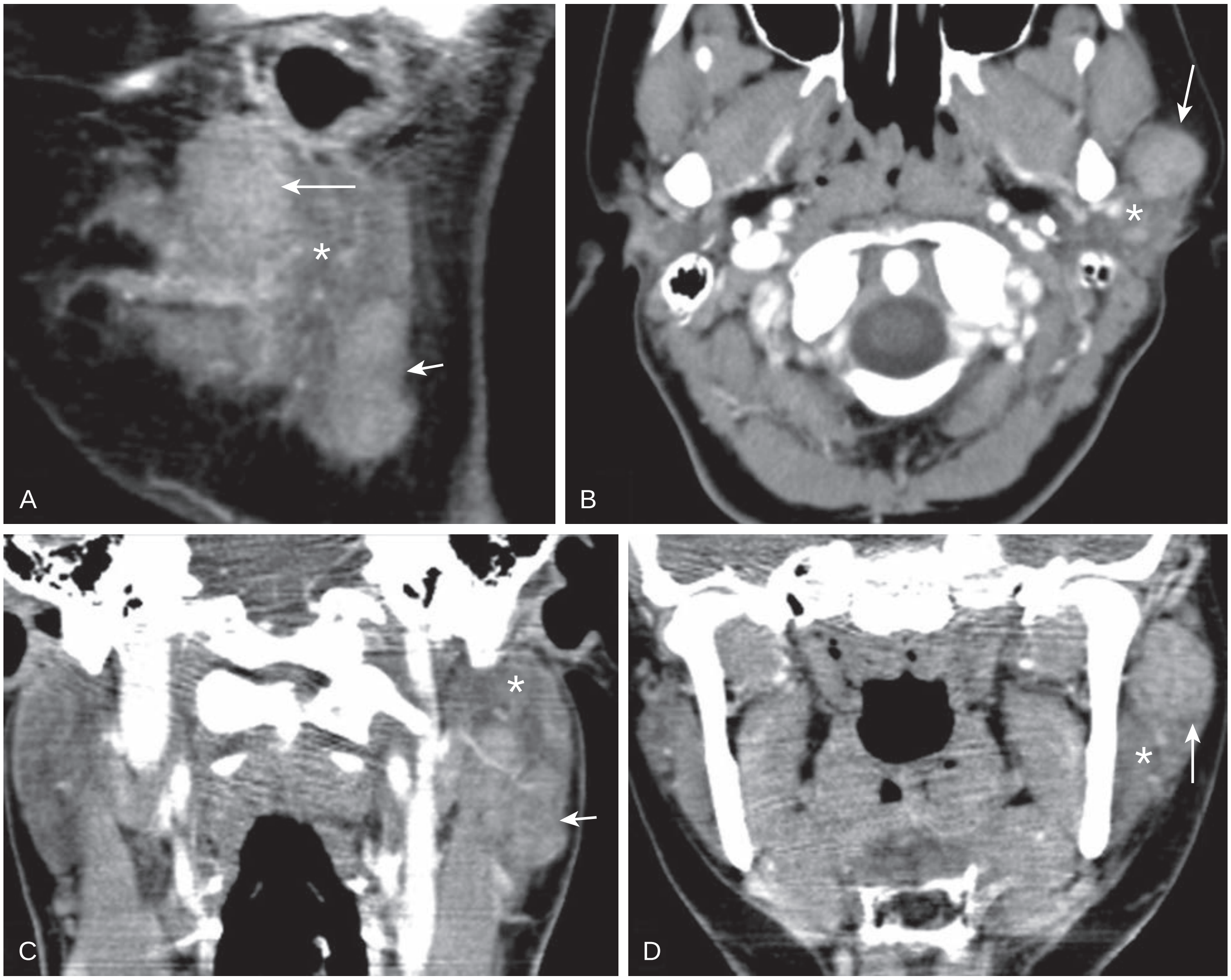

**e-Figure 15.8. Cat scratch disease in a 16-year-old girl with a left-sided neck mass for 6 weeks.** (A) Sagittal, (B) axial and (C–D) coronal contrast-enhanced CT images show enhancing lobular masses anterosuperior *(arrow)* and posteroinferior to the left parotid gland *(asterisk).*

## INFECTIOUS MONONUCLEOSIS

***Overview.*** Infectious mononucleosis is a common disorder usually seen in teenagers and young adults. The annual incidence in the United States is 500 cases for every 100,000 persons.[24] The diagnosis is clinical and can be confirmed with a rapid monospot test for heterophile antibodies. Imaging is rarely indicated.

***Etiology.*** Infectious mononucleosis is an acute self-limiting disorder caused by Epstein–Barr virus, characterized by acute pharyngotonsillitis, fever, malaise, and cervical or generalized lymphadenopathy. Splenomegaly is common.

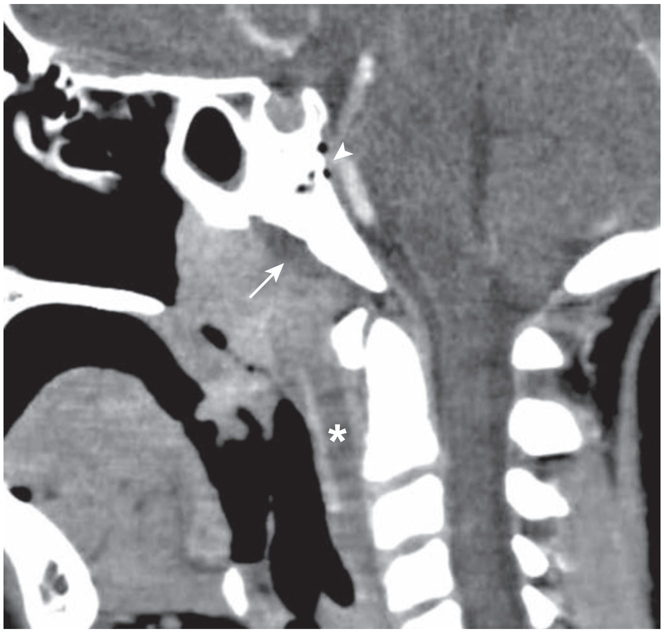

**Figure 15.3. Lemierre syndrome complicated by osteomyelitis in a 9-year-old with fever, neck pain, and sore throat.** Sagittal reconstructed contrast-enhanced CT demonstrates enlarged adenoids, a low-attenuation retropharyngeal fluid collection *(asterisk),* and a subperiosteal fluid collection along the ventral clivus *(arrow).* Air within and dorsal to the clivus due to osteomyelitis *(arrowhead)* and venous occlusion *(not shown)* were also present.

***Imaging.*** Imaging is unnecessary; however, this disease may mimic other infectious or malignant processes, and imaging may be obtained to determine the extent of disease. CT findings are nonspecific and including tonsillar and lymph node enlargement, with little surrounding inflammation (e-Fig. 15.9).[25]

***Treatment.*** Treatment for infectious mononucleosis is supportive. It is recommended that contact sports be avoided for at least 3 weeks following diagnosis to reduce the risk of splenic rupture.[24] The prognosis is excellent, except in cases complicated by splenic rupture.

## HUMAN IMMUNODEFICIENCY VIRUS

***Overview.*** Children infected with human immunodeficiency virus (HIV) often have cervical, mediastinal, or generalized lymphadenopathy. Since these findings are nonspecific, imaging is not required for the diagnosis, but may be considered along with biopsy to rule out malignancy if a neck mass persists or worsens.

***Etiology.*** Lymphadenopathy of HIV is usually symmetric, painless, and extensive. The differential includes Kaposi sarcoma, non-Hodgkin lymphoma, metastatic disease, or reactive lymphadenopathy from underlying head and neck infections.[26] Children with HIV may present with parotid enlargement from lymphocytic infiltration.

***Imaging.*** Prominent adenoids are present in 35% of HIV positive patients.[27] Numerous bilateral enlarged nodes are also common. Parotid US and CT may show multiple cystic and solid (lymphoproliferative) lesions of varying size.[26,27]

***Treatment.*** Highly active antiretroviral therapy (HAART) with multiple antiretroviral drugs is the frontline therapy for HIV treatment. HIV-associated lymphadenopathy does not require specific treatment; however, biopsy may be necessary to rule out other etiologies.

## SIALOADENITIS

***Overview.*** Sialoadenitis most often affects the parotid and submandibular glands in children. It is usually self-limiting. The diagnosis is typically clinical and imaging is usually not indicated.

***Etiology.*** Sialoadenitis presents as a swollen, enlarged gland with fever, most commonly caused by viruses and sialoliths. Mumps is by far the most common viral cause, and affects both parotid glands.[28-30] Other viruses include HIV, influenza, and Coxsackie. Acute bacterial (suppurative) sialoadenitis is uncommon in children.

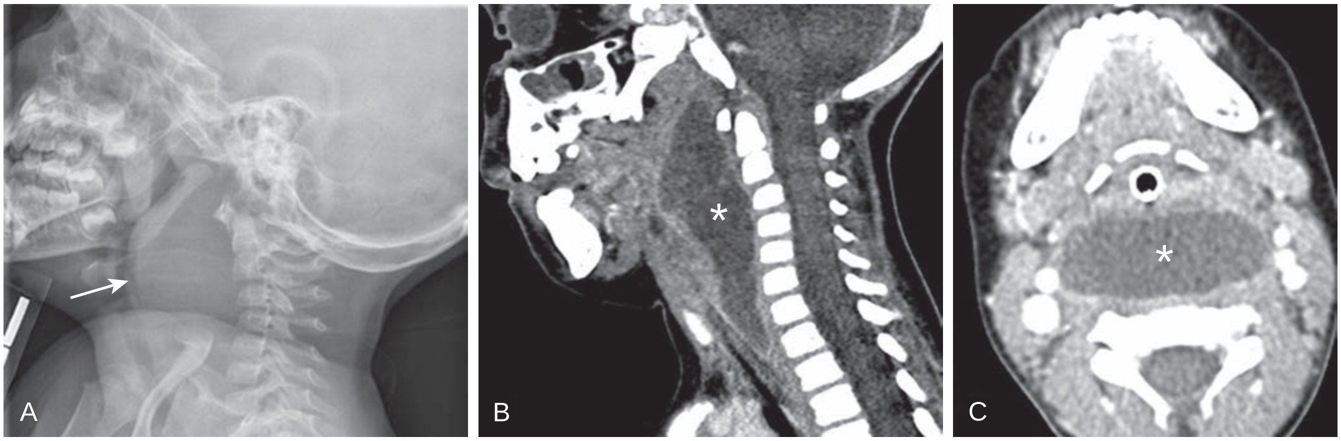

**Figure 15.4. Retropharyngeal abscess in a 2-year-old girl with sore throat, muffled voice, drooling, stridor, and intermittent fever.** (A) Lateral soft tissue neck radiograph reveals extensive swelling displacing the airway anteriorly *(arrow).* (B) Sagittal and (C) axial contrast-enhanced CT confirm a large peripherally enhancing low-attenuation retropharyngeal fluid collection consistent with abscess *(asterisk).*

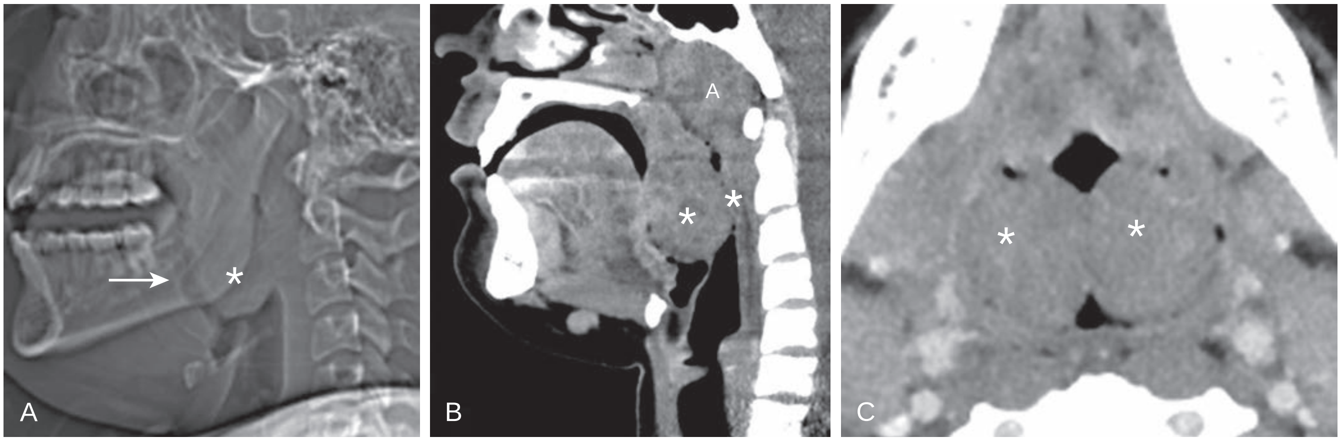

**e-Figure 15.9. Infectious mononucleosis in a 17-year-old girl with sore throat.** (A) Scout image and subsequent (B) sagittal and (C) axial contrast-enhanced CT images show nonspecific marked palatine tonsil *(asterisks)* and adenoid enlargement *(A),* with resultant airway narrowing *(arrow).*

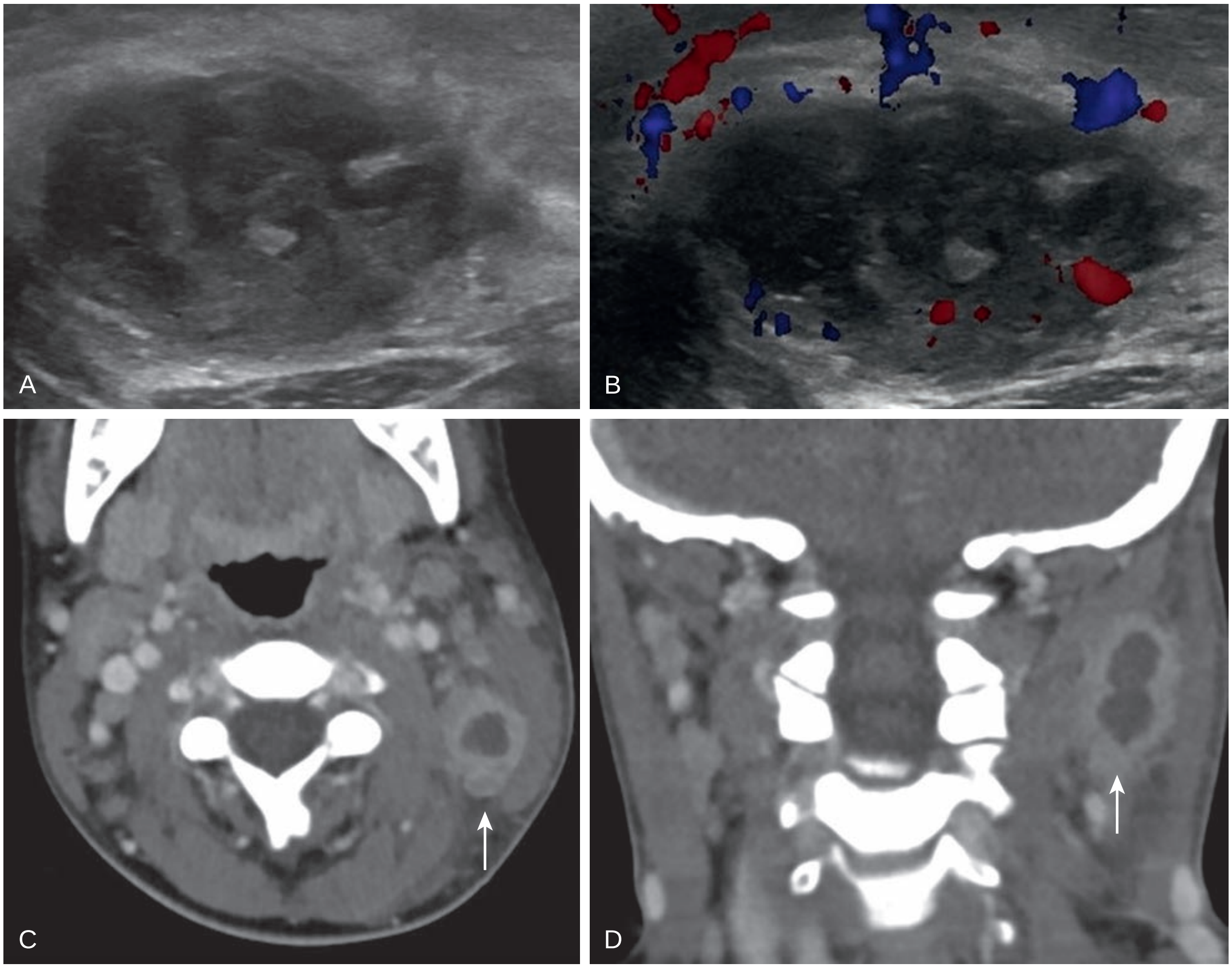

**Figure 15.5. Suppurative lymphadenitis in a 13-year-old boy with a history of combined B-cell immunodeficiency and neck pain.** (A) US with (B) color Doppler images show a heterogeneously hypoechoic mass with surrounding hyperemia. (C) Axial and (D) coronal CT images reveal a conglomerate of enlarged nodes in the left posterior triangle with central necrosis *(arrows).*

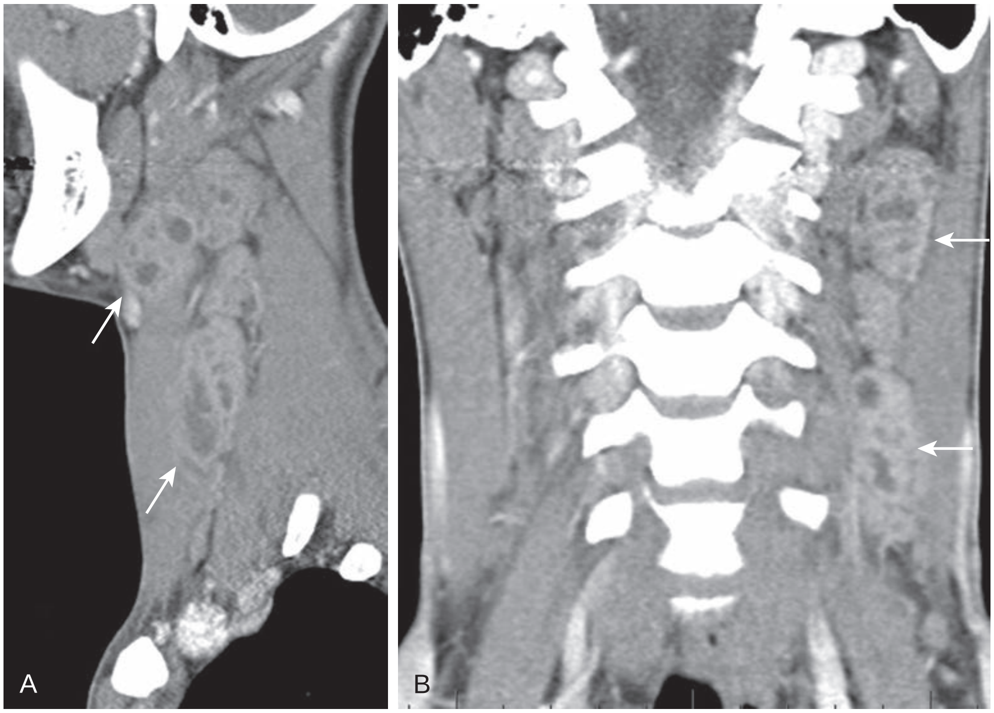

**Figure 15.6. Extrapulmonary tuberculosis in a 15-year-old boy with persistent lymphadenopathy for 5 months despite antibiotics and normal chest radiograph, who emigrated from Thailand 2 years prior.** (A) Sagittal and (B) coronal contrast-enhanced CT images show enlargement and enhancement of the left cervical chain lymph nodes, with central necrosis.

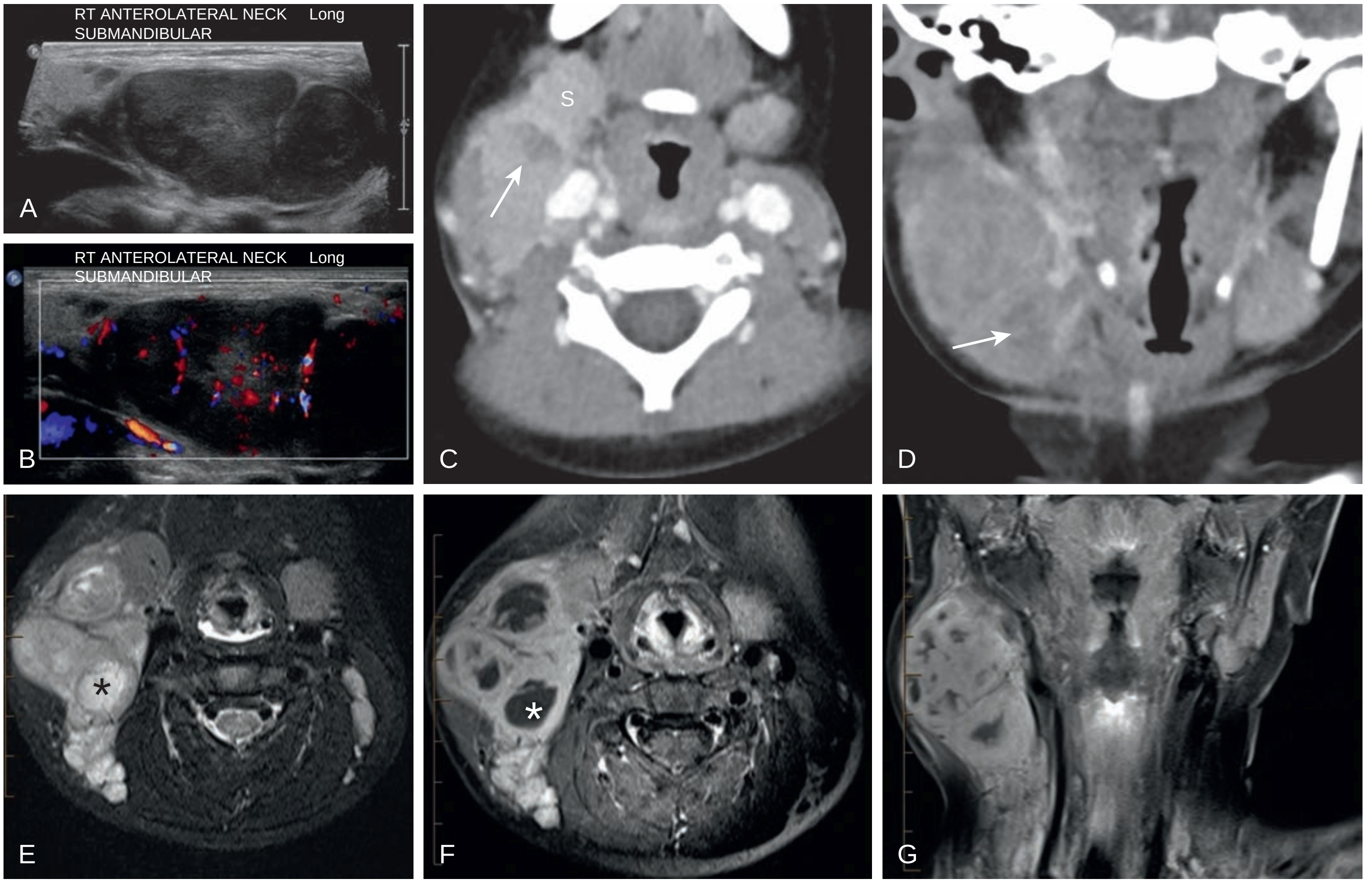

**Figure 15.7. Nontuberculous mycobacterial infection in a 3-year-old boy with fever, upper respiratory symptoms, and right-sided neck swelling.** (A) Gray scale and (B) color Doppler US images show an enlarged and heterogeneous lymph node with internal vascularity. (C) Axial and (D) coronal contrast-enhanced CT images show an aggregate of enlarged nodes in the right neck displacing the submandibular gland anteriorly *(S).* Note a small central low-attenuation necrotic component *(arrows).* At that time, no pathogen was identified. Due to lack of symptomatic improvement, (E) axial T2, (F) axial T1 postcontrast, and (G) coronal T1 postcontrast MRI images were obtained 2 months later, which show increased size of the nodal aggregate, now with multiple fluid pockets *(asterisks).* Excisional biopsy revealed *Mycobacterium avium-intracellulare*.

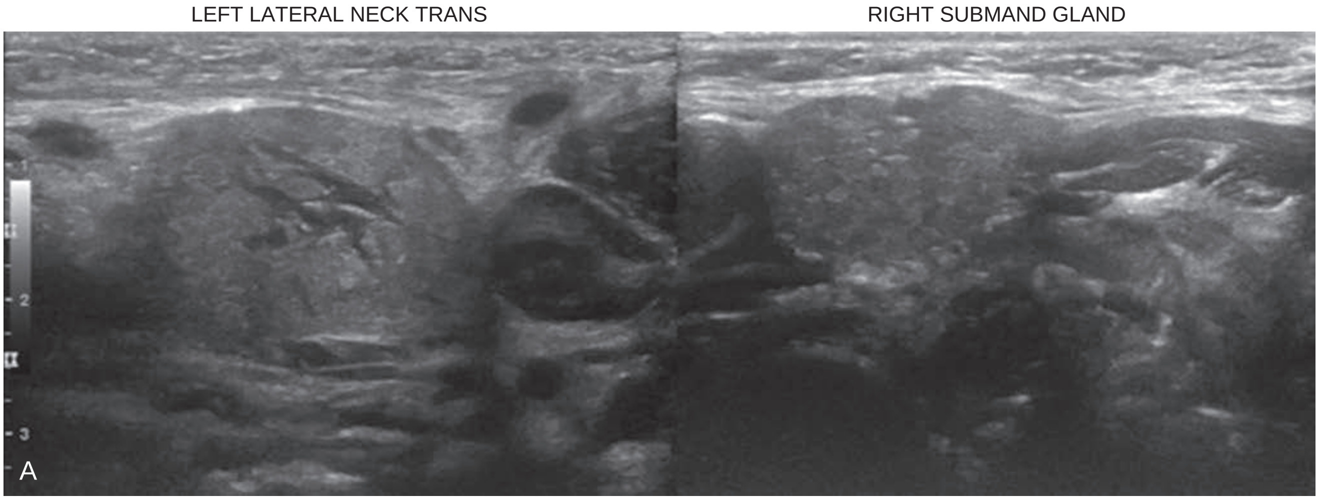

**Figure 15.10. Sialoadenitis in a 4-year-old boy with left-sided jaw swelling.** (A) Gray scale and (B) color Doppler US comparing the submandibular glands demonstrate asymmetric enlargement, edema, and hyperemia on the left.

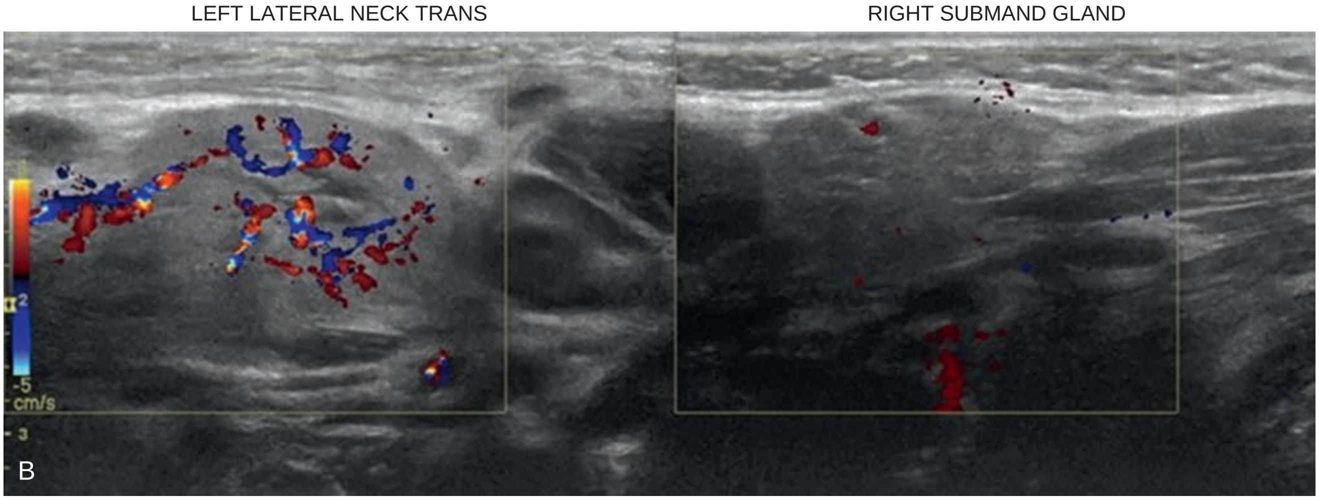

**Figure 15.10, cont'd**

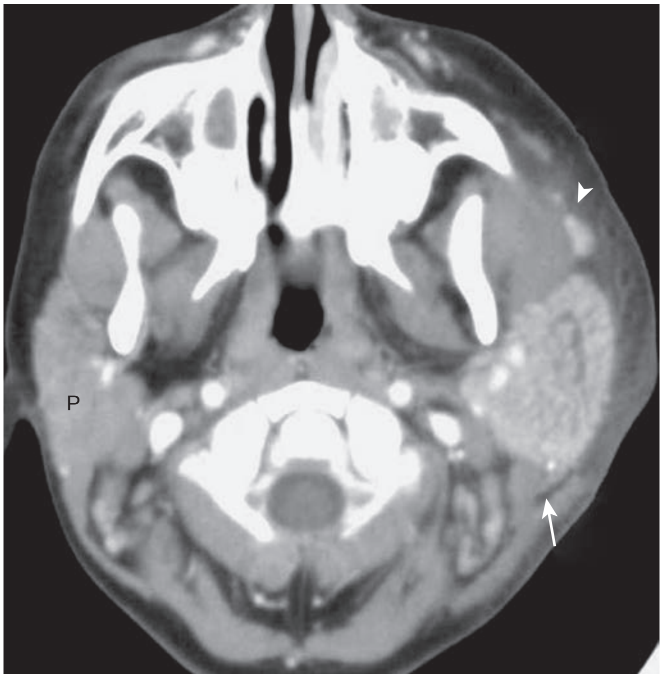

**Figure 15.13. Parotitis in a 6-year-old boy with painful left cheek swelling.** Axial CT demonstrates an enlarged enhancing left parotid gland *(arrow),* with similar changes in the accessory parotid tissue *(arrowhead)* along the course of the parotid (Stensen) duct. Note inflammatory stranding in the left cheek subcutaneous fat and the normal right parotid gland *(P).*

Recurrent submandibular sialoadenitis is most often caused by Wharton's duct sialoliths.[28] Chronic salivary gland inflammation is caused by recurrent bacteria including *Streptococcus viridians*, autoimmune disorders such as Sjögren syndrome, or sarcoidosis. Enlargement of intraparotid nodes can occur due to lymphadenitis affecting other regions of the neck.

***Imaging.*** On US, parotitis reveals as an enlarged gland, with heterogeneous decreased echogenicity and irregular margins. Small intraparenchymal hypoechoic foci may be present, representing salivary fluid, nodes, or abscesses (Fig. 15.10).[29,30] Hyperemia is seen on color Doppler. CT is best to identify salivary calculi (e-Fig. 15.11). Contrast-enhanced CT shows gland enlargement with enhancement (e-Fig. 15.12A). A low-attenuation collection with peripheral enhancement suggests an abscess (see e-Fig. 15.12B and Fig. 15.13).[29]

***Treatment.*** Viral sialoadenitis usually only requires supportive treatment. Patients with sialoliths can be treated medically with hydration, gland massage, and sialogogues to increase saliva production and flush out stones. If medical therapy is unsuccessful, surgery may be required. Total gland excision may be necessary if multiple stones are present.[28]

## KEY POINTS

- Many infectious and inflammatory conditions of the neck do not require imaging for diagnosis; however, imaging may help limit the differential diagnosis.
- Imaging is useful to determine disease extent and identify complications such as abscess, osteomyelitis, thrombophlebitis, and septic emboli, which require more aggressive treatment.
- Abscesses may require drainage for symptom relief, accelerated recovery, and determination of appropriate antibiotic therapy.

## SUGGESTED READINGS

Boyd ZT, Goud AR, Lowe LH, et al. Pediatric salivary gland imaging. *Pediatr Radiol*. 2009;39:710–722.
McKellop JA, Bou-Assaly W, Mukherji SK. Emergency head & neck imaging: infections and inflammatory processes. *Neuroimaging Clin N Am*. 2010;20(4):651–661.
Meuwly JY, Lepori D, Theumann N, et al. Multimodality imaging evaluation of the pediatric neck: techniques and spectrum of findings. *Radiographics*. 2005;25(4):931–948.
Rana RS, Moonis G. Head and neck infection and inflammation. *Radiol Clin North Am*. 2011;49(1):165–182.

## REFERENCES

Full references for this chapter can be found on www.expertconsult.com.

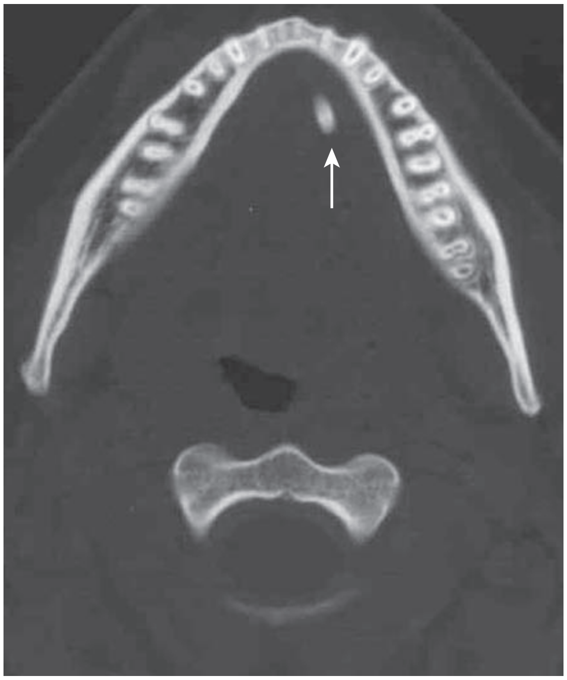

**e-Figure 15.11. Sialoadenitis in a 17-year-old boy with left-sided jaw pain and tenderness.** Axial CT image shows a large calcification in the expected location of the submandibular (Wharton) duct *(arrow).*

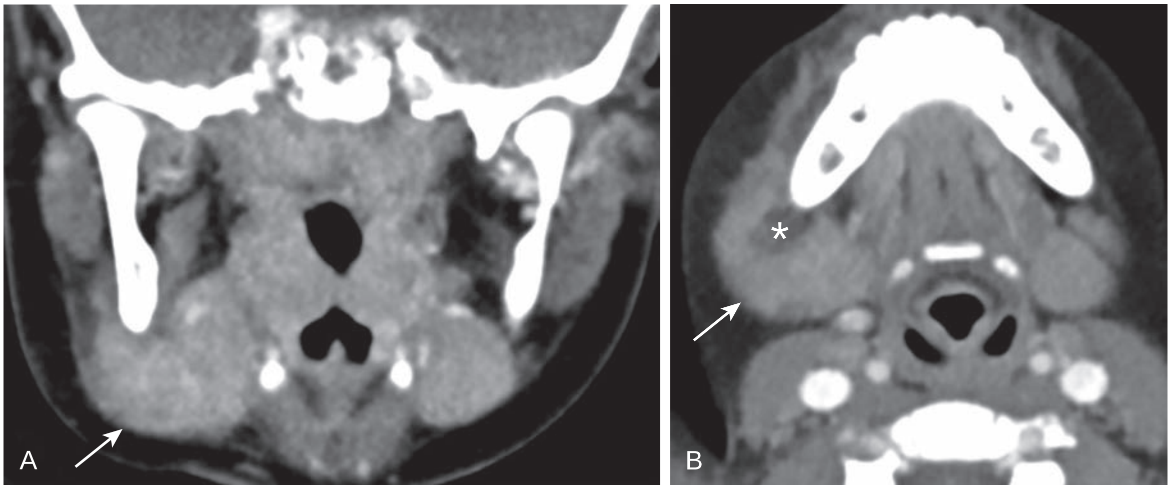

**e-Figure 15.12. Sialoadenitis in a 2-year-old boy with right-sided jaw swelling and fever.** (A) Coronal and (B) axial CT images show diffuse enlargement and enhancement of the right submandibular gland *(arrows)* with mild surrounding edema. A small central region of decreased attenuation suggests necrosis or phlegmon *(asterisk).*

## REFERENCES

1. Gerber MA. Diagnosis and treatment of pharyngitis in children. *Pediatr Clin North Am*. 2005;52(3):729–747.
2. Novis SJ, Pritchett CV, Thorne MC, et al. Pediatric deep space neck infections in U.S. children, 2000-2009. *Int J Pediatr Otorhinolaryngol*. 2014;78(5):832–836.
3. Scott PM, Loftus WK, Kew J, et al. Diagnosis of peritonsillar infections: a prospective study of ultrasound, computerized tomography and clinical diagnosis. *J Laryngol Otol*. 1999;113(3):229–232.
4. Weber AL, Siciliano A. CT and MR imaging evaluation of neck infections with clinical correlations. *Radiol Clin North Am*. 2000;38(5):941–968.
5. Kushawaha A, Popalzai M, El-Charabaty E, et al. Lemierre's syndrome, reemergence of a forgotten disease: a case report. *Cases J*. 2009;2:6397.
6. Gudinchet F, Maeder P, Neveceral P, et al. Lemierre's syndrome in children: high-resolution CT and color Doppler sonography patterns. *Chest*. 1997;112(1):271–273.
7. Megged O, Assous MV, Miskin H, et al. Neurologic manifestations of Fusobacterium infections in children. *Eur J Pediatr*. 2013;172(1):77–83.
8. Peer Mohamed B, Carr L. Neurological complications in two children with Lemierre syndrome. *Dev Med Child Neurol*. 2010;52(8):779–781.
9. Masterson T, El-Hakim H, Magnus K, et al. A case of the otogenic variant of Lemierre's syndrome with atypical sequelae and a review of pediatric literature. *Int J Pediatr Otorhinolaryngol*. 2005;69(1):117–122.
10. Righini CA, Karakas A, Tourniaire R, et al. Lemierre syndrome: study of 11 cases and literature review. *Head Neck*. 2014;36(7):1044–1051.
11. Reilly BK, Reilly JS. Retropharyngeal abscess: diagnosis and treatment update. *Infect Disord Drug Targets*. 2012;12(4):291–296.
12. Restrepo R, Oneto J, Lopez K, et al. Head and neck lymph nodes in children: the spectrum from normal to abnormal. *Pediatr Radiol*. 2009;39(8):836–846.
13. Gosche JR, Vick L. Acute, subacute, and chronic cervical lymphadenitis in children. *Semin Pediatr Surg*. 2006;15(2):99–106.
14. Hudgins PA. Nodal and nonnodal inflammatory processes of the pediatric neck. *Neuroimaging Clin N Am*. 2000;10(1):181–192, ix.
15. Nozaki F, Kusunoki T, Tomoda Y, et al. Grisel syndrome as a complication of Kawasaki disease: a case report and review of the literature. *Eur J Pediatr*. 2013;172(1):119–121.
16. Amir J. Non-tuberculous mycobacterial lymphadenitis in children: diagnosis and management. *Isr Med Assoc J*. 2010;12(1):49–52.
17. Lindeboom JA, Smets AM, Kuijper EJ, et al. The sonographic characteristics of nontuberculous mycobacterial cervicofacial lymphadenitis in children. *Pediatr Radiol*. 2006;36(10):1063–1067.
18. Nwawka OK, Nadgir R, Fujita A, et al. Granulomatous disease in the head and neck: developing a differential diagnosis. *Radiographics*. 2014;34(5):1240–1256.
19. Robson CD, Hazra R, Barnes PD, et al. Nontuberculous mycobacterial infection of the head and neck in immunocompetent children: CT and MR findings. *AJNR Am J Neuroradiol*. 1999;20(10):1829–1835.
20. Rohr A, Saettele MR, Patel SA, et al. Spectrum of radiological manifestations of pediatric cat scratch disease. *Pediatr Radiol*. 2012;42(11):1380–1384.
21. Garcia CJ, Varela C, Abarca K, et al. Regional lymphadenopathy in cat-scratch disease: ultrasonographic findings. *Pediatr Radiol*. 2000;30(9):640–643.
22. Wang CW, Chang WC, Chao TK, et al. Computed tomography and magnetic resonance imaging of cat-scratch disease: a report of two cases. *Clin Imaging*. 2009;33(4):318–321.
23. Florin TA, Zaoutis TE, Zaoutis LB. Beyond cat scratch disease: widening spectrum of Bartonella henselae infection. *Pediatrics*. 2008;121(5):e1413–e1425.
24. Luzuriaga K, Sullivan JL. Infectious mononucleosis. *N Engl J Med*. 2010;362(21):1993–2000.
25. Ludwig BJ, Foster BR, Saito N, et al. Diagnostic imaging in nontraumatic pediatric head and neck emergencies. *Radiographics*. 2010;30(3):781–799.
26. Reisacher WR, Finn DG, Stern J, et al. Manifestations of AIDS in the head and neck. *South Med J*. 1999;92(7):684–697.
27. Yousem DM, Loevner LA, Tobey JD, et al. Adenoidal width and HIV factors. *AJNR Am J Neuroradiol*. 1997;18(9):1721–1725.
28. Francis CL, Larsen CG. Pediatric sialadentis. *Otolaryngol Clin North Am*. 2014;47(5):763–778.
29. Lowe LH, Stokes LS, Johnson JE, et al. Swelling at the angle of the mandible: imaging of the pediatric parotid gland and periparotid region. *Radiographics*. 2001;21(5):1211–1227.
30. Kanekar SG, Mannion K, Zacharia T, et al. Parotid space: anatomic imaging. *Otolaryngol Clin North Am*. 2012;45(6):1253–1272.

# 16

# Neoplasia

Karen K. Moeller

Cancer is a leading cause of death during childhood, second only to trauma in children between the ages of 5 and 14 years. Head and neck involvement can be seen in up to 12% of childhood cancers.[1]

Lymphoma (50%) and rhabdomyosarcoma (30%) account for the majority of primary malignant pediatric head and neck tumors. Other malignant head and neck tumors include thyroid carcinoma, nasopharyngeal carcinoma, other sarcomas, and salivary gland tumors. Important benign tumors are hemangioma, juvenile angiofibroma, teratoma, and nerve sheath tumors. Ultrasound is frequently the initial study for evaluation, especially in lesions involving the thyroid gland. Subsequently, computed tomography (CT) and magnetic resonance imaging (MRI) provide a more complete evaluation and often offer complementary insights into the tumor type and disease extent. Positron emission tomography (PET) is utilized for malignant tumor staging.

## MALIGNANT TUMORS

### Non-Hodgkin Lymphoma

Non-Hodgkin lymphoma (NHL) occurs over a wide age range, although it is rare in children under the age of 2 years. It is a malignant neoplasm of B or T cells that is further classified as low, intermediate, or high grade. The vast majority in childhood are high grade[2] and of B cell origin. The histologic subtypes encountered in children include Burkitt, large B cell, lymphoblastic T or B cell, and anaplastic large cell. NHL in the head and neck can be nodal, nonnodal lymphatic (tonsils and adenoids), or nonnodal. Burkitt lymphoma is more common in children compared with adults and has an established association with Epstein-Barr virus (EBV). Furthermore, the development of Burkitt lymphoma is dependent on B cells acquiring a translocation involving the c-Myc proto-oncogene located on chromosome 8.

NHL initially presents in the head and neck in up to 10% of cases.[3] Children most commonly present with cervical lymphadenopathy and are otherwise asymptomatic. At imaging, the cervical lymphadenopathy is typically bilateral and symmetric. The enlarged lymph nodes are homogeneous and lack stranding of the surrounding fat on CT (Fig. 16.1). On T2-weighted MRI, the lymph nodes are lower in signal compared with reactive nodes and can show decreased diffusivity. These imaging characteristics are also true for nonnodal NHL. NHL disease is fludeoxyglucose (FDG) avid, and PET has a higher sensitivity compared with MRI and CT alone in establishing disease extent.[4] Unlike in adults, radiation therapy is not typically indicated, and these patients are treated primarily with combination chemotherapy.

### Hodgkin Lymphoma

Hodgkin lymphoma (HL) is the most common childhood cancer in the 15- to 19-year age group. It is histologically classified as nodular lymphocyte-predominant or classical. The classical type has four subtypes and is characterized by the presence of Reed-Sternberg (HRS) cells. Up to 50% of cases are found to have an EBV association, and the virus can be detected in HRS cells. When it occurs in the head and neck, HL is rarely extranodal. The most common presentation for pediatric head and neck HL is marked unilateral and painless cervical lymphadenopathy. Although imaging cannot distinguish NHL from HL, and both commonly present with cervical lymphadenopathy, an extranodal mass suggests NHL, and markedly asymmetric cervical lymphadenopathy favors the diagnosis of HL (Fig. 16.2). Hodgkin lymphoma in children is treated with chemotherapy and radiation therapy.

### Rhabdomyosarcoma

Rhabdomyosarcoma (RMS) is the most common soft tissue tumor of childhood, and up to 35% of these cancers occur in the head and neck. RMS has an incidence that peaks in children under the age of 6 years and then again in adolescence. It typically occurs in children who are otherwise healthy; however, it also has an increased occurrence in patients with Noonan syndrome, neurofibromatosis type 1 (NF-1), Beckwith-Wiedemann syndrome, and Li-Fraumeni syndrome (P53 gene mutation). This tumor has its origin from immature mesenchymal cells that are destined to form skeletal muscle, but it can arise in sites where skeletal muscle is not typically found. At histology, these tumors have small round blue cells, similar to other childhood tumors, so advanced immunohistochemical staining and molecular genetic evaluation are needed to establish the diagnosis. The histopathologic subtypes are embryonal, alveolar, and undifferentiated anaplastic. In head and neck RMS, the histology is most often embryonal, and regional lymph nodes are rarely involved.

Head and neck RMS is divide into three types based on location: orbit, parameningeal (masticator space, middle ear, sinus, parapharyngeal space, and pterygopalatine fossa), and nonorbit nonparameningeal. Of these, the most commonly encountered locations are masticator space and orbit. Recognizing parameningeal tumors is important because 55% of tumors at these sites will have intracranial extension. Patients with parameningeal tumors are treated with more aggressive protocols due to an increased incidence of central nervous system (CNS) relapse even in the absence of intracranial extension at presentation. All patients with parameningeal rhabdomyosarcoma are evaluated with lumbar puncture and brain MRI to assess for possible intracranial disease. Intracranial extension is defined as tumor that touches, displaces, invades, or distorts the dura.

On CT, these tumors lack calcification and are isoattenuated compared with muscle. They can remodel or erode bone. RMS is isointense on T1-weighted and hyperintense on T2-weighted MRI compared with muscle with homogenous or heterogeneous contrast enhancement (Fig. 16.3). Decreased diffusivity is often but not always seen. In the temporal bone, RMS can be distinguished from Langerhans cell histiocytosis (LCH) by its tendency to occur more anteromedial involving the middle ear or petrous apex, compared with LCH that has a predilection for the mastoid temporal bone.

Depending on disease extent and location, treatments include resection and chemotherapy. Almost all patients also require radiation therapy.[5] Cure rates for RMS now approach 70%. These improved outcomes are the direct result of risk-based multimodality therapeutic protocols developed by large international cooperative groups.

### Nasopharyngeal Carcinoma

Nasopharyngeal carcinoma (NPC) has a peak incidence during middle age where it is endemic in Southern China and to a lesser

## Abstract:

Cancer is a leading cause of death during childhood, second only to trauma in children between the ages of 5 and 14 years. Head and neck involvement can be seen in up to 12% of childhood cancers. This chapter reviews the imaging findings for common and less commonly encountered head and neck tumors in the pediatric population. Benign and malignant tumors are reviewed with an emphasis on cross sectional radiographic findings that can aid in diagnosis of these lesions.

## Keywords:

cancer
lymphoma
rhabdomyosarcoma

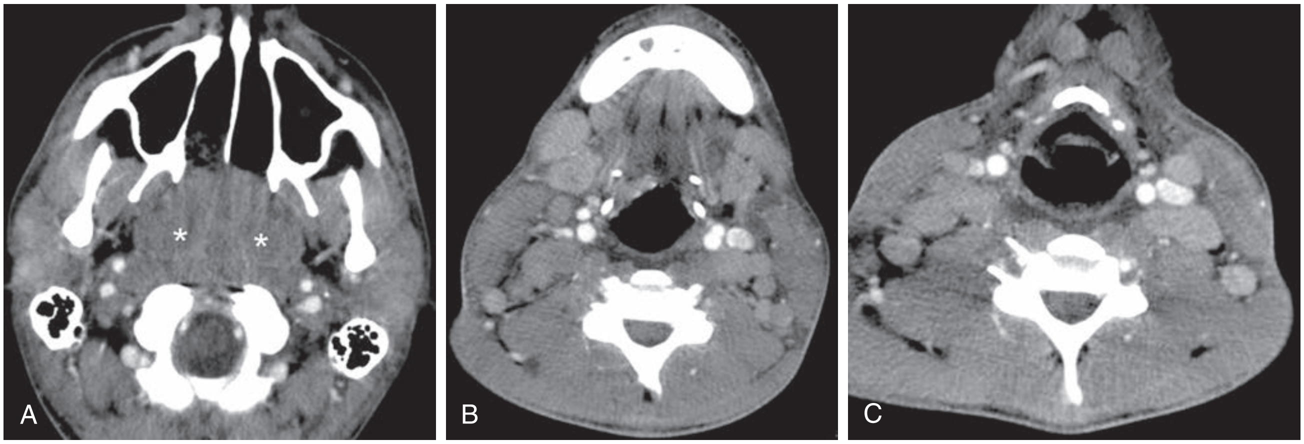

**Figure 16.1. Non-Hodgkin lymphoma in a 16-year-old boy.** (A) Axial contrast-enhanced CT image shows homogeneous enlargement of the adenoids *(asterisks)*. (B and C) There is mild to moderate cervical lymphadenopathy involving level I, level II, and level III nodal groups bilaterally.

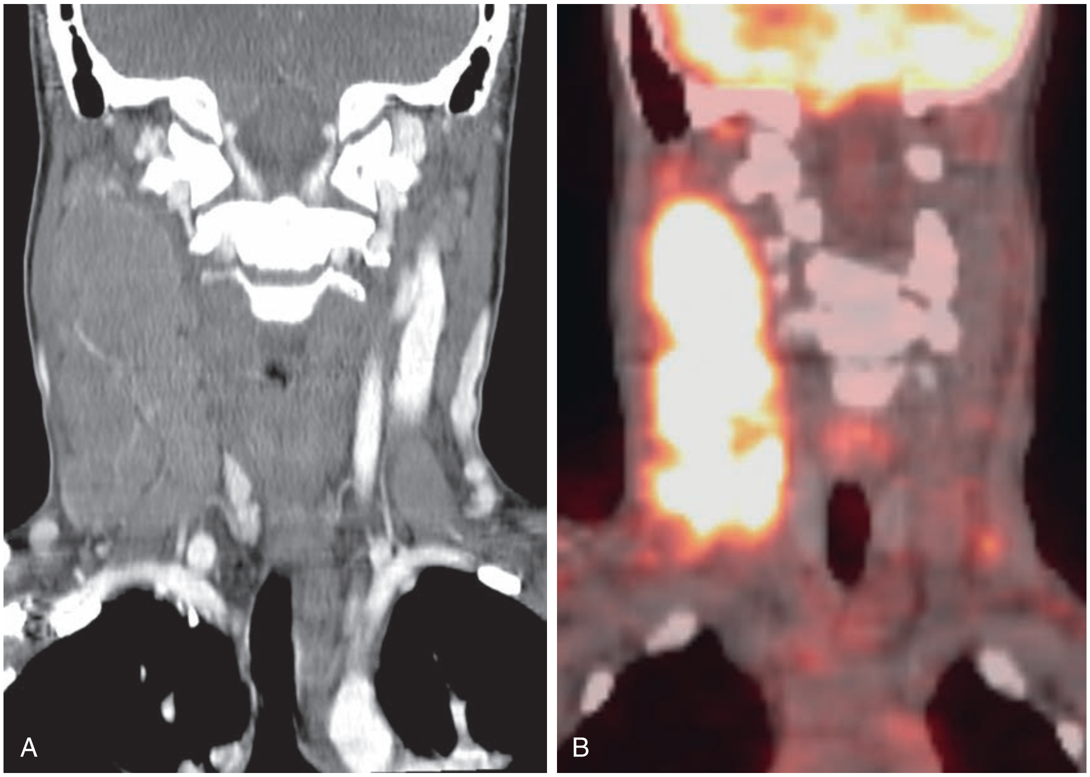

**Figure 16.2. Hodgkin lymphoma in a 10-year-old boy.** (A) Coronal reformatted contrast-enhanced CT image shows massive adenopathy in right neck. (B) PET scan image shows marked FDG avidity of the enlarged lymph nodes.

extent in Southeast Asia, Northern Africa, and the Arctic. There is a smaller incidence peak in adolescence that is not confined to these endemic areas and also includes the United States. It is more frequently encountered in boys and in the United States is more common in African Americans. The histologic subtype encountered in pediatrics is nonkeratinizing undifferentiated NPC, which has an association with previous EBV infection. In general, adolescents with NPC present with advanced stage disease. Imaging findings for these patients include asymmetric adenoid enlargement and mastoid fluid. Adenopathy and skull base invasion are also commonly encountered at presentation (Fig. 16.4).[6] Radiation is the mainstay of treatment for nasopharyngeal carcinoma due to the radiosensitivity of this tumor and because its anatomic location limits surgical resection.

## Thyroid Carcinoma

It is important to remember that an incidentally discovered thyroid nodule in a child is more likely to be malignant (20%) compared with an incidental nodule encountered in an adult (5%) (see also Chapter 17).[7] Fine needle aspiration is the best way to distinguish malignant from benign nodules, and the accuracy is similar to

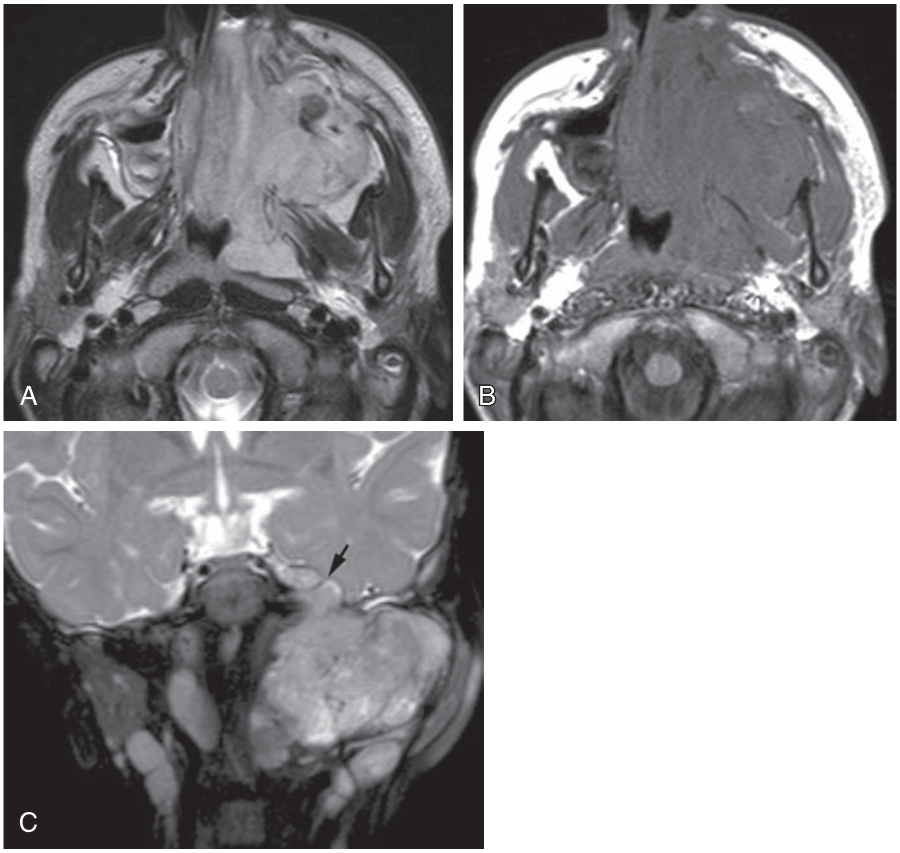

**Figure 16.3. Maxillary sinus rhabdomyosarcoma in a 14-year-old boy.** (A) Axial T2-weighted MR image shows a large left maxillary sinus mass extending into and filling the nasal cavity and nasopharynx. It is hyperintense compared with muscle. (B) The lesion is isointense compared with muscle on T1-weighted MRI. Notice displacement and destruction of surrounding structures. (C) In a different 18-month-old boy, coronal fat-saturated T2-weighted MR image shows a masticator space rhabdomyosarcoma with intracranial extension and tumor reaching the cavernous sinus via a widened foramen ovale *(arrow)*.

that achieved in adults. The majority of thyroid carcinomas in children are of the differentiated type with most of those having papillary or mixed papillary-follicular histology. Differentiated follicular carcinoma is less common and is also less likely to have metastatic lymphadenopathy at presentation compared with papillary thyroid carcinoma.

Patients most often present with an enlarging neck mass that can be from the thyroid tumor itself or from nodal metastases. Ultrasound features that are concerning for thyroid carcinoma include nodules that are tall compared with their width, microcalcifications, and hypervascularity. On pre- and postcontrast CT, the tumors are typically hypodense compared with the rest of the gland. Nodal metastases can vary in size and density (Fig. 16.5) and not uncommonly appear cystic. Because tumors are often multifocal, treatment includes total thyroidectomy. This allows for postoperative administration of radioactive iodine and the use of serial thyroglobulin measurement for surveillance. Children with primary tumors confined to the thyroid with no or only microscopic metastases to central compartment nodes do not require I-131 therapy.[8]

Medullary thyroid carcinoma is rare and is typically sporadic in adults. In pediatrics, it is almost always inherited in the setting of one of the multiple endocrine neoplasia syndromes. These syndromes, which include MEN2a, MEN2b, and the familial medullary thyroid carcinoma syndrome (a subtype of MEN2a), have an autosomal dominant inheritance pattern resulting from a mutation of the *RET* proto-oncogene located on the long arm of chromosome 10. In these patients, the leading cause of morbidity and mortality is the medullary carcinoma since this tumor spreads early and is resistant to chemotherapy. The treatment in children with these syndromes is prophylactic thyroidectomy, and preoperative imaging is typically not obtained.

## Primary Cervical Neuroblastoma

Neuroblastoma most often arises in the retroperitoneum, and primary cervical neuroblastoma is rare, making up less than 5% of cases.[9] This tumor arises from primitive neural crest cells of the sympathetic nervous system. The key to considering this diagnosis is to remember that the sympathetic chain lies very near the common and internal carotid artery, typically medial or posteromedial to it. At imaging, calcifications and/or adjacent adenopathy may be seen. In the neck, these tumors tend to displace vessels rather than encase them (Fig. 16.6). Treatment involves surgery, in most cases, with adjuvant chemotherapy. Radiotherapy is reserved for unresectable tumors or for those that progress despite chemotherapy.

Neuroblastoma is the most common malignancy to metastasize to the head and neck, especially in children under the age of 2 years,[10] and is encountered more frequently than primary cervical neuroblastoma. At imaging, enhancing soft tissue masses with an aggressive periosteal reaction are seen, which can involve the skull base, orbits, temporal bone, or calvarium. This finding can lose its conspicuity when it is bilateral and symmetric

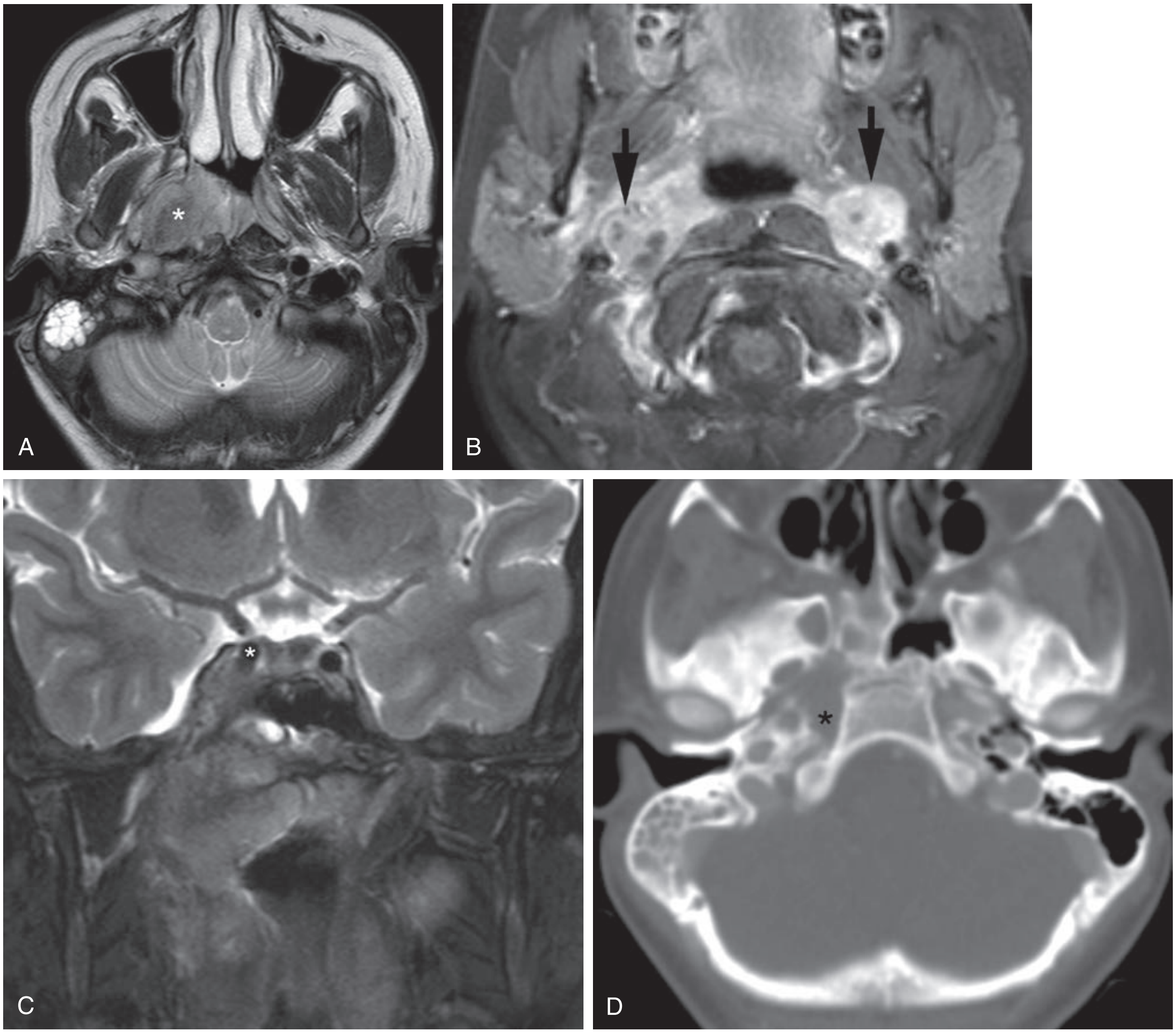

**Figure 16.4. Nasopharyngeal carcinoma in a 13-year-old boy.** (A) Axial T2-weighted MR image shows asymmetric adenoid enlargement *(asterisk)* and right mastoid fluid. (B) Axial contrast-enhanced fat-saturated T1-weighted MR image more inferiorly, there are abnormal necrotic retropharyngeal nodes *(arrows)*. (C) Coronal T2-weighted MR image shows skull base invasion and intracranial tumor surrounding the right cavernous ICA *(asterisk)*. (D) Axial CT image with bone windows depict a widened petroclival fissure on the right *(asterisk)* compared with the normal left side. Notice the skull base erosion posteromedial to right foramen ovale.

(Fig. 16.7). Less commonly, metastatic cervical lymphadenopathy is visualized.

## BENIGN TUMORS

### Juvenile Angiofibroma

Juvenile angiofibroma (also called *juvenile nasopharyngeal angiofibroma*) is a benign, highly vascular, locally aggressive neoplasm that occurs almost exclusively in males. It typically occurs in adolescents with a median age of 15 years. Juvenile angiofibroma is a biphasic tumor that has vascular and fibroblastic components. The etiology for this tumor is debated, but a variety of growth factors (including vascular endothelial growth factor) and chromosomal alterations are thought to play a role.[11] One theory is that a persistent fetal vascular malformation or hamartoma grows in response to hormonal surges that occur during puberty. It has an increased incidence in patients with the familial adenomatous polyposis syndrome.[12] This tumor originates in the posterolateral nasal cavity, specifically at or near the sphenopalatine foramen. It has the propensity to grow into the pterygopalatine fossa, where it can extend intracranially or gain access to the masticator space or orbit. At imaging there is a soft tissue mass in the posterolateral nasal cavity with variable extension into the pterygopalatine fossa. Surrounding bone can be remodeled or destroyed. It has variable signal on T2-weighted MRI, sometimes appearing hypointense, presumably from the fibrous content. Punctate or serpentine flow voids may be seen within the tumor. It has vivid enhancement on postcontrast images (Fig. 16.8, and see Fig. 8.27). Angiography shows an intense capillary tumor blush with vascular supply typically from internal maxillary and ascending pharyngeal branches of the external carotid artery, and occasionally from internal carotid artery

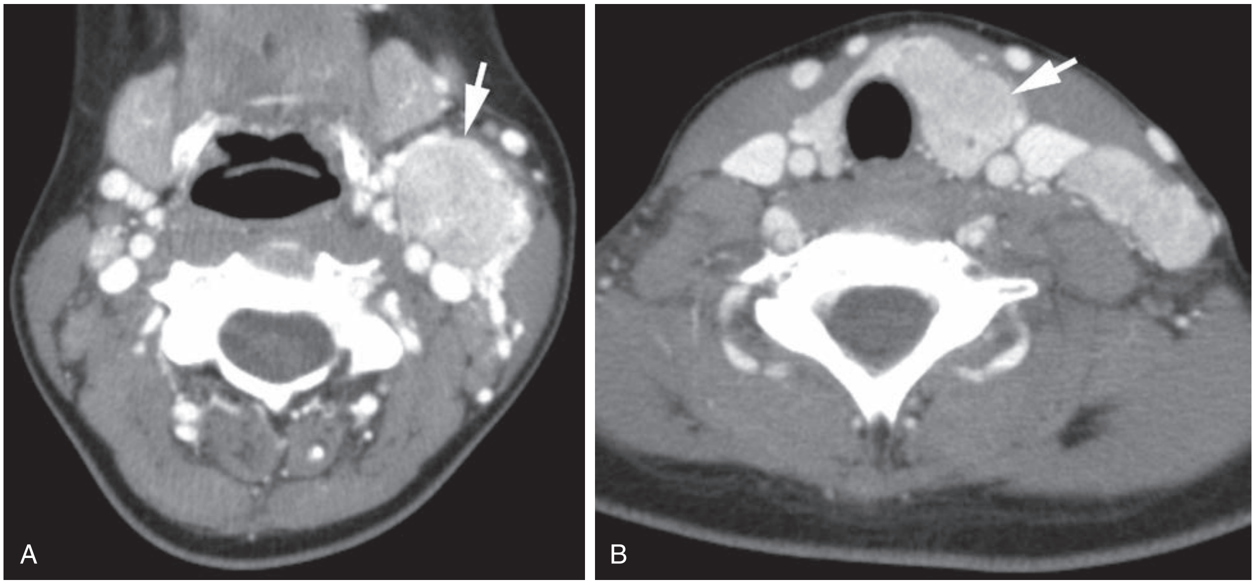

**Figure 16.5. Papillary thyroid carcinoma with nodal metastases in a 13-year-old girl.** (A) Axial contrast-enhanced CT image at the site of the palpable abnormality shows a hyperdense mass *(arrow)* situated between the submandibular gland and the sternocleidomastoid muscle. (B) More inferiorly, there is abnormal enlargement of the left thyroid lobe *(arrow)* and additional hyperdense cervical lymphadenopathy.

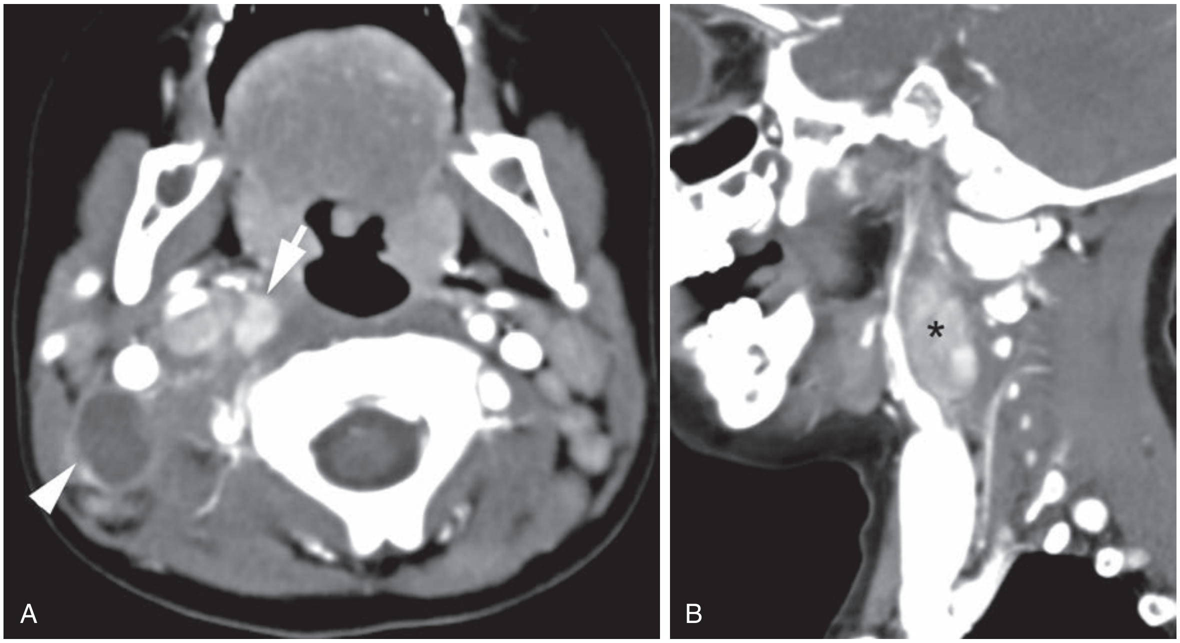

**Figure 16.6. Primary cervical neuroblastoma and metastatic node in a 3-year-old girl.** (A) Axial contrast-enhanced CT image shows a cystic level II node *(arrowhead)*. More anteriorly, there is a solid mass medial to the vessels of the carotid space *(arrow)*. (B) Sagittal reformatted CT image shows anterior displacement of the common and internal carotid artery by the lesion *(asterisk)*.

(ICA) branches. Treatment includes preoperative embolization followed by surgical resection. Residual tumor supply from ICA branches after embolization upstages these tumors and predicts a more difficult surgical resection.[13]

## Nerve Sheath Tumors

Neurofibromas are benign peripheral nerve sheath tumors that are rare in children in the absence of NF-1. In the setting of NF-1, neurofibromas can be located in the skin, along peripheral nerves subjacent to the skin, or along spinal nerve roots. Plexiform neurofibromas, a major cause of disfigurement and morbidity in patients with NF-1, extend longitudinally along a nerve and involve multiple nerve fascicles. Both lesions comprise a mixture of Schwann cells, fibroblasts, perineural cells, and mast cells. The Schwann cells may be abnormal in NF-1 patients, and they can have angiogenic and invasive properties in plexiform neurofibromas.[14] At imaging, these lesions are hypodense on CT. Neurofibromas

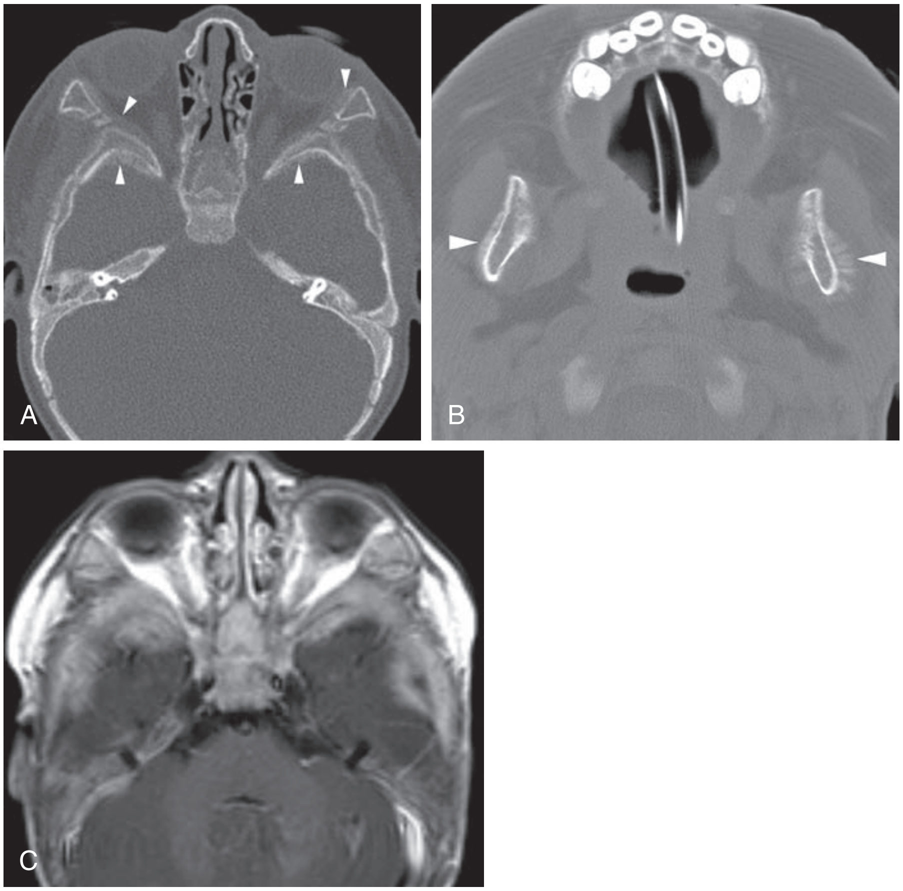

**Figure 16.7. Metastatic neuroblastoma in an 8-month-old boy.** (A and B) Axial noncontrast CT images depict abnormal aggressive appearing periosteal reaction lining orbits, middle cranial fossa, and mandibular rami bilaterally *(arrowheads)*. (C) Axial contrast-enhanced T1-weighted MR image shows that these regions have abnormal thick enhancement.

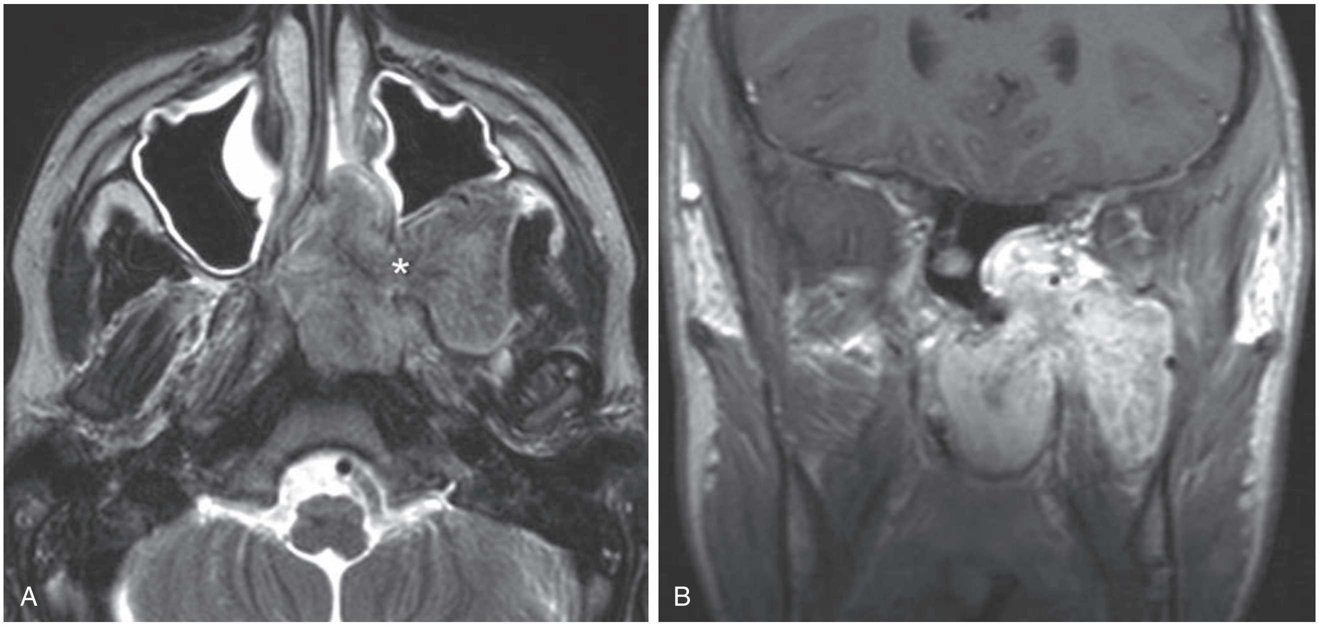

**Figure 16.8. Juvenile angiofibroma in a 14-year-old boy.** (A) Axial fat-saturated T2-weighted MR image shows a hypointense mass in the left posterior nasal cavity and nasopharynx. (B) Coronal contrast-enhanced fat-saturated T1-weighted MR image shows intense enhancement of the mass. There is involvement of the left pterygopalatine fossa and extension to the masticator space via the pterygomaxillary fissure (*asterisk* in A).

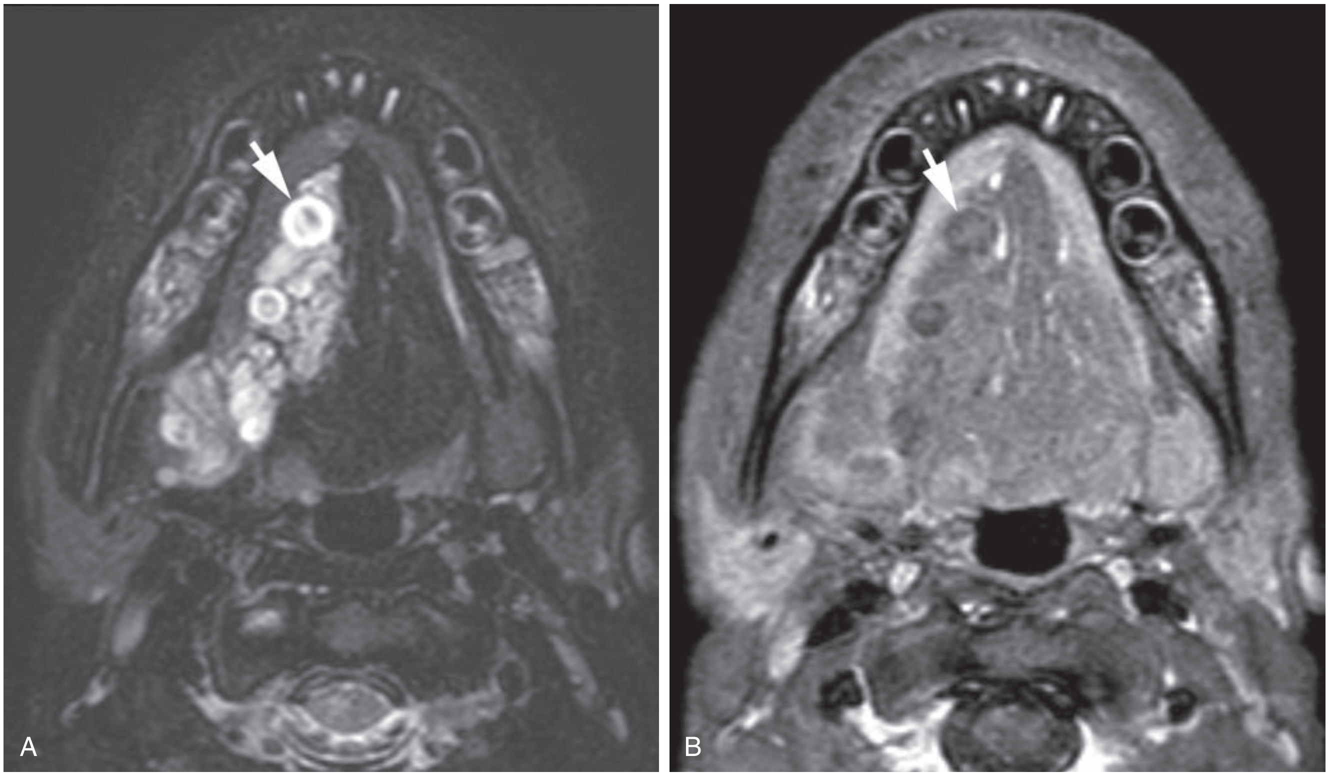

**Figure 16.9. Plexiform neurofibroma in a 7-year-old boy with NF-1.** (A) Axial fat-saturated T2-weighted and (B) axial contrast-enhanced fat-saturated T1-weighted MR images demonstrate a heterogeneous elongated lesion of the right sublingual and submandibular space. Note the "target sign" with central T2 hypointensity and enhancement *(arrows)*.

are well-circumscribed enhancing lesions. Plexiform neurofibromas are more extensive and can appear infiltrative. At MRI, the target sign is frequently seen in plexiform neurofibromas, in which central portions of the lesion have T2 hypointensity and postcontrast enhancement (Fig. 16.9). Malignant peripheral nerve sheath tumors (MPNST) are highly malignant lesions that usually arise from a preexisting plexiform or nodular fibroma in patients with NF-1. These tumors can also arise in patients who are otherwise healthy with up to 50% of MPNST occurring in children without NF-1.[15] MPNST are rapidly enlarging lesions that demonstrate enhancement and FDG avidity.

Schwannomas are rare in pediatrics, even in the setting of neurofibromatosis type 2, where they tend to arise after the second decade. These lesions demonstrate contrast enhancement and may have cystic components.

## Teratoma

Teratomas, although rare, are the most common congenital tumor of the head and neck. This tumor is composed of tissue foreign to the site of origin that histologically contains all three germ cell layers.[16] The World Health Organization classification designates these tumors as mature teratomas, immature teratomas, and teratomas with malignant transformation.[10,17] Compared with adults, pediatric teratomas are less often malignant. In the head and neck, these tumors can be cervical, naso/oropharyngeal, facial, or orbital in location. The term epignathus is applied to teratomas of the oropharynx and oral cavity in neonates. Teratomas may be diagnosed prenatally with ultrasound or MRI. At imaging, these tumors are typically heterogeneous, containing cystic and solid components. Calcifications and fat can be appreciated on both CT and MRI. Treatment is surgical resection. If airway compression by the lesion is demonstrated prenatally, the ex-utero intrapartum procedure is preferred, a technique in which the airway is secured during elective cesarean section while the neonate remains on placental support.

## Hemangioma

Infantile hemangioma is the most common vascular tumor of childhood and is prevalent in the head and neck region. These lesions are more commonly encountered in girls. Infantile hemangioma is not present at birth, becoming apparent in the first days to months of life and then undergoing a proliferative phase during the first year of life. This is followed by a period of involution that typically begins after 1 year and lasts a variable number of years. Glucose transporter 1 (GLUT1) and placenta-associated vascular antigens are highly expressed in the endothelial cells of infantile hemangiomas during both the proliferative and involuting phase. At imaging, these lesions have a characteristic appearance, having a lobulated contour and intense color Doppler flow on ultrasound and contrast enhancement on CT and MRI. Flow voids are typically present, visualized on both T1- and T2-weighted magnetic resonance (MR) images (Fig. 16.10). Children with PHACES association (*P*osterior fossa malformations, *H*emangioma, *A*rterial anomalies, *C*oarctation of the aorta, *E*ye abnormalities, *S*ternal malformation, and paraumbilical raphe) have hemangiomas that are large and plaquelike, or regional hemangiomas involving the face, sometimes with a beardlike distribution.[10,18] Hemangiomas are treated conservatively given the expected involution in most cases. If there is compression of vital structures or potential for disfigurement, oral propranolol is the treatment of choice.[19,20]

The much rarer congenital hemangioma proliferates in utero and then has a variable postnatal involution. They appear to be

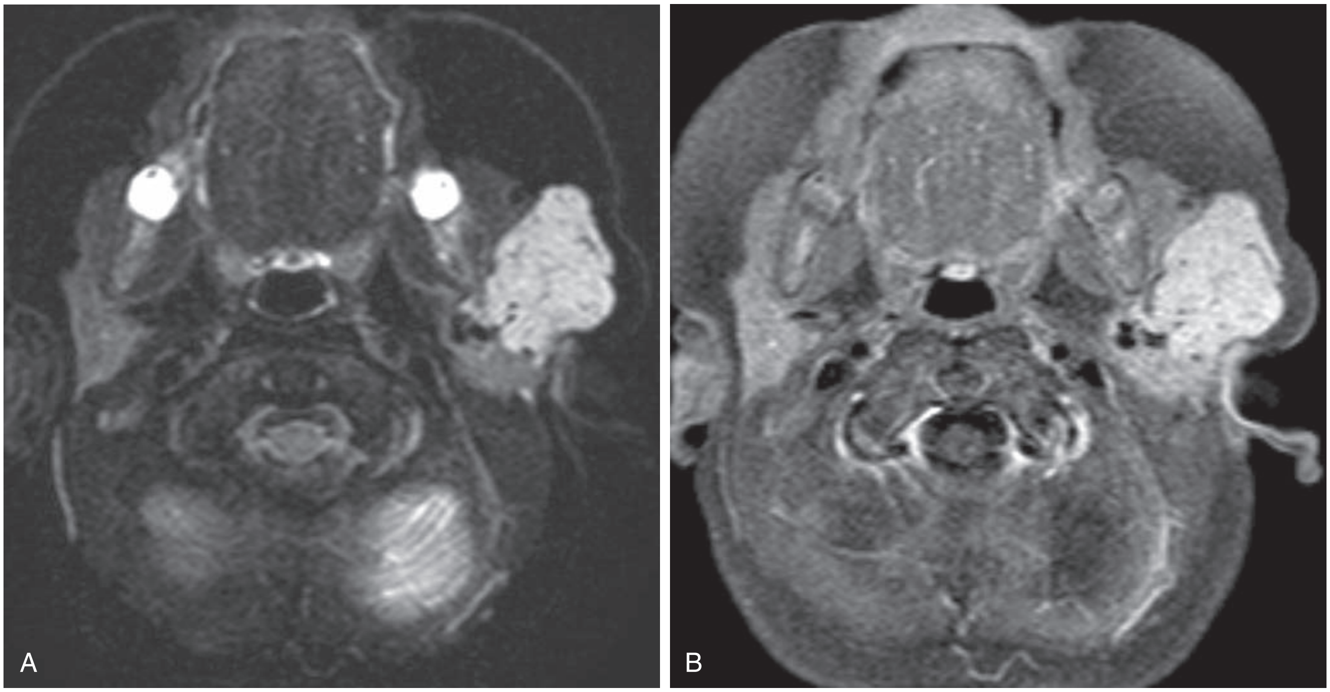

**Figure 16.10. Infantile hemangioma in a 2-month-old girl.** (A) Axial fat-saturated T2-weighted and (B) axial contrast-enhanced fat-saturated MR images show a hyperintense and enhancing lobular mass infiltrating and enlarging the left parotid gland. Flow voids are visualized within the mass.

hybrid lesions histopathologically, having features of both vascular tumor and malformation. Those that involve completely are termed *RICH* (rapidly involuting congenital hemangioma) and those that involute incompletely are termed *NICH* (noninvoluting congenital hemangioma). Cases of RICH evolving into NICH have been reported.[21] Surgical resection is the treatment of choice in NICH cases in which there is functional impairment or a cosmetic concern.

## KEY POINTS

- Lymphoma and rhabdomyosarcoma are the most common pediatric head and neck malignancies.
- Both NHL and HL present with cervical adenopathy, but HL tends to be unilateral.
- Isolated thyroid nodules in children are more likely to be malignant than those in adults.
- Neurofibromas almost always are in the setting of NF-1 and can degenerate into MPNST.
- Infantile hemangioma is the most common vascular tumor of childhood and usually involves in during the first few years of life.

## SUGGESTED READINGS

Francis GL, Waguespack SG, Bauer AJ, American Thyroid Association Guidelines Task Force, et al. Management guidelines for children with thyroid nodules and differentiated thyroid cancer. *Thyroid*. 2015;25(7):716–759. doi:10.1089/thy.2014.0460.

Qaisi M, Eid I. Pediatric head and neck malignancies. *Oral Maxillofac Surg Clin North Am*. 2016;28(1):11–19. doi:10.1016/j.coms.2015.07.008.

Stern JS, Ginat DT, Nicholas JL, Ryan ME. Imaging of pediatric head and neck masses. *Otolaryngol Clin North Am*. 2015;48(1):225–246. doi:10.1016/j.otc.2014.09.015.

## REFERENCES

Full references for this chapter can be found on www.expertconsult.com.

## REFERENCES

1. Albright JT, Topham AK, Reilly JS. Pediatric head and neck malignancies: US incidence and trends over 2 decades. *Arch Otololaryngol Head Neck Surg*. 2002;128:655–659.
2. Sandlund JT, Downing JR, Crist WM. Non-Hodgkin's lymphoma in childhood. *N Engl J Med*. 1996;334:1238–1248.
3. Chaha NK, Forte V. Pediatric head and neck malignancies. *Curr Opin Otolaryngol Head Neck Surg*. 2009;17:471–476.
4. Mody RJ, Bui C, Hutchinson RJ, et al. Comparison of (18)F Fluorodeoxyglucose PET with Ga-67 scintigraphy and conventional imaging modalities in pediatric lymphoma. *Leuk Lymphoma*. 2007;48(4):699–707.
5. Chevallier KM, Wiggins RH, Quinn NA, Gurgel RK. Differentiating pediatric rhabdomyosarcoma and Langerhans cell histiocytosis of the temporal bone by imaging appearance. *AJNR Am J Neuroradiol*. 2016;37:1185–1189.
6. Stambuk HE, Patel SG, Mosier KM, Wolden SL. Holdny AI. Nasopharyngeal carcinoma: recognizing the radiographic features in children. *AJNR Am J Neuroradiol*. 2005;26:1575–1579.
7. Dinauer CA, Breuer C, Rivkees SA. Differentiated thyroid cancer in children: diagnosis and management. *Curr Opin Oncol*. 2008;20:59.
8. Francis GL, Waguespack SG, Bauer AJ, et al. Management guidelines for children with thyroid nodules and differentiated thyroid carcinoma. *Thyroid*. 2015;25:716.
9. Haddad M, Triglia JM, Helardot P, et al. Localized cervical neuroblastoma: prevention of surgical complications. *Int J Pediatric Otorhinolaryngol*. 2003;67:1361–1367.
10. Robson C. Imaging of head and neck neoplasms in children. *Pediatr Radiol*. 2010;40:499–509.
11. Coutinho-Camillo CM, Brentani MM, Nagai MA. Genetic alterations in juvenile nasopharyngeal angiofibromas. *Head Neck*. 2008;30(3):390–400.
12. Ponti G, Losi L, Pellacani G, et al. Wnt pathway, angiogenetic and hormonal markers in sporadic and familial adenomatous polyposis-associated juvenile nasopharyngeal angiofibromas (JNA). *Appl Immunohistochem Mol Morphol*. 2008;16(2):173–178.
13. Alshaikh AN, et al. Juvenile nasopharyngeal angiofibroma staging: an overview. *Ear Nose Throat J*. 2015;94(6):E12–E22.
14. Sheela S, Riccardi VM, Ratner N. Angiogenic and invasive properties of neurofibroma Schwann cells. *J Cell Biol*. 1990;111:645.
15. Ducatman BS, Scheithauer BW, Piepgras DG, et al. Malignant peripheral nerve sheath tumors. A clinicopathologic study of 120 cases. *Cancer*. 1986;57:2006.
16. Chakravarti A, Shashidhar TB, Naglot S, et al. Head and neck teratomas in children: a case series. *Indian J Otolaryngol Head Neck Surg*. 2011;63(2):193–197.
17. Cardesa A, Luna MA. *World Health Classification of head and neck tumors: germ cell tumors*. 2005; 76–77.
18. Metry DW, Haggstron AN, Drolet BA, et al. A prospective study of PHACE syndrome in infantile hemangiomas: demographic features, clinical findings, and complications. *Am J Med Genet*. 2006;140(9):975–986.
19. Sans V, Dumas de la Roque E, Berge J, et al. Propranolol for severe infantile hemangiomas: follow-up report. *Pediatrics*. 2009;124(3):e423–e431.
20. Darrow DH, Green AK, Mancini AJ, et al. Diagnosis and management of infantile hemangioma. *Pediatrics*. 2015;136:e1060.
21. Mulliken JB, Enjolras O. Congenital hemangiomas and infantile hemangioma: missing links. *J Am Acad Dermatol*. 2004;50:875.

# 17 Thyroid and Parathyroid

Hollie A. Lai

## THYROID GLAND

### Embryology

The name "thyroid" is derived from the Greek word for *shield* due to the gland's shape and relationship with the laryngeal thyroid cartilage. The human thyroid gland has a dual embryonic origin.[1–3] The two thyroid cell types, follicular cells (thyrocytes) and parafollicular (C-cells), are derived from all three germ cell layers.[3] The most abundant cells, the follicular cells, arise from the thyroid anlage. The development of the thyroid gland begins when a median epithelial proliferation appears in the floor of the primitive pharynx between the developing tuberculum impar and copula of the tongue anlage, which is first visible as a bud around 24 days gestation.[4] This thickening, known as the median or thyroid anlage, soon forms a ventral outgrowth known as the thyroid diverticulum. The diverticulum is initially hollow but later becomes solid. The progenitor follicular cells continue to proliferate distally and then begin to proliferate laterally, which leads to the characteristic bilobed appearance of the gland connected by an isthmus. While the thyroid cells continue to proliferate, the embryo elongates and the tongue grows. As this happens, the developing thyroid gland descends anterior to the hyoid bone and larynx forming the thyroglossal duct. Because of the close association of the developing thyroid gland and embryonic heart, it is thought that the descent of the heart results in the thyroid gland being pulled.[3,5] The thyroid gland remains connected to the tongue by the thyroglossal duct. At approximately 7 weeks gestation, the thyroid gland has reached its final site in front of the trachea and the thyroglossal duct has disappeared.[4] The original opening of the thyroglossal duct persists as a vestigial pit called the foramen cecum[6,7]. 15% to 75% of people have a pyramidal lobe,[8] which is derived from the lower part of the thyroglossal duct and extends upwards from the isthmus. At about the time the thyroid gland reaches its final position, it merges with the two lateral anlagen or ultimobranchial bodies, resulting in the incorporation of the C-cells (parafollicular cells) into the thyroid gland. The ultimobranchial bodies are a pair of transient embryonic structures derived from the endoderm of the fourth pharyngeal pouch and the ectoderm of the fifth pharyngeal pouch.[9] The C-cell precursors migrate from the neural crest[10] bilaterally to the fourth pharyngeal pouches and become localized in the ultimobranchial bodies. As the cells of the thyroid anlage and the ultimobranchial bodies migrate from their respective sites of origin and complete the merging process, they disappear as individual structures and the cells contained within them disperse in the thyroid gland. The follicular cells continue to organize the thyroid follicles, where the C-cells scatter within the interfollicular space.[4] Remnants of the ultimobranchial bodies, or solid cell nests, can be seen postnatally and are usually located in the middle third of the thyroid lateral lobes.[11]

### Physiology

The thyroid gland's primary function is to produce hormones that play a vital role in regulating many cellular and physiologic activities such as growth, development, and metabolism.

The thyroid gland synthesizes and secretes two hormones, thyroxine ($T_4$) and triiodothyronine ($T_3$). The synthesis and secretion of these hormones is closely regulated through a complex feedback mechanism known as the hypothalamic-pituitary-thyroid-axis.

The hypothalamus synthesizes and secretes thyrotropin-releasing hormone (TRH),[12–14] which is carried to the pituitary gland by the hypothalamic-pituitary portal venous system. Once in the pituitary gland, TRH stimulates the synthesis and secretion of thyrotropin (thyroid-stimulating hormone, TSH) by the thyrotrophs in the anterior pituitary gland. TSH binds to its receptor in the thyroid gland, stimulating the production and secretion of $T_4$ and $T_3$ within the thyroid follicular cells. Thyroid secretion and serum concentrations of $T_4$ and $T_3$ are maintained by a negative feedback loop involving inhibition of TSH and TRH secretion by $T_4$ and $T_3$.[15,16]

Iodide is actively transported into the follicular cells from the circulating plasma by the sodium-iodide symporter (NIS) at the basolateral membrane.[17–21] Thyroid peroxidase (TPO) oxidizes iodide into its chemically active form. Thyroglobulin in the follicular lumen serves as a matrix for the synthesis of $T_4$ and $T_3$. First, TPO catalyzes the iodination of selected tyrosyl residues in thyroglobulin in a process known as iodination and organification. This results in the formation of mono- and diiodotyrosines (MIT, DIT). TPO then catalyzes a coupling reaction in which two iodotyrosines are coupled to form $T_4$ or $T_3$. Iodinated thyroglobulin is stored as colloid in the follicular lumen. When needed, thyroglobulin is internalized into the follicular cell by micro- and macropinocytosis and digested in lysosomes. Subsequently, $T_4$ (80%) and $T_3$ (20%) are released into the bloodstream. MIT and DIT are deiodinated, and released iodide is recycled for hormone synthesis.[3]

C-cells produce thyrocalcitonin, which is important in calcium homeostatis.

### Anatomy

The thyroid gland is composed of a right and left lobe usually joined by an isthmus anteriorly. The thyroid gland extends superiorly to the level of the thyroid cartilage and inferiorly to the level of the fifth or sixth tracheal ring. Occasionally, there is an extra lobe called the pyramidal lobe. This lobe extends superiorly from the isthmus at the midline.

The thyroid gland is located in the visceral space of the infrahyoid neck, anterior and lateral to the trachea and posterior to the infrahyoid strap muscles. Anterolaterally to the thyroid gland are the sternocleidomastoid muscles. The carotid space, containing the carotid arteries and jugular veins, is located posterolaterally. Posteromedially to the thyroid gland are the tracheoesophageal grooves containing the recurrent laryngeal nerves, paratracheal lymph nodes, and parathyroid glands.

The middle layer of the deep cervical fascia surrounds the visceral space and ensheaths the thyroid gland. The fascia condenses to form the suspensory ligament of Berry, affixing the thyroid gland to the trachea and larynx, causing the thyroid gland to move with the larynx during deglutition. A thin fibrous capsule also covers the thyroid gland. From this true capsule, septae extend into the gland dividing the gland into lobes and lobules.

## Abstract:

The signs and symptoms can be similar in pediatric and adult thyroid and parathyroid disease however there are important differences. This chapter discusses the embryology, anatomy, and physiology of these glands and the specific pediatric diseases associated with them. Imaging and treatment option are explored to help the clinician better manage the pediatric patients afflicted with thyroid and parathyroid disorders.

## Keywords:

Pediatric thyroid parathyroid imaging radiology nuclear medicine

The lobules are each made up of multiple follicles. The follicles consist of an outer layer of follicular cells, which enclose a lumen that contains thyroglobulin-rich colloid. Each thyroid follicle is surrounded by a basement membrane. C-cells are found within the basement membrane and are in contact with the follicular cells, but they do not abut the lumen. Follicular cells secrete thyroid hormones and C-cells secrete thyrocalcitonin.[3,22]

The thyroid gland is highly vascular being supplied by paired superior thyroidal arteries (first anterior branches of the external carotid arteries) and inferior thyroidal arteries (branches of the thyrocervical trunks that originate from the subclavian arteries). The thyroidea ima is an inconstant single vessel that has a variable origin but usually arises directly from the aortic arch or innominate artery and helps supply the inferior thyroid gland. Venous drainage of the thyroid gland is via the superior and middle thyroid veins that drain to the internal jugular veins and the inferior thyroid veins that often join to form a single trunk draining to the left brachiocephalic vein. Lymphatic drainage is extensive and multidirectional. The thyroid gland is innervated by the vagus nerve and the cervical sympathetic neural plexus.[22]

## Normal Findings

Ultrasonography (US) is a usually one of the first choices of imaging in pediatrics because it is noninvasive, readily available, and does not utilize radiation. A normal thyroid gland will have homogenous echotexture that is slightly hyperechoic relative to adjacent neck muscles.[23,24] Colloid follicles are commonly seen as small (less than 3 mm in diameter) anechoic cystic areas. Occasionally, the follicles contain inspisated colloid, which appear as punctate echogenic foci (Fig. 17.1).[25]

Morphologic and functional information about the thyroid gland can be achieved with nuclear scintigraphy. Thyroid scintigraphy is performed using intravenous Tc-99m pertechnetate ($^{99m}$TcO4) or oral Na I-123 (I$^{123}$) (Table 17.1). Because of the large radiation dose to the thyroid gland (approximately 1–3 rads per uCi administered), I$^{131}$ is not used for routine diagnostic imaging.[26,27] The normal thyroid gland shows homogenous radiopharmaceutical uptake and distribution in both lobes. The isthmus of the thyroid gland often demonstrates slightly less activity than the right and left thyroid lobes. Normal I$^{123}$ 24-hour uptake ranges from 10% to 30%.

Computed tomography (CT) and magnetic resonance imaging (MRI) provide important adjunctive anatomic information by delineation of lesions within the thyroid gland, detection of lymph node metastases, and detection of thyroid disease extension into adjacent neck structures. The anatomic information provided by CT and MRI is also valuable in guiding the surgical approach. The normal thyroid gland (due to its iodide content) has a density of approximately 80 to 100 HU on CT. In fact, a well-visualized gland usually indicates a normally functioning thyroid. Conversely, a poorly seen gland correlates with poor thyroid function. The injection of iodinated contrast material diffusely and homogenously enhances the gland.[22] Remember that the use of iodinated contrast agents will alter radioactive iodine uptake, whereas gadolinium contrast material used for MRI will not. The normal thyroid gland shows homogenous signal intensity slightly greater than muscle on precontrast T1-weighted images. On T2-weighted images, the thyroid gland is relatively hyperintense to muscle. Following contrast administration, the gland enhances diffusely and homogenously.

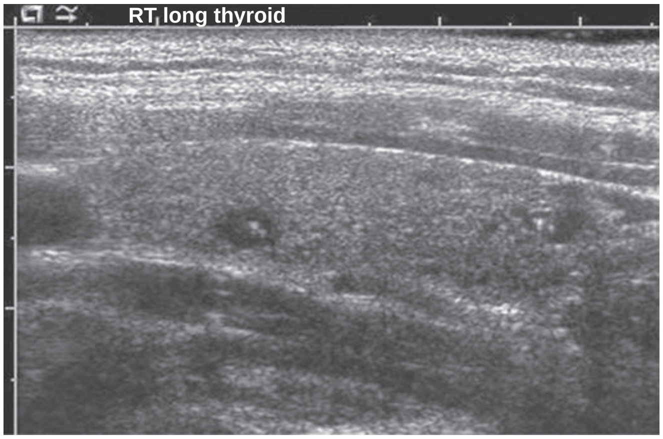

**Figure 17.1. Normal thyroid ultrasound.** Small anechoic foci with a central hyperechoic focus represent colloid follicles, which are a normal finding.

## Hypothyroidism

***Overview.*** Hypothyroidism is the most common disturbance of thyroid function in children. It can be congenital (Box 17.1) or acquired in childhood or adolescence (Box 17.2). Whatever its cause, hypothyroidism can have deleterious effects. Untreated congenital hypothyroidism in early infancy results in profound retardation of growth and neurocognitive development (cretinism). Untreated hypothyroidism in older children leads to growth failure as well as slowed metabolism and impaired memory.

### Congenital Hypothyroidism

***Overview.*** Hypothyroidism in the newborn can be permanent or transient. Congenital hypothyroidism is a condition in which lower than normal thyroxin (T$_4$) causes retardation of growth and neurocognitive development if left untreated. The incidence of congenital hypothyroidism in the United States has dramatically increased over the last 2 decades,[28] from 2.9 cases per 10,000 births in 1991 to nearly 4 cases per 10,000 births in 2000.[29]

***Etiologies, Pathophysiology, and Clinical Presentation.*** The majority of cases of primary congenital hypothyroidism are caused by thyroid gland dysgenesis (see Table 17.2). Thyroid dysgenesis refers to a developmental defect of thyroid morphogenesis. There are three types: ectopia, aplasia (athyrosis), and hypoplasia.

Dyshormonogenesis is the second largest cause of primary congenital hypothyroidism which is often inherited as an autosomal recessive trait. Dyshormonogenesis is an abnormality of one or more of the enzymes involved in the pathway of thyroid hormone synthesis and secretion. Most inborn errors of thyroid hormone synthesis are caused by defects in iodide organification with the most common defect being TPO deficiency. This results in a failure of iodide oxidation which is necessary for organification. A small percentage of infants with congenital hypothyroidism will have hypothalamic-pituitary hypothyroidism or thyroid-stimulating hormone resistance, whereas the remainder will have a transient form of congenital hypothyroidism.

Less than 5% of congenital hypothyroidism patients are diagnosed clinically at birth; most are identified by newborn screening. Newborn screening involves measuring TSH and T$_4$ concentrations. T$_4$ concentrations are decreased and TSH concentrations are elevated in patients with congenital hypothyroidism, except in central hypothyroidism where the TSH is not elevated. The laboratory abnormalities tend to be more marked in cases of thyroid aplasia than in thyroid ectopia. Patients with transient hypothyroidism will also have elevated TSH concentrations and low or normal T$_4$ concentrations that subsequently normalize.

***Imaging.*** Imaging is not routinely used to diagnose congenital hypothyroidism. The most recent recommendations discuss thyroid imaging in congenital hypothyroidism as optional because of controversy regarding the risk-benefit ratio of early thyroid scanning

**TABLE 17.1** Thyroid Scintigraphy

| | Sodium Iodide (Capsule or Liquid) (1-23I) | Tc99m-Pertechnatate (99mTcO4) | Perchlorate Discharge or Washout |
|---|---|---|---|
| Advantages | Better visualization of retrosternal thyroid tissue<br>Yields better images when uptake is low | Less expensive<br>More readily available<br>More rapid examination<br>Can be performed while the patient is on thionamides | Can determine organification defects |
| Disadvantages | Higher cost<br>Longer imaging times<br>Patient must be off thionamides | Trapped, but not organified<br>Activity in esophagus or vascular structures may be misleading<br>Poor image quality when uptake is low | Cannot detect enzymatic defects beyond the point of organification |
| Dose | 1.5 μCi/kg<br>Minimum dose = 25 μCi<br>Maximum dose = 100 μCi | 0.1 mg/kg<br>Minimum dose = 0.5 mCi<br>Maximum dose = 1.0 mCi | Same dosing as I-123<br>Potassium perchlorate:<br>Infant = 10 mg/kg<br>Child = 400 mg<br>Adult = 1000 mg |
| Route of administration | Oral | Intravenous | Oral |
| Time until imaging | 4–6 hours<br>24 hours (for uptake determination) | 20–30 minutes | Do I-123 thyroid uptake at 3 hours. If thyroid appears normal and uptake >10% give perchlorate<br>Do second thyroid uptake 60–90 minutes after perchlorate administration |
| Radiation dosimetry (5 year old)[27]<br>Administered activity<br>Critical organ<br>Effective dose equivalent | Assuming 25% uptake<br>0.1–0.3 MBq<br>0.003–0.01 mCi/kg<br>Thyroid<br>16 mGy/MBq<br>59 rad/mCi<br>0.54 mSv/MBq<br>2.0 rem/mCi | 1.8–9.2 MBq/kg<br>0.05–0.25 mCi/kg<br>Upper large intestine<br>0.21 mGy/MBq<br>0.78 rad/mCi<br>0.04 mSv/MBq<br>0.15 rem/mCi | Same as I-123 |
| Notes | Approximate normal uptake values (may vary greatly)<br>4 hours = 10%–35%<br>24 hours = 6%–18% | | $\text{Discharge }\% = 100 \times \frac{\text{Initial uptake} - \text{Final uptake}}{\text{Initial uptake}}$<br>No change = normal<br>>10%–15% decrease (discharge) suggests an organification defect<br>>50% discharge suggests complete organification defect<br>20%–50% discharge suggests partial organification defect |

## BOX 17.1 Causes of Congenital Hypothyroidism

**PRIMARY (THYROID GLAND)**

Thyroid dysgenesis (80%)
- Ectopia (75%)
- Aplasia or athyrosis (25%)
- Hypoplasia (rare)

Dyshormonogenesis (15%–20%)
- Peroxidase deficiency (most common)
- Other deficiencies (less common)
- Iodide transport defect
- Iodotyrosine deiodinase defect

**SECONDARY (PITUITARY) AND TERTIARY (HYPOTHALAMUS)**

Pituitary and hypothalamic defects (uncommon)

**MISCELLANEOUS**

Thyroid-stimulating hormone resistance

Transient congenital hypothyroidism
- Functional immaturity-common in premature infants
- Transplacental transfer of maternal medication
- Transplacental transfer of maternal thyroid-blocking antibodies
- Maternal antithyroid medications
- Iodine deficiency
- Iodine excess

of infants with suspected hypothyroidism.[30] There are also clinicians who do not order imaging studies because they believe the results would not alter their management of congenital hypothyroidism.

Diagnostic studies for a patient with congenital hypothyroidism can include US and thyroid scintigraphy with $^{123}$I or $^{99m}$TcO4. Use of both US and thyroid scintigraphy has been shown to provide a more complete depiction of congenital hypothyroidism in the newborn than either study performed alone.[31]

The role of US is to identify the presence or absence of thyroid tissue, distinguish rudimentary glands from anatomically normal thyroid glands, and identify an enlarged gland or goiter.

$^{99m}$TcO4 or $^{123}$I can be used to help determine if the cause of hypothyroidism may be due to thyroid dysgenesis (see Table 17.1). In patients with thyroid agenesis, the examination fails to demonstrate functional thyroid tissue. It is important that the images include the oropharynx and upper neck as well as the upper portion of the chest so that an ectopic location of the thyroid gland can be excluded.

$^{99m}$TcO4 scintigraphy demonstrates a round or oval area of uptake in the midline of the upper neck in most cases of ectopia (Fig. 17.2). The ectopic gland may occupy a lingual (most common), sublingual, or prelaryngeal location. Mediastinal and lateral locations are rare. Functional thyroid tissue may be identified in more than one location, most commonly in the lingual and sublingual regions. It is unusual to identify thyroid tissue in its normal location at the base of the neck in the presence of an ectopic gland. Usually patients with an ectopic thyroid gland will have hypothyroidism. Unusual cases do occur in which the ectopic gland is capable of secreting sufficient thyroid hormone such that hypothyroidism is not apparent on neonatal screening. These patients often present with signs of ectopia later in life when the hyperstimulated gland enlarges and causes local symptoms.

$^{99m}$TcO4 scintigraphy in cases of dyshormonogenesis will demonstrate a normally positioned thyroid gland that may or may not be enlarged (e-Fig. 17.3). If dyshormonogenesis is suspected, a perchlorate washout test may be performed. Perchlorate is actively transported into the thyroid gland similar to iodide but with a greater affinity for the transporter and is therefore a competitive inhibitor of the thyroid iodide trap. During unimpaired thyroid hormonogenesis, iodide entering the thyroid gland is rapidly oxidized and iodinates tyrosine, forming MIT and DIT, with subsequent coupling of MIT and DIT to generate $T_4$ and $T_3$. Intrathyroid deiodination of the iodinated tyrosines and thyronines results in a very small pool of thyroidal inorganic iodide. Any congenital or acquired condition associated with a defect in iodide organification may yield a higher intrathyroidal inorganic iodide concentration. The perchlorate discharge/washout test is a means of estimating the size of this intrathyroidal "free" iodide pool, thereby detecting and roughly quantifying disturbances in iodide organification. The perchlorate discharge/washout test is performed by giving the patient an oral dose of $^{123}$I followed by a dose of perchlorate and measuring the "washout" (see Table 17.1). The perchlorate test will be negative in patients who do not have an organification defect, but also when enzymatic defects are present in the synthetic pathway beyond the point of organification.[32–34]

***Treatment.*** Levothyroxine ($T_4$) is the treatment of choice for children with hypothyroidism. The goals of the treatment are to restore normal growth and development.

## Hypothyroidism in Children and Adolescents

### Chronic Autoimmune (Hashimoto) Thyroiditis

***Overview.*** There are many causes of acquired hypothyroidism in the pediatric population (see Table 17.2) Chronic autoimmune (Hashimoto) thyroiditis is by far the most common cause of acquired

**BOX 17.2** Causes of Hypothyroidism in Children and Adolescents

**PRIMARY (THYROID GLAND)**

Chronic autoimmune (Hashimoto) thyroiditis (most common cause in the United States, increased incidence in some chromosomal abnormalities and syndromes)
Iodine deficiency (most common cause worldwide)
Iodine excess
External radiation therapy
Radioactive iodine therapy
Thyroidectomy
Goitrogen foods
Medications (e.g., thionamides, lithium, anticonvulsants)
Late-onset congenital hypothyroidism
- Thyroid dysgenesis
- Inborn errors of thyroid metabolism

**SECONDARY (PITUITARY) AND TERTIARY (HYPOTHALAMUS)**

Central hypothyroidism caused by:
- Craniopharyngioma and other tumors pressing on hypothalamus or pituitary
- Septo-optic dysplasia
- Infiltrative processes
- Langerhans cell histiocytosis
- Neurosurgery
- Cranial irradiation
- Head trauma

**MISCELLANEOUS**

Thyroid hormone resistance
Infection (usually not permanent)
Hemangiomas of the liver

**TABLE 17.2** Causes of Hyperthyroidism and Thyrotoxicosis in Children and Adolescents

| Name | Synonyms | Mechanism of Hyperthyroidism/ Thyrotoxicosis | Laboratory Tests | RAIU Appearance on Scintigraphy | Imaging Appearance of Thyroid Gland |
|---|---|---|---|---|---|
| **HYPERTHYROIDISM, THYROID GLAND HYPERFUNCTION (INCREASED SYNTHESIS OF THYROID HORMONE)** | | | | | |
| Graves disease | Hyperthyroid goiter<br>von Basedow disease | TRS-Ab | Low TSH<br>Elevated free $T_4$<br>Elevated $T_3$<br>High thyroglobulin<br>TSI positive<br>TRS-Ab positive<br>TPO-Ab positive or negative<br>TBII positive | Elevated, often >80%<br>Diffuse increased uptake | Ultrasonography: Enlarged gland; hypoechoic but may be normal; may be nodular; increased vascularity, "thyroid inferno"[51]<br>CT and MRI: Nonspecific findings; enlarged gland; avid, diffuse enhancement<br>Decreased attenuation on noncontrast CT reflecting decrease in iodine concentration |
| Multinodular goiter | Toxic multinodular goiter<br>Adenomatous goiter<br>Nodular hyperplasia<br>Adenomatous hyperplasia | Autonomous overproduction of thyroid hormones by nodules | Low TSH<br>Elevated free $T_4$<br>Elevated $T_3$<br>High thyroglobulin<br>All thyroid antibodies negative | Normal or elevated<br>Heterogeneous uptake; multiple foci increased uptake | Ultrasonography: Enlarged gland; multiple heterogeneous nodules; cystic changes |

*Continued*

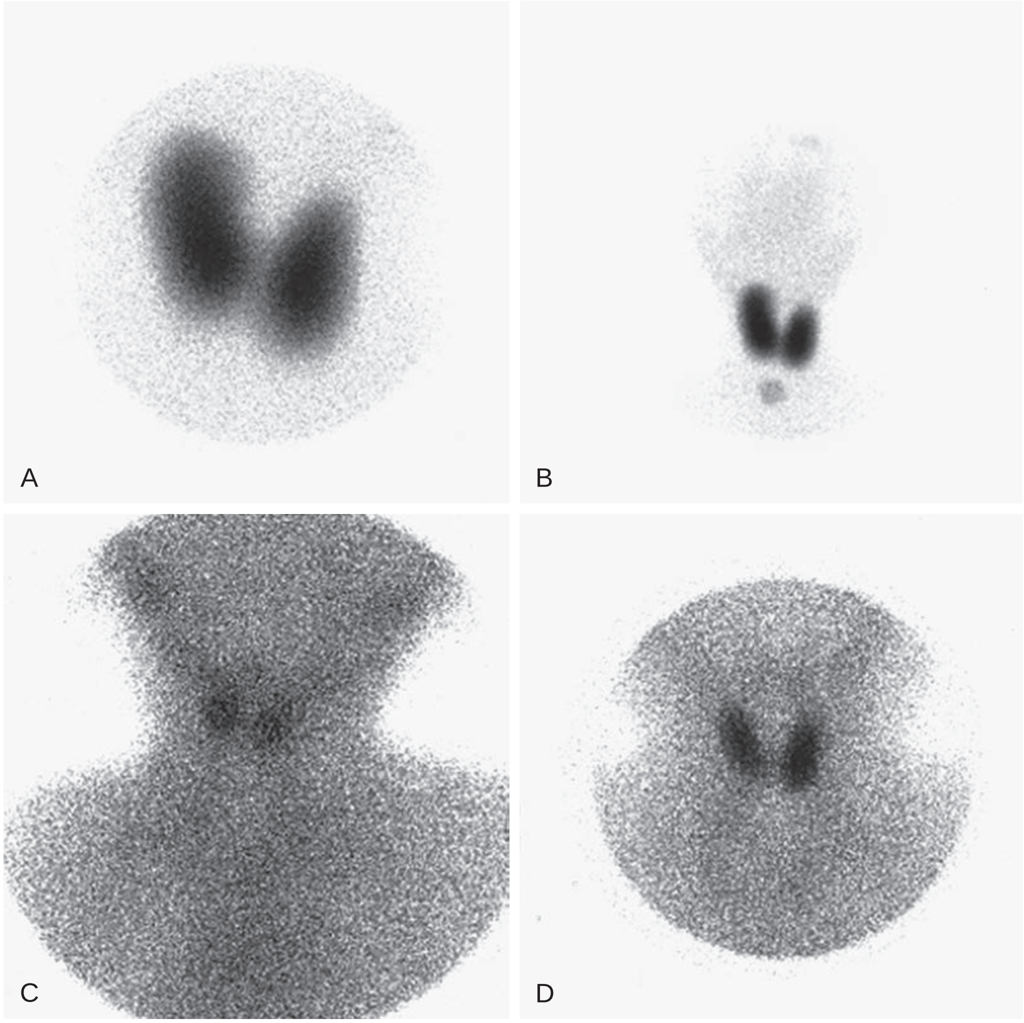

**e-Figure 17.3. Abnormal thyroid scans.** (A and B) Organification defect. (A) Anterior pinhole view. A bilobed thyroid is present in the neck and shows diffusely increased uptake. (B) Anterior prominently sized thyroid compared with the neck and the head. (C and D) Anterior pinhole views of poorly functioning thyroid from two patients. A bilobed thyroid is normally located within the neck. Trapping by the thyroid is poor with high body background. The thyroid may appear small (C) or normal (D). This pattern can be seen in patients with thyroid gland hypoplasia or a transient insult, such as maternal antibodies. Scintigraphically, these entities cannot be distinguished.

**TABLE 17.2** Causes of Hyperthyroidism and Thyrotoxicosis in Children and Adolescents—cont'd

| Name | Synonyms | Mechanism of Hyperthyroidism/ Thyrotoxicosis | Laboratory Tests | RAIU Appearance on Scintigraphy | Imaging Appearance of Thyroid Gland |
|---|---|---|---|---|---|
| Autonomous nodule | Plummer disease<br>Toxic nodule | Uncommon in children; autonomous overproduction of thyroid hormones by solitary nodule; usually produce $T_3$ | Low TSH<br>Normal or elevated free $T_4$<br>Elevated $T_3$<br>High thyroglobulin<br>All thyroid antibodies negative | Elevated<br>Single hot focus; rest of gland suppressed | |
| TSH-producing pituitary adenoma | | Autonomous overproduction of TSH | Normal TSH<br>Elevated free $T_4$<br>High serum TSH alpha subunit concentration<br>All thyroid antibodies negative | High | Pituitary adenoma on MRI |
| Pituitary resistance to thyroid hormone | | Autosomal-dominant; thyroid beta-receptor gene mutation[52]; overproduction of TSH | Normal or slightly elevated TSH<br>Elevated free $T_4$<br>Elevated $T_3$ (less than $T_4$)<br>All thyroid antibodies negative | High<br>Diffuse uptake | |
| **THYROTOXICOSIS-EXCESS SECRETION OF PREFORMED THYROID HORMONES** | | | | | |
| Thyrotoxic phase of chronic lymphocytic (Hashimoto) thyroiditis | Hashitoxicosis<br>Lymphadenoid goiter | Autoimmune; release of preformed hormones | Low TSH<br>Elevated free $T_4$<br>Elevated $T_3$<br>High thyroglobulin<br>TPO-Ab positive; Thyroglobulin positive; TRS-Ab positive or negative | Elevated<br>Diffuse increased uptake | Ultrasonography: Findings are nonspecific; enlarged gland; hypoechoic, heterogeneous echotexture |
| Subacute lymphocytic thyroiditis | Painless sporadic thyroiditis<br>Silent thyroiditis | Autoimmune; release of preformed hormones<br>May be associated with drugs (interferon-alpha, interleukin-2, lithium) | Low TSH<br>Elevated free $T_4$<br>Elevated $T_3$<br>High thyroglobulin<br>TPO-Ab positive | Very low<br>Diffuse decreased uptake | Ultrasonography: Findings are nonspecific; enlarged gland; hypoechoic, heterogeneous echotexture |
| Thyrotoxic phase of subacute granulomatous thyroiditis | Subacute thyroiditis<br>Painful subacute thyroiditis<br>de Quervain thyroiditis<br>Granulomatous giant cell thyroiditis | Viral; release of preformed hormone | Low TSH<br>Elevated free $T_4$<br>Elevated $T_3$<br>High thyroglobulin<br>TPO-Ab negative; elevated ESR | Low<br>Diffuse decreased uptake | Ultrasonography: Findings are nonspecific; enlarged gland; hypoechoic, heterogeneous echotexture |
| Factitious thyroiditis | Thyrotoxicosis factitia | Intentional ingestion of too much thyroxine | Low TSH<br>Elevated free $T_4$<br>Elevated $T_3$<br>Low thyroglobulin | Low | |
| Iodine-induced hyperthyroidism | | Underlying multinodular goiter; thyroid hormone release triggered by exposure to iodine (contrast agents), amiodarone | Low TSH<br>Elevated free $T_4$<br>Elevated $T_3$ | Increased | |

*CT*, Computed tomography; *ESR*, erythrocyte sedimentation rate; *MRI*, magnetic resonance imaging; *RAIU*, radioactive iodine uptake; *$T_3$*, triiodothyronine; *$T_4$*, thyroxine; *TBII*, thyrotropin-binding inhibitor immunoglobulin; *TPO-Ab*, thyroid peroxidase antibodies; *TRS-Ab*, thyrotropin-receptor stimulating antibodies; *TSH*, thyroid-stimulating hormone; *TSI*, thyroid stimulating immunoglobulin.

primary hypothyroidism in children and adolescents in iodine sufficient areas. It is more common in girls than boys and increases in frequency with age during childhood and adolescence. Euthyroid goiter is more common than hypothyroidism.[35–37]

***Etiologies, Pathophysiology, and Clinical Presentation.*** Chronic autoimmune thyroiditis is a complex, thyroid-specific T-cell mediated disease with a strong genetic component.[38–40] It often coexists with other autoimmune diseases[41] and can also be expressed as part of an autoimmune polyendocrine syndrome type 2 (APS-2).[42] The two major forms of the disorder are goitrous autoimmune thyroiditis and atrophic autoimmune thyroiditis, with the common pathologic feature being lymphocytic infiltration and the common serologic feature being the presence of high serum concentrations of antibodies to TPO and thyroglobulin.

The National Health and Nutrition Examination Survey (NHANES III) from 1988 to 1994, demonstrated 7.4% of adolescents (ages 12–19) had positive antithyroglobulin antibodies (Tg Ab) and 4.8% had positive antithyroid peroxidase antibodies (TPO Ab). Approximately 2% of all surveyed adolescents had serum TSH levels indicting hypothyroidism.[43]

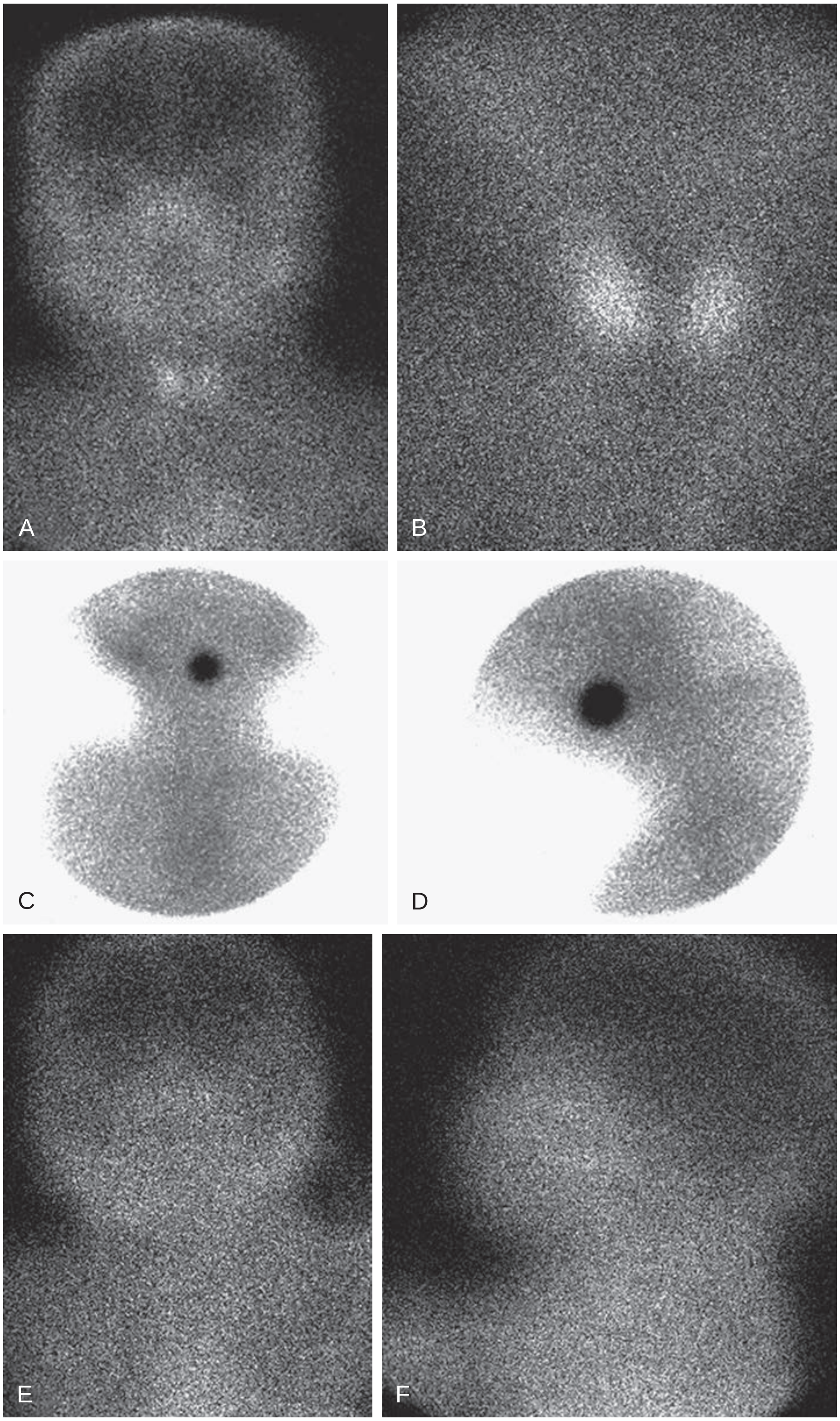

**Figure 17.2. Normal and abnormal thyroid scintigraphy.** (A and B) Normal thyroid anatomy. Anterior and pinhole views show normal bilobe architecture and normal position. Thyroid function cannot be meaningfully estimated from these images in an infant with known thyroid insufficiency. (C and D) Thyroid ectopia. Anterior and lateral views of the neck show a solitary rounded focus of radiopharmaceutical trapping at the base of the tongue. No clinical difference exists between the terms *lingual* and *sublingual*, and they are used interchangeably. (E and F) No thyroid is identified. Anterior and lateral views show no functioning thyroid tissue. Although this finding suggests thyroid agenesis, it is nonspecific because severely decreased thyroid function, particularly resulting from maternal thyrotropin receptor–blocking antibody, also may have this appearance.

The most common physical finding at presentation is a goiter.[35] The most common manifestation of hypothyroidism in children is stunted growth, often resulting in short stature. The growth delay is usually insidious in onset and may be present for several years before other, if any, symptoms occur.[44] Other common symptoms that may occur include altered school performance, sluggishness, lethargy, cold intolerance, constipation, dry skin, brittle hair, facial puffiness, and muscle aches. If the cause is from hypothalamic or pituitary disease, the patients may have headaches, visual symptoms, or pituitary disease manifestations.

***Imaging.*** Most physicians consider the presence of serum antithyroid antibodies as sufficient evidence for chronic autoimmune thyroiditis and that thyroid US or radionuclide scanning are rarely indicated. Children with central hypothyroidism however should undergo cranial MRI (with contrast) and tests for other pituitary hormone deficiencies.

Ultrasound findings are nonspecific but include an enlarged relatively hypoechoic gland with coarse heterogeneous echotexture. Less commonly, the echogenicity of the gland is increased relative to adjacent muscle. Fibrotic septations in the chronic form may produce a pseudolobulated appearance of the parenchyma. Multiple discrete hypoechoic, 1 to 6 mm, micronodules may also be seen (Fig. 17.4A–C).

In the early (preclinical) stage of Hashimoto thyroiditis, elevated $^{123}$I uptake values with diffusely increased radionuclide activity throughout the thyroid may be seen. This happens because there is an initial mild decline in circulating thyroid hormones sensed by the pituitary gland causing a compensatory rise in TSH secretion, which stimulates the gland to synthesize more thyroid hormone so that $T_3$ and $T_4$ levels return to normal. In some instances, thyroid follicles demonstrate a variable response to the chronic TSH stimulation, leading to patchy proliferation of these follicles. On a thyroid scan, this phenomenon manifests as areas of increased activity (follicles that respond to TSH) and of decreased activity (those that do not respond). As more thyroid parenchyma is replaced by fibrous tissue and the $T_3$ and $T_4$ levels decrease as the gland fails to respond to the elevated TSH level, the radionuclide uptake becomes nonuniformly decreased (Fig. 17.4D).[45]

***Treatment.*** Levothyroxine ($T_4$) is the treatment of choice for children with hypothyroidism. The goals of the treatment are to restore normal growth and development. Patients with autoimmune thyroiditis who have a suspicious thyroid examination such as a suspected nodule or significant gland asymmetry, especially if associated with palpable cervical lymphadenopathy, should be evaluated by an experienced thyroid sonologist with consideration of fine needle aspiration (FNA) for any suspicious sonographic features.[46]

## Hypertyhroidism and Thyrotoxicosis

***Overview.*** Hyperthyroidism refers to overproduction of thyroid hormone by the thyroid gland. Thyrotoxicosis refers to the clinical and biochemical manifestations of excess thyroid hormones. There are multiple causes of hyperthyroidism and thyrotoxicosis in children (Box 17.2). Most cases of thyrotoxicosis in children are associated with hyperthyroidism. Graves disease is the most common cause of the hyperthyroidism in the pediatric population.

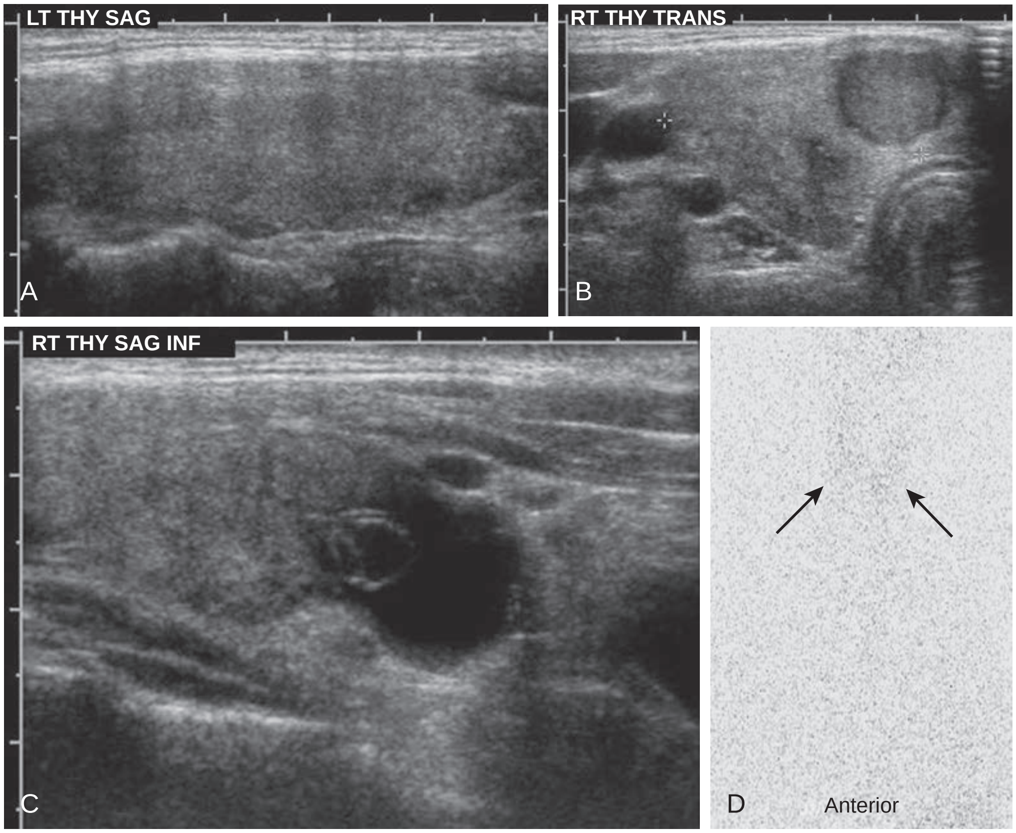

**Figure 17.4. Chronic autoimmune (hashimoto) thyroiditis.** (A) Ultrasonography demonstrates an enlarged gland that is relatively hypoechoic with heterogeneous echotexture. (B and C) The right lobe of the same patient has a hypoechoic nodule and cystic changes. (D) The $^{123}$I scan shows diffuse decreased uptake *(arrows)*. The 24-hour uptake was only 0.5%.

A 2008 study estimating the incidence of hyperthyroidism using the number of new prescriptions of thionamides and data from the 2008 U.S. census concluded that the incidence among individuals aged 0 to 11 years was 0.44 cases per 1000 population; the incidence among individuals aged 12 to 17 years was 0.26 cases per 1000 population; and the incidence among individuals aged 12 to 17 years was 0.59 cases per 1000 population.[47]

### Graves Hyperthyroidism

***Etiologies, Pathophysiology, and Clinical Presentation.*** Graves disease is the most common cause of hyperthyroidism in children and adolescents. The general cause TSH is receptor-stimulating antibodies (TRS-Ab), which activate the TSH receptor.

Many of the clinical features of hyperthyroidism are similar in children, adolescents, and adults. Most children with Graves disease have a diffuse goiter.[48] Hyperthyroidism also affects growth and pubertal development in children. Acceleration of growth with advanced epiphyseal maturation can be seen in untreated hyperthyroidism. The acceleration of growth is usually subtle and the degree depends on the duration of hyperthyroidism before diagnosis. Pubertal development, on the other hand, tends to be delayed in children with untreated hyperthyroidism. In those children who have already begun puberty, it slows until the hyperthyroidism is treated.

Graves disease causes other unique problems not associated to the high serum thyroid hormone concentrations, including ophthalmopathy and pretibial myxedema. Graves ophthalmopathy is common in children but is generally less severe than in adults. The clinical manifestations stem from a combination of increased orbital fat and extraocular muscle volume. The exact etiology is unknown, however, it may result from antibodies against a TSH receptor-like protein in retro-orbital connective tissue. Thyrotropin receptor (TSHr) mRNA and functional protein have been demonstrated in orbital fibroblasts. Studies have suggested TSHr autoantibodies (TRAbs) are potent stimulators of adipogenesis in Graves ophthalmopathic orbital cells. Therefore it is possible that circulating TRAbs in Graves patients that stimulate overproduction of thyroid hormones also increase orbital adipose tissue volume. Although originally thought to represent another causative agent, antibodies to extraocular muscles are now generally thought to be secondary to extraocular muscle inflammation and damage.[49,50]

***Imaging.*** In the majority of patients no imaging is needed. The diagnosis can be made by physical exam, laboratory tests, and onset or chronicity of symptoms. Onset of symptoms may be documented by prior laboratory studies or inferred from the review of symptoms. If thyrotoxicosis has been present for less than 8 weeks, transient thyrotoxicosis secondary to subacute thyroiditis or the thyrotoxic phase of autoimmune/silent thyroiditis should be considered. These are self-limited and refractory to therapy with thionamides. Thyrotoxicosis that has been present for more than 8 weeks suggests true hyperthyroidism thyrotoxicosis. However, if the diagnosis cannot be made clinically, an $^{123}$I uptake, with or without a scan, should be performed.[51]

***Treatment.*** Graves disease can be treated pharmacologically, surgically, or with radioiodine ablation. The thionamide antithyroid drugs propylthiouracil (PTU) and methimazole (MMI) continue to be the most commonly used treatment medications in the United States.[52,53] Thionamides exert their antithyroid effects primarily by inhibiting thyroid hormone synthesis through interference with the oxidation and organic binding of iodide into thyroglobulin.[53] In addition, PTU, but not MMI, inhibits the peripheral conversion of $T_4$ to $T_3$ by type 1 deiodinase.[54,55] Some patients are unable to take these medications or become noncompliant. In these patients, their disease may be treated by radioiodine ablation or thyroidectomy. Concerns over the potential long-term complications of pediatric radiation exposure have traditionally made endocrinologists hesitant about using radioiodine in the treatment of Graves disease. The use of radioactive iodine has now been detailed for more than 1000 children, which found remission rates that top 95% with very few complications.[56] Despite reassurances found in the literature regarding the safety of $^{131}$I in children, it has been shown total-body radiation doses after $^{131}$I therapy vary with age, and the same absolute dose of $^{131}$I will result in more radiation exposure to a young child than to an adolescent or adult.[57–61] Children are also more sensitive to the effects of radiation than adults. Therefore when treating children with radioactive iodine, in addition to selecting a dose that will achieve adequate thyroid tissue destruction, the age of the patient and the total $I^{131}$ dose need to be considered.

### Infection

***Overview.*** Acute suppurative thyroiditis is an infection of the thyroid gland that is rarely seen during childhood but is potentially life-threatening.[62,63]

***Etiologies, Pathophysiology, and Clinical Presentation.*** Acute suppurative thyroiditis is usually caused by a bacterial infection. *Staphylococcus aureus*, *Streptococcus pyogenes*, *Streptococcus epidermidis*, and *Streptococcus pneumoniae* are the most common aerobic bacteria. The predominant anaerobic bacteria are Gram-negative bacilli and *Peptostreptococcus* spp.[64]

Suppurative thyroiditis can be related to a pyriform sinus fistula or thyroglossal duct remnant, especially when recurrent infections occur.[62,65–67]

The classic clinical features of this illness include fever; neck pain; and a swollen, tender mass over the thyroid gland.

***Imaging.*** US is the modality of choice, often demonstrating unilobar or diffuse swelling and/or abscess formation. CT or MRI is not usually necessary. On MRI, the thyroid gland will demonstrate focal or diffuse swelling with decreased signal on T1-weighted and increased signal on T2-weighted images. MRI is superior to ultrasound in detecting capsule rupture into the adjacent soft tissues.

***Treatment.*** The primary treatment is antimicrobial therapy, directed against the likely bacterial pathogens. Surgery may be needed to drain abscesses and repair any developmental anomaly that led to the infection.

## Benign Masses

***Overview.*** Thyroid nodules and cysts are uncommon in healthy children before puberty.[67–71] Most thyroid nodules are benign, but multiple studies have demonstrated an increased risk of malignancy in pediatric thyroid nodules with an overall 26.4% risk of cancer[69] Risk factors associated with the development of thyroid nodules in children include iodine deficiency, prior radiation exposure, history of antecedent thyroid disease, and several genetic syndromes.[46]

### Benign Nodules

***Overview.*** The most common type of benign solitary thyroid nodules is follicular adenomas (hyperplastic nodules).[71]

***Etiologies, Pathophysiology, and Clinical Presentation.*** Follicular adenomas are thought to be the result of cycles of hyperplasia and colloid involution of thyroid nodules.[22,25] They are encapsulated lesions that are usually solitary and nonfunctioning. They are usually asymptomatic or may present as a palpable nodule. Sudden enlargement and pain is usually caused by spontaneous hemorrhage within the lesion. With the increasing performance of cross-sectional studies, thyroid nodules are often found incidentally.[72]

***Imaging.*** The findings of ultrasound, CT, and MRI are nonspecific and can be seen in both benign and malignant nodules.

On US, follicular adenomas are usually hypoechoic relative to normal thyroid tissue, although some are hyperechoic and a few isoechoic. A thin hypoechoic "halo" or rim around the lesion can often be seen. The cause of the "halo" is unknown but may be due to the fibrous capsule, compressed thyroid parenchyma, or pericapsular inflammatory infiltration.[25,73] Adenomas may also contain hypoechoic or anechoic areas from internal hemorrhage and necrosis. Calcifications may also be present (e-Fig. 17.5). Thyroid scintigraphy may be used in the evaluation of a thyroid nodule. Increased uptake in a nodule almost always indicates that the nodule is benign.

***Treatment.*** In 2015 the American Thyroid Association (ATA) published management guidelines for children and adolescents with thyroid nodules and differentiated thyroid cancer (DTC) based on scientific evidence and expert opinion. Biopsy or excision may be performed to exclude malignancy.[74] The ATA recommends "the evaluation and treatment of thyroid nodules in children should be the same as in adults with the following exceptions that: 1. Ultrasound characteristics and clinical context should be used rather than size alone to identify nodules that warrant fine needle aspiration (FNA), 2. All FNA in children should be performed under US-guidance, 3. Preoperative FNA of a hyperfunctioning nodule in a child is not warranted as long as the lesion is removed, 4. A diffusely infiltrative form of PTC [papillary thyroid carcinoma] may occur in children and should be considered in a clinically suspicious gland, and 5. Surgery (lobectomy + isthmusectomy) is favored over repeat FNA for most nodules with indeterminate cytology."[46]

Lesions with benign cytology should be followed by serial US and undergo repeat FNA if suspicious features develop or if the lesion continues to grow. A lobectomy may be performed in patients with compressive symptoms, cosmetic concerns, or patient/parent preference. Lobectomy should be also be considered in all apparently benign solid thyroid nodules >4 cm, those lesions demonstrating significant growth, or other clinical concerns for malignancy.[46]

For pediatric patients with a thyroid nodule and suppressed TSH, thyroid scintigraphy should be performed. Increased uptake within the nodule is consistent with autonomous nodular function. Surgical resection, most commonly lobectomy, is the recommended approach for most autonomous nodules in children and adolescents.[46]

## Cysts

***Overview.*** Cysts are often thought to be due to benign degenerative thyroid diseases. However, as with thyroid nodules, there is a great heterogeneity in these disease processes in children ranging from benign pure cysts to malignant lesions.[70]

***Etiologies, Pathophysiology, and Clinical Presentation.*** True simple cysts lined by epithelium are rare. The majority of benign thyroid cysts are felt to be the result of cystic degeneration of a follicular adenoma, rather than a true cyst.[70] Hemorrhagic cysts are usually the result of bleeding into a follicular adenoma.

Thyroglossal duct cysts are the result of incomplete degeneration of the thyroglossal duct. The duct remnant, which is an epithelium-lined tract, has the potential for obstruction and forming a cyst because of retained secretions. They can occur anywhere along the path of migration of the thyroid gland from the foramen cecum at the tongue base to the anterior lower neck. Most thyroglossal duct cysts are asymptomatic until they become infected. Large cysts can be clinically detected as a palpable midline or near-midline neck mass that moves with swallowing or tongue protrusion.

***Imaging.*** Simple benign cysts are anechoic on US and hypodense on CT. On MRI, they will follow the signal characteristics of water, with low signal on T1-weighted and high signal on T2-weighted images. Hemorrhagic cysts will have high signal on T1-weighted images and will be hyperdense on CT.

Thyroglossal duct cysts are usually anechoic or hypoechoic on US. The cyst may have a high protein content that can result in some internal echoes, or may appear complex with septations and solid appearing areas during or after hemorrhage or infection. On CT, a noninfected thyroglossal duct cyst will be well circumscribed with a thin rim of enhancement. Thick peripheral enhancement suggests the cyst is infected. The attenuation of the cystic component varies on CT from hypodense (low protein content) to hyperdense (high protein content or hemorrhage). On MRI, thyroglossal duct cysts usually have low T1-weighted signal and high T2-weighted signal intensities. However, when the cyst is proteinaceous, it may be hyperintense on T1-weighted images. Thyroid scintigraphy is not necessary in the evaluation of thyroglossal duct cysts except when a thyroid gland cannot be identified. In this case, scintigraphy may be necessary to determine if the cyst contains the patient's only functional thyroid tissue.

***Treatment.*** Thyroid cysts and thyroglossal duct cysts may be excised for diagnosis or if they become secondarily infected, cause mass effect resulting in pain or dysphagia, or for cosmesis.

## Malignant Masses

***Overview.*** According to the Surveillance, Epidemiology, and End Results (SEER) program, 2.8% of all new cases of thyroid cancer in the United States are in people between the ages of 15 to 19,[75] and the incidence appears to be increasing.[76] Papillary thyroid carcinoma accounts for the majority all pediatric cases. Follicular thyroid carcinomas are uncommon, whereas medullary, anaplastic, and poorly differentiated carcinomas are almost unheard of in young children.[77] Other rare thyroid neoplasms include teratomas[78] and non-Hodgkin lymphoma.[79] Because most childhood thyroid malignancies are of the papillary type, the discussion in this section will mainly pertain to papillary carcinomas.

***Etiologies, Pathophysiology, and Clinical Presentation.*** Exposure to head and neck irradiation is associated with an increased risk for the development of thyroid carcinoma. Prior studies have shown a high rate of thyroid cancers in children who have received previous irradiation for treatment of benign conditions.[80] Children are more sensitive than adults to the carcinogenic effect of irradiation, perhaps because of their higher proliferative index of thyroid cells.[81]

Some thyroid cancers have a genetic predisposition and can be associated with certain syndromes. A positive family history is seen in medullary carcinoma[82] and in 3% of papillary carcinomas (chromosome 19p13.2).[83] A high incidence of papillary thyroid carcinomas is seen in familial adenomatosis polyposis coli[84] and Cowden disease.[85] Inherited medullary carcinoma is seen in multiple endocrine neoplasia type 2a and 2b (MEN 2a and 2b) or as part of familial medullary carcinoma.[86]

Thyroid carcinoma in children is biologically and clinically different from that seen in adults. The most common clinical presentation is a solitary thyroid nodule.[87] Other presenting manifestations such as dysphonia or dysphagia due to local invasion of surrounding structures are rare in children. Children present with cervical node involvement (60%) and pulmonary metastases (13%)[88] more often than adults.[89] They have more advanced disease and a higher rate of recurrence.[89] The pulmonary metastases are almost always functional and tend to be miliary.[90] Lymph nodes are the most common site of dissemination followed by the lungs. Bone metastases are rare.[90]

***Imaging.*** The imaging appearance of papillary carcinoma is variable. US is often used in the evaluation a thyroid nodule. The presence of indistinct margins, hypoechogenicity, predominantly solid composition, vascularity, absence of a hypoechoic halo, and calcifications on ultrasound are more suggestive of malignancy.[91] Ultrasound can also help guide the clinician while performing a FNA.[92] Although a solitary nodule is most common in

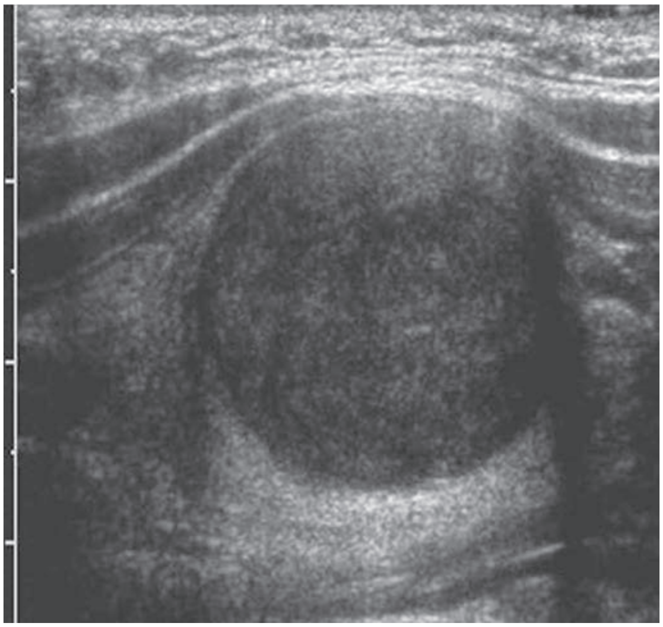

**e-Figure 17.5. Follicular adenoma.** Ultrasound demonstrates a well-circumscribed hypoechoic lesion.

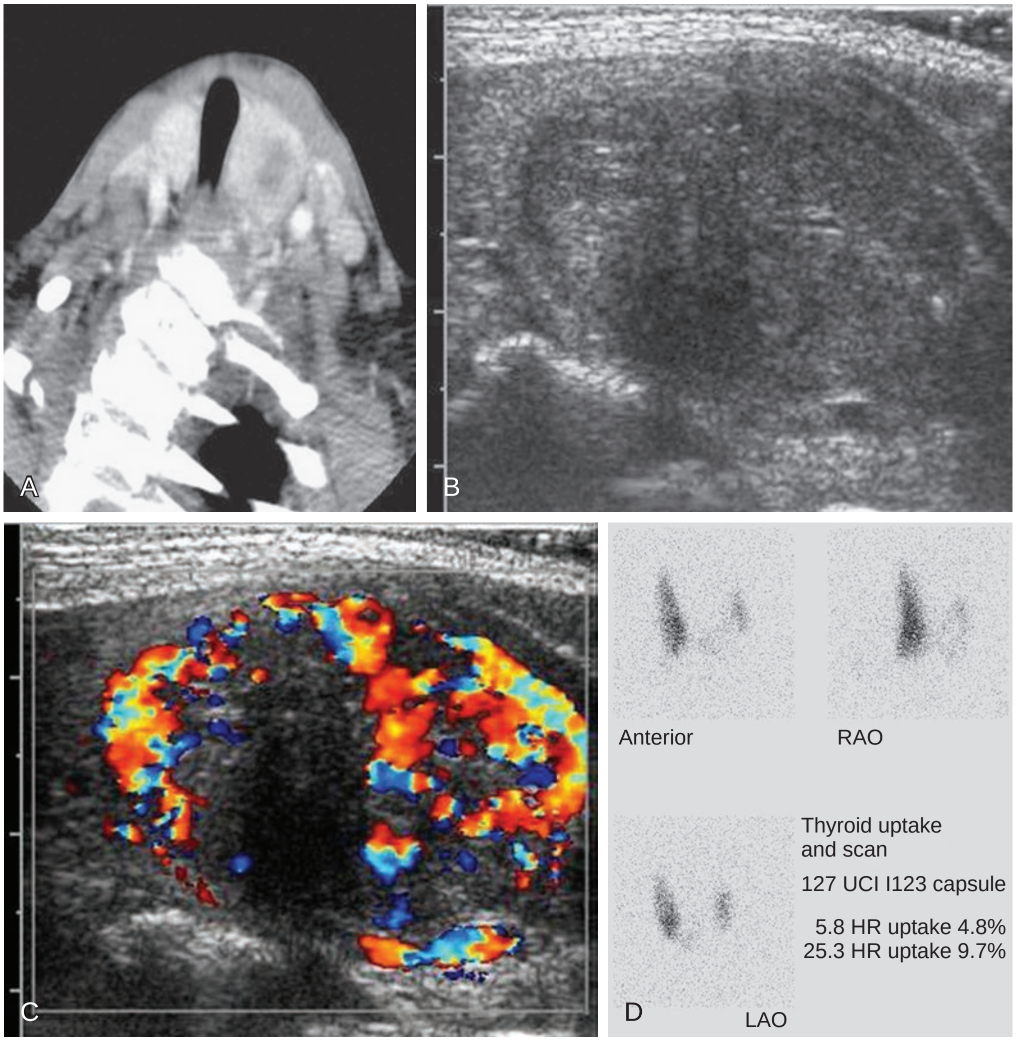

**Figure 17.6. Papillary carcinoma.** (A) Contrast-enhanced CT performed to assess for infection shows a low attenuation lesion in the left lobe of the thyroid gland. (B and C) Ultrasound images demonstrate a relatively heterogeneous nodule with punctate echogenicities and an eccentric round region of hypoechogenicity. Peripherally the lesion has increased vascularity. (D) The $^{123}$I uptake and scan demonstrates decreased uptake in the left gland and a focal "cold" lesion.

children, multifocal nodules, diffuse infiltration with heterogeneous hypodensity, or a normal appearing thyroid gland may be found.[22] Metastatic lymph nodes are usually enlarged, may be calcified, cystic, hemorrhagic, or contain colloid (Fig. 17.6).[93]

Thyroid scintigraphy is often used in the evaluation of a thyroid nodule. Cold nodules are suggestive of malignancy but can also be seen in benign lesions. Some very rare thyroid carcinomas can demonstrate increased radioisotope uptake on thyroid scintigraphy. There are also rare cases of a benign adenoma or carcinoma that have the ability to trap the radioisotope but do not organify the iodide resulting in a discordant nodule that is hot on $^{99m}$TcO4 studies but cold on radioiodine ($^{123}$I) studies.

A comprehensive neck ultrasound of all neck regions is required to optimize the preoperative surgical plan. FNA of suspicious lateral neck lymph nodes is recommended. Anatomic imaging by MRI or CT should be considered in patients with large or fixed thyroid masses, vocal cord paralysis, or bulky metastatic lymphadenopathy to optimize surgical planning.[46] MRI can be helpful in evaluating and delineating the extent of local invasion and lymph node metastases. Chest CT is more sensitive than radiography and can detect micronodular and interstitial patterns of metastases[94] much better than conventional chest radiographs (Fig. 17.7).

As with adults, cytopathology findings on pediatric thyroid FNA are categorized according to The Bethesda System for Reporting Thyroid Cytopathology.[95]

***Treatment.*** The ATA recommends a total thyroidectomy for the majority of pediatric patients. The rationale for this approach is based on multiple studies showing an increased incidence of bilateral and multi-focal disease. Bilateral lobar resection compared with lobectomy has been shown to decrease the long-term risk for persistent or recurrent disease.[46,96–98] Thyroidectomy also enables the use of thyroglobulin levels and whole body radioiodine scans for monitoring disease persistence and recurrence.

Central neck dissection is recommended for children with malignant cytology and evidence of gross extrathyroidal invasion and/or locoregional metastasis on preoperative staging or intraoperative findings. For patients with no clinical evidence of gross extrathyroidal invasion and/or locoregional metastasis, prophylactic central neck dissection may be selectively considered based upon tumor focality and size and the experience of the surgeon. For patients with unifocal disease, ipsilateral central neck dissection,

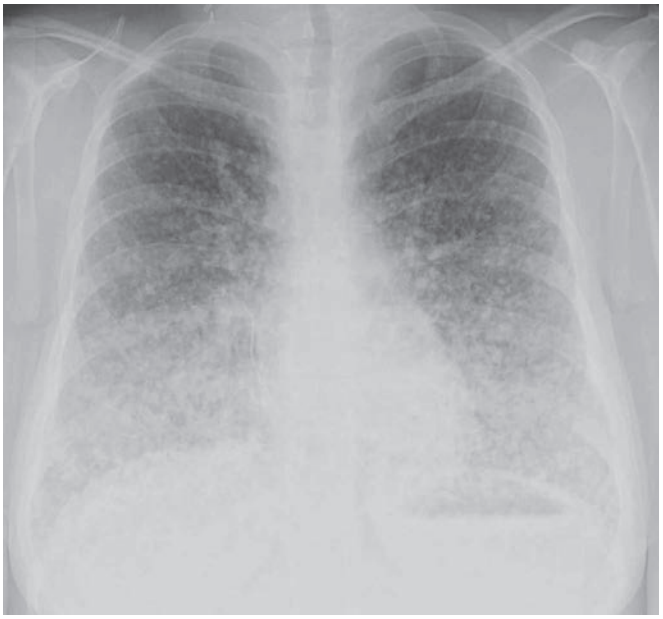

**Figure 17.7. Pulmonary metastases from papillary thyroid carcinoma.** Chest radiograph shows innumerable diffuse small pulmonary nodules (miliary disease).

with pursuit of contralateral central neck dissection based on intraoperative findings, may help balance the risks and benefits. The ATA also recommends compartment-oriented lymph node resection. "Berry picking" and attempting to use palpation to determine if metastatic disease is present in a lymph node are not recommended.[46]

The ATA recommends pediatric thyroid surgery to be performed in a hospital with the full spectrum of pediatric specialty care, to include, but not be limited to: endocrinology, radiology (ultrasound and anatomic imaging), nuclear medicine, anesthesia, a high volume thyroid surgeon, and intensive care. The surgery should ideally be performed by an experienced surgeon who performs at least 30 or more cervical endocrine procedures annually.[46]

Postoperative staging is usually performed within 12 weeks after surgery. ATA Pediatric classified Low-Risk patients may be initially assessed and followed with a TSH-suppressed thyroglobulin (Tg) alone. In contrast, a TSH-stimulated Tg and a diagnostic whole body $^{123}$I scan is typically recommended to assess for evidence of persistent disease in ATA classified Pediatric Intermediate- and High-Risk patients. Additional imaging, to include neck ultrasound and/or hybrid imaging using SPECT/CT, may be used conjunctively to more accurately define the anatomic location of radioactive iodine uptake noted on a whole body scan.[46] Although $^{131}$I can be used, $^{123}$I should be used whenever possible for whole body scans.[99–101]

$^{131}$I is indicated for treatment of iodine-avid persistent locoregional or nodal disease that cannot be resected, as well as known or presumed iodine-avid distant metastases. For patients with persistent disease after $^{131}$I administration, the decision to pursue additional $^{131}$I therapy should be individualized according to clinical data and previous response. The potential risks and benefits must be weighed on an individual basis.[46]

The uptake of radioiodine is dependent on TSH stimulation of thyroid tissue and carcinoma tissue. The TSH level should be greater than 30 uU/mL for optimum radioiodine uptake. A diagnostic scan followed by ablation is performed 6 weeks after thyroidectomy. Thyroid hormone medications must be withheld for a sufficient time to permit an adequate rise in the TSH level. Additionally, the patient should be placed on a low iodine diet for 2 weeks before the scan, to increase tissue avidity for iodine.[46,90] $T_3$ has a short half-life and can be given until 2 weeks before the scan.[94]

The normal thyroid remnant tissue is more efficient than the carcinoma tissue at concentrating radioiodine. As a result, the first diagnostic whole body radioiodine scan done after thyroidectomy might not detect residual tumor or metastases. These may show up on the scan obtained after radioablation, as much higher doses of radioiodine are used for ablation.

The maximally safe radioiodine dose in children can be calculated based on quantitative blood and whole body dosimetry, and the minimally effective dose can be calculated based on lesion dosimetry.[102] Because this is complicated, most centers use a fixed dose of 30 mCi.[103] Rarely, a second treatment may be needed to completely ablate the remnant. A much higher dose of up to 175 to 200 mCi is required to ablate pulmonary metastases.[104] It is customary to obtain a scan 4 to 7 days after radioablation, which will demonstrate avid uptake in the thyroid remnant and may show metastases not apparent on the previous diagnostic radioiodine scan.[94]

Based on the belief that thyroid carcinoma cells are dependent on TSH stimulation for growth, TSH suppressive therapy with thyroxine is also used to suppress tumor growth. The optimum TSH level that needs to be maintained is not known. Initially, TSH levels of less than 0.1 uU/mL are recommended, but once remission has been achieved, levels of less than 0.5 uU/mL may be acceptable.[96]

## PARATHYROID GLANDS

### Embryology

The parathyroid glands are endodermal in origin and develop from the third and fourth pharyngeal pouches. There are usually four glands (two superior and two inferior); however, supernumerary and less than four glands may occur.

The third pharyngeal pouches expand into solid dorsal bulbar portions and hollow ventral elongate portions. During the fifth week, each cranial dorsal portion begins to differentiate into the inferior parathyroid glands. The caudal ventral portions migrate medially and eventually meet and fuse to form the thymus. As both primitive parathyroid glands lose their connection with the pharyngeal wall, they descend with the thymus. This migration of the inferior parathyroid glands with the thymus accounts for their lower position than the superior parathyroid glands that are derived from the fourth pharyngeal pouches.[105] The glands are usually distributed evenly between the lower pole of the thyroid gland and isthmus, but can be found anywhere along their course of descent.[106]

As with the third pharyngeal pouches, the fourth pharyngeal pouches also expand into solid dorsal bulbar portions and ventral elongate portions. During the fifth week each dorsal portion begins to differentiate into the superior parathyroid glands. As they lose their attachment with the pharyngeal wall, they attach to the posterior surface of the descending thyroid. They have a much shorter migration distance compared with the inferior parathyroid glands, which accounts for their more predictable location. Generally, the superior parathyroid glands are located posterior at the level of the upper two-thirds of the thyroid gland, approximately 1 cm above the crossing point of the recurrent laryngeal nerve and inferior thyroid artery.[107] The ventral portions of the fourth pharyngeal pouches develop into the ultimobranchial bodies, which fuse with the developing thyroid gland.

The epithelium of the dorsal parts of the third and fourth pouches proliferates during the fifth week and forms small nodules on the dorsal aspect of each pouch. Vascular mesenchyme soon grows into these nodules, forming a capillary network. The chief cells differentiate during the embryonic period and are believed to become functional in the fetus. The oxyphil cells do not differentiate until about 5 to 7 years after birth.[108]

## Physiology

The function of the parathyroid glands is to produce parathyroid hormone (PTH), which is one of two major hormones involved in calcium and phosphate homeostasis. Chief cells within the parathyroid glands produce PTH. Oxyphil cells may also secret PTH, but their true function is unknown. PTH regulates serum-ionized calcium by maintaining concentrations in a narrow range through stimulation of renal tubular calcium reabsorption and bone resorption.[108] PTH also stimulates the conversion of calcidiol (25-hydroxyvitamin D) to calcitriol (1,25-dihydroxyvitamin $D_3$) in renal tubular cells, thereby stimulating intestinal calcium absorption. PTH secretion is, in turn, regulated by serum-ionized calcium acting via a calcium-sensing receptor (CaSR) on the surface of parathyroid cells.[109] When the CaSR is activated by a small increase in serum-ionized calcium, PTH secretion is inhibited. Conversely, the effect of deactivation of the receptor by a small decrease in serum-ionized calcium stimulates PTH secretion.

## Anatomy

The paired superior parathyroid glands are fairly constant in their position near the upper surface of the thyroid lobes. The inferior parathyroid glands are found in close proximity to the lower pole of the thyroid gland. The glands however can be ectopic. Ectopic superior parathyroid glands can be found at the level of the upper pole of the thyroid gland (2%) and above the upper pole (0.8%). Other ectopic positions of the superior parathyroid glands such as in the posterior neck, retropharyngeal, retroesophageal, or intrathyroid regions, glands are even rarer (1% total).[106,107] Ectopic inferior parathyroid glands can be found anywhere along their area of descent up to the superior border of the pericardium.[106] Supernumerary glands, when present, are often found in the mediastinum associated with the thymus.

The parathyroid glands are encapsulated and well vascularized. The glands are composed of chief cells and oxyphil cells embedded within a fibrous capsule intermixed with adipose tissue. The vascular supply of the parathyroid glands is predominately the inferior thyroid artery,[110] although the superior parathyroid glands can also be supplied by the superior thyroid artery.[107,111] The venous drainage is predominately to the inferior thyroid veins.[112]

The parathyroids are meagerly supplied with vasomotor nerve fibers from either the superior, middle, or inferior cervical sympathetic ganglia.[113,114]

## Normal Findings

Normal glands are difficult to visualize because of their small size (less than 5 mm in length). On ultrasound, a normal parathyroid gland will have an echotexture similar to the adjacent thyroid parenchyma, which adds to the difficulty in identifying the normal glands.[25]

## Hyperparathyroidism

***Overview.*** Primary hyperparathyroidism is rare in children.[115,116] The exact incidence is unknown but is estimated to be 2 to 5 in 100,000.[115] Primary hyperparathyroidism is caused by overproduction of PTH by a pathologically changed parathyroid gland.

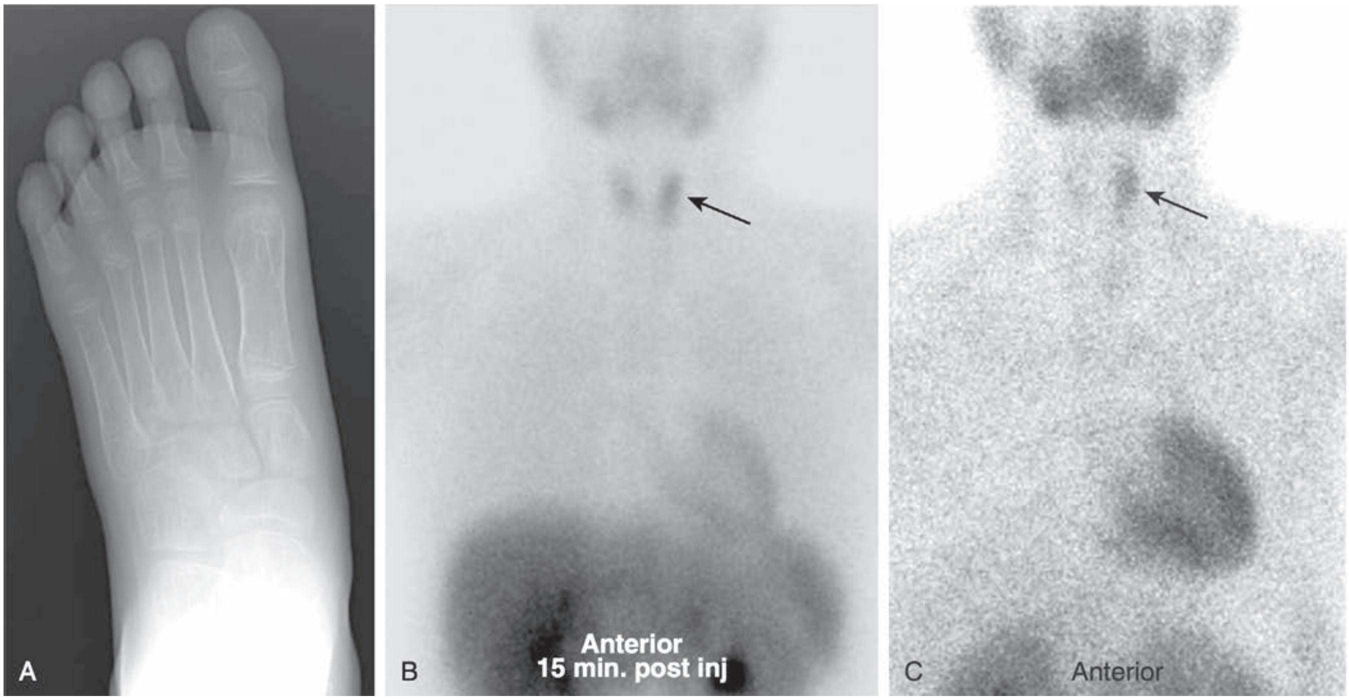

**Figure 17.8. Parathyroid adenoma in a patient presenting with foot pain.** (A) Radiograph of the foot demonstrates diffuse severe osteopenia. Laboratory studies revealed marked hypercalcemia and elevated parathyroid hormone. Initial ultrasonography failed to identify an adenoma. (B) Nuclear scintigraphy shows increased uptake is noted in the left lobe of the thyroid gland *(arrow)* on the initial 99mTc-sestamibi images. (C) Incomplete washout of the radiopharmaceutical is seen on 2-hour delayed images *(arrow)*, suggesting a parathyroid adenoma. The lesion was surgically excised, and the patient’s symptoms resolved.

***Etiologies, Pathophysiology, and Clinical Presentation.*** Primary hyperparathyroidism in children is most often caused by a parathyroid adenoma.[115–117] Multiple endocrine neoplasia (MEN)-I or -II syndromes or familial non-MEN hyperparathyroidism have also been documented and can constitute as much as 30% to 50% of pediatric hyperparathyroid disease.[117–119]

The parathyroid gland(s) becomes overactive and secretes excess amounts of PTH leading to an increase in serum calcium levels. PTH stimulates calcium and phosphate mobilization through osteoclastic bone resorption. In the kidney, PTH stimulates the synthesis of calcitriol, decreases urinary calcium excretion, and increases phosphate excretion. PTH enhances the gut absorption of minerals directly and through calcitriol.

The symptoms of hyperparathyroidism can be nonspecific and include joint aches, fatigue, weakness, loss of appetite, depression, and difficulty concentrating. The commonest clinical signs in children with primary hyperparathyroidism have been reported to be skeletal (bone resorption) and renal disease (hematuria, nephrocalcinosis, or nephrolithiasis).[118]

***Imaging.*** Imaging is rarely used to diagnose hyperparathyroidism. Evaluation of serum calcium and PTH levels is diagnostic. Occasionally, a patient may have an elevated calcium level and a normal or minimally elevated PTH level. Because PTH should normally be low when calcium is elevated, a minimally elevated PTH is considered abnormal and indicates hyperparathyroidism.

Imaging can help in localization for surgical planning. US is a reliable noninvasive method for confirming parathyroid pathology in children preoperatively. A parathyroid adenoma will appear well defined and hypoechoic on ultrasound, although differentiating an adenoma from hyperplasia or a lymph node can often be difficult.

Other reliable studies include $^{99m}$TcO4/$^{201}$Tl subtraction imaging and $^{99m}$Tc-sestamibi scans, which have been reported to have a sensitivity of 67% to 80% for localizing adenomas and a sensitivity of 45% to 60% for hyperplasia in adults; however, data in children are not well established (Fig. 17.8).[120,121]

The most specific radiographic manifestation of hyperparathyroidism is subperiosteal bone resorption. Brown tumors (osteoclastomas) are rare sequelae of hyperparathyroidism occurring in fewer than 5% of all cases.[122] The incidence in pediatric patients with hyperthyroidism is unknown. The lesions localize in areas of intense bone resorption, and the bone defect becomes filled with fibroblastic tissue.

***Treatment.*** Regardless of etiology, parathyroid resection is the treatment of choice for hyperparathyroidism in children.[118,121]

## KEY POINTS

- Ultrasound is the primary imaging modality for evaluating the thyroid and parathyroid glands, and for guiding aspiration and biopsy.
- The majority of cases of congenital hypothyroidism are caused by thyroid gland dysgenesis.
- Chronic autoimmune thyroiditis (Hashimoto thyroiditis) is the most common cause of acquired hypothyroidism in children.
- Graves disease is the most common cause of hyperthyroidism in children.
- Thyroid nodules are less common in children than in adults, but have a higher incidence of malignancy.

## SUGGESTED READINGS

Braverman LE, Utiger RD. *Werner and Ingbar's The Thyroid A Fundamental and Clinical Text*. 9th ed. Philadelphia, PA: Lippincott Williams & Wilkins; 2005

Francis GL, Waguespack SG, Bauer AJ, et al. Management guidelines for children with thyroid nodules and differentiated thyroid cancer. *Thyroid*. 2015;25(7):716-759.

Parekh C, Jackson HA. Thyroid cancer in children. In: Carroll WL, Finlay JL, eds. *Cancer in Children and Adolescents*. Sudbury, MA: Jones and Bartlett; 2010:459–466.

Smith JR, Oates ME. Radionuclide imaging of the parathyroid glands: patterns, pearls, and pitfalls. *Radiographics*. 2004;24(4):1101–1115.

Sofferman RA, Ahuja AT. *Ultrasound of the Thyroid and Parathyroid Glands*. New York, NY: Springer; 2012.

## REFERENCES

Full references for this chapter can be found on www.expertconsult.com.

## REFERENCES

1. Manley NR, Cappecci MR. Hox group 3 paralogs regulate the development and migration of the thymus, thyroid, and parathyroid. *Dev Biol*. 1998;195(1):1–15.
2. De Felice M, De Lauro R. Thyroid development and its disorders: genetics and molecular mechanisms. *Endocr Rev*. 2004;25(5):722–746.
3. Santisteban P. Development and anatomy of the hypothalamic-pituitary-thyroid axis. In: Braverman LE, Utiger RD, eds. *Werner and Ingbar's The Thyroid A Fundamental and Clinical Text*. 9th ed. Philadelphia, PA: Lippincott Williams & Wilkins; 2005:8–25.
4. VanVliet G. Development of the thyroid gland: lessons from congenitally hypothyroid mice and men. *Clin Genet*. 2003;63:445–455.
5. Boyd JD. *Development of the thyroid and parathyroid glands and the thymus. Lecture delivered at the Royal College of Surgeons of England. 30th June, 1950*: 455-471.
6. Jinkins JR. *Atlas of Neuroradiologic Embryology, Anatomy, and Variants*. Philadelphia, PA: Lippincott Williams & Wilkins; 2000:52–53.
7. Moore KL. *The Developing Human Clinically Oriented Embryology*. Philadelphia, PA: W. B. Saunders Company; 1973:146.
8. Braun EM, Windisch G, Wolf G, et al. The pyramidal lobe: clinical anatomy and its importance in thyroid surgery. *Surg Radiol Anat*. 2007;29:21–27.
9. Stone JA, Figuerora RE. Embryology and anatomy of the neck. *Neuroimaging Clin N Am*. 2000;10:55–73.
10. LeDouarin N, Fontaine J, LeLievre C. New studies on neural crest origin of the avian ultimobranchial glandular cells. *Histochemistry*. 1974;38(4):297–305.
11. Harach HR. Solid cell nests of the thyroid. *J Pathol*. 1988;155(3):191–200.
12. Jackson I. Thyrotropin-releasing hormone. *N Engl J Med*. 1982; 306:145–155.
13. Gershengorn MC. Thyrotropin releasing hormone. A review of the mechanisms of acute stimulation of pituitary hormone release. *Mol Cell Biochemistry*. 1982;45(2):163–179.
14. O'Leary R, O'Connor B. Thyrotropin-releasing hormone. *J Neurochem*. 1995;65(3):953–963.
15. Harris ARC, Christianson D, Smith MS, et al. The physiological role of thyrotropin-releasing hormone in the regulation of thyroid-stimulating hormone and prolactin secretion in the rat. *J Clin Invest*. 1978;61(2):441–448.
16. Nikrodhanond AA, Ortiga-Carvalho TM, Shibusawa N, et al. Dominant role of thyrotropin-releasing hormone in the hypothalamic-pituitary-thyroid axis. *J Bio Chem*. 2006;281(8):5000–5007.
17. Alexander WD, Wolff I. Cation requirements for iodide transport. *Arch Biochem Biophys*. 1964;106:525–528.
18. Bagchi N, Fawcett DM. Role of sodium ion in active transport of iodide by cultured thyroid cells. *Biochem Biophys Acta*. 1973;318:235–251.
19. O'Neill B, Magnolato D, Semenza G. The electrogenic, $Na^+$-dependent $I^-$ transport system in plasma membrane vesicles from thyroid glands. *Biochim Biophys Acta*. 1987;896:263–274.
20. Weiss SJ, Philip NJ, Ambesi-Impiombato FS, et al. Thyrotropin-stimulated iodide transport mediated by adenosine 3′,5′-monophosphate and dependent on protein synthesis. *Endocrinology*. 1984;114: 1099–1107.
21. De la Vieja A, Dohan O, Levy O, et al. Molecular analysis of the sodium/iodide symporter: impact on thyroid and extrathyroid pathophysiology. *Physiol Rev*. 2000;80(3):1083–1105.
22. Loevner LA. Thyroid and parathyroid glands: anatomy and pathology. In: Som PM, Curtin HD, eds. *Head and Neck Imaging*. 4th ed. St. Louis MI: Mosby; 2003:2134–2171.
23. James EM, Charboneau JW. High-frequency (10 MHz) thyroid ultrasonography. *Semin Ultrasound CT MR*. 1985;6:294–309.
24. Solbiati L, Cioffi V. Ballarati E. Ultrasonography of the neck. *Radiol Clin North Am*. 1992;30:941–954.
25. Siegel MJ. Face and neck. In: Siegel MJ, ed. *Pediatric Sonography*. 3rd ed. Philadelphia, PA: Lippincott Williams & Wilkins; 2002: 123–166.
26. Balon HR, Silberstein EB, Meier DA, et al. *Society of Nuclear Medicine Procedure Guideline for Thyroid Scintigraphy*. 2006. V3.0.
27. Balon HR, Silberstein EB, Meier DA, et al. *Society of Nuclear Medicine Procedure Guideline for Thyroid Uptake Measurement*. 2006. V3.0.
28. Harris KB, Pass KA. Increase in congenital hypothyroidism in New York State and in the United States. *Mol Genet Metab*. 2007;91(3):268–277.
29. Hinton CF, Harris KB, et al. Trends in incidence rates of congenital hypothyroidism related to select demographic factors: Data from the United States, California, Massachusetts, New York, and Texas. *Pediatrics*. 2010;125:S37–S40.
30. American Academy of Pediatrics, American Thyroid Association and Lawson Wilkins Pediatric Endocrine Society. Update of newborn screening and therapy for congenital hypothyroidism. *Pediatrics*. 2006;117:2290–2303.
31. Chang YW, Lee DH, Hong YH, et al. Congenital hypothyroidism: analysis of discordant US and scintigraphic findings. *Radiology*. 2011;258(3):872–879.
32. el-Deskouki M, al-Juaryyan N, al-Nuaim A, et al. Thyroid scintigraphy and perchlorate discharge test in the diagnosis of congenital hypothyroidism. *Eur J Nucl Med*. 1995;22(9):1005–1008.
33. Frieta JE, Gross MD, Sarkar SD. Laboratory (in vitro) assessment of thyroid function. In: Martin WH, Sandler MP, eds. *Diagnostic Nuclear Medicine*. 4th ed. Phildelphia, PA: Lippincott Williams & Wilkins; 2003:611.
34. Wells RG, Sty JR. Thyroid scintigraphy. In: Miller JH, Gelfand MJ, eds. *Pediatric Nuclear Imaging*. 1st ed. Philadelphia, PA: W.B. Saunders Company; 1994:47.
35. De Vries L, Bulvik S, Phillip M. Chronic autoimmune thyroiditis in children and adolescents: at presentation and during long-term follow up. *Arch Dis Child*. 2009;94(1):33–37.
36. Rallison ML, Dobyns BM, Meikle AW, et al. Natural history of thyroid abnormalities: prevalence, incidence, and regression of thyroid diseases in adolescents and young adults. *Am J Med*. 1991;91(4):363–370. Erratum in: *Am J Med*. 1992;92(5):582.
37. Demirbilek H, Kandemir N, Gonc EN, et al. Hashimoto's thyroiditis in children and adolescents: a retrospective study on clinical, epidemiological and laboratory properties of the disease. *J Pediatr Endocrinol Metab*. 2007;20(11):1199–1205.
38. Chistiakov DA. Immunogenetics of Hashimoto's thyroiditis. *J Autoimmune Dis*. 2005;2:1–21.
39. Vaidya B, Kendall-Taylor P, Pearce SHS. The genetics of autoimmune thyroid disease. *J Clin Endocrinol Metab*. 2002;87(12):5385–5397.
40. Phillips D, McLachlan S, Stephenson A, et al. Autosomal dominant transmission of autoantibodies to thyroglobulin and thyroid peroxidase. *J Clin Endocrinol Metab*. 1990;70:742–746.
41. Jenkins RC, Weetman AP. Disease associations with autoimmune thyroid disease. *Thyroid*. 2002;12:977–988.
42. Betterle C, Zanchetta R. Update on autoimmune polyendocrine syndromes (APS). *Acta Biomed Ateneo Parmense*. 2003;74:9–33.
43. Hollowell JG, Staehling NW, Flanders WD, et al. T(4), and thyroid antibodies in the United States population (1988 to 1994): National Health and Nutrition Examination Survey (NHANES III). *J Clin Endocrinol Metab*. 2002;87(2):489–499.
44. Ozer G, Yuksel B, Kozanoglu M, et al. Growth and development of 280 hypothyroidic patients at diagnosis. *Acta Paediatr Jpn*. 1995;37(2):145–149.
45. Intezno CM, Capuzzi DM, Jabbour S, et al. Scintigraphic features of autoimmune thyroiditis. *Radiographics*. 2001;21:957–964.
46. Francis GL, Waguespack SG, Bauer AJ, et al. Management guidelines for children with thyroid nodules and differentiated thyroid cancer. *Thyroid*. 2015;25(7):716–759.
47. Emiliano AB, Governale L, Parks M, et al. Shifts in propylthiouracil and methimazole prescribing practices: antithyroid drug use in the United States from 1991 to 2008. *J Clin Endocrinol Metab*. 2010;95(5):2227–2233.
48. Nordyke RA, Gilbert FI Jr, Harada AS. Graves' disease. Influence of age on clinical findings. *Arch Intern Med*. 1988;148:626–631.
49. Khoo TK, Bahn RS. Pathogenesis of Graves' ophthalmopathy: the role of autoantibodies. *Thyroid*. 2007;17(10):1013–1018.
50. Bahn RS, Heufelder AE. Pathogenesis of Graves' ophthalmopathy. *N Engl J Med*. 1993;329:1468–1475.
51. Huang SA. Thyroid. In: Treves ST, ed. *Pediatric Nuclear Medicine/PET*. 3rd ed. New York, NY: Springer; 2007:57–71.
52. Refetoff S. Resistance to thyroid hormone: an historical overview. *Thyroid*. 1994;4(3):345–349.
53. Cooper DS. Hyperthyroidism. *Lancet*. 2003;362:459–468.
54. Cooper DS. Antithyroid drugs. *N Engl J Med*. 2005;352:905–917.
55. Cooper DS, Saxe VC, Meskell M, et al. Acute effects of propylthiouracil (PTU) on thyroidal iodide organification and peripheral iodothyronine deiodination: correlation with serum PTU levels measured by radioimmunoassay. *J Clin Endocrinol Metab*. 1982;54: 101–107.

56. Abuid J, Larsen PR. Triiodothyronine and thyroxine in hyperthyroidism: comparison of the acute changes during therapy with antithyroid agents. *J Clin Invest*. 1974;54:201–208.
57. Rivkees SA, Sklar C, Freemark M. Clinical review 99: the management of Graves' disease in children, with special emphasis on radioiodine treatment. *J Clin Endocrinol Metab*. 1998;83:3767–3776.
58. Fahey FH, Treves ST, Adelstein SJ. Minimizing and communicating radiation risk in pediatric nuclear medicine. *J Nucl Med*. 2011;52(8):1240–1251.
59. Rivkees SA. The management of hyperthyroidism in children with emphasis on the use of radioactive iodine. *Pediatr Endocrinol Rev*. 2003;1(2):212–222.
60. Toohey RE, Stabin MG. *Comparative analysis of dosimetry parameters for nuclear medicine. ORISE Report 99-1064, 1999. Proc Sixth International Radiopharmaceutical Dosimetry Symposium*. Gatlinburg, TN: 1996:532–551.
61. Toohey RE, Stabin MG, Watson EE. The AAPM/RSNA physics tutorial for residents: internal radiation dosimetry: principles and applications. *Radiographics*. 2000;20:533–546.
62. Szabo SM, Allen DB. Thyroiditis. Differentiation of acute suppurative and subacute case report and review of the literature. *Clin Pediatr*. 1989;28(4):171–174.
63. Rich EJ, Mendelman PM. Acute suppurative thyroiditis in pediatric patients. *Pediatr Infect Dis J*. 1987;6(10):936–940.
64. Brook I. Microbiology and management of acute suppurative thyroiditis in children. *Int J Ped Otorhinolaryngol*. 2003;67(5):447–451.
65. Chi H, Lee YJ, Chiu NC, et al. Acute suppurative thyroiditis in children. *Pediatr Infect Dis J*. 2002;21(5):384–387.
66. Lucaya J, Berdon WE, Enriquez G, et al. Congenital pyriform sinus fistula: a cause of acute left-sided suppurative thyroiditis and neck abscess in children. *Pediatr Radio*. 1990;21(1):27–29.
67. Rallison ML, Dobyns BM, Keating FR Jr, et al. Thyroid nodularity in children. *JAMA*. 1975;233(10):1069–1072.
68. Niedziela M. Pathogenesis, diagnosis and management of thyroid nodules in children. *Endocr Relat Cancer*. 2006;13:427–453.
69. Yip FW, Reeve TS, Poole AG, et al. Thyroid nodules in childhood and adolescence. *Aust N Z J Surg*. 1994;64:676–678.
70. Yoskovitch A, Laberge J-M, Rodd C, et al. Cystic thyroid lesion in children. *J Pediatr Surg*. 1998;33:866–870.
71. Hung W, Anderson KD, Chandra RS, et al. Solitary thyroid nodules in 71 children and adolescents. *J Pediatric Surg*. 1992;27(11):1407–1409.
72. Ahmed S, Horton KM, Jeffrey BR, et al. Incidental thyroid nodules on chest CT: review of the literature and management suggestions. *AJR*. 2010;195(5):1066–1071.
73. Propper RA, Skolnick ML, Weinstein BJ, et al. The nonspecificity of the thyroid halo sign. *J Clin Ultrasound*. 1980;8(2):129–132.
74. Sidoti M, Marino G, Resemini E, et al. The rational use of fine needle aspiration biopsy (FNAB) in diagnosing thyroid nodules. *Minerva Endocrinol*. 2006;31(2):159–172.
75. Howlader N, Noone AM, Krapcho M, et al, eds. *SEER Cancer Statistics Review, 1975-2013*. Bethesda, MD: National Cancer Institute; 2016. http://seer.cancer.gov/csr/1975_2013/. based on November 2015 SEER data submission, posted to the SEER web site.
76. Vergamini LB, Frazer AL, Abrantes FL, et al. Increase in the incidence of differentiated thyroid carcinoma in children, adolescents, and young adults: a population-based study. *J Pediatr*. 2014;164:1481–1485.
77. *Carcinomas and other malignant epithelial neoplasms ICCCC xi Leslie Bernstein, James C Gurney. Cancer Incidence and Survival among Children and Adolescents: United States SEER Program*, 1975-1995.
78. Thompson LD, Rosai J, Heffess CS. Primary thyroid teratomas: a clinicopathologic study of 30 cases. *Cancer*. 2000;88(5):1149–1158.
79. Hart S, Horsman JM, Radstone CR, et al. Localised extranodal lymphoma of the head and neck: the Sheffield Lymphoma Group experience (1971-2000). *Clin Oncol (R Coll Radiol)*. 2004;16(3):186–192.
80. Winship T, Rosvoll R. Thyroid carcinoma in children: final report of a 20-year study. *Clin Proc Child Hosp DC*. 1970;26:11.
81. Williams ED. Biological mechanisms underlying radiation induction of thyroid carcinoma. In: Thomas G, Karaoglou A, Williams ED, eds. *Radiation and Thyroid Cancer*. Singapore: World Scientific; 1999:177–188.
82. Chi DD, Moley JF. Medullary thyroid carcinoma: genetic advances, treatment recommendations, and the approach to the patient with persistent hypercalcitoninemia. *Surg Oncol Clin N Am*. 1998;7(4):681–706.
83. Canzian F, Amati P, Harach HR, et al. A gene predisposing to familial thyroid tumors with cell oxyphilia maps to chromosome 19p13.2. *Am J Hum Genet*. 1998;63(6):1743–1748.
84. Herraiz M, Barbesino G, Faquin W, et al. Prevalence of thyroid cancer in familial adenomatous polyposis syndrome and the role of screening ultrasound examinations. *Clin Gastroenterol Hepatol*. 2007;5(3):367–373.
85. Haggitt RC, Reid BJ. Hereditary gastrointestinal polyposis syndromes. *Am J Surg Pathol*. 1986;10(12):871–887.
86. Marini F, Falchetti A, Del Monte F, et al. Multiple endocrine neoplasia type 2. *Orphanet J Rare Dis*. 2006;1:45.
87. Harness JK. Childhood thyroid carcinoma. In: Clark OH, Duh Q-Y, eds. *Textbook of Endocrine Surgery*. 2nd ed. Philadelphia, PA: Elsevier Saunders; 1997:75–81.
88. Grigsby PW, Gal-or A, Michalski JM, et al. Childhood and adolescent thyroid carcinoma. *Cancer*. 2002;95(4):724–729.
89. Zimmerman D, Hay ID, Gough IR, et al. Papillary thyroid carcinoma in children and adults: long-term follow-up of 1039 patients conservatively treated at one institution during three decades. *Surgery*. 1988;104(6):1157–1166.
90. Jarzab B, Handkiewicz-Junak D, Wloch J. Juvenile differentiated thyroid carcinoma and the role of radioiodine in its treatment: a qualitative review. *Endocr Relat Cancer*. 2005;12(4):773–803.
91. Frates MC, Benson CB, Charboneau JW, et al. Management of thyroid nodules detected at US: Society of Radiologists in Ultrasound consensus conference statement. *Ultrasound Q*. 2006;22(4):231–238, discussion 239–240.
92. Dinauer C, Francis GL. Thyroid cancer in children. *Endocrinol Metab Clin North Am*. 2007;36(3):779–806, vii.
93. Som PM, Brandwin M, Lidov M, et al. The varied appearance of papillary carcinoma cervical nodal disease: CT and MR findings. *AJNR Am J Neuroradiol*. 1994;15:1129–1138.
94. Piekarski JD, Schlumberger M, Leclere J, et al. Chest computed tomography (CT) in patients with micronodular lung metastases of differentiated thyroid carcinoma. *Int J Radiat Oncol Biol Phys*. 1985;11(5):1023–1027.
95. Cibas ES, Ali SZ. The Bethesda system for reporting thyroid cytopathology. *Thyroid*. 2009;19:1159–1165.
96. Hung W, Sarlis NJ. Current controversies in the management of pediatric patients with well-differentiated non-medullary thyroid cancer: a review. *Thyroid*. 2002;12(8):683–702.
97. Harness JK, Thompson NW, McLeod MK, et al. Differentiated thyroid carcinoma in children and adolescents. *World J Surg*. 1992;16(4):547–553, discussion 553–554.
98. La Quaglia MP, Black T, Holcomb GW 3rd, et al. Differentiated thyroid cancer: clinical characteristics, treatment, and outcome in patients under 21 years of age who present with distant metastases. A report from the Surgical Discipline Committee of the Children's Cancer Group. *J Pediatr Surg*. 2000;35(6):955–959.
99. Sisson JC. Selection of the optimal scanning agent for thyroid cancer. *Thyroid*. 1997;7(2):295–302.
100. Muratet JP, Daver A, Minier JF, et al. Influence of scanning doses of iodine-131 on subsequent first ablative treatment outcome in patients operated on for differentiated thyroid carcinoma. *J Nucl Med*. 1998;39(9):1546–1550.
101. Silberstein EB. Comparison of outcomes after (123) I *versus* (131) I pre-ablation imaging before radioiodine ablation in differentiated thyroid carcinoma. *J Nucl Med*. 2007;48(7):1043–1046.
102. Maxon HR. Quantitative radioiodine therapy in the treatment of differentiated thyroid cancer. *Q J Nucl Med*. 1999;43(4):313–323.
103. Yeh SD, La Quaglia MP. 131-I therapy for pediatric thyroid cancer. *Semin Pediatr Surg*. 1997;6(3):128–133.
104. Beierwaltes WH, Nishiyama RH, Thompson NW, et al. Survival time and "cure" in papillary and follicular thyroid carcinoma with distant metastases: statistics following University of Michigan therapy. *J Nucl Med*. 1982;23(7):561–568.
105. Moore KL. *The Developing Human Clinically Oriented Embryology*. Philadelphia, PA: W. B. Saunders Company; 1973:144–145.
106. Wang Y, Ji Q, Li D, et al. Preoperative CT diagnosis of right nonrecurrent inferior laryngeal nerve. *Head Neck*. 2010;33:232–238.
107. Akerstrom G, Malmaeus J, Bergstrom R. Surgical anatomy of human parathyroid glands. *Surgery*. 1984;95:14–21.
108. Brown EM. Four-parameter model of the sigmoidal relationship between parathyroid hormone release and extracellular calcium concentration in normal and abnormal parathyroid tissue. *J Clin Endocrinol Metab*. 1983;56(3):572–581.
109. Brown EM, Pollak M, Seidman CE, et al. Calcium-ion-sensing cell-surface receptors. *N Engl J Med*. 1995;333(4):234.

110. Alveryd A. Parathyroid glands in thyroid surgery. I. Anatomy of parathyroid glands. II. Postoperative hypoparathyroidism—Identification and autotransplantation of parathyroid glands. *Acta Chir Scand*. 1968;389:1–120.
111. Nobori M, Saiki S, Tanaka N, et al. Blood supply of the parathyroid gland from the superior thyroid artery. *Surgery*. 1994;115(4):417–423.
112. Shimkin PM, Doppman JL, Pearson KD, et al. Anatomic considerations in parathyroid venous sampling. *AJR*. 1973;118(3):654–662.
113. Rhinehart DA. The nerve of the thyroid and parathyroid bodies. *Am J Anat*. 1912;13:91–99.
114. Raybuck HE. The innervation of the parathyroid glands. *Anat Rec*. 1952;112(1):117–123.
115. Li CC, Yang C, Wang S, et al. A 10-year retrospective study of primary hyperparathyroidism in children. *Exp Clin Endocrinol Diabetes*. 2012;120(4):229–233.
116. Kollars J, Zarroug AE, van Heerden J, et al. Primary hyperparathyroidism in pediatric patients. *Pediatrics*. 2005;114(4):974–980.
117. Huang CB, Huang SC, Chou FF, et al. Primary hyperparathyroidism in children: report of a case and a brief review of the literature. *J Formos Med Assoc*. 1993;92:1095–1098.
118. Allo M, Thompson NW, Harness JK, et al. Primary hyperparathyroidism in children, adolescents, and young adults. *World J Surg*. 1982;6:771–776.
119. Marx SJ. New insights into primary hyperparathyroidism. *Hosp Pract (Off Ed)*. 1984;19:55–63.
120. Heller KS, Attie JN, Dubner S. Parathyroid localization: inability to predict multiple gland involvement. *Am J Surg*. 1993;166:357–359.
121. Lee VS, Wilkinson RH Jr, Leight GS Jr, et al. Hyperparathyroidism in high-risk surgical patients: evaluation with double-phase technetium-99m sestamibi imaging. *Radiology*. 1995;197:627–633.
122. Horowitz M, Wishart JM, Need AG, et al. Primary hyperparathyroidism. *Clin Geriatr Med*. 1994;10:757–775.

# SECTION 3 Neuroradiology

## PART 1 Cranium and Face

# 18 Embryology, Anatomy, Normal Findings, and Imaging Techniques

Thomas L. Slovis, Kristin A. Fickenscher, and Andrew Johansen

## ANATOMY OF THE SKULL

The skull is divided into three portions: the neurocranium, the face, and the base. The neurocranium is composed of the membranous portions of the occipital, parietal, frontal, and temporal bones, and is bounded inferiorly by the base of the skull, which includes the sphenoid and ethmoid bones. The face is between the forehead and chin.

Routine skull radiographs include the frontal projection, Towne view of the occipital bone, and the lateral view. Submentovertical, Waters, and Caldwell (posteroanterior 15 degrees) views may be added for specific indications.

The radiation dose (with the thyroid and lens being the most sensitive structures) varies with the view obtained and the age of the patient. Best practice skin doses for a lateral skull range from 0.09 mGy in the first year of life to 0.46 mGy in a 10- to 15-year-old child (see Huda in Suggested Readings).

Indications for skull radiographs are listed in Box 18.1. Computed tomography (CT) and magnetic resonance imaging (MRI) are used for evaluation of intracranial contents, facial structures, craniosynostosis, and trauma.

## NEONATAL AND INFANT SKULL

### Size and Shape

During infancy, the neurocranium is larger relative to the face. Neurocranium to face ratios in the lateral projection are roughly 3 : 1 to 4 : 1 at birth, and decrease to 2 : 1 to 2.5 : 1 by age 6 years. The calvarium is an incompletely mineralized membranous capsule with individual bones divided from one another by connective tissue sutures and fontanelles. The six major fontanelles are located at the four corners of the parietal bones—two in the skull midline and two pairs on each side (Fig. 18.1). Accessory fontanelles may occur in several locations but usually are in the sagittal suture. The sutures and the skull base synchondroses are prominent in newborns but diminish in width during the first 2 to 3 months. Obliteration of the sutures does not begin until the second to third decades. Figs. 18.1 through 18.4 and e-Fig. 18.5 illustrate sutures, fontanelles, and synchondroses.

The sphenoid bone at birth consists of a single central mass composed of the body, lesser wings, and two symmetric lateral masses, each of which includes a greater wing and a pterygoid process. The pituitary fossa is round with smooth margins; the dorsum sella is short and blunt, and the clinoid processes are rudimentary. The angle between the body of the neonatal mandible and the ramus in lateral projection is about 160 degrees; the bodies are separated by a midline cartilaginous symphysis mentalis (see Fig. 18.3). Early tooth calcification is seen in the fifth fetal month.[1]

Components of the individual ununited bones in infancy may cause confusion if they are not correctly recognized. The frontal bone is divided in half by the metopic suture (see Figs. 18.1 and 18.3). Apparent discontinuity of the sphenoid bone with the frontal bone superiorly and the occipital bone posteriorly indicates sites of the sphenoid synchondroses (see Fig. 18.2). The four components of the occipital bone (see Fig. 18.2 and e-Fig. 18.5) likewise may simulate discontinuities.

## GROWTH AND DEVELOPMENT

Most of the postnatal skull growth occurs during the first 2 years of life, after which most of the features of the adult skull are present. During the first 2 years, the bone thickness increases. The inner and outer tables, diploic space, vascular markings, and grooves for the dural sinuses develop by the end of the second year.

With increasing age, the fontanelles and sutures become smaller and narrower. The anterior fontanelle is reduced to fingertip size during the first half of the second year; the posterior fontanelle may be closed at birth (range of closure: birth to several months). Closure of the fontanelles occurs clinically before it is visible radiographically. The metopic suture is variable and may close from birth to the third year; however, it persists in about 10% of adults. In the occipital bone, the mendosal suture (see Fig. 18.4

**BOX 18.1** Indications for Plain Film Examination of the Skull

**DEFINITE**

- Trauma in possible child abuse cases (as part of a skeletal survey)
- Syndrome evaluation
- Craniosynostosis (initial test)
- Physical findings in patient without neurologic symptoms
- Cephalhematoma
- “Bump”
- Foreign body (initial test)
- Metastatic workup for small round cell tumor

**POSSIBLE**

- Initial evaluation in facial trauma

**NOT AN INDICATION**

- Mild trauma
- Neurologic abnormalities (use computed tomography or magnetic resonance imaging)
- Sinusitis evaluation

## Abstract:

The pediatric skull is remarkably variable in size, shape, thickness and mineralization and undergoes significant change as a result of normal childhood development. This chapter discusses the embryology, anatomy and age related development of the pediatric calvarium and paranasal sinuses. This chapter emphasizes normal and developmental variants including Wormian bones, calvarial sutures, fontanelles, and vascular and diploic spaces, as well as the best imaging techniques for the pediatric calvarium and parnasal sinuses.

## Keywords:

pediatric skull
fontanelle
Wormian bones
sutures
paranasal sinuses

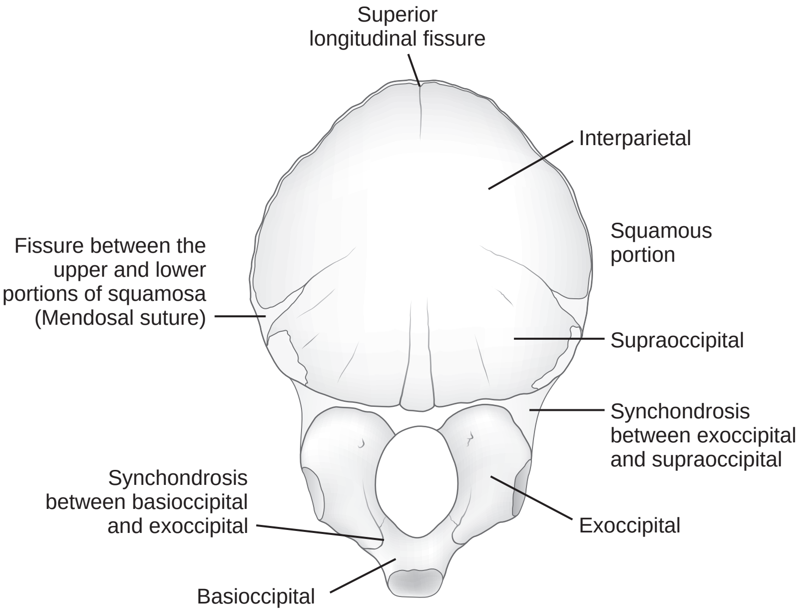
Superior longitudinal fissure
Interparietal
Squamous portion
Fissure between the upper and lower portions of squamosa (Mendosal suture)
Supraoccipital
Synchondrosis between exoccipital and supraoccipital
Synchondrosis between basioccipital and exoccipital
Exoccipital
Basioccipital

**e-Figure 18.5.** Occipital bone at birth, internal surface.

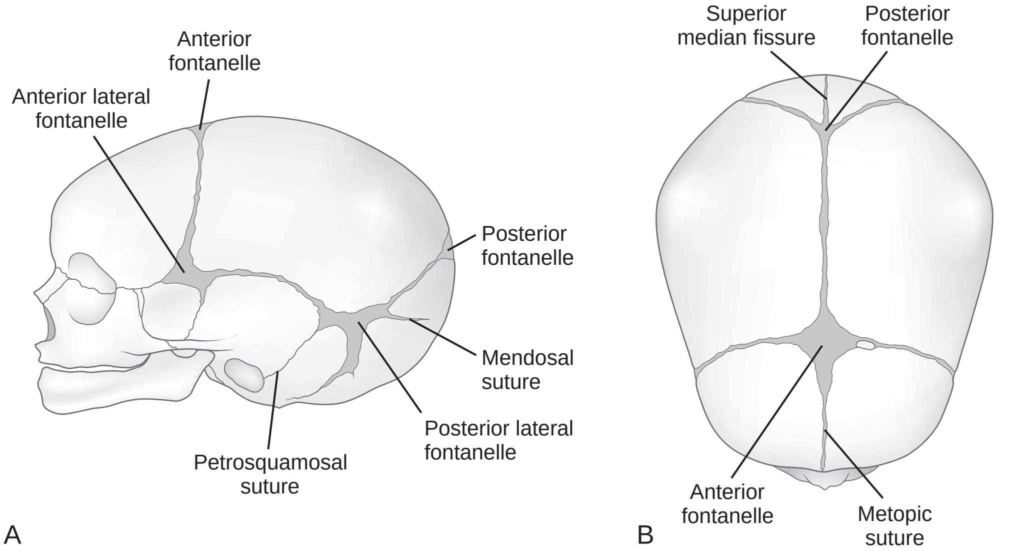

**Figure 18.1.** Schematics of the cranium at birth showing the greater and lesser fontanelles. Lateral (A) and superior (B) views.

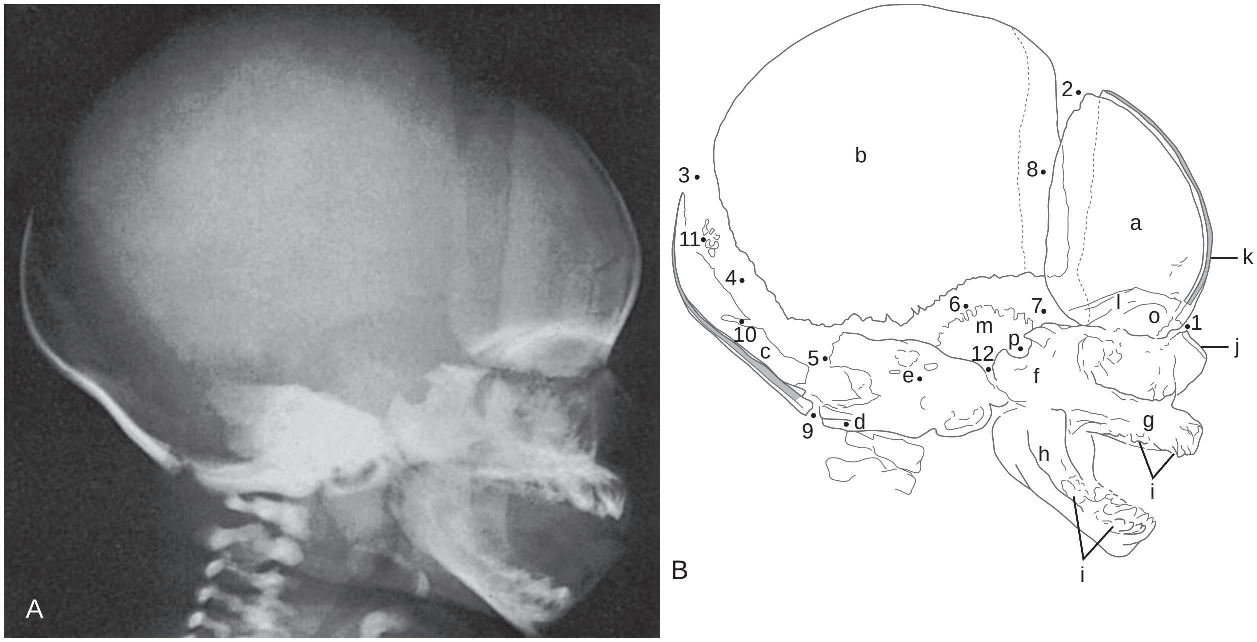

**Figure 18.2.** (A) Lateral radiograph of the normal neonatal skull. (B) Corresponding schematic of (A). *a,* Frontal bone; *b,* parietal bone; *c,* squamous portion of the occipital bone; *d,* exoccipital portion of the occipital bone; *e,* superimposed petrous pyramids of the temporal bone; *f,* body of the sphenoid; *g,* upper maxilla; *h,* mandible; *i,* partially mineralized deciduous teeth and dental crypts; *j,* nasal bone; *k,* squamosa of the frontal bone; *l,* horizontal plates of the frontal bone; *m,* squamosa of the temporal bone; *o,* orbit; *p,* pituitary fossa; *1,* frontonasal suture; *2,* anterior fontanelle; *3,* posterior fontanelle; *4,* lambdoid suture; *5,* posterolateral fontanelle; *6,* squamosal suture; *7,* anterolateral fontanelle; *8,* coronal suture; *9,* synchondrosis between exoccipital and supraoccipital portions of the occipital bone; *10,* mendosal suture; *11,* multiple ossification centers (wormian bones) in the lambdoid suture; *12,* occipitosphenoid synchondrosis.

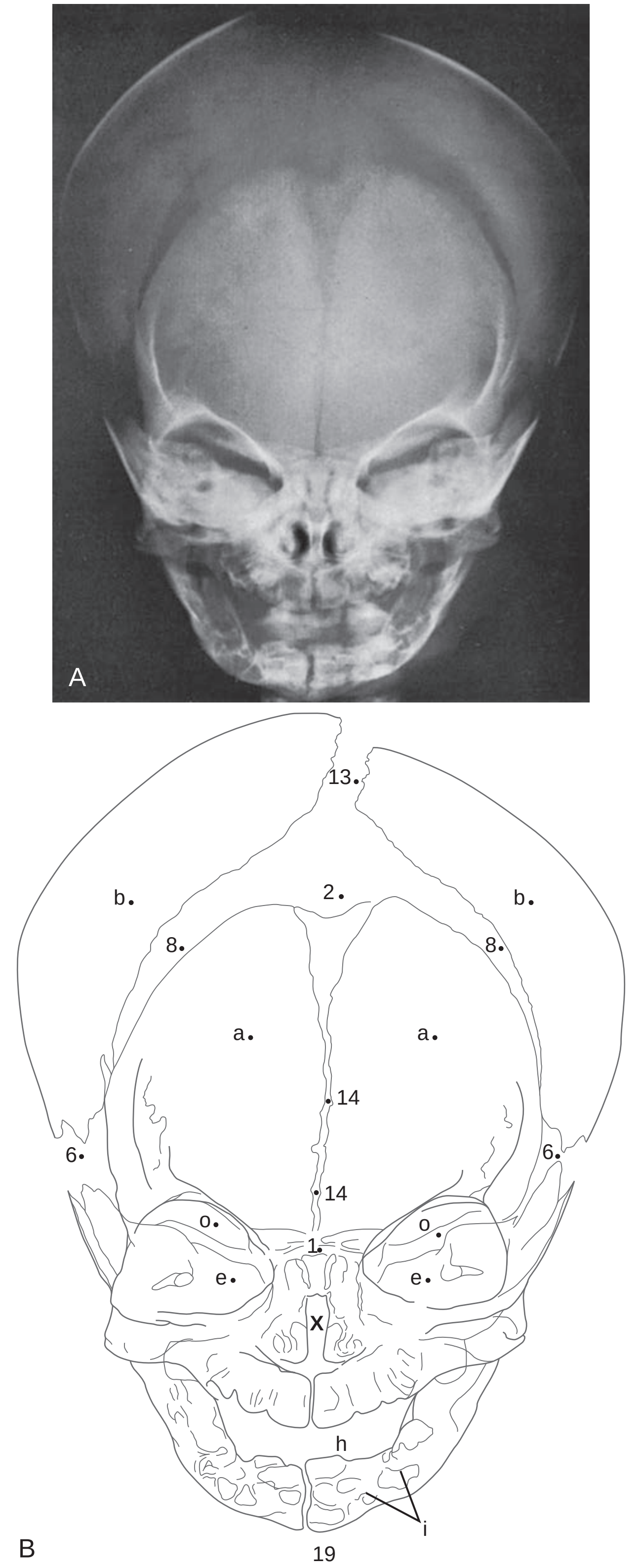

**Figure 18.3.** (A) Posteroanterior radiograph of the normal skull. (B) Corresponding schematic of (A). *a,* Frontal bone; *b,* parietal bone; *e,* superimposed petrous pyramids of the temporal bone; *h,* mandible; *i,* partially mineralized deciduous teeth and dental crypts; *o,* orbit; *x,* nasal septum; *1,* frontonasal suture; *2,* anterior fontanelle; *6,* squamosal suture; *8,* coronal suture; *13,* sagittal suture; *14,* metopic suture dividing the frontal bone; *19,* symphysis of the mandible.

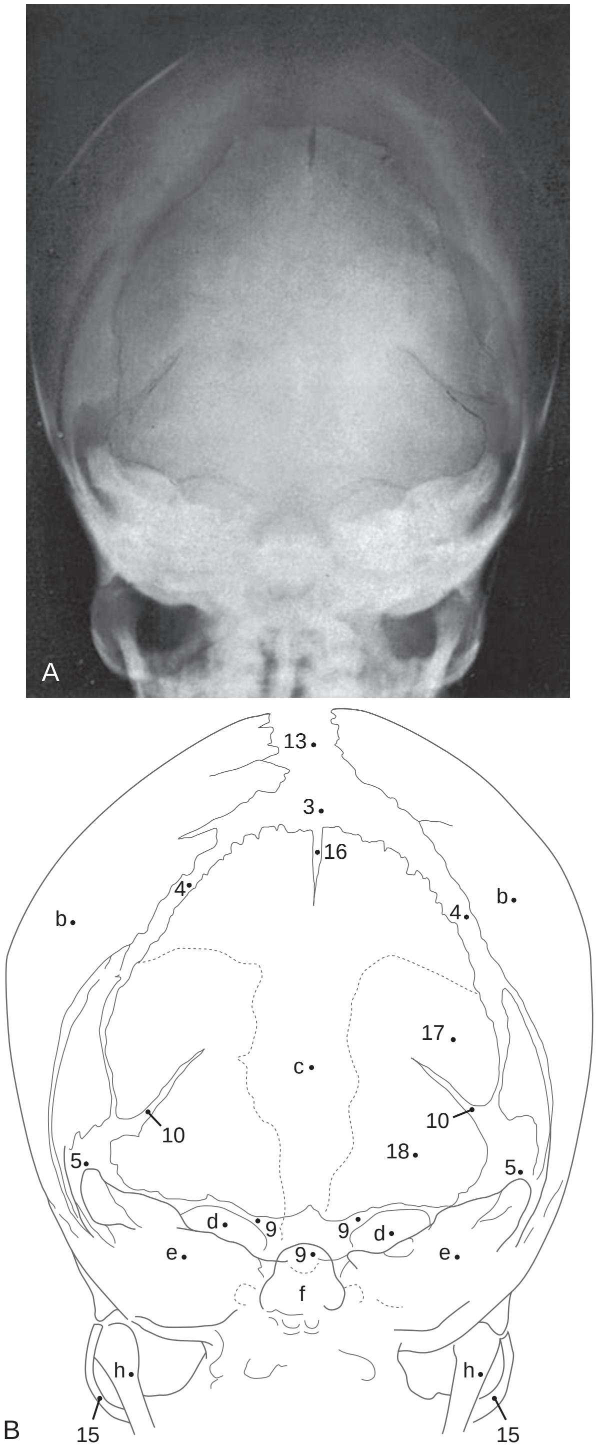

**Figure 18.4.** (A) Towne's radiograph of the normal neonatal skull. (B) Corresponding schematic of (A). *b,* Parietal bone; *c,* squamous portion of the occipital bone; *d,* exoccipital portion of the occipital bone; *e,* superimposed petrous pyramids of the temporal bone; *f,* body of the sphenoid; *g,* basioccipital portion of the occipital bone; *h,* mandible; *3,* posterior fontanelle; *4,* lambdoid suture; *5,* posterolateral fontanelle; *9,* synchondrosis between exoccipital and supraoccipital portions of the occipital bone; *10,* mendosal suture; *13,* sagittal suture; *15,* zygomatic arch; *16,* superior median fissure of the occipital bone; *17,* interparietal portion of the occipital bone; *18,* supraoccipital portion of the occipital bone.

and e-Fig. 18.5) disappears during the first 2 years, but can persist. The synchondrosis between the supraoccipital and exoccipital (supracondylar) portions disappears during the second or third year. The spheno-occipital synchondrosis begins to close near puberty but may persist until the 20th year. Extensive variation makes sutures an unreliable criterion for estimation of age. Around the 20th year, the skull attains its definitive size.

## Normal Variations

Intrasutural, or wormian, bones occur most frequently along the lambdoid sutures (Fig. 18.6 and e-Fig. 18.7; Box 18.2), and less frequently in the fontanelles (see e-Fig. 18.7). The interparietal or Inca bone (Fig. 18.8) results from division of the supraoccipital portion of the occipital bone into two parts by the mendosal suture, with the superior part arising from membranous bone and the inferior part from cartilage continuous with the supracondylar basiocciput. A rare synchondrosis runs vertically through the squamous occipital bone (e-Fig. 18.9); persisting superior and inferior portions of the line are known as the *superior longitudinal fissure* (bi-interparietal suture) and the *cerebellar synchondrosis* (median cerebellar suture). Where the supraoccipital portion of the occipital bone forms the posterior border of the foramen magnum, accessory supraoccipital bones occasionally are found (e-Fig. 18.10). An outward bulge of the occipital squamosa just above the torcular Herophili in a newborn (Fig. 18.11) is called *bathrocephaly*. Rarely, a horizontal interparietal suture divides the parietal bones into superior and inferior moieties (e-Fig. 18.12).

Compression of the fetal skull, molding, during passage through the maternal pelvis produces dysmorphic findings after birth (Fig. 18.13).[2] During the first weeks and months of life, suture widths vary so much that caution is required for the diagnosis of increased intracranial pressure, particularly because superimposition of sutures can produce spurious widening (Fig. 18.14).

## JUVENILE SKULL

After 2 years of age, skull radiographs are similar to adults (Fig. 18.15). During childhood, growth continues at a reduced velocity with a slight postpubertal spurt. The skull grows until late in childhood developing adult characteristics (Figs. 18.16–18.8, e-Fig. 18.19).

### BOX 18.2 Conditions in Which Wormian Bones May Be Present

**TREATABLE**

- Hypothyroid (cretinism)

**COMMONLY FOUND**

- Normal
- Cleidocranial dysplasia
- Osteogenesis imperfecta

**OTHERS (NONINCLUSIVE)***

- Chondrodysplasia punctata
- Copper deficiency: Menkes syndrome
- Hypophosphatasia
- Progeria
- Pyknodysostosis
- Zellweger syndrome

*Many other syndromes may have incidental wormian bones.

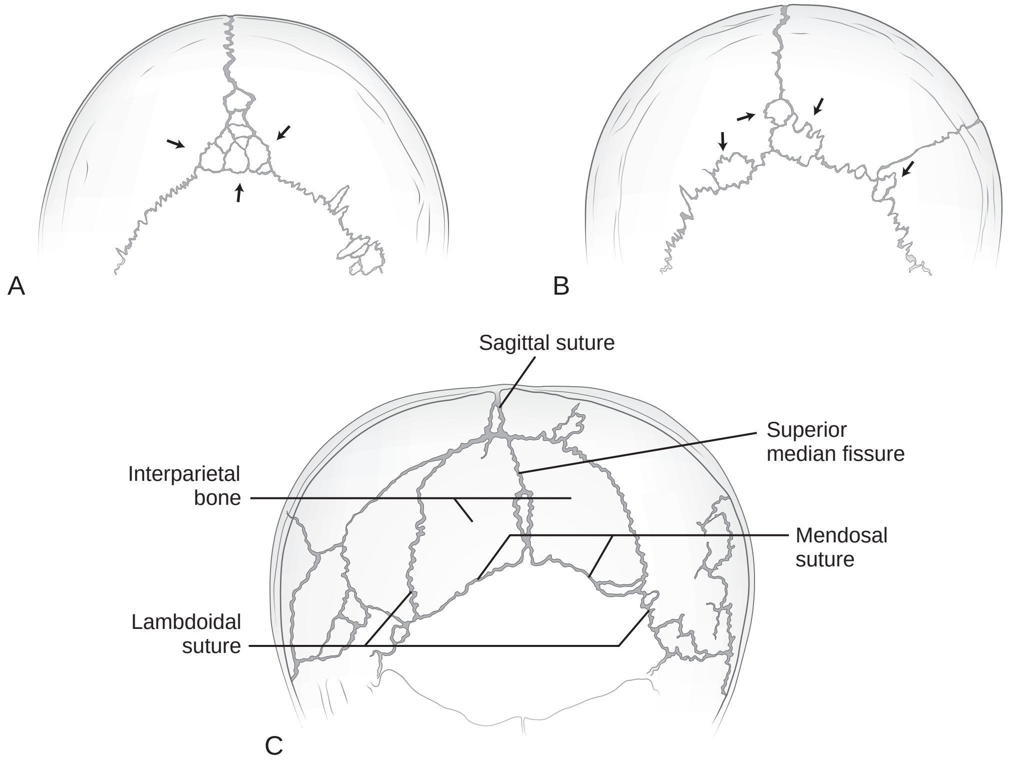

**Figure 18.6. Schematics of wormian bones.** (A) Multiple wormian bones *(arrows)* in the sagittal suture. (B) Multiple wormian bones *(arrows)* in the sagittal and lambdoid sutures. (C) Interparietal bone bounded by the lambdoid and persistent mendosal sutures. The superior median fissure also is still present and divides the interparietal bone into right and left halves.

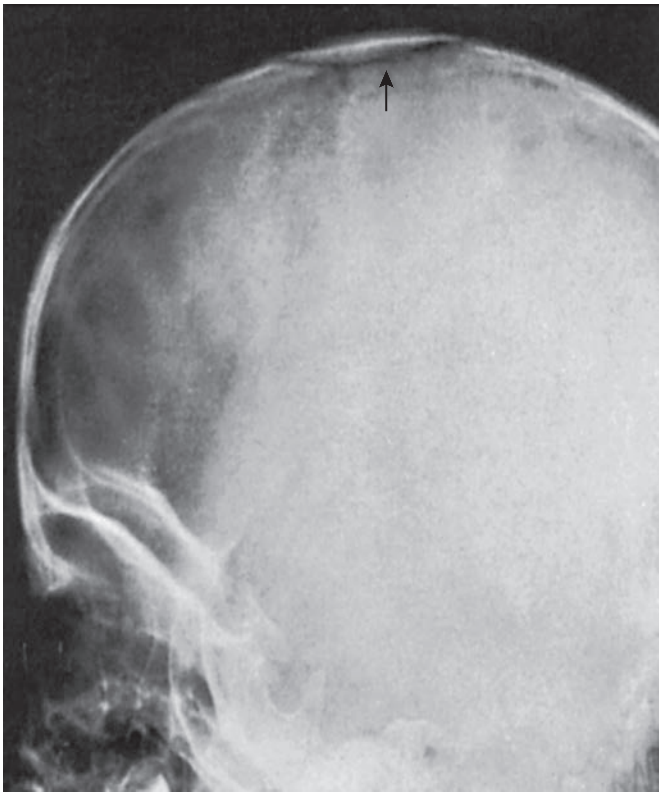

**e-Figure 18.7. A large independent bone *(arrow)* in the anterior fontanelle of a normal 2.5-year-old girl.** Normal variants of this type must be kept in mind when evaluating radiographs trauma. *(Courtesy of Dr. B.R. Girdany, Pittsburgh, PA.)*

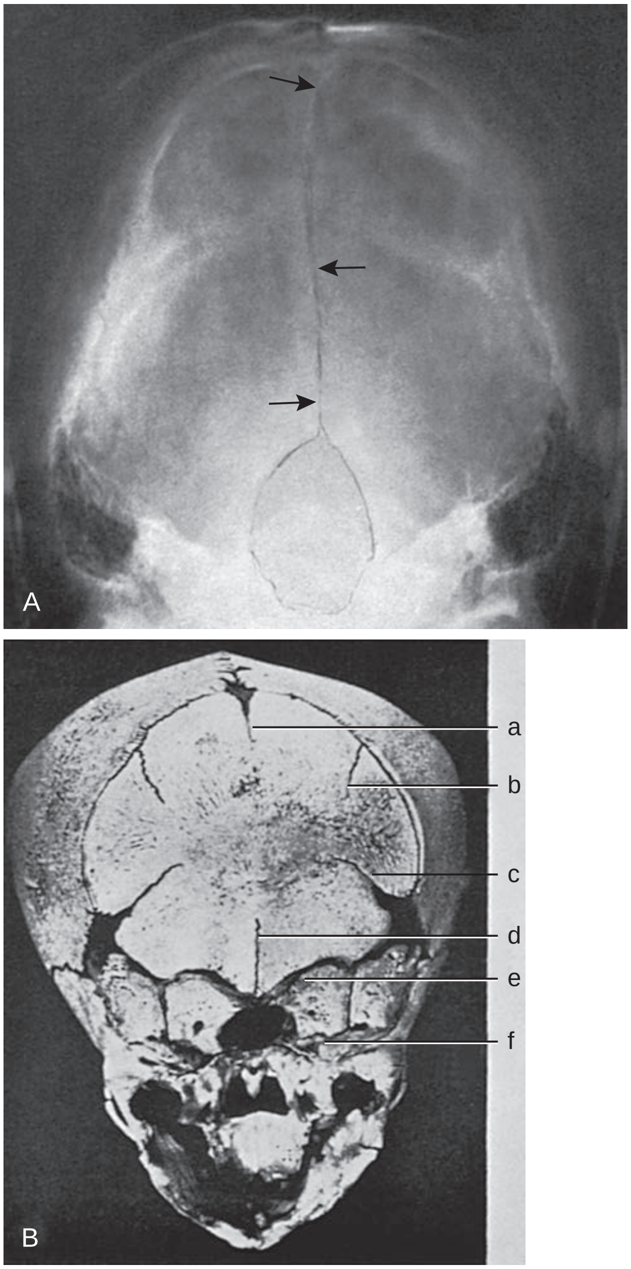

**e-Figure 18.9. Occipital bone.** (A) Towne projection showing radiolucent midline longitudinal or cerebellar synchondrosis *(arrows)* in the occipital squamosa of an 11-year-old girl, which resulted from failure of fusion mediad of its lateral paired ossification centers. This radiolucent strip can be mistaken for a fracture line. (Sutures were retouched with a pencil.) (B) Persistent longitudinal or cerebellar synchondrosis *(d)* in the occipital squamosa of a skull of a newborn; only the caudal segment of the synchondrosis is still open in this case. *a,* Superior median longitudinal fissure; *b,* superior lateral longitudinal fissure; *c,* mendosal suture; *e,* synchrondrosis between exoccipital and supraoccipital bones; *f,* synchrondrosis between basioccipital and exoccipital bones. *(From Koehler A, Zimmer EA.* Borderlands of the Normal and Early Pathologic in Skeletal Roentgenology. *3rd ed. Philadelphia: Grune & Stratton [translated from German ed 11 by S.P. Wilk]; 1968.)*

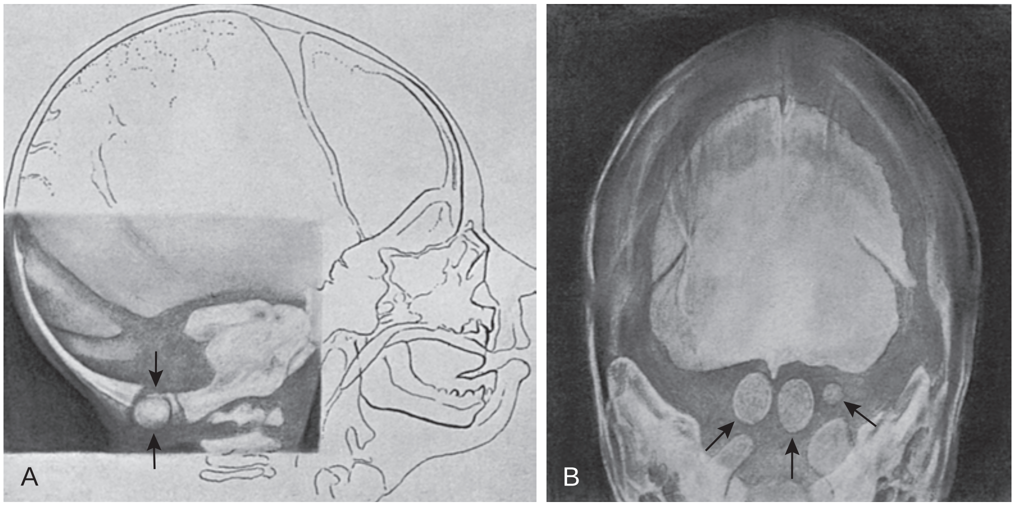

**e-Figure 18.10. Accessory bones of the supraoccipital bone.** (A) Lateral projection on the second day of life shows separate bony images *(arrows)* in the innominate synchondrosis. (A) A Towne projection of the same skull on the 20th day of life. Three ossicles *(arrows)* are present in the cartilage above the foramen magnum, along with a midline bony process on the under edge of the supraoccipital that is similar to the fetal process in this same site described by Kerckring in *Spicilegium Anatomicum* (Amsterdam, 1670).

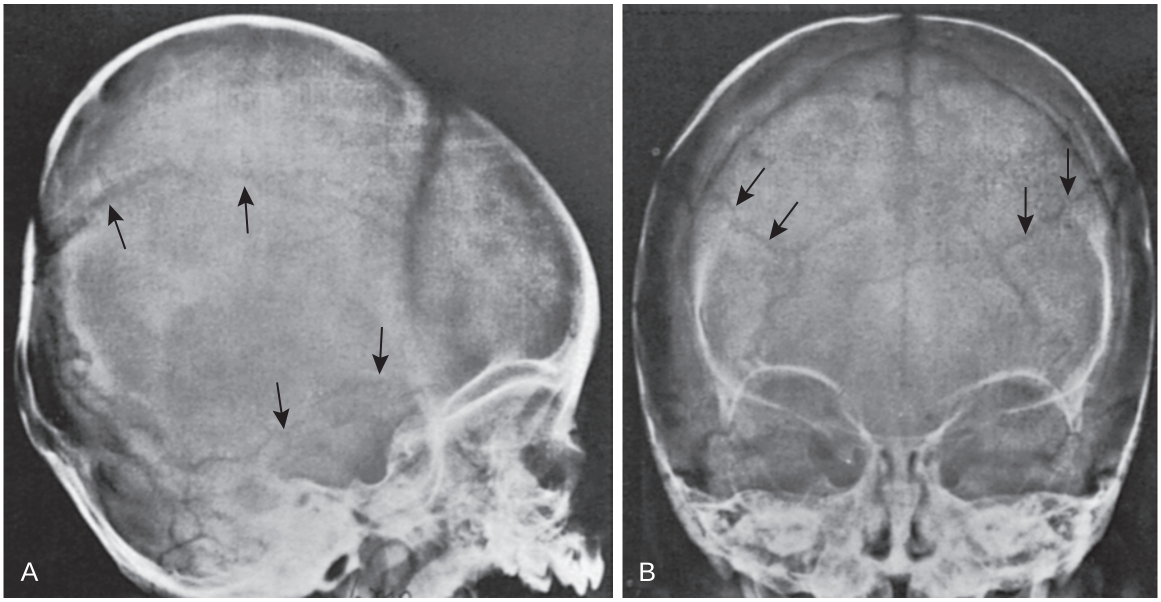

**e-Figure 18.12. Bilateral bifid parietal bones, each of which is divided into an upper and lower segment by an extra horizontal suture.** The flattening of the occipital squamosa is postural in origin. The infant was 6 months old and had not experienced a head injury. Lateral (A) and frontal (B) projections are shown. *Upper arrows* point to the anomalous horizontal intraparietal sutures, and *lower arrows* point to the normal squamosal (parietotemporal) sutures. *(Courtesy of Dr. B.R. Girdany, Pittsburgh, PA.)*

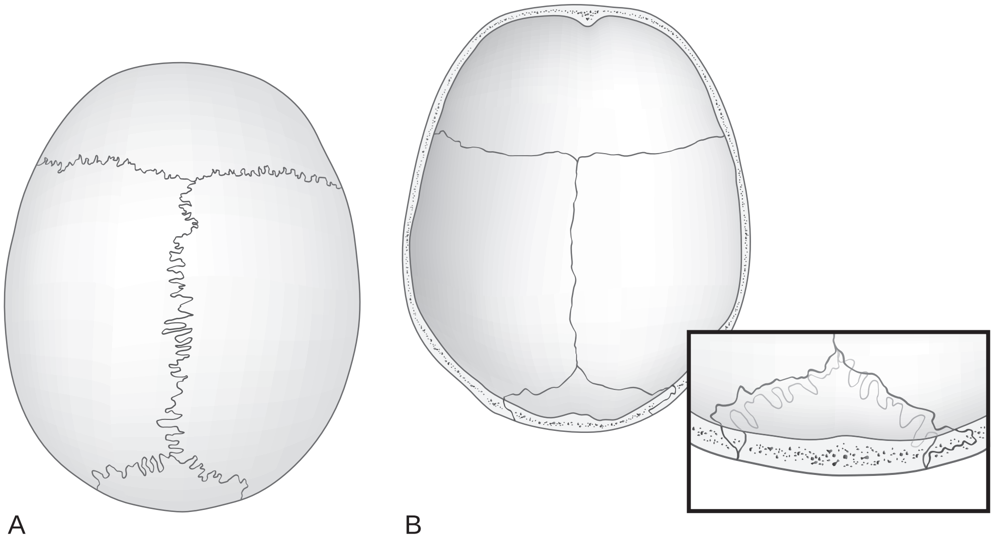

**e-Figure 18.19. Drawings of anatomic specimens show the relationship of the outer and inner tables and diploic space of the calvaria to the great sutures.** (A) External aspect of the calvaria shows deep serrations in sutures of the outer table. (B) Internal aspect shows the straight, nonserrated sutures of the inner table. The *inset* drawing depicts the lambdoid suture near the lambda; the differences in position and course of the sutures of the outer and inner tables are shown. In the diploic space, the suture runs in a plane at approximately right angles to the course of the sutures in the tables.

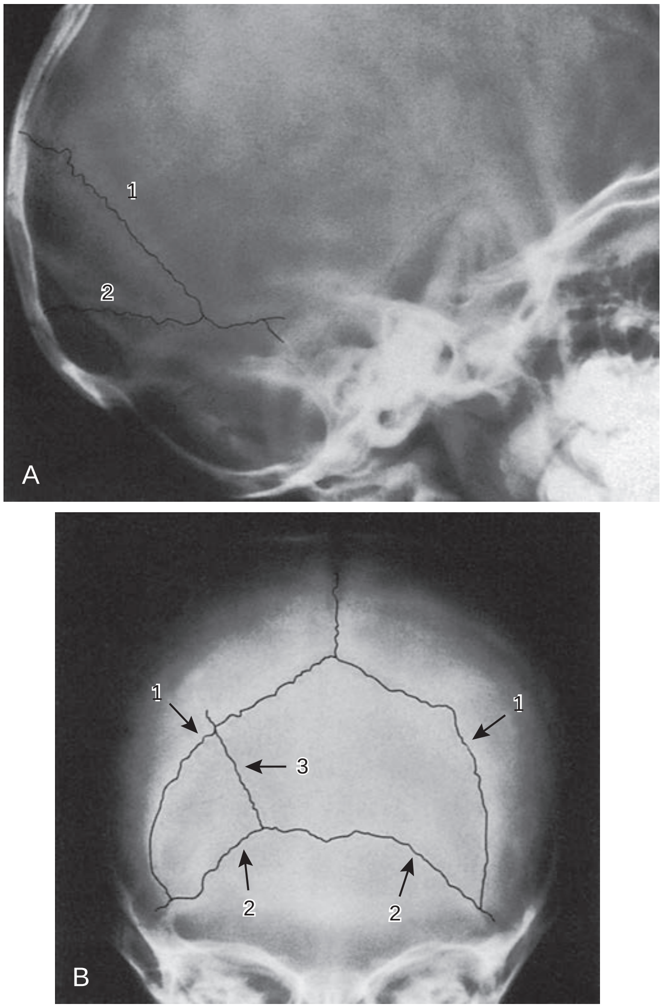

**Figure 18.8. Interparietal (Inca) bone.** (A) Lateral projection. (B) Towne projection. *1,* Right and left lambdoid sutures; *2,* mendosal suture; *3,* accessory suture in interparietal bone. *(Courtesy of Dr. J.P. Dorst, Baltimore, MD.)*

## Normal Variations

The juvenile skull is remarkably variable in size, shape, thickness, mineralization, depth of dural sinus grooves, diploic space pattern, convolutional markings, degree of temporal bone and paranasal pneumatization, and pituitary fossa morphology. In children older than 2 years, the sutures extend through both tables and the diploic space. The outer table portion of the suture may be deeply serrated when the inner table portion is practically a straight line (see e-Fig. 18.19) and may be erroneously interpreted as a fracture. Persistence of the metopic suture may simulate a vertical occipital bone fracture in anteroposterior, caudally angulated radiographs. The frontal crest on the internal surface of the frontal squamosa in the midsagittal plane may be sufficiently prominent to simulate calcification of the falx cerebri (e-Fig. 18.20).

### Convolutional (Digital) Markings

Convolutional (digital) markings are areas of diminished calvarial density separated by strips of normal density (Fig. 18.21). These areas correspond closely to the cerebral convolutions.[3] Convolutional markings are formed by localized pressure of pulsating brain on the inner table of the neurocranium.

### Diploic and Vascular Markings

The diploic space is filled with cancellous osseous bone varying in volume and pattern giving the calvarial vault a fine, honeycomb texture. Radiographically, the diploic veins lie in large, irregular channels of diminished density that extend through the cranial vault in all directions (e-Fig. 18.22 and Fig. 18.23). They vary in size, course, and visibility.

Venous and atrial grooves on the internal calvarial surface are seen as strips of diminished density on radiographs (Fig. 18.24). Compared with the venous grooves, the arterial grooves tend to taper more. The most constant of these channels is the middle meningeal artery, which courses upward and backward from the pterion. The largest vascular markings manifest as osseous thinning over the dural venous sinuses. The superior sagittal sinus lies in a shallow groove on the internal surface at the median plane of the vault near the falx cerebri attachment. At the torcular Herophili, the channels for the superior sagittal and transverse sinuses meet; one transverse sinus is often larger (dominant) compared with the other (see Fig. 18.18). The torcular Herophili in lateral projections may simulate an abnormal defect when it is unusually deep (e-Fig. 18.25). At the bend of the transverse sinus near the mastoid process, superimposition of the transverse and sigmoid sinuses may produce a rounded, radiolucent focus when these sulci are especially deep (e-Fig. 18.26). Often the groove for the bregmatic vein is a conspicuous strip of hypodensity on one or both lateral calvarial walls (e-Fig. 18.27); this groove, also called the *sphenoparietal sinus*, is a misnomer because the true sinus runs underneath the lesser wing of the sphenoid bone and does not always communicate with the bregmatic vein.

### Pacchionian Bodies

The Pacchionian, or arachnoid, granulations (e-Fig. 18.28) are attached to the undersurface of the dura. Originally, they were thought to be the site of cerebrospinal fluid absorption, but this theory has been disputed.[4] These structures are irregular, sharply defined impressions located along the parasagittal inner table of skull. These normal structures appear after age 18 months of age.

### Symmetric Parietal Foramina

About 60% of skulls show small defects (parietal foramina) in the superior posterior angles of the parietal bones through which emissary veins penetrate. The veins communicate with the sagittal sinus internally and occipital vein tributaries externally. Occasionally, large defects are seen and have been termed *enlarged parietal foramina*.[5] Occasionally, they are palpable and, less frequently, they unite to form one large, single defect (Figs. 18.29 and 18.30). The defects result from a failure of mineralization of the membranous bone, and thus the term "enlarged parietal foramina" is a misnomer. The defects are not associated with other skeletal anomalies and have no clinical significance except in the differential diagnosis of cranial defects.

Large parietal foramina have been recognized as an inherited trait ever since Goldsmith found them in 56 members of the Catlin family, giving rise to the term "Catlin mark."[6] They may persist throughout life, although they tend to become smaller or disappear leaving focal sclerotic residua.

## ANATOMY OF THE PARANASAL SINUSES

## Normal Paranasal Sinuses

The paranasal sinuses are paired pneumatic cavities that communicate with the nasal fossae and are located in the maxilla, ethmoid, frontal, and sphenoid bones. Because of the air cell mucosa

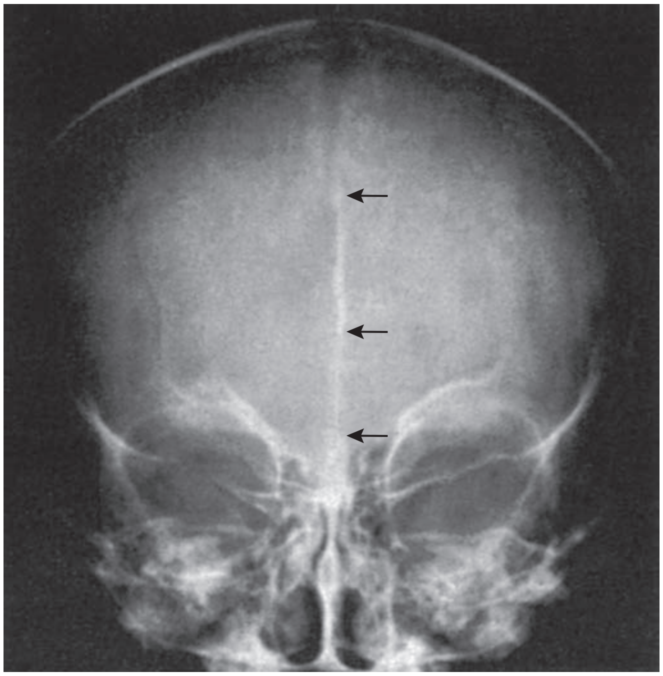

**e-Figure 18.20. Long, dense, normal frontal crest *(arrows)* on the internal surface of the frontal squamosa in its midsagittal plane in a 5-year-old boy.** A lateral projection *(not shown)* revealed that the falx cerebri behind the frontal crest was prematurely calcified.

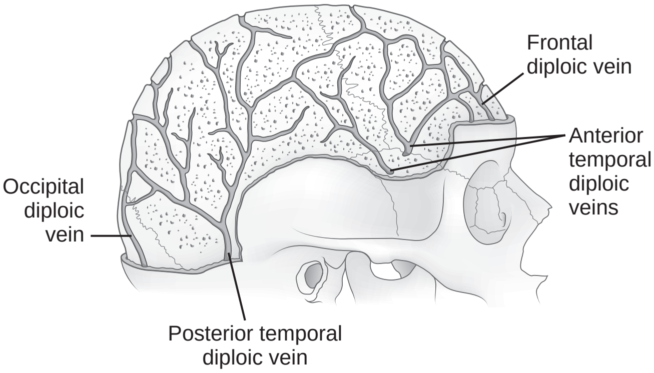
Frontal diploic vein
Anterior temporal diploic veins
Occipital diploic vein
Posterior temporal diploic vein

**e-Figure 18.22. The veins of the diploic space.**

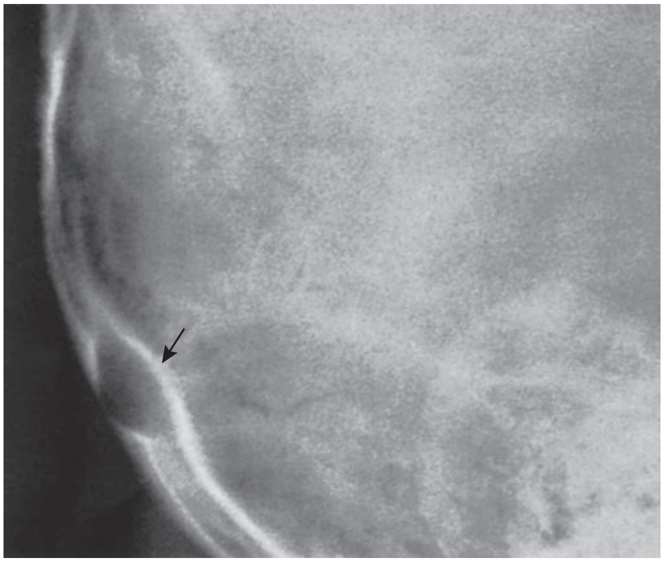

**e-Figure 18.25. Deep sinus confluens (torcular Herophili) and the transverse sinus of a healthy 11-year-old boy.** A radiolucent patch *(arrow)* in the occipital squamosa.

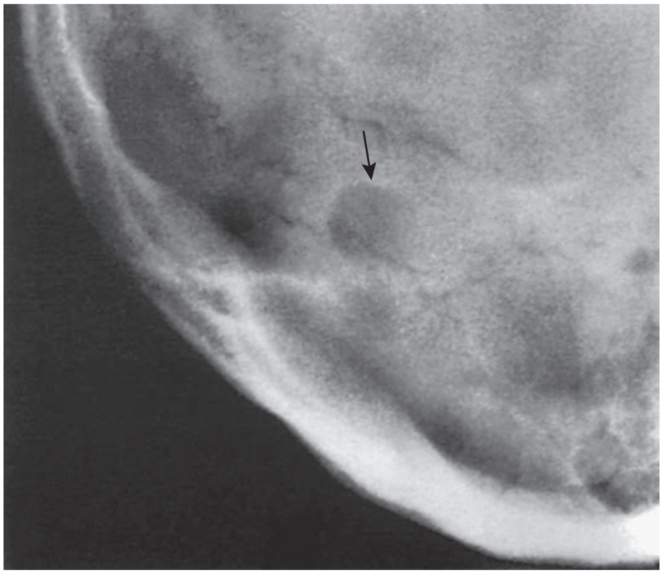

**e-Figure 18.26.** A radiolucent patch *(arrow)* caused by the superimposition of the sulci of an unusually deep transverse sinus and lateral sinus at their junction where the transverse sinus turns caudad. The patient was a healthy 10-year-old boy.

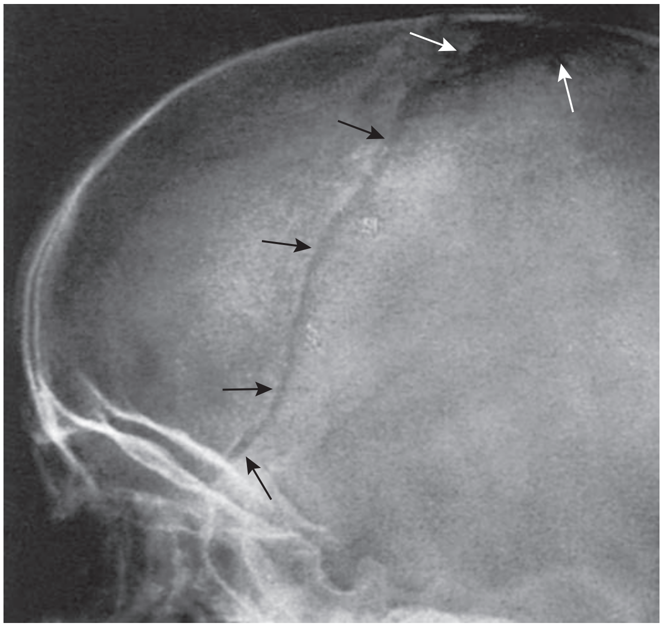

**e-Figure 18.27. Grooves of the bregmatic veins *(arrows)* in a healthy 11-year-old girl near the ventral edge of the left parietal bone.** This groove may be unilateral or bilateral. *(From Lindblom K. Radiographic study of the vascular channels of the skull, with special reference to intracranial tumors and arteriovenous aneurysms.* Acta Radiol Suppl [Stockh]. *1918;30.)*

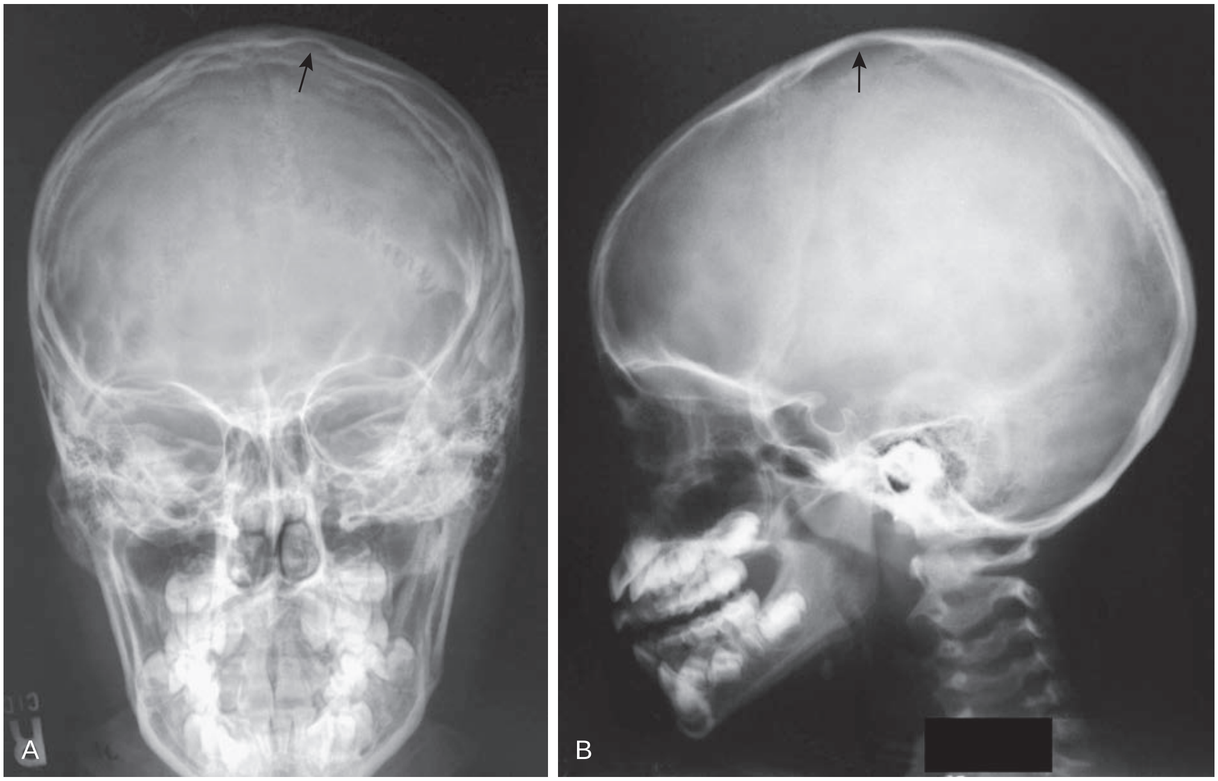

[redacted]

**e-Figure 18.28. Pacchionian granulation seen as a sharply defined impression *(arrows)* on the inner table of the skull in the parasagittal location in two patients.** (A) Caldwell projection. (B) Lateral projection.

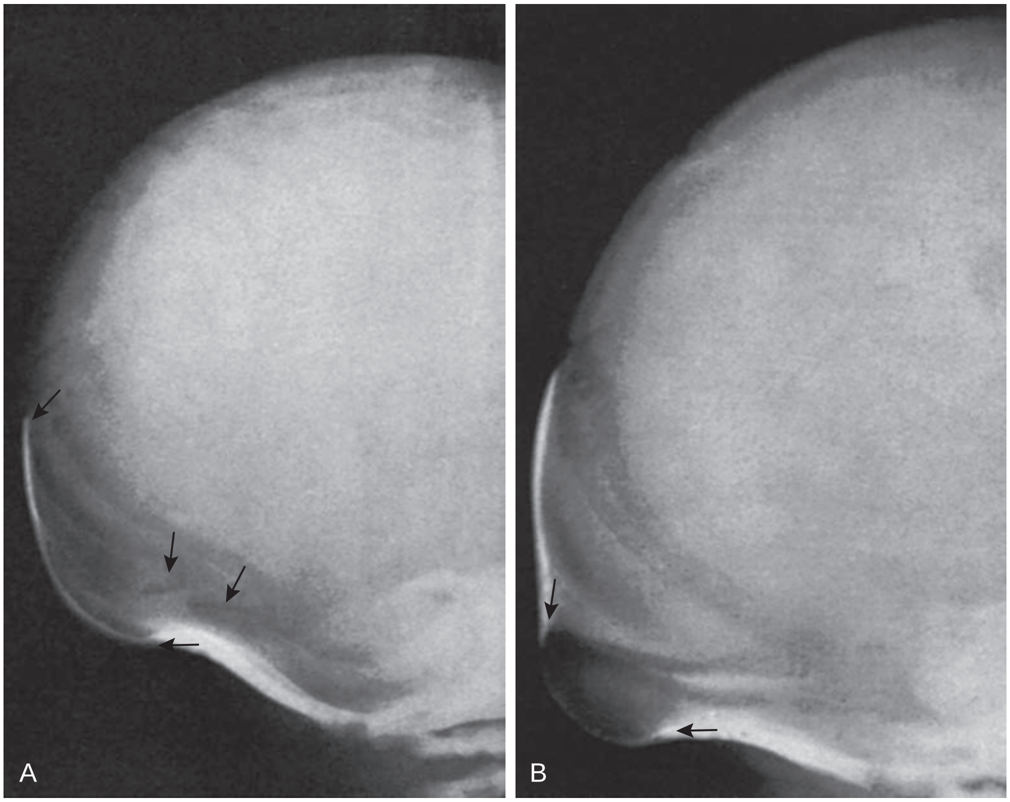

**Figure 18.11. Bathrocephaly in a newborn.** (A) The external bulge *(arrows)* extends from the lambda downward to the mendosal suture in this normal 3-day-old infant. (B) The bulge *(arrows)* in this normal 5-day-old infant begins below the mendosal suture.

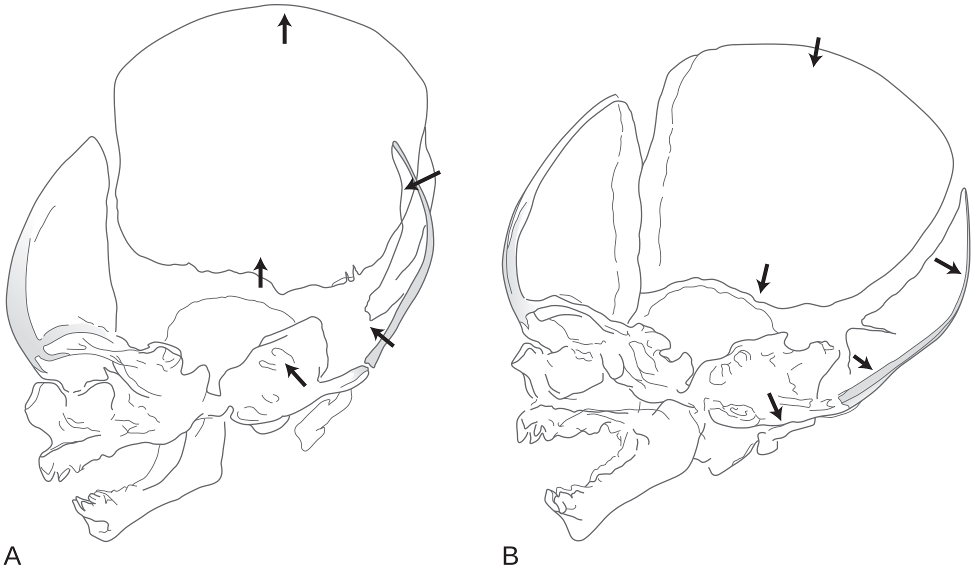

**Figure 18.13.** (A) Lateral illustration of the neonatal skull on the first day of life shows molding of the bones of the calvaria with overlapping of their edges and narrowing of the sutures caused by compression during passage of the head through the birth canal. The parietal bones are displaced upward, and the temporal bones and occipital bone are rotated counterclockwise *(arrows)*. (B) Lateral illustration on day of life 3 shows expansion of the cranium and widening of the sutures compared with (A) after the parietal, occipital, and temporal bones have returned to normal positions *(arrows)*. *(Courtesy of Dr. H.C. Moloy.)*

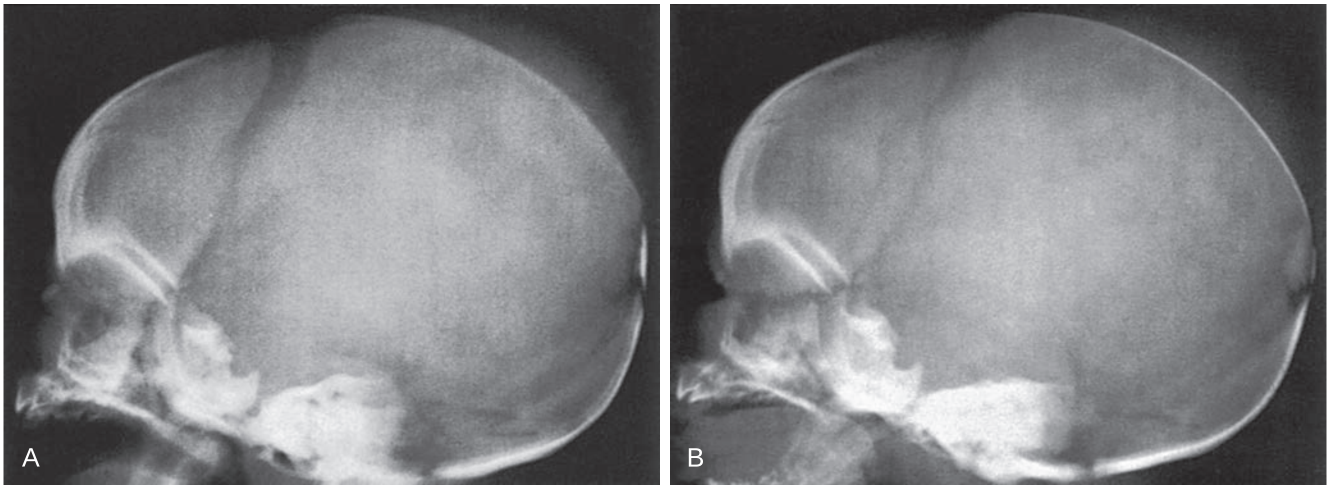

**Figure 18.14. Factitious widening of the coronal suture.** (A) Slightly oblique radiograph in which the right and left limbs of the coronal suture overlap. (B) Radiograph that is a more oblique than (A) reveals the individual, narrower, right and left limbs.

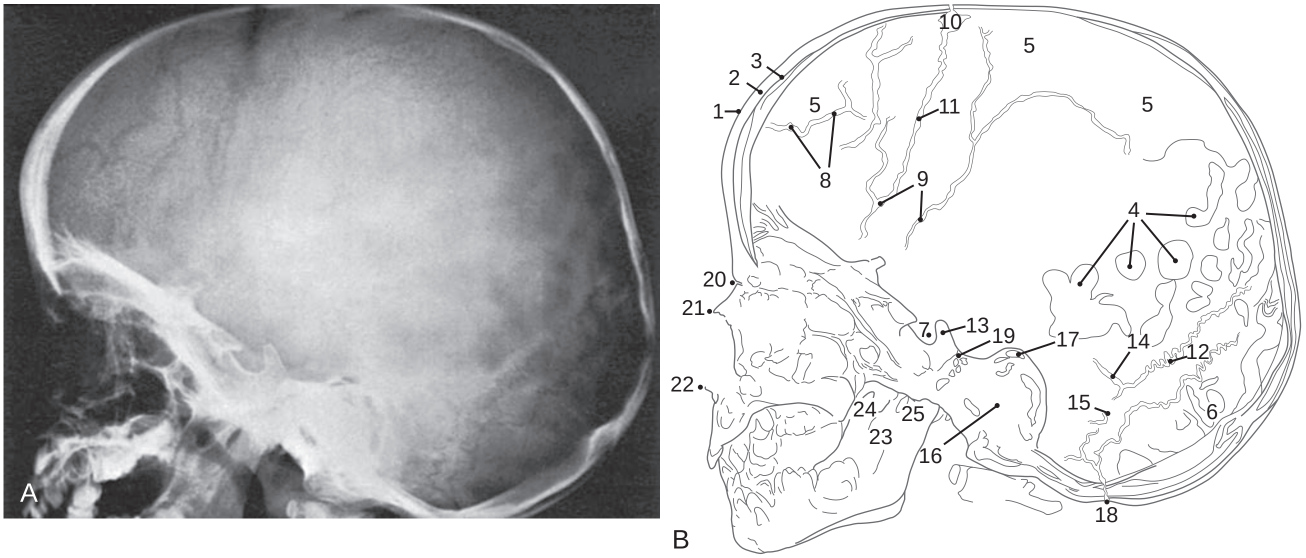

**Figure 18.15. Radiograph of the normal skull at 2 years.** (A) Lateral projection. (B) Tracing of (A). *1,* Outer table; *2,* diploic space; *3,* inner table; *4,* convolutional markings; *5,* fine honeycomb of diploic structure; *6,* internal occipital protuberance; *7,* pituitary fossa; *8,* diploic veins; *9,* vascular grooves; *10,* anterior fontanelle; *11,* coronal suture; *12,* lambdoid suture; *13,* dorsum sellae; *14,* parietomastoid suture; *15,* occipitomastoid suture; *16,* petrous pyramids; *17,* small temporal pneumatic cell; *18,* synchondrosis between exoccipital and supraoccipital; *19,* spheno-occipital synchondrosis; *20,* nasofrontal suture; *21,* nasal bone; *22,* anterior nasal spine; *23,* mandible; *24,* coronoid process of the mandible; *25,* condyloid process of the mandible.

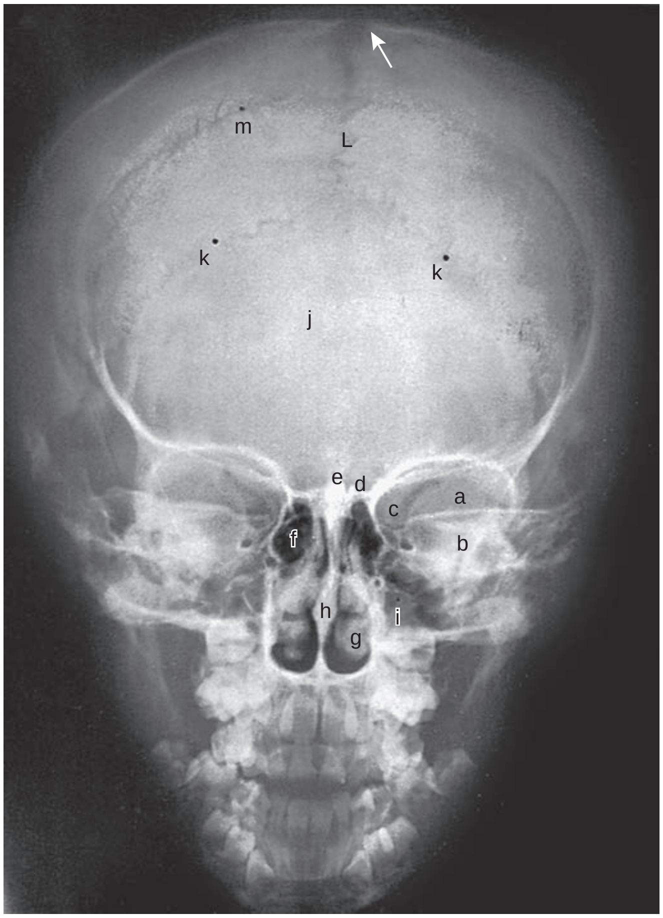

**Figure 18.16. Radiographic features on a normal Water's projection of the skull in a 6-year-old.** *a,* Orbit; *b,* petrous pyramid; *c,* superior orbital fissure; *d,* frontal sinus; *e,* crista galli; *f,* ethmoid cells; *g,* inferior turbinate; *h,* nasal septum; *i,* maxillary sinus; *j,* frontal bone; *k,* lambdoid suture; *m,* coronal suture; *L, arrow,* sagittal suture.

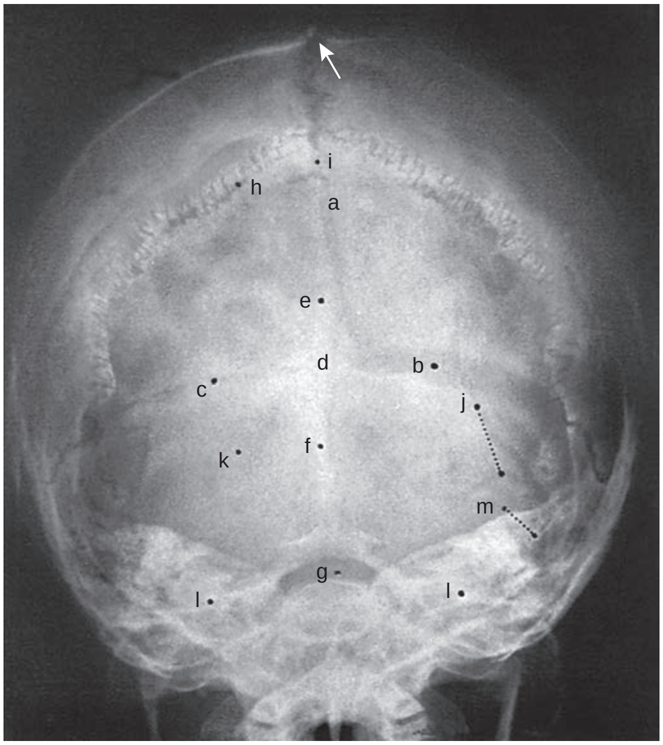

**Figure 18.17. Radiographic features of the normal skull at 3 years of age on a Towne's view.** *a,* Groove for superior sagittal sinus; *b,* groove for right transverse sinus; *c,* groove for left transverse sinus; *d,* torcular Herophili and superimposed external and internal occipital protuberances; *e,* superior half of cruciate ridge; *f,* inferior half of cruciate ridge; *g,* foramen magnum; *h,* lambdoid suture; *i,* lambda; *j,* superimposed vascular markings in frontal bone; *k,* posterior fossa; *l,* petrous pyramid; *m,* mastoid pneumatic cells; *arrow,* sagittal sinus.

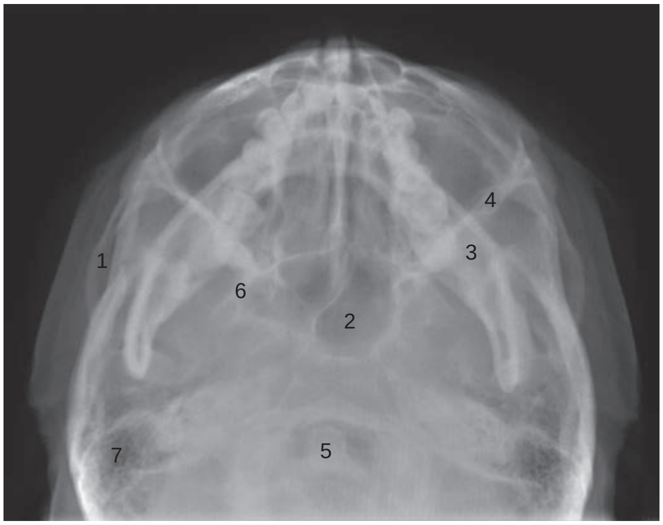

**Figure 18.18. Submental vortex image.** The following structures are labeled: *1,* Zygomatic arch; *2,* sphenoid sinus; *3,* body of mandible; *4,* greater wing of sphenoid (orbital surface); *5,* odontoid; *6,* pterygoid plates; and *7,* mastoid air cells.

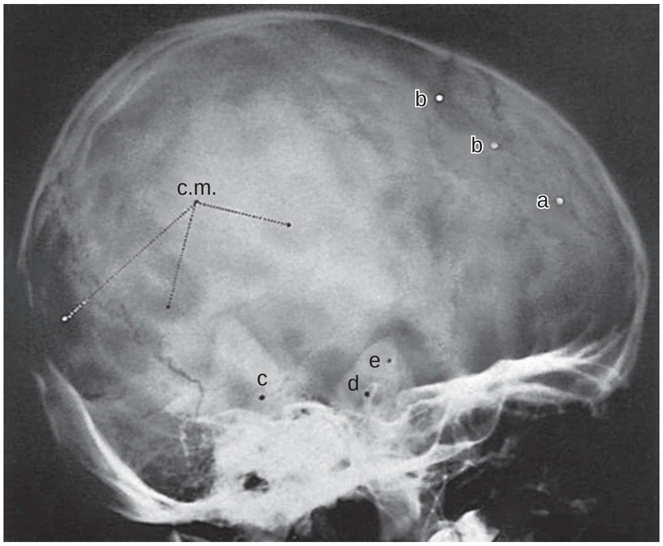

**Figure 18.21. Prominent convolutional markings *(c.m.)* in an asymptomatic 6-year-old girl.** *a,* Diploic veins; *b,* coronal suture; *c,* squamoparietal suture; *d,* dorsum sellae; *e,* shadow of external ear.

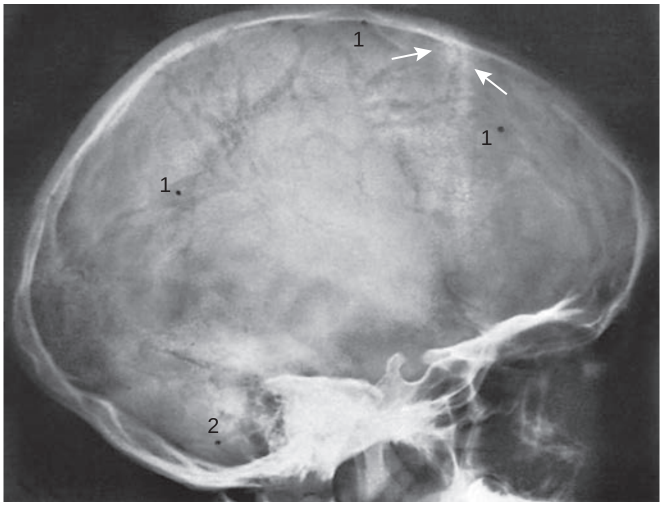

**Figure 18.23. Large diploic veins in the frontal and parietal bones of an 8-year-old girl.** The veins appear as wide strips of diminished density coursing through the frontal and parietal bones. *Arrows* denote the hyperostotic ridges on either side of the coronal suture. *1,* Diploic venous lake; *2,* groove for the emissary vein of the mastoid.

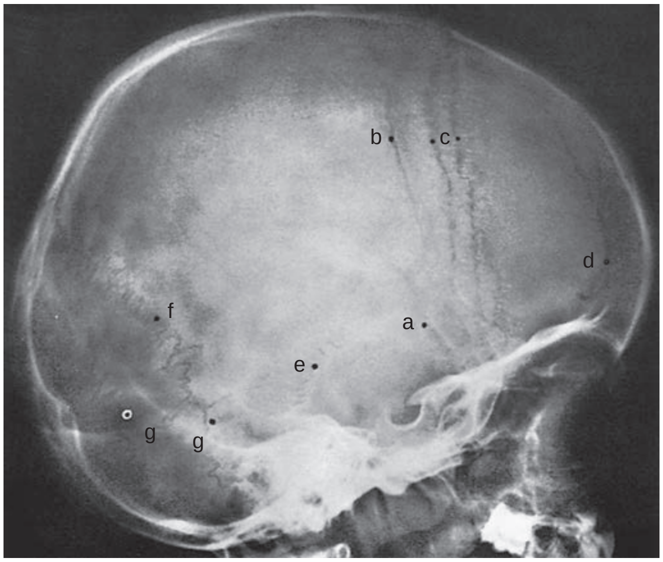

**Figure 18.24. Vascular markings.** *a,* Grooves for the middle meningeal artery; *b,* parietal diploic vein; *c,* coronal suture; *d,* frontal diploic veins; *e,* squamoparietal suture; *f,* lambdoid suture; *g,* large groove for the transverse dural sinus.

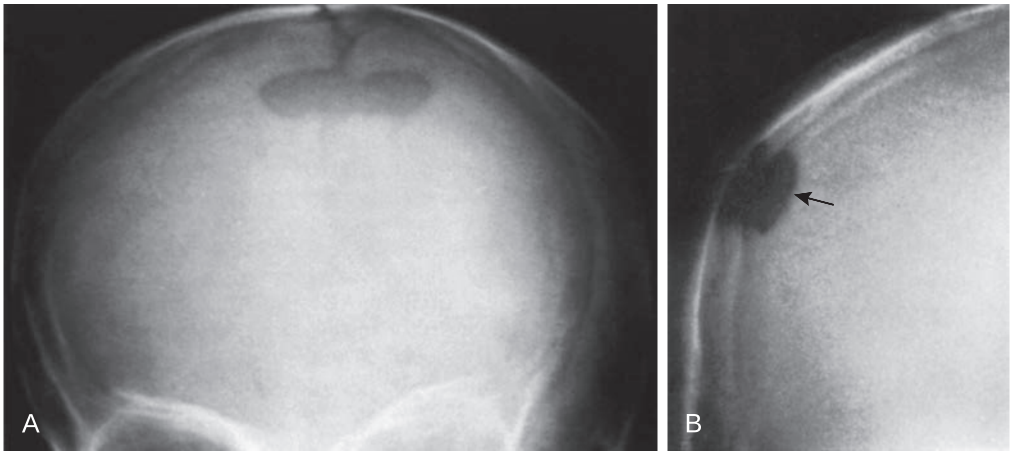

**Figure 18.29. A persistent interparietal fontanelle (parietal foramen) *(arrow)* in an otherwise healthy 5-year-old boy.** (A) Frontal projection. (B) Caldwell projection.

continuity with the nasal cavity via the Eustachian tubes, the mastoid air cells can be considered an additional component. The size and shape of the cavities vary with age, among persons, and on the two sides of the same person.[7,8]

The sinus openings into the nasal cavity are shown in Figs. 18.31 and e-Fig. 18.32. The postnatal growth and sinus extension are shown in e-Fig. 18.33. The fully developed maxillary, frontal, and ethmoid sinuses are illustrated in e-Figs. 18.34 and 18.35. CT shows sinus extensions into the orbital roofs and apices of the petrous temporal bone that are not visible on conventional radiographs.

## Maxillary Sinuses

Changes in maxillary sinus development are shown in e-Fig. 18.35 and Fig. 18.36. The maxillary sinuses are present at birth, expand steadily, and are mature by puberty.[9] Developmental variations include unilateral hypoplasia and prominent septa that compartmentalize the sinus (Fig. 18.37). The roots of the maxillary molars occasionally impinge on the sinus walls (e-Fig. 18.38) and sometimes produce mucous membrane folds. In oblique ventrodorsal skull radiographs, the roots of the teeth may be superimposed on the sinuses and artifactually appear to project into them. A molar that fails to migrate is found in its fetal position near the superomedial angle of the maxillary sinus (Figs. 18.39 and 18.40). The height of the antral floor and morphology of the nasal cavity may influence surgical approaches.

## Frontal Sinuses

Morphologic variation in the frontal sinuses is common. The frontal sinuses are not sufficiently developed for radiographic

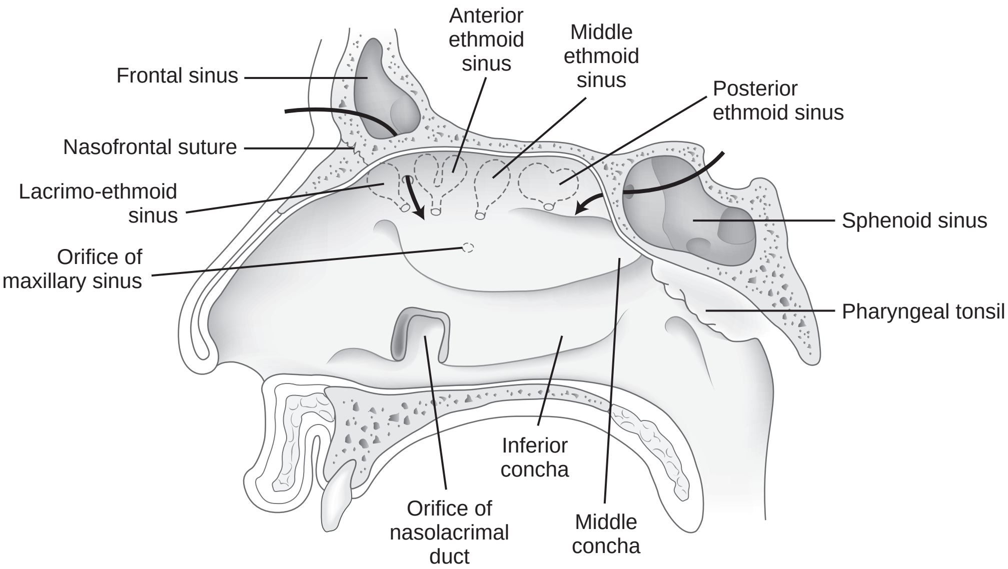

**e-Figure 18.32.** Schematic lateral nasal wall with labeled anatomy.

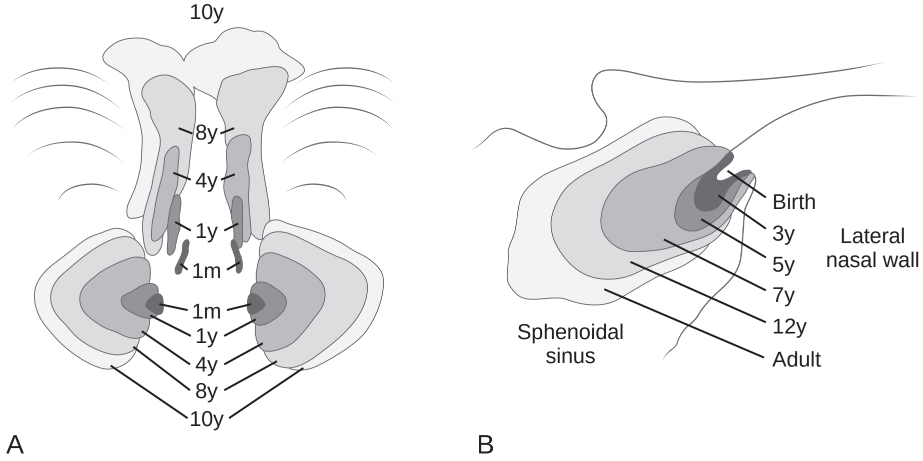

**e-Figure 18.33.** (A) Composite drawing showing the changes in size and shape of the maxillary and frontal sinuses in one person during infancy and childhood. (B) Illustration of the postnatal growth of the sphenoid sinus from birth to maturity. *(A, Modified from Maresh MM. Paranasal sinuses from birth to late adolescence, 1: Size of the paranasal sinuses as observed in routine posteroanterior roentgenograms.* Am J Dis Child*. 1940;60:55–78. B, Modified from Scammon RE. A summary of the anatomy of the infant and child. In: Abt IA, ed.* Pediatrics*. Vol 1. Philadelphia: Saunders; 1923:257–444.)*

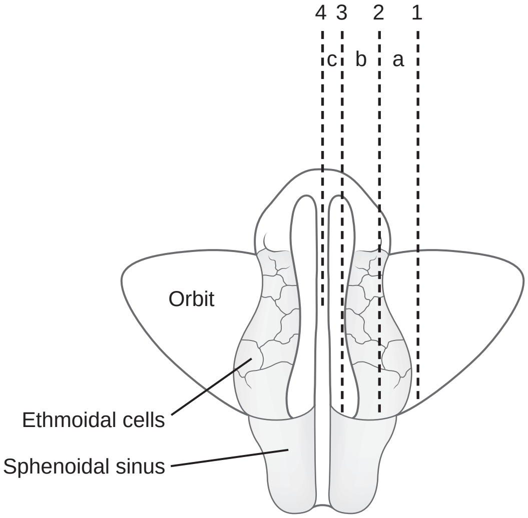

**e-Figure 18.34. Illustration of the ethmoid labyrinths, sphenoid sinuses, and orbits as reviewed in horizontal section.** In segment *a,* the posterior ethmoid cells are located on the margins of the orbit lying lateral to the anterior and middle groups and thus are not superimposed on them or the sphenoid sinus in the dorsoventral radiographic projection. In segment *b,* the three groups of ethmoid cells lie in the same dorsoventral axis and are superimposed on one another and on the sphenoid sinus in the dorsoventral radiographic projection. In segment *c,* a portion of the anterior wall of the sphenoid sinus lies medial to the ethmoid labyrinth and is not superimposed on it in the dorsoventral radiographic projection. *(Modified from Köhler A.* Roentgenography: The Borderlands of the Normal and Early Pathological in the Skiagram*. New York: William Wood & Co; 1928.)*

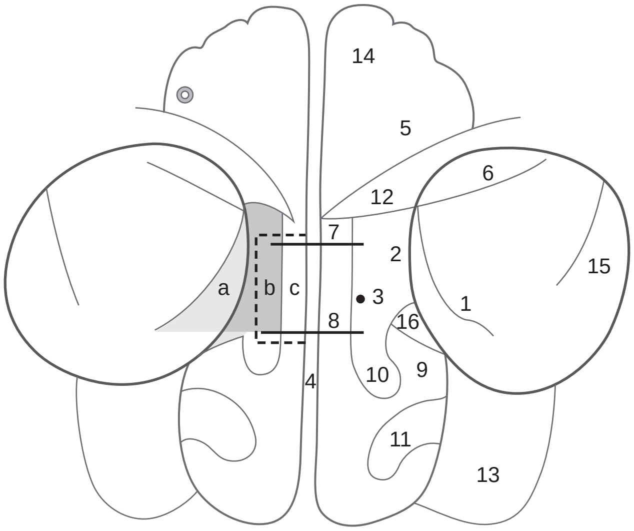

**e-Figure 18.35. Schematic of the paranasal sinuses in a dorsoventral projection.** *a,* Posterior ethmoid cells; *b,* superimposed anterior, middle, and posterior ethmoid cells; *c,* sphenoid sinus without superimposed ethmoid cells; *1,* inner edge of the inferior orbital fissure; *2,* inner margin of the orbit; *3,* medial border of the lateral mass of the ethmoid bone; *4,* nasal septum; *5,* superciliary ridge; *6,* upper border of the superior orbital fissure; *7,* nasofrontal and nasomaxillary sutures; *8,* roof of the superior nasal meatus; *9,* uncinate process; *10,* middle turbinate; *11,* inferior turbinate; *12,* internal projection of the superior orbital margin; *13,* maxillary sinus; *14,* frontal sinus; *15,* sphenozygomatic suture; *16,* ethmoid bulla. *(Redrawn from Köhler A.* Roentgenography: The Borderlands of the Normal and Early Pathological in the Skiagram*. New York: William Wood & Co.; 1928.)*

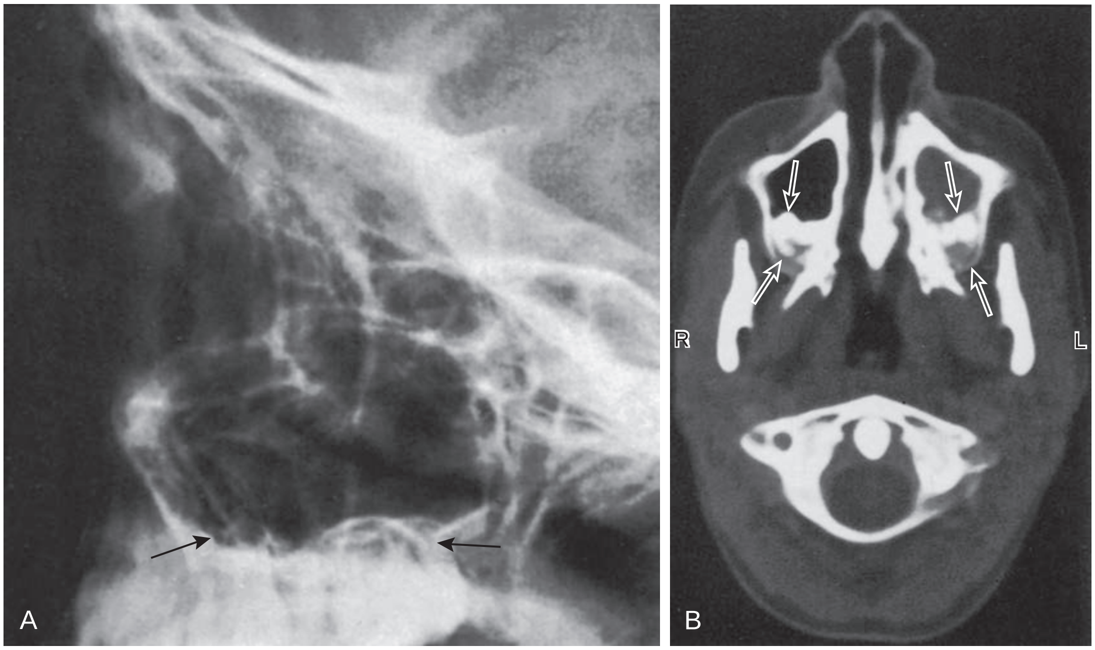

**e-Figure 18.38. Maxillary sinuses.** (A) Lateral maxillary sinus radiograph shows the roots of the molars and bicuspids in contact with the floor of the maxillary sinus *(arrows)* in an 11-year-old child. (B) Molar-indenting maxillary sinuses in a 12-year-old child who had a CT because of sinus disease. Unerupted molars indent the posterior aspects of both maxillary sinuses *(arrows)*. The left sinus is opaque because of sinus disease.

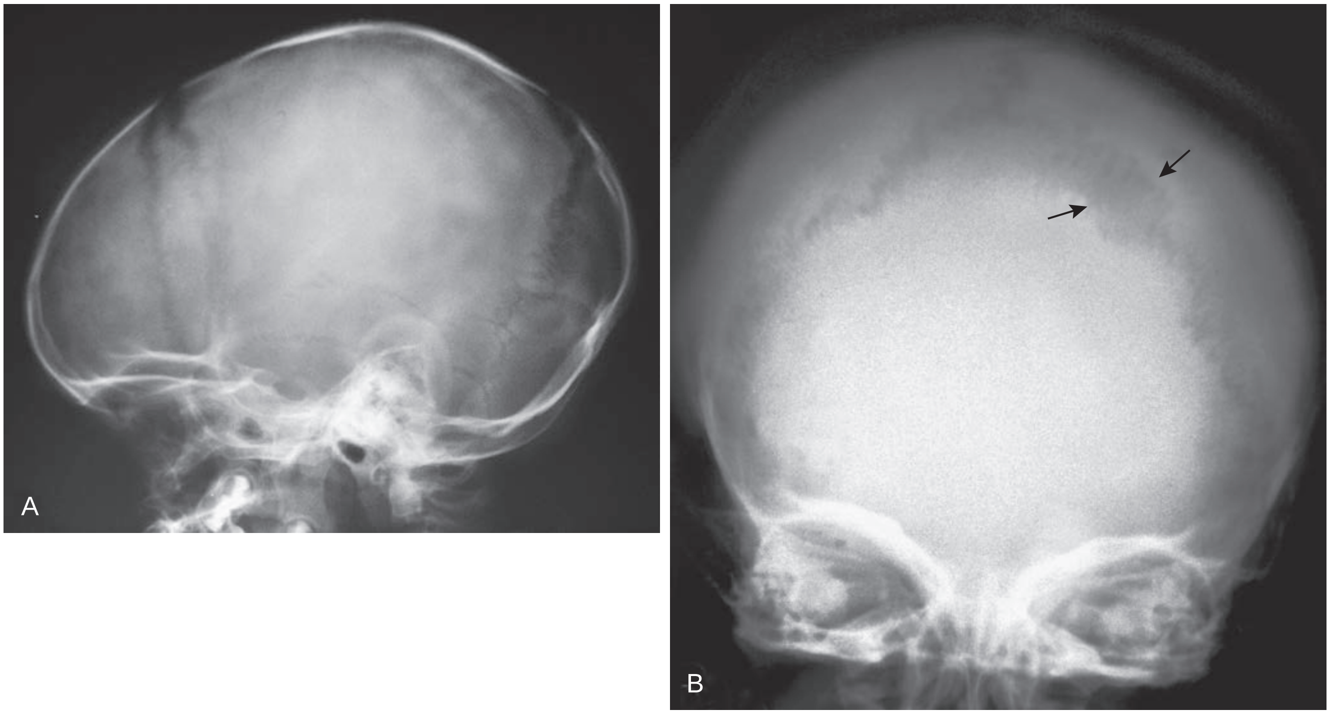

**Figure 18.30. Split sutures.** (A) A lateral radiograph reveals a widened coronal suture caused by acute increased intracranial pressure. (B) A radiograph shows the results of chronic increased intracranial pressure. The interdigitations of the lambdoid suture are widened, but the sutures are not frankly split *(arrows)*. This radiograph shows an attempt of the sutures to reunite with continual increased pressure.

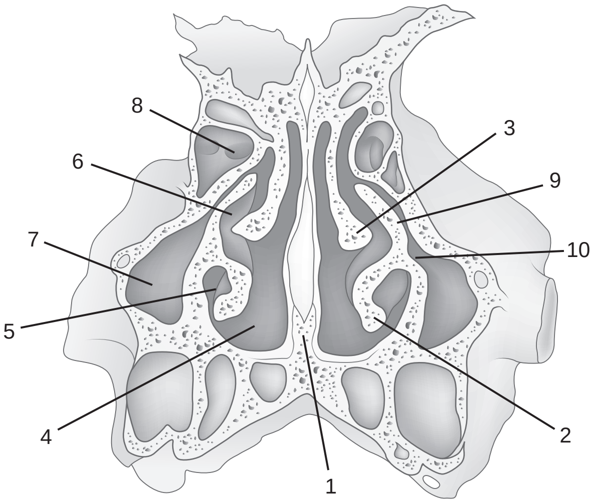

**Figure 18.31. Schematic frontal section through the nasal fossa and paranasal sinuses at the level of the ostium of the maxillary sinus in a 7-year-old child.** *1,* Nasal septum; *2,* inferior turbinate; *3,* middle turbinate; *4,* nasal fossa; *5,* inferior meatus; *6,* middle meatus; *7,* maxillary sinus; *8,* ethmoid cells; *9,* infundibulum; *10,* ostium. *(Modified from Schaeffer JP.* The Nose, Paranasal Sinuses, Naso-Lacrimal Passageways and the Olfactory Organ in Man. *Philadelphia: P. Blakiston's Sons; 1920.)*

identification until 6 years of age. The rate of expansion varies, and they extend to the orbital roof between 6 and 12 years. By puberty, most frontal sinuses have reached adult size. Some are extensions of the anterior ethmoid cells. In some cases (especially in instances of hypoplasia of the frontal lobes of the brain), exaggerated extension into the horizontal plates of the frontal bones may occur. This phenomenon is easily recognized in lateral projections.

## Ethmoid Sinuses

The ethmoid sinuses are composed of a series of cells of variable number, forming paired bony labyrinths suspended from the horizontal plate of the ethmoid bone on each side of the vertical plate, with the lateral walls forming the medial orbits. They are separated by thin osseous septa covered with mucous membranes. They communicate with the nasal cavities directly or indirectly through cells of the same group. They are present at birth, expand rapidly during the first 5 years, expand less quickly until about 8 years, and typically are complete by age 12 years. They usually form three groups: anterior, middle, and posterior (see e-Fig. 18.32 and 18.35). The ethmoid cells often extend into the turbinates, crista galli, and neighboring frontal, maxillary, sphenoid, and palate bones. Three anatomic variants of ethmoid cells are found: Agger nasi, Haller, and Onodi cells (see Chapter 8). Extension of sinus infection to the orbit can occur easily via the lamina papyracea (see Chapter 8).

## Sphenoid Sinus

The paired cavities in the sphenoid bone are separated by an osseous partition that may be displaced to one side so that the

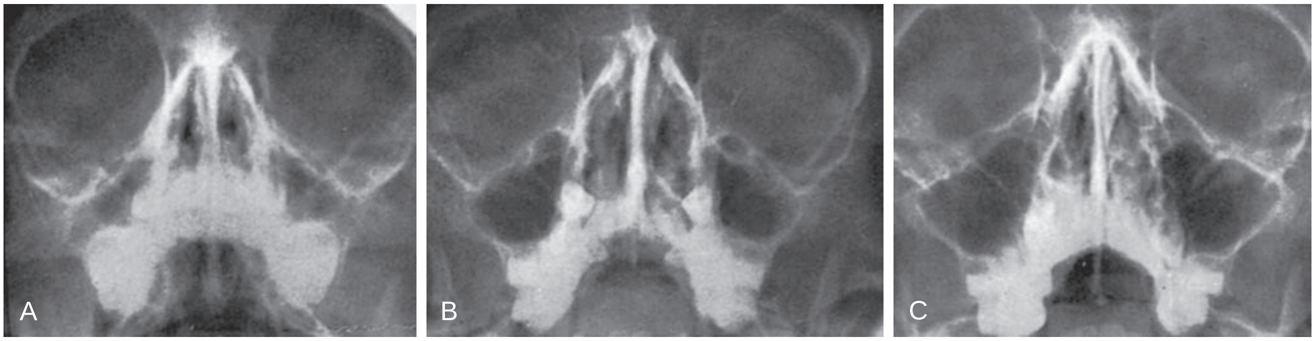

**Figure 18.36. Waters projection of normal maxillary sinuses in a child at ages 4 years.** (A) 7 years, (B and C) 11 years.

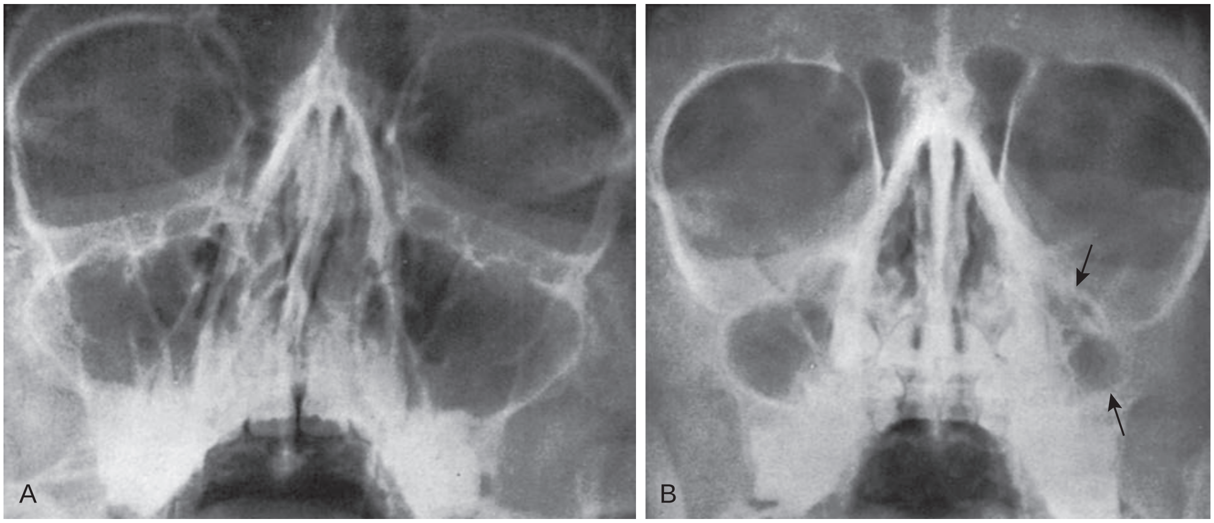

**Figure 18.37. Variants of the maxillary sinus.** (A) Several septa and ridges dividing the maxillary sinus into small cavities in an 11-year-old girl. (B) Hypoplasia of the left maxillary sinus *(arrows)* in a 7-year-old boy.

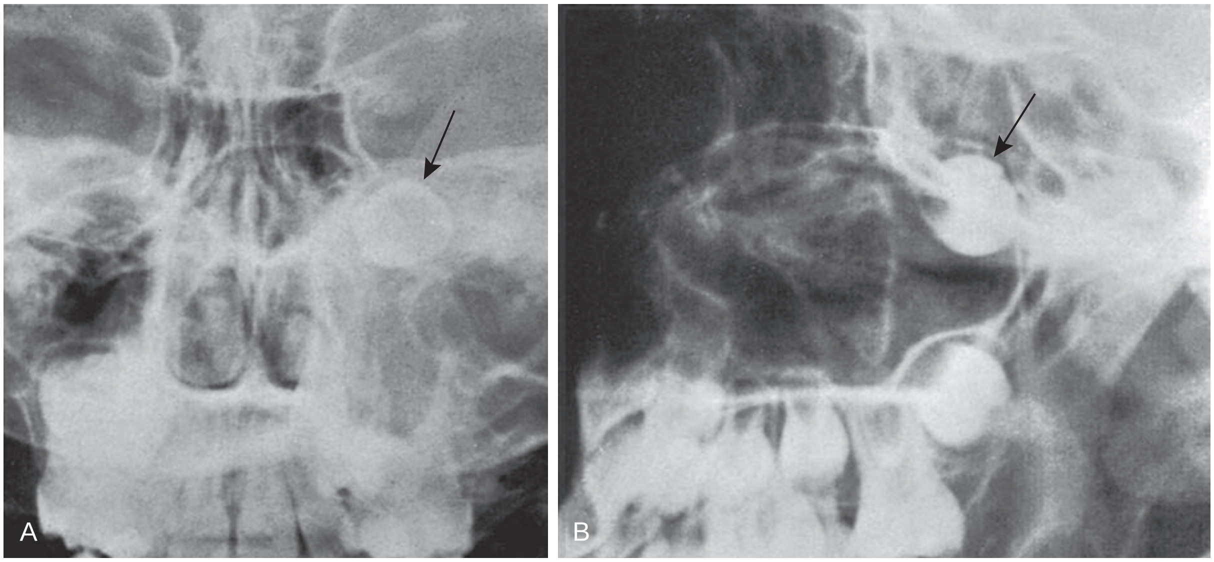

**Figure 18.39. Abnormal molar.** Frontal (A) and lateral (B) projections show an ectopic third molar *(arrows)* in the fetal position because of a failure of normal migration.

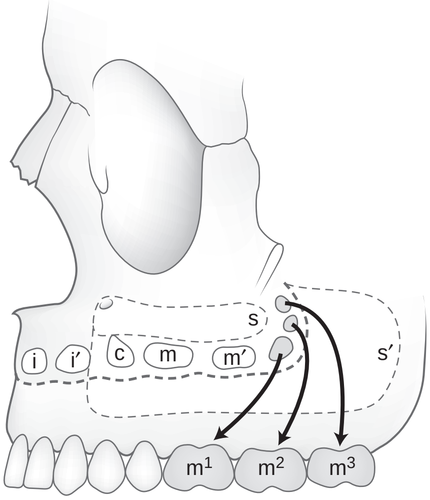

**Figure 18.40. Schematic of postnatal growth of the maxillary sinus, upper maxilla, and superior dental arch.** The *broken line* outlines the maxilla at birth; the adult bone is drawn in *(solid line)*. *c,* Deciduous canine; *i* and *i′,* deciduous incisors; *m* and *m′,* deciduous molars; $m^1$, $m^2$, and $m^3$, permanent molars *(shaded); s,* maxillary sinus at birth; *s′,* maxillary sinus at maturity. *(Modified from Keith A.* Human Embryology and Morphology. *4th ed. London: Edward Arnold & Co.; 1921.)*

two cavities vary in size and shape.[10–12] The cavities can be visualized when superimposed in lateral radiographs or side by side in submentovertical projections (e-Fig. 18.41). Ridges and septa sometimes divide each cavity into compartments. The air cells are not present at birth; by age 4 years, they are 4 to 8 mm in diameter, and become adult size between 7 and 11 years (Fig. 18.42).

## Osteomeatal Unit

The components of the osteomeatal unit (OMU; the central sinus drainage anatomy) are present at birth, albeit crowded (see Figs. 18.31, 18.43, and 18.44). This anatomy is clearly shown with CT obtained either directly coronal or reconstructed from axial images.

## IMAGING OF THE SINUSES

### Plain Radiographs

In general, radiographs are unnecessary for the diagnosis of paranasal sinus disease, particularly in children less than 6 years.[13,14] Nor are they valuable for assessing suitability for, or complications from, sinusitis or sinus surgery.[15,16] Plain radiographs have dubious value in children less than 2 years and certainly infants less than 1 year because of high false-positive rate.[17–19] In older children, a single Waters view may prove useful. See Chapter 8 for further discussion of sinus imaging.

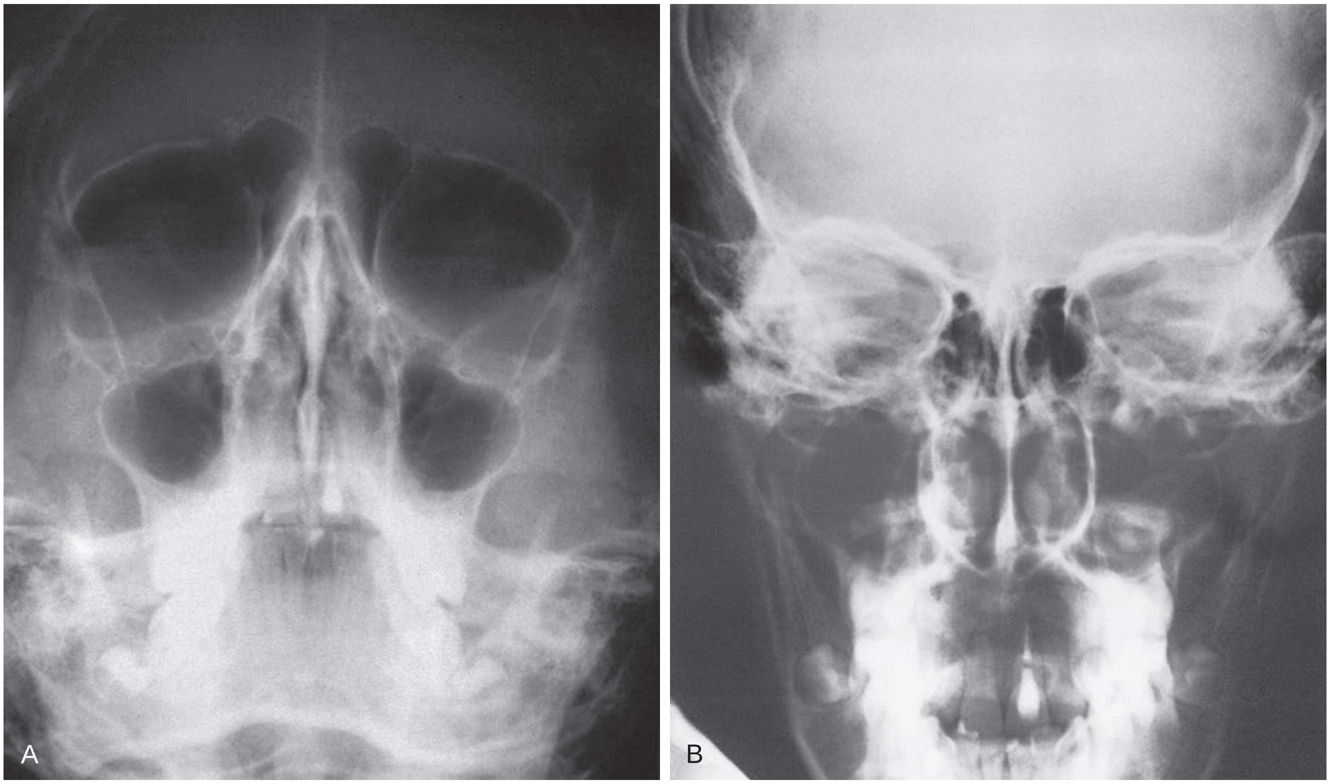

**Figure 18.42. Radiographs of the paranasal sinuses.** (A) Normal Waters (parietocanthial), (B) Posteroanterior axial, (C) Caldwell and (D) Lateral views.

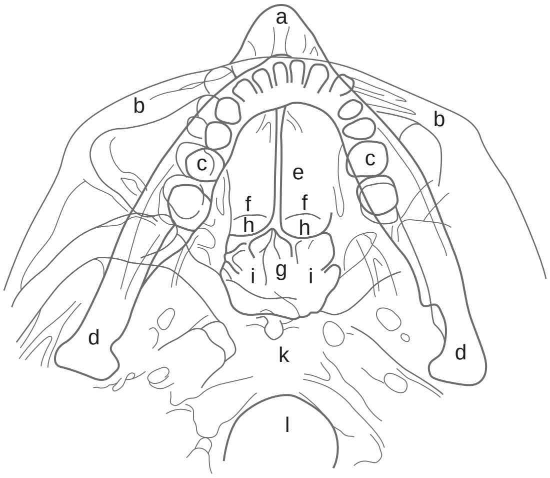

**e-Figure 18.41. Schematic of the sphenoid sinus in a submentovertical projection.** *a,* External nose; *b,* frontal bone; *c,* superimposed upper and lower teeth; *d,* mandible; *e,* hard palate; *f,* posterior margin of hard palate; *g,* septum between the sphenoid sinuses; *h,* anterior wall of the sphenoid sinus; *i,* cavities of the sphenoid sinus; *k,* basiocciput; *l,* foramen magnum. *(Modified from Köhler A.* Roentgenography: The Borderlands of the Normal and Early Pathological in the Skiagram*. New York: William Wood & Co.; 1928.)*

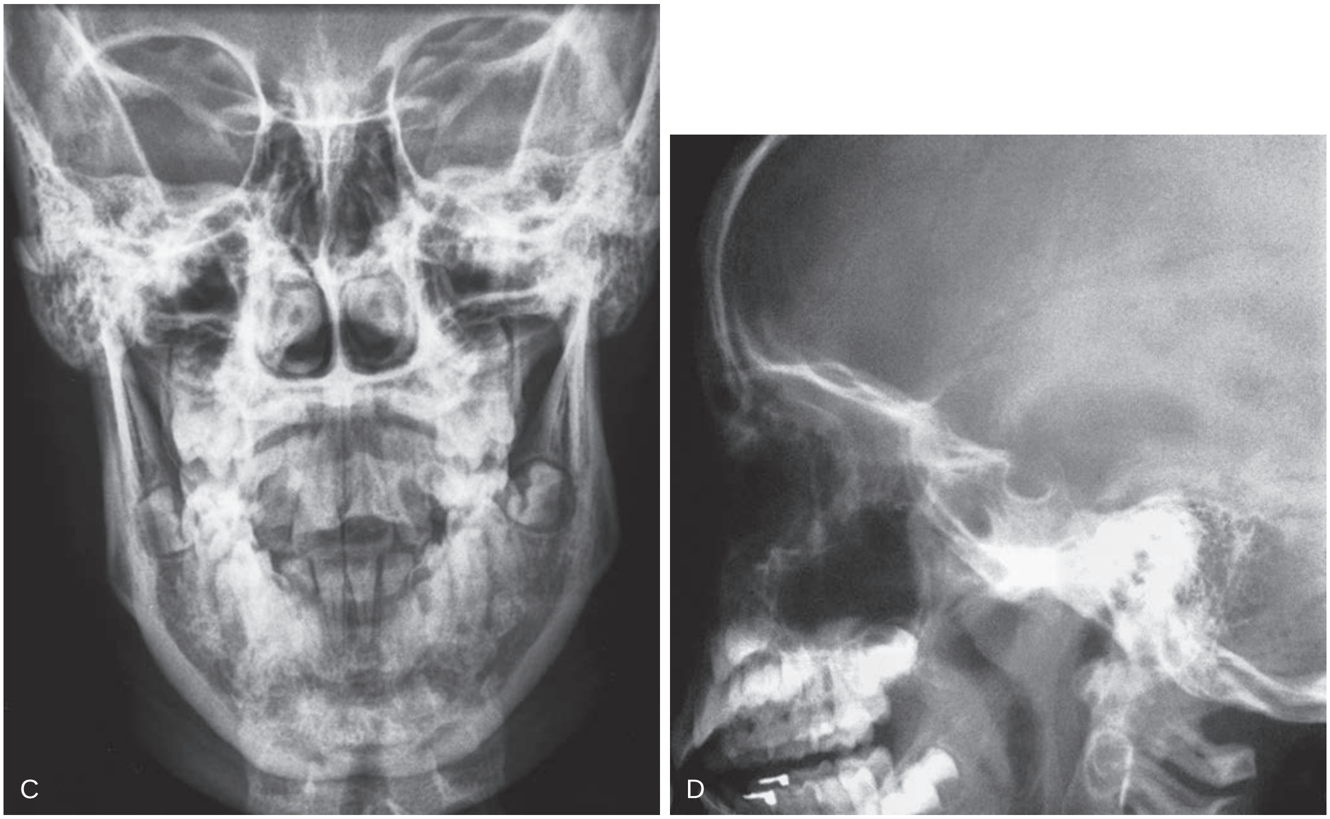

**Figure 18.42, cont'd.**

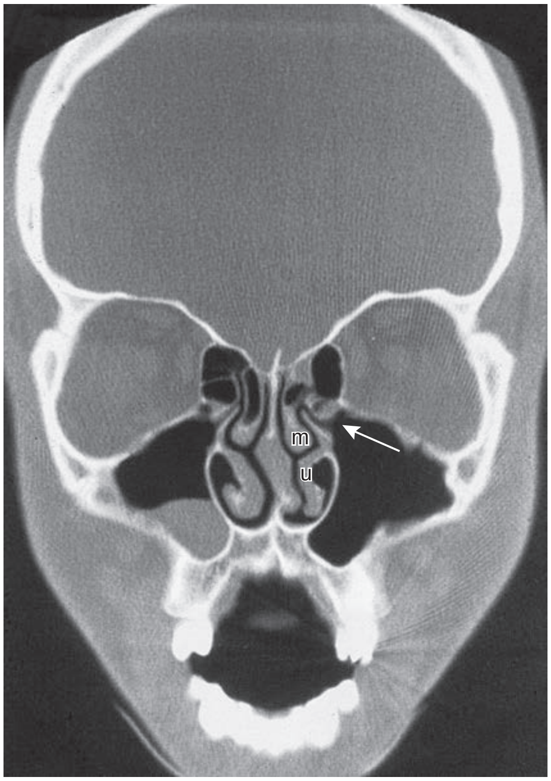

**Figure 18.43. Coronal CT through the midsinuses and nose showing the osteomeatal unit.** Note the mucous retention cyst in the right maxillary antrum and concha bullosa in the right middle turbinate. The patient has no history or evidence of sinus disease. The ostium (opening) *(arrow)*, infundibulum (airspace superior to ostia and lateral to the uncinate process of the inferior turbinate *[u]*), and middle turbinate *(m)* are shown. The circular airspace above the uncinate process is the hiatus semilunaris.

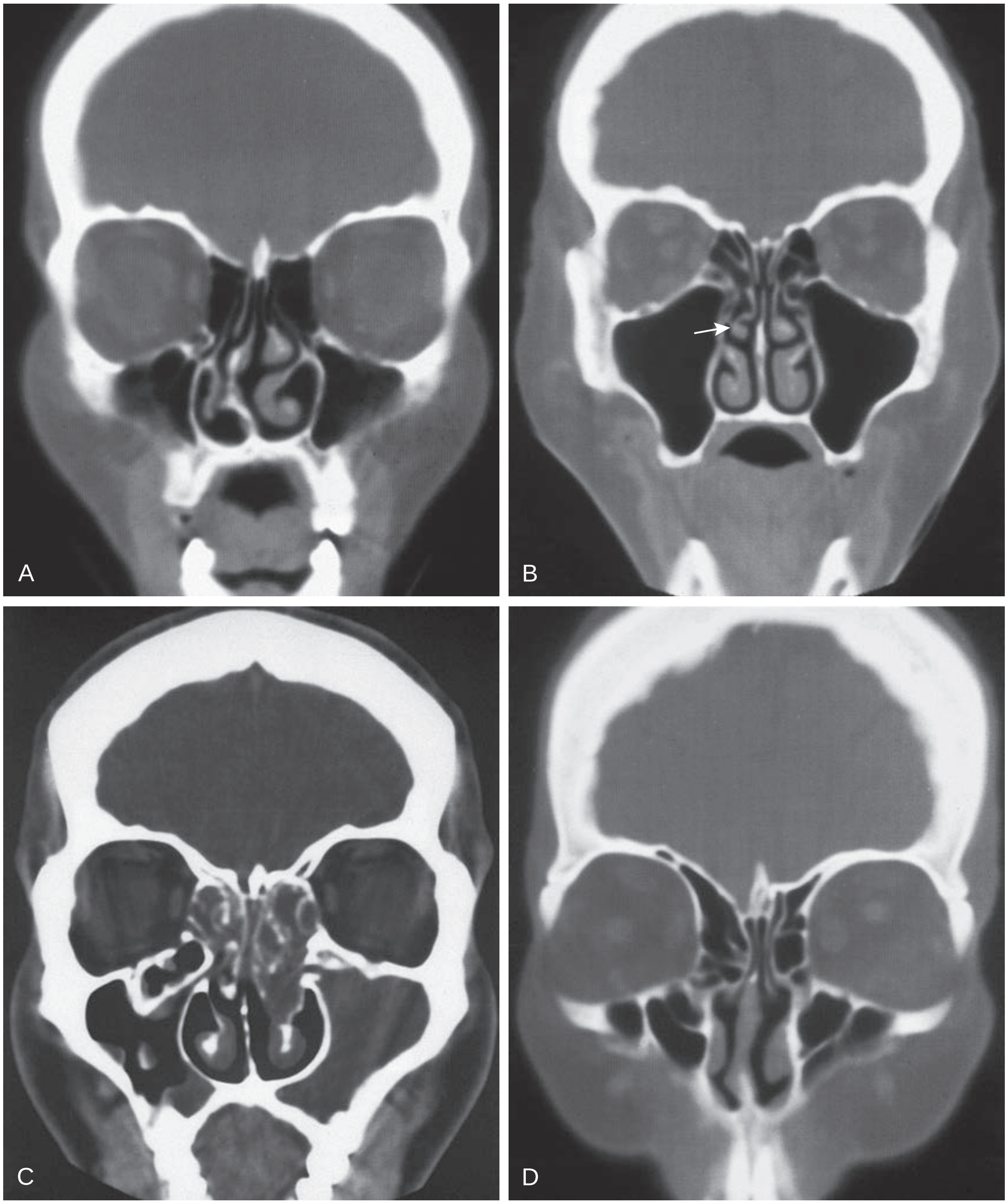

**Figure 18.44. Normal coronal CT variants of the nose.** (A) Deviated nasal septum, (B) a paradoxically bent middle turbinate *(arrow)*, (C) Haller air cell (ethmoid cells located along the rim of the ostia and protruding into the maxillary antrum), and (D) large Agger nasi air cells—the most anterior air cells.

## KEY POINTS

- The head is larger relative to the face in neonates and infants.
- Obliteration of the sutures is not complete until the second to third decade of life.
- Wormian bones, Inca bone, and bathrocephaly are normal cranial variants in children under 2 years of age.
- Cranial variants of normal children and juveniles include the paracondylar process, digital markings, and Pacchionian bodies (arachnoid granulations).
- Plain sinus radiographs have extremely limited utility, especially in children under 2 years, and are unnecessary for diagnosing sinusitis, particularly in children under 6 years old.
- Maxillary and ethmoid air cells are present at birth.
- Sphenoid air cell pneumatization begins around 2 years of age.[20]
- Frontal sinuses are seen between 6 and 12 years of age.

## SUGGESTED READINGS

Barghouth G, Prior JO, Lepori D, et al. Paranasal sinuses in children: size evaluation of maxillary, sphenoid, and frontal sinuses by magnetic resonance imaging and proposal of volume index percentile curves. *Eur Radiol*. 2002;12:1451–1458.

Belden CJ. The skull base and calvaria: adult and pediatric. *Neuroimaging Clin N Am*. 1998;8:1–20.

Bhattacharyya N, Jones DT, Hill M, et al. The diagnostic accuracy of computed tomography in pediatric chronic rhinosinusitis. *Arch Otolaryngol Head Neck Surg*. 2004;130:1029–1032.

Huda W. Assessment of the problem: pediatric doses in screen-film and digital radiography. *Pediatr Radiol*. 2004;34(suppl 3):S173–S182.

Mann SS, Naidich TP, Towbin RB, et al. Imaging of postnatal maturation of the skull base. *Neuroimaging Clin N Am*. 2000;10:1–22.

## REFERENCES

Full references for this chapter can be found on www.expertconsult.com.

## REFERENCES

1. Kier EL. Fetal skull. In: Newton TH, Potts DG, eds. *Radiology of the Skull and Brain*. Vol. 1. St. Louis: Mosby; 1971.
2. Moloy HG. Studies on head molding during labor. *Am J Obstet Gynecol*. 1942;44:962–982.
3. Vignaud-Pasquier J, Lichtenbert R, Laval-Jeantet M, et al. Les impressions digitales de la naissance á neuf ans. *Biol Neonate*. 1964;6:250–276.
4. Greitz D, Hannerz J. A proposed model of cerebrospinal fluid circulation: observations with radionuclide cisternography. *AJNR Am J Neuroradiol*. 1996;17:431–438.
5. Fink AM, Maixner W. Enlarged parietal foramina: MR imaging features in the fetus and neonate. *AJNR Am J Neuroradiol*. 2006;27:1379–1381.
6. Goldsmith WM. Catlin mark: inheritance of unusual opening in parietal bones. *J Hered*. 1941;32:301–309.
7. Maresh MM. Paranasal sinuses from birth to late adolescence. *Am J Dis Child*. 1940;60:841–861.
8. Maresh MM. Paranasal sinuses from birth to late adolescence, 1: size of the paranasal sinuses as observed in routine posteroanterior roentgenograms. *Am J Dis Child*. 1940;60:55–78.
9. Odita JC, Akamaguna AI, Ogisi FO, et al. Pneumatisation of the maxillary sinus in normal and symptomatic children. *Pediatr Radiol*. 1986;16:365–367.
10. Fujioka M, Young LW. The sphenoidal sinuses: radiographic patterns of normal development and abnormal findings in infants and children. *Radiology*. 1978;129:133–136.
11. Kazkayasi M, Kardeniz Y, Arikan OK. Anatomic variations of the sphenoid sinus on computed tomography. *Rhinology*. 2005;43:109–114.
12. Reittner P, Doerfler O, Goritschnig T, et al. Magnetic resonance imaging patterns of the development of the sphenoid sinus: a review of 800 patients. *Rhinology*. 2001;39:121–124.
13. American Academy of Pediatrics, Subcommittee on Management of Sinusitis and Committee on Quality Improvement. Clinical practice guideline: management of sinusitis. *Pediatrics*. 2001;108:798–808.
14. American College of Radiology. Sinusitis in the pediatric population: ACR appropriateness criteria. *Radiology*. 2000;215:811–818.
15. McAlister WH, Kronemer K. Imaging of sinusitis in children. *Pediatr Infect Dis J*. 1999;18:1019–1020.
16. Kronemer KA, McAlister WH. Sinusitis and its imaging in the pediatric population. *Pediatr Radiol*. 1997;27:837–846.
17. Diament MJ, Senac MO, Gilsanz V, et al. Prevalence of incidental paranasal sinus opacification in pediatric patients: a CT study. *J Comput Assist Tomogr*. 1987;11:426–431.
18. Kovatch AL, Wald ER, Ledesma-Medina J, et al. Maxillary sinus radiographs in children with nonrespiratory complaints. *Pediatrics*. 1984;73:306–308.
19. Kristo A, Alho O-P, Luotonen J, et al. Cross-sectional survey of paranasal sinus magnetic resonance imaging findings in schoolchildren. *Acta Paediatr*. 2003;92:34–36.
20. Güldner C, Pistorius SM, Diogo I, et al. Analysis of pneumatization and neurovascular structures of the sphenoid sinus using cone-beam tomography (CBT). *Acta Radiol*. 2012;53(2):214–219.

# 19

# Prenatal Imaging

Ashley James Robinson, Susan Blaser, and A. Michelle Fink

The fetal abnormalities described in this chapter are those most likely to be assessed by a pediatric radiologist who primarily performs fetal magnetic resonance imaging (MRI), computed tomography (CT), radiography, and ultrasound. These additional modalities are particularly useful for acquiring further characterization of fetal abnormalities, especially when a fetal autopsy will be declined but a couple needs to be counseled regarding future pregnancies.

In most of the references provided, a combination of prenatal ultrasound plus MRI and/or CT was performed. The suggested readings list includes references to several standard ultrasound texts that deal with the subject matter from the perspective of ultrasound as the primary imaging modality.

## SCALP

A scalp cyst, although infrequently encountered, is likely to require further assessment by fetal MRI. The most important differential diagnosis is between an ectodermal cyst and a meningocele or encephalocele.[1-6] A fetus with an ectodermal cyst should have no underlying skull defect or transiting vessels or membranes, and the underlying brain should be normal. Because of limitations of resolution, small defects and thus the diagnosis of meningocele can be missed when MRI is used (e-Fig. 19.1).[7]

Hemangioma is another scalp abnormality that occurs infrequently (Fig. 19.2). The main differential diagnosis is encephalocele.[8,9] Further evaluation by fetal MRI can be helpful in demonstrating the absence of a skull defect or an abnormality of the underlying brain.[1,10-14]

Other lesions that should be considered in the differential diagnosis of scalp abnormalities include lymphatic malformation, edema, nevus sebaceous, sarcoma, and a teratoma perforating the skull.[1,15,16] Rare abnormalities that have been described on antenatal imaging include gyriform thickening of the scalp in fetuses with cutis verticis gyrata associated with Noonan syndrome[17] and hamartomata of the scalp in fetuses with encephalocraniocutaneous lipomatosis.[18]

## SKULL

Skull defects are a result of errors in dorsal induction, the process whereby the neural tube forms and closes (neurulation).[19,20] A spectrum of anomalies is characterized by absent flat bones of the skull.

### Large Bony Defects

#### Acalvaria

*Acalvaria* is the term used when the bony skull vault, meninges, and scalp muscles are absent and a normal brain is covered by skin only.[21] *Acrania* is the term used when the skull vault, scalp muscles, and skin are absent and a dysplastic brain is covered by meninges only.[22]

#### Exencephaly

Exencephaly is the combination of acrania with abnormal brain tissue[22] and has been demonstrated to be the predecessor of anencephaly.[23,24] Exencephaly can be seen in association with amniotic band sequence[25-28] and limb body wall complex,[29,30] but can be distinguished from them because they generally form asymmetric skull defects (e-Fig. 19.3).[19] MRI can help to differentiate exencephaly from other cranial vault defects.[31]

#### Anencephaly

Anencephaly, which is the single most common open neural tube defect,[32] is characterized by acrania with complete absence of a normal brain above the brainstem (e-Fig. 19.3A).[19,20] It is the end result of exencephaly with mechanical and chemical attrition of the abnormal brain tissue in utero[22]; the remaining tissue constitutes a mass of exposed vascular neural tissue. The cartilaginous skull is intact. This condition invariably is fatal. When accompanied by dysraphism of the entire spine, it is known as craniorachischisis.[19] Fetal MRI findings have been described in cases associated with omphalocele,[33] gastroschisis,[34] and pentalogy of Cantrell.[35,36]

### Focal Bony Defects

#### Cephaloceles

Focal defects in the skull can allow internal structures to herniate. The terminology changes depending on whether the contents of the hernia include just meninges and cerebrospinal fluid (cephalocele), brain matter (encephalocele), or a ventricle (encephalocystocele). Most defects are in the midline, are occipital (Fig. 19.4),[19,20] and usually contain dysplastic brain tissue and venous sinuses.[20] They can be part of syndromes such as the ciliopathies (e.g., Meckel-Gruber), the congenital muscular dystrophies (e.g., Walker–Warburg), and Chiari III malformation.[19,20,37,38] The most common type of encephalocele in Southeast Asia is frontoethmoidal.[39]

Fetal MRI can be useful to differentiate a cephalocele from a scalp cyst and to determine if it contains brain tissue, with diffusion-weighted imaging being particularly helpful for detecting displaced brain, and echo-planar imaging for detecting draining veins.[1,40,41] Care must be exercised to differentiate a cephalocele from an encephalocystocele with very thin parenchyma.[42] Large encephaloceles can appear similar to anencephaly, although the calvarium typically has developed to some extent.[19] An atretic cephalocele typically presents as a midline subcutaneous nodule or cyst,[43] and underlying venous anomalies often are present that are similar to those seen with enlarged parietal foramina.[44-46]

#### Enlarged Parietal Foramina

Enlarged parietal foramina are thought to be the result of defective ossification of the membranous skull. During fetal life they comprise a large central defect that, because of subsequent ossification, including midline ossification (Fig. 19.5), become bilateral symmetric defects.[47] In contradistinction, encephaloceles typically are midline or unilateral. Enlarged parietal foramina can be large defects, typically closing almost completely during childhood, leaving only small bilateral foramina.[43,48] Although typically benign, they can be associated with hypoplasia or atresia of the straight sinus with a persistent falcine sinus draining to the straight sinus at the level of the anomaly.[43,47] Associated abnormalities of occipital cortical infolding can be seen postnatally.[49] Enlarged parietal foramina can be hereditary (autosomal dominant), associated with genes *MSX2* and *ALX4*.[50,51] Enlarged parietal foramina also can be syndromic, as in Potocki–Shaffer syndrome.[52]

## Abstract:

Detailed assessment of the fetus is primarily performed by ultrasound, with fetal magnetic resonance imaging used as a secondary complimentary modality for further characterisation. Increasingly computed tomography is being used in the assessment of the fetal axial and appendicular skeleton. This chapter describes the most common scalp and cranial vault abnormalities that are encountered in the fetus, including large bony defects such as acalvaria, exencephaly and anencephaly, focal bony defects such as cephaloceles and enlarged partietal foramina, mineralization defects of various skeletal dysplasia, and size and shape abnormalities typical of spina bifida aperta, skeletal dysplasia and various forms of craniosynostosis.

## Keywords:

skeletal dysplasia
abnormalities
spina bifida aperta
skeletal dysplasia
craniosynostosis

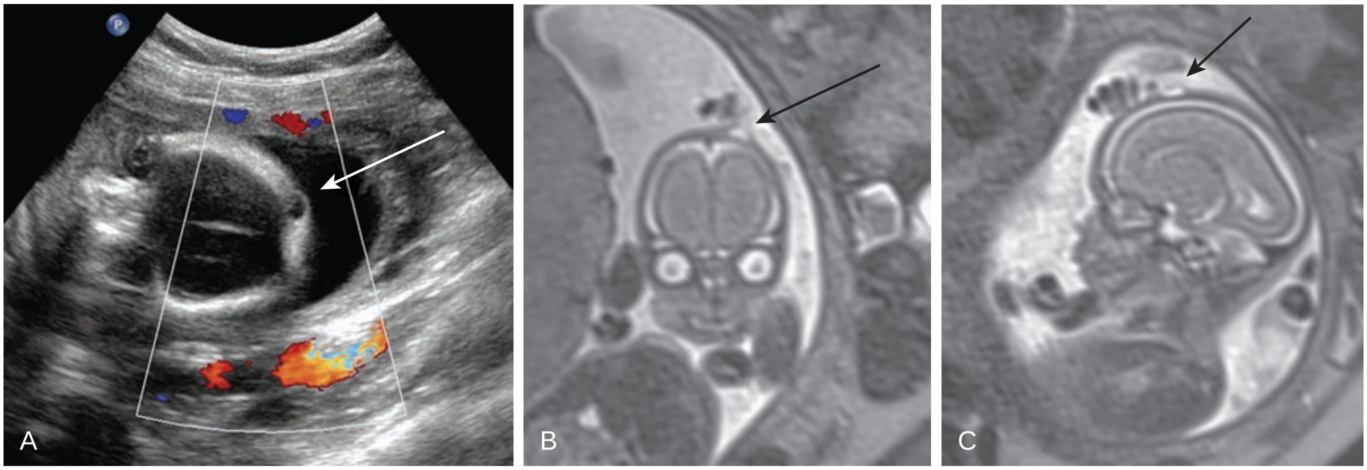

**e-Figure 19.1. Scalp cyst.** (A) Prenatal sonogram shows a parasagittal scalp cyst *(arrow).* No clear intracranial communication or intracyst contents are present. (B) Coronal fetal MRI shows a cyst *(arrow).* The subjacent brain appears normal. No skull defect is seen. (C) Sagittal fetal MRI shows a cyst *(arrow)* in the sagittal view.

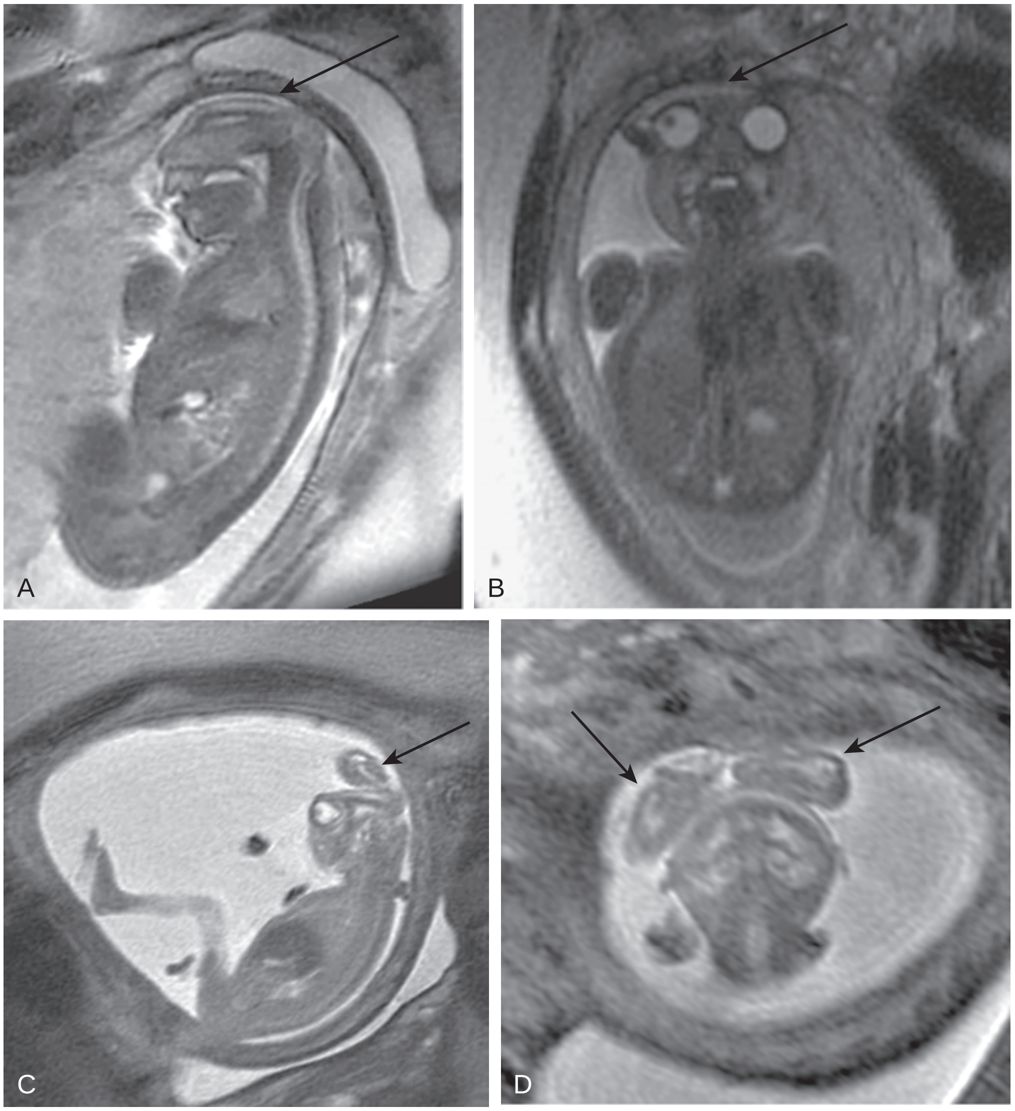

**e-Figure 19.3. Anencephaly/exencephaly.** (A) Sagittal and (B) coronal fetal MRI images show anencephaly. The cranium and brain are completely absent *(arrow)* above the orbits. (C) Sagittal MRI in another fetus shows exencephaly. The cranium is absent, and persistent dysplastic brain tissue is present *(arrow).* (D) Coronal image shows bilateral dysplastic hemispheres *(arrows).*

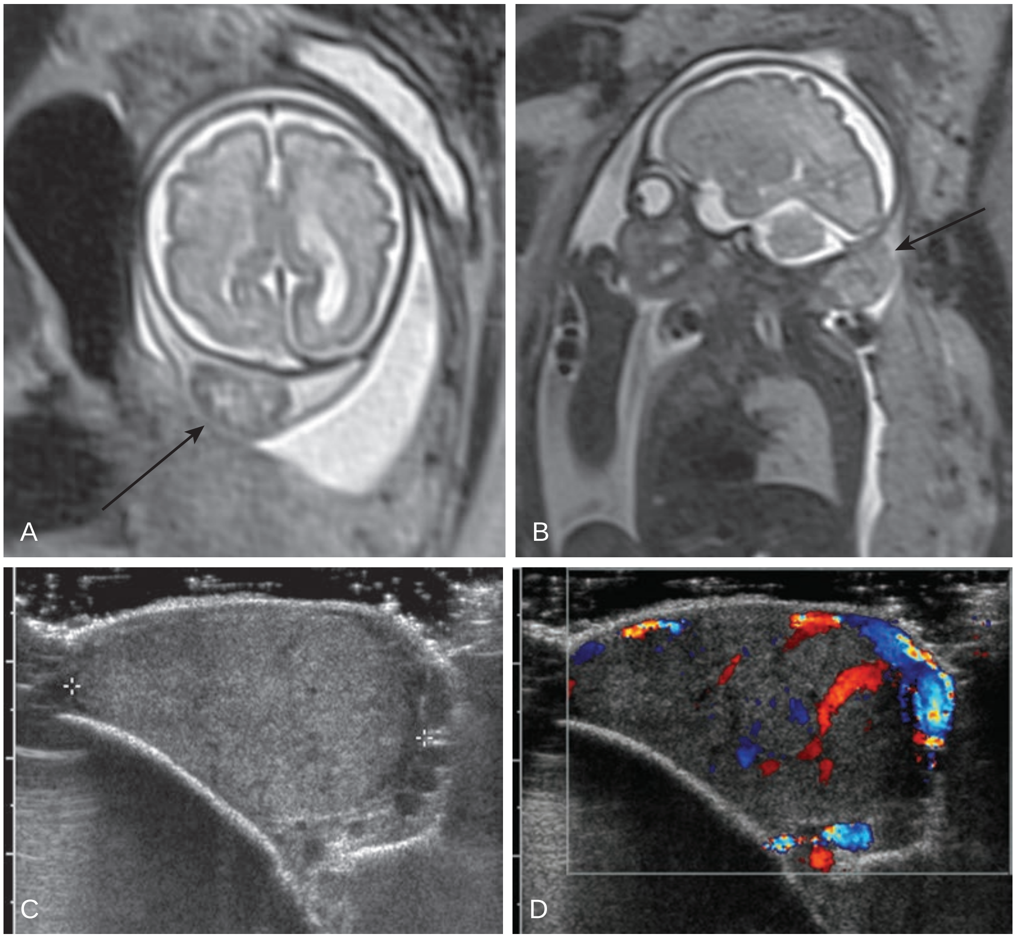

**Figure 19.2. Scalp hemangioma.** (A) Axial fetal MRI shows a heterogeneous mass in the occipital scalp *(arrow)*. The skull appears intact. (B) Sagittal fetal MRI shows a sagittal view of a mass in the occipital scalp *(arrow)*. (C) Postnatal sonogram shows a heterogeneous mass in the scalp. The skull appears to be intact. (D) Color Doppler sonogram shows vascular flow throughout.

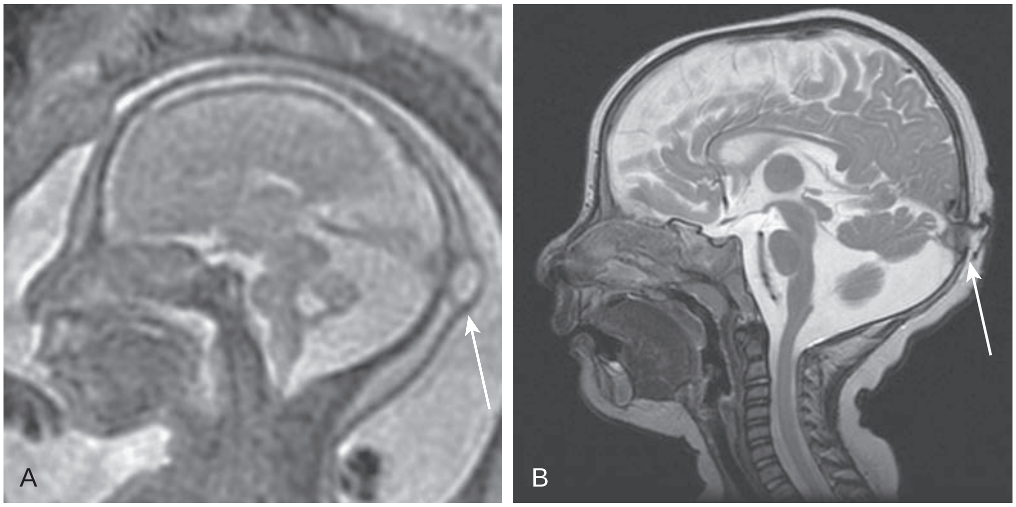

**Figure 19.4. Cephalocele.** (A) Sagittal fetal MRI shows a small occipital cyst *(arrow)* with abnormal cerebellar vermis. (B) Postnatal sagittal T2-weighted MRI shows an atretic cephalocele with a scalp abnormality *(arrow)*. *(From Robinson AJ, Blaser S, Toi A, et al. The fetal cerebellar vermis: assessment for abnormal development by ultrasonography and magnetic resonance imaging.* Ultrasound Q. *2007;23(3):211–223.)*

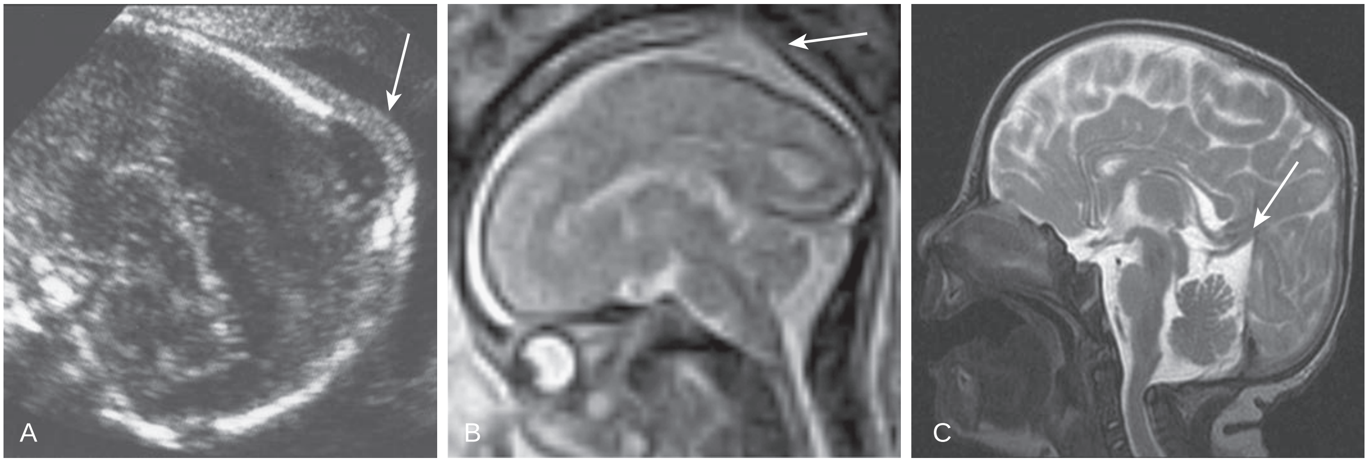

**Figure 19.5. Enlarged parietal foramina.** (A) Sagittal fetal sonogram shows a skull defect with intact overlying scalp *(arrow).* (B) Sagittal fetal MRI shows a skull defect that does not contain brain *(arrow).* (C) Sagittal T2-weighted postnatal MRI shows a skull defect that now contains brain. An abnormal course of a straight sinus is present *(arrow). (From Fink AM, Maixner W. Enlarged parietal foramina: MR imaging features in the fetus and neonate.* AJNR Am J Neuroradiol*. 2006;27:1379–1381.)*

**TABLE 19.1** Skull Abnormalities in Common Lethal Skeletal Dysplasias

| Skull Type | Mineralization | Size | Shape | Trunk Length | Fractures |
|---|---|---|---|---|---|
| Osteogenesis imperfecta (type IIa) | Demineralized | Normal | Deformable | Short | Many |
| Hypophosphatasia | Demineralized | Normal | Deformable | Normal | Few |
| Achondrogenesis | Type I demineralized<br>Type II normal | Large | Normal | Short | Few |
| Thanatophoric dysplasia | Normal | Large (megalencephaly) | Type I normal<br>Type II cloverleaf | Normal | None |

*Modified from Glanc P, Chitayat D, Unger S. The fetal musculoskeletal system. In: Rumack CM, Wilson SR, Charboneau JW, eds.* Diagnostic Ultrasound, *3rd ed. St. Louis: Elsevier; 2005.*

## Mineralization Defects

Prenatal ultrasound may reveal defective skull mineralization in fetuses with several skeletal dysplasias, primarily osteogenesis imperfecta type IIa (e-Fig. 19.6), hypophosphatasia congenita, and achondrogenesis.[53-55] A summary of distinguishing features is provided in Table 19.1. Radiography of the pregnant patient increasingly is being used, and fetal three-dimensional CT is an emerging technique in the evaluation of fetal skeletal dysplasias.[1,20,32,53,56-66]

## Size and Shape Abnormalities

Microcrania and macrocrania are defined when the head circumference differs more than three standard deviations from the mean in either direction.[32]

### Microcrania

The birth incidence of microcrania is 1:1000.[60] Microcrania often is the result of an underlying small brain, that is, microencephaly[1] (e-Fig. 19.7). Causes include genetic syndromes,[60] chromosomal defects (typically trisomy 13),[20] hemorrhage, teratogens, infection, radiation,[60] and encephalocele.[1,20]

### Macrocrania

Macrocrania typically is seen as a result of fetal hydrocephalus. Other causes include hydranencephaly,[20,61] intracranial teratoma or astrocytoma, and, occasionally, rarer tumors.[1,62] Skeletal dysplasias that cause enlargement of the head include achondrogenesis (type 1)[53] and skeletal dysplasias and craniosynostosis syndromes caused by fibroblast growth factor receptors 2 and 3 (*FGFR2* and *FGFR3*) mutations, such as thanatophoric dysplasia (e-Fig. 19.8) due to an enlarged brain (megalencephaly), with preferential enlargement of the temporal lobes and coexistent cerebral malformations, in particular, abnormal premature temporal lobe sulcation, which has been demonstrated by both fetal ultrasound and MRI.[63-72] Partial callosal dysgenesis also has been reported in fetuses with this condition.[66] Table 19.1 summarizes these distinguishing features.

### Dysmorphism

**Lemon-Shaped Skull and Spina Bifida.** A lemon-shaped skull, characterized by a concave or linear contour at the level of the coronal sutures (the “lemon sign”), is a well-known morphologic finding that is highly sensitive for open neural tube defects (e-Fig. 19.9).[73-75] However, it has a poor positive predictive value in low-risk fetuses and is seen in fetuses with other pathologies, including encephalocele and a variety of non–neural tube structural anomalies.[32,76-78]

**Cloverleaf Skull (Kleeblattschädel).** A cloverleaf appearance occurs as a result of bilateral coronal and lambdoid synostosis and is found in fetuses with type II thanatophoric dysplasia (Fig. 19.10).[1,53,64] Cloverleaf skull also has been used to describe the dysmorphic appearance of the skull in fetuses with syndromic craniosynostosis,[79-81] and which in prenatal life is often associated with abnormal karyotype, as described in Chapter 20. Several case reports have described the use of fetal MRI in its antenatal diagnosis.[79,82,83]

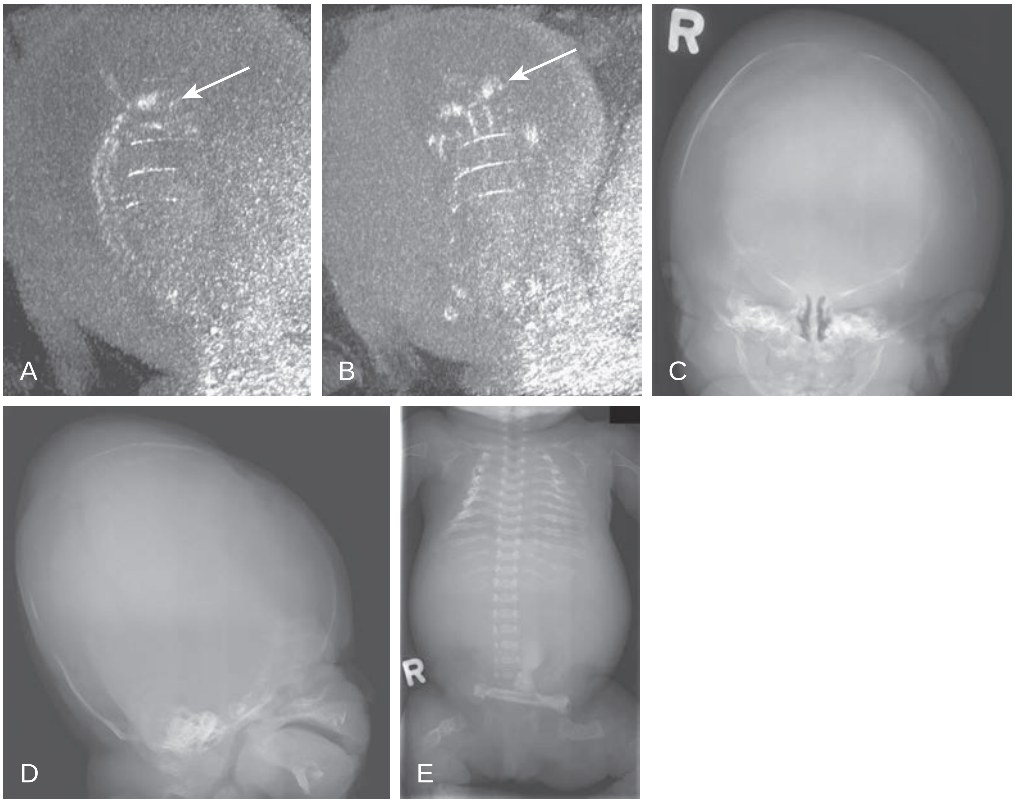

**e-Figure 19.6. Osteogenesis imperfecta.** (A) Fetal CT scan with sagittal reformatting shows that only the skull base *(arrow)* and spine are visible. The cranial vault is severely undermineralized. (B) Fetal CT scan with coronal reformatting shows that only the skull base is mineralized *(arrow).* (C) Postmortem frontal and (D) lateral radiographs show a severely undermineralized skull vault. (E) Postmortem radiograph shows short fractured long bones and ribs.

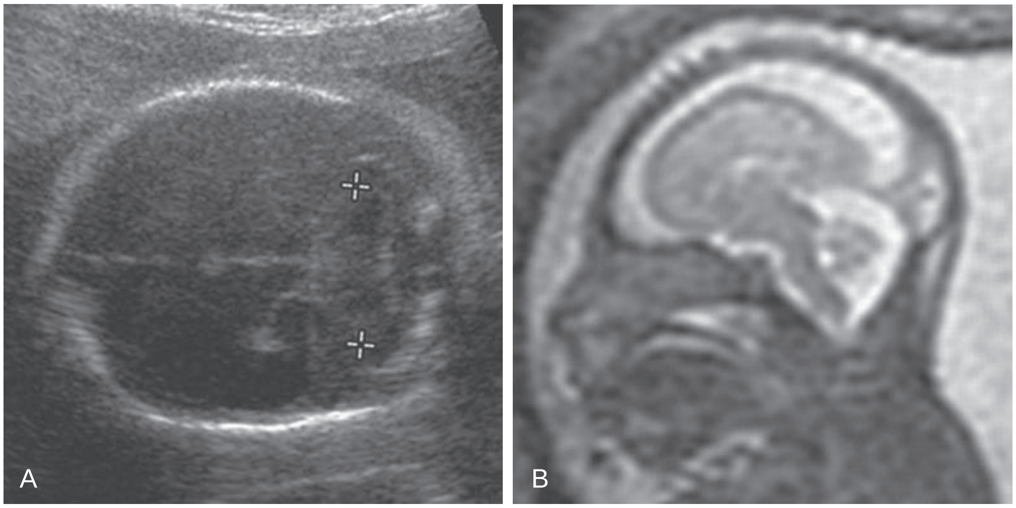

**e-Figure 19.7. Microencephaly.** (A) Transverse fetal sonogram shows a small cerebellum *(calipers).* The head circumference and biparietal diameter also were small. (B) Sagittal fetal MRI shows a small, smooth brain and a backward sloping forehead. *(From Robinson AJ, Blaser S, Toi A, et al. The fetal cerebellar vermis: assessment for abnormal development by ultrasonography and magnetic resonance imaging.* Ultrasound Q*. 2007;23(3):211–223.)*

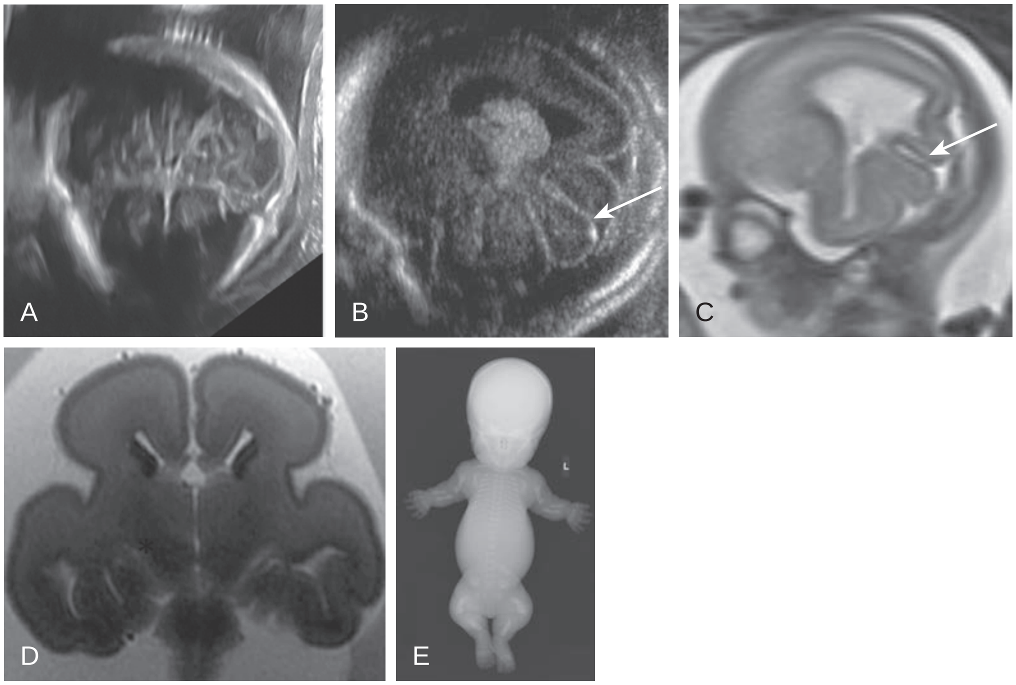

**e-Figure 19.8. Thanatophoric dysplasia.** (A) Axial fetal sonogram shows a strawberry skull caused by relative enlargement of the temporoparietal lobes compared with the frontal lobe. (B) Fetal sonogram shows the parasagittal oblique and thickened abnormal sulci in the temporal lobe *(arrow).* (C) Sagittal fetal MRI shows thickened abnormal temporal lobe sulci *(arrow).* (D) Postmortem T2-weighted MRI shows relative enlargement of the temporal lobes compared with the frontal lobes. (E) Postmortem radiograph shows typical skeletal features including severe micromelia, a curved femora, and platyspondyly. *(*A, B, *and* C, *From Fink AM, Hingston T, Sampson A, et al. Malformation of the fetal brain in thanatophoric dysplasia: US and MRI findings.* Pediatr Radiol*. 2010;40(suppl 1):S134–S137.* D, *From Miller E, Blaser S, Shannon P, et al. Brain and bone abnormalities of thanatophoric dwarfism.* AJR Am J Roentgenol*. 2009;192[1]:48–51.)*

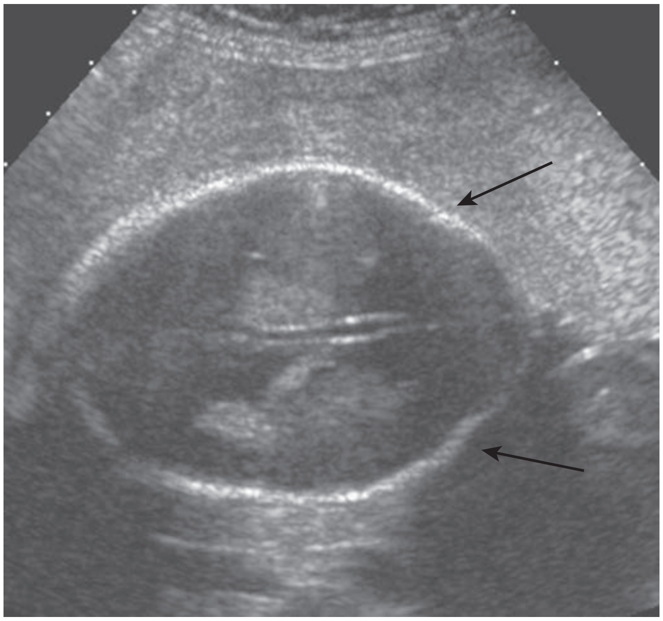

**e-Figure 19.9. Lemon skull.** Axial fetal sonogram of the head shows bilateral indentation of the frontal bones *(arrows).*

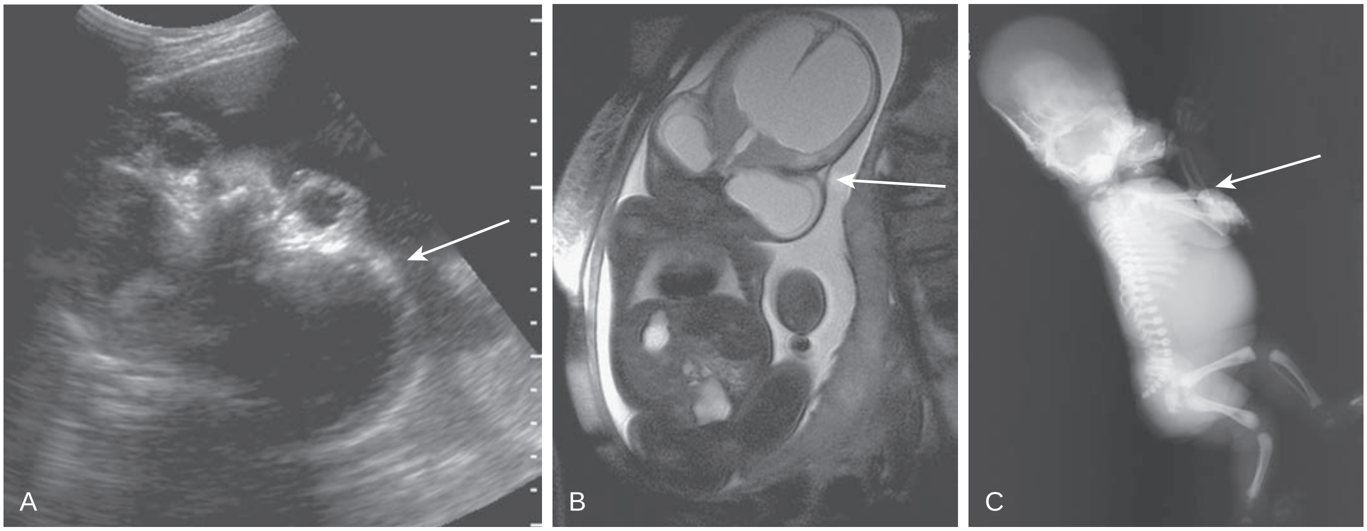

**Figure 19.10. Cloverleaf skull.** (A) Axial fetal sonogram shows bossing of the temporal bones *(arrow)* and bulging eyes in a case of acrocephalosyndactyly. (B) Coronal fetal MRI shows bossing of temporal bones *(arrow)* and frontal bones. Severe ventriculomegaly is noted. (C) Postmortem radiograph shows a severe cloverleaf skull with midface hypoplasia. Note elbow ankylosis typical of Pfeiffer syndrome. *(A, From Robinson AJ, Blaser S, Toi A, et al. Magnetic resonance imaging of the fetal eyes—morphologic and biometric assessment for abnormal development with ultrasonographic and clinicopathologic correlation.* Pediatr Radiol. *2008;38:971–981.)*

**Strawberry Skull.** A strawberry-shaped skull, characterized by flattening of the occiput and pointing of the frontal bones, is seen by ultrasound on the submentobregmatic section and is characteristic of fetuses with trisomy 18.[84] This appearance also has been described in fetal thanatophoric dwarfism.[85]

## KEY POINTS

- Prenatal MRI can be used to differentiate between simple ectodermal cysts and meningoceles or encephaloceles.
- Prenatal MRI can be used to differentiate between solid extracranial masses and encephaloceles or perforating intracranial tumors.
- Prenatal MRI can be used to differentiate (benign) skull foramina from more serious skull defects.
- Use of prenatal three-dimensional CT in the workup of skeletal dysplasias is growing.

## SUGGESTED READINGS

Glanc P, Chitayat D, Unger S. The fetal musculoskeletal system. In: Rumack CM, Wilson SR, Charboneau JW, eds. *Diagnostic Ultrasound*. 3rd ed. St. Louis, MO: Mosby Elsevier; 2005:1433–1440.

McGahan JP. Fetal head and brain. In: McGahan JP, Goldberg BB, eds. *Diagnostic Ultrasound*. 2nd ed. New York: Informa Healthcare; 2008.

Toi A. The fetal head and brain. In: Rumack CM, Wilson SR, Charboneau JW, eds. *Diagnostic Ultrasound*. 3rd ed. St. Louis: Mosby; 2005.

## REFERENCES

Full references for this chapter can be found on www.expertconsult.com.

## REFERENCES

1. Stoustrup-Smith A, Levine D. MR imaging of the fetal skull, face, and neck. In: Levine D, ed. *Atlas of Fetal MRI*. Boca Raton, FL: Taylor & Francis; 2005.
2. Sepulveda W, Wong AE, Sepulveda S, et al. Fetal scalp cyst or small meningocele: differential diagnosis with three-dimensional ultrasound. *Fetal Diagn Ther*. 2011;30(1):77–80.
3. Shahabi S, Busine A. Prenatal diagnosis of an epidermal scalp cyst simulating an encephalocoele. *Prenat Diagn*. 1998;18:373–377.
4. Timor-Tritsch IE, Monteagudo A, Santos R. Fine-tuning the diagnosis of fetal scalp cysts: the value of high-frequency sonography. *J Ultrasound Med*. 2008;27:1363–1368.
5. Ogle RF, Jauniaux E. Fetal scalp cysts—dilemmas in diagnosis. *Prenat Diagn*. 1999;19:1157–1159.
6. Okaro E, Broussin B, Ville Y. Prenatal diagnosis of atypical cystic lesions of the fetal scalp. *Ultrasound Obstet Gynecol*. 1998;12:442–444.
7. Timor-Tritsch IE, Monteagudo A, Santos R. Fine-tuning the diagnosis of fetal scalp cysts: the value of high-frequency sonography. *J Ultrasound Med*. 2008;27:1363–1368.
8. Bronshtein M, Bar-Hava I, Blumenfeld Z. Early second trimester sonographic appearance of occipital haemangioma simulating encephalocele. *Prenat Diagn*. 1992;12:695–698.
9. Sherer DM, Perillo AM, Abramowicz JS. Fetal hemangioma overlying the temporal occipital suture, initially diagnosed by ultrasonography as an encephalocele. *J Ultrasound Med*. 1993;12:691–693.
10. Kashima H, Unno N, Hyodo H, et al. Antenatal sonographic and magnetic resonance images of a giant hemangioma of the fetal skull. *Ultrasound Obstet Gynecol*. 2005;25:522–523.
11. Boulot P, Deschamps F, Montoya F, et al. Prenatal aspects of giant fetal cranial haemangio-endothelioma. *Prenat Diagn*. 1996;16:357–359.
12. Miyakoshi K, Tanaka M, Matsumoto T, et al. Occipital scalp hemangioma: prenatal sonographic and magnetic resonance images. *J Obstet Gynaecol Res*. 2008;34:666–669.
13. Richard F, Garel C, Cynober E, et al. Prenatal diagnosis of a rapidly involuting congenital hemangioma (RICH) of the skull. *Prenat Diagn*. 2009;29:533–535.
14. Elia D, Garel C, Enjolras O, et al. Prenatal imaging findings in rapidly involuting congenital hemangioma of the skull. *Ultrasound Obstet Gynecol*. 2008;31:572–575.
15. Koizumi K, Abe E, Kusanagi Y, et al. Giant immature intracranial teratoma with antenatal cranial perforation. *J Obstet Gynaecol Res*. 2010;36:1252–1255.
16. Dhombres F, Kolanska K, Garel C, et al. Prenatal diagnosis of exophytic nevus sebaceous of the scalp. *Prenat Diagn*. 2013;33:1305–1307.
17. Kennedy A, Perry D, Battin M. Antenatal imaging of cutis verticis gyrata. *Pediatr Radiol*. 2008;38:583–587.
18. Nowaczyk MJ, Mernagh JR, Bourgeois JM, et al. Antenatal and postnatal findings in encephalocraniocutaneous lipomatosis. *Am J Med Genet*. 2000;91:261–266.
19. Toi A. The fetal head and brain. In: Rumack CM, Wilson SR, Charboneau JW, eds. *Diagnostic Ultrasound*. 3rd ed. St. Louis: Elsevier Mosby; 2005.
20. Robertson RL, Ball WS, Barnes PD. Skull and brain. In: Kirks DR, ed. *Practical Pediatric Imaging*. Philadelphia: Lippincott Williams and Wilkins; 1998.
21. Raupp P, Nork M, Kappel I. Antenatal imaging of a near-term fetus with primary acalvaria. *Am J Perinatol*. 2003;20:293–296.
22. Evans C, Marton T, Rutter S, et al. Cranial vault defects: the description of three cases that illustrate a spectrum of anomalies. *Pediatr Dev Pathol*. 2009;12:96–102.
23. Wilkins-Haug L, Freedman W. Progression of exencephaly to anencephaly in the human fetus—an ultrasound perspective. *Prenat Diagn*. 1991;11:227–233.
24. Timor-Tritsch IE, Greenebaum E, Monteagudo A, et al. Exencephaly-anencephaly sequence: proof by ultrasound imaging and amniotic fluid cytology. *J Matern Fetal Med*. 1996;5:182–185.
25. Rohrbach M, Chitayat D, Drake J, et al. Prenatal diagnosis of fetal exencephaly associated with amniotic band sequence at 17 weeks of gestation by fetal magnetic resonance imaging. *Fetal Diagn Ther*. 2007;22:112–115.
26. Ferris NJ, Tien RD. Amnion rupture sequence with "exencephaly": MR findings in a surviving infant. *AJNR Am J Neuroradiol*. 1994;15:1030–1033.
27. Huppert BJ, Brandt KR, Ramin KD, et al. Single-shot fast spin-echo MR imaging of the fetus: a pictorial essay. *Radiographics*. 1999;19:S215–S227.
28. Chandran S, Lim MK, Yu VY. Fetal acalvaria with amniotic band syndrome. *Arch Dis Child Fetal Neonatal Ed*. 2000;82:F11–F13.
29. Chen CP, Cheng SJ, Lin YH, et al. Prenatal imaging of limb-body wall complex by magnetic resonance imaging. *Prenat Diagn*. 2005;25:521–523.
30. Lee SH, Lee MJ, Kim MJ, et al. Fetal MR imaging of constriction band syndrome involving the skull and brain. *J Comput Assist Tomogr*. 2011;35:685–687.
31. Sharif A, Zhou Y. Fetal MRI Characteristics of exencephaly: a case report and literature review. *Case Rep Radiol*. 2016;2016:9801267.
32. McGahan JP. Fetal head and brain. In: McGahan JP, Goldberg BB, eds. *Diagnostic Ultrasound*. 2nd ed. New York: Informa Healthcare; 2008.
33. Chen CP, Liu YP, Tsai FJ, et al. Concomitant craniorachischisis and omphalocele in a male fetus: prenatal magnetic resonance imaging findings and literature review. *Taiwan J Obstet Gynecol*. 2009;48:286–291.
34. Jha T, Bhattacharya AR, Ganguly RP, et al. Anencephaly and gastroschisis in the same foetus: a rarity. *J Indian Med Assoc*. 2012;110:503.
35. Doganay S, Kantarci M, Tanriverdi EC. Pentalogy of Cantrell with craniorachischisis: MRI and ultrasonography findings. *Ultraschall Med*. 2008;29:278–280.
36. Kachare MB, Patki VK, Saboo SS, et al. Pentalogy of Cantrell associated with exencephaly and spinal dysraphism: antenatal ultrasonographic diagnosis. Case report. *Med Ultrason*. 2013;15:237–239.
37. Sepulveda W, Wong AE, Andreeva E, et al. Sonographic spectrum of first-trimester fetal cephalocele: review of 35 cases. *Ultrasound Obstet Gynecol*. 2015;46:29–33.
38. Robinson AJ, Ederies ME. Diagnostic imaging of posterior fossa anomalies in the fetus. *Semin Fetal Neonatal Med*. 2016;21:312–320.
39. Dutta HK, Deori P. Anterior encephaloceles in children of Assamese tea workers. *J Neurosurg Pediatr*. 2010;5:80–84.
40. Kojima K, Suzuki Y, Miyajima S, et al. Antenatal evaluation of an encephalocele in a dizygotic twin pregnancy using fast magnetic resonance imaging. *Fetal Diagn Ther*. 2003;18:338–341.
41. Kasprian GJ, Paldino MJ, Mehollin-Ray AR, et al. Prenatal imaging of occipital encephaloceles. *Fetal Diagn Ther*. 2015;37:241–248.
42. Dankovcik R, Vyhnalkova V, Muranska S, et al. Encephalocystocele—uncommon diagnosis in prenatal medicine. *Fetal Diagn Ther*. 2012; 32:295–298.
43. Fink AM, Maixner W. Enlarged parietal foramina: MR imaging features in the fetus and neonate. *AJNR Am J Neuroradiol*. 2006;27:1379–1381.
44. Bartels RHMA, Merx JL, van Overbeeke JJ. Falcine sinus and occipital encephalocele: a magnetic resonance venography study. *J Neurosurg*. 1998;89:738–741.
45. Otsubo Y, Sato H, Sato N, et al. Cephaloceles and abnormal venous drainage. *Childs Nerv Syst*. 1999;15:329–332.
46. Brunelle F, Baraton J, Renier D, et al. Intracranial venous anomalies associated with atretic cephalocoeles. *Pediatr Radiol*. 2000;30:743–747.
47. Chung HY, Uster-Friedberg T, Pentaz S, et al. Enlarged parietal foramina: findings on prenatal ultrasound and magnetic resonance imaging. *Ultrasound Obstet Gynecol*. 2010;36:521–522.
48. Wilkie AOM, Mavrogiannis LA. Enlarged parietal foramina/cranium bifidum (March 30, 2004 [updated March 30, 2010]). In: Pagon RA, Bird TD, Dolan CR, et al, eds. *Gene Reviews [Internet]*. Seattle (WA): University of Washington; 1993. http://www.ncbi.nlm.nih.gov/books/NBK1128. Accessed September 14, 2012.
49. Reddy AT, Hedlund GL, Percy AK. Enlarged parietal foramina: association with cerebral venous and cortical anomalies. *Neurology*. 2000;14(54):1175–1178.
50. Mavrogiannis LA, Taylor IB, Davies SJ, et al. Enlarged parietal foramina caused by mutations in the homeobox genes ALX4 and MSX2: from genotype to phenotype. *Eur J Hum Genet*. 2006;14:151–158.
51. Saraç Sivrikoz T, Altunoglu U, Kalelioglu İH, et al. ALX4 related parietal foramina mimicking encephalocele in prenatal period. *Prenat Diagn*. 2016;36:591–593.
52. Wu YQ, Badano JL, McCaskill C, et al. Haploinsufficiency of ALX4 as a potential cause of parietal foramina in the 11p11.2 contiguous gene-deletion syndrome. *Am J Hum Genet*. 2000;67:1327–1332.
53. Glanc P, Chitayat D, Unger S. The fetal musculoskeletal system. In: Rumack CM, Wilson SR, Charboneau JW, eds. *Diagnostic Ultrasound*. 3rd ed. St. Louis: Elsevier Mosby; 2005.
54. Chen CP, Su YN, Chang TY, et al. Osteogenesis imperfecta type II: prenatal diagnosis and association with increased nuchal translucency and hypoechogenicity of the cranium. *Taiwan J Obstet Gynecol*. 2012;51:315–318.

55. Suzumori N, Hasegawa T, Sugiura-Ogasawara M. Prenatal diagnosis of osteogenesis imperfecta type II by three-dimensional ultrasound and computed tomography. *J Obstet Gynaecol Res*. 2011;37:664–665.
56. Ulla M, Aiello H, Cobos MP, et al. Prenatal diagnosis of skeletal dysplasias: contribution of three-dimensional computed tomography. *Fetal Diagn Ther*. 2011;29:238–247.
57. Miyazaki O, Nishimura G, Sago H, et al. Prenatal diagnosis of chondrodysplasia punctata tibia-metacarpal type using multidetector CT and three-dimensional reconstruction. *Pediatr Radiol*. 2007;37:1151–1154.
58. Cassart M, Massez A, Cos T, et al. Contribution of three-dimensional computed tomography in the assessment of fetal skeletal dysplasia. *Ultrasound Obstet Gynecol*. 2007;29:537–543.
59. Bonnefoy O, Delbosc JM, Maugey-Laulom B, et al. Prenatal diagnosis of hypochondroplasia: three-dimensional multislice computed tomography findings and molecular analysis. *Fetal Diagn Ther*. 2006;21:18–21.
60. Cicero S, Johnson J, Nicolaides K. Sonographic markers of fetal chromosomal defects in diagnostic ultrasound. In: Rumack CM, Wilson SR, Charboneau JW, eds. *Diagnostic Ultrasound*. 3rd ed. St. Louis: Elsevier Mosby; 2005.
61. Aguirre Vila-Coro A, Dominguez R. Intrauterine diagnosis of hydranencephaly by magnetic resonance. *Magn Reson Imaging*. 1989;7:105–107.
62. Hocwald O, McFadden D, Osiovich H, et al. Congenital gliosarcoma: detailed clinicopathologic documentation of a rare neoplasm. *Pediatr Dev Pathol*. 2009;12:398–403.
63. Fink AM, Hingston T, Sampson A, et al. Malformation of the fetal brain in thanatophoric dysplasia: US and MRI findings. *Pediatr Radiol*. 2010;40:S134–S137.
64. Miller E, Blaser S, Shannon P, et al. Brain and bone abnormalities of thanatophoric dwarfism. *AJR Am J Roentgenol*. 2009;192:48–51.
65. Kalache KD, Lehmann K, Chaoui R, et al. Prenatal diagnosis of partial agenesis of the corpus callosum in a fetus with thanatophoric dysplasia type 2. *Prenat Diagn*. 2002;22:404–407.
66. Tsutsumi S, Sawai H, Nishimura G, et al. Prenatal diagnosis of thanatophoric dysplasia by 3-D helical computed tomography and genetic analysis. *Fetal Diagn Ther*. 2008;24:420–424.
67. Pugash D, Lehman AM, Langlois S. Prenatal ultrasound and MRI findings of temporal and occipital lobe dysplasia in a twin with achondroplasia. *Ultrasound Obstet Gynecol*. 2014;44:365–368.
68. Stark Z, McGillivray G, Sampson A, et al. Apert syndrome: temporal lobe abnormalities on fetal brain imaging. *Prenat Diagn*. 2015;35:179–182.
69. Itoh K, Pooh R, Kanemura Y, et al. Brain malformation with loss of normal FGFR3 expression in thanatophoric dysplasia type I. *Neuropathology*. 2013;33:663–666.
70. Blaas HG, Vogt C, Eik-Nes SH. Abnormal gyration of the temporal lobe and megalencephaly are typical features of thanatophoric dysplasia and can be visualized prenatally by ultrasound. *Ultrasound Obstet Gynecol*. 2012;40:230–234.
71. Cesaretti C, Spaccini L, Rustico M, et al. Prenatal magnetic resonance imaging detection of temporal lobes and hippocampal anomalies in hypochondroplasia. *Prenat Diagn*. 2014;34:1015–1017.
72. Rubio EI, Blask A, Bulas DI. Ultrasound and MR imaging findings in prenatal diagnosis of craniosynostosis syndromes. *Pediatr Radiol*. 2016;46:709–718.
73. Nyberg DA, Mack LA, Hirsch J, et al. Abnormalities of fetal cranial contour in sonographic detection of spina bifida: evaluation of the "lemon" sign. *Radiology*. 1988;167:387–392.
74. Van den Hof MC, Nicolaides KH, Campbell J, et al. Evaluation of the lemon and banana signs in one hundred thirty fetuses with open spina bifida. *Am J Obstet Gynecol*. 1990;162:322–327.
75. Saleem SN, Said AH, Abdel-Raouf M, et al. Fetal MRI in the evaluation of fetuses referred for sonographically suspected neural tube defects (NTDs): impact on diagnosis and management decision. *Neuroradiology*. 2009;51:761–772.
76. Gabbe SG, Mintz MC, Mennuti MT, et al. Detection of open spina bifida by the lemon sign: pathologic correlation. *J Clin Ultrasound*. 1988;16:399–402.
77. Ball RH, Filly RA, Goldstein RB, et al. The lemon sign: not a specific indicator of meningomyelocele. *J Ultrasound Med*. 1993;12:131–134.
78. Thomas M. The lemon sign. *Radiology*. 2003;228:206–207.
79. Weber B, Schwabegger AH, Vodopiutz J, et al. Prenatal diagnosis of Apert syndrome with cloverleaf skull deformity using ultrasound, fetal magnetic resonance imaging and genetic analysis. *Fetal Diagn Ther*. 2010;27:51–56.
80. Nazzaro A, Della Monica M, Lonardo F, et al. Prenatal ultrasound diagnosis of a case of Pfeiffer syndrome without cloverleaf skull and review of the literature. *Prenat Diagn*. 2004;24(11):918–922.
81. David DJ, Cooter RD, Edwards TJ. Crouzon twins with cloverleaf skull malformations. *J Craniofac Surg*. 1991;2:56–60, discussion 61.
82. Tonni G, Panteghini M, Rossi A, et al. Craniosynostosis: prenatal diagnosis by means of ultrasound and SSSE-MRI. Family series with report of neurodevelopmental outcome and review of the literature. *Arch Gynecol Obstet*. 2001;283:909–916.
83. Itoh S, Nojima M, Yoshida K. Usefulness of magnetic resonance imaging for accurate diagnosis of Pfeiffer syndrome type II in utero. *Fetal Diagn Ther*. 2006;21:168–171.
84. Nicolaides KH, Salvesen DR, Snijders RJ, et al. Strawberry-shaped skull in fetal trisomy 18. *Fetal Diagn Ther*. 1992;7:132.
85. Seymour R, Jones A. Strawberry-shaped skull in fetal thanatophoric dysplasia. *Ultrasound Obstet Gynecol*. 1994;4:434–436.

# 20

# Craniosynostosis, Selected Craniofacial Syndromes, and Other Abnormalities of the Skull

Jason F. Tobler, Thomas L. Slovis, and Arlene A. Rozzelle

The clinical and radiologic features of craniosynostosis result from lack of sutural formation or premature fusion across membranous sutures. The premature sutural closure prevalence is displayed in e-Table 20.1.[1] Normal sutures permit skull growth perpendicular to their long axes. With early closure of one suture, there is compensation and excess growth in others resulting in a craniofacial deformity (e-Table 20.2; e-Fig. 20.1 and Figs. 20.2–20.4).

Calvarial deformities present before sutural changes. Only a portion of the bony suture needs to be closed to have craniosynostosis (e-Fig. 20.5). Abnormal head shape secondary to suture maldevelopment can present in utero at 13 weeks' gestational age.[2,3] Craniosynostosis is associated with genetic abnormalities (e-Box 20.1) and is a secondary finding in many systemic disorders (e-Box 20.2).[4]

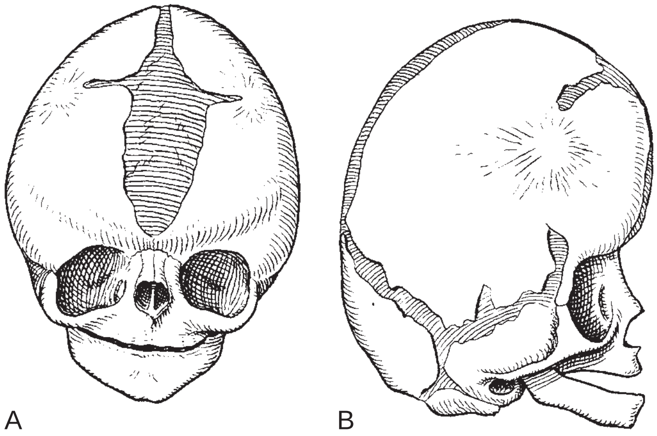

**Figure 20.2. Schematics of bilateral coronal suture synostosis in a child with Apert syndrome.** (A) Frontal, and (B) lateral schematics reveal coronal suture fusion except for short, open terminal segments and open segments near the sagittal suture and anterior fontanel. The metopic, sagittal, lambdoid, and temporoparietal sutures all are open. The calvarium shows anteroposterior shortening and craniocaudal elongation.

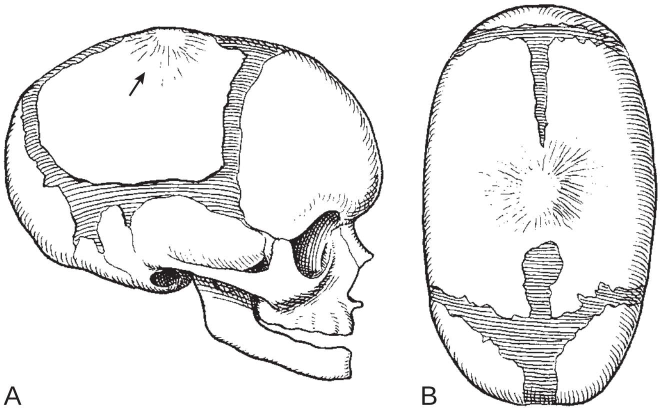

**Figure 20.3. Schematic drawings of premature sagittal suture synostosis.** (A) Lateral and (B) superior schematics are shown.

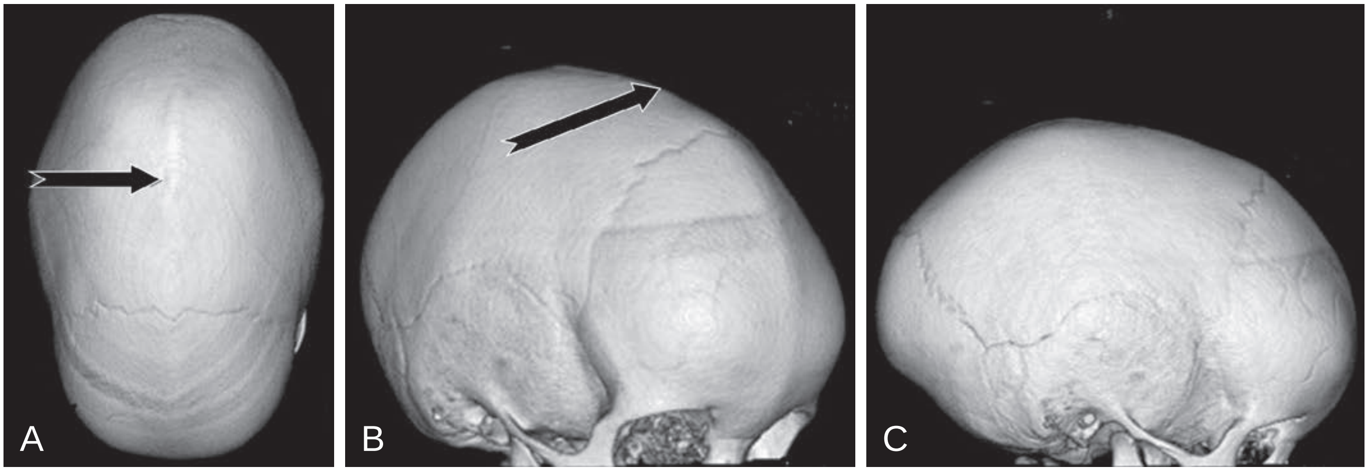

**Figure 20.4. Premature synostosis of the sagittal suture in a 3-year-old female.** (A) Vertex, (B) oblique, and (C) lateral reformatted 3D CT images show occipital-frontal elongation and decreased calvarial width. The sagittal suture *(arrows)* is fused and ridged.

## Abstract:

The subject of this chapter is craniosynostosis, craniofacial syndromes and other abnormalities of the skull that pertain to pediatric radiology. There is brief discussion of normal skull development. The different types of craniosynostosis are discussed with emphasis on the specific growth pattern abnormality and resultant radiology findings. Syndromes associated with craniosynostosis are highlighted. Radiologic hallmarks of major craniofacial syndromes are also discussed.

## Keywords:

Craniosynostosis
craniofacial syndromes
Apert syndrome
plagiocephaly
normal skull
trigonencephaly
scaphocephaly

**e-TABLE 20.1** Prevalence of Individual Premature Suture Closure per 1 Million Live Births

| Suture | No. per 1 Million Live Births | Sporadic (%) | Male/ Female Ratio | % of Total | Comment |
|---|---|---|---|---|---|
| Sagittal | 190 | 72 | 3.5 : 1 | 56 | |
| Coronal | 94 | 61 | 1 : 2 | 26 | Bilateral > unilateral |
| Multiple | — | — | — | 14 | |
| Metopic | 67 | — | 3.3 : 1 | 4 | |
| Lambdoid | — | — | — | <1 | |

*Modified from Cohen Jr MM. Epidemiology of craniosynostosis. In: Cohen Jr MM, MacLean RE, eds.* Craniosynostosis, *New York: Oxford University Press; 2000:113.*

**e-TABLE 20.2** Calvarial Configurations in Primary Craniosynostosis

| Suture | Calvarial Configuration | Descriptive Terms |
|---|---|---|
| Sagittal | Long, narrow head | Scaphocephaly or dolichocephaly |
| Bilateral coronal | Short, wide head; hypertelorism; proptosis; small anterior fossa | Brachycephaly or bradycephaly |
| Metopic | Frontal wedging or keel-shaped head | Trigonocephaly |
| Bilateral lambdoid | Shallow posterior fossa, prominent bregma | Turricephaly |
| Unilateral coronal | Unilateral frontal flattening, uptilting of orbit and tilting of nasal septum | Plagiocephaly |
| Unilateral lambdoid | Unilateral posterior flattening | Plagiocephaly |
| All sutures | Small, round head | Microcephaly |

*From Vannier MW. Radiologic evaluation of craniosynostosis. In: Cohen Jr MM, MacLean RE, eds.* Craniosynostosis, *New York: Oxford University Press; 2000:148.*

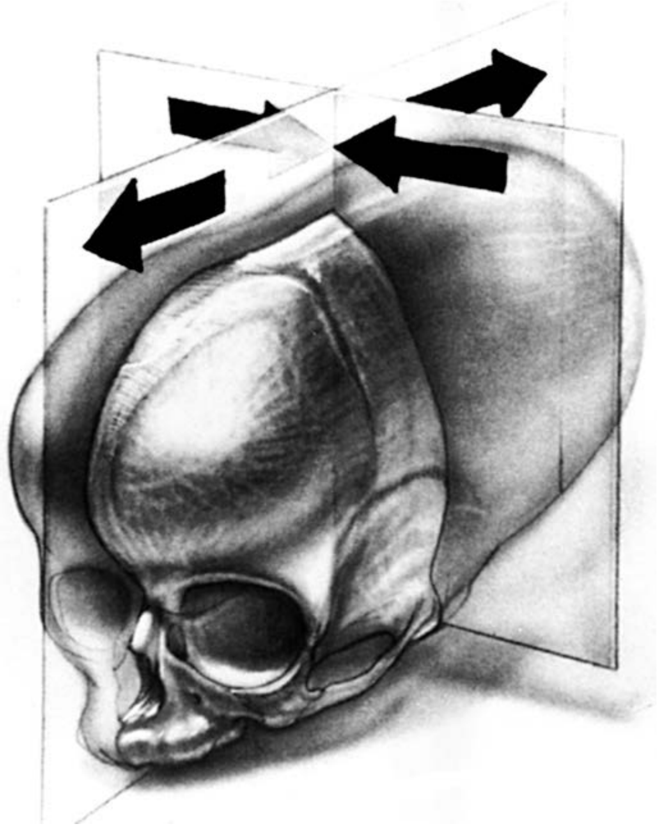

**e-Figure 20.1. Schematic drawing of a child's skull with sagittal synostosis.** Growth of the skull is restricted transversely, the plane perpendicular to the fused suture and increased anteroposteriorly, the plane parallel to that fused suture. *(From Sulica RL, Grunfast KM. Otologic manifestations of craniosynostosis syndromes. In: Cohen Jr MM, MacLean RE, eds.* Craniosynostosis, *New York: Oxford University Press; 2000:211.)*

**e-BOX 20.1** Genes Bearing Known Mutations for Craniosynostosis

- *FGFR1*
  - Pfeiffer syndrome
- *FGFR2*
  - Apert syndrome
  - Pfeiffer syndrome
  - Crouzon syndrome
  - Jackson-Weiss syndrome
  - Beare-Stevenson cutis gyrata syndrome
  - Nonclassifiable and variable craniosynostosis
- *FGFR3*
  - Thanatophoric dysplasia, type I
  - Thanatophoric dysplasia, type II
  - Crouzonodermoskeletal syndrome
  - *FGFR3*-associated coronal synostosis syndrome (Muenke craniosynostosis)
- *TWIST*
  - Saethre-Chotzen syndrome
- *MSX2*
  - Boston-type craniosynostosis

*From Cohen Jr MM. History, terminology, and classification of craniosynostosis. In: Cohen Jr MM, MacLean RE, eds.* Craniosynostosis, *New York: Oxford University Press; 2000:107.*

### **e-BOX 20.2** Conditions With Secondary Craniosynostosis

- Metabolic disorders
    - Hyperthyroidism
    - Rickets (various forms)
- Mucopolysaccharidoses and related disorders
    - Hurler syndrome
    - Morquio syndrome
    - β-glucuronidase deficiency
    - Mucolipidosis III
    - α-mannosidase deficiency
- Hematologic disorders
    - Thalassemia
    - Sickle cell anemia
    - Polycythemia vera
    - Congenital hemolytic icterus
- Teratogens
    - Diphenylhydantoin
    - Retinoids
    - Valproate
    - Aminopterin
    - Fluconazole
    - Cyclophosphamide
- Malformations
    - Holoprosencephaly
    - Microcephaly
    - Encephalocele
- Iatrogenic disorders
    - Hydrocephalus with shunt
    - Atrophy of brain

*Modified from Cohen Jr MM. Sutural pathology. In: Cohen Jr MM, MacLean RE, eds.* Craniosynostosis, *New York: Oxford University Press; 2000:55.*

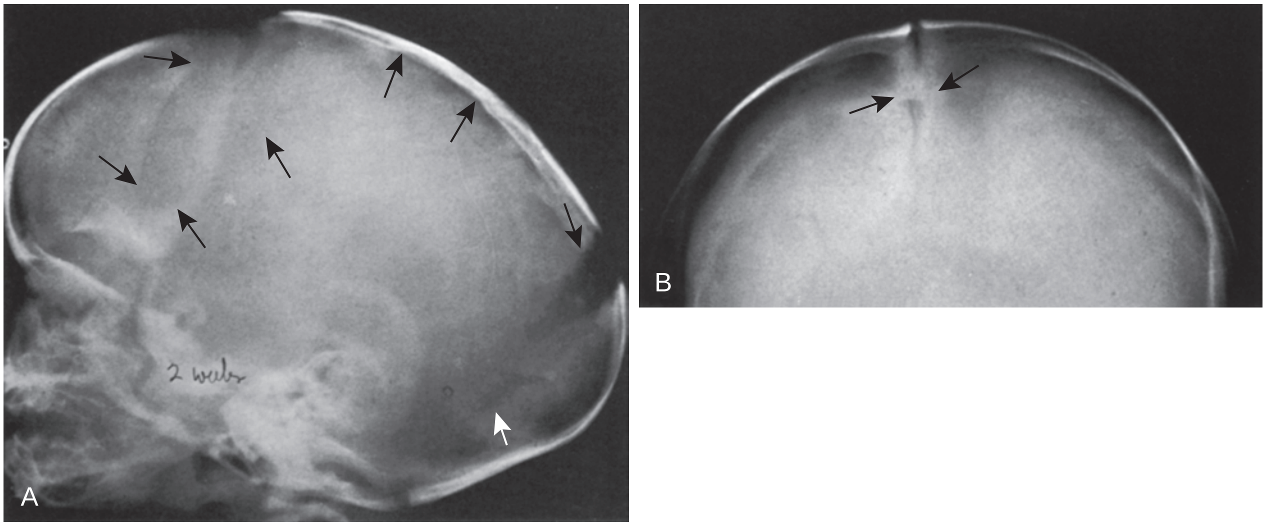

**e-Figure 20.5. Severe sagittal suture synostosis in a 2-week-old infant with scaphocephaly.** (A) Lateral radiograph reveals a deformity resulting from craniostenosis, but the sagittal suture is not seen *(superior black arrows).* Coronal *(black arrows)* and lambdoid sutures *(white arrow)* are widened. (B) Frontal radiograph demonstrates an open sagittal suture except for a short segment *(arrows)* only a few millimeters long.

Specific head shapes are associated with particular suture synostoses (e-Fig. 20.6). The normal head is oval, being widest in the parietal area with a rounded forehead (Fig. 20.7).[5]

*Sagittal synostosis* (scaphocephaly or dolichocephaly) is characterized by increased AP skull length, decreased width, bitemporal pinching, and a tendency for the vertex to be anterior rather than posterior (see Figs. 20.3 and 20.4). *Metopic synostosis* (trigonocephaly) results in a triangular, pointed forehead (Fig. 20.8A-C and e-Fig. 20.9, also see e-Fig. 20.6). The premature fusion of the metopic suture often results in what has been termed the "omega" sign as opposed to the normal "M" sign present in normal physiologic fusion of the metopic suture (Fig. 20.8D and E).

*Unilateral coronal synostosis* results in flattening of the ipsilateral forehead and occipital area, a "harlequin eye" (the sphenoid is drawn up toward the closed suture), contralateral forehead bossing, and deviation of the nose away from the synostosed side

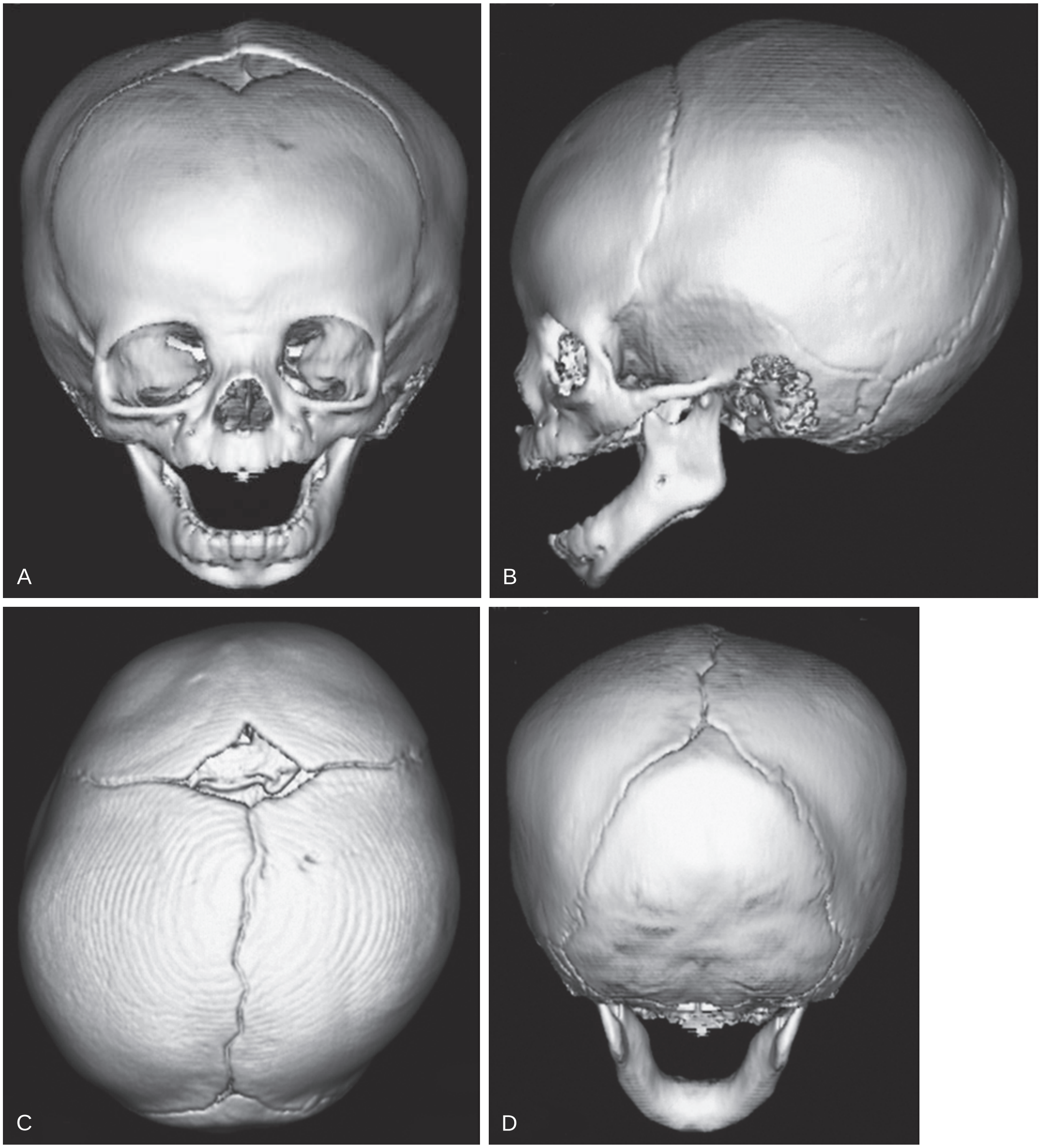

**Figure 20.7. Normal 3D CT of a 7-month-old infant.** (A) Frontal image shows the open anterior fontanel and coronal sutures. The metopic suture has closed. (B) Lateral view identifies the lambdoid, squamosal and coronal sutures. (C) Vertex image identifies the coronal, sagittal, and lambdoid sutures. (D) Posterior view shows the sagittal and lambdoid sutures. The normal head is egg (oval)-shaped, widest at the biparietal area.

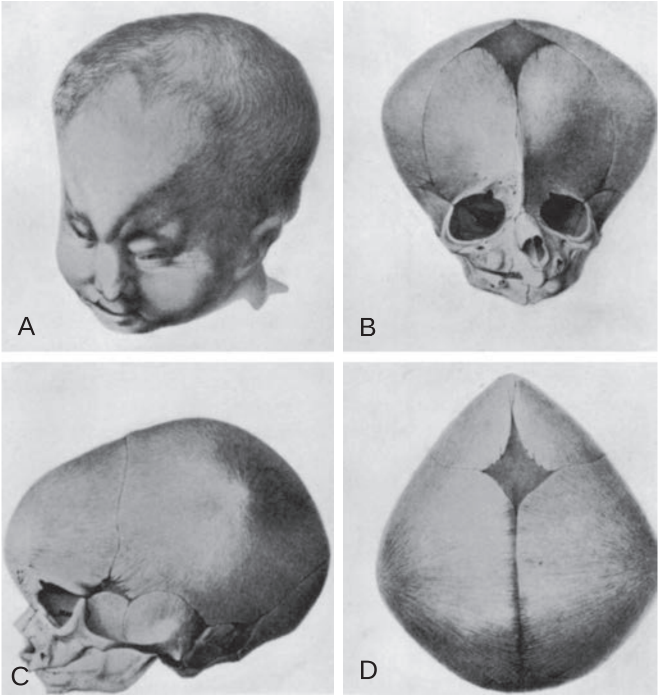

**e-Figure 20.6. Trigonocephaly in a newborn.** (A) Photograph of the calvarium, (B) frontal, (C) lateral and, (D) superior views of the skull. Note the ridge on the forehead, shaped like the keel of a boat. *(From Welcker H.* Untersuchungen über Wachstum und Bau des menschlichen Schädels, *Leipzig: W. Engelmann; 1862.)*

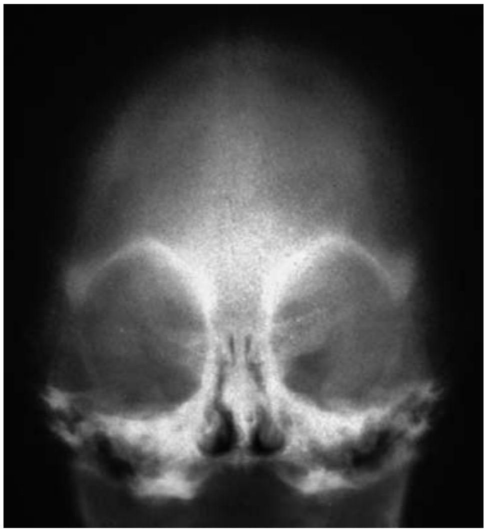

**e-Figure 20.9. Trigonocephaly.** Frontal radiograph shows the characteristic orbital hypotelorism and narrowing of the forehead. The metopic suture is invariably closed.

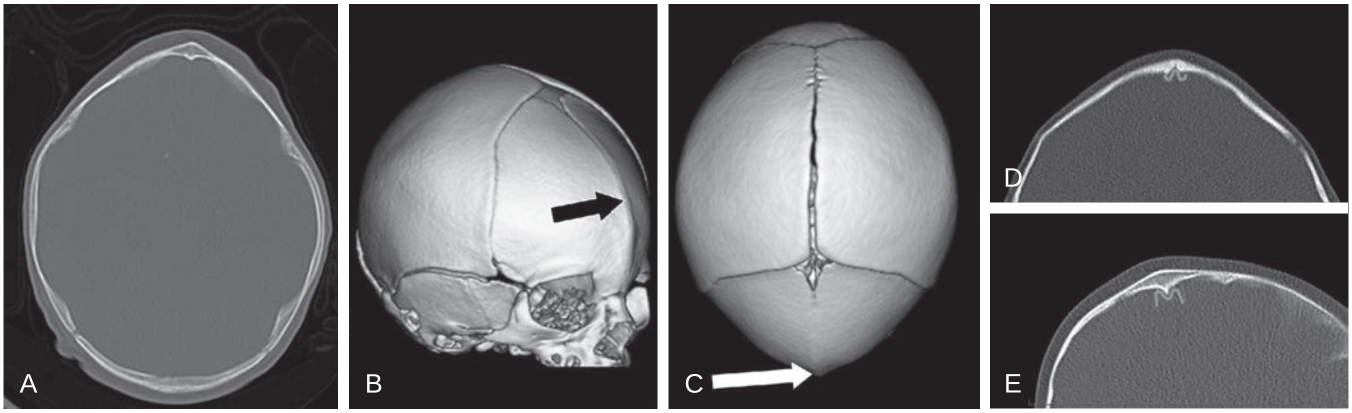

**Figure 20.8. Trigonocephaly in a 3-week-old male.** (A) Axial CT, (B) and (C) 3D CT images reveal metopic suture synostosis with sutural ridging *(black arrow)* and trigonocephaly *(white arrow).* Note that bicoronal and lambdoid sutures override without fusion. (D) and (E) Axial CT images demonstrated the "omega" sign of premature suture fusion, versus the "M" sign of normal physiologic fusion.

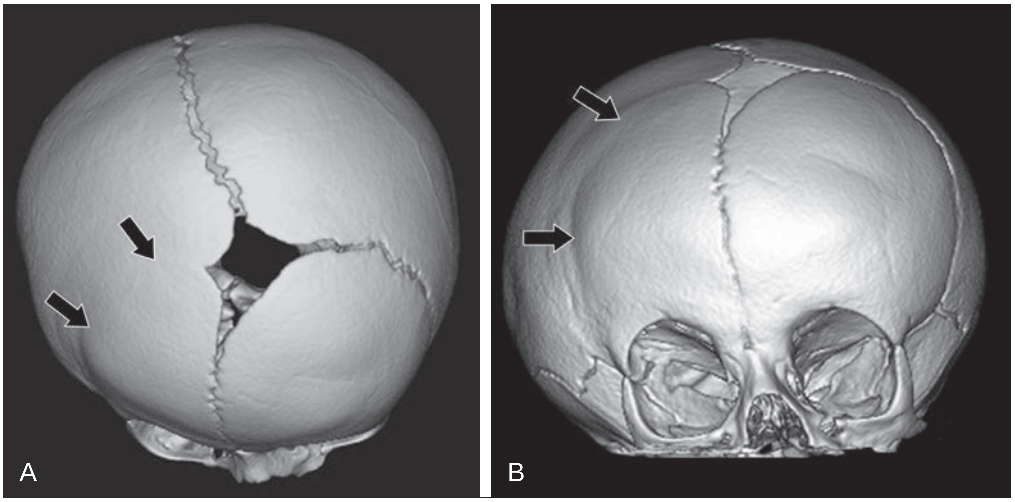

**Figure 20.10. Unilateral coronal suture synostosis in a 6-month-old infant.** (A and B) 3D CT images demonstrate complete fusion of the right coronal suture *(arrows).* The anterior fontanelle and left coronal suture remain patent. The cranial vault demonstrates pronounced right frontal flattening, mild right orbital roof elevation, contralateral frontal bossing and deviation of the nose away from the affected side.

(Fig. 20.10 and e-Fig. 20.11). Features distinguishing unicoronal synostosis from anterior deformational plagiocephaly are listed in e-Table 20.3.

*Bicoronal synostosis* causes brachycephaly (i.e., wide, short head). The supraorbital rims and forehead are recessed with bitemporal and forehead bulging (Fig. 20.12 and e-Fig. 20.13).

*Lambdoid synostosis* results in ipsilateral occipital flattening and elongation along the axis of the synostosed lambdoid with contralateral superior parietal bulge (Fig. 20.14 and e-Fig. 20.15). The features differentiating unilateral lambdoid synostosis from deformational plagiocephaly are listed in e-Table 20.4.

Multiple suture synostosis occurs in 14% of cases, and the head shape depends on which sutures are closed.[1] The *Kleeblattschädel*, or cloverleaf skull anomaly, occurs when all sutures except the squamosal are closed resulting in severe temporal and vertex bulging (Fig. 20.16 and e-Fig. 20.17). Isolated synostosis of the squamosal and skull base sutures can also occur particularly in syndromic cases.[6,7]

Microcrania, or a small cranium, may result when all sutures are closed. This usually occurs with failure of brain growth.[8] Rarely, it occurs without failure of brain growth, and increased intracranial pressure may develop (Fig. 20.18).

## DEFORMITIES MIMICKING CRANIOSYNOSTOSIS

Cranial deformities mimicking synostosis may result from static forces such as intrauterine crowding or prolonged recumbency. The term *plagiocephaly* refers to flattening of the calvarium without denoting an etiology and is preceded by terms that describe the location (e.g., right posterior plagiocephaly). Postnatal deformational plagiocephaly primarily affects the forehead or occipital area. Since the 1993 American Academy of Pediatrics recommendation to put infants to sleep on their backs, occipital deformational plagiocephaly cases have increased (Fig. 20.19). The ipsilateral occiput and contralateral forehead are flattened. Malposition of the ipsilateral pinna, protrusion of the ipsilateral cheek, and

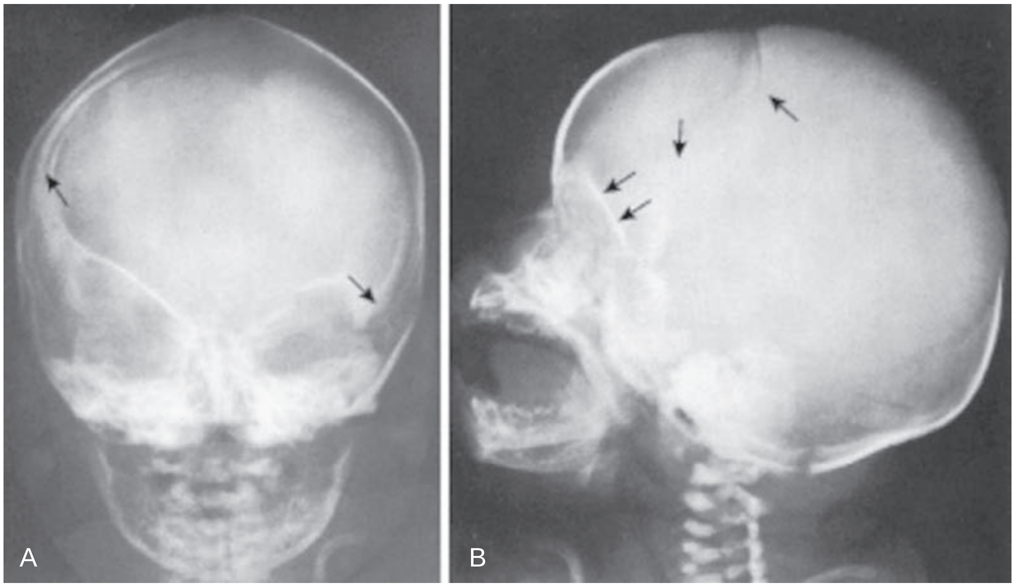

**e-Figure 20.11. Premature synostosis of the caudal segment of the right limb of the coronal suture in a 3-week-old infant.** (A) On the frontal radiograph, *arrows* are directed at the caudal ends of the right and left limbs of the coronal suture. The roof of the right orbit is lifted into a more oblique position, as is the right wing of the sphenoid. (B) On the lateral projection, the right limb of the coronal suture stops abruptly a few centimeters below the anterior fontanel. The lifting of the right orbital roof also is well seen *(two lower arrows).*

**e-TABLE 20.3** Features That Differentiate Unilateral Coronal Synostosis From Anterior Deformational Plagiocephaly

| Features | Synostotic | Deformational |
|---|---|---|
| Ipsilateral superior orbital rim | Up | Down |
| Ipsilateral ear | Anterior, high | Posterior, low |
| Nasal root | Ipsilateral | Midline |
| Ipsilateral malar eminence | Forward | Backward |
| Chin deviation | Contralateral | Ipsilateral |
| Ipsilateral palpebral fissure | Wide, low | Narrow, high |
| Anterior fontanel deviation | Contralateral | None |

*Modified from Cohen Jr MM, MacLean RE. Anatomic, genetic, nasologic, diagnostic, and psychosocial considerations. In: Cohen Jr MM, MacLean RE, eds.* Craniosynostosis, *New York: Oxford University Press; 2000:126.*

**e-TABLE 20.4** Features That Differentiate Unilateral Lambdoid Synostosis From Posterior Deformational Plagiocephaly

| Features | Synostotic | Deformational |
|---|---|---|
| Contralateral posterior bossing | Parieto-occipital | Occipital |
| Forehead | Contralateral frontal bossing | Ipsilateral frontal bossing |
| Ipsilateral occipitomastoid bossing | Present | Absent |
| Ipsilateral ear | Anterior, anteroinferior, posterior, or symmetric | Anterior |
| Skull base and face | Ipsilateral inferior tilt | Normal* |
| Head shape, vertex view | Trapezoid-shaped or parallelogram-shaped depending on severity | Parallelogram |
| Head shape, posterior view | Parallelogram | Normal |
| Lambdoid suture | Unilateral synostosis† | Patent suture |

*Ipsilateral face prominent.

†Bulges at inferior and superior axes of location where suture should be.

*Modified from Cohen Jr MM, MacLean RE. Anatomic, genetic, nasologic, diagnostic, and psychosocial considerations. In: Cohen Jr MM, MacLean RE, eds.* Craniosynostosis, *New York: Oxford University Press; 2000:127.*

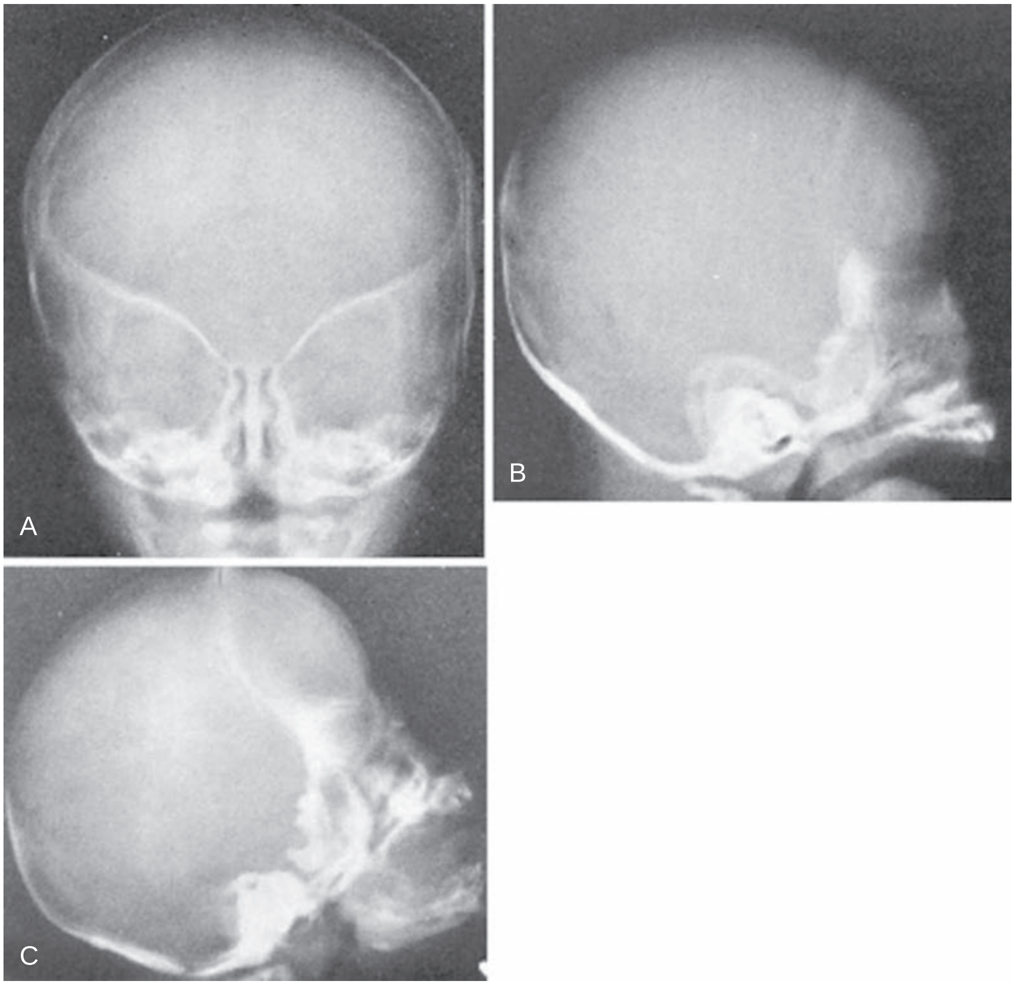

**e-Figure 20.13. Bilateral coronal synostosis.** (A) Frontal radiograph shows the elevated orbital roofs. (B) On the lateral radiograph, the height of the skull is increased from caudad to cephalad and decreased in the anteroposterior dimension. The coronal suture is not seen. (C) Other lateral projection showing the absence of a complete coronal suture. The head is tall (towering) and short in the anteroposterior direction.

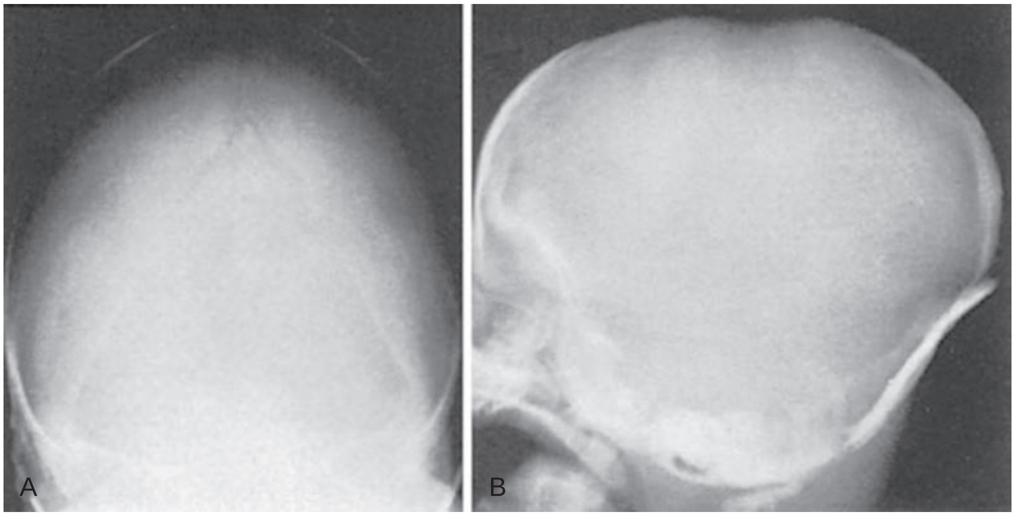

**e-Figure 20.15. Premature closure and ridging of the caudal two-thirds of both lambdoid sutures and flattening of the occipital squamosa in a 1-month-old infant.** The uppermost segment of the lambdoid suture is still open, and a small sutural bone is visible at the lambda itself. The sides of the occipital squamosa are straight, rather than convex, and the squamosa is narrower than is normal. (A) and (B) Anteroposterior (A) and left lateral (B) projections.

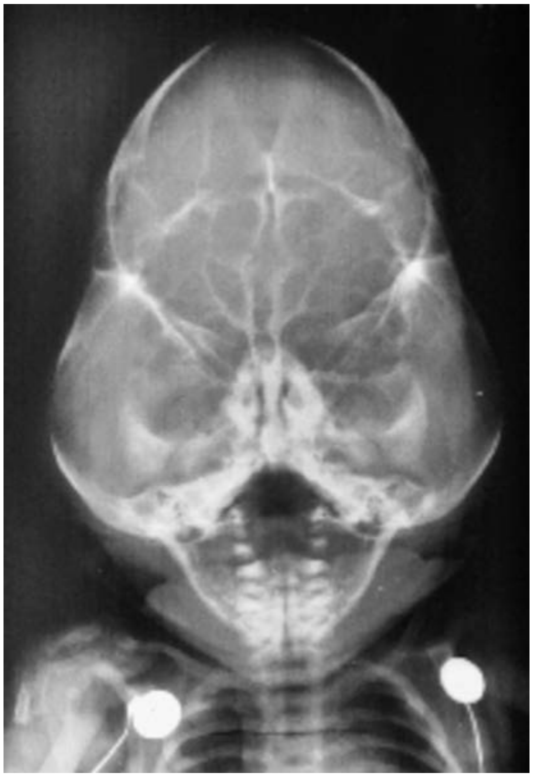

**e-Figure 20.17. Kleeblattschädel (cloverleaf skull) anomaly.** Multisuture closure has occurred, and a bizarre configuration of the face and head with bulging of the temporal region is seen on this frontal radiograph.

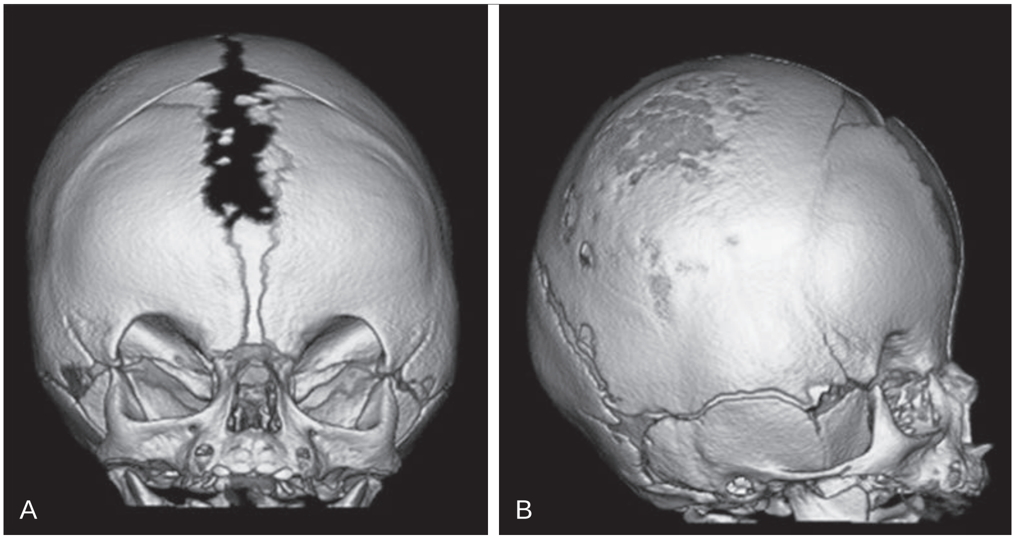

**Figure 20.12. Bilateral coronal synostosis in a 2-month-old male.** (A and B) 3D CT images demonstrate bilateral coronal suture fusion, elevated orbital roofs, a towering calvarium and anteroposterior shorting.

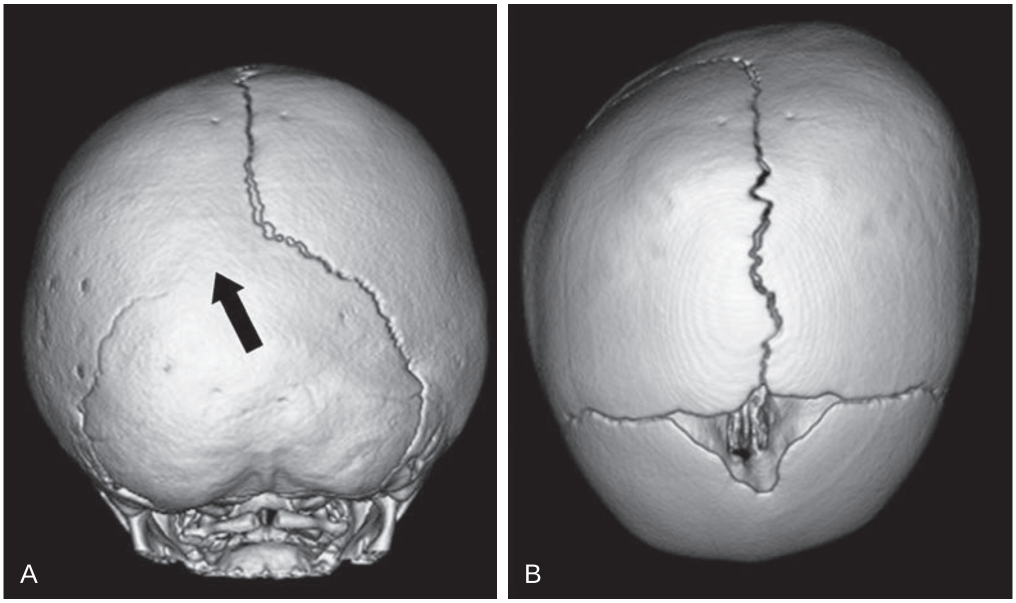

**Figure 20.14. Lambdoid synostosis in an 11-month-old male.** (A and B) 3D CT images show right occipital flattening and partial closure of the right lambdoid suture *(arrow).*

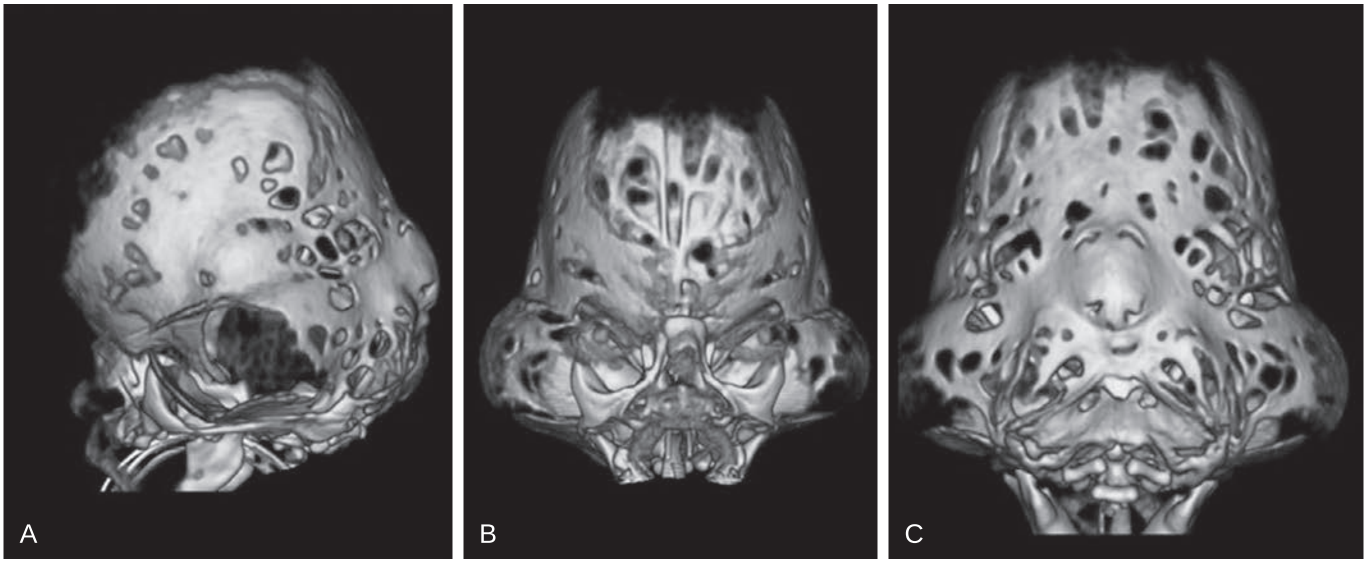

**Figure 20.16. Kleeblattschädel (cloverleaf skull) anomaly in a 1-day-old infant.** (A–C) 3D CT images reveal multiple closed sutures, a misshapen face, towering of the cranium, and temporal bulging.

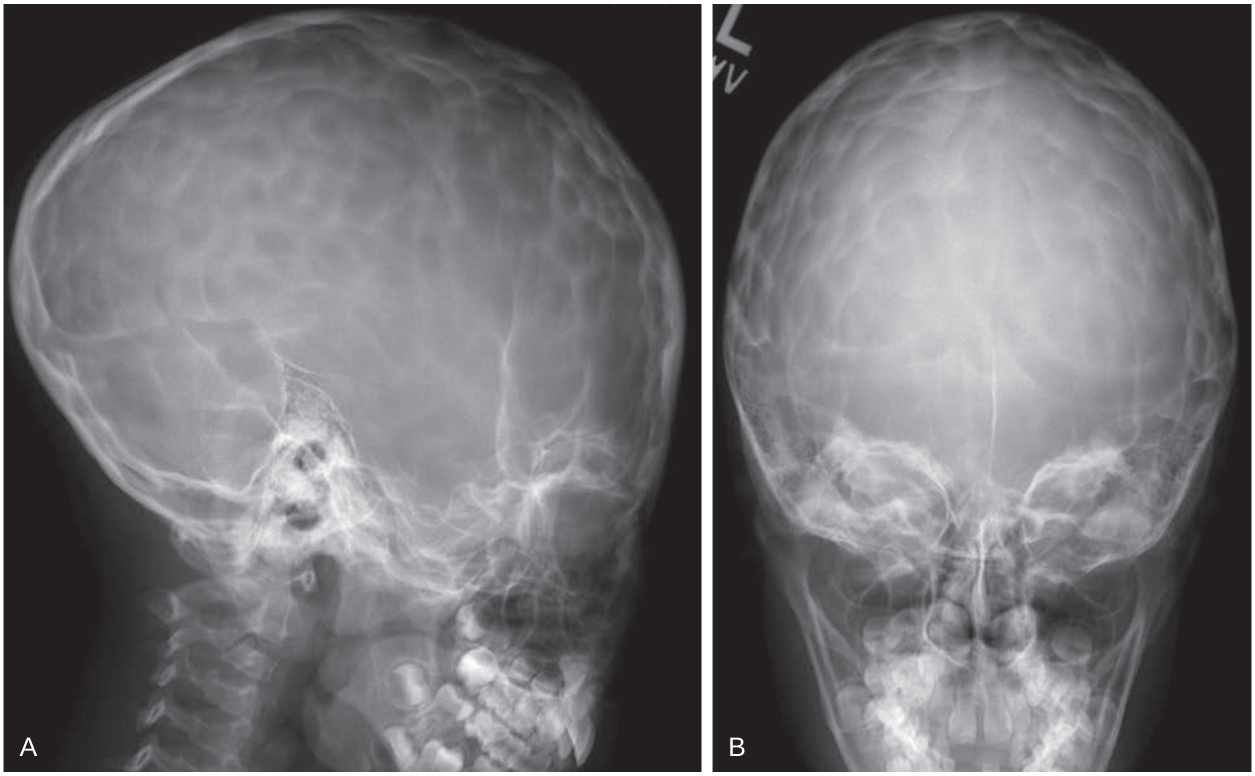

**Figure 20.18. Microcephalic type of craniostenosis in a 6-year-old child.** (A) Lateral and (B) frontal radiographs show obliteration of all sutures, and skull shortening. Long-standing increased intracranial pressure is indicated by heavy convolutional markings. Note poor visualization of the sella.

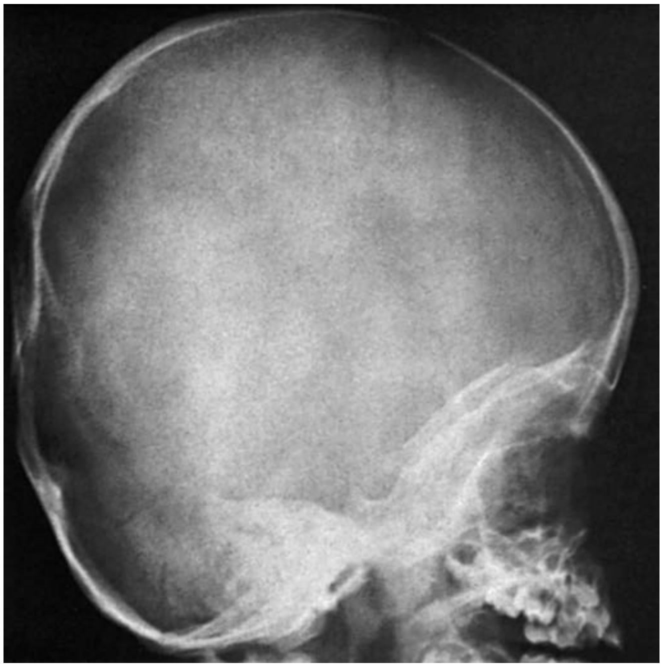

**Figure 20.19. Deformational (postural) plagiocephaly in a 22-month-old infant.** The occipital flattening shown on this lateral radiograph suggests coronal suture synostosis in general. However, the coronal sutures are open, the anterior fossa is deep, and the posterior fossa is shallow.

compensatory bulging of the ipsilateral forehead and contralateral occipital area are noted. Viewed from above, the head has a parallelogram shape (Fig. 20.20).

Perisutural lambdoid sclerosis may be seen on a plain radiograph; however, the suture is open. The concept of a "sticky lambdoid suture" is no longer considered valid.[9,10] Plagiocephaly also may occur with bony, muscular, or ocular torticollis.

In deformational plagiocephaly, the skull base (i.e., aligned from the crista galli through the foramen magnum) remains straight, with less than 7 degrees' angulation, whereas in unilateral coronal or lambdoid synostosis, the skull base curves (see Figs. 20.20 and 20.21). Pseudoscaphocephaly occurs when premature infants lie on the sides of their heads in the neonatal intensive care unit. Although the head is long and narrow, the sagittal suture is open.

## Radiographic Findings

Radiographic examination of the skull consists of anteroposterior or Caldwell, Towne, and both lateral views. The sagittal, coronal, and lambdoid sutures are all normally identified. The anterior fontanel is visible at least until 7 months of age. Although the metopic suture closes any time from before birth to after 3 months of age, as many as 10% remain open into adulthood.[11] The same head deformity results from partial and total suture synostosis (see e-Fig. 20.5). The key findings to diagnosis craniosynostosis are (1) abnormal head shape and (2) suture obliteration.

Cranial restructuring techniques have focused on (1) release of sutural synostosis, (2) cranial remodeling, (3) reduction of abnormal skull expansion, and (4) expansion of abnormally narrow areas.[12]

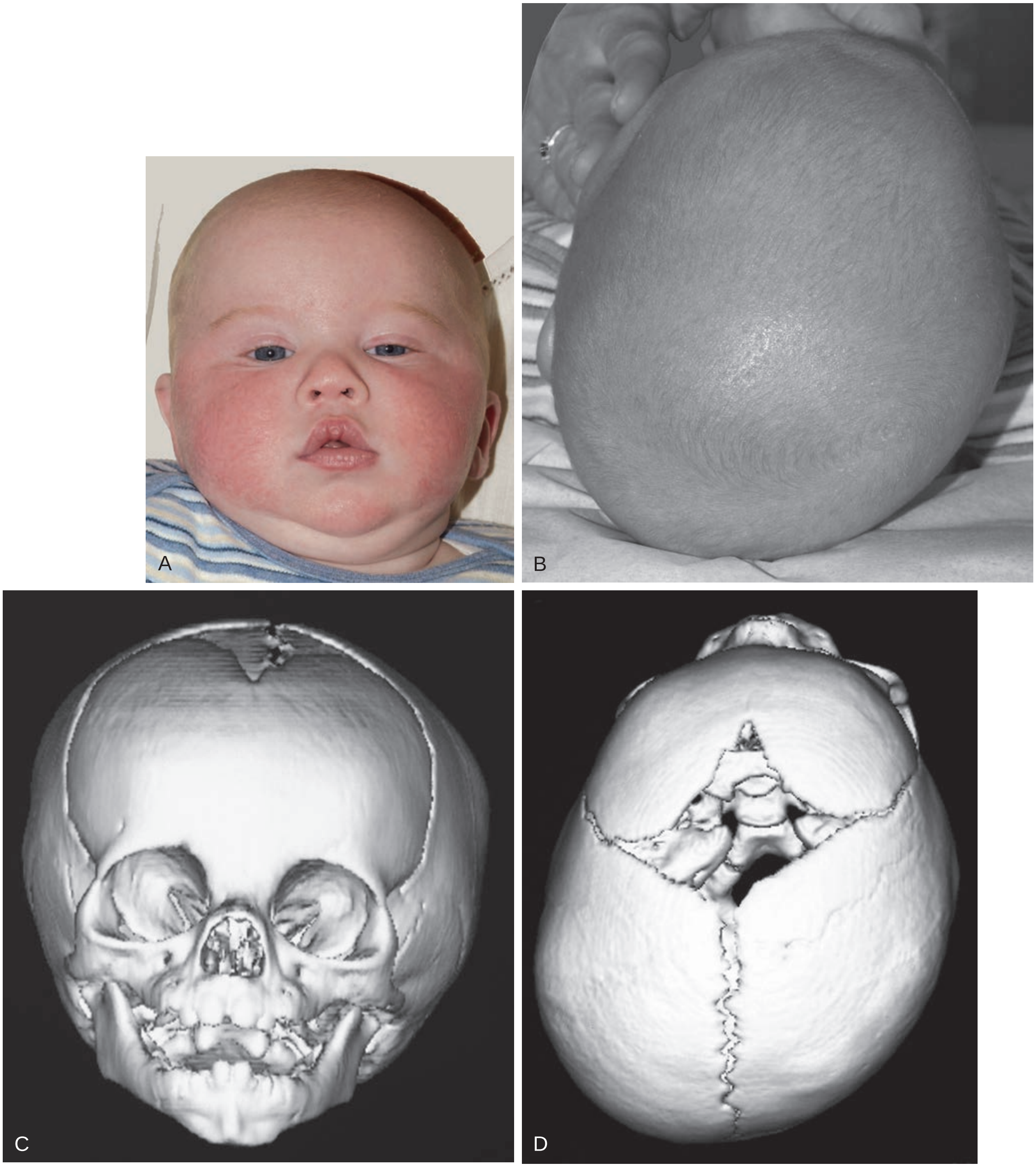

**Figure 20.20. Deformational plagiocephaly in an infant.** (A) Frontal and (B) bird's eye view photographs demonstrate a parallelogram skull shape. (C) Frontal and (D) vertex 3-D CT images confirm the clinical plagiocephaly with open sutures.

*Continued*

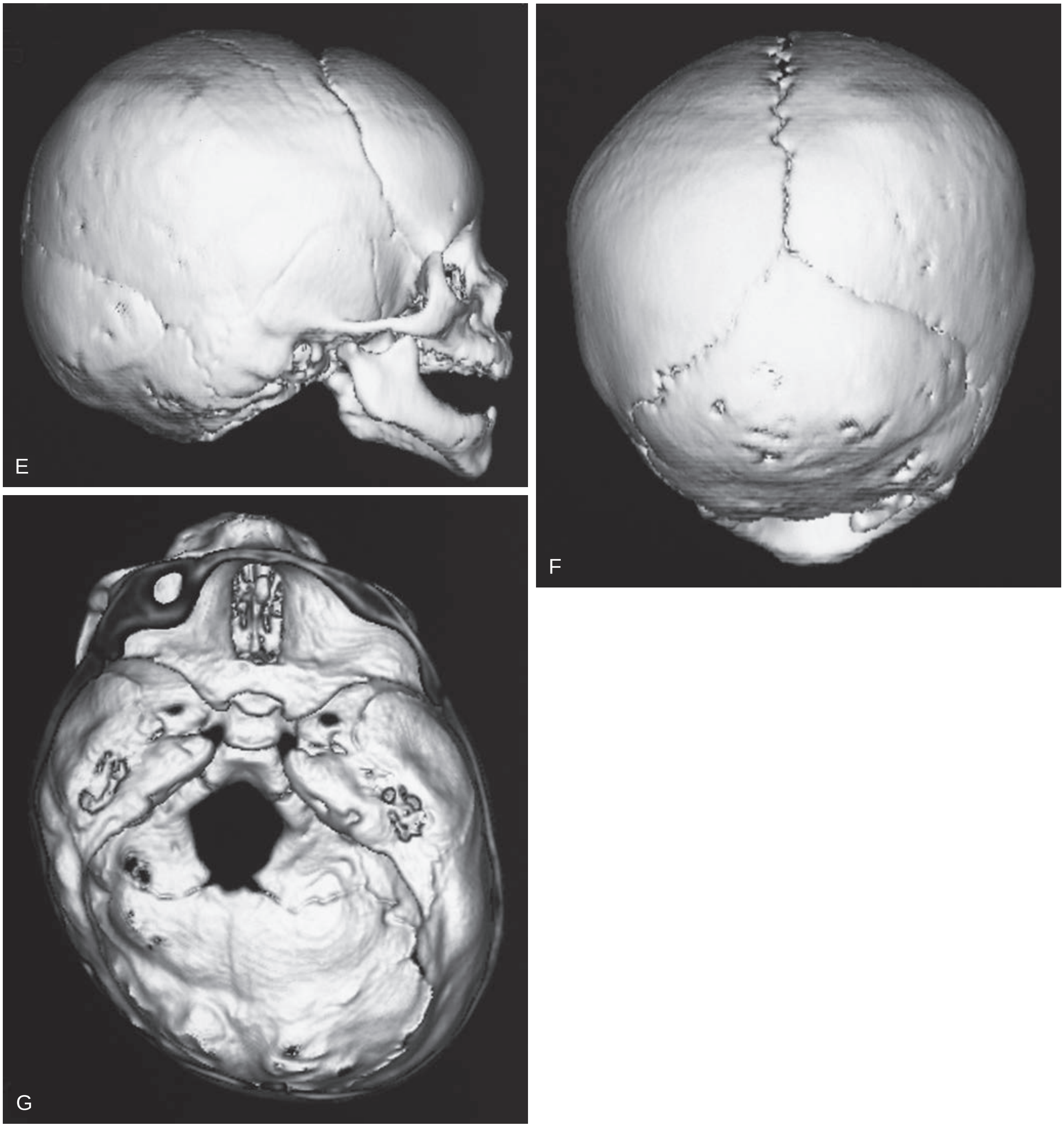

**Figure 20.20, cont'd.** (E) Lateral, (F) posterior, and (G) basilar CT images again confirm open sutures. Right occipital and left frontal flattening with compensatory right frontal and left occipital bulging are seen. No skull base angulation is present.

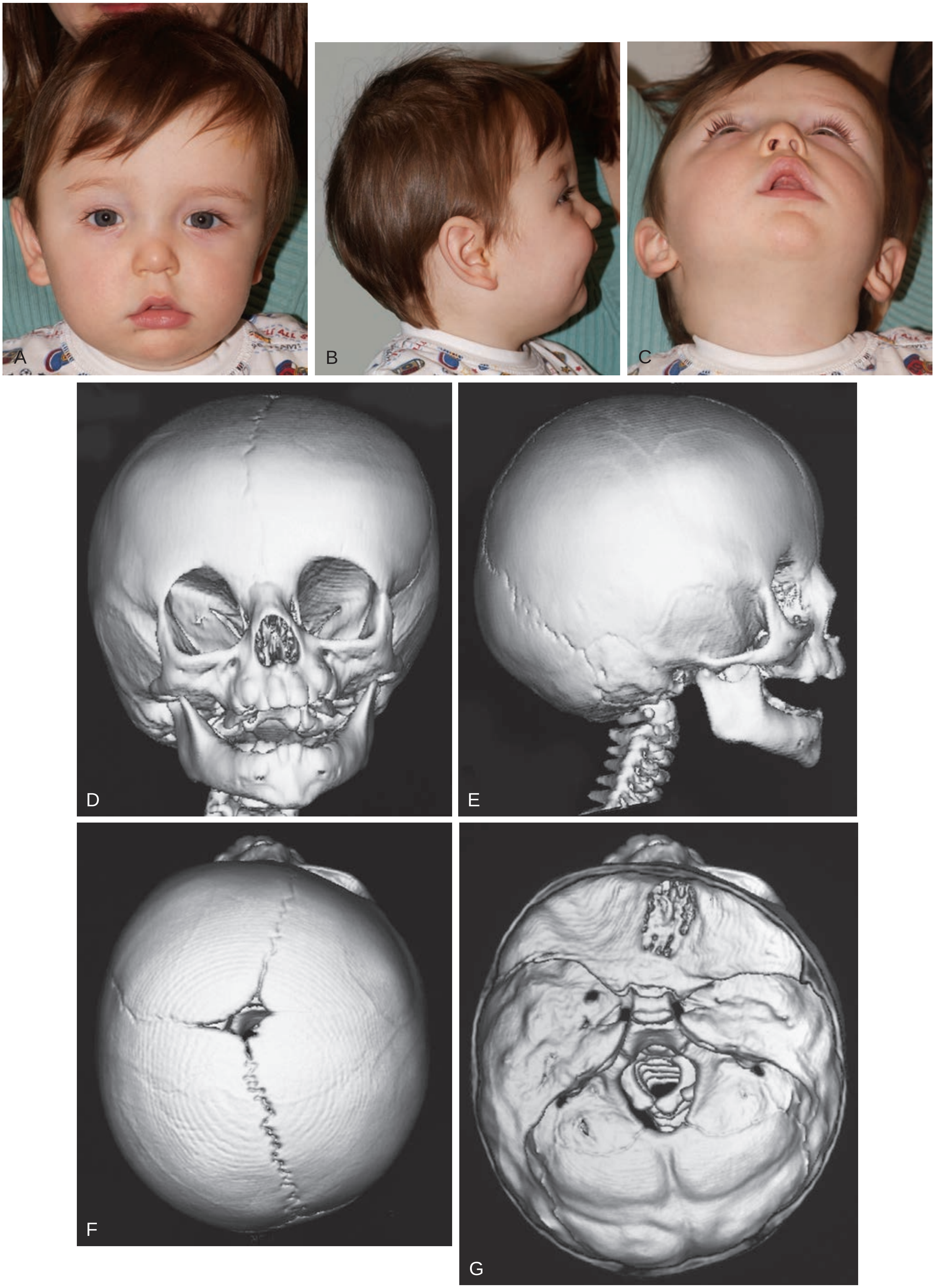

**Figure 20.21. Unilateral right coronal synostosis in an infant.** (A–C) Facial photographs show right frontal and occipital flattening with some right orbital recession. Note craniocaudal skull elongation (scaphocephaly) and anteroposterior shortening (D) Frontal, (E) lateral, (F) vertex, and (G) basilar 3D CT images confirm right coronal suture fusion, elevation of the sphenoid wing, right frontal and occipital flattening, compensatory ipsilateral and temporal contralateral frontal bulging. Also, note angulation of skull base toward side of coronal synostosis.

In most instances, three-dimensional (3D) computed tomography (CT) is required to plan for cranial restructuring. Radiation dose can be lowered to 65 mA and 80 kV at 0.5 second with a slice thickness of 1.25 mm and a CT dose index "dose" of approximately 2.37 mGy. Images are reconfigured to 0.625 mm for various reconstructions (Figs. 20.22–20.24 and e-Fig. 20.25).

Magnetic resonance imaging (MRI) is not well suited for identifying cranial sutures. However, a recently reported gradient echo sequence has been used to minimize soft tissue contrast allowing the cranial sutures to be hyperintense against the signal void of the cranial bones. In syndromic children, brain MRI is performed for developmental anomalies.

While there are reports of successfully using ultrasound for diagnosing synostosis, this has not gained widespread acceptance and, if positive, requires further imaging to be performed.

## Associated Abnormalities

Limb defects are the most common anomalies associated with craniosynostosis, occurring in up to 84%.[1] Syndactyly and polysyndactyly constitute 30% of the limb defects, and deficiencies account for 22%.

Several types of acrocephalosyndactyly and acrocephalopolysyndactyly have been described. Some are clearly defined; others are less clear and may undergo reclassification as further information becomes available.

The best-known acrocephalosyndactyly is *Apert syndrome* (acrocephalosyndactyly type I), in which bicoronal synostosis is associated with symmetric syndactyly of the second, third, and fourth digits, resulting in the "mitten or paddle hand" (e-Fig. 20.26). Developmental delay is variably present. Evaluation of

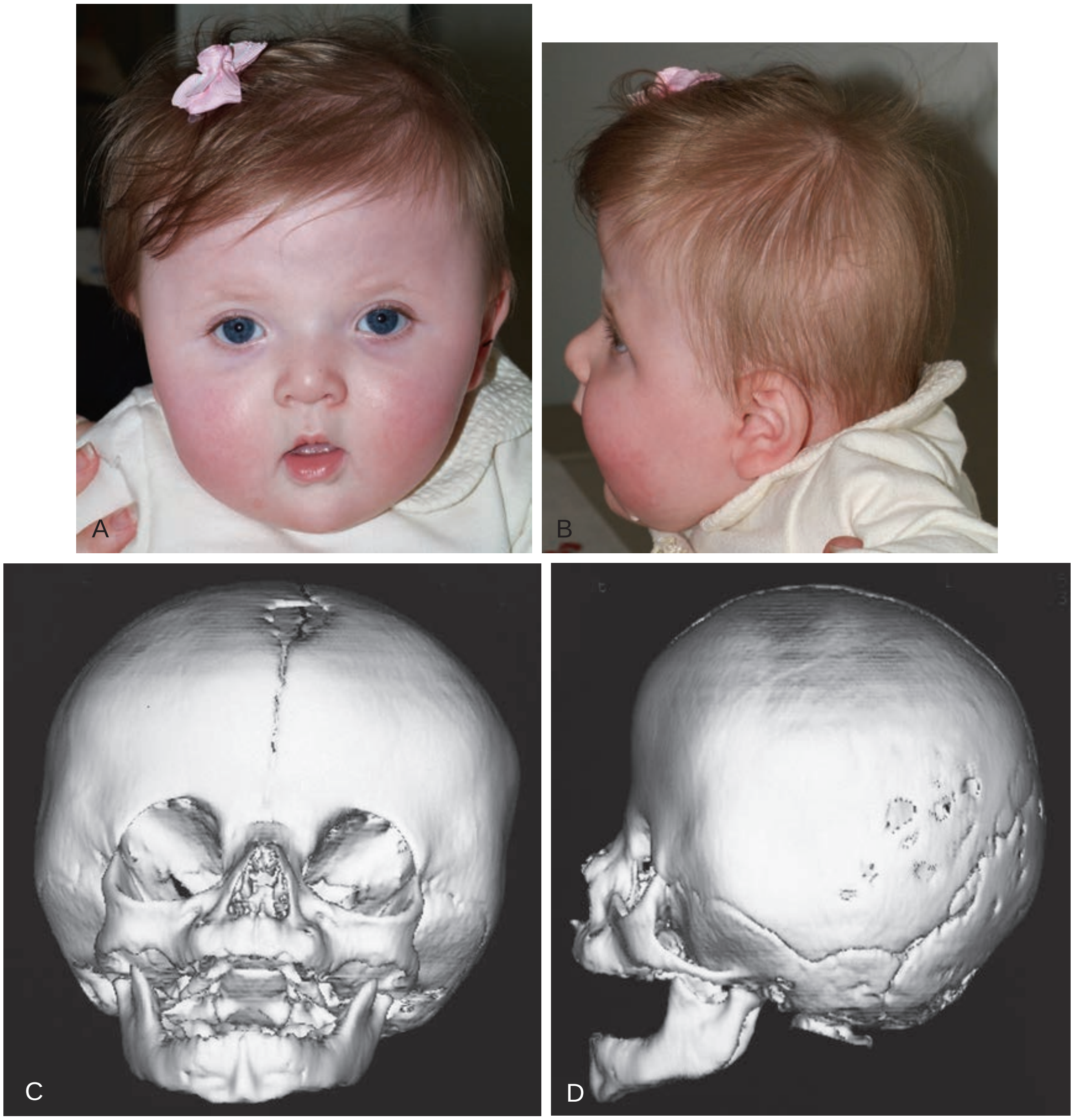

**Figure 20.22. Bilateral coronal synostosis in an infant with brachycephaly.** (A) Frontal and (B) lateral photographs show a towering calvarium with some temporal bulging and orbital recession. (C) Frontal, (D) lateral, and (E) vertex 3-D CT images, in addition to (F) sagittal and (G) axial CT reconstructions reveal coronal suture closure, a towering skull, decreased anteroposterior skull dimension, temporal bulging, and orbital recession.

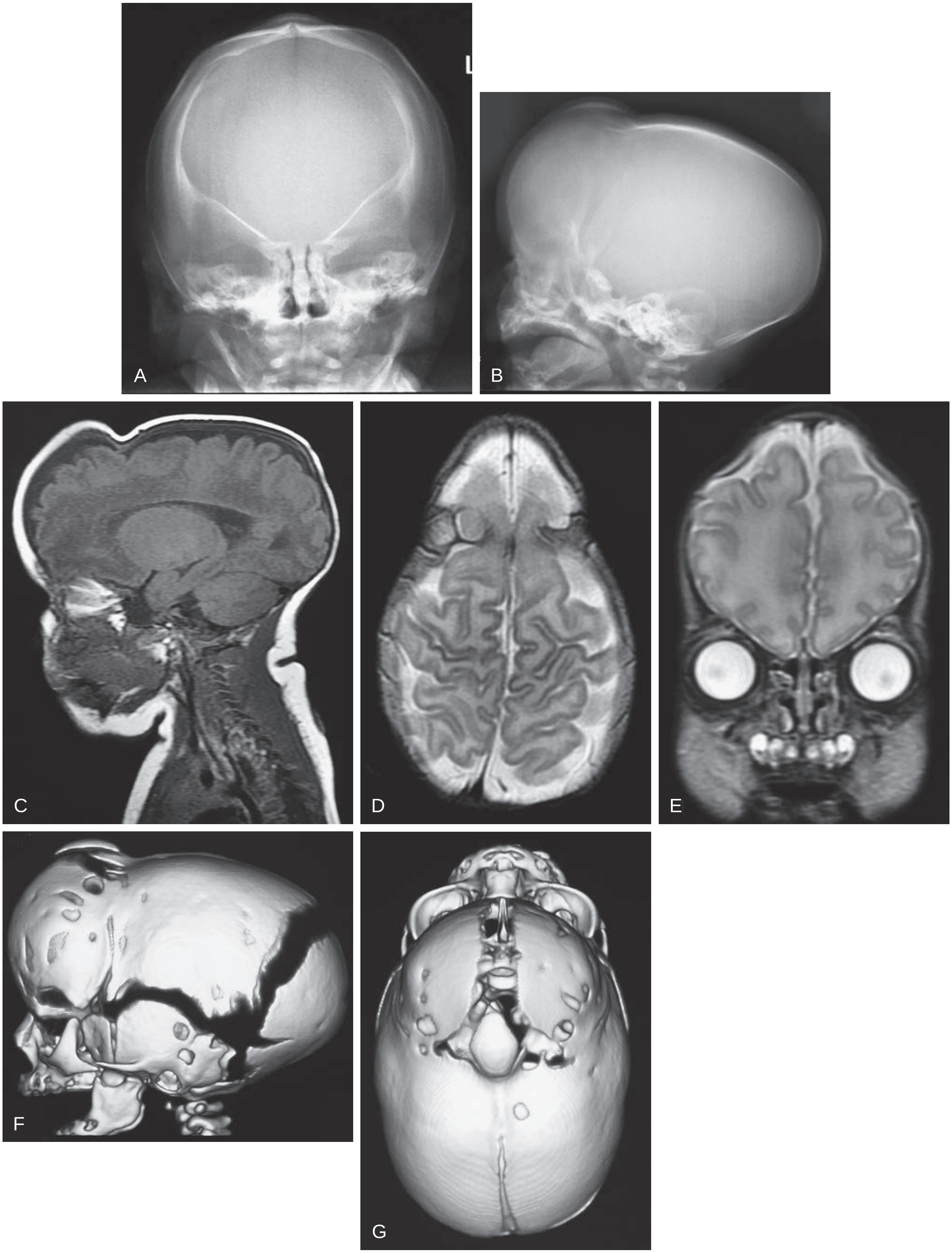

**e-Figure 20.25. Multiple suture closure.** (A) Frontal and (B) lateral radiographs show elevated orbital ridge, upper coronal suture closure, and ridging and closure of the sagittal suture. MRI sequences (C) sagittal T1-, (D) axial T2-, and (E) coronal T2-weighted images reveal normal brain, but severe deformity. (F) Lateral, and (G) vertex 3D CT images show coronal and sagittal suture closure.

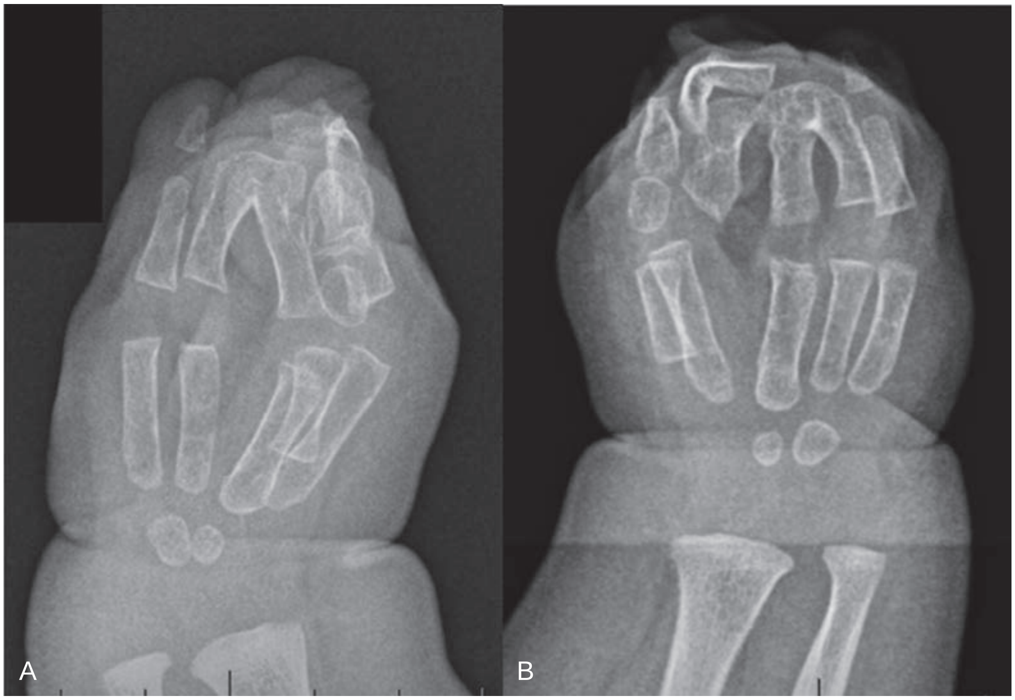

**e-Figure 20.26. Bilateral acrocephalosyndactyly, type I (Apert syndrome).** (A and B) Osseous and soft tissue syndactyly of the phalanges are present. Typical of Apert syndrome, the findings are bilateral and symmetric.

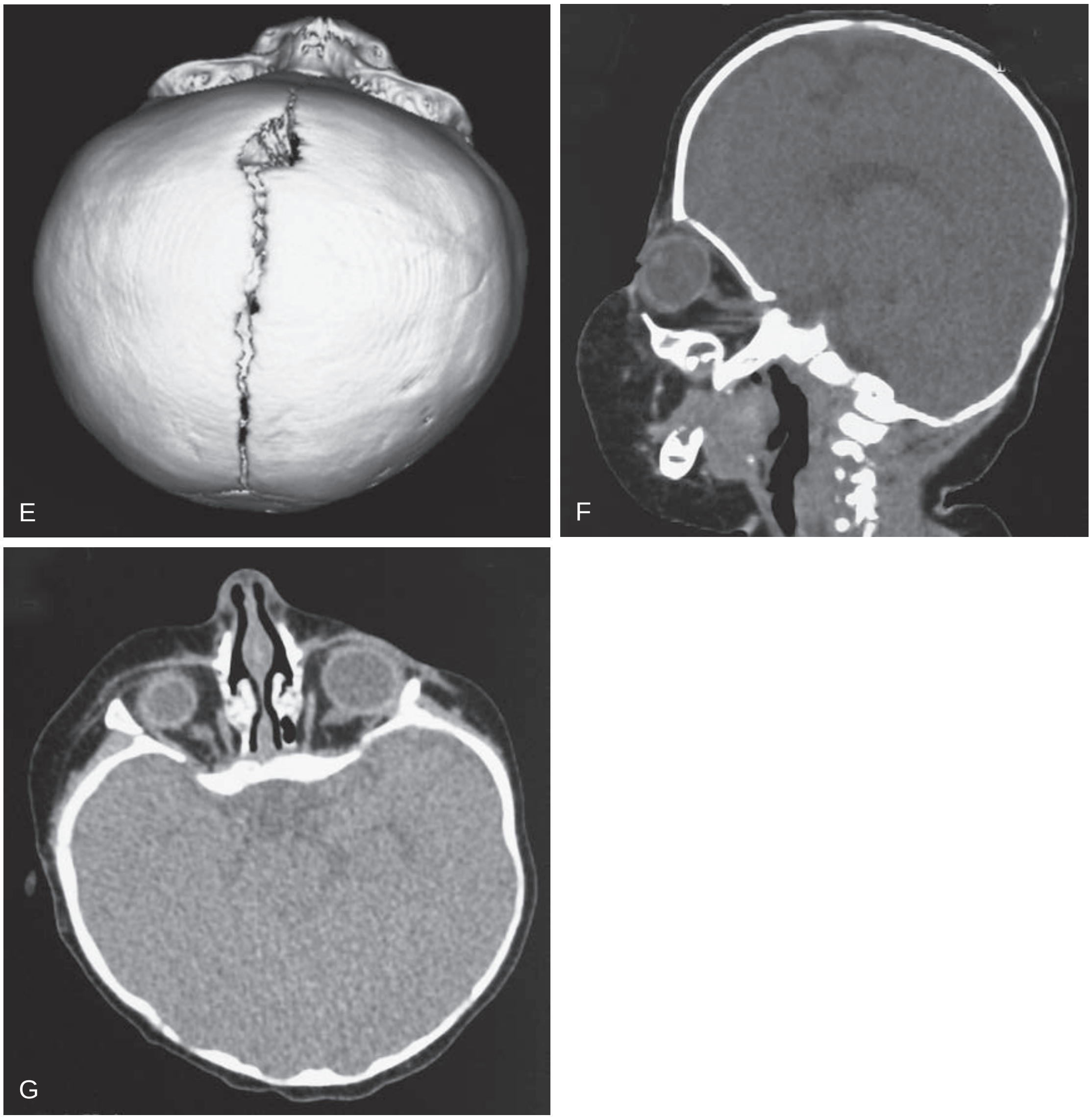

**Figure 20.22, cont'd.**

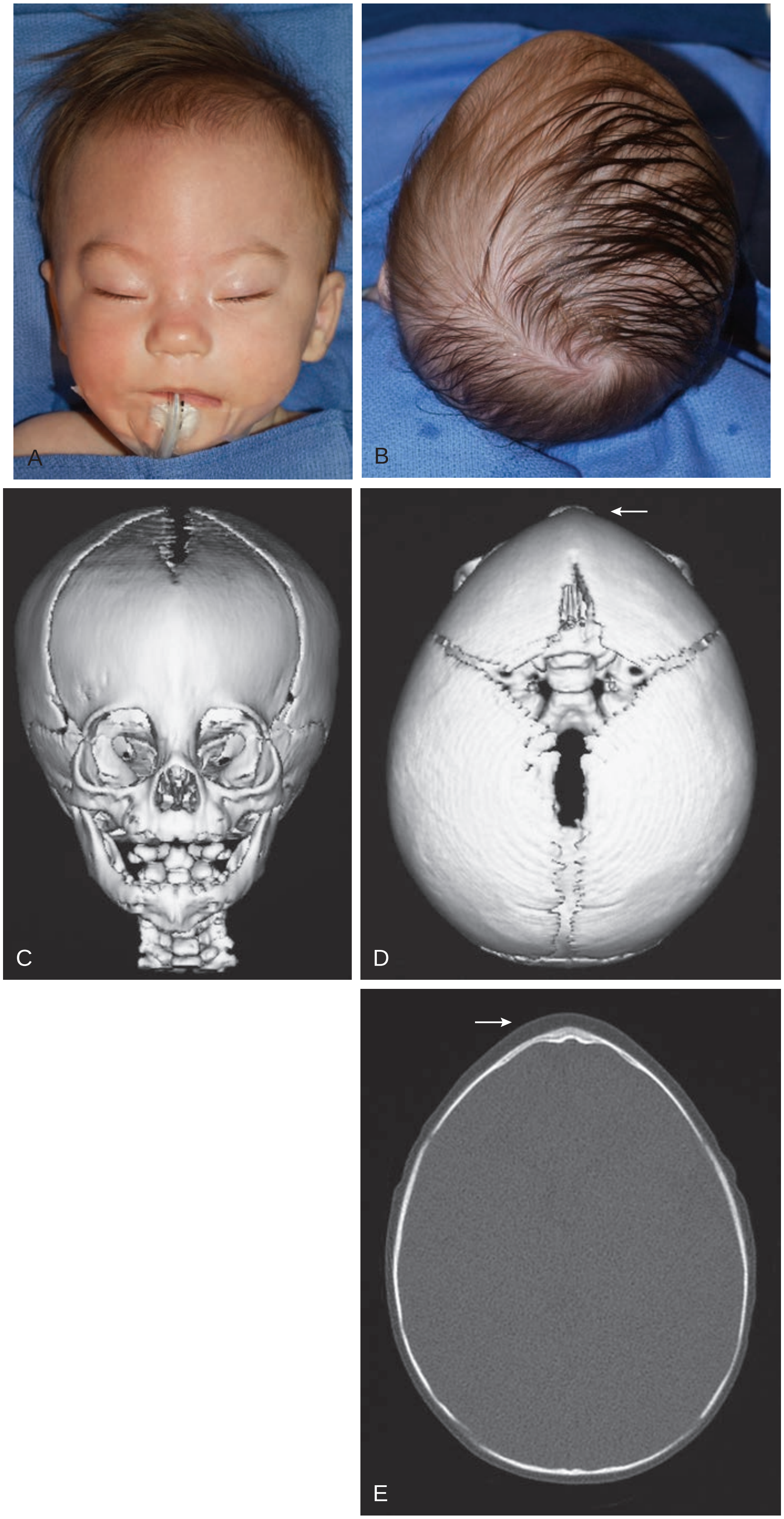

**Figure 20.23. Metopic synostosis in an infant with trigonencephaly and hypotelorism.** (A) Frontal and (B) vertex photographs show a keel-shaped, triangular forehead typical of trigonencephaly. (C) Frontal, (D) vertex, and (E) axial CT images reveal metopic suture fusion and confirm trigonencephaly *(arrow).*

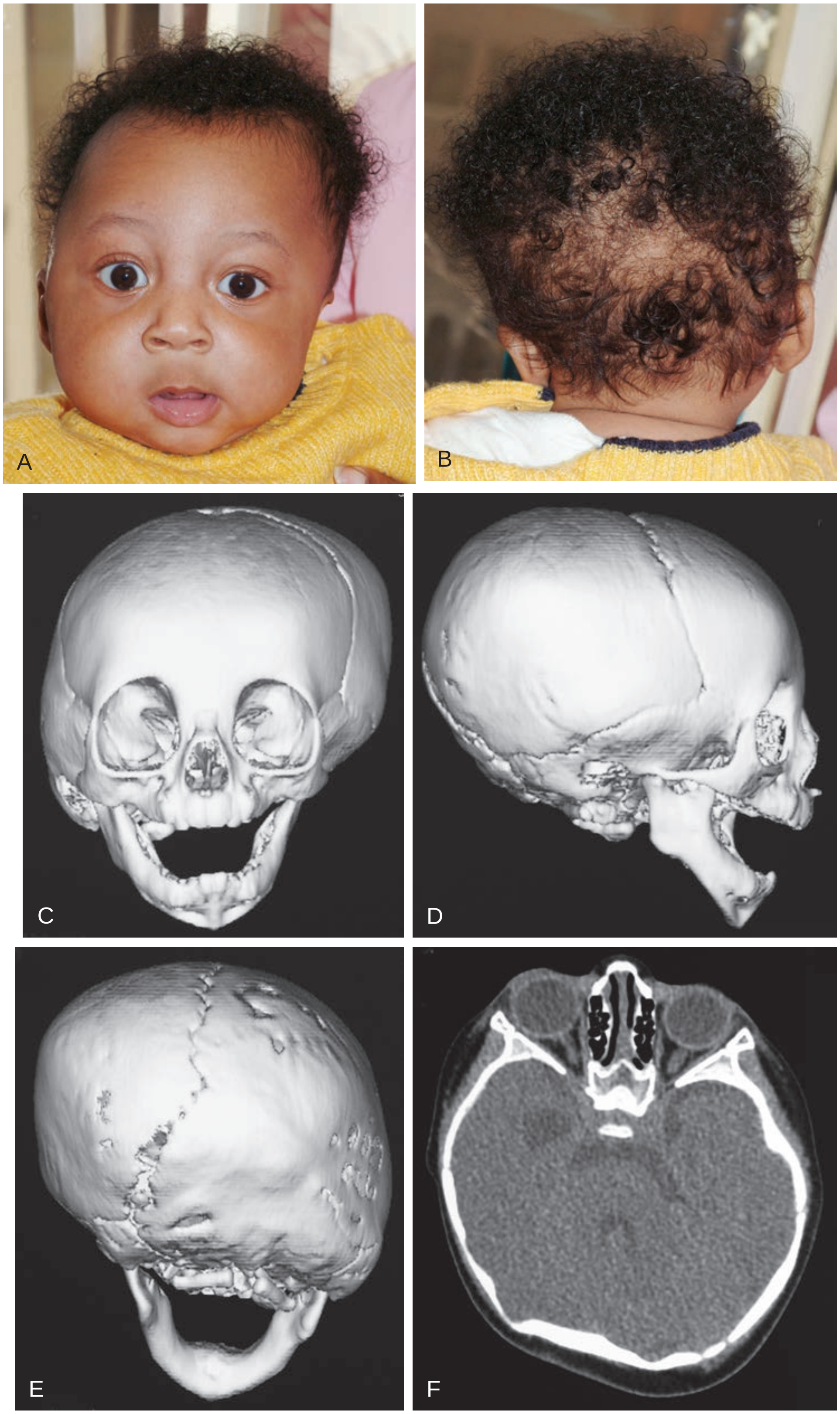

**Figure 20.24. Unilateral right lambdoid synostosis in an infant.** (A) Frontal and (B) posterior photographs show asymmetric bulging of the right inferior occipital region and compensatory left parietal bulging superiorly. (C) Frontal, (D) lateral, and (E) posterior 3D CT and (F) axial CT images demonstrate right lambdoid suture absence with compensatory bulging of the superior and inferior ends of the synostosal suture (i.e., left parietal and right occipital region). Skull-base angulation is evident.

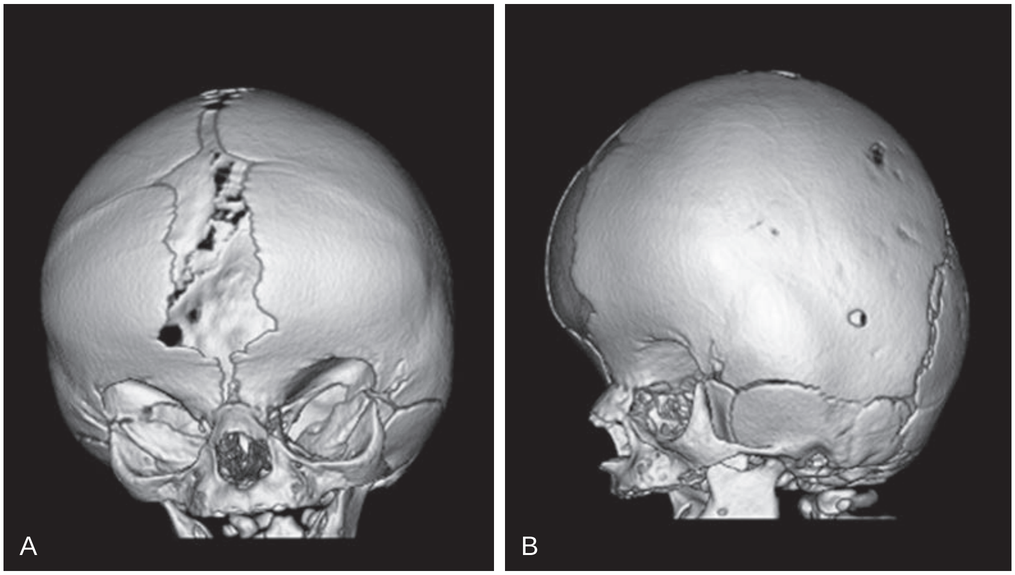

**Figure 20.28. Apert syndrome in an 8-day-old infant.** (A) Frontal and (B) lateral 3D CT images show classic bilateral coronal synostosis with brachycephaly and a towering skull with a gaping metopic suture. Also noted are exophthalmos, hypertelorism, and maxillary retrusion.

craniofacial deformities may be assisted by CT (e-Fig. 20.27, Fig. 20.28, and e-Fig. 20.29).

Acrocephalosyndactyly types II, III, and IV are known as *Apert-Crouzon disease*, *Saethre-Chotzen syndrome*, and *Waardenburg syndrome*, respectively; they involve varying degrees of facial abnormality and syndactylies in patterns particular for each type. Acrocephalosyndactyly type V, *Pfeiffer syndrome*, has only moderate soft tissue syndactyly, but the thumbs and great toes are deformed and broad (Fig. 20.30).

*Carpenter syndrome* (acrocephalopolysyndactyly type II) is characterized by developmental delay and preaxial polydactyly of the feet. Types I and III are known as *Noack syndrome* and *Sakati-Nyhan syndrome*.

In *Crouzon syndrome*, the cardinal elements originally included (1) brachycephaly, (2) facial dysostosis with a hooked parrot nose and small maxilla, (3) bilateral exophthalmos, and (4) genetic transmission and familial incidence (e-Fig. 20.31 and Fig. 20.32).

The complications of these syndromes include exophthalmos, loss of vision, increased intracranial pressure, and developmental delay. Maxillary hypoplasia may cause upper airway obstruction and sleep apnea. Surgical procedures are performed to improve the airway, dental occlusion, and deformities.

Kleeblattschädel (cloverleaf skull) results from closure of all sutures except the squamosal sutures, leading to severe temporal and vertex bulging with exophthalmos (see Fig. 20.16 and e-Fig. 20.17). Hydrocephalus develops in utero, deforming the skull into a superiorly elongated calvarium with dilated frontal and temporal regions. Most patients do not survive infancy (see Fig. 20.16). Kleeblattschädel may be found in thanatophoric dysplasia type II.

## CRANIOFACIAL SYNDROMES

A large number of conditions fall under the category of craniofacial syndromes; most are uncommon and beyond the scope of this book. Four of the relatively more common syndromes are discussed: Goldenhar, hemifacial microsomia, Treacher Collins, and Pierre Robin sequence (PRS).

### Goldenhar Syndrome and Hemifacial Microsomia

Goldenhar syndrome is part of the oculo-auricular-vertebral spectrum, which includes hemifacial macrosomia (HFM).[13,14] Most cases are sporadic, although there is an increased incidence of Goldenhar in infants of diabetic mothers. The phenotype has been associated with other conditions, including trisomy 18, maternal thalidomide, primidone, and retinoic acid use.

The hallmarks of Goldenhar syndrome are epibulbar dermoids, preauricular appendages, mandibular hypoplasia, microtia, and vertebral anomalies. Extreme variability of expression is characteristic of this anomaly. Most frequently, the orbital lesions, mandibular hypoplasia (Fig. 20.33), and microtia are ipsalateral.[15] Colobomas occur in 60% of patients, requiring urgent repair to prevent ulceration. Deafness is common because of associated anomalies of the middle and inner ear.[16] Vertebral anomalies, most often cervical, occur in 60% of patients including basilar invagination, occipitalization of the atlas, C1-2 instability, hemivertebra, butterfly vertebrae, scoliosis, kyphosis, and Sprengel deformities (e-Fig. 20.34).[17] Verterbral anomalies below the cervical spine are found in only 10% of patients but may be severe.

Hemifacial microsomia is a variable malformation of asymmetric facial hypoplasia, microsomia, unilateral microtia, and ipsilateral mandibular hypoplasia. HFM implies unilateral involvement, but the structures affected are bilateral and affected to different degrees. HFM may be caused by a hemorrhagic event involving the stapedial artery during early stages of craniofacial development.[18] Patients with HFM resemble those with Goldenhar syndrome, but the presence of epibulbar dermoids, lipodermoids, auricular appendices, pretragal blind-ending fissures, and vertebral anomalies favors a Goldenhar diagnosis.

The mode of inheritance is autosomal or X-linked dominant in most cases.

### Treacher Collins Syndrome

The condition has been diagnosed in utero by ultrasonography and is autosomal dominant with variable penetrance and expression.

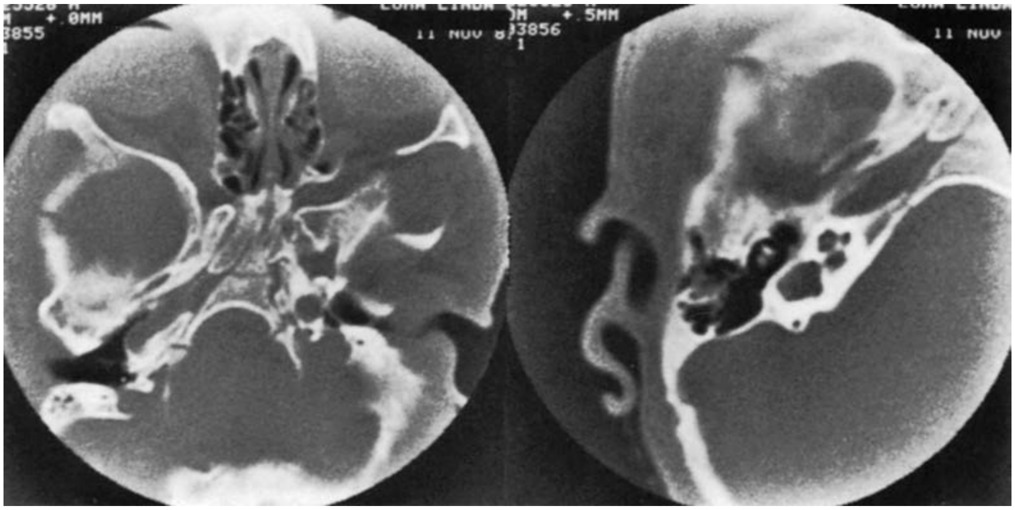

**e-Figure 20.27. Bizarre skull base deformity due to asymmetric craniosynostosis in a child with Apert syndrome.** *Left,* CT image demonstrates spheno-occipital synchondrosis. The basiocciput shows asymmetry and a partial cleft in the sphenoid body. *Right,* Magnified right inner ear view reveals a single cavity replacing the vestibule and semicircular canals. The ossicles are normal. *(Courtesy of Anton N. Hasso, MD.)*

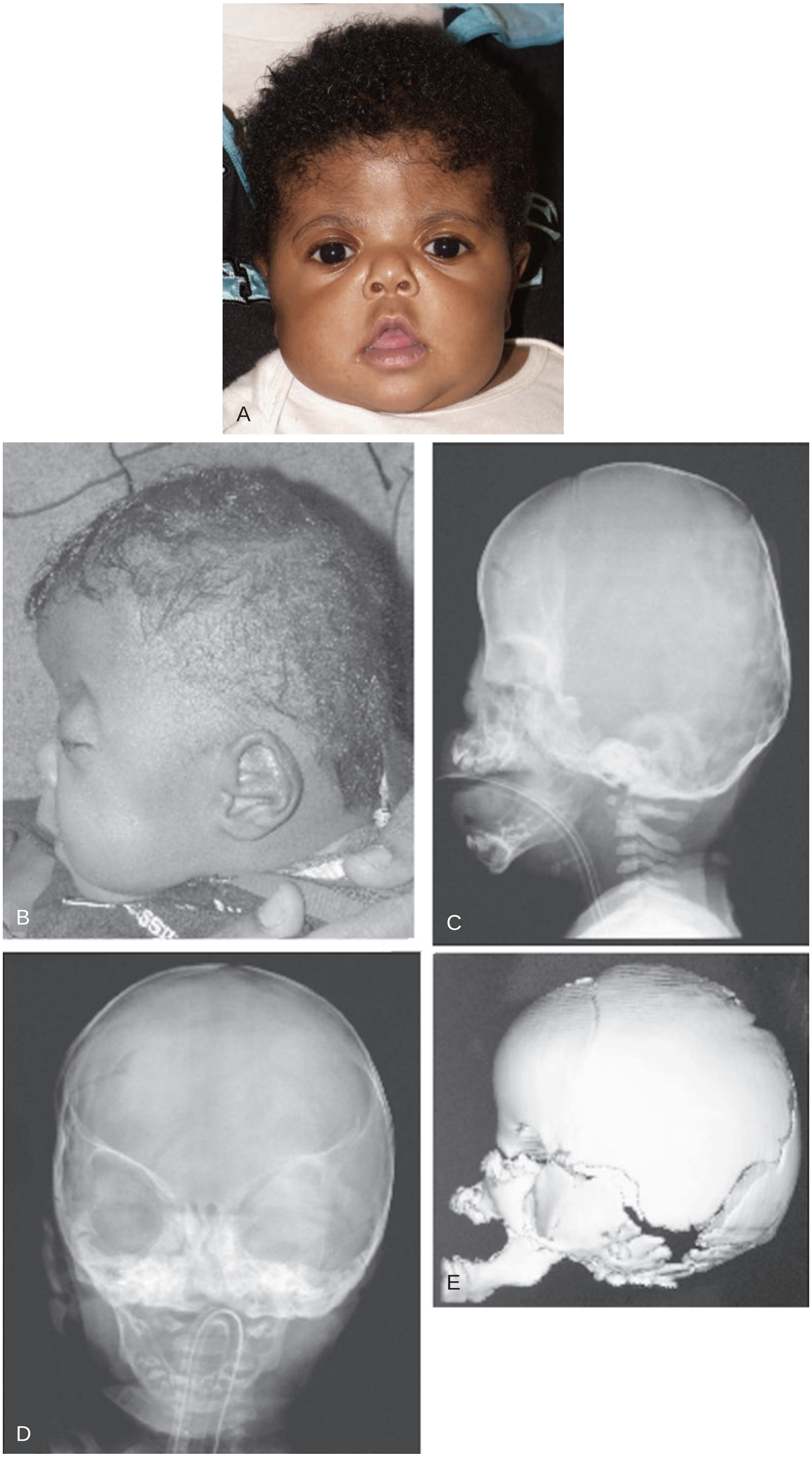

**e-Figure 20.29. Apert syndrome.** (A) Frontal and (B) lateral photographs show brachycephaly and increased caudad-to-cephalad dimension suggesting bilateral coronal synostosis. (C) Frontal and (D) lateral radiographs of the same patient show the bilateral coronal synostosis and the expected contour of the calvarium. (E) 3D CT lateral view confirms closure of inferior coronal suture and maxillary retrusion.

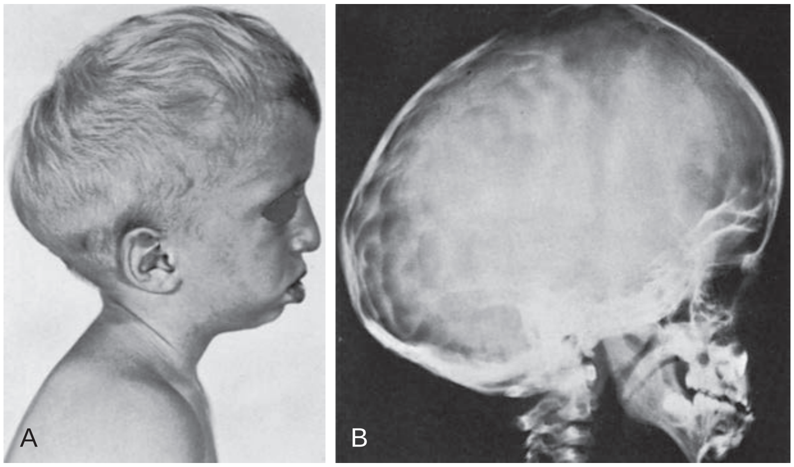

**e-Figure 20.31. Crouzon disease (craniofacial dysostosis).** (A) Lateral photograph shows an enlarged, ventrodorsally elongated calvarium. Also noted are a small face, beaked nose, and marked bilateral exophthalmos. (B) Lateral radiograph reveals a large frontal squamosa, and externally bulging edges of the frontal and parietal bones at the anterior fontanel. Convolutional markings are heavy in the occipital squamosa. The facial segment is small, with a small maxilla and relatively larger mandible; the latter has an increased obtuse angle. The anterior cranial fossa is small and shallow compared with the middle and posterior fossae.

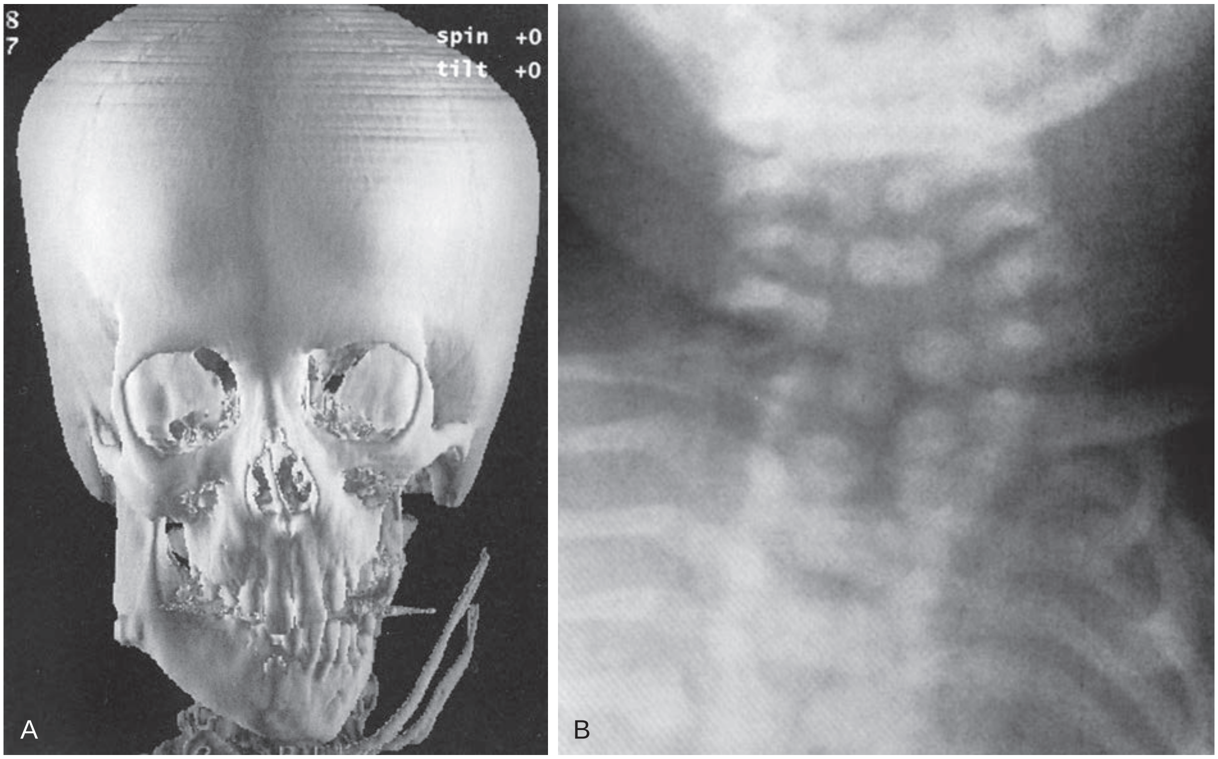

**e-Figure 20.34. Goldenhar syndrome (hemifacial microsomia).** (A) Marked left hemimandibular hypoplasia is present on 3D CT image. (B) Frontal cervical spine radiograph shows multiple segmentation anomalies.

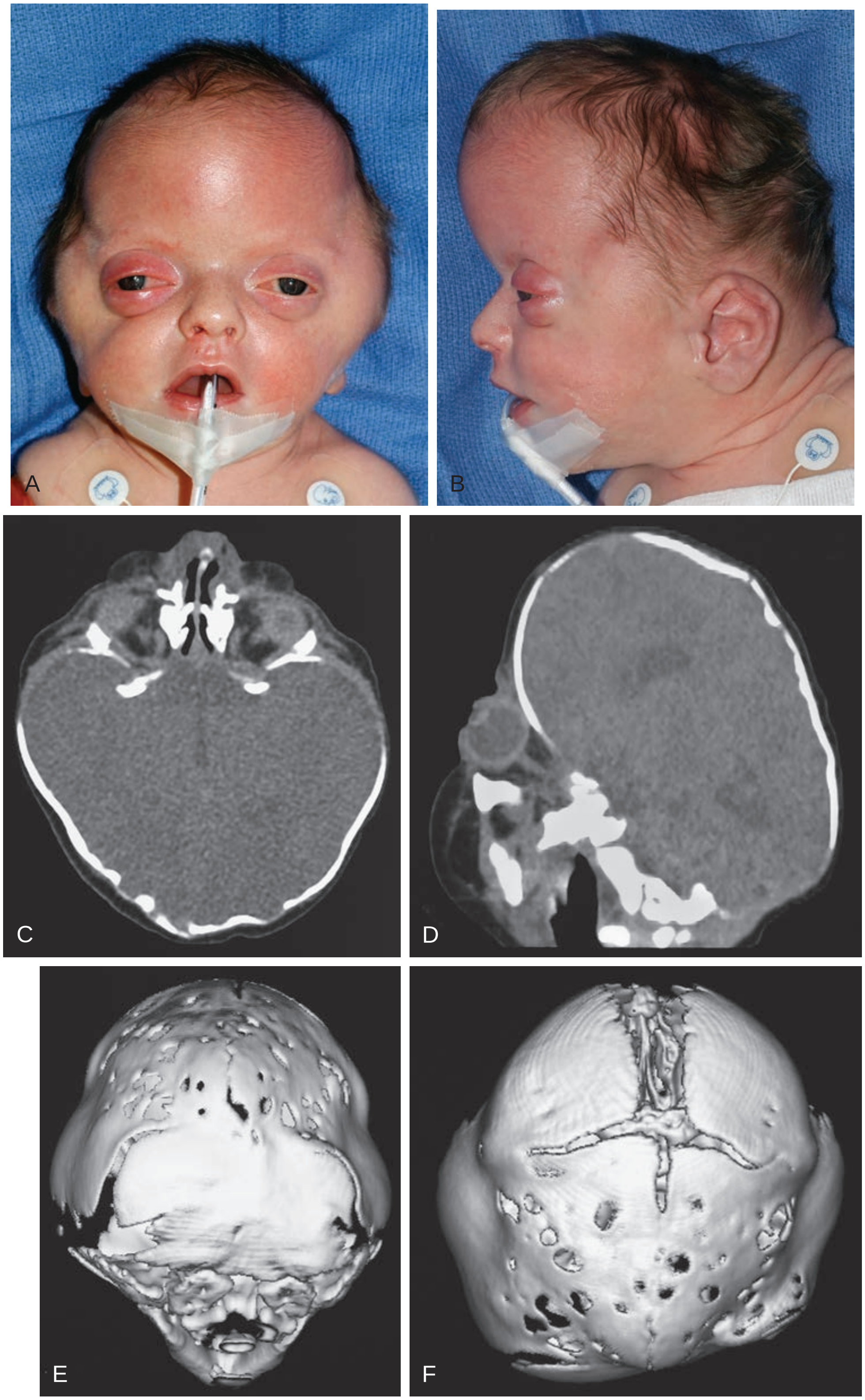

**Figure 20.30. Pfeiffer syndrome.** (A) Frontal and (B) lateral photographs show cloverleaf skull shape due to multisutural synostosis (bilateral coronal, bilateral lambdoid, and sagittal synostosis). (C) Axial and (D) reconstructed sagittal CT images show temporal bulging, bony fenestrations, maxillary retrusion, and exophthalmos. (E) Posterior and (F) vertex 3D CT images confirm coronal, bilateral lambdoid and sagittal suture closures.

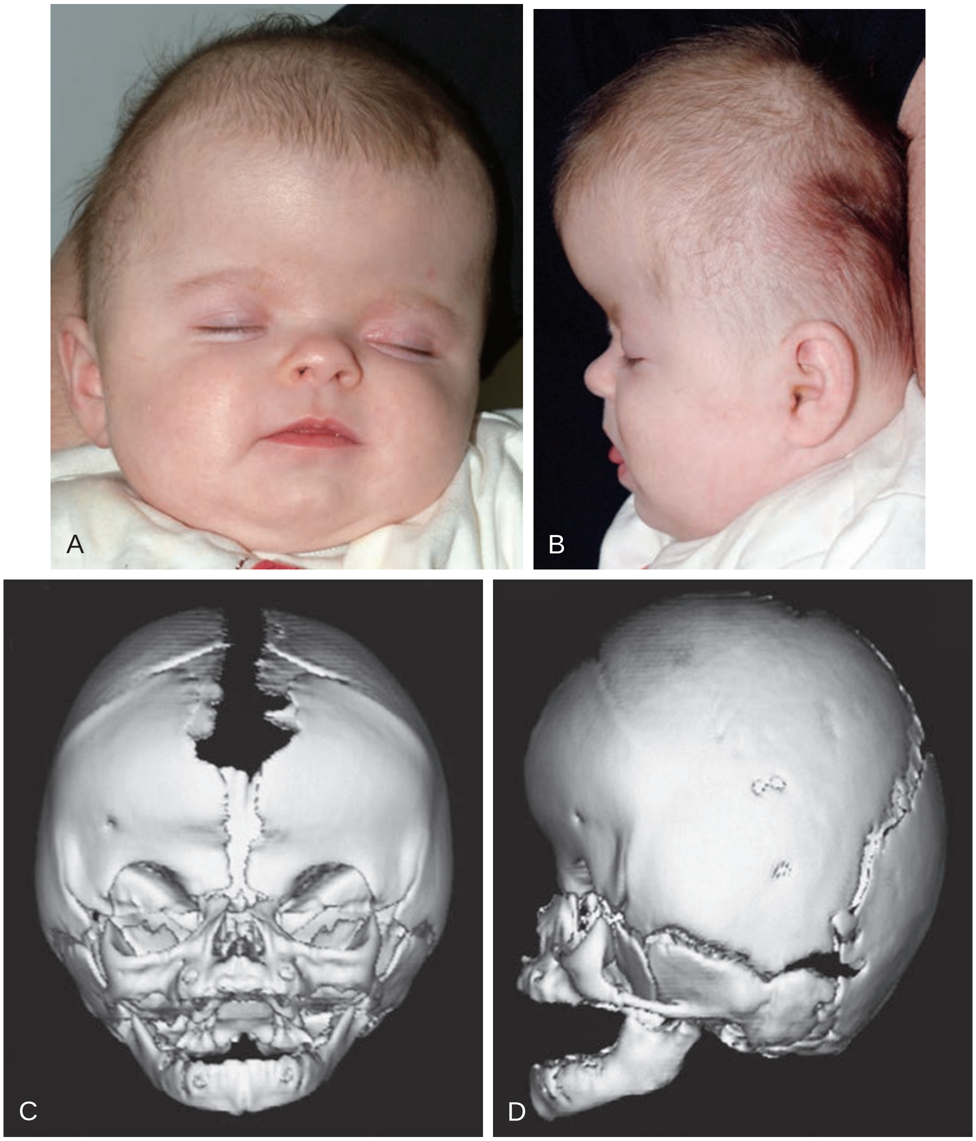

**Figure 20.32. Crouzon syndrome in an infant with brachycephaly.** (A) Frontal and (B) lateral photographs show increased craniocaudal and decreased anteroposterior dimensions. (C) Frontal and (D) lateral 3D CT images reveal brachycephaly due to bilateral coronal synostosis.

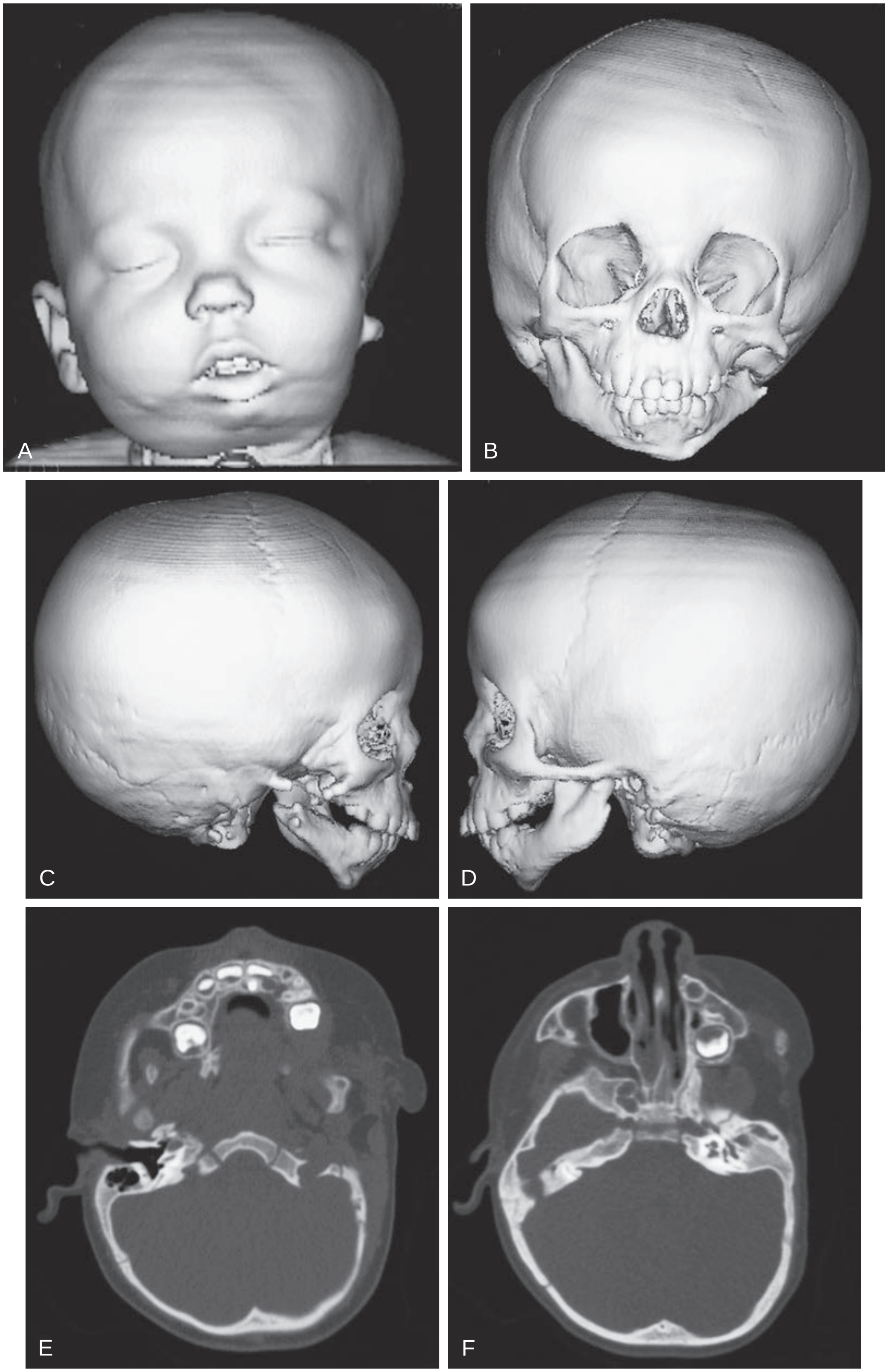

**Figure 20.33. Goldenhar syndrome in an infant with microtia.** (A) 3D CT surface rendering shows left hemifacial microsomia and left ear microtia. (B) Frontal 3D CT reveals a hypoplastic left mandible and zygomatic arch. (C and D) Lateral 3D CT images confirm asymmetry and left microsomia. (E and F) Axial CT images of the skull base reveal normal right external canal and temporal bone. The left face is hypoplastic and the external auditory canal is absent.

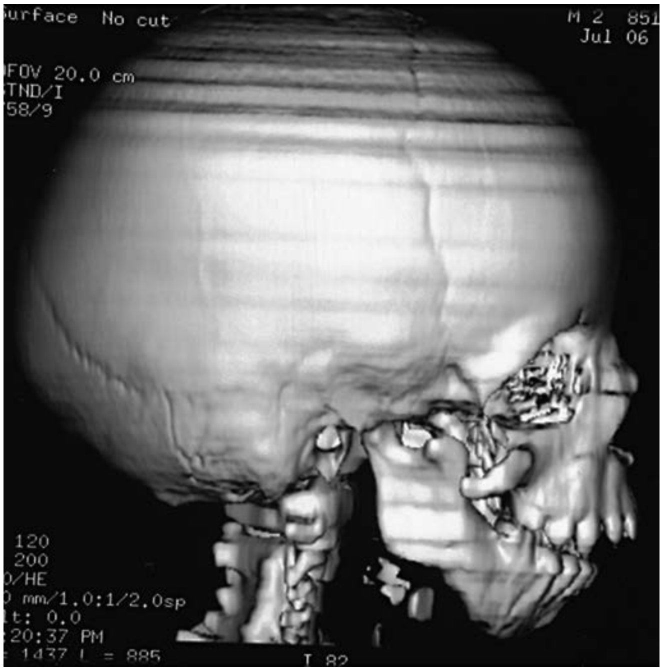

**Figure 20.35. Treacher Collins syndrome in a 3-month-old boy with micrognathia.** Lateral 3D CT image shows mandibular hypoplasia and absence of the zygomatic arch.

The facial features of Treacher Collins syndrome (TCS) are characteristic including bilateral, symmetric micrognathia, narrow face, depressed cheekbones, antimongoloid slant of eyes, malformed small ears, downturned mouth, high-arched or cleft palate, and conductive hearing loss.[19,20] The features are characterized by abnormalities derived from the first and second branchial arches.[20] Mutations in the *TCOF1* gene are associated with TCS.[21] The imaging features are primarily facial including mandibular, zygomatic, maxillary, and supraorbital hypoplasia. The orbits are described as egg-shaped. The mandible has a characteristic short body and ramus varying with patient age. The mandibular condyle and coronoid process may be severely hypoplastic, flat, or even absent (Fig. 20.35). Ear abnormalities include hypoplasia or absence of the middle ear. The ossicles and vestibular apparatus may be malformed. Zygomatic hypoplasia or aplasia is an important imaging finding for the diagnosis. Craniofacial 3D CT has become invaluable for surgical planning.[22]

### Pierre Robin Sequence

PRS, or Robin sequence, represents a nonrandom association of micrognathia, cleft palate, and glossoptosis.[23] PRS is causally heterogeneous, pathogenetically, and phenotypically variable.[24] Patients with PRS are classified as isolated (most common), syndromic, or with associated anomalies. Numerous syndromes, including Stickler and velocardiofacial syndromes, are associated with PRS.[25] Respiratory compromise from mechanical and central nervous system causes are common. The mandible may be small or normal-sized with retrognathia due to a large cranial base. Typically, a reduction in cranial base, maxillary and mandibular lengths are seen.[26]

Cardiovascular anomalies include septal defects and patent ductus arteriosus. Numerous skeletal anomalies of the ribs, sternum, spine, and limbs occur. Airway management is similar in both nonsyndromic and syndromic PRS. Infants may be managed with positioning, nasal pharyngeal airway, tongue-tie adhesions, or mandibular distraction.[27–30] Cine MRI or CT give dynamic and 3D information useful in airway evaluation of these patients.

## OTHER ABNORMALITIES OF THE SKULL

### Cranioschisis (Cranium Bifidum)

Cranioschisis usually occurs in the median sagittal plane, anteriorly or posteriorly (Fig. 20.36). It is characterized by bony defects and may accompany a meningocele or meningoencephalocele.[31] Meningoceles are characterized by a hernia sac, which is covered with skin and contains only meninges and cerebrospinal fluid (e-Fig. 20.37). Meningoencephaloceles also contain brain (e-Fig. 20.38). Rarely, cranioschisis may be heralded by a scalp nodule, with or without intracranial communication. Occasionally, small cranial defects (cranium bifidum occultum) through which no herniation occurs are encountered (e-Fig. 20.39). MRI is effective for evaluation.

Cranium bifidum with encephalocele often occurs in the sphenoid bone or the cribriform plate. In such cases, the protruding mass of brain and covering meninges may extend into the nasal cavity, nasopharynx, sphenoid sinus, posterior orbit, or pterygoid fossae. Important clinical signs include facial deformity hypertelorism and a broad nasal base.

### Lacunar Skull of the Newborn (Lückenschädel, Craniolacunia)

Lacunar skull develops during fetal life and is present at birth.[32] It is nearly always associated with meningomyelocele, myelocele, encephalocele or Chiari II malformation. The cause is unknown, but it is probably a dysplasia of the calvarium and the internal calvarial periosteum (i.e., the dura). It is not caused by increased intracranial pressure because it is found in infants whose skulls are normal or are small in size without hydrocephalus. The characteristic "soap bubble" rarefactions in the upper part of the calvarium are easily recognized (e-Fig. 20.40). These begin to fade after birth and usually disappear by 4 to 5 months of age. Normal convolutional rarefactions differ from lacunar rarefactions in that they are not obvious until the end of the first year and appear first in the posterolateral calvarium.

### *Sinus Pericranii*

The term *sinus pericranii* is used for a soft, fluctuant, red-to-blue scalp mass over the sagittal or transverse sinuses. It changes size in response to maneuvers that increase intracranial pressure and may be associated with an underlying calvarial defect. It results from abnormal communication between the intracranial and extracranial venous systems, and its significance is cosmetic.[33–35] It must be differentiated from more serious lesions such as arteriovenous malformations, angiomas and hemangiomas, cephaloceles, and abscess. Ultrasound can suggest the diagnosis, but MRI is the best modality for demonstrating the abnormal vascular communication (Fig. 20.41).

KEY POINTS

- Craniosynostosis deformities are complex, and secondary abnormalities at the base of the skull add to the structural changes.
- Plagiocephaly denotes abnormal skull shape (usually flattening) without defining a cause.
- Lacunar skull is not related to increased intracranial pressure.

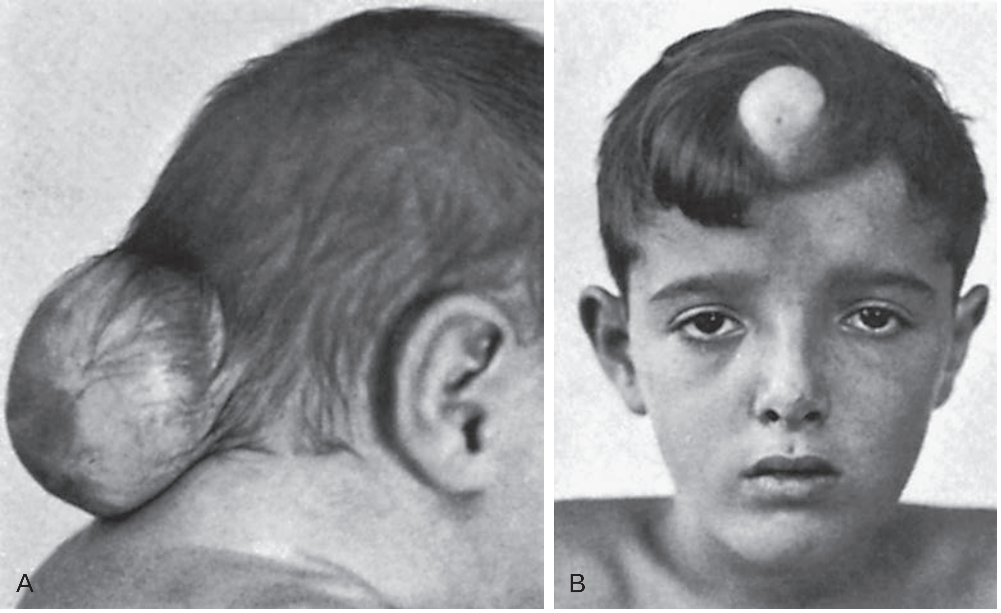

**e-Figure 20.37. Photographs of two children with skull defects and meningoceles.** (A) Lateral photograph of a 1-week-old neonate with an occipital meningocele. (B) Photograph of a 9-year-old male with a frontal meningocele.

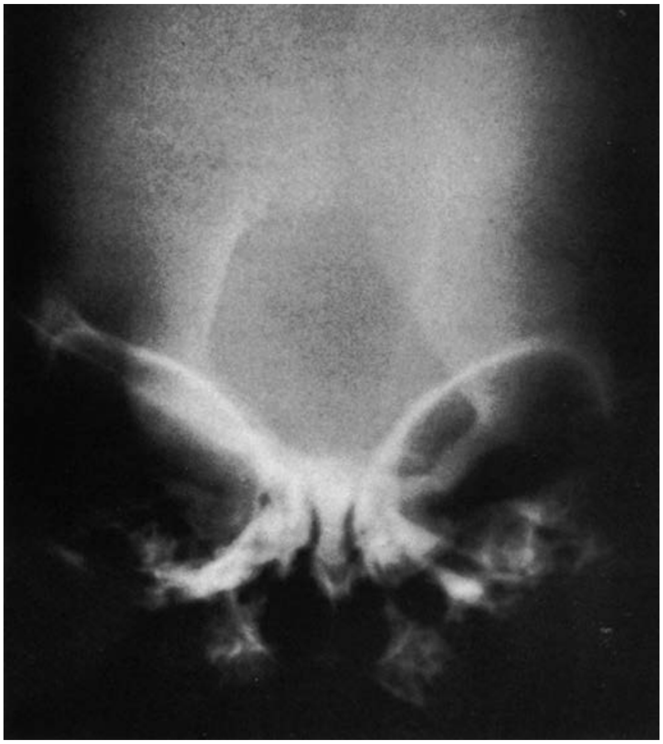

**e-Figure 20.38. Cranium bifidum and occipital cephalocele in an infant with macrocrania.** Lucent osseous defect shown is in continuity with the foramen magnum. A Dandy-Walker cyst protruded through the bony defect *(not shown).*

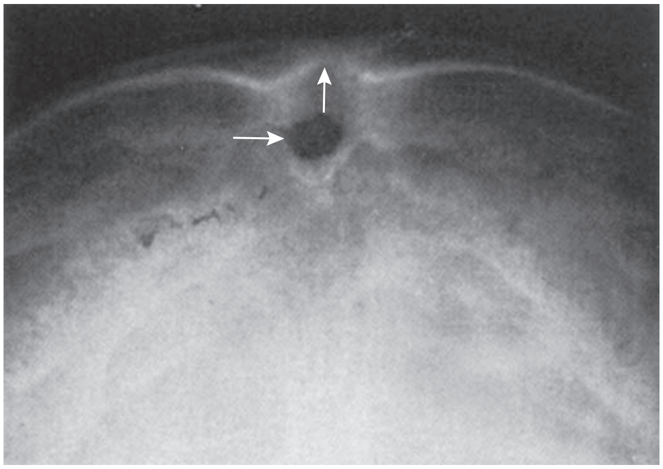

**e-Figure 20.39. Cranium bifidum occultum in a 7-year-old infant.** Small round bony defect in the sagittal suture *(horizontal arrow)* without protrusion of a hernia sac. The groove for the sagittal sinus is shown *(vertical arrow).*

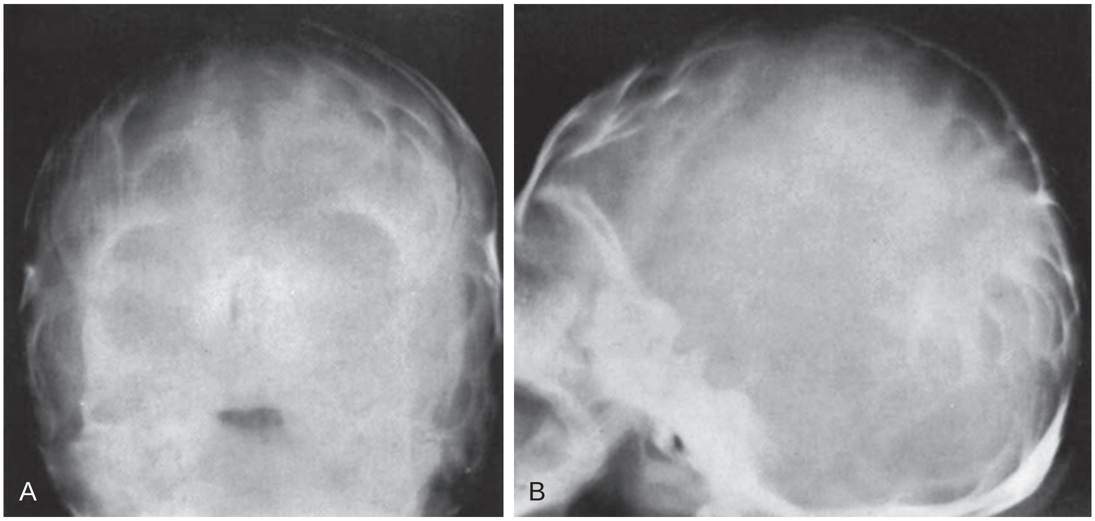

**e-Figure 20.40. Lacunar skull with occipital meningocele in a newborn.** (A) Frontal and (B) lateral radiographs demonstrate checkered skull rarefaction separated by bands of heavier density (lacunar pattern) resembling beaten copper or silver.

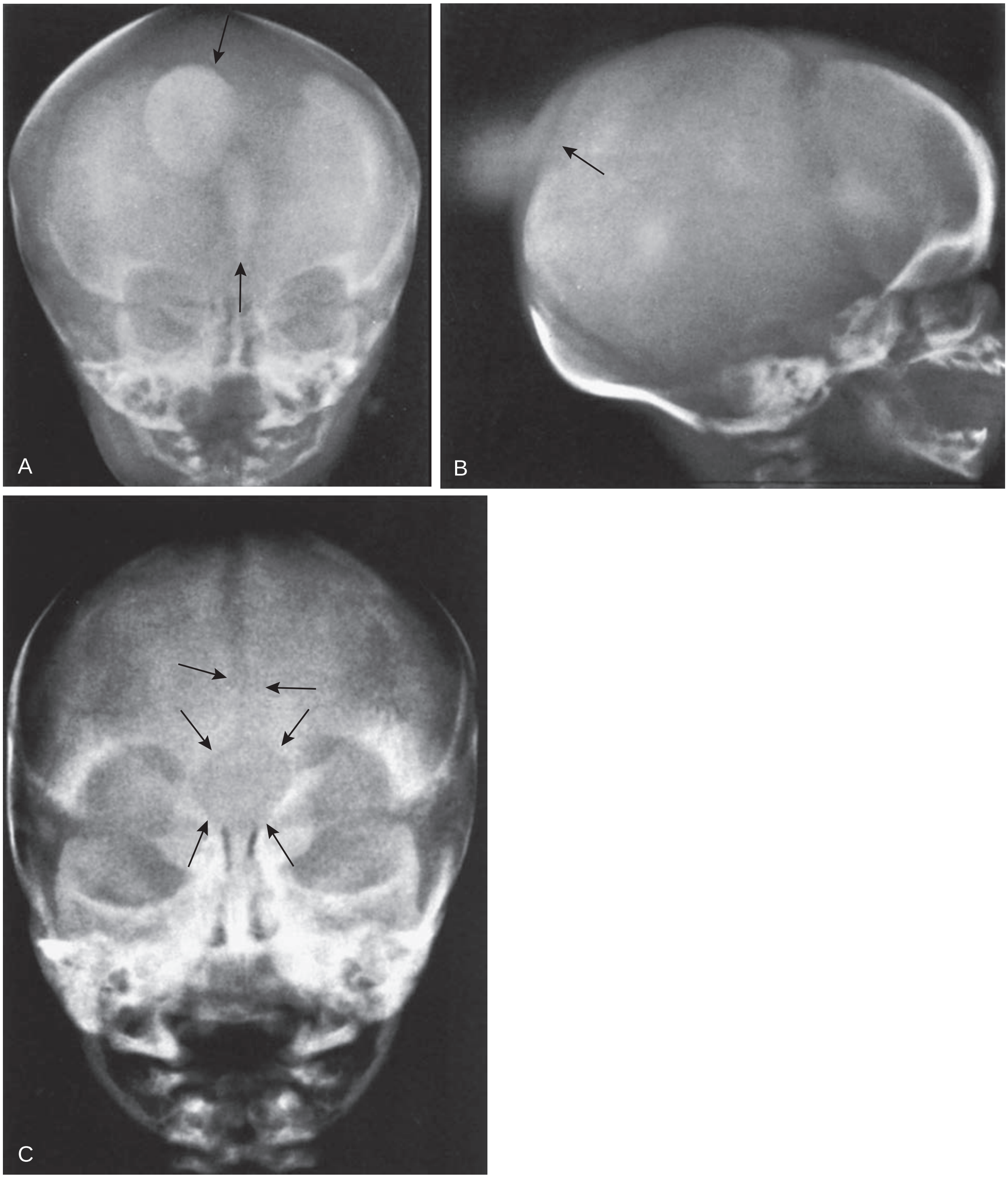

**Figure 20.36. Cranium bifidum and cephalocele in a 2-day-old girl.** (A) Frontal and (B) lateral radiographs show cranium bifidum in the metopic and sagittal suture, with protrusion of a meningoencephalocele at anterior and posterior sites. The metopic suture is open wide, and a smaller mass of soft tissue bulges externally between the frontal bones. In A, the larger superior patch of increased density *(upper arrow)* represents the interparietal protrusion, and the lower small patch *(lower arrow)* represents the smaller intrafrontal protrusion. (B) *(Arrow)* again denotes the protruding cephalocele. (C) Large circular glabellar osseous defect (cranium bifidum) in the metopic suture with an associated cephalocele *(arrows)* are shown.

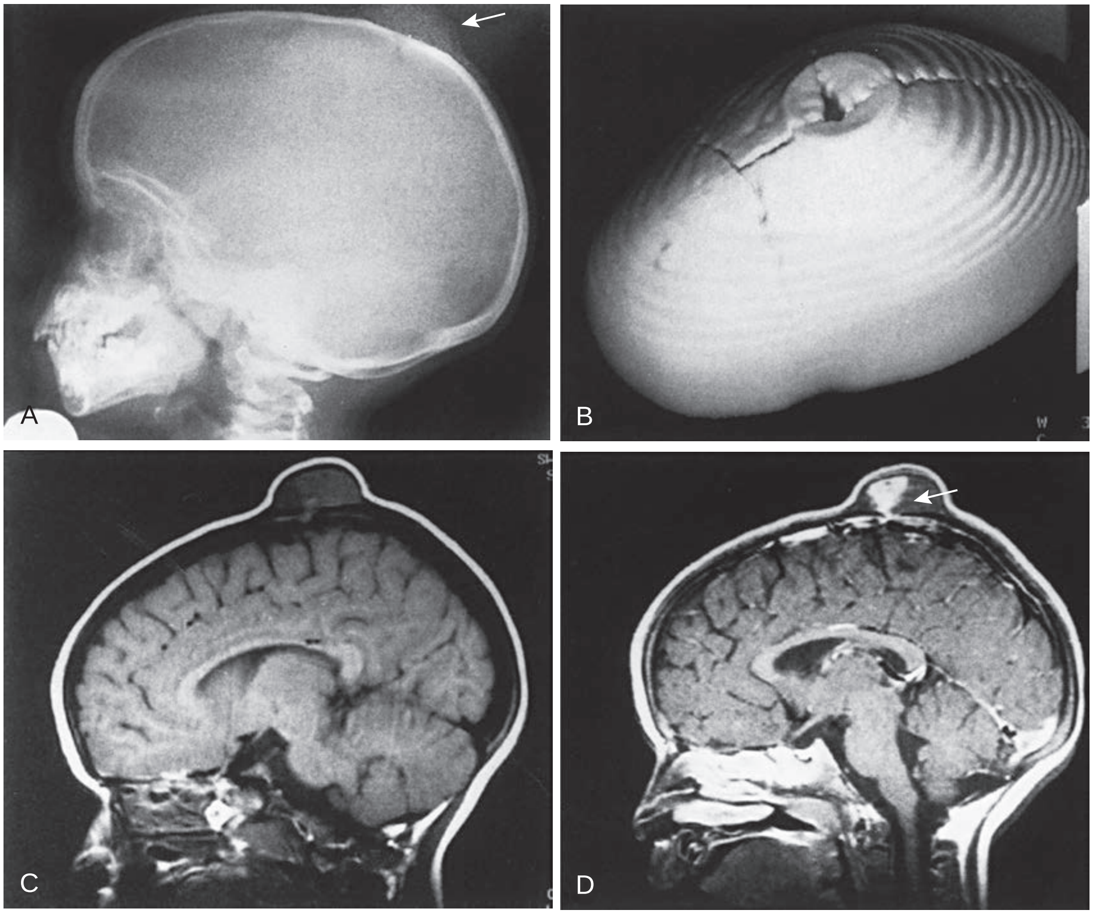

**Figure 20.41. Sinus pericranii.** (A) Lateral skull radiograph shows a soft tissue mass *(arrow)* and a well-defined defect in the midline of the parietal bones. (B) 3D CT image demonstrates erosion of both tables. (C) Precontrast T1-weighted magnetic resonance (MR) image confirms a midline interparietal mass with mixed signal intensity and areas of signal void indicating flowing blood. (D) Postcontrast T1-weighted MR image reveals heterogeneous enhancement and an emissary vein extending from the parietal bone to the superior sagittal sinus *(arrow). (From Bigot J-L, Iacona C, Lepreux A, et al. Sinus pericranii: advantages of MR imaging.* Pediatr Radiol. *2000;30:710–712.)*

## SUGGESTED READINGS

Glass RB, Fernbach SK, Norton KI, et al. The infant skull: a vault of information. *Radiographics*. 2004;24:507–522.

Kirmi O, Lo SJ, Johnson D, et al. Craniosynostosis: a radiological and surgical perspective. *Semin Ultrasound CT MRI*. 2009;30:492–512.

Sood S, Rozzelle A, Shaqiri B, et al. Effect of molding helmet on head shape in nonsurgically treated sagittal craniosynostosis. *J Neurosurg Pediatr*. 2011;7:1–6.

## REFERENCES

Full references for this chapter can be found on www.expertconsult.com.

## REFERENCES

1. Cohen MM Jr, MacLean RE, eds. *Craniosynostosis*. New York: Oxford University Press; 2000.
2. Hefler TM, Peixoto AB, Tonni G, et al. Craniosynostosis: prenatal diagnosis by 2D/3D ultrasound, magnetic resonance imaging and computed tomography. *Med Ultraso*. 2016;18(3):375–385.
3. Fjortoft MI, Sevely A, Boetto S, et al. Prenatal diagnosis of craniosynostosis: value of MR imaging. *Neuroradiology*. 2007;49:515–521.
4. Currarino G. Sagittal synostosis in X-linked hypophosphatemic rickets and related diseases. *Pediatr Radiol*. 2007;37:805–812.
5. Greene AK, Mulliken JB, Proctor MR, et al. Phenotypically unusual combined craniosynostoses: presentation and management. *Plast Reconstr Surg*. 2008;122:853–862.
6. Rogers GF, Greene AK, Oh AK, et al. Zygomaticotemporal synostosis: a rare cause of progressive facial asymmetry. *Cleft Palate Craniofac J*. 2007;44:106–111.
7. Rogers GF, Proctor MR, Mulliken JB. Unilateral fusion of the frontosphenoidal suture: a rare cause of synostotic frontal plagiocephaly. *Plast Reconstr Surg*. 2002;110:1011–1021.
8. Kim HJ, Roh HG, Lee IW. Craniosynostosis: updates in radiologic diagnosis. *J Korean Neurosurg Soc*. 2016;59(3):219–226.
9. Rollins N, Sklar F. Factitious lambdoid perisutural sclerosis: does the "sticky suture" exist? *Pediatr Radiol*. 1996;26:356–358.
10. Regelsberger J, Schmidt T, Busse B, et al. Synchrotron—microcomputed tomography studies of normal and pathological cranial sutures: further insight. *J Neurosurg Pediatr*. 2010;5:238–242.
11. Vu HL, Panchal J, Parker EE, et al. The timing of physiologic closure of the metopic suture: a review of 159 patients using reconstructed 3D CT scans of the craniofacial region. *J Craniofac Surg*. 2001;12:527–532.
12. Choi JW, Lim SY, Shin HJ. Craniosynostosis in growing children: pathophysiological changes and neurosurgical problems. *J Korean Neurosurg Soc*. 2016;59(3):197–203.
13. Martelli-Junior H, de Miranda RT, Fernandes CM, et al. Goldenhar syndrome: clinical features with orofacial emphasis. *J Appl Oral Sci*. 2010;18:646–649.
14. Tasse C, Bohringer S, Fischer S, et al. Oculo-auriculo-vetebral spectrum (OAVS): clinical evaluation and severity scoring of 53 patients and proposal for a new classification. *Eur J Med Genet*. 2005;48:397–411.
15. Santos DT, Miyazaki O, Cavalcanti MGP. Clinical-embryological and radiological correlations of oculo-auriculo-vertebral spectrum using 3D-CT. *Dentomaxillofac Radiol*. 2003;32:8–14.
16. Johnson JM, Moonis G, Green GE, et al. Syndromes of the first and second branchial arches, part 1: embryology and characteristic defects. *AJNR Am J Neurol Radiol*. 2011;32:14–19.
17. Anderson PJ, David DJ. Spinal anomalies in Goldenhar syndrome. *Cleft Palate Craniofac J*. 2005;42:477–480.
18. Werler MM, Starr JR, Cloonan YK, et al. Hemifacial microsomia: from gestation to childhood. *J Craniofac Surg*. 2009;20(suppl 1):664–669.
19. Thompson JT, Anderson PJ, David DJ. Treacher Collins syndrome: protocol management from birth to maturity. *J Craniofac Surg*. 2009;20:2028–2035.
20. Trainor PA, Dixon J, Dixon MJ. Treacher Collins syndrome: etiology, pathogenesis and prevention. *Eur J Hum Genet*. 2009;17:275–283.
21. Plomp RG, van Lieshout MJ, Joosten KF, et al. Treacher Collins Syndrome: a systematic review of evidence-based treatment and recommendations. *Plast Reconstr Surg*. 2016;137(1):191–204.
22. Senggen E, Laswed T, Meuwiy JY, et al. First and second branchial arch syndromes: multimodality approach. *Pediatr Radiol*. 2011;41:549–561.
23. Bütow KW, Koogendijk CF, Zwahlen RA. Pierre Robin sequence: appearances and 25 years of experience with an innovative treatment protocol. *J Pediatr Surg*. 2009;44:2112–2118.
24. Evans AK, Rahbar R, Rogers GE, et al. Robin sequence: a retrospective review of 115 patients. *Int J Pediatr Othrhinolaryngol*. 2006;70:973–980.
25. Cohen MM. Robin sequences and complexes. Editorial comment: causal heterogeneity and pathogenetic/phenotypic variability. *Am J Med Genet*. 1999;83:311–315.
26. Suri S, Ross RB, Tompson BD. Craniofacial morphology and adolescent facial growth in Pierre Robin sequence. *Am J Orthod Dentofacial Orthop*. 2010;137:763–774.
27. Al-Samkari HT, Kane AA, Molter DW, et al. Neonatal outcomes of Pierre Robin sequence: an institutional experience. *Clin Pediatr (Phila)*. 2010;49:1117–1122.
28. Mackay DR. Controversies in the diagnosis and management of the Robin sequence. *J Craniofac Surg*. 2011;22:415–420.
29. Evans KN, Sie KC, Hopper RA, et al. Robin sequence: from diagnosis to development of an effective management plan. *Pediatrics*. 2011;127:936–948.
30. Pruzansky S. Not all dwarfed mandibles are alike. *Birth Defects*. 1969;1:120–129.
31. Diebler D, Dulac O. Cephaloceles: clinical and neuroradiological appearance: associated cerebral malformation. *Neuroradiology*. 1983;25:188–216.
32. Van Wyhe RD, Chamata ES, Hollier LH. Midline craniofacial masses in children. *Semin Plast Surg*. 2016;30(4):176–180.
33. Pavanello M, Melloni I, Antichi E, et al. Sinus pericranii: diagnosis and management in 21 pediatric patients. *J Neurosurg Pediatr*. 2015;15(1):60–70.
34. Carnes JT. Sinus pericranii: demonstration using three-dimensional surface shading. *J Comput Assist Tomogr*. 2002;26:285–286.
35. Yanik B, Keyik B, Conk Bayir I, et al. Sinus pericranii: color Doppler ultrasonographic findings. *J Ultrasound Med*. 2006;25:679–682.

# 21

# Neoplasms, Neoplasm-like Lesions, and Infections of the Skull

*Travis H. Kauffman, David B. Nielsen, and Thomas L. Slovis*

## PRIMARY NEOPLASMS

Primary neoplasms of the skull are rare. The most common lesions in children with a solitary nontraumatic lump on the head are dermoid tumors (61%), cephalhematomas (9%), Langerhans cell histiocytosis (LCH) (7%), and occult meningoceles and encephaloceles (4%).[1,2]

Osteochondromas may arise from the cartilaginous bones of the skull base. Osteoblastomas have been reported in the calvaria of infants, and aneurysmal bone cysts have been noted in the skull base and the calvaria (Fig. 21.1). Osteomas are small and usually limited to the outer table, although osteoid osteomas may occur in the diploë. Osteoid osteomas may present as a button sequestrum. Malignant bone tumors are unusual, but osteogenic sarcoma and Ewing sarcoma have been reported (e-Fig. 21.2).[3-5]

Angiomas and neurofibromas of the scalp may affect the underlying skull and cause deformities, bony defects, and regional hyperostoses. Plain radiographs of neurofibromatosis (NF) most commonly show lytic defects in the lambdoid suture, but also include absence of the orbital roof and floor, partial absence of the greater sphenoid wing, anteroposterior enlargement of the middle cranial fossa with possible bony erosive changes, enlarged cranial nerve foramina, and J-shaped sella (Fig. 21.3).[6,7]

Venolymphatic malformations (formerly known as cavernous hemangiomas) of the skull are characterized by rounded areas of diminished density in which there may be a honeycomb or radial pattern of spiculation. These malformations (e-Fig. 21.4) thicken the outer table externally and are radially striated. They do not displace the inner table.

Epidermoids are ectodermal rests or inclusions that may be in the scalp, the diploic spaces, or between the internal surface of the inner table and the dura. Epidermoids are typically benign and grow slowly. When epidermoids involve bone, they produce lucent, sharply demarcated lesions with smooth, sometimes scalloped, margins (Fig. 21.5). These lesions are treated with surgical excision.[8,9]

Meningiomas are rare in children. Radiographic changes include reactive hyperostosis, an increase in the caliber and number of grooves for regional blood vessels, and calcifications in the meningioma itself. Occasionally, there are radiolucent patches due to overlying bone loss. Rarely, interosseous meningiomas occur (e-Fig. 21.6). Multiple meningiomas suggest NF. Calvarial lesions, like the lesions in NF, can occur in congenital fibromatosis.[10]

Chordomas are malignant neoplasms that are more aggressive in children than in adults.[11] Children and adolescents account for less than 5% of all chordomas, with the majority being in the clivus. They may present with headaches (due to increased intracranial pressure), cranial nerve palsies, and long tract signs. Children less than 5 years may present with torticollis. On magnetic resonance imaging (MRI) chordomas are lobulated masses with septations. They are predominantly T1 isointense/hypointense and T2 hyperintense with marked heterogeneous enhancement (Fig. 21.7).[12]

Melanotic neuroectodermal tumor of infancy (melanotic progonoma, retinal anlage) is rare. More than 90% of cases involve the head and neck; 70% in the maxilla, and about 11% in the calvarium, arising in the sutures with roughly half at the anterior fontanelle.[13] In the calvarium, the tumor most often presents during the first year of life as a movable scalp nodule that subsequently invades the bone, becomes fixed to it (often adhering to the dura), and grows very rapidly. Bone destruction creates a sunburst appearance tangential to the mass (e-Fig. 21.8). Occasionally, the mass presents as a soft tissue density. MRI signal is variable on T1- and T2-weighted images, but consistently shows marked enhancement. Malignancy has not been reported for tumors in the calvarium, whereas malignancy has been noted in extracalvarial tumors.[14-17]

## SECONDARY NEOPLASMS

Secondary tumors of the calvarium are more common than primary tumors and include leukemia, neuroblastoma, small round cell tumors, and LCH (Figs. 21.9 through 21.11 and e-Fig. 21.12).

## NEOPLASM-LIKE LESIONS

### Langerhans Cell Histiocytosis

LCH is addressed in more detail in Chapter 139; only the calvarial manifestations are presented here. Lesions in the skull are common, with an incidence of 28% to 54%.[18,19] The calvarium is affected more frequently than the skull base with the parietal bone being the most common. Multiple lesions are most frequently in children younger than 5 years. A solitary calvarial lesion in a child older than 5 years is likely to be LCH (Figs. 21.13 and 21.14). Sphenoid bone involvement may be associated with diabetes insipidus. Exophthalmos may occur when the bones of the orbit are involved.[20]

Mandibular LCH is more common than maxillary involvement and begins characteristically in the molar areas of the alveolar processes, where osseous destruction results in a characteristic finding of “floating teeth.” The teeth are frequently loose, and spontaneous shedding of teeth is common.

The radiographic hallmark of skull LCH is a “punched-out” radiolucent defect with little or no adjacent reaction. LCH lesions involve the full thickness of the calvarium and have a classic beveled edge. Lesions often have a soft tissue mass and may extend across sutures. LCH is the most common cause of a button sequestrum (which is also seen with infection). During healing, the margins of the lesions lose their sharpness, and the lesion gradually disappears.

### Fibrous Dysplasia

Fibrous dysplasia of the pediatric calvarium usually involves the frontal, sphenoid, and ethmoid bones (Fig. 21.15).[21] It most often presents with painless progressive scalp masses. Rarely, children may present with vision changes due to compression of the orbital apex or ischemia of the optic nerve.[22]

There are three CT patterns of fibrous dysplasia: ground-glass matrix (56%), homogeneously dense bone (23%), and cystic lucencies (21%).[23] On MRI, fibrous dysplasia shows well-defined geographic margins. It is T1 hypointense, and heterogeneous on T2-weighted images.[24,25] Fibrous tissue may markedly enhance, simulating a tumor.

## Abstract:

Primary neoplasms of the pediatric skull are rare but include a vast differential which can be focused by imaging features, anatomic location and patient age. Most primary skull neoplasms are benign. Secondary neoplasms of the skull are more common. Neoplasm-like lesions of the skull include Langerhans Cell Histiocytosis and fibrous dysplasia which are typically distinguished radiographically and can be symptomatic. Infections of the skull are due to direct extension or hematogenous spread. Specific infectious processes may have similar imaging appearances, but are usually distinguished by clinical history. Lesions involving the pediatric skull can be divided into primary neoplasms, secondary neoplasms, neoplasm-like lesions, and infections. Imaging features in conjunction with clinical history will help radiologists to narrow the sometimes broad differential and assist in arriving at a timely diagnosis to initiate appropriate treatment.

## Keywords:

Skull
Calvarium
Primary Neoplasms
Langerhan's Cell Histiocytosis
Fibrous Dysplasia
Infection
Osteomyelitis

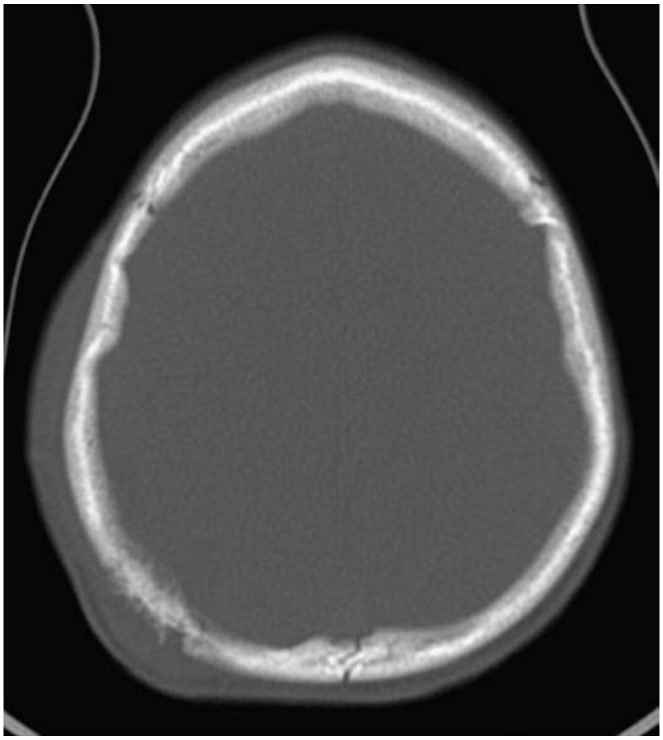

**e-Figure 21.2. Osteogenic sarcoma of the skull.** Axial CT bone window reveals a right parieto-occipital soft tissue mass with permeation and periosteal spiculation.

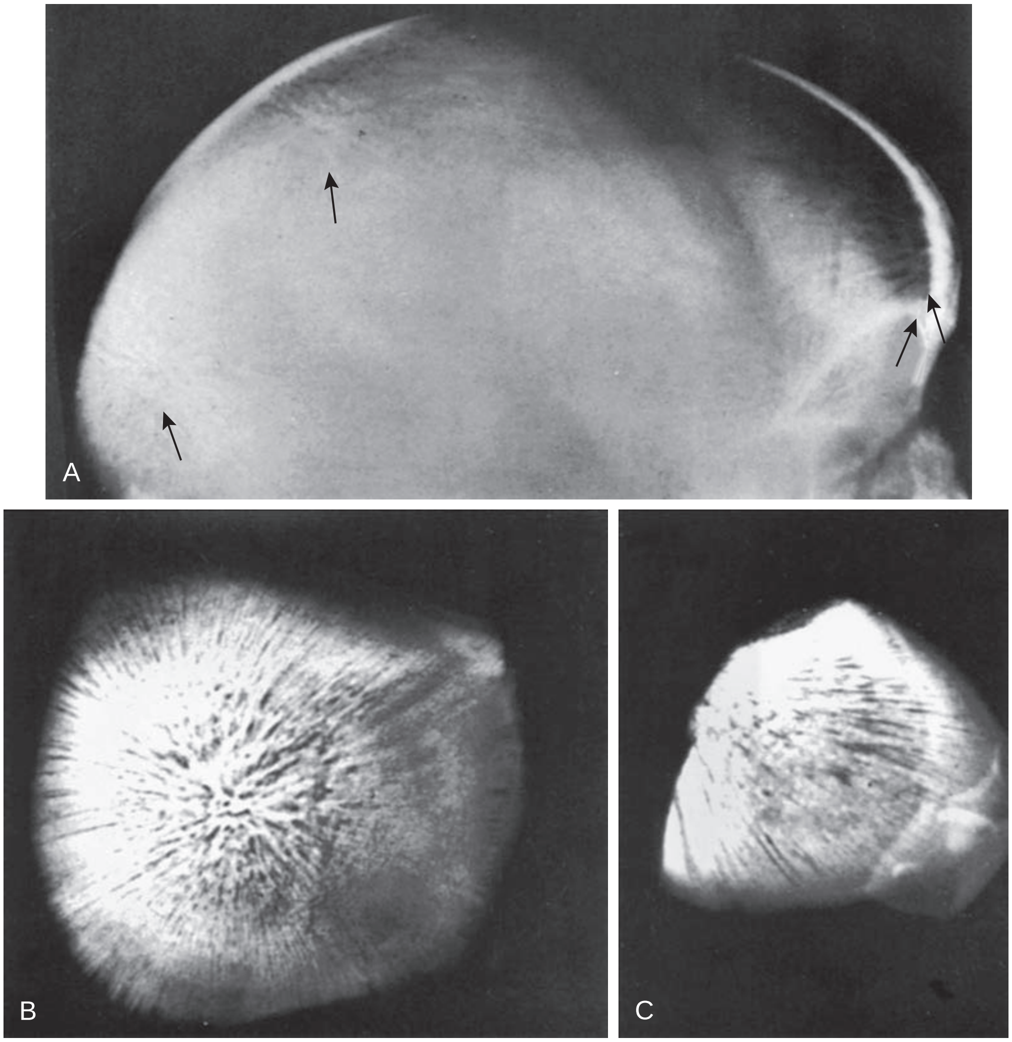

**e-Figure 21.4. Radially striated venous malformation *(arrows)* in the frontal, occipital squamosal, and parietal bones of a child who also had vascular lesions of the neck, shoulder, and upper thorax.** (A) Lateral radiograph of the head. (B and C) Necropsy specimens from the occipital squamosa. *(Courtesy of Marie Capitanio, MD.)*

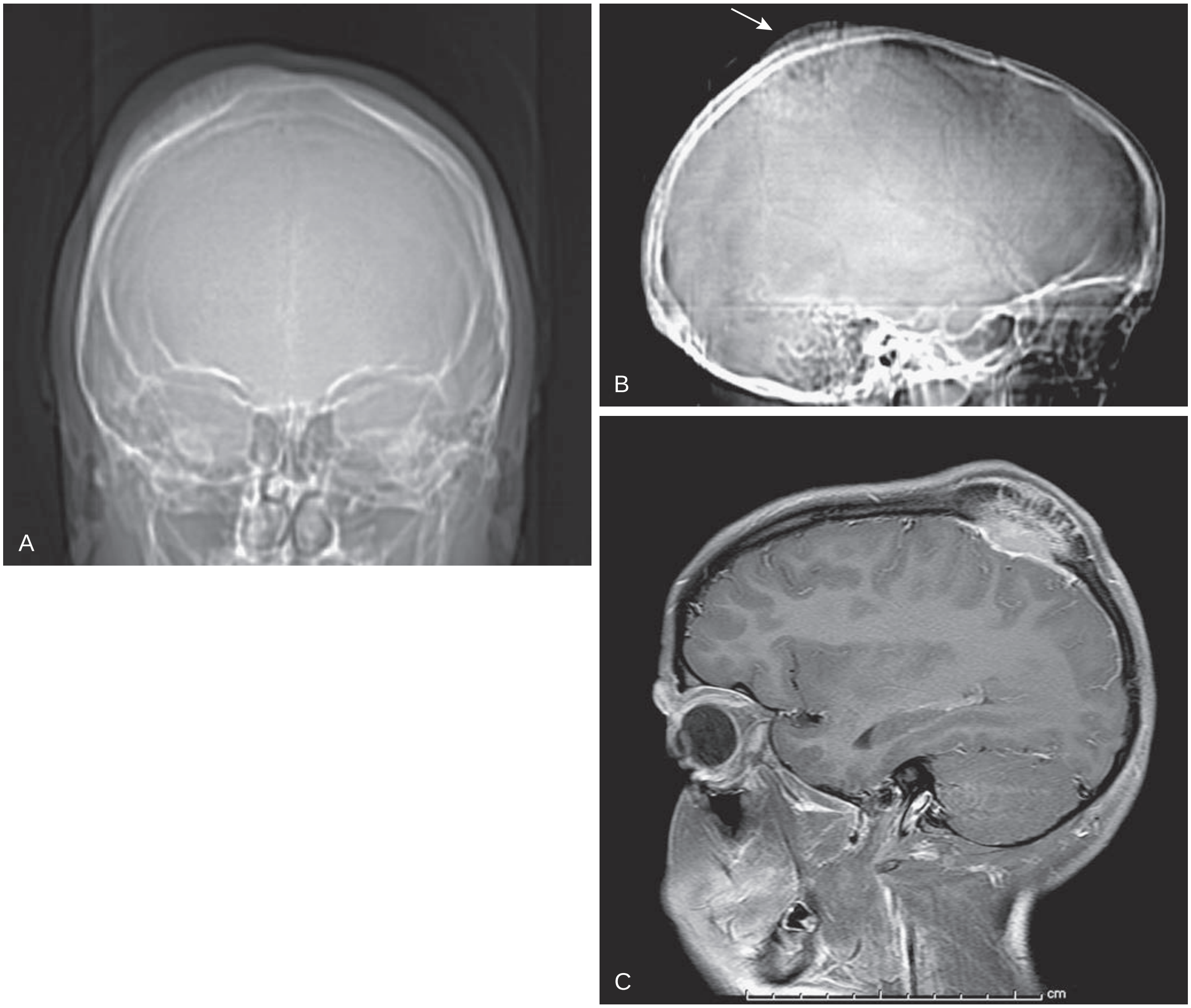

**e-Figure 21.6. Interosseous meningioma in a child with a hard skull mass.** (A and B) Frontal and lateral scout CT images show a right bony mass *(arrow).* (C) Sagittal enhanced MRI demonstrates the enhancing mass and shows spiculated bone. *(Courtesy of Tina Young Poussaint, MD, Boston, MA.)*

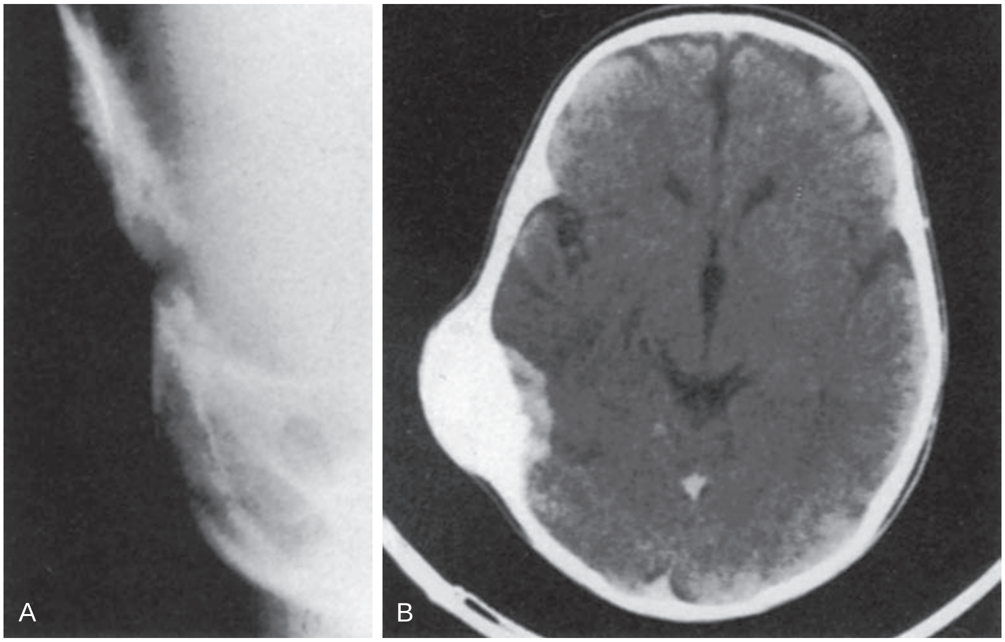

**e-Figure 21.8. Melanotic neuroectodermal tumor of infancy.** (A) Tangential radiograph of the posterolateral fontanelle shows the typical bone reaction and spiculation. (B) Unenhanced CT image shows internal tumor expansion and extensive bone reaction. *(From Jones HH, Parker BR, Ballerio CG, et al. Case report 617: melanotic neuroectodermal tumor of infancy in the calvaria.* Skeletal Radiol. *1990;19:317–318.)*

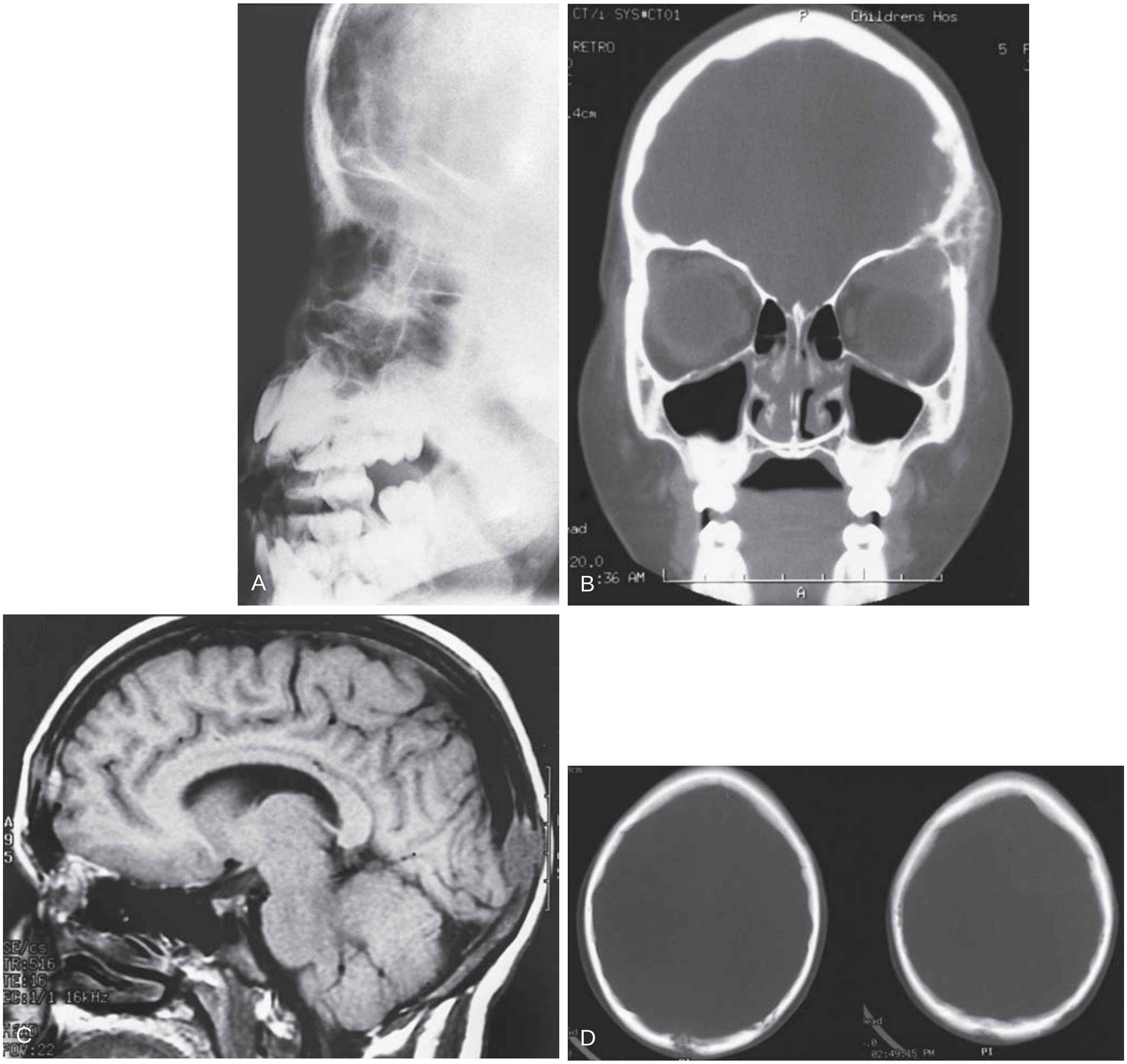

**e-Figure 21.12. Ewing sarcoma metastatic to the calvarium.** (A) Lateral skull radiograph shows frontal permeative changes. (B) Coronal CT identifies frontal bone destruction of the left lateral orbital wall due to a large intraorbital mass. (C) Sagittal T1 MRI of another child with metastatic Ewing sarcoma reveals an extraaxial occipital lesion. (D) Two axial bone window CT images demonstrates osseous destruction.

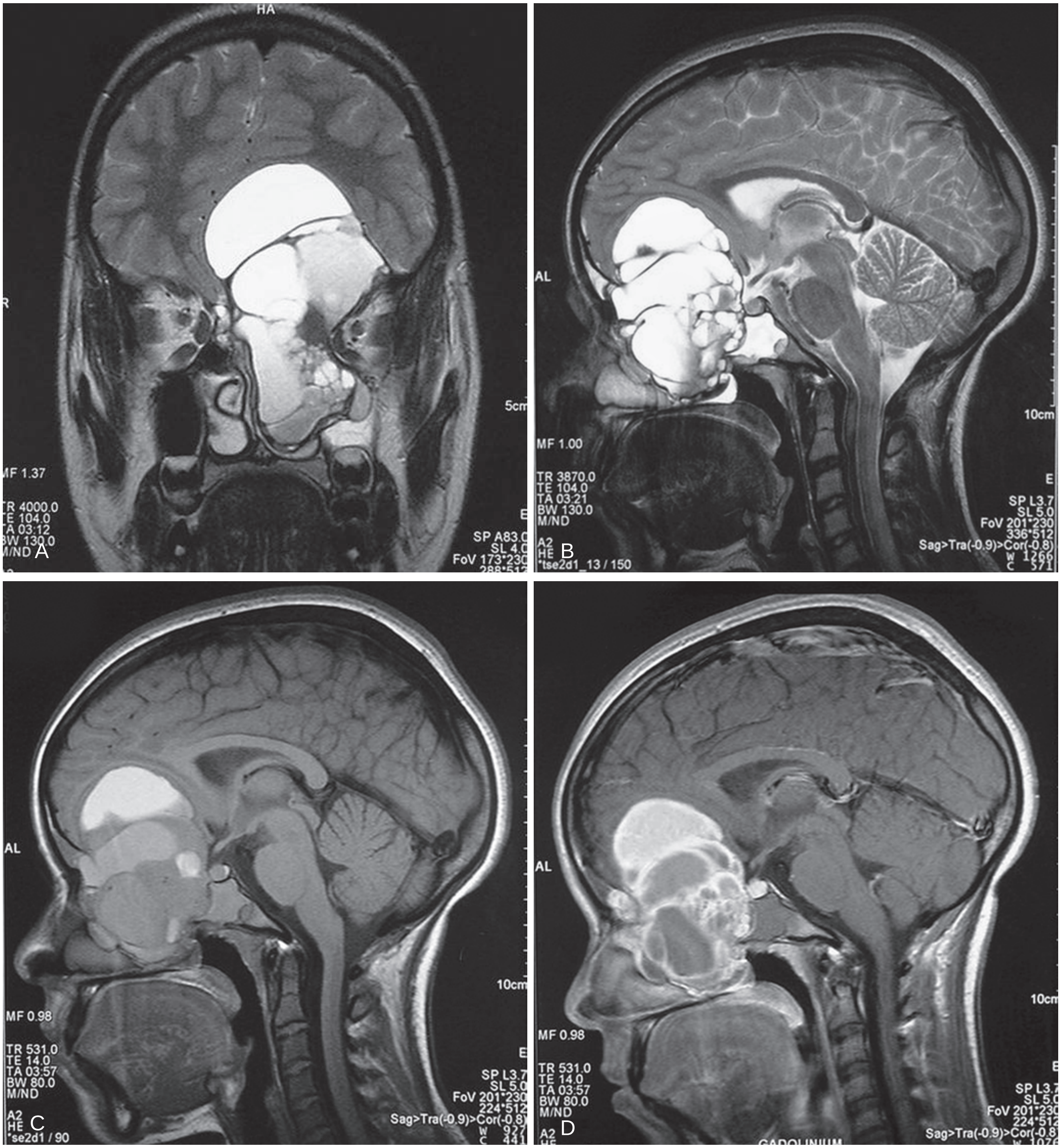

**Figure 21.1. Aneurysmal bone cyst of the skull base.** (A) Coronal T2-weighted MRI shows a multicystic, expansile anterior skull base mass that extends into the anterior cranial fossa, left ethmoid bone, and clivus. (B) Sagittal T2. (C) Sagittal T1 precontrast and (D) postcontrast images reveal multiple fluid levels and heterogeneous enhancement of the lesion periphery and internal septations. *(A and* B, *Courtesy of Theron S, Steyn F. An unusual cause of proptosis: aneurysmal bone cyst of the anterior skull base.* Pediatr Radiol*. 2006;36:997.)*

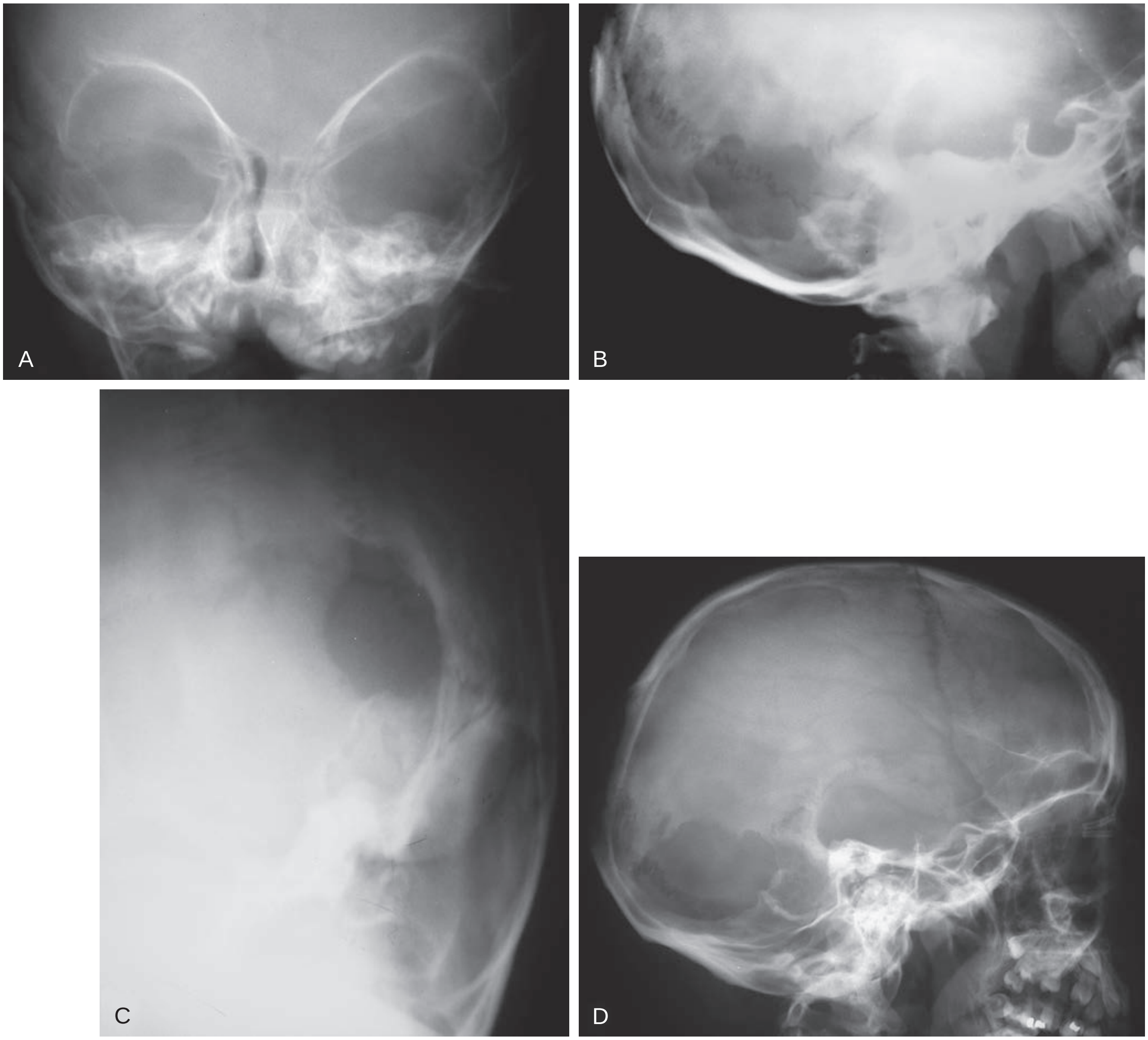

**Figure 21.3. Skull changes of neurofibromatosis (NF) type 1 in three children.** (A) Frontal orbital radiograph reveals bilateral elevated sphenoid wings and left sphenoid hypoplasia. (B) Lateral, and (C) oblique radiographs in a 5-year-old boy show a left lambdoid suture defect. (D) Lateral view of another child with NF shows a large skull defect in the left lambdoid suture. *(Courtesy of Peter Strouse, MD, Ann Arbor, MI.)*

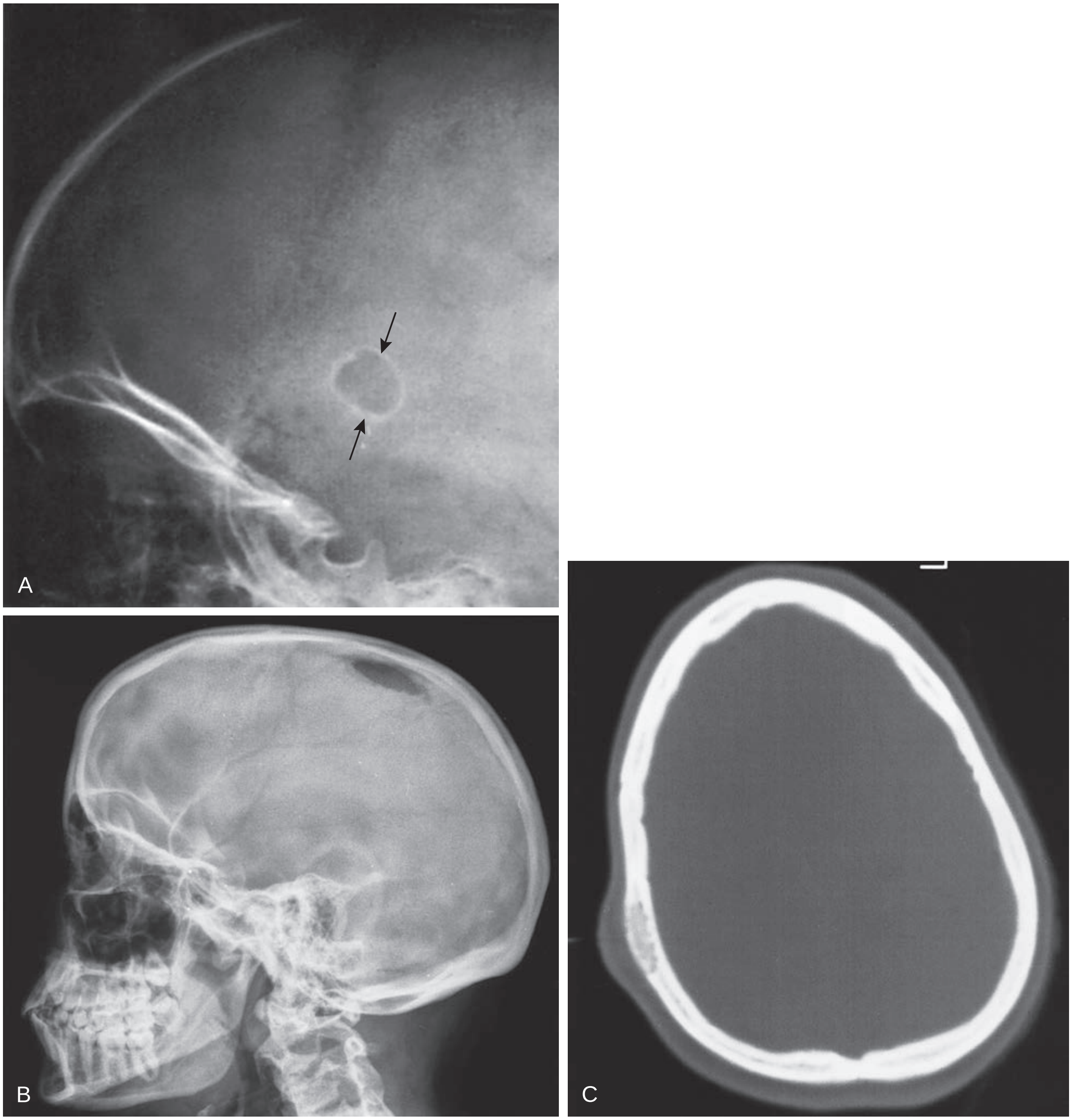

**Figure 21.5. Epidermoid in a 1-year-old infant.** (A) Lateral radiograph demonstrates a small oval defect with sharply defined sclerotic margins in the parietal bone *(arrows).* (B) Radiograph and (C) axial CT image of another child with an epidermoid show a less well demarcated lesion and identify soft tissue swelling.

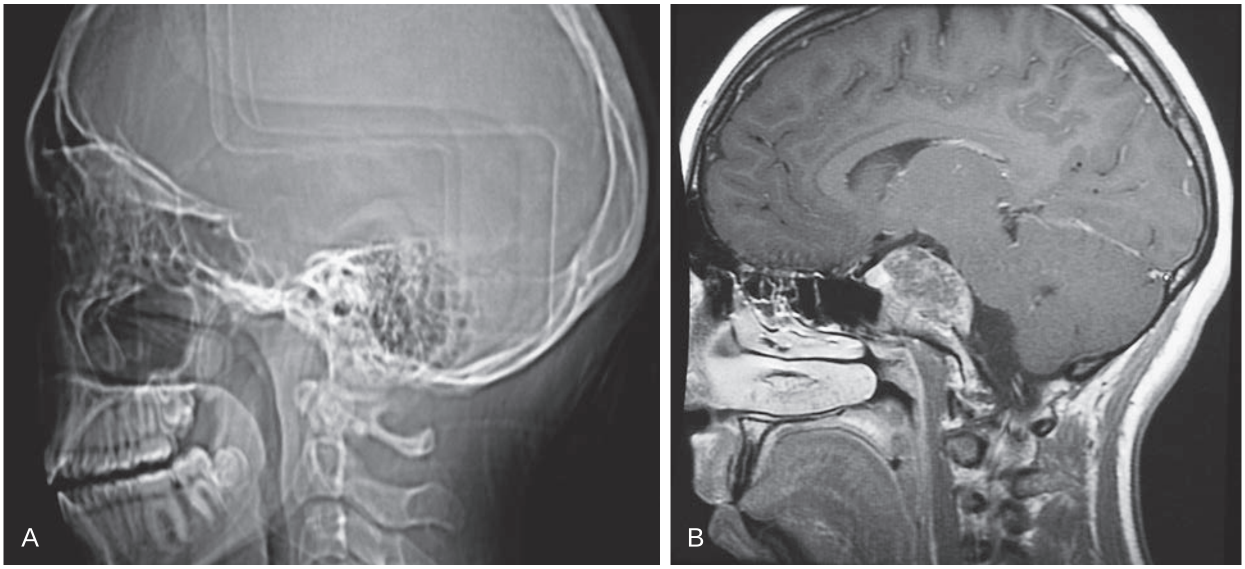

**Figure 21.7. Chordoma.** (A) Lateral CT scout image reveals nonvisualization of the clivus. (B) Sagittal T1-weighted contrast-enhanced MRI shows a large enhancing clival and sphenoid mass compressing the brainstem.

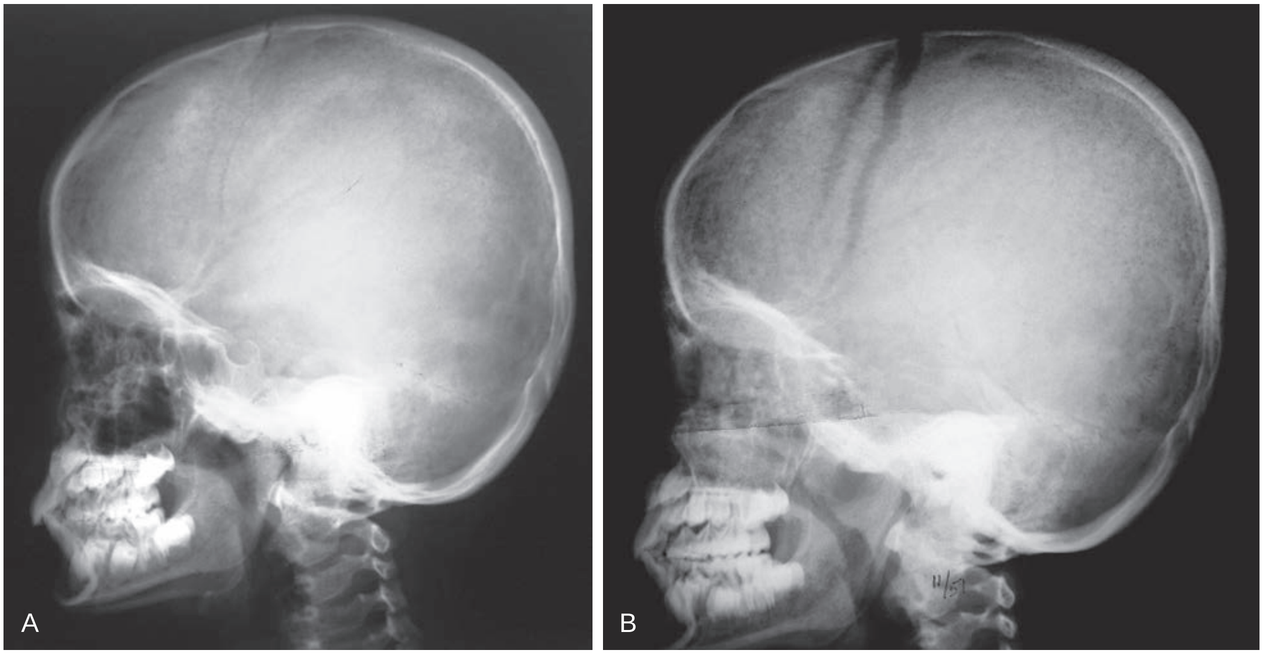

**Figure 21.9. Leukemia.** (A) Radiograph demonstrates a permeative area in the frontal calvarium with osseous spiculation in the parietal bone. (B) Radiograph in another child shows more pronounced osseous heterogeneity and widened coronal sutures indicating increased intracranial pressure.

## INFECTIONS OF THE CALVARIA

### Osteomyelitis

Osteomyelitis of the skull is rare in children and has many different etiologies.[26] Trauma is a common precursor.[27] Secondary infection after halo placement for traumatic injuries may occur. In such cases, halo pins may become loose.[28] Bones adjacent to the paranasal sinuses may become infected from direct extension of sinusitis. Clival osteomyelitis resulting from the spread of infection through the fossa navicularis magna has been reported after retropharyngeal abscess.[29] Systemic diseases can alter the body's defense and predispose to infections.

Hematogenous osteomyelitis may develop during bacteremia, by direct extension from scalp cellulitis or after fractures. Osteomyelitis can spread intracranially causing meningitis, or forming epidural or subdural abscesses. It may also cause extracranial subgaleal or subcutaneous abscesses. CT and MRI are useful to characterize infection extent.

Radiographic findings are normal during early osteomyelitis. However, when inflammatory lesions become visible, they involve the full thickness of the skull, including the diploic space, inner tables, and outer tables. Osteomyelitic lesions may be single or multiple, and are more common in the frontal and parietal bones. Lesions begin with fine lytic osseous foci that enlarge and coalesce, forming a permeative lesion. When chronic, osteomyelitis may

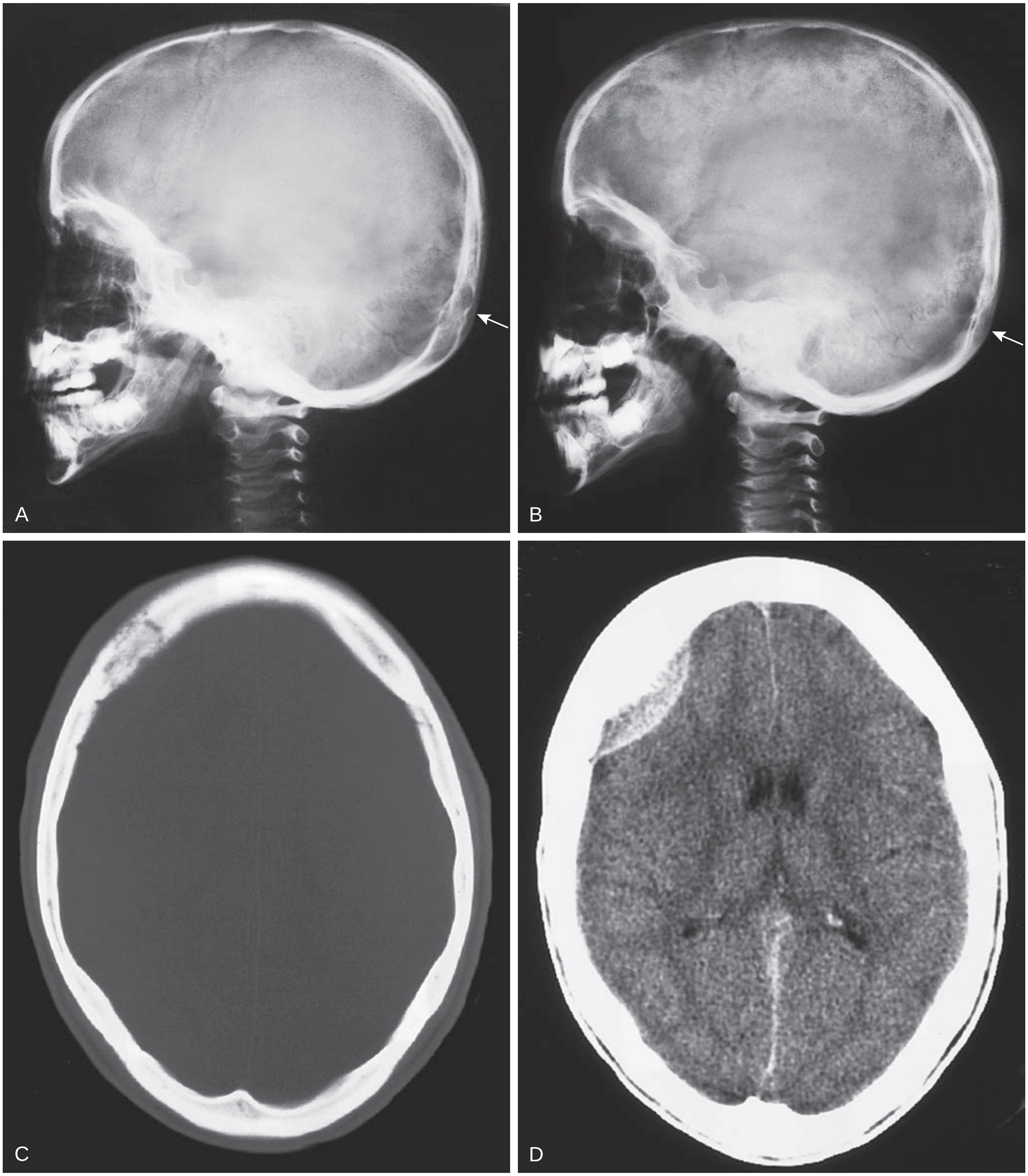

**Figure 21.10. Metastatic neuroblastoma in a child presenting with scalp pain.** (A and B) Plain radiographs demonstrate a destructive occipital lesion. Mild permeative changes are present in the frontal and occipital regions *(arrow).* Image (B) shows the finding to best advantage. (C) Bone and (D) soft tissue postcontrast CT images in another patient reveal a permeative right frontal lesion with an enhancing epidural mass.

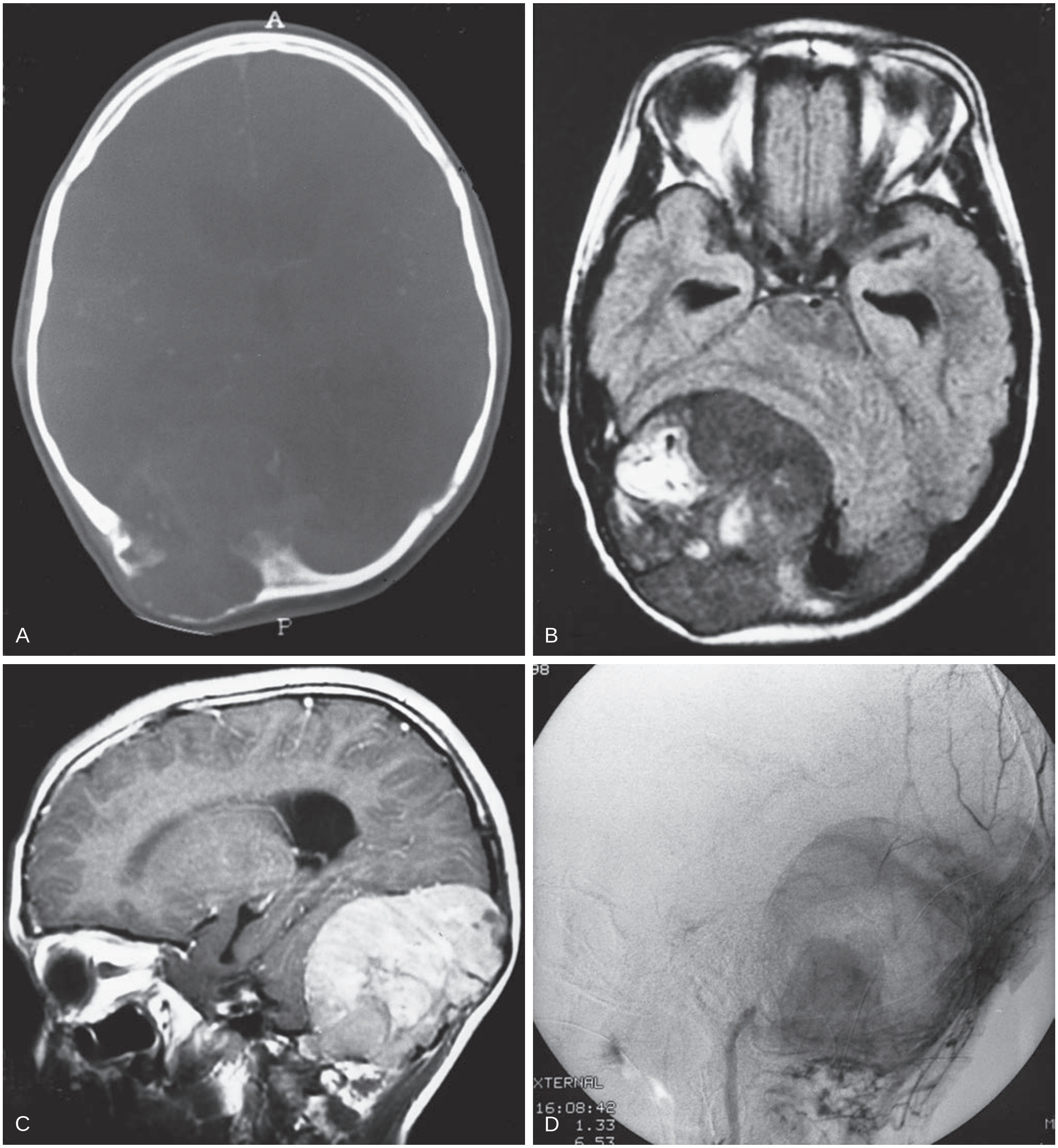

**Figure 21.11. Metastatic neuroblastoma.** (A) Axial CT shows an occipital mass with bone destruction. (B) Axial FLAIR and (C) sagittal T1-weighted enhanced MRI show the extradural mass. (D) Angiography shows a vascular mass.

develop peripheral sclerosis. In infants, the avascular sutures act as barriers to spread. The differential diagnosis of permeative skull lesions includes osteomyelitis, leukemia, metastatic neuroblastoma, and metastatic small round cell tumors (Ewing sarcoma, medulloblastoma, and retinoblastoma).[30]

Infection of a cephalhematoma, usually after bacteremia or attempted needle aspiration, may be complicated by osteomyelitis, septicemia, meningitis, or dural venous sinus thrombosis.

The accuracy of diagnosing an infected cephalhematoma is poor because infected and uninfected cephalhematomas both demonstrate radiolucencies. CT is the best modality to show bony changes, and MRI is superior for detecting intracranial complications such as venous sinus thrombosis and abscess.

Pott's puffy tumor, described in 1760 by Sir Percival Pott, consists of a subperiosteal abscess and osteomyelitis of the frontal bone.[31,32] It may result from acute frontal sinusitis or trauma

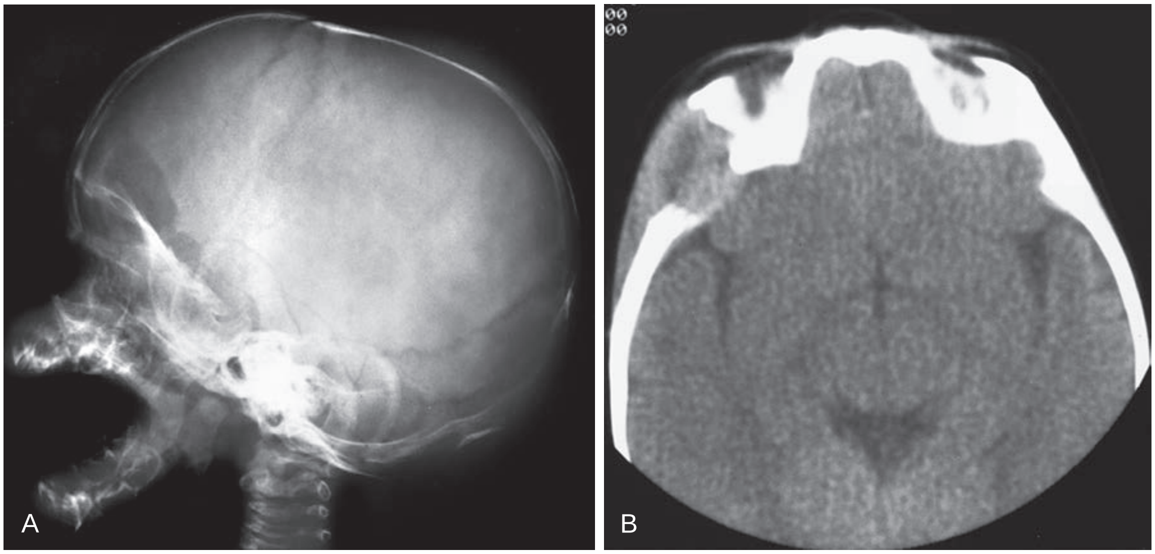

**Figure 21.13. Langerhans cell histiocytosis.** (A) Lateral skull radiograph shows a lytic, well-defined supraorbital, frontal lesion. (B) CT reveals bony destruction with a soft tissue mass. Note the beveled margins with greater outer than inner table destruction.

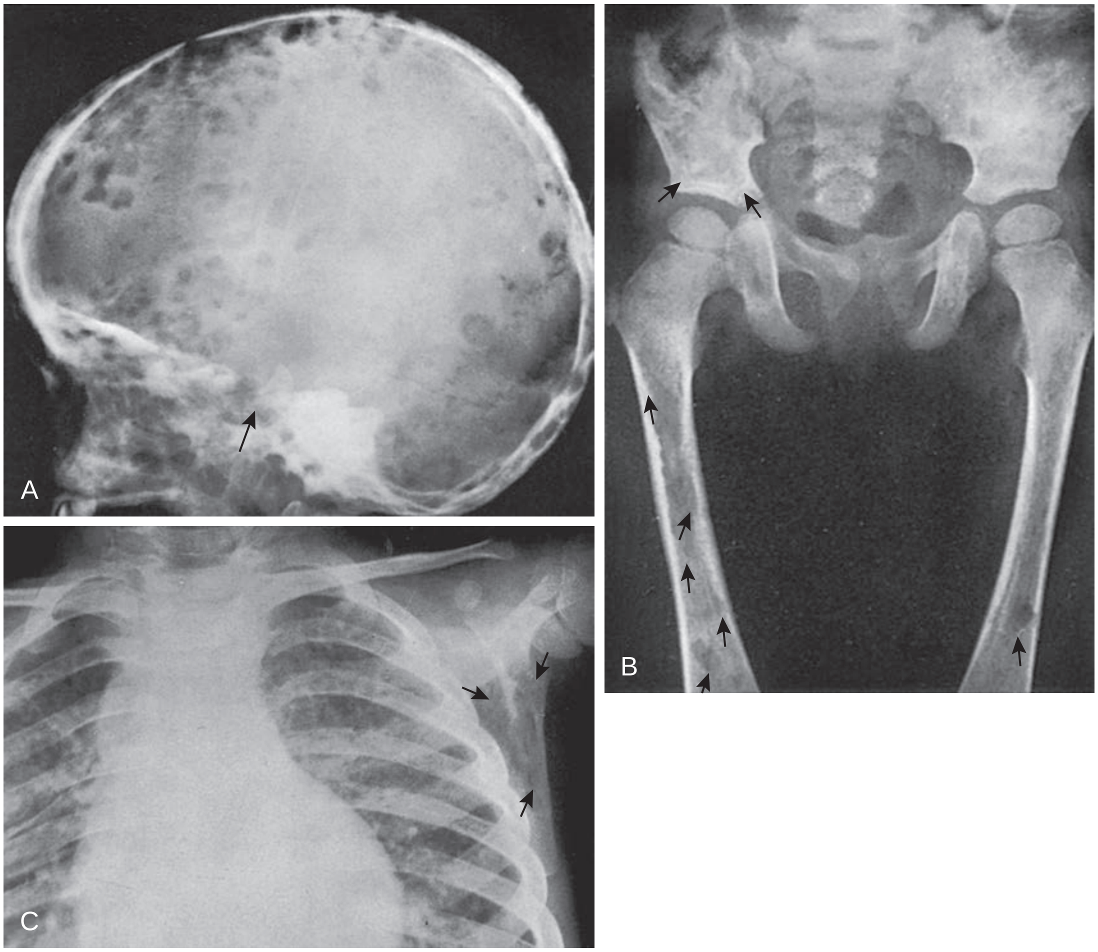

**Figure 21.14. Langerhans cell histiocytosis in a 3-year-old boy.** (A) Lateral skull radiograph shows numerous rounded defects in the calvaria and skull base *(arrow).* (B) Multiple defects *(arrows)* in the ilia and femora, the latter of which shows cortical erosion indicating a medullary cavity origin. (C) Scapular defects *(arrows)* and infiltration of the lungs and pleura.

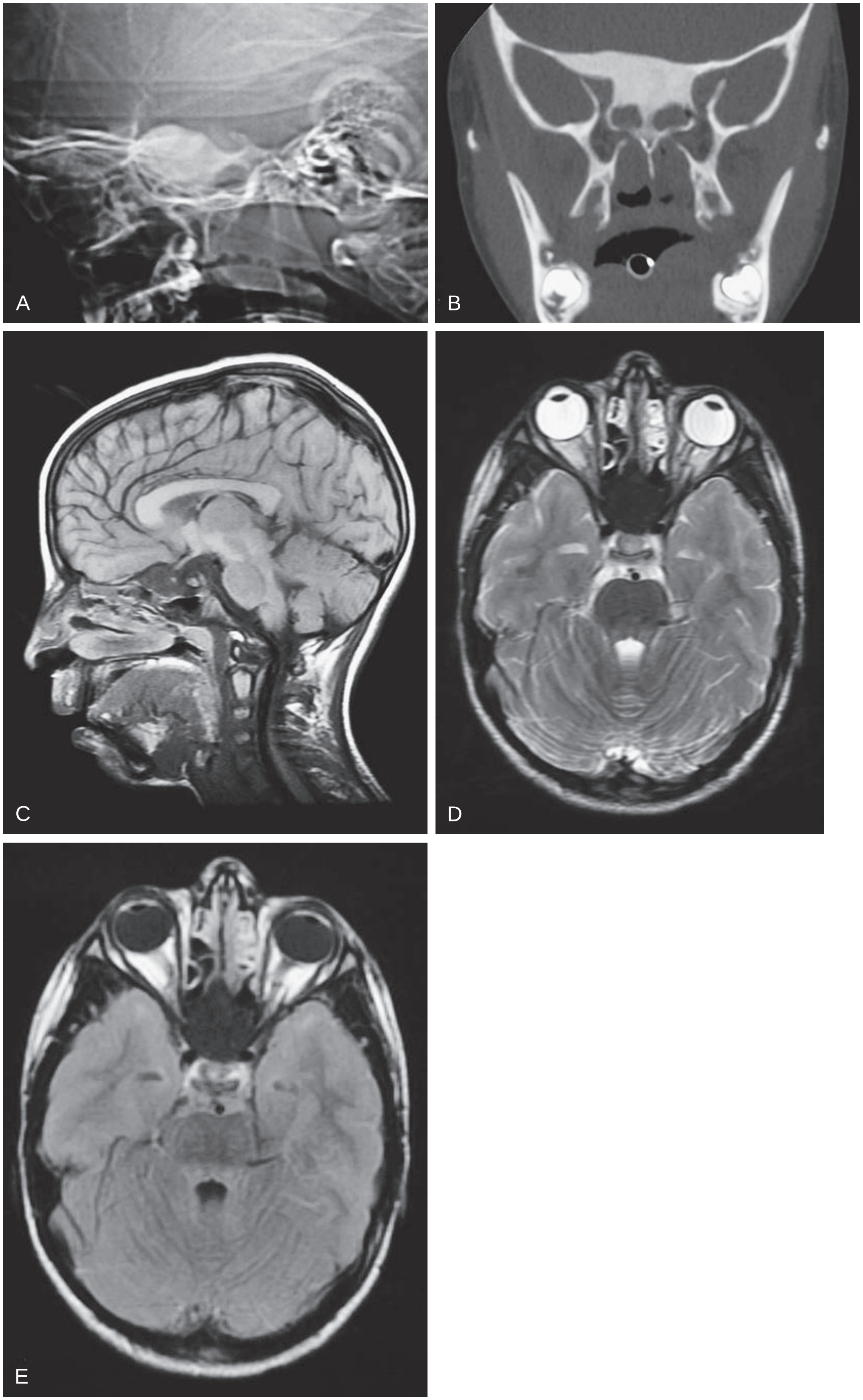

**Figure 21.15. Fibrous dysplasia of the skull.** (A) Scout CT image reveals a dense sphenoid bone. (B) Coronal CT image confirms the dense lesion with ground glass matrix. (C) Sagittal T1 image shows the lesion is hypointense. (D) On T2 and (E) FLAIR it is hyperintense.

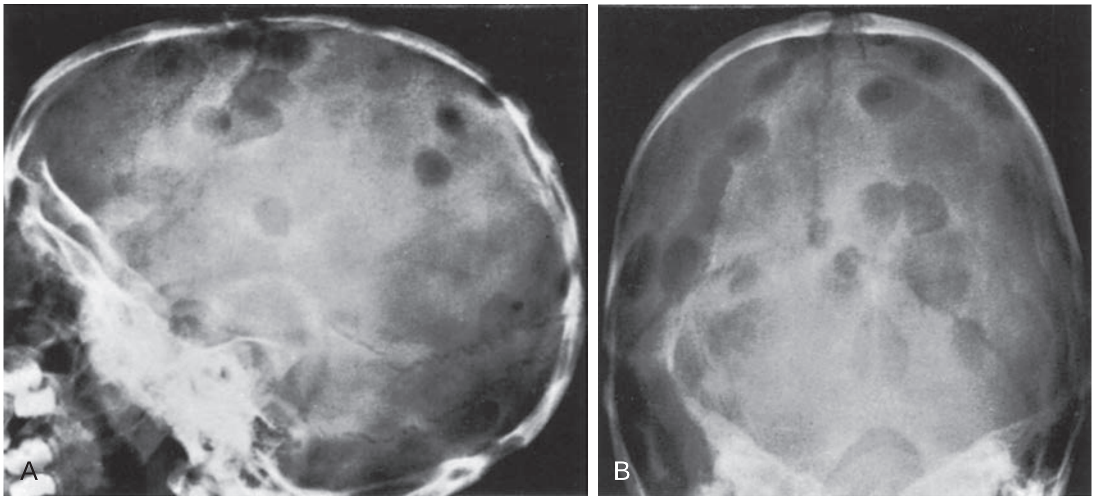

**Figure 21.17. Calvarial tuberculosis in a 3-year-old girl.** (A) Lateral and (B) frontal radiographs show multiple lytic foci.

(e-Fig. 21.16). The valveless diploic veins that drain the sinuses allow spread of septic emboli. Sonography can show subgaleal abscesses. However, CT and MRI are needed to demonstrate frontal sinusitis, osteomyelitis, and intracranial abscesses.

Petrous apicitis (Gradenigo syndrome) typically presents with middle ear disease, headache, cranial neuropathy, and elevated erythrocyte sedimentation rate. Characteristic CT and MRI findings include petrosal marrow T1 hypointensity, T2 hyperintensity, soft tissue inflammation, and bone destruction.

Unusual causes of calvarial osteomyelitis include cochlear implants and, rarely, cat scratch disease. The frontal and sphenoid bones have also been involved in chronic recurrent multifocal osteomyelitis.[33]

## Tuberculosis

Tuberculosis of the calvaria usually manifests as painless subgaleal scalp swelling with a discharging sinus. The lesions may be small, punched-out lytic areas (Fig. 21.17), spreading circumscribed sclerotic areas, or a combination.[34]

## Sarcoidosis

Sarcoidosis of the diploic space is associated with large radiolucent patches in the frontal, parietal, and occipital bones (e-Fig. 21.18).[35]

## Syphilis

The cranium can be involved in infantile syphilis in association with severe syphilitic osteitis of the long bones. Destructive and productive changes may be present, usually in the parietal and frontal bones.

## Mycotic Osteomyelitis

The cranium may be involved in chronic fungal infections, including actinomycosis, blastomycosis, coccidiomycosis, cryptococcosis, and candidiasis.[36] The radiographic features are similar to tuberculous, syphilis, and chronic osteomyelitis. The diagnosis requires identification of a responsible organism, and underlying immunodeficiency is frequent.[37]

### KEY POINTS

- Primary neoplasms are rare in children and most are benign.
- Secondary neoplasms are more common than primary neoplasms.
- LCH can have many appearances.
- Trauma and sinusitis are common precursors to osteomyelitis.
- Pott's puffy tumor includes osteomyelitis of the frontal bone and subperiosteal abscess.

### SUGGESTED READINGS

Atkinson GO, Davis PC, Patrick LE, et al. Melanotic neuroectodermal tumour of infancy: MR findings and a review of the literature. *Pediatr Radiol*. 1989;20:20–22.

Koch BL. Imaging extracranial masses of the pediatric head and neck. *Neuroimaging Clin N Am*. 2000;10:193–214.

Lui YW, Dasari SB, Young RJ. Sphenoid masses in children: radiologic differential diagnosis with pathologic correlation. *AJNR Am J Neuroradiol*. 2011;32:617–626.

Willatt JMG, Quagheberu G. Calvarial masses of infants and children. A radiological approach. *Clin Radiol*. 2004;59:474–486.

### REFERENCES

Full references for this chapter can be found on www.expertconsult.com.

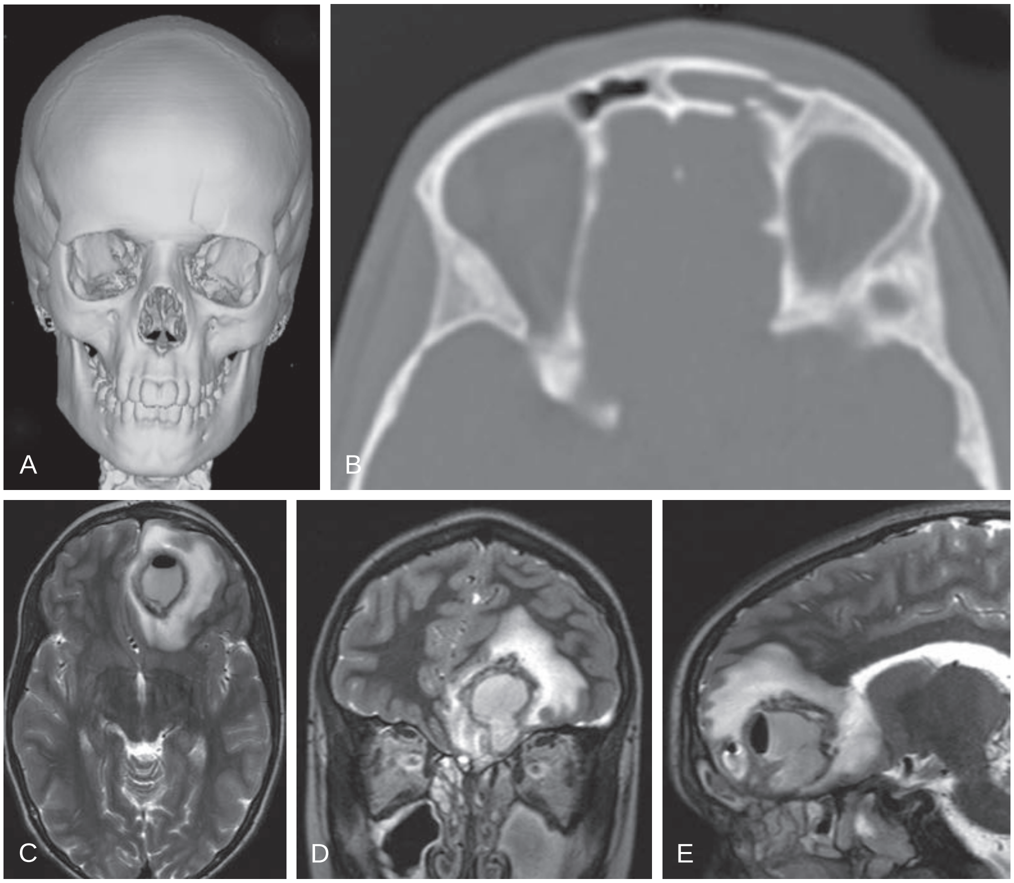

**e-Figure 21.16. Frontal osteomyelitis with brain abscess in a 12-year-old after a sledding accident.** (A) Three-dimensional CT and (B) axial CT images show a left frontal sinus fracture. Three weeks later, (C–E) axial, coronal, and sagittal T2 images show a large hyperintense, gas-containing left frontal lobe abscess with surrounding edema. Sinus disease is also present.

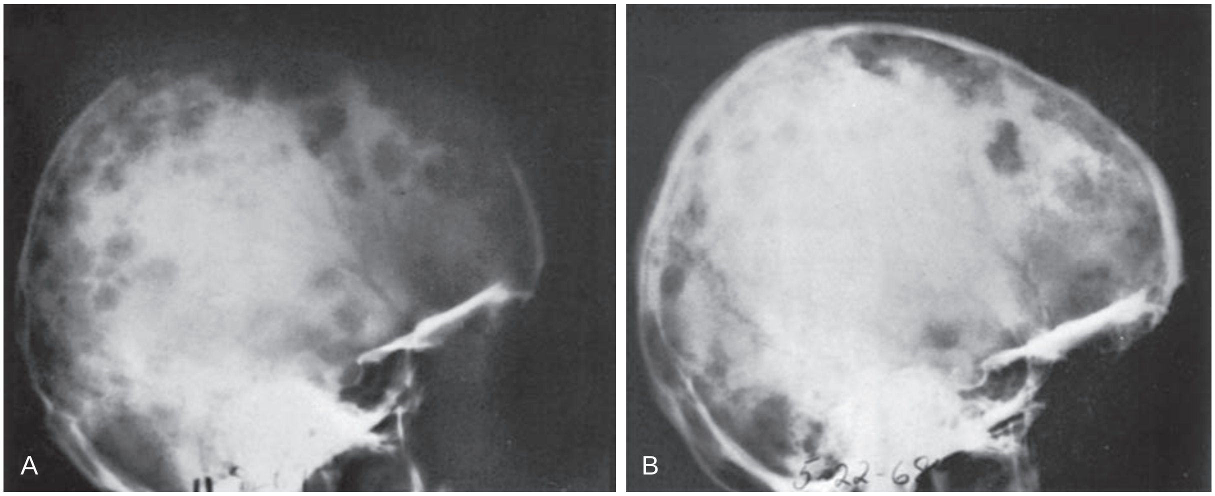

**e-Figure 21.18. Sarcoidosis of the diploic space in a 14-year-old girl.** (A) Lateral radiograph before treatment reveals multiple radiolucent defects scattered throughout the frontal, parietal, and occipital bones. Microscopically, the radiolucent patches represent sarcoid destruction of internal and external tables in the diploic space. (B) Lateral radiograph 7 months after steroid therapy show that many of the radiolucencies have decreased in size or resolved. *(From Toomey F, Bautista A. Rare manifestations of sarcoidosis in children.* Radiology. *1970;94:569-573.)*

## REFERENCES

1. Ruge JR, Tomila T, Naidich TP, et al. Scalp and calvarial masses of infants and children. *Neurosurgery*. 1988;22:1037–1042.
2. Moron FE, Morriss MC, Jones JJ, et al. Lumps and bumps on the head of children: use of CT and MR imaging in solving the clinical diagnostic dilemma. *Radiographics*. 2004;24:1655–1674.
3. Salvati M, Ciapetta P, Capone R, et al. Osteosarcoma of the skull in a child: case report and review of the literature. *Childs Nerv Syst*. 1993;9:437–439.
4. Sato J, Himi T, Tamakawa M. Osteosarcomatosis involving craniofacial bones presenting with cranial nerve palsies. *J Laryngol Otol*. 2000;114:214–217.
5. Sharma A, Garg A, Mishra NK, et al. Primary Ewing's sarcoma of the sphenoid bone with unusual imaging features: a case report. *Clin Neurol Neurosurg*. 2005;107:528–531.
6. Jacquemin C, Bosley TM, Svedberg H. Orbit deformities in craniofacial neurofibromatosis type 1. *AJNR Am J Neuroradiol*. 2003;24:1678–1682.
7. Arrington D, Danehy A, Peleggi A, et al. Calvarial defects and skeletal dysplasia in patients with neurofibromatosis type 1. *J Neurosurg Pediatrics*. 2013;11:410–416.
8. Holthusen W, Lassrich MA, Steiner C. Epidermoids and dermoids of the calvarian bones in early childhood: their behavior in the growing skull. *Pediatr Radiol*. 1983;13:189–194.
9. Gibson S, Prayson R. Primary skull lesions in the pediatric population: a 25-year experience. *Arch Pathol Lab Med*. 2007;131:761–766.
10. Briselli MF, Soule EH, Gilchrist DS. Congenital fibromatosis: report of 18 cases of solitary and 4 cases of multiple tumors. *Mayo Clin Proc*. 1980;55:554–562.
11. Hoch B, Nielsen G, Liebsch N, et al. Base of skull chordomas in children and adolescents: a clinicopathologic study of 73 cases. *Am J Surg Pathol*. 2006;30(7):811–818.
12. Beccaria K, Sainte-Rose C, Zerah M, et al. Paediatric chordomas. *Orphanet J Rare Dis*. 2015;10:116.
13. Cutler LS, Chaudhry AP, Topazian R. Melanotic neuroectodermal tumor of infancy: an ultrastructural study, literature review, and reevaluation. *Cancer*. 1981;48:257–270.
14. Nishio S, Morioka T, Murakami N, et al. Melanotic neuroectodermal tumour of infancy at the anterior fontanelle. *Neuroradiology*. 1999;41:202–204.
15. Saleem S, Altinok D. Melanotic neuroectodermal tumor of the calvarium. *Pediatr Radiol*. 2010;40(suppl 1):S159.
16. Smith AB, Rushing EJ, Smirniotopoulos JG. Pigmented lesions of the central nervous system: radiologic-pathologic correlation. *Radiographics*. 2009;29:1503–1524.
17. Haque S, McCarville MB, Sebire N, et al. Melanotic neuroextodermal tumour of infancy: CT and MR findings. *Pediatr Radiol*. 2012;42(6):699–705.
18. D'Ambrosio N, Soohoo S, Warshall C, et al. Craniofacial and intracranial manifestations of Langerhans cell histiocytosis: report of findings in 100 patients. *Am J Roentgenol*. 2008;191:589–597.
19. Kirks DR, Taybi H, Histiocytosis X. Parker BR, Castellino RA, eds. *Pediatric oncologic radiology*. St. Louis: Mosby-Year Book; 1977.
20. Prayer D, Grois N, Prosch H, et al. MR imaging presentation of intracranial disease associated with Langerhans cell histiocytosis. *AJNR Am J Neuroradiol*. 2004;25:880–891.
21. DiRocco C, Marchese E, Velardi F. Fibrous dysplasia of the skull in children. *Pediatr Neurosurg*. 1992;18:117–126.
22. Maher CO, Friedman JA, Meyer FB, et al. Surgical treatment of fibrous dysplasia of the skull in children. *Pediatr Neurosurg*. 2002;37:87–92.
23. Brown EW, Megerian CA, McKenna MJ, et al. Fibrous dysplasia of the temporal bone. *AJR Am J Roentgenol*. 1995;164:679–682.
24. Chong VFH, Khoo JBK, Fan Y-K. Fibrous dysplasia involving the base of the skull. *AJR Am J Roentgenol*. 2002;178:717–720.
25. Utz JA, Kransdorf MJ, Jelinek JS, et al. MR appearances of fibrous dysplasia. *J Comput Assist Tomogr*. 1989;13:845–851.
26. Pincus DJ, Armstrong MB, Thaller SR. Osteomyelitis of the craniofacial skeleton. *Semin Plast Surg*. 2009;23:73–79.
27. Hanifan WC, Olivero WC, Duff JJ, et al. Lawn dart injury in children: report of two cases. *Pediatr Emerg Care*. 1986;2:247–249.
28. Limpaphayom N, Skaggs DL, McComb G, et al. Complications of halo use in children. *Spine*. 1990;34:779–784.
29. Prabhu SP, Zinkus T, Cheng AG, et al. Clival osteomyelitis resulting from spread of infection through the fossa navicularis magna in a child. *Pediatr Radiol*. 2009;39:995–998.
30. Ozgen B, Oguz KK, Cila A. Diffusion MR imaging features of skull base osteomyelitis compared with skull base malignancy. *AJNR Am J Neuroradiol*. 2001;32:179–184.
31. Rabiu TB. Pott's puffy tumour in the paediatric population. *Childs Nerv Syst*. 2010;26:729.
32. Tsai BY, Lin KL, Lin TY, et al. Pott's puffy tumor in children. *Child Neuro*. 2010;26:53–60.
33. Khanna G, Satot S, Ferguson P. Imaging of chronic recurrent multifocal osteomyelitis. *Radiographics*. 2009;29(4):1159–1177.
34. Ramdurg SR, Gupta DK, Suri A, et al. Calvarial tuberculosis: uncommon manifestation of common disease—a series of 21 cases. *Br J Neurosurg*. 2010;24:572–577.
35. Toomey F, Bautista A. Rare manifestations of sarcoidosis in children. *Radiology*. 1970;94:569–573.
36. Budenz CL, Tajudeen BA, Roehm PC. Actinomycosis of the temporal bone and brain: case report and review of the literature. *Ann Otol Rhinol Laryngol*. 2010;119:313–318.
37. Marsot-Dupuch K, Quillard J, Meyohas MC. Head and neck lesions in the immunocompromised host. *Eur Radiol*. 2004;14:E155–E167.

# PART 2 Mandible

# 22 The Mandible

*Laura Dinneen and Thomas L. Slovis*

## ANATOMY

At birth, the mandible consists of two lateral halves united in the midline at the symphysis by a bar of cartilage (Fig. 22.1, e-Fig. 22.2, and Fig. 22.3). Bony fusion of the symphysis usually occurs before the second year, but segments of the fissures may persist beyond puberty. The body of the mandible is large at birth compared with the relatively short vertical rami with poorly differentiated coronoid and condylar processes. The rami form an angle of about 160 degrees with the body at birth.

The mandible is the only freely movable bone of the face; it articulates with the temporal bone in the temporomandibular fossa anterior to the external auditory canal (see Fig. 22.3). The range of motion is free in all directions, and the condyle moves downward and forward in the articular fossa upon opening of the jaw.

The temporomandibular joint (TMJ) (see Fig. 22.3) is a complex joint in which a biconcave fibrous disk divides the articular space into upper and lower compartments. Gliding movements occur in the upper compartment, whereas the lower compartment functions as a true hinge joint. The articulating bony surfaces are not covered by hyaline cartilage as in other synovial joints but by fibrocartilage separated from the underlying bone of the condyle by growth cartilage.

## DENTITION

By approximately the sixth week of embryologic development, the dental lamina develops along the length of the upper and lower jaws. It is the predecessor to dental bud formation and ultimately tooth development.

Teeth are situated in bony prominences along the mandible and maxilla known as *alveolar processes*. The alveolar processes and mandibular body atrophy when teeth are absent (e-Fig. 22.4). There are two sets of dentition, primary/deciduous teeth and permanent teeth. There are 20 total primary teeth and 32 total permanent teeth in the mouth in a normal situation (Fig. 22.5).[1] The developmental absence of some or all teeth, hypodontia and anodontia respectively, is demonstrated in a rare inherited disorder called *anhidrotic/hypohidrotic ectodermal dysplasia* (Fig. 22.6). Hyperdontia or supernumerary teeth may occur sporadically or in association with conditions such as Gardner syndrome and cleidocranial dysplasia. Other dental abnormalities in cleidocranial dysplasia include markedly delayed shedding of primary teeth and delayed or failed eruption of permanent teeth.[2]

Natal and neonatal teeth are uncommon but do occur in 1:2000–3000 live births. In the majority of cases, this is an isolated, nonsyndromic occurrence with early premature eruption of a normal primary tooth/teeth. Complications with suckling may occur for baby and mother.[3]

## EMBRYOLOGY

The branchial apparatus, also known as *pharyngeal apparatus*, comprises a series of paired embryologic structures—arches, pouches, clefts, and membranes—associated with the pharynx from which many adult craniofacial structures are derived. Branchial apparatus neural crest cells contribute to skeletal development in the face.

Between weeks 4 and 5 of development, the stomodeum (rudimentary mouth) forms in the center of the face surrounded by the first and second branchial pairs. The first branchial arch, the so-called mandibular arch, and its corresponding neural crest cells give rise to the mandible.[4]

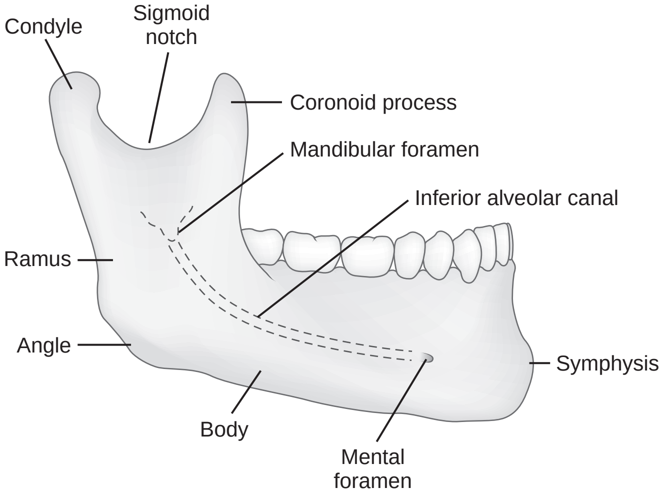

**Figure 22.1.** Important anatomic features of the normal mandible.

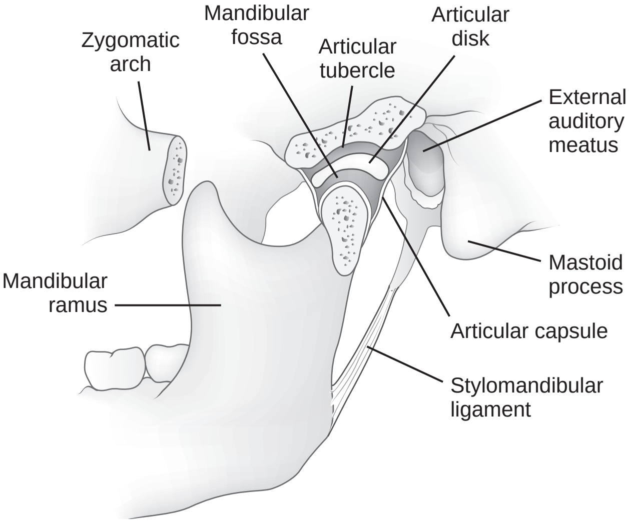

**Figure 22.3.** Anatomy of a normal temporomandibular joint. The zygomatic arch and a portion of the ramus of the mandible are cut away to expose the articular disk.

## Abstract:

Morphogenesis and anatomy of the mandible including teeth discussed. Craniofacial malformation as it pertains to mandible touched upon. Imaging pediatric mandibular pathology to include arthritic and nonarthritic TMJ disorders, mandibular fractures, osteomyelitis and CRMO, odontogenic and nonodontogenic mandibular cysts and masses, metastatic disease and other generalized skeletal diseases involving the mandible including fibrous dysplasia, infantile cortical hyperostosis and metabolic bone disorders like renal osteodystrophy highlited. CT, MRI and radiography including Panorex emphasized. Advances in fetal MRI included where applicable.

## Keywords:

Mandible
teeth
temporomandibular joint(s)
mandible cyst
mandible tumor
osteomyelitis

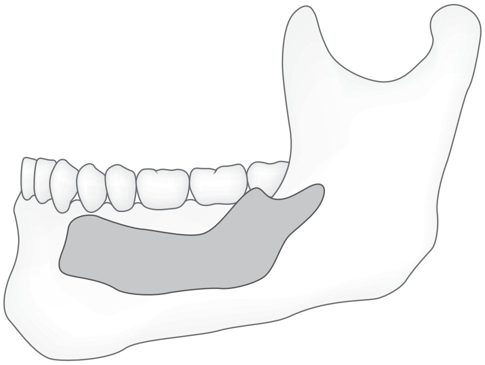

**e-Figure 22.2.** The relative size and shape of neonatal and adult mandibles. The rami form an angle with the body of 160 degrees at birth; this angle is reduced to 130 degrees at adolescence and 120 degrees in adulthood. *(Modified from Arey LB.* Developmental Anatomy. *Philadelphia: Saunders; 1942.)*

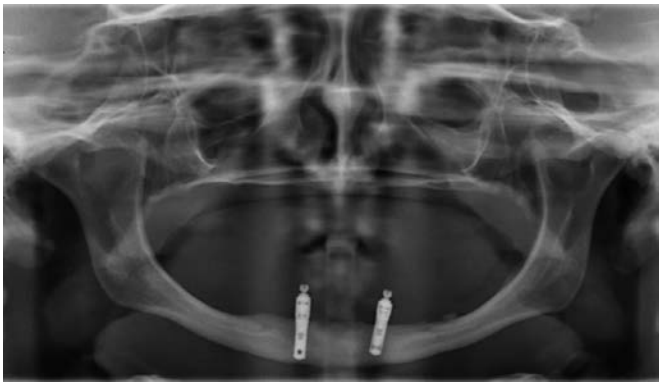

**e-Figure 22.4.** Edentulous mandibular hypoplasia. Panorex from a 10-year-old female with chronic neutropenia status after a full-mouth dental extraction for innumerable caries and peridontal pathology. Two mandibular post implants are in place for affixing dentures. The alveolar bone, which exists for the sake of the teeth, has resorbed postextraction.

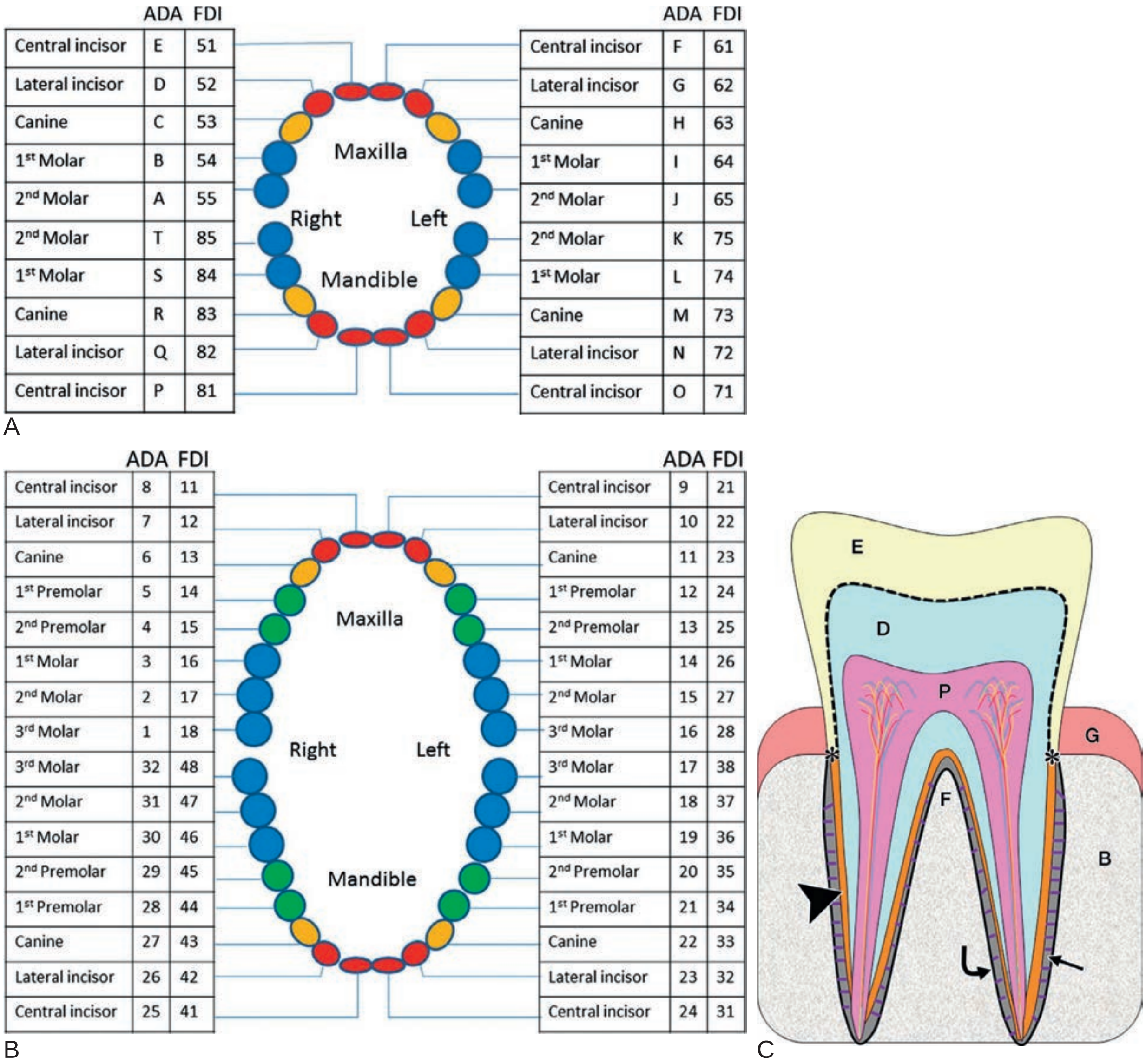

**Figure 22.5.** Tooth numbering nomenclature for (A) primary and (B) permanent teeth. *ADA,* American Dental Association; *FDI,* Feberation Dentaire Internationale. (C) Normal tooth anatomy. Enamel *(E)* covers the crown, and a thin layer of cementum *(arrowhead)* covers the roots. Dentin *(D)*, a calcified matrix, lies between the enamel or cementum and the pulp chamber *(P)* or root canal. Cementum and dentin cannot be distinguished at imaging because they have similar mineralization. The pulp chamber and root canal contain neurovascular elements. Gingiva *(G)* covers the maxillary and mandibular alveolar processes *(B)*. In teeth with multiple roots, the space between the roots is called the *furcation (F)*. Lamina dura *(curved arrow)*, a thin layer of dense bone, lines the socket. The periodontal ligament *(straight arrow)* lies between the lamina dura and cementum. * = cementoenamel junction, dashed line = dentinoenamel junction. *(C from Scheinfeld MH, Shifteh K, Avery LL, et al. Teeth: what radiologists should know.* RadioGraphics. *2012;32[7]:1927–1944. doi:10.1148/rg.327125717; A and B from Errata.* RadioGraphics. *2013;33[1]:312–312. doi:10.1148/rg.331125717.)*

First branchial arch neural crest cell insufficiency results in mandibular insufficiency (i.e., micrognathia). Micrognathia describes an undersized hypoplastic mandible (Fig. 22.7). Retrognathia describes a retropositioned mandible. Often micrognathia and retrognathia go hand-in-hand; a small jaw is also a retropositioned jaw. Prognathia describes an oversized mandible. Partial duplication of the mandible is very rare.

Transformation of the first branchial apparatus explains a developmental relationship between the jaw and the ear. The principal derivatives of the first arch include not only the bony mandible but also middle ear ossicles malleus and incus. The endodermal-lined first branchial pouch derivatives include the pharyngotympanic (Eustachian) tube and middle ear cavity. The ectodermal-lined first branchial cleft principal derivative is the external auditory canal. The intervening first branchial membrane develops into tympanic membrane.[5] Genetic conditions and environmental factors can adversely affect the complex transformation of the branchial apparatus. Gone awry, the interrelated transformations of the first and second branchial pairs can result in isolated mandibular anomalies (rare) to major syndromic categories of craniofacial malformation termed the *otomandibular dysplasias*, which include Goldenhar (hemifacial microsomia), Treacher Collins (mandibulofacial dysostosis), branchio-oto-renal syndrome, Nager preaxial/radial acrofacial dysostosis, and Pierre Robin sequence (PRS) (see also Chapter 20).[6]

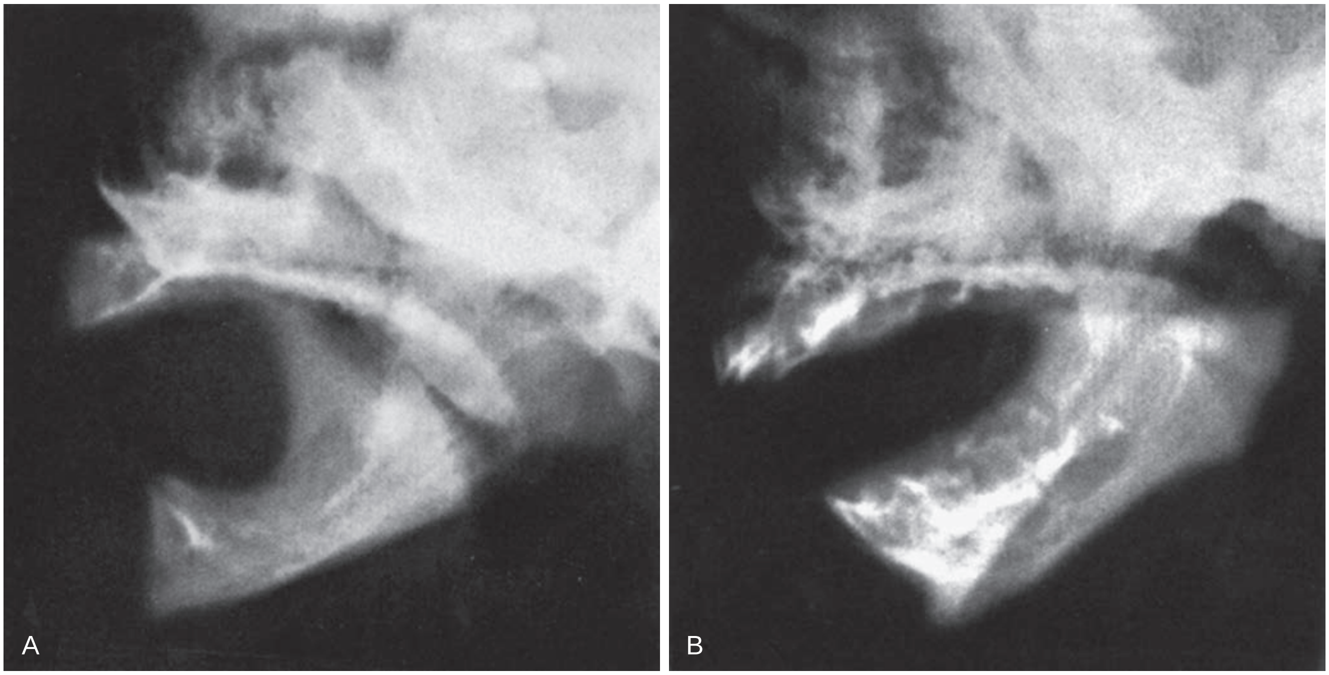

**Figure 22.6.** (A) A mandible in an 8-week-old infant with hereditary ectodermal dysplasia shows failure of calcification of dental crowns and defective dental sacs. (B) A radiograph of a normal 8-day-old newborn shows normal dental development in the neonatal period.

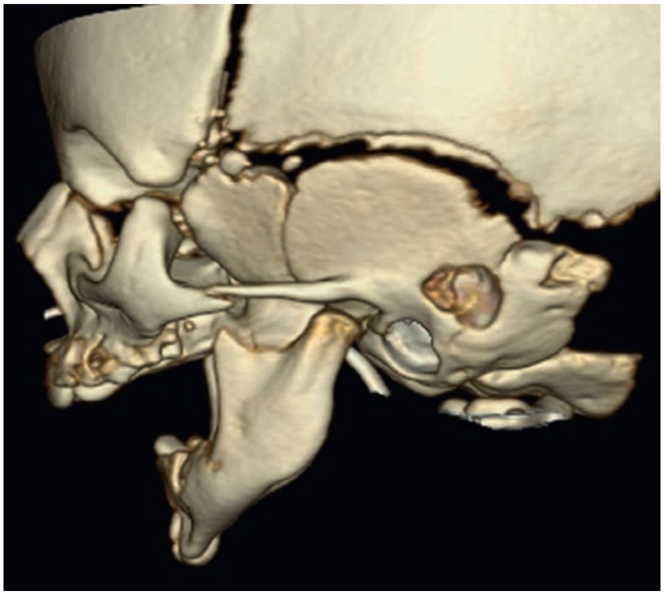

**Figure 22.7. Micrognathia in Pierre Robin sequence.** Newborn with a small retropositioned jaw, glossioptosis and cleft palate developed respiratory distress in the delivery room due to airway obstruction. Note short dorsoventral diameter of the micrognathic mandible on this sagittally oriented 3D craniofacial CT rendering.

Craniofacial and more specifically mandibular development is increasingly assessed in utero using prenatal magnetic resonance imaging (MRI) as an adjunct to screening ultrasound (US). MRI-based reference data for fetal mandibular growth with validated metrics to quantitatively evaluate fetal mandibular size and position (jaw index and inferior facial angle) have been derived improving the antenatal diagnosis of micrognathia and retrognathia.[7] Improved antenatal diagnosis of micrognathic conditions such as PRS, characterized by cleft palate, small jaw, and occlusive retropositioned tongue, could preclude perinatal airway emergencies and improve survival.[8]

## PATHOLOGY

### Temporomandibular Joint Disorders

Juvenile idiopathic arthritis (JIA) is the most common rheumatic disease of childhood. It affects synovial joints. TMJ involvement in JIA is a well-recognized feature of the disease. TMJ involvement is often asymptomatic and clinically undetectable, so delayed diagnosis is not uncommon. The risk for growth disturbances in the TMJ is high and irreversible mandibular asymmetry, malocclusion, and dysfunction can occur. MRI is used for early diagnosis and to monitor for ongoing active inflammatory disease.[9] MRI signs of ongoing active inflammation can result in escalation of therapy or site-specific therapy such as intraarticular steroid injection (e-Fig. 22.8). Bone marrow edema, joint effusion, and synovial enhancement signal active disease (Fig. 22.9). Articular surface flattening, widening, and irregularity are signs of erosive remodeling (Fig. 22.10).[10]

Nonarthritic TMJ dysfunction can also occur and is best assessed with dynamic open- and closed-mouth MRI techniques to evaluate the integrity of the articular disk and the retrodiskal soft tissues vital to normal TMJ function (Fig. 22.11).[11]

Trauma and infection also affect the TMJ. Delayed or nontreatment could result in permanent joint damage and disability as in other joints.

### Mandibular Fractures

Direct trauma is the usual cause of fractures in the pediatric mandible. The incidence of traumatic mandibular fractures increases with age. Below age 5, fractures are rare. The incidence rises in school-age children and peaks during adolescence. In early life,

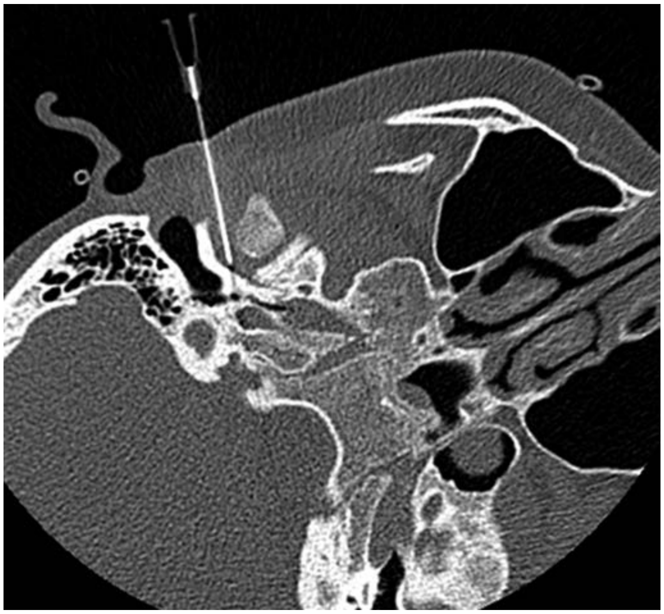

**e-Figure 22.8. CT-guided temporomandibular joint (TMJ) injection.** Site-specific therapeutic steroid injection for ongoing active unilateral TMJ inflammatory arthritis. Injections of the TMJ are frequently imaging guided as up to 20% of injections given using landmarks alone are extraarticular.

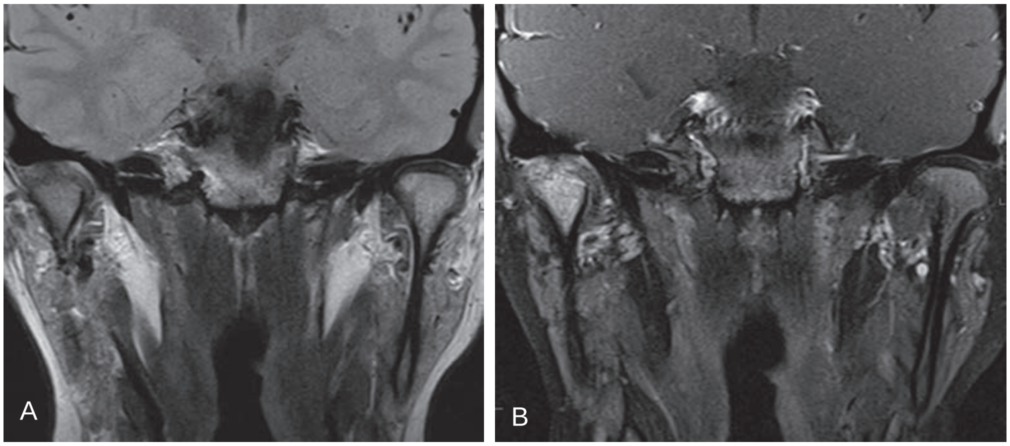

**Figure 22.9. Mild ongoing right temporomandibular joint (TMJ) arthritis on therapy.** An 11-year-old female with polyarticular juvenile idiopathic arthritis (JIA) on etanercept. (A) Coronal PD MR image shows a dysmorphic right mandibular condyle with an irregular eroded articular surface. (B) T1W FS +C image demonstrates unilateral right TMJ synovial enhancement and condylar bone marrow enhancement.

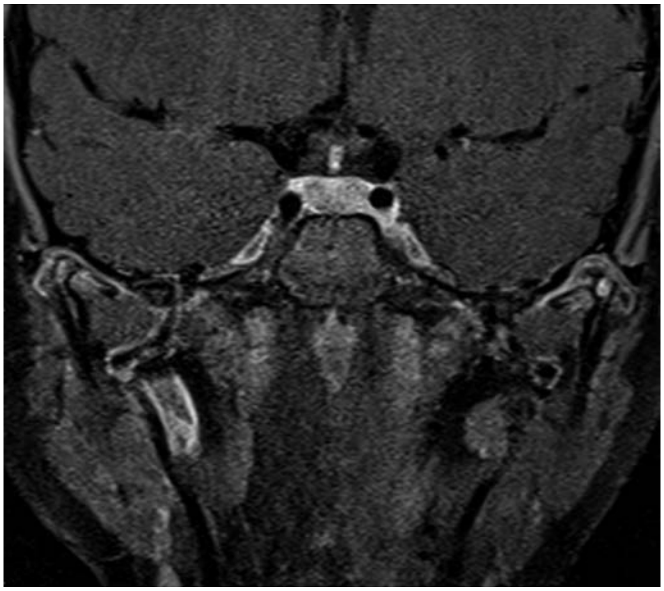

**Figure 22.10. Ongoing deforming bilateral temporomandibular joint arthritis.** A 13-year-old female with juvenile idiopathic arthritis. Coronal contrast-enhanced fat-saturated T1-weighted MR image shows severely whittled down dysplastic bilateral mandibular condyles with continued enhancement in the condylar marrow and joint soft tissues bilaterally.

the midface and mandible are retruded relative to the cranial vault, and the incidence of fracture is low. With increasing age and skeletal maturity, the midface and mandible become more protrusive relative to the neurocranium, and the incidence of fracture increases. This changing craniofacial ratio along with decreasing mandibular plasticity and more independent and unsupervised activity as a child grows coincide with the increased incidence of mandibular fracture. The most common causes of mandibular fracture in childhood are vehicular trauma and falls. The most common site of pediatric mandible fracture is the condyle. The alveolar bone of the mandible, containing teeth in different stages of eruption, is also subject to fracture along the lines of developing dental crypts. When one mandibular fracture is seen, another should be sought. Many double mandibular fractures are of the coup-contracoup variety with ipsalateral condyle and contralateral body being a common combination (Fig. 22.12).

Though treatment goals for fracture are similar in children and adults—restoration of the preinjury skeletal and dentoalveolar anatomy and function—management is different. In children, rapid union of mandibular fractures occurs, so fractures must be detected and reduced without delay. Immobilization periods are shorter in children. Closed reduction methods are preferred. With open reduction and internal fixation (ORIF) techniques, miniplate(s) and screws can be used at the inferior non–tooth-bearing border of the mandible. Applied screws are directed away from the developing dental buds (e-Fig. 22.13). Mandibular fractures without displacement or malocclusion are observed with clinical management of diet and analgesia. Ankylosis of the TMJ is a complication of a high/intracapsular condylar fracture and may be avoided by a shorter immobilization period and early physical therapy.[12] In patients with facial trauma, multidetector CT with reformations is important for not only accurate diagnosis but also multidisciplinary treatment planning. Treatment progress can be monitored using plain film techniques such as the panoramic radiograph.[13]

## Mandibular Osteomyelitis

Osteomyelitis due to infection in the mandible is rare but can occur as a result of dental infection or trauma. Hematogenous spread of infection to the mandible is rare. Risk factors for bacterial osteomyelitis include impaired immunity and conditions that affect blood supply such as sickle cell anemia, collagen vascular disease, and metabolic bone disorders such as osteopetrosis. Bone necrosis, sequestrum formation, sinus tract formation through the buccal and lingual cortices, and cloaking periosteal new bone formation are all features.[14]

Chronic recurrent multifocal osteomyelitis (CRMO) is non-bacterial osteomyelitis of children and young adults that causes multifocal bone pain, tenderness, and swelling secondary to sterile osseous inflammation. The disease is defined by a protracted course, involvement of more than one bone, and relapses at old and new sites. Mandibular CRMO, also known as *diffuse sclerosing osteomyelitis of the mandible*, can be isolated or multifocal. In its initial phases, it is actually more lytic with associated soft tissue inflammation but no abscess. In time, it becomes more sclerosing causing mandibular hyperostosis and bone enlargement. When mandibular disease is present, other craniofacial sites may be present. Biopsy

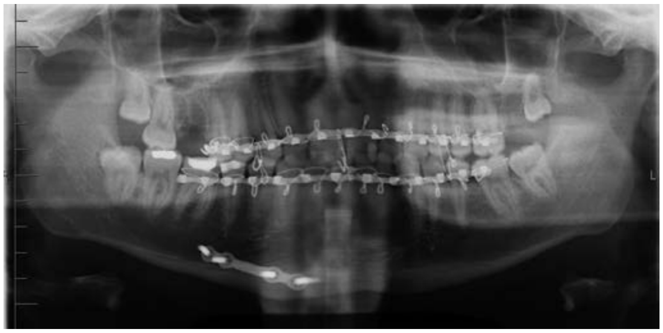

**e-Figure 22.13. Mandible fractures, postreduction.** An 18-year-old male was assaulted. Panorex status post maxillomandibular closed reduction of a left subcondylar fracture and open reduction internal fixation (ORIF) of a right parasymphyseal fracture with plate and screws applied well below the dentition along the inferior border of the mandible.

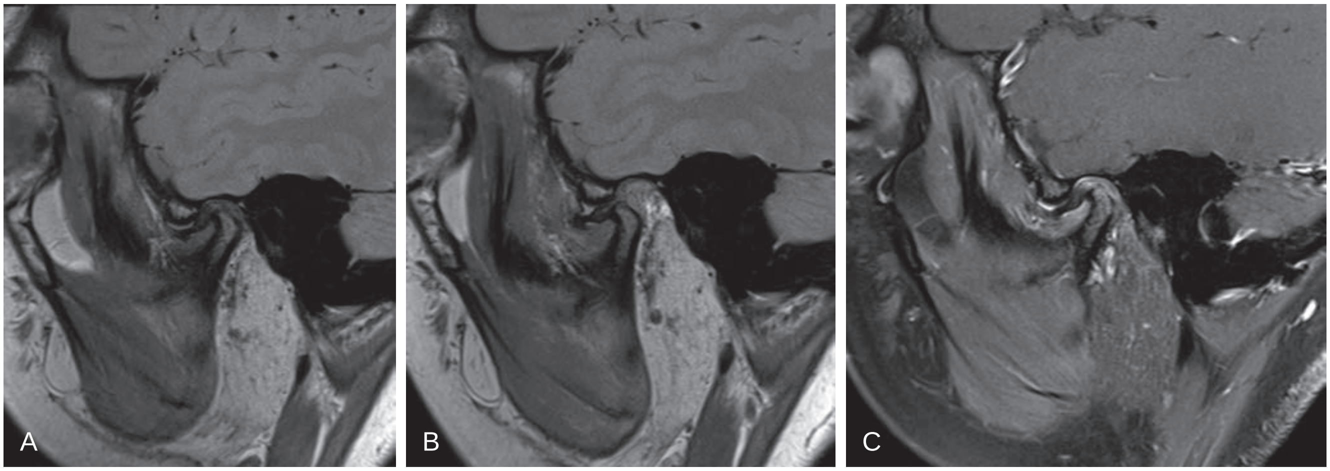

**Figure 22.11. Right temporomandibular dysfunction (TMJ) dysfunction due to an irreducible articular disk.** Proton-density MRI sagittal (A) closed- and (B) open-mouth views right TMJ demonstrate an irreducible anteriorly displaced articular disk with crumpling of the posterior band when the jaw is open. (C) T1-weighed fat-saturated contrast-enhanced MRI demonstrates abnormal enhancement in the retrodiskal soft tissues and condylar marrow.

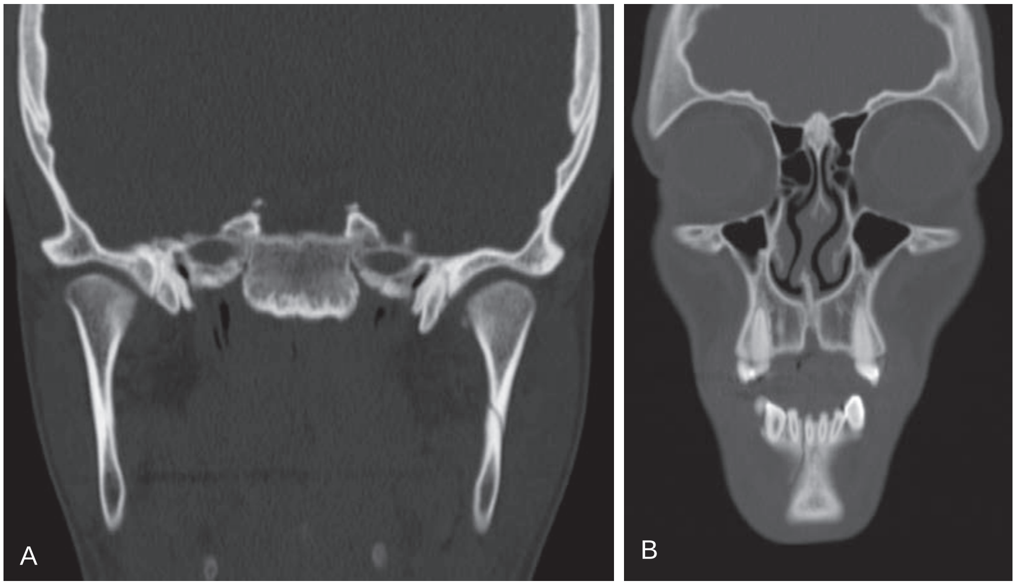

**Figure 22.12. Traumatic mandible fractures.** An 18-year-old male was assaulted. Coronal CT images of the mandible. Nondisplaced mandibular fractures (A) left subcondylar and (B) right parasymphyseal.

results yield a culture-negative chronic osteomyelitis. Recognizing CRMO as a distinct entity will help to avoid unnecessary invasive procedures and antibiotic therapy.[15]

## Mandibular Cysts and Masses

Primary mandibular lesions can develop from odontogenic and nonodontogenic tissues. Lesions originating superior to the inferior alveolar canal are odontogenic and inferior to the canal are nonodontogenic. Most primary mandibular lesions are odontogenic with cysts seen 2.25 times more frequently than tumors. CT and MRI can help to differentiate cysts from tumors and very precisely localize lesions for treatment planning.

Benign odontogenic cysts of the mandible classified mainly by location include periapical (also known as *radicular cyst*), pericoronal (also known as *dentigerous* or *follicular cyst*), or lateral periodontal cysts. Periapical cysts are often small, less than 1 cm, and always acquired resulting from inflammation at the apices or roots of a tooth due to caries or trauma (Fig. 22.14). In contradistinction pericoronal cysts may become very large and are developmental in origin forming around the crown of an unerupted tooth typically the mandibular third molar (Fig. 22.15). Another benign odontogenic cystic lesion despite its aggressive behavior and growth pattern is the odontogenic keratocyst (OKC). Though reclassified by the World Health Organization in 2005 as keratocystic odontogenic tumor (KOT), use of the outdated nomenclature OKC is widespread. OKCs contain keratinaceous “cheesy” debris and have aggressive behavior and high postresection recurrence rates. Most arise in the posterior mandible. OKCs are unilocular or multilocular, have scalloped margins, and grow along the long axis of the mandible resorbing dental roots and displacing or extruding teeth. Multiple OKCs in a young patient raise the possibility of nevoid

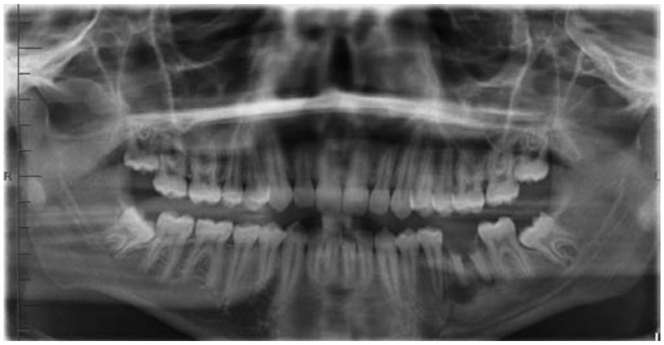

**Figure 22.14. Periapical abscess.** A 15-year-old male with 2 days of left facial pain, swelling, and fever. Panorex image shows a carious crown left first mandibular molar and rounded radiolucencies at the root apices along with root resorption. Periapical dental abscess diagnosed, incised, and drained.

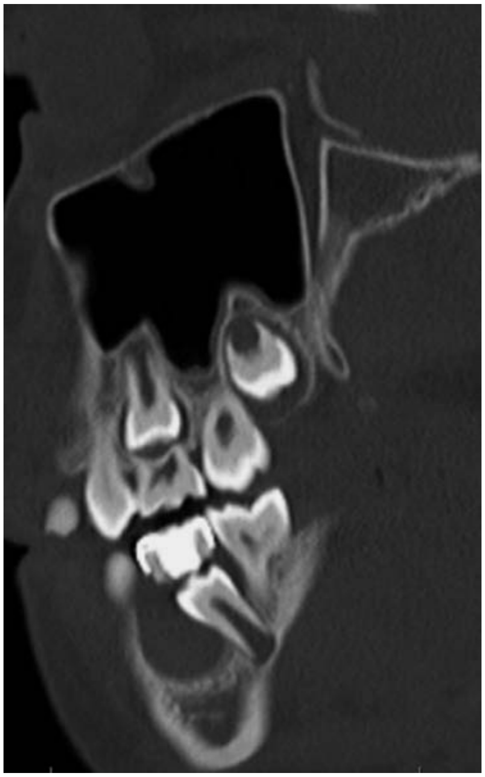

**Figure 22.15. Pericoronal or dentigerous cyst.** A 10-year-old male with a painless left mandibular cyst discovered incidentally on a dental x-ray. Sagittal CT image shows a well-circumscribed lucency enclosing the crown of the unerupted left second premolar tooth. No significant adjacent tooth displacement nor root resorption. Patient underwent cyst enucleation and extractions of the left second premolar (unerupted, permanent) and left second molar (erupted, deciduous) teeth.

basal cell carcinoma syndrome (NBCCS, also known as *basal cell nevus syndrome*, also known as *Gorlin-Goltz syndrome*) (Fig. 22.16). Incidence of OKCs in the maxilla and mandible of children with NBCCS is reported between 66% and 92%. Besides multiple OKCs, NBCCS patients have many basal cell epitheliomas and carcinomas of the skin and can develop posterior fossa medulloblastoma. As NBCCS children are more susceptible to developing secondary cancers with ultraviolet and ionizing radiation exposure, early diagnosis of NBCCS is absolutely key to avoiding unnecessary medical radiation (e.g., CT imaging of multiple OKCs, radiotherapy for posterior fossa medulloblastoma). A vigilant radiologist who can link multiple OKCs to the diagnosis of NBCCS will dramatically affect a patient's long-term outcome.[16]

Benign nonodontogenic cysts, simple and aneurysmal, can also occur in the mandible, mainly posterior.

Benign solid mandibular tumors of dental origin include odontoma, ameloblastoma, and cementoblastoma. Odontoma is the most common odontogenic "tumor" of the mandible typically diagnosed in the first two decades of life and subdivided into two types: compound (e-Fig. 22.17) and complex (Fig. 22.18). Odontomas are hamartomatous lesions consisting of various tooth components; a compound odontoma is better differentiated than a complex odontoma. Ameloblastomas arise from enamel-forming cells and can occur in the pediatric age group. Ameloblastomas are slow-growing, expansile, admixed solid and cystic masses most commonly found in the posterior mandible third molar region classically described as "soap-bubbly" in appearance. Despite their typically benign pathology (ameloblastoma can only be distinguished from ameloblastic carcinoma histopathologically), it can erode cortex, resorb dental roots, and expand into the oral and perioral soft tissues (Fig. 22.19).[17] Cementoblastoma is a rare jaw tumor occurring primarily in children and young adults, 50% in the first two decades of life, 75% in the first three decades of life. It is sharply marginated and sclerotic (cementum-laden) with a low-attenuation halo. Located periapically, it fuses to the root(s) of the involved premolar or molar tooth (usually first molars).

Benign mandibular tumors not of dental origin include two fibro-osseous lesions with ground-glass attenuation, ossifying fibroma and fibrous dysplasia, and one giant cell lesion called *central giant cell granuloma (CGCG)*. Ossifying fibromas (also known as cemento-ossifying or cementifying fibroma) occur over a wide age range but can be seen in pediatrics. Classically ossifying fibroma is described as solitary, sharply marginated, focally expansile ground-glass lesion in the posterior mandible without a lucent halo that becomes more radioopaque over time as the osteoid component of its matrix mineralizes. It has a centrifugal growth pattern perpendicular to the long axis of the bone. Tooth displacement is common. Juvenile ossifying fibroma is a notable destructive variant of ossifying fibroma seen in boys under 15 years of age with highly aggressive growth. Fibrous dysplasia, another ground-glass attenuation lesion, can be distinguished from ossifying fibroma because it causes less of a focal alteration in the shape of the bone expanding along, rather than perpendicular to, the mandible's long axis. Unlike ossifying fibroma's narrow zone of transition, fibrous dysplasia has a wide zone of transition but does not displace teeth. Histopathologically, osteoblastic rimming is seen with ossifying fibroma but not fibrous dysplasia.[14] CGCGs are thought to result due to altered vascular and reactive responses within bone and are also referred to as *giant cell reparative cysts*. Seen most frequently in adolescent and young adult females, CGCGs are classically radiolucent, located in the anterior mandible, and have a multilocular honeycomb appearance due to "wispy" internal bony septae, which orient perpendicular to the edge of the lesion. These slow-growing lesions may expand, erode, and remodel cortex and resorb dental roots.[18] Multiple giant cell lesions of the mandible and maxilla are described in a molecular variant of Noonan syndrome.[19] Other benign nonodontogenic tumors that are defined by their relationship to the inferior alveolar canal include neural and vascular lesions such as neurofibroma and schwannoma, central hemangioma, and arteriovenous malformation. Finally, exophytic and nonexophytic osteomas can occur in the mandible.

Malignant tumors of the mandible are usually not primary. Neuroblastoma is the most common metastatic disease to the mandible (e-Fig. 22.20). Other malignancies seen in the pediatric mandible include leukemia, lymphoma (including Burkitt), and sarcomas (including Ewing, osteosarcoma, rhabdomyosarcoma, and chondrosarcoma) (Fig. 22.21). Originally described and thought pathognomonic for

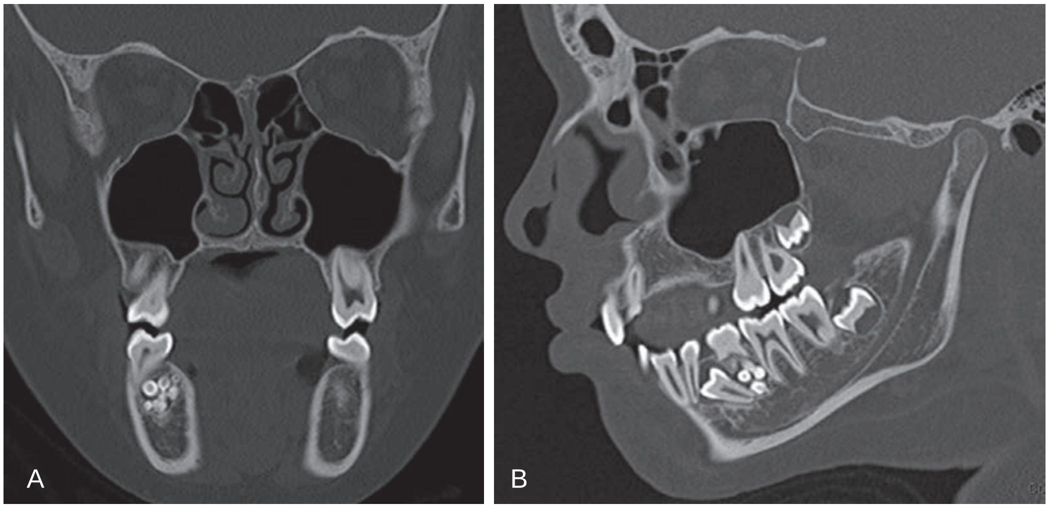

**e-Figure 22.17. Compound odontoma.** A 12-year-old asymptomatic female. Unenhanced (A) coronal and (B) sagittal oblique reformat CT images show a hamartomatous mass of well-differentiated tooth structure that comprises multiple miniteeth (denticles) surrounded by a radiolucent rim resembling, in this case, a tiny bag of teeth. It is developing above the inferior alveolar nerve canal (where a tooth would normally develop). Note the conspicuity of the inferior alveolar nerve canal on the sagittal oblique reformat image.

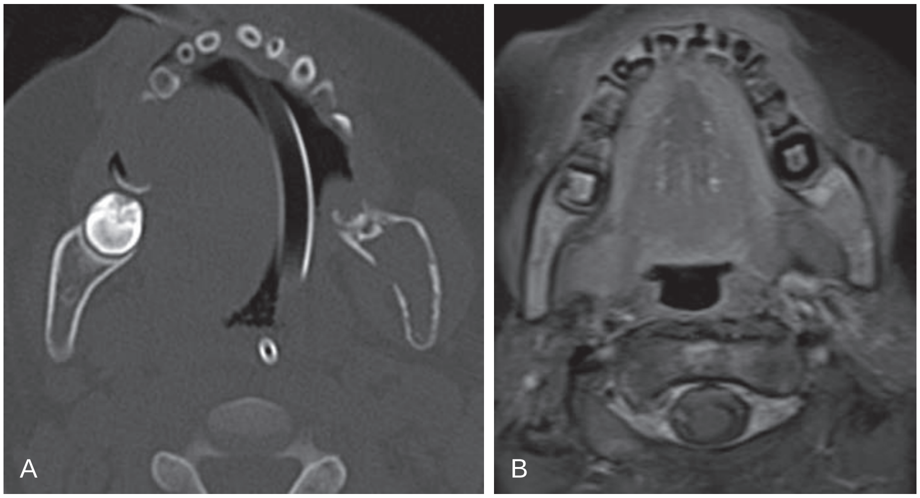

**e-Figure 22.20. Metastatic neuroblastoma.** A 4-year-old female with right suprarenal neuroblastoma and metastatic disease to the mandible at initial presentation. (A) Unenhanced axial CT image through the mandible with an endotracheal tube in place demonstrates a permeated “disappearing” cortex at the expanded angle of the left mandible. (B) T1-weighted contrast-enhanced fat-saturated axial MR image demonstrates a corresponding hypoenhancing but aggressive mass, a path-proven neuroblastoma metastasis.

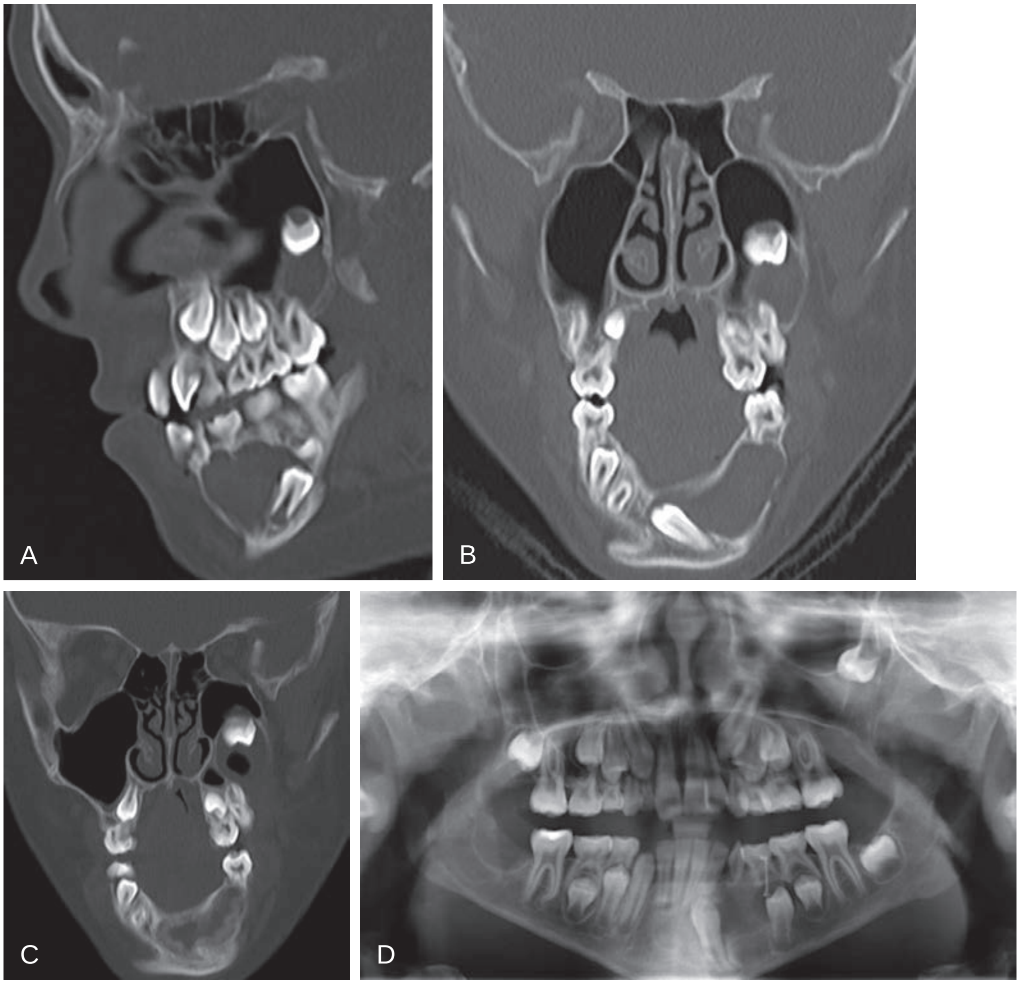

**Figure 22.16. Multiple odontogenic keratocysts (OKCs) in nevoid basal cell carcinoma syndrome (NBCCS).** A 9-year-old female with NBCCS. Initial (A) sagittal and (B) coronal CT images show multiple OKCs, left parasymphyseal mandibular, and left maxillary. (C) Coronal CT image 3–4 months postmarsupialization shows a shrinking, sclerosing left parasymphyseal OKC. Left maxillary OKC is enlarging after drainage tube fell out prematurely. (Both lesions were subsequently enucleated.) (D) Note how difficult it is to identify the large left maxillary OKC on this panorex, even with unnaturally high left maxillary molar tooth displacement. Also take note of progressive shrinkage left parasymphyseal OKC and a new right posterior mandibular OKC.

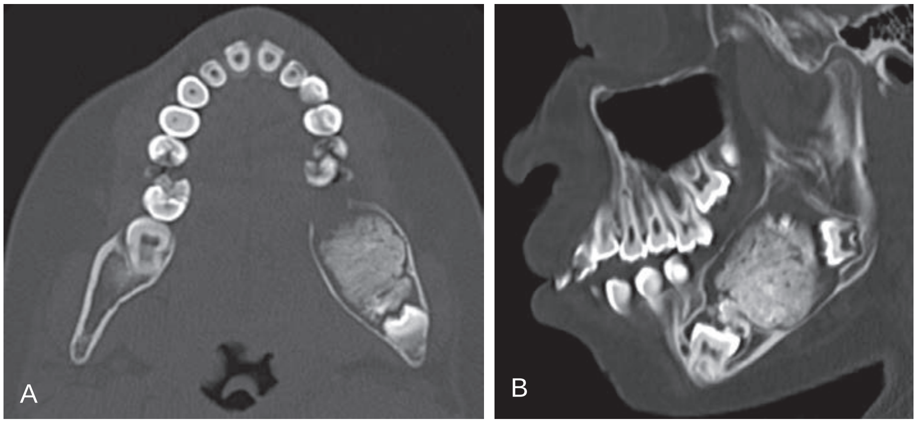

**Figure 22.18. Complex odontoma.** A 9-year-old female with left facial swelling and a palpable mandibular abnormality. Unenhanced (A) axial and (B) sagittal oblique MPR CT images show an amorphous mineralized mass of enamel and dentin resembling a clump of cotton in the molar region of the mandible associated with the crown of an impacted molar tooth. Note the characteristic perilesional lucent halo.

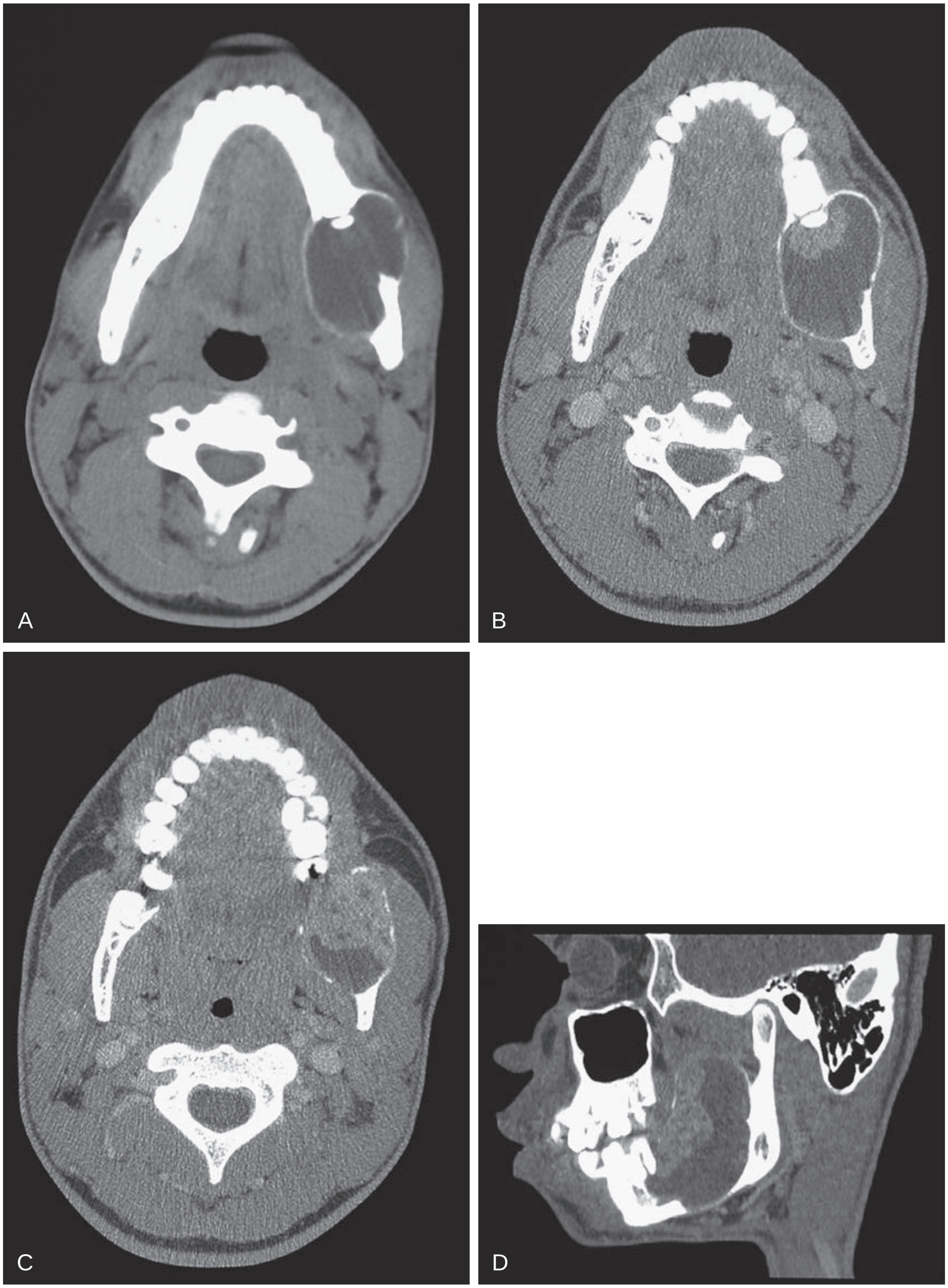

**Figure 22.19.** A 4-year-old patient with ameloblastoma of the left mandible. (A) An axial computed tomography (CT) scan shows the large destructive lesion of the left mandible. (B) Contrast-enhanced axial CT. With further windowing, the two components of the lesion are demonstrated: a more solid component anteriorly and a more cystic component posteriorly. (C) An image slightly inferior to that shown in (B) reveals the solid component. (D) The sagittal reconstruction shows the effect on the mandible; solid and cystic components of the lesion are seen.

Langerhans cell histiocytosis (LCH), the radiographic appearance of "floating teeth" has been observed in the context of other tumors that destroy the alveolar ridge (Figs. 22.22 and 22.23).[20]

In pediatric patients in whom there is ongoing mandibular growth and odontogenesis, surgical techniques, especially for large cystic lesions, aim to spare tissue, maintain continuity, and preserve function.[21]

## Cherubism

Cherubism is a benign condition characterized by progressive painless cheek swelling due to bilateral symmetric mandibular and maxillary multilocular giant cell-containing cystic lesions. Lesions tend to extend from the region of the molar teeth toward the anterior midline. Stretching of the skin as a result of maxillary involvement tends to pull the lower eyelids down, revealing a band of white sclerae between the eyelid and the iris (e-Fig. 22.24). This cherubic "eyes raised to heaven" expression has led to the term "cherubism." Once thought to be exclusively familial and dubbed "familial fibrosis of jaws," we now know cherubism can be nonfamilial. Once thought to be a subtype of craniofacial fibrous dysplasia, genetic analysis reveals that cherubism and craniofacial fibrous dysplasia are distinct entities despite their radiologic mimicry. Cherubism usually presents before age 5, most often between 12

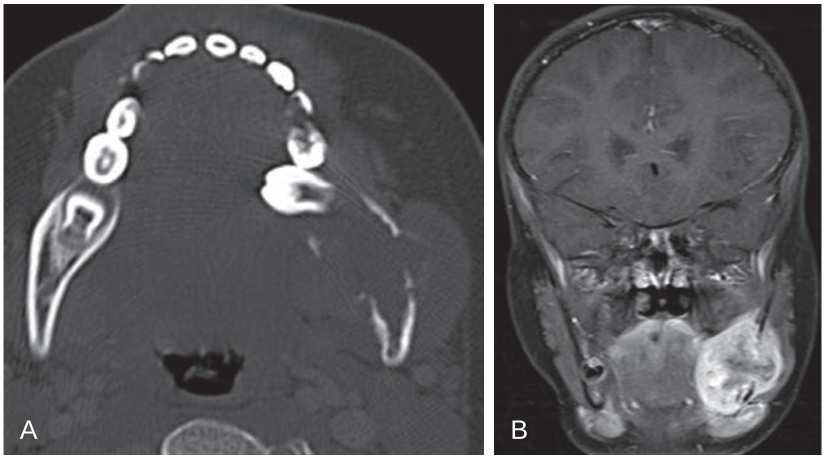

**Figure 22.21. Left mandibular rhabdomyosarcoma.** A 5-year-old female evaluated by her dentist for left mandibular swelling. (A) Contrast-enhanced axial CT image through the mandible demonstrates a destructive and deforming lytic mass in the left posterior mandible. (B) T1-weighted contrast-enhanced fat-saturated coronal MR image demonstrates a bulky, avidly-enhancing, aggressive left mandibular mass encroaching on the oral cavity with the very large extraosseous soft tissue component perhaps underestimated by CT.

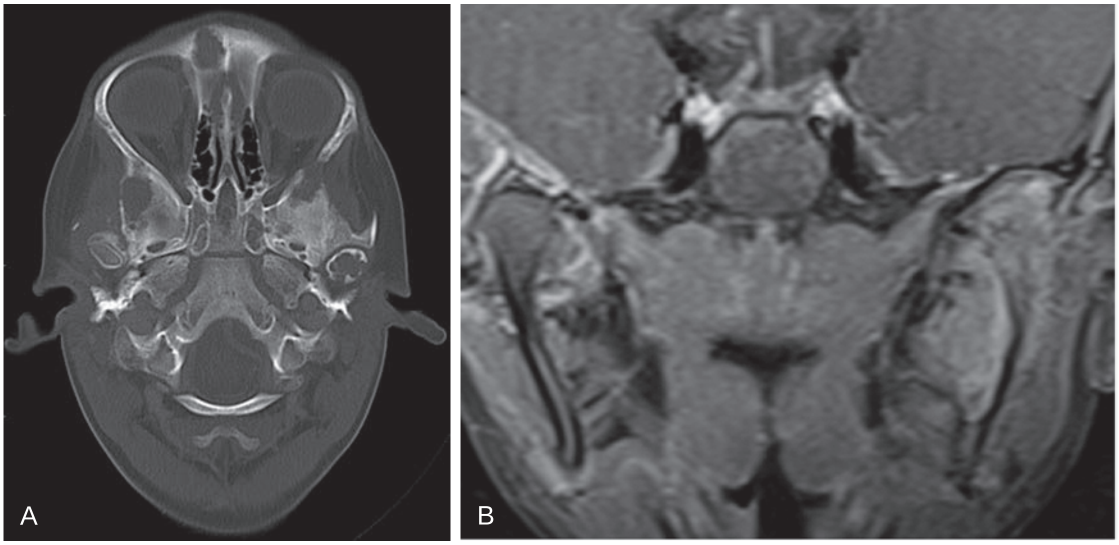

**Figure 22.22. Langerhans cell histiocytosis (LCH).** A 4-year-old male with facial swelling. (A) Axial unenhanced CT image shows multiple destructive lytic lesions at the skull base and left temporomandibular joint. (As in 25% of children with LCH involving the facial bones or anterior or middle cranial fossae, this child went on to develop CNS involvement with infiltration of the posterior pituitary and resultant diabetes insipidus.) (B) T1-weighted contrast-enhanced fat-saturated coronal MR image shows a destructive heterogeneously enhancing mandibular mass centered in the left condylar neck and vertical ramus breaking through the buccal and lingual cortices and also extending to the condylar articular surface.

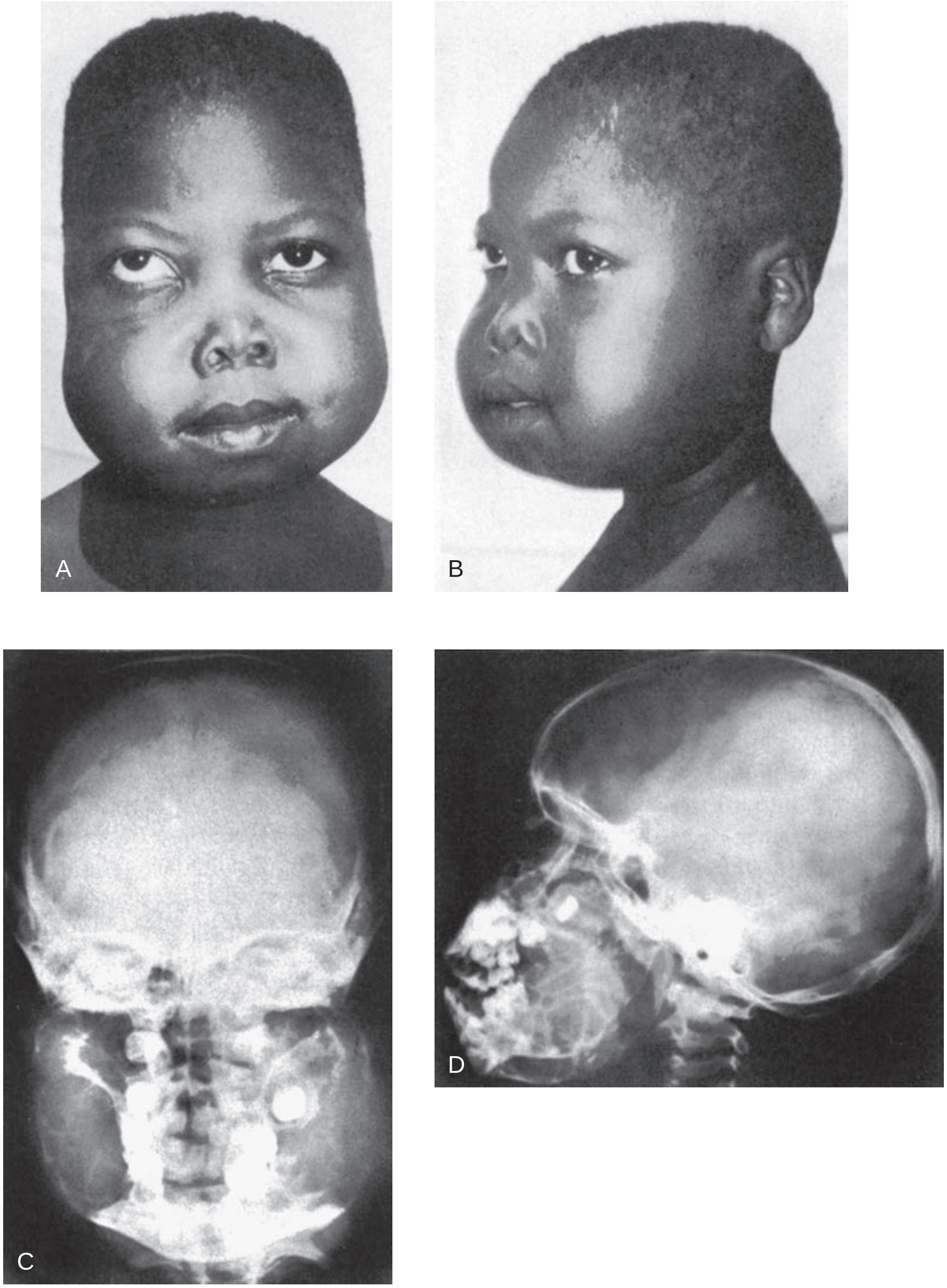

**e-Figure 22.24.** Familial fibrosis of the jaws (cherubism) in a 6-year-old boy whose two siblings and father were affected. (A and B) Clinical photographs. Massive painless swelling extends to the preauricular level and obscures the normal external ears in the frontal view. The downward displacement of the lower lids explains the term cherubism ("eyes raised to heaven"). (C and D) Frontal (C) and lateral (D) skull projections show cystic swelling of the mandible and, to a lesser degree, the maxilla. The teeth are displaced medially except for the unerupted left maxillary molar. The unerupted right molar and the swollen maxilla impinge on the right maxillary sinus, partially obliterating its cavity. The clouding of the left maxillary sinus extends to the left ethmoid, indicating bony involvement or ostial occlusion. *(From Shuler RK, Silverman FN. Familial fibrous dysplasia of the jaws of "cherubism" in a Haitian family.* Ann Radiol. *1965;8:45–52.)*

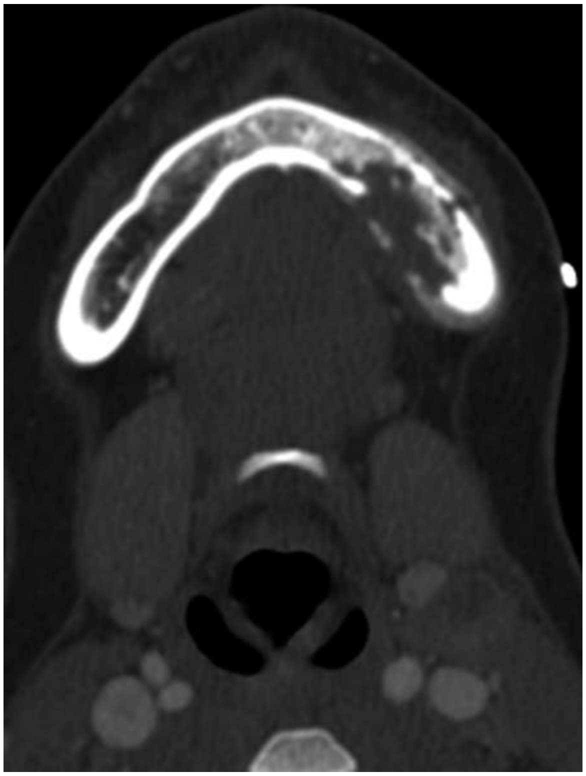

**Figure 22.23. Langerhans cell histiocytosis (LCH) mimicking chronic osteomyelitis.** A 10-year-old female with left jaw pain and swelling for 6+ weeks with clinical concern for osteomyelitis. Lesion in left mandible debrided by an oral surgeon. Histopathology compatible with LCH. Contrast-enhanced axial CT image through the mandible predebridement shows a destructive mixed lytic and sclerotic lesion in the body of the left mandible with cortical breakthrough, cloaking periosteal reaction, and periosseous soft tissue fullness.

and 36 months, and progresses until puberty, after which there is a partial to complete spontaneous involution. Nondevelopment, maldevelopment, displacement, and/or premature loss of both deciduous and permanent teeth are commonly present. Not all patients have the typical features and course.

Cherubism is rare. There is no active disease treatment. Surgical interventions are reserved for functional impairment or cosmesis.[22]

With the molecular basis of diseases being derived, what we now know about cherubism, initially described in 1933, will continue to evolve. Already various clinical and radiologic mimics that are genetically distinct, like craniofacial fibrous dysplasia and SOS-1-related Noonan syndrome, exist (Fig. 22.25).

## Other Generalized Diseases of the Skeleton Involving the Mandible

Monoostotic fibrous dysplasia is far more common than the polyostotic form of the disease. There is craniofacial involvement with both forms.

Infantile cortical hyperostosis (Caffey disease) is an asymmetric polyostotic process. Acute inflammation in periosseous soft tissues and periosteal bone causes localized thickening of adjacent bone cortex. The infant mandible is involved in 80% of cases.

Metabolic bone disorders may cause lesions in the mandible that are similar to lesions occurring elsewhere in the body. For example, renal osteodystrophy is a skeletal response to longstanding kidney disease. As in other parts of the skeleton, early renal osteodystrophy of the jaw is characterized by diffuse ground-glass attenuation replacing normal trabeculation with the blurring of cortical lines, a mimic of diffuse fibrous dysplasia of the jaw. Deforming osteosclerosis is seen in more advanced stages of renal osteodystrophy. Brown tumors of the jaw can also be seen.

Bisphosphonates are medications that inhibit pathologic bone loss and have become widely accepted in the treatment of pediatric bone disorders such as osteogenesis imperfecta. In adult patients, bisphosphonate use has been linked to osteonecrosis of the jaw. Thus far, bisphophonate-related osteonecrosis of the jaw has not been reported in children.[23]

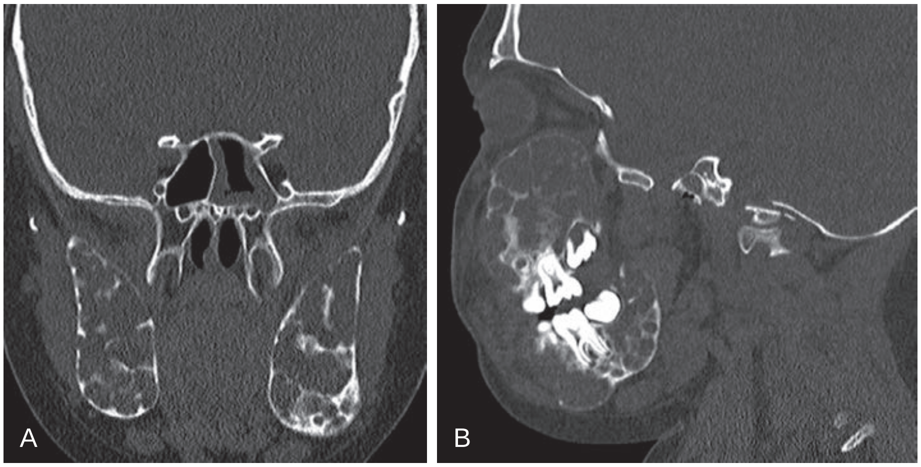

**Figure 22.25. Noonan syndrome with multiple giant cell lesions.** A 9-year-old female with Noonan syndrome and cherubic facies. (A) Coronal CT image of vertical rami of the mandible and (B) sagittal CT of the infraorbital maxilla show massive honeycomb-like expansion of the bone, diffusely thinned and eroded cortex, and blunted dental roots due to root tip resorption. There is bulging of the bilateral orbital floors contributing to the “eyes raised to heaven”/cherubic facies. These biopsy-proven giant cell-containing lesions are seen with a rare molecular variant of Noonan syndrome.

## KEY POINTS

- Abnormal development of the first and second branchial pairs can result in isolated mandibular anomalies or syndromes such as the otomandibular dysplasias.
- Mandibular development is increasingly assessed in utero using fetal MRI as an adjunct to screening US.
- TMJ involvement in JIA is well known but often asymptomatic and clinically undetectable. MRI is important for initial diagnosis and assessing response to therapy.
- The condyle is the most common site of pediatric mandibular fracture.
- Most primary mandibular lesions are benign and odontogenic in origin with cysts more prevalent than tumors.
- Malignant tumors of the mandible are usually not primary. Neuroblastoma is the most common metastatic disease to the pediatric mandible.

## SUGGESTED READINGS

Gohel A, Villa A, Sakai O. Benign jaw lesions. *Dent Clin North Am*. 2016;60(1):125–141. doi:10.1016/j.cden.2015.08.005.

Plunk MR, Oda D, Parnell SE, et al. Focal benign disorders of the pediatric mandible with radiologic-histopathologic correlation: mandibular development and lucent lesions. *AJR Am J Roentgenol*. 2017;208(1):180–192. doi:10.2214/ajr.16.16587.

Scheinfeld MH, Shifteh K, Avery LL, et al. Teeth: what radiologists should know. *Radiographics*. 2012;32(7):1927–1944. doi:10.1148/rg.327125717.

von Kalle T, Stuber T, Winkler P, et al. Early detection of temporomandibular joint arthritis in children with juvenile idiopathic arthritis—the role of contrast-enhanced MRI. *Pediatr Radiol*. 2014;45(3):402–410. doi:10.1007/s00247-014-3143-5.

## REFERENCES

Full references for this chapter can be found on www.expertconsult.com.

## REFERENCES

1. Errata. *Radiographics*. 2013;33(1):312–312. doi:10.1148/rg.331125717.
2. Gonzalez GE, Caruso PA, Small JE, et al. Craniofacial and temporal bone CT findings in cleidocranial dysplasia. *Pediatr Radiol*. 2008;38(8):892–897. doi:10.1007/s00247-008-0866-1.
3. Leung AKC, Robson WLM. Natal teeth: a review. *J Natl Med Assoc*. 2006;98(2). https://www.ncbi.nlm.nih.gov/pmc/articles/PMC2595049/. Accessed December 10, 2016.
4. Kline-Fath BM, Bulas DI, Bahado-Singh R. *Fundamental and advanced fetal imaging ultrasound and MRI*. Philadelphia, PA, United States: Wolters Kluwer Health; 2015.
5. Sadler TW, Leland J, Sadler-Redmond SL. *Langman's Medical Embryology*. 11th ed. Philadelphia, PA: Lippincott Williams and Wilkins; 2009.
6. Senggen E, Laswed T, Meuwly J-Y, et al. First and second branchial arch syndromes: multimodality approach. *Pediatr Radiol*. 2010;41(5):549–561. doi:10.1007/s00247-010-1831-3.
7. Nemec U, Nemec SF, Brugger PC, et al. Normal mandibular growth and diagnosis of micrognathia at prenatal MRI. *Prenat Diagn*. 2014;35(2):108–116. doi:10.1002/pd.4496.
8. Kaufman MG, Cassady CI, Hyman CH, et al. Prenatal identification of Pierre Robin sequence: a review of the literature and look towards the future. *Fetal Diagn Ther*. 2015;39(2):81–89. doi:10.1159/000380948.
9. Cannizzaro E, Schroeder S, Muller LM, et al. Temporomandibular joint involvement in children with juvenile idiopathic arthritis. *J Rheumatol*. 2010;38(3):510–515. doi:10.3899/jrheum.100325.
10. Abramowicz S, Cheon J-E, Kim S, et al. Magnetic resonance imaging of temporomandibular joints in children with arthritis. *J Oral Maxillofac Surg*. 2011;69(9):2321–2328. doi:10.1016/j.joms.2010.12.058.
11. Tomas X, Pomes J, Berenguer J, et al. MR imaging of temporomandibular joint dysfunction: a pictorial review. *Radiographics*. 2006;26(3):765–781. doi:10.1148/rg.263055091.
12. Glazer M, Joshua BZ, Woldenberg Y, et al. Mandibular fractures in children: analysis of 61 cases and review of the literature. *Int J Pediatr Otorhinolaryngol*. 2011;75(1):62–64. doi:10.1016/j.ijporl.2010.10.008.
13. Avery LL, Susarla SM, Novelline RA. Multidetector and three-dimensional CT evaluation of the patient with Maxillofacial injury. *Radiol Clin North Am*. 2011;49(1):183–203. doi:10.1016/j.rcl.2010.07.014.
14. Curé JK, Vattoth S, Shah R. Radiopaque jaw lesions: an approach to the differential diagnosis. *Radiographics*. 2012;32(7):1909–1925. doi:10.1148/rg.327125003.
15. Khanna G, Sato TSP, Ferguson P. Imaging of chronic recurrent multifocal osteomyelitis. *Radiographics*. 2009;29(4):1159–1177. doi:10.1148/rg.294085244.
16. Sartip K, Kaplan A, Obeid G, et al. Neuroimaging of nevoid basal cell carcinoma syndrome (NBCCS) in children. *Pediatr Radiol*. 2012;43(5):620–627. doi:10.1007/s00247-012-2516-x.
17. Dunfee BL, Sakai O, Pistey R, et al. Radiologic and pathologic characteristics of benign and malignant lesions of the mandible. *Radiographics*. 2006;26(6):1751–1768. doi:10.1148/rg.266055189.
18. Gupta M, Kaste SC, Hopkins KP. Radiologic appearance of primary jaw lesions in children. *Pediatr Radiol*. 2002;32(3):153–168. doi:10.1007/s00247-001-0633-z.
19. Beneteau C, Cavé H, Moncla A, et al. SOS1 and PTPN11 mutations in five cases of Noonan syndrome with multiple giant cell lesions. *Eur J Hum Genet*. 2009;17(10):1216–1221. doi:10.1038/ejhg.2009.44.
20. Zaveri J, La Q, Yarmish G, et al. More than just Langerhans cell histiocytosis: a radiologic review of histiocytic disorders. *Radiographics*. 2014;34(7):2008–2024. doi:10.1148/rg.347130132.
21. Bodner L, Woldenberg Y, Bar-Ziv J. Radiographic features of large cystic lesions of the jaws in children. *Pediatr Radiol*. 2003;33(1):3–6. doi:10.1007/s00247-002-0816-2.
22. Jain V, Sharma R. Radiographic, CT and MRI features of cherubism. *Pediatr Radiol*. 2006;36(10):1099–1104. doi:10.1007/s00247-006-0261-8.
23. Brown JJ, Ramalingam L, Zacharin MR. Bisphosphonate-associated osteonecrosis of the jaw: does it occur in children? *Clin Endocrinol (Oxf)*. 2008;68(6):863–867. doi:10.1111/j.1365-2265.2008.03189.x.

# 23

# Traumatic Lesions of the Skull and Face*

*Erin K. Opfer and Thomas L. Slovis*

## CONGENITAL DEPRESSIONS

Congenital depressions of the calvaria result from mechanical factors that occur before or during birth.[1] During labor, calvarial depressions are caused by excessive localized pressure on the head by the bony prominences in the maternal pelvis, including the sacral promontory, pubic symphysis, and sciatic spines (e-Fig. 23.1). Application of forceps to the fetal head and traction with excessive force is another less common cause of congenital depressions.

Deformities also may develop from sustained abnormal fetal positions (e-Fig. 23.2). Grooves in the calvarium and face may be caused by excessive pressure of an ectopic limb and represent restrictions of the usual active movements of the fetus. Deformities also may arise as a result of pressure from amniotic bands. Depressions due to long-standing fetal position are present at birth and are not associated with edema or hemorrhage.

These calvarial depressions are usually visible by direct inspection, but radiographs often are obtained to search for associated fractures. Spontaneous elevation of prenatal depressions during the first year after birth without adverse residual effects have been reported.[1] Acute depressions as a result of the application of forceps, often called "ping-pong ball depressions," have been elevated by simple tangential digital pressure on opposite sides of the depression and by suction with a vacuum extractor.[2,3]

## HEMORRHAGE

Hemorrhage in the neonatal scalp has an increased incidence with difficult or traumatic deliveries. It may occur at three different levels: subcutaneous (caput succedaneum), subaponeurotic (subgaleal), and subperiosteal (cephalhematoma). More superficial bleeds cross suture lines and may extend widely into the face ventrally, onto the neck dorsally, and onto the zygomatic arches and mastoid processes laterally.

## CAPUT SUCCEDANEUM

Caput succedaneum is a local subcutaneous swelling of the scalp that contains edema and blood and can extend across suture lines (Fig. 23.3). It is usually a result of pressure on the presenting head. The swelling is recognized at birth and disappears after a few days. Local scalp swelling casts a shadow of water density on skull radiographs that disappears without residual bone changes. Rarely, the hemorrhage can be so massive that hypovolemic shock occurs. In such cases, intracranial hemorrhage often is present.

## SUBGALEAL HEMATOMAS/HYGROMA

Subgaleal hemorrhages, also known as cephalhematoceles, result from an accumulation of cerebrospinal fluid (CSF) and blood beneath the epicranial aponeurosis caused by the rupture of emissary veins. The abnormal fluid extends across the sutures into a potential space that can develop slowly postdelivery.[4] Clinically, they present as a fluctuant mass and may simulate a cephalhematoma or caput succedaneum. Radiographically, the swellings are usually in the parietal regions and can have associated fractures (Fig. 23.4). Trauma from use of obstetric forceps or vacuum extraction is a common cause of subgaleal hematomas. In older children, a subgaleal hygroma may result from hair-pulling in cases of child abuse or accidental entrapment of long hair in mechanical equipment. A subgaleal hematoma may occur without trauma in patients with coagulation abnormalities.

## CEPHALHEMATOMA

Subperiosteal hemorrhages are known as cephalhematomas. Cephalhematomas are confined by sutures, and shells of bone form over them during resolution, arising from the elevated periosteum that covers them (Fig. 23.5). The usual cause of cephalhematomas is trauma to the fetal head during labor, and the incidence is higher in instrument-assisted delivery.[5,6] The incidence of neonatal cephalhematomas in two large series was found to be 1.5% to 2.5%.[5,6] Associated fractures were found in 25% of the cephalhematomas studied radiographically and generally are of no clinical significance.[5]

Clinically, subperiosteal cephalhematomas are localized swellings, usually over the parietal and occipital bone (Fig. 23.6). Fresh

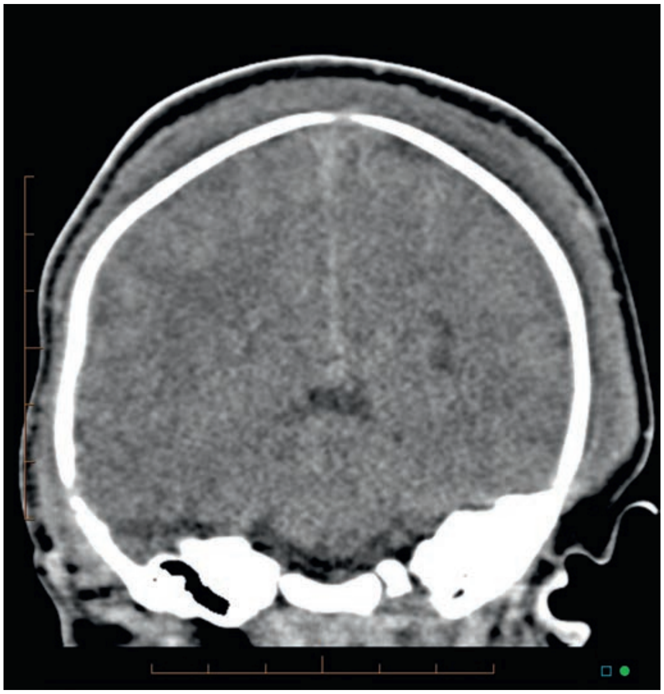

**Figure 23.3. Caput succedaneum in a 14-hour-old neonate with seizures after prolonged labor.** Coronal reconstructed CT image shows soft tissue scalp swelling/hematoma surrounding the calvarium and extending across the sagittal and lamboidal *(not shown)* sutures.

---

*This chapter originally was written by Dr. John Caffey and revised by Dr. Frederic Silverman. Although some of the images in this chapter appeared in the first edition in 1945, they are still excellent examples of clinical and radiographic imaging.

## Abstract:

Imaging of traumatic lesions of the pediatric skull can be helpful in the assessment and management of pediatric cranial skull fractures and soft tissue scalp injury. Deformities of the neonatal skull can be secondary to congenital depressions or post traumatic fractures during delivery. Other post traumatic injuries may include soft tissue scalp injuries such as caput succedaneum, subgaleal hematoma and cephalhematoma which are most commonly seen with traumatic delivery. The imaging features on plain film and cross sectional imaging can help differentiate level of the hemorrhage. Cranial fractures can occur in all pediatric age groups and usually nonabusive fractures of the pediatric skull heal well with no sequela. Imaging may be helpful if there are clinical signs that warrant assessment for associated intracranial evaluation.

## Keywords:

Caput Succedaneum
Subgaleal Hematoma
Cephalhematoma
Leptomeningeal cyst
congenital depressions

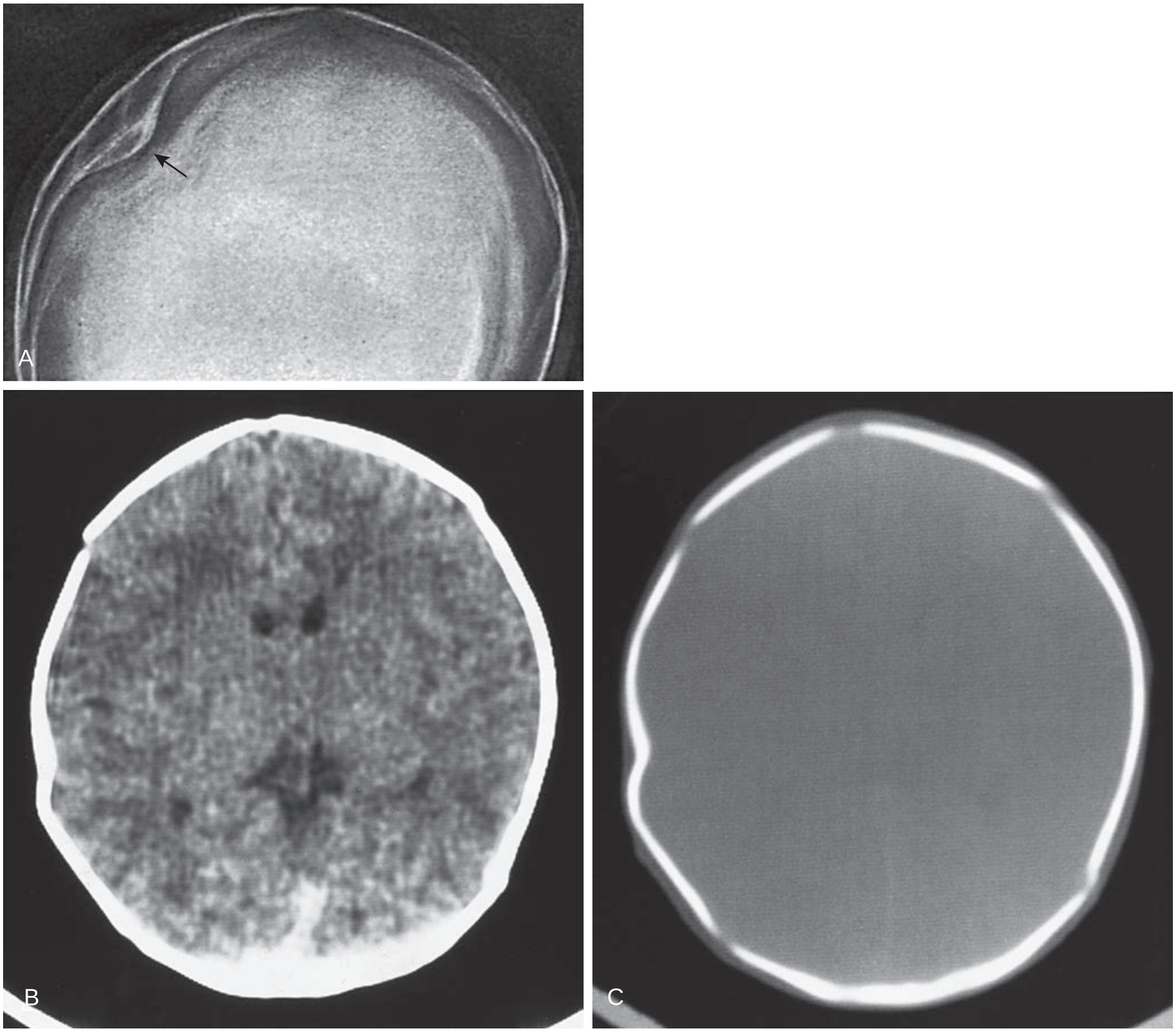

**e-Figure 23.1. Congenital parietal depression in a 37-day-old infant.** (A) Radiograph shows a congenital parietal depression *(arrow)*. (B) Brain and (C) bone windows of another infant with a depressed right parietal fracture.

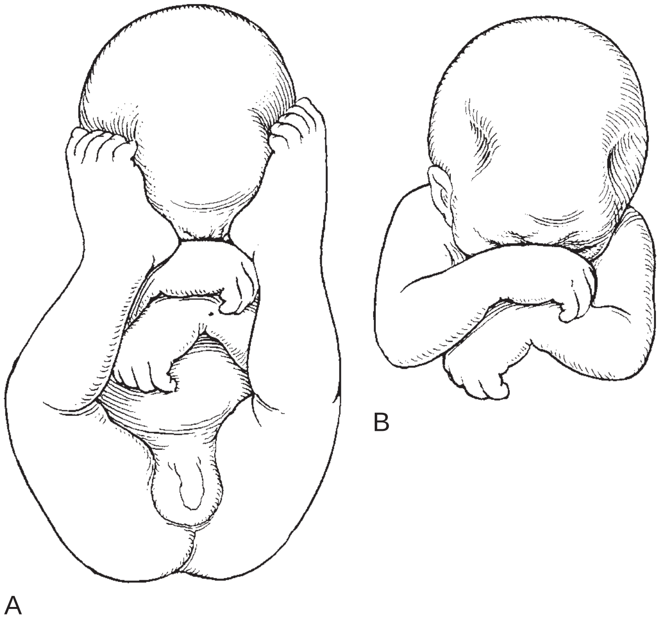

**e-Figure 23.2. Schematic rendering of the pathogenesis of congenital calvarium depressions due to faulty fetal posture.** (A) An abnormal fetal position in which the feet indent the calvaria. (B) Lateral frontoparietal depressions in the calvaria after removal of the feet from the depressions.

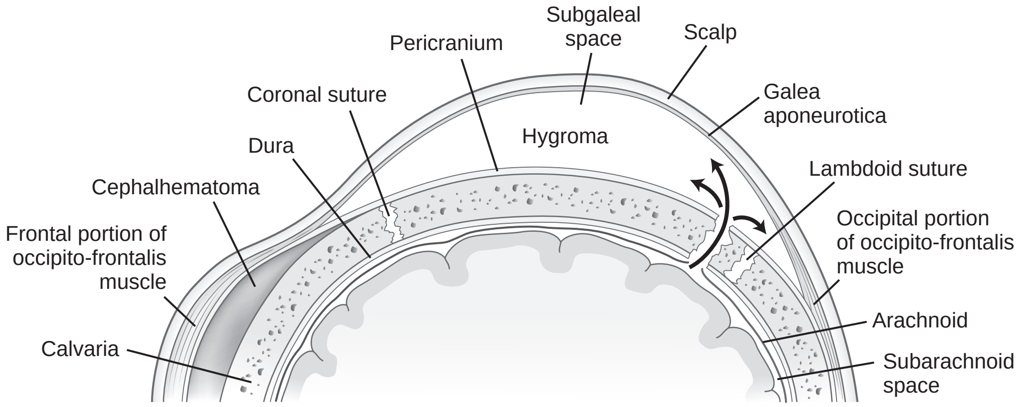

**Figure 23.4. Course of flow of the cerebrospinal fluid after fracture of the calvarium.** Tears of the arachnoid and dura internally and of the periosteum externally into the subgaleal (epicranial) space form a large subgaleal hygroma under the galea aponeurotica. *(Modified from Epstein JA, Epstein BS, Small M. Subepicranial hygromas: a complication of head injuries in infants and children.* J Pediatr. *1961;59:562–566.)*

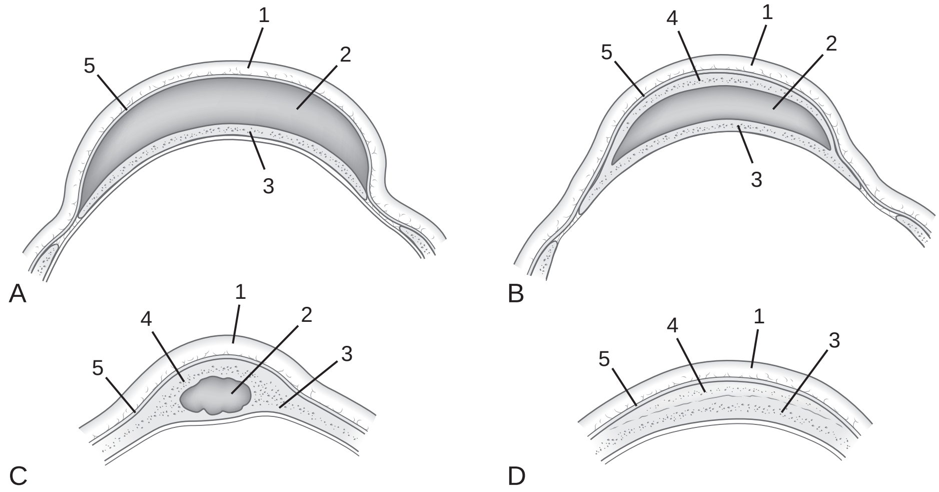

**Figure 23.5. Schematics of anatomic changes that occur in cephalhematoma.** (A) A fresh subperiosteal hematoma. (B) The healing phase, which shows a shell of subperiosteal bone over the hematoma. (C) Persistence of organized hematoma in the diploic space. (D) Residual external thickening of the outer table after complete resorption of subperiosteal blood. (C and D) represent late residuals that may persist into adult life. *1,* Scalp; *2,* hematoma; *3,* normal calvaria; *4,* new subperiosteal bone; *5,* periosteum.

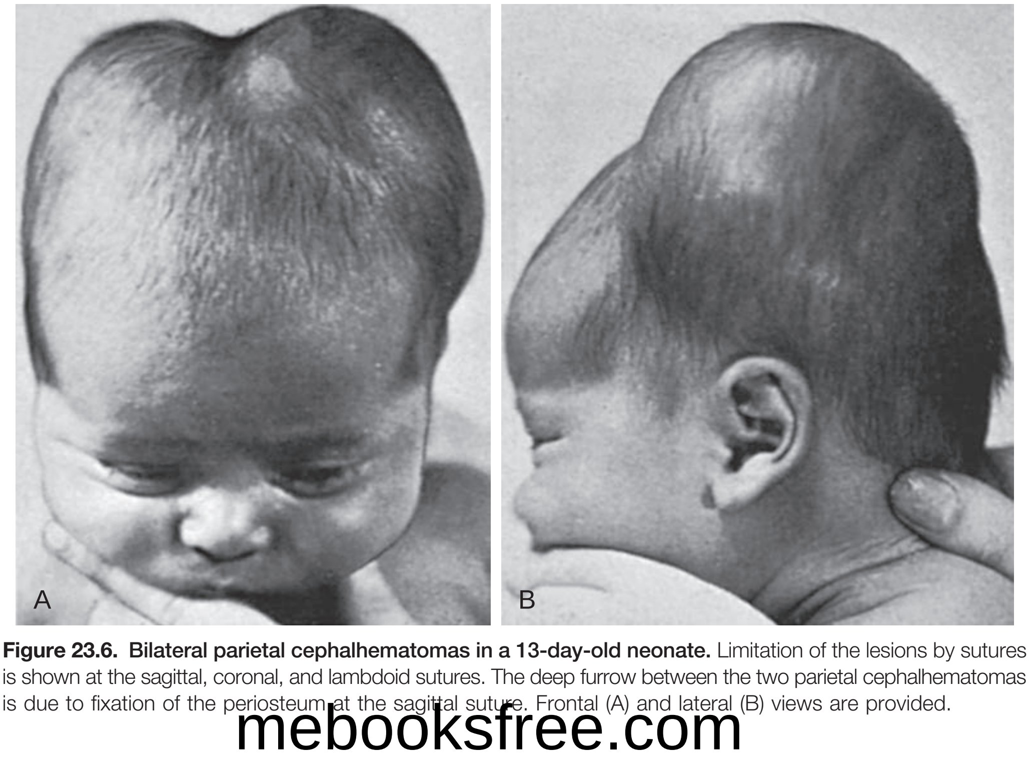

**Figure 23.6. Bilateral parietal cephalhematomas in a 13-day-old neonate.** Limitation of the lesions by sutures is shown at the sagittal, coronal, and lambdoid sutures. The deep furrow between the two parietal cephalhematomas is due to fixation of the periosteum at the sagittal suture. Frontal (A) and lateral (B) views are provided.

lesions often extend over the surface of the affected bone and are sharply limited by the tightly bound periosteum of the sutures. Occipital lesions are common and may be confused with occipital meningoceles during the first days of life. Frontal cephalhematomas are very rare.

The radiographic findings vary with the age of the cephalhematomas. During the first 2 weeks, the lesion is composed of fluid blood (Fig. 23.7). Near the end of the second week, bone begins to form under the elevated periosteum. It appears first at the margins, but soon the entire cephalohematoma is overlaid with a complete shell of bone (see Fig. 23.7; e-Fig. 23.8). Depending on their size, cephalhematomas are absorbed over 2 weeks to 3 months. The radiographic findings can persist long after the clinical signs have disappeared (e-Fig. 23.9). The outer table usually remains thickened as a flat, irregular hyperostosis for several months and is gradually resorbed (e-Fig. 23.10). Fresh cephalhematomas may become infected during bacteremia or needle aspiration.[7] Ultrasonography may be used for early diagnosis, thus avoiding radiation (Fig. 23.11).

In some cases, the space between a new shell of bone and the inner table remains widened for many years, and the space originally occupied by the hematoma becomes filled with normal diploic bone (Fig. 23.12). In other cases, large and small cystlike defects persist in the sites of cephalhematomas (e-Fig. 23.13).[8] Infantile cephalhematoma occasionally persists into adult life, when symptomless large segments of bone production and destruction still may be visible in the calvarium (cephalhematoma deformans) (e-Fig. 23.14).[9] The possibility of a prior neonatal cephalhematoma

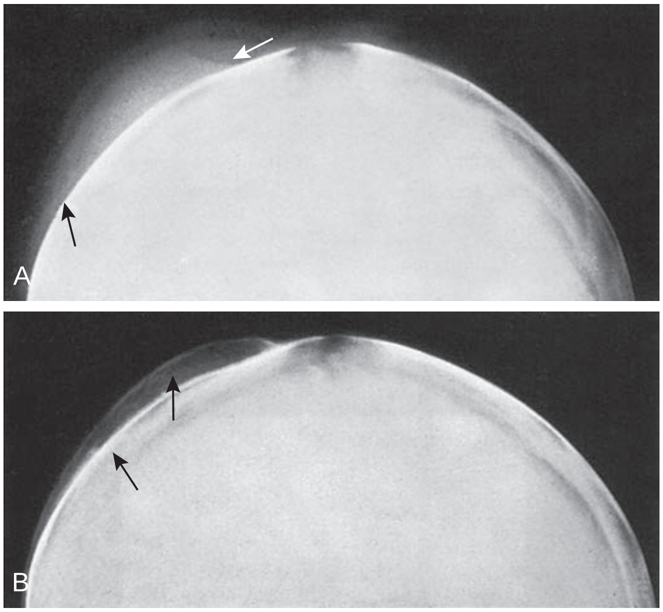

**Figure 23.7. Cephalhematoma in a newborn with scalp deformity.** (A) Rounded soft tissue swelling *(arrows)* of water density over the left parietal bone at age 7 days. (B) The same skull at age 32 days shows a thin shell of newly formed subperiosteal bone *(upper arrow)* overlying the margin of the partially resorbed hematoma *(lower arrow)*.

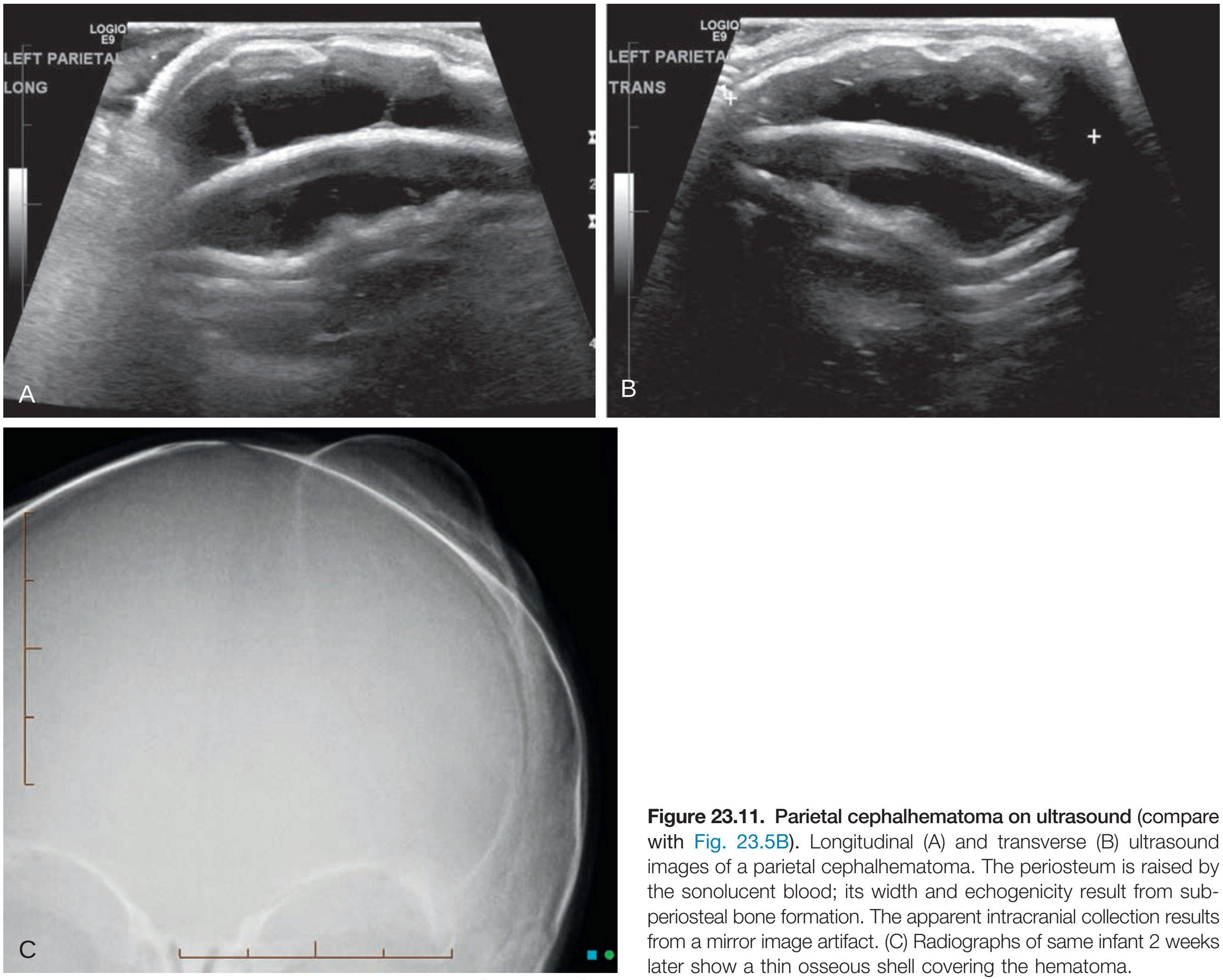

**Figure 23.11. Parietal cephalhematoma on ultrasound** (compare with Fig. 23.5B). Longitudinal (A) and transverse (B) ultrasound images of a parietal cephalhematoma. The periosteum is raised by the sonolucent blood; its width and echogenicity result from subperiosteal bone formation. The apparent intracranial collection results from a mirror image artifact. (C) Radiographs of same infant 2 weeks later show a thin osseous shell covering the hematoma.

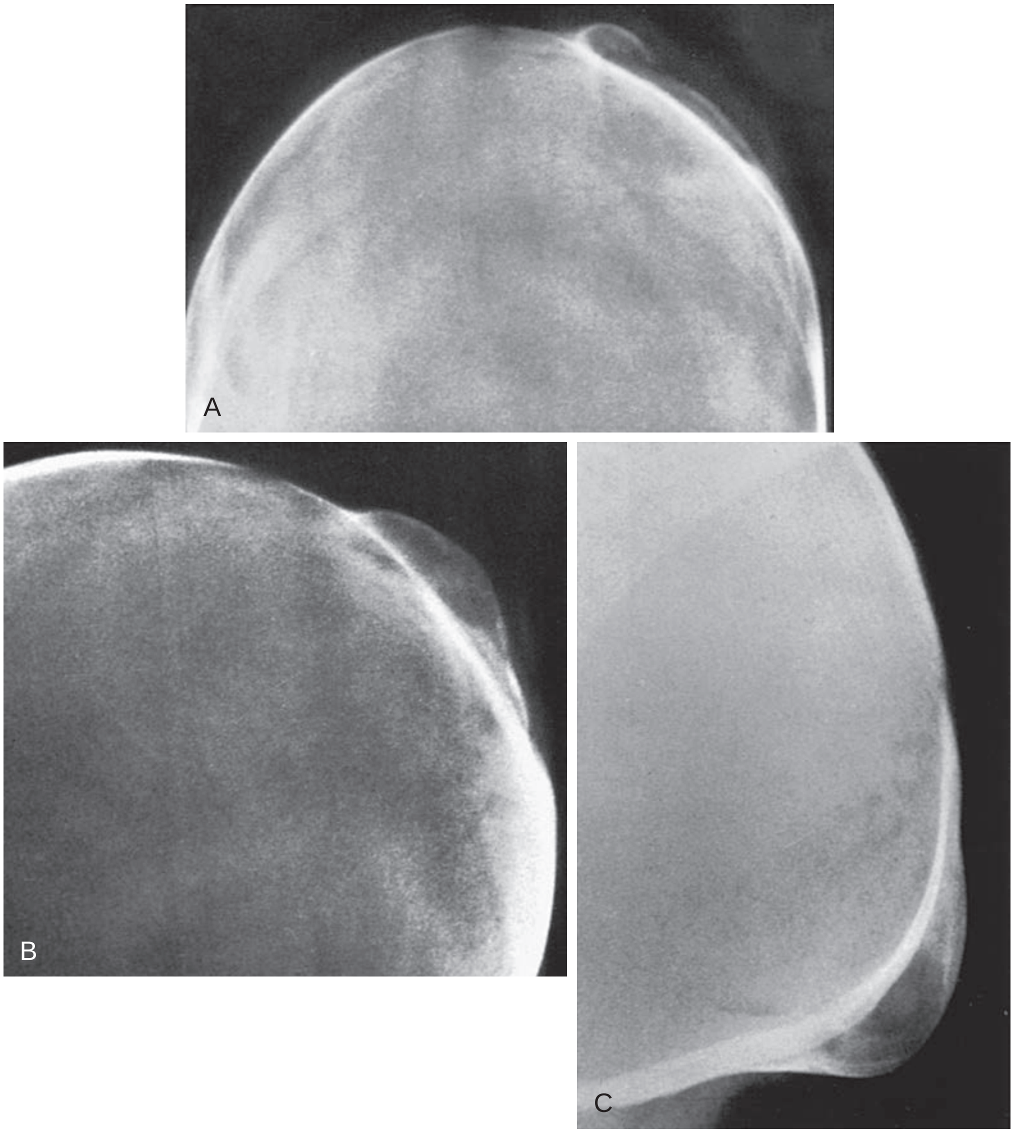

**e-Figure 23.8. Ossifying subperiosteal hematoma in a 6-week-old infant delivered by forceps.** Frontal (A) and lateral (B) projections demonstrate a thin, but incomplete, shell of bone covering the hematoma. (C) An occipital subperiosteal cephalhematoma with a complete, thicker shell of bone over the radiolucent hematoma, which is limited by the mendosal suture.

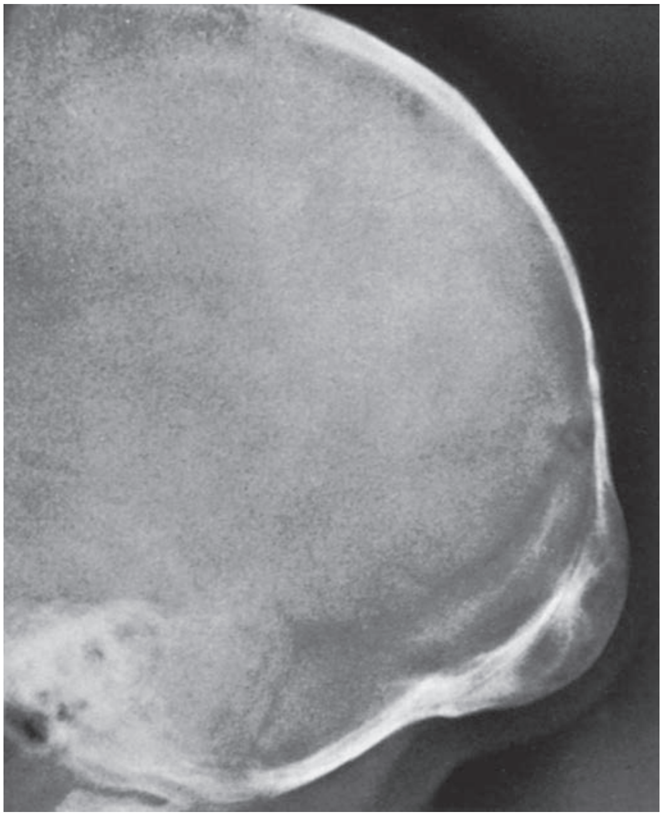

**e-Figure 23.9. An ossifying occipital subperiosteal cephalhematoma in a 4-month-old infant.** The cephalhematoma extends from the lambdoid suture above to the level of the mendosal suture below, which is already fused. The large radiolucent patches beneath the subperiosteal shell of newly formed bone are cast by masses of blood in varying degrees of organization and resorption.

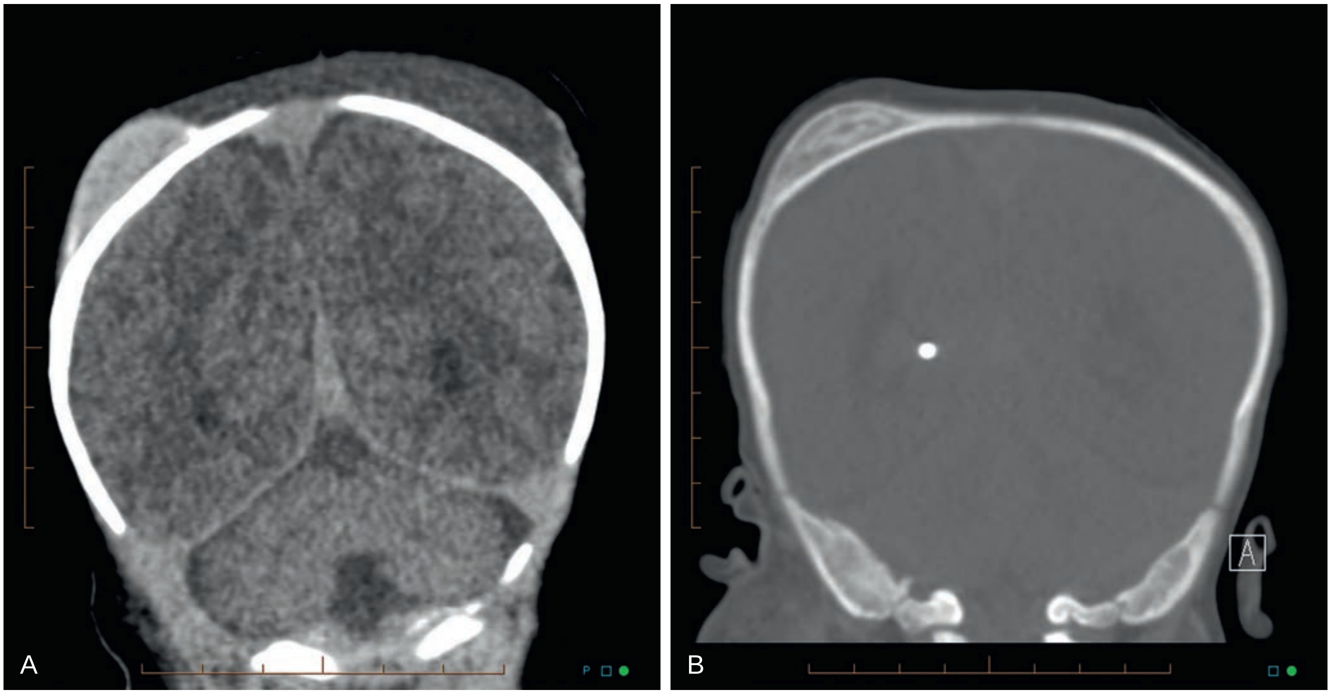

**e-Figure 23.10. Right parietal cephalhematoma and caput succedaneum in a 15-day-old infant with seizures.** (A) Coronal reconstructed CT in soft tissue windows shows a hyperdense right parietal cephalhematoma with bone forming at the margins of the hematoma. (B) Follow up CT 5 months of age after placement of VP shunt reveals diploic bone filling in hematoma with small cystic area.

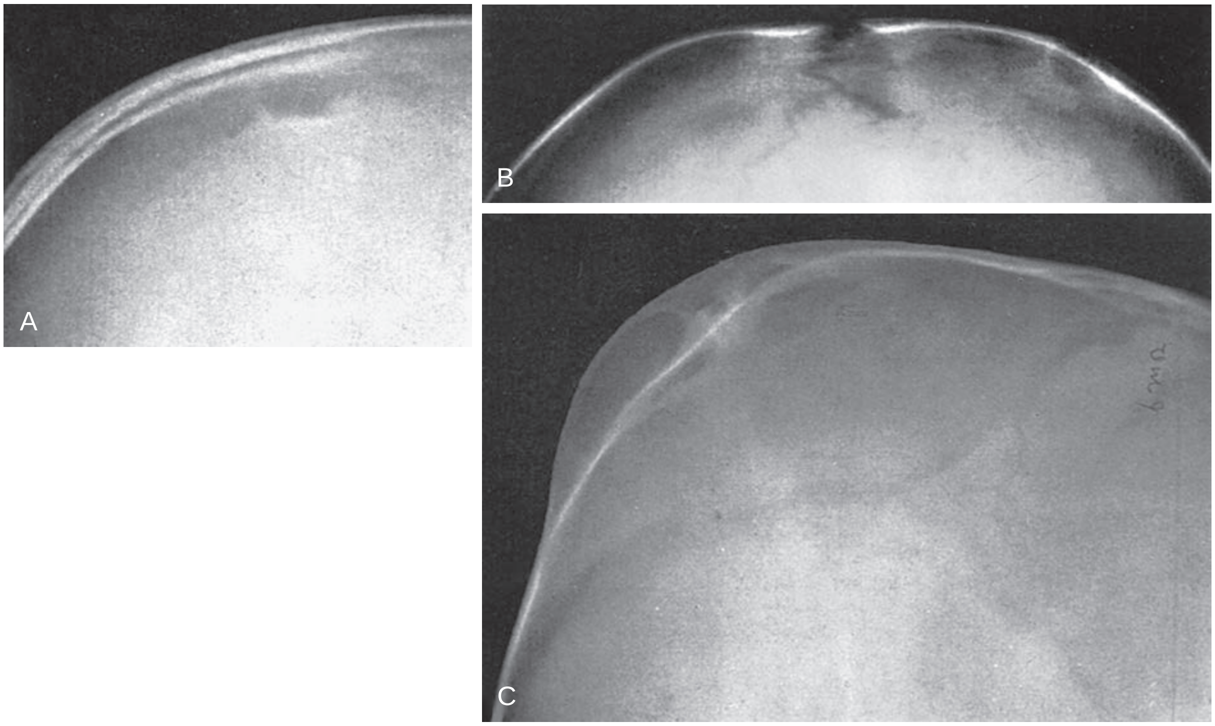

**e-Figure 23.13. Cephalhematoma with cystlike residuals in an 11-month-old infant.** (A) Lateral and (B) frontal projections show a parietal defect with residual thickening. (C) Residual parietal thickening in a different 6-month-old infant reveals large cystlike defects in the area of thickening.

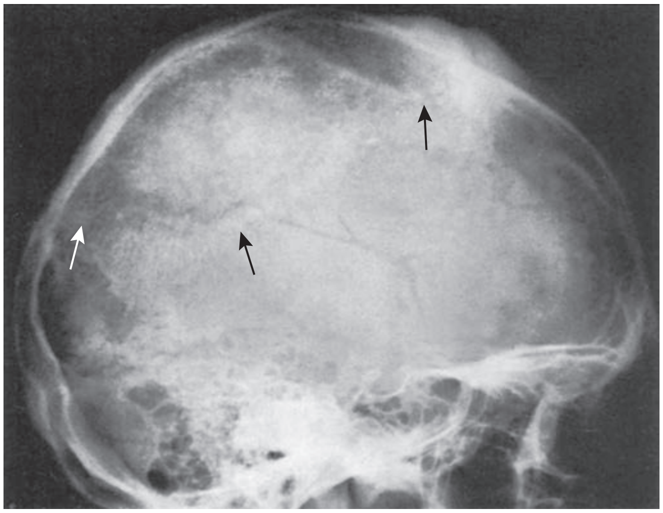

**e-Figure 23.14. Cephalhematoma deformans parietalis in a 20-year-old patient whose cranium was injured when he was 2 years old.** A large segment of one parietal bone is irregularly dense and rarefied *(arrows)*, with a heavy peripheral rim of sclerosis and thickening. *(Courtesy of Juan M. Taveras, MD.)*

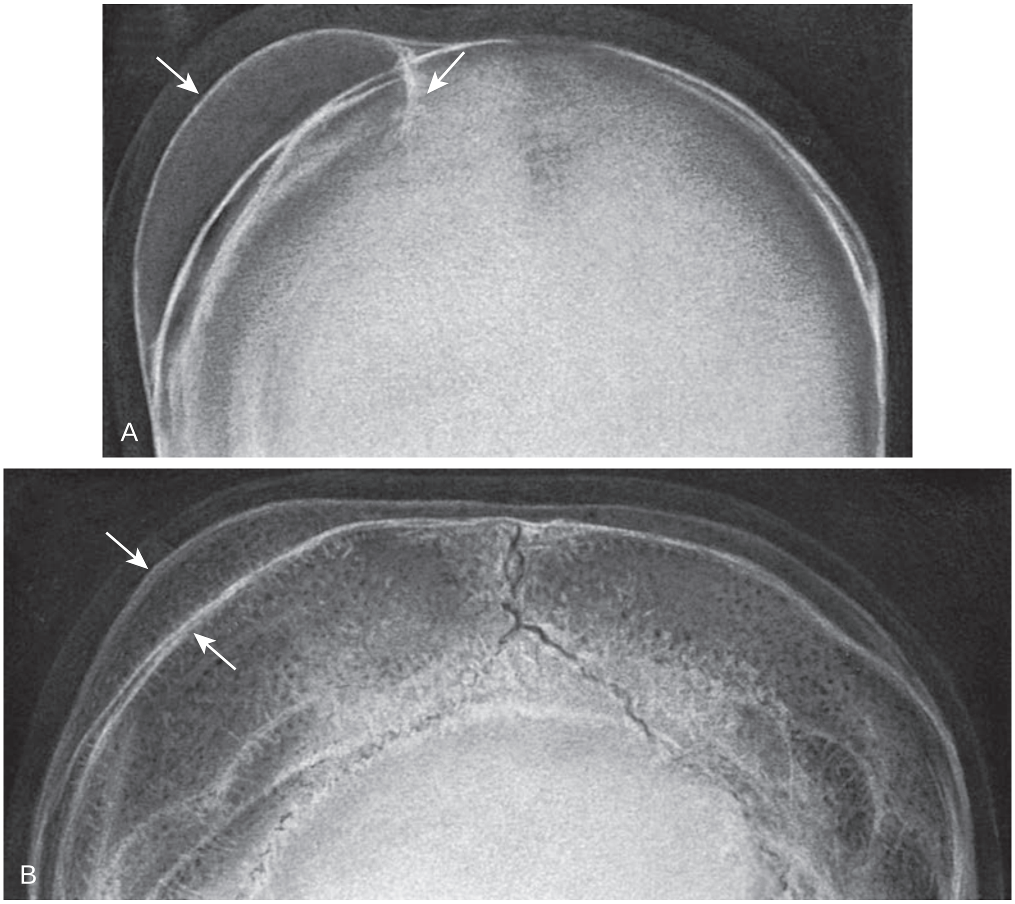

**Figure 23.12. Radiographs show late residual thickening of the calvaria resulting from neonatal cephalhematoma.** (A) At 7 weeks of age, a large right parietal hematoma *(arrows)* is covered by a thin osseous shell. (B) At 3 years and 11 months of age, a widening of the diploic space *(arrows)* is seen where the neonatal hematoma was located.

should be considered in lesions of parietal and occipital bones. To avoid unneeded radiation, history should be obtained before radiographic evaluation.

## CRANIAL FRACTURES

### Neonates

Occasionally, the skull is fractured during delivery. Simple linear or fissure fractures occur commonly and are seen as linear lucencies on radiographs. Basilar fractures are rare. A 12% incidence of skull fractures, all depressed, was reported in a large series of birth-related head injuries.[10] Forceps were used in most of these deliveries, and the fractures were almost all in the parietal and occipital bones. When clinical signs warrant intracranial evaluation, computed tomography (CT) may be used in emergent situations, but magnetic resonance imaging (MRI) will provide more detailed brain evaluation.

### Infants and Children

Skull radiographs have little to offer in nonabusive head trauma. The presence or absence of a fracture has no impact on management.[11–16] In a series of 256 children younger than 5 years who fell out of bed at home or in the hospital, only three skull fractures were found, and clinically these fractures were insignificant.[16] Serious injuries attributed to falls from a bed must be evaluated very carefully for possible child abuse factors.

The major indication for skull radiographs is suspected abuse. A prospective study including more than 7,000 patients suggests that, if certain clinical criteria are present singly or in combination, CT or MRI examination is warranted to evaluate for intracranial injury.[17–23] The selection criteria are (1) unconsciousness or a documented decreasing level of consciousness; (2) a history of a craniotomy with a shunt in place; (3) the probability of a skull depression or identification of a skull depression by probing through a laceration or a puncture wound; (4) blood in the ear or fluid discharge from the ear; (5) CSF discharge from the nose; (6) ecchymosis behind the ear (Battle sign); (7) bilateral orbital ecchymoses; and (8) unexplained focal neurologic signs. If cephalhematoma, drowsiness, and age less than 1 year were added as criteria, no fractures would have been missed.

In a multi-institutional study in which more than 42,000 children with head trauma and a Glasgow Coma Scale score of 14 or 15 were evaluated, a negative predictive value of almost 100% and a sensitivity of greater than 96.8% were found when the criteria in Box 23.1 were absent.

Depressed skull fractures occur most frequently when strong forces are involved, as in vehicular accidents or direct local trauma or after forceps deliveries in the neonate. Many fractures are comminuted and/or complicated by associated lacerations or communication with the nasal or aural cavities. Dural tears are common with depressed fractures, whereas extradural and subdural hematomas are far less common.[10]

When examining young patients with open sutures for potential fractures, it is necessary to remember normal suture variability. Widened sutures may result from long-term prostaglandin $E_1$ administration and during recovery from nutritional deprivation.[24,25] Whether or not the fractures are depressed, they may result in dural sinus tears. The position of the bone edges after trauma may give no indication of how much displacement took place when the fracture occurred. In some cases, especially depressed fractures, the fracture fragments may overlap. CT is the optimal modality for evaluating the depressed fragments and their relation to the underlying brain (Fig. 23.15). Several radiographic features of cranial

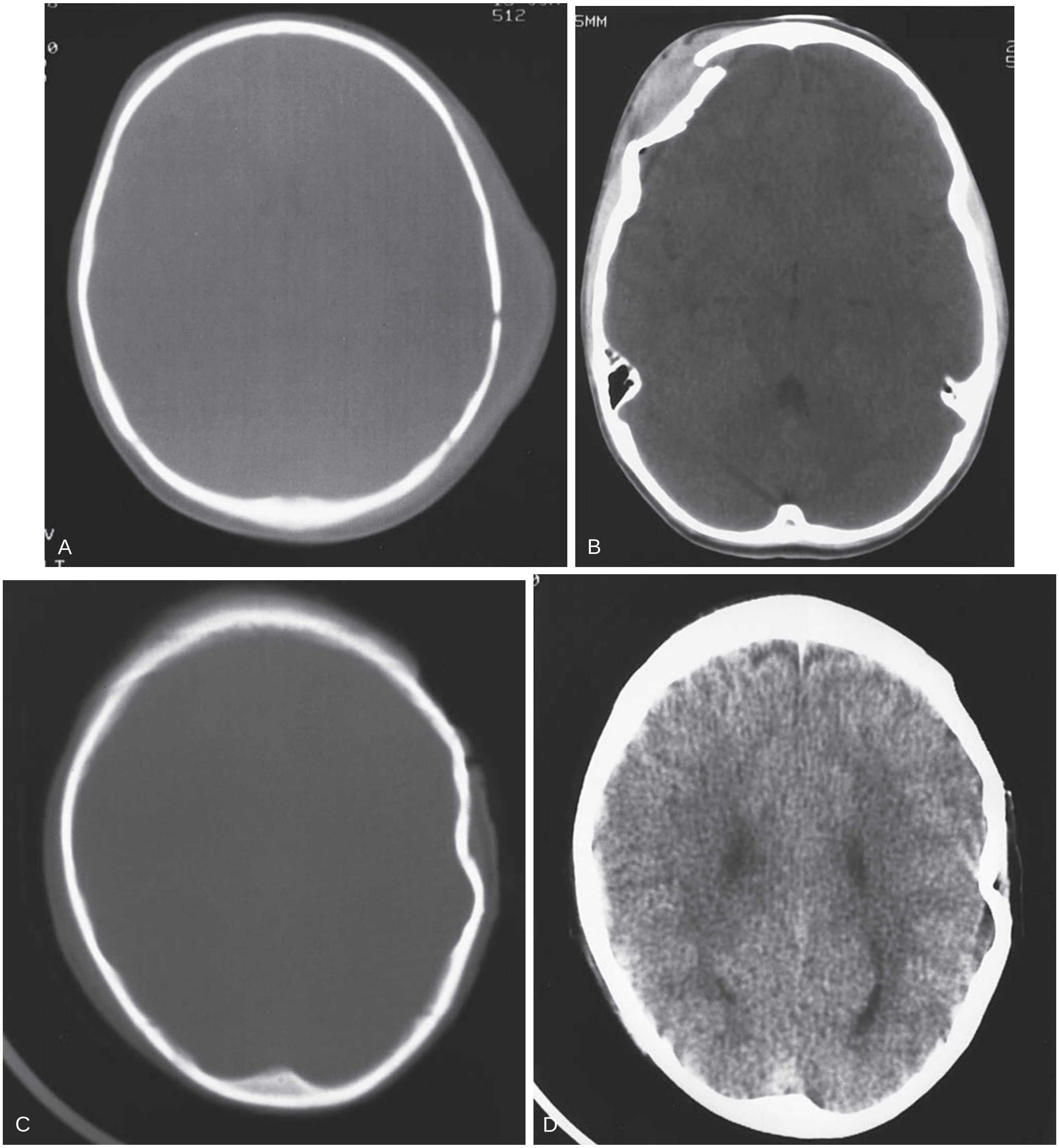

**Figure 23.15. Calvarial and intracranial trauma on CT.** (A) A CT scan with bone windows shows a large soft tissue hematoma and left linear parietal fracture. (B) CT image of another child shows a depressed right frontal fracture with a large external hematoma and a small epidural anteriorly. Bone (C) and brain (D) windows reveal lack of intracranial involvement, but the child has sustained a left parietal fracture and scalp lacerations.

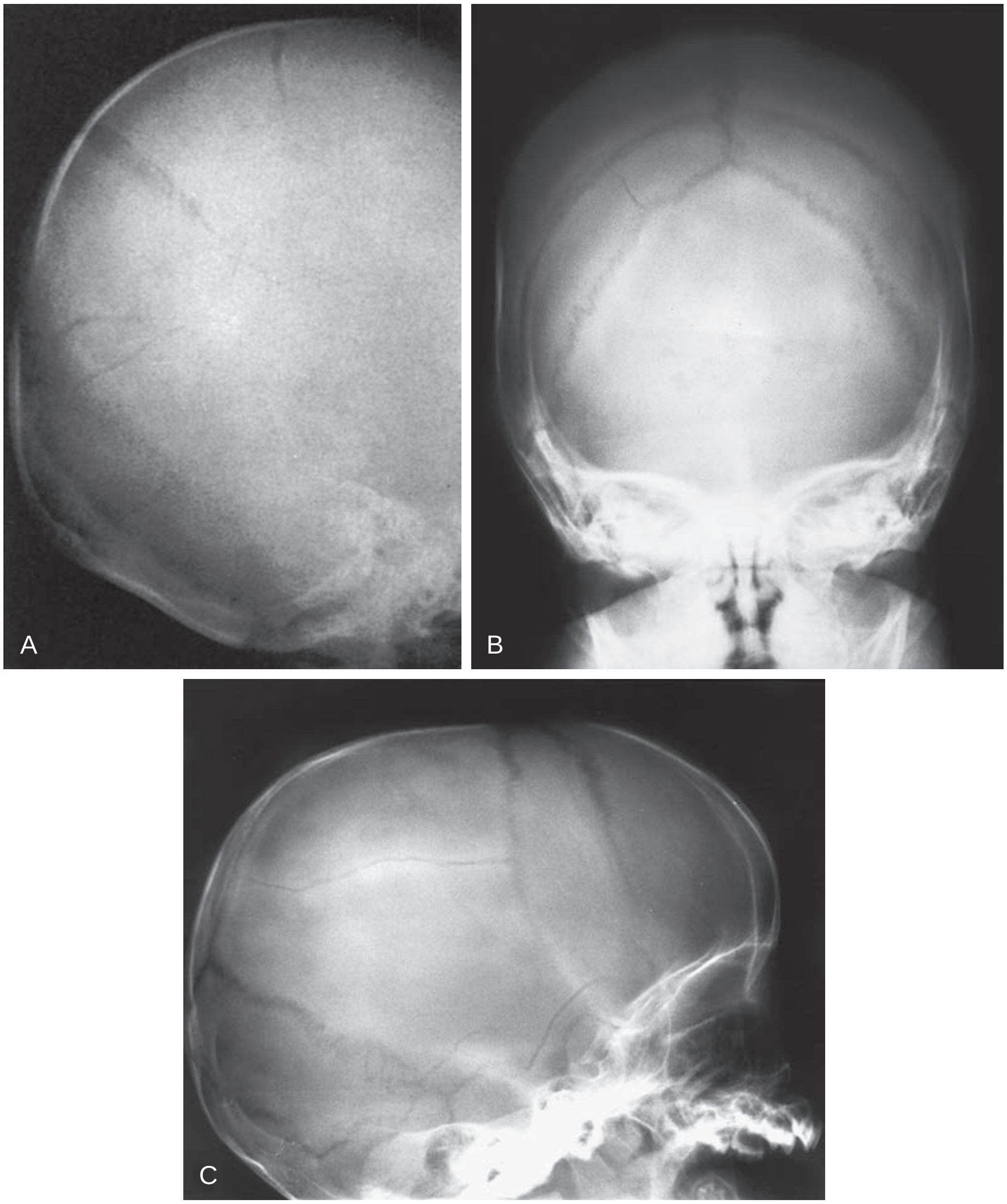

**Figure 23.17. Linear fractures alone and with signs of increased intracranial pressure.** (A) Multiple fractures of the right parietal bone in a 9-month-old infant. (B and C) Linear parietal fracture in another child, who also has diastatic sutures denoting increased intracranial pressure.

fractures are shown in e-Fig. 23.16, Figs. 23.17 through 23.19, and e-Fig. 23.20.

Linear fractures in infants and children generally heal with few or no sequelae. The fracture margins become hazy, and gradually disappear over several months. When comminution has occurred, bone may be resorbed locally, leaving a defect. If the dura has been disrupted at the time of the fracture, the edges of the fracture may separate allowing the local leakage of CSF and formation of a leptomeningeal cyst.[26,27] Cysts are thought to be most common in fractures involving sutures. Further, associated widening of one coronal suture has been reported after vacuum extraction when cup placement was too anterior.[28]

By transmitting the pulsations of the brain, the cyst causes pressure atrophy of bone unprotected by dura, and a large defect may develop after many months or years (Figs. 23.21 and 23.22). Progressive enlargement of the calvarial defect has given rise to the term "growing fracture." Scalloped defect margins results from differential erosion of inner and outer tables.

Gas may accumulate in scalp soft tissues contiguous to fractures, often through breaks in the paranasal sinuses or mastoid air cells. If air escapes from the sinuses into the subaponeurotic space of the scalp, the result is called extracranial traumatic pneumocephalus. Air also may leak into the cranial cavity, causing internal pneumocephalus.

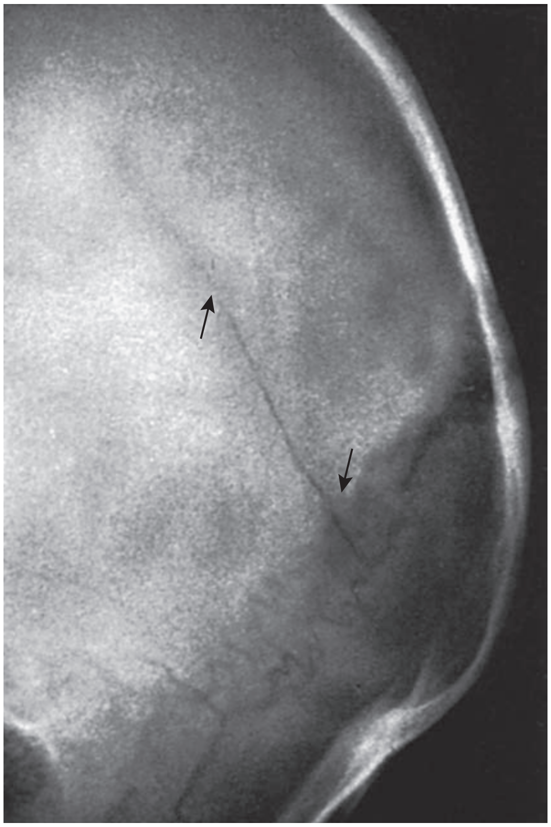

**e-Figure 23.16.** A fine linear fracture of the parietal bone *(arrows)* in a 15-month-old infant who fell from a highchair.

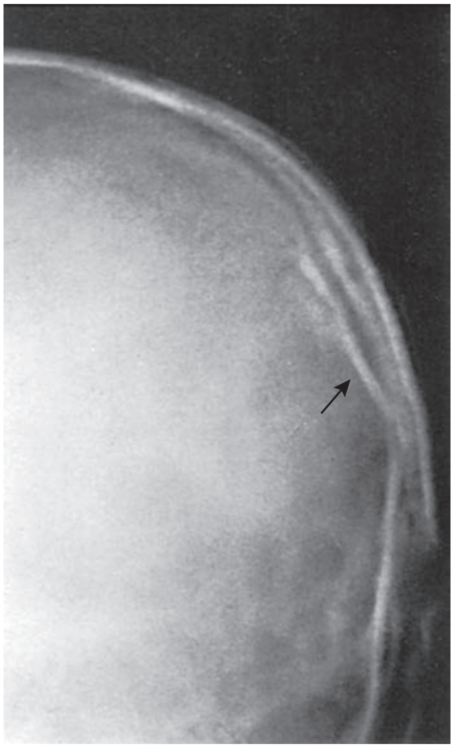

**e-Figure 23.20. Depressed parietal fracture in a 7-year-old girl with plagiocephaly.** The left calvarium is smaller than the right due to a fracture that caused hypoplasia and flattening of the left producing a segment of inner table of the smaller parietal bone that is central to the larger right parietal bone.

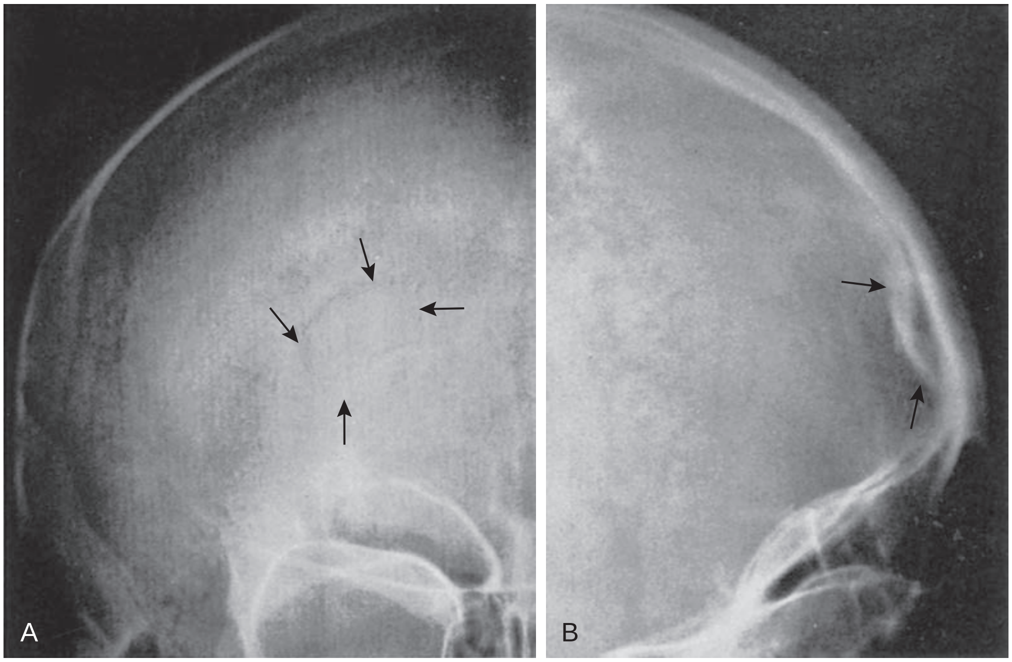

**Figure 23.18. Depressed fracture of the frontal bone in a 9-year-old child.** (A) A radiograph shows fracture *(arrows)*. In the medial inferior segment, the arcuate shadow of diminished density is replaced by a curved linear shadow of increased density that is caused by overlapping of bone fragments. (B) Lateral projection demonstrating the depression of the calvarial tables *(arrows)*.

**BOX 23.1** Criteria for Head Computed Tomography in Children With a Glasgow Coma Scale Score of 14

**A. <2 YEARS OLD**

1. Altered mental status
2. Palpable skull fracture
3. Occipital, parietal, or temporal scalp hematoma
4. Loss of consciousness >5 seconds
5. Severe mechanism of injury
6. Not acting normally, per parent

**B. >2 YEARS OLD**

1. Altered mental status
2. Signs of basilar skull fracture
3. Loss of consciousness
4. Vomiting
5. Severe mechanism of injury
6. Severe headache

*Modified from Kuppermann N, Holmes JF, Dayan PS, et al. Identification of children at very low risk of clinically important brain injuries after head trauma: a prospective cohort study.* Lancet. *2009;374:1160–1170.*

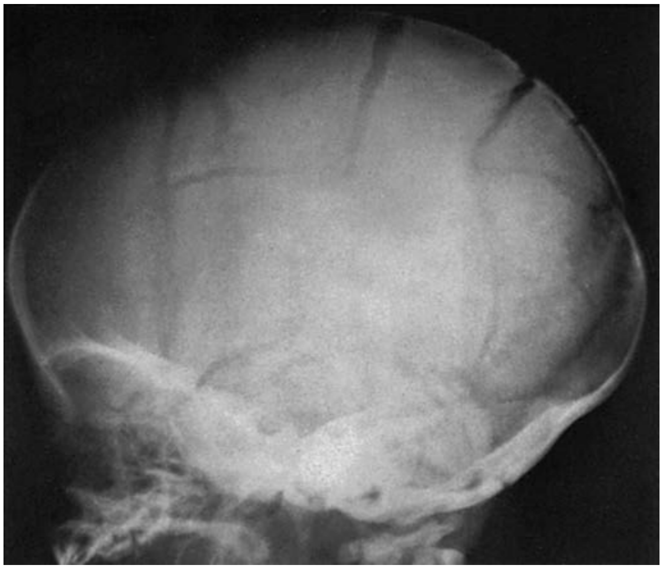

**Figure 23.19. Comminuted diastatic fractures in a 2-month-old infant due to nonaccidental trauma.** Comminuted diastatic fractures of the parietal bones are shown. Both ocular fundi contained retinal hemorrhages, and bilateral subdural hematomas were noted.

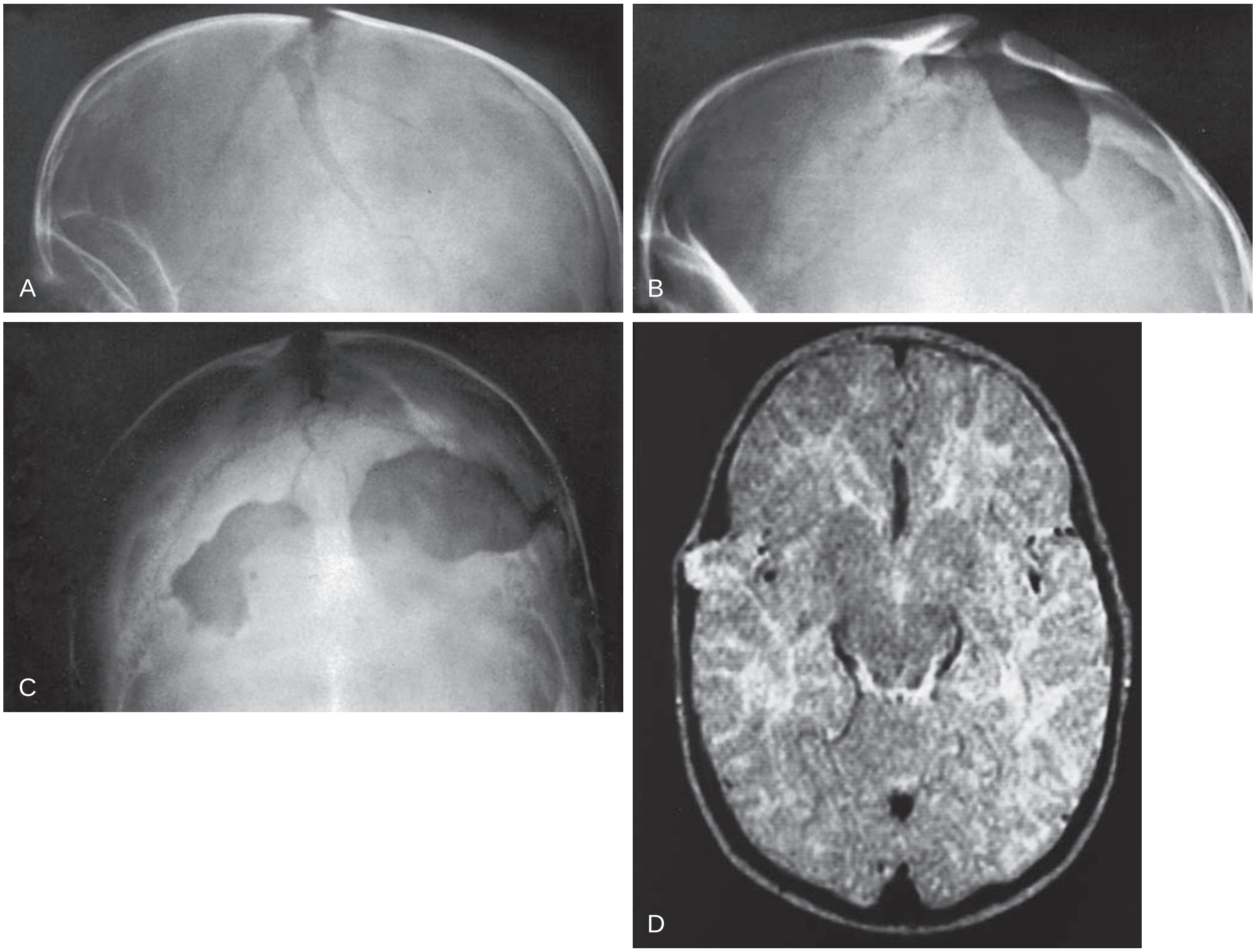

**Figure 23.21. A pulsating leptomeningeal cyst with residual bilateral large defects in the calvaria.** (A) Diastatic bilateral comminuted parietal fractures after a head injury during infancy. Lateral (B) and frontal (C) projections 5 years later show large bilateral defects in the sites of the earlier parietal fractures. At surgery, the dura beneath the fractures was torn. The bone on the margins of the defect is sclerotic and thickened. (D) Magnetic resonance imaging in another child with a leptomeningeal cyst reveals herniation of the brain outward in the right parietal region. *(A, B, and C, Courtesy of Walter E. Berdon, MD.)*

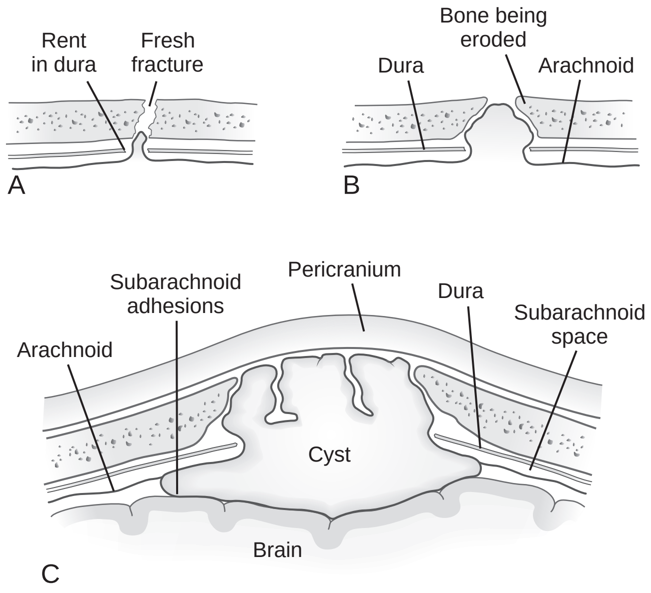

**Figure 23.22. Schematic representation of leptomeningeal cyst formation.** (A) Immediately after an injury occurs, fresh parietal bone fractures, fresh dural rents, and early protrusion of the arachnoid membrane through the fracture are seen. (B) Lateral marginal erosion of bone and widening of the dural defect. (C) Later incomplete cyst formation in the arachnoid due to adhesions, depression, and pressure atrophy of the underlying brain and leptomeninges and increases the defect. *(Courtesy of Juan M. Taveras, MD.)*

## KEY POINTS

- Cranial fractures seldom correlate with the clinical situation or management except in child abuse.
- Plain skull radiographs have little to offer in the management of pediatric nonabusive head trauma.
- Leptomeningeal cyst (i.e., a growing fracture of childhood) is uncommon after 5 years of age.

## SUGGESTED READINGS

Chadwick LM, Pemberton PJ, Kurinczuk JJ. Neonatal subgaleal haematoma: associated risk factors, complications and outcome. *J Paediatr Child Health*. 1996;32:L228–L232.

Masters SJ, McClean PM, Arcarese JS, et al. Skull x-ray examinations after head trauma: recommendations by a multidisciplinary panel and validation study. *N Engl J Med*. 1987;316:84–91.

Oman JA, Cooper RJ, Holmes JF, et al. Performance of a decision rule to predict need for computed tomography among children with blunt head trauma. *Pediatrics*. 2006;117:e238–e246.

## REFERENCES

Full references for this chapter can be found on www.expertconsult.com.

## REFERENCES

1. Axton JHM, Levy LF. Congenital moulding depressions of the skull. *BMJ*. 1965;1:1644–1647.
2. Schrager GO. Elevation of depressed skull fracture with a breast pump. *J Pediatr*. 1970;77:300–301.
3. Amin AA, Al-Zeky AM, El-Azm M. Vacuum extraction as a treatment modality of neonatal skull depression in a twin infant. *Saudi Med J*. 2007;28(7):1122–1124.
4. Chadwick LM, Pemberton PJ, Kurinczuk JJ. Neonatal subgaleal haematoma: associated risk factors, complications and outcome. *J Paediatr Child Health*. 1996;32:32L228.
5. Kendall N, Woloshin H. Cephalhematoma associated with fracture of the skull. *J Pediatr*. 1952;41:125–132.
6. Zelson C, Lee SJ, Pearl M. The incidence of skull fractures underlying cephalhematomas in newborn infants. *J Pediatr*. 1974;85:371–373.
7. Chan MSM, Wong YC, Lau SPC, et al. MRI and CT findings of infected cephalhaematoma complicated by skull vault osteomyelitis, transverse venous sinus thrombosis and cerebellar haemorrhage. *Pediatr Radiol*. 2002;32:376–379.
8. Chorobski J, Davis L. Cyst formation of the skull. *Surg Gynecol Obstet*. 1934;58:12–31.
9. Schüller A, Morgan F. Cephalhematoma deformans: late developments of infantile cephalhematoma. *Surgery*. 1946;19:651–660.
10. Harwood-Nash DC, Hendrick EB, Hudson AR. The significance of skull fractures in children: a study of 1,187 patients. *Radiology*. 1971;101:151–155.
11. Lloyd DA, Carty H, Patterson M, et al. Predictive value of skull radiography for intracranial injury in children with blunt head injury. *Lancet*. 1997;349:821–824.
12. Frush DP, O'Hara SM, Kliewer MA. Pediatric imaging perspective: acute head trauma—is the skull radiography useful? *J Pediatr*. 1998;132:553–554.
13. Leonidas JC, Ting W, Binkiewicz A, et al. Mild head trauma in children: when is a roentgenogram necessary? *Pediatrics*. 1982;69:139–143.
14. Lloyd DA. Skull radiographs and children with blunt head injury. *Br J Surg*. 1998;85:580–581.
15. Masters SJ, McClean PM, Arcarese JS, et al. Skull x-ray examinations after head trauma: recommendations by a multidisciplinary panel and validation study. *N Engl J Med*. 1987;316:84–91.
16. Helfer RE, Slovis EL, Black M. Injuries resulting when small children fall out of bed. *Pediatrics*. 1977;60:533–535.
17. Haydel MJ. Clinical decision instruments for CT scanning in minor head injury. *JAMA*. 2005;294:1551–1553.
18. Klassen TP, Reed MH, Stiell IG, et al. Variation in utilization of computed tomography scanning for the investigation of minor head trauma in children: a Canadian experience. *Acad Emerg Med*. 2000;7:739–744.
19. Oman JA, Cooper RJ, Holmes JF, et al. Performance of a decision rule to predict need for computed tomography among children with blunt head trauma. *Pediatrics*. 2006;117:e238–e246.
20. Palchak MJ, Holmes JP, Vance CW, et al. Does an isolated history of loss of consciousness or amnesia predict brain injuries in children after blunt head trauma? *Pediatrics*. 2004;113:e507–e513.
21. Schutzman SA, Barnes P, Duhaime AC, et al. Evaluation and management of children younger than two years old with apparently minor head trauma: proposed guidelines. *Pediatrics*. 2001;107:983–993.
22. Smits M, Dippel DWJ, de Haan GG, et al. External validation of the Canadian CT head rule and the New Orleans criteria for CT scanning in patients with minor head injury. *JAMA*. 2005;294:1519–1525.
23. Stiell IG, Clement CM, Rowe BH, et al. Comparison of the Canadian CT head rule and the New Orleans criteria in patients with minor head injury. *JAMA*. 2005;294:1511–1518.
24. Beitzke A, Stein J. Pseudo-widening of cranial sutures as a feature of long-term prostaglandin E1 therapy. *Pediatr Radiol*. 1986;16:57–58.
25. Capitanio MA, Kirkpatrick JA. Widening of the cranial sutures: a roentgen observation during periods of accelerated growth in patients treated for deprivation dwarfism. *Radiology*. 1969;92:53–59.
26. Roy S, Sarkar C, Tandon PN, et al. Cranio-cerebral erosion (growing fracture of the skull in children), Part I: pathology. *Acta Neurochir*. 1987;87:112–118.
27. Tandon PN, Banerji AK, Bhatia R, et al. Cranio-cerebral erosion (growing fracture of the skull in children), Part II: clinical and pathological observations. *Acta Neurochir*. 1987;88:1–9.
28. Hansen KN, Pedersen H, Pedersen MB. Growing skull fracture—rupture of coronal suture caused by vacuum extraction. *Neuroradiology*. 1987;29:502.

# 24

# Embryology and Brain Development

*Marvin D. Nelson Jr.*

The human brain undergoes four phases of development: (1) dorsal induction (primary and secondary neurulation), (2) ventral induction (patterning of the forebrain), (3) neuronal proliferation and migration, and (4) myelination. During the third week of embryogenesis, initiation of the central nervous system evolves with the development of the notochordal process. This derivative of ectoderm grows rapidly in length so that by 20 days it is converted from a hollow tube to a solid rod—the notochord (Fig. 24.1; e-Table 24.1). The notochord works with the axial mesoderm to induce the neural plate. The neuroepithelium of the neural plate begins the formation of the brain and spinal cord. It appears initially at the cranial end of the embryo and differentiates craniocaudally. At the beginning of the fourth week, the neural plate is composed of a broad cranial portion and a narrow caudal portion—the fetal brain and spinal cord.

## DORSAL INDUCTION

The process of neurulation or formation of the neural tube occurs when the lateral edges of the neural plate elongate to become neural folds and join together in the midline to form the neural tube (Fig. 24.2).[1] The process starts in the craniocervical region and proceeds superiorly and inferiorly. The space within the neural tube, the neural canal, initially is open at the cranial (or rostral) and caudal ends (cranial and caudal neuropores), which communicates with the amniotic cavity. The neuropores gradually decrease in size and close between the 24th and 26th day.[1] The lowest portion of the spinal cord, the inferior sacral and coccygeal levels, are formed by a different process called *secondary neurulation* (see Chapter 40). Pluripotent tissue within the caudal eminence forms a solid neural cord; this neural cord forms a lumen that fuses with the caudal end of the neural tube to form a portion of the conus medullaris and the filum terminale (e-Fig. 24.3). This secondary process is not completed until the eighth week after fertilization of the ovum.[1]

Some neural crest cells (the population of neural cells arising at the lateral edge of the neural plate during neural tube formation) detach during neurulation and form many different tissues (e.g., melanocytes and chromaffin cells of the adrenal medulla), including the major components of the peripheral and autonomic nervous system (e-Fig. 24.4).[1]

## VENTRAL INDUCTION

The prechordal plate cephalic to the neural tube and notochord induces this stage of development. The three major divisions of the brain—the prosencephalon or forebrain, mesencephalon or midbrain, and rhombencephalon or hind brain—are more clearly differentiated during the rostral expansion of the neural tube (the formation of the primary brain vesicles).[1,2] During the fourth and fifth weeks, a series of brain flexures occur in the midbrain, cervical, and later pontine regions so that by the end of the fifth week, five secondary brain vesicles are present (Fig. 24.5). With further development, the prosencephalon becomes subdivided into the telencephalon and the diencephalon. The rhombencephalon subdivides into the metencephalon and myelencephalon. The mesencephalon does not divide. Within each of these five vesicles, the neural canal expands into a primary ventricle. The central canal of the spinal cord is continuous with the brain ventricles. The fate of these structures is shown in Fig. 24.5. The cranial nerve nuclei appear in the brainstem during the fifth week (see the next section).[1,2]

## NEURONAL PROLIFERATION AND MIGRATION

During the period of morphologic development of the brain, cytodifferentiation occurs. Formation of the cerebral neocortex is a complex process with proliferation, migration, and differentiation varying in time from one site to another. Several patterns of neuronal migration occur, including (1) radial migration along the path of radial glial cells from the ventricles toward the surface and (2) tangential migration along transverse surfaces (e-Fig. 24.6).[1–3]

Although details of the migration process vary for each region of the brain, general principles include the following: (1) the ultimate migration is from deep (ventricle) to superficial regardless of trajectory differences; (2) the migration establishes layers of the cortex (Figs. 24.7 and 24.8); and (3) neurons of each later wave of migration pass through the preceding layers to form a more superficial layer.[4]

During the 10th to 20th weeks of gestation, neuronal genesis occurs. The proliferative cells of the ventricular zone (also known as *germinal matrix*) form waves of migrating neuroblasts that pass through the intermediate zone to form the cortical subplate. Each new layer migrates through the preceding layer to become more superficial. The mature cortex has six layers, and neuronal migration concludes between 20 and 24 weeks' gestation.

The subplate and cortical plate form the cortex, whereas the intermediate zone becomes white matter (see Fig. 24.7). The germinal matrix also produces the glial cells, that is, astrocytes and oligodendrocytes.[4] The microglial cells are of mesodermal origin and are the resting tissue histiocytes of the brain. In contrast to cortical migration, glial cell migration and differentiation continues for more than 1 year after birth.[4]

Excessive cells of the fetal neurosystem ranging from 30% to 70% are produced when compared with the number of mature cells. These "surplus" cells undergo programmed death or apoptosis if they are not utilized.

The steps of neurulation, cell proliferation, and migration are induced by multiple neurotransmitters, and genes controlling these transmitters have been identified.[5]

The brainstem and spinal cord are similar in development. Two basal (ventral) columns and two alar (dorsal) columns are formed. These columns form a dorsal sensory and ventral motor configuration and are found in both the brainstem and spinal cord. The cranial nerves IX through XII come from the myelencephalon (medulla) and cranial nerves IV through VII from the metencephalon (pons) (see Fig. 24.5). The pons is largely composed of white matter tracts of the cerebellum. The cerebellum is also derived from the metencephalon (see Fig. 24.5).

## Abstract:

This chapter reviews what we know about the process of normal development of the human brain.

## Keywords:

Brain
Development
Normal
Embryology
Central Nervous System

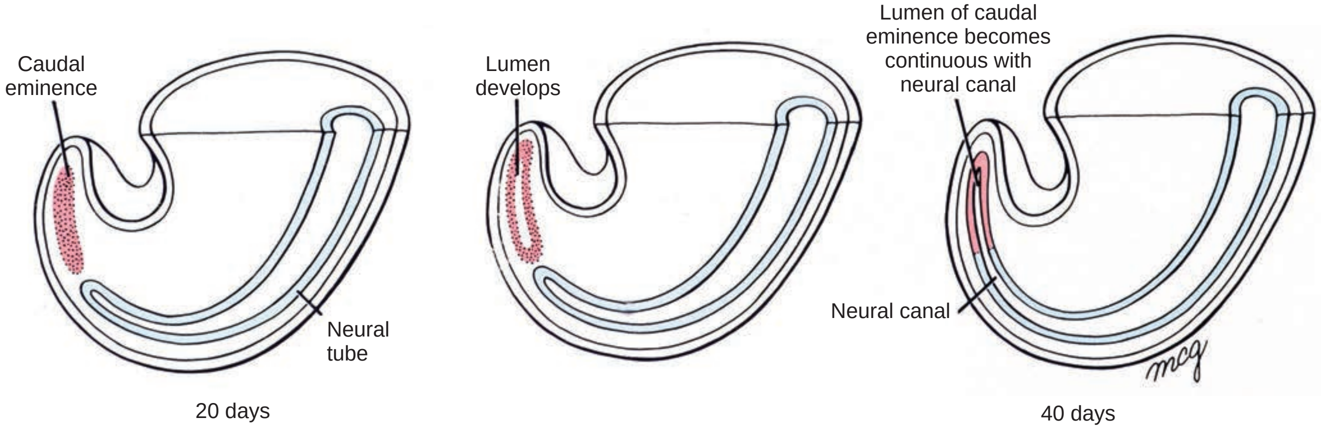

**e-Figure 24.3. Secondary neurulation and formation of the neural tube inferior to the second sacral level.** Mesoderm invading this region during gastrulation condenses into a solid rod called the *caudal eminence*, which later develops a lumen. At the end of the sixth week, this structure fuses with the neural tube. *(From Larsen WJ.* Human Embryology. *2nd ed. New York: Churchill Livingstone; 1997.)*

**e-TABLE 24.1** Schematic Chronology of the Major Events During Human Neocortical Development

| Event | Time Event Occurs |
|---|---|
| Neuroectoderm induction | Third GW |
| Neurulation | Third to end of fourth GW |
| Proencephalic and hemispheric formation | Fifth to tenth GW |
| Neuronal proliferation | Tenth to twentieth GW |
| Neuronal migration | Twelfth to twenty-fourth GW |
| Programmed neuronal cell death | Twenty-eighth to forty-first GW |
| Neurogenesis | Fifteenth to twentieth GW to well into postnatal months or years |
| Synaptogenesis | Twentieth GW to puberty |
| Gliogenesis | Twenty to twenty-fourth GW to well into postnatal years |
| Myelination | Twenty-sixth to twenty-eighth GW to 2 to 3 postnatal years |
| Angiogenesis | Fifth to tenth GW to well into postnatal years |

*GW,* Gestational week.
*From Gressens P, Helppi PS. Normal and abnormal brain development. In Martin R, Fanaroff A, Walsh M, eds.* Neonatal-Perinatal Medicine. *8th ed. Philadelphia: Elsevier Mosby; 2005.*

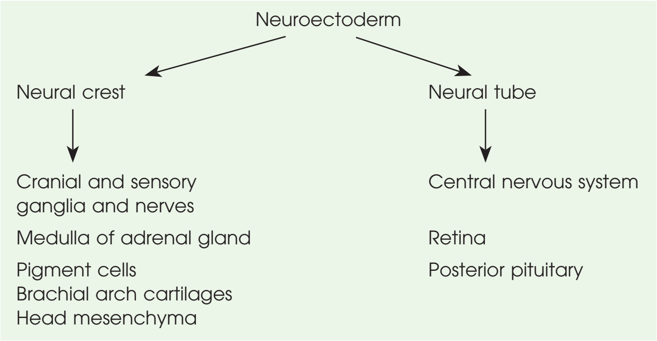

From Moore KL: *The developing human*, ed. 4, Philadelphia, 1988, WB Saunders.

**e-Figure 24.4. Neuroectoderm derivatives.** *(From Moore KL.* The Developing Human*. 4th ed. Philadelphia: WB Saunders, 1999.)*

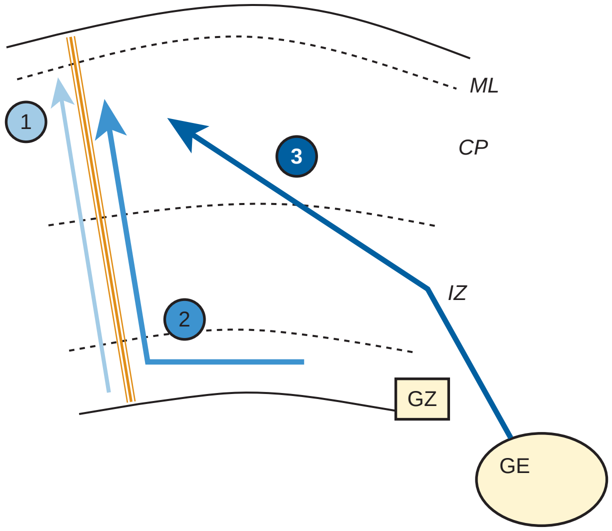

**e-Figure 24.6. Schematic representation of the different neuronal migratory pathways.** *1,* Radial migration along radial glial cell guides of neurons originating from the periventricular germinative zone *(GZ). 2,* Tangential migration in the GZ followed by a radial migration along glial guides. *3,* Tangential migration in the intermediate zone (*IZ,* prospective white matter) of neurons originating from the ganglionic eminence (GE). *CP,* Cortical plate; *ML,* molecular layer. *(From Martin RJ, Fanaroff AA, Walsh MC, eds.* Fanaroff and Martin's Neonatal Perinatal Medicine*. 8th ed. Philadelphia: Mosby Elsevier; 2006.)*

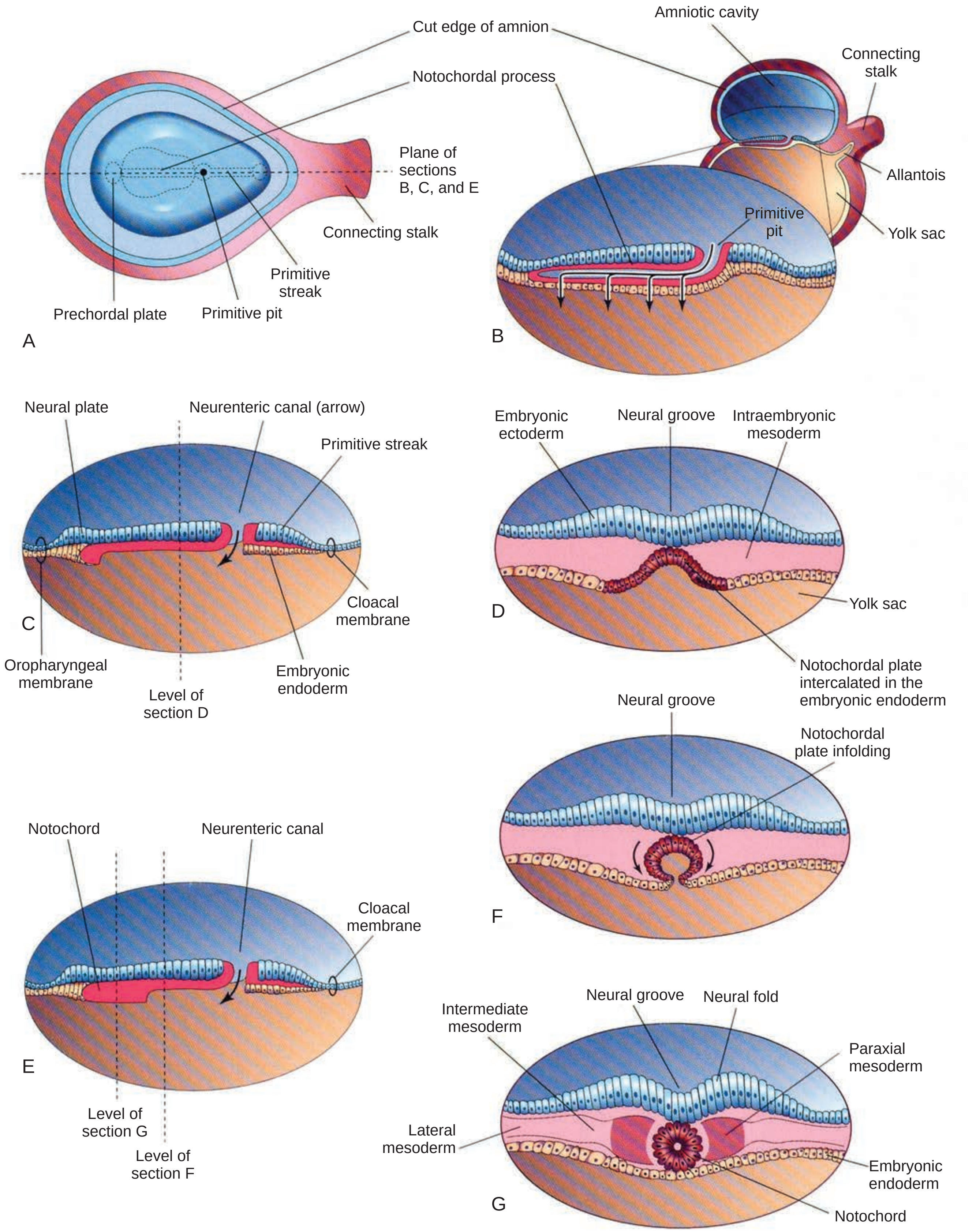

**Figure 24.1. Development of the notochord by transformation of the notochordal process.** (A) Dorsal view of the embryonic disc (about 18 days), exposed by removing the amnion. (B) Three-dimensional median section of the embryo. (C and E) Similar sections of slightly older embryos. (D, F, and G) Transverse sections of the trilaminar embryonic disc shown in (C) and (E). *(From Moore KL, Persaud TVN.* Before We Are Born. *5th ed. Philadelphia: WB Saunders; 1998.)*

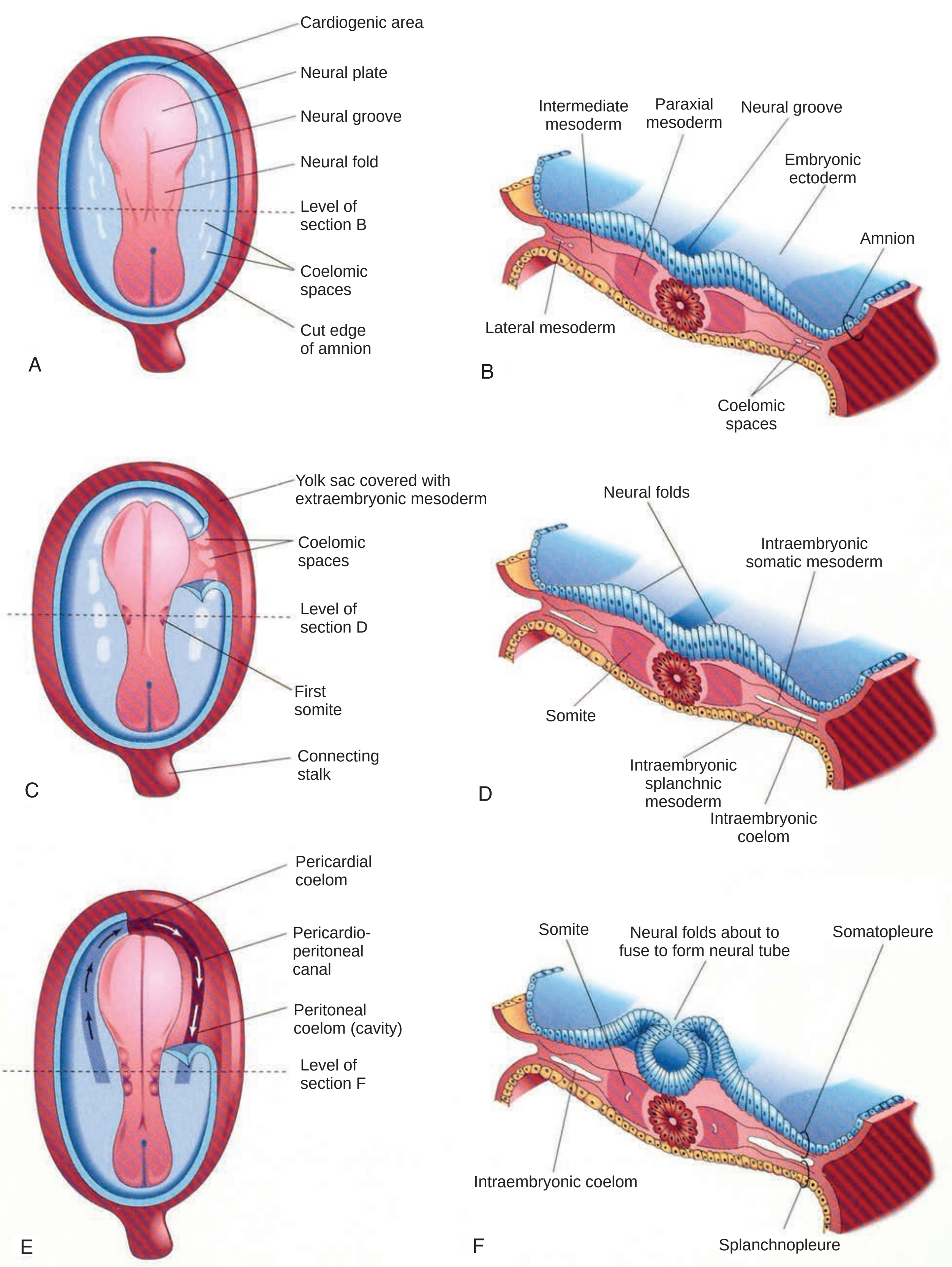

**Figure 24.2. Drawings of embryos of 19 to 21 days, illustrating development of the somites and intraembryonic coelom.** (A, C, and E) Dorsal view of the embryo, exposed by removal of the amnion. (B, D, and F) Transverse sections through the embryonic disc at the levels showing. (A) Presomite embryo of about 18 days. (C) An embryo of about 20 days, showing the first pair of somites. A portion of the somatopleure on the right has been removed to show the isolated coelomic spaces in the lateral mesoderm. (E) A three-somite embryo (about 21 days) showing the horseshoe-shaped intraembryonic coelom, exposed on the right by removal of a portion of the somatopleure. *(From Moore KL, Persaud TVN.* Before We Are Born. *5th ed. Philadelphia: WB Saunders; 1998.)*

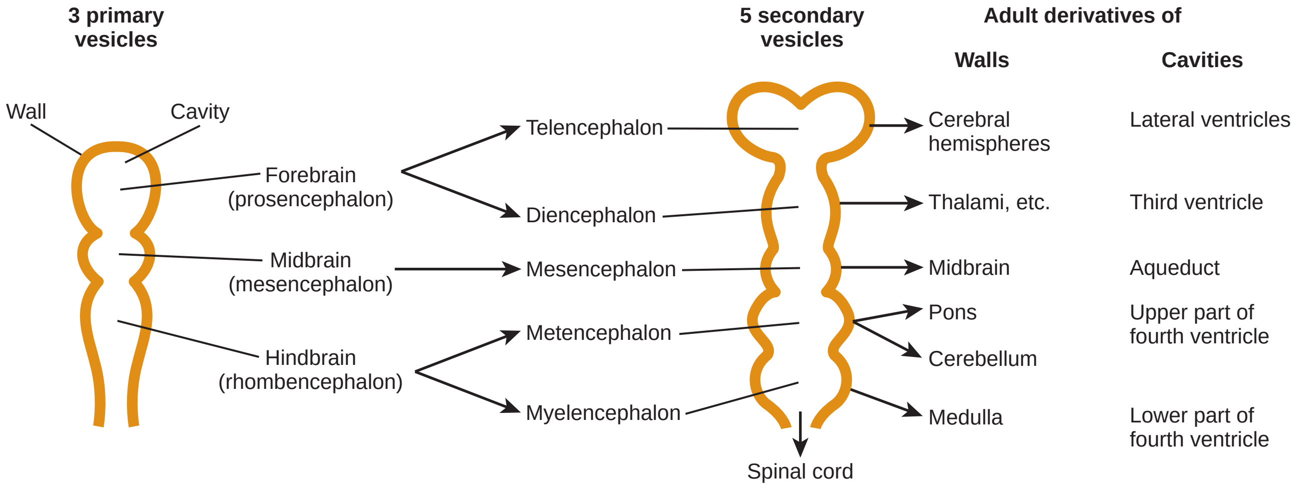

**Figure 24.5. Ventral induction.** *(From Moore KL, Persaud TVN.* Before We Are Born. *5th ed. Philadelphia: WB Saunders; 1988.)*

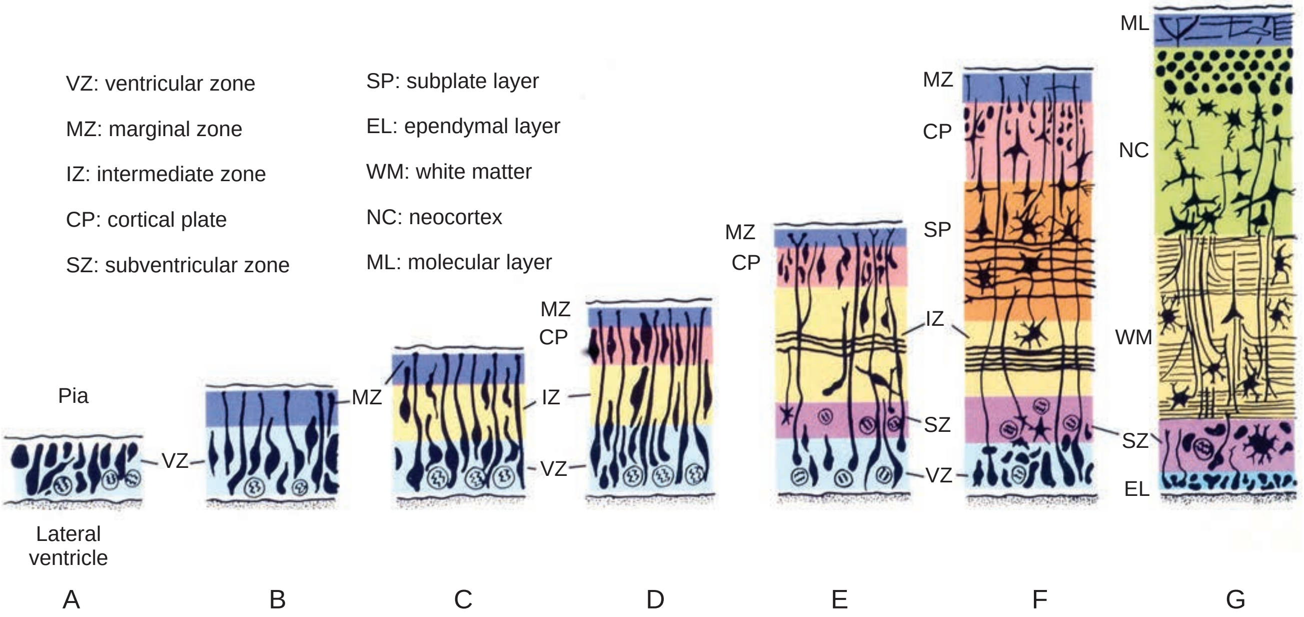

**Figure 24.7. Cytodifferentiation of the cerebral neocortex.** Although the timing of neuroblast formation varies widely in different regions of the cerebral hemispheres, the general scheme illustrated here (A–G) is typical for all regions. *(From Larsen WJ.* Human Embryology. *2nd ed. New York: Churchill Livingstone; 1997.)*

## FETAL DEVELOPMENT IN THE PRETERM INFANT

The normal brain anatomy of the fetus is in many ways quite different from the normal anatomy of the term infant. The following differences are noted:

1. The fetal ventricles are large relative to the size of the brain and have a posterior (occipital) predominance that decreases after 25 weeks.
2. The fluid-filled spaces of the brain are large; subarachnoid spaces are increased in size relative to size of the brain, and the cisterna magna is larger than at term.
3. The germinal matrix, for aforementioned reasons, is quite large, peaks at 26 weeks then regresses and is grossly gone by 34 weeks.
4. Primary and secondary sulcation and gyration follow a predictable course (Figs. 24.9 and 24.10).[6]

The normal biochemical profile follows the type and amount of cells present in any given stage of development. This can be seen through the normal but different spectrographic patterns (e-Fig. 24.11).[3] Normal myelination occurs via a defined order from the third trimester onward through adolescence (Table 24.2).[7,8] Generally, myelination proceeds caudal to rostral and posterior to anterior.

## NORMAL ANATOMY

The result of these complex processes result in the mature brain and spinal cord. Neuroanatomic descriptions in detail are beyond the scope of this text, but many atlases of anatomy and imaging are available. Comparison of normal development with pathologic development will be discussed in Chapter 31.

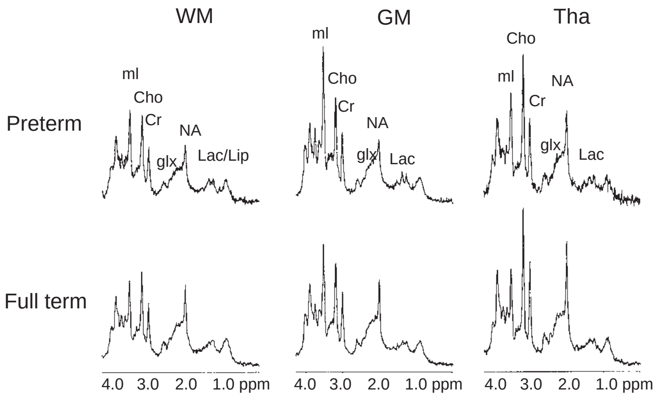

**e-Figure 24.11. Spectra during human functional development in different regions of the brain.** Metabolites identified are lactate *(Lac)*, lactate/lipid *(Lac/lip)*, N-acetyl aspartate *(NA)*, glutamine and glutamate *(Glx)*, creatine and phosphocreatine *(Cr)*, choline *(Cho)*, and myo-inositol *(mI)*. Spectra are all scaled identically. Developmental changes in metabolic concentrations are illustrated by different peak heights comparing spectra from preterm and full-term newborns. *GM,* Gray matter; *Tha,* thalamus; *WM,* white matter. *(Spectra analyzed by Roland Kreis, MR Center, Inelspital, University of Berne, Berne, Switzerland.) (From Martin RJ, Fanaroff AA, Walsh MC, eds.* Fanaroff and Martin's Neonatal Perinatal Medicine*. 8th ed. Philadelphia: Mosby; 2006.)*

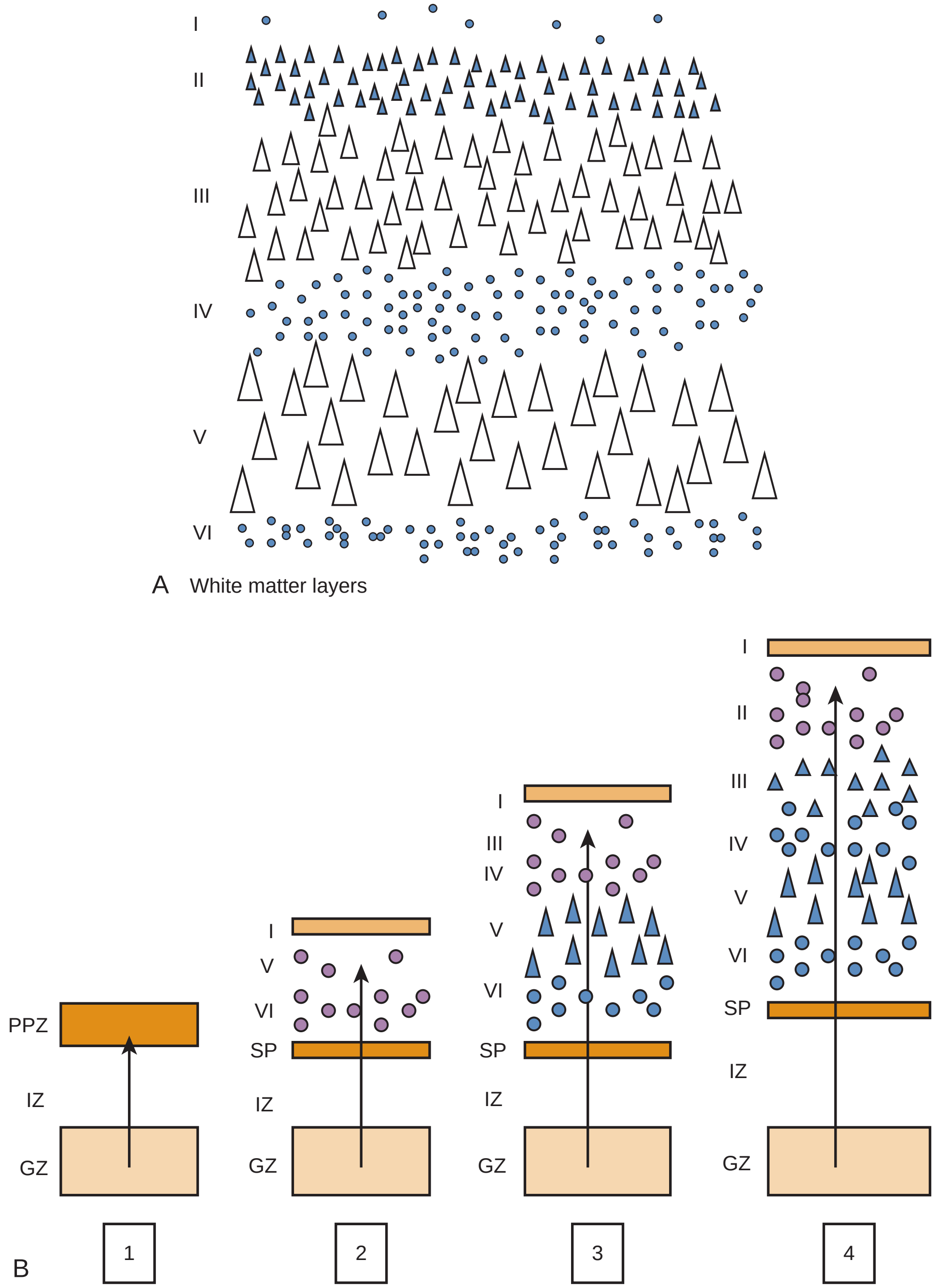

**Figure 24.8. Schematic illustration of mammalian neocortical formation and neuronal migration.** *Arrows* and *light gray circles* indicate migrating neurons; *black circles* and *triangles* represent postmigratory neurons. *GZ,* Germinative zone; *IZ,* intermediate zone (prospective white matter); *PPZ,* primitive plexiform zone; *SP,* subplate; *I,* cortical layer I or molecular layer; *II* or *VI,* cortical layers II to VI. *(From Martin RJ, Fanaroff AA, Walsh MC, eds.* Fanaroff and Martin's Neonatal Perinatal Medicine. *8th ed. Philadelphia: Mosby Elsevier; 2006.)*

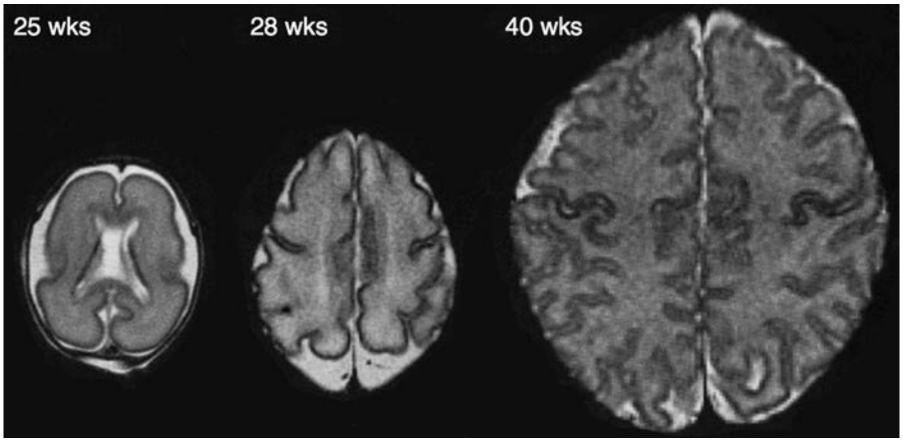

**Figure 24.9. Cortical folding.** Axial T2-weighted in vivo magnetic resonance (MR) images obtained at 25, 28, and 40 weeks' gestational age. *(From Martin RJ, Fanaroff AA, Walsh MC, eds.* Fanaroff and Martin's Neonatal Perinatal Medicine. *8th ed. Philadelphia: Mosby Elsevier; 2006.)*

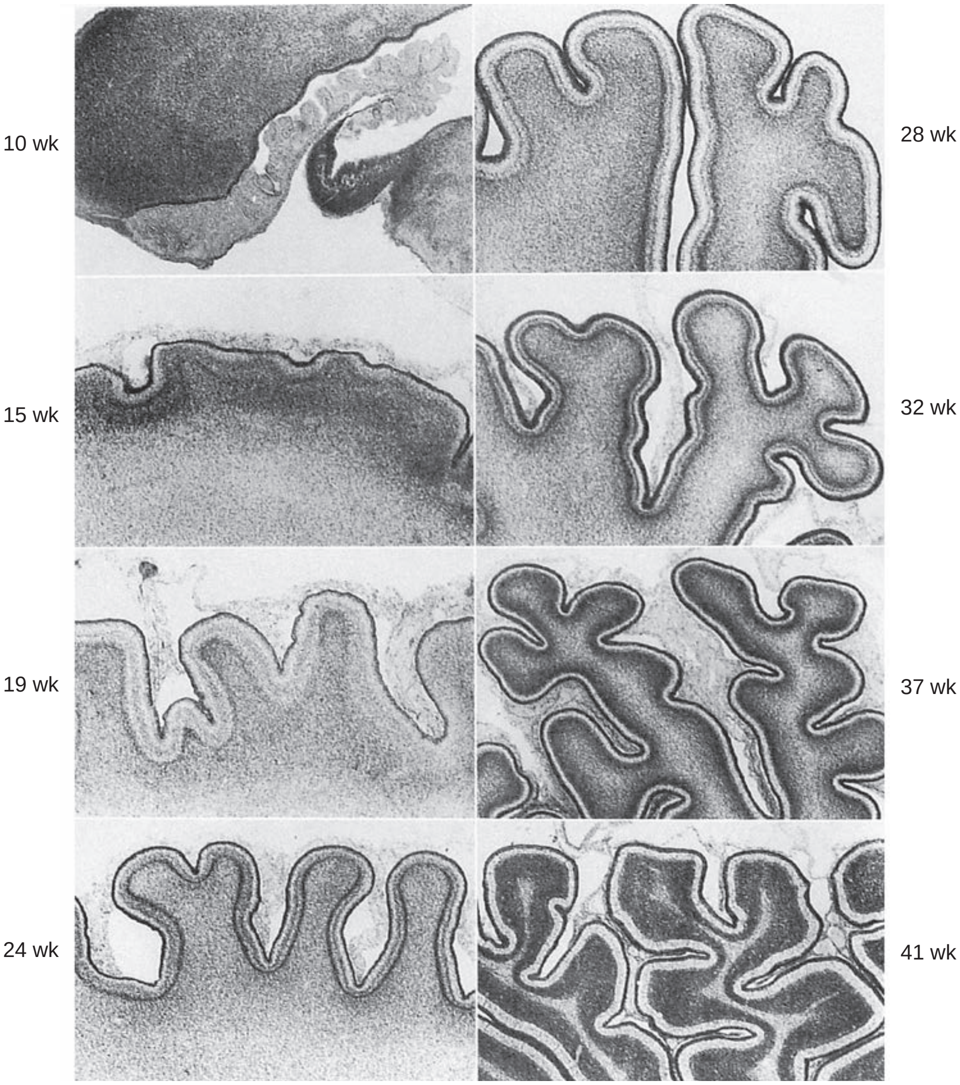

**Figure 24.10. Morphologic appearance of the developing neocortex from 10 to 41 weeks.** *(From Gilbert-Barness, ed.* Potter's Pathology of the Fetus and Infant*. Vol 2. St Louis: Mosby; 1997.)*

**TABLE 24.2** Sequence of Myelination Based on Histologic Analysis and Magnetic Resonance Imaging

| Anatomic Region | Median Age for Detection of Myelin Histology | Age for Detection of Myelin: Magnetic Resonance Imaging | |
|---|---|---|---|
| | | **T1-Weighted Images** | **T2-Weighted Images** |
| Ventrolateral thalamus | 28–30 wk | 32–34 wk | |
| Posterior limb of internal capsule | 38–44 wk* | 38–40 wk | Posterior portion 40–48 wk<br>Anterior portion 56–70 wk |
| Anterior limb of the internal capsule | 50–87 wk | 48–53 wk | 70–90 wk |
| Central corona radiata | 37–52 wk | 28–56 wk | 52–65 wk |
| Genu corpus callosum | 50–53 wk | 56–64 wk | 64–72 wk |
| Splenium corpus callosum | 54–65 wk | 52–56 wk | 56–64 wk |
| Occipital white matter | | | |
| Central | 47–87 wk | 52–60 wk | 76–96 wk |
| Peripheral | 56–122 wk | 56–70 wk | 90–102 wk |
| Frontal white matter | | | |
| Central | 50–119 wk | 52–64 wk | 90–106 wk |
| Peripheral | 72–119 wk | 70–90 wk | 96–114 wk |

*The first number corresponds to earliest identification of some myelin tubules by microscopic examination of hematoxylin and eosin stained sections. The second number corresponds to mature myelin stained with blue dye by eye observation.

*From Martin RJ, Fanaroff AA, Walsh MC, eds.* Fanaroff and Martin's Neonatal Perinatal Medicine. *8th ed. Philadelphia: Mosby Elsevier; 2006.*

## KEY POINTS

- The neural tube differentiates into the brain and spinal cord. The neural crest gives rise to the peripheral and autonomic nervous system.
- Neuronal migration proceeds from the ventricular zone to the superficial regions of the brain along radial glial cells.
- In general, myelination proceeds caudal to rostral and posterior to anterior.

## SUGGESTED READING

Gilles FH, Nelson MD Jr. *The Developing Human Brain. Growth and Adversities*. London: Mac Keith Press; 2012.

## REFERENCES

Full references for this chapter can be found on www.expertconsult.com.

## REFERENCES

1. O'Rahilly R, Muller F. *Human Embryology & Teratology*. 3rd ed. New York: Wiley Liss; 2001.
2. O'Rahilly R, Muller F. *The Embryonic Human Brain. An Atlas of Developmental Stages*. 3rd ed. New York: Wiley Liss; 2006.
3. Gilles FH, Nelson MD Jr. *The Developing Human Brain. Growth and Adversities*. London: Mac Keith Press; 2012.
4. Marin O, Rubenstein JLR. Cell migration in the forebrain. *Annu Rev Neurosci*. 2003;26:441–483.
5. Clark GD. Brain development and the genetics of brain development. *Neurol Clin N Am*. 2002;20:917–939.
6. Chi JG, Dooling EC, Gilles FH. Gyral development of the human brain. *Ann Neurol*. 1977;1(1):86–93.
7. Brody BA, Kinney HC, Kloman AS, et al. Sequence of central nervous system myelination in human infancy, I: an autopsy study of myelination. *J Neuropathol Exp Neurol*. 1987;46:283–301.
8. Kinney HC, Brody BA, Kloman AS, et al. Sequence of central nervous system myelination in human infancy, II: patterns of myelination of autopsied infants. *J Neuropathol Exp Neurol*. 1988;47:217–234.

# 25

# Magnetic Resonance Spectroscopy and Positron Emission Tomography

*Andre Dietz Furtado, Celso Hygino da Cruz Jr., Wael Abdalla, Stefan Bluml, and Ashok Panigrahy*

Magnetic resonance spectroscopy (MRS) capability is available in most clinical magnetic resonance (MR) scanners. The additional information from MRS allows the assessment of cellular metabolism noninvasively. For the brain in particular, it has been proved that MRS of protons or hydrogen (1H MRS) provides additional clinically relevant information for several disease processes such as brain tumors, metabolic disorders, and systemic diseases, and it is the most accessible method for studying and monitoring patients with neurometabolic disorders (Table 25.1).

## THEORETICAL BACKGROUND OF MAGNETIC RESONANCE SPECTROSCOPY

In MR imaging (MRI), the signal from hydrogen nuclei in water molecules is used to create images or anatomic maps. In contrast, 1H MRS analyzes the signal of protons attached to other molecules. The output of MRS is a collection of peaks at different radiofrequencies representing proton nuclei in different chemical environments, that is, the spectrum (typical MR spectra of normal occipital gray matter is shown in Fig. 25.1). MRS can measure a variety of metabolites (Table 25.2). The $x$ axis, or chemical shift axis, is a measure of the frequency shift of a proton relative to a universally fixed reference substance (tetramethylsilane at 0 parts per million [ppm]). In spectra in vivo, the protons of water (usually not shown) resonate at 4.7 ppm. The ppm scale has been selected instead of Hertz ($\text{Hz} = \text{sec}^{-1}$) because it is independent of the magnetic field strength. The $y$ axis is a measure of the signal intensity, which is proportional to the concentration of the metabolite or chemical.

## MAIN METABOLITES OF THE IN VIVO PROTON SPECTRUM

### N-Acetylaspartate

The most prominent peak of the 1H spectrum is the resonance at 2.0 ppm from three equivalent protons of the acetyl group of the N-acetylaspartate (NAA) molecule (see Fig. 25.1). The role of NAA and its regulation in vivo are not well understood. In the normal brain, NAA is synthesized in neurons, diffuses along axons, and is broken down in oligodendrocytes. NAA is present in high concentrations only in normal neurons and axons,[1,2] and from an MRS perspective, it is a marker of viability for mature neurons and axons. The concentrations of NAA increase after birth, becoming the dominant peak around 6 months.[3–5] Proton spectra of any disease associated with neuronal or axonal loss will exhibit a reduction of NAA. Brain NAA increases rapidly as the brain matures, peaks at approximately 10 to 15 years, and then decreases slightly over time as the number of neurons and axons declines even in the normal brain.[4]

### Total Choline

The next prominent peak at 3.2 ppm is commonly referred to as *choline* or *trimethylamines*. Choline is a complex peak comprising several metabolites that contain choline, and therefore the term total choline (tCho) is used in this chapter. Compounds that contain choline are involved in the synthesis and breakdown of phosphatidylcholine (lecithin). Phosphatidylcholine is the major phospholipid component of eukaryotic cells, accounting for approximately 60% of total cellular phospholipids.

### Creatine

The second tallest peak in occipital gray matter spectra is creatine (Cr) at 3.0 ppm. For normal brain tissue, the Cr peak comprises contributions from free Cr and phosphocreatine in approximately equal proportions. Phosphocreatine is in rapid chemical exchange with free Cr and is used to replenish adenosine triphosphate (ATP) levels, if required. Like NAA, Cr levels also are low in the newborn.

### Myo-inositol

tCho, Cr, and NAA can be detected readily and quantified in long echo time (TE) MRS. Short TE acquisition methods are necessary for reliable quantitation of myo-inositol (mI), which is a sugar-like molecule that resonates at 3.6 ppm in the proton spectrum. It has been identified as a marker for astrocytes and is an osmolyte.[6,7] mI also is involved in the metabolism of phosphatidyl inositol, a membrane phospholipid. Similar to choline, mI is altered in response to alteration of membrane metabolism or membrane damage. Both tCho and mI are high in the newborn brain but decrease rapidly to normal levels within the first 12 to 24 months after birth.

### Lactate

Lactate (1.33 ppm) indicates anaerobic metabolism. Lactate is the product of anaerobic glycolysis and increases when subsequent oxidation of lactate in the tricarboxylic acid cycle is impaired (for example, by lack of oxygen or mitochondrial disorders). With the exception of healthy-term neonates who may have trace amounts of lactate in the brain in the first days of life (lactate/choline <0.15),[8] significantly elevated lactate concentrations is indicative of pathologic tissue. Lactate is typically elevated in brain infarcts, contusions, infections, tumor necrosis, metabolic disorders, and cysts. Lactate (1.33 ppm) can be differentiated from other lipids and macromolecules (0.9–1.3 ppm) using TE = 144 ms that causes the lactate peak to reverse (Fig. 25.2).

### Lipids and Macromolecules

The protons of the methyl groups ($\text{-CH}_3$) of lipid molecules resonate at 0.9 ppm, whereas protons of the methylene groups ($\text{-CH}_2\text{-}$) resonate at 1.3 ppm in the $^1$H spectrum. Both resonances are broad and also may comprise contributions from other macromolecules. In normal tissue, the concentration of free lipids is small, and very little signal should be present in this part of the spectrum. Lipid signals increase upon breakdown of cell membranes and release of fatty acids, therefore lipids are marker of severity of brain imaging. NAA and lactate can be detected using either short echo (35 ms) or long echo (144 or 288 ms) time. MI, glutamate/

## Abstract:

Magnetic resonance spectroscopy allows the assessment of cellular metabolism noninvasively. In MR imaging, the signal from hydrogen nuclei in water molecules is used to create images or anatomic maps. In contrast, MRS of hydrogen protons (1H MRS) analyzes the signal of protons attached to other molecules, expressed as parts per million. N-acetylaspartate is present in high concentrations only in normal neurons and axons and is a marker of viability and maturation of neurons and axons. Choline compounds are involved in the synthesis and breakdown of phosphatidylcholine (lecithin), a major component of the cellular membranes and is typically elevated in regions with high cellularity and high mitoses. Lactate is the product of anaerobic glycolysis and indicates anaerobic metabolism. For the brain in particular, it has been proved that 1H MRS provides additional clinically relevant information in several disease processes such as neonatal hypoxic-ischemic encephalopathy, metabolic diseases and white matter disorders, pediatric brain tumors, hepatic encephalopathy and pediatric brain trauma. Additional metabolic information may be obtained with positron emission tomography (PET). PET is able to quantify the intracellular concentration of the compounds. PET using F18-fluorodeoxyglucose is a well-established biomarker of cellular metabolism, particularly in pediatric brain tumors and epilepsy. 68Gallium-labeled somatostatin analogues has been recently introduced for clinical use. Uptake 68Gallium-labeled somatostatin analogues have been reported in glioma, medulloblastoma, meningioma, and pituitary macroadenoma.

## Keywords:

Advanced Imaging
Magnetic Resonance Spectroscopy
Positron Emission Tomography
F18-fluorodeoxyglucose

glutamine, and lipids can be detected only during use of the short echo technique (see Fig. 25.2).

## MAGNETIC RESONANCE SPECTROSCOPY METHODS

### Data Acquisition Techniques

#### Localized Single-Voxel Spectroscopy

Single-voxel MRS measures the MR signal of a single selected region of interest, whereas signal outside this area is suppressed. For single-voxel MRS, the magnetic field and other parameters are optimized to get the best possible spectrum from a relatively small region of the brain. Manufacturers generally provide point-resolved spectroscopy,[9,10] stimulated echo acquisition mode,[11] and image-selected in vivo spectroscopy.[12] These sequences differ in how radiofrequency pulses and so-called gradient pulses are arranged to achieve localization. It is beyond the scope of this review to discuss details about localization methods; the interested reader is referred to the aforementioned publications.

**TABLE 25.1** Common Indications for Pediatric Magnetic Resonance Spectroscopy

| | |
|---|---|
| Tumors | New tumor |
| | Evaluate progression |
| | Tumor vs. encephalitis/other lesions |
| Hypoxic ischemic injury | Patients at risk for cerebral malperfusion (congenital heart defects—status, postoperative) |
| | Status, postoperative cardiac arrest, apneic episodes |
| | Trauma, nonaccidental trauma |
| | Birth asphyxia |
| Other | New seizures, worsening seizures |
| | Unknown neurologic condition, altered mental state, developmental delay, global hypotonia |
| | Metabolic disorders, phenylketonuria |
| | Leukodystrophies—monitoring |
| | Liver problems/failure—preliver transplant |

#### Two-Dimensional or Three-Dimensional Chemical Shift Imaging

With chemical shift imaging (CSI) approaches, multiple spatially arrayed spectra (typically more than 100 spectra per slice) from slices or volumes are acquired simultaneously. Slice selection can be achieved with a selective radiofrequency pulse, as for MRI

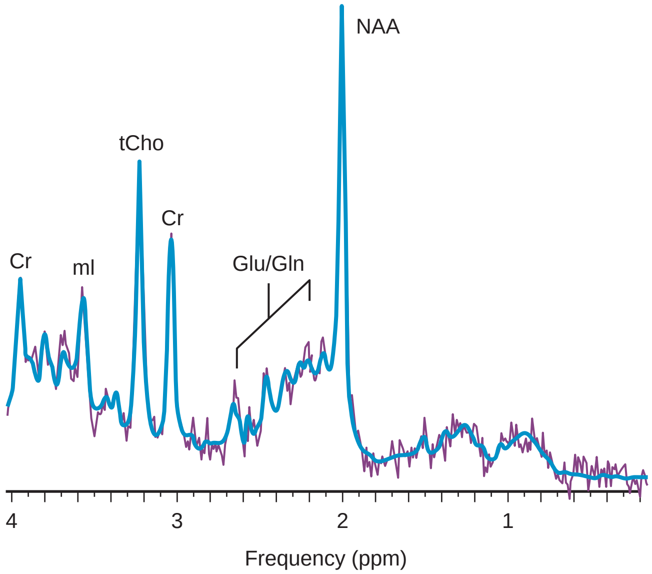

**Figure 25.1. $^1$H spectra of occipital gray matter acquired in a control subject.** Magnetic resonance imaging uses the signal provided by the protons of water to generate an anatomic map of the brain. In contrast, $^1$H magnetic resonance spectroscopy uses the signal from the protons of chemicals to generate a biochemical fingerprint of a "region of interest." Spectra were acquired using a point resolved spectroscopy sequence with echo time of 35 ms. *Cr,* creatine; *Glu,* glutamate; *Gln,* glutamine; *mI,* myo-inositol; *NAA,* N-acetylaspartate; *ppm,* parts per million; *tCho,* choline containing metabolites.

**TABLE 25.2** Summary of Chemicals Detectable With In Vivo Hydrogen Magnetic Resonance Spectroscopy

| | Long Name | Role, Regulation, Location | Altered in Magnetic Resonance Spectrum When: |
|---|---|---|---|
| NAA | N-acetylaspartate | Synthesized in neurons, diffuses along axons, broken down in oligodendrocytes, high in neurons and axons | Nonspecific but quantitative marker for neuronal/axonal damage |
| Cr | Creatine (creatine + phosphocreatine) | Synthesized in liver; functions as "battery" to replenish adenosine triphosphate levels | Abnormal in diseases of creatine synthesis, absent in cells that lack creatine kinase |
| tCho | Choline-containing metabolites | Involved in membrane synthesis and breakdown, osmolyte (GPC) | High in proliferative tumors, gliosis, leukodystrophies, low in hypoosmotic conditions, after radiation therapy |
| mI | Myo-inositol | High in astrocytes, osmolyte, sugar-like molecule, involved with phosphatidyl inositol (membrane lipid) metabolism | High in glial-based tumors (but low in glioblastoma multiforme), adrenoleukodystrophy, depleted in hepatic encephalopathy, low in other encephalitis (infections), liver disease |
| Glu | Glutamate | Excitatory neurotransmitter, high in neurons | High in seizures? Low in hepatic encephalopathy |
| Gln | Glutamine | Glutamate detoxification, osmolyte, high in glial cells, ammonia detoxification | High in hepatic encephalopathy, encephalitis (infections), ischemic-hypoxic injury |
| Lac | Lactate | End product of glycolysis, accumulates in cystic necrotic tissue, anaerobic metabolism indicator | Often high in tumors, (secondary) hypoxic-ischemic injury, mitochondrial disorders |
| Lip | Lipids | Membrane degeneration marker, necrosis marker | Aggressive tumors, infections, diseases associated with membrane breakdown |
| Glc | Glucose | Principle substrate for energy metabolism | Diabetes, disrupted energy metabolism |
| Tau | Taurine | Membrane stabilization | Elevated in medulloblastoma and possibly other primitive tumors |

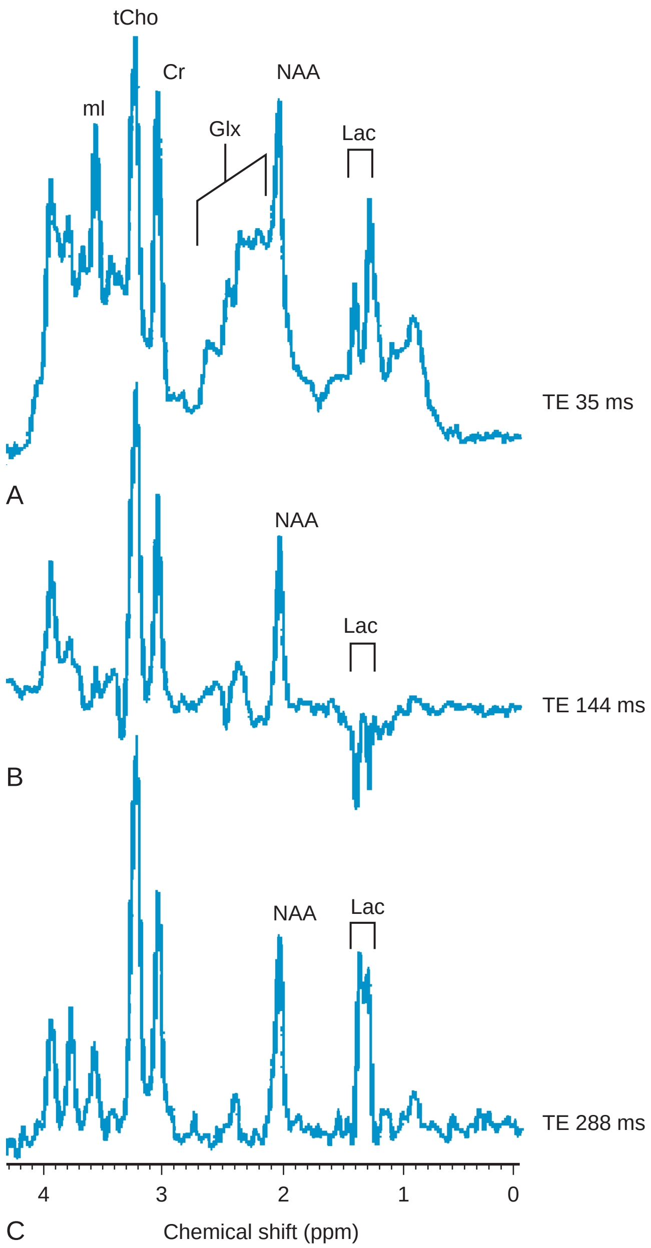

**Figure 25.2. Comparison of magnetic resonance spectroscopy (MRS) of neonatal hypoxic-ishemic encephalopathy (acquired at multiple echo times [TEs]) with neonatal metabolic disease.** (A–C) Single-voxel MRS at three different echo times in the basal ganglia of a hypoxic-ischemic term infant. Note the characteristic modulation of lactate *(Lac)*. (A) A spectrum acquired using short TE (35 ms), which shows a myo-inositol *(mI)* peak (left side of the spectrum), an elevated glutamine/glutamine *(Glx)* peak next to a reduced N-acetylaspartate *(NAA)* peak (middle spectrum), and an elevated lactate doublet next to a lipid peak (right side of the spectrum). (B) A spectrum acquired using long TE (144 ms) that shows a lactate doublet peak inverted and reduced NAA, but nonvisualization of myo-inositol, glutamate, and lipids. (C) A spectrum acquired using longer TE (288 ms) that is similar to 144 ms, except that the lactate doublet reverts to the other side of the spectrum.

(Fig. 25.3). When it is desired that the region of interest be limited to a smaller volume, for example, to avoid bone and fat from the skull, CSI is usually combined with point-resolved spectroscopy, stimulated echo acquisition mode, or image-selected in vivo spectroscopy but with a significantly larger volume selected than for single-voxel MRS. CSI is a very efficient method for acquiring information from different parts of the brain. An important feature is that, within the examined volume of interest, any region of interest can be selected retrospectively by a process termed *voxel shifting*.

### Parameters

The most important parameter is the TE. Indeed, MRS can be separated into long TE (typically >135 ms) and short TE (≈30 ms) methods. Long TE has been easier to use in clinical practice because of a flat baseline and because three peaks (NAA, Cr, and tCho) can be unequivocally separated. Short TE MRS allows the detection of an increased number of metabolites and has a signal-to-noise advantage over long TE.

## CLINICAL APPLICATIONS

### Neonatal Hypoxic-Ischemic Encephalopathy

MRS can detect neonates with acute hypotensive injury even when diffusion imaging and conventional imaging are negative.[13–24] The lactate from the acute event is rapidly cleared within the first 24 hours after resuscitation. The lactate/NAA peak ratio, measured in deep gray matter, is an accurate prognosticator for neonatal hypoxic-ischemic encephalopathy.[13,19,25–32] A generalized elevation of lactate would indicate global disruption or impairment of perfusion consistent with hypoxia and eventual poor outcome.[16]

### Metabolic Diseases and White Matter Disorders

Metabolic disease may be classified as acquired metabolic disorders or inborn errors of metabolism. Inborn errors of metabolism can present in the neonatal period.[33] Some examples of acquired metabolic disorders include hyperbilirubinemia and hypoglycemia, both of which may result in brain injury. Inborn errors of metabolism can be classified broadly into organic acidemias, disorders of amino acid oxidation, disorders of fatty acid oxidation, primary lactic acidosis, mitochondria function, lysosomal storage disorders, and peroxisomal disorders.[34–37]

Examples of organic acid disorders include methylmalonic acidemia and propionic aciduria, in which enzymatic defects occur in the conversion of valine, isoleucine, threonine, and methionine to propionic acid, succinic acid, and methylmalonic acid. Conventional MR findings include abnormal signal change corresponding to edema in both myelinated and unmyelinated structures. The edema in the myelinated structures is characterized by a vacuolating (or spongiform) myelinopathy, which can be seen in amino acid and organic acid disorders. In vacuolating myelinopathy, water is trapped within vacuoles that can be found within the myelin sheath layers, resulting in restricted diffusion of water. MRS of these organic acid disorders detects reduction in mI and NAA levels and elevation of glutamine and lactate levels as a result of hyperammonia, ketoacidosis, and mitochondrial dysfunction.[34–38]

The classic phenotype of maple syrup urine disease is a disturbance in the metabolism of the essential amino acids leucine, isoleucine, and valine. Symptoms occur by the first week of life and include seizures, vomiting and dystonia, fluctuating ophthalmoplegia, and coma. Conventional MR findings include abnormal edema in the deep cerebellar white matter, brainstem tegmentum, posterior limb of the internal capsule, perirolandic white matter, and pre- and postcentral gyrus. The accumulation of abnormal branched-chain amino acids and branched-chain α-keto acids results in a peak at 0.9 ppm. Both the changes detected by diffusion imaging and MRS may normalize after treatment is started.[39,40]

Urea cycle defects are characterized by a total of five disorders that involve different defects in the biosynthesis of enzymes of the urea cycle, including ornithine carbamyl transferase deficiency,

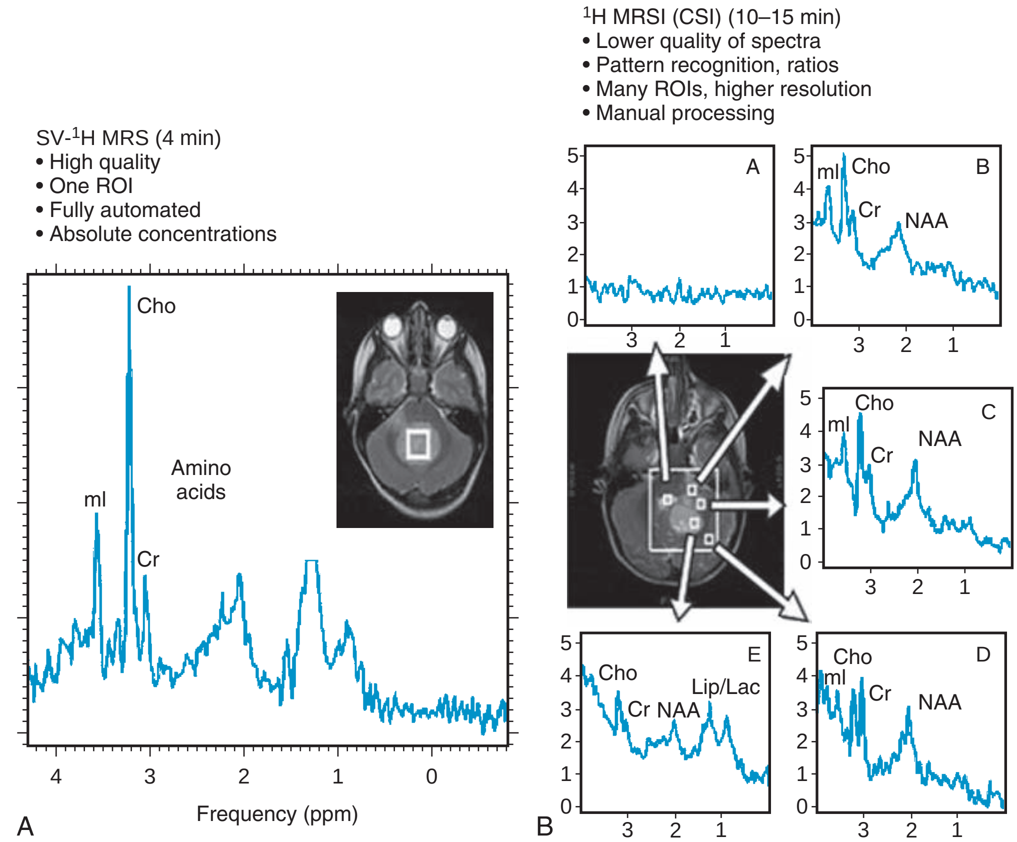

**Figure 25.3.** Differences between single-voxel (A) and multivoxel (B) acquisition. *Cho,* Choline; *Cr,* creatine; *CSI,* chemical shift imaging; *Lip/Lac,* lipid/lactate; *MRS,* magnetic resonance spectroscopy; *MRSI,* magnetic resonance spectroscopy imaging; *NAA,* N-acetylaspartate; *ppm,* parts per million; *ROI,* region of interest.

carbamyl phosphate synthetase deficiency, argininosuccinic aciduria, citrullinemia, and hyperargininemia.[41,42] In patients with these disorders, MRS can detect elevated glutamine levels resulting from hyperammonemia, which can be reversed with treatment.

Mitochondrial disorders are caused by defects of intracellular energy metabolism and result in decreased ATP production.[43–45] Leigh disease is a multisystem disorder in which the defect may be at different enzymatic mitochondrial levels, including the pyruvate dehydrogenase complex, cytochrome c oxidase, or ATP synthase. Conventional and diffusion imaging shows abnormalities in signal intensity and mean diffusivity in the brainstem (pons, periaqueductal gray, substantia nigra, and medulla), the subthalamic nucleus, and the globus pallidus. MRS is used to detect lactate in these disorders. It should be noted, however, that an elevated lactate level is not specific for a mitochondrial disorder. Similarly, failure to detect lactate does not exclude the possibility of a mitochondrial abnormality.

Leukoencephalopathies include a broad spectrum of inherited and acquired diseases that affect white matter that are associated with genetic enzyme defects leading to myelin dysfunction and breakdown. These disease processes tend to present in infancy or childhood. Leukoencephalopathies can be classified in multiple ways, including (1) involvement of the primary cellular organelle; (2) biochemistry; and (3) location of primary involvement (periventricular, subcortical, white matter only, and gray and white matter). The MRS correlate of these white-matter disorders have been reviewed extensively.[33] One of the most exclusive pathognomonic MRS diagnoses is that of Canavan disease. Canavan disease is an autosomal-recessive disorder arising from a deficiency of the enzyme aspartoacyclase[46] that results in an accumulation of NAA in the brain. MRS shows marked elevation of the NAA peak (Fig. 25.4).

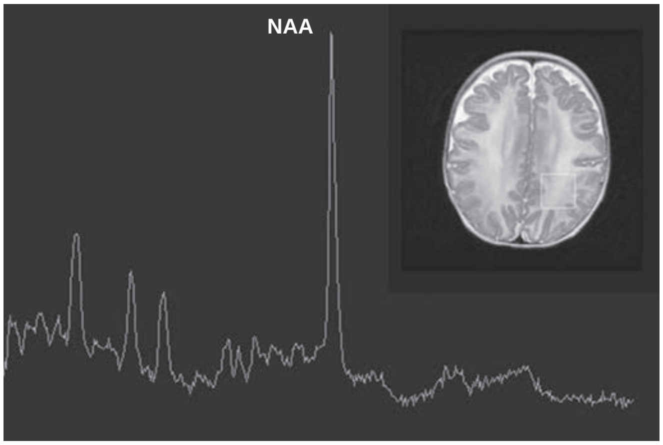

**Figure 25.4.** Elevated N-acetylaspartate *(NAA)* in a patient with Canavan disease.

## Pediatric Brain Tumors

### Posterior Fossa Lesions

Approximately 60% of all pediatric tumors arise from the posterior fossa. In most cases, these tumors are grade IV medulloblastoma or grade I pilocytic astrocytoma; grade II or III ependymoma are

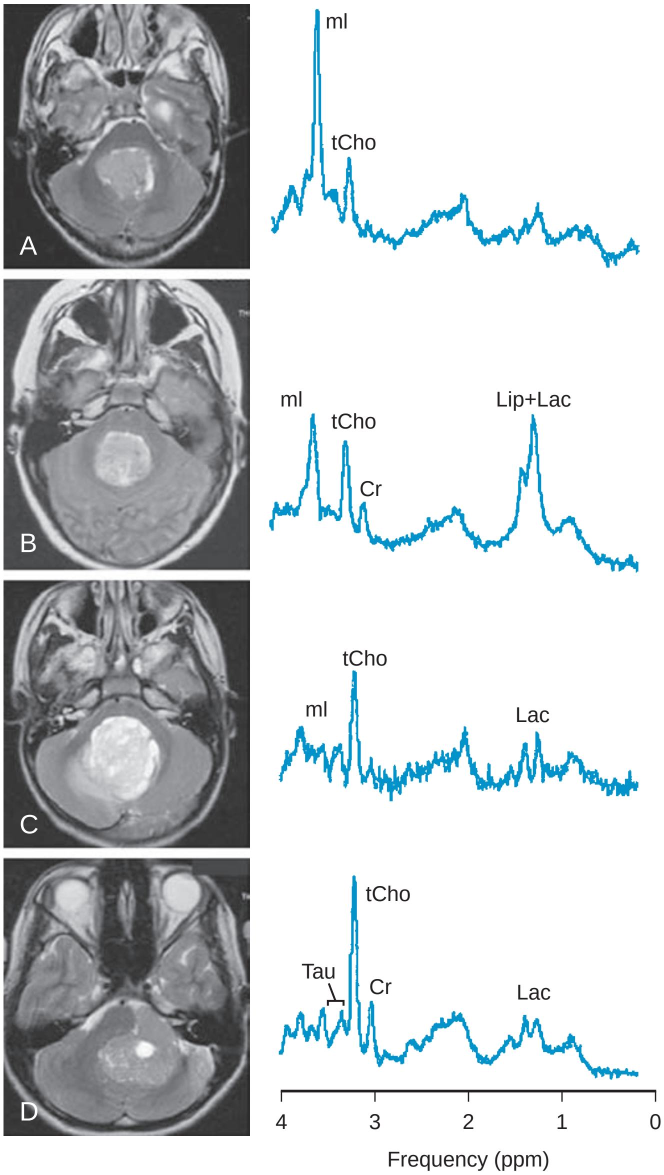

**Figure 25.5. T2-weighted MR images and MR spectra of posterior fossa tumors.** (A) Choroid plexus papilloma. (B) Ependymoma (grade II). (C) Pilocytic astrocytoma. (D) Classic medulloblastoma. All spectra were acquired from lesions with no partial volume of surrounding tissue using a single-voxel point resolved spectroscopy sequence with a short echo time of 35 ms. Shown are the original unfiltered spectra *(thin line)* and the LCModel fits to the data *(thick line)* (Stephen Provencher Inc., version 6.1-G4). In all four cases presented, MR spectroscopy provided clues to the correct diagnosis, which was different from the impression of the routine anatomic MR image. *Cr,* Creatine; *Lac,* lactate; *Lip,* lipid; *mI,* myo-inositol; *tCho,* total choline; *Tau,* taurine.

less common. Occasionally, a cystic/necrotic medulloblastoma may have imaging characteristics that overlap with posterior fossa pilocytic astrocytoma (Fig. 25.5). Grade I pilocytic astrocytomas may have high Cho/Cr and elevated lactate, similarly to high grade tumors. Taurine (Tau) elevation has been observed in medulloblastomas[47–50] and is an important differentiator of medulloblastoma from other tumors of the posterior fossa. Medulloblastomas also have higher levels of choline than other posterior fossa tumors.[51,52] The hallmark of pilocytic astrocytomas is very low Cr concentrations, low mI, and low tCho concentrations, consistent with their low cellularity. Lipids also are low in pilocytic astrocytomas, but mean lactate levels are higher than in other tumors. Ependymomas have higher mI levels than medulloblastomas or pilocytic astrocytomas; their choline levels are variable but generally fall between that of medulloblastomas and pilocytic astrocytomas.

### Supratentorial Tumors

Approximately 40% of all pediatric brain tumors arise outside the posterior fossa. Embryonal tumors outside the posterior fossa are central nervous system primitive neuroectodermal tumors (PNETs) or atypical teratoid/rhabdoid tumors (AT/RT). Supratentorial PNETs have metabolic profiles comparable to that of posterior fossa medulloblastomas, with prominent choline levels and presence of taurine. Atypical teratoid/rhabdoid tumors may have more moderate choline levels and typically no detectable taurine. A pilocytic astrocytoma outside the posterior fossa may show a slightly more prominent mI signal, but the metabolic pattern otherwise is quite comparable with that of cerebellar pilocytic lesions.

### Treatment Response

Conventional imaging does not reliably distinguish between recurrent/residual disease and postoperative changes or necrosis after radiation. Postradiation changes sometimes occur many months after therapy, and the correct diagnosis is a major challenge for patient management. Spectroscopy is an important tool to assess response to therapy in pediatric and adult brain tumors.[53–59] Effective therapy causing cell death will result in generally reduced metabolite concentrations (including tCho) and increased lipids because of the release of fatty acids from cell membranes. On the other hand, increasing levels of tCho (or tCho/NAA) are indicators for failed therapy and high risk for progressing disease.

## Neoplasia Versus Encephalitis

Accurate initial diagnoses are needed not only to distinguish different types of tumors but also to separate neoplastic from nonneoplastic disease. Acute encephalitis (mostly viral) can mimic conventional MRI characteristics of primary brain tumors. Accurate noninvasive diagnosis of encephalitis is important because it may prevent the risks of a more invasive procedure. Brain lesions resulting from acute encephalitis (mostly viral) can have reduced levels of mI compared with neoplastic processes.[60]

## Hepatic Encephalopathy

Hepatic encephalopathy refers to a broad spectrum of neurologic derangements associated with liver disease. MRS of hepatic encephalopathy typically demonstrates decreased levels of mI and choline and increased concentration of glutamate/glutamine (Glx) (Fig. 25.6). More recently, it has been demonstrated that MRS metabolites are correlated with plasma ammonia levels and the ratio of branched-chain to aromatic amino acids and can be useful to help establish a diagnosis of minimal hepatic encephalopathy in pediatric patients.[61]

## Pediatric Brain Trauma

Traumatic brain injury is the leading cause of morbidity and mortality in children and adolescents in the United States. Two age groups are at greatest risk: ages 0 to 4 years and 15 to 19 years. MRS may improve detection of parenchymal brain injury in children with severe head trauma and infants with suspected

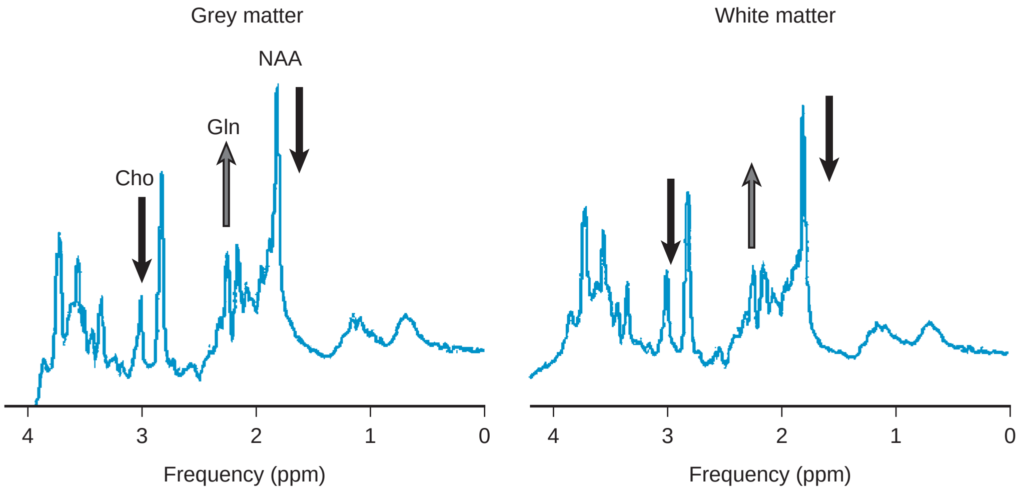

**Figure 25.6. Hepatic encephalopathy in a pediatric patient with iron intoxication and acute liver failure.** Magnetic resonance spectroscopy performed at 3T with point resolved spectroscopy and a time echo of 35 ms. Three voxel locations show an elevated glutamine *(Gln)* level, a reduced choline level, and a reduced myo-inositol level, indicating poor liver function. N-acetylaspartate *(NAA)* also is reduced, which may indicate neuronal/axonal loss/damage. Conventional magnetic resonance imaging was within normal limits. *ppm,* Parts per million.

inflicted head trauma. In pediatric head trauma, reduced NAA/Cr level and presence of lipid/lactate predicted poor outcome with high sensitivity and specificity.[62,63]

## QUANTIFICATION IN POSITRON EMISSION TOMOGRAPHY IMAGING

Positron emission tomography (PET) is able to quantify radioactivity concentration within a given region of interest. Analysis of tracer activity and its distribution can provide meaningful information on available receptor binding sites or biochemical processes. Three categories of methods in analyzing data are available: (1) qualitative analysis (visual assessment), (2) semiquantitative assessment such as standardized uptake value (SUV) and lesion-to-background ratio, and (3) absolute quantitative analysis using nonlinear regression, Patlak graphical analysis, and simplified quantitative methods.[64] Qualitative analysis requires minimal effort but has the least accuracy, whereas an absolute quantification method requires more complex procedures such as compartmental kinetic modeling to measure the individual rate constant based on data from dynamic image acquisition and serial blood sampling. Because of its complexity and time-consuming nature, this method is impractical in most clinical settings.

In clinical fluorodeoxyglucose (FDG)-PET studies, SUV is the most commonly used semiquantitative parameter. SUV is defined by lesion concentration of tracer per injected dose of normalized patient body weight multiplied by a decay factor:

$$\begin{aligned}\text{SUV} = {} & \text{Tissue activity concentration (MBq/mL)} \\ & \text{(Injected dose [MBq/mL]/Body weight [g]} \\ & \times \text{Decay factor of 18 F)}\end{aligned}$$

Compared with kinetic modeling, the SUV calculation is simple (without any need for arterial blood sampling) and faster (without dynamic image acquisition). Tissue SUV is known to have a highly correlative linear relationship with the rate of glucose metabolism measured by kinetic modeling.[65,66]

## POSITRON EMISSION TOMOGRAPHY AND BRAIN DEVELOPMENT

The FDG-PET metabolic pattern of a developing brain follows the order of anatomic, evolutional, and behavioral development.[67] Increased glucose metabolism demonstrated in the visual cortex, sensorimotor cortex, and cerebellum is correlated with early visuospatial and sensorimotor function and primitive reflexes. It also is known that hypermetabolism in the basal ganglia is associated with developing movement and sensorimotor function.

The degree of glucose metabolism of infants is known to be significantly lower than that of adults based on the quantitative analysis of brain FDG-PET. The current hypothesis is that increased metabolism is associated with increased metabolic demands from neuronal plasticity development. The metabolic level of the neonatal brains is about 30% that of adults, and it continues to increase with age. By the age of 3 years, the degree of metabolic activity exceeds that of adults, reaching its plateau between ages 4 and 9 years, with a value 1.3 times higher than that of healthy adults.[68] After this period, the metabolic activity continues to decrease to adult levels by the end of the second decade.[67] The overall degree of cortical metabolism significantly decreases with age, a consistent finding related to normal aging.[69]

The distribution of glucose metabolism of a pediatric brain becomes similar to that of young adults by the age of 1 year. The frontal lobe demonstrates more significant age-related metabolic changes compared with other parts of the brain. For the first 4 months of life, the frontal lobe has relatively low glucose levels, and the metabolic levels in this area gradually increase as frontal lobe–mediated cognitive function and complicated social interaction develops.

The remaining cortical areas such as the parietal, occipital, and temporal lobes have significant variations within and across age groups. The metabolic activity in the basal ganglia, thalami, hippocampi, cerebellum, visual cortices, and posterior cingulate gyrus is shown to remain stable at different ages, whereas the metabolic activity in the brainstem increases with age.[69]

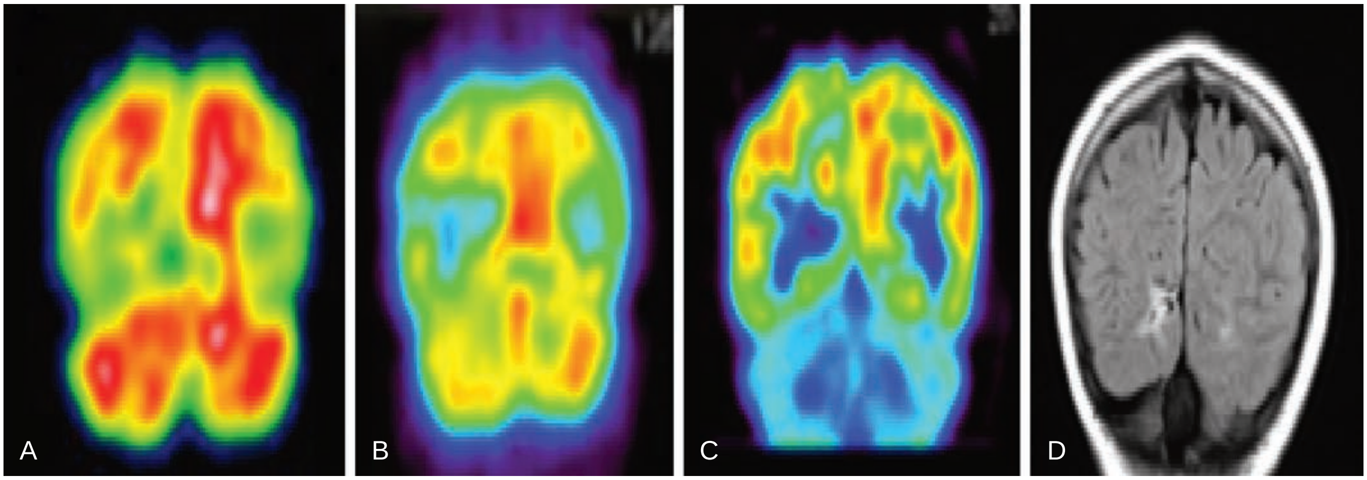

**Figure 25.7. Extratemporal lobe (right occipital) epilepsy in a 13-year-old girl with with localizing epileptogenic focus shown in interictal single photon emission computed tomography (SPECT), positron emission tomography (PET), magnetic resonance imaging (MRI), and nonlocalizing ictal SPECT.** (A) Ictal SPECT scan demonstrates an asymmetric perfusion pattern with relative hypoperfusion in the right occipital lobe. No focal hyperperfusion is noted. (B) Interictal SPECT scan demonstrates hypoperfusion in the right occipital lobe with an epileptogenic focus. (C) Fluorodeoxyglucose-PET scan demonstrates hypometabolism in the right occipital lobe with an epileptogenic focus. (D) Fluid attenuated inversion recovery MR image demonstrates hyperintensity in the right occipital lobe, suggesting an epileptogenic focus.

## POSITRON EMISSION TOMOGRAPHY IN PEDIATRIC EPILEPSY

The PET tracer most widely used in clinical practice for evaluation of brain glucose metabolism to localize epileptogenic focus is fluorine-18-deoxyglucose ($^{18}$F-FDG). FDG-PET is better suited for capturing the interictal state of epilepsy rather than the ictal state because of its long uptake period (40–60 minutes). The typical pattern of PET glucose metabolism of an epileptic focus is hypometabolism of the ipsilateral temporal lobe with or without less severe hypometabolism in the extratemporal structures such as the frontal lobe, parietal lobe, and contralateral temporal lobe. When anatomic lesions are associated with epilepsy, the extent of hypometabolism is known to be greater than the size of the structural lesion.[70]

The pathophysiology of regional hypometabolism in interictal FDG-PET is not clearly known, although several hypotheses have been proposed, including neuronal cell loss, neuronal inhibition, and diaschisis associated with hippocampal neuronal loss (Fig. 25.7).[71] However, conflicting evidence also exists, such as temporal hypometabolism without neuronal loss or gliosis[72] and a poor correlation between metabolic change in the temporal lobe and hippocampal cell count.[73]

Additional proposed hypotheses to explain interictal hypometabolism include an inhibitory process and reduction in synaptic density. Findings of several studies suggest that this secondary inhibition or neuronal loss in the area surrounding the epileptic zone can cause larger and more extensive hypometabolism in FDG-PET[71,74,75] and hypoperfusion in single photon emission computed tomography (SPECT)[76] than the area of involvement seen on electroencephalography or a pathologic correlate. Interictal FDG-PET is known to be more sensitive than MRI in localizing epileptogenic foci in cases of temporal and extratemporal epilepsy.[77]

About 29% of patients with partial or focal epilepsy have normal MRI findings.[78] Intracranial electroencephalography has limitations in this situation because of a lack of electrode targeting precision to the areas of suspected seizure origin. FDG-PET and ictal SPECT correctly localized epileptogenic zones in greater than 80% of patients in temporal lobe epilepsy.[79] In two studies, the localization rates by FDG-PET in patients with normal MRI findings were 57% and 32%.[80,81]

## PET/CT IMAGING OF PEDIATRIC BRAIN TUMORS

Recently, the use of PET for brain tumor imaging has increased. Currently the only radiotracer approved by the FDA is $^{18}$F-FDG, although other investigational agents show promise in specific situations.[82,83] In clinical practice, FDG-PET is being used as an adjunct tool in cases in which CT and MRI are unable to address a specific clinical question. The most common clinical indications of PET imaging include: (1) confirmation of the presence or absence of tumor; (2) help in establishing the grade of malignancy; (3) determination of the degree of treatment of the tumor or tumor response; and (4) distinguishing tumor recurrence from radiation necrosis (Figs. 25.8 and 25.9).[84] FDG-PET is known to be very sensitive in detecting high-grade gliomas. The high background uptake of FDG normally seen in the cortex results in less accurate detection of low-grade gliomas.[85]

## PET/MRI

Combined PET/MRI is a promising newer technology offering the potential application for novel molecular imaging with excellent soft tissue differentiation, lack of ionizing radiation from the MRI component, and simultaneous anatomic and functional data acquisition.

The first PET/MRI studies in humans demonstrated an excellent simultaneous performance of PET and MRI imaging without degrading image quality.[86] The diagnostic advantages of fused PET and MR images over PET/CT were shown by a 2006 study.[87] Moreover, PET/MRI is more beneficial to pediatric patients because it entails less radiation exposure compared with PET/CT. The ultimate role and utility of combined PET/MRI studies versus separately acquired and fused PET and MRI studies remain to be determined.

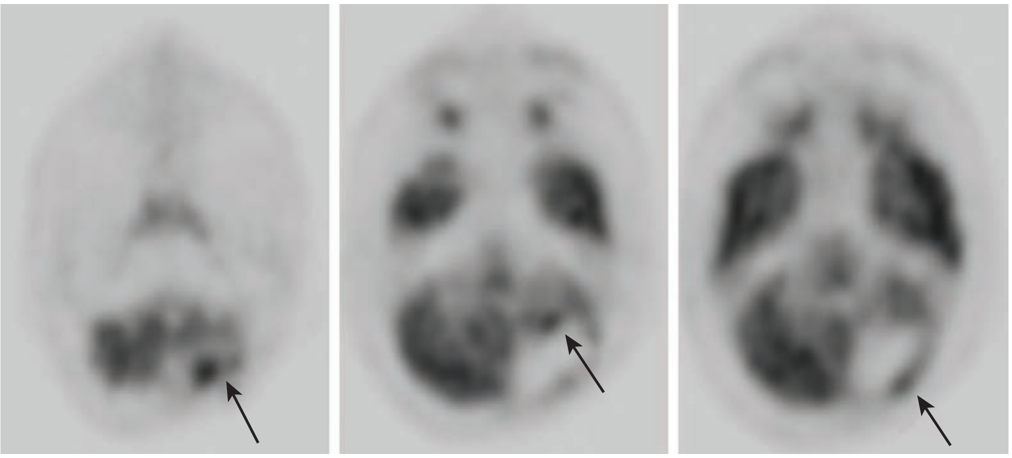

**Figure 25.8. An 18-year-old male with a history of anaplastic ependymoma in the left cerebellum, after having multiple surgeries.** FDG-PET brain scan demonstrates multiple areas of increased activity in the anterior and posterior resection margin consistent with malignant disease *(arrows)*.

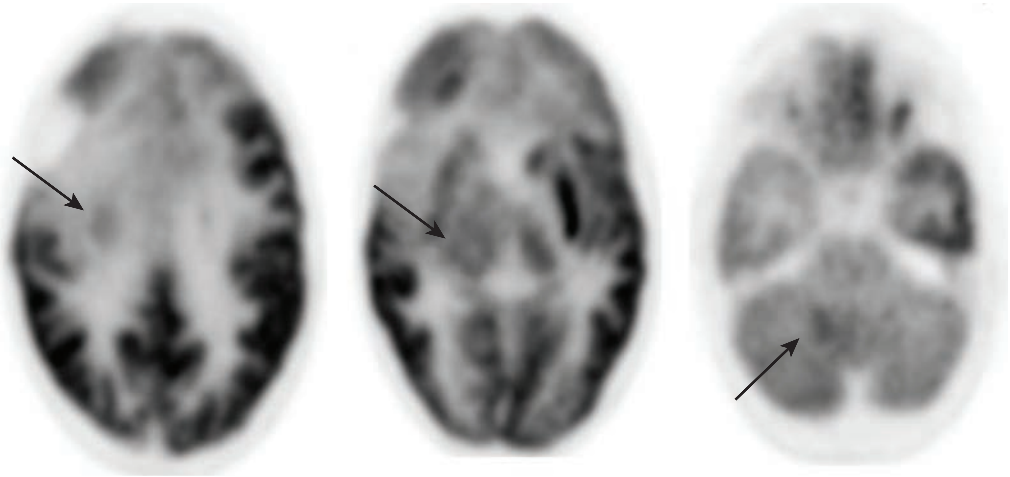

**Figure 25.9. A 9-year-old boy with an anaplastic astrocytoma after undergoing resection in the right frontal lobe.** Multiple areas of increased metabolic activity *(arrows)* are noted involving the right posterior medial frontal lobe, right basal ganglia, right thalamus, and the right cerebellum corresponding to areas of tumor infiltration seen with magnetic resonance imaging.

## KEY POINTS

- Proton magnetic resonance spectroscopy can provide metabolic information that can lead to more specific diagnoses of metabolic and neoplastic conditions.
- The presence of lactate indicates anaerobic metabolism.
- Long TE MRS is easier to use in clinical practice, although short TE MRS detects an increased number of metabolites and has a signal-to-noise advantage over long TE.
- Epileptic foci are typically hypometabolic at FDG-PET imaging. When anatomic lesions are present, the extent of hypometabolism is usually greater than the size of the structural lesion.

## SUGGESTED READINGS

Cecil KM, Kos RS. Magnetic resonance spectroscopy and metabolic imaging in white matter diseases and pediatric disorders. *Top Magn Reson Imaging*. 2006;17:275–293.

Panigrahy A, Nelson MD Jr, Bluml S. Magnetic resonance spectroscopy in pediatric neuroradiology: clinical and research applications. *Pediatr Radiol*. 2010;40(1):3–30.

## REFERENCES

Full references for this chapter can be found on www.expertconsult.com.

## REFERENCES

1. Baslow MH. Functions of N-acetyl-L-aspartate and N-acetyl-L-aspartylglutamate in the vertebrate brain: role in glial cell-specific signaling. *J Neurochem*. 2000;75:453–459.
2. Tallan HH. Studies on the distribution of N-acetyl-L-aspartic acid in brain. *J Biol Chem*. 1957;224:41–45.
3. Kimura H, Fujii Y, Itoh S, et al. Metabolic alterations in the neonate and infant brain during development: evaluation with proton MR spectroscopy. *Radiology*. 1995;194:483–489.
4. Kreis R, Ernst T, Ross BD. Development of the human brain: in vivo quantification of metabolite and water content with proton magnetic resonance spectroscopy. *Magn Reson Med*. 1993;30:424–437.
5. van. der Knaap MS, van der Grond J, van Rijen PC, et al. Age-dependent changes in localized proton and phosphorus MR spectroscopy of the brain. *Radiology*. 1990;176:509–515.
6. Lien YH, Shapiro JI, Chan L. Effects of hypernatremia on organic brain osmoles. *J Clin Invest*. 1990;85:1427–1435.
7. Videen JS, Michaelis T, Pinto P, et al. Human cerebral osmolytes during chronic hyponatremia. A proton magnetic resonance spectroscopy study. *J Clin Invest*. 1995;95:788–793.
8. Bartha AI, Yap KR, Miller SP, et al. The normal neonatal brain: MR imaging, diffusion tensor imaging, and 3D MR spectroscopy in healthy term neonates. *AJNR Am J Neuroradiol*. 2007;28:1015–1021.
9. Bottomley PA. Selective volume method for performing localized NMR spectroscopy. *USA patent 4 480 228*. 1984.
10. Bottomley PA. Spatial localization in NMR spectroscopy in vivo. *Ann N Y Acad Sci*. 1987;508:333–348.
11. Frahm J, Bruhn H, Gyngell ML, et al. Localized high-resolution proton NMR spectroscopy using stimulated echoes: initial applications to human brain in vivo. *Magn Reson Med*. 1989;9:79–93.
12. Ordidge RJ, Connelly A, Lohman JA. Image-selected in-vivo spectroscopy (ISIS). A new technique for spatially selective NMR spectroscopy. *J Magn Reson*. 1986;283–294.
13. Penrice J, Cady EB, Lorek A, et al. Proton magnetic resonance spectroscopy of the brain in normal preterm and term infants, and early changes after perinatal hypoxia-ischemia. *Pediatr Res*. 1996;40:6–14.
14. Hanrahan JD, Sargentoni J, Azzopardi D, et al. Cerebral metabolism within 18 hours of birth asphyxia: a proton magnetic resonance spectroscopy study. *Pediatr Res*. 1996;39:584–590.
15. Leth H, Toft PB, Peitersen B, et al. Use of brain lactate levels to predict outcome after perinatal asphyxia. *Acta Paediatr*. 1996;85:859–864.
16. Holshouser BA, Ashwal S, Luh GY, et al. Proton MR spectroscopy after acute central nervous system injury: outcome prediction in neonates, infants, and children. *Radiology*. 1997;202:487–496.
17. Groenendaal F, Veenhoven RH, Van Der Grond J, et al. Cerebral lactate and N-acetyl-aspartate/choline ratios in asphyxiated full-term neonates demonstrated in vivo using proton magnetic resonance spectroscopy. *Pediatr Res*. 1994;35:148–151.
18. Huppi PS, Posse S, Lazeyras F, et al. Magnetic resonance in preterm and term newborns: 1H-spectroscopy in developing human brain. *Pediatr Res*. 1991;30:574–578.
19. Cheong JL, Cady EB, Penrice J, et al. Proton MR spectroscopy in neonates with perinatal cerebral hypoxic-ischemic injury: metabolite peak-area ratios, relaxation times, and absolute concentrations. *AJNR Am J Neuroradiol*. 2006;27:1546–1554.
20. Moorcraft J, Bolas NM, Ives NK, et al. Spatially localized magnetic resonance spectroscopy of the brains of normal and asphyxiated newborns. *Pediatrics*. 1991;87:273–282.
21. Peden CJ, Cowan FM, Bryant DJ, et al. Proton MR spectroscopy of the brain in infants. *J Comput Assist Tomogr*. 1990;14:886–894.
22. Barkovich AJ, Baranski K, Vigneron D, et al. Proton MR spectroscopy for the evaluation of brain injury in asphyxiated, term neonates. *AJNR Am J Neuroradiol*. 1999;20:1399–1405.
23. Vigneron DB, Barkovich AJ, Noworolski SM, et al. Three-dimensional proton MR spectroscopic imaging of premature and term neonates. *AJNR Am J Neuroradiol*. 2001;22:1424–1433.
24. Kreis R, Hofmann L, Kuhlmann B, et al. Brain metabolite composition during early human brain development as measured by quantitative in vivo 1H magnetic resonance spectroscopy. *Magn Reson Med*. 2002;48:949–958.
25. Shanmugalingam S, Thornton JS, Iwata O, et al. Comparative prognostic utilities of early quantitative magnetic resonance imaging spin-spin relaxometry and proton magnetic resonance spectroscopy in neonatal encephalopathy. *Pediatrics*. 2006;118:1467–1477.
26. Amess PN, Penrice J, Wylezinska M, et al. Early brain proton magnetic resonance spectroscopy and neonatal neurology related to neurodevelopmental outcome at 1 year in term infants after presumed hypoxic-ischaemic brain injury. *Dev Med Child Neurol*. 1999;41:436–445.
27. Robertson NJ, Cox IJ, Cowan FM, et al. Cerebral intracellular lactic alkalosis persisting months after neonatal encephalopathy measured by magnetic resonance spectroscopy. *Pediatr Res*. 1999;46:287–296.
28. Roelants-Van. Rijn AM, van der Grond J, de Vries LS, et al. Value of (1)H-MRS using different echo times in neonates with cerebral hypoxia-ischemia. *Pediatr Res*. 2001;49:356–362.
29. L'Abee C, de Vries LS, van der Grond J, et al. Early diffusion-weighted MRI and 1H-magnetic resonance spectroscopy in asphyxiated full-term neonates. *Biol Neonate*. 2005;88:306–312.
30. Robertson NJ, Lewis RH, Cowan FM, et al. Early increases in brain myo-inositol measured by proton magnetic resonance spectroscopy in term infants with neonatal encephalopathy. *Pediatr Res*. 2001;50:692–700.
31. Brissaud O, Chateil JF, Bordessoules M, et al. Chemical shift imaging and localised magnetic resonance spectroscopy in full-term asphyxiated neonates. *Pediatr Radiol*. 2005;35:998–1005.
32. Meyer-Witte S, Brissaud O, Brun M, et al. [Prognostic value of MR in term neonates with neonatal hypoxic-ischemic encephalopath: MRI score and spectroscopy. About 26 cases]. *Arch Pediatr*. 2008;15:9–23.
33. Cecil KM, Kos RS. Magnetic resonance spectroscopy and metabolic imaging in white matter diseases and pediatric disorders. *Top Magn Reson Imaging*. 2006;17:275–293.
34. Kinnala A, Rikalainen H, Lapinleimu H, et al. Cerebral magnetic resonance imaging and ultrasonography findings after neonatal hypoglycemia. *Pediatrics*. 1999;103:724–729.
35. Cecil KM. MR spectroscopy of metabolic disorders. *Neuroimaging Clin N Am*. 2006;16:87–116, viii.
36. van. der Knaap MS, Valk J. *Magnetic Resonance of Myelin, Myelination, and Myelin Disorders*. 2nd ed. Berlin: Springer; 1995.
37. Barkovich AJ. *Toxic and Metabolic Brain Disorders. Pediatric Neuroimaging*. 5th ed. Philadelphia: Lippincott Williams & Wilkins; 2005:76–189.
38. Enns GM, Barkovich AJ, Rosenblatt DS, et al. Progressive neurological deterioration and MRI changes in cblC methylmalonic acidaemia treated with hydroxocobalamin. *J Inherit Metab Dis*. 1999;22:599–607.
39. Jan W, Zimmerman RA, Wang ZJ, et al. MR diffusion imaging and MR spectroscopy of maple syrup urine disease during acute metabolic decompensation. *Neuroradiology*. 2003;45:393–399.
40. Cavalleri F, Berardi A, Burlina AB, et al. Diffusion-weighted MRI of maple syrup urine disease encephalopathy. *Neuroradiology*. 2002;44:499–502.
41. Takanashi J, Barkovich AJ, Cheng SF, et al. Brain MR imaging in acute hyperammonemic encephalopathy arising from late-onset ornithine transcarbamylase deficiency. *AJNR Am J Neuroradiol*. 2003;24:390–393.
42. Choi CG, Yoo HW. Localized proton MR spectroscopy in infants with urea cycle defect. *AJNR Am J Neuroradiol*. 2001;22:834–837.
43. Bianchi MC, Tosetti M, Battini R, et al. Proton MR spectroscopy of mitochondrial diseases: analysis of brain metabolic abnormalities and their possible diagnostic relevance. *AJNR Am J Neuroradiol*. 2003;24:1958–1966.
44. Cross JH, Connelly A, Gadian DG, et al. Clinical diversity of pyruvate dehydrogenase deficiency. *Pediatr Neurol*. 1994;10:276–283.
45. Zand DJ, Simon EM, Pulitzer SB, et al. In vivo pyruvate detected by MR spectroscopy in neonatal pyruvate dehydrogenase deficiency. *AJNR Am J Neuroradiol*. 2003;24:1471–1474.
46. Madhavarao CN, Moffett JR, Moore RA, et al. Immunohistochemical localization of aspartoacylase in the rat central nervous system. *J Comp Neurol*. 2004;472:318–329.
47. Moreno-Torres A, Martinez-Perez I, Baquero M, et al. Taurine detection by proton magnetic resonance spectroscopy in medulloblastoma: contribution to noninvasive differential diagnosis with cerebellar astrocytoma. *Neurosurgery*. 2004;55:824–829; discussion 829.
48. Wilke M, Eidenschink A, Muller-Weihrich S, et al. MR diffusion imaging and 1H spectroscopy in a child with medulloblastoma. A case report. *Acta Radiol*. 2001;42:39–42.
49. Tong Z, Yamaki T, Harada K, et al. In vivo quantification of the metabolites in normal brain and brain tumors by proton MR spectroscopy using water as an internal standard. *Magn Reson Imaging*. 2004;22:1017–1024.
50. Kovanlikaya A, Panigrahy A, Krieger MD, et al. Untreated pediatric primitive neuroectodermal tumor in vivo: quantitation of taurine with MR spectroscopy. *Radiology*. 2005;236:1020–1025.

51. Wang Z, Sutton LN, Cnaan A, et al. Proton MR spectroscopy of pediatric cerebellar tumors. *AJNR Am J Neuroradiol*. 1995;16:1821–1833.
52. Panigrahy A, Krieger MD, Gonzalez-Gomez I, et al. Quantitative short echo time 1H-MR spectroscopy of untreated pediatric brain tumors: preoperative diagnosis and characterization. *AJNR Am J Neuroradiol*. 2006;27:560–572.
53. Warren KE, Frank JA, Black JL, et al. Proton magnetic resonance spectroscopic imaging in children with recurrent primary brain tumors. *J Clin Oncol*. 2000;18:1020–1026.
54. Lazareff JA, Gupta RK, Alger J. Variation of post-treatment H-MRSI choline intensity in pediatric gliomas. *J Neurooncol*. 1999;41:291–298.
55. Tzika AA, Astrakas LG, Zarifi MK, et al. Spectroscopic and perfusion magnetic resonance imaging predictors of progression in pediatric brain tumors. *Cancer*. 2004;100:1246–1256.
56. Wald LL, Nelson SJ, Day MR, et al. Serial proton magnetic resonance spectroscopy imaging of glioblastoma multiforme after brachytherapy. *J Neurosurg*. 1997;87:525–534.
57. Preul MC, Leblanc R, Caramanos Z, et al. Magnetic resonance spectroscopy guided brain tumor resection: differentiation between recurrent glioma and radiation change in two diagnostically difficult cases. *Can J Neurol Sci*. 1998;25:13–22.
58. Isobe T, Matsumura A, Anno I, et al. [Changes in 1H-MRS in glioma patients before and after irradiation: the significance of quantitative analysis of choline-containing compounds]. *No Shinkei Geka*. 2003;31:167–172.
59. Schlemmer HP, Bachert P, Herfarth KK, et al. Proton MR spectroscopic evaluation of suspicious brain lesions after stereotactic radiotherapy. *AJNR Am J Neuroradiol*. 2001;22:1316–1324.
60. Panigrahy A, Krieger M, Gonzalez-Gomez I, et al. *Differentiation of Encephalitis from Astrocytomas in Pediatric Patients by Quantitative in vivo MR Spectroscopy*. Chicago: American Society of Neuroradiology; 2007.
61. Foerster BR, Conklin LS, Petrou M, et al. Minimal hepatic encephalopathy in children: evaluation with proton MR spectroscopy. *AJNR Am J Neuroradiol*. 2009;30:1610–1613.
62. Ross BD, Ernst T, Kreis R, et al. 1H MRS in acute traumatic brain injury. *J Magn Reson Imaging*. 1998;8:829–840.
63. Makoroff KL, Cecil KM, Care M, et al. Elevated lactate as an early marker of brain injury in inflicted traumatic brain injury. *Pediatr Radiol*. 2005;35:668–676.
64. Basu S, Zaidi H, Houseni M, et al. Novel quantitative techniques for assessing regional and global function and structure based on modern imaging modalities: implications for normal variation, aging and diseased states. *Semin Nucl Med*. 2007;37:223–239.
65. Minn H, Leskinen-Kallio S, Lindholm P, et al. [18F]fluorodeoxyglucose uptake in tumors: kinetic vs. steady-state methods with reference to plasma insulin. *J Comput Assist Tomogr*. 1993;17:115–123.
66. Kole AC, Nieweg OE, Pruim J, et al. Standardized uptake value and quantification of metabolism for breast cancer imaging with FDG and L-[1-11C]tyrosine PET. *J Nucl Med*. 1997;38:692–696.
67. Chugani HT, Phelps ME, Mazziotta JC. Positron emission tomography study of human brain functional development. *Ann Neurol*. 1987;22:487–497.
68. Chugani HT. Functional brain imaging in pediatrics. *Pediatr Clin North Am*. 1992;39:777–799.
69. Loessner A, Alavi A, Lewandrowski KU, et al. Regional cerebral function determined by FDG-PET in healthy volunteers: normal patterns and changes with age. *J Nucl Med*. 1995;36:1141–1149.
70. Koepp MJ, Woermann FG. Imaging structure and function in refractory focal epilepsy. *Lancet Neurol*. 2005;4:42–53.
71. Engel J Jr, Brown WJ, Kuhl DE, et al. Pathological findings underlying focal temporal lobe hypometabolism in partial epilepsy. *Ann Neurol*. 1982;12:518–528.
72. Henry TR, Mazziotta JC, Engel J Jr. Interictal metabolic anatomy of mesial temporal lobe epilepsy. *Arch Neurol*. 1993;50:582–589.
73. Henry TR, Babb TL, Engel J Jr, et al. Hippocampal neuronal loss and regional hypometabolism in temporal lobe epilepsy. *Ann Neurol*. 1994;36:925–927.
74. Duncan JD, Moss SD, Bandy DJ, et al. Use of positron emission tomography for presurgical localization of eloquent brain areas in children with seizures. *Pediatr Neurosurg*. 1997;26:144–156.
75. Theodore WH. MRI, PET, SPECT: interrelations, technical limits, and unanswered questions. *Epilepsy Res Suppl*. 1992;5:127–134.
76. Markand ON, Spencer SS, Anderson AR. SPECT in epilepsy. *J Neuroimaging*. 1995;5(suppl 1):S23–S33.
77. Spencer SS. The relative contributions of MRI, SPECT, and PET imaging in epilepsy. *Epilepsia*. 1994;35(suppl 6):S72–S89.
78. Semah F, Picot MC, Adam C, et al. Is the underlying cause of epilepsy a major prognostic factor for recurrence? *Neurology*. 1998;51:1256–1262.
79. Lee JJ, Kang WJ, Lee DS, et al. Diagnostic performance of 18F-FDG PET and ictal 99mTc-HMPAO SPET in pediatric temporal lobe epilepsy: quantitative analysis by statistical parametric mapping, statistical probabilistic anatomical map, and subtraction ictal SPET. *Seizure*. 2005;14:213–220.
80. Chugani HT, Shields WD, Shewmon DA, et al. Infantile spasms: I. PET identifies focal cortical dysgenesis in cryptogenic cases for surgical treatment. *Ann Neurol*. 1990;27:406–413.
81. Swartz BE, Brown C, Mandelkern MA, et al. The use of 2-deoxy-2-[18F] fluoro-D-glucose (FDG-PET) positron emission tomography in the routine diagnosis of epilepsy. *Mol Imaging Biol*. 2002;4:245–252.
82. Cleary JO, Yeung J, McMeekin H, et al. The significance of incidental brain uptake on 68Ga-DOTATATE PET-CT in neuroendocrine tumour patients. *Nucl Med Commun*. 2016;37:1197–1205.
83. Win Z, Al-Nahhas A, Towey D, et al. 68Ga-DOTATATE PET in neuroectodermal tumours: first experience. *Nucl Med Commun*. 2007;28:359–363.
84. Van. Heertum RL, Greenstein EA, Tikofsky RS. 2-deoxy-fluorglucose-positron emission tomography imaging of the brain: current clinical applications with emphasis on the dementias. *Semin Nucl Med*. 2004;34:300–312.
85. Di. Chiro G, Delapaz RL, Brooks RA, et al. Glucose utilization of cerebral gliomas measured by [18F] fluorodeoxyglucose and positron emission tomography. *Neurology*. 1982;32:1323–1329.
86. Schlemmer HP, Pichler BJ, Schmand M, et al. Simultaneous MR/PET imaging of the human brain: feasibility study. *Radiology*. 2008;248:1028–1035.
87. Muller-Horvat C, Radny P, Eigentler TK, et al. Prospective comparison of the impact on treatment decisions of whole-body magnetic resonance imaging and computed tomography in patients with metastatic malignant melanoma. *Eur J Cancer*. 2006;42:342–350.

# 26

# Diffusion-Weighted Magnetic Resonance Imaging: Principles and Implementation in Clinical and Research Settings

*Jessica L. Wisnowski, Rafael C. Ceschin, and Vincent J. Schmithorst*

Of the advanced magnetic resonance imaging (MRI) modalities, diffusion-weighted (DW) MRI has probably garnered the most excitement in both clinical and research settings during the past decade. Standard now in nearly every neuroimaging MR protocol, DW-MRI has demonstrated substantial clinical utility in the detection of acute ischemia, the differential diagnosis of intracranial lesions, and the evaluation of white matter. Diffusion tensor imaging (DTI) and other high-angular resolution diffusion imaging (HARDI) models have been applied to the evaluation of normal developmental processes and pathology, particularly that which involves the white matter. Numerous postprocessing methods have been developed that not only allow for group level comparisons of the underlying "tissue microstructure" but also allow for estimation (and visual representation) of the underlying white matter "tracts." In this chapter, we will review (1) underlying principles of DW-MRI acquisitions; (2) basic diffusion-weighted imaging (DWI) acquisitions (its application in clinical settings); (3) DTI models and postprocessing methods, with emphasis on the strengths and potential pitfalls in both clinical and research settings; and (4) advanced diffusion imaging models.

## UNDERLYING PRINCIPLES OF DW-MRI ACQUISITION

At its core, DW-MRI involves the application of two additional pulses of magnetic field gradient (called "diffusion-encoding" or "diffusion-sensitizing" gradients) to a T2-weighted sequence after the excitation pulse but before the readout. During the first gradient pulse, spin precession is accelerated in accordance with the spatial position of the individual water molecules; spins associated with water molecules with a high Z coordinate, for example, will precess more quickly after administration of a gradient pulse along the Z direction, whereas spins associated with water molecules with a low Z coordinate will precess more slowly. Therefore the net effect of the first gradient pulse on the ensemble of spins is that the spins begin precessing at different rates and consequently "dephase," resulting in signal attenuation. The second gradient pulse is equal in direction, magnitude, and duration ($\delta$) to the first and is either of opposite polarity (in the case of a gradient echo acquisition) or of the same polarity (in the case of a spin echo acquisition) but placed after a 180-degree refocusing pulse. Assuming that the spins do not move from their original locations, the effect of the second gradient pulse will be to precisely undo the effect of the first and thus "rephase" the spins so there is no longer any signal attenuation due to spin dephasing. However, under physiologic conditions, water molecules possess thermal energy and therefore will move a finite distance away from their original locations during the time between gradient pulses ($\Delta$). Thus, the rephasing is incomplete and the signal will be attenuated compared with the signal with no diffusion-sensitizing gradients.

Assuming that the movement of water molecules is not hindered by any form of barrier (so-called "free diffusion"), the mean squared distance that the spins will move over a given period is described by the Einstein-Smoluchowsky equation and is linearly proportional to the time ($\Delta$) and to the self-diffusion coefficient $D$. The amount of attenuation is a function of the gradient strength $G$, gradient duration $\delta$, time between gradient pulses $\Delta$, and diffusion coefficient $D$. Typically $G$, $\delta$, and $\Delta$ are combined to derive the "b-value"; the higher the b-value, the greater the signal attenuation in the resultant DW images (Fig. 26.1). In fact, signal attenuation is exponential, where $S$ is the measured signal and $S_0$ is the signal in the absence of diffusion weighting. As a result, $D$ (measured in $mm^2/s$) can be estimated by obtaining DW images at different b-values or by obtaining images with and without diffusion weighting.

However, the diffusion of water molecules in the brain differs in two important respects from free diffusion. First, the diffusion of water is hindered by a variety of barriers, including axon sheaths and glial cell and astrocyte membranes. Hence the measured diffusion coefficient is not a self-diffusion coefficient and therefore is referred to as an *apparent* diffusion coefficient (ADC). Furthermore, the diffusion of water in the brain is not isotropic (i.e., independent of direction). For instance, diffusivity along an axon direction will be larger than diffusivity perpendicular to the axon. Hence, DW images often are obtained using a variety of gradient directions to infer information about the diffusivity of water molecules in different directions; the amount of attenuation in the DW images is dependent on the diffusion of water molecules only in the direction of the applied diffusion-encoding gradients.

It also is important to note that, because DW measurements reflect an *attenuation* of signal at a given spatial location, maintenance of sufficient signal to noise in the resultant data is an inherent challenge in DWI. Moreover, the time needed to acquire data sufficient for some of the most advanced postprocessing techniques, which require acquisitions at many different gradient direction and b-values, is often well outside of what is typically feasible in clinical settings and in many pediatric populations. Thus in practice, most pediatric DW-MRI studies generally are limited to the more basic DW-MRI models (i.e., DTI, described in a later section of this chapter), although recent developments provide hope that other techniques will become clinically feasible.

## DIFFUSION WEIGHTING, APPARENT DIFFUSIVITY, AND THEIR APPLICATION IN CLINICAL SETTINGS

Clinically relevant information is available even from a single DWI acquisition. For instance, diffusion is restricted in regions of cytotoxic edema after a stroke, and these regions therefore will be hyperintense on DW images. However, typical DWI acquisitions are strongly T2-weighted, because a long echo time is necessary as a result of the time needed to apply the diffusion-sensitizing gradients. Therefore it is important to distinguish hyperintensity on DWI that represents true diffusion restriction from hyperintensity that reflects tissue T2 prolongation (often termed "T2 shine-through"). This differentiation usually is performed by the additional acquisition of an image without diffusion weighting (e.g., $b = 0\ s/mm^2$) and quantifying ADC on a pixel-by-pixel basis, which subsequently can be represented in gray scale as an ADC map. Additionally, instead of a single DW acquisition, three DW

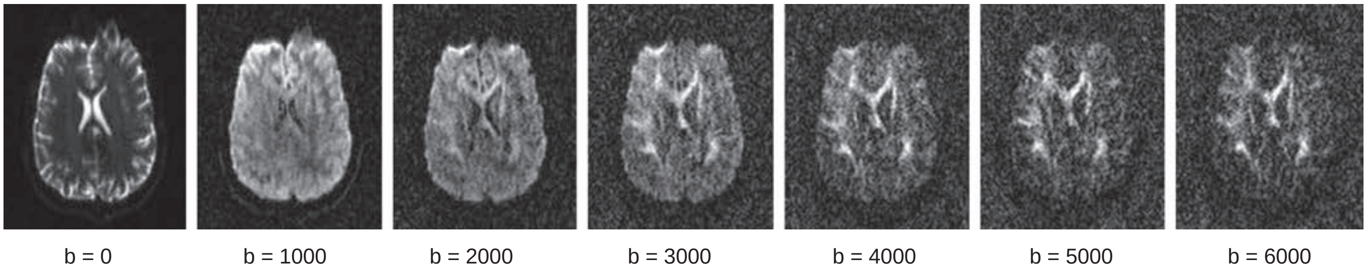

**Figure 26.1. Changing b-value.** Displayed are corresponding slices from a single subject imaged at multiple b-values. Notice how contrast between gray and white matter increases with the increasing b-value, whereas overall signal/noise ratio decreases. *(Author's Original.)*

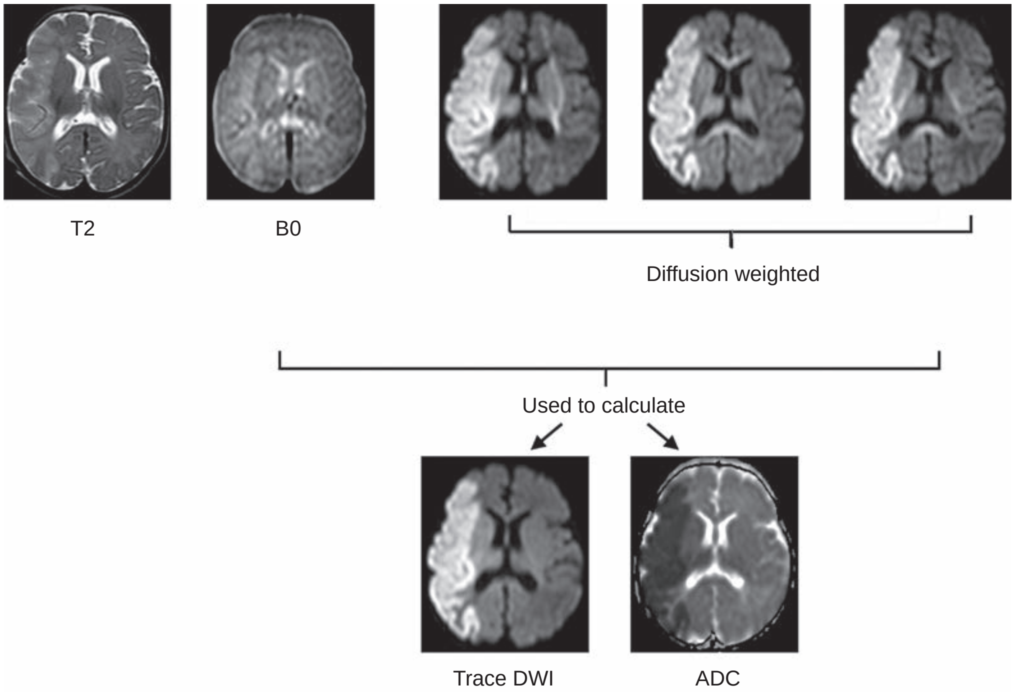

**Figure 26.2. Diffusion-weighted imaging demonstrated in a 3-week-old neonate with an acute stroke.** *(top row)* Corresponding slices from an axial T2-weighted and DW-MRI scan. In most protocols, three diffusion-encoding directions (rather than one) are acquired, averaged, and compared with the image without diffusion encoding (B0) to generate *(bottom row)* trace-weighted and apparent diffusivity maps that demonstrate areas of restricted diffusion as areas of high and low signal, respectively. Note that areas of directional anisotropy are visualized in each of the diffusion-encoding directions, but as a result of averaging, these areas are not apparent in the trace-weighted and ADC maps.

images typically are acquired using three orthogonal gradient directions, and the results are averaged to obtain *directionally averaged* DW images and ADC maps to minimize the effects of anisotropy. The directionally averaged ADC map is proportional to the trace of the diffusion tensor (described later), and thus the DWI images and ADC maps often are referred to as "trace-weighted DWI" and "trace diffusion tensor maps," respectively (Fig. 26.2).

As previously noted, in the past 2 decades, trace DW images with corresponding ADC values have demonstrated remarkable clinical utility in the detection of cerebral ischemia, before such injuries become apparent on T2-weighted MRI. Acutely, ischemia leads to energy failure, and more specifically, a failure of the Na+/K+–adenosine triphosphatase pumps in the cell membrane. This phenomenon, in turn, leads to an influx of sodium (and other ions) and water into the cell, resulting in cytotoxic edema and a concomitant decrease in ADC.

ADC values decrease within minutes after the onset of cerebral ischemia and reach a nadir around 3 days after onset, although this timing can be variable depending on the magnitude of initial insult, tissue reperfusion, and application of neuroprotective therapies (e.g., therapeutic hypothermia).[1–3] Subsequently, ADC values begin to rise, reaching "normal values" approximately 1 week after onset (i.e., pseudonormalization) and then continuing higher in the subacute/chronic phase, paralleling cell death and the resultant decrease in cell density.

Because ADC is not only sensitive to edema but also cell density, DWI is becoming the method of choice for imaging cancerous lesions. DWI has advantages over positron emission tomography

(PET) in that it does not use ionizing radiation or require injection of any radioactive tracer. Water diffusion decreases as cellularity increases; thus a low ADC is usually associated with a high degree of malignancy (Fig. 26.3). By contrast, high ADC values are typically observed in low-grade lesions or in association with a positive treatment response. Recent studies have now combined serial ADC measurements with quantitative postprocessing techniques (i.e., parametric response mapping), which not only allow treatment response to be characterized on a voxelwise basis but also provide quantitative biomarkers for use in clinical trials and in clinical practice.[4]

## DIFFUSION TENSOR IMAGING

Although three diffusion-sensitizing gradients are sufficient for calculating a directionally averaged ADC image, a minimum of six directions is needed to characterize diffusion anisotropy. Anisotropic diffusion is directionally dependent, as within white matter fiber bundles, and is distinguishable from isotropic diffusion, which is observed in free fluids (e.g., the lateral ventricles) (Fig. 26.4).

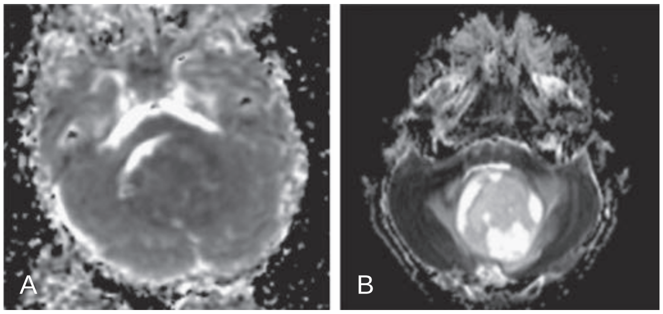

**Figure 26.3. Apparent diffusion coefficient and intracranial lesions.** (A) The ADC map demonstrates restricted diffusion in a tumor with high cellularity (a medulloblastoma). (B) The ADC map demonstrates increased diffusion in a tumor with low cellularity (a pilocytic astrocytoma).

To calculate anisotropy, DTI models diffusion as a tensor quantity (a 3 × 3 matrix) on a voxel-by-voxel basis. Typically, the matrix is rotated such that anisotropy may be described in terms of three coordinate axes ("eigenvectors"), with the principal axis (the one corresponding to the largest "eigenvalue" $\lambda_1$, also known as $\lambda_{\parallel}$, or axial diffusivity [AD]) being along the axis of preferred diffusion and the remaining two eigenvalues ($\lambda_2$ and $\lambda_3$) corresponding to vectors perpendicular to the principal axis. Eigenvalues $\lambda_2$ and $\lambda_3$ often are combined (averaged) to generate another metric referred to as radial diffusivity (RD) ($\lambda_{\perp}$). Importantly, although the 3 × 3 *diffusion tensor* may be ideal for estimating diffusion in a three-dimensional (3D) structure characterized by fiber bundles aligned in a single orientation, this model falls short if the underlying structure includes fiber bundles of different orientations (e.g., "crossing fibers"). Potential pitfalls associated with DTI will be discussed in further detail later.

The most common anisotropy metric derived from DTI data is fractional anisotropy (FA). FA is a scalar metric (rather than a vector) and represents the degree of anisotropy at a given voxel. It is calculated by comparing the estimated diffusion along each of the three eigenvalues in accordance with the following equation:

$$\mathrm{FA} = \frac{\sqrt{(\lambda_1-\lambda_2)^2+(\lambda_2-\lambda_3)^2+(\lambda_3-\lambda_1)^2}}{\sqrt{2(\lambda_1^2+\lambda_2^2+\lambda_3^2)}}$$

As can be determined from this equation, FA can range from 0 (when $\lambda_1 = \lambda_2 = \lambda_3$, i.e., isotropic diffusion) to 1 (when $\lambda_2 = \lambda_3 = 0$, i.e., fully anisotropic). In adults, typical white-matter values range between 0.9 and 0.4 depending on whether the measurement is obtained in a region where fiber bundles are heavily myelinated, tightly packed, and uniformly oriented (e.g., in the corpus callosum) or in a region where the organization deviates from that (such as in the vicinity of crossing fibers), respectively. FA values are much lower in neonates (ranging between 0.45 and 0.1) but rapidly increase toward the adult range in the first 2 years of life and then continue to increase at a much lower rate through adolescence into adulthood.[5–7]

Because of the higher water content in the neonatal brain and the fact that this increase in extracellular water is associated with increased diffusivity and increased signal attenuation in the setting

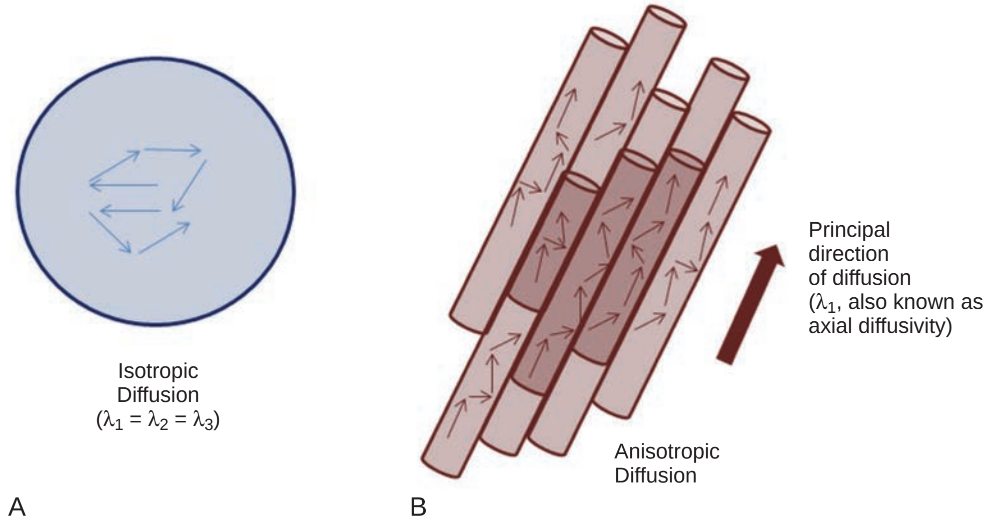

**Figure 26.4. Isotropic and anisotropic diffusion.** (A) Isotropic diffusion is exemplified by free diffusion such as in a large glass of water. (B) Anisotropic diffusion occurs when diffusion is greater in one direction compared with the others, such as in axons. By convention, the principal eigenvalue ($\lambda_1$) represents diffusion along the preferred axis.

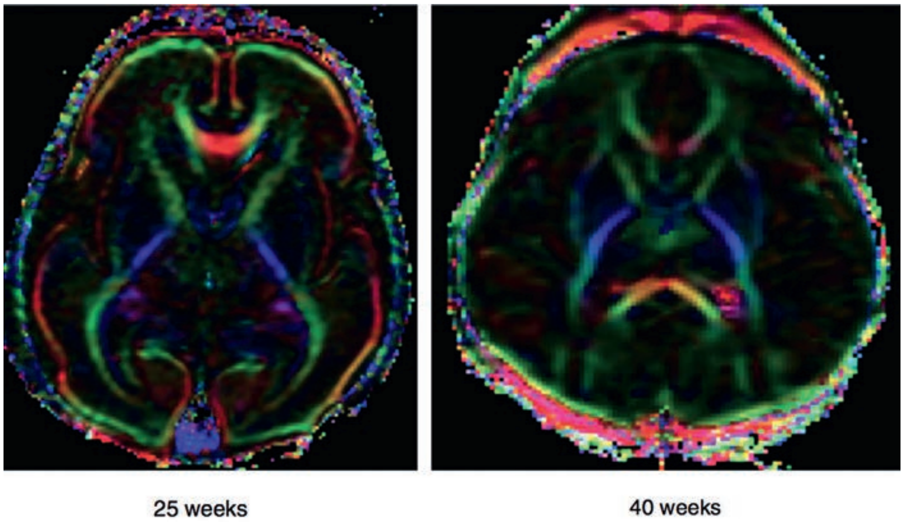

**Figure 26.5. Color fractional anisotropy maps reconstructed from diffusion tensor imaging data acquired from a preterm neonate at 25 weeks and a term neonate at 40 weeks.** By convention, voxels in which the principal eigenvector ($\lambda_1$) is in a left-right orientation (relative to the slice) are colored in *red,* voxels in which $\lambda_1$ is in an anterior-posterior orientation are colored *green,* and voxels in which $\lambda_1$ is in a superior-inferior orientation are colored *blue.* Note the presence of high anisotropy in the cortex of the neonate at 25 weeks and that, by term, the cortex has lower anisotropy than the adjacent white matter.

of diffusion encoding gradients, neonates often undergo imaging at a lower b-value (e.g., b = 700 s/mm$^2$).

To further enhance clinical utility, FA often is combined with information regarding the direction of the principal eigenvector, yielding a color FA map (Fig. 26.5). The typical convention is to color pixels red when the principal eigenvector is in the left-right direction relative to the 3D coordinate space, green when the principal eigenvector is anterior-posterior, and blue when the principal eigenvector is inferior-superior.

## Microstructural Integrity

The sensitivity of DTI to local (“microstructural”) tissue properties has rendered the technique a popular instrument for investigating the neuroanatomic underpinnings of various conditions (e.g., traumatic brain injury, multiple sclerosis, white-matter injury of prematurity, autism, and dyslexia, but also such areas as normal development, learning, and musical training) at the level of gray- and white-matter tissue microstructure. Moreover, DTI sequences are readily available in most commercial MRI scanners, with the acquisition time necessary for a typical 30- to 60-direction DTI sequence being between 5 minutes to less than 15 minutes. Accordingly, DTI is not only feasible in most pediatric patients but also is a potential key to understanding the neuroanatomic basis for a wide range of conditions, many of which are not associated with visible changes on conventional T1- and T2-weighted imaging.

However, the precise interpretation for many of the differences in DTI measures of microstructure remains to be determined. Pioneering laboratory work by Sheng-Kwei Song and colleagues in mouse models demonstrated that myelin loss alone (without loss or degeneration of axons) results in an increase in RD, leaving AD unchanged.[8] By contrast, direct axonal damage results in a decrease in AD.[9] Based on these findings, many researchers have drawn inverse conclusions on their own data—namely, that an increase in RD in a given white-matter region reflects primarily damage to myelin, whereas a decrease in AD reflects primarily damage to axons. Unfortunately, the inverse conclusion is not necessarily valid. First, most of the laboratory work supporting the interpretation of AD and RD in relation to axonal pathology versus myelin has been carried out in the optic nerve, spinal cord, or corpus callosum.[8–10] These structures are unique in the central nervous system in that they contain fiber bundles essentially aligned in parallel along a principal axis. By contrast, it has been estimated that as many as 90% of white-matter voxels in the cerebrum contain crossing fibers,[11] and it is not yet known how altering myelination or axonal integrity along a single fiber bundle, in the setting of multiple crossing fibers, would alter AD or RD. Accordingly, in the cerebrum, given available knowledge at this point, a more appropriate interpretation may be “altered microstructure,” with more specific conclusions being drawn from collateral information.

## Tractography

Some of the increasingly common—and most important—questions that researchers and neuroradiologists have aimed to address with use of DTI concerns anatomic connectivity (e.g., “Which cortical and subcortical regions are connected and by which fiber pathways?” “How strong are the connections between X and Y? … in this population compared with that one?”). To address these types of questions, most researchers and clinicians begin by constructing a visual representation of the white-matter fibers (or tracts). This task is carried out with the use of computer algorithms that regard fiber tracts as a continuous trajectory derived from local (voxel or pixel) estimates of fiber orientation (e.g., eigenvectors; Fig. 26.6). This technique is commonly known as tractography. It should be emphasized that no tractography method is capable of reconstructing axonal fibers or even fiber bundles. Rather, these methods compute trajectories or pathways represented by the data, which, it is hoped, parallel the predominant trajectories of the underlying axonal fiber bundles.

One of the most commonly used algorithms for tractography is known as fiber assignment by continuous tracking (FACT, also known as deterministic tractography).[12] This algorithm proceeds from an initially determined point (seed region) and propagates pixel by pixel in the direction of the principal eigenvector until a predetermined lower FA threshold or maximal turning angle is reached, at which point the fiber path is terminated (see Fig. 26.6). The result is a streamline, a visual representation of anisotropic diffusion, and importantly, not an actual visual representation of

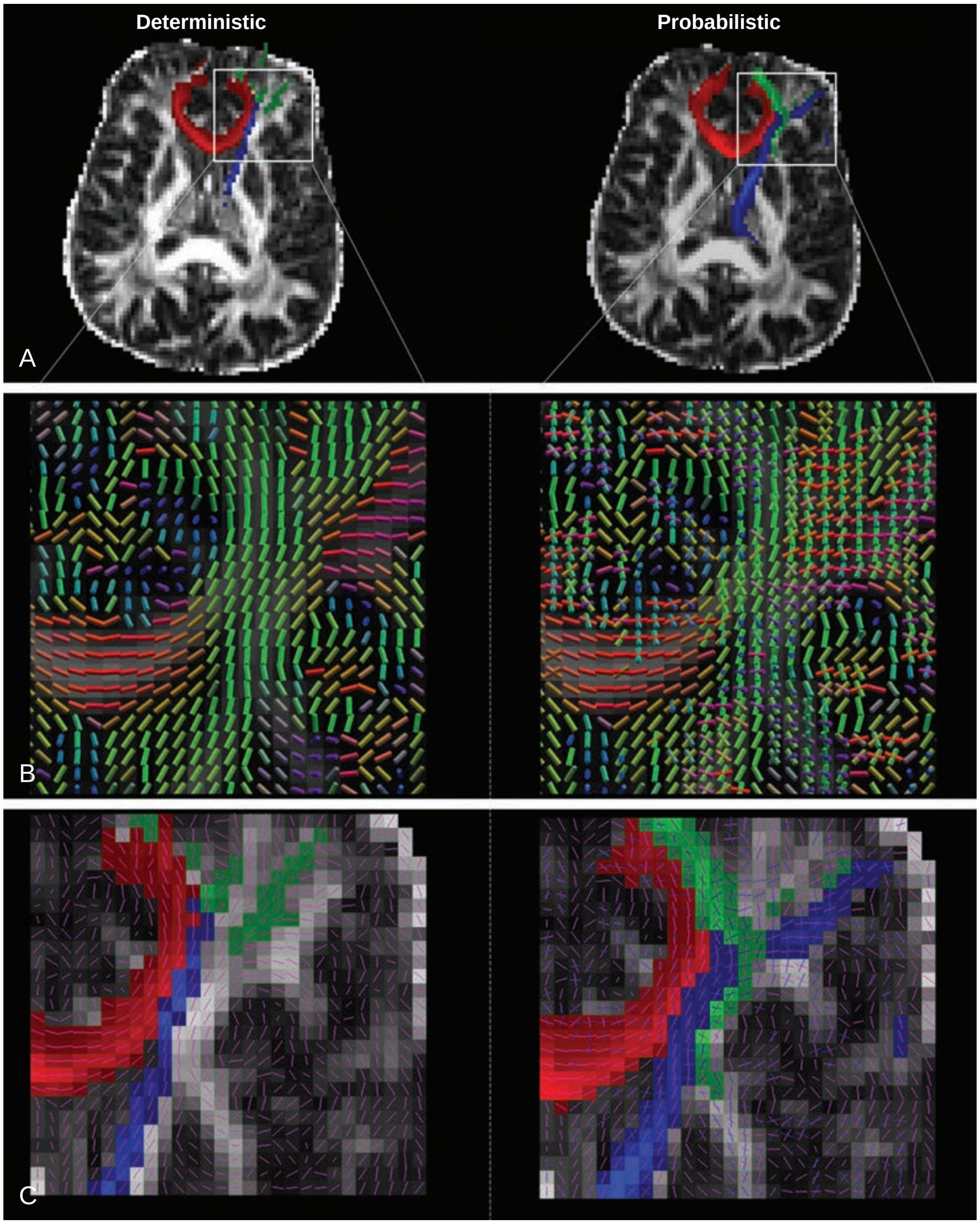

**Figure 26.6. Deterministic and probabilistic tractography.** (A) The same seed and waypoints were used to track anterior thalamic radiation *(blue),* genu of corpus callosum *(red),* and inferior frontooccipital fasciculus using deterministic *(left)* and probabilistic *(right)* algorithms on the same dataset acquired on a single subject. (B) In deterministic tractography, the direction of anisotropy is considered to be along the axis of a single, principal eigenvector, which is represented voxelwise in the image on the left. (Color convention is as described in Fig. 26.5.) In contrast, probabilistic tractography models anisotropy as a probability distribution and allows for a two-fiber solution, which is represented on the right, with the major axis being larger in scale compared with the minor axis. (C) The difference in output is clearly visualized in the region of the crossing fibers where, on the *left,* deterministic tractography (principal eigenvector overlaid as *pink lines*) fails to yield as many tracks as the output from the probabilistic algorithm on the *right* (again, principal and secondary eigenvectors are overlaid in *pink* and *blue,* respectively).

axons or fiber bundles. Moreover, the number of streamlines originating from a particular seed region is directly proportional to the number of seed points within a given voxel, and accordingly, not directly related to the underlying anatomic connectivity. However, assuming the same number of seed points per given voxel are used across populations of interest (which, in most software packages, is not a number that can be manipulated by the operator), the number of streamlines can be considered a proxy for the underlying tissue microstructure, and accordingly, may be used as a metric in group-level comparisons.

One of the key limitations in tractography is that the mathematical model used to reconstruct DTI data assumes that a single fiber population exists in each voxel. However, at the resolution of a typical DTI acquisition (≥2 mm in each dimension), many voxels contain populations of fibers oriented in some manner other than parallel (from one-third to 90%), including fibers that are crossing, fanning, branching, or bottlenecking.[11,13,14] This crossing fiber problem is a significant concern if one is trying to carry out tractography on DTI data. First, the main effect of crossing or other nonparallel fiber orientations on the principal eigenvectors is to decrease the principal eigenvalue. This effect, in turn, results in a decrease in FA, which can cause tractography algorithms to prematurely stop if the FA value has fallen below the predetermined threshold. Second, because the algorithm follows only the principal eigenvector, it may generate spurious streamlines (e.g., a streamline that propagates into a crossing region perpendicular to the principal eigenvector could be made to bend and then continue in the new direction).

One method to address limitations associated with using deterministic tractography and DTI parameters is to use the information derived from the diffusion tensor fit to generate a 3D probability distribution regarding the diffusion of water molecules instead of constraining the molecules to only move along the direction of the principal eigenvector.[13,15,16] In this way, probabilistic tractography algorithms allow water molecules to follow more than one orientation when passing through a voxel in a crossing region. Current probabilistic algorithms allow for the modeling of uncertainty of two (or more) fiber directions at each voxel. Tracking is done by launching a high number of streamlines from a seed region, and at each voxel—instead of deterministically following the principal eigenvector—drawing from the previously determined 3D probability distribution to propagate the tracts. Coherent fiber orientation is preserved by following the sampled direction most closely parallel to the previous location's direction, as opposed to only following an arbitrary angle threshold. After a sufficient number of samples, the output is a probabilistic mapping of the uncertainty of fiber tracts at each voxel, with the dominant streamline surfacing as most probable (see Fig. 26.6). Notably, this method does not resolve the crossing fiber problem with 100% certainty, but the resulting probabilistic map yields a much more robust estimate of the dominant fiber path when compared with deterministic approaches.[13,17] Moreover, it also shows improvements in the rendering of the lateral corticospinal and corticobulbar tracts and the medial portion of the superior longitudinal fasciculus, which typically are not visualized by deterministic tractography. Fig. 26.6 shows the comparison between deterministic and probabilistic algorithms in modeling fibers passing through a densely packed, high-fiber–crossing region of the brain. The probabilistic output shows significant improvement in delineating crossing fiber tracts, such as the inferior frontooccipital fasciculus and anterior thalamic radiation. Similar performance is noted in a single direction tract, as in the genu of the corpus callosum. Despite improved performance in modeling regions with crossing fiber tracts, probabilistic tractography still cannot completely overcome the limitation that the diffusion tensor model is not an adequate model for the underlying physiology in crossing fiber regions. This limitation requires more advanced approaches, as described in the next section.

## Advanced Diffusion Imaging Techniques

Advanced diffusion imaging techniques have been proposed to address the two major limitations of the DTI model: multiple/crossing fiber bundles and signal attenuation that deviates from an exponential decay with increasing b-value. Currently, these approaches have found limited clinical use because of their greater acquisition time and the greater computational resources needed for data analysis. However, with the increasing availability of multiband and other fast imaging techniques, higher order diffusion techniques will become possible in clinical settings.[18]

To address the problem of crossing fibers, HARDI methods (sometimes called "Q-ball")[16,17,19,20] sample a much larger number of diffusion directions (e.g., 64–256) than typical DTI acquisitions (e.g., ~30, although DTI analysis is possible with as few as 6). In addition to more directions, HARDI acquisitions utilize higher b-values (~3000 s/mm$^2$). As discussed earlier in this chapter, higher b-values allow for greater signal decay (see Fig. 26.1). At the same time, this signal decay will be most pronounced for the faster-diffusing extracellular water, thereby increasing the sensitivity toward slower-diffusing intracellular water (note the increased conspicuity of the white-matter tracks in the higher b-value images in Fig. 26.1). The HARDI sampling technique allows for modeling of orientation distribution functions (ODF) in lieu of simple tensors, in turn improving angular resolution and fiber detection. With these techniques, it is possible to model two, three, or even more crossing fiber bundles.

Higher b-values not only support better fiber detection, but also, when combined with additional b-weightings, further delineation of tissue microstructure due to the non-exponential nature of the signal decay. Biophysical models such as composite hindered and restricted model of diffusion (CHARMED) and neurite orientation dispersion and density imaging (NODDI) combine diffusion acquisitions at multiple high b-values (i.e., "multishelled" acquisitions) and advanced reconstruction techniques to model cellular geometry, diameter, and density/dispersion in grey and white matter.[21,22] Likewise, techniques such as diffusion kurtosis imaging (DKI) utilize multishelled acquisitions (albeit typically with fewer diffusion directions) to increase sensitivity toward pathologic changes, such as discriminating high and low grade glioma.[23,24]

The "ultimate" in DWI acquisition combines high directional resolution and multiple b-values, which allows for the most accurate specification of the water diffusion profiles, enabling the simultaneous modeling of crossing fiber bundles as well as nonexponential decay. This technique is called diffusion spectrum imaging (DSI) or Q-space imaging.[25,26] The acquisition demands are intense; a typical DSI protocol involves 512 separate DWI acquisitions, making the total acquisition time longer than 1 hour for a typical DWI acquisition protocol; however, ongoing efforts to optimize imaging parameters may soon make this feasible in clinical settings.[26]

### KEY POINTS

- The diffusion of water is hindered by a variety of barriers, including axon sheaths and glial cell and astrocyte membranes.
- The amount of attenuation in the DW images is dependent on the diffusion of water molecules only in the direction of the applied diffusion-encoding gradients.
- In addition to fluid homeostasis and intracellular water, DWI and ADC also are sensitive to the relative properties of water in the extracellular space.
- Because of the higher water content in the neonatal brain and because of the fact that this increase in extracellular water is associated with increased diffusivity and increased signal attenuation in the setting of diffusion encoding gradients, neonates often undergo imaging at a lower b-value (e.g., b = 700 s/mm$^2$).
- Tractography methods compute trajectories or pathways represented by the data, which, it is hoped, parallel the predominant trajectories of the underlying axonal fiber bundles.
- Advanced diffusion imaging techniques address the two major limitations of conventional tractography: multiple/crossing fiber bundles and signal attenuation that deviates from an exponential decay with increasing b-value.

## SUGGESTED READINGS

Bihan DL, Iima M. Diffusion magnetic resonance imaging: what water tells us about biological tissues. *PLoS Biol*. 2015;13:e1002246. doi:10.1371/journal.pbio.1002246.

Jones DK, Knösche TR, Turner R. White matter integrity, fiber count and other fallacies: the do's and don'ts of diffusion MRI. *Neuroimage*. 2013;73:239–254. doi:10.1016/j.neuroimage.2012.06.081.

Wu W, Miller KL. Image formation in diffusion MRI: a review of recent technical developments. *J Magn Reson Imaging*. 2017;46(3):646–662. doi:10.1002/jmri.25664.

## REFERENCES

Full references for this chapter can be found on www.expertconsult.com.

## REFERENCES

1. Robertson RL, Ben-Sira L, Barnes PD, et al. MR Line-scan diffusion-weighted imaging of term neonates with perinatal brain ischemia. *AJNR Am J Neuroradiol*. 1999;20:1658–1670.
2. van der Aa NE, Benders MJNL, Vincken KL, et al. The course of apparent diffusion coefficient values following perinatal arterial ischemic stroke. *PLoS ONE*. 2013;8:1–6. doi:10.1371/journal.pone.0056784.
3. Bednarek N, Mathur A, Inder T, et al. Impact of therapeutic hypothermia on MRI diffusion changes in neonatal encephalopathy. *Neurology*. 2012;78:1420–1427. doi:10.1212/WNL.0b013e318253d589.
4. Ceschin R, Kurland BF, Abberbock SR, et al. Parametric response mapping of apparent diffusion coefficient as an imaging biomarker to distinguish pseudoprogression from true tumor progression in peptide-based vaccine therapy for pediatric diffuse intrinsic pontine glioma. *AJNR Am J Neuroradiol*. 2015;36:2170–2176. doi:10.3174/ajnr.A4428.
5. Schmithorst VJ, Wilke M, Dardzinski BJ, et al. Correlation of white matter diffusivity and anisotropy with age during childhood and adolescence: a cross-sectional diffusion-tensor MR imaging study. *Radiology*. 2002;222:212–218.
6. Gao W, Lin W, Chen Y, et al. Temporal and spatial development of axonal maturation and myelination of white matter in the developing brain. *AJNR Am J Neuroradiol*. 2009;30:290–296. doi:10.3174/ajnr.A1363.
7. Asato MR, Terwilliger R, Woo J, et al. White matter development in adolescence: a DTI study. *Cereb Cortex*. 2010;20:2122–2131. doi:10.1093/cercor/bhp282.
8. Song SK, Sun SW, Ramsbottom MJ, et al. Dysmyelination revealed through MRI as increased radial (but unchanged axial) diffusion of water. *Neuroimage*. 2002;17:1429–1436.
9. Song SK, Sun SW, Ju WK, et al. Diffusion tensor imaging detects and differentiates axon and myelin degeneration in mouse optic nerve after retinal ischemia. *Neuroimage*. 2003;20:1714–1722. doi:10.1016/j.neuroimage.2003.07.005.
10. Kim JH, Loy DN, Liang H-F, et al. Noninvasive diffusion tensor imaging of evolving white matter pathology in a mouse model of acute spinal cord injury. *Magn Reson Med*. 2007;58:253–260. doi:10.1002/mrm.21316.
11. Jeurissen B, Leemans A, Tournier JD, et al. Investigating the prevalence of complex fiber configurations in white matter tissue with diffusion magnetic resonance imaging. *Hum Brain Mapp*. 2013;34:2747–2766. doi:10.1002/hbm.22099.
12. Mori S, Crain BJ, Chacko VP, et al. Three-dimensional tracking of axonal projections in the brain by magnetic resonance imaging. *Ann Neurol*. 1999;45:265–269. doi:10.1002/1531-8249(199902)45:2<265::AID-ANA21>3.0.CO;2-3.
13. Behrens TEJ, Berg HJ, Jbabdi S, et al. Probabilistic diffusion tractography with multiple fibre orientations: what can we gain? *Neuroimage*. 2007;34:144–155. doi:10.1016/j.neuroimage.2006.09.018.
14. Mori S, Van Zijl PCM. Fiber tracking: principles and strategies - a technical review. *NMR Biomed*. 2002;15:468–480. doi:10.1002/nbm.781.
15. Descoteaux M, Deriche R, Knösche T, et al. Deterministic and probabilistic tractography based on complex fiber orientation distributions. *IEEE Trans Med Imaging*. 2009;28:269–286. doi:10.1109/TMI.2008.2004424.
16. Pontabry J, Rousseau F, Oubel E, et al. Probabilistic tractography using Q-ball imaging and particle filtering: application to adult and in-utero fetal brain studies. *Med Image Anal*. 2013;17:297–310. doi:10.1016/j.media.2012.11.004.
17. Berman JI, Chung SW, Mukherjee P, et al. Probabilistic streamline q-ball tractography using the residual bootstrap. *Neuroimage*. 2008;39:215–222. doi:10.1016/j.neuroimage.2007.08.021.
18. Wu W, Miller KL. Image formation in diffusion MRI: a review of recent technical developments. *J Magn Reson Imaging*. 2017;1–17:doi:10.1002/jmri.25664.
19. Tuch DS. Q-ball imaging. *Magn Reson Med*. 2004;52:1358–1372. doi:10.1002/mrm.20279.
20. Hess CP, Mukherjee P, Han ET, et al. Q-ball reconstruction of multimodal fiber orientations using the spherical harmonic basis. *Magn Reson Med*. 2006;56:104–117. doi:10.1002/mrm.20931.
21. Assaf Y, Basser PJ. Composite hindered and restricted model of diffusion (CHARMED) MR imaging of the human brain. *Neuroimage*. 2005;27:48–58. doi:10.1016/j.neuroimage.2005.03.042.
22. Zhang H, Schneider T, Wheeler-Kingshott CA, et al. NODDI: practical in vivo neurite orientation dispersion and density imaging of the human brain. *Neuroimage*. 2012;61:1000–1016. doi:10.1016/j.neuroimage.2012.03.072.
23. Differences M, Raab P, Hattingen E, et al. *Cerebral Gliomas : Diffusional Kurtosis Imaging Analysis of Purpose : Methods : Results :*, 254 (2010).
24. Winfeld M, Jensen JH, Adisetiyo V, et al. Differentiating high and low grade pediatric brain tumors using diffusional kurtosis imaging. *J Pediatr Neuroradiol*. 2013;2:301–305. doi:10.3233/PNR-13072.
25. Basser PJ. Relationships between diffusion tensor and q-space MRI. *Magn Reson Med*. 2002;47:392–397. doi:10.1002/mrm.10052.
26. Westin CF, Knutsson H, Pasternak O, et al. Q-space trajectory imaging for multidimensional diffusion MRI of the human brain. *Neuroimage*. 2016;135:345–362. doi:10.1016/j.neuroimage.2016.02.039.

# 27

# Functional Magnetic Resonance Imaging

James Leach

## PHYSIOLOGIC BASIS OF FUNCTIONAL MAGNETIC RESONANCE IMAGING

Functional magnetic resonance imaging (fMRI) is based on the blood oxygen level–dependent (BOLD) contrast effect and neuronal activity–cerebrovascular flow coupling. Oxygenated blood (oxyhemoglobin) is diamagnetic, producing little susceptibility-related dephasing on magnetic resonance (MR) signal. Deoxyhemoglobin is paramagnetic and elicits a more prominent effect on local field homogeneity and phase coherence, resulting in signal loss. Changes in the relative concentrations of oxyhemoglobin and deoxyhemoglobin in the vascular bed therefore result in changes in regional MR signal. The increase in cerebral blood flow that accompanies neuronal activity results in a relative increase in oxyhemoglobin concentration and a resultant localized increase in MR signal.[1] The actual physiology underlying the BOLD response is complex and is the subject of ongoing research.[2] Many anatomic and physiologic changes occur during brain development that have the potential to alter the BOLD response in children compared with adults.[3-6] Despite these physiologic differences, the basic BOLD response in children is generally similar to that in adults,[3,7] albeit with some task-related differences.[8] Neonates and infants may exhibit significantly different BOLD responses than do older children and adults, complicating interpretation in this age group.[9-11]

## TECHNICAL CONSIDERATIONS FOR FUNCTIONAL MAGNETIC RESONANCE IMAGING PERFORMANCE IN CHILDREN

The requirements for fMRI performance include an MRI scanner with gradient hardware capable of performing fMRI useable sequences, stimulation/presentation hardware and software linked to the scanner to allow for synchronization of stimuli and MR imaging, hardware and software for documenting patient responses, and postprocessing software for producing activation maps. The small BOLD effect changes in MR signal typically are detected by echo-planar imaging (EPI) T2*-sensitive gradient recalled echo techniques. Because of increased signal to noise and sensitivity for BOLD contrast effects, 3T scanners are preferred for fMRI studies.[12,13]

Performance of useful clinical fMRI examinations in children requires specialized preparation and resources. The patient is assessed for underlying neurologic deficits, developmental level, and ability to complete the fMRI paradigms. Explanation of the MR procedure and fMRI paradigms to the patient and parents in a calm, child-centered environment is critical. Practicing the fMRI paradigms is important to maximize performance and to adapt the tasks for the patient's clinical and developmental level. Video presentations and mock scanners are highly useful in preparing children for the fMRI environment.[14,15] Patient comfort should be maximized.

Patient motion can influence fMRI performance in children.[14,16] Despite some ability to retrospectively correct for head motion, gross head movement typically results in unusable fMRI data. Head coil bite bars, inflatable head cushions, and forehead and chin straps may be used but can be difficult to implement. Head motion is more pronounced in younger children and in boys.[16] Older children and girls have a higher rate of successfully completed examinations.[14] With care and adequate preparation, most children presenting for clinical fMRI studies can complete fMRI examinations with multiple administered paradigms.[17] The routine application of real-time fMRI processing can reduce the number of inadequate studies.[18]

For task-based fMRI examinations, repeated samplings of the brain (one brain volume scan during each repetition time period) while the subject alternates between active cognitive and control tasks typically is performed (the fMRI "paradigm"). Typical fMRI paradigms require 3 to 7 minutes of imaging time for acquisition of 100 or more image volumes during three to five cycles of alternating behavior. Although many approaches are possible, clinical fMRI is most commonly performed in a "blocked-periodic" design in which blocks of task and control (baseline) conditions are administered sequentially.[19] The fMRI paradigm that is used ideally will result in activation of brain regions involved with the sensory, motor, or cognitive task presented, without activation in other regions. The proper choice of control and task conditions is important to allow this distinction and must be carefully matched to elicit detectable BOLD signal and isolate the function of interest.[20,21] For successful performance of fMRI examinations in children, utilization of age and developmentally appropriate paradigms is mandatory.[14,21]

Imaging processing is required for fMRI and should involve the interpreting radiologist. After acquisition of images during the fMRI paradigm, the images typically are processed to diminish EPI artifacts, correct for susceptibility-related distortions, limit effects from patient movement during the paradigm, align and transform the T2* EPI images to a higher resolution anatomic dataset, and statistically analyze the images for BOLD signal changes between the task conditions on a voxel-by-voxel basis (the statistical map) (Fig. 27.1).[22,23] Increasingly, streamlined, clinically oriented options are being offered on most clinical MR systems or by a growing number of third-party vendors. The most common statistical tests used for clinical fMRI are the general linear model[22] and the cross-correlation method.[19] Determination of the optimum statistical threshold for use in individual clinical patients is a complex issue.[23,24] Evaluating fMRI studies at multiple different thresholds is important to maximize clinical effectiveness.

## CLINICAL APPLICATIONS OF FUNCTIONAL MAGNETIC RESONANCE IMAGING IN CHILDREN

Although many indications for pediatric fMRI are undergoing active research evaluation, the most common clinical use of fMRI in children is for presurgical assessment of language and memory function for patients with intractable epilepsy and evaluation of potentially eloquent cortex in patients with brain lesions (e.g., tumors and cavernous malformations).

### Limitations

Some fundamental concepts must be kept in mind when performing and interpreting fMRI studies in clinical patients.[25] For example, fMRI activation regions are not functionally specific, and lack of activation in a brain region does not indicate lack of critical brain function. The fMRI procedure is an indirect evaluation of neuronal function and relies on statistical mapping techniques that are not clinically standardized. The BOLD effect can be directly altered by pathologic states with changes in cerebrovascular autoregulation

## Abstract:

Clinical fMRI use in children primarily is used to assess eloquent brain regions before surgery relating to lesions or epilepsy. Clinical fMRI in children requires special preparation and resources, as well as developmentally appropriate fMRI paradigms. Somatosensory and language assessments are the most commonly performed fMRI examinations in clinical patients. Standardization of fMRI paradigms and interpretation, as well as better validation and outcome studies, are needed in pediatric patients. Newer techniques such as resting state fMRI hold promise to expand clinical fMRI applications to children who currently are unable to perform task-directed fMRI examinations.

## Keywords:

functional MRI
fMRI
pediatrics
epilepsy
language
children

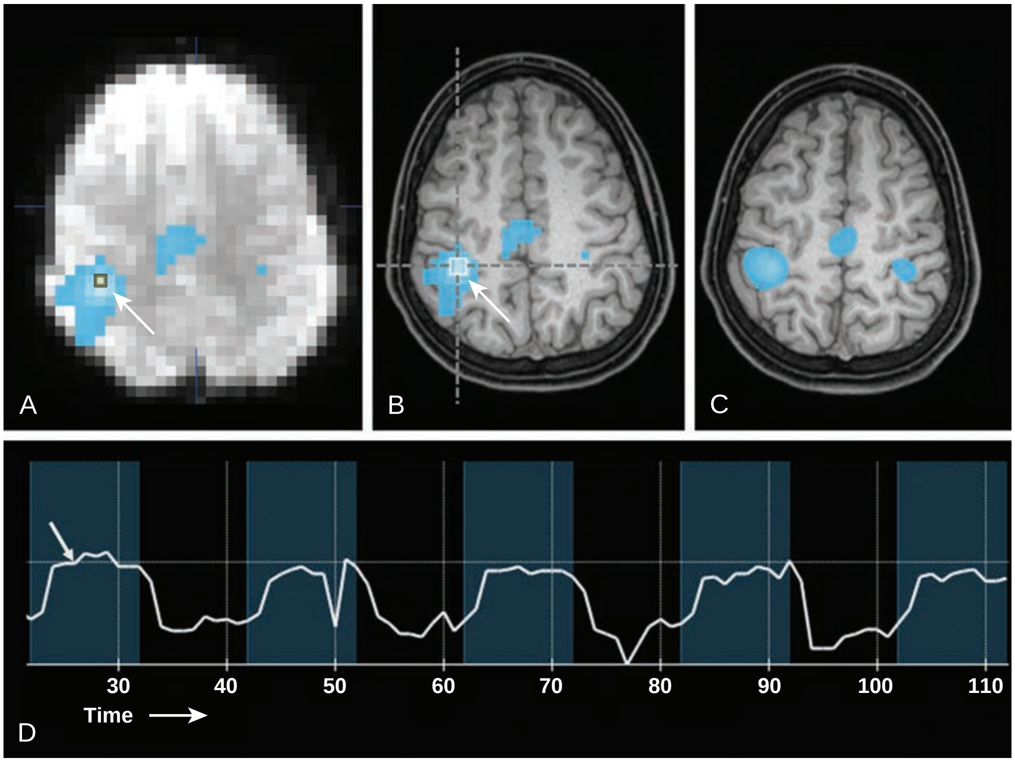

**Figure 27.1. Example of bilateral finger tapping functional magnetic resonance imaging (fMRI) and the effect of smoothing on the appearance of fMRI statistical maps.** (A) A source echo-planar image with an overlaid nonsmoothed statistical activation map. A single voxel region of interest *(arrow)* is located in the region of maximal statistical significance. (B) A nonsmoothed fMRI statistical activation map overlaid onto a 1-mm isotropic T1-weighted image shows activation overlying the right central sulcus in the hand motor region *(arrow).* Overlay onto anatomic MRI images allows the spatial relationships of the fMRI activation areas to be appreciated and related to anatomy and pathology. (C) An fMRI statistical activation map overlaid on a 1-mm isotropic T1-weighted image with smoothing applied to fMRI data. (D) Actual signal intensity within a voxel of interest (*arrow* in A) during the fMRI paradigm. Blue time periods are during finger tapping. Black periods are times of rest. Note the delay in the signal increase (hemodynamic response, *arrow*) after task initiation.

and neurovascular coupling,[26] including vascular steno-occlusion, tumors with high vascularity, and arteriovenous malformations.[26-28] Artifacts from regions of susceptibility effect (e.g., skull base, sinuses, hemorrhage, and prior surgery) may limit fMRI sensitivity. Sedation also can alter the BOLD response significantly.[29,30]

## Sensorimotor System Evaluation

The most common and reproducible application of fMRI in clinical patients is assessment of the sensorimotor system (Fig. 27.2).[25,31] The fMRI activation areas are somatotopically arranged along the central sulcus. Secondary regions, including the supplementary motor area and premotor cortex, often are identified. Validation with direct electrocortical simulation (ECoS), the surgical gold standard, generally has been excellent,[32-35] with studies demonstrating nearly 100% concordance.[31] Sensorimotor fMRI evaluation is most useful when the normal anatomic relationships relating to the central sulcus are distorted by adjacent mass lesions; fMRI can help guide operative approaches in these cases (Fig. 27.3). High success rates of motor fMRI (93%) in children undergoing surgery for epilepsy have been documented.[36]

## Language Evaluation

Multiple clinical and fMRI studies have established that a left hemispheric dominance exists for semantic and phonologic language functions in most persons. Most fMRI studies of language lateralization in children have shown similar patterns of activation compared with adults, supporting the theory that language networks are established by early childhood. However, multiple cross-sectional and longitudinal fMRI studies have demonstrated changes in BOLD localization[21,37-41] with multiple language paradigms during development. In general, greater and more widespread activation is present in children compared with adults, which likely is related to differential brain maturation and performance differences. Hemispheric language dominance is related to handedness, with approximately 93% to 95% of normal right-handed adults and children being left hemispheric dominant for language, whereas approximately 15% to 20% of non–right-handed subjects (those who are ambidextrous or left handed) exhibit atypical (nonlateralizing or right-sided) hemispheric language dominance.[42,43] These findings should be kept in mind when interpreting language fMRI examinations in children.

### Paradigms for Language Assessment

Multiple fMRI paradigms have been created to assess different aspects of language function (Fig. 27.4 and e-Fig. 27.5). It is important to use multiple language tasks in clinical patients to more fully define language processing.[21,44-46] The use of multiple tasks reduces the likelihood of nondiagnostic findings, improves interrater reliability, and helps in the confirmation of language

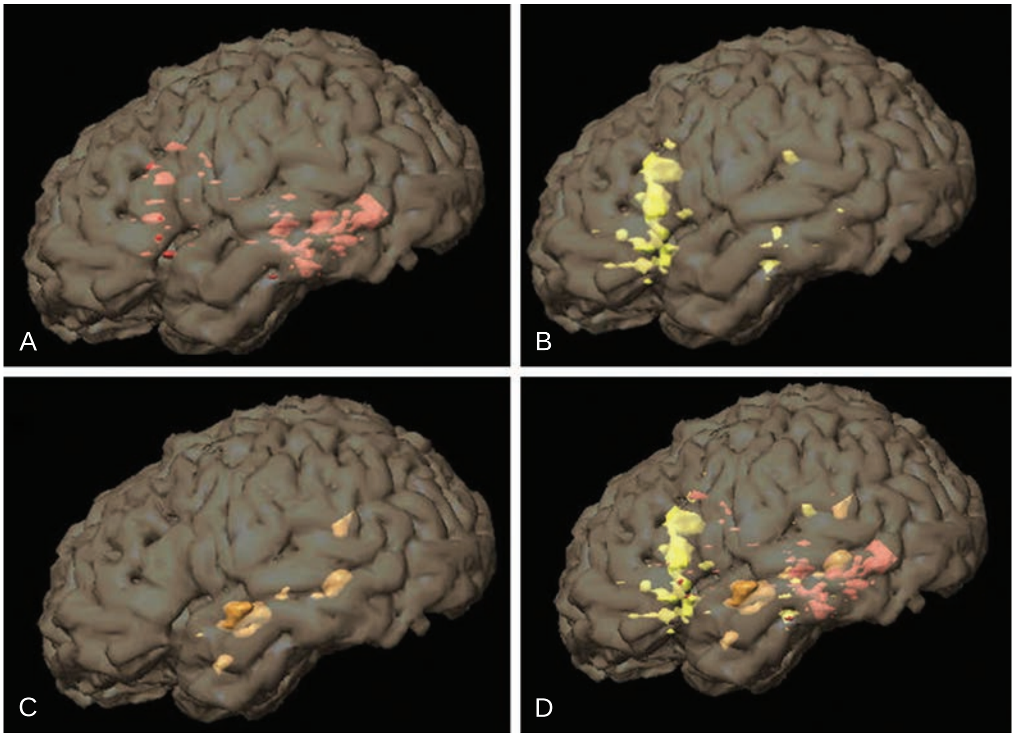

**e-Figure 27.5.** Left hemispheric activation areas from language tasks in Fig. 27.4 are superimposed on three-dimensional (3D) segmented brain images, a very useful tool for presurgical mapping and understanding the 3D relationships between functional magnetic resonance imaging activation regions. (A) Verb generation. (B) Semantic decision. (C) Story processing (temporal lobe regions). (D) Combined activation regions.

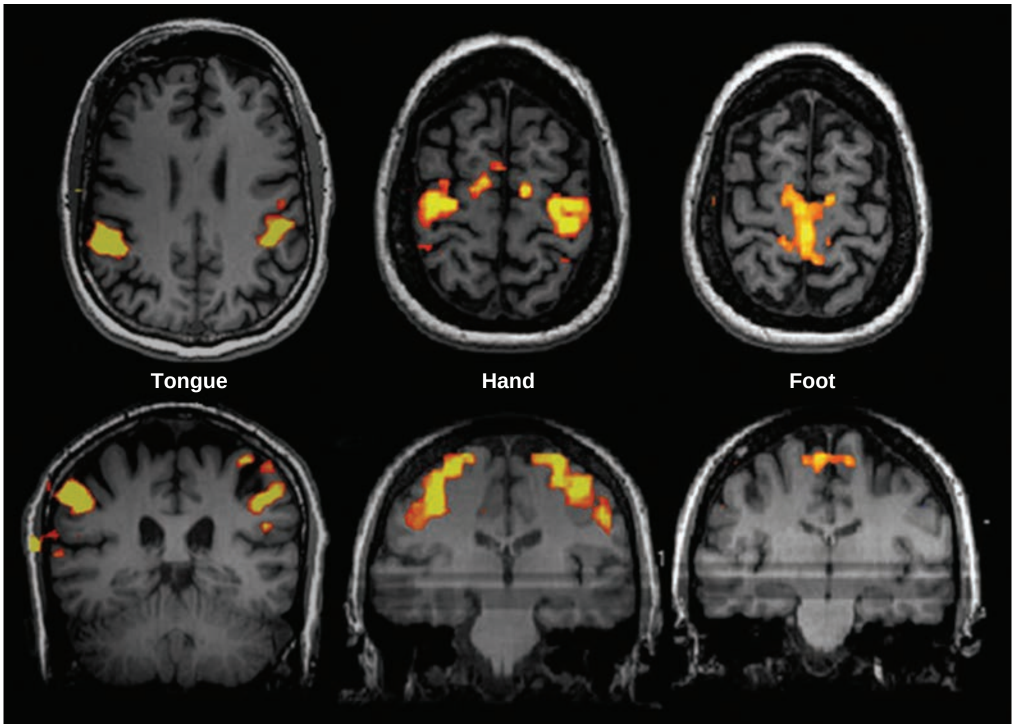

**Figure 27.2. Examples of different motor paradigms useful for clinical functional magnetic resonance imaging.** *Tongue:* Sequential tongue movement while the mouth is closed. *Hand:* Sequential bilateral finger tapping. *Foot:* Sequential bilateral foot flexion and extension. Typically performed clinical paradigms include sequential finger thumb opposition, hand grasping, wrist flexion and extension, foot flexion and extension, lip puckering, and tongue movement for motor strip assessment and tactile stimulation with brushes or air puffs for sensory component evaluation.

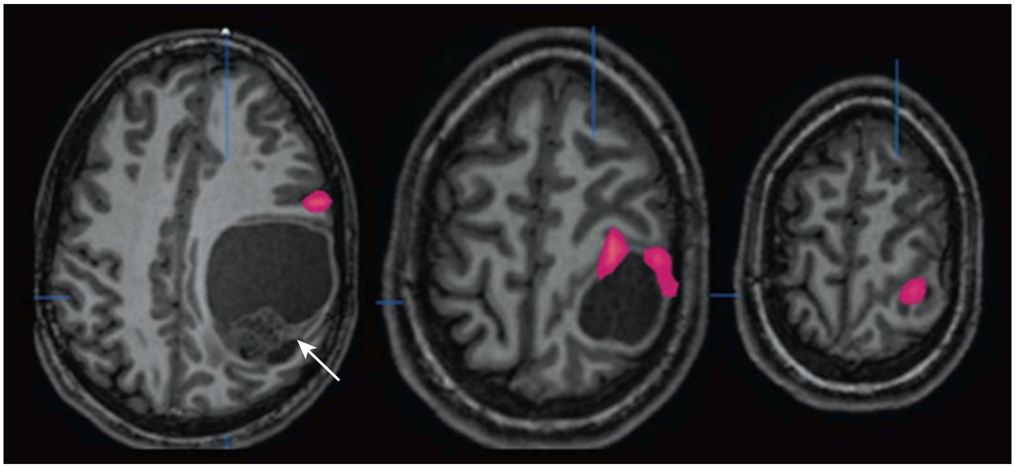

**Figure 27.3. A 15-year-old boy with progressive right-sided motor weakness.** Anatomic magnetic resonance imaging revealed a large cystic and solid mass within the left parietal lobe *(arrow)* that was markedly distorting normal anatomy; functional magnetic resonance imaging (fMRI) was requested to outline the location of the motor strip more definitively. An fMRI image obtained during right-sided sequential finger tapping demonstrates activation along the superior and anterior aspects of the mass. A posterior surgical approach was performed with gross total resection and no new deficit. Pathology revealed that the mass was an anaplastic ependymoma.

laterality.[46] Three of the most studied paradigms in children are verb generation, semantic decision, and story processing (see Fig. 27.2).

The verb generation task[37] (see Fig. 27.4A) involves the auditory presentation of a series of concrete nouns. The patient covertly (silently) generates as many verbs associated with the noun as possible. Control tasks include rest or bilateral sequential finger tapping.[37,38,47] The semantic decision task has been modified for children and involves the auditory presentation of single words (animal names)[44,48] (see Fig. 27.4B). The child makes a button press if the animal fits a target semantic property (e.g., “Does the

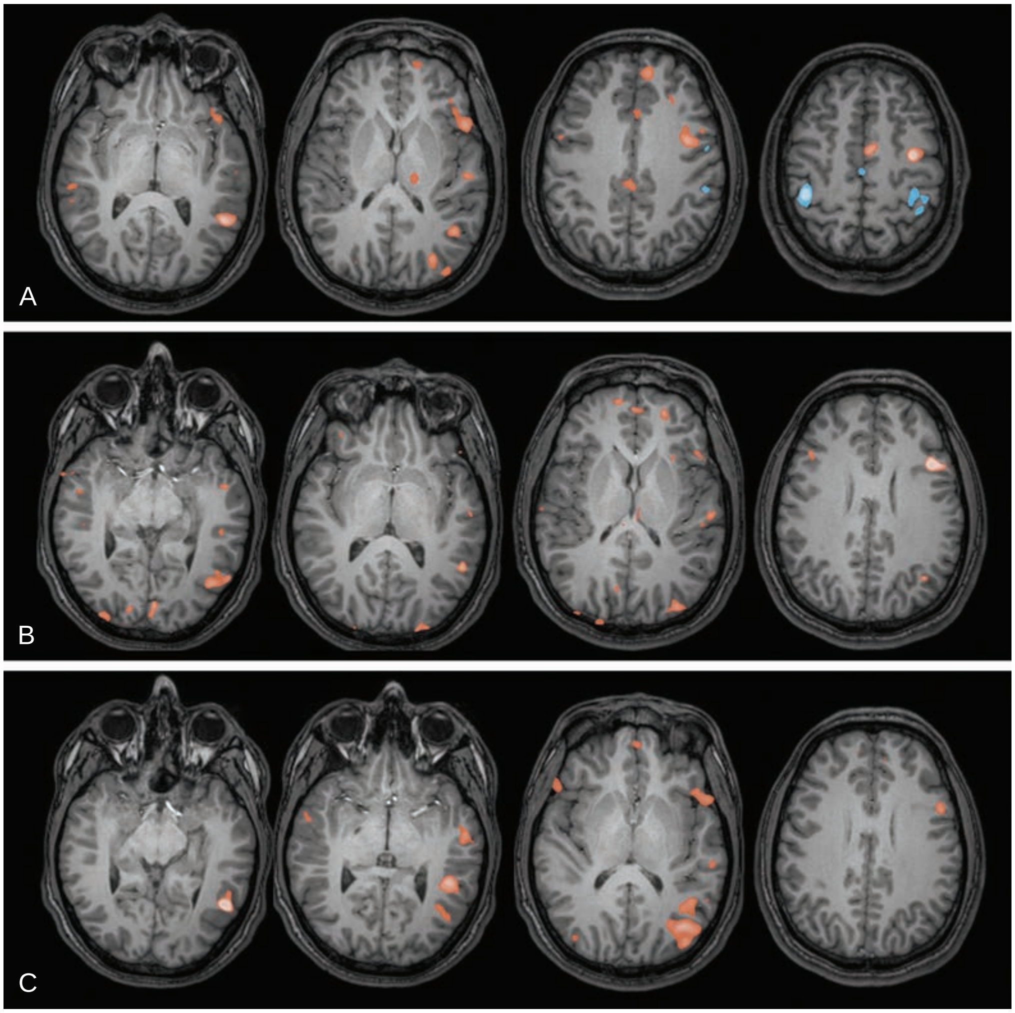

**Figure 27.4. Examples of language functional magnetic resonance imaging (fMRI) paradigms in a 12-year-old right-handed girl with intractable epilepsy.** (A) Verb generation (control task: finger tapping). A statistical map of fMRI activation during verb generation *(orange areas)* demonstrates left lateralization, particularly in the left inferior frontal lobe and left temporal lobe, which is typical for this paradigm. Activation during finger tapping is noted along both central sulci in the hand motor regions, as well as the putative supplementary motor area in the midline. (B) Semantic decision (control task: tone discrimination). A similar left lateralizing pattern is noted with robust inferior frontal and temporal parietal activation, which is typical for this paradigm. The semantic decision task provides an additional assessment of frontal and temporal language areas and has the added capability of allowing direct assessment of patient performance. (C) Story processing (control task: backwards speech). Clear left lateralizing activation is noted in the temporal lobe. Left lateralizing inferior frontal activation also is noted. These paradigms together indicate typical left lateralization of language in this patient.

animal walk on four legs?"). In the control condition, the patient listens to a series of tones for a specific tonal sequence. The story processing task[44,49,50] typically involves the auditory presentation of simple stories, each composed of sentences with specifically formulated complex syntactic constructions (see Fig. 27.4C). The control tasks are listening to various tonal sequences,[21] speech shaped noise, or identical periods of temporally reversed speech.[50] Other tasks such as linguistic prosody, read response naming, and auditory and reading sentence comprehension also have been used successfully with children.[44,51,52]

## Clinical Examination Interpretation

Interpretation of language fMRI in children can be difficult. Descriptions of language laterality and hemispheric dominance in clinical and research contexts typically have been described on the basis of a region of interest (ROI) "laterality" or "asymmetry" index (LI).[21,25] LI calculations are dependent on the statistical technique and threshold used for calculating activated voxels, ROI, and fMRI task.[53,54] They are more robust when ROIs targeted to typical language areas are used.[55,56] Use of multiple thresholds and fMRI tasks in individual patients to more completely assess language laterality is recommended.[53] Interestingly, visual assessment of lateralization in individual patients actually may be as good as ROI-based LI calculations.[52,57] Recent studies have shown that cerebellar activation laterality is an additional helpful feature when assessing language tasks. Contralateral cerebellar activation is typically seen[58] and can provide additional evidence for language laterality. fMRI examinations are interpreted in clinical patients as left hemispheric dominant (typical activation pattern), right hemispheric dominant, and bilateral or nonlateralizing language representation. Bilateral activation patterns can be problematic in evaluation of individual clinical patients because this fMRI pattern often cannot be conclusively interpreted.[53] Epilepsy,[59,60] perinatal stroke,[61] and prenatally or perinatally acquired lesions[62] can effect language development and lead to altered lateralization of language function (e-Fig. 27.6).

## Validation of Language Functional Magnetic Resonance Imaging

The traditional method for determining language dominance before surgery has been the Wada or intracarotid amobarbital procedure (IAP). Another method of language mapping is direct ECoS either during surgery with the patient awake or with use of subdural grid electrodes.[63] The IAP is expensive, invasive, and more difficult to perform in children.[63,64] It carries with it a small but definite risk of complications,[64-66] and its invasive nature limits repeated assessments.[67] Although it provides lateralization information, the IAP cannot spatially localize language functions in the brain, which is an advantage for fMRI.

Correlation studies between fMRI and IAP for language lateralization consistently have shown an 85% to 90% concordance rate,[20,65,66,68,69] with the use of multiple tasks increasing the degree of concordance.[55,56] Discrepancies are most common in patients who exhibit atypical language lateralization, particularly patients with bilateral, nonlateralized representation.[67,68,70] Discordance between fMRI and the IAP also is more common in patients with neocortical epilepsy (a more common scenario in pediatric patients than in the adult epilepsy population) and left temporal lobe seizure origin.[57] The few studies that have specifically compared language-based fMRI with the IAP in children have demonstrated concordance in 80% to 100% of patients.[67,71] The IAP is still useful when fMRI is not typically lateralizing, or when memory function is a critical concern. Although fMRI may not be able to replace the IAP in all circumstances, routine fMRI can diminish IAP utilization significantly.[72]

fMRI has been used in an attempt to guide resections near eloquent language regions. Because fMRI will demonstrate areas of the brain that are associated with, but not necessarily essential to, a particular task, fMRI will always exhibit a lack of specificity for language mapping in this scenario. Few direct comparisons between language fMRI and ECoS for regional language mapping have been performed, and the results have been variable. The sensitivity of fMRI in identifying critical language areas as established by ECoS varies from 22% to 100%, with specificities of between 61% and 100%.[73] A detailed study in adult patients with a brain tumor found an overall fMRI sensitivity of 80% and a specificity of 78% for critical language areas compared with the results of ECoS.[74] Despite the variable reported correlations, fMRI may be very useful to guide intraoperative ECoS procedures and for counseling parents and children regarding surgery in eloquent areas.[18,75,76]

## Other Indications

The fMRI procedure has been used to investigate a wide variety of clinical conditions in children, including the evaluation of reading and dyslexia, attention deficit–hyperactivity disorder, autism, and hearing loss,[77-79] to name a few. Clinical applications in these conditions are evolving and at present should be regarded as research tools.

Assessment of memory by fMRI is possible and has begun to be assessed in clinical patients. Clinical research studies have been performed that correlate fMRI activation patterns with the IAP[80,81] and postoperative memory after temporal lobe resection in adults,[81] with encouraging results; however, evaluation of the application in pediatric patients is incomplete. Hemispheric language laterality appears to be closely linked with verbal memory lateralization and has been used to predict verbal memory outcome after temporal lobectomy.[82]

The fMRI procedure, often in combination with other functional modalities (e.g., diffusion tensor imaging and magnetoencephalography), may allow for guidance during surgical access and resection using modern neuronavigation systems (functional neuronavigation).[83] Use of fMRI in conjunction with ECoS and frameless stereotaxy has been found to help facilitate tumor resection in children with a wide variety of lesions near eloquent cortical regions (e-Figs. 27.7 and 27.8).[84]

## ADDITIONAL TECHNIQUES

Newer techniques of fMRI acquisition and processing hold promise to expand the utility of fMRI in children. These techniques include advanced connectivity analyses of fMRI data and fMRI performed in the so-called *resting state*.[85] Resting state fMRI (rsfMRI) analyses have begun to be used in evaluating the functional networks in the developing brain[86,87] (e-Fig. 27.9) and may have particular clinical use in identifying functionally important cortex and networks in patients in which task-based fMRI examinations are not feasible (e.g., in neonates, infants, and sedated patients). Although currently primarily a research tool, initial clinical applications have been described in adults and children.[88,89] Evaluation of rsfMRI data does require more sophisticated analysis tools; however, some institutions are applying rsfMRI techniques routinely to presurgical planning with good results.[90]

### KEY POINTS

- Clinical fMRI in children primarily is used to assess eloquent brain regions before surgery relating to lesions or epilepsy.
- Clinical fMRI in children requires special preparation and resources, as well as developmentally appropriate fMRI paradigms.
- Somatosensory and language assessments are the most commonly performed fMRI examinations in clinical patients.
- Standardization of fMRI paradigms and interpretation, as well as better validation and outcome studies, are needed in pediatric patients.
- Newer techniques such as resting state fMRI hold promise to expand clinical fMRI applications to children who currently are unable to perform task-directed fMRI examinations.

### SUGGESTED READINGS

Altman NR, Bernal B. Pediatric applications of functional magnetic resonance imaging. *Pediatr Radiol*. 2015;45(suppl 3):S382–S396.

Holland SK, Vannest J, Mecoli M, et al. Functional MRI of language lateralization during development in children. *Int J Audiol*. 2007;46:533–551.

Kotsoni E, Byrd D, Casey BJ. Special considerations for functional magnetic resonance imaging of pediatric populations. *J Magn Reson Imaging*. 2006;23:877–886.

Leach JL, Holland SK. Functional MRI in children: clinical and research applications. *Pediatr Radiol*. 2010;40:31–49.

Wilke M, Holland SK, Myseros JS, et al. Functional magnetic resonance imaging in pediatrics. *Neuropediatrics*. 2005;34(5):225–233.

### REFERENCES

Full references for this chapter can be found on www.expertconsult.com.

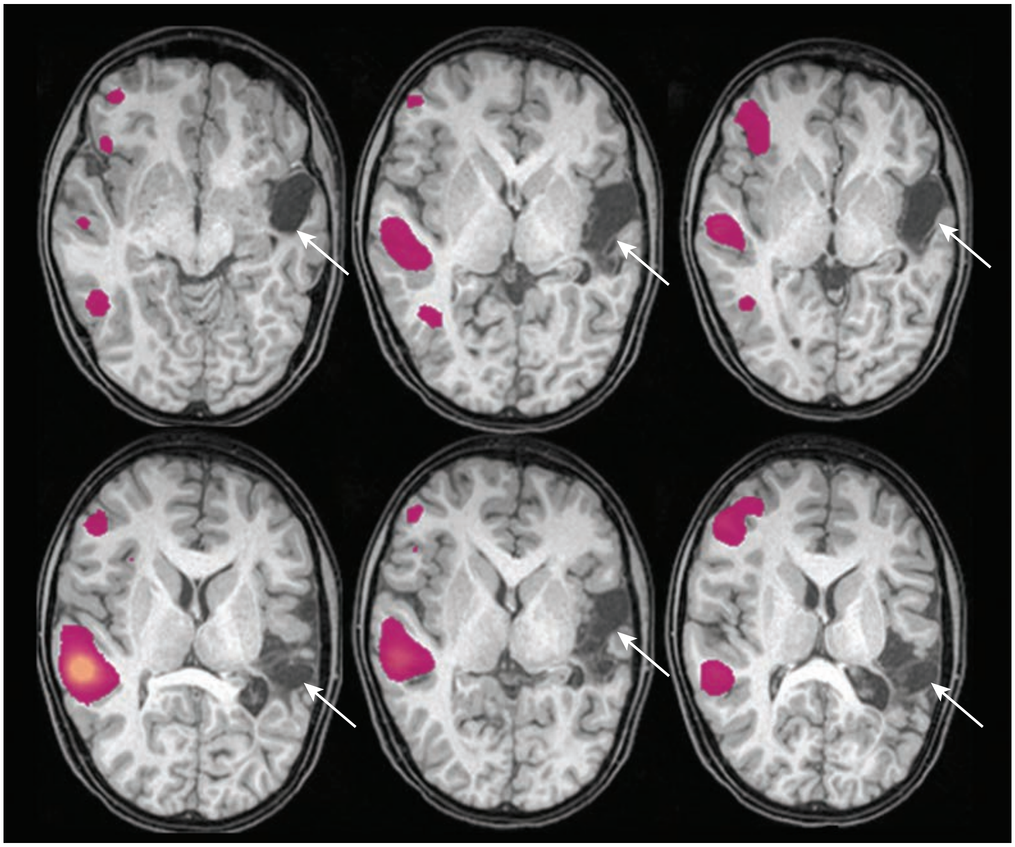

**e-Figure 27.6. An 11-year-old boy with intractable epilepsy and a history of perinatal left middle cerebral artery infarct.** Large areas of encephalomalacia are identified in the left hemisphere *(arrows).* Statistical activation maps demonstrate clear right lateralization of activation with verb generation in right hemispheric homologous regions. Right hemispheric dominance for language was confirmed by an intraarterial amobarbital procedure.

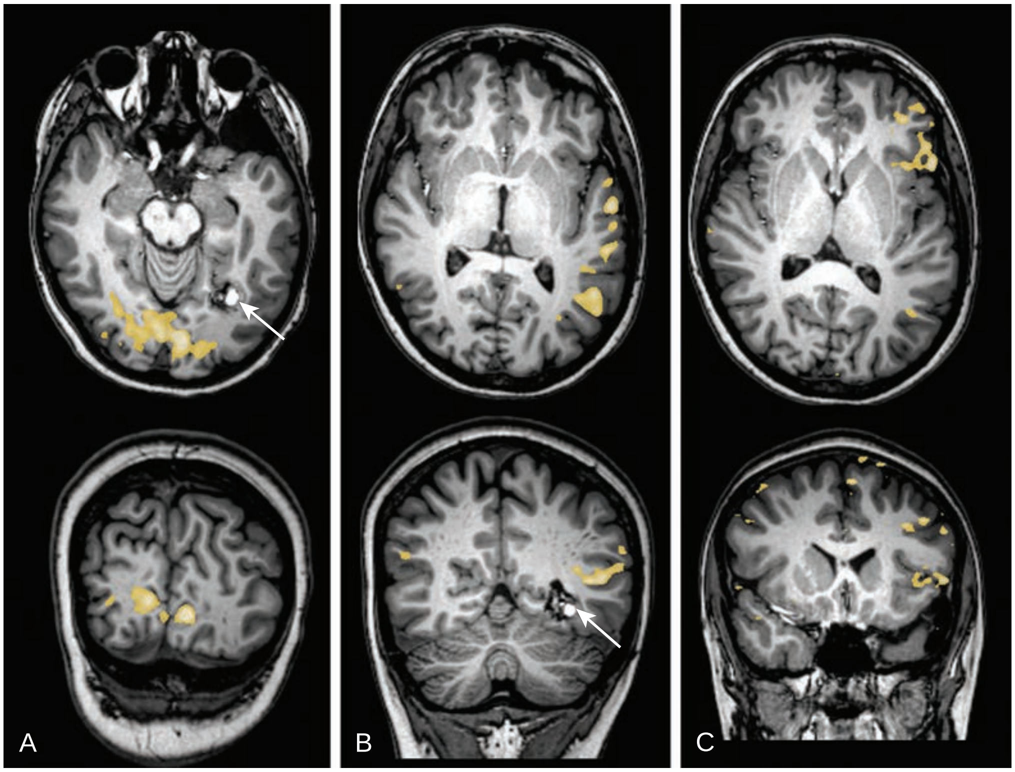

**e-Figure 27.7. A 15-year-old boy with seizures and headache.** A cavernous malformation *(arrows)* is identified in the left inferior medial occipital lobe along the temporal occipital junction. The patient was referred for functional magnetic resonance imaging and diffusion tensor imaging–tractography to aid in operative planning. (A) A visual stimulation paradigm demonstrates activation along the calcarine fissure medial to the lesion. (B) A story processing task demonstrates activation along the left temporal lobe very asymmetric to the right, lateral, and slightly superior to the plane of the lesion. (C) A verb generation task demonstrates clear left lateralization of activation in the frontal and temporal parietal regions. Verb generation and story processing tasks were consistent with left hemispheric lateralization of language.

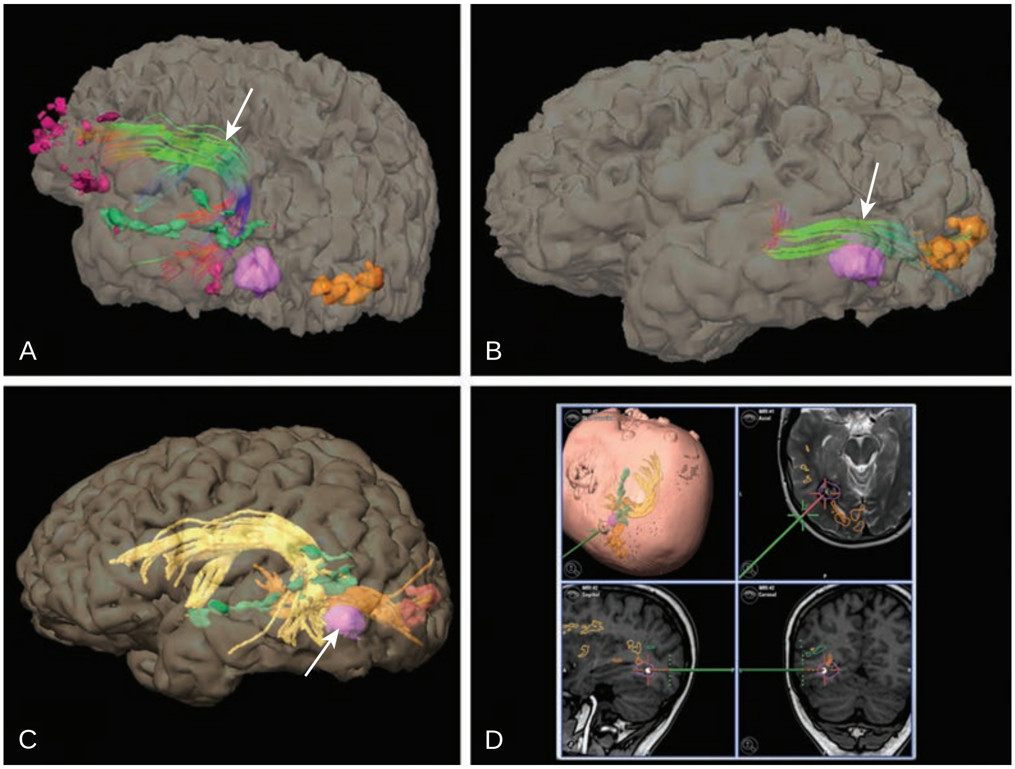

**e-Figure 27.8. Utility of combined functional magnetic resonance imaging (fMRI) and tractography for operative planning** (same patient shown in e-Fig. 27.6). (A) Tractography is performed to outline the arcuate fasciculus orientation *(arrow)* using fMRI activation regions to guide seed points. *Dark purple areas:* fMRI activation regions from verb generation. *Green areas:* fMRI activation areas from a story processing task. *Light purple area:* cavernous malformation (surgical target). *Orange areas:* fMRI activation regions from visual stimulation. The posterior arcuate fasciculus is anterior to the lesion. (B) Tractography is performed to outline the geniculocalcarine tract *(arrow).* The geniculocalcarine tract lies directly above and touches the superior aspect of the lesion. (C) Because of the close proximity of the lesion *(arrow)* to functionally important regions, integration of the tractography and fMRI data with anatomic images was performed. Objects were created from the lesion, temporal lobe language areas as demonstrated by a story processing task, arcuate fasciculus, and geniculocalcarine tract. (D) Images captured during surgery demonstrating the operative approach, which was guided by anatomic and functional imaging. Complete resection was performed with no neurologic deficit. *(Intraoperative images courtesy of Francesco Mangano, DO.)*

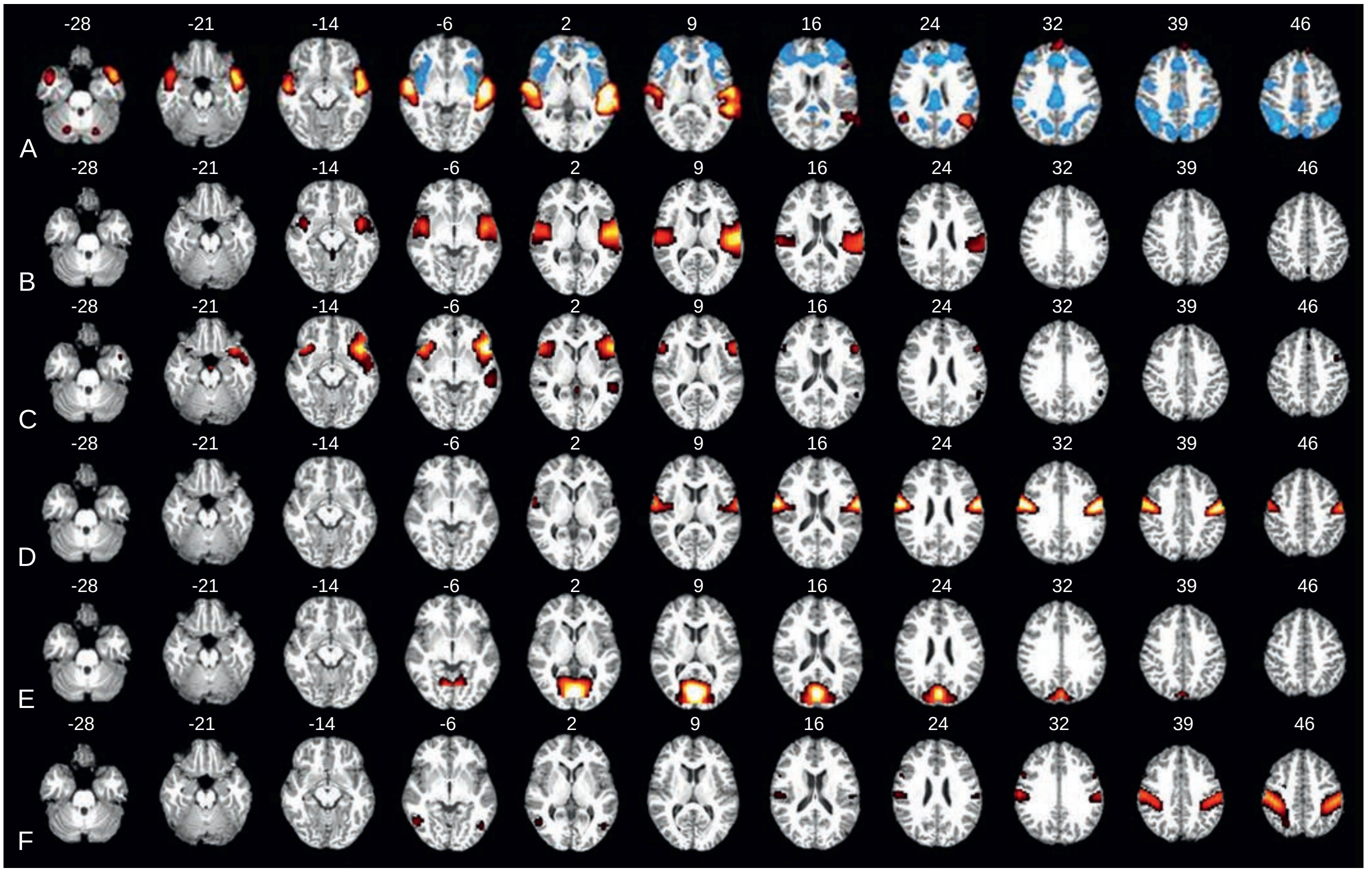

**e-Figure 27.9. Group analysis of functional magnetic resonance imaging (fMRI) in a group of normally developing children.** (A) Task-based fMRI during story processing. (B–F) Independent component analysis of resting state fMRI (rsfMRI) in the same group of children demonstrating some of the identified networks. (B) Auditory. (C) Language. (D) Motor. (E) Primary visual. (F) Dorsal attention. *(Images courtesy of Dr. Mark DiFrancesco, PhD, Cincinnati Children's Hospital Medical Center. Imaging data from the CMIND study, https://research.cchmc.org/c-mind/.)*

## REFERENCES

1. Huettel SA, Song AW, McCarthy G. Spatial and temporal properties of fMRI. In: Huettel SA, Song AW, McCarthy G, eds. *Functional Magnetic Resonance Imaging*. Sunderland, MA: Sinauer Associates; 1992.
2. Logothetis NK. The underpinnings of the BOLD functional magnetic resonance imaging signal. *J Neurosci*. 2003;23:3963–3971.
3. Gaillard WD, Grandin CB, Xu B. Developmental aspects of pediatric fMRI: considerations for image acquisition, analysis, and interpretation. *Neuroimage*. 2001;13:239–249.
4. Chugani HT, Phelps ME, Mazziotta JC. Positron emission tomography study of human brain functional development. *Ann Neurol*. 1987;22:487–497.
5. Levin JM, Frederick B, Ross MH, et al. Influence of baseline hematocrit and hemodilution on BOLD fMRI activation. *Magn Reson Imaging*. 2001;19:1055–1062.
6. Chiang LK, Dunn AE. Cardiology. In: Siberry GK, Iannone R, eds. *The Harriet Lane Handbook: A Manual for Pediatric House Officers*. St. Louis: Mosby; 2001.
7. Schlaggar BL, Brown TT, Lugar HM, et al. Functional neuroanatomical differences between adults and school aged children in the processing of single words. *Science*. 2002;296:1476–1479.
8. Brauer J, Neumann J, Friederici AD. Temporal dynamics of perisylvian activation during language processing in children and adults. *Neuroimage*. 2008;41:1484–1492.
9. Heep A, Scheef L, Janowski J, et al. Functional magnetic resonance imaging of the sensorimotor system in preterm infants. *Pediatrics*. 2009;123:294–300.
10. Morita T, Kochiyama T, Yamada H, et al. Difference in the metabolic response of the lateral geniculate nucleus and the primary visual cortex of infants: a fMRI study. *Neurosci Res*. 2000;38:63–70.
11. Born AO, Rostrup E, Miranda MJ, et al. Visual cortex reactivity is sedated children examined with perfusion MRI (FAIR). *Magn Reson Imaging*. 2002;20:199–205.
12. Kruger G, Kastrup A, Glover GH. Neuroimaging at 1.5 T and 3.0 T: comparison of oxygenation-sensitive magnetic resonance imaging. *Magn Reson Med*. 2001;45:595–604.
13. Voss HU, Zevin JD, McCandliss BD. Functional MR imaging at 3.0T versus 1.5T: a practical review. *Neuroimaging Clin N Am*. 2006;16(2):285–297.
14. Byars AW, Holland SK, Strawsburg RH, et al. Practical aspects of conducting large scale functional magnetic resonance image studies in children. *J Child Neurol*. 2002;17:885–889.
15. Altman NR, Bernal B. Pediatric applications of fMRI. In: Faro S, Mohamed FB, eds. *Functional MRI. Basic Principles and Clinical Applications*. New York: Springer; 2006.
16. Yuan W, Altaye M, Ret J, et al. Quantification of head motion in children during various fMRI language tasks. *Hum Brain Mapp*. 2009;30(5):1481–1489.
17. Rajagopal A, Byars A, Schapiro M, et al. Success rates for functional MR imaging in children. *AJNR Am J Neuroradiol*. 2014;35(12):2319–2325.
18. Kesavadas C, Thomas B, Sujesh S, et al. Real-time functional MRI (fMRI) for presurgical evaluation of pediatric epilepsy. *Pediatr Radiol*. 2007;37:964–974.
19. Bandettini P, Jesmanowicz E, Wong E, et al. Processing strategies for time course data sets in functional MRI of the human brain. *Magn Reson Med*. 1993;30:161–173.
20. Binder JR, Swanson SJ, Hammeke TA, et al. A comparison of five fMRI protocols for mapping speech comprehension systems. *Epilepsia*. 2008;49(12):1980–1997.
21. Holland SK, Vannest J, Mecoli M, et al. Functional MRI of language lateralization during development in children. *Int J Audiol*. 2007;46:533–551.
22. Friston K, Jezzard P, Turner R. Analysis of functional MRI time series. *Hum Brain Mapp*. 1998;6:283–300.
23. Goebel R. Localization of brain activity using functional magnetic resonance imaging. In: Stippich C, ed. *Clinical Functional MRI. Presurgical Functional Neuroimaging*. 1st ed. Heidelberg: Springer-Verlag; 2007.
24. Peck KK. Methods of analysis. In: Holodny A, ed. *Functional Neuroimaging. A Clinical Approach*. New York: Informa Healthcare; 2008.
25. Stippich C, Blatow M, Krakow K. Presurgical functional MRI in patients with brain tumors. In: Stippich C, ed. *Clinical Functional MRI. Presurgical Functional Neuroimaging*. Heidelberg: Springer-Verlag; 2007.
26. Ulmer JL, Hacein-Bev L, Matthews VP, et al. Lesion induced pseudo-dominance at functional magnetic resonance imaging: implications for preoperative assessments. *Neurosurgery*. 2004;55(3):569–579.
27. Rossini PM, Altamura C, Ferretti A, et al. Does cerebrovascular disease affect the coupling between neuronal activity and local haemodynamics? *Brain*. 2004;127:99–110.
28. Kamba M, Sung Y-W, Ogawa S. Alteration of blood oxygen level-dependent signaling by local circulatory condition. *J Magn Reson Imaging*. 2007;26:1506–1513.
29. Qiu M, Ramani R, Swetye M, et al. Anesthetic effects on regional CBF, BOLD, and the coupling between task-induced changes in CBF and BOLD: an fMRI study in normal human subjects. *Magn Reson Med*. 2008;60(4):987–996.
30. DiFrancesco MW, Robertson SA, Karunanayaka P, et al. BOLD fMRI in infants under sedation: comparing the impact of pentobarbital and propofol on auditory and language activation. *J Magn Reson Imaging*. 2013;38(5):1184–1195.
31. Roessler K, Donat M, Lanzenberger R. Evaluation of preoperative high magnetic field motor functional MRI (3 Tesla) in glioma patients by navigated electrocortical stimulation and postoperative outcome. *J Neurol Neurosurg Psychiatry*. 2005;76:1152–1157.
32. Yetkin FZ, Mueller WM, Morris GL, et al. Functional MR activation correlated with intraoperative cortical mapping. *AJNR Am J Neuroradiol*. 1997;18:1311–1315.
33. Lehericy S, Duffau H, Cornu P, et al. Correspondence between functional magnetic resonance imaging somatotopy and individual brain anatomy of the central region: comparison with intraoperative stimulation in patients with brain tumors. *J Neurosurg*. 2000;92:589–598.
34. Shinoura N, Yamada R, Kodama T, et al. Intraoperative cortical mapping has low sensitivity for the detection of motor function in the proximity to a tumor in the primary motor area. *Stereotact Funct Neurosurg*. 2005;83:135–141.
35. Krishnan R, Raabe A, Hattingen E, et al. Functional magnetic resonance imaging-integrated neuronavigation: correlation between lesion to motor cortex distance and outcome. *Neurosurgery*. 2004;55:904–915.
36. De Tiège X, Connelly A, Liégeois F, et al. Influence of motor functional magnetic resonance imaging on the surgical management of children and adolescents with symptomatic focal epilepsy. *Neurosurgery*. 2009;64(5):856–864.
37. Holland SK, Plante E, Byars AW, et al. Normal fMRI brain activation patterns in children performing a verb generation task. *Neuroimage*. 2001;14:837–843.
38. Schapiro MB, Schmithorst VJ, Wilke M, et al. BOLD-fMRI signal increases with age in selected brain regions in children. *Neuroreport*. 2004;15(17):2575–2578.
39. Weiss-Croft LJ, Baldeweg T. Maturation of language networks in children: a systematic review of 22 years of functional MRI. *Neuroimage*. 2015;123:269–281. doi:10.1016/j.neuroimage.2015.07.046. Review. PubMed PMID: 26213350.
40. Gaillard WD, Hertz-Pannier L, Mott SH, et al. Functional anatomy of cognitive development: fMRI of verbal fluency in children and adults. *Neurology*. 2000;54:180–185.
41. Gaillard WD, Balsamo LM, Ibrahim Z, et al. fMRI identifies regional specialization of neural networks for reading in young children. *Neurology*. 2003;60:94–100.
42. Szaflarski JP, Binder JR, Possing ET. Language lateralization in left handed and ambidextrous people: fMRI data. *Neurology*. 2002;59:238–244.
43. Szaflarski JP, Rajagopal A, Altaye M, et al. Left-handedness and language lateralization in children. *Brain Res*. 2012;1433:85–97.
44. Vannest J, Karunanayaka PR, Schmithorst VJ, et al. Language networks in children: evidence from functional MRI studies. *AJR Am J Roentgenol*. 2009;192:1190–1196.
45. Wilke M, Lidzba K, Staudt M, et al. An fMRI task battery for assessing hemispheric language dominance in children. *Neuroimage*. 2006;32:400–410.
46. Gaillard WD, Balsamo L, Xu B, et al. fMRI language task panel improves determination of language dominance. *Neurology*. 2004;63:1403–1408.
47. Szaflarski JP, Holland SK, Schmithorst VJ, et al. An fMRI study of language lateralization in children and adults. *Hum Brain Mapp*. 2006;27(3):202–212.
48. Binder JR, Frost JA, Hammeke TA, et al. Human brain language areas identified by functional magnetic resonance imaging. *J Neurosci*. 1997;17:353–362.
49. Karunanayaka PR, Holland SK, Schmithorst VJ, et al. Age related connectivity changes in fMRI data from children listening to stories. *Neuroimage*. 2007;34:349–360.

50. Ahmad Z, Balsamo LM, Sachs BC, et al. Auditory comprehension of language in young children. Neural networks identified with fMRI. *Neurology*. 2003;60:1598–1605.
51. Gaillard WD, Pugilese M, Grandin CB, et al. Cortical localization of reading in normal children. An fMRI language study. *Neurology*. 2001;57:47–54.
52. Gaillard WD, Balsamo MA, Xu B, et al. Language dominance in partial epilepsy patients identified with an fMRI reading task. *Neurology*. 2002;59:256–265.
53. Wellmer J, Weber B, Weis S, et al. Strongly lateralized activation in language fMRI of atypical dominant patients—implications for presurgical work-up. *Epilepsy Res*. 2008;80:67–76.
54. Ruff IM, Petrovich Brennan NM, Peck KK, et al. Assessment of the language laterality index in patients with brain tumor using functional MR imaging: effects of thresholding, task selection, and prior surgery. *AJNR Am J Neuroradiol*. 2008;29:528–535.
55. Rutten GJ, Ramsey NF, van Rijen PC, et al. Reproducibility of fMRI-determined language lateralization in individual subjects. *Brain Lang*. 2002;80:421–437.
56. Arora J, Pugh K, Westerveld M, et al. Language lateralization in epilepsy patients: fMRI validated with the Wada procedure. *Epilepsia*. 2009;50(10):2225–2241.
57. Woerman FG, Joeckert H, Luerding R, et al. Language lateralization by the Wada test and fMRI in 100 patients with epilepsy. *Neurology*. 2003;61(5):699–701.
58. Gelinas JN, Fitzpatrick KP, Kim HC, et al. Cerebellar language mapping and cerebral language dominance in pediatric epilepsy surgery patients. *Neuroimage Clin*. 2014;12(6):296–306.
59. Yuan W, Szaflarski JP, Schmithorst VJ, et al. fMRI shows atypical language lateralization in pediatric epilepsy patients. *Epilepsia*. 2006;47(3):593–600.
60. Ibrahim GM, Morgan BR, Doesburg SM, et al. Atypical language laterality is associated with large-scale disruption of network integration in children with intractable focal epilepsy. *Cortex*. 2015;65:83–88.
61. Tillema J-M, Byars AW, Jacola LM, et al. Cortical reorganization of language functioning following perinatal left MCA stroke. *Brain Lang*. 2008;105:99–111.
62. Staudt M, Grodd W, Niemann G, et al. Early left periventricular brain lesions induce right hemispheric organization of speech. *Neurology*. 2001;57:122–125.
63. Schevon CA, Carlson C, Zaroff CM, et al. Pediatric language mapping: sensitivity of neurostimulation and Wada testing in epilepsy surgery. *Epilepsia*. 2007;48(3):539–545.
64. Baxendale SA, Thompson PJ, Duncan JS. Evidence-based practice: a reevaluation of the intracarotid amobarbital procedure (Wada test). *Arch Neurol*. 2008;65(6):841–845.
65. Abou-Khalil B. An update on determination of language dominance in screening for epilepsy surgery: the Wada test and newer non-invasive alternatives. *Epilepsia*. 2007;48(3):442–455.
66. Kloppel S, Buchel C. Alternatives to the Wada test: a critical view of functional magnetic resonance imaging in preoperative use. *Curr Opin Neurol*. 2005;18:418–423.
67. Anderson DP, Harvey SA, Saling MM, et al. fMRI lateralization of expressive language in children with cerebral lesions. *Epilepsia*. 2006;47(6):988–1008.
68. Lee D, Swanson SJ, Sabsevitz DS, et al. Functional MRI and Wada studies in patients with interhemispheric dissociation of language functions. *Epilepsy Behav*. 2008;13:350–356.
69. Sabsevitz DS, Swanson SJ, Hammeke TA, et al. Use of preoperative functional neuroimaging to predict language deficits from epilepsy surgery. *Neurology*. 2003;60:1788–1792.
70. Benke T, Koylu B, Visani P, et al. Language lateralization in temporal lobe epilepsy: a comparison between fMRI and the Wada test. *Epilepsia*. 2006;47(8):1308–1319.
71. Liegois F, Cross HJ, Gadian DG, et al. Role of fMRI in the decision making process: epilepsy surgery for children. *J Magn Reson*. 2006;23:933–940.
72. Bauer PR, Reitsma JB, Houweling BM, et al. Can fMRI safely replace the Wada test for preoperative assessment of language lateralisation? A meta-analysis and systematic review. *J Neurol Neurosurg Psychiatry*. 2014;85(5):581–588.
73. Smits M, Visch-Brink E, Schraa-Tam C, et al. Functional MR imaging of language processing: an overview of easy-to-implement paradigms for patient care and clinical research. *Radiographics*. 2006;26:S145–S158.
74. Bizzi A, Blasi V, Falini A, et al. Presurgical functional MRI of language and motor functions: validation with intraoperative electrocortical mapping. *Radiology*. 2008;248(2):579–589.
75. Ojemann JG, Ojemann GA, Lettich E. Cortical stimulation mapping of language cortex by using a verb generation task: effects of learning and comparison to mapping based on object naming. *J Neurosurg*. 2002;97:33–38.
76. de Ribaupierre S, Fohlen M, Bulteau C, et al. Presurgical language mapping in children with epilepsy: clinical usefulness of functional magnetic resonance imaging for the planning of cortical stimulation. *Epilepsia*. 2012;53(1):67–78.
77. Patel AM, Cahill LD, Ret J, et al. Functional magnetic resonance imaging of hearing impaired children under sedation before cochlear implantation. *Arch Otolaryngol Head Neck Surg*. 2007;133(7):677–683.
78. Seyffert M, Castellanos FX. Functional MRI in pediatric neurobehavioral disorders. *Int Rev Neurobiol*. 2005;67:239–284.
79. Kelly AMC, Margulies DS, Castellanos FX. Recent advances in structural and functional brain imaging studies of attention–deficit/hyperactivity disorder. *Curr Psychiatry Rep*. 2007;9:401–407.
80. Szfalrski JP, Holland SK, Schmithorst VJ, et al. High resolution functional MRI at 3T in healthy and epilepsy subjects: hippocampal activation with picture encoding task. *Epilepsy Behav*. 2004;5:244–252.
81. Rabin ML, Narayan VM, Kimberg DY. Functional MRI predicts post-surgical memory following temporal lobectomy. *Brain*. 2004;127:2286–2298.
82. Binder JR. Preoperative prediction of verbal episodic memory outcome using FMRI. *Neurosurg Clin N Am*. 2011;22(2):219–232.
83. Nimsky C, Ganslandt O, Buchfelder M, et al. Intraoperative visualization for resection of gliomas: the role of functional neuronavigation and intraoperative 1.5T MRI. *Neurol Res*. 2006;28:482–487.
84. Stapleton SR, Kiriakopoulos E, Mikulis D, et al. Combined utility of functional MRI, cortical mapping, and frameless stereotaxy in resection of lesions in eloquent areas of brain in children. *Pediatr Neurosurg*. 1997;26:68–82.
85. Fox MD, Greicius M. Clinical applications of resting state functional connectivity. *Front Syst Neurosci*. 2010;4(19):1–13.
86. Smyser CD, Snyder AZ, Neil JJ. Functional connectivity MRI in infants: exploration of the functional organization of the developing brain. *Neuroimage*. 2011;56(3):1437–1452.
87. Xiao Y, Friederici AD, Margulies DS, et al. Longitudinal changes in resting-state fMRI from age 5 to age 6 years covary with language development. *Neuroimage*. 2016;128:116–124.
88. Shimony JS, Zhang D, Johnston JM, et al. Resting-state spontaneous fluctuations in brain activity: a new paradigm for presurgical planning using fMRI. *Acad Radiol*. 2009;16(5):578–583.
89. Böttger J, Margulies DS, Horn P, et al. A software tool for interactive exploration of intrinsic functional connectivity opens new perspectives for brain surgery. *Acta Neurochir (Wien)*. 2011;153(8):1561–1572.
90. Lee MH, Miller-Thomas MM, Benzinger TL, et al. Clinical resting-state fMRI in the preoperative setting: are we ready for prime time? *Top Magn Reson Imaging*. 2016;25(1):11–18.

# 28 Perfusion Imaging and Magnetoencephalography

*Arastoo Vossough*

## PERFUSION IMAGING

In the cerebrovascular literature, perfusion imaging refers to an all-encompassing term of various methods to measure hemodynamically derived functional parameters in the brain.[1,2] In radiology, the three most common parameters that are assessed and utilized clinically are cerebral blood volume (CBV), cerebral blood flow (CBF), and mean transit time (MTT). CBV refers to the amount (volume) of blood within a given mass of brain tissue at a given time and is measured in mL/100 g. CBF refers to the flow of blood through an area of the brain and is usually measured in mL/100 g of brain tissue per minute. MTT refers to the time it takes for blood to flow between the arterial inflow and venous outflow in the brain, that is, the time that blood spends in the cerebral capillary circulation and is often measured in seconds. The general relationship between these three parameters is depicted by the central volume theorem:

$$\text{CBV} = \text{CBF} \times \text{MTT}$$

A parameter that is being increasing used recently along with MTT is Tmax, or the time to maximum tissue residue function after deconvolution of the tissue contrast agent concentration. Evaluation of these various perfusion parameters can give us an understanding of the physiologic state of the brain and cerebral vasculature in various disorders and help in patient management. Cerebral perfusion can be measured by a variety of methods including magnetic resonance imaging (MRI), computed tomography (CT), and nuclear medicine techniques. These techniques differ in terms of image acquisition duration, spatial resolution, the types of endogenous or exogenous tracers used, and their ability or accuracy in measuring different perfusion parameters.[1] The clinical applications of perfusion imaging include investigation of cerebrovascular disease, brain tumors, and the effect of other diseases on cerebral perfusion.

## Perfusion Magnetic Resonance Imaging

Perfusion MRI can be performed via the injection of dynamic gadolinium-based contrast material or without contrast material injection by tagging intravascular protons using MR labeling schemes (i.e., arterial spin labeling [ASL]).

### Dynamic Susceptibility Contrast Perfusion Magnetic Resonance Imaging

Dynamic susceptibility contrast (DSC) perfusion MRI is based on susceptibility effects using T2-weighted or, more commonly, T2*-weighted images and is the most commonly studied and clinically used perfusion technique in assessment of brain masses and stroke. This method is based on the principle that the signal change that occurs during passage of a high-concentration bolus of gadolinium contrast material in the vessels causes a difference in susceptibility between the vessels that contain contrast material and brain tissue, and this signal change can be converted to a relaxation rate change proportional to the fraction of blood volume within each voxel.[3,4] Data generally are acquired during first-pass perfusion over approximately 1 minute, during which time a high-concentration bolus of gadolinium chelate is rapidly injected intravenously. Time-signal intensity curves drawn during this acquisition will show a rapid decline in signal as the contrast enters the brain, with return of the signal to near baseline after the first pass (Fig. 28.1). These measurements are used to construct a relative CBV map, and the time signal intensity curve can be used to derive other perfusion parameters by various mathematical methods.[1,5,6]

To provide adequate temporal resolution during dynamic contrast administration, most centers currently use gradient echo planar imaging sequences to perform clinical DSC perfusion MRI.[7–9] This technique is very sensitive to structures that cause magnetic field inhomogeneity such as blood, calcium, bone, metals, or air interfaces such as the skull base. The use of DSC imaging entails multiple technical considerations.[10,11] Accuracy of CBV maps can vary substantially depending on the acquisition and postprocessing methods used.[6] It is important to take into consideration the type of acquisition used in applying research results for characterization of lesions, because the results and thresholds may vary.[12] Derivation of the perfusion parameters also depends on the mathematical models used by the processing software, and caution must be exercised in comparing results from different calculation methods.[13,14] Sometimes a small prebolus dose of contrast material is given before the actual DSC acquisition to correct for leakage and more accurate calculation of the perfusion parameters.[6,10]

DSC perfusion applications are used predominantly to assess cerebrovascular disease and in brain tumor evaluation (e-Fig. 28.2). DSC perfusion can assess the ischemic penumbra in persons who have had an acute stroke and aid in their imaging triage and management.[15,16] DSC perfusion has been used in differentiation of brain tumors from other mass-like lesions in the brain, preoperative grading of brain tumors (higher grades generally have higher CBV), differentiation of primary high grade from metastatic tumors, assessment of treatment response, and as an adjunct in differentiation of radiation necrosis from a recurrent tumor.[1,17–23]

### Arterial Spin Labeling Perfusion Magnetic Resonance Imaging

ASL perfusion imaging does not require exogenous contrast injection. It uses magnetically labeled arterial blood water as an endogenous flow tracer.[24] A general scheme of the ASL technique is illustrated in Fig. 28.3. Two sets of images are obtained, one as a baseline image of the brain and the other after labeling (or tagging) blood arterial water protons in the neck using an inversion or saturation radiofrequency pulse. This second set is obtained after a short time delay that allows the labeled blood to flow into the imaging slices. If the baseline and postlabel images are subtracted from each other, the resulting subtracted image is proportional to blood flow that has entered the brain. Quantitative measures of CBF can then be derived from the subtracted images. Numerous schemes exist for ASL tagging and imaging (such pulsed ASL, pseudocontinuous ASL, velocity-selective ASL, and their subtypes).[25] Typically, echoplanar or spiral nonechoplanar techniques are used for image acquisition. ASL imaging takes significantly longer than DSC perfusion MRI because the signal change resulting from the ASL is very small (in the order of 0.5%–3%), and therefore numerous signal averages need to be acquired to gain acceptable signal to noise. Imaging at 3 Tesla significantly increases the signal and quality of ASL images. Given the requirement for image

## Abstract:

Cerebral perfusion imaging encompasses various methods of measuring hemodynamically derived functional parameters in the brain. These various parameters provide important physiologic insights into cerebrovascular health and disease. Other applications of perfusion imaging including neuro-oncologic uses and the assessment of various disease states on cerebral perfusion. There are various techniques including computed tomography, magnetic resonance imaging, or nuclear medicine radioisotopes to assess cerebral perfusion. Arterial spin labeling is a group of magnetic resonance techniques for assessing cerebral blood without the administration of exogenous contrast and has a number of purported and demonstrable benefits in certain pediatric disorders. Magnetoencephalography (MEG) records and analyzes the small magnetic fields produced by the electrical fields of neuronal activity in the brain using highly sensitive magnetic sensor. MEG can be combined with MRI to enable magnetic source imaging for localization of electromagnetic abnormalities. The main clinical utility of MEG is in the detection and localization of abnormal electrical activity and epileptiform discharges in the brain in patients with epilepsy. Meg can be helpful in presurgical assessment and localization of the epileptogenic or ictal onset zones. Additional MEG can be used as a tool for presurgical mapping of motor and sensory cortical areas. We will present the basic principles and applications of these two advanced neuroimaging applications, cerebral perfusion imaging and magnetoencephalography, in pediatric neurological disorders.

## Keywords:

MRI
Cerebral perfusion
Perfusion imaging
arterial spin labeling
magnetoencephalography
magnetic source imaging
epilepsy
preoperative localization

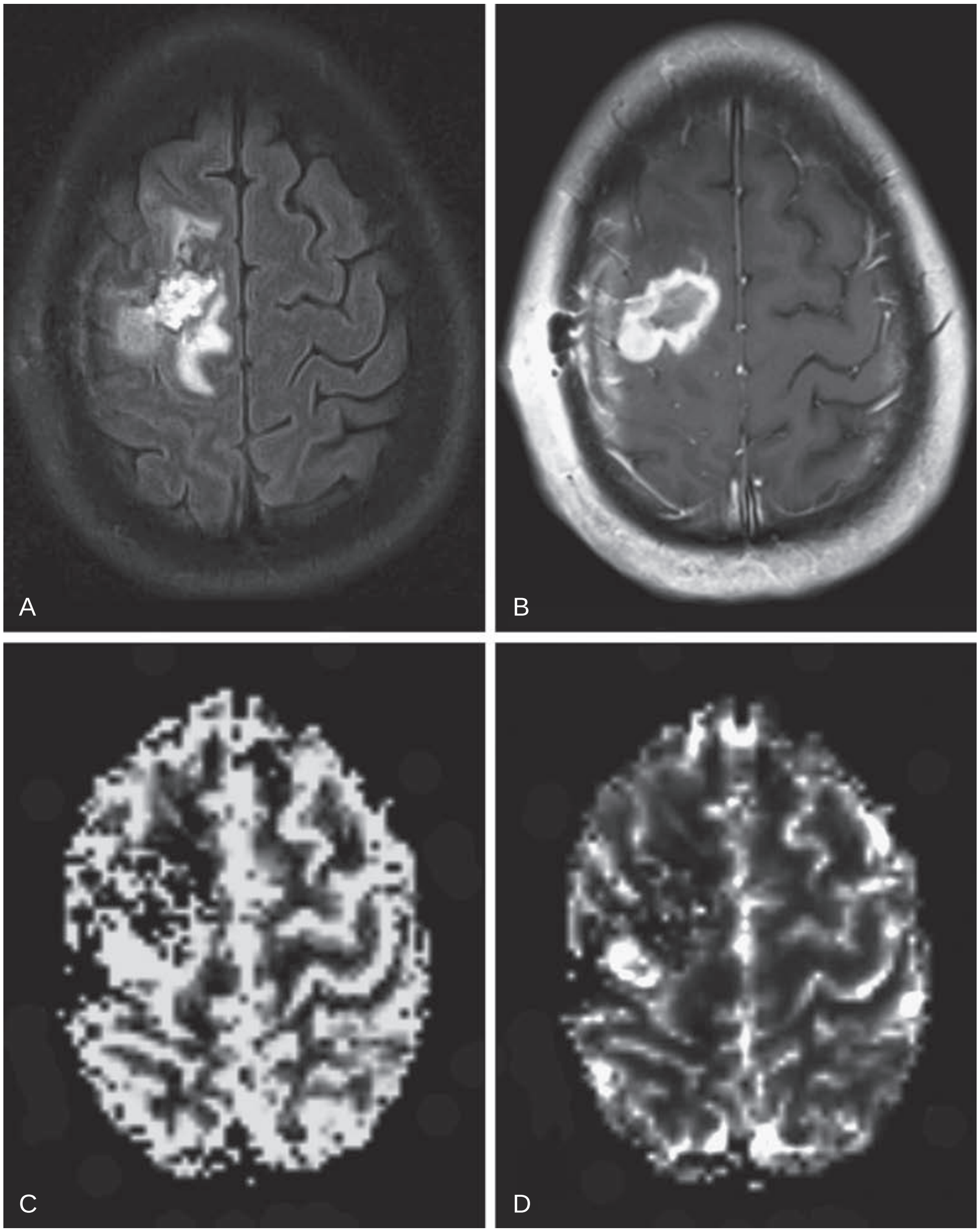

**e-Figure 28.2. Perfusion MRI in a 17-year-old patient with an anaplastic astrocytoma a few months after surgical resection and chemoradiation therapy.** An axial fluid-attenuated inversion recovery image (A) and postcontrast T1-weighted image (B) demonstrate a surgical resection cavity with signal abnormality and enhancement around the cavity. Relative blood volume (C) and blood flow (D) maps derived from dynamic susceptibility contrast MR perfusion demonstrate a focus of abnormally increased perfusion posterolateral to the surgical resection cavity consistent with recurrence and progression of the neoplasm.

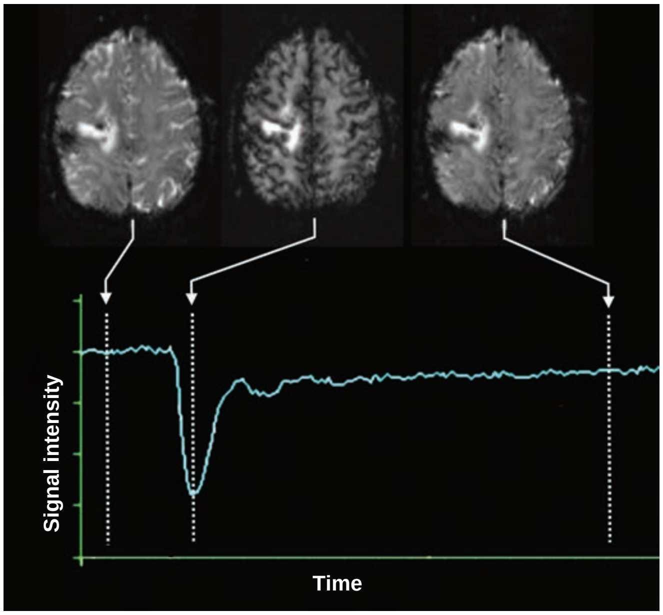

**Figure 28.1. Acquisition of dynamic susceptibility contrast perfusion magnetic resonance imaging.** Typically, a rapid echo planar acquisition is obtained through the head continuously over the course of approximately 1 or 1.5 minutes. A rapid injection of gadolinium-based contrast material is injected, which results in a transient dip in the signal intensity during the course of the first pass of contrast through the brain. After this first pass, the signal returns toward normal, although often not completely. A time-signal intensity curve is plotted before, during, and after the first pass bolus for each voxel, including brain tissue and vascular structures, which in turn is used to derive various perfusion parameters.

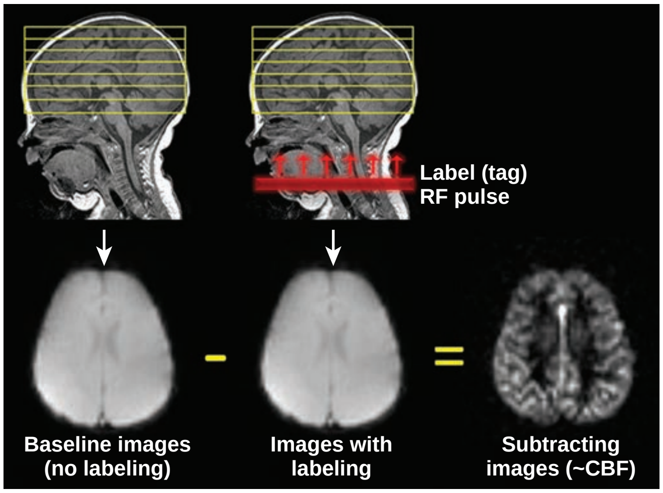

**Figure 28.3. Schematic demonstration of the general principle of arterial spin labeling perfusion MRI.** Images of the head are obtained once without and once with labeling of blood water protons using a radiofrequency (RF) pulse. The labeled (or tagged) blood flows into the brain, and if the images without and with label are subtracted from each other, the difference image results from these labeled blood protons and is proportional to cerebral blood flow (CBF).

subtraction and longer acquisition times, ASL perfusion is very sensitive to motion artifacts.

ASL has a number of potential advantages compared with exogenous contrast–based perfusion methods. ASL does not require rapid injection of a large bolus of contrast, which sometimes can be a problem in young children because of a lack of large bore intravenous access. ASL has the potential to provide quantitative perfusion data and also can be repeated in the same imaging session if the child moves. The disadvantages of ASL perfusion include longer imaging times, sensitivity to patient motion, lack of an easy way to derive CBV and MTT parameters, and specific artifacts as a result of arterial transit delays between the labeling and imaging planes, for example, when blood passes through collateral circulation channels.

Applications of ASL perfusion include cerebrovascular disease, detection of changes during complicated migraine, hypoxic-ischemic injury, depiction of hypoperfusion in mesial temporal sclerosis, and emerging applications in brain tumors.[26–32] In complicated or hemiplegic migraine, ASL can show either hyperperfusion or hypoperfusion depending on the timing of the exam in relation to vasodilation or vasoconstriction[33] (e-Fig. 28.4). After hypoxic ischemic injury or even after cases of arterial ischemic stroke when the vessels are open, a pattern of hyperperfusion may be demonstrated on ASL in the areas of ischemic injury (Fig. 28.5). Changes in perfusion can be detected during acute stroke and chronic cerebrovascular disease, but lack of easy calculation of MTT or Tmax and the presence of arterial transit delay artifacts limits its usefulness. It is perhaps still not reliable and informative enough to be concretely used in triage of acute arterial stroke management. ASL can show arteriovenous shunting in vascular disorders of the brain,[34] but other vascular pathophysiology may also be detected (e-Fig. 28.6). For example, residual high signal in the large brain vessels (with appropriate timing) can be indicative of slow flow due to a stenosis or clot. Similarly, delayed flow via collateral vessels may also sometimes be demonstrated.

ASL has some utility in imaging evaluation of pediatric brain tumors.[35] In general, higher grade or vascular tumors have higher CBF whereas lower grade or cystic tumors have lower perfusion (Fig. 28.7). Hemangiomas show very high CBF. In one study in children, patients with pilomyxoid astrocytoma could be distinguished from pilocytic astrocytoma.[36] The distinction among grades of adult glioma by DSC perfusion seems more reliable than between various posterior fossa tumor histologies in children.[35] Areas of active or recent seizures can show increased perfusion whereas areas of gliosis and chronic encephalomalacia will show normal to decreased perfusion. Further research is needed to further establish the role of ASL imaging in pediatrics.

## Computed Tomographic Perfusion Imaging

Dynamic CT perfusion imaging bears some similarity to DSC perfusion MRI, in that perfusion parameters are derived from a time-concentration curve obtained during continuous scanning of the first pass of a rapid injection of iodinated contrast material through the brain.[1,37,38] Quantitative maps of CBV, CBF, MTT, and Tmax can be obtained. Dynamic CT perfusion imaging has the advantage of widespread availability and speed, which can be important in the setting of acute stroke or in patients with contraindications to MRI. CT perfusion imaging often is performed in conjunction with CT angiography in the evaluation of cerebrovascular disease. Although continuous scanning of the head for CT perfusion can lead high radiation exposure, CT perfusion can be performed satisfactorily with 80 kVp and a low mA technique, which considerably decreases the radiation dose.[1,39] CT perfusion imaging has been studied extensively in the evaluation of patients with cerebrovascular disease, especially in the setting of acute ischemic stroke.[37,40] It can demonstrate the ischemic penumbra and tissues at risk and can be helpful in patient selection for stroke management (Fig. 28.8).[1,37,41]

## Other Perfusion Imaging Methods

Xenon CT perfusion uses stable nonradioactive Xenon gas inhaled over the course of a few minutes to act as a contrast agent for

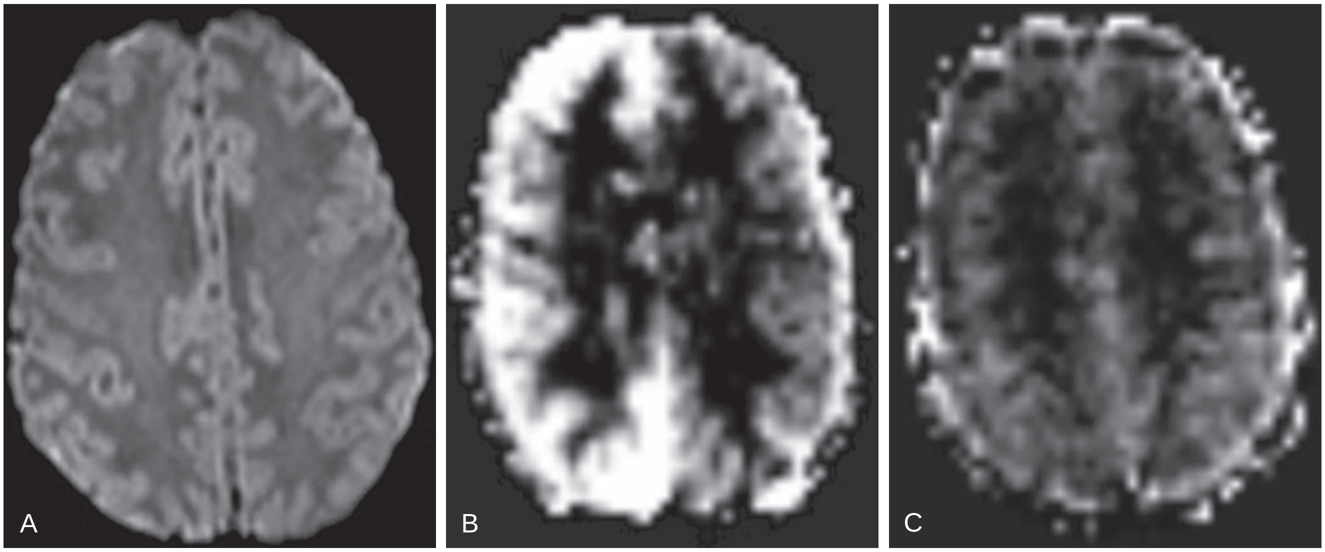

**e-Figure 28.4. Arterial spin labeling in a child with hemiplegic migraine.** The patient presented with acute onset left-sided weakness in the face and both the upper and lower extremities, along with headache. MRI was emergently performed to exclude an arterial ischemic stroke. No abnormality was found on diffusion-weighted imaging (A), but ASL perfusion MRI demonstrated increased cerebral blood flow in the right cerebral hemisphere (B). Two days later, the patient's symptoms have completely resolved and a repeat MRI demonstrated normal appearance of the brain on ASL perfusion imaging (C).

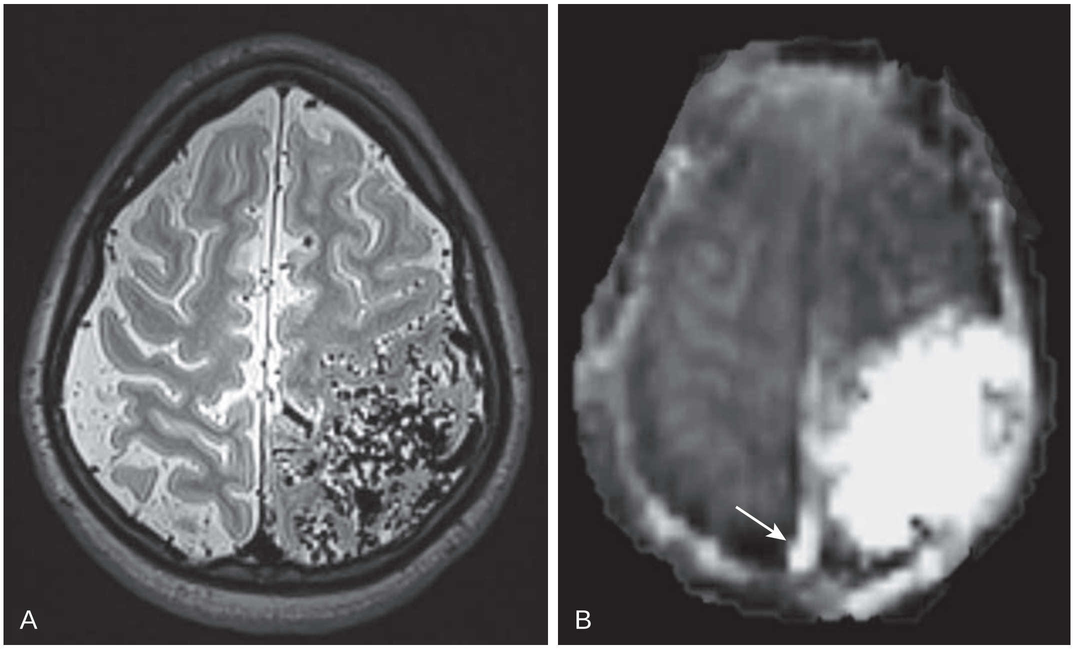

**e-Figure 28.6. ASL perfusion imaging in a patient with an arteriovenous malformation (AVM).** There is a large AVM in the left parietal region (A). ASL perfusion imaging shows markedly elevated cerebral blood flow in the lesion. There is also elevated signal in the superior sagittal sinus (B) which shows the drainage pathway of the AVM *(arrow).* ASL can physiologically depict whether there is superficial or deep drainage in most cases of AVM.

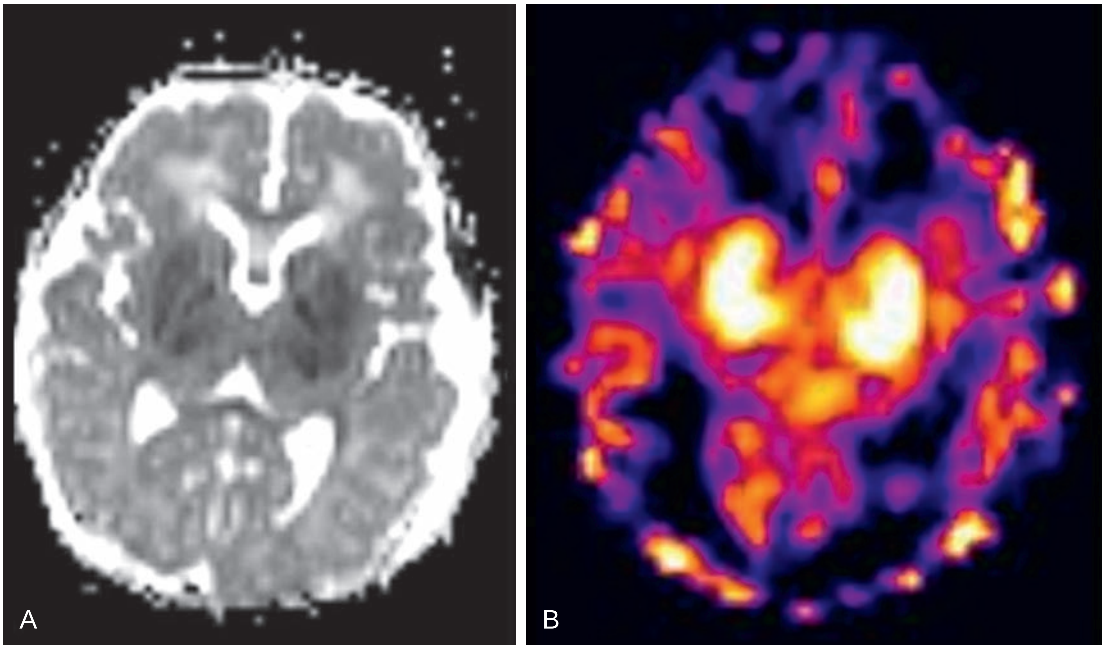

**Figure 28.5. ASL perfusion in an infant with hypoxic ischemic encephalopathy.** Axial apparent diffusion coefficient (ADC) maps show reduced diffusion in the bilateral deep grey nuclei (A) three days after a profound hypoxic event. (B) ASL perfusion map shows markedly elevated cerebral blood flow and hyperperfusion in the areas of reduced diffusion.

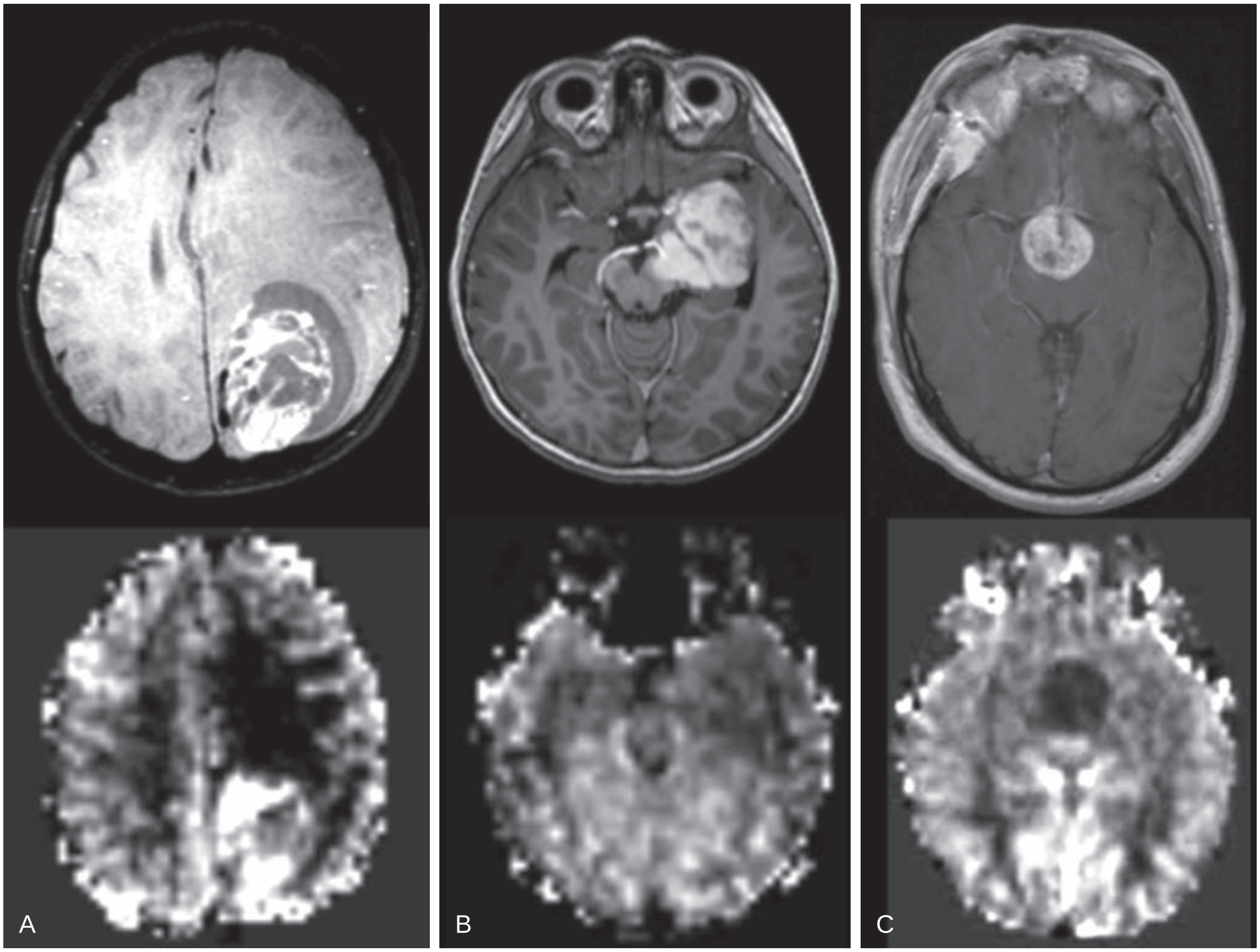

**Figure 28.7. ASL perfusion in three contrast enhancing brain masses.** (A) Elevated perfusion in a patient with a high grade malignant glioma. (B) No elevated perfusion in a patient with a low grade glioma (pilocytic astrocytoma). (C) Low perfusion in a patient with craniopharyngioma.

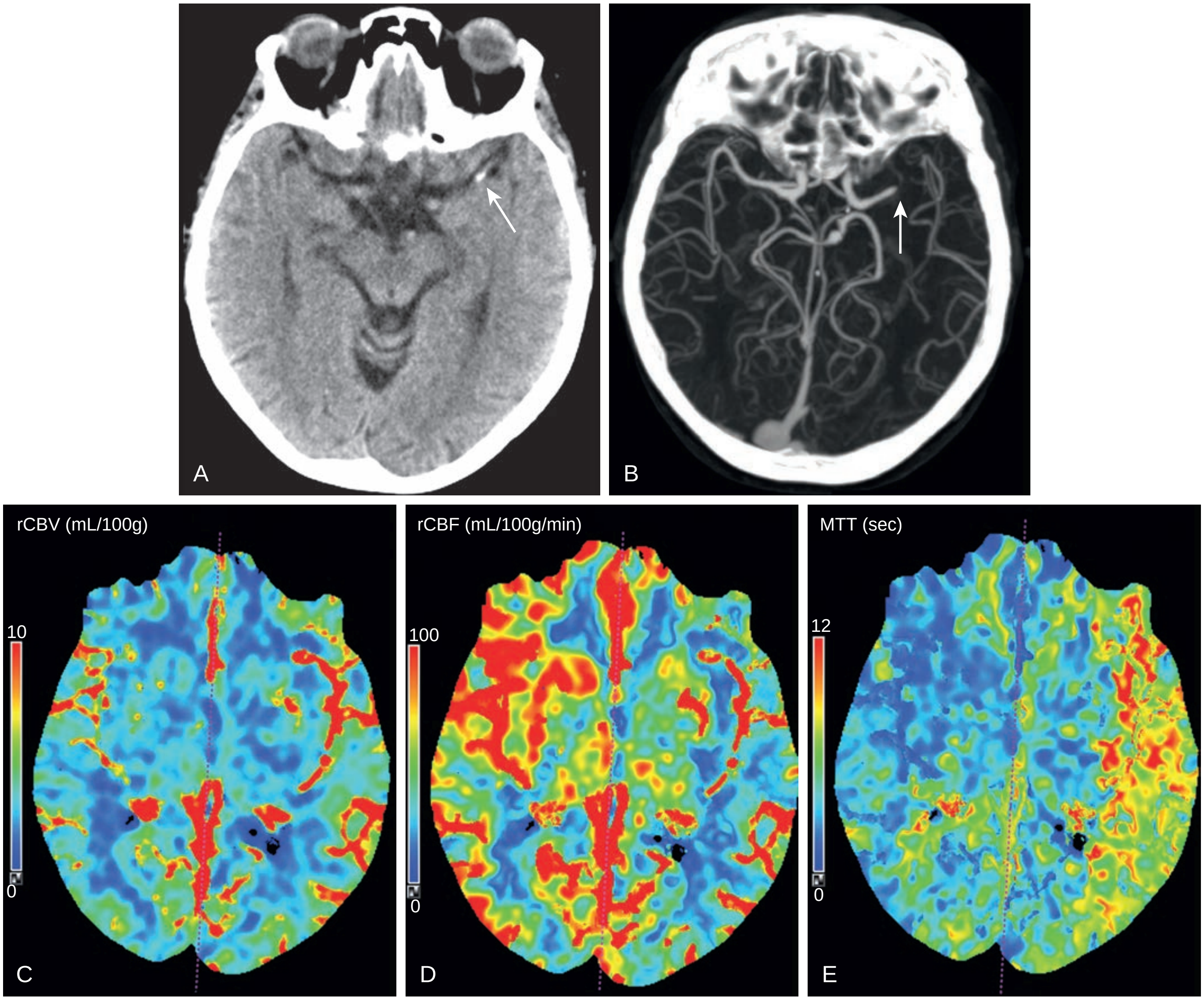

**Figure 28.8. CT perfusion imaging in a patient with acute right-sided weakness and aphasia.** Noncontrast CT examination (A) demonstrated a focus of high density *(arrow)* in the M1 segment of the left middle cerebral artery. No loss of gray white differentiation or edema was seen on CT at this time. CT angiography (B) showed an abrupt cutoff in the left middle cerebral artery *(arrow)*. CT perfusion imaging done immediately after CT angiography showed no large change in relative cerebral blood volume (C), but the relative cerebral blood flow (D) was decreased and mean transit time (E) was elevated in the distribution of the left middle cerebral artery compared with the contralateral side.

perfusion after crossing the blood-brain barrier. Xenon CT perfusion can produce accurate quantitative CBF measurements and even can be used to assess cerebrovascular reserve after a vasodilatory challenge in patients with occlusive or stenotic cerebrovascular disease.[1,42,43] Various nuclear medicine techniques also have been used to quantitatively assess cerebral perfusion. These techniques include positron emission tomography using $H_2{}^{15}O$, $^{15}O_2$, and $C^{15}O_2$ and single photon emission CT using $^{99m}$Tc-HMPAO and $^{133}$Xe. Xenon CT and nuclear medicine perfusion methods are not often performed in pediatric patients because of a lack of widespread availability and clinical expertise with these techniques, and potential concerns about the radiation dose.

## MAGNETOENCEPHALOGRAPHY AND MAGNETIC SOURCE IMAGING

Magnetoencephalography (MEG) is a noninvasive technique that records and analyzes the magnetic fields produced by the electrical currents of neural activity in the brain. MEG signals arise from intracellular currents that flow from dendrites to the cell body.[44] These magnetic signals are extremely weak, on the order of 10 to 1000 femtoTesla ($10^{-15}$ T),[45] requiring special sensors for detection. These magnetic fields induce electrical current in an array of special detector coils coupled to a superconducting quantum interference device.[45] Modern-day MEG machines typically have a few hundred sensor channels that surround the head (e-Fig. 28.9). Given the very weak magnetic fields generated by brain activity and the very high sensitivity of the superconducting quantum interference device sensors, MEG is very prone to interference from external magnetic sources, and thus siting in a highly-shielded room is required to prevent electromagnetic contamination. MEG provides excellent temporal resolution (less than 1 ms), and compared with standard electroencephalography, it provides very good spatial resolution (down to 3–15 mm depending on depth) in the detection of normal and abnormal brain waveforms. The most important current clinical applications of MEG relate to evaluating epileptic disorders and presurgical functional mapping.

In a typical clinical MEG examination, multiple sequential recordings are made via the various channels. The MEG waveform analysis results often are coregistered to a volumetric MRI of the head for source spatial localization of the abnormal waveforms or functional mappings. This combination of MEG with MRI is known as *magnetic source imaging*. For clinical purposes, when one uses the term MEG, it usually refers to magnetic source imaging with MRI coregistration. The registration of MEG and MRI typically is performed by using fiducial markers in predetermined regions.[46] The same fiducial markers can be used for determining patient motion and motion correction, which is important for clinical interpretation. After acquisition of the MEG waveform data, various complex mathematical models and algorithms are used for source localization, along with the ability to provide information from a "virtual depth electrode" in the brain.[45,46]

Various artifacts almost always occur during an MEG examination. Muscle twitching, eye blinking, and cardiac electrical activity can cause changes in MEG waveforms. The presence of dental and orthodontic hardware, vagal nerve stimulators (even when turned off), and metallic piercings will cause artifacts on MEG as well.

## Magnetoencephalography in the Evaluation of Children With Epilepsy

The major goal in the presurgical evaluation of patients with epilepsy is identification of the epileptogenic or ictal onset zones.[47,48] It is hoped that surgical removal of this epileptogenic region will result in a seizure-free state (or at least a significant decrease in seizure frequency) with minimal postsurgical neurologic deficits. Due to lack of methods that measure the epileptogenic zone directly, this area is indirectly identified based on concordant data from a multitude of presurgical noninvasive imaging modalities, electrophysiologic tests, and intracranial recordings. However, the results of these tests are sometimes insufficiently concordant or even inconclusive. The excellent temporal and very good spatial resolution of MEG makes it a very useful tool in the evaluation of patients with epilepsy, especially those who are medically refractory. MEG evaluation typically is performed by passive interictal recording of spontaneous electromagnetic activity and discharges. Patients often are instructed to be sleep deprived overnight to increase interictal activity. In young children, typically 5 years or younger, or in patients with developmental delay or psychiatric issues, general anesthesia may be required to perform the MEG examination. The choice of anesthetic medication is important so as to avoid interference with the detection of epileptiform changes on MEG.[46]

MEG has the potential to be used in the following clinical scenarios in the evaluation of patients with epilepsy:

1. Investigation of inconclusive electroencephalogram (EEG) results (Fig. 28.10)
2. Investigation of discrepancy between EEG and neuroimaging findings
3. When no structural lesion is found on MRI in a patient with epilepsy, MEG results may be used to guide a targeted "second look" at the MRI for possible detection of subtle abnormalities that initially may have been difficult to identify
4. In patients with multiple structural lesions on MRI, determination of whether one of the lesions is primarily responsible for the patient's refractory seizures, indicating surgical feasibility
5. Determination of multiple epileptogenic zones, suggesting an unfavorable outcome or contraindication for surgery

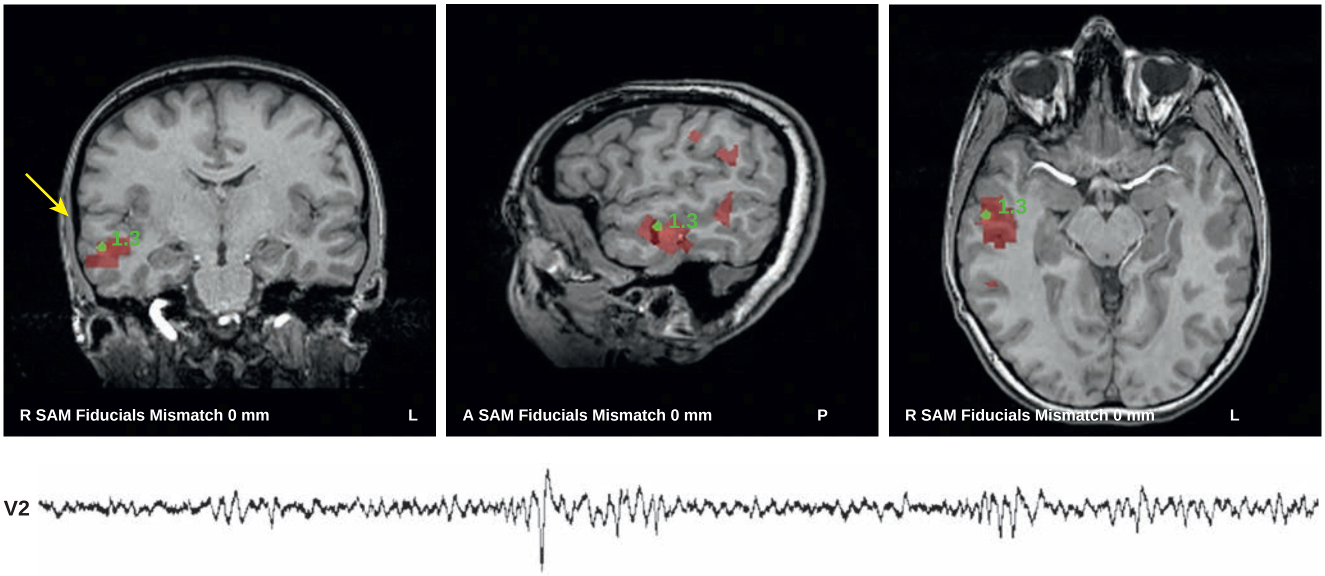
1.3
R SAM Fiducials Mismatch 0 mm
L
1.3
A SAM Fiducials Mismatch 0 mm
P
1.3
R SAM Fiducials Mismatch 0 mm
L
V2

**Figure 28.10. Magnetoencephalography and magnetic source imaging in a patient with inconclusive EEG localization results.** An interictal MEG shows spike and wave and sharp activity localizing to the lateral aspect of the right temporal lobe *(arrow)*. No lesion could be identified on MRI and there was no mesial temporal sclerosis.

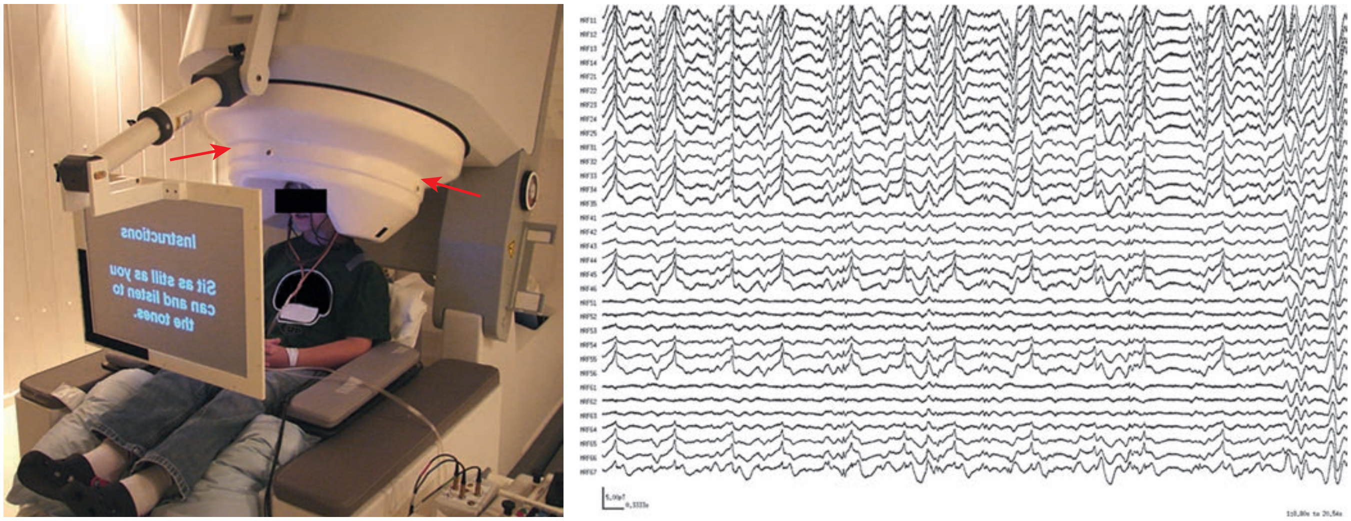

**e-Figure 28.9. Magnetoencephalography.** The image on the left demonstrates a typical MEG machine (biomagnetometer) and patient setup for recordings and functional mapping. The patient's head is situated within the helmet-like head element, which houses the multiple arrays of sensors around the head *(arrows)* within an insulated dewar. The image on the right demonstrates a small sample of representative MEG wave recordings from just 33 channels over the course of approximately 20 seconds. Typically, many more channels are recorded and the recordings are done for much longer periods, resulting in a tremendous amount of data to be analyzed for magnetic source imaging.

6. Confirmation of localization based on other methods, allowing surgery to proceed without long-duration invasive intracranial EEG monitoring
7. More accurate spatial localization of the epileptogenic zone to decrease the extent of craniotomy and grid placement for invasive EEG monitoring
8. Evaluation of recurrence of epilepsy after surgery to plan for possible re-resection (e-Fig. 28.11)
9. Delineation of eloquent cortex to aid presurgical decision making

Careful visual scrutiny of the source MEG waves is necessary to help determine the presence or absence of significant epileptiform activity or artifacts. High-frequency oscillations have emerged as new potential biomarkers for the delineation of the epileptogenic zone. Various automated software waveform analyses and statistical tests can be performed to determine the significance of the waveforms detected on MEG. One such measure is determining kurtosis, or "spikiness" of the waves, which can help in identifying areas of significant activity. The addition of MEG to the evaluation of patients with epilepsy has been shown to improve the quality of medical care and surgical outcomes and provides important nonredundant information in a significant proportion of patients.[47–50]

## Brain Functional and Presurgical Mapping Using Magnetoencephalography

Currently, the clinical gold standard for functional mapping of eloquent cortex is intraoperative direct cortical stimulation and mapping. Noninvasive examinations such as functional MRI (fMRI) are often used for preoperative localization and mapping before resection of tumors, vascular malformations, and epileptogenic foci. The blood oxygenation level dependent response used in fMRI localization is a measurement of the hemodynamic response to neuronal activity rather than direct measurement of the neuronal activity (see Chapter 27). Many pathophysiologic processes are known to adversely affect and/or blunt the hemodynamic response measured with fMRI, such as arteriovenous malformations or even some tumors. MEG can be used as another noninvasive method for functional identification of eloquent cortical regions.[51–53] Motor, somatosensory, and language areas typically are examined by MEG in the clinical setting. Auditory and visual centers are also occasionally investigated. Similar to fMRI, MEG recordings are used to evaluate responses to task performance and/or evoked stimulation.

Motor mapping can be performed with self-paced button pressing, for example using left and right index fingers, and recording the MEG response. Typically these motor actions result in event-related desynchronization (ERD) in the beta wave band, approximately 200 to 300 ms after the button press. Depending on the area of interest for motor mapping, occasionally other areas such as the great toes, elbows, or oral musculature also could be used. Somatosensory testing can be performed with use of various stimuli while recording the MEG response as well. Alternatively, and especially in patients who are sedated or anesthetized, somatosensory testing can be performed via painless electric stimulation of the median or tibial nerves. Typically, MEG activity at 20 ms after stimulus is used to map somatosensory function.

Language mapping is another area in which MEG may be useful, either in evaluation of language lateralization or localization. The language tasks used are similar to those used with fMRI; common language tasks in children may include picture naming, word recall, stem completion, and verb generation, among others. The tasks typically are displayed via a screen in front of the patient, with the operator giving audio instructions when they are needed. Similar to motor mapping, ERD associated with neuronal activity can be exploited for assessing language-related centers in the brain, approximately 400 to 500 ms before the patient's response. In our experience, MEG is more successful in language lateralization than language center localization.

After the functional mapping tasks and stimulations are performed, areas of target activity or statistically significant ERD are overlaid on volumetric MRI to visualize the functional areas mapped by MEG (Fig. 28.12). In small children and in patients who are anesthetized, it generally is not feasible to perform motor and language mapping. Somatosensory mapping only via median or tibial nerve stimulation may be a viable choice. The functional mappings performed by means of MEG are used in determining the feasibility and risks of surgery and occasionally in planning the surgical approach to lesions. Depending on the results and the experience of the center, MEG may be used in conjunction with or in lieu of fMRI.

## Other Current and Future MEG Applications

MEG has many other current and future potential applications in evaluation of brain disorders beyond epilepsy. The strength lies in the combination of electrophysiology and imaging localization capabilities, although there remain challenges in localization and analysis of the complex MEG signals. Many disorders that affect the brain will cause changes in brain electromagnetic oscillations, such as traumatic brain injury, genetic and developmental disorders, autism, disorders of consciousness, and a variety of psychiatric disorders. Many of these disorders do not have overt changes on MR imaging of the brain. However, there may be changes in the electrographic signatures of various parts of the brain that can be detected and evaluated by MEG. For example, autistic children can demonstrate particular changes and delays in the MEG auditory signature.[54] In some patients, these can change over time as the child gets older and there may be correlation with outcome.[55] Somatosensory evoked potentials have been traditionally used to evaluate and predict clinical outcome in at-risk infants. MEG can highlight many key changes in somatosensory processing in typical and atypical development and be used in this cohort.[56] In traumatic brain injury, MEG features such as slow waves and high frequency oscillations may be identified including in patients without overt conventional imaging findings.[57] The potential of MEG is still largely untapped and remains an active area for further investigation.

### KEY POINTS

- Perfusion imaging includes a number of imaging techniques used to measure hemodynamically derived functional parameters in the brain.
- DSC perfusion MRI provides measures of CBV, CBF, and MTT, which are useful in the imaging evaluation of cerebrovascular diseases and brain neoplasms. ASL perfusion MRI is a noninvasive method that uses magnetically labeled arterial blood water as an endogenous tracer to measure CBF.
- Perfusion imaging methods have a large number of applications in evaluation of various aspects of cerebrovascular diseases, neuro-oncology, and effect of other brain disorders on cerebral perfusion.
- MEG is a robust and sensitive tool in the depiction of abnormal epileptiform activity in the brain and can be coregistered with MRI to localize these abnormal discharges in children with epilepsy.
- MEG can be used for presurgical functional mapping of motor, somatosensory, and language areas in the brain. MEG is being increasingly investigated and used in evaluation of a wide spectrum of brain disorders.

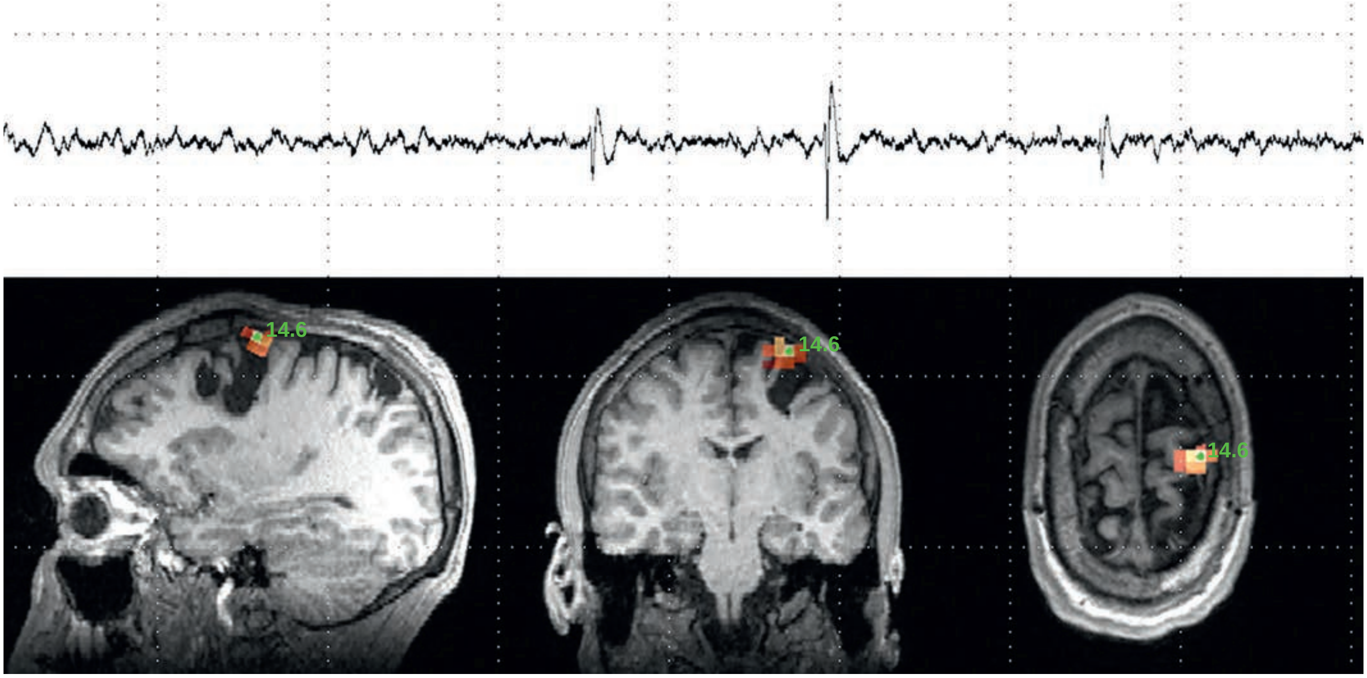

**e-Figure 28.11. Magnetoencephalography and magnetic source imaging in a patient with continued seizures even after epilepsy surgery.** The patient had undergone multiple cortical resections after an extensive epilepsy workup and invasive cortical mapping a few years earlier. However, although some improvement in the frequency of seizures occurred, the patient continued to have medically refractory epilepsy. An interictal MEG shows multiple isolated spike and slow wave abnormalities during multiple recordings localized to a focus along the superomedial aspect of the site of surgical resection.

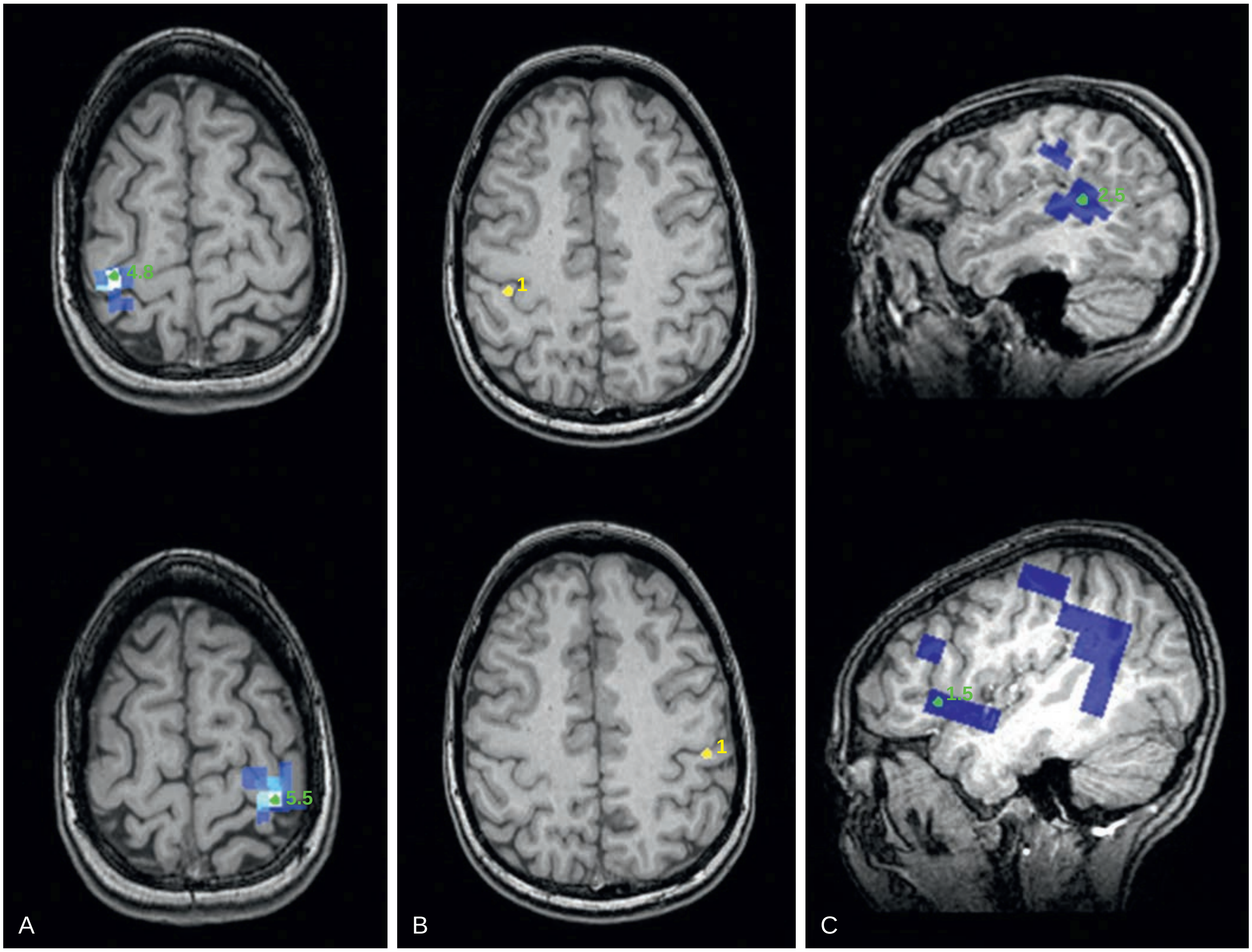

**Figure 28.12. Presurgical functional motor, somatosensory, and language mapping using magnetoencephalography.** Motor mapping (A) of the left and right index fingers by simple finger tapping mapped to the right and left precentral gyri, respectively. Somatosensory mapping (B) using stimulation of the fingers by a puff of air shows mapping to the banks of the contralateral postcentral gyri. Language mapping was performed using various tasks that predominantly localized to the posterior aspect of the left superior temporal gyrus and anterior opercular region of the lateral left frontal lobe (C).

## SUGGESTED READINGS

Alsop DC, Detre JA, Golay X, et al. Recommended implementation of arterial spin-labeled perfusion MRI for clinical applications: A consensus of the ISMRM perfusion study group and the European consortium for ASL in dementia. *Magn Reson Med*. 2015;73:102–116.

Chuang NA, Otsubo H, Pang EW, et al. Pediatric magnetoencephalography and magnetic source imaging. *Neuroimaging Clin N Am*. 2006;16:193–210.

Schwartz ES, Dlugos DJ, Storm PB, et al. Magnetoencephalography for pediatric epilepsy: how we do it. *AJNR Am J Neuroradiol*. 2008;29:832–837.

Wintermark M, Sesay M, Barbier E, et al. Comparative overview of brain perfusion imaging techniques. *Stroke*. 2005;36:e83–e99.

Wolf RL, Detre JA. Clinical neuroimaging using arterial spin-labeled perfusion magnetic resonance imaging. *Neurother*. 2007;4:346–359.

Zaharchuk G. Theoretical basis of hemodynamic MR imaging techniques to measure cerebral blood volume, cerebral blood flow, and permeability. *AJNR Am J Neuroradiol*. 2007;28:1850–1858.

## REFERENCES

Full references for this chapter can be found on www.expertconsult.com.

## REFERENCES

1. Wintermark M, Sesay M, Barbier E, et al. Comparative overview of brain perfusion imaging techniques. *Stroke*. 2005;36:e83–e99.
2. Zaharchuk G. Theoretical basis of hemodynamic MR imaging techniques to measure cerebral blood volume, cerebral blood flow, and permeability. *AJNR Am J Neuroradiol*. 2007;28:1850–1858.
3. Rosen BR, Belliveau JW, Vevea JM, et al. Perfusion imaging with NMR contrast agents. *Magn Reson Med*. 1990;14:249–265.
4. Belliveau JW, Rosen BR, Kantor HL, et al. Functional cerebral imaging by susceptibility-contrast NMR. *Magn Reson Med*. 1990;14:538–546.
5. Rosen BR, Belliveau JW, Aronen HJ, et al. Susceptibility contrast imaging of cerebral blood volume: human experience. *Magn Reson Med*. 1991;22:293–299, discussion 300-303.
6. Paulson ES, Schmainda KM. Comparison of dynamic susceptibility-weighted contrast-enhanced MR methods: recommendations for measuring relative cerebral blood volume in brain tumors. *Radiology*. 2008;249:601–613.
7. Boxerman JL, Bandettini PA, Kwong KK, et al. The intravascular contribution to fMRI signal change: Monte Carlo modeling and diffusion-weighted studies in vivo. *Magn Reson Med*. 1995;34:4–10.
8. Schmainda KM, Rand SD, Joseph AM, et al. Characterization of a first-pass gradient-echo spin-echo method to predict brain tumor grade and angiogenesis. *AJNR Am J Neuroradiol*. 2004;25:1524–1532.
9. Donahue KM, Krouwer HG, Rand SD, et al. Utility of simultaneously acquired gradient-echo and spin-echo cerebral blood volume and morphology maps in brain tumor patients. *Magn Reson Med*. 2000;43:845–853.
10. Calamante F, Willats L, Gadian DG, et al. Bolus delay and dispersion in perfusion MRI: implications for tissue predictor models in stroke. *Magn Reson Med*. 2006;55:1180–1185.
11. Calamante F. Perfusion MRI using dynamic-susceptibility contrast MRI: quantification issues in patient studies. *Top Magn Reson Imaging*. 2010;21:75–85.
12. Sugahara T, Korogi Y, Kochi M, et al. Perfusion-sensitive MR imaging of gliomas: comparison between gradient-echo and spin-echo echo-planar imaging techniques. *AJNR Am J Neuroradiol*. 2001;22:1306–1315.
13. Wu O, Ostergaard L, Koroshetz WJ, et al. Effects of tracer arrival time on flow estimates in MR perfusion-weighted imaging. *Magn Reson Med*. 2003;50:856–864.
14. Wu O, Ostergaard L, Sorensen AG. Technical aspects of perfusion-weighted imaging. *Neuroimaging Clin N Am*. 2005;15:623–637, xi.
15. Grandin CB. Assessment of brain perfusion with MRI: methodology and application to acute stroke. *Neuroradiology*. 2003;45:755–766.
16. Toth G, Albers GW. Use of MRI to estimate the therapeutic window in acute stroke: is perfusion-weighted imaging/diffusion-weighted imaging mismatch an EPITHET for salvageable ischemic brain tissue? *Stroke*. 2009;40:333–335.
17. Law M, Yang S, Wang H, et al. Glioma grading: sensitivity, specificity, and predictive values of perfusion MR imaging and proton MR spectroscopic imaging compared with conventional MR imaging. *AJNR Am J Neuroradiol*. 2003;24:1989–1998.
18. Law M, Hamburger M, Johnson G, et al. Differentiating surgical from non-surgical lesions using perfusion MR imaging and proton MR spectroscopic imaging. *Technol Cancer Res Treat*. 2004;3:557–565.
19. Vossough A, Nabavizadeh SA. Functional imaging based diagnostic strategy: intra-axial brain masses. In: Faro S, Mohamed FB, eds. *Functional Neuroradiology: Principles and Clinical Applications*. Berlin: Springer; 2011.
20. Law M, Cha S, Knopp EA, et al. High-grade gliomas and solitary metastases: differentiation by using perfusion and proton spectroscopic MR imaging. *Radiology*. 2002;222:715–721.
21. Cha S. Dynamic susceptibility-weighted contrast-enhanced perfusion MR imaging in pediatric patients. *Neuroimaging Clin N Am*. 2006;16:137–147, ix.
22. Barajas RF Jr, Chang JS, Segal MR, et al. Differentiation of recurrent glioblastoma multiforme from radiation necrosis after external beam radiation therapy with dynamic susceptibility-weighted contrast-enhanced perfusion MR imaging. *Radiology*. 2009;253:486–496.
23. Essock-Burns E, Lupo JM, Cha S, et al. Assessment of perfusion MRI-derived parameters in evaluating and predicting response to antiangiogenic therapy in patients with newly diagnosed glioblastoma. *Neuro Oncol*. 2011;13:119–131.
24. Williams DS, Detre JA, Leigh JS, et al. Magnetic resonance imaging of perfusion using spin inversion of arterial water. *Proc Natl Acad Sci USA*. 1992;89:212–216.
25. Deibler AR, Pollock JM, Kraft RA, et al. Arterial spin-labeling in routine clinical practice, part 1: technique and artifacts. *AJNR Am J Neuroradiol*. 2008;29:121234.
26. Deibler AR, Pollock JM, Kraft RA, et al. Arterial spin-labeling in routine clinical practice, part 3: hyperperfusion patterns. *AJNR Am J Neuroradiol*. 2008;29:141435.
27. Wang J, Licht DJ, Jahng GH, et al. Pediatric perfusion imaging using pulsed arterial spin labeling. *J Magn Reson Imaging*. 2003;18:404–413.
28. Detre JA, Alsop DC. Perfusion magnetic resonance imaging with continuous arterial spin labeling: methods and clinical applications in the central nervous system. *Eur J Radiol*. 1999;30:115–124.
29. Wolf RL, Detre JA. Clinical neuroimaging using arterial spin-labeled perfusion magnetic resonance imaging. *Neurother*. 2007;4:346–359.
30. Wang J, Licht DJ. Pediatric perfusion MR imaging using arterial spin labeling. *Neuroimaging Clin N Am*. 2006;16:149–167, ix.
31. Chen J, Licht DJ, Smith SE, et al. Arterial spin labeling perfusion MRI in pediatric arterial ischemic stroke: initial experiences. *J Magn Reson Imaging*. 2009;29:282–290.
32. Deibler AR, Pollock JM, Kraft RA, et al. Arterial spin-labeling in routine clinical practice, part 2: hypoperfusion patterns. *AJNR Am J Neuroradiol*. 2008;29:1235–1241.
33. Rigual DA, Stence NV, Fenton LZ, et al. The spectrum of imaging findings in pediatric hemiplegic migraine. *Neurographics*. 2016;6:372–376.
34. Nabavizadeh SA, Edgar JC, Vossough A. Utility of susceptibility-weighted imaging and arterial spin perfusion imaging in pediatric brain arteriovenous shunting. *Neuroradiology*. 2014;56(10):877–884.
35. Yeom KW, Mitchell LA, Lober RM, et al. Arterial spin-labeled perfusion of pediatric brain tumors. *AJNR Am J Neuroradiol*. 2014;35(2):395–401.
36. Nabavizadeh SA, Assadsangabi R, Hajmomenian M, et al. High accuracy of arterial spin labeling perfusion imaging in differentiation of pilomyxoid from pilocytic astrocytoma. *Neuroradiology*. 2015;57:527–533.
37. Shetty SK, Lev MH. CT perfusion in acute stroke. *Neuroimaging Clin N Am*. 2005;15:481–501, ix.
38. Allmendinger AM, Tang ER, Lui YW, et al. Imaging of stroke: part 1, perfusion CT—overview of imaging technique, interpretation pearls, and common pitfalls. *AJR Am J Roentgenol*. 2012;198:52–62.
39. Wintermark M, Maeder P, Verdun FR, et al. Using 80 kVp versus 120 kVp in perfusion CT measurement of regional cerebral blood flow. *AJNR Am J Neuroradiol*. 2000;21:1881–1884.
40. Wintermark M. Brain perfusion-CT in acute stroke patients. *Eur Radiol*. 2005;15(suppl 4):DD31.
41. Campbell BC, Mitchell PJ, Kleinig TJ, et al. Endovascular therapy for ischemic stroke with perfusion-imaging selection. *N Engl J Med*. 2015;372:1009–1018.
42. Gupta R, Jovin TG, Yonas H. Xenon CT cerebral blood flow in acute stroke. *Neuroimaging Clin N Am*. 2005;15:531–542, x.
43. Nemoto EM, Yonas H, Kuwabara H, et al. Differentiating hemodynamic compromise by the OEF response to acetazolamide in occlusive vascular disease. *Adv Exp Med Biol*. 2005;566:135–141.
44. Okada YC, Wu J, Kyuhou S. Genesis of MEG signals in a mammalian CNS structure. *Electroencephalogr Clin Neurophysiol*. 1997;103:474–485.
45. Schwartz ES, Edgar JC, Gaetz WC, et al. Magnetoencephalography. *Pediatr Radiol*. 2010;40:50–58.
46. Schwartz ES, Dlugos DJ, Storm PB, et al. Magnetoencephalography for pediatric epilepsy: how we do it. *AJNR Am J Neuroradiol*. 2008;29:832–837.
47. Grondin R, Chuang S, Otsubo H, et al. The role of magnetoencephalography in pediatric epilepsy surgery. *Childs Nerv Syst*. 2006;22:779–785.
48. Chuang NA, Otsubo H, Pang EW, et al. Pediatric magnetoencephalography and magnetic source imaging. *Neuroimaging Clin N Am*. 2006;16:193–210.
49. Otsubo H, Snead OC 3rd. Magnetoencephalography and magnetic source imaging in children. *J Child Neurol*. 2001;16:227–235.
50. Stufflebeam SM, Tanaka N, Ahlfors SP. Clinical applications of magnetoencephalography. *Hum Brain Mapp*. 2009;30:1813–1823.
51. Gaetz W, Cheyne D, Rutka JT, et al. Presurgical localization of primary motor cortex in pediatric patients with brain lesions by the use of spatially filtered magnetoencephalography. *Neurosurgery*. 2009;64:177–185, discussion 186.
52. Merrifield WS, Simos PG, Papanicolaou AC, et al. Hemispheric language dominance in magnetoencephalography: sensitivity, specificity, and data reduction techniques. *Epilepsy Behav*. 2007;10:120–128.
53. Gaetz WC, Cheyne DO. Localization of human somatosensory cortex using spatially filtered magnetoencephalography. *Neurosci Lett*. 2003;340:161–164.

54. Roberts TP, Cannon KM, Tavabi K, et al. Auditory magnetic mismatch field latency: a biomarker for language impairment in autism. *Biol Psychiatry*. 2011;70:263–269.
55. Port RG, Edgar JC, Ku M, et al. Maturation of auditory neural processes in autism spectrum disorder - a longitudinal MEG study. *Neuroimage Clin*. 2016;11:566–577.
56. Saby JN, Meltzoff AN, Marshall PJ. Beyond the N1: a review of late somatosensory evoked responses in human infants. *Int J Psychophysiol*. 2016;110:146–152.
57. Wilde EA, Bouix S, Tate DF, et al. Advanced neuroimaging applied to veterans and service personnel with traumatic brain injury: state of the art and potential benefits. *Brain Imaging Behav*. 2015;9:367–402.

# 29

# Prenatal Imaging

Dorothy Bulas

Central nervous system (CNS) anomalies occur in 1.4 to 1.6 per 1,000 live births and 3% to 6% of still births.[1] Whereas some anomalies can be detected as early as the first trimester (such as anencephaly), others may not develop or become apparent until later in gestation.[2]

Ultrasound is the initial imaging modality used for the assessment of fetal CNS anomalies. When ultrasound is carefully performed using established guidelines, it can be very sensitive in evaluating the fetal brain.[3] Axial images are important for the assessment of biparietal diameter and head circumference measurements, ventricular size, and cerebellar configuration. Coronal and sagittal images can confirm the presence of the cavum septum pellucidum and corpus callosum. However, because of limitations from skull shadowing, fetal lie, maternal obesity, and oligohydramnios, evaluation of the fetal brain by ultrasound may be incomplete. When a fetal CNS anomaly is suspected, magnetic resonance imaging (MRI) is an adjunct that can provide additional information.[4–7]

The multiplanar capability of MRI allows for the evaluation of the brain in any plane regardless of fetal lie, oligohydramnios, and overlying bone and gas. Single shot rapid acquisition with relaxation enhancement sequences decrease movement artifact. Slices as thin as 2 mm can be obtained and provide excellent anatomic detail. T1 sequences take longer to obtain and may require thicker slices for sufficient signal, but they are useful for detecting hemorrhage, calcification, and gliosis.

Advanced techniques include diffusion-weighted imaging (DWI), echo planar imaging (EPI), diffusion tensor imaging (DTI), spectroscopy, and functional MRI.[8] The apparent diffusion coefficient normally decreases after 30 weeks' gestational age (GA),[9] but higher apparent diffusion coefficient (ADC) values have been reported in high-risk fetuses.[10] DWI can help detect hemorrhage and acute ischemia (Fig. 29.1). DTI measures the magnitude and direction of diffusion (fractional anisotropy). Although intrinsic anisotropy is low in the fetal brain, imaging improvements will help understand the onset and timing of delayed white matter connectivity.[11,12] Proton MR spectroscopy has advanced the investigation of fetal brain metabolism. Creatine and N-acetylaspartate peaks appear to have a progressive increase, whereas choline decreases in the third trimester.[13] Alterations in these peaks may help identify conditions associated with fetal compromise.

Ongoing enhancement of ultrafast MR sequences and postprocessing methodology has resulted in imaging techniques that can evaluate growth, organization, and remodeling processes that occur during fetal brain development.[14,15] Three-dimensional volumetric studies have demonstrated the value of quantitative assessment of brain growth in healthy versus high-risk fetuses. Fetuses with congenital heart disease have been shown to have impaired third-trimester brain growth compared with control subjects, offering a method to evaluate timing and progression of abnormal brain development.[16] Three-dimensional reconstruction of the fetal brain can provide cortical measures such as surface area and gyrification indices.

Fetal MRI is routinely performed with 1.5 Tesla units, with centers now moving to 3 Tesla. Issues regarding increased specific absorption rate heating and movement artifacts need to be addressed with these higher Tesla units.[17–19]

These advanced neuroimaging techniques improve our ability to assess anomalies and provide methods for monitoring high-risk pregnancies, leading to improved counseling, planning of fetal intervention, and perinatal management. In a large recent multicenter prospective cohort study, fetal MRI was shown to improve the diagnostic accuracy of brain evaluation in 23% of cases age 18 to 24 weeks GA and 29% in cases greater than 24 weeks GA. Diagnostic accuracy was 68% for ultrasound and 93% for MRI. MRI provided additional information in 49% of cases, changed the prognostic information in 20%, and changed clinical management in 30%. This large series helps demonstrate that a fetus with a brain anomaly identified by ultrasound can benefit from a fetal MRI to improve counseling and management planning.[20]

## NORMAL DEVELOPMENT OF THE FETAL BRAIN

Knowledge of normal fetal morphology and development is important when evaluating anomalies. From 18 to 24 weeks' gestation, the brain is smooth, with minimal sulcation. The ventricles and extraaxial subarachnoid space, including the cisterna magna, are prominent until the third trimester[21] (Fig. 29.2).

Neuronal migration patterns can be documented by MRI.[22–25] Before 20 weeks' gestation, three layers are visualized, including the germinal matrix, intermediate/cell sparse zone, and cortex. The germinal matrix has a low signal on T2-weighting and high signal on T1-weighting along the lateral ventricular walls and involutes from posterior to anterior after 28 weeks' gestation. The intermediate zone represents migrating glial cells and eventually becomes the white matter. With a high water content, it appears low on T1-weighting and high on T2-weighting with high ADC due to low cellularity. The cortical ribbon has high T1 and low T2 signal due to high cellularity with low ADC.

From 20 to 28 weeks' gestation, a five-layer pattern is observed. This includes the germinal matrix, subventricular periventricular fiber-rich zone, subventricular cellular/intermediate zone, subplate, and cortical plate. The germinal matrix and cortical plate have low T2 signal and high T1 signal due to high cellularity. The subventricular cellular/intermediate zone is slightly low signal on T2 and high signal on T1, while the subventricular periventricular fiber-rich zone and subplate are of low signal on T1 and high signal on T2.

The fetal cortical mantle follows a predictable course in maturation. Gyration progresses throughout the second and third gestation and can be used to assess GA (Box 29.1). By 32 weeks' gestation, extensive gyration and sulcation is present (Fig. 29.3).[21–26]

## FETAL VENTRICULOMEGALY

The fetal ventricles are prominent in relation to the brain parenchyma until the third trimester. After 25 weeks' gestation, the ventricles lose their colpocephalic configuration. Fetal ventriculomegaly (VM) is defined as an atrial measurement greater than 10 mm with separation of choroid from the medial wall (i.e., floating choroid). VM can be due to obstruction, atrophy, maldevelopment, or, rarely, overproduction of cerebrospinal fluid. Ultrasound and MRI should be used to carefully assess for findings that suggest chromosomal anomalies (e.g., trisomy 13, 18, or 21), malformations (e.g., Chiari 2, Dandy–Walker, agenesis of the corpus callosum [ACC], or holoprosencephaly), or destructive lesions (e.g., infarction or infection).[26–28]

## Abstract:

Central nervous system (CNS) anomalies occur in 1.4 to 1.6 per 1000 live births and 3% to 6% of still births. Whereas some anomalies can be detected as early as the first trimester (such as anencephaly), others may not develop until—or only become apparent—later in gestation.

Ultrasound is the initial imaging modality used for the assessment of fetal CNS anomalies. When ultrasound is carefully performed using established guidelines, it can be very sensitive in evaluating the fetal brain. However, because of limitations from skull shadowing, fetal lie, maternal obesity, and oligohydramnios, evaluation of the fetal brain by ultrasound may be incomplete. The multiplanar capability of MRI allows for the evaluation of the brain regardless of fetal lie, oligohydramnios, and overlying bone and gas. Advanced fetal MR techniques include diffusion-weighted imaging, echo planr imaging, diffusion tensor imaging, spectroscopy and functional MRI. Ongoing enhancement of ultrafast MR sequences and postprocessing methodology has resulted in imaging techniques that can evaluate growth, organization, and remodeling processes that occur during fetal brain development. Three-dimensional volumetric studies have demonstrated the value of quantitative assessment of brain growth in healthy versus high-risk fetuses.

It is hoped that use of these advanced neuroimaging techniques will improve our ability to assess anomalies and provide methods for monitoring high-risk pregnancies, leading to improved counseling, planning of fetal intervention, and perinatal management.

## Keywords:

Fetal central nervous system
Fetal Brain
Fetal MRI
hydrocephalus
cortical dysplasia
posterior fossa anomalies
Holoprosencephaly

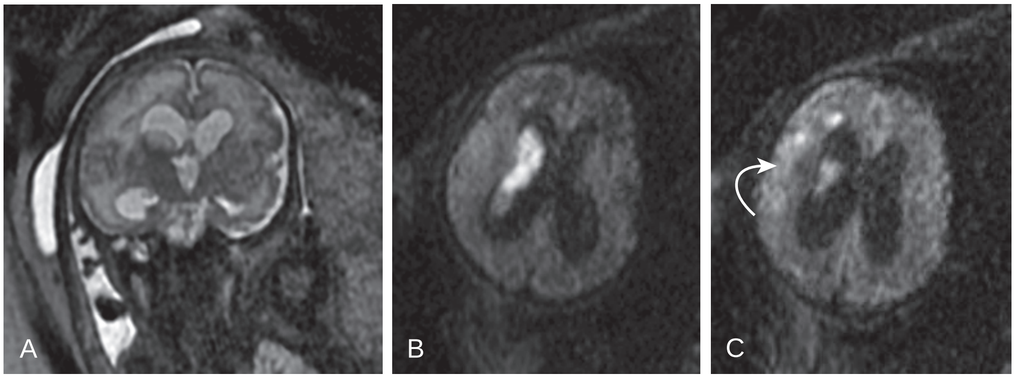

**Figure 29.1. Periventricular hemorrhagic infarction in a fetus at 32 weeks' gestation.** (A) Coronal single-shot fast spin-echo T2-weighted MR image shows moderate ventriculomegaly, intraventricular material, and abnormal high signal in the right periventricular white matter. Axial diffusion-weighted sequence demonstrates increased diffusion signal within the lateral ventricle (B) and deep frontal white matter (C, *arrow*) consistent with intraventricular hemorrhage and a periventricular hemorrhagic infarct.

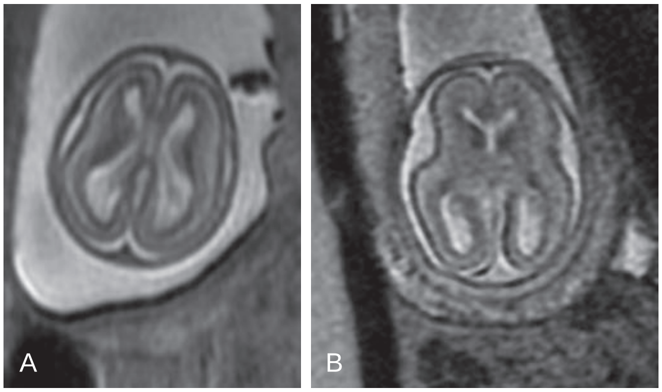

**Figure 29.2. Normal development.** (A) Axial single-shot fast spin-echo T2-weighted MR image at 19 weeks' gestation shows a smooth cortex, prominent ventricles, and subarachnoid space. Low-signal germinal matrix is present along the lateral ventricular walls with a three layer pattern. (B) At 22 weeks' gestation, mild infolding of the Sylvian fissure has occurred with progression to a five-layer pattern.

**BOX 29.1** Gyrus Maturation by Week of Gestation

- 18, the Sylvian fissure
- 20–23, the parieto-occipital fissure
- 22–23, the callosal sulcus
- 24–25, the calcarine fissure
- 24–26, the central sulcus
- 26–28, the precentral and postcentral sulci
- 28, the superior temporal sulcus
- 30 to 32, the anterior superior temporal sulcus

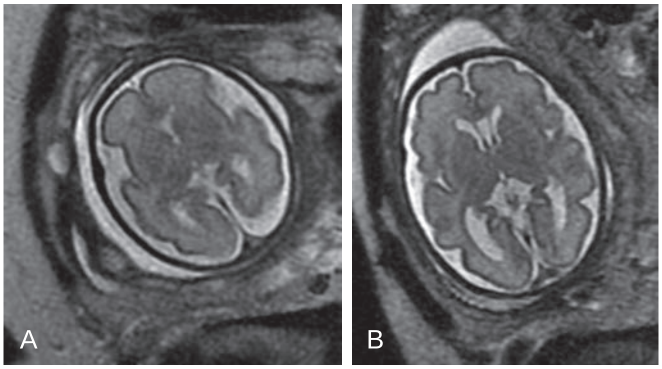

**Figure 29.3. Progression of sulcation.** (A) Axial single-shot fast spin-echo T2-weighted MR image at 28 weeks' gestation shows progression of the sulcation with involution of the germinal matrix. (B) By 32 weeks' gestation, all primary sulcation is present.

The degree of VM has been shown to be associated with the incidence of live birth and survival beyond the neonatal period. Moderate VM (>12–15 mm) is more likely to demonstrate associated anomalies (56%) compared with mild VM (10–12 mm) (6%).[29] Isolated VM has abnormal outcomes in 10% to 25% of cases.[30]

If other anomalies are present, outcome is worse, with only 50% to 80% of fetuses having a normal neurodevelopmental outcome.[31–34] Motor outcomes are more severely affected than cognitive or adaptive outcomes, although prenatal atrial diameter was not consistently associated with postnatal developmental outcome.[35] If VM is severe due to aqueductal stenosis, the overall mortality is 40%; perinatal mortality is 23%, with only 10% of those surviving having normal outcome.[33]

## AGENESIS OF THE CORPUS CALLOSUM

The corpus callosum forms between the eighth and twentieth week from genu to splenium. The rostrum forms last, between 18 to 20 weeks' gestation. Agenesis can be complete (ACC) or partial (hypogenesis). The corpus callosum may be difficult to visualize sonographically, particularly in the early weeks of gestation and/or with hypogenesis.[36] Sonographic and MRI findings include colpocephaly of the occipital horns with parallel orientation of the lateral ventricles, an absent septum pellucidum, and a high-riding third ventricle (Fig. 29.4). Coronal images are particularly helpful in demonstrating the presence or absence of the cavum septum pellucidum and corpus callosum. With ACC, the frontal horns tend to be narrow with straight medial borders secondary to the bundles of Probst, which represent the callosal fibers that have not crossed the midline. The third ventricle may extend superiorly into an interhemispheric cyst. The cerebral convolutions have a radial arrangement on sagittal imaging. An associated lipoma may be present, which will be echogenic on ultrasound and isointense to gray matter on T2-weighted MRI. If associated anomalies are detected, the outcome is typically poor.[27–29,37–39] While isolated ACC may have a good outcome, up to 20% of cases diagnosed

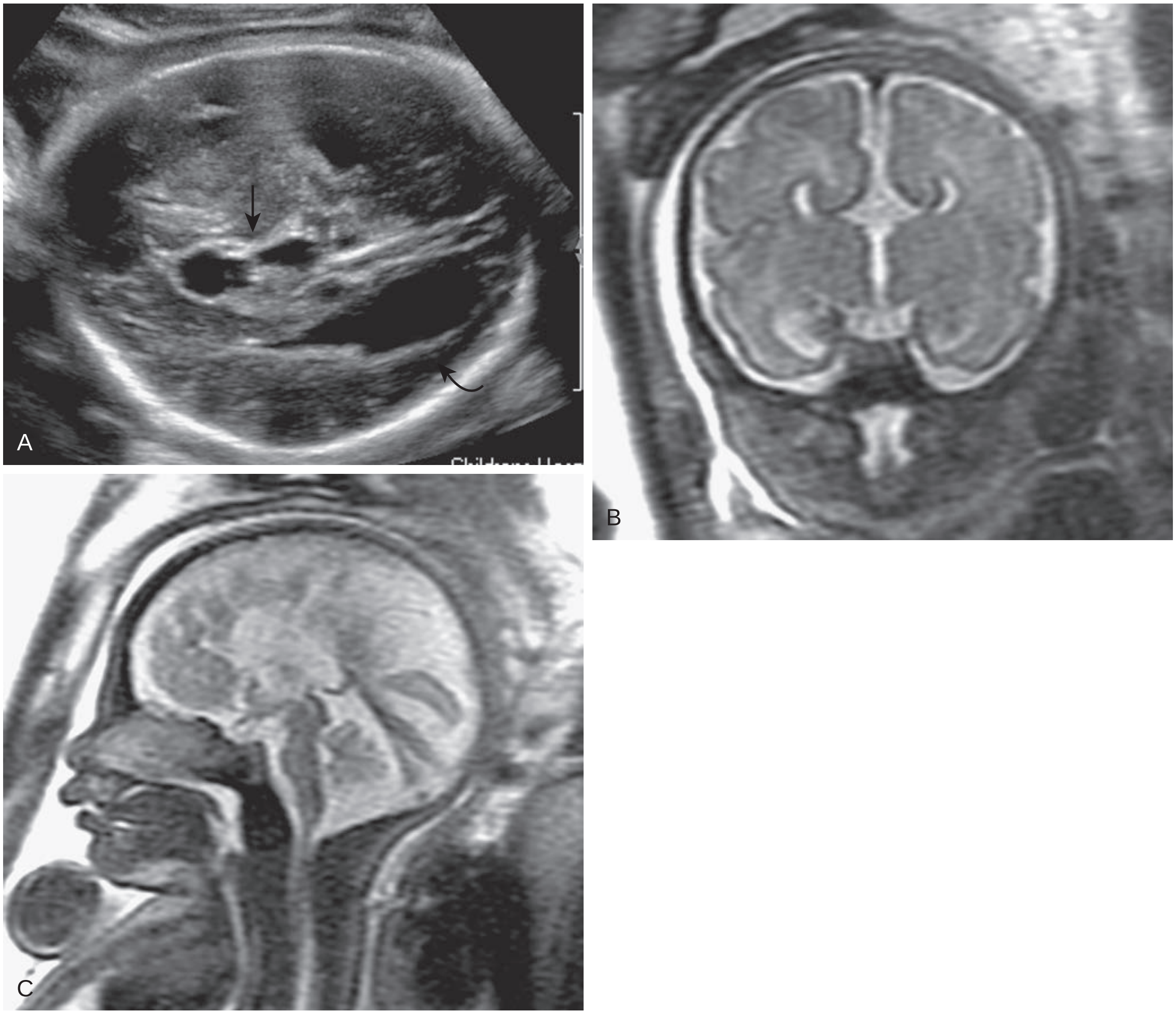

**Figure 29.4. Agenesis of the corpus callosum.** (A) Transverse sonogram of the fetal brain shows dilatation of the occipital horns *(curved arrow)* and a high-riding third ventricle *(arrow)*. (B) Coronal T2-weighted MR image shows that the cavum septum pellucidum is absent, along with a high-riding third ventricle. The medial walls of the anterior horns are indented by the bundles of Probst. (C) Sagittal T2-weighted MR image shows medial sulci radiating perpendicular to the expected course of the corpus callosum. The pericallosal sulcus is absent.

prenatally have additional anomalies noted postnatally. Long-term outcome remains unknown, with several studies suggesting that delays become more apparent in later years and can be associated with autism, attention deficit disorder, and schizophrenia.[40]

## NEURAL TUBE DEFECTS

Cranial neural tube defects can be assessed by ultrasound and include anencephaly, iniencephaly (cervical dysraphism and fixed fetal head extension), Chiari 2 malformation (low occipital/high cervical encephalocele), and cranial encephaloceles (e-Figs. 29.5 and 29.6). Ultrasound can identify many of these anomalies, but MRI is useful to further evaluate the amount of herniated brain and associated cranial anomalies.

Meningomyeloceles associated with Chiari 2 malformation are the most common neural tube defect. Cranial findings identifiable sonographically include a small or absent cisterna magna, cerebellar herniation (banana sign), frontal concavity (lemon sign), and VM.[41,42] MRI can further delineate the amount of brainstem and cerebellar herniation, beaking of the tectum, heterotopias, small subarachnoid space, and callosal dysgenesis. If fetal surgery is performed, hindbrain herniation may reverse, decreasing the need for shunting postnatally.[43,44]

## HOLOPROSENCEPHALY

Failure of prosencephalic cleavage results in holoprosencephaly; septo-optic dysplasia is the mildest form, and alobar holoprosencephaly is the most severe form.[45] These anomalies are associated with several genetic syndromes including Meckel–Gruber, Smith–Lemli–Opitz, trisomy 13 and 18, and teratogen exposure. Midline and facial structures often are abnormal as well and can include proboscis, trigonocephaly, cyclopia, hypotelorism, and facial clefts (Fig. 29.7). Ultrasound can identify the most severe

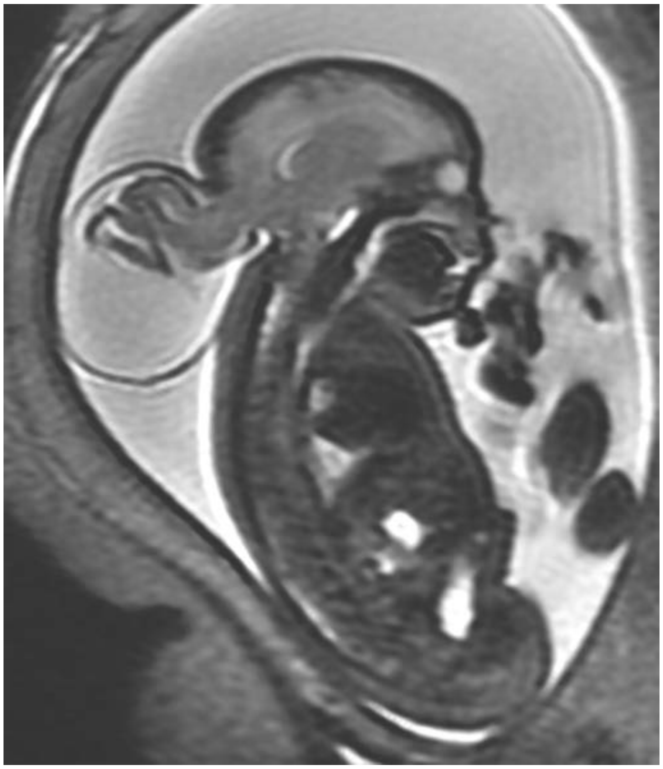

**e-Figure 29.5. Occipital encephalocele.** Sagittal T2-weighted MR image at 33 weeks' gestation demonstrates a large posterior skull defect with brain tissue herniating into a skin-covered sac. Note the obliterated subarachnoid space.

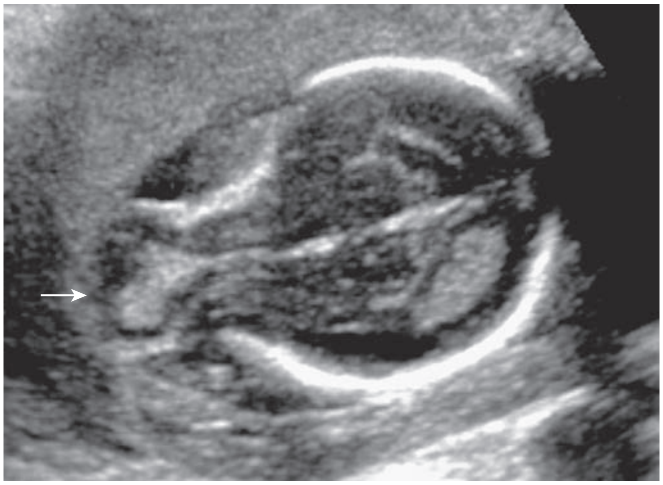

**e-Figure 29.6. Frontal encephalocele.** Axial sonogram of the fetal brain at 16 weeks' gestation shows a frontal skull defect with brain contents herniated anteriorly *(arrow)*.

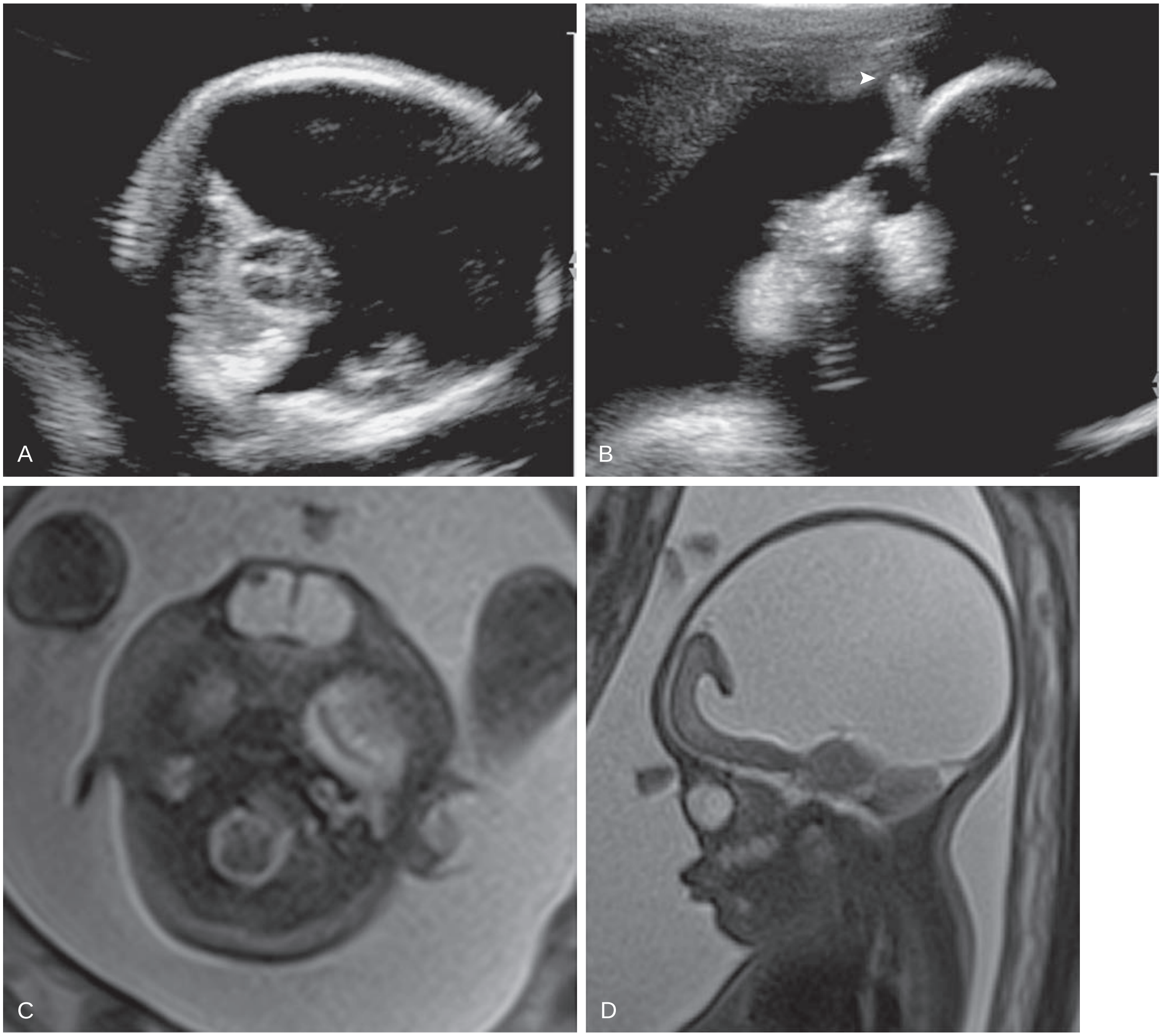

**Figure 29.7. Cyclopia.** (A) Axial sonogram of the fetal brain demonstrates alobar holoprosencephaly with a monoventricle, absent falx, and fused thalami. (B) Sagittal image of the fetal face shows a single midline orbit, absent nose, and supraorbital proboscis *(arrowhead)*. (C) Axial T2-weighted MR at 30 weeks' gestation demonstrates a single midline orbit with partially fused globes. (D) Sagittal T2-weighted image of the fetal brain and face demonstrates a proboscis superior to the orbit. There is a large posterior dorsal cyst.

alobar form, but subtle cases of lobar holoprosencephaly may be difficult to diagnose, even with MRI.

Alobar holoprosencephaly is complete failure of division of the promesencephalic vesicle. A monoventricle is identified with "kissing choroid" by ultrasound. The thalami and basal ganglia are fused. The falx, corpus callosum, and interhemispheric fissure are absent (Fig. 29.8). With semilobar and lobar forms, a posterior interhemispheric fissure is present, with absence of the genu of the corpus callosum. Lobar holoprosencephaly may have a normally formed thalamus and callosal splenium. The anterior frontal lobes are fused and the frontal lobes typically are hypoplastic. The septum pellucidum and anterior falx are absent. Syntelencephaly is a variant in which the anterior parietal lobe or posterior frontal lobes are contiguous across the midline.[46,47]

Septo-optic dysplasia may be identified by the presence of ventricular dilation, an absent septum pellucidum, and flat roof of the frontal horns. Schizencephaly, heterotopias, and callosal dysgenesis often are associated with this sporadic anomaly and are better seen by MRI.[27]

## POSTERIOR FOSSA MALFORMATIONS

Malformations of the cerebellum and brainstem can be categorized by posterior fossa size: small, normal, or large. The cisterna magna is measured by ultrasound from the midline posterior aspect of the vermis to the inner occiput and normally measures between 3 to 10 mm. Although ultrasound can identify many posterior fossa anomalies, MRI is particularly useful in evaluating the vermis, brainstem, and location of the tentorium.[48–50]

When a small posterior fossa is noted, a Chiari malformation should be considered, with a close search for an associated meningomyelocele. The tentorium is low, and the cisterna magna

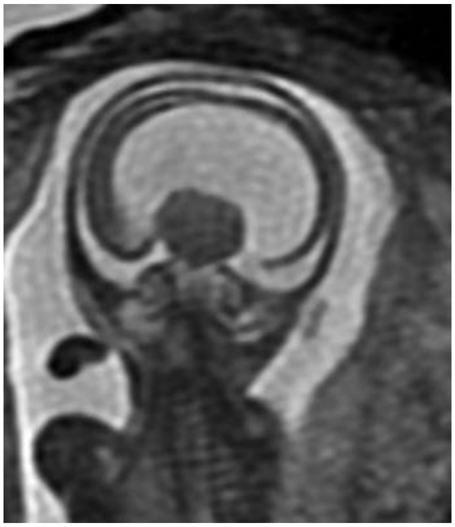

**Figure 29.8.** Alobar holoprosencephaly at 17 weeks' gestation. Coronal T2-weighted MR image shows a single mantle of neural tissue with a monoventricle and fused thalami.

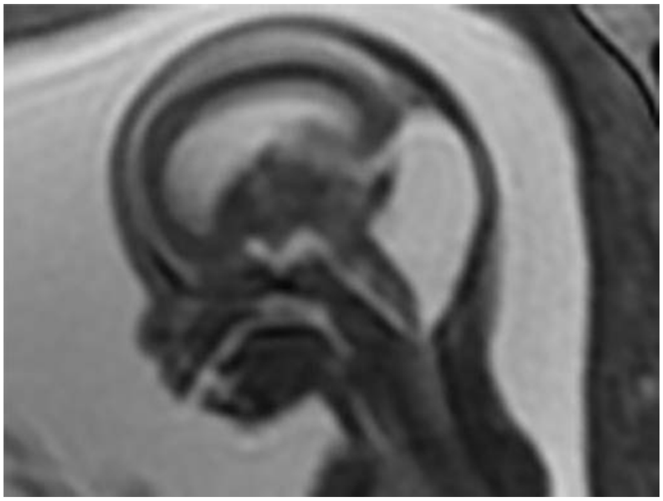

**Figure 29.11. Dandy–Walker malformation.** Sagittal single-shot fast spin-echo T2-weighted MR image at 18 weeks' gestation demonstrates an enlarged posterior fossa, elevated torcula, hypoplastic rotated vermis, and retrocerebellar fluid collection connected to the fourth ventricle.

and fourth ventricle are small. The differential diagnosis includes cerebellar hypoplasia.

When the posterior fossa is normal in size, abnormalities include cerebellar/pontocerebellar hypoplasia and vermian dysgenesis (partial or total absence of the vermis). Rarely, rhombencephalosynapsis (agenesis of the vermis with fusion of cerebellum) can be identified prenatally (e-Fig. 29.9). The fetal vermis is not completely developed until 18 weeks' gestation, and the fetal cerebellum continues to form in the third trimester, with cellular migration occurring through the first year of life. Thus mild cerebellar hypoplasia may be difficult to diagnose prenatally.[51–54] Volume measurements may aid in the diagnosis. Although pontocerebellar hypoplasia has a poor prognosis, the outcome for vermian dysgenesis is not as clear.

When the posterior fossa is enlarged, the differential diagnosis includes mega cisterna magna, Blake's pouch cyst, Dandy–Walker malformation, or arachnoid cyst. Mega cisterna magna is a wide cistern (anteroposterior greater than 10 mm) with a normal vermis and cerebellum (e-Fig. 29.10). The tentorium is located in a normal position. Mega cisterna magna can be a normal finding, although it has been associated with aneuploidy. If no additional anomalies are found and chromosomes are normal, the outcome should be good.[55]

Blake's pouch cyst is a posterior protuberance of the inferior medullary velum into the cistern. This fluid collection is posterior inferior to the vermis and communicates with the fourth ventricle. The vermis typically is intact, with mass effect and elevation of the tentorium. The cyst does not communicate with the subarachnoid space.[56]

Dandy–Walker malformation is a retrocerebellar cyst that communicates with the fourth ventricle. The posterior fossa is enlarged, with an elevated tentorium. The vermis is incomplete, elevated, and rotated (Fig. 29.11). Hydrocephalus usually is present. Prognosis depends on the degree of vermian hypoplasia, brainstem hypoplasia, and associated anomalies such as ACC, heterotopias, and encephaloceles.

Arachnoid cysts can develop in the posterior fossa, causing mass effect on the vermis, which otherwise is normally formed (e-Fig. 29.12). These cysts do not communicate with the fourth ventricle. The tentorium may be elevated. Symptoms can occur if hydrocephalus develops or the brainstem is compressed.

## CORTICAL DEVELOPMENT

Disorders of neuronal cell migration can be difficult to recognize in the fetal brain both by ultrasound and by MRI.[57,58] The cortex is poorly visualized by ultrasound, and whereas MRI demonstrates the cortical mantle relatively well, the cortex is not well developed in the second trimester. Thus a relatively smooth brain at 20 weeks that is normal can be indistinguishable from smooth pachygyria.

Abnormalities of cellular differentiation include unilateral megalencephaly and tuberous sclerosis (TS).[59] Subependymal hamartomas are present in up to 80% of patients with TS. Subependymal and subcortical tubers may be noted as intermediate-signal lesions on T2-weighted images and high-signal lesions on T1-weighted images in the third trimester (e-Fig. 29.13).

Neuronal heterotopias result when neurons fail to reach their destination at the cortical plate. Clusters can remain in the subependymal region or subcortical layer or form bands in the subcortical white matter. Subependymal heterotopias may be unilateral or bilateral, projecting as small lumps into the ventricles. The differential diagnosis includes hamartomas of TS and subependymal hemorrhage. Subcortical heterotopias are clumps of neurons and glial cells in the white matter that often are associated with ACC or neuroepithelial cysts. Associated microcephaly may not develop until the late third trimester or postnatally.

Agyria/pachygyria results from arrest of migration of neuroblasts with abnormal cortical lamination and failure of sulcation. Classic lissencephaly has few sulci, whereas pachygyria is less severe. In fetuses with cobblestone lissencephaly, cellular overmigration is present with hydrocephalus. Prenatally, ventricles typically are enlarged. Fetal MRI may show abnormal cortical sulcation in the third trimester (Fig. 29.14).[60]

Polymicrogyria is excessive folding of cerebral cortical cell layers with fusion of the gyral surface. It is common after cytomegalovirus infection in the second trimester and is difficult to diagnose before the third trimester. Multiple small, irregular sulci may be noted with mild VM.

## SUMMARY

Interpreting fetal MR images can be challenging because structures are small and change with fetal maturation. Great care must be

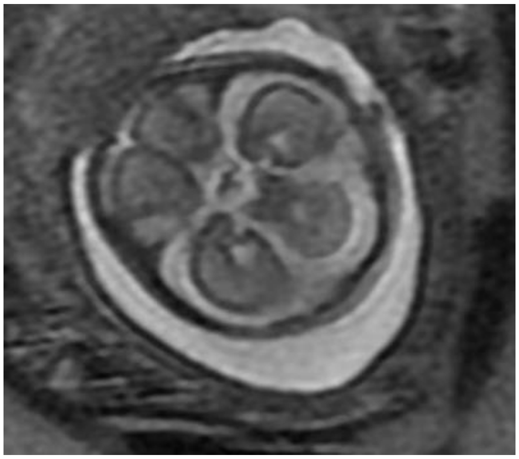

**e-Figure 29.9. Rhombencephalosynapsis.** Axial T2-weighted MR image of the posterior fossa at 23 weeks' gestation demonstrates cerebellar hemispheric folia continuous across the midline with absence of the anterior vermis.

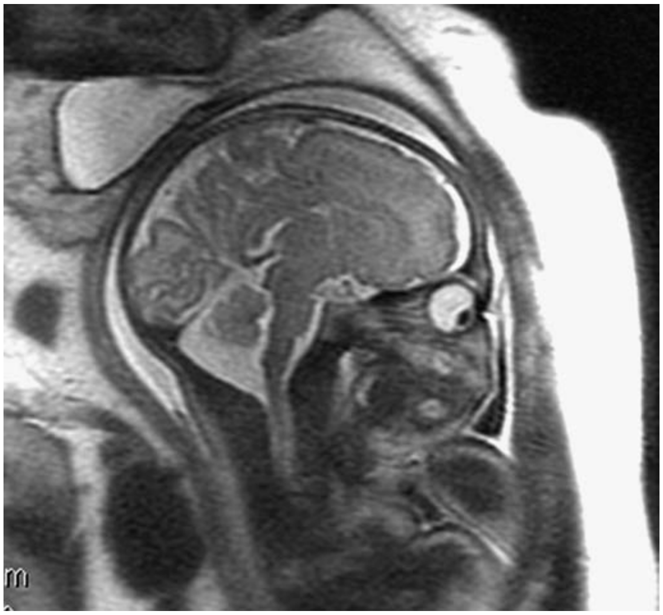

**e-Figure 29.10. Mega cisterna magna.** Sagittal single-shot fast spin-echo T2-weighted magnetic resonance image shows a prominent cisterna magna. The vermis is intact. The cerebellar volume and brainstem are normal for gestational age.

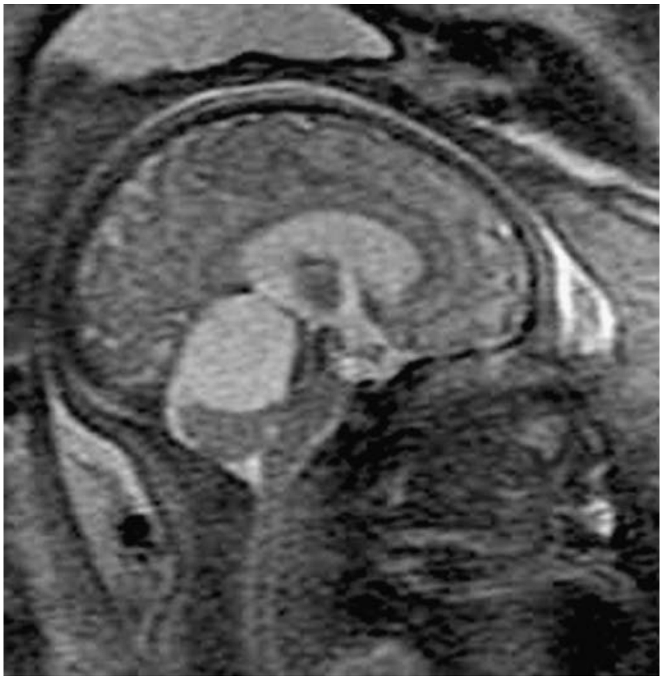

**e-Figure 29.12. Arachnoid cyst.** Sagittal single-shot fast spin-echo T2-weighted MR image of a 37-week fetus shows an enlarged posterior fossa with a cystic structure deviating the vermis inferiorly. The cyst does not connect to the fourth ventricle. A sonogram at 21 weeks' gestation was normal.

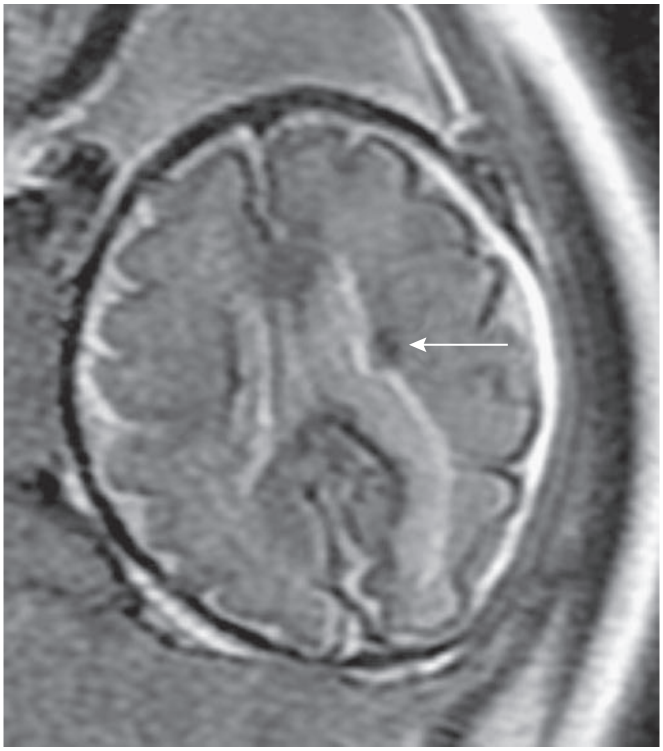

**e-Figure 29.13. Subependymal hamartoma.** Axial single-shot fast spin-echo T2-weighted MR image shows a low-signal subependymal mass *(arrow),* which had high signal on T1-weighted imaging. The fetus had rhabdomyomas involving the heart as well. After delivery, tuberous sclerosis was confirmed.

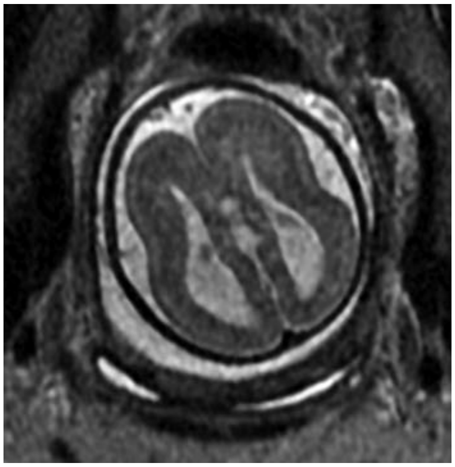

**Figure 29.14. Lissencephaly.** Axial single-shot fast spin-echo T2-weighted MR image of a 36-week gestation fetus demonstrates an abnormal smooth surface with lack of gyri and sulci. The cortical and subcortical layers are disorganized. Colpocephaly is present with dilated atria. The infant was diagnosed with Miller–Dieker syndrome after delivery.

taken when performing and interpreting these studies. Prognosis of abnormalities can be varied, making counseling difficult, even when anomalies are well delineated. Long-term follow-up studies are necessary to provide accurate data. Ultrasound remains the screening modality of choice in the assessment of the fetal brain. However, when a CNS anomaly is identified, MRI has become an important adjunct in further assessment.

## KEY POINTS

- Neuronal migration and gyration follows a predictable course throughout the second and third trimester.
- Fetal VM outcome is variable. Associated anomalies and aneuploidy bode for a worse prognosis.
- The fetal vermis does not develop until 18 weeks' gestation and the cerebellum continues to form in the third trimester. Thus vermian and cerebellar hypoplasia may be difficult to diagnosis accurately in the second trimester.
- Cortical dysplasias may not be visualized in the second trimester.

## SUGGESTED READINGS

Barzilav E, Bar-Yosef O, Dorembus S, et al. Fetal brain anomalies associated with ventriculomegaly or asymmetry: an MRI based study. *AFNR*. 2016;Epub.

Garel C. *MRI of the fetal brain: normal development and cerebral pathologies*. Berlin: Springer-Verlag; 2005.

Griffiths P, Bradburn M, Campbell M, et al. Use of MRI in the diagnosis of fetal brain abnormalities in utero (Meridian): a multicenter, prospective cohort study. *Lancet*. 2016;Epub.

Kline Fath B. Normal brain imaging. In: Kline FB, Bulas D, Bahado-Singh R, eds. *Fundamental and Advanced Fetal Imaging*. Philadelphia: Wolters Kluwer; 2015.

Limperopoulos C, Clouchoux C. Advancing fetal brain MRI. Targets for the future. *Semin Perinatol*. 2009;33:289–298.

Yamaski M, Nonaka M, Bamba Y, et al. Diagnosis, treatment and long term outcomes of fetal hydrocephalus. *Semin Fetal Neonatal Med*. 2012;17:330–335.

## REFERENCES

Full references for this chapter can be found on www.expertconsult.com.

## REFERENCES

1. Chitty LS, Pilu G. The challenge of imaging the fetal central nervous system: an aid to prenatal diagnosis, management and prognosis. *Prenat Diagn*. 2009;29:301–302.
2. Malinger G, Lerman-Sagie T, Watemberg N, et al. A normal second trimester ultrasound does not exclude intracranial structural pathology. *Ultrasound Obstet Gynecol*. 2009;20:51–56.
3. Malinger G, Monteagudo A, Pilu G, et al. Sonographic examination of the fetal central nervous system: guidelines for performing the “basic examination” and the “fetal neurosonogram. *Ultrasound Obstet Gynecol*. 2007;29:109–116.
4. Salomon LF, Garel C. Magnetic resonance imaging examination of the fetal brain. *Ultrasound Obstet Gynecol*. 2007;30:1019–1032.
5. Giboud L. Contribution of fetal cerebral MRI for diagnosis of structural anomalies. *Prenat Diagn*. 2009;29:420–433.
6. Hagmann DF, Roberson NJ, Leung WC, et al. Fetal brain imaging: US or MRI: a comparison between magnetic resonance imaging and a dedicated multidisciplinary neurosonographic opinion. *Acta Paediatr*. 2007;97:414–419.
7. Prayer D. Investigation of the normal organ development with fetal MRI. *Eur Radiol*. 2006;17:2458–2471.
8. Limperopoulos C. Advanced neuroimaging techniques: their role in the development of future fetal and neonatal neuroprotection. *Semin Perinatol*. 2010;34:93–101.
9. Righini A, Bianchini E, Parazzini C, et al. Apparent diffusion coefficient determination in normal fetal brain: a prenatal MR imaging study. *AJNR Am J Neuroradiol*. 2003;24:799–804.
10. Berman JI, Hamrick SE, McQuillen PS, et al. Diffusion-weighted imaging in fetuses with severe congenital heart defects. *AJNR Am J Neuroradiol*. 2011;32:E21–E22.
11. Kasprian G, Brugger PC, Weber M, et al. In utero tractography of fetal white matter development. *Neuroimage*. 2008;43:213–224.
12. Jiang S, Xue H, Counsell S, et al. In-utero three dimension high resolution fetal brain diffusion tensor imaging. *Med Image Comput Assist Interv*. 2007;10(Pt 1):18–26.
13. Borowska-Matwiejczuk K, Lemancewicz A, Tarasow E, et al. Assessment of fetal distress based on magnetic resonance examinations: preliminary report. *Acad Radiol*. 2003;10:1274–1282.
14. Rousseau F, Glenn OA, Iordanova B, et al. Registration-based approach for reconstruction of high-resolution in utero fetal MR brain images. *Acad Radiol*. 2006;13:1072–1081.
15. Sandrasegaran K, Laal C, Aisen AA, et al. Fast fetal magnetic resonance imaging. *J Comput Assist Tomogr*. 2005;29:487–498.
16. Limperopoulos C, Tworetzky W, McElhinney DB, et al. Brain volume and metabolism in fetuses with congenital heart disease: evaluation with quantitative magnetic resonance imaging and spectroscopy. *Circulation*. 2010;121:26–33.
17. Bulas D, Egloff A. Benefits and risks of MRI in pregnancy. *Semin Perinatol*. 2013;37:301–304.
18. Welsh R, Nemec U, Thomason M. Fetal MRI at 3.0 T. *Top Magn Reson Imaging*. 2011;1:1–13.
19. Victoria T, Johnson AM, Edgar JC, et al. Comparison between 1.5 T and 3T MRI for fetal imaging: is there an advantage to imaging with a higher filed strength? *AJR Am J Roentgenol*. 2016;206:195–201.
20. Griffiths PD, Bradburn M, Campbell MJ, et al. Use of MRI in the diagnosis of fetal brain abnormalities in utero (MERIDIAN): a multicentre, prospective cohort study. *Lancet*. 2016;Epub.
21. Blaas HG, Eik-Nes SH. Sonoembryology and early prenatal diagnosis of neural anomalies. *Prenat Diagn*. 2009;29:312–325.
22. Garel C, Chantrel E, Birsse H, et al. Fetal cerebral cortex: normal gestation landmarks identified. *AJNR Am J Neuroradiol*. 2001;22:184–189.
23. Kline Fath B. Normal brain. In: Kline F, Bulas D, Bahado-Singh R, eds. *Imaging in Fundamental and Advanced Fetal Imaging*. Philadelphia: Wolters Kluwer; 2015.
24. Hu H, Guo W, Chen H, et al. Morphological regionalization using fetal MRI of normal developing brains. *Eur J Neurosci*. 2009;29:1560–1567.
25. Kasprian G, Langs G, Bruddet PC, et al. The prenatal origin of hemispheric asymmetry an in utero neuroimaging study. *Cereb Cortex*. 2010;21:1076–1083.
26. Girard N, Rayboud C, Bambarelli D, et al. Fetal brain MR imaging. *Magn Reson Imaging Clin N Am*. 2001;9:19–56.
27. Li Y, Sansgiri RK, Estroff JA, et al. Outcome of fetuses with cerebral ventriculomegaly and septum pellucidum leaflet abnormalities. *AJR Am J Roentgenol*. 2011;196(1):W83–W92.
28. Sadan S, Malinger G, Schweiger AS, et al. Neuropsychological outcome of children with asymmetric ventricles or unilateral mild ventriculomegaly identified in utero. *BJOG*. 2007;114:596–602.
29. Melchiorre K, Bhide A, Gika AD, et al. Counseling in isolated mild fetal ventriculomegaly. *Ultrasound Obstet Gynecol*. 2009;34:212–224.
30. Quahba I, Luton D, Vuillardf F, et al. Prenatal isolated mild ventriculomegaly: outcome in 127 cases. *BIOG*. 2006;113:1072–1079.
31. Pier DB, Levine D, Kataoka ML, et al. Magnetic resonance volumetric assessments of brains in fetuses with ventriculomegaly correlated to outcomes. *J Ultrasound Med*. 2011;30(5):595–603.
32. Gaglioti P, Oberto M. Todrdos T. The significance of fetal ventriculomegaly: etiology, short and long term outcomes. *Prenat Diagn*. 2009;29:381–388.
33. Alexander MP, Murdoch E, et al. Obstetric and neonatal outcomes in severe fetal ventricuolomegaly. *Prenat Diagn*. 2007;27:124–129.
34. Li Y, Estroff JA, Mehta TS, et al. Ultrasound and MRI of fetuses with ventriculomegaly: can cortical development be used to predict postnatal outcome? *AJR Am J Roentgenol*. 2011;196(6):1457–1467.
35. Beeghly M, Ware J, Soul J, et al. Neurodevelopmental outcome of fetuses referred for ventriculomegaly. *Ultrasound Obstet Gynecol*. 2010;35(4):405–416.
36. Achiron R, Achiron A. Development of the human fetal corpus callosum: a high resolution cross section sonographic study. *Ultrasound Obstet Gynecol*. 2001;21:116–120.
37. Volpe P, Paldini D, Resta M, et al. Characteristic associations and outcome of partial agenesis of the corpus callosum in the fetus. *Ultrasound Obstet Gynecol*. 2006;27:509–516.
38. Glenn OA, Goldstein RB, Li KC, et al. Fetal MRI in the evaluation of fetuses referred for sonographically suspected abnormalities of the corpus callosum. *J Ultrasound Med*. 2005;24:791–804.
39. Fratelli N, Papgeorghious AT, Prefumo F, et al. Fetal outcome of prenatally diagnosed agenesis of the corpus callosum. *Prenat Diagn*. 2007;27:512–517.
40. Szabo N, Gerger G, Bovor L, et al. Corpus callosum anomalies birth prevalence and clinical spectrum in Hungary. *Pediatr Neurol*. 2011;44:420–426.
41. Cameron M, Moran P. Prenatal screening and diagnosis of neural tube defect. *Prenat Diagn*. 2009;29:402–411.
42. Sepulveda W, Corral E, Ayal C, et al. Chromosomal abnormalities in fetuses with open neural tube defects: prenatal identification with US. *Ultrasound Obstet Gynecol*. 2004;23:352–356.
43. Bebbington MW, Danzer E, Johnson PM, et al. Open fetal surgery for myelomeningocele. *Prenat Diagn*. 2011;31(7):689–694.
44. Adzick NM. Fetal myelomeningocele: natural history, pathophysiology, and in-utero intervention. *Semin Fetal Neonatal Med*. 2010;15(1):9–14.
45. Volpe P, Campobsso G, De Robertis V, et al. Disorders of prosencephalic development. *Prenat Diagn*. 2009;29:340–354.
46. Simon EM, Hevner RJ, Pinter JD, et al. The middle interhemispheric variant of holoprosencephaly. *AJNR Am J Neuroradiol*. 2002;23:151–156.
47. Oba H, Barkovich AJ. Holoprosencephaly an analysis of callosal formation and its relation to development of the interhemispheric fissure. *AJNR Am J Neuroradiol*. 1995;16:453–460.
48. Guiboud L. Practical approach to prenatal posterior fossa abnormalities using MRI. *Pediatr Radiol*. 2003;34:700–711.
49. Guiboud L, des Portes V. Pleas for an anatomical approach to abnormalities of the posterior fossa in prenatal diagnosis. *Ultrasound Obstet Gynecol*. 2006;27:477–481.
50. Patel S, Barkovich AJ. Analysis and classification of cerebellar malformations. *AJNR Am J Neuroradiol*. 2002;23:1074–1087.
51. Malinget G, Lev D, Lerman-Sagie T. The fetal cerebellum: pitfalls in diagnosis and management. *Prenat Diagn*. 2009;20:372–380.
52. Forzano F, Mansour S, Ierullo A, et al. Posterior fossa malformation in fetuses: a report of 56 further case and a review of the literature. *Prenat Diagn*. 2007;27:495–501.
53. Limperopoulos C, Roberston RI Jr, Khwaja OS, et al. How accurately does current fetal imaging identify posterior fossa anomalies? *AJR Am J Roentgenol*. 2008;190:1637–1643.
54. Limperopoulos C, Robertson RL, Estroff JA, et al. Diagnosis of inferior vermian hypoplasia for fetal MRI potential pitfalls and neurodevelopmental outcome. *Am J Obstet Gynecol*. 2006;194:1070–1076.
55. Malinger G, Dror R, Ber Sira L, et al. Developmental outcome of children with a large cisterna magna diagnosed in utero. *Ultrasound Obstet Gynecol*. 2008;32:253–259.

56. Calbro F, Arcuri T, Jinkins JR. Blake's pouch cysts: an entity within the Dandy Walker continuum. *Neuroradiology*. 2000;42:290–295.
57. Barkovich AJ, Kuzniecky RI, Jackson GD, et al. A developmental and genetic classification for malformations of cortical development. *Neurology*. 2005;65:1873–1887.
58. Toi A, Chitayar D, Blaser S. Abnormalities of the fetal cerebral cortex. *Prenat Diagn*. 2009;17:105–114.
59. Wortmann SB, Reimer A, Creemers JW, et al. Prenatal diagnosis of cerebral lesions in tuberous sclerosis complex: case report and review of the literature. *Eur J Pediatr Neurol*. 2008;12:123–126.
60. Ghai S, Fong KW, Toi A, et al. Prenatal US and MR imaging findings of lissencephaly: review of fetal cerebral sulcal development. *Radiographics*. 2006;26:389–405.

# 30

# Neonatal Brain Injury

Andre Dietz Furtado, Jessica L. Wisnowski, and Ashok Panigrahy

A significant number of deaths and permanent neurologic disabilities occur during the first month of life, the neonatal period. During the first month of life, term infants and particularly preterm neonates are vulnerable to a wide range of adverse events that may cause brain injury. Imaging is used not only to diagnose and understand neonatal brain injury but also to predict the neurodevelopmental outcome.[1]

Because of its portability, cranial ultrasound is usually the first imaging modality to be performed and can be used serially to monitor the evolution of certain injuries. Ultrasound is usually sufficient for evaluation of germinal matrix hemorrhage (GMH) and intraventricular hemorrhage (IVH), serial assessment of ventricular size in hydrocephalus, cystic white matter changes, and severe brain malformations. Ultrasound is less sensitive than computed tomography (CT) or magnetic resonance imaging (MRI) in the detection of small calcifications and is less sensitive than MRI in the detection of hypoxic-ischemic injury and subtle brain malformations. MRI also is excellent for the evaluation of punctate white matter lesions, which are seen in the setting of premature white matter.

Because of the associated ionizing radiation, the use of CT is mainly restricted to instances in which there is a suspicion of intracranial calcifications, lesions that contain fat, acute intracranial hemorrhage, and to evaluate the bones. MRI is the most sophisticated modality to evaluate the neonatal brain, and with advanced imaging techniques such as diffusion-weighted imaging (DWI), functional magnetic resonance imaging (fMRI), and magnetic resonance spectroscopy (MRS), it has the advantage of providing information regarding physiology, function, and metabolism. Arterial spin labeling techniques provide assessment of brain perfusion in the neonate without the use of intravenous contrast material. Intravenous contrast is not routinely used because of the physiologic renal immaturity in the first few days to weeks after birth.

## IMAGING TECHNIQUES

High-resolution images with good tissue contrast are essential for an adequate evaluation of the neonatal brain. Ultrasound provides high-resolution images of the neonatal brain, but it has limitations regarding visualization of deeper structures and the cerebellum. Because increased tissue contrast in CT usually is achieved at the expense of increased radiation dose, CT usually is performed with use of low radiation dose protocols and is reserved for a limited number of situations.

MRI is the imaging modality with the highest sensitivity for differentiating abnormalities from normal brain. Conventional MRI, including T1-weighted, T2-weighted, DWI, and gradient-echo sequences or susceptibility-weighted images, provide the most useful diagnostic information. Sequences should be modified to optimize signal to noise for the neonatal brain. Structurally, the brains of preterm infants and neonates have much higher water content and much lower lipid content compared with brains of older children. With myelination, these compositions invert. Myelination begins along specific tracts in the third trimester and continues well into the postnatal years. Longer echo times are useful for younger patients because of the differences of extracellular lengthening of the T2-relaxation time with decreasing age. Similarly, the T1 relaxation is longer for infants and young children and varies with the magnetic field strength. Longer inversion times of T1-weighted scans provide additional contrast between myelinated and unmyelinated white matter in infants. Finally, the higher water content and lower anisotropy in infants necessitate a lower b-values (600–700 s/mm$^2$) to optimize signal to noise in DWI.

Dedicated neonatal MR head coils improve image contrast and resolution at the smaller field of view optimal for neonatal imaging.[2,3] These dedicated coils improve gray-white matter differentiation and provide better visualization of the brainstem and posterior fossa. If a dedicated neonatal head coil is not available, coils for small body parts (i.e., knee coil) should be used to improve image quality.

### Patient Preparation, Safety, and Hazards

Ultrasound can be performed at the bedside and does not use contrast material or ionizing radiation. The only precaution with ultrasound is prevention of infection, which can be achieved with use of sterile gel and a probe cover. CT scanning time is short but usually requires transportation of the neonate to the scanner. Portable CT scanners may be useful in selected patients. Contrast material is rarely needed and should be avoided in neonates because of their physiologic renal immaturity, which is present in the first few days to weeks after birth.

Because of the magnetic resonance (MR) environment and length of most MRI examinations, MR safety is a particular concern for neonates. Before the MR examination, any patient, including neonates, should be screened for possible cardiac devices, implants, non–MR-compatible leads, or surgically implanted wires. The compatibility of any device must always be verified with the manufacturer. Continuous monitoring and support for respiratory and cardiovascular functions can be achieved with MR-compatible equipment. Thermoregulation, which can be a particular concern for preterm neonates, can be supported through use of MR-compatible incubators and monitored through use of an MR-compatible temperature probe. Special attention should be given for loops in conductive cables, which may cause burns and possibly fires.

Increasingly, neonates undergoing MRI are scanned during natural sleep (“feed and bundle” procedures). Although acoustic noise and table vibration from the MR scanner may awaken an older infant (i.e., >3 months of age, a developmental stage at which infants normally begin to awaken to startling noises), young infants (<3 months) often tolerate even long MR protocols when imaging is performed during natural sleep. At our institution, we routinely use MR-compatible noise-canceling headphones designed for neonates. When imaging during natural sleep is not possible, neonates and older infants are scanned while sedated. Sedation should be performed only by properly trained and credentialed clinicians.

## BIRTH TRAUMA

Birth trauma is more common in vaginal delivery, particularly if forceps or vacuum extraction is used. The most common traumatic birth lesions are extracranial hematomas, skull fractures, osteodiastasis, and subdural hematomas.

## Abstract:

A significant number of deaths and permanent neurologic disabilities occur during the first month of life, the neonatal period. During the first month of life, term infants and particularly preterm neonates are vulnerable to a wide range of adverse events that may cause brain injury, namely birth trauma, hypoxic-ischemic encephalopathy, infarction, hemorrhage, hydrocephalus, white matter injury, and metabolic disorders. Because of its portability, ultrasound is usually the first imaging modality to be performed and can be used serially to monitor the evolution of certain injuries. Ultrasound is usually sufficient for evaluation of germinal matrix hemorrhage and intraventricular hemorrhage, Computed tomography (CT) or magnetic resonance imaging are more sensitive in the detection of small calcifications and is less sensitive than MRI in the detection of hypoxic-ischemic injury and subtle brain malformations. Because of the ionizing radiation, the use of CT is mainly restricted to instances in which there is a suspicion of intracranial calcifications, lesions that contain fat, acute intracranial hemorrhage, and to evaluate the bones. MRI is the most sophisticated modality to evaluate the neonatal brain, providing information regarding physiology, function, and metabolism.

## Keywords:

Neonatal
Brain
Injury
Neuroimaging

## Extracranial Hematomas

The major types of extracranial hematomas are cephalohematoma, caput succedaneum, and subgaleal hematoma (also see Chapter 23). In subgaleal hematomas, the hemorrhage accumulates between the epicranial aponeurosis of the scalp and the periosteum (e-Fig. 30.1). The hematoma may enlarge rapidly and lead to potentially life-threatening hypovolemia. Anemia, coagulopathy, metabolic acidosis, renal impairment, and skull fracture have been reported as predictors of poor outcome. Early recognition and management are essential. Upon imaging, extracranial hematomas appear as a hemorrhagic collection overlying the calvarium and crossing the sutures. They may extend underneath the attachments of the occipitofrontalis muscle to the orbital margins anteriorly, the temporal fascia laterally, and the nuchal ridge posteriorly (e-Fig. 30.2).

Caput succedaneum is common after vaginal delivery, particularly when vacuum extraction is used. Typically, resolution occurs within a few days without complications. Caput succedaneum represents edema, which may be accompanied by hemorrhage, within the subcutaneous tissues, which are not limited by the cranial sutures (see e-Fig. 30.2).

Cephalohematomas are rarely associated with complications but may be associated with skull fracture and epidural hematomas. Blood degradation within a hematoma may cause jaundice. Cephalohematomas are subperiosteal hemorrhages confined by cranial sutures. Typically, hematomas increase in size after birth, and a small proportion of them calcify and may cause skull deformity (calcified cephalohematoma).

## Subdural Hematomas

The most common intracranial hemorrhage in term neonates is subdural hematoma, and most common is asymptomatic in parafalcine location or over the tentorium. The incidence of these small subdural hematomas in neonates has been reported as high as 46% in the first 72 hours after birth.[5] Most subdural hematomas are venous in origin related to tearing of the dura, inferior sagittal sinus, and cortical veins. The typical appearance of subdural hematomas is of an extraaxial collection that may cross under sutures, but respect the dural reflection, such as the falx and tentorium (see e-Fig. 30.2). Arterial subdural hematomas caused by arterial bleeding are rare but should be suspected in large hyperacute subdural hematomas. Most lethal cases are related to large infratentorial hemorrhages with compression of the brainstem. Associated small subarachnoid hemorrhages related to tearing of cortical veins are not infrequent. Large subdural hematomas may cause parenchymal infarction as a result of impaired arterial supply and venous drainage, leading to hemorrhagic venous infarction. Large subdural hematomas may interfere with cerebrospinal fluid (CSF) reabsorption and cause hydrocephalus. Subdural hematomas that are not evacuated undergo absorption or evolve into subdural hygromas, which can persist for several months.

Finally, late subdural hematomas after the first week of life may be a presentation of a nonaccidental trauma, in addition to late hemorrhagic disease of the newborn (vitamin K deficiency).

## Spontaneous Superficial Parenchymal and Leptomeningeal Hemorrhage

Spontaneous superficial parenchymal and leptomeningeal (subpial) hemorrhage may also occur in otherwise healthy asymptomatic neonates. They are most common in the temporal lobes, adjacent to a suture. The hemorrhage may extend into the adjacent sulci but is confined by the pia matter (e-Fig. 30.3). Mild surrounding decreased diffusion is typically present.[6]

# HYPOXIC-ISCHEMIC ENCEPHALOPATHY

Brain damage in the term neonate is highly variable and depends on the severity and duration of insult. Moreover, the imaging findings vary dramatically in relation to the timing of imaging studies. Imaging before 72 hours may underestimate the severity because of delayed cell death. Therapeutic hypothermia, which typically is applied for 72 hours beginning within 6 hours of life, may further delay this process.

## Central Pattern of Hypoxic-Ischemic Encephalopathy

The central pattern of hypoxic-ischemic encephalopathy (HIE) usually occurs with profound asphyxia, when there is an abrupt interruption of the blood supply, depriving the neonatal brain of oxygen and glucose. Highly metabolic structures such as the thalami, basal ganglia, and brainstem are more vulnerable to hypoxia and ischemia, more specifically the ventral lateral thalami, posterolateral lentiform nuclei, posterior midbrain, hippocampi, lateral geniculate nuclei, and perirolandic cerebral cortex (Fig. 30.4).[7] Quadriparesis,

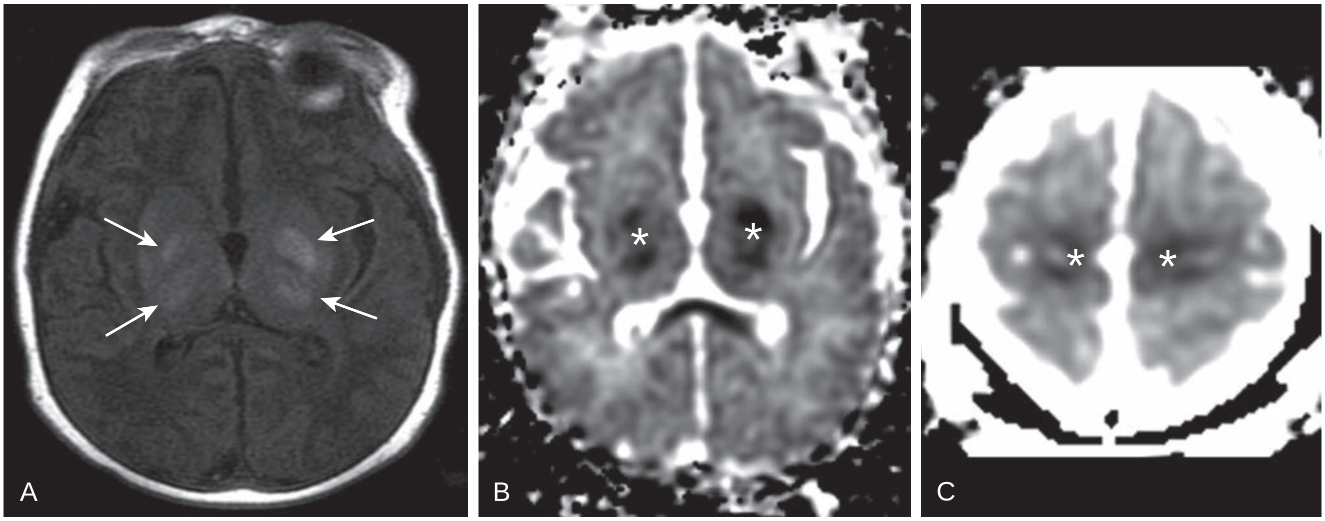

**Figure 30.4. Central hypoxic-ischemic injury.** (A) Axial T1-weighted MR image shows increased T1 signal in the globi pallidi and ventrolateral thalami bilaterally *(arrows)*. (B and C) Reduced apparent diffusion coefficient is seen in the globi pallidi and thalami and in the perirolandic regions bilaterally *(asterisks)*.

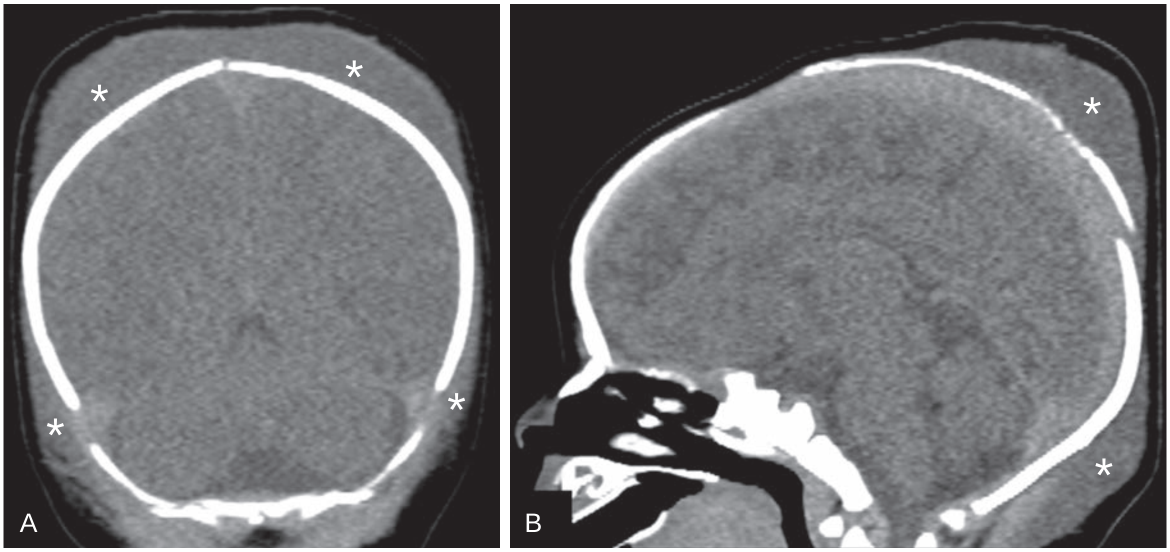

**e-Figure 30.1. Subgaleal hematoma in a newborn.** (A) Coronal and (B) sagittal CT images show large subgaleal hematoma crossing the cranial sutures and extending into the suboccipital region *(asterisks)*.

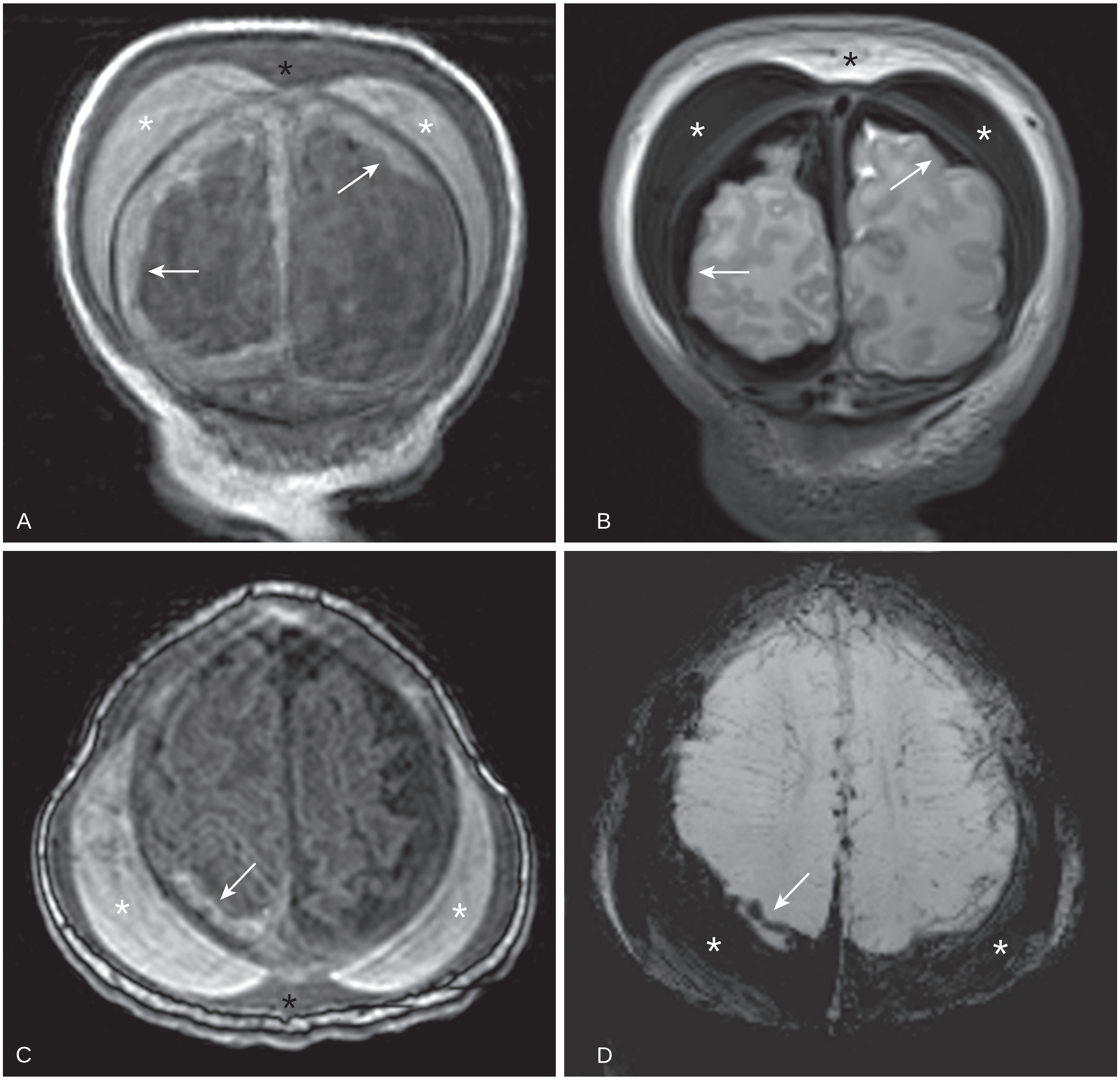

**e-Figure 30.2. Caput succedaneum, cephalohematoma, and subdural hematoma in a newborn.** Caput succedaneum crossing over the sagittal suture *(black asterisk)*, cephalohematoma respecting the sagittal and bilateral coronal sutures *(white asterisk)*, subdural hematoma along the posterior hemispheres, falx, and tentorium *(arrows)*. (A and C) T1-weighted MR images. (B) T2-weighted MR image. (D) Susceptibility-weighted MR image.

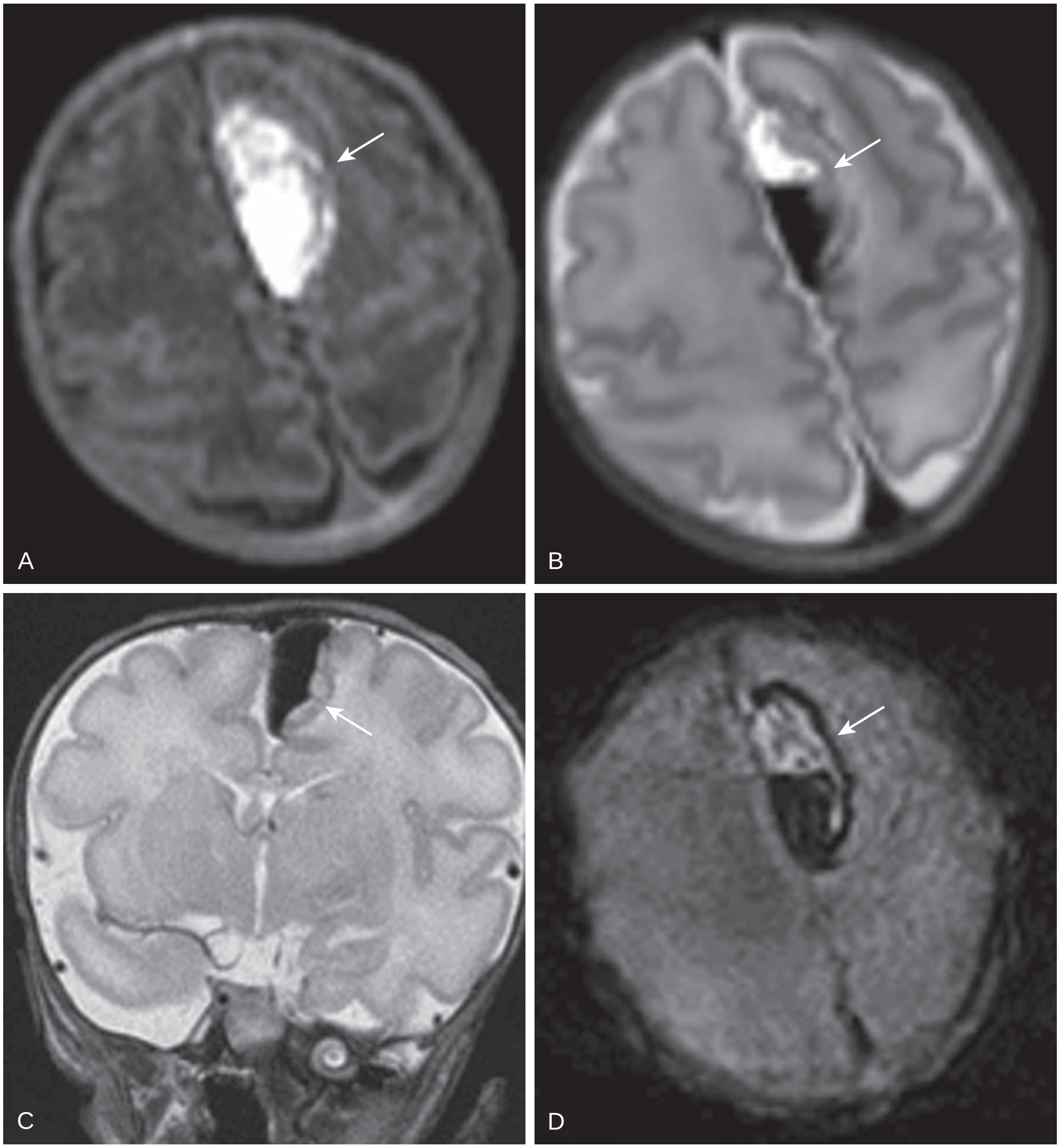

**e-Figure 30.3. Spontaneous superficial parenchymal and leptomeningeal (subpial) hemorrhage.** (A) T1-weighted MR image; (B and C) T2-weighted MR images; (D) susceptibility-weighted MR image *(arrows)*.

choreoathetosis, seizures, mental retardation, and cerebral palsy have been associated with profound asphyxia.[8] Ultrasound and CT have low sensitivity to detect early ischemic changes in the deep structures of the brain. The most common pattern on ultrasound is transient or persistent hyperechogenicity, which may progress to cavitation in the basal ganglia and thalami, particularly in the globus pallidus and ventral lateral nuclei of the thalamus. With more severe insults involving the cortex and subcortical white matter, ultrasound and CT may depict indirect evidence of edema, such as effacement of the sulci, loss of gray-white matter differentiation, and compressed lateral ventricles.

MRI is the imaging modality of choice for neonatal encephalopathy. MRS performed 24 hours after the insult is considered sensitive for hypoxic-ischemic brain injury. Elevated lactate and diminished N-acetyl-aspartate (NAA) are the most common MRS findings in neonates with neurologic and developmental abnormalities (e-Fig. 30.5). Lactate rises after the hypoxic-ischemic event, peaking at 3 to 5 days, whereas NAA starts to decline around the third day. Although a minimally elevated lactate level (lactate/choline ratio <0.15) may be detected in the normal neonatal brain at term, an increased lactate level relative to the total creatine peak in the basal ganglia provides an early indication of brain injury. It has been suggested that resuscitation may rapidly clear lactate and that a secondary increase in lactate may occur after 12 to 24 hours. This may cause false-negative MRS with normal spectra but abnormal outcomes. The metabolites tend to normalize after about day 5, although in some cases abnormal metabolite ratios persist. Persistently elevated lactate levels in the basal ganglia provide prognostic information about the severity of the brain injury and the subsequent adverse neurodevelopmental outcome.

DWI is a sensitive technique for assessment of acute brain injury and shows deep gray matter and perirolandic gray matter lesions before they are seen with conventional MRI. If DWI is performed in the first few hours after the injury, it may underestimate the extent of the injury or even show normal results. Paralleling the clinical presentation of HIE, in which neonates may actually transiently improve before demonstrating a more permanent decline in neurologic functioning because of delayed cell death via apoptotic mechanisms, some patients demonstrate mild brain damage for the first few days and then proceed to demonstrate extensive brain involvement around 5 days after the injury. Apparent diffusion coefficient (ADC) values always evolve over time; they decrease initially after the injury, with the nadir around 3 to 5 days, and increase (via facilitated diffusion) later in the chronic phase. As ADC values increase, a point of transient "pseudonormalization" exists in which injured tissue can be misdiagnosed as "normal." Conventional MRI findings are usually unremarkable during the first few days but then begin to demonstrate first an increased T1-weighted signal and a decreased T2-weighted signal in the subacute period followed by an increased T2-weighted signal in the more chronic period. Evidence suggests that hypothermia therapy delays the onset of MR changes (in metabolic, diffusion, and conventional imaging) associated with injury and, in particular, delays the onset of pseudonormalization in the ADC signal.[9]

## Peripheral Pattern of Hypoxic-Ischemic Encephalopathy

The peripheral pattern of HIE usually results from a period of decreased blood supply to the brain (rather than a near total and abrupt interruption) and is thought to develop as a result of a compensatory shunting of blood to vital brain structures, such as the brainstem, thalami, basal ganglia, hippocampi, and cerebellum, at the expense of less metabolically active structures, namely the cerebral cortex and white matter (Fig. 30.6). Therefore the brainstem, cerebellum, and deep gray matter structures generally are spared from injury in mild to moderate hypoxic-ischemic insults. More prolonged insults result in injury to the intervascular border (watershed) zones, which are relatively hypoperfused as a result of this shunting. Neurologic examination varies depending on the severity of the insult, from asymptomatic in mild cases to proximal extremity weakness or spasticity and cerebral palsy in persons who sustain severe insults.[8] Increasing severity of watershed-distribution injury is associated with impaired neurocognitive functioning, including language, visuoperceptual, and executive functioning impairments.

Ultrasound lacks sensitivity in assessing partial prolonged hypoxia-ischemia because it provides poor visualization of the triple watershed zone. CT also is not sensitive to the early changes but may show effacement of the gray-white junction, hypoattenuation with mass effect from acute edema, or hypoattenuation with volume loss in the watershed zone. Similar to central HIE, in the acute phase, MRI can detect lactate and restricted diffusion with corresponding low ADC values in the affected brain regions, which predominantly involve the cortex and underlying white matter along the parasagittal frontal-parietal cortex. With time, increased T2/fluid-attenuated inversion recovery signal and mass effect related to edema may develop. Chronically, gliosis and volume loss mainly involving the deep portion of the gyri result in mushroom-shaped gyri (known as ulegyria), which sometimes is associated with an epileptogenic focus. Atrophic changes and gliosis predominately involve the subcortical white matter in the border zone between the anterior and the middle cerebral arteries, in the parasagittal watershed zone, and in the parietal lobes at the border zone of the three major cerebral arteries, that is, the triple watershed zone.

## NEONATAL ARTERIAL INFARCTION

Infarctions involving the vascular territory of a major artery, most commonly the middle cerebral artery, are more common in term than in preterm neonates. Symptoms are subtle and nonspecific, and many neonatal arterial infarcts may be unrecognized until motor or cognitive symptoms develop later in infancy or childhood. In the neonatal period, the most common presenting symptom is a focal motor seizure involving the contralateral limbs, which may secondarily generalize. Infarcts of the anterior and posterior cerebral arteries are underdetected because they may be asymptomatic and difficult to visualize on ultrasound. Several causes have been described, including sepsis, bacterial meningitis, inherited or acquired coagulopathies, and cardiac abnormalities, but often no specific cause is identified. Initial imaging shows a loss of gray-white matter differentiation, which in severe instances may be detected on ultrasound but is most readily visualized on MRI as increased signal on DWI with low ADC values (Fig. 30.7). Later (after 24–48 hours) the edema becomes apparent as increased echogenicity on ultrasound, hypoattenuation on CT, increased signal on T2-weighted MRI, and decreased signal on T1-weighted MRI. Although the high water content of the unmyelinated neonatal brain poses significant challenges for the detection of edema on CT or conventional MRI sequences, loss of gray-white matter differentiation frequently is present. This lack of contrast between the normal brain and the infarction is particularly relevant at 5 to 10 days after infarction when the ADC may be pseudonormalized. With time, ADC values increase (via facilitated diffusion); after a few weeks, volume loss and encephalomalacia become apparent. Hemorrhagic transformation of an ischemic stroke is rare in neonates, but increased signal on T1-weighted imaging along the cortex related to laminar necrosis is not uncommon. Interestingly, acutely after a perinatal ischemic infarct, hyperperfusion as demonstrated on arterial spin label sequences frequently is observed in the regions corresponding to areas of low ADC on diffusion-weighted MRI.

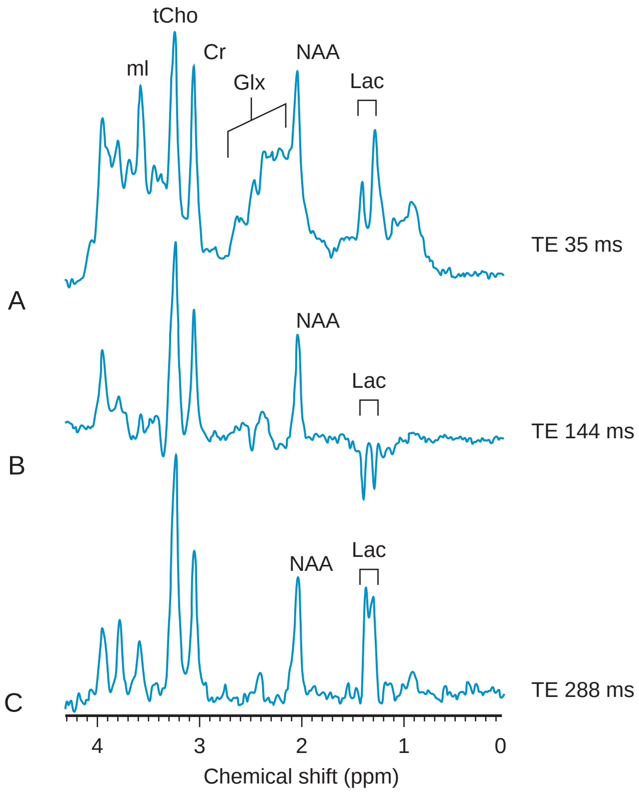

**e-Figure 30.5. Magnetic resonance (MR) spectroscopy in hypoxic-ischemic encephalopathy.** Increased lactate on MR spectroscopy performed with TE of 35 ms (A), 288 ms (C) and inverted with TE of 144 ms (B). *Cr,* Creatine; *Glx,* glutamate/glutamine; *lac,* lactate; *ml,* myo-inositol; *NAA,* N-acetyl asparatate; *tCho,* total choline.

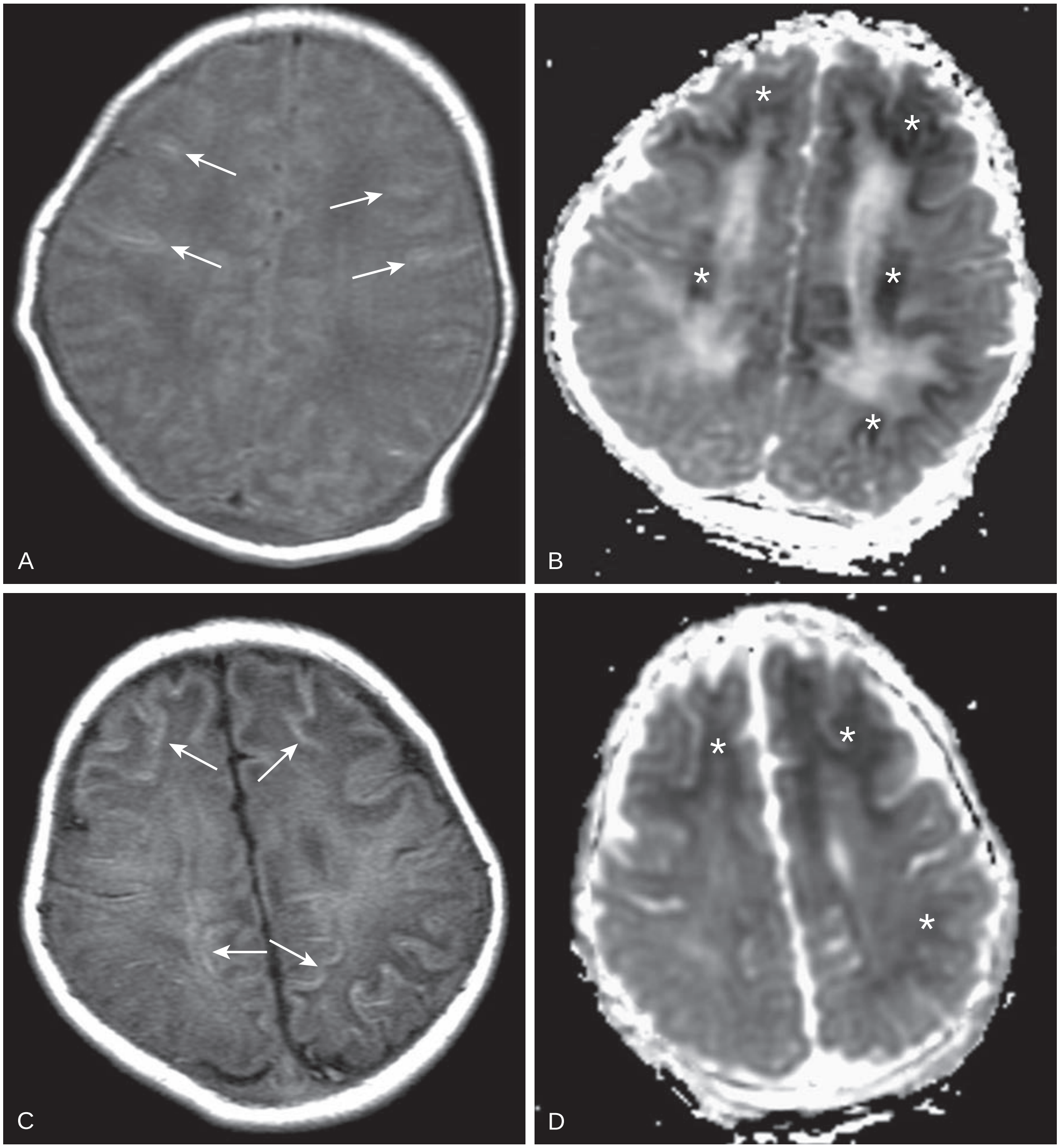

**Figure 30.6. Peripheral pattern of hypoxic-ischemic injury.** (A and B) At day 2 after the ischemic insult, increased signal on axial T1-weighted MR images *(arrows)* and reduced apparent diffusion coefficient (ADC) *(asterisks)* mainly involving the juxtacortical white matter *(arrows)*. (C and D) At 7 days after the insult, axial T1-weighted images demonstrate progression on the areas of increased signal *(arrows)* and less conspicuously reduced ADC *(asterisks)*.

## INTRAVENTRICULAR AND LARGE PARENCHYMAL HEMORRHAGE

Intraparenchymal hemorrhage occurs infrequently in full-term neonates. Most parenchymal bleeding in the term infant involves the thalamus, is associated with IVH, and develops in infants at risk for venous thrombosis. The most documented cause of intraparenchymal hemorrhage is cerebrovenous sinus thrombosis, followed by coagulopathy, infection, hypoglycemia, vascular malformation, tumor, and genetic disorders. A hemorrhagic and thrombotic screening is the first step in any neonate with intracranial hemorrhage. Additionally, confirmation of vitamin K administration and examination of alloimmune antibodies in the mother's blood should be obtained. Although hemorrhage may occur anywhere in the term neonatal brain, the thalamus and the choroid plexus are the most common locations. Rarely, hemorrhages occur in areas of residual germinal matrix (GM). Blood degradation products without surrounding edema or hydrocephalus with chronic blood products in the first days of life are suggestive of intrauterine hemorrhage, which are most commonly caused by maternal factors such as anticoagulants, vasogenic agents (including illicit drugs), diabetes, and trauma. Less commonly, fetal conditions such as

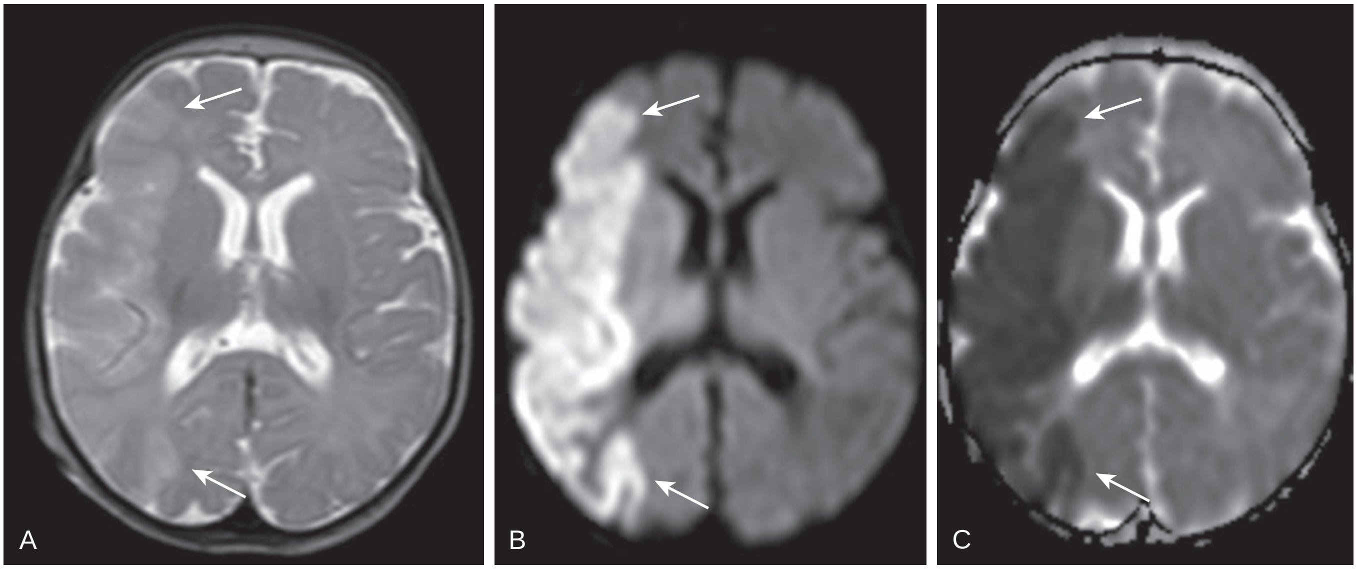

**Figure 30.7. Ischemic infarct.** (A) Axial T2-weighted MR image shows developing edema with loss of the gray-white matter differentiation involving the territory of the right middle cerebral artery *(arrows)*. (B) Corresponding restricted diffusion *(arrows)* and (C) low apparent diffusion coefficient values *(arrows)*.

arteriovenous malformation (AVM and vein of Galen malformation), congenital brain tumor, and genetic disorders may lead to prenatal hemorrhage.

## NEONATAL CEREBROVENOUS SINUS THROMBOSIS

Neonatal cerebrovenous sinus thrombosis (CVST) is a rare but devastating condition. It may be a result of trauma, increased hematocrit, sepsis, dehydration, cardiac failure, and thrombotic disorders such as factor V Leiden. The impaired venous drainage commonly results in cytotoxic edema, vasogenic edema, and parenchymal hemorrhage, and in more severe cases acute or chronic hydrocephalus. Although venous infarction can occur anywhere in the brain, the most characteristic locations are the thalami, resulting from thrombosis of the straight sinus and vein of Galen, and the bilateral parasagittal cortex and subcortical white matter, resulting from thrombosis of the superior sagittal sinus. Diffuse cerebral swelling may be a result of extensive CVST.

The diagnosis of CVST may be achieved by demonstrating the thrombus or the lack of normal venous flow in the venous sinuses. Doppler ultrasound may detect superior sagittal sinus thrombosis in neonates, but it has limited sensitivity in evaluating the remainder of the venous system (Fig. 30.8). Serial Doppler ultrasound is an easily performed and inexpensive alternative for monitoring sinovenous thrombosis. CT without contrast may demonstrate a hyperattenuating sinus with a large thrombus but has limited value for small thrombi. False-positive results can occur with unenhanced CT because of relative hyperattenuation of normal neonatal blood due to the high hematocrit and the adjacent hypoattenuating nonmyelinated brain tissue. Moreover, hyperattenuating subdural hematomas that are present in up to a third of the neonates can be misinterpreted as a thrombus. The demonstration of filling defects using CT venography is confirmatory of CVST. Beam hardening artifact from dense bone adjacent to the dural sinus and normal arachnoid granulations may mimic a filling defect. The normal dural sinus and veins have flow voids on unenhanced MRI. Phase-contrast MR venography and two-dimensional time-of-flight MR venography are specific for flow and are valuable in demonstrating obstruction. High signal on unenhanced MRI or lack of flow-related signal on two-dimensional time-of-flight MR venography can be related to thrombus or slow flow. Thin-slice images oriented perpendicular to the flow in the sinus with an abnormal signal is usually sufficient to correct for this “artifact.” MR venography and contrast-enhanced MRI are complementary to unenhanced MRI to show the filling defect and to differentiate venous thrombosis from adjacent subdural hematoma. The best unenhanced conventional MR sequences for detection of sinus venous thrombosis are spin echo T1 and proton density images (see Fig. 30.8). Although full anticoagulation is controversial in the neonatal period, CVST is a medical emergency, and a definite diagnosis should be confirmed as soon as possible. When the aforementioned diagnostic modalities are inconclusive, digital subtraction angiography is the gold standard.

## VASCULAR MALFORMATIONS

Most vascular malformations are silent during the neonatal period but may be diagnosed prenatally or incidentally. A full description of all the major vascular malformations is beyond the scope of this chapter. Instead, we will focus on those that more commonly manifest in the neonatal period: cerebral (pial) vascular malformations, aneurismal malformation of the vein of Galen, and malformation of the dural sinuses.

### Arteriovenous Malformations

AVMs are abnormal thin-walled vessels that connect arteries to veins without intervening capillaries. Most cases of AVM manifest later in childhood or in early adulthood. Neonates with an AVM tend to present with systemic cardiac manifestations or seizures related to parenchymal hypoperfusion. Macrocephaly and hydrocephalus related to abnormally increased venous pressure and spontaneous hemorrhage are less common manifestations of AVMs in the neonatal period.

In symptomatic patients, early diagnosis and emergency endovascular embolization is important because progression to atrophy and leukomalacia may occur rapidly. Unenhanced CT is useful to detect acute hemorrhaging, but it lacks the sensitivity necessary to detect the underlying vascular malformation. CT angiography (CTA) involves radiation exposure but provides exquisite anatomic detail of a nidus (if present), feeding arteries, draining veins, and the presence of possible aneurysms. MR

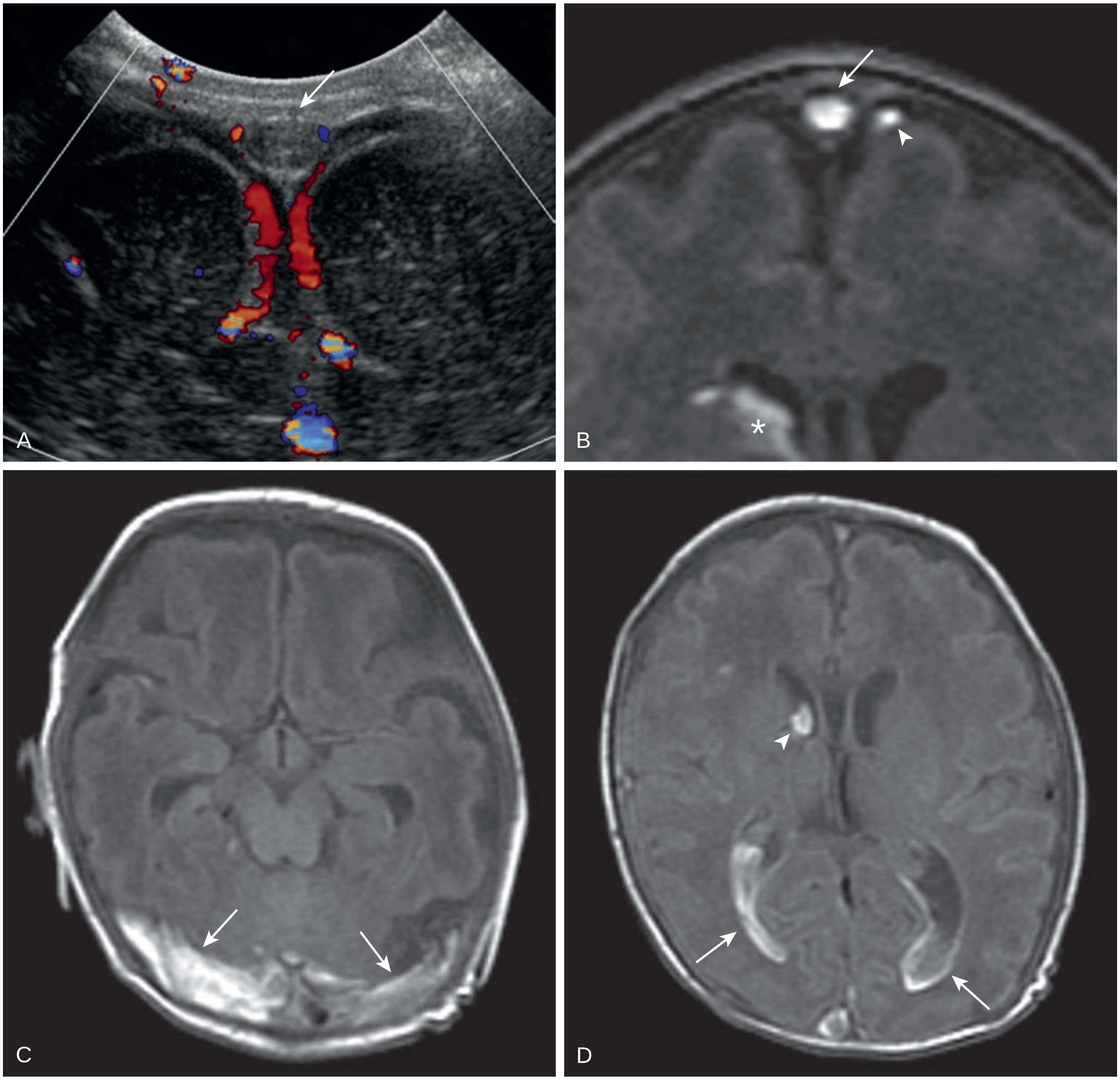

**Figure 30.8. Venous sinus thrombosis.** (A) Coronal color Doppler sonogram shows an enlarged superior sagittal sinus without Doppler flow *(arrow)*. (B) Axial T1-weighted MR image shows increase signal within the sagittal sinus *(arrow)*, and thrombosis of a cortical vein *(arrowhead)* and right germinal matrix hemorrhage *(asterisk)*. (C) Axial T1-weighted MR image shows increase signal within the bilateral transverse sinus *(arrows)*. (D) Axial T1-weighted MR image shows right germinal matrix hemorrhage *(arrowhead)* and intraventricular hemorrhage layering in the occipital horns *(arrows)*.

angiography (MRA) is excellent for the detection of hemorrhage and to delineate the AVM, although smaller vascular malformations may go undetected. The flow void seen in the tangled vessel of the nidus has been described as a “bag of black worms.” High-resolution T1-weighted sequences are important to define the location of the nidus. Three-dimensional (3D) time-of-flight MRA has slightly less special resolution than does CTA, but it does not expose the neonate to radiation. Time-resolved MRA has less special resolution than 3D time-of-flight (TOF) MRA and CTA, but it may provide sufficient information to differentiate feeding arteries and draining veins.

## Vein of Galen Malformation

Malformations involving the vein of Galen are true congenital arteriovenous connections between thalamic perforating, choroidal, and anterior cerebral arteries with the embryonic median prosencephalic vein. Associated cardiovascular anomalies may be present, such as aortic coarctation and secundum atrial septal defect.[10] The most common clinical presentation is high-output cardiac failure (e-Fig. 30.9). The prognosis is mainly related to the number of abnormal arteriovenous connections and the amount of associated parenchymal injury from arterial steal and hypoperfusion. The

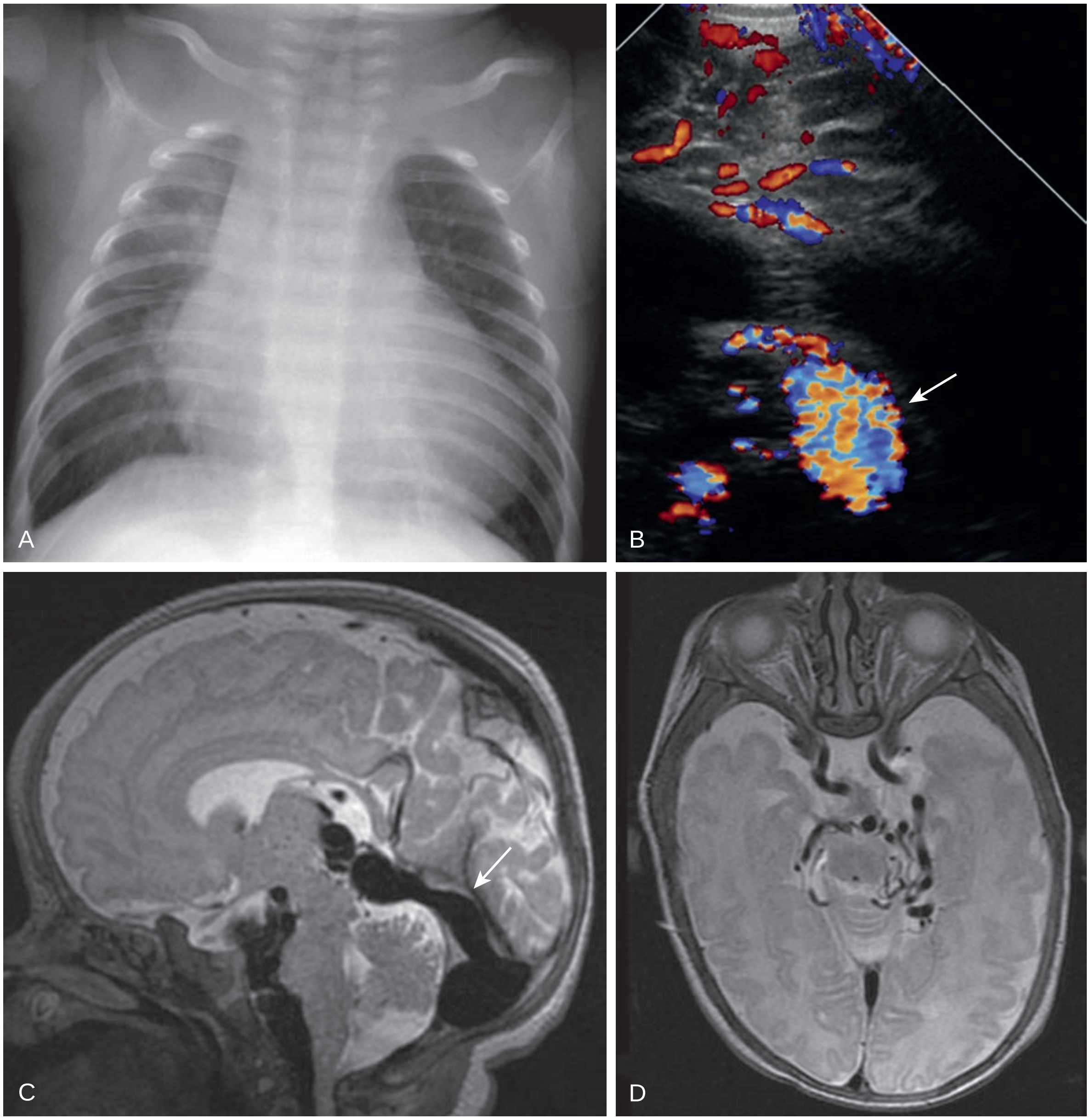

**e-Fig. 30.9. Vein of Galen malformation.** (A) Chest radiograph shows enlargement of the cardiac silhouette and high-output pulmonary vascular congestion. (B) Oblique sagittal color Doppler sonogram and (C) sagittal T2-weighted MR image shows a dilated median prosencephalic vein *(arrow)*. (D) Axial T2-weighted MR image shows enlarged posterior choroidal arteries.

most common is the choroidal type with innumerous connections, which usually is fatal. The mural type with one to four connections has a better prognosis and is less likely to present in the neonatal period. This type usually presents during infancy as developmental delay, hydrocephalus, and seizures, or in older children as hemorrhage. Endovascular therapy is the treatment of choice. Prenatal and postnatal spontaneous thrombosis has been reported.

### Malformation of the Dural Sinuses

Saccular malformations of the dural sinus are rare; when they occur, they are associated with thrombosis, likely related to slow flow. The neonatal venous system has poor capacity to establish collateral circulation, and the drainage to the cavernous sinus is not yet developed. The propagation of the venous thrombosis within a dural sinus malformation may cause venous infarcts. The treatment of choice is preventive anticoagulation.

### Encephalopathy of Prematurity

For more than a century, it has been recognized that the developing white matter is exceptionally vulnerable to injury during the second half of fetal gestation (i.e., the period during which preterm infants are born, and in most cases, survive beyond infancy). Several terms have been used (e.g., white matter injury of prematurity, periventricular leukomalacia, venous infarcts, ischemic coagulation necrosis). It is increasingly recognized that injury to the preterm neonate can involve many regions in the central nervous system (CNS), from gray matter (thalamus, cortex, and basal ganglia) to white matter to the brainstem and cerebellum. As a result, we use a more comprehensive term, “encephalopathy of prematurity” (see Suggested Readings).

## GERMINAL MATRIX AND INTRAVENTRICULAR HEMORRHAGE

The GM is a transient area of proliferation and migration of the neuronal and glial precursor cells located within the walls of the ventricles (ventricular/subventricular zones). The GM is highly vascular; it has thin-walled vessels with limited capability to compensate for hemodynamic and oxygen tension changes, which makes it susceptible to hemorrhage after hypoperfusion followed by reperfusion. GMH may extend into the lateral ventricles (IVH), and in severe instances, it may result in hydrocephalus. The choroid plexus also may hemorrhage, usually in association with GMH. During the end of the second trimester, the GM starts to involute. One of the last areas to involute is the ganglionic eminence located deep to the ependyma in the caudothalamic notch, a groove between the head of the caudate nucleus and the thalamus. After 34 weeks of gestational age, the GM matures, and hemorrhage becomes very unlikely to occur. Most infants with a small area of GMH are asymptomatic or demonstrate subtle signs that are easily overlooked. An unexplained drop in the hematocrit may occur with larger areas of bleeding.

Hemorrhagic brain injury of prematurity has been classified into four groups. Grade I is hemorrhage confined to the GM; grade II is GMH extending into the ventricles without evidence of ventricular dilatation; grade III is IVH with evidence of ventriculomegaly; and grade IV is IVH with an associated parenchymal infarction, as a result of congestion of the venous outflow (Table 30.1). Grades I and II of GMH/IVH have a low morbidity and mortality, whereas grades III and IV have higher mortality rates and a substantial risk of poor neurodevelopmental outcome among survivors (Fig. 30.10). Posthemorrhagic ventricular dilation can be managed with a temporizing neurosurgical procedure, including a ventricular reservoir, a subgaleal shunt, or a ventriculoperitoneal shunt.

**TABLE 30.1** Classification of Germinal Matrix Hemorrhage/Intraventricular Hemorrhage

| Grade | Definition |
|---|---|
| 1 | Hemorrhage confined to germinal matrix |
| 2 | Intraventricular without ventriculomegaly |
| 3 | Intraventricular with ventriculomegaly |
| 4 | Parenchymal hemorrhage related to venous infarction (not directly related to grades 1–3) |

The cerebellum also has a GM, located in the granular layer. Hemorrhage into the immature cerebellum is an underrecognized complication of premature birth. Large cerebellar hemorrhage often occurs concomitantly with supratentorial hemorrhage and is associated with high mortality and cerebral palsy. Cerebellar hemorrhage involving the medial part of the cerebellum (vermis) is particularly associated with cerebral palsy. Isolate petechial hemorrhages are of uncertain clinical significance. Multiple hemorrhages, especially if of different types and in different locations, may be a manifestation of an underlying clotting disorder.

### White Matter Injury in Preterm Neonates

The pattern of injury in preterm neonates has changed during the past several decades in parallel with advances in neonatal intensive care. Historically, cystic periventricular leukomalacia, characterized by multiple areas of cavitary necroses in the periventricular and deep white matter with surrounding astrogliosis, was a frequent observation, particularly among neonates who underwent autopsy. In the modern era, subtle changes in the white matter are more often observed on neuroimaging (microscopic necroses 1–2 mm or less visualized on MRI as punctate lesions with high T1-signal intensity in the periventricular and deep white matter).[7,11] A transient mild elevation of the concentration of lactate may be detected in preterm neonates and neonates who are small for gestational age using MRS and is often considered a “normal” finding unless it persists for more than a week or is associated with other findings (Fig. 30.11).

Several other pathologic and nonpathologic processes may be confused with encephalopathy of prematurity. Viral encephalitis and venous thrombosis may also present with periventricular and/or subcortical lesions, which may demonstrate reduced diffusivity. Metabolic disorders such as organic acidemia and neuromuscular disorders such as Fukuyama muscular dystrophy are other causes of increased T2 signal in the white matter. Signal abnormality involving the gray matter may be seen in organic acidemias, particularly propionic acidemia, cortical dysplasia, and also in newborns with Fukuyama muscular dystrophy. The normal developmental congenital periventricular cysts of the frontal horns should not be misdiagnosed as cystic white matter changes. The location of these anatomic variants is very characteristic and therefore is useful in distinguishing the variants from injury. Periventricular connatal cysts, septations, and coarctations of the frontal horns are normal variants located at or below the level of the ventricular angles, often following the normal contour of the ventricular wall.

As previously noted, ultrasound is most often the first neuroimaging modality used in the evaluation of a preterm neonate. Normal periventricular white matter is relatively echogenic in preterm neonates. To be considered “normal” in a diagnostic setting, the echogenicity in the white matter must be bilaterally homogenous and symmetric. Asymmetry, heterogeneity, and focal areas of increased echogenicity relative to the choroid plexus are all considered to be a concern for abnormality. Serial ultrasound often is performed before white matter injury is more definitively diagnosed. Abnormally increased periventricular echogenicity representing edema or hemorrhage most commonly occurs in the

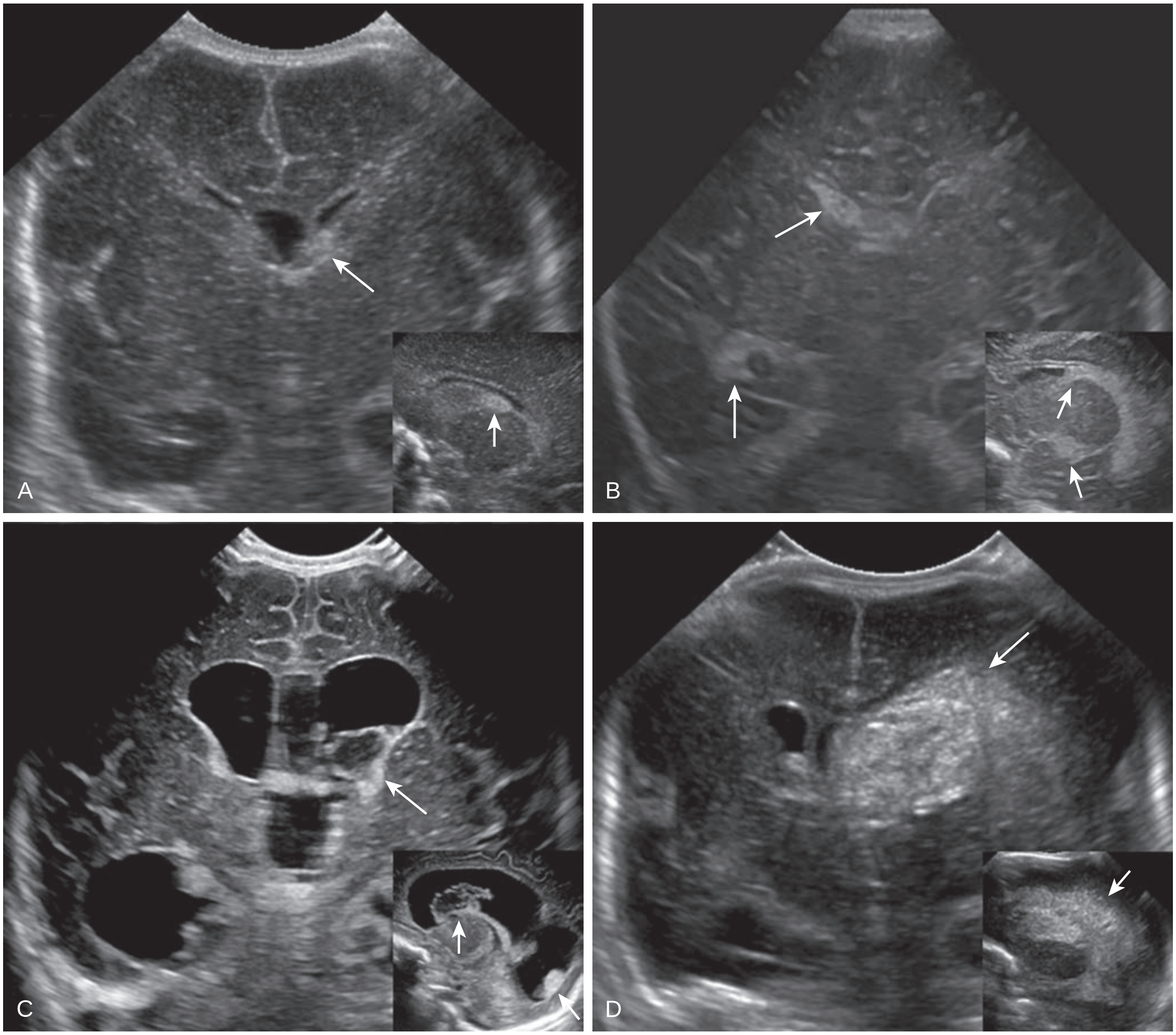

**Figure 30.10. Germinal matrix hemorrhages on ultrasound.** Coronal images with sagittal image insets. (A) Grade 1: hemorrhage confined to the left germinal matrix *(arrows)*. (B) Grade 2: right germinal matrix hemorrhage extending into the lateral ventricle *(arrows)*. (C) Grade 3: left germinal matrix hemorrhage extending into the lateral ventricle with ventriculomegaly *(arrows)*. (D) Large intraparenchymal hemorrhage *(arrows)*.

first week of life, and when present, the cystic changes develop at approximately 3 to 4 weeks of age. Ultrasound shows unilateral or bilateral linear hyperechoic hemorrhagic material in the region of the caudothalamic notch, choroid plexus, ventricles, and periventricular white matter. Ultrasound findings of extensive periventricular cystic lesions and white matter damage portends a poor prognosis, but normal ultrasound findings do not necessarily imply a normal neurodevelopmental outcome.

## CONGENITAL AND NEONATAL INFECTION

Neonatal brain infections are an important cause of severe long-term neurologic morbidity. Viral, bacterial, and parasitic infections may be transmitted to the fetus or newborn in utero (congenital), intrapartum, or postnatally. As a general rule, bacterial and fungal infections are most commonly transmitted intrapartum or postnatally, whereas toxoplasmosis, syphilis, rubella, and cytomegalovirus (CMV) are most commonly transmitted in utero. The transmission of herpes simplex virus infection and human immunodeficiency virus (HIV) may occur in utero, intrapartum, or postnatally.

### Bacterial Infections

The most common bacterial neonatal brain infections are caused by group B streptococcus, *Escherichia coli*, *Streptococcus pneumoniae*, *Haemophilus influenzae* type B, and *Listeria monocytogenes*. Imaging should be performed in neonates with bacterial meningitis if a rapid response to treatment does not occur or if a focal neurologic deficit develops. Complications of meningitis include empyema, ventriculitis, hydrocephalus, infarction, sinovenous thrombosis, cerebritis, or abscess. In uncomplicated meningitis, imaging is usually normal. Leptomeningeal enhancement may be seen as a result of vascular engorgement.

Ventricular enlargement resulting from impaired CSF absorption by fibrinous inflammatory exudate is the most common imaging finding in persons with meningitis and does not necessarily indicate

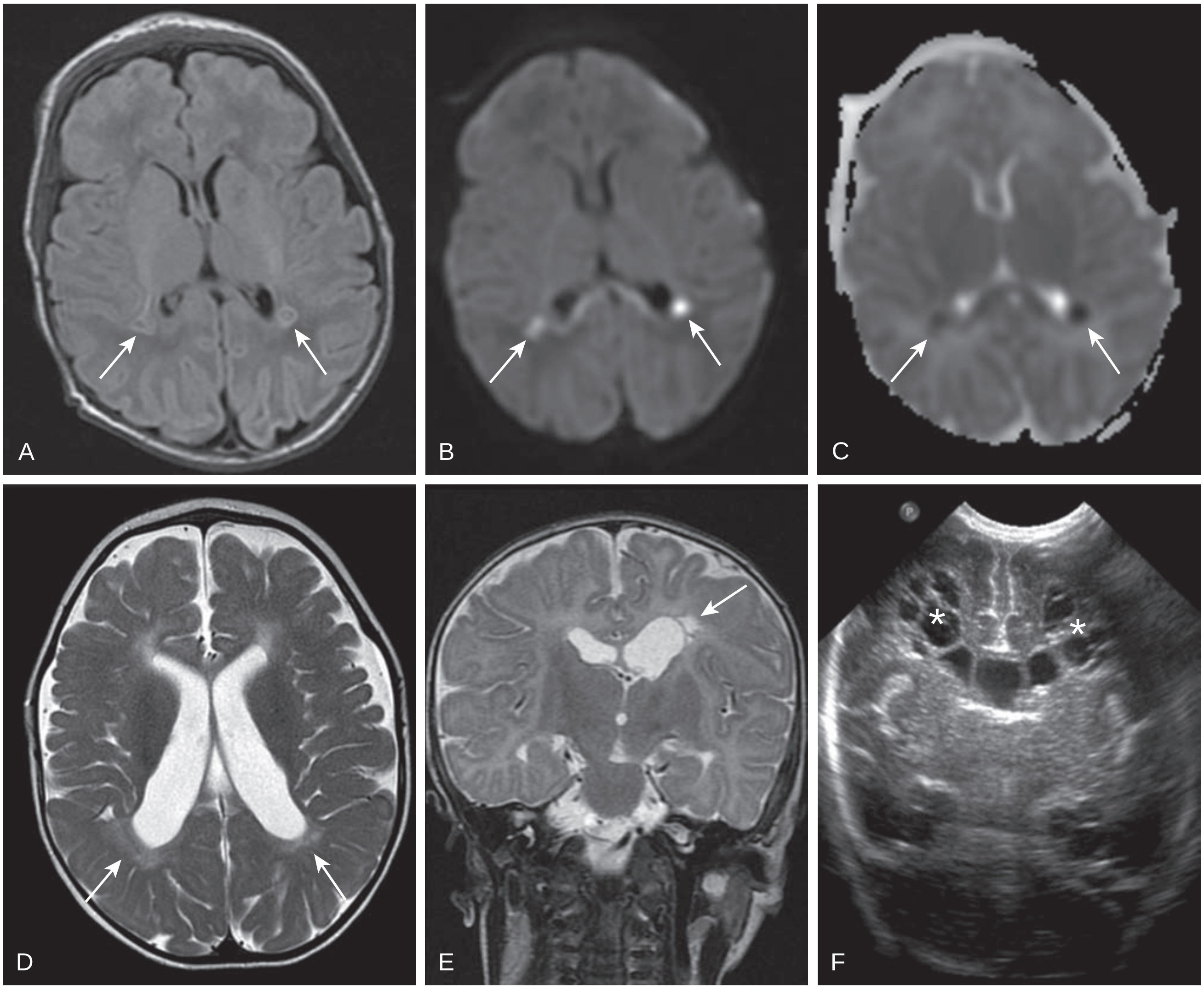

**Figure 30.11. White matter injury of prematurity.** (A) Acutely, focal areas of necrosis with increased signal are seen on this axial T1-weighted MR image *(arrows)*. (B and C) Restricted diffusion and low apparent diffusion coefficient *(arrows)*. (D) Axial T2-weighted MR image in a different patient at 2 years of age shows increased T2 signal and volume loss involving the periventricular white matter bilaterally *(arrows)*. (E) Coronal T2-weighted MR image shows unilateral white matter injury with small cysts *(arrow)*. (F) Coronal sonogram shows bilateral cystic white matter lesions *(asterisk)*.

ventriculitis. Ventriculitis usually presents with ependymal enhancement and sometimes with a pus-fluid level. Ventriculitis often is associated with hydrocephalus and sometimes with intraventricular abscess. Sterile subdural effusions are not uncommon in neonates with meningitis; however, in approximately 2% of cases empyemas develop. Subdural collection with a signal intensity different from that of CSF, peripheral enhancement sometimes with septa, and signal abnormality involving the brain parenchyma are suggestive of empyema. Cerebritis is not uncommon in autopsies of neonates with meningitis despite normal findings of in vivo imaging. When imaging findings are present, cerebritis appears as an area of vasogenic edema with or without patchy areas of enhancement and/or cortical enhancement that may resolve with treatment. If the infection progresses, the enhancing areas become more confluent, and later an abscess forms with restricted water diffusivity and an enhancing capsule. Neonatal *Citrobacter koseri (diversus)* meningitis is rare but often is complicated by formation of abscesses, with a predilection for the frontal lobes. Neonatal pneumocephalus also has been reported as a complication of *C. koseri* meningitis. *Citrobacter* meningitis usually has a poor neurologic outcome (e-Fig. 30.12).

## Fungal Infection *(Candida)*

*Candida* is a neonatal commensal fungus. Infection is caused by organisms that are already present in the intestine and other locations. The key risk factors are catheters and use of wide-spectrum antibiotics; premature infants are particularly susceptible. It causes meningitis, multiple enhancing hemorrhagic microabscesses, macroabscesses, and extensive brain necrosis. Multiple macroabscesses within the subcortical and periventricular regions and basal ganglia are the most common imaging findings in the neonate; however, imaging findings may be normal.

## Herpes Simplex Virus Type 2 Infections

Women who have their first outbreak of herpes simplex virus type 2 genital herpes during pregnancy are at high risk of miscarriage

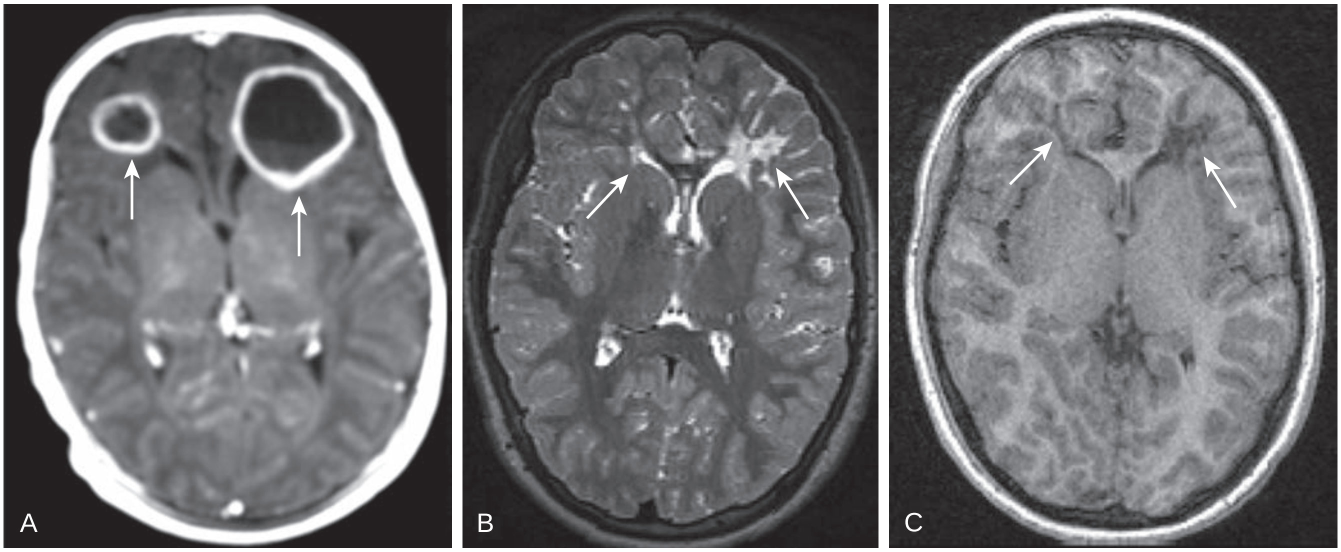

**e-Figure 30.12.** ***Citrobacter.*** (A) Axial contrast-enhanced T1-weighted MR image shows bilateral frontal abscesses *(arrows)*. After resolution of acute infection, there is volume loss and gliosis/encephalomalacia *(arrows)* on T2-weighted (B) and T1-weighted (C) MR images.

or delivering a baby with a low birth weight. The infection can be passed to the neonate in utero or, most commonly, during birth. The most serious risk to the infant is herpes simplex virus type 2 encephalitis. Signs and symptoms in the newborn are nonspecific, with irritability, a high-pitched cry, fever, and poor feeding. Diagnosis is made via a viral culture or polymerase chain reaction (PCR) of the CSF. If the infection occurs early in pregnancy, it may cause hydranencephaly, basal ganglia calcifications, and microphthalmia (the classic TORCH pattern). Late pregnancy or intrapartum transmission involves the bilateral gray-white matter diffusely, which rapidly develops into whole brain necrosis. Multiple cortical hemorrhagic foci and sometimes leptomeningeal enhancement often are present. With time, cystic white matter changes develop (Fig. 30.13).[12]

## Enterovirus and Parechovirus Infection

Enterovirus and parechovirus belong to the family *Picornaviridae*. Enteroviruses are well known for causing neonatal hepatitis, myocarditis, and meningoencephalitis, which can lead to death or severe long-term morbidity. Parechoviruses recently have been reported as causing severe neonatal infection, including involvement of the CNS. The diagnosis is made by PCR; however, PCR for enterovirus does not detect parechovirus. Meningoencephalitis in the neonatal period causes extensive white matter abnormalities, which appear as hyperechogenicity on ultrasound, hypoattenuation on CT, increased signal on T2-weighted MRI images, and decreased signal on T1-weighted MRI images, with or without restricted water diffusivity (e-Fig. 30.14). This pattern of injury easily may

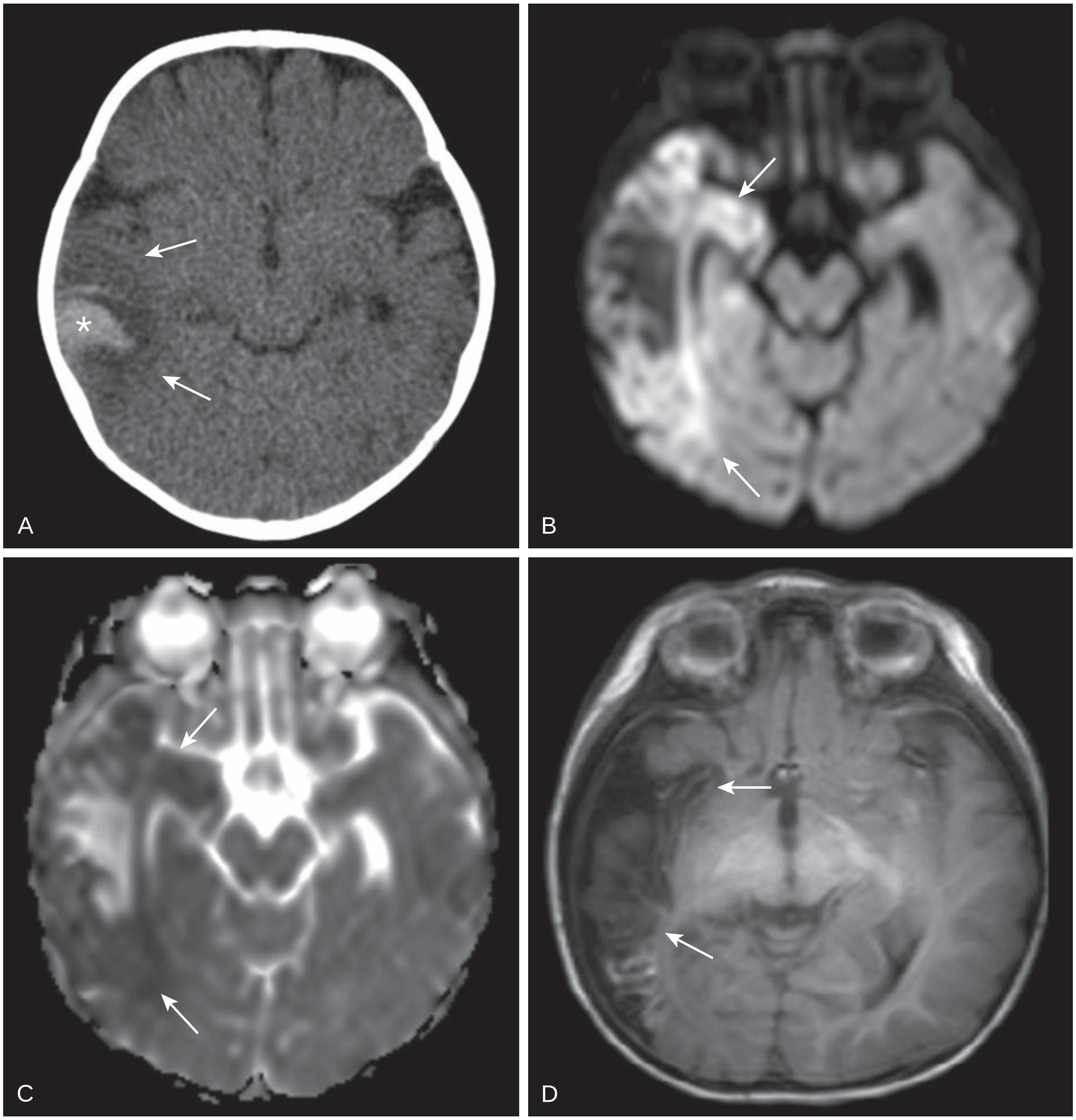

**Figure 30.13. Herpes encephalitis.** (A) Axial noncontrast CT showing parenchymal edema in the right temporal lobe *(arrows)*. Peripheral area of increased attenuation represents confluent petechial hemorrhages *(asterisk)*. (B and C) Axial diffusion-weighted MRI demonstrating restricted diffusion on DWI and low ADC values. (D) Axial T1-weighted MR image, 30 days after the first CT, shows encephalomalacia.

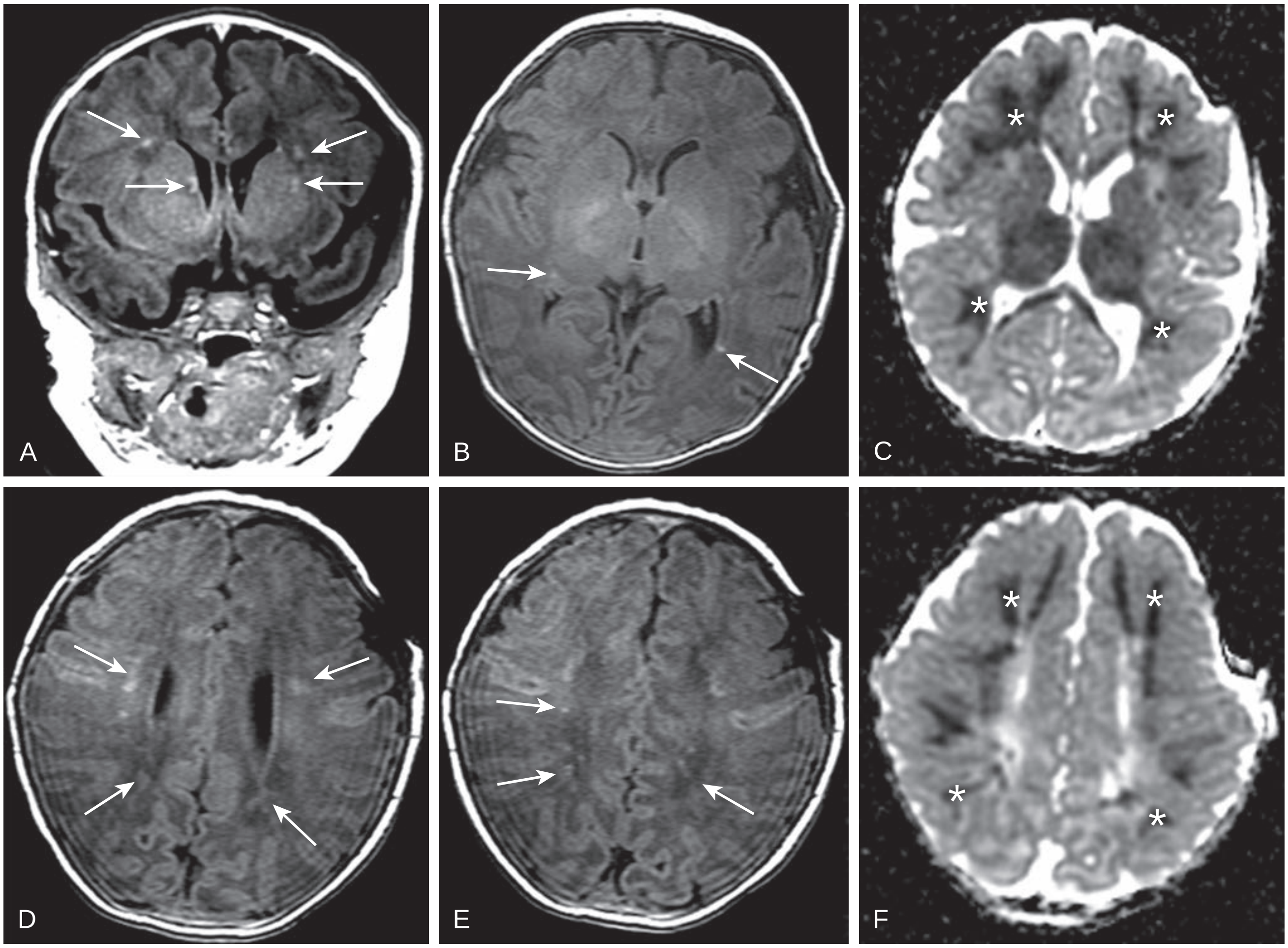

**e-Figure 30.14. Parechovirus.** (A, B, D, and E) T1-weighted MR images demonstrate multiple necrotic foci in the matter and basal ganglia bilaterally *(arrows)*. (C and F) Diffusion-weighted images show reduced ADC involving the white matter, basal ganglia, and thalami bilaterally *(asterisk)*.

be misinterpreted as white matter injury of prematurity or as being caused by hypoxic-ischemic injury, particularly the partial prolonged type.[13]

## Congenital Cytomegalovirus Infection

CMV is the most common congenital viral infection in the United States. Between 30% and 50% of women of childbearing age in the United States have never been infected with CMV, and about 1% to 4% have a primary CMV infection during a pregnancy. The transmission rate to the fetus is about 33%. More than 5000 children each year experience permanent problems caused by CMV infection in the United States. Maternal antibodies, which protect the fetus from rubella and toxoplasmosis, do not prevent fetal transmission of CMV, but they do lessen the severity of the disease. Chorioretinitis occurs in 15% to 20% of cases. Diagnosis of CMV infection in the newborn is usually made via a urine culture. No cure exists for CMV infection. Treatment is primarily supportive.

The brain is the most commonly affected organ. CMV interferes with normal fetal brain development and is associated long term with mental retardation, blindness, deafness, or epilepsy. Depending on the timing of infection during fetal development, neonates with congenital CMV may have microcephaly, predominately periventricular calcifications, ventriculomegaly, lissencephaly, polymicrogyria, cerebellar hypoplasia, dysplastic white matter, and porencephaly (Fig. 30.15).[14] Other findings include intrauterine growth restriction, hepatosplenomegaly, cardiomyopathy, echogenic bowel, and hydrops. CT can detect and characterize diminutive periventricular and subependymal calcifications. CMV is also the leading infectious cause of sensorineural hearing loss; CT may demonstrate a Mondini malformation with an absent interscalar septum, a large vestibule, and an enlarged vestibular aqueduct.

## Congenital Toxoplasmosis Infection

It is estimated that 400 to 4000 cases of congenital toxoplasmosis occur each year in the United States. In the first trimester, maternal infection is less likely to result in congenital infection (2%–10%), but when it occurs, it is more likely to be severe or to result in abortion. Severe congenital toxoplasmosis meningoencephalitis is associated with intrauterine growth restriction, hydrocephalus, microcephaly, calcifications, porencephaly, or hydranencephaly. Maternal infection after 20 weeks of gestation has a much higher rate of transmission to the fetus (20%–30%). The sequelae are generally less severe but still include blindness, epilepsy, and mental retardation.

Although the neurologic outcome is good in the absence of brain abnormalities, congenital toxoplasmosis may be unrecognized until late in infancy when infants present with seizures or other neurologic symptoms. Nonshadowing cerebral and hepatic calcifications are the most typical ultrasound findings. Intracranial calcifications may be periventricular or random in distribution. Other less specific imaging findings are subependymal cysts, echogenic lenticulostriate and thalamostriate arteries (candlestick sign), and cystic white matter changes. CT is sensitive for the detection and characterization of cerebral calcifications and may demonstrate hydrocephalus and microcephaly. The ocular calcifications seen on CT may mimic retinoblastoma. Because of its high sensitivity and absence of ionizing radiation, MRI may be used serially throughout pregnancy to evaluate for the development of brain abnormalities. Acutely, the fetal brain abnormality consists of white matter signal abnormality such as loss of the intermediate zone layer in young fetuses. In fetuses with advanced gestational age, cystic lesions with a mural nodule are characteristic; however, MRI is not sensitive for small calcifications. After birth, calcifications, variable degrees of white matter dysplasia and gliosis, and cortical malformations all may be detected on MRI.

## Congenital HIV Infection

HIV transmission to the fetus or neonate occurs in utero, intrapartum, or postpartum via breast milk. Without treatment, about 30% of pregnant women with HIV pass the infection to their fetus. Intrapartum treatment with protease inhibitors, elective caesarean section, and avoiding breast-feeding decreases the transmission to the fetus to less than 2%. HIV penetrates the blood-brain barrier via macrophages very early in the course of disease and incites a subacute encephalitis with perivascular mononuclear inflammatory cell infiltration. Neuroimaging findings usually are normal in neonates with HIV. The onset of neurologic decline generally occurs between 2 months to 5 years. Atrophy, delayed myelination, corticospinal tract degeneration, cervical lymphadenopathy, benign lymphoepithelial cysts in the parotid glands, aneurysms, opportunistic infections, progressive multifocal leukoencephalopathy, and CNS lymphoma are all associated late findings of congenital HIV infection.

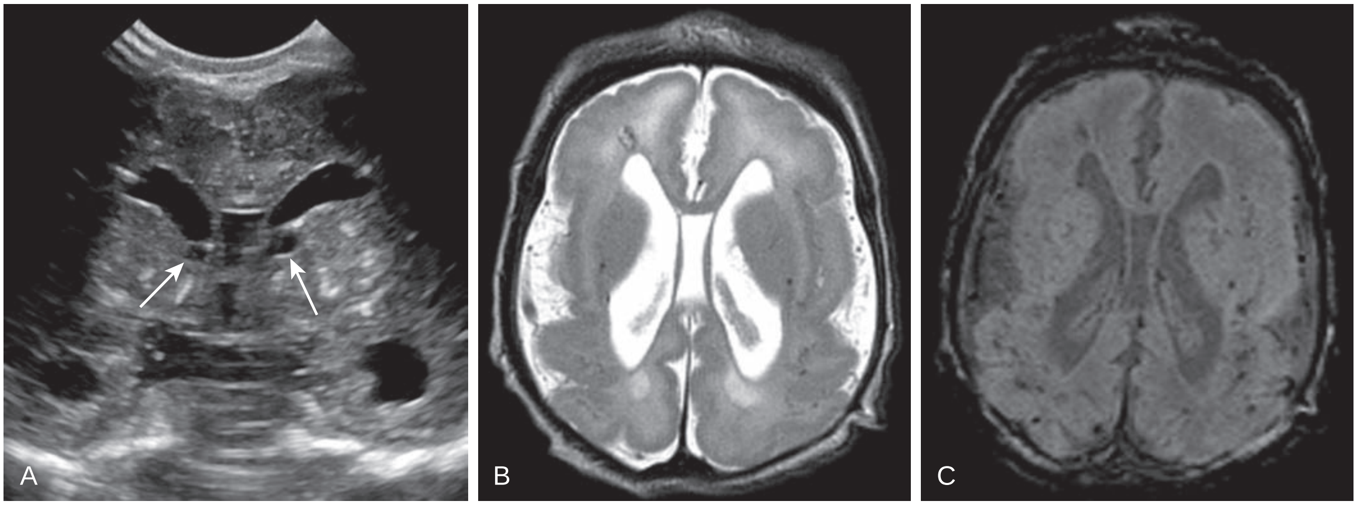

**Figure 30.15. Cytomegalovirus.** (A) Coronal sonogram demonstrates white matter volume loss, multiple calcifications in the brain parenchyma, nonshadowing echogenic foci, and germinolytic cysts *(arrows)*. (B) Axial T2-weighted MR image depicts extensive cortical malformation bilaterally. (C) Axial susceptibility-weighted MR image shows multiple dark foci bilaterally due to susceptibility effect from the calcifications in the brain parenchyma.

## Congenital Rubella Infection (German Measles)

Congenital rubella infection is extremely rare as a result of vaccination and screening of pregnant women. The most common manifestation is rash, fever, and symptoms of an upper respiratory tract infection. Rubella infection during early pregnancy can pass through the placenta to the fetus and cause serious birth defects, including heart abnormalities, mental retardation, blindness, and deafness. Imaging usually shows nonspecific findings such as microcephaly, ventriculomegaly, abnormal myelination, and calcifications, particularly of the basal ganglia.

## Congenital Syphilis Infection

Syphilis is a sexually transmitted bacterial infection that can be transferred from mother to fetus through the placenta. It is estimated that in up to 50% of cases of congenital syphilis, the neonate is born prematurely, is stillborn, or dies shortly after birth. Nevertheless, congenital syphilis rarely manifests with neurologic symptoms in the neonatal period. Only a few patients present with meningitis, choroiditis, hydrocephalus, or seizures. Severe ischemic-hemorrhagic lesions involving predominantly unilateral periventricular white matter, which are thought to be a result of endarteritis, have been reported in neonates. Other findings of congenital syphilis are generalized lymphadenopathy, hepatosplenomegaly, jaundice, and rash. The findings of CNS syphilis, such as leptomeningeal enhancement (particularly involving the basal meninges) and intraparenchymal mass (gumma), as well as frontal bossing, saddle nose deformity, mulberry molars, peglike upper frontal incisor, and saber shin, typically are observed later in infancy or childhood.

## Congenital Varicella Infection

The incidence of congenital varicella syndrome after maternal varicella infection during the first two trimesters is less than 1%. As with CMV and toxoplasmosis, intrahepatic and intracranial calcifications are very common. Intrauterine encephalitis, cortical atrophy, and porencephaly have been reported in cases of congenital varicella infection before 20 weeks of gestational age. Other possible fetal abnormalities are polyhydramnios, limb hypoplasia, and contractures, as well as paradoxical diaphragmatic motion as a result of unilateral paralysis. Neonates may demonstrate dysfunction of the autonomic nervous system (neurogenic bladder), hydroureter, esophageal dilation, aspiration pneumonia, and cutaneous lesions in a dermatomal distribution.[15]

## Congenital Lymphocytic Choriomeningitis Virus

Lymphocytic choriomeningitis virus (LCMV) primarily infects rodents, but it also can infect humans through inhalation of aerosolized particles of rodent urine, feces, or saliva; through ingestion of contaminated food; or through direct contact of open wounds to virus-infected blood. Human-to-human transmission may occur via the placenta or through solid-organ transplantation. The disease is usually mild in healthy individuals, but it may cause serious consequences to immunosuppressed persons and pregnant women. Miscarriage, birth defects, and long-term neurologic problems may result from congenital LCMV. LCMV causes chorioretinitis, ependymitis with ependymal calcifications, polymicrogyria, and microcephaly or hydrocephalus. These findings are similar to those of congenital toxoplasmosis and CMV; however, hepatosplenomegaly usually is not present in persons with LCMV.

## Zika Virus

Zika virus is a single-stranded RNA virus of the Flaviviridae family. The transmission from human to human occurs primarily through the bite of infected mosquitos of the genus *Aedes*; however, it has been reported that Zika virus can be sexually transmitted and could be passed from the mother to the fetus. Growing evidence suggests that vertical transmission of Zika during pregnancy is associated with severe brain damage and resultant microcephaly. Although proving Zika virus is linked to microcephaly is challenging at least in part due to lack of resources in epidemic areas, there has been an increase in the incidence in infants born with microcephaly in Brazil coinciding with an epidemic of Zika infection and, of those, approximately one-third have been confirmed to have Zika infection during pregnancy. Cases have since been reported in other Latin American countries and the southern United States. The most common neuroimaging findings reported in cases of presumed Zika infection during pregnancy are generalized brain parenchyma volume loss, ventriculomegaly, malformation of cortical development, and calcifications in the basal ganglia, periventricular white matter, and in the junction between the cortex and the juxtacortical white matter (Fig. 30.16).[16]

# ACQUIRED METABOLIC DISORDERS

## Kernicterus (Bilirubin Encephalopathy)

Kernicterus is caused by markedly elevated or sustained unconjugated hyperbilirubinemia. Kernicterus usually develops in the first week of life; however, it may occur as late as the third week. Severe hemolytic conditions, especially Rh hemolytic disease with hydrops fetalis, are the most common causes. Other risk factors include prematurity, polycythemia, resolving hematomas, sulphonamide administration, glucose-6-phosphate dehydrogenase deficiency, and Crigler-Najjar and Gilbert syndromes. Although risk factors are usually present, kernicterus has been reported in otherwise healthy babies. Acutely, kernicterus manifests as lethargy, decreased feeding, hypotonia or hypertonia, a high-pitched cry, spasmodic torticollis, opisthotonus, the setting sun sign, fever, seizures, and even death. In severe cases, kernicterus results in a tetrad of movement disorder, auditory dysfunction, oculomotor impairments, and dental enamel hypoplasia of the deciduous teeth. Persons with mild cases are still at risk for isolated hearing loss or some degree of neurologic, cognitive, learning, and movement disorders.

Pathologically, kernicterus causes damage to the globi pallidi, subthalamic nuclei, hippocampi (CA2 and CA3 regions), pars reticulata of the substantia nigra, and dentate nuclei. Ultrasound and CT are not sensitive in detecting early abnormalities in persons with kernicterus. On MRI, the classic description of a transient increased signal seen on T1-weighted images seems to be inconsistent particularly in infants with mild or moderate hyperbilirubinemia. Moreover, conventional T1 spin echo images appear to be more reliable than 3D T1 spoiled gradient echo images, because the latter are associated with a high signal in normal subthalamic nuclei, which may cause false-positive results. Increased signal on T2-weighted images of affected areas that develops later is a more reliable finding (e-Fig. 30.17), when hyperechogenicity may appear on ultrasound and hypoattenuation may appear on CT.[17] Acutely, these areas may demonstrated restricted diffusion[18]; however, when restricted diffusion is present, other conditions such as hypoxia-ischemia should also be considered. Hypoxic-ischemic injury typically involves the putamen more than the globus pallidus, and kernicterus typically involves the globus pallidus and subthalamic nuclei more than the putamen. A metabolite signature of acute kernicterus has been proposed on MRS using an echo time of 35 ms with elevated ratios of taurine, glutamate, glutamine, and myoinositol, and a decreased ratio of choline relative to creatine with no significant elevation of lactate.

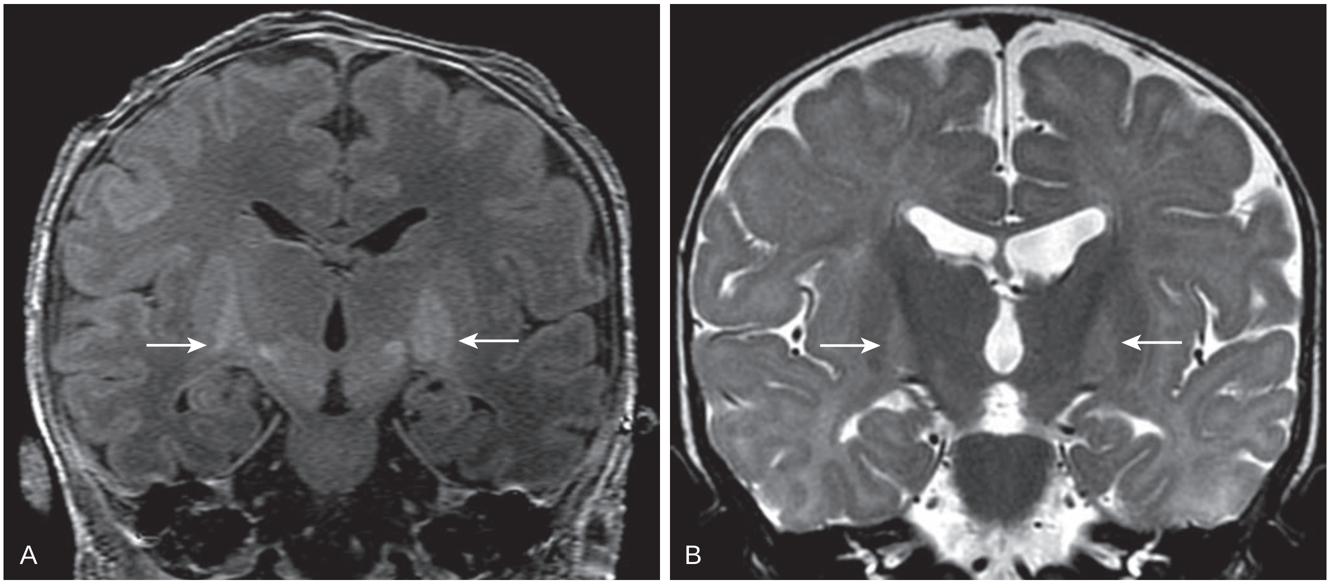

**e-Figure 30.17. Kernicterus.** (A) Coronal T1-weighted MR image shows increased signal in the bilateral globus pallidus at 1 week of age *(arrows)*. (B) Coronal T2-weighted MR image 1 month later shows increased T2 signal *(arrows)*.

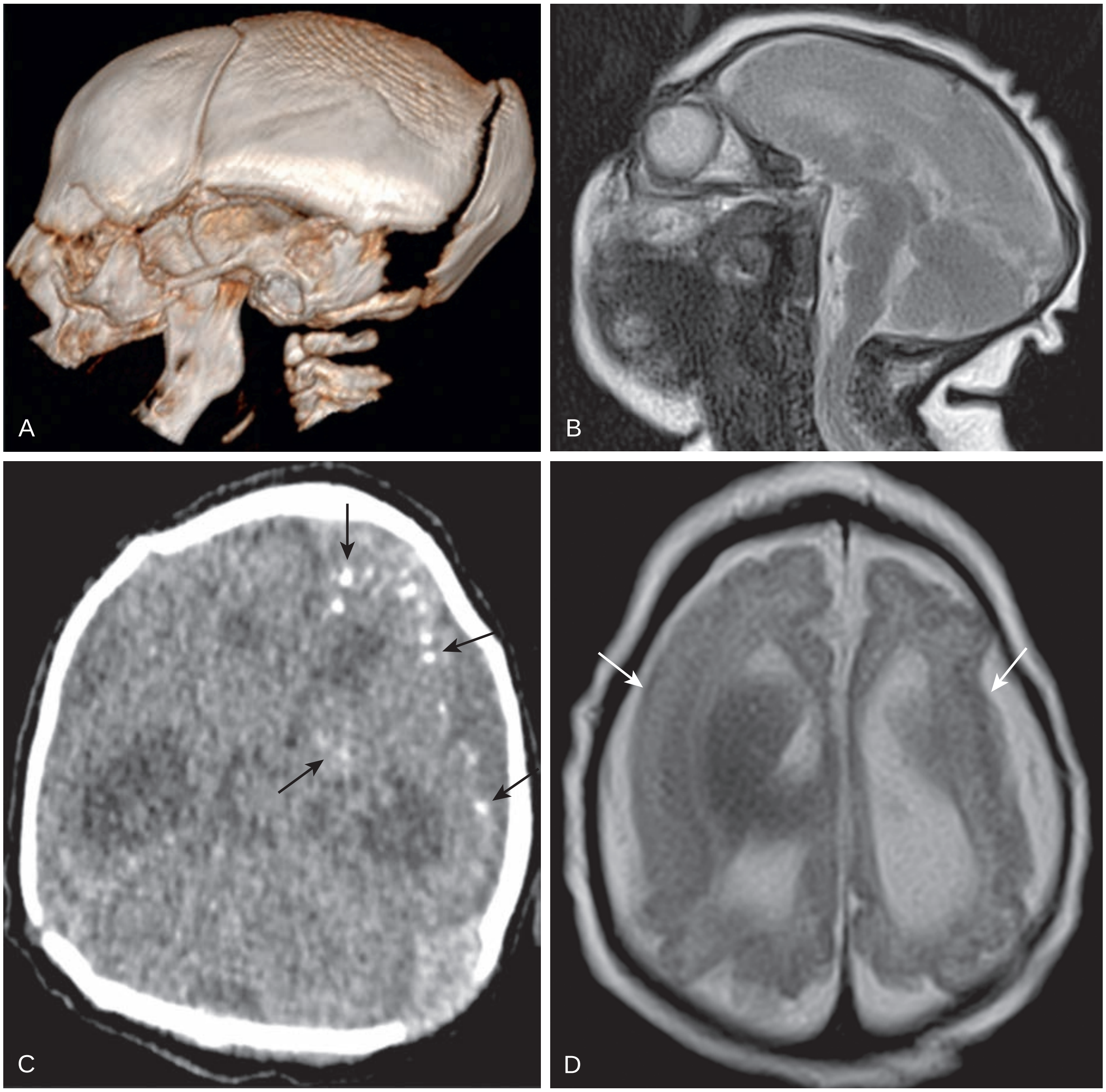

**Figure 30.16. Zika-linked microcephaly.** (A) 3D reconstructed CT shows severe microcephaly. (B) Sagittal T2-weighted MR image shows severe volume loss involving the cerebral hemispheres. (C) Axial unenhanced CT shows juxtacortical and basal ganglia calcifications *(black arrows)*. (D) Axial T2-weighted MR image shows brain parenchyma volume loss with ex-vacuo dilation of the lateral ventricles and extensive bilateral cortical malformation *(white arrows)*. *(Case courtesy Dr. Celso Hygino.)*

### Hypoglycemia

Neonatal encephalopathy resulting from hypoglycemia typically occurs when glucose concentrations are less than 30 mg/dL in the term infant and less than 20 mg/dL in the preterm infant. The clinical presentation of neonatal hypoglycemia may be subtle, including stupor, jitteriness, seizures, respiratory abnormalities, and hypotonia. MRI is the imaging modality of choice, showing abnormalities in the posterior parietal and occipital cortex and adjacent white matter. Acutely, there is restricted diffusion on DWI as well as edema on T1- and T2-weighted imaging (Fig. 30.18). MRS with an echo time of 30 ms exhibits an increased lactate-lipid peak and a decreased NAA peak in the involved areas. In the chronic phase, the involved areas evolve into encephalomalacia and atrophy. If the hypoglycemia is severe and prolonged, progression to diffuse brain damage occurs with involvement of the hippocampus, corpus striatum, and cerebellum.[19]

## INBORN ERRORS OF METABOLISM

Inborn errors of metabolism present with signs and symptoms related to the involvement of one or more of the organ systems, including the CNS. Inborn errors of metabolism are classified into organic acidemia, disorders of amino acid oxidation, disorders of fatty acid oxidation, primary lactic acidosis, mitochondria function, lysosomal storage disorders, and peroxisome disorders (also see Chapter 33). Whereas some inborn errors of metabolism manifest immediately at birth (e.g., primary lactic acidosis, type 2 glutaric aciduria, long-chain acyl coenzyme A dehydrogenase, hydroxymethylglutaryl-CoA lyase, ornithine transcarbamylase, and carbamyl phosphatase synthetase deficiencies), in others, it takes a few days for signs and symptoms to develop (e.g., isovaleric acidemia, methylmalonic acidemia, propionic acidemia, nonketotic hyperglycinemia, citrullinemia, argininosuccinic aciduria, and maple syrup urine disease).

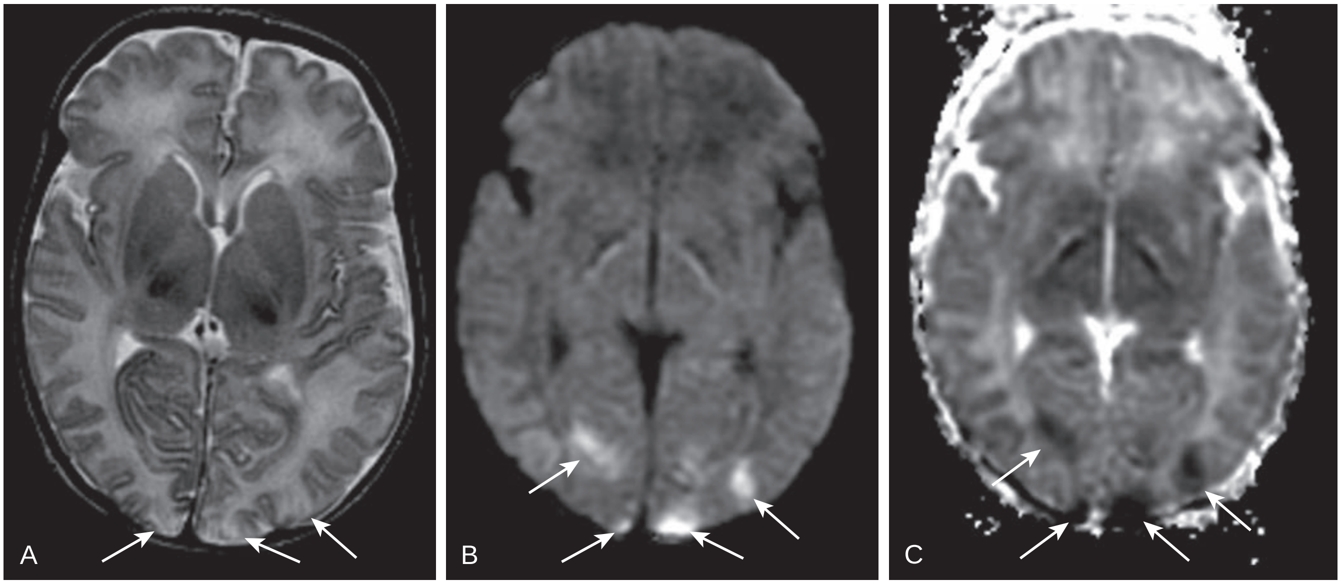

**Figure 30.18. Hypoglycemia.** (A) Axial T2-weighted MR image shows edema with increased signal in the occipital lobes *(arrows)*. (B and C) Axial diffusion weighted images show decreased diffusion and low ADC values *(arrows)*.

The inborn errors of metabolism that affect the nervous system exclusively (namely l-2-hydroxyglutaric aciduria, glutaric aciduria type 1, 4-hydroxybutyric aciduria, alpha-ketoglutaric aciduria, mevalonic aciduria, and N-acetylaspartic aciduria [Canavan disease]) present later in life and are not encountered in neonates. MRS can provide valuable information regarding specific metabolites in certain neonatal metabolic disorders: increased branched-chain amino acids (e.g., l-leucine, l-isoleucine, and valine) in persons with maple syrup urine disease, increased glycine in persons with nonketotic hyperglycinemia, and absence of creatine in persons with guanidinoacetate methyltransferase deficiency (also see Chapter 25).

## Organic Acid Disorders

Methylmalonic acidemia and proprionic aciduria are examples of organic acid disorders. These disorders cause ketoacidosis, often leading to severe acidosis, vomiting, tachycardia, lethargy, seizures, coma, and death. In these disorders, edema is present in both myelinated and unmyelinated structures. The edema involving the myelinated white matter is related to vacuolating or spongiform myelinopathy, which acutely demonstrates restricted water diffusivity because the water is trapped within vacuoles. Findings on conventional imaging include edema with increased T2 signal and decreased T1 signal involving the white matter. In more severe cases, the deep gray structures may be involved, with a predilection for the globi pallidi in persons with methylmalonic acidemia and for the putamina and caudate nuclei in persons with proprionic aciduria. MRS detects a reduction in myoinositol and NAA and an elevation of glutamine. Elevation of lactate as a result of hyperammonia, ketoacidosis, and/or mitochondrial dysfunction also may be present during an acute metabolic crisis.

## Amino Acid Disorders

Maple syrup urine disease results from an interruption of the metabolism of the essential amino acids leucine, isoleucine, and/or valine. The most severe form manifests in the first week of life with seizures, vomiting, dystonia, fluctuating ophthalmoplegia, and coma. The imaging findings are almost pathognomonic. Conventional MR shows edema in the deep cerebellar white matter, brainstem tegmentum, posterior limb of the internal capsule, perirolandic white matter, and precentral and postcentral gyrus. Restricted water diffusivity is seen acutely in the areas of vacuolating edema in the myelinated white matter. MRS shows a peak at 0.9 parts per million (ppm) related to the accumulation of abnormal branched-chain amino acids and branched-chain alpha-ketoacids. The imaging findings by diffusion imaging and MRS may resolve with treatment.[20]

## Urea Cycle Disorders

Urea cycle enzyme defects include ornithine carbamyl transferase deficiency, carbamyl phosphate synthetase deficiency, argininosuccinic aciduria, citrullinemia, and hyperargininemia, resulting in hyperammonemia and elevation of glutamate. Cases with severe impairment of elimination of nitrogen waste products manifest as irritability, lethargy, poor feeding, hypothermia, and seizures during the neonatal period.

Imaging in the acute phase shows markedly diffuse vasogenic edema, predominantly in the unmyelinated white matter, with early involvement of the subcortical U fibers and relative preservation of the myelinated white matter. The underlying pathophysiology of the urea cycle defects is related to vasogenic edema, in contrast to vacuolating myelinopathy in persons with maple syrup urine disease. As a result, the mean diffusivity maps in the urea cycle defect will show increased signal intensity in the unmyelinated white matter. In some cases, the lentiform nuclei (particularly the globi pallidi), the posterior insular cortex, and the perirolandic cortex also may be involved with increased T1 signal. This presentation causes some overlap between the conventional imaging findings of urea cycle disorders and hypoxic-ischemic injury. However, involvement of the globi pallidi and putamina in urea cycle disorders is predominant as opposed to thalami in cases of hypoxia-ischemia. MRS in patients with urea cycle defects typically demonstrates increased levels of glutamate and glutamine and decreased levels of myoinositol, NAA, choline, and creatine.

## Nonketotic Hyperglycinemia

Nonketotic hyperglycinemia is caused by a defect of the glycine cleavage system, which is present in the liver, kidney, and brain, leading to the accumulation of glycine in blood, urine, and CSF. The diagnosis is established by calculating the CSF/plasma glycine concentration ratio. A value of greater than 0.08 is diagnostic. Confirmation of the diagnosis requires measurement of the activity of the glycine cleavage system in liver tissue. The neonatal (classic) form of nonketotic hyperglycinemia is far more common than the infantile, late-onset, or transient phenotypes. The neonatal form presents in the first days of life with encephalopathy, hypotonia, lethargy, seizures, and characteristic hiccups, which can progress rapidly to intractable seizures, coma, and respiratory failure. The outcome is invariably poor.

On MRI, abnormal myelination and a hypoplastic or dysgenic corpus callosum are seen, which progresses to diffuse cerebral atrophy. Increased T2 signal and restricted water diffusivity involving the myelinated portion of the posterior limb of the internal capsules, pyramidal tracts, middle cerebellar pedicles, and dentate nuclei have been reported. The underdevelopment of the corpus callosum is difficult to assess in the neonate because of its small size and lack of myelin, but it becomes evident later. Atrophy and delayed myelination also are common findings in other metabolic disorders, particularly in organic acidurias. MRS exhibits a large glycine peak at 3.55 ppm.

## Peroxisomal Disorders

Peroxisomal disorders that manifest in the neonate are primarily a result of the failure to form viable peroxisomes (peroxisomal biogenesis disorders), resulting in multiple metabolic abnormalities. Zellweger syndrome and neonatal adrenoleukodystrophy are the most common peroxisomal disorders in the neonate, and both have pathognomonic findings on conventional MRI. Zellweger syndrome is characterized by delayed myelination, temporal and parietal polymicrogyria, and subependymal germolytic cysts adjacent to the frontal horns of the lateral ventricles. In contrast to Zellweger syndrome, neonatal adrenoleukodystrophy causes dysmyelination, mainly involving the occipital lobes, the splenium of the corpus callosum, and/or the cerebellum. Often these lesions demonstrate restricted water diffusion and peripheral enhancement. MRS in persons with Zellweger syndrome is not specific, showing a marked decrease in NAA levels in the gray-white matter, thalamus, and/or cerebellum, a decreased myoinositol level in the gray matter if concomitant hepatic dysfunction is present, and in some cases, elevated glutamine levels.

## Molybdenum Cofactor Deficiency

Molybdenum cofactor deficiency is a rare, usually underrecognized, autosomal-recessive disorder caused by genetic mutation of the genes that produce enzymes essential for the formation of molybdenum cofactor. The absence of molybdenum cofactor leads to toxic levels of sulphite, which may be detected by hypouricemia, elevated urine sulfate, and elevated S-sulfocysteine. Clinically, molybdenum cofactor deficiency manifests in the first few days of life with seizures and encephalopathy, and usually leads to death within months. Imaging shows edema and cystic changes involving predominantly the basal ganglia and severe volume loss of the gray-white matter. Reduced water diffusivity may be present in the affected areas.

## Mitochondrial Disorders

Mitochondrial disorders are a group of diseases caused by enzymatic defects leading to primary lactic acidosis and decreased ATP production. Pyruvate transcarboxylase, pyruvate dehydrogenase, and cytochrome c oxidase deficiencies are the most common enzymatic defects leading to primary lactic acidosis in the neonatal period. MRI is the imaging modality of choice for its capability to detect areas of reduced water diffusivity and the presence of lactate typically associated with these disorders. Characteristically, areas of increased T2 signal and reduced water diffusivity are found in the brainstem, the subthalamic nucleus, and the globus pallidum. MRS detects elevated lactate levels in the areas with abnormal signal, as well as in the normal-appearing brain. It should be noted, however, that elevated lactate is not always indicative of a mitochondrial disorder, and nondetectable lactate levels do not preclude the possibility of a mitochondrial disorder. Sometimes specific spectroscopic peaks can be detected—for example, elevated succinate peak at 2.4 ppm in persons with succinate dehydrogenase deficiency and an elevated pyruvate peak at 2.36 ppm in persons with pyruvate dehydrogenase complex deficiency.

### KEY POINTS

- MRI is the imaging modality with the highest sensitivity for detecting abnormalities in the neonatal brain.
- The central pattern of HIE usually occurs with profound asphyxia, when an abrupt interruption occurs in the oxygen supply to the neonatal brain.
- The peripheral pattern of HIE usually results from a period of decreased supply of oxygen to the neonatal brain.
- Arterial infarctions are more common in term neonates and most frequently involve the middle cerebral artery and its branches.
- Birth trauma is more common in vaginal delivery, particularly if forceps or vacuum extraction is used.
- Small subdural hematomas are seen in up to 46% of the newborns in the first week of life.
- The most common bacterial neonatal brain infections are caused by group B streptococcus, *Escherichia coli*, *Streptococcus pneumoniae*, *Haemophilus influenzae* type B, and *Listeria monocytogenes*.
- Kernicterus is caused by markedly elevated or sustained unconjugated hyperbilirubinemia.
- Neonatal encephalopathy resulting from hypoglycemia typically occurs when glucose concentrations are less than 30 mg/dL in the term infant and less than 20 mg/dL in the preterm infant.
- Inborn errors of metabolism are classified into organic acidemia, disorders of amino acid oxidation, disorders of fatty acid oxidation, primary lactic acidosis, mitochondria function, lysosomal storage disorders, and peroxisomal disorders.

### SUGGESTED READINGS

Barkovich AJ. *Pediatric Neuroradiology*. 5th ed. Philadelphia: Lippincott Williams & Wilkins; 2012.

Barkovich AJ. MR imaging of the neonatal brain. *Neuroimaging Clin N Am*. 2006;16(1):117–135, viii-ix.

Huang BY, Castillo M. Hypoxic-ischemic brain injury: imaging findings from birth to adulthood. *Radiographics*. 2008;28(2):417–439, quiz 617.

Rutherford MA. *MRI of the neonatal brain (website)*: www.mrineonatalbrain.com.

Volpe JJ. The encephalopathy of prematurity—brain injury and impaired brain development inextricably intertwined. *Semin Pediatr Neurol*. 2009;16(4):167–178.

### REFERENCES

Full references for this chapter can be found on www.expertconsult.com.

## REFERENCES

1. Lemons JA, Bauer CR, Oh W, et al. Very low birth weight outcomes of the National Institute of Child Health and Human Development Neonatal Research Network, January 1995 through December 1996. NICHD Neonatal Research Network. *Pediatrics*. 2001;107(1):E1.
2. Panigrahy A, Borzage M, Bluml S. Basic principles and concepts underlying recent advances in magnetic resonance imaging of the developing brain. *Semin Perinatol*. 2010;34(1):3–19.
3. Bluml S, Friedlich P, Erberich S, et al. MR imaging of newborns by using an MR-compatible incubator with integrated radiofrequency coils: initial experience. *Radiology*. 2004;231(2):594–601.
4. Kanal ESF. *Safety Reference Manual on Magnetic Resonance Imaging Contrast agents*. New York: Lippincott-Raven; 1996.
5. Rooks VJ, Eaton JP, Ruess L, et al. Prevalence and evolution of intracranial hemorrhage in asymptomatic term infants. *AJNR Am J Neuroradiol*. 2008;29(6):1082–1089.
6. Huang AH, Robertson RL. Spontaneous superficial parenchymal and leptomeningeal hemorrhage in term neonates. *AJNR Am J Neuroradiol*. 2004;25(3):469–475.
7. Sie LT, van der Knaap MS, Oosting J, et al. MR patterns of hypoxic-ischemic brain damage after prenatal, perinatal or postnatal asphyxia. *Neuropediatrics*. 2000;31(3):128–136.
8. Martinez-Biarge M, Diez-Sebastian J, Kapellou O, et al. Predicting motor outcome and death in term hypoxic-ischemic encephalopathy. *Neurology*. 2011;76(24):2055–2061.
9. Bednarek N, Mathur A, Inder T, et al. Impact of therapeutic hypothermia on MRI diffusion changes in neonatal encephalopathy. *Neurology*. 2012;78(18):1420–1427.
10. McElhinney DB, Halbach VV, Silverman NH, et al. Congenital cardiac anomalies with vein of Galen malformations in infants. *Arch Dis Child*. 1998;78(6):548–551.
11. Dyet LE, Kennea N, Counsell SJ, et al. Natural history of brain lesions in extremely preterm infants studied with serial magnetic resonance imaging from birth and neurodevelopmental assessment. *Pediatrics*. 2006;118(2):536–548.
12. Whitley R. Neonatal herpes simplex virus infection. *Curr Opin Infect Dis*. 2004;17(3):243–246.
13. Gupta S, Fernandez D, Siddiqui A, et al. Extensive white matter abnormalities associated with neonatal Parechovirus (HPeV) infection. *Eur J Paediatr Neurol*. 2010;14(6):531–534.
14. Barkovich AJ, Lindan CE. Congenital cytomegalovirus infection of the brain: imaging analysis and embryologic considerations. *AJNR Am J Neuroradiol*. 1994;15(4):703–715.
15. Smith CK, Arvin AM. Varicella in the fetus and newborn. *Semin Fetal Neonatal Med*. 2009;14(4):209–217.
16. de Fatima Vasco Aragao M, van der Linden V, Brainer-Lima AM, et al. Clinical features and neuroimaging (CT and MRI) findings in presumed Zika virus related congenital infection and microcephaly: retrospective case series study. *BMJ*. 2016;353:i1901.
17. Gkoltsiou K, Tzoufi M, Counsell S, et al. Serial brain MRI and ultrasound findings: relation to gestational age, bilirubin level, neonatal neurologic status and neurodevelopmental outcome in infants at risk of kernicterus. *Early Hum Dev*. 2008;84(12):829–838.
18. Wisnowski JL, Panigrahy A, Painter MJ, et al. Magnetic resonance imaging abnormalities in advanced acute bilirubin encephalopathy highlight dentato-thalamo-cortical pathways. *J Pediatr*. 2016;174:260–263.
19. Kim SY, Goo HW, Lim KH, et al. Neonatal hypoglycaemic encephalopathy: diffusion-weighted imaging and proton MR spectroscopy. *Pediatr Radiol*. 2006;36(2):144–148.
20. Jan W, Zimmerman RA, Wang ZJ, et al. MR diffusion imaging and MR spectroscopy of maple syrup urine disease during acute metabolic decompensation. *Neuroradiology*. 2003;45(6):393–399.

# 31 Congenital Brain Malformations

Nancy Rollins

Advances in gene sequencing and genotype-phenotype profiling have furthered understanding of many brain malformations.[1–4] Some malformations previously considered disparate in terms of gestational timing and etiology are now considered phenotypic variants of common pathways while others previously considered variants of a specific malformation are now known to result from mutations affecting disparate molecular pathways (e.g., the lissencephalies).[1–4] Given the large number of congenital human brain malformations, the complexity of the molecular genetics, and the degree of anatomic variability, an in-depth discussion of some malformations is beyond the scope of this chapter. This chapter will address malformations seen most often in clinical practice and malformations that, although less common, are distinctive and have a profound impact on early childhood development. The malformations presented herein are grouped according to presumed dominant defect in embryologic or fetal development. Diffusion tensor imaging (DTI) is included for malformations in which aberrant white matter tracts are a dominant feature of the malformation.

A rudimentary description of relevant embryology is needed. Around 26 to 28 days after conception, primary neurulation occurs, in which the lateral edges of the neural plate elevate into neural folds under the control of signaling genes such as sonic hedgehog *(SHH)*, which is also important in prosencephalic differentiation.[5,6] The folds then fuse medially to form the neural tube; initial fusion is in the middle of the embryo with subsequent closure of the cranial and caudal ends (neuropores) of the neural tube.[5,6] The primitive brain vesicles (e.g., the prosencephalon, mesencephalon, and rhombencephalon) form at the cranial end of the neural tube.[5,6] The prosencephalon divides into the telencephalon, which gives rise to the cerebral hemispheres, lateral ventricles, and corpus striatum, and the diencephalon, which gives rise to the thalami and hypothalamus. The cerebral peduncles and midbrain arise from the mesencephalon while the rhombencephalon gives rise to the metencephalon, which forms the pons and cerebellum, and the myelencephalon from which arises the medulla[5,6].

## DEFECTS OF NEURULATION

***Clinical.*** Failure of closure of the cranial neuropore results in anencephaly (e.g., absent forebrain, skull, and scalp), a lethal malformation. Less severe disorders of cranial neuropore closure result in meningoceles and encephaloceles, which are protrusions of meninges or brain respectively through a congenital defect of the skull and dura occurring in about 1/5000 live births.[7] Encephaloceles in Asian children tend to be anterior,[1] whereas those in occidental children tend to be posterior and both are most often midline. Frontal encephaloceles include interorbital frontal, nasofrontal, nasoethmoidal, and nasoorbital lesions.[7–9] Interorbital frontal encephaloceles protrude through a defect in the frontal bone (Fig. 31.1). Nasofrontal encephaloceles involve the region of nasal bridge and/or the floor of the anterior cranial fossa (e-Fig. 31.2). Nasofrontal encephaloceles are also referred to as *nasal gliomas*, although they are not neoplastic. These masses of neuroglial tissue are categorized as extranasal (60%), intranasal (30%), or mixed (10%).[6] When there are telangiectasias on the skin overlaying an external nasal glioma, the lesion may be mistaken for a hemangioma. There is often hypertelorism with a broad nasal bridge. Intranasal glioma present as an intranasal mass; biopsy should be avoided before imaging due to the risk of meningitis. With nasoethmoidal encephaloceles, the frontal bone is intact. The neural tissue bulges into the ethmoid sinus through a defect in the floor of the anterior cranial fossa, and the nasal septum defines the posterior margin of the encephalocele. A defect in the medial orbital wall results in a nasoorbital encephalocele, which protrudes into the orbit with unilateral exophthalmos. Other facial anomalies seen with anterior encephaloceles include a bifid nasal tip or complete midline splitting of the nose in an uncommon malformation known as *frontonasal dysplasia*. Basal encephaloceles result from defects in the sphenoid bone (Fig. 31.3); the encephalocele herniates into the posterior nasopharynx anterior to the dorsum sella and may contain pituitary tissue, optic nerves, and/or branches of the circle of Willis. Parietal encephaloceles range from large, deforming, "towering" lesions to small meningoceles (e-Fig. 31.4). Atretic parietal encephaloceles or meningoceles present as a small vertex subcutaneous fibrofatty masses, often painful to palpation (e-Fig. 31.5).[8] Occipital encephaloceles may contain dysplastic cerebellar tissue alone or with cerebral cortex (Fig. 31.6). Rarely, the brainstem may be within the encephalocele making this malformation lethal. The prognosis depends on the severity of associated brain anomalies and the amount of dysplastic brain contained within the encephalocele.[6–9] Although dysplastic nonfunctional neural tissue is usually resected during encephalocele closure, major dural venous sinuses are preserved if possible. Hydrocephalus is common after closure of large parietal and occipital encephaloceles.

Occipital encephaloceles are seen in trisomy 13 and 18, amniotic band syndrome, Meckel-Gruber syndrome, dyssegmental dwarfism, Knobloch syndrome, Walker-Warburg (Type II lissencephaly) syndrome, cryptophthalmos, and Voss syndrome. Frontal encephaloceles are seen in morning glory syndrome includes midline facial defects, callosal agenesis, and characteristic eye anomalies.

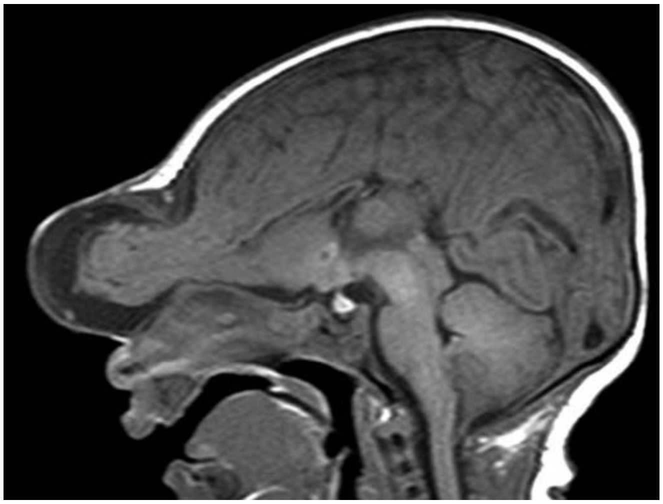

**Figure 31.1. Frontal encephalocele in a neonate.** Sagittal T1-weighted MR image shows agenesis of the corpus callosum associated with an encephalocele at the glabella.

## Abstract:

Advances in MR imaging, gene sequencing, and development of mouse models of congenital brain malformations have advanced the understanding of the etiologies and mechanisms of many congenital brain malformations. Congenital brain malformations have historically been grouped by gestational stage at time of teratogenic insult or expression of gene mutation; e.g. malformations of neural tube closure, malformations of diverticulation. However, malformations occurring at seemingly different gestational stages may have commonalities. Examples are the fused thalami seen in neural tube defects and holoprosencephaly and malformations of cortical development seen in many diverse malformations. Conventional MR imaging provides exquisite surface detail of the brain and allows white matter to be differentiated from grey matter. However, little information is provided about the white matter tracts that connect different regions of the brain. By virtue of sensitivity to different orientation of white matter tracts, diffusion imaging provides insight into malformations of axonal path finding and migration in diverse supra and infra tentorial brain malformations and expands the spectrum of anomalies in the malformed brain.

## Keywords:

Congenital brain malformations
MRI
diffusion tensor imaging
mid hindbrain malformations

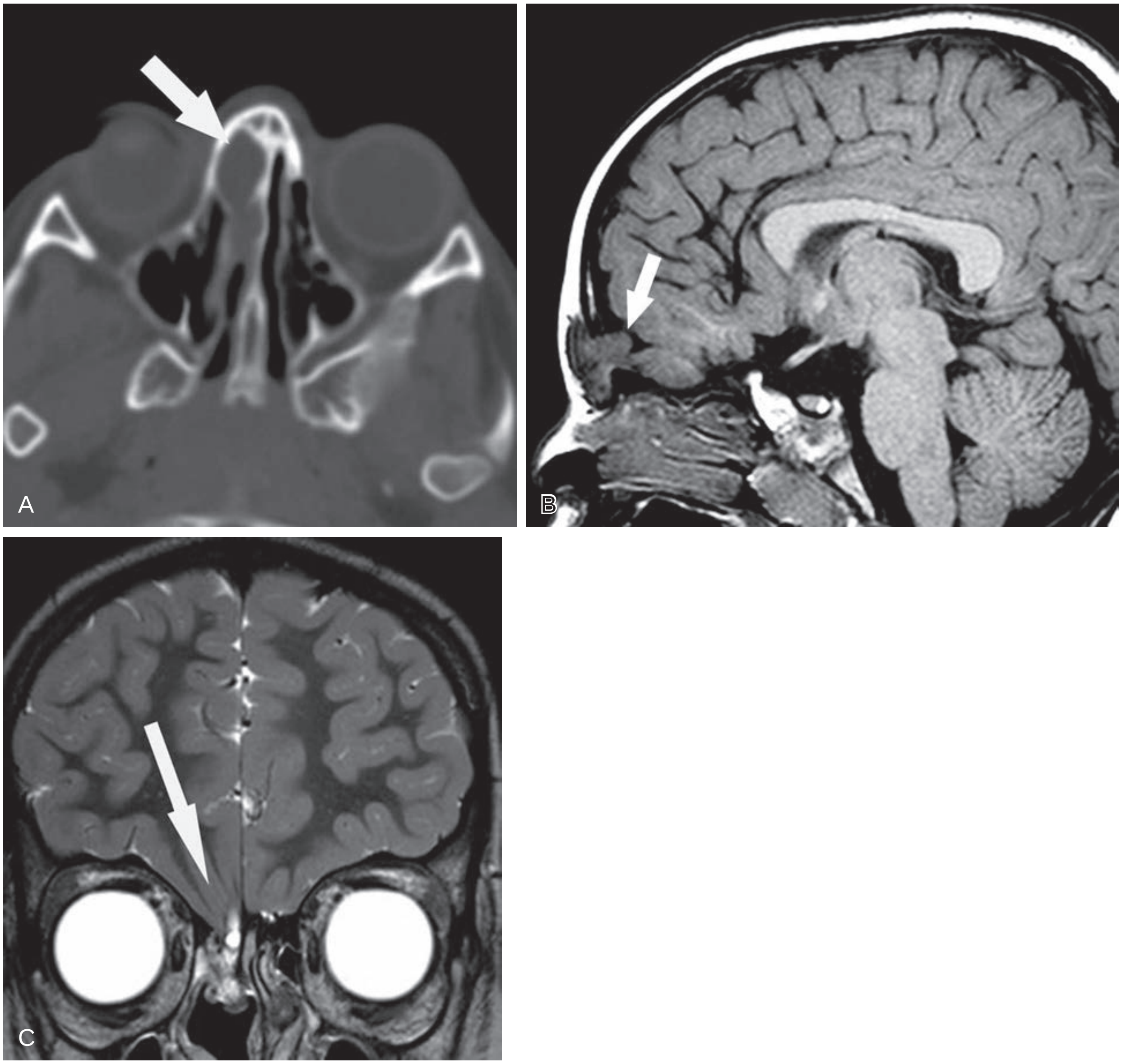

**e-Figure 31.2. Incident nasofrontal encephalocele found on CT done for trauma.** (A) Axial CT image shows a focally expansile lesion within the right ethmoid sinus *(arrow)*. (B) Sagittal T1-weighted MR image shows a small skin-covered mass *(arrow)* in the region of the glabella. (C) Coronal T2-weighted MR image shows hypertelorism and protrusion of brain and meninges *(arrow)* through a defect in the right cribriform plate.

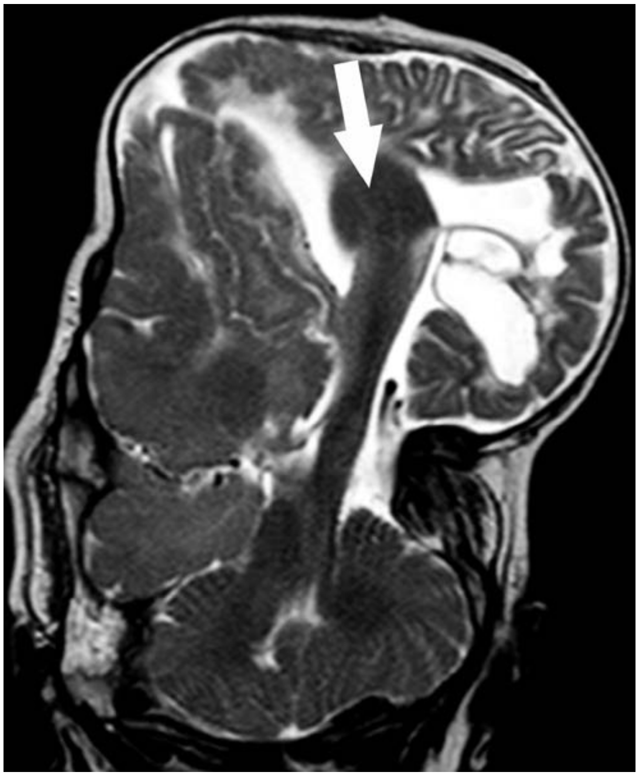

**e-Figure 31.4. Large parietal encephalocele.** Coronal T2-weighted MR image shows extremely dysmorphic brain and diencephalic structures contained within the massive parietal encephalocele.

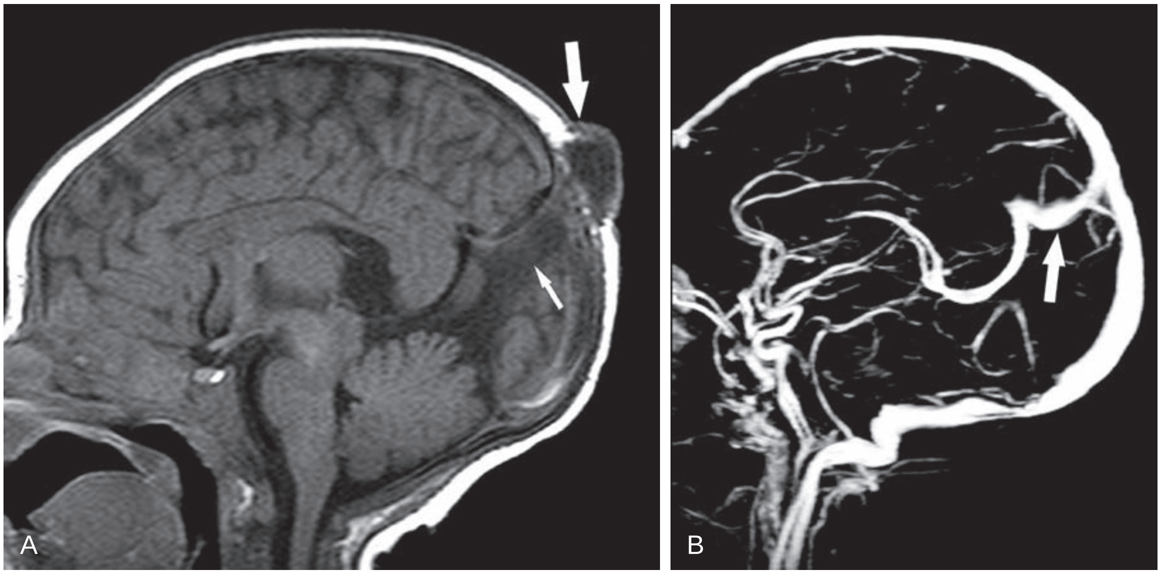

**e-Figure 31.5. Atretic parietal meningocele.** (A) Sagittal T1-weighted MR image shows the small meningocele *(arrow)* over the parietal vertex. There is focal expansion of the posterior interhemispheric subarachnoid space *(small arrow)*. (B) Sagittal view from gadolinium-enhanced MR venogram shows a persistent falcine sinus *(arrow)* draining the deep medullary venous system; there is no straight sinus.

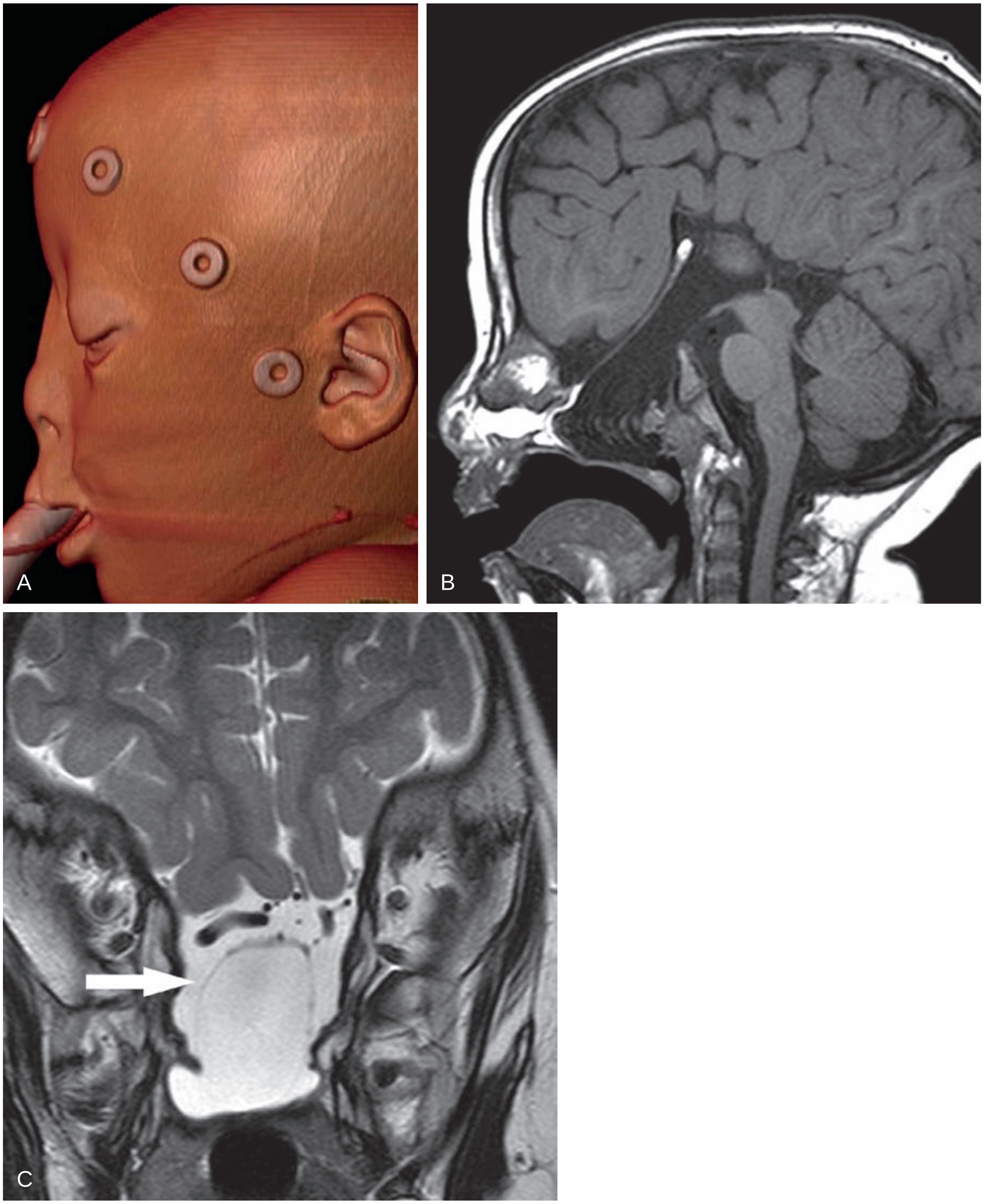

**Figure 31.3. Basal encephalocele.** (A) Lateral reformatted image from three-dimensional CT shows depressed nasal bridge. (B) Sagittal T1-weighted MR image shows callosal agenesis with a tiny lipoma. There is a large defect in the basisphenoid. Note absence of the pituitary, floor of the third ventricle, and optic pathways. (C) Coronal high-resolution T2-weighted MR image shows the pituitary-hypothalamic structures, and hypoplastic optic nerves *(arrow)* are contained within the encephalocele.

***Imaging.*** High-resolution magnetic resonance imaging (MRI) is performed soon after birth to define contents of the encephalocele and the severity of associated brain anomalies, which include callosal agenesis, malformations of cortical formation, and variable anomalies of the cerebellum, diencephalon, and brainstem. Magnetic resonance (MR) venography is essential with large occipital and midline parietal encephaloceles that may contain dural venous sinuses. Atretic parietal encephaloceles are characterized by posterior tenting of the tectal plate, a persistent falcine sinus with hypoplasia or atresia of the straight sinus, and focal expansion of posterior interhemispheric subarachnoid space.

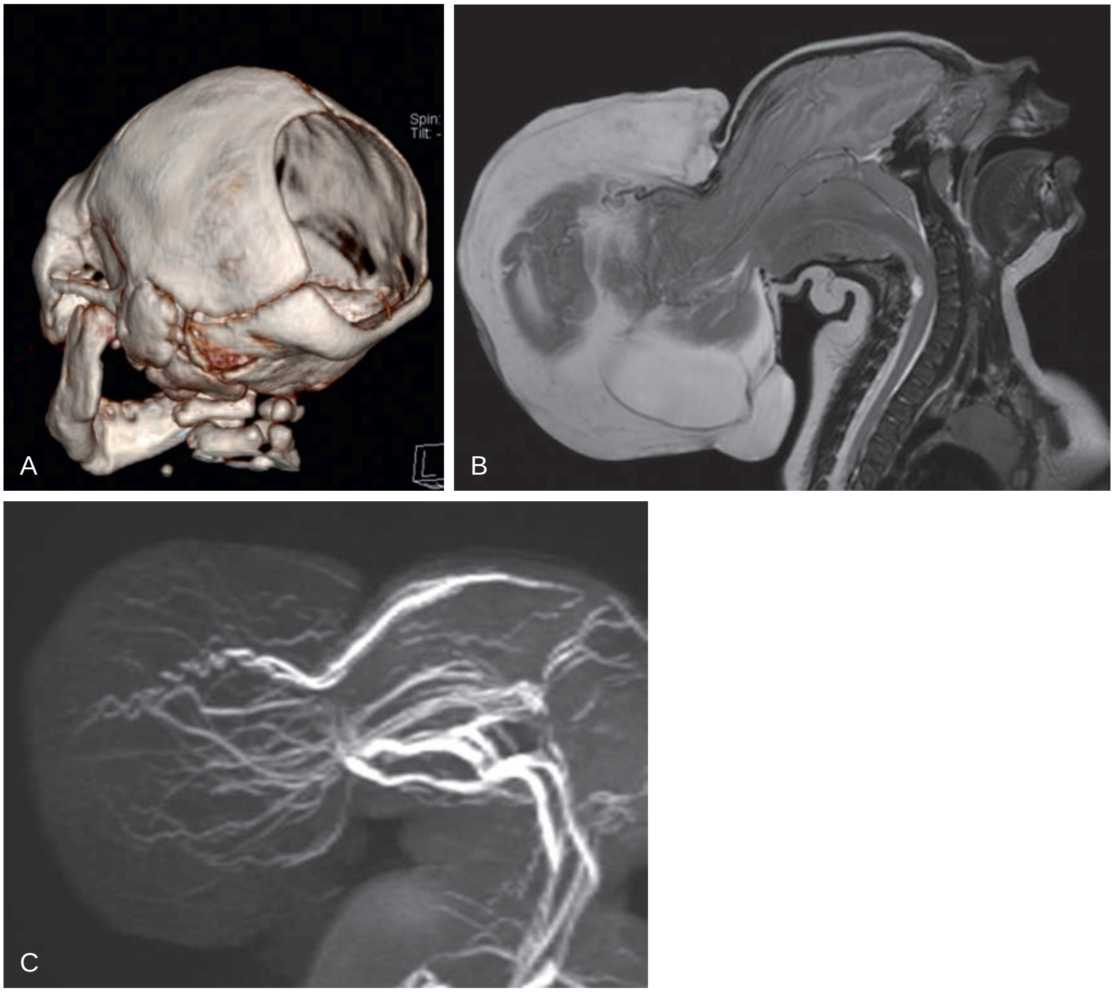

**Figure 31.6. Occipital encephalocele.** (A) Three-dimensional CT shows a large parietooccipital bony defect. (B) Sagittal T2-weighted MR image in this patient shows the encephalocele contains cerebellum and dysplastic cerebrum. (C) MR angiography shows numerous extracranial arteries and veins contained within the encephalocele.

## CHIARI II MALFORMATION

***Clinical.*** The Chiari II malformation is the intracranial manifestation of failure of closure of the caudal neuropore, which results in failure of the temporary occlusion of the neural tube needed to distend the primary brain vesicles.[10–14] Failure of distension of the primitive ventricular system results in premature fusion of the mesenchymal components that form the calvarium while the hindbrain manifestations result from leakage of cerebrospinal fluid (CSF) through the neural tube defect.[10–14]

Neural tube defects have been reported with multiple chromosomal abnormalities, including trisomies 18, 13, and 9, triploidies, unbalanced translocations and deletions, and in syndromes such as Turner, DiGeorge, and velocardiofacial syndrome.[15] The genes in the region of *22q11* have been implicated in the development of neural tube defects, although neural tube defects and the associated Chiari II malformation are probably due to a combination of genetic polymorphisms and environmental factors, including dietary folate intake and maternal folate metabolism.

The Chiari II malformation is characterized by mesodermal dysplasia, small and dysplastic lower cranial nerve ganglia, deficient tentorium cerebelli, hypoplastic and dysmorphic cerebellum, and thickened basal meninges.[10–14] As in holoprosencephaly (HPE), these anomalies are attributable to defective or deficient mesenchyme, which presumably deprived the skull base, hindbrain, and rhombencephalon of normal inductive effects.[4] Clinical problems related specifically to the malformed hindbrain include apnea, aspiration, feeding difficulties, and recurrent respiratory infections. Prenatal closure of myelomeningoceles reportedly decreases the need for ventricular shunting, decreases hindbrain herniation, and marginally improves the level of the motor deficit compared with those patients who undergo postnatal closure of the spinal dysraphic defect.[16]

***Imaging.*** The calvarial manifestations of the Chiari II malformation include a bifid frontal bone and lückenschädel or lacunar skull. Lückenschädel is due to nonossified fibrous bone in the inner and outer tables of the skull that results in the apparent scalloping of the cranium (Fig. 31.7); the affected cranium ossifies by 6 months of age. Lückenschädel is not the result of increased intracranial pressure and is not synonymous with the beaten copper skull.

The intracranial stigmata of the Chiari II malformation are typically infratentorial and less pronounced in patients who have undergone prenatal closure of the myelomeningocele.

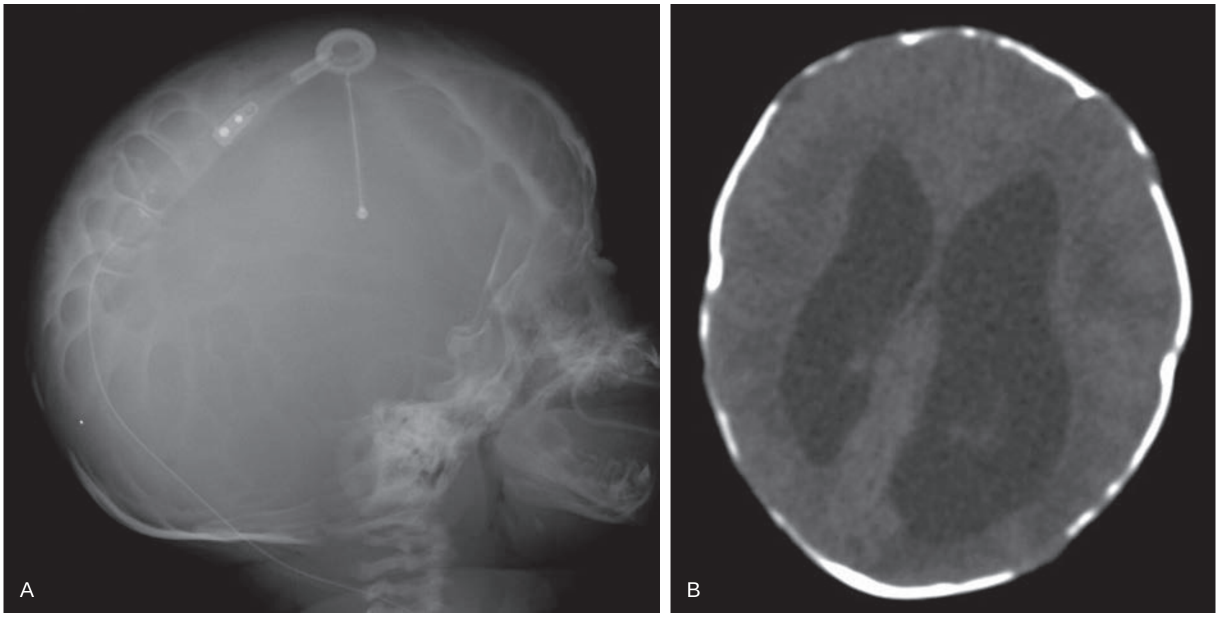

**Figure 31.7. Chiari II malformation and lückenschädel.** (A) Lateral skull radiograph shows a lacelike appearance to the cranium, which is a manifestation of mesodermal dysplasia not due to increased intracranial pressure. (B) Axial CT shows scalloping of the inner and outer tables of the calvarium.

MRI shows caudal displacement of dysplastic brainstem and hypoplastic cerebellum into the upper cervical canal with "kinking" of the cervicomedullary brainstem (Fig. 31.8). The fourth ventricle is effaced and caudally displaced. The torcula and transverse sinuses are low-lying, which presents a potential surgical hazard during decompressive suboccipital craniectomy performed for relief of symptomatic hindbrain compression. There is a "beaked" tectal plate and a variably thickened massa intermedia that may be so thick that the thalami appear virtually fused with partial atresia of the third ventricle.[6] There is an enlarged foramen magnum and constriction of the posterior cranial fossa with effacement of CSF spaces in the posterior cranial fossa; the cerebellum wraps around the ventral aspect of the brainstem, and the clivus and petrous ridges are concave. Common supratentorial abnormities include callosal dysgenesis, neuronal migration anomalies, and hydrocephalus seen in 95% of patients. After CSF diversion, the cerebral hemispheres drop away from the inner table of the skull, allowing the cortex to interdigitate across the midline under the hypoplastic falx while the superior cerebellar vermis projects upward across a widened tentorial incisura. These findings may also be seen after CSF diversion of severe congenital obstructive hydrocephalus. DTI of Chiari II malformations associated with more severe degrees of cerebellar hypoplasia show variable hypoplasia of the dorsal pontocerebellar tracts with preservation of the corticospinal tracts and medial-lateral lemniscus fibers (Fig. 31.9). The cingulum may be anomalous, crossing the midline above the corpus callosum (see Fig. 31.9).

The variants of Chiari malformations (e.g., Chiari III) are seen with high cervical/low occipital encephaloceles with variable cerebellar hypo- or aplasia. Defects of neurulation have been reported to coexist in patients with HPE; the latter malformation is considered a disorder of differentiation of the dorsal neural plate.[17] The coexistence of these malformations traditionally considered disparate in embryologic timing and insult may explained in part by mutations in genes implicated in both neural tube defects and HPE.

## DISORDERS OF DIFFERENTIATION OF DORSAL NEURAL PLATE

### Holoprosencephaly

***Clinical.*** HPE is the most common anomaly of the ventral forebrain, occurring in 1/250 embryos and 1/8300–16,000 live births.[4,18] HPE results from inductive failure of the median and paramedian structures, which are most pronounced in the ventral forebrain and declines in severity from rostral to caudal and from median to lateral.[19] HPE is due to a combination of genetic polymorphisms and environmental factors; the incidence of HPE is increased 200-fold in maternal diabetes mellitus and in prenatal retinoic acid and fetal alcohol exposure. HPE is notable for its genetic heterogeneity; at least 12 HPE loci are implicated in midline brain development.[19,20–23] Although 24% to 45% of affected live-born individuals have chromosomal abnormalities, there are no strong correlations between the type or severity of the holoprosencephalic defect and the specific mutation. Frequent facial anomalies include flattening of the nasal bridge, hypotelorism without metopic synostosis, a single central maxillary incisor, cleft lip/palate to facial clefting, and cyclopia with a central proboscis.[4,19–22] More severe facial anomalies are seen with more severe variants of HPE, whereas mild facial anomalies may occur in the absence of brain anomalies. Clinical problems include developmental delay, seizures, hypothalamic and brainstem dysfunction with swallowing problems, thermal instability and respiratory problems, pituitary dysfunction, and erratic sleeping.

***Imaging.*** There is considerable topographic variation in HPE, which is most often characterized as alobar, semilobar, or lobar.[19–22] The hallmark of HPE is incomplete separation of the forebrain, variable hypoplasia of the frontal lobes, absence of the anterior interhemispheric falx, and variable fusion of central grey nuclei with absent septum pellucidum.

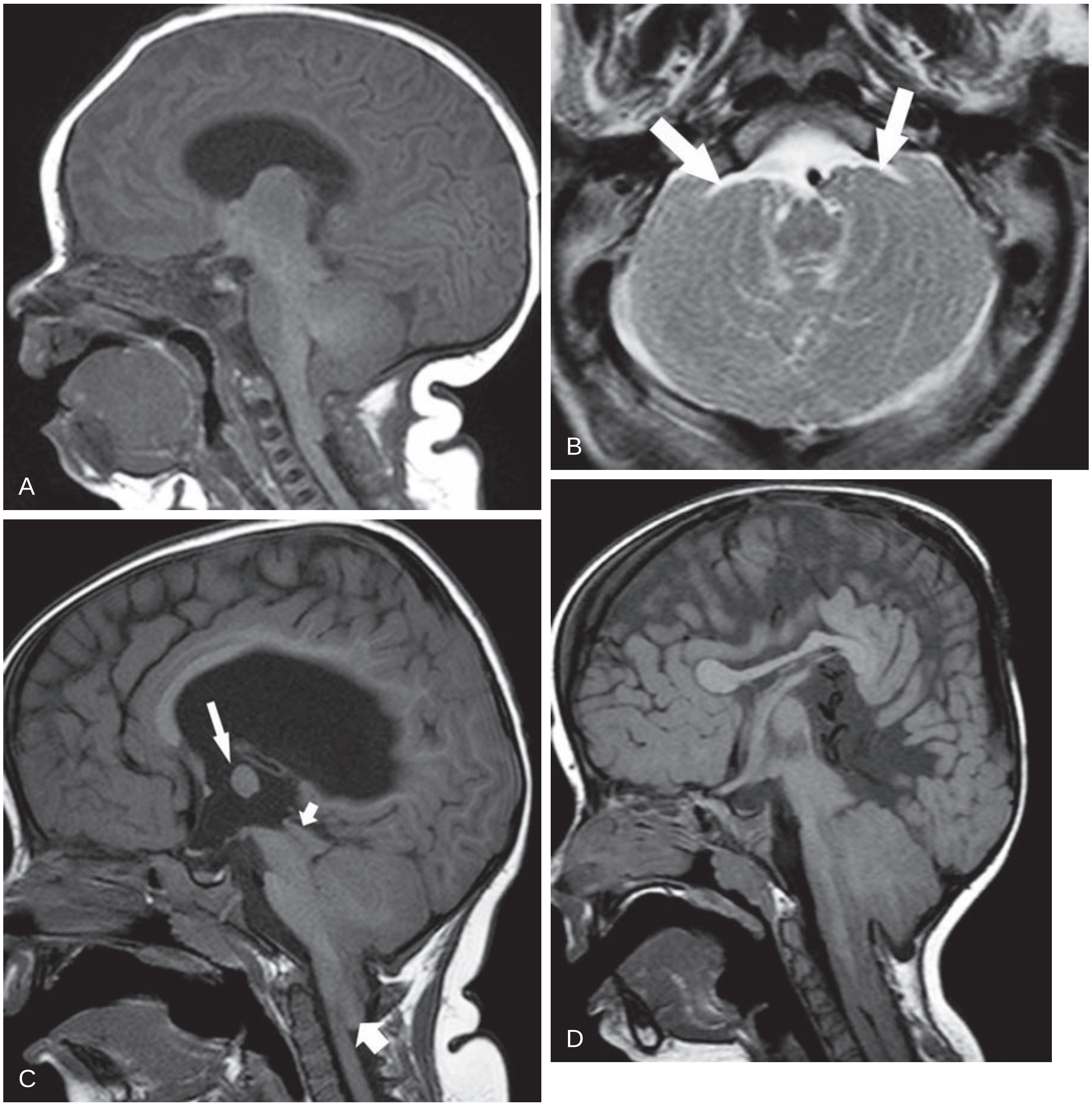

**Figure 31.8. Chiari II malformation.** (A) Neonate with Chiari II malformation. Sagittal T1-weighted MR image shows that the fourth ventricle is caudally displaced and effaced. The posterior cranial fossa is small. There is herniation of hindbrain into the upper cervical canal. (B) Axial T2-weighted MR image through the posterior fossa shows cerebellar tissue wrapping around the brainstem *(arrows)*. (C) Sagittal T1-weighted MR image in another patient shows the cerebellum and brainstem are more hypoplastic and the tectal plate *(small arrow)* is beaked. Note the large massa intermedia *(large arrow)* and the hydrocephalus. Hindbrain herniation is at the C2 level *(thick arrow)*. (D) Sagittal T1-weighted MR image shows a hypoplastic brainstem with absence of the ventral pons. The cerebellum is small, dysplastic, and caudally herniated. The fourth ventricle is not apparent.

## Alobar Holoprosencephaly

In this most severe form of HPE, there is complete lack of separation between the cerebral hemispheres with absence of the falx. The corpus callosum and septum pellucidum are absent, the central grey nuclei are fused, and the rudimentary single ventricle has a "U" configuration that may communicate with a dorsal cyst (Fig. 31.10A).[20–22]

## Semilobar Holoprosencephaly

There is relative preservation of the lateral and posterior cerebrum and the splenium (Fig. 31.10B-D). The posterior interhemispheric fissure and falx are present while the hypoplastic frontal lobe is undivided.[4,20–22] Frontal lobe hypoplasia results in the anterior position of the Sylvian fissures, termed a *wide Sylvian angle*.[23] The globus pallidi are absent or hypoplastic, and the caudate nuclei are fused, resulting in obliteration of or lack of formation of the septal region. The posterior limbs of the internal capsules are ventral to partially or totally fused thalami.[24] The hippocampus is virtually always present, although usually incompletely or abnormally developed. There may be a dorsal cyst. DTI shows fornices imbedded in dysplastic thalami and bands of anomalous white matter crossing the forebrain.[25]

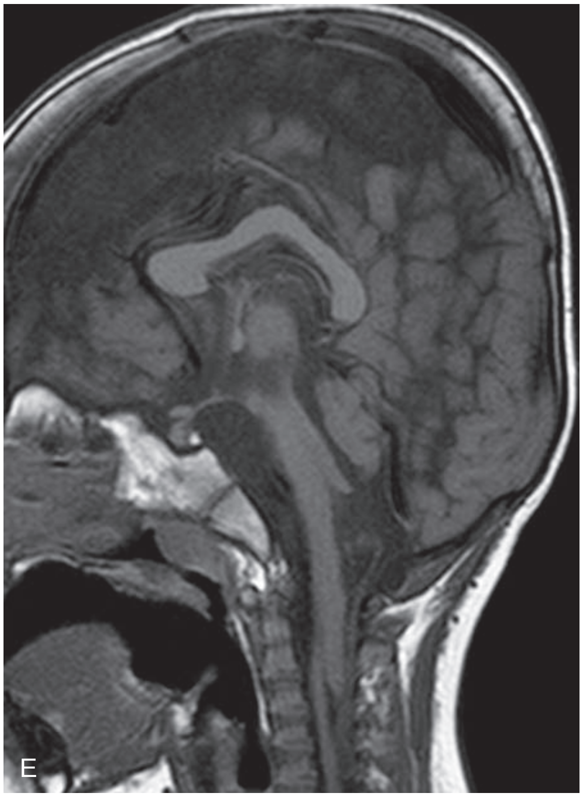

**Figure 31.8, cont'd.** (E) Sagittal T1-weighted MR image shows aplasia of the cerebellar hemispheres, sometimes referred to as *Chiari IV malformation*. This entity is probably best described as Chiari II malformation with cerebellar aplasia.

## Lobar Holoprosencephaly

In this mildest form of HPE, there is hypoplasia of the frontal poles, agenesis of the septal pellucidum, and incomplete separation of the basal forebrain, which is best depicted with high resolution coronal images (Fig. 31.11). The posterior frontal, parietal, and occipital lobes are more normally formed.[4,20–22] The callosal body and splenium are preserved.

## Syntelencephaly (Middle Frontal Variant)

The middle frontal variant is an unusual variant of lobar HPE characterized by separation of the frontal and occipital poles, fusion of the middle portions of the cerebral hemispheres (Fig. 31.12), preservation of portions of the commissural fibers of the corpus callosum, and neuronal migration anomalies; thalamic fusion is variable.[26,27]

## Septo-optic Dysplasia

***Clinical.*** Septo-optic dysplasia (SOD) is considered along the continuum of disorders of ventral forebrain differentiation.[4] Patients typically present in early childhood with nystagmus, optic nerve atrophy, short stature due to growth hormone deficiency, or panhypopituitarism with or without diabetes insipidus. Affected patients are at risk for Addisonian crisis due to subclinical adrenal insufficiency, which may become clinically apparent only during illness or severe stress. Most cases of isolated SOD are sporadic.

***Imaging.*** SOD is characterized by absence of the septum pellucidum and variable optic nerve hypoplasia (Fig. 31.13). The neurohypophysis may be ectopic and the pituitary stalk may be interrupted. However, agenesis of the septum pellucidum may be isolated with normal optic pathways and intact neuroendocrine function. Absence of the septal leaves results in downward displacement of the fornices into the third ventricle. SOD is seen in multiple malformations such as schizencephaly, neuronal migration anomalies, and neural tube defects.

## Corpus Callosal Agenesis/Dysgenesis

***Clinical.*** Agenesis of the corpus callosum (ACC), one of the most common central nervous system (CNS) malformations (0.5–70/10,000 live births), is genetically and phenotypically heterogeneous with clinical phenotype dependent on coexistent malformations and numerous chromosomal abnormalities and syndromes.[4,28] Affected patients have variable developmental delay, including speech, problems with vision and feeding, and seizures.[28]

Formation of the corpus callosum begins around 6 weeks' gestation, with initial axonal crossing around 11 to 12 weeks' gestation, and completion of callosal formation around 18 to 20 weeks. The first axons to cross the midline arise from neurons destined for the cingulate cortex and provide a path for subsequent migrating callosal axons arising elsewhere in the developing neocortex.[4,5,28–30] The crossing axons are controlled by the glial wedge composed of radial glial cells that geographically limits the passage of axons and then repel the axons away from the midline by expressing molecular guidance cues.[1,4,5,29] Other embryonic structures important in callosal formation include the indusium griseum above the callosal body and the subcallosal sling.[28] After crossing the midline, callosal axons grow into the contralateral hemisphere; their ultimate destination mirrors their region of origin and the cortical layer of the parent neuron.[28–30] Many of the crossing callosal axons undergo programmed cell death after reaching their final destination, which starts during the second trimester with postnatal pruning of axonal axons.[1,28] When the axons fail to cross the midline and remain in their hemisphere of origin, the misrouted callosal axons may course along the medial aspect of the lateral ventricle forming the longitudinal callosal bundles of Probst.[4,31,32] Alternately, aberrant axons may project to the contralateral hemisphere across a rudimentary callosal genu as nonhomotopic fibers.[33] Patients with isolated ACC and well-developed Probst bundles may be developmentally intact and processing deficits detected only with neurocognitive assessment.[34]

***Imaging.*** The anterior commissure (AC) is a variably sized tract embedded in the cranial aspect of the lamina terminalis, which demarcates the anterior wall of the third ventricle and may be enlarged, normal, or small in ACC. The hippocampal commissure is a thin sheet of white matter connecting the fornices, which is not routinely visualized on MRI of the normal brain. Absence of the corpus callosum, AC, and hippocampal commissure is described as "complete commissural agenesis" (Fig. 31.14).[4,31,32] Preservation of the AC in the absence of the corpus callosum and hippocampal commissure is "calloso-hippocampal agenesis," whereas the anterior and hippocampal commissures may be preserved, resulting in "isolated callosal agenesis." Calloso-hippocampal agenesis is the most common malformation, although it might be argued these classifications are somewhat academic. By MRI, the sulci over the mesial surface of the frontal lobes have a radial configuration and the lateral ventricles have a characteristic parallel orientation. Absence of the temporal segments of the cingulum results in dilatation of the temporal horns while hypoplasia of association fibers connecting the occipital and temporal lobe allows dilatation of trigones of the lateral ventricles, referred to as *colpocephaly*. Callosal agenesis may be associated with interhemispheric diencephalic pseudocyst (e.g. high-riding third ventricle) or interhemispheric cysts that do not communicate with the ventricles. In patients with a rudimentary callosal genu, diffusion tractography shows the nonhomotopic aberrant callosal connections described as "asymmetric sigmoid

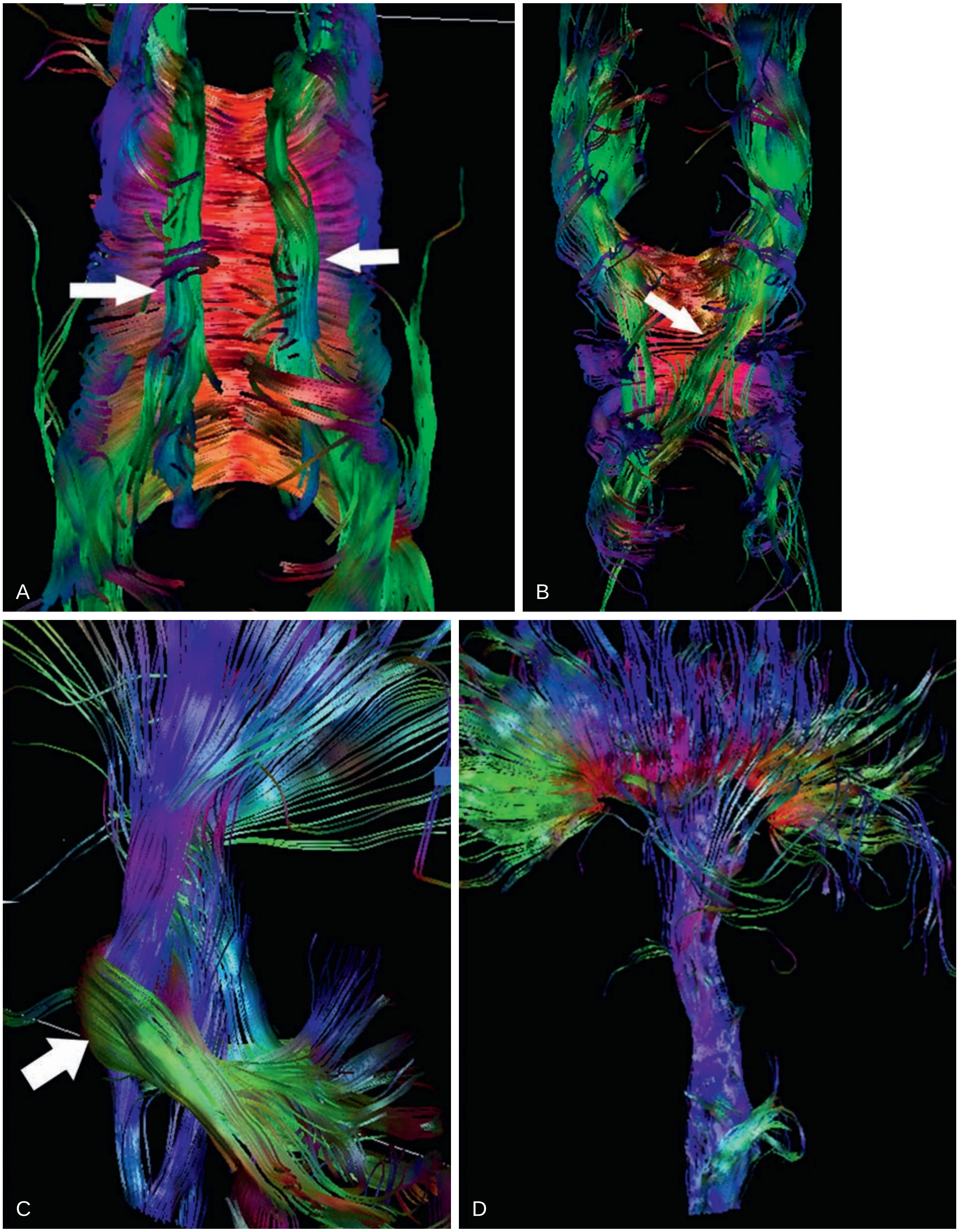

**Figure 31.9. Diffusion tensor imaging in Chiari II malformation.** (A) Diffusion tractography from a normal patient shows paired association fibers forming the cingulum *(arrows)* above the corpus callosum. The green orientation indicates the fibers are oriented back-front. By definition, association fibers do not cross the midline. (B) In a patient with Chiari II malformation, diffusion tractography shows the left cingulum is deficient and there are anomalous supracallosal fibers *(arrow)*. (C) Normal pontocerebellar tracts *(arrow)* in a normal patient. (D) Absence of the middle cerebellar peduncles and pontocerebellar tracts in patient illustrated in Fig. 31.8D.

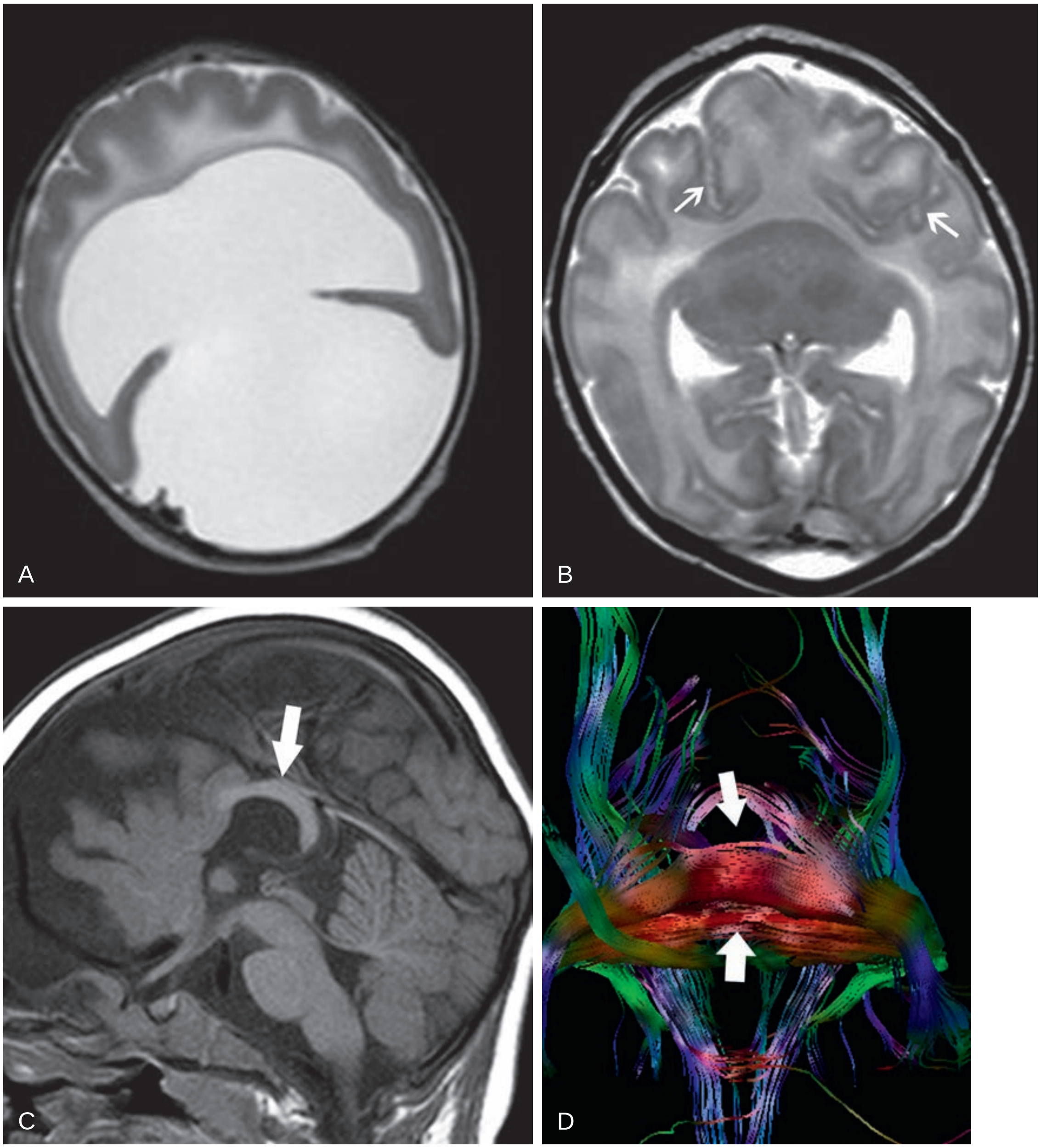

**Figure 31.10. Holoprosencephaly (HPE).** (A) Alobar HPE. Axial T2-weighted MR image shows a monoventricle with a large dorsal cyst. Note absence of an interhemispheric fissure and falx. (B) Semilobar HPE. Axial T2-weighted MR image shows the Sylvian fissures *(arrow)* are more anterior displaced in another patient with more severe frontal lobe hypoplasia. (C) Sagittal T1-weighted MR image shows underdeveloped frontal lobes. The splenium *(arrow)* is formed. (D) DTI of semilobar HPE. Tractography viewed in the coronal plane shows bands of anomalous white matter *(arrows)* crossing the midline.

bundles" and have also been reported in patients with aberrantly shaped corpus callosum.[33]

Callosal agenesis may be isolated or associated with aqueductal stenosis, Chiari II malformations, and malformations of cortical development (MCD), brainstem, and cerebellum.[31,32] There are numerous syndromes associated with complete or partial ACC. Aicardi syndrome is a rare sporadic X-linked dominant malformation seen in females characterized by callosal agenesis, interhemispheric neuroepithelial cysts, and MCD (Fig. 31.15); affected males have Klinefelter syndrome (47,XXY). Ocular abnormalities include chorioretinal lacunae and coloboma; the cerebellum may be malformed. CRASH syndrome (corpus callosum agenesis, retardation, adducted thumbs, spastic paraplegia, and hydrocephalus) is caused by mutations in the L1 cell adhesion molecule gene that codes for a transmembrane cell adhesion protein involved in axonal migration.[4]

## Callosal Hypoplasia/Hyperplasia

The corpus callosum may be incompletely formed, diffusely hypoplastic, or segmentally deficient (e-Fig. 31.16). Partial callosal agenesis is usually characterized by absence of the splenium and dorsal body with relative preservation of the genu and rostral body, although the reverse may be seen. Diffuse callosal hypoplasia

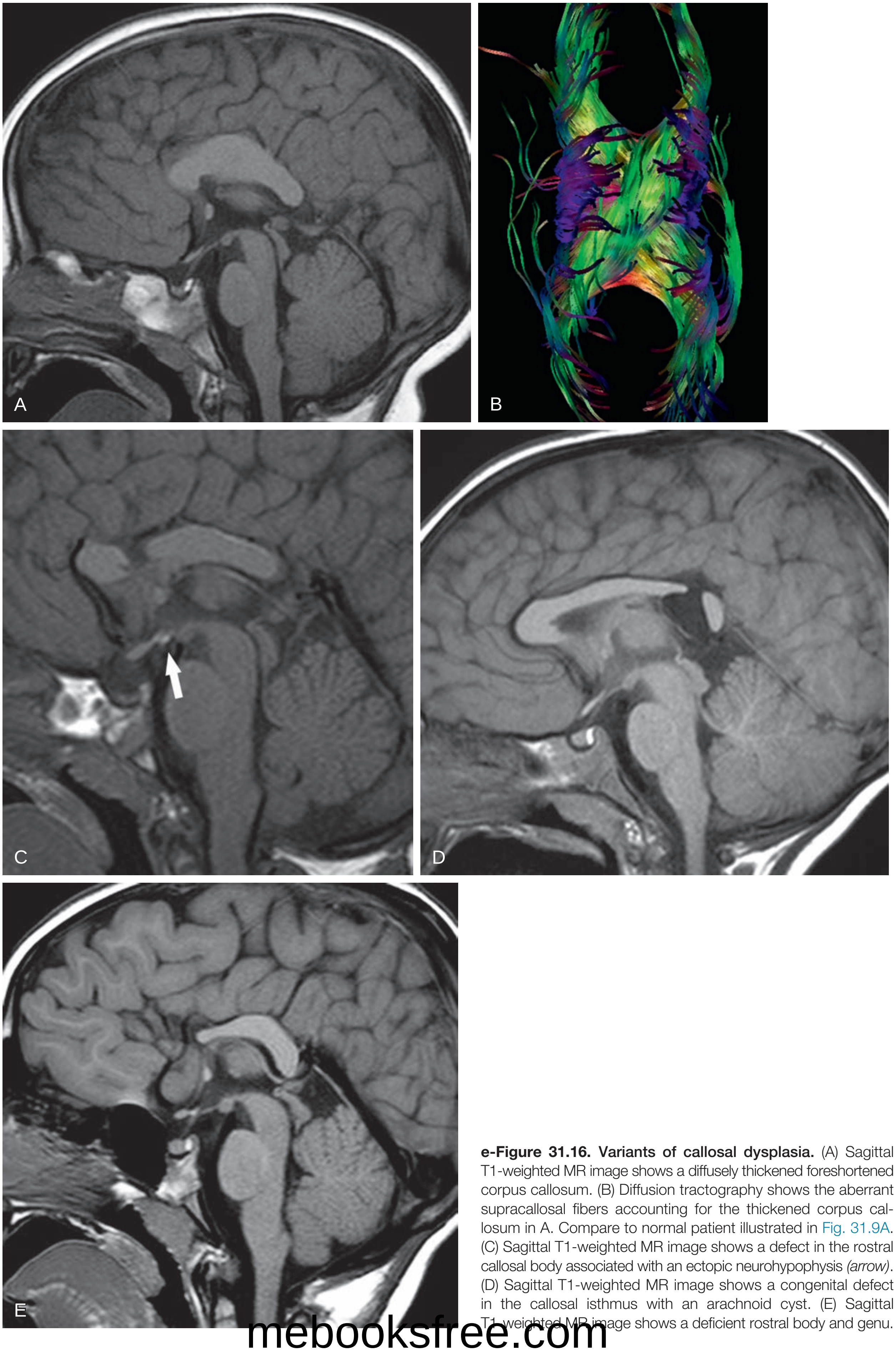

**e-Figure 31.16. Variants of callosal dysplasia.** (A) Sagittal T1-weighted MR image shows a diffusely thickened foreshortened corpus callosum. (B) Diffusion tractography shows the aberrant supracallosal fibers accounting for the thickened corpus callosum in A. Compare to normal patient illustrated in Fig. 31.9A. (C) Sagittal T1-weighted MR image shows a defect in the rostral callosal body associated with an ectopic neurohypophysis *(arrow)*. (D) Sagittal T1-weighted MR image shows a congenital defect in the callosal isthmus with an arachnoid cyst. (E) Sagittal T1-weighted MR image shows a deficient rostral body and genu.

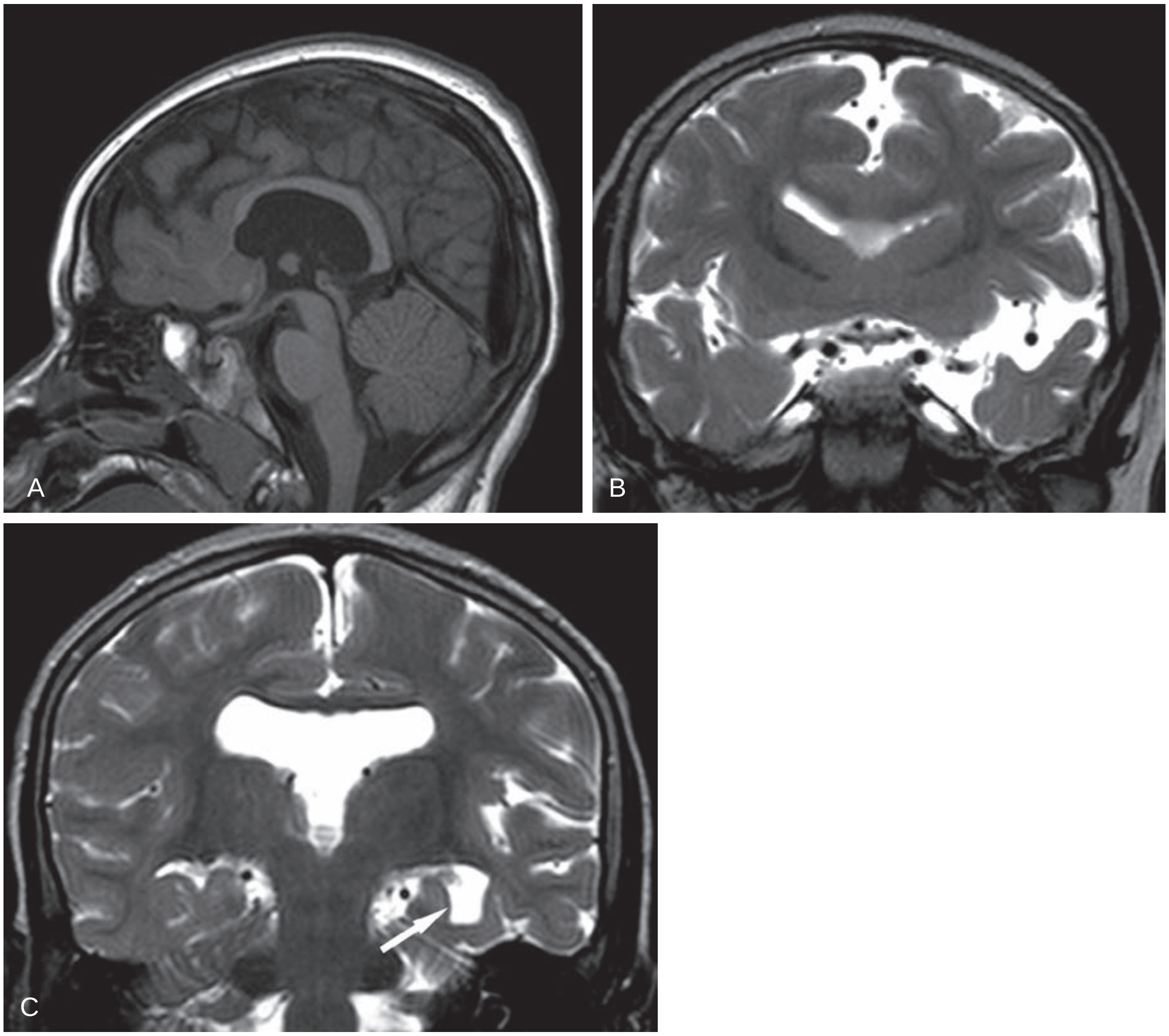

**Figure 31.11. Lobar holoprosencephaly.** (A) Sagittal T1-weighted MR image shows that the callosal rostrum and genu are deficient. (B) Coronal T2-weighted image shows a lack of separation of basal forebrain and caudate nuclei. (C) Coronal T2-weighted MR image shows that the septal leaves are absent. The hippocampi are globular with lateral insertion of the forniceal fimbria *(arrow)* onto the dysplastic hippocampus.

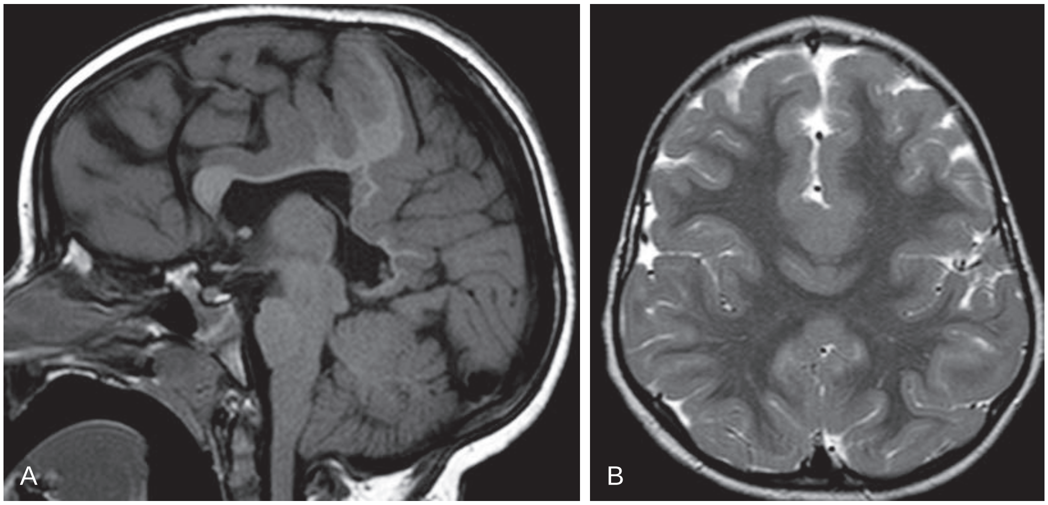

**Figure 31.12. Syntelencephaly (middle frontal variant of holoprosencephaly).** (A) Sagittal T1-weighted MR image shows the callosal genu is formed; the callosal body appears formed but is hypoplastic. There is partial fusion of the frontal lobes. (B) Axial T2-weighted MR image shows fusion of cortex and white matter in the middle frontal region. The anterior and posterior interhemispheric fissures are well developed.

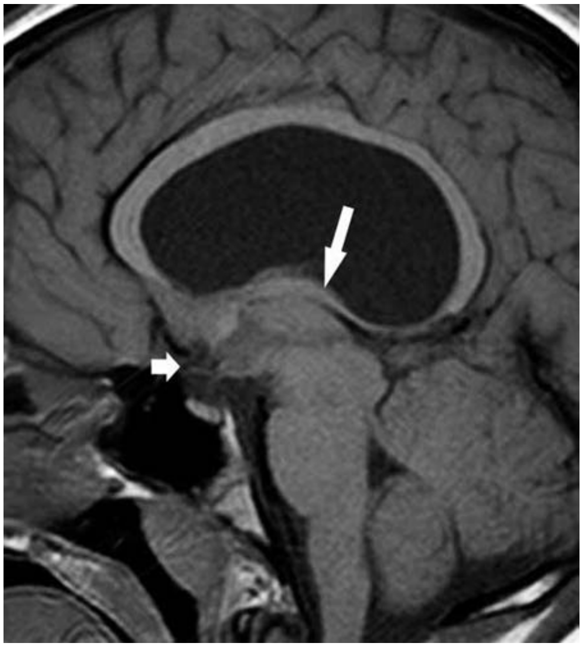

**Figure 31.13. Septo-optic dysplasia with agenesis of the septum pellucidum.** Sagittal T1-weighted MR image shows that fornices are inferiorly positioned *(arrow)*. The optic apparatus is hypoplastic *(short arrow)*; there is no identifiable neurohypophysis.

is characterized by diffuse thinning, while segmental callosal hypoplasia involves an intermediate portion of the corpus callosum. The segmental defects may result from a secondary callosal destruction or injury to regional white matter. Callosal hyperplasia may be diffuse, as seen in neurofibromatosis type 1, or limited to the midcallosal body, in which case the corpus callosal is often foreshortened. DTI of the congenitally thickened corpus callosum often shows anomalous longitudinal supracallosal fibers that represent misrouted callosal axons.[34]

Callosal lipomas are rare and are thought to result from abnormal differentiation of pluri-potential mesenchymal tissue.[4] Most of cases are associated with agenesis or incomplete formation of the corpus callosum. Anterior lipomas are more common than posterior. The lipoma itself is an incidental finding and may be seen with a fully formed corpus callosum.

## Primary Microcephaly

There are more than 400 phenotypes associated with microcephaly, discussion of which is beyond the scope of this chapter. Primary nonsyndromic microcephaly is autosomal recessive and genetically diverse. Genes implicated in primary microcephaly affect the centrosomes, centrioles, and spindle fibers of neuronal precursors adversely affecting neuronal proliferation and migration; the net result is diffuse thinning of the cerebral cortex.[35,36] Seizure disorders are uncommon; 15% of patients have normal neurodevelopmental outcomes.

MR may show a small, otherwise normal brain or diffuse undersulcation. DTI may show unsuspected anomalous white matter tracts, suggesting axonal migration defects in addition to defective neuronal proliferation and migration.

## Brain Overgrowth Syndromes (Megalencephaly)

***Clinical.*** Brain overgrowth may be diffuse or focal. Diffuse megalencephaly may be isolated or associated with polymicrogyria (PMG) and ventriculomegaly.[2,36] Megalencephaly is associated with gene mutations affecting protein products in the mammalian target of Rapamycin (mTOR) pathways, which regulate cell metabolism, growth, proliferation, and survival and are implicated in tuberous sclerosis and refractory epilepsy.[36–38] Hemimegalencephaly reflects focal megalencephaly with somatic mutations affecting only the dysmorphic overgrown tissues. Hemimegalencephaly may be isolated or associated with neurocutaneous syndromes such as epidermal nevus syndrome, Proteus syndrome, unilateral hypomelanosis of Ito, neurofibromatosis type I, Klippel-Trenaunay syndrome, and tuberous sclerosis.[36–38] Hemispherectomy may be required for relief of severe intractable epilepsy.

***Imaging.*** MRI of diffuse megalencephaly shows diffuse enlargement of the cerebrum and cerebellum with crowding of the posterior cranial fossa and secondary tonsillar herniation; there may be PMG (e-Fig. 31.17)

MRI of hemimegalencephaly shows diffusely enlarged hemisphere or lobe (Fig. 31.18) with abnormal sulcation pattern that may include PMG, agyria, and grey matter heterotopias. The regional white matter is thickened and gliotic. A hallmark is enlargement of the ipsilateral ventricle, which becomes more pronounced with age, with expansion of the overlaying hemicranium; the affected occipital lobe bulges across the midline. Lobar brain overgrowth may be subtle in the neonatal period. DTI shows anomalous white matter tracts that will be transected during hemispherotomy.

## Encephaloclastic/Destructive Lesions

Hydranencephaly describes near complete to total absence of the cerebral hemispheres with preservation of the brainstem, central grey nuclei, and cerebellum, and is thought to be due to intrauterine ischemic insult.[4] There may be remnants of the inferior frontal, anterior temporal, or occipital lobes (Fig. 31.19). Affected patients appear neurologically normal at birth due to the intact brainstem.

The differential diagnosis of hydranencephaly is aqueductal stenosis with severe hydrocephalus. In the latter conditions, CSF diversion results in variable reexpansion of the cerebral cortex, whereas shunt placement in patients with hydranencephaly serves to prevent progressive massive macrocephaly but does not affect the appearance of the rudimentary cerebral cortex. Other encephaloclastic lesions include porencephaly, which are CSF-containing spaces that usually communicate with the ventricular system. Porencephaly may occur from intrauterine vascular insult, trauma, infection, and nontraumatic hemorrhage. Unlike schizencephalic defects, porencephalic defects are not lined with dysplastic grey matter.

## MALFORMATIONS OF CORTICAL DEVELOPMENT

These malformations include a wide spectrum of developmental malformations of the cortex caused by disruption of neuronal cell proliferation, migration, and/or organization.[2,4,39] Neuronal proliferation commences in the germinal matrix along the subependymal layer of the walls of the lateral ventricles at 7 to 8 weeks' postconception.[2–4] The radial glia in the ventricular zone function as progenitor cells and also provide scaffolding on which the neurons migrate in waves out to the cortical plate.[2–4] Neurons in cortical layer VI are the first to reach the cortex followed by those destined for layers V, IV, III, etc. in an "inside-out" sequence. The trailing processes of the migrating neurons form the axons, which migrate away from the parent neuron toward their final destinations concurrent with the ventriculofugal migration of the parent neurons. Neuronal migration and axonal path finding are driven by complex molecular signaling controlled by genes that switch the signaling molecules on and off.[2,38,39] At the completion of migration, the cortex becomes organized with synaptic contacts developing between neurons throughout the six-layered cortex. Disruptions of neuronal proliferation,

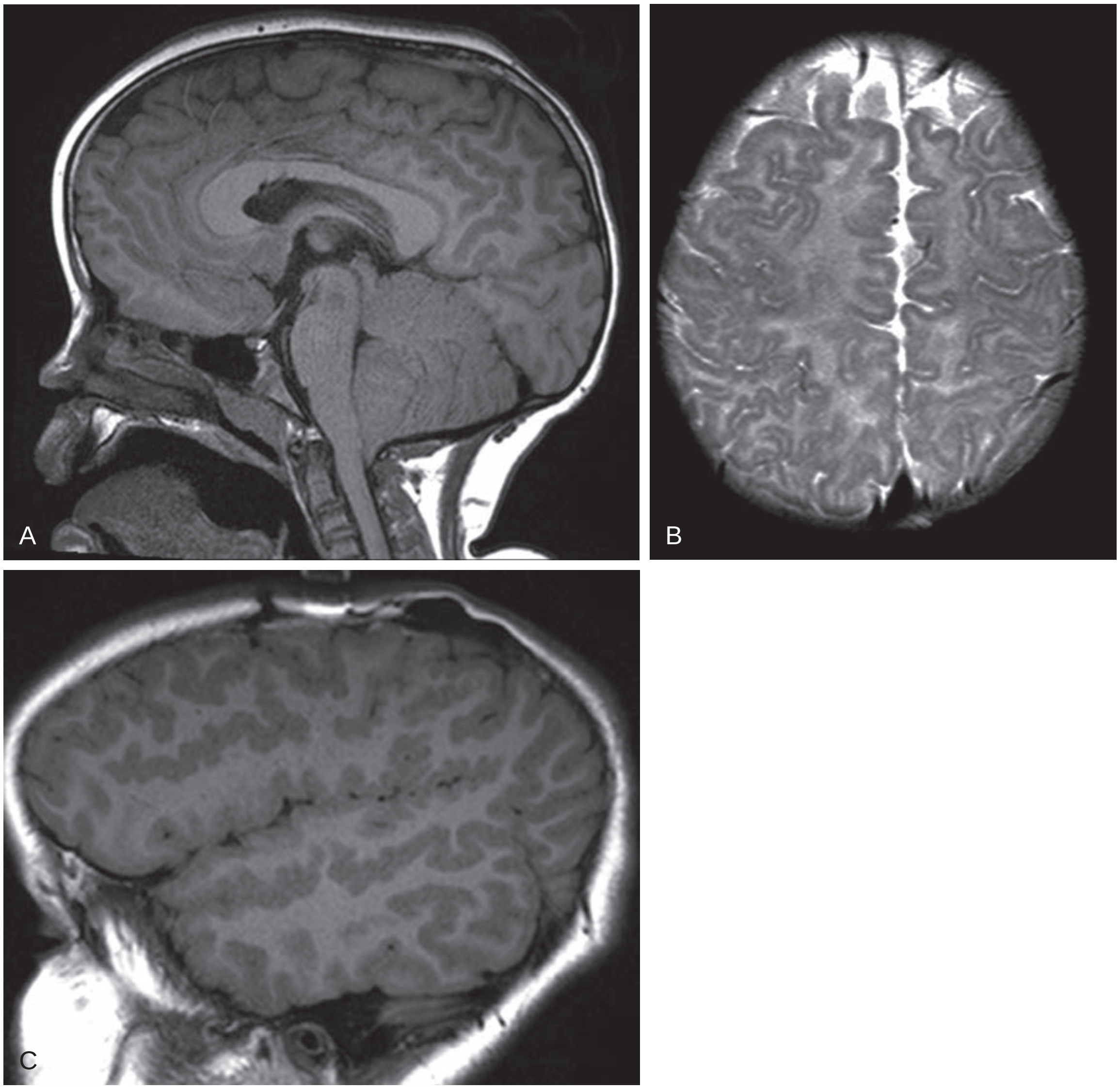

**e-Figure 31.17. Diffuse megalencephaly.** (A) Sagittal T1-weighted MR image shows a diffusely enlarged cerebrum and cerebellum with secondary tonsillar herniation. (B) Axial T2 image shows asymmetric polymicrogyria. (C) Parasagittal T1 image shows extensive polymicrogyria.

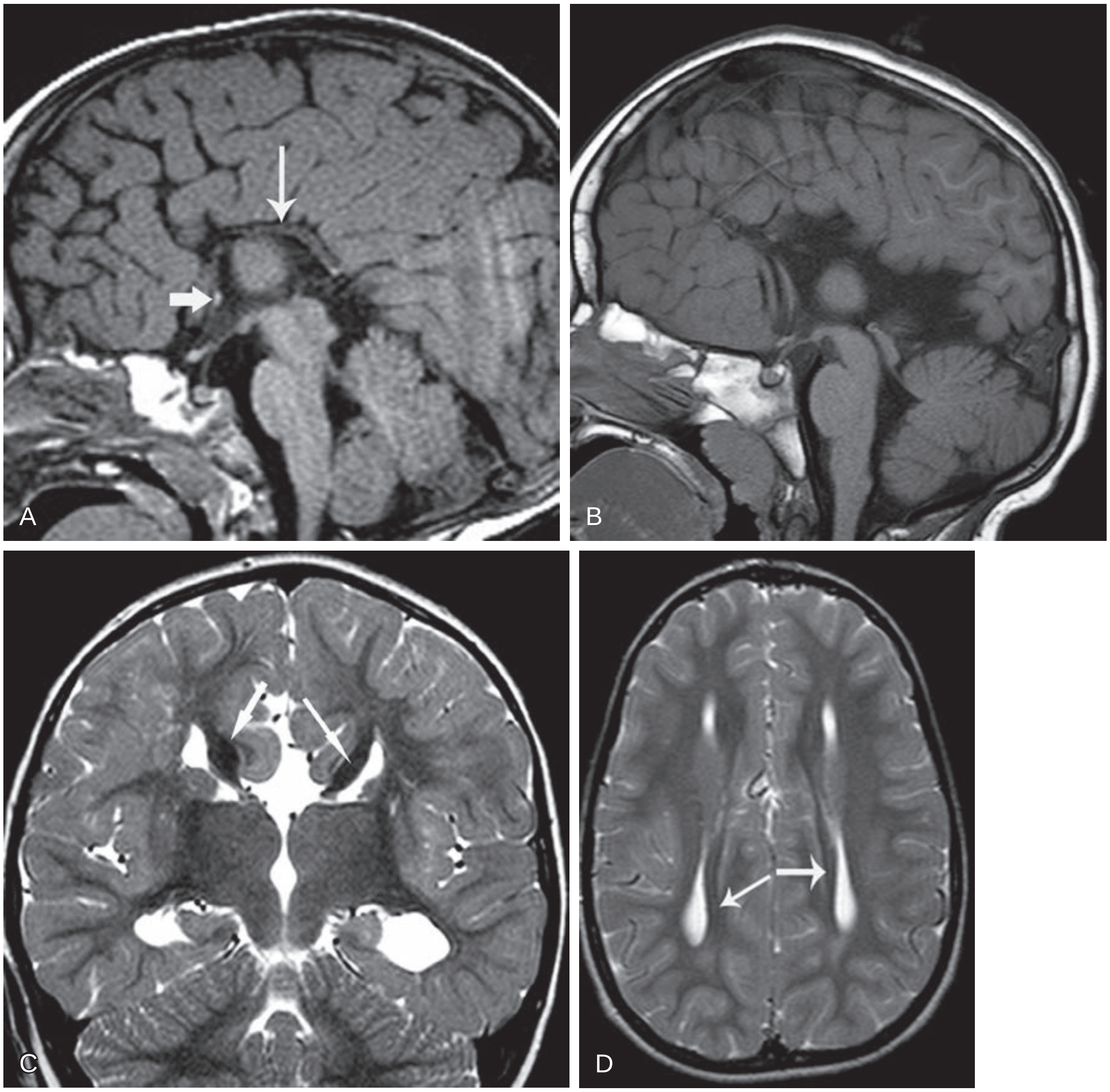

**Figure 31.14. Variants of corpus callosal agenesis.** (A) Sagittal T1-weighted MR image shows callosal agenesis with preservation of the anterior and hippocampal commissures. There is a thin midline commissural structure *(arrows)*, which represents the hippocampal commissure rather than a severely hypoplastic corpus callosum. (B) Sagittal T1-weighted MR image shows that the anterior and hippocampal commissures are also absent. (C) Coronal T2-weighted MR image shows the bundles of Probst *(arrows)* along the medial walls of the lateral ventricles. (D) Axial T2-weighted MR image shows that the ventricles have a characteristic parallel orientation in callosal agenesis. The variable enlargement of the ventricles is due to lack of regional white matter rather than to hydrocephalus. Note Probst bundles *(arrows)* along the lateral ventricles.

migration, and organization can result from infections (e.g., TORCH, Zika[39,40]), intrauterine ischemic insults, toxins, radiation exposure, genetic anomalies, and without known cause.[4] Affected patients have seizures, developmental delay, and variable focal neurologic deficits.

Based on advances in the understanding of cortical development, an updated classification has been proposed for MCD.[2]

- Group I: Malformations secondary to abnormal neuronal and glial proliferation or apoptosis, which includes microcephaly and diffuse megalencephalies, some forms of focal cortical dysplasia (FCD), and tuberous sclerosis complex.
- Group II: Malformations secondary to abnormal neuronal migration, which includes periventricular heterotopia, the various complete and incomplete lissencephalies, subcortical heterotopia, and the cobblestone lissencephalies.
- Group III: Malformations secondary to abnormal postmigrational development, which includes PMG, schizencephaly, some forms of FCD, and microcephaly.

## Microlissencephaly

***Clinical.*** Unlike lissencephaly, patients with microlissencephaly have severe microcephaly (<3 SD) at birth often with dysmorphic craniofacial features, abnormal genitalia, and arthrogryposis.[4] Developmental delay is pervasive and profound with accompanying epilepsy. Mode of inheritance is thought to be autosomal recessive, related in some patients to the *RELN* gene. Mutations in ACTG1, a cytoplasmic

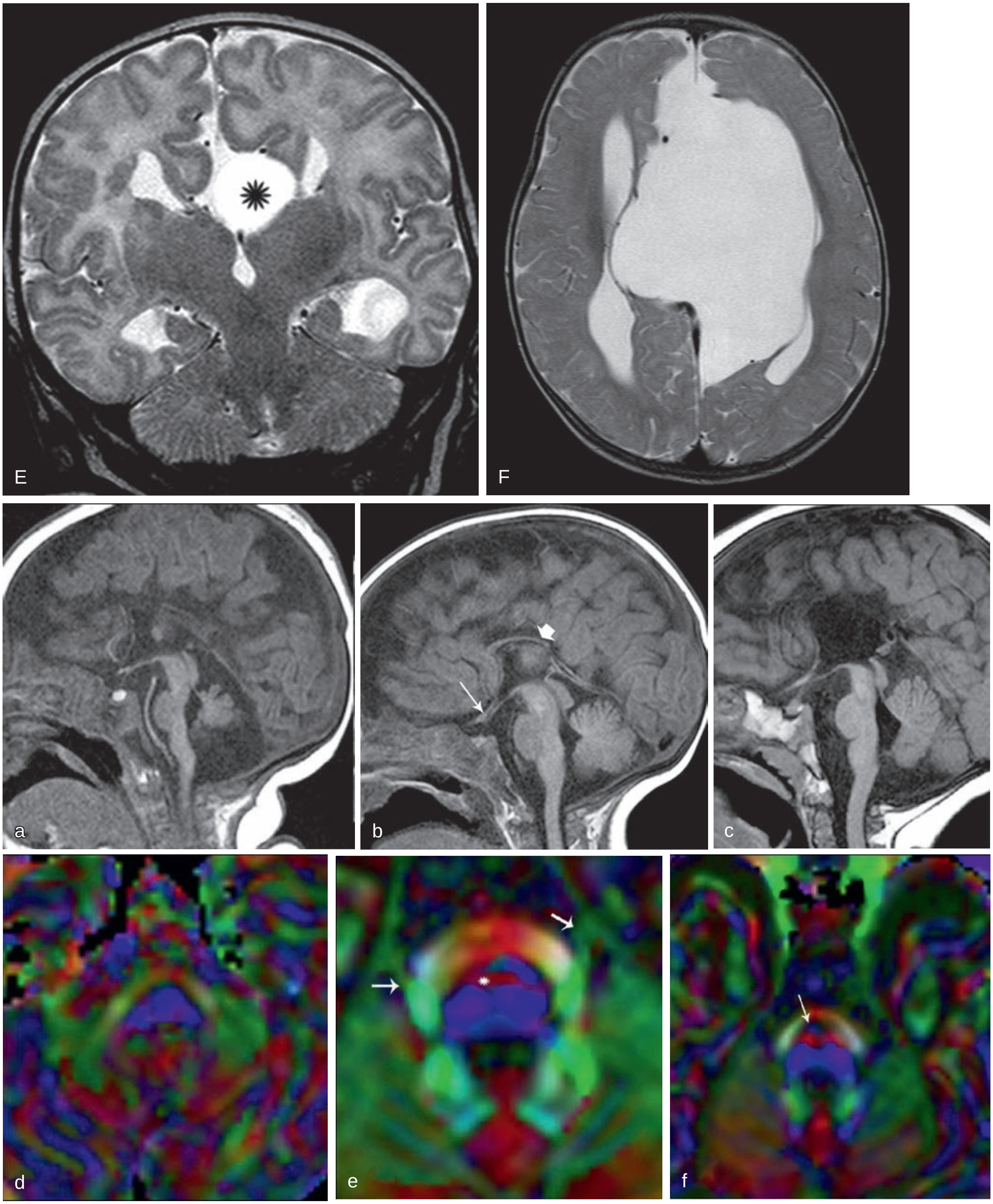

**e-Figure 31.14.** (E) Coronal T2-weighted MR image shows a small interhemispheric cyst *(asterisk)* versus high-riding third ventricle. (F) Axial T2-weighted MR image shows a large interhemispheric cyst in ACC. Patient is developmentally normal. (G) Composite of pontine anomalies by DTI in ACC. a, d; pontocerebellar dysplasia with a single ventral pontocerebellar tract. b, e; persistent hippocampal commissure *(short arrow)* and optic pathway *(arrow)* hypoplasia, with hyperplastic ventral pontocerebellar tract, hypoplastic dorsal pontocerebellar tract *(asterisk)*, and dislocated hypoplastic corticospinal tracts. *Arrows* indicate Vth nerves. c, f; ACC with a single hypoplastic corticospinal tract *(arrow)*. Patients b and c had absent gag and respiratory drive.

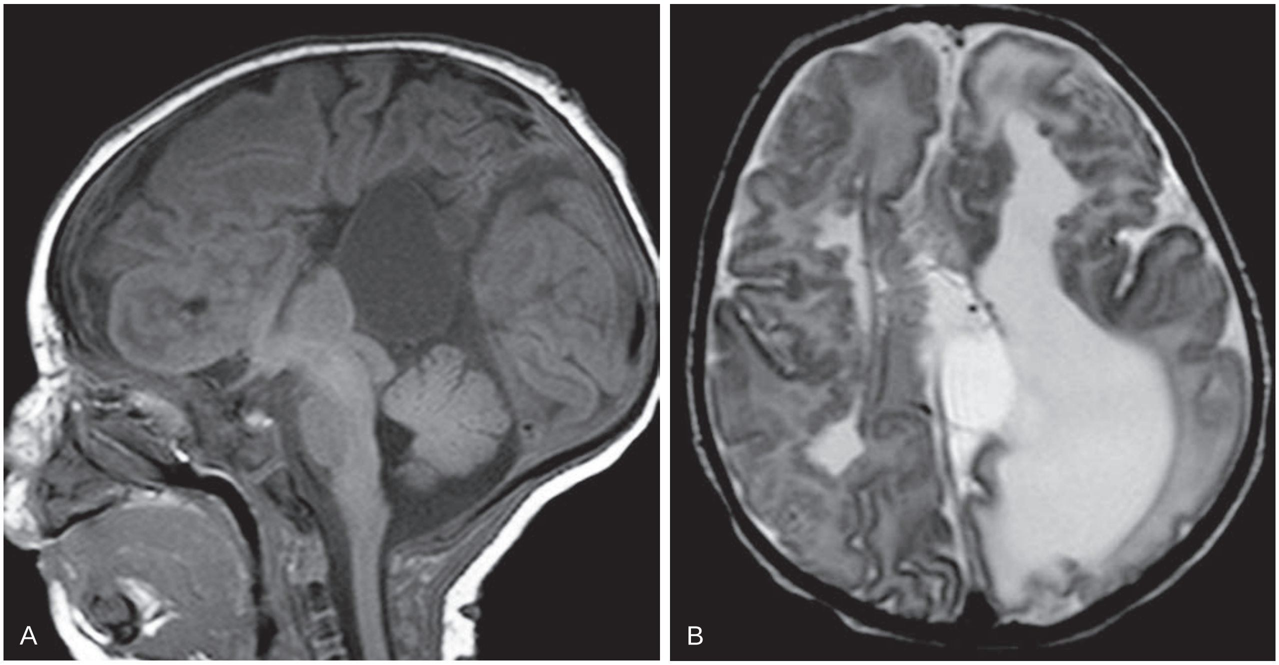

**Figure 31.15. Aicardi syndrome.** (A) Sagittal T1-weighted MR image shows callosal agenesis with an interhemispheric cyst. (B) Axial T2-weighted MR image shows extensive asymmetric cortical dysplasia, interhemispheric cyst, and asymmetric ventriculomegaly.

actin, are implicated in Baraitser-Winter syndrome characterized by microlissencephaly and distinctive facies in addition to congenital nonsyndromic neurosensory hearing loss.[40,41] Prenatal infections causing microlissencephaly include cytomegalovirus (CMV) and Zika.[42,43]

***Imaging.*** MRI shows diffuse cortical thinning with agyria-pachygyria and/or PMG (Fig. 31.20) and variable hypoplasia of the corpus callosum, brainstem, and cerebellum. Imaging abnormalities in congenital Zika infection include microlissencephaly with cortical-subcortical dystrophic calcifications, pachygyria and PMG, and ex vacuo ventriculomegaly often with cerebellar hypoplasia.[43] The calvarium is collapsed around the atrophic brain; there may be a prominent occipital ridge.[43]

## Focal Cortical Dysplasia (FCD)

***Clinical.*** FCD is probably caused by mutations in multiple genes but is not associated with a known single genetic mutation.[2,44,45] The histologic hallmark of FCD is lack of normal cortical lamination. FCD is classified into types I, II, and more recently type III, based on cortical laminar structure, cytoarchitectural disruption, cell composition, and the presence of associated destructive brain lesions.[44] Type I FCD has alterations in cortical layering, with distortion of the normal radial cortical lamination and lack of the normal six-layered neocortex, but by definition, type I FCD has no balloon cells. Type II FCD is characterized by cortical dyslamination and dysmorphic neurons without or with balloon cells and is considered a malformation resulting from abnormal proliferation.[2] Type III FCD is found in association with encephaloclastic lesions such as traumatic brain injury, perinatal ischemia, Rasmussen encephalitis, or low-grade tumors and is considered a malformation resulting from abnormal postmigrational development reflecting cortical injury during later stages of cortical development.[2,44] FCD presents as medication-resistant focal epilepsy and/or variable cognitive impairment.[44,45]

***Imaging.*** Even with high-resolution MRI and knowledge of the seizure semiology, FCD may not be detected. The most common histopathologic finding in surgical specimens removed for cryptogenic epilepsy (e.g., no lesion is identifiable by imaging) is type I FCD.[44] Findings of type I FCD include focal cortical thickening often within the depth of a sulcus and blurring of the gray–white junction. MRI of type II FCD may show focal thickening of cortex with regional subcortical increased signal on T2-weighted and FLAIR sequences viewed with using narrow tissue contrast windowing (Fig. 31.21). There may be radial extension of balloon cells and ectopic neurons into the deep white matter (e.g., "transmantle sign" of FCD), which may be the sole visible evidence of FCD.[44] The differential diagnosis of type II FCD is low-grade tumor. Although type II FCD can be suggested on the basis of MR findings, there is overlap in imaging findings between type I and II, and the ultimate diagnosis is based on histopathology.[44]

## Grey Matter Heterotopias

***Clinical.*** Grey matter heterotopias include periventricular nodular heterotopias (PNH), subcortical heterotopia, and subcortical band heterotopia. PNH results from mutations in the genes that code for proteins involved in neuronal migration including the *FLNA* gene on Xq28.[2,44,45] These nodular masses of normal neurons and glial cells devoid of laminar organization are intrinsically epileptogenic; seizures result from hyperexcitable circuitries between the ectopic neurons and the overlaying cortex and may not manifest until adolescence.[2,44–46] More severe and generalized seizure activity and cognitive delay are seen with bilateral PNH.

***Imaging.*** MRI of PNH shows variable-sized nodules in the subependymal periventricular white matter (Fig. 31.22) with the same signal intensity as cortex.

## Polymicrogyria

***Clinical.*** PMG results from disruption of normal terminal neuronal migration and organization and is defined by excessive convolutions of the cerebral cortex.[47–51] PMG is seen in conjunction with inborn errors of metabolism (e.g., cobblestone lissencephaly,

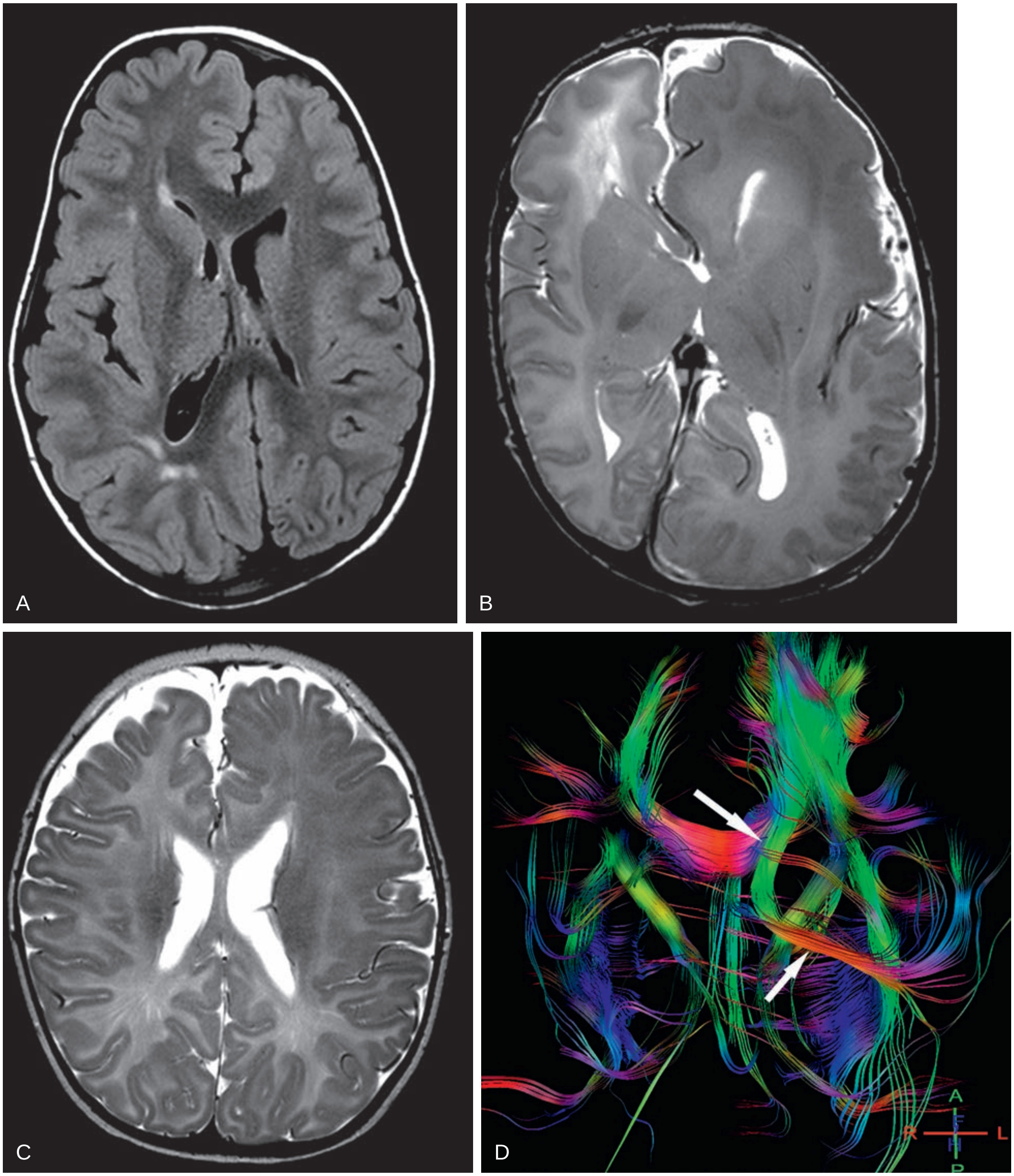

**Figure 31.18. Hemimegalencephaly.** (A) Axial FLAIR MR image shows an overgrown dysplastic right hemisphere with ipsilateral ventriculomegaly. The white matter is thickened and focally gliotic. (B) Axial T2-weighted MR image in another patient shows more striking hamartomatous overgrowth of the left hemisphere, particularly the frontal lobe. (C) Axial T2-weighted MR image in a neonate with intractable seizures shows subtle hamartomatous overgrowth of the left frontal pole. (D) DTI of patient in C shows anomalous white matter tracts *(arrows)*. The left frontal pole is composed of bands of grey and white matter that are in a highly parallel configuration, resulting in high anisotropy.

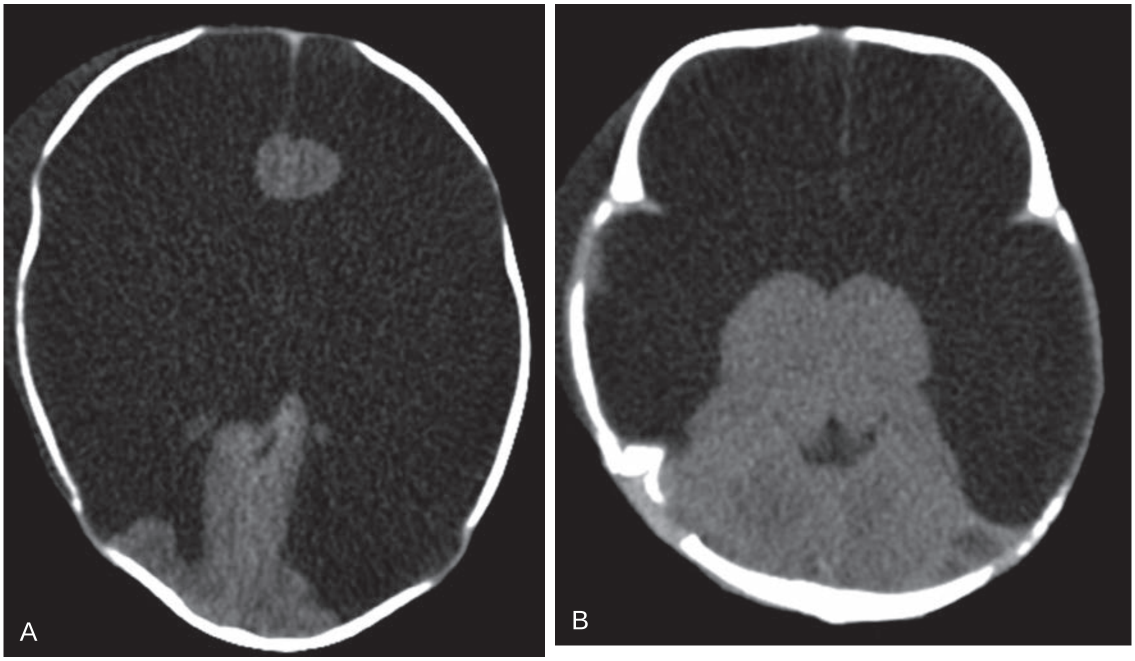

**Figure 31.19. Hydranencephaly.** (A) Axial CT image shows hydrocephalus with split sutures and absence of large portions of the cortical mantle. (B) The basal ganglia are compressed by the supratentorial ventriculomegaly.

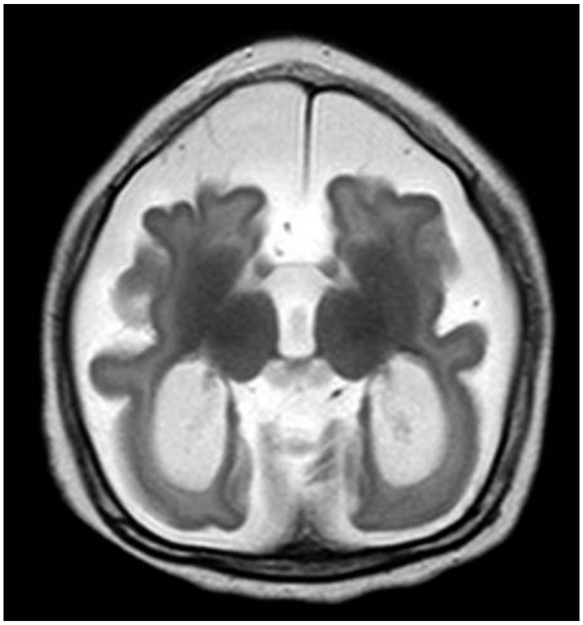

**Figure 31.20. Microlissencephaly.** Axial T2-weighted MR image shows that the brain is diffusely undersulcated with callosal agenesis and dilated ventricles.

Zellweger) and with multiple congenital anomalies, including schizencephaly, callosal agenesis, Aicardi syndrome, and Joubert syndrome and related disorders (JSRD).[2,47–51] PMG may also occur from CMV infection and intrauterine ischemic injury. Regardless of etiology, PMG is associated with thickened dysplastic overlaying leptomeninges.[43–44] The severity of seizures and developmental impairment correlates with the location and severity of the malformation. Focal PMG may be clinically occult or associated with seizures, often medically uncontrollable. Bilateral perisylvian PMG is associated with epilepsy, delayed development, strabismus, dysphagia and speech problems, and paresis.

***Imaging.*** MRI shows increased cortical thickness and irregularity at the cortical–white matter junction (Fig. 31.23). PMG may be focal, bilateral but asymmetric, or symmetric, most often bifrontal or biparietal; the pattern of the PMG appears to differ with location.[2,48] The appearance of the PMG may change with brain maturation, and PMG visible in the unmyelinated brain as T2 hypointensity may be less conspicuous as myelination progresses.

### Schizencephaly

***Clinical.*** Schizencephaly is a congenital cleft extending from the pial surface to the ventricles.[46] Affected patients may present with seizures and/or motor deficits or may be asymptomatic. Larger or bilateral defects are associated with poorer neurodevelopmental outcome.[4,52]

***Imaging.*** The lips of the defects may be in apposition (closed lip) or separated (open lip). The clefts are lined with dysplastic grey matter that extends the full length of the cleft. Discontinuity of the ventricular ependyma and the subpial membrane in open lip schizencephaly results in communication between the lateral ventricles and the subarachnoid space. The pulsations of the CSF may cause remodeling and outward expansion of the calvarium overlaying the open cleft (Fig. 31.24). The septum pellucidum is absent in most cases of schizencephaly involving the frontoparietal regions. Unilateral schizencephaly is often associated with contralateral peri-Sylvian PMG.[48] With open-lip defects, the corticospinal tract ipsilateral to the defect is hypoplastic by DTI.

## DIFFUSE MALFORMATIONS OF CORTICAL DEVELOPMENT

### Type I (Classic) Lissencephaly

Type 1 or classic lissencephaly (LIS1) is considered a malformation due to generalized abnormal transmantle migration,[2,53,54]

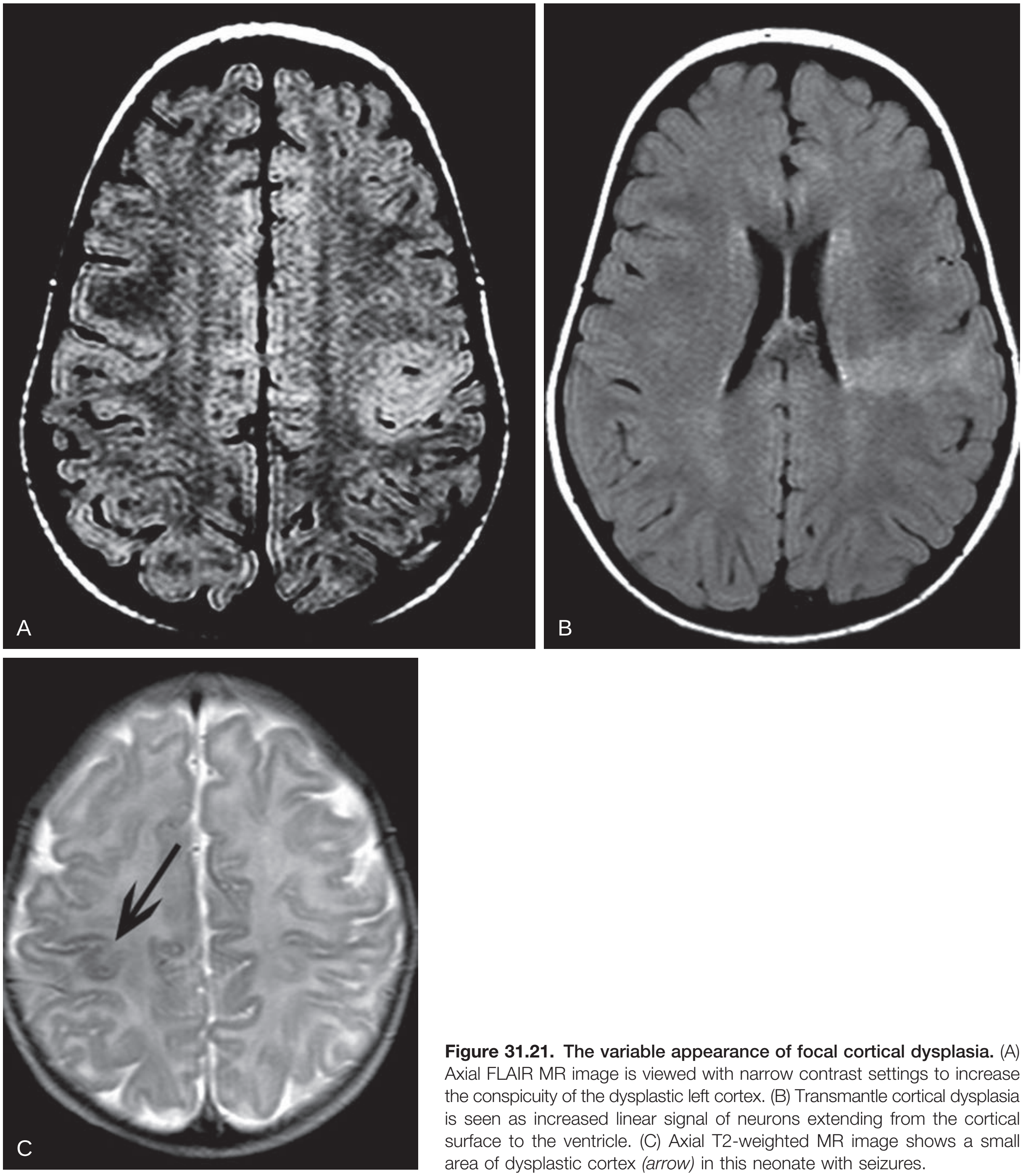

**Figure 31.21. The variable appearance of focal cortical dysplasia.** (A) Axial FLAIR MR image is viewed with narrow contrast settings to increase the conspicuity of the dysplastic left cortex. (B) Transmantle cortical dysplasia is seen as increased linear signal of neurons extending from the cortical surface to the ventricle. (C) Axial T2-weighted MR image shows a small area of dysplastic cortex *(arrow)* in this neonate with seizures.

and the phenotype includes classic anterior, posterior, or diffuse LIS1 with and without known genetic causes, and agyria/pachygyria with and without cerebellar hypoplasia.[2,53,54] LIS1 occurs in 1/500,000 live births with gender predominance only in the less-common X-linked forms. The most common mutations in LIS1 occur in the *PAFAH1B1* (platelet-activating factor acetylhydrolase isoform 1b regulatory subunit 1) of 17p13.3 (LIS1 gene), Xq22.3–q23 DCS, and in tubulinopathies such as *TUBA1A*, *TUBB2B*, and *TUBB3*.[56–58] *PAFAH1B1* is integral to neuronal division and migration by coupling the nucleus to centrosomes. The tubulinopathies disrupt centrosome and nuclear movement and the integrity of the microtubules, growth cones, filaments, and other components of the cytoskeleton required for normal migration of cerebral, precerebellar, and cerebellar neurons, which also affect axonal path finding and migration.[39,54]

Histopathology of LIS1 shows inversion of cortical laminar architecture; the normal six-layered cortex is replaced with a two-, three-, or four-layered cortex.[48] The four layers include a superficial molecular layer, layer II of pyramidal cells resembling the fifth and sixth layers of the normal neocortex, followed by a sparse cellular layer (layer III), and a thick band of disorganized neurons

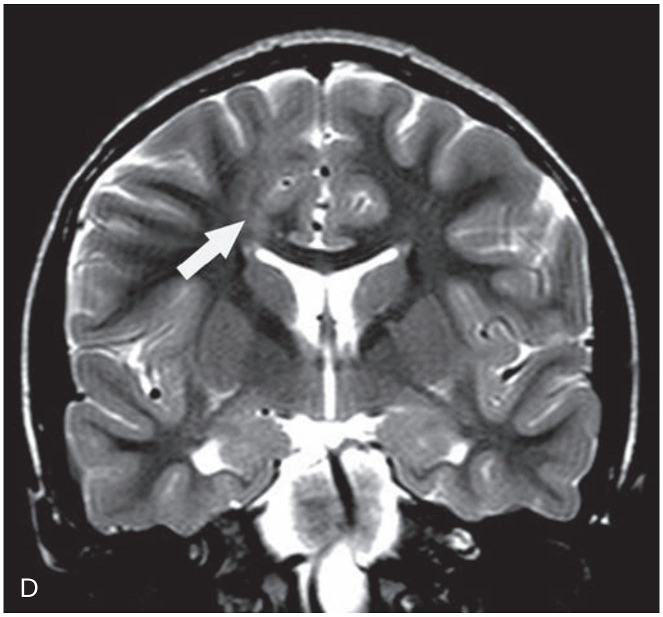

**e-Figure 31.21.** (D) Coronal T2-weighted MR image shows transmantle cortical dysplasia *(arrow)*.

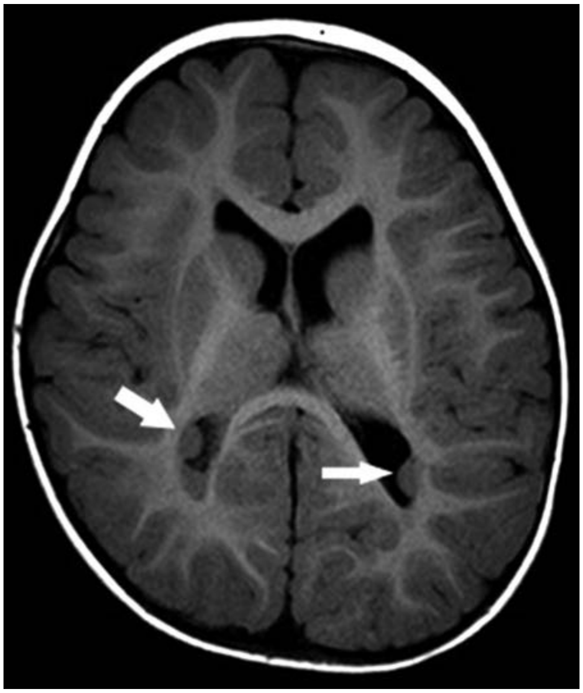

**Figure 31.22. Grey matter heterotopia.** Axial T1-weighted MR image shows variable-sized nodules of grey matter along the surface of the ventricle *(arrows)*.

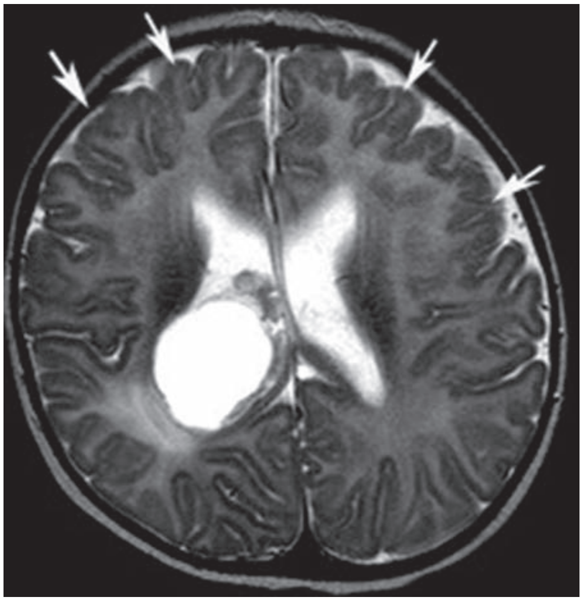

**Figure 31.23. Polymicrogyria.** Axial T2-weighted MR image shows bifrontal polymicrogyria *(arrows)* and large intraventricular cyst.

of variable size (layer IV), which extends into the regional white matter.[48]

***Clinical.*** The hallmarks of LIS1 are profound mental retardation with a normal to small head size, intractable seizures, hypertonia, and hyperreflexia. LIS is classified according to brain and extra-CNS anomalies.[2,4] Patients with Miller-Dieker syndrome have LIS1 and abnormal facies. Males with the X-linked *DCX* mutation have classic LIS1 by MRI, whereas females will have variable cognitive delay and subcortical band heterotopias (SBH) by MRI without seizures. The presence of an unexplained seizure disorder or cognitive problems in the mother of a male child with lissencephaly should trigger a screening MRI of the mother for possible SBH. Females with the *ARX* mutation have ambiguous genitalia without lissencephaly; males have lissencephaly with ambiguous genitalia (XLAG) syndrome. Lissencephaly due to the *RELN* mutation is associated with congenital lymphedema.

***Imaging.*** The most severe LIS1 is diffuse agyria with no gradient in severity from anterior to posterior.[2,4] There may be posterior predominant agyria with variable frontal pachygyria; posterior predominant pachygyria, or SBH.[48] DTI of classic LIS1 shows a highly organized laminated pattern reflecting the persistent radial pattern of the neurons arrested during migration (Fig. 31.25). The lissencephalic pattern in males with the sex-linked *DCX* mutation is similar to L1S1 but more severe anteriorly. Females with the *DCX* mutation have SBH (e.g., the "double cortex"[2,4]) with bands of heterotopic neurons embedded in white matter between normal appearing cortex and the ventricles. *TUBA1A* LIS is posterior predominant with variable cerebellar and callosal hypoplasia, dysplastic basal ganglia, and ventriculomegaly.[57]

The severe supratentorial malformation in LIS1 overshadows the infratentorial anomalies. The severity of the lissencephaly is reflected by the degree of brainstem hypoplasia on MRI.[58] DTI shows derangement of pontine fibers in LIS1, which does not appear to correlate with the severity of the LIS or the brainstem hypoplasia.[59]

The other tubulinopathies have marked phenotypic variability including congenital fibrosis of the extraocular muscles type 3 (CFEOM3), MCD including PMG, gyral disorganization, fusion of the basal ganglia with thin corpus callosum, hypoplastic brainstem and corticospinal tracts (e-Fig. 31.26), and dysplastic cerebellar vermis.[56,57]

## Type II Cobblestone Lissencephaly

Cobblestone lissencephaly reflects abnormal glycosylation of α-dystroglycan due to *DAG* gene mutations.[2,39,51,60] The nodular surface of the brain reflects the structural defects in the glial-pial limiting membrane that normally prevent migrating neurons from traversing the pial surface and accumulating on the surface of the brain. There is variable pachygyria and PMG with thickened cortex lacking the normal six-layered cortex, fibroglial proliferation of the leptomeninges, and focal interhemispheric fusion.

***Clinical.*** *DAG* is also expressed in skeletal muscle and the eye. The clinical presentation of the cobblestone lissencephalies is congenital muscular dystrophy (CMD), which is a heterogeneous group of inherited disorders presenting with diffuse symmetric hypotonia at birth or in infancy.[2,39,51,60] CMD is categorized as CMD without and with CNS abnormalities; the latter includes Fukuyama congenital muscular dystrophy (FCMD), muscle-eye-brain disease (MEBD), and Walker-Warburg syndrome (WWS).[2] Depending on the specific syndrome, affected patients also have psychomotor retardation, seizures, micropthalmia, optic nerve hypoplasia, and colobomas. Scoliosis and contractures develop during early childhood. Death is often respiratory due to chest wall rigidity and weakness of the diaphragm or aspiration, or from cardiomyopathy. The specific diagnosis is made based on clinical findings, serum creatine kinase, neuroimaging, muscle and/or skin biopsy, and molecular genetic testing.[60]

Fukuyama CMD is an autosomal recessive disorder most common in Japan, where the incidence approaches 3/100,000 individuals.[60] The syndrome results from mutations in the *FKTN* gene on chromosome 9, which codes for the protein fukutin that interacts with α-dystroglycan in the extracellular matrix. MEBD is an autosomal recessive disorder rare outside of Finland caused by mutations in the *POMT1*, *POMT2*, *POMGnT1*, *fukutin*, and *FKRP* genes; phenotypes may overlap with FCMD. WWS is the

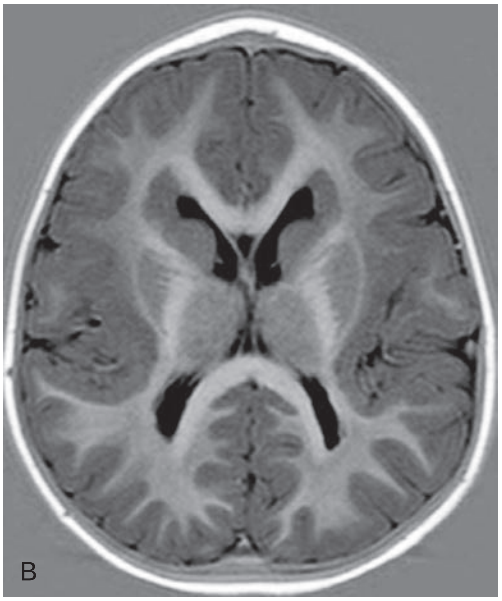

**e-Figure 31.23.** (B) Axial T1-weighted image shows bifrontal polymicrogyria and periventricular grey matter heterotopia.

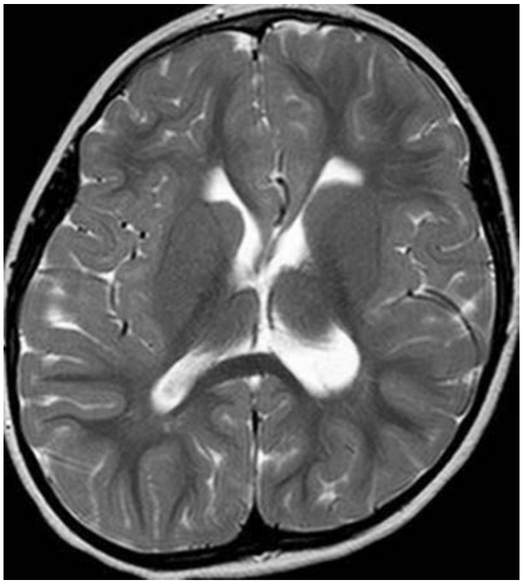

**e-Figure 31.26.** The tubulinopathies can result in phenotypes identical to LIS1. There is phenotypic heterogeneity. This patient with a TUBB3 mutation has dysmorphic basal ganglia, asymmetric ventriculomegaly, and gyral disorganization.

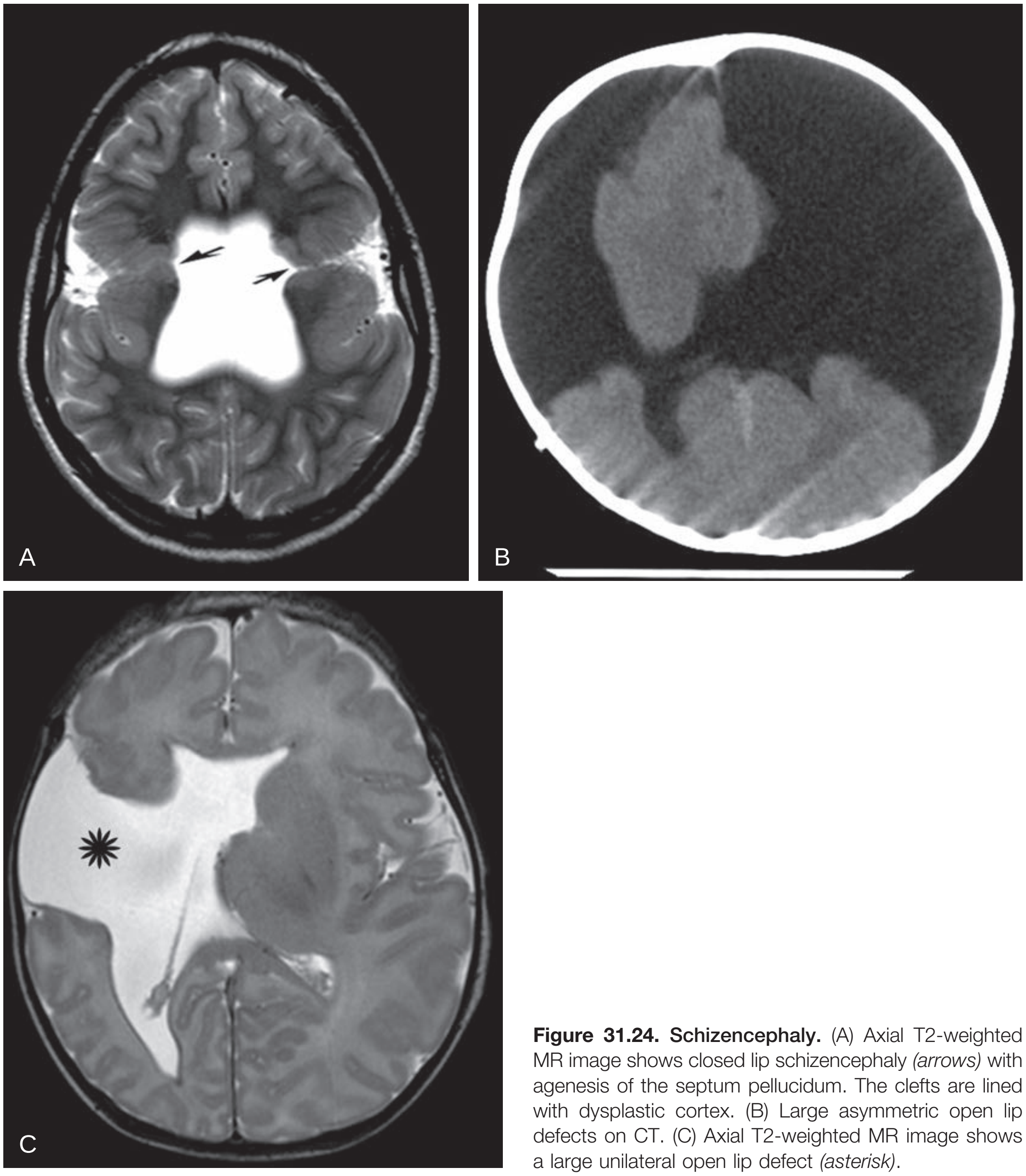

**Figure 31.24. Schizencephaly.** (A) Axial T2-weighted MR image shows closed lip schizencephaly *(arrows)* with agenesis of the septum pellucidum. The clefts are lined with dysplastic cortex. (B) Large asymmetric open lip defects on CT. (C) Axial T2-weighted MR image shows a large unilateral open lip defect *(asterisk)*.

most severe form of CMD with CNS manifestations and is also associated with mutations in the *POMT1*, *POMT2*, *fukutin*, and fukutin-related protein genes.[2,60]

***Imaging.*** The MR abnormalities are less severe in FCMD than in WWS and MEBD.[2,4,60] In mild cases of FCMD, the cerebrum may be relatively normal or have a simplified gyral pattern. More severe malformations have variable pachygyria and PMG; the white matter is gliotic with cysts. Neurons may be seen lining the ependymal surface of the ventricle, contrasted on T2-weighted images by hyperintense signal of the CSF and the abnormal white matter (Fig. 31.27). The lateral ventricles are enlarged. The cerebellum consistently shows small cysts with variable PMG. The most severe cerebellar hypoplasia is seen with WWS, which is also associated with occipital encephalocele (Fig. 31.28). The brainstem is usually normal in FCMD, hypoplastic in MEBD, and small and kinked posteriorly in WWS. Hydrocephalus is rare in FCMD, common in MEBD, and almost invariable in WWS; the hydrocephalus may mask the malformation.

## HINDBRAIN AND CEREBELLAR MALFORMATIONS

### Brainstem Malformations

The embryonic hindbrain is transiently divided into distinct segments or rhombomeres (r1-8), giving rise to rhombomeric-specific neurons and physiologic regulatory circuits.[61,62] The pontine nuclei are populated by mossy fibers that arise from the rhombic lip of the hindbrain and traverse the pons tangentially along the subpial surfaces of the developing brainstem changing migration from tangential to radial at the site where precerebellar nuclei develop.[63] The pontine nuclei are the primary targets for the corticopontine tracts, most of which of cross the midline in the basal pons, terminating in the contralateral cerebellar hemisphere.

A malformed brainstem may occur as a relatively localized developmental defect or in conjunction with and overshadowed by cerebral malformations.[61,62] Localized malformations affecting

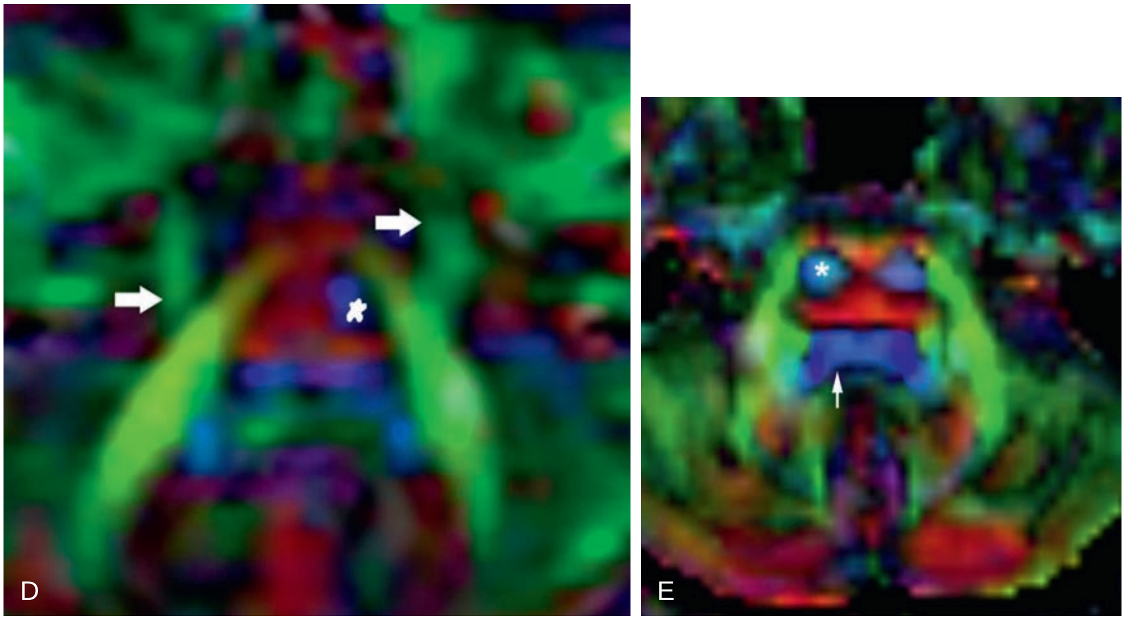

**e-Figure 31.24.** (D) DTI of the pons from patient in C shows severe hypoplasia of the corticospinal tract ipsilateral to the schizencephaly. Note normal contralateral corticospinal tract *(asterisk)*. *Arrows* indicates the fifth cranial nerves. (E) DTI of normal pons. Asterisk *(asterisk)* denotes the normal corticospinal tract, and the *arrow* indicates the dorsal column medial lemniscus complex.

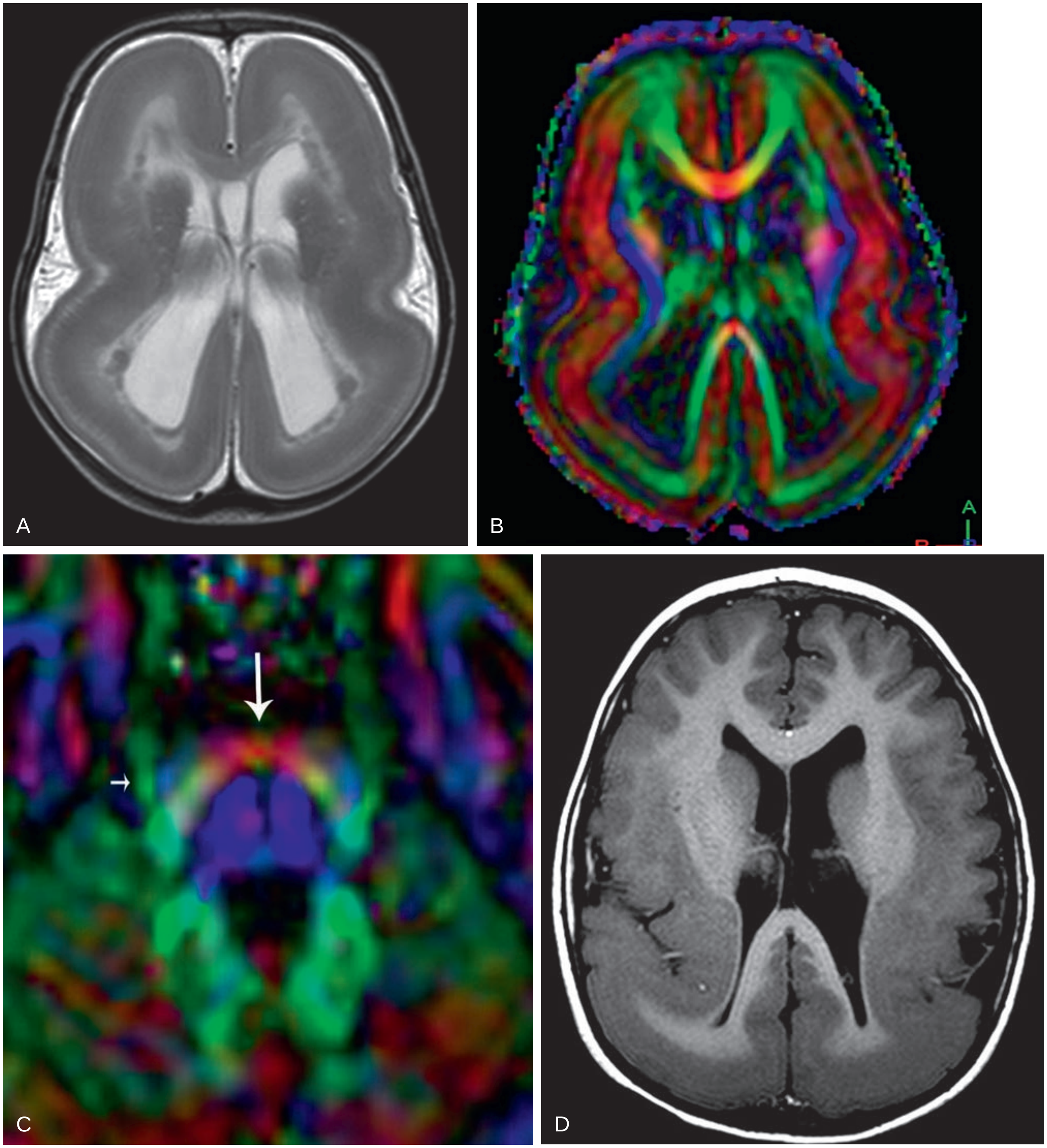

**Figure 31.25. Lissencephaly type I.** (A) Axial t2 MR image showed complete agyria. The brain is smooth with bands of arrested neurons imbedded in the hemispheres. There are subependymal grey matter heteropias. (B) DTI shows the bands of grey matter *(arrows)* in arrested migration. (C) Axial DTI through pons from the patient illustrated in A and B. There is a single red band of pontine fibers *(arrow)* instead of the 2 red bands seen in the normal pons (compare to e-Fig 31.24c). Small arrow indicates the Vth cranial nerve. (D) Axial T1 image in another patient shows posterior predominant agyria.

*Continued*

the brainstem and cerebellum are uncommon, characterized by deficient or defective formation of cranial nerve nuclei resulting in problems with ocular movement and lid control, facial palsy, and/or neurosensory hearing loss. Conventional MR imaging is useful in the diagnosis of brainstem malformations in which brainstem surface morphology and size are affected, although DTI provides more information about white matter tracts and may show absence or hypoplasia of dorsal pontocerebellar tracts.[59] The Chiari I malformation is included here for convenience, although it is not considered a true brainstem malformation.

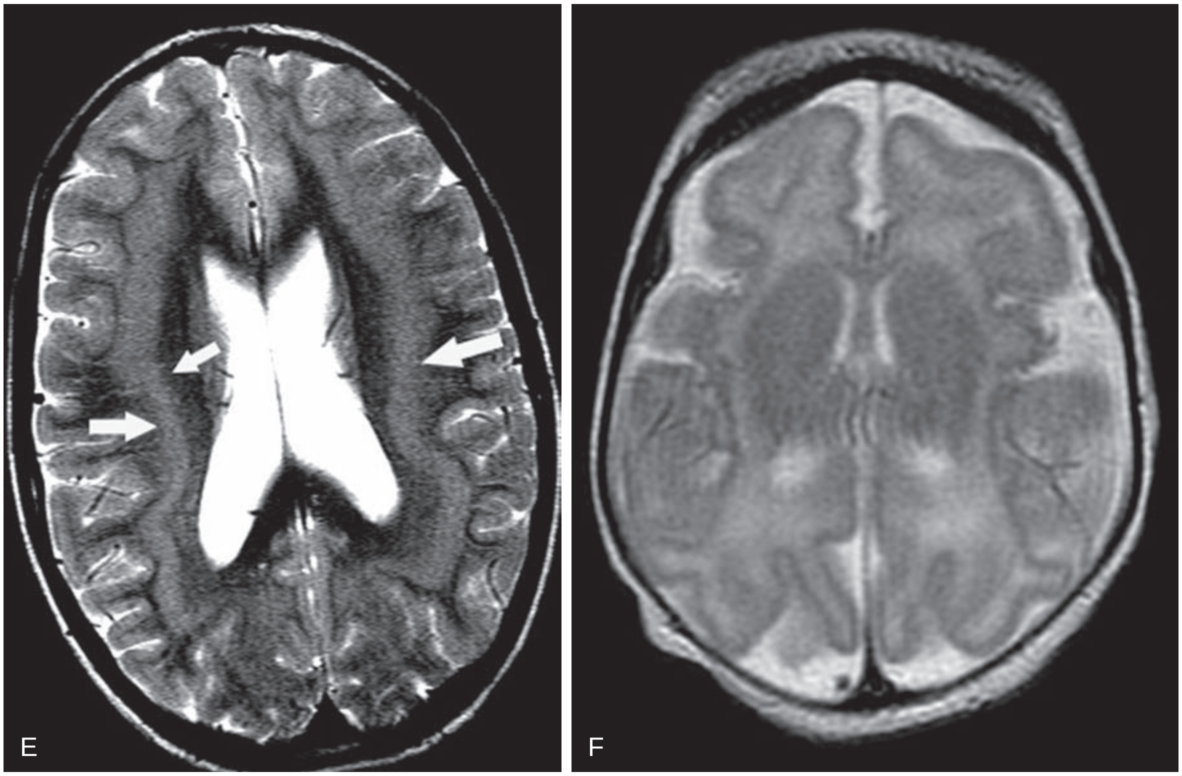

**Figure 31.25, cont'd.** (E) Axial T2-weighted image shows subocrtical band heterotopia. Bands of grey matter arrested during radial ventriculofugal migration are imbedded in the deep white matter. (F) Axial T2-weighted image shows diffuse pachygyria.

## Molar Tooth Syndrome (Joubert Syndrome and Related Disorders)

***Clinical.*** JSRD-causing mutations are usually autosomal recessive and involve one of multiple genes involved in the nonmotile cilia integral to neuronal and axonal migration. The clinical syndrome is markedly diverse and characterized by hypotonia; episodic hypo- and hyperventilation, which tend to improve with age; truncal ataxia that develops during early childhood; oculomotor apraxia; nystagmus; pigmentary retinopathy; endocrinopathies; and abnormal facial features, which include ptosis, hypertelorism, and low-set ears.[64] There may be hepatic and/or kidney dysfunction reflecting the extra CNS role of nonmotile cilia.

***Imaging.*** MR findings include variable hypoplasia of the superior vermis with enlargement of the superior aspect of the fourth ventricle and elevation of the fastigium. The superior cerebellar peduncles are thickened and elevated, forming the "molar tooth" seen in the axial plane at the pontomesencephalic junction.[4,64,65] DTI of Joubert syndrome shows consistent absence of both the decussation of the superior cerebellar peduncle within the midbrain (e.g., the "red dot") and the pyramidal tracts in the medulla with variable anomalies of pontocerebellar fibers (Fig. 31.29).[65–67]

## Horizontal Gaze Palsy With Progression Scoliosis

***Clinical.*** Horizontal gaze palsy with progression scoliosis (HGPPS) is the expression of mutation of the *ROBO3* gene, which codes for proteins involved in axonal guidance and neuronal migration.[61,62] Expression of the defective gene appears to be limited to decussating fibers in the brainstem. Patients with HGPPS tend to be cognitively normal but have congenital nystagmus and are unable to perform lateral eye movements due to lack of decussating fibers in the brainstem. Progressive scoliosis develops during early childhood.

***Imaging.*** MRI shows pontine hypoplasia with a dorsal midsagittal cleft.[66,67] The facial colliculi are absent, the inferior olivary nuclei prominent, and the medulla lacks the normal dorsal convexities formed by the gracile and cuneate nuclei (Fig. 31.30). DTI of HGPPS shows hypoplasia of the ventral transverse pontine fibers and absence of the dorsal transverse pontine fibers with small middle cerebellar peduncles, and small superior cerebellar peduncles with absent decussating fibers within the midbrain.[66,67]

## Pontine Tegmental Cap Dysplasia

***Clinical.*** Pontine tegmental cap dysplasia is a rare brainstem malformation associated with variable developmental delay, ataxia, and restricted horizontal gaze, failure initiating fast eye movements, facial weakness, deafness, and swallowing problems, which reflect deficient lower cranial nerves.[68]

***Imaging.*** MRI shows pontine hypoplastic; the ventral surface is flattened and there is ectopic tissue protruding dorsally into the fourth ventricle referred to as the *tegmental cap*. The superior cerebellar vermis is hypoplastic, which along with the elongated and laterally misplaced superior cerebellar peduncle results in a molar-tooth-like deformity. By DTI, the tegmental cap is transversely oriented ectopic pontine fibers (e-Fig. 31.31). DTI shows absence of the normal decussations of the superior and middle cerebellar peduncles.[66–68]

## Brainstem Disconnection Syndrome

***Clinical.*** This is a rare and usually lethal malformation for which no gene mutations have been identified; intrauterine ischemia has been postulated as etiology.[61,62]

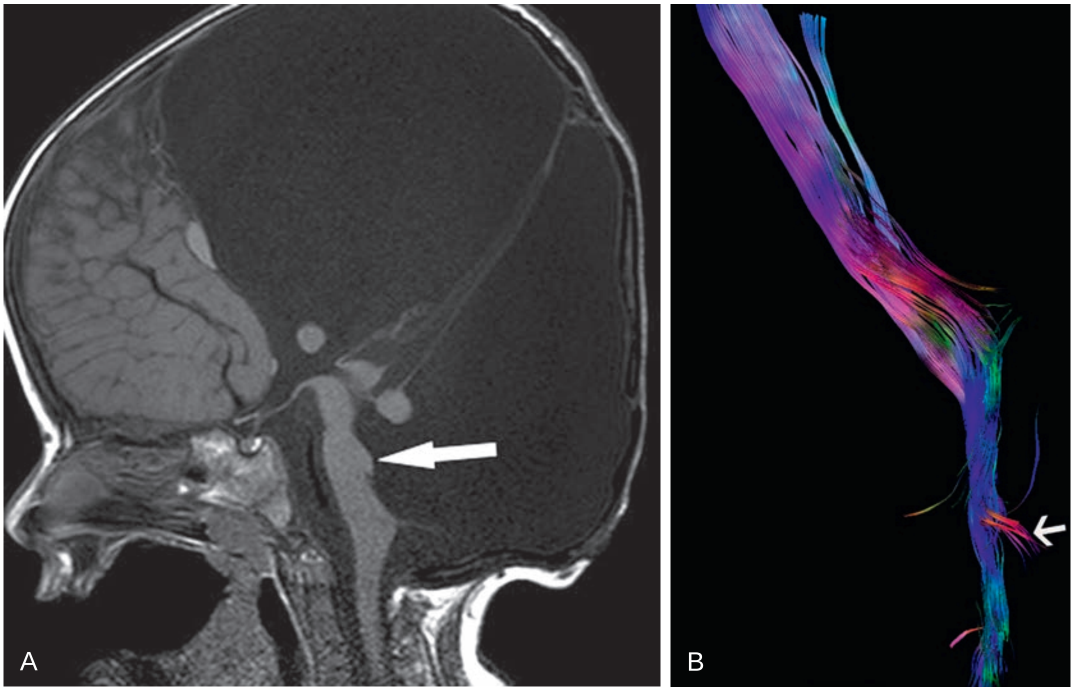

**e-Figure 31.31. Pontine tegmental cap dysplasia.** (A) The pons is severely hypoplastic with a dorsal cap *(arrow)*. There is hydrocephalus and a Dandy-Walker malformation; rare in this entity. (B) DTI shows absence of crossing brainstem fibers with the exception of a transverse band of dorsal fibers corresponding to the cap *(arrow)*.

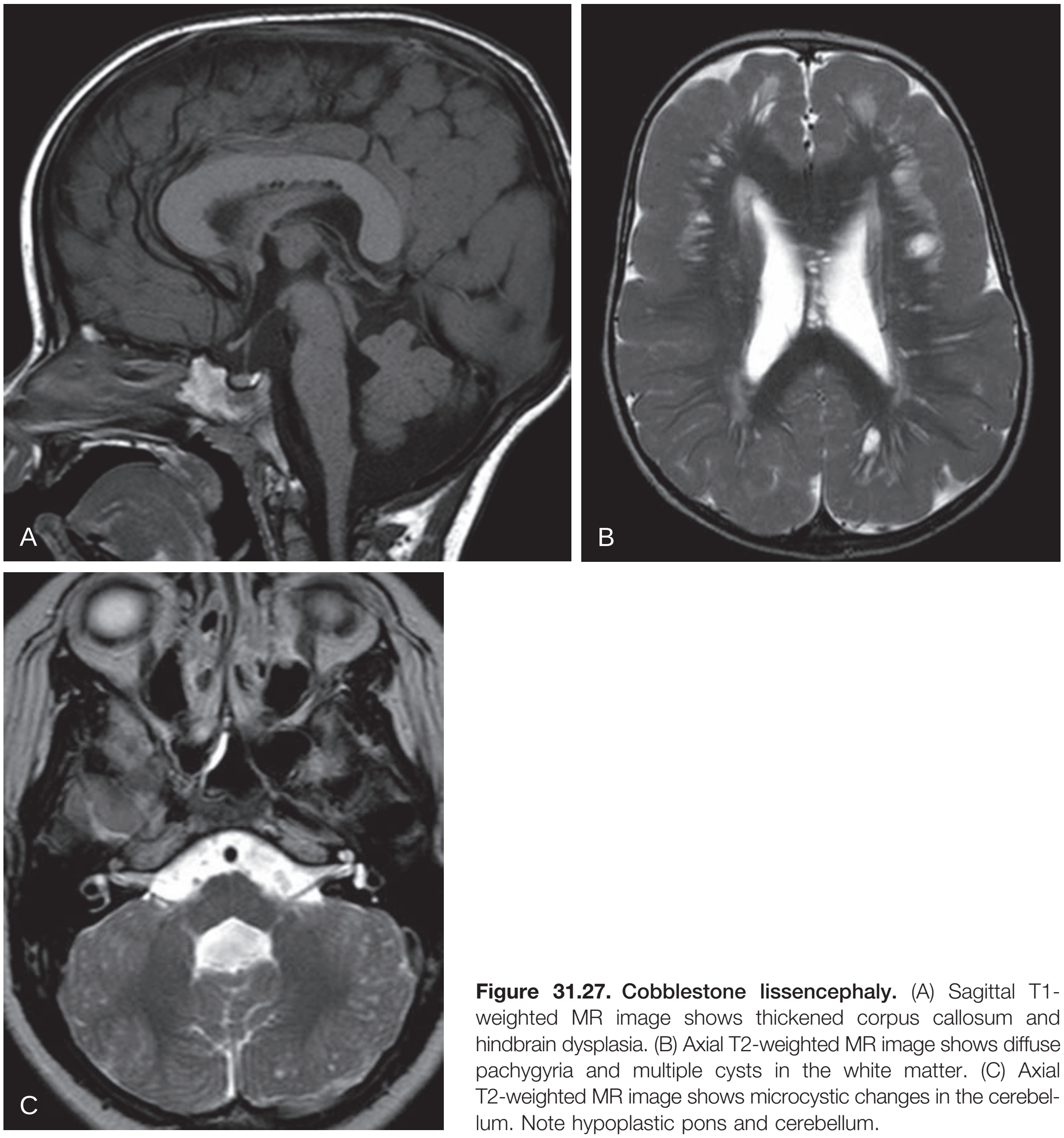

**Figure 31.27. Cobblestone lissencephaly.** (A) Sagittal T1-weighted MR image shows thickened corpus callosum and hindbrain dysplasia. (B) Axial T2-weighted MR image shows diffuse pachygyria and multiple cysts in the white matter. (C) Axial T2-weighted MR image shows microcystic changes in the cerebellum. Note hypoplastic pons and cerebellum.

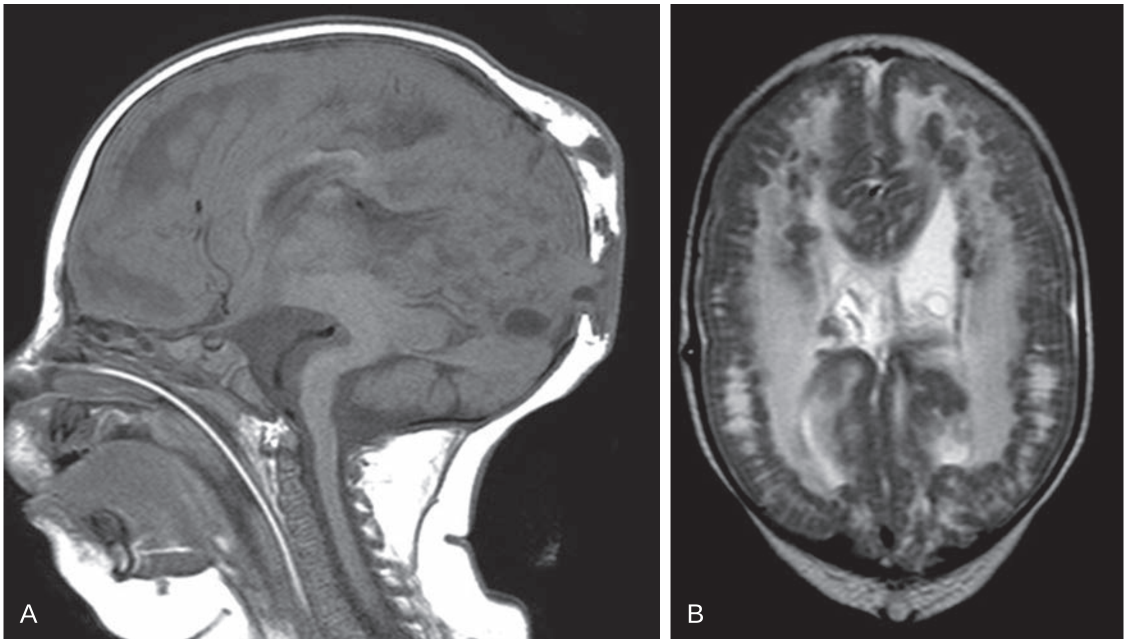

**Figure 31.28. Walker-Warburg type II cobblestone lissencephaly.** (A) Sagittal T1-weighted MR image shows "Z-shaped" configuration to the brainstem. There is severe cortical dysplasia. Note multiple atretic parieto-occipital encephaloceles. (B) Axial T2-weighted MR image shows severe hemispheric dysplasia with microcysts and grey matter heterotopias within the deep white matter.

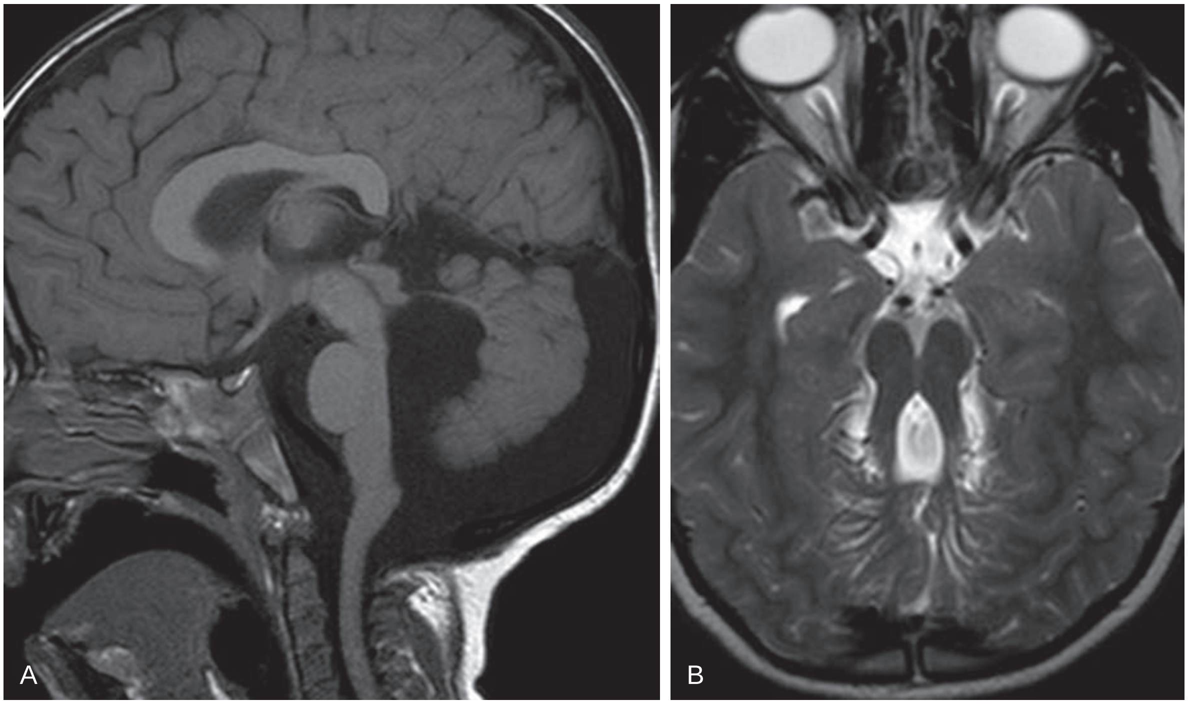

**Figure 31.29. Molar tooth syndrome.** (A) Sagittal T1-weighted MR image shows hypoplasia of the superior cerebellar vermis with upward bowing of the roof of the fourth ventricle. (B) Axial T2-weighted image shows the molar tooth at the level of the midbrain, the hallmark of Joubert syndrome and related disorders (JSRD).

***Imaging.*** MRI shows a severely constricted hindbrain with cerebellar dysplasia; the basilar artery is absent (e-Fig. 31.32). The clivus may be dysplastic. There are usually no supratentorial anomalies.

## Chiari I Malformation

***Clinical.*** Chiari I malformation is defined as downward displacement of cerebellar tonsils below the foramen magnum and may be acquired or spontaneously resolve.[4,11,13] It is not associated with defective neural tube closure. Although many patients with Chiari I malformations are asymptomatic, some patients experience suboccipital headaches, neck pain, ataxia, dysmetria, nystagmus, and disequilibrium due to brainstem or cerebellar compression and/or upper extremity weakness and pain due to cervical cord myelopathy.[69] Treatment of a symptomatic Chiari I malformation with or without syrinx is a suboccipital decompressive craniectomy with duraplasty; the cerebellar tonsils may be resected.

***Imaging.*** The Chiari I malformation is defined by cerebellar tonsils greater than 6 mm below the posterior lip of the foramen magnum. In symptomatic patients, the low-lying tonsils disrupt CSF flow across the foramen magnum, which predisposes to syringomyelia in the thoracic or cervical spinal cord (Fig. 31.33). Flow of CSF across the foramen magnum is further impaired when the odontoid is elongated and dorsally angulated or with platybasia (e.g., the complex Chiari I variant). The dynamic significance of the low-lying tonsils is best depicted using single slice multiple phase gated two-dimensional (2D) phase contrast MR images in the sagittal and/or axial plane with a velocity encoding of 5 cm/sec. Obstruction of CSF flow results in abnormal bidirectional movement of hindbrain across the foramen magnum seen as changes in signal intensity on the phase contrast sequence. In patients with a Chiari I malformation, increased intracranial pressure resulting from a tumor or hydrocephalus resulting in secondary tonsillar herniation should be excluded with screening images through the brain.

Bony anomalies of the craniovertebral junction may be seen with low-lying cerebellar tonsils including an elongated retroflexed odontoid and a short clivus (e.g., platybasia) with impingement on the ventral surface of the cervicomedullary brainstem by the high-riding odontoid (Table 31.1).[69]

## Cerebellar Malformations

This section addresses malformations of the cerebellum in which the cerebellum is hypoplastic or dysplastic but not cerebellar atrophy.[70] Cerebellar hypoplasia is defined by a small cerebellum with fissures of normal size compared with the folia. Cerebellar dysplasia describes disorganized development and includes an abnormal folial pattern or cerebellar grey

**TABLE 31.1** Comparison of Chiari I and II Malformations

| Chiari I | Chiari II |
|---|---|
| Headache and neck pain increased by cough or Valsalva; dysarthria, dysphagia, downbeat nystagmus, upper extremity weakness/numbness | Brainstem dysfunction; swallowing/feeding difficulties, stridor, apnea, weak cry, nystagmus |
| Downward herniation of cerebellar tonsils resulting in compression of cervicomedullary brainstem; impeded CSF flow. Odontoid may be elongated and retroflexed | Downward herniation of dysplastic lower brainstem and cerebellar vermis |
| Brain usually normal<br>Syringomyelia 30%-70% | Callosal dysgenesis, neuronal migration anomalies, hydrocephalus ~95% |

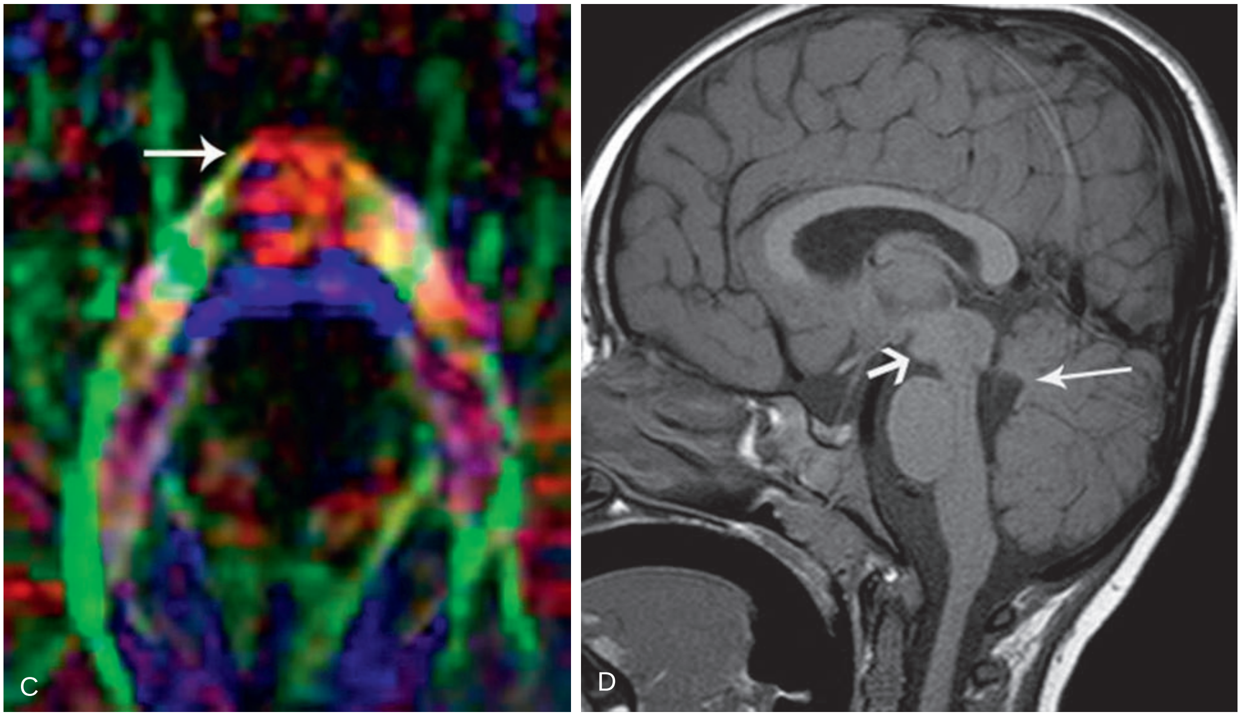

**e-Figure 31.29, cont'd.** (C) Axial DTI shows the decussation of the cerebellar peduncles (e.g. the red dot) is absent in JSRD and several other hindbrain malformations, along with the decussation of the pyramidal tracts. DTI may also show pontine dysplasia. The right CST is fragmented *(arrow)* and the left CST is absent. (D) Sagittal T1-weighted MR image from another patient with JSRD shows elevation of the fastigium *(long arrow)* of the 4th ventricle and a dysplastic midbrain with ventral cap *(arrow)*.

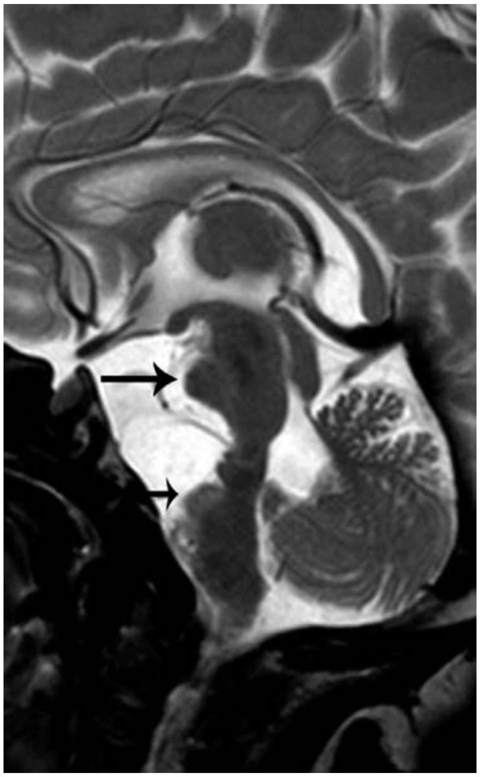

**e-Figure 31.32. Brainstem disconnection syndrome.** Sagittal T2-weighted image shows the cranial and caudal limits of the severely constricted pons *(arrows)*. The basilar artery is absent and the clivus is dysplastic.

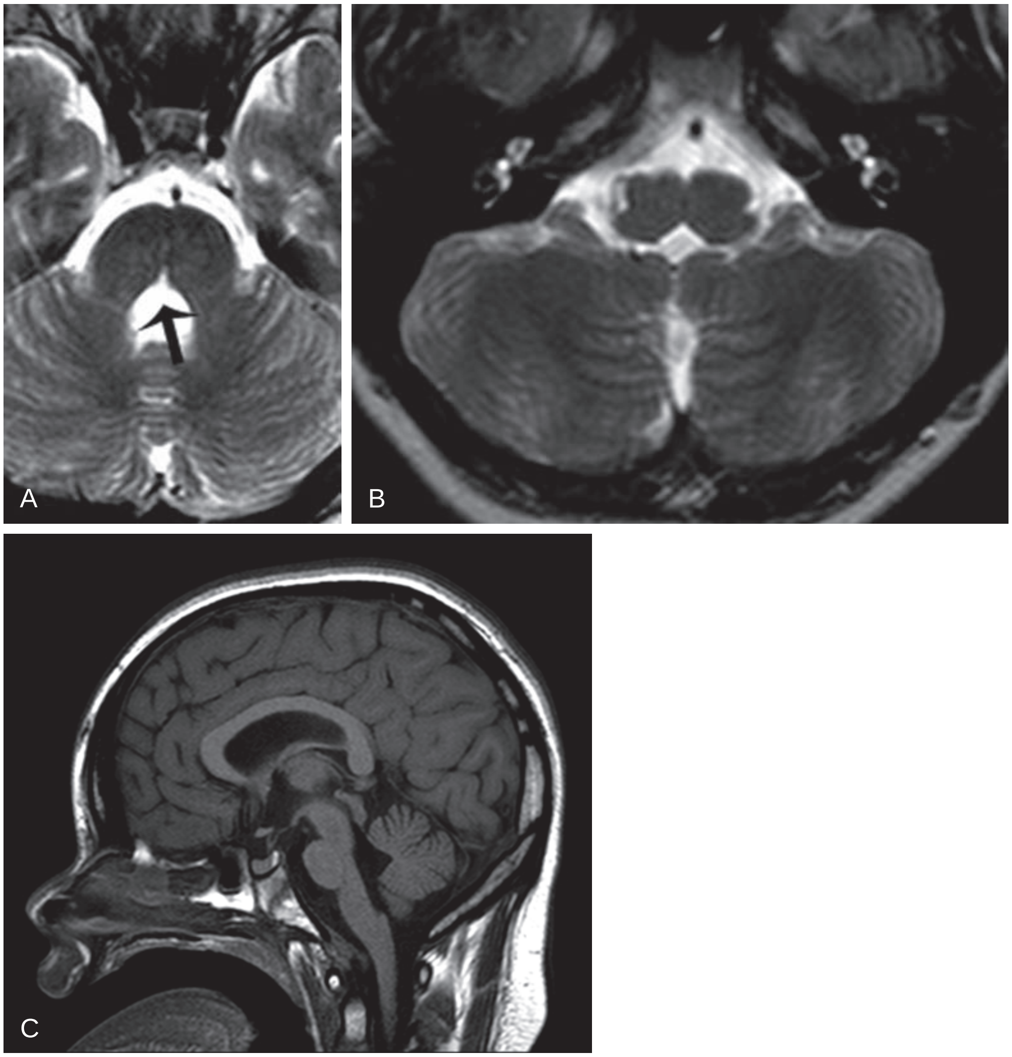

**Figure 31.30. Horizontal gaze palsy with progression scoliosis.** (A) Axial T2-weighted MR image shows a cleft *(arrow)* along the dorsal pons. (B) Axial T2-weighted MR image and (C) sagittal T1-weighted MR image show that the medulla lacks the normal dorsal convexities and the facial nerve colliculi are absent.

matter heterotopias, which may be generalized and involving cerebellar hemispheres and vermis, or focal and limited to a hemisphere or vermis. Cerebellar hypoplasia includes the Dandy-Walker continuum and isolated focal cerebellar hypoplasia.[70,71]

## Dandy-Walker Continuum

The Dandy-Walker malformation is defined by complete or partial agenesis of the vermis, cystic dilatation of the fourth ventricle, and an enlarged posterior fossa with cranial displacement of the torcular (Fig. 31.34), often associated with supratentorial hydrocephalus. Associated anomalies occurring in 70% of patients include an abnormal or absent corpus callosum, callosal lipoma, and neuronal migration anomalies.[70,71] The Dandy-Walker variants are controversial and defined by inferior vermian hypoplasia with nonobstructive cystic dilatation of the fourth ventricle; the posterior fossa is not enlarged. In contrast to the Dandy-Walker continuum, the posterior fossa arachnoid cyst and mega cisterna magna are associated with a fully formed cerebellum. Retrocerebellar arachnoid cysts (Fig. 31.35) cause anterior displacement of the fourth ventricle and cerebellum. The mega cisterna magna consists of enlarged retrocerebellar CSF spaces with no mass effect on the normally formed cerebellum.

## Cerebellar Dysplasia

Unlike focal cerebellar dysplasia, diffuse cerebellar dysplasia is usually associated with severe supratentorial MCD such as LIS1 and cobblestone LIS (e-Fig. 31.36).[70]

## Rhombencephalosynapsis

***Clinical.*** This is a relatively rare major malformation of the cerebellum in which the two halves of the cerebellum fail to form.

***Imaging.*** The hallmark of this malformation is fusion of the cerebellar hemispheres (Fig. 31.37).[70–72] Associated brainstem abnormalities include fused colliculi, atresia or dilatation of the fourth ventricle, and cranial nerve and inferior olivary nuclei abnormalities. The corpus callosum may be hypoplastic or absent, and there may be failure of formation of diencephalic structures

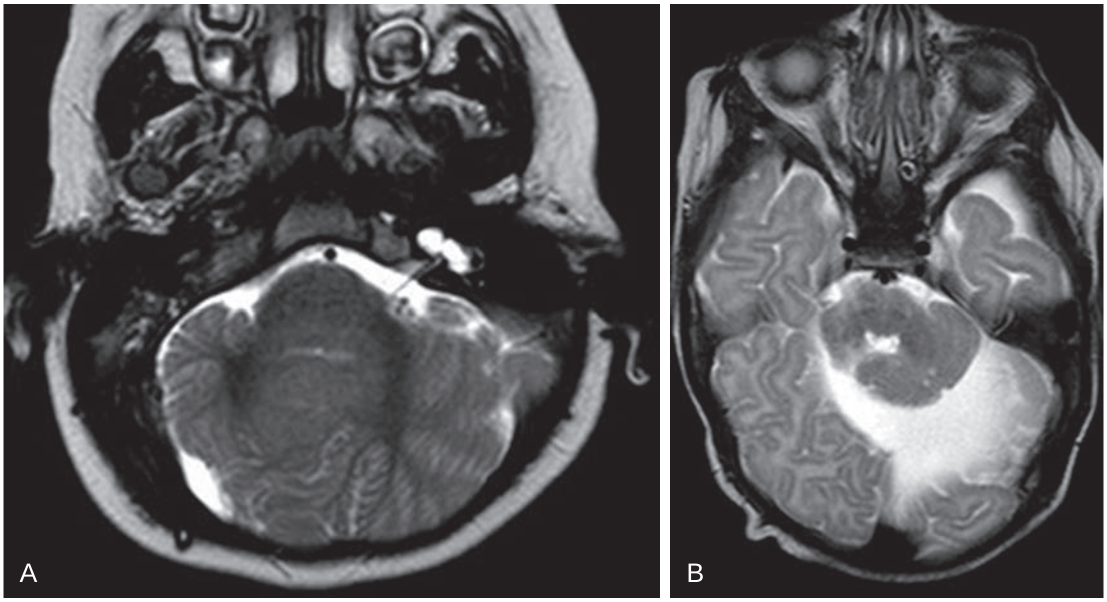

**e-Figure 31.36. Cerebellar dysplasia.** (A and B) Axial T2-weighted MR images shows asymmetric cerebellar hemispheres and vermian dysplasia.

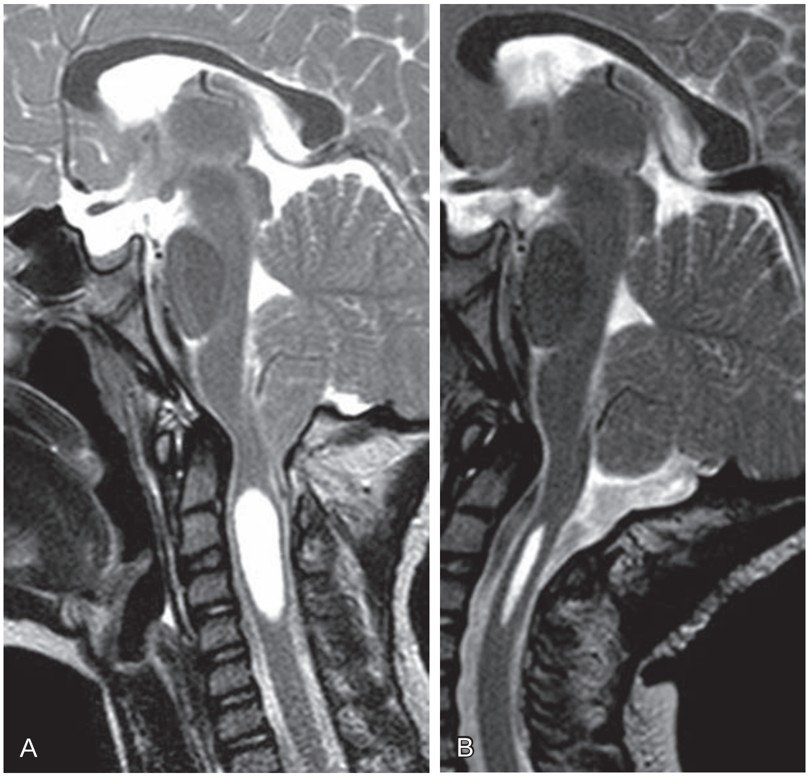

**Figure 31.33. Chiari I malformation.** (A) Sagittal T2-weighted image shows that the cerebellar tonsils are caudally displaced. The blockage to the flow of CSF across the foramen magnum has resulted in dilatation of the central spinal canal and syrinx formation. Previous decompressive suboccipital craniectomy was inadequate. (B) Sagittal T2-weighted image after repeat surgery reestablished normal CSF flow across the foramen magnum shows that the syrinx has improved.

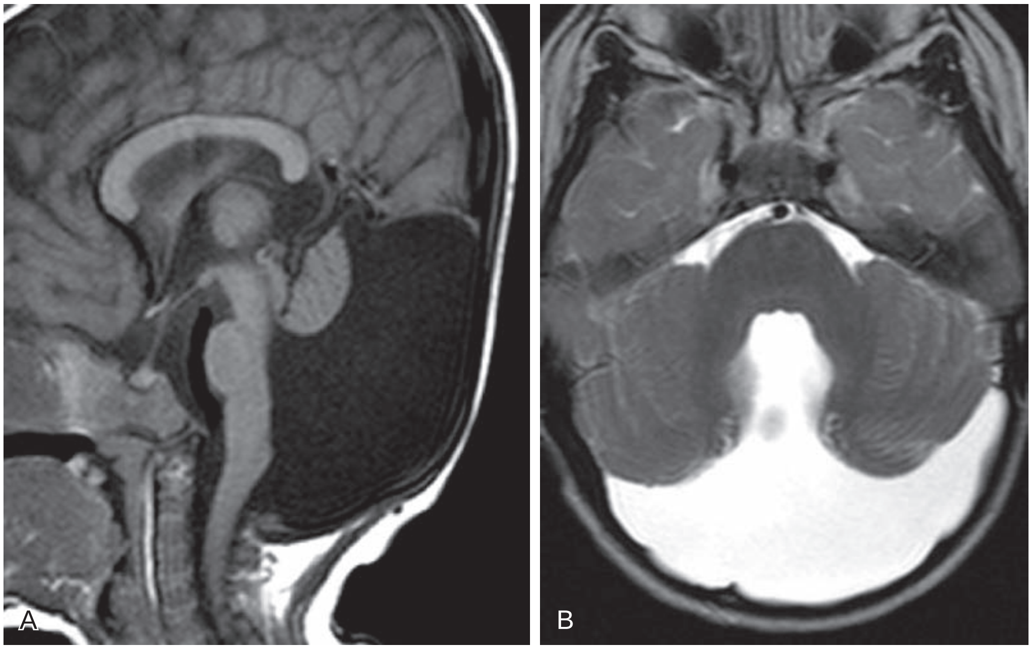

**Figure 31.34. Dandy-Walker malformation.** (A) Sagittal T1-weighted MR image shows an elevated torcular and cerebellar hypoplasia. (B) Axial T2-weighted MR image shows that the vermis is deficient and the retrocerebellar fluid communicates with the fourth ventricle; the hemispheres are relatively normal.

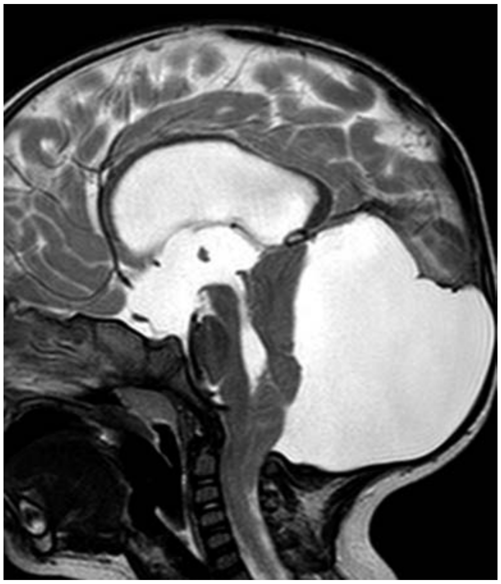

**Figure 31.35. Retrocerebellar arachnoid cyst.** Sagittal T2-weighted MR shows that the cerebellum is compressed by a large CSF collection causing obstruction to fourth ventricle outflow and resultant hydrocephalus.

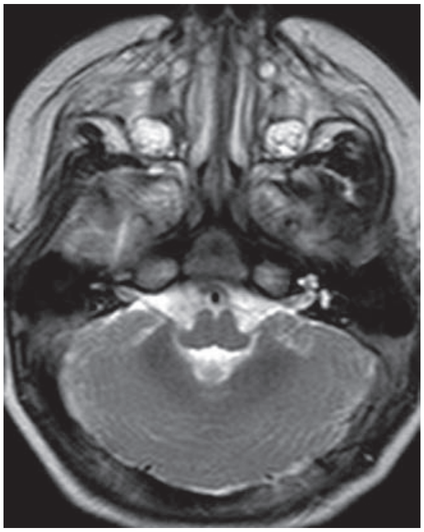

**Figure 31.37. Rhombencephalosynapsis.** Axial T2-weighted MR image shows fusion of the cerebellar hemispheres and absent vermis. A band of white matter is seen posterior to the third ventricle.

with thalamic fusion, hydrocephalus, and malformations of cortical development. Clinical problems vary with the severity of associated malformations. Isolated rhombencephalosynapsis may be associated with normal cognition or behavioral disorders, hypotonia, and ataxia.

## KEY POINTS

- Advances in developmental genetics have furthered understanding of many congenital brain malformations and their associated extra CNS manifestations.
- DTI shows anomalies of white matter tracts in malformations dominated by cortical anomalies by conventional MR techniques.
- The relative contribution of genetics versus epigenetics in some brain malformations remains poorly defined.
- A given gene mutation may have variable phenotypic expression.

## SUGGESTED READINGS

Barkovich AJ, Guerrini R, Kuzniecky RI, et al. A developmental and genetic classification for malformations of cortical development: update 2012. *Brain*. 2012;135(Pt 5):1348–1369.

Doherty D, Millen KJ, Barkovich AJ. Midbrain and hindbrain malformations: advances in clinical diagnosis, imaging, and genetics. *Lancet Neurol*. 2013;12(4):381–393.

Parrini E, Conti V, Dobyns WB, et al. Genetic basis of brain malformations. *Mol Syndromol*. 2016;7(4):220–233.

## REFERENCES

Full references for this chapter can be found on www.expertconsult.com.

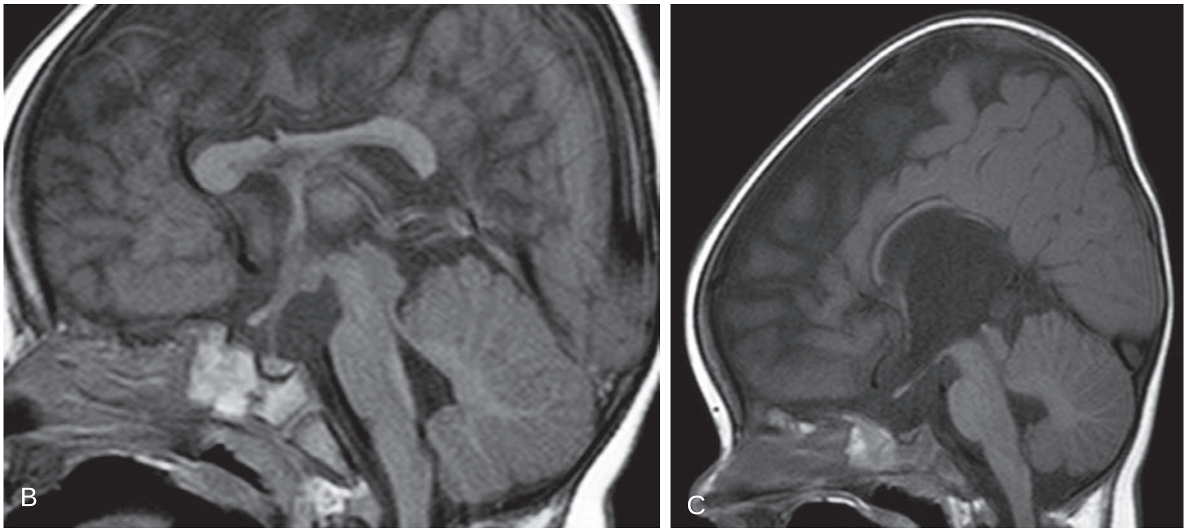

**e-Figure 31.37.** (B) Sagittal T1-weighted MR image shows a dysmorphic corpus callosum after CSF diversion. There is aqueductal stenosis and pontine hypoplasia. The cerebellar primary fissure is absent. (C) Sagittal T1-weighted image from another patient shows diffuse callosal hypoplasia and septal agenesis. The cerebellum is dysplastic with absent fissures.

## REFERENCES

1. Dyment DA, Sawyer SL, Chardon JM, et al. Recent advances in the genetic etiology of brain malformations. *Curr Neurol Neurosci Rep*. 2013;13(8):364.
2. Barkovich AJ, Guerrini R, Kuzniecky RI, et al. A developmental and genetic classification for malformations of cortical development: update 2012. *Brain*. 2012;135(Pt 5):1348–1369.
3. Parrini E, Conti V, Dobyns WB, et al. Genetic basis of brain malformations. *Mol Syndromol*. 2016;7(4):220–233.
4. Tortori-Donati P, Rossi A, Biancheri R. Brain malformations. In: Tortori-Donati P, Rossi A, eds. *Pediatric Neuroradiology: Brain, Head, Neck and Spine*. 1st ed. Berlin, Germany: Springer; 2005. [Chapter 4].
5. Catala M. Embryology of the brain. In: Tortori-Donati P, Rossi A, eds. *Pediatric Neuroradiology: Brain, Head, Neck and Spine*. 1st ed. Berlin, Germany: Springer; 2005. [Chapter 1].
6. Stiles J, Jernigan TL. The basics of brain development. *Neuropsychol Rev*. 2010;20(4):327–348.
7. David DJ, Proudman TW. Cephaloceles: classification, pathology, and management. *World J Surg*. 1989;13(4):349–357.
8. Gao Z, Massimi L, Rogerio S, et al. Vertex cephaloceles: a review. *Childs Nerv Syst*. 2014;30(1):65–72.
9. Naidich TP, Altman NR, Braffman BH, et al. Cephaloceles and related malformations. *AJNR Am J Neuroradiol*. 1992;13(2):655–690.
10. McLone DG, Knepper PA. The cause of Chiari II malformation: a unified theory. *Pediatr Neurosci*. 1989;15(1):1–12.
11. Tortori-Donati P, Rossi A, Biancheri R, et al. Magnetic resonance imaging of spinal dysraphism. *Top Magn Reson Imaging*. 2001;12(6):375–409.
12. Barkovich AJ. Congenital anomalies of the spine. In: Barkovich AJ, ed. *Pediatric Neuroimaging*. 4th ed. Philadelphia, PA: Lippincott Williams and Wilkins; 2005:704–772.
13. Tortori-Donati P, Rossi A, Biancheri R, et al. Congenital malformations of the spine and spinal cord. In: Tortori-Donati P, Rossi A, eds. *Pediatric Neuroradiology: Brain, Head, Neck and Spine*. Berlin, Germany: Springer; 2005:1567–1568.
14. McLone DG, Naidich TP. Developmental morphology of the subarachnoid space, brain vasculature, and contiguous structures, and the cause of the Chiari II malformation. *AJNR Am J Neuroradiol*. 1992;13(2):463–482.
15. Au KS, Northrup H. Genetic complexity of human myelomeningocele. *Genetics*. 2013;2:116. doi:10.4172/2161-1041.1000116.
16. Adzick NS, Thom EA, Spong CY, et al. A randomized trial of prenatal versus postnatal repair of myelomeningocele. *N Engl J Med*. 2011;364(11):993–1004.
17. Rollins N, Joglar J, Perlman J. Coexistent holoprosencephaly and Chiari II malformation. *AJNR Am J Neuroradiol*. 1999;20(9):1678–1681.
18. Muller F, O'Rahilly R. Mediobasal prosencephalic defects, including holoprosencephaly and cyclopia, in relation to the development of the human forebrain. *Am J Anat*. 1989;185(4):391–414.
19. Solomon BD, Gropman A, Muenke M. Holoprosencephaly overview. In: Pagon RA, Adam MP, Ardinger HH, et al., eds. *GeneReviews® [Internet]*. Seattle (WA): University of Washington, Seattle; 1993-2017; 2000 Dec 27 [Updated 2013 Aug 29]. Available from: https://www.ncbi.nlm.nih.gov/books/NBK1530/.
20. Petryk A, Graf D, Marcucio R. Holoprosencephaly: signaling interactions between the brain and the face, the environment and the genes, and the phenotypic variability in animal models and humans. *Wiley Interdiscip Rev Dev Biol*. 2015;4(1):17–32.
21. Winter TC, Kennedy AM, Woodward PJ. Holoprosencephaly: a survey of the entity, with embryology and fetal imaging. *Radiographics*. 2015;35(1):275–290.
22. Solomon BD, Mercier S, Vélez JI, et al. Analysis of genotype-phenotype correlations in human holoprosencephaly. *Am J Med Genet C Semin Med Genet*. 2010;154C(1):133–134.
23. Barkovich AJ, Simon EM, Clegg NJ, et al. Analysis of the cerebral cortex in holoprosencephaly with attention to the sylvian fissures. *AJNR Am J Neuroradiol*. 2002;23(1):143–150.
24. Simon EM, Hevner R, Pinter JD, et al. Assessment of the deep gray nuclei in holoprosencephaly. *AJNR Am J Neuroradiol*. 2000;21(10):1955–1961.
25. Rollins N. Semilobar holoprosencephaly seen with diffusion tensor imaging and fiber tracking. *AJNR Am J Neuroradiol*. 2005; 26(8):2148–2152.
26. Simon EM, Hevner R, Pinter JD, et al. The middle interhemispheric variant of holoprosencephaly. *AJNR Am J Neuroradiol*. 2002;23(1):151–156. Erratum in *AJNR Am J Neuroradiol* 2002;23(4):742.
27. Verschuuren S, Poretti A, Meoded A, et al. Diffusion tensor imaging and fiber tractography in syntelencephaly. *Neurographics*. 2013;3(4):164–168.
28. Schell-Apacik CC, Wagner K, Bihler M, et al. Agenesis and dysgenesis of the corpus callosum: clinical, genetic and neuroimaging findings in a series of 41 patients. *Am J Med Genet A*. 2008;146A(19):2501–2511.
29. Chinn GA, Hirokawa KE, Chuang TM, et al. Agenesis of the Corpus Callosum due to defective glial wedge formation in Lhx2 mutant mice. *Cereb Cortex*. 2015;25(9):2707–2718.
30. Paul LK, Brown WS, Adolphs R, et al. Agenesis of the corpus callosum: genetic, developmental and functional aspects of connectivity. *Nat Rev Neurosci*. 2007;8(4):287–299.
31. Barkovich AJ, Norman D. Anomalies of the corpus callosum: correlation with further anomalies of the brain. *AJNR Am J Neuroradiol*. 1988;9(3):493–501.
32. Hetts SW, Sherr EH, Chao S, et al. Anomalies of the corpus callosum: an MR analysis of the phenotypic spectrum of associated malformations. *AJR Am J Roentgenol*. 2006;187(5):1343–1348.
33. Wahl M, Strominger Z, Jeremy RJ, et al. Variability of homotopic and heterotopic callosal connectivity in partial agenesis of the corpus callosum: a 3T diffusion tensor imaging and Q-ball tractography study. *AJNR Am J Neuroradiol*. 2009;30(2):282–289.
34. Rollins NK. Diffusion imaging of the congenitally thickened corpus callosum. *AJNR Am J Neuroradiol*. 2013;34(3):660–665.
35. Thornton GK, Woods CG. Primary microcephaly: do all roads lead to Rome? *Trends Genet*. 2009;25(11):501–510.
36. Mirzaa GM, Ashwal S, Dobyns WB. Disorders of brain size. In: Swaiman KF, Ashwal S, Ferriero DM, et al, eds. *Swaiman's Pediatric Neurology: Principles and Practice*. 5th ed. Edinburgh: Elsevier Saunders; 2012:173–201.
37. Mirzaa GM, Conway RL, Gripp KW, et al. Megalencephaly-capillary malformation (MCAP) and megalencephaly-polydactyly-polymicrogyria-hydrocephalus (MPPH) syndromes: two closely related disorders of brain overgrowth and abnormal brain and body morphogenesis. *Am J Med Genet A*. 2012;158A(2):269–291.
38. Sim JC, Scerri T, Fanjul-Fernández M, et al. Familial cortical dysplasia caused by mutation in the mammalian target of rapamycin regulator NPRL3. *Ann Neurol*. 2016;79(1):132–137.
39. Liu JS. Molecular genetics of neuronal migration disorders. *Curr Neurol Neurosci Rep*. 2011;11(2):171–178.
40. Rivière JB, van Bon BW, Hoischen A, et al. De novo mutations in the actin genes ACTB and ACTG1 cause Baraitser-Winter syndrome. *Nat Genet*. 2012;44(4):440–444, S1-2.
41. van Wijk E, Krieger E, Kemperman MH, et al. A mutation in the gamma actin 1 (ACTG1) gene causes autosomal dominant hearing loss (DFNA20/26). *J Med Genet*. 2003;40(12):879–884.
42. Fink KR, Thapa MM, Ishak GE, et al. Neuroimaging of pediatric central nervous system cytomegalovirus in. *Radiographics*. 2010;30(7):1779–1796.
43. Baptista T, Quaghebeur G, Alarcon A. Neuroimaging findings of babies with microcephaly and presumed congenital Zika virus infection. *BMJ*. 2016;353:i219.
44. Guerrini R, Dobyns WB. Malformations of cortical development: clinical features and genetic causes. *Lancet Neurol*. 2014;13(7):710–726.
45. Blümcke I, Thom M, Aronica E, et al. The clinicopathologic spectrum of focal cortical dysplasias: a consensus classification proposed by an ad hoc Task Force of the ILAE Diagnostic Methods Commission. *Epilepsia*. 2011;52(1):158–174.
46. Watrin F, Manent JB, Cardosa C, et al. Causes and consequences of grey matter heterotopia. *CNS Neurosci Ther*. 2015;21(2):112–122.
47. Leventer RJ, Jansen A, Pilz DT, et al. Clinical and imaging heterogeneity of polymicrogyria: a study of 328 patients. *Brain*. 2010;133(Pt 5):1415–1427.
48. Barkovich AJ. Current concepts of polymicrogyria. *Neuroradiology*. 2010;52(6):479–487.
49. Judkins AR, Martinez D, Ferreira P, et al. Polymicrogyria includes fusion of the molecular layer and decreased neuronal populations but normal cortical laminar organization. *J Neuropathol Exp Neurol*. 2011;70(6):438–443.
50. Crino PB. mTOR: A pathogenic signaling pathway in developmental brain malformations. *Trends Mol Med*. 2011;17(12):734–742.
51. Aronica E, Becker AJ, Spreafico R. Malformations of cortical development. *Brain Pathol*. 2012;22(3):380–401.
52. Packard AM, Miller VS, Delgado MR. Schizencephaly: correlations of clinical and radiologic features. *Neurology*. 1997;48(5):1427–1434.
53. Fry AE, Cushion TD, Pilz DT. The genetics of lissencephaly. *Am J Med Genet C Semin Med Genet*. 2014;166C(2):198–210.

54. Keays DA, Tian G, Poirier K, et al. Mutations in alpha-tubulin cause abnormal neuronal migration in mice and lissencephaly in humans. *Cell*. 2007;128(1):45–57.
55. [deleted in review]
56. Poirier K, Saillour Y, Bahi-Buisson N, et al. Mutations in the neuronal ß-tubulin subunit TUBB3 result in malformation of cortical development and neuronal migration defects. *Hum Mol Genet*. 2010;19(22):4462–4473.
57. Kumar RA, Pilz DT, Babatz TD, et al. TUBA1A mutations cause wide spectrum lissencephaly (smooth brain) and suggest that multiple neuronal migration pathways converge on alpha tubulins. *Hum Mol Genet*. 2010;19(14):2817–2827.
58. Jissendi-Tchofo P, Kara S, Barkovich AJ. Midbrain-hindbrain involvement in lissencephalies. *Neurology*. 2009;72(5):410–418.
59. Rollins NK, Booth TN, Chahrour MH. Variability of Ponto-cerebellar fibers by diffusion tensor imaging in diverse brain malformations. *J Child Neurol*. 2016;pii: 0883073816680734. [Epub ahead of print].
60. Devisme L, Bouchet C, Gonzalès M, et al. Cobblestone lissencephaly: neuropathological subtypes and correlations with genes of dystroglycanopathies. *Brain*. 2012;135(Pt 2):469–482.
61. Doherty D, Millen KJ, Barkovich AJ. Midbrain and hindbrain malformations: advances in clinical diagnosis, imaging, and genetics. *Lancet Neurol*. 2013;12(4):381–393.
62. Barkovich AJ, Millen KJ, Dobyns WB. A developmental and genetic classification for midbrain-hindbrain malformations. *Brain*. 2009;132(Pt 12):3199–3230.
63. Watanabe H, Murakami F. Real time analysis of pontine neurons during initial stages of nucleogenesis. *Neurosci Res*. 2009;64(1):20–29.
64. Quisling RG, Barkovich AJ, Maria BL. Magnetic resonance imaging features and classification of central nervous system malformations in Joubert syndrome. *J Child Neurol*. 1999;14(10):628–635.
65. Parisi M, Glass I. Joubert syndrome and related disorders. In: Pagon RA, Adam MP, Ardinger HH, et al., eds. *GeneReviews® [Internet]*. Seattle (WA): University of Washington, Seattle, 1993-2017; 2003 Jul 9 [Updated 2013 Apr 11]. Available from: https://www.ncbi.nlm.nih.gov/books/NBK1325/.
66. Widjaja E, Blaser S, Raybaud C. Diffusion tensor imaging of midline posterior fossa malformations. *Pediatr Radiol*. 2006;36(6):510–517.
67. Poretti A, Meoded A, Rossi A, et al. Diffusion tensor imaging and fiber tractography in brain malformations. *Pediatr Radiol*. 2013;43(1):28–54.
68. Barth PG, Majoie CB, Caan MW, et al. Pontine tegmental cap dysplasia: a novel brain malformation with a defect in axonal guidance. *Brain*. 2007;130(Pt 9):2258–2266.
69. Moore HE, Moore KR. Magnetic resonance imaging features of complex Chiari malformation variant of Chiari 1 malformation. *Pediatr Radiol*. 2014;44(11):1403–1411.
70. Patel S, Barkovich AJ. Analysis and classification of cerebellar malformations. *AJNR Am J Neuroradiol*. 2002;23(7):1074–1087.
71. Bosemani T, Orman G, Boltshauser E, et al. Congenital abnormalities of the posterior fossa. *Radiographics*. 2015;35(1):200–220.
72. Ishak GE, Dempsey JC, Shaw DW, et al. Rhombencephalosynapsis: a hindbrain malformation associated with incomplete separation of midbrain and forebrain, hydrocephalus and a broad spectrum of severity. *Brain*. 2012;135(Pt 5):1370–1386.

# 32 Hydrocephalus

Giulio Zuccoli and Subramanian Subramanian

Hydrocephalus means "water in the brain." It is the morphologic end result of many different processes related to enlarging ventricles with compression on brain parenchyma and subarachnoid spaces leading to raised intracranial pressure (ICP). The active enlargement of cerebrospinal fluid (CSF) space in the ventricles eventually leads to loss of brain tissue. By convention, ventriculomegaly associated with increased ICP is termed *hydrocephalus*. It is crucial to differentiate it from *ex vacuo* enlargement of the ventricles secondary to volume loss or from anomalies that may alter the morphology of the ventricular system thus mimicking hydrocephalus.

Hydrocephalus is one of the most common sequelae of any insult to a child's central nervous system (CNS). Hydrocephalus occurs in 1 in 2000 live births and is associated with one-third of all CNS malformations. Since the 1970s, the incidence of spinal dysraphism–related hydrocephalus has declined[1] primarily due to maternal folate therapy, and vaccinations have decreased the number of patients with meningitis who may have been progressed to hydrocephalus.

## PHYSIOLOGY OF CEREBROSPINAL FLUID

CSF appears in response to degeneration of the primitive mesenchyma that surrounds the brain. Although the precise timing of CSF formation is not clear, CSF circulation from the ventricles to the subarachnoid space does not occur until after formation of the fourth ventricle outlet foramina at the ninth to tenth week of gestation.

Approximately 60% of CSF is produced by the choroid plexus, and the rest is produced extrachoroidally, possibly across parenchymal capillaries or by the ependyma itself. The rate of choroid plexus CSF production in adults is approximately 500 mL/24 hr. Normal CSF volume in an adult is estimated to be approximately 150 mL. The CSF volume in a neonate is approximately 50 mL.

The sites of CSF absorption remain controversial. It is widely accepted that arachnoid villi are one of the major sites in adults and older children.[2] The arachnoid villi (pacchionian granulations) are not developed in children until the closure of the fontanels. Studies suggest that a portion of CSF drains through the perivascular and perineural spaces into the lymphatic system or through the capillaries of the brain and spinal cord.[3] Others suggest that the arachnoid villi and granulation are poorly formed in neonates and that the majority of CSF absorption occurs through the lymphatic and venous system.[4]

## MECHANISMS OF HYDROCEPHALUS

Several theories have been used to explain the pathophysiology of hydrocephalus. Two widely accepted theories include the bulk flow theory and the Greitz model (hydrodynamic theory).

### Bulk Flow Theory

According to the bulk flow theory, hydrocephalus occurs as a result of imbalance between the production and the absorption of CSF. An obstruction inside the ventricular system proximal to fourth ventricle foramen of Lushka and Magendie causes obstructive hydrocephalus, whereas an obstruction outside the ventricular system causes communicating hydrocephalus.

Increased CSF production is rare but may occur with choroid plexus papilloma. Decreased CSF uptake occurs as a result of obstruction to CSF flow anywhere along the CSF pathway. The common sites of obstruction along the CSF pathway are the foramen of Monro, the aqueduct of Sylvius, the fourth ventricle outlet foramina, the basal cisterns, and the arachnoid villi.

### Hydrodynamic Model for Cerebrospinal Fluid Circulation

The hydrodynamic model is based on the concept that the absorption of CSF occurs through the capillaries in the CNS rather than through the arachnoid granulations and villi.[3] The skull is a nonelastic housing for brain tissue; blood, CSF, and brain tissue are almost incompressible. As stated by the Monro-Kellie doctrine, the total volume of arteries, veins, CSF, and brain confined within the skull cavity and dura mater is constant, and any increase in volume in one or more compartments causes a decrease in volume in the others. The skull and dura mater of children are more compliant. The elasticity of these structures plays a pivotal role in the hydrodynamic theory of hydrocephalus. During the cardiac systole, the expansion of the intracranial arteries increases the ICP, causing CSF displacement into the spinal canal and an increase in the venous outflow. During the cardiac diastole, there is inflow of CSF from the spinal canal, which causes elevation of pressure in the subarachnoid space. Therefore there is increased pressure in the CSF spaces during the entire cardiac cycle, which in turn compresses the venous outlets, causing an increase in outlet resistance and venous "counter" pressure. This pressure is necessary to keep the intracerebral veins sufficiently distended to accommodate the normal cerebral flow.

## CLASSIFICATION

Tully and colleagues identified five subtypes of hydrocephalus without evident extrinsic cause: "developmental hydrocephalus." This new classification is based on the apparent level of obstruction identified on magnetic resonance imaging (MRI): (1) hydrocephalus associated with myelomeningocele; (2) hydrocephalus with apparent aqueductal obstruction; (3) hydrocephalus associated with posterior fossa crowding; (4) hydrocephalus associated with cysts or cephaloceles; and (5) communicating hydrocephalus.[5]

## IMAGING

### Computed Tomography and Magnetic Resonance Imaging

Computed tomography (CT) and MRI are the primary modalities to assess ventricular size. Head ultrasound (US) is used as the initial study in infants with macrocephaly. Several parameters can help in differentiating between hydrocephalus and *ex vacuo* dilatation of ventricles from cerebral atrophy in infants. The parameters that favor the diagnosis of hydrocephalus are listed in Box 32.1.

The most reliable sign of hydrocephalus is the enlargement of anterior and posterior recesses of the third ventricle (Fig. 32.1). This does not occur in *ex vacuo* enlargement of the ventricles and strongly favors a diagnosis of hydrocephalus. The disproportionate enlargement of the recesses occurs because the thin hypothalamus

## Abstract:

Hydrocephalus is the most common end result of insult to pediatric central nervous system. The physiology of cerebrospinal fluid production and mechanism of development of hydrocephalus including bulk flow theory and hydrodynamic model for cerebrospinal fluid circulation has been discussed. The newer classification system of developmental hydrocephalus is based on MRI including hydrocephalus associated with myelomeningocele, hydrocephalus with apparent aqueduct obstruction, hydrocephalus associated with posterior fossa crowding, hydrocephalus associated with cyst or cephaloceles and communicating hydrocephalus. The various imaging findings in hydrocephalus on ultrasound, CT and MRI has been reviewed with emphasis on differentiating ventriculomegaly from hydrocephalus. Genetic factors have a role in development of hydrocephalus and role of ciliary dyskinesia, L1CAM mutation and X-linked inheritance has been discussed. Ultrasound is preferred modality when anterior fontanelle is open. Radiographs and CT scan play an important role in evaluation of shunt malfunction. Rapid MRI protocol is increasingly used to assess shunt malfunction resulting in substantial reduction of radiation. Use of third ventriculostomy in hydrocephalus and assessment of patency of third ventriculostomy by imaging techniques have been discussed.

## Keywords:

Hydrocephalus
CT
MRI
ultrasound
radiograph
aqueduct obstruction
third ventriculostomy
ciliary dyskinesia

### **BOX 32.1** Imaging Characteristics of Hydrocephalus*

Enlargement of the third ventricle, particularly the anterior and posterior recesses
Commensurate dilation of the temporal horn with the lateral ventricles
Narrowing of the mamillopontine distance
Narrowing of the ventricular angle
Widening of the frontal horn radius
Periventricular interstitial edema
Effacement of cortical sulci

*From Barkovich AJ. Hydrocephalus. In Barkovich AJ, ed.* Pediatric Neuroimaging, *4th ed, Philadelphia: Lippincott Williams & Wilkins; 2005:663.*
*Listed in order of diagnostic value.

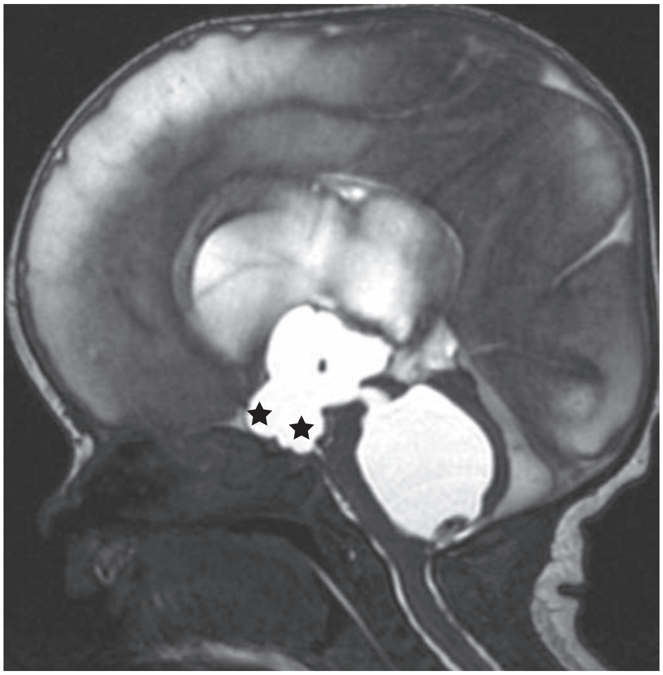

**Figure 32.1. Hydrocephalus and third ventricular enlargement.** Midline sagittal balanced steady-state free precession (SSFP) MR image demonstrates the dilatation of the chiasmatic and infundibular recess of the third ventricle *(asterisks)*. A dilated fourth ventricle is also noted in this patient with fourth ventricular outflow obstruction (entrapped fourth ventricle) from neonatal hemorrhage.

and cisterns surrounding these recesses provide relatively little resistance to expansion. In contrast, the body of the third ventricle is restricted by the rigid thalami, which provide more resistance to expansion. The anterior recesses (i.e., the chiasmal and infundibular) expand earlier than the posterior recesses (i.e., the pineal and suprapineal).[6] These findings are best appreciated on midsagittal magnetic resonance (MR) images.[5] On axial CT, dilation of the anterior recesses of the third ventricle is detected when the third ventricle is larger at the level of the optic chiasm than at the middle of the ventricle.

The enlargement and inferior displacement of the anterior recesses may cause flattening of the pituitary gland with erosion of the dorsum sellae, giving the classical plain film appearance of increased ICP in older children and adults. The recesses may compress the infundibulum and decrease the flow in the hypothalamic-pituitary portal venous system, resulting in hypothalamic-pituitary dysfunction. The enlargement of the suprapineal and pineal recesses may displace the pineal gland inferiorly, and it occasionally elevates the vein of Galen. A large diverticulum of this recess may compress the tectum inferiorly and shorten it in the rostrocaudal direction, mimicking a neoplasm.

Commensurate dilation of the temporal horns with the lateral ventricles is also a strong indicator of hydrocephalus. Temporal horn dilation is best viewed on coronal T2-weighted MR images. The choroidal fissure is enlarged, and the hippocampus is compressed and displaced inferomedially (Fig. 32.2). Studies have suggested that temporal horns dilate less than the bodies of the lateral ventricles in generalized atrophy.[7] This may be related to the small size of the temporal lobes and to their relatively small volume of white matter.

In *ex vacuo* dilatation of ventricles associated with cerebral atrophy, the superior and inferior walls of temporal horns remain parallel and are smaller than the lateral ventricle body. The hippocampus is normally placed, and the choroidal fissures are not enlarged. The Sylvian fissure is enlarged in patients with temporal lobe atrophy. In children with temporal lobe atrophy, temporal horn enlargement is not a reliable sign of hydrocephalus.

The mamillopontine distance is measured on sagittal MRI from the anterior root of the mamillary body to the top of the pons parallel to the anterior mesencephalon (e-Fig. 32.3).[6] The normal average distance is 3.8 mm. The floor of the third ventricle as seen on a sagittal MR images is usually concave downward. With enlargement of the third ventricle, it becomes straightened or convex downward, resulting in reduction of the mamillopontine distance.

The ventricular angle, as defined by Heinz and colleagues, measures the divergence of the frontal horns (e-Fig. 32.4).[7] Concentric enlargement of the frontal horns in hydrocephalus causes diminution of this angle as seen on axial or coronal images and produces an enlargement of the frontal horn radius with a rounded configuration of the frontal horns, or a “Mickey Mouse ears” appearance.

Enlargement of the ventricles disproportionate to enlargement of the cortical sulci favors a diagnosis of hydrocephalus. This parameter is not reliable in children, especially in the first couple of years of life, because patients with communicating hydrocephalus and atrophy have enlargement of both the fluid spaces. Also, the sizes of the ventricles and the subarachnoid spaces may vary tremendously, as seen in infants with benign macrocephaly. Therefore it is important to evaluate ventricular size in conjunction with the patient’s neurologic evaluation and serial head circumference measurements. A large or rapidly enlarging head would favor a diagnosis of hydrocephalus, whereas a small or diminishing head circumference would suggest atrophy.

The presence of periventricular interstitial edema is indicative of hydrocephalus (Fig. 32.5). With elevation of pressure within the ventricles, the normal centripetal flow toward the ventricles is reversed. The CSF is forced out through the ependyma into the surrounding extracellular spaces to be absorbed by alternative routes. This increase in periventricular fluid constitutes interstitial edema. It is best recognized on MRI with fluid-attenuated inversion–recovery (FLAIR) and proton density sequences. It is more difficult to appreciate on T2-weighted images because of the bright signal from the ventricles. Periventricular interstitial edema is difficult to appreciate in neonates and young infants because it is masked by bright signal from immature myelin, with its high water content. On CT, periventricular interstitial edema is seen as hypoattenuation in the periventricular region, with indistinct ventricular margins.

A CSF “flow void” in the third ventricle, aqueduct of Sylvius, and fourth ventricle is accentuated in hydrocephalus as a result of hyperdynamic flow (e-Fig. 32.6). The specificity of this finding has been disputed by some authors.

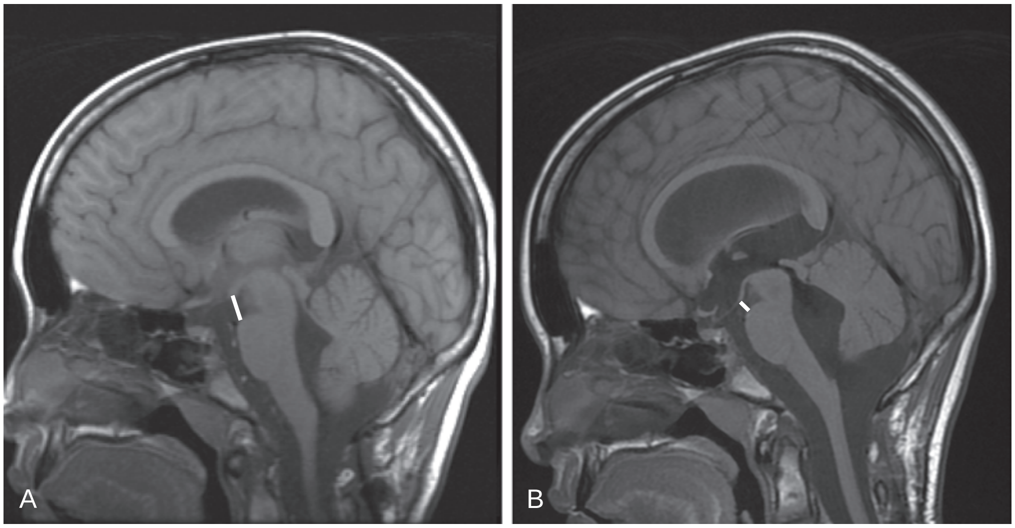

**e-Figure 32.3. Mamillopontine distance.** (A) Baseline MRI in this 11-year-old patient demonstrates normal mamillopontine distance on T1-weighted sagittal midline image. The distance *(bar)* is measured from the anterior base of the mamillary body to the top of the pons parallel to the anterior aspect of the mesencephalon. (B) Reduction in the mamillopontine distance within 6 months due to interval development of hydrocephalus from intraventricular hemorrhage. Note the stretching of corpus callosum and the third ventricular dilatation.

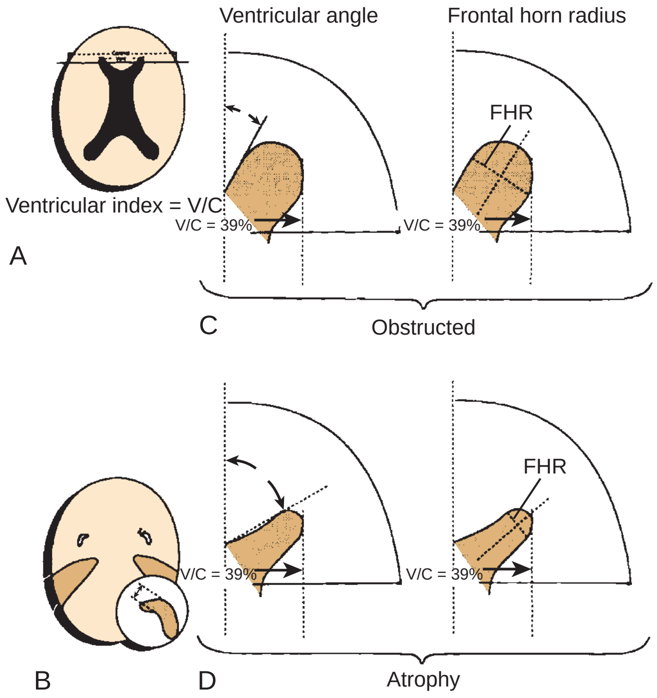

**e-Figure 32.4. Methods of radiographically diagnosing hydrocephalus.** (A) The ventricular index is the ratio of the ventricular diameter at the level of the frontal horns to the diameter of the brain measured at the same level. This is not very sensitive because the ventricular index is enlarged in cerebral atrophy as well as in hydrocephalus. (B) Temporal horns that have enlarged commensurately with the bodies of the lateral ventricles are probably the most sensitive and reliable sign in the differentiation of hydrocephalus from atrophy. There is significantly less dilation of the temporal horns than of the bodies of the lateral ventricles in cerebral atrophy. (C) The ventricular angle measures the divergence of the frontal horn. In theory, the angle made by the anterior or superior margins of the frontal horn at the level of the foramina of Monro is diminished when concentric enlargement of the frontal horns occurs. Compare the illustration of hydrocephalus (top) with that of atrophy (bottom). The ventricular index in both cases is 39%, but the ventricular angle is markedly reduced in hydrocephalus. (D) Concentric dilation produces an enlargement of the frontal horn radius *(FHR)* with a rounded configuration of the frontal horns, or a "Mickey Mouse ears" appearance. *(From Barkovich AJ.* Pediatric Neuroimaging, *4th ed, Philadelphia: Lippincott Williams & Wilkins; 2005:631.)*

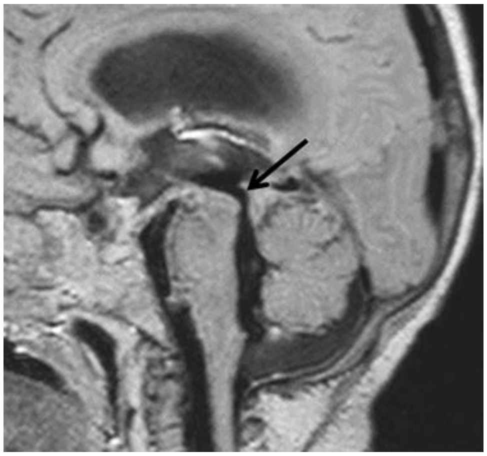

**e-Figure 32.6. Aqueductal flow cerebrospinal fluid flow void.** Sagittal fluid-attenuated–inversion recovery (FLAIR) image demonstrates flow void in the aqueduct of Sylvius *(arrow)* with enlarging lateral ventricles *(not shown),* indicative of hydrocephalus.

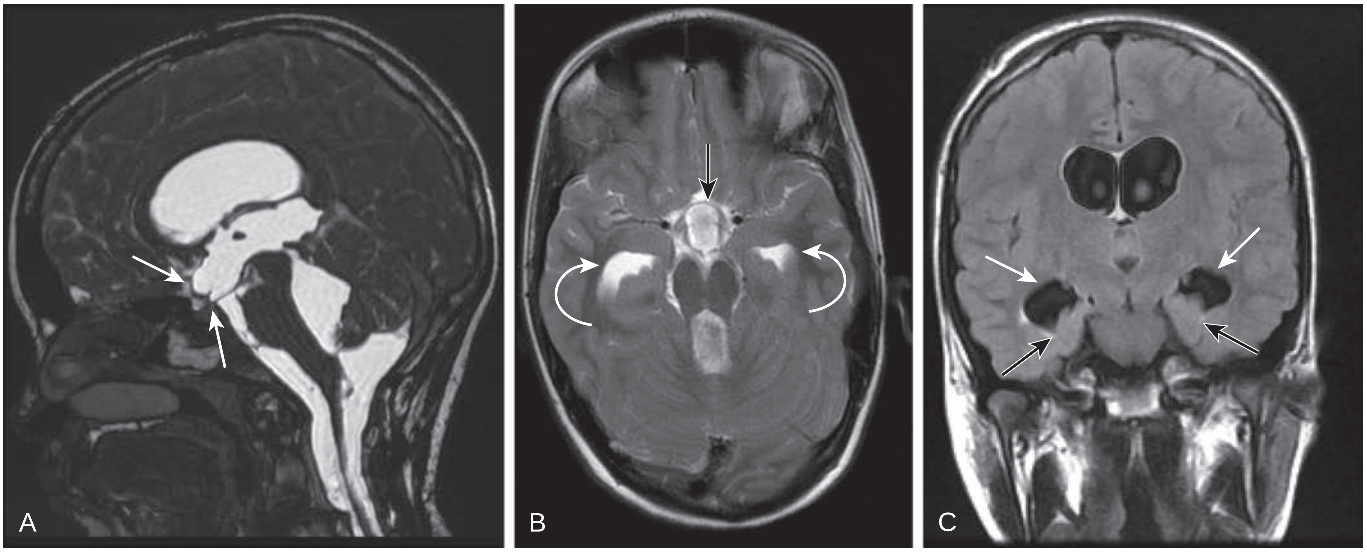

**Figure 32.2. MRI findings in hydrocephalus.** (A) Midsagittal T2-weighted MR image in a 10-year-old girl with tectal glioma demonstrates dilation of the chiasmatic and infundibular recesses *(arrows)*. (B) Axial T2-weighted MR image shows dilated anterior recess *(straight arrow)*. The temporal horns are also dilated *(curved arrows)*. (C) Coronal fluid-attenuated–inversion recovery (FLAIR) MR image shows the characteristic dilation of the temporal horns *(white arrows)* with enlargement of the choroidal fissure and inferomedial displacement of the hippocampi *(black arrows)* and with surrounding increase in signal suggesting increased transependymal cerebrospinal fluid resorption.

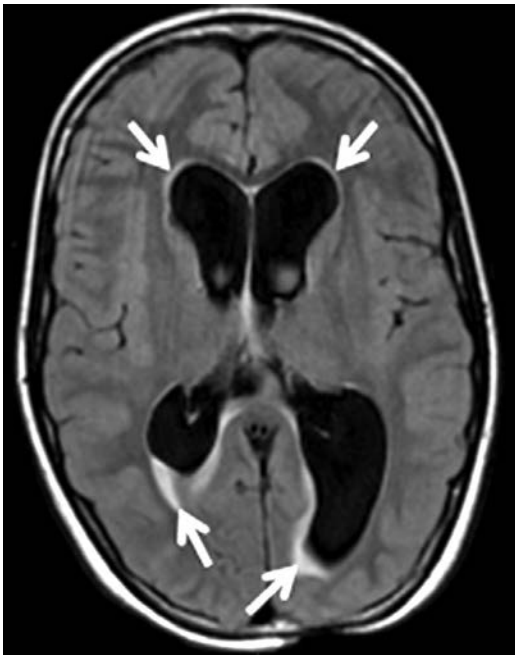

**Figure 32.5. Periventricular interstitial edema.** Axial fluid-attenuated–inversion recovery (FLAIR) MR image at the level of lateral ventricles demonstrates characteristically increased periventricular hyperintensities *(arrows)* indicating transependymal flow of cerebrospinal fluid.

Ventriculomegaly secondary to hydrocephalus causes mass effect and distortion of adjacent brain structures. There is stretching, upward displacement, and smooth, uniform thinning of the corpus callosum as a result of lateral ventricular enlargement. Corpus callosum thinning also occurs in atrophy. It is typically not elevated superiorly and may not be uniformly thin, as seen in hydrocephalus.

Marked hydrocephalus may lead to formation of atrial diverticula, which is herniation of the ventricular wall through the choroidal fissure of the ventricular trigone into the supracerebellar and quadrigeminal cisterns. The atrial diverticula may cause compression and distortion of the tectum. They may also mimic arachnoid cysts in the region of the quadrigeminal cistern.[8]

MRI in hydrocephalus frequently involves utilization of three-dimensional balanced steady-state free precession (SSFP). This sequence is particularly useful in demonstrating arachnoid membranes, intraventricular cysts, and aqueductal stenosis.

Qualitative and quantitative CSF analysis can be performed using phase contrast cine MRI. The technique is useful in demonstration of pulsatile flow at the craniocervical junction, aqueduct of Sylvius, and across a surgically created third ventriculostomy (Fig. 32.7).[9]

## Ultrasound

Head US is a useful initial examination for evaluation of macrocephaly in infants if the anterior fontanelle is open. Transcranial Doppler techniques may be helpful to identify infants with raised ICP, and they may help to determine the need for shunt placement. Under experimental conditions, with elevated ICP, arterial flow tends to be maximally affected during diastole, resulting in elevated pulsatility. Many researchers have demonstrated elevated resistive indices in infants with raised ICP and a subsequent decrease after ventricular tapping. These results, however, have not been uniformly reproducible.[10–12]

## Plain Radiographs

The changes related to elevated ICP on the plain radiograph of the skull depend on the age of the child. In children up to 8 or 10 years of age, sutural diastasis may occur within a few days of elevated pressures (e-Fig. 32.8). After 12 to 13 years of age, sutural diastasis is uncommon early, and the first sign of longstanding hydrocephalus may be erosion of the sellar cortex. The anterior part of the base of the dorsum is the earliest to be eroded. The

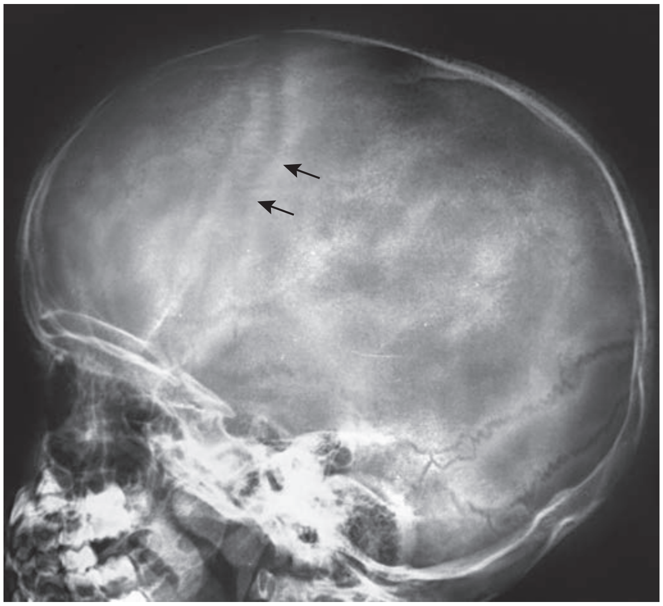

**e-Figure 32.8. Elevated intracranial pressure.** Lateral radiograph of the skull in an 18-month-old child with signs of elevated intracranial pressure, showing diastasis of the coronal sutures *(arrows)*. Magnetic resonance imaging performed subsequently demonstrated a supratentorial ependymoma.

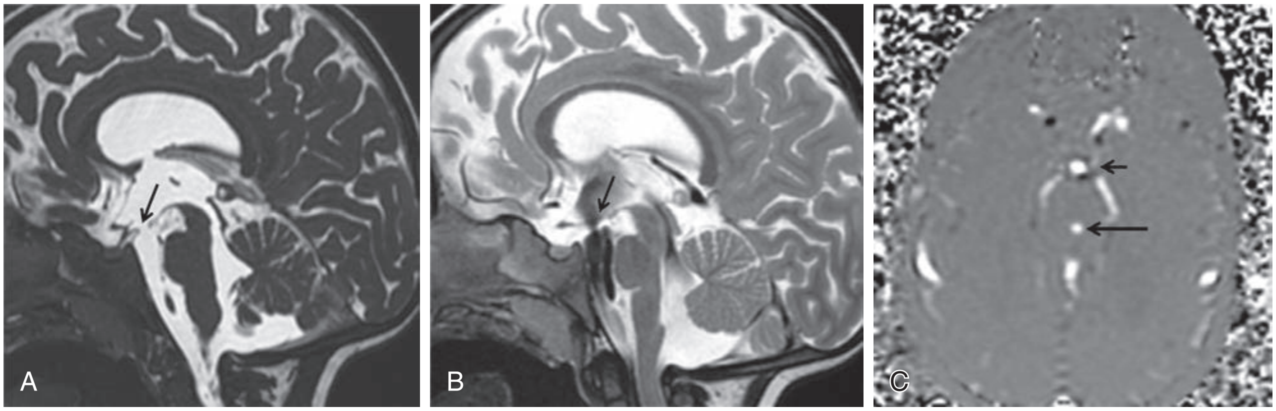

**Figure 32.7. Phase contrast cine MRI.** Images are acquired throughout the cardiac cycle and demonstrate pulsatile cerebrospinal fluid (CSF) motion. (A) Midsagittal steady-state free precession MR image shows patent third ventriculostomy *(arrow)*. (B) Sagittal T2-weighted MR image demonstrates flow void in third ventriculostomy *(arrow)*. (C) Axial phase contrast MR image demonstrates pulsatile CSF flow in third ventriculostomy *(short arrow)* and aqueduct of Sylvius *(long arrow)*.

**BOX 32.2** Hydrocephalus Without Known Extrinsic Causes[5]

**MYELOMENINGOCELE-ASSOCIATED HYDROCEPHALUS**

Proximal obstruction:

1. Aqueduct stenosis *L1CAM* mutation
2. Muscle-Eye-Brain syndrome

Distal obstruction: Posterior fossa crowding leading to Chiari 1

1. Crouzon syndrome
2. Pfeiffer syndrome
3. Carpenter syndrome
4. Achondroplasia
5. Thanatophoric dysplasia
6. Spondyloepiphyseal dysplasia
7. MPPH syndrome (megalencepahly, polydactyly, polymicrogyria, and hydrocephalus)

Hydrocephalus associated with cyst and cephaloceles:
  Oro-Facial-Digital syndrome
  Chudley-McCullough syndrome
  Aicardi syndrome

Communicating hydrocephalus:
  Cardio-facio-cutaneous with pulmonic stenosis
  Gorlin syndrome

Hydrocephalus with known extrinsic causes
Intraventricular hemorrhage
Infection
Trauma tumor vein of Galen malformation
Thrombosis of dural venous sinuses or other causes of obstruction to venous drainage

erosion may spread to involve the floor of the sella. The enlargement of the anterior recesses of the third ventricle is responsible for these changes.

## ETIOLOGY OF HYDROCEPHALUS

### In Newborns and Infants

The common etiologies for hydrocephalus in newborns and infants are listed in Box 32.2.

Infants with ventriculomegaly typically present with macrocephaly. It is critical and often difficult to differentiate between ventriculomegaly caused by communicating hydrocephalus, which requires shunting, and ventriculomegaly related to benign extraaxial fluid of infancy, which is a benign self-limiting condition and does not require intervention. These infants should be assessed clinically for other signs of elevated ICP, such as dilated scalp veins, bulging fontanelles, and sutural diastasis. They may have ocular signs and spasticity in the lower extremities secondary to disproportionate stretching of the corticospinal tracts arising from the leg area in the motor cortex by the enlarged ventricles. Infants with macrocephaly should be evaluated with imaging to assess for ventricular dilation. US is the most common initial modality for imaging infants with macrocrania. However, in patients with macrocephaly presenting with nonspecific symptoms, abusive head trauma should be included in the differential considerations. In these patients, CT or MRI could be obtained as a screening tool.[13]

### Benign ExtraAxial Collections of Infancy

The most common cause of macrocephaly in this age group is benign extraaxial collections of infancy. This condition has been variously called *benign enlargement of subarachnoid spaces in infancy*, *benign external hydrocephalus*, *benign macrocrania*, and *benign subdural collection of infancy*. It is a fairly common condition and rarely comes to clinical attention unless there is rapid increase in head size. These infants typically present between 2 and 6 months of age and have normal neurologic development with no clinical signs of raised ICP. The head circumference is above the 95th percentile and stabilizes along a curve parallel to the 95th percentile by 18 months of age. The subarachnoid spaces are mildly enlarged and return to normal size by 18 to 24 months of age. The CSF spaces are disproportionately larger, with the ventricles only mildly prominent. This condition likely represents transient communicating hydrocephalus from delay in maturation of the arachnoid villi.

Imaging demonstrates mild prominence of the subarachnoid spaces along the frontoparietal convexities, the cortical sulci, the Sylvian fissures, and the anterior interhemispheric fissures (Fig. 32.9). The ventricles are typically normal in size, but they may be mildly enlarged. The extraaxial fluid must be symmetric and have the same signal intensity as CSF, and it should not be associated with mass effect. If the fluid collection is of higher attenuation than CSF, is asymmetric, or exerts mass effect on adjacent structures, MRI may be performed to evaluate for blood or blood byproducts in a traumatic subdural hematoma. Both MRI and US can help differentiate between subarachnoid fluid and subdural hematoma. With enlarged subarachnoid spaces, the cortical veins course through the fluid and lie adjacent to the inner table of the calvarium.

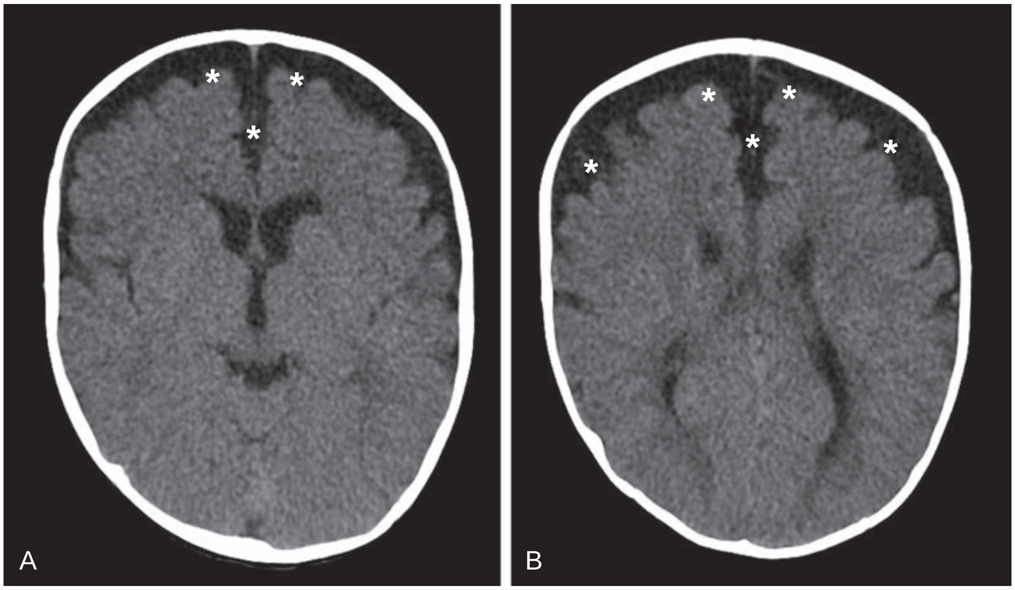

**Figure 32.9. Benign extraaxial collections of infancy.** (A and B) Axial computed tomography shows prominent subarachnoid extraaxial fluid spaces and interhemispheric fissure *(asterisks)*. The ventricles are also mildly prominent.

If the subdural space is enlarged, the cortical veins should be displaced away from the inner table toward the cerebral cortex. The signal intensity of chronic subdural hematoma also differs from that of CSF on MRI.[14] It has been questioned whether enlarged CSF spaces may make these patients more susceptible to subdural hemorrhage from minor trauma, as occurs in children with arachnoid cysts.

The diagnosis of benign extraaxial collection of infancy is a diagnosis of exclusion. Other causes of prominent CSF subarachnoid spaces include congenital anomalies, communicating hydrocephalus, infection, hypercortisolism, dehydration, cerebral atrophy, and drug induced (parenteral nutrition and chemotherapy).

In communicating hydrocephalus, the ventricles are typically disproportionately larger than the subarachnoid spaces (e-Fig. 32.10). At times, the two conditions cannot be differentiated on imaging. The imaging findings should always be interpreted in the context of the clinical history and serial head circumference measurements. Infants with communicating hydrocephalus usually have other signs of raised ICP and an abnormal neurologic examination. When the imaging findings and clinical examination are equivocal, a CSF cisternogram may help to differentiate between the two conditions. Rarely, the issue has to be resolved by invasive ICP monitoring.

### Older Children

Common causes of ventriculomegaly in older children are listed in Box 32.3. Because of the inability of their cranium to expand as quickly as in infants and young children, older children with hydrocephalus have a more acute presentation. They may have the classical triad of headache, vomiting, and lethargy. Children developing chronic hydrocephalus as a result of slowly expanding lesions typically present with persistent morning headaches and intermittent vomiting. Papilledema is often encountered. Focal neurologic deficits from the primary lesion may be present, and pyramidal tract signs, more marked in the lower extremities, are found. Hypothalamic-pituitary dysfunction may also develop as a result of compression of these structures by enlarging anterior recesses of the third ventricle.

**BOX 32.3** Causes of Ventriculomegaly in Older Children

Ventriculomegaly without elevated ICP
*Ex vacuo* dilation secondary to atrophy
Congenital anomalies
Ventriculomegaly with elevated intracranial pressure
Infection
Trauma
Superficial siderosis from prior hemorrhage (see e-Fig. 32.10)
Tumors: Direct pressure or leptomeningeal metastases
Delayed identification of congenital abnormality

## NORMAL PRESSURE HYDROCEPHALUS

Intermittent high CSF pressures with consequent reduced cerebral blood flow may lead to brain damage and can lead to hydrocephalus if there is concomitant reduction in the compliance in the cranial cavity (Greitz model). This is the postulated pathogenesis for normal pressure hydrocephalus (NPH). The loss of compliance is felt to be due to damage to arachnoid membranes or loss of dural elasticity. NPH is mainly a disease of adults with pediatric cases seen in association with prior history of meningitis or intraventricular bleed. CSF volume is displaced at the craniovertebral junction during systole, and the venous stroke volume is decreased. Intracranial CSF pulse pressure is increased (though mean CSF pressure is normal) commensurate with reduced compliance in the meninges.

The CSF pressure assessed at lumbar puncture is normal. On imaging, fast flow or increased velocity flow at the aqueduct is seen on phase contrast cine MRI.

## GENETICS IN HYDROCEPHALUS

Genetic factors may play an important role in development of congenital hydrocephalus. Various animal models of congenital hydrocephalus have demonstrated abnormalities in cerebral

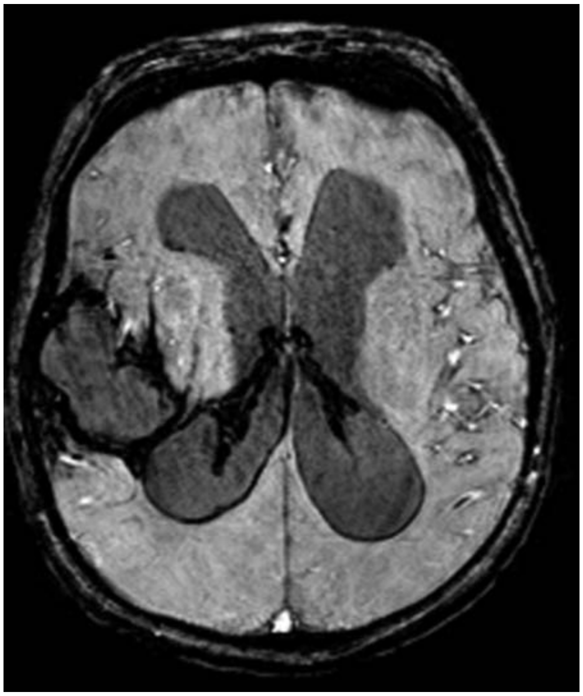

**e-Figure 32.10. Superficial siderosis leading to communicating hydrocephalus.** Axial GRE MR image in a patient with prior hemorrhage demonstrates low signal susceptibility changes in lateral ventricular wall leading to decreased absorption of cerebrospinal fluid. There is encephalomalacia with susceptibility changes in right temporal lobe from prior hemorrhage.

aqueduct or subarachnoid space.[15] There is a higher incidence of aqueduct stenosis in patients with ciliary dyskinesia suggesting abnormalities in ciliary processes in the ependyma may play a role.[15] In children with aqueduct stenosis, up to 14% have defined syndromes, and some patients have L1CAM mutations.[5] Children with congenital hydrocephalus and posterior fossa crowding had craniosynostosis or skeletal dysplasia and frequently demonstrated fibroblast growth factor receptor mutations.[5] Developmental communicating hydrocephalus is noted in children with family members having macrocephaly, with male children being more affected, suggesting X-linked inheritance.[5]

## ASSESSMENT OF CHILDREN WITH VENTRICULAR SHUNTS

### Methods of Shunting

Different methods have been used for CSF shunting, with the goal to decrease ICP by providing an alternative pathway for CSF absorption. The shunt catheters have a proximal intracranial segment connected in series to a valve and distal tubing. The proximal catheter may be inserted through the occipital, frontal, or posterior temporal approach. The placement of the ventriculostomy catheter is optimal if the tip and the side holes of the catheter are not in direct contact with the choroid plexus; this is most possible if the tip of the catheter lies in the frontal horn anterior to the foramen of Monro or in the atrium. This serves to minimize the chances of tissue ingrowth into the holes and occlusion of the proximal catheter. The distal catheter may be placed in various locations, including the peritoneal cavity, pleural cavity, central veins or right atrium, and gallbladder. The peritoneal cavity is the overwhelmingly favored location. The only relative contraindications to its use are active intraperitoneal infection, significant risk of future peritoneal infections, severe adhesions, and previous failure of peritoneal shunts as a result of inadequate absorption.

### Shunt Malfunction

One of the most common acute complications from insertion of the proximal catheter is hemorrhage, occurring in approximately 1% of patients (Box 32.4). It is even more common when an old catheter is removed. Neuronal injury may result in focal deficits such as hemiparesis if the catheter traverses the internal capsule. Seizures can occur and are more common with catheters placed through a frontal trajectory. With lumbar catheters, there is a 5% reported risk of radiculopathy and a 1% risk of myelopathy.

It is an axiom in pediatric medicine that, when a child with a ventricular shunt has a medical problem, the shunt is the cause of the problem until proven otherwise. The causes of shunt malfunction can be broadly divided into mechanical shunt failure involving the shunt apparatus[1] and shunt infection.[2] The most common time for the shunt to fail is in the first 6 months after insertion. Multiple studies indicate that patients younger than 6 months are at a higher risk of shunt malfunction. The overall 1-year failure rate is 40% for patients with a corrected median age of 55 days and 30% in older age groups.

#### Mechanical Failure of the Shunt

The leading cause of shunt malfunction is mechanical failure. Obstruction is most common at the proximal end and can result from occlusion by brain parenchyma, choroid plexus, protein plug, or tumor cells.[16] Disconnection may occur at any point in the shunt apparatus, but it is most frequent at the site of connection between the valve and the peritoneal catheter (e-Fig. 32.11) and at the site of increased mobility (i.e., the lateral neck). The shunt may migrate to a variety of sites.

**BOX 32.4** Complications of Catheter Insertion

Intracranial hemorrhage
Damage to neuronal tissue
Pneumocephalus; air lock in the shunt
Altered CSF flow dynamics: Loculated fourth ventricle
Slit ventricles
Subdural hematoma
Meningeal fibrosis
Craniosynostosis

*CSF*, Cerebrospinal fluid.

**BOX 32.5** Abdominal Complications of Distal Shunt Catheter

Acute abdomen
Ascites
Cerebrospinal fluid: Enteric fistula
Inflammatory pseudotumor of mesentery
Inguinal hernia
Intrahepatic abscess
Omental cyst
Perforation of bowel
Perforation of gallbladder
Pseudocyst
Small bowel obstruction
Umbilical fistula
Ureter obstruction
Volvulus

*From Martin AE, Gaskill SJ. Cerebrospinal fluid shunts: complication and results. In McLone DG, ed.* Pediatric Neurosurgery: Surgery of the Developing Nervous System, *4th ed, Philadelphia: WB Saunders; 2001:223.*

Preperitoneal displacement of the catheter may be evidenced by the sudden onset of shunt malfunction. This appears on a shunt survey as double-backing of the catheter through the peritoneal opening. The distal catheter has its own unique set of complications (Box 32.5), which are best evaluated with abdominal imaging. A pseudocyst may occur at the distal end, with or without infection, causing impairment of CSF absorption.

Chronic shunt placement may alter CSF flow dynamics, resulting in isolated ventricles. Isolated fourth ventricle may occur with shunting of noncommunicating hydrocephalus. On shunting, enlarged lateral ventricles collapse, resulting in obstruction of the aqueduct of Sylvius that over time becomes irreversible. The CSF being produced in the fourth ventricle cannot be drained from above because of obstruction at the aqueduct or below (because there is original outlet obstruction), causing progressive dilation of the fourth ventricle (e-Figs. 32.12 and 32.13).

Other chronic complications include subdural hematomas, which occur because of rapid decompression of the ventricular system before the brain parenchyma can expand to fill the cranial vault. Meningeal fibrosis may rarely occur, possibly as a reaction to chronic subdural hematoma. The meninges show profuse enhancement on postcontrast images. Craniosynostosis is a rare complication occurring only in patients shunted before 6 months of age.

#### Shunt Infections

Shunt infections remain an important and distressing cause of shunt failure, with an overall infection rate of 5% to 10%. The

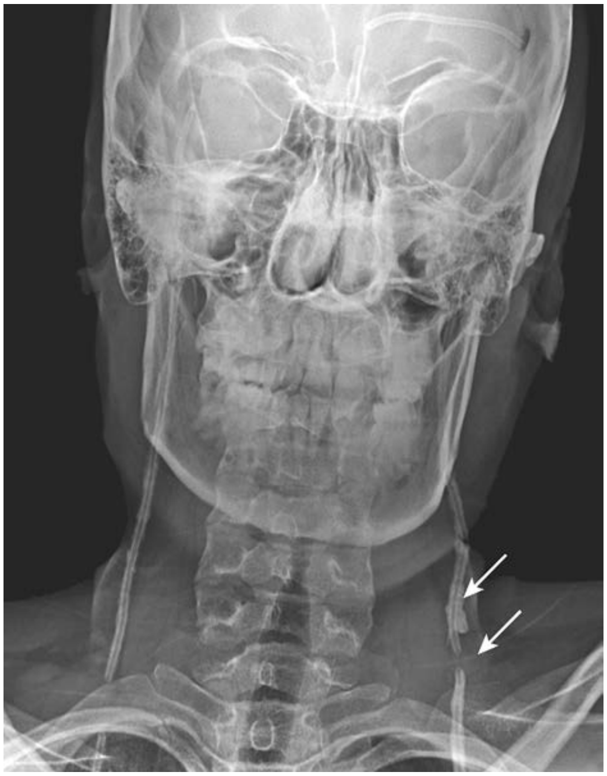

**e-Figure 32.11. Broken shunt.** Frontal radiograph of the neck in a patient with shunt malfunction new onset irritation and vomiting shows pericatheter calcification and break in the distal tubing *(arrows)*.

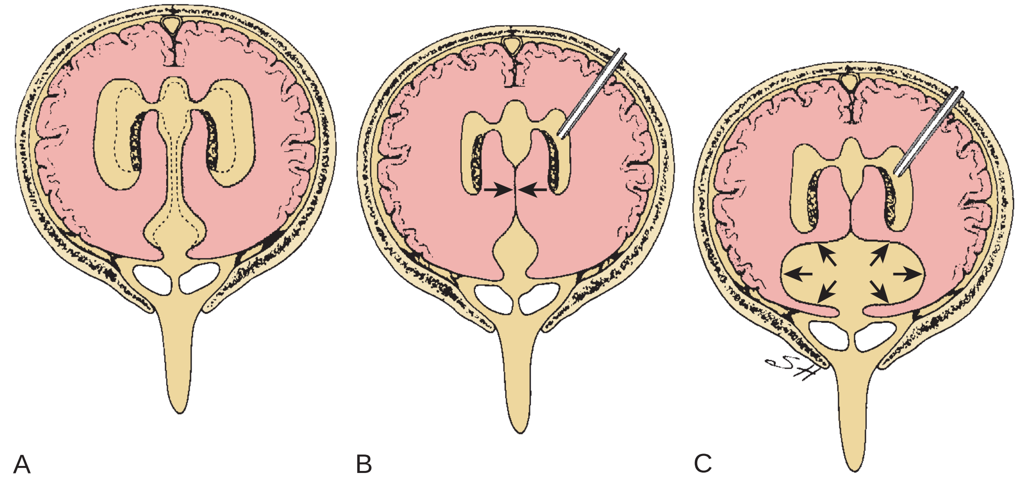

**e-Figure 32.12. Diagram of the pathophysiology of the isolated fourth ventricle.** (A) Panventricular hydrocephalus with dilation of the aqueduct of Sylvius and blockage of the basal cisterns. (B) The shunting of the lateral ventricles leads to collapse of the aqueduct of Sylvius *(arrows)* that, with time, becomes irreversible. (C) Because cerebrospinal fluid is still being produced in the fourth ventricle and cannot be drained from above or below, it causes progressive dilation of the fourth ventricle *(arrows)*. *(From Rekate HL. Treatment of hydrocephalus. In McLone DG, ed.* Pediatric Neurosurgery: Surgery of the Developing Nervous System, *4th ed, Philadelphia: WB Saunders; 2001:213.)*

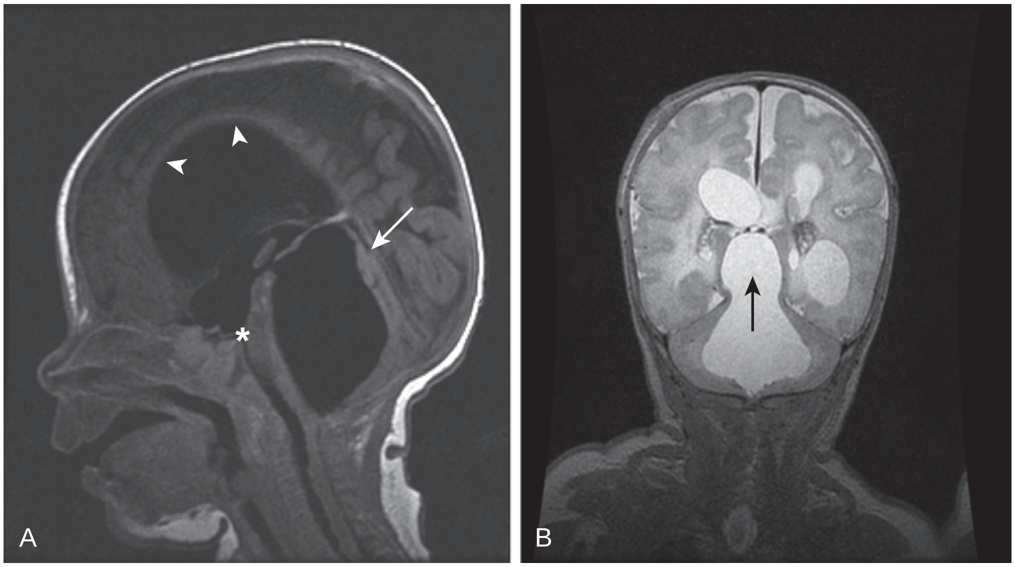

**e-Figure 32.13. Trapped fourth ventricle.** (A) Midsagittal T1-weighted MR image in a 12-week-old infant with neonatal ventriculitis and intraventricular abscess shows marked dilatation and superior herniation of the enlarged fourth ventricle *(arrow)*. Note also the dilated anterior recess of third ventricle *(asterisk)* and thinning of corpus callosum *(arrowheads)*. (B) Coronal T2-weighted MR image shows fourth ventricular enlargement and supratentorial herniation *(arrow)* with cystic hydrocephalus as a result of resolving intraventricular infection.

rate of infection in infants is much higher (10%–20%). Most infections present within 2 months of surgery, indicating that they occur during the surgery. Shunt infection can also occur from other abdominal surgical procedures, such as bladder augmentation and gastrostomy tube placement.

## EVALUATION OF SHUNT MALFUNCTION

Diagnosis of shunt malfunction is based primarily on the clinical signs and symptoms with which the patient presents. The shunts may be evaluated by static or dynamic methods (Box 32.6).

Plain radiographs of the shunt and CT or MRI of the head are the primary radiologic investigations for evaluating shunt malfunction. The advantages of CT are that it is widely available and relatively inexpensive, and it allows quick examination and reproducible assessment of ventricular size and catheter position. However, children with hydrocephalus undergo many imaging procedures in their lifetime, so minimizing radiation exposure is especially important to reduce potential risks.

MRI is an alternative to CT for shunt evaluation, often performed with steady-state gradient recalled sequence and balanced SSFP sequences (Fig. 32.14). Fast MRI sequences such as single-shot or half-Fourier T2-weighted sequences and T1-weighted spoiled gradient sequences reduce the scan time dramatically, decreasing or eliminating the need for sedation. These sequences provide reliable visualization of the catheter, assessment of ventricular size, and anatomic detail without the need for sedation.[18]

**BOX 32.6** Evaluation of Shunt Malfunction

Static methods
Plain radiographs
Imaging: CT, MRI, US
Dynamic methods
Shunt injection studies (shuntogram)
Nuclear medicine studies
Others: Cine phase contrast MRI, Doppler

Plain radiographs of the entire shunt are obtained with frontal and lateral views of the skull, and with frontal views of the chest and abdomen. These assess for discontinuity or migration of the shunt. Calcification along the tubing is common in old shunts, which are prone to fracture (see e-Fig. 32.11). Abdominal complications such as mass effect from a pseudocyst, bowel perforation, and adhesions resulting in bowel obstruction are also evaluated on plain radiographs. If preperitoneal placement of distal tubing is suspected, with tight coiling of the peritoneal catheter, a lateral radiograph should be obtained.[17]

Imaging of the head is performed to assess changes in the shape and size of the ventricles as well as any other collections or loculated compartments. Imaging is usually obtained only when the patient is sick, so there is often no valid baseline comparison when the patient is well. The position and course of the catheter can be assessed. Dilation of ventricles compared with previous images is the clearest sign of shunt malfunction. However, some patients with shunt malfunction may demonstrate little if any enlargement, and some may have small ventricles. Therefore the ventricular size alone, especially in the absence of previous studies, may be misleading. Enlarged ventricles are seen in approximately 70% of patients with mechanical obstruction and 30% of those with shunt infection.

The subset of symptomatic patients with little or no change in ventricular size, or with small ventricles, may benefit from shunt tapping and, rarely, from a shuntogram. Tapping of the shunt is also helpful for CSF sampling if shunt infection is suspected. The shunt is tapped proximal to the reservoir with a 25-gauge butterfly needle after meticulous preparation of the site. Free flow of CSF may indicate adequate patency of the proximal catheter. Manometric measurements can also be performed. Contrast can be injected into the valve chamber at the time of shunt tapping and a shuntogram obtained with radiographs taken at 1 and 15 minutes. Shunt injection studies are more helpful in diagnosing distal malfunction, and peritoneal spill of contrast proves patency of the distal tubing. The results of the shuntogram may be inconclusive in patients with partially obstructed shunts, and there is a 25% to 40% rate of false-positive results in patients with proximal malfunction (i.e., failure of proximal CSF to pass through the distal tubing despite patent tubing). Similarly, radioisotope studies are occasionally used to assess shunt patency and obtain physiologic information about CSF flow through the shunt.

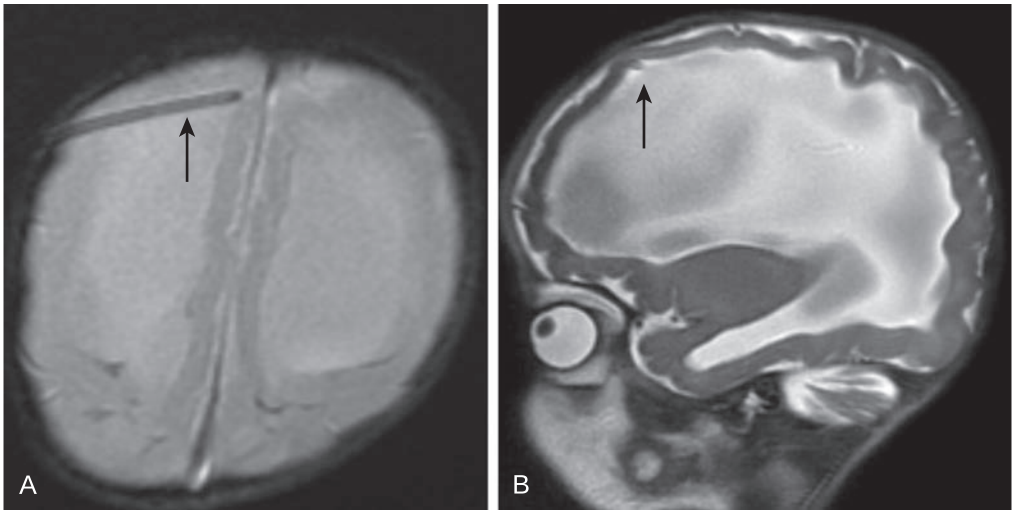

**Figure 32.14. Shunt evaluation.** (A) Axial steady-state gradient sequence demonstrates the course of the catheter in the right lateral ventricle *(arrow)*. (B) Sagittal balanced steady-state free precession (SSFP) sequence demonstrates the tip of the catheter within an enlarged lateral ventricle *(arrow)*.

## Slit Ventricle Syndrome

In general, small ventricles in a child with a shunt are good, and large ventricles are bad. A small subset of 1% to 5% of patients with very small, or slit, ventricles becomes symptomatic with acute or chronic headaches, nausea, vomiting, and lethargy. These patients have been lumped together under the term slit ventricle syndrome (Fig. 32.15). This terminology is confusing as it has been used for multiple clinical entities.[19] At one end of the spectrum is a child with small ventricles who is very sick as a result of intracranial hypertension. At the other end of the spectrum is an asymptomatic child with a harmless and inconsequential CT finding.

## ENDOSCOPIC THIRD VENTRICULOSTOMY

There is increasing interest in treating hydrocephalus with endoscopic procedures (Box 32.7). The major attraction is to give these children freedom from lifelong dependency on shunts and their numerous inherent complications. Endoscopic third ventriculostomy (ETV) is most often used for obstructive hydrocephalus, where the success rate is reportedly 60% to 70%. The technique involves using an endoscope to perforate the floor of the third ventricle just anterior to the mammillary bodies, thereby establishing communication between the ventricles and cisterns. Endoscopic fourth ventricular aqueductoplasty, with or without stent placement, has recently been described as an alternative method when ETV is not feasible.[20] This is especially useful in patients with a trapped fourth ventricle. In patients who have an intrathird ventricular tumor causing obstruction of the foramen of Monro or of the mouth of the aqueduct, direct endoscopic removal of the tumor may effectively relieve the obstruction. Large intrathird ventricular arachnoid cysts can be endoscopically fenestrated and fulgurated to reconstruct the floor of the third ventricle and restore the CSF pathways.

On postoperative imaging, there is a gradual decrease in the size of the ventricles over months to years. This is contrary to postshunting imaging, when there is rapid reduction in size of the ventricles. The third ventricle responds early and decreases in size over 3 months, while the lateral ventricles decrease over 2 years. It is therefore difficult to assess for third ventriculostomy patency on the basis of ventricular size.[21]

Fast spin echo T2-weighted sequences are sensitive in assessing patency of the third ventriculostomy. Midline sagittal images show hypointensity in the region of the ventriculostomy as a result of CSF-related flow-void if the ventriculostomy is patent (Fig. 32.16). Balanced SSFP images can also demonstrate closure of the ventriculostomy by the absence of a defect. Please note that the flow void may not be detected using balanced SSFP images.

Phase contrast cine MRI is helpful to assess ventriculostomy patency.[9] Using cardiac gating, phase contrast images can demonstrate pulsatile CSF flow through the ventriculostomy and determine flow velocity. Velocity ratios between the flow in prepontine cistern from the ventriculostomy and posterior cervical spine have been used for assessing the patency of the third ventriculostomy. A caveat of phase contrast cine MRI is the presence of turbulent or pulsatile flow secondary to third ventricular floor motion (e-Fig. 32.17). Third ventriculostomy may fail if the liliquist membrane is not perforated (e-Fig. 32.18).

**BOX 32.7** Common Indications for Third Ventriculostomy

Delayed-onset aqueductal obstruction CSF shunt obstruction in patients with obstructive hydrocephalus
Older patients with spina bifida and blocked shunts
Obstructive hydrocephalus caused by pineal and posterior fossa tumors

KEY POINTS

- Hydrocephalus is one of the most common sequelae of any insult to a child's CNS.
- The most common cause of macrocephaly in infants is benign extraaxial collections of infancy.
- US of the head is a useful initial examination if the anterior fontanelle is open. After fontanelle closure, CT or MRI is required for evaluation of the ventricular system and shunts.
- The most reliable sign of hydrocephalus is enlargement of the anterior and posterior recesses of the third ventricle.

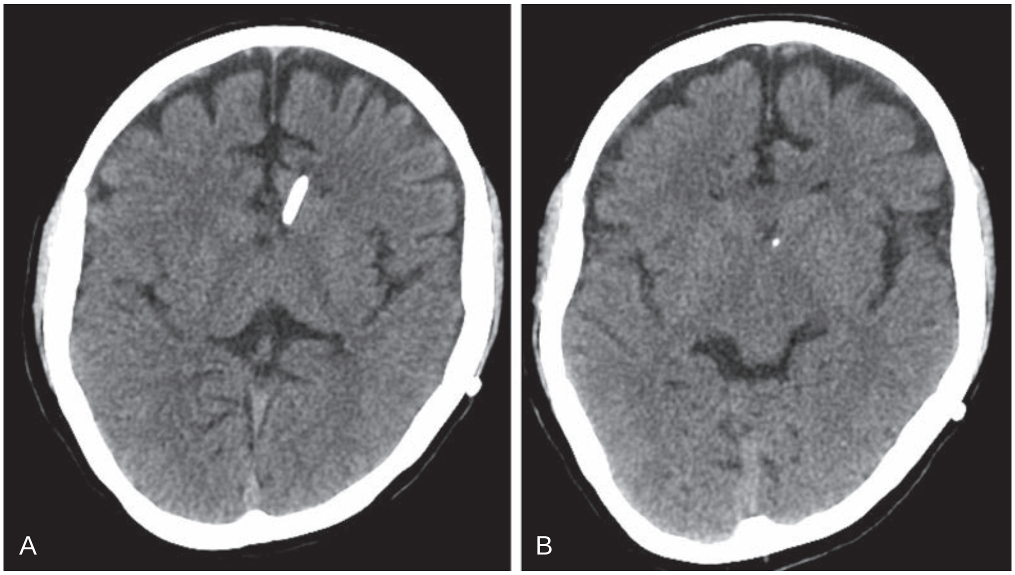

**Figure 32.15. Slit ventricle syndrome.** CT images in a 13-year-old with shunted hydrocephalus with the tip of VP shunt in left frontal horn (A) resulting in slit-like ventricles (B).

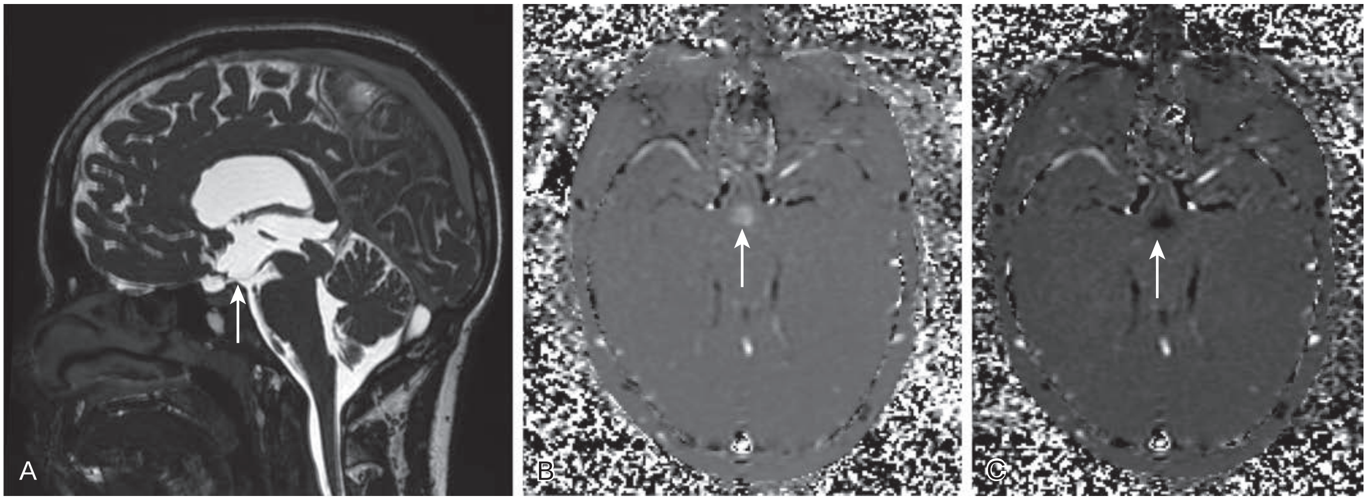

**e-Figure 32.17. Failed third ventriculostomy.** (A) Midsagittal T2-weighted MR image through the third ventricle floor demonstrates absence of the third ventriculostomy defect. (B and C) Axial phase contrast image may be deceiving as the signal noted is secondary to the on-off motion of the floor of third ventricle and not flow of cerebrospinal fluid through the third ventricle floor.

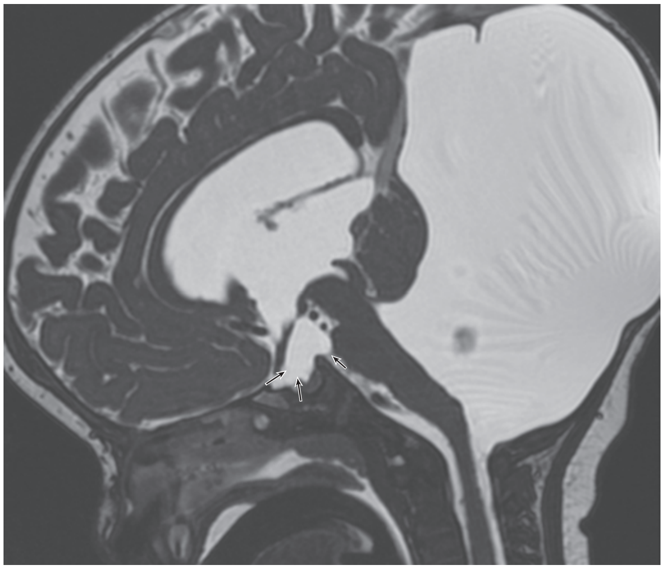

**e-Figure 32.18. Failed third ventriculostomy.** Sagittal steady-state free precession MR image in a patient with Dandy-Walker malformation and failed third ventriculostomy demonstrates failure to perforate the liliquist membrane *(arrows)*.

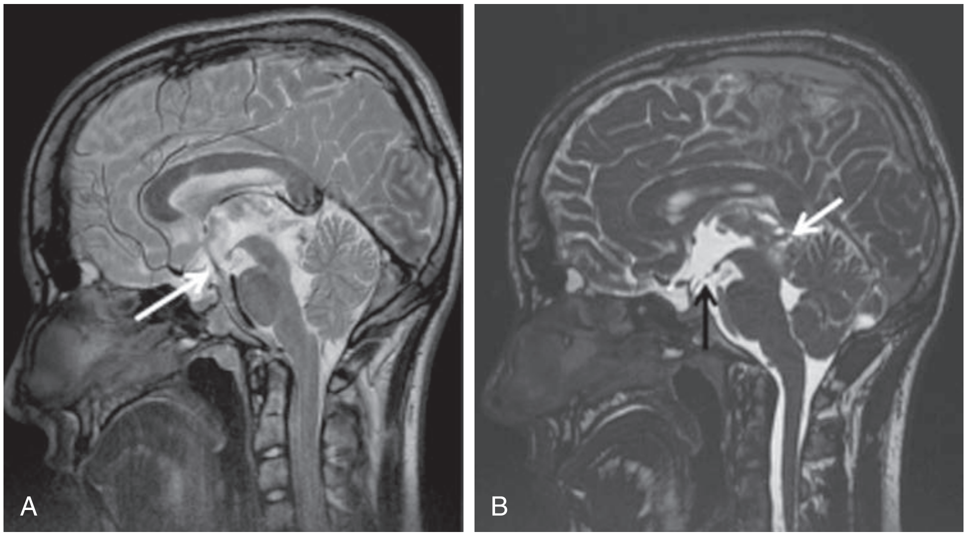

**Figure 32.16. Third ventriculostomy.** (A) Midsagittal T2-weighted image through the third ventricle at 2-mm section thickness and 512 × 512 matrix demonstrates the flow void through the ventriculostomy in a patient affected by tectal tumor. (B) Midsagittal balanced steady-state free precession image shows the ventriculostomy defect *(dark arrow)* and the tectal tumor *(white arrow)*.

## SUGGESTED READINGS

Barkovich AJ, Raybaud C, eds. *Pediatric Neuroimaging*. 5th ed. Philadelphia: Lippincott Williams & Wilkins; 2012:808–856.
Kahle KT, Kulkarni AV, Limbrick DD Jr, Warf BC. Hydrocephalus in children. *Lancet*. 2016;387:788–799. doi:10.1016/S0140-6736(15)60694-8.
Li V. Methods and complications in surgical cerebrospinal fluid shunting. *Neurosurg Clin N Am*. 2001;12:685–693.
Raybaud C. MR assessment of pediatric hydrocephalus: a road map. *Childs Nerv Syst*. 2016;32:19–41. doi:10.1007/s00381-015-2888-y.

## REFERENCES

Full references for this chapter can be found on www.expertconsult.com.

## REFERENCES

1. Chi JH, Fullerton HJ, Gupta N. Time trends and demographics of deaths from congenital hydrocephalus in children in the United States: National Center for Health Statistics data, 1979 to 1998. *J Neurosurg*. 2005;103:113–118.
2. Bergsneider M. Evolving concepts of cerebrospinal fluid physiology. *Neurosurg Clin N Am*. 2001;36:631–638.
3. Greitz D, Greitz T, Hindmarsh T. A new view on the CSF circulation with the potential for pharmacological treatment of childhood hydrocephalus. *Acta Pediatr*. 1997;86:125–132.
4. Papaiconomou C, Zakharov A, Azizi N, et al. Reassessment of the pathways responsible for cerebrospinal fluid absorption in the neonate. *Childs Nerv Syst*. 2004;20:29–36.
5. Tully HM, Ishak GE, Rue TC, et al. Two hundred and 36 children with developmental hydrocephalus: causes and clinical consequences. *J Child Neurol*. 2016;31:309–320.
6. El Gammal TE, Allen MB Jr, Brooks BS, Mark EK. MR evaluation of hydrocephalus. *Am J Roentgenol*. 1987;149:807–813.
7. Heinz ER, Ward A, Drayer BP, DuBois PJ. Distinction between obstructive and atrophic dilatation of ventricles in children. *J Comput Assist Tomogr*. 1980;4:320–325.
8. Naidich T, McLone D, Hahn Y, Hanaway J. Atrial diverticula in severe hydrocephalus. *AJNR Am J Neuroradiol*. 1982;3:257–266.
9. Lev S, Bhadelia RA, Estin D, et al. Functional analysis of third ventriculostomy patency with phase-contrast MRI velocity measurements. *Neuroradiology*. 1997;39:175–179.
10. Chadduck WM, Seibert JJ, Adametz J, et al. Cranial Doppler ultrasonography correlates with criteria for ventriculoperitoneal shunting. *Surg Neurol*. 1989;31:122–128.
11. Goh D, Minns RA, Pye SD, Steers AJ. Cerebral blood flow velocity changes after ventricular taps and ventriculoperitoneal shunting. *Childs Nerv Syst*. 1991;7:452.
12. Taylor GA, Madsen JR. Hemodynamic response to fontanelle compression in neonatal hydrocephalus: correlation with intracranial pressure and need for shunt placement. *Radiology*. 1996;201:685–689.
13. Flom L, Fromkin J, Panigrahy A, et al. Development of screening MRI for infants at risk for abusive head injury. *Pediatr Radiol*. 2016;46:519–526.
14. Wilms G, Vanderschueren G, Demaerel PH, et al. CT and MR in infants with pericerebral collections and macrocephaly: benign enlargement of the subarachnoid spaces versus subdural collections. *AJNR Am J Neuroradiol*. 1993;14:855–860.
15. Zhang J, Williams MA, Rigamonti D. Genetics of human hydrocephalus. *J Neurol*. 2006;253:1255–1266.
16. Di Rocco C, Marchese E, Verladi F. A survey of the first complication of newly implanted CSF shunt devices for the treatment of nontumoral hydrocephalus: cooperative survey of the 1991–1992 Education Committee on the ISPN. *Childs Nerv Syst*. 1994;10:321–327.
17. Desai KR, Babb JS, Amodio JB. The utility of the plain radiograph "shunt series" in the evaluation of suspected ventriculoperitoneal shunt failure in pediatric patients. *Pediatr Radiol*. 2007;37:452–456.
18. Iskandar BJ, Sansone JM, Medow J, Rowley HA. The use of quick magnetic resonance imaging in the evaluation of shunt-treated hydrocephalus. *J Neurosurg*. 2004;101:147–151.
19. Bruce DA, Weprin B. The slit ventricle syndrome. *Neurosurg Clin N Am*. 2001;12:709–717.
20. Sansone JM, Iskandar BJ. Endoscopic cerebral aqueductoplasty: a trans- fourth ventricle approach. *J Neurosurg*. 2005;103:388–392.
21. Schwartz TH, Yoon SS, Cutruzzola FW, Goodman RR. Third ventriculostomy: postoperative ventricular size and outcome. *Minim Invasive Neurosurg*. 1996;39:122–129.

# 33

# Inherited Metabolic and Neurodegenerative Disorders

Giulio Zuccoli and Kim M. Cecil

## INHERITED METABOLIC BRAIN DISORDERS

Inherited metabolic brain disorders produce changes in brain metabolism and structure as a result of genetic mutations. Clinically, children with metabolic brain disorders often present with nonspecific symptoms, such as hypotonia, seizures, and developmental delay, which often makes diagnosis difficult. A combination of neurologic symptoms with and without visceral manifestation and age at onset of symptoms often are important factors indicating an underlying inherited metabolic brain disorder. The diagnosis traditionally has been accomplished by laboratory analyses of biologic specimens (urine or blood) and tissue (muscle or fibroblast) biopsy. However, the increased availability of imaging studies incorporating advanced techniques, specifically magnetic resonance imaging (MRI) with diffusion-weighted imaging (DWI) and MR spectroscopy (MRS), offers more diagnostic features, thereby improving the ability to recognize disease patterns and classify patients for metabolic and genetic investigations with candidate diseases prioritized from imaging and clinical features. Although the number of metabolic brain disorders is significant, neuroradiologists should be able to recognize the features of the key disorders outlined in this chapter.

Because these disorders generally are progressive, the classification of neurodegenerative features also is used appropriately as imaging findings worsen—for example, cortical volume loss, gliosis, and hypomyelination. The generic term "hypomyelination" is used to describe abnormal myelination, whether it is improperly formed or altered after formation, because distinguishing demyelination from dysmyelination is a pathologic diagnosis not distinguished objectively by imaging alone. Because these diseases frequently or primarily involve the white matter, they often are put into a general category of leukodystrophy. The known leukodystrophies are genetic diseases involving defects in oligodendroglia function and myelinogenesis. The term "leukodystrophy" describes a chronic, progressive, destructive process of the white matter within the central nervous system (CNS) characterized by a metabolic disorder of myelin sheath formation and maintenance, often with a slow but progressive loss of nervous system structures. The clinical course is progressive and typically includes mental retardation with signs of long tract dysfunction, such as pyramidal and cerebellar disturbances, with abnormal conduction of visual auditory and somatic sensory input as measured by evoked potentials.

In young children, more heavily T2-weighted sequences with a repetition time of 2,500 to 3,000 msec and time to echo (TE) of 100 to 200 msec should be obtained. It is difficult to evaluate the degree of myelination in children younger than 2 years because the normal myelination process does not begin until the fifth month of fetal gestation and proceeds rapidly during the first 2 years of life. Fluid-attenuated inversion recovery (FLAIR) imaging may be misleading before 18 months of age because it sharpens the difference between myelinated and even physiologically unmyelinated white matter. By 2 years of age, 90% of all the white matter fiber tracts have become myelinated, but myelination is incomplete, and some variability exists in the meeting of various milestones. In children younger than 2 years, destructive processes may not be adequately demonstrated on T2-weighted images. However, by 2 years of age and older, destructive processes resulting in white matter fiber abnormal T2 hyperintensity is demonstrated in the leukodystrophies. In recent reports, contrast enhancement has been helpful because many of the newly recognized leukodystrophies have disruption of the blood-brain barrier. The end-stage appearance of all the leukodystrophies on computed tomography (CT) or MRI is marked generalized volume loss. Most leukodystrophies involve the central white matter in a symmetric fashion; Canavan disease is the exception. Patients with delayed myelination or symmetrically abnormal myelination from an earlier insult may have an imaging appearance similar to an early leukodystrophy, making radiologic diagnosis less accurate. Symptoms in these children may be similar to those in children with a leukodystrophy.

DWI provides information about the gross mobility of water (see also Chapter 26). Cytotoxic and myelinic edema can produce a hyperintense signal of diffusion-weighted images. To distinguish this signal from a hyperintense signal arising from T2 weighting, an apparent diffusion coefficient (ADC) map can be generated. On an ADC map, cytotoxic and myelinic edema generates a hypointense signal, indicating a restriction of water diffusion. Diffusion tensor imaging holds the promise of providing white matter microstructural details by revealing the magnitude and direction of water movement along the axons. As myelination is detected, water molecules demonstrate reduced diffusivity and increased diffusion anisotropy. Abnormal myelin can be quantitated from changes in these properties using measures such as mean diffusivity and fractional anisotropy.

MRS is useful in the evaluation of metabolic diseases in children because many laboratory studies that test for systemic metabolic diseases often do not reveal abnormalities, especially when the metabolic derangements are within localized regions of the brain. When CNS involvement is demonstrated on anatomic MR images, the MRS spectrum is usually abnormal. In some metabolic disorders, abnormalities are observed in the MRS spectrum in the absence of anatomic MR abnormalities (e.g., creatine deficiency syndromes).

In the evaluation of a possible metabolic disorder, acquiring both short- and long-echo spectra offers the most diagnostic utility. The use of a short echo time allows for the detection of metabolites with faster T2 decay, especially glutamine/glutamate and myo-inositol (mI). The long-echo spectra have a flatter baseline, which is important for the detection of lactate, a double resonance at 1.3 ppm. Identification of lactate within cerebral tissue typically reflects mitochondrial impairment and should raise suspicion of mitochondrial disease, with confirmation by a muscle biopsy and possibly laboratory analyses of serum or cerebrospinal fluid (CSF). Mitochondrial enzyme systems are involved in many key cell metabolic pathways—oxidative phosphorylation, oxidation of fatty acids and amino acids, and processes involved in the Krebs cycle and part of the urea cycle. Abnormal lactate accumulation detected in patients with mitochondrial disorders can reflect the following mechanisms: (1) a high degree of nonoxidative glycolysis resulting from impaired oxidative energy metabolism, (2) the use of anaerobic metabolism by infiltrating macrophages, and (3) damage to or loss of viable neuroaxonal tissue.

## Abstract:

Inherited metabolic brain disorders cause changes in brain metabolism and structure due to genetic mutations involving enzymatic function, protein, and mitochondrial expression. In inherited metabolic brain disorders, the presentation symptoms are often non-specific. In lysosomal storage disorders, mechanical disruption of the cell results from storage of nondegradable material leading to cellular dysfunction. Lysosomal disorders primarily targeting the gray matter include the gangliosidoses, mucopolysaccharidoses, and neuronal ceroid lipofuscinoses (NCLs). Metachromatic leukodystrophy (MLD) and Krabbe disease also known as Globoid Cell Leukodystrophy, demonstrate abnormalities in the white matter, cranial nerves and cauda equina roots. Mitochondrial disorders usually refer to disorders of the mitochondrial respiratory chain resulting in impaired respiratory chain function and reduced adenosine triphosphate production. Imaging findings of mitochondrial disorders include bilateral symmetrical signal intensity alterations involving the brainstem and the basal ganglia with restricted diffusion on DWI (Leigh Syndrome, Subacute Necrotizing Encephalomyelopathy). Brain MRIs of patients suffering from mitochondrial encephalomyopathy, lactic acidosis, and stroke-like symptoms (MELAS) are characterized by abnormal signal involving the brain cortex in a non-territorial distribution mimicking cortical infarcts on DWI. Magnetic Resonance Spectroscopy (MRS) can be very useful during the early phases of a mitochondrial disorder since it may reveal metabolic anomalies in an otherwise normal appearing brain parenchyma. In patients affected by neurodegeneration with brain iron accumulation (NBIA), Susceptibility Weighted Imaging discloses iron accumulation within the basal ganglia and cerebellar atrophy.

## Keywords:

Mitochondrial Diseases
Leigh Syndrome
Lysosomal storage disease
Magnetic Resonance Spectroscopy
Magnetic Resonance Imaging
Glutaric Aciduria
Menkes Disease

This chapter includes as a reference a large listing of metabolic brain diseases encountered in imaging (Tables 33.1 to 33.10). For convenience, the recognized metabolic or genetic defect and the patterns of inheritance are summarized. However, because of space limitations, the following discussion will address only the most commonly encountered of these rare disorders.

## LYSOSOMAL STORAGE DISEASES

Many neurodegenerative diseases are characterized by the accumulation of nondegradable molecules in cells or at extracellular sites in the brain. Lysosomes are intracellular organelles responsible for degrading lipids, proteins, and complex carbohydrates. In most lysosomal disorders, the genetic mutation resulting in the absence or deficiency of an enzyme or protein is known and functionally understood. In most, the substrate for the defective enzyme builds up, leading to intralysosomal storage. Although the diseases are complex, storage of nondegradable material primarily leads to neuronal dysfunction rather than neuronal loss. Exceptions are the differential loss of Purkinje cells that characterize several storage diseases (including Niemann-Pick disease type C) and the massive cell loss that occurs in the neuronal ceroid lipofuscinoses (NCLs). It is not known whether the storage material affects cellular function only when it begins to accumulate in extralysosomal sites or if problems in cell homeostasis are triggered while the material is still confined to the lysosome.

Lysosomal disorders typically are inherited as autosomal-recessive traits, usually afflict infants and young children, and are untreatable. The collective frequency of lysosomal storage diseases is estimated to be approximately 1 in 8,000 live births, with some occurring at higher frequency in select populations.

**TABLE 33.1** Summary of Metabolic Disorders Encountered in the Pediatric Neuroimaging Setting: Adrenoleukodystrophy—Argininosuccinate Lyase Deficiency

| Disorder | Gene Name; Abbreviation (Locus) | OMIM | Mode of Inheritance | Primary Classification | Primary Defect |
|---|---|---|---|---|---|
| Neonatal adrenoleukodystrophy | *PTS1* and Peroxin genes | 202370 | Autosomal recessive | Peroxisomal | Deficiency in oxidizing VLCFA |
| X-linked adrenoleukodystrophy | Adrenoleukodystrophy; *ALD/ABCD1* (Xq28) | 300100 | X-linked | Peroxisomal | Inability to oxidize VLCFA into shorter chain fatty acids |
| Alexander disease | Glial fibrillary acidic protein; *GFAP* (17q21.31) | 203450 | Autosomal dominant | Leukodystrophy | Presence of Rosenthal fibers, glial fibrillary acid proteins in astrocytes |
| Alpers disease | Nuclear encoded mitochondrial DNA polymerase-gamma; *POLG* (15q26.1) | 203700 | Autosomal recessive | Mitochondrial | Respiratory chain abnormalities |
| Argininemia (arginase deficiency) | Arginase; *ARG1* (6q23.2) | 207800 | Autosomal recessive | Urea cycle | Defect encoding enzyme *ARG1* |
| Argininosuccinate lyase deficiency | Argininosuccinate lyase; *ASL* (7q11.21) | 207900 | Autosomal recessive | Urea cycle | Defect encoding enzyme *ASL* |

*OMIM,* Online Mendelian Inheritance in Man Database; *VLCFA,* very-long-chain fatty acid.
*Modified from Cecil KM. MR spectroscopy of metabolic disorders.* Neuroimaging Clin North Am. *2006;16:87–116; used with permission. Data from The Johns Hopkins University, Online Mendelian Inheritance in Man (OMIM), McKusick-Nathans Institute for Genetic Medicine, Johns Hopkins University (Baltimore, MD) and the National Center for Biotechnology Information, National Library of Medicine (Bethesda, MD), 2000. Available at http://www.ncbi.nlm.nih.gov/omim/.*

**TABLE 33.2** Summary of Metabolic Disorders Encountered in the Pediatric Neuroimaging Setting: Biotinidase Deficiency—Citrullinemia

| Disorder | Gene Name; Abbreviation (Locus) | OMIM | Mode of Inheritance | Primary Classification | Primary Defect |
|---|---|---|---|---|---|
| Biotinidase deficiency | Biotinidase gene; *BTD* (3p25.1) | 253260 | Autosomal recessive | Organic or amino acid | Biotinidase deficiency with elevated lactate, β-hydroxyisovalerate |
| Canavan disease | Aspartoacylase; *ASPA* (17p13.2) | 271900 | Autosomal recessive | Leukodystrophy | Enzyme deficiency; aspartoacylase deficiency; inability to metabolize NAA into aspartate and acetate |
| Carbamoyl phosphate synthetase I deficiency | Carbamoyl phosphate synthetase I; *CPS1* (2q34) | 237300 | Autosomal recessive | Urea cycle | Defect encoding enzyme; *CPS1* enzyme deficiency; catalyzes first committed step in the urea cycle |
| Cerebrotendinous xanthomatosis | 27-sterol hydroxylase: *CYP27* (2q35) | 213700 | Autosomal recessive | Lysosomal | Enzyme deficiency—sterol 27-hydroxylase |
| Childhood ataxia with diffuse CNS hypomyelination (vanishing white matter) | *EIF2B1-5* (12q24.31, 14q24.3, 1p34.1, 2p23.3, 3q27) | 603896 | Autosomal recessive | Leukodystrophy | Gene defect in eukaryotic translation initiation factor (mRNA translated into proteins) |
| Citrullinemia, classic (argininosuccinate synthetase deficiency) | Argininosuccinate synthetase; *ASS* (9q34.11) | 215700 | Autosomal recessive | Urea cycle | Gene defect encoding enzyme argininosuccinate synthetase |

*CNS,* Central nervous system; *mRNA,* messenger ribonucleic acid; *NAA,* N-acetylaspartate; *OMIM,* online Mendelian Inheritance in Man Database.
*Modified from Cecil KM. MR spectroscopy of metabolic disorders.* Neuroimaging Clin N Am. *2006;16:87–116; used with permission. Data from The Johns Hopkins University, Online Mendelian Inheritance in Man (OMIM), McKusick-Nathans Institute for Genetic Medicine, Johns Hopkins University (Baltimore, MD) and the National Center for Biotechnology Information, National Library of Medicine (Bethesda, MD), 2000. Available at http://www.ncbi.nlm.nih.gov/omim/.*

**TABLE 33.3** Summary of Metabolic Disorders Encountered in the Pediatric Neuroimaging Setting: Cockayne Disease—Creatine Deficiency

| Disorder | Gene Name; Abbreviation (Locus) | OMIM | Mode of Inheritance | Primary Classification | Primary Defect |
|---|---|---|---|---|---|
| Cockayne disease | Excision-repair cross-complementing group 8 gene; *ERCC8* (5q12.1) | 216400 | Autosomal recessive | Miscellaneous | Defective DNA repair |
| Congenital muscular dystrophies | Fukuyama: fukutin; *FCMD* (9q31.2) | 253800 | Autosomal recessive | Congenital muscular dystrophy | Defect in dystrophin-associated proteins |
|  | Merosin-deficient: laminin alpha-2-gene; *LAMA2* (6q22.33) | 607855 | Autosomal recessive | Congenital muscular dystrophy | Absence of merosin in muscle |
|  | Duchenne: dystrophin *DMD* (Xp21.2–p21.1) | 310200 | X-linked recessive | Congenital muscular dystrophy | Absence of dystrophin in muscle |
| Creatine deficiency—creatine transporter defect | *SLC6A8* (Xq28) | 300352 | X-linked | Miscellaneous | Creatine transport impaired to the brain |
| Creatine deficiency—arginine:glycine amidinotransferase deficiency | *GATM* (15q21.1) | 612718 | Autosomal recessive | Miscellaneous | Creatine synthesis impaired |
| Creatine deficiency—guanidinoacetate methyltransferase deficiency | *GAMT* (19p13.3) | 612736 | Autosomal recessive | Miscellaneous | Creatine synthesis impaired |

*DNA,* Deoxyribonucleic acid; *OMIM,* online Mendelian Inheritance in Man Database.

*Modified from Cecil KM. MR spectroscopy of metabolic disorders.* Neuroimaging Clin N Am. *2006;16:87–116; used with permission. Data from The Johns Hopkins University, Online Mendelian Inheritance in Man (OMIM), McKusick-Nathans Institute for Genetic Medicine, Johns Hopkins University (Baltimore, MD) and the National Center for Biotechnology Information, National Library of Medicine (Bethesda, MD), 2000. Available at http://www.ncbi.nlm.nih.gov/omim/.*

**TABLE 33.4** Summary of Metabolic Disorders Encountered in the Pediatric Neuroimaging Setting: Ethylmalonic Aciduria—Hydroxyglutaric Aciduria

| Disorder | Gene Name; Abbreviation (Locus) | OMIM | Mode of Inheritance | Primary Classification | Primary Defect |
|---|---|---|---|---|---|
| Ethylmalonic aciduria | *ETHE1* (19q13.31) | 602473 | Autosomal recessive | Organic or amino acid | Ethylmalonic aciduria with cytochrome c oxidase deficiency in skeletal muscle; lactic acidemia |
| Galactosemia | galactose-1-phophate uridylyltransferase; *GALT* (9p13.3) | 230400 | Autosomal recessive | Miscellaneous | Defect encoding galactose-1-phosphate uridyltransferase |
| Globoid cell leukodystrophy (Krabbe disease) | Galactocerebrosidase; *GALC* (14q31.3) | 245200 | Autosomal recessive | Lysosomal | Enzyme deficiency—galactocerebroside beta-galactosidase deficiency |
| Glutaric aciduria | Type I glutaryl-CoA-dehydrogenase; *GCDH* (19p13.13) | 231670 | Autosomal recessive | Organic or amino acid | Enzyme deficiency altering metabolism of lysine, hydroxylysine, tryptophan |
| Glutaric aciduria | Type II multiple acyl CoA-dehydrogenase genes (19q13.41, 15q24.2–q24.3, 4q32.1) | 231680 | Autosomal recessive | Organic or amino acid | Disorder of fatty acid, amino acid, and choline metabolism |
| Homocystinuria | Cystathionine β-synthase; *CBS* (21q22.3) | 236200 | Autosomal recessive | Organic or amino acid | Increased urinary homocystine and methionine |
| L-Hydroxyglutaric aciduria | *L2HGDH* 14q21.3 | 236792 | Autosomal recessive | Organic or amino acid | Increase of L-2-hydroxy glutaric acid in urine |

*OMIM,* Online Mendelian Inheritance in Man Database.

*Modified from Cecil KM. MR spectroscopy of metabolic disorders.* Neuroimaging Clin N Am. *2006;16:87–116; used with permission. Data from The Johns Hopkins University, Online Mendelian Inheritance in Man (OMIM), McKusick-Nathans Institute for Genetic Medicine, Johns Hopkins University (Baltimore, MD) and the National Center for Biotechnology Information, National Library of Medicine (Bethesda, MD), 2000. Available at http://www.ncbi.nlm.nih.gov/omim/.*

Lysosomal disorders primarily affecting gray matter include the gangliosidoses, mucopolysaccharidoses, and NCLs. Two of the more common lysosomal disorders, metachromatic leukodystrophy (MLD) and Krabbe disease, demonstrate abnormalities in white matter. However, broader involvement of gray and white matter often occurs in later stages of lysosomal disease progression.

## Gangliosidoses

The gangliosidoses are divided into two groups, referred to as GM1 and GM2. In the GM1 group, the primary enzyme deficiency is in β-galactosidase, and in the GM2 group there is a hexosaminidase deficiency.

**TABLE 33.5** Summary of Metabolic Disorders Encountered in the Pediatric Neuroimaging Setting: Isovaleric Acidemia—Ketothiolase Deficiency

| Disorder | Gene Name; Abbreviation (Locus) | OMIM | Mode of Inheritance | Primary Classification | Primary Defect |
|---|---|---|---|---|---|
| Isovaleric acidemia | Isovaleryl CoA dehydrogenase; *IVD* (15q15.1) | 243500 | Autosomal recessive | Organic or amino acid | Accumulation of isovaleric acid |
| Juvenile Huntington disease | Huntington; *HTT* (4p16.3) | 143100 | Autosomal dominant | Miscellaneous | Neural cell death from production of quinolinic acid |
| Kearns-Sayre syndrome | Various mitochondrial deletions | 530000 | Mitochondrial | Mitochondrial | Lactic acidosis, decreased Co-Q |
| Kernicterus | Uridine diphosphate-glucuronosyltransferase; *UGT1A1* (2q37.1) | 237900 | Autosomal recessive | Miscellaneous | Hyperbilirubinemia |
| b-Ketothiolase deficiency | Acetyl-Co-A-acetyltransferase 1; *ACAT1* (11q22.3) | 203750 | Autosomal recessive | Organic or amino acid | Increased urinary 2-methyl-3-hydroxybutyric acid |
| Leigh syndrome | Nuclear and mitochondrial-encoded genes involved in energy metabolism | 256000 | Autosomal recessive, mitochondrial | Mitochondrial | Lactic acidosis |
| Leukoencephalopathy with brainstem and spinal cord involvement with elevated lactate | *DARS2* (1q25.1), mitochondrial aspartyl-tRNA synthetase | 611105 | Autosomal recessive | Leukodystrophy | Lactic acidosis |
| Lowe disease | Phosphatidylinositol polyphosphate 5-phosphatase; *OCRL* (Xq26.1) | 309000 | X-linked recessive | Organic or amino acid | Increased phosphatidylinositol-4,5-biphosphate |

*OMIM,* Online Mendelian Inheritance in Man Database.

*Modified from Cecil KM. MR spectroscopy of metabolic disorders.* Neuroimaging Clin N Am. *2006;16:87–116; used with permission. Data from The Johns Hopkins University, Online Mendelian Inheritance in Man (OMIM), McKusick-Nathans Institute for Genetic Medicine, Johns Hopkins University (Baltimore, MD) and the National Center for Biotechnology Information, National Library of Medicine (Bethesda, MD), 2000. Available at http://www.ncbi.nlm.nih.gov/omim/.*

**TABLE 33.6** Summary of Metabolic Disorders Encountered in the Pediatric Neuroimaging Setting: Maple Syrup Urine Disease—Molybdenum Cofactor Deficiency

| Disorder | Gene Name; Abbreviation (Locus) | OMIM | Mode of Inheritance | Primary Classification | Primary Defect |
|---|---|---|---|---|---|
| Maple syrup urine disease | Mutations in the catalytic subunit genes of the branched chain alpha ketoacid dehydrogenase complex; *BCKD, DBT, DLD* (19q13.2, 6q14.1, 1p21.2) | 248600 | Autosomal recessive | Organic or amino acid | Defect in the genes of the branched chain alpha ketoacid dehydrogenase blocking oxidative decarboxylation |
| MELAS | Multiple mitochondrial genes | 540000 | Mitochondrial | Mitochondrial | Lactic acidosis |
| Menkes disease | Cu(2+) transporting ATPase, alpha polypeptide; *ATP7A* (Xq21.1) | 309400 | X-linked recessive | Mitochondrial | Low copper |
| Metachromatic leukodystrophy | Arylsulfatase A; *ASA/ARSA* (22q13.33) | 250100 | Autosomal recessive | Lysosomal | Decreased arylsulfatase A, *ARSA* activity |
| Methylmalonic aciduria | Methylmalonyl-CoA mutase; *MUT* (6p12.3) | 251000 | Autosomal recessive | Organic or amino acid | Defect in methylmalonyl-CoA mutase; disorder of methylmalonate and cobalamin metabolism |
| Molybdenum cofactor deficiency | Molybdenum cofactors; *MOCS1* (6p21.3); *MOCS2* (5q11.2); gephyrin *GPHN* (14q23.3) | 252150 | Autosomal recessive | Miscellaneous | Increased urinary sulfite, taurine, and xanthine |

*ATPase,* Adenosine triphosphatase; *MELAS,* mitochondrial encephalomyopathy, lactic acidosis, and strokelike symptoms; *OMIM,* online Mendelian Inheritance in Man Database.

*Modified from Cecil KM. MR spectroscopy of metabolic disorders.* Neuroimaging Clin N Am. *2006;16:87–116; used with permission. Data from The Johns Hopkins University, Online Mendelian Inheritance in Man (OMIM), McKusick-Nathans Institute for Genetic Medicine, Johns Hopkins University (Baltimore, MD) and the National Center for Biotechnology Information, National Library of Medicine (Bethesda, MD), 2000. Available at http://www.ncbi.nlm.nih.gov/omim/.*

**TABLE 33.7** Summary of Metabolic Disorders Encountered in the Pediatric Neuroimaging Setting: Mucopolysaccharidoses (MPS)

| Disorder | Gene Name; Abbreviation (Locus) | OMIM | Mode of Inheritance | Primary Classification | Primary Defect |
|---|---|---|---|---|---|
| MPS IH—Hurler | alpha-L-iduronidase; *IDUA* (4p16.3) | 607014 | Autosomal recessive | Lysosomal | α-L-Iduronidase deficiency |
| MPS II—Hunter | duronate 2-sulfatase; *IDS* (Xq28) | 309900 | X-linked recessive | Lysosomal | Iduronate sulfatase deficiency |
| MPS III—San Fillipo | N-sulfoglucosamine sulfonhydrolase; *SGSH* (17q25.3) | 252900 | Autosomal recessive | Lysosomal | Heparan sulfate deficiency |
|  | N-alpha-acetylglucosaminidase; *NAGLU* (17q21.2) | 252920 | Autosomal recessive | Lysosomal | N-Acetyl-α-D-glucosaminidase, α-Glucosamine-N-acetyltransferase, N-acetylglucosamine-6-sulfate sulfatase |
| MPS IV—Morquio | galactosamine-6-sulfate sulfatase; GALNS (16q24.3) | 253000 | Autosomal recessive | Lysosomal | N-Acetylgalactosamine-6-sulfate sulfatase, B galactosidase |
| MPS IS—Scheie | *IDUA* (4p16.3) | 607016 | Autosomal recessive | Lysosomal | α-L-Iduronidase |
| MPS VI—Maroteaux-Lamy | arylsulfatase; *ARSB* (5q14.1) | 253200 | Autosomal recessive | Lysosomal | Arylsulfatase B |
| MPS VII—Sly | beta-glucuronidase; *GUSB* (7q11.21) | 253220 | Autosomal recessive | Lysosomal | β-Glucuronidase |

*OMIM,* Online Mendelian Inheritance in Man Database.

*Modified from Cecil KM. MR spectroscopy of metabolic disorders.* Neuroimaging Clin N Am. *2006;16:87–116; used with permission. Data from The Johns Hopkins University, Online Mendelian Inheritance in Man (OMIM), McKusick-Nathans Institute for Genetic Medicine, Johns Hopkins University (Baltimore, MD) and the National Center for Biotechnology Information, National Library of Medicine (Bethesda, MD), 2000. Available at http://www.ncbi.nlm.nih.gov/omim/.*

**TABLE 33.8** Summary of Metabolic Disorders Encountered in the Pediatric Neuroimaging Setting: Neuronal Ceroid Lipofuscinosis—Phenylketonuria

| Disorder | Gene Name; Abbreviation (Locus) | OMIM | Mode of Inheritance | Primary Classification | Primary Defect |
|---|---|---|---|---|---|
| Neuronal ceroid lipofuscinosis | *CLN3* (16p11.2) | 204200 | Autosomal recessive | Lysosomal | Defects involve lysosomal function |
| Niemann-Pick type C | *NPC1* (18q11.2) | 257220 | Autosomal recessive | Lysosomal | Defective cholesterol esterification due to a deficiency of sphingomyelinase |
| Nonketotic hyperglycinemia | Multiple genes (*GLDC* [9p24.1], *GCSH* [16q23.2], *AMT* [3p21.31]) | 605899 | Autosomal recessive | Amino aciduria | Defective mitochondrial enzyme involved in glycine cleavage |
| Ornithine transcarbamylase deficiency | Ornithine carbamoyltransferase; *OTC* (Xp11.4) | 311250 | X-linked recessive | Urea cycle | Gene defect encoding enzyme ornithine carbamoyltransferase |
| Pantothenate kinase (Hallervorden-Spatz) | Pantothenate kinase; *PANK* (20p13) | 234200 | Autosomal recessive | Mitochondrial | Iron deposition in globus pallidus, caudate, and substantia nigra |
| Pelizaeus-Merzbacher | Proteolipid protein; *PLP1* (Xq22.2) | 312080 | X-linked | Leukodystrophy | Duplication or deficiency of *PLP* gene results in altered myelin |
| Phenylketonuria | Phenylalanine hydroxylase (12q23.2) | 261600 | Autosomal recessive | Amino aciduria | Phenylalanine hydroxylase deficiency |

*OMIM,* Online Mendelian Inheritance in Man Database.

*Modified from Cecil KM. MR spectroscopy of metabolic disorders.* Neuroimaging Clin N Am. *2006;16:87–116; used with permission. Data from The Johns Hopkins University, Online Mendelian Inheritance in Man (OMIM), McKusick-Nathans Institute for Genetic Medicine, Johns Hopkins University (Baltimore, MD) and the National Center for Biotechnology Information, National Library of Medicine (Bethesda, MD), 2000. Available at http://www.ncbi.nlm.nih.gov/omim/.*

## GM1 Gangliosidosis

Three types of GM1 gangliosidosis exist: type I (infantile), type II (late infantile/juvenile), and type III (adult). An intermediate form between infantile and juvenile has been reported.[1] The clinical presentation of GM1 gangliosidosis typically occurs in infancy; its features include seizures, decerebrate posturing, pitting edema of the face, hypotonia, developmental delay, hepatosplenomegaly, macrocephaly, and cherry-red spots involving the macula of the retina. Additional features include broad digits, kyphoscoliosis, skeletal dysplasia with widening of the metaphyses, and dermal pigmentary lesions.[2] The course is progressive, with death common by 2 years of age. The juvenile form presents during the second year of life with progressive ataxia, but without many features of the infantile variety.

The underlying deficiency of β-galactosidase results in accumulation of GM1 ganglioside in both gray and white matter of the cerebrum, brainstem, cerebellum, and spinal cord. Results of cerebral MRI initially are normal, with subsequent loss of cortical gray matter. Secondary changes to the white matter manifest later and typically exhibit an abnormal, nonspecific, patchy, hyperintense T2 signal within the centrum semiovale. Hypointensity of the thalami on T2-weighted images also has been reported.[3]

## GM2 Gangliosidosis

The most common forms of GM2 gangliosidoses include Tay-Sachs disease and Sandhoff disease. Tay-Sachs disease arises with β-*N*-acetylhexosaminidase-A isoenzyme deficiency in Jewish children

**TABLE 33.9** Summary of Metabolic Disorders Encountered in the Pediatric Neuroimaging Setting: Propionic Aciduria—Sandhoff Disease

| Disorder | Gene Name; Abbreviation (Locus) | OMIM | Mode of Inheritance | Primary Classification | Primary Defect |
|---|---|---|---|---|---|
| Propionic aciduria | Propionic-CoA carboxylase; *PCCB* (3q22.3) and *PCCA* (13q32.3) | 232050 | Autosomal recessive | Organic or amino acid | Defect in propionic-CoA carboxylase |
| Pyruvate decarboxylase deficiency | E1-alpha polypeptide of pyruvate dehydrogenase; *PDHA1* (Xp22.12) | 312170 | X-linked | Mitochondrial | Defect in first of 3 enzymes in PDH-glycolysis and TCA cycle |
| Pyruvate dehydrogenase deficiency | Multiple genes of the pyruvate dehydrogenase complex | Multiple | Multiple | Mitochondrial | Defect in enzymes coupling glycolysis and TCA cycle for conversion of pyruvate to acetyl-CoA |
| Refsum disease | Infant: *PEX1* 7q21.2, *PXMP3* 8q21.11, *PEX26* 22q11.21 Adult: *PHYH* 10p13, *PEX7* 6q23 | 266510, 266500 | Autosomal recessive | Peroxisomal | Phytanic acid oxidase deficiency |
| Ribose 5-phosphate isomerase deficiency | Ribose 5-phosphate isomerase deficiency; *RPIA* 2p11.2 | 608611 | Autosomal recessive | Leukodystrophy | Deficiency in ribose 5-phosphate isomerase |
| Salla disease | *SLC17A5* (6q13) | 604369 | Autosomal recessive | Lysosomal | Defect in sialic acid transport at the lysosomal membrane |
| Sandhoff disease | Hexosaminidase; *HEXB* 5q13.3 | 268800 | Autosomal recessive | Lysosomal | Defect in beta subunit of hexosaminidase A and B isoenzymes |

*CoA,* coenzyme A; *OMIM,* Online Mendelian Inheritance in Man Database; *PDH,* pyruvate dehydrogenase; *TCA,* tricarboxylic acid.

*Modified from Cecil KM. MR spectroscopy of metabolic disorders.* Neuroimaging Clin N Am. *2006;16:87–116; used with permission. Data from The Johns Hopkins University, Online Mendelian Inheritance in Man (OMIM), McKusick-Nathans Institute for Genetic Medicine, Johns Hopkins University (Baltimore, MD) and the National Center for Biotechnology Information, National Library of Medicine (Bethesda, MD), 2000. Available at http://www.ncbi.nlm.nih.gov/omim/.*

**TABLE 33.10** Summary of Metabolic Disorders Encountered in the Pediatric Neuroimaging Setting: Sjögren-Larsson Syndrome—Zellweger Syndrome

| Disorder | Gene Name; Abbreviation (Locus) | OMIM | Mode of Inheritance | Primary Classification | Primary Defect |
|---|---|---|---|---|---|
| Sjögren-Larsson syndrome | Fatty aldehyde dehydrogenase; ALDH3A2 (17p11.2) (17p11.2) | 270200 | Autosomal recessive | Lysosomal | Fatty alcohol oxidation failure |
| Succinate semialdehyde dehydrogenase deficiency | Succinic semialdehyde dehydrogenase; *ALDH5A1* (6p22.3) | 271980 | Autosomal recessive | Organic or amino acid | Succinic semialdehyde dehydrogenase deficiency with 4-hydroxybutyricaciduria |
| Tay-Sachs disease | Hexosaminidase A; *HEXA* 15q23 | 272800 | Autosomal recessive | Lysosomal | Defect in alpha subunit of hexosaminidase A |
| Vacuolating megalencephalic leukoencephalopathy (with subcortical cysts, MLC) | *MLC1* (22q13.33) | 604004 | Autosomal recessive | Leukodystrophy | Defect in MLC1 |
| Walker-Warburg syndrome | protein O-mannosyltransferase-1; *POMT1* (9q34.13) | 236670 | Autosomal recessive | Congenital muscular dystrophy | Elevated creatine kinase; defective glycosylation of alpha-dystroglycan |
| Wilson disease | *ATP7B* (13q14.3) | 277900 | Autosomal recessive | Miscellaneous | Defect in copper transport |
| Zellweger syndrome | Several genes involved in peroxisome biogenesis, *PEX1* (7q21.2) | 214100 | Autosomal-recessive | Peroxisomal | Decreased dihydroxyacetone phosphate acyltransferase (DHAP-AT) activity |

*OMIM,* Online Mendelian Inheritance in Man Database.

*Modified from Cecil KM. MR spectroscopy of metabolic disorders.* Neuroimaging Clin N Am. *2006;16:87–116; used with permission. Data from The Johns Hopkins University, Online Mendelian Inheritance in Man (OMIM), McKusick-Nathans Institute for Genetic Medicine, Johns Hopkins University (Baltimore, MD) and the National Center for Biotechnology Information, National Library of Medicine (Bethesda, MD), 2000. Available at http://www.ncbi.nlm.nih.gov/omim/.*

of eastern European descent. Onset is usually before the age of 1 year with irritability, hypotonia, seizures, blindness, and cherry-red spots on the macula in 90% of patients. Death usually results by 2 to 3 years of age. Sandhoff disease is attributed to a deficiency of A and B isoenzymes of hexosaminidase. The clinical course is similar to that of Tay-Sachs disease. There is visceral involvement, including hepatomegaly and cardiac and renal tubular abnormalities. Brain MRI in the early stages demonstrates increased T2 signal in the basal ganglia, particularly with enlarged caudate nuclei. Later, cortical and deep gray matter volume loss occurs with patchy increases in T2 signal in the white matter. Thalamic involvement is more reflective of Sandhoff disease. In adult-onset Sandhoff disease, lower motor neuron involvement has been reported. Cerebellar atrophy is variable and does not correlate with clinical severity.[4] In persons with Tay-Sachs disease, the thalami may be hypointense on T2-weighted images and hyperintense on T1-weighted images because of calcium deposition. T2-weighted hyperintensity in cerebral matter may indicate abnormal myelin production and active demyelination.[5] Elevated levels of cytokines have been reported, possibly indicating inflammation as a contributing factor to the progression of gangliosidosis.[6] In the B1 variant of GM2 gangliosidosis, the thalami may appear hyperdense/hyperintense on CT and T1-weighted MRI and show T2-hypointense signal in the ventral thalami and a hyperintense signal in the posteromedial thalami. Other findings in this variant include involvement of the medullary lamellae, bilateral T2 hyperintense/swollen basal ganglia, diffuse white matter hyperintensity on T2-weighted images, and brain atrophy in later stages.[7]

## Mucopolysaccharidoses

The mucopolysaccharidoses are the best known of the lysosomal abnormalities affecting predominately gray matter. The primary metabolic defect is a failure to break down sulfates (dermatan, heparan, and keratan); mucopolysaccharides fill and overburden the lysosomes within histiocytes of the brain, bone, skin, and other organs. Glycosaminoglycans accumulate with target organs such as the bone, liver, and brain. Eight subtypes have been defined; however, six distinct forms are now recognized within this classification scheme, based on which metabolite is involved. The six are referred to as Hurler (IH), Hunter (II), Sanfilippo (III), Morquio (IV), Maroteaux-Lamy (VI), and Sly (VII), with the classic prototypical disease being Hurler syndrome. All of these diseases are autosomal recessive except Hunter (type II), which is an X-linked recessive condition. Coarse facial features and complex skeletal manifestations are well-known clinical characteristics for all of these disorders. Without treatment, death usually comes within the first decade of life.

MRI demonstrates two major abnormalities (Fig. 33.1): (1) diffuse patches of hyperintensity on T2-weighted images resulting from accumulation of mucopolysaccharide in neurons and astrocytes and degenerative effects on myelin, and (2) prominent cystic or perivascular spaces resulting from metabolite accumulation within histiocytes located in perivascular areas, which is the most characteristic imaging feature; reversal of these changes after bone marrow transplantation has been reported. Hydrocephalus is common, probably as a result of plugging of the pacchionian granulations. Spinal stenosis is especially common in Morquio and Maroteaux-Lamy variants but may be demonstrated in other variants. Bullet-shaped vertebral bodies are characteristic.

For the mucopolysaccharidoses, proton MRS reveals a broad resonance at 3.7 ppm, which is attributed to a composite of mucopolysaccharide molecules. After bone marrow transplantation, the resonance at 3.7 ppm decreases in the brain of some patients, which may aid in determining the efficacy of the therapy. N-acetylaspartate (NAA) levels may improve in response to treatment.

## Neuronal Ceroid Lipofuscinoses

NCL is a group of disorders characterized by striking volume loss of brain parenchyma. NCL, which can be divided into six subtypes based on age at onset, is one of the most common neurodegenerative syndromes, with an incidence of 1 per 25,000 live births. The various subtypes are associated with different mutations in the *CLN* genes and have similar clinical manifestations occurring at different ages. These manifestations include seizures and abnormal eye movements with subsequent vision loss, dementia, hypotonia, and speech and motor deficits. CSF neurotransmitter abnormalities have been reported.[8] At pathology, these disorders are characterized by distinctive granular inclusions in neuronal lysosomes (granular osmiophilic deposits). Imaging findings lag the clinical presentation in all but the infantile form of NCL and are dominated by progressive cerebral and cerebellar volume loss. Later disease stages are characterized by the development of a band of hyperintense signal in the periventricular white matter on T2-weighted images. In palmitoyl protein thioesterase-1 related NCL, isolated, symmetric dentate nucleus T2 hyperintensities have been reported in early stages.[9] Proton MRS has shown progressive decreases in NAA and relative increases in mI in persons with NCL.

## Metachromatic Leukodystrophy

The primary metabolic defect in MLD is a deficiency in the enzyme arylsulfatase A, resulting in lysosomal accumulation of cerebroside sulfate. MLD has four subtypes: congenital, late infantile, juvenile, and adult. The late infantile subtype is the most common and presents from around 14 months to 4 years of age. The early presentations are an unsteady gait that progresses to severe ataxia and flaccid paralysis, dysarthria, mental retardation, and decerebrate posturing. Gallbladder involvement has been reported, possibly appearing before the onset of neurologic symptoms. Intestinal involvement also has been reported, specifically polypoid masses in one patient.[10]

Histologic analysis of the abnormal nervous tissue demonstrates a complete loss of myelin (demyelination) followed by axonal degeneration. Metachromatic granules are reported within engorged lysosomes in white matter and neurons, and on peripheral nerve biopsies. Oligodendrocytes are reduced in number, and areas of demyelination predominate throughout the deep white matter region. An inflammatory response typically is absent, which accounts for a lack of enhancement, but eventually even myelinated white matter is replaced by astrogliosis and scarring. The corpus callosum is involved early, whereas subcortical arcuate white matter fibers ("U" fibers) remains unaffected until the disease has progressed; atrophy is a late sign. Demyelination also can be seen in the posterior limbs of the internal capsule, descending pyramidal tracts, and the cerebellar white matter.[11] Thalamic changes may be common in primary MLD, and isolated cerebellar atrophy may be seen in some atypical later-onset variants. On T2-weighted images, there is marked hyperintensity of the white matter fiber tracts involving the cerebral hemispheres that may extend to the cerebellum, brainstem, and spinal cord. The findings initially are focal and patchy, but later, a diffuse, hyperintense T2 signal of the centrum semiovale develops. Two distinct white matter appearances have been noted that mimic what was previously considered to be pathognomonic of Pelizaeus-Merzbacher disease (PMD) and globoid cell leukodystrophy (Krabbe disease). Punctate areas of hypointensity ("leopard skin" appearance) and radiating patterns of linear tubular structures of T2 hypointensity ("tigroid" appearance) are seen, with areas of relatively normal-appearing white matter within the areas of demyelination. On T1-weighted images, the white matter fibers may be isointense with, or hypointense to, gray matter (Fig. 33.2).

Proton MRS studies have demonstrated reduced NAA, which is expected with neuroaxonal loss, but they also have revealed disturbances in glial cell metabolism associated with elevated mI and choline. The levels of NAA in white matter have been found to correlate with motor function in children with MLD.[12]

## Globoid Cell Leukodystrophy (Krabbe Disease)

Globoid cell leukodystrophy (Krabbe disease) arises from a deficiency in the enzyme β-galactocerebrosidase, leading to the accumulation of cerebroside and galactosylsphingosine, which induces apoptosis in oligodendrocyte cell lines. It is an autosomal-recessive disorder with a frequency of 2 in 100,000. Onset of symptoms usually begins between 3 and 5 months after birth with irritability. Disease progression leads to symptoms mimicking encephalitis with motor deterioration and atypical seizures. At the

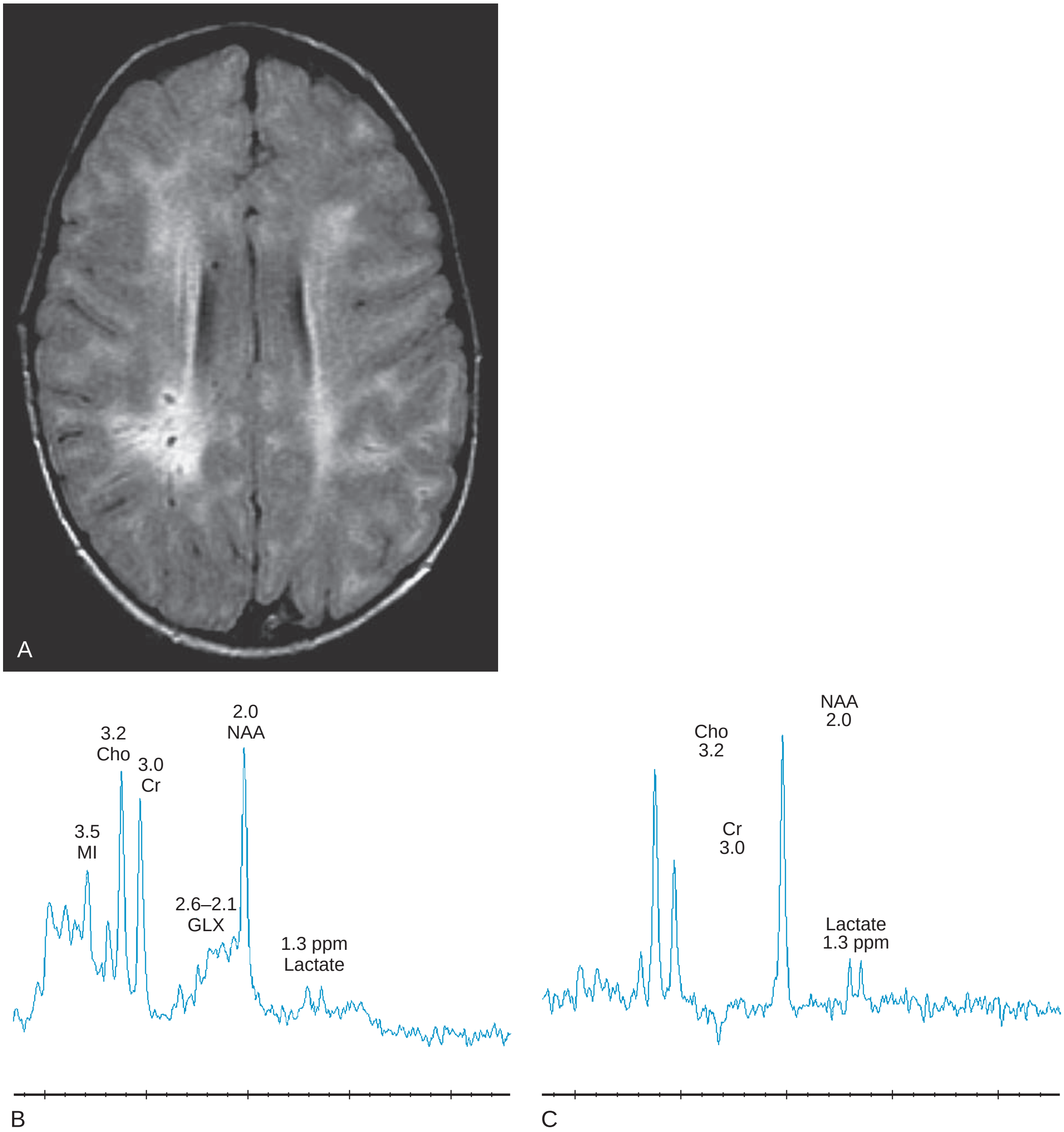

**Figure 33.1. Hunter syndrome, mucopolysaccharidoses type II, in a 2-year-old boy.** Axial fluid-attenuated inversion recovery (A), short echo (time to echo [TE] 35 milliseconds [msec]) magnetic resonance spectroscopy (MRS) (B), and long echo (TE 288 msec) MRS (C) images are shown. The patient underwent scanning within months of a stem cell transplant. Prominent perivascular spaces are demonstrated with a diffuse, abnormal, hyperintense signal throughout the periventricular and subcortical white matter. The spectra demonstrate diminished N-acetylaspartate levels with elevated lactate, which may reflect histiocytic cell infiltration of the perivascular spaces and brain parenchyma. PPM, parts per million. *(From Cecil KM. MR spectroscopy of metabolic disorders.* Neuroimaging Clin N Am*. 2006;16:87–116; used with permission.)*

end stage of the disease, the child is in a vegetative state with decerebrate posturing. Elevated CSF protein has been reported, more so in adult phenotypes than in phenotypes affecting younger people.[13] In nerve conduction studies, the severity of abnormalities appears to correlate with the severity of clinical symptoms.[14,15]

The disease predominantly involves the white matter of the cerebral hemispheres, cerebellum, and spinal cord. Pathologic changes include a marked toxic reduction in the number of oligodendrocytes. Globoid multinucleated cells and reactive macrophages are scattered throughout the white matter. Hypomyelination may be extensive and eventually leads to white matter gliosis and scarring. Gray matter involvement in the basal ganglia region also can be found with punctate calcification.

In infantile Krabbe disease, MRI findings may be normal or show delayed myelination, but as the disease progresses, classic Krabbe features emerge.[16] The appearance of Krabbe disease on MRI is featured as one of either two patterns. The first is a patchy hyperintense periventricular signal on T2-weighted

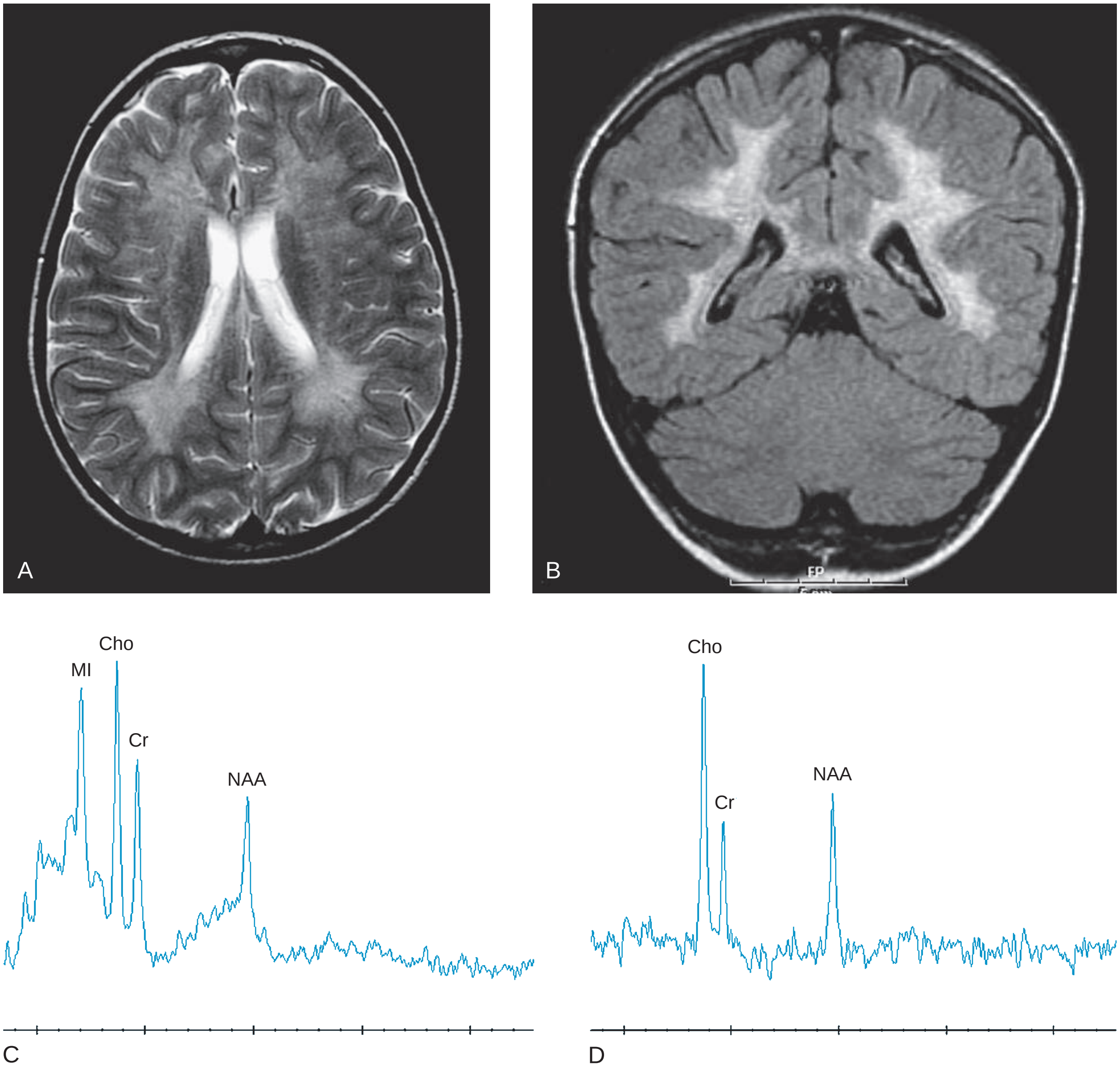

**Figure 33.2. Metachromatic leukodystrophy in a 7-year-old boy.** Axial T2-weighted (A), coronal fluid-attenuated inversion recovery (B) with left parietal white matter short echo magnetic resonance spectroscopy (MRS) (C) and long echo MRS (D) images reveal an abnormal hyperintense signal in the periventricular white matter throughout the cerebrum, sparing the subcortical U fibers. The signal has a "tigroid" appearance on T2-weighted images. The spectra demonstrate significant elevations of choline and myo-inositol with diminished N-acetylaspartate reflecting neuroaxonal loss, demyelination, and glial activation. *(From Cecil KM. MR spectroscopy of metabolic disorders.* Neuroimaging Clin N Am*. 2006;16:87–116; used with permission.)*

images, consistent with hypomyelination, which eventually may become more diffuse; involvement of the thalami is often present as well. The second pattern is a patchy low signal on T2-weighted images in a similar distribution to the hyperdense regions seen on CT, which is suspected to represent a paramagnetic effect from calcium deposition in the region. Additional early changes include increased density in the distribution of the thalami, cerebellum, caudate heads, and brainstem that may precede the abnormally low attenuation of white matter in the centrum semiovale. Symmetric enlargement of the optic nerves also has been described. The distal optic nerves are primarily involved; however, a case has been described with proximal prechiasmatic enlargement of the nerves.[17] T2 hyperintensity within the cerebellar white matter has been reported. The findings within the spinal cord are visualized as atrophic changes. Diffuse volume loss and periventricular white matter abnormalities predominate in the latter stages of this disease (Fig. 33.3). Midbrain morphology on midsagittal MR images reflects the extent of neurodegeneration in Krabbe disease. The morphology of the midbrain (i.e., convex, flat, concave) appears to be a reliable tool in assessing the clinical progression of the disease.[18] On MRI of the spine, abnormal thickening of the cauda equina roots is observed in Krabbe disease.[19]

Proton MRS demonstrates the reduced NAA expected with neuroaxonal loss but also has revealed disturbances in glial cell metabolism associated with hypomyelination. Elevated levels of choline and mI also have been reported, which is consistent with the general neurodegenerative pattern seen on proton spectroscopy. DWI also has been applied in a limited number of patients with

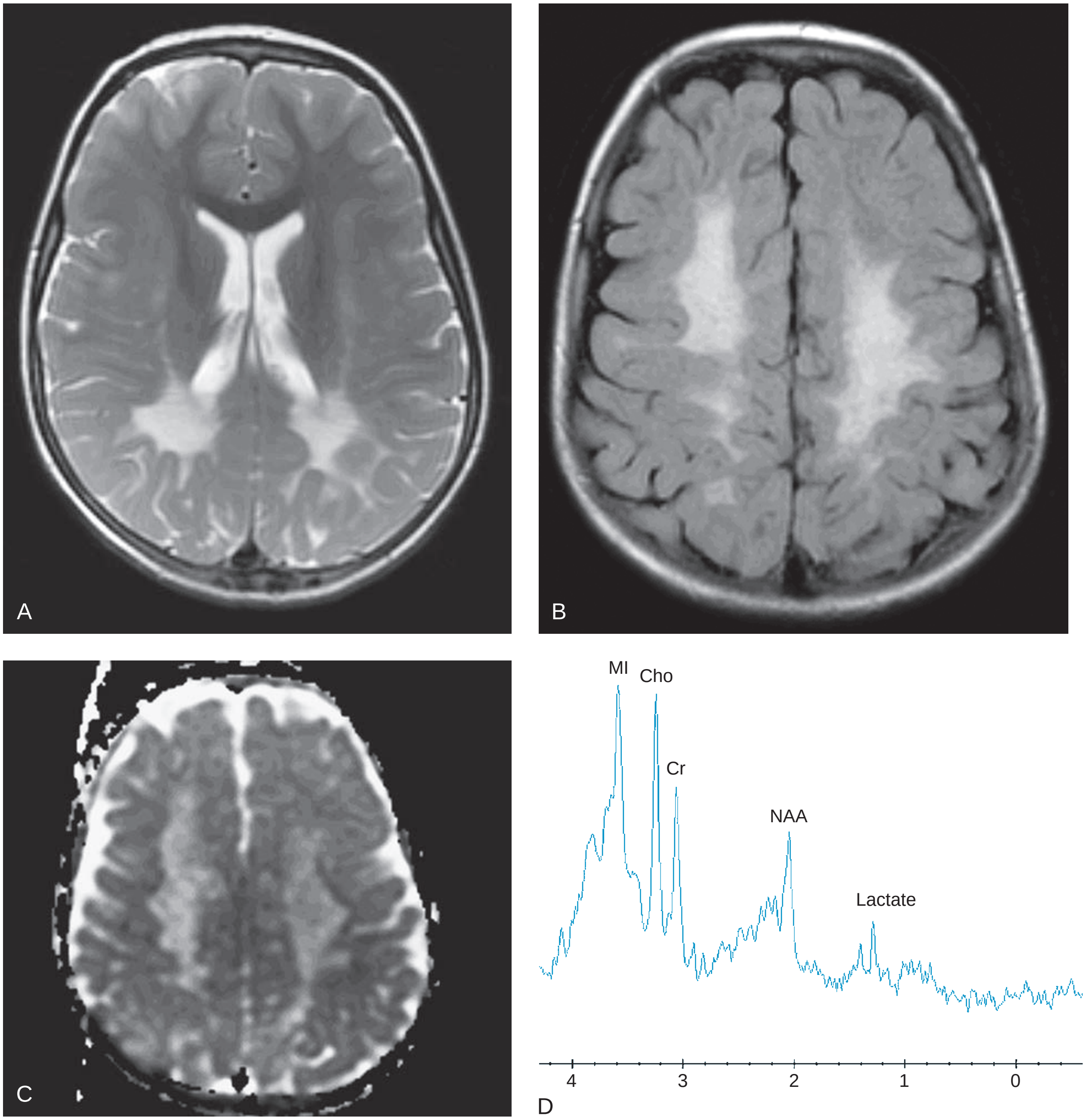

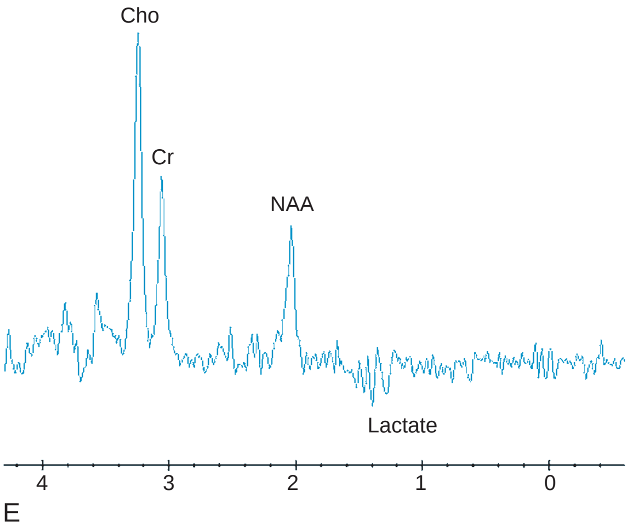

**Figure 33.3. Krabbe disease in a 4-year-old girl.** Axial T2-weighted fast spin echo (A), axial fluid attenuated inversion recovery (FLAIR) (B), axial apparent diffusion coefficient (ADC) map (C), short echo magnetic resonance spectroscopy (MRS) (D), and intermediate (time to echo 144 milliseconds [msec]) echo MRS (E) images are shown. Abnormal hyperintense T2 and FLAIR signals are noted within the centrum semiovale with sparing of the subcortical U fibers and posterior limbs of the internal capsules. Relatively increased diffusion is seen in the periatrial and parietal white matter. The spectra demonstrate significant elevations of lactate, choline, and myo-inositol, with diminished N-acetylaspartate reflecting neuroaxonal loss, demyelination, and glial activation.

Krabbe disease; loss of diffusion relative anisotropy preceded changes in T2 hyperintensity.

## PEROXISOMAL DISORDERS

Peroxisomes are organelles within a cell that contain enzymes responsible for critical cellular processes, including biosynthesis of membrane phospholipids, cholesterol, and bile acids; conversion of amino acids into glucose; oxidation of fatty acids; reduction of hydrogen peroxide by catalases; and prevention of excess oxalate synthesis. Peroxisomal disorders are subdivided into two major categories: (1) peroxisomal biogenesis disorders (PBDs) that arise from a failure to form viable peroxisomes, resulting in multiple metabolic abnormalities, and (2) disorders resulting from the deficiency of a single peroxisomal enzyme. Four different disorders constitute the genetically heterogeneous PBD group: Zellweger syndrome (ZS), infantile Refsum disease, neonatal adrenoleukodystrophy (ALD), and rhizomelic chondrodysplasia punctata.

### Zellweger Syndrome (Cerebrohepatorenal Syndrome)

ZS is an autosomal-recessive disease characterized by defective peroxisomal functions. Infants are symptomatic early, with hypotonia, seizures, hepatomegaly, and limb and facial anomalies that are easily recognizable at birth. MRI shows a diffuse lack of myelination throughout the white matter, combined with cortical dysplasia. The gyri are broad, with shallow intervening sulci found mainly in the anterior frontal and temporal lobes but also over the convexities in the perirolandic area (e-Fig. 33.4). The presence of a germinolytic cyst in the caudothalamic groove is common and may have hemorrhage.[20] In one case, signal abnormality suggestive of demyelination was identified almost solely in the brainstem corticospinal tracts.[21] Clinical overlap may occur with other conditions, including neonatal ALD, infantile Refsum disease, and hyperpipecolic acidemia. Death usually comes with many of these conditions within the first 2 years of life.

MRS in older patients with ZS and Refsum disease reveals similar features, with dramatic lipid and choline elevations, minor mI elevations, and reduced NAA levels in sampled white matter. For rhizomelic chondrodysplasia punctata, two studies report elevations of mobile lipids, mI-glycine, and acetate and reduced choline. In contrast to ZS, infantile Refsum disease, and neonatal ALD, rhizomelic chondrodysplasia punctata does not feature liver disease, which is significant to account for the mI differences. To detect mI levels, a short echo technique (i.e., TE ≤35 msec) must be used to recognize a resonance appearing at 3.5 ppm. For MRS performed at 1.5 T, the mI resonance normally is distinct, with four of the molecule's six methine protons magnetically indistinguishable, thereby coresonating at the same location (3.5 ppm). However, increased spectral dispersion inherent at higher field strengths (3 T) produces two distinct resonances (3.5 and 3.6 ppm) for the four protons, effectively reducing the signal by half. Although some reports have found improved detection of mI at high field strength arising from increased signal/noise ratio, it may be problematic depending on the acquisition conditions.

### Neonatal Adrenoleukodystrophy

Neonatal ALD is characterized by the presence of multiple recognizable enzyme deficiencies with grossly normal but deficient numbers of peroxisomes. Specific conditions include pipecolic and phytanic acidemia, and a deficiency of plasmalogen synthetase. This condition presents with hypotonia in the first months of life but without many of the facial features of ZS. Cortical dysplasia can be found, as well as hypomyelination, in cerebral white matter (Fig. 33.5).

### Adrenoleukodystrophy

X-linked ALD is the prototypical peroxisomal disorder in which organelle morphology is normal on electron microscopy but a single enzyme defect, acyl-CoA synthetase, along with a failure of incorporation into cholesterol esters for myelin synthesis, leads to the accumulation of very-long-chain fatty acids and progressive CNS deterioration in the form of a chronic progressive encephalopathy. This "classic" form of ALD is an X-linked disorder with a clinical onset between the ages of 5 to 7 years, followed by a rapidly progressive decline in neurologic function and death within the ensuing 5- to 8-year period. The first indication of this condition may include mental status changes or a decline in school performance, progressing to subtle alterations in neurocognitive function, and ultimately resulting in severe spasticity and visual deficits, leading finally to a vegetative state and death. Childhood cerebral ALD, although rare, can present with raised intracranial pressure (ICP) and an elevated level of CSF protein.[22]

CT and MRI findings in X-linked ALD show predominately posterior involvement that, over time, progresses anteriorly into the frontal lobes and from the deep white matter to the peripheral subcortical white matter. On CT, the involvement appears as symmetrical low attenuation in a butterfly distribution across the splenium of the corpus callosum, surrounded on its periphery by an enhancing zone (inflammatory intermediate zone). Three zones are readily distinguished on MR: an inner zone of astrogliosis and scarring corresponds to the low density zone seen on CT that appears hypointense on T1-weighted images and hyperintense on T2-weighted sequences; an intermediate zone of active inflammation that appears isointense on T1-weighted images and isointense or hypointense on T2-weighted images; and an outer zone of active demyelination that appears minimally hypointense on T1-weighted images and hyperintense on T2-weighted scans. Enhancement after administration of gadolinium is demonstrated within the intermediate zone of active inflammation and may disappear as the first change after bone marrow transplantation (Fig. 33.6).

Proton MRS demonstrates abnormal spectra within regions of abnormal signal, as well as white matter that appears normal. The spectral profile for normal-appearing white matter of neurologically asymptomatic patients is characterized by slightly elevated concentrations of composite choline compounds, with an increase of both choline and mI reflecting the onset of demyelination. Markedly elevated concentrations of choline, mI, and glutamine in affected white matter suggest active demyelination and glial proliferation. A simultaneous reduction of the concentrations of NAA and glutamate is consistent with neuronal loss and injury. An elevated lactate level is consistent with inflammation and/or macrophage infiltration. The more severe metabolic disturbances in persons with ALD correspond to progressive demyelination, neuroaxonal loss, and gliosis leading to clinical deterioration and death. The detection of MRS abnormalities before the onset of neurologic symptoms may help in the selection of patients for bone marrow transplantation and stem cell transplantation, and monitoring after treatment. Stabilization and partial reversal of metabolic abnormalities is demonstrated in some patients.

## MITOCHONDRIAL DISEASES

Mitochondrial diseases generally refer to disorders of the mitochondrial respiratory chain, the only cellular metabolic pathway under control by both the mitochondrial genome (mtDNA) and the nuclear genome (nDNA). Mitochondrial diseases demonstrate impaired respiratory chain function and reduced adenosine triphosphate production. The mtDNA mutations can be divided into two categories: those that impair mitochondrial protein synthesis *in toto* and those that affect respiratory chain subunits. Disorders

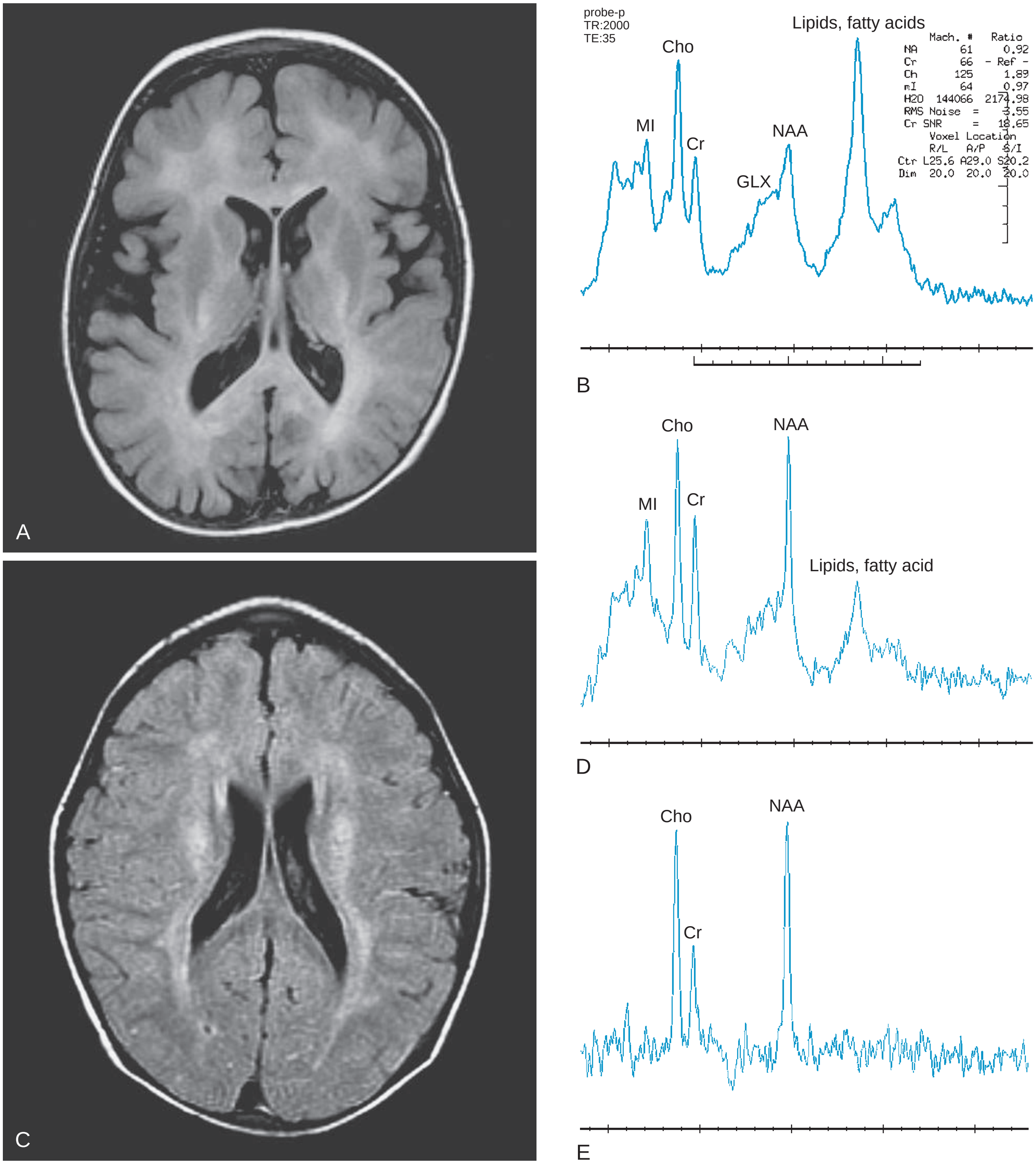

```
      Mach. #   Ratio
  NA       61     0.92
  Cr       66   - Ref -
  Ch      125     1.89
  mI       64     0.97
  H2O  144066  2174.98
  RMS Noise  =    3.55
  Cr SNR     =   18.65
      Voxel Location
      R/L    A/P   S/I
 Ctr L25.6 A29.0 S20.2
 Dim  20.0  20.0  20.0
```

**e-Figure 33.4. Zellweger syndrome (A and B) and Refsum disease (C, D, and E).** Axial fluid attenuated inversion recovery (FLAIR) (A) and short echo magnetic resonance spectroscopy (MRS) (B) images were acquired in the left frontal lobe of a 3-year-old boy with Zellweger syndrome. Imaging demonstrates mildly enlarged ventricles and extraaxial spaces consistent with parenchymal volume loss with abnormal hyperintense signal throughout the white matter. Axial FLAIR (C), short echo MRS (D), and long echo MRS (E) images were acquired in the periventricular white matter of a 6-year-old boy with Refsum disease. An abnormal hyperintense signal is demonstrated in the periventricular white matter and is noted along the course of the corticospinal tracts. Spectra from both patients demonstrate an elevated lipid peak, representing stored fatty acids. Reduced N-acetylaspartate with elevated choline and myo-inositol levels also are demonstrated in the spectra. *(From Cecil KM. MR spectroscopy of metabolic disorders.* Neuroimaging Clin N Am. *2006;16:87–116; used with permission.)*

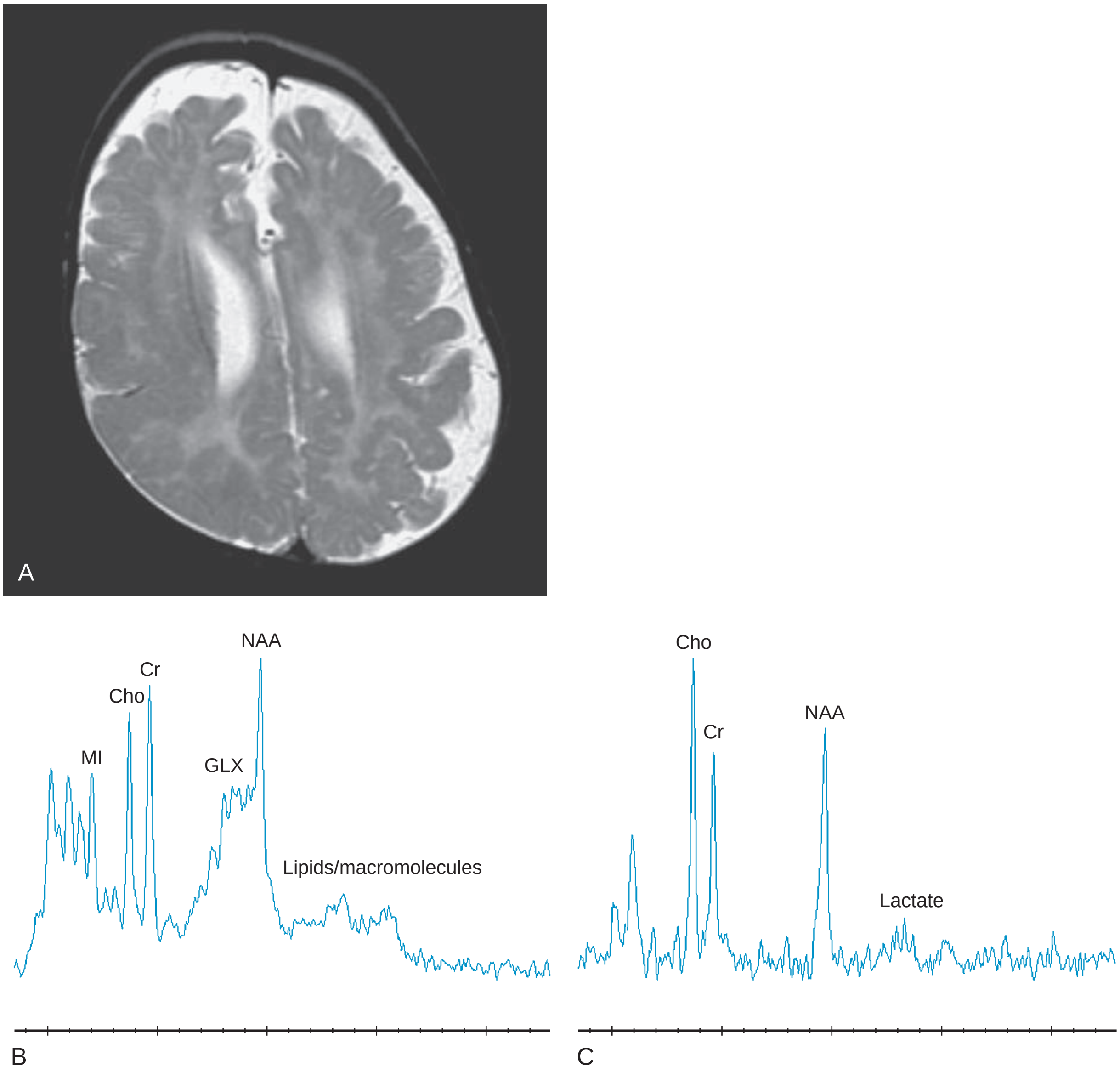

**Figure 33.5. Neonatal adrenoleukodystrophy in a 12-month-old boy.** Axial T2-weighted (A), short echo magnetic resonance spectroscopy (MRS) (B), and long echo MRS (C) images are shown. The imaging reveals an abnormal hyperintense signal within the central white matter and an abnormal cerebral gyral pattern consistent with polymicrogyria. The lateral ventricles and extraaxial spaces are prominent in size with a thin corpus callosum. The spectroscopy performed in the left parietal cortex and white matter reveals elevated glutamate and glutamine with a slightly elevated lactate signal and reduced N-acetylaspartate levels. *(From Cecil KM. MR spectroscopy of metabolic disorders.* Neuroimaging Clin N Am. *2006;16:87–116; used with permission.)*

attributed to mtDNA mutations follow lax rules of mitochondrial genetics. However, disorders arising from nDNA mutations are governed by Mendelian genetics. The disorders attributed to mutations in nDNA are more abundant because most respiratory chain subunits are nucleus-encoded and the correct assembly and functioning of the entire respiratory chain require numerous steps. The clinical phenotypes of nDNA-related mitochondrial disorders tend to be uniform, whereas both the spectrum and severity of clinical manifestations associated with mtDNA-related disorders are extremely variable. Marked genotype-phenotype variability is characteristic of mtDNA-related disorders. The clinical diversity observed in patients with mtDNA-related disorders can be partially explained by heteroplasmy, the coexistence of mutant and wild-type mtDNA within a cell. Only when the proportion of mutant genomes exceeds a particular level is the disease expressed.

## Kearns-Sayre Syndrome

A group of clinical syndromes arising from mtDNA rearrangements, either deletions or duplications, includes Kearns-Sayre syndrome, Pearson syndrome, and progressive external ophthalmoplegia.

Kearns-Sayre syndrome is characterized by external ophthalmoplegia, retinal pigmentary degeneration, and conductive hearing block. Ragged red fibers indicative of a defect in the respiratory chain of mitochondria are demonstrated on muscle biopsy, in common with mitochondrial encephalomyopathy, lactic acidosis,

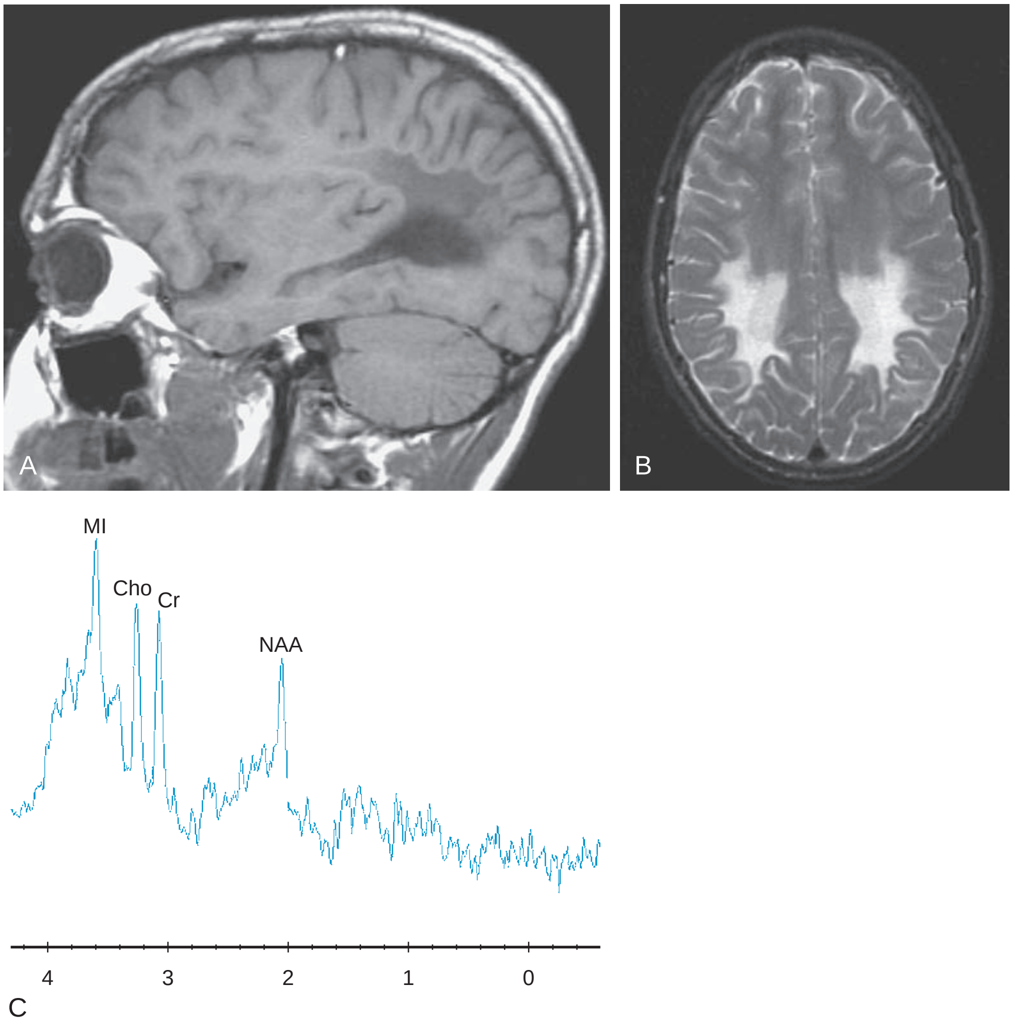

**Figure 33.6. X-linked adrenoleukodystrophy in a 16-year-old boy, 8 months after a bone marrow transplant.** Sagittal T1-weighted (A), axial T2-weighted (B), and short echo magnetic resonance spectroscopy (MRS) (C) images are shown. The imaging demonstrates an abnormal signal in the posterior portion of the cerebrum. The spectra sampled in the right posterior parietal white matter reveals a diminished N-acetylaspartate level with an elevated myo-inositol level. Imaging and spectroscopy reflected disease stability for this patient.

and strokelike symptoms (MELAS) and myoclonic epilepsy with ragged red fibers (MERRF) syndromes. The heart is often affected, causing conduction defects, which progress to heart block and heart failure.[23] Choroid plexus failure also has been reported.[24] Cerebral MRI demonstrates diffuse, patchy areas of hyperintensity on T2-weighted images. In the presence of calcification, both the basal ganglia and dentate nuclei may show hyperintense T1-weighted signal. On T2-weighted and FLAIR images, bilateral involvement of the thalamus, basal ganglia, and brainstem are observed. Cerebral and, more frequently, cerebellar atrophy often are observed.[25] Ocular myopathy characterizes some patients affected by Kearns-Sayre syndrome (e-Fig. 33.7).

## MELAS Syndrome

There are several clinical syndromes arising from point mutations in mtDNA, the most notable being MELAS syndrome, MERRF syndrome, neurogenic weakness and ataxia with retinitis pigmentosa syndrome, and Leber hereditary optic neuropathy. MELAS syndrome often is caused by an A3243G point mutation in $\text{tRNA-leu}^{\text{UUR}}$ or the *MTTL1* gene (80% of cases). Other phenotypes can result in the A3243G point mutation (e.g., maternally inherited deafness and diabetes). The clinical presentation of MELAS syndrome resembles that of cerebral infarction; however, the “infarcts” lack the usual arterial stroke distribution. Age of onset is usually between 2 and 11 years. The basal ganglia and parietal, temporal, and occipital lobes are most commonly involved. MRI demonstrates areas of T2 hyperintensity with volume loss a late development.

Proton MRS has been used to aid diagnosis of mitochondrial disorders, with the assumption that elevation of lactic acid is a primary feature. However, positive lactate at spectroscopy does not necessarily equal the presence of a mitochondrial disorder, and the absence of lactate on MRS does not rule out a defect in mitochondrial function. Proton MRS in patients with MELAS syndrome can demonstrate variable results as strokelike lesions emerge and evolve. Proton MRS details energy failure with increased lactate and decreased creatine. Elevation of lactate in the acute and subacute stages typically is observed, with subsequent declines in NAA and creatine, consistent with neuroaxonal injury that may or may not be reversible. It has been reported that increase of lactate peaks in MRS and hyperperfusion with arterial spin label imaging both indicate active lesions.[26] MELAS syndrome shows a gradual spread of the core of edematous lesions, a

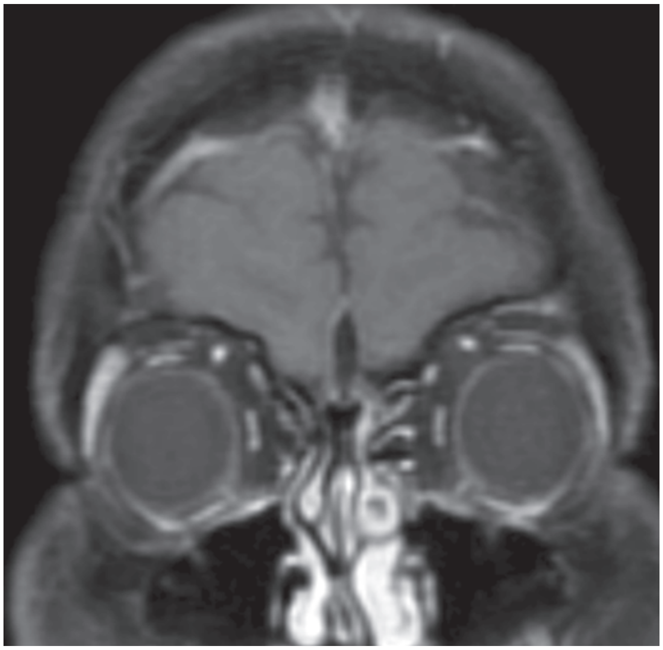

**e-Figure 33.7. Kearns-Sayre syndrome.** Coronal contrast-enhanced T1-weighted fat-saturated MR image shows atrophic extraocular muscles.

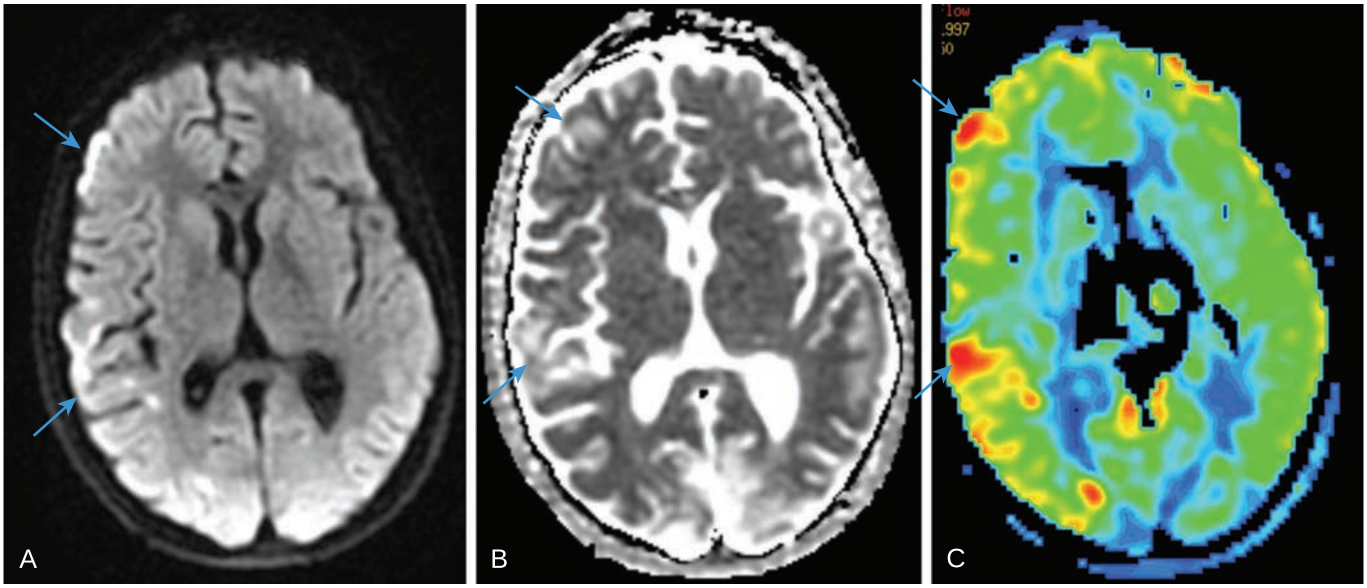

**Figure 33.8. Mitochondrial encephalomyopathy, lactic acidosis, and strokelike symptoms (MELAS) in a 13-year-old boy.** Axial diffusion-weighted imaging (A), axial apparent diffusion coefficient (ADC) map (B), and an axial arterial spin labeling color map (C) are shown. Scattered foci of vasogenic edema denoted by *arrows* corresponding to increased perfusion are identified in the acute phase of the disease in the right cerebral hemisphere.

contributing factor to the prolonged ADC decline, which helps differentiate it from ischemic stroke[27] (Fig. 33.8).

## Leigh Syndrome (Subacute Necrotizing Encephalomyelopathy)

Disorders arising from defects in nDNA are numerous, but the most commonly encountered is Leigh syndrome. The genetic defect of Leigh syndrome can arise from several sources, including pyruvate dehydrogenase complex deficiency, complex I deficiency, complex V deficiency with adenosine triphosphatase 6 mutation, and cytochrome oxidase deficiency with *SURF1* mutation. This group of disorders characteristically presents at 3 months to 2 years of age but may begin with symptoms of hypotonia in the newborn period or even in adulthood. Clinical signs include ophthalmoplegia, cerebellar signs, and spasticity, which are slowly progressive. Other features include psychomotor regression, extrapyramidal signs, blindness, nystagmus, respiratory compromise, or cranial nerve palsies. Onset of symptoms within the first years of life typically portends a rapid downhill course. A later onset of symptoms is generally associated with slower progression.

Pathologically, this syndrome involves both gray and white matter of the brain and spinal cord. Common sites of anatomic involvement include the basal ganglia, specifically the globus pallidus and putamina, and the thalami, midbrain, pons, cerebellum, and medulla. Pathologic changes include spongiform degeneration, demyelination, and vascular compromise and proliferation.

Abnormal low signal on T1-weighted images or a high signal on T2-weighted images in the basal ganglia, periaqueductal gray matter, and brainstem/cerebellum are characteristic of this group of disorders. Bilateral symmetric lesions in the basal ganglia (globus pallidus and putamen) characterized by hypointensity on T1-weighted images and hyperintensity on T2-weighted images is highly suggestive of this condition and should prompt further clinical investigation for signs of lactic acid in the serum or CSF. Late involvement may manifest as regions of an abnormal hyperintense signal on T2-weighted images in the centrum semiovale (Fig. 33.9 and e-Fig. 33.10).

Proton MRS images obtained from the basal ganglia, occipital cortex, and brainstem show elevations in lactate, which are most pronounced in regions where abnormalities are seen with routine T2-weighted MRI. Proton MRS images in regions of abnormal MRI signal also reveal a decrease in the NAA/creatine ratio and an increase in the choline/creatine ratio, representing neuronal loss and breakdown of membrane phospholipids. Some evidence indicates that a reduction of lactate levels may correlate with response to therapy, such as with dichloroacetate and coenzyme Q10.

## Pantothenate Kinase-Associated Neurodegeneration

Pantothenate kinase-associated neurodegeneration, also called neurodegeneration with brain iron accumulation (NBIA), is caused by mutations in the gene that encodes pantothenate kinase 2 *(PANK2)*. *PANK2* is necessary for the production of coenzyme A in mitochondria. Other similar mutations result in atypical presentations of the same syndrome. "Classic" NBIA has an early onset of disease in infancy, with rapid progression of gait impairment, development of choreoathetoid movements, rigidity, dysarthria, and cognitive decline. Dystonia is a prominent feature of this disorder. All of these clinical manifestations reflect the impact of the disease upon the basal ganglia and striatum. Atrophy of the cerebellum and iron accumulation in the basal ganglia on susceptibility weighted images (SWI) are prominent imaging features of these disorders. Atypical NBIA has a later presentation with slower progression (Fig. 33.11).

## Menkes Disease

Menkes disease (also known as trichopoliodystrophy or kinky-hair syndrome) is an X-linked recessive mitochondrial cytopathy. The disease may commence in utero and has been recognized at birth. It appears in males with the clinical features of hypotonia, seizures, spastic quadriplegia, and profound retardation with sparse, fragile hair that is easily broken. Growth failure and microcephaly are common. Absorption of copper from the gastrointestinal tract is

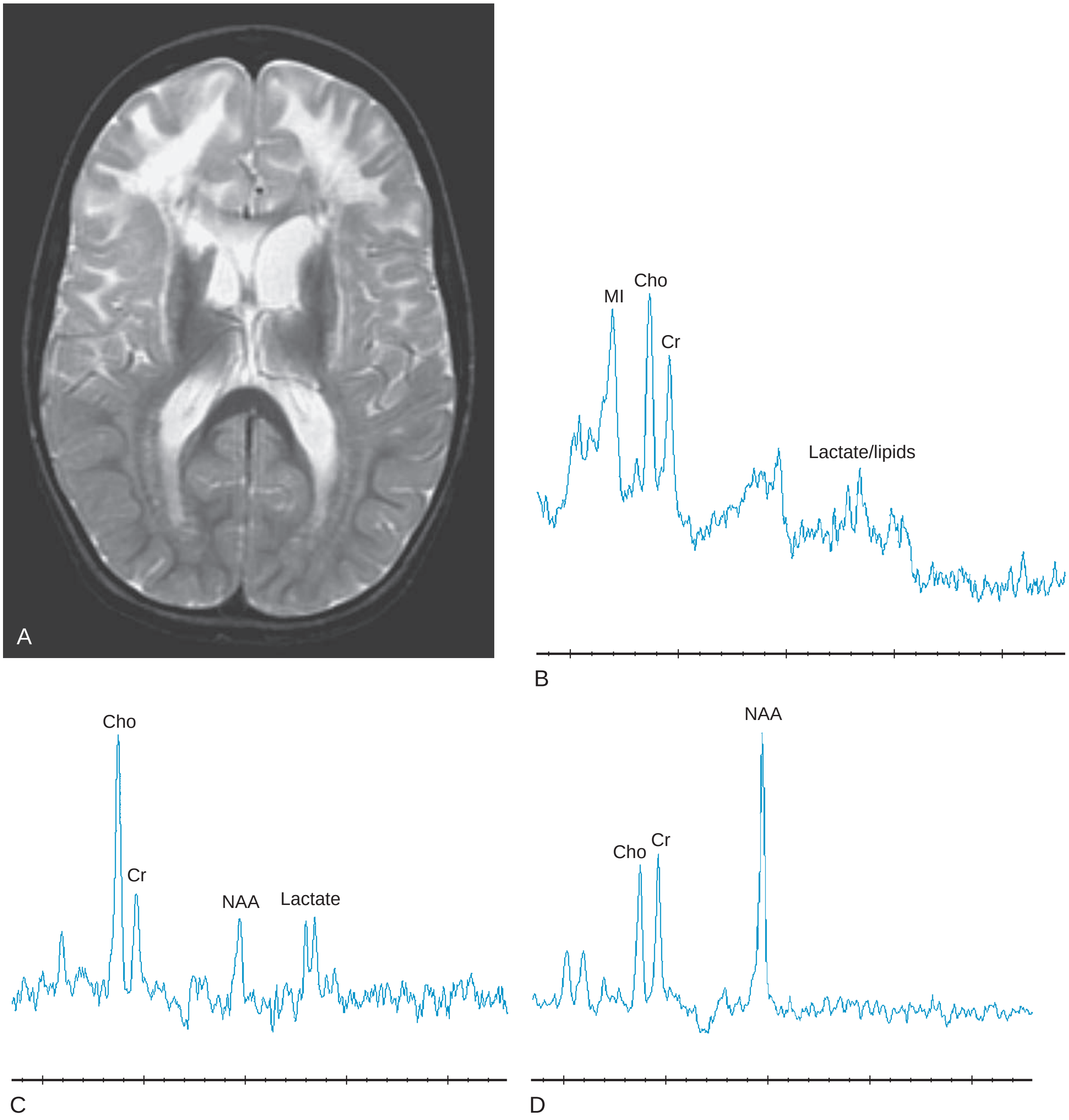

**e-Figure 33.10. Complex I deficiency acquired in a 4-year-old girl.** Note the dramatic differences in the imaging and spectroscopy compared with Fig. 33.9. Axial T2-weighted image (A), a short echo magnetic resonance spectroscopy (MRS) image in the frontal white matter (B), a long echo MRS image in the frontal white matter (C), and a long echo MRS image in the posterior cortex parasagittally (D) are shown. The imaging reveals an abnormal hyperintense signal within the white matter of frontal lobe, including the U fibers but sparing the internal capsule with enlarged ventricles, suggesting volume loss of the caudates. Within the frontal lobe, decreased N-acetylaspartate with lactate, choline, and myo-inositol elevations are seen, representing mitochondrial dysfunction, demyelination, axonal loss, and astrocytosis. The sampled spectrum within the posterior cortex is unremarkable. *(From Cecil KM. MR spectroscopy of metabolic disorders.* Neuroimaging Clin N Am. *2006;16:87–116; used with permission.)*

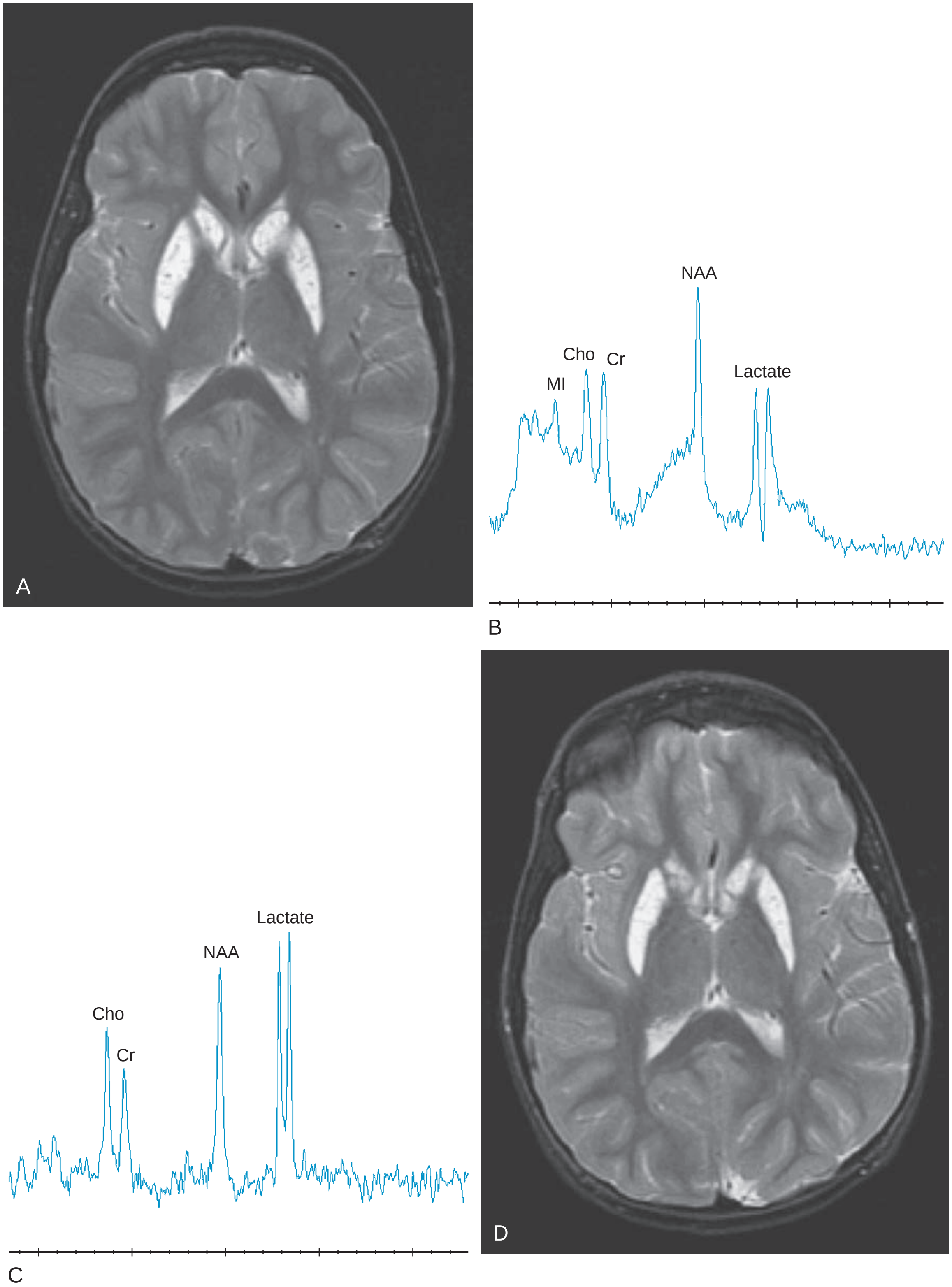

**Figure 33.9. Complex I deficiency in an 8-year-old girl with magnetic resonance examinations acquired approximately 3 months apart.** Axial T2-weighted (A), short echo magnetic resonance spectroscopy (MRS) (B), and long echo MRS (C) images were obtained. The imaging reveals a pattern characteristic of "Leigh syndrome" with an abnormal hyperintense signal bilaterally within the caudate and globus pallidus. The MRS image acquired in the left basal ganglia at a period of clinical exacerbation caused by febrile illness demonstrates a dramatic elevation of lactate compared with her routinely observed levels as shown in axial T2-weighted (D), short echo MRS (E), and long echo MRS (F) images. The spectra acquired 3 months later demonstrates a significant reduction in lactate. A comparison of the imaging data is unremarkable between the examinations. The dramatic elevation of lactate revealed on MRS in (B) and (C) corresponds to worsening clinical symptoms (seizures and leg stiffening). The lactate levels observed in (E) and (F) are typical and consistent with this mitochondrial defect. *(From Cecil KM. MR spectroscopy of metabolic disorders.* Neuroimaging Clin N Am. *2006;16:87–116; used with permission.)*

*Continued*

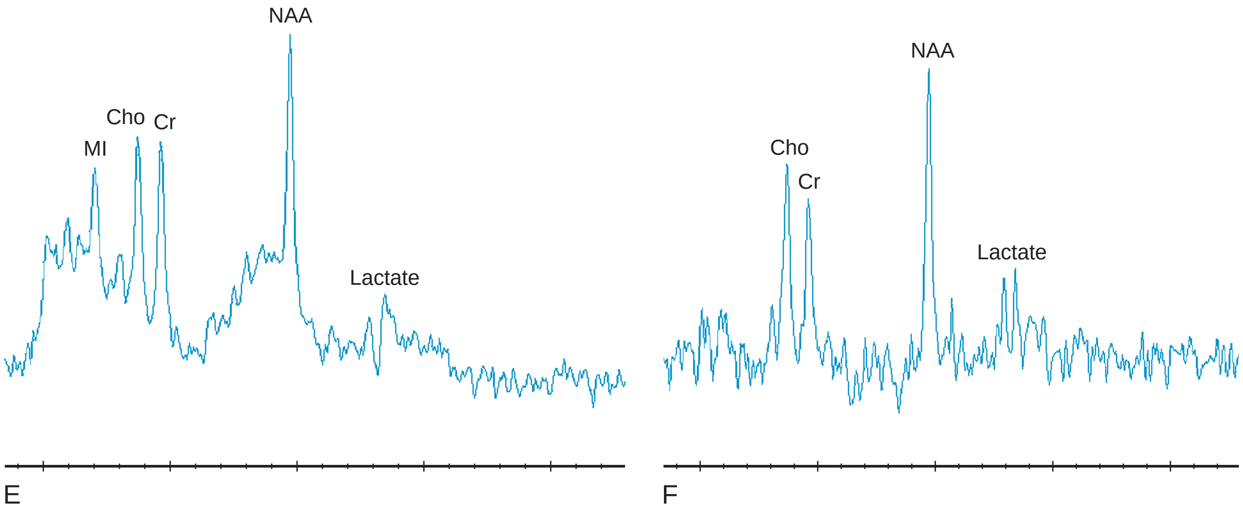

**Figure 33.9, cont'd.**

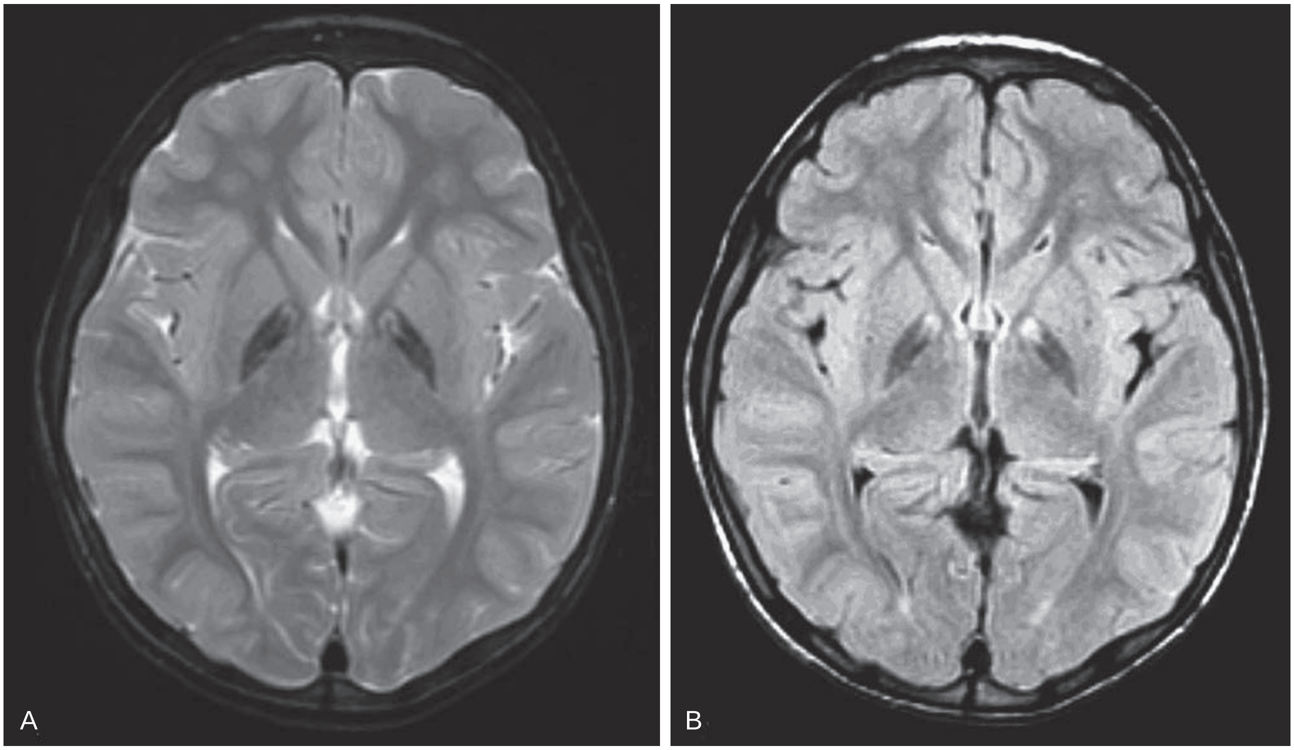

**Figure 33.11. Pantothenate kinase-associated neurodegeneration or neurodegeneration with brain iron accumulation, traditionally referred to as Hallervorden-Spatz syndrome in a 6-year-old girl.** Axial T2-weighted (A) and axial fluid attenuated inversion recovery (FLAIR) (B) MR images are shown. An abnormal hypointense signal is demonstrated bilaterally in the globus pallidus.

decreased. The defective intracellular binding and membrane transport of copper are related to an abnormal metallothionein, a copper-binding protein. Decreased activity of copper-dependent enzymes is found in the liver, brain, and white cells.

Radiographs may demonstrate wormian bones in the skull, rib fractures, and metaphyseal infarctions in long bones. Neuroimaging findings include cerebral volume loss and subdural collections, and cerebral angiography shows dilated and tortuous vessels within the circle of Willis. Basal ganglia lesions have been reported in advanced stages; however, reports of basal ganglia involvement in the early stages of Menkes disease exist.[28] Hyperintense white matter T2 signal indicates a lack of myelination but may also be related to a relative lack of blood flow as a result of the vascular involvement (Fig. 33.12). The combination of extracerebral collections and metaphyseal infarctions may simulate battered child syndrome.

## ORGANIC AND AMINO ACID DISORDERS

Many disorders of organic acid metabolism affect mitochondrial function, and as such they demonstrate imaging features similar to those of mitochondrial disorders. Two key disorders are glutaric aciduria and methylmalonic acidemia. Myelin formation is dependent on amino acids. Defects in amino acid metabolism lead

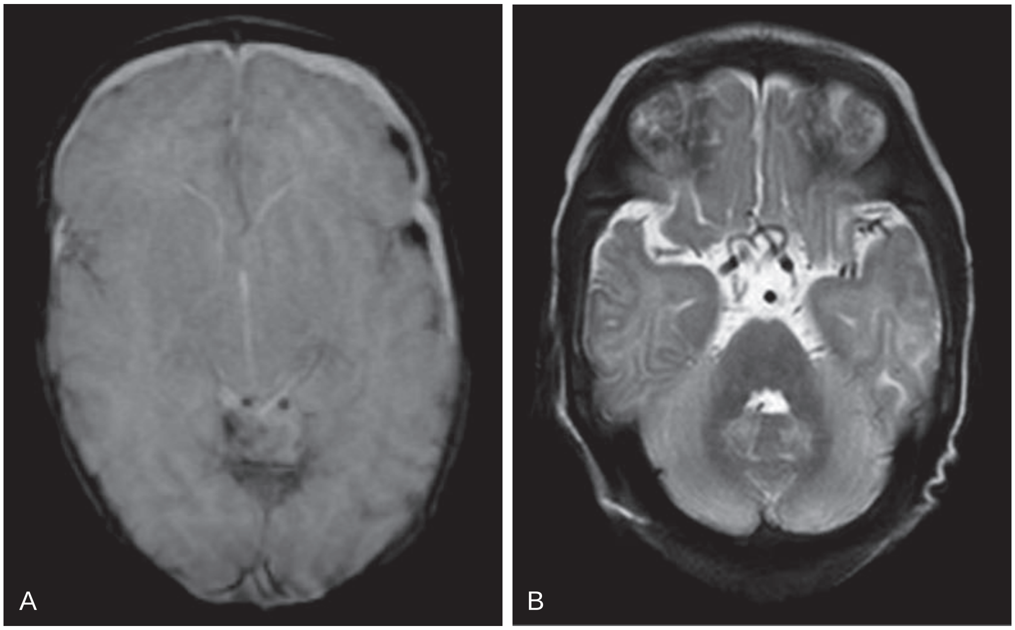

**Figure 33.12. Menkes disease in a male patient.** (A) Axial multiple planar gradient recalled MR image reveals bilateral subdural collections with evidence of hemorrhage at 6 weeks. (B) Axial T2-weighted MR image at the cerebellum at 4 months.

to failure of formation and maintenance of normal myelin. Disorders primarily of amino acid metabolism include phenylketonuria, maple syrup urine disease (MSUD), homocystinuria/hyperhomocysteinemia, and nonketotic hyperglycinemia.

## Glutaric Aciduria

Glutaric aciduria type I is an autosomal recessive organic aciduria resulting from deficiency of the enzyme glutaryl-CoA dehydrogenase, which is involved in the metabolism of hydroxylysine, lysine, and tryptophan. Presentation may be acute with encephalopathy or chronic with multiple neurologic abnormalities, including hypotonia, ataxia, dysmetria, and delayed achievement of milestones.

MRI demonstrates T2 hyperintensity in the basal ganglia, especially the putamen, but also in the caudate nucleus and globus pallidus. Myelination is delayed. Bilateral temporal arachnoid cysts and enlarged frontotemporal spaces with subdural hematomas may be found. As a consequence, this rare disorder is sometimes considered as a differential diagnosis in children with abusive head trauma. The development of T2 prolongation in the basal ganglia and periventricular white matter would support the diagnosis of glutaric aciduria type I in such cases. The enlargement of extraaxial spaces makes glutaric aciduria type I one of the metabolic diseases associated with macrocrania. Unlike in Alexander disease and Canavan disease, the macrocrania does not reflect megalencephaly. Enlargement of the Sylvian fissure has been correlated with severity of the enzyme deficiency. Acute striatal necrosis is the main cause of death during infancy; it can be visualized as usually symmetric, strokelike signal hyperintensity on T2-weighted and diffusion-weighted MRI, bilateral striatal lucency on CT, or a sharp decline of fluorodeoxyglucose uptake on positron emission tomography.[29] Prenatal MRI has been shown to be useful in identifying GA1, revealing focal reduction of the anterior pole of both temporal lobes with widening of CSF spaces[30] (Fig. 33.13).

## Methylmalonic and Proprionic Acidemias

Methylmalonic acidemia results from a deficiency in methylmalonyl CoA mutase, an enzyme required for the conversion of methylmalonic CoA to succinyl CoA, which is necessary for the proper metabolism of the amino acids methionine, threonine, isoleucine, and valine. The high levels of methylmalonic acid resulting from the enzyme deficiency inhibit succinate dehydrogenase, which disrupts aerobic metabolism in the mitochondria. A relatively milder form of the disease is caused by deficiency of the cobalamin coenzyme. Propionic aciduria is a result of a deficiency in propionyl-CoA carboxylase and presents in a similar fashion.

Epilepsy is common in patients with methylmalonic acidemia, and cardiac involvement, including cardiomyopathy, arrhythmias, carnitine deficiency, and structural heart disease, have been reported.[31,32] Hyperglycemia also has been reported.[33] On imaging, parenchymal volume often is decreased, with delays in myelination. Optic neuropathy also has been reported.[34] Like other mitochondrial-based syndromes, the organic acidemias have a strong tendency to cause lesions in the basal ganglia, most particularly the globus pallidus. Lesions in the globus pallidus are striking in their stereotypical appearance from patient to patient. Affected areas will appear low in attenuation on CT and hyperintense on T2-weighted MRI (e-Fig. 33.14). Strokelike episodes similar to MELAS occasionally may be encountered. DWI will show restricted diffusion in affected regions. Proton MRS has shown decreases in NAA and elevation of lactate levels. Lactate elevation also can be found in the CSF, which is important for narrowing the differential diagnosis.

## Phenylketonuria

Phenylketonuria is an autosomal-recessive disorder resulting from enzyme deficiencies (phenylalanine hydroxylase, dihydrobiopterin reductase, and dihydrobiopterin biosynthesis) that impair the ability to convert phenylalanine to tyrosine, thereby producing the accumulation of neurotoxic acids. Its frequency is on the order of 1:14,000 live births.

MRI initially demonstrates symmetric hyperintense areas on T2-weighted images in the periatrial white matter. Extension occurs into the optic radiations and periventricular frontal white matter with more severe involvement and contrast enhancement. In untreated patients, it has been reported that diffuse white matter

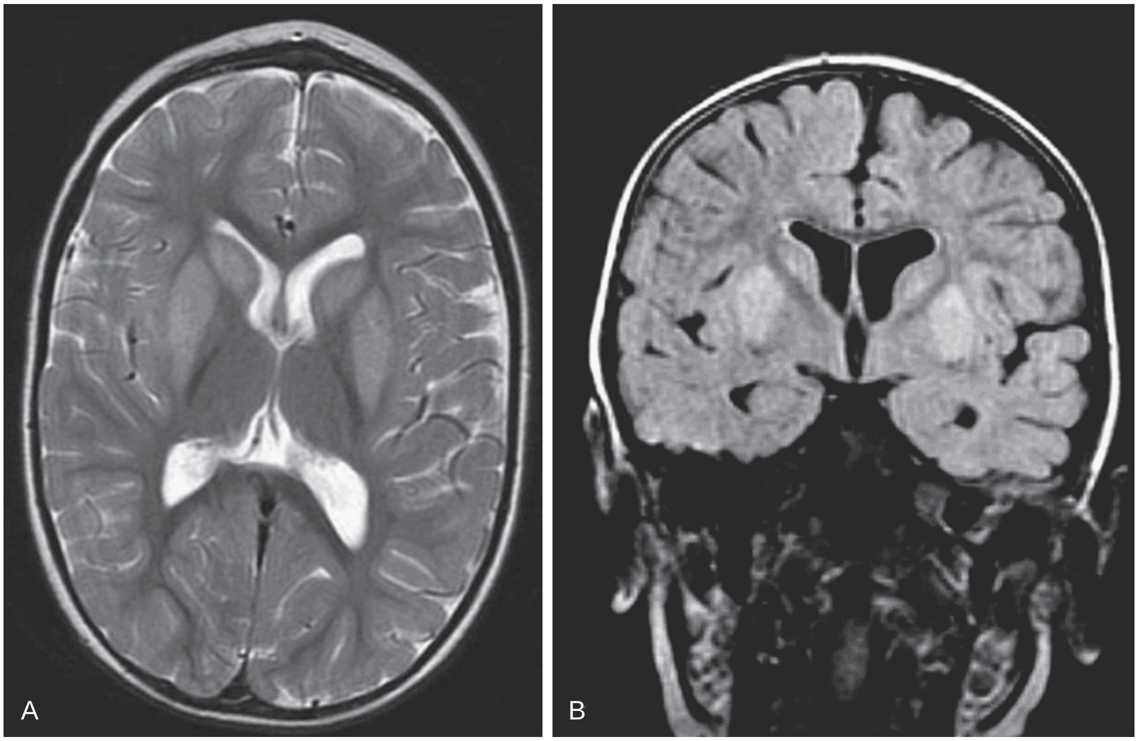

**e-Figure 33.14. Propionic aciduria in a 2-year-old boy.** Axial T2-weighted fast spin echo (A) and coronal fluid attenuated inversion recovery (FLAIR) MR images (B) reveal an abnormal hyperintense signal bilaterally within the putamen without evidence of volume loss.

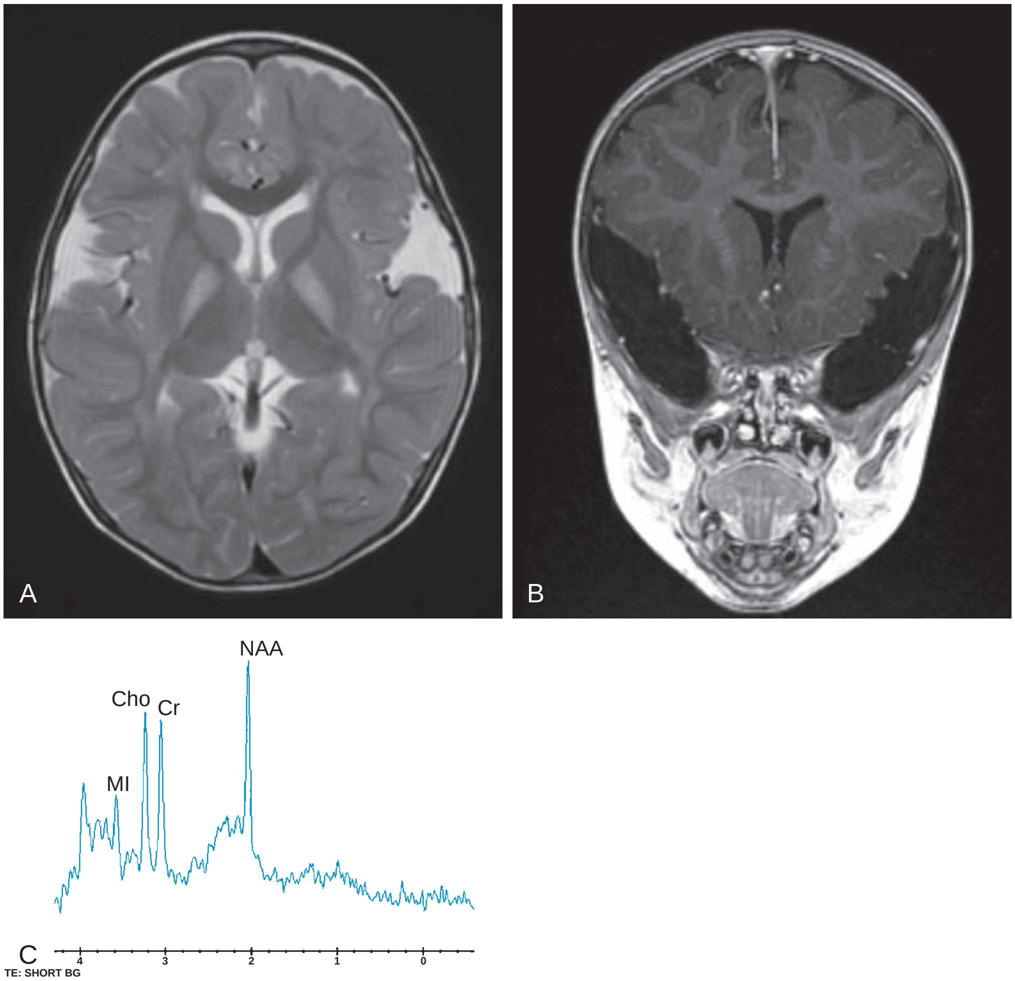

**Figure 33.13. Glutaric aciduria I in a 22-month-old boy.** (A) Axial fast spin echo T2-weighted MR image demonstrates a hyperintense signal bilaterally within the globus pallidus. (B) Coronal spoiled gradient echo MR image features the prominent symmetric, bilateral widening of the Sylvian fissures with frontotemporal hypoplasia. (C) A short echo (time to echo 35 milliseconds [msec]) magnetic resonance spectroscopy (MRS) image acquired within the basal ganglia demonstrates an elevation of choline.

pathology is evidence of hypomyelination; however, white matter abnormalities in patients who are treated early are indicative of intramyelinic edema.[35] Hyperintensity in multiple areas on T1-weighted images has been reported, corresponding to subcortical parenchymal calcification.

MRI white matter alterations in patients with phenylketonuria correlated to blood phenylalanine concentrations and to brain phenylalanine concentrations measured by proton MRS. MRS may demonstrate an abnormal peak at 7.30 ppm resulting from elevated phenylalanine. Interindividual variations of blood-brain barrier phenylalanine transport constants and variations of the individual brain phenylalanine consumption rate are responsible for the patient differences.

## Maple Syrup Urine Disease

MSUD is a rare autosomal-recessive disorder caused by defective oxidative decarboxylation of three branched-chain amino acids: valine, isoleucine, and leucine. The accumulation of metabolites in the urine leads to the characteristic odor, which resembles that of maple syrup. Although cerebral imaging findings initially may be unremarkable, diffuse cerebral edema develops with subsequent residual areas of hyperintensity in the dorsal brainstem and pons. Proton MRS of the brain appears to be useful for examining patients who have MSUD in different metabolic states. The accumulation of abnormal branched-chain amino acids and branched-chain alpha-ketoacids appear as a broad peak at 0.9 ppm accompanied by an elevated lactate level. The presence of cytotoxic or intramyelinic edema as evidenced by restricted water diffusion on DWI, with the presence of lactate on spectroscopy, could imply cell death. However, in the context of metabolic decompensation in MSUD, it appears that changes in cell osmolarity and metabolism can reverse completely after metabolic correction. Classification of MSUD includes a form responsive to thiamine (e-Fig. 33.15).

## Nonketotic Hyperglycinemia

Nonketotic hyperglycinemia occurs when a metabolic defect impairs the conversion of glycine to serine, resulting in CNS accumulation of glycine. The toxic effects of an elevated glycine level present in the neonatal period as lethargy, hypotonia, myoclonus, and seizures that may lead to an unresponsive state with apnea. Prognosis is poor, with few patients surviving beyond the neonatal period.

Pathology in nonketotic hyperglycinemia is characterized by vacuolation, astrocytosis, and demyelination, also called vacuolating

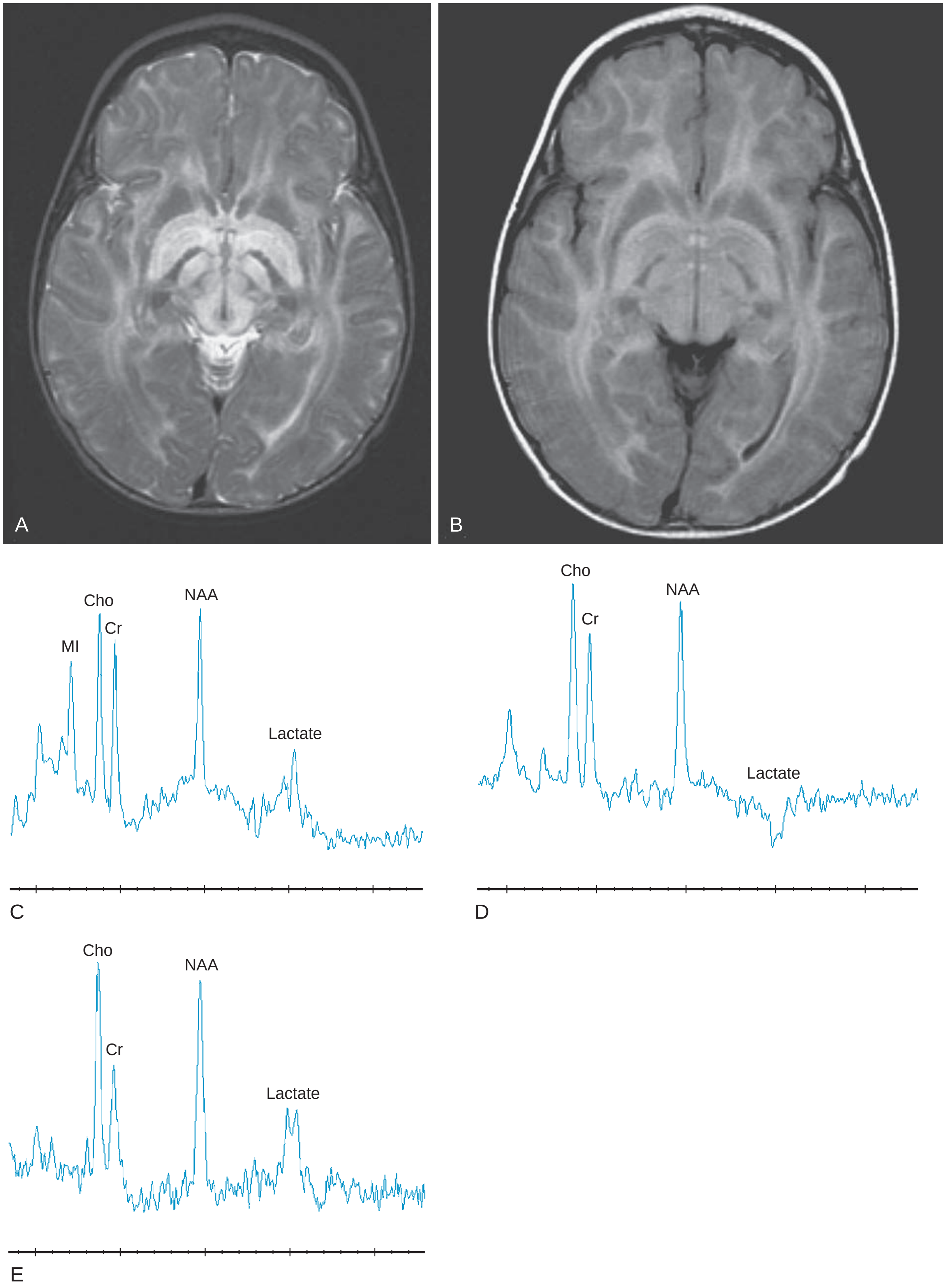

**e-Figure 33.15. Maple syrup urine disease in an infant.** Axial T2-weighted (A), axial fluid attenuated inversion recovery (FLAIR) (B), short echo magnetic resonance spectroscopy (MRS) (C), intermediate echo MRS (D), and long echo MRS (E) images reveal an abnormal signal within the brainstem, internal capsule, and globus pallidus. On short echo MRS, a composite of branched chain amino acids (0.9 parts per million [ppm]) with lactate (1.35 ppm) is inverted on intermediate echo and upright on long echo MRS. Notice the reduced signal intensity associated with the inversion at time to echo (TE) 144 milliseconds (msec) with partial restoration of the signal intensity at TE 288 msec. *(From Cecil KM. MR spectroscopy of metabolic disorders.* Neuroimaging Clin N Am. *2006;16:87–116; used with permission.)*

myelinopathy. Because these changes only occur in myelinated white matter, in the neonate they are restricted to the dorsal limbs of the internal capsule, dorsal brainstem, pyramidal tracts in the coronal radiata, and lateral thalamus. A long tractlike lesion involving the spinal cord has been reported in persons with late-onset disease.[36] On MR, these areas will show a hyperintense signal on T2-weighted images and restricted diffusion on DWI. Volume loss ensues and may be present at birth as a result of the toxic effects of glycine in utero. Proton MRS can detect the accumulated glycine itself, as a distinct resonance at 3.55 ppm. In patients with nonketotic hyperglycinemia, elevated cerebral glycine can be measured with proton MRS. Using long echo times, such as 288 ms, MRS reveals glycine at 3.5 ppm. With use of short echo times, the resonance at 3.5 is a composite of mI and glycine. Select metabolite ratios (NAA, mI, and glycine) appear to correlate with the patient's course (Fig. 33.16).

## PRIMARY DISORDERS OF WHITE MATTER (LEUKODYSTROPHIES)

The term "leukodystrophy" generally is reserved for conditions that are both progressive and genetically determined. Although

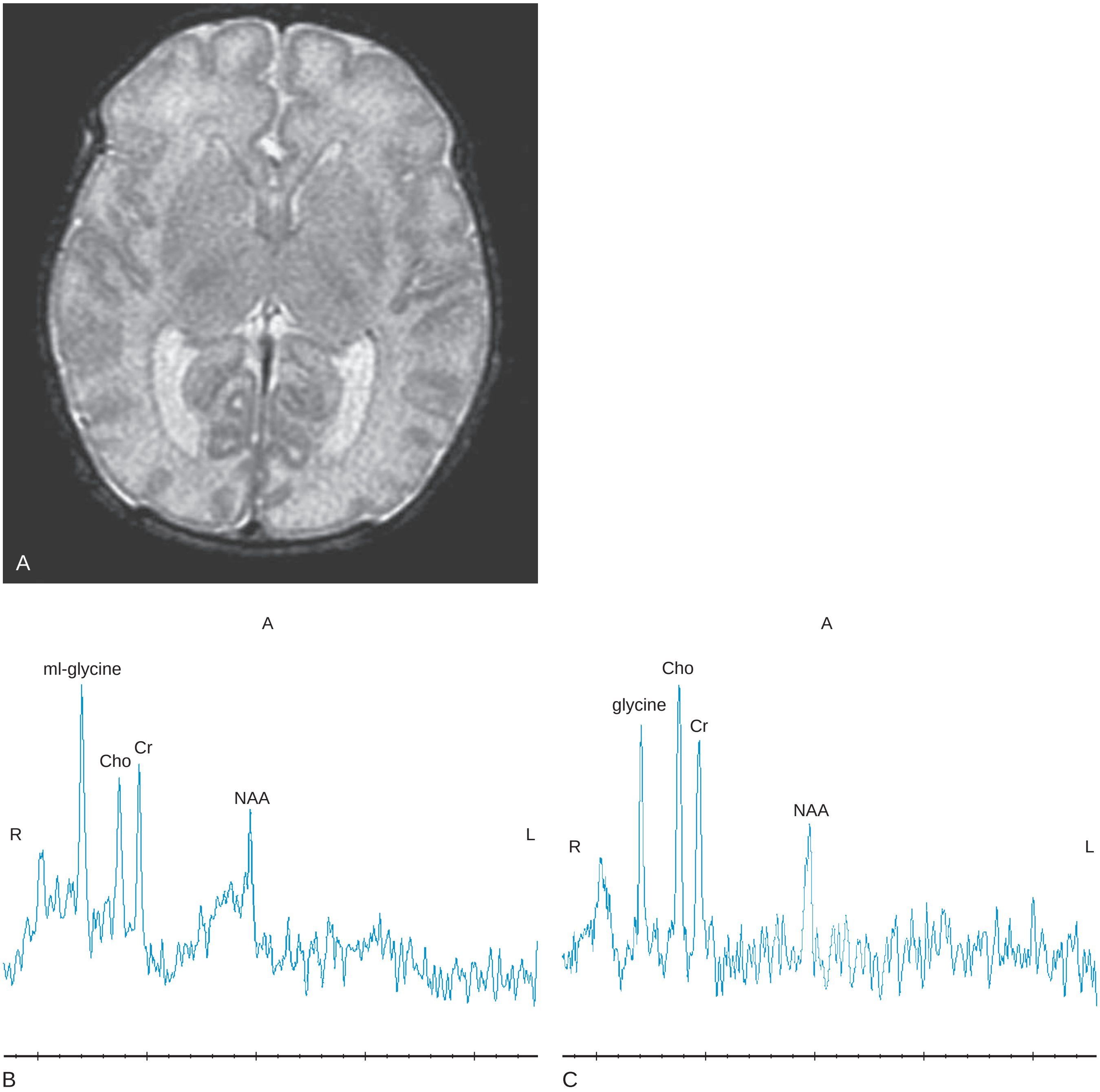

**Figure 33.16. Nonketotic hyperglycinemia in a neonate.** Axial T2-weighted (A), short echo magnetic resonance spectroscopy (MRS) (B), and intermediate (144 milliseconds [msec]) MRS (C) images are shown. The short echo spectrum demonstrates a composite myo-inositol and glycine resonance at 3.5 parts per million (ppm). The intermediate echo demonstrates glycine. *(From Cecil KM. MR spectroscopy of metabolic disorders.* Neuroimaging Clin N Am. *2006;16:87–116; used with permission.)*

these conditions eventually may involve and alter gray matter, the primary features affect the white matter.

## Canavan Disease

Canavan disease is an autosomal-recessive disorder arising from a deficiency of the enzyme aspartoacylase, which results in the accumulation of NAA in the brain. Three clinical subtypes—infantile, juvenile, and adult—are recognized. The most common is the infantile type, which usually presents within the first 6 months of life with hypotonia, irritability, and enlarging head size, leading to spasticity, blindness, choreoathetoid movement, and myoclonic seizures.

The diagnosis is made by demonstrating increased amounts of NAA in the urine and plasma. On histologic examination, the disease is seen to begin in a peripheral location, involving the U fibers of the subcortical white matter of the cerebral hemispheres. Later, the abnormality involves the deep white matter structures of both cerebral hemispheres, and eventually it extends to the cerebellum and spinal cord. The involvement of the U fibers of the white matter is diffuse, with evidence of vacuoles within the subcortical white matter and extending into the adjacent cortex.

The MRI findings are related to the myelin degeneration of the white matter tracts. The first change detected is hyperintensity on T2-weighted images of the subcortical U fibers. Eventually, there is diffuse involvement of all the white matter fiber tracts in both cerebral hemispheres. In the later stages of the disease, volume loss of the cerebral hemispheres occurs. Enlarged perivascular spaces, likely reflecting spongiform degeneration of the white matter, has been described.[37] MRS demonstrates marked elevation of the NAA peak, which is diagnostic for Canavan disease (Fig. 33.17).

## Alexander Disease

Missense mutations in the gene encoding for glial fibrillary acidic protein (GFAP) are found in all three clinical variants (infantile, juvenile, and adult) of Alexander disease. In brain biopsy specimens, Rosenthal fibers label extensively for GFAP upon immunocytochemistry. The mutations in Alexander disease are heterozygous and dominant, and accordingly most cases are sporadic. The most commonly encountered variant of Alexander disease is the infantile form, which presents in the first 2 years of life with megalencephaly and developmental delay, frequently with seizures. Children with the infantile form of the disease rarely survive to the second decade. The juvenile form presents after 4 years of age with speech and swallowing difficulties, ataxia, and spasticity. Progression is slower, with a more prolonged survival. Adult-onset disease has a more variable clinical presentation and occasionally is diagnosed incidentally at autopsy.

The diagnosis traditionally has been performed via a brain biopsy. The predominant histologic feature is a considerable amount of Rosenthal fibers within the white matter. Most commonly, the disease begins in the periventricular white matter, usually involving the frontal lobes and then extending into the parietotemporal and then the occipital regions. Eventually, involvement of the cerebellar white matter and spinal cord occurs. CSF oligoclonal bands have been reported in the adult-onset variant.[38]

The MRI findings demonstrate macrocephaly with hyperintensity on T2-weighted images involving the white matter areas, which commonly is seen in the frontal areas with progression posteriorly to involve other parts of the cerebral hemispheres (Fig. 33.18). Five MRI characteristics can be applied to suspected cases of Alexander disease to make a presumptive diagnosis: (1) extensive cerebral white matter changes with frontal predominance, (2) a periventricular rim with a high signal on T1-weighted images and a low signal on T2-weighted images, (3) signal abnormalities with swelling or volume loss in the basal ganglia and thalami, (4) brainstem signal abnormalities, and (5) contrast enhancement of one or more of the following structures: ventricular lining, periventricular rim, white matter of the frontal lobes, optic chiasm, fornix, basal ganglia, thalamus, dentate nucleus, or brainstem structures. Although many of these abnormalities may be seen in other leukodystrophies, the association of four or more appears to be relatively specific for Alexander disease (see Fig. 33.18).[39,40] The extent and pattern of contrast enhancement and the distinctive periventricular rim of abnormal signal are not encountered in many other processes, making contrast administration useful in this specific diagnosis.

Proton MRS has shown elevated concentrations of mI in conjunction with normal or increased choline compounds in gray and white matter, basal ganglia, and cerebellum, that indicate astrocytosis and demyelination.[41] Neuroaxonal degeneration, as reflected by a reduction of NAA, was most pronounced in cerebral and cerebellar white matter.

## Megalencephalic Leukoencephalopathy With Subcortical Cysts

Megalencephalic leukoencephalopathy with subcortical cysts typically presents in infancy or childhood with macrocrania, developmental delay, seizures, and motor disability. MRI demonstrates widespread signal abnormalities throughout the white matter, with sparing of deep structures. Cysts typically are identified in the subcortical temporal lobes and less frequently in the frontal, parietal, or occipital lobes. Despite the extensive abnormalities on imaging, many affected patients achieve a high level of normal function. The genetic source of the condition has been traced to the *MLC1* gene on the long arm of chromosome 22 (22q13.33). The disease is inherited in an autosomal-recessive pattern, and because of the variable phenotype, identification of a single case should prompt further investigation and genetic counseling (e-Fig. 33.19).

## Leukoencephalopathy With Brainstem and Spinal Cord Involvement and Elevated White Matter Lactate

Leukoencephalopathy with brainstem and spinal cord involvement and elevated white matter lactate recently has been described based on the MRI characteristics. Initial childhood development is generally unremarkable, with motor deterioration occurring later in childhood. The MRI pattern is quite distinct. The progressive white matter abnormalities spread from the periventricular region outward with sparing of the subcortical U fibers (e-Fig. 33.20). The corpus callosum is affected with posterior preference. The pyramidal tracts are affected over their entire length from the posterior limb of the internal capsule and brainstem into the lateral corticospinal tracts of the spinal cord. The sensory tracts are involved from the dorsal columns in the spinal cord, the medial lemniscus through the brainstem up to the level of the thalamus, and the corona radiata above the level of the thalamus. The cerebellar involvement progresses over time to the point of significant volume loss. Clinical severity and the extent of neurologic abnormalities on MRI do not appear to correlate.[42]

## Galactosemia

Galactosemia is the result of a deficiency in galactose-1-phosphate uridyl transferase, an enzyme essential for the metabolism of galactose. It presents in infants soon after the introduction of cow's milk into the diet. Clinical features include failure to thrive, hepatomegaly with jaundice, vomiting and diarrhea, cataracts, increased ICP, and mental deterioration. It can be identified by the presence of increased reducing substances in the stool. Neurologic

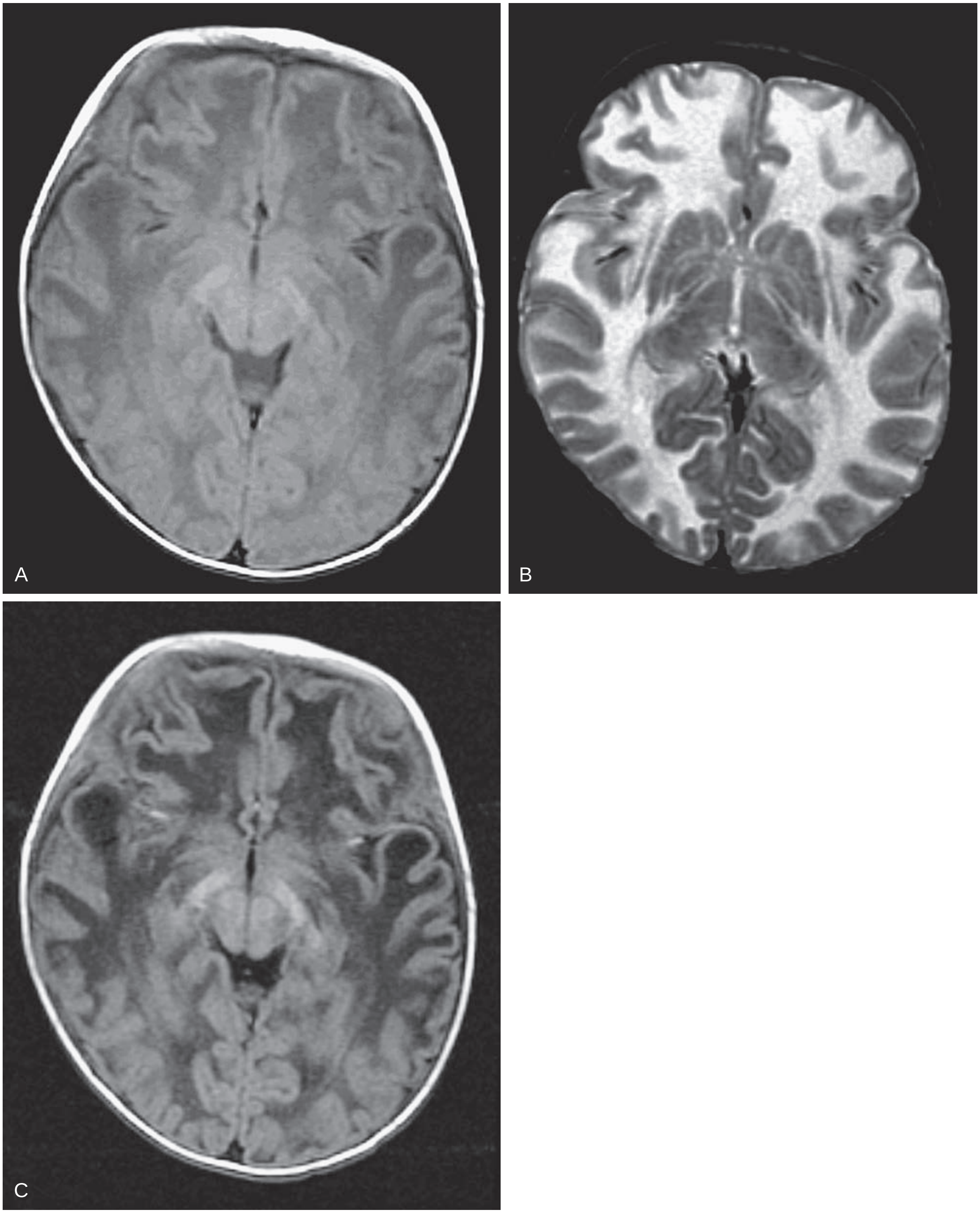

**e-Figure 33.19. Megalencephalic leukoencephalopathy with subcortical cysts in a 7-month-old boy.** Axial T1-weighted (A), axial T2-weighted (B), and axial fluid attenuated inversion recovery (FLAIR) (C) MR images are shown. A decreased signal throughout the hemispheric white matter is demonstrated on the T1-weighted and FLAIR images, with a corresponding hyperintense signal on the T2-weighted images. The basal ganglia are spared.

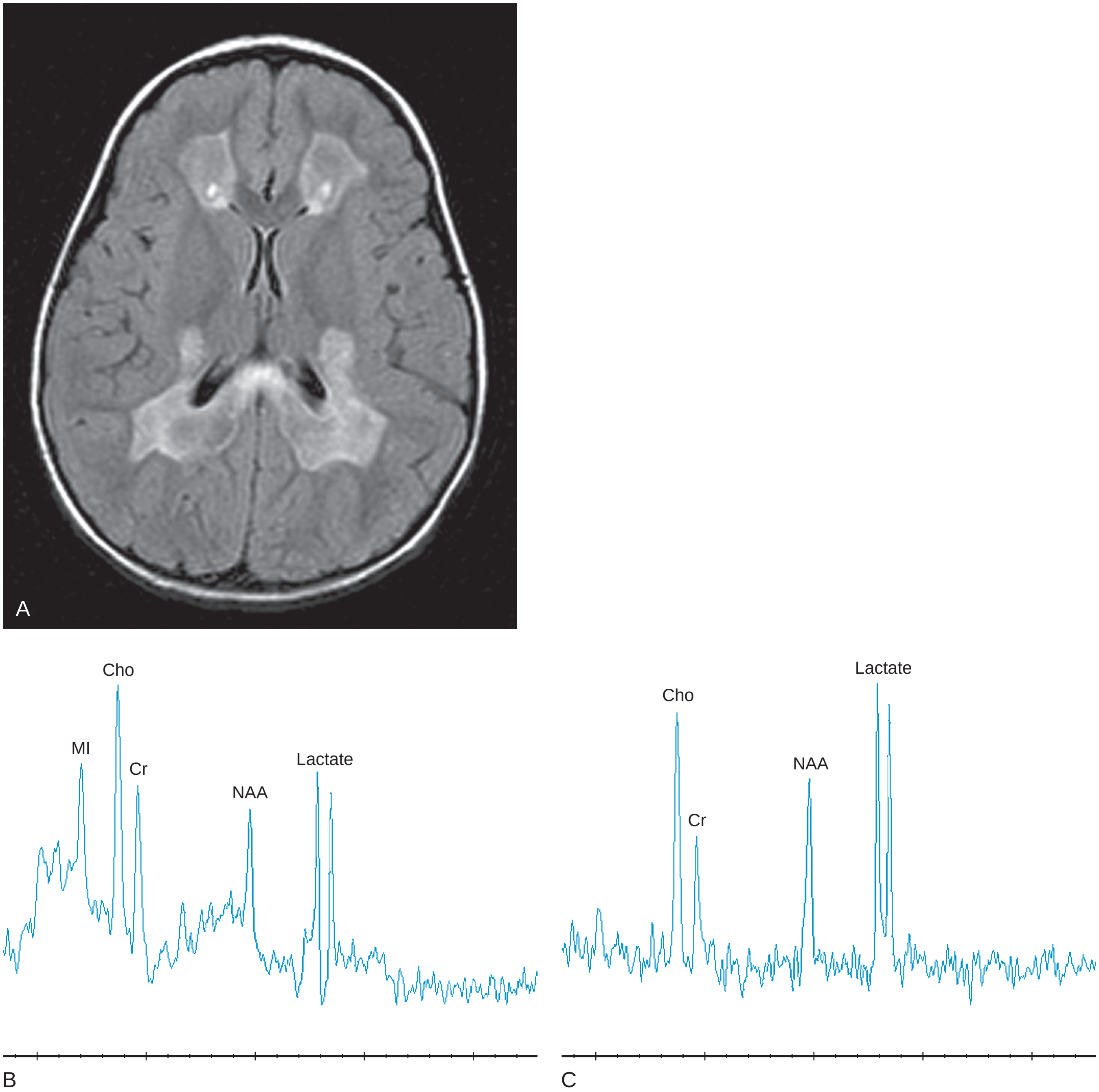

**e-Figure 33.20. Leukodystrophy with brainstem and spinal cord involvement and high lactate levels in a 2-year-old girl.** Axial T2-weighted (A), short echo magnetic resonance spectroscopy (MRS) (B), and long echo MRS (C) images are shown. The T2-weighted image (A) reveals a confluent, hyperintense signal in the central white matter with sparing of subcortical U fibers. Elevated lactate, choline, and myo-inositol levels with diminished N-acetylaspartate are demonstrated in white matter regions with an abnormal signal. Not shown are normal spectra from unaffected gray matter. *(From Cecil KM. MR spectroscopy of metabolic disorders.* Neuroimaging Clin N Am*. 2006;16:87–116; used with permission.)*

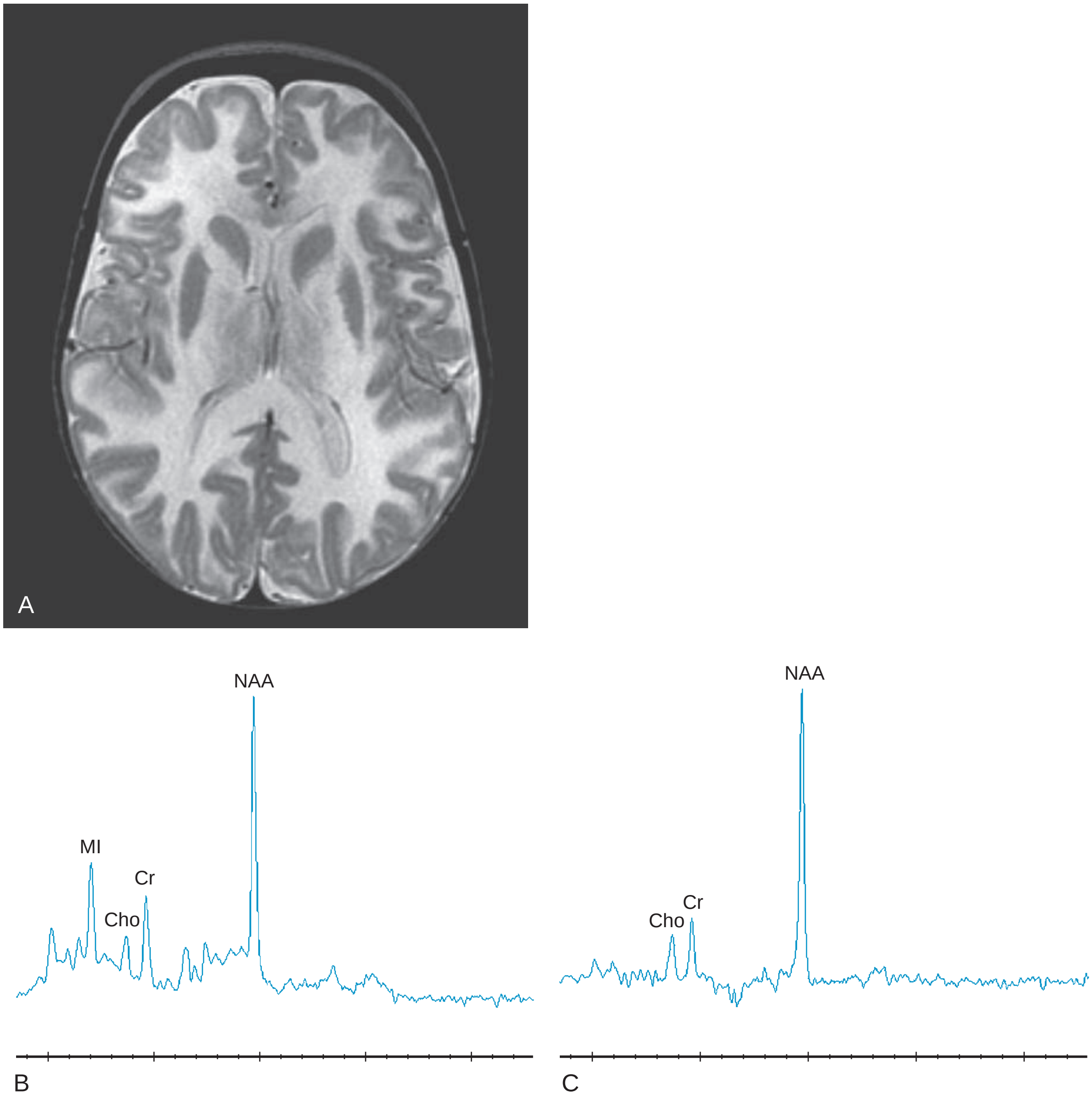

**Figure 33.17. Canavan disease in a 12-month-old girl.** Axial T2-weighted (A), short echo magnetic resonance spectroscopy (MRS) (B), and long echo MRS (C) images are shown. Diffuse hypomyelination is revealed on the T2-weighted image. Elevated N-acetylaspartate (NAA) is the key feature with secondary myo-inositol elevation representing gliosis. Because of the deficiency in aspartoacylase, NAA accumulates in the mitochondria, impairing myelin synthesis. *(From Cecil KM. MR spectroscopy of metabolic disorders.* Neuroimaging Clin N Am. *2006;16:87–116; with permission.)*

dysfunction is the result of hypoglycemia and the accumulation of galactose, galactose-1-phosphate, and galactitol in the brain and eye. In adult forms, low bone density often is observed.[43]

On CT, diffuse low attenuation of white matter mimicking diffuse edema often is present. The most consistent early MRI finding is a delay in myelination, which may appear as persistence of a hyperintense T2 signal in the peripheral white matter. These signal abnormalities may be more widespread in older children as a result of demyelination. Patchy areas of focal increased signal on T2-weighted images also have been reported and are thought to represent damaged areas of white matter. Eventually, a pattern of mild cerebral or cerebellar volume loss is found. Brain edema may occur in infants with galactosemia and has been associated with accumulation of galactitol.

## Creatine Deficiency

Inborn errors of creatine metabolism, specifically defects in creatine synthesis and transport, recently have been reported involving arginine glycine amidinotransferase (AGAT) and guanidinoacetate methyltransferase (GAMT).[44] Patients may have epilepsy and severe developmental delay. Proton MRS clinical studies have led to the discovery of three creatine deficiency syndromes: creatine transporter deficiency syndrome, AGAT deficiency, and GAMT deficiency. Several patients have been found to have a markedly diminished or absent creatine signal with proton MRS. If proton MRS reveals the absence of creatine in the brain, serum and urine creatine assessments may give a preliminary indication of whether there is a synthesis defect (diminished creatine) or a transport

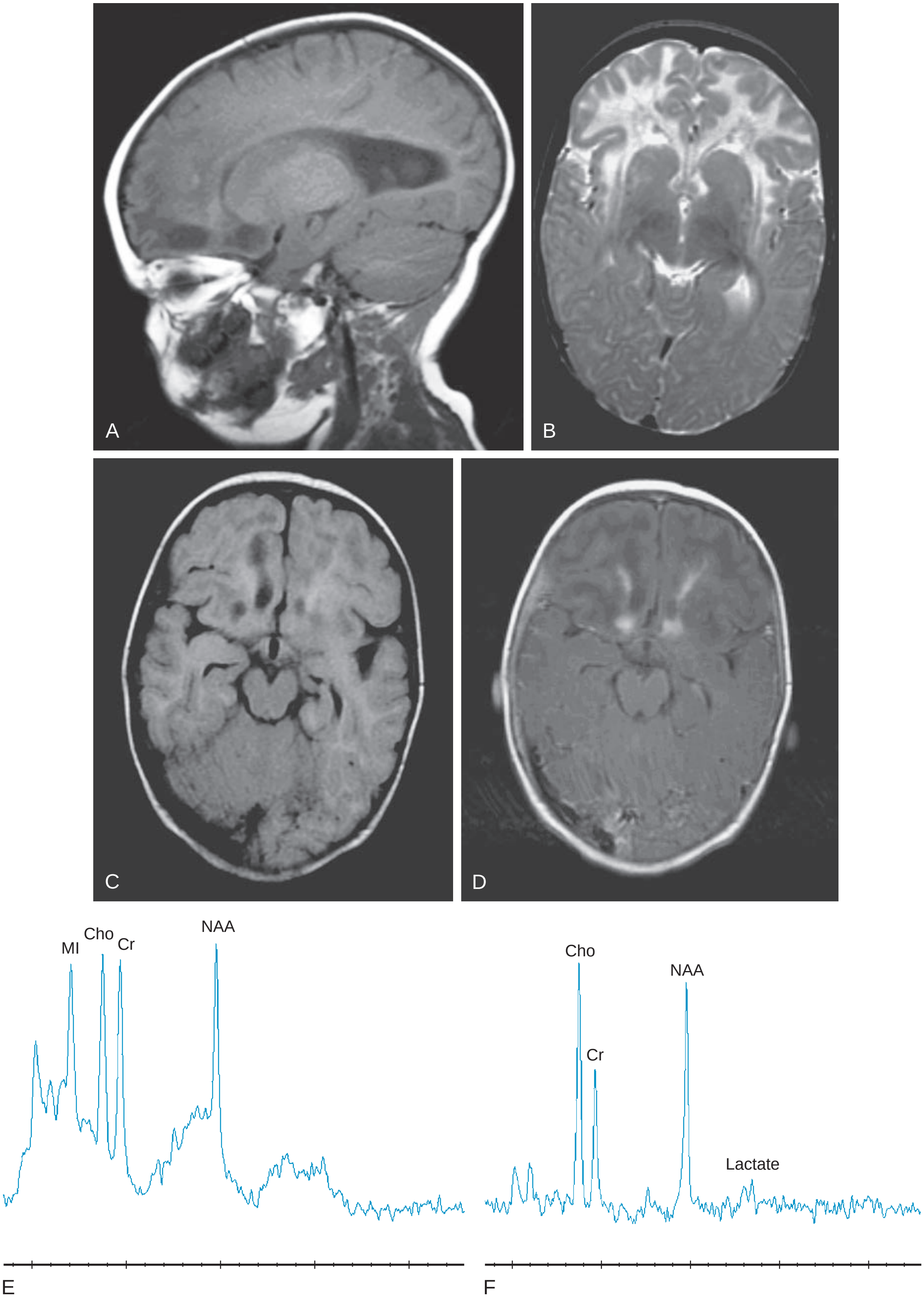

**Figure 33.18. Alexander disease in an 8-month-old girl.** Sagittal T1-weighted (A), axial T2-weighted (B), axial fluid attenuated inversion recovery (FLAIR) (C), axial T1-weighted postcontrast (D), short echo magnetic resonance spectroscopy (MRS) (E), and long echo MRS (F) MR images were acquired in the frontal white matter. The deep frontal and periventricular white matter demonstrate a hypointense T1-weighted and hyperintense T2-weighted signal. The frontal lobe cavitations are revealed on the FLAIR image with hypointense signal and demonstrate enhancement at the borders. Volume enlargement of the caudate heads is seen. Decreased N-acetylaspartate with lactate, choline, and myo-inositol elevations representing macrophage infiltration, demyelination, and astrocytosis are indicated from the MRS image.

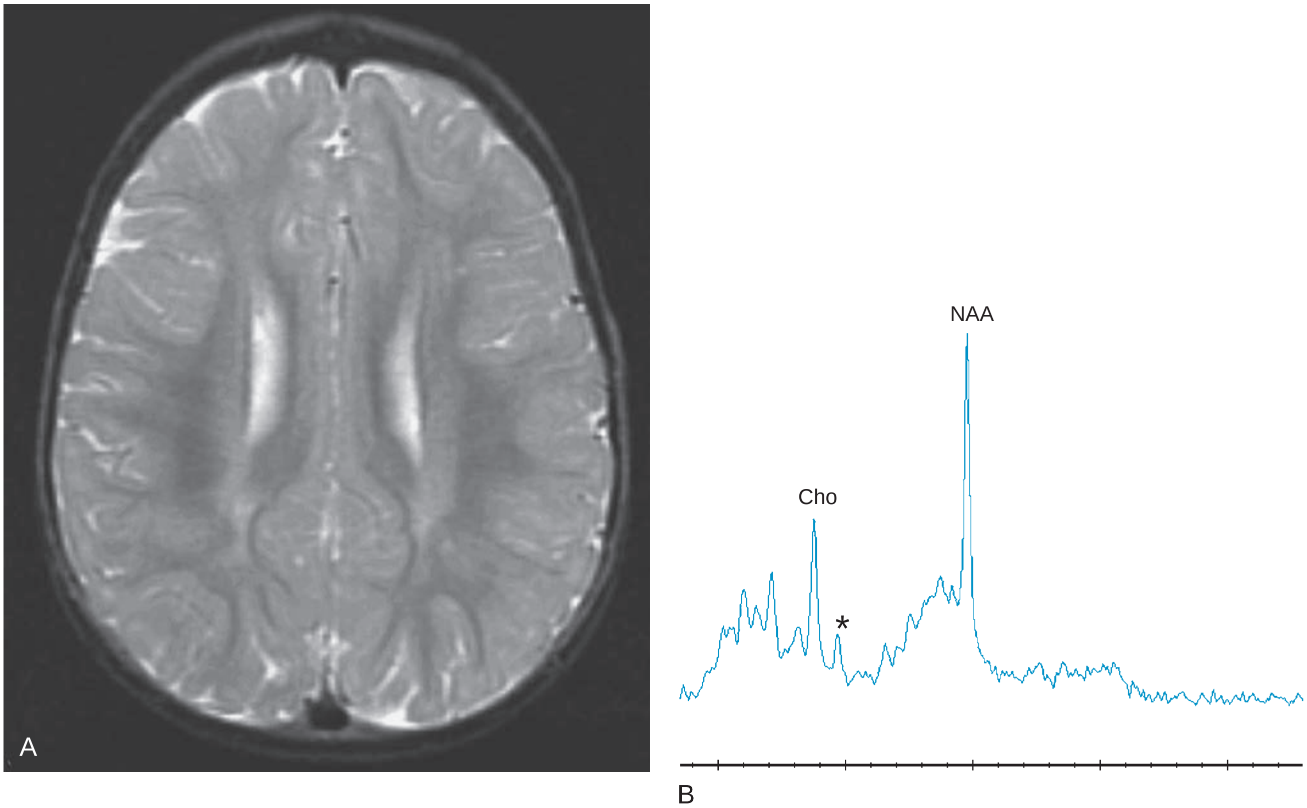

**Figure 33.21. Creatine transporter mutation in a 2-year-old boy.** Axial T2-weighted (A) and short echo magnetic resonance spectroscopy (MRS) (B) images reveal an abnormal signal within the periventricular white matter, representing hypomyelination. Short echo spectroscopy reveals a marked reduction of creatine signal *(asterisk)*.

defect (elevated creatine) (Fig. 33.21). In cases of synthesis defects, proton MRS can monitor increasing brain creatine concentration with oral supplementation, which offers improvement of some symptoms but not recovery of normal function.

## MISCELLANEOUS WHITE MATTER DISORDERS

### Pelizaeus-Merzbacher Disease and Disorders of Myelin Proteolipid Protein

PMD is condition that manifests as a primary defect in myelin formation. It is the prototypical hypomyelination syndrome, in that the imaging appearance is of an otherwise normal brain that is severely delayed in its formation of myelin.

Mutations or duplications of the gene-encoding myelin proteolipid protein (*PLP*; Xq22.2) produce variable clinical manifestations. Spastic paraplegia type 2 is characterized by lower limb spasticity alone. Persons with "complicated" spastic paraplegia type 2 exhibit cerebellar ataxia, nystagmus, and a pyramidal syndrome. The more severe phenotypic manifestations traditionally have been categorized as PMD and result in alterations of multiple functional systems, with symptoms including nystagmus and compromises in respiratory function, with associated severe disability and morbidity.

The classic descriptions of PMD divide it into several different subtypes. The most common presentation is that of the slowly progressive "classic" form that presents in infancy with early nystagmus ("dancing eyes"), poor head control, spasticity, ataxia or extrapyramidal movement disorders, and severe developmental delay. These findings slowly progress, usually leading to death in late adolescence or young adulthood. A second pattern (connatal, or the Seitelberger type) begins in the neonatal period and is more rapidly progressive, with death typically occurring in the first decade.

Imaging demonstrates a marked delay in myelination from the onset. Whereas many metabolic or neurodegenerative processes are associated with delayed myelination, the absence of other imaging findings is characteristic of the early stages of the *PLP* gene disorders. On CT, hypomyelination can be appreciated as diffuse low attenuation of white matter. The characteristic normal progression of myelination as detected by MRI in the first 2 years of life is entirely absent or severely slowed in persons with the *PLP* gene disorders. Myelination that does occur tends to be patchy, without the characteristic predictable distribution within the white matter tracts. In the later stages of disease, white matter volume may decrease, with thinning of the corpus callosum and excess mineralization in the basal ganglia.

Diffusion tensor imaging has been reported to be effective for detecting subtle changes in the microstructure of the white matter, such as abnormal myelination, even when findings of MRI and MRS are normal.[45]

Proton MRS has shown diminished values of NAA and mild elevations of choline, indicating axonal injury and secondary gliosis. Heterogeneous cerebral metabolite patterns have been found in patients with PMD and Pelizaeus-Merzbacher–like disease, indicating a mixture of nonspecific changes as a result of primary hypomyelination and secondary gliosis and demyelination.[46] However, neither MRI nor MRS provided unique patterns to allow differentiation between patients with PMD and Pelizaeus-Merzbacher–like disease.

# OTHER DISORDERS AFFECTING THE BASAL GANGLIA

## Huntington Disease

Huntington disease (HD) is an autosomal-recessive degenerative disorder, with most cases presenting after the fourth decade. HD is characterized by a movement disorder. Cerebellar symptoms, seizures, rigidity, and mental retardation are common. Caudate volume loss is demonstrated on MRI, although cortical changes also may be detected.[47] Bilateral areas of T2 hyperintensity may be seen in the basal ganglia. Global atrophy in persons with HD shows a disproportionate relationship to caudate involvement.[48] In preHD, gray matter change has been reported to be specific to basal ganglia-thalamocortical pathway regions, whereas white matter changes were much more generalized.[49] White matter diffusivity abnormalities also have been reported in the corpus callosum and external/extreme capsules.[50] In premanifest gene carriers, the white matter pathway of the sensorimotor cortex is impaired.[51] Changes in the hypothalamic region have been reported in prodromal HD and appear to be one of the earliest evident features of this disease.[52]

## Fahr Disease

Fahr disease comprises a group of disorders that have basal ganglia calcification. Mental deterioration and growth retardation have been described. MRI demonstrates areas of signal void within the basal nuclei and dentate nuclei on T1- and T2-weighted images. The appearances correlate with the areas of calcification on CT. Transcranial sonography also has been reported to be useful for visualizing calcifications of the basal ganglia.[53]

## Wilson Disease

Hepatolenticular degeneration, or Wilson disease, is an autosomal-recessive inborn error in copper metabolism. Ceruloplasmin, the serum transport protein for copper, is deficient, with resultant copper deposition in various sites. This disease typically presents in young adults with chronic hepatic insufficiency and neurologic deterioration. Copper fails to be excreted in the bile and thus accumulates in the body, especially in liver, brain, kidney, and red blood cells. The clinical presentation is primarily that of extrapyramidal signs, hepatic insufficiency, and the presence of Kayser-Fleischer corneal rings. Either the hepatic toxicity or the neurologic findings may predominate. Neurologic dysfunction begins with changes in mentation, abnormalities in speech or language, and difficulty swallowing, all of which may progress with time.

On CT, the basal ganglia are typically low in attenuation, especially the globus pallidus and putamen arising from copper accumulation. Volume loss of these structures eventually follows. The white matter also may appear low in attenuation, with volume loss eventually leading to compensatory dilatation of the lateral ventricles. On MRI, the basal ganglia are hyperintense on T1-weighted images and the first echo of the T2-weighted sequence, as seen with other causes of hepatic dysfunction. These same regions typically are hyperintense on T2-weighted images early in the course of the disease, but the hyperintense signal may decrease late in the disease associated with an increase in signal on the T1-weighted images. The white matter demonstrates progressive increase in T2-signal as a result of demyelination and gliosis. Corpus callosum abnormalities also have been reported.[54] The presence of signal changes involving the basal ganglia, thalami, and brainstem; the "face of giant panda" sign; midbrain tectal plate signal changes; or central pontine myelinolysis-like changes all can be considered to be diagnostic of Wilson disease.[55]

## KEY POINTS

### Clinical Features Suggestive of a Metabolic or Neurodegenerative Disorder

- Loss of developmental milestones or unexplained developmental delay
- Predisposing conditions are absent
- Basal ganglia symptoms such as hypotonia and hypertonia
- Progressive features of encephalopathy
- An unexplained clinical course inconsistent with imaging findings

### General Imaging Features of a Metabolic or Neurodegenerative Disorder

- Progressive changes with time coupled with clinical progression
- Progressive hypomyelination
- Symmetric involvement of white matter tracts
- Pervasive and symmetric involvement of white and gray matter
- Contrast enhancement appears in later stages of the disease course

### Clinical Indications for Incorporating MRS into the Imaging Evaluation

- Developmental regression or progressive condition
- Feeding difficulties
- Parental consanguinity
- Previously affected siblings
- Family history of mental retardation
- Multiple organ involvement
- Delayed myelination on conventional anatomic images

### Genetic Origins of Select Mitochondrial Disorders

- Deletions in mtDNA
  - Kearns-Sayre syndrome
- Mitochondrial DNA point mutations
  - Adenosine triphosphate 6 mutation
  - Maternally inherited myopathy/cardiomyopathy
  - MELAS
  - MERRF
  - Multiple inherited subcutaneous lipomatosis
  - Leber hereditary optic neuropathy
- Nuclear DNA abnormalities
  - Infantile cytochrome oxidase deficiency
- Leigh syndrome
- Mitochondrial myopathy, peripheral neuropathy, gastrointestinal encephalopathy

## SUGGESTED READINGS

Dali C, Hanson LG, Barton NW, et al. Brain N-acetylaspartate levels correlate with motor function in metachromatic leukodystrophy. *Neurology*. 2010;75(21):1896–1903.

Kamate M, Hattiholi V. Normal neuroimaging in early-onset Krabbe disease. *Pediatr Neurol*. 2011;44(5):374–376.

Miller E, Widjaja E, Nilsson D, et al. Magnetic resonance imaging of a unique mutation in a family with Pelizaeus–Merzbacher disease. *Am J Med Genet A*. 2010;152A:748–752.

van der Knaap MS, Wassmer E, Wolf NI, et al. MRI as diagnostic tool in early-onset peroxisomal disorders. *Neurology*. 2012;78(17):1304–1308.

Zuccoli G, Narayanan S, Panigrahy A, et al. Midbrain morphology reflects extent of brain damage in Krabbe disease. *Neuroradiology*. 2015;57(7):739–745.

## REFERENCES

Full references for this chapter can be found on www.expertconsult.com.

## REFERENCES

1. Caciotti A, Garman SC, Rivera-Colon Y, et al. GM1 gangliosidosis and Morquio B disease: an update on genetic alterations and clinical findings. *Biochi Biophys Acta*. 2011;1812(7):782–790.
2. Dweikat I, Libdeh BA, Murrar H, et al. Gm1 gangliosidosis associated with neonatal-onset of diffuse ecchymoses and mongolian spots. *Indian J Dermatol*. 2011;56(1):98–100.
3. Sharma S, Sankhyan N, Kabra M, et al. Teaching neuroimages: T2 hypointense thalami in infantile GM1 gangliosidosis. *Neurology*. 2010;74(12):e47.
4. Delnooz CC, Lefeber DJ, Langemeijer SM, et al. New cases of adult-onset Sandhoff disease with a cerebellar or lower motor neuron phenotype. *J Neurol Neurosurg Psychiatry*. 2010;81(9):968–972.
5. Aydin K, Bakir B, Tatli B, et al. Proton MR spectroscopy in three children with Tay-Sachs disease. *Pediatr Radiol*. 2005;35:1081–1085.
6. Hayase T, Shimizu J, Goto T, et al. Unilaterally and rapidly progressing white matter lesion and elevated cytokines in a patient with Tay-Sachs disease. *Brain Dev*. 2010;32(3):244–247.
7. Bano S, Prasad A, Yadav SN, et al. Neuroradiological findings in GM2 gangliosidosis variant B1. *J Pediatr Neurosci.* 2011;6(2):110–113.
8. Le NM, Parikh S. Late infantile neuronal ceroid lipofuscinosis and dopamine deficiency. *J Child Neurol*. 2012;27(2):234–237.
9. Kamate M, Hattiholi V. Novel neuroimaging finding in palmitoyl protein thioesterase-1 related neuronal ceroid lipofuscinosis. *Pediatr Neurol*. 2012;46(5):325–328.
10. Yavuz H, Yükeskkaya A. Intestinal involvement in metachromatic leukodystrophy. *J Child Neurol*. 2011;26:117–120.
11. Gieselmann V, Krägeloh-Mann I. Metachromatic leukodystrophy—an update. *Neuropediatrics*. 2010;41(1):1–6.
12. Dali C, Hanson LG, Barton NW, et al. Brain N-acetylaspartate levels correlate with motor function in metachromatic leukodystrophy. *Neurology*. 2010;75(21):1896–1903.
13. Duffner PK, Barczykowski A, Kay DM, et al. Later onset phenotypes of Krabbe disease: results of the world-wide registry. *Pediatr Neurol*. 2012;46(5):298–306.
14. Brodsky MC, Hunter JS. Positional ocular flutter and thickened optic nerves as sentinel signs of Krabbe disease. *J AAPOS*. 2011;15(6):595–597.
15. Kohlschütter A, Eichler F. Childhood leukodystrophies: a clinical perspective. *Expert Rev Neurother*. 2011;11:1485–1496.
16. Kamate M. Hattiholi V. Normal neuroimaging in early-onset Krabbe disease. *Pediatr Neurol*. 2011;44(5):374–376.
17. Hussain SA, Zimmerman HH, Abdul-Rahman OA, et al. Optic nerve enlargement in Krabbe disease: a pathophysiologic and clinical perspective. *J Child Neurol*. 2011;26(5):642–644.
18. Zuccoli G, Narayanan S, Panigrahy A, et al. Midbrain morphology reflects extent of brain damage in Krabbe disease. *Neuroradiology*. 2015;57(7):739–745.
19. Hwang M, Zuccoli G, Panigrahy A, et al. Thickening of the cauda equina roots: a common finding in Krabbe disease. *Eur Radiol*. 2016;26(10):3377–3382.
20. Takenouchi T, Raju GP. Germinal matrix hemorrhage in Zellweger syndrome. *J Child Nerurol*. 2010;25(11):1398–1400.
21. Kulkarni KS, Baranano KW, Lin DD, et al. Contrast enhancement of brainstem tracts in Zellweger spectrum disorder: evidence of inflammatory demyelination? *Neuropediatrics*. 2011;42(1):32–34.
22. Bansal AR, Baheti NN, Rathore C, et al. Teaching neuroimages: adrenoleukodystrophy presenting as raised intracranial pressure. *Neurology*. 2010;74(21):e93.
23. Ergül Y, Nişli K, Sagygili A, et al. Kearns-Sayre syndrome presenting as somatomedin C deficiency and complete heart block. *Turk Kardiyol Dern Ars*. 2010;38(8):568–571.
24. Spector R, Johanson CE. Choroid plexus failure in the Kearns-Sayre syndrome. *Cerebrospinal Fluid Res*. 2010;7:14.
25. Phadke M, Lokeshwar MR, Bhutada S, et al. Kearns Sayre syndrome—case report with review of the literature. *Indian J Pediatr*. 2012;79(5):650–654.
26. Tsujokawa T, Yoneda M, Shimizu Y, et al. Pathophysiologic evaluation of MELAS strokes by serially quantified MRS and CASL perfusion images. *Brain Dev*. 2010;32(2):143–149.
27. Kim JH, Lim MK, Jeon TY, et al. Diffusion and perfusion characteristics of MELAS (mitochondrial myopathy, encephalopathy, lactic acidosis, and stroke-like episode) in thirteen patients. *Korean J Radiol*. 2011;12(1):15–24.
28. Koprivsek K, Lucic M, Kozic D, et al. Basal ganglia lesions in the early stage of Menkes disease. *J Inherit Metab Dis*. 2010;33:301–302.
29. Sen A, Pillay RS. Striatal necrosis in type 1 glutaric aciduria: different stages in two siblings. *J Pediatr Neurosci.* 2011;6(2):146–148.
30. Righini A, Fiori L, Parazzini C, et al. Early prenatal magnetic resonance imaging of glutaric aciduria type 1: case report. *J Comput Assist Tomogr*. 2010;34(3):446–448.
31. Ma X, Zhang Y, Yang Y, et al. Epilepsy in children with methylmalonic academia: electroclinical features and prognosis. *Brain Dev*. 2011;33:790–795.
32. Prada CE, Al Jasmi F, Kirk EP, et al. Cardiac disease in methylmalonic academia. *J Pediatr*. 2011;159:862–864.
33. Imen M, Hanene B, Ichraf K, et al. Methylmalonic academia and hyperglycemia: an unusual association. *Brain Dev*. 2012;34:113–114.
34. Traber G, Baumgartner MR, Schwarz U, et al. Subacute bilateral visual loss in methylamalonic acidemia. *J Neuro Opthalmol*. 2011;31:344–346.
35. Anderson PJ, Leuzzi V. White matter pathology in phenylketonuria. *Mol Genet Metab*. 2010;99:3–9.
36. Wei SH, Weng WC, Lee NC, et al. Unusual spinal cord lesions in late-onset non-ketoic hyperglycinemia. *J Child Neurol*. 2011;26(7):900–903.
37. Pradhan S, Goyal G. Teaching neuroimages: honeycomb appearance of the brain in patient with Canavan disease. *Neurology*. 2011;76(13):e68.
38. Tschampa HJ, Greschus S, Vinahl M, et al. MS-like presentation of Alexander disease with multifocal lesions and oligoclonal bands. *J Neurol*. 2011;258:935–937.
39. van der Knapp MS, Salomons GS, Li R, et al. Unusual variants of Alexander's disease. *Ann Neurol*. 2005;57:327–338.
40. van der Knaap MS, Ramesh V, Schiffmann R, et al. Alexander disease: ventricular garlands and abnormalities of the medulla and spinal cord. *Neurology*. 2006;66:494–498.
41. Brockmann K, Dechent P, Meins M, et al. Cerebral proton magnetic resonance spectroscopy in infantile Alexander disease. *J Neurol*. 2003;250:300–306.
42. Labauge P, Dorboz I, Eymard-Pierre E, et al. Clinically asymptomatic adult patient with extensive LBSL MRI pattern and DARS2 mutations. *J Neurol*. 2011;258:335–337.
43. Batley LA, Welt CK, Rohr F, et al. Skeletal health in adult patients with classic galactosemia. *Osteoporos Int*. 2013;24(2):501–509.
44. Braissant O, Henry H, Beard E, et al. Creatine deficiency syndromes and the importance of creatine synthesis in the brain. *Amino Acids*. 2001;40:1315–1324.
45. Miller E, Widjaja E, Nilsson D, et al. Magnetic resonance imaging of a unique mutation in a family with Pelizaeus–Merzbacher disease. *Am J Med Genet A*. 2010;152A:748–752.
46. Plecko B, Stockler-Ipsiroglu S, Gruber S, et al. Degree of hypomyelination and magnetic resonance spectroscopy findings in patients with Pelizaeus Merzbacher phenotype. *Neuropediatrics*. 2003;34:127–136.
47. Caixeta L. Huntington's disease presenting as posterior cortical atrophy. *Arq Neuropsiquiatr*. 2011;69(2B):407–408.
48. Hobbs NZ, Barnes J, Frost C, et al. Onset and progression of pathologic atrophy in Huntington disease: longitudinal MR imaging study. *AJNR Am J Neuroradiol*. 2010;31:1036–1041.
49. Stoffers D, Sheldon S, Kuperman JM, et al. Contrasting gray and white matter changes in preclinical Huntington disease. *Neurology*. 2010;74:1208–1216.
50. Bohanna I, Georgiou-Karistianis N, Sritharan A, et al. Diffusion tensor imaging in Huntington's disease reveals distinct patterns of white matter degeneration associated with motor and cognitive deficits. *Brain Imaging Behav*. 2011;5:171–180.
51. Dumas EM, van den Bogaard SJ, Ruber ME, et al. Early changes in white matter pathways of the sensorimotor cortex in premanifest Huntington's disease. *Hum Brain Mapp*. 2012;33(1):203–212.
52. Soneson C, Fontes M, Zhou Y, et al. Early changes in the hypothalamic region in prodromal Huntington disease revealed by MRI analysis. *Neurobiol Dis*. 2010;40(3):531–543.
53. Toscano M, Canevelli M, Giacomelli E, et al. Transcranial sonography of basal ganglia in calcifications in Fahr disease. *J Ultrasound Med*. 2011;30:1030–1036.
54. Trocello JM, Guichard JP, Leyendecker A, et al. Corpus callosum abnormalities in Wilson's disease. *J Neurol Neurosurg Psychiatry*. 2011;82:1119–1121.
55. Prashanth LK, Sinha S, Taly AB, et al. Do MRI features distinguish Wilson's disease from other early onset extrapyramidal disorders? An analysis of 100 cases. *Mov Disord*. 2010;25(6):672–678.

# 34

# Infection and Inflammation

Alexis B. Rothenberg Maddocks and Avrum N. Pollock

## BRAIN INFECTIONS

Bacterial, viral, fungal, and parasitic organisms are all causative factors in central neurologic system (CNS) infection. Brain infection manifests as encephalitis, cerebritis, and meningitis. Encephalitis refers to diffuse infection of the brain parenchyma, whereas cerebritis is due to a more focal parenchymal infection. Meningitis refers to infection of the pia, arachnoid, and dural membranes as well as the cerebrospinal fluid (CSF). Ventriculitis is often present in cases of meningitis. Infectious complications most often include abscess and/or empyema. These infectious collections, in association with infectious symptomatology, are straightforward in their diagnosis. Infection in the setting of tumor or hemorrhage often presents a diagnostic conundrum.

Imaging of CNS infection is most often initially performed by means of computed tomography (CT) to assess for hydrocephalus or increased intracranial pressure before the performance of a lumbar puncture. Nonspecific parenchymal hypoattenuation indicative of edema on CT is sometimes appreciated in cases of more focal infection. In more complicated cases, CT is superior in the evaluation of bone erosion and destruction. More advanced imaging utilizing magnetic resonance imaging (MRI) is warranted in the assessment of infectious complications such as abscess, empyema, vasculitis, and/or ischemia in the setting of a worsening clinical condition or lack of clinical improvement. Infection is most often manifested on MRI by hyperintense signal abnormality on T2-weighted and proton density sequences. The most sensitive magnetic resonance (MR) sequence is fluid-attenuated inversion–recovery (FLAIR). There is often corresponding hypointense signal on T1-weighted sequences. Postcontrast T1-weighted images are essential in the evaluation for infectious collections and meningeal enhancement. Postcontrast images or magnetic resonance venography (MRV) sequences help to visualize suspected venous sinus thrombosis as a complication of infection. Diffusion-weighted imaging (DWI) and apparent diffusion coefficient (ADC) maps help in localizing abscess collections and infection associated with ischemia and can at times help distinguish lymphoma from abscess, especially in immunocompromised patients. DWI may also demonstrate lesions earlier than conventional sequences in detecting viral infections such as herpes and West Nile virus (e-Fig. 34.1). MR spectroscopy (MRS) may be helpful in distinguishing pyogenic abscesses from those composed of more atypical organisms, with the former often demonstrating the presence of amino acids and lack of choline.

## BACTERIAL INFECTIONS

Nearly two-thirds of cases of bacterial meningitis in the United States occur in children. Routes of transmission include hematogenous, direct traumatic, congenital, as well as via direct extension from adjacent sinus or mastoid disease (e-Fig. 34.2, Figs. 34.3 and 34.4, and e-Fig. 34.5). Imaging plays a key role in determining the course of treatment for bacterial infection. It is essential to distinguish between a focal cerebritis (Fig. 34.6), in which surgery is contraindicated and tends to respond to antibiotics, and frank abscess that often requires surgical intervention in addition to antibiotic therapy.

Hypoattenuation on CT, indicative of edema, and corresponding hyperintense T2-weighted and hypointense T1-weighted signal on MRI with patchy nonspecific postcontrast enhancement are typical imaging characteristics of cerebritis. Mild to moderate mass effect is often present. Sequential imaging is essential in the assessment of the response to antibiotics or progression to an abscess. Progression from cerebritis to an abscess generally takes 1 to 2 weeks but can progress more rapidly in the neonatal population. *Citrobacter*, *Serratia*, and *Proteus* are the most common causes of neonatal brain abscess. *Citrobacter* and *Serratia* infections may cause neonatal medullary vein thrombosis and associated hemorrhage (Fig. 34.7). In general, abscesses tend to be situated at gray-white matter junctions in the region where the diameter of the end arterioles changes (Fig. 34.8). Opportunistic organisms are common culprits in immunocompromised neonates. Differential considerations of a peripherally contrast-enhancing fluid-filled structure in the brain includes infectious abscess and tumor. DWI is often helpful when evaluating for an abscess, as lesions on DWI will appear hyperintense (and dark on ADC), indicating restricting material. On both MRI and CT, abscesses tend to have smooth regular inner margins and are often thinner-walled along their medial edge than along their lateral margins. Intraventricular rupture of an abscess portends a poor outcome. MRS of abscesses is notable for the presence of amino acids and lactate (Fig. 34.9) and the absence of normal metabolite peaks. In neonates, ultrasound (US) may depict a hypoechoic abscess with peripheral hyperechogenicity, which at times may contain dependent echogenic debris.

Bacterial meningitis is the most common form of pediatric CNS infection (Fig. 34.10). Although not diagnosed by imaging, imaging is warranted if a diagnosis is unclear, persisting seizures are present, and/or symptoms persist despite treatment. It is more common in preterm infants as well as full-term infants within the first month of life. The subarachnoid space tends to resist infection in older normal children, making meningitis in this age group a rarity. Most cases of neonatal meningitis in the United States are caused by group B streptococcus (GBS) (Fig. 34.11) and *Escherichia coli*. Other less common organisms (e.g., *Serratia*, enterococci, and *Listeria*) tend to inflict more extensive destruction. In infants greater than 1 month of age, the most common causative organisms are *Haemophilus influenza* type b, *Streptococcus pneumonia* (Fig. 34.12), *Neisseria meningitides*, and *E. coli*. Complications of meningitis include cerebritis, abscess, empyema, hydrocephalus, venous thrombosis, infarction (venous and/or arterial), ventriculitis (e-Fig. 34.13), mycotic aneurysms (e-Fig. 34.14), and sensorineural hearing loss (Fig. 34.15).

### Tuberculosis Infection

CNS infection with *Mycobacterium tuberculosis* (TB) differs clinically and radiographically from pyogenic infection. Other granulomatous and fungal organisms are rare in the pediatric age group and often present with similar imaging characteristics as TB. The pathogenesis of tuberculous meningitis is different from that of other bacterial meningitides. Hematogenous spread to the CNS may produce miliary tuberculosis (rare in children) but more typically produce tuberculomas in the meninges and/or brain at the gray-white junction, spinal cord, or rarely in the choroid plexus. After a variable period of time, organisms from one or more of these foci are discharged into the CSF/subarachnoid space and causing meningitis. Isolated meningeal tuberculomas tend to localize in the region of the Sylvian fissures, producing meningitis in the basal

*Text continued on p. 334*

## Abstract:

Brain infections in children may manifest as encephalitis, cerebritis, or meningitis. Causative pathogens may be bacterial, viral, fungal or parasitic, and their incidence is dependent upon where in the world the child lives.

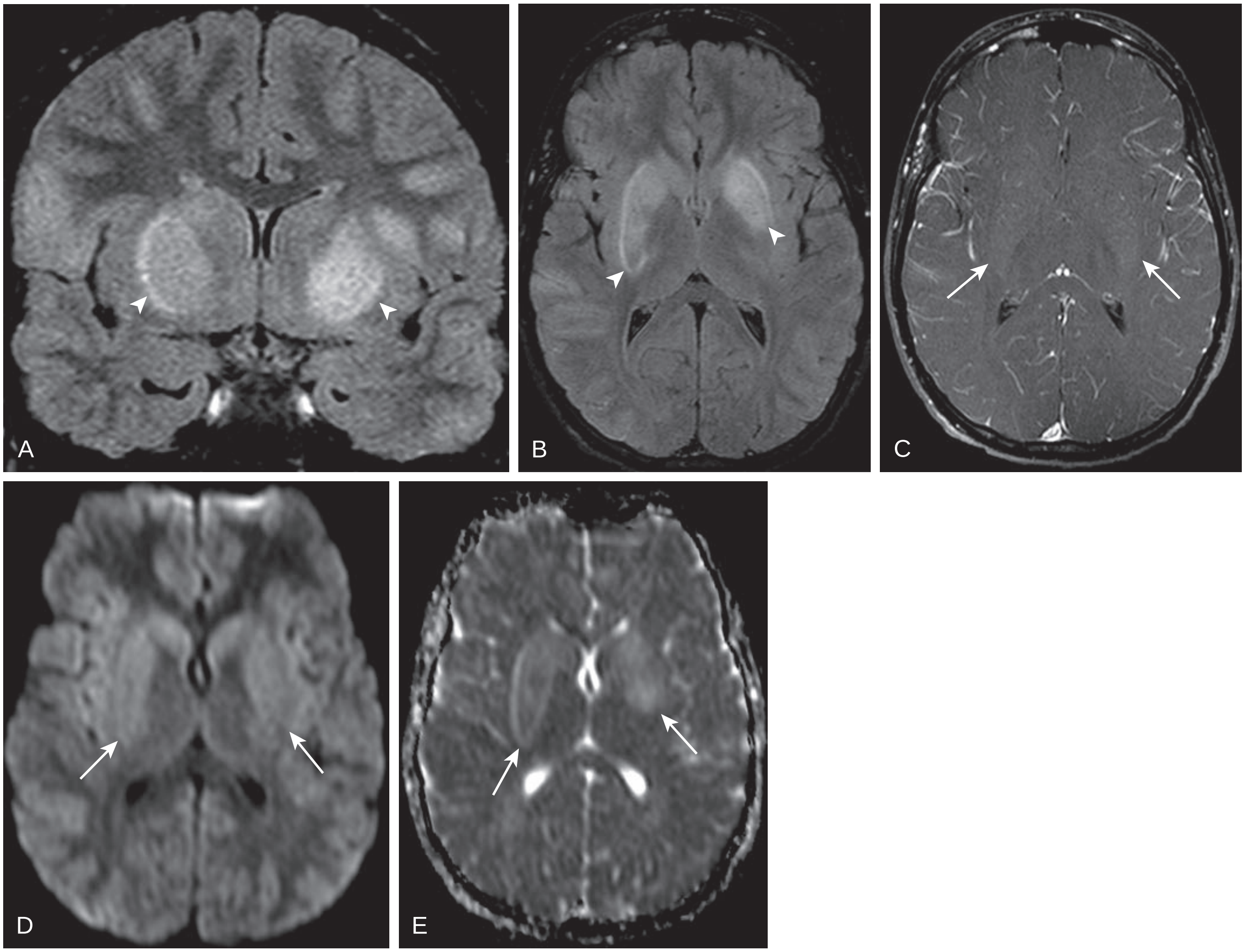

**e-Figure 34.1. West Nile virus.** Patient with loss of consciousness and questionable history of mosquito bite. (A) Coronal, (B) axial fluid-attenuated inversion–recovery, (C) axial contrast-enhanced T1-weighted, (D) axial diffusion-weighted imaging (DWI), and (E) apparent diffusion coefficient (ADC) map MR images show T2 prolongation within the basal ganglia bilaterally (*arrowheads* in A and B), with some questionable contrast enhancement or magnetization transfer effect as seen on postcontrast images (C). There is increased signal on DWI as well as ADC maps (*arrows* in D and E), in keeping with T2 shine-through.

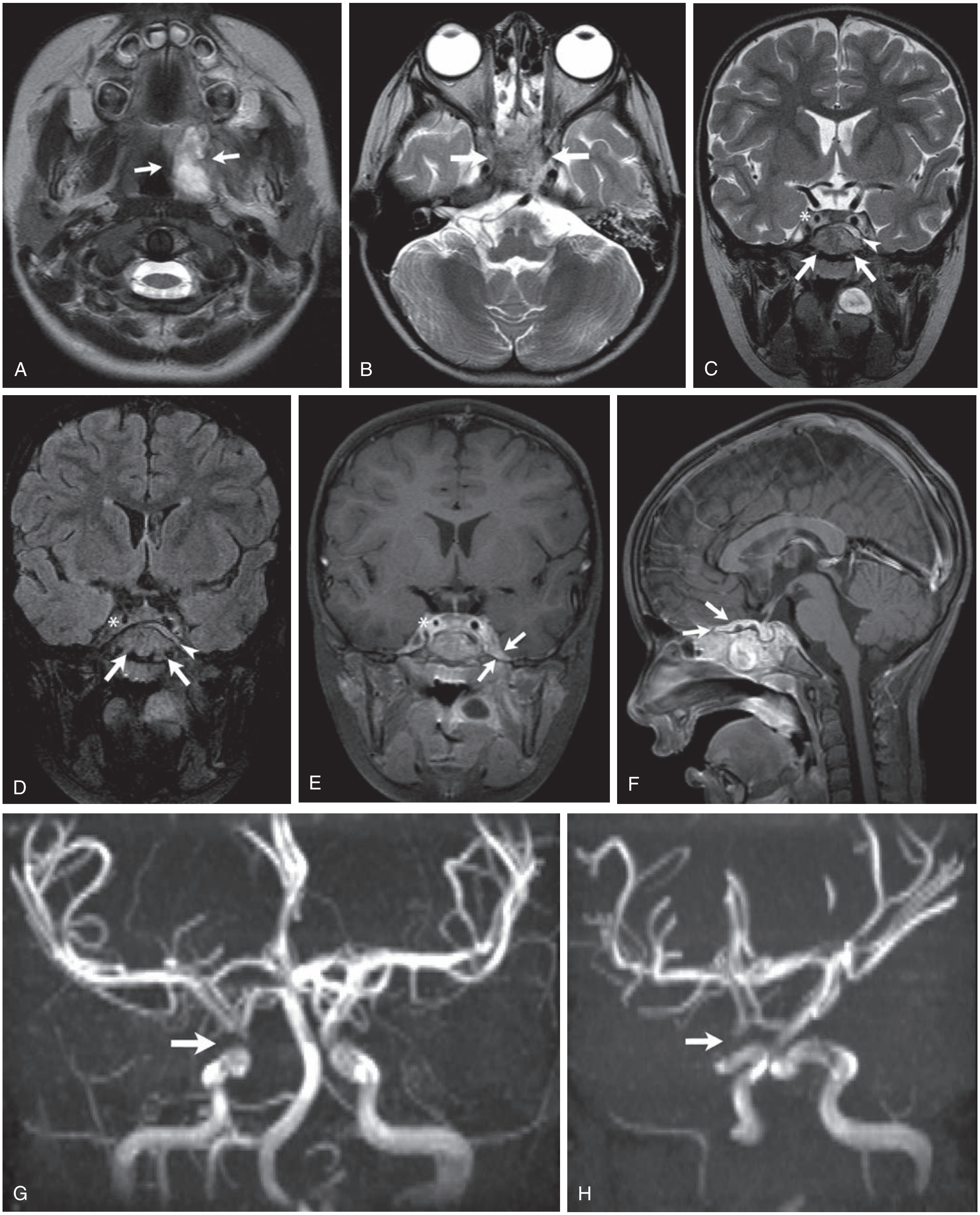

**e-Figure 34.2. Parameningeal spread of retropharyngeal infection.** Three-year-old female with retropharyngeal abscess, now with fever, headache, emesis, and left sixth nerve palsy. Axial T2-weighted MR images at the level of the (A) adenoids and (B) sphenoid bone. (C) Coronal T2-weighted and (D) fluid-attenuated inversion–recovery (FLAIR) (E) coronal and (F) contrast-enhanced T1-weighted MR images, as well as 3D time of flight (TOF) MRA in the (G) frontal and (H) left anterior oblique (LAO) projections. Note the inflammatory process within the left retropharyngeal region (*arrows* in A). There is abnormal marrow signal within the sphenoid bone (*arrows* in B, C, and D). In addition, there is abnormal soft tissue seen extending superior to the sphenoid bone on the coronal T2-weighted and FLAIR sequences (*arrowhead* in C and D). There is corresponding abnormal contrast enhancement along the region of the skull base and planum sphenoidale seen on the postcontrast images (*arrows* in E and F). Note the diminution in size of the right internal carotid artery (*asterisks* in C, D, and E) with corresponding narrowing of the right supraclinoid carotid artery (*arrows*

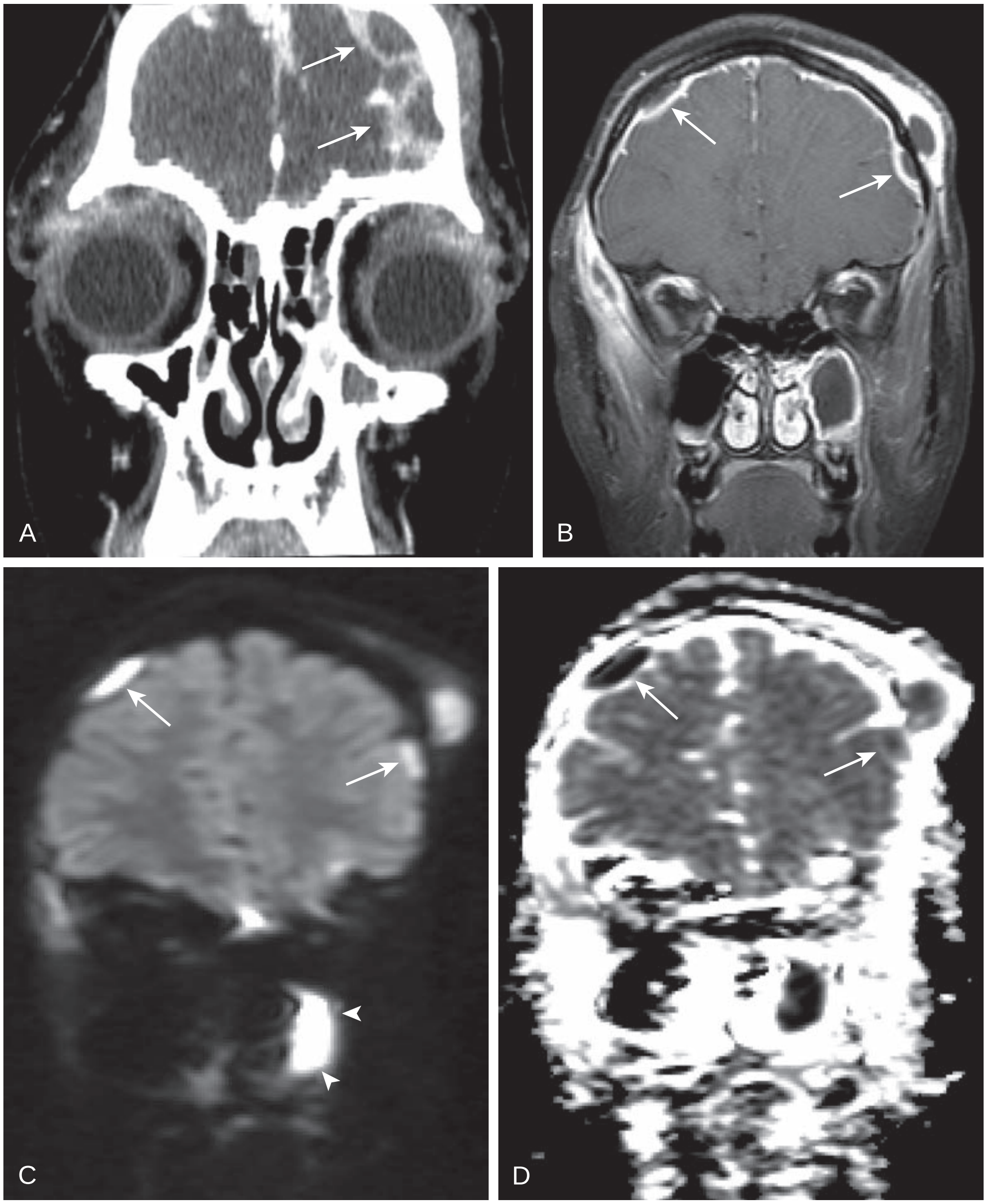

**e-Figure 34.5. Pott puffy tumor, with associated intracranial and extraaxial pus.** Eleven-year-old female with orbital swelling, preseptal cellulitis, and increase in forehead swelling associated with pansinusitis. The patient initially presented with syncope, fever, and bilateral orbital swelling. (A) Coronal contrast-enhanced CT, (B) coronal fat-saturated contrast-enhanced T1-weighted MRI through the frontal region, and (C) coronal diffusion-weighted image (DWI) with (D) apparent diffusion coefficient map. Note the abnormal extraaxial collections (*arrows* in A, B). There is corresponding restricted diffusion in the extraaxial space over the right cerebral hemisphere (*arrows* in C, D). Note also that corresponding to the area of apparent fluid collection within the left maxillary sinus, there is an area of corresponding restricted diffusion on the DWI (*arrowheads* in C), corresponding to pus within the left maxillary sinus.

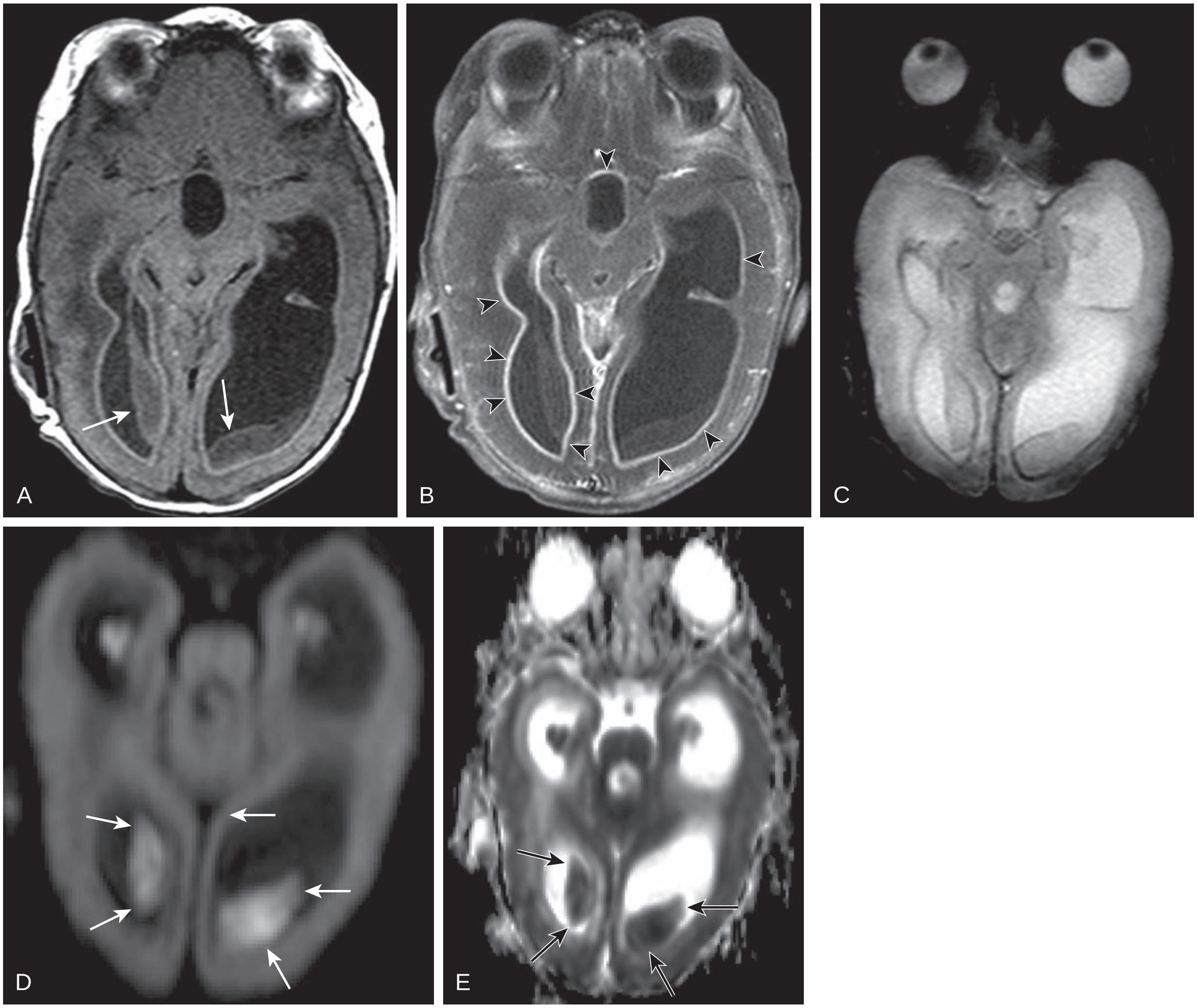

**e-Figure 34.13. Ventriculitis.** Four-month-old, ex-24-week preterm infant with IVH, ventricular peritoneal shunt, status postshunt revision for *E. coli* meningitis and ventriculitis. (A) Axial T1-weighted pre- and (B) postcontrast MR images, (C) axial gradient echo, and (D) axial diffusion-weighted image (DWI) with (E) apparent diffusion coefficient map demonstrate intraventricular soft tissue masses (*arrows* in A–E), which fail to demonstrate contrast enhancement (B), and do not show significant T2* effect on the gradient echo image (C). These masses demonstrate restricted diffusion on the DWI (*arrows* in D, E), in keeping with infected ependyma and clot. There is avid contrast enhancement along the lining of the ventricles (*arrowheads* in B), indicating ventriculitis.

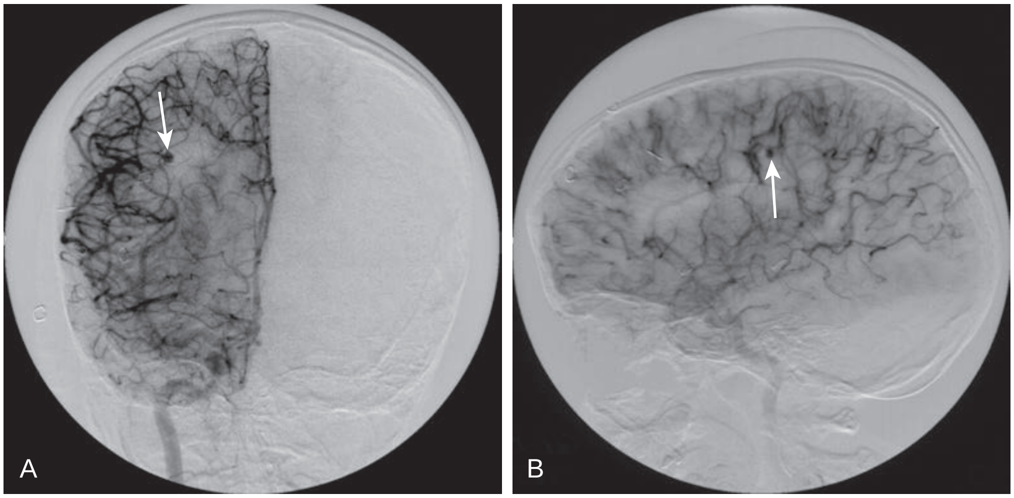

**e-Figure 34.14. Mycotic aneurysm.** Nine-year-old male with complex congenital heart disease and subacute bacterial endocarditis who presents with hemorrhage and left-sided hemiparesis, with a normal angiogram 2 weeks earlier. (A) Frontal and (B) lateral views from digital subtraction angiogram demonstrate a small outpouching from a right middle cerebral artery branch *(arrows),* indicating a mycotic aneurysm secondary to hematogenous spread of *Staphylococcus aureus*.

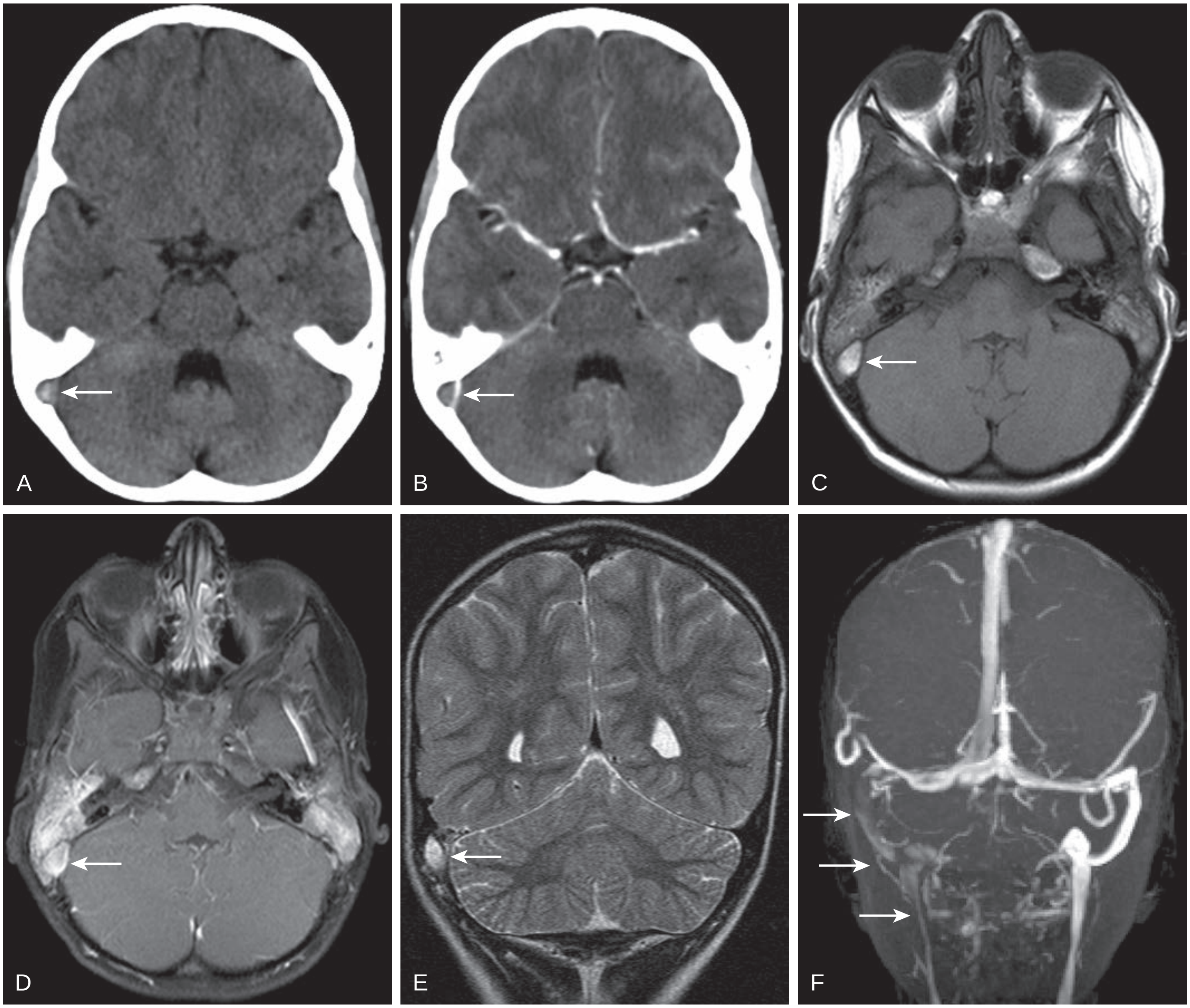

**Figure 34.3. Transverse sinus thrombosis associated with otomastoiditis and middle ear disease.** Patient presented with otitis media, headache, and papilledema. (A) Axial noncontrast and (B) contrast-enhanced CT of the head through the level of the posterior fossa, axial magnetization transfer T1-weighted MRI (C) precontrast and (D) fat-saturated postcontrast, (E) coronal T2-weighted, and (F) coronal multiple intensity projection (MIP) image from a 3D TOF MRV were obtained. Note the dense appearance of the dural sinus within the right transverse sinus region (*arrow* in A), with corresponding lack of contrast filling within the same region on the contrast-enhanced CT study (*arrow* in B). There is corresponding T1 shortening on the precontrast MRI (*arrow* in C), with corresponding abnormal signal on the postcontrast images indicating clot/slow flow within the region of the right transverse sinus/sigmoid sinus region (*arrow* in D). There is corresponding T2 prolongation on the coronal T2-weighted image (*arrow* in E). Note the striking asymmetry of flow within the right posterior fossa dural venous system/internal jugular vein on (*arrows* in F).

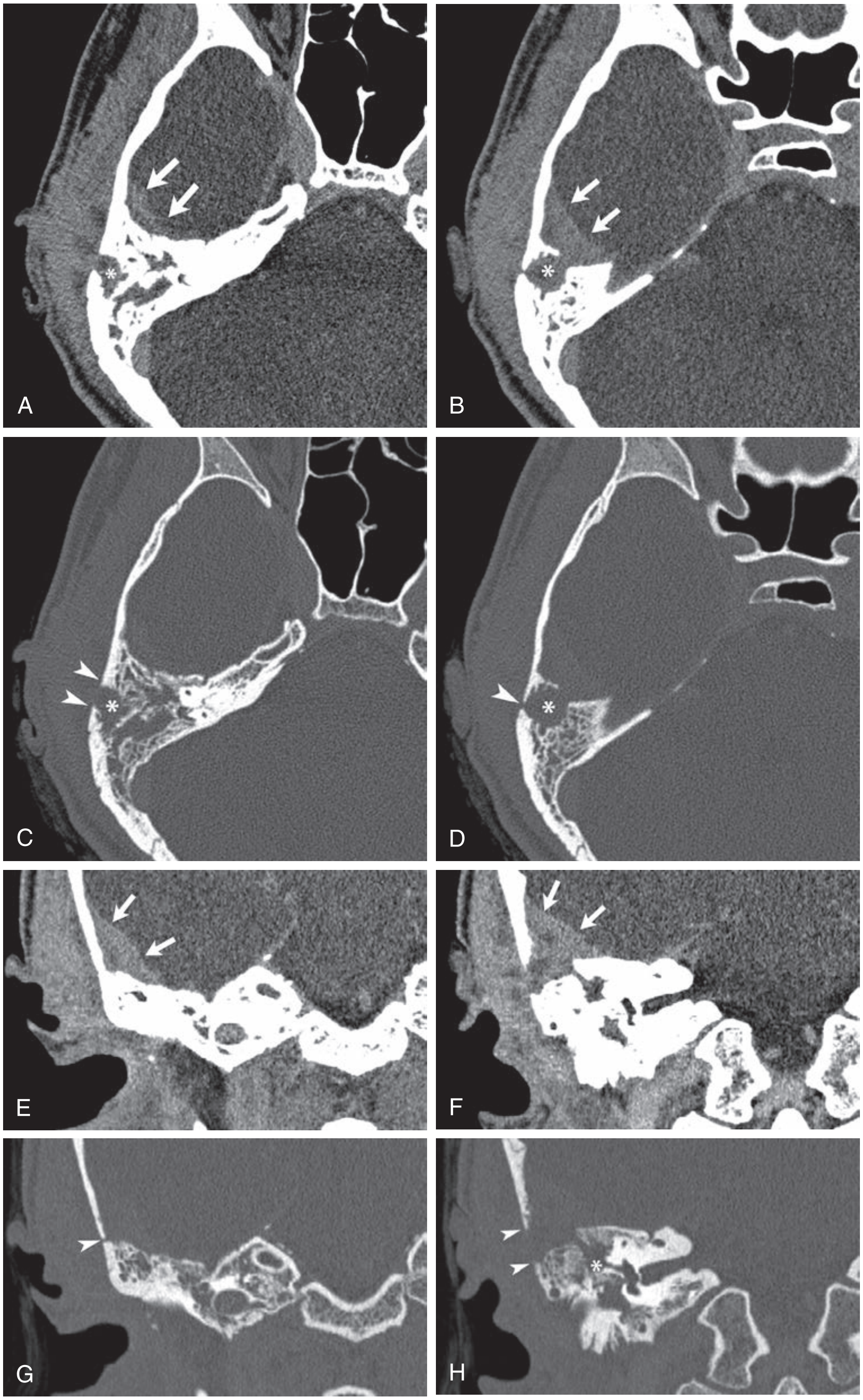

**Figure 34.4. Mastoiditis with associated epidural abscess.** A 17-year-old male with 5-month history of otitis media, now with severe right-sided mastoid pain. Axial contrast-enhanced CT images through the right mastoid region, including soft tissue (A and B), as well as bone windows (C and D), and direct coronal images in soft tissue (E) and (F), and bone windows (G and H). Note the abnormal soft tissue opacification within the right mastoid region (*asterisks* in A–D). There is associated abnormal soft tissue swelling along the external surface of the skull/scalp with an abnormal soft tissue component seen extending intracranially (*arrows* in A, B, E, F), corresponding to epidural abscess formation. There is bony resorption and breakdown seen within the mastoid cortex laterally (*arrowheads* in C, D, G, H). In addition, note the erosion of the lateral semicircular canal (*asterisk* in H).

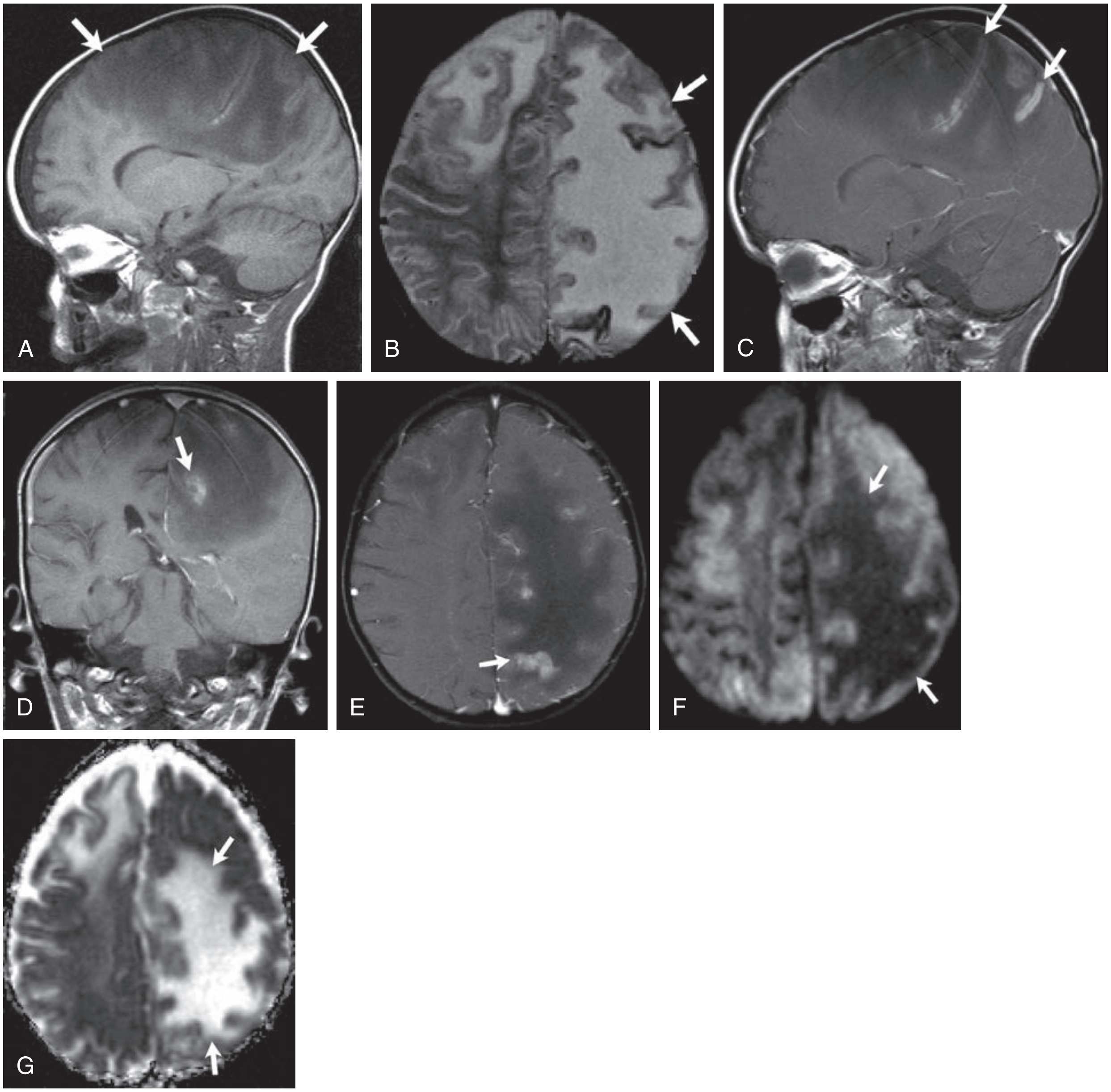

**Figure 34.6. Cerebritis.** A 2-year-old male with *Staphylococcus aureus* bacteremia and persistent fevers with new onset of hypertension. (A) Sagittal T1-weighted, (B) axial T2-weighted, and (C) sagittal, (D) coronal, and (E) axial contrast-enhanced spin echo MR images, as well as (F) axial diffusion-weighted image (DWI) and (G) apparent diffusion coefficient maps demonstrate T1 and T2 prolongation (*arrows* in A and B, respectively), with some mild cortical enhancement (*arrows* in C, D, E), and increased diffusion *(arrows)* as evidenced by decreased signal on DWI and increased signal on the DWI images.

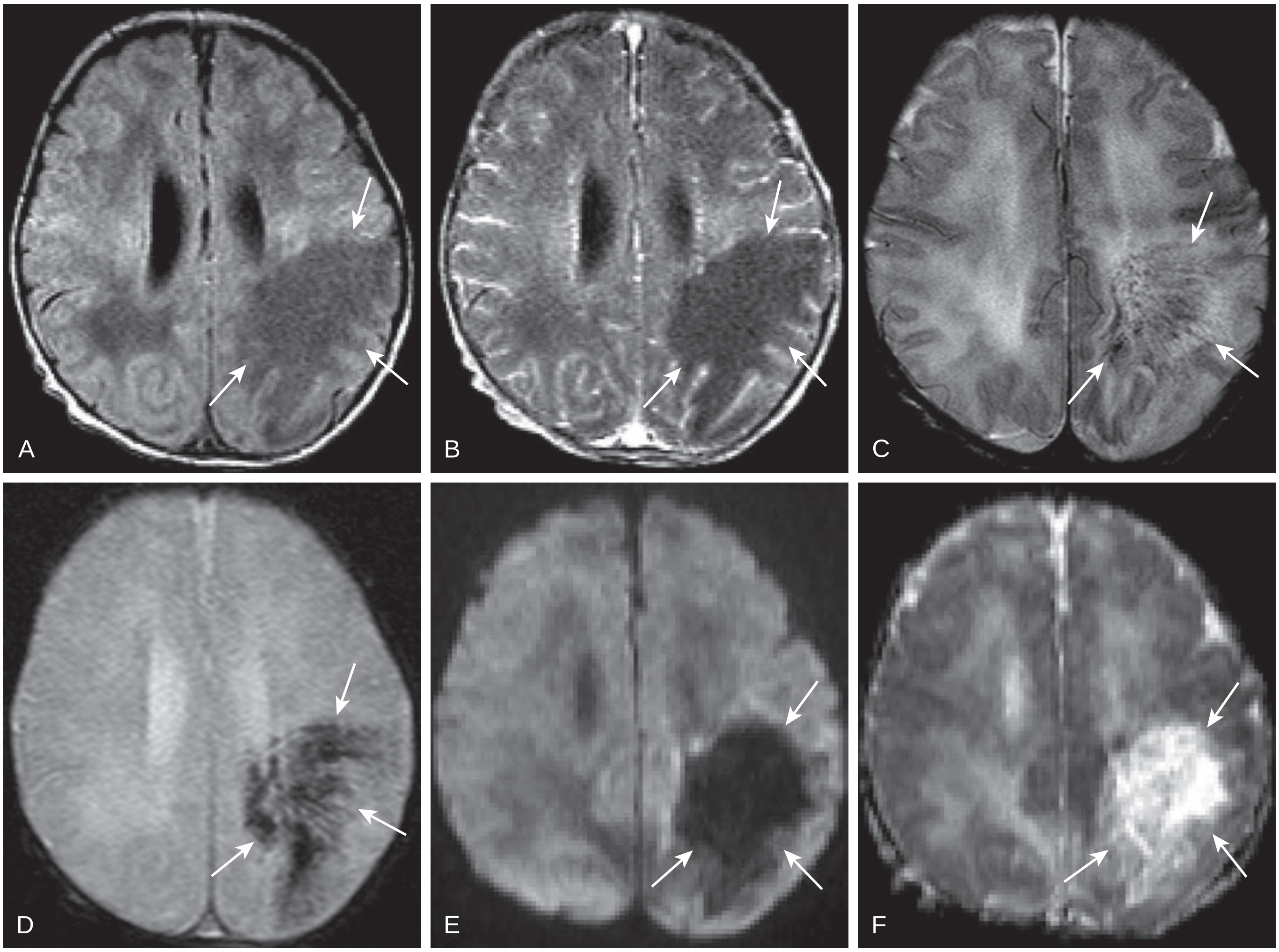

**Figure 34.7.** ***Citrobacter*** **infection with secondary venous thrombosis.** Seven-day-old full-term female neonate with seizures, gram-negative sepsis, and increased white blood cell count on lumbar puncture. Axial pre- (A) and postcontrast (B) T1-weighted MR images, (C) axial T2-weighted, (D) axial gradient echo MR images, as well as (E) axial diffusion-weighted image (DWI) and (F) apparent diffusion coefficient map. Note the area of T1 prolongation within the left posterior frontal parietal region (*arrows* in A, B), corresponding to areas with linear signal voids on both T2-weighted and gradient echo sequences (*arrows* in C, D), corresponding to distended medullary veins. Note that there is no diffusion restriction, but rather increase in diffusion on the corresponding area on DWI (*arrows* in E, F).

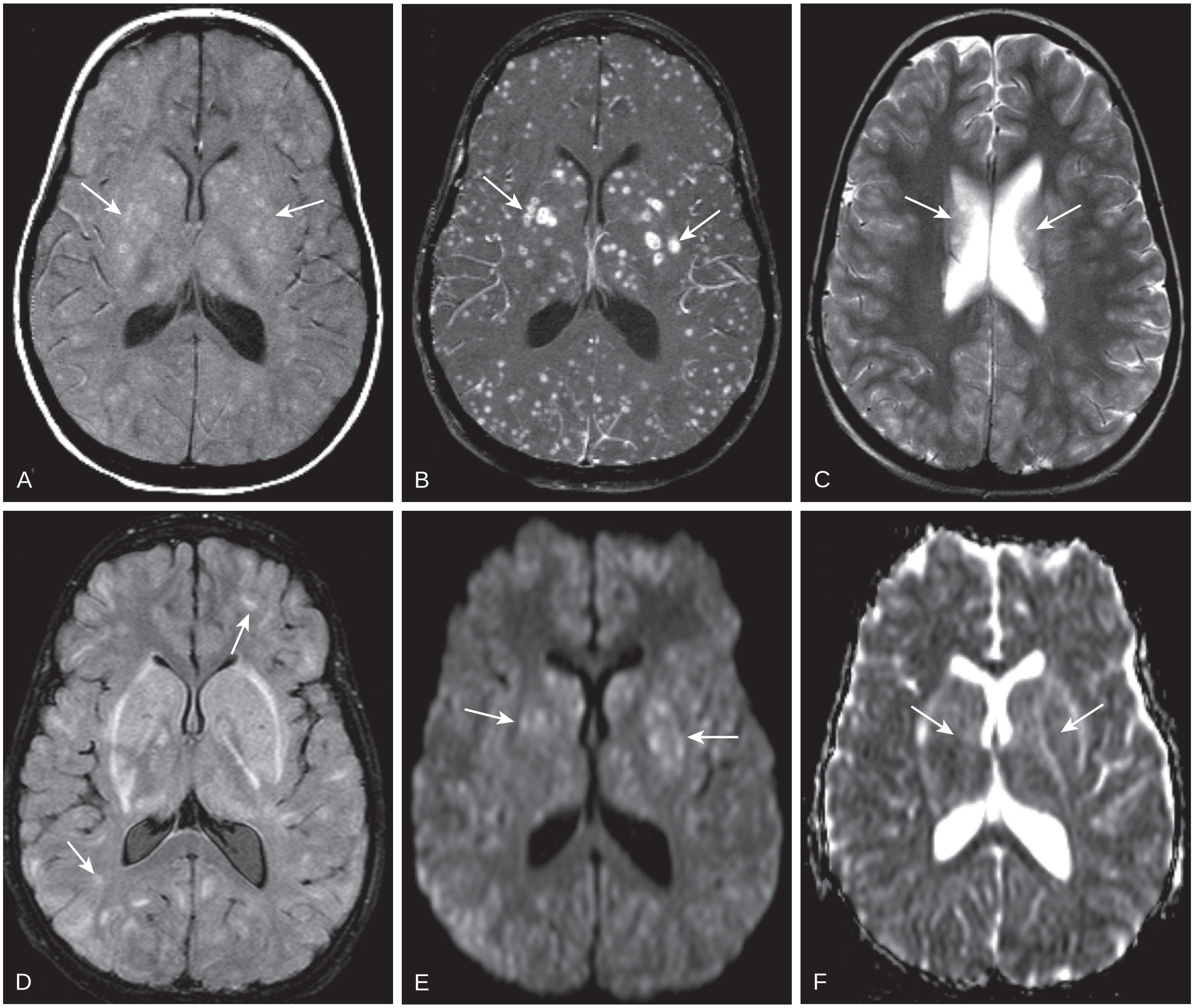

**Figure 34.8. Streptococcus viridans abscesses.** Twelve-year-old female with acute myelogenous leukemia and mental status changes. Axial T1-weighted magnetization transfer MR images, (A) pre- and (B) postcontrast, (C) axial T2-weighted and (D) fluid-attenuated inversion–recovery (FLAIR), and (E) axial diffusion-weighted imaging with (F) apparent diffusion coefficient map. Note the areas of T1 shortening on precontrast (*arrows* in A), and the corresponding marked gadolinium enhancement within multiple bilateral intraparenchymal nodules of differing size (*arrows* in B). There is T2 prolongation noted on the axial T2W and FLAIR sequences in some corresponding areas (*arrows* in C, D), but this is markedly less conspicuous than on the postcontrast images. There is subtle restricted diffusion noted in some of the nodular areas, specifically within the basal ganglia, corresponding to the largest lesions seen on postcontrast images (*arrows* in E, F).

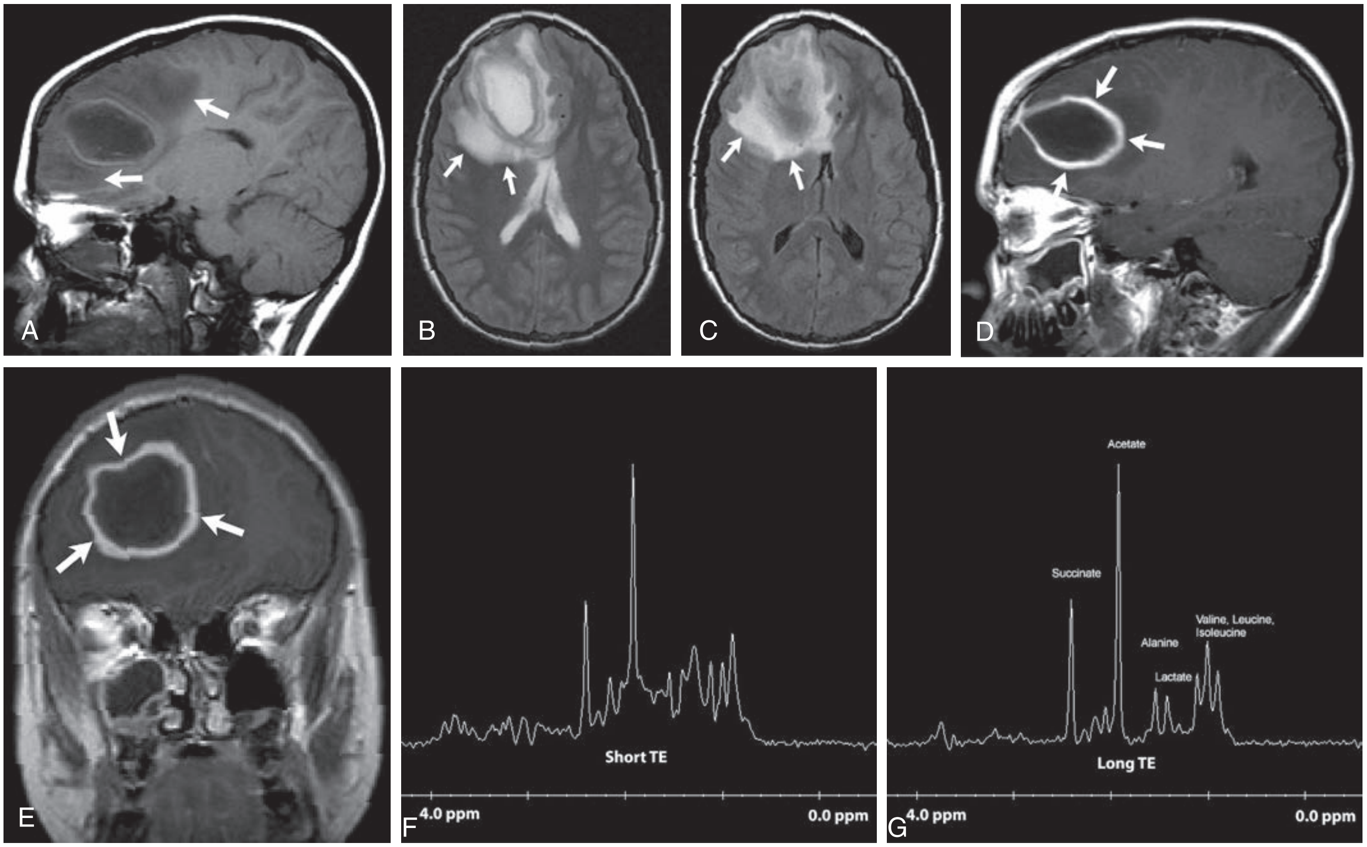

**Figure 34.9. Cerebral abscess.** Patient with seizures and fever. (A) Sagittal T1-weighted, (B) axial T2-weighted, (C) axial fluid-attenuated inversion–recovery, postcontrast, (D) sagittal, and (E) coronal spin echo MR images, as well as (F) short TE and (G) long TE magnetic resonance spectroscopy (MRS) images. Note the areas of T2 prolongation (*arrows* in B, C), with some central low signal intensity (C) in the region of abscess with surrounding vasogenic edema. There is thick, rindlike enhancement of the periphery of the right frontal abscess (*arrows* in D, E). MRS images demonstrate abnormal amino acid peaks, at around 1 ppm, and a doublet lactate peak deflected upward at 1.33 ppm. *(Case courtesy Kim M. Cecil, PhD, Cincinnati, OH.)*

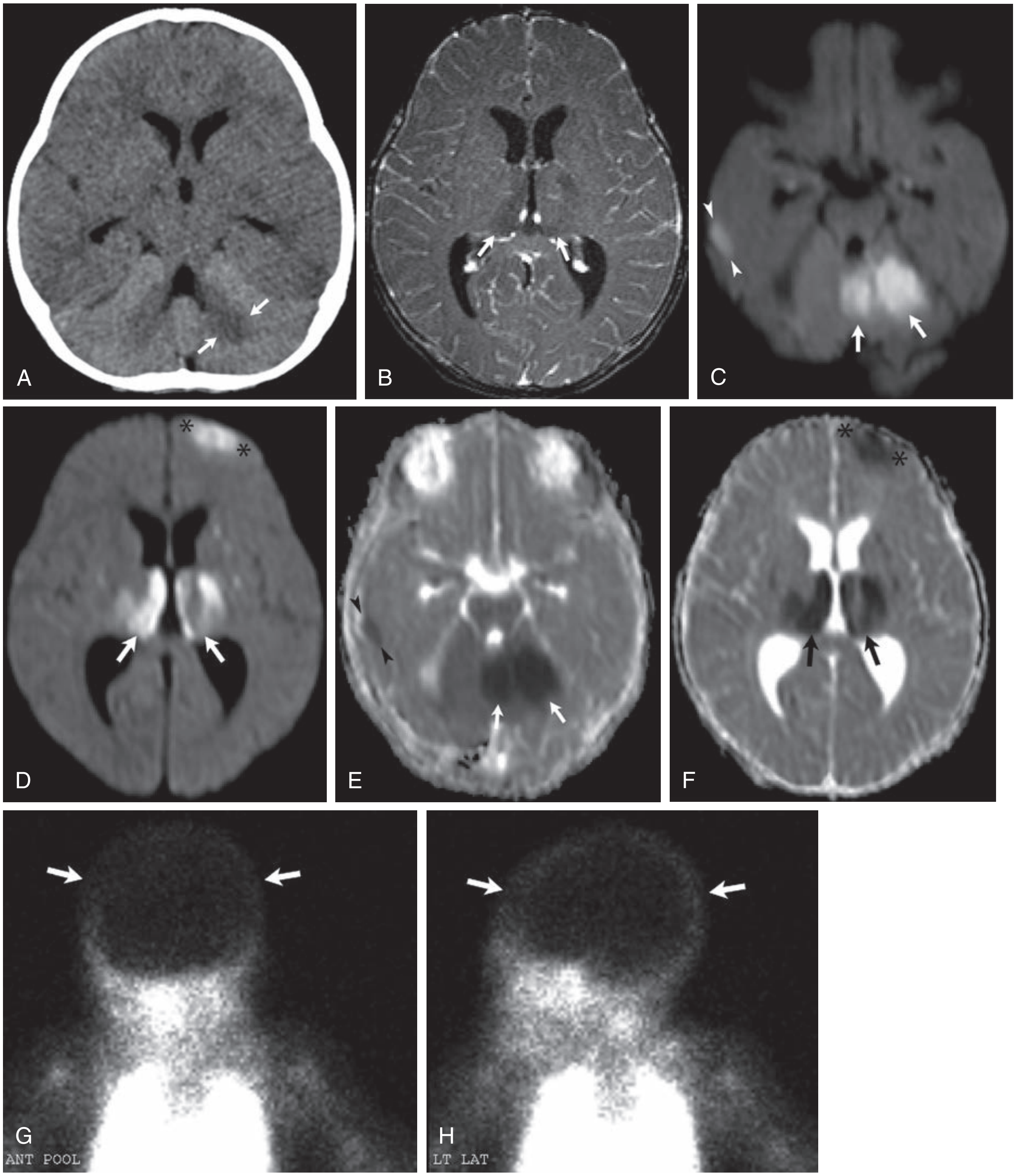

**Figure 34.10. Meningitis and brain death.** Six-month-old male with seizures and fever due to gram-positive cocci meningitis. (A) Axial noncontrast CT, (B) axial postcontrast T1-weighted spin echo, axial diffusion-weighted images (DWI) at the level of the (C) posterior fossa and (D) thalami, and (E and F) axial ADC maps at the same levels as C and D, and (G) frontal and (H) lateral Neurolite nuclear medicine brain flow study. Note the subtle decreased attenuation within the left cerebellar hemisphere (*arrows* in A), and the areas of T1 prolongation within the thalami (*arrows* in B). There are corresponding areas of restricted diffusion on the DWI and apparent diffusion coefficient images (*arrows* in C–F). In addition, there are areas of restricted diffusion within the right temporal lobe *(arrowheads),* and left frontal lobe *(asterisks)* on the diffusion-weighted sequences (C–F). There is no identifiable perfusion to the brain, as evidenced by lack of accumulation of radiotracer (*arrows* in G, H).

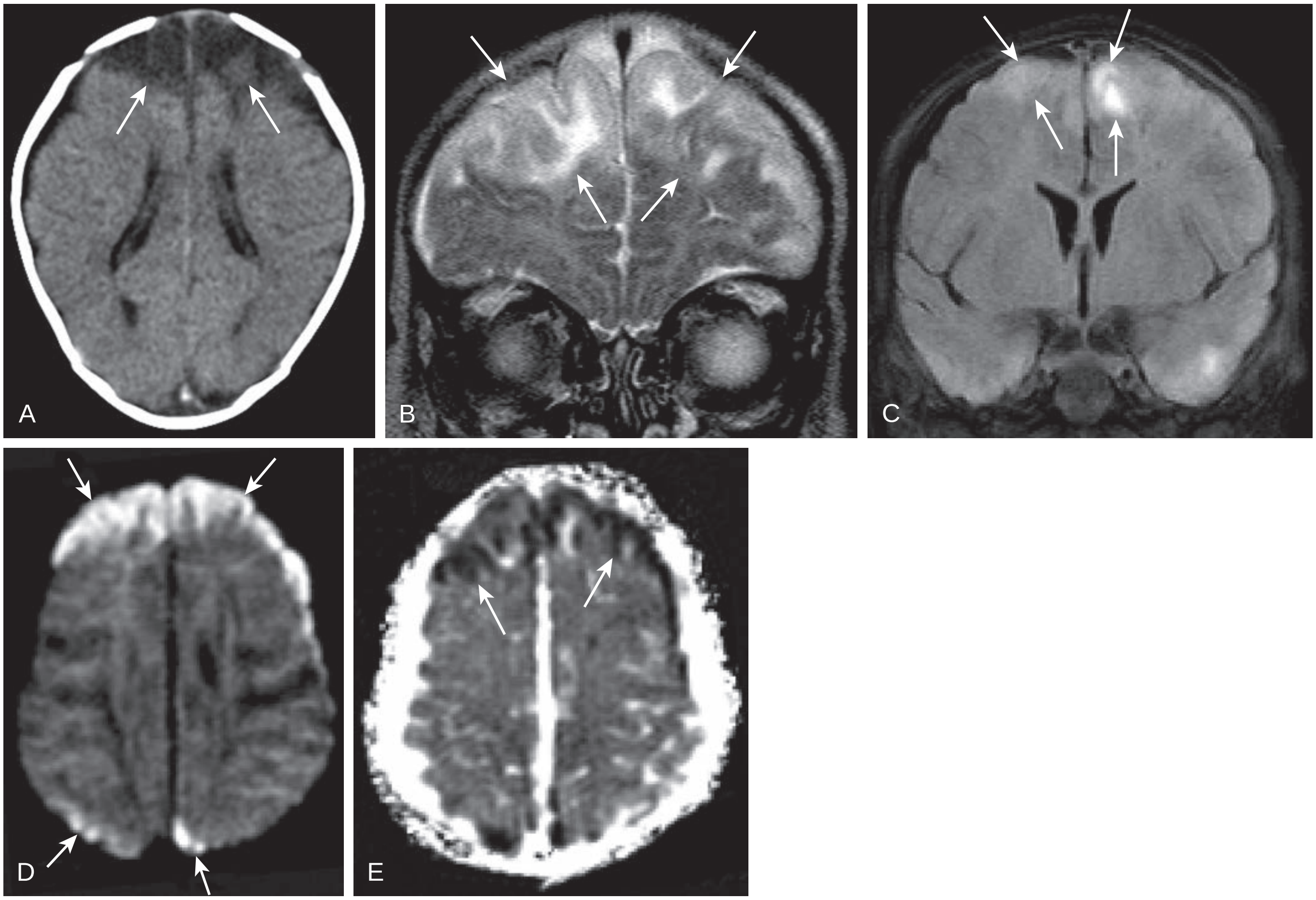

**Figure 34.11. Group B streptococcus (GBS) meningitis.** A 10-week-old female with GBS sepsis and meningitis. (A) Axial noncontrast CT of the head, (B) coronal T2-weighted and (C) fluid-attenuated inversion–recovery (FLAIR) MR images, and (D) diffusion-weighted image with (E) apparent diffusion coefficient (ADC) maps. Note the low attenuation within the frontal lobes bilaterally (*arrows* in A), with corresponding T2 prolongation and abnormal increased FLAIR signal (*arrows* in B, C). In addition, there is restricted diffusion within the frontal and parietal regions bilaterally (*arrows* in D, E), in keeping with ischemic changes secondary to meningitis.

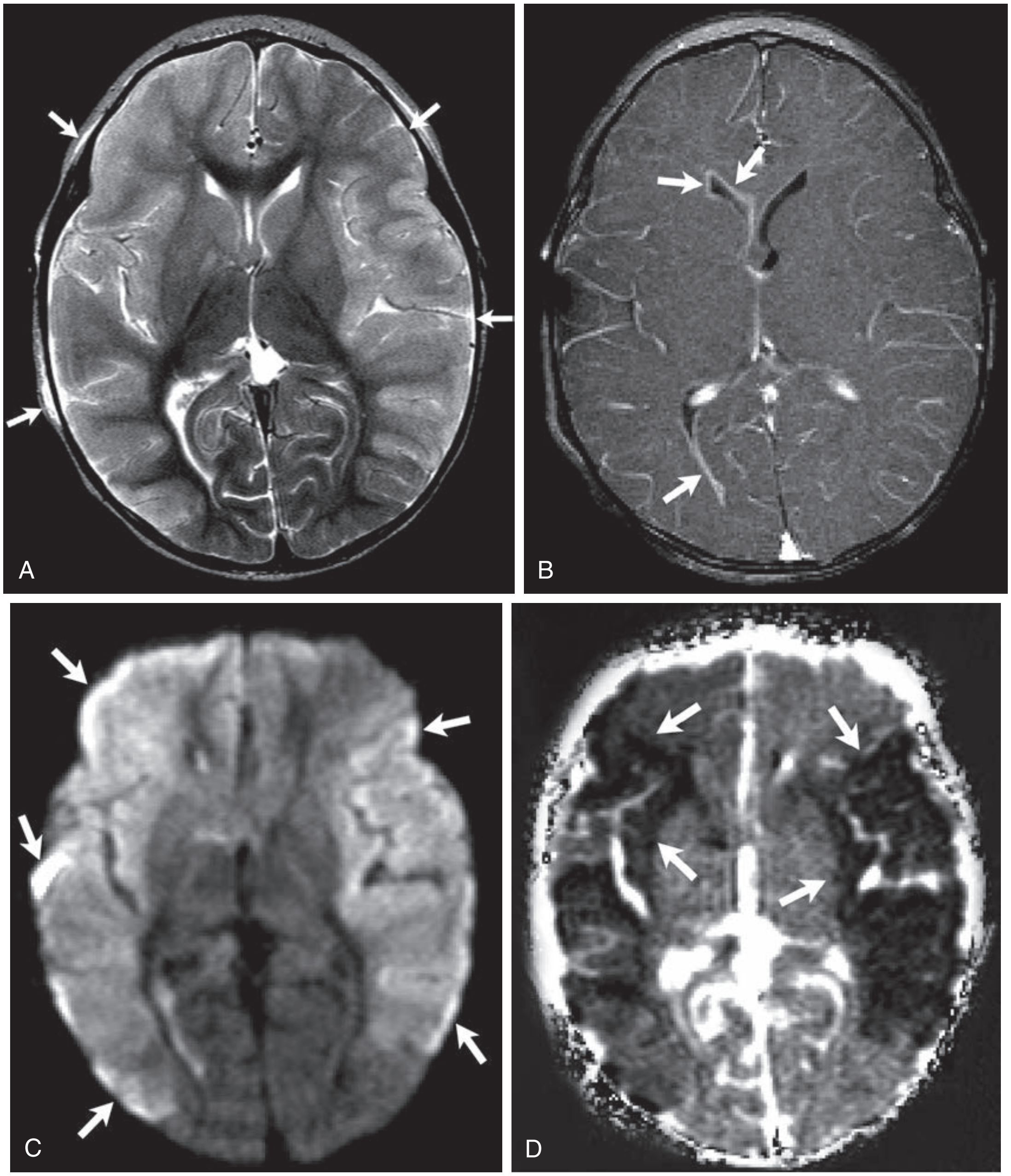

**Figure 34.12. Pneumococcal meningitis with infarctions.** Eleven-month-old female with ventriculostomy and mental status changes, with suspected meningitis. (A) Axial T2-weighted, (B) axial postcontrast T1-weighted MR images, (C) axial diffusion-weighted image and (D) apparent diffusion coefficient maps, and (E) 3D time of flight MRA frontal and (F) compressed cranio-caudad views. There is diffuse T2 prolongation within the cerebral cortex bilaterally (*arrows* in A), with associated abnormal enhancement along the ventricular lining (*arrows* in B), indicating ventriculitis. Note the marked restricted diffusion within both hemispheres (*arrows* in C, D) in keeping with cytotoxic edema secondary to infection. There is bilateral middle cerebral artery narrowing, right greater than left *(arrows),* and narrowing of the supraclinoid carotid arteries bilaterally (*arrowheads* in E).

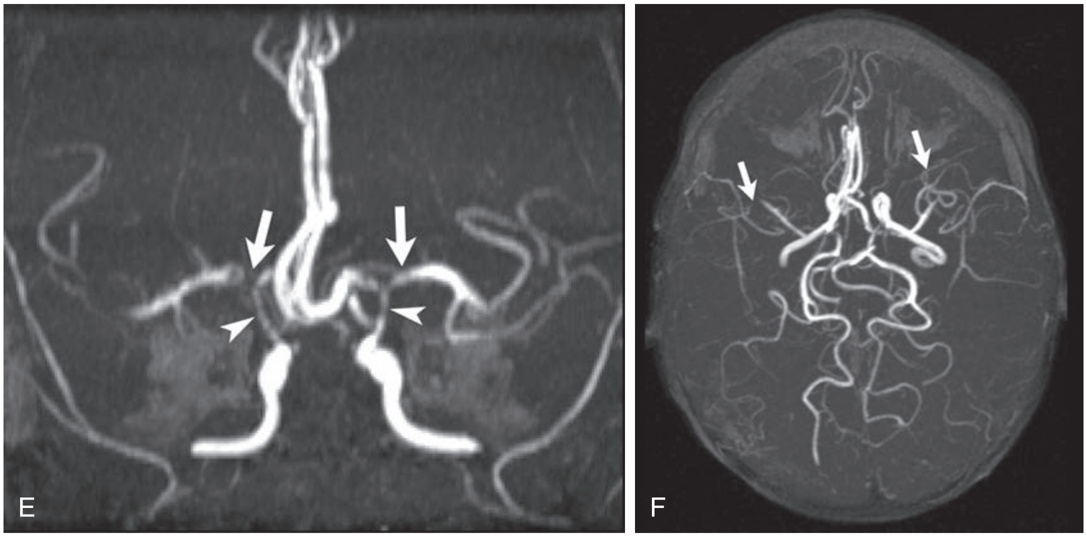

**Figure 34.12, cont'd.**

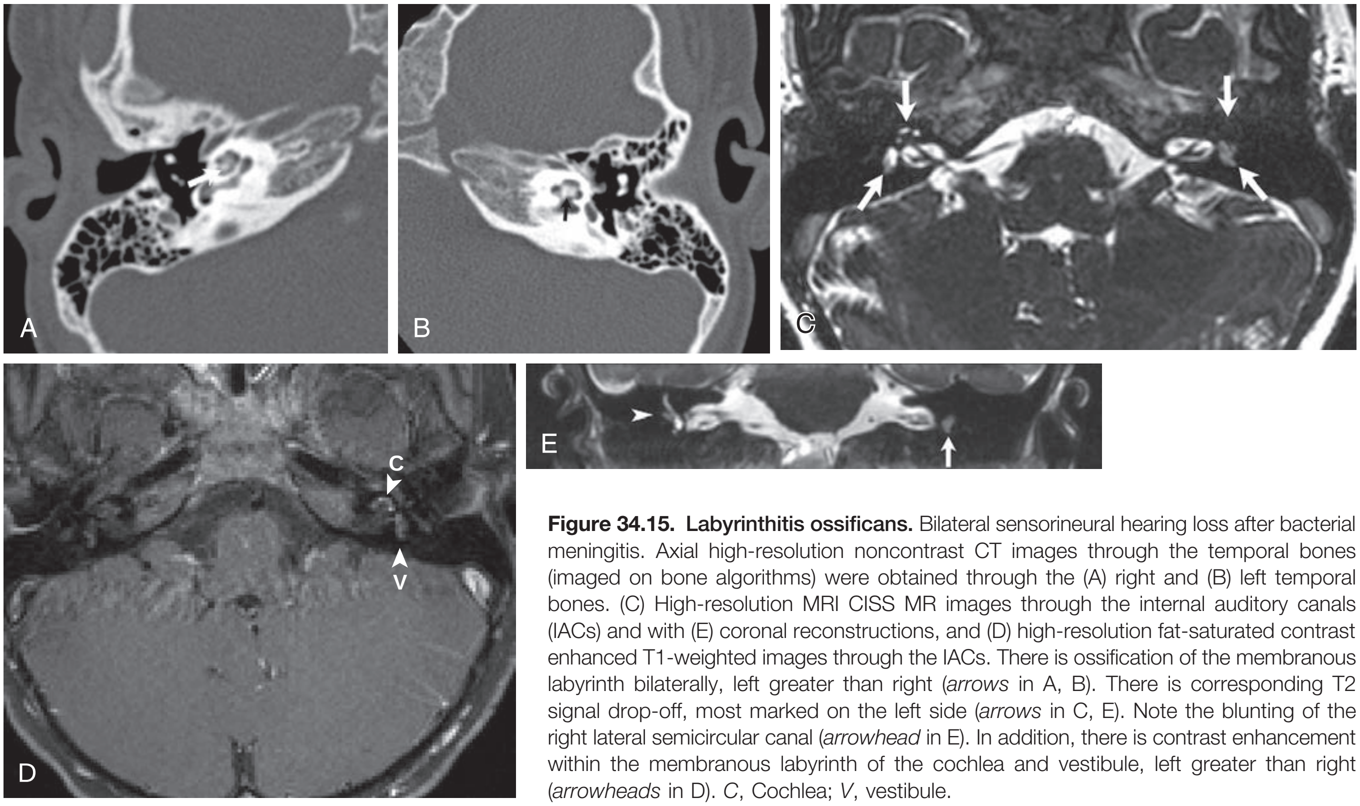

**Figure 34.15. Labyrinthitis ossificans.** Bilateral sensorineural hearing loss after bacterial meningitis. Axial high-resolution noncontrast CT images through the temporal bones (imaged on bone algorithms) were obtained through the (A) right and (B) left temporal bones. (C) High-resolution MRI CISS MR images through the internal auditory canals (IACs) and with (E) coronal reconstructions, and (D) high-resolution fat-saturated contrast enhanced T1-weighted images through the IACs. There is ossification of the membranous labyrinth bilaterally, left greater than right (*arrows* in A, B). There is corresponding T2 signal drop-off, most marked on the left side (*arrows* in C, E). Note the blunting of the right lateral semicircular canal (*arrowhead* in E). In addition, there is contrast enhancement within the membranous labyrinth of the cochlea and vestibule, left greater than right (*arrowheads* in D). *C*, Cochlea; *V*, vestibule.

cisterns. This leads to secondary complications including cranial nerve palsies, infarction consequent to vasculitis, and hydrocephalus secondary to blockage of fourth ventricular outlet foramina.

Hematogenous dissemination of tuberculous bacilli is believed to occur about 1 week after the infected inhalation. Three stages of tuberculous meningitis have been described that progress over approximately a 3-week period. Clinical presentation ranges from personality change and anorexia to coma and death, with nuchal rigidity being the most common presenting clinical sign. Pathologically, tuberculous exudate fills the subarachnoid spaces. Most affected patients demonstrate hydrocephalus. On CT, exudate within the cisterns is manifested by attenuation greater than CSF. On contrast-enhanced MRI there is marked subarachnoid and cisternal enhancement on T1-weighted sequences (Fig. 34.16), with T2-weighted sequences demonstrating obscuration of the cisterns due to inherent hyperintense signal within these affected regions. Microinfarctions are common. Tuberculomas often manifest at gray-white junctions and are more common above the tentorium cerebelli. On CT, they demonstrate high attenuation and ring enhancement (Fig. 34.17), yet on MRI they demonstrate hyperintense T1-weighted and hypointense T2-weighted signal. When less than 2 cm, tuberculomas enhance uniformly, and when greater than 2 cm, they show more peripheral enhancement. The rare tuberculous abscess can be differentiated from a tuberculoma by its central hyperintense T2-weighted signal and more pronounced associated vasogenic edema. While DWI is not particularly helpful in making a diagnosis, lipid detection on MRS has been reported as helpful in certain cases.

## Lyme Disease

Lyme disease is the most common tick-borne disease in the United States and Europe. More than one in five cases have been reported in children or adolescents. This multisystemic disorder involves the neurologic system in approximately one-fifth of affected children, manifesting as lymphocytic meningitis, meningoencephalitis, pseudotumor cerebri-like syndrome, or cranial neuropathy. It is unclear whether the mechanism of CNS involvement is a result

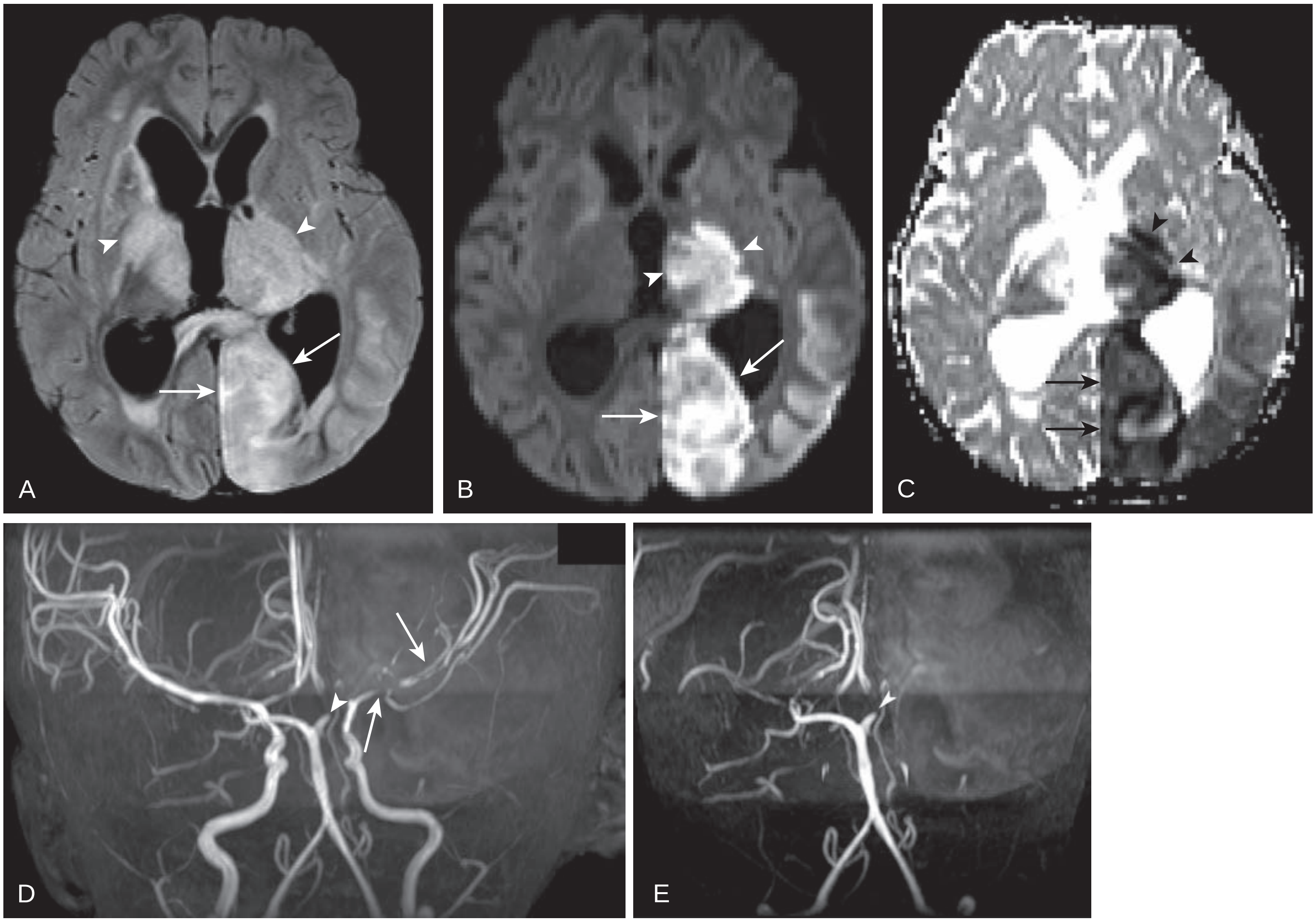

**Figure 34.16. Tuberculous (TB) meningitis.** Two-year-old female with suspected TB meningitis and left-sided posterior cerebral artery territory stroke. (A) Axial fluid-attenuated inversion–recovery (FLAIR) MR image, (B) axial diffusion-weighted image (DWI) and (C) apparent diffusion coefficient (ADC) map, and 3D time of flight MRA in the (D) anterior projection and (E) craniocaudad collapsed view, (F) frontal angiographic view of the posterior cerebral arteries (PCA) circulation, as well as sequential axial contrast-enhanced T1-weighted images through the level of the brainstem (G–I) demonstrating worsening changes of tuberculous meningitis over time. Note the abnormal FLAIR signal seen within the left occipital lobe *(arrows)* and bilateral thalami *(arrowheads)* on the axial FLAIR sequence. There is corresponding restricted diffusion within the left thalamus *(arrowheads)* and occipital lobes *(arrows)* as seen on DWI sequences. There is marked irregularity of the left middle cerebral artery (*arrows* in D, F), as well as cutoff of the left PCA (*arrowheads* in D–F). Note the marked abnormal contrast enhancement along the basal meninges bilaterally, outlining the base of the brain (*arrows* in G–I), secondary to TB meningitis.

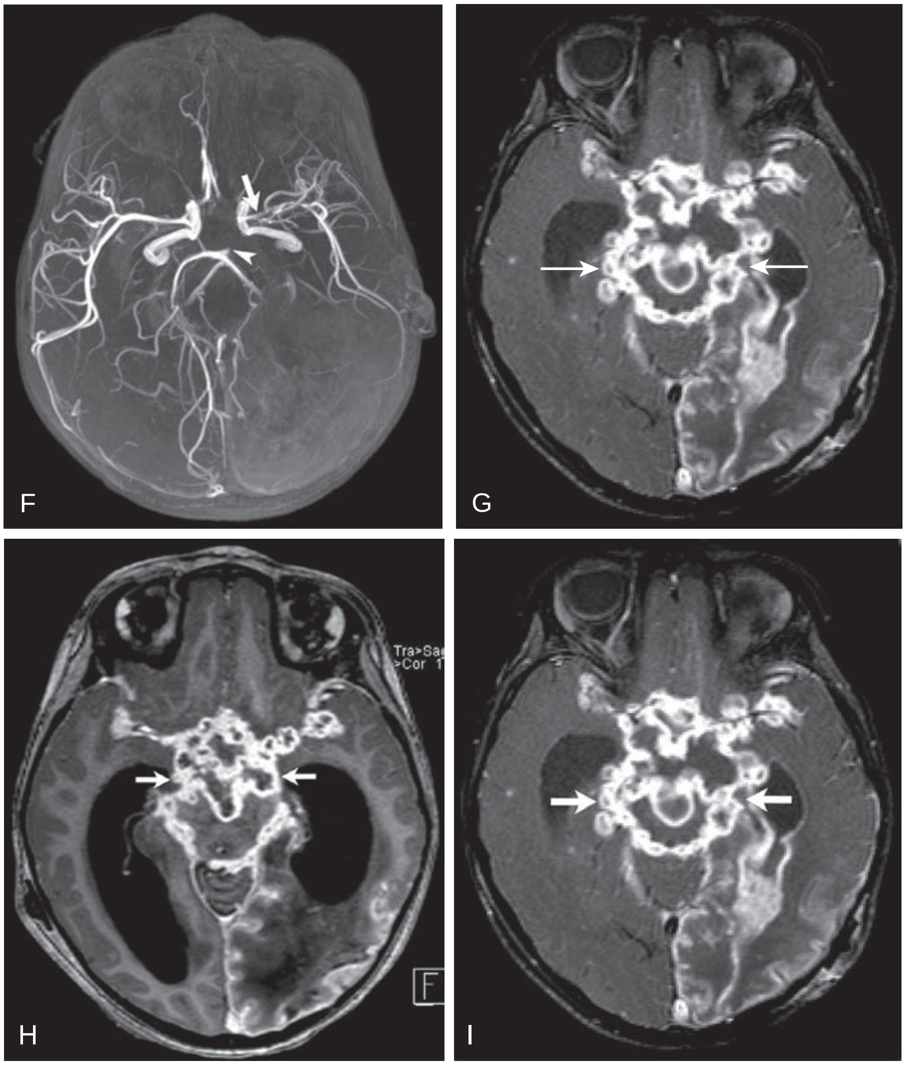

**Figure 34.16, cont'd.**

of direct invasion by the *Borrelia burgdorferi* organism or due to an autoimmune phenomenon.

CT scans are usually normal in Lyme disease, although focal areas of hypoattenuation have been reported. Focal white matter lesions, which are hyperintense on T2-weighted images, are seen in about one in four neurologically affected patients. Contrast-enhanced MRI may show leptomeningeal enhancement, with or without enhancement of the affected cranial nerves, in children with cranial neuropathy (Fig. 34.18).

## PARASITIC INFECTIONS

In the United States, parasitic CNS infection in children is rare. While cysticercosis is not very common per se, it often presents in immigrants from endemic regions. The most common presenting symptoms of pediatric neurocysticercosis include seizures, developmental delay, and hydrocephalus. The most common form, parenchymal cysticercosis, is caused by inflammatory reaction secondary to the death of the parasite. Focal lesions are cystic and solid and present with peripheral enhancement and calcification, respectively. They are most often situated at the cortex and/or gray-white matter junction (Fig. 34.19). Parenchymal lesions follow CSF signal intensity on DWI, which helps differentiate them from pyogenic abscesses. The typical calcification seen in adults is not always seen in children. Surrounding inflammatory reaction demonstrates hyperintense T2-weighted signal. Intraventricular cysterci often cause obstructive hydrocephalus. Thin-slice T1-weighted imaging best depicts the causative intraventricular scolex (e-Fig. 34.20). The leptomeningeal form of cysticercosis mimics the radiographic appearance of TB, with marked postcontrast subarachnoid enhancement. Subarachnoid granulomata mimic their parenchymal counterparts. Hydrocephalus and vasculitis are common associated findings. Racemose cysts are large cysts that are most often found in the cerebellopontine angle, Sylvian fissures, as well as the basilar and suprasellar cisterns. Multiple coexisting forms of cysticercoids often suggest the diagnosis. On MRI, clusters of cysts are most commonly depicted.

## VIRAL INFECTIONS

Viruses affecting the brain (e-Fig. 34.21) all produce inflammation and neuronal necrosis to a greater or lesser extent. Some viruses such as herpes simplex virus (HSV) and Coxsackieviruses may also produce white matter necrosis, whereas the primary inflammatory process involves the parenchyma. There is usually a meningeal inflammatory reaction or even ventriculitis. In general, acute viral infection typically causes marked edema (e-Fig. 34.22). Hyperechogenicity on US, hypoattenuation on CT, as well as hyperintense signal on T2-weighted and FLAIR sequences are typical imaging findings of CNS viral infection. Restricted diffusion on DWI is the earliest sign of viral encephalitis. Fortunately differences in presentation and location help suggest one viral

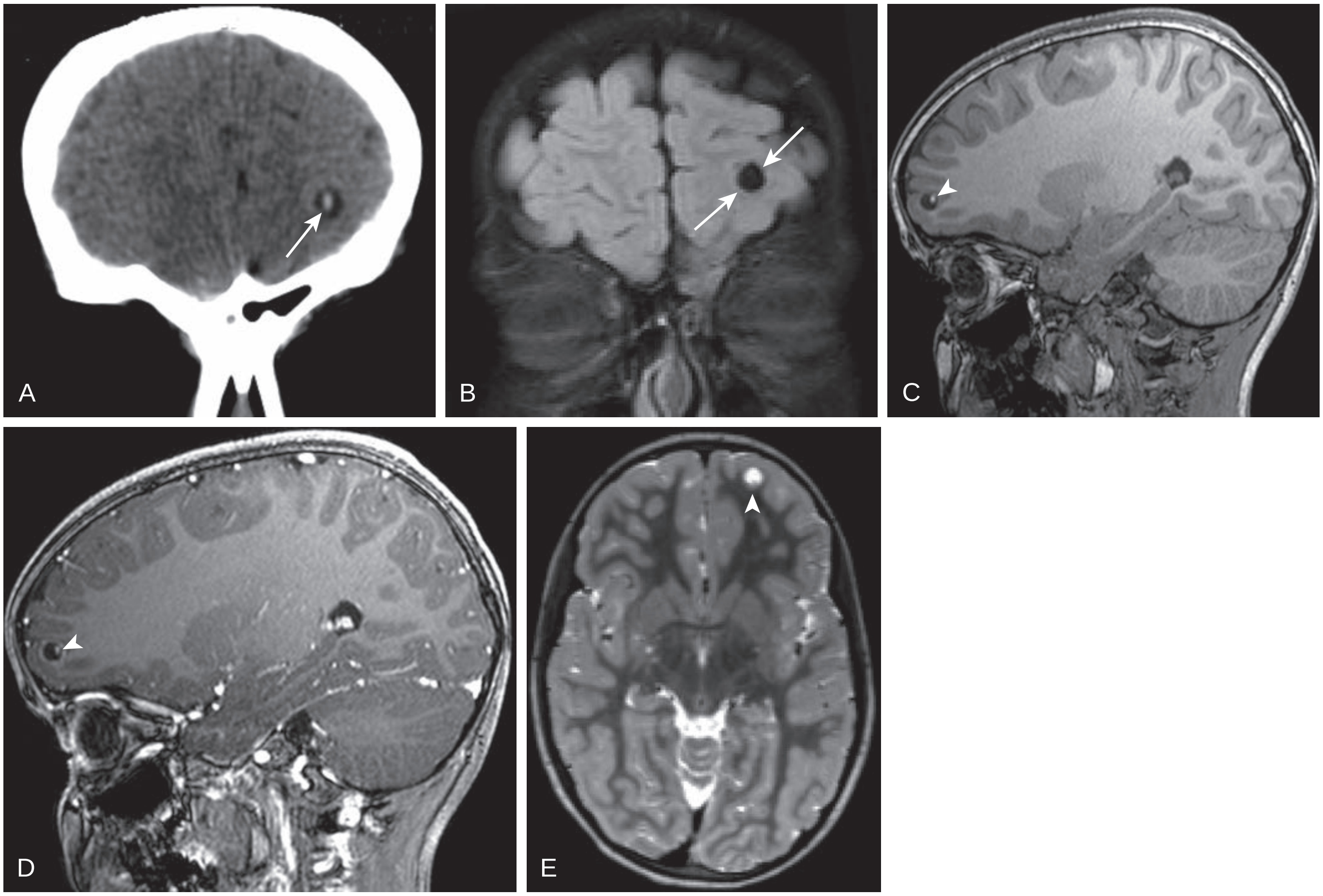

**e-Figure 34.20. Cysticercosis.** Seven-year-old female with left frontal cystic lesion. (A) Coronal noncontrast CT of the head, (B) coronal fluid-attenuated inversion–recovery MR image, sagittal (C) pre- and (D) contrast-enhanced 3D-SPGR images through the level of the left frontal lobe, and (E) reconstructed axial 3D T2-weighted image through the same area. Note the area of high attenuation within the center of the lesion (*arrow* in A), corresponding to the scolex within a cystic rim (*arrows* in B). Note the bright appearance of the scolex on the sagittal images (*arrowheads* in C, D) and the subtle area of T2 shortening at the base of the cyst within the frontal lobe (*arrowhead* in E).

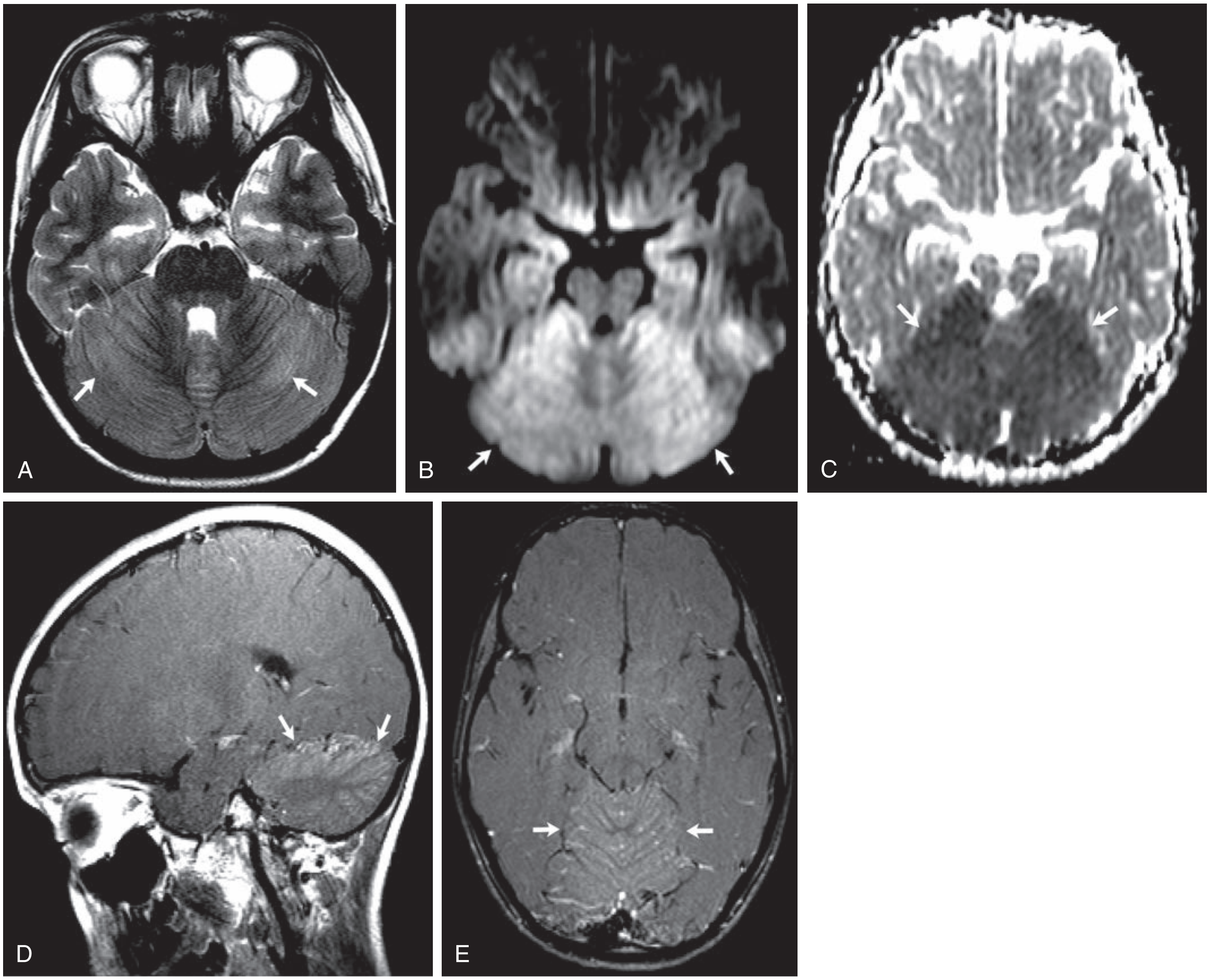

**e-Figure 34.21. Cerebellitis.** Ten-year-old female with headache, fever, and dysmetria. (A) Axial T2-weighted, (B) axial diffusion-weighted image (DWI), and (C) apparent diffusion coefficient (ADC) map, and (D) sagittal and (E) axial contrast-enhanced magnetization transfer T1-weighted MR images were obtained. Note the subtle T2 prolongation within the cerebellum (*arrows* in A). There is corresponding restricted diffusion on the DWI and ADC (*arrows* in B, C). There is gyriform type enhancement within the cerebellar hemisphere (*arrows* in D), and within the cerebellar vermis (*arrows* in E).

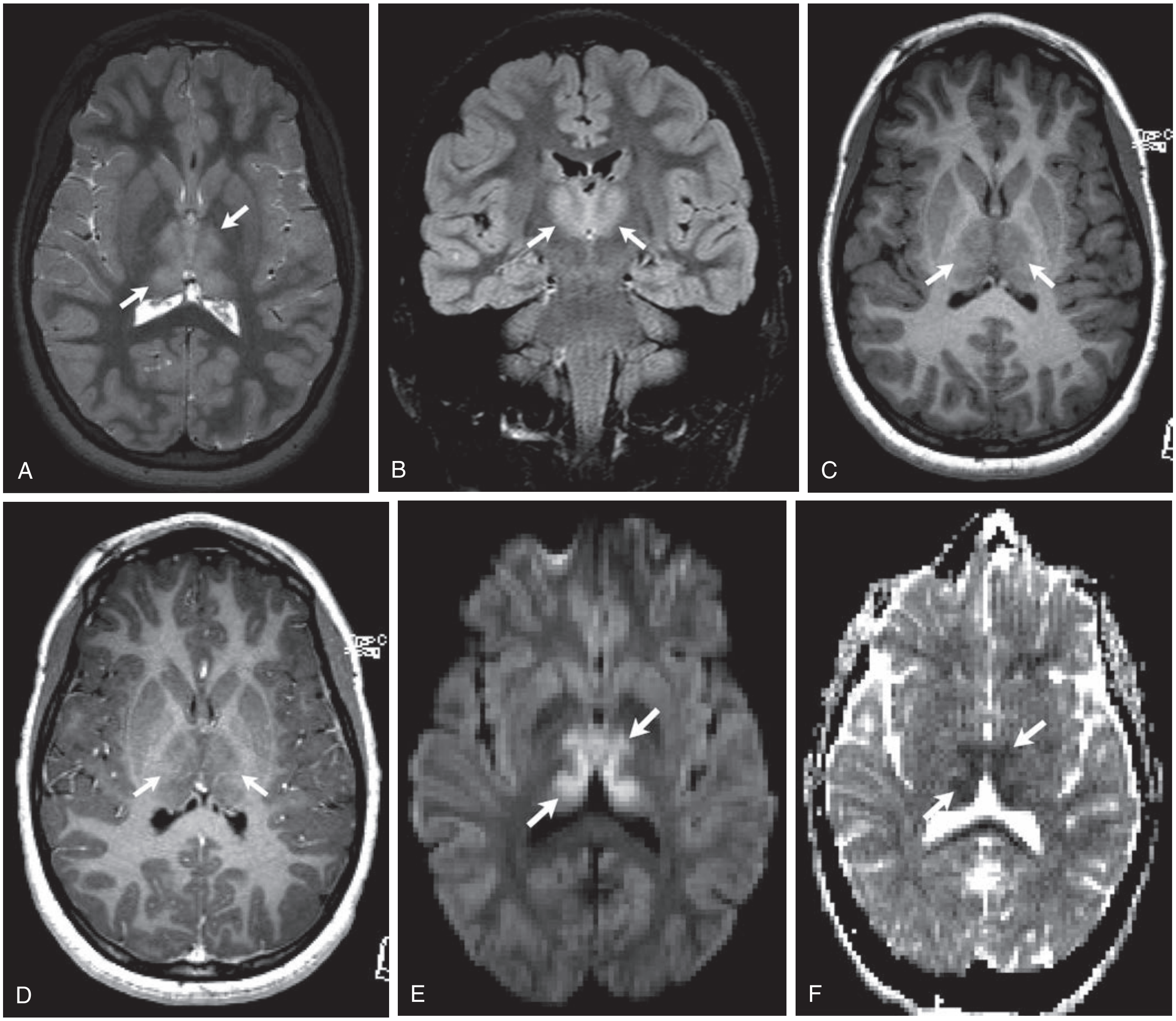

**e-Figure 34.22. Thalamic viral encephalitis.** Nine-year-old boy with new onset of seizures and fever, as well as disorientation, with concern for encephalitis. (A) Axial T2-weighted, (B) coronal fluid-attenuated inversion–recovery, (C) axial pre- and (D) contrast-enhanced reconstructed T1-weighted 3D SPGR images, and axial (E) diffusion-weighted image and (F) apparent diffusion coefficient map were obtained on a 3T system. Note the T2 prolongation within the thalami bilaterally (*arrows* in A, B), with corresponding T1 prolongation in similar areas (C, D). There is diffusion restriction within the thalami bilaterally (*arrows* in E, F).

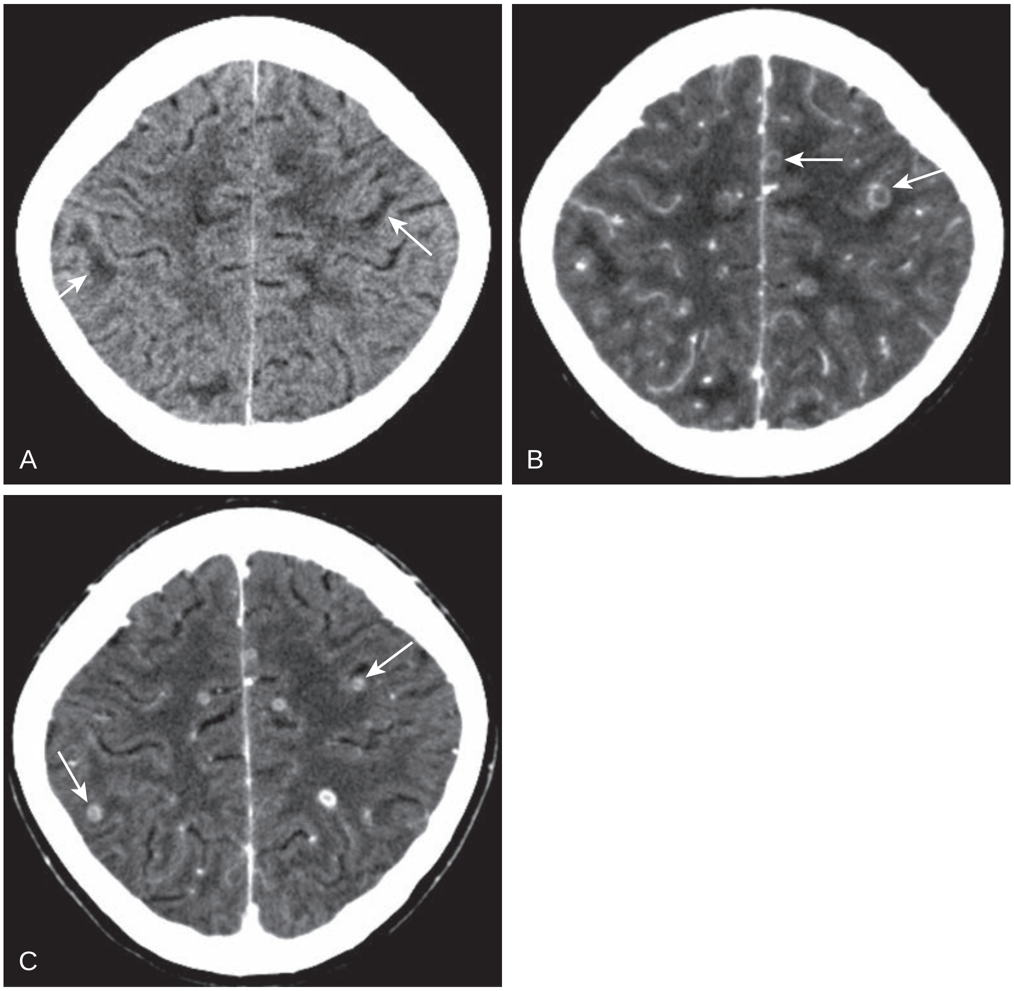

**Figure 34.17. Tuberculosis and microabscesses.** Thirteen-year-old female with headaches, vomiting, and vertigo. Patient also has a positive PPD and abnormal chest x-ray. (A) Axial noncontrast CT and (B) contrast-enhanced CT of the head, and (C) contrast-enhanced CT image 1 month later. Note the areas of low attenuation at the gray-white matter junction at the time of presentation (*arrows* in A). There are multiple ring enhancing lesions noted bilaterally within the gray-white matter junction (*arrows* in B, C), corresponding to multiple microabscesses, secondary to TB.

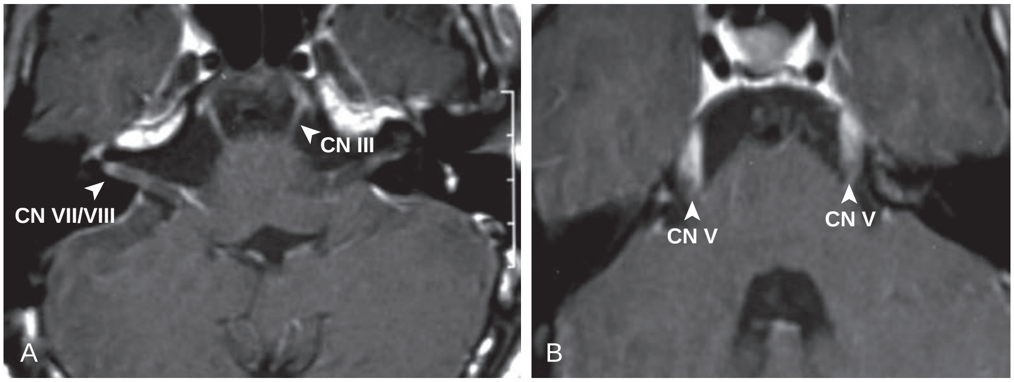

**Figure 34.18. Lyme disease.** Fifteen-year-old male with multiple cranial nerve neuropathies and suspected tuberculosis exposure. (A and B) Axial contrast-enhanced T1-weighted MR images were obtained through the region of the posterior fossa. Note the symmetric abnormal contrast enhancement along the cranial nerves *(CN)* as labeled by their respective numbers adjacent to the *arrowheads*.

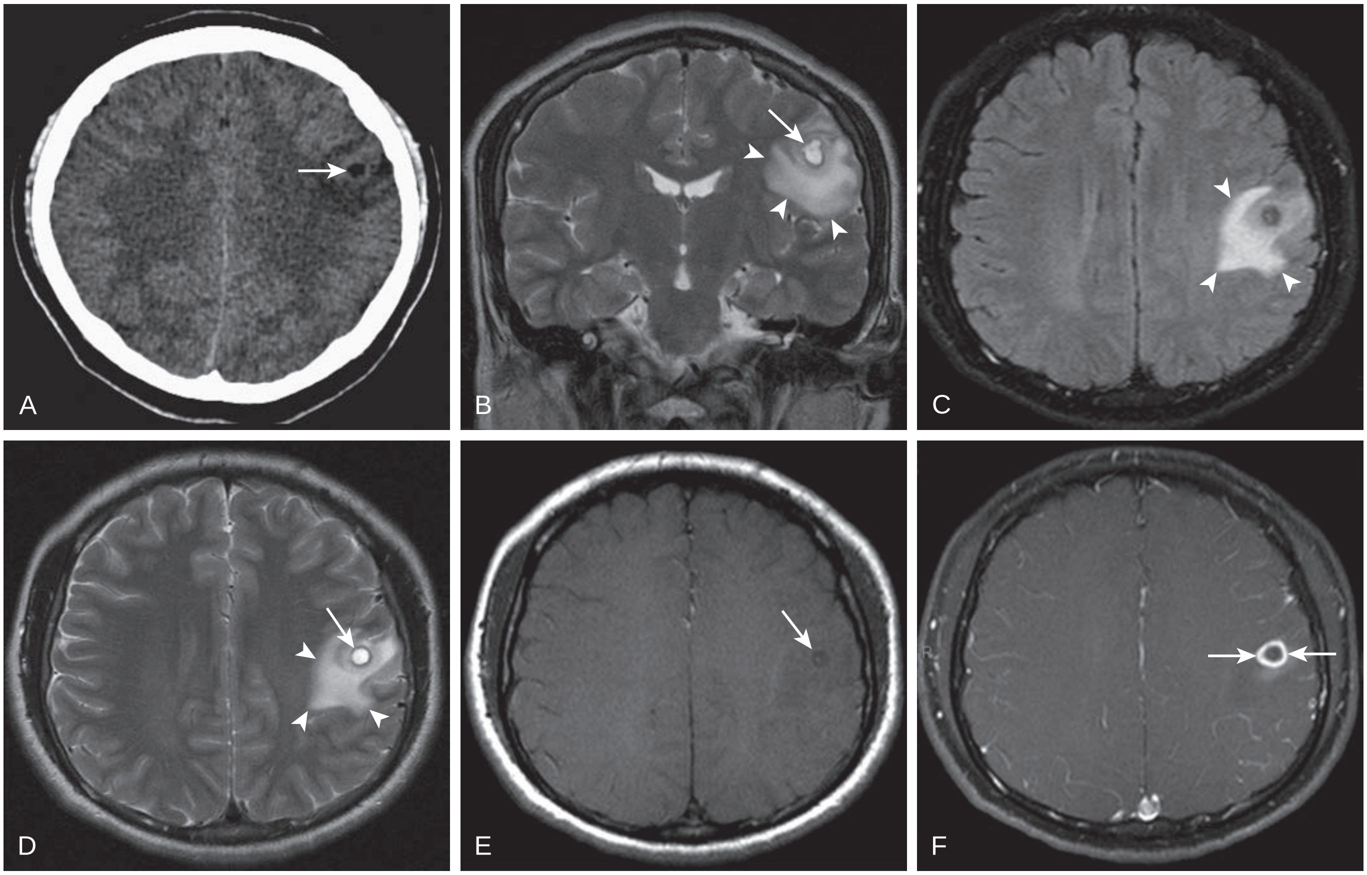

**Figure 34.19. Cysticercosis.** History of ingestion of uncooked pork. (A) Axial noncontrast CT of the head, (B) coronal T2-weighted MR image, (C) axial fluid-attenuated inversion–recovery and (D) T2-weighted sequences, and (E) axial pre- and (F) contrast-enhanced T1-weighted MR images. Note the area of decreased attenuation on CT (*arrow* in A). There is corresponding cystlike T2 prolongation within the center of this region (*arrows* in B, D). This is surrounding vasogenic edema (*arrowheads* in B–D). In addition, there is a subtle area of T1 shortening within the center of the lesion (*arrow* in E) corresponding to the scolex. Note the thick reactive rim enhancement around the area of the parasite (*arrows* in F).

etiology over another. Viral-like syndromes with autoimmune associations, such as acute disseminated encephalomyelitis (ADEM) and posttransplantation lymphoproliferative disorders (PTLD) (e-Fig. 34.23), often demonstrate imaging characteristics similar to viral infections.

## Herpes Simplex Virus 1

Herpes simplex virus 1 (HSV-1), as opposed to the perinatally acquired HSV-2 (see later), is a spontaneous infection most often caused by reactivation of an orofacial HSV infection, which occurs in all ages but has a pediatric predominance. Early symptoms of fever and malaise can progress to seizures and hemiparesis. Restricted diffusion on MRI is the earliest radiologic manifestation with unilateral or bilateral medial temporal lobe hyperintense signal on T2-weighted and FLAIR sequences, with more heterogeneous diffusion appearing several days later. CT findings of low attenuation within the temporal lobe and insular cortex do not manifest until several days after the onset of symptoms. Leptomeningeal and cortical enhancement, as well as foci of calcification and hemorrhage, may also be present.

## Human Immunodeficiency Virus

In the United States, greater than 90% of children with human immunodeficiency virus (HIV) are infected as a result of maternal transmission to the fetus. Radiologic CNS manifestations of congenital HIV include atrophy with resultant ventricular and subarachnoid space prominence, as well as basal ganglia and subcortical calcifications. The calcifications are best seen on CT (Fig. 34.24). Superinfection and neoplasm, which are not uncommon in the adult HIV population, are seldom seen in children. In children, progressive multifocal leukoencephalitis (PML) caused by the Jakob-Creutzfeldt polyomavirus, is radiologically identical to its presentation in adults. PML demonstrates white matter hypoattenuation on CT, as well as hyperintense signal on T2-weighted and FLAIR MRI sequences. These lesions characteristically lack mass effect and do not enhance after contrast administration. HIV infection can also lead to vasculitis (Fig. 34.25).

## Acute Disseminated Encephalomyelitis

ADEM is a monophasic focal or multifocal, perivascular inflammatory and demyelinating disorder often affecting both the brain and spinal cord after a vaccination or viral infection. Lesions are generally hyperintense on T2-weighted sequences and have corresponding hypointensity or isointensity on T1-weighted sequences. MRI characteristics of ADEM (Fig. 34.26) are variable, with enhancement patterns including solid or ringlike enhancement, to no enhancement at all, in lesions that range from small to large, and that affect gray matter, white matter, or both. A clinical history

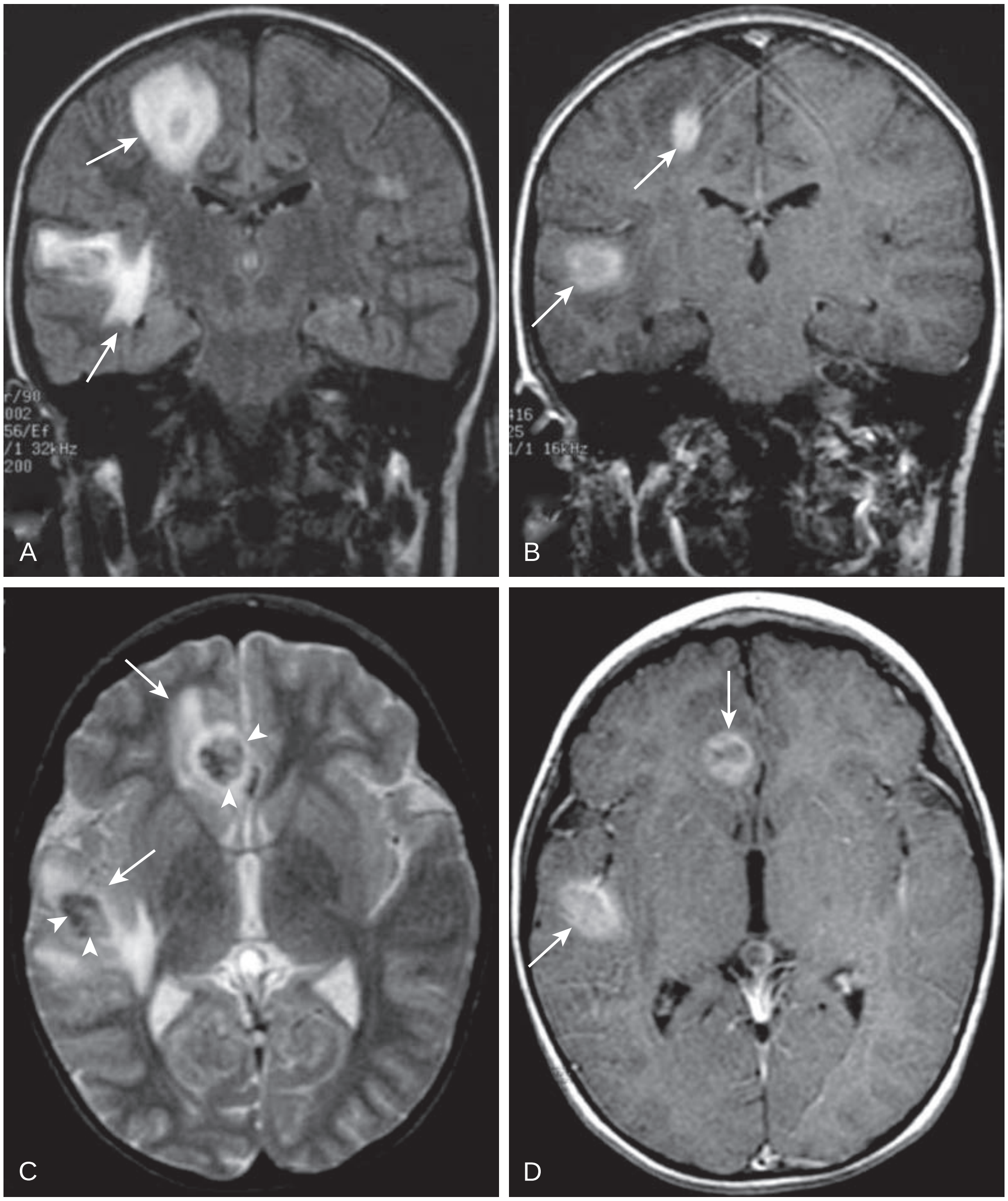

**e-Figure 34.23. Posttransplant lymphoproliferative disease (PTLD).** Seven-year-old male, status post heart transplant for underlying complex congenital heart disease, now with headache and visual changes. (A) Coronal fluid-attenuated inversion–recovery, (B) coronal postcontrast T1-weighted, (C) axial T2-weighted, and (D) axial postcontrast T1-weighted MR images were obtained. Note the multiple areas of T2 prolongation within the right cerebral hemisphere (*arrows* in A and C). There is central T2 shortening, suggesting an element of hemorrhage (*arrowheads* in C). There is avid contrast enhancement evidenced on the postcontrast images (*arrows* in B and D).

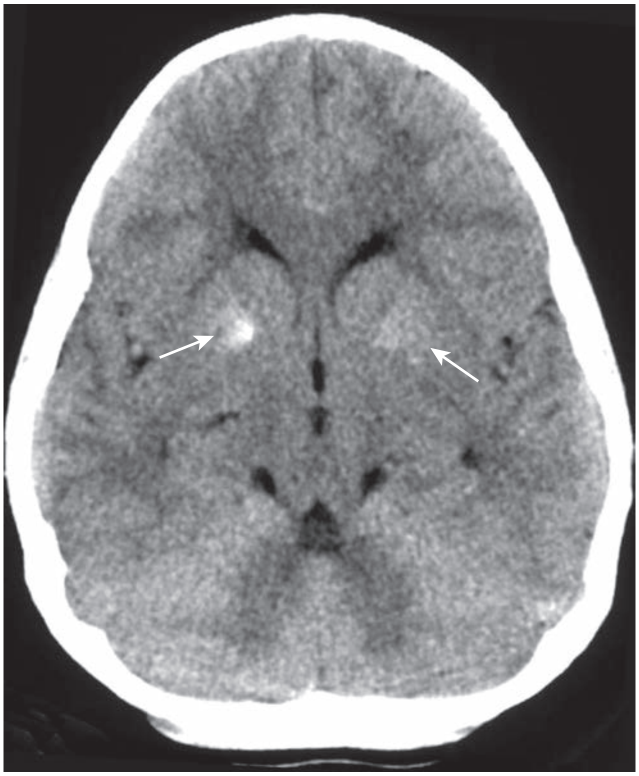

**Figure 34.24. Human immunodeficiency virus (HIV).** Nine-year-old male with known HIV infection. Noncontrast CT of the head at the level of the basal ganglia demonstrates calcific areas within the basal ganglia bilaterally *(arrows),* right greater than left, commonly seen in patients with HIV.

of a recent viral illness or vaccination is the key to properly diagnosing these lesions.

## Subacute Sclerosing Panencephalitis

Subacute sclerosing panencephalitis is believed to represent a response to reactivation of the measles virus years after an infection. MRI reveals cortical and basal ganglia predominant hyperintense signal on T2-weighted and FLAIR sequences.

## Rasmussen's Encephalitis

Rasmussen's encephalitis is one of the leading causes of intractable epilepsy in children, presenting between 1 and 15 years of age, and is characterized by seizures, progressive hemiplegia, and progressive psychomotor deterioration. It is characteristically localized to one hemisphere. Initial imaging studies are normal, with MRI later demonstrating hemispheric atrophy (Fig. 34.27) and hyperintense signal on T2-weighted and FLAIR sequences in the frontal and temporal lobes, predominantly within the white matter as well as the basal ganglia.

## Congenital Infections

Transplacental, and less often, transvaginal transfer of infection to the fetus is often the result of TORCH (Toxoplasmosis, Other, Rubella, Cytomegalovirus, Herpes) infection (e-Fig. 34.28). Insults occurring during the first two trimesters most often manifest as severe congenital malformations. Those occurring during the third trimester often result in destructive lesions.

## Cytomegalovirus

Cytomegalovirus (CMV) is the most common serious viral infection to affect newborns in the United States, occurring in nearly 1% of all live births. Up to 25% of infected infants develop neurologic or developmental abnormalities in the first year of life, which include microcephaly, hearing impairment, chorioretinitis, and seizures. Neonatal US in affected patients often demonstrates nonspecific mineralizing vasculopathy of the basal ganglia (Fig. 34.29). MRI and CT demonstrate the sequelae of infection in the third trimester as periventricular calcification and/or hemorrhage, ventricular and sulcal prominence, as well as periventricular and subcortical white matter changes. Intrauterine infection with this virus is associated with polymicrogyria, especially in the region of the Sylvian fissures (Figs. 34.30 and 34.31).

## Toxoplasmosis

Symptomatic congenital toxoplasmosis infection is far less common than CMV. The parasite *Toxoplasma gondii* is believed to be transmitted to the pregnant mother by ingestion of uncooked oocysts in infected birds and/or mammals. Principle clinical findings include hydrocephalus, abnormal CSF, bilateral chorioretinitis, and intracranial calcifications. Fetal infection before 20 weeks' gestation leads to severe neurologic deficits; infection between 20 and 30 weeks leads to a more variable outcome. Beyond 30 weeks, CT manifestations often include intracerebral and periventricular calcifications, which are nearly identical to the distribution in CMV-affected children and is rarely accompanied by ventricular dilatation. Cortical malformations, which are fairly typical with CMV infection, are most often absent in cases of toxoplasmosis.

## Herpes Simplex Virus 2

Most cases of neonatal HSV-2 are contracted transvaginally as the child passes through the birth canal. Neonatal CNS HSV infection is believed to occur in approximately 1 in 10,000 births. CNS manifestations generally present between 2 to 4 weeks of life and include meningoencephalitis with seizures, lethargy, and fever. Sequelae include mental retardation, severe neurologic deficits, or even death, secondary to virulent destruction of the brain. The disease may progress to produce ischemic infarction of parts of or all of the brain, necrosis, atrophy, encephalomalacia, demyelination, and gliosis. Watershed distribution ischemia is also fairly common in areas remote from the primary herpetic lesions. Hypointense signal on ADC images, which may be multifocal or limited to the temporal lobes, brainstem, or cerebellum, is the first MRI sign of HSV brain destruction (Fig. 34.32). CT changes in early disease are either normal or demonstrate mild abnormalities. Later, patchy white matter low attenuation on CT and corresponding hyperintense T2-weighted MRI signal with rapid progression is demonstrated. Meningeal enhancement reflects the extent of the disease. Also of note is classic persisting hyperattenuation of cortical gray matter on CT (Fig. 34.33) and corresponding T1 and T2 shortening on MRI. Eventually, diffuse cerebral and cerebellar (in about 50% of cases) atrophy and encephalomalacia ensue. It should be noted that HSV-1 encephalitis, which affects older children and adults (Fig. 34.34), is different from neonatal HSV infection (see previous section).

## Zika Virus

Zika virus infection or exposure in pregnancy has recently been described in association with increased risk of microcephaly and intracranial calcifications in affected fetuses. The center of the epidemic is in Brazil, where the majority of the cases have been

*Text continued on p.344*

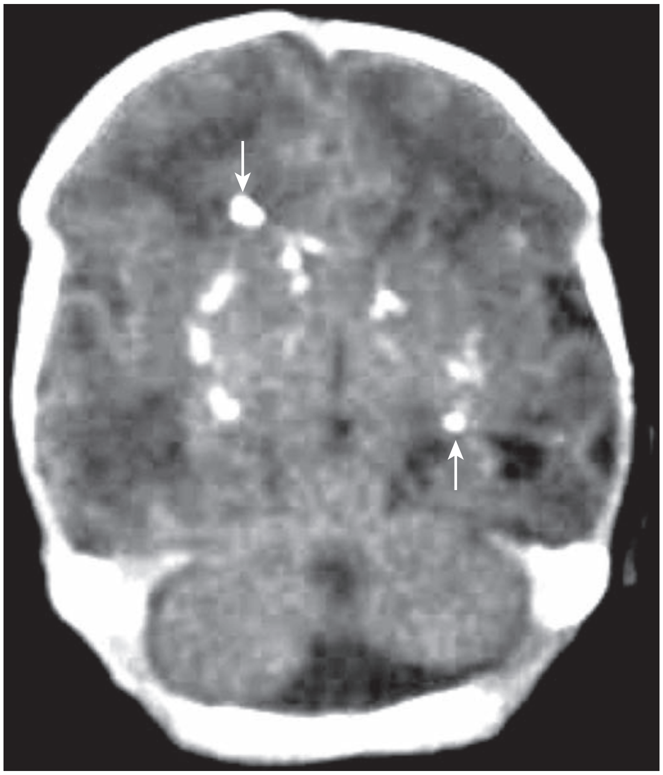

**e-Figure 34.28. Toxoplasmosis, other, rubella, cytomegalovirus, herpes (TORCH) infection.** Newborn female with seizures and questionable intracranial hemorrhage. Noncontrast CT of the head demonstrates multiple scattered punctate calcifications *(arrows)* seen bilaterally, slightly greater on the right than on the left, in a more random fashion than is expected with cytomegalovirus infection. This likely represents calcification from another TORCH-type infection, such as toxoplasmosis.

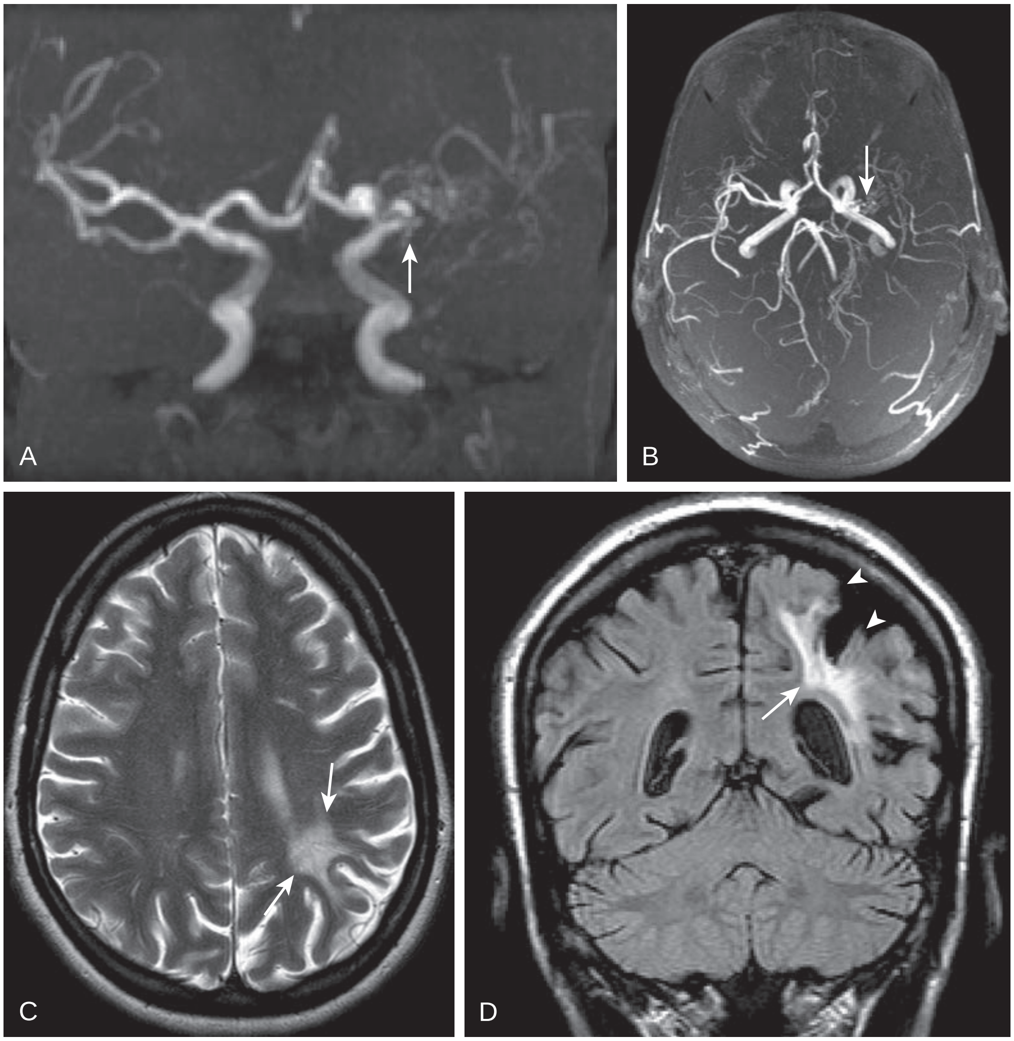

**Figure 34.25. Human immunodeficiency virus (HIV) vasculitis.** Eighteen-year-old female with HIV and right hemiplegia. Coronal and collapsed CC view of the intracranial circulation from a 3D time of flight (TOF) MRA (A and B, respectively), axial T2-weighted (C), and coronal fluid-attenuated inversion–recovery (D) MR images. Note the marked narrowing of the left MCA on the TOF MRA (*arrows* in A and B). There is corresponding T2 prolongation within the left parietal subcortical white matter (*arrows* in C and D), corresponding to gliosis. There is associated overlying cortical volume loss (*arrowheads* in D).

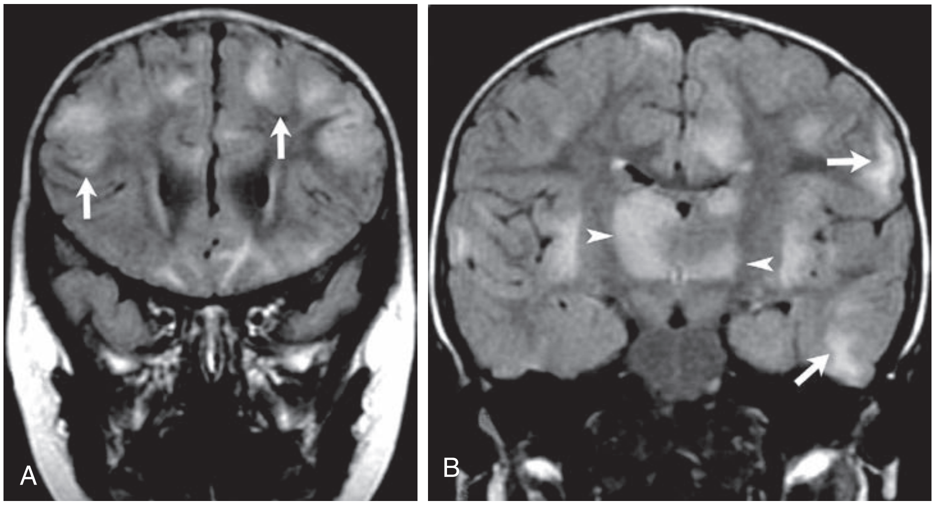

**Figure 34.26. Acute disseminated encephalomyelopathy (ADEM).** Twenty-two-month-old male with lethargy, hypotonia, ataxia, and decreased righting reflexes preceded by an antecedent upper respiratory illness. Sequential coronal fluid-attenuated inversion–recovery images from anterior to posterior (A–C), (D) axial T2-weighted, and (E) axial postcontrast T1-weighted MR images. There are patchy areas of bilateral subcortical white matter T2 prolongation (*arrows* in A–D), as well as abnormal T2 prolongation within the central gray structures (*arrowheads* in B and D). There is no significant contrast enhancement noted; however, the central gray structures appear to standout in relief on the postcontrast images (*arrows* in E) likely secondary to abnormal T1 prolongation.

*Continued*

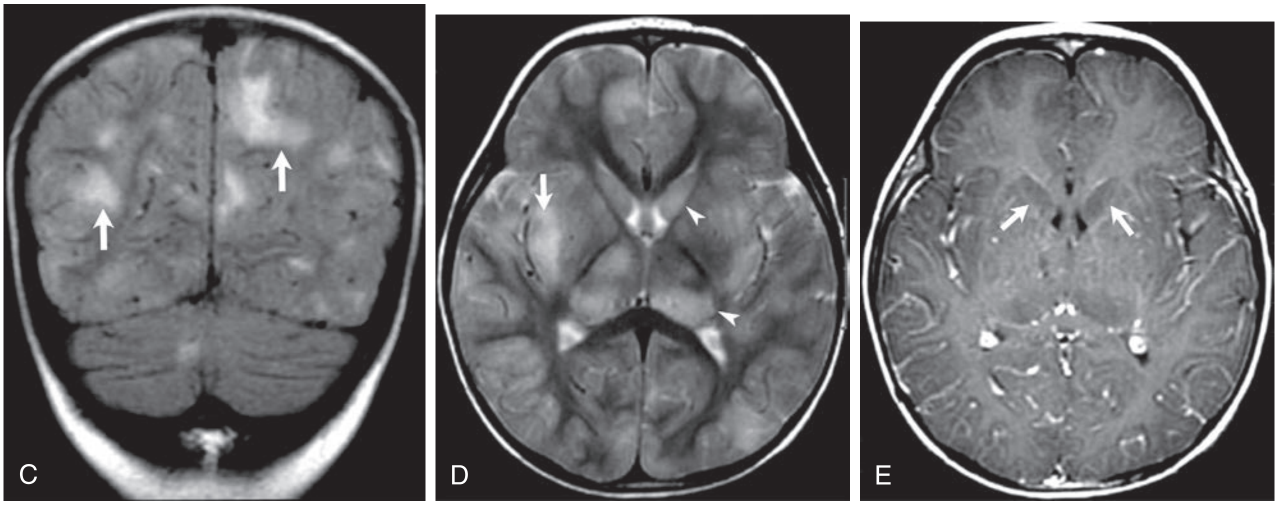

**Figure 34.26, cont'd.**

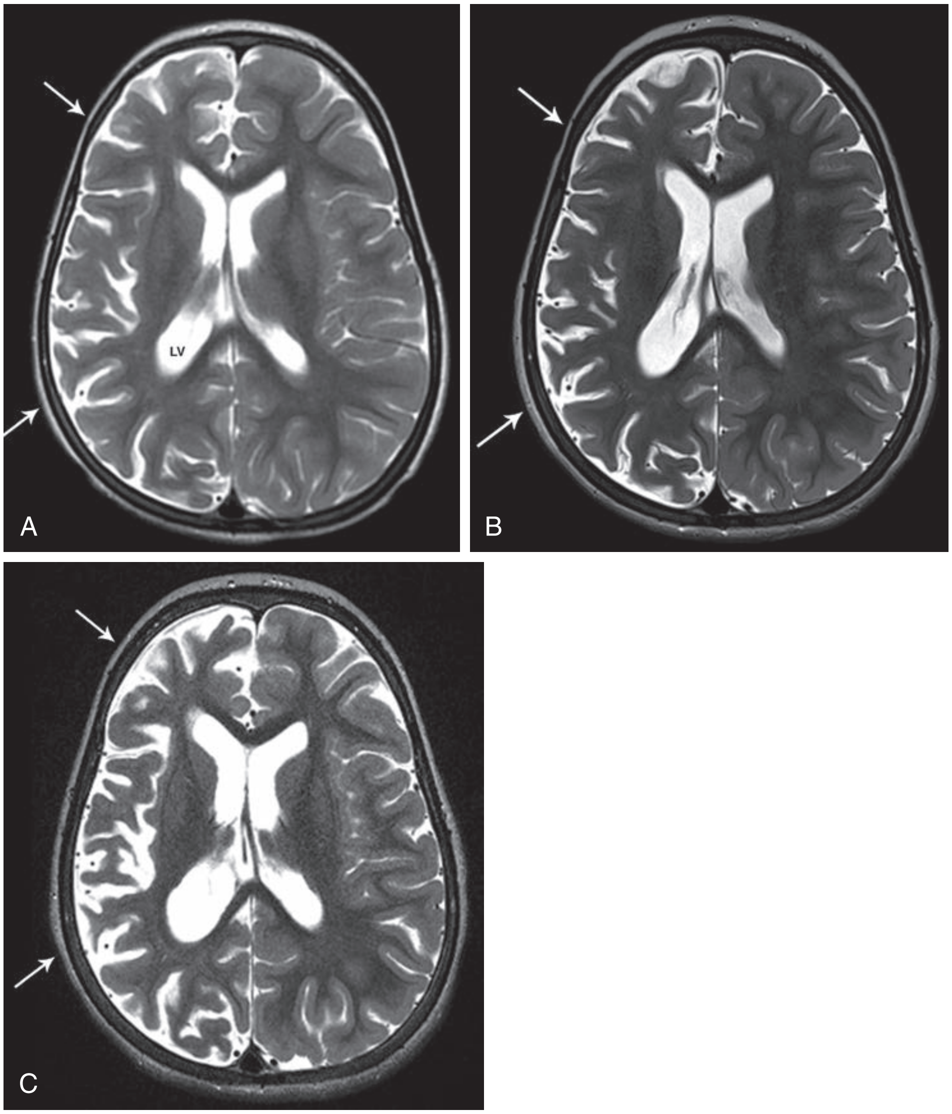

**Figure 34.27. Rasmussen's encephalitis.** Three-year-old female with recent explosive onset of simple partial seizures left hemiparesis and epilepsia partialis continua on EEG. (A) Axial T2-weighted MR images obtained at presentation, (B) at 4 months, and (C) 6 months from original MRI. There is diffuse right hemispheric volume loss *(arrows)* with associated *ex vacuo* prominence of the right lateral ventricle *(LV)*. Note the mild progression on the 4- and 6-month follow-up studies.

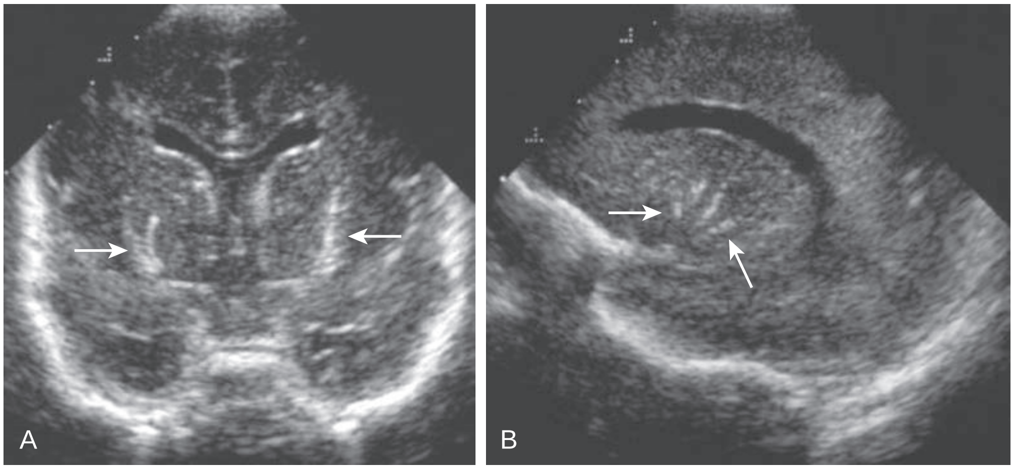

**Figure 34.29. Mineralizing vasculopathy.** Three-week-old, former preterm infant with positive cytomegalovirus titers. (A) Coronal and (B) sagittal US images through the anterior fontanelle were obtained. Note the linear branching areas of increased echogenicity seen within the distribution of the perforating vessels *(arrows)*.

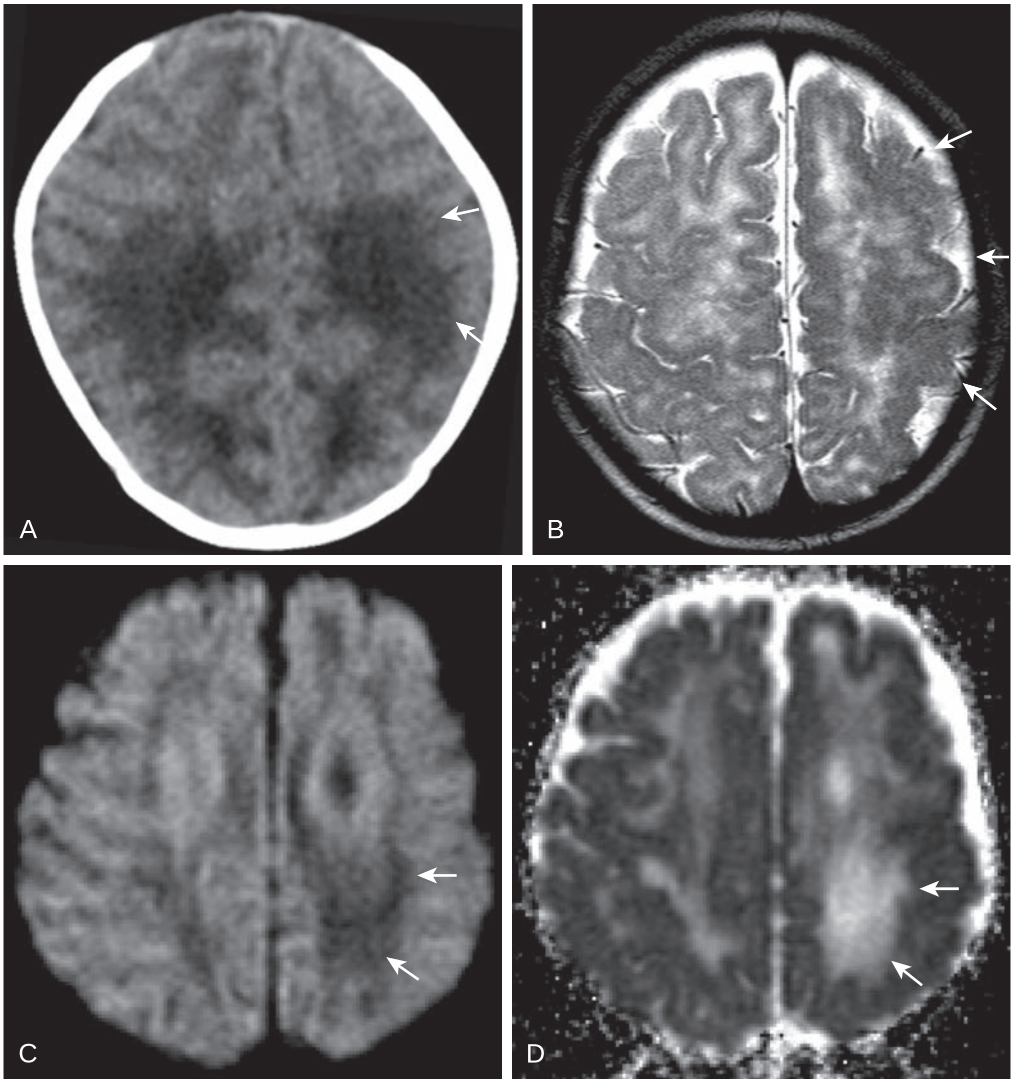

**Figure 34.30. Cytomegalovirus (CMV).** Patient with congenital CMV, pale left optic nerve, and failed hearing test. (A) Axial noncontrast CT of the head, (B) axial T2-weighted MR image, and (C) axial diffusion-weighted imaging and (D) apparent diffusion coefficient map. Note the abnormal low attenuation within the white matter (*arrows* in A). Note the abnormal sulcal pattern of the left hemisphere in (B) in keeping with associated polymicrogyria (*arrows* in A). Note that there is, in fact, increased diffusion within the corresponding white matter, left greater than right (*arrows* in C and D).

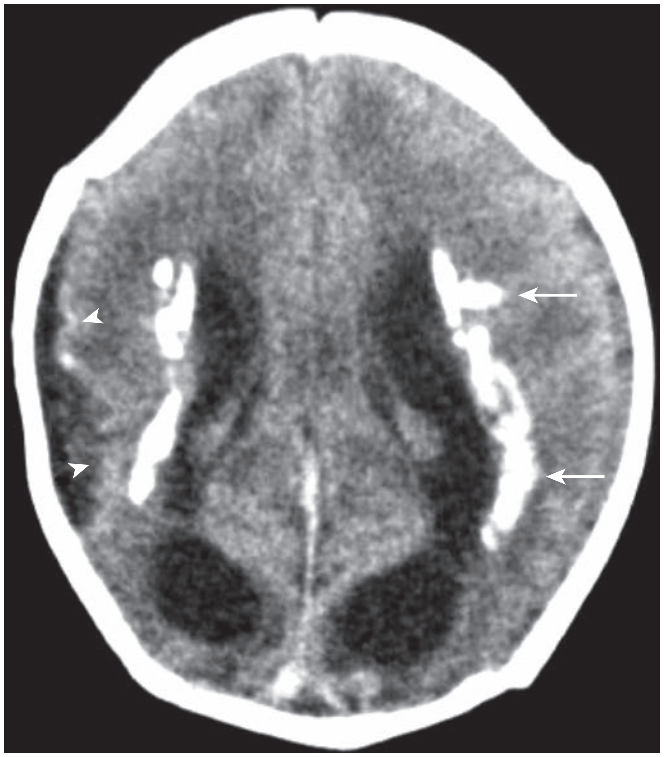

**Figure 34.31. Cytomegalovirus (CMV).** One-day-old with congenital CMV infection. Noncontrast CT of the head demonstrates multiple areas of confluent calcifications within the periventricular regions bilaterally (*arrows),* typical of the expected distribution of calcification secondary to CMV. Note the abnormal sulcal pattern of the right hemisphere, indicating associated polymicrogyria *(arrowheads)*.

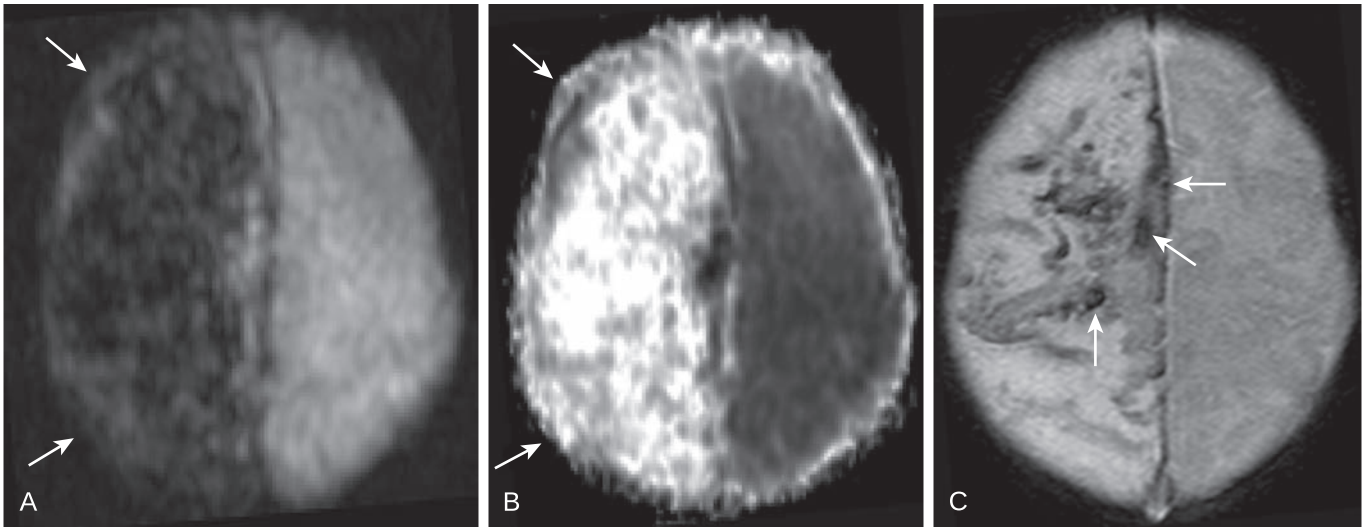

**Figure 34.32. Herpes simplex virus cerebritis/encephalitis (hemorrhagic type).** One-month-old female with several-day history of seizures and positive cerebrospinal fluid herpes simplex virus culture. (A) Diffusion-weighted image and (B) apparent diffusion coefficient map, (C) axial gradient echo, (D) sagittal T1-weighted, (E) axial fluid-attenuated inversion–recovery, and (F) axial fat-saturated postcontrast T1-weighted MR images. Note the increased diffusion throughout the right cerebral hemisphere (*arrows* in A and B). There is corresponding T2* effect within the superior right cerebral hemisphere corresponding to hemorrhage (*arrows* in C). There is corresponding T1 shortening near the midline midline (*arrows* in D) corresponding to mineralization. Note the mass effect due to edema of the right cerebral hemisphere (*arrows* in E), and the paucity of abnormal contrast enhancement (F).

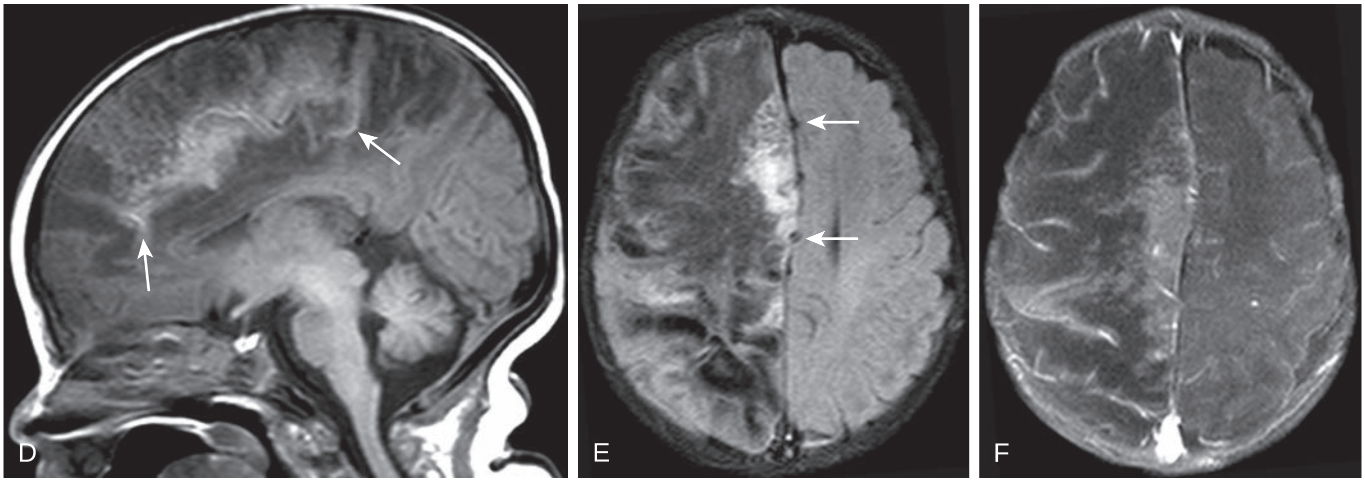

**Figure 34.32, cont'd.**

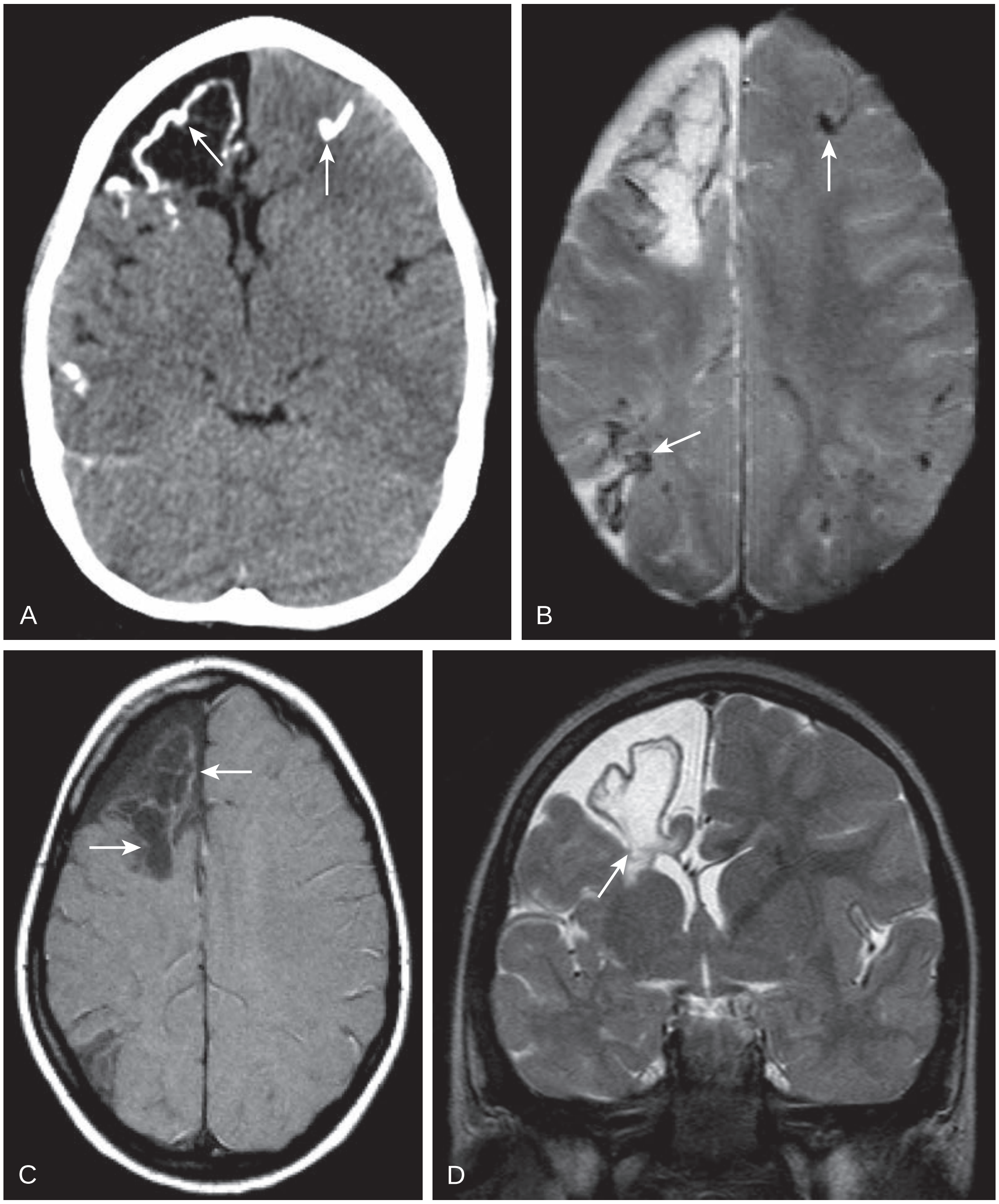

**Figure 34.33. Chronic changes of herpes simplex virus (HSV).** Five-year-old female with fulminant hepatic failure, renal failure, and lethargy with a prior history of HSV encephalitis. (A) Axial noncontrast CT of the head, (B) axial gradient echo, (C) axial magnetization transfer T1-weighted, and (D) coronal T2-weighted MR images. Note the calcification seen within both hemispheres (*arrows* in A), with corresponding areas of T2* effect within both cerebral hemispheres (*arrows* in B), in keeping with mineralization. There is slight T1 shortening effect (*arrows* in C), corresponding to mineralization. There is volume loss within the frontal lobe and associated T2 prolongation (*arrows* in D).

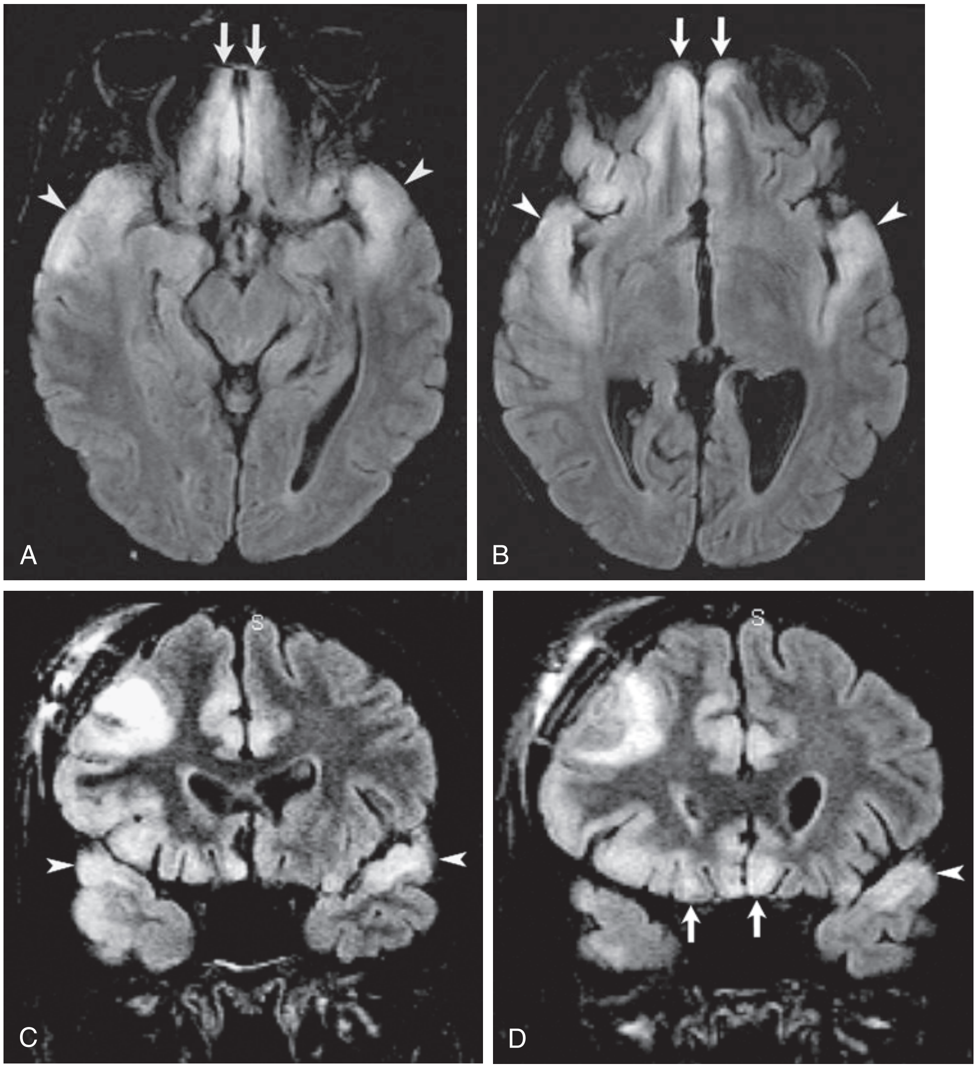

**Figure 34.34. Herpes simplex virus (HSV).** Patient with seizures and decreased level of consciousness. Axial fluid-attenuated inversion–recovery (FLAIR) (A and B) and coronal FLAIR (C and D) MR images were obtained. There is abnormal signal intensity within both frontal lobes *(arrows)* and temporal lobes *(arrowheads)* indicative of HSV encephalitis. The bilateral temporal lobe involvement is a clue to the underlying causative agent.

reported. The World Health Organization declared Zika virus to be a global health emergency in February 2016. Imaging findings reported in association with Zika virus include ventriculomegaly, cortical abnormalities (simplified gyral pattern, polymicrogyria, pachygyria), corpus callosum abnormalities, cerebellar abnormalities, and brainstem hypoplasia/atrophy (Fig. 34.35). Zika virus can be confirmed by molecular and serologic testing.

## Congenital Rubella, Varicella, and Syphilis

Congenital rubella is rare in western countries and now has an incidence in the United States of about 1 in 1,000,000 births. Congenital varicella is also rare, as even when the pregnant mother is affected with varicella zoster, the fetus is most often unaffected. Congenital syphilis is unlikely to cause neurologic symptoms in the neonatal period.

### KEY POINTS

- In bacterial CNS infections, imaging plays a role in differentiating cerebritis from abscess.
- Tuberculous meningitis often involves the basilar cisterns and can result in cranial nerve palsies, infarctions, and hydrocephalus.
- Restricted diffusion on MRI is the earliest imaging sign of viral brain infections.
- HSV-1 usually occurs in older children and is related to reactivation of orofacial infections, whereas HSV-2 infections are acquired perinatally and affect infants.
- Cytomegalovirus is the most common serious viral infection of newborns.

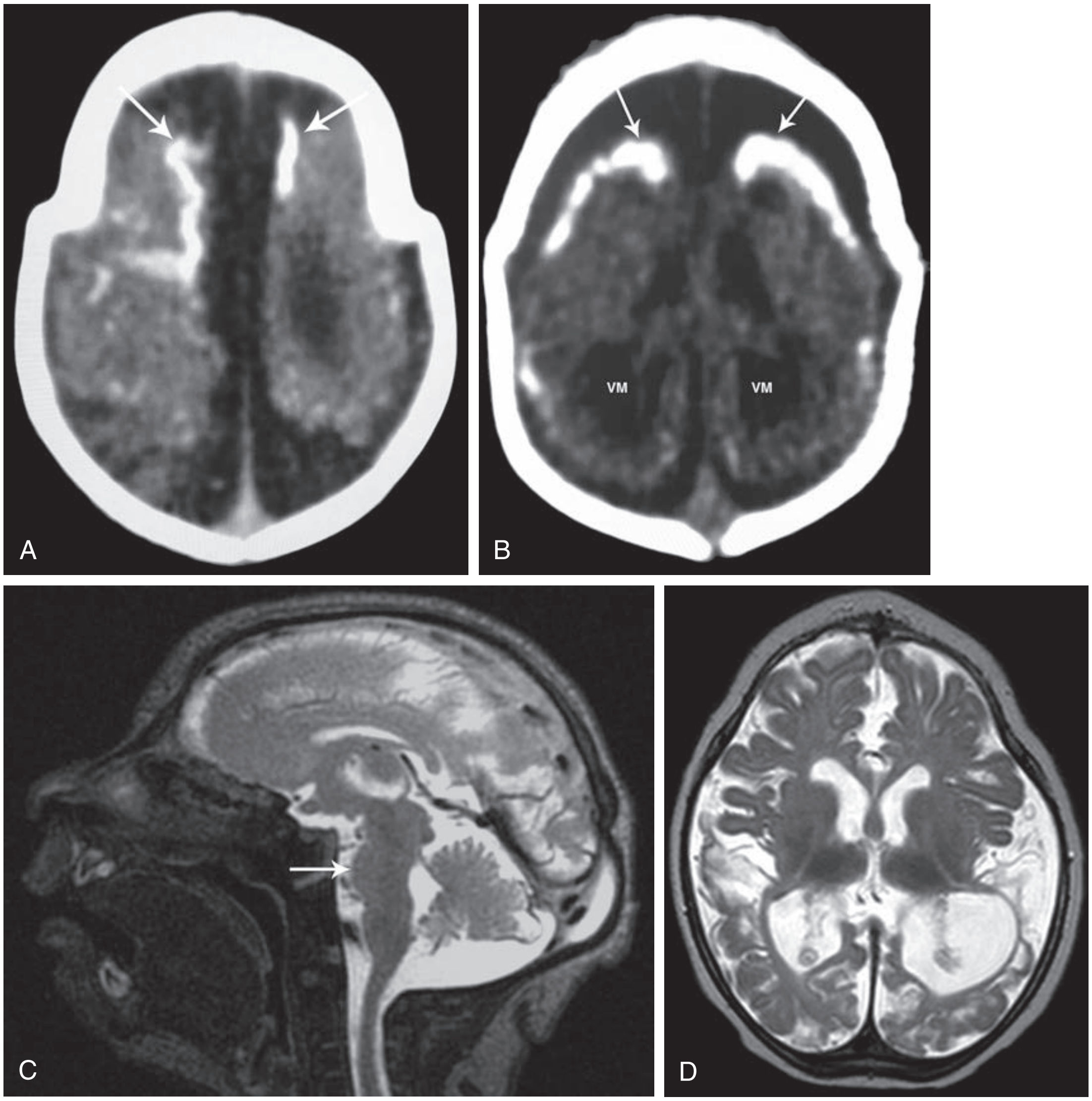

**Figure 34.35. Zika virus.** Neonate with known Zika virus exposure in utero. (A and B) Axial noncontrast CT, (C) sagittal T2-weighted, and (D) axial T2-weighted MR images show predominantly cortical-based calcifications (*arrows* in A and B). There is marked microcephaly and mild brainstem hypoplasia particularly at the level of the pons (*arrow* in C). There is bilateral ventriculomegaly *(VM)* and mild simplification of gyral pattern. *(Images provided by Henrique M. Lederman, MD, PhD, and Sergio Cavalheiro, MD, PhD, Sao Paulo, Brazil.)*

## SUGGESTED READINGS

Bien CG, Widman G, Urbach H, et al. The natural history of Rasmussen's encephalitis. *Brain*. 2002;125:1751–1759.

Bonfield CM, Sharma J, Dobson S. Pediatric intracranial abscesses. *J Infect*. 2015;71(suppl 1):S42–S46.

Murthy SN, Faden HS, Cohen ME, Bakshi R. Acute disseminated encephalomyelitis in children. *Pediatrics*. 2002;110:E21.

Nickerson JP, Richner B, Santy K, et al. Neuroimaging of pediatric intracranial infection–part 1: techniques and bacterial infections. *J Neuroimaging*. 2012;22(2):e42–e51.

Nickerson JP, Richner B, Santy K, et al. Neuroimaging of pediatric intracranial infection–part 2: TORCH, viral, fungal, and parasitic infections. *J Neuroimaging*. 2012;22(2):e52–e63.

Parmar H, Ibrahim M. Pediatric intracranial infections. *Neuroimaging Clin N Am*. 2012;22(4):707–725.

Rossi A, Martinetti C, Morana G, Severino M, Tortora D. Neuroimaging of infectious and inflammatory diseases of the pediatric cerebellum and brainstem. *Neuroimaging Clin N Am*. 2016;26(3):471–487.

## REFERENCES

Full references for this chapter can be found on www.expertconsult.com.

## REFERENCES

1. Agarwal R, Sze G. Neuro-lyme disease: MR imaging findings. *Radiology*. 2009;253(1):167–173.
2. Barkovich AJ, Raybaud C. *Pediatric Neuroimaging*. 5th ed. Philadelphia: Lippincott Williams and Wilkins; 2011.
3. Byrd S, Locke G, Biggers S, Percy A. The CT appearance of cerebral cysticercosis in adults and children. *Radiology*. 1982;144:819–823.
4. Chiapparini L, Granata T, Farina L, et al. *Diagnostic imaging in 13 cases of Rasmussen's encephalitis: can early MRI suggest the diagnosis?*
5. De Fatima Vasco Aragao M, van der Linden V, Brainer-Lima AM, et al. Clinical features and neuroimaging (CT and MRI) findings in presumed Zika virus related congenital infection and microcephaly: retrospective case series study. *BMJ*. 2016;353:i1901.
6. Diebler C, Dusser A, Dulac O. Congenital toxoplasmosis: clinical and neuroradiological evaluation of the cerebral lesions. *Neuroradiology*. 1985;27:125–130.
7. Fink KR, Thapa MM, Ishak GE, Pruthi S. Neuroimaging of pediatric central nervous system cytomegalovirus infection. *Radiographics*. 2010;30:1779–1796.
8. Gasparetto EL, Cabral RF, da Cruz LC Jr, Dominues RC. Diffusion imaging in brain infections. *Neuroimaging Clin N Am*. 2011;21(1):89–113, viii.
9. Gilden DH. Brain imaging abnormalities in CNS virus infections. *Neurology*. 2008;70:84.
10. Gupta RK, Vatsal DK, Husain N, et al. Differentiation of tuberculous from pyogenic brain abscesses with in vivo proton MR spectroscopy and magnetization transfer MR imaging. *AJNR Am J Neuroradiol*. 2001;22:1503–1509.
11. Jaremko JL, Moon AS, Kumbla S. Patterns of complications of neonatal and infant meningitis on MRI by organism: a 10 year review. *Eur J of Radiology*. 2011;80:821–827.
12. Kastrup O, Wenke I, Maschke M. Neuroimaging of infection. *NeuroRx*. 2005;2(2):324–332.
13. Kim TK, Chang KH, Kim CJ, et al. Intracranial tuberculoma: comparison of MR with pathologic findings. *AJNR Am J Neuroradiol*. 1995;16:1903–1908.
14. Kopelovich JC, Germiller JA, Laury AM, et al. Early *Prediction of Postmeningitic Hearing Loss in Children Using Magnetic Resonance Imaging*. *Arch Otolaryngol Head Neck Surg*. 2011;137(5):441–447.
15. Nickerson JP, Richner B, Santy K, et al. Neuroimaging of pediatric intracranial infection-part 1: techniques and bacterial infections. *J Neuroimaging*. 2012;22(2):e42–e51.
16. Nickerson JP, Richner B, Santy K, et al. Neuroimaging of pediatric intracranial infection—part2: TORCH, viral, fungal, and parasitic infections. *J Neuroimaging*. 2012;22(2):e52–e63.
17. Noorbehesht B, Enzmann DR, Sullinder W, Bradley JS, Arvin AM. Neonatal herpes simplex encephalitis: correlation of clinical and CT findings. *Radiology*. 1987;162:813–819.
18. Parayni S, Arvin A. Intrauterine infection with varicella-zoster virus after maternal varicella. *N Engl J Med*. 1986;314:1542–1546.
19. Preblud SE, Alford CA. Rubella. In: Remington JS, Kleain JO, eds. *Infectious Diseases of the Fetus and Neonate*. Philadelphia: Saunders; 1990:155–164.
20. Santy K, Nan P, Chantana Y, et al. The diagnosis of brain tuberculoma by (1)H-magnetic resonance spectroscopy. *Eur J Pediatr*. 2011;170(3):379–387.
21. Schrier LA, Schopps JH, Feigin RD. Bacterial and fungal infections of the central nervous system. In: Berg BO, ed. *Principles of Child Neurology*. New York: McGraw-Hill; 1996:766–771.
22. Snyder RD. Bacterial infections of the nervous system. In: Berg BO, ed. *Neurological Aspects of Pediatrics*. Boston: Butterworth-Heinemann; 1992:195–226.
23. Soares de Oliveira-Szejnfeld P, Levine D, Suely de Oliveira Melo AS, et al. Congenital brain abnormalities and Zika Virus: what the radiologist can expect to see prenatally and postnatally. *Radiology*. 2016;382(1):203–218.
24. Tucker KA, Robertson KR, Lin W, et al. Neuroimaging in human immunodeficiency virus infection. *J Neuroimmunology*. 2004;157(1–2):153–162.
25. Vossough A, Zimmerman RA, Bilaniuk LT, Schwartz EM. Imaging findings of neonatal herpes simplex virus type 2 encephalaitis. *Neuroradiology*. 2008;50(4):355–366.
26. Whitley RJ, Hutto C. Neonatal herpes simplex virus infections. *Pediatric Reviews*. 1985;7:119–126.
27. Yow MD. Congenital cytomegalovirus disease: a now problem. *J Infect Dis*. 1989;159:163–167.

# 35

# Pediatric Brain Neoplasms

Sanjay P. Prabhu and Tina Young Poussaint

## OVERVIEW

Brain tumors are the most common solid pediatric tumors and are the leading cause of death in children from solid tumors.[1] The incidence rate of all childhood primary brain and central nervous system (CNS) tumors is estimated to be 5.47 cases per 100,000 person-years.[2] An estimated 4830 new cases of childhood primary malignant and nonmalignant brain and other CNS tumors are expected to be diagnosed in the United States in 2017.[2] The incidence of brain tumors is highest in infants (<1 year of age), followed by children ages 1 to 4 years.[3] The most common site of childhood brain tumors is the cerebellum (18.7%), followed by the frontal, temporal, parietal, and occipital lobes (15.7%).[3]

The most recent World Health Organization (WHO) classification of central nervous system tumors represents a major restructuring of the diffuse gliomas, medulloblastomas, and other embryonal tumors, and incorporates new entities defined by both histology and molecular features.[4] Of particular note, the embryonal tumors have also undergone substantial changes in their classification, most notably with removal of the term *primitive neuroectodermal tumor (PNET)* from the diagnostic lexicon. The following description tries to incorporate some of these more recent changes while acknowledging the previously accepted terminology that is still currently used in clinical discussions.

## ETIOLOGY

The etiology of pediatric brain tumors is an area of continuing research beyond the scope of this chapter, requiring understanding of genetic alterations, signaling systems, and molecular genetics and pathways. No specific risk factor explains more than a small proportion of childhood brain tumors. Known risk factors for childhood brain tumors include therapeutic doses of ionizing radiation to the head for brain tumors and radiation for leukemia,[5,6] and certain genetic syndromes. Some genetic inherited syndromes have an association with brain tumors including neurofibromatosis types 1 and 2, Gorlin syndrome (basal cell nevus syndrome), tuberous sclerosis, Turcot syndrome, von Hippel–Lindau syndrome, and Li–Fraumeni syndrome.[7]

## IMAGING

Wide availability of computed tomography (CT) has resulted in its use for diagnosis for patients with brain tumors presenting acutely. Its advantages include the ability to detect a mass, to identify lesion mass effect, to check for ventricular effacement and/or enlargement, lesional hemorrhage, calcification, and osseous involvement.

Magnetic resonance imaging (MRI) with contrast is the modality of choice at diagnosis to determine lesion size, location, and characterization due to its superior soft tissue resolution, multiplanar capability, and lack of ionizing radiation. Presence of contrast enhancement reflects disruption of the blood-brain barrier. The degree of contrast enhancement does not always correlate with tumor grade. For example, benign tumors such as choroid plexus papillomas and pilocytic astrocytomas can enhance avidly, whereas anaplastic astrocytomas may not enhance at all.[8]

The definition of lesion margins and accurate staging of the tumor by confirming the presence or absence of tumor spread through the neural axis are essential for treatment planning. In addition, diffusion tractography and functional MRI can be used to show the relationship of the tumor to eloquent brain and other vital structures to minimize treatment damage to these regions. Intraoperative MRI systems are being increasingly used to guide tumor resection and stereotactic and minimally invasive tumor resection.

MRI can be used to assess tumor response and progression and to monitor treatment effects. After surgical resection, MRI is used to determine the presence of residual tumor, to look for postoperative complications, and for routine follow-up. Advanced techniques (discussed later in this chapter) are used to complement structural imaging and provide insight into tumor physiology.[9]

## ROLE OF ADVANCED IMAGING TECHNIQUES IN IMAGING BRAIN TUMORS

### Diffusion-Weighted Imaging

Contrast on diffusion-weighted imaging (DWI) reflects the mean distance travelled by free water protons in tissue due to Brownian motion.[10,11] Diffusivity of tissues is indicated by the apparent diffusion coefficient (ADC), which is a scalar parameter with units of $mm^2$/sec. Diffusion occurs freely in the direction of tract orientation and is restricted in orthogonal planes.

Diffusion tensor imaging (DTI) is an adaptation of DWI, and is performed by acquiring diffusion data in six or more directions, enabling determination of the direction and magnitude of water diffusion. The degree of anisotropy is expressed by a variety of quantitative measures, the most common of which is fractional anisotropy (FA), which reflects the presence of myelinated white matter tracts and related processes such as axonal transport in tissues. Connecting the directions of diffusion in each voxel to those of neighboring voxels using a variety of mathematical algorithms enables creation of a three-dimensional white matter tract map, termed *tractography*.[12]

DWI can help assess cellularity of a lesion, as markedly decreased ADC usually correlates well with the histologic measures of tumor cellularity in brain neoplasms. The ADC value depends on the complexity of the cytoarchitecture and the rapid exchange of protons between different compartments. The cytoarchitecture of the tumor can inhibit random Brownian motion and thus causes water diffusion to deviate from strict Gaussian behavior.[9] Generally, highly cellular tumors have reduced diffusivity, whereas vasogenic edema and necrosis show increased diffusion.[8,13,14] However, overlap between tumor grades makes it imperative that the ADC values are interpreted in conjunction with the structural MRI sequences.[8,15]

DWI can be extremely useful in the postoperative period, when low ADC values at the surgical margins or within the resection cavity may be indicative of ischemia, residual cellular tumor, or abscess, and in conjunction with conventional MRI helps exclude artifact from hematoma.[16] ADC values can also be used to assess treatment response, detect tumor recurrence, and may help differentiate tumor recurrence from pseudoprogression.[17]

DTI can help identify the patterns of tumor interaction with white matter fiber tracts: deviation, edema, infiltration, and destruction.[18] DTI in conjunction with volumetric data can guide surgical resection and predict possible postoperative deficits resulting from white matter tract damage (e-Fig. 35.1). Reduction in FA has been

## Abstract:

Brain tumors are the most common solid pediatric tumors and are the leading cause of death in children from solid tumors. Radiologists play a very important role in the diagnosis and management of pediatric patients with brain tumors. The most recent World Health Organization (WHO) classification of central nervous system tumors represents a major restructuring of the diffuse gliomas, medulloblastomas, and other embryonal tumors, and incorporates new entities defined by both histology and molecular features. The following description incorporates some of these more recent changes while acknowledging the previously accepted terminology that is still currently used in clinical discussions. In addition to describing characteristic imaging features of the more commonly encountered pediatric brain tumors in practice, this chapter describes the role of advanced imaging techniques in the management of pediatric patients with brain tumors including functional MRI, MR spectroscopy and perfusion-weighted imaging is also discussed. Special emphasis is placed on some of the genetic alterations in tumors that have an important role in the management of these patients.

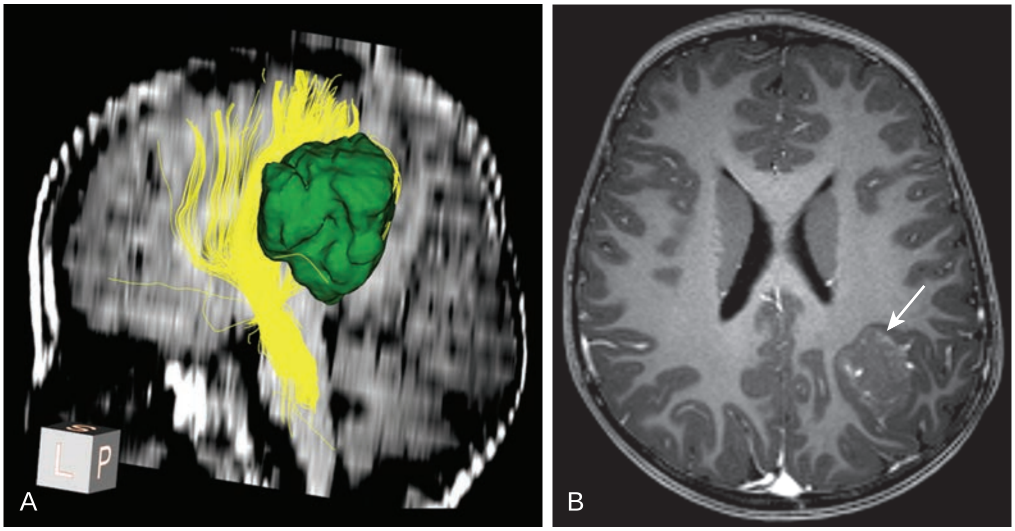

**e-Figure 35.1. Presurgical tractography.** (A) Tractography of the portion of the posterior limb of the internal capsule that forms the left corticospinal tract (shown in *yellow*) in a patient with a left parietal lobe tumor (segmented and shown in *green*). The tract is displaced medially by the solid tumor in the left parietal lobe, but still intact. (B) Axial postcontrast MPRAGE MRI shows the cortical-based enhancing tumor *(arrow).*

found in the white matter of medulloblastoma patients, even in the absence of abnormalities on structural sequences.[19] Deceased FA values correlate with the age at which radiation was administered and with worse school performance, and may be a biomarker of the effects of radiotherapy.[20]

Other applications include ADC histogram technique in diffuse midline tumors of the pons, which has demonstrated significant correlation between diffusion metrics and survival, with lower diffusion values (increased cellularity), and increased enhancement associated with shorter survival.[21] Functional diffusion mapping (fDM) has been suggested as a tool for early detection of tumor treatment efficacy, although interpretation requires careful correlation with structural sequences and the underlying biology of both tumor and healthy tissue.[22] Serial parametric response mapping of ADC, performed at multiple time points of therapy, has the potential to distinguish pseudoprogression from true progression of tumors.[23]

## Magnetic Resonance Spectroscopy

Magnetic resonance spectroscopy (MRS) enables detection and quantification of normal and abnormal metabolites in the brain. MRS can help identify tumor tissue, differentiate tumor types, and separate active tumor from radiation necrosis or scar formation. MRS can be performed on most standard MRI scanners, typically incorporating either the point resolved spin echo (PRESS) or stimulated echo acquisition mode (STEAM) techniques. Simultaneous acquisition of MRS from multiple voxels increases spatial resolution and is called chemical shift imaging (CSI) or magnetic resonance spectroscopic imaging (MRSI).[24]

Normal metabolites detected in the brain include N-acetylaspartate (NAA), a neuronal marker; choline (Cho), a membrane marker; and creatine (Cr), a marker of energy metabolism. Myoinositol (mI), a glial marker, can be better resolved with short echo-time MRS techniques. Concentrations of metabolites are usually expressed in the form of metabolite ratios.

Most brain tumors are characterized by the presence of increased Cho/Cr and decreased NAA/Cr ratios, indicating loss of neuroaxonal integrity and increased cell membrane turnover. Presence of lactate, an indicator of anaerobic metabolism, indicates impaired energy metabolism.[25]

Tumor characterization has been attempted using MRS. In general, high-grade tumors have higher Cho/Cr and lower NAA/Cr ratios than low-grade ones. One exception is juvenile pilocytic astrocytoma, in which the choline peak can be markedly elevated. Necrotic areas in rapidly growing malignant tumors such as medulloblastomas and atypical teratoid rhabdoid tumors may contain lipid resonances.[26] In adults, lactate is typically associated with high-grade gliomas. In children, lactate is frequently paradoxically elevated in pilocytic astrocytomas, a low-grade tumor.[23] The presence of specific metabolites such as alanine in meningiomas (an inverted doublet at 1.44 parts per million [ppm]), and taurine (peak at 3.3–3.4 ppm) in medulloblastoma may help in narrowing the differential diagnosis[27,28] (e-Fig. 35.2). Citrate has been described in pediatric brain tumors and can be particularly high in pontine gliomas[29] and in Grade 2 astrocytomas that have progressed.[30]

## Perfusion-Weighted Imaging

Perfusion-weighted imaging (PWI) measures cerebral hemodynamics at the microcirculation level (e-Fig. 35.3). Measured parameters include cerebral blood volume (CBV), cerebral blood flow (CBF), and mean transit time (MTT). CBV is defined as the volume of blood in an area of brain tissue expressed in mL/100 g, and is the most commonly used parameter in brain tumor evaluation.[31]

Three main techniques are available to measure perfusion within the brain: T2*-weighted dynamic susceptibility contrast (DSC) imaging, T1-weighted dynamic contrast-enhanced (DCE) perfusion, and arterial spin labeling (ASL).

DSC is the most widely available technique, and, consists of a rapid bolus of intravenous paramagnetic contrast agent administration, followed by a rapid acquisition of a series of echo-planar images during the first pass of contrast material through the capillary bed. The contrast medium in the blood passes through the tissues and results in a signal drop proportional to the blood volume.[32] Challenges to routine use in children include the need to use power injectors and large-bore intravenous catheter placement.[33]

DCE T1-weighted permeability perfusion pharmacokinetic parameters have been useful for discriminating low-grade and high-grade pediatric tumors.[34] In one study, the rate constant from the blood plasma into the extracellular extravascular space ($K^{trans}$), rate constant from extracellular extravascular space back into blood plasma ($K_{ep}$), and extracellular extravascular volume fraction ($V_e$) were all significantly correlated with tumor grade; high-grade tumors showed higher $K^{trans}$, higher $K_{ep}$, and lower $V_e$.

ASL uses endogenous blood as a tracer agent. Differences in signal intensity changes on ASL are smaller when compared with contrast-enhanced perfusion techniques and depend on other parameters such as the T1 relaxation time of blood and time delay between the tagging pulses and the readout time of the images.[33] ASL has shown promise for hemodynamic evaluation of brain tumors.[35-37] High-grade pediatric brain tumors display higher CBF compared with low-grade tumors, and CBF is correlated with tumor microvascular density.[38] Lower-grade astrocytomas have relatively lower regional blood volume (rCBV) than higher-grade tumors such as anaplastic astrocytomas and glioblastomas.[39] However, in pediatric patients, low-grade pilocytic astrocytomas can have a high relative blood volume.[32]

## Functional Magnetic Resonance Imaging

Functional MRI (fMRI) is a technique that relies on the fact that oxyhemoglobin is diamagnetic and deoxyhemoglobin is paramagnetic. Due to the relative increased blood flow and consequent increased utilization of oxygen within the activated portions of the brain, the magnetic resonance signal (called the blood oxygen level–dependent [BOLD] signal) is measurably different compared with other parts of the brain. Event-related paradigms (short bursts of stimuli followed by rest) or block design paradigms (alternating blocks of same type of stimuli) are described for use in presurgical planning.[40] fMRI has been successfully used in sedated younger pediatric patients.[41-43] The primary value of fMRI is in localizing eloquent areas in the brain controlling language, motor functions, and memory. This information helps guide therapeutic approaches to minimize damage to eloquent cortex.[44] The acceptance of fMRI and its capabilities has largely replaced the invasive Wada test in determining hemispheric dominance of memory and language functions.[45] It is important to note that changes in blood flow in and around hypervascular tumors can affect the regional reliability and accuracy of fMRI.[46]

## Single Positron Emission Computed Tomography and Positron Emission Tomography

Assessment of regional cerebral blood flow by single positron emission computed tomography (SPECT) has been largely replaced by magnetic resonance perfusion and functional MRI techniques. Positron emission tomography (PET) is an adjunct to MRI and CT brain tumor evaluation, used to determine metabolic activity at diagnosis, to determine response to therapy, and to distinguish between treatment effect and tumor recurrence. Fluorodeoxyglucose ($[^{18}F]$ FDG) is the most commonly used isotope for PET studies in children. Other labeled agents such as amino acid analogues, $[^{11}C]$ methionine and $[^{11}C]$ tyrosine, have shown promise in detecting low-grade tumors in adults, but their role in children is yet to be established.[47] These amino acid analogues are incorporated into tumor proteins, and degree of uptake reflects tumor

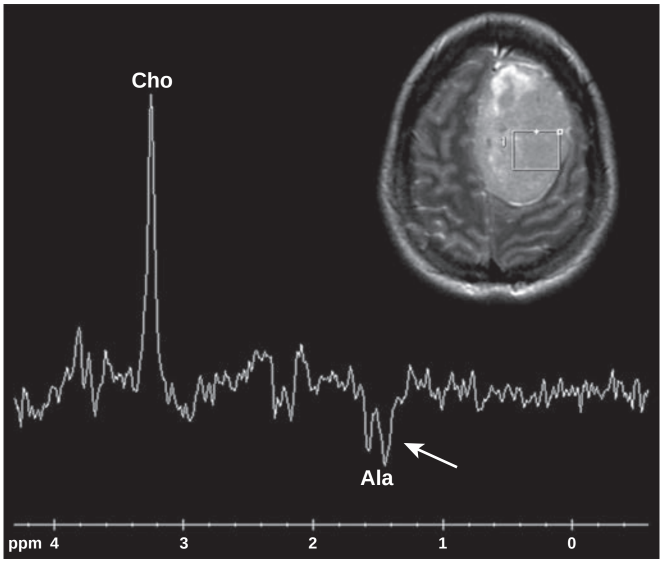

**e-Figure 35.2. Magnetic resonance spectroscopy.** Single-voxel MRS (TE 144 msec) over the extraaxial dural-based lesion in the left frontal lobe (see *inset* T2-weighted image) shows a prominent choline peak (Cho) and reduced creatine and NAA peaks. The inverted doublet centered at approximately 1.55 to 1.6 ppm is consistent with an alanine peak, reported in meningioma. Note the small inverted doublet peak centered at 2.3 ppm, which is of uncertain etiology.

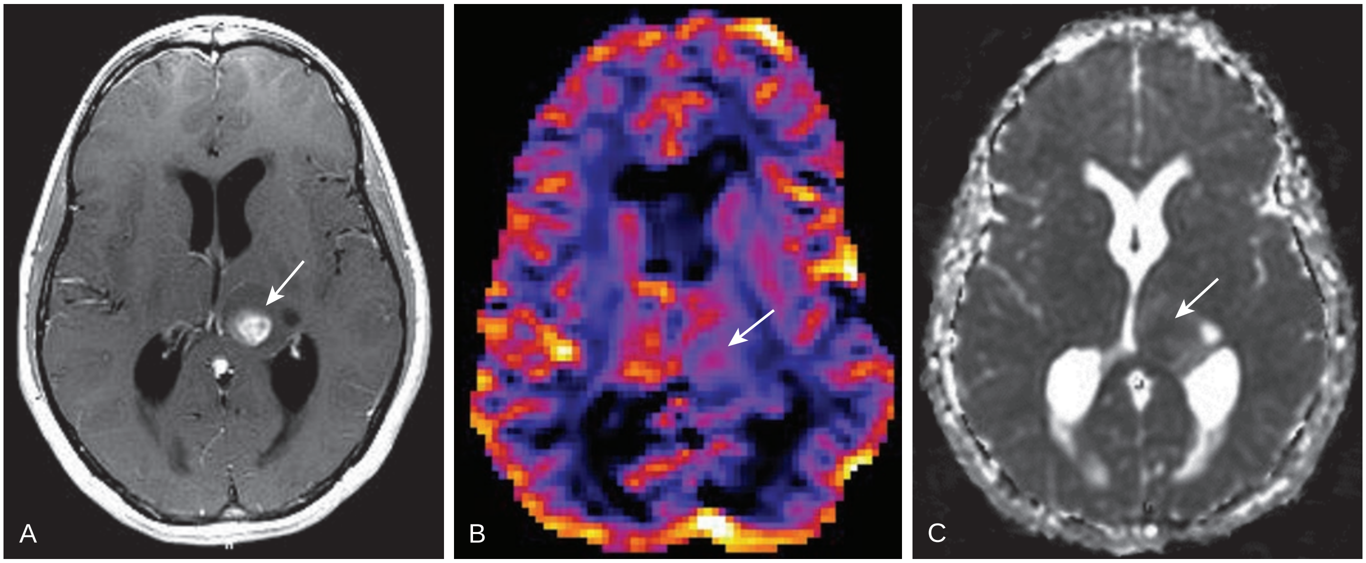

**e-Figure 35.3. Perfusion-weighted imaging.** (A) Axial T1-weighted MRI shows a rounded central enhancing mass lesion in the left thalamus *(arrow).* (B) Axial perfusion image shows a focal area of increased perfusion corresponding to the enhancing solid portion of the tumor in the left thalamus *(arrow)* suggesting high-grade lesion and pathology was glioblastoma multiforme. (C) ADC map shows areas of decreased diffusion corresponding to the solid component of the left thalamic tumor *(arrow).*

protein synthesis.[48,49] Other agents being investigated include cell proliferation agents such as [$^{11}$C]-labeled fluorothymidine and cell hypoxia imaging agents such as fluoromisonidazole ([$^{18}$F] MISO) and Cu-diacetyl-bis (N4-methylthiosemicarbazone (Cu-ATSM).

## WORLD HEALTH ORGANIZATION CLASSIFICATION OF TUMORS

The new 2016 WHO Classification of Tumors of the Central Nervous System uses molecular parameters in addition to histology to define many tumor entities, formulating how CNS tumor diagnoses should be structured in the molecular era.[4] This classification presents major restructuring of the diffuse gliomas, medulloblastomas, and other embryonal tumors, and incorporates new entities that are defined by both histology and molecular features. Some of these tumors are relevant to pediatric practice and will be addressed below. It is hoped that this classification of tumors will further evolve and facilitate epidemiologic studies and improved treatments.

## CLASSIFICATION OF PEDIATRIC BRAIN TUMORS BY LOCATION

Classification of tumors by location helps limit the differential diagnosis in conjunction with the appearance of the lesion on conventional MRI and advanced imaging techniques (Box 35.1).

## TUMORS OF THE CEREBRAL HEMISPHERES

### Astrocytomas

The most recent WHO classification of brain tumors divides astrocytomas into two broad groups. The first group consists of diffuse astrocytic and oligodendroglial tumors, which includes diffuse and anaplastic astrocytoma and glioblastoma. Each of these types is further subdivided into three subtypes based on the presence or absence of isocitrate dehydrogenase (IDH) mutations.[4] For both grade II and III tumors, the great majority falls into the IDH-mutant category. The second group consists of other astrocytic tumors, which includes pilocytic astrocytomas (with pilomyxoid astrocytomas as subtype), subependymal giant cell astrocytomas, and pleomorphic xanthoastrocytoma (with and without anaplastic features).

### Pilocytic and Pilomyxoid Astrocytomas

Pilocytic astrocytomas (PA) are grade I WHO tumors that account for 20% to 30% of all childhood brain tumors.[50] They arise typically in the first two decades of life and there is no definite gender predominance. The most common locations are in the optic pathways, hypothalamus, thalamus, basal ganglia, cerebral hemispheres, cerebellum, and brainstem. Patients with neurofibromatosis type 1 (NF1) have an increased risk of developing pilocytic astrocytomas, including optic pathway tumors, which tend to have a better long-term prognosis than in patients without NF1.[51]

On CT and MRI, a pilocytic astrocytoma is usually a well-defined lesion that demonstrates contrast enhancement of its solid component (Fig. 35.4). Tumoral “cystic” components containing proteinaceous fluid are seen more often in cerebellar lesions. They often contain a contrast-enhancing mural nodule. Increased ADC values due to their low cellularity help to distinguish them from higher-grade astrocytomas. The enhancing components of pilocytic astrocytomas tend to have low perfusion with decreased rCBV, although nodules with increased perfusion may be seen.[52]

Rarely, pilocytic astrocytomas can present with diffuse leptomeningeal spread, most often seen in association with the diencephalic syndrome (discussed later) or with the pilomyxoid variant. These tumors have an indolent course, but their propensity for slow-growing persistent recurrences makes them difficult to treat.[53] Pilomyxoid astrocytoma (PMA) represents a variant of classical PA with more invasive growth and increased risk of recurrences and dissemination.

**BOX 35.1** Classification of Pediatric Brain Tumors Based on the Location of the Tumors

1) **TUMORS OF THE CEREBRAL HEMISPHERES**
    a) Astrocytomas (WHO grades I-IV)
    b) Supratentorial embryonal tumors
    c) Atypical teratoid rhabdoid tumor
    d) Supratentorial ependymoma
    e) Thalamic astrocytoma
    f) Dysembryoplastic neuroepithelial tumor (DNET)
    g) Meningioangiomatosis
    h) Germinoma
    i) Choroid plexus tumors—papilloma and carcinoma
    j) Neuronal and mixed neuronal-glial tumors (including desmoplastic infantile ganglioglioma [DIG])
2) **SELLAR AND SUPRASELLAR TUMORS**
    a) Craniopharyngioma
    b) Chiasmatic/hypothalamic glioma
    c) Hypothalamic hamartomas
    d) Pituitary adenoma
    e) Germ cell tumors
    f) LCH
    g) Rathke cleft cyst
    h) Arachnoid cysts
    i) Dermoid/epidermoid cysts
3) **POSTERIOR FOSSA TUMORS**
    **Intraaxial**
        a) Medulloblastoma
        b) Cerebellar astrocytoma
        c) Tectal glioma
        d) Brainstem neoplasms including diffuse midline gliomas
        e) Atypical teratoid rhabdoid tumors (ATRT)
        f) Ependymomas
        g) Teratoma
        h) Hemangioblastoma
    **Extraaxial**
        a) Dermoid
        b) Epidermoid
        c) Teratoma
        d) Schwannoma
        e) Meningioma
        f) Skull base neoplasms
4) **PARAMENINGEAL TUMORS**
    a) Osseous, chondroid, or myeloid origin
    b) Other mesenchymal origin tumors
    c) Tumors from notochordal elements
    d) Metastatic disease including leptomeningeal disease from dissemination of primary brain tumors
5) **PINEAL REGION TUMORS**
    a) Germ cell tumors
    b) Pineal parenchymal tumors
    c) Tumors of supporting tissues of the pineal gland or adjacent structures

Typically, pilocytic astrocytomas exhibit distinct histology with biphasic architecture of loose, microcystic and compact, fibrillary areas. However, some tumors display a heterogeneous histopathologic appearance that can mimic other glial neoplasms. Not infrequently, pilocytic astrocytomas exhibit atypical histologic features suggestive of anaplasia that can suggest a diffuse high-grade glioma. Genetic alterations resulting in aberrant signaling of the mitogen-activated protein kinase (MAPK) pathway have been implicated in the development of pilocytic astrocytomas. The presence of the most commonly identified BRAF-KIAA1549 fusion gene mutation may be associated with improved clinical outcomes.[54,55]

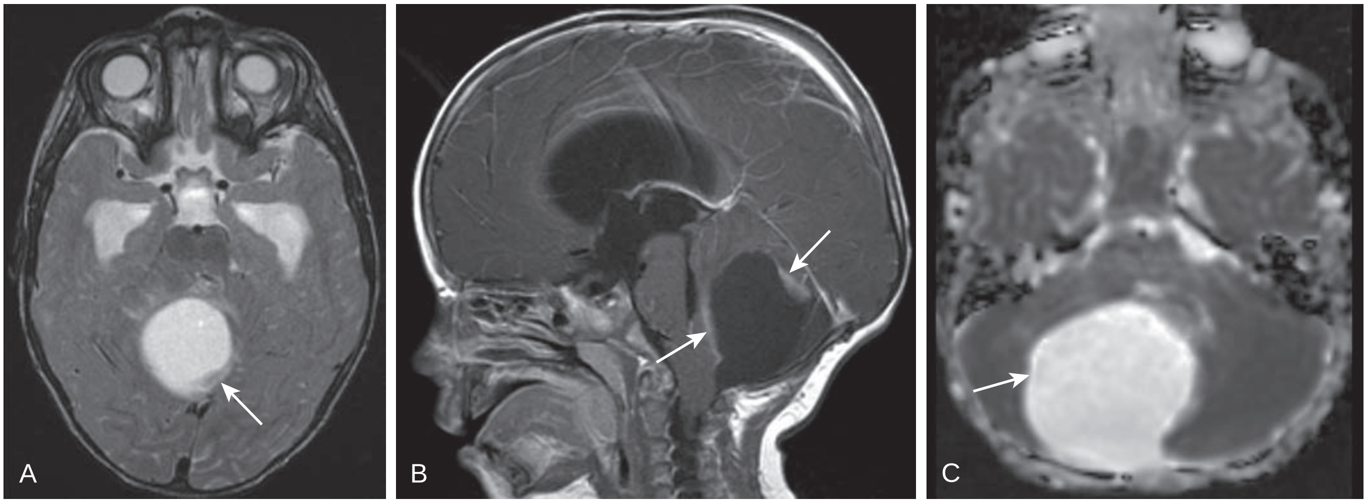

**Figure 35.4. Cerebellar astrocytoma.** (A) Axial T2-weighted MRI shows a large cystic mass centered in the right cerebellar hemisphere with small solid components along the posterior and anterior aspects *(arrow).* (B) Postcontrast sagittal MPRAGE MRI shows the solid components *(arrows)* along the anterior and posterior margins enhance after paramagnetic contrast administration. (C) ADC map shows increased diffusion within the lesion *(arrow)* consistent with the relatively low cellularity within the lesion.

Gross total resection is often curative, but micrometastases may occur. Recent treatment trials for unresectable recurrent disease have incorporated molecular *BRAF* status in low-grade glioma treatment with MEK inhibitor drugs. The role of Ras/MAPK alterations seems to be dominant in all pediatric low grade gliomas, but specifically in hemispheric tumors.[56]

## Diffuse Astrocytomas

Diffuse astrocytomas are low-grade tumors (WHO grade II) that are rare compared with pilocytic astrocytomas.[57] Around one-third arise in the frontal or parietal lobes, which represents the most common location.[57] On MRI, they have relatively ill-defined margins but they are uniformly hypointense on T1- and hyperintense on T2-weighted sequences. They do not enhance on postcontrast images and they do not show restricted diffusion.[58] Anaplastic transformation to a higher-grade tumor occurs in only about 10% of pediatric cases.[59] Diffuse astrocytomas do not show significantly increased rCBV and may show elevated myoinositol on MRS.[60,61]

## Anaplastic Astrocytoma

Anaplastic astrocytomas represent close to 2% of all CNS tumors in children.[62] They are poorly circumscribed infiltrative lesions with rapid growth rates.[58] They most commonly occur in the cerebral hemispheres, particularly the frontal and temporal lobes. They typically do not enhance on postcontrast images, and do not show evidence of hemorrhage or necrosis, which differentiate them from glioblastomas.[58,63] Anaplastic astrocytomas have lower ADC values and increased rCBV compared with lower-grade tumors.[61] On MRS, anaplastic astrocytomas show increased choline and decreased N-acetylaspartate, with decreased myoinositol compared with the spectra of lower-grade tumors.[60]

## Glioblastomas

Glioblastomas are rare in children, accounting for about 3% of primary brain tumors.[64] These tumors occur most commonly in the frontotemporal region but can affect other lobes or deep gray structures. They present typically as heterogeneously enhancing tumors with areas of necrosis with marked surrounding edema. The solid components show restricted diffusion, and increased perfusion and permeability parameters. These features may help differentiate them from lower-grade tumors and can help differentiate between tumor recurrence and treatment response. On MRS, in addition to elevated choline, reduced NAA, and reduced myoinositol, glioblastomas typically have elevated lactate due to anaerobic metabolism and elevated lipids resulting from tumor necrosis.[61] Prognosis is poor, but survival rates are better compared with adult glioblastomas.[65]

## Diffuse Gliomas

Under the new WHO classification, diffuse gliomas include the WHO grade II and grade III astrocytic tumors, the grade II and III oligodendrogliomas, the grade IV glioblastomas, and the related diffuse gliomas of childhood.[4] Astrocytomas that have a more circumscribed growth pattern, lack IDH gene alterations, and frequently have *BRAF* alterations (pilocytic astrocytoma, pleomorphic xanthoastrocytoma) or *TSC1/TSC2* mutations (subependymal giant cell astrocytoma) are considered distinct from the diffuse gliomas. The WHO grade II diffuse astrocytomas and WHO grade III anaplastic astrocytomas are now each divided into IDH-mutant, IDH-wildtype, and not otherwise specified (NOS) categories. Although prognostic differences between grade II diffuse astrocytomas and IDH-mutant WHO grade III anaplastic astrocytomas are not as marked, this has not been noted in all studies.[66,67] The current recommendation is that WHO grading is retained for both IDH-mutant and IDH-wildtype astrocytomas, although the prognosis of the IDH-mutant cases appears more favorable in both grades.

## High-Grade Gliomas

High-grade gliomas are relatively rare in children compared with adults. Supratentorial high-grade gliomas comprise a third of pediatric high-grade gliomas and occur most commonly in adolescents (Fig. 35.5). Most high-grade gliomas in children are purely astrocytic and classified as either anaplastic astrocytomas (WHO grade III) or glioblastomas (WHO grade IV); other mixed or non–astrocytic types are rare.[63]

# Supratentorial Embryonal Tumors

The term *primitive neuroectodermal tumor (PNET)* has been removed from the diagnostic lexicon in the most recent WHO classification.

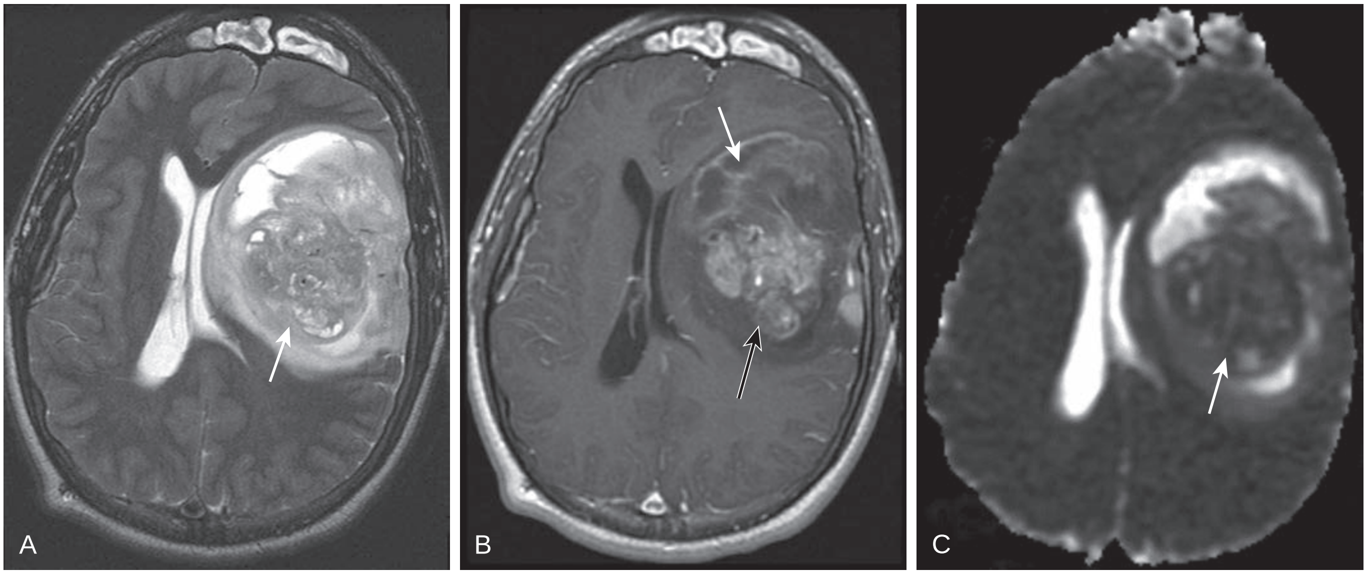

**Figure 35.5. Supratentorial high-grade glioma.** (A) Axial T2-weighted MRI shows a large heterogeneous mass *(arrow)* in the left frontal, temporal, and parietal lobes with marked mass effect, subfalcine herniation, surrounding edema, and rightward midline shift. (B) Postcontrast T1-weighted MRI shows heterogeneous enhancement of the solid components of the tumor *(black arrow)* and nonenhancing components anteriorly *(white arrow)* suggestive of necrosis. (C) ADC map reveals decreased diffusion within the solid component *(arrow)* indicating high cellularity.

This reclassification was driven by the recognition that many of these rare tumors display amplification of the C19MC region on chromosome 19 (19q13.42). C19MC-amplified tumors include the lesions previously known as ETANTR (embryonal tumors with abundant neuropil and true rosettes, but also referred to as embryonal tumors with multilayered rosettes), ependymoblastoma, and, in some cases, medulloepithelioma.[53] In the 2016 CNS WHO classification, the presence of C19MC amplification results in a diagnosis of embryonal tumor with multilayered rosettes (ETMR), C19MC-altered. In the absence of C19MC amplification, a tumor with histologic features conforming to ETANTR/ETMR should be diagnosed as embryonal tumor with multilayered rosettes, NOS, and a tumor with histologic features of medulloepithelioma should be diagnosed as medulloepithelioma (recognizing that some medulloepitheliomas do not have C19MC amplification). 2016 CNS WHO classification has created a probable additional category of CNS embryonal tumor, NOS that includes tumors previously designated as CNS PNET.

Although supratentorial embryonal tumors are relatively rare, they are more common in the first decade, with peak incidence from birth to 5 years of age.[68] They account for 5% of all supratentorial tumors in childhood. They are often large at presentation and are well-defined lesions, occurring either in the cerebral hemispheres or lateral ventricles. They may be solid and homogenous, or can be heterogeneous with cyst formation.[69] Calcification is often seen on CT. On MRI, solid areas have restricted diffusion and T2-hypointense areas, reflecting the high nuclear-to-cytoplasm ratio and increased cellularity, as well as increased CBV on perfusion imaging. Necrosis and hemorrhage can also occur. Heterogeneous enhancement is seen after contrast administration interspersed with variable hypodense foci of necrosis (Fig. 35.6). Leptomeningeal dissemination and drop metastases occur frequently, necessitating imaging of the entire neuraxis at presentation and on follow-up.

## Supratentorial Ependymoma

Ependymomas constitute approximately 10% of all intracranial tumors in children; 90% of ependymomas occur intracranially, with two-thirds located in the posterior fossa and one-third within the supratentorial compartment.[70,71] These tumors are thought to arise from embryonic rests of ependymal tissue trapped in the developing cerebral hemispheres.[72] They are isointense to hyperintense to gray matter on T2-weighted MRIs.[73] On MRI, there is usually avid enhancement of the soft tissue components of the tumor, intermixed with poorly enhancing or nonenhancing areas.[73] Calcification, necrosis, and hemorrhage may be seen within these lesions, accounting for their heterogeneous appearance.

A recent study defined nine molecular subgroups, three in each anatomic compartment of the CNS: the spine, posterior fossa, and supratentorial compartment.[74,75] Two supratentorial subgroups are characterized by prototypic fusion genes involving *RELA* and *YAP1*, respectively. Patients with supratentorial *RELA*-positive ependymoma have a dismal prognosis. Risk stratification by molecular subgrouping is superior to histologic grading and the classification proposed was suggested as a basis for the new WHO classification.

## Thalamic Astrocytomas

Thalamic tumors account for less than 5% of pediatric intracranial tumors.[76] Most thalamic tumors are unilateral and around half are low-grade astrocytomas. They can be either well-circumscribed pilocytic astrocytomas or infiltrating diffuse gliomas. Imaging characteristics of lower-grade tumors are similar to pilocytic astrocytomas elsewhere.

Diffuse infiltrating thalamic tumors are less common in children. They are classified as low-grade diffuse astrocytomas, anaplastic astrocytomas, and glioblastoma multiforme. The low-grade diffuse astrocytomas are T1-hypointense and of intermediate or high signal intensity on T2-weighted images, and demonstrate no or variable enhancement.

A specific type of thalamic tumor called bithalamic glioma has also been recognized. This is a large symmetric lesion in both thalami that may extend to the basal ganglia and midbrain. Their deep location makes them difficult to access for surgical resection, and radiation with or without chemotherapy is still the treatment of choice. Somatic mutations of genes encoding for histone H3

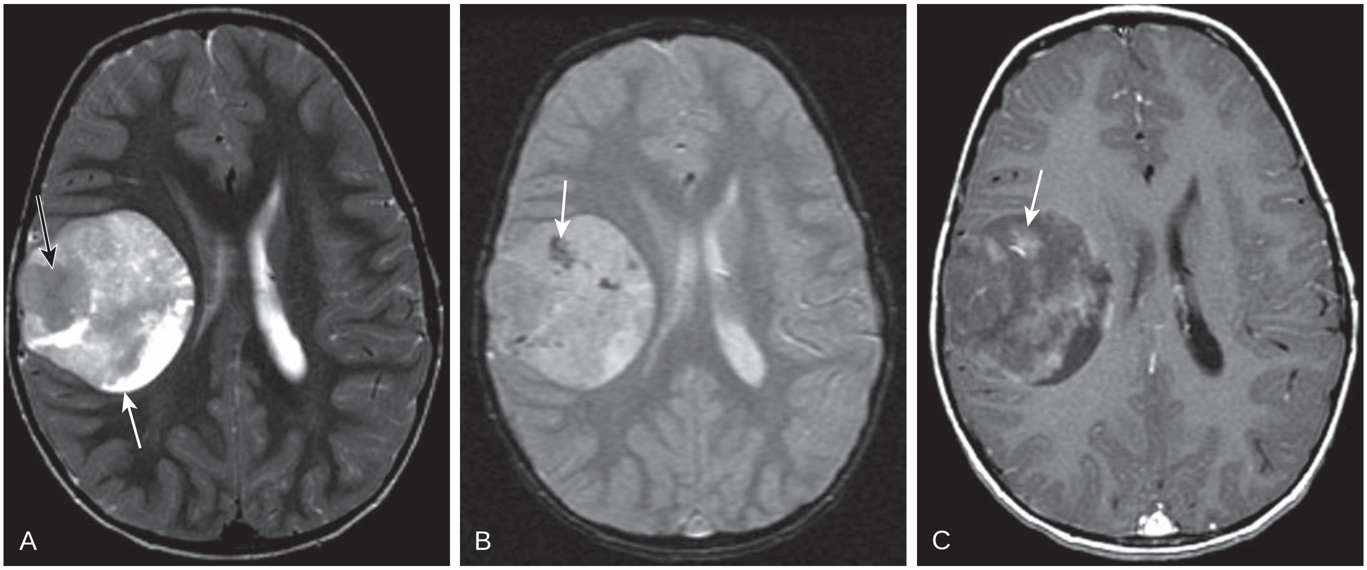

**Figure 35.6. Supratentorial CNS embryonal tumor (previously designated as primitive neuroectodermal tumor).** (A) Axial T2-weighted MRI shows a large well-defined heterogeneous mass lesion in the right cerebral hemisphere with a predominant solid T2-hypointense component *(black arrow)* and smaller areas of T2 prolongation *(white arrow).* (B) Axial gradient-recall echo MRI shows scattered foci of susceptibility *(arrow)* suggestive of calcification or blood products within the lesion. (C) Axial postcontrast T1-weighted MRI shows patchy heterogeneous enhancement within the lesion *(arrow).*

variants have been identified in a subgroup of high-grade gliomas arising in the thalamus, leading to inclusion of this subgroup into the group of tumors called diffuse midline gliomas.[77] However, the presence of the specific H3.3 K27M mutation results in poorer prognosis in brainstem gliomas compared with thalamic gliomas, although data currently exist only for adults.[78,79]

## Choroid Plexus Tumors

Choroid plexus tumors account for approximately 3% of pediatric brain tumors.[80] Of these, 10% to 20% arise in the first decade of life and 80% occur in the first 2 years of life, including a considerable number of tumors diagnosed in utero.[81] Choroid plexus papillomas account for most choroid plexus tumors (up to 85%) with the remainder being choroid plexus carcinomas.

These tumors typically occur in the trigone of the lateral ventricles in children, compared with adults where they occur in the fourth ventricle. On CT, they present typically as isodense to hypodense lobulated masses that enhance avidly and homogenously. They may contain punctate calcifications. On MRI, they present as homogenous intraventricular masses that are hypointense on T1-weighted images and predominantly hyperintense on T2-weighted images, with focal hypointense foci (Fig. 35.7).

Choroid plexus carcinomas may be hyperdense on CT reflecting increased cellularity. Carcinomas almost always invade the adjacent brain through the ventricular wall and cause vasogenic edema.[82] They are characterized by areas of heterogeneous signal intensity on both T1- and T2-weighted images because of hemorrhage and necrosis. Imaging differentiation between papillomas and carcinomas may be difficult. Extensive parenchymal invasion and peritumoral vasogenic edema are suggestive of malignancy.[82] MRS will demonstrate significantly higher mI levels in choroid plexus papillomas. Choroid plexus carcinomas, on the other hand, have significantly elevated levels of choline compared with choroid plexus papillomas.[83]

Spinal drop metastases can occur with both choroid plexus papilloma and carcinoma, although this is more frequent with carcinoma. Screening of the spine for possible metastasis should be part of the routine preoperative protocol.

## Neuronal and Neuronal-Glial Tumors

### Neurocytomas

Neurocytomas are rare tumors, accounting for less than 0.5% of all brain tumors.[84] They usually occur in adolescents and young adults. They arise in the lateral ventricles, close to the foramen of Monro and the third ventricle, and are called central neurocytomas. Extraventricular neurocytomas also occur, and are confined to the brain parenchyma.

On MRI, these tumors present as well-circumscribed lobulated masses in the anterior aspect of the lateral ventricles. They are isointense to slightly hypointense to gray matter on T1-weighted images and hyperintense on T2-weighted images, and may enhance after contrast administration. In a small subset of patients, MRS has demonstrated a glycine peak at 3.55 ppm in addition to a high choline peak and decreased NAA peak.[85]

### Desmoplastic Infantile Ganglioglioma/Astrocytoma

Desmoplastic infantile ganglioglioma/astrocytomas are rare supratentorial tumors that occur in young children less than 18 months of age with an incidence of around 1.25%. These tumors typically involve the cerebral surface and overlying dura.[86,87] They are often large at presentation and are predominantly cystic with a solid peripheral component, and most commonly occur in the frontal and parietal lobes. On CT, the cystic component is similar to cerebrospinal fluid, and the superficial solid component is isodense or slightly hyperdense and enhances postcontrast.[86] On MRI, T1-weighted images characteristically show a hypointense cystic mass with a peripheral solid component that enhances intensely after gadolinium administration.[86,88] Extension of the enhancement to the leptomeninges is characteristic and correlates with the dural attachment of the solid component. The solid portion is heterogeneous on T2-weighted images. Meningeal thickening and enhancement adjacent to the solid tumor component, calcifications, and osseous thinning are common associated features. The prognosis is often good if surgical resection can be carried out without damage to adjacent structures.

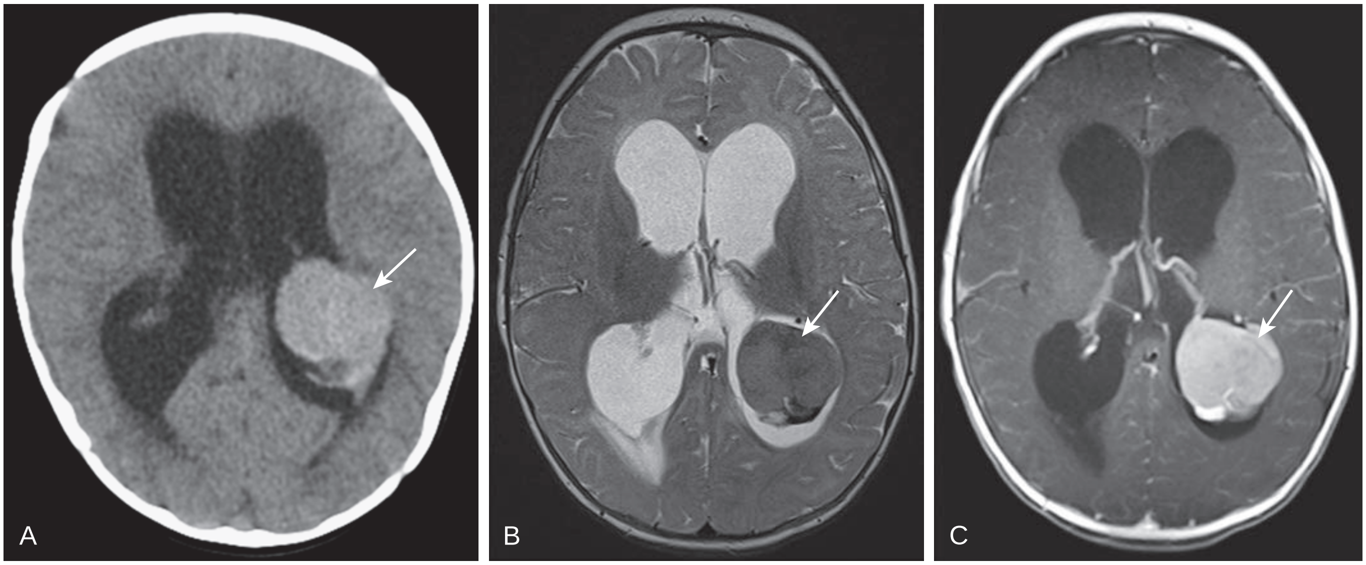

**Figure 35.7. Choroid plexus papilloma.** (A) Axial noncontrast CT shows a lobulated hyperdense mass in the left lateral ventricle *(arrow)*. (B) Axial T2-weighted MRI shows the mass in the left lateral ventricle is hypointense compared with the brain parenchyma *(arrow)*. (C) Axial postcontrast T1-weighted MRI shows homogenous enhancement of the lesion *(arrow)* after contrast administration.

## SELLAR AND PARASELLAR TUMORS

### Craniopharyngiomas

Craniopharyngiomas are slow-growing, benign, nonglial tumors arising in the sellar and parasellar region that comprise between 3% and 10% of all pediatric brain tumors.[70] They are classified as WHO grade I tumors and arise from ectodermal remnants of the Rathke's pouch. They have a bimodal incidence with peak incidence in the first and fifth decades. The adamantinous variant occurs more often in children, whereas the squamous-papillary variant tends to occur in adults.[70] Although histologically benign, they can invade surrounding structures eliciting a gliotic response making resection challenging.

Imaging reflects the mixed cystic and solid nature of these tumors with 90% having calcification and cyst formation. On MRI, high signal intensity on both T1- and T2-weighted images is seen within areas of the lesions with high protein content or as result of subacute hemorrhage (Fig. 35.8). Hypointensity seen on T1-weighted images reflects presence of keratin in some of the cystic areas. CT can demonstrate calcification, which is important for diagnosis and surgical planning. Calcification, vascular encasement, and tumor recurrence are more common in the adamantinous type. Heterogeneous enhancement is seen in the solid components of the tumor.

Surgical treatment remains the mainstay, with radiotherapy having a role in cases that are not amenable to gross total resection. Recurrence-free 5-year survival is close to 87%, but falls to less than 50% with subtotal resection.[89] Follow-up imaging must be directed toward identifying recurrence, second tumors, and associations with moyamoya syndrome.

### Chiasmatic/Optic Pathway/Hypothalamic Gliomas

Optic pathway gliomas are low-grade pilocytic astrocytomas (WHO grade I), which represent 15% of supratentorial tumors.[90] Although sporadic lesions are not uncommon, there is a strong association of optic nerve gliomas with NF1 and bilateral optic nerve tumors are virtually pathognomonic of this diagnosis.[91] From 20% to 50% of optic gliomas occur in patients with NF1, whereas the prevalence of optic pathway gliomas in the NF1 population is between 1.5% and 19%.[91] The tumors may involve the optic nerves, optic chiasm, optic tract, lateral geniculate bodies, and optic radiations. Tumors in children with NF1 are less aggressive than those in children without NF1.[92]

Optic pathway gliomas are usually isointense to the cortex and hypointense to white matter on T1-weighted images. On T2-weighted images, lesions demonstrate mixed signal intensity, predominantly isointense to hyperintense relative to white matter and the cortex (Fig. 35.9). After contrast administration, intense enhancement is common. Use of coronal and axial fat-suppressed thin-section postcontrast T1-weighted images and inversion recovery or T2-weighted images with fat saturation enables optimal visualization of the optic pathways.[93] T2-hyperintensity extends along the optic radiations, although rarely beyond the lateral geniculate bodies. In these cases, it is difficult to differentiate between nonenhancing tumor and edema.

Diencephalic syndrome may be seen in a proportion of patients with hypothalamic/chiasmatic astrocytomas. These children are severely emaciated, although they have normal linear growth. Tumors associated with this syndrome are often larger, occur at a younger age, and are more aggressive. Further, these tumors may seed throughout the CSF pathways.[94] Chemotherapeutic treatment of optic pathway gliomas is started in younger patients, patients with progressive symptoms, and those with extensive CNS involvement.[92]

## POSTERIOR FOSSA TUMORS

### Medulloblastoma

Medulloblastoma (MB) is the most common posterior fossa tumor in childhood, representing up to 38% of posterior fossa tumors and approximately 15% to 20% of all pediatric brain tumors. It is an embryonal neural tumor, histologically classified in five groups by the WHO in its most recent classification: classic MB, anaplastic MB, large cell MB, desmoplastic-nodular MB, and MB with extensive nodularity. A simpler, more practical classification into three groups is used: classic MB (the most common), desmoplastic-nodular MB, and large cell-anaplastic (LCA) MB, the most malignant. This classification correlates relatively well with structural MRI.

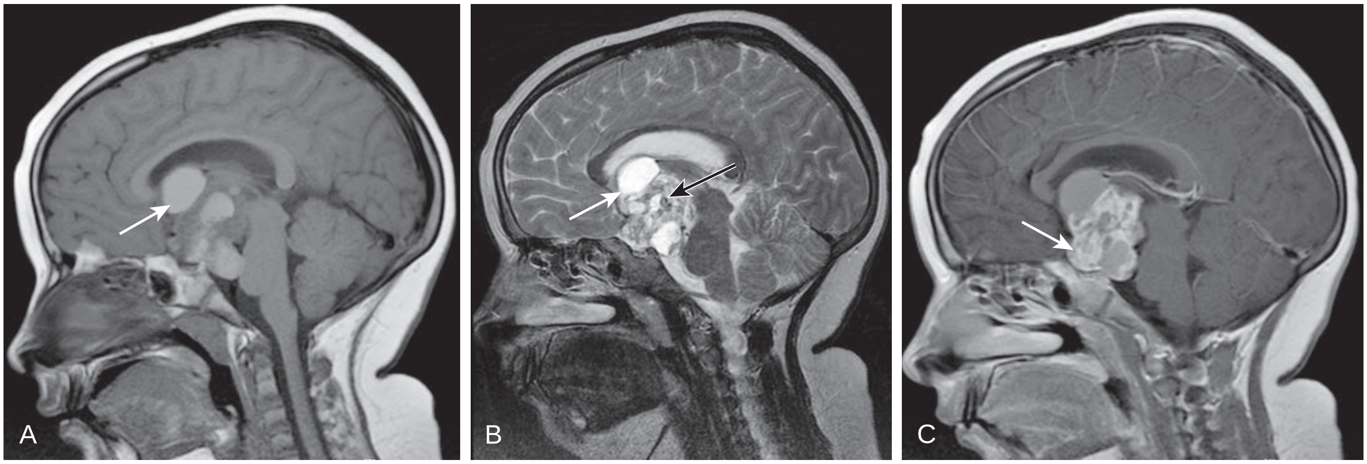

**Figure 35.8. Craniopharyngioma.** (A) Sagittal T1-weighted MRI shows a large suprasellar lesion containing solid and cystic components, with T1-shortening within the cystic components *(arrow)* consistent with proteinaceous content. (B) Sagittal T2-weighted MRI shows T2 hyperintensity within the cystic components *(white arrow)* and scattered hypointensity consistent with foci of calcification *(black arrow).* (C) Sagittal postcontrast T1-weighted MRI shows avid enhancement of the solid component *(arrow).*

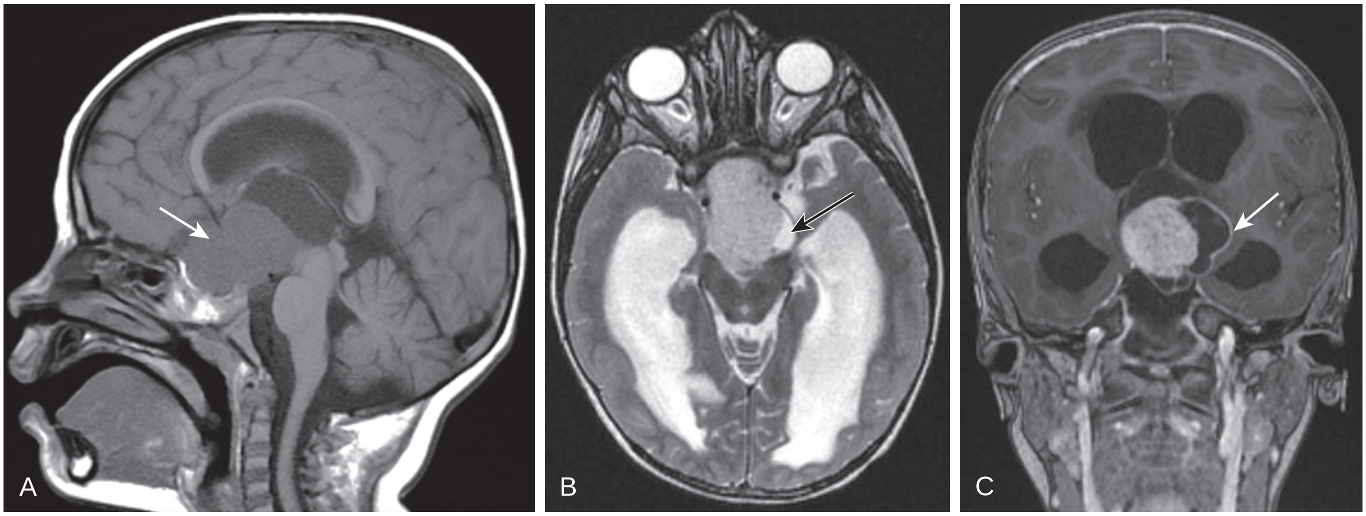

**Figure 35.9. Chiasmatic/hypothalamic glioma.** (A) Sagittal T1-weighted MRI shows a large lobulated suprasellar mass *(arrow)* in the region of the optic chiasm with superior extension into the third ventricle and pontine cistern. (B) Axial T2-weighted MRI shows the lesion is hyperintense compared with brain parenchyma and there is a more hyperintense cystic component along its superior and right aspects *(black arrow).* (C) Coronal T1-postcontrast image shows marked enhancement of the central solid component and peripheral enhancement of the cystic components *(arrow).*

Classic MB presents as a homogenous, compact and well-circumscribed central posterior fossa mass filling the fourth ventricle and causing hydrocephalus. The mass is moderately hypointense on T1, minimally hyperintense to hypointense on T2-weighted images (mildly hyperattenuating on CT), moderately bright on FLAIR, and shows markedly restricted diffusion (Fig. 35.10). This reflects the high cellularity of the tumor and its high nuclear to cytoplasmic ratio. Focal hemorrhage or cystic necrosis may be seen. Enhancement is variable; most tumors enhance in a diffuse, patchy, or ringlike manner, but some do not, although prominent vascular signal voids may be seen within the lesion. Macroscopic intracranial and/or spinal leptomeningeal dissemination may be demonstrated, but not commonly at presentation.

Desmoplastic nodular MB is located within the cerebellar hemispheres away from the midline. They are well circumscribed, compact, somewhat multinodular, and have markedly restricted diffusion. They avidly enhance in a multinodular manner. Large cell anaplastic MB is the most malignant. It has low T1, slightly elevated T2 and FLAIR signal, demonstrates markedly restricted diffusion, and usually enhances diffusely. The most typical (although not most common) presentation is a small tumor in the fourth ventricle, often without hydrocephalus, but already associated with early leptomeningeal dissemination. However, they most often present with a nonspecific pattern on MRI.

As molecular expression may relate to different anatomic origins, anatomically oriented MRI may correlate well with the molecular classification. Currently, four subgroups are identified: WNT subgroup, sonic hedgehog (SHH) subgroup, group 3, and group 4 (these last two subgroups lack specific molecular markers, but the tumors in each group cluster together). WNT MB is characterized by a good long-term prognosis. It presents mostly with the classic histology, affects girls and boys equally, but is uncommon in infants.

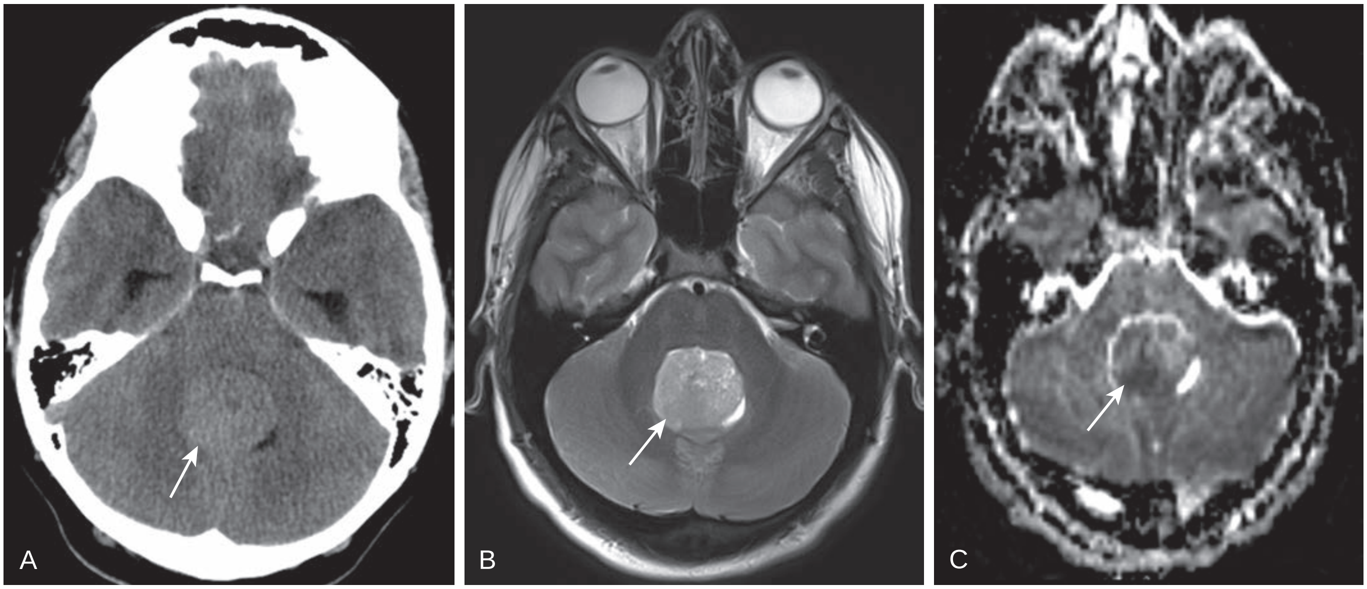

**Figure 35.10. Medulloblastoma.** (A) Axial T2-weighted MRI shows a solid T2-hypointense mass centered in the midline within the cerebellum *(arrow).* (B) Postcontrast axial T1-weighted MRI shows heterogeneous enhancement of the lesion. (C) Apparent diffusion coefficient map shows restricted diffusion in parts of the mass *(arrow),* indicating high cellularity.

It often seems to develop from the lower rhombic lip, which has a strong Wnt expression and therefore 75% of WNT tumors occur along the cerebellopontine angle or cerebellar peduncle.[95] SHH signaling modulates the development of the external granular layer and the production of granule cells; accordingly, tumors of the SHH MB subgroup arise from the cerebellar hemispheres.[95] Tumors of both *group 3* and *group 4* develop in the midline in the immediate vicinity of the fourth ventricle, and may be histologically classic or LCA, with metastatic dissemination.[95,96] Group 3 is found mostly in infants, is associated with *MYC* amplifications, and has the worst prognosis. Group 4 corresponds to the typical MB, with an intermediate prognosis. A notable MRI feature of group 4 lesions is the absence of enhancement after contrast administration, implying a specific "preservation" of the tumoral blood-brain barrier. At recurrence, SHH MB recurs most frequently locally in the resection cavity, whereas group 3 and group 4 recur almost exclusively with leptomeningeal dissemination.[96]

As a practical summary, medulloblastomas should be considered high in the list of differential diagnoses of a posterior fossa tumor that has a vermian location, signs of increased cellularity, restricted diffusion, and intratumoral hemorrhage. MRI of the spine should be obtained at presentation, as the overall incidence of CSF dissemination at diagnosis is between 20% and 30%.[97]

Treatment of medulloblastoma is multimodal, consisting of surgery, radiation therapy, and chemotherapy. e-Table 35.1 summarizes the correlation between the genetic profile, histology, and clinical prognosis.

## Cerebellar Astrocytomas

Features of cerebellar astrocytomas are similar to astrocytomas elsewhere in the brain as discussed in detail previously.

## Tectal Gliomas

Patients with tectal gliomas present with symptoms of obstructive hydrocephalus, caused by growth located adjacent to the aqueduct of Sylvius. Tectal plate lesions can be diagnosed based on imaging findings alone. Imaging appearance is similar to pilocytic astrocytomas elsewhere. Most tectal gliomas do not enhance after contrast enhancement (Fig. 35.11). They may require CSF diversion procedures to relieve hydrocephalus, but do not usually require biopsy or resection. Careful observation suffices for slowly progressing asymptomatic tumors. Rarely, tumors greater than 10 cm may require surgical debulking and/or chemotherapy.[98,99]

## Brainstem Gliomas

Brainstem tumors account for up to 12% of all brain tumors in children.[3] Based on MRI, four types are described: focal, dorsal exophytic, cervicomedullary, and diffuse midline glioma.

### Diffuse Intrinsic Pontine Glioma (Diffuse Midline Glioma)

These tumors are typically centered in the pons. Tumors previously referred to as diffuse intrinsic pontine gliomas are now classified under a newly defined entity called diffuse midline gliomas characterized by K27M mutation in the histone H3 gene *H3F3A* or less commonly in the *HIST1H3B/C* histones.[4] The peak incidence is from ages 6 to 8 years, coinciding with an expansion of a neural precursor–like cell population in the ventral pons, proposed as the possible cell-of-origin.[100]

On CT, pontine gliomas are hypodense or isodense. Calcification or hemorrhage is rare. On MRI, these tumors are isointense to hypointense on T1-weighted images and hyperintense on T2-weighted images. Typically, they partially surround the basilar artery. Enhancement is minimal or absent at presentation in most patients, but in the later stages of tumor progression, diffuse enhancement and necrosis may be present (Fig. 35.12).

These tumors have increased ADC values and reduced FA at presentation with reduction in ADC after initiation of radiotherapy.[101-103] Increased ADC values are thought to be secondary to a larger extracellular volume, possibly arising from a combination of vasogenic edema and a lower number of tumor cells.[104] Volumetric ADC histogram metrics demonstrate significant correlations between diffusion metrics and survival, with lower diffusion values (increased cellularity), increased skewness, and enhancement associated with shorter survival.[21,103] DTI suggests that the tracts are initially infiltrated[105] but not fully disrupted, with better visualization of white matter tracts after radiation.

**e-TABLE 35.1** Medulloblastomas: Summary of Genetic Profile, Histology, and Clinical Prognosis

| Genetic Profile | Histology | Prognosis |
|---|---|---|
| **Medulloblastoma, WNT-activated** | Classic | Low-risk tumors—classic morphology is a feature of almost all WNT-activated tumors |
| | Large cell/anaplastic (rare) | Clinicopathologic significance uncertain |
| **Medulloblastoma, SHH-activated, TP53-mutant** | Classic | Uncommon high-risk tumor |
| | Large cell/anaplastic | High-risk tumor; prevalent in children ages 7-17 years |
| | Desmoplastic/nodular (rare) | Clinicopathologic significance uncertain |
| **Medulloblastoma, SHH-activated, TP53-wildtype** | Classic | Standard-risk tumor |
| | Large cell/anaplastic | Clinicopathologic significance uncertain |
| | Desmoplastic/nodular | Low-risk tumor that occurs in infants, prevalent in infants and adults |
| | Extensive nodularity | Low-risk tumor that occurs in young infants |
| **Medulloblastoma, non-WNT/non-SHH, Group 3** | Classic | Standard-risk tumor |
| | Large cell/anaplastic | High-risk tumor |
| **Medulloblastoma, non-WNT/non-SHH, Group 4** | Classic | Standard-risk tumor, classic morphology seen in most group 4 tumors |
| | Large cell/anaplastic | Clinicopathologic significance uncertain |

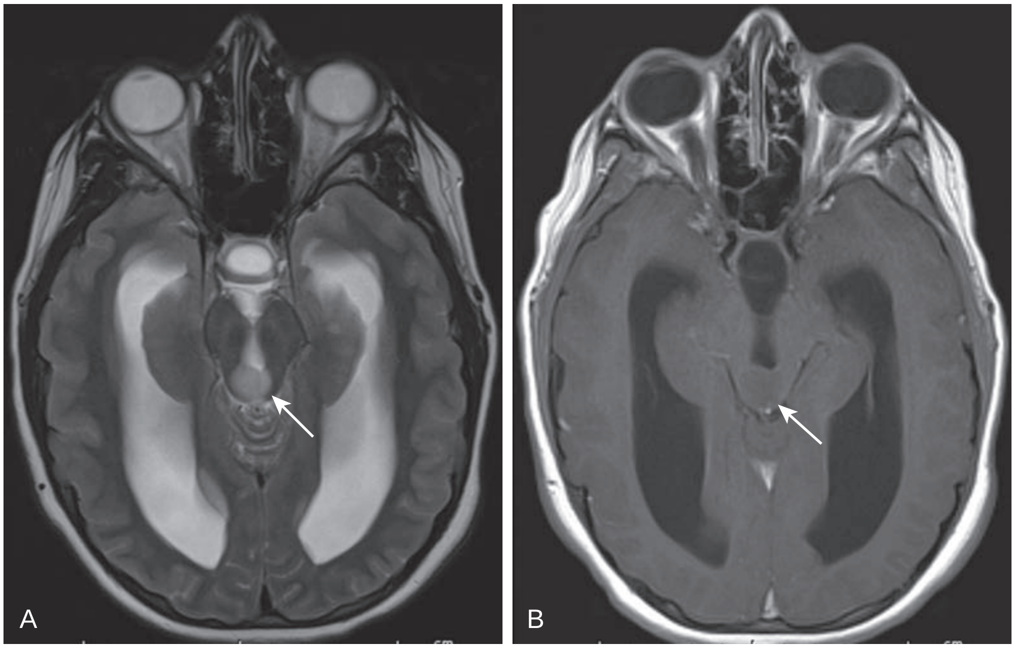

**Figure 35.11. Tectal plate glioma.** (A) Axial T2-weighted MRI shows a hyperintense lesion *(arrow)* involving the tectum causing obstruction of the aqueduct. (B) Axial postcontrast T1-weighted MRI shows the mass is T1-isointense to brain parenchyma *(arrow)* and does not enhance after contrast administration.

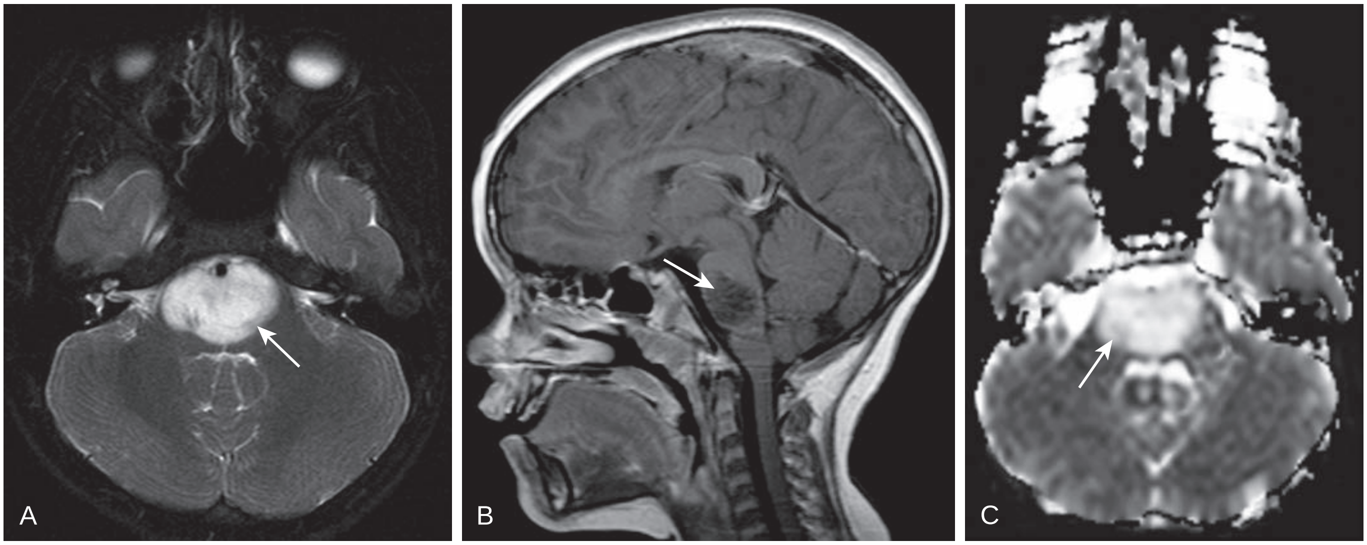

**Figure 35.12. Diffuse midline glioma of the pons.** (A) Axial T2-weighted MRI shows a rounded, hyperintense mass centered in the pons *(arrow)* surrounding the basilar artery and narrowing the pontine cistern. (B) Postcontrast sagittal T1 MRI shows that the lesion does not enhance *(arrow)* after contrast administration. (C) ADC map shows increased diffusion within the lesion *(arrow),* a typical finding at initial presentation.

Tumor progression then results in complete loss of anisotropy possibly due to tract infiltration and disruption.[21,101]

These tumors have a poor long-term survival and were previously considered inoperable. Biopsy of some of these lesions is now being performed allowing the development of new molecular analyses using very small amounts of tissue.[106-108] These tumors usually respond initially to radiation therapy, which has improved the median overall survival from weeks to months.[109] Adjuvant therapies such as radiation sensitizers, differentiation agents, cytotoxic drugs, molecularly targeted drugs, and immunotherapy have been tried. Although they have shown preliminary evidence of immunologic and clinical response, outcomes for patients have not changed significantly.[107,109-111]

### Low-Grade Brainstem Astrocytomas

Low-grade brainstem tumors are usually pilocytic astrocytomas. These are focal tumors that arise in the brainstem and typically extend in an exophytic fashion from its dorsal margin.[112] Imaging features are similar to pilocytic astrocytomas elsewhere.

## Atypical Teratoid Rhabdoid Tumors

Atypical teratoid/rhabdoid tumors (AT/RT) are highly malignant tumors seen in young children, with a peak incidence between birth and 3 years.[113] They are the most common malignant CNS tumor in children below 1 year of age.[3] These tumors account for almost 10% of CNS tumors in children and approximately 1% to 2% of all pediatric brain tumors.[114] Almost 60% of these tumors are seen in the posterior fossa at the cerebellopontine angle. However, supratentorial AT/RTs are also frequently seen in the pineal region, spine, and suprasellar region.[115]

AT/RT has been identified as pathologically distinct entities from medulloblastoma and other embryonal tumors. In the recent WHO classification, AT/RT is now defined by alterations of either the *INI1* or, very rarely, *BRG1 genes*. If a tumor has histologic features of AT/RT but does not harbor either of the diagnostic genetic alterations, only a descriptive diagnosis of CNS embryonal tumor with rhabdoid features is available; in other words, the diagnosis of AT/RT requires confirmation of the characteristic molecular defect.[4,116]

Imaging appearances are similar to medulloblastoma: isointense on T1-weighted images and hypointense signal intensity on T2-weighted images (e-Fig. 35.13). Cystic areas are common. Due to their highly cellular nature, T2 hypointensity is often seen in the solid areas, associated with restricted diffusion. Hemorrhage and calcification is not uncommon.[117] Subarachnoid spread throughout the CNS with spinal drop metastases is common, with frequency ranging between 25% and 46%.[118,119]

Survival rates for patients with AT/RT are generally poor but have improved in recent years with aggressive multimodality therapies and development of trials specifically designed for this entity.[120] Although some older studies quoted 2-year survival rates as low as 18%, more recent studies have reported improved 2-year survival rates up to 60% for patients with gross total resection of the primary tumor.[120,121] Survival rates are higher in children older than 3 years of age. Poor prognosis is related to the young age of the affected patients, as well as the high propensity for CSF tumor dissemination. Distant metastases to the lungs and abdomen also may be seen.

### Infratentorial Ependymomas

Infratentorial ependymomas constitute 8% to 15% of posterior fossa tumors in children. The molecular features were previously discussed. They arise from the ventricular ependymal lining and grow out of the fourth ventricle via the foramina of Luschka and Magendie into the cerebellopontine angles and cisternal spaces around the brainstem and cervicomedullary junction. These tumors are T1 hypointense and isointense to gray matter on T2-weighted images, and demonstrate heterogeneous enhancement (Fig. 35.14). Up to 50% contain foci of calcification. Disseminated disease is present in 7% to 15% of patients at diagnosis.[122] Posterior fossa ependymomas demonstrate significantly higher ADC values than medulloblastomas and lower ADC values than astrocytomas,[123] which may help in preoperative tumor differentiation.

Extent of surgical resection is the most important prognostic factor. Complete surgical resection followed by other treatments has a more than 80% 3-year disease-free survival rate.[124,125] Older age and favorable histologic grading indicate a better prognosis.[126]

## PINEAL REGION TUMORS

Pineal tumors comprise between 3% and 8% of all pediatric brain tumors.[127] Pineal region tumors can be divided into four categories: germ cell tumors, pineal cysts, pineal parenchymal tumors, and tumors of the supporting tissues of the pineal gland or adjacent structures (such as pineal gliomas, dermoids, and epidermoids).

The most common pineal region tumors are germ cell tumors, of which 65% are pure germinomas.[128] Other variants such as nongerminomatous germ cell tumors (NGGCTs), mixed germ cell tumors, teratomas, embryonal cell carcinoma, yolk sac tumor, and choriocarcinoma constitute the remainder.

### Germ Cell Tumors

Germinomas are hyperdense on CT and enhance homogenously. The typical appearance on CT is a calcified pineal gland surrounded by noncalcified tumor. On MRI, these lesions have homogenous signal isointense to gray matter on all sequences with intense contrast enhancement. These tumors grow anteriorly into the floor of the third ventricle and may infiltrate the thalami and midbrain (Fig. 35.15). Spinal dissemination is seen in up to 36% of cases.[129]

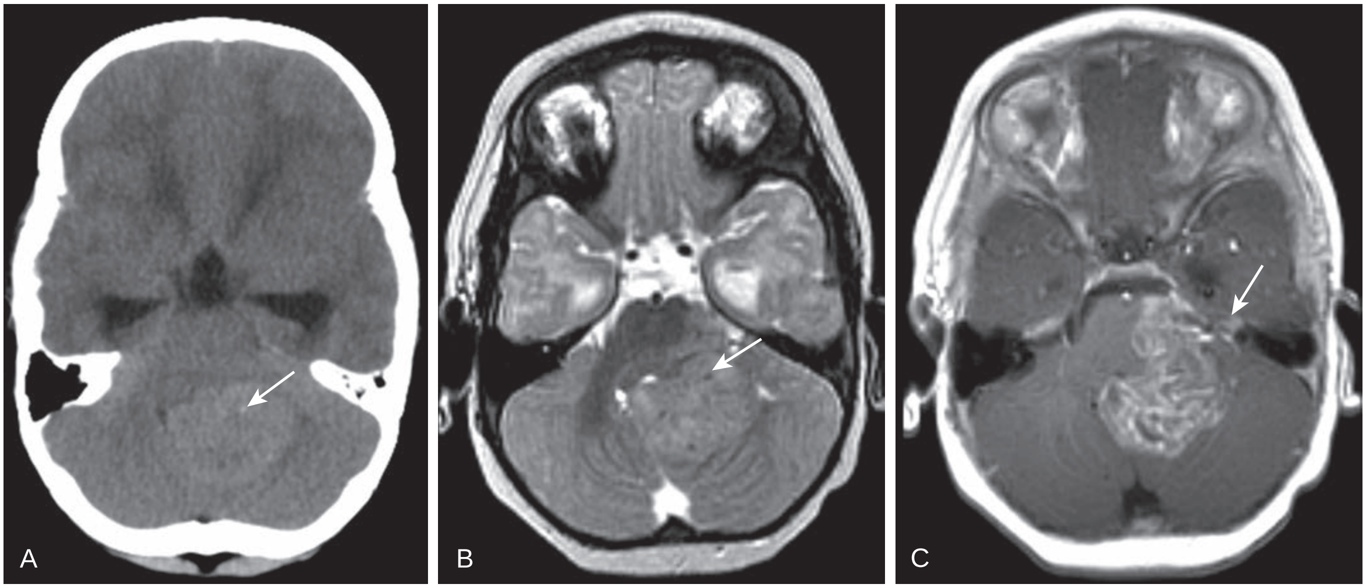

**Figure 35.14. Ependymoma.** (A) Axial noncontrast CT shows a hyperdense mass lesion occupying the fourth ventricle and extending through the left foramen of Luschka. Note several tiny punctate areas of calcification *(arrow).* (B) Axial T2-weighted MRI shows the lesion *(arrow)* is isointense compared with gray matter. (C) Axial postcontrast MPRAGE MRI shows heterogeneous enhancement of the lesion and its extension toward the left foramen of Luschka *(arrow).*

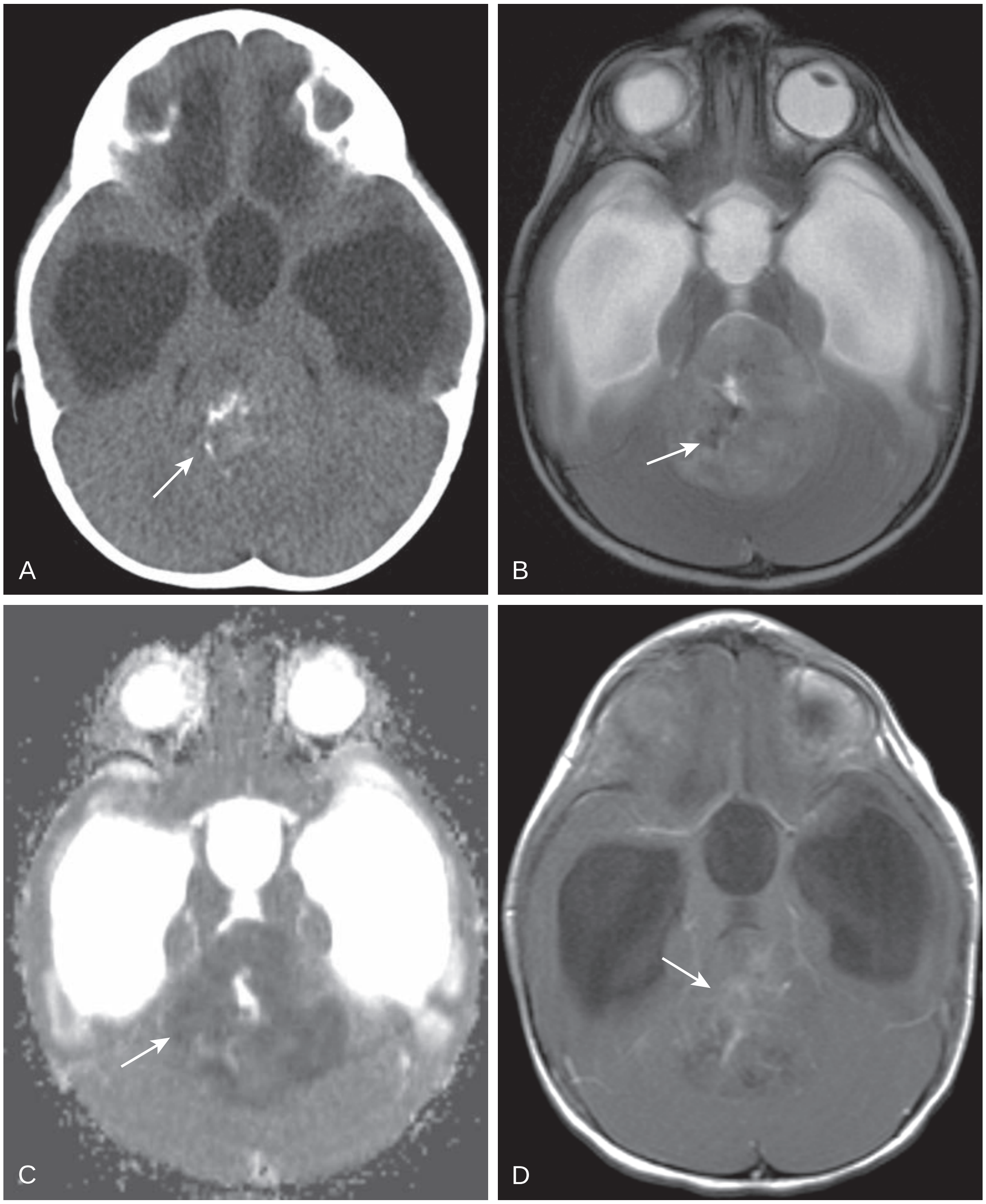

**e-Figure 35.13. Infratentorial atypical teratoid/rhabdoid tumor.** (A) Axial non contrast CT head shows a large posterior fossa mass with areas of calcification *(arrow)*. (B) The axial T2-weighted image, the predominant solid component is hypointense compared with gray matter. Foci of even lower signal intensity *(arrow)* correspond to the foci of calcification seen on the CT. (C) Apparent diffusion coefficient (ADC) map shows restricted diffusion within the mass reflecting the hypercellularity within the tumor *(arrow)*. (D) Axial post-contrast T1-weighted MRI shows patchy enhancement of the mass *(arrow)*.

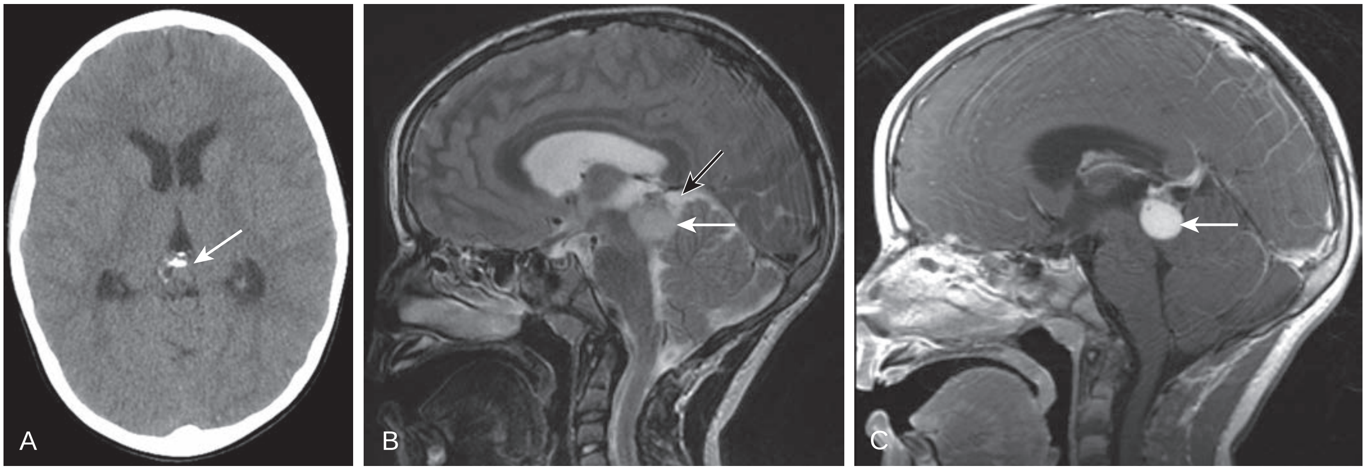

**Figure 35.15. Pineal germinoma.** (A) Axial unenhanced CT shows a partially calcified lesion *(arrow)* in the pineal region. Note presence of hydrocephalus resulting from third ventricular obstruction. (B) Sagittal T2-weighted MRI shows a rounded mass *(white arrow)* hyperintense to gray matter centered in the pineal region. Note the presence of cystic T2-hyperintense component along the superior aspect *(black arrow).* (C) Postcontrast T1-weighted MRI shows homogenous enhancement of the solid component *(arrow)* of the lesion.

Imaging appearances of NGGCTs are nonspecific, with intratumoral cysts and calcifications being a relatively common finding. For example, teratomas are heterogeneous and contain cysts and calcification and demonstrate variable enhancement. The presence of fat is a specific feature. The presence of hemorrhage is more suggestive of a choriocarcinoma.

## Pineal Parenchymal Tumors

Pineocytomas are well-differentiated tumors that retain morphologic features of the pineal parenchymal cells. They are slow-growing, circumscribed, but noncapsulated tumors. They are more commonly solid tumors, although cystic variants have been described. Solid tumors are either hypointense or isointense to gray matter and T2-hyperintense. Enhancement is homogenous and calcification is common. Cystic variants are often indistinguishable from pineal cysts.[130]

Pineoblastomas are malignant, unencapsulated tumors that resemble embryonal tumors NOS, but are distinct from such tumors in other locations due to their photosensory differentiation.[131] On MRI, these lesions are hypointense to isointense on T1-weighted images and variable low, high, or mixed signal on T2-weighted images. They have lobulated contours and enhance homogenously (e-Fig. 35.16). They calcify less often then pineocytomas. The "exploded pattern" of calcification with peripheral displacement of pineal gland calcification is considered more typical of pineal parenchymal tumors, differentiating them from germ cell tumors.[132] Pineoblastomas are resected surgically with adjuvant craniospinal radiation and multiagent chemotherapy. Prognosis is relatively poor.[133]

## CONCLUSION

Advances in neuroimaging coupled with advances in molecular biology and neurosurgery over the past decade have improved our ability to detect, diagnose, characterize, and treat pediatric CNS tumors. It is important to recognize the typical features of each of these tumors on imaging studies, as this forms the basis for further management. Accurate characterization and reporting of a tumor at presentation and its relation to eloquent areas can help plan immediate and, in some cases, long-term management (e-Box 35.2). In the future, it is hoped that imaging studies will become further refined to enable rapid and more accurate diagnoses, helping design treatment regimens tailored to the needs of an individual patient, and enable improved assessment of treatment response and early detection of recurrence.

### KEY POINTS

1. MRI with contrast is the imaging modality of choice for the diagnosis of pediatric brain tumors.
2. Advanced imaging techniques can help understand tumor physiology and map out the surgical plan by defining relationship of tumors to eloquent areas.
3. The latest WHO classification emphasizes molecular parameters in addition to histological features in the classification of brain tumors, which relate increasingly to the management and outcome.
4. In addition to providing a complete description of imaging features of a new tumor, the radiologist's report should include information that can help inform surgical planning and other treatment measures.
5. Increasing use and availability of minimally invasive techniques and intraoperative imaging calls for greater radiologist involvement in planning surgical management of pediatric brain tumors.

### SUGGESTED READINGS

Brandão LA, Young Poussaint T. Posterior fossa tumors. *Neuroimaging Clin N Am*. 2017;27:1–37.

Lequin M, Hendrikse J. Advanced MR imaging in pediatric brain tumors, clinical applications. *Neuroimaging Clin N Am*. 2017;27:167–190.

Louis DN, Perry A, Reifenberger G, et al. The 2016 World Health Organization Classification of Tumors of the Central Nervous System: a summary. *Acta Neuropathol*. 2016;131:803–820.

Ostrom QT, de Blank PM, Kruchko C, et al. Alex's Lemonade Stand Foundation Infant and Childhood Primary Brain and Central Nervous System Tumors Diagnosed in the United States in 2007-2011. *Neuro Oncol*. 2015;16(suppl 10):x1–x36.

### REFERENCES

Full references for this chapter can be found on www.expertconsult.com.

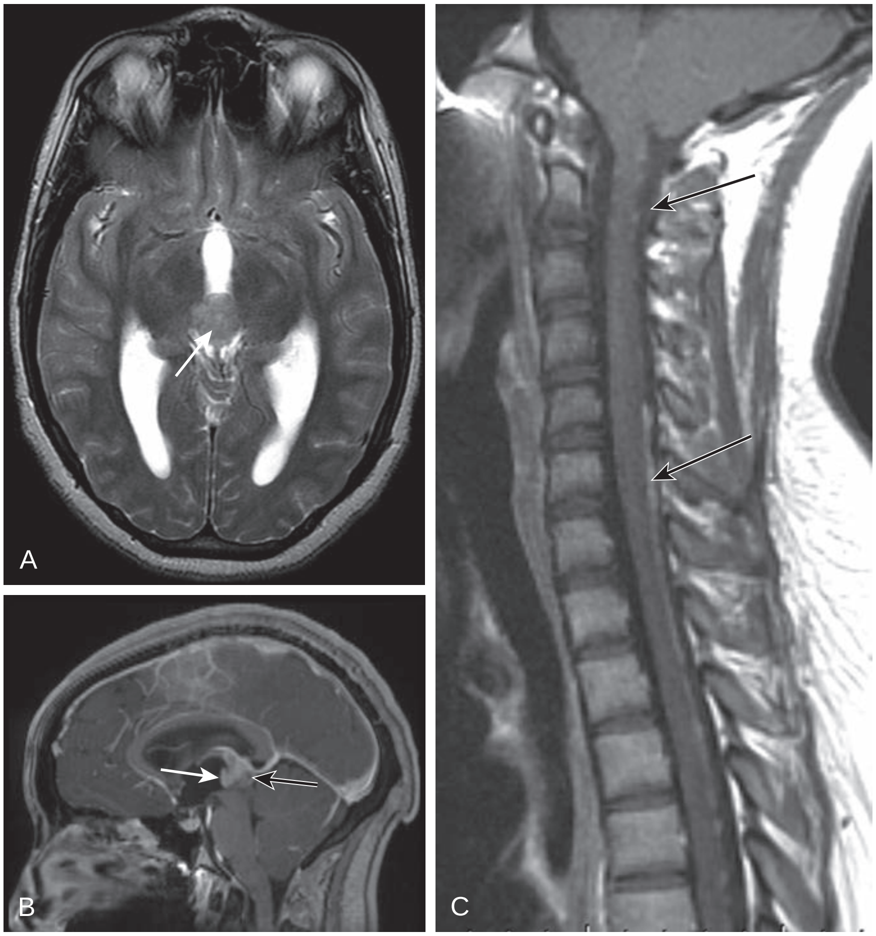

**e-Figure 35.16. Pineoblastoma.** (A) Axial T2-weighted MRI shows a heterogeneous lobulated hypointense mass *(arrow)* in the pineal region causing obstructive hydrocephalus. (B) Postcontrast sagittal T1-weighted MRI shows heterogeneous enhancement of the mass *(white arrow)* with a small focus of nonenhancement in its posterior aspect *(black arrow).* (C) Sagittal T1-postcontrast MRI through the cervical and upper thoracic spine shows linear and nodular enhancement *(arrows)* along the surface of the cervical and upper thoracic spinal cord consistent with leptomeningeal seeding of the tumor.

### **e-BOX 35.2** Key Points to Include in the Report When a New Tumor Is Identified

- Signal characteristics, including enhancement characteristics, presence of calcification and/or hemorrhage
- Intraaxial or extraaxial location
- Lesion extent
- Surrounding edema or white matter infiltration
- Relationship to adjacent structures (e.g., optic chiasm, pituitary gland, and eloquent cortical areas)
- Relationship and effect on arterial and venous structures
- Mass effect, midline shift, and subfalcine, transtentorial, or uncal herniation
- Presence of leptomeningeal enhancement and craniospinal dissemination
- Osseous involvement in cases of extraaxial tumors
- Reduced or increased diffusivity
- Perfusion characteristics
- Magnetic resonance spectroscopy

## REFERENCES

1. Gurney J, Smith M, Bunin G. CNS and miscellaneous intracranial and intraspinal neoplasms. In: Ries LA, Smith M, Gurney J, eds. *Cancer Incidence and Survival among Children and Adolescents: United States SEER Program 1975-1995 NIH Publication No 99-4649*. Philadelphia: National Cancer Institute SEER Program; 1999:51–63.
2. Ostrom QT, Gittleman H, Xu J, et al. CBTRUS Statistical Report: Primary Brain and Other Central Nervous System Tumors Diagnosed in the United States in 2009–2013. *Neuro Oncol*. 2016;18 (suppl 5):v1–v75.
3. Ostrom QT, de Blank PM, Kruchko C, et al. Alex's Lemonade Stand Foundation Infant and Childhood Primary Brain and Central Nervous System Tumors Diagnosed in the United States in 2007-2011. *Neuro Oncol*. 2015;16(suppl 10):x1–x36.
4. Louis DN, Perry A, Reifenberger G, et al. The 2016 World Health Organization Classification of Tumors of the Central Nervous System: a summary. *Acta Neuropathol*. 2016;131(6):803–820.
5. Neglia JP, Meadows AT, Robison LL, et al. Second neoplasms after acute lymphoblastic leukemia in childhood. *N Engl J Med*. 1991;325(19):1330–1336.
6. Vinchon M, Leblond P, Caron S, et al. Radiation-induced tumors in children irradiated for brain tumor: a longitudinal study. *Childs Nerv Syst*. 2011;27(3):445–453.
7. Bunin GR. Nongenetic causes of childhood cancers: evidence from international variation, time trends, and risk factor studies. *Toxicol Appl Pharmacol*. 2004;199(2):91–103.
8. Poussaint TY, Rodriguez D. Advanced neuroimaging of pediatric brain tumors: MR diffusion, MR perfusion, and MR spectroscopy. *Neuroimaging Clin N Am*. 2006;16(1):169–192, ix.
9. Lequin M, Hendrikse J. Advanced MR imaging in pediatric brain tumors, clinical applications. *Neuroimaging Clin N Am*. 2017;27(1):167–190.
10. Mukherjee P, Berman JI, Chung SW, et al. Diffusion tensor MR imaging and fiber tractography: theoretic underpinnings. *AJNR Am J Neuroradiol*. 2008;29(4):632–641.
11. Mukherjee P, Chung SW, Berman JI, et al. Diffusion tensor MR imaging and fiber tractography: technical considerations. *AJNR Am J Neuroradiol*. 2008;29(5):843–852.
12. Mukherjee P, McKinstry RC. Diffusion tensor imaging and tractography of human brain development. *Neuroimaging Clin N Am*. 2006;16(1):19–43, vii.
13. Gauvain KM, McKinstry RC, Mukherjee P, et al. Evaluating pediatric brain tumor cellularity with diffusion-tensor imaging. *AJR Am J Roentgenol*. 2001;177(2):449–454.
14. Cha S. Update on brain tumor imaging: from anatomy to physiology. *AJNR Am J Neuroradiol*. 2006;27(3):475–487.
15. Poretti A, Meoded A, Cohen KJ, et al. Apparent diffusion coefficient of pediatric cerebellar tumors: a biomarker of tumor grade? *Pediatr Blood Cancer*. 2013;60(12):2036–2041.
16. Ozturk A, Oguz KK, Akalan N, et al. Evaluation of parenchymal changes at the operation site with early postoperative brain diffusion-weighted magnetic resonance imaging. *Diagn Interv Radiol*. 2006;12(3):115–120.
17. Lee WJ, Choi SH, Park CK, et al. Diffusion-weighted MR imaging for the differentiation of true progression from pseudoprogression following concomitant radiotherapy with temozolomide in patients with newly diagnosed high-grade gliomas. *Acad Radiol*. 2012;19(11):1353–1361.
18. Jellison BJ, Field AS, Medow J, et al. Diffusion tensor imaging of cerebral white matter: a pictorial review of physics, fiber tract anatomy, and tumor imaging patterns. *AJNR Am J Neuroradiol*. 2004;25(3):356–369.
19. Khong PL, Kwong DL, Chan GC, et al. Diffusion-tensor imaging for the detection and quantification of treatment-induced white matter injury in children with medulloblastoma: a pilot study. *AJNR Am J Neuroradiol*. 2003;24(4):734–740.
20. Khong PL, Leung LH, Chan GC, et al. White matter anisotropy in childhood medulloblastoma survivors: association with neurotoxicity risk factors. *Radiology*. 2005;236(2):647–652.
21. Poussaint TY, Vajapeyam S, Ricci KI, et al. Apparent diffusion coefficient histogram metrics correlate with survival in diffuse intrinsic pontine glioma: a report from the Pediatric Brain Tumor Consortium. *Neuro Oncol*. 2016;18(5):725–734.
22. Grech-Sollars M, Saunders DE, Phipps KP, et al. Challenges for the functional diffusion map in pediatric brain tumors. *Neuro Oncol*. 2014;16(3):449–456.
23. Hwang JH, Egnaczyk GF, Ballard E, et al. Proton MR spectroscopic characteristics of pediatric pilocytic astrocytomas. *AJNR Am J Neuroradiol*. 1998;19(3):535–540.
24. Young GS, Xia S. Advanced MR techniques in Clinical Brain Tumor Imaging. In: Newton HB, Jolesz FA, eds. *Handbook of Neuro-oncology Neuroimaging*. vol. 1. USA: Academic Press; 2008.
25. Warren KE. NMR spectroscopy and pediatric brain tumors. *Oncologist*. 2004;9(3):312–318.
26. Astrakas LG, Zurakowski D, Tzika AA, et al. Noninvasive magnetic resonance spectroscopic imaging biomarkers to predict the clinical grade of pediatric brain tumors. *Clin Cancer Res*. 2004;10(24):8220–8228.
27. Cho YD, Choi GH, Lee SP, et al. (1)H-MRS metabolic patterns for distinguishing between meningiomas and other brain tumors. *Magn Reson Imaging*. 2003;21(6):663–672.
28. Moreno-Torres A, Martinez-Perez I, Baquero M, et al. Taurine detection by proton magnetic resonance spectroscopy in medulloblastoma: contribution to noninvasive differential diagnosis with cerebellar astrocytoma. *Neurosurgery*. 2004;55(4):824–829, discussion 9.
29. Seymour ZA, Panigrahy A, Finlay JL, et al. Citrate in pediatric CNS tumors? *AJNR Am J Neuroradiol*. 2008;29(5):1006–1011.
30. Bluml S, Panigrahy A, Laskov M, et al. Elevated citrate in pediatric astrocytomas with malignant progression. *Neuro Oncol*. 2011;13(10):1107–1117.
31. Rossi A, Gandolfo C, Morana G, et al. New MR sequences (diffusion, perfusion, spectroscopy) in brain tumours. *Pediatr Radiol*. 2010;40(6):999–1009.
32. Ball WS Jr, Holland SK. Perfusion imaging in the pediatric patient. *Magn Reson Imaging Clin N Am*. 2001;9(1):207–230, ix.
33. Panigrahy A, Bluml S. Neuroimaging of pediatric brain tumors: from basic to advanced magnetic resonance imaging (MRI). *J Child Neurol*. 2009;24(11):1343–1365.
34. Vajapeyam S, Stamoulis C, Ricci K, et al. Automated processing of dynamic contrast-enhanced MRI: correlation of advanced pharmacokinetic metrics with tumor grade in pediatric brain tumors. *AJNR Am J Neuroradiol*. 2017;38(1):170–175.
35. Lehmann P, Monet P, de Marco G, et al. A comparative study of perfusion measurement in brain tumours at 3 Tesla MR: Arterial spin labeling versus dynamic susceptibility contrast-enhanced MRI. *Eur Neurol*. 2010;64(1):21–26.
36. Noguchi T, Yoshiura T, Hiwatashi A, et al. Perfusion imaging of brain tumors using arterial spin-labeling: correlation with histopathologic vascular density. *AJNR Am J Neuroradiol*. 2008;29(4):688–693.
37. Yeom KW, Mitchell LA, Lober RM, et al. Arterial spin-labeled perfusion of pediatric brain tumors. *AJNR Am J Neuroradiol*. 2014;35(2):395–401.
38. Dangouloff-Ros V, Deroulers C, Foissac F, et al. Arterial spin labeling to predict brain tumor grading in children: correlations between histopathologic vascular density and perfusion MR imaging. *Radiology*. 2016;281(2):553–566.
39. Di Costanzo A, Pollice S, Trojsi F, et al. Role of perfusion-weighted imaging at 3 Tesla in the assessment of malignancy of cerebral gliomas. *Radiol Med*. 2008;113(1):134–143.
40. Birn RM, Cox RW, Bandettini PA. Detection versus estimation in event-related fMRI: choosing the optimal stimulus timing. *Neuroimage*. 2002;15(1):252–264.
41. DiFrancesco MW, Robertson SA, Karunanayaka P, et al. BOLD fMRI in infants under sedation: comparing the impact of pentobarbital and propofol on auditory and language activation. *J Magn Reson Imaging*. 2013;38(5):1184–1195.
42. Gemma M, de Vitis A, Baldoli C, et al. Functional magnetic resonance imaging (fMRI) in children sedated with propofol or midazolam. *J Neurosurg Anesthesiol*. 2009;21(3):253–258.
43. Suarez RO, Taimouri V, Boyer K, et al. Passive fMRI mapping of language function for pediatric epilepsy surgical planning: validation using Wada, ECS, and FMAER. *Epilepsy Res*. 2014;108(10):1874–1888.
44. Gupta A, Shah A, Young RJ, et al. Imaging of brain tumors: functional magnetic resonance imaging and diffusion tensor imaging. *Neuroimaging Clin N Am*. 2010;20(3):379–400.
45. Bauer PR, Reitsma JB, Houweling BM, et al. Can fMRI safely replace the Wada test for preoperative assessment of language lateralisation? A meta-analysis and systematic review. *J Neurol Neurosurg Psychiatry*. 2014;85(5):581–588.
46. Holodny AI, Schulder M, Liu WC, et al. The effect of brain tumors on BOLD functional MR imaging activation in the adjacent motor cortex: implications for image-guided neurosurgery. *AJNR Am J Neuroradiol*. 2000;21(8):1415–1422.

47. Jager PL, Vaalburg W, Pruim J, et al. Radiolabeled amino acids: basic aspects and clinical applications in oncology. *J Nucl Med*. 2001;42(3):432–445.
48. Kubota K, Yamada K, Fukada H, et al. Tumor detection with carbon-11-labelled amino acids. *Eur J Nucl Med*. 1984;9(3):136–140.
49. Herholz K, Holzer T, Bauer B, et al. 11C-methionine PET for differential diagnosis of low-grade gliomas. *Neurology*. 1998;50(5):1316–1322.
50. Scheithauer BW, Hawkins C, Tihan T. Pilocytic astrocytomas. In: Louis DN, Ohgaki H, Wiestler OD, eds. *Classification of Tumours of the Central Nervous System*. Geneva: World Heath Organization Press; 2007:14–21.
51. Deliganis AV, Geyer JR, Berger MS. Prognostic significance of type 1 neurofibromatosis (von Recklinghausen Disease) in childhood optic glioma. *Neurosurgery*. 1996;38(6):1114–1118, discussion 8-9.
52. Grand SD, Kremer S, Tropres IM, et al. Perfusion-sensitive MRI of pilocytic astrocytomas: initial results. *Neuroradiology*. 2007;49(7):545–550.
53. Komotar RJ, Burger PC, Carson BS, et al. Pilocytic and pilomyxoid hypothalamic/chiasmatic astrocytomas. *Neurosurgery*. 2004;54(1):72–79, discussion 9-80.
54. Hawkins C, Walker E, Mohamed N, et al. BRAF-KIAA1549 fusion predicts better clinical outcome in pediatric low-grade astrocytoma. *Clin Cancer Res*. 2011;17(14):4790–4798.
55. Collins VP, Jones DT, Giannini C. Pilocytic astrocytoma: pathology, molecular mechanisms and markers. *Acta Neuropathol*. 2015;129(6):775–788.
56. Lassaletta A, Zapotocky M, Bouffet E, et al. An integrative molecular and genomic analysis of pediatric hemispheric low-grade gliomas: an update. *Childs Nerv Syst*. 2016;32(10):1789–1797.
57. Pfister S, Witt O. Pediatric gliomas. *Recent Results Cancer Res*. 2009;171:67–81.
58. Borja MJ, Plaza MJ, Altman N, et al. Conventional and advanced MRI features of pediatric intracranial tumors: supratentorial tumors. *AJR Am J Roentgenol*. 2013;200(5):W483–W503.
59. Pfister S, Hartmann C, Korshunov A. Histology and molecular pathology of pediatric brain tumors. *J Child Neurol*. 2009;24(11):1375–1386.
60. Castillo M, Smith JK, Kwock L. Correlation of myo-inositol levels and grading of cerebral astrocytomas. *AJNR Am J Neuroradiol*. 2000;21(9):1645–1649.
61. de Fatima Vasco Aragao M, Law M, Batista de Almeida D, et al. Comparison of perfusion, diffusion, and MR spectroscopy between low-grade enhancing pilocytic astrocytomas and high-grade astrocytomas. *AJNR Am J Neuroradiol*. 2014;35(8):1495–1502.
62. Kaatsch P, Rickert CH, Kuhl J, et al. Population-based epidemiologic data on brain tumors in German children. *Cancer*. 2001;92(12):3155–3164.
63. Zamora C, Huisman TA, Izbudak I. Supratentorial tumors in pediatric patients. *Neuroimaging Clin N Am*. 2017;27(1):39–67.
64. Perkins SM, Rubin JB, Leonard JR, et al. Glioblastoma in children: a single-institution experience. *Int J Radiat Oncol Biol Phys*. 2011;80(4):1117–1121.
65. Song KS, Phi JH, Cho BK, et al. Long-term outcomes in children with glioblastoma. *J Neurosurg Pediatr*. 2010;6(2):145–149.
66. Olar A, Wani KM, Alfaro-Munoz KD, et al. IDH mutation status and role of WHO grade and mitotic index in overall survival in grade II-III diffuse gliomas. *Acta Neuropathol*. 2015;129(4):585–596.
67. Reuss DE, Mamatjan Y, Schrimpf D, et al. IDH mutant diffuse and anaplastic astrocytomas have similar age at presentation and little difference in survival: a grading problem for WHO. *Acta Neuropathol*. 2015;129(6):867–873.
68. Kleihues P, Cavenee WK. *International Agency for Research on Cancer. Pathology and Genetics of Tumours of the Nervous System*. Lyon: IARC Press; 2000. 314 p.
69. Figeroa RE, el Gammal T, Brooks BS, et al. MR findings on primitive neuroectodermal tumors. *J Comput Assist Tomogr*. 1989;13(5):773–778.
70. Kieran M, Chi SN, Samuel D, et al. Tumors of the brain and spinal cord. In: Orkin SH, Fisher DE, Look AT, et al, eds. *Oncology of Infancy and Childhood*. vol. 1. USA: Saunders Elsevier; 2009:602–685.
71. Kilday JP, Rahman R, Dyer S, et al. Pediatric ependymoma: biological perspectives. *Mol Cancer Res*. 2009;7(6):765–786.
72. Koeller KK, Sandberg GD. From the archives of the AFIP. Cerebral intraventricular neoplasms: radiologic-pathologic correlation. *Radiographics*. 2002;22(6):1473–1505.
73. Yuh EL, Barkovich AJ, Gupta N. Imaging of ependymomas: MRI and CT. *Childs Nerv Syst*. 2009;25(10):1203–1213.
74. Pajtler KW, Mack SC, Ramaswamy V, et al. The current consensus on the clinical management of intracranial ependymoma and its distinct molecular variants. *Acta Neuropathol*. 2016.
75. Pajtler KW, Witt H, Sill M, et al. Molecular classification of ependymal tumors across all CNS compartments, histopathological grades, and age groups. *Cancer Cell*. 2015;27(5):728–743.
76. Fernandez C, Maues de Paula A, Colin C, et al. Thalamic gliomas in children: an extensive clinical, neuroradiological and pathological study of 14 cases. *Childs Nerv Syst*. 2006;22(12):1603–1610.
77. Solomon DA, Wood MD, Tihan T, et al. Diffuse midline gliomas with histone H3-K27M mutation: a series of 47 cases assessing the spectrum of morphologic variation and associated genetic alterations. *Brain Pathol*. 2016;26(5):569–580.
78. Aihara K, Mukasa A, Gotoh K, et al. H3F3A K27M mutations in thalamic gliomas from young adult patients. *Neuro Oncol*. 2014;16(1):140–146.
79. Feng J, Hao S, Pan C, et al. The H3.3 K27M mutation results in a poorer prognosis in brainstem gliomas than thalamic gliomas in adults. *Hum Pathol*. 2015;46(11):1626–1632.
80. Wolff JE, Sajedi M, Brant R, et al. Choroid plexus tumours. *Br J Cancer*. 2002;87(10):1086–1091.
81. Cavalheiro S, Moron AF, Hisaba W, et al. Fetal brain tumors. *Childs Nerv Syst*. 2003;19(7–8):529–536.
82. Naeini RM, Yoo JH, Hunter JV. Spectrum of choroid plexus lesions in children. *AJR Am J Roentgenol*. 2009;192(1):32–40.
83. Horska A, Ulug AM, Melhem ER, et al. Proton magnetic resonance spectroscopy of choroid plexus tumors in children. *J Magn Reson Imaging*. 2001;14(1):78–82.
84. Hassoun J, Soylemezoglu F, Gambarelli D, et al. Central neurocytoma: a synopsis of clinical and histological features. *Brain Pathol*. 1993;3(3):297–306.
85. Yeh IB, Xu M, Ng WH, et al. Central neurocytoma: typical magnetic resonance spectroscopy findings and atypical ventricular dissemination. *Magn Reson Imaging*. 2008;26(1):59–64.
86. Tenreiro-Picon OR, Kamath SV, Knorr JR, et al. Desmoplastic infantile ganglioglioma: CT and MRI features. *Pediatr Radiol*. 1995;25(7):540–543.
87. Paulus W, Schlote W, Perentes E, et al. Desmoplastic supratentorial neuroepithelial tumours of infancy. *Histopathology*. 1992;21(1):43–49.
88. Tamburrini G, Colosimo C Jr, Giangaspero F, et al. Desmoplastic infantile ganglioglioma. *Childs Nerv Syst*. 2003;19(5–6):292–297.
89. Di Rocco C, Caldarelli M, Tamburrini G, et al. Surgical management of craniopharyngiomas–experience with a pediatric series. *J Pediatr Endocrinol Metab*. 2006;19(suppl 1):355–366.
90. Burkhard C, Di Patre PL, Schuler D, et al. A population-based study of the incidence and survival rates in patients with pilocytic astrocytoma. *J Neurosurg*. 2003;98(6):1170–1174.
91. Chung EM, Specht CS, Schroeder JW. From the archives of the AFIP: Pediatric orbit tumors and tumorlike lesions: neuroepithelial lesions of the ocular globe and optic nerve. *Radiographics*. 2007;27(4):1159–1186.
92. Janss AJ, Grundy R, Cnaan A, et al. Optic pathway and hypothalamic/chiasmatic gliomas in children younger than age 5 years with a 6-year follow-up. *Cancer*. 1995;75(4):1051–1059.
93. Simon J, Szumowski J, Totterman S, et al. Fat-suppression MR imaging of the orbit. *AJNR Am J Neuroradiol*. 1988;9(5):961–968.
94. Poussaint TY, Barnes PD, Nichols K, et al. Diencephalic syndrome: clinical features and imaging findings. *AJNR Am J Neuroradiol*. 1997;18(8):1499–1505.
95. Perreault S, Ramaswamy V, Achrol AS, et al. MRI surrogates for molecular subgroups of medulloblastoma. *AJNR Am J Neuroradiol*. 2014;35(7):1263–1269.
96. Raybaud C, Ramaswamy V, Taylor MD, et al. Posterior fossa tumors in children: developmental anatomy and diagnostic imaging. *Childs Nerv Syst*. 2015;31(10):1661–1676.
97. Meyers SP, Wildenhain SL, Chang JK, et al. Postoperative evaluation for disseminated medulloblastoma involving the spine: contrast-enhanced MR findings, CSF cytologic analysis, timing of disease occurrence, and patient outcomes. *AJNR Am J Neuroradiol*. 2000;21(9):1757–1765.
98. Bowers DC, Georgiades C, Aronson LJ, et al. Tectal gliomas: natural history of an indolent lesion in pediatric patients. *Pediatr Neurosurg*. 2000;32(1):24–29.
99. Poussaint TY, Kowal JR, Barnes PD, et al. Tectal tumors of childhood: clinical and imaging follow-up. *AJNR Am J Neuroradiol*. 1998;19(5):977–983.

100. Monje M, Mitra SS, Freret ME, et al. Hedgehog-responsive candidate cell of origin for diffuse intrinsic pontine glioma. *Proc Natl Acad Sci USA*. 2011;108(11):4453–4458.
101. Prabhu SP, Ng S, Vajapeyam S, et al. DTI assessment of the brainstem white matter tracts in pediatric BSG before and after therapy: a report from the Pediatric Brain Tumor Consortium. *Childs Nerv Syst*. 2011;27(1):11–18.
102. Helton KJ, Edwards M, Steen RG, et al. Neuroimaging-detected late transient treatment-induced lesions in pediatric patients with brain tumors. *J Neurosurg*. 2005;102(suppl 2):179–186.
103. Poussaint TY, Kocak M, Vajapeyam S, et al. MRI as a central component of clinical trials analysis in brainstem glioma: a report from the Pediatric Brain Tumor Consortium (PBTC). *Neuro Oncol*. 2011;13(4):417–427.
104. Chen HJ, Panigrahy A, Dhall G, et al. Apparent diffusion and fractional anisotropy of diffuse intrinsic brain stem gliomas. *AJNR Am J Neuroradiol*. 2010;31(10):1879–1885.
105. Helton KJ, Phillips NS, Khan RB, et al. Diffusion tensor imaging of tract involvement in children with pontine tumors. *AJNR Am J Neuroradiol*. 2006;27(4):786–793.
106. Roujeau T, Machado G, Garnett MR, et al. Stereotactic biopsy of diffuse pontine lesions in children. *J Neurosurg*. 2007;107(suppl 1):1–4.
107. Puget S, Beccaria K, Blauwblomme T, et al. Biopsy in a series of 130 pediatric diffuse intrinsic Pontine gliomas. *Childs Nerv Syst*. 2015;31(10):1773–1780.
108. Puget S, Blauwblomme T, Grill J. Is biopsy safe in children with newly diagnosed diffuse intrinsic pontine glioma? *Am Soc Clin Oncol Educ Book*. 2012;629–633.
109. Packer RJ, Boyett JM, Zimmerman RA, et al. Hyperfractionated radiation therapy (72 Gy) for children with brain stem gliomas. A Childrens Cancer Group Phase I/II Trial. *Cancer*. 1993;72(4):1414–1421.
110. Hargrave D, Bartels U, Bouffet E. Diffuse brainstem glioma in children: critical review of clinical trials. *Lancet Oncol*. 2006;7(3):241–248.
111. Pollack IF, Jakacki RI, Butterfield LH, et al. Antigen-specific immunoreactivity and clinical outcome following vaccination with glioma-associated antigen peptides in children with recurrent high-grade gliomas: results of a pilot study. *J Neurooncol*. 2016;130(3):517–527.
112. Pollack IF, Hoffman HJ, Humphreys RP, et al. The long-term outcome after surgical treatment of dorsally exophytic brain-stem gliomas. *J Neurosurg*. 1993;78(6):859–863.
113. Reddy AT. Atypical teratoid/rhabdoid tumors of the central nervous system. *J Neurooncol*. 2005;75(3):309–313.
114. Biegel JA. Molecular genetics of atypical teratoid/rhabdoid tumor. *Neurosurg Focus*. 2006;20(1):E11.
115. Hilden JM, Meerbaum S, Burger P, et al. Central nervous system atypical teratoid/rhabdoid tumor: results of therapy in children enrolled in a registry. *J Clin Oncol*. 2004;22(14):2877–2884.
116. Judkins AR. Immunohistochemistry of INI1 expression: a new tool for old challenges in CNS and soft tissue pathology. *Adv Anat Pathol*. 2007;14(5):335–339.
117. Meyers SP, Khademian ZP, Biegel JA, et al. Primary intracranial atypical teratoid/rhabdoid tumors of infancy and childhood: MRI features and patient outcomes. *AJNR Am J Neuroradiol*. 2006;27(5):962–971.
118. Parmar H, Hawkins C, Bouffet E, et al. Imaging findings in primary intracranial atypical teratoid/rhabdoid tumors. *Pediatr Radiol*. 2006;36(2):126–132.
119. Chi SN, Zimmerman MA, Yao X, et al. Intensive multimodality treatment for children with newly diagnosed CNS atypical teratoid rhabdoid tumor. *J Clin Oncol*. 2009;27(3):385–389.
120. Fruhwald MC, Biegel JA, Bourdeaut F, et al. Atypical teratoid/rhabdoid tumors-current concepts, advances in biology, and potential future therapies. *Neuro Oncol*. 2016;18(6):764–778.
121. Athale UH, Duckworth J, Odame I, et al. Childhood atypical teratoid rhabdoid tumor of the central nervous system: a meta-analysis of observational studies. *J Pediatr Hematol Oncol*. 2009;31(9):651–663.
122. Robertson PL, Zeltzer PM, Boyett JM, et al. Survival and prognostic factors following radiation therapy and chemotherapy for ependymomas in children: a report of the Children's Cancer Group. *J Neurosurg*. 1998;88(4):695–703.
123. Rumboldt Z, Camacho DL, Lake D, et al. Apparent diffusion coefficients for differentiation of cerebellar tumors in children. *AJNR Am J Neuroradiol*. 2006;27(6):1362–1369.
124. Timmermann B, Kortmann RD, Kuhl J, et al. [Interdisciplinary therapy of childhood ependymomas]. *Strahlenther Onkol*. 2002;178(9):469–479.
125. Timmermann B, Kortmann RD, Kuhl J, et al. Combined postoperative irradiation and chemotherapy for anaplastic ependymomas in childhood: results of the German prospective trials HIT 88/89 and HIT 91. *Int J Radiat Oncol Biol Phys*. 2000;46(2):287–295.
126. Tihan T, Zhou T, Holmes E, et al. The prognostic value of histological grading of posterior fossa ependymomas in children: a Children's Oncology Group study and a review of prognostic factors. *Mod Pathol*. 2008;21(2):165–177.
127. Hoffman HJ, Yoshida M, Becker LE, et al. Pineal region tumors in childhood. Experience at the Hospital for Sick Children. 1983. *Pediatr Neurosurg*. 1994;21(1):91–103, discussion 4.
128. Smirniotopoulos JG, Rushing EJ, Mena H. Pineal region masses: differential diagnosis. *Radiographics*. 1992;12(3):577–596.
129. Maity A, Shu HK, Janss A, et al. Craniospinal radiation in the treatment of biopsy-proven intracranial germinomas: twenty-five years' experience in a single center. *Int J Radiat Oncol Biol Phys*. 2004;58(4):1165–1170.
130. Engel U, Gottschalk S, Niehaus L, et al. Cystic lesions of the pineal region–MRI and pathology. *Neuroradiology*. 2000;42(6):399–402.
131. Hirato J, Nakazato Y. Pathology of pineal region tumors. *J Neurooncol*. 2001;54(3):239–249.
132. Zee CS, Segall H, Apuzzo M, et al. MR imaging of pineal region neoplasms. *J Comput Assist Tomogr*. 1991;15(1):56–63.
133. Dirks PB, Harris L, Hoffman HJ, et al. Supratentorial primitive neuroectodermal tumors in children. *J Neurooncol*. 1996;29(1):75–84.

# 36 Cerebrovascular Disorders

Jordan Smith, Ross Holwerda, and Lisa H. Hutchison

Stroke is defined as a neurologic deficit persisting for more than 24 hours and may be caused by cerebral ischemia or intracranial hemorrhage. The annual incidence of stroke in children ranges from 2 to 13 cases per 100,000 patients and is among the top 10 causes of death in childhood.[1] Among children diagnosed with stroke, more than 40% will have major neurologic sequelae and more than 75% will have perceptible residual neurologic deficits.[2]

The clinical presentation of stroke in children is sometimes heralded by the abrupt onset of focal neurologic deficits; however, the symptoms are often nonspecific, resulting in delayed diagnosis.

The most common predisposing conditions in children include cerebrovascular arteriopathy, vascular anomalies, aneurysms, congenital heart disease, sickle cell disease, and hematologic abnormalities.[1] Over half of all strokes in children are ischemic caused by intrinsic vasculopathy or embolic phenomenon, and vascular malformations, aneurysms, and venous sinus thrombosis are the most common causes of hemorrhagic stroke.[2] This chapter focuses on pediatric vascular abnormalities as causes of ischemic and hemorrhagic stroke.

## ARTERIOPATHY

Ischemic stroke in children has an annual incidence of between 2 and 3 per 100,000 children in the United States.[3] Identifiable causes of ischemic stroke occur in approximately 70% of cases, including arterial dissection, moyamoya disease, sickle cell disease, vasculitis/angiitis of the central nervous system, and coagulopathy. The remaining cases are often idiopathic in origin. Twenty-five percent of children with ischemic stroke have coexistent cardiac disease, suggesting a component of embolic etiology.[2]

The most common symptoms of ischemic stroke in children are hemiplegia, seizures, fever, dysphagia, headache, and altered level of consciousness. Headache and seizures are especially common in chronic ischemic conditions such as moyamoya disease.[4]

***Imaging.*** The imaging features of ischemic stroke in children are variable and depend on the underlying cause. In acute arterial dissection, large vessel arterial distribution infarction is often present on computed tomography (CT) or magnetic resonance imaging (MRI). By contrast, in proximal, chronic steno-occlusive disease such as moyamoya disease (Fig. 36.1), infarctions may be absent, conform to an arterial territory, or lie within the watershed zones between the major vascular territories.

Noninvasive vascular imaging such as computed tomographic angiography (CTA) or magnetic resonance angiography (MRA) may show dissection as an abrupt vascular cutoff intracranially or as tapering stenosis, commonly seen with involvement of the neck vasculature. In moyamoya disease, stenosis or occlusion of the supraclinoid segment of the internal carotid artery and/or proximal middle and anterior cerebral arteries is usually present, with collateral vessel formation in the basal ganglia and along the pial surfaces.[5] Vasculitis causes irregular narrowing of medium or small vessels and is inconsistently demonstrated on CTA or MRA.[6] Catheter angiography remains the gold standard for the imaging diagnosis of cerebrovascular disease in children and should be considered whenever a small vessel vasculitis is suspected or when surgical treatment is contemplated.

## VASCULAR ANOMALIES

Vascular anomalies are disorders of vascular development. Although congenital, they may only become symptomatic many months or years after birth. Intracranial vascular malformations are classified according to the vascular channels involved and the hemodynamics of the lesion (high-flow vs. low-flow).[7]

### High-Flow Vascular Anomalies

High-flow vascular anomalies occur when there is an abnormal connection between an artery and a vein that bypasses the normal arteriolar-capillary network. In arteriovenous fistula (AVF), the supplying artery communicates directly with the draining vein through a macroscopic fistula. In arteriovenous malformation (AVM), the supplying artery connects with the draining vein through a plexiform network of abnormal vessels, termed the *nidus*. Both AVF and AVM can be further subdivided, on the basis of anatomic location, as dural, subarachnoid (vein of Galen malformation), pial, or parenchymal (Figs. 36.2, 36.3, and 36.5; e-Fig. 36.4).[7,8]

High-flow vascular malformations may produce clinical manifestations by different methods.[7,9,10] The presence of a direct channel between a supplying artery and a draining vein allows for potentially rapid blood flow. In the absence of venous outflow obstruction, the malformation may cause high-output cardiac failure. Additionally, the lower resistance through the malformation may result in diversion of blood away from the normal brain parenchyma ("steal" phenomenon), producing cerebral ischemia. High-flow malformations also expose the draining veins to arterial pressure, which may cause progressive stenosis of the vein (termed *high-flow venopathy*) or the development of a varix or venous aneurysm that predisposes to hemorrhage. High-flow venopathy may be a cause of seizures or cerebral atrophy due to impaired tissue perfusion from venous hypertension. Hydrocephalus can develop from increased venous pressures that result in impaired resorption of cerebrospinal fluid (see Fig. 36.3A).

### Dural High-Flow Anomalies

Dural AV fistulas in the pediatric population are most frequently congenital, as opposed to acquired AV fistulas in the adult population. The malformation is formed by an abnormal connection between the meningeal arterial supply from the external carotid vasculature with a dural venous sinus (see Fig. 36.2).[7,10,11] The abnormal connections are frequently located in the vicinity of the torcular herophili, and may be associated with high-output heart failure.

### Vein of Galen Malformations

Vein of Galen malformation (VOGM) is a fistulous connection with arterial supply from the deep choroidal arteries and venous drainage through a persistent dilated embryonic median prosencephalic vein, one of the embryologic precursors of the vein of Galen (see Fig. 36.3).[7,11,12] The symptoms, signs, and age at presentation associated with VOGMs depend on the angioarchitecture of the anomaly and the degree of venous outflow obstruction. In the absence of venous outflow obstruction, VOGMs may produce

## Abstract:

Cerebrovascular disorders in the pediatric population can have devastating, long lasting effects resulting from complications such as ischemic or hemorrhagic stroke. The most common predisposing conditions for stroke in children include cerebrovascular arteriopathy, vascular anomalies, aneurysms, congenital heart disease, sickle cell disease, and hematologic abnormalities. Over half of all strokes in children are ischemic caused by intrinsic vasculopathy or embolic phenomenon. Vascular malformations, aneurysms, and venous sinus thrombosis are the most common causes of hemorrhagic stroke. Among children with stroke, more than 40% will have major neurologic sequelae and more than 75% will have perceptible residual neurologic deficits. In this chapter, cerebrovascular disorders are broadly categorized into arteriopathy, high and low flow vascular anomalies, and aneurysms highlighting important clinical and imaging findings that point to a specific diagnosis. Case examples are provided to familiarize the reader with expected imaging manifestations of both common and uncommon cerebrovascular disorders. Knowledge and early recognition of cerebrovascular disorders is imperative as they often predispose patients to ischemic or hemorrhagic stroke. Understanding the variable clinical presentations as well as imaging manifestations of these vascular phenomena is necessary to make a timely diagnosis and initiate prompt treatment when necessary.

## Keywords:

Stroke
Vascular anomalies
Vascular malformations
Aneurysm
Arteriopathy
Telangiectasia

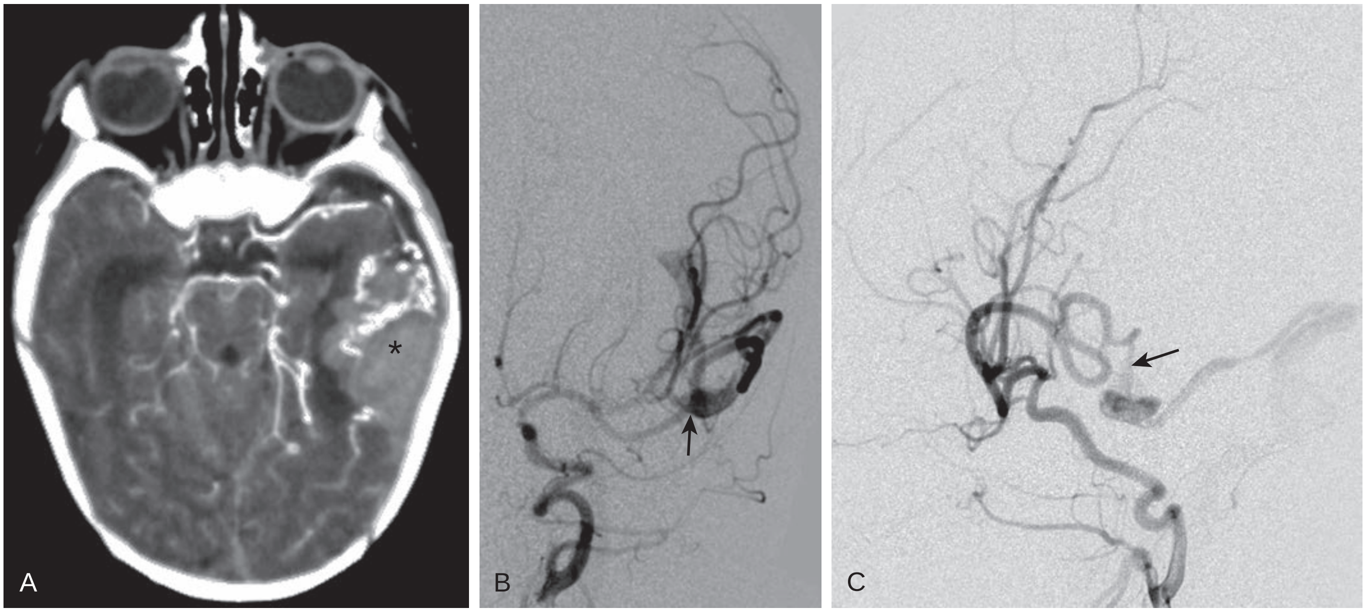

**e-Figure 36.4. Pial arteriovenous fistula and left temporal hemorrhage in an 18-day-old child presenting with irritability, poor feeding, and vomiting.** (A) Contrast-enhanced CT image shows hemorrhage *(asterisk)* in the left temporal lobe associated with enlarged vessels. (B) Frontal digital subtraction angiogram shows a pial arteriovenous fistula *(arrow)* supplied by the left middle cerebral artery. (C) The lateral angiogram demonstrates a fistula *(arrow)* between the middle cerebral artery and the dilated cortical vein.

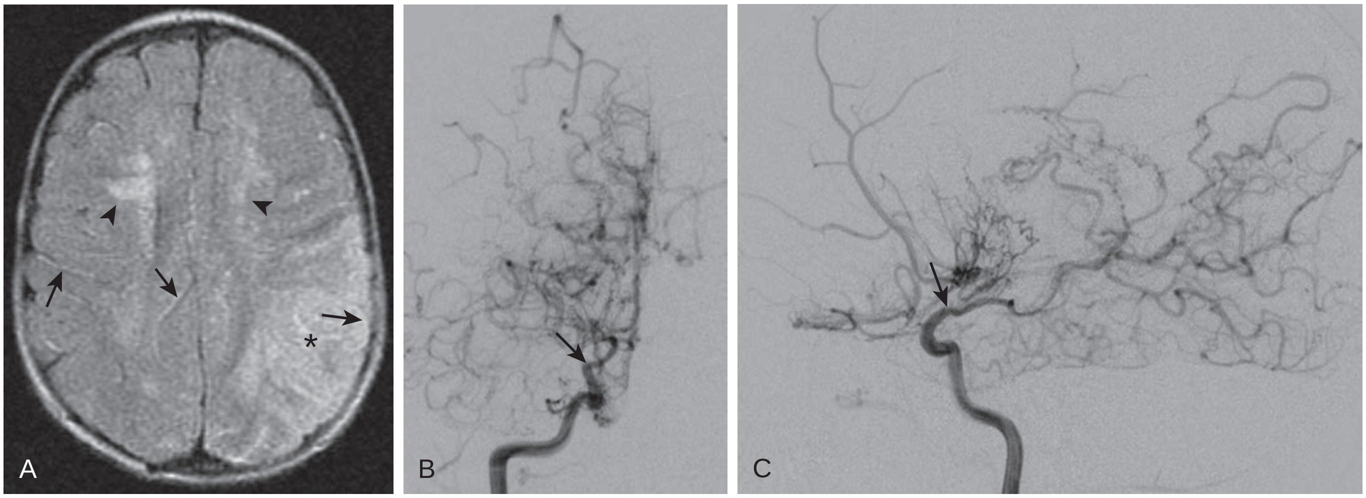

**Figure 36.1. Moyamoya disease in a 2-year-old child presenting with new-onset right-sided hemiplegia.** (A) Axial fluid-attenuated inversion recovery MRI shows a subacute infarct involving the left middle cerebral artery–posterior cerebral artery watershed territory *(asterisk).* There is periventricular white matter T2 prolongation due to chronic ischemic change *(arrowheads).* Linear sulcal signal abnormality is demonstrated bilaterally, consistent with slow flow *(arrows)* in leptomeningeal vessels. (B) Frontal projection from digital subtraction angiogram shows severe steno-occlusive changes involving the distal right internal carotid artery *(arrow),* with occlusion of the middle and anterior cerebral arteries and multiple basal collaterals. (C) Lateral projection again shows the distal tapering and occlusion of the supraclinoid internal carotid artery *(arrow),* multiple basal collaterals, and anterior shift of the posterior cerebral territory through pial collaterals to supply the posterior portions of the middle and anterior cerebral territories.

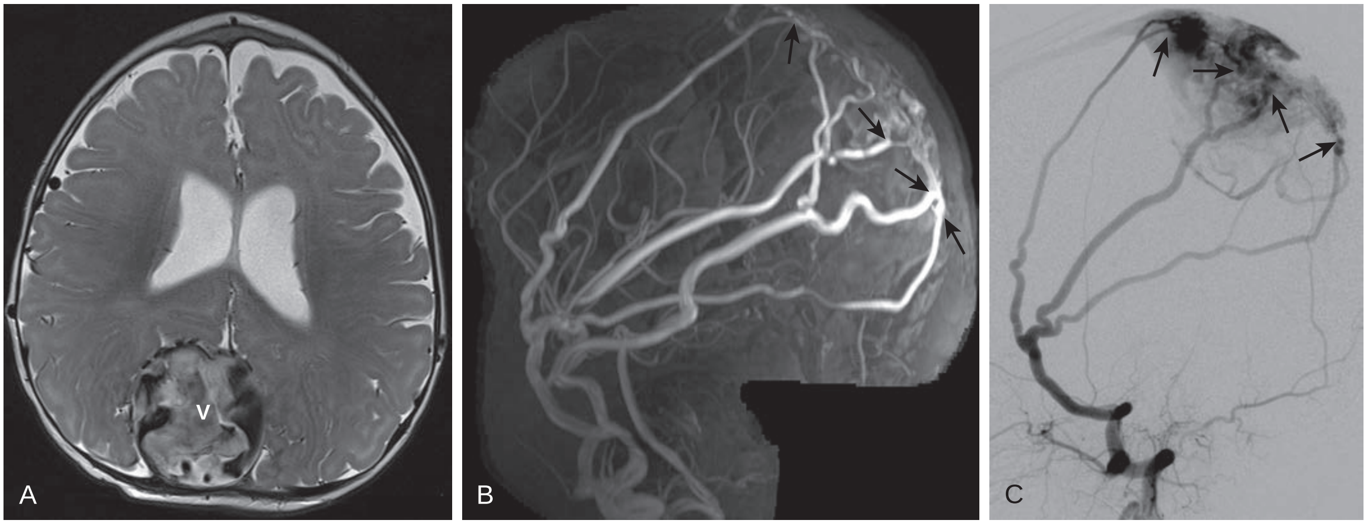

**Figure 36.2. Dural arteriovenous fistula in a 5-month-old girl presenting with vomiting, lethargy, macrocephaly, and distended pulsating scalp veins.** (A) Axial T2-weighted MRI shows an enlarged, partially thrombosed superior sagittal sinus *(V).* Also noted are prominent middle meningeal arterial branches along the dural surface bilaterally. (B) Coronal maximum intensity projection reconstruction of a magnetic resonance venogram shows bilaterally enlarged middle meningeal arteries with fistulae *(arrows)* to the dilated, partially thrombosed superior sagittal sinus. (C) Lateral digital subtraction angiogram demonstrates the dural arteriovenous fistulae with the markedly enlarged middle meningeal artery branches directly communicating through several fistulae *(arrows)* with the superior sagittal sinus near the torcular herophili.

congestive heart failure in the fetus or neonate due to the shunting of blood through the malformation. Additionally, intracranial hemorrhage can occur from rupture of the varix. VOGMs with fewer arteriovenous connections often present later in infancy or childhood with hydrocephalus or brain atrophy caused by progressive venous hypertension and impaired parenchymal perfusion (see Fig. 36.3).

## Pial High-Flow Anomalies

Pial AVM comprise a pial arterial supply with cortical venous drainage (see e-Fig. 36.4).[7] Pial AVMs are rarely detected in the neonate and usually come to medical attention in late infancy or early childhood. The fistulous connections occur along the surface of the brain, resulting in dilation of the superficial cortical draining

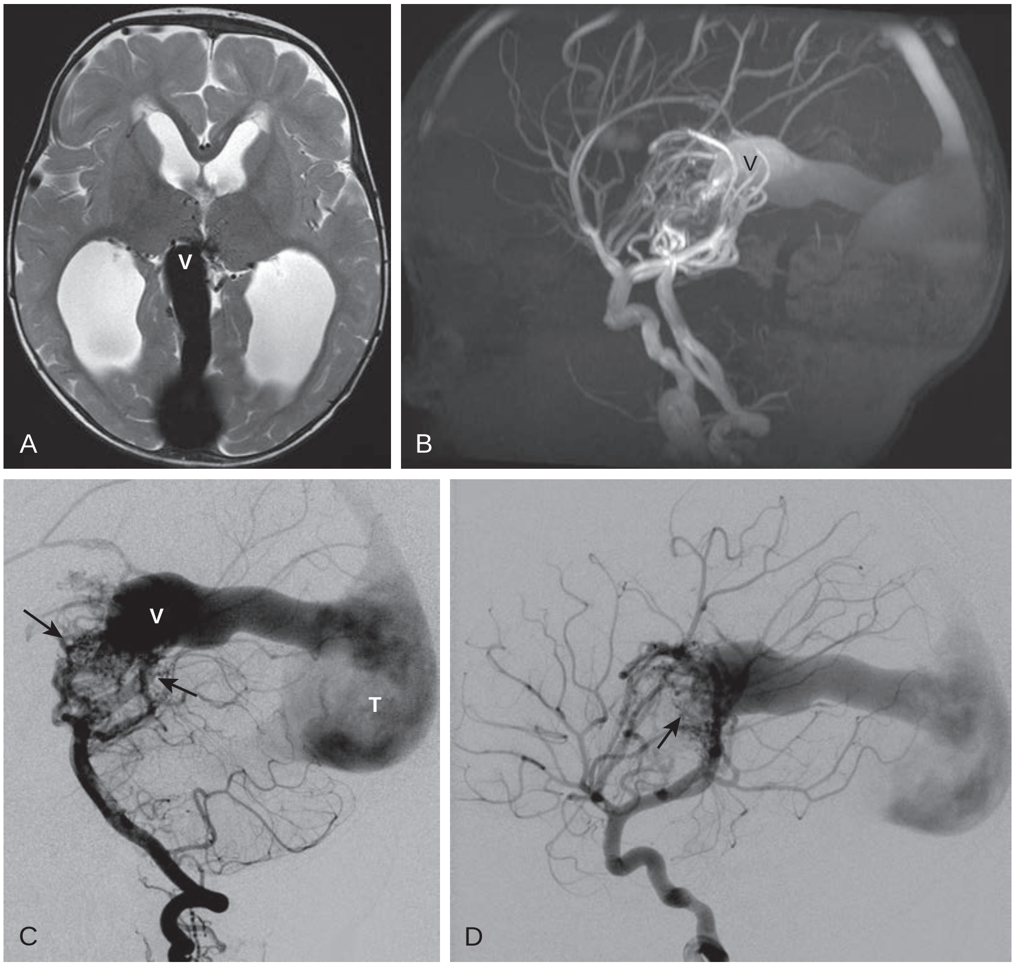

**Figure 36.3. Vein of Galen malformation in a 12-month-old child presenting with macrocephaly and developmental delay.** (A) Axial T2-weighted MRI shows a dilated median vein of the prosencephalon *(V).* The straight sinus and torcular herophili are enlarged. Multiple small serpiginous signal voids are present medially between the thalami from enlarged branches of a primitive arterial arcade. Hydrocephalus is present from venous hypertension. (B) Sagittal maximum intensity MRA confirms a high-flow arteriovenous connection with marked flow related enhancement in the varix and draining sinuses. (C) Lateral digital subtraction angiogram of the left vertebral artery injection shows enlarged left vertebral, basilar, and posterior cerebral arteries supplying a primitive arterial arcade with a vascular nidus of abnormal vessels draining into the enlarged prosencephalic vein. (D) Lateral right internal carotid artery injection demonstrates additional anterior circulation supply to the malformation *(arrow).*

veins. Pial AVM may be asymptomatic for long periods, being discovered only incidentally on imaging performed for other reasons, or the high-flow anomaly may be a cause of catastrophic intracranial hemorrhage.

## Parenchymal High-Flow Anomalies

Intraparenchymal AVMs, like pial anomalies, derive their arterial supply from either the anterior or posterior cerebral circulation (see Fig. 36.5). Parenchymal AVMs usually present after infancy, most often as a cause of intracranial hemorrhage.[7,9,10] Intranidal aneurysms and varices occur commonly; however, aneurysmal dilation of the supplying arteries is much less frequent than in adults.

***Imaging.*** Imaging in high-flow vascular malformations is directed toward delineation of the vascular anomaly and demonstration of complications. Dural AVF and VOGM may be diagnosed in utero on either obstetrical sonography or fetal MRI.[7,8,11] Fetal ultrasound (US) or MRI of dural AVF shows an off-midline vascular mass with enlarged meningeal arteries. Fetal US or MRI of VOGM demonstrates a midline vascular mass, with increased flow in the supplying arteries and draining veins on color Doppler examination. In dural AVF, as well as VOGM, fetal cardiomegaly and congestive heart failure with hydrops may be present. In addition to showing the vascular mass, fetal and postnatal MRI scans may show T1 shortening in the white matter, indicating chronic ischemic brain injury. Postnatal CT is now used less frequently but may show chronic ischemic brain injury with loss of gray/white matter contrast and parenchymal calcification, in addition to the vascular anomaly.

Treatment of dural malformations and VOGMs is typically performed via an endovascular approach.[9,10,13] Successful treatment of the anomaly requires occlusion of the arteriovenous connection. AVFs may be treated by placement of coils across the lesion, whereas closure of AVMs requires obliteration of the nidus and is best accomplished by using a liquid embolic agent.[10,13] Pial and parenchymal malformations are often treated with endovascular embolization, surgical resection, or combined preoperative embolization followed by surgical resection.[9,10,13] Malformations

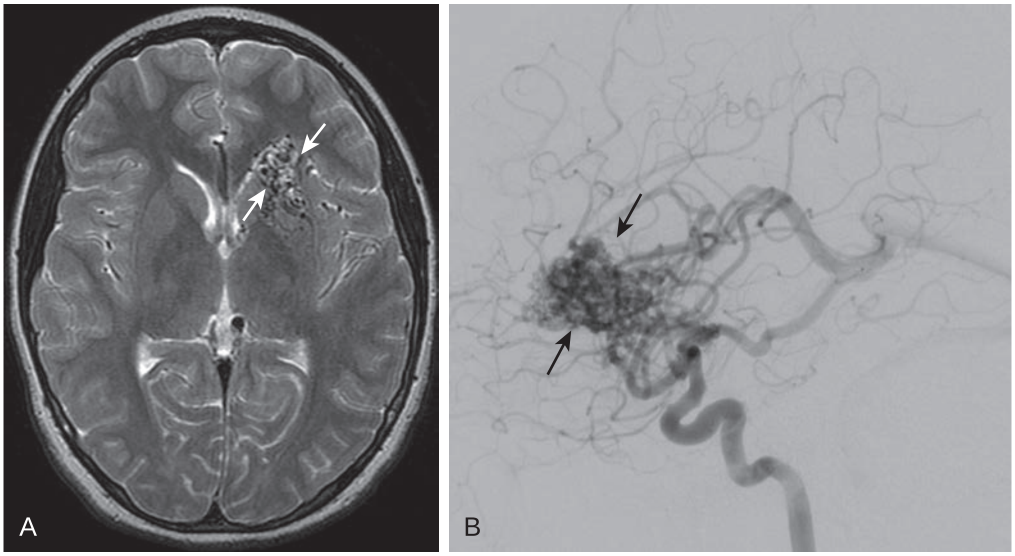

**Figure 36.5. Frontal arteriovenous malformation and intraventricular hemorrhage in an 11-year-old girl presenting with severe headache, vomiting, and left leg weakness.** (A) Axial T2-weighted MRI shows multiple signal voids in the left inferior frontal lobe involving the caudate head and basal ganglia. (B) Lateral cerebral angiogram demonstrates the large vascular nidus *(arrows)* with early opacification of the internal cerebral veins and straight sinus.

that are not surgically accessible may be treated by using endovascular techniques or focused radiation therapy, including proton beam treatment.[14,15]

## Low-Flow Vascular Anomalies

Low-flow vascular anomalies include capillary telangiectasias, cavernous malformations, and developmental venous anomalies (DVAs).[16-21] Each of these entities consists of a malformed, endothelial-lined, blood-filled vascular structure.

### Capillary Telangiectasia

Capillary telangiectasias are composed of dilated capillaries and are found most frequently within the pontine tegmentum.[16-18] Capillary telangiectasias are usually clinically silent and are noted incidentally on imaging performed for other reasons. Rare cases of pontine hemorrhage in which no cause is determined may be caused by capillary telangiectasia.

***Imaging.*** Capillary telangiectasias are typically not apparent on noncontrast imaging and appear as a faint focus of T2 prolongation without an associated mass effect (e-Fig. 36.6). After the administration of contrast, subtle enhancement is seen.

### Cavernous Malformation (Cavernoma)

Cavernous malformations are localized collections of venous blood.[18-21] They can occur in isolation but may also occur very close to DVAs, which suggests a venous origin. Cavernous malformations may be single or multiple; when multiple, they may be familial, or they may develop in response to radiation therapy for treatment of neuro-oncologic disease.[8,21] Cavernous malformations may be discovered incidentally on imaging or may produce symptomatic intracranial hemorrhage or symptoms due to mass effect. Pediatric cavernous malformations behave more aggressively compared with their adult counterparts and are two to three times more likely to hemorrhage.[21]

***Imaging.*** On imaging, small cavernous malformations are typically occult or very subtle on spin-echo imaging but appear as foci of signal loss on long echo, gradient echo, or susceptibility-weighted imaging because of the presence of the magnetic susceptibility effects from associated blood products (Fig. 36.7).[8] Larger lesions are centrally hyperintense on T1-weighed and T2-weighted imaging, with a hypointense rim from the deposition of hemosiderin around the margin of the lesion. Cavernous malformations are usually found within the brain parenchyma but are occasionally superficial and exophytic, simulating an extra-axial mass. Faint post contrast enhancement is also a common feature.

### Developmental Venous Anomaly

DVAs are abnormal veins typically draining normal brain parenchyma. The usual appearance of a DVA is of a cluster of medullary veins radially arranged around the end of an abnormally dilated collecting vein.[19,22] DVAs may be small or provide the entire venous drainage for a cerebral lobe or hemisphere. DVAs are usually asymptomatic and discovered incidentally but are occasionally associated with intracranial hemorrhage, especially when associated with a cavernous malformation. Intracranial DVAs may be seen in association with venous malformation or other vascular anomalies of the scalp and face.[22] DVAs are occasionally identified in association with cortical malformations in the evaluation of seizures.[23]

***Imaging.*** On contrast-enhanced CT or MRI, DVAs are seen as multiple enhancing medullary veins draining into a single collecting vein, an appearance often referred to as the *caput medusa* (Fig. 36.8). DVAs are also visible on catheter angiography and should opacify with contrast at the same time as normal intracerebral veins.[19,22]

## ANEURYSMS

Intracranial aneurysms in children differ in many respects from aneurysms in adults.[24-26] Pediatric aneurysms account for less than 5% of all aneurysms and are rare in the first year of life.[25,27,28] Intracranial aneurysms in children are more likely to be fusiform, involve the posterior circulation, and be larger at the time of presentation than in adults.[25] Symptoms of mass effect are at least as common as those from subarachnoid hemorrhage. Aneurysms

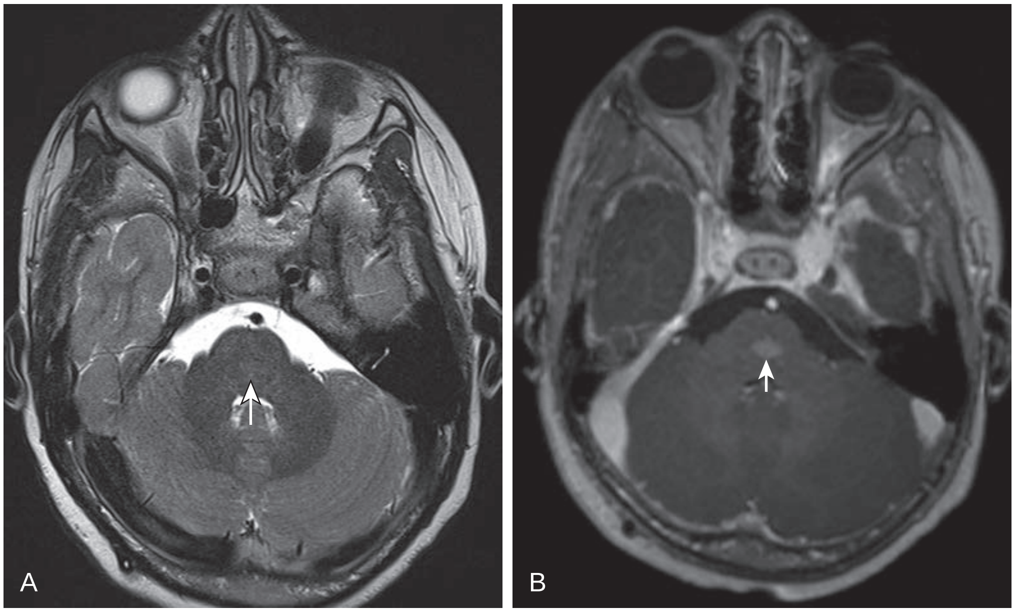

**e-Figure 36.6. Pontine capillary telangiectasia in a 5-year-old with optic pathway glioma.** (A) Axial T2-weighted MRI demonstrates nearly imperceptible T2 prolongation in the pontine tegmentum *(arrow).* (B) Postcontrast axial T1-weighted image shows a blush of enhancement without mass effect typical of capillary telangiectasia.

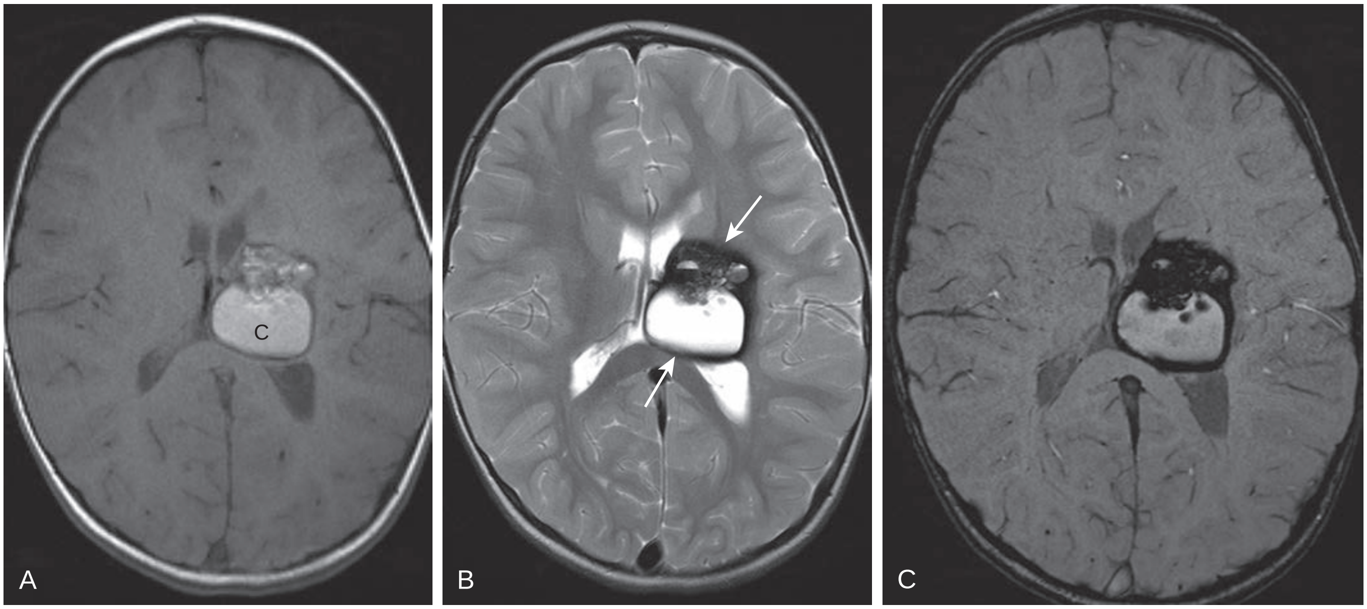

**Figure 36.7. Cavernous malformation involving the left basal ganglia and the thalamus in a 3-year-old presenting with early left hand preference and speech delay.** (A) Axial T1-weighted MRI reveals a large heterogeneous lesion with areas of T1 shortening suggestive of blood products. (B) Axial T2-weighted image demonstrates a low signal intensity rim of hemosiderin *(arrows)* surrounding the lesion. (C) Susceptibility-weighted sequence demonstrates "blooming" of the susceptibility artifact from hemosiderin.

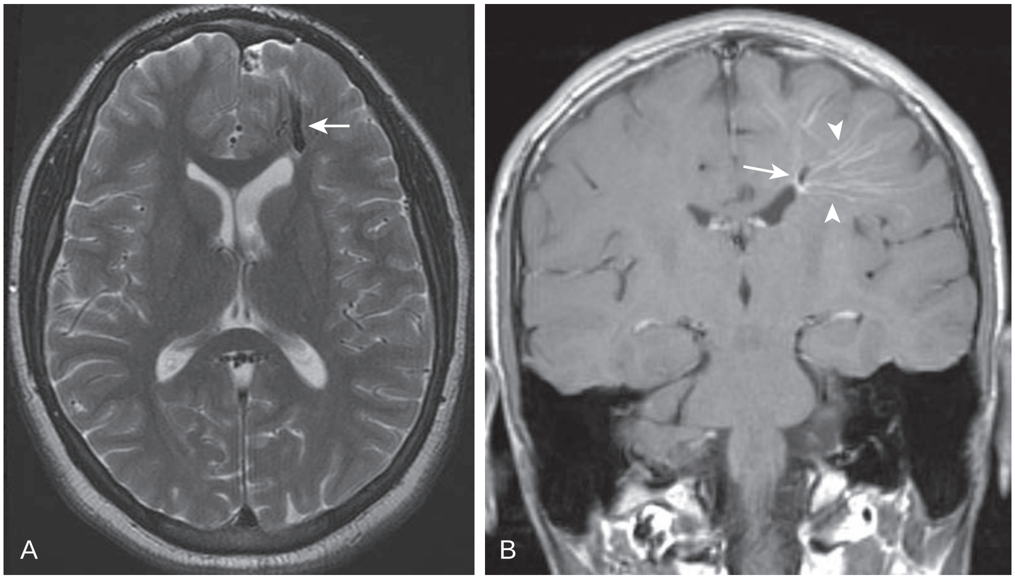

**Figure 36.8. Developmental venous anomaly in a 15-year-old with remote history of trauma presenting with increasing headaches.** (A) Axial T2-weighted MRI shows a prominent intraparenchymal dilated vein in the anterior left frontal lobe *(arrow).* (B) Postcontrast coronal T1-weighted images show the cluster of radially arranged medullary veins *(arrowheads),* the "caput medusa," associated with the abnormally dilated collecting vein *(arrow)* of a developmental venous anomaly.

in children, especially those that are giant or fusiform, may also be discovered incidentally on neuroimaging performed for unrelated reasons. Unlike in adults, in whom aneurysms show a female predominance, in children, boys are more likely to be affected than girls.[25] Comorbidities such as collagen vascular disease, polycystic kidney disease, dwarfism, moyamoya disease, and infections are present with roughly 25% of intracranial aneurysms in children.[25,29]

Saccular aneurysms, the most common form in adults, tend to occur at vessel bifurcations and are believed to be caused by chronic hemodynamic stress on the vessel wall (Fig. 36.9).[25] However, because of the time required for vascular stresses to have an effect, saccular aneurysms are much less common in children. Saccular aneurysms tend to occur most frequently at the origin of the posterior communicating artery but are also found at the origin of the anterior communicating artery and basilar artery bifurcation in children.

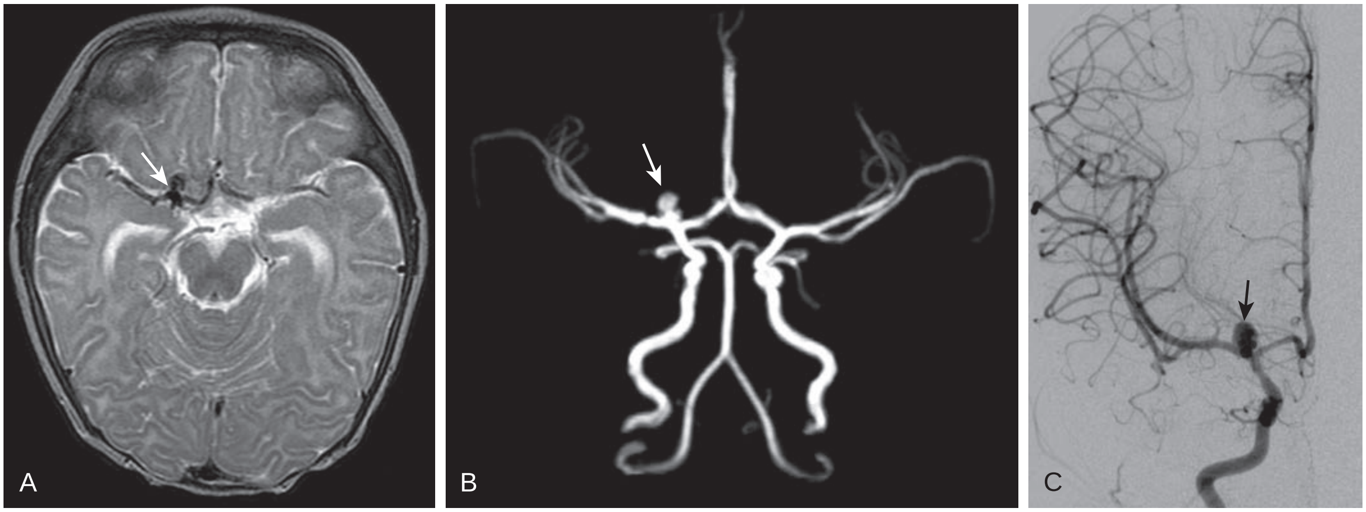

**Figure 36.9. Aneurysmal subarachnoid hemorrhage in a 5-month-old girl with new-onset seizure.** (A) Axial T2-weighted MRI demonstrates a region of signal void *(arrow)* near the right internal carotid artery–middle cerebral artery bifurcation. (B) Time-of-flight MRA demonstrates flow-related enhancement in a lobulated saccular aneurysm *(arrow)* involving the proximal M1 segment of the right middle cerebral artery. (C) The saccular aneurysm *(arrow)* is confirmed on the frontal view from a right internal carotid artery catheter angiogram.

Fusiform aneurysms can be congenital or caused by vessel dissection.[25,30] Common sites of involvement in children include the supraclinoid internal carotid artery, the proximal middle cerebral artery, and the basilar artery. Fusiform aneurysms are more likely to result in symptoms due to mass effect (e-Fig. 36.10) but can also result in subarachnoid hemorrhage, particularly when vessel dissection is the underlying cause.

Mycotic aneurysms tend to occur along distal vascular segments.[24,25] Aneurysms caused by infections are likely to lead to subarachnoid hemorrhage and may rapidly increase in size or number. Posttraumatic aneurysms may also occur in distal vascular segments.

***Imaging.*** CT is often the first study performed when an intracranial aneurysm is suspected. Subarachnoid, intraventricular, or parenchymal hemorrhage may be seen on non–contrast-enhanced CT. In giant aneurysms, a hyperdense mass in proximity to the parent artery is typically evident.[8] CTA may be used to delineate the relationship of the aneurysm to the parent vessel, the size of the aneurysm neck, intraaneurysmal thrombus, and potential collateral vessels, all factors important in treatment planning.

On MRI, an aneurysm may appear as a localized signal void, adjacent to an intracranial vessel or as a fusiform expansion of the vascular signal void. Giant aneurysms may have a lamellated appearance, with alternating areas of T1 shortening and signal void because of the presence of both thrombus and intraaneurysmal flow. Adjacent artifacts from vascular pulsation may be present in the phase encode direction of the images (see e-Fig. 36.10A). MRA can visualize aneurysm features relevant to endovascular or surgical treatment planning. Although MRA avoids radiation and can be performed without contrast, it is often limited by flow artifacts in high-flow lesions.

Catheter angiography remains the gold standard for the evaluation of intracranial aneurysms and is often performed with the intent of endovascular treatment during the procedure.[22,26] Catheter angiography, especially when combined with rotational imaging, shows the anatomic features of the aneurysm and provides information on aneurysm hemodynamics.

## KEY POINTS

- Pediatric stroke can be caused by either cerebral ischemia or intracranial hemorrhage.
- The presenting symptoms of stroke in children are frequently nonspecific, which often results in delay in diagnosis and initiation of therapy.
- The majority of children with stroke will have a persistent neurologic deficit on follow-up.
- Ischemic infarctions may be in an arterial territory or in a vascular watershed zone distribution, depending on the nature of the underlying vasculopathy.
- Vascular anomalies are classified on the basis of hemodynamics, angioarchitecture, and anatomic location.
- Aneurysms are less common in children than in adults and may come to clinical attention because of either subarachnoid hemorrhage or symptoms of local mass effect.

## SUGGESTED READINGS

Amlie-Lefond C, Bernard TJ, Buillaume S, et al. Predictors of cerebral arteriopathy in children with arterial ischemic stroke: results of the International Pediatric Stroke Study. *Circulation*. 2009;119:1417–1423.

Gemmete JJ, Davagnanam I, Toma AK, et al. Arterial ischemic stroke in children. *Neuroimaging Clin N Am*. 2013;23(4):781–798.

Huisman TA, Singhi S, Pinto PS. Non-invasive imaging of intracranial pediatric vascular lesions. *Childs Nerv Syst*. 2010;26(10):1275–1295.

Mackay MT, Monagle P, Babl FE. Brain attacks and stroke in children. *J Paediatr Child Health*. 2016;52(2):158–163.

Niazi TN, Klimo P, Anderson RC, et al. Diagnosis and management of arteriovenous malformations in children. *Neurosurg Clin N Am*. 2010;21:443–456.

Smith ER. Structural causes of ischemic and hemorrhagic stroke in children: moyamoya and arteriovenous malformations. *Curr Opin Pediatr*. 2015;27(6):706–711.

## REFERENCES

Full references for this chapter can be found on www.expertconsult.com.

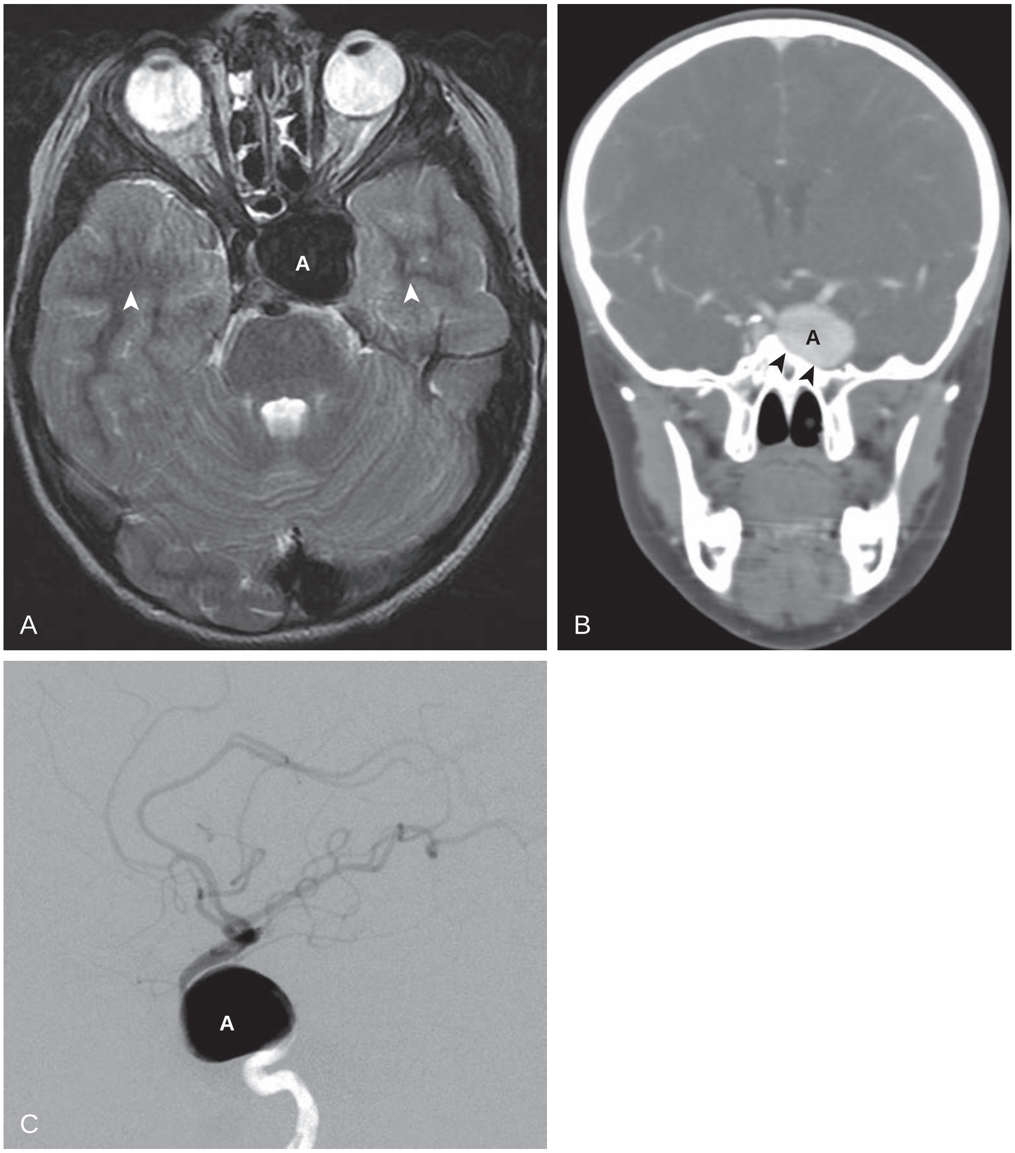

**e-Figure 36.10. Aneurysm in an 8-year-old boy with new onset of diplopia and cranial nerve VI palsy.** (A) Axial T2-weighted images shows a large signal void *(A)* in the cavernous sinus. Pulsations from the aneurysm produce phase encoding artifact seen as alternating bright and dark bands *(arrowheads)* extending away from the aneurysm along the phase encode direction. (B) Reformatted coronal CTA image confirms the presence of a large aneurysm originating from the cavernous portion of the internal carotid artery. The aneurysm *(A)* has caused remodeling of the adjacent lateral wall of the sphenoid sinus *(arrowheads).* (C) Lateral cerebral angiogram confirms a giant aneurysm *(A)* arising from the cavernous portion of the carotid artery.

## REFERENCES

1. Beslow LA, Jordan LC. Pediatric stroke: the importance of cerebral arteriopathy and vascular malformations. *Childs Nerv Syst*. 2010;26:1263–1273.
2. Bowen MD, Burak CR, Barron TF. Childhood ischemic stroke in a nonurban population. *J Child Neurol*. 2005;20:194–197.
3. Lynch JK, Hirtz DG, DeVeber G, et al. Report of the National Institute of Neurological Disorders and Stroke workshop on perinatal and childhood stroke. *Pediatrics*. 2002;109:116–123.
4. Smith ER, Scott RM. Moyamoya: epidemiology, presentation, and diagnosis. *Neurosurg Clin North Am*. 2010;21:543–551.
5. Ibrahimi DM, Tamargo RJ, Ahn ES. Moyamoya disease in children. *Childs Nerv Syst*. 2010;26:1297–1308.
6. Aviv RI, Benseler SM, Silverman ED, et al. MR imaging and angiography of primary CNS vasculitis of childhood. *AJNR Am J Neuroradiol*. 2006;27:192–199.
7. Burrows PE, Robertson RL. Neonatal central nervous system vascular disorders. *Neurosurg Clin North Am*. 1998;9:155–180.
8. Huisman TA, Singhi S, Pinto PS. Non-invasive imaging of intracranial pediatric vascular lesions. *Childs Nerv Syst*. 2010;26:1275–1295.
9. Rubin D, Santillan A, Greenfield JP, et al. Surgical management of pediatric cerebral arteriovenous malformations. *Childs Nerv Syst*. 2010;26:1337–1344.
10. Thiex R, Williams A, Smith E, et al. The use of Onyx for embolization of central nervous system arteriovenous lesions in pediatric patients. *AJNR Am J Neuroradiol*. 2010;31:112–120.
11. Brunelle F. Brain vascular malformations in the fetus: diagnosis and prognosis. *Childs Nerv Syst*. 2003;19:524–528.
12. Lasjaunias PL, Alvarez H, Rodesch G, et al. Aneurysmal malformations of the vein of Galen. Follow-up of 120 children treated between 1984 and 1994. *Interv Neuroradiol*. 1996;2:15–26.
13. Jankowitz BT, Vora N, Jovin T, et al. Treatment of pediatric intracranial vascular malformations using Onyx-18. *J Neurosurg Pediatr*. 2008;2:171–176.
14. Zadeh G, Andrade-Souza YM, Tsao MN, et al. Pediatric arteriovenous malformation: University of Toronto experience using stereotactic radiosurgery. *Childs Nerv Syst*. 2007;23:195–199.
15. Vernimmen FJ, Slabbert JP, Wilson JA, et al. Stereotactic proton beam therapy for intracranial arteriovenous malformations. *Int J Radiat Oncol Biol Phys*. 2005;62:44–52.
16. Barr RM, Dillon WP, Wilson CB. Slow-flow vascular malformations of the pons: capillary telangiectasias? *AJNR Am J Neuroradiol*. 1996;17:71–78.
17. Guibaud L, Pelizzari M, Guibal AL, et al. Slow-flow vascular malformation of the pons: congenital or acquired capillary telangiectasia. *AJNR Am J Neuroradiol*. 1996;17:1798–1800.
18. Rigamonti D, Johnson PC, Spetzler RF, et al. Cavernous malformations and capillary telangiectasia: a spectrum within a single pathological entity. *Neurosurgery*. 1991;28:60–64.
19. San Millan Ruiz D, Gailloud P. Cerebral developmental venous anomalies. *Childs Nerv Syst*. 2010;26:1395–1406.
20. Abla AA, Lekovic GP, Garrett M, et al. Cavernous malformations of the brainstem presenting in childhood: surgical experience in 40 patients. *Neurosurgery*. 2010;67:1589–1599.
21. Acciarri N, Galassi E, Giulioni M, et al. Cavernous malformations of the central nervous system in the pediatric age group. *Pediatr Neurosurg*. 2009;45:81–104.
22. Burrows PF, Robertson RL, Barnes PD. Angiography and the evaluation of cerebrovascular disease in childhood. *Neuroimaging Clin N Am*. 1996;6:561–588.
23. Rasalkar DD, Paunipagar BK. Developmental venous anomaly associated with cortical dysplasia. *Pediatr Radiol*. 2010;40(suppl 1):S165.
24. Lasjaunias P, Wuppalapati S, Alvarez H, et al. Intracranial aneurysms in children aged under 15 years: review of 59 consecutive children with 75 aneurysms. *Childs Nerv Syst*. 2005;21:437–450.
25. Requejo F, Ceciliano A, Cardenas R, et al. Cerebral aneurysms in children: are we talking about a single pathological entity? *Childs Nerv Syst*. 2010;26:1329–1335.
26. Sanai N, Auguste KI, Lawton MT. Microsurgical management of pediatric intracranial aneurysms. *Childs Nerv Syst*. 2010;26:1319–1327.
27. Pasqualin A, Mazza C, Cavazzani P, et al. Intracranial aneurysms and subarachnoid hemorrhage in children and adolescents. *Childs Nerv Syst*. 1986;2:185–190.
28. Proust F, Toussaint P, Garnieri J, et al. Pediatric cerebral aneurysms. *J Neurosurg*. 2001;94:733–739.
29. Liang J, Bao Y, Zhang H, et al. The clinical features and treatment of pediatric intracranial aneurysm. *Childs Nerv Syst*. 2009;25:317–324.
30. Mizutani T, Miki Y, Kojima H, et al. Proposed classification of nonatherosclerotic cerebral fusiform and dissecting aneurysms. *Neurosurgery*. 1999;45:253–259.

# 37 Pediatric Stroke

*Susan Sotardi, Michael Rivkin, Katyucia De Macedo Rodrigues, and P. Ellen Grant*

Stroke is a leading cause of disability and death in children. Three distinct time periods can be used to categorize stroke in the pediatric population: fetal (14 weeks of gestation until the onset of labor), perinatal/neonatal (between late third trimester and the first month of life), and childhood (beyond the first month of life until adulthood). The true incidence of fetal stroke is unknown, particularly because the causes of fetal demise are often uncertain, and neurologic deficits in a surviving fetus are largely undetectable until birth. The incidence of stroke observed in the perinatal/neonatal period is between 1 per 1,600 and 1 per 5,000 live births.[1] Therefore neonates constitute the second most common age group, after adults, in which stroke occurs. In children, ages 30 days to 19 years, the overall incidence is approximately 2 per 100,000.[2] Among children who survive the neurologic insult, more than 50% will develop permanent neurologic or cognitive sequelae,[3] frequently resulting in a large economic burden to the family and society.

Detection rates of stroke across fetal, neonatal, and childhood populations are rising due to improved imaging techniques, as well as higher awareness of pediatric stroke among medical professionals. However, despite improved diagnostic modalities, the cause of the stroke often cannot be determined with certainty; delays in diagnosis along with multiple, overlapping risk factors frequently complicate the clinical picture. The causes of stroke in the pediatric population are shown in Box 37.1. These etiologies can be categorized by both patient age and the vessel of origin: arterial versus venous. In the United States, the epidemiology of pediatric stroke has shifted from infectious etiologies, still common in the developing world, to congenital and genetic disorders, such as congenital heart disease, sickle cell anemia, extracranial carotid dissection, and thrombophilia.

Delayed recognition of pediatric stroke is common and leads to important delays in treatment. Clinical presentation of pediatric stroke differs by age and etiology, which frequently confounds early diagnosis. In a study of perinatal stroke, clinical presentations included seizures (72%), diffuse neurologic signs (63%), abnormal tone (38%), or encephalopathy (39%).[4] In children presenting to emergency rooms, several symptoms independently associated with stroke include: being well the week before presentation, face weakness, arm weakness, and inability to walk.[5] In children presenting with venous thrombosis, 58% of the children had seizures, 76% had diffuse neurologic signs, and 42% had focal neurologic signs.[6] Because the presentation, causes, diagnosis, treatment, and outcomes of pediatric stroke differ significantly from adults, approaches to adult stroke are not necessarily applicable to the pediatric population. While treatment guidelines have been established for adults, the hyperacute management of pediatric stroke continues to emerge.[7] Tissue plasminogen activator is now being administered in several pediatric stroke centers to children over the age of 2 years with stroke of less than 4.5 hours duration, and the use of endovascular thrombectomy, while nascent, is emerging in children over the age of 2 years with a somewhat longer timeframe.[8]

## FETAL STROKE

Fetal stroke is defined as occurring between 14 weeks of gestation until the onset of labor. Although diagnosis may be made by prenatal ultrasound, it has a low sensitivity for identifying fetal infarcts, and strokes identified by antenatal ultrasound screening are typically large.[3] Detection of fetal stroke is often delayed until the neonatal period or even later in life, when deficits become clinically perceptible and the child is diagnosed with presumed perinatal stroke. These poor detection rates limit the assessment of fetal stroke incidence rates.

### Risk Factors

Fetal stroke has different risk factors, clinical presentation, and outcomes compared with perinatal or childhood strokes. In more than 50% of cases of fetal stroke, no obvious cause is determined.[3] Maternal conditions associated with fetal stroke include: diabetic ketoacidosis, immune thrombocytopenic purpura, warfarin use, trauma, maternal fever with gastroenteritis, and antiepileptic medications.[3] Pregnancy-related factors include: fetal alloimmune thrombocytopenia, placental hemorrhage/thrombosis, abruptio placenta, multiple gestations, and twin-twin transfusion syndrome. Fetal conditions include: pyruvate decarboxylase deficiency, cytomegalovirus infection, non-A/non-B hepatitis, von Willebrand disease, and protein C deficiency.[3]

### Imaging Findings

Prenatal ultrasound is the most common screening tool for fetal brain abnormalities but is limited for the evaluation of stroke. Ultrasound detection rates are low for small and acute infarcts, and imaging findings are often not specific to stroke.[3] Injury location and suggestion of a vascular distribution may raise concern for infarction; however, ultrasound cannot provide a definitive diagnosis.

Detection of a brain abnormality on prenatal ultrasound is often further evaluated with fetal magnetic resonance imaging (MRI).[9] Fetal MRI has improved detection for ischemia and is the imaging modality of choice for confirming and assessing the extent of fetal ischemic brain injury (e-Fig. 37.1). Single-shot turbo (fast) spin echo T2-weighted sequences are most frequently utilized to minimize motion artifacts. It is also possible to obtain T1-weighted images, T2*-weighted images, T2/T1-weighted images, diffusion-weighted imaging (DWI), and spectroscopic data. Importantly, unlike in older children and adults, fetal diffusion-weighted MRI sequences may not be reliable in predicting the approximate onset of an ischemic event.[10]

The most common findings associated with fetal stroke are intraparenchymal hemorrhage (91%), ventriculomegaly (59%), porencephaly (13%), and hydrocephalus.[3] The pattern of parenchymal injury can suggest a venous or arterial origin of the stroke. Arterial ischemic strokes (AIS) in the prenatal period usually involve the major arterial territories, most commonly the middle cerebral artery (MCA). Venous strokes frequently result in hemorrhage, and hemorrhagic infarct should raise concern for venous thrombosis.

The age of the fetus at the time of infarct can contribute to the subsequent pathology and pattern of injury.[11] As early as 12 weeks' gestation, supratentorial hydranencephaly can be seen as the result of bilateral internal carotid artery infarcts. If an ischemic

## Abstract:

Stroke is a leading and under-recognized cause of disability in the pediatric population. Limited data on the detection of pediatric infarcts, as well as the causative etiology, contributes to a lack of understanding about stroke in children. Fetal stroke is defined as occurring between 14 weeks of gestation until the onset of labor and differs significantly in its clinical risk factors, presentation, imaging features and outcomes, when compared with perinatal or childhood infarcts. Perinatal stroke occurs between late third trimester and the first month of life. Arterial ischemic, venous and hemorrhagic strokes in the neonatal/perinatal period are separate entities with differing risk profiles and imaging characteristics. Childhood stroke occurs between 30 days and 18 years of age. Childhood stroke is distinct from neonatal and fetal stroke, with independent risk factors including vasculopathies/vasculitis, hypercoagulable states and genetic disorders. While imaging features of pediatric stroke may overlap, important patterns which help to distinguish these entities are presented in this chapter.

## Keywords:

Fetal infarct
Neonatal infarct
Pediatric infarct
Ischemic event
Stroke

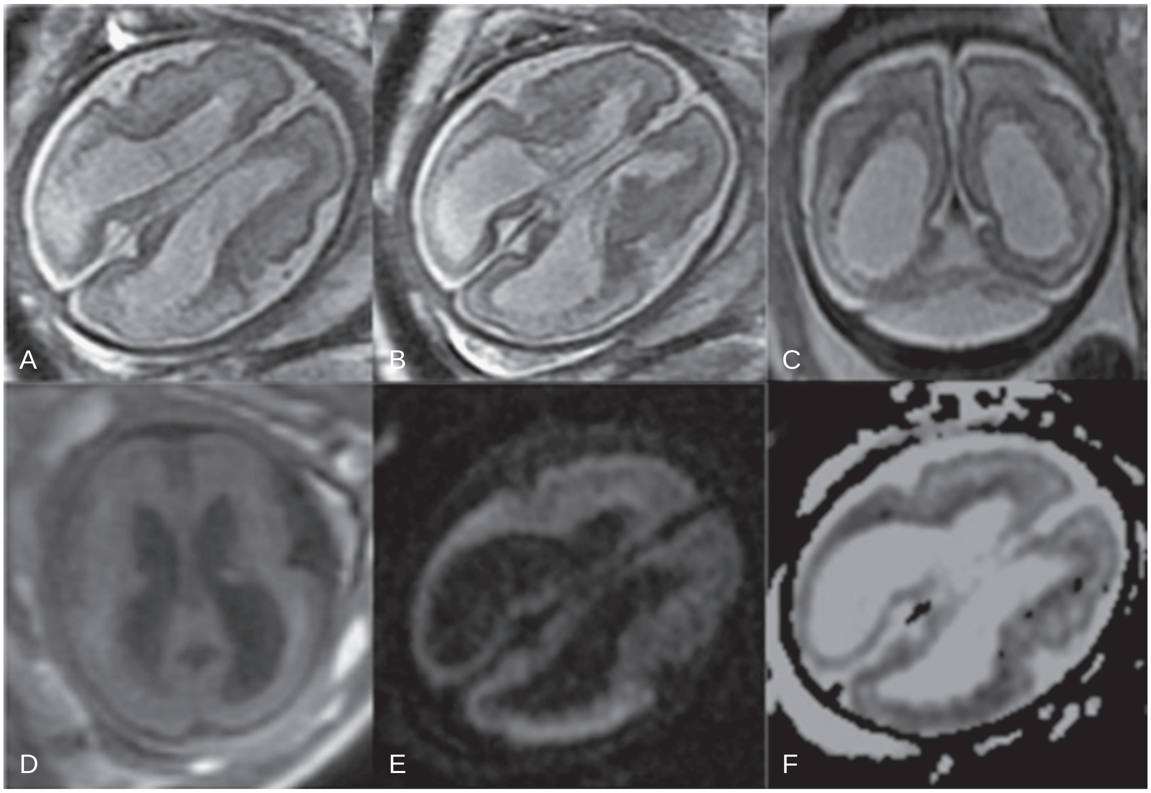

**e-Figure 37.1. Fetal infarct.** A 30-year-old female underwent MRI scan after fetal ventriculomegaly was found on routine prenatal ultrasound at 29 weeks' gestational age. (A–C) T2-weighted MR images show dilatation of the lateral ventricles associated with mixed decreased and increased T2 signal, and thinning and irregularity of the periatrial white matter. (D) T1-weighted MR image shows that the regions of decreased T2 signal are associated with increased T1 signal consistent with evolving hemorrhage. (E) DWI and (F) ADC map also demonstrate decreased diffusion within the periventricular white matter, suggesting associated ischemic necrosis.

### BOX 37.1 Causes of Pediatric Stroke

**ARTERIAL ISCHEMIC STROKE**

**Cardiac**

Congenital heart disease
Valvular heart disease
Neoplasm, myxomas
Cardiac surgery
Myocarditis, cardiomyopathy

**Cerebral Vasculopathy**

Infection (e.g., meningitis)
Collagen vascular disease (e.g., systemic lupus erythematosus, giant cell arteritis, Takayasu arteritis, Kawasaki arteritis)
Primary angiitis of the central nervous system
Viral infection (e.g., varicella)
Trauma, dissection

**Disorders of Coagulation**

Protein C or S deficiency
Antithrombin III deficiency
Anticardiolipin antibodies
Lupus anticoagulant
Dysfibrinogenemia
Polycythemia and hyperviscosity

**Moyamoya**

Idiopathic/familial (Japanese)
Secondary (e.g., sickle cell disease)
Neurofibromatosis 1
Radiation vasculopathy

**Inborn Errors of Metabolism**

Fabry disease
Hyperhomocysteinemia
Ehlers-Danlos syndrome (type IV)

**SINOVENOUS THROMBOSIS**

Infection of the head and neck
Dehydration
Hypercoagulable states
Chemotherapeutic agents
Iatrogenic

event occurs during neuronal migration, particularly between 22 to 24 weeks' gestational age, the injury may result in cortical disorganization and polymicrogyria.[12,13] Before approximately 27 weeks' gestational age, the fetal brain lacks a glial response to injury; after 27 weeks, the fetal brain can demonstrate a glial response, which is typically seen as T2 hyperintense signal at the periphery of the infarct.[14] Schizencephaly occurs at less than 24 weeks of gestation and is thought to be due to destruction and defective development of a segment of the immature prosencephalic cortical mantle, potentially a consequence of ischemic etiologies.[11] Porencephaly resulting from cystic degeneration, without gliosis, can be seen before 27 weeks' gestation. The transmantle variant of porencephaly that follows prenatal AIS results from insults greater than 24 weeks' gestation.[11]

## Outcomes

There is minimal data available regarding outcomes in fetal stroke. In one study, 78% (35/45) of in utero strokes resulted in either death or adverse neurodevelopmental outcome at ages 3 months to 6 years.[3] Survivors may have developmental delay, cerebral palsy, and seizures.[3] In another small study, those with resulting cystic encephalomalacia plus atrophy had worse cognitive outcomes than children with atrophy or gliosis alone.[15] However, generalization of these data to individual fetuses is difficult due to the small numbers of cases as well as variability in infarct location and size.

# PERINATAL/NEONATAL STROKE

Perinatal stroke occurs between late third trimester and the first month of life, usually defined between 28 weeks' gestational age to 28 days old.[3] The incidence of AIS in newborns is reported as 1 in 2,300 to 5,000 deliveries,[16] and the yearly incidence of cerebral sinovenous thrombosis (SVT) in term newborns is reported as 1.4 to 12 per 100,000.[17] In this age group, the differentiation of ischemic stroke from hypoxic-ischemic injury may be challenging, particularly due to significant overlap in imaging findings, as well as coexisting pathophysiology. However, accurate interpretation is important given the differences in management and prognosis.

## Risk Factors

Risk factors differ by arterial and venous etiologies, as well as by hemorrhagic infarct. Risk factors for perinatal stroke in term infants can be categorized by maternal, fetal and placental factors. However, the cause of perinatal stroke is not identified in over half of patients.

In AIS, maternal factors include: thrombophilia, infertility, prolonged rupture of membranes, preeclampsia/hypertension, gestational diabetes, abnormal maternal gestational bleeding, smoking, illegal drug use, intrauterine growth retardation, infection, and maternal fever. Fetal conditions include: thrombophilia, congenital heart disease, arteriopathy, hypoglycemia, perinatal asphyxia, infection, need of resuscitation, and Apgar score of less than 7 at 5 minutes. Placental factors include: chorioamnionitis, placental infarcts, and placenta weighing less than tenth percentile.[16,18–20]

In SVT, maternal risk factors include: preeclampsia/HELLP syndrome, diabetes, maternal shock, maternal surgery, and history of clotting disorder. Perinatal risk factors include: complicated delivery, perinatal asphyxia, and fetomaternal transfusion. Neonatal risk factors include: sepsis or meningitis, dehydration, congenital heart defect, and extracorporeal membrane oxygenation (ECMO). Prothrombotic risk factors include: antithrombin level, protein C and S levels, factor V Leiden, prothrombin factor II, and other abnormalities.[17] Independent risk factors for idiopathic hemorrhagic stroke are lower maternal age, primiparity, prior spontaneous abortion, difficult fetal transition (bradycardia and low Apgar scores), and being small for gestational age.[21]

## Imaging Findings

### Arterial Ischemic Stroke

Causes of neonatal AIS are shown in Box 37.1. Perinatal AIS leads to focal ischemic necrosis in an arterial distribution, most commonly in the MCA territory.[22] Regions of AIS can evolve into focal volume loss, glial scarring, or cystic encephalomalacia, depending on the severity of the injury.

Computed tomography (CT) can detect hemorrhage and areas of advanced infarction; however, CT can be falsely negative in small acute infarcts, particularly in the context of some low-dose techniques. MR is the preferred modality for detection and evaluation of acute neonatal AIS (Fig. 37.2). Areas of acute infarct are easily identified as regions of bright signal on DWI and decreased signal on apparent diffusion coefficient (ADC) maps, typically in a vascular territory. The reduction in ADC can persist for up to 2 weeks and is more conspicuous during the first 4 days.[23] Subtle loss of gray-white matter differentiation may be identified on T2-weighted images; however, T2 signal changes may be imperceptible within the first hours after the ischemic event. MR angiography (MRA) may be helpful in evaluating the occlusion of a major intracranial artery but is frequently limited by the type

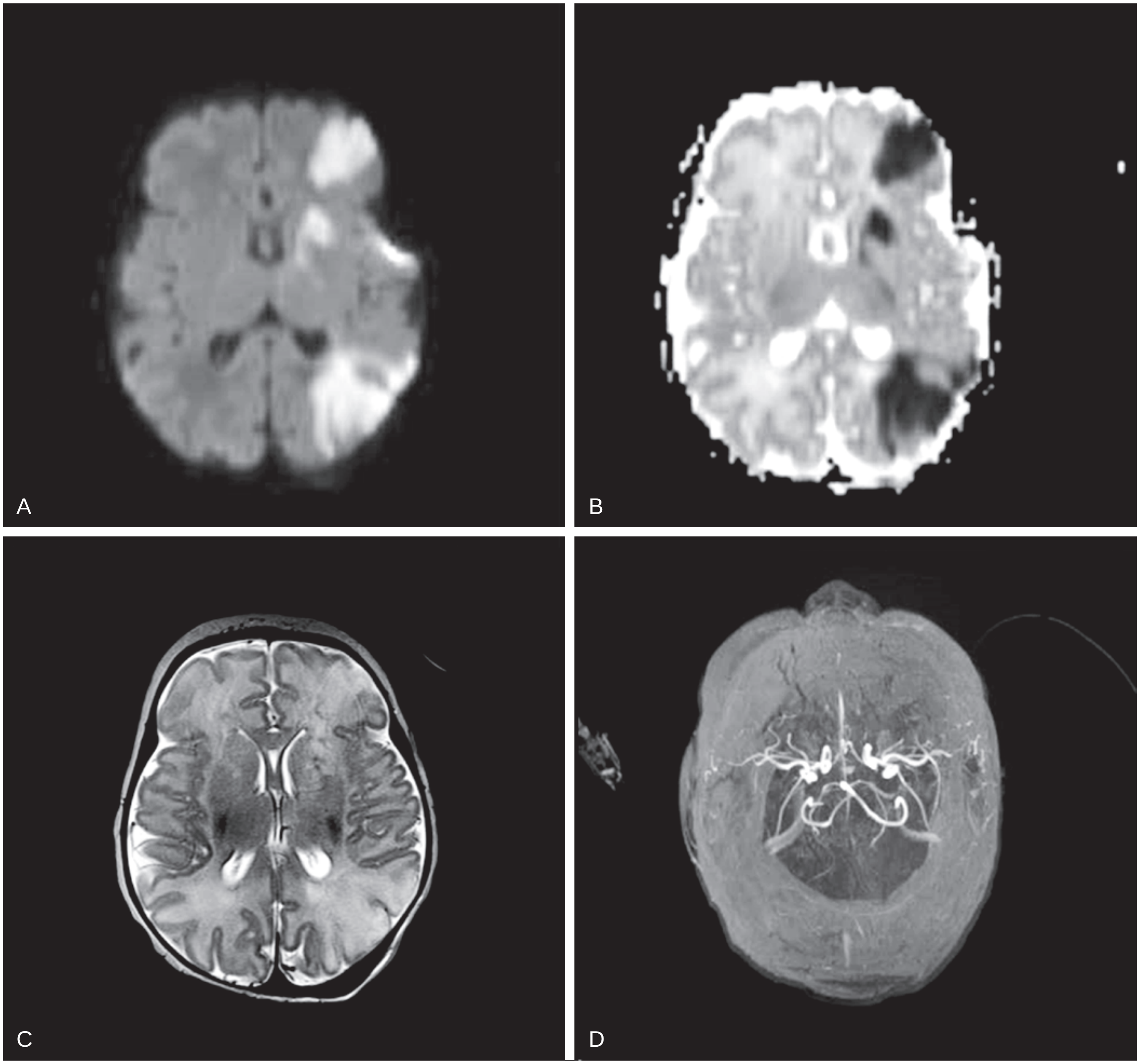

**Figure 37.2. Neonatal arterial ischemic strokes.** A 1-day-old full-term neonate with focal right-sided seizures and lip smacking. This neonate was found to have renal vein thrombosis, along with a PFO and VSD as well as the risk factor of maternal type 1 diabetes. (A) DWI and (B) ADC map demonstrate multiple acute/subacute arterial ischemic infarcts, throughout the left hemisphere in an MCA distribution, likely embolic in etiology. (C) Axial FSE T2-weighted MR image shows loss of gray-white differentiation and edema in involved regions. (D) TOF MRA image shows no evidence of luminal thrombus. *ADC,* Apparent diffusion coefficient; *DWI,* diffusion weighted images; *MCA,* middle cerebral artery; *PFO,* patent foramen ovale; *TOF MRA,* time of flight magnetic resonance angiogram; *VSD,* ventricular septal defect.

of MRA acquisition. With time-of-flight MRA sequences, turbulent or fast flow can result in the loss of normal flow-related signal, which may be mistaken for partially occlusive thrombus. Several sequences, such as arterial spin labeling (ASL)[24] and MR perfusion, may assist in determining cerebral perfusion. ASL can be used to obtain cerebral blood flow measurements and is particularly useful in determining the presence of reperfusion in areas of abnormal ADC.[25] ASL has shown hyperperfusion in the infarct core in 73% of neonatal arterial ischemic infarcts, frequently without a penumbra.[26]

Ultrasound has a high false negative rate and has limited utility in the evaluation of acute infarct,[22] but combined with color and pulsed Doppler, it remains a useful technique to evaluate the circle of Willis. It may be helpful for confirming or disproving areas of concern seen on MRA. If an intraluminal clot is identified, bedside Doppler can be used to monitor for recanalization.

## Venous Stroke

Venous strokes occur as a result of venous outflow obstruction. This may result from occlusion of a vein or venous sinus by thrombus, or by venous hypertension. Determining the exact mechanism is often complicated by the fact that venous thrombus is often not visualized and may have been resorbed before imaging.[27]

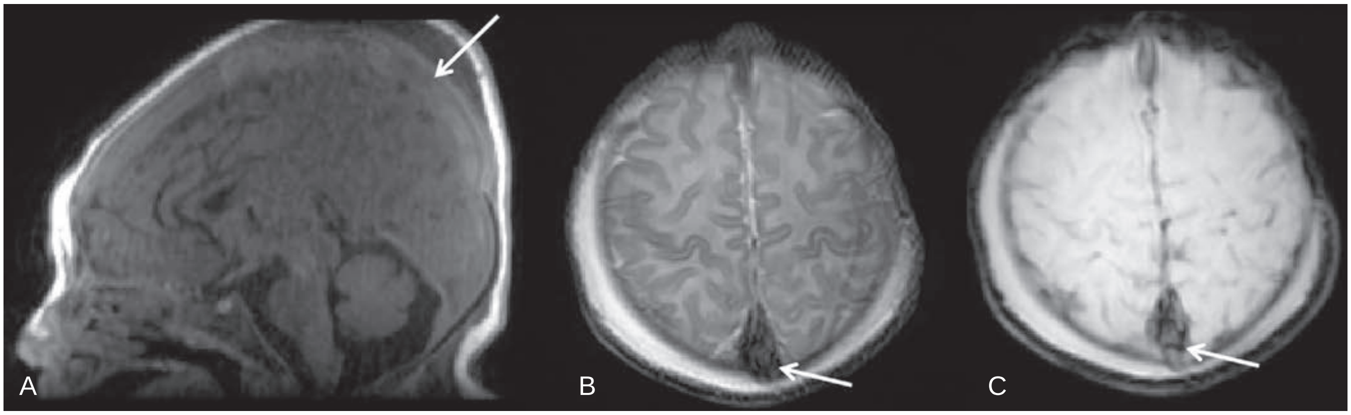

**Figure 37.3. Cerebral sinovenous thrombosis.** Neonate with Apgars of 5 and 9, presenting at 1 day of life with focal seizures. Mother had known Factor V Leiden heterozygosity. (A) Sagittal T1-weighted MR image demonstrates T1 hyperintense signal within the superior sagittal sinus *(arrow)*, consistent with SVT. (B) Axial T2-weighted and (C) gradient echo T2 MR images demonstrate hypointense signal within the superior sagittal sinus *(arrow)*, consistent with thrombus.

The common associated imaging findings of recent venous infarcts are: venous congestion, hemorrhage, and/or parenchymal ischemic injury, which may be cortical, subcortical, white matter-based, or involve deep gray matter.[28] Prior periventricular venous infarcts are assumed when unilateral parenchymal injury is identified with at least four of the following conditions: focal periventricular encephalomalacia, internal capsule T2 prolongation, cortical sparing, basal ganglia sparing, or remote hemorrhage.[29]

Preterm and term neonates show different patterns of brain lesions associated with SVT. Extensive white matter damage is predominant in preterm neonates, whereas, intraventricular and thalamic hemorrhage with punctate white matter lesions are more often seen in term infants.[30] However, intraventricular hemorrhage is common in both groups.[28] Over time, the affected brain parenchyma may show encephalomalacia or gliosis; however, some infarcts may demonstrate apparent resolution on follow-up imaging.

As with AIS, ultrasound has limited sensitivity in detecting SVT, especially peripheral cortical infarction.[22] Ultrasound may visualize an echogenic clot and lesions associated with a thrombosis (such as thalamic hemorrhage), and can monitor infarct evolution and screen for complications (such as hydrocephalus secondary to intraventricular hemorrhage). There is a high incidence of SVT (4.4%) in preterm infants with a gestational age of less than 29 weeks, and a recent report suggests that serial head ultrasound may have utility in this population.[31]

Noncontrast CT is helpful for the evaluation of intracranial hemorrhage and may rarely show hyperdense clot in the involved vein or venous sinus. Contrast-enhanced CT may demonstrate filling defects within the venous structures. However, MRI is the preferred modality for confirming the diagnosis and determining the extent of associated parenchymal injury (Figs. 37.3 and 37.4). MR venography (MRV) is helpful for evaluation of thrombosis and can be performed without contrast. However, all forms of MRV, particularly the most common time-of-flight acquisition, are prone to artifacts, which may simulate clot. Correlation with gradient-echo (GRE) or susceptibility-weighted images (SWI) can confirm venous thrombosis, which "blooms" on these sequences. GRE and SWI are also useful in detecting subtle intraparenchymal hemorrhage. High-resolution, contrast-enhanced T1-weighted images are more reliable for delineation of filling defects in the venous system and may be confirmatory for suspected findings on MRV.[32] However, given the unknown risks of gadolinium exposure,[33,34] contrast should only be given if MRV and GRE/SWI results are equivocal and confirmation of an intraluminal clot would alter management.

### Neonatal Hemorrhagic Stroke

Although hemorrhagic stroke is most often the result of SVT and less often AIS, a significant proportion of cases are idiopathic and some have suggested the process constitutes a separate disease entity. Neonatal hemorrhagic stroke occurs with a reported incidence of 1 in 6,300 live births.[21] Cole et al. demonstrated that 63% of neonatal hemorrhagic strokes were idiopathic and 37% were hemorrhagic transformation of primary ischemic injuries.[21] The primary etiologies included: cerebral SVT, AIS, hypoxic ischemic encephalopathy, and presumed perinatal hemorrhagic stroke. Additional underlying abnormalities included trauma, coagulopathies, and vascular abnormalities (such as arteriovenous malformation, cavernous malformations, and aneurysm). The imaging findings of hemorrhage may be identified on ultrasound, CT, and/or MR depending on the size of the hemorrhage. MR GRE and SWI sequences are the most sensitive modalities for detecting intracranial hemorrhage (e-Fig. 37.5). Underlying structural abnormalities that may have been a source of hemorrhage usually cannot be evaluated in the acute period, so follow-up imaging is recommended to assess the underlying parenchyma once the size of hematoma has decreased or resolved.

### Outcomes

Outcomes after neonatal stroke depend on numerous factors, such as etiology, extent, and location of infarct. Perinatal stroke may result in cerebral palsy, cognitive impairments, epilepsy, and sensory impairments. Large infarctions, bilateral infarctions, and seizures tend to be associated with worse outcomes but are not definitely predictive.[35] Imaging findings of injury to specific brain regions may assist in the prediction of clinical outcomes.[36]

## CHILDHOOD STROKE

Childhood stroke can be defined as occurring after perinatal/neonatal stroke, between ages 30 days to 18 years. Based on imaging findings, the annual incidence of childhood stroke are estimated to be 2.4 cases per 100,000 patient population, higher than previously thought.[37] Recurrence of stroke in childhood also presents a significant challenge; in a recent study, 16% (56/355) of children with AIS experienced a recurrent ischemic event (stroke or transient ischemic attack [TIA]) during a follow-up period of at least 1 year.[38]

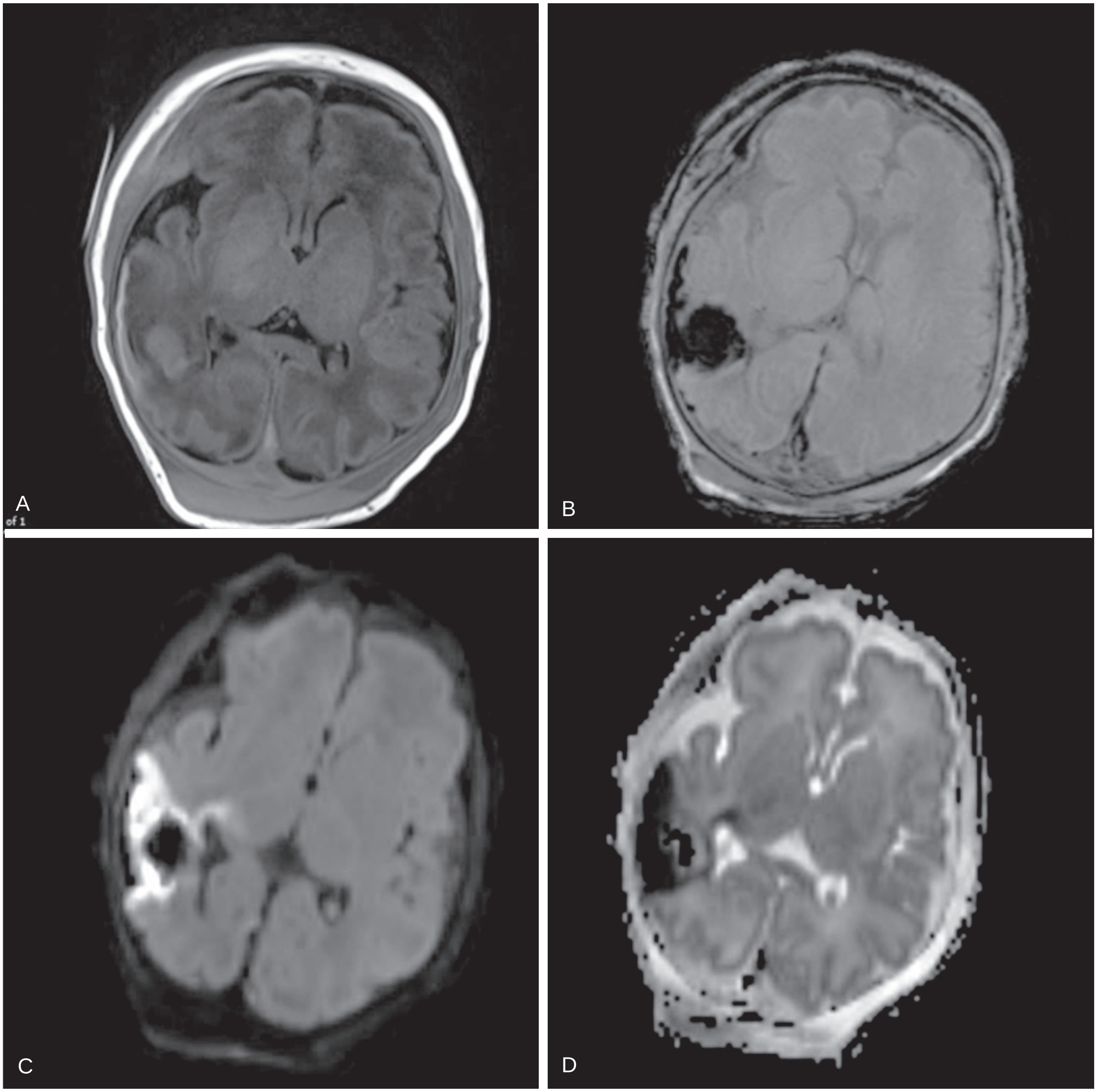

**e-Figure 37.5. Neonatal hemorrhagic infarct.** A 3-day-old female with unexplained anoxia and shoulder dystocia status after vacuum-assisted delivery. (A) Axial T1-weighted MR images demonstrate hyperintense signal consistent with hemorrhage in the right temporal lobe with overlying subpial hemorrhage. (B) SWI image confirms the right temporal lobe hemorrhage with subpial involvement. (C) High signal on DWI and (D) low signal on ADC map surrounds the hemorrhage confirming associated ischemic injury. Vessel imaging was unremarkable *(not shown)*.

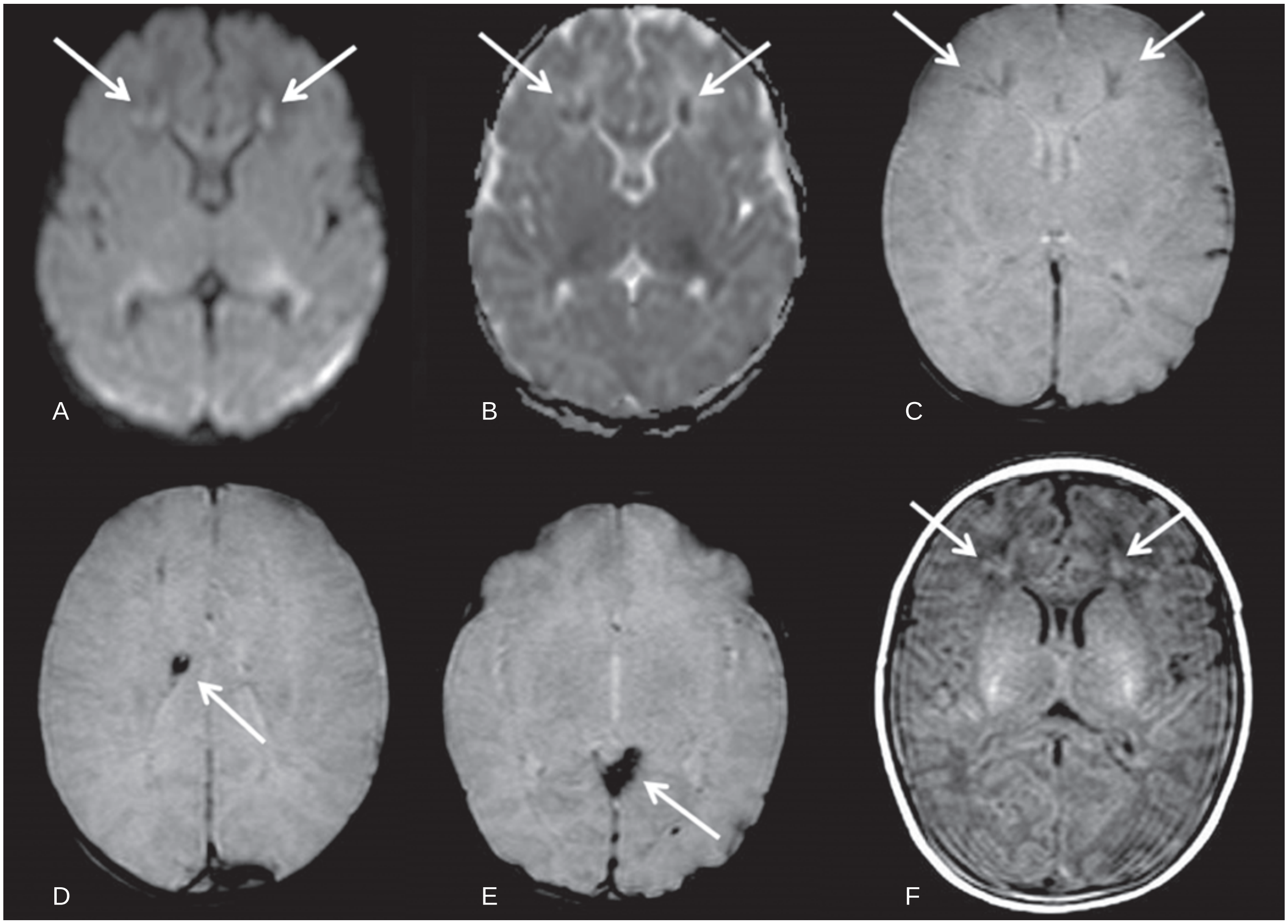

**Figure 37.4. Neonatal venous infarcts.** A 1-day-old full-term neonate with normal Apgars with multiple episodes of rhythmic jerking of the extremities in the first 24 hours of life, consistent with seizures. No known maternal risk factors. Pregnancy was complicated by small placental separation at 15 to 25 weeks. Tight nuchal cord was noted at delivery. (A) DWI and (B) ADC map demonstrate decreased diffusion in the frontal periventricular regions, in a medullary venous distribution *(arrows)*. (C–E) Axial gradient echo T2-weighted MR images demonstrate foci of blooming consistent with microhemorrhage and thrombus within the deep periventricular veins *(arrows)*. (F) Axial T1-weighted MR image demonstrates hyperintense signal in the frontal white matter in same region as blooming, likely hemorrhage *(arrows)*.

## Risk Factors

Childhood stroke is a distinct entity from neonatal and fetal stroke, with independent risk factors. The most common risk factors for stroke in children include: vasculopathies, cerebral vasculitis, primary and secondary hypercoagulable states, and genetic disorders.[39] SVT in children has been associated with numerous etiologies such as: dehydration, hypoxic-ischemic injury, postlumbar puncture, infections, medications, and multiple systemic conditions.[28]

## Imaging Findings

Boxes 37.2 and 37.3 demonstrate general guidelines for the time-course of findings of stroke seen in CT and MR, respectively.

### Arterial Ischemic Stroke

Numerous etiologies are associated with childhood AIS, as seen in Box 37.1. In approximately one-third of childhood AIS, the cause of stroke is undetermined.[40] The major sources of childhood AIS are arteriopathy, hypercoagulable states, and thromboembolism.[41,42] Arteriopathies have numerous underlying etiologies, including transient cerebral arteriopathy, trauma-related vascular injury such as arterial dissection (Fig. 37.6) or vasospasm after subarachnoid hemorrhage (e-Fig. 37.7), postinfectious vasculitis (Fig. 37.8), immune-related arteritides, and sickle cell disease arteriopathy. Hypercoagulable states, such as protein C or S deficiency, antithrombin III, or factor V Leiden mutation, are also known causes of AIS. Thromboembolism may originate from intracranial or extracranial vessels, as well as cardiac disorders such as congenital or acquired heart disease, intracardiac shunts, and procedures.[41,42]

Arteriopathies are responsible for up to two-thirds of first-time stroke in previously healthy children.[43,44] The most common arteriopathy, known as transient cerebral arteriopathy (TCA), presents as a unilateral arteriopathy involving the anterior circulation, such as the distal internal carotid, proximal middle cerebral, or proximal anterior cerebral arteries.[45] Differentiating TCA from arterial dissection can be challenging, given that both are unilateral. However, the time course of the diseases differs significantly. In TCA, the stenosis increases over a period of 3 months and then stabilizes beyond 6 months, whereas arterial dissection usually improves over the initial 3 months.[45]

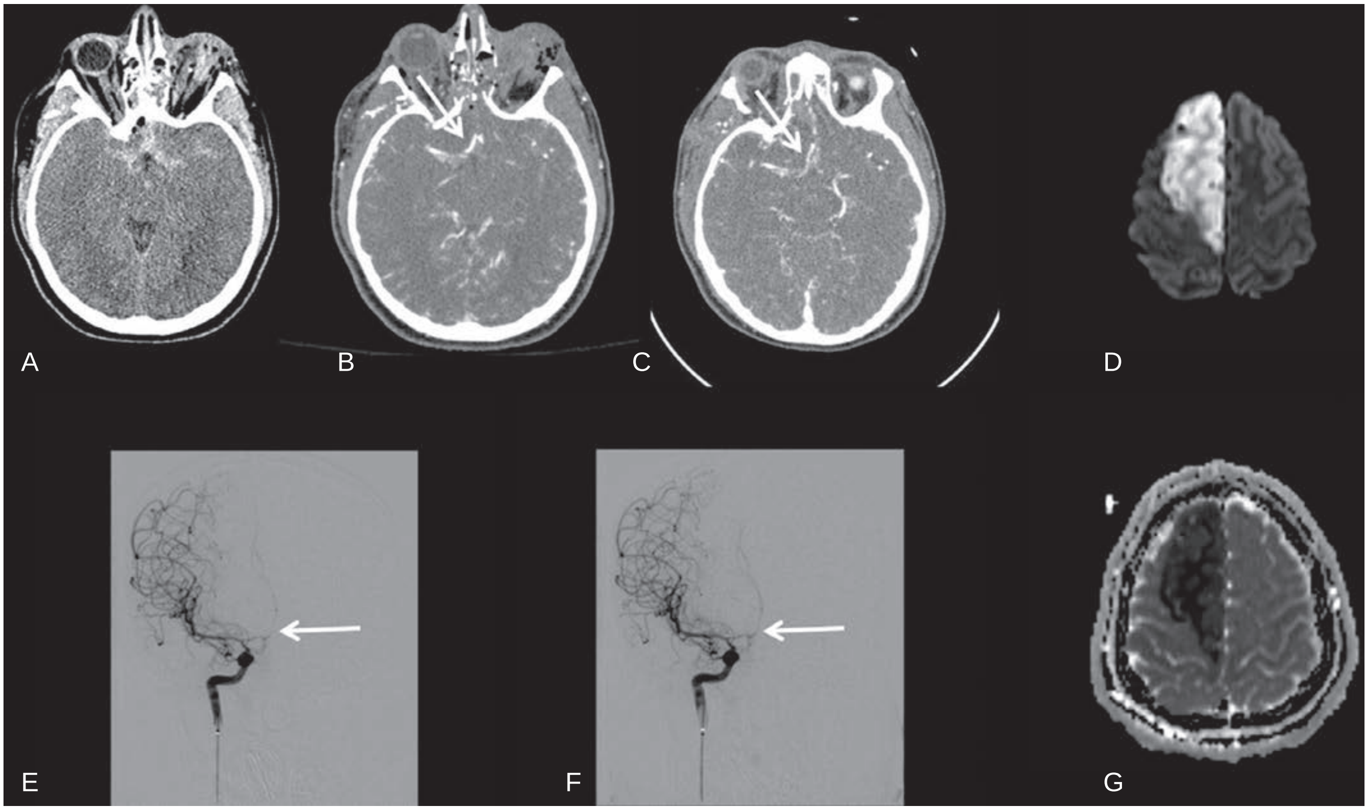

**e-Figure 37.7. Traumatic subarachnoid hemorrhage with vasospasm and infarct.** A 15-year-old male who suffered a gunshot wound to the face, globe trauma, with intracranial subarachnoid and intraparenchymal hemorrhage. Five days later, the patient developed right anterior cerebral artery territory infarct, consistent with vasospasm associated with traumatic subarachnoid hemorrhage. (A) CT shows subarachnoid hemorrhage seen in the suprasellar cistern. (B) At admission, the proximal right anterior cerebral artery (ACA) demonstrates normal caliber *(arrow)*. (C) Five days later, the proximal right ACA demonstrates irregular narrowing, consistent with vasospasm *(arrow)*. (D) DWI and (G) ADC map show acute infarct in the right ACA territory. (E) Digital subtraction angiogram demonstrates vasospasm of the right ACA *(arrow)* (F) with slight improvement *(arrow)* on postverapamil angiogram.

### BOX 37.2 Cerebral Infarction: Computed Tomographic Findings

**HYPERACUTE INFARCT (<12 HR)**

Normal (50%–60%)
Hyperdense artery (25%–50%)

**ACUTE (12–24 HR)**

Low-density basal ganglia
Loss of gray–white interfaces (insular ribbon sign, obstruction of cortex–medullary white matter border)
Sulcal effacement

**1–3 DAYS**

Increasing mass effect
Wedge-shaped low-density area that involves both gray and white matter
Hemorrhagic transformation may occur (basal ganglia and cortex are common sites)

**4–7 DAYS**

Gyral enhancement
Mass effect and edema persist

**1–8 WEEKS**

Contrast enhancement persists
Mass effect resolves
Transient calcification can occur (pediatric strokes)

**MONTHS TO YEARS**

Encephalomalacic change, volume loss
Calcification rare

*Data from Osborn AG.* Diagnostic neuroradiology: A text atlas, *St. Louis: Mosby-Year Book; 1994.*

### BOX 37.3 Cerebral Infarction: Magnetic Resonance Imaging Findings

**IMMEDIATE**

Absence of normal flow void
Intravascular contrast enhancement
Low apparent diffusion coefficient
Perfusion alterations

**<12 HOURS**

Anatomic alterations on T1-weighted image (T1WI)
Sulcal effacement
Gyral edema
Loss of gray–white interface

**12–24 HOURS**

Hyperintensity develops on T2-weighted image (T2WI)
Meningeal enhancement adjacent to infarct
Mass effect

**1–3 DAYS**

Intravascular and meningeal enhancement begins decreasing
Early parenchymal contrast enhancement
Signal abnormalities striking on T1WI, T2WI
Hemorrhagic transformation may become evident

**4–7 DAYS**

Striking parenchymal contrast enhancement
Hemorrhage apparent in 25%
Mass effect and edema begin to diminish
Intravascular and meningeal enhancement disappear

**1–8 WEEKS**

Contrast enhancement often persists
Mass effect resolves
Decrease in abnormal signal on T2WI sometimes noted (fogging effect)
Hemorrhagic changes evolve, become chronic

**MONTHS TO YEARS**

Encephalomalacic changes, volume loss in affected vascular distribution
Hemorrhagic residua (hemosiderin/ferritin)

*Data from Osborn AG.* Diagnostic neuroradiology: A text atlas, *St. Louis: Mosby-Year Book; 1994.*

Arterial dissection may occur spontaneously or after trauma. The mechanism of infarct is formation of an intramural thrombus that can result in occlusion of the vessel or distal emboli. MRI with MRA is the initial diagnostic modality of choice (see Fig. 37.6). If noncontrast MRA sequences are degraded by flow-related artifacts, CTA may be helpful in confirming the lumen diameter. Imaging findings suggestive of dissection are: abrupt segmental narrowing with an intimal flap, a beaded appearance of the vessel, or pseudoaneurysm formation.[46] T1-weighted fat-saturated MR sequences can occasionally demonstrate eccentric hyperintense signal from the intramural hematoma of the dissection.

There are two classes of immunologic arteritides causing pediatric stroke: those associated with a systemic disease such as lupus, scleroderma, or polyarteritis nodosum, and primary central nervous system (CNS) arteritides.[44] Childhood primary angiitis of the CNS (cPACNS) is an increasingly recognized vasculitic inflammatory brain disease in previously healthy children. Three types of cPACNS have been described: nonprogressive angiography-positive large-medium vessel, progressive angiography-positive large-medium vessel, and angiography-negative small vessel disease.[44] For large vessel cPACNS, MRI and MRA with contrast should be performed. MRI most commonly shows unilateral ischemic lesions in large vessel territories;[47] however, bilateral involvement may occur. MRA of the affected vessel segment may reveal wall thickening and enhancement due to inflammation, as well as unilateral or bilateral stenosis, with beading and irregularity (e-Fig. 37.9). Children with small vessel, angiography-negative cPACNS have normal MRA and conventional angiography studies; meningeal contrast enhancement is relatively specific but infrequently seen.[44] Brain biopsy is often required for diagnosis.

Moyamoya syndrome is an arteriopathy associated with sickle cell disease, neurofibromatosis type 1, and trisomy 21[48]; if the cause remains undetermined, the findings are referred to as moyamoya disease. The annual risk of stroke in moyamoya disease is 3.2%,[49] and the risk of stroke in moyamoya syndrome depends on the etiology. In both moyamoya syndrome and disease, progressive vasculopathy results in stenosis of the intracranial arteries, with predilection for terminal portions of the internal carotid arteries. Thin, irregular collateral vessels, classically from the lenticulostriate arteries, lead to a classic "puff-of-smoke" appearance on angiography. MRI may demonstrate loss of the normal flow void in the distal carotid branches on T2-weighted images, as well as development of abnormally large and irregular collateral vessels (Fig. 37.10). FLAIR images often show increased signal in distal vessels, as a result of slow flow. Carotid stenosis may be seen on MRA, but is frequently overestimated in severity.[50] Postcontrast MRA and CTA can improve assessment of the vasculature. DWI is both sensitive and specific for the evaluation of acute infarct. Perfusion-weighted and ASL sequences may be helpful for assessing alterations in cerebral flow.

Sickle cell disease carries a significantly increased risk of stroke in children.[51,52] The rigid, sickle-shaped red blood cells lead to vascular occlusion, and chronic vessel wall damage results in stenotic vessels. The proximal MCA or distal internal carotid artery (ICA)

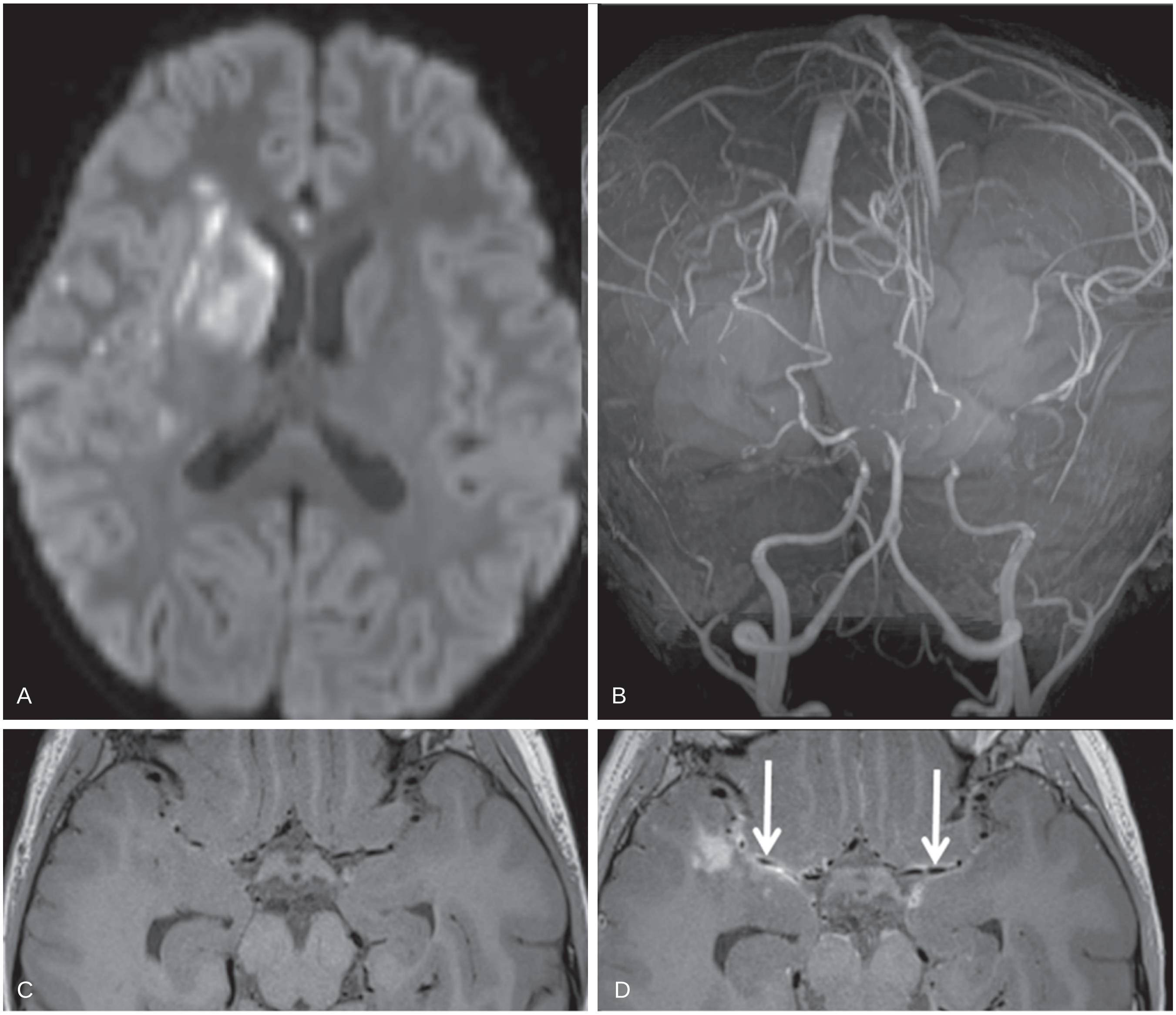

**e-Figure 37.9. Large vessel arteritis.** Bilateral progressive large vessel cerebral arteritis in a 6-year-old female presenting with a stuttering course of progressive motor deficits. Evaluation of blood and CSF was negative for infection or malignancy and did not reveal evidence of a systemic inflammatory disorder. This patient improved with treatment with high dose steroids. (A) Axial DWI shows decreased diffusion in a multifocal distribution. (B) TOF MRA shows loss of flow related enhancement in both intracranial internal carotid arteries beginning proximal to bifurcation, and the proximal bilateral MCAs and PCAs. (C) Axial T1-weighted 3D fast spin echo MR image at the level of the circle of Willis shows bilateral MCA beading and irregularity. (D) Axial postcontrast T1-weighted 3D fast spin echo MR image (vessel wall imaging) shows bilateral MCA enhancement *(arrows)* consistent with vasculitis.

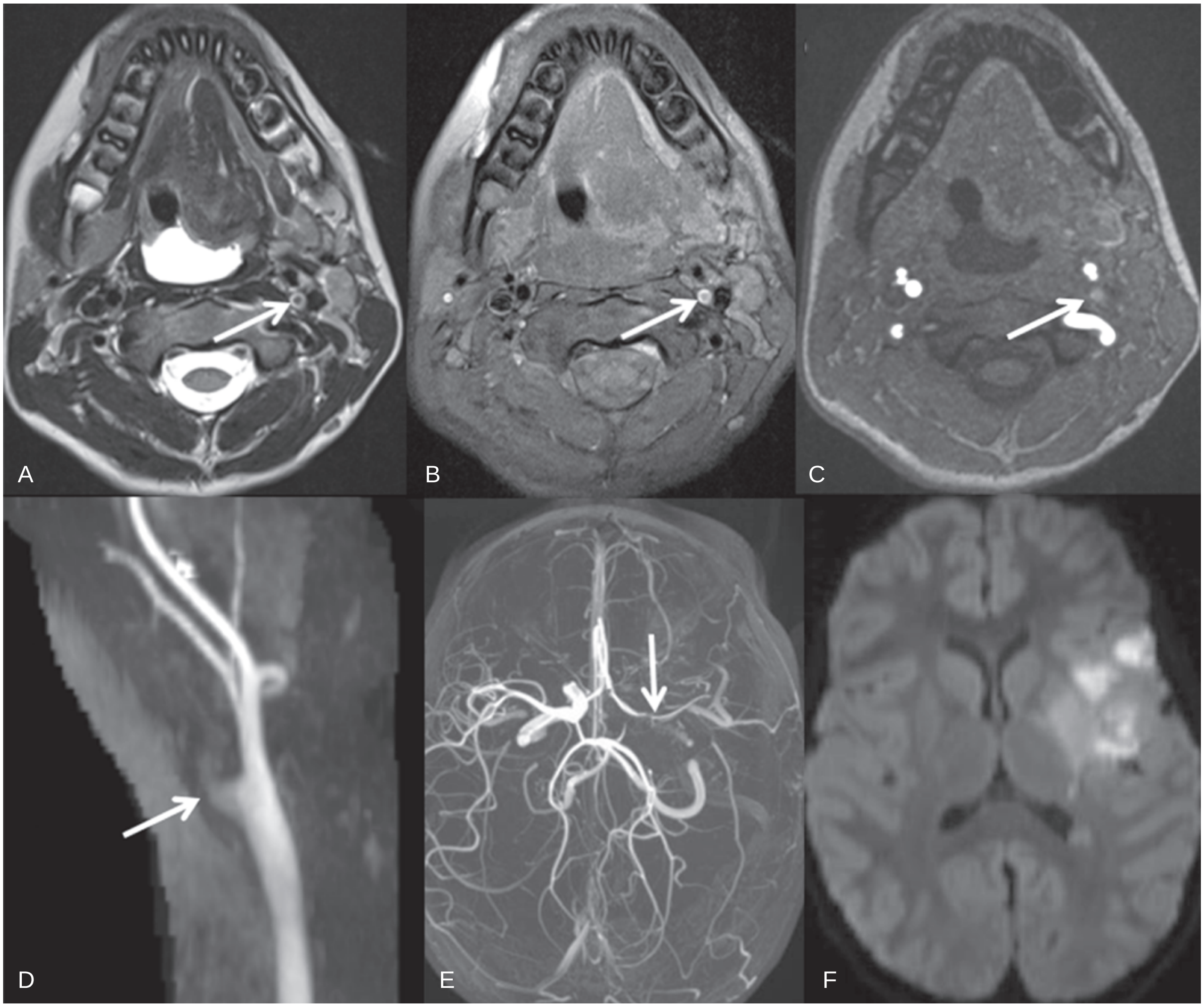

**Figure 37.6. Carotid dissection with acute infarction.** An 8-year-old female who presented with an episode of decreased responsiveness, right-sided weakness, and left eye deviation after emerging from a swimming pool without clear history of trauma. (A) Axial FSE T2-weighted MR image demonstrates T2 hyperintense signal circumferentially in the left carotid *(arrow)*, suggesting subintimal hematoma/dissection. (B) Fat-saturated T1-weighted MR image also shows the circumferential hyperintense signal *(arrow)* confirming intramural hematoma/dissection. (C) TOF MRA of the neck shows loss of normal flow related enhancement in the same region *(arrow)*. (D) MIP from the same TOF MRA of the neck and (E) MIP from the 3D TOF brain demonstrates loss of flow-related signal in the left internal carotid artery from just distal to the bifurcation to its bifurcation with decreased flow-related enhancement in the left MCA *(arrow)*. (F) DWI demonstrating associated left MCA infarction. *FSE,* Fast spin echo; *MIP,* maximum intensity projection; *TOF MRA,* time of flight magnetic resonance angiogram; *MCA,* middle cerebral artery.

branches are the most commonly involved vessels. Biannual screening with transcranial Doppler (TCD) imaging is routinely performed, and abnormally elevated velocities from stenotic arteries necessitates blood transfusion to prevent stroke.[53] Prior to TCD screening, stroke occurred in 5% to 10% of children.[51] Brain MRI is usually performed to evaluate children with sickle cell anemia presenting with acute onset of symptoms such as seizures, or motor or sensory deficits. Acute infarcts may be superimposed on a diseased brain with atrophy and chronic changes. In the setting of moyamoya syndrome, MRA commonly shows irregular stenotic arteries involving the anterior circulation with leptomeningeal collaterals. CTA has restricted use in the evaluation of patients with sickle cell disease, as iodinated contrast predisposes to sickling. Low osmolar agents should be used, along with transfusion and hydration to reduce the risk of complications.

## Venous Stroke

In children, SVT is the primary cause of venous stroke, with incidence of approximately 0.67 case per 100,000 children per year.[6] Risk factors include head and neck disorders (29%), acute systemic illnesses (54%), chronic systemic diseases (36%), and prothrombotic states (41%).[6] Dehydration, complicated otitis media, and sinusitis are the major risk factors in older children. Without treatment, 30% of SVT patients will have propagation of the thrombus, which are associated with new venous infarcts in 40% of children.[54]

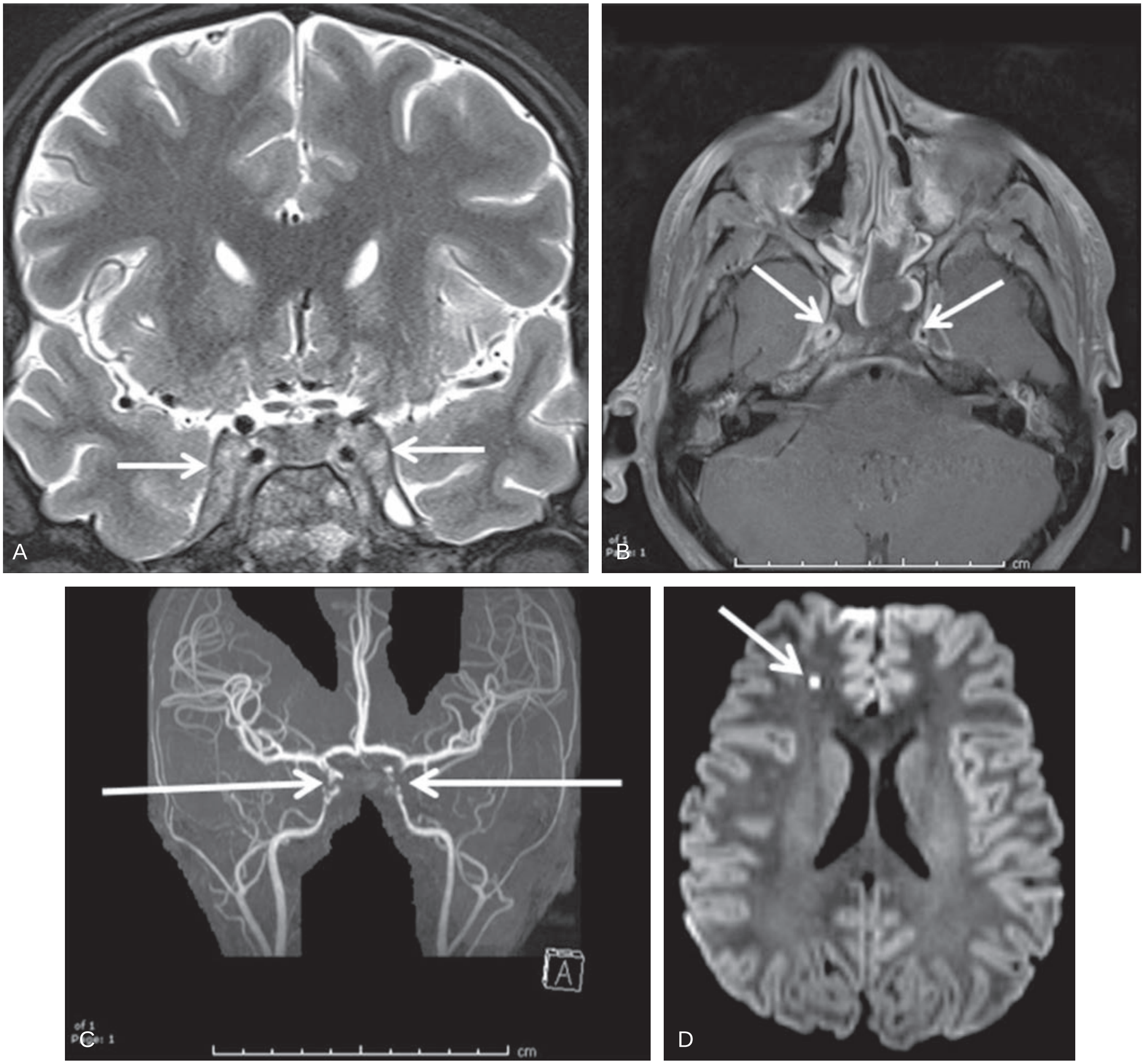

**Figure 37.8. Postinfectious vasculitis with infarct.** A 15-year-old female with bilateral sinusitis, cavernous venous thrombosis, gram-negative bacteremia, and skull base osteomyelitis with high fevers and new impaired horizontal eye movements. (A) Coronal fat-saturated FSE T2-weighted MR image demonstrates enlarged thrombosed bilateral cavernous sinuses *(arrows)*. (B) Axial fat-saturated postcontrast T1-weighted MR image demonstrates wall thickening and stenosis of the cavernous internal carotid arteries *(arrows)*, consistent with arteritis. Extensive sinusitis is present. (C) 3D TOF MRA confirms bilateral cavernous carotid involvement with irregular narrowing *(arrows)*. (D) DWI demonstrates a punctate acute embolic infarct *(arrow)* in the right frontal deep white matter.

Imaging findings of SVT in children are similar to those discussed previously. CT should only be considered in children who cannot obtain an adequate MR without sedation or for whom sedation risks during MRI outweigh the risks of radiation exposure. MR sequences are helpful for evaluation of SVT and venous infarct include DWI, GRE/SWI, MRV, and T1-weighted precontrast and postcontrast high-resolution sequences. DWI is both sensitive and specific for the evaluation of venous infarct. GRE or SWI may be useful for demonstrating thrombus, which frequently "blooms" on these sequences. MRV is prone to artifacts that may simulate clot; contrast-enhanced T1-weighted images are more reliable for delineation of venous filling defects and may be confirmatory for suspected findings on MRV.[32]

## ALTERNATIVE DIAGNOSES

Numerous diseases have similar clinical presentations as stroke and should be considered before diagnosis, including migraine

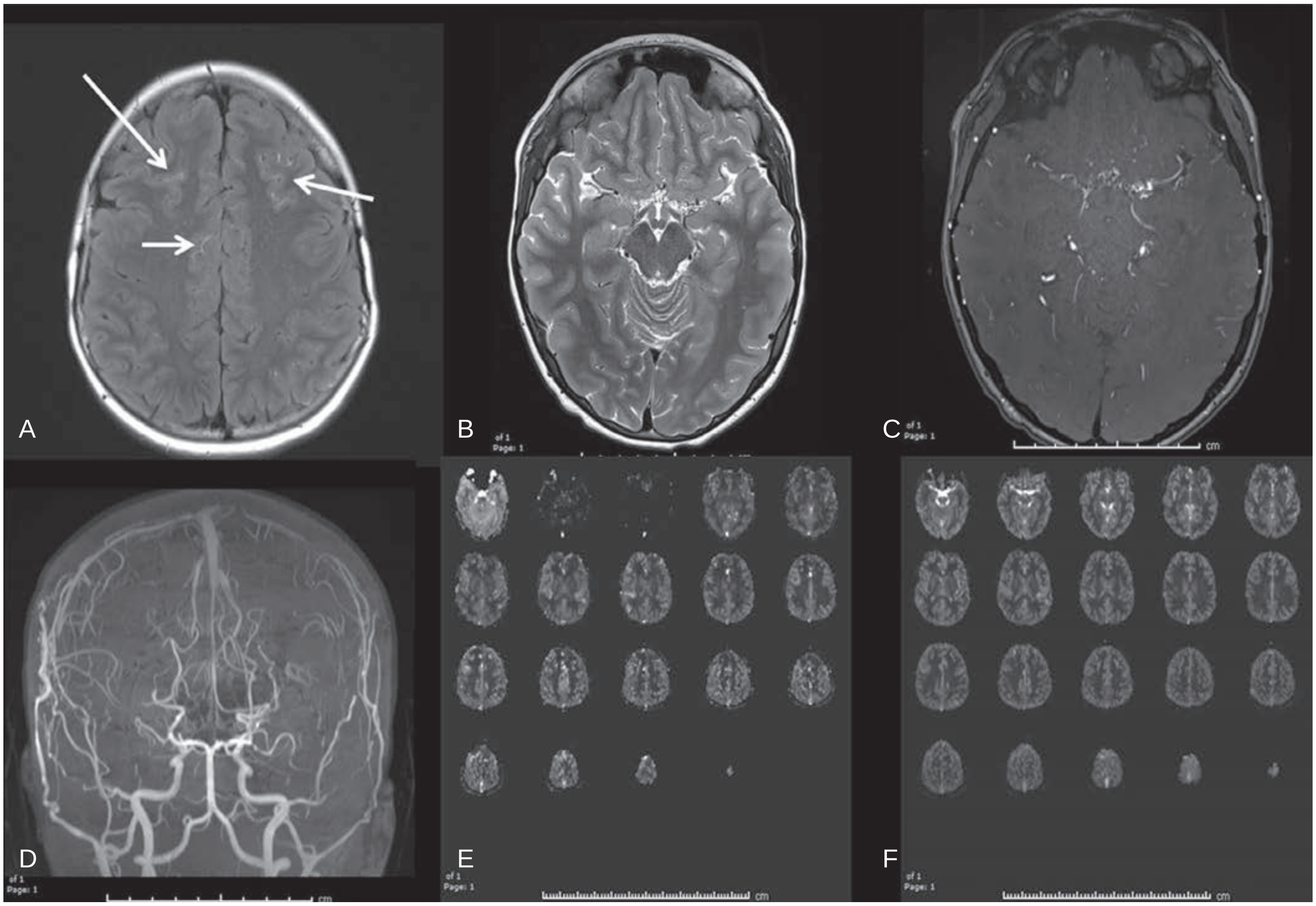

**Figure 37.10. Moyamoya disease vasculopathy.** Asymptomatic 13-year-old male with moyamoya disease status postpial synangioses. No known history of sickle cell disease or other causative etiologies. (A) Axial FLAIR image demonstrates hyperintense pial vessels *(arrows)*, consistent with slow flow in collateral vessels. (B) FSE T2-weighted, (C) TOF MRA and (D) coronal MIP from MRA show extensive lenticulostriate collateral vessels within the expected regions of the bilateral MCAs. (E) Perfusion ASL images show bright signal within the bilateral ACAs and MCAs due to delayed arrival of the labeled blood to the parenchyma. (F) Velocity selective ASL shows symmetric cerebral perfusion in the parenchyma consistent with successful synangiosis and current asymptomatic state.

disorders, postictal state, Bell palsy, and conversion disorders.[5] Additionally, several disease processes have imaging findings of decreased diffusion on MRI DWI sequences, which could be confused with ischemic infarcts. Hemiplegic migraine, mitochondrial disorders, demyelinating disease, and status epilepticus may have regions of decreased diffusion that should not be mistaken for acute infarct. Transient neurologic symptoms in patients with migraine can simulate stroke symptoms clinically, and decreased diffusion has been described in hemiplegic migraine disorders.[55] Migraine with aura has an increased risk of stroke in the adult population, and some case reports indicate a relationship between infarcts and migraine in adolescents.[56] The association between migraine and stroke may be related to a dysfunction of cerebral arteries during migraine attacks. Mitochondrial disorders, such as MELAS (mitochondrial encephalopathy, lactic acidosis, and strokelike episodes), are frequently complicated by strokelike events. These disorders can be clinically indistinguishable from AIS, but the imaging findings do not conform to a vascular territory (e-Fig. 37.11). Demyelinating disease, such as multiple sclerosis, typically presents with white matter lesions that may demonstrate decreased diffusion acutely. However, clinical history and multiple lesions of differing ages on imaging may argue for a demyelinating disorder, as opposed to infarct. Status epilepticus or prolonged seizures can also result in transient decreased diffusion in the peri-ictal phase. On imaging, this finding usually does not conform to a vascular distribution. However, caution is required, particularly in neonates, as neonatal infarcts often present as seizures.

## SUMMARY

Stroke is an important cause of morbidity and mortality in the pediatric population across all ages. Despite advances in imaging, stroke poses numerous diagnostic challenges, particularly because the diagnosis is frequently not considered until the subacute to chronic phase, when imaging findings may be more difficult to interpret. The often complex, overlapping risk factors and disease processes in pediatric stroke are in striking contrast to the adult population, in which stroke is usually attributed to atherosclerotic vascular disease. Management of pediatric stroke is controversial due to the current lack of large-scale, disease-specific risk and outcomes data. As such, pediatric stroke treatment is an important, active area of research. Increased awareness of pediatric stroke is necessary to facilitate prevention, early diagnosis and intervention in children of all ages.

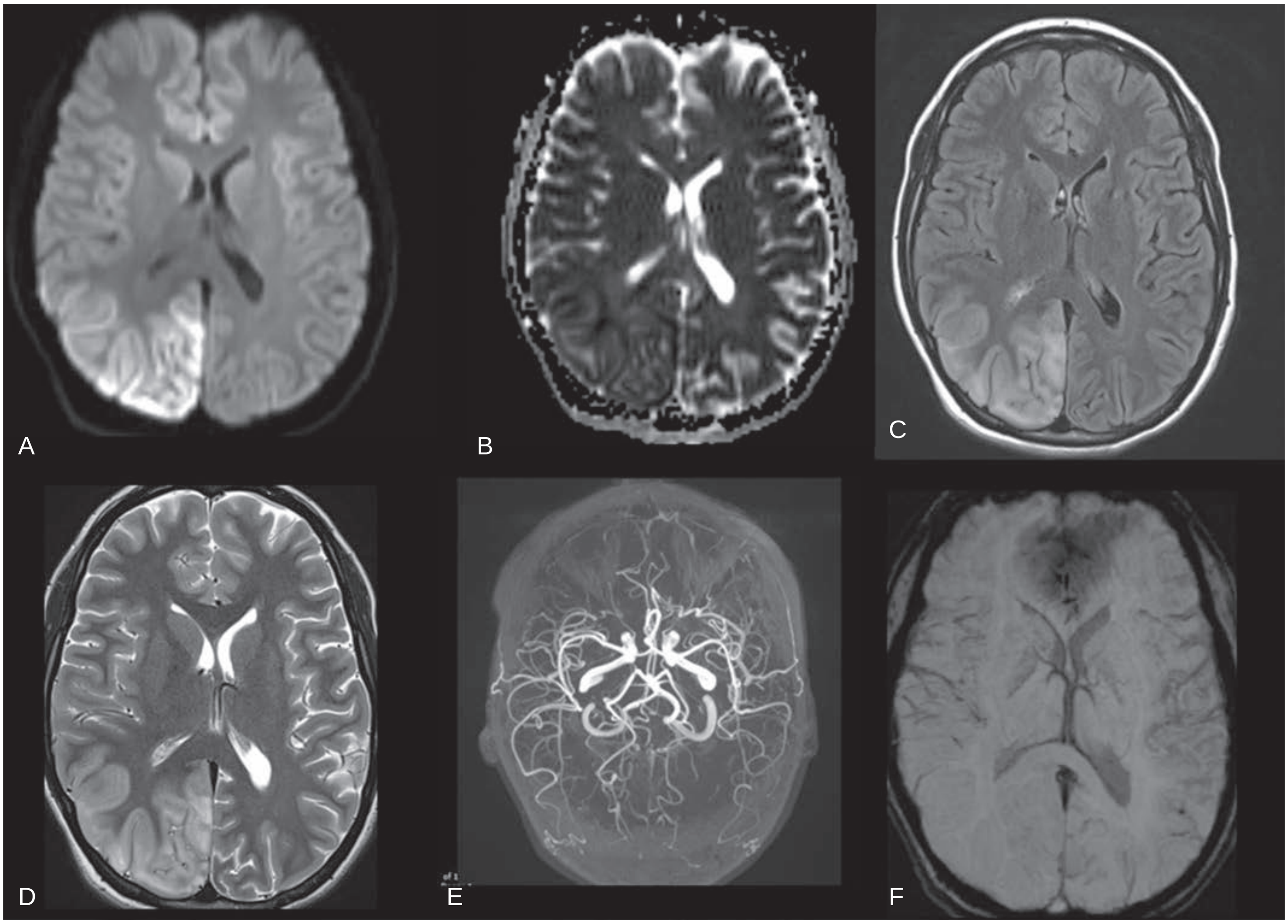

**e-Figure 37.11. Alternative considerations in the setting of decreased diffusion—MELAS.** A 15-year-old with MELAS and new neurologic symptoms of numbness of LLE and blurry vision. (A) DWI and (B) ADC map demonstrate decreased diffusion in a nonvascular distribution involving the right parietal region. In addition, the ADC is atypical for arterial ischemic infarct, as there is subcortical edema. (C) FLAIR and (D) T2 hyperintense signal with significant swelling is inconsistent with an acute AIS. (E) 3D TOF MRA shows no evidence of vascular occlusion and, in fact, shows slight prominence of the right PCA. (F) SWI shows decreased venous deoxyhemoglobin in the involved region consistent with increased perfusion.

## KEY POINTS

- Stroke is a significant cause of morbidity and mortality in all pediatric age groups but particularly common in the neonatal population.
- Determining the etiology of a stroke is often not possible. No definite cause of perinatal AIS is determined in 25% to 50% of cases. In venous infarcts, the true incidence is difficult to determine as venous thrombus is often not visualized at imaging.
- The patterns of stroke indicate the mechanism of injury. Perinatal AIS leads to focal ischemic injury in an arterial distribution, most commonly in the MCA territory and may be hyperperfused at diagnosis. Venous infarcts may involve superficial or deep medullary venous territories, with quite different patterns.
- In fetal stroke, the age of the fetus at the time of infarct can contribute to the subsequent pathology and pattern of injury.
- The diagnosis of stroke in children is frequently not considered until the subacute to chronic phase, when imaging findings may have partially resolved and become more difficult to interpret. Early consideration of stroke as part of the differential diagnosis and timely imaging is therefore important for treatment and prognosis.

## SUGGESTED READINGS

Berfelo FJ, Kersbergen KJ, van Ommen CH, et al. Neonatal cerebral sinovenous thrombosis from symptom to outcome. *Stroke*. 2010;417:1382–1388.

Kirton A, Armstrong-Wells J, Chang T, et al. Symptomatic neonatal arterial ischemic stroke: the International Pediatric Stroke Study. *Pediatrics*. 2011;1286:e1402–e1410.

Rodrigues K, Grant PE. Diffusion-weighted imaging in neonates. *Neuroimaging Clin N Am*. 2011;211:127–151. http://iapediatricstroke.org/home.aspx.

Rutherford MA, Ramenghi LA, Cowan FM. Neonatal stroke. *Arch Dis Child Fetal Neonatal Ed*. 2012;975:F377–F384.

## REFERENCES

Full references for this chapter can be found on www.expertconsult.com.

## REFERENCES

1. Lynch JK. Epidemiology and classification of perinatal stroke. *Semin Fetal Neonatal Med*. 2009;14(5):245–249.
2. Fullerton HJ, Wu YW, Zhao S, et al. Risk of stroke in children: ethnic and gender disparities. *Neurology*. 2003;61(2):189–194.
3. Ozduman K, Pober BR, Barnes P, et al. Fetal stroke. *Pediatr Neurol*. 2004;30(3):151–162.
4. Kirton A, Armstrong-Wells J, Chang T, et al. Symptomatic neonatal arterial ischemic stroke: the International Pediatric Stroke Study. *Pediatrics*. 2011;128(6):e1402–e1410.
5. Mackay MT, Yock-Corrales A, Churilov L, et al. Differentiating childhood stroke from mimics in the emergency department. *Stroke*. 2016;47(10):2476–2481.
6. deVeber G, Andrew M, Adams C, et al. Cerebral sinovenous thrombosis in children. *N Engl J Med*. 2001;345(6):417–423.
7. Ellis MJ, Amlie-Lefond C, Orbach DB. Endovascular therapy in children with acute ischemic stroke: review and recommendations. *Neurology*. 2012;79(13 suppl 1):S158–S164.
8. Rivkin MJ, Bernard TJ, Dowling MM, et al. Guidelines for urgent management of stroke in children. *Pediatr Neurol*. 2016;56: 8–17.
9. Reddy UM, Abuhamad AZ, Levine D, et al. Fetal imaging: executive summary of a joint Eunice Kennedy Shriver National Institute of Child Health and Human Development, Society for Maternal-Fetal Medicine, American Institute of Ultrasound in Medicine, American College of Obstetricians and Gynecologists, American College of Radiology, Society for Pediatric Radiology, and Society of Radiologists in Ultrasound Fetal Imaging workshop. *Obstet Gynecol*. 2014;123(5): 1070–1082.
10. Tanner SF, Ramenghi LA, Ridgway JP, et al. Quantitative comparison of intrabrain diffusion in adults and preterm and term neonates and infants. *AJR Am J Roentgenol*. 2000;174(6):1643–1649.
11. Govaert P. Prenatal stroke. *Semin Fetal Neonatal Med*. 2009;14(5):250–266.
12. Griffiths PD, Sharrack S, Chan KL, et al. Fetal brain injury in survivors of twin pregnancies complicated by demise of one twin as assessed by in utero MR imaging. *Prenat Diagn*. 2015;35(6):583–591.
13. Barkovich AJ. Current concepts of polymicrogyria. *Neuroradiology*. 2010;52(6):479–487.
14. Barkovich AJ, Millen KJ, Dobyns WB. A developmental and genetic classification for midbrain-hindbrain malformations. *Brain*. 2009;132(Pt 12):3199–3230.
15. Bava S, Archibald SL, Trauner DA. Brain structure in prenatal stroke: quantitative magnetic resonance imaging (MRI) analysis. *J Child Neurol*. 2007;22(7):841–847.
16. Lehman LL, Rivkin MJ. Perinatal arterial ischemic stroke: presentation, risk factors, evaluation, and outcome. *Pediatr Neurol*. 2014;51(6):760–768.
17. Berfelo FJ, Kersbergen KJ, van Ommen CH, et al. Neonatal cerebral sinovenous thrombosis from symptom to outcome. *Stroke*. 2010;41(7):1382–1388.
18. Golomb MR, MacGregor DL, Domi T, et al. Presumed pre- or perinatal arterial ischemic stroke: risk factors and outcomes. *Ann Neurol*. 2001;50(2):163–168.
19. Nelson KB. Perinatal ischemic stroke. *Stroke*. 2007;38(2 suppl):742–745.
20. Golomb MR, Garg BP, Edwards-Brown M, et al. Very early arterial ischemic stroke in premature infants. *Pediatr Neurol*. 2008;38(5):329–334.
21. Cole L, Dewey D, Letourneau N, et al. Clinical characteristics, risk factors, and outcomes associated with neonatal hemorrhagic stroke: a population-based case-control study. *JAMA Pediatri*. 2017;171:203.
22. Rutherford MA, Ramenghi LA, Cowan FM. Neonatal stroke. *Arch Dis Child Fetal Neonatal Ed*. 2012;97(5):F377–F384.
23. Rodrigues K, Grant PE. Diffusion-weighted imaging in neonates. *Neuroimaging Clin N Am*. 2011;21(1):127–151, viii.
24. Engelsen BA, Tzoulis C, Karlsen B, et al. POLG1 mutations cause a syndromic epilepsy with occipital lobe predilection. *Brain*. 2008;131(Pt 3):818–828.
25. Chen J, Licht DJ, Smith SE, et al. Arterial spin labeling perfusion MRI in pediatric arterial ischemic stroke: initial experiences. *J Magn Reson Imaging*. 2009;29(2):282–290.
26. Watson CG, Dehaes M, Gagoski BA, et al. Arterial spin labeling perfusion magnetic resonance imaging performed in acute perinatal stroke reveals hyperperfusion associated with ischemic injury. *Stroke*. 2016;47(6):1514–1519.
27. Eichler F, Krishnamoorthy K, Grant PE. Magnetic resonance imaging evaluation of possible neonatal sinovenous thrombosis. *Pediatr Neurol*. 2007;37(5):317–323.
28. Dlamini N, Billinghurst L, Kirkham FJ. Cerebral venous sinus (sinovenous) thrombosis in children. *Neurosurg Clin N Am*. 2010;21(3): 511–527.
29. Kirton A, Deveber G, Pontigon AM, et al. Presumed perinatal ischemic stroke: vascular classification predicts outcomes. *Ann Neurol*. 2008;63(4):436–443.
30. Kersbergen KJ, Groenendaal F, Benders MJ, et al. The spectrum of associated brain lesions in cerebral sinovenous thrombosis: relation to gestational age and outcome. *Arch Dis Child Fetal Neonatal Ed*. 2011;96(6):F404–F409.
31. Raets MM, Sol JJ, Govaert P, et al. Serial cranial US for detection of cerebral sinovenous thrombosis in preterm infants. *Radiology*. 2013;269(3):879–886.
32. Jackson BF, Porcher FK, Zapton DT, et al. Cerebral sinovenous thrombosis in children: diagnosis and treatment. *Pediatr Emerg Care*. 2011;27(9):874–880, quiz 81-3.
33. McDonald RJ, McDonald JS, Kallmes DF, et al. Intracranial gadolinium deposition after contrast-enhanced MR imaging. *Radiology*. 2015;275(3):772–782.
34. Olchowy C, Cebulski K, Lasecki M, et al. The presence of the gadolinium-based contrast agent depositions in the brain and symptoms of gadolinium neurotoxicity - a systematic review. *PLoS ONE*. 2017;12(2):e0171704.
35. Golomb MR. Outcomes of perinatal arterial ischemic stroke and cerebral sinovenous thrombosis. *Semin Fetal Neonatal Med*. 2009;14(5):318–322.
36. Kirton A, Shroff M, Visvanathan T, et al. Quantified corticospinal tract diffusion restriction predicts neonatal stroke outcome. *Stroke*. 2007;38(3):974–980.
37. Agrawal N, Johnston SC, Wu YW, et al. Imaging data reveal a higher pediatric stroke incidence than prior US estimates. *Stroke*. 2009;40(11):3415–3421.
38. Fullerton HJ, Wintermark M, Hills NK, et al. Risk of recurrent arterial ischemic stroke in childhood: a prospective international study. *Stroke*. 2016;47(1):53–59.
39. Roach ES, Golomb MR, Adams R, et al. Management of stroke in infants and children: a scientific statement from a Special Writing Group of the American Heart Association Stroke Council and the Council on Cardiovascular Disease in the Young. *Stroke*. 2008;39(9): 2644–2691.
40. Nowak-Gottl U, Strater R, Heinecke A, et al. Lipoprotein (a) and genetic polymorphisms of clotting factor V, prothrombin, and methylenetetrahydrofolate reductase are risk factors of spontaneous ischemic stroke in childhood. *Blood*. 1999;94(11):3678–3682.
41. Beslow LA, Jordan LC. Pediatric stroke: the importance of cerebral arteriopathy and vascular malformations. *Childs Nerv Syst*. 2010;26(10):1263–1273.
42. Mackay MT, Wiznitzer M, Benedict SL, et al. Arterial ischemic stroke risk factors: the International Pediatric Stroke Study. *Ann Neurol*. 2011;69(1):130–140.
43. Fullerton HJ, Wu YW, Sidney S, et al. Risk of recurrent childhood arterial ischemic stroke in a population-based cohort: the importance of cerebrovascular imaging. *Pediatrics*. 2007;119(3):495–501.
44. Twilt M, Benseler SM. CNS vasculitis in children. *Mult Scler Relat Disord*. 2013;2(3):162–171.
45. Dlamini N, Freeman JL, Mackay MT, et al. Intracranial dissection mimicking transient cerebral arteriopathy in childhood arterial ischemic stroke. *J Child Neurol*. 2011;26(9):1203–1206.
46. Stence NV, Fenton LZ, Goldenberg NA, et al. Craniocervical arterial dissection in children: diagnosis and treatment. *Curr Treat Options Neurol*. 2011;13(6):636–648.
47. Aviv RI, Benseler SM, Silverman ED, et al. MR imaging and angiography of primary CNS vasculitis of childhood. *AJNR Am J Neuroradiol*. 2006;27(1):192–199.
48. Smith ER. Structural causes of ischemic and hemorrhagic stroke in children: moyamoya and arteriovenous malformations. *Curr Opin Pediatr*. 2015;27(6):706–711.
49. Kuroda S, Hashimoto N, Yoshimoto T, et al. Radiological findings, clinical course, and outcome in asymptomatic moyamoya disease: results of multicenter survey in Japan. *Stroke*. 2007;38(5):1430–1435.
50. Smith ER, Scott RM. Spontaneous occlusion of the circle of Willis in children: pediatric moyamoya summary with proposed evidence-based practice guidelines. A review. *J Neurosurg Pediatr*. 2012;9(4): 353–360.
51. Ware RE, de Montalembert M, Tshilolo L, et al. Sickle cell disease. *Lancet*. 2017;390:311.

52. Ohene-Frempong K, Weiner SJ, Sleeper LA, et al. Cerebrovascular accidents in sickle cell disease: rates and risk factors. *Blood*. 1998;91(1):288–294.
53. Adams RJ, McKie VC, Hsu L, et al. Prevention of a first stroke by transfusions in children with sickle cell anemia and abnormal results on transcranial Doppler ultrasonography. *N Engl J Med*. 1998;339(1):5–11.
54. Moharir MD, Shroff M, Stephens D, et al. Anticoagulants in pediatric cerebral sinovenous thrombosis: a safety and outcome study. *Ann Neurol*. 2010;67(5):590–599.
55. Jacob A, Mahavish K, Bowden A, et al. Imaging abnormalities in sporadic hemiplegic migraine on conventional MRI, diffusion and perfusion MRI and MRS. *Cephalalgia*. 2006;26(8):1004–1009.
56. Ming X, Yacoub H, Khanna A, et al. Two young patients with stroke in conjunction with migraineus headache. *Open Neurol J*. 2010;4:111–116.

# 38 Neuroimaging in Pediatric Epilepsy

Elysa Widjaja

## OVERVIEW

Epilepsy is a common pediatric neurologic disorder. In North America, the overall incidence of epilepsy is approximately 50/100,000 per year, highest for children below 5 years of age and the elderly.[1,2] Children are at higher risk for developing epilepsy than adults. Atypical, idiopathic, and focal epilepsy as well as epileptic syndromes require evaluation with magnetic resonance imaging (MRI). Approximately 30% of children with epilepsy become refractory to medical therapy.[3] In this group of children with refractory focal epilepsy, neuroimaging is critical for identifying an epileptogenic substrate responsible for the epilepsy, particularly in those potentially undergoing surgery. Epilepsy surgery in those with normal MRI has been reported to have poorer surgical outcomes compared with those with an identifiable lesion.[4] Epileptogenic substrates include malformations of cortical development (MCD), developmental tumors, anoxic-ischemic injuries, prior cerebrovascular disease, neurocutaneous syndromes, and Rasmussen encephalitis. Concurrent lesions such as MCD, hippocampal sclerosis, and developmental tumors can occur in approximately 13% to 20% of cases.[5,6] Another important role of imaging in presurgical epilepsy evaluation is to identify the location of eloquent cortex and white matter tracts.

MRI is the imaging study of choice for identifying an epileptogenic substrate. Higher field strengths such as 3 T is preferred. A dedicated epilepsy protocol is required to improve lesion detection and has been shown to improve seizure-free surgical outcome.[7] The epilepsy protocol in children should include volumetric T1-weighted imaging, and T2-weighted and fluid attenuation inversion recovery (FLAIR) imaging in at least two orthogonal planes covering the entire brain.[8] Additional sequences such as proton density, 3D FLAIR, inversion recovery, and gradient echo/susceptibility-weighted imaging may be helpful. Epilepsy protocols in neonates and infants younger than 1 year require a different set of sequences due to immature myelination and should include volumetric T1-weighted, and axial and coronal T2-weighted images covering the entire brain. FLAIR and proton density images are less helpful in neonates and infants due to lack of myelination. Volumetric imaging section thickness of less than or equal to 1 mm provides excellent gray-white matter contrast, can be reformatted into any orthogonal or nonorthogonal planes, and can be used for anatomic integration of functional data, stereotactic electrode placement, and neuronavigation.[9–11] In temporal lobe epilepsy, the coronal plane should be acquired perpendicular to the long axis of the hippocampus. Contrast injection does not improve lesion detection but may help with lesion characterization. In cases where an epileptogenic focus is not identified, further evaluation with dedicated higher resolution MRI, image postprocessing, or additional imaging techniques including diffusion tensor imaging, magnetic resonance spectroscopy, functional imaging with interictal positron emission tomography (PET) or ictal/interictal single-photon emission computed tomography (SPECT), and magnetoencephalography (MEG) may help in identifying a lesion or the epileptogenic zone.[12,13]

## MALFORMATIONS OF CORTICAL DEVELOPMENT

MCD are a major cause of drug-resistant epilepsy,[14] in particular focal cortical dysplasia (FCD), hemimegalencephaly, and tuberous sclerosis. Other MCD such as lissencephaly, gray matter heterotopia, polymicrogyria, and schizencephaly are also associated with epilepsy.[15–18]

### Focal Cortical Dysplasia

***Overview.*** FCD is one of the most common causes of intractable epilepsy in children and accounts for up to 39% of pediatric epilepsy surgical cases.[19,20] The mechanism of epilepsy is still unclear. Postulated possibilities include abnormal firing from the dysplastic neurons rather than from balloon cells,[21] dysfunction of synaptic circuits with abnormal synchronization of the neuronal population, and abnormal organization of the inhibitory interneurons.[22] A consensus classification has been proposed by the International League Against Epilepsy (ILAE) in 2011 (Table 38.1).[23]

***Imaging.*** FCD can be located in any cortex of the cerebral hemisphere and can have variable size, from one gyrus to more than one lobar involvement. The MRI features of FCD include increased cortical thickness, blurring of the cortical–white matter junction, increased T2 or FLAIR signal in the cortex and subcortical white matter, high T1 signal in the cortex, and abnormal sulcation and gyration pattern. Taylor's FCD or FCD type IIB are more likely to demonstrate high T2/FLAIR signal that tapers toward the ventricle.[24–26] Type I FCD is more likely to demonstrate hypoplasia or atrophy of the white matter and mild increased T2 signal of the white matter. The high T2 signal in the white matter may be secondary to abnormal myelination, either due to the underlying disease or secondary to seizures. FCD, in particular FCD type I, are associated with hippocampal sclerosis.[27] The MR appearance of FCD may change with brain myelin maturation. In patients with focal epilepsy, MR during infancy may be normal, and repeat imaging after the age of 2 years may reveal FCD.[28] Therefore even when the MRI appears normal in an infant with refractory focal seizures, a repeat study is recommended at a later age[28] (Fig. 38.1). In contrast to the high T2/FLAIR signal in the white matter of FCD in children, the white matter adjacent to the dysplastic cortex may demonstrate low T2 and high T1 signal in neonates and infants. This is postulated to be secondary to early myelination in the white matter from repeated seizures.[29]

***Treatment and Follow-up.*** Up to 50% to 70% of patients with FCD achieve good seizure control or seizure-free outcome after surgical resection of FCD.[30–32] This compares favorably with the outcome of patients with hippocampal sclerosis[33] and low-grade neoplasms.[34] The reported surgical outcomes of subtypes of FCD are variable. Some studies reported better surgical outcome in those with Taylor's FCD,[26,35,36] while others reported better surgical outcomes in those with other subtypes of FCD, including type I FCD and mild MCD.[37,38] Differences in outcomes of subtypes of FCD may in part be related to the preponderance of type I FCD and mild MCD in the temporal lobe.[37]

### Hemimegalencephaly

***Overview.*** Hemimegalencephaly is a MCD characterized by one hemisphere being larger than the contralateral side. It may be sporadic or associated with a variety of syndromes, including proteus syndrome, epidermal nevus syndrome, hypomelanosis of Ito, linear nevus sebaceous syndrome, neurofibromatosis type I, and tuberous sclerosis. The sporadic form is considered a hemispheric variant of FCD.[39] On histology, the appearance is similar

## Abstract:

Epilepsy is a common pediatric neurologic disorder. Approximately 30% of children with epilepsy become refractory to medical therapy, and some of these patients are amenable to surgical treatment. MRI is important for identifying a lesion responsible for epilepsy. Detection of a lesion on MRI may influence epilepsy surgery outcome, and those with a lesion seen on MRI have better seizure-free surgical outcome relative to those with normal MRI. Lesion identification on MRI can be improved through the use of high-resolution dedicated epilepsy protocol on 3T and meticulous review of MRI, with knowledge of the clinical semiology, EEG, and functional imaging information such as PET, SPECT or MEG.

There is a wide range of brain abnormalities that can cause epilepsy. The two most common causes of intractable focal epilepsy are malformations of cortical development (MCD) and developmental tumors. Focal cortical dysplasia, a MCD, is one of the most challenging lesions to identify on imaging, as the MRI features can be subtle. The MRI appearance of focal cortical dysplasia may vary by age, with lower T2 and high T1 signal in the subcortical white matter in neonates and infants, postulated to be secondary to early myelination from repeated seizures. Hippocampal sclerosis is less common in children compared to adults with focal intractable epilepsy. Other less common lesions responsible for epilepsy include hypothalamic hamartoma, Rasmussen encephalitis, vascular lesions such as cavernomas, and meningioangiomatosis. Dual pathology may be encountered in about 15% of cases.

## Keywords:

Pediatric epilepsy
MRI
malformations of cortical development
developmental tumors
hypothalamic hamartoma
Rasmussen encephalitis
meningioangiomatosis

**TABLE 38.1** Histopathologic Classification of Focal Cortical Dysplasia[23,122]

| | |
|---|---|
| ***FCD Type I (isolated)*** | **Type Ia:** Focal cortical dysplasia with abnormal radial cortical lamination<br>**Type Ib:** Focal cortical dysplasia with abnormal tangential cortical lamination<br>**Type Ic:** Focal cortical dysplasia with abnormal radial and tangential lamination |
| ***FCD Type II (isolated)*** | **Type IIa:** Cortical dyslamination and dysmorphic neurons without balloon cells<br>**Type IIb:** Cortical dyslamination and dysmorphic neurons with balloon cells |
| ***FCD Type III (associated with principal lesion)*** | **With associated lesion**<br>**Type IIIa:** Hippocampal sclerosis<br>**Type IIIb:** Epilepsy-associated tumors<br>**Type IIIc:** Vascular malformation<br>**Type IIId:** Other lesion |

to FCD with abnormal gyration of the cortex, dyslamination, blurring of gray-white matter junction, giant neurons in both gray and white matter, and balloon cells in 50% of cases. The most common clinical presentation is early intractable epilepsy; other clinical presentations include hemiparesis, hemianopia, and intellectual disability.

***Imaging.*** The affected hemisphere is larger than the contralateral side. The cortex is dysplastic and thick, with broad gyri and shallow sulci (e-Fig. 38.2). The ipsilateral lateral ventricle may be enlarged. The ipsilateral white matter also demonstrates signal changes that are variable, depending on the age of the patient. Neonates and infants usually demonstrate high T1/low T2 white matter signal, suggestive of early myelination, while in older children, the white matter shows low T1/high T2 signal, suggestive of gliosis, and may be associated with calcification.[40–42] With recurrent seizures or status epilepticus, the enlarged hemisphere may later become atrophic.[43]

***Treatment and Follow-up.*** Hemispherectomy or functional hemispherotomy may be required.

### Tuberous Sclerosis Complex

***Overview and Imaging.*** Tuberous sclerosis complex (TSC) is an autosomal dominant neurocutaneous syndrome characterized by multisystem involvement including brain, eyes, heart, kidney, skin, and lungs. Seizures occur in about 80% to 90% of patients and are intractable in 25% to 30%.[44] Children with medically refractory epilepsy usually have multiple cortical/subcortical tubers that exhibit broad gyri, thick cortex, and abnormal signal in the cortex and subcortical white matter. The cortical/subcortical tubers may occasionally demonstrate calcification and cystic degeneration. A combination of structural and functional imaging such as FDG-PET, ictal/interictal SPECT, and MEG can be used to identify the epileptogenic tubers[45–48] (Fig. 38.3). Cerebellar tubers can also be identified and are more commonly seen in patients with high cerebral tuber burden. The subependymal nodules commonly calcify. Another manifestation of TSC is subependymal giant cell astrocytomas, which commonly occur in the region of the foramen of Monro.

## STURGE–WEBER SYNDROME

***Overview and Imaging.*** Sturge–Weber syndrome (encephalotrigeminal angiomatosis) is characterized by facial capillary vascular malformation or “port wine stain” in the trigeminal nerve distribution, ipsilateral leptomeningeal angiomatosis, and angiomatosis of the choroid in ipsilateral eye. Seizures are usually the initial neurologic manifestation in the first year of life. Children with early onset of epilepsy are more likely to have hemiparesis, status epilepticus, and developmental delay compared with those whose seizures start later in life.[49] Imaging findings include leptomeningeal angiomatosis, enlargement of the choroid plexus, parenchymal atrophy, calvarial changes, and calcification (Fig. 38.4). Leptomeningeal angiomatosis and choroid plexus hyperplasia appear earlier, while atrophy and calcification usually are evident later. Contrast-enhanced MRI is considered the most sensitive modality for depicting leptomeningeal enhancement, to reveal subtle bilateral hemispheric involvement, compensatory venous drainage, enlarged choroid plexus in the atria, as well as cerebellar and eye involvement.[50–52]

***Treatment and Follow-up.*** Medical therapy is the first line of treatment for controlling seizures. Functional hemispherotomy may be indicated when seizures are refractory to medical therapy.

## MESIAL TEMPORAL SCLEROSIS

***Overview and Imaging.*** Mesial temporal sclerosis (MTS) or hippocampal sclerosis is less frequently encountered in children compared with adults.[53–56] The etiology of MTS is unknown, but a link with febrile seizures has been suggested.[57,58] MTS is characterized by neuronal loss and gliosis in the hippocampus.[59] MRI features include atrophy and increased T2/FLAIR signal in the hippocampus[59–62] (Fig. 38.5). Other findings include loss of interdigitations of the hippocampal head,[63] atrophy of the ipsilateral mamillary body and fornix,[64] dilatation of the ipsilateral temporal horn, volume loss of the temporal lobe, and atrophy of the collateral white matter between the hippocampus and collateral sulcus.[62]

***Treatment and Follow-up.*** In patients who have medically refractory epilepsy, surgery offers good seizure control in 70% to 90% of cases.[65–68]

## EPILEPSY ASSOCIATED DEVELOPMENTAL TUMORS

***Overview and Imaging.*** Epilepsy associated tumors account for up to two-thirds of pathologic substrates[69–72] in epilepsy surgery. They are usually associated with benign behavior and low proliferation index. The tumors include ganglioglioma, desmoplastic infantile ganglioglioma, dysembryoplastic neuroepithelial tumor (DNET), pleomorphic xanthoastrocytoma (PXA), and low-grade astrocytoma.[73]

### Gangliogliomas

The most common clinical presentation of this tumor is seizures; often complex partial and medically intractable.[74] They are larger in children than in adults[75] and are located mostly in the temporomesial (50%) or temporolateral (29%) location.[76] Gangliogliomas are composed of glial cells and neurons, and may present as a solid mass in 43%, a cyst in 5%, and a mixed lesion in 52%.[77,78] They involve the cortex and may cause remodeling of the adjacent bone. On CT, most are hypodense (38%), but iso- (15%), hyper- (15%), or mixed density masses (32%) can be found,[79] and calcification is seen in 30% to 50% of cases. On MRI, the solid part of the tumor may appear hypo- or isointense to gray matter on T1-weighted images and hyperintense on T2-weighted images (Fig. 38.6). Enhancement is present in up to 60% of cases; it can be nodular, ringlike, or solid. Gangliocytoma is a variant of ganglioglioma without any glial component and affects older children and young adults. On MRI, gangliocytoma may demonstrate low T1 and high T2 signal, and show enhancement.[80,81]

### Dysembryoplastic Neuroepithelial Tumor

DNET is a benign supratentorial cortical tumor that shows predilection for the temporal and frontal lobes. The tumor may

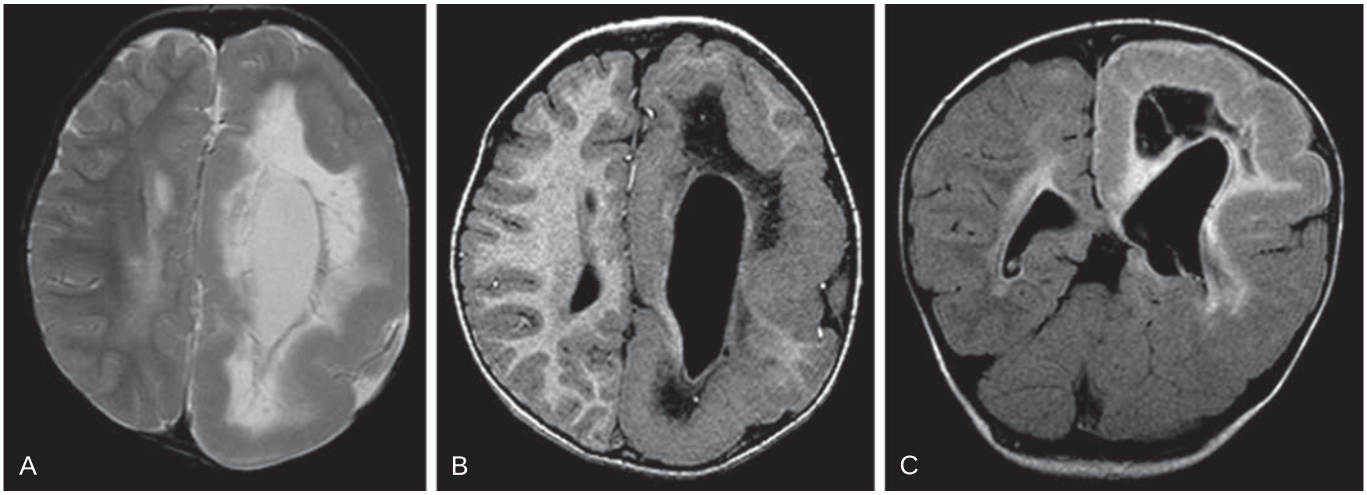

**e-Figure 38.2. Hemimegalencephaly in a 2-year-old.** (A) Axial T2-weighted, (B) axial volumetric T1-weighted, and (C) coronal FLAIR MR images demonstrate diffuse enlargement of the left cerebral hemisphere, associated with abnormally thick cortex, abnormal sulcation, and gyration pattern, as well as dysmorphic and enlarged left lateral ventricle. There is also abnormal increased T2 and FLAIR signal, and reduced T1 signal in the white matter of the affected hemisphere.

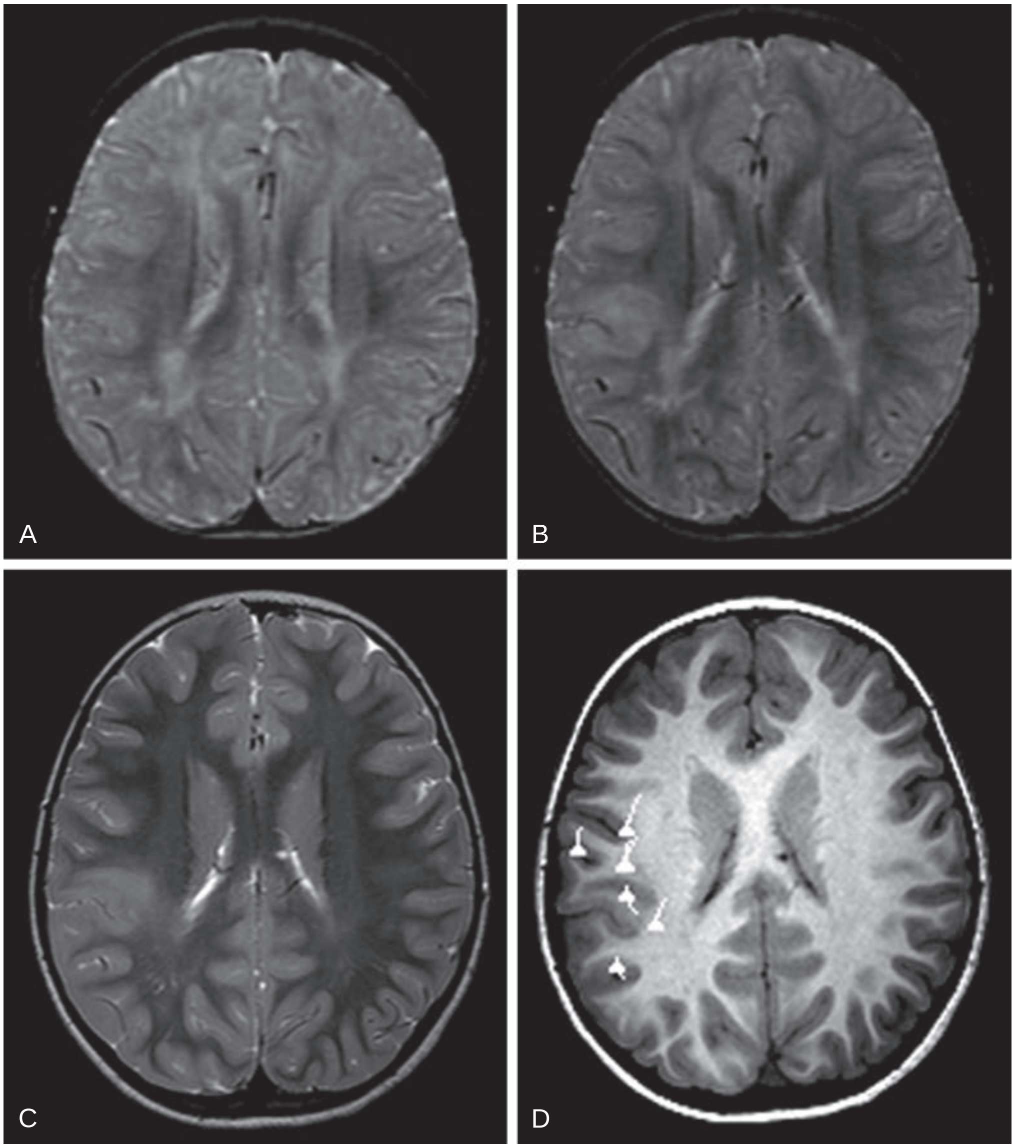

**Figure 38.1. Focal cortical dysplasia in a 5-year-old girl.** (A) Axial T2-weighted MR image at 12 months does not show a lesion. However, at 19 months (B) and 5 years of age (C), axial T2-weighted MR images demonstrate abnormal signal in the cortex and subcortical white matter, associated with blurring of gray-white matter junction. (D) MEG projected onto axial T1-weighted MR image demonstrates the dipoles, indicative of the epileptogenic zone, are located in and around the lesion. Surgical resection of the lesion and epileptogenic zone confirmed focal cortical dysplasia type IIB.

be associated to broadening of the gyri, effacement of the sulci, distortion of the ventricles, and remodeling of the overlying skull vault.[82,83] On CT, DNET tends to be hypoattenuated with a cystic appearance.[84] Calcification has been reported in 20% to 36% of cases.[83] On MRI, DNET demonstrates low T1/high T2 signal, often with multi-cystic and "bubbly" appearance,[82] and may have a thin rim of high FLAIR signal[85,86] (Fig. 38.7). Approximately one-third of cases show nodular, patchy or ring enhancement. The tumor may extend to the ventricle in 30% of cases. Hemorrhagic changes are rare.[85,87]

## Pleomorphic Xanthoastrocytoma

PXA is a rare localized glioma of astrocytic origin affecting children and young adults.[88] It is mostly temporal (49%) in location and less commonly parietal, frontal, or occipital.[89,90] They are large hemispheric cystic/solid mass close to the cortex. On CT, the tumor is predominantly hypodense with a mixed density enhancing nodule. On MRI, the cystic portion of the tumor are isointense to cerebrospinal fluid (CSF); the solid tumor is hypo- to isointense to gray matter on T1-weighted imaging and hyper to isointense on T2-weighted imaging. There is enhancement of the nodular solid component and adjacent meninges ("dural tail")[91] (e-Fig. 38.8). PXA may be associated with FCD.[92,93]

***Treatment and Follow-up.*** Patients with ganglioglioma have the best surgical outcome with respect to epilepsy control compared with other types of epilepsy associated tumors.[71,76,94] DNET has less favorable seizure outcome compared with ganglioglioma, which could be related to longer duration of epilepsy, incomplete resection of the tumor, or the presence of FCD beyond the margins of resected DNET.[94–96] The prognosis of PXA is generally good, but it may recur, and malignant degeneration occurs in 20%.[97]

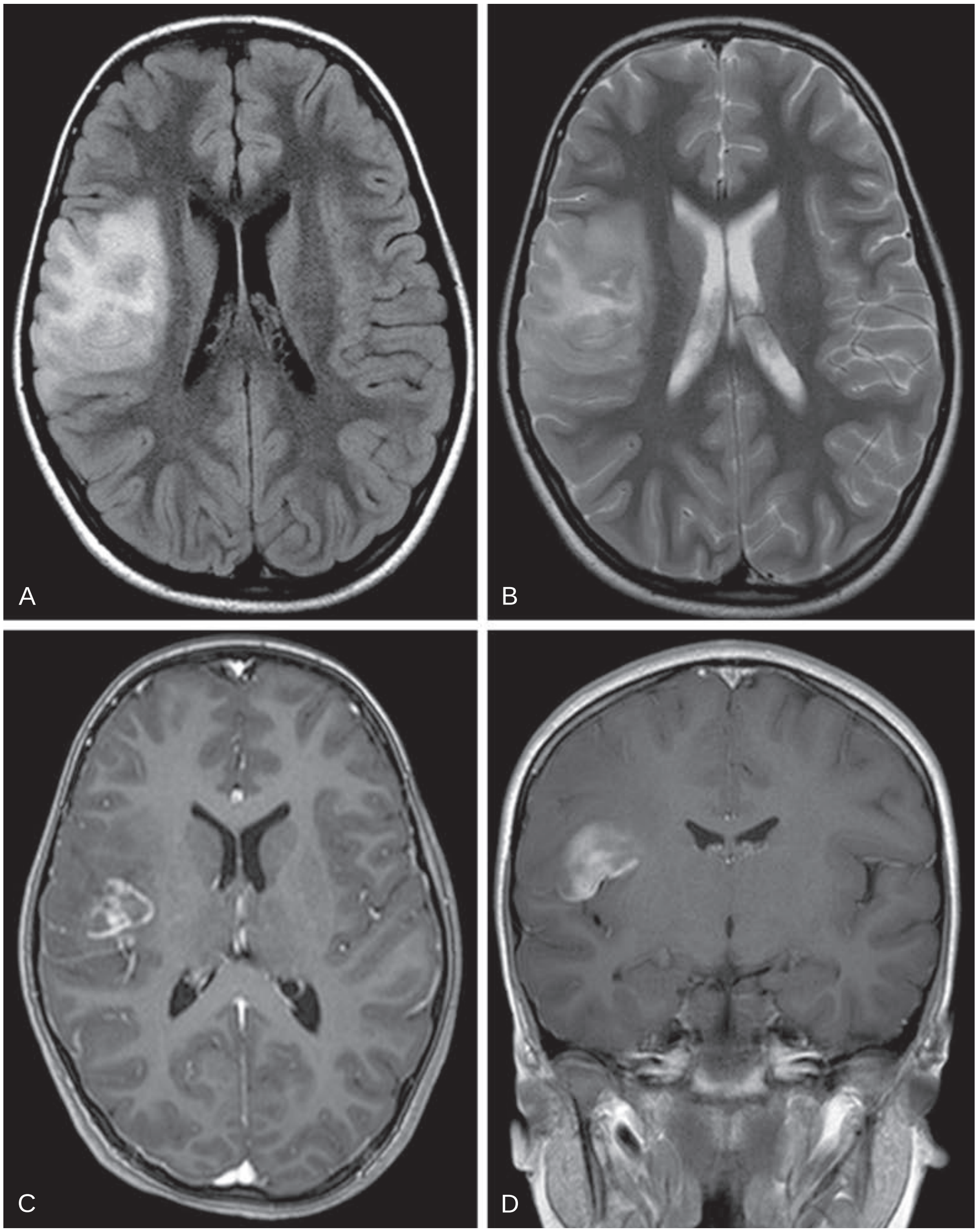

**e-Figure 38.8. Pleomorphic xanthoastrocytoma in a 6-year-old.** (A) Axial FLAIR, (B) axial T2-weighted, (C) axial, and (D) coronal T1-weighted contrast enhanced MR images demonstrate a mass in the right inferior frontal gyrus that involves the cortex and subcortical white matter. The tumor demonstrates enhancement medially, and there is surrounding edema.

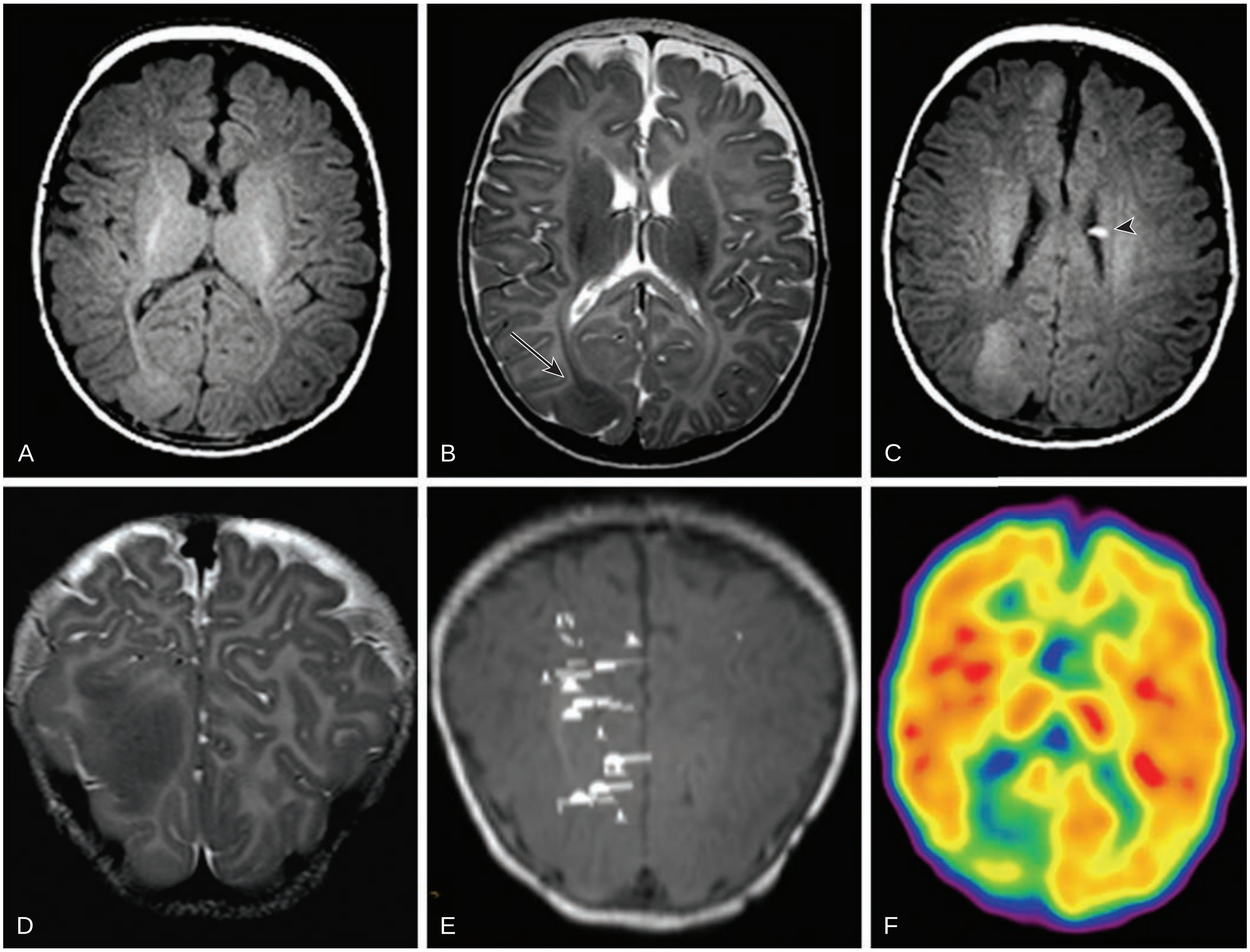

**Figure 38.3. Tuberous sclerosis complex (TSC) and right occipital lobe intractable epilepsy in a 3-month-old.** On (A and C) axial T1-weighted, (B) axial T2-weighted, and (D) coronal T2-weighted MR images, there are several cortical/subcortical tubers in the right frontal and occipital lobes *(arrow)* that demonstrate high T1 and lower T2 signal. There are also several subependymal nodules *(arrowhead)*. (E) MEG dipoles projected onto coronal T1 image demonstrates dipole cluster in the right occipital lobe. (F) FDG PET study shows hypometabolism that is more extensive than the right occipital tuber.

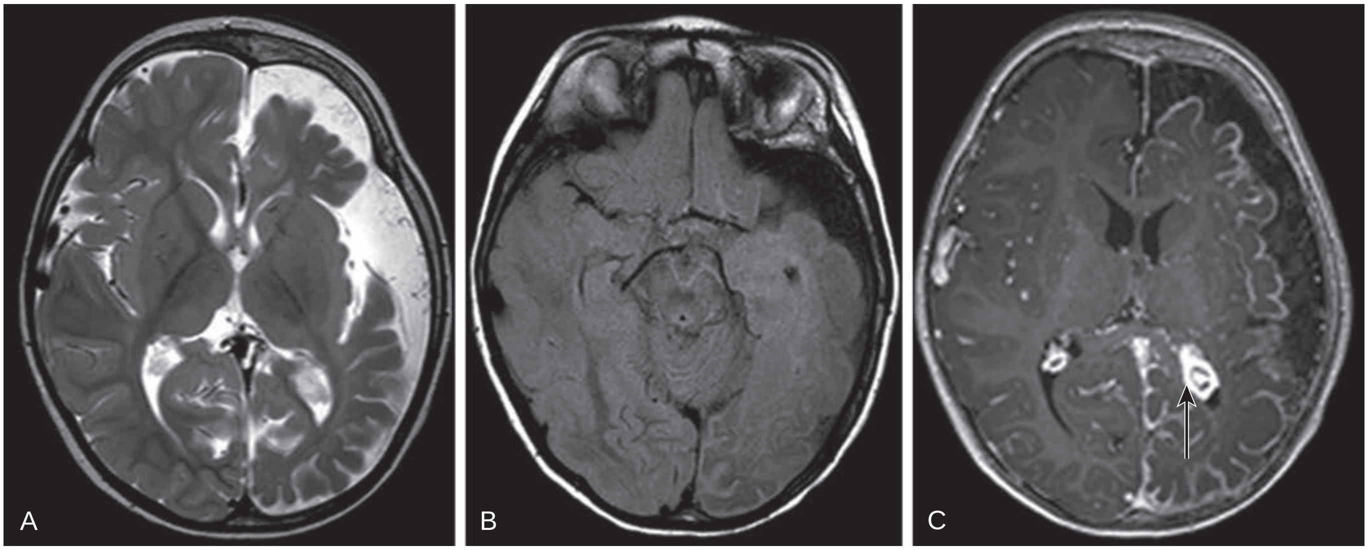

**Figure 38.4. Sturge–Weber syndrome in a 15-month-old boy.** (A) Axial T2-weighted and (B) axial FLAIR MR images show volume loss in the left cerebral hemisphere with enlargement of subarachnoid spaces, and high FLAIR signal in the left cerebral sulci. (C) Axial T1-weighted contrast-enhanced MR image shows pial enhancement over the left cerebral hemisphere, as well as enlarged choroid plexus in the left trigone *(arrow)*.

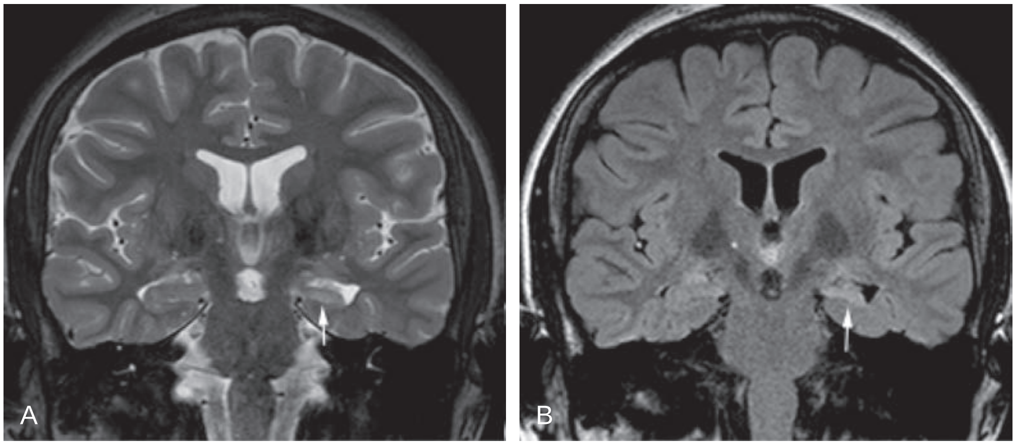

**Figure 38.5. Left mesial temporal sclerosis in an 11-year-old girl.** (A) Coronal T2-weighted and (B) coronal FLAIR MR images demonstrate high T2 and FLAIR signal, associated with volume loss in the left hippocampus *(arrow)*.

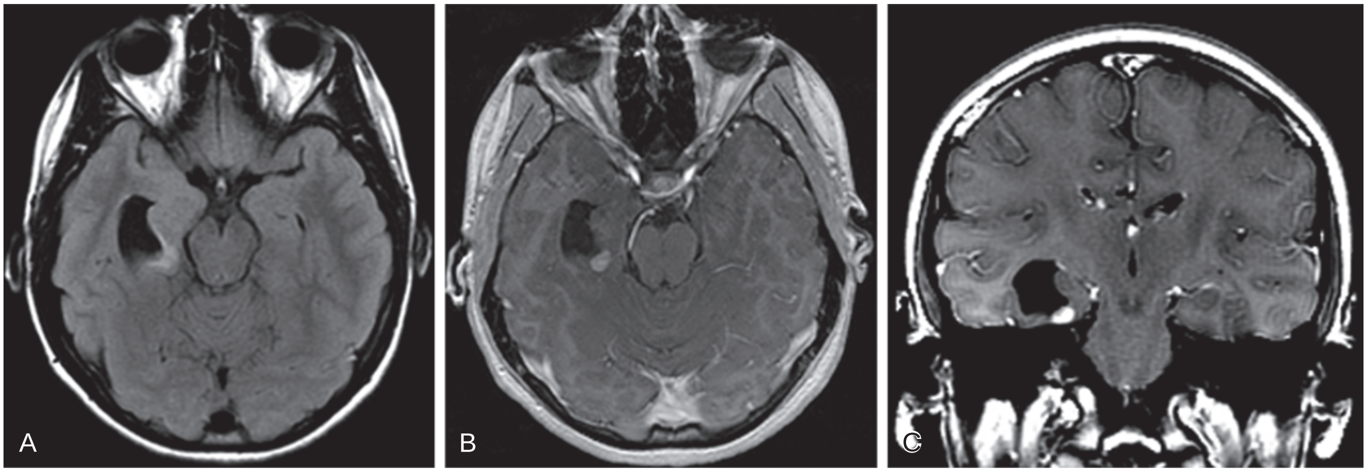

**Figure 38.6. Ganglioglioma in a 16-year-old girl.** (A) Axial FLAIR, (B) axial, and (C) coronal T1-weighted contrast-enhanced MR images show a cystic tumor with mural enhancing nodule in the right mesial temporal lobe.

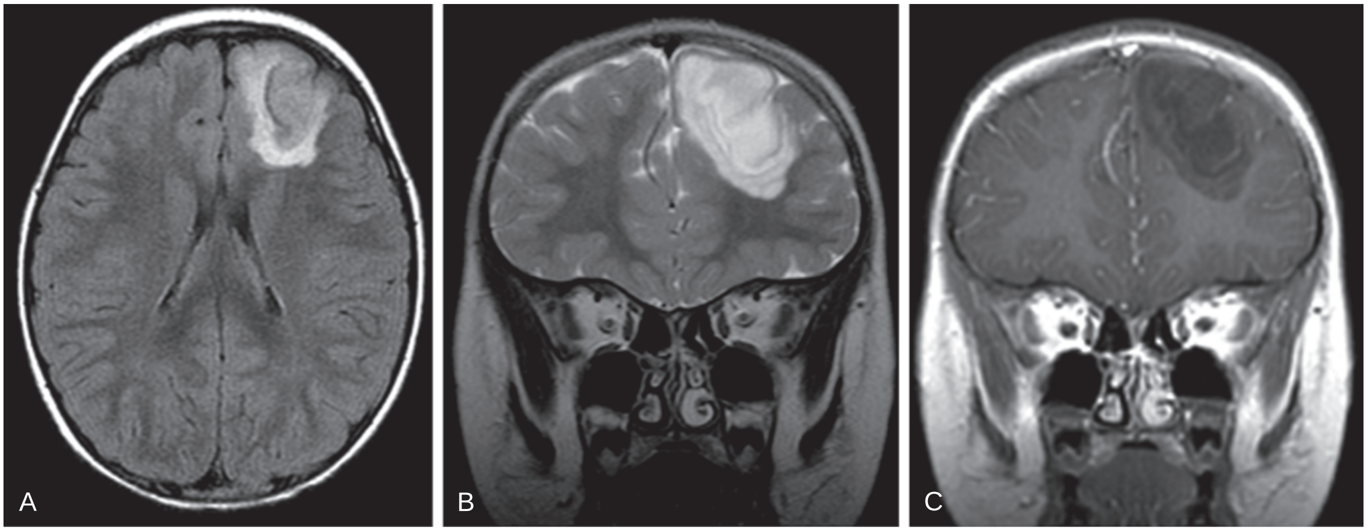

**Figure 38.7. Dysembryoplastic neuroepithelial tumor (DNET) in a 4-year-old boy.** (A) Axial FLAIR, (B) coronal T2-weighted, and (C) contrast-enhanced coronal T1-weighted MR images demonstrate a well-defined tumor in the left frontal lobe involving the cortex and white matter. The tumor extends to the margin of the frontal horn of the left lateral ventricle, has a rim of high FLAIR signal, and does not show enhancement.

## Hypothalamic Hamartoma

***Overview and Imaging.*** Hypothalamic hamartoma, also known as hamartoma of the tuber cinereum, is a congenital malformation of the hypothalamus that may be asymptomatic or manifest with precocious puberty or gelastic seizures.[98] Intrahypothalamic hamartomas that invade the third ventricle are associated with early occurrence of epilepsy, while the parahypothalamic hamartomas that do not involve the third ventricle more commonly present with central precocious puberty.[99,100] MRI demonstrates a mass at the tuber cinereum that is T1 hypointense, T2 iso- or hyperintense relative to gray matter, and FLAIR hyperintense. There is no enhancement and no calcification (e-Fig. 38.9). Careful examination of the hypothalamic region on MRI is needed, as hamartomas can be small and nonpedunculated.

***Treatment and Follow-up.*** The first line treatment is medical treatment with hormonal therapy and antiepileptic medications. However, if the child becomes refractory to medical treatment, surgical resection, radiosurgery, or laser therapy should be considered.[101–104]

## RASMUSSEN ENCEPHALITIS

***Overview and Imaging.*** Rasmussen encephalitis is a rare, chronic progressive encephalitis characterized by severe refractory epilepsy and unilateral brain atrophy.[105] Clinically, seizures begin abruptly in previously normal children and include focal seizures and epilepsia partialis continua. With disease progression, the patients develop hemiparesis or hemiplegia and cognitive decline. There is a possible autoimmune basis for the disease.[106–108] The histological findings include chronic encephalitis with lymphocytic infiltrations and perivascular cuffing; in the later stage of the disease, nonspecific findings such as atrophy and gliosis with minimal inflammatory cellular infiltrate are found.[109] In the acute stages, MRI can be entirely normal[110,111] or demonstrate cortical swelling with low T1 and hyperintense T2 and FLAIR signal, with no enhancement. With disease progression, MR shows progressive volume loss and progressive abnormal signal in the white matter and cortex[112] (Fig. 38.10). It is predominantly a unilateral disease, and the frontal and temporal lobes are more commonly involved.

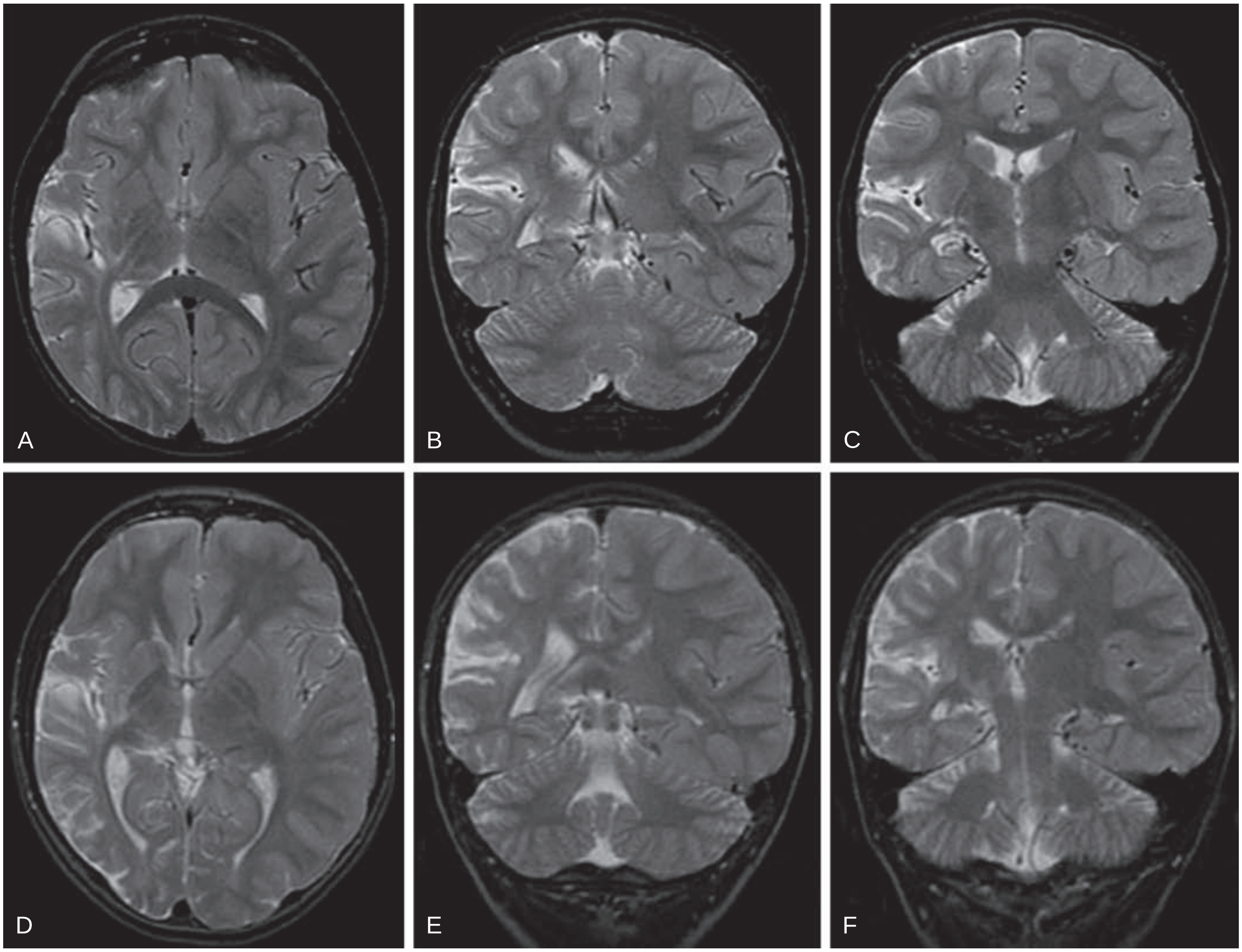

**Figure 38.10. Rasmussen encephalitis in a 5-year-old boy with presenting with epilepsia partialis continua.** At presentation, (A–C) axial and coronal T2-weighted MR images demonstrate mild volume loss in the right Sylvian and temporal lobe. Three years later, (D–F) axial and coronal T2-weighted MR images demonstrate progressive volume loss in the right Sylvian, temporal, and parietal lobes, with ex-vacuo dilatation of the right lateral ventricle.

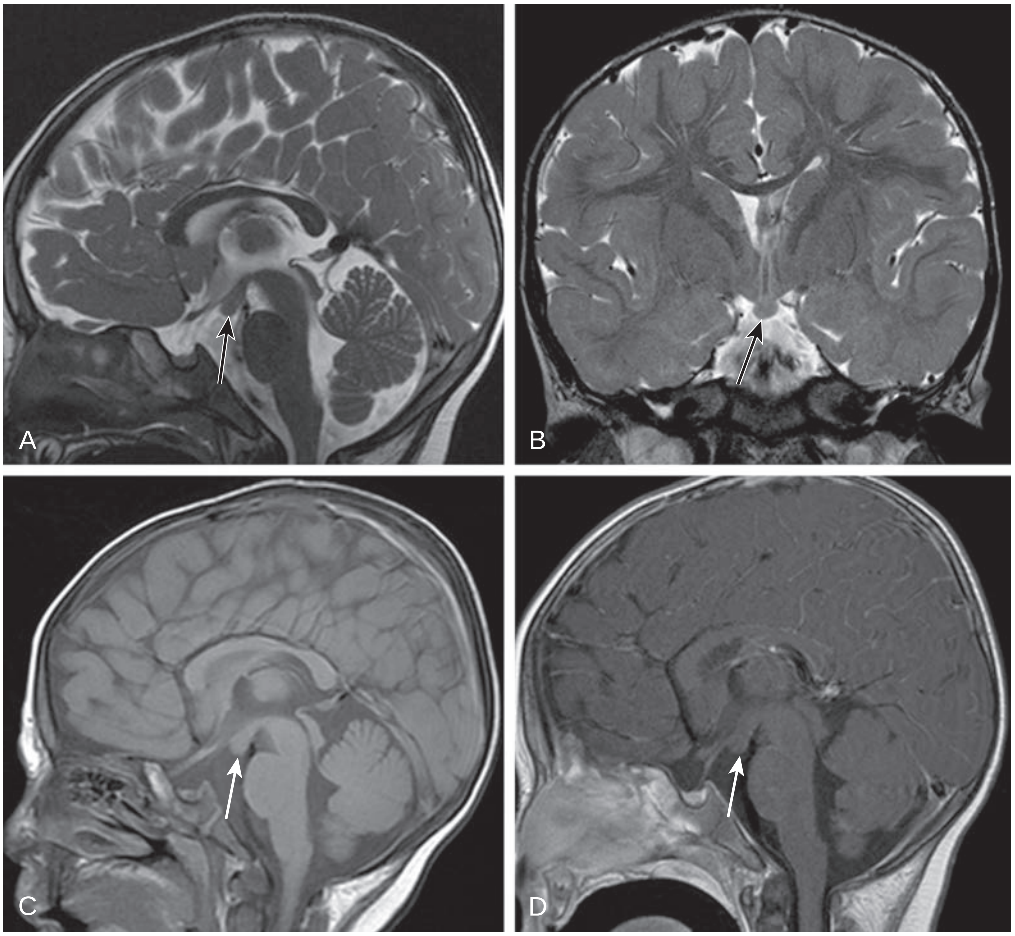

**e-Figure 38.9. Two-year-old with hypothalamic hamartoma *(arrow)*.** (A) Sagittal T2-weighted, (B) coronal T2-weighted, and (C) sagittal T1-weighted MR images show a focal lesion in the tuber cinereum *(arrow)* that has signal similar to gray matter on T1- and T2-weighted sequences. There is no enhancement of the lesion after gadolinium administration (D).

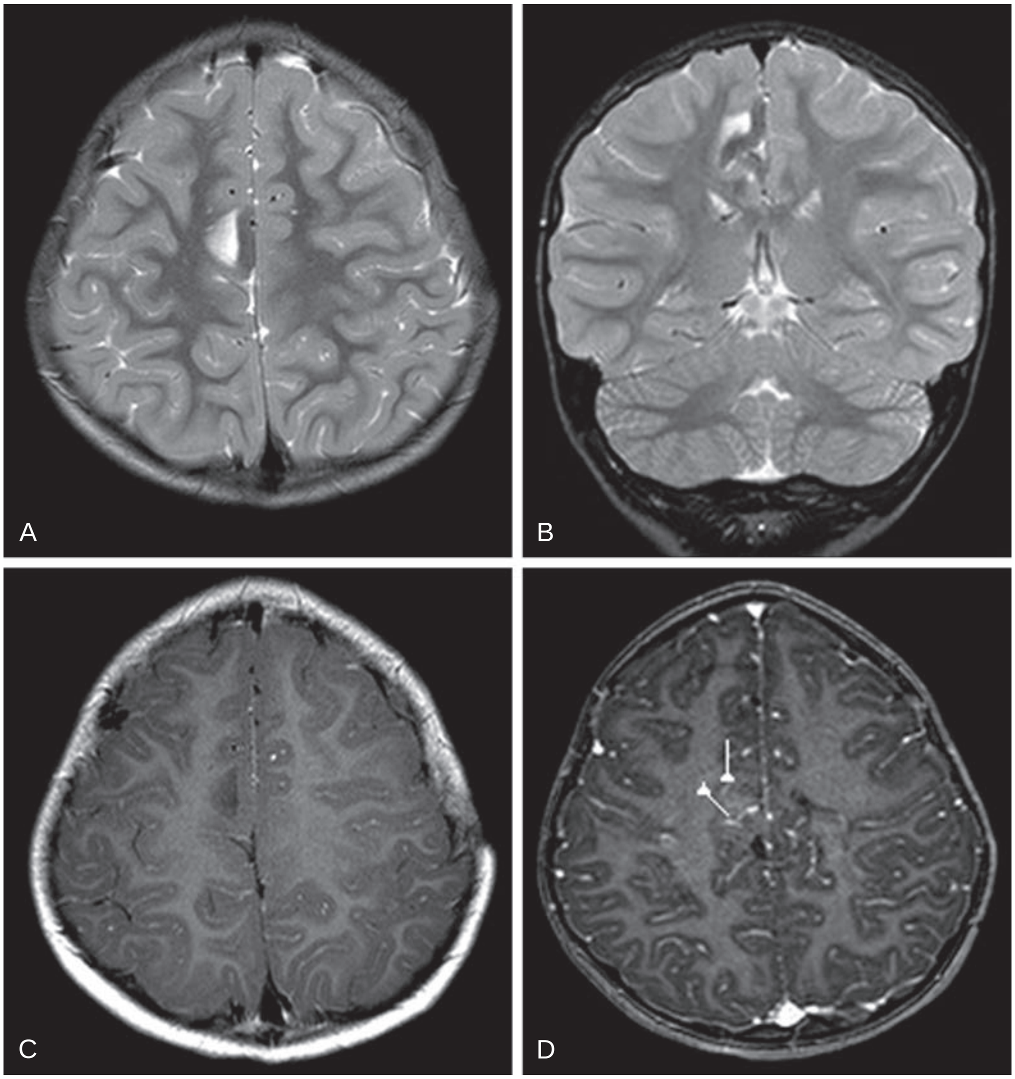

**Figure 38.11. Meningioangiomatosis in a 5-year-old boy with right frontal lobe epilepsy.** (A) Axial and (B) coronal T2-wrighted MR images show low T2 signal in the cortex and high T2 signal in the subcortical white matter of the lesion in right mesial frontal lobe. (C) Axial T1-weighted contrast-enhanced MR image shows no enhancement of the lesion. (D) MEG projected onto the contrast-enhanced MR image shows dipoles around the lesion.

***Treatment and Follow-up.*** Medical treatment include intravenous immunoglobulin, plasmapheresis, or immunosuppressive medications. Hemispherectomy or functional hemispherotomy is frequently necessary for seizure control and to prevent progression of cognitive impairment.

## CAVERNOMAS

***Overview and Imaging.*** In children, seizures are the most common symptom of cavernomas at presentation.[113–115] Cavernomas are more commonly supratentorial (80%) and can have variable size. On MRI, cavernomas have a combination of mixed high and low T1 and T2 signals, surrounding hemosiderin rim,[116] and are best depicted on T2* gradient echo imaging. Calcification may be seen on CT.

***Treatment and Follow-up.*** Cavernomas that present with refractory epilepsy should be treated surgically. The longer the duration of preoperative seizures, the greater the likelihood of continued seizures postoperatively.[117,118]

## MENINGIOANGIOMATOSIS

***Overview and Imaging.*** Meningioangiomatosis is a rare lesion characterized by vascular proliferation involving the cortex and leptomeninges. Sporadic lesions are usually solitary and present with refractory epilepsy. Those associated with neurofibromatosis type 2 are often multiple.[119] On CT, the lesion is hypodense and may contain calcification. On MRI, the cortex may have hypointense T1 and T2 signal due to calcification, the subcortical white matter may be T2 hyperintense, and enhancement may be seen (Fig. 38.11). Meningioangiomatosis may mimic other disorders such as tumors, FCD, and arteriovenous malformation.[120] Treatment is surgical resection, but seizure outcome is poorer compared with those with tumors or hippocampal sclerosis.[121]

## CONCLUSION

Neuroimaging plays a crucial role in identifying anatomic lesions responsible for epilepsy and can assist in localizing the eloquent cortex and white matter tracts for presurgical planning. In those with MRI-negative epilepsy, functional imaging with PET, SPECT, and MEG may help localize the epileptogenic zone and assist with the detection of subtle lesions.

## KEY POINTS

- Approximately 30% of patients with epilepsy become refractory to medical therapy, and surgery may be necessary to control seizures in some of these patients. Lesion identification on neuroimaging impacts surgical outcome.
- There is a wide range of brain abnormalities that can cause epilepsy. In children, the two most common causes of intractable focal epilepsy are MCD and developmental tumors. Hippocampal sclerosis is less common in children compared with the adult population with intractable focal epilepsy.
- Dual lesions can occur in approximately 15% of patients.
- Meticulous review of MRI is necessary to identify subtle lesions such as focal cortical dysplasia. MRI should be reviewed with knowledge of the clinical information, including seizure semiology and electroencephalography (EEG) findings.
- In patients with MRI-negative epilepsy, functional imaging with PET, ictal/interictal SPECT, and MEG may help to localize the epileptogenic zone.

## SUGGESTED READINGS

Colombo N, Salamon N, Raybaud C, et al. Imaging of malformations of cortical development. *Epileptic Disord*. 2009;11(3):194–205.

Martinez-Rios C, McAndrews MP, Logan W, et al. Magnetic resonance imaging in the evaluation of localization-related epilepsy. *J Magn Reson Imaging*. 2016;44(1):12–22.

Rastogi S, Lee C, Salamon N. Neuroimaging in pediatric epilepsy: a multimodality approach. *Radiographics*. 2008;28(4):1079–1095.

Rubinger L, Chan C, D'Arco F, et al. Change in presurgical diagnostic imaging evaluation affects subsequent pediatric epilepsy surgery outcome. *Epilepsia*. 2016;57(1):32–40.

Widjaja E, Raybaud C. Advances in neuroimaging in patients with epilepsy. *Neurosurg Focus*. 2008;25(3):E3.

## REFERENCES

Full references for this chapter can be found on www.expertconsult.com.

## REFERENCES

1. Theodore WH, Spencer SS, Wiebe S, et al. Epilepsy in North America: a report prepared under the auspices of the global campaign against epilepsy, the International Bureau for Epilepsy, the International League Against Epilepsy, and the World Health Organization. *Epilepsia*. 2006;47(10):1700–1722.
2. Hauser WA. The prevalence and incidence of convulsive disorders in children. *Epilepsia*. 1994;35 Suppl 2:S1–S6.
3. Snead OC 3rd. Surgical treatment of medically refractory epilepsy in childhood. *Brain Dev*. 2001;23(4):199–207.
4. Tellez-Zenteno JF, Hernandez Ronquillo L, Moien-Afshari F, et al. Surgical outcomes in lesional and non-lesional epilepsy: a systematic review and meta-analysis. *Epilepsy Res*. 2010;89(2–3):310–318.
5. Berg AT, Testa FM, Levy SR, et al. Neuroimaging in children with newly diagnosed epilepsy: a community-based study. *Pediatrics*. 2000;106(3):527–532.
6. Gaillard WD, Chiron C, Cross JH, et al. Guidelines for imaging infants and children with recent-onset epilepsy. *Epilepsia*. 2009; 50(9):2147–2153.
7. Rubinger L, Chan C, D'Arco F, et al. Change in presurgical diagnostic imaging evaluation affects subsequent pediatric epilepsy surgery outcome. *Epilepsia*. 2016;57(1):32–40.
8. Martinez-Rios C, McAndrews MP, Logan W, et al. MRI in the evaluation of localization-related epilepsy. *J Magn Reson Imaging*. 2016;44(1):12–22.
9. Bastos AC, Comeau RM, Andermann F, et al. Diagnosis of subtle focal dysplastic lesions: curvilinear reformatting from three-dimensional magnetic resonance imaging. *Ann Neurol*. 1999;46(1):88–94.
10. Bastos AC, Korah IP, Cendes F, et al. Curvilinear reconstruction of 3D magnetic resonance imaging in patients with partial epilepsy: a pilot study. *Magn Reson Imaging*. 1995;13(8):1107–1112.
11. Montenegro MA, Li LM, Guerreiro MM, et al. Focal cortical dysplasia: improving diagnosis and localization with magnetic resonance imaging multiplanar and curvilinear reconstruction. *J Neuroimaging*. 2002;12(3):224–230.
12. Widjaja E, Raybaud C. Advances in neuroimaging in patients with epilepsy. *Neurosurg Focus*. 2008;25(3):E3.
13. Grondin R, Chuang S, Otsubo H, et al. The role of magnetoencephalography in pediatric epilepsy surgery. *Childs Nerv Syst*. 2006;22(8):779–785.
14. Guerrini R, Barba C. Malformations of cortical development and aberrant cortical networks: epileptogenesis and functional organization. *J Clin Neurophysiol*. 2010;27(6):372–379.
15. Barkovich AJ, Kuzniecky RI, Jackson GD, et al. A developmental and genetic classification for malformations of cortical development. *Neurology*. 2005;65(12):1873–1887.
16. Cascino GD, Buchhalter JR, Sirven JI, et al. Peri-ictal SPECT and surgical treatment for intractable epilepsy related to schizencephaly. *Neurology*. 2004;63(12):2426–2428.
17. Dubeau F, Tyvaert L. Understanding the epileptogenicity of lesions: a correlation between intracranial EEG and EEG/fMRI. *Epilepsia*. 2010;51(suppl 1):54–58.
18. Kobayashi E, Bagshaw AP, Grova C, et al. Grey matter heterotopia: what EEG-fMRI can tell us about epileptogenicity of neuronal migration disorders. *Brain*. 2006;129(Pt 2):366–374.
19. Jay V, Becker LE, Otsubo H, et al. Pathology of temporal lobectomy for refractory seizures in children. Review of 20 cases including some unique malformative lesions. *J Neurosurg*. 1993;79:53–61.
20. Farrel M, DeRosa M, Curran J, et al. Neuropathological findings in cortical resection (including hemispherectomies) performed for the treatment of intractable childhood epilepsy. *Acta Neuropathol*. 1992;83:246–259.
21. Cepeda C, Andre VM, Vinters HV, et al. Are cytomegalic neurons and balloon cells generators of epileptic activity in pediatric cortical dysplasia? *Epilepsia*. 2005;46 Suppl 5:82–88.
22. Guerrini R, Sicca F, Parmeggiani L. Epilepsy and malformations of the cerebral cortex. *Epileptic Disord*. 2003;5 Suppl 2:S9–S26.
23. Blumcke I, Thom M, Aronica E, et al. The clinicopathologic spectrum of focal cortical dysplasias: a consensus classification proposed by an ad hoc Task Force of the ILAE Diagnostic Methods Commission(1). *Epilepsia*. 2011;52(1):158–174.
24. Urbach H, Scheffler B, Heinrichsmeier T, et al. Focal cortical dysplasia of Taylor's balloon cell type: a clinicopathological entity with characteristic neuroimaging and histopathological features, and favorable postsurgical outcome. *Epilepsia*. 2002;43(1):33–40.
25. Colombo N, Citterio A, Galli C, et al. Neuroimaging of focal cortical dysplasia: neuropathological correlations. *Epileptic Disord*. 2003;5 Suppl 2:S67–S72.
26. Tassi L, Colombo N, Garbelli R, et al. Focal cortical dysplasia: neuropathological subtypes, EEG, neuroimaging and surgical outcome. *Brain*. 2002;125(Pt 8):1719–1732.
27. Colombo N, Salamon N, Raybaud C, et al. Imaging of malformations of cortical development. *Epileptic Disord*. 2009;11(3):194–205.
28. Yagishita A, Arai N, Maehara T, et al. Focal cortical dysplasia: appearance on MR images. *Radiology*. 1997;203(2):553–559.
29. Demerens C, Stankoff B, Logak M, et al. Induction of myelination in the central nervous system by electrical activity. *Proc Natl Acad Sci USA*. 1996;93(18):9887–9892.
30. Widjaja E, Li B, Schinkel CD, et al. Cost-effectiveness of pediatric epilepsy surgery compared to medical treatment in children with intractable epilepsy. *Epilepsy Res*. 2011;94(1–2):61–68.
31. Kral T, Clusmann H, Blumcke I, et al. Outcome of epilepsy surgery in focal cortical dysplasia. *J Neurol Neurosurg Psychiatry*. 2003;74(2):183–188.
32. Keene DL, Ventureyra EC. Epilepsy surgery for 5- to 18-year old patients with medically refractory epilepsy - is it cost efficient? *Childs Nerv Syst*. 1999;15(9):433.
33. Sperling MR, O'Connor MJ, Saykin AJ, et al. Temporal lobectomy for refractory epilepsy. *JAMA*. 1996;276(6):470–475.
34. Britton JW, Cascino GD, Sharbrough FW, et al. Low-grade glial neoplasms and intractable partial epilepsy: efficacy of surgical treatment. *Epilepsia*. 1994;35(6):1130–1135.
35. Widdess-Walsh P, Kellinghaus C, Jeha L, et al. Electro-clinical and imaging characteristics of focal cortical dysplasia: correlation with pathological subtypes. *Epilepsy Res*. 2005;67(1–2):25–33.
36. Chassoux F, Devaux B, Landre E, et al. Stereoelectroencephalography in focal cortical dysplasia: a 3D approach to delineating the dysplastic cortex. *Brain*. 2000;123(Pt 8):1733–1751.
37. Fauser S, Schulze-Bonhage A, Honegger J, et al. Focal cortical dysplasias: surgical outcome in 67 patients in relation to histological subtypes and dual pathology. *Brain*. 2004;127(Pt 11):2406–2418.
38. Palmini A, Gambardella A, Andermann F, et al. Operative strategies for patients with cortical dysplastic lesions and intractable epilepsy. *Epilepsia*. 1994;35 Suppl 6:S57–S71.
39. Robain O, Gelot A. Neuropathology of hemimegalencephaly. In: Guerrini R, Andermann F, Canapicchi R, et al, eds. *Dysplasias of Cerebral Cortex and Epilepsy*. Philadelphia PA: Lippincott-Raven; 1996:89–92.
40. Barkovich AJ, Chuang SH. Unilateral megalencephaly: correlation of MR imaging and pathologic characteristics. *AJNR Am J Neuroradiol*. 1990;11(3):523–531.
41. Broumandi DD, Hayward UM, Benzian JM, et al. Best cases from the AFIP: hemimegalencephaly. *Radiographics*. 2004;24(3):843–848.
42. Yagishita A, Arai N, Tamagawa K, et al. Hemimegalencephaly: signal changes suggesting abnormal myelination on MRI. *Neuroradiology*. 1998;40(11):734–738.
43. Wolpert SM, Cohen A, Libenson MH. Hemimegalencephaly: a longitudinal MR study. *AJNR Am J Neuroradiol*. 1994;15(8):1479–1482.
44. Roach ES, Gomez MR, Northrup H. Tuberous sclerosis complex consensus conference: revised clinical diagnostic criteria. *J Child Neurol*. 1998;13(12):624–628.
45. Jansen FE, Huiskamp G, van Huffelen AC, et al. Identification of the epileptogenic tuber in patients with tuberous sclerosis: a comparison of high-resolution EEG and MEG. *Epilepsia*. 2006;47(1): 108–114.
46. Jozwiak S, Schwartz RA, Janniger CK, et al. Usefulness of diagnostic criteria of tuberous sclerosis complex in pediatric patients. *J Child Neurol*. 2000;15(10):652–659.
47. Wu JY, Salamon N, Kirsch HE, et al. Noninvasive testing, early surgery, and seizure freedom in tuberous sclerosis complex. *Neurology*. 2010;74(5):392–398.
48. Juhasz C, Chugani HT. Imaging the epileptic brain with positron emission tomography. *Neuroimaging Clin N Am*. 2003;13(4):705–716, viii.
49. Bourgeois M, Crimmins DW, de Oliveira RS, et al. Surgical treatment of epilepsy in Sturge-Weber syndrome in children. *J Neurosurg*. 2007;106(1 suppl):20–28.
50. Griffiths PD. Sturge-Weber syndrome revisited: the role of neuroradiology. *Neuropediatrics*. 1996;27(6):284–294.
51. Di Rocco C, Tamburrini G. Sturge-Weber syndrome. *Childs Nerv Syst*. 2006;22(8):909–921.

52. Puttgen KB, Lin DD. Neurocutaneous vascular syndromes. *Childs Nerv Syst*. 2010;26(10):1407–1415.
53. Harvey AS, Berkovic SF, Wrennall JA, et al. Temporal lobe epilepsy in childhood: clinical, EEG, and neuroimaging findings and syndrome classification in a cohort with new-onset seizures. *Neurology*. 1997;49(4):960–968.
54. Harvey AS, Grattan-Smith JD, Desmond PM, et al. Febrile seizures and hippocampal sclerosis: frequent and related findings in intractable temporal lobe epilepsy of childhood. *Pediatr Neurol*. 1995;12(3):201–206.
55. Grattan-Smith JD, Harvey AS, Desmond PM, et al. Hippocampal sclerosis in children with intractable temporal lobe epilepsy: detection with MR imaging. *AJR Am J Roentgenol*. 1993;161(5):1045–1048.
56. Mohamed A, Wyllie E, Ruggieri P, et al. Temporal lobe epilepsy due to hippocampal sclerosis in pediatric candidates for epilepsy surgery. *Neurology*. 2001;56(12):1643–1649.
57. Cendes F. Febrile seizures and mesial temporal sclerosis. *Curr Opin Neurol*. 2004;17(2):161–164.
58. Scott RC, King MD, Gadian DG, et al. Hippocampal abnormalities after prolonged febrile convulsion: a longitudinal MRI study. *Brain*. 2003;126(Pt 11):2551–2557.
59. Bronen RA. Epilepsy: the role of MR imaging. *AJR Am J Roentgenol*. 1992;159(6):1165–1174.
60. Jack CR Jr, Sharbrough FW, Cascino GD, et al. Magnetic resonance image-based hippocampal volumetry: correlation with outcome after temporal lobectomy. *Ann Neurol*. 1992;31(2):138–146.
61. Cascino GD, Jack CR Jr, Parisi JE, et al. Magnetic resonance imaging-based volume studies in temporal lobe epilepsy: pathological correlations. *Ann Neurol*. 1991;30(1):31–36.
62. Meiners LC, van Gils AD, De Kort G, et al. Fast fluid-attenuated inversion recovery (FLAIR) compared with T2-weighted spin-echo in the magnetic resonance diagnosis of mesial temporal sclerosis. *Invest Radiol*. 1999;34(2):134–142.
63. Oppenheim C, Dormont D, Biondi A, et al. Loss of digitations of the hippocampal head on high-resolution fast spin-echo MR: a sign of mesial temporal sclerosis. *AJNR Am J Neuroradiol*. 1998;19(3):457–463.
64. Baldwin GN, Tsuruda JS, Maravilla KR, et al. The fornix in patients with seizures caused by unilateral hippocampal sclerosis: detection of unilateral volume loss on MR images. *AJR Am J Roentgenol*. 1994;162(5):1185–1189.
65. Engel J Jr, McDermott MP, Wiebe S, et al. Design considerations for a multicenter randomized controlled trial of early surgery for mesial temporal lobe epilepsy. *Epilepsia*. 2010;51(10):1978–1986.
66. Ozkara C, Uzan M, Benbir G, et al. Surgical outcome of patients with mesial temporal lobe epilepsy related to hippocampal sclerosis. *Epilepsia*. 2008;49(4):696–699.
67. Spencer SS. When should temporal-lobe epilepsy be treated surgically? *Lancet Neurol*. 2002;1(6):375–382.
68. Smyth MD, Limbrick DD Jr, Ojemann JG, et al. Outcome following surgery for temporal lobe epilepsy with hippocampal involvement in preadolescent children: emphasis on mesial temporal sclerosis. *J Neurosurg*. 2007;106(3 suppl):205–210.
69. Benifla M, Otsubo H, Ochi A, et al. Multiple subpial transections in pediatric epilepsy: indications and outcomes. *Childs Nerv Syst*. 2006;22(8):992–998.
70. Mittal S, Montes JL, Farmer JP, et al. Long-term outcome after surgical treatment of temporal lobe epilepsy in children. *J Neurosurg*. 2005;103(5 suppl):401–412.
71. Luyken C, Blumcke I, Fimmers R, et al. The spectrum of long-term epilepsy-associated tumors: long-term seizure and tumor outcome and neurosurgical aspects. *Epilepsia*. 2003;44(6):822–830.
72. Clusmann H, Kral T, Gleissner U, et al. Analysis of different types of resection for pediatric patients with temporal lobe epilepsy. *Neurosurgery*. 2004;54(4):847–859, discussion 859-860.
73. Raybaud C, Shroff M, Rutka JT, et al. Imaging surgical epilepsy in children. *Childs Nerv Syst*. 2006;22(8):786–809.
74. Matsumoto K, Tamiya T, Ono Y, et al. Cerebral gangliogliomas: clinical characteristics, CT and MRI. *Acta Neurochir (Wien)*. 1999; 141(2):135–141.
75. Provenzale JM, Ali U, Barboriak DP, et al. Comparison of patient age with MR imaging features of gangliogliomas. *AJR Am J Roentgenol*. 2000;174(3):859–862.
76. Luyken C, Blumcke I, Fimmers R, et al. Supratentorial gangliogliomas: histopathologic grading and tumor recurrence in 184 patients with a median follow-up of 8 years. *Cancer*. 2004;101(1):146–155.
77. Koeller KK, Henry JM. From the archives of the AFIP: superficial gliomas: radiologic-pathologic correlation. Armed Forces Institute of Pathology. *Radiographics*. 2001;21(6):1533–1556.
78. Castillo M, Davis PC, Takei Y, et al. Intracranial ganglioglioma: MR, CT, and clinical findings in 18 patients. *AJNR Am J Neuroradiol*. 1990;11(1):109–114.
79. Tampieri D, Moumdjian R, Melanson D, et al. Intracerebral gangliogliomas in patients with partial complex seizures: CT and MR imaging findings. *AJNR Am J Neuroradiol*. 1991;12(4):749–755.
80. Peretti-Viton P, Perez-Castillo AM, Raybaud C, et al. Magnetic resonance imaging in gangliogliomas and gangliocytomas of the nervous system. *J Neuroradiol*. 1991;18(2):189–199.
81. Altman NR. MR and CT characteristics of gangliocytoma: a rare cause of epilepsy in children. *AJNR Am J Neuroradiol*. 1988;9(5):917–921.
82. Ostertun B, Wolf HK, Campos MG, et al. Dysembryoplastic neuroepithelial tumors: MR and CT evaluation. *AJNR Am J Neuroradiol*. 1996;17(3):419–430.
83. Stanescu Cosson R, Varlet P, Beuvon F, et al. Dysembryoplastic neuroepithelial tumors: CT, MR findings and imaging follow-up: a study of 53 cases. *J Neuroradiol*. 2001;28(4):230–240.
84. Shin JH, Lee HK, Khang SK, et al. Neuronal tumors of the central nervous system: radiologic findings and pathologic correlation. *Radiographics*. 2002;22(5):1177–1189.
85. Fernandez C, Girard N, Paz Paredes A, et al. The usefulness of MR imaging in the diagnosis of dysembryoplastic neuroepithelial tumor in children: a study of 14 cases. *AJNR Am J Neuroradiol*. 2003;24(5):829–834.
86. Parmar HA, Hawkins C, Ozelame R, et al. Fluid-attenuated inversion recovery ring sign as a marker of dysembryoplastic neuroepithelial tumors. *J Comput Assist Tomogr*. 2007;31(3):348–353.
87. Thom M, Gomez-Anson B, Revesz T, et al. Spontaneous intralesional haemorrhage in dysembryoplastic neuroepithelial tumours: a series of five cases. *J Neurol Neurosurg Psychiatry*. 1999;67(1):97–101.
88. Petropoulou K, Whiteman ML, Altman NR, et al. CT and MRI of pleomorphic xanthoastrocytoma: unusual biologic behavior. *J Comput Assist Tomogr*. 1995;19(6):860–865.
89. Giannini C, Scheithauer BW, Burger PC, et al. Pleomorphic xanthoastrocytoma: What do we really know about it? *Cancer*. 1999;85(9):2033–2045.
90. Tien RD, Cardenas CA, Rajagopalan S. Pleomorphic xanthoastrocytoma of the brain: MR findings in six patients. *AJR Am J Roentgenol*. 1992;159(6):1287–1290.
91. Lipper MH, Eberhard DA, Phillips CD, et al. Pleomorphic xanthoastrocytoma, a distinctive astroglial tumor: neuroradiologic and pathologic features. *AJNR Am J Neuroradiol*. 1993;14(6):1397–1404.
92. Im SH, Chung CK, Kim SK, et al. Pleomorphic xanthoastrocytoma: a developmental glioneuronal tumor with prominent glioproliferative changes. *J Neurooncol*. 2004;66(1–2):17–27.
93. Lach B, Duggal N, DaSilva VF, et al. Association of pleomorphic xanthoastrocytoma with cortical dysplasia and neuronal tumors. A report of three cases. *Cancer*. 1996;78(12):2551–2563.
94. Benifla M, Otsubo H, Ochi A, et al. Temporal lobe surgery for intractable epilepsy in children: an analysis of outcomes in 126 children. *Neurosurgery*. 2006;59(6):1203–1213, discussion 1213-1204.
95. Nolan MA, Sakuta R, Chuang N, et al. Dysembryoplastic neuroepithelial tumors in childhood: long-term outcome and prognostic features. *Neurology*. 2004;62(12):2270–2276.
96. Sakuta R, Otsubo H, Nolan MA, et al. Recurrent intractable seizures in children with cortical dysplasia adjacent to dysembryoplastic neuroepithelial tumor. *J Child Neurol*. 2005;20(4):377–384.
97. Marton E, Feletti A, Orvieto E, et al. Malignant progression in pleomorphic xanthoastrocytoma: personal experience and review of the literature. *J Neurol Sci*. 2007;252(2):144–153.
98. Harvey AS, Freeman JL. Epilepsy in hypothalamic hamartoma: clinical and EEG features. *Semin Pediatr Neurol*. 2007;14(2):60–64.
99. Arita K, Kurisu K, Kiura Y, et al. Hypothalamic hamartoma. *Neurol Med Chir (Tokyo)*. 2005;45(5):221–231.
100. Freeman JL, Coleman LT, Wellard RM, et al. MR imaging and spectroscopic study of epileptogenic hypothalamic hamartomas: analysis of 72 cases. *AJNR Am J Neuroradiol*. 2004;25(3):450–462.
101. Frazier JL, Goodwin CR, Ahn ES, et al. A review on the management of epilepsy associated with hypothalamic hamartomas. *Childs Nerv Syst*. 2009;25(4):423–432.
102. Calisto A, Dorfmuller G, Gohlen M, et al. Endoscopic disconnection of hypothalamic hamartomas: safety and feasibility of

robot-assisted, thulium laser-based procedures. *J Neurosurg Pediatr*. 2014;14(6):563–572.
103. Curry DJ, Gowda A, McNichols RJ, et al. MR-guided stereotactic laser ablation of epileptogenic foci in children. *Epilepsy Behav*. 2012;24(4):408–414.
104. Wilfong AA, Curry DJ. Hypothalamic hamartomas: optimal approach to clinical evaluation and diagnosis. *Epilepsia*. 2013;54(suppl 9):109–114.
105. Rasmussen T, Olszewski J, Lloydsmith D. Focal seizures due to chronic localized encephalitis. *Neurology*. 1958;8(6):435–445.
106. Rogers SW, Andrews PI, Gahring LC, et al. Autoantibodies to glutamate receptor GluR3 in Rasmussen's encephalitis. *Science*. 1994;265(5172):648–651.
107. McNamara JO, Whitney KD, Andrews PI, et al. Evidence for glutamate receptor autoimmunity in the pathogenesis of Rasmussen encephalitis. *Adv Neurol*. 1999;79:543–550.
108. He XP, Patel M, Whitney KD, et al. Glutamate receptor GluR3 antibodies and death of cortical cells. *Neuron*. 1998;20(1):153–163.
109. Aguilar MJ, Rasmussen T. Role of encephalitis in pathogenesis of epilepsy. *Arch Neurol*. 1960;2:663–676.
110. Fukuda T, Oguni H, Yanagaki S, et al. Chronic localized encephalitis (Rasmussen's syndrome) preceded by ipsilateral uveitis: a case report. *Epilepsia*. 1994;35(6):1328–1331.
111. Geller E, Faerber EN, Legido A, et al. Rasmussen encephalitis: complementary role of multitechnique neuroimaging. *AJNR Am J Neuroradiol*. 1998;19(3):445–449.
112. Chiapparini L, Granata T, Farina L, et al. Diagnostic imaging in 13 cases of Rasmussen's encephalitis: can early MRI suggest the diagnosis? *Neuroradiology*. 2003;45(3):171–183.
113. Giulioni M, Acciarri N, Padovani R, et al. Results of surgery in children with cerebral cavernous angiomas causing epilepsy. *Br J Neurosurg*. 1995;9(2):135–141.
114. Pozzati E, Padovani R, Morrone B, et al. Cerebral cavernous angiomas in children. *J Neurosurg*. 1980;53(6):826–832.
115. Lee JW, Kim DS, Shim KW, et al. Management of intracranial cavernous malformation in pediatric patients. *Childs Nerv Syst*. 2008;24(3):321–327.
116. Kim DS, Park YG, Choi JU, et al. An analysis of the natural history of cavernous malformations. *Surg Neurol*. 1997;48(1):9–17, discussion 17-18.
117. Cohen DS, Zubay GP, Goodman RR. Seizure outcome after lesionectomy for cavernous malformations. *J Neurosurg*. 1995;83(2): 237–242.
118. Acciarri N, Galassi E, Giulioni M, et al. Cavernous malformations of the central nervous system in the pediatric age group. *Pediatr Neurosurg*. 2009;45(2):81–104.
119. Jallo GI, Kothbauer K, Mehta V, et al. Meningioangiomatosis without neurofibromatosis: a clinical analysis. *J Neurosurg*. 2005;103(4 suppl):319–324.
120. Arcos A, Serramito R, Santin JM, et al. Meningioangiomatosis: clinical-radiological features and surgical outcome. *Neurocirugia (Astur)*. 2010;21(6):461–466.
121. Wiebe S, Munoz DG, Smith S, et al. Meningioangiomatosis. A comprehensive analysis of clinical and laboratory features. *Brain*. 1999;122(Pt 4):709–726.
122. Palmini A, Najm I, Avanzini G, et al. Terminology and classification of the cortical dysplasias. *Neurology*. 2004;62(6 suppl 3):S2–S8.

# 39 Trauma*

*Joshua D. Wermers and Lisa H. Hutchison*

## INCIDENCE AND ETIOLOGY

Head trauma and resulting traumatic brain injury (TBI) are among the most common causes of morbidity and mortality in children. Head trauma alone is responsible for 50% of deaths in children ages 1 to 14 years. Approximately 475,000 cases of TBI occur annually in children less than 14 years in the United States. Half of the cases occur in children under 5 years. Infants and children under 4 years and adolescents between 15 and 19 years of age are the two pediatric age groups at highest risk for TBI. Boys are more frequently injured than are girls (2:1). Motor vehicle accidents, especially car-versus-pedestrian accidents, are responsible for approximately 30% of TBI cases.

In infants younger than 2 years, the most common causes of head trauma are falls, an object striking the head, the infant being dropped, and nonaccidental trauma (NAT). NAT accounts for more than 80% of deaths from head trauma in this group. Skull fractures, subdural hematomas, cerebral edema, and parenchymal contusions are common injuries before 2 years of age. In children ages 3 to 14 years, falls, sporting activities, and all-terrain and motor vehicle accidents are the most common causes of head trauma. Fractures and parenchymal contusions are the most common injuries in this group. In older adolescents (>14 years), diffuse axonal injury (DAI) related to motor vehicle accidents predominates. Birth trauma is discussed in Chapter 23.

## IMAGING IN PEDIATRIC HEAD TRAUMA

### Computed Tomography

In general, computed tomography (CT) is the initial imaging modality used to evaluate patients with known or suspected head trauma to detect potentially life-threatening conditions that may require immediate surgical intervention. CT is widely available, easy to obtain, and quickly performed. Multidetector CT scanners have the advantage of producing multiplanar and three-dimensional (3D) images. These advances have increased the sensitivity of CT in detecting the sequelae of head trauma. CT angiography (CTA) is useful in the evaluation of traumatic vascular injury and has the advantage of speed and fewer flow-related artifacts compared with magnetic resonance angiography (MRA).

CT limitations include low contrast in the immature brain and beam hardening artifacts, which may obscure small extraaxial collections or subtle cortical contusions adjacent to bone. Although advances in CT scanners have improved their sensitivity in detecting TBI, CT underestimates the degree and extent of traumatic parenchymal injuries compared with magnetic resonance imaging (MRI). Nonetheless, acute CT findings have been proposed as criteria for grading and predicting outcome in TBI (the Marshall Classification and subsequent modifications by Maas et al.).[1]

Importantly, exposure of children to excess radiation has become a concern after Pearce et al.[2] demonstrated that children who underwent head CT had an increased risk of brain tumors years later. For patients with a minor head injury (Glasgow Coma Scale [GCS] score of 13 to 15), clinical guidelines for obtaining a head CT are available including the New Orleans Criteria, the Canadian CT Head Rule, and guidelines from the Pediatric Emergency Care Applied Research Network. These criteria are highly sensitive for detecting injuries that require neurosurgical intervention.[3] The American College of Radiology (ACR) also publishes Appropriateness Criteria for imaging in pediatric head trauma, including children under 2 years in whom clinical criteria are less reliable compared with older children.[4]

Adaptive statistical iterative reconstruction and other postprocessing techniques reduce image noise and improve low-contrast detectability and image quality. They provide higher diagnostic performance at a lower dose without loss of image quality.[5]

### Magnetic Resonance Imaging

Because of its more limited availability and longer scanning times, MRI is a secondary modality in acute head trauma evaluation. However, recent studies have compared the efficacy of rapid sequence MRI to CT in detecting intracranial injury. MRI demonstrated detection rates similar to CT in a select population without the risk of radiation.[6] MRI is more often performed in subacute and chronic trauma, especially when the CT findings do not correlate with the patient's clinical condition, or when patients have unexpected neurologic deterioration. MRI offers the advantages of multiplanar imaging and greater overall sensitivity and specificity for the detection of TBI. It is particularly useful in the detection of extraaxial hematomas, nonhemorrhagic intraaxial contusions, brain edema, posterior fossa abnormalities, and DAI.[7]

Specific MRI sequences are invaluable in TBI. Fluid attenuation inversion recovery sequences (FLAIR) null signal from cerebrospinal fluid (CSF) increasing detection of abnormal signal foci in the subarachnoid spaces and adjacent to ventricles.

T2* gradient-echo sequences (GREs) use a pair of bipolar gradient pulses to enhance magnetic susceptibility caused by magnetic field distortion. Susceptibility-weighted imaging (SWI) uses the signal loss from out-of-phase protons with different magnetic susceptibilities and is more sensitive than GRE for detection of blood products.[8]

Diffusion-weighted imaging (DWI) assesses the diffusion of water protons, which is normally along the MRI gradient signal. Areas of restricted diffusion retain the magnetic resonance signal, indicating ischemia/hypoxia due to acute injury. Reduced diffusion is also present in lesions with low nucleus-cytoplasm ratios. DWI is susceptible to the intrinsic T2* signal of the tissue because it is a gradient sequence. This is known as the T2 shine-through effect. To separate DWI signal from T2 shine through, the apparent water diffusion coefficient (ADC) is calculated by acquiring images with different gradient duration and amplitude (b-values), thus eliminating the T1 and T2* values.[9] Diffusion tensor imaging (DTI) assesses anisotropy of brain tissue by evaluating differences in direction of water diffusion in tissues. Although DTI can provide information about white matter tract integrity, it is currently mostly used for research purposes.

MRA and magnetic resonance venography, typically using the time-of-flight technique, are useful if a vascular injury is suspected.

Magnetic resonance spectroscopy (MRS) assesses the distribution and quantification of molecules within the central nervous system (see Chapter 25). The point-resolved spectroscopy sequence using

---

*We acknowledge the contributions of the authors of the prior version of this chapter: Andre D. Furtado, Ajaya R. Pande, and Vera R. Sperling.

## Abstract:

Head trauma and resulting traumatic brain injury (TBI) are among the most common causes of morbidity and mortality in children. Head trauma alone is responsible for 50% of deaths in children ages 1 to 14 years. Approximately 475,000 cases of TBI occur annually in children less than 14 years in the United States. Half of the cases occur in children under 5 years. Head injury after nonaccidental trauma (NAT) is an important consideration in the pediatric population. Radiologic findings are an integral part of the workup and diagnosis of NAT as the clinical presentation is often nonspecific and highly variable. In general, CT is the initial imaging modality used to evaluate patients with known or suspected head trauma. In this chapter, head trauma is broadly classified by mechanism of head injury. Scalp hematoma, skull fractures, extraaxial and intraventricular hemorrhage, subarachnoid and traumatic parenchymal injury including non-accidental trauma are discussed highlighting important clinical and imaging findings that point to a specific diagnosis. Case examples are provided to familiarize the reader with expected imaging manifestations of both common and uncommon manifestations of head trauma. Head trauma is a frequent cause of morbidity and mortality in the pediatric population. A wide spectrum of traumatic head injuries occurs in children, many of which are unique to the pediatric population. Understanding the variable clinical presentations as well as imaging manifestations of head trauma is necessary to make a timely diagnosis and initiate prompt treatment when necessary.

## Keywords:

Head trauma
Traumatic brain injury
epidural hematoma
subdural hematoma
subarachnoid hemorrhage
nonaccidental trauma

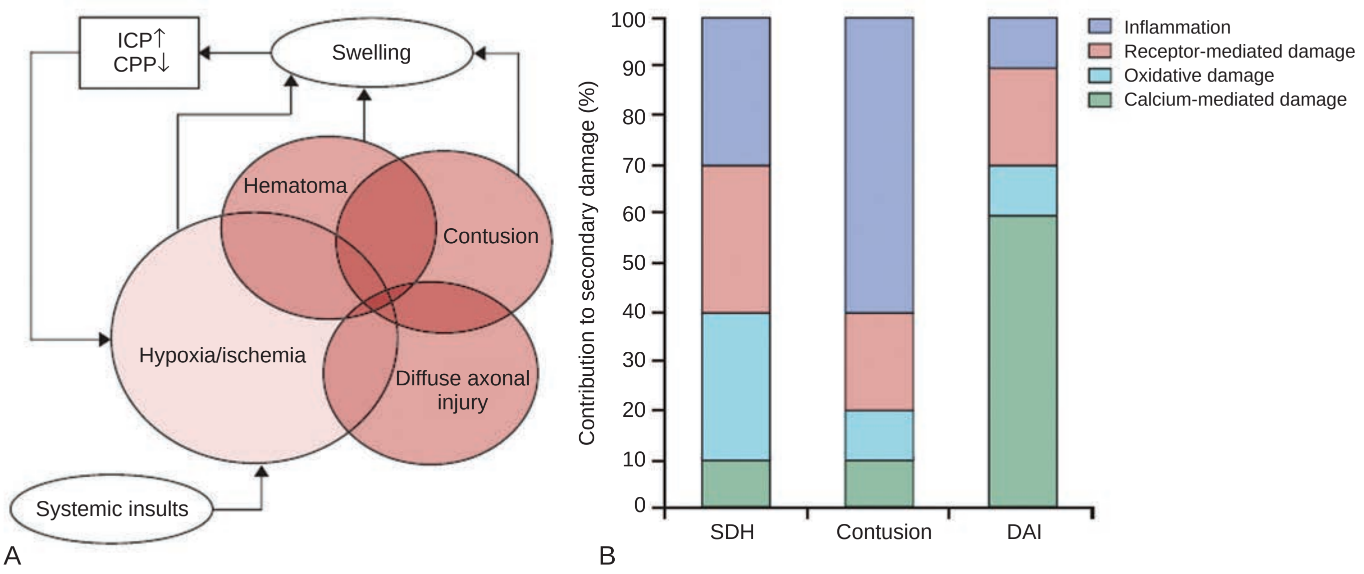

**Figure 39.1.** Components of TBI and various pathophysiologic mechanisms. *CPP,* Cerebral perfusion pressure; *DAI,* diffuse axonal injury; *ICP,* intracranial pressure; *SDH,* subdural hematoma. *(From Maas AIR, Stocchetti N, Bullock R. Moderate and severe traumatic brain injury in adults.* Lancet Neurol. *2008;7:728–741.)*

short and long time to echo (TE) acquisitions are the most commonly used techniques. MRS provides a noninvasive analysis of brain metabolites and biochemical changes. Decreased N-acetyl aspartate (NAA) has been correlated with abnormal neuropsychologic function in TBI. Significant lactate elevations have been correlated with a poor prognosis.[10]

### Nuclear Imaging Modalities

Single-photon emission CT (SPECT) can detect abnormalities in cerebral blood flow, but these alterations are not always associated with traumatic lesions on imaging. However, a negative initial SPECT scan after trauma is a strong predictor of favorable clinical outcome. A worse prognosis is associated with large and/or multiple lesions, as well as lesions located in the brainstem, basal ganglia, and temporal or parietal lobes.

Positron emission tomography (PET) measures the cerebral metabolism of various substrates (see Chapter 25). Fluorodeoxyglucose, the primary substrate used in the measurement of glucose metabolism, correlates to neuronal viability. Although rarely used in children, PET can be used in DAI to determine damage extent, predict prognosis, and determine lesion reversibility. The major limitation of PET is its inability to distinguish functional abnormalities from structural damage.

## CLASSIFICATION AND MECHANISMS OF HEAD INJURY

The sequelae of head trauma can be classified into direct injury from impact loading forces and indirect injury from acceleration/deceleration and rotational forces. Brain injury may result from direct (coup) or indirect (contrecoup) impact. The most common sequelae of direct head injury are scalp hematoma, skull fracture, brain contusion, laceration of the brain parenchyma, subarachnoid hemorrhage (SAH), and epidural or subdural hematomas beneath the site of impact. Nonimpact (acceleration/deceleration) injuries are the result of linear translational forces, acceleration/deceleration, and rotational acceleration causing shear-strain on axons, neurons, and blood vessels. These injuries include contusions, DAI, deep gray matter injury, brainstem injuries, and intraparenchymal and extraaxial hematomas. Brain axons are the most vulnerable, and blood vessels are the most resistant to injury from acceleration/deceleration forces (Fig. 39.1).[11]

Based on the GCS, head injuries are classified as mild (GCS score 13 to 15), moderate (GCS score 9 to 12), and severe (GCS score 3 to 8). Most head trauma results in mild injury with a nearly 0% risk of death in children. Moderate pediatric head injury has a similar occurrence rate as in adults, but a lower mortality rate. Severe pediatric head injury occurs less frequently than in adults, but has a significantly lower mortality rate. The exception is in infants under 2 years who have a higher rate due to severe head injuries from NAT.[12]

### Scalp Hematoma

Scalp contusions and hematomas usually resolve without complications with the exception of subgaleal hematomas in infants, which may pose the risk of life-threatening hypovolemia. When evaluating pediatric scalp contusions, size, location, and patient age are important factors because large scalp hematomas (particularly in infants under 12 months) are associated with an increased risk of fractures and intracranial injury.

### Skull Fractures

The likelihood of intracranial injury in children increases significantly when a skull fracture is present. However, the absence of a skull fracture does not preclude intracranial injury and has little prognostic significance in children. Younger children have thinner, more pliable skulls than adults. Therefore children have a higher incidence of traumatic intracranial injury without the presence of a fracture, particularly in children age 6 to 24 months. Falls and motor vehicle accidents account for most skull fractures in children.

Fractures in infants may be linear, depressed, diastatic, compound (stellate), "ping pong" (buckled), or penetrating. In this age group, fractures are often the result of being dropped by a caregiver or an object striking the head. Fractures tend to course toward a suture, synchondrosis, foramen, or canal. As the calvarium becomes more mature, comminuted fractures may occur.

Linear calvarial fractures are more frequent in all age groups, followed by depressed or comminuted calvarial and basilar fractures. Linear fractures usually heal without complication. Complex fractures, in which the dura mater is torn, may be complicated by herniation of arachnoid layers, creating a leptomeningeal cyst. CSF pulsations cause progressive erosion of fracture margins, known as a "growing fracture," which appears as a lytic skull lesion with scalloped margins (see Chapter 23). Underlying brain contusion is common.

Depressed fractures occur when osseous fragments are displaced inward and usually result from blunt force trauma. These fractures may result in increased intracranial pressure (ICP), epidural hematoma, parenchymal contusion, and/or laceration. Depressed fractures are treated surgically for cosmetic reasons and to prevent complications. Those involving the dural sinuses are treated conservatively due to the risk of fatal hemorrhage with intervention (e-Fig. 39.2). Depressed fractures are categorized as compound when associated with a scalp laceration and as penetrating when an underlying dural tear is present. Pneumocephalus indicates a compound fracture (e-Fig. 39.3). CSF leaks and infection are a concern with compound fractures that have visible contamination, a meningeal tear, and delayed treatment for more than 8 hours after the initial injury.

Diastatic skull fractures (sutures >2 mm) most frequently involve the lambdoid sutures of newborns and infants, but may occur at any age. However, asymmetric sutures, even those less than 2 mm, should raise suspicion for a diastatic fracture.

Skull base fractures are associated with increased risk of vascular or cranial nerve injury. Basilar fractures involving the temporal bone may cause bleeding into the middle ear and mastoid air cells. Temporal bone fractures are classified according to their orientation (longitudinal or transverse) and the portion of the temporal bone involved (petrous or squamous). These classifications are helpful in determining the risk of complications. Although longitudinal fractures are more common (70%–90%), transverse fractures are at higher risk of permanent injury to the facial and vestibulocochlear nerves, cochlear disruption, facial paralysis, sensorineural hearing loss, and perilymph fistula. Temporal bone fractures involving the petrous apex or the carotid canal are associated with increased risk of carotid artery and/or jugular vein injury.

Studies report sensitivities between 94% and 99% for detection of skull fractures on plain radiographs. These radiographs are routinely obtained in suspected cases of NAT as part of the skeletal survey. Previously, axial CT has had a lower sensitivity for detection of linear fractures parallel to the imaging plane. However, reconstructed planes and 3D CT are often diagnostic in difficult cases. CT is sensitive for the detection of depressed and basilar skull fractures, fractures of the facial bones, sinuses, and orbits. In children, skull fractures heal in 6 to 8 weeks, but may remain radiographically visible for 1 year.

## Extraaxial and Intraventricular Hemorrhage

### Epidural Hematoma

Epidural hematomas are uncommon in infants and increase in incidence with age, peaking in adulthood. The etiology of epidural hematomas in children differs from adults. Venous epidural hematomas usually occur in younger children due to tearing of a dural venous sinus, an emissary or diploic vein. Venous epidural hematomas occur in the posterior fossa and occipital region from laceration of the transverse or sigmoid sinus. Middle cranial fossa and parasagittal hematomas result from injuries of the sphenoparietal sinus and superior sagittal sinus, respectively. In older children and adolescents, arterial epidural hematomas are more common. They often involve injuries to the meningeal artery with hematomas accumulating over the temporal or parietal convexities (Fig. 39.4). Fractures associated with epidural hematomas are slightly less frequent in children than adults (83% vs. 93%).

The presentation of epidural hematomas in children may include a loss of consciousness at the time of injury, with a lucid interval in the first 24 hours. Factors associated with a poor outcome in children with epidural hematomas include absence of an immediate lucid period, the presence of additional intracranial injuries, a delayed diagnosis, and surgical intervention.

Epidural collections do not cross suture lines, but do extend over the falx and tentorium. Posterior fossa epidural hematomas may extend into the supratentorial compartment, whereas subdural hematomas are confined to one compartment. Moreover, frontal epidural collections may cross the midline along the superior sagittal sinus, whereas subdural hematomas accumulate along the falx. These features are much more reliable than lentiform versus biconvex shape at differentiating epidural from subdural hematomas. Venous epidural hematomas are frequently concave in the posterior fossa, are often larger, and carry an overall worse prognosis than arterial epidural hematomas because of their delayed presentation.

On CT, acute epidural hematomas are hyperattenuated with progression to intermediate attenuation in the subacute phase and hypoattenuation, possibly with membranes, in the chronic phase. Mixed attenuation may represent active bleeding, hypercoagulable states, a dural tear with mixed CSF and blood in the epidural space, or layering serum as a result of clot retraction. Mixed attenuation hyperacute hematomas (active hemorrhage) occur in the hours after an injury and have frequent associated severe brain injury, edema, and mass effect.

On MRI, the signal characteristics of extraaxial collections are more variable than on CT and depend on several factors such as the patient's hematocrit, local partial pressure of oxygen, pH level, protein concentration, presence of an associated dural tear with CSF mixing, and the magnetic field strength. Signal changes over time of intracranial hematomas have been mainly studied in adults with parenchymal, not subdural, hemorrhages. Because of this, the age of intraaxial, but not extraaxial, blood products can be reliably dated with MRI. Although aging of extraaxial hematomas based on MRI signal characteristics have not been validated in children, signal patterns are similar to parenchymal blood (Table 39.1).

MRI is useful in distinguishing small epidural from subdural hematomas, in which the displaced dura in an epidural hematoma is visualized as a thin, uniform line of hypointense signal on intermediate and T2-weighted sequences. The inner membrane of a subacute or chronic subdural hematoma may have a similar appearance, but the membrane is thicker and more irregular.

### Subdural Hematoma

Subdural hematomas are more common in infants than in older children and adolescents. They may result from shear-strain forces disrupting small veins that traverse the potential subdural space. In infants, up to 85% of subdural hematomas are bilateral. Trauma is the most common cause of subdural hematomas, both accidental and NAT. Most subdural hematomas in infants under 2 years are caused by NAT. Other findings suggestive of NAT include interhemispheric location of subdural hematomas, multilayered subdural hematomas containing blood at different stages of degradation, and associated parenchymal contusions. Retinal hemorrhages are also suggestive of NAT and usually found on funduscopic examination.

Infants with subdural hematomas have various presentations ranging from asymptomatic to vomiting, poor feeding, irritability, a bulging fontanelle, or an increasing head circumference. Older children more commonly present with the signs of raised ICP, headache, altered level of consciousness, systemic hypertension, decreased heart rate, irregular respiration, asymmetric pupils, and hemiparesis. Large subdural hematomas may cause anemia due to blood loss, especially in infants.

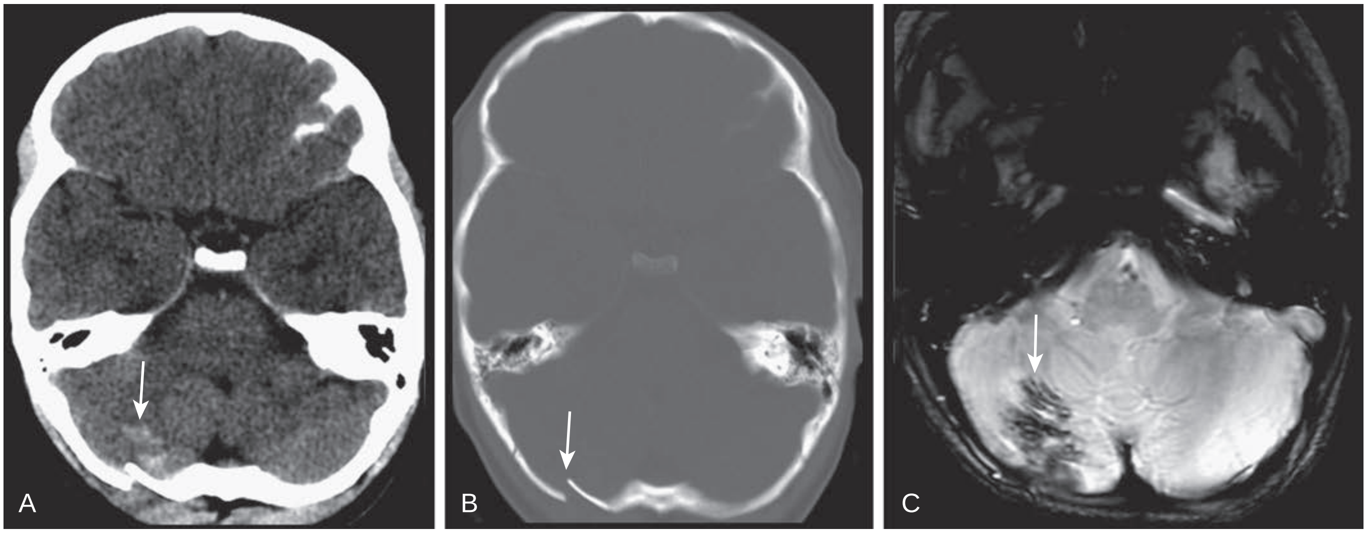

**e-Figure 39.2. Occipital fracture and cerebellar contusion.** (A) Unenhanced CT shows an area of hyperdensity in the right cerebellum representing a hemorrhagic contusion *(arrow).* (B) Bone reconstruction shows a depressed right occipital bone fracture *(arrow).* (C) Susceptibility-weighted MRI sequence shows low signal susceptibility artifact due to blood products *(arrow).* Depressed fractures adjacent to venous sinuses may not be suitable for surgical repair.

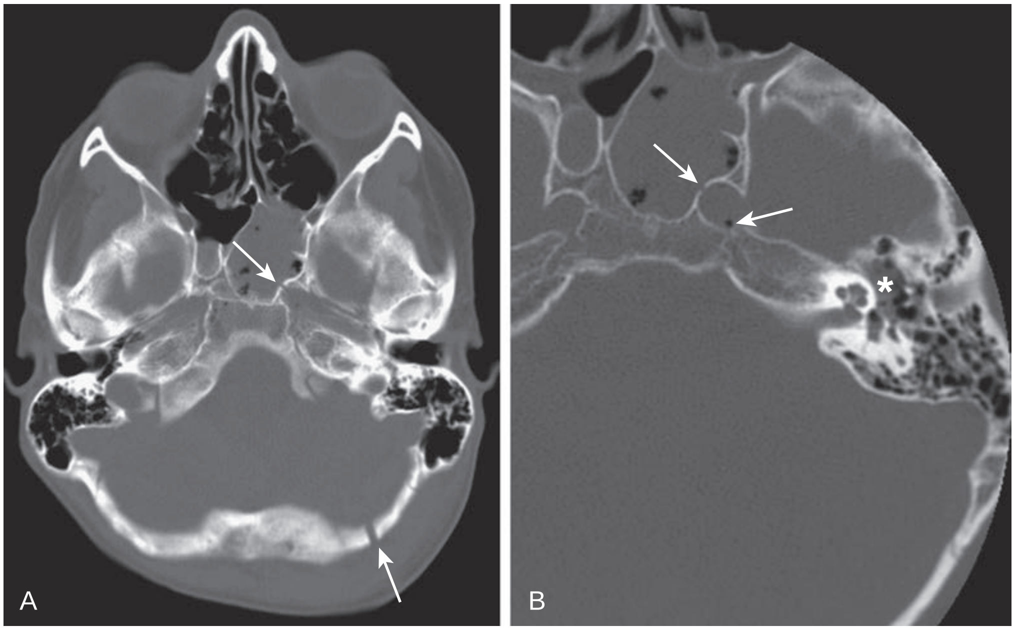

**e-Figure 39.3. Skull base fracture.** (A) A compound fracture through the left occipital bone and petrous apex extending into the sphenoid sinus *(arrows).* (B) Reconstructed CT image shows involvement of the left carotid canal *(arrow)* with a locule of air within the carotid canal *(thin arrow)* and partial opacification of the middle ear *(asterisk).*

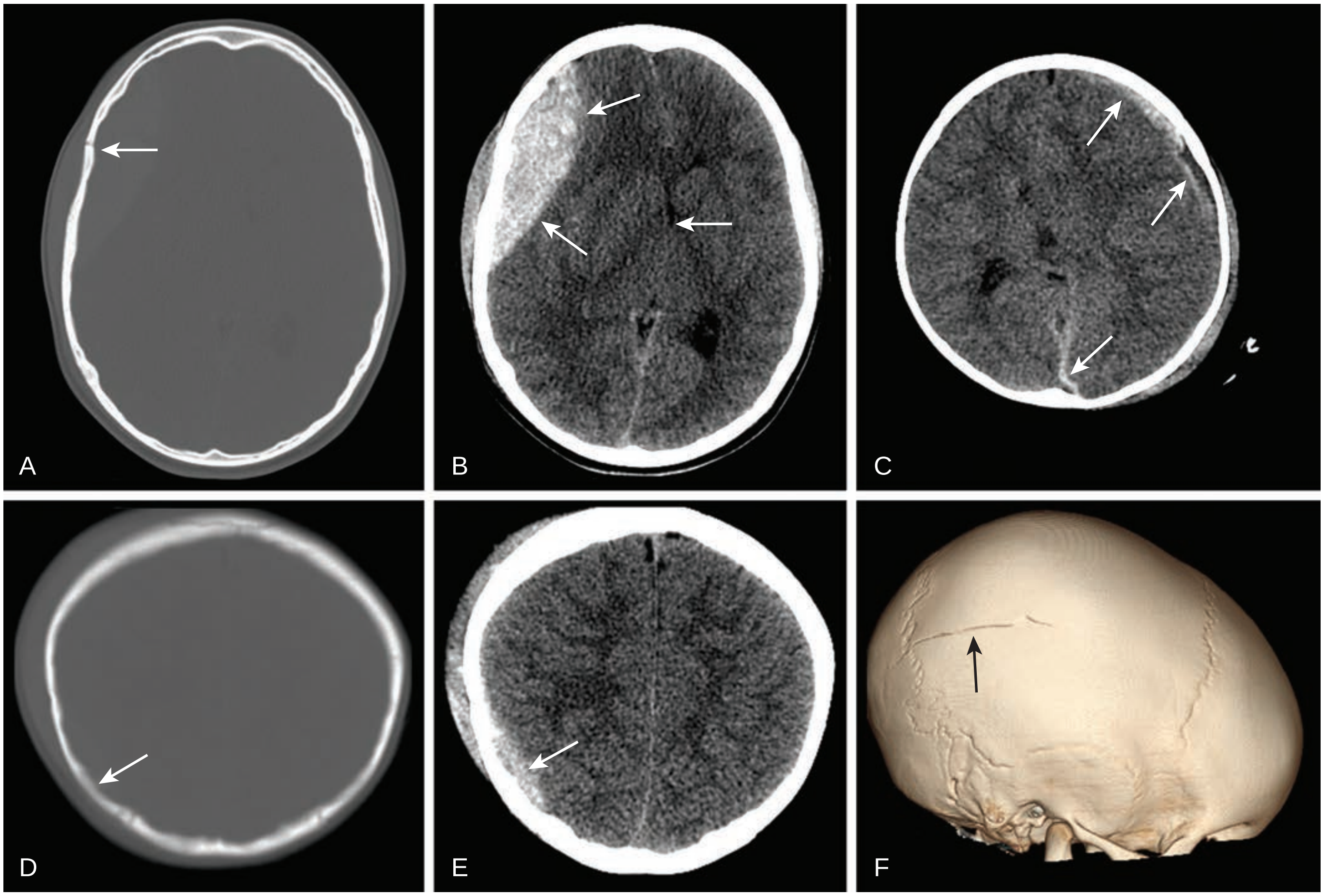

**Figure 39.4. Skull fractures and extraaxial hematomas.** Unenhanced CT images show a pterional fracture *(arrow)* (A) and an acute epidural hematoma with midline shift (B). (C) A hyperacute mixed attenuation (actively bleeding) left frontal subdural hematoma extending to the left occipital lobe is shown *(arrows).* (D) A skull fracture parallel to the image plane is noted *(arrow).* (E) An acute epidural hematoma adjacent to the fracture *(arrow)* in the same patient as *D*. (F) The poorly visualized fracture on axial images is well demonstrated on 3D volume rendering *(arrow).*

**TABLE 39.1** MRI of Blood at Different Stages at 1.5 Tesla

| Age of Blood | T1 | T2 | GRE |
|---|---|---|---|
| Hyperacute (4–6 hours) | Isointense | Hyperintense | Hypointense |
| Acute (7–72 hours) | Isointense | Central hypointense and peripheral hyperintense | Hypointense |
| Early subacute (4–7 days) | Peripheral hyperintensity and central isointense | Hypointense with some central hyperintense | Hypointense |
| Late subacute (1–4 weeks) | Hyperintense | Hyperintense | Hypointense |
| Early chronic (months) | Peripheral isointensity to hypointensity and central hyperintensity | Peripheral hypointense and central hyperintense | Hypointense |
| Late chronic (months to years) | Hypointense | Hypointense | Hypointense |

*GRE,* Gradient echo.

Subdural hematomas are most commonly located over the frontal, parietal, and temporal lobes. Posterior fossa subdurals, approximately 10% of cases, may result from tearing of the dural sinuses or tentorium. Subdural hematomas cross sutures, but do not cross the falx or tentorium. Occasionally, a normal hyperdense falx may mimic a subdural hematoma on CT. The normal falx is distinguished by a thin, smooth, symmetric contour. Conversely, subdural hematomas are asymmetric, are more irregular, and cause thickening of the falx or tentorium.

CT characteristics of subdural hematomas depend on hematoma age. Hyperacute hematomas represent unclotted blood and show mixed attenuation. After a few hours, hyperacute hemorrhage coagulates converting to an acute hematoma, which is homogenously hyperattenuated. The hyperattenuated acute blood may mix with CSF resulting from a tear in the arachnoid (see Fig. 39.4). Within 1 to 3 weeks, subacute hematomas become isodense to brain parenchyma. After 2 to 3 weeks, the attenuation becomes similar to CSF indicating a chronic hematoma. Hematomas that are isointense to brain may be difficult to detect, save for associated mass effect heralding their presence. If the presence of a subacute or chronic hematoma is questionable, intravenous contrast may show enhancing membranes. If the size of the collection increases or if the attenuation is heterogeneous, rebleeding should be suspected. Spontaneous rebleeding is common in subdural hematomas and does not indicate additional trauma. Membranes calcify in under 3% of cases.

MRI is more sensitive than CT for the detection of subdural hematomas, particularly when their attenuation is similar to brain parenchyma or CSF. Proton-density and FLAIR are the most sensitive sequences for detection of subdural hematomas that are isointense to CSF on T1- and T2-weighted images. The signal of subdural hematomas on MRI varies, depending on the phase of blood products and the presence or absence of CSF leakage. The evolution of signal characteristics of subdural hematomas are similar to those previously described for epidural hematomas.

Subdural hygromas are caused by laceration of the arachnoid with accumulation of CSF in the subdural space. They may occur alone or in combination with acute hemorrhage after trauma. Subdural hygromas generally manifest 3 to 5 days after injury and are bilateral in up to 50% of cases. Hygromas are distinguishable from chronic subdural hematomas in that they are isointense to CSF on all sequences, including FLAIR and proton-density.

## Subarachnoid and Intraventricular Hemorrhage

Traumatic SAH is due to damage of pia-arachnoid vessels and associated parenchymal injury. It is seen in 18% to 25% of pediatric closed head injury (CHI) cases. The amount of blood in the subarachnoid space is typically small and rarely persists longer than 1 week. If a large SAH is seen without parenchymal damage or extraaxial hematomas, there may be an underlying aneurysm or arteriovenous malformation. SAH may obstruct normal CSF resorption at the arachnoid granulations resulting in communicating hydrocephalus.

Traumatic intraventricular hemorrhage (IVH) is related to subependymal vein injury or decompression of a parenchymal hematoma into the ventricles. The most common location of subependymal vein injury is along the anterior corpus callosum, posterior fornix, or septum pellucidum.

CT is the imaging modality of choice for acute SAH and IVH, showing increased attenuation within the sulci (Fig. 39.5), or ventricles, respectively. The most common location of traumatic SAH is in the posterior interhemispheric fissure and along the tentorium. On CT, hyperdense SAH is initially detected adjacent to the source of bleeding. With time, it accumulates in the subarachnoid cisterns (particularly the interpeduncular cistern), the Sylvian fissures, over the convexities, and in the occipital horns.

MRI is more sensitive than CT in detecting small amounts of SAH, showing increased signal on FLAIR sequences. Although GRE and SWI sequences are less sensitive than FLAIR, when visible, SAH is hypointense on these sequences. While extensive or recurrent SAH is rare in children, it may lead to superficial siderosis, hemosiderin laden macrophages within the leptomeninges. Vasospasm due to traumatic SAH is rare in children.

## Traumatic Parenchymal Injury

### Contusion and Laceration

Brain contusions invariably involve the cortex, with variable underlying white matter injury. They are twice as common in children as adults. Brain contusions occur at the site of impact (coup), opposite the site of impact (contrecoup), along the rough calvarial surfaces in the anterior temporal and orbitofrontal regions, and against the free margins of falx cerebri, and tentorium. Cerebellar contusions are often associated with occipital fractures, and frequently involve the cerebellar tonsils. Brain edema develops over the first 1 to 2 days, and is maximal 3 to 5 days after the initial injury. Approximately 50% of brain contusions are hemorrhagic. With increasing severity, microhemorrhages may coalesce into focal hematomas. After 1 month, contused areas progress to form areas of cystic encephalomalacia.

On CT, contusions show hypoattenuation with loss of the gray-white differentiation and sulcal effacement. Hemorrhagic contusions show hyperattenuated central foci (see Fig. 39.5). After the contusion, cortical enhancement may occur in 1 to 2 weeks due to proliferation of immature capillaries lacking a blood-brain barrier.

MRI is the most sensitive modality for detection of brain contusions. In particular, DWI sequences are able to detect parenchymal contusions and shear injury in the first hours after an injury. After 1 to 2 days, contused areas become hyperintense on FLAIR and T2-weighted sequences due to edema and hemorrhagic foci (hypointense on T2 GRE or SWI) (e-Fig. 39.6). High signal on T1-weighted images may be seen in the subacute phase, related to methemoglobin. FLAIR is insensitive to parenchymal contusion in infants because of low contrast in the unmyelinated white matter. T2-weighted images are particularly useful in these cases, showing loss of gray-matter differentiation and hyperintensity relative to the normal brain.

Lacerations of brain parenchyma cause cortical hemorrhage with variable extension into the white matter. They result from penetrating and CHI with or without associated fractures (see Fig. 39.5). Posttraumatic hematoma may rapidly increase in size requiring follow-up imaging in the first 24 to 48 hours. Parenchymal lacerations are most common in the inferior frontal and anterior temporal lobes. Corpus callosum and brainstem lacerations may occur in association with DAI.

### Diffuse Axonal Injury

DAI is one of the most devastating types of TBI, and is the most common cause of posttraumatic neurologic and cognitive disability. DAI is more common in children than previously recognized, with infants being particularly susceptible. DAI results from rapid acceleration/deceleration resulting in angular and rotational forces that stretch the axons causing damage to their cytoskeleton. Subsequent brain swelling and calcium influx into injured axons is thought to cause further damage.

Children with DAI may present with immediate loss of consciousness and coma. Clinical symptoms are often disproportionate to imaging findings, and CT findings may be normal. Although high-speed motor vehicle accidents are the most common cause of DAI, it may result from any type of head trauma. The mechanism of shear-strain injury in infants younger than 12 months is different from older children and adults. The dominant histologic abnormality in infants is hypoxia, which leads to acute brain swelling, encephalomalacia, volume loss, and potentially death.

Imaging underestimates the extent of DAI, with only 20% to 50% of CT images showing findings initially. Findings of DAI on CT include foci of abnormal attenuation, which are usually bilateral, less than 1 cm, and oriented parallel to white matter tracts. DAI occurs most at the gray-white matter junction of the frontal and temporal lobes, splenium of corpus callosum, and brainstem. An important indirect sign of DAI is intraventricular hemorrhage from adjacent corpus callosum involvement (Fig. 39.7). In infants with severe DAI, CT demonstrates diffuse brain edema. Within 2 to 3 weeks, encephalomalacia and volume loss may also develop.

MRI is more sensitive than CT in detecting shear injuries, and is best performed 3 to 7 days after injury when cellular necrosis and restricted diffusion are maximal. MRI using SWI and GRE sequences detect DAI in 30% of patients with mild head injury and an initially normal CT scan. DAI reveals multiple small, ovoid

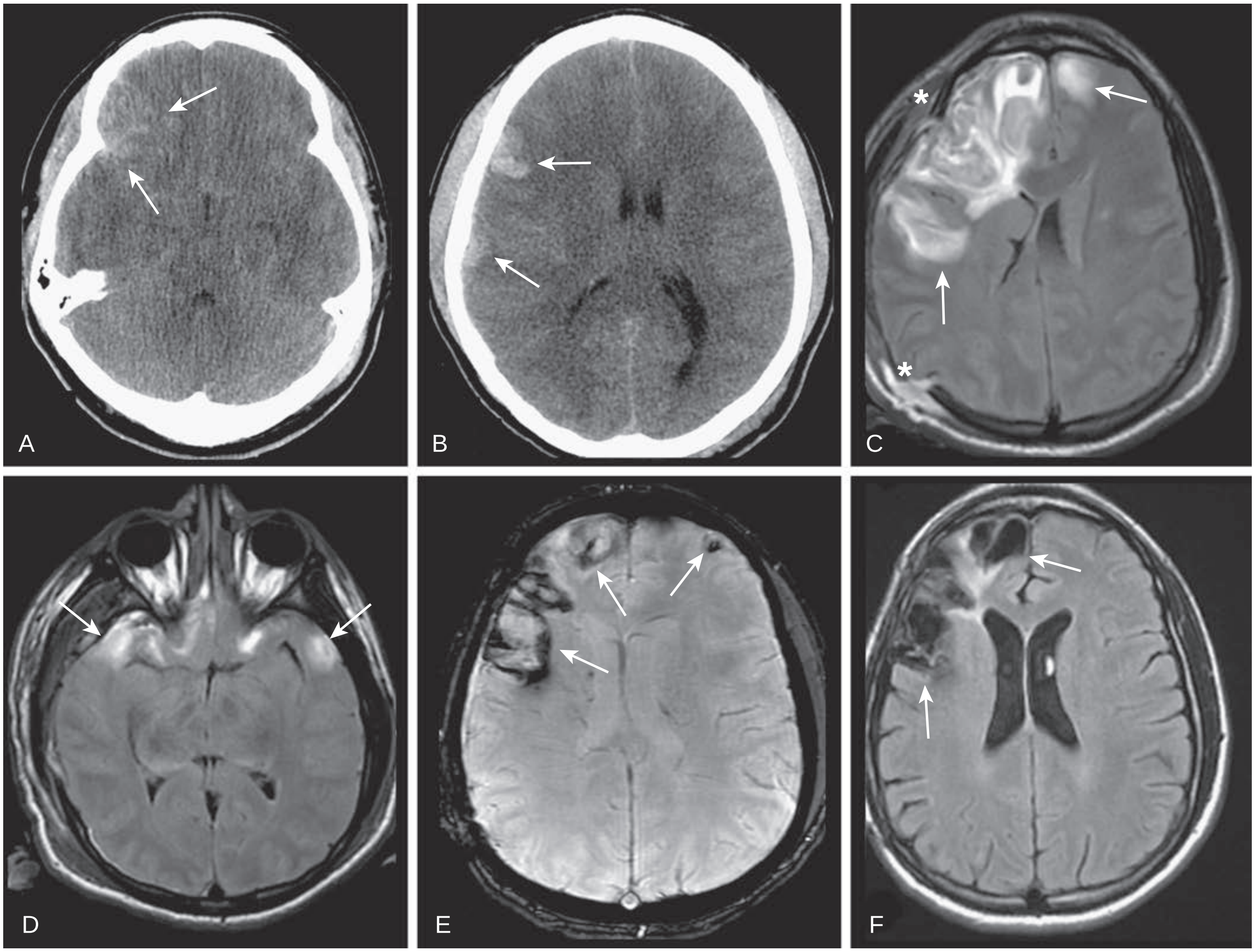

**e-Figure 39.6. Progression of imaging characteristics in a parenchymal contusion.** (A and B) Unenhanced CT images demonstrate an acute right frontal contusion *(arrows)* with minimal midline shift. (C and D) A few days later, MRI FLAIR image reveals extensive edema, increasing midline shift, and additional contusions in the left frontal lobe and temporal lobes *(arrows).* Postsurgical findings are related to right hemispherical craniotomy *(asterisks).* (E and F) A few months later, a peripheral rim of susceptibility related to chronic blood products *(arrows)* is seen on SWI sequence (E), and encephalomalacia and volume loss are seen on FLAIR (F).

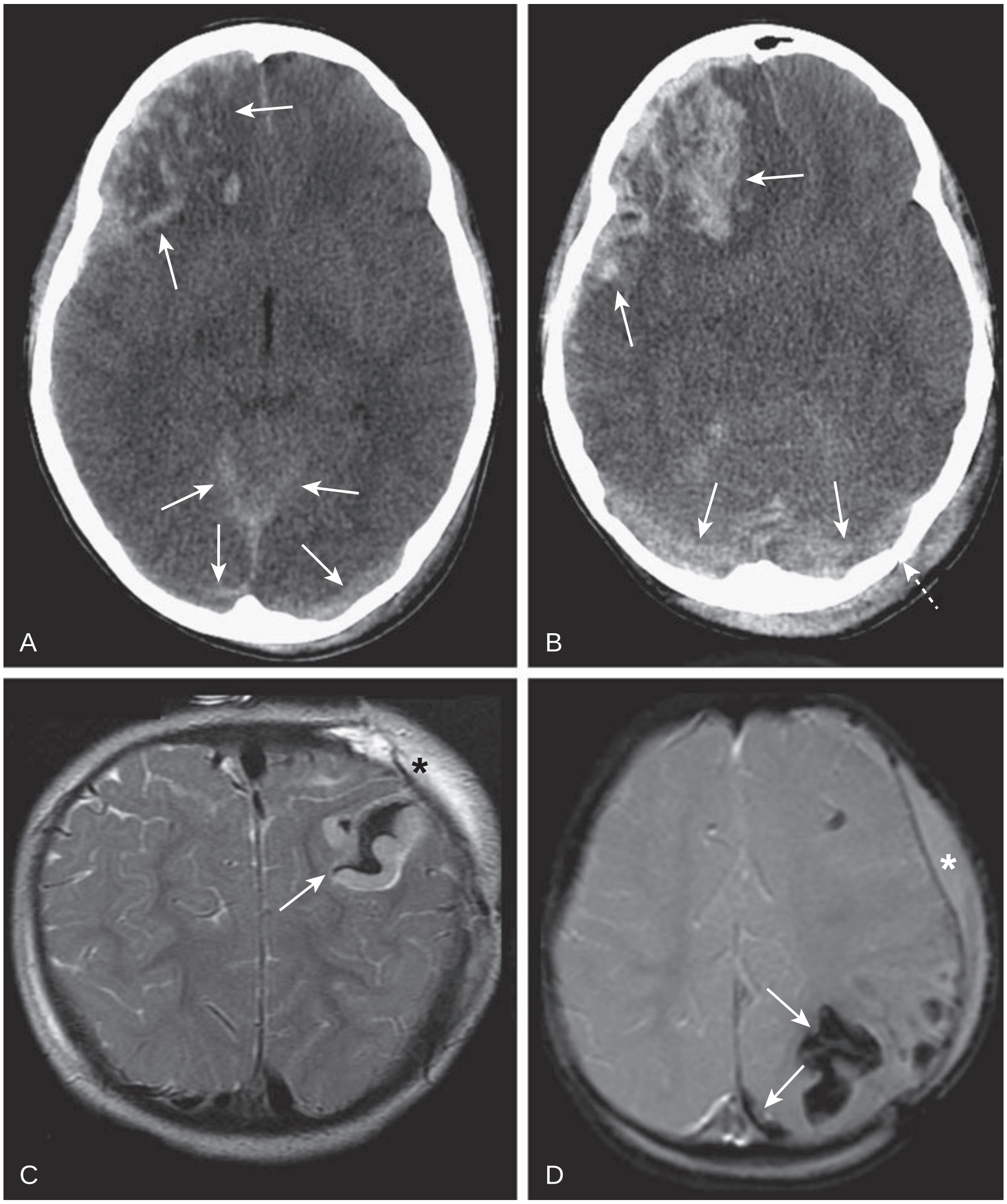

**Figure 39.5. Parenchymal contusion, subarachnoid hemorrhage, and laceration.** Unenhanced CT images (A and B) show a contrecoup right frontal and temporal contusion with associated subarachnoid hemorrhage *(arrows)*. Acute bilateral subdural hematomas are present along with a left occipital fracture and a scalp hematoma *(broken arrow).* MRI T2-weighted (C) and SWI sequence (D) show a parenchymal laceration with a hematoma *(arrows).* Also note postcraniectomy findings *(asterisks).*

areas of decreased T1, increased T2, increased FLAIR, and abnormal DWI signal. Hemorrhagic lesions cause susceptibility effect, with hypointensity on T2* and SWI (see Fig. 39.7). Initial nonhemorrhagic lesions may convert to hemorrhagic foci with time, showing change of signal characteristics of blood, with increasing size due to hemorrhage and edema. DWI depicts additional lesions that exhibit restricted diffusion. ADC values decrease over a longer period of approximately 18 days after injury, which is beyond the usual time frame for cytotoxic edema related to ischemia.[13]

A reduction in fractional anisotropy has been shown with DTI in early imaging after TBI. DTI tractography has shown acute axonal shearing injuries and may have prognostic value for post-traumatic cognitive and neurologic sequelae.

A grading scheme for DAI based on the severity of head trauma and lesion location has been proposed, with mild trauma resulting in more superficial lesions and increasingly severe trauma resulting in involvement of deeper structures. A greater number of lesions correlates with poorer outcomes.

## Deep Gray Matter Injury

Deep gray matter injury, which occurs in severely injured patients, constitutes less than 5% of all primary intraaxial injuries. This type of injury is found in the thalami, basal ganglia, and upper brainstem, from shear-strain forces disrupting small perforating vessels with or without hemorrhage. Surviving patients have profound neurologic deficits. CT is often normal,

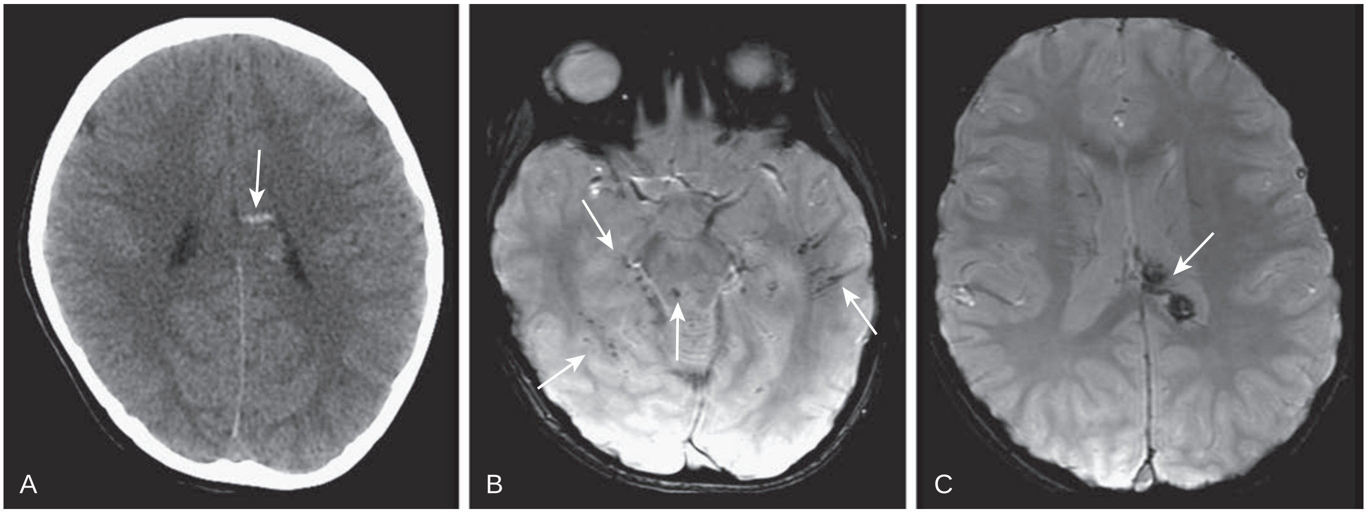

**Figure 39.7. Diffuse axonal injury.** (A) An unenhanced CT image with hyperdense foci in the corpus callosum compatible with a shear injury *(arrow).* (B and C) An MRI SWI sequence shows multiple susceptibility foci of hypointensity/blooming *(arrows)* consistent with parenchymal (B) and intraventricular (C) hemorrhage.

but may show foci of petechial hemorrhage. FLAIR is the most sensitive MRI sequence for nonhemorrhagic deep gray matter injury.

### Brainstem Injury

Although brainstem injury is uncommon in the pediatric population, it is likely underestimated. Clinically, patients with a brainstem injury recover poorly warranting further MRI evaluation.

Injuries include brainstem contusion, shear injury, pontomedullary separation, and hypoxic-ischemic injury. Brainstem injuries cause death in up to 50% of blunt head trauma cases.

Primary brainstem injury can occur from direct or indirect forces characteristically involving the dorsolateral midbrain and superior pons. Indirect forces resulting in brainstem injury can have variable associated DAI in the corpus callosum and deep white matter. Pontomedullary separation is a result of hyperextension forces and is often fatal.

Secondary brainstem injury can result from transtentorial herniation, global hypoxic-ischemic injury, or hypotensive hypoperfusion. If the cause of transtentorial herniation can be treated, its sequelae may be reversible. Prolonged compression of the brainstem and brainstem injury are usually terminal.

### Diffuse Brain Swelling and Hypoperfusion Injury

Diffuse brain swelling has been reported to occur in 21% of pediatric head trauma cases and is 3.5 times more common in this group, particularly in infants and young children.

After a young child sustains a traumatic injury, the immature vasoregulatory system responds with vasodilation and increased blood flow, resulting in a hyperemic state and subsequent diffuse cerebral swelling or edema. In addition, the release of excitatory amines also causes vasodilation and increased blood volume, and the redistribution of intracranial blood from pial to intraparenchymal vessels contributes further to the hyperemic state.

The imaging findings in both conditions primarily affect the cerebrum with loss of the gray-white interface, diffuse decreased attenuation, and effacement of the subarachnoid cisterns and ventricles on CT. The decreased attenuation can cause the circulating blood to erroneously appear hyperdense on CT giving it a “pseudo-SAH” appearance. Further, the cerebellum may be relatively hyperdense compared with the cerebral hemispheres (“white cerebellar sign,” Fig. 39.8).

DWI, MRS, and SWI are helpful in differentiating the two conditions. Increased blood flow and vasogenic edema have increased diffusion on DWI, whereas acute axonal shear injury with cytotoxic edema shows restricted diffusion. MRS shows decreased NAA and increased lactate, choline, and neurotransmitter levels as a result of neuronal injury in acute DAI, with metabolites near normal early in the course of cerebral edema. SWI has a high sensitivity for the detection of hemorrhagic lesions in the setting of DAI.

Progressive edema and increased ICP can result in transtentorial, subfalcine, and tonsillar herniation with subsequent vascular complications and death in 7% of pediatric cases. Overall, these complications occur less frequently in children than adults.

Hypoperfusion injury after trauma may be due to severe cerebral edema, hypotension, and shock. Imaging shows diffuse loss of gray-white interface with relative preservation of extraaxial spaces, subarachnoid cisterns, and ventricle size.

The reversal sign, decreased attenuation of the cerebral cortex compared with the thalami, brainstem, and cerebellum, is a striking CT finding in children with anoxic-ischemic injury. Its presence also portends a poor prognosis.

## SEQUELAE OF TRAUMA

Various clinical and imaging sequelae occur after trauma ranging from neurologic disability and seizures to hydrocephalus and encephalomalacia. Pediatric traumatic vascular injury, such as arterial dissection, may result in infarction (Fig. 39.9). Pseudoaneurysms after skull base fractures, and carotid cavernous fistulas, are less common sequelae after trauma. Venous injury to the dural sinuses is most common after birth trauma and is often associated with fractures, subdural hematomas, or epidural hematomas. Venous sinuses thrombosis can be caused by compression resulting from intracranial bleeding, adjacent fracture, or increased ICP.

CTA is used for imaging vascular injuries such as laceration, occlusion, dissection, pseudoaneurysm, or arteriovenous fistula. CSF leaks can also be evaluated with CT, radionuclide cisternography, and high-resolution long T2-weighted MRI. Infection is an uncommon sequela of penetrating injuries that may present with meningitis, empyema, cerebritis, or intracranial abscess.

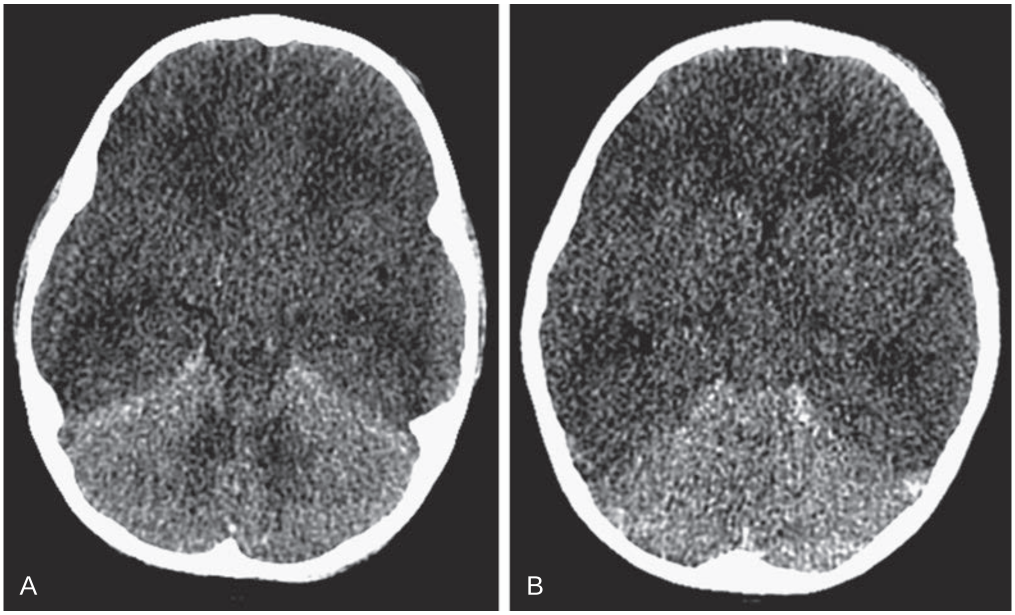

**Figure 39.8. White cerebellum sign.** (A and B) A noncontrast CT image shows diffuse decrease in attenuation of cerebral parenchyma, with increased attenuation of the cerebellum.

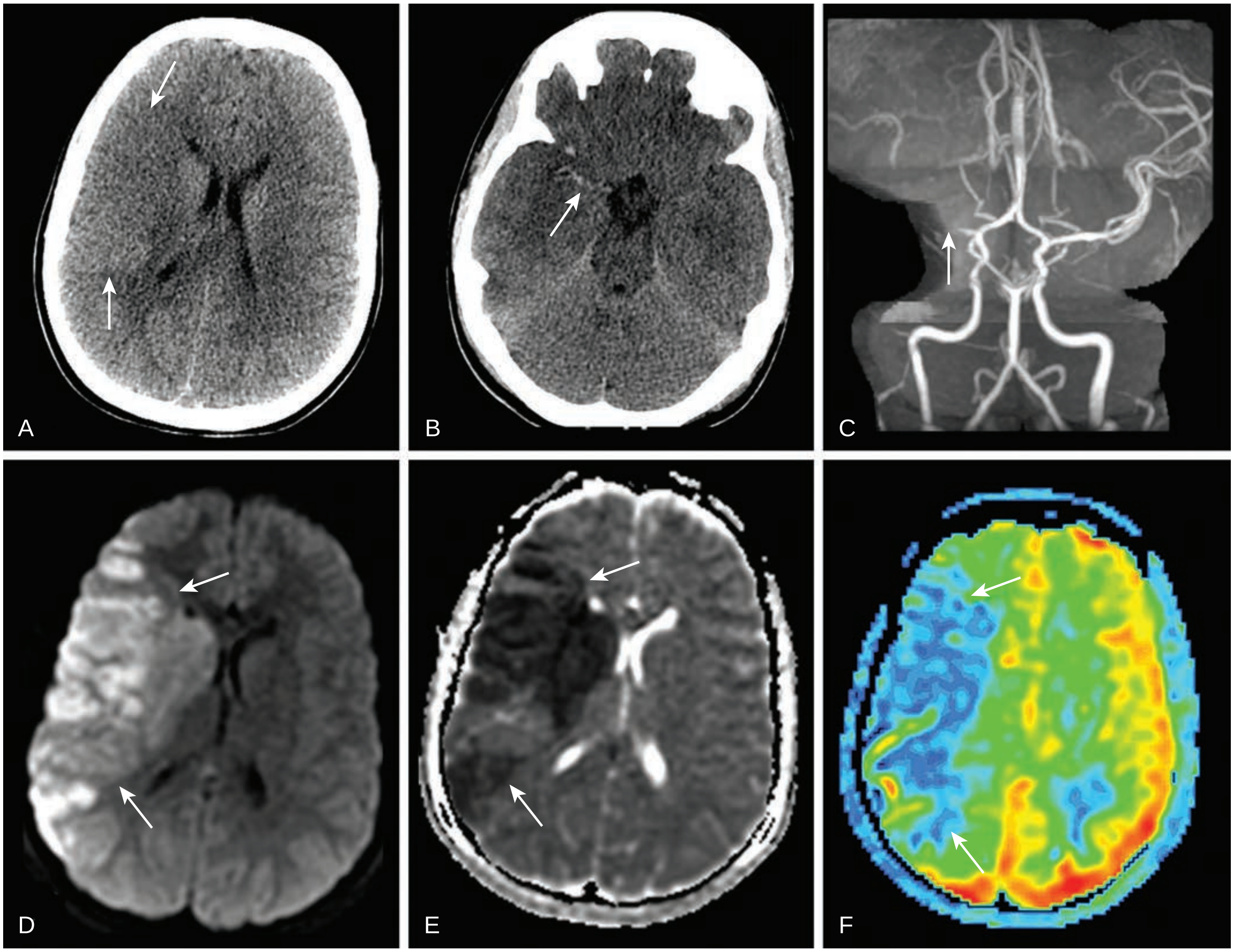

**Figure 39.9. Traumatic dissection of the right middle cerebral artery (MCA).** (A) An unenhanced CT image of the brain demonstrate poor gray-white matter differentiation in the right frontal and temporal lobes *(arrows).* (B) An unenhanced CT image at the level of the circle of Willis and midbrain demonstrates the "hyperdense MCA sign" *(arrow).* (C) Occlusion of the right MCA *(arrow)* on 3D time-of-flight MRA. (D and E) Restricted diffusion and low ADC values *(arrows).* (F) An arterial spin label perfusion image shows decreased cerebral blood flow in the right MCA territory *(arrows).*

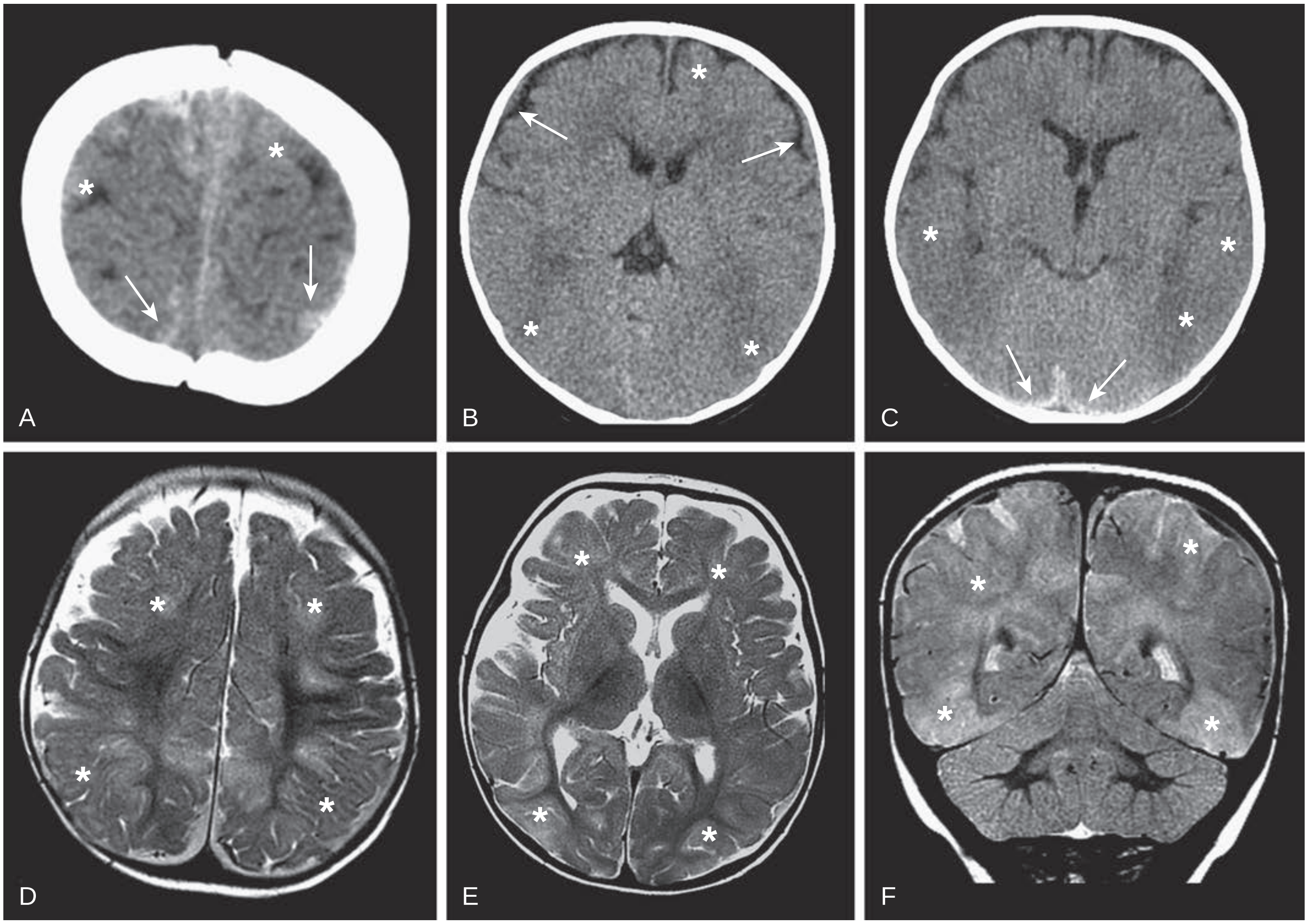

**Figure 39.10. Nonaccidental trauma.** (A–C) An unenhanced CT image demonstrates multiple areas of loss of gray-white matter differentiation *(asterisks)* and bilateral acute and subacute subdural hematomas *(arrows)*. (D–F) MRI T2-weighted images show the extent of parenchymal injury with multifocal cortical and subcortical injuries *(asterisks).*

## NONACCIDENTAL TRAUMA

Head injury after NAT is one of the leading causes of mortality and morbidity in infants and children. Radiologic findings are an integral part of the workup and diagnosis of NAT (see Chapter 143). Head injuries in these infants and children include skull fractures, intracranial and retinal hemorrhages, and parenchymal brain injury such as contusions, edema, ischemia, and infarction.

The clinical presentation of NAT head trauma is often nonspecific and highly variable ranging from a normal neurologic examination to irritability, lethargy, or seizures. Imaging findings of NAT may provide the first clues to the diagnosis. As in accidental trauma or other causes of acute altered mental status, CT is the initial imaging modality, with MRI used to further define injury extent and assess for possible craniocervical injury.

Intracranial hemorrhages, especially subdural hematomas, are common in NAT. Bleeding into the subarachnoid space may coexist and is seen in the sulci and subarachnoid cisterns. Epidural hemorrhages are uncommon in infants and young children who have sustained NAT. Most acute subdural hematomas are hyperdense on CT, but this finding varies because mixing with CSF from a dural tear may also present.

On MRI, the signal intensity of parenchymal injuries varies with time, and when correlated with other clinical findings, it can be helpful to clinicians and child advocacy services. However, the precise aging of parenchymal lesions and extraaxial hematomas should be undertaken with caution. CT hyperdensity is the only reliable indicator of hemorrhage age (Fig. 39.10). Subdural hematomas in infants under 2 years and subdural hematomas of different ages are highly suspicious for NAT. Although rarely seen on imaging, retinal hemorrhages are a cardinal manifestation of NAT that are best assessed on a dilated funduscopic examination (Fig. 39.11). Their number and severity (multiple, bilateral, multilayered, peripheral extension) correlates with the likelihood of NAT and the severity of associated brain injury.

Mortality and morbidity in children with NAT are often due to parenchymal brain injury. Posttraumatic hypoxic ischemic injury and brain edema are more common than parenchymal contusions and DAI. Hypoxic ischemic injury due to NAT is typically diffuse, and although the exact mechanism is unclear, it is likely related to hypoperfusion. Key imaging findings include diffuse loss of gray-white matter differentiation (brain edema) with sparing of the basal ganglia. Severe insults demonstrate basal ganglia and posterior fossa involvement. Hypoxia after strangulation involves various portions of the anterior circulation bilaterally, with relative sparing of the vertebral circulation. MRI and DWI are useful to delineate the extent and severity of ischemic injury. MRS may show a decrease in NAA, indicating neuronal loss, and an increase in lactate, indicating anaerobic metabolism and a worse prognosis (see Fig. 39.11).

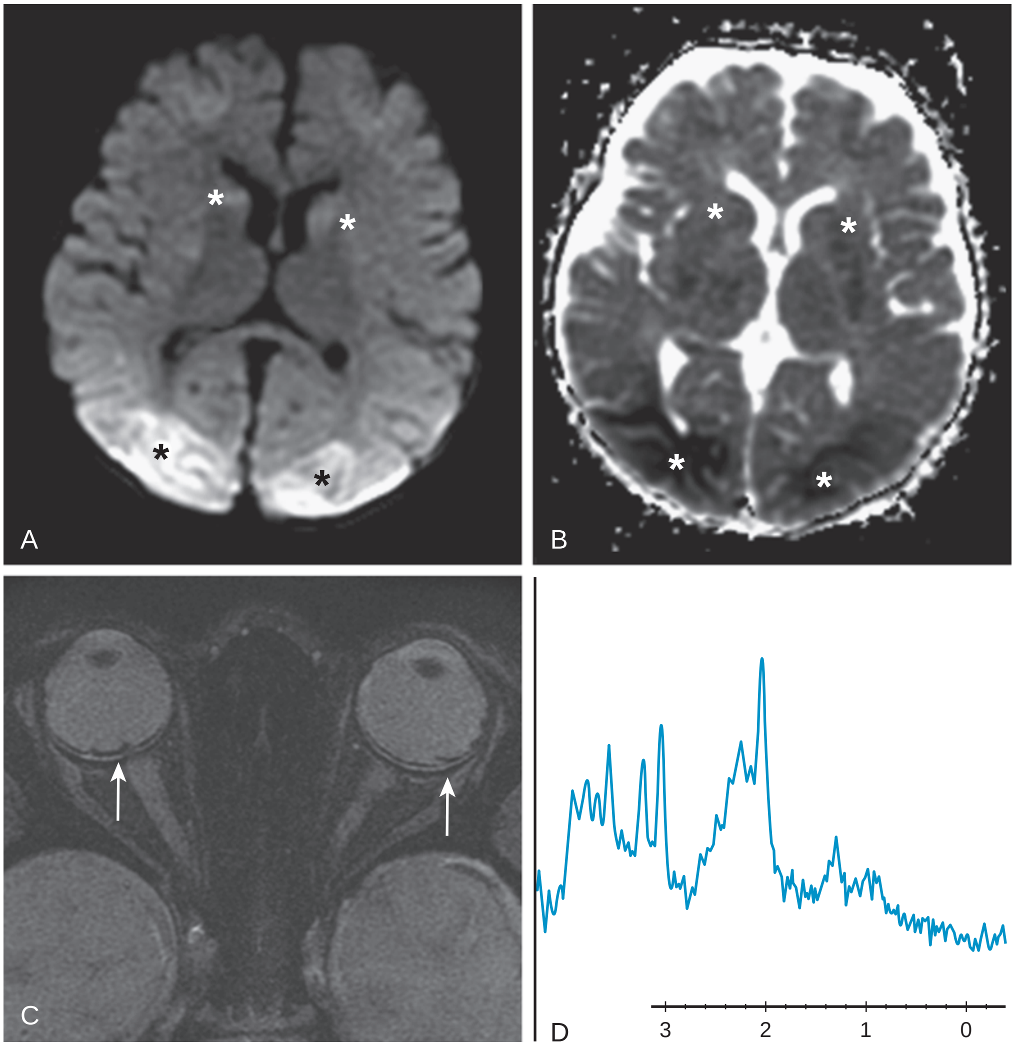

**Figure 39.11. Nonaccidental trauma.** (A and B) MRI diffusion sequences show multiple areas of restriction that are more pronounced in the occipital lobes and caudate nuclei *(asterisks)* (A) and ADC (B). (C) A high-resolution SWI sequence shows susceptibility related to retinal hemorrhages bilaterally *(arrows).* (D) MRS at the level of the occipital lobes demonstrates a decrease in NAA level (2.0 ppm), elevated lactate/lipids (0.8–1.2 ppm), and glutamate/glutamine (2.2–2.4 ppm) levels.

A multidisciplinary approach should be used in the diagnosis of NAT when radiologic findings are suspicious or inconsistent with the clinical history. Radiologists must also consider coagulopathies, severe meningoencephalitis, certain rare metabolic disorders (such as glutaric aciduria type 1) that can present with subdural hematomas, and birth trauma in the differential diagnoses. Intracranial hemorrhage in infants due to birth trauma generally resolves within 4 to 6 weeks.

Vigilance, familiarity with the radiologic findings, communication with the referring physician, relevant clinical history, and recommendation for further imaging to identify or document injuries for evidentiary reasons, if needed, all aid in the workup, diagnosis, and prosecution of NAT.

### Prognosis

Children are more likely than adults to recover from focal brain injury and have a higher likelihood of survival after severe injury. However, children are more vulnerable to long-term cognitive and behavioral dysfunction after diffuse brain injury. Some degree of learning disability is found in 50% of pediatric head trauma survivors. Overall, children under 6 years have the worst prognosis, likely because of the increased risk and prevalence of shear injury in the immature brain. Ultimately, functional outcome depends on injury extent and the ability of existing neurons to recover function.

## SUMMARY

Head trauma is a frequent cause of morbidity and mortality in the pediatric population. A wide spectrum of traumatic head injuries occurs in children, many of which are unique to the pediatric population. The type of injury depends on the mechanism, the force sustained, and patient age. Although CT is the acute imaging modality of choice, various newer imaging techniques such as CTA and MRI with DWI and MRS are useful to better predict recovery and outcome in pediatric patients.

## KEY POINTS

- Head trauma and resulting TBI are the most common causes of morbidity and mortality in children.
- In general, CT is the initial imaging modality used to evaluate patients with known or suspected head trauma.
- The mortality rate from minor head injury in childhood approaches 0%.
- The likelihood of intracranial injury increases when a skull fracture is present, but skull fracture absence does not preclude intracranial injury and has little prognostic significance in pediatric head trauma.
- In younger children, epidural hematomas are more often venous than arterial.
- DAI is one of the most devastating types of TBI and is the most common cause of posttraumatic neurologic and cognitive disability.
- Diffuse brain swelling and hypoperfusion injuries are more common in children and can be differentiated using MRI.
- Children are more likely than adults to recover from focal brain injury and have a higher likelihood of survival after severe injury. However, children are more vulnerable to long-term cognitive and behavioral dysfunction after diffuse brain injury.

## SUGGESTED READINGS

Barkovich AJ. *Diagnostic Imaging: Pediatric Neuroradiology*. 2nd ed. Salt Lake City, Utah Philadelphia, PA: Amirsys Publishing, Inc., Elsevier; 2014.

Barkovich AJ. *Pediatric Neuroradiology*. 5th ed. Philadelphia: Lippincott Williams & Wilkins; 2012.

Provenzale JM. Imaging of traumatic brain injury: a review of the recent medical literature. *AJR Am J Roentgenol*. 2010;194(1):16–19.

Tortori-Donati P, Rossi A. *Pediatric Neuroradiology: Brain, Head, Neck and Spine*. New York: Springer; 2005.

## REFERENCES

Full references for this chapter can be found on www.expertconsult.com.

## REFERENCES

1. Maas AI, et al. Prediction of outcome in traumatic brain injury with computed tomographic characteristics: a comparison between the computed tomographic classification and combinations of computed tomographic predictors. *Neurosurgery*. 2005;57(6):1173–1182.
2. Pearce MS, Salotti JA, Little MP, et al. Radiation exposure from CT scans in childhood and subsequent risk of leukaemia and brain tumours: a retrospective cohort study. *Lancet*. 2012;380(9840):499–505.
3. Bouida W, Marghli S, Souissi S, et al. Prediction value of the Canadian CT head rule and the New Orleans criteria for positive head CT scan and acute neurosurgical procedures in minor head trauma: a multicenter external validation study. *Ann Emerg Med*. 2013;61(5):521–527.
4. Ryan ME, Palasis S, Saigal G, et al. ACR Appropriateness Criteria head trauma—child. *J Am Coll Radiol*. 2014;11(10):939–947.
5. McKnight CD, Watcharotone K, Ibrahim M, et al. Adaptive statistical iterative reconstruction: reducing dose while preserving image quality in the pediatric head CT examination. *Pediatr Radiol*. 2014;44(8):997–1003.
6. Young JY, Duhaime AC, Caruso PA, et al. Comparison of non-sedated brain MRI and CT for the detection of acute traumatic injury in children 6 years of age or less. *Emerg Radiol*. 2016;23(4):325–331.
7. Lee H, et al. Focal lesions in acute mild traumatic brain injury and neurocognitive outcome: CT versus 3T MRI. *J Neurotrauma*. 2008;25(9):1049–1056.
8. Mittal S, Wu Z, Neelavalli J, et al. Susceptibility-weighted imaging: technical aspects and clinical applications, part 2. *AJNR Am J Neuroradiol*. 2009;30(2):232–252.
9. Provenzale JM. Imaging of traumatic brain injury: a review of the recent medical literature. *AJR Am J Roentgenol*. 2010;194(1):16–19.
10. Tollard E, et al. Experience of diffusion tensor imaging and 1H spectroscopy for outcome prediction in severe traumatic brain injury: preliminary results. *Crit Care Med*. 2009;37(4):1448–1455.
11. Zhu GW, Wang F, Liu WG. Classification and prediction of outcome in traumatic brain injury based on computed tomographic imaging. *J Int Med Res*. 2009;37(4):983–995.
12. Maas AI, Stocchetti N, Bullock R. Moderate and severe traumatic brain injury in adults. *Lancet Neurol*. 2008;7(8):728–741.
13. Galloway NR, et al. Diffusion-weighted imaging improves outcome prediction in pediatric traumatic brain injury. *J Neurotrauma*. 2008;25(10):1153–1162.

# 40

# Embryology, Anatomy, and Normal Findings

*Peter Winningham and Lisa H. Hutchison*

## EMBRYOLOGY

The spinal cord forms in three stages beginning in the third gestational week.[1] The first stage, neurulation, involves progression from neural plate to neural tube.[1] The notochord becomes the nucleus pulposus of the intervertebral disks.[2] The second stage, canalization, involves formation of cysts within the caudal cell mass that coalesce and fuse to the distal neural tube forming the primitive spinal cord. The third stage, retrogressive differentiation, involves programmed cell death with regression of the primitive distal cord to form the fetal conus, filum terminale and ventriculus terminalis[1,2] (Fig. 40.1).

The vertebral bodies develop from somites originating from sclerotomes.[3] The caudal and cranial portions of sclerotomes fuse to become single vertebrae. Failure of this process leads to congenital segmentation anomalies such as block and hemivertebrae (Fig. 40.2).[4,5]

## ANATOMY AND PHYSIOLOGY

The spinal cord is largest in the cervical and lumbar regions. Dorsal and ventral nerve roots arise from each level, and the cord is held in place by the lateral dentate ligaments. The distal spinal cord and thecal sac extend to the L2–L3 disc space and the S2 level, respectively.

Although 5% of humans have differing numbers of vertebrae, most have 7 cervical, 12 thoracic, and 5 lumbar segments, as well as 5 sacral and 4 coccygeal segments.[6] Running craniocaudal are the anterior and posterior longitudinal ligaments, supraspinous and interspinous ligaments, and ligamentum flavum.

The arterial supply to the spinal cord is via the anterior spinal and paired posterior spinal arteries. The anterior spinal artery, which originates from branches of the vertebral arteries, courses along the ventral cord. Similarly, the posterior spinal arteries arise from the intradural vertebral arteries and course along the dorsal cord.[7] Radicular artery branches contribute to the cord arterial supply with one particularly large branch, the artery of Adamkiewicz, entering the spinal canal between T9 and T12. It is recognized by its characteristic proximal hairpin turn.[8]

## Normal Findings

The pediatric spine may be imaged with plain radiographs, ultrasound, computed tomography (CT), and magnetic resonance imaging (MRI). Radiographs and CT are used to screen for osseous anomalies, including acute trauma. In neonates, spine sonography and MRI are the most frequently used modalities. Sonography is used to screen infants younger than 6 months due to its excellent resolution and lack of radiation. It provides sufficient characterization of spinal anomalies to determine if urgent intervention or MRI is required. In older infants and children, MRI is the study of choice for spine evaluation.

Indications for spine sonography include screening neonates with multiple congenital anomalies, dimples with skin stigmata, and infants with soft tissue masses suggesting possible (occult) spinal dysraphism. It is also used to determine the cause of failed lumbar puncture (LP) and localize cerebrospinal fluid (CSF) for reattempts at LP.[9,10] High-risk skin stigmata include atypical dimples (>5 mm) above the gluteal crease (>2.5 cm from the anus), and dimples with skin stigmata such as a hairy patch, hemangioma, mound of soft tissue, skin tag, or tail.[11] Simple sacral dimples do not require imaging.[12] MRI is the study of choice for anomalies requiring surgery and dimples draining CSF.[13,14] Additionally, MRI is best performed immediately before therapeutic intervention.[9]

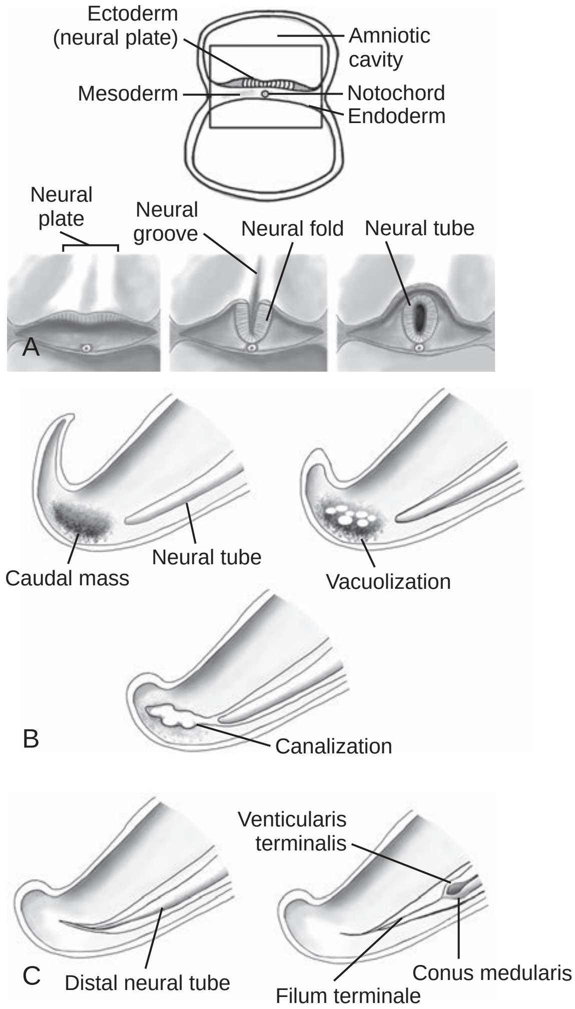

**Figure 40.1. Embryologic development of the spinal cord.** (A) Neurulation schematic illustrates progression from neural plate to groove to neural tube. (B) Canalization schematic depicts coalescence of cysts within the caudal cell mass that fuse to the distal neural tube. (C) A retrogressive differentiation schematic reveals the process of programmed cell death forming the conus medullaris and filum terminale.

## Abstract:

This chapter presents a brief overview of normal embryological development and anatomy of the spinal cord. This chapter also covers when specific modalities (radiography, ultrasound, CT, MRI) should be performed to evaluate the spine in the setting of certain clinical scenarios. The majority of the chapter is focused on discussing normal findings and anatomic variants. These normal variants of the lower spine include ventriculus terminalis, filar cyst, fatty filum, and prominent filum terminale which are discussed in detail with accompanying images.

## Keywords:

spinal cord
vertebral column
normal variants
ventriculus terminalis
filar cyst
fatty filum

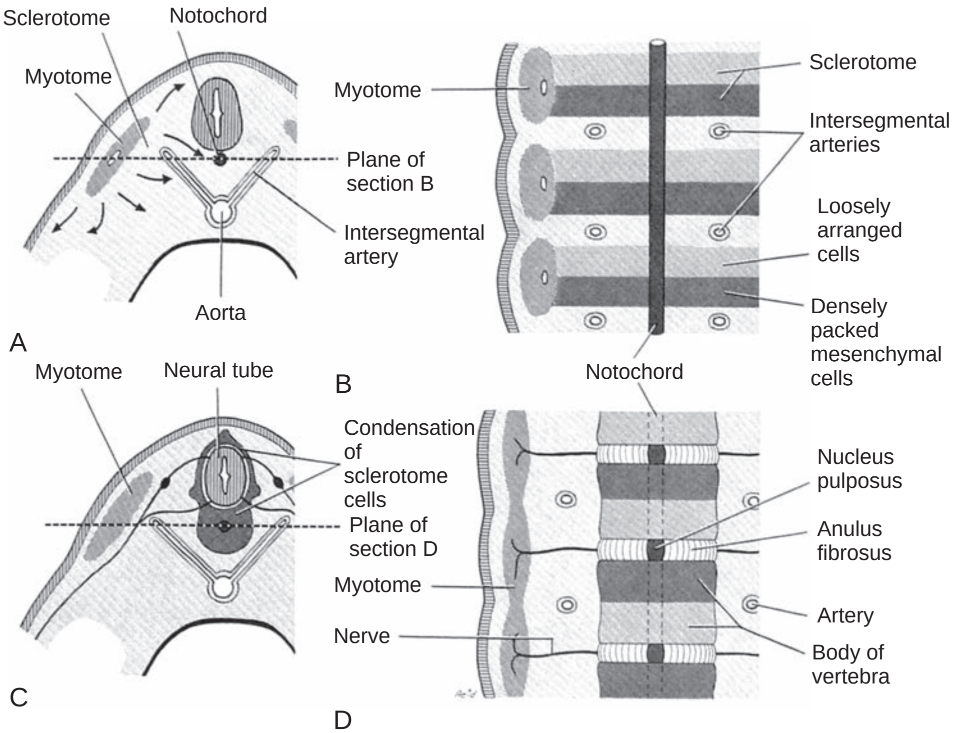

**Figure 40.2. Embryologic development of the vertebra.** (A) A partial transverse section through a 4-week embryo shows *arrows* indicating the spread of mesenchymal cells from the sclerotome region of the somite on the right. (B) A diagrammatic frontal section of this embryo shows that condensation of sclerotome cells around the notochord consists of a cranial area of loosely packed cells and a caudal area of densely packed cells. (C) A partial transverse section through a 5-week embryo shows the condensation of sclerotome cells around the notochord and the neural tube, which forms a mesenchymal vertebra. (D) A diagrammatic frontal section illustrates the vertebral body forms from the cranial and caudal halves of two successive sclerotomes. The intersegmental arteries cross the bodies of the vertebrae, and the spinal nerves lie between the vertebrae. The notochord persists as the nucleus pulposus within the intervertebral disks. *(From Moore KL.* The developing human: clinically oriented embryology. *4th ed. Philadelphia: Saunders; 1988:338.)*

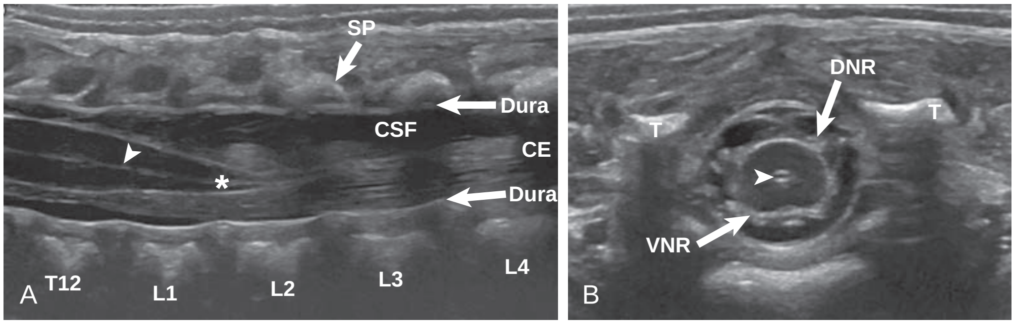

**Figure 40.3. Normal spine sonogram in a 1-day-old male infant with multiple congenital anomalies.** Longitudinal (A) and transverse (B) images demonstrate normal anatomy. Note the dura, central echo complex *(arrowheads),* and conus medullaris *(asterisk).* Other labeled structures include the vertebra (T12–L4); *CE,* cauda equina; *CSF,* cerebrospinal fluid; *DNR,* dorsal nerve roots; *SP,* spinous processes; *T,* transverse processes; *VNR,* ventral nerve roots.

The conus location is determined by counting down from the twelfth rib, as well as up from the lumbosacral junction.[11,13,15] In some cases, one may need to count down from the cervical level as well.[14] The end of the thecal sac ends at S2, and can be used as a landmark. If the conus level is still uncertain, follow-up ultrasound may be performed. Rarely, an immediate determination is important in patient management, in which case a BB can be placed at the tip of conus level (as determined by ultrasound) and a radiograph of the entire spine obtained for clarification.[16]

Spine sonography requires knowledge of normal anatomy and variants that may simulate pathology to prevent unnecessary referral and MRI. The spinal cord and conus medullaris are easily seen within the hypoechoic CSF (Fig. 40.3). Nerve roots may be observed pulsating (oscillating) with the cardiac cycle, which can be documented with cine or M-mode ultrasound. However, this motion

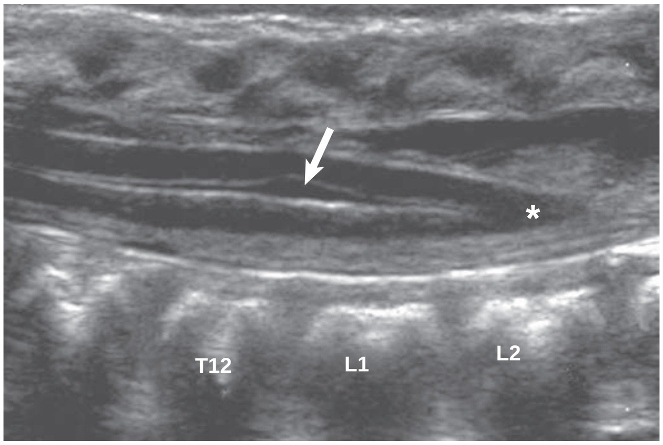

**Figure 40.4. Ventriculus terminalis in a 3-month-old girl with a deep dimple.** Longitudinal sonogram demonstrates focal distension of the distal central spinal canal *(arrow)* in the lumbar cord just above the conus medullaris *(asterisk).*

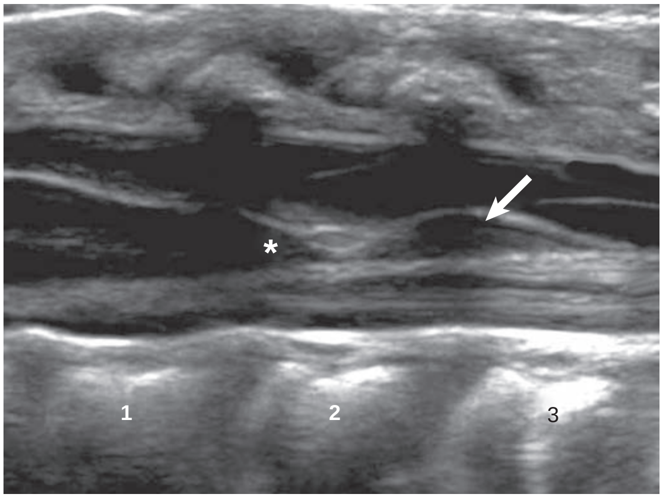

**Figure 40.5. Filar cyst in a 6-week-old male infant with an asymmetric gluteal crease.** Longitudinal sonogram shows a fusiform, midline hypoechoic cyst *(arrow)* just below the conus medullaris *(asterisk).*

is variably present in newborns.[15] The normal filum terminale, an echogenic linear structure that extends from the conus medullaris to the distal thecal sac, should be homogeneous in echotexture and morphology throughout its length, measuring less than 1 to 1.5 mm. The normal conus is located at or above the superior end plate of L3.[17] Recent reports indicate that infants with isolated borderline low conus position extending to the midbody of L3 are normal and will develop normally.[18] A conus tip below the midbody of L3 is abnormal.[17]

Common normal variants include the ventriculus terminalis, filar cysts, a prominent filum terminale, a pseudosinus tract, a cauda equina pseudomass, and a dysmorphic coccyx. The ventriculus terminalis, which is seen mostly in children younger than 5 years, and occasionally in adults, involves persistence of the normal fetal terminal ventricle. It is characterized by contiguity with the spinal canal, which forms a small fluid containing space (Fig. 40.4). It must be distinguished from a syrinx, which is larger and may grow over time.

Filar cysts are midline, fusiform, well-defined hypoechoic fluid spaces located in the cauda equina immediately below the conus medullaris (Fig. 40.5). They are seen on ultrasound in 11.8% of infants, typically are not seen on MRI, and lack pathologic description, indicating that they may be structural pseudocysts.[19] As isolated sonographic findings, they are of no known clinical significance.[19]

The normal filum terminale is more prominent than the rest of the cauda equina. It is distinguished as normal by its thickness (<1–1.5 mm) and midline location (e-Fig. 40.6). A prominent filum must be distinguished from a fibrofatty filum and a filar lipoma, which are suspected when focal hyperechogenicity and thickening (>2 mm) of the filum terminale are seen (Fig. 40.7).[20] A fibrofatty filum is most often incidental, but has been described as part of the "tight filum terminale syndrome," the symptoms of which include lower extremity weakness, spasticity, foot deformities, bladder dysfunction, scoliosis, and back pain.[21]

A pseudomass due to nerve root clumping may be seen when infants undergo sonography in the decubitus position. The finding is easily clarified by rescanning the infant prone, which resolves the mass. Pseudosinus tracts, normal fibrous cords extending from the base of dimples to the coccyx tip, are a frequent normal variant (Fig. 40.8). These echogenic cords do not have an associated mass or drain fluid as they do not connect to the thecal sac, as occurs with true dermal sinus tracts. True sinus tracts are caused by incomplete disjunction of cutaneous ectoderm from neuroectoderm.[22] A final normal variant, the misshapen or dysmorphic coccyx, is a common finding that may be discovered on physical examination when a "mass" is palpated.[23] Although the variety of dysmorphic coccygeal shapes may be impressive, the finding is of no significance (e-Fig. 40.9).

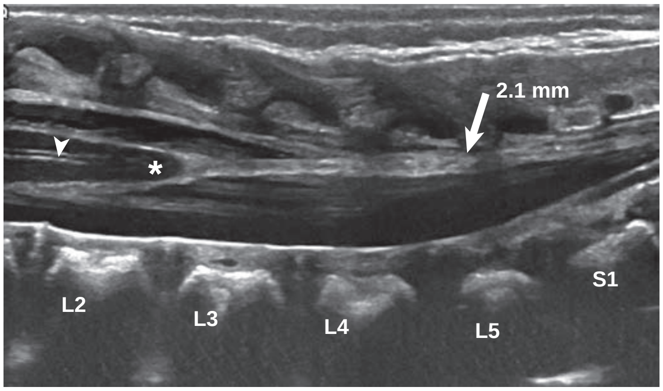

**Figure 40.7. Fatty filum in a 2-day-old male infant with VATER syndrome.** Longitudinal sonogram reveals a linear, hyperechoic, thickened (2.1 mm) filum *(arrow)* extending from the conus medullaris to the distal thecal sac. Note the normal central echo complex *(arrowhead).*

## KEY POINTS

- Spine ultrasonography and MRI are the imaging modalities of choice for the pediatric spine.
- Imaging requires knowledge of normal anatomy and variants to prevent improper clinical referral and unnecessary imaging.
- Frequent normal variants include a ventriculus terminalis, filar cyst, prominent filum terminale, pseudomass due to positional nerve root clumping, pseudosinus tract, and a dysmorphic coccyx.

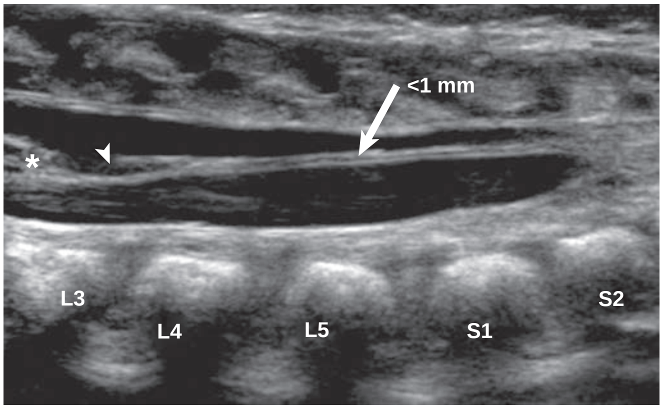

**e-Figure 40.6. Prominent filum terminale in a 1-day-old male infant with multiple congenital anomalies.** Longitudinal sonogram reveals a midline linear filum terminale *(arrow)* of normal size (<1 mm) measured at L5–S1. The filum extends from the conus tip *(asterisk)* to the distal thecal sac. Note the incidental filar cyst *(arrowhead).*

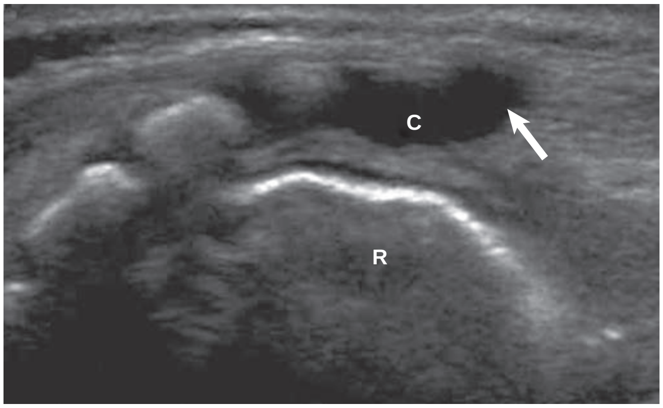

**e-Figure 40.9. Dysmorphic coccyx in a 4-week-old male infant with a palpable lump beneath a dimple high in the gluteal crease.** Longitudinal sonogram shows the normal hypoechoic coccyx *(C)* with a dysmorphic dorsal curve *(arrow).* Note the gas-filled rectum *(R).*

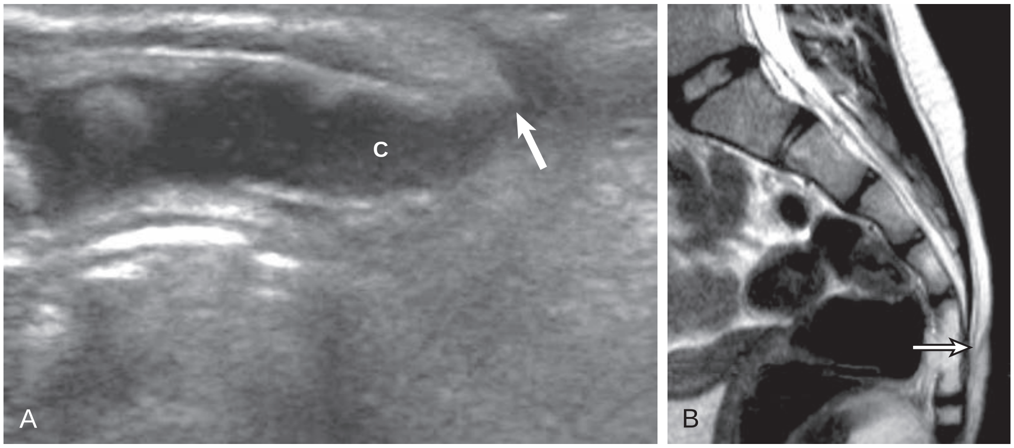

**Figure 40.8. Pseudosinus tract in a 3-month-old girl with a deep dimple in the gluteal crease.** (A) Longitudinal sonogram identifies the normal coccyx *(C)* with a cordlike hypoechoic pseudotract *(arrow)* extending to the skin dimple. (B) Follow-up MRI at age 6 months confirms the incidental pseudosinus tract *(arrow).*

## SUGGESTED READINGS

Bulas D. Fetal evaluation of spine dysraphism. *Pediatr Radiol*. 2010; 40(6):1029–1037.

Johanek AJ, Lowe LH, Moore AW. Sonography of the neonatal spine: part 1, normal anatomy, imaging pitfalls and variations that may simulate disorders. *Am J Roentgenol*. 2007;188:733–738.

Johanek AJ, Lowe LH, Moore AW. Sonography of the neonatal spine: part 2, spinal disorders. *Am J Roentgenol*. 2007;188:739–744.

## REFERENCES

Full references for this chapter can be found on www.expertconsult.com.

## REFERENCES

1. Carlson BM. *Human Embryology and Developmental Biology*. 5th ed. Philadelphia: Elsevier; 2016.
2. Moore KL, Persaud TVN, Torchia MG. *The Developing Human: Clinically Oriented Embryology*. 10th ed. Philadelphia: Elsevier; 2015.
3. Sasaki N, Kurisu J, Kengaku M. Sonic hedgehog signaling regulates actin cytoskeleton via Tiam1-Rac1 cascade during spine formation. *Mol Cell Neurosci*. 2010;45(4):335–344.
4. Nolting D, Hansen BF, Keeling J, et al. Prenatal development of the normal human vertebral corpora in different segments of the spine. *Spine*. 1998;23(21):2265–2271.
5. Turnpenny PD. Defective somitogenesis and abnormal vertebral segmentation in man. *Adv Exp Med Biol*. 2008;638:164–189.
6. Karasick D, Schweitzer ME, Vaccaro AR. The traumatized cervical spine in Klippel-Feil syndrome: imaging features. *AJR Am J Roentgenol*. 1998;170(1):85–88.
7. Drake RL, Vogel AW, Mitchell AWM. *Gray's Anatomy for Students*. Philadelphia: Churchill Livingstone/Elsevier; 2015.
8. Takase K, Sawamura Y, Igarashi K, et al. Demonstration of the artery of Adamkiewicz at multi-detector row helical CT. *Radiology*. 2002;223(1):39–45.
9. Robinson AJ, Russell S, Rimmer S. The value of ultrasonic examination of the lumbar spine in infants with specific reference to cutaneous markers of occult spinal dysraphism. *Clin Radiol*. 2005;60(1):72–77.
10. Filippigh P, Clapuyt P, Debauche C, et al. Sonographic evaluation of traumatic spinal cord lesions in the newborn infant. *Pediatr Radiol*. 1994;24(4):245–247.
11. Byrd SE, Darling CF, McLone DG. Developmental disorders of the pediatric spine. *Radiol Clin North Am*. 1991;29(4):711–752.
12. Kucera JN, Coley I, O'Hara S, et al. The simple sacral dimple: diagnostic yield of ultrasound in neonates. *Pediatr Radiol*. 2015;45(2):211–216. doi:10.1007/s00247-014-3110-1.
13. Hughes JA, De Bruyn R, Patel K, et al. Evaluation of spinal ultrasound in spinal dysraphism. *Clin Radiol*. 2003;58(3):227–233.
14. Korsvik HE, Keller MS. Sonography of occult dysraphism in neonates and infants with MR imaging correlation. *Radiographics*. 1992;12(2):297–306, discussion 307-308.
15. Unsinn KM, Geley T, Freund MC, et al. US of the spinal cord in newborns: spectrum of normal findings, variants, congenital anomalies, and acquired diseases. *Radiographics*. 2000;20(4):923–938.
16. DiPietro MA, Garver KA. Sonography of the neonatal spinal canal. In: Haller JO, ed. *Textbook of Neonatal Ultrasound*. 1st ed. New York: Parthenon; 1998.
17. Robbin ML, Filly RA, Goldstein RB. The normal location of the fetal conus medullaris. *J Ultrasound Med*. 1994;13(7):541–546.
18. Thakur NH, Lowe LH. Borderline low conus medullaris on infant lumbar sonography: what is the clinical outcome and the role of neuroimaging follow-up? *Pediatr Radiol*. 2011;41(4):483–487.
19. Irani N, Goud AR, Lowe LH. Isolated filar cyst on lumbar spine sonography in infants: a case-control study. *Pediatr Radiol*. 2006;36(12):1283–1288.
20. Rypens F, Avni EF, Matos C, et al. Atypical and equivocal sonographic features of the spinal cord in neonates. *Pediatr Radiol*. 1995;25(6):429–432.
21. Cornips EM, Vereijken IM, Beuls EA, et al. Clinical characteristics and surgical outcome in 25 cases of childhood tight filum syndrome. *Eur J Paediatr Neurol*. 2012;16(2):103–117.
22. Sewell MJ, Chiu YE, Drolet BA. Neural tube dysraphism: review of cutaneous markers and imaging. *Pediatric Dermatol*. 2015;32(2):161–170.
23. Kriss VM, Desai NS. Occult spinal dysraphism in neonates: assessment of high-risk cutaneous stigmata on sonography. *AJR Am J Roentgenol*. 1998;171(6):1687–1692.

# 41

# Spinal Cord Imaging Techniques

*Sumit Pruthi and Lisa H. Hutchison*

Pediatric spinal cord imaging relies heavily on ultrasound (US) in infants under 6 months of age and magnetic resonance imaging (MRI) thereafter.[1,2] Other imaging modalities, such as radiography, computed tomography (CT), and nuclear scintigraphy, have a limited role but may provide useful information in cases with specific questions.

## PLAIN RADIOGRAPHY

Plain radiographic spine series include frontal and lateral radiographs of the cervical, thoracic, or lumbar region. Oblique or odontoid views may be added depending on the clinical indication. Although they have limited ability to evaluate the spinal cord, radiographs are used to screen the pediatric spine and determine the most appropriate next study, particularly in acute trauma.[3] The PECARN (Pediatric Emergency Care Applied Research Network) study has identified eight variables that are highly associated with cervical spine injury (CSI). These data provide evidence-based risk stratification for pediatric CSI and help determine appropriate imaging after blunt trauma.[4]

## CONTRAST RADIOGRAPHY

Contrast radiography includes conventional angiography and myelography. As with plain radiography, contrast radiography has a limited role in pediatric spinal cord evaluation. Myelography, with or without CT, is used rarely to assess the spinal cord and thecal sac in situations where MRI is contraindicated.[5] Similarly, conventional angiography in spinal imaging is limited to diagnostic and therapeutic evaluation of dural fistulas and arteriovenous malformations, both of which are rare in children.[1]

## COMPUTED TOMOGRAPHY

CT plays a role in pediatric spinal imaging with the added risk of radiation. Multiplanar reconstructions provide superior sensitivity and specificity in delineating bony abnormalities compared with radiography and is complementary to MRI for spinal cord evaluation (Figs. 41.1 and 41.2).[3]

CT protocols must be optimized in children to limit radiation exposure. Examinations should be single phase, tailored to the specific indication, size of the patient, and region of interest. CT spine technique typically includes high-resolution 3-mm images obtained axially. Images are reformatted to submillimeter axial, sagittal, and coronal planes. Three-dimensional images may also be obtained if desired. Intravenous and, rarely, intrathecal contrast may be added for specific indications.

## ULTRASOUND

US is used for evaluation of the neonatal spinal canal and its contents.[2,6] Incompletely ossified spinal arches serve as excellent acoustic windows in infants; however, progressive ossification diminishes the window, limiting visualization of the spinal cord.[6] Because of this, US may not adequately demonstrate the spinal contents in infants over 6 months of age.[2]

Spinal US is performed with a high-frequency 7- to 12-MHz linear-array or 8- to 10-MHz curved-array transducer.[2] Imaging is performed with the infant prone in the longitudinal (sagittal) and transverse (axial) planes from the craniocervical junction to the coccyx (Fig. 41.3). Paramedian scanning is useful in older infants with smaller acoustic windows.[2] Vertebral body level is determined in multiple ways, often using an extended (panoramic) field of view to identify the lumbosacral junction and lowermost rib to confirm levels.[2,7] In cases when the level of the conus cannot be definitively assessed, correlation with radiographs is helpful. A radiopaque marker can be placed on the skin overlying the conus to correlate with the US level on spine radiographs. Real-time cine loops are obtained routinely to demonstrate the normal undulating cauda equina nerve roots during the cardiac cycle.[2] M-mode US can also be helpful in documenting motion of the cord and nerve roots.

Common indications for spine US include screening lumbosacral anomalies associated with low conus position (tethered cord), evaluation of atypical sacral dimples located greater than 2.5 cm above the anus, deep dimples in which the base cannot be visualized, and dimples with cutaneous stigmata.[7] Other indications include guidance for lumbar puncture and assessment of cause after failed lumbar puncture.[8]

## MAGNETIC RESONANCE IMAGING

### Overview

MRI is the primary modality for imaging the pediatric spinal cord because of its superior tissue contrast characteristics.[1] Not only does MRI provide detailed spinal cord evaluation, it also allows assessment of the surrounding soft tissues and osseous structures. Additional evaluation of cerebrospinal fluid flow characteristics are possible with velocity encoded phase contrast imaging, which is used most often to assess the craniocervical junction[9] (Fig. 41.4). Bone marrow changes associated with various disorders may be assessed with T1- and T2-weighted sequences.[10,11] MRI can be used to further define abnormalities identified on prenatal or antenatal US, conventional radiography, and CT.[1,10]

### Indications

The indications for pediatric spinal MRI are numerous, including evaluation of known or suspected masses, inflammatory processes, spinal trauma, metastatic spread of an intracranial primary neoplasm, spinal dysraphism, and dorsal dermal sinuses.[1,10,12]

### Pediatric Imaging Challenges

MRI is challenging when performed in infants and younger children who are unwilling or unable to cooperate for the examination. In these patients, it is crucial to use methods to control patient motion, such as swaddling, sleep deprivation, and sedation.[1] Likewise, imaging techniques that are less sensitive to motion such as noncartesian spiral or PROPELLER acquisitions can be helpful. Various sedation techniques may be used including oral and intravenous drug administration. No single recipe works for all patients and in all circumstances. Thus the sedation approach used depends on the resources available.

To produce high-quality pediatric spinal MRI, various technical challenges must be overcome. Because of the small spinal cord size, a smaller field of view, higher resolution, and decreased (or no) interslice gap must be used.[13,14] Because increasing resolution

## Abstract:

Pediatric spinal cord imaging is a complex and interesting area that relies predominantly on magnetic resonance imaging (MRI) for the evaluation, assessment of severity, and follow-up of diseases of the pediatric spinal cord. US is still utilized in neonates younger than 6 months to assess for spinal contents, its utility however diminishes significantly afterwards due to lack of an adequate acoustic window. Various other imaging modalities such as plain radiography, contrasted radiography, computed tomography (CT), and nuclear scintigraphy serve a limited role but can provide useful adjunctive information in cases with a specific question. Spinal MRI is one of the most sensitive imaging tests for detecting anatomic abnormalities of the cord and adjacent structures. That been said findings may be misleading if not closely correlated with the clinical history, clinical examination, and other tests. In this chapter, we will discuss the role of various imaging modalities and techniques available for assessment of pediatric spinal cord. The chapter will highlight the role of magnetic resonance imaging (MRI) with emphasis on optimizing the use of this modality and the challenges encountered in pediatric population.

## Keywords:

Spinal Cord
Pediatric
Imaging Techniques
Magnetic resonance imaging
Ultrasound

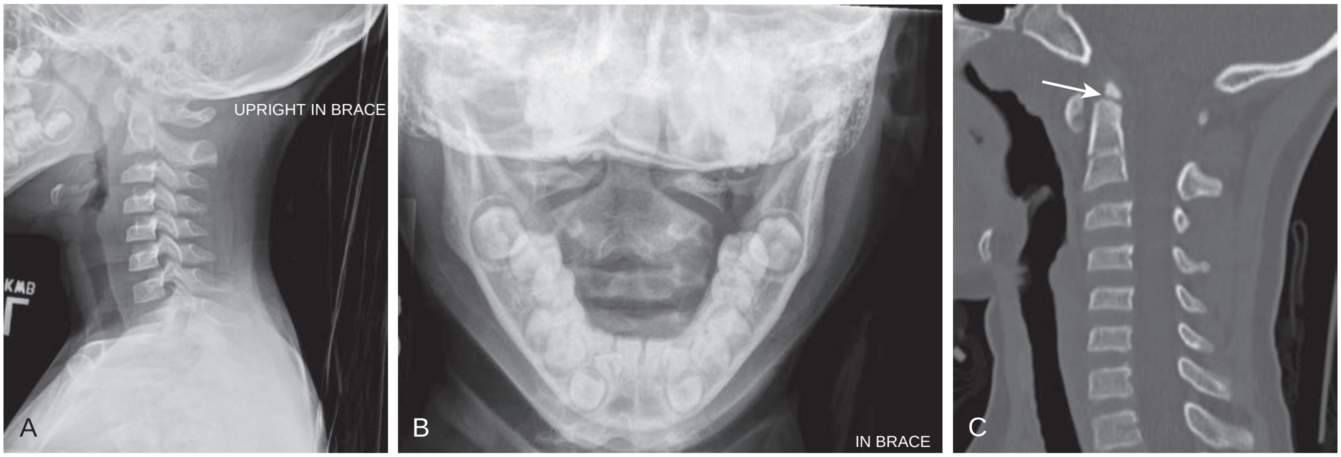

**Figure 41.1. An 8-year-old girl status post-MVC.** (A) Lateral and (B) odontoid cervical spine radiographs are normal. The alignment is normal and the dens is not completely visualized on odontoid view. (C) Sagittal reformatted CT image reveals a nondisplaced dens fracture. CT is very accurate for imaging bony spine trauma, but adds radiation risk.

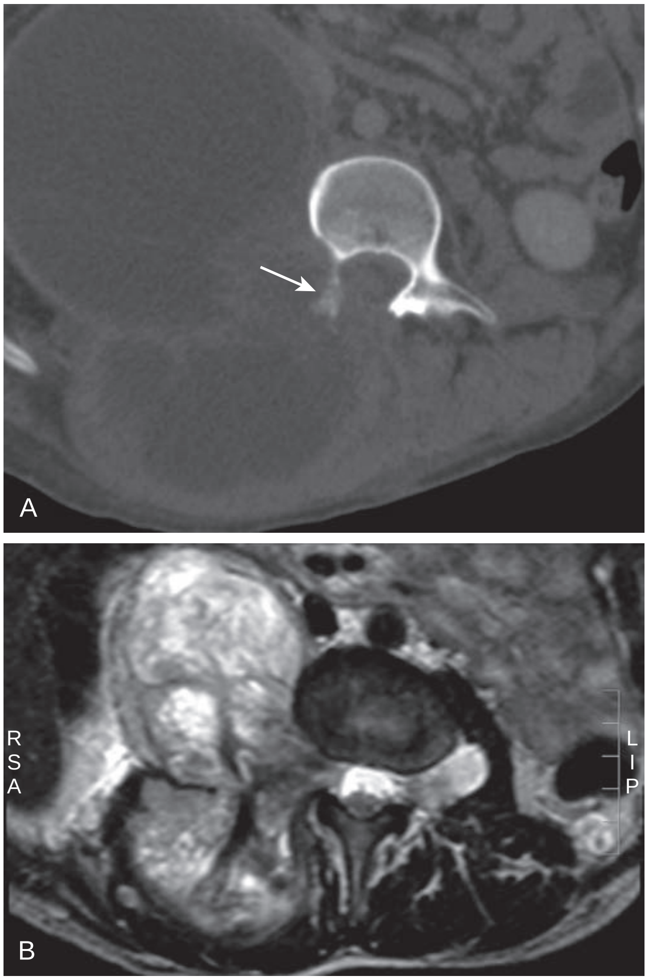

**Figure 41.2. Malignant peripheral nerve sheath tumor in a 16-year-old with neurofibromatosis.** (A) Axial CT image of the thoracolumbar spine demonstrate a large lobulated mass along the right side of the L2–L3 neural foramina. Associated bony destruction is shown on CT, whereas (B) axial T2-weighted MRI better demonstrates the internal characteristics of the mass and its intraspinal extension.

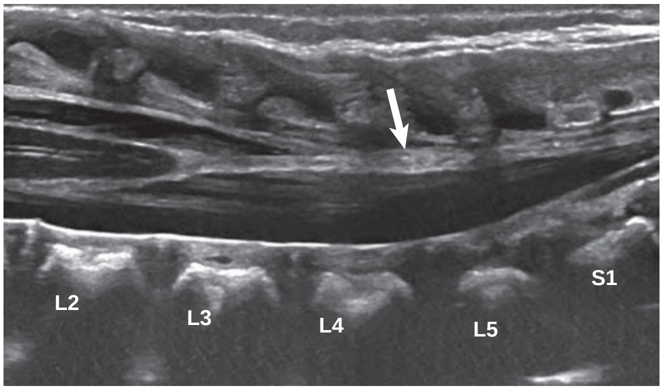

**Figure 41.3. Fatty filum in a neonate with VATER syndrome.** A longitudinal US reveals a normally positioned conus medullaris at L2–L3. Focal hyperechoic fat within the filum terminale *(arrow)* is noted. The child had normal development at 2 years of age.

and decreasing voxel volume leads to a decrease in signal-to-noise ratio (SNR), multiple image averages are frequently required, which increases the total imaging time. With longer imaging times, motion becomes more of an issue, even with proper sedation. Useful technical advances include prospective motion tracking and correction techniques, among others. Motion artifacts arising from fluid flow or respiration can be diminished with the application of flow compensation (gradient moment nulling), respiratory gating, and saturation bands.[14,15]

## High Field Strength Magnetic Resonance Imaging

With the increased utilization of 3-Tesla (T) MRI scanners, the inherent SNR limitations at 1.5 T may be overcome in some cases. With scan parameter modifications to account for differences produced by the increased field strength, 3-T MRI provides superior image quality and detail compared with 1.5 T.[16] This improvement is due to higher SNR and improved contrast between some tissues due to changes in their transverse and longitudinal relaxation times. The surplus of SNR can be used in children to decrease imaging times while maintaining image quality, potentially reducing sedation duration and increasing MRI throughput.[15-17]

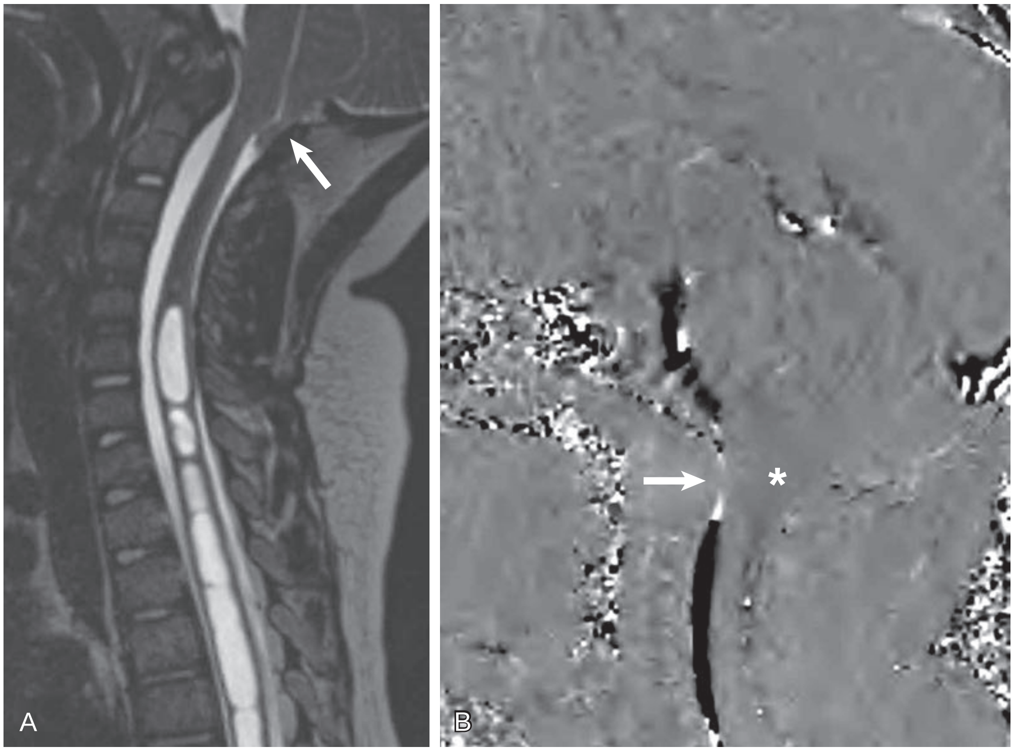

**Figure 41.4. Chiari 1 malformation in a 6-year-old boy with levothoracic scoliosis.** (A) A sagittal isometric heavily T2-weighted MRI reconstructed along the scoliotic curve shows the cerebellar tonsils extending into the posterior aspect of the upper cervical spinal canal *(arrow),* and a large multiseptated cervicothoracic syrinx. (B) Phase-contrast cerebrospinal fluid (CSF) cine (velocity encoded to 5 cm/sec) image reveals decreased CSF flow across the foramen magnum *(arrow)* and slight cerebellar tonsil motion *(asterisk).*

Although useful in the spine, high field strength MRI is not without limitations, including increased magnetic susceptibility artifact, chemical shift artifact, and specific absorption rate (SAR).[15,16] Higher field strengths markedly increase magnetic susceptibility artifact from metallic objects, tissue-bone interfaces, and tissue-air interfaces. Signal loss due to susceptibility artifact can be minimized with shorter echo times, though this can decrease tissue contrast. Metal artifacts can distort the slice profile in two-dimensional acquisitions and cause displacements in the frequency encoding direction of many sequences. These effects may be minimized by increasing the band width (slice select and/or frequency encoding), though this causes lower SNR.[18]

Chemical shift artifacts also increase with increasing field strength, carrying with it the same tradeoff of artifact reduction at the cost of lower SNR due to increased bandwidth. Finally, the increased SAR is a potential limiting factor at 3 T, although standard rates are rarely exceeded with routine imaging and can be decreased with use of multitransmit radiofrequency (RF) excitations.[16]

## Coil Selection

Use of whole body transmit coils for RF excitation is the best choice in the spine due to homogeneous excitation profile. For signal reception, surface coil arrays are the standard practice with the number of channels providing increasing image quality. Only coils covering the region of interest should be used.[19]

## Parameters

The choice of MRI pulse sequences is guided by the clinical history and study indications. Standard pediatric spinal MRI sequences include two-dimensional axial and sagittal T1- and T2-weighted images.[1,12] Coronal T2 sequences are helpful in patients with scoliosis or paraspinal lesions. Isometric sequences allow volumetric imaging with curved reformations in severe scoliosis.[20,21] Short tau inversion recovery (STIR) methods increase conspicuity of osseous and ligamentous lesions. T1 sequences with fat saturation are used with intravenous contrast administration.

Diffusion-weighted imaging (DWI) in the pediatric spine is challenging, but increasingly used. A major issue is image distortion due to single-shot echo planar imaging (EPI) methods. Read-out segmented EPI sequence is a newer technique that helps decrease distortion in diffusion data, thus improving the evaluation of many pediatric spine pathologies, including tumors, infarcts, infection, inflammatory and/or autoimmune diseases, and trauma.[22]

For example, DWI (e-Fig. 41.5) can distinguish dermoids from arachnoid cysts.[5,14] The role of diffusion tensor imaging, though currently limited, is expected to increase in future.

## Contrast Material

Contrast enhancement occurs in some lesions, allowing them to be better visualized.[23] Contrast is routinely administered when assessing neoplastic and inflammatory pathologies.[1,12] Recently, residual gadolinium has been found within the brain tissue of patients receiving multiple gadolinium-based contrast doses over their lifetimes. Although there are no known adverse clinical consequences associated with gadolinium deposition, caution should be used when using contrast media. This is particularly true in children who may receive contrast studies throughout their lives.[24]

## NUCLEAR SCINTIGRAPHY

Nuclear scintigraphy has limited use in the evaluation of the pediatric spine and surrounding structures. Other than very rare use in assessment of shunt patency and cerebrospinal fluid leaks,

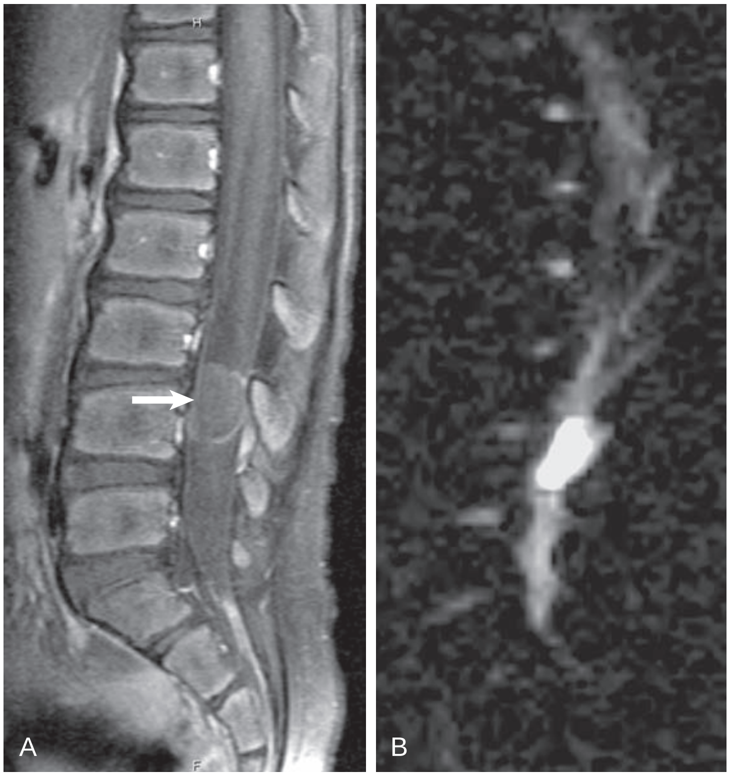

**e-Figure 41.5. Epidermoid in a 6-year-old boy with back pain.** (A) Sagittal fat-suppressed, contrast-enhanced, T1-weighted MRI identifies a well-circumscribed mass with minimal peripheral enhancement in the spinal canal posterior to L4 *(arrow)*. (B) Sagittal DWI shows hyperintense signal within the mass.

scintigraphy occasionally is used to evaluate osseous structures, such as gallium scanning for vertebral osteomyelitis and bone scintigraphy for metastatic disease. However, with the increasing utilization of positron emission tomography (PET) with[23] 18F-fluorodeoxyglucose, PET may develop a larger role in some disorders, particularly in tumors in which treatment response can be assessed.[25]

## KEY POINTS

- US can provide detailed evaluation of the pediatric spinal cord up to 6 months of age, after which time vertebral ossification limits visualization of anatomic detail.
- MRI is the primary imaging modality for pediatric spinal cord evaluation because of its superior soft tissue contrast.
- Recent advances in MRI techniques allow for the use of higher field strength and modern imaging sequences to fully evaluate pediatric spinal pathology.

## SUGGESTED READINGS

Lowe LH, Johanek AJ, Moore CW. Sonography of the neonatal spine: part 1, normal anatomy, imaging pitfalls, and variations that may simulate disease. *AJR Am J Roentgenol*. 2007;188(3):733–738.

Lowe LH, Johanek AJ, Moore CW. Sonography of the neonatal spine: part 2. Spinal disorders. *AJR Am J Roentgenol*. 2007;188(3):739–744.

Vertinsky AT, Krasnokutsky MV, Augustin M, et al. Cutting-edge imaging of the spine. *Neuroimaging Clin N Am*. 2007;17(1):117–136.

## REFERENCES

Full references for this chapter can be found on www.expertconsult.com.

## REFERENCES

1. Byrd SE, Darling CF, McLone DG, et al. MR imaging of the pediatric spine. *Magn Reson Imaging Clin N Am*. 1996;4(4):797–833.
2. Unsinn KM, Geley T, Freund MC, et al. US of the spinal cord in newborns: spectrum of normal findings, variants, congenital anomalies, and acquired diseases. *Radiographics*. 2000;20(4):923–938.
3. Moore JM, Hall J, Ditchfield M, et al. Utility of plain radiographs and MRI in cervical spine clearance in symptomatic non-obtunded pediatric patients without high-impact trauma. *Childs Nerv Syst*. 2016;[Epub ahead of print].
4. Leonard JC, Kuppermann N, Olsen C, et al. Factors associated with cervical spine injury in children after blunt trauma. *Ann Emerg Med*. 2011;58(2):145–155.
5. Khosla A, Wippold FJ Jr. CT myelography and MR imaging of extramedullary cysts of the spinal canal in adult and pediatric patients. *AJR Am J Roentgenol*. 2002;178(1):201–207.
6. Ladino Torres MF, DiPietro MA. Spine ultrasound imaging in the newborn. *Semin Ultrasound CT MR*. 2014;35(6):652–661.
7. Kriss VM, Desai NS. Occult spinal dysraphism in neonates: assessment of high-risk cutaneous stigmata on sonography. *AJR Am J Roentgenol*. 1998;171(6):1687–1692.
8. Coley BD, Shiels WE Jr, Hogan MJ. Diagnostic and interventional ultrasonography in neonatal and infant lumbar puncture. *Pediatr Radiol*. 2001;31(6):399–402.
9. Sharma A, Parsons MS, Pilgram TK. Balanced steady-state free-precession MR imaging for measuring pulsatile motion of cerebellar tonsils during the cardiac cycle: a reliability study. *Neuroradiology*. 2012;54(2):133–138.
10. Koeller KK, Rosenblum RS, Morrison AL. Neoplasms of the spinal cord and filum terminale: radiologic-pathologic correlation. *Radiographics*. 2000;20(6):1721–1749.
11. Nouh MR, Eid AF. Magnetic resonance imaging of the spinal marrow: basic understanding of the normal marrow pattern and its variant. *World J Radiol*. 2015;7(12):448–458.
12. Walker HS, Dietrich RB, Flannigan BD, et al. Magnetic resonance imaging of the pediatric spine. *Radiographics*. 1987;7(6):1129–1152.
13. Bammer R. Fazekas F. Diffusion imaging of the human spinal cord and the vertebral column. *Top Magn Reson Imaging*. 2003;14(6):461–476.
14. Vorona GA, Berman JI. Review of diffusion tensor imaging and its application in children. *Pediatr Radiol*. 2015;45(suppl 3):S375–S381.
15. Vargas MI, Delavelle J, Kohler R, et al. Brain and spine MRI artifacts at 3Tesla. *J Neuroradiol*. 2009;36(2):74–81.
16. Phalke VV, Gujar S, Quint DJ. Comparison of 3.0 T versus 1.5 T MR: imaging of the spine. *Neuroimaging Clin N Am*. 2006;16(2):240–248.
17. Fries P, Runge VM, Kirchin MA, et al. Magnetic resonance imaging of the spine at 3 Tesla. *Semin Musculoskelet Radiol*. 2008;12(3):238–252.
18. Tanenbaum LN. Clinical 3T MR imaging: mastering the challenges. *Magn Reson Imaging Clin N Am*. 2006;14(1):1–15.
19. Moriya S, Miki Y, Yokobayashi T, et al. Optimization of the number of selectable channels for spine phased array coils for transverse imaging. *Jpn J Radiol*. 2011;29(3):166–170.
20. Rumboldt Z, Marotti M. Magnetization transfer, HASTE, and FLAIR imaging. *Magn Reson Imaging Clin N Am*. 2003;11(3):471–492.
21. Weiss KL, Sun D, Weiss JL. Pediatric MR imaging with automated spine survey iterative scan technique (ASSIST). *AJNR Am J Neuroradiol*. 2009;30(4):821–824.
22. Hayes LL, Alazraki A, Wasilewski-Masker K, et al. Diffusion-weighted imaging using readout-segmented EPI reveals bony metastases from neuroblastoma. *J Pediatr Hematol Oncol*. 2016;38(7):e263–e266.
23. Hahn G, Sorge I, Gruhn B, et al. Pharmacokinetics and safety of gadobutrol-enhanced magnetic resonance imaging in pediatric patients. *Invest Radiol*. 2009;44(12):776–783.
24. McDonald RJ, McDonald JS, Kallmes DF, et al. Intracranial gadolinium deposition after contrast-enhanced MR imaging. *Radiology*. 2015;275(3):772–782.
25. Kamoto Y, Sadato N, Yonekura Y, et al. Visualization of the cervical spinal cord with FDG and high-resolution PET. *J Comput Assist Tomogr*. 1998;22(3):487–491.

# 42 Prenatal Imaging

Erin Simon Schwartz

Vast improvements have been made in the diagnosis and therapy of fetal anomalies as a result of advances in imaging and surgical technology. Nowhere is this more applicable than in the fetal spine. Ultrasonography is the primary imaging modality for fetal evaluation and helps distinguish normal from abnormal spine development and provides valuable information about spinal anomalies. Magnetic resonance imaging (MRI) is complementary to ultrasonography, as it has the advantage of better detection and depiction of associated central nervous system (CNS) and non-CNS anomalies that may have a significant impact on postnatal neurologic function and quality of life.

The major lesion of the CNS currently amenable to fetal diagnosis and intervention, and a driving force behind the use of highly detailed prenatal imaging, is open spinal dysraphism, commonly referred to as *myelomeningocele (MMC)*. The osseous detail and real-time evaluation of lower extremity configuration, position, and motion detectable with ultrasonography, combined with soft tissue and parenchymal assessments with MRI, provide the maternal-fetal-medicine specialist and pediatric neurosurgeon with highly detailed anatomic information. Because fetal surgery is not without risk to the mother and the fetus, obtaining accurate information is essential for determining surgical appropriateness and presurgical planning. When significant congenital anomalies are present outside of the CNS, information about associated spinal abnormalities is valuable for counseling and parental decision making regarding the management of the pregnancy, labor, and delivery or interruption of the pregnancy.

## IMAGING TECHNIQUES

The accuracy of identifying spinal anomalies during nontargeted screening ultrasonography varies, depending on the skill and experience of the operator. The accuracy of a referral center performing detailed targeting studies for a suspected neural tube defect (elevated maternal serum $\alpha$-fetoprotein) is close to 100%. A detailed protocol should be performed. Axial and longitudinal views of the spine should be obtained. Spine ossification progresses from 10 to 22 weeks' gestation. By 16 weeks' gestation, neural arch ossification is complete to L5. By 19 weeks, S1 is typically ossified, and by 22 weeks, S2 as well. Everted pedicles are best visualized in the transverse plane. An overlying sac may be imaged in transverse and longitudinal planes, with higher-frequency transducers showing cord tethering and placode contents (Fig. 42.1).

Because fetuses with open neural tube defects typically have Chiari II malformations, the fetal brain should be scanned initially. A small cisterna magna with rounded, small cerebellum is termed the *banana sign* and is 99% sensitive in the diagnosis of a Chiari II malformation (e-Fig. 42.2). The frontal bones may be concave and is termed the *lemon sign*. This sign is less specific, however, being present in 1% to 2% of normal fetuses, and may resolve by the third trimester. Ventriculomegaly may be present.

Fetal MRI is typically performed on 1.5 Tesla (T) magnets, although some centers are now performing fetal MRI at 3.0 T. A surface coil (torso, cardiac, or body phased-array) is used to maximize image quality. A standard localizer sequence generally facilitates quick identification of fetal position. This is used to guide the initial imaging plane, which should be appropriately aligned with the fetal anatomy in question. Subsequent imaging sequences are prescribed in orthogonal planes with respect to the fetal spine, each adjusted from the preceding image set, to account for changes in fetal position.

Ultrafast sequences are used to minimize image degradation by maternal and fetal movements. T2-weighted images provide most of the diagnostic information for the examination: single-shot fast spin echo (SSFSE) or half-Fourier acquisition single-shot turbo spin echo (HASTE) sequences at 2- to 4-mm slice thickness. Fast T1-weighted gradient echo imaging is frequently attempted but shows satisfactory contrast resolution and signal-to-noise ratio only after approximately 26 weeks' gestation. Extremely rapid gradient echo, echo planar imaging, or susceptibility weighted imaging, with their high sensitivity to paramagnetic susceptibility effect, may be used to identify osseous and vascular structures, hemorrhage, and mineralization. Steady-state free precession imaging, particularly at 3T, can improve visualization of spinal segments. Diffusion-weighted imaging can assess for acute ischemia.

## OPEN SPINAL DYSRAPHISM

### Etiology

Abnormalities in formation of the primitive neural tube (neurulation) may result from defects in disjunction, the process by which the neural tube separates from the overlying ectoderm (see also Chapter 43). MMC occurs in the third week of gestation, when a localized failure of disjunction occurs. This failure may occur anywhere along the length of the spinal cord, but it is most common in the lumbar region. The resulting lesion is an open spinal canal with a flat neural placode instead of a cylindrical spinal cord. Prenatally, ultrasonography and MRI reveals the failure of neurulation in as a posterior osteocutaneous defect. In the presence of elevation of the neural placode, secondary to expansion of the subarachnoid space, the lesion is referred to as MMC (Fig. 42.3). This is distinguished from myeloschisis, also known as *myelocele*, where an open neural tube defect exists, but the subarachnoid space is not expanded, and the neural placode remains within the confines of the dysraphic spinal canal (Fig. 42.4).

The neurologic deficits sustained by the fetus are postulated to occur in stages, a "two-hit" hypothesis. The first "hit" is the original defect in neurulation that creates the dysraphism and any associated myelodysplasia. The second "hit" is the secondary chemical or physical trauma (or both) to the neural tissue as a result of its exposure to the intrauterine environment.

A unified theory regarding the pathogenesis of the associated Chiari II malformation suggests that the open spinal canal and associated free drainage of cerebrospinal fluid (CSF) promote collapse of the primitive ventricular system and cause lack of expansion of the rhombencephalic vesicle, from which the posterior fossa develops. This lack of distension leads to an abnormally small posterior fossa and subsequent hindbrain herniation. However, the Chiari II malformation is a pancerebral anomaly, affecting broad areas of the brain. Abnormalities include herniation of the medulla, cerebellar tonsils, and vermis through the foramen magnum; a small posterior fossa; "beaking" of the tectum of the midbrain; an enlarged massa intermedia of the thalami; partial or complete callosal dysgenesis; and structural changes in the skull (Fig. 42.5). Migrational abnormalities, particularly subependymal gray matter heterotopia, are commonly seen. The cause of hydrocephalus in patients with MMC is debated. Current theories

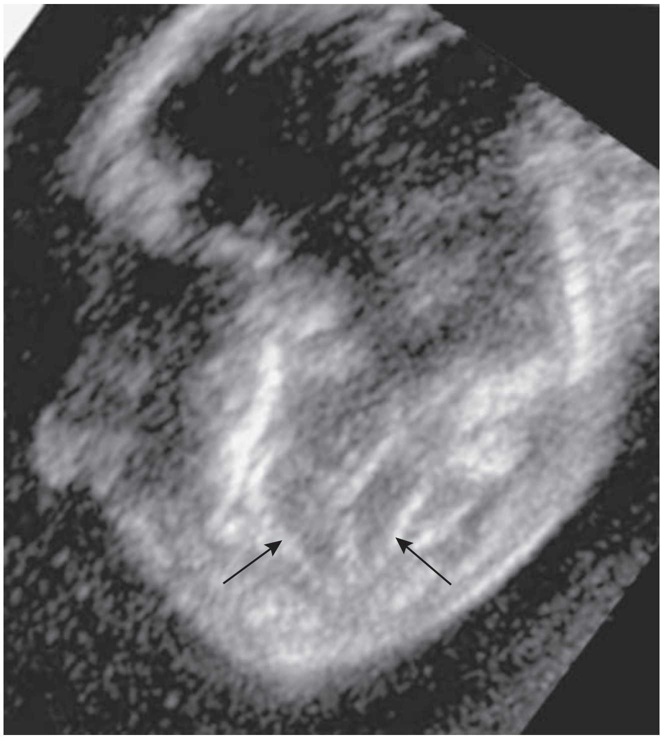

**e-Figure 42.2. Banana sign.** Axial sonogram through the posterior fossa in a 21-week fetus with a Chiari II malformation shows the crowding of the cerebellum around the brainstem that has been termed the *banana sign (arrows)*.

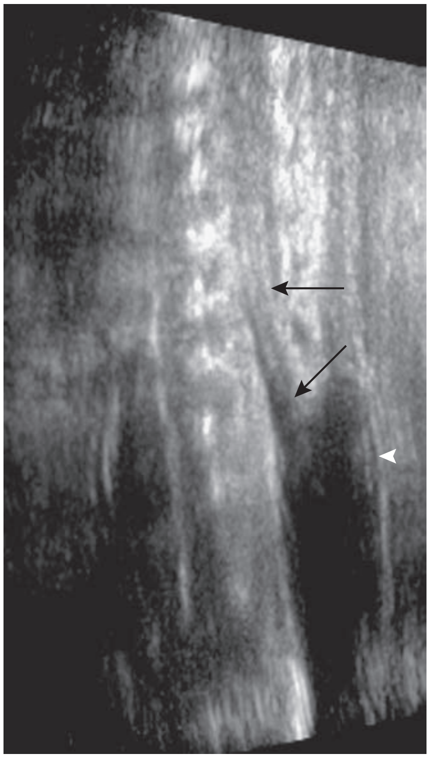

**Figure 42.1. Myelomeningocele.** Longitudinal sonogram through the lumbosacral spine in a 20-week fetus shows the defect in the posterior elements *(white arrow),* with the abnormally low spinal cord extending to the level of the defect *(black arrows)*.

include mechanical obstruction secondary to anatomic changes associated with the Chiari II malformation and dysfunctional CSF absorption. Clinically, hydrocephalus may not be present at birth but may become apparent after early postnatal closure of the defect.

## Treatment

Prenatal repair of MMC is now standard of care in the United States. While the initial intent was to preserve distal neurologic function by covering the exposed spinal cord, and some improvement in distal sensorimotor function is expected, the primary benefit of prenatal repair is the reduction in hindbrain herniation (Fig. 42.6) and substantially decreased need for ventricular shunting.

Ultrasound examination of fetuses with MMC at 18 weeks' gestational age frequently shows lower limb movements that correlate with the movements of unaffected fetuses, indicating that loss of motor function in these patients likely occurs later in gestation. Another argument for in utero repair of MMC came from the lesser degrees of neurologic deficits in many of the forms of closed spinal dysraphism in which the neural elements remain covered by skin (e.g., lipomyelomeningocele). The Management of Myelomeningocele Study (MOMS) trial found that fetuses who underwent in utero MMC repair demonstrated superior standardized test scores for motor skills and that twice as many children were walking independently at 30 months of age compared with those randomized to postnatal surgery. MMC is generally not a fatal disease in utero or postnatally, and most prenatally diagnosed infants survive to lead productive lives. Fetal surgery is associated with premature delivery and its attendant complications, including fetal/neonatal loss. Maternal complications may range from uterine rupture and hemorrhage to deep venous thrombosis.

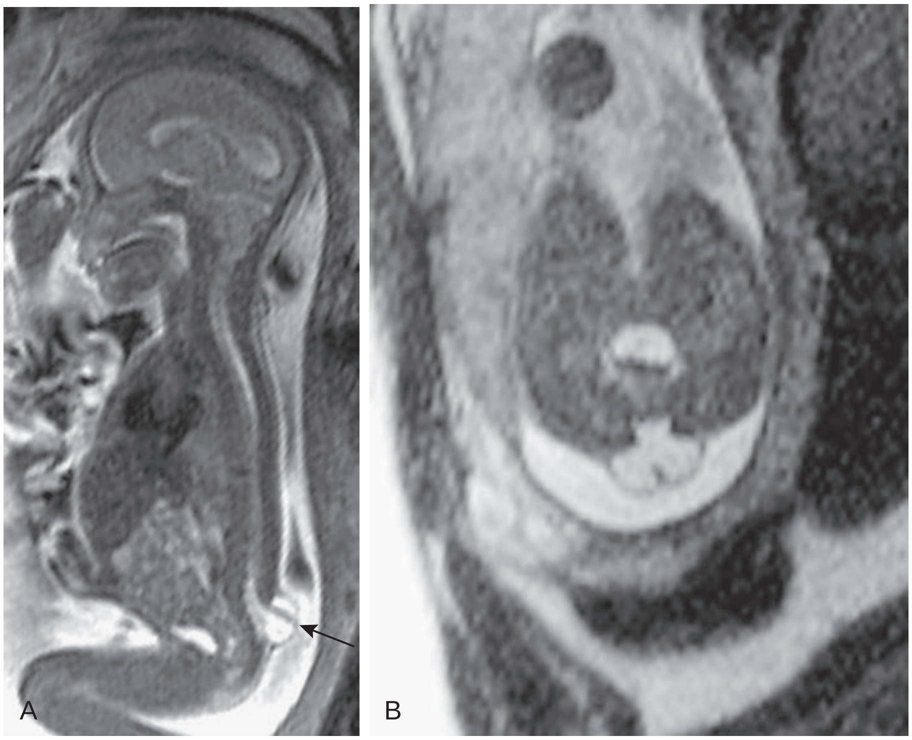

**Figure 42.3. Myelomeningocele.** (A) Sagittal HASTE magnetic resonance (MR) image in a 21-week fetus with a small myelomeningocele sac protruding at the lumbosacral junction level. The neural tissue can be readily identified traversing the sac *(arrow)*. Note the Chiari II malformation findings. (B) Axial HASTE image at the lumbosacral level shows the expanded subarachnoid space protruding through the wide posterior element deficiency. Note the neural placode outside the confines of the canal, traversing the sac.

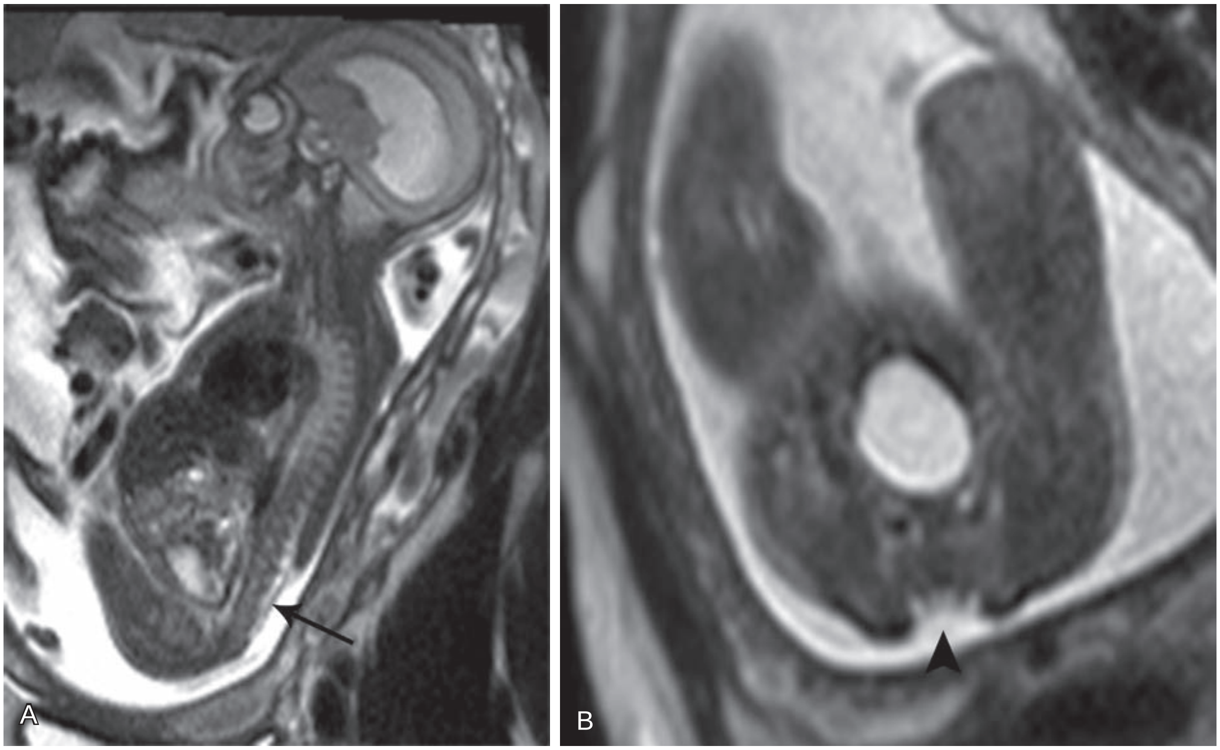

**Figure 42.4. Myeloschisis.** (A) Sagittal HASTE MR image of the spine in a 22-week fetus with a posterior spinal defect. The placode remains within the spinal canal *(arrow)*. (B) Axial HASTE image at the lumbosacral level shows the wide posterior element deficiency and neural placode within the confines of the broad canal *(arrowhead)*.

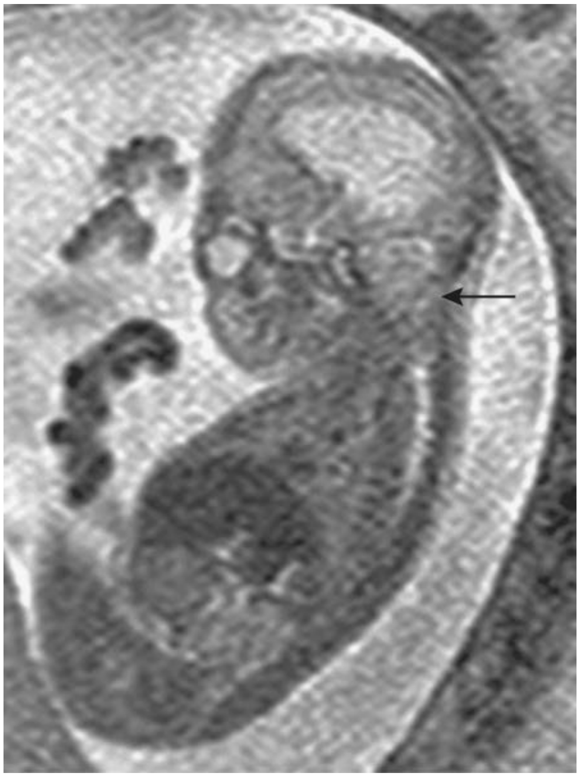

**Figure 42.5. Chiari II malformation.** Sagittal HASTE MR image at the craniocervical junction in a 19-week fetus shows the hindbrain herniation and funneling of the posterior fossa of the Chiari II malformation *(arrow)*. Note the ventriculomegaly and loss of the supratentorial subarachnoid spaces.

## CLOSED SPINAL DYSRAPHISM

Many other spinal anomalies may be recognized in utero. Although none are candidates for prenatal surgery at this time, it is important to recognize these anomalies and distinguish them from MMC to allow for proper patient counseling.

Spinal dysraphism, particularly the terminal myelocystocele, is frequently seen in association with systemic anomalies, most commonly anomalies of the genitourinary and lower gastrointestinal systems (cloacal anomalies). This is likely caused by the relative proximity of the embryonic caudal cell mass to the cloaca. The caudal cell mass is the origin of the conus medullaris, filum terminale, and lower lumbar and sacral nerve roots. Constellations of anomalies that commonly have associated congenital spinal malformations include the OEIS (*o*mphalocele, *e*xstrophy, *i*mperforate anus, *s*pinal anomalies), VACTERL (*v*ertebral, *a*nal atresia, *c*ardiac, *t*racheal, *e*sophageal, *r*enal, *l*imb), and Currarino triad (sacral hypogenesis, anorectal malformations, presacral teratoma or meningocele). The vertebral anomalies seen with OEIS and VACTERL are most commonly hemivertebrae or butterfly vertebrae can be difficult to diagnose in utero; however, they may be detected prenatally, particularly if they distort spinal alignment. More severe anomalies have been reported as well. The association of the notochord with the induction of visceral organ formation is a likely explanation of the associations between congenital vertebral and spinal cord anomalies, and thoracic or abdominal anomalies, including the VACTERL association and congenital diaphragmatic hernia.

### Lipoma With Dorsal Defect

Premature disjunction of the cutaneous ectoderm from the neuroectoderm allows mesenchyme to contact the inner portion of the developing neural tube. As the tube begins to close, the

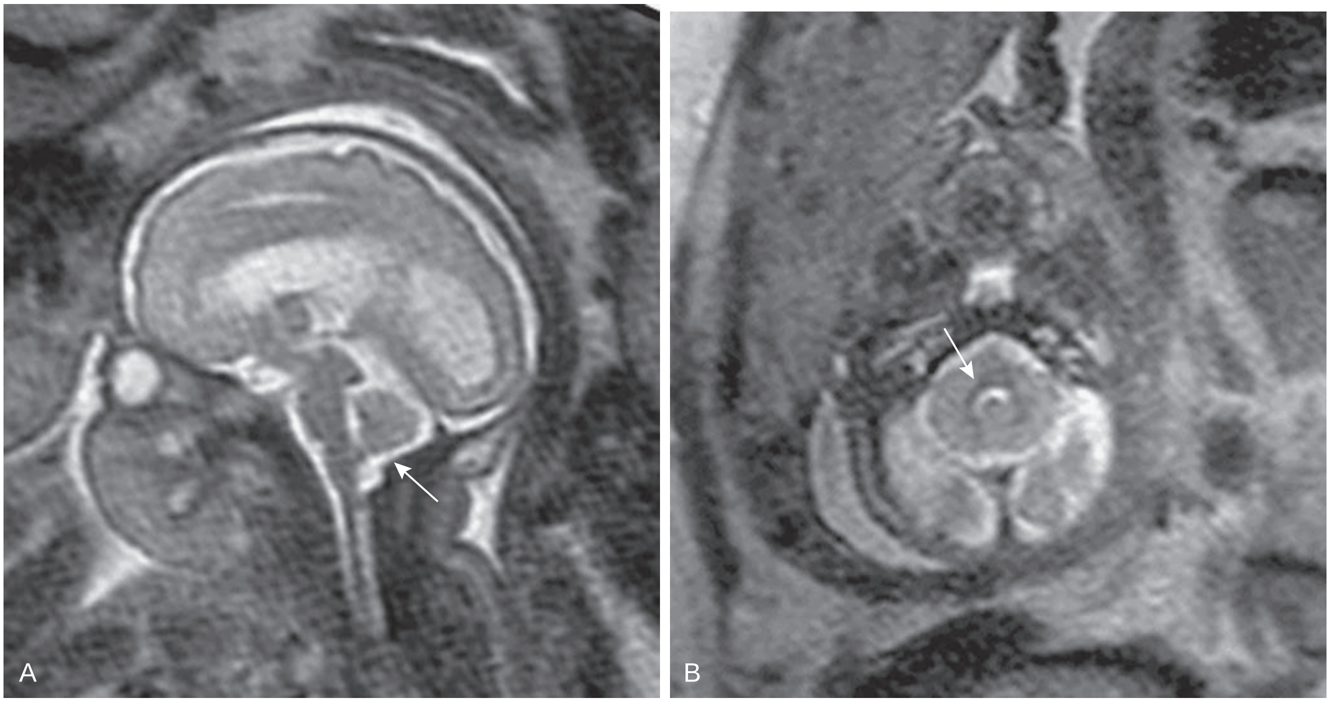

**Figure 42.6. Reversal of hindbrain herniation after fetal myelomeningocele repair.** (A) Sagittal HASTE MR image of the same fetus as in Fig. 42.5 reveals the dramatic improvement in the appearance of the brain 6 weeks after surgery. The hindbrain herniation has resolved, with return of the posterior fossa subarachnoid spaces *(arrow)*. The supratentorial subarachnoid spaces are now normal, but the ventricles remain enlarged. (B) Axial HASTE MR image through the posterior fossa shows the now normal appearance of the fourth ventricle *(arrow)*.

mesenchyme is induced to become fat, the presence of which may interfere with neurulation. This may result in a lipoma with dorsal defect—the lipomyelomeningocele or lipomyeloschisis. These lesions are skin covered and consequently not associated with the Chiari II malformation or abnormal elevation of maternal serum or amniotic fluid α-fetoprotein and acetylcholinesterase (markers of an open neural tube). A small lipomyelomeningocele may be harder to detect with screening ultrasonography but should be apparent with MRI, particularly later in the second trimester and in the third trimester (Fig. 42.7). As in the case of MMC, the distinction between lipomyelomeningocele and lipomyeloschisis lies in the location of the placode–lipoma interface with respect to the plane of the back. The expansion of the subarachnoid space characterizes the lipomyelomeningocele but, in contrast to MMC, it is much less common than its flat counterpart. The placode in the lipomyelomeningocele is much more likely to be deformed, being rotated toward the lipoma and away from the protrusion of the meninges. This poses an additional problem for the pediatric neurosurgeon performing postnatal repair because the spinal nerve roots are similarly deformed, with shortened roots on the side of the lipoma, which tether the cord. The elongated roots on the side of the meninges must be carefully negotiated as the surgeon attempts to access the placode–lipoma interface.

## Split Cord Malformation

Split cord malformation (SCM) is a developmental abnormality of the notochord. It is not always possible on imaging to distinguish between diastematomyelia (spinal cord and canal splitting) and diplomyelia (spinal cord and canal duplication). As such, SCM is the preferred terminology.

The spinal cord is split into two hemicords, often asymmetrically. This may involve the entire anteroposterior aspect of the cord or a portion of the spinal cord, the latter being quite rare. Each hemicord contains a central canal, and at least one dorsal horn and one ventral horn, from which nerve roots arise. An osseous septum between dual dural tubes (type I) or fibrous septum within a single dural tube (type II) may separate the hemicords. Occasionally, no intervening septum exists in type II lesions. SCM most commonly occurs in the lumbar region, and the type I is frequently associated with vertebral body anomalies. Cervicothoracic junction lesions may be more common than is currently reported because they are often asymptomatic owing to the absence of spinal cord tethering.

Type I SCM is readily recognized with fetal imaging (e-Fig. 42.8). An often-subtle alteration in spinal alignment from the associated anomalous vertebral bodies should be a clue that a spinal anomaly is present. When present, the osseous septum may appear on ultrasonography as an echogenic structure traversing the spinal canal. Echo planar or susceptibility weighted MRI techniques may be valuable in assessing for the osseous septum, which commonly tethers the spinal cord, and is significant in determining the extent of postnatal surgical intervention. The simple fibrous septum or cord duplication without intervening septum (type II) may be difficult to visualize prenatally, particularly when imaging is performed in the second trimester. SCM is reported to be present in 40% of MMC, although this most commonly involves only duplication or splitting of the placode, which may be impossible to detect prenatally. It is imperative to search for SCM when MMC is encountered because the spinal cord may remain tethered by the septum after MMC repair.

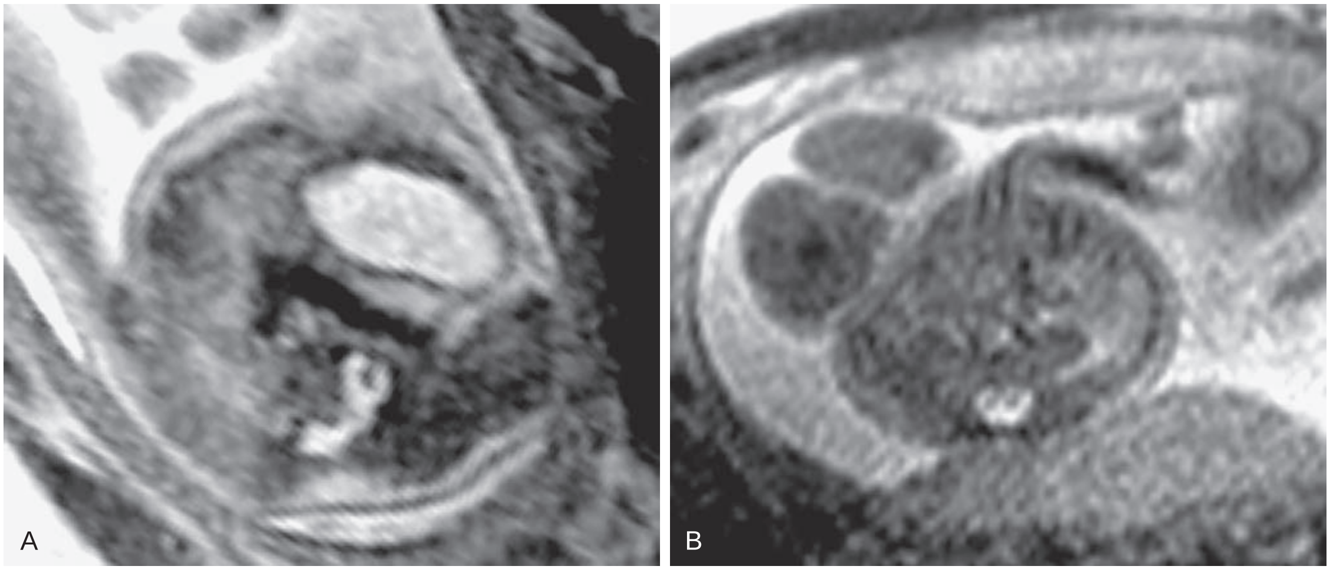

**e-Figure 42.8. Split cord malformation.** (A) Axial HASTE MR image through a type I split cord malformation. The osseous septum traversing the two canals is visible. (B) Axial HASTE MR image through a type II split cord malformation. No septum is visible between the two hemicords.

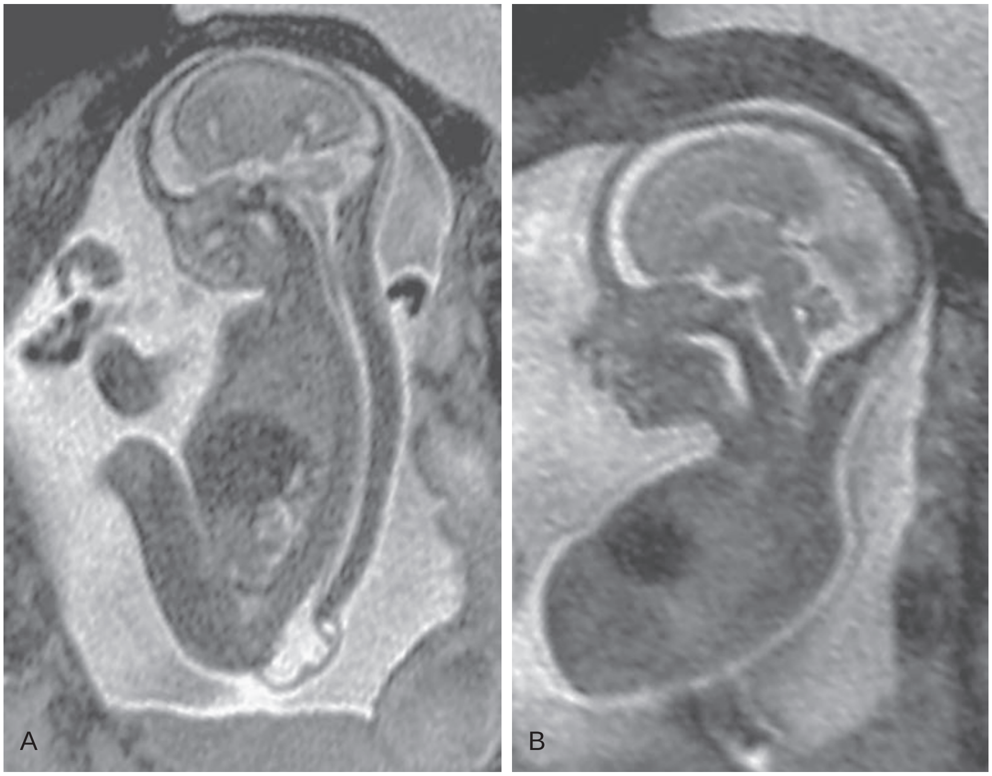

**Figure 42.7. Lipomyelomeningocele.** (A) Sagittal HASTE MR image of a 21-week fetus shows a large lumbosacral defect with neural tissue traversing the sac. The sac appears slightly thicker walled than that of a myelomeningocele, although correlation with open neural tube defect markers is required. (B) Sagittal HASTE MR image through the midline of the brain shows normal morphology, including a normal corpus callosum. No Chiari II malformation is present.

## Terminal Myelocystocele

This rare malformation may represent a severe manifestation of the persistent terminal ventricle, resulting from an inability of CSF to escape from the neural tube during its formation. The marked dilation of the distal central canal is also referred to as the *terminal ventricle* of the spinal cord, which herniates through a posterior lumbosacral spinal defect. The leptomeninges herniate around the bulbous distal spinal cord (Fig. 42.9). With prenatal imaging, terminal myelocystocele may sometimes be distinguished from the MMC with close attention to the morphology and wall thickness of the protruding sac, the absence of Chiari II malformation, and the lack of elevation of maternal serum and amniotic fluid markers of an open neural tube defect. A degree of downward displacement of the cerebellar tonsils through the foramen magnum and reduction of the infratentorial and supratentorial subarachnoid spaces may develop late in gestation with a large terminal myelocystocele, but this should not be mistaken for the Chiari II malformation.

## Meningocele

The simple posterior meningocele is characterized by a meningeal-lined CSF sac, which protrudes through a posterior osseous spinal defect (e-Fig. 42.10). The spinal cord does not enter the sac, although it may be associated with hypertrophy of the filum terminale or spinal cord tethering. Its etiology is not well understood, but some postulate that CSF pulsations cause the meninges to herniate through a focal posterior osseous defect. Most commonly encountered in the thoracic spine, these anomalies rarely may be present in utero and must be differentiated from thoracic MMC. Similar to the terminal myelocystocele and lipomyelomeningocele, these skin-covered (closed) lesions do not have an associated Chiari II malformation, and the maternal serum or amniotic fluid does not contain markers of an open neural tube defect.

## CAUDAL REGRESSION SYNDROME

Caudal regression syndrome represents a wide spectrum of anomalies, ranging from coccygeal or lumbosacral hypogenesis to sirenomelia. Infants of mothers with diabetes are the most susceptible, and the incidence is 1:7500 live births. This entity may be diagnosed prenatally, by a single lower extremity in the most extreme form to an absence or reduction in number of lower vertebral segments in lesser degrees of involvement. The less severe forms may not be detectable prenatally.

The lower extent of the spine determines the type of caudal regression and the severity of the clinical and imaging findings. The more severe form is diagnosed (type I) when the spine ends at or above the S1 level. The lowest formed level may even be in the midthoracic region. The spinal cord terminates abnormally high, with an abrupt, blunted tip, rather than the smooth taper that should be seen with a normal conus medullaris. Associated deformation of the cauda equina is common, with anterior and posterior separation of nerve roots. A spine terminating at or below the S2 level (type II) contains many fewer malformations, although the distal-most portion of the conus medullaris is absent, resulting in a blunted appearance. Typically, the spinal cord is tethered by a tight filum terminale or filum lipoma.

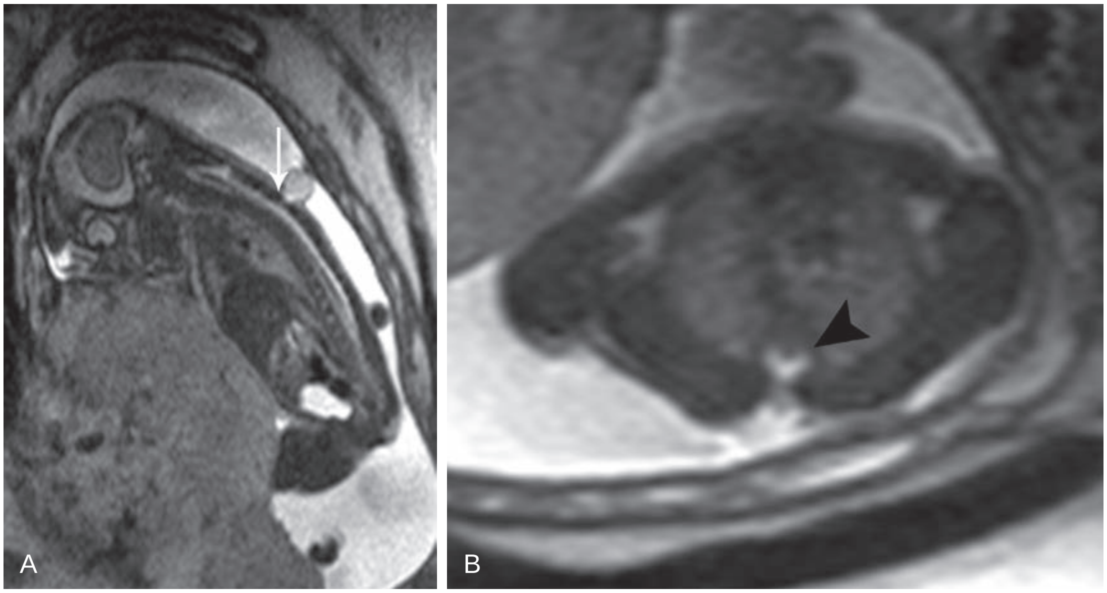

**e-Figure 42.10. Dorsal meningocele.** (A) Sagittal HASTE MR image in a 22-week fetus shows the sac protruding through the posterior osseous defect *(arrow).* (B) Note the spinal cord traversing, and not entering, the sac on the axial image *(arrowhead)*.

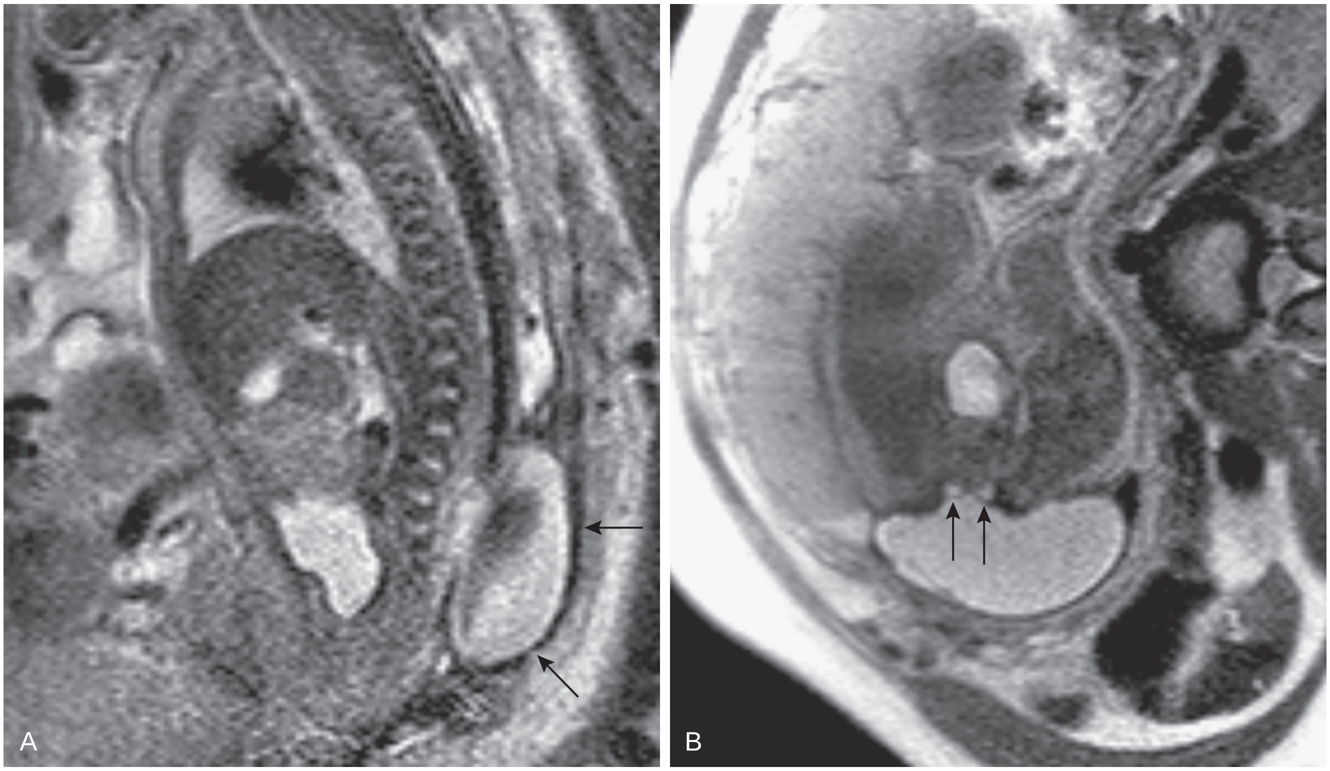

**Figure 42.9. Terminal myelocystocele.** (A) Sagittal HASTE MR image in a 32-week fetus shows the thick-walled posterior sac *(arrows)* protruding through a focal lower lumbar osseous defect. (B) Axial HASTE MR image through the osseous defect and large sac shows the distal spinal cord *(arrows)* splitting around the dilated central canal.

In unusual cases of mild caudal regression syndrome, only the tip of the conus medullaris may be absent, and the spinal cord may not be tethered. It is not expected that these findings would be detectable prenatally. This complex continuum is also associated with syndromes, including OEIS, VACTERL, and the Currarino triad.

## SEGMENTAL SPINAL DYSGENESIS

Segmental spinal dysgenesis is a rare entity in which a focal segment of the lumbar or thoracic spine is agenetic or markedly hypogenetic. The spinal cord at this level is segmentally disrupted, the distal spinal cord is often abnormally large, and a sharply angled focal kyphosis develops after birth. Some authors believe that segmental spinal dysgenesis falls within the caudal regression spectrum and that the morphology depends on the level of notochordal disruption. If the notochordal development is affected distally, caudal regression syndrome ensues, but if the lesion occurs more proximally, segmental spinal dysgenesis is seen. No known treatment is currently available to improve function in this condition, although postnatal surgical decompression has been reported to prevent worsening neurologic function.

## SECONDARY SPINAL MALALIGNMENT

Severe neurologic abnormalities, such as forms of congenital muscular dystrophy, or extensive non-CNS anomalies, including limb-body wall complex (Fig. 42.11), may result in acquired spinal malalignment. Fetal spinal malalignment can also be the secondary result of intrauterine factors, such as synechiae. While a careful evaluation of the spinal column should be performed to assess for associated vertebral anomalies, in utero scoliosis may have a purely neuromuscular or mechanical origin.

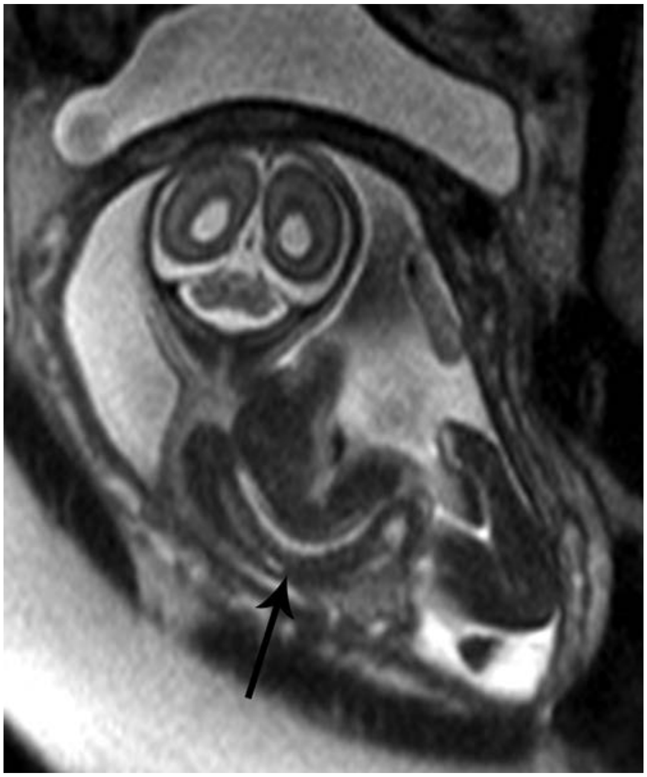

**Figure 42.11. Fetal scoliosis.** MRI in a fetus with limb-body-wall complex, the fetal spine is markedly scoliotic, turning nearly 90 degrees *(arrow)* in this 20-week fetus.

## KEY POINTS

- Careful attention to morphology in the prenatal evaluation of spinal dysraphism may aid in distinguishing between entities with similar features (i.e., MMC, lipomyelomeningocele, and meningocele).
- Prenatal surgical repair is the standard of care for the treatment of open spinal dysraphism in the United States.

## SUGGESTED READINGS

Adzick NS, Thom EA, Spong CY, et al. A randomized trial of prenatal versus postnatal repair of myelomeningocele. *N Engl J Med*. 2011;364(11):993–1004.

Glenn OA, Barkovich AJ. Magnetic resonance imaging of the fetal brain and spine: an increasingly important tool in prenatal diagnosis, part 1. *AJNR Am J Neuroradiol*. 2006;27(8):1604–1611.

Glenn OA, Barkovich AJ. Magnetic resonance imaging of the fetal brain and spine: an increasingly important tool in prenatal diagnosis: part 2. *AJNR Am J Neuroradiol*. 2006;27(9):1807–1814.

Griffiths PD, Paley MN, Widjaja E, et al. In utero magnetic resonance imaging for brain and spinal abnormalities in fetuses. *BMJ*. 2005;331(7516):562–565.

Rossi A, Gandolfo C, Morana G, et al. Current classification and imaging of congenital spinal abnormalities. *Semin Roentgenol*. 2006;41(4): 250–273.

## REFERENCES

Full references for this chapter can be found on www.expertconsult.com.

## REFERENCES

1. Adzick NS, Sutton LN, Crombleholme TM, et al. Successful fetal surgery for spina bifida [letter]. *Lancet*. 1998;352:1666–1675.
2. Bruner JP, Tulipan N, Paschall RL, et al. Fetal surgery for myelomeningocele and the incidence of shunt-dependent hydrocephalus. *JAMA*. 1999;282:1819–1825.
3. Dias MS, McLone DG. Hydrocephalus in the child with dysraphism. *Neurosurg Clin N Am*. 1993;4:715–726.
4. Hasan SJ, Keirstead HS, Muir GD, et al. Axonal regeneration contributes to repair of injured brainstem-spinal neurons in embryonic chick. *J Neurosci*. 1993;13:492–507.
5. Heffez DS, Aryanpur J, Rotellini NA, et al. Intrauterine repair of experimental surgically created dysraphism. *Neurosurgery*. 1993;32:1005–1010.
6. Inagaki T, Schoenwoif GC, Walker ML. Experimental model: change in the posterior fossa with surgically induced spina bifida aperta in mouse. *Pediatr Neurosurg*. 1997;26:185–189.
7. Johnson MP, Sutton LN, Rintoul N, et al. Fetal myelomeningocele repair: short-term clinical outcomes. *Am J Obstet Gynecol*. 2003;189:482–487.
8. Korenromp MJ, van Gool JD, Bruinese HW, et al. Early fetal leg movements in myelomeningocele [letter]. *Lancet*. 1986;1:917–918.
9. Larsen WJ. *Human Embryology*. 2nd ed. New York: Churchill Livingstone; 1997.
10. Levine D, Barnes PD, Madsen JR, et al. Central nervous system abnormalities assessed with prenatal magnetic resonance imaging. *Obstet Gynecol*. 1999;94:1011–1019.
11. McLone DG, Knepper PA. The cause of Chiari II malformation: a unified theory. *Pediatr Neurosci*. 1989;15:1–12.
12. Meuli M, Meuli-Simmen C, Hutchins GM, et al. The spinal cord lesion in human fetuses with myelomeningocele: implications for fetal surgery. *J Pediatr Surg*. 1997;32:448–452.
13. Paek BW, Farmer DL, Wilkinson CC, et al. Hindbrain herniation develops in surgically created myelomeningocele but is absent after repair in fetal lambs. *Am J Obstet Gynecol*. 2000;183:1119–1123.
14. Pilu G, Falco P, Perolo A, et al. Ultrasound evaluation of the fetal neural axis. In: Callen P, ed. *Ultrasonography in Obstetrics and Gynecology*. 4th ed. Philadelphia, PA: Saunders; 2000:277–306.
15. Sutton LN, Adzick NS, Bilaniuk LT, et al. Improvement in hindbrain herniation demonstrated by serial fetal magnetic resonance imaging following fetal surgery for myelomeningocele. *JAMA*. 1999;282:1826–1831.
16. Tulipan N, Bruner JP, Hernanz-Schulman M, et al. Effect of intrauterine myelomeningocele repair on central nervous system structure and function. *Pediatr Neurosurg*. 1999;31:183–188.
17. Tulipan N, Hernanz-Schulman M, Lowe LH, et al. Intrauterine myelomeningocele repair reverses preexisting hindbrain herniation. *Pediatr Neurosurg*. 1999;31:137–142.
18. Victoria T, Johnson AM, Edgar JC, et al. Comparison between 1.5T and 3T for fetal imaging: is there an advantage to imaging with a higher field strength? *AJR Am J Roentgenol*. 2016;206:195–201.
19. Walsh DS, Adzick NS, Sutton LN, et al. The rationale for in utero repair of myelomeningocele. *Fetal Diagn Ther*. 2001;16:312–322.

# 43

# Congenital Abnormalities of the Spine

Kevin R. Moore

## EMBRYOLOGY AND DEVELOPMENTAL ANATOMY

Spine formation begins early in gestation, commencing at the end of the second gestational week with formation of the Hensen node and continuing into the beginning of the third week with the appearance of the neural plate during gastrulation. The notochordal process forms at day 16 or 17, with transient communication of the amnion through the notochordal canal to the yolk sac and through the neurenteric canal of Kovalevsky. The spine develops in a mostly orderly progression, with the vertebral axis and spinal cord developing synchronously. The rostral spinal cord (to about the level of S2) forms by the process of primary neurulation, whereas the caudal spinal cord (below the S2 level) forms by secondary neurulation, previously referred to as canalization and retrogressive differentiation. Most congenital spinal anomalies can be explained by one or more events going awry during these processes.

The neural tube folds and closes at the end of the third gestational week, during primary neurulation; this leaves temporary cranial and caudal openings called neuropores. Normal neural tube closure by day 25 to 27 signals the end of primary neurulation. Meanwhile, the neural tube separates from the overlying ectoderm during the related process of disjunction. If disjunction occurs prematurely, perineural mesenchyme is permitted access to the neural groove and ependymal lining. This mesenchyme may differentiate into fat and prevent complete neural tube closure, which leads to the lipomatous malformation spectrum. If disjunction fails to occur (nondisjunction), an ectodermal–neuroectodermal tract forms that prevents mesenchymal migration. Nondisjunction results in posterior dysraphism, producing the open neural tube defect spectrum of myelomeningocele (MMC), dorsal dermal sinus, and myelocystocele.

The neuroepithelial cells (neuroblasts) around the inner neural tube form the mantle layer, which produces the spinal cord gray matter. The outermost layer forms the marginal layer, which subsequently myelinates to produce the spinal cord white matter. The central neuroepithelial cells differentiate into ependymal cells along the central canal. Neural crest cells along each side of the neural tube form the dorsal root ganglia, autonomic ganglia, Schwann cells, leptomeninges, and adrenal medulla.

Concurrent with the neural tube folding during primary neurulation, spinal cord development below the caudal neuropore commences within the pluripotent tissue at the caudal eminence in the process of secondary neurulation. The initially solid cell mass canalizes and becomes contiguous with the rostral neural tube that was formed by primary neurulation. By day 48, a transient ventriculus terminalis appears in the future conus. If this persists after birth, it is noted incidentally as a normal variant ventriculus terminalis (“fifth ventricle”), usually of no clinical significance. Failure of proper secondary neurulation leads to caudal spine anomalies in the caudal regression, tethered cord, or sacrococcygeal teratoma (SCT) spectra in addition to terminal myelocystocele and anterior sacral meningocele.

By the third gestational month, the spinal cord extends the entire length of the developing spinal column. In fact, the more rapid elongation of the vertebral column and dura relative to the cord produces the apparent ascent of the cord during the remainder of gestation. Most important, the conus should be at adult level soon after birth, and persistent cord termination below L2–L3 after the first month of life in a full-gestation infant is probably abnormally low-lying.

Occurring simultaneously with spinal cord development is vertebral formation. During neurulation, the notochord induces the surrounding paraxial mesoderm derived from the primitive streak to form paired somite blocks (myotomes and sclerotomes). The myotomes form the paraspinal muscles and skin cover, and the sclerotomes divide into medial and lateral formations to produce the vertebral bodies, intervertebral disks, meninges, spinal ligaments (medial), and posterior spinal elements (lateral). Failure of correct notochordal induction leads to incomplete splitting of the neural plate from the notochord, producing the split notochord syndromes (neurenteric cyst and diastematomyelia).

From day 24 until the fifth week, sclerotomal resegmentation commences, during which a horizontal sclerotomal cleft appears in the vertebra, and the caudal half of one vertebra combines with the rostral half of the vertebra below to form a “new” vertebral body. The notochord within the vertebral body degenerates, and the intervertebral notochord remnant becomes the intervertebral disk nucleus pulposus. Between days 40 and 60, the vertebrae undergo chondrification followed by subsequent ossification at distinct centers within the vertebral body and arches. This process continues past birth and into young adulthood. Ossification begins in the lower thoracic and upper lumbar regions and diverges cranially and caudally. In the cervical region, the vertebral primary ossification centers appear after the neural arch centers, beginning in the lower cervical spine (C6, C7) and proceeding rostrally. Aberrances occurring during the chondrification and ossification process produce myriad segmentation and fusion anomalies (SFAs; hemivertebrae, butterfly vertebrae, block vertebrae).[1]

## SPINAL DYSRAPHISM

*Spinal dysraphism* is a broad term that encompasses a variety of disorders that have as a common feature abnormal dorsal spine formation; it is defined as incomplete or absent fusion of midline mesenchymal, osseous, and neural structures. This term refers to large spinal defects, and not to the common spina bifida occulta, in which there is only a small cleft within a spinous process or a minor incomplete fusion of the L5 or S1 laminae. Use of the older term *spina bifida occulta* is strongly discouraged in favor of the preferred term *incomplete posterior element fusion*, because this finding is generally incidental and without clinical significance.

The osseous abnormalities associated with true spinal dysraphism may involve multiple vertebrae. Spina bifida (Latin, “cleft into two parts”) is characterized by incomplete neural arch fusion with absence of all or parts of the affected posterior elements (laminae and spinous processes). Associated segmentation anomalies of the vertebral bodies may be present, such as hemivertebrae, butterfly vertebrae, and block vertebrae.

Children with spinal dysraphism may come to medical attention with a back mass, abnormal cutaneous manifestations, gait disturbance, and bowel and bladder incontinence. Classically, spinal dysraphism is classified into two categories, based on the clinical presence or absence of a back mass. Two categories of dysraphism with back mass are described. The first category is spinal dysraphism with back mass that is not covered by skin (e.g., spina bifida aperta or cystica, MMC, myelocele); the second is spinal dysraphism

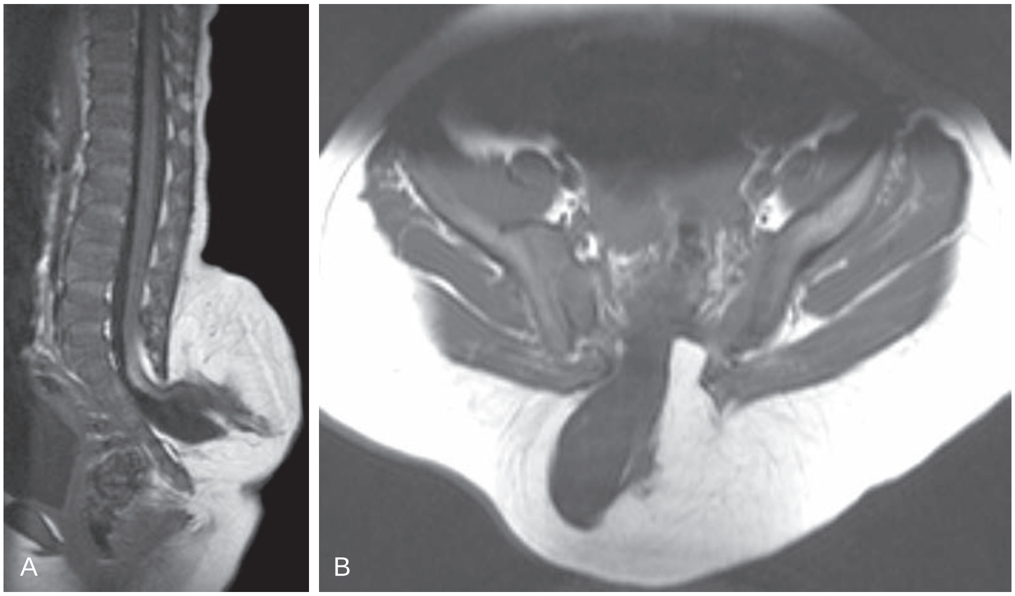

**Figure 43.1. Lipomyelomeningocele.** Sagittal (A) and axial (B) T1-weighted MRI demonstrated a typical lipomyelomeningocele, with a low-lying cord tethered into a large lipomatous malformation contiguous with the subcutaneous fat through a posterior dysraphic defect.

with skin-covered back mass (e.g., lipomyelomeningocele, myelocystocele, dorsal meningocele).

## ABNORMALITIES OF PRIMARY NEURULATION

Primary neurulation abnormalities result from premature disjunction, nondisjunction, or a combination of both.

### Premature Disjunction

Premature disjunction of the neural tube from overlying ectoderm permits perineural mesenchyme to access the neural groove and ependymal lining. This mesenchyme differentiates into fat and prevents complete neural tube closure, resulting in skin-covered lipomatous malformations with or without posterior spinal dysraphism. The most commonly observed anomalies are lipomyelocele and lipomyelomeningocele (LMC, LMMC) (Fig. 43.1) and intradural spinal lipoma (Fig. 43.2).

An LMC is a skin-covered, closed dysraphism anomaly in which the neural placode is complexed with a lipoma that is contiguous with the subcutaneous fat through a dysraphic defect, attaching to and tethering the cord. An LMMC is an LMC with enlargement of the subarachnoid space that displaces the neural placode outside of the spinal canal. In both cases, syringomyelia is a common associated finding. LMC and LMMC account for 20% to 56% of occult spinal dysraphism and 20% of skin-covered lumbosacral masses. LMMC is not affected by maternal folate metabolism, unlike the less common MMC.

Multiplanar magnetic resonance imaging (MRI) best delineates the critical anatomy and facilitates the search for additional associated sacral dysgenesis, segmentation anomalies, or visceral organ anomalies. Early surgery can arrest or prevent neurologic deficits, and progressive deterioration after untethering prompts a search for retethering or for other previously undiagnosed congenital spinal anomalies.

The spinal lipoma is subdivided into intradural (juxtamedullary, subpial) and terminal lipomas. Intradural lipomas are most common in the cervicothoracic or thoracic spine and commonly occur near the conus. They are more often dorsal than ventral, variable in size, and grow proportionally with the infant. Neurologic symptoms are representative of the lipoma level and usually progress slowly. More distal lipomas within the filum or at the filum insertion (terminal lipoma) may also present with tethered cord symptoms. A focal sacral dysraphism is frequently seen in terminal lipoma.

MRI is the imaging modality of choice for lipoma diagnosis and treatment planning. A lipoma follows fat signal on all sequences, assisting differentiation from dermoid or proteinaceous cysts. Spinal lipoma and dermal sinus are occasionally detected concurrently, so a dedicated search for multiple nondisjunction or premature disjunction anomalies is always merited.

The fatty filum (filum fibrolipoma) is an exception to the previously described clinical presentations. It is common, occurs in up to 4% to 6% of people, and is seldom symptomatic. When it does produce symptoms, they are those of a tethered cord. It is always prudent to search for other occult anomalies before ascribing responsibility for neurologic symptoms to the fatty filum.

All lipomatous lesions may be asymptomatic, but frequently they produce the clinical symptoms of tethered spinal cord. For simplicity, some authorities lump all premature disjunction disorders that feature abnormal fat together under the unifying term *lipomatous malformation*. Given the overlap of neurologic symptoms and imaging appearance between LMMC and lipoma, this simplified classification is plausible. In all cases, it is critical to assess how much fat is present and where it is located, the status and level of the spinal cord involved, the levels and extent of spinal dysraphism, and the presence or absence of other visceral or neuraxial anomalies for treatment planning because symptomatic patients usually require lipoma resection and cord untethering. MRI is the best modality for both preoperative planning and for follow-up after symptom recurrence.

### Nondisjunction

In contrast to lipomatous malformations, anomalies that result from nondisjunction occur when the neural tube fails to dissociate from adjacent cutaneous tissue. The simplest and least extensive variation is the dorsal dermal sinus, which occurs when a single connection persists and forms a fibrous cord from a skin dimple to the dural sac, conus, or central spinal cord canal.[2] It is important to distinguish dermal sinus from its clinically asymptomatic mimic,

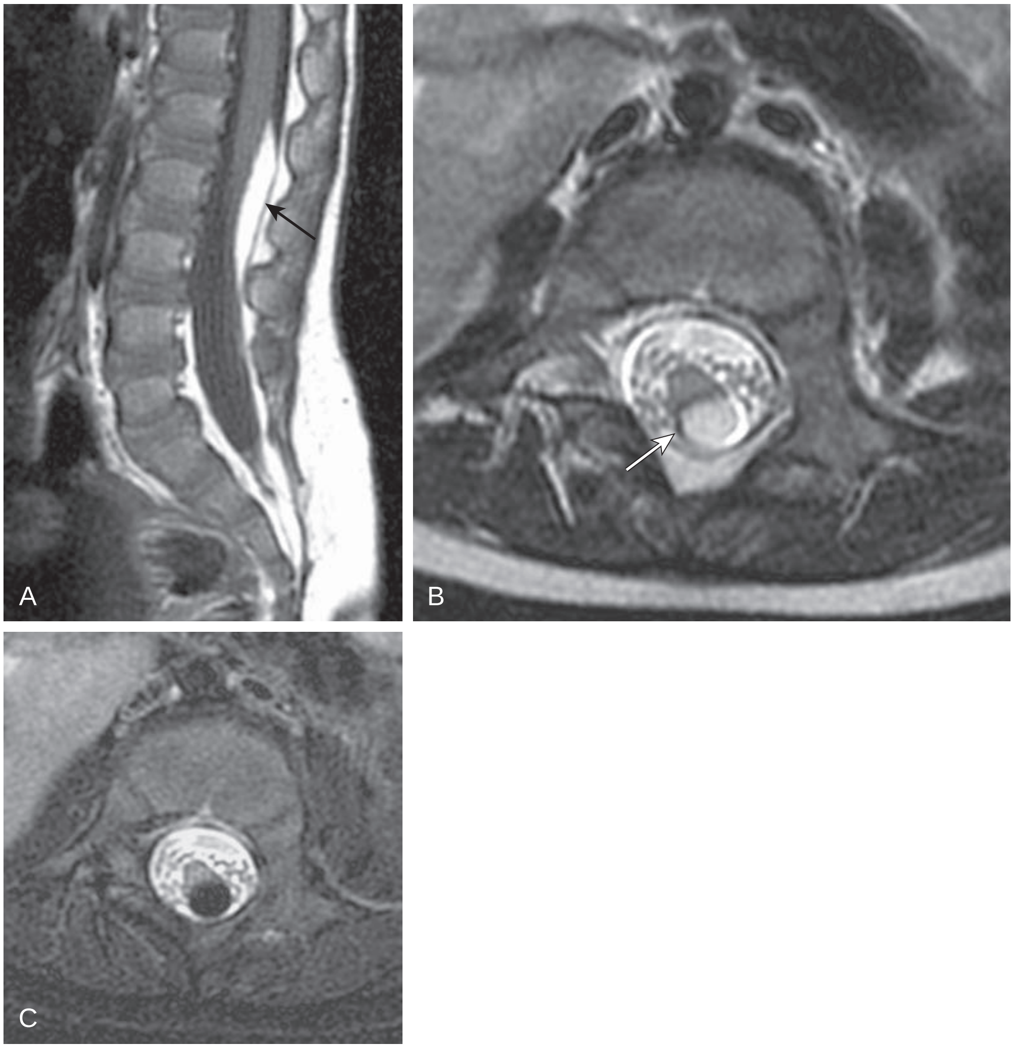

**Figure 43.2. Juxtamedullary (subpial) spinal lipoma.** (A) Sagittal T1-weighted MRI shows a small subpial intradural lipoma *(arrow)* adherent to the dorsal conus surface. (B) Axial T2-weighted MRI confirms direct contiguity of the neural placode with the lipoma. Note chemical shift artifact *(arrow)* in the frequency encoding direction, indicating fat. (C) Axial fat-saturated T2-weighted MRI confirms fat content by homogeneous signal loss within the lipoma.

simple coccygeal dimple (Fig. 43.3). The low sacral or coccygeal sinus originates from a low skin dimple and attaches to the coccyx via a short fibrous tract. These dimples are nearly always found within the intergluteal cleft, never communicate with the spinal canal, and require no treatment or imaging if there are no associated abnormalities.

Conversely, the true congenital dorsal dermal sinus tract (DST; Fig. 43.4) usually has an atypical dimple at the ostium that is larger (>5 mm), often asymmetric, and remote (>2.5 cm) from the anus. It may also be found in combination with other cutaneous anomalies, such as a hair patch or vascular lesion. The most common DST location is in the lumbosacral spine, followed by the occiput. In all dermal sinus cases, there is some degree of focal dysraphism, which may be as subtle as a bifid spinous process. The sinus tract cord is epithelial-cell lined and may or may not be canalized. When patent, it exposes the patient to an elevated risk of meningitis. It is critical to look for this anomaly in all patients with atypical skin dimples, cutaneous back lesions, or lipomas. Additionally, 30% to 50% of DSTs may have an associated dermoid or epidermoid cyst. These patients should be imaged with MRI. The best MRI sequence is usually sagittal T1-weighted MRI, windowed widely so that the hypointense tract is visualized as a gray cord immersed in bright fat that passes inferiorly and ventrally to the lumbodorsal fascia; it then turns upward to ascend within the spinal canal, often tenting the dorsal dura at the point of entry. Dermal sinuses are surgically excised to prevent meningitis and to untether the spinal cord.

More extensive nondisjunction produces MMC (Fig. 43.5). Infants come to medical attention with an open, red, weeping skin defect on the back that features protruding neural elements. Most MMC lesions are either lumbosacral or thoracolumbar, but cervical and thoracic MMCs occur. Lesion level and severity of associated hydrocephalus determine the patient's prognosis. MMCs are linked to methylenetetrahydrofolate-reductase (MTHFR) mutations with abnormal folate metabolism, and are associated with maternal folate deficiency. *PAX3* paired box gene derangements and trisomy 13 or 18 (14% of fetuses with neural tube defect) are also described. These gene derangements and folate metabolism abnormalities are postulated to interfere with carbohydrate molecule expression on the neuroectodermal surface, which causes neural tube closure to fail. Prevalence in the United States is 2 in 10,000 live births, and it is more common in females by a ratio of 3 : 1. The prevalence

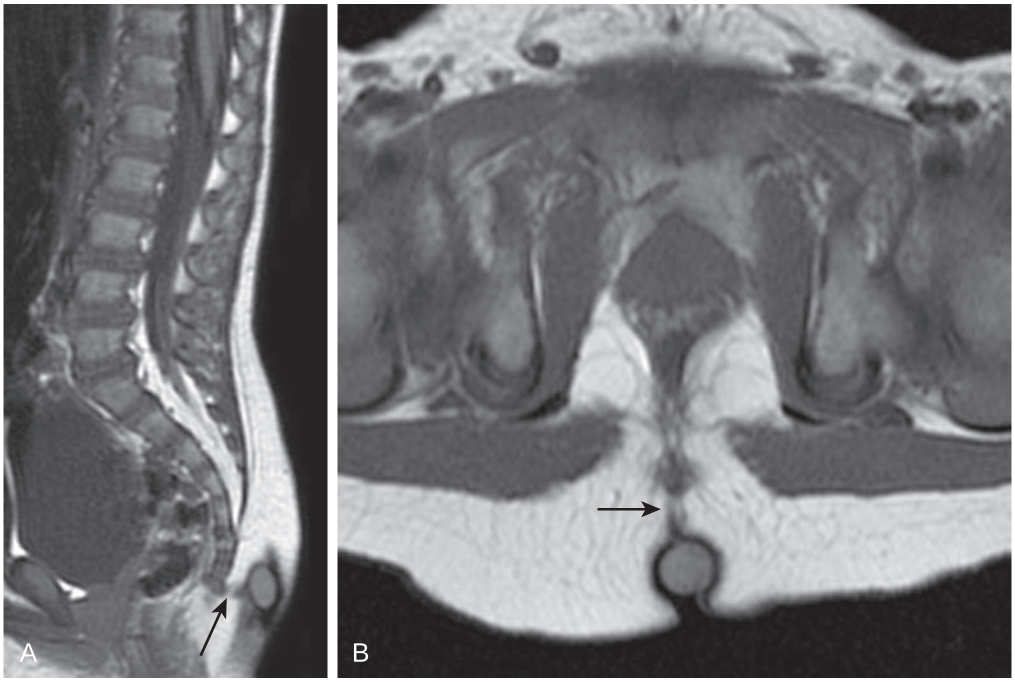

**Figure 43.3. Simple sacrococcygeal dimple.** Sagittal (A) and axial (B) T1-weighted MRI demonstrates a low sacral dimple within the intergluteal cleft, marked by a hyperintense vitamin E capsule. The short fibrous tract *(arrow)* that extends from the dimple to the coccyx tip confirms the diagnosis.

of MMC decreased 23% from 1995 to 2004, attributed to more widespread folate fortification of food.

Associated orthopedic and neuraxial anomalies are common, and Chiari II malformation is universally present. Complications of the Chiari II malformation are the major cause of death in these patients. MMC patients should have a stable neurologic deficit after MMC closure, and a progressive or new neural deficit should prompt an imaging search for other occult spinal abnormalities, such as diastematomyelia, or complications of MMC repair, such as cord tethering, dural ring constriction, spinal cord ischemia, or syrinx. MRI is the best modality for postoperative imaging in the clinical context of progressive deficits. Imaging before MMC closure is rarely indicated.

## ANOMALIES OF THE CAUDAL CELL MASS

Caudal cell mass anomalies are a diverse group of anomalies that result from aberrant secondary neurulation, postulated to be an insult to the caudal cell mass before the fourth gestational week. Most cases are sporadic, although a dominantly inherited defect in the *HLXB9* gene has been described. The mothers of 15% to 20% of these infants are diabetic, the offspring of 1% of diabetic mothers are afflicted, and an association has been found with VACTERL syndrome (***v***ertebral, ***a***nal atresia, ***c***ardiac, ***t***racheal, ***e***sophageal, ***r***enal, ***l***imb), omphalocele, bladder exstrophy, imperforate anus, and the Currarino triad. The range of severity is substantial, from clinically unapparent mild dysgenesis to absence of the lower body.

Hypogenesis or agenesis of the caudal cell mass produces caudal regression syndrome (CRS; Fig. 43.6). Two types are described. The more severe type 1 CRS features a foreshortened terminal vertebral column, high-lying wedge-shaped conus termination, and more severe associated visceral and orthopedic anomalies. The less severe type 2 CRS has a low-lying tethered spinal cord with milder associated malformations. In general, the higher the cord termination, the more severe the sacral anomalies. The most severe CRS presentations are lumbosacral agenesis, in which the spine terminates at the lower thoracic level, and severe sacral dysgenesis, with fused lower extremities in a "mermaid" configuration (sirenomelia).[4] In contrast, the mildest CRS cases may manifest merely as a missing terminal sacral segment identified on imaging that is clinically asymptomatic. CRS is associated with myriad other visceral abnormalities, including renal or pulmonary hypoplasia and anorectal malformations. Other commonly associated spinal malformations include open dysraphism, vertebral SFAs, and split-cord malformations.

Segmental spinal dysgenesis (SSD) is a very rare dysraphic anomaly characterized by segmental thoracolumbar or lumbar vertebral and spinal cord dysgenesis or agenesis. Congenital thoracic or lumbar kyphosis is characteristic, with a palpable dorsal bone spur located at the gibbous apex. The upper spinal cord is normal, but the cord segment below the dysgenetic segment is bulky, thickened, and low-lying. The spinal canal proximal and distal to the dysgenetic level is of normal caliber. Some authors believe that SSD and CRS represent different phenotypes along a single malformation spectrum, and that spinal morphology depends on the level of developmental disruption. If development is affected distally, CRS results, but if the lesion occurs more proximally, SSD is observed.

Perhaps the most common entity within the caudal cell mass dysplasia spectrum is tethered cord syndrome (TCS), which manifests clinically as gait spasticity, low back and leg pain that is worse in the morning, lower extremity sensory abnormalities, and/or bladder dysfunction. TCS patients are most likely to present during periods of rapid somatic growth. TCS refers strictly to patients with a low-lying cord and thickened filum, not those with other spine and cord abnormalities, although in fact those patients may be similar in clinical presentation and may be considered "clinically tethered." It is important to consider TCS a distinct clinical diagnosis, with imaging relegated to the role of preoperative planning rather than establishing the primary diagnosis. On imaging, TCS manifests either as a taut spinal cord without definitive conus or a low-lying conus (Fig. 43.7). The filum is frequently thickened and shortened, and an associated terminal

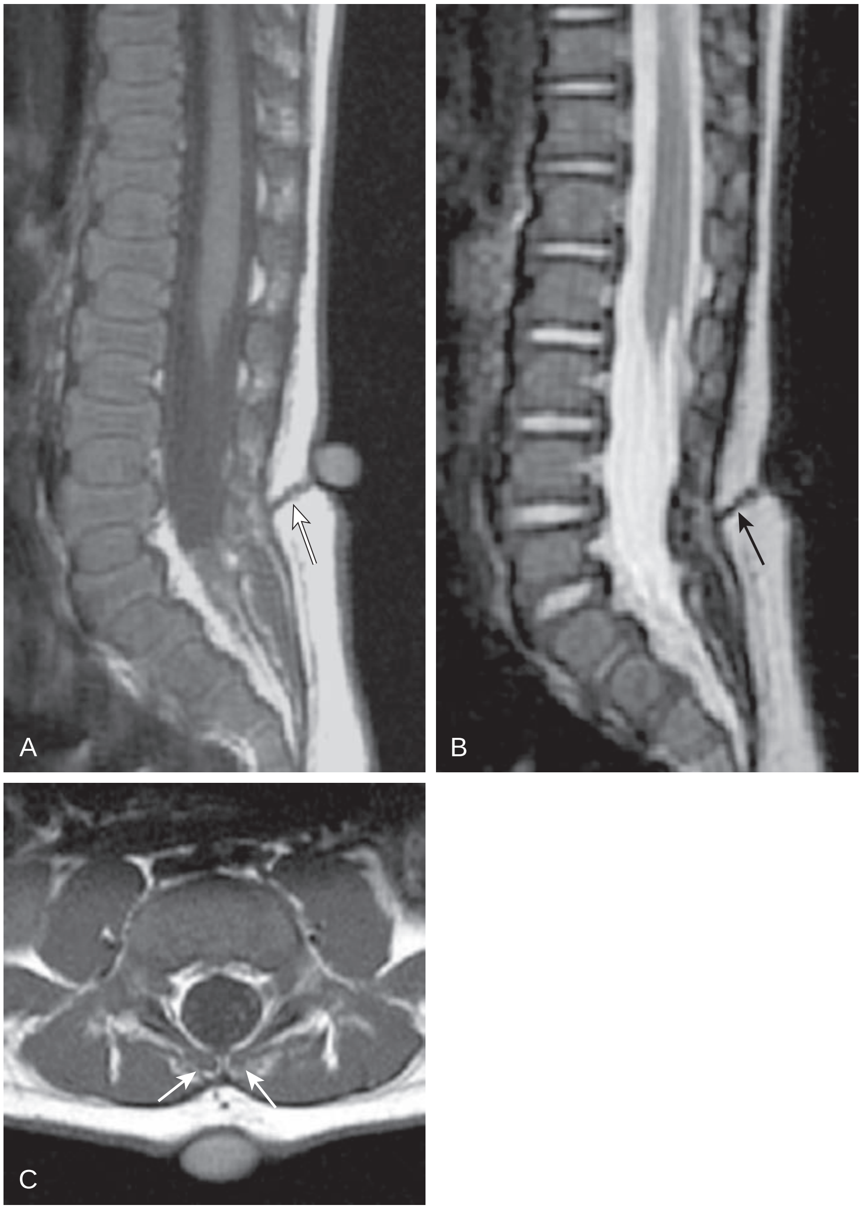

**Figure 43.4. Dorsal dermal sinus.** Sagittal T1-weighted (A) and T2-weighted (B) MRI demonstrates a low-lying spinal cord tethered by a dorsal dermal sinus tract *(arrows).* The skin opening is marked by a vitamin E capsule. Axial T1-weighted MRI (C) confirms the tract accessing the dural sac through a bifid spinous process *(arrows).*

lipoma may be present. Symptomatic patients may benefit from surgery, but it is crucial to exclude other associated anomalies.

Two other important rare presentations of caudal cell mass dysplasia are the anterior sacral meningocele (ASM) and the terminal myelocystocele. ASM features a large anterior meningocele outpouching that traverses an enlarged sacral foramen and produces a presacral cystic mass. This may be clinically mistaken for a SCT and may prompt neuroimaging. Most ASMs are sporadic, but a minority show an inherited predisposition within the Currarino triad or in syndromes that feature dural dysplasia, such as neurofibromatosis type 1 (NF1) and Marfan syndrome. As with other caudal cell mass dysplasias, additional congenital abnormalities may be found, such as anorectal malformations, caudal dysgenesis, and dermoid or epidermoid cysts. Fortunately, imaging is highly characteristic in the more common simple form, with a presacral cystic mass that connects to the thecal sac through an enlarged sacral neural foramen (Fig. 43.8). Complex ASMs with fat or neural elements are also recognized by their extension through the neural foramen. Terminal myelocystocele is a very rare malformation that manifests as a hydromyelic spinal cord that traverses a meningocele to terminate in a skin-covered myelocystocele (e-Fig. 43.9). Associated anorectal and visceral anomalies are common. Infants with terminal myelocystocele may be neurologically intact at birth but subsequently lose neurologic function.

Finally, if the primitive streak incompletely regresses and leaves a caudal totipotential cell rest remnant, an SCT (Fig. 43.10) may result. SCTs demonstrate tissue from all three cell layers and contain varying proportions of mature and immature elements. These are surgically graded, according to the American Academy of Pediatrics (AAP) classification, based on the proportion of internal (pelvic) and external components from type 1 (all external) to type 4 (all internal). Prognosis is determined by the grade and by the presence or absence of mature or malignant components. External tumors, mature elements, and younger patient age predict

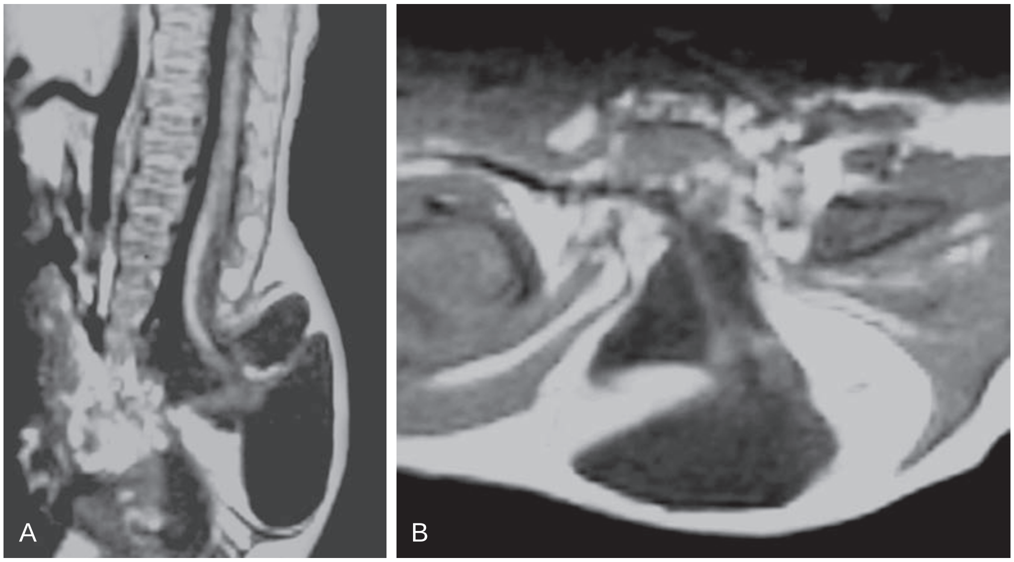

**e-Figure 43.9. Terminal myelocystocele.** Sagittal T1-weighted MRI (A) depicts a low-lying hydromyelic cord with terminal cyst projecting through a sacral meningocele. Axial T1-weighted MRI (B) confirms the origin of the terminal cyst as the hydromyelic terminal central canal.

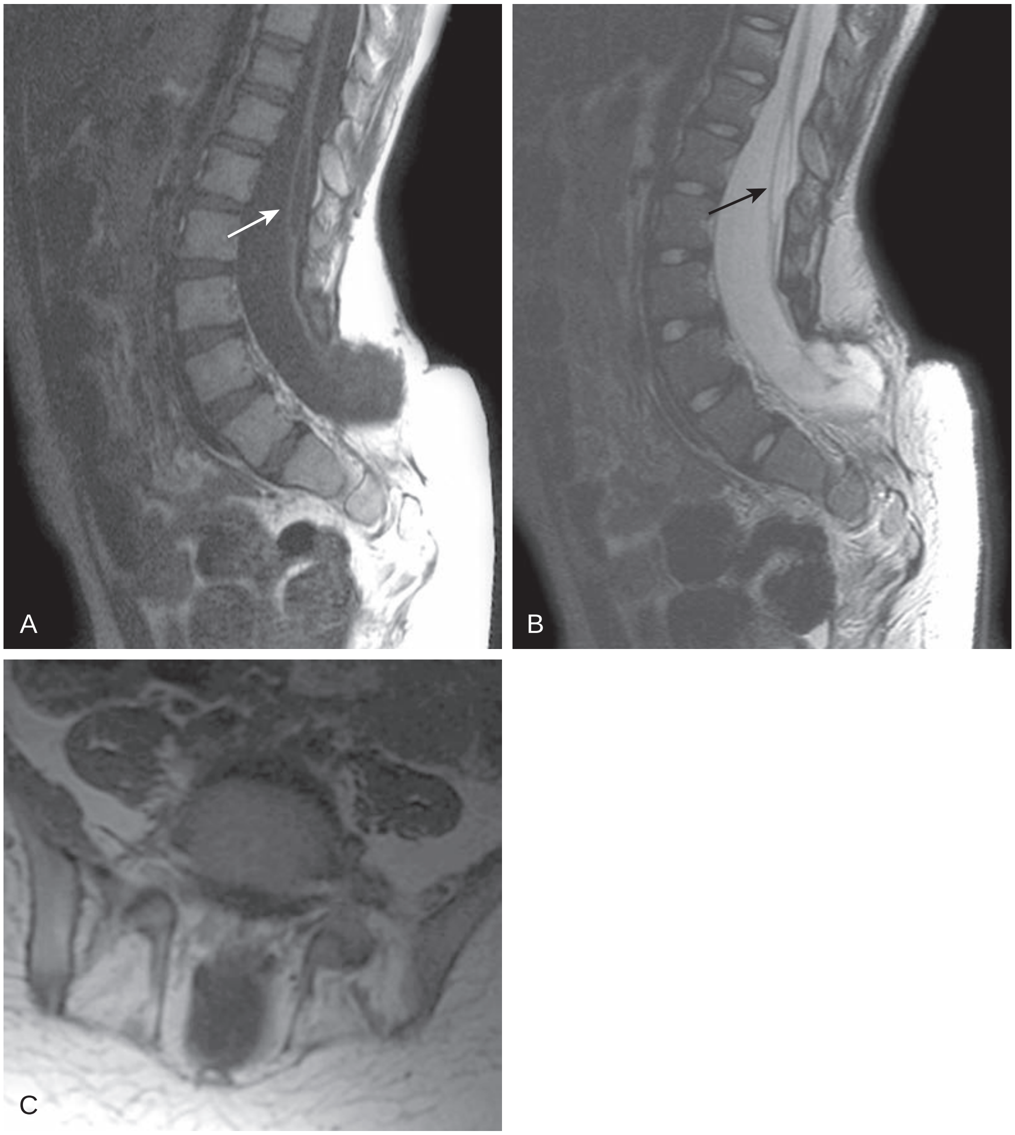

**Figure 43.5. Myelomeningocele.** Sagittal T1-weighted (A) and T2-weighted (B) MRI shows the postoperative appearance of the spine after myelomeningocele closure. The large dysraphic defect is now covered with skin, and the attenuated distal spinal cord is scarred into the closure. A small syrinx is present *(arrow).* Axial T1-weighted MRI (C) reveals the protrusion of the distal sac through parallel dysraphic posterior elements.

a better outcome. The surgeon must resect the coccyx to prevent recurrence. Fetal and early infancy morbidity and mortality are related mostly to cardiac failure from intratumoral shunting and associated visceral anomalies, whereas later mortality is related to lesion malignancy.

MRI is the best modality for preoperative planning and staging for all caudal cell mass anomalies.[8] Computed tomography (CT) has a more limited role, such as in screening for visceral organ anomalies or evaluating bones. Ultrasonography may be helpful for initial newborn screening, because it can be performed portably in the newborn nursery, but it usually does not provide all the necessary information for surgical planning.

## ANOMALIES OF NOTOCHORD DEVELOPMENT

Neurenteric cyst (e-Fig. 43.11) consists of an intraspinal cyst lined by enteric mucosa, and is most common in the thoracic spine, followed by the cervical spine. Such cysts putatively arise from an abnormal connection between primitive endoderm and ectoderm that persists beyond the third embryonic week. Whereas normally the notochord separates ventral endoderm (foregut) and dorsal ectoderm (skin, spinal cord) during embryogenesis, in a neurenteric cyst a separation failure "splits" the notochord and hinders the development of mesoderm, which traps a small piece of primitive gut within the developing spinal canal. This gut remnant may become isolated, forming a cyst, or it may maintain connections with gut or skin (or both); this produces the spectrum of fistulas and sinuses that constitute the spectrum of dorsal-enteric spinal anomalies. The most severe malformations remain in communication through the primitive vertebral osseous canal of Kovalevsky, but even mild cases usually show some vertebral segmentation anomalies on close inspection. MRI best demonstrates the cyst and its relationship to the spinal cord, as well as connections to the mediastinal or abdominal viscera. CT, particularly with multiplanar and three-dimensional reformats, optimally demonstrates osseous vertebral anomalies for preoperative planning.

Diastematomyelia (DSM) arises from an aberrant process similar to that of the neurenteric cyst and results in a splitting

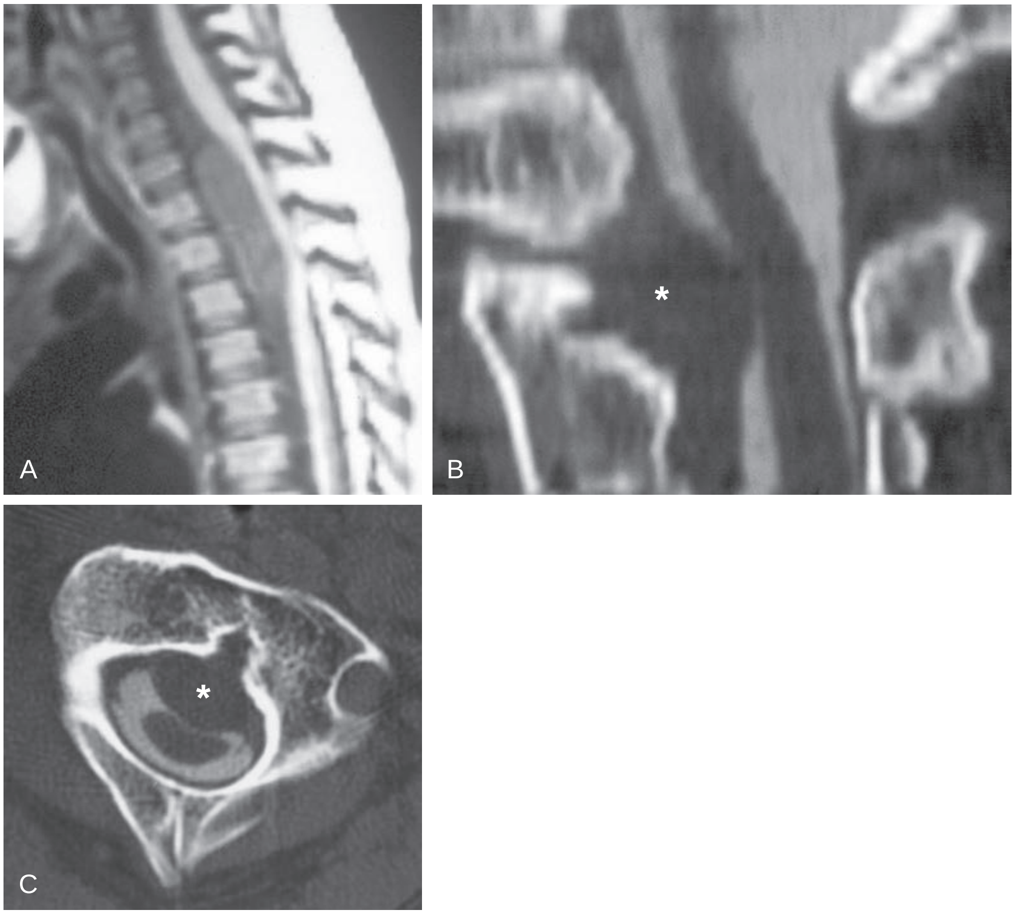

**e-Figure 43.11. Neurenteric cyst.** Sagittal T1-weighted MRI (A) shows a ventral neurenteric cyst in the spinal canal that compresses the spinal cord. Additionally, a small cyst of similar signal characteristics was found along the anterior spine that on axial imaging (not shown) was contiguous with the neurenteric cyst through a midline sagittal vertebral cleft. Sagittal (B) and axial (C) CT myelogram images in a different patient with Klippel–Feil syndrome show a ventral extradural neurenteric cyst *(asterisk)* compressing the ventral thecal sac and spinal cord, contiguous with a sagittal vertebral body cleft.

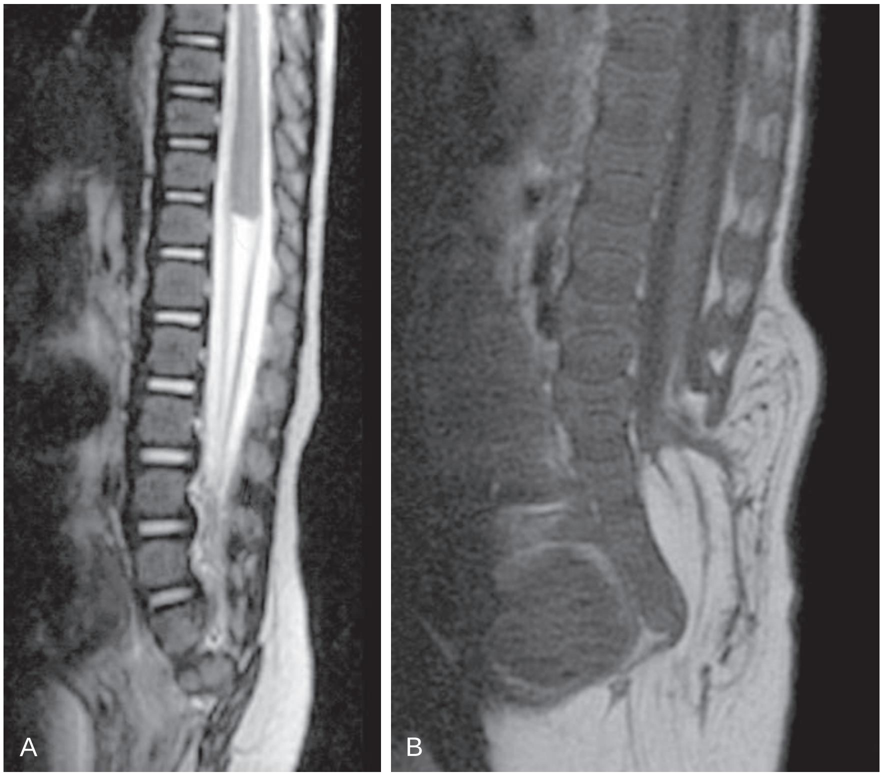

**Figure 43.6. Caudal regression syndrome.** Sagittal T2-weighted MRI (A) shows the typical appearance of type 1 CRS, with severe sacral dysplasia and the characteristic wedge-shaped high conus termination. Sagittal T1-weighted MRI (B) contrasts the appearance of type 2 CRS (with a less severe sacral dysgenesis) with an elongated spinal cord that inserts distally into a terminal lipoma.

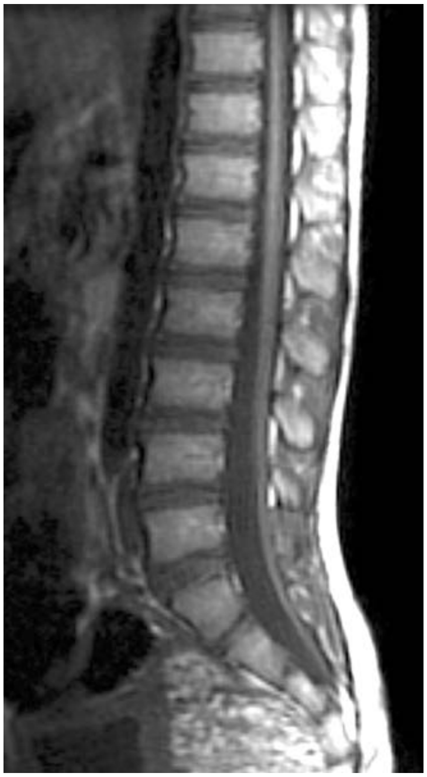

**Figure 43.7. Tethered cord syndrome.** Sagittal T1-weighted MRI reveals an elongated spinal cord, indistinguishable from the filum, inserting into the terminal thecal sac.

of the spinal cord into two hemicords, each with one ventral and one dorsal root. The hemicords may be symmetric, or they may be asymmetric, known as partial DSM; one or both may feature hydromyelia or be tethered. The much rarer (perhaps mythical) diplomyelia, or duplicated spinal cord, is the only other differential entity to consider; it occurs probably in the context of a duplicated spinal axis, and many authorities think it most likely represents a very severe DSM rather than true spinal cord duplication.

Because the notochord influences vertebral development, vertebral segmentation anomalies are very commonly associated with DSM. Therefore important factors for preoperative planning include the presence (type 1 DSM; Fig. 43.12) or absence (type 2 DSM; Fig. 43.13) of an osseous or fibrous spur and whether the cords reside in separate or single dural tubes. Occasionally in type 2 DSM, a nerve root or roots may become adherent to the dura and may tether the spinal cord, producing the meningocele manqué malformation. DSM may be isolated or found in conjunction with other spinal anomalies, particularly MMC, thus it is critical to search for DSM before any spinal anomaly repair or scoliosis correction. A patient with MMC whose symptoms progress after surgical closure is a relatively common presentation of undiagnosed DSM. Cutaneous abnormalities such as skin dimples or discoloration, vascular lesions, or hair patches are sometimes present and can guide attention to the most likely level of DSM.

## OTHER CONGENITAL AND DEVELOPMENTAL ANOMALIES

Other uncommon but important congenital spinal anomalies whose etiology is not definitively known include the simple dorsal meningocele and the lateral meningocele.

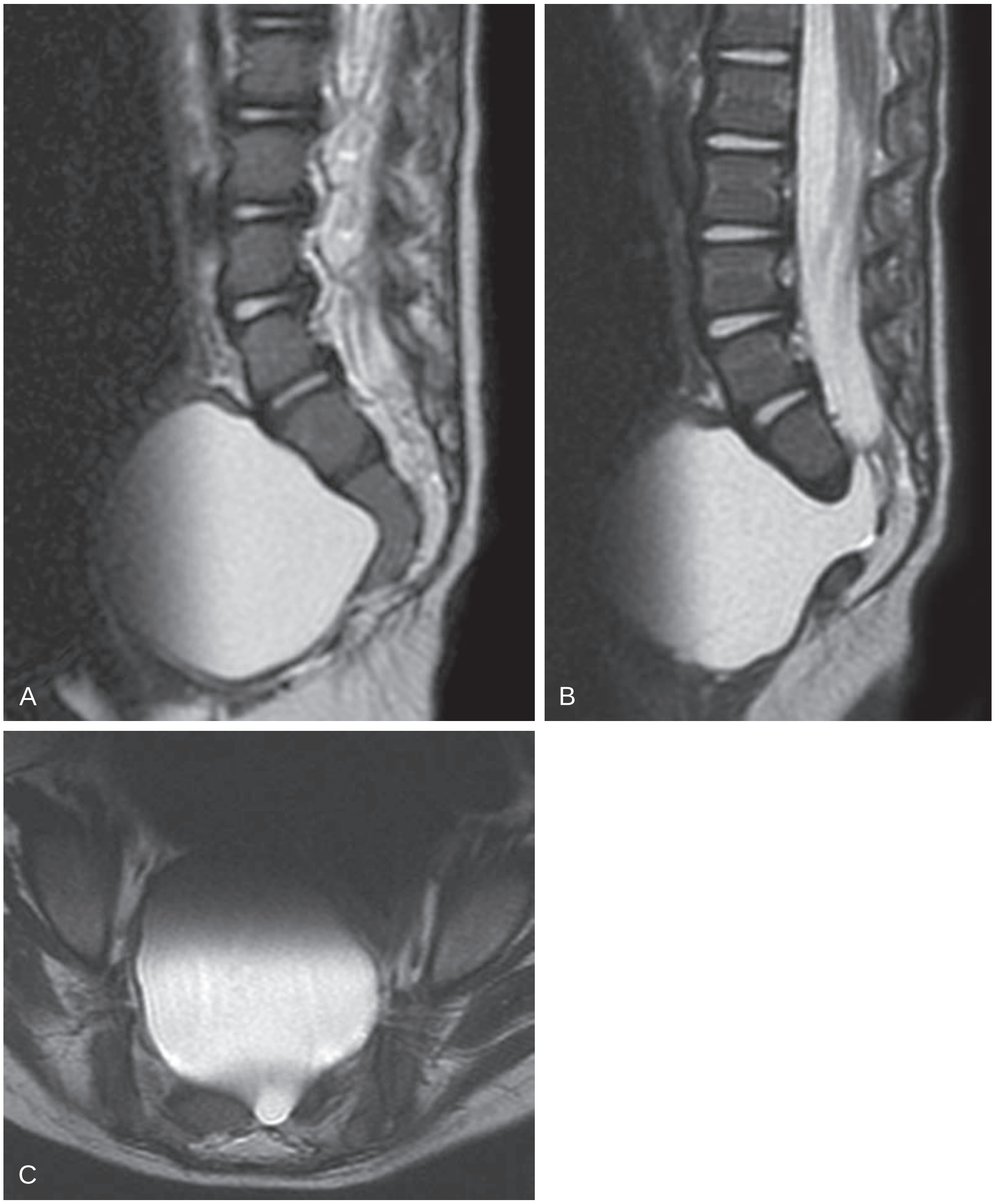

**Figure 43.8. Anterior sacral meningocele.** Sagittal midline T2-weighted MRI (A) shows the characteristic scimitar shape of the sacrum. Parasagittal (B) and axial (C) T2-weighted MRI confirms a typical, simple, anterior sacral meningocele that appears as a presacral cyst contiguous with the thecal sac through an enlarged left sacral neural foramen.

Dorsal meningoceles by definition occur dorsally, most often over the lumbosacral spine, and feature a skin-covered meningocele devoid of neural elements that protrudes through a posterior dysraphic defect (e-Fig. 43.14). In practice, however, it is not uncommon to find a dysplastic nerve root or other neural tissue within a meningocele.

Lateral meningoceles manifest as paraspinal masses filled with cerebrospinal fluid that are contiguous with the thecal sac and extend through the neural foramen, with adjacent pedicular and foraminal osseous remodeling (e-Fig. 43.15). They are generally “simple,” but some may contain fat or neural tissue and are then better termed “complex.” Important associations include Marfan syndrome and NF1.

In both anomalies, MRI is the best modality to demonstrate the soft tissue components. CT is helpful for clarifying the osseous anatomy, and is usually done before surgery. If MRI is contraindicated or inconclusive, CT myelography can demonstrate the meningocele and confirm its continuity with the dural sac.

## VERTEBRAL FORMATION AND SEGMENTATION ANOMALIES

Anomalies of vertebral formation and segmentation arise from aberrancies in vertebral column formation. These are generally divided into anomalies that result from either partial or total failure of vertebral formation and failure to correctly segment after vertebral formation (vertebral segmentation failure). The abnormal vertebra may be supernumerary, or it may replace a normal vertebral body. Abnormal *PAX1* expression is a postulated etiology in the development of segmentation anomalies, and other

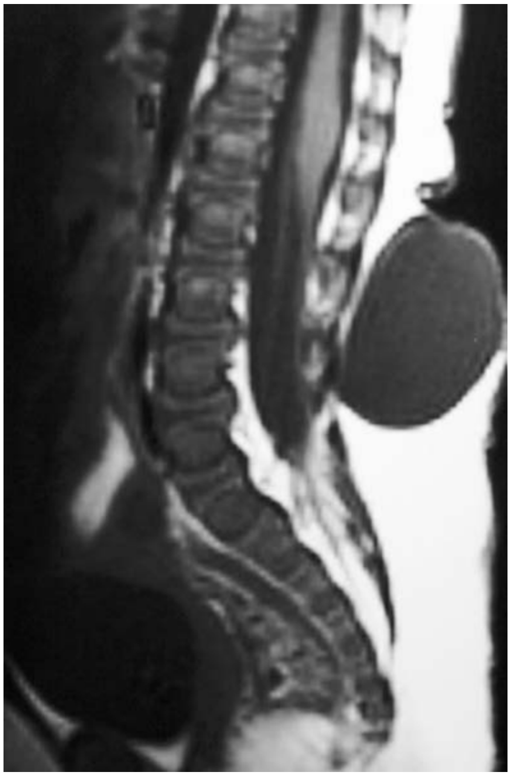

**e-Figure 43.14 Dorsal meningocele.** Sagittal T1-weighted MRI shows a large, skin-covered cystic back mass connected to the thecal sac by a thin cerebrospinal fluid–filled stalk. The tethered conus terminates at L2–L3. *(Image courtesy of Marvin Nelson Jr, MD.)*

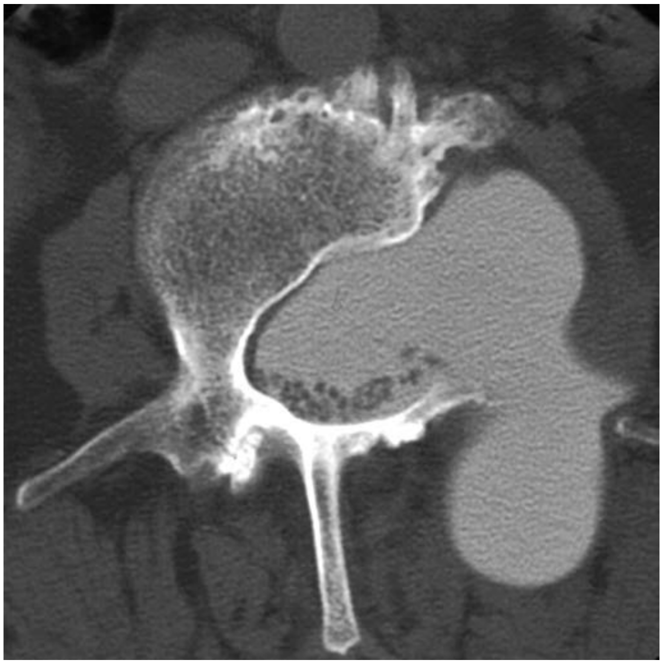

**e-Figure 43.15 Lateral meningocele.** Axial CT myelogram image shows a large left lateral meningocele with pedicular erosion in a patient with neurofibromatosis type 1. The image confirms vertebral remodeling and contiguity of the meningocele with the thecal sac. In addition to lateral extension, the meningocele also extends posteriorly into the paraspinal muscles.

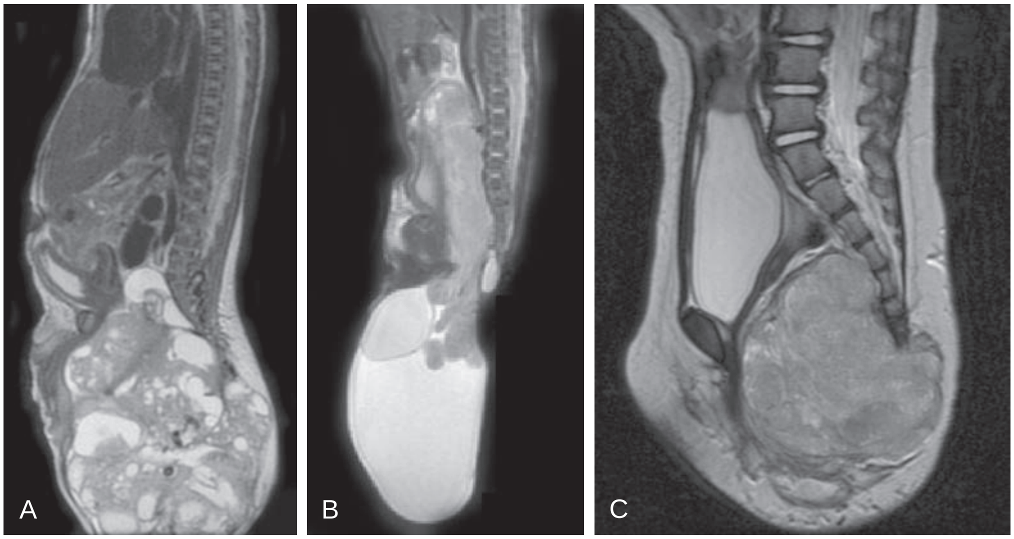

**Figure 43.10. Sacrococcygeal teratoma.** Sagittal T2-weighted MRI in three different infants shows large, mixed cystic and solid pelvic masses confirmed pathologically as sacrococcygeal teratomas. The proportions of internal and external tumor produce diagnoses of grade 1 (A), grade 2 (B), and grade 3 (C) using the American Academy of Pediatrics classification.

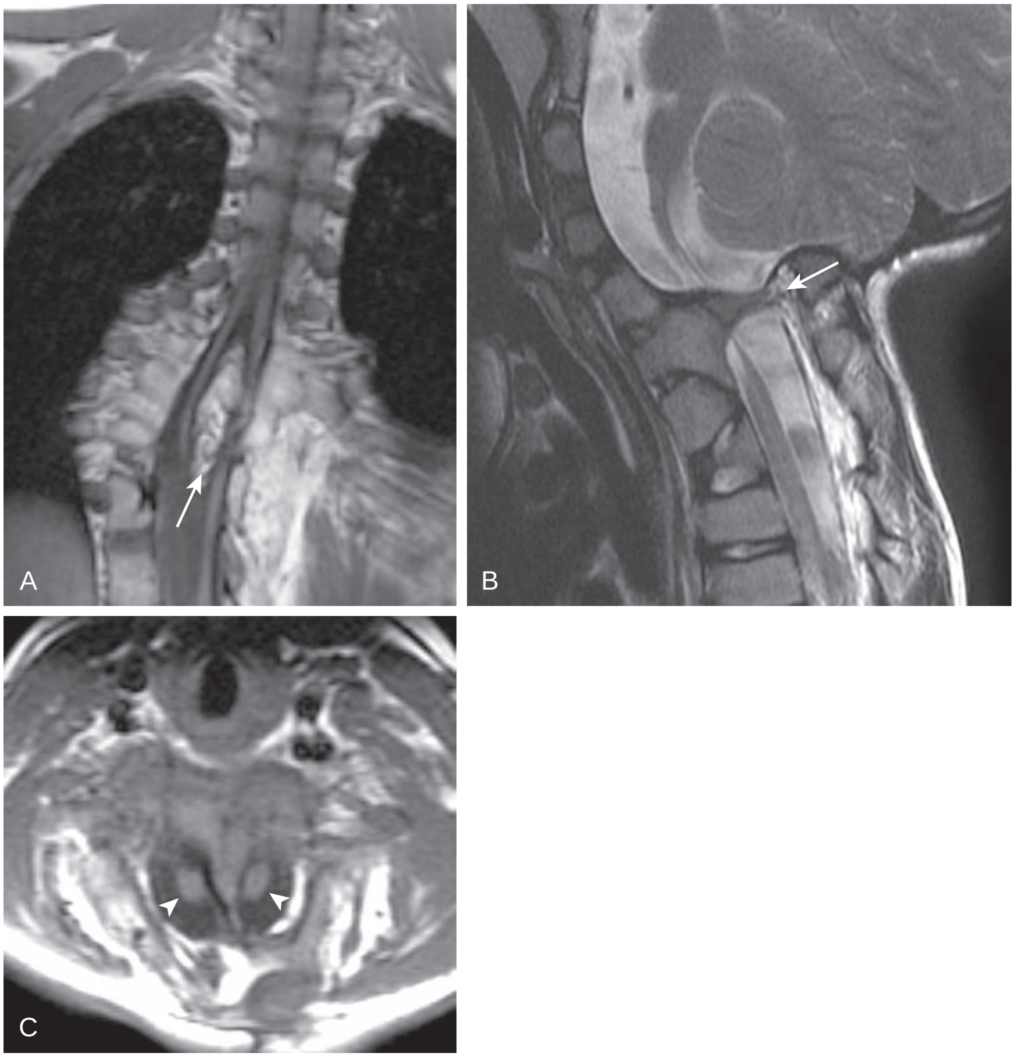

**Figure 43.12. Diastematomyelia type 1.** Coronal (A) T1-weighted MRI in a patient with type 1 DSM shows a large ossified spur *(arrow)* that splits the thoracic spinal cord. Numerous vertebral segmentation anomalies with posterior rib fusions are present. Sagittal T2-weighted (B) and axial T1-weighted (C) MRI of a different patient shows a type 1 cervical DSM with ossified spur (*arrow* in B) and two hemicords (*arrowheads* in C).

visceral and neuraxis anomalies are also commonly identified. More severe SFAs tend to have a higher incidence of concurrent visceral organ or other neuraxis anomalies. The degree and location of vertebral formation failure predicts morphology; unilateral chondral center deficiency and failure of ossification produces a hemivertebra, whereas central failure of ossification centers to unite produces a butterfly vertebra (Fig. 43.16). Conversely, vertebral segmentation failure presents with composite or "block" vertebra and posterior element fusions (Fig. 43.17 and e-Fig. 43.18). Not surprisingly, block vertebrae frequently coexist with hemivertebrae and butterfly vertebrae (Fig. 43.19), leading many to lump these various vertebral anomalies together into the working term SFAs. Many clinical syndromes prominently feature SFAs, including Klippel–Feil and Jarcho–Levin (spondylothoracic dysplasia) syndromes. SFAs are imaging markers that should prompt further consideration of a possible syndromic process.

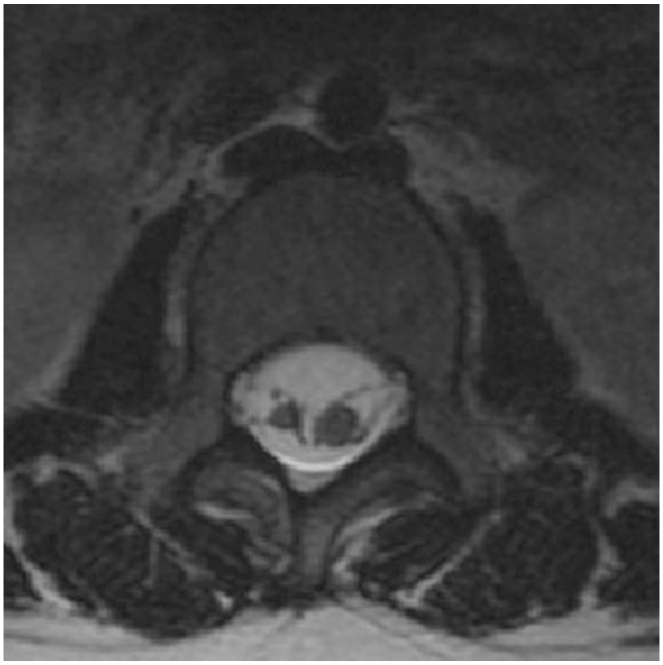

**Figure 43.13. Diastematomyelia type 2.** Axial T2-weighted MRI in a patient with type 2 DSM shows the spinal cord split into two hemicords within a single dural tube. No fibrous or osseous septum was identified.

## KEY POINTS

- The conus is normally at adult level (L2 or above) soon after birth; conus termination below L2–L3 is probably abnormally low-lying.
- LMC and LMMC account for 20% to 56% of occult spinal dysraphism and 20% of skin-covered lumbosacral masses.
- The simple coccygeal sinus that originates from a low sacral dimple found within the intergluteal cleft never communicates with the spinal canal, is usually incidental, and does not require imaging.
- The offspring of 1% of diabetic mothers have a caudal cell mass anomaly.
- TCS is a specific clinical entity that usually presents during periods of rapid somatic growth.
- MRI is the best modality for preoperative planning and staging of caudal cell anomalies, as well as assessing postoperative recurrence.
- Anomalies that reflect failure of vertebral formation and vertebral segmentation failure frequently coexist.

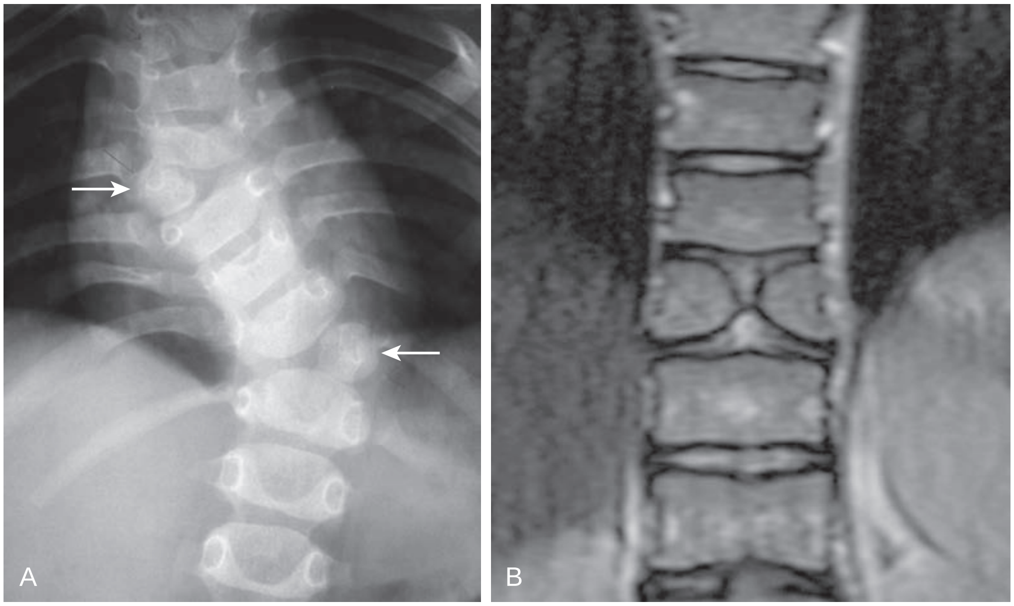

**Figure 43.16. Failure of vertebral formation.** (A) Frontal radiograph demonstrates balanced thoracic hemivertebrae *(arrows)* detected during evaluation of congenital scoliosis. (B) Coronal T2-weighted MRI shows a classic butterfly vertebra. Both of these may coexist with each other and with malformations of vertebral segmentation failure.

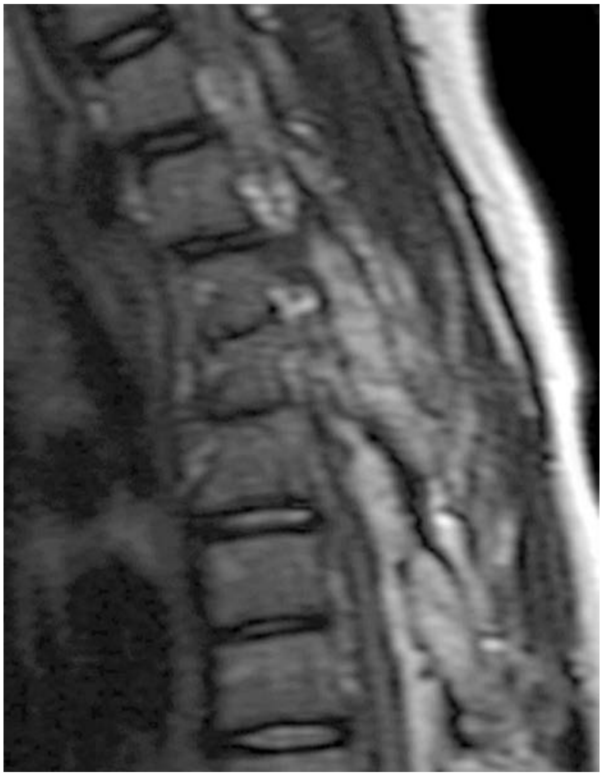

**e-Figure 43.18 Posterior element segmentation failure with fusion.** Sagittal T2-weighted MRI shows a multilevel pedicular and facet bar associated with vertebral segmentation failure at the same levels.

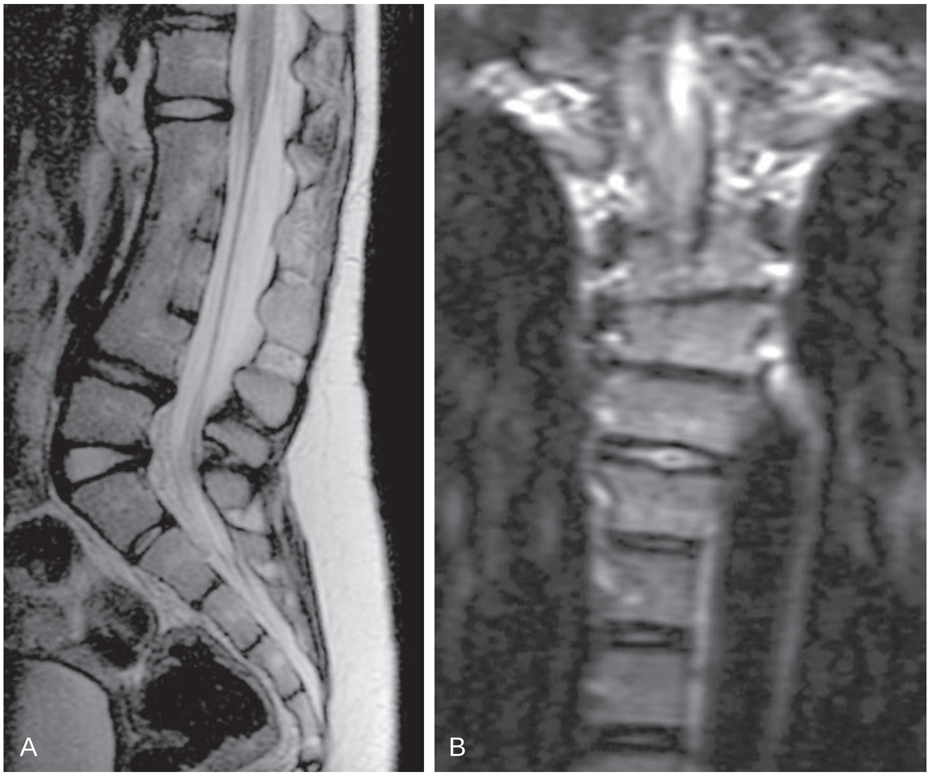

**Figure 43.17. Vertebral segmentation failure.** (A) Sagittal T2-weighted MRI demonstrates multilevel vertebral segmentation failure producing a large block vertebra and kyphotic lumbar curve. Incomplete segmentation of the posterior elements is also evident. (B) Coronal T2-weighted imaging in a different patient shows a three-level thoracic block vertebra and mild scoliotic curve related to a slightly better attempt at segmentation on the left.

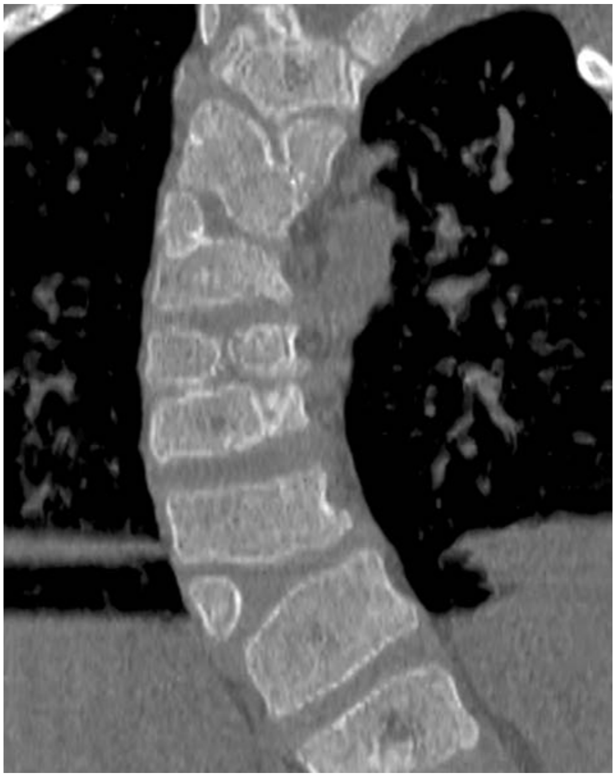

**Figure 43.19. Coexistent vertebral segmentation and vertebral formation failure anomalies.** Coronal CT image in a patient with VACTERL syndrome shows multiple combinations of both segmentation and formation failure with resultant congenital dextroscoliosis.

## SUGGESTED READINGS

Giampietro PF, Dunwoodie SL, Kusumi K, et al. Progress in the understanding of the genetic etiology of vertebral segmentation disorders in humans. *Ann N Y Acad Sci*. 2009;1151:38–67.

Rufener S, Ibrahim M, Parmar HA. Imaging of congenital spine and spinal cord malformations. *Neuroimaging Clin N Am*. 2011;21:659–676. doi:10.1016/j.nic.2011.05.011.

Schwartz ES, Rossi A. Congenital spine anomalies: the closed spinal dysraphisms. *Pediatr Radiol*. 2015;45(suppl 3):S413–S419. doi:10.1007/s00247-015-3425-6.

## REFERENCES

Full references for this chapter can be found on www.expertconsult.com.

## REFERENCES

1. Giampietro PF, Dunwoodie SL, Kusumi K, et al. Progress in the understanding of the genetic etiology of vertebral segmentation disorders in humans. *Ann N Y Acad Sci*. 2009;1151:38–67.
2. Kucera JN, Coley I, O'Hara S, et al. The simple sacral dimple: diagnostic yield of ultrasound in neonates. *Pediatr Radiol*. 2015;45(2):211–216.
3. Pang D, Dias MS, Ahab-Barmada M. Split cord malformation: part I. A unified theory of embryogenesis for double spinal cord malformations. *Neurosurgery*. 1992;31:451–480.
4. Pang D. Sacral agenesis and caudal spinal cord malformations. *Neurosurgery*. 1993;32:755–778, discussion 778-779.
5. Rufener SL, Ibrahim M, Raybaud CA, et al. Congenital spine and spinal cord malformations—pictorial review. *AJR Am J Roentgenol*. 2010;194(suppl 3):S26–S37.
6. Rufener S, Ibrahim M, Parmar HA. Imaging of congenital spine and spinal cord malformations. *Neuroimaging Clin N Am*. 2011;21:659–676. doi:10.1016/j.nic.2011.05.011.
7. Schwartz ES, Rossi A. Congenital spine anomalies: the closed spinal dysraphisms. *Pediatr Radiol*. 2015;45(suppl 3):S413–S419. doi:10.1007/s00247-015-3425-6.
8. Tortori-Donati P, Rossi A, Biancheri R, et al. Magnetic resonance imaging of spinal dysraphism. *Top Magn Reson Imaging*. 2001;12:375–409.
9. Tortori-Donati P, Rossi A, Cama A. Spinal dysraphism: a review of neuroradiological features with embryological correlations and proposal for a new classification. *Neuroradiology*. 2000;42:471–491.

# 44

# Infections of the Spine and Spinal Cord

*Alexis B. Rothenberg Maddocks and Avrum N. Pollock*

Spinal infections in children occur uncommonly. Etiologies include direct and indirect (hematogenous) inoculation by bacterial, viral, parasitic, and fungal agents. Direct bacterial infectious inoculation may be as a result of trauma, instrumentation, or via a preexisting congenital sinus tract or area of spinal dysraphism (i.e., meningocele). Lyme disease (Fig. 44.1), caused by a *Borrelia burgdorferi*-infected tick bite, is also a cause of spinal cord infection, especially in the Northeastern United States. Mosquito-borne West Nile virus (e-Fig. 44.2), with cases initially appearing along the east coast of the US, has emerged as an infectious cause of spinal cord infection. Enterovirus D68 (Fig. 44.3) is a respiratory illness that has been recently described to be a cause of spinal cord infection, which can result in acute flaccid paralysis. Tuberculosis (TB) (Fig. 44.4) of the spinal cord usually occurs in the thoracic region in children and manifests as an intramedullary tuberculoma, most often seen in patients with AIDS or other immunocompromised states. TB is most prevalent in India but is also widespread in Africa and Southeast Asia. Cysticercosis (e-Fig. 44.5) is the most common parasitic infection encountered within the spinal cord. It occurs after ingestion of uncooked pork infected with *Taenia solium* and is most prevalent in South America and Southeast Asia. The parasitic infection Gnatosthomasis (e-Fig. 44.6), caused by the nematode *Gnathostoma spinigerum*, can lead to the clinical presentation of myeloradiculitis. Acquired by ingesting contaminated fish or meat, it is endemic in Southeast Asia and is virtually unknown in North America, other than in cases acquired abroad.

Inflammatory entities, related in some form to infections, are often how spinal cord infections manifest. Neurologic deficits often prompt imaging in the search for a diagnostic explanation for the patient’s symptoms. Magnetic resonance imaging (MRI) remains the gold standard examination for the evaluation of spinal cord infection. In general, central nervous system infections present with hyperintensity on fluid-sensitive T2-weighed sequences, and with variable enhancement on gadolinium-enhanced T1-weighted sequences. Like infections elsewhere, increase in cord caliber often occurs secondary to an increase in water content/edema. Rare related hemorrhages can at times be more clearly seen using gradient echo sequences.

## DISCITIS AND OSTEOMYELITIS

Disc space infection often coexists with vertebral osteomyelitis in children secondary to hematogenous spread, through capillary tufts in vertebral body endplates, and vascular channels of immature intervertebral disc spaces. Contrast-enhanced MRI is the study of choice and should be performed without delay

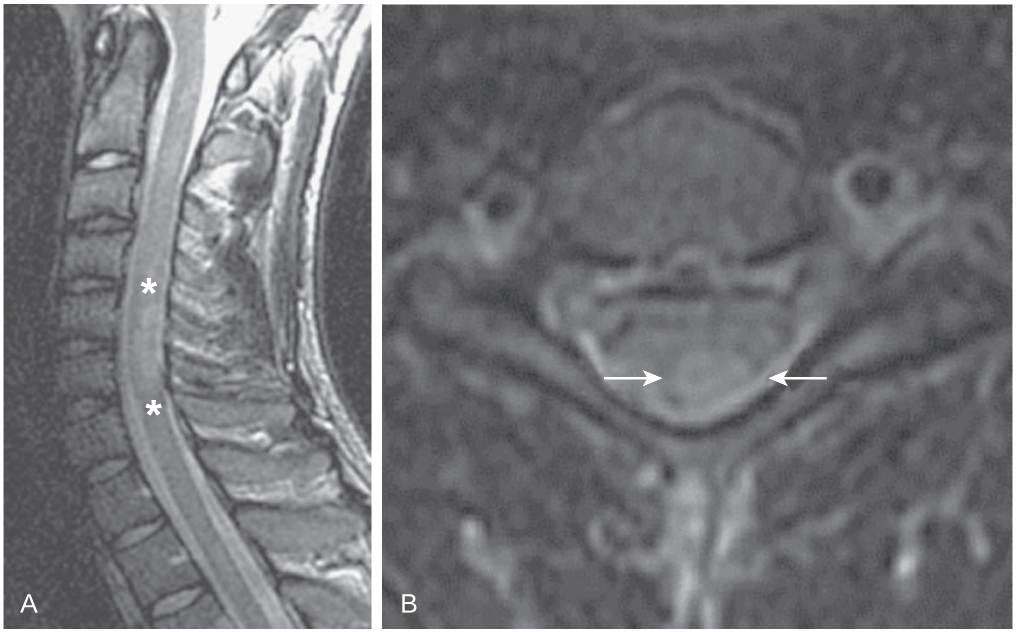

**Figure 44.1. Lyme disease in a patient with prior tick bite.** (A) Sagittal and (B) axial T2-weighted magnetic resonance (MR) images of the cervical spine demonstrates T2 prolongation (*asterisks* in A and *arrows* in B) within the dorsal spinal cord at the level of C5/C6 secondary to demyelination, similar to those seen in the brain in patients with Lyme disease. *(Case courtesy of Dr. Gul Moonis, MD, Beth Israel Deaconess Medical Center, Division of Neuroradiology.)*

## Abstract:

Although spinal cord infections are rare in children, when they do occur, the causative pathogens may be bacterial, viral, fungal or parasitic, and their incidence is dependent upon where in the world the child lives.

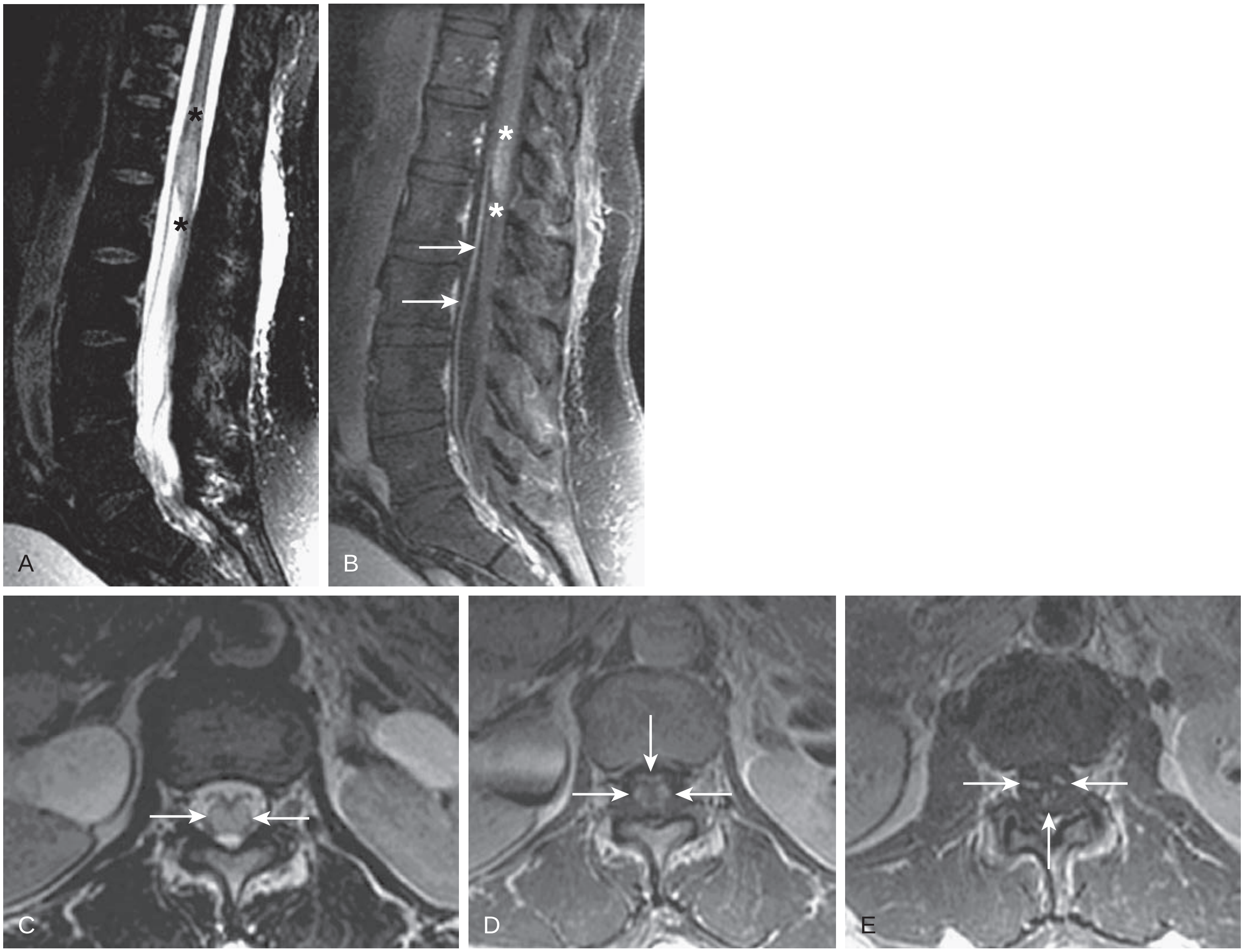

**e-Figure 44.2. (A–E) West Nile virus in a patient after mosquito bite.** (A) Sagittal and (C) axial T2-weighted MR images (Fig. 44.2A and 44.2C, respectively), as well as sagittal (Fig. 44.2B) and axial (Fig. 44.2D and 44.2E) postgadolinium T1-weighted images of the lumbar spine demonstrate T2 prolongation (*asterisks* in A and *arrows* in C) within the distal spinal cord/conus medullaris as well as contrast enhancement of the distal cord *(asterisks)*/ conus medullaris (*arrows* in B and D) and within the cauda equina (*arrows* in E) secondary to viral myeloradiculitis. *(Case courtesy of Dr. Gul Moonis, MD, Beth Israel Deaconess Medical Center, Division of Neuroradiology.)*

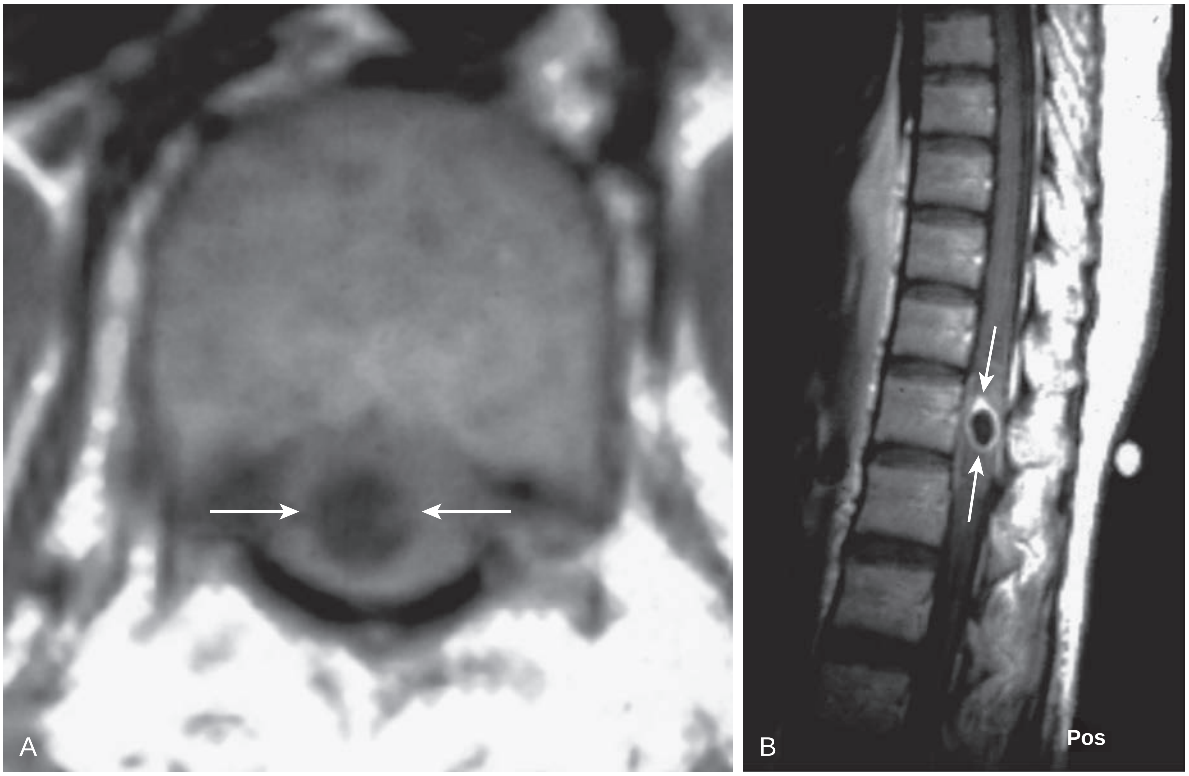

**e-Figure 44.5. Cysticercosis in 20-year-old male presenting with paraparesis developing over 2 weeks.** (A) Axial T1-weighted and (B) sagittal postcontrast T1-weighted MR images of the thoracic spine demonstrate central T1 prolongation within the spinal cord proper (*arrows* in A), with corresponding rim enhancement on the postcontrast images (*arrows* in B). *(Case courtesy of Dr. Manu Shroff of the Hospital for Sick Children in Toronto, Canada.)*

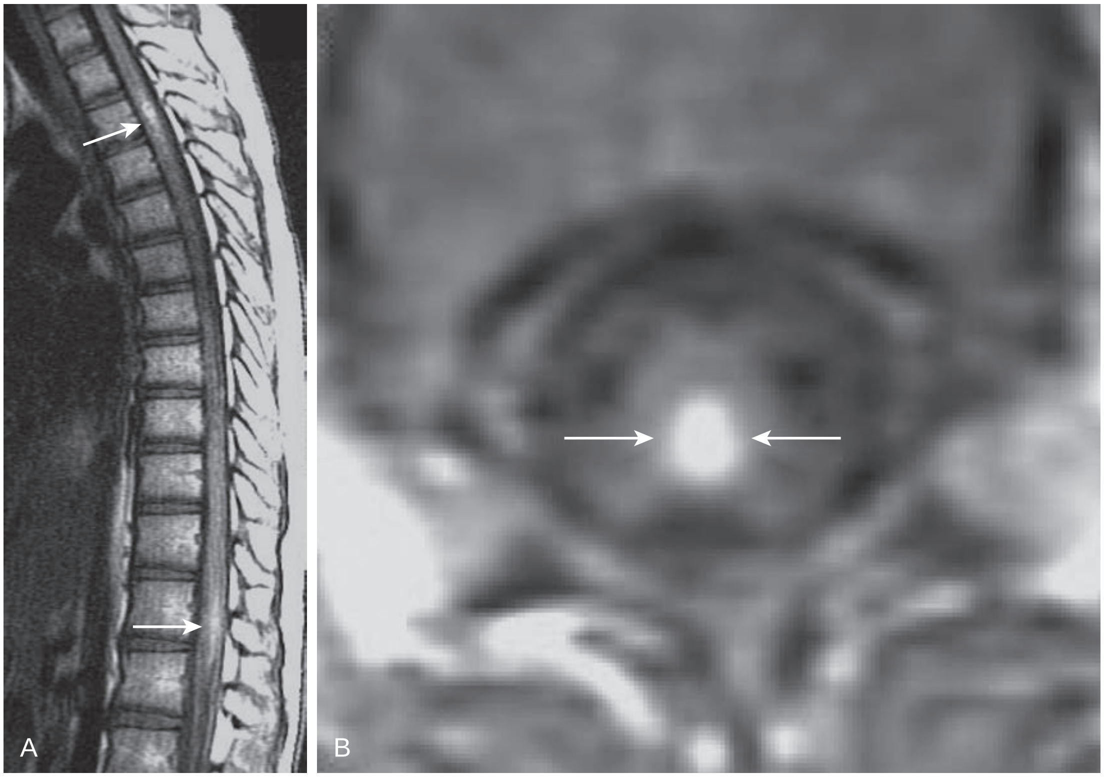

**e-Figure 44.6. Gnathosthomiasis.** A 17-year-old boy from Thailand with exposure to Gnathostoma parasite. (A) Sagittal and (B) axial postcontrast T1-weighted MR images of the thoracic spine demonstrate enhancing nodules *(arrows)* within the spinal cord secondary to parasitic infection. *(Case courtesy of Dr. Jiraporn Laothamatas of Mahidol University, Bangkok, Thailand.)*

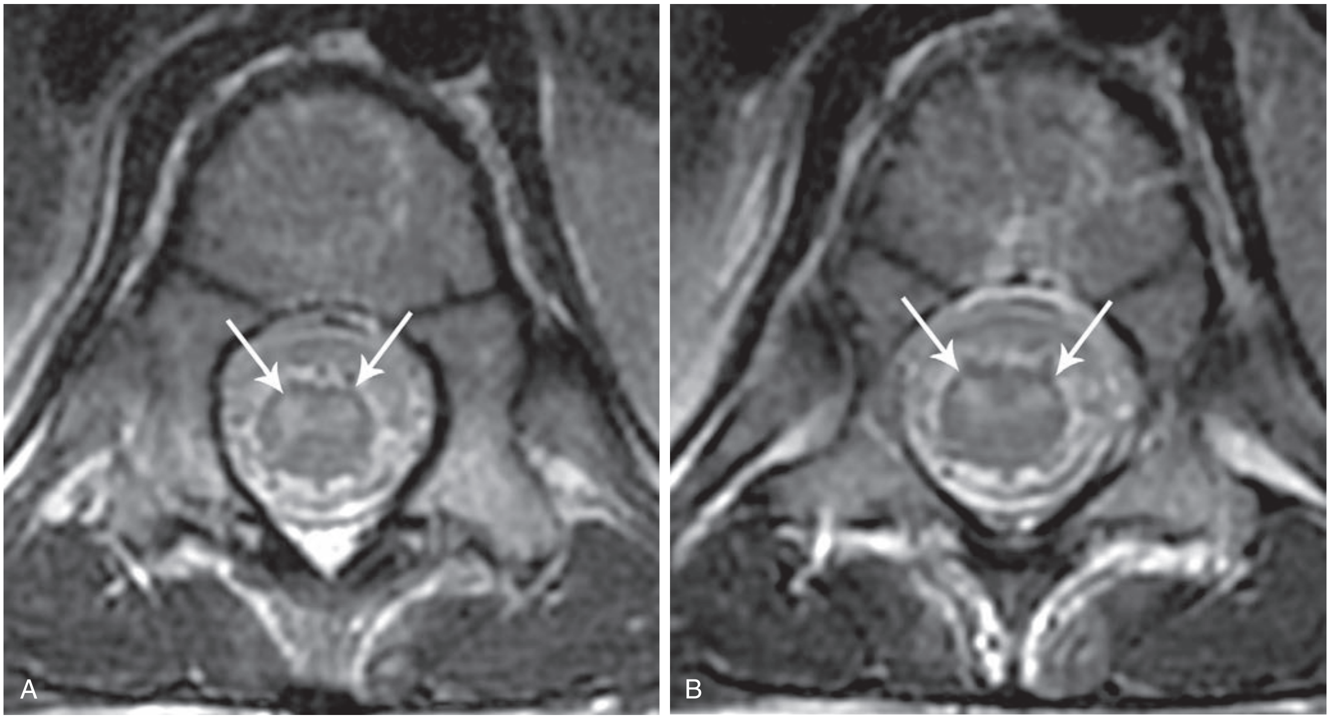

**Figure 44.3. Enterovirus D68.** Axial T2-weighted images (A and B) through the lower thoracic spine demonstrate T2 prolongation involving the central gray matter of the spinal cord with predominant involvement of the anterior horn cells *(arrows)*.

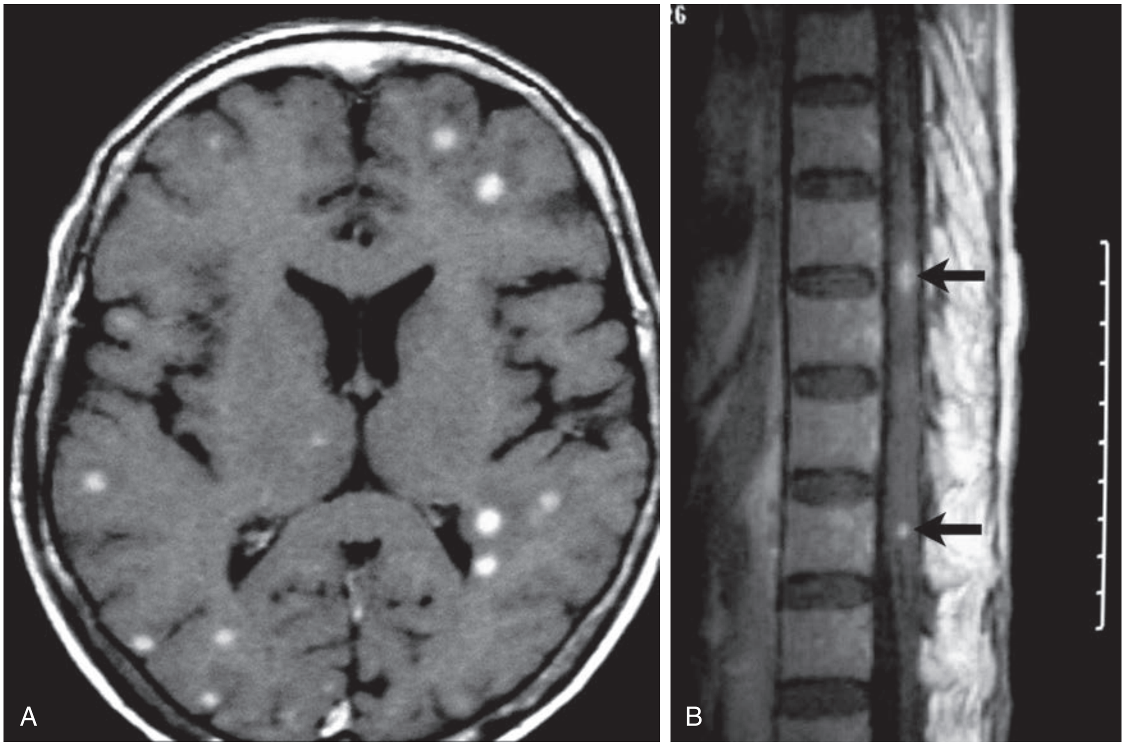

**Figure 44.4. Tuberculosis.** Adult patient with TB exposure. (A) Axial postcontrast T1-weighted MR images of the brain and (B) thoracic spine demonstrate multiple enhancing intraaxial nodules corresponding to tuberculomas (*arrows* in B). *(Case Courtesy of Drs. Pranjal Goswami, Nirod Medhi, and Pratul Kr. Sarma of Primus Institute in Guwahati, India.)*

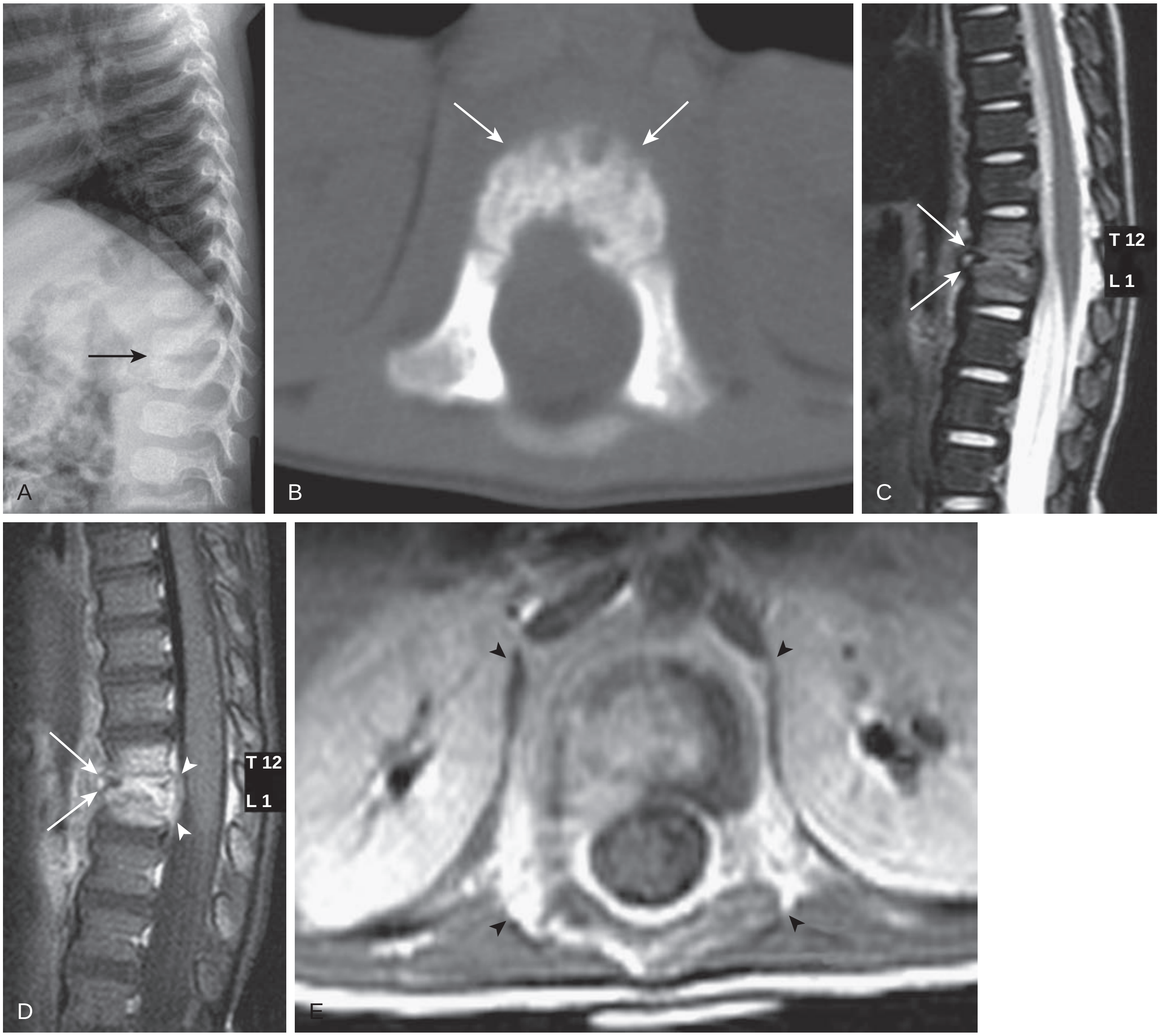

**Figure 44.7. Discitis/Osteomyelitis.** A 15-month-old female with abnormal gait and concern for intraspinal mass. (A) Lateral spine radiographs demonstrate narrowing of the T12-L1 intervertebral disc space *(arrow)*. (B) Axial noncontrast CT of the spine demonstrates irregularity to the vertebral endplates *(arrows)*. (C) Sagittal T2-weighted and (D) sagittal fat-saturated postcontrast T1-weighted image, and (E) axial postcontrast T1-weighted MR images of the thoracolumbar junction demonstrate loss of height of the T12-L1 intervertebral disc space with T2 prolongation of the adjacent endplates (*arrows* in C), with corresponding abnormal enhancement in the same regions (*arrows* in D), and surrounding masslike soft tissue enhancement (*arrowheads* in E).

in suspected cases (Fig. 44.7). While infection can occur at any level, the midlumbar spine is most often affected. *Staphylococcus aureus* represents the most common etiologic organism. Worldwide, atypical etiologic organisms such as TB are not uncommon. The first radiographic sign of infection is irregularity of the vertebral body endplates. The affected disc space is most often narrowed and demonstrates low signal intensity on T2-weighted sequences. Edema and postcontrast enhancement in adjacent vertebral body endplates indicate the presence of associated osteomyelitis and possible disc space abscess. Complicated cases demonstrate epidural/paravertebral abscess/phlegmon, which are well seen on MRI. Signs of late detection include vertebral body collapse and spinal deformity (Fig. 44.8). After treatment, vertebral body and disc space findings may persist for up to 24 and 34 months, respectively. Chronic recurrent multifocal osteomyelitis (CRMO) is the most severe form of chronic

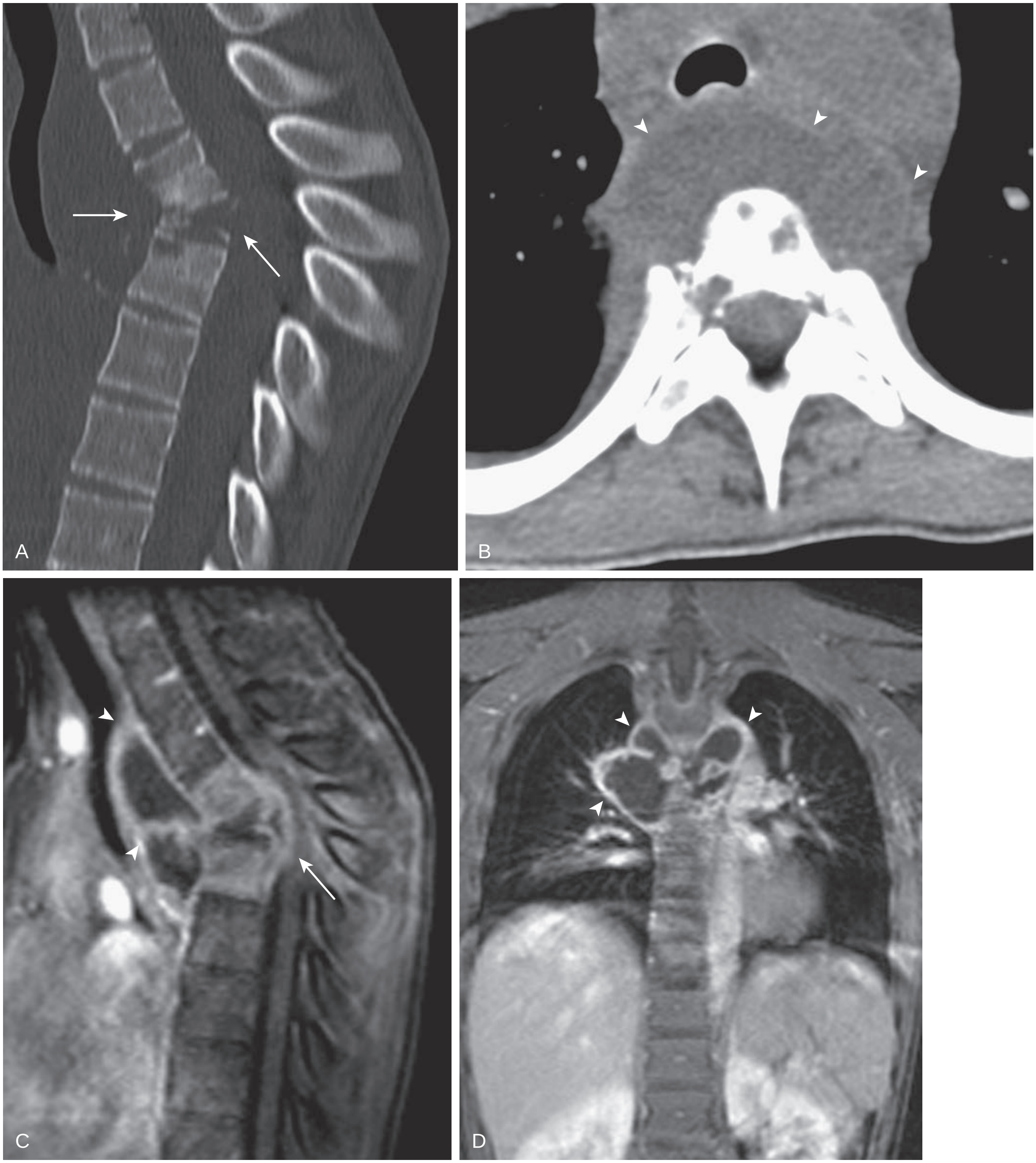

**Figure 44.8. Tuberculous osteomyelitis in 13-year-old female with progressive loss of strength and coordination in legs.** (A) Sagittal reformatted and (B) axial soft-tissue window images from a CT of the spine, and (C) sagittal and (D) coronal fat-saturated postcontrast T1-weighted MR images of the thoracic spine demonstrate marked kyphosis at site of bony collapse at the level of the midthoracic spine (*arrows* in A and C), as well as surrounding soft tissue abscess (*arrowheads* in B–D), predominately anteriorly, at the same level.

nonbacterial osteomyelitis. The etiology remains unknown, and it is a diagnosis of exclusion. Although CRMO most commonly affects the metaphyses of long bones and medial clavicles, vertebral column and pelvic involvement is relatively common (Fig. 44.9).

## GUILLAIN-BARRÉ SYNDROME

Since the eradication of poliomyelitis, Guillain-Barré syndrome (GBS), or acute inflammatory demyelinating polyradiculoneuropathy has become the most common cause of acute motor paralysis in children. It is believed to arise from an abnormal T-cell response precipitated by a preceding infection. Infectious etiologies include Epstein-Barr virus, cytomegalovirus, hepatitis, varicella, *Mycoplasma pneumonia*, and *Campylobacter jejuni*. MRI of the spinal axis in patients with GBS often shows thickening of the cauda equina and intrathecal nerve roots as well as anterior predominant nerve root gadolinium enhancement, even beyond the time period of the initial presentation (Fig. 44.10). Imaging findings have been described to be 83% sensitive for acute GBS and are present in 95% of typical cases. Chronic inflammatory demyelinating polyneuropathy (CIDP) (e-Fig. 44.11) is thought to be a chronic form of GBS that shares similar imaging characteristics but often shows marked nerve root thickening.

## TRANSVERSE MYELITIS

Transverse myelitis (TM) is an inflammatory condition that traverses a focal area of the spinal cord and extends over three or more vertebral segments. The midthoracic spine is most often affected, and patients present with symmetrical bilateral sensory and motor deficits related to the affected region. While viral etiologies are believed to be the leading infectious cause of TM, as many as 60% of cases are thought to be idiopathic in nature. In most cases, a specific viral etiology is never determined. Vasculidites seen with autoimmune diseases such as systemic lupus erythematosus have also been described as potential etiologies. TM manifests on MRI (Fig. 44.12) with increased T2 signal encompassing more than two-thirds of the spinal cord's diameter on fluid-sensitive sequences, generally extending along more than three vertebral segments, with variable enlargement of the spinal cord secondary to edema, and variable degrees of enhancement after administration of intravenous contrast.

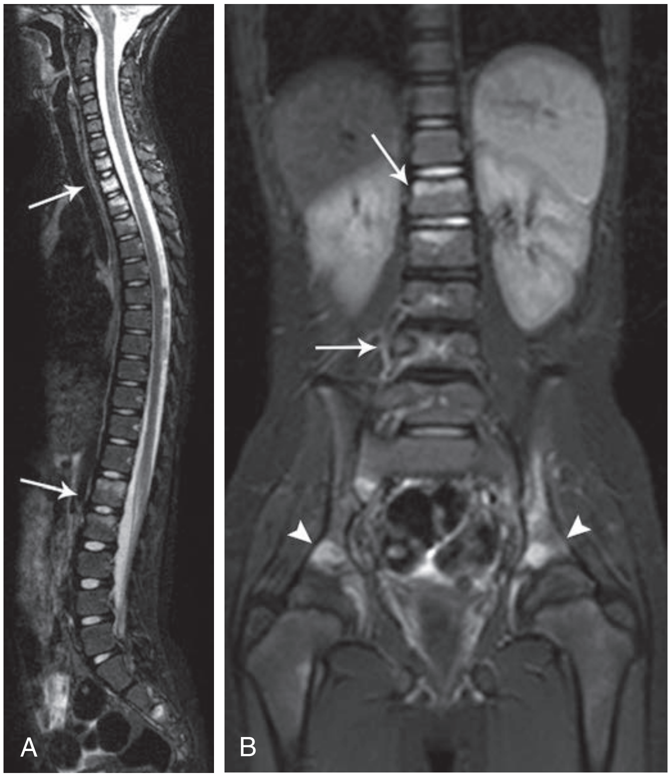

**Figure 44.9. Chronic recurrent multifocal osteomyelitis.** (A) Sagittal and (B) coronal STIR images demonstrate multilevel vertebral increased signal *(arrows)* as well as bilateral pelvic involvement *(arrowheads)*. *(Courtesy of Dr. Nancy Chauvin, Philadelphia, PA.)*

## ACUTE DISSEMINATED ENCEPHALOMYELITIS

Acute disseminated encephalomyelitis (ADEM) is a monophasic focal or multifocal perivascular inflammatory and demyelinating disorder, which often presents after a vaccination or viral infection. Lesions are generally hyperintense on T2-weighted sequences and have corresponding hypointensity or isointensity on T1-weighted sequences. These lesions often present as a diagnostic dilemma in which the differential diagnosis also includes neoplasm of the spinal cord and can in isolation often be indistinguishable from the demyelinating lesions of multiple sclerosis (MS). The lack of abnormal apparent diffusion coefficients (ADC) within the corpus callosum (brain) may aid in diagnosing ADEM, as opposed to those seen with MS, which classically demonstrates abnormal ADC within the corpus callosum. A clinical history of a recent viral illness and/or vaccination is the key to properly diagnosing these lesions. MRI characteristics of ADEM (Fig. 44.13) are variable, with enhancement patterns including solid or ringlike enhancement, to no enhancement at all, in lesions that range from small to large, and which affect gray matter, white matter, or both. These lesions often show dramatic response to plasmapheresis, corticosteroids, and immunoglobulin therapies, with consequent improvement or resolution of the imaging findings.

## MULTIPLE SCLEROSIS

Although it is much more prevalent in the adult population, MS is also seen in children. Its presentation and diagnosis mimics that seen in adults. While the cause is not known, viral and immune diseases are believed to be etiologic factors. MRI is part of the McDonald diagnostic criteria for diagnosis of MS and demonstrates disease in most patients presenting with compatible clinical symptoms. The majority of patients affected by MS will have spinal lesions (Fig. 44.14), and there is cervical cord predominance. MS can involve the white matter as well as gray matter and most often manifests as eccentrically situated lesions involving the dorsolateral aspect of the spinal cord. Spinal MS is associated with concomitant brain lesions in 80% of cases, making brain imaging essential when MS is a differential consideration. Concomitant presence of optic neuritis, in addition to spinal cord involvement, constitutes Devic disease, also known as *neuromyelitis optica*. MS lesions usually span less than two vertebral bodies in length and demonstrate hypointense signal on T1-weighted images and corresponding hyperintense signal on T2-weighted images. Prompt contrast enhancement occurs in active lesions. Studies have shown the greater sensitivity of fast-STIR (short tau inversion recovery) sequences when compared with fast spin echo sequences.

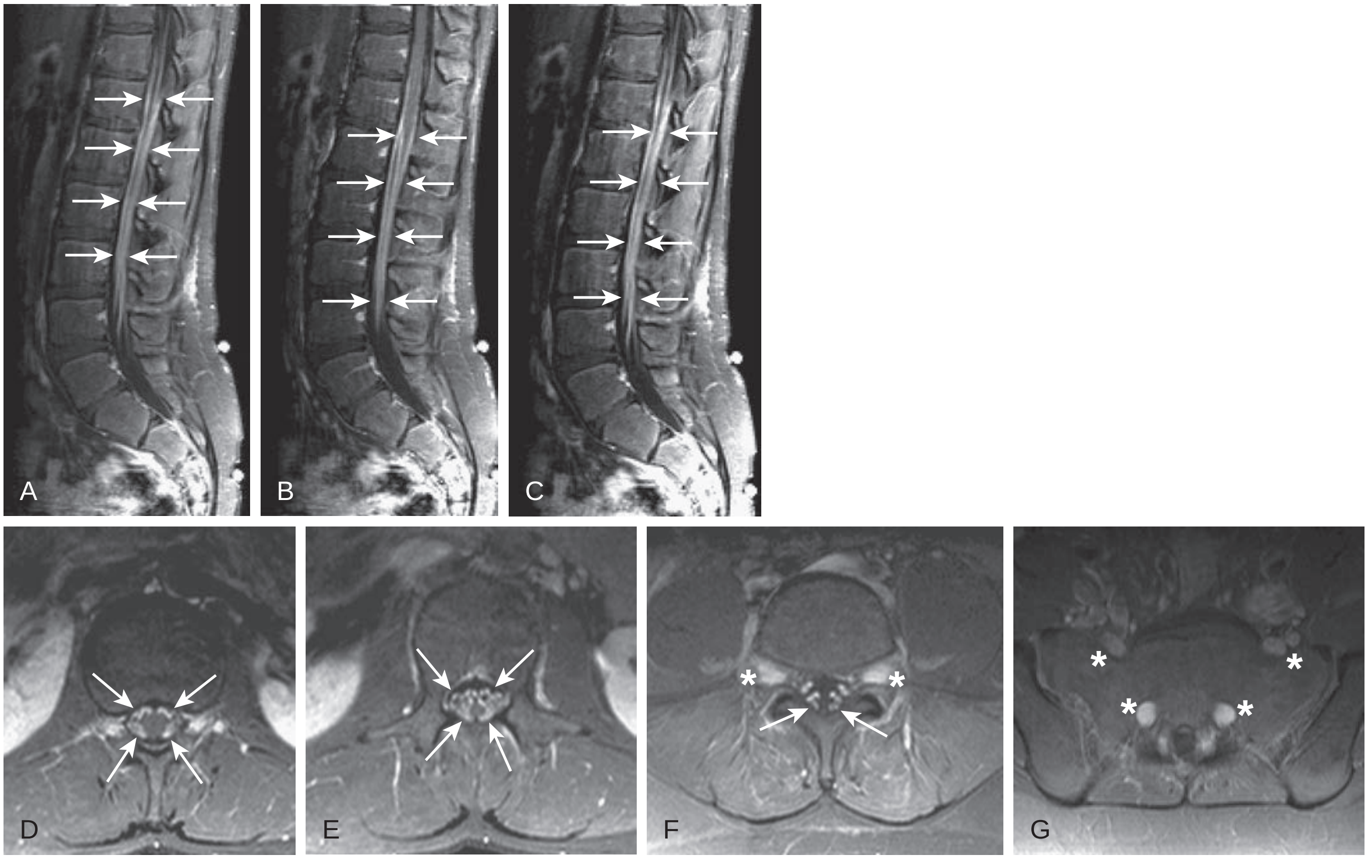

**e-Figure 44.11. Chronic inflammatory demyelinating polyneuropathy (CIDP).** A 13-year-old male with peripheral neuropathy and gait disturbances. Sagittal fat-saturated T1-weighted MR images off midline to the right, at midline, and off midline to the left (Fig. 44.11A–C, respectively), and axial fat-saturated postcontrast T1-weighted MR images through the lower thoracolumbar junction, conus medullaris, and proximal as well as distal nerve roots (Fig. 44.11D–G, respectively), demonstrate marked enhancement of the spinal nerve roots *(arrows)*, with expansion of the nerve roots seen as they exit the neural foramina *(asterisks)*. This enlargement and enhancement is typical of CIDP.

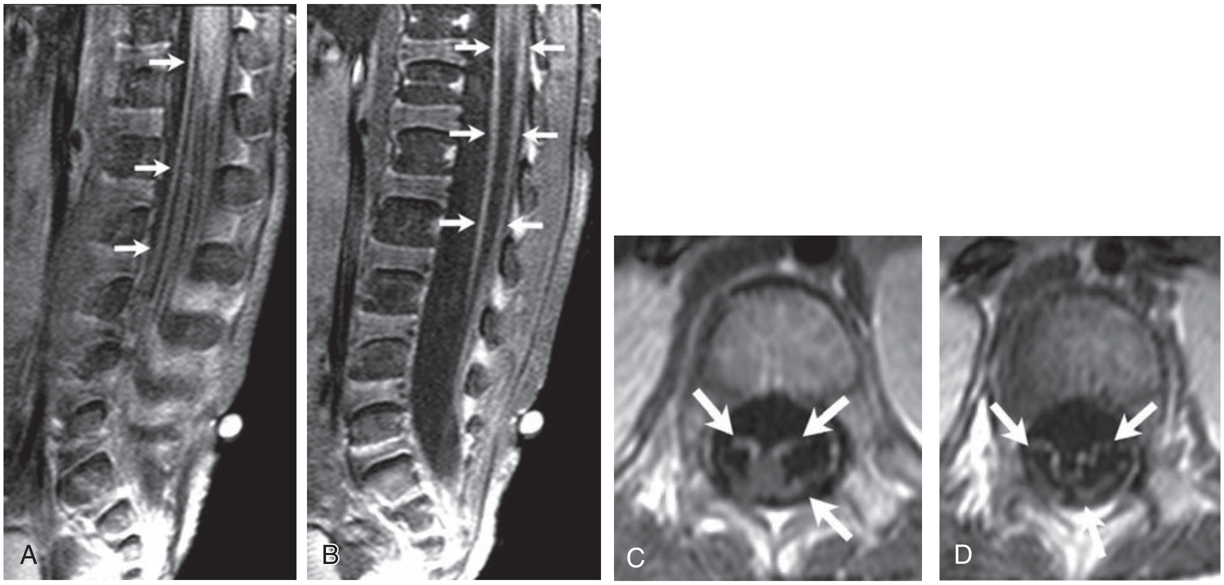

**Figure 44.10. Guillain-Barré Syndrome.** (A) Sagittal off midline and (B) midline fat-saturated postcontrast T1-weighted MR images through the lumbar spine, demonstrate extensive contrast enhancement of nerve roots *(arrows)*, typical of Guillain-Barré.

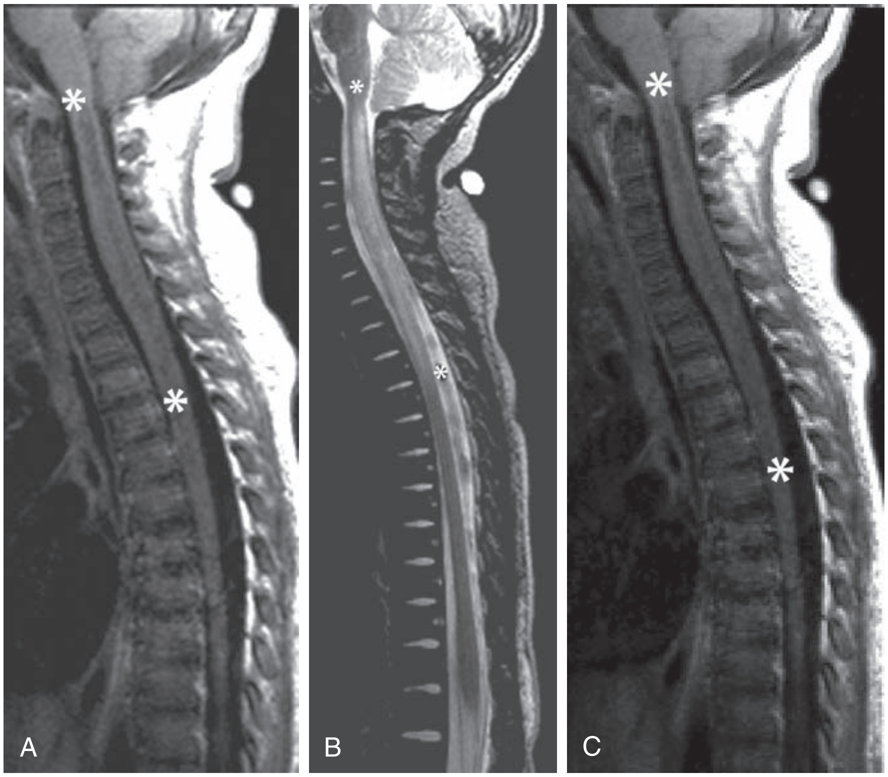

**Figure 44.12. Transverse myelitis.** Fever and rapidly ascending paralysis in a 17-month-old boy. (A) Sagittal T1-weighted, (B) sagittal T2-weighted, and (C) sagittal postcontrast T1-weighted MR the lower cervical and upper thoracic spinal cord. Note the diffuse T1 and T2 prolongation *(asterisks)* of the entire cervical and upper thoracic spinal cord, with associated expansion of the cervical cord. There is no associated contrast enhancement (*asterisks* in C).

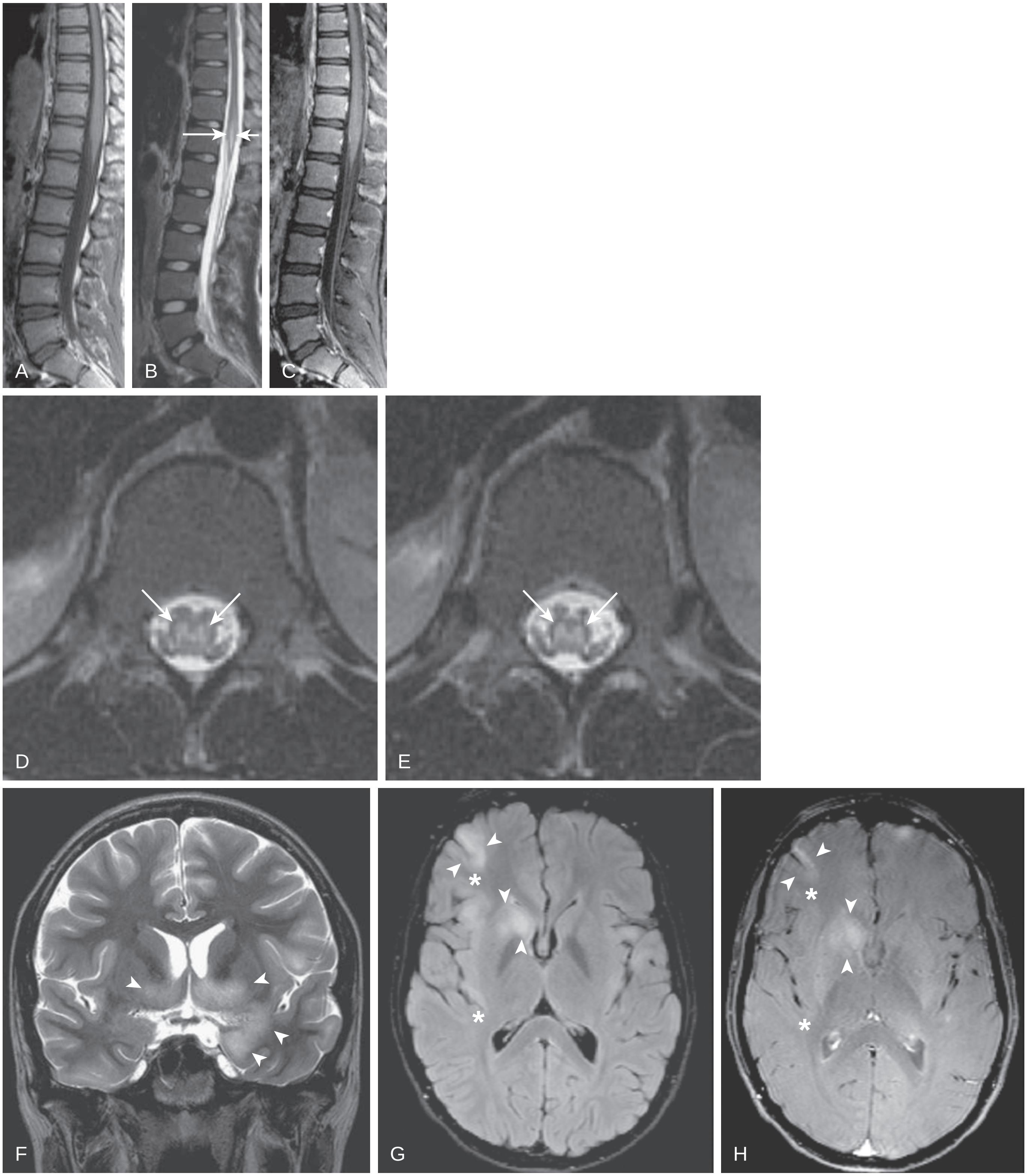

**Figure 44.13. Acute disseminated encephalomyelitis (ADEM).** A 16-year-old male history of constipation, urinary retention, lower extremity weakness, and numbness. Sagittal T1-weighted, sagittal T2-weighted, and sagittal postcontrast T1-weighted MR images (A–C, respectively), axial T2-weighted MR images through the lower thoracolumbar region (D and E), coronal T2-weighted MR image of the brain (F), axial FLAIR image through the brain (G), and axial postcontrast magnetization transfer T1-weighted image through the brain (H). Note the nonexpansive T2 prolongation *(arrows)* of the central spinal cord (D and E). In addition, there are areas of T2 prolongation within the brain (F and G), with involvement of both superficial gray and deep gray structures *(arrowheads)*, including the right insula *(asterisks)*.

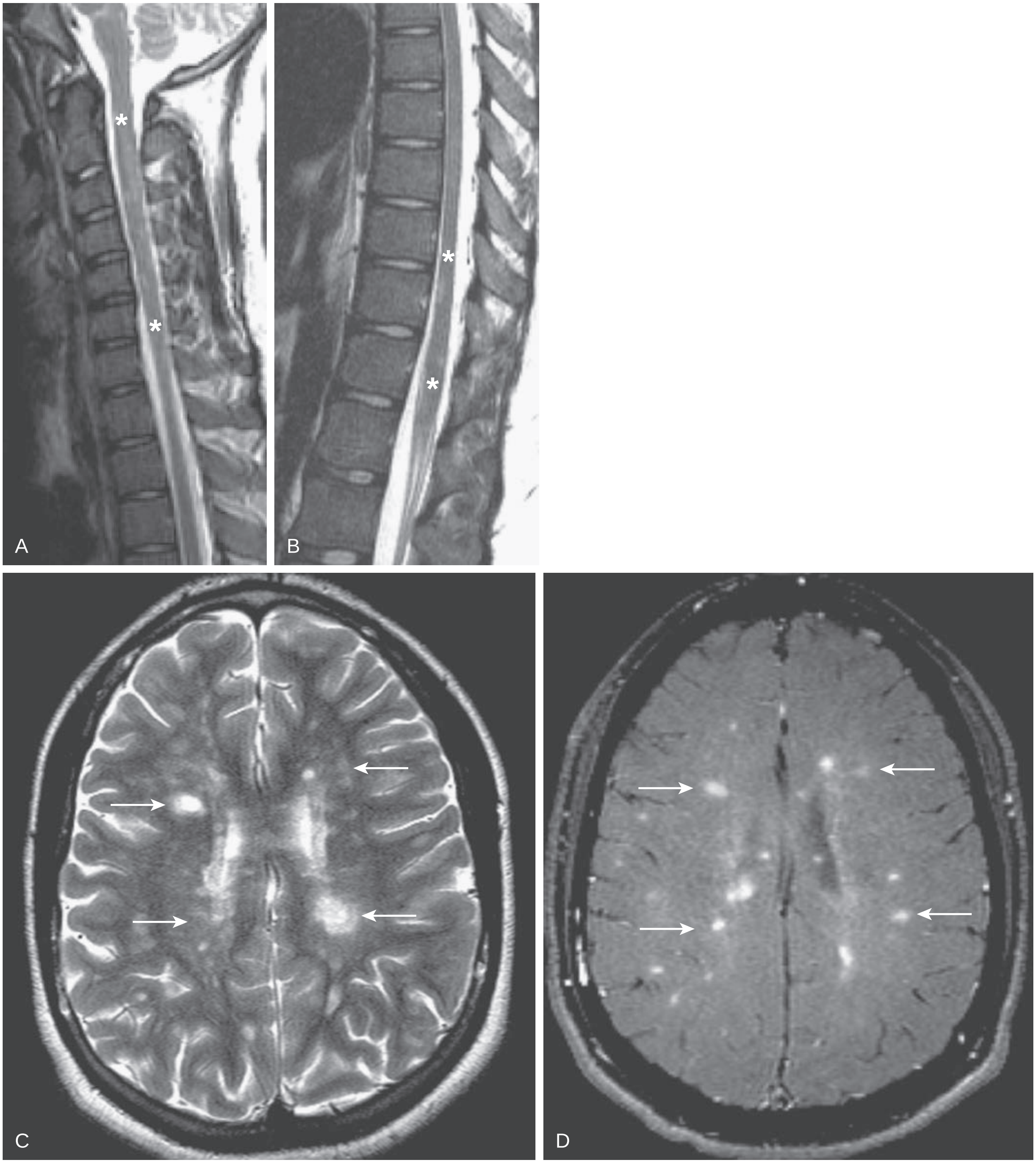

**Figure 44.14. Multiple sclerosis (MS).** Child with sensory changes and decreased vision. Sagittal T2-weighted MR images through the (A) cervical and (B) thoracic spine shows nonexpansive T2 prolongation *(asterisks)* of the spinal cord. (C) Axial T2-weighted and (D) axial postcontrast T1-weighted magnetization transfer MR images of the brain show multiple areas of T2 prolongation (*arrows* in C) within the deep white matter of the cerebrum, running perpendicular to the lateral ventricles (the so-called Dawson's fingers), associated with enhancement (*arrows* in D), suggesting acuity to the demyelinating plaques.

## KEY POINTS

- MRI is the imaging modality of choice for infectious and inflammatory conditions of the spine and spinal cord.
- *Staphylococcus aureus* is the most common infectious agent causing vertebral discitis and osteomyelitis.
- Guillain-Barré syndrome has become the most common cause of acute motor paralysis in children.
- Spinal cord lesions in transverse myelitis generally extend over three or more vertebral body segments, whereas those in multiple sclerosis generally extend over fewer than two vertebral body segments.

## SUGGESTED READINGS

Rossi A. Pediatric spinal infection and inflammation. *Neuroimaging Clin N Am*. 2015;25(2):173–191.

Ryan MM. Guillain-Barre syndrome in childhood. *J Paediatric Child Health*. 2005;41(5–6):237–241.

Wang PI, Gomez-Hassan DM, Stenberg L, Sundgren P. Infections and inflammatory conditions of the pediatric spine and spinal cord. *Appl Radiol*. 2014;16–22.

## REFERENCES

Full references for this chapter can be found on www.expertconsult.com.

## REFERENCES

Alper G, Petropoulou KA, Fitz CR, Kim Y. Idiopathic acute transverse myelitis in children: an analysis and discussion of MRI findings. *Mult Scler*. 2011;17(1):74–80.

Banwell B, Shroff M, Ness JM, et al. MRI features of pediatric multiple sclerosis. *Neurology*. 2007;68:S46–S53.

Brown R, Hussain M, McHugh K, Novelli V, Jones D. Discitis in young children. *J Bone Joint Surg Br*. 2001;83:106–111.

Cameron ML, Durack DT. Helminthic infections. In: Scheld WM, Whitley RJ, Durack DT, eds. *Infections of the Central Nervous System*. Lippincott Williams & Wilkins; 1997:845–878.

Choi KH, Lee KS, Chung SO, Park JM, Kim YJ. Idiopathic tranverse myelitis: MR characteristics. *AJNR Am J Neuroradiol*. 1996;17(6):1151–1160.

Coskun A, Kumandas S, Pac A. Childhood Guillain-Barre syndrome. MR imaging in diagnosis and follow-up. *Acta Radiol*. 2003;44(2):230–235.

Fischer GW, Popich GA, Sullivan DE, et al. Discitis: a prospective diagnostic analysis. *Pediatrics*. 1978;62:543–544.

Fuchs PM, Meves R, Yamada HH. Spinal infections in children: a review. *Int Orthop*. 2012;36(2):387–395.

Goh C, Phal PM, Desmond PM. Neuroimaging in acute transverse myelitis. *Neuroimaging Clin N Am*. 2011;21(4):951–973.

Hughes RA, Rees JH. Clinical and epidemiological features of Guillain-Barre syndrome. *J Infect Dis*. 1997;176:S92–S98.

Iyer RS, Thapa MM, Chew FS. Chronic recurrent multifocal osteomyelitis: review. *AJR Integrative Imaging*. 2011;196(suppl 2):S87–S91.

Kesselring J, Miller DH, Robb SA. Acute disseminated encephalomyelitis. MRI findings and the distinction from multiple sclerosis. *Brain*. 1990;113(Pt 2):291–302.

Khanna G, Sato TS, Ferguson P. Imaging of chronic recurrent multifocal osteomyelitis. *Radiographics*. 2009;29(4):1159–1177.

Kincaid O, Lipton HL. Viral myelitis: an update. *Curr Neurol Neurosci Rep*. 2006;6(6):469–474.

MacDonnell AH, Baird RW, Bronze MS. Intramedullary tuberculomas of the spinal cord: case report and review. *Rev Infect Dis*. 1990;12: 432–439.

Maloney JA, Mirsky DM, Messacar K, et al. MRI findings in children with acute flaccid paralysis and cranial nerve dysfunction occurring during the 2014 Enetrovirus D68 outbreak. *Amer J Neuroradiol*. 2015;36(2): 245–250.

Noseworthy JH, Lucchinetti C, Rodriguez M, Weinshenker BG. Multiple sclerosis. *N Engl J Med*. 2000;343(13):938–952.

Rocca MA, Mastronardo G, Horsfield MA, et al. Comparison of three MR sequences for the detection of cervical cord lesions in patients with multiple sclerosis. *AJNR Am J Neuroradiol*. 1999;20(9):1710.

Ryan MM. Guillain-Barre syndrome in childhood. *J Paediatric Child Health*. 2005;41(5–6):237–241.

Shalmon B, Nass D, Ram Z, Achiron A. Giant lesions in multiple sclerosis—a diagnostic challenge. *Harefuah*. 2000;138:936–939.

Singh S, Alexander M, Korah IP. Acute disseminated encephalomyelitis: MR imaging features. *Am J Roentgenol*. 1999;173:1101–1107.

Sithinamsuwan P, Chairangsaris P. Images in clinical medicine. Gnathostomiasis -Neuroimaging of larval migration. *N Engl J Med*. 2005;353(2):188. [Medline].

Straus Farber R, Devilliers L, Miller A, et al. Differentiating multiple sclerosis from other causes of demyelization using diffusion weighted imaging of the corpus callosum. *J Magn Reson Imaging*. 2009;30(4):732–736.

# 45

# Spinal Tumor and Tumor-like Conditions

*Lisa H. Hutchison and Kalie Adler*

## SPINAL NEOPLASMS

***Overview.*** Spinal tumors occur predominantly in young or middle-aged adults and are rare in children. The most common presentation is vague pain, gait disturbance, change in spinal curvature, motor weakness, and bowel and bladder dysfunction. In this chapter, general concepts regarding spinal neoplasms are discussed, followed by anatomic categories of lesions. Categories include neoplasms located in the intramedullary, intradural-extramedullary, or extradural compartments.[1]

***Imaging.*** The imaging features of spinal neoplasms are often nonspecific and findings overlap. Familiarity with age at diagnosis, key imaging findings, and associations can narrow the differential diagnosis, as summarized in Table 45.1.

Although osseous erosion can occur as a late finding with pediatric spinal cord tumors, plain radiographs are of limited utility. Computed tomography (CT) is helpful in imaging primary osseous lesions, but is less useful in cord evaluation. Instead, magnetic resonance imaging (MRI) is the study of choice to characterize and define spinal cord lesions. Differentiating intramedullary (within the cord) versus intradural-extramedullary (outside the cord, but inside the dura) versus extradural (outside the thecal sac) location is important to narrow the differential diagnosis. Intramedullary lesions show cord expansion, whereas extramedullary lesions will be separate from the cord in at least one plane. Baseline postoperative MRI is deferred for at least 12 weeks because surgical changes make early postoperative scans difficult to interpret.[2]

***Treatment.*** Treatment differs depending on the grade and type of neoplasm (see Table 45.1). The goal with lower-grade, noninfiltrative spinal neoplasms is complete excision of both the solid tumor and associated syrinx cavities. Although tumors may recur or have drop metastasis with suboptimal resection, they are generally amenable to repeat resection. In subtotal resection, adjuvant radiotherapy is useful in adults, but is controversial in children due to increased morbidity from damage to an immature cord.[3] Infiltrative or higher-grade neoplasms may preclude total surgical resection.[4]

Intraoperative ultrasound is often used to determine tumor margins during surgical planning and resection.[2] Electrophysiologic monitoring techniques can be helpful as the periphery of the tumor is approached to prevent damage to the uninvolved portions of the spinal cord.[3]

***Prognosis.*** Prognosis varies depending on tumor grade with high-grade tumors having the worst prognosis, presence or absence of cerebrospinal fluid (CSF) dissemination, and degree of resection. Preoperative neurologic deficits may persist postoperatively, but most tumors can be removed without causing new morbidity. With most cord neoplasms, contrast enhanced MRI of the entire cerebrospinal axis is warranted.

## INTRAMEDULLARY NEOPLASMS

***Overview.*** Pediatric intramedullary tumors occur most commonly in the cervicothoracic cord.[5] Nonspecific symptoms often lead to a delay in diagnosis. Younger children may present with spinal pain (dull and aching) or root pain, rigidity, persistent torticollis, and muscle spasm. Older children may present with gait disturbance and/or progressive scoliosis. Extremity weakness and paresthesias are common.[6] A subset of patients may present with symptoms of increased intracranial pressure (ICP) and hydrocephalus.

### Astrocytoma

***Overview and Origin.*** Up to 60% of intramedullary tumors in children are astrocytomas and the cervical cord is most commonly involved.[3] Spinal astrocytomas usually occur in children around 10 years of age, with an equal sex predilection. Spinal astrocytomas are rarely seen in neonates and infants and may present with irritability, torticollis, and loss or absence of developmental milestones.[6]

Astrocytomas arise from astrocytes and range from benign (grade I) to malignant (grade IV).[7] Spongioblastomas and pilocytic astrocytomas are at the benign end of the spectrum, and high-grade astrocytomas and glioblastoma multiforme tumors are at the malignant end of the spectrum.

Spinal astrocytomas may be cystic, mixed cystic and solid, solid, or contain necrotic components. Malignant astrocytomas can mimic spinal vascular malformations as a result of hypervascularity with possible intratumoral hemorrhage. Lesion size varies from focal to involvement of the entire spinal cord (holocord), which usually is seen during the first year of life.[8]

***Imaging.*** Key features of astrocytomas include cord expansion, eccentric location, hypointense to isointense T1 signal, heterogeneous hyperintense T2 signal, and variable enhancement, sometimes of a mural nodule, on postcontrast images (Figs. 45.1 and 45.2). T2 heterogeneity depends on the presence of solid, cystic, and necrotic components. Tumors may be small with associated syringohydromyelia and subarachnoid seeding.[5]

### Ependymoma

***Overview and Origin.*** Up to 30% of intramedullary tumors in children are ependymomas and the thoracic cord is most commonly involved. Ependymomas present in an older age group than do astrocytomas with a slight female predilection.[3] Ependymomas originate from ependymal cells within the central cord and frequently span multiple vertebral segments.[9] A variety of histologic subtypes exist, with cellular ependymoma being the most common.

Myxopapillary ependymoma occurs exclusively in the lower cord and filum terminale. When located in the cauda equina, this subtype may be associated with subarachnoid hemorrhage, back pain, lower extremity weakness, numbness, pain, and bowel and bladder incontinence.[10]

***Imaging.*** Ependymomas are distinguished by the findings of central cord location, cord expansion, heterogeneous signal intensity on all sequences, and a T2-hypointense hemosiderin cap along the cranial or caudal aspects of the tumor (Figs. 45.3 and 45.4). Contrast-enhanced spinal MRI is useful in the evaluation of drop metastasis, a common feature of ependymomas.[11,12] Multiple ependymomas should prompt consideration of neurofibromatosis type 2 (NF2).[13]

### Ganglioglioma

***Overview and Origin.*** Gangliogliomas contain both neoplastic glial and neuronal components. They present in the first three decades with an average presentation age of 12 years.[5,14]

**TABLE 45.1** Pediatric Spinal Neoplasms: Location, Key Imaging Features, and Other Comments

| Location | Neoplasm | Key Imaging Features | Other Comments |
|---|---|---|---|
| IM | Astrocytoma | Cervical most common<br>Tend to be eccentric in cord ± syrinx<br>Cystic with enhancing nodule | 10 years of age<br>Treatment: surgical debulking ± chemotherapy and radiation |
| | Ependymoma | Tend to be central in cord<br>Cervical most common<br>Hemosiderin cap on T2 sequences<br>Drop metastases | 13–14 years of age<br>If multiple lesions, consider NF2<br>Treatment: surgery ± radiation and chemotherapy |
| | Ganglioglioma | Similar imaging to ependymoma | 7 years; associated with NF2<br>Treatment: surgical resection |
| | Hemangioblastoma | Cystic with an enhancing mural nodule<br>Flow voids | Associated with von Hippel–Lindau disease<br>Treatment: surgery |
| EM | Leptomeningeal metastasis | Lumbosacral involvement<br>Variable size and number of lesions | Common with ependymomas, medulloblastomas, higher-grade astrocytomas<br>Treatment: depends on primary lesion |
| | Nerve sheath tumor (schwannoma, neurofibroma) | Target sign<br>Expansion of intervertebral foramina<br>Posterior vertebral body scalloping | Associated with NF1 and NF2<br>Treatment: conservative; rarely, debulking |
| | Meningioma | Isointense on noncontrast imaging<br>Homogeneous, vigorous enhancement | Teenagers; multiple lesions in setting of NF2<br>Treatment: surgical resection |
| ED | Osteoblastoma | Posterior element, solid, expansile, enhancing mass | 10–30 years; 40% occur in spine<br>Treatment: surgical resection |
| | Aneurysmal bone cyst | Posterior element, expansile, multicystic, fluid-fluid levels | 10–30 years; 20% occur in spine<br>Treatment: embolization, surgical curettage, and packing |
| | Osteoid osteoma | Posterior element lucent nidus with marked surrounding enhancement, ± central calcification | 90% <25 years of age; 10% occur in spine<br>Treatment: radiofrequency ablation |
| | Lymphoma | Vertebral body lesion with little or no loss of height; single > multiple | Spinal involvement with systemic disease; rarely primary lesion<br>Treatment: chemotherapy |
| | Leukemia | Vertebral body lesion with slight loss of height; multiple > single | Spinal involvement with systemic disease<br>Treatment: chemotherapy |
| | Langerhans cell histiocytosis | Vertebral body lesion(s) with severe loss of height (vertebra plana) and soft tissue mass; single > multiple | Ranges from single osseous lesion (histiocytosis X) to systemic disease<br>Treatment: usually chemotherapy |
| | Neuroblastoma | Paraspinous (adrenal is most common) mass encasing vessels with calcifications | 1–5 years of age<br>Treatment: chemotherapy and surgery |
| | Sacrococcygeal teratoma | Heterogeneous signal intensity; enhancement of solid tumor portions; ± osseous erosions; mature types are mostly cystic | 80% <6 months, found in utero; female > male; 4 types based on intrapelvic or extrapelvic location |

*ED,* Extradural (50%); *EM,* extramedullary (15%–20%); *IM,* intramedullary (30%–35%); *MRI,* magnetic resonance imaging; *NF1,* neurofibromatosis type 1; *NF2,* neurofibromatosis type 2.

Gangliogliomas are usually low grade with low malignant potential, but have a propensity for local recurrence.[14]

***Imaging.*** Gangliogliomas may be solid, cystic, calcified, or hemorrhagic. They demonstrate heterogeneous signal intensity on all sequences.[15] Notable features include a lack of peritumoral edema, and adjacent osseous erosion (Fig. 45.5). Given this lesion's similar appearance to an ependymoma on MRI and its association with patients who have NF2, it should be included in the differential diagnosis when ependymoma is a diagnostic consideration.[14]

### Hemangioblastoma

***Overview and Origin.*** Hemangioblastomas are most commonly intramedullary, but can be pial, subpial, or combined intramedullary-extramedullary.[16] Their presence should prompt consideration of von Hippel–Lindau disease and an appropriate workup should be initiated. Treatment includes chemotherapy and surgical resection.[17,18]

***Imaging.*** Hemangioblastomas are typically cystic masses with variable T1 signal, T2 hyperintensity, variable enhancement of mural nodules, and a syrinx in up to 50% of patients (Fig. 45.6). Flow voids are produced by the lesion's arterial and venous supply. Associated hemorrhage and peritumoral edema are common.[19]

## INTRADURAL-EXTRAMEDULLARY NEOPLASMS

***Overview.*** Intradural-extramedullary spinal neoplasms in children include various lesions such as neurofibromas/schwannomas, meningiomas, and leptomeningeal metastases.

### Nerve Sheath Tumors

***Overview and Origin.*** The two main spinal nerve sheath tumors are neurofibromas and schwannomas, with the focus in this chapter on neurofibromas.[20] Neurofibromas are derived from an intermediate cell or from a combination of Schwann cells and perineural fibroblasts. Most spinal neurofibromas are

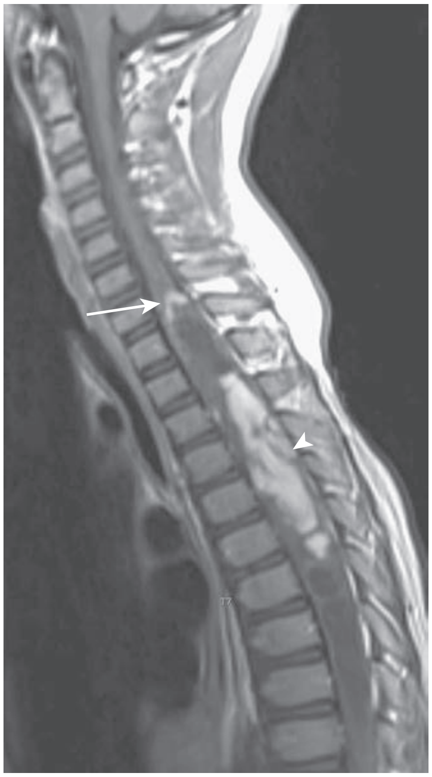

Figure 45.1. Astrocytoma in an 8-year-old boy with back pain. A sagittal T1-weighted contrast-enhanced image demonstrates an intramedullary cystic mass with dorsal nodular *(arrowhead)* and peripheral cranial *(arrow)* enhancement.

intradural-extramedullary lesions. The two morphologic types are fusiform (arising from a single nerve fascicle) and plexiform (involving multiple nerve branches). Lesions may be single, multiple, or diffuse. Neurofibromas are often encountered in children with neurofibromatosis type 1 (NF1), but they may occur as an isolated lesion.[21]

***Imaging.*** Neurofibromas have variable T1 signal, are T2 hyperintense, and enhance after contrast administration. Key imaging features include remodeling and expansion of the intervertebral foramina, indicative of slow indolent growth, and a target appearance (central low signal with peripheral high signal) on T2 images (Fig. 45.7). Rib erosion may be seen, and when extensive, may cause "ribbon ribs." Malignant degeneration into a neurofibrosarcoma is uncommon, but should be considered in large lesions with bone destruction or necrosis.

## Meningioma

***Overview and Imaging.*** Meningiomas of the spinal cord are rare in childhood.[22] When they are seen in patients with neurofibromatosis type 2 (NF2), they may occur intracranially and intraspinally. Meningiomas are T1 hypointense to isointense, T2 hyperintense, uniformly enhance after contrast, and may contain calcifications (Fig. 45.8).[23]

## Leptomeningeal Metastases

***Overview and Origin.*** Metastatic spread to the spinal canal occurs via CSF due to drop metastases from primary supratentorial and posterior fossa brain neoplasms, such as medulloblastoma, ependymoma, and atypical teratoid-rhabdoid tumors.[24]

***Imaging.*** CSF metastases may be solitary, multiple, or diffuse, coating the spinal cord and nerve roots. Metastatic nodules may range in size from 1 mm to a several cm, and may obstruct CSF flow (Fig. 45.9). The most common site is the distal thecal sac, followed by the thoracic, and lastly the cervical spine.[22] The spinal cord should be scanned before surgery for newly diagnosed brain tumors with a propensity to spread via the CSF. If preoperative

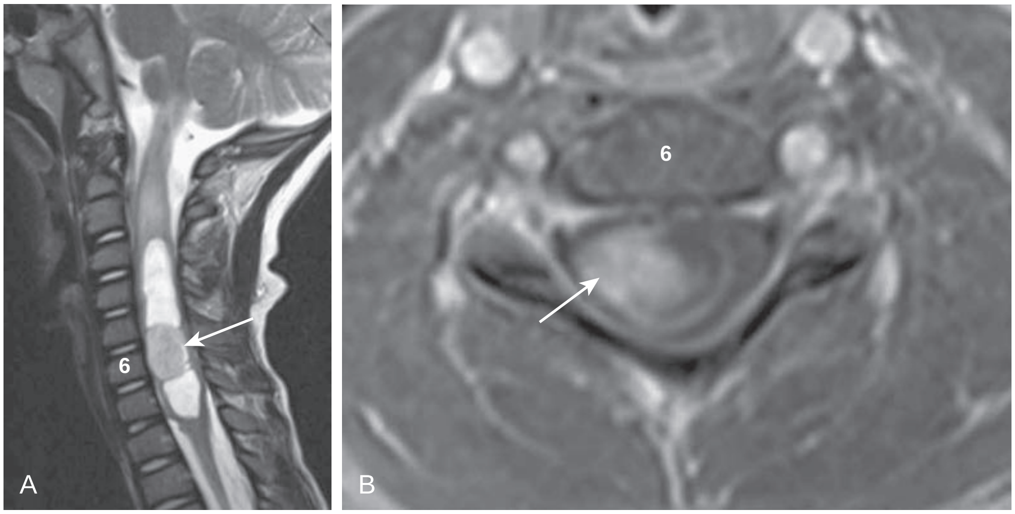

Figure 45.2. Astrocytoma in a 6-year-old boy with pain and decreased right arm use. (A) A sagittal T2-weighted image shows an intramedullary cystic cervical cord mass with a mural nodule *(arrow)*. Note T2 bright cord edema above the mass. (B) An axial T1-weighted postcontrast image through the enhancing nodule shows it is eccentrically located.

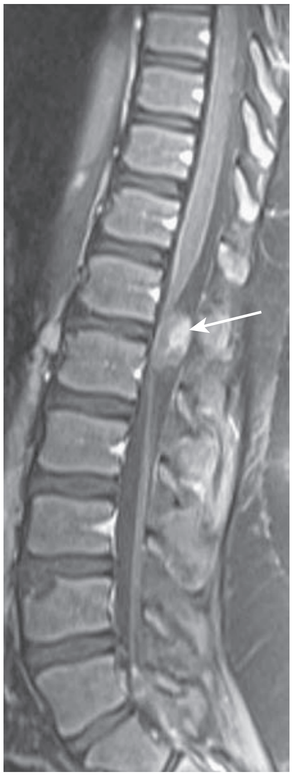

**Figure 45.3. Ependymoma in an 11-year-old boy with unexplained altered mental status.** A sagittal fat suppressed T1-weighted MR image demonstrates an extramedullary heterogeneously enhancing mass *(arrow)* at T12–L1 displacing the nerve roots ventrally.

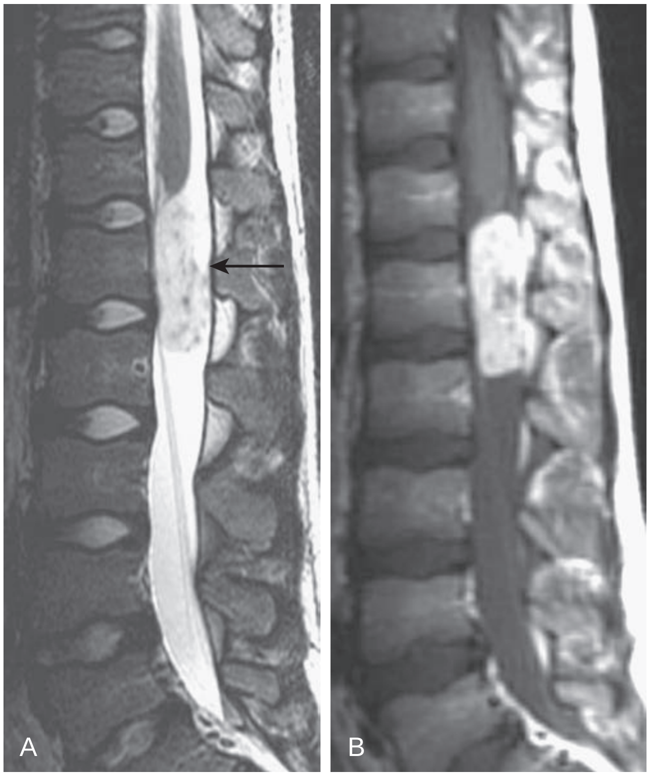

**Figure 45.4. Myxopapillary ependymoma in an 11-year-old girl with back pain.** (A) Sagittal T2-weighted MR image demonstrates a hyperintense, well-defined mass with internal flow voids just below the conus medullaris *(arrow)*. (B) A sagittal postcontrast T1-weighted image reveals avid enhancement.

MRI is not feasible, MRI should be delayed for 4 to 6 weeks after surgery to avoid confusion and possible false-positive results.[11]

## EXTRADURAL TUMORS

***Overview.*** Most childhood extradural neoplasms arise in the vertebral bodies or the paravertebral soft tissues and invade the spinal canal via the intervertebral foramina, such as neuroblastomas and sacrococcygeal teratomas. Primary osseous lesions, such as aneurysmal bone cysts, lymphoma, and Ewing sarcoma, as well as metastatic lesions, also may involve the vertebra and the spinal canal. Imaging is used to determine the extent of spinal involvement, the degree of neural element compression, and the degree of spinal column destabilization due to osseous destruction.[12,25]

### Neuroblastoma

***Overview and Origin.*** Tumors of neural crest cell origin include neuroblastomas, ganglioneuroblastomas, and ganglioneuromas. Neuroblastoma is by far the most common extracranial solid neoplasm, usually presenting between 1 and 5 years of age. Neuroblastomas are classified as primitive neuroectodermal tumors (PNETs) when they involve the central nervous system.

Neuroblastomas originate from neuroblasts along the sympathetic chain and arise most often in the adrenal gland. Metastatic spine involvement can be osseous or involve sympathetic chain ganglia. Spinal metastases may be single or multilevel, and may extend into the epidural space potentially causing cord compression. Larger lesions may have hemorrhage and necrosis. Ganglioneuroblastoma and ganglioneuroma are progressively less malignant forms of neuroblastoma that are composed of mature ganglion cells and nerve fibers. They are well encapsulated and similar in appearance to neuroblastoma, although usually smaller and better defined.

***Imaging.*** Neuroblastomas are paraspinal soft tissue masses, with frequent intraspinal extension. They are hypointense to isointense on T1-weighted images. On T2-weighted images, they range from hypointense to mildly T2 hyperintense and show variable contrast enhancement (Fig. 45.10). Hypointense areas on T1- and T2-weighted imaging may indicate calcifications. Fat-suppressed T2-weighted imaging is useful to determine the extent of disease. Evaluating for tumor extension across the midline is needed for staging.[1]

### Sacrococcygeal Teratomas

***Overview and Origin.*** Sacrococcygeal teratomas (SCTs) are neoplasms derived from all three germinal layers and may be benign or malignant. These neoplasms can contain neural elements, squamous and intestinal epithelium, skin appendages, teeth, and calcium. Four types of SCTs exist; type 1 is external to the pelvis, type 2 is predominantly external with a small intrapelvic portion, type 3 is predominantly intrapelvic with a small external component, and type 4 is completely intrapelvic. All four types may present as an extradural mass and may be associated with bony erosions. SCTs can be cystic, mixed cystic-solid, or solid lesions. Lesions with a more favorable prognosis are type 1 (external), those in younger or female patients, and those lesions that are cystic, homogenous, and contain calcifications.

***Imaging.*** CT is used to demonstrate osseous findings, as well as intrinsic calcifications. On MRI, cystic components of SCT are T1 hypointense and T2 hyperintense. The signal of hemorrhagic components will depend on the age of the hemorrhage. Solid components may enhance (Fig. 45.11).

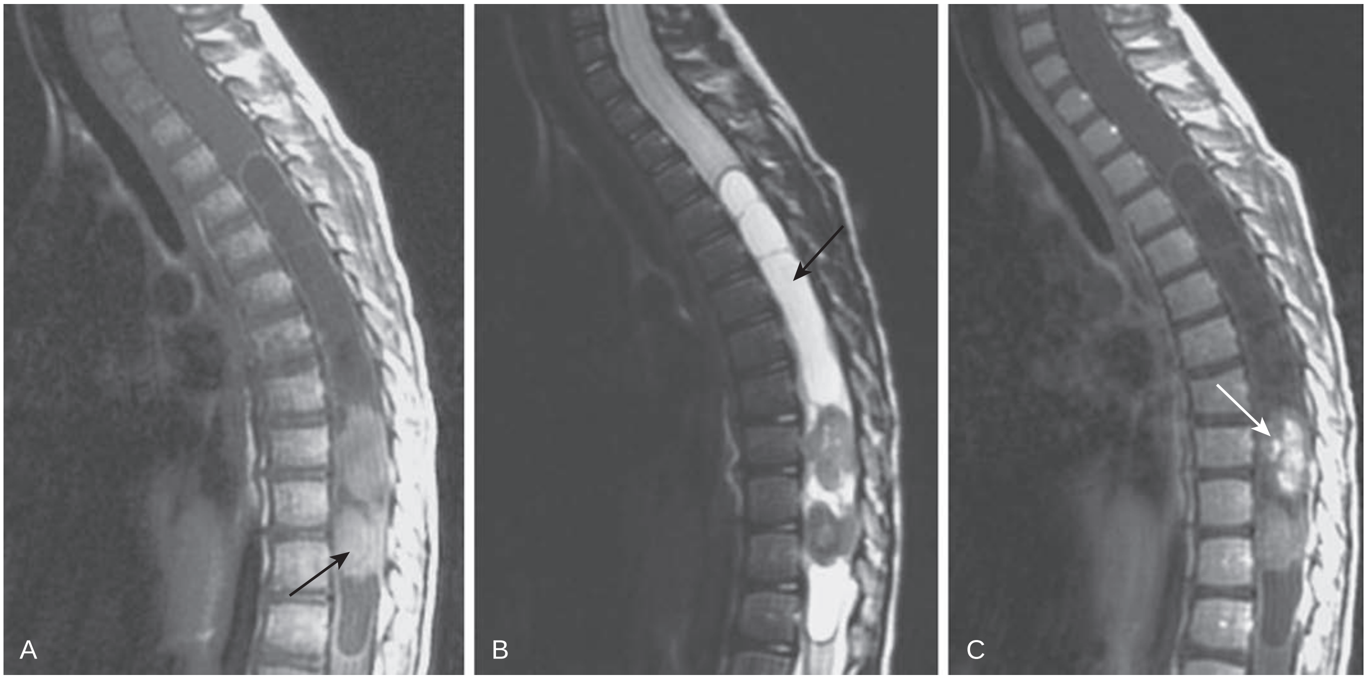

**Figure 45.5. Ganglioglioma.** (A) A sagittal T1-weighted MR image shows a holocord tumor. Rounded hyperintense elements at the thoracolumbar junction were found during surgery to represent hemorrhagic tumor components *(arrow).* (B) A sagittal fat-suppressed T2-weighted image shows the hemorrhagic components of the lesion as hypointense masses. Note the tumor cyst in the midthoracic cord *(arrow).* (C) A sagittal postcontrast T1-weighted image reveals enhancement of the caudal tumor *(arrow).*

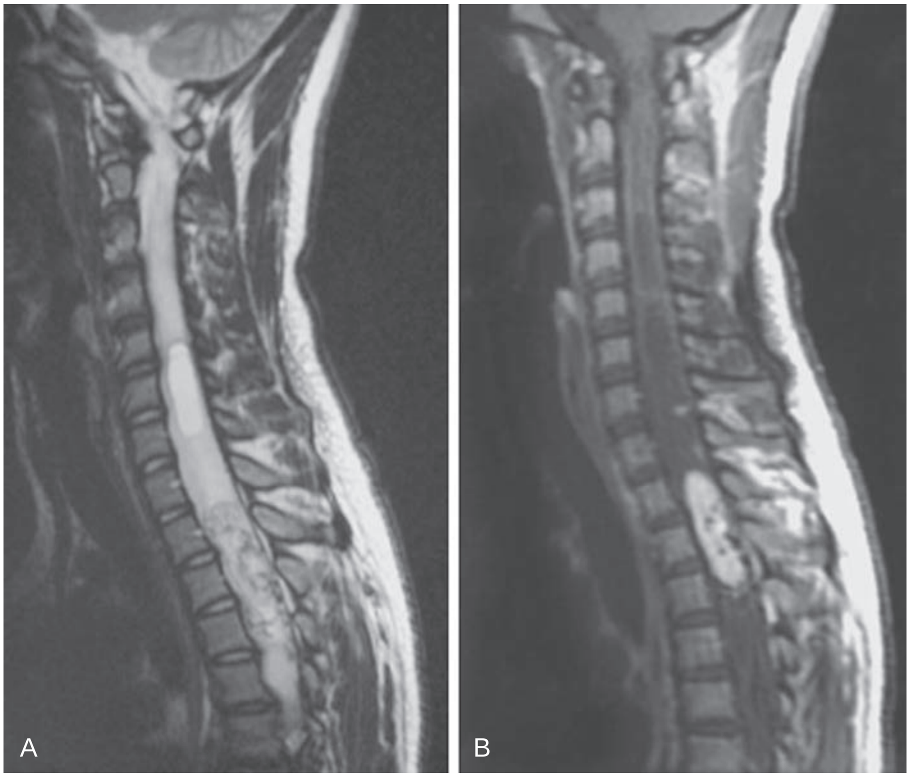

**Figure 45.6. Hemangioblastoma in a 14-year-old child with von Hippel–Lindau disease.** (A) A sagittal T2-weighted MR image shows a cystic component superior to the heterogeneous spinal cord lesion containing flow voids. (B) A sagittal postcontrast T1-weighted image demonstrates marked tumor enhancement and multiple bright foci of other hemangioblastomas in the cystic portion of the cord mass. A low signal cystic component is again seen.

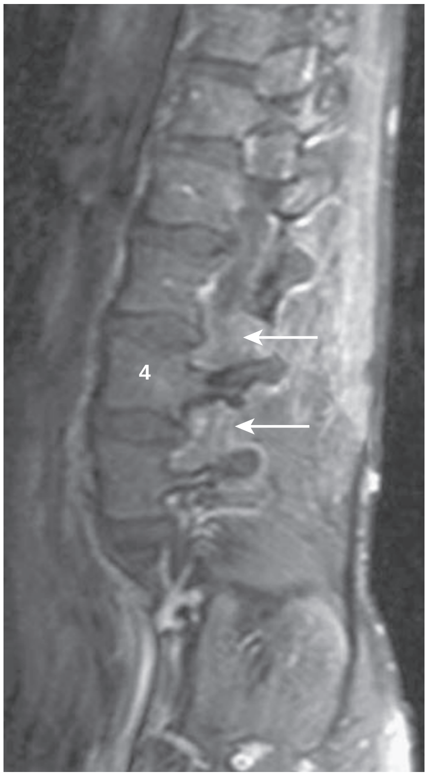

**Figure 45.7. Plexiform neurofibroma in a 13-year-old girl with NF1 and scoliosis.** Sagittal fat-suppressed T1-weighted MR image with contrast identifies neural foraminal stenosis at multiple contiguous lumbar levels *(arrows).*

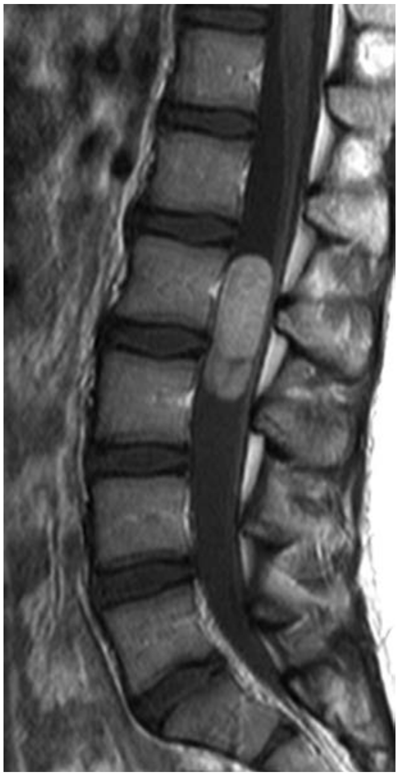

**Figure 45.8. Meningioma in a 15-year-old girl with leg and back pain.** Sagittal contrast-enhanced fat-suppressed T1-weighted MR image shows a well-defined enhancing mass in the lumbar spinal canal.

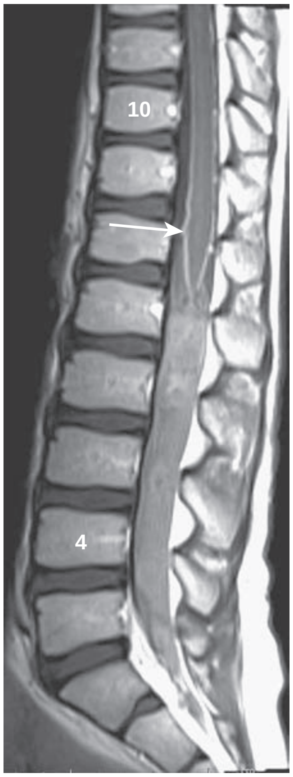

**Figure 45.9. Leptomeningeal metastases in a 9-year-old girl with an atypical rhabdoid teratoid tumor who has undergone radiation.** A sagittal postcontrast T1-weighted MR image demonstrates leptomeningeal enhancement *(arrow)* from the lower thoracic cord to the conus medullaris. Extensive enhancing solid tissue fills the distal thecal sac.

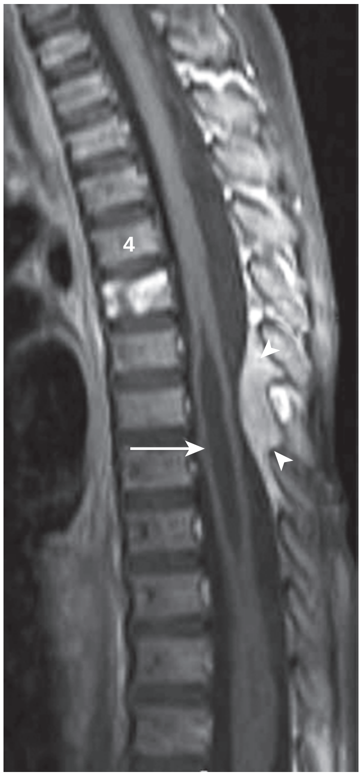

**Figure 45.10. Metastatic neuroblastoma in a 2-year-old boy with leg weakness and diarrhea.** A sagittal T1-weighted, fat-suppressed MR image identifies an enhancing metastatic lesion in the T5 vertebral body, a syrinx from T5 to T11 *(arrow),* and a hyperintense, enhancing dorsal epidural lesion *(arrowheads).* A primary right adrenal mass was found (not shown).

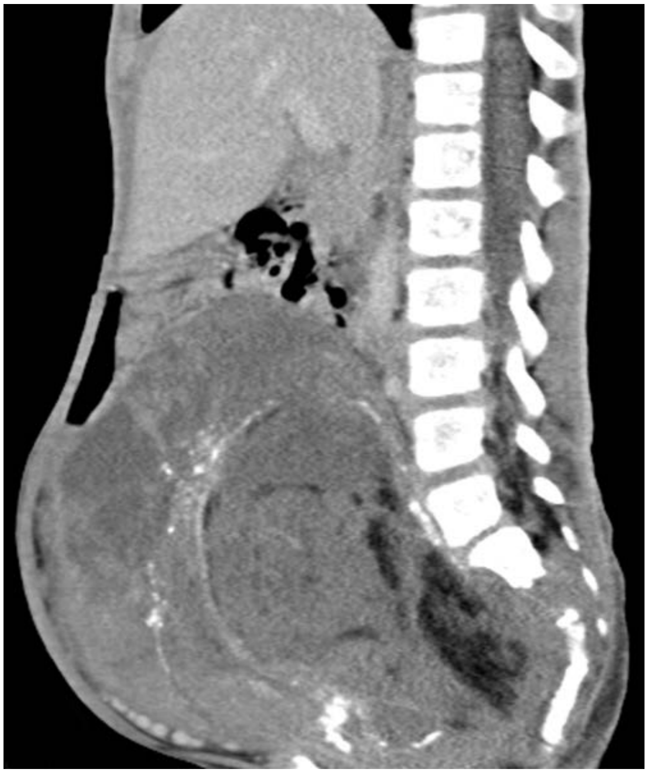

**Figure 45.11. Sacrococcygeal teratoma, type 4, in a 6-day-old girl with an abdominal mass.** Sagittal reconstructed postcontrast CT image shows a large mass anterior to and invading the sacrum. The heterogeneous mass contains low-attenuation fat, soft tissue, and scattered calcifications.

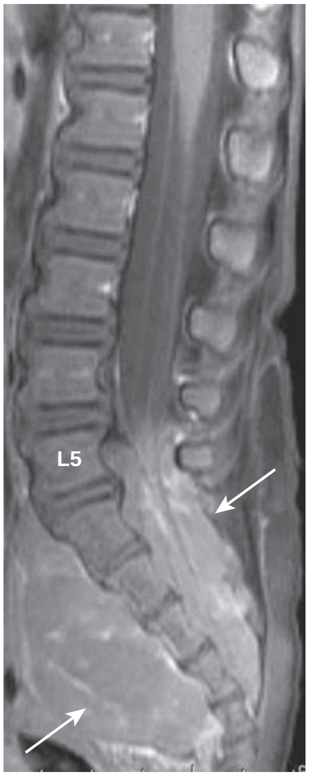

**Figure 45.13. Megakaryocytic leukemia in a 1-year-old boy with thrombocytopenia.** A sagittal T1-weighted postcontrast, fat-suppressed MR image identifies an enhancing mass arising from the sacrum with extensive lumbosacral epidural involvement *(arrows).*

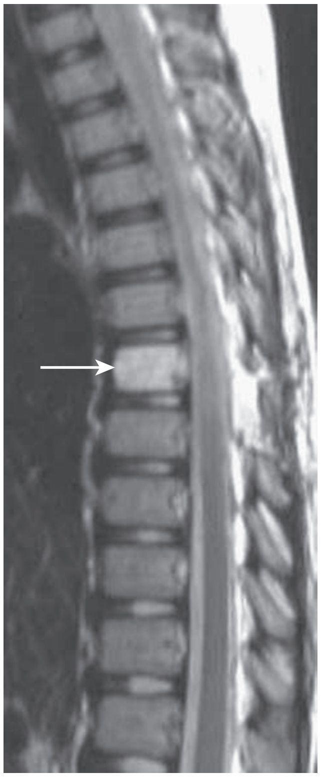

**Figure 45.12. Burkitt lymphoma in a 5-year-old boy with back pain and urinary retention.** A sagittal T2-weighted MR image demonstrates a hyperintense T7 vertebral body lesion. Note postsurgical changes of the posterior elements.

The location of the SCT in relationship to the gluteal fold helps differentiate this lesion from masses associated with spinal dysraphic conditions. Specifically, SCTs typically extend below the gluteal fold and masses associated with spinal dysraphism typically extend above the gluteal fold.[26]

## LYMPHOMA AND LEUKEMIA

***Overview and Origin.*** Lymphoma involves the spine less commonly than it does other reticuloendothelial system structures, such as lymph nodes. Single or multiple vertebral bodies may be involved, especially with non-Hodgkin–type lymphoma (Fig. 45.12). A diffuse epidural infiltration, a localized epidural mass, a primary osseous or paraspinal mass with epidural extension, or spinal cord masses may be present. Single or multiple vertebral levels may be involved. Epidural deposits from leukemia more commonly produce clinical symptoms in children than in adults, with myelogenous leukemia more likely presenting as a focal mass (Fig. 45.13).[27]

***Imaging.*** Epidural involvement in patients with lymphoma and leukemia is usually isointense on noncontrast T1-weighted, and slightly hypointense on T2-weighted sequences. Homogeneous enhancement is seen after contrast administration. A key imaging finding is the presence of normal vertebral body height and no osseous destruction despite abnormal marrow signal.[28]

### Leptomeningeal Melanosis

***Overview.*** Neurocutaneous melanosis is a rare, nonfamilial phakomatosis caused by melanocyte proliferation within the epidermis and leptomeninges. A forme fruste may occur in which only leptomeningeal involvement is present without cutaneous

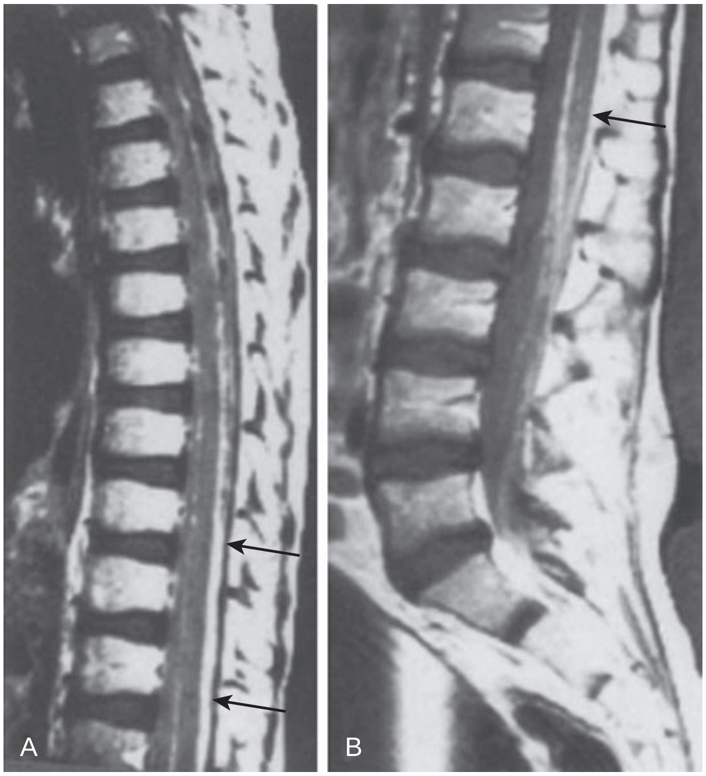

**Figure 45.14. Leptomeningeal melanosis.** A postcontrast sagittal T1-weighted MR image reveals diffuse enhancement *(arrows)* of the thoracic (A) and lumbosacral (B) spinal cord leptomeninges.

manifestations. In the pediatric population, leptomeningeal involvement may present with signs of raised ICP and hydrocephalus.

***Imaging.*** The most common finding is diffuse leptomeningeal thickening and enhancement after contrast administration, as can be seen with leptomeningeal metastases. However, hyperintense signal on noncontrast T1-weighted sequences, indicating melanin, should prompt consideration of melanosis (Fig. 45.14).[29]

## Extradural Bony Lesions

***Overview.*** Numerous vertebral osseous abnormalities may produce extradural mass effect. Spinal lesions tend to arise either from the posterior elements or vertebral bodies. Common posterior element lesions include osteoid osteomas, aneurysmal bone cysts, and osteoblastomas. Common primary pediatric vertebral masses include Ewing sarcoma (a peripheral PNET), lymphoma, leukemia, Langerhans cell histiocytosis, and metastatic disease, such as neuroblastoma.

***Imaging.*** Imaging findings vary depending on the specific type of lesion. CT plays a greater role in imaging osseous masses and is best used complementary to MRI. Posterior element lesions, which include osteoid osteomas, have a focal sclerotic nidus surrounded by a lucent halo on CT and show a "double density sign" on nuclear bone scintigraphy. On MRI, these lesions show impressive surrounding edema. Aneurysmal bone cysts are classically expansile, multilocular lesions with fluid-fluid levels due to internal hemorrhage (Fig. 45.15). Osteoblastomas are expansile solid masses of the posterior elements and rarely have fluid levels (Fig. 45.16). Lesions that involve the marrow space of a single vertebral body, such as Ewing sarcoma and lymphoma, tend to be T1 hypointense and T2 hyperintense with enhancement after contrast. They usually cause little, if any, loss of vertebral body height.[30]

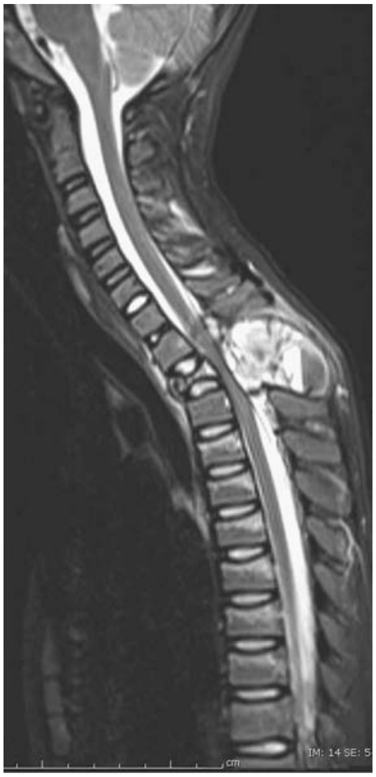

**Figure 45.15. An aneurysmal bone cyst in a 10-year-old girl with back pain.** A sagittal T2-weighted MR image demonstrates a multiloculated, expansile lesion with fluid levels in the T3 posterior elements. Compression of T3 causes effacement of the adjacent spinal canal.

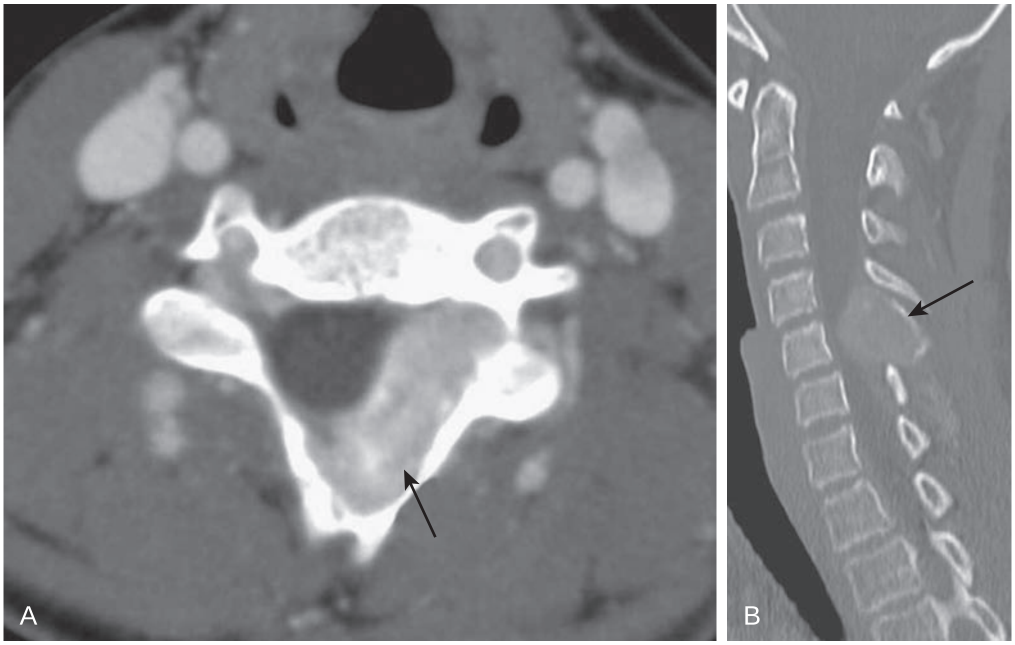

**Figure 45.16. Osteoblastoma in 14-year-old boy with left neck pain and paresthesias.** (A) Axial postcontrast CT image shows an enhancing epidural lesion *(arrow)* with rightward cord displacement. (B) Sagittal cervical spine CT demonstrates a C5 posterior element expansile mass *(arrow).*

## KEY POINTS

- The differential diagnosis of spinal neoplasms in children can be narrowed by determining the lesion compartment: intramedullary, intradural-extramedullary, or extradural.
- The most common pediatric spinal cord mass is astrocytoma, an intramedullary, expansile, infiltrative, often eccentric lesion with an enhancing component.
- The second most common pediatric spinal cord neoplasm is ependymoma, an intramedullary, often central, circumscribed mass often having a hemosiderin cap and necrosis.

## SUGGESTED READINGS

Crawford JR, Zaninovic A, Santi M, et al. Primary spinal cord tumors of childhood: effects of clinical presentation, radiographic features, and pathology on survival. *J Neurooncol*. 2009;95:259–269.

Menashe SJ, Iyer RS. Pediatric spinal neoplasia: a practical overview of intramedullary, intradural and osseous tumors. *Curr Probl Diagn Radiol*. 2013;42(6):249–265.

Rossi A, Gandolfo C, Morana G, et al. Tumors of the spine in children. *Neuroimaging Clin N Am*. 2007;17(1):17–35.

## REFERENCES

Full references for this chapter can be found on www.expertconsult.com.

## REFERENCES

1. Dietrich RB, Kangarloo H. Retroperitoneal mass with intradural extension: value of magnetic resonance imaging in neuroblastoma. *AJR Am J Roentgenol*. 1986;146(2):251–254.
2. Keiper MD, Zimmerman RA, Bilaniuk LT. MRI in the assessment of the supportive soft tissues of the cervical spine in acute trauma in children. *Neuroradiology*. 1998;40(6):359–363.
3. Smith AB, Soderlund KA, Rushing EJ, et al. Radiologic-pathologic correlation of pediatric and adolescent spinal neoplasms: Part 1, Intramedullary spinal neoplasms. *AJR Am J Roentgenol*. 2012;198(1):34–43.
4. Sakai Y, Matsuyama Y, Katayama Y, et al. Spinal myxopapillary ependymoma: neurological deterioration in patients treated with surgery. *Spine*. 2009;34(15):1619–1624.
5. Soderlund KA, Smith AB, Rushing EJ, et al. Radiologic-pathologic correlation of pediatric and adolescent spinal neoplasms: Part 2, Intradural extramedullary spinal neoplasms. *AJR Am J Roentgenol*. 2012;198:44–51.
6. Young Poussaint T, Yousuf N, Barnes PD, et al. Cervicomedullary astrocytomas of childhood: clinical and imaging follow-up. *Pediatr Radiol*. 1999;29(9):662–668.
7. Roonprapunt C, Houten JK. Spinal cord astrocytomas: presentation, management, and outcome. *Neurosurg Clin N Am*. 2006;17(1):29–36.
8. Schittenhelm J, Ebner FH, Tatagiba M, et al. Holocord pilocytic astrocytoma—case report and review of the literature. *Clin Neurol Neurosurg*. 2009;111(2):203–207.
9. Sarikaya S, Acikgoz B, Tekkok IH, et al. Conus ependymoma with holocord syringohydromyelia and syringobulbia. *J Clin Neurosci*. 2007;14(9):901–904.
10. Wippold FJ 2nd, Smirniotopoulos JG, Moran CJ, et al. MR imaging of myxopapillary ependymoma: findings and value to determine extent of tumor and its relation to intraspinal structures. *AJR Am J Roentgenol*. 1995;165(5):1263–1267.
11. Khan SN, Donthineni R. Surgical management of metastatic spine tumors. *Orthop Clin North Am*. 2006;37(1):99–104.
12. Gebauer GP, Farjoodi P, Sciubba DM, et al. Magnetic resonance imaging of spine tumors: classification, differential diagnosis, and spectrum of disease. *J Bone Joint Surg Am*. 2008;90(suppl 4):146–162.
13. Aguilera DG, Mazewski C, Schniederjan MJ, et al. Neurofibromatosis-2 and spinal cord ependymomas: report of two cases and review of the literature. *Childs Nerv Syst*. 2011;27(5):757–764.
14. Patel U, Pinto RS, Miller DC, et al. MR of spinal cord ganglioglioma. *AJNR Am J Neuroradiol*. 1998;19(5):879–887.
15. Jallo GI, Freed D, Epstein FJ. Spinal cord gangliogliomas: a review of 56 patients. *J Neurooncol*. 2004;68(1):71–77.
16. Bostrom A, Hans FJ, Reinacher PC, et al. Intramedullary hemangioblastomas: timing of surgery, microsurgical technique and follow-up in 23 patients. *Eur Spine J*. 2008;17(6):882–886.
17. Sardi I, Sanzo M, Giordano F, et al. Monotherapy with thalidomide for treatment of spinal cord hemangioblastomas in a patient with von Hippel-Lindau disease. *Pediatr Blood Cancer*. 2009;53(3):464–467.
19. Vougioukas VI, Glasker S, Hubbe U, et al. Surgical treatment of hemangioblastomas of the central nervous system in pediatric patients. *Childs Nerv Syst*. 2006;22(9):1149–1153.
20. Kim NR, Suh YL, Shin HJ. Thoracic pediatric intramedullary schwannoma: report of a case. *Pediatr Neurosurg*. 2009;45(5):396–401.
22. Jinnai T, Koyama T. Clinical characteristics of spinal nerve sheath tumors: analysis of 149 cases. *Neurosurgery*. 2005;56(3):510–515, discussion 510-515.
23. Liu PI, Liu GC, Tsai KB, et al. Intraspinal clear-cell meningioma: case report and review of literature. *Surg Neurol*. 2005;63(3):285–288, discussion 288-289.
24. Solero CL, Fornari M, Giombini S, et al. Spinal meningiomas: review of 174 operated cases. *Neurosurgery*. 1989;25(2):153–160.
25. Parmar H, Hawkins C, Bouffet E, et al. Imaging findings in primary intracranial atypical teratoid/rhabdoid tumors. *Pediatr Radiol*. 2006;36(2):126–132.
26. Sciubba DM, Hsieh P, McLoughlin GS, et al. Pediatric tumors involving the spinal column. *Neurosurg Clin N Am*. 2008;19(1):81–92.
27. Fadler KM, Askin DF. Sacrococcygeal teratoma in the newborn: a case study of prenatal management and clinical intervention. *Neonatal Netw*. 2008;27(3):185–191.
28. Vazquez E, Lucaya J, Castellote A, et al. Neuroimaging in pediatric leukemia and lymphoma: differential diagnosis. *Radiographics*. 2002;22(6):1411–1428.
29. Hayashi M, Maeda M, Maji T, et al. Diffuse leptomeningeal hyperintensity on fluid-attenuated inversion recovery MR images in neurocutaneous melanosis. *AJNR Am J Neuroradiol*. 2004;25(1):138–141.
30. Beltran J, Noto AM, Chakeres DW, et al. Tumors of the osseous spine: staging with MR imaging versus CT. *Radiology*. 1987;162(2):565–569.

# 46

# Vascular Lesions

*Joseph V. Loeb, Lisa H. Hutchison, and Kay North*

Vascular lesions of the spine are uncommon in children. Vascular lesions are subdivided into fast-flow lesions, such as arteriovenous malformations (AVMs) and arteriovenous fistulas (AVFs), and slow-flow lesions, such as venous (formerly "cavernous") malformations. Rarely, children suffer spinal cord infarcts. Several syndromes are associated with spinal cord AVMs and AVFs, including hereditary hemorrhagic telangiectasia (Osler–Weber–Rendu), neurofibromatosis, and Parkes–Weber, Cobb, and CLOVES (congenital, lipomatous, overgrowth, vascular malformations, epidermal nevi, and spinal/skeletal anomalies or scoliosis) syndromes.[1,2,5]

## CLASSIFICATION

Vascular lesions of the spine have undergone various classifications,[1,6-10] in part because of the complexity of their diagnosis and features. The term *spinal arteriovenous shunt* is used to denote both types of high-flow lesions (AVMs and AVFs). Because AVMs and AVFs are found in various locations (i.e., intramedullary, intradural extramedullary, and extradural sites) with variable feeding vessels, structural features, drainage, and hemodynamic changes, additional subclassifications have been proposed.[6,8,9] Due to recent histopathologic discoveries, pediatric vascular anomalies have been classified using the International Society for the Study of Vascular Anomalies (ISSVA) system first published by Mulliken and Glowacki in 1996 and updated in 2014.[3,11,12] This system, which allows for correlation between lesion histology, clinical presentation, and treatment, is now used widely by pediatric subspecialists including dermatologists, interventional radiologists, plastic surgeons, and neurosurgeons.[10] The ISSVA classification system divides lesions into two broad categories: neoplasms and vascular malformations.[10-12] Vascular anomalies are further divided into simple, combined (containing more than one type of vessels), or associated with other anomalies.[3] This chapter discusses pediatric vascular anomalies, emphasizing the most common lesions, including AVMs and AVFs, and venous malformations. Spinal cord infarcts are also discussed in this chapter, though they fall outside the ISSVA system.

## ARTERIOVENOUS MALFORMATIONS

***Overview and Etiology.*** AVMs are high-flow malformations that contain a nidus (nest), or vascular network, that communicates between the arteries and veins. AVMs may be sporadic or seen in patients with various disorders. The high-flow dynamics within the AVM predisposes the involved arteries and veins to the formation of aneurysms and varices, respectively.[10] AVMs can be characterized further by the location of the nidus (intramedullary or extramedullary), as well as by morphology of the nidus (the central, tightly formed "glomus" type, or the diffuse, extensive, extramedullary "juvenile" or "metameric" type). In children, the glomus spinal cord fast-flow AVM is the most common. In one large series, twice as many children had AVMs as had AVFs.[6] AVMs may occur anywhere along the spine, and do so in approximate proportion with each segment, including 30% to 40% cervical and 60% to 70% thoracolumbar.

***Clinical Presentation.*** The initial clinical presentation varies from acute paraparesis to slowly progressive myelopathy with weakness, sensory loss, and bowel and bladder dysfunction. Hemorrhage is more common in children (78%) compared with adults, especially in cervical cord AVMs. In 56% of cases, children present acutely due to AVM hemorrhage.[6]

***Imaging.*** Magnetic resonance imaging (MRI) is the best noninvasive modality for initial diagnosis and follow-up of a spinal arteriovenous shunt.[6,13] Imaging findings of cord AVMs include tortuous dilated vessels within or on the surface of the cord that are identified by flow-voids. Hemorrhage has a variable appearance on T1-weighted and T2-weighted images depending on chronicity. T2-weighted images may demonstrate spinal cord edema and expansion.[3] MRI also documents the presence of cord cavitation, atrophy, and venous thrombosis. Images obtained after administration of gadolinium may reveal cord enhancement due to venous stasis, ischemia, or cord infarction[1] (Fig. 46.1). Distinguishing normal physiologic cerebrospinal fluid (CSF) pulsation and flow (particularly in the dorsal extramedullary midthoracic region) from vascular abnormalities requires optimization of spine imaging, which may include switching the phase and frequency encoding directions to decrease the effect of physiologic CSF pulsation. Computed tomography (CT) has a limited role in imaging AVMs, but may document bony changes, often seen in large, diffuse metameric-type lesions. Ultimately, spinal angiography remains the gold standard for diagnosis and delineation of AVMs.

***Treatment.*** Endovascular embolization is the primary line of treatment for fast-flow vascular anomalies, except for lesions at the conus, which are managed surgically.[1,3,6] In some patients, complete lesion embolization or resection is not possible because of unacceptably high risk of morbidity or mortality. In these cases, the treatment goal is to reach a hemodynamic equilibrium between the lesion and the spinal cord that will reduce the risk of ischemia and hemorrhage.[14,15]

***Prognosis.*** A spectrum of outcomes may occur depending on the lesion location, presentation, and treatment.[15] The severity of symptoms at the time of diagnosis is directly related to patient outcome, with most symptoms persisting partially or completely after treatment.[14]

## ARTERIOVENOUS FISTULA

***Overview and Etiology.*** The term *AVF* is used to describe fast-flow lesions with a direct artery to vein connection without a focal nidus, as seen in AVMs. Converse to AVMs, which are congenital lesions, AVFs are believed to be acquired anomalies resulting from microvascular injury and reparative healing.[8,16] In a large combined pediatric and adult series, a higher percentage of multiple cord fistulas were observed in pediatric (46%) compared with adult patients (27%).[6] AVFs are divided by location into two groups, spinal cord and spinal dural. Spinal cord AVFs are perimedullary in location and one-third as common as AVMs in children. Spinal dural AVFs are extremely rare in the pediatric population.[6]

***Clinical Presentation.*** The clinical presentation of AVFs is similar to AVMs, including slowly progressive weakness, sensory loss, and bowel and bladder dysfunction due to venous congestion, venous hypertension, and resultant myelopathy. However, AVFs hemorrhage less than AVMs, and acute presentations are uncommon.[6]

***Imaging.*** Imaging findings of pediatric spinal cord AVFs are virtually identical to spinal cord AVMs.[1] Dural AVFs, which are common in adults, are uncommon in children.[6]

## Abstract:

Spinal vascular lesions in children are rare, but have significant neurologic presentations and sequelae. The lesions can be subdivided into fast flow lesions, such as AVM's and AVF's, and slow flow lesions, such as venous malformations. Rarely, children suffer spinal cord infarcts.

## Keywords:

Vascular malformations
Arteriovenous malformation
Arteriovenous fistula
Venous malformations
Spinal infarcts

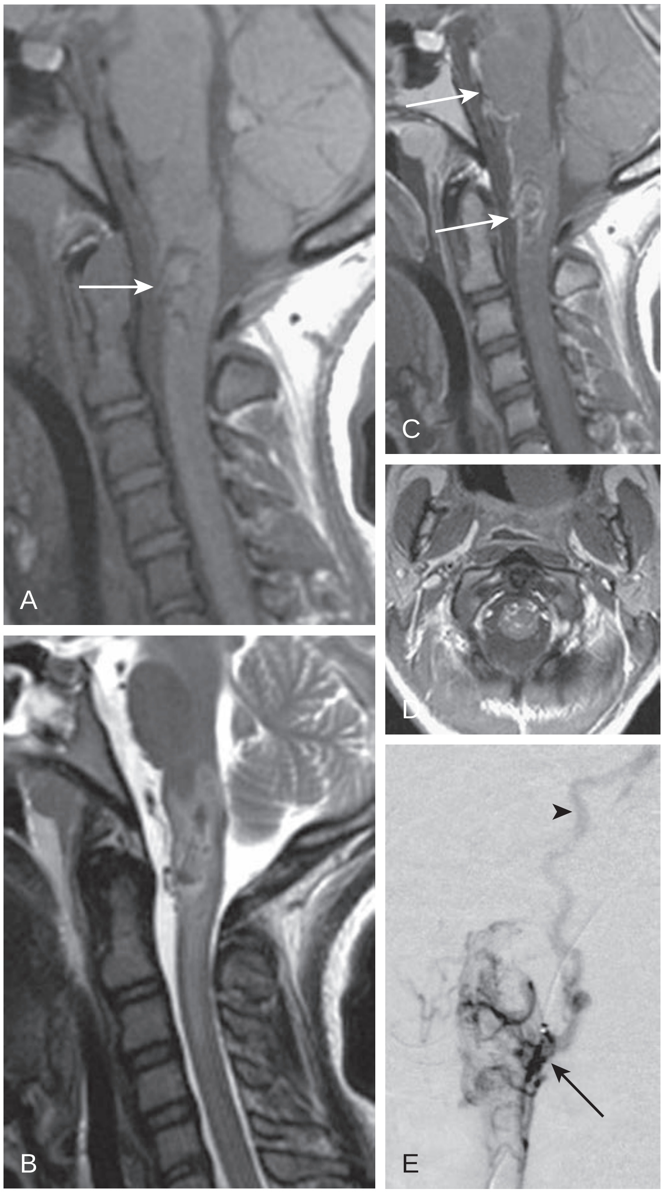

**Figure 46.1. AVM in a 14-year-old girl with sudden severe headache, left-sided weakness, and loss of consciousness.** Head CT (not shown) revealed intraventricular hemorrhage. (A) Sagittal T1-weighted MRI shows a hypointense lesion with subtle foci of high signal hemorrhage *(arrow).* (B) Sagittal T2-weighted MRI confirms low-signal central hemorrhage with hyperintense surrounding edema. (C and D) Postcontrast T1-weighted sagittal and axial MRI demonstrates enhancing superficial serpiginous vessels and peripheral intramedullary enhancement *(arrows).* (E) A catheter angiogram injection of the vertebral artery reveals an intramedullary nidus *(arrow)* with arterial supply from anterior and lateral spinal artery contributors. Venous drainage is toward the jugular bulb via a recurrent perimedullary vein *(arrowhead).*

***Treatment.*** Because each spinal AVF is unique, treatment must be tailored to the specific lesion, taking into account location, size, number of fistulous sites, and associated symptoms.[3] Therapies are the same as for other fast-flow anomalies, including endovascular embolization, microsurgical resection, radiation therapy (used rarely), or a combination of these therapies.[1,3,17] Endovascular embolization has the advantage of being less invasive than the other therapies, but the feeding arteries may not be accessible, and thus open surgery is needed in some cases.[18]

***Prognosis.*** Early diagnosis of AVFs is essential to preserve neurologic function. Patient outcome is proportional to the severity of symptoms at the time of diagnosis. Patients who are nonambulatory and those with poor bladder or bowel function before treatment are unlikely to regain neurologic functions after therapy.[17,18]

## VENOUS MALFORMATIONS

***Overview.*** Slow-flow venous (formerly known as cavernous) malformations (VMs), also previously termed *cavernous angiomas* and *cavernomas*, are congenital vascular malformations composed of dysmorphic venous channels lined by a single layer of endothelial cells with no intervening neural tissue.[19] Per the ISSVA classification system, VMs of the spinal cord have been reclassified as simple vascular malformations III. Rather than the misnomer cavernoma, the term *venous (cavernous) malformation* is used to avoid confusion with true neoplasms that enlarge through cell division (mitosis). VMs increase in size by distention of vascular channels, often due to inflammation or hemorrhage. Spinal cord VMs are less common than similar lesions found in the brain, with one study showing that 5% of pediatric VMs located within the spine.[20]

***Etiology.*** The specific etiology of spinal VMs is unclear. However, the presentation of multiple brain and/or spinal VMs in any child should prompt a careful history and genetic analysis. Associated mutations predisposing patients to multiple VMs have been found on chromosomes 3 and 7, with an autosomal dominant variable penetrance pattern of inheritance.[20] Deep venous anomalies are associated with sporadic VMs in up to 40% of cases. Patients who previously have undergone radiation therapy, typically of the craniospinal axis, are predisposed to the development of VMs. Approximately 12% to 16% of pediatric patients have multiple VM lesions.[20,21]

***Clinical Presentation.*** The clinical presentation of VMs is variable, often resulting from hemorrhage. They may present at any age with variable symptoms, from being nearly asymptomatic to having severe neurologic symptoms. Pediatric patients are more likely to have a sudden clinical onset compared with adults, with up to 75% presenting acutely.[20]

***Imaging.*** MRI findings of spinal cord VMs are similar to their intracranial counterparts, with T1-weighted signal heterogeneity within the lesion caused by blood products of varying age. On T2-weighted imaging, a classic hypointense rim representing hemosiderin is key, with an internal heterogeneous T2 signal. Cord edema may be seen if recent hemorrhage has occurred (Fig. 46.2). On T2* gradient recalled echo imaging and susceptibility-weighted imaging (SWI), a prominent blooming effect is noted because of hemorrhage degradation products.[22] SWI has been shown to be significantly better than T2* gradient imaging to detect hemorrhage.[22] Distinguishing a spinal cord VM from other pathologies can be difficult in some cases, but usually is based on identification of the classic hemosiderin rim (or ring), and the absence of other morphologic features that would suggest a neoplasm, such as an enhancing mass.[19] Because VMs are very slow-flow lesions, they are not seen on catheter angiography. Therefore catheter angiography has no role in the imaging evaluation of VMs.

***Treatment.*** Asymptomatic VMs and those located in delicate regions are treated conservatively. Although symptomatic VMs located elsewhere in the body may be treated initially with sclerotherapy, this treatment is not an option for intramedullary spinal cord lesions. Instead, patients with symptomatic spinal cord lesions may undergo surgical resection or, rarely, radiotherapy when the lesions are in hard-to-reach locations.[19,21]

***Prognosis.*** The immediate postoperative outcome after VM resection in one study showed that 11% of patients had worse symptoms, 83% were the same, and 6% were improved. At 5-year follow-up, the percentages of patients who were the same and

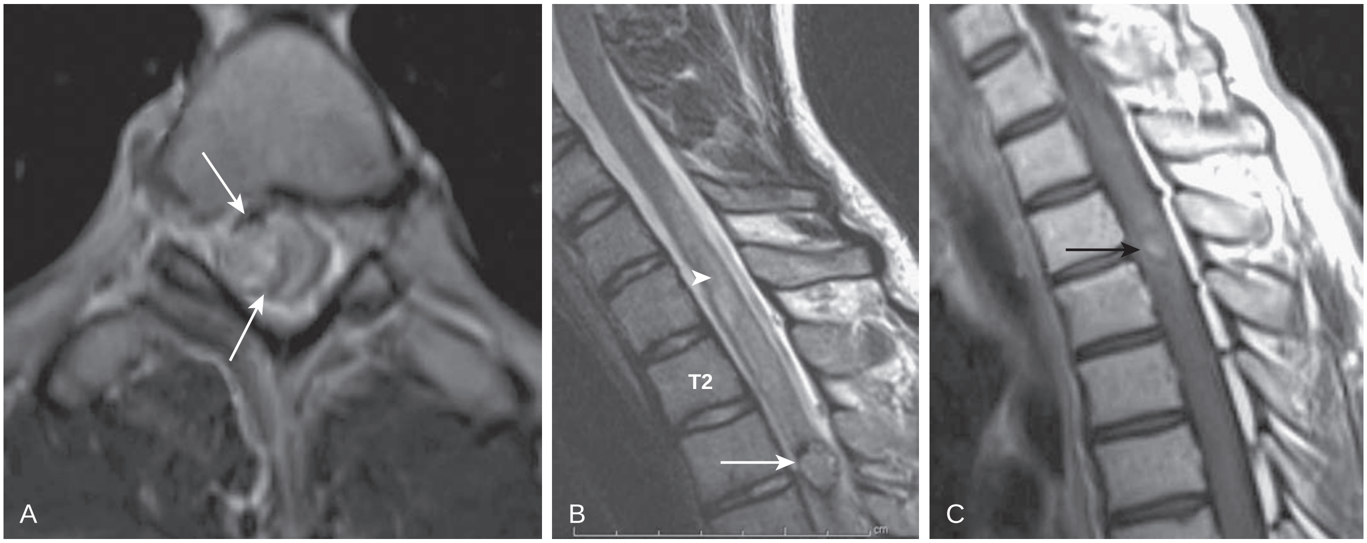

**Figure 46.2. Vascular malformation in a 16-year-old boy with arm weakness.** (A and B) Axial and sagittal T2-weighted MRI demonstrates a centrally hyperintense intramedullary lesion with a hypointense rim *(arrows).* Central bright signal cord edema is noted proximally as well *(arrowhead).* (C) Postcontrast T1-weighted MRI shows no enhancement. Central hyperintense hemorrhage within the lesion *(arrow)* also was seen on precontrast images (not shown).

improved were 68% and 23%, respectively,[23] showing a moderate response to treatment.

## SPINAL CORD INFARCTION

***Overview.*** Infarction of the spinal cord is uncommon, particularly in children. The most vulnerable region of the spinal cord is the anterior half, which is supplied by the single anterior spinal artery. The posterior spinal cord is supplied by paired paramedian posterior spinal arteries, allowing more extensive collateral circulation.

***Etiology.*** Trauma and infection (e.g., meningitis) are the most common causes of cord infarction in children.[24] Other causes of spinal cord infarction include thrombotic and/or embolic phenomena from cardiac disease, hypercoagulable states, umbilical arterial lines, or fibrocartilaginous embolization, as well as hypoperfusion and cardiac arrest.[24,25,29]

***Clinical Presentation.*** Spinal cord infarction most often presents with acute paraparesis or quadriparesis depending on the level of cord involvement.[26]

***Imaging.*** Because the single anterior artery supplies the anterior two-thirds of the spinal cord, infarction often shows anterior cord involvement of both gray and white matter, seen as T1 hypointensity and T2 hyperintensity (Fig. 46.3). T2 hyperintensity may not be seen initially if MRI is performed in the hyperacute (first few hours after the event) setting. Cord edema and swelling can be seen acutely, and contrast enhancement can occur in the subacute (>5 days) phase.[27] Current MRI techniques allow diffusion-weighted imaging (DWI) of the spinal cord as a supplement to standard sequences to confirm ischemia[27,28] (Fig. 46.4). In the differential diagnosis of cord infarction is transverse myelitis, which is more common than cord infarction (see Chapter 44). Isolated involvement of the spinal cord gray matter suggests an infectious or postinfectious autoimmune process rather than infarction. Careful review of the patient's history, spinal fluid, and anatomic distribution of signal abnormality in spinal gray and/or white matter are helpful to distinguish cord infarct from transverse myelitis.[24,29]

***Treatment.*** Supportive care is largely the only treatment for spinal cord infarct (Fig. 46.5). Methylprednisone may be given in the acute setting to help limit cord edema, but its utility is questionable.[25,29]

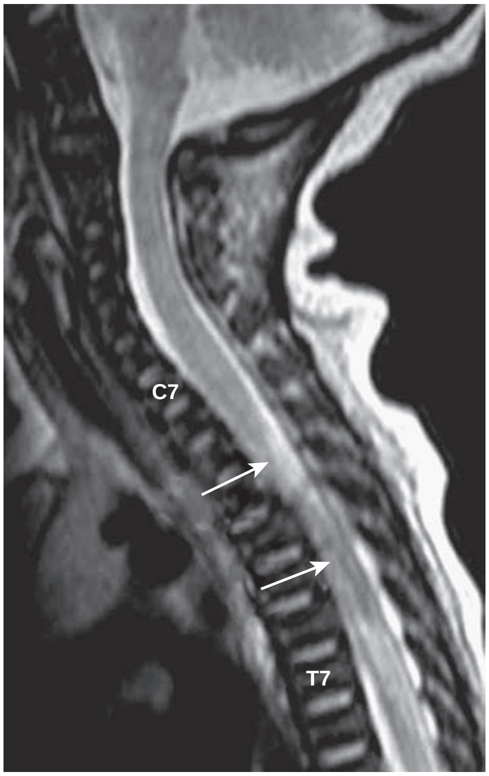

**Figure 46.3. Spinal cord infarct in a newborn male with paraplegia due to traumatic delivery.** Sagittal T2-weighted MRI reveals a large region of heterogeneous signal intensity *(arrows)* due to thoracic cord transection. Proximal hyperintense edema also is seen. Labeled are the seventh cervical (C7) and thoracic (T7) vertebrae.

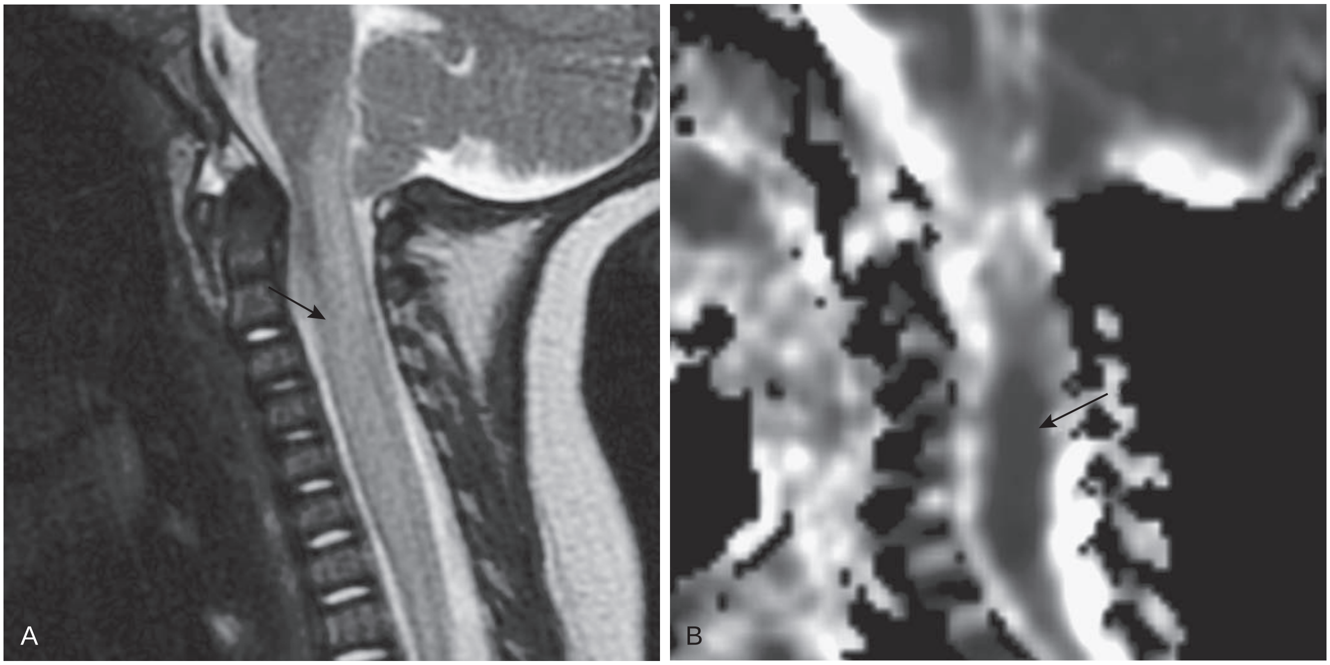

**Figure 46.4. Cord ischemia due to herpes simplex virus type 6.** (A) A sagittal fast spin echo T2-weighted MRI shows T2 hyperintensity and cord swelling because of edema *(arrow).* (B) Apparent diffusion coefficient (ADC) map of a sagittal echo planar diffusion-weighted image shows hypointensity representing cytotoxic cord edema *(arrow).* The findings are consistent with necrotizing myelitis.

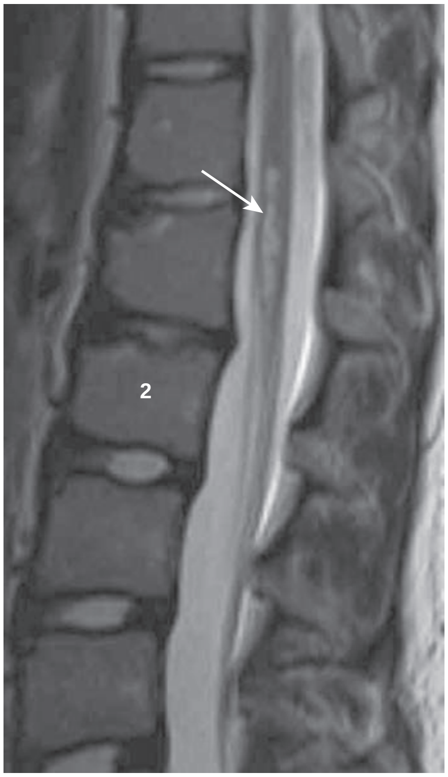

**Figure 46.5. Lumbar spinal cord infarct in a 13-year-old girl with pain and leg weakness for 2 weeks.** Sagittal T2-weighted MRI reveals a well-defined region of oblong hyperintensity *(arrow).* Irregularity at the anterior superior margin of L1 and L2 are consistent with Schmorl nodes suggesting possible fibrocartilaginous etiology.

***Prognosis.*** The outcome of cord infarction depends on the initial symptoms. Unfortunately, symptoms such as paraparesis and paraplegia seen at presentation often persist.[25,26]

## KEY POINTS

- Spinal vascular lesions in children are rare, but have significant neurologic presentations and sequelae. Diagnosis of such a lesion should prompt evaluation for an underlying cause, syndrome, or genetic predisposition.
- Advances in histopathologic knowledge have led to development of the ISSVA classification system, which allows consistent correlation between the type of pediatric vascular anomaly, lesion treatment, and outcome.
- Newer MRI techniques, such as SWI and DWI, can help characterize fast-flow spinal cord arteriovenous shunts, as well as slow-flow vascular lesions and spinal cord infarcts.

## SUGGESTED READINGS

Boo S, Hartel J, Hogg JP. Vascular abnormalities of the spine: an imaging review. *Curr Probl Diagn Radiol*. 2010;39(3):110–117.
Nagib MG, O'Fallon MT. Intramedullary cavernous angiomas of the spinal cord in the pediatric age group: a pediatric series. *Pediatr Neurosurg*. 2002;36:57–63.
Nozaki T, Nosaka S, Miyazaki O. Syndromes associated with vascular tumors and malformations: a pictorial review. *Radiographics*. 2013;33(1):175–195.
Rangel-Castilla L, et al. Contemporary management of spinal AVFs and AVMs: lessons learned from 110 cases. *Neurosurg Focus*. 2014;37(3):E14.
Wassef M, et al. Vascular Anomalies Classification: Recommendations From the International Society for the Study of Vascular Anomalies. *Pediatrics*. 2015;136(1):e203–e214.

## REFERENCES

Full references for this chapter can be found on www.expertconsult.com.

## REFERENCES

1. Cullen S, Krings T, Ozanne A, et al. Diagnosis and endovascular treatment of pediatric spinal arteriovenous shunts. *Neuroimaging Clin N Am*. 2007;17(2):207–221.
2. Krings T, Chng SM, Ozanne A, et al. Hereditary hemorrhagic telangiectasia in children: endovascular treatment of neurovascular malformations: results in 31 patients. *Neuroradiology*. 2005;47(12):946–954.
3. Cahill AM, Nijs EL. Pediatric vascular malformations: pathophysiology, diagnosis, and the role of interventional radiology. *Cardiovasc Intervent Radiol*. 2011;34(4):691–704.
4. [deleted in review].
5. Alomari AI, Chaudry G, Rodesch G, et al. Complex spinal-paraspinal fast-flow lesions in CLOVES syndrome: analysis of clinical and imaging findings in 6 patients. *AJNR Am J Neuroradiol*. 2011;32(10):1812–1817.
6. Niimi Y, Berenstein A, Song J. Spinal vascular malformations. In: Albright AL, Pollack IF, Adelson PD, et al, eds. *Principles and Practice of Pediatric Neurosurgery*. New York: Thieme Medical Publishers; 2008.
7. Anson JA, Spetzler RF. Interventional neuroradiology for spinal pathology. *Clin Neurosurg*. 1992;39:388–417.
8. Spetzler RF, Detwiler PW, Riina HA, et al. Modified classification of spinal cord vascular lesions. *J Neurosurg*. 2002;96(suppl 2):145–156.
9. Zozulya YP, Slin'ko EI, Al Q II. Spinal arteriovenous malformations: new classification and surgical treatment. *Neurosurg Focus*. 2006;20(5):E7.
10. Dubois J, Garel L. Imaging and therapeutic approach of hemangiomas and vascular malformations in the pediatric age group. *Pediatr Radiol*. 1999;29(12):879–893.
11. Kollipara R, Dinneen L, Rentas KE, et al. Current classification and terminology of pediatric vascular anomalies. *AJR Am J Roentgenol*. 2013;201(5):1124–1135.
12. Wassef M, et al. Vascular anomalies classification: recommendations from the International Society for the Study of Vascular Anomalies. *Pediatrics*. 2015;136(1):doi:10.1542/peds.2014-3673.
13. Dormont D, Gelbert F, Assouline E, et al. MR imaging of spinal cord arteriovenous malformations at 0.5 T: study of 34 cases. *AJNR Am J Neuroradiol*. 1988;9(5):833–838.
14. Veznedaroglu E, Nelson PK, Jabbour PM, et al. Endovascular treatment of spinal cord arteriovenous malformations. *Neurosurgery*. 2006;59(5 suppl 3):S202–S209, discussion S203-S213.
15. Juszkat R, Zabicki B, Checinski P, et al. Endovascular treatment of arteriovenous malformation. *Aesthetic Plast Surg*. 2009;33(4):639–642.
16. Spetzler RF, Zabramski JM. Surgical management of large AVMs. *Acta Neurochir Suppl (Wien)*. 1988;42:93–97.
17. Patsalides A, Knopman J, Santillan A, et al. Endovascular treatment of spinal arteriovenous lesions: beyond the dural fistula. *AJNR Am J Neuroradiol*. 2011;32(5):798–808.
18. Song D, Garton HJ, Fahim DK, et al. Spinal cord vascular malformations in children. *Neurosurg Clin N Am*. 2010;21(3):503–510.
19. Mottolese C, Hermier M, Stan H, et al. Central nervous system cavernomas in the pediatric age group. *Neurosurg Rev*. 2001;24(2–3):55–71, discussion 72-73.
20. Acciarri N, Galassi E, Giulioni M, et al. Cavernous malformations of the central nervous system in the pediatric age group. *Pediatr Neurosurg*. 2009;45(2):81–104.
21. Deutsch H, Shrivistava R, Epstein F, et al. Pediatric intramedullary spinal cavernous malformations. *Spine*. 2001;26(18): E427–E431.
22. Wang M, Dai Y, Han Y, et al. Susceptibility weighted imaging in detecting hemorrhage in acute cervical spinal cord injury. *Magn Reson Imaging*. 2011;29(3):365–373.
23. Mitha AP, Turner JD, Abla AA, et al. Outcomes following resection of intramedullary spinal cord cavernous malformations: a 25-year experience. *J Neurosurg Spine*. 2011;14(5):605–611.
24. Nance JR, Golomb MR. Ischemic spinal cord infarction in children without vertebral fracture. *Pediatr Neurol*. 2007;36(4): 209–216.
25. Tosi L, Rigoli G, Beltramello A. Fibrocartilaginous embolism of the spinal cord: a clinical and pathogenetic reconsideration. *J Neurol Neurosurg Psychiatry*. 1996;60(1):55–60.
26. Raghavan A, Onikul E, Ryan MM, et al. Anterior spinal cord infarction owing to possible fibrocartilaginous embolism. *Pediatr Radiol*. 2004;34(6):503–506.
27. Krings T, Lasjaunias PL, Hans FJ, et al. Imaging in spinal vascular disease. *Neuroimaging Clin N Am*. 2007;17(1):57–72.
28. Manara R, Calderone M, Severino MS, et al. Spinal cord infarction due to fibrocartilaginous embolization: the role of diffusion weighted imaging and short-tau inversion recovery sequences. *J Child Neurol*. 2010;25(8):1024–1028.
29. Han JJ, Massagli TL, Jaffe KM. Fibrocartilaginous embolism—an uncommon cause of spinal cord infarction: a case report and review of the literature. *Arch Phys Med Rehabil*. 2004;85(1):153–157.

# 47

# Trauma

Peter Winningham and Lisa H. Hutchison

The mortality rate of spine-related trauma in children is higher than in adults and is estimated at 25% to 32%.[1] Fortunately, children with incomplete neurologic lesions fare better than adults, with up to 90% having partial recovery and 60% having full recovery.[1,2]

## ETIOLOGY

Motor vehicle accidents (MVAs), falls, and sports injuries are the most common causes of pediatric spinal trauma. Young athletes are at higher risk than adults for developing stress-related injuries.[3,4] Congenital spine anomalies such as os odontoideum, block vertebrae, Klippel–Feil syndrome, and Down syndrome increase the risk of cervical spinal injury. Nerve root avulsion may result from birth trauma, MVAs, or penetrating injury (Fig. 47.1).[5]

Younger children are more susceptible to upper cervical injuries because of their relatively large-sized, heavy craniums and weaker neck muscles.[6] This anatomy causes a more cranial fulcrum of movement at C2–C3 in younger children versus C5–C6 in older children and adults.[1] Injuries in younger children, especially those younger than 8 years, differ from those in older children. Because of greater cervical mobility and ligament laxity in the spine of younger children, they tend to have injuries at higher levels (occiput to C3). These injuries are more likely associated with a neurologic deficit and extend through synchondroses.[7]

## SPINAL CORD INJURY WITHOUT RADIOGRAPHIC ABNORMALITY

The unique biomechanical properties of young children causes increased occurrence of spinal cord injury without radiographic abnormality (SCIWORA).[8] With the introduction of magnetic resonance imaging (MRI), injuries in children with SCIWORA could be visualized and the general prognosis predicted on the basis of the findings.[9,10] MRI can show the findings of cord contusion, hemorrhage, and transection (Fig. 47.2).[11] The presence of intramedullary hemorrhage and transection portend a poor prognosis.[8]

## ATLANTO-OCCIPITAL DISASSOCIATION

Because of their relatively small occipital condyles and more horizontal atlanto-occipital joints, young children are at increased risk for atlanto-occipital disassociation.[2,9,12] Devastating spinal cord injury often occurs, and many cases are fatal. A diagnosis is made by measuring a condylar gap greater than 5 mm (Kaufman condylar gap) or a basion-to-axis interval (BAI) greater than 12 mm (Fig. 47.3).[2] One pitfall is that in children under 13 years, the BAI is less reliable.[12] See Table 47.1 for pediatric cervical spine measurements.[13] Atlanto-occipital disassociation requires urgent stabilization.

## ATLAS OR JEFFERSON FRACTURE

Cervical spine compression loading forces can result in a C1 burst, or Jefferson, fracture. This injury is most common in adolescents from MVAs and diving accidents. Jefferson fractures show between one and four defects in the C1 ring. The fracture may be stable or unstable, depending on whether or not the transverse ligament is intact or ruptured, respectively. A single C1 ring defect is usually stable, whereas three or four defects are unstable.[9] A dens to C1 lateral mass distance greater than 8 mm suggests instability. Forty percent of Jefferson fractures have an associated C2 fracture.[12] Lateral cervical spine radiographs are of little value, and the diagnosis is made on the odontoid view or computed tomography (CT) by showing offset of the C1 on C2 lateral masses (Fig. 47.4).[13] Pitfalls to avoid include head rotation on the open-mouth view, which may cause the lateral mass to appear laterally displaced; hypermobility in young children that may have minimal normal lateral displacement of C1 on C2; and the normal developmental offset of C1 lateral masses in children less than 2 years of age because of differential C1 versus C2 growth.[9]

## ATLANTOAXIAL ROTATORY FORCE INJURY

The atlantoaxial joint is responsible for 50% of the normal neck range of motion. Temporary ligamentous laxity after neck infection or surgery may cause mild atlantoaxial rotatory subluxation (AARS), or Grisel syndrome. A similar situation, referred to as “wry neck,” occurs in normal children who simply awaken with a stiff neck unable to turn their head to one side.[9] Grisel syndrome and wry neck represent a mild, self-limiting form of C1 on C2 rotatory subluxation caused by muscle spasm. In frank rotatory dislocation, children present with torticollis, holding their heads in a peculiar “cock robin” position (head rotated to one side and tilted to the other).[2] The duration of subluxation is proportional to the risk of morbidity. When rotatory injury is fixed, the term *atlantoaxial rotatory fixation (AARF)* is applied. Atlantoaxial rotatory injury is classified into four types, according to Fielding and Hawkins (Table 47.2).[14] Mild rotatory anomalies are treated with muscle relaxers and physical therapy, but more aggressive management may include traction and, rarely, surgery, to prevent C1–C2 osseous fusion.[2] An imaging diagnosis of AARS is suggested by the presence of asymmetry in the dens to C1 lateral mass distance on open-mouth odontoid radiographs and CT (Fig. 47.5). CT signs of rotatory disorders include loss of articulation of the occiput and C1, as well as sclerosis on both sides of the joint with impending fusion (Fig. 47.6).

## ODONTOID (DENS) FRACTURES

Dens, or odontoid, fractures are common in children. The rigid, upright nature of dens makes it susceptible to a variety of flexion, loading, and extension forces.[9] In young children, the odontoid is separated from the body of C2 by a cartilaginous synchondrosis, which fuses between 5 and 7 years.[9] The presence of the synchondrosis in infants and young children allows fractures to occur frequently through this growth plate, but fortunately these fractures heal readily (Fig. 47.7). In adults these fractures are often complicated by nonunion or pseudoarthroses.[1] Dens fractures are classified into three types with type 2 being unstable. Type 1 is through the tip of the dens, type 2 is through the base of the dens, and type 3 is through the body of C2.[2,9]

A pitfall of odontoid fractures is the presence of an os odontoideum. This variant is a well-corticated ossicle of variable size in the expected location of the odontoid process. Small os odontoideums are normal variants of no significance; however, when large enough to extend inferior to the annular ligament, they may be unstable and susceptible to injury.[9] The origin is

## Abstract:

This chapter reviews spine related trauma in children. Specific diagnoses covered with accompanying images include: atlanto-occipital disassociation, Jefferson fracture, atlantoaxial rotatory force injury, odontoid fracture, hangman fracture, chance and burst fractures. The concept of spinal cord injury without radiographic abnormality (SCIWORA) is discussed. Tables within the chapter include the Fielding classification of atlantoaxial rotatory subluxation and typical radiographic measurements used in pediatric cervical spine trauma.

## Keywords:

Jefferson fracture
atlantoaxial rotatory subluxation
odontoid fracture
hangman fracture
chance fracture
burst fracture
SCIWORA

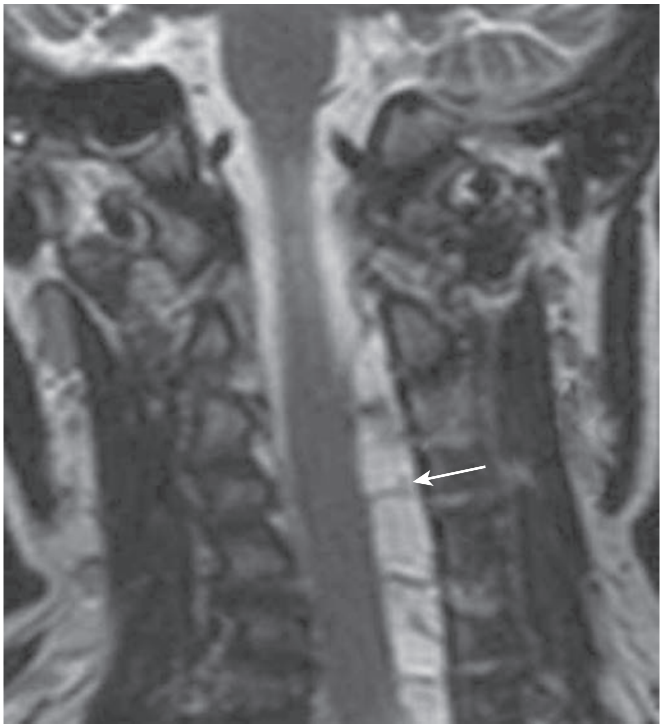

**Figure 47.1. Avulsed nerve roots in a 13-year-old girl unable to use her left arm after an all-terrain vehicle accident.** Coronal T2-weighted MRI shows an extensive intradural cerebrospinal fluid collection *(arrow)* shifting the spinal cord to the right due to C2 to T1 nerve root avulsions.

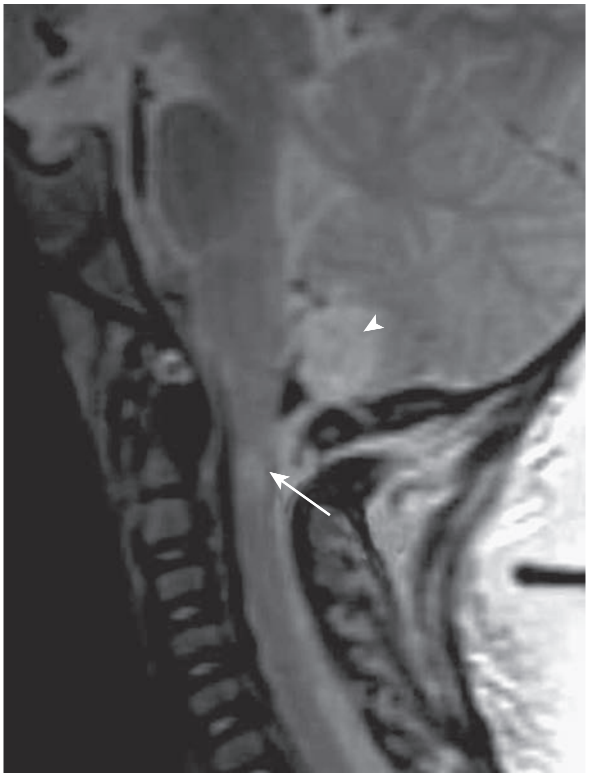

**Figure 47.2. Spinal cord injury without radiographic abnormality (SCIWORA) in a 6-year-old boy with paraplegia after a fall from a horse and normal cervical spine radiographs.** Sagittal MRI of the craniocervical junction reveals hyperintense T2 contusions within the cervical cord *(arrow)* and the inferior cervical vermis *(arrowhead).* Note T2 dark hemorrhage in the cerebrospinal fluid at the level of the foramen magnum just below the vermian contusion.

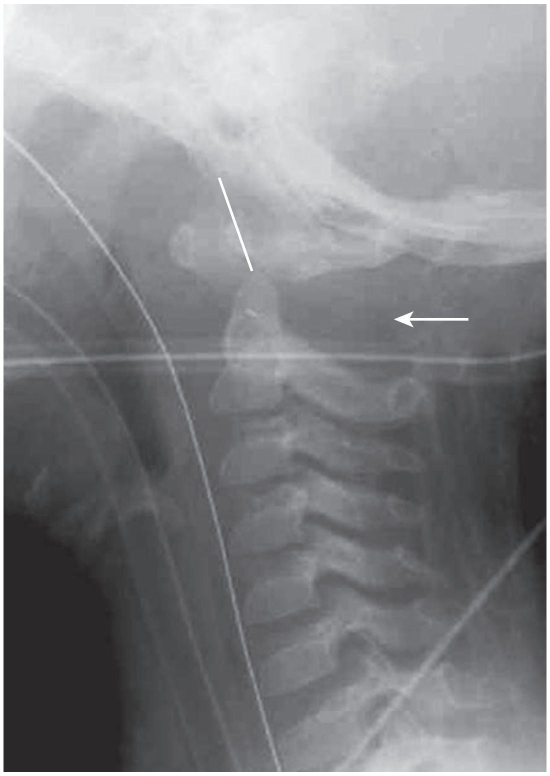

**Figure 47.3. Atlantoaxial dissociation in a 5-year-old unrestrained girl after a motor vehicle accident.** Lateral cervical spine radiograph demonstrates abnormally increased basion to dens distance of 15 mm *(white line).* The C1–C2 interspinous distance is also increased at greater than 12 mm *(arrow).*

controversial, but they are likely both posttraumatic and congenital.[2,15]

## HANGMAN FRACTURE

Hyperextension forces may cause fractures through the C2 pars interarticularis, known as *hangman fractures*. Often, these fractures are complex in morphology being associated with flexion and extension forces in the same patient.[9] The C2 fracture lucency is diagnostic, but may be difficult to visualize on lateral radiographs (Fig. 47.8). They are more easily detected with flexion views. Application of the posterior cervical line (see Table 47.1) is helpful to diagnose the injury.[9] Hangman fractures may be unilateral or bilateral, in which case they are stable or unstable, respectively. In infants, one must be aware of the pitfall of congenital defects of C2 being confused with a hangman fracture. Congenital defects are distinguished by smooth, sclerotic, narrow margins.[9,16]

## THORACIC AND LUMBAR SPINE FRACTURES

Cervicothoracic junction injuries are associated with breech delivery often presenting as SCIWORA or brachial plexus injuries.[2] Associated T1 and T2 transverse process fractures also occur.

Lower thoracic and upper lumbar spine injuries are most often caused by MVAs, with up to 50% having associated small bowel injury from seatbelt trauma.[2,17] Common lower thoracic and lumbar fractures include anterior column compressions, which are typically stable, and posterior column burst fractures, which are typically unstable (Fig. 47.9). Burst fractures occur with axial compression forces, causing endplate fracture extending into the anterior and posterior column (Fig. 47.10). Chance, or seatbelt, fractures are

**TABLE 47.1** Cervical Spine Measurements Useful in Evaluation of Pediatric Trauma

| Imaging Sign | Definition | Normal | Injury |
|---|---|---|---|
| Predental distance | Distance between posterior inferior C1 arch to anterior dens | Age 0–8years: <5 mm<br>Age 8+ years: <3 mm<br>Flexion/extension: <2 mm change | C1–C2 ligamentous injury |
| C1–C2 interspinous interval | Distance between C1–C2 spinous processes | <12 mm | C1–C2 ligamentous injury |
| Basion dens interval | Distance between basion to superior tip of dens | <12 mm | Atlanto-occipital distraction |
| Condylar gap | Distance between occipital and C1 condyles | <5 mm | Atlanto-occipital distraction |
| Dens to C1 lateral masses | Distance from dens to bilateral lateral C1 masses | Must be symmetric right to left<br>>8 mm suggests instability | AARS, AARF, Jefferson fracture |
| Spinolaminar line | Line between C1 and C3 anterior spinous process cortex | Anterior spinous process cortex of C2 is missed by <1.5 mm | Hangman fracture |

*AARF,* Atlantoaxial rotatory fixation; *AARS,* atlantoaxial rotatory subluxation.

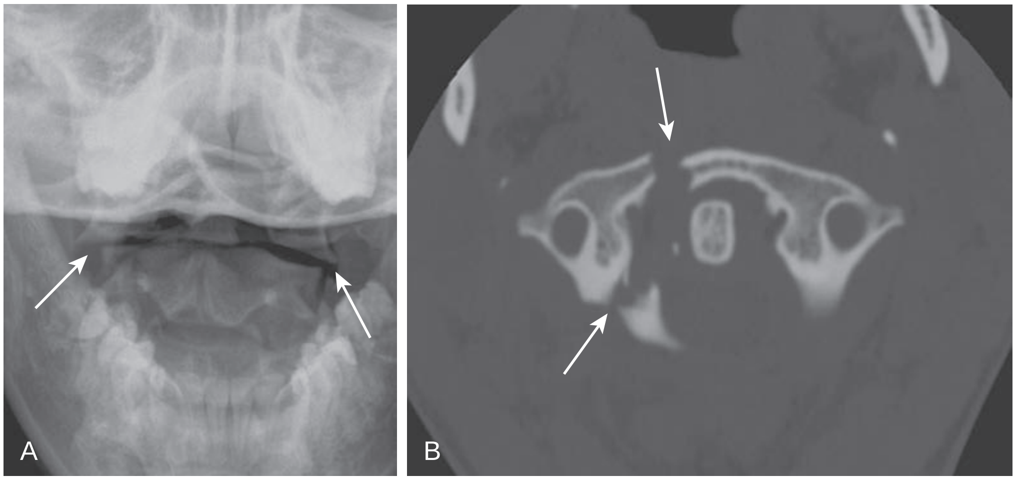

**Figure 47.4. Jefferson fracture in an adolescent with unspecified trauma.** (A) Open-mouth odontoid view shows asymmetric bilateral offset of the lateral masses of C1 on C2 *(arrows).* (B) An axial CT image reveals fracture lucencies in the right anterior and posterior C1 arches *(arrows).*

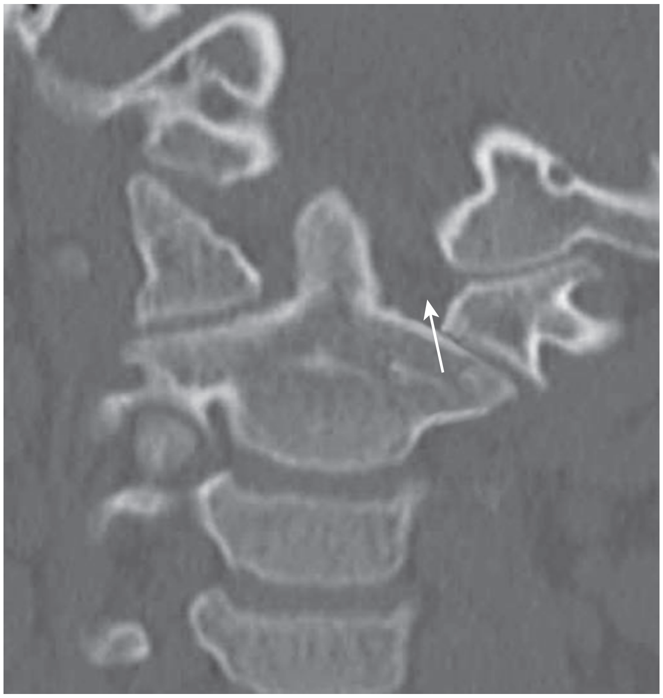

**Figure 47.5. Atlantoaxial rotatory subluxation in a 13-year-old girl with torticollis for 2 weeks and no history of infection or trauma.** Coronal reconstructed cervical spine CT shows widening of the atlantodental distance on the left *(arrow)* compared with the normal right side. This distance widened and narrowed when turning the head to the left and the right, respectively (dynamic CT not shown).

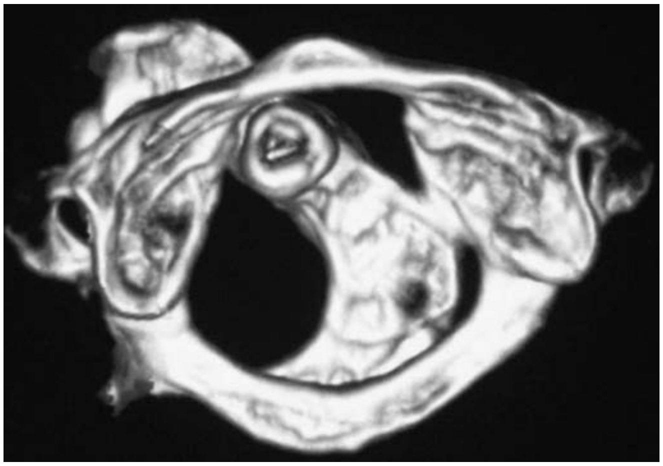

**Figure 47.6. Atlantoaxial rotatory fixation (Fielding type 1) in a 15-year-old girl with rigid torticollis for 4 weeks after spinal manipulation.** Axial three-dimensional cervical CT reveals rotation of C1 on C2 with loss of articulation of the condyles, but without anterior displacement of C1. Note normal distance between C1 and dens, which indicates a Fielding type 1 injury.

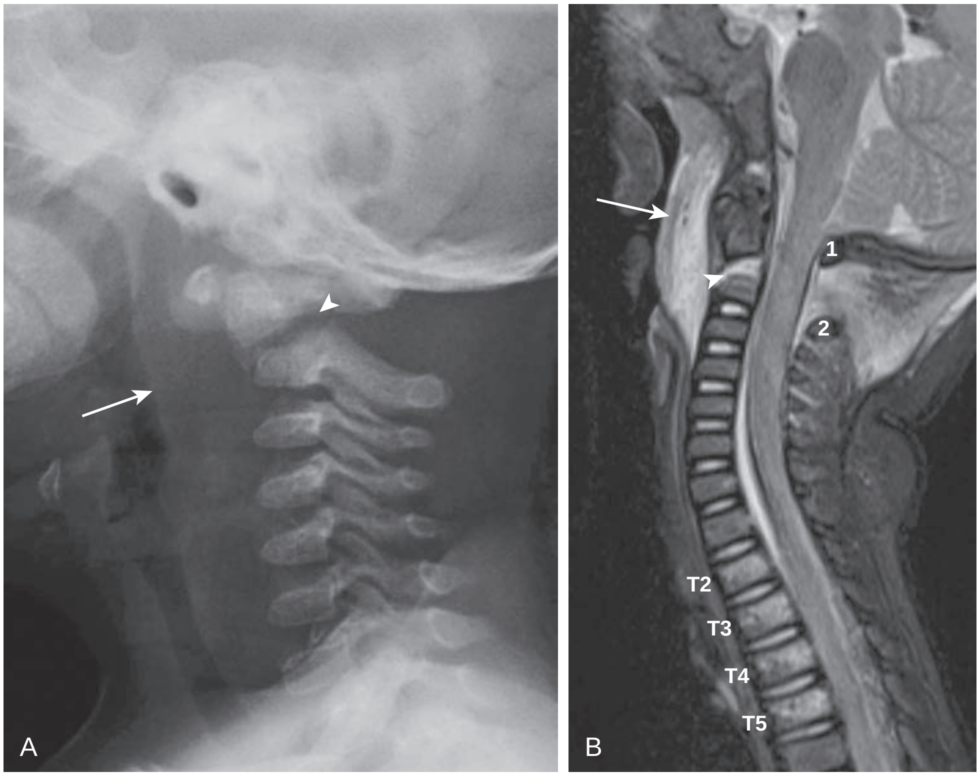

**Figure 47.7. Odontoid fracture in a 12-month-old girl after a motor vehicle accident.** (A) Lateral cervical radiograph shows prevertebral soft tissue swelling *(arrow),* widening of the C2 synchondrosis *(arrowhead),* and anterior subluxation of the dens on the body of C2. (B) Sagittal T2-weighted fat-suppressed MRI confirms the radiographic findings and also reveals additional vertebral contusions as hyperintense marrow signal of T2–T5. Ligamentous injury is seen as increase in the C1–C2 interspinous interval, which contains T2 bright soft tissue edema.

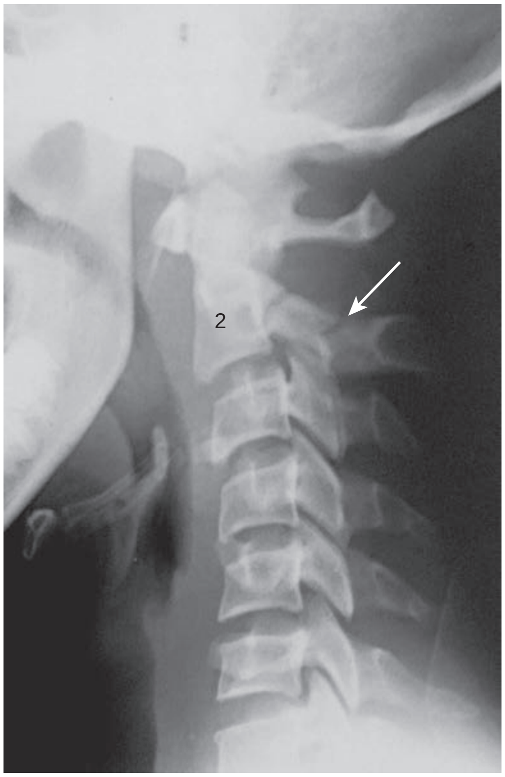

**Figure 47.8. Hangman fracture in a 15-year-old boy after an accidental fall.** A lateral cervical spine radiograph identifies lucency through the C2 posterior elements *(arrow).*

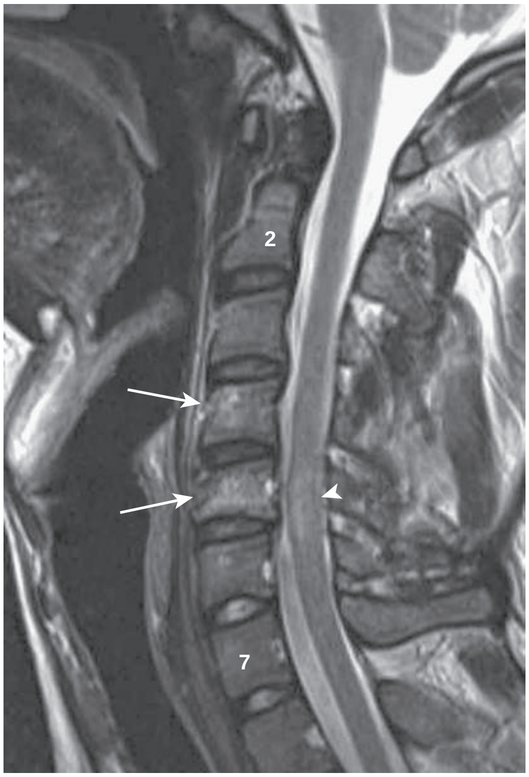

**Figure 47.9. Cervical spine compression fractures and cord contusion in a 17-year-old boy after an all-terrain vehicle accident.** Sagittal T2-weighted MRI shows hyperintense signal and decreased height of the anterior C4 and C5 vertebral bodies *(arrows).* T2 bright signal cord contusion is seen at the C5 level *(arrowhead).*

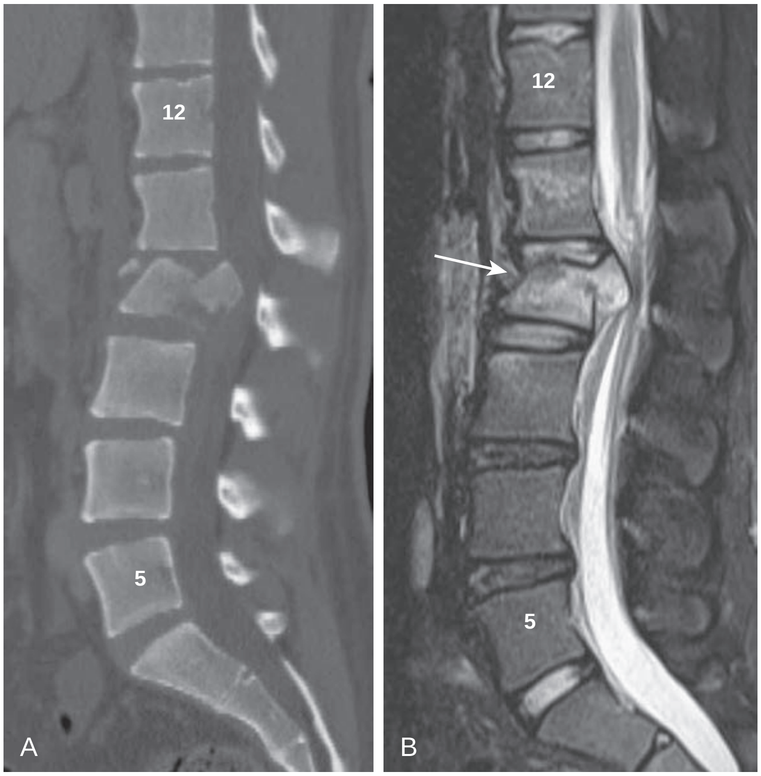

**Figure 47.10. Burst fracture in a 16-year-old boy with leg pain and weakness after a motor vehicle accident.** (A) Sagittal reformatted CT identifies a comminuted L2 fracture with a retropulsed fragment in the spinal canal. (B) Sagittal short tau inversion recovery (STIR) MRI confirms the fracture with retropulsed fragment compressing the cauda equina *(arrow).* In addition, T2 bright signal contusions in the adjacent L1 and L3 vertebral bodies are present.

**TABLE 47.2** Fielding Classification of Atlantoaxial Rotatory Subluxation

| Type | Description |
|---|---|
| I | Rotatory displacement of C1 on dens without anterior displacement; most common type |
| II | 3–5 mm of anterior C1 displacement with rotation centered on the lateral facets possibly disrupting the transverse ligaments |
| III | >5 mm anterior C1 displacement with rotation centered on lateral facets possibly disrupting the transverse ligament, alar ligament, and facet capsule |
| IV | Posterior C1 displacement on C2 of both lateral facets; rarely seen in adults with rheumatoid arthritis |

caused by flexion injury with horizontal extension through the posterior vertebrae (Fig. 47.11).[2]

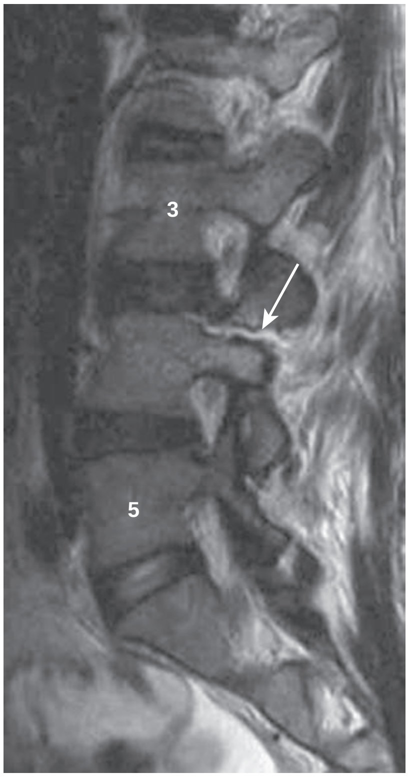

**Figure 47.11. Chance fracture in a 5-year-old-boy unable to move his legs after a motor vehicle accident.** Sagittal T2-weighted MRI shows a horizontal fracture through the superior endplate and pedicles of L4 *(arrow).* Associated surrounding T2 bright soft tissue edema is also seen.

## SPONDYLOLYSIS

Spondylolysis may be a congenital deformity or an acquired stress fracture extending through the pars interarticularis. It is believed due to repetitive flexion and extension of the adolescent spine and is often seen in athletes, having been reported in 11% of female gymnasts.[18] Defects extend through the pars on radiography, CT, and MRI. Spondylolysis without spondylolisthesis is treated conservatively. Spondylolisthesis may require stabilization depending on severity.

## SPINAL CORD CONTUSIONS AND TRANSECTIONS

Spinal cord contusions and transections are a continuum of injuries occurring alongside fractures, ligamentous injuries, or both.

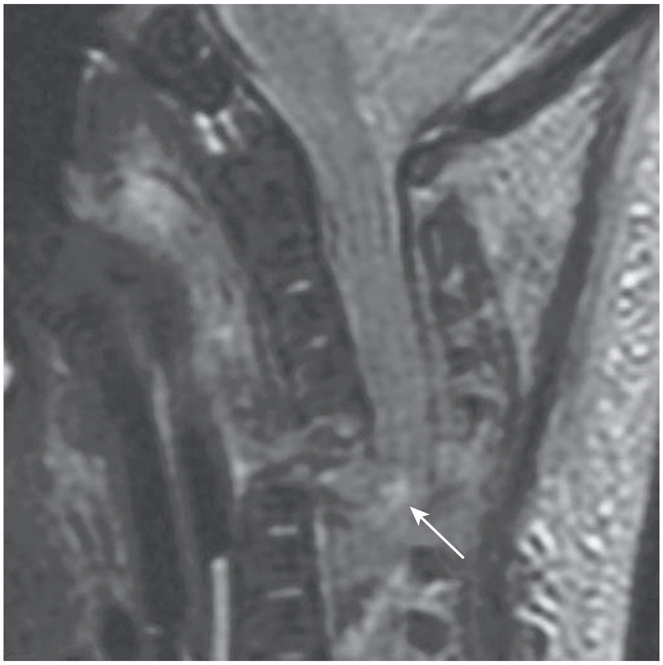

**Figure 47.12. Cord transection in a newborn with distractive birth injury.** Sagittal STIR MRI shows disruption of the cervical vertebral column at C5–C6, transection of the spinal cord, and focal hyperintense signal within cord consistent with hyperacute edema and hemorrhage *(arrow).*

Contusions are areas of edema secondary to shearing injuries. Severe cases have rupture of intramedullary vessels with cord hemorrhage and vascular compromise.[17] Complete cord transection results from extreme distraction or severe shear injury, and has a very poor prognosis (Fig. 47.12).[10]

### KEY POINTS

- Infants and young children have a higher likelihood of upper cervical injury with greater risk of permanent morbidity.
- MRI is used to detect spinal cord and ligament injuries, including SCIWORA.
- In the evaluation of spinal cord injury, MRI is able to determine the extent of intramedullary hemorrhage, which correlates with patient outcome.

## SUGGESTED READINGS

Egloff AM, Kadom N, Vezina G, et al. Pediatric cervical spine trauma imaging: a practical approach. *Pediatr Radiol*. 2009;39:447–456.

Gore PA, Chang S, Theodore N. Cervical spine injuries in children: attention to radiographic differences and stability compared to those in the adult patient. *Semin Pediatr Neurol*. 2009;16:42–58.

## REFERENCES

Full references for this chapter can be found on www.expertconsult.com.

## REFERENCES

1. Arvin B, Fournier-Gosselin MP, Fehlings MG. Os odontoideum: etiology and surgical management. *Neurosurgery*. 2010;66(suppl 3):22–31.
2. Lustrin ES, Karakas SP, et al. Pediatric cervical spine: normal anatomy, variants, and trauma. *Radiographics*. 2003;23:539–560.
3. Maxfield BA. Sports-related injury of the pediatric spine. *Radiol Clin North Am*. 2010;48(6):1237–1248.
4. Cirak B, Ziegfeld S, Knight VM, et al. Spinal injuries in children. *J Pediatr Surg*. 2004;39(4):607–612.
5. Sasaka KK, Phisitkul P, Boyd JL, et al. Lumbosacral nerve root avulsions: MR imaging demonstration of acute abnormalities. *AJNR Am J Neuroradiol*. 2006;27(9):1944–1946.
6. Junewick JJ. Pediatric craniocervical junction injuries. *AJR Am J Roentgenol*. 2011;196:1003–1010.
7. Khanna G, El-Khoury GY. Imaging of cervical spine injuries of childhood. *Skeletal Radiol*. 2007;36(6):477–494.
8. Pang D, Wilberger JE Jr. Spinal cord injury without radiographic abnormalities in children. *J Neurosurg*. 1982;57(1):114–129.
9. Swischuk LE. Imaging of the cervical spine in children. In: Swischuk LE, ed. *Imaging of the Cervical Spine in Children*. 2nd ed. New York: Springer; 2013:112–113.
10. Grabb PA, Pang D. Magnetic resonance imaging in the evaluation of spinal cord injury without radiographic abnormality in children. *Neurosurgery*. 1994;35(3):406–414, discussion 414.
11. Goldberg AL, Kershaw SM. Advances in imaging of vertebral and spinal cord injury. *J Spinal Cord Med*. 2010;33(2):105–116.
12. Harris JH Jr, Carson GC, Wagner LK, et al. Radiologic diagnosis of traumatic occipitovertebral dissociation: 2. Comparison of three methods of detecting occipitovertebral relationships on lateral radiographs of supine subjects. *AJR Am J Roentgenol*. 1994;162(4):887–892.
13. el-Khoury GY, Kathol MH, Daniel WW. Imaging of acute injuries of the cervical spine: value of plain radiography, CT, and MR imaging. *AJR Am J Roentgenol*. 1995;164(1):43–50.
14. Fielding JW, Hawkins RJ. Atlanto-axial rotatory fixation. (Fixed rotatory subluxation of the atlanto-axial joint). *J Bone Joint Surg Am*. 1977;59(1):37–44.
15. Arvin B, Fournier-Gosselin MP, Fehlings MG. Os odontoideum: etiology and surgical management. *Neurosurgery*. 2010;66:22–31.
16. Giguere JF, St-Vil D, Turmel A, et al. Airbags and children: a spectrum of C-spine injuries. *J Pediatr Surg*. 1998;33(6):811–816.
17. Green NE, Swiontkowski MF. *Skeletal Trauma in Children*. 4th ed. Philadelphia, PA: Saunders; 2009.
18. Ogden JA. *Skeletal Injury in the Child*. 2nd ed. Philadelphia, PA: Saunders; 1990.

# 48 Embryology, Anatomy, and Neonatal Lung Pathophysiology

Beverley Newman

## OVERVIEW

The respiratory system consists of conducting and gas exchange components, with the bifurcating airways and accompanying pulmonary arteries (PAs) bringing air and blood to peripheral capillary-lined airspaces for gas exchange. In understanding and evaluating pulmonary pathologic processes, it is useful to view the lung as consisting of multiple sets of branching trees including airways, arterial and venous pulmonary vasculature, systemic vasculature, and lymphatics.[1] This chapter reviews the developmental biology, clinical anatomy, and pathophysiology of the respiratory system. Medical lung diseases in the neonate are used as illustrative examples, although the relevance of the discussion extends to the entire pediatric age group and beyond.

There are a large number of causes of newborn respiratory distress. They have been classified as congenital and acquired, medical versus surgical, and intrapulmonary versus extrapulmonary/extrathoracic.[2–4] Chest radiographic findings are often nonspecific (Table 48.1); close clinical correlation is needed for intelligent interpretation.[3] This chapter will not exhaustively review neonatal lung disorders but rather selected conditions not covered elsewhere in this book that are relevant to the anatomy/physiology discussed.

## DEVELOPMENTAL BIOLOGY AND PATHOPHYSIOLOGY

### Airways

The larynx, trachea, and bronchi develop from a ventromedial diverticulum of the foregut known as the laryngotracheal groove. Proliferation of the laryngeal mesenchyme produces arytenoid swellings that grow toward the tongue, converting the primordial glottis into a T-shaped laryngeal inlet. In the infant, the larynx is high in location, with its inferior border located at the C4 level. During childhood, the larynx descends and eventually reaches its adult location at the C6–C7 level by age 15 years. Functions of the larynx include breathing, phonation, and protection of the lower airway against aspiration.[5–7]

The laryngotracheal groove grows caudally, forming the trachea. It lies ventral and parallel to the dorsal foregut, which becomes the esophagus. The separation of the trachea and esophagus progresses cranially and is complete by 6 weeks' gestation. The endodermal lining will produce the epithelium and glandular structures of the trachea, whereas the connective tissue, cartilage, and smooth muscle come from the surrounding splanchnic mesenchyme.[5–7] Faulty separation of the trachea and esophagus gives rise to esophageal atresia/tracheoesophageal fistula (see Chapter 96). Disproportionate growth of the esophagus at the expense of the trachea may give rise to tracheal stenosis or, in the most severe form, tracheal agenesis (see Chapter 52).

### Lungs

The lung bud arises from the caudal end of the laryngotracheal groove by the end of the fourth week and soon divides into two bronchial buds.[5,8,9] The bronchial buds grow laterally into the pericardioperitoneal canals. Early in the fifth week, the connection of the bronchial buds to the trachea enlarges to form the mainstem bronchi. The right main stem bronchus bifurcates into a superior secondary bronchus, supplying the right upper lobe and an inferior secondary bronchus that subdivides into two bronchi, supplying the right middle and lower lobes. The left main stem bronchus divides into two secondary bronchi that supply the upper and lower lobes of the left lung. The bronchi continue to divide, and all airway divisions are complete by 16 weeks' gestation (Fig. 48.1). Cartilage appears at 10 weeks in the trachea and is found in the segmental bronchi by 16 weeks. Unequal growth of the lung buds can lead to the development of unilateral pulmonary agenesis or hypoplasia. Prolonged oligohydramnios, space-occupying thoracic or abdominal lesions that compress one or both hemithoraces, chest wall deformities, neuromuscular disorders, and conditions producing PA hypoperfusion are associated with pulmonary hypoplasia.[5,8,10,11]

Lung development has been divided into five stages (Table 48.2). After completion of tracheobronchial and peripheral airway branching during the embryonic (26–52 days) and pseudoglandular (52 days–16 weeks) stages, the bronchi and terminal bronchioles enlarge during the canalicular stage (17–28 weeks). The capillary bed begins to approximate the future air spaces, and gas exchange is possible. Type I and type II pneumocytes can be identified in the fetal lung by 20 to 22 weeks, but the capillary-alveolar interface is not adequate for extrauterine survival until 23 to 24 weeks of gestation.[5,8,9,12]

The saccular stage (29–36 weeks) is characterized by the development of terminal air sacs with flattening of the epithelium in the distal air spaces. The type II pneumocytes produce surfactant, which is stored as lamellar bodies. During the alveolar stage (36 weeks to infancy), the size and number of alveoli increase. When birth occurs at full term, it is estimated that 50 million alveoli are present. Alveolar formation continues postnatally until about 8 years, with most development in the first 2 years of life. The mature human lung ultimately has 300 million alveoli. Further lung growth occurs via enlargement of existing lung components (Table 48.3).

Acinar or alveolar dysplasia and alveolar capillary dysplasia (ACD) are rare, usually lethal disorders with early lung developmental arrest with lack of normal formation of terminal air spaces and distal vessels resulting in markedly impaired gas exchange. In ACD, there is often misalignment of the pulmonary veins centrally adjacent to pulmonary arterioles and bronchioles instead of their normal peripheral interlobular location[11,13,14] (see Chapter 56).

## Surfactant

Surfactant is composed of phospholipids, protein, and neutral lipids (e-Fig. 48.2). Surfactant lines the alveoli and decreases surface tension, which leads to decreased work of breathing and stabilizes the terminal air spaces, preventing alveolar atelectasis, especially at low lung volumes.[15] Surfactant can be detected as early as 24 to 26 weeks' gestation, although mature surfactant usually is not present until 34 to 36 weeks' gestation. Surfactant maturation can be affected by a variety of substances. Insulin delays surfactant maturation (propensity for infants of diabetic mothers to have surfactant deficiency), whereas other substances, such as glucocorticoids and thyroid hormone, accelerate it.[16] Administration of glucocorticoid to mothers 24 to 48 hours before preterm delivery accelerates surfactant maturation and results in a significant decrease in the incidence and severity of respiratory distress syndrome of the newborn (RDS), also known as hyaline membrane disease or

**TABLE 48.1** Common Medical Diseases of the Newborn Chest[2]

| Pattern | Lung Disease* |
|---|---|
| Hazy granular | RDS<br>Pneumonia<br>CHF |
| Confluent alveolar | RDS<br>Pneumonia<br>Hemorrhage<br>CHF |
| Patchy opacities | Aspiration<br>Pneumonia<br>Hemorrhage |
| Streaky interstitial | TTN<br>Pneumonia<br>CHF |

*RDS, CHF, and TTN tend to be symmetric. Aspiration and hemorrhage tend to be asymmetric. Pneumonia can mimic almost all patterns.

*CHF*, Congestive heart failure; *RDS*, respiratory distress syndrome; *TTN*, transient tachypnea of the newborn.

**TABLE 48.2** Classification of Phases of Human Intrauterine Lung Growth

| Phase | Time of Occurrence | Significance |
|---|---|---|
| Embryonic | 26–52 days | Development of trachea and major bronchi |
| Pseudoglandular | 52 days to 16 wk | Development of remaining conducting airways |
| Canalicular | 17–28 wk | Development of vascular bed, framework of acinus; flattening of epithelium |
| Saccular | 29–36 wk | Increased complexity of saccules |
| Alveolar | 36 wk to term | Presence and development of alveoli |

*From Thurlbeck WL. Lung growth and development. In Thurlbeck W, Churg AM, eds.* Pathology of the Lung, *2nd ed, New York: Thieme Medical Publishers; 1995;38.*

**TABLE 48.3** Changes in Lung Size With Growth

| | 30 Weeks' Gestation | Full Term | Adult | Fold Increase After Birth |
|---|---|---|---|---|
| Lung volume | 25 mL | 150–200 mL | 5 L | 23 |
| Lung weight | 20–25 g | 50 g | 800 g | 16 |
| Alveolar number | — | 50 m | 300 m | 6 |
| Surface area | 0.3 m$^2$ | 3–4 m$^2$ | 75–100 m$^2$ | 23 |
| Surface area/kg | | 0.4 m$^2$ | 1 m$^2$ | 2.5 |
| Alveolar diameter | 32 μm | 150 μm | 300 μm | 22 |
| No. of airways | 24 | 23–24 | 22–24 | 22 |
| Tracheal length | | 26 mm | 184 mm | 7 |
| Main bronchi length | | 26 mm | 254 | 10 |

*From Hodson WA: Normal and abnormal structural development of the lung. In Polin RA, Fox WW, eds.* Fetal and Neonatal Physiology, *ed 2, Philadelphia: WB Saunders; 1998:1037.*

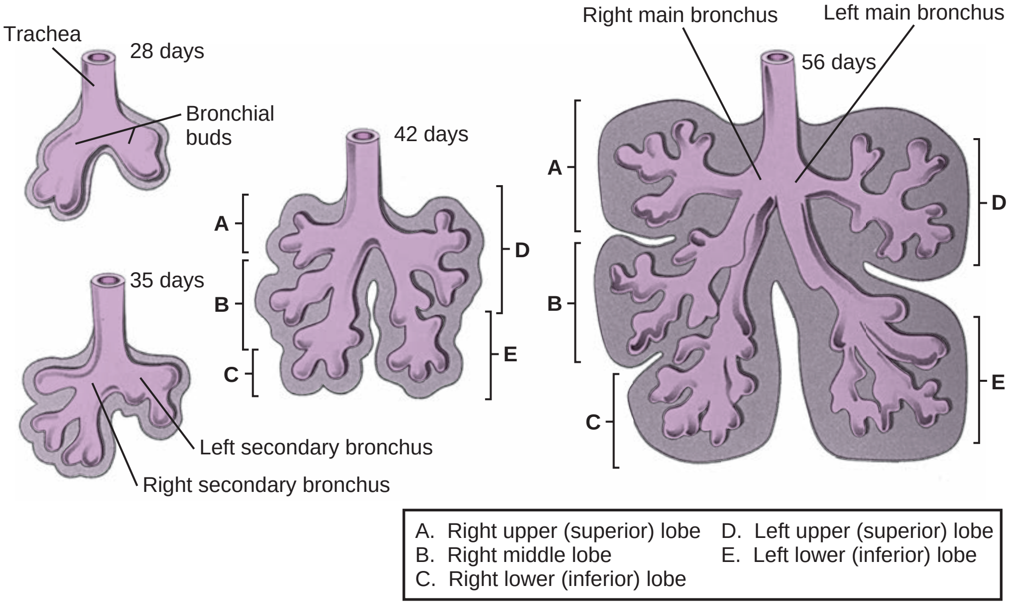

**Figure 48.1. Progressive stages in the development of the bronchi and lungs.** *(From The respiratory system. In: Moore KL, Persaud TVN, eds.* Before we are born: Essentials of Embryology and Birth Defects, *5th ed, Philadelphia: WB Saunders; 1998:247. Reprinted with permission.)*

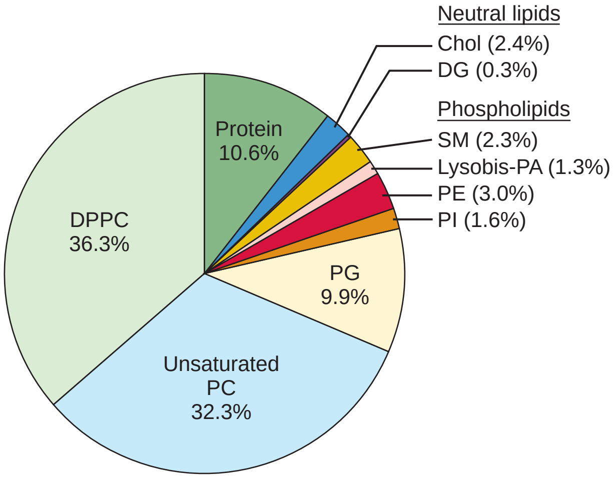

**e-Figure 48.2. The composition of bovine pulmonary surfactant.** *Chol,* Cholesterol; *DG,* diacylglycerol; *DPPC,* dipalmitoylphosphatidylcholine; *PC,* phosphatidylcholine; *PE,* phosphatidylethanolamine; *PG,* phosphatidylglycerol; *PI,* phosphatidylinositol; *SM,* sphingomyelin. *(From Possmayer F. Physicochemical aspects of pulmonary surfactant. In: Polin RA, Fox WW, eds.* Fetal and Neonatal Physiology, *2nd ed, Philadelphia: WB Saunders; 1998:1260. Reprinted with permission.)*

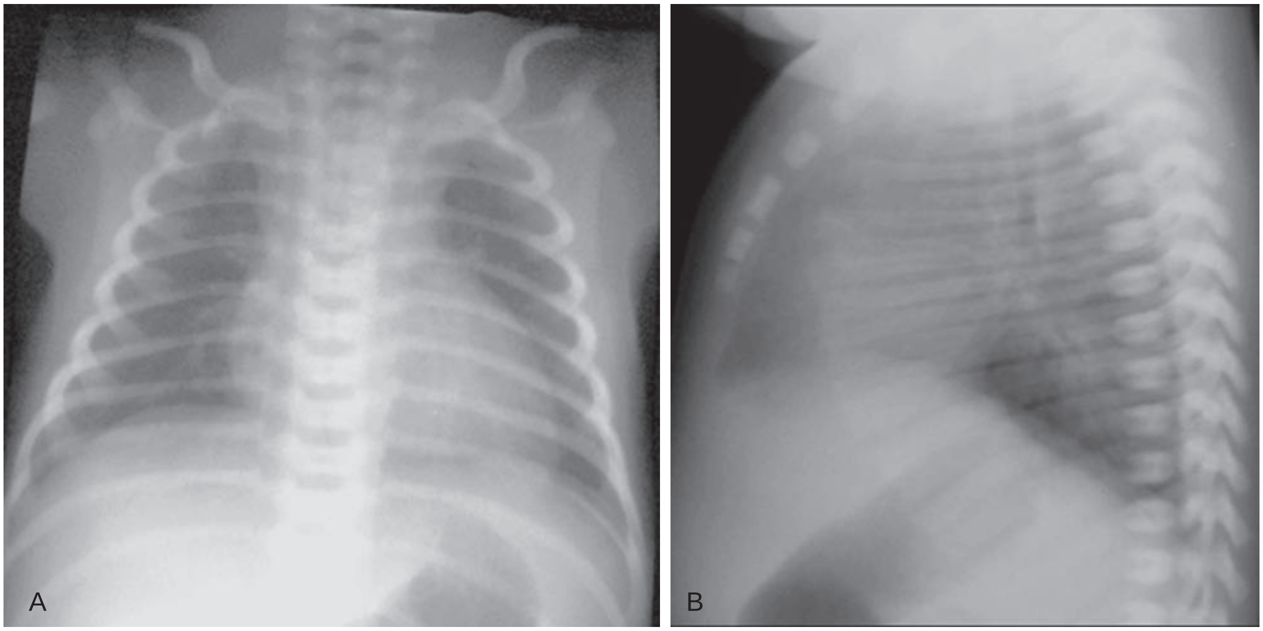

**Figure 48.3. Normal newborn chest radiograph.** Normal frontal (A) and lateral (B) newborn chest radiographs. Aeration is typically six to eight anterior ribs. The central pulmonary vessels are distinct and not enlarged. The lungs are symmetric and clear, and the airways are visible. The superior mediastinum often appears wide due to normal thymus, but there is no mass effect. Similarly, the cardiac silhouette may look slightly prominent on frontal view (due to thymus) but not on lateral (thymus anterior). The bony structures are normal, and the ribs horizontal.

surfactant deficiency disease.[12] RDS is largely encountered in premature infants less than 36 weeks' gestation related to absence or immaturity of pulmonary surfactant. Other risk factors include maternal diabetes, multigestation, and caesarian section. Secondary surfactant insufficiency also may accompany asphyxia, infection, and meconium aspiration.[3] RDS of prematurity is characterized clinically by cyanosis, tachypnea, and retractions within a few hours of delivery. As opposed to the normal radiographic appearance of the newborn chest radiograph (Fig. 48.3), the lungs in RDS are underinflated and without therapeutic intervention exhibit diffuse ground glass opacity ranging from mild fine granularity to complete lung opacification with air bronchograms (Fig. 48.4) (see Table 48.1).[2–4,12] Tracheal instillation of exogenous surfactant can ameliorate the natural course of RDS significantly.[3,17] With early treatment including continuous positive airway pressure (CPAP) and surfactant at birth, underaeration may be less apparent radiographically, and a more coarse granular lung pattern is seen due to partial reaeration of alveoli. Because of nonuniform distribution of surfactant, lung involvement may become patchy or asymmetric (Fig. 48.5).[2,3,12] Other complications including atelectasis, air leak such as pulmonary interstitial emphysema, pneumomediastinum, pneumothorax and pneumopericardium, as well as pulmonary edema related to shunting through a patent ductus arteriosus, pulmonary hemorrhage, and superimposed infection may occur during the course of the disease and its treatment. The incidence and severity of these are somewhat modified with modern management.[2,3,12] Progression of neonatal lung disease (not confined to RDS) to chronic lung disease is less common and less severe than was encountered previously, especially in more mature infants. However, the survival of very small premature infants, as young as 23 to 24 weeks with very immature lungs, has resulted in a different pattern of chronic lung disease, reflecting arrested and disordered alveolar and pulmonary vascular development (see Chapter 56).[12,13]

In addition, there are a number of rare congenital genetic disorders of surfactant production and metabolism that may be causes of respiratory distress and diffuse hazy lung opacification, usually in the term neonate (see Chapter 56).[13]

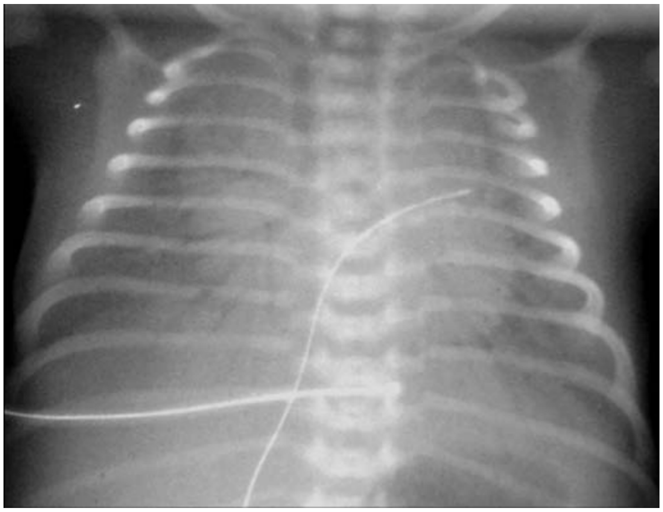

**Figure 48.4. RDS in a premature 29-week-gestation newborn infant.** The lungs are underaerated with symmetric ground-glass opacification. Note central air bronchograms.

## Fetal Lung Liquid

The fetal lung is filled with fluid during gestation. This fluid is produced by pulmonary epithelial cells, and its composition is different from that of amniotic fluid.[18] As the fetus matures, surfactant can be found in this lung fluid. Fetal lung liquid is under higher pressure than amniotic fluid, and efflux of lung liquid into the amniotic fluid occurs, forming the basis of amniotic fluid analysis for surfactant to determine fetal pulmonary maturity.

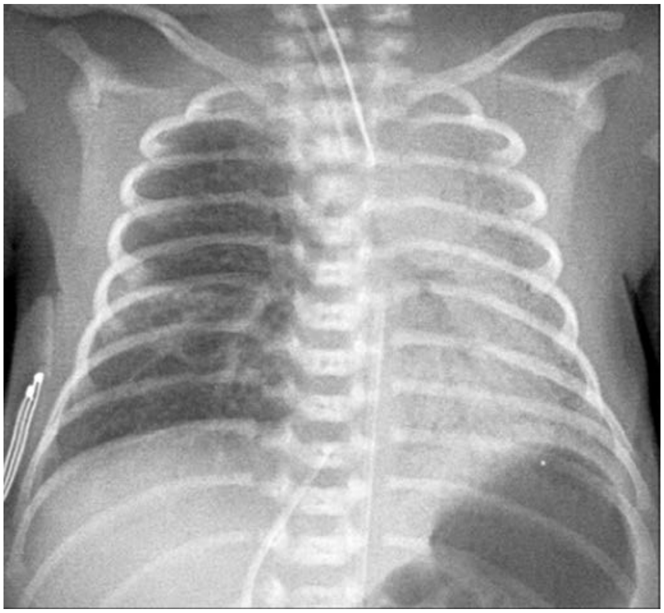

**Figure 48.5. RDS with asymmetric clearing post surfactant in a 26-week-gestation infant.** Note UA and UV lines in place with tips in the descending aorta and IVC/right atrial junction, respectively. A hazy granular pattern is seen on the left consistent with persistent RDS, with partial reaeration on the right with a more coarse streaky appearance. The hyperlucent right lung raises the question of possible airleak such as anterior pneumothorax. No pneumothorax was present on a later decubitus view *(not shown)*. However, the right perihilar linear lucencies may represent mild interstitial emphysema.

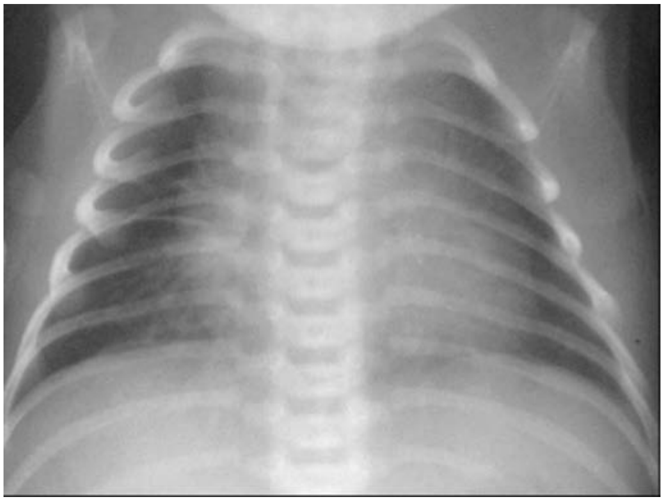

**Figure 48.6. Transient tachypnea of the newborn (TTN) in a full-term infant born by cesarean section.** There are mild streaky interstitial markings, right greater than left, with fluid in the minor fissure. Note prominent thymus with thymic wave appearance at margins. The lungs cleared by day 2 of life *(not shown)*.

Removal of liquid from the lung begins shortly before delivery and continues for several hours after delivery. The majority of the lung fluid is expelled during passage through the birth canal. The major routes for postnatal clearance of fetal lung fluid are the pulmonary circulation and lymphatics. Delayed clearance of fetal lung fluid results in mild to moderate respiratory distress and is seen more commonly in infants delivered by cesarean section. This disorder, also known as transient tachypnea of the newborn, is predominantly seen in full-term infants and is characterized radiographically by transient abnormality (usually normalizes in 24–48 hours) with a similar appearance to mild pulmonary edema including mild hyperinflation, increased perihilar markings, and small pleural effusions, features likely related to the presence of fluid in lymphatic channels (Fig. 48.6).[2–4]

## Pulmonary Vasculature/Circulation

The fetal lung is the only organ that does not perform its postnatal function before birth. All gas exchange occurs via the placenta and oxygenated blood returns to the fetus via the umbilical vein to the ductus venosus, inferior vena cava (IVC), and right atrium (RA). Most of the IVC return entering the RA crosses the foramen ovale into the left atrium. The remaining IVC and superior vena cava (SVC) blood flow to the RA enters the right ventricle. Most of the right ventricle output crosses the ductus arteriosus (DA) into the aorta. These shunts at the foramen ovale and DA result in most of the fetal cardiac output bypassing the lungs (see Chapter 70).[19]

Dramatic pulmonary circulatory changes occur at delivery. The lungs expand with air, the partial pressure of oxygen rises, and the umbilical cord is clamped. These changes result in a decrease in pulmonary vascular resistance, ductal constriction, and functional closure of the foramen ovale so that all of the blood entering the RA passes through the lungs. In term and near-term infants, this process may go awry with the persistence of high pulmonary vascular resistance and continued shunting of blood away from the lungs via the foramen ovale and DA. This mechanism results in hypoxemia and is known as persistent pulmonary hypertension of the newborn. It usually is seen in infants with underlying pulmonary hypoplasia (e.g., congenital diaphragmatic hernia) or with perinatal stresses such as asphyxia, often associated with meconium aspiration, infection, or hypoglycemia.[2,3] Management of persistent pulmonary hypertension of the newborn currently is aimed at treating the underlying disease and promoting pulmonary vasodilatation. Inhalation of nitric oxide often results in relaxation of the pulmonary vasculature with improved oxygenation. Infants who do not respond to conventional treatment or nitric oxide frequently require extracorporeal membrane oxygenation. Persistent pulmonary hypertension in and of itself does not produce characteristic radiographic findings; the lungs may be clear or exhibit oligemia. Radiographs may show cardiomegaly and congestion in the presence of significant myocardial ischemia. In meconium aspiration, typical findings include hyperinflation and asymmetric patchy opacities with or without airleak (Fig. 48.7). Acute infection (e.g., group B Streptococcus) can have a variable appearance ranging from streaky interstitial or scattered patchy to diffuse granular changes mimicking many other neonatal lung conditions (Fig. 48.8) (see Table 48.1).[2–4]

# CLINICAL ANATOMY

## Airways

Basic airway anatomy to the level of the terminal bronchiole (the last purely conducting, i.e., nonalveolated, airway) is not substantially different in children compared with adults except in size. The right lung has three lobes, and the left lung has two lobes (Fig. 48.9). The pleural fissures separating the lobes of the lungs often are anatomically incomplete. Portions of the fissures occasionally are radiographically visualized as fine lines in healthy infants. The lungs are subdivided further into 8 to 10 segments on the left and 10 on the right, each served by a segmental bronchus (Figs. 48.10 and 48.11).[20–22]

The trachea, which is the largest of the conducting airways, is a fibromuscular tube lined principally by ciliated columnar

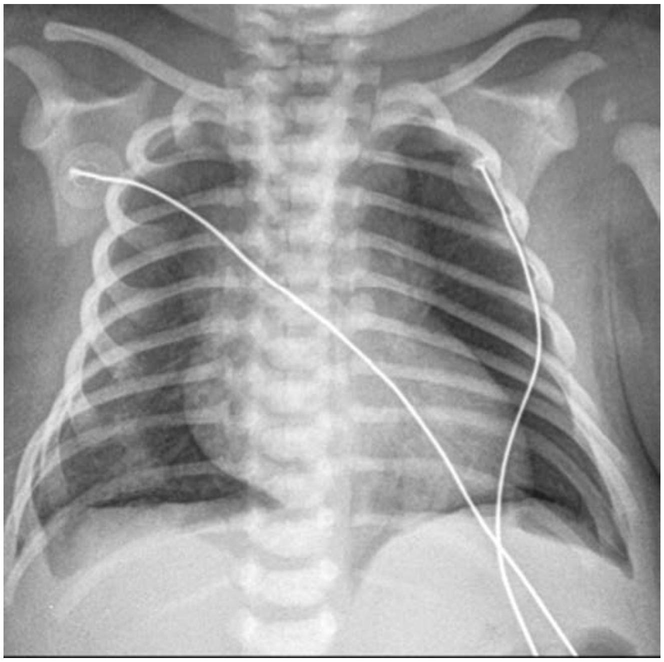

**Figure 48.7. Perinatal asphyxia and meconium aspiration during delivery in a full-term newborn with respiratory distress at birth.** There are streaky increased interstitial markings with patchy opacities at both lung bases consistent with meconium aspiration. In addition, there are bilateral pneumothoraces as evidenced by the hyperlucent left and medial right hemithoraces, subpulmonic air bilaterally, with accentuation of the inferior pleural margins.

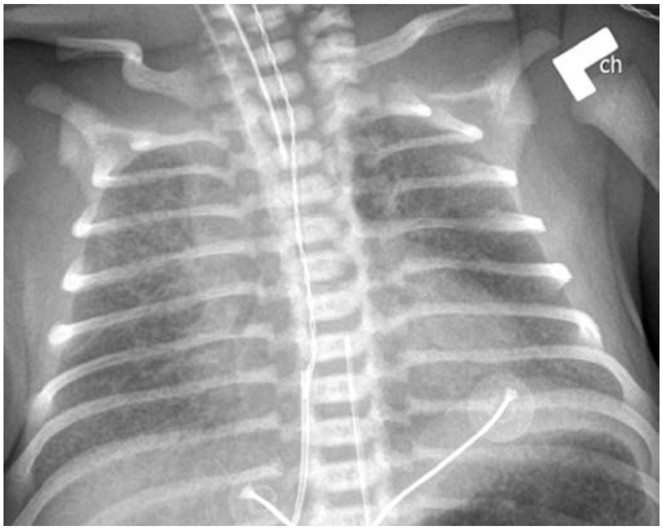

**Figure 48.8. Group B streptococcal pneumonia in a full-term newborn.** The lungs are mildly underaerated with diffuse hazy to streaky bilateral opacities. No pleural effusion is evident (a common finding in neonatal pneumonia).

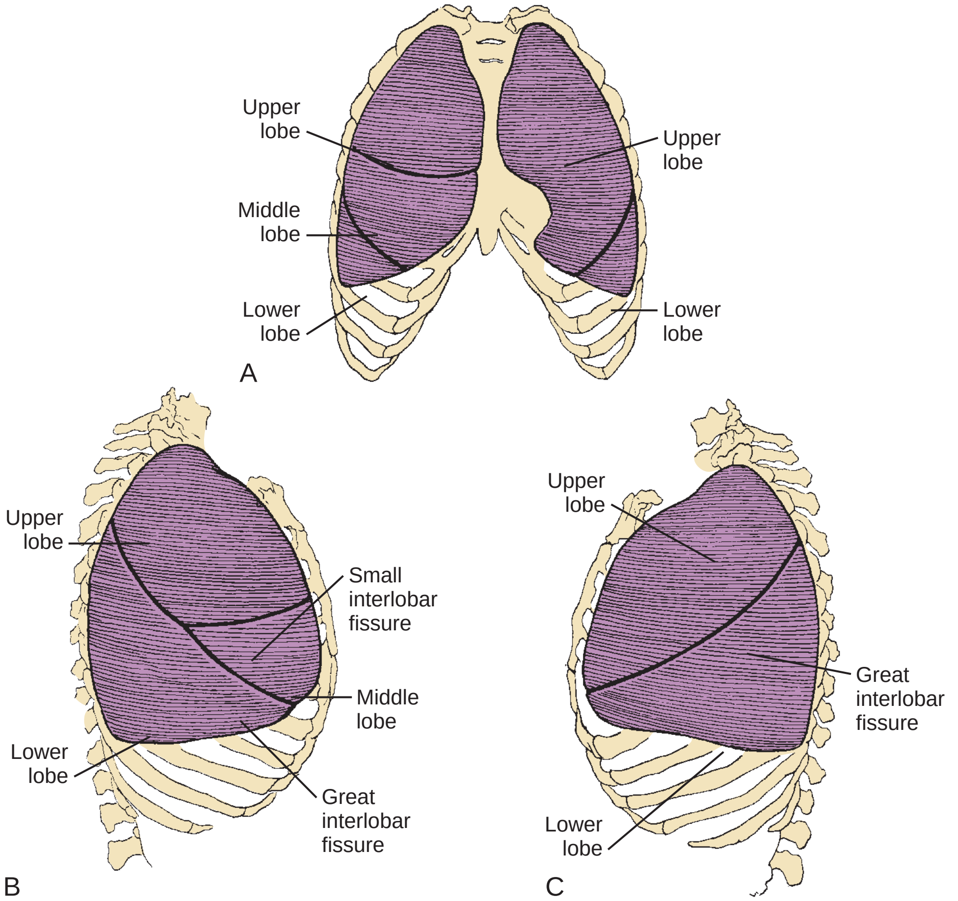

**Figure 48.9. Lobes and fissures of normal lungs.** (A) Frontal aspect of both lungs. (B) Lateral aspect of the right lung. (C) Lateral aspect of the left lung.

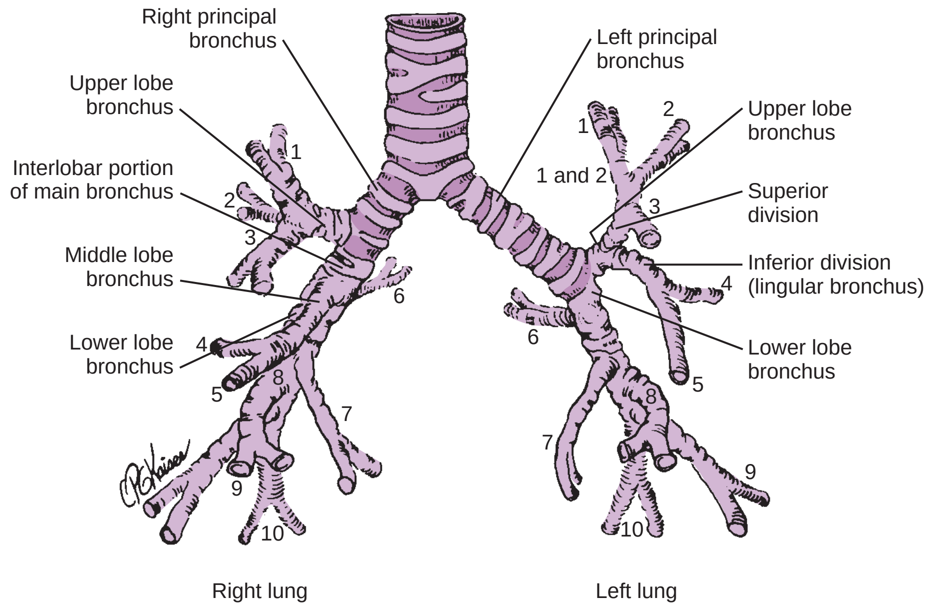

UPPER LOBE
1. Apical
2. Posterior
3. Anterior
MIDDLE LOBE
4. Lateral
5. Medial
LOWER LOBE
6. Superior
Basal segments:
7. Medial basal
8. Anterior basal
9. Lateral basal
10. Posterior basal

UPPER LOBE
Superior division:
1, 2. Apicoposterior
(1 Apical; 2 Posterior)
3. Anterior
Inferior division (lingular bronchus):
4. Superior lingular
5. Inferior lingular
LOWER LOBE
6. Superior
Basal segments:
7. Medial basal
8. Anterior basal
9. Lateral basal
10. Posterior basal

**Figure 48.10.** Tracheobronchial tree with the segmental bronchi identified by name and number. *(From Rosse C, Gaddum-Rosse P.* Hollingsched's textbook of anatomy, *5th ed, Philadelphia: Lippincott-Raven; 1997:447.)*

epithelium and mucous cells. The trachea is supported by 16 to 20 cartilaginous rings, which are incomplete posteriorly, where the tracheal wall is composed of fibrous, muscular, and elastic tissue. The trachea extends from the cricoid cartilage at the C4 level to the carina near the T4 level at birth and at a lower level with increasing age. Congenital tracheal stenosis is characterized by complete cartilaginous rings; a short or long segment may be affected (see Chapter 52). The tracheal cross-sectional area has been analyzed by computed tomography (CT) and grows predictably with age.[23,24] The cross-sectional shape may vary considerably in the normal population and depending on the phase of respiration.[25]

The first four bronchial generations (through the segmental branches) are strongly supported by cartilaginous plates that aid in keeping the bronchi patent. The smaller cartilaginous bronchial branches, from the fifth to the eleventh generation, double in number with each branching generation and decrease in size down to approximately 1 mm in diameter (Fig. 48.12).[26] They are in a common fibrous sheath with an accompanying PA branch.

The bronchioles are the conducting airways that extend to the sixteenth generation and lack cartilage in their walls. They are dependent for their patency on the support of the surrounding lung parenchyma. As the lung expands, the bronchioles dilate. Unless they are abnormal, bronchioles are usually not visible on imaging beyond the eighth generation (1.5 mm) (see Fig. 48.12). The last purely conducting branch of the airway is the terminal bronchiole, which arborizes into three generations of respiratory bronchioles, each giving rise to progressively greater numbers of alveoli. The alveoli and the alveolar ducts and sacs that give rise to them constitute the gas-exchange portion of the lung (see Fig. 48.12).

## The Respiratory Portion of the Lungs

The two subunits of the peripheral airspaces that are most important to the radiologist are the acinus and the secondary pulmonary lobule. The alveolus, which in an adult averages approximately 200 to 300 µm in diameter, is below the limits of visibility on imaging. The acinus is the unit of lung tissue peripheral to the terminal bronchiole and consists of a cluster of 50 to 400 alveoli. It occasionally is visible in the pediatric lung and typically ranges in diameter from 1 to 2 mm in infants younger than 1 year old to 7 to 9 mm in adolescents and adults (Fig. 48.13 and e-Fig. 48.14).[27]

The secondary pulmonary lobule is a cluster of about 3 to 24 acini that are separated from other lobules by interlobular septa composed of fibrous tissue. The secondary lobules and their septa are much better developed in the periphery of the lung than in the center. The mean diameter of the secondary lobule at birth is 3 mm and by 12 years measures 15 mm (see e-Fig. 48.14).[27] The pulmonary veins and lymphatics course through the interlobular septa, and the PAs and bronchioles are positioned centrally within the lobule (see Fig. 48.13). Thickened septa are visible on

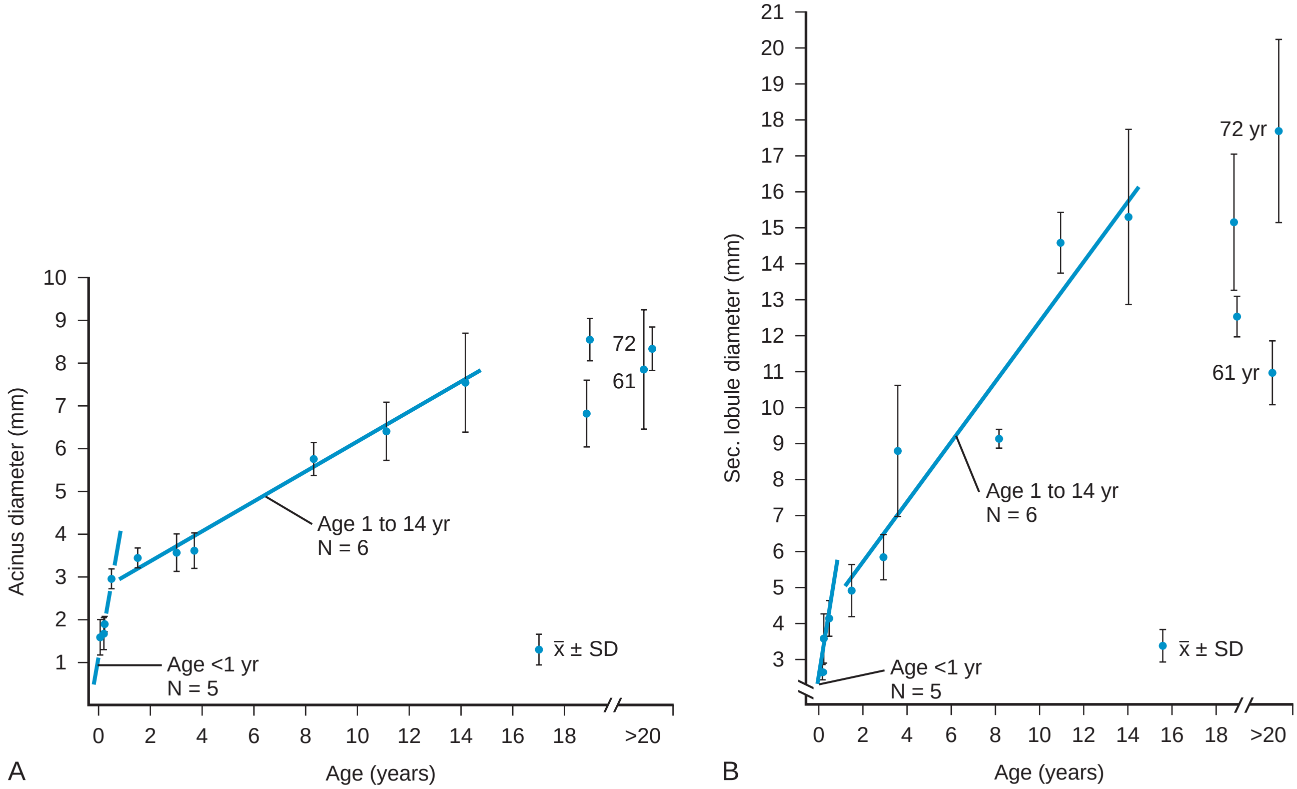

**e-Figure 48.14. Size of the pulmonary acinus and secondary lobule in children.** The relationship of mean acinar diameter (A) and secondary lobular diameter (B) with respect to age. *SD,* Standard deviation. *(From Osborne DRS, Effmann EL, Hedlund LW. Postnatal growth and size of the pulmonary acinus and secondary lobule in man.* AJR Am J Roentgenol*. 1983;140:449).*

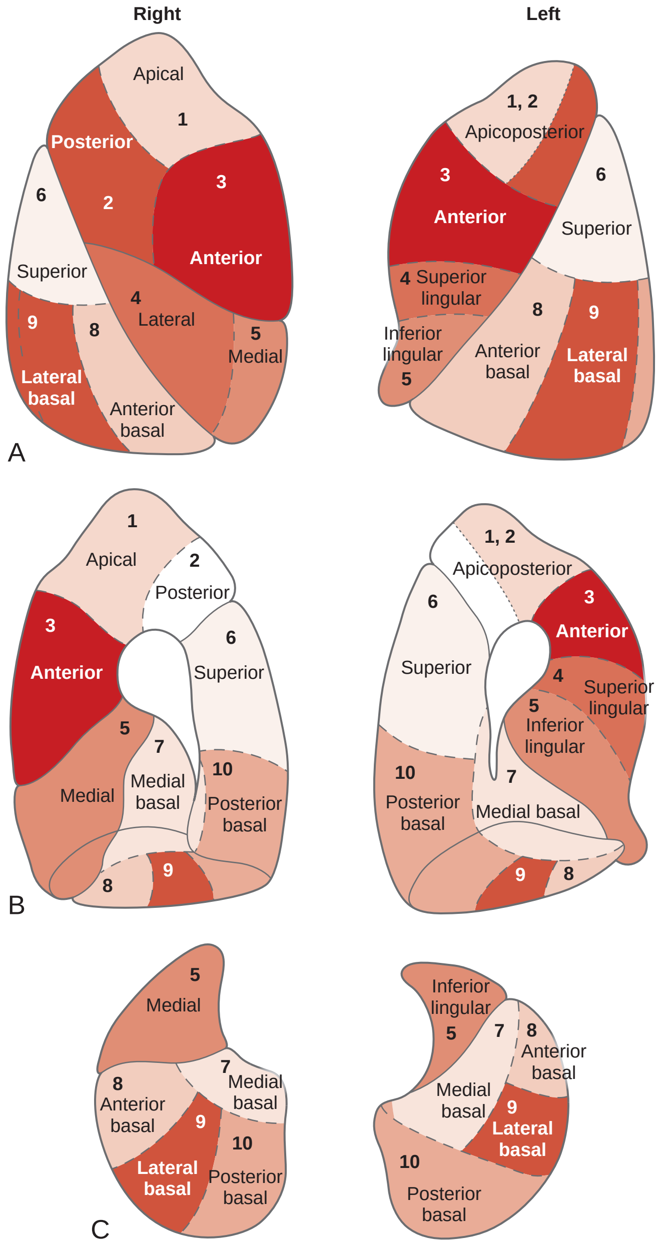

**Figure 48.11. Bronchopulmonary segments as seen on the surface of the lungs.** (A) Lateral surface. (B) Medial surface. (C) Base or diaphragmatic surface. *(Adapted from Boyden EA.* The segmental anatomy of the lungs, *New York: McGraw-Hill; 1955; and from Rosse C, Gaddum-Rosse P.* Hollingsched's textbook of anatomy, *5th ed, Philadelphia: Lippincott-Raven; 1997:457.)*

chest radiographs as Kerley B lines and directly on high-resolution CT (Fig. 48.15).

Multiple imaging modalities have been used to determine prenatal and postnatal lung volumes and growth. CT postprocessing tools can provide accurate measurement of lung volume as well as sizes of airway wall/lumen and arterial area from an axial multidetector CT dataset.[28–30]

Mean CT density decreases with age and increases in an anterior to posterior gradient in a quietly breathing supine child.[31] Patient age, anterior versus posterior location, and apical versus basal location are significant predictors of regional lung density at inspiratory and expiratory volumes.[32]

Collateral ventilation can occur across pulmonary segments because no pleurae separate them. It also may occur between lobes when fissures are incomplete. There are three routes of collateral ventilation: (1) alveolar pores of Kohn (2- to 10-microns circular apertures in the alveolar walls); (2) canals of Lambert (epithelial-lined tubular structures between preterminal, terminal, or respiratory bronchioles and the alveoli surrounding them); and (3) direct small airway anastomoses.[21] Collateral ventilatory pathways are less well developed in young infants than in older children and adults.

## Pulmonary Vasculature/Circulation

The pulmonary circulation develops in concert with the airways, as the two systems are strongly interdependent (see Chapter 53). The development of the vascular system of the lung requires exquisite regulation of cell migration, proliferation, and differentiation; complex molecular pathway interactions are just beginning to be elucidated.[14] The lung has a dual blood supply consisting of a PA and a systemic arterial supply. The main PA arises from the right ventricle distal to the pulmonic valve and forms a segment of the left heart border before it bifurcates at the level of the carina. The left PA curves superiorly and posteriorly to the left hilum anterior to the left main bronchus, where it divides into two branches. The lower branch is directed posteriorly and crosses over the left upper lobe bronchus, descending parallel with but lateral to the left lower lobe bronchus. This vessel gives branches to the lingula segment, to the superior segment of the lower lobe, and to the basilar segments. The smaller superior branch divides, and its branches parallel the bronchial divisions to the upper lobe. The right PA is almost horizontal and divides into its two major branches while still within the pericardium. It lies posterior to the ascending aorta and SVC, and anterior to the right main bronchus. The main upper lobe branch, the truncus anterior, ascends anterior to the right upper lobe bronchus and subdivides into three branches that parallel the three segmental bronchi to the right upper lobe. The largest branch of the right PA is the interlobar artery, which passes anterior to the bronchus intermedius and descends lateral to it, giving branches, in order, to the middle lobe, the superior segment of the lower lobe, and four branches to the basilar segments of the right lower lobe.

In the lung parenchyma, the PA branches travel and divide with the bronchial branches, although they also give off unaccompanied supernumerary branches. There are approximately 23 divisions of airway branching and approximately 28 divisions of PA branching. These vessels can be visualized on high-resolution CT to about the level of the sixteenth generation, which is a few millimeters from the pleural surface and corresponds to the level of the terminal bronchioles, allowing identification of the secondary pulmonary lobule (the parenchyma supplied by three to five or more terminal bronchioles). The arterioles continue to divide until they form a dense capillary network surrounding the alveolus. This network ultimately consists of 280 billion capillary segments with a total blood volume of 140 mL; pulmonary blood volume can nearly double during exercise.[33]

The primary role of the pulmonary circulation is to transport deoxygenated blood from the heart to the alveolar capillaries, where oxygenation occurs, and then transport oxygenated blood through the pulmonary veins back to the left atrium. The pressure in the pulmonary circuit is about one-sixth that of the systemic circuit; total pulmonary blood flow is determined primarily by cardiac output, although the control of pulmonary blood flow is complex and also depends on the relative systemic and pulmonary pressures, gravity, and local pulmonary factors. Large numbers of lung capillaries normally are not perfused or are only minimally perfused, which allows for increased arterial flow without increased PA pressure. Gravity is an important determinant of regional pulmonary blood flow, with the more dependent regions receiving

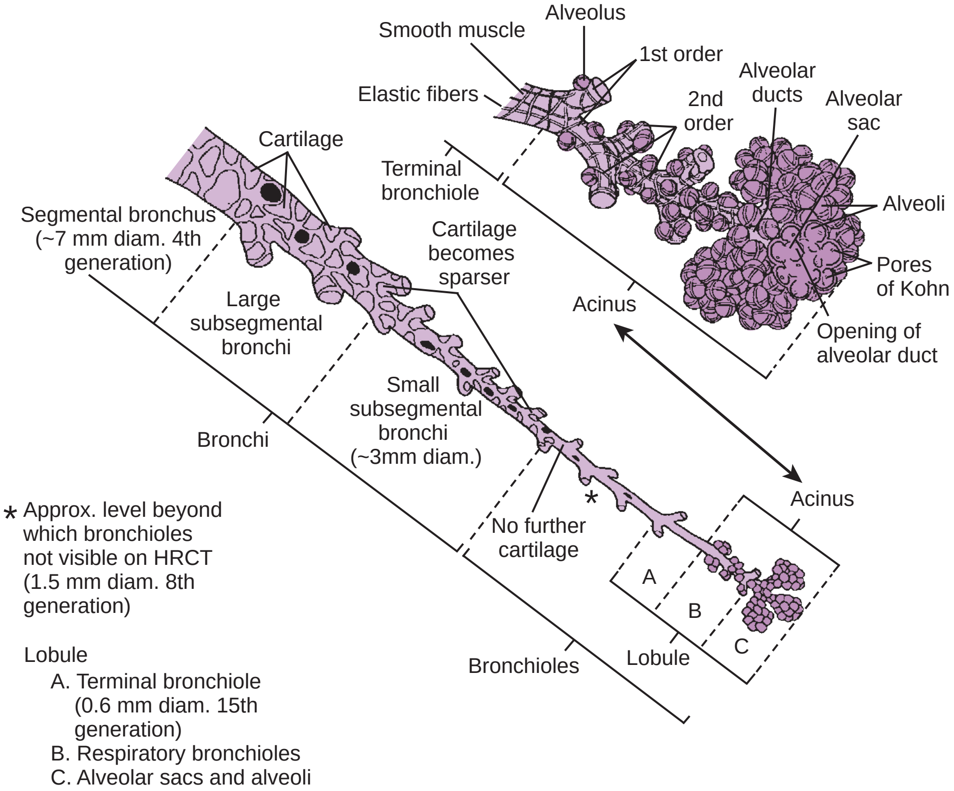
Alveolus
Smooth muscle
1st order
Alveolar ducts
Alveolar sac
Elastic fibers
2nd order
Cartilage
Terminal bronchiole
Alveoli
Segmental bronchus (~7 mm diam. 4th generation)
Cartilage becomes sparser
Pores of Kohn
Acinus
Large subsegmental bronchi
Opening of alveolar duct
Small subsegmental bronchi (~3mm diam.)
Bronchi
Acinus
*
* Approx. level beyond which bronchioles not visible on HRCT (1.5 mm diam. 8th generation)
No further cartilage
A
B
C
Lobule
Bronchioles
Lobule
A. Terminal bronchiole (0.6 mm diam. 15th generation)
B. Respiratory bronchioles
C. Alveolar sacs and alveoli

**Figure 48.12. Bronchial generations.** The bronchi and airways from the fourth generation (the segmental bronchus) to the last generation (the alveolar sacs and alveoli) are represented. Bronchi contain cartilage within their walls, to the level of small (3-mm diameter) subsegmental branches. They are readily visible on high-resolution computed tomography (HRCT). Bronchioles, which do not contain cartilage but rather an extensive network of fibers within their walls, are seen only to the eighth generation, which corresponds to a diameter of about 1.5 mm. Beyond the eighth generation, the bronchiolar walls are not visible by HRCT unless they are abnormal. The terminal bronchioles are the sixteenth-generation bronchioles and conduct air into the lobules. Beyond the terminal bronchioles, four to eight respiratory bronchioles lead to distal acini. Respiratory bronchioles are characterized by the presence of outpouchings representing alveolar ducts and terminal groupings of alveolar sacs. *(From Armstrong P. The normal chest. In: Armstrong P, Wilson AG, Dee P, et al, eds.* Imaging of Diseases of the Chest, *3rd ed, London: Mosby; 2000:26.)*

a greater volume of blood. The smaller, muscular PA branches vasoconstrict under conditions of hypoxia in an attempt to maintain the ventilation-perfusion balance. When lung disease becomes severe enough, this protective mechanism is overwhelmed, and poorly ventilated alveoli are perfused, which results in right-to-left shunting and systemic desaturation. Hypoxemia and accompanying acidosis increase pulmonary vascular resistance, which leads to right ventricular hypertrophy and eventually to cor pulmonale.

The vast pulmonary capillary bed serves the function of gas exchange. Its endothelial cell lining has important metabolic functions and is quite sensitive to toxins, including infectious agents and high oxygen concentrations. When endothelial cells are damaged, increased permeability pulmonary edema often results.[2]

The pulmonary venous radicles arise distal to the capillary meshwork and travel in the interlobular septa, which form the walls of the secondary pulmonary lobules; the veins do not accompany the PA and bronchial branches. They drain toward the hilum and gradually increase in size. Usually two large central pulmonary veins are found on each side. The upper lobe veins are more vertical in orientation, and the lower ones are more horizontal before they enter the left atrium. The right superior vein is located posterior to the SVC and anterior to the right interlobar PA. The left superior pulmonary vein is located anterior to the left main PA and is just anterior to the left upper lobe bronchus. The right inferior branch enters the left atrium anterior to the right lower lobe bronchus, and the left inferior pulmonary vein enters the left atrium at a point just anterior to the descending aorta and posterior to the left lower lobe bronchus.

The systemic circulation to the lung is via two to four (most commonly one right and two left) bronchial arteries that are branches of the thoracic aorta. These vessels provide blood supply to the airways and central mediastinum. In the presence of PA obstruction, collateral circulation to the pulmonary capillaries can develop through precapillary anastomotic channels.

## Lymphatics

Pulmonary lymphatics are essential to removal of initial fetal lung liquid and to the removal of protein and water outside the vascular space.[34,35] This fluid is returned to the circulation via the right lymphatic duct and the thoracic duct. Lymphatic vessels travel beside blood vessels in the bronchovascular spaces and in the connective tissues of the pleura. No lymphatics are present within the alveolar walls, but juxta-alveolar lymphatics represent the initial part of the lung lymphatic system. Enlargement of lymphatic channels in secondary lobular septa may be visualized on chest radiography and with CT (see Fig. 48.15). Lymphangiectasia and lymphatic malformations may be primary, congenital, or acquired related to

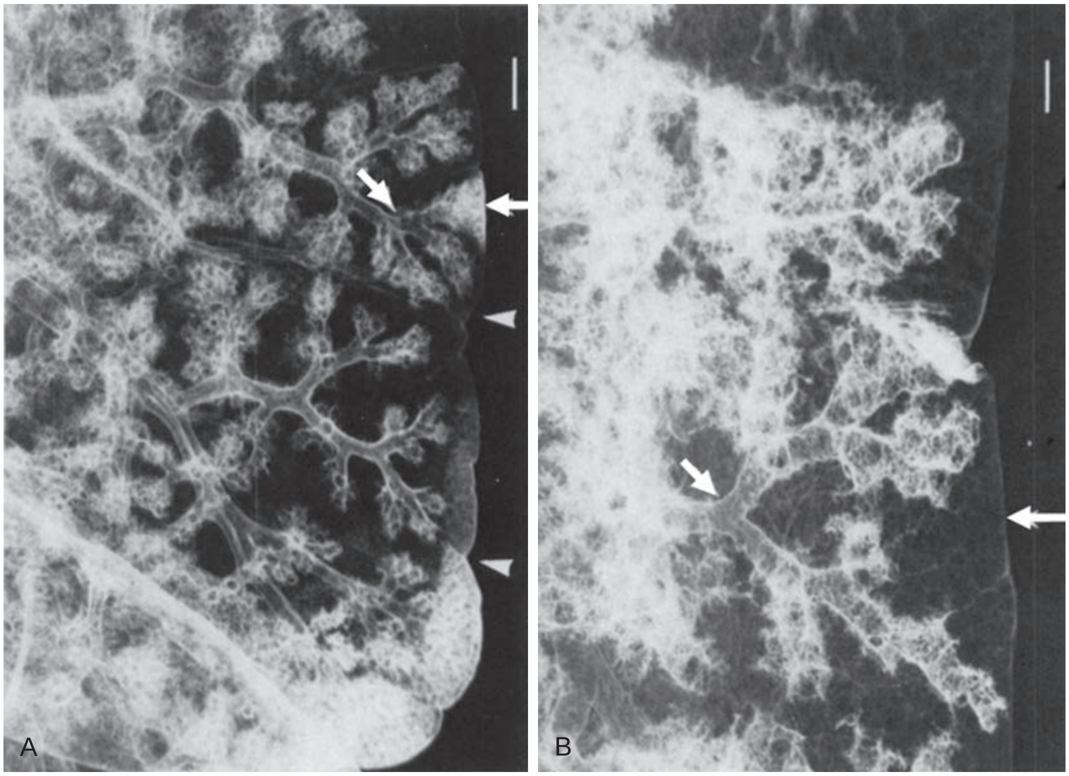

**Figure 48.13. Acinar and secondary lobular anatomy in children.** Radiographs of selected sections of human lung obtained from postmortem examination and prepared by silver nitrate bronchoacinography. (A) (left) The lung from a 2-month-old infant showing the diameter of one acinus extending between the terminal bronchial and acinar surface *(arrows)*. A subjacent underfilled secondary lobule is delimited by interlobular septa *(arrowheads)*. (B) (right) The lung from a 19-year-old showing a mean acinar diameter *(arrows)* that is considerably larger. Both images are at the same magnification, with the marker bar *(upper right)* equal to 1 mm (corrected for specimen shrinkage). *(From Osborne DRS, Effmann EL, Hedlund LW. Postnatal growth and size of the pulmonary acinus and secondary lobule in man.* AJR Am J Roentgenol*. 1983;140:449).*

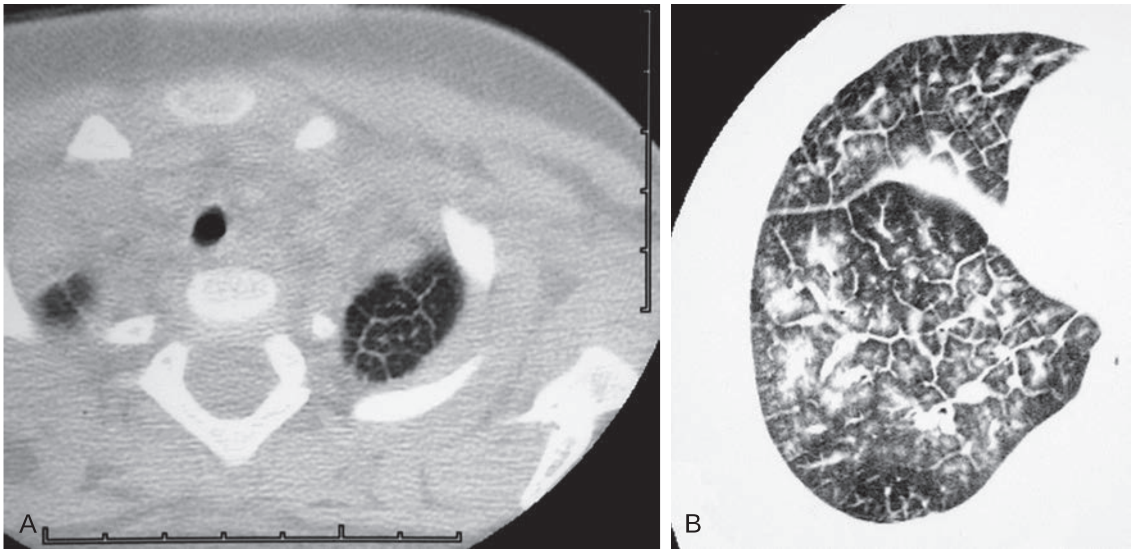

**Figure 48.15. Secondary lobular septal thickening in two patients.** (A) A 1-year-old child with Noonan syndrome showing polygonal-shaped secondary lobules in the left lung apex. Respiratory motion degraded lower sections, which also showed patchy septal thickening. (B) A 15-year-old girl with mixed connective tissue disease shows moderately severe septal thickening and patchy distribution of ground-glass opacities within some lobules.

absent, malformed, obstructed, congested, or disrupted lymphatic channels.[13,36] Some genetic syndromes especially Turner, Noonan, and Down syndrome are associated with lymphatic abnormalities. Dilated pulmonary/pleural and/or mediastinal lymphatics, focal lymphatic collections, and chylothorax may produce mild to severe respiratory distress (see Chapters 55 and 56).

## KEY POINTS

- An understanding of normal airway and pulmonary development, physiology, and anatomy is essential in appreciating the clinical and imaging findings in pulmonary pathologic conditions.
- Airway, lung, and vascular development and physiologic function are interdependent and follow an orderly progression. Arrest or disruption of these processes often results in newborn respiratory distress with a wide variety of conditions including genetic disorders, congenital lung anomalies, thoracic compressive lesions, lung disease of prematurity, abnormal retention of fetal lung liquid, perinatal asphyxia, meconium aspiration, and pulmonary infection.
- The number of alveoli increases sixfold after birth with the process accelerated in early life and completed by age 8 years, with further lung growth by enlargement of existing lung components.
- Two clinically useful subunits of airspace disease are the acinus and secondary pulmonary lobule. The acinus is the unit of lung peripheral to the terminal bronchiole and consists of 50 to 400 alveoli, whereas the secondary lobule is a cluster of 3 to 24 acini separated by interlobular septa.
- The peripheral pulmonary vasculature divides and accompanies bronchial branching. It may be visualized to at least the sixteenth generation of division within a few millimeters of the peripheral surface and corresponds to the level of the terminal bronchioles.

## SUGGESTED READINGS

Hansell DM, Armstrong P, Lynch DA, et al. The normal chest. In: Hansell DM, Armstrong P, Lynch DA, et al, eds. *Imaging of Diseases of the Chest*. 5th ed. Philadelphia: Mosby; 2010.

Lobo L. The neonatal chest. *Eur J Radiol*. 2006;60(2):152–158.

Newman B, Varich L. Neonatal imaging. In: Daldrup-Link H, Gooding C, eds. *Essentials of Pediatric Radiology. A Multimodality Approach*. New York: Cambridge University Press; 2010:19–30.

Polin RA, Fox WW, Abman SH, eds. *Fetal and Neonatal Physiology*. 3rd ed. Philadelphia: Saunders; 2004.

Webb WR, Müller N, Naidich DP. Normal lung anatomy. In: Webb WR, Müller N, Naidich DP, eds. *High Resolution CT of the Lung*. 4th ed. Philadelphia: Lippincott; 2009.

## REFERENCES

Full references for this chapter can be found on www.expertconsult.com.

## REFERENCES

1. Bush A. Congenital lung disease: a plea for clear thinking and clear nomenclature. *Pediatr Pulmonol*. 2001;32(4):328–337.
2. Newman B, Varich L. Neonatal imaging. In: Daldrup-Link H, Gooding C, eds. *Essentials of Pediatric Radiology. A Multimodality Approach*. New York: Cambriage University Press; 2010:19–30.
3. Lobo L. The neonatal chest. *Eur J Radiol*. 2006;60(2):152–158.
4. Arthur R. The neonatal chest x-ray. *Paediatr Respir Rev*. 2001;2(4): 311–323.
5. O'Rahilly R, Müller F. *Human Embryology & Teratology*. 2nd ed. New York: Wiley-Liss New York; 1996.
6. Saacson G. Developmental anatomy and physiology of the larynx, trachea, and esophagus. In: Bluestone CD, Stool SE, et al, eds. *Pediatric Otolaryngology*. 4th ed. Philadelphia: Saunders; 2003.
7. Wood RE. Physiology of the larynx, airway, and lungs. In: Bluestone CD, Stool SE, et al, eds. *Pediatric Otolaryngology*. 4th ed. Philadelphia: Saunders; 2003.
8. Wert SE. Normal and abnormal structural development of the lung. In: Polin RA, Fox WW, Abman SG, eds. *Fetal and Neonatal Physiology*. Philadelphia: Saunders; 2004:784–794.
9. Avery ME, Fletcher DD, Williams RG. *The Lung and its Disorders in the Newborn Infant*. 4th ed. Philadelphia: Saunders; 1981.
10. Porter HJ. Pulmonary hypoplasia. *Arch Dis Child Fetal Neonatal Ed*. 1999;81(2):F81–F83.
11. Newman B. Congenital bronchopulmonary foregut malformations: concepts and controversies. *Pediatr Radiol*. 2006;36(8):773–791.
12. Agrons GA, Courtney SE, Stocker JT, et al. From the archives of the AFIP: lung disease in premature neonates: radiologic-pathologic correlation. *Radiographics*. 2005;25(4):1047–1073.
13. Guillerman RP, Brody AS. Contemporary perspectives on pediatric diffuse lung disease. *Radiol Clin North Am*. 2011;49(5):847–868.
14. Kool H, Mous D, Tibboel D, et al. Pulmonary vascular development goes awry in congenital lung abnormalities. *Birth Defects Res C Embryo Today*. 2014;102(4):343–358.
15. Possmayer F. *Physicochemical aspects of pulmonary surfactant*. Vol 2 2004.
16. Gross I, Ballard P. *Hormonal therapy for prevention of respiratory distress syndrome*. 1997.
17. Jobe AH. Surfactant treatment. In: Polin RA, Fox WW, Abman SG, eds. *Fetal and Neonatal Physiology*. 3rd ed. Philadelphia: Saunders; 2004.
18. Barker PM, Southern KW. Regulation of liquid secretion and absorption by the fetal and neonatal lung. In: *Fetal and Neonatal Physiology*. 3rd ed. Philadelphia: Saunders; 2004:822–834.
19. Rabinovitch M. Physiologic development of the cardiovascular system in the fetus. In: Polin RA, Fox WW, Abman SG, eds. *Fetal and Neonatal Physiology*. 3rd ed. Philadelphia: Saunders; 2004.
20. Rosse C, Gaddum-Rosse P. *Hollingsched's Textbook of Anatomy*. 5th ed. Lippincott-Raven; 1997.
21. Fraser RS, Muller NL, Colman N, et al. The normal chest. In: Fraser RS, Pare PD, eds. *Diagnosis of Diseases of the Chest*. Vol. 1. 4th ed. Philadelphia: Saunders; 1999.
22. Hansell DM, Armstrong P, Lynch DA. et al. The normal chest. In: Hansell DM, Armstrong P, Lynch DA, et al, eds. *Imaging of Diseases of the Chest*. 5th ed. London: Mosby; 2010.
23. Griscom NT. Computed tomographic determination of tracheal dimensions in children and adolescents. *Radiology*. 1982;145(2):361–364.
24. Effmann EL, Fram EK, Vock P, et al. Tracheal cross-sectional area in children: CT determination. *Radiology*. 1983;149(1):137–140.
25. Griscom NT, Wohl ME. Tracheal size and shape: effects of change in intraluminal pressure. *Radiology*. 1983;149(1):27–30.
26. Armstrong P. The normal chest. In: Armstrong P, Wilson AG, Dee P, et al, eds. *Imaging of Diseases of the Chest*. 3rd ed. London: Mosby; 2000.
27. Osborne DRS, Effmann EL, Hedlund LW. Postnatal growth and size of the pulmonary acinus and secondary lobule in man. *AJR Am J Roentgenol*. 1983;140(3):449–454.
28. Mueller KS, Long FR, Flucke RL, et al. Volume-monitored chest CT: a simplified method for obtaining motion-free images near full inspiratory and end expiratory lung volumes. *Pediatr Radiol*. 2010;40(10):1663–1669.
29. Gollogly S, Smith JT, White SK, et al. The volume of lung parenchyma as a function of age: a review of 1050 normal CT scans of the chest with three-dimensional volumetric reconstruction of the pulmonary system. *Spine*. 2004;29(18):2061–2066.
30. de Jong PA, Long FR, Wong JC, et al. Computed tomographic estimation of lung dimensions throughout the growth period. *Eur Respir J*. 2006;27(2):261–267.
31. Vock P, Malanowski D, Tschaeppeler H, et al. Computed tomographic lung density in children. *Invest Radiol*. 1987;22(8):627–631.
32. Long FR, Williams RS, Castile RG. Inspiratory and expiratory CT lung density in infants and young children. *Pediatr Radiol*. 2005;35(7): 677–683.
33. Weibel ER. *Morphometry of the Human Lung*. New York: Academic Press; 1963.
34. Ohtani O, Ohtani Y. Organization and developmental aspects of lymphatic vessels. *Arch Histol Cytol*. 2008;71(1):1–22.
35. El-Chemaly S, Levine SJ, Moss J. Lymphatics in lung disease. *Ann N Y Acad Sci*. 2008;1131:195–202.
36. Faul JL, Berry GJ, Colby TV, et al. Thoracic lymphangiomas, lymphangiectasis, lymphangiomatosis, and lymphatic dysplasia syndrome. *Am J Respir Crit Care Med*. 2000;161:1037–1046.

# 49

# Imaging Techniques

*Hyun Woo Goo, Laura A. Drubach, and Edward Y. Lee*

## OVERVIEW

Various imaging modalities—conventional radiography, fluoroscopy, ultrasound, computed tomography (CT), magnetic resonance imaging (MRI), and nuclear medicine studies—are used to assess the pediatric respiratory system. Although having abundant air in the respiratory system is beneficial when performing conventional radiography, fluoroscopy, and CT, it complicates assessment of the respiratory system with ultrasound and MRI.

When answers to specific clinical questions are sought, radiologists and clinicians ideally should work together to select appropriate imaging modalities. Up-to-date knowledge about the advantages and disadvantages of each imaging modality should be carefully considered when making a selection because the imaging techniques for the pediatric respiratory system are continuously evolving. Furthermore, the imaging techniques should be tailored to the individual pediatric patient for optimal results. This chapter discusses indications, contraindications, benefits, risks, and other relevant issues pertaining to each imaging modality currently being used.

## CONVENTIONAL RADIOGRAPHY

Conventional radiography is the creation of a projection image with the use of x-rays to view parts of the human body. This primary, cost-effective imaging method currently is the modality used most frequently for evaluation of the respiratory system in children. Conventional radiography is associated with a very low level of ionizing radiation exposure (in the range of 0.01–0.02 mSv for chest posteroanterior [PA] radiography).[1,2] Soft tissue neck study and chest radiography are the two radiographic imaging studies used most frequently to assess the pediatric respiratory system.

### Soft Tissue Neck Study

Inspiratory stridor resulting from an upper airway obstruction is the most frequent indication for a soft tissue neck study in pediatric patients.[3] The common causes of inspiratory stridor in infants and children include croup, epiglottitis, a foreign body, and an upper airway mass. To obtain optimal diagnostic quality, the neck of the patient should be extended and images should be obtained at full inspiration. The standard views consist of both an anteroposterior (AP) view and a lateral view. An additional expiratory lateral view of the neck subsequently may be obtained; this can be helpful in differentiating a fixed large airway disorder (e.g., subglottic stenosis) from a dynamic large airway disorder (e.g., tracheomalacia).

Use of the high-kilovoltage technique with added filtration and coned magnification may facilitate visualization of the upper airway and adjacent soft tissue. Immobilization may be necessary for infants and young children (<5 years) who may not be able to follow verbal instructions. However, great care should be taken not to exacerbate airway obstruction when positioning a child with respiratory distress. For instance, the upright position is preferred and the supine position is contraindicated in the setting of acute epiglottitis. When necessary, careful manual immobilization of the head and neck during the study by the child's parents or by an experienced technologist may be considered. A clinician should accompany the child with respiratory distress, and an emergency kit should be available in the examination room. In most conditions resulting in upper airway obstruction in pediatric patients, a soft tissue neck study is sufficient to make the diagnosis. However, when the underlying cause of upper airway obstruction is not evident, fluoroscopy, CT, or MRI may be necessary as a next step in the imaging evaluation.

### Chest Radiography

Chest radiography is the imaging study obtained most frequently to evaluate the respiratory system in pediatric patients. Immobilization is usually required in uncooperative infants and young children (<5 years) to achieve consistent image quality by decreasing motion artifacts and poor positioning.[4] Chest radiography is obtained during quiet inspiration in uncooperative infants and young children, and during full inspiration in cooperative older pediatric patients. The standard chest radiographic views consist of the AP view in infants and young children (<5 years) and either AP or PA views in older children, in addition to a lateral view. AP, PA, and lateral views of the chest can be obtained with the patient in the supine or erect position. Exposure parameters for chest radiography should be appropriately optimized. Unnecessary radiation to nonthoracic structures such as the lower neck, proximal upper extremity, and upper abdomen should be avoided by using appropriate collimation and shielding.[5,6]

In contrast to a radiographic screen-film system, image acquisition and display are decoupled in digital radiography, which allows increased versatility of image manipulations.[7,8] Recently, optimization of digital radiographic techniques has been emphasized to reduce unnecessary overexposure to pediatric patients.[6,9] The increased likelihood of overexposure in digital radiography, the so-called *dose creep*, is attributed not only to the lack of a standardized exposure index but also to the difficulty in recognizing overexposed radiographs by radiologic technologists and radiologists. Fortunately, a new standardized exposure index for digital radiography was proposed recently.[10]

Optimized techniques of digital chest radiography in children often are different from those in adults. For instance, automatic exposure control and grids are not particularly helpful in small pediatric patients. Additional views such as expiratory, decubitus, and oblique views sometimes are necessary to clarify abnormalities detected on standard AP or PA views or to solve unanswered clinical questions. Expiratory views may be used to confirm air trapping due to an underlying airway obstruction. The lateral decubitus view generally is used to detect freely shifting pleural effusion or air; it is used infrequently to demonstrate an air-fluid level in an intraparenchymal cavitary lesion. In addition, the lateral decubitus view may be used to demonstrate air trapping in the dependent lung or to clarify poorly defined lung opacities in the nondependent lung in uncooperative infants and young children.[11,12] Oblique views may be helpful for evaluating rib, soft tissue, hilar, carinal, and peripheral lung abnormalities.

## FLUOROSCOPY

Fluoroscopy can be used to evaluate dynamic large airway and lung abnormalities, such as airway obstruction, air trapping, and diaphragmatic paresis/paralysis. Use of fluoroscopic techniques and equipment should be optimized to minimize radiation exposure

## Abstract:

Various imaging modalities—conventional radiography, fluoroscopy, ultrasound, computed tomography (CT), magnetic resonance imaging (MRI), and nuclear medicine studies—currently are available and are used to assess the pediatric respiratory system in clinical practice. The presence of air in the airways and lungs can be beneficial and challenging with regard to imaging the respiratory system. Although having abundant air in the respiratory system is beneficial when performing conventional radiography, fluoroscopy, and CT, it complicates assessment of the respiratory system with ultrasound and MRI.

## Keywords:

Respiratory system
Children
Imaging techniques
Radiography
Fluoroscopy
Ultrasonography
Computed tomography
Magnetic resonance imaging
Nuclear medicine imaging

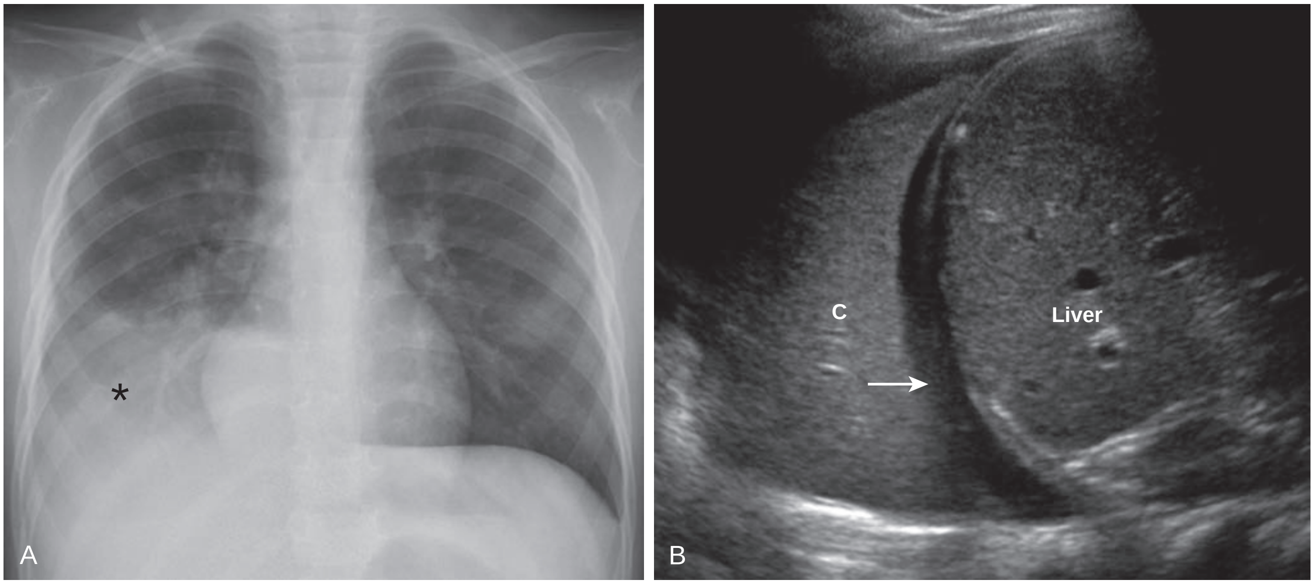

**Figure 49.1. Plain radiography and ultrasound in a 3-year-old girl with fever, cough, and respiratory distress.** (A) Frontal chest radiograph shows an opacity *(asterisk)* projecting over the right lower lung zone. (B) Longitudinal sonogram of the right lower hemithorax demonstrates consolidated lung *(C),* small effusion *(arrow),* and liver.

of both the patient and operator by following the “imaging gently” and “step lightly” principles.[13]

## Fluoroscopy-Guided Airway Study

A fluoroscopy-guided airway study may be helpful in demonstrating dynamic airway abnormalities, such as laryngomalacia, tracheomalacia, obstructive sleep apnea, and vocal cord dysfunction syndrome.[14-16] Additionally, a fixed airway disorder such as stenosis or stricture can be identified and differentiated from a dynamic airway disorder. Compared with endoscopic procedures, a fluoroscopy-guided airway study generally is inexpensive and less invasive.[17] In recent years, fluoroscopy-guided airway studies have begun to be replaced by dynamic airway CT with a low radiation dose technique.[18] Dynamic airway CT is more accurate than a fluoroscopy for evaluation of the location, degree, and extent of both the dynamic and fixed airway abnormalities. Furthermore, dynamic airway CT can provide additional information about other intrathoracic structures, which is a valuable benefit.[18]

## ULTRASOUND

Ultrasound (US) is a valuable and commonly used imaging modality for evaluating the chest in pediatric patients, because it is widely available, is relatively easy to perform, and does not expose patients to radiation.[19,20] Its real-time evaluation capability and portability are important additional benefits. Furthermore, crucial information regarding associated vascular structures or underlying blood flow also can be obtained with color Doppler US.[19,20] US is useful in assessing and triaging selected lung and pleural lesions, as well as juxtadiaphragmatic and mediastinal structures, as long as there is a sonographic window without intervening aerated lung.

### Evaluation of Lungs and Mediastinum

The main clinical indication for ultrasound of the lungs in pediatric patients is to characterize a peripheral lung opacity (i.e., parenchymal versus pleural disease) that has been detected with chest radiography.[19] Frequent underlying etiologies include atelectasis, consolidation, lung necrosis, a lung abscess, congenital lung lesions, and a primary or metastatic lung neoplasm (Fig. 49.1).[19,20] For evaluation of these abnormalities, conventional chest radiography should be carefully reviewed to localize the area of interest so the clinical question can be specifically answered with the US evaluation.[19,20] Lung US has shown utility as a primary imaging modality to diagnose pediatric pneumonia, and is also being used to assess for interstitial disease, whether from edema, inflammatory, or fibrotic processes.[21]

Ultrasound evaluation of the lungs typically is performed with the patient in the supine or upright position. However, to improve the visualization in some selected situations, the lateral decubitus view or the supraclavicular and/or suprasternal notch view may be beneficial. Optimal views can be achieved by placing a pillow or blanket on the dependent side or behind the shoulder to help extend the neck of the patient.[19] The choice of US transducer depends primarily on three factors: the age of the patient, the size of the patient, and the location of the abnormality.[19,20] Although curved or linear array transducers typically are used to evaluate peripheral lung opacity, smaller sector or vector transducers may be necessary for imaging in infants or young children who have a small available acoustic window (such as between the ribs). High-frequency transducers (e.g., 7.5–15.0 MHz) are helpful in evaluating the chest in infants and young children who do not have substantial subcutaneous tissue and provide higher resolution images.[19] Conversely, use of low-frequency transducers (e.g., <5 MHz) may be necessary when evaluating older children who required greater soft tissue penetration, although image resolution is decreased.[19] Color Doppler US is useful for evaluating lung lesions with underlying vascular structures in cases of pulmonary sequestration or blood flow in cases involving a neoplasm.

Mediastinal lesions can also be evaluated initially by US, especially in small children. One of the major uses of US is to differentiate normal thymus from a mediastinal mass and prevent further unnecessary CT or MRI. Characterizing lesions as cystic or solid is also useful.

### Evaluation of Pleura

In emergent and critical care settings, US can reliably detect a pneumothorax, and may be more sensitive than radiography in supine patients.[20,22] US can be useful in differentiating pleural fluid from atelectasis and/or consolidation when the diagnosis is equivocal on the basis of conventional radiography. Furthermore, US is more sensitive and accurate than conventional radiography or CT for characterizing pleural fluid, which may be simple or complex (Fig. 49.2).[19] US evaluation of patients in both the erect and lateral decubitus positions can be useful for differentiating between freely flowing and loculated pleural fluid. In addition, ultrasound can visualize the internal debris, septations, and pleural thickening often associated with parapneumonic collections. Such complex pleural effusion often requires a drainage procedure that can be facilitated with ultrasound guidance.

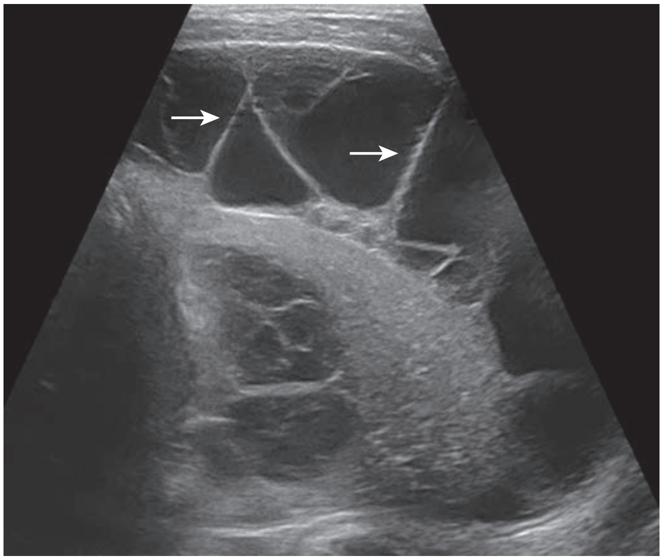

**Figure 49.2. Ultrasound for pleural fluid in a 5-year-old boy with recurrent pneumonia in the right lung.** Longitudinal sonogram of the right hemithorax shows a complex pleural effusion with thick septations *(arrows)*.

## COMPUTED TOMOGRAPHY

CT is a valuable cross-sectional imaging study for evaluating the pediatric chest, mainly because its images provide excellent air-tissue contrast. Current multidetector CT allows short scan times with a decreased rate of sedation, and has increased the role of CT assessment of pediatric airways and lungs.[23] Respiratory motion artifacts can degrade CT image quality in infants and young children who breathe freely during the scan. These artifacts can be reduced with the use of general anesthesia and controlled ventilation.[24,25] These techniques also can be used to control either the inspiratory or expiratory phases of respiration.[24-26] In addition, newer high-pitch dual-source spiral CT scanning is very helpful in reducing motion artifacts on non–breath-hold chest CT scans in children.[27] Virtual monoenergetic dual-energy CT with energy domain noise reduction can provide higher iodine contrast-to-noise ratio compared with conventional single-energy CT further improving image quality (Fig. 49.3).[28]

Reducing the CT radiation dose while maintaining diagnostic image quality is of critical importance in pediatric patients because of the greater radiosensitivity and longer life expectancy of children, coupled with increasing CT use. Low-dose, body size–adapted chest CT protocols using variable tube voltages and tube currents have been established, usually on the basis of body weight.[29,30] However, recent studies demonstrate that cross-sectional dimensions provide better CT dose adaptation to body habitus.[30-34] The tube current always should be modulated if applicable because this allows CT dose reduction without degrading image quality.[35-37] Electrocardiogram-triggered sequential scanning may be used in CT of the chest in children to achieve fewer motion artifacts and a lower radiation dose.[25,38]

CT image quality may be further improved by adjusting kilovolt levels and reconstruction algorithms: a low kilovolt level for contrast-enhanced CT and a high kilovolt level for unenhanced CT, a high-frequency reconstruction algorithm for lung evaluation, and a standard reconstruction algorithm for mediastinal evaluation. In addition to axial CT images, postprocessed and reconstructed images such as multiplanar reformatted (MPR) and

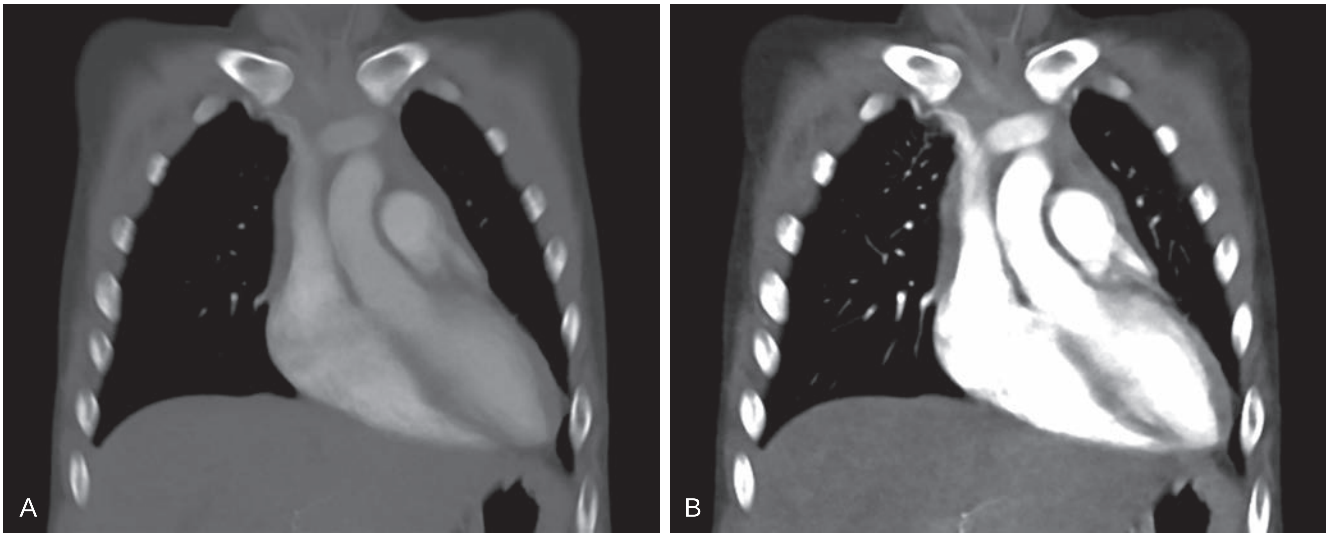

**Figure 49.3. Coronal dual-energy enhanced chest CT (window level, 200 HU; window width 1000 HU) using dual-source technique (80 kVp and 140 kVp with tin filter).** Compared with linear blending image (A) with mixed ratio of 0.4 (40% from 80 kVp data), virtual monoenergetic 40 keV image (B) with energy domain noise reduction demonstrates markedly increased iodine contrast-to-noise ratio.

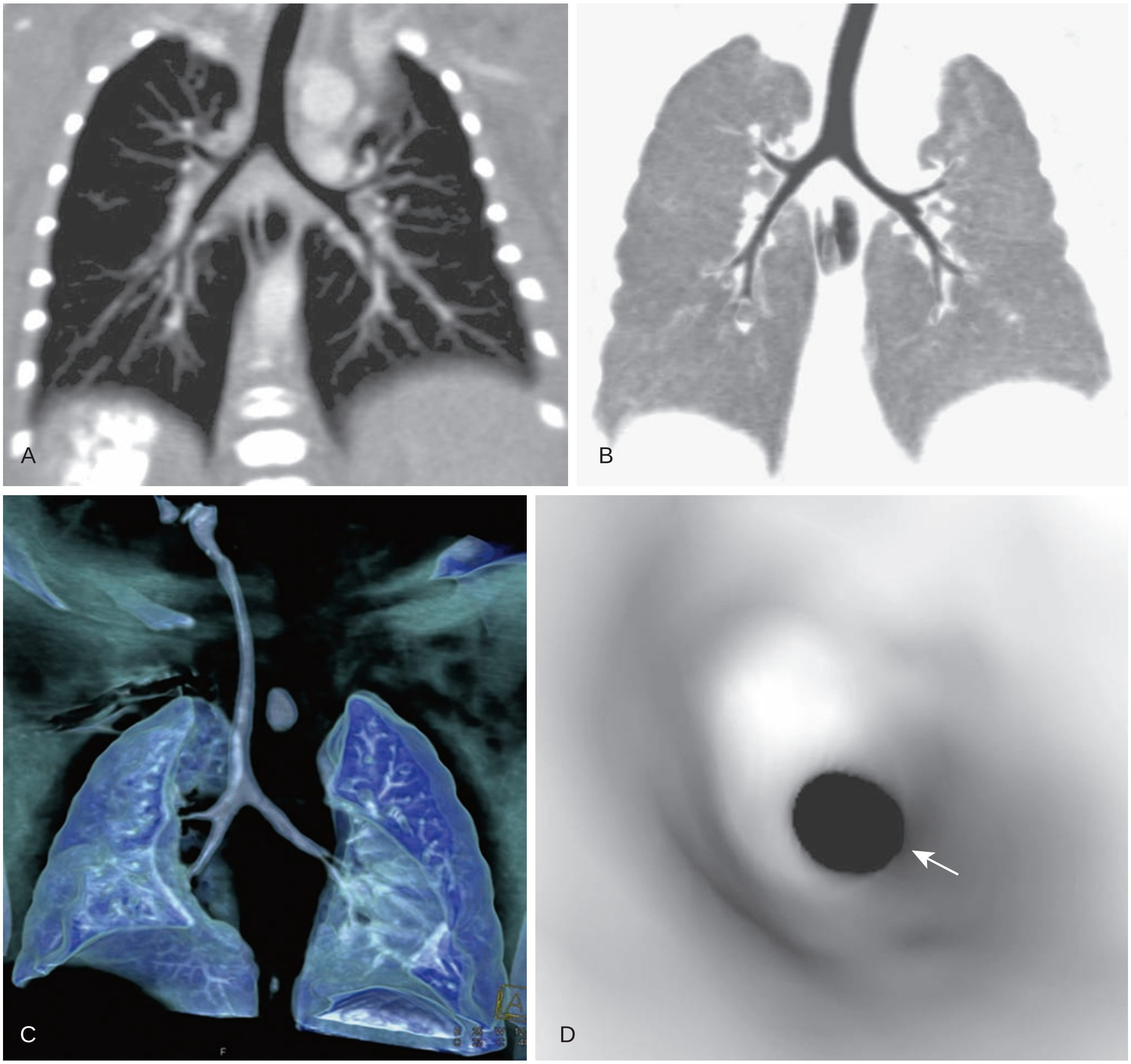

**Figure 49.4. Multiplanar reformatted and 3D CT imaging.** (A) Coronal thin-slab CT image shows normal relationships between the airway and the pulmonary artery, indicating thoracic situs solitus. (B) Coronal minimum-intensity projection CT image shows anatomic details of the central airways. (C) Volume-rendered CT image shows the 3D appearance of the lungs and airways. (D) Virtual bronchoscopic image providing an endoscopic view of the trachea shows concentric narrowing *(arrow)* from a tracheal web.

three-dimensional (3D) images considerably increase diagnostic accuracy of pediatric chest CT (Fig. 49.4).[39] CT scanning with thinner collimation (<1 mm) offers better-quality MPR and 3D images. Various visualization techniques including maximum intensity projection, minimum intensity projection, volume rendering, and virtual bronchoscopy can help further visualize thoracic abnormalities (see Fig. 49.4).

## Evaluation of Airways

Anatomic details of the pediatric airways can readily be imaged with CT.[40,41] However, small airways distal to the subsegmental level (i.e., airways <0.5–1.5 mm in diameter) often are invisible on CT. CT is less invasive than bronchoscopy in evaluating pediatric airways and provides cross-sectional imaging without superimposition. Various airway abnormalities, including fixed or dynamic obstruction, bronchiectasis, and wall thickening, can be diagnosed. Contrast-enhanced CT allows for evaluation of airway/vascular relationships. MRI may be used to evaluate large airways with comparable diagnostic accuracy, but MRI is inferior to CT in evaluating small airways because of lower spatial resolution and lower signal/noise ratio.

### Static Airway Computed Tomography Study

A static airway CT study is performed mainly to assess a fixed airway narrowing or stenosis. Axial CT data are acquired in infants and young children while they breathe freely and in older children while they hold their breath at the end of an inspiration (Fig. 49.4C). Anatomic details of the airway typically are well visualized,

**TABLE 49.1** Tube Current and Kilovoltage by Patient Weight for Central Airway Multidetector Computed Tomography

| Weight (kg) | Tube Current (mAs) Inspiration/Expiration | Kilovoltage |
|---|---|---|
| <10 | 40/20 | 80 |
| 10–14 | 50/25 | 80 |
| 15–24 | 60/30 | 80 |
| 25–34 | 70/35 | 80 |
| 35–44 | 80/40 | 80 |
| 45–54 | 90/40 | 90 |
| 55–70 | 100–120/40 | 100–120 |

For tube current and kilovoltage by patient weight for end-expiratory multidetector computed tomography (MDCT) examination, mAs should be reduced by 50% to a maximum of 40 mAs while maintaining the same level of kilovoltage for end-inspiratory MDCT examination.

*From Lee EY, Boiselle PM. Tracheobronchomalacia in infants and children: multidetector CT evaluation.* Radiology. *2009;252(1):7–22.*

even in free-breathing studies, because of the fast scan speed of multidetector CT. The extent and cause of airway abnormalities can be better evaluated with MPR and 3D CT images than with axial CT images alone.

### Dynamic Airway Computed Tomography Study

A paired inspiratory and expiratory CT study is performed for the dynamic evaluation of a large airway disorder, most commonly tracheobronchomalacia.[18] Expiratory CT is performed with a low radiation dose technique during this dual-phase study (Table 49.1). The resultant effective dose from this paired study typically is in the range of 3.5 to 7.5 mSv.[18] Expiratory CT can be obtained with two different respiratory maneuvers: (1) holding the breath at the end of an expiration during end-expiratory CT and (2) forced exhalation during dynamic expiratory CT. In uncooperative infants and young children, general anesthesia with intubation, controlled ventilation, or respiratory triggering can be used.[18,24,25,41]

### Cine Airway Computed Tomography Study

In cine airway CT, axial sequential scans are acquired continuously at predefined noncontiguous slices with high resolution and low radiation dose technique throughout the respiratory cycle.[42] This technique allows changes in the cross-sectional area and shape of the airway to be demonstrated throughout the entire respiratory cycle, thus making the diagnosis of tracheobronchomalacia possible. To achieve the high temporal resolution required for cine airway CT, the fastest gantry rotation speed is used. The total scan time should be tailored to a range of one to two respiratory cycles to minimize the radiation dose. As a result, the radiation dose of cine airway CT is quite low—in the range of 0.2 mSv to 0.3 mSv.[25] Cine airway CT is performed in infants and young children as they breathe freely or with a coughing maneuver in cooperative older children.[18,43] Coughing exaggerates the expiratory collapse of the airway because it produces a higher intrathoracic extra-airway pressure than does normal or forced exhalation, and thus it is the preferred technique for a cine airway CT study. In addition to dynamic airway evaluation, cine airway CT also can be used to detect pulmonary air trapping, which often is a secondary sign of underlying small airway disease.[42]

### Four-Dimensional Airway Computed Tomography Study

Increased longitudinal coverage of up to 16 cm with modern CT makes four-dimensional (4D) airway CT study feasible.[44] As in a cine airway CT study, an axial sequential CT scan is continuously acquired without table movement throughout the respiration cycle in 4D airway CT. The major difference from cine airway CT is the real-time volumetric coverage of almost the entire central airway in infants and young children (Fig. 49.5).

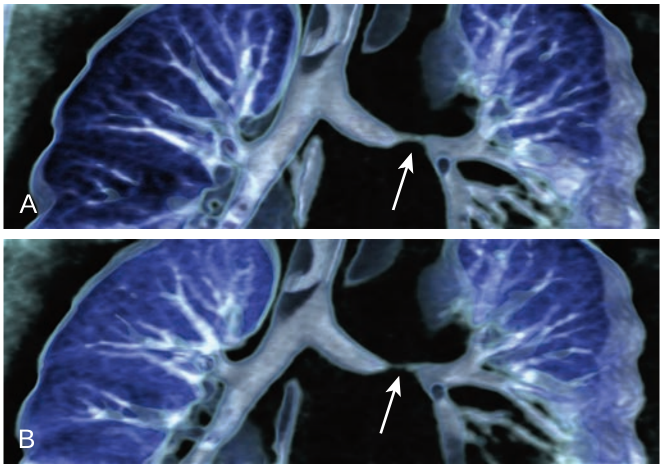

**Figure 49.5. Four-dimensional airway CT study.** (A) Peak inspiration. (B) Peak expiration. A fixed narrowing *(arrow)* is noted at the distal left main bronchus.

## Evaluation of Lungs

CT is valuable in evaluating not only the air spaces, but also interstitial and vascular abnormalities, and parenchymal nodules or masses in the lung. In addition, mediastinal, hilar, and chest wall abnormalities also can be assessed. However, soft tissue contrast resolution of CT is inferior to that of MRI, and MRI is better in evaluating intraspinal and paraspinal regions.

Expiratory CT is necessary to confirm air trapping accurately.[42,45] To obtain proper expiratory CT data, patient cooperation or anesthesia is required. In uncooperative infants and young children, lateral decubitus CT may be used as an altenative.[46] In this position, dependent and nondependent lungs show different lung volumes that mimic inspiration and expiration, respectively (Fig. 49.6A). A drawback of the lateral decubitus CT technique is the need to change the position of the patient, different location between the dependent and nondependent lungs, and exaggerated respiratory motion artifacts in the nondependent lung. Cine CT in the supine position can overcome some of the limitations of lateral decubitus CT (Fig. 49.6B and C).[42] Recently, dual-energy chest CT has been used in pediatric patients to assess regional lung perfusion and ventilation.[47-53] Quantitative analysis to determine lung volume or density can be performed using 3D CT data.

### Routine Chest Computed Tomography Study

Routine chest CT is performed without or with intravenous administration of an iodinated contrast agent, depending on the clinical questions being addressed. High tube voltage should be used for an unenhanced chest CT scan, whereas low tube voltage should be selected for an enhanced chest CT scan. The use of precontrast and postcontrast (dual-phase) chest CT should be avoided in pediatric patients as much as possible to minimize exposure to radiation. Virtual unenhanced CT imaging using the dual-energy technique may substitute for real unenhanced CT imaging, reducing radiation dose.[53]

### High-Resolution Computed Tomography Study

High-resolution CT (HRCT) originally was developed in the 1980s as a special technique in which noncontiguous thin sections,

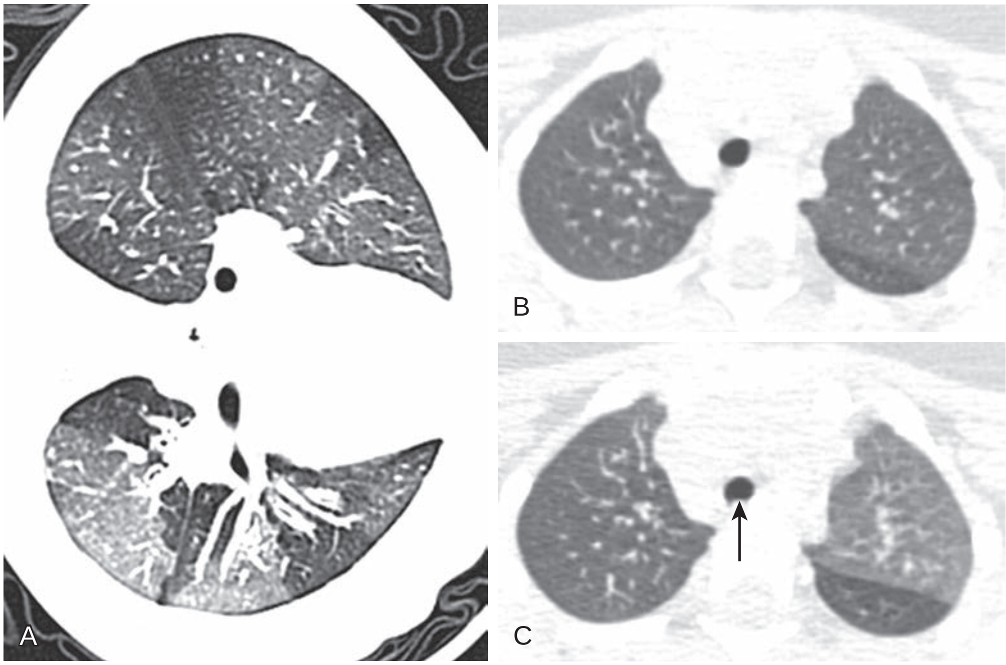

**Figure 49.6. Expiratory CT techniques in children breathing freely.** (A) Left-side-down lateral decubitus CT scan shows geographic hyperlucent areas due to trapping of air, so-called mosaic lung attenuation, in the dependent left lung of a child with bronchiolitis obliterans. Inspiratory (B) and expiratory (C) cine CT images show the normal left upper lobe and the abnormal right upper and left lower lobes with trapping of air. The normal posterior flattening of the trachea *(arrow)* is noted at expiration (C).

approximately 1 mm in slice thickness, are acquired at 5- to 20-mm intervals depending on the size of the patient.[54] To illustrate fine details of the lung anatomy and pathology, a high spatial frequency reconstruction algorithm is used. This classic HRCT study has been used principally as a follow-up imaging study of diffuse lung abnormalities, such as interstitial lung disease or cystic fibrosis, while delivering a very low radiation dose. The development of MDCT allows contiguous thin sections of the entire lung to be viewed with a reasonably low radiation dose and MPR capabilities, which changes the technical concept of HRCT of the lung. MDCT with thin collimation (<1 mm), single spiral CT scanning can provide both thick sections (for a routine chest CT with standard reconstruction algorithm) and thin sections (for HRCT of the lung with high spatial frequency reconstruction algorithm) without additional scanning radiation exposure. It has been reported that reconstructed HRCT images from volumetric MDCT acquisition have significantly less motion artifact than images obtained with traditional axial HRCT acquisition in pediatric patients.[54-57] Nonetheless, the classic HRCT technique still may be used in pediatric patients because of the overall decreased radiation exposure compared with volumetric data acquisition.

## MAGNETIC RESONANCE IMAGING

Chest MRI has inherent limitations because of the low signal-to-noise ratio of the lung, cardiac and respiratory motion artifacts, and susceptibility artifacts that occur at air-tissue interfaces in the lung. A lengthy examination time is another important disadvantage of MRI, leading to a greater requirement for sedation or anesthesia in pediatric patients. However, recent technical advances in MRI, such as parallel imaging and multichannel body-array coils, allow substantial reduction of examination time. In addition, vector electrocardiogram triggering, respiratory triggering, and navigator gating may be used separately or together to suppress motion artifacts.

Lack of ionizing radiation exposure and excellent soft tissue contrast are advantages of MRI. Different tissue characteristics can be evaluated with T1- and T2-weighted imaging and, more recently, balanced steady-state free precession imaging. Fat saturation may be added to the pulse sequence if necessary. The use of gadolinium contrast agents can further improve tissue characterization on T1-weighted imaging. A variety of functional thoracic assessments, including perfusion, ventilation, and respiratory mechanics, can be performed with MRI.[58-60] Water diffusivity or cellularity of thoracic masses may be evaluated with diffusion-weighted imaging (Fig. 49.7). Hyperpolarized gas MRI allows excellent static and dynamic visualization of the lung and airway and may overcome the limitations of proton MRI of the thorax.[61] However, hyperpolarized gas MRI has markedly limited availability, which is the main obstacle to its clinical use and the primary reason it remains in the research realm. Chest MRI examination cannot be performed in some circumstances (e.g., when contraindications for MRI exist, such as the presence of a permanent cardiac pacemaker, the presence of a cardioverter-defibrillator, or claustrophobia).

### Evaluation of Airways

Central airways and their relationships to adjacent cardiovascular structures can be assessed with noncontrast black-blood MRI (Fig. 49.8).[62] Tracheobronchomalacia can be diagnosed with real-time dynamic airway MRI. CT is generally preferred for airway evaluation as the detailed delineation of the airway, especially smaller peripheral airways on MRI, is somewhat limited because of lower spatial resolution.

### Evaluation of Lungs

Despite the inherent limitations of lung MRI, magnetic resonance is rapidly advancing as a viable lung imaging modality. One study

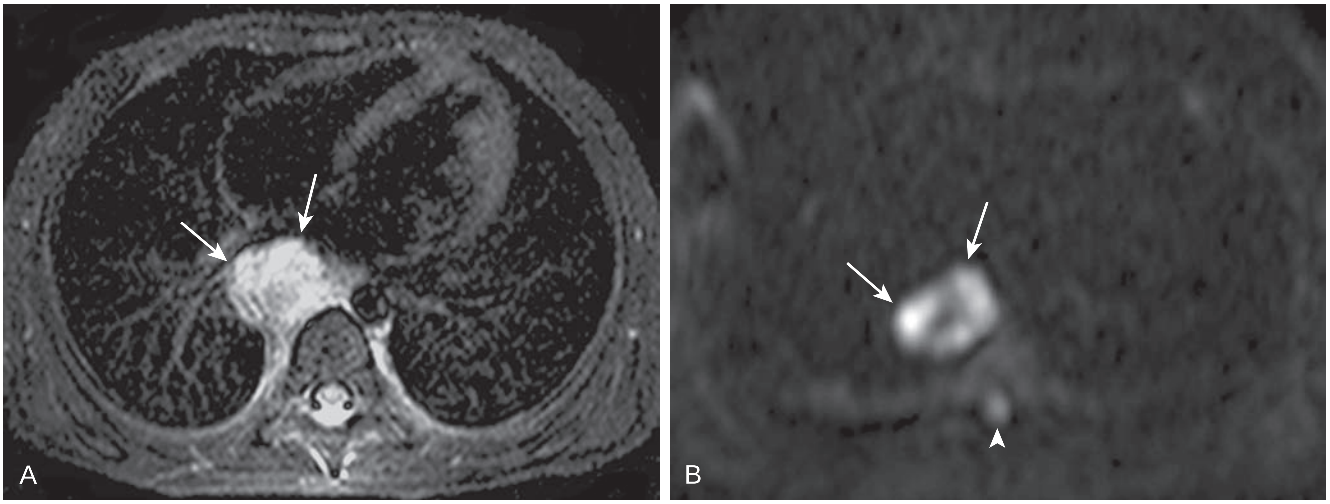

**Figure 49.7. Diffusion-weighted MRI.** (A) Axial T2-weighted chest MRI using a short tau inversion recovery sequence shows a metastatic neuroblastoma involving a paraesophageal lymph node *(arrows).* (B) On axial diffusion-weighted MRI (b-value, 800 sec/mm$^2$), hyperintense areas are predominant in the lesion *(arrows),* indicating restricted water diffusion or hypercellularity. Of note, the normal spinal cord *(arrowhead)* appears modestly hyperintense.

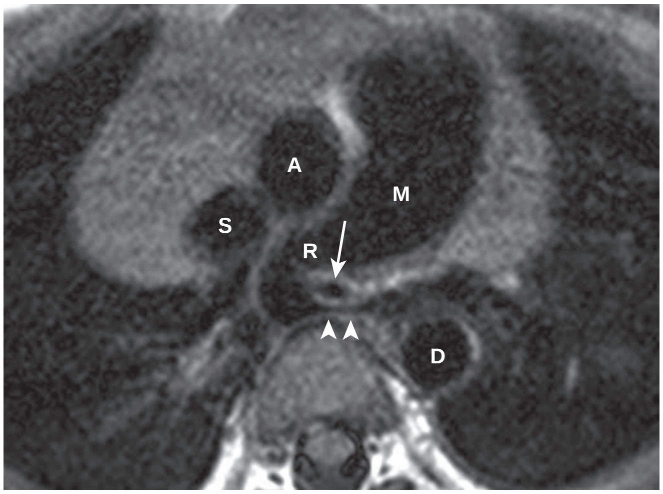

**Figure 49.8. Black-blood MRI.** An axial T1-weighted, electrocardiogram-triggered chest MRI using spin-echo echo-planar imaging and the black-blood technique shows an intimate relationship between the left pulmonary artery sling and congenital tracheal stenosis *(arrow),* the so-called “sling-ring” complex. Note a severe focal stenosis *(arrowheads)* of the left pulmonary artery between the trachea and the spine. *A,* Ascending aorta; *D,* descending aorta; *M,* main pulmonary artery; *R,* right pulmonary artery; *S,* superior vena cava.

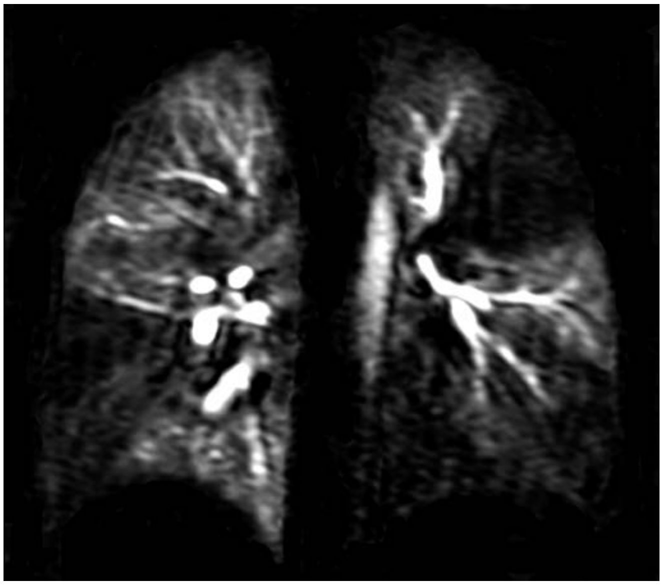

**Figure 49.9. Contrast-enhanced lung perfusion MRI.** A coronal image obtained from time-resolved MRA shows maximal contrast enhancement in the normal lung areas and multiple lung perfusion defects. The signal outside the lung is suppressed by means of subtraction.

showed that lung nodules of a diameter larger than 3 to 4 mm can be detected with MRI with use of 1.5-T systems.[63] Contrast-enhanced time-resolved magnetic resonance angiography (MRA) offers not only anatomic details of pulmonary vessels but also hemodynamics of the pulmonary circulation. Because contrast bolus timing is not needed and less motion artifact occurs because of high temporal resolution (e.g., <1 second for the entire lung), time-resolved MRA often replaces static high-resolution MRA in pediatric patients.[64] Lung perfusion MRI can be obtained with either the contrast-enhanced or non–contrast-enhanced technique (Fig. 49.9). Real-time dynamic chest MRI with the patient breathing freely may be used to demonstrate normal and abnormal respiratory dynamics.[65] Regional ventilation may be assessed with oxygen-enhanced MRI or hyperpolarized gas (${}^{3}$helium or ${}^{129}$xenon) MRI. Diffusion-weighted imaging using hyperpolarized gas enables calculation of the size of peripheral air spaces. Hyperpolarized xenon MRI has an additional capability of assessing diffusing capacity in the lung. Newer free-breathing proton MRI techniques without any contrast agents allow both lung perfusion and lung tissue density determination in a single data acquisition.[66]

## NUCLEAR MEDICINE STUDIES

In some clinical settings, nuclear medicine techniques have an important advantage over anatomic imaging methods because they

**TABLE 49.2** Recommended Administered Activities Based on the North American Consensus Guidelines for Administered Radiopharmaceutical Activities in Children and Adolescents

| Radiopharmaceutical Agent | Recommended Administered Activity | Minimum Administered Activity | Maximum Administered Activity |
|---|---|---|---|
| $^{99m}$Tc macroaggregated albumin | If $^{99m}$Tc is used for ventilation, 2.59 MBq/kg (0.07 mCi/kg)<br>If no $^{99m}$Tc ventilation study is performed, 1.11 MBq/kg (0.03 mCi/kg) | 14.8 MBq (0.4 mCi) | |
| $^{99m}$Tc methylene diphosphonate | 9.3 MBq/kg (0.25 mCi/kg) | 37 MBq (1.0 mCi) | |
| $^{123}$I metaiodobenzylguanidine | 5.2 MBq/kg (0.14 mCi/kg) | 37 MBq (1.0 mCi) | 370 MBq (10.0 mCi) |
| 18F deoxyglucose | 3.7–5.2 MBq/kg (0.10–0.14 mCi/kg) | 37 MBq (1.0 mCi) | |

*This research was originally published in JNM. Gelfand MJ, Parisi MT, Treves ST, Pediatric radiopharmaceutical administered doses: 2010 North American consensus guidelines.* J Nucl Med. *2011;52:318–322. Copyright by the Society of Nuclear Medicine and Molecular Imaging, Inc.*

evaluate physiologic processes. Several radionuclide techniques are commonly used to evaluate pediatric diseases of the respiratory system or chest wall, as listed in Table 49.2. Most nuclear medicine studies are performed with an intravenous injection of a radiopharmaceutical agent. Many nuclear medicine procedures carry inherently higher radiation exposure to the patient than plain film radiographic procedures, but the radiation exposure is comparable to or less than that of CT examinations. It is important to use the lowest possible injected tracer dosage that allows good-quality images to be recorded. Although accepted standard adult radiopharmaceutical dosages often are established, dosage determination in children is best calculated on the basis of weight, which in turn is derived from the adult reference administered activity.[67] Current recommendations are presented in Table 49.2.

The acquisition time for nuclear medicine images often is quite long compared with radiographic techniques, and gentle immobilization and distraction is necessary in small children. Sedation occasionally is required during lengthy imaging sessions. Currently available nuclear medicine studies that are used to assess thoracic disorders in pediatric patients include the lung perfusion and ventilation study, salivagram, neuroendocrine imaging study, bone scan, and positron emission tomography. Only those studies that are specific to the chest are discussed here.

## Lung Perfusion and Ventilation Study

Lung perfusion imaging, although largely supplanted by CT techniques for the diagnosis of pulmonary embolus, remains an important technique for the evaluation of lung physiology and pathology. The incidence of pulmonary embolism in the pediatric population is lower than in the adult population, but occasionally perfusion imaging is used with patients who have significant risk factors to evaluate for an embolus when a contraindication to the administration of radiographic contrast material exists. Nuclear ventilation and perfusion imaging is much more commonly used to evaluate relative function in diseases in which knowledge of physiology helps guide clinical care. Both relative ventilation and perfusion can be quantitated, which permits treatment planning and follow-up evaluation in a variety of clinical entities such as lung malformations resulting from congenital lobar emphysema and congenital pulmonary airway malformations (Fig. 49.10). The quantitative analysis of relative lung perfusion and ventilation also is useful in preoperative cases before pneumonectomy to evaluate for the estimated postsurgical lung capacity.[68]

Patients with congenital heart disease frequently undergo perfusion imaging to quantitate relative perfusion between the right and left lungs at baseline and after catheter intervention, as well as long term (e-Fig. 49.11). A recent study evaluated the utility of lung perfusion scans in patients with primary pulmonary vein stenosis. The findings showed a good correlation of lung scan and cardiac catheterization angiography.[69]

The perfusion study is performed with technetium-99m ($^{99m}$Tc) macroaggregated albumin (MAA). The dosage in pediatrics is based on patient weight (see Table 49.2). In cases of congenital heart disease when differential lung perfusion is evaluated, a specially prepared radiopharmaceutical agent with a low concentration of particles of MAA is recommended. The tracer is always injected with the patient supine so a hydrostatic gradient is not present from lung apex to base. Imaging can be performed with the patient either upright or supine, but supine imaging typically is performed in children. If imaging is being performed to evaluate pulmonary physiology, typically only anterior and posterior planar views are acquired. The differential lung perfusion is then calculated by drawing a region of interest around each lung and calculating the geometric mean (i.e., the square root of the product of anterior and posterior views) of counts in each lung. If the perfusion scan is being performed to evaluate for a pulmonary embolism, additional anatomic information is recorded, with a standard of eight planar images (i.e., anterior, posterior, left and right lateral, right anterior oblique, left anterior oblique, right posterior oblique, and left posterior oblique views). Alternatively, single-photon emission computed tomography (SPECT) imaging of the lungs can be performed. When evaluating for a possible pulmonary embolus, a correlation should be made with a chest radiograph obtained within 24 hours of the study.

The ventilation study can be performed either with a radioactive gas (xenon-133) that demonstrates air flow or a radio aerosol ($^{99m}$Tc diethylenetriaminepentaacetic acid [DTPA]) that localizes in alveoli without significant large airway deposition. 133Xe gas has a principal photon energy of 81 keV, which is lower than $^{99m}$Tc. The DTPA aerosol study uses the same $^{99m}$Tc label as MAA perfusion imaging, but much less aerosol tracer activity localizes in the lungs than is present with the intravenous MAA injection. Thus both xenon and aerosol ventilation imaging must be performed before the perfusion agent is administered.

133Xe gas is administered by inhalation. The recommended dose is 10 to 20 mCi. The dynamic nature of the xenon study limits the projections that can be obtained, and thus imaging typically is acquired in the posterior view with a single-head camera. If a dual-head camera is used, simultaneous anterior and posterior imaging can be acquired. The presence of the anterior detector over the child's face and thorax can cause anxiety, and thus in young children only the posterior image typically is acquired.

$^{99m}$Tc DTPA aerosol is administered via a shielded nebulizer; the child inhales long enough to accumulate sufficient aerosol in the lung for imaging. The aerosol remains in the lungs long enough for imaging to be performed in multiple projections, matching those acquired with perfusion imaging. When SPECT perfusion imaging is performed, SPECT aerosol images also can be acquired for comparison.

## Salivagram

Radionuclide evaluation for salivary aspiration (i.e., a salivagram) offers a safe and easily performed test with minimal radiation exposure to the patient. The sensitivity of the salivagram has been

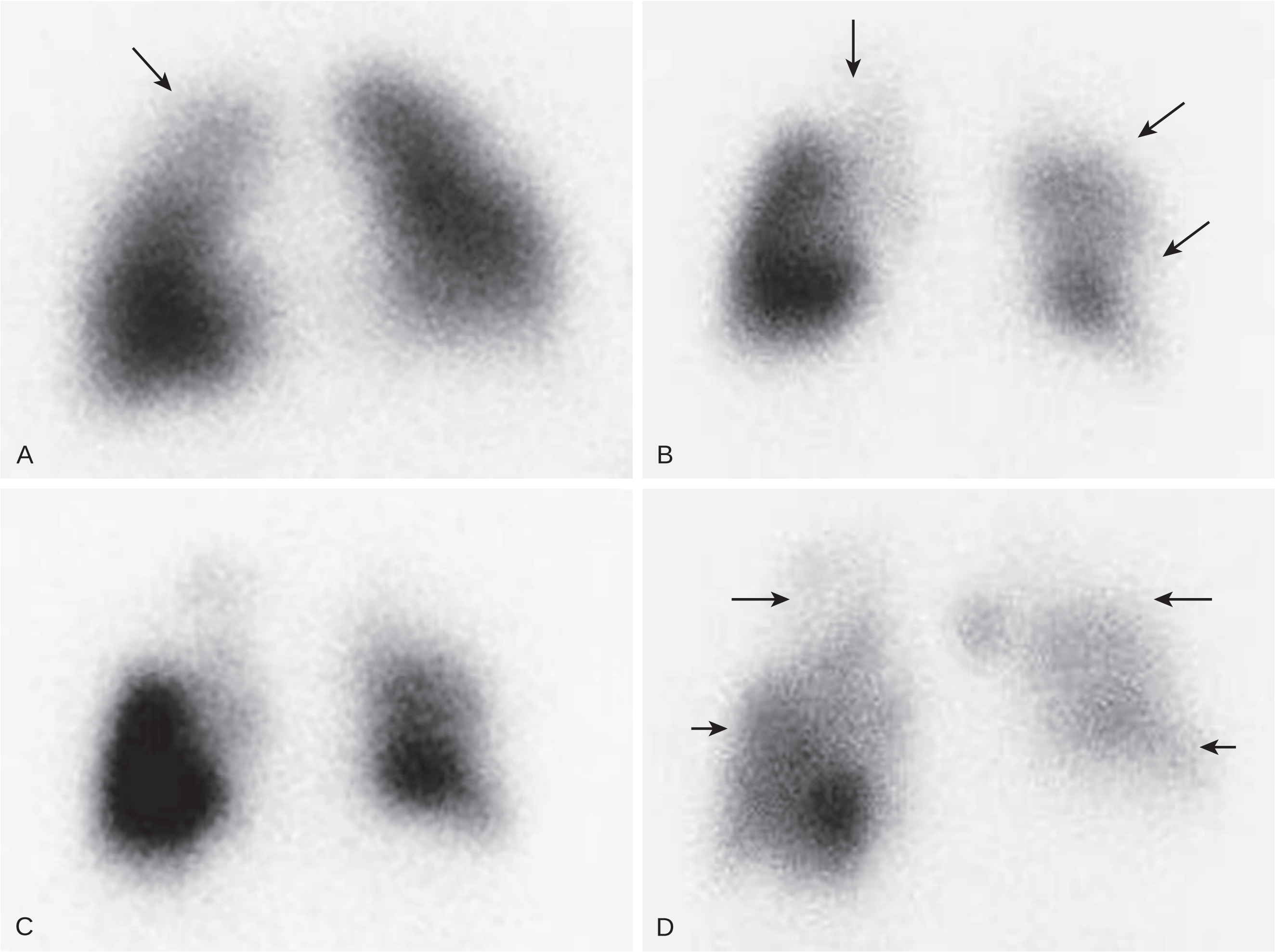

**e-Figure 49.11. Nuclear medicine perfusion imaging of an 8-year-old boy with diagnosis of pulmonary vein stenosis of all four pulmonary veins.** (A) Posterior view of the lung scan showing the relative decreased perfusion of the left upper lung *(arrow).* (B) Follow-up lung scan showing worsening perfusion to the right lung, in addition to the decreased perfusion of the left upper lung. (C) Follow-up study after repair of the stenosis of the right inferior pulmonary vein, now showing better perfusion to the right lower lung. (D) The patient presents again with increasing symptoms and lung scan shows worsening perfusion to the right lung and left upper lung suggestive of restenosis of the pulmonary veins *(arrows)*.

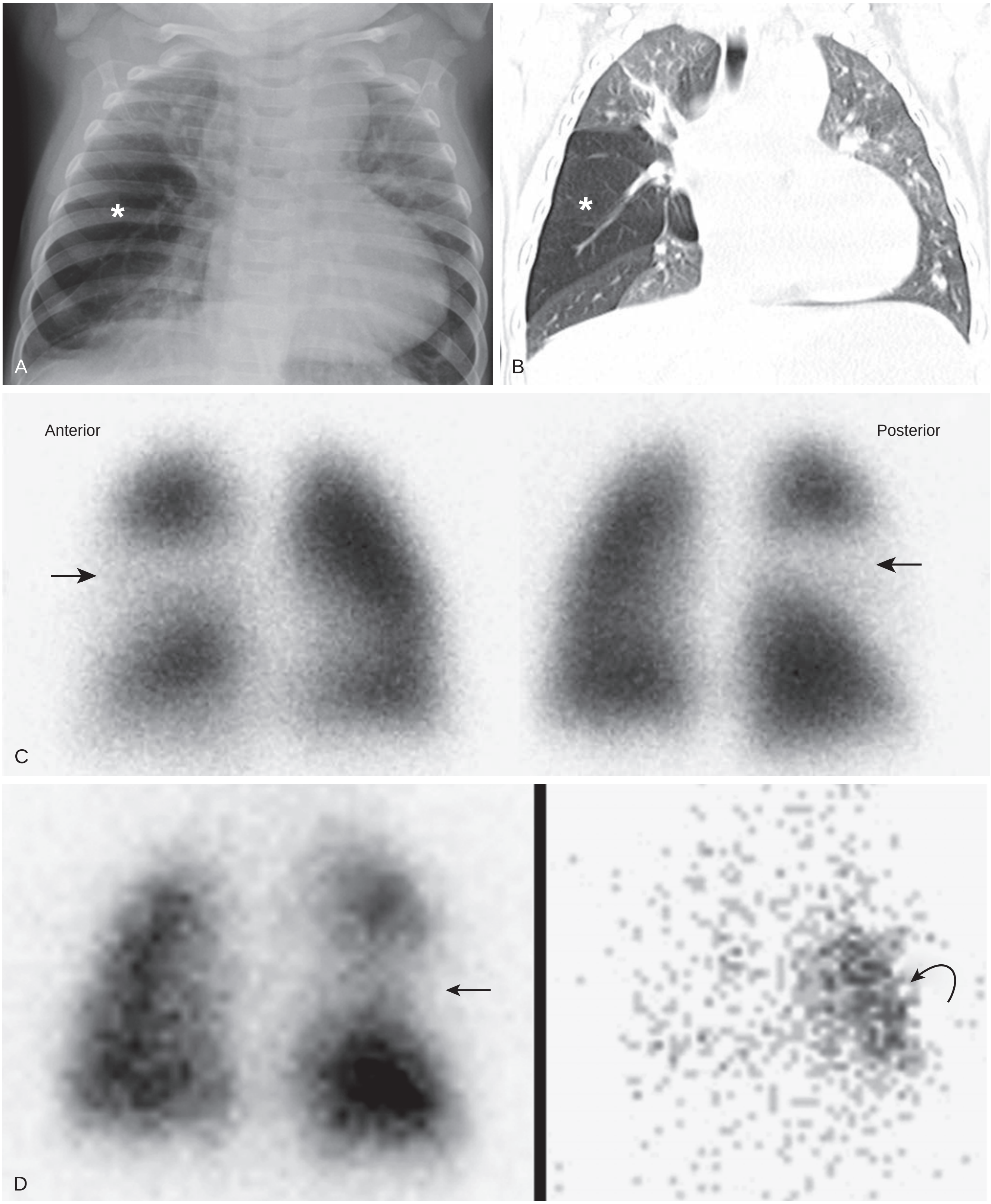

**Figure 49.10. Multimodality imaging of a 7-month-old girl with congenital lobar emphysema.** (A) Frontal chest radiograph shows hyperlucency *(asterisk)* in the right mid to lower lung zone. (B) Coronal lung window CT demonstrates hyperinflation and oligemia of the right middle lobe *(asterisk),* consistent with congenital lobar emphysema. (C) Perfusion lung scan shows no perfusion to the right middle lobe *(arrow)* on the anterior view *(Anterior)* and posterior view *(Posterior).* (D) Posterior image from a ventilation scan on the left showing initial decreased ventilation to the right middle lung *(straight arrow)* with air trapping in the same area on the later images *(curved arrow).*

reported to range between 26% and 73%.[70-72] The salivagram can be performed with the administration of a small drop (approximately 100 µL) of $^{99m}$Tc sulfur colloid (300 µCi [11.1 MBq]) that is placed in the oral cavity while the patient is lying in a supine position in the imaging bed. After administration of the radiopharmaceutical agent, the patient is allowed to swallow normally and posterior planar imaging of the mouth, chest, and upper abdomen is obtained dynamically for 60 minutes. Imaging is acquired using a low-energy, high-resolution or ultra–high-resolution collimator, with consecutive dynamic images recorded every 30 seconds for a total of 120 frames. A positive salivagram for aspiration shows the radiopharmaceutical agent entering the bronchi (Fig. 49.12).

## Positron Emission Tomography

Positron emission tomography (PET) is useful in evaluating many primary and metastatic intrathoracic tumors in pediatric patients (Fig. 49.13). Pediatric tumors commonly evaluated with PET include Hodgkin lymphoma, non-Hodgkin lymphoma, rhabdomyosarcoma, osteosarcoma, Ewing sarcoma, neuroblastoma, and other less common malignancies.

The recommended dosage of fluorine-18–labeled deoxyglucose (FDG) is 150 µCi/kg (5.55 MBq) (minimum 500 µCi [18.5 MBq] and maximum 10 mCi [370 MBq]). Imaging is performed about 60 minutes after the injection to allow adequate accumulation of the tracer in the tumor. Images of the torso or of the entire body can be obtained according to the indication of the study. Several elements of patient preparation for the study are important. Because FDG is taken up competitively with glucose, the patient must fast (i.e., no solid food and nothing to drink except water) for at least 4 hours before the PET scan. The patient must not receive any form of glucose, including intravenous fluids containing glucose, for at least 4 hours before administration. The blood glucose level is measured routinely at the time of tracer administration and should be between 50 and 200 mg/dL. Patients who are diabetic and/or dependent on insulin should take their diabetic medication and/or insulin 2 hours before the examination with a small amount of juice and dry toast or plain crackers. The patient should avoid any strenuous exercise 24 hours before the study because such exercise might lead to an increase in muscle uptake that hinders the interpretation of the study.

Another important aspect of pediatric PET studies is the high incidence of metabolically active brown fat activation compared with the adult population. The presence of brown fat increases

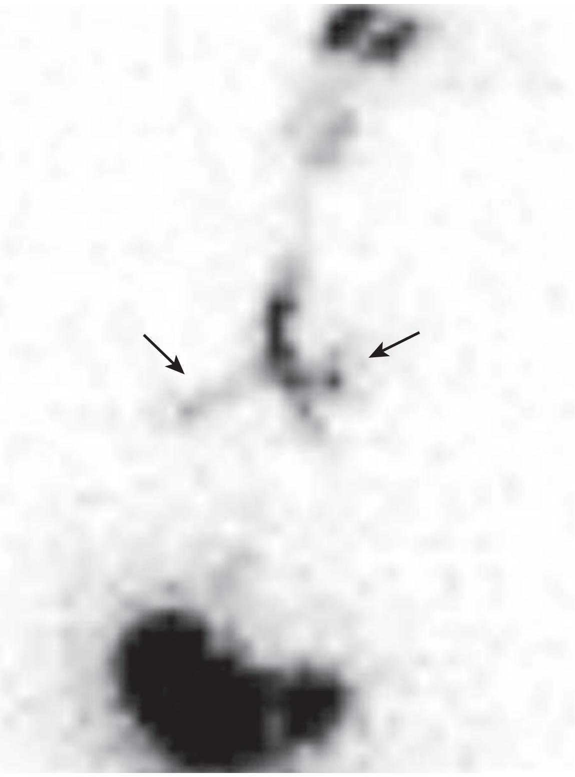

**Figure 49.12. Salivagram.** A posterior view of the neck, chest, and upper abdomen shows bilateral aspiration into the proximal bronchi *(arrows).*

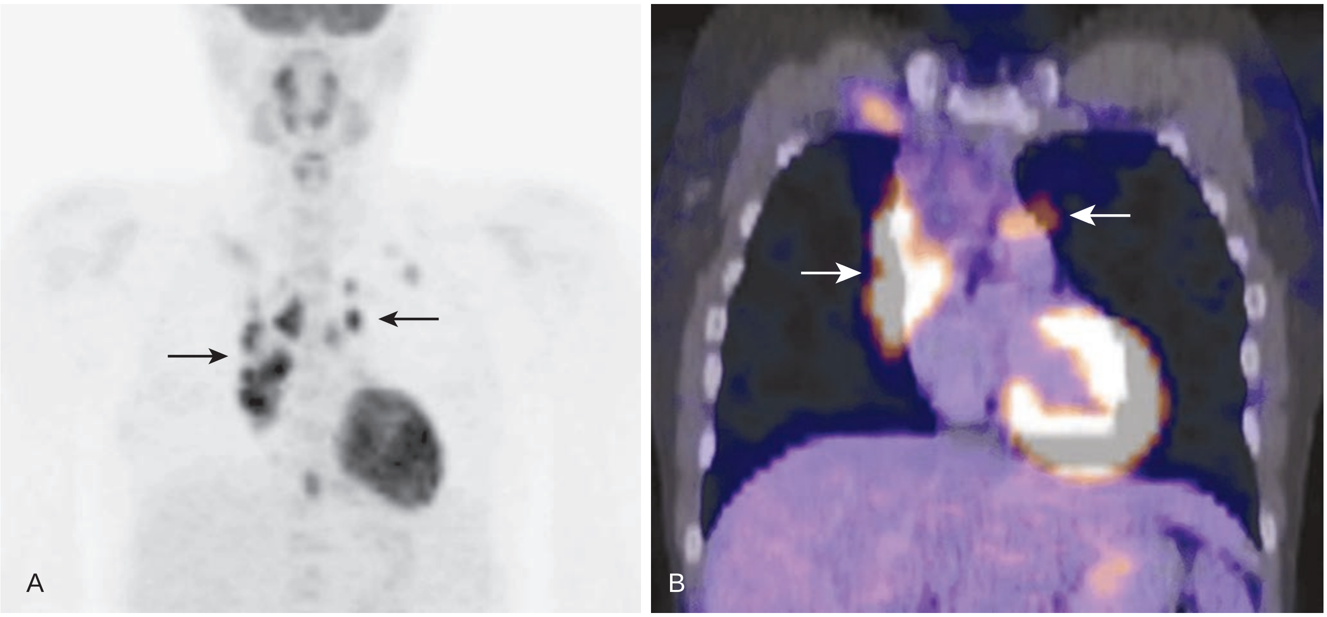

**Figure 49.13. PET imaging in a 19-year-old with newly diagnosed Hodgkin disease.** (A) Coronal PET image shows multiple sites of abnormal uptake in the anterior mediastinum *(arrows).* (B) Fusion of PET and CT images shows the abnormal areas of uptake corresponding to enlarged lymph nodes on CT *(arrows).*

the number of equivocal studies.[73] Keeping patients at an ambient temperature of 24°C before and during the FDG uptake phase decreases the incidence of brown fat activation significantly.[74]

In the evaluation of tumors, PET provides an advantage over anatomic imaging because it detects metabolically active viable tissue. Use of PET in the evaluation of Hodgkin lymphoma has been shown to increase the detection of metastases when compared with CT alone.[75]

## KEY POINTS

- Up-to-date knowledge regarding imaging techniques is essential to achieve optimum diagnostic performance and to choose an appropriate imaging method for evaluation of the pediatric respiratory system.
- Imaging parameters should be tailored to each individual pediatric patient for optimal results.
- Risks related to diagnostic imaging, such as radiation exposure, the use of a contrast agent, and sedation, should be minimized.

## SUGGESTED READINGS

Coley BD. Chest sonography in children: current indications, techniques, and imaging findings. *Radiol Clin North Am*. 2011;49(5):825–846.
Goo HW. State-of-the-art CT imaging techniques for congenital heart disease. *Korean J Radiol*. 2010;11:4–18.
Lee EY. Advancing CT and MR imaging of the lungs and airways in children: imaging into practice. *Pediatr Radiol*. 2008;38:S208–S212.
Lee EY, Greenberg SB, Boiselle PM. Multidetector computed tomography of pediatric large airway diseases: state-of-the-art. *Radiol Clin North Am*. 2011;49(5):869–893.
Treves ST, Baker A, Fahey FH, et al. Nuclear medicine in the first year of life. *J Nucl Med*. 2011;52(6):905–925.
Willis CE. Optimizing digital radiography of children. *Eur J Radiol*. 2009;72:266–273.

## REFERENCES

Full references for this chapter can be found on www.expertconsult.com.

## REFERENCES

1. Linet MS, Kim KP, Rajaraman P. Children's exposure to diagnostic medical radiation and cancer risk: epidemiologic and dosimetric considerations. *Pediatr Radiol*. 2009;39(suppl 1):S4–S26.
2. Mettler FA Jr, Huda W, Yoshizumi TT, et al. Effective doses in radiology and diagnostic nuclear medicine: a catalog. *Radiology*. 2008;248:254–263.
3. John SD, Swischuk LE. Stridor and upper airway obstruction in infants and children. *Radiographics*. 1992;12:625–643.
4. Kohda E, Tsutsumi Y, Nagamoto M, et al. Revisit image control for pediatric chest radiography. *Radiat Med*. 2007;25:60–64.
5. Soboleski D, Theriault C, Acker A, et al. Unnecessary irradiation to non-thoracic structures during pediatric chest radiography. *Pediatr Radiol*. 2006;36:22–25.
6. Willis CE. Computed radiography: a higher dose? *Pediatr Radiol*. 2002;32:745–750.
7. MacMahon H, Vyborny C. Technical advances in chest radiography. *AJR Am J Roentgenol*. 1994;163:1049–1059.
8. Willis CE. Optimizing digital radiography of children. *Eur J Radiol*. 2009;72:266–273.
9. Don S. Pediatric digital radiography summit overview: state of confusion. *Pediatr Radiol*. 2011;41:567–572.
10. Seibert JA, Morin RL. The standardized exposure index for digital radiography: an opportunity for optimization of radiation dose to the pediatric population. *Pediatr Radiol*. 2011;41:573–581.
11. Capitanio MA, Kirkpatrick JA. The lateral decubitus film. An aid in determining air-trapping in children. *Radiology*. 1972;103:460–462.
12. Kaufman AS, Kuhns LR. The lateral decubitus view: an aid in evaluating poorly defined pulmonary densities in children. *AJR Am J Roentgenol*. 1977;129:885–888.
13. Strauss KJ, Kaste SC. The ALARA (as low as reasonably achievable) concept in pediatric interventional and fluoroscopic imaging: striving to keep radiation doses as low as possible during fluoroscopy of pediatric patients—a white paper executive summary. *Pediatr Radiol*. 2006;36(suppl 2):110–112.
14. Berg E, Naseri I, Sobol SE. The role of airway fluoroscopy in the evaluation of children with stridor. *Arch Otolaryngol Head Neck Surg*. 2008;134:415–418.
15. Thakkar K, Yao M. Diagnostic studies in obstructive sleep apnea. *Otolaryngol Clin North Am*. 2007;40:785–805.
16. Nastasi KJ, Howard DA, Raby RB, et al. Airway fluoroscopic diagnosis of vocal cord dysfunction syndrome. *Ann Allergy Asthma Immunol*. 1997;78:586–588.
17. Donnelly LF, Strife JL, Myer CM 3rd. Is sedation safe during dynamic sleep fluoroscopy of children with obstructive sleep apnea? *AJR Am J Roentgenol*. 2001;177:1031–1034.
18. Lee EY, Boiselle PM. Tracheobronchomalacia in infants and children: multidetector CT evaluation. *Radiology*. 2009;252:7–22.
19. Lee EY, Siegel MJ. Paediatric chest. In: Allan PL, Baxter GM, Weston MJ, eds. *Clinical Ultrasound*. 3rd ed. London: Churchill Livingstone Elsevier; 2011.
20. Coley BD. Chest sonography in children: current indications, techniques, and imaging findings. *Radiol Clin North Am*. 2011;49(5):825–846.
21. Audette LD, Parent MC. Bedside lung ultrasound for the diagnosis of pneumonia in children. *Emerg Med J*. 2016;33(8):589–592. doi:10.1136/emermed-2016-206047.3. Review. PMID: 27440771.
22. Rambhia SH, D'Agostino CA, Noor A, et al. Thoracic ultrasound: technique, applications, and interpretation. *Curr Probl Diagn Radiol*. 2016; pii: S0363-0188(16)30128-1. doi:10.1067/j.cpradiol.2016.12.003. [Epub ahead of print]; Review. PMID: 28185691.
23. Lemos AA, Siegel MJ, Rossi G, et al. Single- versus multidetector-row CT: comparison of sedation rates, conventional angiograms and motion artifacts in young children following liver transplantation. *Radiol Med*. 2006;111:911–920.
24. Long FR, Williams RS, Adler BH, et al. Comparison of quiet breathing and controlled ventilation in the high-resolution CT assessment of airway disease in infants with cystic fibrosis. *Pediatr Radiol*. 2005;35:1075–1080.
25. Goo HW. State-of-the-art CT imaging techniques for congenital heart disease. *Korean J Radiol*. 2010;11:4–18.
26. Mueller KS, Long FR, Flucke RL, et al. Volume-monitored chest CT: a simplified method for obtaining motion-free images near full inspiratory and end expiratory lung volumes. *Pediatr Radiol*. 2010;40:1663–1669.
27. Lell MM, May M, Deak P, et al. High-pitch spiral computed tomography: effect on image quality and radiation dose in pediatric chest computed tomography. *Invest Radiol*. 2011;46:116–123.
28. Leng S, Yu L, Fletcher JG, et al. Maximizing iodine contrast-to-noise ratios in abdominal CT imaging through use of energy domain noise reduction and virtual monoenergetic dual-energy CT. *Radiology*. 2015;276:562–570.
29. Yang DH, Goo HW. Pediatric 16-slice CT protocol: radiation dose and image quality. *J Korean Radiol Soc*. 2008;59:333–347.
30. Kim JE, Newman B. Evaluation of a radiation dose reduction strategy for pediatric chest CT. *AJR Am J Roentgenol*. 2010;194:1188–1193.
31. Boone JM, Geraphty EM, Seibert JA, et al. Dose reduction in pediatric CT: a rational approach. *Radiology*. 2003;228:352–360.
32. Nyman U, Ahl TL, Kristiansson M, et al. Patient-circumference-adapted dose regulation in body computed tomography. A practical and flexible formula. *Acta Radiol*. 2005;46:396–406.
33. Jung YY, Goo HW. The optimal parameter for radiation dose in pediatric low dose abdominal CT: cross-sectional dimensions versus body weight. *J Korean Radiol Soc*. 2008;58:169–175.
34. Goo HW. Individualized volume CT dose index determined by cross-sectional area and mean density of the body to achieve uniform image noise of contrast-enhanced pediatric chest CT obtained at variable kV levels and with combined tube current modulation. *Pediatr Radiol*. 2011;41:839–847.
35. Goo HW, Suh DS. Tube current reduction in pediatric non-ECG-gated heart CT by combined tube current modulation. *Pediatr Radiol*. 2006;36:344–351.
36. Goo HW, Suh DS. The influences of tube voltage and scan direction on combined tube current modulation: a phantom study. *Pediatr Radiol*. 2006;36:833–840.
37. Peng Y, Li J, Ma D, et al. Use of automatic tube current modulation with a standardized noise index in young children undergoing chest computed tomography scans with 64-slice multidetector computed tomography. *Acta Radiol*. 2009;50:1175–1181.
38. Pauls S, Aschoff AJ, Whal J, et al. Multi-detector row CT: is prospective electrocardiographic triggering improving the detection of small pulmonary tumors? *Acad Radiol*. 2005;12:614–619.
39. Siegel MJ. Multiplanar and three-dimensional multi-detector row CT of thoracic vessels and airways in the pediatric population. *Radiology*. 2003;229:641–650.
40. Papaioannou G, Young C, Owen CM. Multidetector row CT for imaging the paediatric tracheobronchial tree. *Pediatr Radiol*. 2007;37:515–529.
41. Long FR. Imaging evolution of airway disorders in children. *Radiol Clin North Am*. 2005;43:371–389.
42. Goo HW, Kim HJ. Detection of air trapping on inspiratory and expiratory phase images obtained by 0.3-sec cine-CT in the lungs of free breathing young children. *AJR Am J Roentgenol*. 2006;187:1019–1023.
43. Goo HW. Free-breathing cine CT for the diagnosis of tracheomalacia in young children. *Pediatr Radiol*. 2013;43:922–928.
44. Wagnetz U, Roberts HC, Chung T, et al. Dynamic airway evaluation with volume CT: initial experience. *Can Assoc Radiol J*. 2010;61:90–97.
45. Lee EY, Tracy DA, Bastos M, et al. Expiratory volumetric MDCT evaluation of air trapping in pediatric patients with and without tracheomalacia. *AJR Am J Roentgenol*. 2010;194:1210–1215.
46. Choi SJ, Choi BK, Kim HJ, et al. Lateral decubitus HRCT: a simple technique to replace expiratory CT in children with air trapping. *Pediatr Radiol*. 2002;32:179–182.
47. Goo HW. Initial experience of dual-energy lung perfusion CT using dual-source CT system in children. *Pediatr Radiol*. 2010;40:1536–1544.
48. Chae EJ, Seo JB, Goo HW, et al. Xenon ventilation CT with a dual-energy technique of dual-source CT: initial experience. *Radiology*. 2008;248:615–624.
49. Goo HW, Chae EJ, Seo JB, et al. Xenon ventilation CT using a dual-source dual-energy technique: dynamic ventilation abnormality in a child with bronchial atresia. *Pediatr Radiol*. 2008;38:1113–1116.
50. Goo HW, Yang DH, Hong SJ, et al. Xenon ventilation CT using dual-source and dual-energy technique in children with bronchiolitis obliterans: correlation of xenon and CT density values with pulmonary function test results. *Pediatr Radiol*. 2010;40:1490–1497.
51. Goo HW, Yang DH, Kim N, et al. Collateral ventilation to congenital hyperlucent lung lesions assessed on xenon-enhanced dynamic dual-energy CT: an initial experience. *Korean J Radiol*. 2011;12:25–33.
52. Goo HW, Yu J. Redistributed regional ventilation after the administration of a bronchodilator and demonstrated on xenon-inhaled dual-energy CT in a patient with asthma. *Korean J Radiol*. 2011;12:386–389.
53. Johnson TR, Krauss B, Sedlmair M, et al. Material differentiation by dual energy CT: initial experience. *Eur Radiol*. 2007;17:1510–1517.
54. Brody AS. Imaging considerations: interstitial lung disease in children. *Radiol Clin North Am*. 2005;43:391–403.

55. Ha HI, Goo HW, Seo JB, et al. Effects of high-resolution CT of the lung using partial versus full reconstruction on motion artifacts and image noise. *AJR Am J Roentgenol*. 2006;187:618–622.
56. Kelly DM, Hasegawa I, Borders R, et al. High-resolution CT using MDCT: comparison of degree of motion artifacts between volumetric and axial methods. *AJR Am J Roentgenol*. 2004;182:757–759.
57. Bastos M, Lee EY, Strauss KJ, et al. Motion artifacts on high-resolution CT images of pediatric patients: comparison of volumetric and axial CT methods. *AJR Am J Roentgenol*. 2009;193:1414–1418.
58. Puderbach M, Kauczor HU. Can lung MR replace CT? *Pediatr Radiol*. 2008;38:S439–S451.
59. Lee EY. Advancing CT and MR imaging of the lungs and airways in children: imaging into practice. *Pediatr Radiol*. 2008;38:S208–S212.
60. Pennati F, Quirk JD, Yablonskiy DA, et al. Assessment of regional lung function with multivolume (1)H MR imaging in health and obstructive lung disease: comparison with (3)He MR imaging. *Radiology*. 2014;273(2):580–590. doi:10.1148/radiol.14132470.
61. Chang YV, Quirk JD, Ruset IC, et al. Quantification of human lung structure and physiology using hyperpolarized 129Xe. *Magn Reson Med*. 2014;71(1):339–344. doi:10.1002/mrm.24992. PMID: 24155277.
62. Yedururi S, Guillerman RP, Chung T, et al. Multimodality imaging of tracheobronchial disorders in children. *Radiographics*. 2008;28:e29.
63. Biederer J, Hintze C, Fabel M. MRI of pulmonary nodules: technique and diagnostic value. *Cancer Imaging*. 2008;19:125–130.
64. Chung T. Magnetic resonance angiography of the body in pediatric patients: experience with a contrast-enhanced time-resolved technique. *Pediatr Radiol*. 2005;35:3–10.
65. Lee CH, Goo JM, Kim YT, et al. The clinical feasibility of using non-breath-hold real-time MR-echo imaging for the evaluation of mediastinal and chest wall tumor invasion. *Korean J Radiol*. 2010;11:37–45.
66. Bauman G, Puderbach M, Deimling M, et al. Non-contrast-enhanced perfusion and ventilation assessment of the human lung by means of Fourier decomposition in proton MRI. *Magn Reson Med*. 2009;62:656–664.
67. Gelfand MJ, Parisi MT, Treves ST. Pediatric radiopharmaceutical administered doses: 2010 North American consensus guidelines. *J Nucl Med*. 2011;52:318–322.
68. Mineo TC, Schillaci O, Pompeo E, et al. Usefulness of lung perfusion scintigraphy before lung cancer resection in patients with ventilatory obstruction. *Ann Thorac Surg*. 2006;82:1828–1834.
69. Drubach LA, et al. Evaluation of primary pulmonary vein stenosis in children: comparison of radionuclide perfusion lung scan and angiography. *AJR Am J Roentgenol*. 2015;205(4):873–877.
70. Bar-Sever Z, Connolly LP, Treves ST. The radionuclide salivagram in children with pulmonary disease and a high risk of aspiration. *Pediatr Radiol*. 1995;25(suppl 1):S180–S183.
71. Levin K, Colon A, DiPalma J, et al. Using the radionuclide salivagram to detect pulmonary aspiration and esophageal dysmotility. *Clin Nucl Med*. 1993;18:110–114.
72. Cook SP, Lawless S, Mandell GA, et al. The use of the salivagram in the evaluation of severe and chronic aspiration. *Int J Pediatr Otorhinolaryngol*. 1997;41:353–361.
73. Bar-Sever Z, Keidar Z, Ben-Barak A, et al. The incremental value of 18F-FDG PET/CT in paediatric malignancies. *Eur J Nucl Med Mol Imaging*. 2007;34:630–637.
74. Zukotynski KA, Fahey FH, Laffin S, et al. Constant ambient temperature of 24 degrees C significantly reduces FDG uptake by brown adipose tissue in children scanned during the winter. *Eur J Nucl Med Mol Imaging*. 2009;36:602–606.
75. Schaefer NG, Hany TF, Taverna C, et al. Non-Hodgkin lymphoma and Hodgkin disease: coregistered FDG PET and CT at staging and restaging—do we need contrast-enhanced CT? *Radiology*. 2004;232:823–829.

# 50

# Prenatal Imaging and Intervention

Dorothy Bulas

With the advances in ultrasound (US) and magnetic resonance imaging (MRI), thoracic lesions are now commonly detected before birth. The most common congenital thoracic lesions include congenital diaphragmatic hernia (CDH); congenital bronchopulmonary malformations, which represent a group of lung anomalies, including congenital pulmonary airway malformation (CPAM), bronchopulmonary sequestration (BPS), and congenital lobar overinflation (CLO); and congenital hydrothorax. Additionally, congenital high airway obstruction (CHAOS), which is caused by obstruction or absence of the trachea, may also present in utero. Pulmonary hypoplasia, agenesis, and aplasia are less common and discussed in Chapter 53.[1-4]

In a fetus, the clinical importance of these lesions lies primarily in the mass effect on surrounding structures. This may result in compression of the airway, blood vessels, lymphatics, and lung parenchyma with development of pleural effusions, polyhydramnios, hydrops, and pulmonary hypoplasia. The outcome depends on the timing of secondary effects and the severity of pulmonary hypoplasia. With improvements in fetal imaging, fetal intervention has also advanced. Masses that resulted in hydrops in the past were typically lethal. Now these masses may be amenable to fetal intervention, including maternal steroids, intrauterine cyst aspiration, fetal thoracentesis, thoracoamniotic shunts, laser therapy, sclerotherapy, and in utero fetoscopic or open fetal surgery.[5-9]

In maternal-fetal surgery, the greatest responsibility is to the mother, who is an innocent bystander in the maldevelopment occurring in utero. She must be aware of the risks and benefits for herself and the fetus and has the potential to undergo an operation that has no direct benefit to her. A limiting factor of invasive fetal therapy is the risk of preterm labor, although fetoscopic surgery carries a lower risk.[7] Women who have undergone open fetal surgery have been able to have children subsequently, although delivery of subsequent pregnancies requires cesarean section.

## COMMON CONGENITAL THORACIC LESIONS IN THE FETUS

### Congenital Diaphragmatic Hernia

***Etiology.*** The diaphragm develops in the fourth week of gestation with fusion of its four embryonic components. By 8 weeks, the pleural–peritoneal cavity separates. There is caudal migration with final diaphragmatic positioning by 12 weeks. The most common CDH occurs secondary to failure of fusion of the left pleuroperitoneal membrane to the remaining primitive diaphragm (Bochdalek hernia). The bowel returns to the abdomen by the 10th week of gestation and may begin to herniate into the chest if a diaphragmatic defect is present.

CDH occurs in 1:3000 to 1:4000 live births. They can be classified by location: posterolateral Bochdalek hernia (70%–75%), anterior Morgagni hernia (23%–28%), and central hernia (2%–7%). They occur on the left in 88%, the right in 10%, and bilaterally in 2% of cases.[10-12]

Herniation can occur in the second trimester and may affect early lung development on the contralateral as well as ipsilateral sides. CDH is typically sporadic; however, a 15% to 45% incidence of associated anomalies is seen. Rare familial cases and syndromes have been described.[11] The presence of additional major malformations significantly increases the mortality rate. Careful evaluation for additional anomalies, fetal echocardiography, and karyotyping are important for appropriate counseling and delivery planning.

***Imaging.*** The diagnosis of CDH in fetuses may be missed by US, particularly when the stomach is not herniated into the chest.[12,13] In these cases, mediastinal shift may be the first finding to suggest the diagnosis. Coronal and sagittal US images help delineate the defect, whereas axial images are important to assess the amount of mediastinal deviation. Contralateral lung volume should be measured. Ipsilateral lung tissue should be looked for but typically is too compressed to be visualized. The stomach and gallbladder are identified, and the location above or below the diaphragm is noted. Polyhydramnios may develop due to esophageal and/or gastric kinking.

Herniation of the liver into the chest is associated with a poorer outcome. Evaluation may be difficult by US because the liver, bowel, and lung have similar echogenicity. An abnormal course of the umbilical, hepatic, and portal veins may help confirm liver herniation.[14] With left CDH, the left lobe of the liver typically herniates into the anterior chest. If the stomach is adjacent to the anterior chest wall, liver herniation is unlikely. The more posterior the stomach is in the chest, the more liver is herniated superiorly. At times, small bowel loops may mimic lung cysts, making it difficult to differentiate hernia from CPAM. Color Doppler of the superior mesenteric artery may be helpful in confirming herniation of bowel loops by following the vessel into the chest. Associated anomalies, particularly cardiac, should be searched for with dedicated fetal echocardiography.

Fetal MRI protocols should include T2-weighted images in all three planes and T1-weighted breath hold gradient recalled echo images in the coronal and sagittal plane to assess for liver and meconium positions (Figs. 50.1 and 50.2). Meconium-filled bowel loops are low signal on T2-weighted images and high signal on T1-weighted images. The liver is high signal on T1-weighted images and intermediate signal on T2-weighted images, making it easier to quantitate amount of liver herniation than with US (e-Fig. 50.3). MRI is particularly helpful in the evaluation of right and bilateral CDH.[15,16] In these cases, with the stomach often located below the diaphragm, it may be difficult to differentiate a CPAM from a CDH by US. MRI easily distinguishes abdominal contents within the chest from cystic pulmonary lesions and provides specific information on hernia content and amount of residual ipsilateral and contralateral lung.

One goal of fetal imaging is predicting severity, important in guiding therapeutic options and delivery planning. Survival rates range from 40% to 90% with an overall survival reported to be 70% to 80%.[17] Currently, no single finding or measurement is an absolute indicator of postnatal outcome. Indications of poor prognosis include large mediastinal shift, low observed to expected lung volumes, and percentage of liver herniation.[18] When liver herniation is present, the survival rate has been reported to be approximately 50%, whereas fetuses without herniation may have up to 90% survival.[15,19,20] Additional findings such as intrathoracic location of the stomach, asymmetric size of cardiac ventricles, and polyhydramnios also may indicate a worse prognosis. Syndromes associated with CDH, including Fryns syndrome, have a poorer prognosis (e-Fig. 50.4).[11] The presence of additional anomalies affects outcome as well. Bilateral CDHs are typically fatal.

## Abstract:

With the advances in high-resolution ultrasonography and magnetic resonance imaging (MRI), thoracic lesions are now commonly detected before birth. The most common congenital thoracic lesions include congenital diaphragmatic hernia (CDH); congenital bronchopulmonary malformations, which represent a group of lung anomalies, including congenital pulmonary airway malformation (CPAM), bronchopulmonary sequestration (BPS), and congenital lobar overinflation (CLO); and congenital hydrothorax. Additionally, congenital high airway obstruction (CHAOS), which is caused by obstruction or absence of the trachea, may also present in utero.

In a fetus, the clinical importance of these lesions lies primarily in the mass effect on surrounding structures. This may result in compression of the airway, blood vessels, lymphatics, and lung parenchyma with development of pleural effusions, polyhydramnios, hydrops, and pulmonary hypoplasia. The outcome depends on the timing of secondary effects and the severity of pulmonary hypoplasia. With improvements in fetal imaging, fetal intervention has also advanced. While in the past lungs masses that developed hydrops were often lethal. Now these masses may be amenable to fetal intervention including maternal steroids, intrauterine cyst aspiration, fetal thoracentesis, thoracoamniotic shunts, laser therapy, sclerotherapy, and in utero fetoscopic or open fetal surgery.

## Keywords:

congenital pulmonary airway malformation
fetal chest
bronchopulmonary sequestration
congenital lobar overinflation
congenital diaphragmatic hernia
congenital high airway obstruction

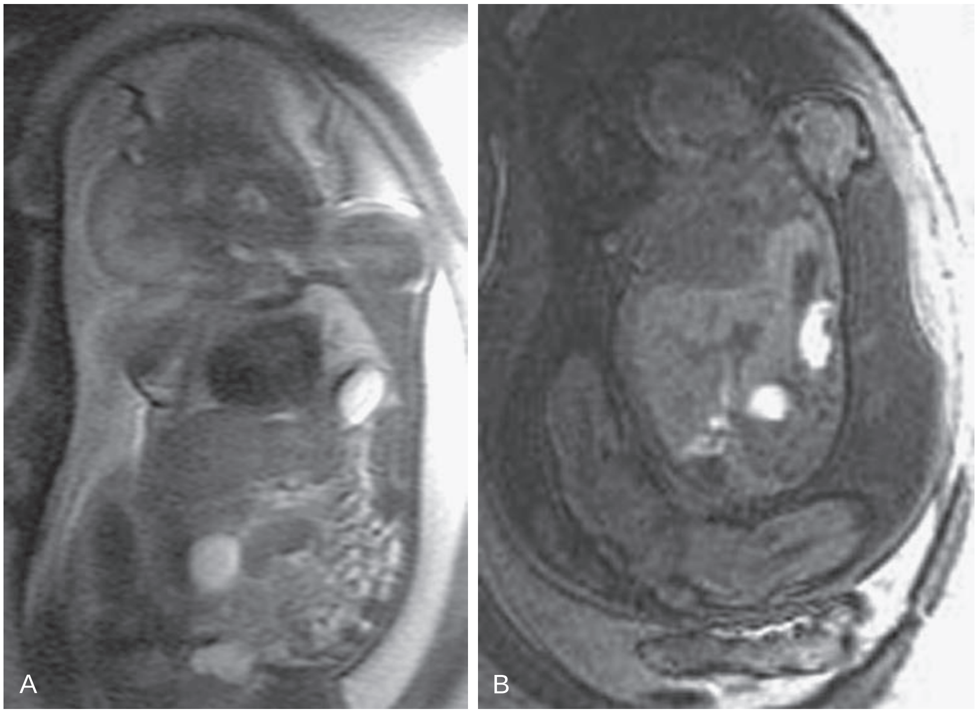

**e-Figure 50.3. Congenital diaphragmatic hernia with covering membrane.** (A) Coronal single-shot fast spin echo T2-weighted MRI shows stomach, bowel, and a portion of the left lobe of the liver herniated into the left hemithorax. Residual left lung parenchyma is noted superior to the stomach. (B) Coronal gradient recalled echo T1-weighted MRI confirms that high signal meconium-filled colon and intermediate high signal liver are herniated into the left hemithorax.

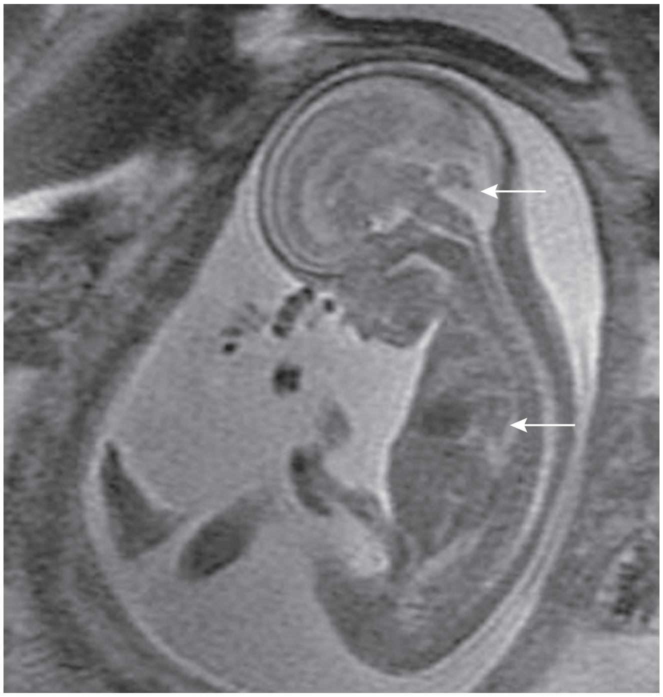

**e-Figure 50.4. Fryns syndrome.** A single-shot fast spin echo T2-weighted right parasagittal MRI of a fetus at 24 weeks of gestational age shows bowel loops *(inferior arrow)* herniated into the hemithorax. Inferior vermian hypoplasia *(superior arrow)* and nuchal thickening are present. This infant was diagnosed with Fryns syndrome at delivery.

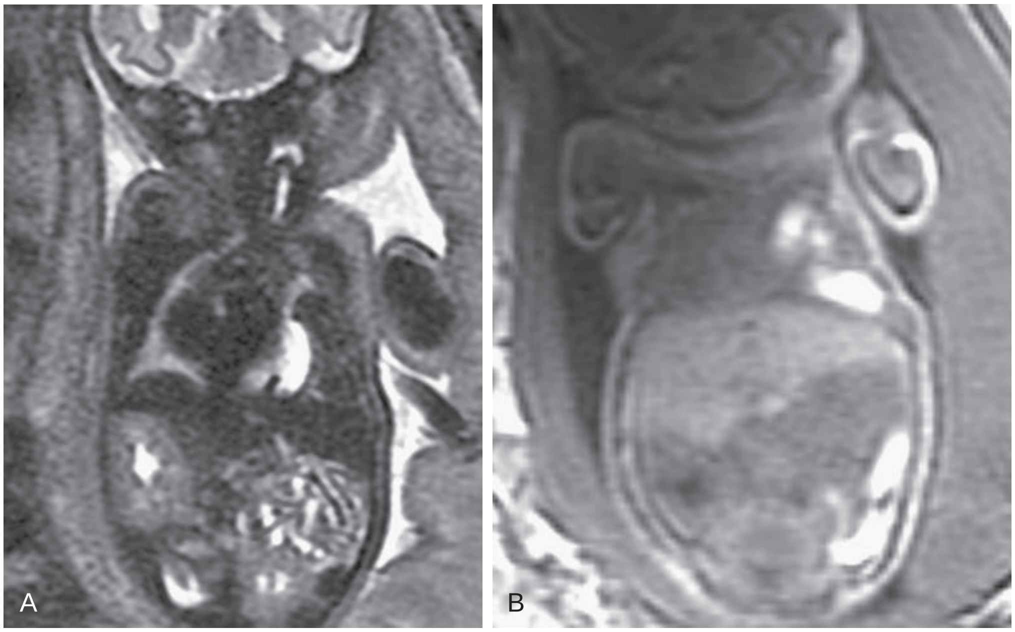

**Figure 50.1. Left congenital diaphragmatic hernia.** (A) Coronal single-shot fast spin echo T2-weighted MRI at 32 weeks of gestation demonstrates deviation of the heart to the right. High-signal fluid-filled stomach and low-signal meconium are herniated into the left chest. The liver appears infradiaphragmatic. (B) Coronal gradient recalled echo T1-weighted image shows high signal meconium-filled colon herniated into the left hemithorax. The intermediate signal liver is infradiaphragmatic.

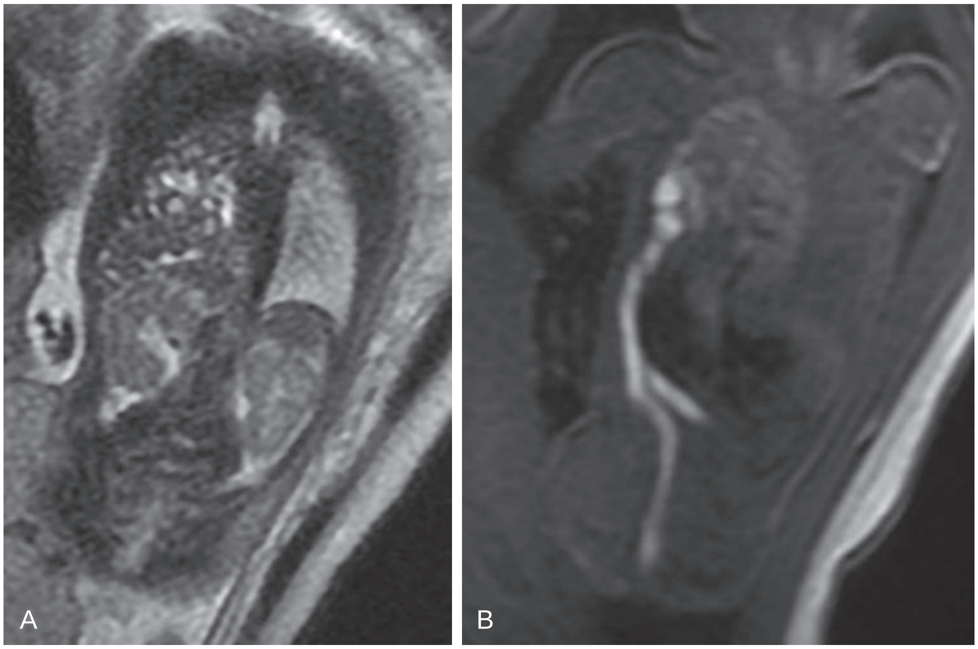

**Figure 50.2. Right congenital diaphragmatic hernia.** (A) Coronal single-shot fast spin echo T2-weighted MRI at 32 weeks of gestation demonstrates loops of fluid filled bowel filling the right hemithorax. (B) Coronal gradient recalled echo T1-weighted MRI demonstrates the right lobe of the liver, as well as loops of colon filled with high signal meconium herniated into the right hemithorax.

Various US and MRI measurement have been proposed to estimate severity of lung hypoplasia and outcome. By US, measurement of the lung-to-head ratio (LHR) and observed to expected LHR are used to estimate residual lung and predict outcome. Lower ratios correlate with higher mortality, with an LHR of less than 0.6 and an observed to expected LHR of less than 25% suggesting a low survival rate. However, measurements can be difficult to reproduce and do not take liver position into account.[20-28]

Various volumetric measurements can be obtained with MRI and used as indicators of outcome. MRI measurements allow assessment of both lungs and can be more reliably obtained than US[29-35] MRI measurements include total lung volume, observed to expected total lung volume (o/e TLV), percent predicted lung volume (PPLV), fetal lung volume to fetal body volume ratio (FLV/FBV), percent liver herniation (%LH), and herniated liver to fetal thoracic volume ratio (LiTR).[36-40]

Total lung MRI volumes have been used to quantify degree of lung hypoplasia. A better prognosis is expected in fetuses with a total lung volume of 25 $cm^3$ or more, compared with fetuses with a lung volume of 18 $cm^3$ or less. Various methods of measuring lung volume ratios all show a correlation of lower numbers with poor outcome.[24-27,37] Similarly a large herniated liver volume predicts higher mortality.[38-40]

Infants struggle with various degrees of pulmonary hypertension after delivery. Pulmonary hypertension may be predicted using the modified McGoon index. From prenatal US or MRI measurements, the right and left pulmonary artery diameters are added, and then divided by the aortic diameter. If the value is less than 0.8, the risk of developing pulmonary hypertension is high; if the value is greater than 1.0, the risk is low.[41,42]

Variables including measurement technique, gestational age at time of the study, right vs left hernia, associated anomalies, and development of pulmonary hypertension limit accuracy for perfect outcome prediction using US or MRI. Developing reliable, reproducible measurements, however, is critical as invasive fetal therapeutic options become more available.[42-44]

***Treatment and Follow-up.*** The severity of pulmonary hypoplasia and pulmonary hypertension affects outcome.

Postnatally, extracorporeal membrane oxygenation (ECMO) is a method of supporting neonatal oxygenation until pulmonary hypertension resolves. Outcome is variable, however, with the most severe cases not surviving despite weeks on ECMO or ex utero intrapartum treatment (EXIT)–to–ECMO strategies. Thus surgeons have turned to in utero surgery as a potential way to improve outcomes of those with the most severe hernias. To help lungs have more space to grow in utero, open fetal surgical diaphragmatic repair was initially attempted. Outcomes were no better than those with postnatal support with complications including umbilical vein kinks and high risk for preterm delivery.[45]

Fetal intervention has evolved with less invasive fetoscopic techniques.[43,46,47] It was noted that fetuses with laryngeal or tracheal atresia have larger than normal lungs. Animal experimentation that revealed that when the trachea was occluded and fetal lung fluid egress blocked, lung growth was stimulated. In utero tracheal occlusion, initially by application of an external tracheal clip and now by fetal bronchoscopic insertion of an occlusive balloon, has been performed with resultant lung growth.[48] At delivery, the EXIT procedure is performed to remove the tracheal occlusion device before separation from the placenta. Temporary tracheal occlusion via fetoscopy is now being attempted in some centers, with a suggestion of early favorable results. Until this study is completed, the standard of care includes supportive care after delivery as close to term as possible with high-frequency ventilation and ECMO, if needed, with some centers advocating an EXIT-to-ECMO approach for high-risk fetuses.[49]

## Congenital Pulmonary Airway Malformation

***Etiology.*** CPAM, previously known as congenital cystic adenomatoid malformation, is the most common congenital lung abnormality, representing 30% to 47% of lung masses diagnosed in utero. CPAM is a hamartomatous lesion characterized by abnormal growth of terminal bronchioles containing cystic and solid tissue. It is currently thought that maldevelopment of the airways results in obstructive dysplastic changes.[50-52] Typically unilobular (85%–95%), CPAMs may be multilobular and bilateral. They contain multiple microcysts or macrocysts lined by respiratory epithelium. Usually, an abnormal communication with the tracheobronchial tree exists, with blood supplied from pulmonary arteries.

Stocker's classification of CPAM includes five different types.[53] This is based on cyst size and underlying histologic resemblance to the bronchial tree and airspaces. Adzick described a classification based on fetal imaging appearance and gross anatomy: (1) macrocystic CPAM (multiple large cysts >5 mm with slow growth and favorable prognosis); and (2) microcystic CPAM (cysts <5 mm with solid appearance, which have the highest risk for developing hydrops).[54]

***Imaging.*** Fetal ultrasonographic appearance of CPAM depends on histology. With macrocystic CPAM, multiple nonconnecting cysts are seen. Often a single lobe is affected, although multiple lobes and bilateral CPAM have been reported. Microcystic CPAMs are homogeneously echogenic and usually more echogenic than the adjacent lung.[55] If the echogenicity of the CPAM is similar to adjacent lung (more common in the third trimester), mass affect may be the only finding to suggest the diagnosis.[56] Vascularity is usually from distorted pulmonary arteries in contradistinction to BPS, in which the vascular supply is from the aorta. Hybrid lesions with mixed features of CPAM (macrocysts) and BPS (aortic supply) are common. CLO can also present as a homogeneous echogenic mass fed by pulmonary arteries branching more normally through the lobe.

MRI is useful in delineating the lung mass and amount of residual normal lung. CPAM usually has high T2-weighted signal with macrocysts and or microcysts (Figs. 50.5 and 50.6).[57] They may be difficult to differentiate from the surrounding normal lung, particularly in the later weeks of gestation when normal lung signal increases. When bilateral, differentiation from CHAOS must be made. In these cases, MRI is useful in showing fetal tracheal obstruction. In cases of CLO, high signal lung that respects the anatomic boundaries of a normal lobe may be seen.

Prognosis of CPAM is typically favorable with spontaneous decrease in size in up to 90% of cases.[58-60] Although some masses may appear to resolve completely prenatally and can have a normal appearing chest radiograph after delivery, computed tomography (CT) often identifies a residual mass. Theories as to the reason for the resolution include decompression into the bronchial tree, outgrowth of blood supply, or vascular pedicle torsion.

***Treatment and Follow-up.*** Rapidly growing CPAM, either solid or with a large dominant cyst, have a higher incidence of hydrops and are associated with a poorer outcome. Hydrops results from severe mediastinal shift causing venous and lymphatic obstruction and ultimately fetal cardiac failure. If no hydrops exists, the outcome is excellent, with greater than 95% survival. If hydrops develops, the fetus may die without intervention.[5,61] The greatest period of growth of a CPAM is between 20 to 26 weeks of gestation.[61] Lesions that are largely solid appearing and rapidly increasing in size are at most risk for causing hydrops.

The CPAM volume ratio (CVR) can be used to predict which fetuses are at risk to progress to hydrops. The lung mass volume is determined using the ellipse formula (length × width × anteroposterior diameter × 0.52), which is then divided by the head circumference. If the CVR is greater than 1.6, the risk is 75% for developing hydrops. Fetuses with CVR less than 1.6 without a dominant cyst have less than a 3% risk of developing hydrops and those with macrocystic lesions have a 14% risk.[61]

In uncontrolled studies, maternal steroid administration reversed hydrops and improved outcome.[62-68] Although it is possible that fetal thoracic growth and/or CPAM regression rather than steroids account for the resolution of hydrops, the current recommendation are to treat large microcystic CPAM with two doses of 12 mg intramuscularly 24 hours apart. Steroids have been used for macrocystic disease as well, but with less promising results.

If hydrops develops after 32 weeks of gestation, delivery is recommended. In the past, fetuses with solid lesions that developed hydrops in the second trimester underwent in utero resection.[69,70] With the current steroid protocol, there has been a decrease in the number of solid/microcystic masses that require in utero

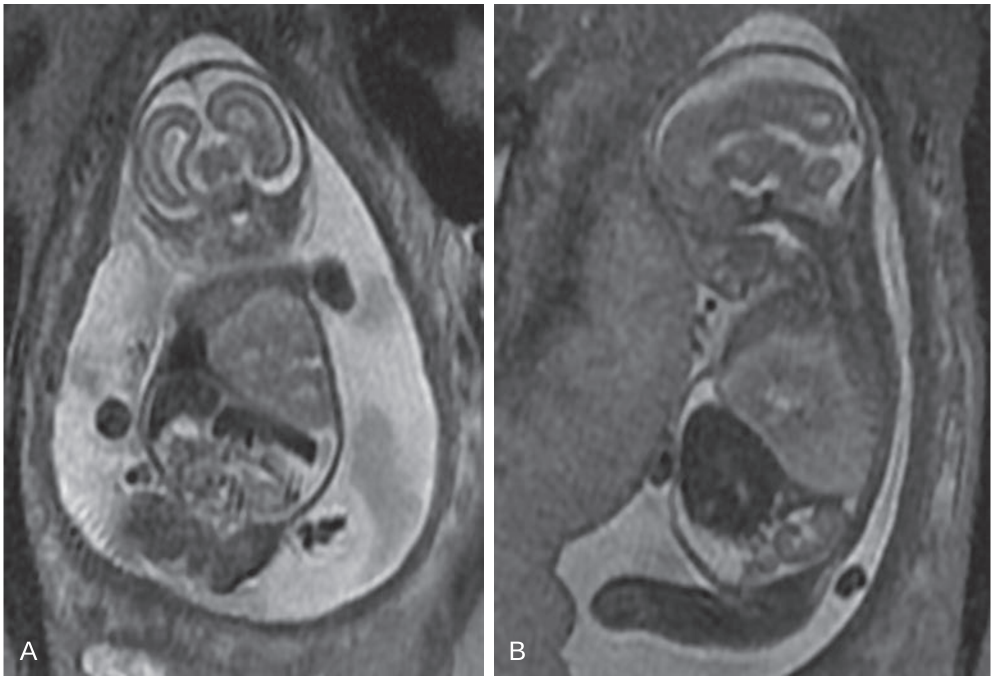

**Figure 50.5. Microcystic congenital pulmonary airway malformation with ascites.** Coronal (A) and sagittal (B) single shot fast spin echo T2-weighted MRI demonstrates a large left lower lobe heterogeneous mass deviating the mediastinum to the left and diaphragm inferiorly. Ascites is present.

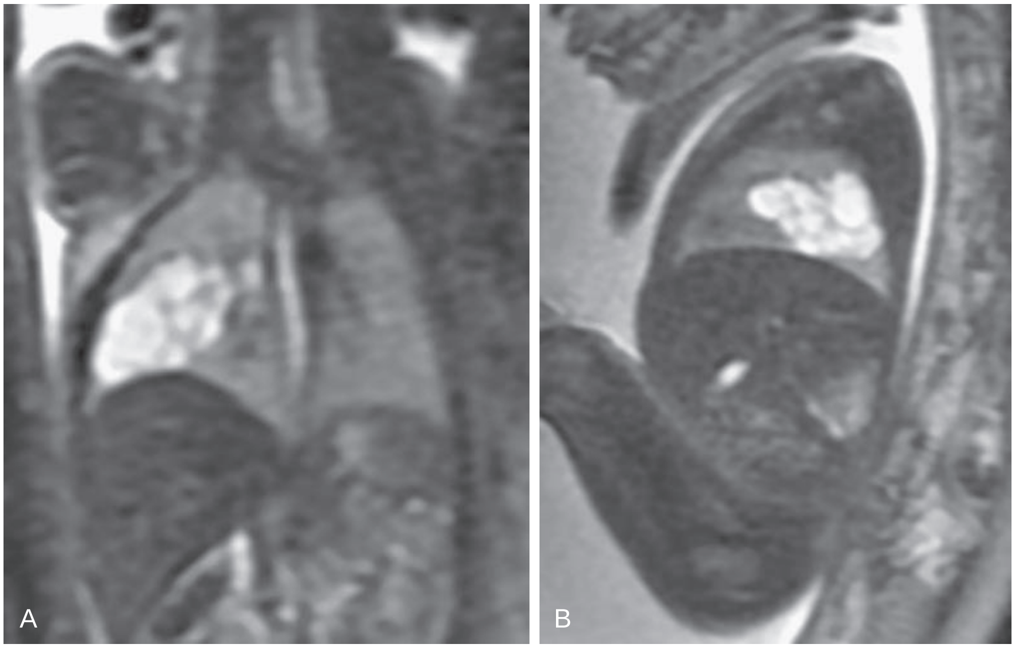

**Figure 50.6. Macrocystic congenital pulmonary airway malformation.** Coronal (A) and sagittal (B) single-shot fast spin echo T2-weighted MRI demonstrates a multicystic high signal mass involving the posterior right lower lobe. No significant mass affect is seen.

resection. In macrocystic lesions where hydrops is less likely to resolve with steroids, aspiration, thoracoamniotic shunting, and laser therapy have been attempted.[71]

After delivery, if the infant is symptomatic, prompt resection is required. The need for resection if the infant is asymptomatic continues to be debated.[72-74] Even if the chest radiograph appears normal, CT scans typically show a residual CPAM (e-Fig. 50.7).[75,76] Residual cysts may develop air trapping or a pneumothorax. Recurrent infections may occur. Rhabdomyosarcoma and bronchoalveolar carcinoma developing from CPAM has been reported.[77-81] Thus surgical resection is currently advocated in asymptomatic patients despite the lack of large long-term outcome studies.

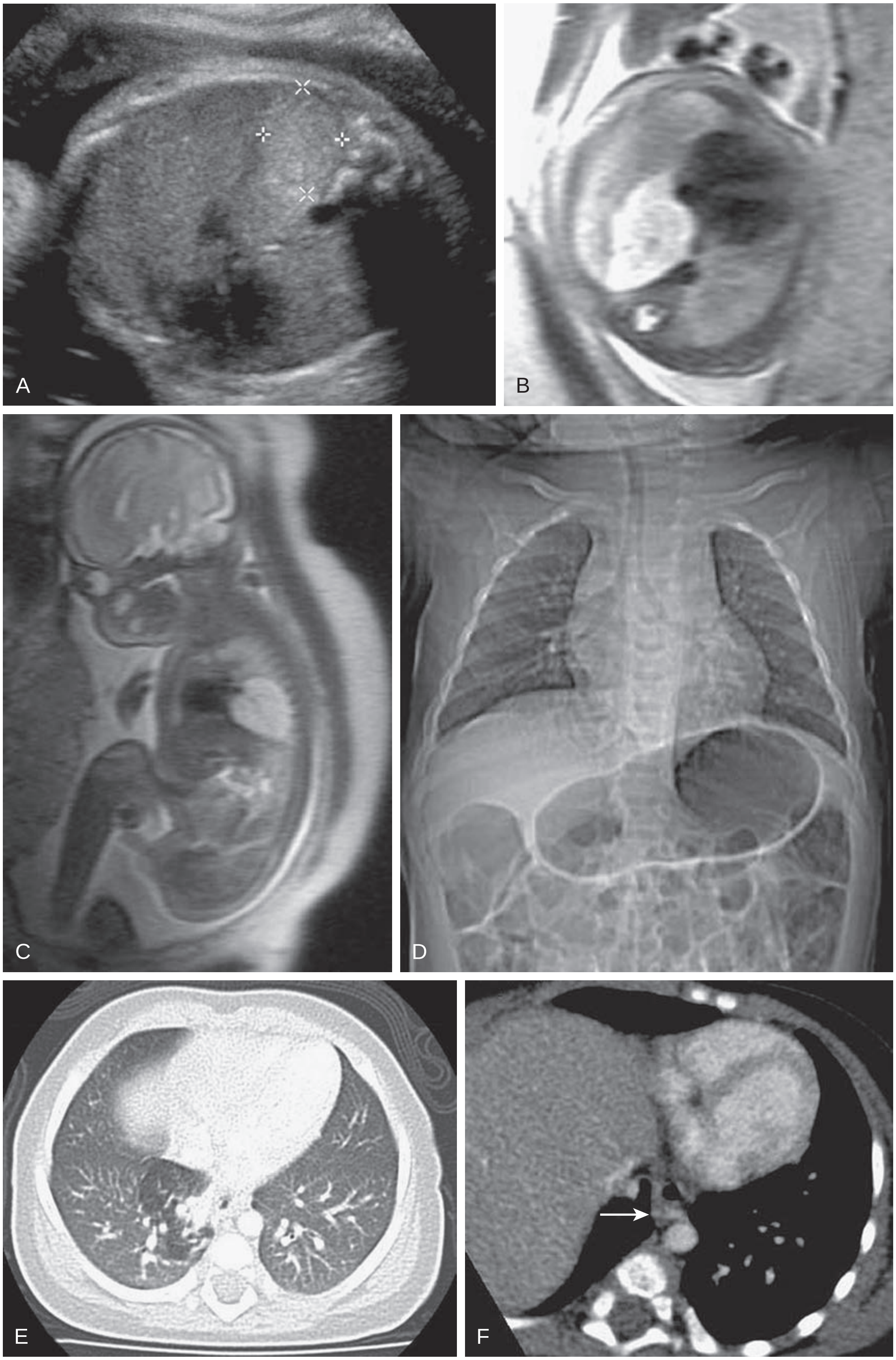

**e-Figure 50.7. Hybrid congenital pulmonary airway malformation-sequestration.** (A) Axial sonogram shows an echogenic mass in the right lower hemithorax *(calipers).* (B and C) Single-shot fast spin echo T2-weighted MRI in the coronal (B) and sagittal (C) planes confirms the presence of a high signal mass in the right lower lobe. At delivery, the infant had no respiratory symptoms. (D) CT scout image of the chest at 3 weeks of gestational age shows no evidence of a residual lung mass. (E) Axial CT scan demonstrates a hyperlucent lesion in the medial right lower lobe. (F) Mediastinal reformatted image shows a feeding vessel *(arrow)* coursing from the aorta. At surgery, a congenital pulmonary airway malformation with a systemic feeding vessel was resected.

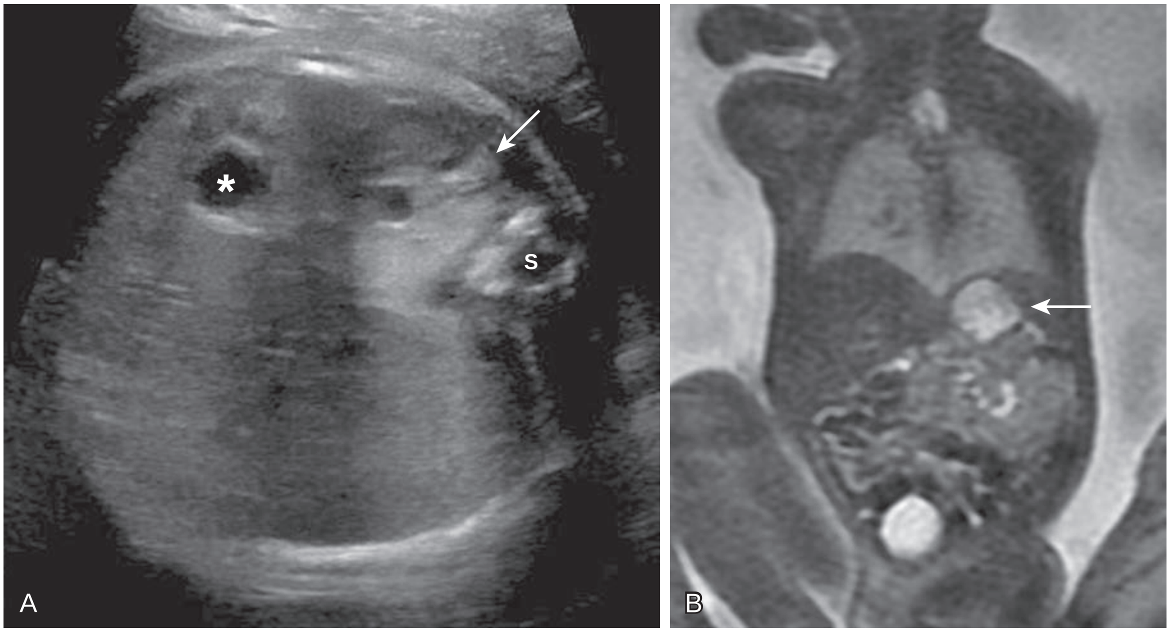

**Figure 50.8. Infradiaphragmatic sequestration.** (A) Axial sonogram of a fetus at 26 weeks of gestational age demonstrates a mixed cystic and solid mass *(arrow)* adjacent to the spine *(S)* and posterior to the stomach *(asterisk).* (B) A coronal single-shot fast spin echo T2-weighted MRI demonstrates a high signal mass below the diaphragm *(arrow).* The systemic feeding vessel was difficult to document prenatally.

## Bronchopulmonary Sequestration

***Etiology.*** BPS is abnormal pulmonary tissue with no connection with the normal tracheobronchial tree and systemic arterial blood supply from the aorta.[82] Typically located in the left posteroinferior thorax, BPSs have been found infradiaphragmatically and within the diaphragm and may mimic a suprarenal neuroblastoma (Fig. 50.8).[83]

There are two types of BPS: extralobar and intralobar. Extralobar sequestration has a separate pleural covering and has systemic venous drainage via the azygos system or inferior vena cava. Intralobar sequestration has no separate pleura with venous drainage via the pulmonary veins. Both types receive arterial blood supply from the systemic circulation, usually the aorta.

Extralobar sequestration has a higher association with anomalies, including CDH, eventration, and foregut anomalies. Hybrid lesions are relatively common with CPAM masses associated with systemic arterial supply (see e-Fig. 50.7).[84] Rarely, sequestrations can present with effusions or hydrops (Fig. 50.9).

***Imaging.*** The prenatal US appearance of BPS is typically a solid triangular hyperechoic mass in the lower hemithorax adjacent to the diaphragm.[85] Hybrid lesions may have a cystic component.[86] The masses are typically small and decrease in size in later gestation in 75% of cases.[87]

Systemic vascular supply should be searched for, typically branching from the aorta below the diaphragm. Color and power Doppler are helpful in identifying the vessel but may be difficult to demonstrate.

On MRI, BPS has homogeneous intermediate high signal on T2-weighted images. Vascular supply may be suggested by a low signal line coursing to the mass but also may be difficult to identify prenatally. As the lesions regress they may appear of lower signal intensity to lung on T2-weighted images.

Torsion of extralobar sequestration has been described as a source of hydrothorax/effusion.[88]

Masses that appeared to resolve in utero are typically still found on postnatal CT.[89] The apparent resolution is likely due to decompression into the normal lung, lesion outgrowing blood supply, or torsion around the vascular pedicle resulting in infarction.[90] As these lesions regress, they become more difficult to visualize on US.

***Treatment and Follow-up.*** Prognosis is typically favorable with only rare reports of associated pleural effusions or hydrops.[91,92] If hydrops develops after 32 weeks of gestation, early delivery is recommended. Before 32 weeks, in utero surgical resection may be considered.[93] Percutaneous laser ablation of the feeding vessel is a less invasive procedure and has been reported to decrease tumor size.[94,95]

In one series, cases complicated by pleural effusion or hydrops treated by laser ablation of the feeding vessel resulted in decrease in BPS size, increase in mass of normal lung parenchyma, and disappearance of pulmonary effusions. After delivery, these patients were all asymptomatic and none of them required surgical intervention.[96]

A macrocyst within BPS suggests a hybrid lesion (macrocystic CPAM and BPS). In these cases, a maternal course of antenatal steroids and cyst drainage are options, as with CPAM.

If the BPS is solid with a large pleural effusion, thoracentesis to prevent pulmonary hypoplasia is possible, but rapid reaccumulation of fluid limits its usefulness. Placement of a thoracoamniotic shunt has been attempted in these cases.[97]

Postnatal CT with contrast enhancement or MRI is useful in identifying the feeding systemic vessel. Symptoms depend on the size of the mass. Because BPS may become infected, elective surgery is often recommended even if the infant is asymptomatic.[98]

## Congenital Lobar Overinflation

***Etiology.*** CLO, also known as congenital lobar hyperinflation or emphysema, is characterized by hyperinflation of a lung segment or lobe with normal pulmonary vascular supply. Microscopically, the alveoli are dilated but not maldeveloped.[2,3,50,52] The alveolar walls are intact, thus the preference of using the term *overinflation* rather than *emphysema*. Two subgroups of CLO seem to exist. The first group presents with respiratory distress postnatally with overinflation secondary to airway cartilage anomalies, absent bronchial cartilage, or extrinsic compression of the airway by a

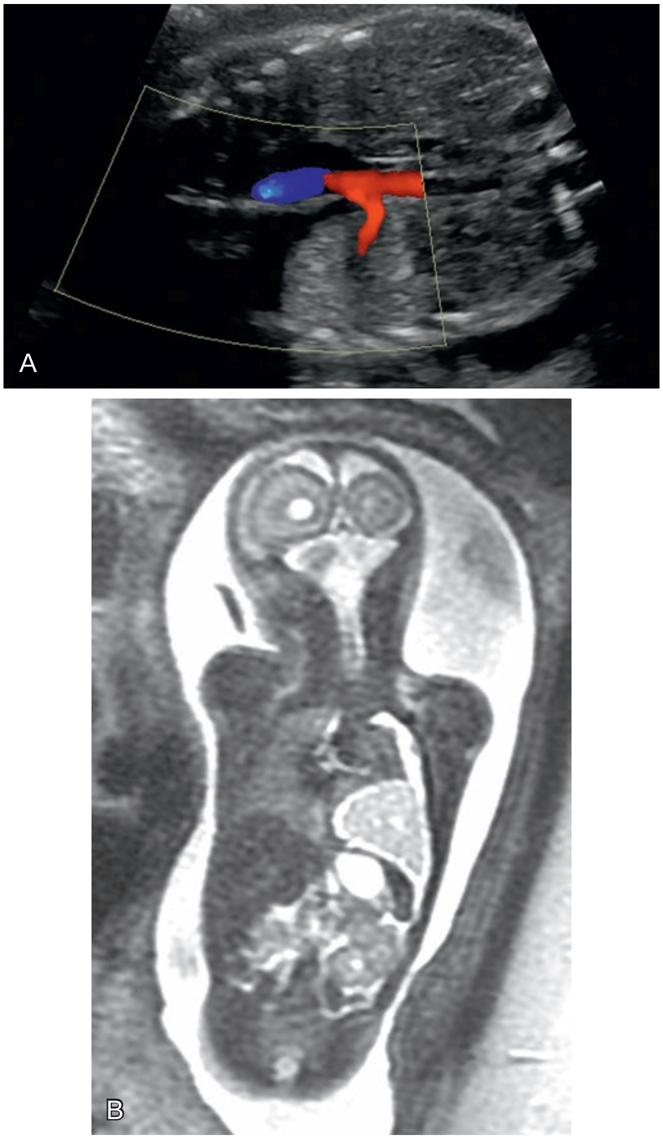

**Figure 50.9. Bronchopulmonary sequestration with pleural effusion at 24 weeks of gestation.** (A) Coronal sonogram of the fetal chest demonstrates a systemic vessel coursing from the aorta into an echogenic left lower lobe mass. (B) Coronal single-shot fast spin echo T2-weighted MRI demonstrates a high signal left lower lobe mass with moderate pleural effusion. The feeding vessel was not as well seen by MRI.

bronchogenic cyst or an enlarged pulmonary artery.[98] The partially obstructed airway results in air trapping. This group most commonly affects the left upper lobe, then the right upper and middle lobes.[99] The second group of CLO is now recognized more frequently prenatally. These cases of segmental or lobar hyperinflation are often associated with bronchial atresia, most common in the lower lobes.[100-102]

***Imaging.*** CLO is often recognized with US in the second trimester as a homogeneously hyperechoic mass. No macrocysts are present. The hyperechogenicity is thought to be secondary to accumulation of fluid within the alveoli.[100] By the third trimester, the mass often becomes isoechoic and difficult to differentiate from adjacent normal lung. Mediastinal deviation may be the only clue that a CLO is present.

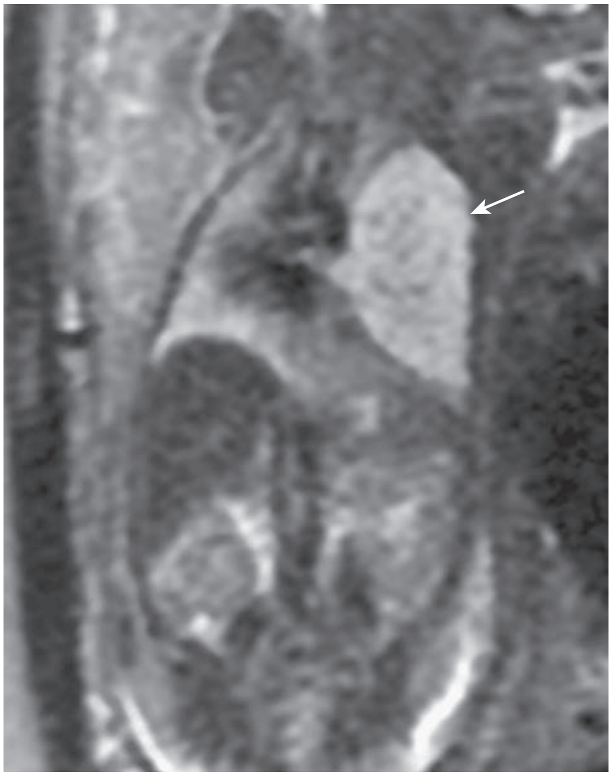

**Figure 50.10. Congenital lobar overinflation.** Coronal single-shot fast spin echo T2-weighted MRI of a fetus at 25 weeks of gestational age demonstrates a high signal homogeneous left upper lobe *(arrow).* Pulmonary vessels can be seen coursing through the parenchyma.

With MRI, the mass is of high signal compared with adjacent lung on T2-weighted images. Mass effect on the adjacent intermediate signal normal lung may be noted. The diaphragm often is flattened.

Differentiation of CLO from microcystic CPAM or sequestration may be difficult prenatally both by US and MRI. One useful differentiation is the assessment of vascularity with Doppler; normal pulmonary vessels course through CLO, with no systemic feeders (Fig. 50.10). Rarely, the mediastinal shift is severe enough to result in polyhydramnios, hydrops, and pulmonary hypoplasia.[103-105]

***Treatment and Follow-up.*** Prognosis is typically favorable. As with other fetal lung masses, follow-up US prenatally is useful to exclude the rare development of hydrops and polyhydramnios. Diagnosis may be confirmed by following delivery with radiography and CT.[104,105] Postnatal surgery is performed if the child is symptomatic.

## Congenital Hydrothorax

***Etiology.*** Fetal pleural fluid may develop without an associated mass and is considered abnormal at any gestational age.[106,107] The fluid collection may be unilateral or bilateral. The incidence is 1:15,000 births. Chylothorax is the most common cause of congenital hydrothorax and may be caused by thoracic duct anomalies. Lesions associated with pleural effusions include masses (CDH, CPAM, BPS), lymphangiectasia, cardiac anomalies, Turner syndrome, trisomy 21, lymphatic malformation, and TORCH (toxoplasmosis, other [congenital syphilis and viruses], rubella, cytomegalovirus, and herpes simplex virus) infection. Thorough evaluation is required to identify associated anomalies. Overall mortality is reported to be as high as 50%. Outcome is best if the

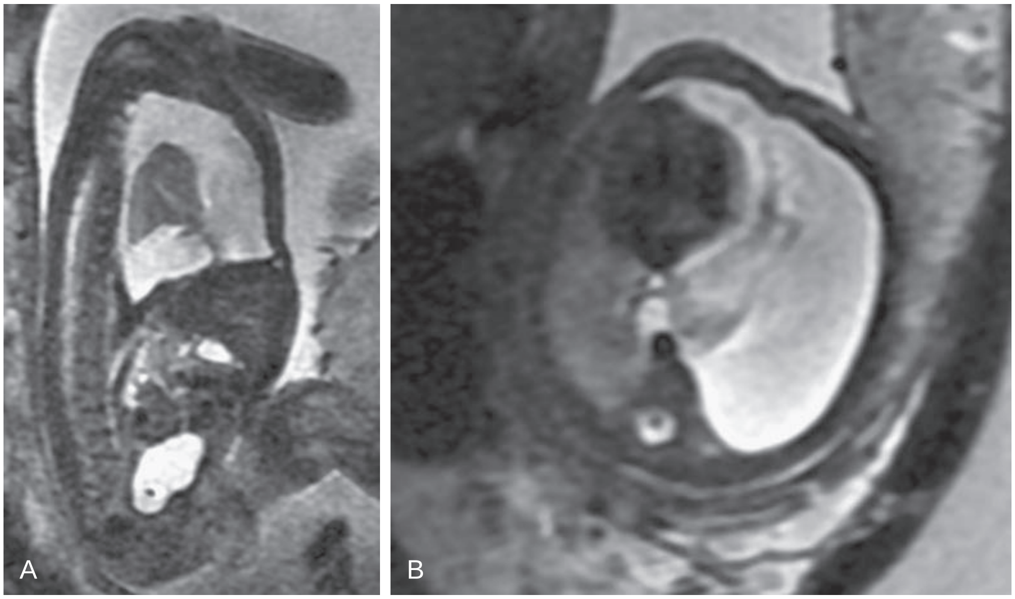

**Figure 50.11. Pleural effusion.** (A) Sagittal single-shot fast spin echo T2-weighted MRI shows a large pleural effusion with compression of the underlying lung parenchyma. (B) Axial single-shot fast spin echo T2-weighted MRI of the chest demonstrates the severity of the mediastinal shift and compression of both ipsilateral and contralateral lung.

effusion is unilateral. Primary chylothorax may resolve spontaneously (22%). If effusions progress to hydrops, mortality increases owing to the development of pulmonary hypoplasia.

***Imaging.*** US demonstrates anechoic fluid in the pleural space. MRI shows high signal fluid surrounding lung parenchyma. MRI may be useful in identifying a cause for the hydrothorax such as an underlying CPAM or BPS (Fig. 50.11).

***Treatment and Follow-up.*** If the effusion is small, conservative observation is appropriate. If the effusion is large, and the infant is less than 32 weeks of gestational age, fetal thoracentesis and thoracoamniotic shunting are potential prenatal treatment options, although reaccumulation of fluid is frequent.

## Congenital High Airway Obstruction

***Etiology.*** CHAOS is caused by obstruction or absence of the trachea. This rare entity may be the result of laryngotracheal atresia, tracheal stenosis, or tracheal web. Aberrant pulmonary budding off the foregut is present and in most cases there is a connection with the esophagus. Other anomalies can be associated with this entity, including Fraser syndrome and DiGeorge syndrome.

***Imaging.*** With US, both lungs are seen to be symmetrically enlarged and echogenic as a result of fluid trapping. The heart is compressed, and the diaphragms are flattened. Hydrops may develop. Increase or decrease in amniotic fluid may occur.[108-110] MRI shows abnormally large high signal lungs on T2-weighted images. Diaphragmatic eversion is present (Fig. 50.12). Identification of a fluid-filled trachea and bronchi confirms the diagnosis. Differential diagnosis includes bilateral CPAM.

***Treatment and Follow-Up.*** EXIT delivery with airway control is the current management of choice in a fetus with CHAOS. The prognosis is typically poor.[111,112]

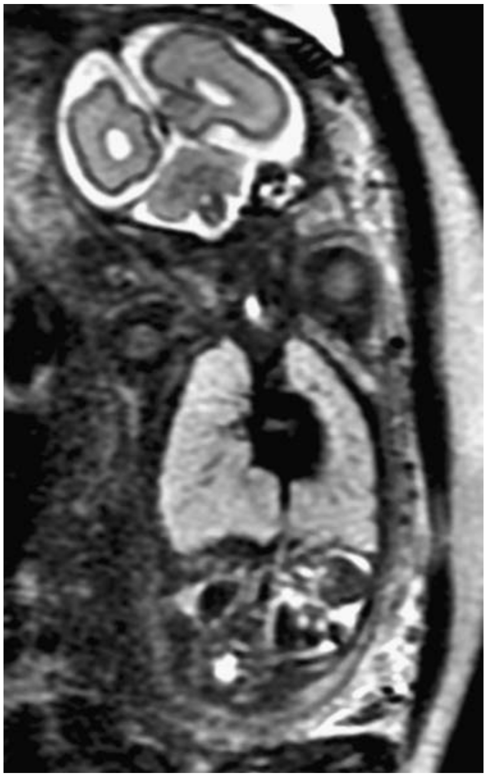

**Figure 50.12. Congenital high airway obstruction secondary to tracheal stenosis.** Coronal T2-weighted MRI of a 27-week-old fetus demonstrates abnormally enlarged high signal lungs. The diaphragms are flattened. Mild ascites is present.

## KEY POINTS

- The most common fetal chest abnormalities include CDH, congenital bronchopulmonary malformations, and congenital hydrothorax.
- Accurate prenatal diagnosis aids in counseling and planning potential fetal therapy, mode of delivery, and postnatal care.
- In a fetus with CDH, low lung-to-head circumference ratio and liver herniation into the chest suggest a worse outcome.
- Prognosis of congenital bronchopulmonary malformations is typically excellent. However, if hydrops develops prenatally, the outcome is poor without intervention.
- Chylothorax is the most common cause of congenital hydrothorax.

## SUGGESTED READINGS

Adzick NS. Management of fetal lung lesions. *Clin Perinat*. 2009;36:363–376.

Barth RA. Imaging of fetal chest masses. *Pediatr Radiol*. 2012;42(suppl 1):862–873.

Bulas D, Egloff A. *Prenatal Diagnosis and Management of Congenital Pulmonary Airway Malformation*. Up to Date. Wolters Kluwer Health.

Daltro P, Werner H, Gasparetto T, et al. Congenital chest malformations: a multimodality approach with emphasis on fetal MR imaging. *Radiographics*. 2010;30(2):385–395.

Deshmukh S, Rubesova E, Barth R. MR assessment of normal fetal lung volumes: a literature review. *AJR*. 2010;194:W212–W217.

Epelman M, Kreiger PA, Servas S, et al. Current imaging of prenatally diagnosed congenital lung lesions. *Semin Ultrasound CT MR*. 2010;31:141–157.

Kline-Fath B. Current advances in prenatal imaging of congenital diaphragmatic hernia. *Pediatr Radiol*. 2012;42(suppl 1):S74–S90.

## REFERENCES

Full references for this chapter can be found on www.expertconsult.com.

## REFERENCES

1. Johnson AM, Hubbard AM. Congenital anomalies of the fetal/neonatal chest. *Semin Roentgenol*. 2004;39:197–214.
2. Epelman M, Kreiger PA, Servas S, et al. Current imaging of prenatally diagnosed congenital lung lesions. *Semin Ultrasound CT MR*. 2010;31:141–157.
3. Daltro P, Werner H, Gasparetto T, et al. Congenital chest malformations: a multimodality approach with emphasis on fetal MR imaging. *Radiographics*. 2010;30(2):385–395.
4. Levine D, Barnewolt CE, Mehta TS, et al. Fetal thoracic abnormalities: MR imaging. *Radiology*. 2003;228:379–388.
5. Witlox RS, Lopriore E, Oepkes D. Prenatal interventions for fetal lung lesions. *Prenat Diagn*. 2011;31:628–638.
6. Bruner JP, Jarnagin BK, Reinisch L. Percutaneous laser ablation of fetal congenital cystic adenomatoid malformation: too little too late? *Fetal Diagn Ther*. 2000;15(6):359–363.
7. Adzick NS. Open fetal surgery for life-threatening fetal anomalies. *Semin Fetal Neonatal Med*. 2010;15:1–8.
8. Adzick NS. Management of fetal lung lesions. *Clin Perinat*. 2009;36:363–376.
9. Bermudez C, et al. Percutaneous fetal sclerotherapy for congenital cystic adenomatoid malformation of the lung. *Fetal Diagn Ther*. 2008;24:237–240.
10. Leeuwen L, Fitzgerald DA. Congenital diaphragmatic hernia. *J Paediatr Child Health*. 2014;50:667–673.
11. Benacerraf BR, Sadow P, Barnewolt C, et al. Cleft of the secondary palate without cleft lip diagnosed with three-dimensional ultrasound and magnetic resonance imaging in a fetus with Fryns' syndrome. *Ultrasound Obstet Gynecol*. 2006;27:566–570.
12. Graham G, Devine C. Antenatal diagnosis of congenital diaphragmatic hernia. *Semin Perinatol*. 2005;20:69–76.
13. Claus F, Sandaite I, Dekoninck P, et al. Prenatal anatomical imaging in fetuses with congenital diaphragmatic hernia. *Fetal Diagn Ther*. 2011;29(1):88–100.
14. Bootstaylor BS, Filly RA, Harrison MR, et al. Prenatal sonographic predictors of liver herniation in congenital diaphragmatic hernia. *J Ultrasound Med*. 1995;14:515–520.
15. Hendrick HL, Crombleholme TM, Flake AW, et al. Right congenital diaphragmatic hernia: prenatal assessment and outcome. *J Pediatr Surg*. 2004;39:319–323.
16. Tsukahar Y, Ohno Y, Itakura A, et al. Prenatal diagnosis of congenital diaphragmatic eventration by MRI. *Am J Perinatol*. 2001;18:241–244.
17. Skari H, Byornlank D, Haugen G, et al. Congenital diaphragmatic hernia: a meta-analysis of mortality factors. *J Pediatr Surg*. 2000;35:1187–1197.
18. Lazar DA, Cass DL, Rodriguez MA, et al. Impact of prenatal evaluation and protocol-based perinatal management on congenital diaphragmatic hernia outcomes. *J Pediatr Surg*. 2011;46(5):808–813.
19. Kitano Y, Nakagawa S, Kuroda T, et al. Liver position in fetal congenital diaphragmatic hernia retains a prognostic value in the era of lung-protective strategy. *J Pediatr Surg*. 2005;40:1827–1832.
20. Shragia L, Paek BW, Filly RA, et al. Congenital diaphragmatic hernia without herniation of the liver: does the lung to head ratio predict survival. *J Ultrasound Med*. 2002;19:845–850.
21. Laudy JA, Van Gucht M, VanDooren MF, et al. Congenital diaphragmatic hernia: an evaluation of the prognostic value of the lung-to-head ration and other prenatal parameters. *Prenat Diagn*. 2003;23:634–639.
22. Hedrick HL, Danzer E, Merchant A. Liver position and lung to head ratio for prediction of extracorporeal membrane oxygenation and survival in isolated left congenital diaphragmatic hernia. *Am J Obstet Gynecol*. 2007;197:422–432.
23. Arkovitz MS, Russo M, Devine P. Fetal lung—head ratio is not related to outcome for antenatal diagnosed congenital diaphragmatic hernia. *Pediatr Surg*. 2007;42:107–111.
24. Jani JC, Peralta CF, Ruano R, et al. Comparison of fetal lung area to head circumference ratio with lung volume in the prediction of postnatal outcome in diaphragmatic hernia. *Ultrasound Obster Gynecol*. 2007;30:850–854.
25. Gorincour G, Boubenot J, Mourot MG, et al. Prenatal prognosis of congenital diaphragmatic hernia using MRI measurement of fetal lung volume. *Ultrasound Obstet Gynecol*. 2005;26:738–744.
26. Rypens F, Metens T, Rocourt N, et al. Fetal lung volume: estimation at MR imaging – initial results. *Radiology*. 2001;219:236–241.
27. Danzer E, Hedrick HL. Controversies in the management of severe congenital diaphragmatic hernia. *Semin Fetal Neonatal Med*. 2014;19:376–384.
28. McHoney M. Congenital diaphragmatic hernia. *Early Hum Dev*. 2014;90:941–946.
29. Benachi A, Cordier A, Cannie M, et al. Advances in prenatal diagnosis of congenital diaphragmatic hernia. *Semin Fetal Neonatal Med*. 2014;19:331–337.
30. Losty PD. Congenital diaphragmatic hernia: where and what is the evidence? *Semin Pediatr Surg*. 2014;13:278–282.
31. Madenci AL, Sjogren AR, Treadwell MC, et al. Another dimension to survival: predicting outcomes with fetal MRI versus prenatal ultrasound in patients with congenital diaphragmatic hernia. *J Pediatr Surg*. 2013;48:1190–1197.
32. Jeanty C, Kunisaki SM, MacKenzie TC. Novel non-surgical prenatal approaches to treating congenital diaphragmatic hernia. *Semin Fetal Neonatal Med*. 2014;19:349–356.
33. Ruano R, Lazar DA, Cass DL, et al. Fetal lung volume and quantification of liver herniation by magnetic resonance imaging in isolated congenital diaphragmatic hernia. *Ultrasound Obstet Gynecol*. 2014;43:662–669.
34. Bouvenot GG, Mourot MG, Sonigo P, et al. Prenatal prognosis of congenital diaphragmatic hernia using magnetic resonance imaging measurement of fetal lung volume. *Ultrasound Obstet Gynecol*. 2005;26:738–744.
35. Walsh DS, Hubbard AM, Olutoye OO, et al. Assessment of fetal lung volumes and liver herniation with MRI in congenital diaphragmatic hernia. *Am J Obstet Gynecol*. 2000;183:1067–1069.
36. Büsing KA, Kilian AK, Schaible T, et al. Reliability and validity of MR image lung volume measurement in fetuses with congenital diaphragmatic hernia and in vitro lung models. *Radiology*. 2008;246:553–561.
37. Barnewolt CE, Kunisaki SM, Fauza DO, et al. Percent predicted lung volumes as measured on fetal MRI: a useful biometric parameter for risk stratification in congenital diaphragmatic hernia. *J Pediatr Surg*. 2007;42:193–197.
38. Cannie M, Jani J, Chaffiotte C, et al. Quantification of intrathoracic liver herniation by magnetic resonance imaging and prediction of postnatal survival in fetuses with congenital diaphragmatic hernia. *Ultrasound Obstet Gynecol*. 2008;32:627–632.
39. Lazar DA, Ruano R, Cass DL, et al. Defining "liver-up": does the volume of liver herniation predict outcome for fetuses with isolated left-sided congenital diaphragmatic hernia? *J Pediatr Surg*. 2012;47:1058–1062.
40. Weidner M, Hagelstein C, Debus A, et al. MRI-based ratio of fetal lung volume to fetal body volume as a new prognostic marker in congenital diaphragmatic hernia. *AJR Am J Roentgenol*. 2014;202:1330–1336.
41. Vuletin JF, Lim FY, Cnota J, et al. Prenatal pulmonary hypertension index: novel prenatal predictor of severe postnatal pulmonary artery hypertension in antenatally diagnosed congenital diaphragmatic hernia. *J Ped Surg*. 2010;45(4):703–708.
42. Mehollin-Ray AR, Caasady CI, Cass DK, et al. Fetal MR imaging of congenital diaphragmatic hernia. *Radiographics*. 2012;32:1067–1084.
43. Deprest JA, Hyett JA, Flake AS, et al. Current controversies in prenatal diagnosis: should fetal surgery be done in all cases of severe diaphragmatic hernia? *Prenat Diagn*. 2009;29:15–19.
44. Deshmukh S, Rubesova E, Barth R. MR assessment of normal fetal lung volumes: a literature review. *AJR*. 2010;194:W212–W217.
45. Harrison MR, Adzick NS, Bullard KM, et al. Correction of CDH in utero. VII. A prospective trial. *J Pediatr Surg*. 1997;32:1637–1642.
46. Sydorak RM, Harrison MR. Congenital diaphragmatic hernia: advances in prenatal therapy. *World J Surg*. 2003;27:68–76.
47. Sydorak RM, Heddrick MH, Longaker MT, et al. Pathophysiologic patterns influencing fetal surgery. *World J Surg*. 2003;27:45–53.
48. Flake AW, Crombleholme TM, Johnson MP, et al. Treatment of severe congenital diaphragmatic hernia by fetal tracheal occlusion: clinical experience with fifteen cases. *Am J Obstet Gynecol*. 2000;183:1059–1066.
49. Kunisaki SM, et al. Ex-utero-intrapartum treatment with placement of extracorporeal membrane oxygenation for fetal thoracic masses. *J Pediatr Surg*. 2007;42(2):420–425.
50. Langston C. New concepts in the pathology of congenital lung malformations. *Semin Pediatr Surg*. 2003;12:17–37.
51. Mackenzie TC, Buttenberg ME, Nisenbaum HL, et al. A fetal lung lesion consisting of bronchogenic cyst, bronchopulmonary sequestration, and congenital cystic adenomatoid malformation: the missing link? *Fetal Diagn Ther*. 2001;16:193–195.

52. Correia-Pinto J, Gonzaga S, Huang Y, et al. Congenital lung lesions- underlying molecular mechanisms. *Semin Pediatr Surg*. 2010;19(3):171–179.
53. Stocker JT, Madewell JE, Drake RM. Congenital cystic adenomatoid malformation of the lung: classification and morphologic spectrum. *Hum Pathol*. 1977;8:155–171.
54. Adzick NS, Harrison MR, Crombleholme TM, et al. Fetal lung lesions: management and outcome. *Am J Obstet Gynecol*. 1998;179(4):884–889.
55. Cavoretto P, et al. Prenatal diagnosis and outcome of echogenic fetal lung lesions. *Ultrasound Obstet Gynecol*. 2008;32:769–783.
56. Lecompte B, et al. Hyperechoic congenital lung lesions in a non-selected population: from prenatal detection till perinatal management. *Prenat Diagn*. 2009;29:1222–1230.
57. Hata N, Wada T, Chiba T, et al. Three-dimensional volume rendering of fetal MR images for the diagnosis of congenital cystic adenomatoid malformation. *Acad Radiol*. 2003;10:209–212.
58. Cass DL, Olutoye OO, Cassady CI, et al. Prenatal diagnosis and outcome of fetal lung masses. *J Pediatr Surg*. 2011;46(2):292–298.
59. Miller JA, Corteville JE, Langer JC. Congenital cystic adenomatoid malformation in the fetus: natural history and predictors of outcome. *J Pediatr Surg*. 1996;31:805–808.
60. Azizkhan RG, Crombleholme TM. Congenital cystic lung disease: contemporary antenatal and postnatal management. *Pediatr Surg Int*. 2008;24:643–657.
61. Crombleholme TM, Coleman B, Hedrick H, et al. Cystic adenomatoid malformation volume ratio predicts outcome in prenatally diagnosed cystic adenomatoid malformation of the lung. *Pediatr Surg*. 2002;37:331–338.
62. Curran PF, Jelin EB, Rand L, et al. Prenatal steroids for microcystic congenital cystic adenomatoid malformations. *J Pediatr Surg*. 2010;45:145–150.
63. Morris LM, Lim FY, Livingston JC, et al. High-risk fetal congenital pulmonary airway malformations have a variable response to steroids. *J Pediatr Surg*. 2009;44:60–65.
64. Peranteau WH, Wilson RD, Liechty KW, et al. Effect of maternal betamethasone administration on prenatal congenital cystic adenomatoid malformation growth and fetal survival. *Fetal Diagn Ther*. 2007;22:365.
65. Loh KC, Jelin E, Hirose S, et al. Microcystic congenital pulmonary airway malformation with hydrops fetalis: steroids vs open fetal resection. *J Pediatr Surg*. 2012;47:36.
66. Peranteau WH, Boelig MM, Khalek N, et al. Effect of single and multiple courses of maternal betamethasone on prenatal congenital lung lesion growth and fetal survival. *J Pediatr Surg*. 2016;51:28–32.
67. Kunisaki SM, Ehrenberg-Buchner S, Dillman JR, et al. Vanishing fetal lung malformations: prenatal sonographic characteristics and postnatal outcomes. *J Pediatr Surg*. 2015;50:978–982.
68. Derderian SC, Coleman AM, Jeanty C, et al. Favorable outcomes in high-risk congenital pulmonary airway malformations treated with multiple courses of maternal betamethasone. *J Pediatr Surg*. 2015;50:515–518.
69. Dommergues M, Louis-Sylvestre C, Mandelbrot L, et al. Congenital adenomatoid malformation of the lung: when is active fetal therapy indicated? *Am J Obstet Gynecol*. 1997;177:953–958.
70. Mann S, et al. Antenatal diagnosis and management of congenital cystic adenomatoid malformation. *Semin Fetal Neonatal Med*. 2007;12:477–481.
71. Peranteau WH, Adzick NS, Boelig MM, et al. Thoracoamniotic shunts for the management of fetal lung lesions and pleural effusions: a single-institution review and predictors of survival in 75 cases. *J Pediatr Surg*. 2015;50:301.
72. Hellmmund A, Berg Ch, Geipel A, et al. Prenatal diagnosis and evaluation of sonographic predictors for intervention and adverse outcome in congenital pulmonary airway malformation. *PLoS ONE*. 2016;11(3):e0150474.
73. Costanzo S, Filisetti C, Vella C, et al. Pulmonary malformations: predictors of neonatal respiratory distress and early surgery. *J Neonatal Surg*. 2016;5(3):27.
74. Ehrenberg-Buchner S, Stapf AM, Berman DR, et al. Fetal lung lesions: can we start to breathe easier? *Am J Obstet Gynecol*. 2013;208:151.e1.
75. Zeidan S, et al. Congenital lung malformation: evaluation of prenatal and postnatal radiologic findings. *Respirology*. 2009;14:1005–1011.
76. Winters WD, Effman EL, Nhgiem HV, et al. Disappearing fetal lung masses: importance of postnatal imaging studies. *Pediatr Radiol*. 1997;27:535–539.
77. Morresi A, Wockel W, Karg O. Adenomatoid cystic lung abnormality in adults with associated bronchioloalveolar carcinoma. *Pathology*. 1995;16:292–298.
78. Murphy JJ, Blair GK, Fraser GC. Rhabdomyosarcoma arising within congenital pulmonary cysts: report of three cases. *J Pediatr Surg*. 1992;27:1364–1367.
79. Ozcan C, Celik A, Ural Z, et al. Primary pulmonary rhabdomyosarcoma arising within cystic adenomatoid malformation: a case report and review of the literature. *J Pediatr Surg*. 2001;36:1062–1065.
80. Prichard MG, Brown PJ, Sterrett GF. Bronchioloalveolar carcinoma arising in longstanding lung cysts. *Thorax*. 1984;39:545–549.
81. Ueda K, Gruppo R, Unger F, et al. Rhabdomyosarcoma of the lung arising in congenital cystic adenomatoid malformation. *Cancer*. 1977;40:383–388.
82. Becmeur F, Horta-Geraud P, Donato L, et al. Pulmonary sequestration: prenatal diagnosis with clinicopathologic correlation. *Curr Opin Obstet Gynecol*. 1998;6:479–496.
83. Becmeur F, Horta-Geraud P, Donato L, et al. Pulmonary sequestrations: prenatal ultrasound diagnosis, treatment and outcome. *J Pediatr Surg*. 1998;33:492–496.
84. Cass DL, Crombleholme TM, Howell LJ, et al. Cystic lung lesions with systemic arterial blood supply: a hybrid of congenital cystic adenomatoid malformation and bronchopulmonary sequestration. *J Pediatr Surg*. 1997;32:986–990.
85. Vijayaraghavan SB, et al. Prenatal sonographic features of intralobar bronchopulmonary sequestration. *J Ultrasound Med*. 2003;22:541–544.
86. Sepulveda W. Perinatal imaging in bronchopulmonary sequestration. *J Ultrasound Med*. 2009;28:89–94.
87. Abbey P, Das CJ, Pangtey GS, et al. Imaging in bronchopulmonary sequestration. *J Med Imaging Radiat Oncol*. 2009;53:22–31.
88. Coleman AM, Merrow AC, Crombleholme TM, et al. Fetal MRI of torsed bronchopulmonary sequestration with tension hydrothorax and hydrops in a twin gestation. *Fetal Diagn Ther*. 2016;40:156–160.
89. Lecomte B, Hadden H, Coste K, et al. Hyperechoic congenital lung lesions in a non-selected population: from prenatal detection till perinatal management. *Prenat Diagn*. 2009;29:1222–1230.
90. Azizkhan RG, Crombleholme TM. Congenital cystic lung disease: contemporary antenatal and postnatal management. *Pediatr Surg Int*. 2008;24:643–657.
91. Lopoo JB, Goldstein RB, Lipshutz GS, et al. Fetal pulmonary sequestration: a favorable congenital lung lesion. *Obstet Gynecol*. 1999;94:567–571.
92. Witlox RS, Lopriore E, Walther FJ, et al. Single-needle laser treatment with drainage of hydrothorax in fetal bronchopulmonary sequestration with hydrops. *Ultrasound Obstet Gynecol*. 2009;34:355–357.
93. Mychaliska GB, Bryner BS, Nugent C, et al. Giant pulmonary sequestration: the rare case requiring the EXIT procedure with resection and ECMO. *Fetal Diagn Ther*. 2009;25:163–166.
94. Mallmann MR, Geipel A, Bludau M, et al. Bronchopulmonary sequestration with massive pleural effusion: pleuroamniotic shunting vs intrafetal vascular laser ablation. *Ultrasound Obstet Gynecol*. 2014;44:441–446.
95. Ruano R, da Silva MM, Salustiano EM, et al. Percutaneous laser ablation under ultrasound guidance for fetal hyperechogenic microcystic lung lesions with hydrops: a single center cohort and a literature review. *Prenat Diagn*. 2012;32:1127–1132.
96. Cruz-Martinez R, Mendez A, Duenas-Riano J, et al. Fetal laser surgery prevents fetal death and avoids the need for neonatal sequestrectomy in cases with bronchopulmonary sequestration. *Ultrasound Obstet Gynecol*. 2015;46:627–632.
97. Knox EM, Kilby MD, Martin WL, et al. In-utero pulmonary drainage in the management of primary hydrothorax and congenital cystic lung lesion: a systematic review. *Ultrasound Obstet Gynecol*. 2006;28:726734.
98. Biyyam DR, Chapman T, Ferguson MR, et al. Congenital lung abnormalities: embryologic features, prenatal diagnosis and postnatal radiologic pathologic correlation. *Radiographics*. 2010;30:1721–1738.
99. Levine D, Jennings R, Barnewolt C. Progressive fetal bronchial obstruction caused by a bronchogenic cyst diagnosed using prenatal MR imaging. *Am J Roentgenol*. 2001;176:49–52.
100. Stigers KB, Wookring JH, Kanga JF. The clinical and imaging spectrum of findings in patients with congenital lobar emphysema. *Pediatr Pulmonol*. 1992;14:160–170.
101. Johnston JH, Kline-Fath BM, Bitters C, et al. Congenital overinflation: prenatal MRI and US findings and outcomes. *Prenat Diagn*. 2016;36(6):568–575.

102. Kunisaki SM, Fauza DO, Nemes L, et al. Bronchial atresia: the hidden pathology within a spectrum of prenatally diagnosed lung masses. *J Pediatr Surg*. 2006;41:61–65.
103. Pariente G, Aviram M, Landau D, et al. Prenatal diagnosis of congenital lobar emphysema: case report and review of the literature. *J Ultrasound Med*. 2009;28:1081–1084.
104. Seo T, Ando H, Kaneko K, et al. Two cases of prenatally diagnosed congenital lobar emphysema caused by lobar bronchial atresia. *J Pediat Surg*. 2006;41:E17–E20.
105. Bush A, Hogg J, Chitty LS. Cystic lung lesions—prenatal diagnosis and management. *Prenat Diagn*. 2008;28:604–611.
106. Aubard Y, Derouineau I, Aubard V, et al. Primary fetal hydrothorax: a literature review and proposed antenatal clinical strategy. *Fetal Diagn Ther*. 1998;13:325–333.
107. Longaker MR, Laberge JM, Dansereau J, et al. Primary fetal hydrothorax: natural history and management. *J Pediatr Surg*. 1989;24:573–576.
108. Vidaeff AC, Szmuk P, Mastrobattista JM, et al. More or less CHAOS: case report and literature review suggesting the existence of a distinct subtype of congenital high airway obstruction syndrome. *Ultrasound Obstet Gynecol*. 2007;30:114–117.
109. Courtier J, Poder L, Wang ZJ, et al. Fetal tracheolaryngeal airway obstruction: prenatal evaluation by sonography and MRI. *Pediatr Radiol*. 2010;40:1800–1805.
110. Roybal JL, Liechty KW, Hedrick HL, et al. Predicting the severity of congenital high airway obstruction syndrome. *J Pediatr Surg*. 2010;45:1633–1639.
111. Mong A, Johnson AM, Kramer SS, et al. Congenital high airway obstruction syndrome: MR/US findings, effect on management, and outcome. *Pediatr Radiol*. 2008;38:1171–1179.
112. Kuwashima S, Kazuhiro K, Yasushi K, et al. MR imaging appearance of laryngeal atresia (congenital high airway obstruction syndrome): unique course in a fetus. *Pediatr Radiol*. 2008;38:344–347.

# 51

# Upper Airway Disease

Bernard F. Laya and Edward Y. Lee

The upper airway, by definition, lies above the thoracic inlet. The anomalies and abnormalities involving the upper airway in children are common and varied. They include a combination of congenital and acquired morphologic, neuromuscular, bony, and cartilaginous abnormalities.[1] The anatomic considerations that predispose children to acute respiratory distress, even with only partial obstruction, are as follows: (1) The nasopharynx is narrower than in adults, (2) the pediatric larynx is more anteriorly and superiorly located, (3) the conus elasticus is susceptible to edema, (4) the vocal cords are more angled anteriorly, (5) the epiglottis is broader and longer, and (6) the tongue is larger.[2]

Affected children usually present with acute respiratory distress associated with stridor, apnea, or even acute pulmonary edema.[3,4] Some children may present with more chronic clinical symptoms characterized by recurrent chest infections or obstructive sleep apnea, which can lead to growth retardation, chronic respiratory failure, cor pulmonale, and even death.[3]

Although a thorough history and physical examination may narrow differential diagnostic considerations of upper airway disease in the pediatric population, imaging evaluation plays an important role in establishing the diagnosis, localizing the anatomic area of abnormality, and defining the extent of disease.[5] Frontal and lateral radiographs of the airway and fluoroscopy have been mainstays in upper airway evaluation. Advances in cross-sectional imaging techniques approaching near-endoscopic detail have been developed to more accurately demonstrate airway anatomy.[3] For practical purposes, the discussion of pathology in this chapter is divided into the supraglottic, glottic, and subglottic regions.

## SUPRAGLOTTIC ABNORMALITIES

### Laryngomalacia

***Etiology.*** Laryngomalacia is abnormal laxity of the pharyngeal tissues that causes the epiglottis, arytenoids, and aryepiglottic folds to involute and partially obstruct breathing during inspiration. The underlying cause of laryngomalacia is attributed to the immaturity of the laryngeal cartilages and muscles, which allows the larynx and the supralaryngeal structures to collapse.[3-6] The unstable epiglottis and redundant arytenoid cartilage mucosa tend to be sucked into the glottis during inspiratory airflow causing obstruction.[7] Laryngomalacia accounts for more than 75% of cases of congenital stridor and is the most common cause of symptomatic partial upper airway obstruction in infants.[8,9] The stridor typically improves when the infant is agitated or active and becomes worse when the infant is at rest.

***Imaging.*** The diagnosis of laryngomalacia can be established with use of airway fluoroscopy, although laryngoscopy is the diagnostic procedure of choice.[10] The characteristic imaging finding in patients with laryngomalacia consists of downward and posterior bending of the epiglottis and anterior buckling of the aryepiglottic folds, which narrow and eventually obliterate the upper airway (Fig. 51.1).[9] Although airway fluoroscopy appears to be reliable because of its high specificity, it has low sensitivity, and thus negative findings of a fluoroscopic study require further diagnostic evaluation in the setting of a high clinical suspicion.[11]

***Treatment and Follow-up.*** In most infants with laryngomalacia, stridor resolves during the first year of life. However, potentially serious complications, including airway obstruction and sudden death, may occur. In severe or life-threatening cases, various surgical treatment options are available including supraglottoplasty, an incision in the aryepiglottic folds, epiglottopexy, and tracheostomy.[7,12]

### Epiglottitis

***Etiology.*** Acute bacterial epiglottitis is a potentially serious cause of upper airway obstruction in children. It is characterized by inflammation and swelling of the epiglottis and the aryepiglottic folds but also can affect the false cords and the subglottic region.[13] Epiglottitis usually is attributed to *Haemophilus influenzae*, although other bacteria including *Streptococcus*, *Staphylococcus*, *Moraxella*, and *Pseudomonas* also have been implicated.[14] Because *H. influenzae* is now preventable by immunization, the incidence of epiglottitis has substantially diminished, although vaccine failures do occur.[15,16] Epiglottitis typically occurs in children between 3 and 6 years of age, but it also can occur in adults.[17] Epiglottitis usually has a sudden onset with no history of a preceding upper respiratory tract infection. Affected children typically appear toxic with acute stridor, dysphagia, fever, restlessness, drooling, and increased respiratory distress in the recumbent position. Epiglottitis is a life-threatening disease that requires potential emergent intubation.

***Imaging.*** Epiglottitis usually is diagnosed with radiography, and endoscopy is obtained for confirmation. A lateral radiograph reveals swelling and marked enlargement of the epiglottis that resembles the shape of a thumb (Fig. 51.2). Associated thickening of the aryepiglottic folds also occurs. Inflammation extends into the glottis and subglottic regions, causing a steeple or funnel configuration of the airway on frontal views. Because of the potentially rapid progression of the condition, which can lead to sudden and complete obstruction of the upper airway, radiographs should be obtained expeditiously with minimal manipulation of the neck. When undergoing imaging, patients should remain upright in their position of maximal comfort. Conditions that mimic bacterial epiglottitis in children include caustic ingestion, angioneurotic edema, chemical or thermal injury, abscess, and epithelial cyst, among others. The omega epiglottis with prominent lateral folds is a normal variant and should not be misinterpreted as epiglottitis. In such cases, the aryepiglottic folds remain thin.[18]

***Treatment and Follow-up.*** Antibiotic therapy is a mainstay of treatment, and steroids are administered to some patients. Direct laryngoscopy with intubation is performed to secure the airway in severely affected patients.[14]

## GLOTTIC ABNORMALITIES

### Laryngeal Atresia

***Etiology.*** Laryngeal atresia, a rare congenital malformation, is usually fatal. The malformation is caused by nondevelopment of the sixth branchial arch during embryogenesis, resulting in failure of the larynx and the trachea to recanalize. Typical presentation of affected patients with laryngeal atresia at birth is severe

## Abstract:

The upper airway, by definition, lies above the thoracic inlet. The anomalies and abnormalities involving the upper airway in children are common and varied. They include a combination of congenital and acquired morphologic, neuromuscular, bony, and cartilaginous abnormalities. The anatomic considerations that predispose children to acute respiratory distress, even with only partial obstruction, are as follows: (1) The nasopharynx is narrower than in adults, (2) the pediatric larynx is more anteriorly and superiorly located, (3) the conus elasticus is susceptible to edema, (4) the vocal cords are more angled anteriorly, (5) the epiglottis is broader and longer, and (6) the tongue is larger.

Affected children usually present with acute respiratory distress associated with stridor, apnea, or even acute pulmonary edema. Some children may present with more chronic clinical symptoms characterized by recurrent chest infections or obstructive sleep apnea, which can lead to growth retardation, chronic respiratory failure, cor pulmonale, and even death.

Although a thorough history and physical examination may narrow differential diagnostic considerations of upper airway disease in the pediatric population, imaging evaluation plays an important role in establishing the diagnosis, localizing the anatomic area of abnormality, and defining the extent of disease. In this chapter, the imaging modalities utilized in the evaluation of upper airway are discussed. Various congenital as well as acquired upper airway diseases in children are presented with emphasis on their typical imaging characteristics.

## Keywords:

Upper Airway Disease in Children
Upper Airway Obstruction in Children
Congenital and Acquired Upper Airway Disorders
Imaging of the Upper Airways
Stridor in Children

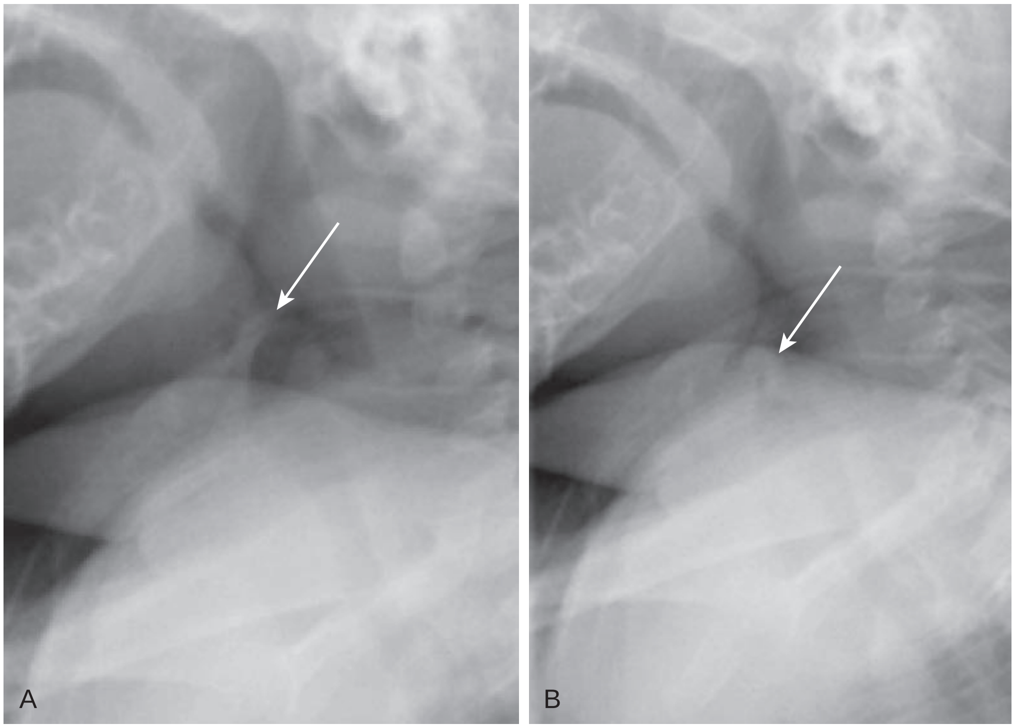

**Figure 51.1. Laryngomalacia in a 3-month-old boy with stridor.** (A) Still lateral image from an airway fluoroscopic study demonstrates the normal position of the epiglottis *(arrow).* (B) Still image from an airway fluoroscopic study during inspiration shows laxity of the epiglottis with posterior, downward movement obstructing the airway *(arrow)* consistent with laryngomalacia.

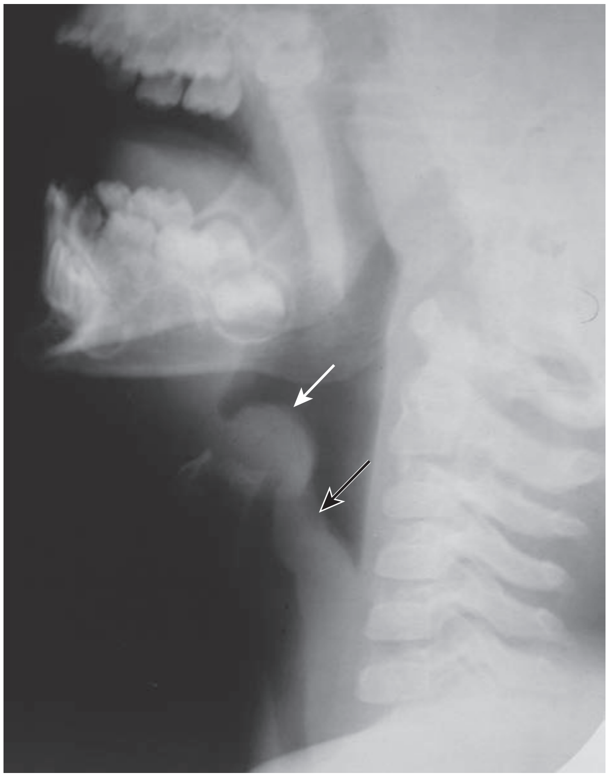

**Figure 51.2. Epiglottitis in a 5-year-old boy with respiratory distress and drooling.** A lateral soft tissue neck radiograph shows a markedly thickened epiglottis *(white arrow),* which is referred to as the "thumb" sign. The aryepiglottic folds *(black arrow)* also are thickened.

respiratory distress despite strong respiratory effort. Associated anomalies include a tracheoesophageal fistula, esophageal atresia, urinary tract abnormalities, limb defects, and low-set ears.[19] Laryngeal atresia is the most common reason for congenital high airway obstruction syndrome (CHAOS), a rare entity causing fluid entrapment within the enlarged trachea and lungs along with flattening of the diaphragm (see also Chapter 50).[20]

***Imaging.*** Laryngeal atresia can be diagnosed with use of prenatal ultrasound by identifying the signs of congenital high airway obstruction syndrome, such as enlarged hyperechogenic lungs, a flattened or inverted diaphragm, a dilated and fluid-filled trachea, fetal hydrops, and polyhydramnios.[20,21] Fetal magnetic resonance imaging (MRI), which correlates highly with prenatal ultrasound, can detect laryngeal atresia with the advantage of having the capability to identify the level of obstruction in most cases (e-Fig. 51.3).[20,22]

***Treatment and Follow-up.*** The treatment of laryngeal atresia focuses on prompt airway intervention at delivery after an accurate prenatal diagnosis, which may allow survival of infants with this otherwise fatal condition. An emergent tracheostomy is required immediately after birth to secure an airway. Ex utero intrapartum treatment (EXIT) procedure has also been used for this condition to facilitate safe delivery and allow some time to secure the airway.[20] Repair of laryngeal atresia requires laryngotracheal reconstruction.

## Laryngeal Web

***Etiology.*** A congenital laryngeal web is an uncommon condition caused by faulty embryogenesis of the laryngotracheal groove. This web is a band of varying thickness, usually located anteriorly at the level of the cords, which obliterates the anterior commissure. A congenital laryngeal web occasionally occurs just below the true cords. Affected infants present with a weak or absent cry, varying

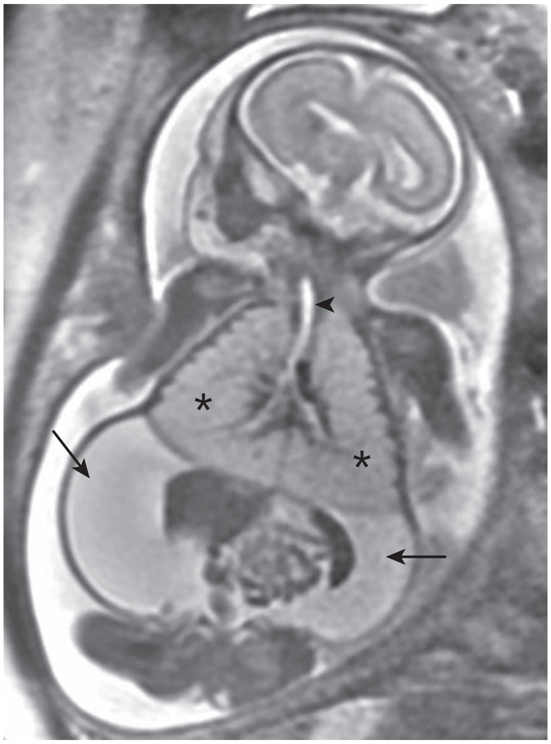

**e-Figure 51.3. Congenital high airway obstruction syndrome in a 20-week-gestation fetus.** A half Fourier acquisition single-shot turbo spin echo sequence of a fetal MRI scan demonstrates a dilated, fluid-filled trachea up to the mid neck *(solid arrows),* enlarged hyperintense lungs *(asterisks)* with inversion of both hemidiaphragms, and ascites *(arrowhead).* *(Image courtesy of Dr. Carl Merrow, MD, Cincinnati, OH.)*

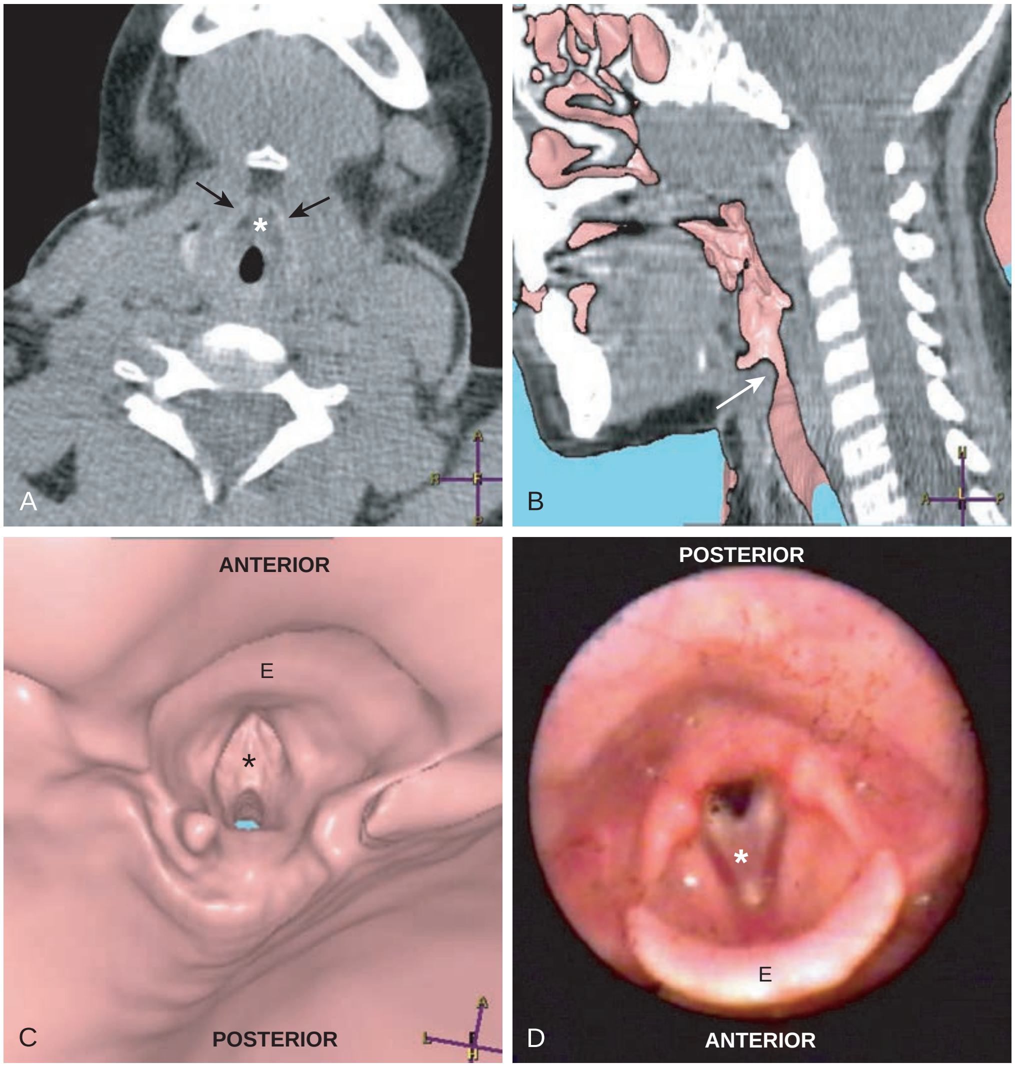

**Figure 51.4. Laryngeal web.** (A) Axial CT scan of the neck at the level of the larynx and the thyroid cartilage *(black arrows)* demonstrates the laryngeal web *(asterisk).* (B) Sagittal virtual endoscopic view superimposed on a sagittal reformatted CT image shows the laryngeal web *(arrow).* Virtual endoscopic view (C) and corresponding laryngoscopy (D) demonstrate the laryngeal web *(asterisk).* The epiglottis *(E)* is well demonstrated on these images. *(Courtesy of Suleymen Men, MD, Izmir, Turkey.)*

degrees of stridor, and respiratory distress; they often have concomitant abnormalities such as subglottic stenosis.[3]

***Imaging.*** A definitive diagnosis of laryngeal web can be provided by direct laryngoscopy, but imaging evaluation plays a role in diagnosis. Plain radiography and fluoroscopy can demonstrate that the abnormality is in the glottis region, but no definitive radiographic findings exist.[6] Computed tomography (CT) with multiplanar imaging and three-dimensional reconstructions can provide precise information with respect to the exact location of the web, its thickness, and extent (Fig. 51.4). Furthermore, CT is able to visualize the structures beyond the area of obstruction, which is a limitation of laryngoscopy.[23]

***Treatment and Follow-up.*** The primary goals of treatment for a congenital laryngeal web are to provide a patent airway and achieve sufficient voice quality. Treatment depends on the thickness and extent of the abnormality. Surgical procedures include laryngotracheal reconstruction, laryngofissure and placement of a stent or keel, and endoscopic lysis with application of mitomycin C.[24,25]

## Laryngocele

***Etiology.*** A laryngocele is a rare lesion characterized by abnormal dilation of the laryngeal saccule, which is a narrow blind pouch arising from the anterior end of the laryngeal ventricle.[20,26,27] Laryngoceles may extend internal or external to the larynx.[21,28]

Most childhood laryngoceles are congenital; acquired laryngocele may develop in older children or adults who experience increased intralaryngeal pressure.

***Imaging.*** CT and MRI have replaced older plain film and fluoroscopic techniques.[20,21,28] A laryngocele typically is a well-defined cystic structure of air or near-water density value in a characteristic location, with a smooth surface, lack of mucosal abnormality, and variable extent of airway narrowing (Fig. 51.5).[22,29,30]

***Treatment and Follow-up.*** Microlaryngoscopic surgery with the use of $CO_2$ laser has become the treatment of choice for internal laryngoceles (those that lie within the larynx). An external approach remains the main surgical treatment of combined or external laryngoceles (those that protrude through the thyrohyoid membrane).[30]

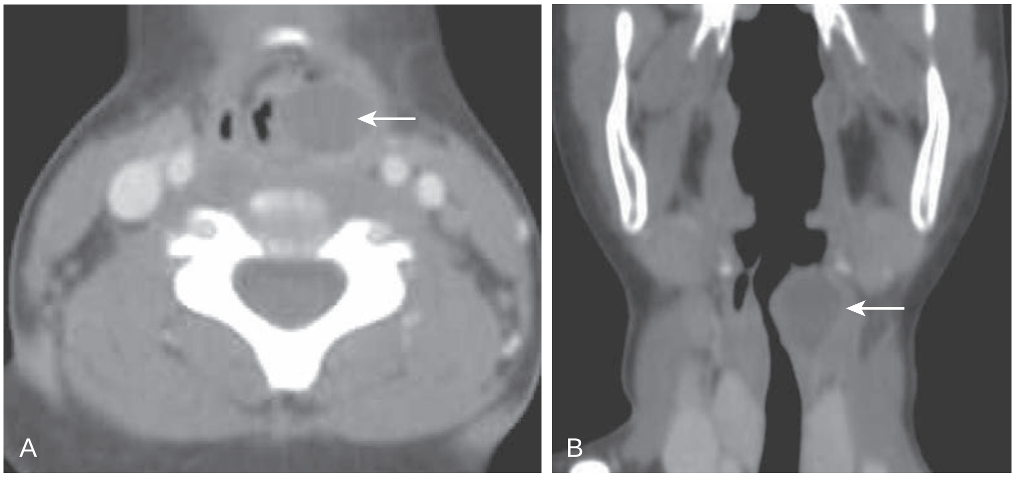

**Figure 51.5. Laryngocele in a 5-year-old boy with chronic stridor.** Axial CT scan (A) with coronal reconstruction (B) of the upper airway reveals a well-demarcated fluid-filled rounded structure *(arrow)* adjacent to the left laryngeal ventricle compatible with a laryngocele. Also noted is a marked narrowing of the upper airway.

## Recurrent Respiratory Papillomatosis

***Etiology.*** Recurrent respiratory papillomatosis (RRP) is the most common benign neoplasm to affect the larynx in children.[31] It is the proliferation of benign squamous papillomas in the aerodigestive tract, usually involving the larynx. The etiology of RRP is infection of the upper airway with human papillomavirus types 6 and 11.[7,32] Vertical transmission occurring during delivery through an infected birth canal is presumed to be the major mode of transmission in children.[33] Maternal vaccination has greatly reduced the incidence of this potentially devastating disease.

Change in voice (e.g., hoarseness, weak cry, and aphonia) and stridor are the most common symptoms in patients with RRP. Less common presenting symptoms include chronic cough, recurrent pneumonia, failure to thrive, dyspnea, dysphagia, and acute respiratory distress, especially in infants with a superimposed upper respiratory tract infection.[34] The age of symptom onset typically ranges from neonates to 6 years. RRP can mimic other diseases including croup, tracheomalacia, or asthma.[35] This diagnosis should be considered in children when other common pediatric airway diseases either do not follow the expected natural history or do not respond to treatment.[36]

***Imaging.*** On plain radiographs, RRP typically appears as irregular filling defect in the glottis (Fig. 51.6). It also can extend into the subglottic region and seed peripherally in the respiratory tract, resulting in pulmonary nodules or nonspecific lung parenchymal changes.[3] A confirmatory diagnosis of RRP is made by direct laryngoscopy and biopsy for tissue diagnosis.[36]

***Treatment and Follow-up.*** Carbon dioxide laser surgery, antiviral therapy, and other adjuvant regimens have been tried, but none of them have proved to be completely successful in treating RRP. Recurrences are very common.[34,37]

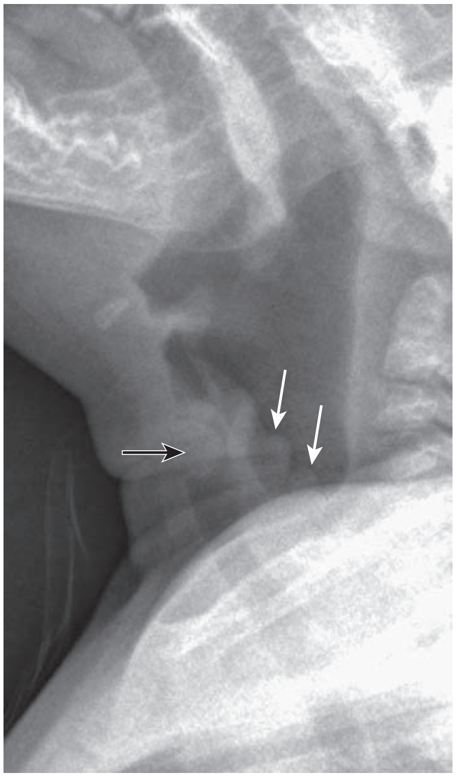

**Figure 51.6. Recurrent respiratory papillomatosis in a 4-year-old boy.** A lateral soft tissue radiograph demonstrates a rounded soft tissue mass in the laryngeal region *(black arrow).* Nodular soft tissue densities also are noted along the aryepiglottic folds *(white arrows). (Courtesy of Elizabeth H. Ey, MD, Dayton, OH.)*

## SUBGLOTTIC ABNORMALITIES

### Subglottic Stenosis

***Etiology.*** Subglottic stenosis is a narrowing of the subglottic airway that can be either congenital or acquired. In pediatric patients, congenital subglottic stenosis is due to faulty recanalization of the fetal laryngeal lumen, whereas the acquired type usually is the result of prolonged endotracheal intubation.[3,7] Because of improved management of neonates who require ventilatory support, the incidence of neonatal subglottic stenosis has diminished substantially.[38] Stridor is the most common clinical presentation. However, an infant or child with a mild degree of congenital or acquired subglottic stenosis may remain asymptomatic until an upper respiratory tract infection results in aggravation of the subglottic airway narrowing.[6]

***Imaging.*** Endoscopy is the reference standard for diagnosis, but imaging plays an important role in the evaluation of subglottic stenosis. Plain radiography and fluoroscopy, which show fixed narrowing of the subglottic airway, usually enable diagnosis.

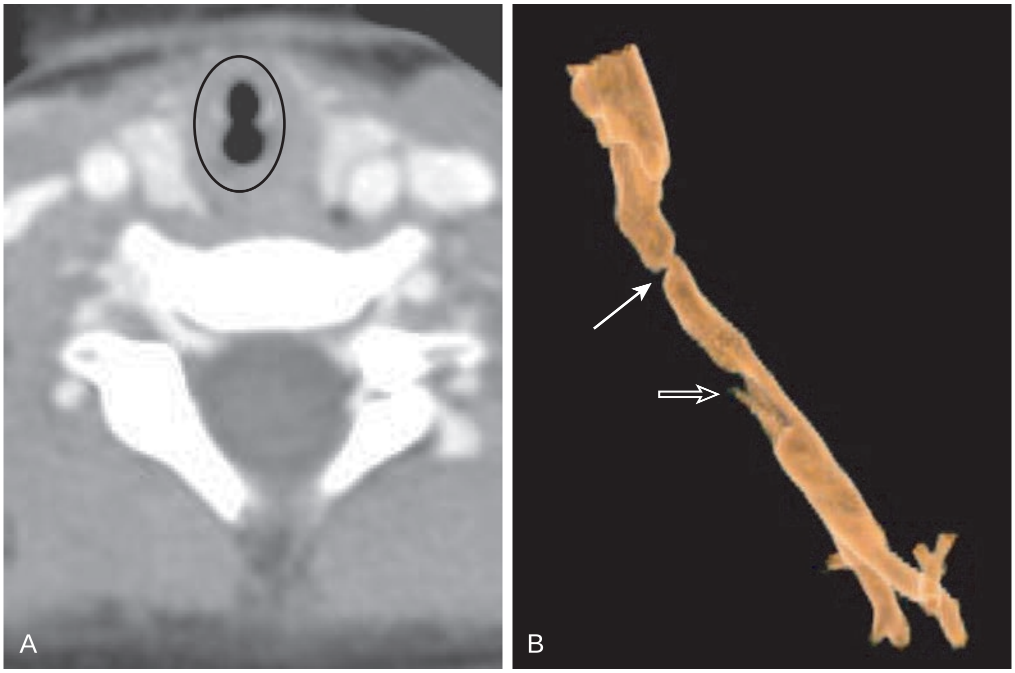

**Figure 51.7. Subglottic stenosis in a 2-year-old girl, a former premature infant who had undergone chronic intubation.** (A) Axial neck CT demonstrates severe transverse narrowing of the subglottic trachea *(circled).* (B) An external surface volume-rendered reconstruction shows severe subglottic stenosis *(solid arrow)* and a defect from the tracheostomy tube *(open arrow).*

However, CT with virtual bronchoscopy and MRI can be useful in assessing the exact site and length of stenosis and the airway distal to the area of narrowing (Fig. 51.7).[6,39]

***Treatment and Follow-up.*** The two major treatment options currently available for subglottic stenosis are endoscopic dilation and surgical reconstruction.[7,40]

## Croup

***Etiology.*** Viral croup or laryngotracheobronchitis is the most common cause of upper airway obstruction in children from 6 months to 3 years of age. Parainfluenza and influenza virus are the two most common etiologic agents for viral croup. They induce a reactive inflammatory response, which results in subglottic edema and subsequent upper airway narrowing. Clinically, viral croup is characterized by a low-grade fever and varying degrees of inspiratory stridor, barking cough, and hoarseness.[2,6,41]

***Imaging.*** Although the diagnosis of viral croup is mainly clinical, airway studies may be obtained for diagnostic confirmation and exclusion of other causes of acute stridor, such as epiglottitis. On a frontal radiograph, the lateral walls of the subglottic larynx normally are convex or shouldered. Mucosal edema in viral croup narrows this space, which results in a loss of lateral convexity, creating a "steeple" shape below the vocal cords (Fig. 51.8). The narrowing can extend 5 to 10 mm below the vocal cords. The steeple sign is not specific for croup and may be seen in some children with epiglottitis. Furthermore, it can be absent in children affected with viral croup. On lateral radiographs, the hypopharynx often is overdistended, and the subglottic region is hazy or indistinct as a result of narrowing of the airway by mucosal edema. The epiglottis, aryepiglottic folds, and prevertebral spaces are normal in persons with viral croup.[2-6]

***Treatment and Follow-up.*** In most pediatric patients with viral croup, the disease is mild and self-limited. Depending on the severity of disease, steroids and nebulized epinephrine have been administered to treat patients.[41,42]

## Bacterial Tracheitis

***Etiology.*** Bacterial tracheitis is a potentially life-threatening cause of upper airway obstruction. Bacterial tracheitis also has been referred as membranous croup, pseudomembranous croup, bacterial croup, purulent tracheobronchitis, and membranous laryngotracheobronchitis. The common etiologic bacteria include *Staphylococcus*, *Moraxella*, *Streptococcus*, and *Haemophilus* species.[43,44] The bacterial infection causes an inflammatory response that produces thick adherent mucopurulent exudates, ulceration, and sloughing of the laryngeal, tracheal, and bronchial mucosa. Affected children usually are preschool- to school-age children and are sicker than those affected with viral croup. Clinically there is typically a recent history of viral respiratory illness, rhinorrhea, cough, fever, and sore throat. With the advent of bacterial tracheitis there is often progression to high fever, a toxic appearance, and severe upper airway obstruction with hoarseness, cough, stridor, and tachypnea.[43-45] A definitive diagnosis of bacterial tracheitis is made on the basis of the history and physical examination, combined with findings from laboratory and bronchoscopic evaluation.[45]

***Imaging.*** Typical radiographic findings of bacterial tracheitis on the frontal radiograph of the cervical airway is narrowing of the subglottic airway. On lateral radiographs of the upper airway, diffuse haziness and marked irregularity of the anterior wall of the trachea may be seen, which is referred to as the "candle-dripping sign" (Fig. 51.9).[43,46] Opaque linear streaks or filling defects, membranes, or plaquelike irregularities can be seen within the airway. Chest radiographic abnormalities are common in children with bacterial tracheitis, with at least 50% showing concomitant findings of pneumonia.[46]

***Treatment and Follow-up.*** When managing symptomatic children with bacterial tracheitis, a patent airway should be established to treat acute respiratory failure.[33] Antibiotic therapy usually is initiated, and laryngoscopy may be required for endoscopic removal of the obstructing purulent secretions and membranes.

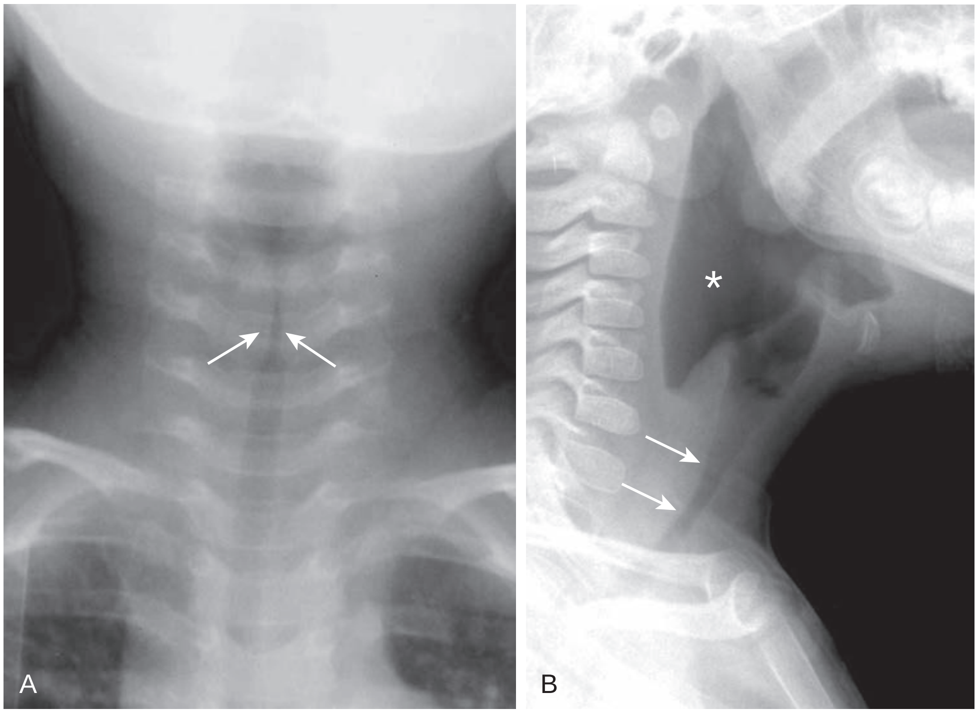

**Figure 51.8. Croup.** (A) Frontal soft tissue neck radiograph demonstrates a "steeple" appearance of the subglottic trachea *(arrows).* (B) Lateral soft tissue neck radiograph in another patient shows a dilated hypopharynx *(asterisk),* as well as haziness and narrowing of the subglottic region *(arrows).*

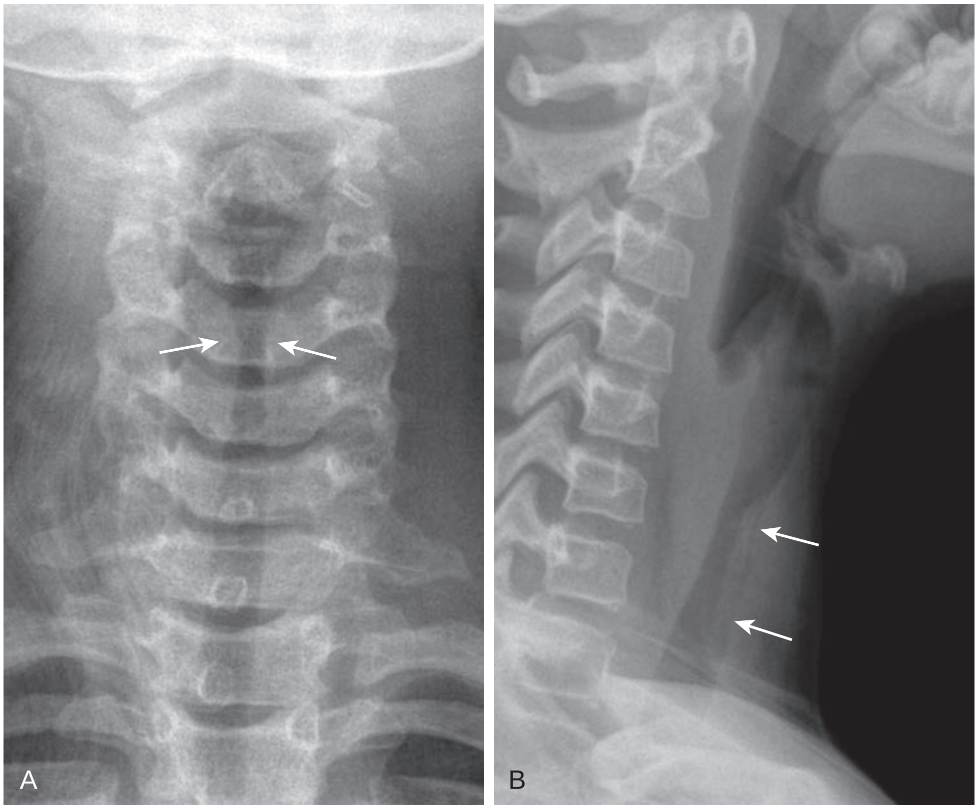

**Figure 51.9. Bacterial tracheitis in a 9-year-old girl with a high fever, cough, and stridor.** (A) Frontal soft tissue neck radiograph shows subglottic tracheal narrowing *(arrows).* (B) Lateral soft tissue neck radiograph shows irregular linear membranous debris within the trachea *(arrows).*

## Retropharyngeal Cellulitis/Abscess

***Etiology.*** Retropharyngeal cellulitis/abscess is a serious and occasionally life-threatening pyogenic infection with the potential to encroach on the upper airway. It occurs as a consequence of infections of the nasopharynx, paranasal sinuses, or middle ear. Suppurative lymph nodes in the retropharyngeal space are the usual cause, but infection can also extend from diskitis, osteomyelitis, mediastinitis, or a penetrating foreign body.[2] Usual etiologic agents are *Streptococcus*, *Staphylococcus*, and *Haemophilus*, although anaerobes and even *Mycobacterium tuberculosis* have been implicated.[47] The infection occurs predominantly in early childhood; typical clinical symptoms are fever, neck stiffness, and dysphagia, with occasional presentation with signs of upper airway obstruction.[1,6,43] Diagnosis is based on clinical suspicion with supportive imaging studies.

***Imaging.*** On a lateral neck radiograph, the normal prevertebral space in infants and children is wide because the vertebrae are not fully ossified. As a general guide, the thickness of the prevertebral soft tissue space from C1 to C4 is equal to half of the adjacent vertebral body width. In the older child, the vertebral bodies become larger and the prevertebral space becomes smaller. However, if the thickness of the prevertebral space is greater than the adjacent vertebral body width below C3, it usually is abnormal.[4] Attention to imaging technique is important; a poorly obtained neck radiograph that is taken obliquely, on expiration, or with the neck flexed can accentuate the retropharyngeal space and mimic pathology. Typical plain film radiographic findings of retropharyngeal cellulitis/abscess include fixed retropharyngeal soft tissue widening, anterior displacement of the airway, and often reversal of the cervical lordotic curvature.[3,6] Retropharyngeal cellulitis or abscess are not distinguishable on a plain radiograph unless retropharyngeal air is seen.[6] CT is the preferred imaging modality to confirm the diagnosis and demonstrate the size, extent, and location of the pus collection from a retropharyngeal abscess.[3,48,49] Lesions with a low-density center surrounded by an enhancing thick rim are more characteristic of a retropharyngeal abscess rather than cellulitis (e-Fig. 51.10).

***Treatment and Follow-up.*** Although retropharyngeal abscesses traditionally have been treated with surgical drainage of the pus collection, some cases may be managed with antibiotics alone.[38,39,48-51]

# OTHER CAUSES OF UPPER AIRWAY ABNORMALITIES

## Obstructive Sleep Apnea

***Etiology.*** Obstructive sleep apnea syndrome (OSA) is a disorder of breathing during sleep characterized by prolonged partial or complete upper airway obstruction that disrupts normal ventilation and sleep patterns. Typical symptoms of OSA include snoring, disturbed sleep, and daytime neurobehavioral problems. Common complications from OSA are neurocognitive impairment, behavioral problems, failure to thrive, and cor pulmonale in severe cases. Risk factors for developing OSA include adenotonsillar hypertrophy, obesity, craniofacial anomalies, and neuromuscular disorders.[52] Nocturnal polysomnography (sleep study) is the only diagnostic technique shown to quantify the ventilatory and sleep abnormalities associated with sleep-disordered breathing.

***Imaging.*** For imaging assessment of OSA, a lateral soft tissue neck radiograph can be obtained to evaluate adenoid size.[3] The adenoidal-nasopharyngeal ratio derived from the lateral soft tissue neck radiograph is a clinically useful index of pharyngeal patency.[6,53,54] Also, the lingual or palatine tonsils are considered enlarged if they narrow the nasopharynx.[2] Videofluoroscopic evaluation of the airway while the child is asleep can be performed to investigate inspiratory collapse of the nasopharynx and oropharynx as a result of proximal airway obstruction acting in concert with sleep-related hypotonia of the pharyngeal musculature.[55] More recently, cine MRI has been advocated as the more accurate diagnostic imaging technique because it shows the volumetric dimension of the adenoids and palatine tonsils (Fig. 51.11). Furthermore, it also can demonstrate dynamic motion of the upper airway, thereby allowing evaluation of the relationship between the size of the adenoid and palatine tonsils and the degree of airway motion.[56]

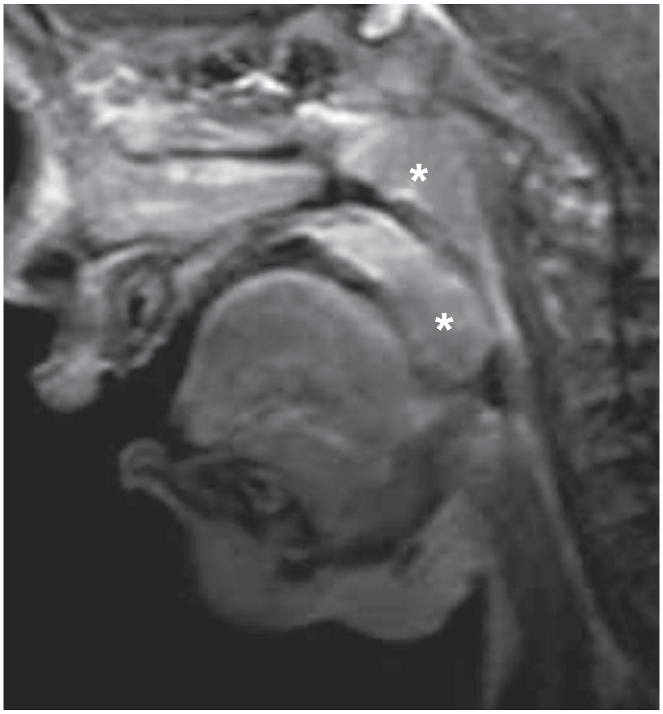

**Figure 51.11. Obstructive sleep apnea in a 2-year-old girl with snoring.** Sagittal MRI sequence of the upper airway shows markedly enlarged adenoids *(upper asterisk)* and palatine tonsils *(lower asterisk)* causing narrowing of the nasopharyngeal airway.

***Treatment and Follow-up.*** Treatment of mild cases of OSA include lifestyle changes such as weight loss. For moderate to severe OSA, the most commonly used treatments include a continuous positive airway pressure or automatic positive airway pressure device that can maintain the patency of the patient's airway during sleep by providing the pressurized air flow into the upper airway. Additionally, several surgical treatments currently are available in patients with anatomic causes of upper airway obstruction, including septoplasty, turbinate surgery, tonsillectomy, and uvulopalatopharyngoplasty.

## Foreign Body

***Etiology.*** Most patients who present with foreign bodies in the upper airway are children between 6 months and 3 years of age. The most commonly aspirated foreign bodies in the upper airway are usually bulky, irregularly shaped, or sharp objects (Fig. 51.12).[2]

Nasal foreign bodies tend to be located on the floor of the nasal passage, just below the inferior turbinate, or in the upper nasal fossa anterior to the middle turbinate (Fig. 51.13).[57] Affected pediatric patients often present with unilateral, foul-smelling nasal discharge. Only 3% of aspirated foreign bodies are lodged in the larynx, but it is a common cause of death in children younger than 2 years old.[2] Patients with a foreign body lodged in the supraglottic region present with cough, dyspnea, salivation, and voice changes; when in the larynx, there is stridor, cough, voice changes, and severe

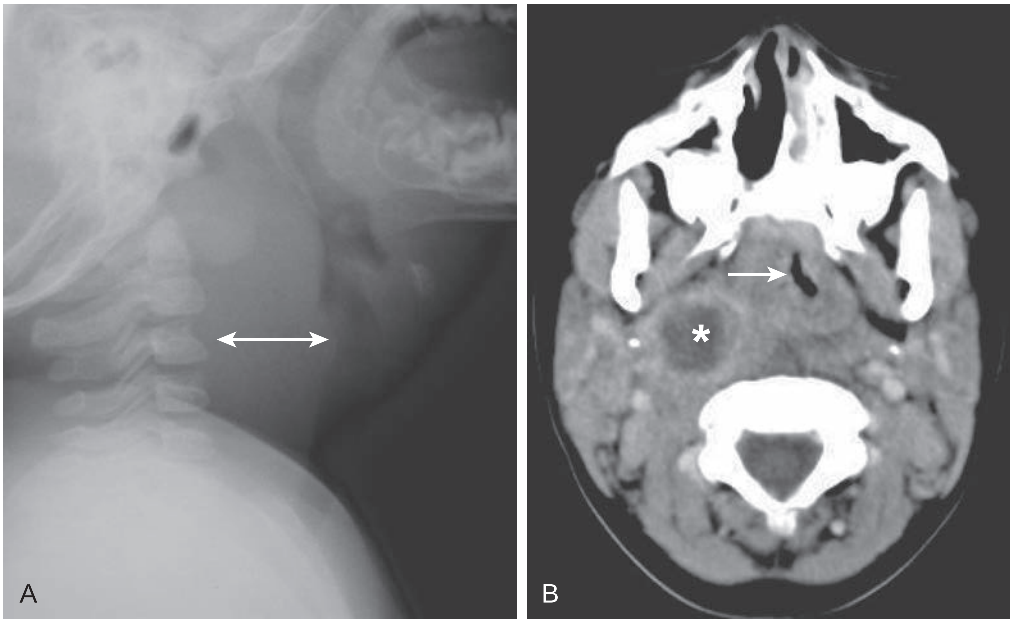

**e-Figure 51.10. Retropharyngeal abscess in a 3-year-old girl.** (A) Lateral soft tissue neck radiograph shows markedly widened retropharyngeal soft tissue *(double arrow).* (B) Axial CT scan through the upper airway demonstrates a rounded area of hypoattenuation with enhancing border compatible with abscess *(asterisk)* and associated soft tissue swelling effacing the airway *(arrow).*

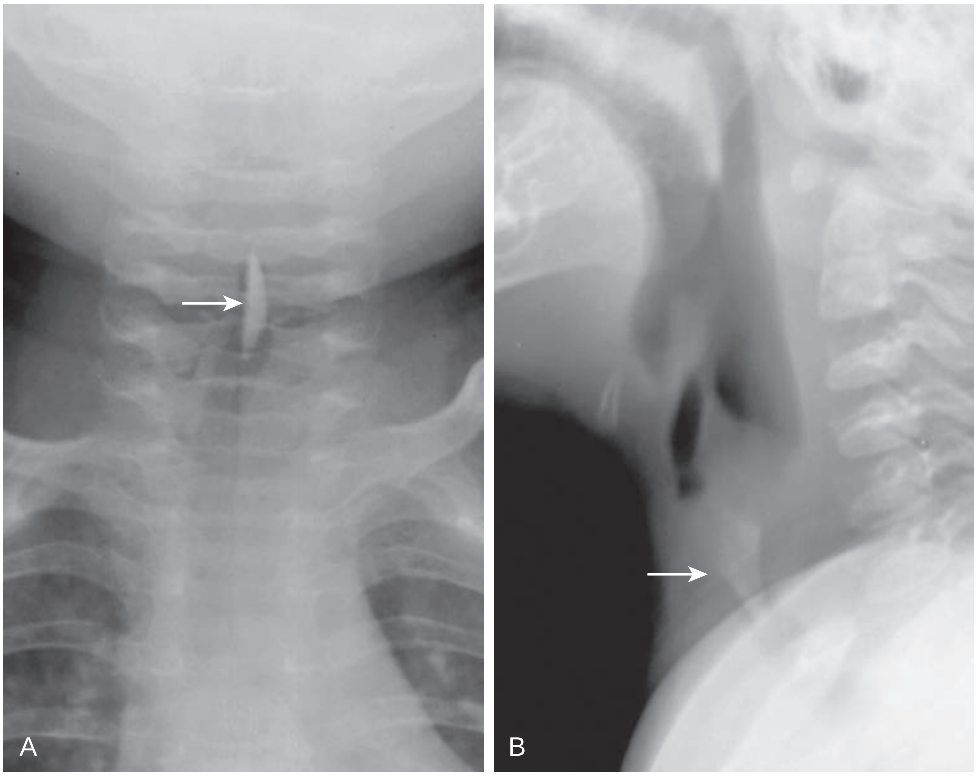

**Figure 51.12. Laryngeal foreign body in a 5-month-old boy who presented with stridor.** Frontal (A) and lateral (B) radiographs of the upper airway reveals an elongated density in the laryngeal region *(arrow)* proven to be a piece of bone.

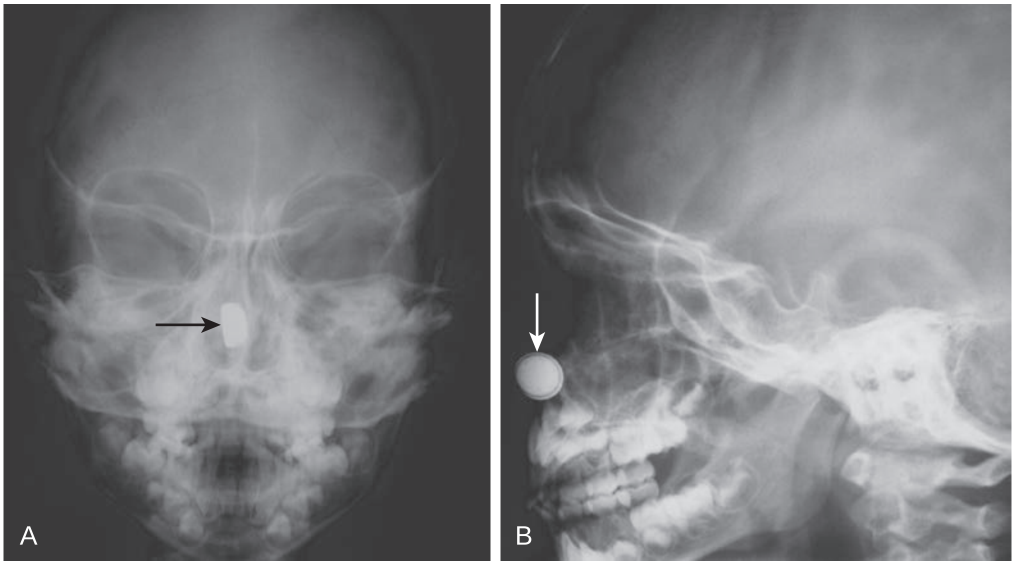

**Figure 51.13. A nasal foreign body in a boy who presented with nasal congestion and foul-smelling discharge for 1 week.** Frontal (A) and lateral (B) radiographs of the nasal airway show a metallic foreign body (battery; *arrow*) in the right nasal cavity. Battery foreign bodies must be removed emergently.

breathing difficulty; when in the extrathoracic trachea, inspiratory stridor and expiratory rhonchi are observed.[58]

***Imaging.*** Radiography can be helpful in localizing radiopaque foreign bodies such as coins, buttons, and batteries, but because most foreign bodies are radiolucent, management should not be based solely on imaging.[59] Plain radiography is sufficient to demonstrate radiopaque upper airway and esophageal foreign bodies. On frontal radiographs, coins in the esophagus are seen en face, whereas coins in the trachea are seen in tangent because of a posterior gap in the tracheal cartilage rings. Indirect signs of airway obstruction include overdistention of the hypopharynx and prevertebral soft tissue swelling. Food and other nonradiopaque foreign bodies in the upper airway often are identified only with endoscopy.[6]

***Treatment and Follow-up.*** Most nasal foreign bodies can be removed by a skilled physician, although attempts at removal may push the nasal foreign body into the pharynx, creating an airway hazard. Pharyngeal and laryngeal foreign bodies are medical emergencies because airway obstruction usually occurs at the time of aspiration and results in immediate respiratory distress. Flexible or rigid endoscopy usually is required to confirm the diagnosis, remove the foreign body, and avoid complications, including airway obstruction, laryngeal edema, and pushing the foreign body into the subglottic space or trachea.[59]

## Traumatic Injuries

***Etiology.*** Pediatric laryngotracheal injuries are infrequent because of the softer cartilage and the protection provided by the prominent mandible.[60,61] Airway compromise is suggested if dysphonia, dysphagia, or dyspnea is present.[62] The most important clinical signs of laryngeal injury include hoarseness and subcutaneous emphysema.[61] Injuries may be subtle and present with minimal initial symptoms that, if undiagnosed, may rapidly progress to loss of the airway. Thus a high index of suspicion is needed to promptly and accurately diagnose and manage pediatric laryngotracheal injuries. Fiberoptic laryngoscopy is mandatory when injury to the larynx and trachea is suspected.[61,62]

***Imaging.*** In any pediatric patient with possible upper airway injury, plain radiographs of the neck and chest may aid in the diagnosis. Radiographs also can be useful to assess the cervical spine. Findings of laryngotracheal injuries in pediatric patients vary considerably according to the mechanism of injury, but radiographic evidence of soft tissue air and wounds opening into the airway are common findings. CT is also useful and can play a primary role in localizing the injury and determining its extent (Fig. 51.14).[60-64]

***Treatment and Follow-up.*** Most laryngotracheal injuries in children can be managed conservatively. However, extensive injuries, including displaced fractures of the cartilage, injuries to the recurrent nerves, and laryngotracheal separation, require surgical intervention.[63]

## Neoplasms

### Subglottic Hemangioma

***Etiology.*** Subglottic hemangioma, a congenital vascular tumor, is the most common primary neoplasm affecting the subglottic trachea. Although the tumor is present at birth, patients with subglottic hemangioma usually become symptomatic between 1 and 6 months of age because of their rapid initial growth. Affected infants usually present with intermittent or acute onset of acute respiratory difficulty that varies in severity and includes stridor and crouplike symptoms. Fifty percent of patients also have concomitant cutaneous hemangiomas. During its initial proliferative phase, the mass grows rapidly during the first 18 months of life, followed by a gradual involution that may last until age 10 years. Generally, a subglottic hemangioma is a self-limiting condition, and the respiratory distress tends to diminish and may disappear. However, the behavior of the individual lesion is unpredictable, and the symptoms are variable in severity.[65]

***Imaging.*** Plain radiographs of infants and children with subglottic hemangiomas typically show an irregular, small, soft tissue mass below the true vocal cords (e-Fig. 51.15A). These lesions have a characteristic radiographic appearance of a soft tissue shadow bulging into the airway lumen, often with asymmetric subglottic narrowing. However, symmetric narrowing of the trachea can be caused by a hemangioma if it is located central to the plane of projection. CT or MRI can show the mass at the subglottic region with intense enhancement after the administration of contrast material (e-Fig. 51.15B).[65]

***Treatment and Follow-up.*** Propranolol has recently emerged as the primary treatment for hemangioma.[66] However, laryngotracheoplasty and direct surgical excision are alternative therapies in patients with severe airway compromise who are refractory to propranolol therapy.[67]

### Malignant Neoplasms

Neoplasms of the head and neck may present with upper airway obstruction. Lymphoma and rhabdomyosarcoma are the most

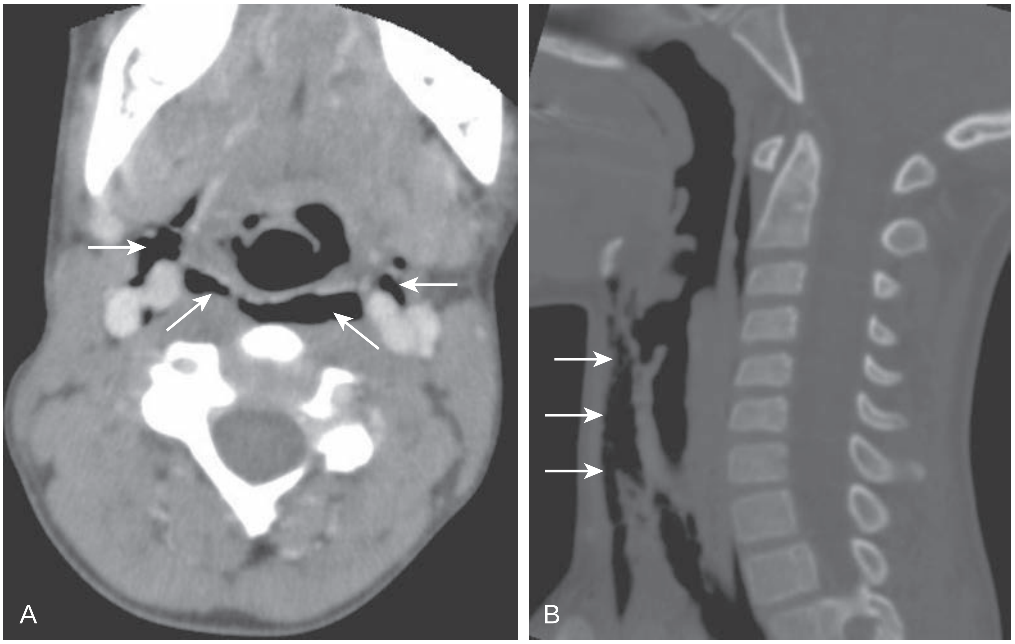

**Figure 51.14. Laryngeal trauma in a 10-year-old boy who tripped and struck his anterior neck across a log.** Axial (A) and sagittal reconstruction (B) CT scans of the neck show air dissecting along the parapharyngeal region *(arrows)* compatible with laryngeal trauma. *(Courtesy of Elizabeth H. Ey, MD, Dayton, OH.)*

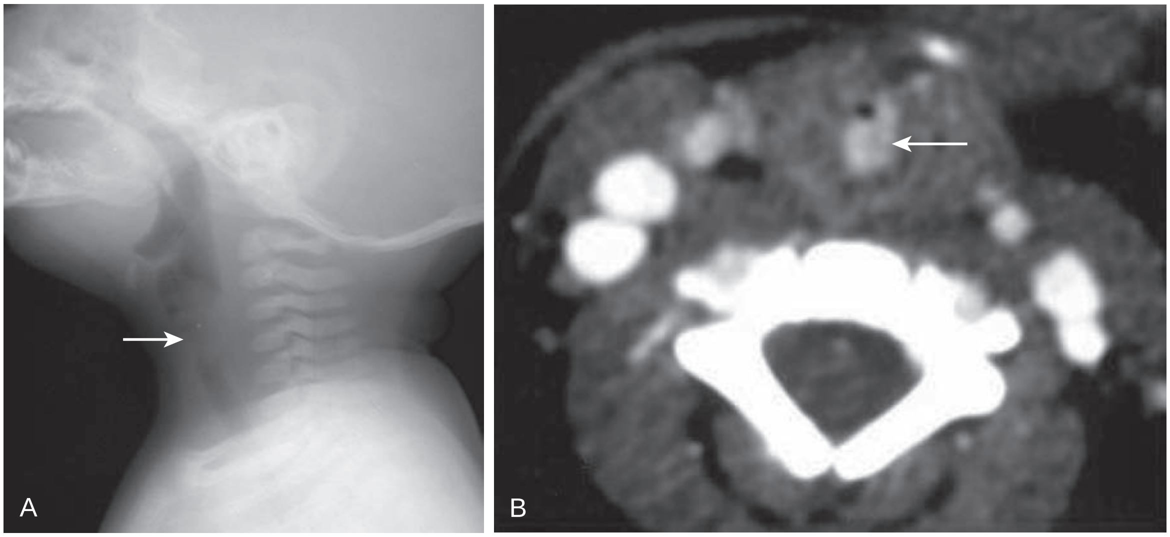

**e-Figure 51.15. Subglottic hemangioma in a 6-month-old boy with stridor.** (A) Lateral neck radiograph demonstrates haziness and soft tissue densities in the subglottic tracheal region *(arrow).* (B) Axial CT scan at the subglottic region shows the hemangioma *(arrow),* an intensely enhancing soft tissue mass causing marked narrowing of the subglottic trachea.

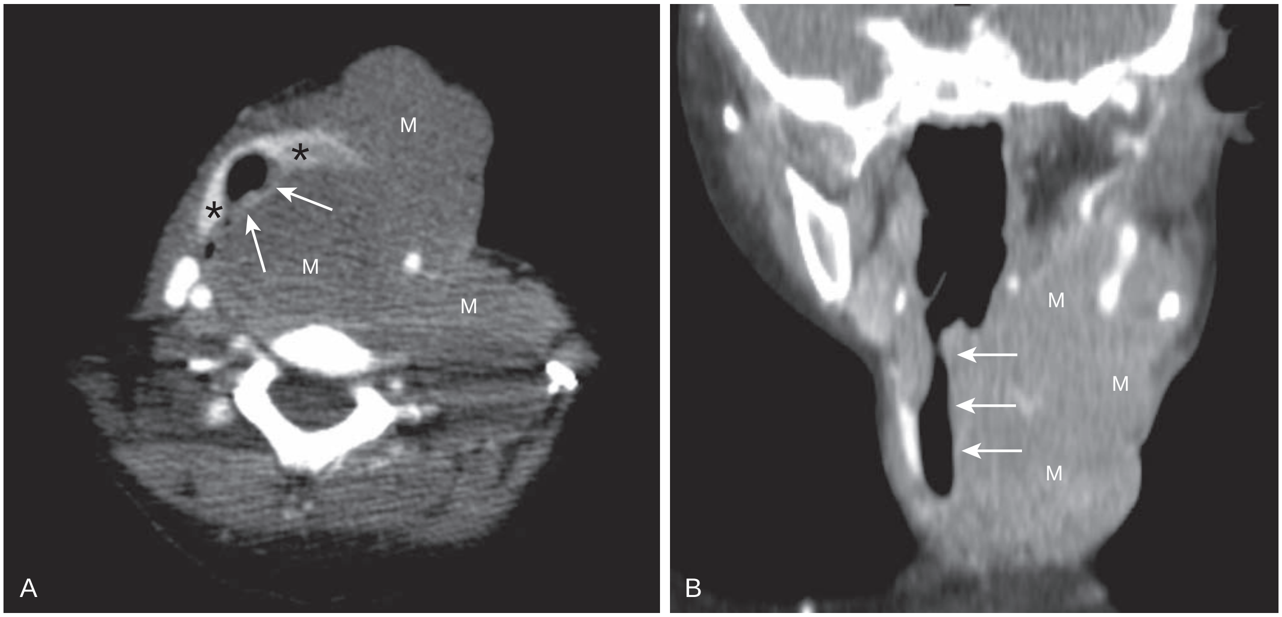

**Figure 51.17. Embryonal rhabdomyosarcoma in a 2-year-old girl with noisy breathing.** Frontal (A) and coronal (B) CT images of the neck reveal a large soft tissue mass *(M)* in the left neck region significantly effacing the upper airway *(arrows)* anteriorly and to the right. The lobes of the thyroid gland *(asterisks)* are also effaced anteriorly.

common malignancies in this region in children.[68–70] CT and MRI are the predominant imaging modalities for evaluating the location, extent, and vascularity of these tumors, as well as the degree of airway compromise (e-Fig. 51.16 and Fig. 51.17). Both CT and MRI with intravenous contrast can be used for diagnosis, staging, and follow-up.[71] These lesions are discussed in detail in Chapter 16.

Other malignant neoplasms involving the head and neck that have the potential to affect the airway include nasopharyngeal carcinoma, thyroid cancers, and salivary gland tumors, although these entities are uncommon in children.

## KEY POINTS

- Upper airway disease is a common problem in infants and children because of the narrow diameter of the airway early in life.
- Upper airway diseases in children can be categorized as acute or chronic, but the etiology is diverse and includes congenital, infectious/inflammatory, foreign body, posttraumatic, and neoplastic causes.
- Radiographs maintain an integral role in the initial evaluation of a patient with upper airway disease, but attention to proper positioning and technique is important to avoid pitfalls.
- Cross-sectional imaging (CT and MRI) is capable of multiplanar reconstruction, which allows a detailed evaluation of airway anatomy and disease in both static and dynamic states.
- Endoscopy is still the gold standard in evaluating upper airway diseases, but CT three-dimensional–virtual endoscopy has the ability to produce a realistic representation of the inner walls of the airway, simulating a real endoscopic examination, with the advantage of depicting the anatomy below a high-grade stenosis, a limitation of endoscopy.

## SUGGESTED READINGS

Bradshaw K. Imaging the upper airways. *Paediatr Respir Rev*. 2001;2:46–56.
Darras KE, Roston AT, Ywchuk LK. Imaging acute airway obstruction in infants and children. *Radiographics*. 2015;35:2064–2079.
John SD, Swischuk LE. Stridor and upper airway obstruction in infants and children. *Radiographics*. 1992;12:625–643.
Laya BF, Lee EY. Congenital causes of upper airway obstruction in pediatric patients: updated techniques and review of imaging findings. *Semin Roentgenol*. 2012;47(2):147–158.
Lee EY, Greenberg SB, Boiselle PM. Multidetector computed tomography of pediatric large airway disease: state-of-the-art. *Radiol Clin North Am*. 2011;49(5):869–893.
Macpherson RI, Leithiser RE. Upper airway obstruction in children: an update. *Radiographics*. 1985;5(3):339–376.

## REFERENCES

Full references for this chapter can be found on www.expertconsult.com.

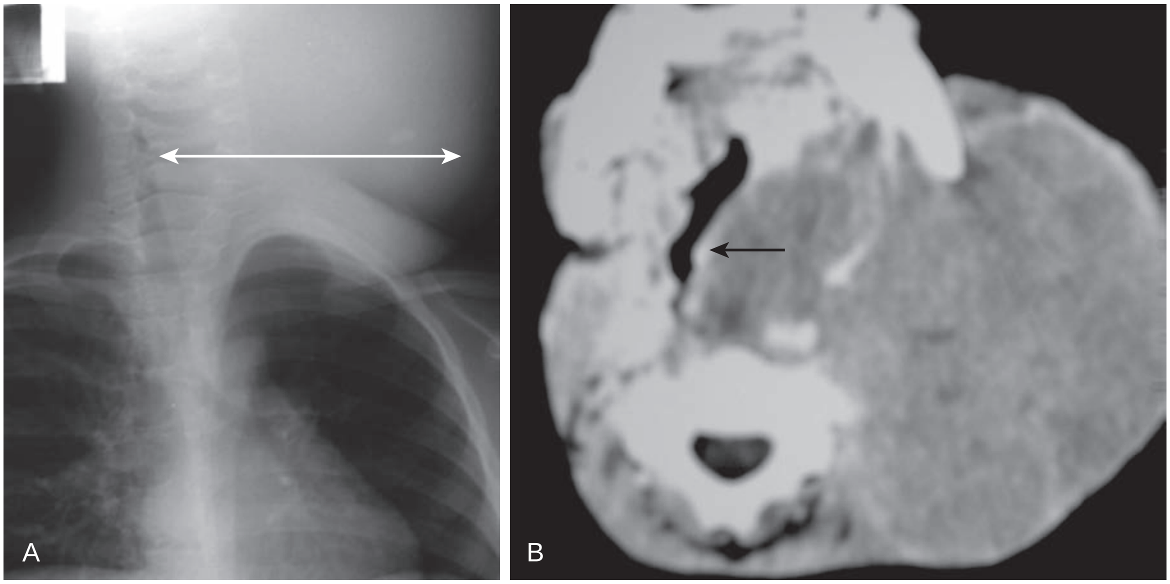

**e-Figure 51.16. Lymphoma in a 9-year-old boy with difficulty breathing.** (A) Frontal neck radiograph shows a large left-sided neck mass *(double arrow).* (B) Axial CT scan of the upper neck demonstrates the large mass effacing and displacing the airway to the right *(arrow).*

## REFERENCES

1. Marcus CL, Smith RJH, Mankarius LA, et al. Developmental aspects of the upper airway: report from an NHLBI workshop, March 5-6, 2009. *Proc Am Thorac Soc*. 2009;6(6):513–520. doi:10.1513/pats.200905-024CB.
2. Darras KE, Roston AT, Ywchuk LK. Imaging acute airway obstruction in infants and children. *Radiographics*. 2015;35:2064–2079.
3. Macpherson RI, Leithiser RE. Upper airway obstruction in children: an update. *Radiographics*. 1985;5(3):339–376.
4. Bradshaw K. Imaging the upper airways. *Paediatr Respir Rev*. 2001;2:46–56.
5. Wiett GJ, Long FR, Shiels WE II, et al. Advances in pediatric airway radiology. *Otolaryngol Clin North Am*. 2000;33(1):15–28.
6. John SD, Swischuk LE. Stridor and upper airway obstruction in infants and children. *Radiographics*. 1992;12:625–643.
7. Sittel C. Pathologies of the larynx and trachea in childhood. *GMS Curr Top Otorhinolaryngol Head Neck Surg*. 2014;13:Doc09. doi:10.3205/cto000112.
8. Tucker GF. Laryngeal development and congenital lesions. *Ann Otol Rhinol Laryngol Suppl*. 1980;74:142–145.
9. Laya BF, Lee EY. Congenital causes of upper airway obstruction in pediatric patients: updated techniques and review of imaging findings. *Semin Roentgenol*. 2012;47(2):147–158.
10. Sivan Y, Ben-Ari J, Soferman R, et al. Diagnosis of laryngomalacia by fiberoptic endoscopy: awake compared with anesthesia-aided technique. *Chest*. 2006;130(5):1412–1418.
11. Berg E, Naseri I, Sobol SE. The role of airway fluoroscopy in the evaluation of children with stridor. *Arch Otolaryngol Head Neck Surg*. 2008;134(4):415–418.
12. Ahmad SM, Soliman AMS. Congenital anomalies of the larynx. *Otolaryngol Clin North Am*. 2007;40:177–191.
13. Shackelford GD, Siegel MJ, McAlister WH. Subacute edema in acute epiglottitis in children. *AJR Am J Roentgenol*. 1978;131:603–605.
14. Shah RK, Roberson DW, Jones DT. Epiglottitis in the Haemophilus type B vaccine era: changing trends. *Laryngoscope*. 2004;114:557–560.
15. McEwan J, Giridharan W, Clarke RW, et al. Paediatric acute epiglottitis: not a disappearing entity. *Int J Pediatr Otorhinolaryngol*. 2003;67(4):317–321.
16. Chandler D, Coonnor M, Breen D. Hib epiglottitis despite fully vaccinated status. *Br J Gen Pract*. 2009;59(565):597–598. doi:10.7860/JCDR/2016/15243.7463. [Epub 2016 Mar 1].
17. Dort JC, Frohlich AM, Tate RB. Acute epiglottitis in adults: diagnosis and treatment in 43 patients. *J Otolaryngol*. 1994;23(4):281–285.
18. Goodman TR, McHugh K. The role of radiology in the evaluation of stridor. *Arch Dis Child*. 1999;81:456–459.
19. Hartnick CJ, Cotton RT. Syndromic and other congenital anomalies of the head and neck. *Otolaryngol Clin North Am*. 2000;33(6):232–238.
20. Sharma R, Dey AK, Alam S, et al. A series of congenital high airway obstruction syndrome - classic imaging findings. *J Clin Diagn Res*. 2016;10(3):TD7–TD9.
21. Onderoglu L, Karamursel BS, Bulun A, et al. Prenatal diagnosis of laryngeal atresia. *Prenat Diagn*. 2003;23(4):277–280.
22. Mong A, Johnson AM, Kramer SS, et al. Congenital high airway obstruction syndrome: MR/US findings, effect on management, and outcome. *Pediatr Radiol*. 2008;38(11):1171–1179.
23. Men S, Ikiz AO, Topcu I, et al. CT and virtual endoscopy findings in congenital laryngeal web. *Int J Pediatr Otorhinolaryngol*. 2006;70(6):202–207.
24. Unal M. The successful management of congenital laryngeal web with endoscopic lysis and topical mitomycin-C. *Int J Pediatr Otorhinolaryngol*. 2004;68(2):231–235.
25. Amir M, Youssef T. Congenital glottic web: management and anatomical observation. *Clin Respir J*. 2004;4:202–207.
26. Glazer HS, Mauro MA, Aronberg DJ, et al. Computed tomography of laryngoceles. *AJR Am J Roentgenol*. 1983;140:549–552.
27. Koeller KK, Alamo L, Adair CF, et al. Congenital cystic masses of the neck: radiologic- pathologic correlation. *Radiographics*. 1999;19(1):121–146.
28. Lindell MM, Jing BS, Fischer EP, et al. Laryngocele. *AJR Am J Roentgenol*. 1978;131:259–262.
29. Kumar G, Bradley PJ, Wastie ML. Case of the month. What a blow. *Br J Radiol*. 1998;71:799–800.
30. Zelenik K, Stanikova L, Smatanova K, et al. Treatment of laryngoceles: What is the progress over the last two decades? *Biomed Res Int*. 2014;819453. doi:10.1155/2014/819453. [Epub 2014 Mar 6].
31. Bauman NM, Smith RJH. Recurrent respiratory papillomatosis. *Pediatr Clin North Am*. 1996;43:1385–1401.
32. Wiatrak BJ, Wiatrak D, Bracken TR, et al. Recurrent respiratory papillomatosis: a longitudinal study comparing severity associated with human papilloma viral types 6 and 11 and other risk factors in a large pediatric population. *Laryngoscope*. 2004;114(suppl 104):1–23.
33. Bennett RS, Powell KR. Human papillomavirus; association between laryngeal papillomas and genital warts. *Pediatr Infect Dis J*. 1987;6:229–232.
34. Derkay CS, Wiatrak B. Recurrent respiratory papillomatosis: a review. *Laryngoscope*. 2008;118(7):1236–1247.
35. Boo WH, Rajan P, Ching SM, et al. Juvenile recurrent respiratory papillomatosis: a rare masquerade of asthma. *Malays Fam Physician*. 2015;10(2):45–48.
36. Zacharisen MC, Conley SF. Recurrent respiratory papillomatosis in children: masquerader of common respiratory diseases. *Pediatrics*. 2006;11(5):1925–1931.
37. Carifi M, Napolitano D, Morandi M, et al. Recurrent respiratory papillomatosis: current and future perspectives. *Ther Clin Risk Manag*. 2015;11:731–738.
38. Walner DL, Loewen MS, Kimura RE. Neonatal subglottic stenosis: incidence and trends. *Laryngoscope*. 2001;111(1):48–51.
39. Seam N, Finkkelstein SE, Gonzales DA, et al. The work up of stridor: virtual bronchoscopy as a complimentary technique in the diagnosis of subglottic stenosis. *Respir Care*. 2007;52(3):337–339.
40. Holinger PH, Kutnick SL, Schild JA, et al. Subglottic stenosis in infants and children. *Ann Otol Rhinol Laryngol*. 1976;85:591–599.
41. Leung AK, Kellner JD, Johnson DW. Viral croup: a current perspective. *J Pediatr Health Care*. 2004;18(6):297–301.
42. Johnson DW. Croup. *BMJ Clin Evid*. 2014;9:321.
43. Jones R, Santos J, Overall J. Bacterial tracheitis. *JAMA*. 1979;242:721–726.
44. Kasian GF, Bingham WT, Steinberg J, et al. Bacterial tracheitis in children. *CMAJ*. 1980;140:46–50.
45. Al-Mutairi B, Kirk V. Bacterial tracheitis in children; approach to diagnosis and treatment. *Paediatr Child Health*. 2004;9(1):25–30.
46. Han BK, Dunbar JS, Striker TW. Membranous laryngotracheobronchitis (membranous croup). *AJR Am J Roentgenol*. 1979;133:53–58.
47. Craig FW, Schunk JE. Retropharyngeal abscess in children: clinical presentation, utility of imaging, and current management. *Pediatrics*. 2003;111(6):1394–1398.
48. Alawad AAM, Khalifa AFM. Images in clinical tropical medicine: a rare cause of retropharyngeal abscess: cervical Pott's disease. *Am J Trop Med Hyg*. 2015;92(5):884.
49. Lalakea M, Messner AH. Retropharyngeal abscess management in children: current practices. *Otolaryngol Head Neck Surg*. 1999;121:398–405.
50. Kirse DJ, Roberson DW. Surgical management of retropharyngeal space infections in children. *Laryngoscope*. 2001;111:1413–1422.
51. Martin CA, Gabrillargues J, Louvrier C, et al. Contribution of CT scan and CT-guided aspiration in the management of retropharyngeal abscess in children based on a series of 18 cases. *Eur Ann Otorhinolaryngol Head Neck Dis*. 2014;131(5):277–282. doi:10.1016/j.anorl.2013.04.007.
52. Section on Pulmonology, Subcommittee on Obstructive Sleep Apnea Syndrome, Amercan Academy of Pediatrics. Clinical practice guideline: diagnosis and management of childhood obstructive sleep apnea syndrome. *Pediatrics*. 2002;109(4):704–712.
53. Fujioka M, Young LW, Girdany BR. Radiographic evaluation of adenoidal size in children: adenoidal-nasopharyngeal ratio. *AJR Am J Roentgnol*. 1979;133:401–404.
54. Villorente FF, Dizon ML, Laya BF, et al. Correlation of adenoidal-nasopharyngeal ratio and palatine tonsil size in lateral soft tissue neck radiograph with polysomnogram among children symptomatic for sleep apnea. *Philippine College Radiol J*. 2010;4(1):26–31.
55. Fernbach SK, Brouillette RT, Riggs TW, et al. Radiologic evaluation of adenoids and tonsils in children with obstructive sleep apnea: plain films and fluoroscopy. *Pediatr Radiol*. 1983;13(5):258–265.
56. Donnelly LF, Casper KA, Chen B. Correlation on cine MR imaging of size of adenoid and palatine tonsils with degree of upper airway motion in asymptomatic sedated children. *AJR Am J Roentgenol*. 2002;179(2):503–508.
57. Chan TC, Ufberg J, Harrigan RA, et al. Nasal foreign body removal. *J Emerg Med*. 2004;26:441–445.
58. Grassi R, Faggian A, Somma F, et al. Application of imaging guidelines in patients with foreign body ingestion or inhalation: literature review. *Semin Ultrasound CT MR*. 2015;36(1):48–56.

59. Silva AB, Muntz HR, Clary R. Utility of conventional radiography in the diagnosis and management of pediatric airway foreign bodies. *Ann Otol Rhinol Laryngol*. 1998;107(10 Pt 1):834–838.
60. Shires CB, Preston T, Thompson J. Pediatric laryngeal trauma: a case series at a tertiary children's hospital. *Int J Pediatr Otorhinolaryngol*. 2011;75(3):401–408.
61. Granholm T, Farmer DL. The surgical airway. *Respir Care Clin N Am*. 2001;7(1):13–23.
62. Francis S, Gaspard DJ, Rogers N, et al. Diagnosis and management of laryngotracheal trauma. *J Natl Med Assoc*. 2002;94(1):21–24.
63. Cicala RS, Kudsk Ka, Butts A, et al. Initial evaluation and management of upper airway injuries in trauma patients. *J Clin Anesth*. 1991;3(2):91–98.
64. Jalisi S, Zoccoli M. Management of laryngeal fractures: a 10 year experience. *J Voice*. 2011;25(4):473–479.
65. Koplewitz BZ, Springer C, Slasky BS. CT of hemangiomas of the upper airways in children. *AJR Am J Roentgenol*. 2005;184:663–670.
66. Li XY, Wang Y, Jin L, et al. Role of oral propranolol in the treatment of infantile subglottic hemangioma. *Int J Clin Pharmacol Ther*. 2016;54(9):675–681.
67. Siegel B, Mehta D. Open airway surgery for subglottic hemangioma in the era of propranolol: Is it still indicated? *Int J PediatrOtorhinolaryngol*. 2015;79(7):1124–1127.
68. Pastore G, Magnani C, Verdecchia A, et al. Survival of childhood lymphomas in Europe, 1978-1992: a report from EUROCARE study. *Eur J Cancer*. 2001;37:703–710.
69. Dagher R, Helman L. Rhabdomyosarcoma: an overview. *Oncologist*. 1999;4:34–44.
70. McHugh K, Boothroyd A. The role of radiology in childhood rhabdomyosarcoma. *Clin Radiol*. 1999;54:2–10.
71. Lloyd C, McHugh K. The role of radiology in head and neck tumors in children. *Cancer Imaging*. 2010;10:49–61.

# 52

# Lower Large Airway Disease

Edward Y. Lee

## OVERVIEW

Disorders of the lower large airways occur frequently in the pediatric population and have the potential to be life threatening.[1-3] Because these disorders are often associated with nonspecific clinical symptoms, the diagnosis frequently is missed or delayed, particularly in infants and young children. After careful investigation of the clinical history and physical examination, imaging evaluation is the next management step. Imaging plays an important role in the diagnosis of congenital and acquired lower large airway disorders. By becoming familiar with the characteristic imaging findings of lower large airway disorders, radiologists can play an important role in ensuring prompt diagnosis, guiding appropriate management, and providing follow-up evaluation of these often acute and complex conditions in pediatric patients.

This chapter reviews the etiology, imaging findings, and management of the frequently encountered congenital and acquired lower large airway disorders in the pediatric population. Large airway disorders due to primary benign neoplasms and extrinsic compression due to mediastinal vascular anomalies are not included in this chapter because they are discussed in other chapters (see Chapters 51 and 76, respectively) in this book.

## SPECTRUM OF LOWER LARGE AIRWAY DISEASE

### Congenital Anomalies

### Tracheobronchial Branching Anomalies

**Tracheal Agenesis**

***Etiology.*** Tracheal agenesis is characterized by either partial or complete tracheal underdevelopment.[4-7] Three main types of tracheal agenesis exist. Type 1 consists of absent upper trachea and connection of the lower trachea to the esophagus; type 2 consists of a common bronchus connecting bilateral main bronchi to the esophagus; and type 3 consists of independent bilateral main bronchi arising from the esophagus (Fig. 52.1A). Of these three types, type 2 is the most common. Affected pediatric patients typically present with severe respiratory distress and absence of an audible cry, and the airway cannot be intubated below the larynx immediately after birth.[4-7] The diagnosis of tracheal agenesis should be considered in any infant who demonstrates improved lung ventilation after placement of the endotracheal tube in the esophagus after an initial unsuccessful intubation attempt. Once tracheal agenesis is diagnosed, radiologists should carefully investigate for other congenital anomalies that frequently are associated with this condition, such as congenital heart disease, duodenal atresia, and radial ray anomalies.[4-7]

***Imaging.*** Chest radiographic imaging findings of tracheal agenesis often are nonspecific, such as unaerated lungs or decreased lung volume. However, the diagnosis of tracheal agenesis should be considered when absence of the normal tracheal air lucency, abnormal carinal position, and placement of the endotracheal tube in the esophagus are seen on chest radiographs immediately after birth (Fig. 52.1B and C). Computed tomography (CT) and/or bronchoesophagoscopy confirm the diagnosis,[4-8] which can show both the partial or complete tracheal underdevelopment and anomalous bronchi connected to the esophagus (Fig. 52.1D).

***Treatment and Follow-up.*** Because of difficulties related to both early diagnosis and treatment, tracheal agenesis usually is a fatal condition.[4-7] The initial management of tracheal agenesis is aimed at early diagnosis at birth and immediate maintenance of airway patency, usually via the esophagus in the presence of a bronchoesophageal fistula. Patients with short-segment tracheal agenesis may be amenable to direct tracheal anastomosis.[5,7]

**Tracheal Bronchus**

***Etiology.*** Tracheal bronchus is a congenital bronchial branching anomaly in which an ectopic (more frequently) or supernumerary bronchial branch arises from the lateral tracheal wall just above the carina.[9-15] This condition also is known as bronchus suis because it is a normal finding in pigs. The incidence of tracheal bronchus in the pediatric population is between 0.1% and 5%.[16] Tracheal bronchus most frequently occurs on the right side. Most pediatric patients with tracheal bronchus are asymptomatic, and it is usually an incidental finding detected on imaging studies obtained for the workup of other medical conditions. However, patients with tracheal bronchus also may present with symptoms of persistent or recurrent upper lobe pneumonia, atelectasis, or air trapping.[11] Additionally, tracheal bronchus may unexpectedly be discovered after intubation as a result of upper lobe atelectasis related to inadvertent occlusion of the ectopic upper lobe bronchial orifice by a low-lying endotracheal tube.[14]

***Imaging.*** On chest radiographs, secondary imaging findings of tracheal bronchus such as upper lobe atelectasis or pneumonia can be detected, but the anomalous upper lobe bronchus cannot be reliably visualized. In the past, tracheal bronchus was evaluated with tracheobronchography. However, CT with two-dimensional (2D) and three-dimensional (3D) reconstructions is the imaging technique of choice for evaluating anomalous tracheal bronchus and associated lung abnormalities[17-19] (Fig. 52.2). Bronchoscopy can confirm the diagnosis of tracheal bronchus when necessary.

***Treatment and Follow-up.*** Patients with incidentally detected tracheal bronchus generally do not require treatment. However, symptomatic children with recurrent upper lobe infection due to tracheal bronchus may require surgical resection, especially if permanent lung damage has developed or they are considered at risk for the development of permanent lung damage.[1]

**Esophageal Bronchus or Lung**

***Etiology.*** Esophageal bronchus or lung is a rare congenital anomaly.[11,20] The term *esophageal bronchus* refers to the condition in which a lobar bronchus, typically the medial basal segment of the right lower lobe, arises directly from the esophagus. The term *esophageal lung* is used when the main bronchus arises directly from the esophagus. It is associated with a wide spectrum of clinical presentations ranging from asymptomatic to recurrent severe pulmonary infections or even death depending on the size and location of the anomaly. In general, symptomatic pediatric patients with esophageal bronchus or lung typically present with feeding difficulties and recurrent respiratory tract infections. Other associated congenital anomalies include congenital heart disease, duodenal atresia, duodenal stenosis, distal tracheoesophageal fistula, and esophageal atresia.

***Imaging.*** Affected pediatric patients typically present as a result of aspiration during feeding, with radiographic findings of air

## Abstract:

Disorders affecting the lower large airways occur frequently in the pediatric population and have the potential to be life threatening. After initial investigation of the clinical history and physical examination, imaging evaluation is the next management step. Imaging plays an important role in the diagnosis of congenital and acquired lower large airway disorders in infants and children. By becoming familiar with the characteristic imaging findings of lower large airway disorders, radiologists can play an important role in ensuring prompt diagnosis, guiding appropriate management, and providing follow-up evaluation of these often acute and complex conditions in pediatric patients. This chapter reviews the etiology, imaging findings, and current management of the congenital and acquired lower large airway disorders in infants and children in daily clinical practice.

## Keywords:

Lower Large Airway Disorder
Congenital Large Airway Disorder
Acquired Large Airway Disorder
Infants
Children
Pediatric Patients

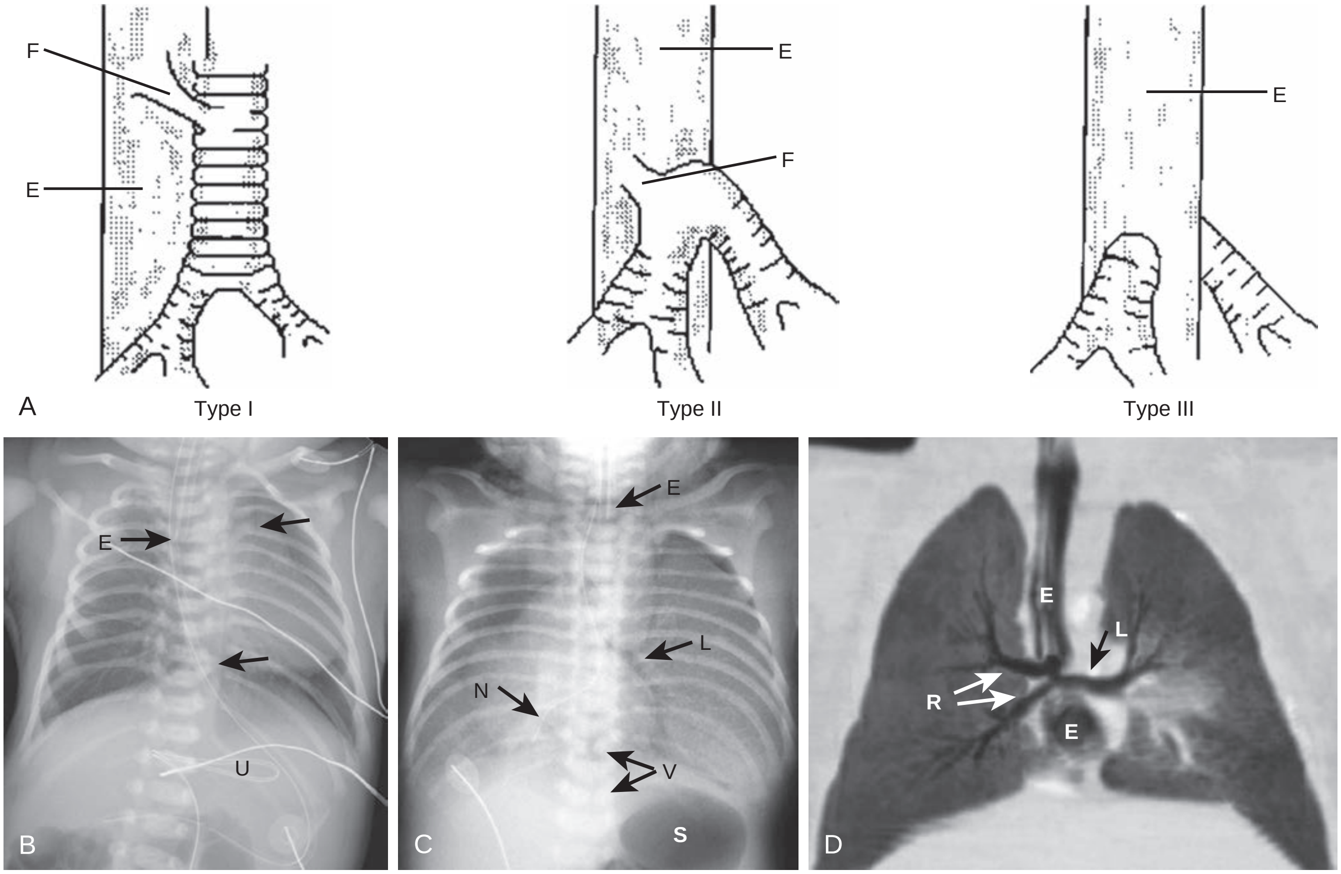

**Figure 52.1. Tracheal agenesis.** (A) Schematic of three types. In type I, part of the proximal trachea is absent with a short distal trachea communicating to the esophagus via a tracheoesophageal fistula. In type II, the most common type, the trachea is completely absent with a carina connecting the two main bronchi. A bronchoesophageal fistula is usually, but not always, present. In type III, the trachea and carina are absent with the bronchial orifices separately arising directly from the esophagus. (B) Newborn with type II tracheal agenesis. Chest radiograph shows lungs that are relatively normal in aeration, although haziness is present, which may represent retained fetal fluid. The endotracheal tube *(E)* is slightly low but otherwise is unremarkable. The nasogastric tube also is present and is in the stomach. Segmentation abnormalities of the spine and upper left ribs are noted *(arrows).* The umbilical venous catheter *(U)* is malpositioned. (C) Newborn with type III tracheal agenesis. Chest radiograph obtained during resuscitation shows poorly aerated lungs with pneumomediastinum and a left pneumothorax. The endotracheal tube *(E)* is at the thoracic inlet level. The nasogastric tube *(N)* is in the right bronchial tree, which appears to originate lower than normal. Note the low position of the left main bronchus *(L).* "Butterfly" vertebrae *(V)* are seen. (D) Newborn with type III trachea agenesis. Coronal maximum intensity projection reformatted CT image shows two right bronchi *(R)* and the left bronchus *(L)* arising near the midline from the esophagus *(E).* The trachea is absent with the possible exception of a small segment connecting the bronchi. A nasogastric tube is present in the esophagus *(E). E,* Esophagus; *F,* fistula; *S,* stomach. (A, *From Effmann EI, Spackman TJ, Berdon WE, et al. Tracheal agenesis.* AJR Am J Roentgenol. *1975;125:767.* B–D, *From Strouse PJ, Newman B, Hernandez RJ, et al. CT of tracheal agenesis.* Pediatr Radiol. *2006;36:920–926.)*

space opacification in the medial lower lobe in the case of esophageal bronchus and air space opacification that involves the entire lung in the case of esophageal lung.[1,11] An esophagram can provide a definitive diagnosis by allowing visualization of a direct communication between a bronchus and the esophagus (Fig. 52.3). CT may be helpful for evaluating associated lung parenchymal abnormalities and guiding surgery.

***Treatment and Follow-up.*** Surgical lobectomy or pneumonectomy is the current management of choice for symptomatic patients with esophageal bronchus or lung, respectively.[20]

## Congenital Tracheal Stenosis

***Etiology.*** Congenital tracheal stenosis is a rare condition characterized by intrinsic narrowing of the tracheal lumen, usually as a result of underlying complete cartilaginous rings.[2,3,21,22] Such cartilaginous rings with an absent or deficient posterior membranous portion render the tracheal lumen smaller and less pliable. Affected pediatric patients typically present in the first year of life with expiratory stridor, wheezing, and respiratory distress.[2,3,21,22] Congenital tracheal stenosis traditionally is classified into three types: (1) focal (50%), (2) generalized (30%), and (3) funnel shaped (20%).[23] Other congenital anomalies often associated with congenital tracheal stenosis are tracheoesophageal fistula, pulmonary agenesis or hypoplasia, pulmonary artery sling type 2, and bronchial stenosis.[2,3,11,24]

***Imaging.*** Although neck and chest radiographs or fluoroscopy may lead to the suspicion of congenital tracheal stenosis when a narrowed trachea is encountered in pediatric patients with respiratory symptoms, CT is the current imaging modality of choice for

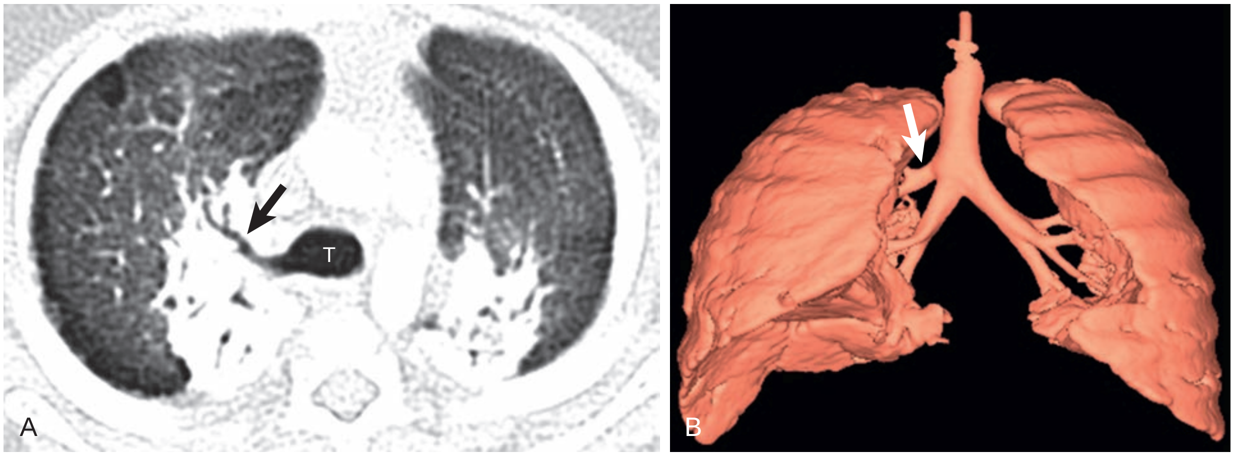

**Figure 52.2. Tracheal bronchus in an 8-month-old girl with recurrent right upper lobe atelectasis.** (A) Axial lung window CT image shows an anomalous right upper lobe bronchus *(arrow)* directly arising from the trachea *(T).* Atelectasis is present adjacent to the tracheal bronchus. (B) Frontal 3D volume-rendered CT image of the central airways and lungs shows an anomalous right upper lobe bronchus *(arrow)* directly arising from the trachea. The location, size, and course of this anomalous tracheal bronchus are better demonstrated than on an axial CT image.

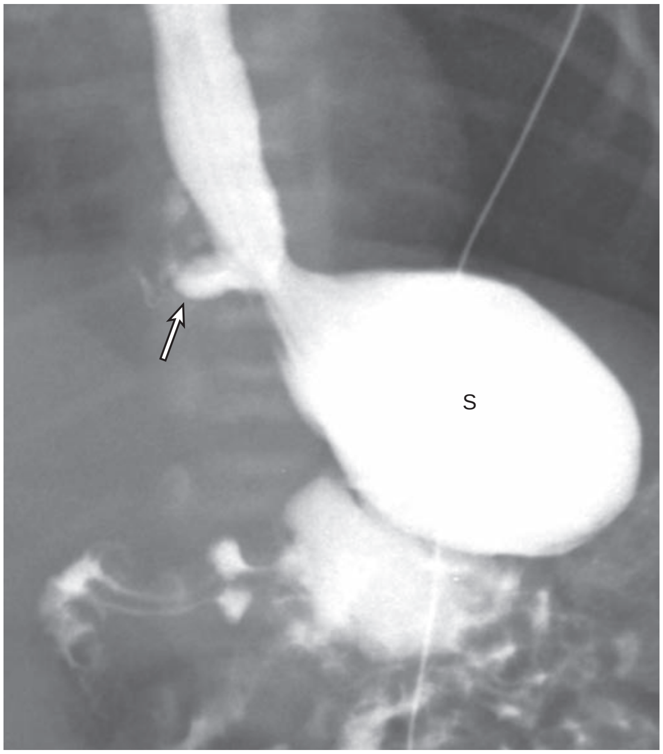

**Figure 52.3. Esophageal bronchus in a 4-day-old infant girl who presented with acute respiratory distress during feeding.** Esophagram shows a barium-filled medial right lower lobe bronchus *(arrow)* directly arising from the distal esophagus. *S,* Stomach.

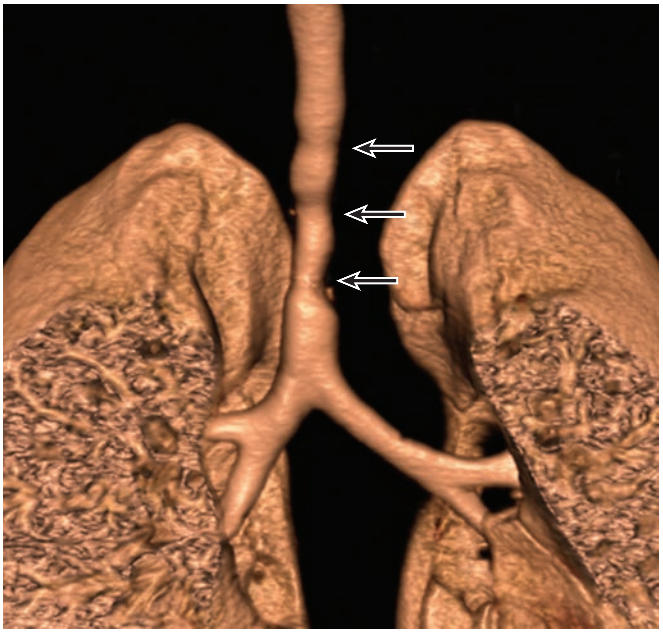

**Figure 52.4. Congenital tracheal stenosis in a 3-month-old boy with expiratory stridor and respiratory distress.** Frontal 3D volume-rendered CT image of the large airways and lungs shows several areas of mild to moderate mid to distal tracheal narrowing *(arrows).*

diagnosis and characterization.[2,4,24] With CT, the diagnosis of congenital tracheal stenosis is based on the identification of decreased caliber with a rounded configuration of the trachea without evidence of tracheal wall thickening. The size of the subglottic region (which does not contain tracheal cartilage) can serve as an internal reference standard. The use of 2D/3D reconstructed CT imaging is particularly helpful for increasing detection of subtle stenoses, improving measurement of craniocaudal extent of disease, and enhancing evaluation of its anatomic relationship with other mediastinal structures for preoperative assessment (Fig. 52.4).[2,4,24-26] This appearance contrasts with the normal appearance in which the C-shaped rings do not extend to the posterior membranous wall.[25] In addition, virtual bronchoscopy can evaluate the airways distal to high-grade tracheal stenoses, beyond which a conventional bronchoscope cannot pass.[2,4,24,25] CT also may aid in the detection of other associated anomalies that often have an abnormal lung component.

***Treatment and Follow-up.*** A short tracheal stenosis may be treated by end-to-end anastomosis, whereas a longer lesion is now typically repaired with sliding tracheoplasty.[22] Other available options for short-segment tracheal stenosis include stent placement or balloon dilation, although these methods are used more commonly to treat acquired tracheal stenosis.

### Tracheobronchomegaly

***Etiology.*** Tracheobronchomegaly, also known as Mounier–Kuhn syndrome, is a rare disorder characterized by dilation of the trachea and main bronchi.[27-29] Although the exact etiology of this condition currently is unknown, a defect in the elastic and muscular tissues of the large airways is presumed to be a potential underlying cause. The increased compliance of the large airway walls as a result of the atrophy of longitudinal elastic fibers with thinning of the muscularis mucosa often results in the development of broad, diverticulum-like protrusions of redundant musculomembranous tissue between the cartilaginous rings. It may occur either as a familial condition or in association with a connective tissue disorder such as Ehlers–Danlos syndrome.[30] It typically occurs in pediatric patients who have received prolonged ventilatory support or who have a chronic pulmonary infection such as cystic fibrosis. Although the clinical manifestations of tracheobronchomegaly are nonspecific, affected patients may present with a harsh cough, copious purulent sputum, occasional hemoptysis, and progressive dyspnea.

***Imaging.*** Chest radiographs alone may be adequate to detect the enlargement of trachea and bronchi in severe cases, but CT is the imaging modality of choice for diagnosing tracheobronchomegaly, potential tracheal diverticulum, and associated lung abnormalities (Fig. 52.5).[1] Because of the increased incidence of tracheobronchomalacia (TBM) in patients with tracheobronchomegaly, a dynamic CT study consisting of both inspiratory and expiratory phase imaging may be beneficial for detecting concomitant TBM.

***Treatment and Follow-up.*** Asymptomatic pediatric patients with tracheobronchomegaly require no specific treatment. For symptomatic patients, treatment usually is conservative, including chest physiotherapy for assistance with clearing of secretions and antibiotics for treatment of pulmonary infections.[31,32]

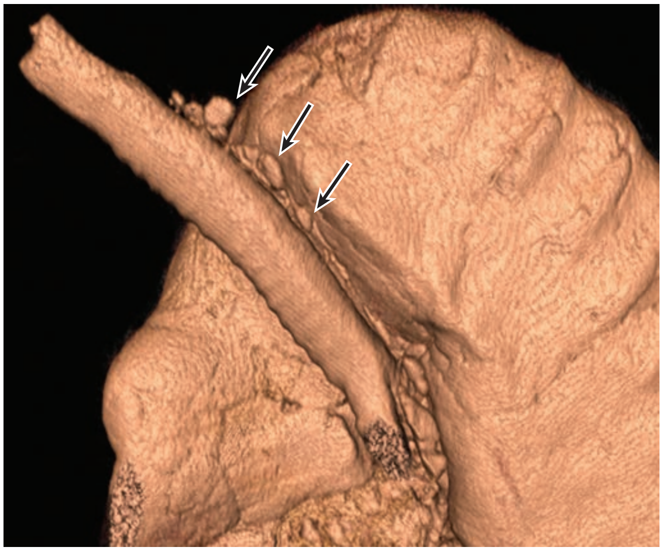

**Figure 52.5. Tracheomegaly with tracheal diverticuli in an adolescent girl with cystic fibrosis.** 3D volume-rendered CT lateral view of the large airway shows multiple diverticuli *(arrows)* arising from the posterior aspect of the enlarged trachea.

## Acquired Abnormalities

### Foreign Body Aspiration

***Etiology.*** Foreign body aspiration into the tracheobronchial airway is a frequent cause of acute respiratory distress in pediatric patients, especially those between 6 months and 3 years of age.[1-3,33,34] Although some pediatric patients may present with a clinical history of possible aspiration followed by cough, wheezing, respiratory distress, or decreased breath sounds, most affected pediatric patients present with a history that is either lacking or misleading.[1-3,33,34] Therefore a high clinical suspicion and thorough investigation are required for any infants and young children with respiratory symptoms suspicious for possible foreign body aspiration.

Only approximately 10% of aspirated foreign bodies within the tracheobronchial airway are radiopaque.[35] The remaining 90% of nonradiopaque foreign bodies are particularly difficult to diagnose early in pediatric patients. Nearly 70% of aspirated foreign bodies lodge in the bronchi, with the right side (52%) affected more frequently than the left side (18%).[33] The remaining 30% of aspirated foreign bodies lodge in the trachea (13%) and less common locations (17%).[33] In the early phase of foreign body aspiration, affected patients typically present with cough, wheezing, respiratory distress, or decreased breath sounds. During the late phase of missed foreign body aspiration, affected patients often present with episodic wheezing and/or recurrent pneumonias.

***Imaging.*** Radiographic findings of foreign body aspiration depend on the size, location, duration, and nature of the aspirated foreign body (e-Fig. 52.6). Radiopaque foreign bodies usually are detected easily with radiographic studies, which should include frontal and lateral films encompassing the upper airway from the nasopharynx to the upper abdomen. When the foreign body is not radiopaque, careful inspection of the tracheobronchial airway with high-kilovoltage films or fluoroscopy may show a faintly visible opacity interrupting the air column within the large airways. If the foreign object is located in the trachea, the chest radiograph may be normal or may show bilateral hypoinflation or hyperinflation depending on the degree of obstruction. Many intratracheal foreign bodies escape detection without the use of CT.

Rather than lodging in the trachea, most foreign bodies lodge in the main bronchi. In approximately 20% of cases, the foreign body migrates into a segmental bronchial branch.[33] The chest radiograph may show a variety of findings, the most common of which is a unilateral hyperlucent lung. If the bronchial obstruction becomes more complete, postobstructive atelectasis, pneumonia, or bronchiectasis may develop. A chest radiograph obtained at full inspiration can appear normal in approximately 20% to 30% of patients with bronchial foreign bodies; close inspection may show relatively increased volume on the normal side with a slight mediastinal shift toward the partially obstructed side. If a foreign body is suspected clinically, an expiratory chest radiograph is useful to demonstrate ipsilateral air trapping. Lateral decubitus films may be diagnostic if satisfactory inspiration-expiration chest radiographs cannot be obtained. When air trapping is present in a dependent lung on the decubitus view, the affected lobe or segment remains hyperlucent rather than deflating, as would normally occur (Fig. 52.7). Fluoroscopic examination of the chest also is valuable for detecting air trapping. It can show inspiratory mediastinal shift toward the affected side and restricted diaphragmatic excursion on the affected side.

The sensitivity and specificity of chest radiographs for foreign body detection were only 74% and 45%, respectively, in a series of 93 patients examined by Silva et al.[36] and 68% and 67%, respectively, in a series of 83 patients examined by Svedstrom et al.[38] Because of this relatively poor accuracy, Silva and colleagues have suggested that chest radiographs should not be relied on for diagnosis, but rather that all patients with suspected foreign body aspiration should undergo bronchoscopy.[36] This approach results

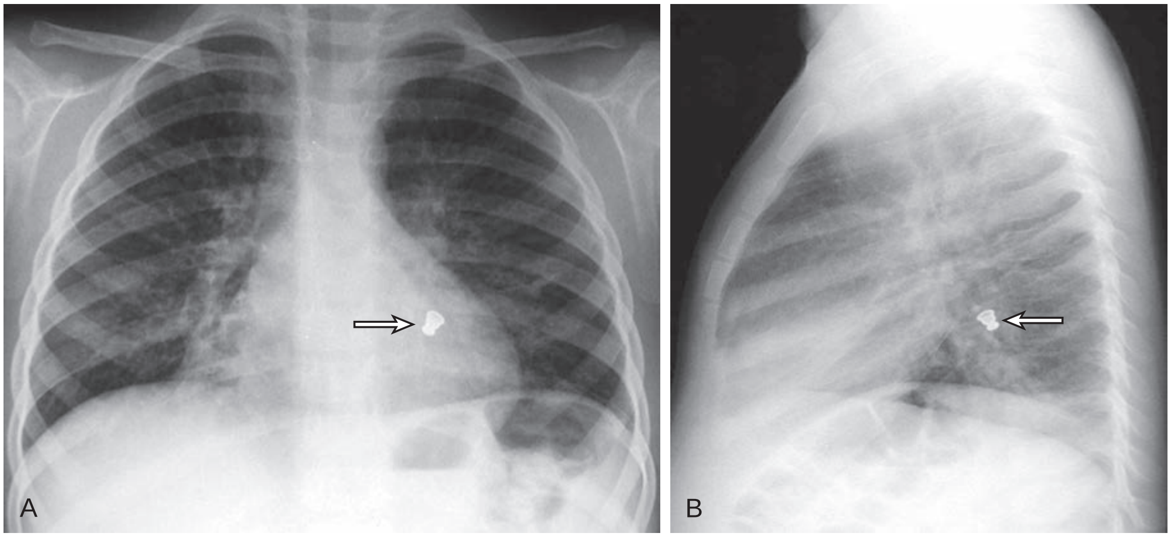

**e-Figure 52.6. Radiopaque foreign body aspiration in a 4-year-old boy who presented with acute onset of coughing and respiratory distress.** (A) Frontal chest radiograph shows a radiopaque foreign body *(arrow)* located in the left lower lobe, retrocardiac region. (B) Lateral chest radiograph confirms the location of the foreign body *(arrow)* in a left lower lobe bronchus. Bronchoscopy showed a metallic bottle cap lodged in the left lower lobe bronchus. *(From Lee EY, Restrepo R, Dillman JR, et al. Imaging evaluation of pediatric trachea and bronchi: systematic review and updates.* Semin Roentgenol. *2012;47(2):183.)*

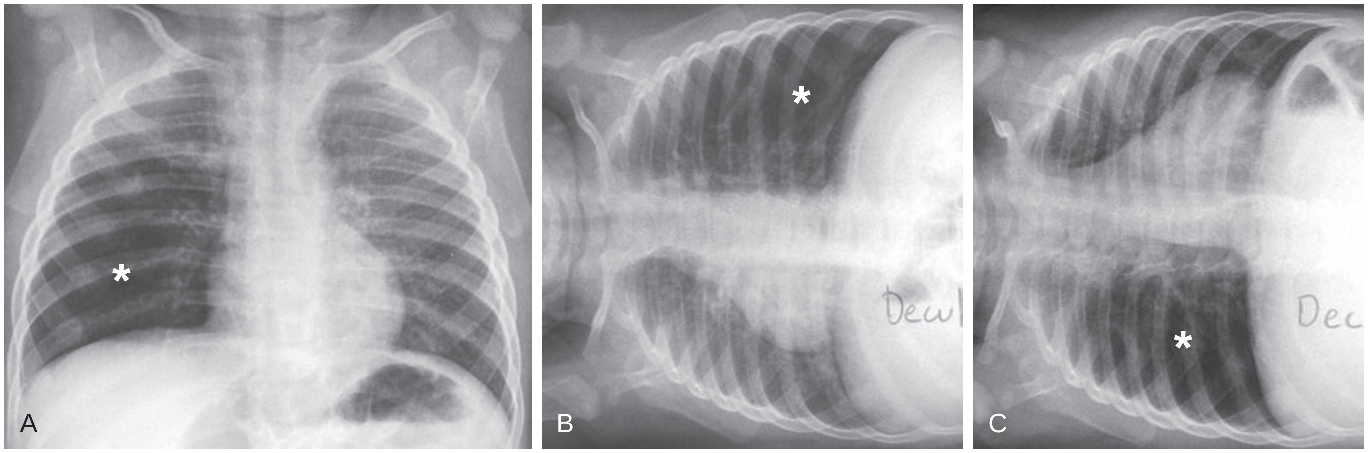

**Figure 52.7. Nonradiopaque foreign body aspiration in a 5-year-old girl who presented with persistent coughing and respiratory distress while eating popcorn.** (A) Frontal chest radiograph obtained at end-inspiration shows mild hyperinflation *(asterisk)* of the right lower lobe. (B) Frontal chest radiograph obtained at end-inspiration in the left lateral decubitus position demonstrates normal volume loss in the left lung and mild hyperinflation *(asterisk)* of the right lower lobe. (C) Frontal chest radiograph obtained at end-inspiration in the right lateral decubitus position shows persistent hyperinflation *(asterisk)* of the right lower lobe.

in a false-negative bronchoscopy rate of at least 20% in most series, however.[36]

CT is the most sensitive diagnostic imaging technique, but in general it should be reserved for patients for whom chest radiography is either normal or nonspecific. With use of CT, the diagnosis of a foreign body can be established with nearly 100% accuracy.[2,38] Either the foreign body is visualized or a focal pulmonary abnormality such as postobstructive air trapping, atelectasis, or consolidation is seen. If none of these findings is present, it is extremely unlikely that a foreign body is present. However, CT is less likely to visualize the foreign body directly if the lung is consolidated unless the foreign body is calcified or opaque.

Preliminary studies of low-dose multidetector computed tomography (MDCT) virtual bronchoscopy suggest that it may be able to (1) identify the precise location of a foreign body before bronchoscopy and (2) exclude a foreign body in children with a low level of suspicion and normal or nonspecific findings on chest radiography.[26,37-41] Because CT is less expensive and less invasive than bronchoscopy, it may be a viable alternative for selected patients.

***Treatment and Follow-up.*** Once an aspirated foreign body is diagnosed on imaging studies, bronchoscopy and removal of the aspirated foreign body should be performed. Although imaging findings may be nonspecific or normal, symptomatic pediatric patients with high clinical suspicion and a convincing history of possible foreign body aspiration require bronchoscopy for a complete assessment.

## Infection/Inflammation

### Tuberculosis

***Etiology.*** Tuberculosis (TB) is caused by *Mycobacterium tuberculosis*. Although advances in diagnosis and treatment have been made in the past 2 decades, TB continues to be a major cause of morbidity and mortality, particularly in infants, elderly persons, and immunocompromised patients.[42,43] In developed countries, TB most commonly is transmitted to infants and children by an adult family member infected with active TB. Although most pediatric patients with primary TB are asymptomatic, some may present with nonspecific symptoms such as a mild cough, a low-grade fever, weight loss, fatigue, and malaise. Respiratory distress may be the primary symptom in pediatric patients with large airway involvement from TB infection. The diagnosis usually can be made by skin testing, whereas sputum and gastric aspirates are confirmatory in anergic patients.

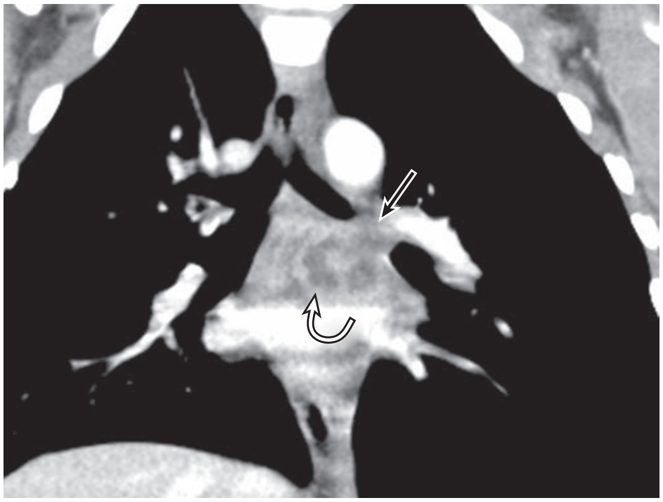

**Figure 52.8. Left main bronchial obstruction due to subcarinal lymphadenopathy from tuberculosis infection in a 4-year-old girl.** Coronal contrast-enhanced CT image shows left main stem bronchial obstruction *(straight arrow)* as a result of the necrotic subcarinal lymphadenopathy *(curved arrow).*

***Imaging.*** Large airway involvement of TB infection mainly results from either extrinsic compression of airways by enlarged mediastinal and/or hilar infectious lymph nodes, or direct infection of the airway wall through peribronchial lymphatic pathways.[1-3,42-45] Although chest radiographs may show mediastinal and/or hilar lymphadenopathy with resultant large airway narrowing, the location, degree, and extent can be better evaluated with CT with 2D/3D reconstructions (Fig. 52.8).[1-3] Direct tracheobronchial infection from TB eventually may result in irreversible large airway stricture/stenosis, again best assessed with CT.[1-3,42-45] Additionally, CT also can show lung abnormalities associated with TB infection such as “tree-in-bud” nodular opacities and airspace consolidation.

***Treatment and Follow-up.*** Pediatric TB patients currently are treated for 6 months with a combination of antibiotics. Large airway narrowing due to extrinsic compression from the enlarged mediastinal lymph nodes often resolves after medical treatment, whereas irreversible stricture/stenosis from direct tracheobronchial TB infection may require surgical management, including primary end-to-end anastomosis after stricture resection.

### Histoplasmosis

***Etiology.*** Histoplasmosis is caused by the dimorphic fungus *Histoplasma capsulatum*. Although *H. capsulatum* is found throughout the world, it is endemic in certain areas, including states bordering the Ohio River valley, the lower Mississippi River, and caves in southern and East Africa. Although acute histoplasmosis is attributed to airborne primary infection, chronic progressive histoplasmosis is the consequence of reactivation of a prior infection. Large airway involvement from histoplasmosis often results from fibrosing mediastinitis.[46-48] Affected pediatric patients may present with respiratory or esophageal symptoms related to complete or partial obstruction of large airways and the esophagus.[47,48] The definitive diagnosis of histoplasmosis is made by finding the fungus in samples taken from sputum, blood, or infected organs, and by identifying antigens in blood or urine samples.

***Imaging.*** On chest radiographs, typical imaging findings include multiple, ill-defined pulmonary nodules (1–3 cm in diameter) and hilar and/or mediastinal lymphadenopathy, both of which often are calcified.[44] CT currently is the imaging modality of choice for evaluating large airway compromise, particularly related to underlying fibrosing mediastinitis.[1-3] These patients typically show heterogeneous and often calcified mediastinal soft tissue densities resulting in complete or partial obstruction of mediastinal structures such as the tracheobronchial airway, superior vena cava, and esophagus (Fig. 52.9).[1-3,47,48] CT also can demonstrate abnormal lung findings from histoplasmosis infection.

***Treatment and Follow-up.*** In severe cases, antifungal medications are used to treat acute, chronic, and disseminated histoplasmosis infection. Unfortunately, no pharmacologic treatment has been shown to affect the outcome of histoplasmosis-related fibrosing mediastinitis. Large airway occlusion due to fibrosing mediastinitis is particularly difficult to treat because surgery often is ineffective and placement of metallic airway stents is avoided because of recurrent obstruction from ingrowth of granulation tissue.

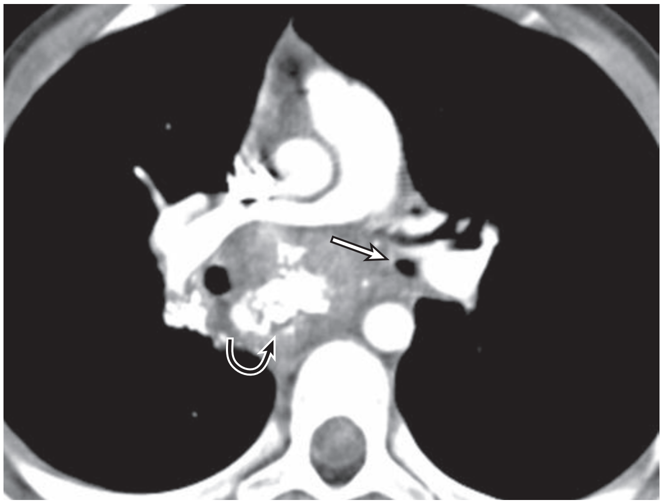

**Figure 52.9. Fibrosing mediastinitis caused by histoplasmosis in a 9-year-old girl who presented with 1 month of cough and dyspnea.** Axial contrast-enhanced CT image shows narrowing of the left main stem bronchus *(straight arrow)* from a heterogeneously enhancing and partially calcified subcarinal soft tissue mass *(curved arrow)*. *(From Lee EY, Greenberg SB, Boiselle PM. Multidetector computed tomography of pediatric large airway diseases: state-of-the-art.* Radiol Clin North Am. *2011;49[5]:886.)*

## Neoplasm

Tracheobronchial tumors are rare in children. Two of the most common primary benign large airway neoplasms, subglottic hemangioma and recurrent respiratory papillomatosis, were discussed in Chapter 51. The most common malignant lower large airway primary neoplasm, carcinoid tumor, is discussed in the next section.

### Carcinoid Tumor

***Etiology.*** A carcinoid tumor is a neuroendocrine neoplasm that encompasses a spectrum of histology ranging from slow-growing, locally infiltrative lesions to a metastasizing neoplasm.[49-54] Carcinoid tumors traditionally have been classified into two types based on typical or atypical histologic findings. Affected patients often present with a cough, wheezing, and recurrent pneumonia as a result of airway obstruction. Because of the underlying hypervascularity of carcinoid tumors, hemoptysis may be the presenting symptom. The carcinoid syndrome rarely occurs in pediatric patients with a large airway carcinoid tumor. The diagnosis is confirmed by bronchoscopy and biopsy.

***Imaging.*** Imaging findings of a carcinoid tumor within the large airway depend on the size and location of the tumor.[49-54] Most tracheobronchial carcinoid tumors are intrabronchial (Fig. 52.10). Centrally located carcinoid tumors may mimic foreign bodies and may cause postobstructive air trapping, atelectasis, recurrent infection, abscess, or bronchiectasis.[53] Peripherally located carcinoid tumors usually are not associated with bronchial obstruction and have the appearance of a pulmonary nodule.[53] Chest radiographs may be normal in 10% of cases or may show either a well-defined hilar or perihilar opacity representing an underlying tumor, or secondary signs such as focal air trapping or consolidation.[49-54] CT characteristically shows an enhancing spherical or ovoid mass with a well-defined lobulated contour.[53,54] Although calcification may not be clearly visible on chest radiographs, either punctate or diffuse calcifications may be detected in up to 30% of cases on CT.[54]

***Treatment and Follow-up.*** The current treatment of choice for large airway carcinoid tumors is complete surgical resection with primary reanastomosis or sleeve resection.

## Trauma

### Acquired Tracheobronchial Stenosis

***Etiology.*** Acquired tracheobronchial stenosis in children usually is caused by previous instrumentation such as endotracheal intubation or use of a tracheostomy tube.[1-3] Granulation tissue and fibrosis can develop at the stoma, at the tip of the tube, or at the site of the cuff. Scott and Kramer[55] reported tracheostomy-related complications in 26% of intubated children. The duration of intubation is a major factor in determining the incidence and severity of complications. Microscopic lesions occur after approximately 48 hours of intubation. Epithelial metaplasia is seen in children intubated for longer than 7 days, although occasionally granuloma may develop after very brief periods of intubation. Bronchial stenosis, like tracheal stenosis, usually is acquired and occurs at the site of surgical anastomosis in pediatric patients after lung transplantation.[1-3]

***Imaging.*** The diagnosis of tracheobronchial stenosis may be suspected on chest radiographs when large airway narrowing is observed. However, CT, which can measure cross-sectional areas of the large airways accurately, is the current choice for evaluating tracheobronchial stenosis, especially preoperatively.[1-3] Such stenosis may be weblike or fusiform, or it may have an irregular shape (e-Fig. 52.11).[1-3,56] Newer techniques such as paired inspiratory and expiratory CT or real-time dynamic four-dimensional CT can help differentiate a fixed tracheobronchial stenosis from TBM.[56-61]

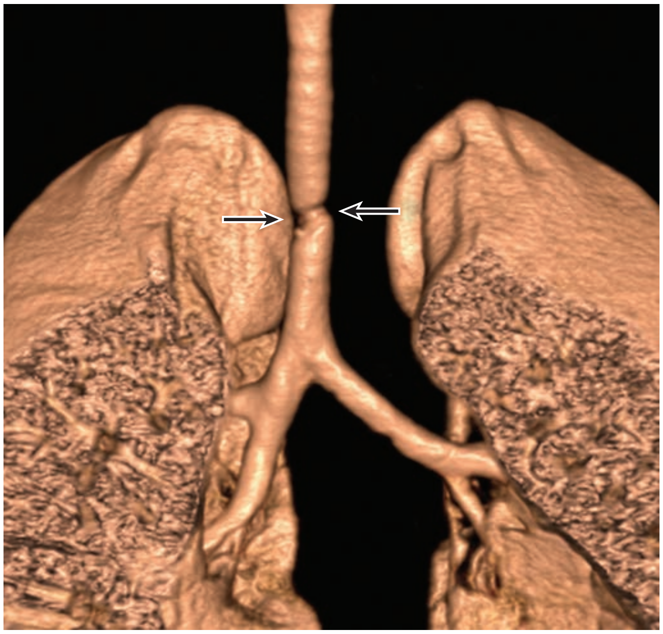

**e-Figure 52.11. Acquired tracheobronchial stenosis in a 4-year-old girl with progressively worsening stridor after long-term endotracheal tube placement.** Frontal 3D volume-rendered CT image of the central airways and lungs shows a focal irregular narrowing *(arrows)* at the level of the previous endotracheal tube placement.

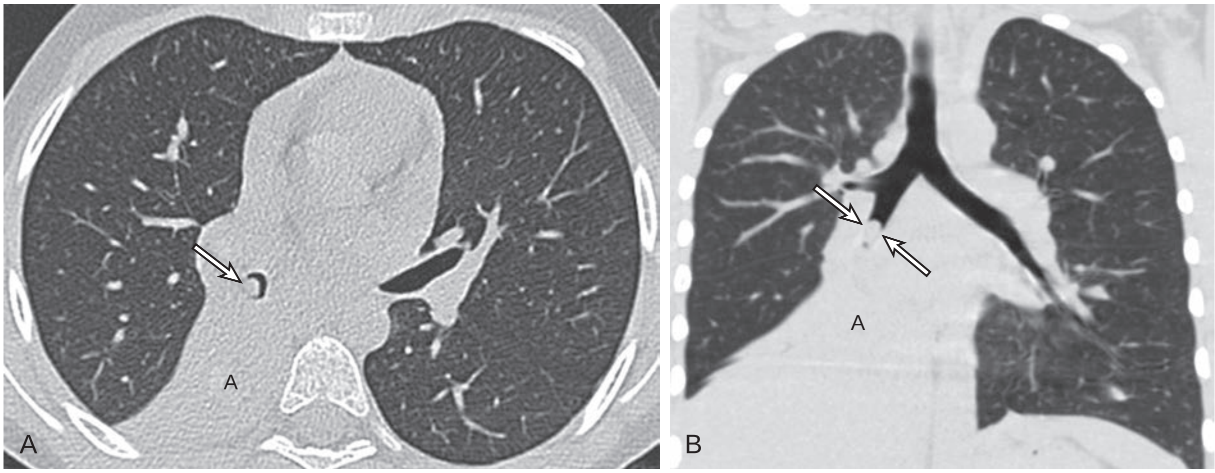

**Figure 52.10. Endobronchial carcinoid tumor in a 17-year-old girl who presented with a cough and recurrent right lower lobe pneumonia for the past 18 months.** Surgical pathology confirmed the diagnosis of an endobronchial carcinoid tumor. (A) Axial bone window CT image shows an endobronchial mass *(arrow)* located within the right bronchus intermedius with postobstructive atelectasis *(A).* (B) Coronal lung window CT image demonstrates an endobronchial mass *(arrows)* in the right bronchus intermedius with postobstructive atelectasis *(A).* The overall shape, size, and location of the mass are better visualized on this coronal image than on the axial image.

***Treatment and Follow-up.*** A short tracheobronchial stenosis may be treated by balloon dilation, stent placement, or end-to-end anastomosis after surgical resection of the stenotic segment. A longer stenosis may require a patch or autograft repair.[60]

### Tracheobronchial Injury

***Etiology.*** Tracheobronchial injury is a potentially life-threatening condition that may be caused by either penetrating or blunt chest trauma.[62-67] Although tracheobronchial injury is relatively rare with a reported incidence between 0.7% and 2.9%, it is associated with a substantial mortality rate of 30%.[62-73] Tracheobronchial injury typically occurs within 2.5 cm of the carina.[62-71] In the setting of trauma, abnormal endotracheal tube position, rib fractures (particularly involving the anterior ends of the first three ribs), and persistent pneumothoraces and/or pneumomediastinum despite the presence of a well-functioning chest tube and/or mediastinal tube should raise the possibility of underlying tracheobronchial injury.[72,73]

***Imaging.*** Radiographic imaging findings of a traumatic tracheobronchial injury depend on the location and degree of injury. In the setting of mild injury, a small amount of pneumothorax and/or pneumomediastinum may be the only findings. Such nonspecific and subtle radiographic findings often delay the accurate diagnosis of tracheobronchial injury, particularly in pediatric patients.[62,63,68] Extensive pneumothorax and/or pneumomediastinum, often extending into subcutaneous tissues of the neck and chest wall, typically are seen with severe injuries such as a displaced laceration or transection.[62-73] MDCT with thin-section axial and 2D/3D reconstruction can provide accurate diagnosis and preoperative guidance (Fig. 52.12).[1,70,72,73]

***Treatment and Follow-up.*** Individualized surgical repairs depend on the location and severity of injury and are performed via primary anastomosis or reimplantation.

## Dynamic Tracheobronchial Disorder

### Tracheobronchomalacia

***Etiology.*** TBM is attributed to an abnormal weakness of the underlying airway walls and/or supporting cartilage.[59,60,74] Despite increasing recognition of this condition in recent years, diagnosing TBM continues to be challenging mainly because clinical symptoms of affected pediatric patients are nonspecific and overlap with those of other chronic respiratory disorders.[59,60,74] TBM can be divided into two types: primary and secondary.[60,74] Primary TBM often is seen in premature infants or children with a variety of syndromes and in persons with systemic disease affecting cartilage, such as Larsen syndrome and relapsing polychondritis.[60,74] Secondary TBM is seen in infants or children with tracheoesophageal fistula, extrinsic pressure by vessels, and mediastinal masses.[60,74] It also may arise as a result of tracheal injury, most commonly intubation. Affected patients typically present with expiratory stridor and a cough that often is described as barking or brassy. Undiagnosed TBM may result in chronic tracheobronchial and lung infections.

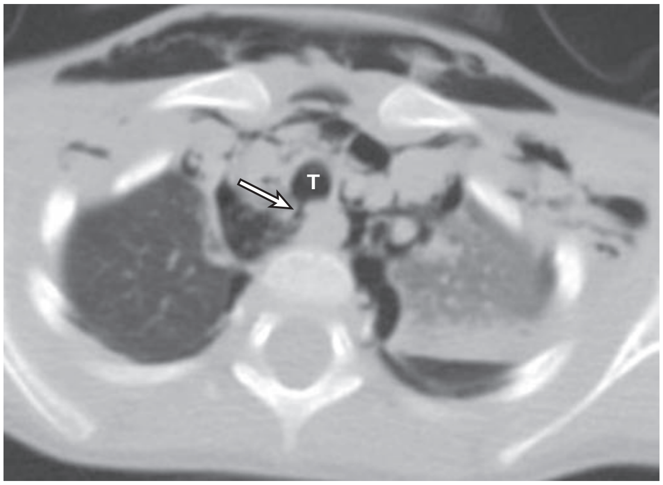

**Figure 52.12. Traumatic tracheal injury in a 3-year-old boy as a result of a motor vehicle accident.** Axial CT image shows a focal disruption *(arrow)* of the posterior wall of the trachea at the 7 o'clock position, with an adjacent collection of air within the mediastinum, indicating tracheal rupture. Extensive pneumomediastinum and subcutaneous emphysema also are seen. *T,* Trachea.

***Imaging.*** Chest radiographs and airway fluoroscopy have been used to evaluate TBM in pediatric patients in the past.[1] Fluoroscopy may show an exaggerated decrease (>50%) in the caliber of the trachea during expiration in patients with tracheomalacia[1,2] (Fig. 52.13); however, evaluation of the bronchi is markedly limited with this technique. MDCT is the imaging modality of choice for a complete assessment of TBM and underlying causes in pediatric populations.[57-61] MDCT provides noninvasive evaluation of TBM with diagnostic accuracy similar to bronchoscopy, and 2D and 3D evaluation with MDCT in particular has become an important preoperative assessment by offering information regarding the precise location, accurate degree and extent, and underlying predisposing conditions of TBM.[59,60,74] For the diagnosis of TBM with MDCT in children, tracheobronchial collapse greater than 50% currently is used (Fig. 52.14).[59,60] The very large detector array CT scanners currently available allow real-time evaluation of large airway collapsibility even in nonsedated infants and young children.[1,2] Magnetic resonance imaging is also becoming a viable technique for the dynamic evaluation of the airway.[75]

***Treatment and Follow-up.*** Conservative therapies such as treatment of underlying respiratory infections, humidified oxygen therapy, and pulmonary physiotherapy are the mainstay of management in pediatric patients with a mild to moderate degree of TBM.[74,76,77] However, pediatric patients with severe and progressively worsening TBM may require more aggressive treatment, including tracheostomy placement, stent placement, and surgical intervention such as a tracheoplasty.[78-89]

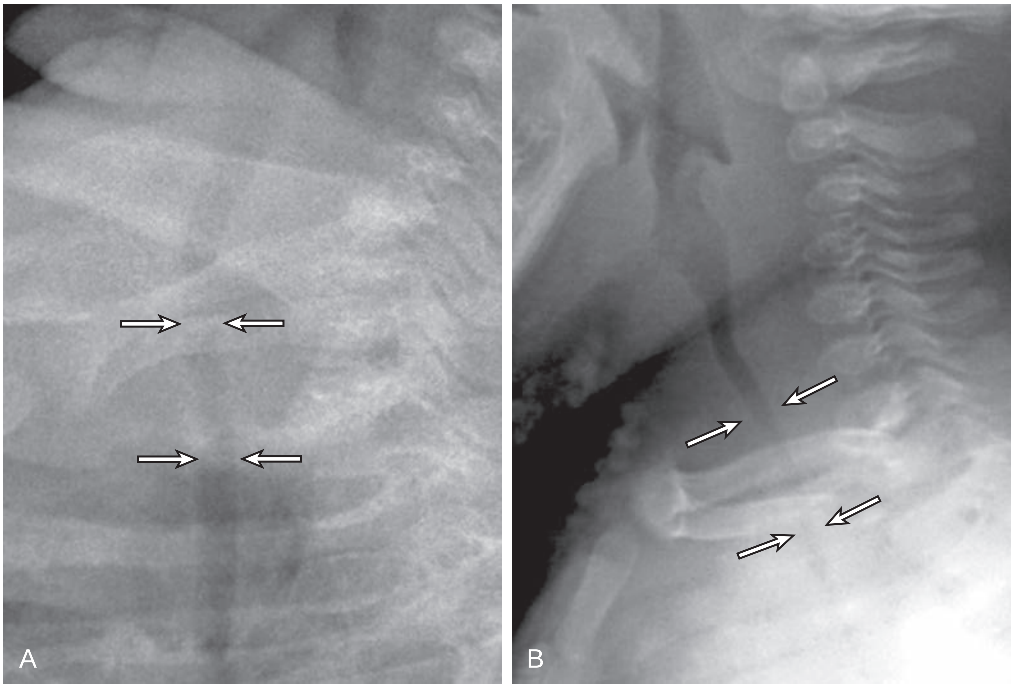

**Figure 52.13. Tracheomalacia in a 2-year-old girl who presented with a chronic cough and recurrent pulmonary infections.** (A) Lateral radiograph obtained at end-inspiration during airway fluoroscopy study shows a patent trachea *(arrows).* (B) Lateral radiograph obtained at end-expiration during airway fluoroscopy study demonstrates marked (>75%) collapse of the trachea *(arrows),* consistent with tracheomalacia.

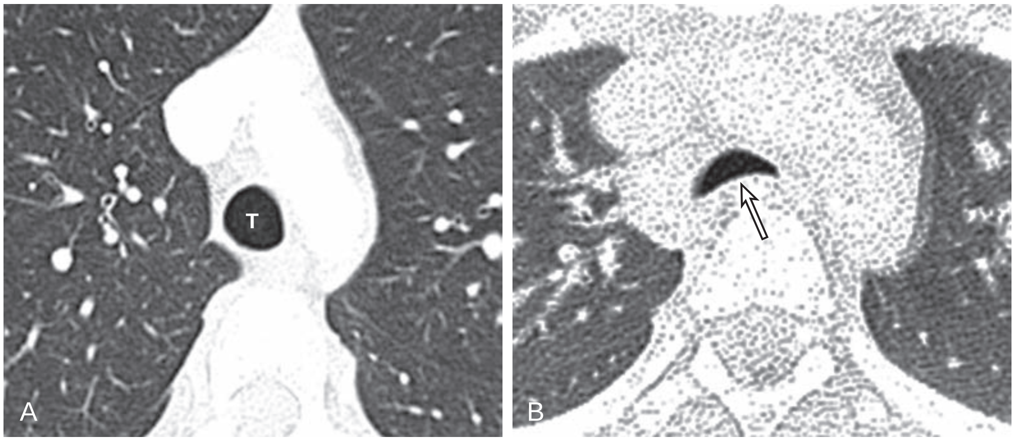

**Figure 52.14. Tracheomalacia in a 15-year-old girl who presented with a chronic cough and recurrent pulmonary infections.** (A) Axial CT image obtained at end-inspiration shows a normal patent trachea *(T).* (B) Axial CT image obtained at end-expiration demonstrates a greater than 50% collapse of the trachea *(arrow),* which is consistent with tracheomalacia. Increased attenuation of the lungs is a result of decreased lung volume related to end-expiration. Bronchoscopy showed marked tracheomalacia.

## KEY POINTS

- Congenital and acquired lower large airway disorders are common and may be life threatening in the pediatric population.
- The diagnosis of lower large airway disorders is frequently missed or delayed, particularly in infants and young children, mainly because of nonspecific clinical symptoms.
- After careful investigation of the clinical history and physical examination, imaging evaluation is the next management step and plays an important role in the diagnosis of a variety of congenital and acquired lower large airway disorders.
- Although conventional radiographs may be sufficient for making an accurate diagnosis of several lower large airway disorders, such as radiopaque foreign body aspiration, CT is often necessary for a complete assessment, particularly for surgical lesions.
- Bronchoscopy is still the reference standard in evaluating lower large airway diseases, but CT with 2D/3D/4D reconstructed images may provide sufficient information to avoid this invasive procedure in many patients. In selected cases, CT may provide information to help guide diagnostic and therapeutic bronchoscopic procedures.

## SUGGESTED READINGS

Carden KA, Boisell PM, Waltz DA, et al. Tracheomalacia and tracheobronchomalacia in children and adults: an in-depth review. *Chest*. 2005;127:987–1005.

Hegde SV, Hui PK, Lee EY. Tracheobronchial foreign bodies in children: imaging assessment. *Semin Ultrasound CT MR*. 2015;36(1):8–20.

Hewitt RJ, Butler CR, Maughan EF, et al. Congenital tracheobronchial stenosis. *Semin Pediatr Surg*. 2016;25(3):144–149.

Lee EY, Restrepo R, Dillman JR, et al. Imaging evaluation of pediatric trachea and bronchi: systematic review and updates. *Semin Roentgenol*. 2012;47(2):182–196.

Lee EY, Zucker EJ, Restrepo R, et al. Advanced large airway CT imaging in children: evolution from axial to 4-D assessment. *Pediatr Radiol*. 2013;43(3):285–297.

## REFERENCES

Full references for this chapter can be found on www.expertconsult.com.

## REFERENCES

1. Lee EY, Restrepo R, Dillman JR, et al. Imaging evaluation of pediatric trachea and bronchi: systematic review and updates. *Semin Roentgenol*. 2012;47(2):182–196.
2. Lee EY, Greenberg SB, Boiselle PM. Multidetector computed tomography of pediatric large airway disease: state-of-the-art. *Radiol Clin North Am*. 2011;49:869–893.
3. Lee EY, Siegel MR. MDCT of tracheobronchial narrowing in pediatric patients. *J Thorac Imaging*. 2007;22:300–309.
4. de Groot-van der Mooren MD, Haak MC, Lakeman P, et al. Tracheal agenesis: approach towards this severe diagnosis. Case report and review of the literature. *Eur J Pediatr*. 2012;17(3):425–431.
5. Kanojia RP, Parikh M, Bhagat H, et al. Tracheal agenesis: case report with review of the current scenario and management reported over the past two decades. *Eur J Pediatr Surg*. 2010;20(1):55–57.
6. Saccardi C, Ludwig K, Cosmi E, et al. Tracheal agenesis with bifurcating common airway arising from midesophagus. *Pediatr Dev Pathol*. 2010;13(3):252–254.
7. Fuchimoto Y, Mori M, Takasato F, et al. A long-term survival case of tracheal agenesis: management for tracheoesophageal fistula and esophageal reconstruction. *Pediatr Surg Int*. 2011;27(1):103–106.
8. Panthagani ID, Santos MC, D'Angio CT. Use of computed tomography to categorize the type of tracheal agenesis. *J Pediatr Surg*. 2009;44(5):1044–1046.
9. Manjunatha YC, Gupta AK. Tracheal bronchus (pig bronchus). *Indian J Pediatr*. 2010;77(9):1037–1038.
10. Panigada S, Sacco O, Girosi D, et al. Recurrent severe lower respiratory tract infections in a child with abnormal tracheal morphology. *Pediatr Pulmonol*. 2009;44(2):192–194.
11. Berrocal T, Madrid C, Novo S, et al. Congenital anomalies of the tracheobronchial tree, lung, and mediastinum: embryology, radiology, and pathology. *Radiographics*. 2004;24(1):e17.
12. Bennett EC, Holinger LD. Congenital malformations of the trachea and bronchi. In: Bluestone CD, Stool SE, eds. *Pediatric Otolaryngology*. 4th ed. Philadelphia: Saunders; 2002.
13. Ghaye B, Szapiro D, Fanchamps JM, et al. Congenital bronchial anomalies revisited. *Radiographics*. 2001;21:105–119.
14. O'Sullivan BP, Frassica JJ, Rayder SM. Tracheal bronchus: a cause of prolonged atelectasis in intubated children. *Chest*. 1998;113:537–540.
15. Doolittle AM, Mair EA. Tracheal bronchus: classification, endoscopic analysis, and airway management. *Otolaryngol Head Neck Surg*. 2002;126(3):240–243.
16. Landing BH, Dixon LG. Congenital malformation and genetic disorders of the respiratory tract. *Am Rev Respir Dis*. 1979;120:151–185.
17. Yasuda M, Nagashima A, Ichiki Y, et al. Operation for trachea bronchus: 3-dimensional reconstruction imaging. *Ann Thorac Surg*. 2011;92(6):e127.
18. Akiba T, Marushima H, Takagi M, et al. Preoperative evaluation of a tracheal bronchus by three-dimensional 64-row multidetector-row computed tomography (MDCT) bronchography and angiography: report of a case. *Surg Today*. 2008;38(9):841–843.
19. Ming Z, Lin Z. Evaluation of tracheal bronchus in Chinese children using multidetector CT. *Pediatr Radiol*. 2007;37(12):1230–1234.
20. Sugandhi N, Sharma P, Agarwala S, et al. Esophageal lung: presentation, management, and review of literature. *J Pediatr Surg*. 2011;46:1634–1637.
21. Webb WR. The trachea. In: Webb WR, Higgins CB, eds. *Thoracic Imaging*. 1st ed. Philadelphia: Lippincott Williams and Wilkins; 2005.
22. Hewitt RJ, Butler CR, Maughan EF, et al. Congenital tracheobronchial stenosis. *Semin Pediatr Surg*. 2016;25(3):144.
23. Beasley SW, Qui BQ. Understanding tracheomalacia. *J Paediatr Child Health*. 1998;34:209-201.
24. Lee EY, Boiselle PM, Shamberger RC. Multidetector computed tomography and 3-dimensional imaging: preoperative evaluation of thoracic vascular and tracheobronchial anomalies and abnormalities in pediatric patients. *J Pediatr Surg*. 2010;45(4):811–821.
25. Boiselle PM, Ernst A, DeCamp MM. CT diagnosis of complete tracheal rings in an adult. *J Thorac Imaging*. 2007;22(2):169–171.
26. Lee EY, Zucker EJ, Restrepo R, et al. Advanced large airway CT imaging in children: evolution from axial to 4-D assessment. *Pediatr Radiol*. 2013;43(3):285–297.
27. Karsh S, Mahboubi S. Tracheomegaly in children. *Clin Imaging*. 1989;13(1):77–81.
28. Menon B, Malik A, Chugh A, et al. Radiological appearances in a rare case of tracheomegaly, tracheal diverticulosis, bronchomegaly and bronchiectasis. *Indian J Chest Dis Allied Sci*. 2005;47(1):39–41.
29. Woodring JH, Barrett PA, Rehm SR, et al. Acquired tracheomegaly in adults as a complication of diffuse pulmonary fibrosis. *AJR Am J Roentgenol*. 1989;152(4):743–747.
30. Ayres JG, Pope FM, Reidy JF, et al. Abnormalities of the lungs and thoracic cage in the Ehlers-Danlos syndrome. *Thorax*. 1985;40:300–305.
31. Schoor JV, Joos G, Pauwels R. Tracheobronchomegaly: the Mounier-Kuhn syndrome: report of two cases and review of the literature. *Eur Respir J*. 1991;4:1301–1306.
32. Guest JL, Anderson JN. Tracheobronchomegaly (Mounier-Kuhn syndrome). *JAMA*. 1977;238:1754–1755.
33. Eren S, Balci AE, Dikici B, et al. Foreign body aspiration in children: experience of 1160 cases. *Ann Trop Paediatr*. 2003;1:31–37.
34. Centers for Disease Control and Prevention. Nonfatal choking-related episodes among children—United States, 2001. *MMWR Morb Mortal Wkly Rep*. 2002;51:945–948.
35. Shin SM, Kim WS, Cheon JE, et al. CT in children with suspected residual foreign body in airway after bronchoscopy. *AJR Am J Roentgenol*. 2009;192:1744–1751.
36. Silva AB, Muntz HR, Clary R. Utility of conventional radiography in the diagnosis and management of pediatric airway foreign bodies. *Ann Otol Rhinol Laryngol*. 1998;107:834–838.
37. Hegde SV, Hui PK, Lee EY. Tracheobronchial foreign bodies in children: imaging assessment. *Semin Ultrasound CT MR*. 2015;36(1):8–20.
38. Svedstrom E, Puhakka H, Kero P. How accurate is chest radiography in the diagnosis of tracheobronchial foreign bodies in children? *Pediatr Radiol*. 1989;19:520–522.
39. Sodhi KS, Aiyappan SK, Saxena AK, et al. Utility of multidetector CT and virtual bronchoscopy in tracheobronchial obstruction in children. *Acta Paediatr*. 2010;99(7):1011–1015.
40. Adaletli I, Kurugolglu S, Ulus S, et al. Utility of low-dose multidetector CT and virtual bronchoscopy in children with suspected foreign body aspiration. *Pediatr Radiol*. 2007;37(1):33–40.
41. Kosucu P, Ahmetoglu A, Koramaz I, et al. Low-dose MDCT and virtual bronchoscopy in pediatric patients with foreign body aspiration. *AJR Am J Roentgenol*. 2004;183(6):1771–1777.
42. Marquez L, Starke JR. Diagnosis and management of TB in children: an update. *Expert Rev Anti Infect Ther*. 2011;9:1157–1168.
43. Cruz AT, Starke JR. A current review of infection control for childhood tuberculosis. *Tuberculosis (Edinb)*. 2011;91(suppl 1):S11–S15.
44. Leung AN, Muller NL, Pineda PR, et al. Primary tuberculosis in childhood: radiographic manifestations. *Radiology*. 1992;182:87–91.
45. Weber AL, Bird KT, Janower ML. Primary tuberculosis in childhood with particular emphasis on changes affecting the tracheobronchial tree. *AJR Am J Roentgenol*. 1968;103:123–132.
46. Fischer GB, Mocelin H, Severo CB, et al. Histoplasmosis in children. *Paediatr Respir Rev*. 2009;10:172–177.
47. Rossi SE, McAdams HP, Rosado-de-Christenson ML, et al. Fibrosing mediastinitis. *Radiographics*. 2001;21:737–757.
48. Sherrick AD, Brown LR, Harms GF, et al. The radiographic findings of fibrosing mediastinitis. *Chest*. 1994;106(2):484–489.
49. Bellah RD, Mahboubi S, Berdon WE. Malignant endobronchial lesions of adolescence. *Pediatr Radiol*. 1992;22:563–567.
50. Chong S, Lee KS, Chung MJ, et al. Neuroendocrine tumors of the lung: clinical, pathologic, and imaging findings. *Radiographics*. 2006;26:41–57.
51. Connor GF, Fishman EK. Endobronchial carcinoid in a child: depiction with three-dimensional volume rendering. *Pediatr Radiol*. 2004;34:1008–1011.
52. Parson RB, Milestone BN, Adler LP. Radiographic assessment of airway tumors. *Chest Surg Clin N Am*. 2003;13:63–77.
53. Yikilmaz A, Lee EY. CT imaging of mass-like nonvascular pulmonary lesions in children. *Pediatr Radiol*. 2007;37:1253–1263.
54. Magid D, Siegelman SS, Eggleston JC, et al. Pulmonary carcinoid tumors: CT assessment. *J Comput Assist Tomogr*. 1989;13:244–247.
55. Scott JR, Kramer SS. Pediatric tracheostomy. II. Radiographic features of difficult decannulations. *AJR Am J Roentgenol*. 1978;130(5):893–898.
56. Lee EY. Advancing CT and MR imaging of the lungs and airways in children: imaging into practice. *Pediatr Radiol*. 2008;38(suppl 2):S208–S212.
57. Lee EY, Mason KP, Zurakowski D, et al. MDCT assessment of tracheomalacia in symptomatic infants with mediastinal aortic vascular anomalies: preliminary technical experience. *Pediatr Radiol*. 2008;38(1):82–88.

58. Lee EY, Zurakowski D, Waltz DA, et al. MDCT evaluation of the prevalence of tracheomalacia in children with mediastinal aortic vascular anomalies. *J Thorac Imaging*. 2008;23(4):248–265.
59. Lee EY, Litmanovich D, Boiselle PM. Multidetector CT evaluation of tracheobronchomalacia. *Radiol Clin North Am*. 2009;47(2):261–269.
60. Lee EY, Boiselle PM. Tracheobronchomalacia in infants and children: multidetector CT evaluation. *Radiology*. 2009;252(1):7–22.
61. Ridge CA, O'Donnell CR, Lee EY, et al. Tracheobronchomalacia: current concepts and controversies. *J Thorac Imaging*. 2011;26(4):278–289.
62. Ozdulger A, Cetin G, Erkmen Gulhan S, et al. A review of 24 patients with bronchial ruptures: is delay in diagnosis more common in children? *Eur J Cardiothorac Surg*. 2003;23:379–383.
63. Nakayama DK, Ramenofsky ML, Rowe MI. Chest injuries in childhood. *Ann Surg*. 1989;201:770–775.
64. Jackimczyk K. Blunt chest trauma. *Emerg Med Clin North Am*. 1993;11:81–96.
65. Harvey-Smith W, Bush W, Northrop C. Traumatic bronchial rupture. *AJR Am J Roentgenol*. 1980;134:1189–1193.
66. Ein SH, Friedberg J, Shandling B, et al. Traumatic bronchial injuries in children. *Pediatr Pulmonol*. 1986;2:60–64.
67. Mahboubi S, O'Hara AE. Bronchial rupture in children following blunt chest trauma. Report of five cases with emphasis on radiologic findings. *Pediatr Radiol*. 1981;10:133–138.
68. Hrkac Pustahija A, Vukelic Markovic M, Ivanac G, et al. An unusual case of bronchial rupture—pneumomediastinum appearing 7 days after blunt chest trauma. *Emerg Radiol*. 2009;16:163–165.
69. Scaglione M, Romano S, Pinto A, et al. Acute tracheobronchial injuries: impact of imaging in diagnosis and management implications. *Eur J Radiol*. 2006;59:336–343.
70. Le Guen M, Beigelman C, Bouhemad B, et al. Chest computed tomography with multiplanar reformatted images for diagnosing traumatic bronchial rupture: a case report. *Crit Care*. 2007;11:R94.
71. Wan YL, Tsai KT, Yeow KM, et al. CT findings of bronchial transaction. *Am J Emerg Med*. 1997;15:176–177.
72. Moore MA, Wallace EC, Westra SJ. Chest trauma in children: current imaging guidelines and techniques. *Radiol Clin North Am*. 2011;49(5):949–968.
73. Hammer MR, Dillman JR, Chong ST, et al. Imaging of pediatric thoracic trauma. *Semin Roentgenol*. 2012;47(2):135–146.
74. Carden KA, Boiselle PM, Waltz DA, et al. Tracheomalacia and tracheobronchomalacia in children and adults: an in-depth review. *Chest*. 2005;127(3):984–1005.
75. Baez JC, Ciet P, Mulkern R, et al. Pediatric chest MR imaging: lung and airways. *Magn Reson Imaging Clin N Am*. 2015;23(2):337–349.
76. Greenholz SK, Karrer FM, Lilly JR. Contemporary surgery of tracheomalacia. *J Pediatr Surg*. 1986;21(6):511–514.
77. Sommer D, Forte V. Advances in the management of major airway collapse: the use of airway stents. *Otolaryngol Clin North Am*. 2000;33(1):163–177.
78. Lee KS, Lunn W, Feller-Kopman D, et al. Multislice CT evaluation of airway stents. *J Thorac Imaging*. 2005;20(2):81–88.
79. Weber TR, Keller MS, Fiore A. Aortic suspension (aortopexy) for severe tracheomalacia in infants and children. *Am J Surg*. 2002;184(6):573–577.
80. Adler SC, Isaacson G, Balsara RK. Innominate artery compression of the trachea: diagnosis and treatment by anterior suspension—25 year experience. *Ann Otol Rhinol Laryngol*. 1995;104(12):924–927.
81. Morabito A, MacKinnon E, Alizai N, et al. The anterior mediastinal approach for management of tracheomalacia. *J Pediatr Surg*. 2000;35(10):1456–1458.
82. Baxter JD, Dunbar JS. Tracheomalacia. *Ann Otol Rhinol Laryngol*. 1963;72:1012–1023.
83. Kiely EM, Spitz L, Brereton R. Management of tracheomalacia by aortopexy. *Pediatr Surg Int*. 1987;2:13–15.
84. Vasko JS, Ahn C. Surgical management of secondary tracheomalacia. *Ann Thorac Surg*. 1968;6(3):269–272.
85. Davis S, Jones M, Kisling J, et al. Effect of continuous positive airway pressure on forced expiratory flows in infants with tracheomalacia. *Am J Respir Crit Care Med*. 1998;158(1):148–152.
86. Reiterer F, Eber E, Zach MS, et al. Management of severe congenital tracheobronchomalacia by continuous positive airway pressure and tidal breathing flow-volume loop analysis. *Pediatr Pulmonol*. 1994;17(6):401–403.
87. Ferguson GT, Benoist J. Nasal continuous positive airway pressure in the treatment of tracheobronchomalacia. *Am Rev Respir Dis*. 1993;147(2):457–461.
88. Page BA, Klein EF Jr. Tracheal stent as an aid in weaning from mechanical ventilation in tracheomalacia. *Anesthesiology*. 1977;47(3):300–301.
89. Altman KW, Wetmore FR, Marsh RR. Congenital airway abnormalities in patients requiring hospitalization. *Arch Otolaryngol Head Neck Surg*. 1999;125(5):525–528.

# 53

# Congenital Lung Anomalies

Monica Epelman, Edward Y. Lee, and Beverley Newman

Congenital lung anomalies represent a heterogeneous group of pulmonary developmental disorders that affect the lung parenchyma, its arterial supply, venous drainage, or a combination thereof. The reported incidence of congenital lung anomalies ranges from 30 to 42 cases per 100,000 population.[1] Although prenatal sonography, fetal magnetic resonance imaging (MRI) and advances in postnatal imaging have enhanced our understanding of congenital lung anomalies, substantial controversy continues regarding the nomenclature, classification, pathogenesis, description, and management of these lesions. In addition, considerable variability exists in their prenatal clinical presentation and outcome, ranging from in-utero involution to severe hydrops and fetal demise. Likewise, their postnatal clinical presentation also is variable, ranging from marked neonatal respiratory distress to a completely asymptomatic newborn to an older child or young adult with recurrent pneumonias. In this chapter, the underlying etiology, clinical presentation, imaging findings, and management of various congenital lung anomalies are discussed.

## SPECTRUM OF CONGENITAL LUNG ANOMALIES

The classification of congenital lung anomalies is challenging and controversial from embryologic, radiologic, pathologic, and clinical viewpoints. Several classifications and terminologies with particular advantages and disadvantages have been suggested.[2–4] Some investigators have used embryology as a basis and have classified congenital lung anomalies according to the stage of intrauterine development in which the insult resulting in the malformation developed.[2] Others have categorized lesions based on their morphologic-radiologic features and divided them into two groups: whole lung malformations (e.g., lung hypoplasia) and focal malformations (e.g., bronchial atresia).[3,5] Recently the Langston[4] classification has become one of the most accepted classification systems for congenital lung anomalies, particularly from the pathologic standpoint, although it is by no means used by all clinical groups. Langston categorizes the wide spectrum of respiratory tract malformations primarily as bronchial atresia, congenital pulmonary airway malformation (CPAM), extralobar bronchopulmonary sequestration (BPS), congenital lobar overinflation (CLO), and bronchogenic cysts. These five congenital lung anomalies comprise approximately 90% of the anomalies seen in clinical practice. However, this classification system is limited because other congenital lung anomalies (e.g., pulmonary arteriovenous malformation [AVM]) are not included.

For the purpose of relatively clear classification, easy differentiation on imaging studies, and preoperative assessment of surgical lesions, congenital lung anomalies discussed in this chapter are categorized according to their morphologic-radiologic-pathologic features. Such a classification system views congenital lung anomalies as a continuum ranging from predominantly parenchymal abnormalities (i.e., abnormal lung parenchyma with variable airway/foregut components and relatively normal vasculature, e.g., CPAM), to combined parenchymal and vascular abnormalities (e.g., pulmonary sequestration and scimitar syndrome) in which foregut and airway components play an important role and the major abnormalities are intertwined (Fig. 53.1), and lastly predominantly vascular abnormalities, such as pulmonary AVM or absent or interrupted pulmonary artery with secondary lung/airway abnormalities.

Given that specific terminology for these lesions may be controversial and occasionally confusing, we and other authors[1,6–10] recommend that radiologists thoroughly describe all imaging findings of congenital lung anomalies rather than try to categorize the lesions by pathologic terminology. Specific imaging findings that need to be evaluated and described include (1) location of lesions; (2) vascular supply and drainage of the lesions; (3) internal architecture, presence of cystic components, and degree of aeration; (4) airway abnormality; (5) exclusion of communication with the gastrointestinal (GI) tract; (6) integrity of the diaphragm; and (7) an assessment of associated anomalies, such as vertebral anomalies.[6,8,11]

## PREDOMINANTLY PARENCHYMAL LESIONS

### Bronchial Atresia

***Etiology.*** Bronchial atresia refers to atresia of a lobar, segmental, or subsegmental bronchus at or near its origin resulting in a blind-ended atretic proximal bronchus. Bronchial atresia has been categorized as proximal or peripheral.[12] While proximal atresia is less common, it is often lethal during pregnancy. Peripheral bronchial atresia most frequently affects a segmental bronchus and may be isolated or part of another congenital lung malformation. Peripheral bronchial atresia may be diagnosed as an incidental finding on chest radiographs later in life in asymptomatic older children or adults.[4] However, it is increasingly being diagnosed in utero, given the widespread use of prenatal imaging.[4,7–9,12,13]

The precise etiology of bronchial atresia remains unknown, but etiologies such as a vascular insult to the involved atretic or stenotic portion have been proposed.[4] Several authors who used modern dissecting techniques found that bronchial atresia is more common than originally thought.[4,13–15] Furthermore, bronchial atresia and BPSs coexist in nearly all cases,[4,13–15] whereas it is found in nearly 70% of CPAM lesions.[14] A malformation sequence resulting from airway obstruction during development has been proposed as the unifying element for such a wide spectrum of imaging appearances of the major bronchopulmonary malformations. Differences in degree, level, and timing of the bronchial obstruction are thought to be responsible for these variations.[4,6,14,15]

***Imaging.*** Prenatally, the involved portion of the lung appears hyperexpanded and shows increased homogenous echogenicity on US and high T2 signal on fetal MRI (Fig. 53.2).[12,16] The appearance may be difficult to distinguish from CLO, pulmonary sequestration, and microcystic CPAM. Identification of a centrally located, mucus-filled bronchocele/mucocele on prenatal US or MRI strongly suggests bronchial atresia (e-Fig. 53.3).[7,12,17]

Characteristically, the apicoposterior segmental bronchus of the left upper lobe is most commonly affected, followed by the segmental bronchi of the right upper, right middle, and lower lobes.[18] In children, radiographic and computed tomography (CT) imaging features of bronchial atresia are characterized by a tubular or glove-shaped opacity representing mucus plugging in the region distal to the atretic bronchus, surrounding segmental hyperlucency

## Abstract:

The most common clinically significant congenital lung anomalies span a continuum of maldevelopment and can be classified into three main groups: predominantly parenchymal abnormalities, combined parenchymal and vascular abnormalities, and predominantly vascular abnormalities.

Despite advancements in pre- and postnatal imaging considerable controversy exists regarding nomenclature, classification, pathogenesis, description, and management of congenital lung anomalies.

Bronchial atresia and other congenital lung anomalies are believed to be the result of an obstruction malformation sequence. Differences in degree, level, and timing of the bronchial obstruction are thought to be responsible for the various imaging appearances. The obstruction is believed to occur at the time of differentiation of the diaphragm and gastrointestinal tract, this could explain some of the associated extrapulmonary anomalies. Given that specific terminology for these lesions may be controversial and occasionally confusing, it is recommended that careful description of all imaging findings is more important than specific categorization of the lesions by pathologic terminology. Imaging findings of congenital lung anomalies that need to be evaluated and described include (1) location of lesions, (2) associated anomalous vascular supply and drainage of the lesions, (3) internal components and the degree of aeration, (4) airway abnormality ,(5)exclusion of communication with the gastrointestinal (GI) tract, (6) integrity of the diaphragm, and (7) an assessment of associated anomalies.

In this chapter, the underlying etiology, clinical presentation, imaging findings, and management of the most common congenital lung anomalies encountered in the pediatric population are discussed and illustrated.

## Keywords:

Bronchial Atresia
bronchogenic cyst
congenital lobar overinflation
congenital pulmonary airway malformation
bronchopulmonary sequestration
hypogenetic lung syndrome
anomalies of the pulmonary arteries and veins

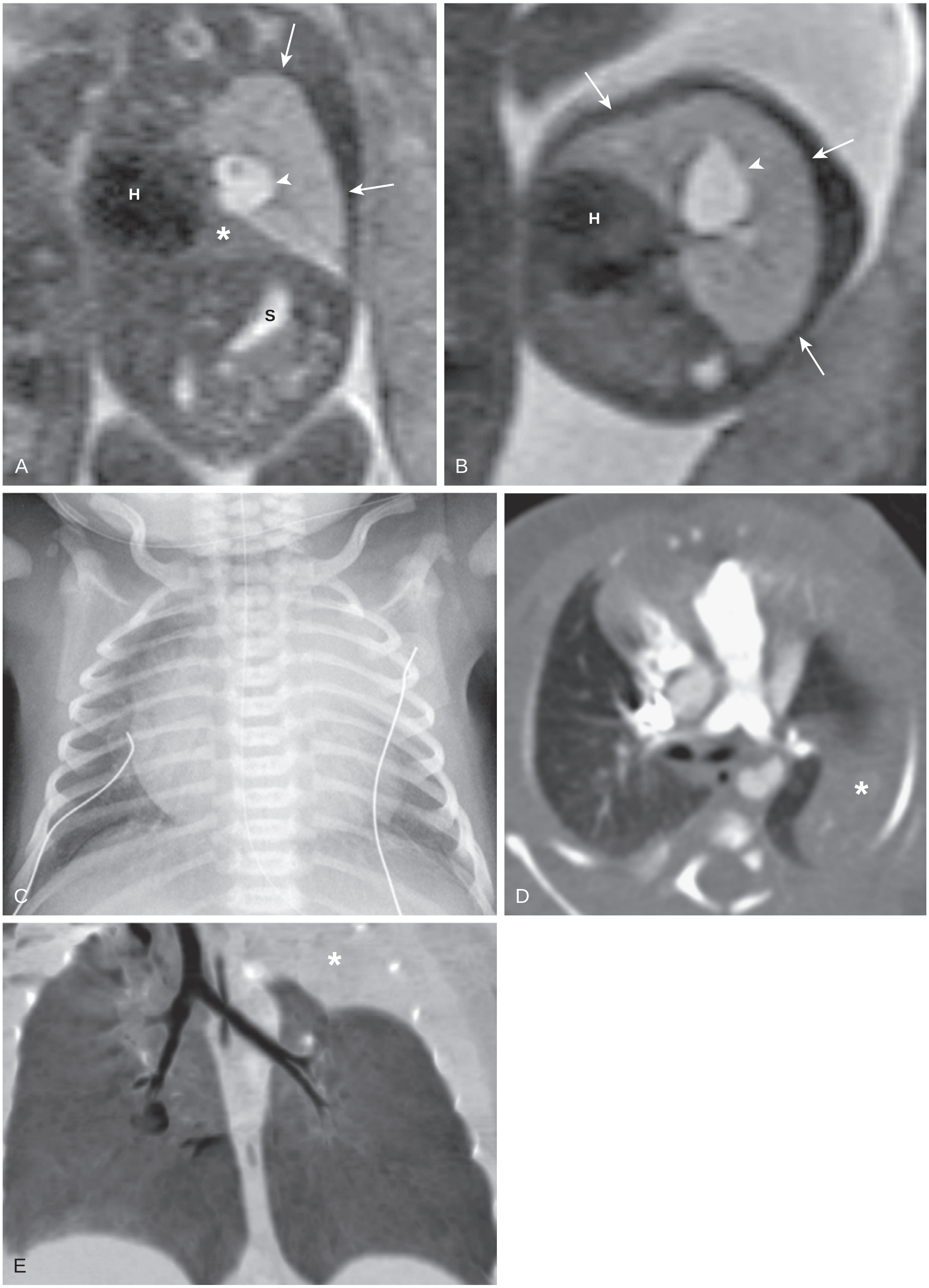

**e-Figure 53.3. Bronchial atresia.** Coronal (A) and axial (B) T2-weighted fetal MR images show a large hyperintense, homogeneous lesion in the left upper lobe *(arrows)* in a 21-week gestational age fetus. The left lower lobe *(asterisk)* is displaced and compressed inferiorly. The heart *(H)* is shifted to the right. Very large central fluid-filled bronchi are noted *(arrowheads)*. *S,* Stomach. (C) Frontal chest radiograph at birth shows complete opacification of the left upper lobe, presumably as a result of retained fetal fluid and mucostasis related to bronchial atresia. Axial CT angiography (D) and minimum intensity projection (E) images performed at day 2 of life show complete collapse of the left upper lobe *(asterisk)*. In addition, the left upper lobe bronchus could not be delineated, a finding suggestive of bronchial atresia. Three-dimensional reconstructions are invaluable in showing the “interrupted connection” to the remainder of the airway.

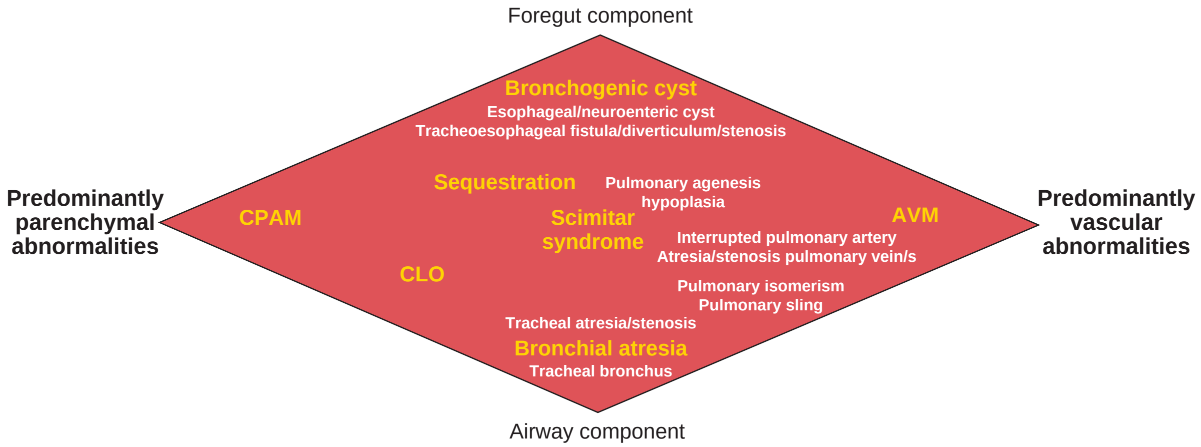
Foregut component
Bronchogenic cyst
Esophageal/neuroenteric cyst
Tracheoesophageal fistula/diverticulum/stenosis
Predominantly parenchymal abnormalities
CPAM
Sequestration
Pulmonary agenesis hypoplasia
Scimitar syndrome
Interrupted pulmonary artery
Atresia/stenosis pulmonary vein/s
AVM
Predominantly vascular abnormalities
CLO
Pulmonary isomerism
Pulmonary sling
Tracheal atresia/stenosis
Bronchial atresia
Tracheal bronchus
Airway component

**Figure 53.1. Diagram of the spectrum of congenital lung anomalies, including foregut and airway components.** The lesions in *yellow* denote those most commonly encountered in this entity, whereas the lesions in *white* represent additional lesions that can be considered part of the spectrum. *AVM,* Arteriovenous malformation; *CPAM,* congenital pulmonary airway malformation; *CLO,* congenital lobar overinflation. *(Adapted from Newman B. Congenital bronchopulmonary foregut malformations: concepts and controversies.* Pediatr Radiol. *2006;36:773–791.)*

due to air trapping (associated with collateral aeration), and decreased underlying vascularity (e-Fig. 53.4).[1,17] However, in neonates, a portion of the lung distal to the atretic segment may remain atelectatic as a result of the in-utero mucostasis. Therefore some authors recommend avoiding immediate postnatal imaging evaluation because the underaerated lung related to bronchial atresia may be difficult to differentiate from the normal lung with expected fetal fluid retention in the newborn period.[8] Identification of the hallmark atretic bronchus and the "bronchocele/mucocele" by means of two-dimensional (2D) multiplanar or three-dimensional (3D) reconstructions either on prenatal or postnatal imaging may be helpful.[6,8,19]

***Treatment and Follow-up.*** In general, surgical resection is the treatment of choice in symptomatic pediatric patients, with conservative management possible in asymptomatic children with small lesions.[12,20,21] Although opinions vary, some centers advocate elective surgical resection of bronchial atresia even in asymptomatic pediatric patients because of potential future lung infection and especially when associated with CPAM.[22]

## Bronchogenic Cysts

***Etiology.*** Bronchogenic cysts result from abnormal tracheobronchial branching and probably originate from an aberrant bud of the developing foregut, similar to other foregut duplication cysts. Bronchogenic cysts typically are unilocular, fluid-filled or mucus-filled cysts lined by respiratory epithelium and are attached to, but usually do not communicate with, the tracheobronchial tree.[1,4,20] Although most bronchogenic cysts are located within the mediastinum (predominantly near the carina), they may be encountered anywhere from the suprasternal area to the retroperitoneum. Bronchogenic cysts also may be found within the lung parenchyma, usually in the lower lobes located close to an adjacent airway.[1,20] Such intrapulmonary bronchogenic cysts usually do not communicate with the airway unless superimposed infection occurs,[4] which may further predispose them to recurrent infections. Symptoms depend on the mass effect the cyst exerts on neighboring structures including the airway, GI tract, and cardiovascular structures. Airway compression is usually mild, but it may be life-threatening in some instances when large bronchogenic cysts are located near the carina.[23]

***Imaging.*** A bronchogenic cyst typically presents as a round or oval-shaped cystic lesion located near the right paratracheal or subcarinal area within the middle mediastinum. Bronchogenic cysts are anechoic on prenatal ultrasound and show high signal intensity on T2-weighted prenatal MRI (e-Fig. 53.5).[16,20] On chest radiographs, a bronchogenic cyst manifests as a well-delineated round or oval-shaped middle mediastinal mass. On CT, approximately 50% of bronchogenic cysts demonstrate fluid attenuation value (~0 Hounsfield unit) (Fig. 53.6). The remaining bronchogenic cysts may have CT attenuation higher than water because of thick mucoid, milk-of-calcium, proteinaceous, or hemorrhagic contents. MRI, which can confirm the cystic nature of the bronchogenic cysts on T2-weighted images, is helpful for differentiating bronchogenic cysts with high attenuation value from a solid mass on CT. Typically, no internal contrast enhancement is seen within uncomplicated bronchogenic cysts. The presence of an air-fluid level, thick wall enhancement, or surrounding inflammatory changes often is associated with superimposed infection.[1,9,18]

***Treatment and Follow-up.*** Complete surgical resection is the current management of choice for bronchogenic cysts, particularly in symptomatic pediatric patients.[24] Temporizing or palliative procedures such as transparietal, transbronchial, or mediastinal aspiration may be considered in symptomatic patients who are not surgical candidates.

## Congenital Lobar Overinflation

***Etiology.*** CLO, also referred to as infantile/congenital lobar emphysema or congenital lobar hyperinflation, is thought to be caused by an intrinsic or extrinsic bronchial narrowing, resulting in marked alveolar overdistension or overinflation of at least one pulmonary segment or lobe.[10,25] The alveolar walls are maintained, therefore true emphysematous change is not present.[10] Intrinsic bronchial narrowing can be caused by weakness or absence of underlying bronchial cartilage, whereas extrinsic bronchial narrowing may be due to the compression from adjacent mediastinal masses or enlarged vessels. Most cases of segmental overinflation, and some with lobar abnormality, are due to underlying bronchial atresia. CLO presents clinically with respiratory distress in the newborn period[1,16,20] in nearly half of the symptomatic cases, and by the age of 6 months in 80% of cases.[26] There is a slight male

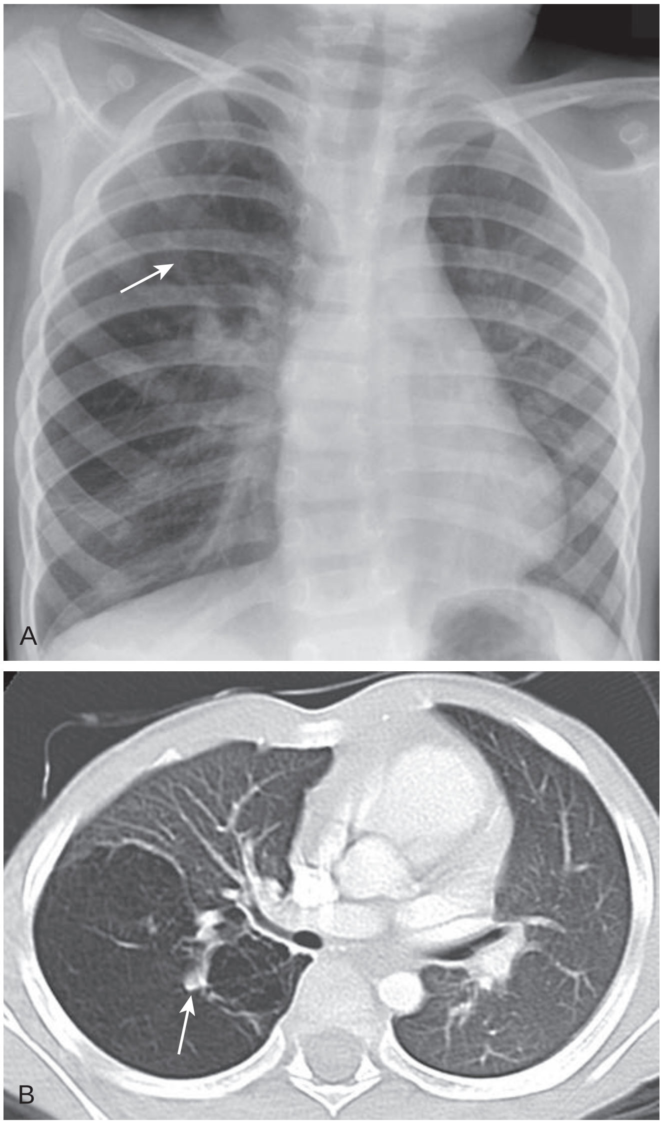

**e-Figure 53.4. Bronchial atresia in an older child.** Frontal chest radiograph (A) and axial CT (B) image in a 3-year-old show right upper lobe hyperlucency and branching linear density *(arrows)* reflecting mucoid impaction in the bronchi distal to the atresia.

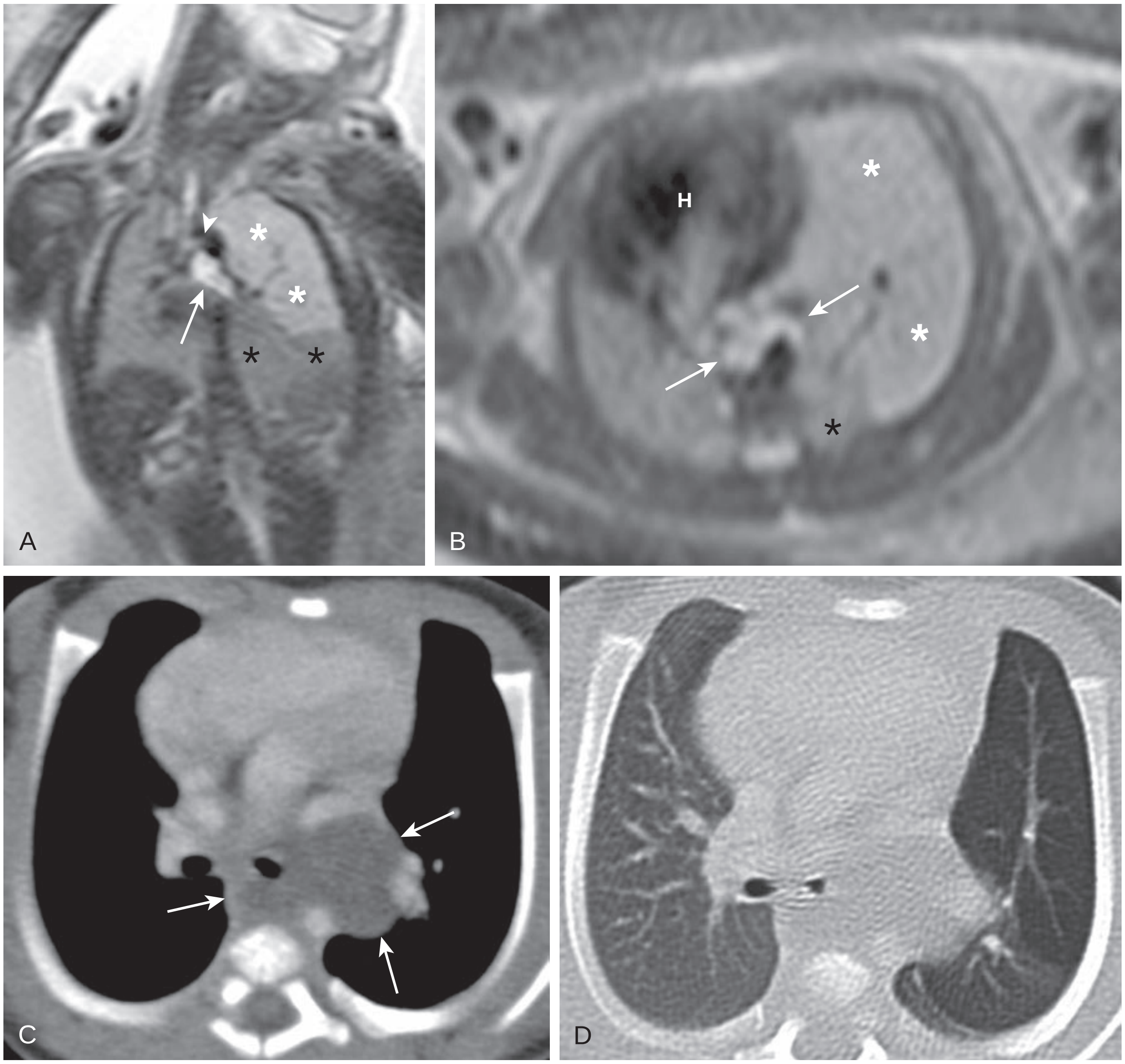

**e-Figure 53.5. Bronchogenic cyst.** Coronal (A) and axial (B) T2-weighted fetal MR images in a 26-week gestational age fetus show a cystic structure in the posterior mediastinum *(arrows)* apparently compressing the left mainstem bronchus *(arrowhead)* and resulting in hyperexpansion with increased fluid signal in the left upper lobe *(white asterisks)*. The left lower lobe is compressed and displaced inferiorly *(black asterisks)*. The fetal heart *(H)* and mediastinum have shifted to the right. Postnatal contrast-enhanced CT images in mediastinal (C) and lung (D) windows show the fluid-filled cystic structure consistent with a bronchogenic cyst *(arrows)* centered at the left hilum and extending posteriorly and inferiorly. The cyst compresses the left mainstem bronchus and results in air trapping in the left upper lobe.

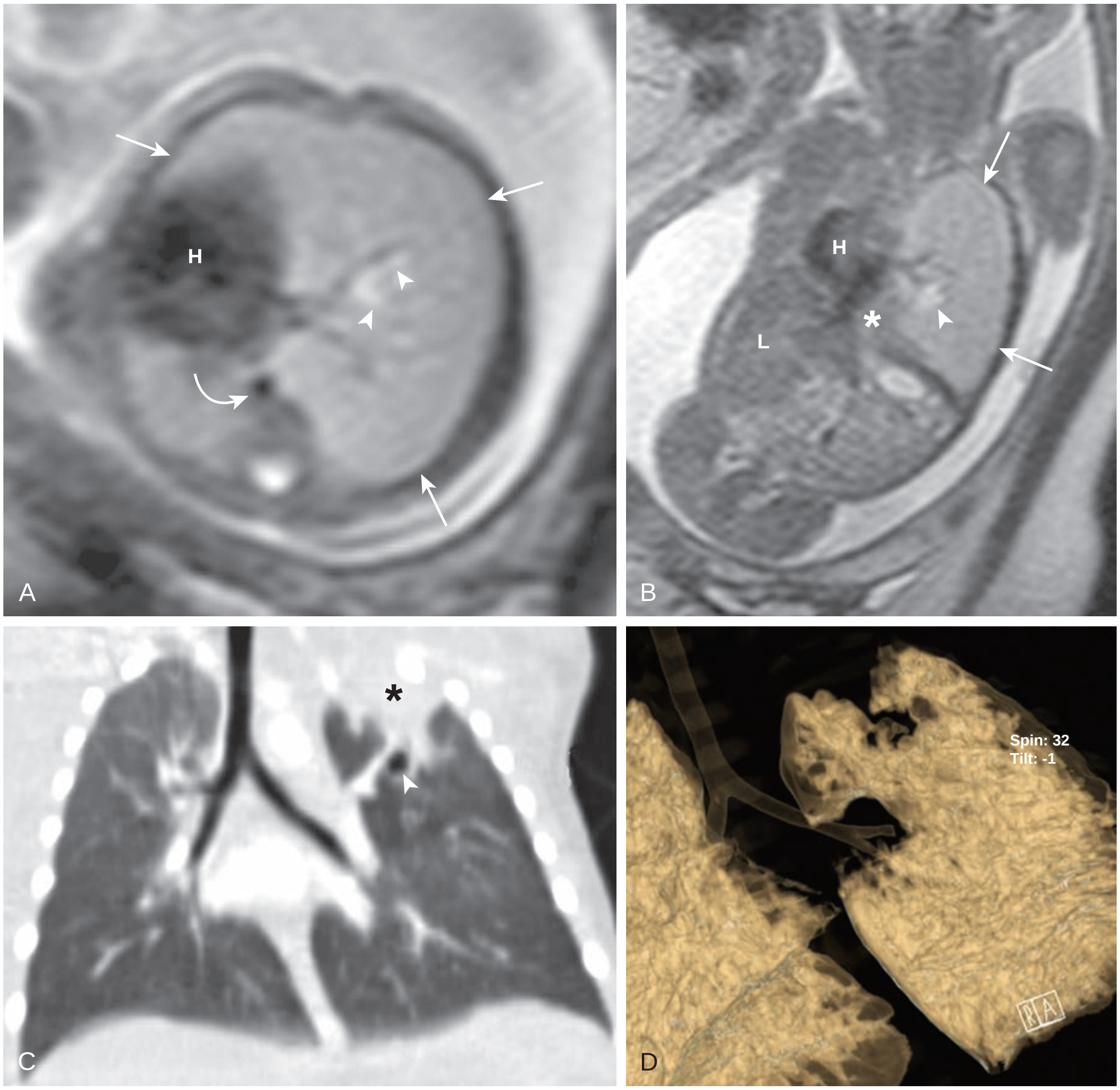

**Figure 53.2. Bronchial atresia.** Axial (A) and coronal (B) T2-weighted fetal MR images in a 22-week gestational age fetus demonstrate a large hyperintense, homogeneous lesion in the left upper lobe *(arrows)*. Central fluid-filled bronchi are noted *(arrowheads)*. The left lower lobe *(asterisk)* is compressed inferiorly and displaced medially adjacent to the fetal heart *(H)*. The *curved arrow* denotes the aorta, which is also displaced to the right. *L,* Liver. (C) Coronal postnatal multiplanar reconstruction CT image shows partial opacification *(asterisk)* of the left upper lobe, presumably due to mucostasis related to bronchial atresia. In addition, a small air bubble is seen *(arrowhead)*, reflecting a bronchocele. (D) Volume-rendered reconstructed CT image could not delineate the left upper lobe bronchus.

predominance, and the upper lobes are affected more frequently than the lower lobes, with the left lung affected more often than the right (see also Chapter 50).[10,26]

***Imaging.*** On prenatal imaging, CLO manifests as a homogeneously hyperechogenic lesion on US or as a T2 hyperintense lesion on MRI without visible cysts. CLO often is indistinguishable from other congenital lung anomalies, particularly in the presence of bronchial atresia.[7,10,27] In the immediate postnatal period, CLO initially may appear as an area of increased opacity related to retained fetal lung fluid, which will clear on subsequent studies.[1,4,20,24] CLO usually is diagnosed postnatally by its typical clinical presentation and characteristic radiographic features of progressive lobar hyperexpansion and hyperlucency, producing displacement or compression of adjacent structures. Similar imaging findings are noted on CT, and the attenuated pulmonary vasculature is a helpful clue to distinguish CLO from a pneumothorax or other entities in cases of inconclusive chest radiographic findings (Fig. 53.7).[1] Similar to bronchial atresia, early CT imaging should be avoided because of a confusing appearance when the affected lung is still fluid-filled.

***Treatment and Follow-up.*** Surgical lobectomy is the current management for symptomatic pediatric patients with CLO.[24,28] Some medical centers advocate expectant management for cases with minimal or no symptoms.[25,28]

## Congenital Pulmonary Airway Malformation

***Etiology.*** CPAMs, formerly known as cystic adenomatoid malformations of the lung, were first described by Ch'In and Tang in 1949 as rare lung lesions occurring in premature or stillborn

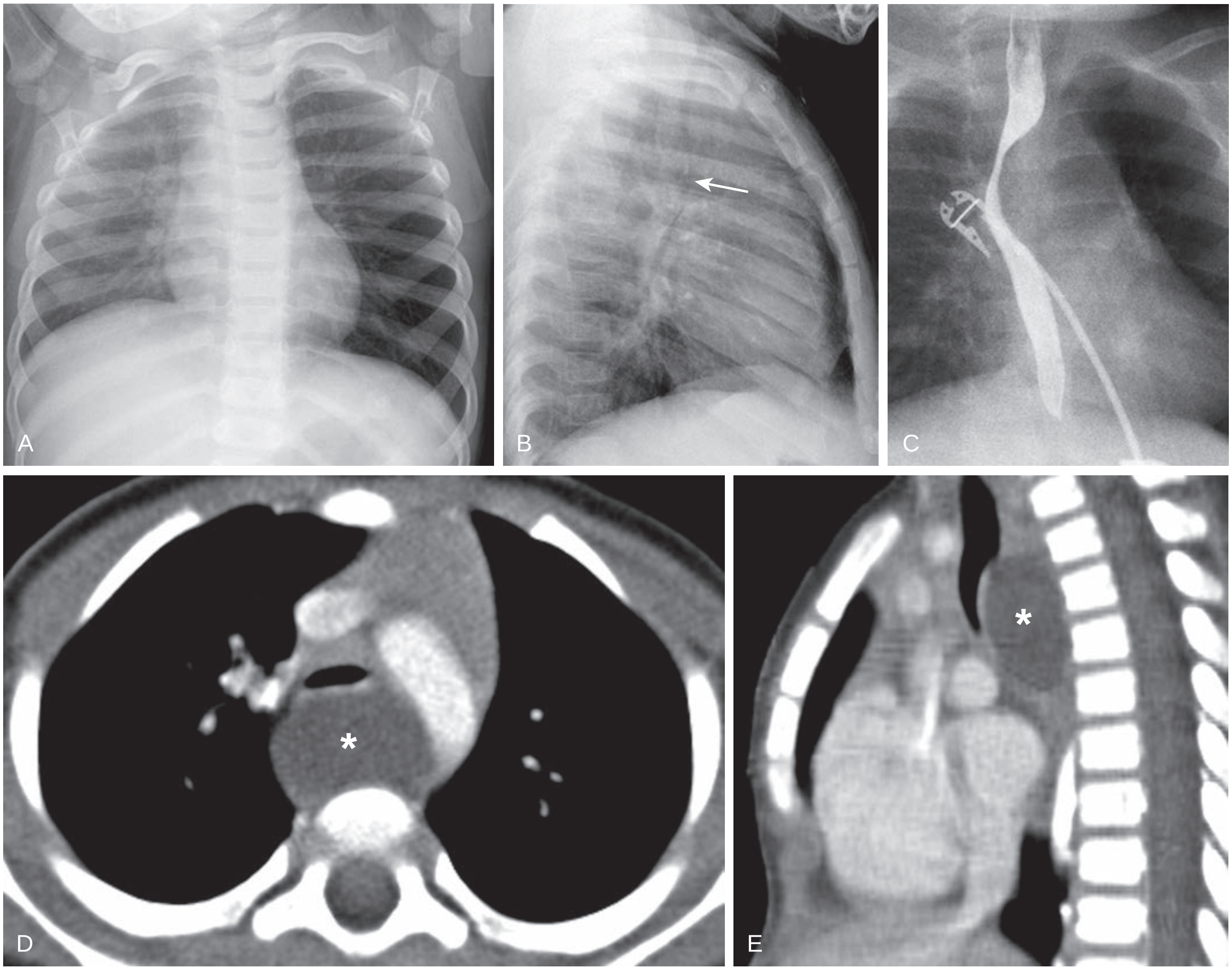

**Figure 53.6. Bronchogenic cyst in a 15-month-old child with stridor.** Frontal chest radiograph (A) shows hyperinflation of the left lung. Lateral radiograph (B) reveals the effect of the mass and anterior displacement of the airway *(arrow)*. (C) Upper gastrointestinal image shows esophageal displacement to the right by a soft tissue density mass. Contrast-enhanced axial (D) and sagittal (E) CT images show a fluid density lesion *(asterisks)* posterior to the lower trachea consistent with a bronchogenic cyst.

infants with significant hydrops.[29,30] CPAMs are currently one of the most common congenital lung anomalies accounting for about 30% to 40% of the cases.[10,15] CPAMs are characterized by a heterogeneous group of congenital cystic lung masses with an abnormal bronchial communication or bronchial atresia.[6,15,31]

In 1977, Stocker et al.[31] classified these lesions based on their clinical and pathologic features, with subdivisions based on the size of the cysts (types 1, 2, and 3) and according to the location of suspected development of the malformation along the airway. Type 1 CPAMs consist of cysts larger than 2 cm, with presumed bronchial/bronchiolar origin. Type 2 CPAMs consist of cysts smaller than 2 cm, with presumed bronchiolar origin. Type 3 CPAMs appear solid/microcystic, with a presumed bronchiolar/alveolar origin. However, Stocker later expanded his classification into five types that included type 0 CPAMs, with presumed tracheobronchial origin (hypoplastic lungs, usually lethal, not recognizable on imaging), and type 4 CPAMs, with presumed distal acinar origin. The term CPAM was implemented instead of cystic adenomatoid malformations, because cystic changes were observed in only three of the aforementioned types (types, 1, 2, and 4), and adenomatoid change was observed only in type 3.[1,7,32,33] This expanded classification has proven problematic with increasing evidence indicating that the type 4 CPAM lesions is the same entity as type 1 cystic pleuropulmonary blastoma.[4,34] Langston[4] classifies CPAM lesions into two types, and terms the Stocker type 1 CPAM as “large cyst-type lesions” and the Stocker type 2 CPAMs as “small cyst-type lesions” based on cyst size and pathologic criteria. Langston proposed that the type 3 CPAM actually represents a form of pulmonary hyperplasia/dysplasia and should be excluded from the CPAM classification.[4] On radiographs and CT imaging, these lesions are typically divided into large cyst (type 1, most common), small cyst (type 2), and solid (microcystic, type 3, very rare) lesions.

***Imaging.*** Prenatally, CPAMs have been classified on the basis of cyst size as microcysts (<5 mm) and macrocysts (≥5 mm) on fetal US and MRI.[35] Type 1 CPAMs may contain one, several, or multiple macrocysts, some of which are ≥5 mm in diameter (Fig. 53.8).[7] Type 2 CPAMs have variable appearances, ranging from

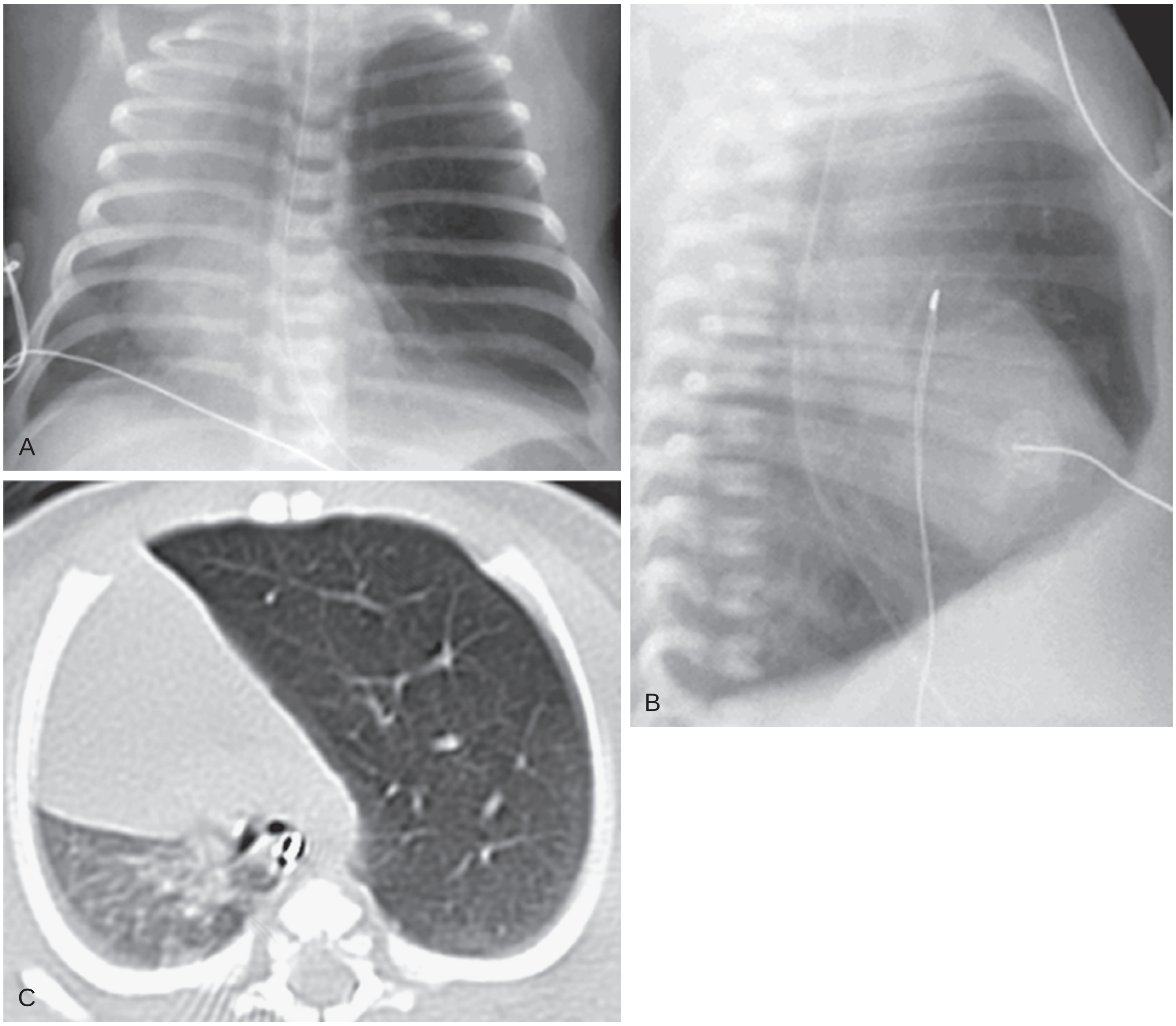

**Figure 53.7. Congenital lobar overinflation in a 3-day-old with increasing tachypnea.** Frontal (A) and lateral (B) chest radiographs and an axial CT image (C) show hyperexpansion and hyperlucency of the left upper lobe with contralateral cardiomediastinal shift consistent with congenital lobar emphysema.

homogeneously hyperechoic or hyperintense lesions to microcystic lesions exhibiting multiple, uniform cysts that measure <5 mm (e-Figs. 53.9 and 53.10).[7,16,20]

Postnatal imaging findings of CPAMs usually correlate with underlying histopathologic features.[1] Large cyst-type CPAMs typically present with one or several larger air-filled cystic structures with intervening solid, unaerated lung parenchyma. The cysts of type 1 CPAMs are larger than 2 cm and may be accompanied by several smaller cysts, whereas small cyst type or type 2 CPAMs usually manifest as partially air-filled multicystic masses, with individual cysts smaller than 2 cm and with variable degrees of solid-appearing, unaerated lung tissue.[1,8] Type 3 CPAMs typically appear as solid lesions with mild contrast enhancement because of microscopic cysts that can be identified only at histologic evaluation. Pleuropulmonary blastoma in infancy usually present as large cysts arising from the peripheral portion of the lung, this lesion may be difficult to distinguish radiographically from other cystic lung lesions (see Chapter 55) (e-Fig. 53.11).

CPAM blood supply is often from the pulmonary artery and venous drainage is into the pulmonary veins, although hybrid sequestration/CPAM lesions with systemic arterial supply are common (especially CPAM type 2). Although unilobar involvement of CPAM is far more common, multilobar and even bilateral lung involvement may occur.[30,33,36] Although any lobe of the lung can be involved, predilection exists for the lower lobe.[36] CPAMs that are complicated as a result of superimposed infection may have an imaging appearance similar to pneumonia or a lung abscess (Fig. 53.12).

***Treatment and Follow-up.*** The generalized consensus is that symptomatic CPAMs should be resected, typically by lobectomy, regardless of the patient's age at presentation.[15,24,28] However, considerable controversy exists with regard to the management of prenatally diagnosed, asymptomatic, small CPAM lesions, and no consensus exists on the timing of or need for resection.[15,37–39] Although there is some support for a nonsurgical strategy with imaging follow-up, most medical centers advocate surgical resection before 1 year of age because of the potential risk of associated complications, such as infection, pneumothorax, and the small risk of malignant transformation, particularly in the case of CPAM type 1 lesions.[23,24,36,40,41]

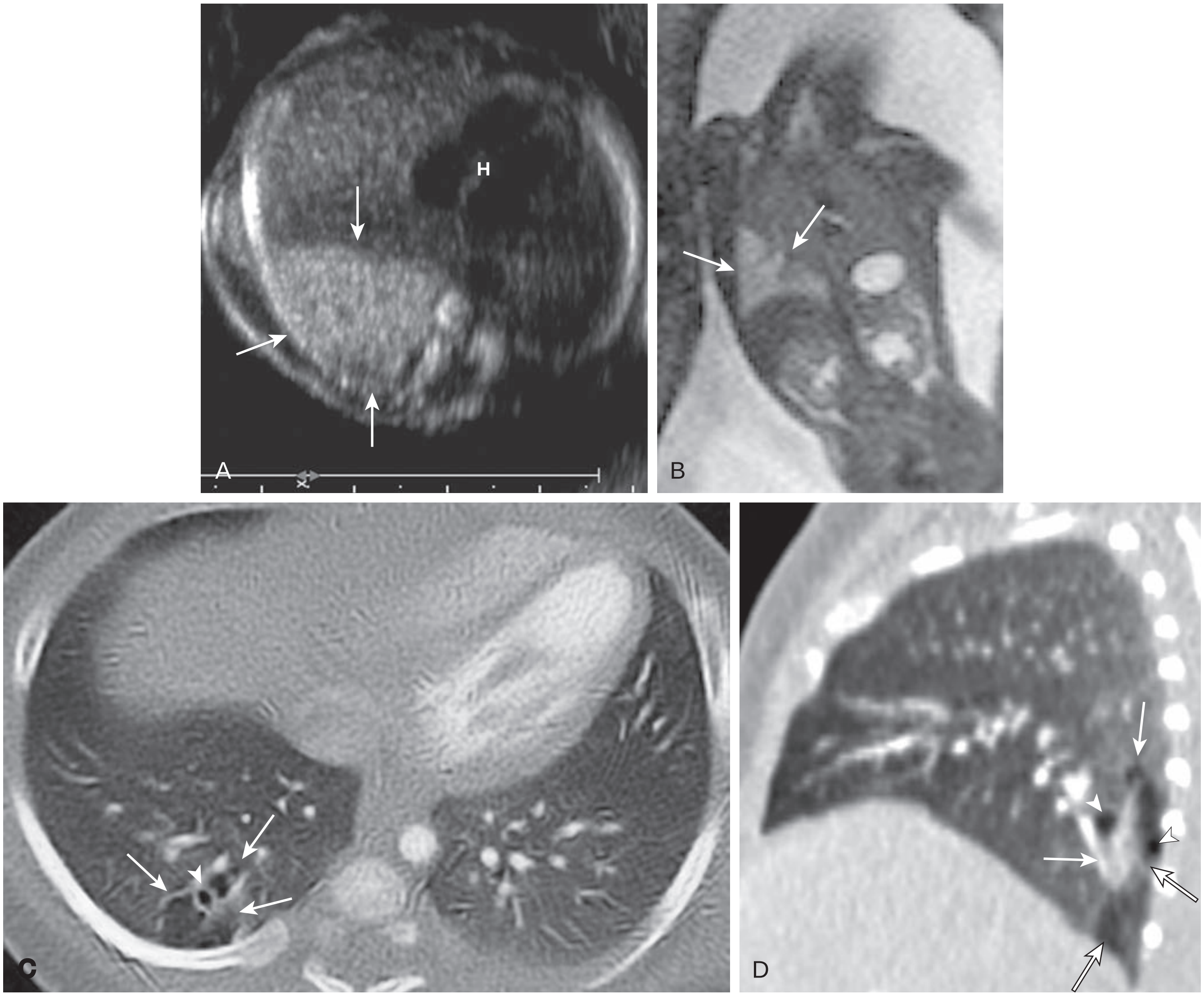

**e-Figure 53.9. Congenital pulmonary airway malformation (CPAM) type 2.** (A) Transverse fetal sonogram through the chest in a 20-week gestational age fetus shows an echogenic right lower lobe lung lesion with tiny cysts only seen on high-resolution images *(not shown)* consistent with a CPAM type 2 lesion *(arrows)*. The heart *(H)* and mediastinum are only mildly shifted without cardiac compression. Coronal (B) fetal T2-weighted MR image shows a mildly heterogeneous lesion *(arrows)* with slightly nodular contours but no visible cysts. Postnatal axial and sagittal CT images (C and D) at 1 month of age show an ill-defined, relatively smaller hyperlucent lesion *(arrows)* in the right lower lobe with tiny, subcentimeter internal cysts *(arrowheads)*. This lesion also demonstrated bronchial atresia components on histologic examination.

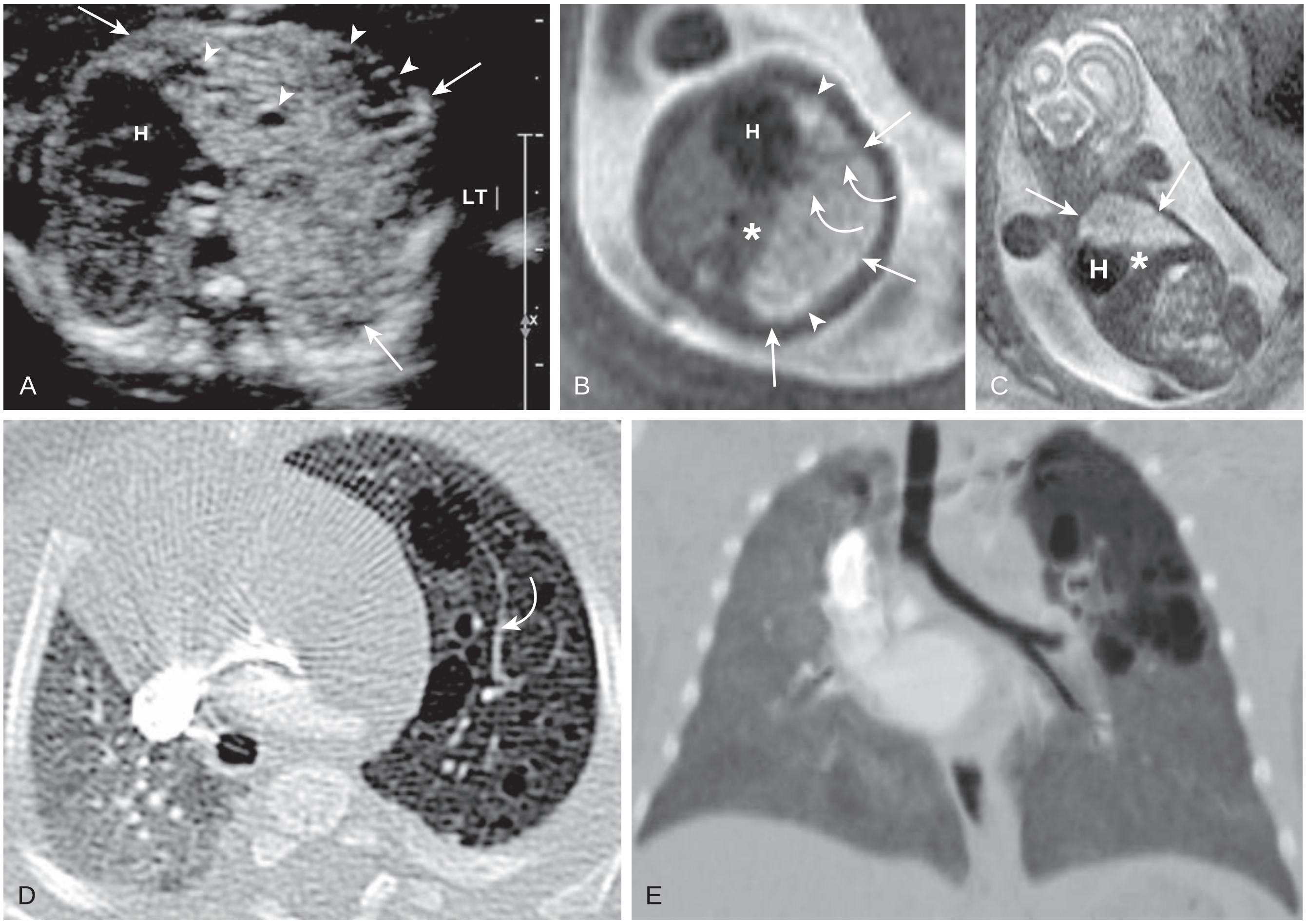

**e-Figure 53.10. Congenital pulmonary airway malformation type 2.** (A) Transverse fetal sonogram through the chest in a 19-week gestational age fetus shows an echogenic left upper lobe lesion with several internal cysts *(arrowheads)*, findings consistent with a CPAM type 2 lesion *(arrows)*. The heart *(H)* and mediastinum are moderately shifted to the right without cardiac compression. *LT,* Left. Axial (B) and coronal (C) fetal T2-weighted MR images show a heterogeneous lesion *(arrows)* with internal cysts *(arrowheads)*; some of them even appear as "macrocysts." Normal-appearing lung tissue is noted as being compressed posteriorly and inferiorly *(asterisks)*. However, on postnatal axial (D) and minimum intensity projection (E) CT images at 3 months of age, the lesion appears relatively smaller and exerts less mass effect and no mediastinal shift. All the cysts are aerated and measure less than 2.0 cm. Note that some slightly prominent, tortuous internal pulmonary vessels are seen within the lesion in both the fetal MR image (B) and the postnatal CT image (D) *(curved arrows)*.

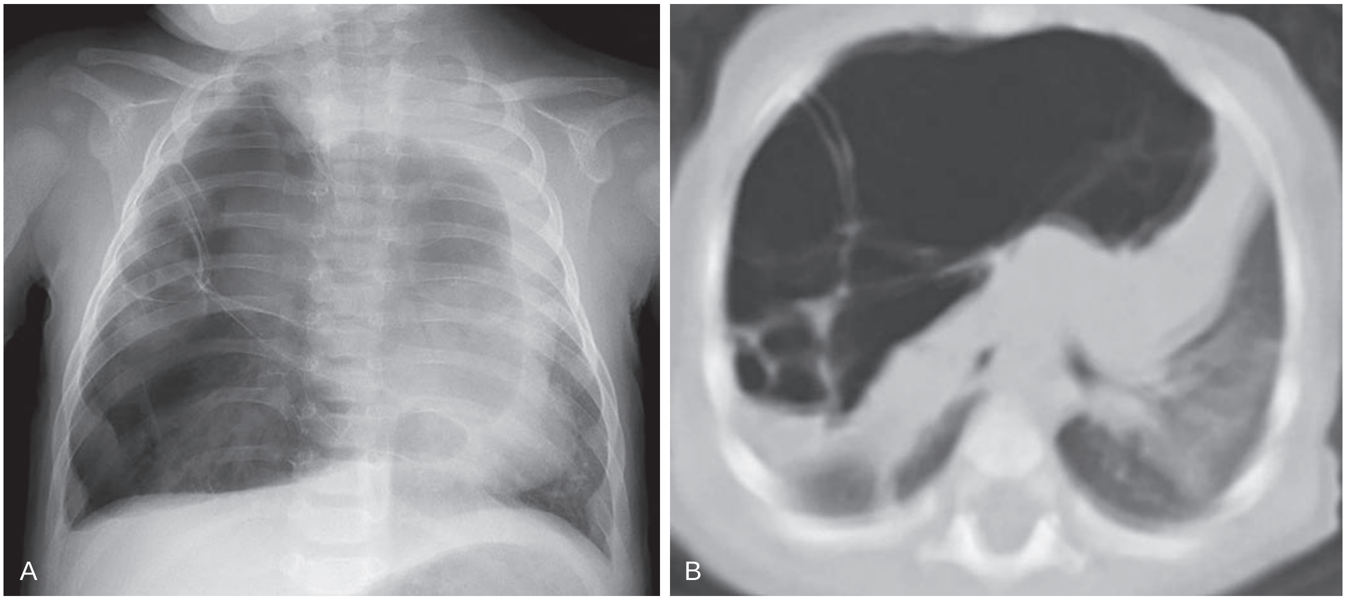

**e-Figure 53.11. Cystic pleuropulmonary blastoma in a 6-month-old with increased work of breathing.** (A) Frontal chest radiograph demonstrates a large radiolucent lesion with fine septations and multiple cysts within the right lung resulting in a mediastinal shift. (B) Axial computed tomography image reveals multiple cysts of varying sizes with mass effect demonstrated on the mediastinum and contralateral left lung.

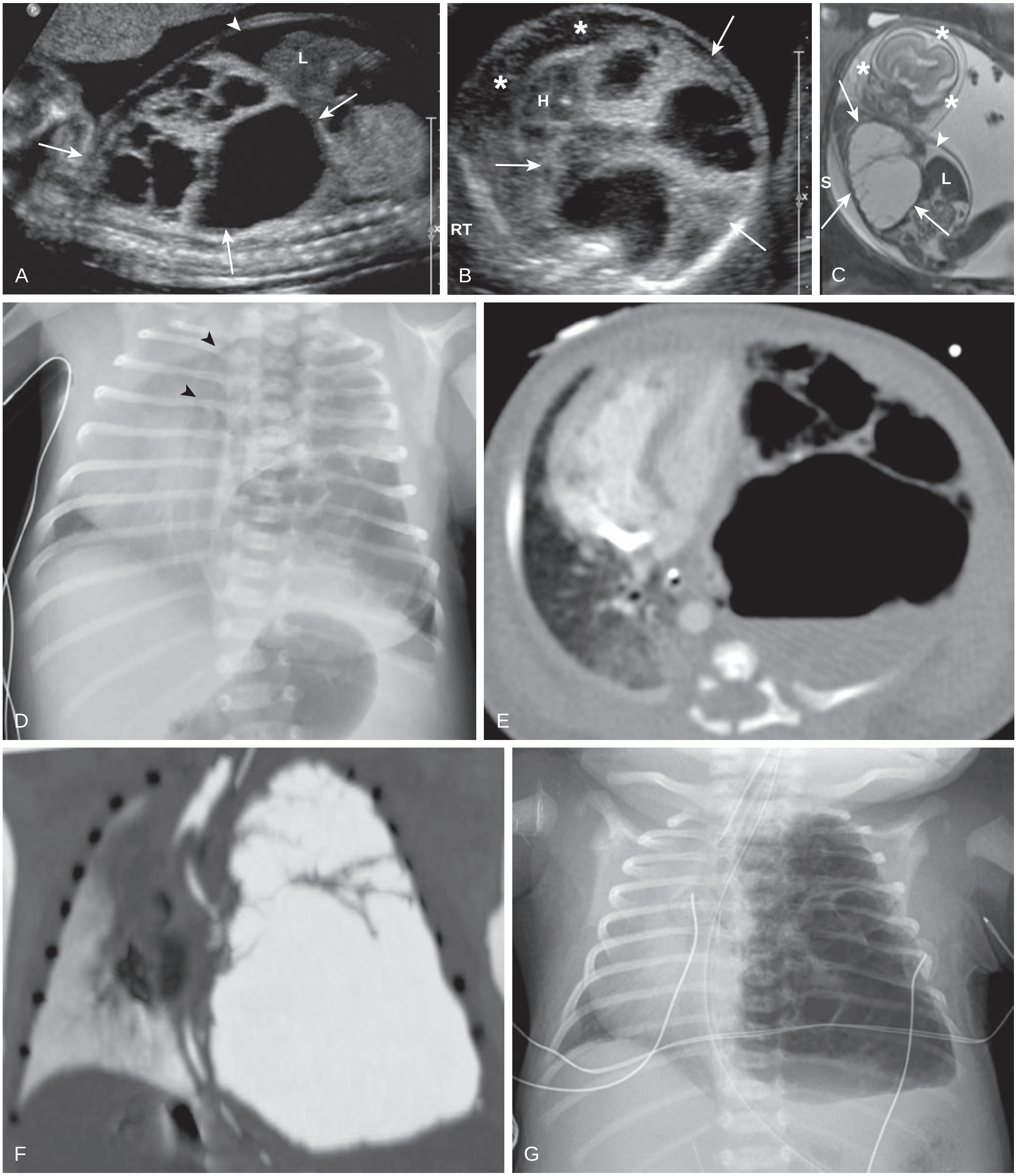

**Figure 53.8. Congenital pulmonary airway malformation type 1.** Sagittal ultrasound (A), axial ultrasound (B), and fetal sagittal T2-weighted MR (C) images in a 22-week gestational age fetus show a large, heterogeneous, multicystic lesion occupying the vast majority of the left hemithorax *(arrows)* and resulting in inversion of the left hemidiaphragm. Note the ascites in the abdomen *(arrowhead)* and the skin thickening and edema *(asterisks)*, which are reflective of hydrops. *H,* Heart; *L,* liver. (D) Radiograph immediately after delivery shows the complex, partially aerated lesion resulting in significant mediastinal shift. The *arrowheads* denote the severe tracheal deviation. Axial computed tomography angiography (E) and coronal inverted minimum intensity projection (F) images obtained the following day show the large, heterogeneous lesion with multiple macrocysts of varying sizes. Fluid is identified in some of the cysts. (G) As fetal fluid is cleared from the lungs, the lesion appears more aerated and further mediastinal shift occurs.

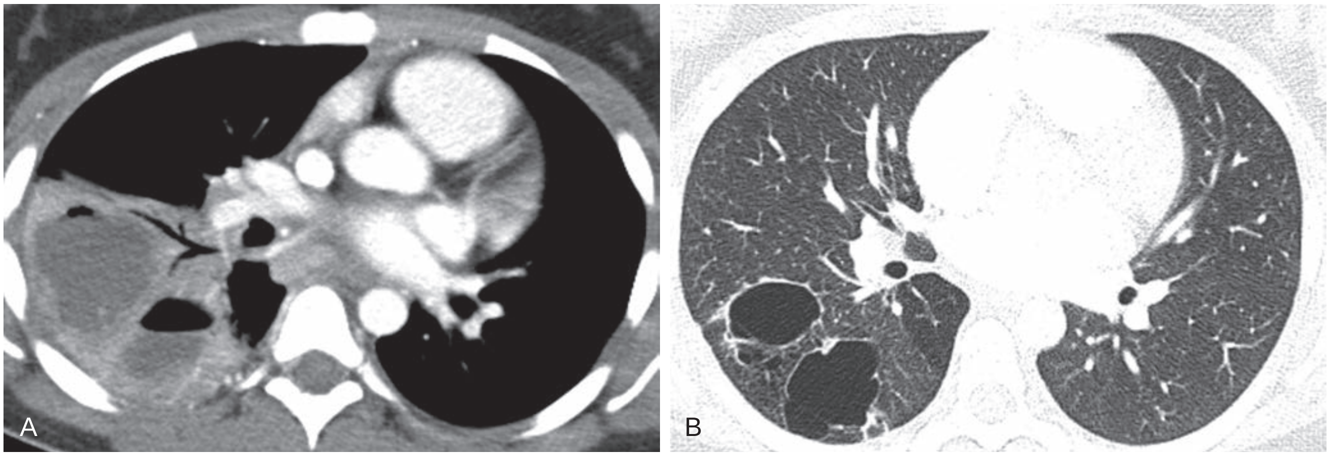

**Figure 53.12. Infected CPAM type 1 in a 15-year-old girl.** (A) Initial axial contrast-enhanced CT image shows consolidation, with areas of low attenuation representing superimposed infection with air–fluid levels in the cystic components. (B) Follow-up CT image obtained 7 months later shows resolution of the infection and visualization of the air-filled CPAM cysts.

## COMBINED PARENCHYMAL AND VASCULAR LESIONS

### Bronchopulmonary Sequestration

***Etiology.*** BPSs are congenital lung malformations that consist of nonfunctioning lung tissue that does not connect with the tracheobronchial tree. A BPS has a systemic arterial supply, usually from the aorta, although occasionally it may arise from branches of the celiac, splenic, intercostal, or subclavian arteries.

Sequestrations are classified as either extralobar (25%) or intralobar (75%). Extralobar sequestration (ELS) is defined as an isolated mass of lung tissue with its own pleural investment and aberrant systemic vascular supply. An ELS is believed to develop from a supernumerary lung bud that separates from the tracheobronchial tree and parasitizes its own vascular supply from the systemic circulation and is usually unaerated.[4,10,42] Venous drainage is into the azygos or hemiazygos systems in most cases. However, an ELS may drain into the pulmonary veins or other systemic veins, including the subclavian and intercostal veins, as well as the portal venous system.[4,8,42] Although most ELSs are identified in isolation, occasionally an ELS may be associated with congenital heart defects, abnormal communications with the GI tract, pulmonary hypoplasia, ectopic pancreas, vertebral anomalies, and congenital diaphragmatic hernia, which is the most commonly associated anomaly.[1,4,8,20,42] ELS may show spontaneous regression.[43] Associated microcystic maldevelopment or CPAM type 2 components have been described in many of these cases,[8,44] referred to as hybrid lesions.[45,46] Most patients with an ELS are asymptomatic.

Intralobar sequestration (ILS) is defined as a developmental malformation composed of isolated, nonfunctioning lung tissue without communication to the tracheobronchial tree and with an aberrant systemic vascular supply, typically embedded within a normal lobe.[4,20,47] Unlike ELS, ILS lesions do not have their own pleural coat, and venous drainage primarily occurs into the pulmonary veins.[8,9,20,47] In the past, ILS has been considered an acquired lesion resulting from a chronic inflammatory process that recruited collateral flow from aortic branch arteries.[47] Increasing reports of antenatal ILS detection, confirmed by postnatal resection, has challenged this previous concept. Pediatric patients with ILS often clinically present with recurrent lung infection.

***Imaging.*** Imaging findings of BPS vary, primarily on the basis of association with superimposed infection (e-Fig. 53.13), CPAM lesions (Fig. 53.14), or GI tract communication.[1,8] In fetal imaging, BPS lesions are echogenic on ultrasound and hyperintense on T2-weighted magnetic resonance (MR) images.[27] The supplying systemic artery may be identified prenatally. Similar to CPAM and bronchial atresia, BPS can be detected as early as in the 12th week of gestation,[24] although most usually are diagnosed on routine ultrasound at 19 to 20 weeks. They exhibit a characteristic increase in volume from the 20th to the 26th week and usually reach a plateau by the 28th week of gestation.[7,24,27,36,41] BPS usually decrease in size during the third trimester and seem to vanish in nearly half of the cases. Because complete regression is extremely unusual, follow-up cross-sectional postnatal imaging is recommended in all cases,[7,27,36] because these lesions may be overlooked on chest radiographs.[48]

On chest radiographs, ELS lesions typically present as a focal nonaerated lung mass. ILS lesions often present as a focal lung mass and/or cyst but also may manifest as an area of consolidation or lung abscess, particularly in the setting of recurrent superimposed infection. Although ELSs may be encountered anywhere from the neck to below the diaphragm, they are found most commonly within the lower hemithorax, more often on the left side.[4,8,42]

On CT, ELS lesions characteristically appear as solid, unaerated lesions, although in nearly half of the cases, coexistent pathology with CPAM type 2 has been reported (Fig. 53.15). In these cases, internal cystic components may be identified.[4,8,44] Because ILS lesions do not have a pleural investment, they typically manifest as aerated lesions, presumably from collateral air drift, if enough time has elapsed to adequately clear any retained fetal lung fluid (Fig. 53.16).[8] Anomalous vascular components of BPS can be evaluated postnatally with either CT or MRI, with interpretation facilitated by multiplanar and 3D reconstructions.[1,8,49]

***Treatment and Follow-up.*** Many authors support the elective surgical resection of ILS because of the risk of complications, such as superimposed infection, pneumothorax, hemorrhage, sudden respiratory compromise, and the small risk of malignant transformation.[23,24,28,40] Lobectomy via video-assisted thoracoscopic surgery is performed in many institutions, because segmentectomies may result in incomplete resection and air leaks.[23,24,40] Segmentectomies are usually reserved for smaller lesions or for children with bilateral, multilobar involvement.[28]

Management of ELS is more controversial, because there is a lower risk of complications.[23] Nonoperative, expectant management frequently is applied to an extrathoracic ELS, whereas an intrathoracic ELS usually is resected. Arterial embolization has been

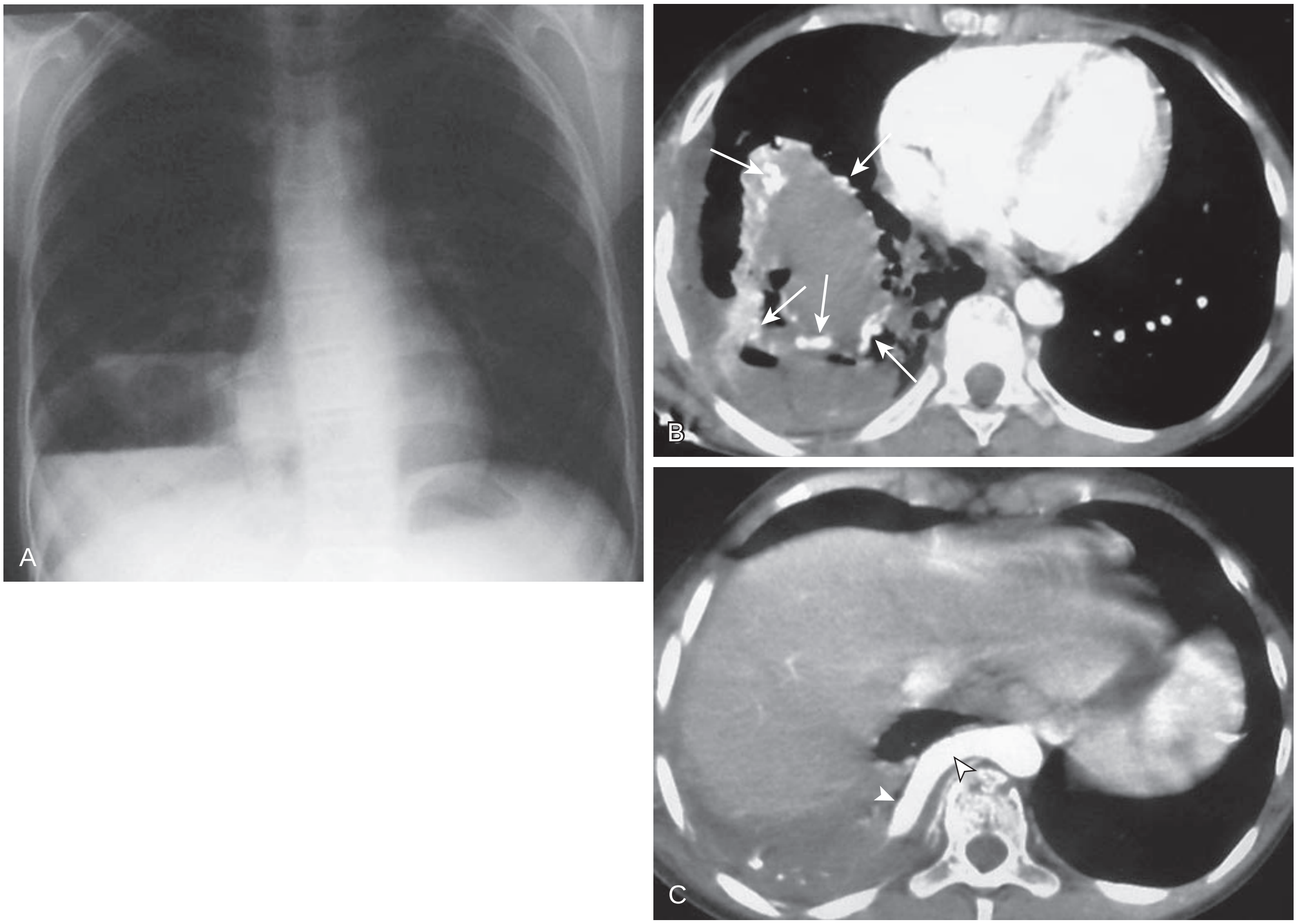

**e-Figure 53.13. Infected hybrid lesion in a 12-year-old girl with a history of recurrent right lower lobe pneumonia.** (A) Frontal chest radiograph shows a large right lower lobe lesion with an air fluid level. (B) Axial CTA image shows rounded, fluid-filled lesions with peripheral brisk, enhancing *(arrows)* margins. A small associated pleural effusion is present. (C) Axial CTA image shows a large aortic feeder *(arrowheads)* providing arterial systemic supply to the lesion.

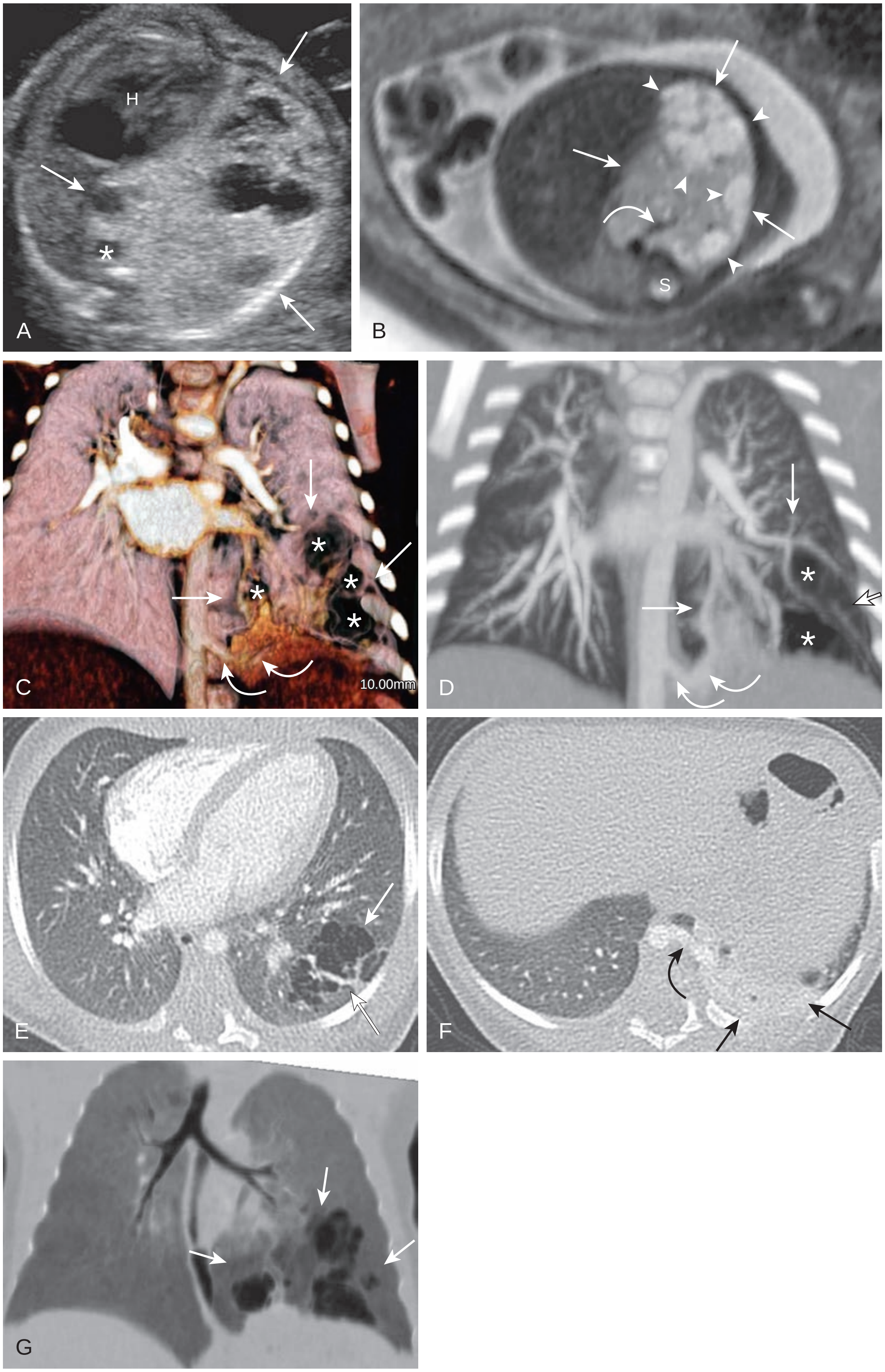

**Figure 53.14. Hybrid lesion, intralobar sequestration, and microcystic maldevelopment (CPAM type 2).** (A) Transverse fetal sonogram shows a large left lower chest lesion *(arrows)* resulting in significant heart *(H)* and aortic *(asterisk)* displacement. Internal cystic components are noted mainly at the periphery of the lesion. (B) Axial T2-weighted fetal MR image shows the extensive hyperintense lesion within the left lower lobe. Cystic peripheral components consistent with CPAM are noted *(arrowheads)*. An aortic feeder *(curved arrow)* is seen supplying the lesion. *S,* Spine. (C–F) Postnatal CT imaging shows a complex, partially aerated left lower lesion supplied by an aberrant aortic vessel *(curved arrows)* with aerated, mainly peripheral cysts *(asterisks)* and overall findings consistent with a hybrid lesion *(arrows)*. The lesion appears relatively smaller when compared with the prenatal images. Coronal volume-rendered (C), maximum intensity projection (D), and axial CTA (E and F) images show a systemic, aortic feeder *(curved arrows)* to the lesion *(arrows)*. Internal cystic components are noted predominantly at the periphery *(asterisks)* of the lesion. A portion of unaerated lung is seen at the base of the lesion. (G) A coronal reformatted minimum intensity projection image shows the internal cystic CPAM components *(arrows)* to better advantage.

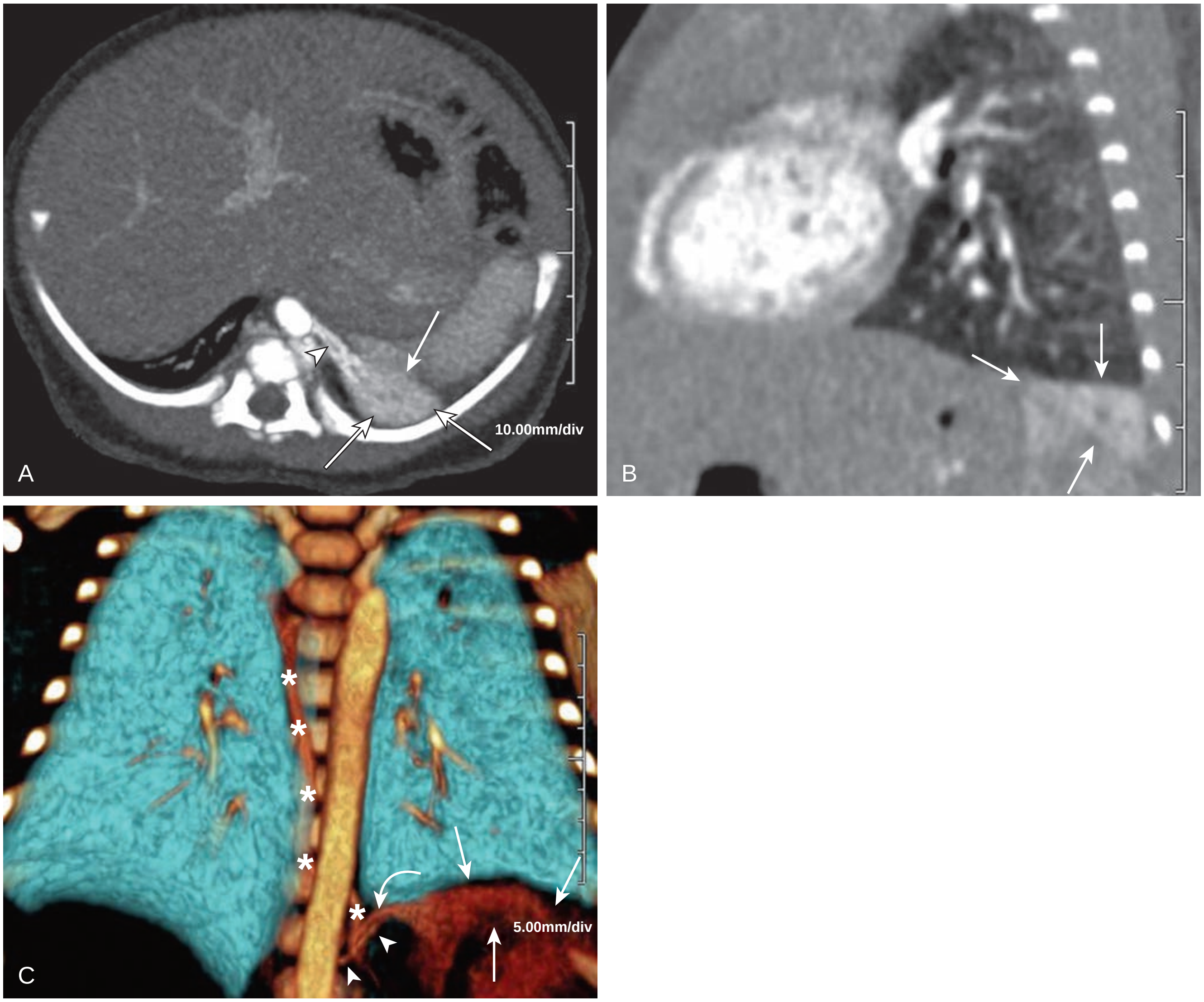

**Figure 53.15. Extralobar bronchopulmonary sequestration in a 1-month-old infant.** Axial maximum intensity projection (A) and a sagittal multiplanar reconstruction (B) CT images show unaerated, enhancing lung tissue in the left costophrenic sulcus with a small aortic feeder *(arrowhead)*, consistent with extralobar sequestration (ELS) *(arrows)*. If the aberrant arterial supply was not identified, the appearance of the lung could easily be ascribed to atelectasis. A coronal volume-rendered three-dimensional image (C) demonstrates the relationship of the small sequestration *(arrows)* to the left lung and depicts the course of the aortic feeder *(arrowheads)* and the draining vein *(curved arrow)* into the azygos system *(asterisks)*.

reported as a successful alternative management for sequestration, particularly for infants presenting with congestive heart failure,[23] as evidenced by shrinkage of the lesion on follow-up imaging.[50,51]

## Hypogenetic Lung Syndrome (Scimitar Syndrome)

***Etiology.*** Hypogenetic lung syndrome, also known as scimitar syndrome, refers to an anomalous connection of the right pulmonary veins to the inferior vena cava, in which an anomalous pulmonary vein drains part of or the entire right lung. The anomalous vein may on occasion drain into the hepatic veins, portal veins, azygos vein, coronary sinus, or right atrium. The anomalous vein often resembles a scimitar, a curved Turkish sword, hence the name “scimitar syndrome.” Hypogenetic lung syndrome frequently is associated with various degrees of right lung hypoplasia and abnormal lobation, and a hypoplastic pulmonary artery along with heart dextroposition.[49] Additional reported anomalies associated with hypogenetic lung syndrome include bronchogenic cyst, horseshoe lung, accessory diaphragm, hernia, and arterial supply of parts of the right lung by collateral arterial blood vessels, usually from the descending aorta.[1,49,52] Affected infants may present with clinical signs and symptoms related to congestive heart failure from right-heart volume overload. Hypogenetic lung syndrome also may be seen as an incidental finding in older children or alternatively may manifest as recurrent right basilar pneumonia (see also Chapter 71).[1,9,15]

***Imaging.*** The classic vertically oriented curvilinear opacity, representing the scimitar vein, which projects over the right lower hemithorax in conjunction with a hypoplastic right lung, is usually seen on frontal chest radiographs. On lateral chest radiographs, a dense retrosternal band of variable width typically is observed, which is a result of the decrease in anteroposterior diameter of the hypoplastic lung, resulting in a lung–soft tissue interface.[5,53] CT or MRI are the preferred imaging modalities for confirming

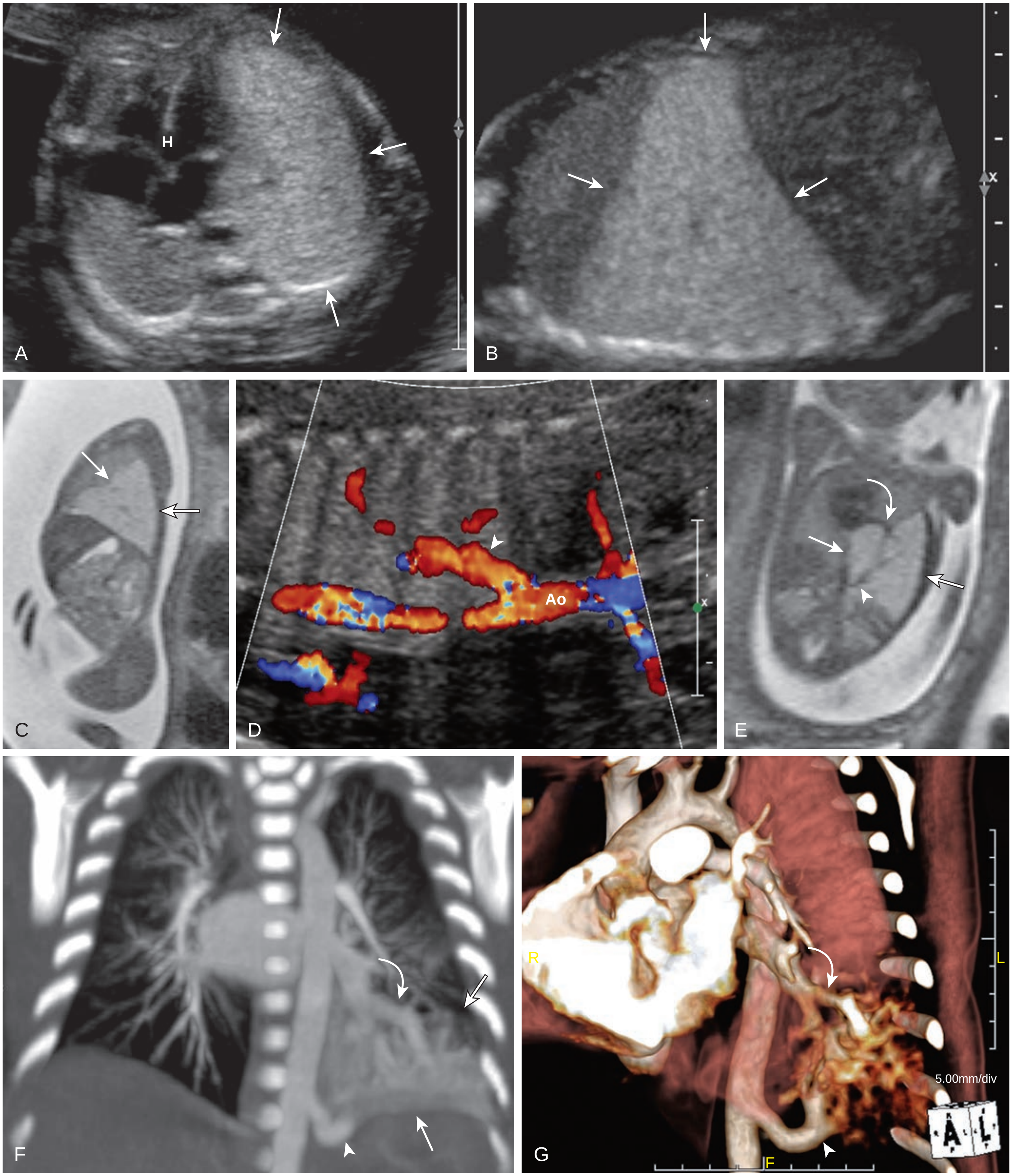

**Figure 53.16. Intralobar sequestration.** (A) Transverse sonogram through the chest shows a large, homogeneously hyperechoic lesion *(arrows)* in the left lower chest resulting in mild mediastinal shift and cardiac heart *(H)* displacement. Sagittal ultrasound (B) and sagittal T2-weighted fetal MR (C) images show a homogeneous large left lower lesion without visible cysts *(arrows)*. (D) Coronal fetal sonogram shows an aortic feeder *(arrowhead)*. *Ao,* Aorta. (E) Coronal oblique T2-weighted fetal MR image also shows a prominent aortic feeder *(arrowhead)* and a slightly prominent pulmonary vein *(curved arrow)* draining the large hyperintense lesion *(arrows)* within the left lower lobe. Coronal maximum intensity projection (F) and volume-rendered (G) CTA images at 7 days of age show a prominent aortic feeder *(arrowhead)*. The lesion *(straight arrows)* is only partially aerated and drains into a prominent pulmonary vein *(curved arrows)* consistent with an intralobar bronchopulmonary sequestration. Note the relative decrease in the size of the lesion compared with prenatal imaging.

and characterizing hypogenetic lung syndrome in pediatric patients (e-Figs. 53.17 and 53.18). Multidetector CT with 2D and 3D reformatted images have are particularly useful for preprocedural evaluation by displaying the entire course of the anomalous vein.[9,49] They are also helpful for evaluating postoperative complications, including thrombosis or stenosis of a reimplanted anomalous vein. Furthermore, abnormal lung parenchymal changes, abnormal lung lobation, and anomalous bronchial branching patterns often are seen in patients with hypogenetic lung syndrome and also can be well evaluated.[9,49] The absence of an ipsilateral inferior pulmonary vein is a helpful finding that supports the diagnosis.

***Treatment and Follow-up.*** For symptomatic pediatric patients with scimitar syndrome, surgical techniques aim to reconnect the anomalous vein to the left atrium with or without the creation of an intracardiac baffle. Complications related to either restenosis or baffle obstruction are not uncommon.[54] In addition, occlusion of the collateral arteries may be necessary in affected patients; this may be performed angiographically to reduce the amount of shunting and to improve the clinical symptoms of congestive heart failure, if present.[55,56] The presence of associated pulmonary hypertension plays an important role in the incidence of postoperative complications.[56]

## PREDOMINANTLY VASCULAR LESIONS

This section emphasizes vascular anomalies that are associated with or produce secondary lung parenchymal or airway abnormalities. Purely vascular lesions such as isolated partial anomalous venous return (see Chapter 71) and pulmonary varix (see Chapter 82) are covered elsewhere in the book.

### Anomalies of the Pulmonary Artery

#### Pulmonary Agenesis, Aplasia, and Hypoplasia

***Etiology.*** Pulmonary underdevelopment may be classified into three main types: (1) lung agenesis, consisting of the absence of the lung, bronchus, and pulmonary artery; (2) lung aplasia, that is, the presence of a rudimentary bronchus but the lack of lung tissue and pulmonary artery; and (3) lung hypoplasia, which consists of a hypoplastic bronchial tree and pulmonary artery with a variable amount of lung parenchyma.[15,57,58]

The etiology of lung agenesis or aplasia remains uncertain. Genetic, teratogenic, and mechanical factors may play a role.[1] Pulmonary agenesis associated with ipsilateral radial ray defects or hemifacial microsomia may be the result of an abnormal development of the first and second arch derivatives or abnormal blood flow at this level inciting the developmental event, given the common association.[59] On the other end of the spectrum, no identifiable cause has been found for primary lung hypoplasia.[1]

Persons with pulmonary agenesis, aplasia, and hypoplasia either are asymptomatic or present with variable degrees of respiratory distress, depending on the extent of lung underdevelopment and associated anomalies. Other congenital malformations occur in 50% to 80% of cases including cardiovascular, GI, musculoskeletal, and genitourinary anomalies.[1,59–61]

***Imaging.*** On chest radiographs, there may be a small, radiopaque or radiolucent hemithorax, depending on the degree of abnormality. Ipsilateral displacement of mediastinal structures and elevation of the hemidiaphragm usually are present. The normal contralateral lung shows compensatory hyperinflation and herniation across the anterior midline, which is best seen on the lateral projections as a band of increased retrosternal lucency (Fig. 53.19).[1] Left lung agenesis is more common than right lung agenesis. CT with multiplanar 2D and 3D imaging capabilities can be used to distinguish among pulmonary agenesis, pulmonary aplasia, and pulmonary hypoplasia by clearly identifying the bronchial stump and/or the rudimentary bronchial tree (e-Figs. 53.20 and 53.21, Fig. 53.22, and e-Fig. 53.23).[1,49] Additional vascular, airway, or lung abnormalities can also be defined.

***Treatment and Follow-up.*** The prognosis of pediatric patients with pulmonary underdevelopment primarily depends on the extent of underdevelopment and the severity of other associated congenital malformations. Treatment usually is aimed at improving the respiratory status and symptoms related to concomitant congenital malformations.

#### Proximal Interruption of the Pulmonary Artery

***Etiology.*** Proximal interruption of the pulmonary artery results from the abnormal involution of the proximal sixth aortic arch. Such involution causes the “absence” of the proximal pulmonary artery and a persistent connection of the hilar pulmonary artery to the distal sixth aortic arch, which ultimately becomes the ductus arteriosus. The hilar pulmonary artery supplying the ipsilateral affected lung continues to develop via the blood supply received from the ductus arteriosus (which originates either from the base of the right innominate artery or occasionally from an aberrant right subclavian artery).[1,6] Progressive closure of the ductus arteriosus eventually results in loss of blood supply to the hilar pulmonary artery and the lung. Perfusion of the affected lung subsequently becomes dependent on collateral systemic vessels, mainly aortopulmonary and bronchial arteries but also transpleural branches of the intercostal, internal mammary, subclavian, and innominate arteries.[62–64] Although asymptomatic pediatric patients with this anomaly may be detected incidentally, some children present with symptoms related to recurrent pulmonary infections, hemoptysis, and pulmonary hypertension.[6,9,15]

***Imaging.*** The interrupted proximal pulmonary artery is characteristically located on the contralateral side to the aortic arch and is more commonly seen on the right side. Interruption of the proximal left pulmonary artery is less common and frequently is associated with congenital heart disease, typically tetralogy of Fallot and ventricular septal defect.[1,6,49] On chest radiographs, the affected lung and hilum are smaller than those of the contralateral side (Fig. 53.24). Ipsilateral mediastinal shift, narrowed intercostal spaces, or rarely rib notching in the case of prominent intercostal collaterals also may be present.[9,15,64] On CT or MRI, the interrupted pulmonary artery terminates within 1 cm of its origin from the main pulmonary artery. However, the hilar portion of the pulmonary artery and the intrapulmonary vascular network remain patent (e-Fig. 53.25). A small ductal diverticulum is usually present at the base of the innominate artery, the remnant of the prior ductal supply to the pulmonary artery. Serrated pleural thickening and subpleural parenchymal bands also may be observed, which reflect the direct anastomosis of transpleural systemic collaterals with peripheral pulmonary arterial branches. Airway branching and pulmonary lobation anomalies are not uncommon. Additional imaging findings may include tiny peripheral cystic and possibly dysplastic lung changes, areas of mosaic attenuation, bronchiectasis, and an asymmetric thoracic cage.[1,6,15,49,63]

***Treatment and Follow-up.*** Prompt diagnosis and early surgical intervention may provide adequate blood supply to the affected lung, allowing improved pulmonary arterial supply and lung growth. Surveillance is indicated for patients with a late presentation who are considered unsuitable for intervention. Patients who present with recurrent hemoptysis or pulmonary hypertension may benefit from coil embolization of large systemic collaterals.[1,6,65]

#### Pulmonary Artery Sling

***Etiology.*** Pulmonary artery sling (PAS) is a rare congenital anomaly in which the left pulmonary artery arises anomalously from the posterior aspect of the right pulmonary artery and courses between the trachea and esophagus to reach the left hilum.[15] The anomalous left pulmonary artery forms a sling around the distal

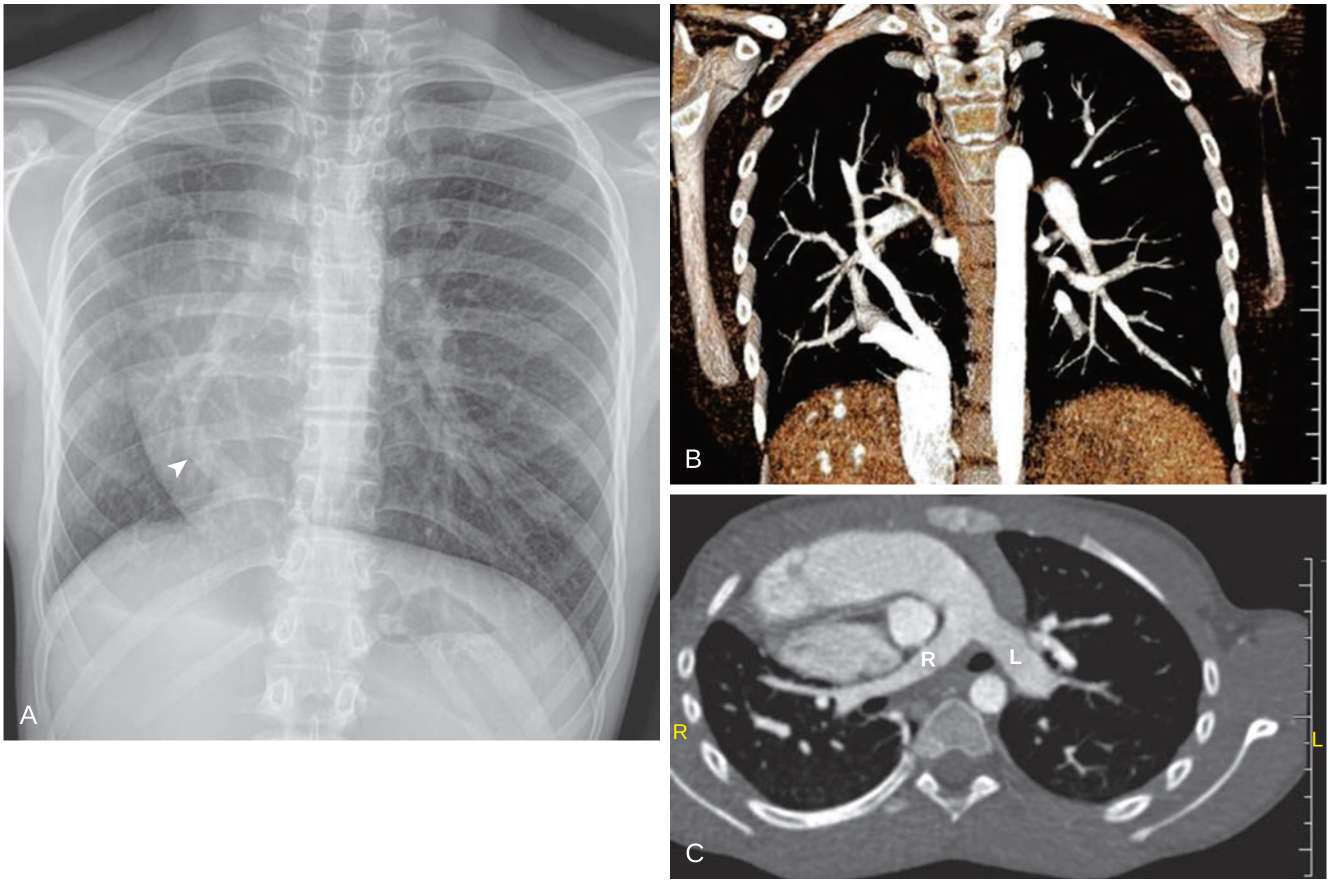

**e-Figure 53.17. Hypogenetic lung syndrome in a 13-year-old with exercise intolerance.** (A) Frontal chest radiograph shows a scimitar vein *(arrowhead)* extending to the medial right hemidiaphragm and heart dextroposition consistent with hypogenetic lung syndrome. (B) Coronal volume-rendered CTA image shows partial anomalous pulmonary venous drainage of the right lung to the inferior vena cava via two scimitar veins. A small portion of the right lung drains as expected into the left atrium. (C) An axial maximum intensity projection CT image shows dextroposition of the heart and hypoplasia of the right pulmonary artery *(R)* relative to the left pulmonary artery *(L)*.

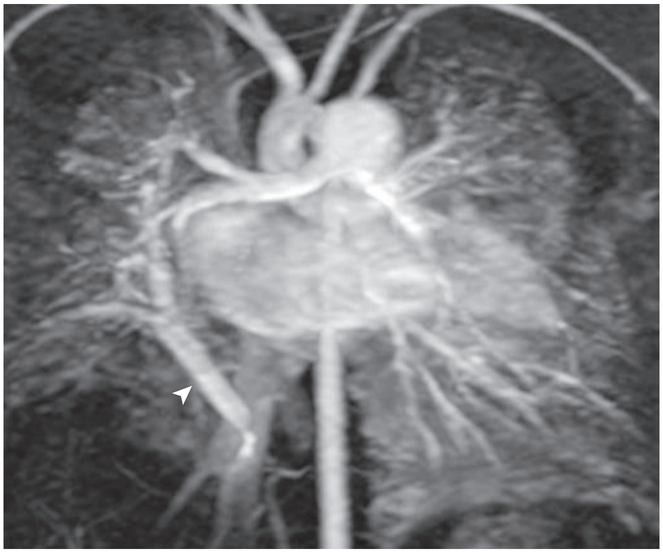

**e-Figure 53.18. Hypogenetic lung syndrome in a 3-month-old with a history of an abnormal chest radiograph.** Coronal maximum intensity projection MR image reveals anomalous pulmonary venous drainage of the right hypoplastic lung via a scimitar vein *(arrowhead)* into the inferior vena cava.

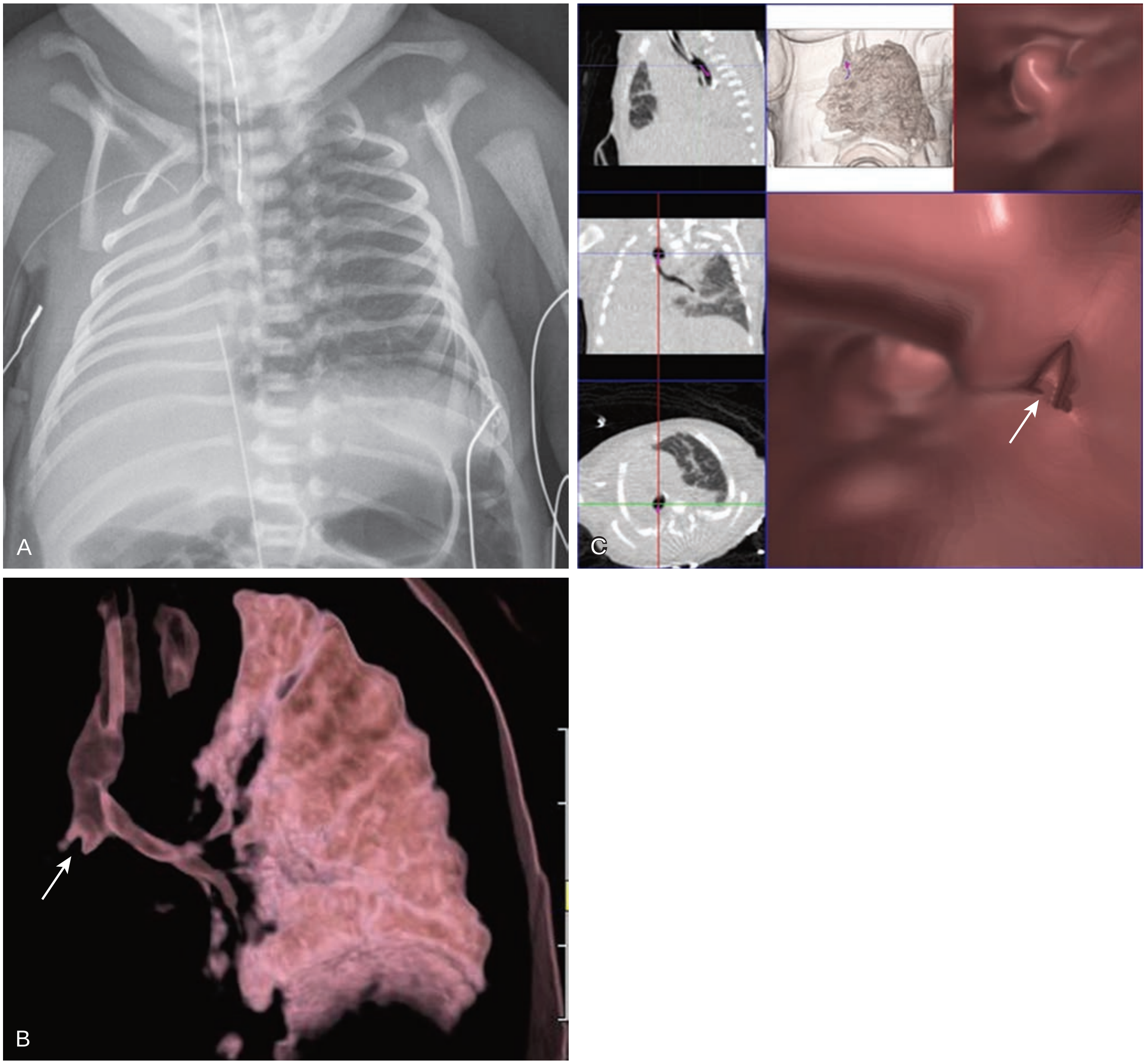

**e-Figure 53.20. Lung aplasia, absent right pulmonary artery, esophageal atresia, and distal tracheoesophageal fistula in a 1-day-old.** (A) Frontal chest radiograph shows complete opacification with volume loss in the right hemithorax. The airway and mediastinum are shifted to the right with associated dextroposition of the heart. A nasogastric tube terminates in the upper esophageal pouch consistent with esophageal atresia. The anterior view of a volume-rendered CT image of the central airway and lungs (B) and virtual bronchoscopic (C) images demonstrate a rudimentary right main stem bronchus *(straight arrows)* consistent with lung aplasia. No right pulmonary artery is identified *(not shown)*.

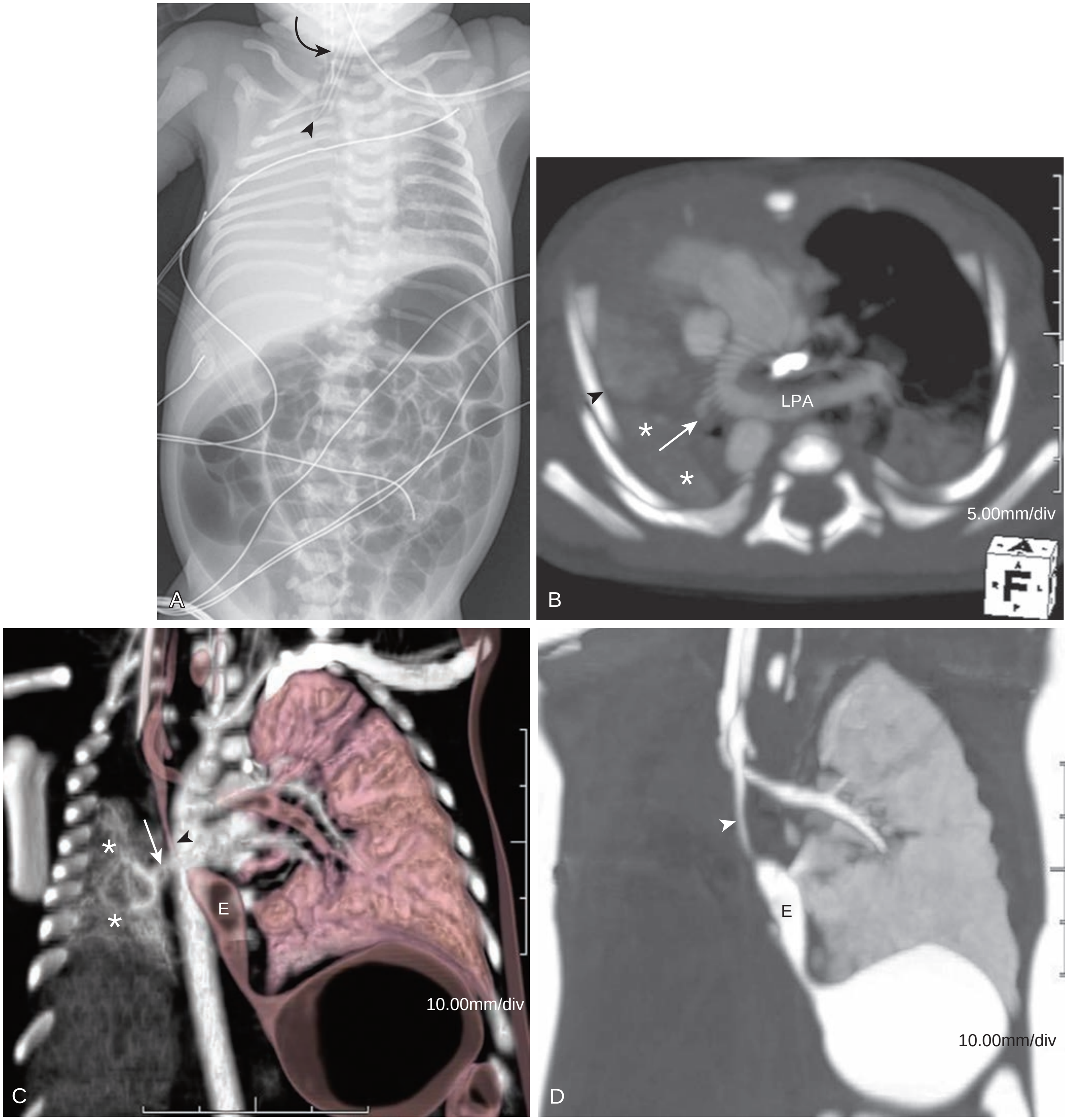

**e-Figure 53.21. Hypoplastic right lung in an ex-34-weeks premature with associated esophageal atresia, distal tracheoesophageal fistula, imperforate anus, and pulmonary sling.** (A) Frontal radiograph of the chest and abdomen shows complete opacification with volume loss in the right hemithorax. The endotracheal tube *(arrowhead)* and mediastinum are shifted to the right with associated dextroposition of the heart. A nasogastric tube *(curved arrow)* terminates in the upper esophageal pouch consistent with esophageal atresia. Pronounced gaseous distension of numerous small and large bowel loops is seen that is consistent with imperforate anus and distal TE fistula. (B) An axial maximum intensity projection CT image shows an anomalous left pulmonary artery *(LPA)* arising from a tiny, hypoplastic right pulmonary artery *(arrow)* and coursing behind the mainstem bronchi in a slinglike configuration. The right lung is severely hypoplastic and collapsed *(asterisks)*. (C) A frontal volume-rendered CT image shows an aerated left lung and a collapsed, unaerated right lung *(asterisks)*. Note the hypoplastic right pulmonary veins *(arrow)*. The *arrowhead* denotes the distal TE fistulous communication. (D) An inverted coronal minimum intensity projection CT image better demonstrates the distal TE fistulous communication *(arrowhead)*. The right bronchi were fluid opacified and could not be depicted with these techniques. *E,* Esophagus.

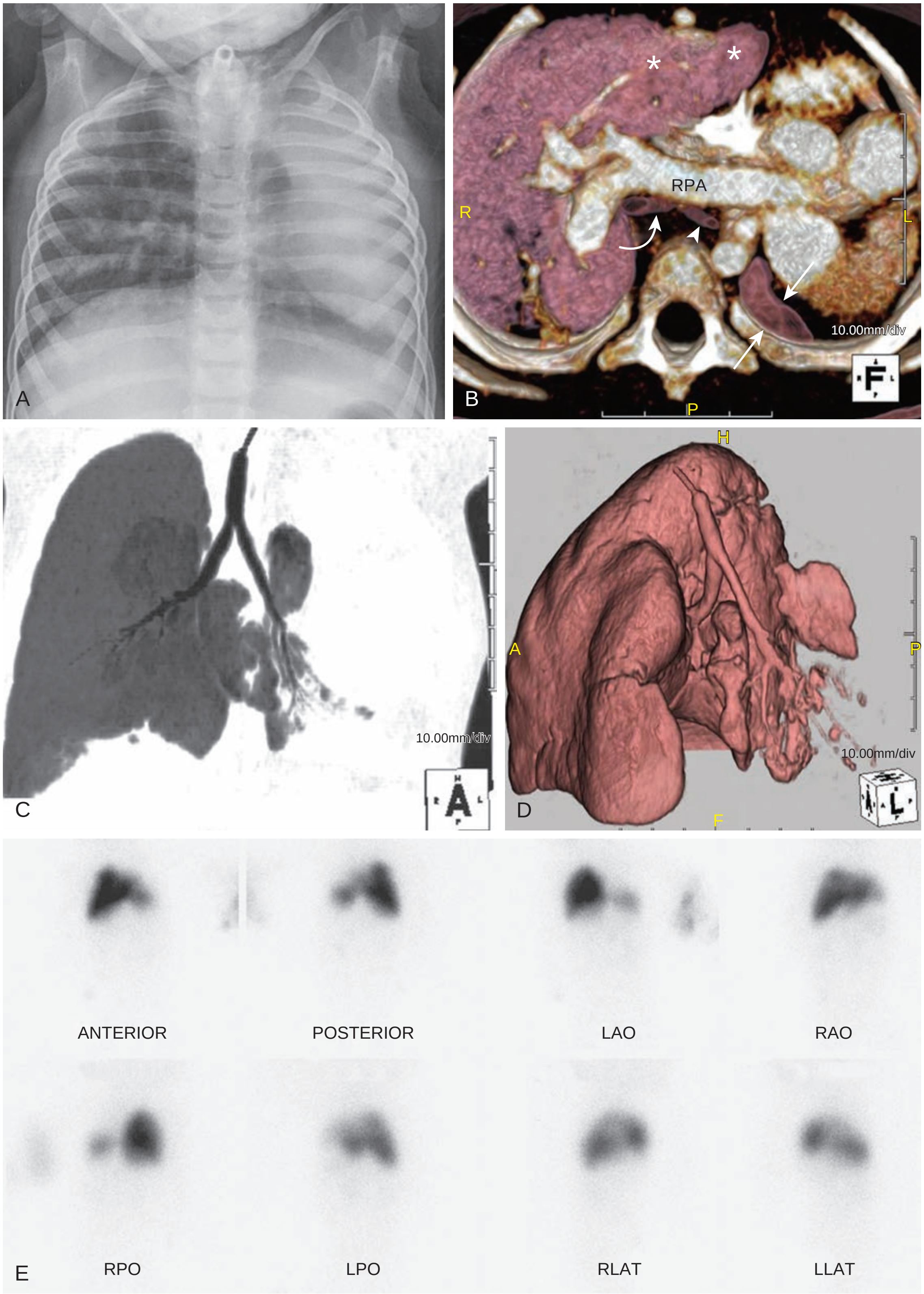

**e-Figure 53.23. Left lung hypoplasia in a 2-year-old with multiple congenital anomalies.** (A) Frontal chest radiograph shows a small, hypoplastic left lung and leftward shift of the mediastinum. (B) Axial volume-rendered CT image confirms leftward shift of the mediastinum and heart and shows a small, hypoplastic left lung *(arrows)*, hypoplastic left bronchus *(arrowhead)* relative to the right *(curved arrow)* and compensatory hyperinflation with herniation of the right upper lobe *(asterisks)* into the left hemithorax. A secondary leftward mediastinal shift with levoposition of the heart is seen. Note the prominent right pulmonary artery *(RPA)* to the right lung. The left pulmonary artery was severely hypoplastic *(image not shown).* Coronal minimum intensity projection (C) and coronal oblique three-dimensional volume-rendered (D) CT images of the central airways and lungs show a hypoplastic left mainstem bronchus and left lung. Technetium-99m lung scan images (E) reveal significantly decreased perfusion of the left lung in comparison to the right lung. *LAO,* Left anterior oblique; *LLAT,* left lateral; *LPO,* left posterior oblique; *RAO,* right anterior oblique; *RLAT,* right lateral; *RPO,* right posterior oblique.

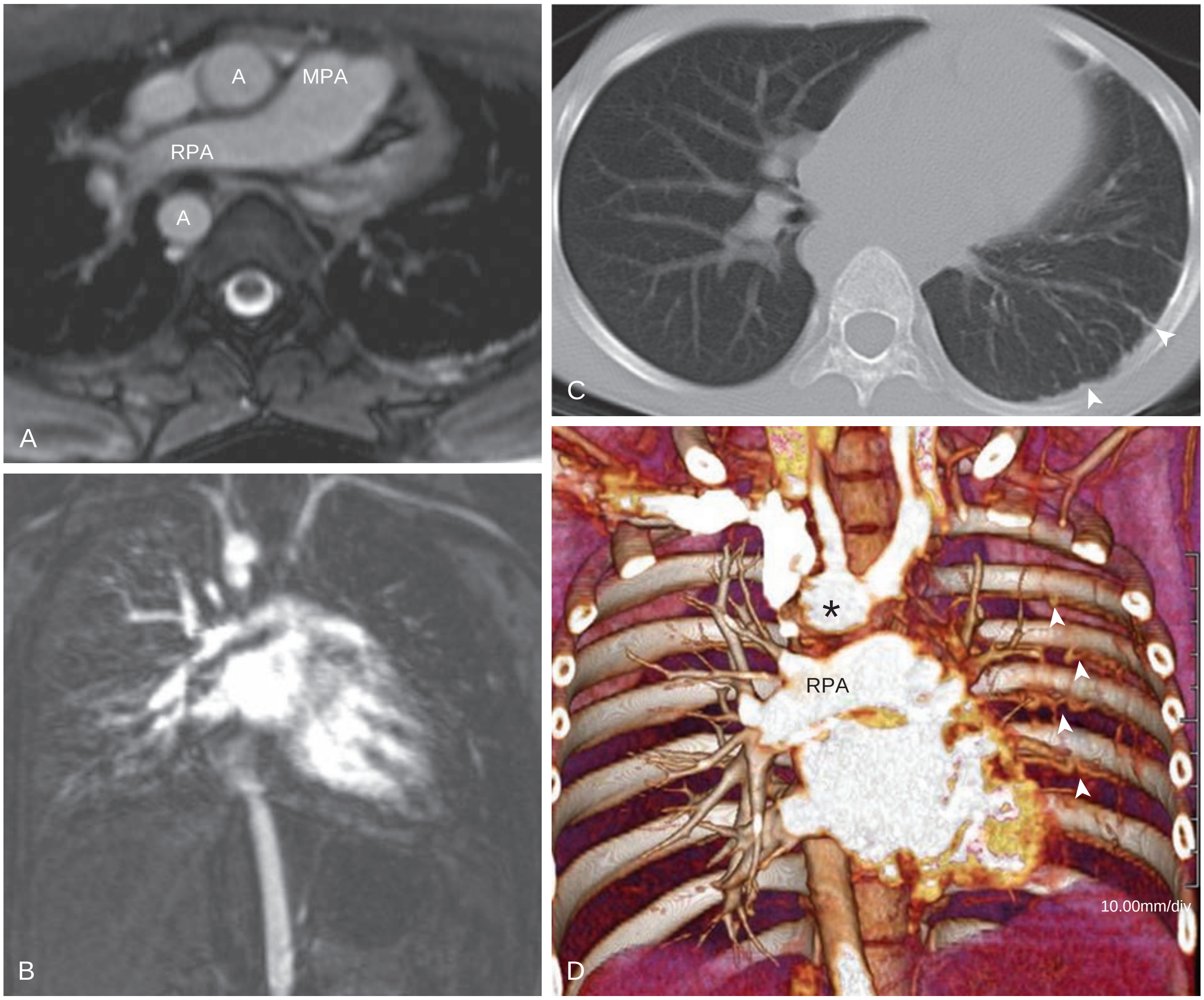

**e-Figure 53.25. Proximal interruption of the left pulmonary artery in a 10-year-old.** (A) Axial T2-weighted MR image shows absence of the left pulmonary artery. Pulmonary blood flow is from the main pulmonary artery *(MPA)* to the right pulmonary artery *(RPA)*. The aortic arch is right-sided. *A,* Aorta. (B) Coronal MRA image in the pulmonary arterial phase shows nearly no enhancement of the left lung. (C) Axial CT image shows a smaller left lung with slight mediastinal shift and serrated pleural thickening *(arrowheads)*, reflective of the direct anastomosis of transpleural systemic collaterals with peripheral branches of the pulmonary arteries. (D) Volume-rendered CTA image shows normal right pulmonary artery *(RPA)* arborization and poor vascularity in the left lung. Prominent left intercostal arteries *(arrowheads)* are providing collateral flow to the left lung. Note the right-sided aortic arch *(asterisk)*.

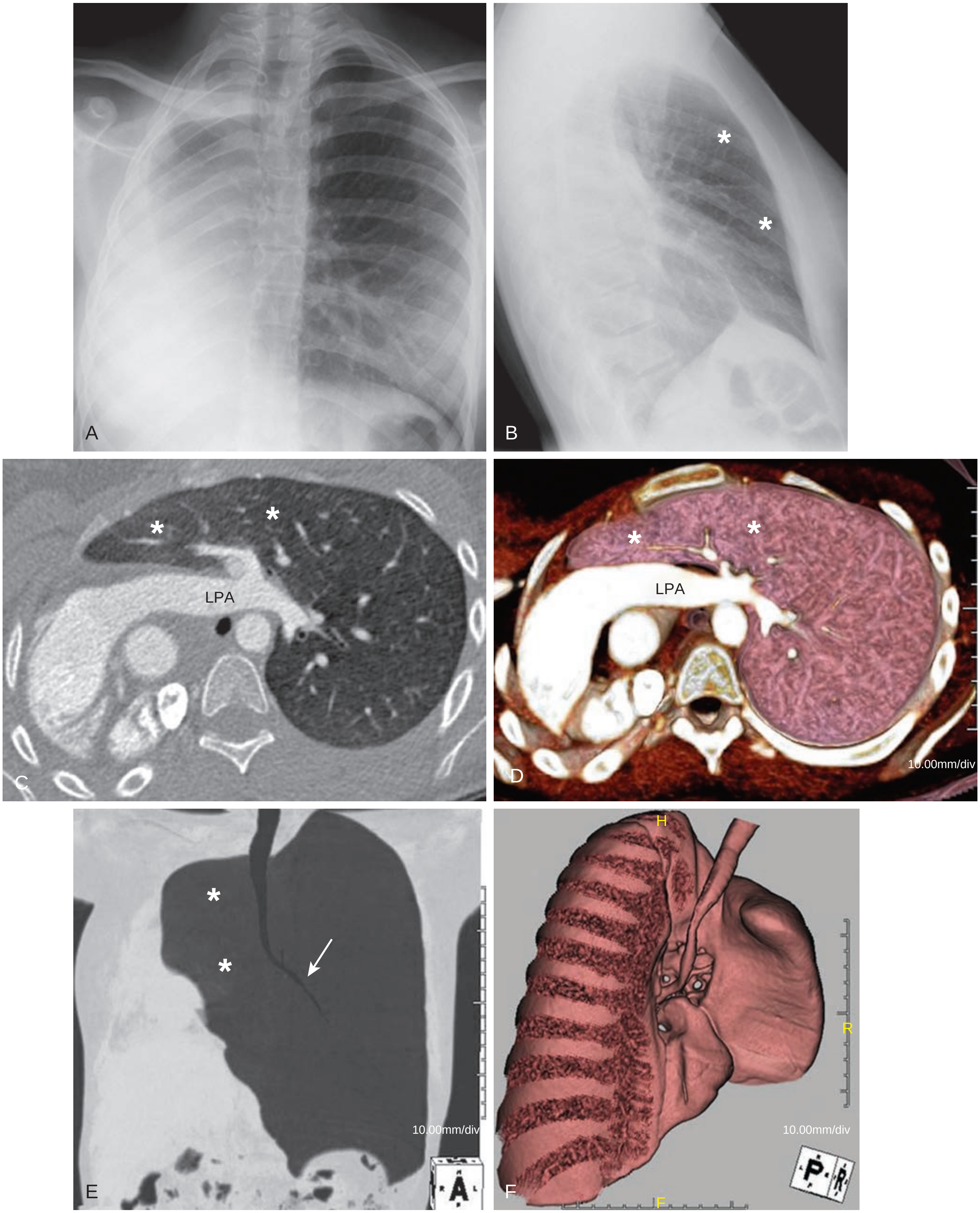

**Figure 53.19. Pulmonary agenesis.** Frontal (A) and lateral (B) radiographs in a 15-year-old with worsening asthma demonstrate marked hyperinflation of the left lung that extends across the midline anteriorly and herniates toward the right, as evidenced by a band of retrosternal lucency on the lateral projection *(asterisks)*. Associated dextroposition of the heart into the right hemithorax is seen. Contrast-enhanced axial CT (C), axial volume-rendered (D), coronal minimum intensity projection (E), and three-dimensional volume-rendered (F) images of the central airway and lungs demonstrate complete agenesis of the right bronchus, absence of the right pulmonary artery and lung. Associated dextroposition of the heart and compensatory hyperexpansion is present, particularly of the left upper lobe *(asterisks)*, which herniates into the right hemithorax. A normal left mainstem bronchus *(arrow)* is seen. *LPA,* Left pulmonary artery.

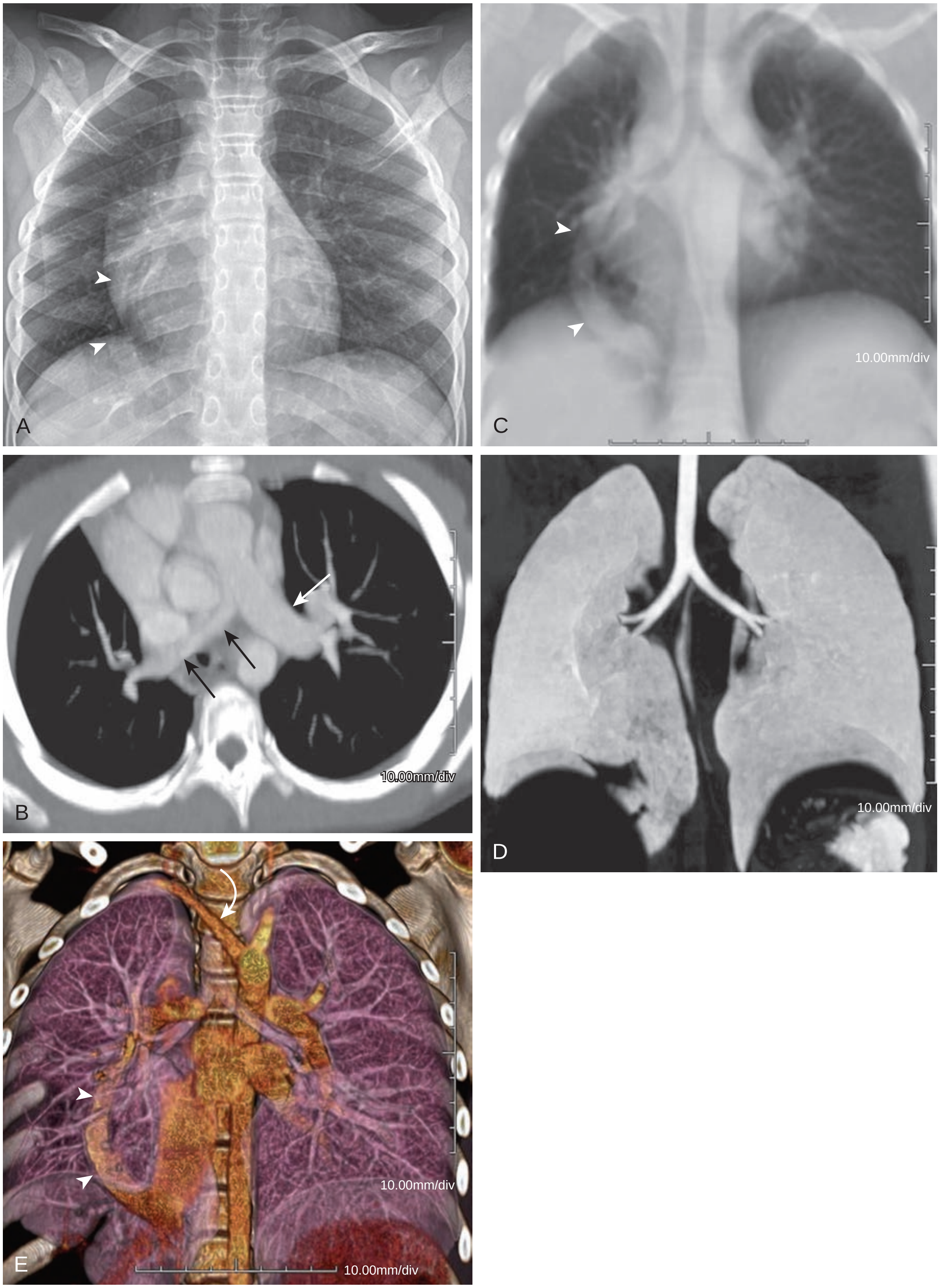

**Figure 53.22. Hypoplastic right lung and scimitar syndrome in an 8-year-old.** (A) Frontal chest radiograph shows asymmetric lung volumes with dextroposition of the heart and a vertically oriented curvilinear opacity *(arrowheads)* projecting over the right lower hemithorax. An axial maximum intensity projection CT image (B) confirms mild dextroposition of the heart and hypoplastic right lung and pulmonary artery (PA) *(black arrows)* relative to the normal left pulmonary artery *(white arrow)*. Coronal thick multiplanar reconstruction (C), inverted minimum intensity projection (D), and three-dimensional volume rendered (E) images show hypoplasia of the right lung with absence of the right upper lobe bronchus and partial anomalous pulmonary venous return of the right lung via a scimitar vein *(arrowheads)* into the inferior vena cava. Incidentally noted is a right aberrant subclavian artery *(curved arrow)*.

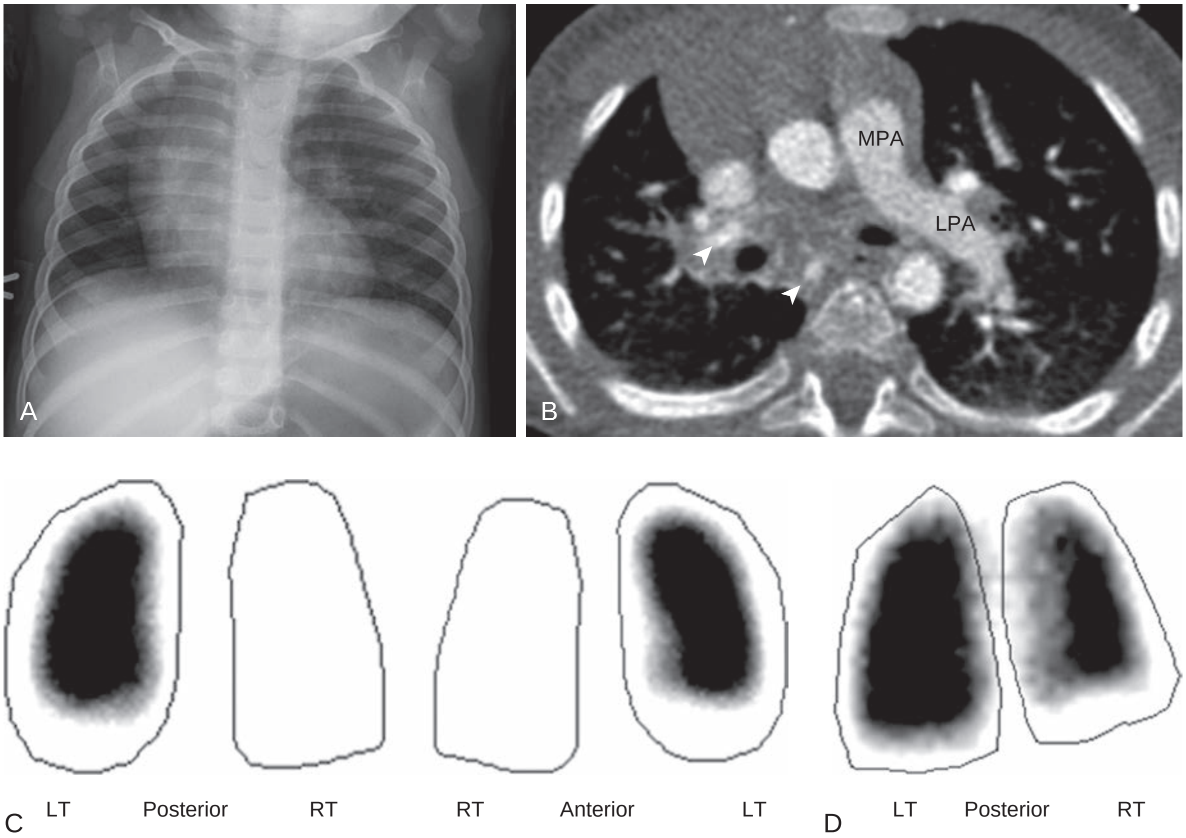

**Figure 53.24. Interrupted proximal right pulmonary artery in a 16-month-old with a persistent abnormal chest radiograph after resolution of respiratory syncytial virus bronchiolitis.** (A) Frontal chest radiograph shows a small right lung, dextroposition of the cardiomediastinal silhouette and mild asymmetry of pulmonary vascularity, decreased on the right. (B) Axial contrast-enhanced CT image reveals absence of the proximal right pulmonary artery. Several collaterals to the right lung are present *(arrowheads)*. The main pulmonary artery *(MPA)* and the left pulmonary artery *(LPA)* are intact. The aortic arch is left-sided, and overall findings are consistent with proximal interruption of the right pulmonary artery. (C) Techtetium-99m macroaggregated albumin first pass lung perfusion images show absent blood flow to the right lung. (D) Xenon-133 posterior planar image of the lungs shows decreased airflow to the right lung. *LT,* Left; *RT,* right.

trachea and/or the proximal right mainstem bronchus.[1,52,63,66] It is hypothesized that PAS develops as a result of proximal left sixth arch involution, and a secondary connection is acquired to the right sixth branchial arch via the embryonic peritracheal primitive mesenchymal vessels.[52,63,66] The concurrent presence of a left ligamentum arteriosum connecting the main or right pulmonary artery and the left descending aorta results in a complete vascular ring that encircles the trachea but spares the esophagus.[15,52]

Two main types of PAS exist. In type I PAS, the position of the carina is normally situated at the T4–T5 level. In these instances, the airway is intrinsically normal or with an associated tracheal bronchus. The aberrant left pulmonary artery may compress the posterior wall of the distal trachea and/or the lateral aspect of the right mainstem bronchus, resulting in right lung air trapping.[6,15,66] Type II PAS is more common[66,67] and is associated with a more inferiorly located carina at the T6 level. Type II PAS often is associated with long-segment tracheal stenosis with complete cartilaginous rings and abnormal bronchial branching, including a T-shaped carina and a right-bridging bronchus. Other cardiovascular, gastrointestinal, and right lung anomalies (e.g., lung hypoplasia, aplasia, agenesis, and scimitar syndrome) may coexist.[1,6,66] Patients usually present as infants with respiratory symptoms, such as stridor, apneic spells, and/or hypoxia. The timing and severity of the respiratory symptoms depend on the severity of the accompanying airway abnormalities.[6,9,66]

***Imaging.*** Imaging findings of PAS depend on its type and other coexisting congenital anomalies. On frontal chest radiographs, either hyperinflation or hypoinflation of the right lung as a result of partial or complete obstruction of the right mainstem bronchus may present in patients with type I PAS. In patients with type II PAS associated with long-segment tracheal stenosis, bilateral hyperinflation may be observed or there may be right lung hypoplasia.[6,66] On occasion, a small, rounded soft tissue density representing the anomalous left pulmonary artery may be seen between the midtrachea and esophagus on lateral chest radiographs in patients with both types of PAS (e-Fig. 53.26A). CT or MRI with 2D and 3D reconstructions are useful for evaluating the origin, size, and entire course of the anomalous vasculature (e-Fig. 53.26B and C). CT is advantageous over MRI for evaluating associated central airway and lung abnormalities (e-Fig. 53.26C). Inspiratory and expiratory imaging is particularly useful for assessing for associated tracheobronchomalacia.[1,68]

***Treatment and Follow-up.*** Asymptomatic pediatric patients with PAS may be followed up clinically. Symptomatic pediatric patients with PAS require surgical reimplantation of the anomalous left pulmonary artery to the main pulmonary artery or anterior translocation in conjunction with excision of the coexisting patent ductus arteriosus or ductal ligament. In patients with type II PAS, reimplantation or anterior translocation of the anomalous left pulmonary artery by itself may not result in respiratory improvement

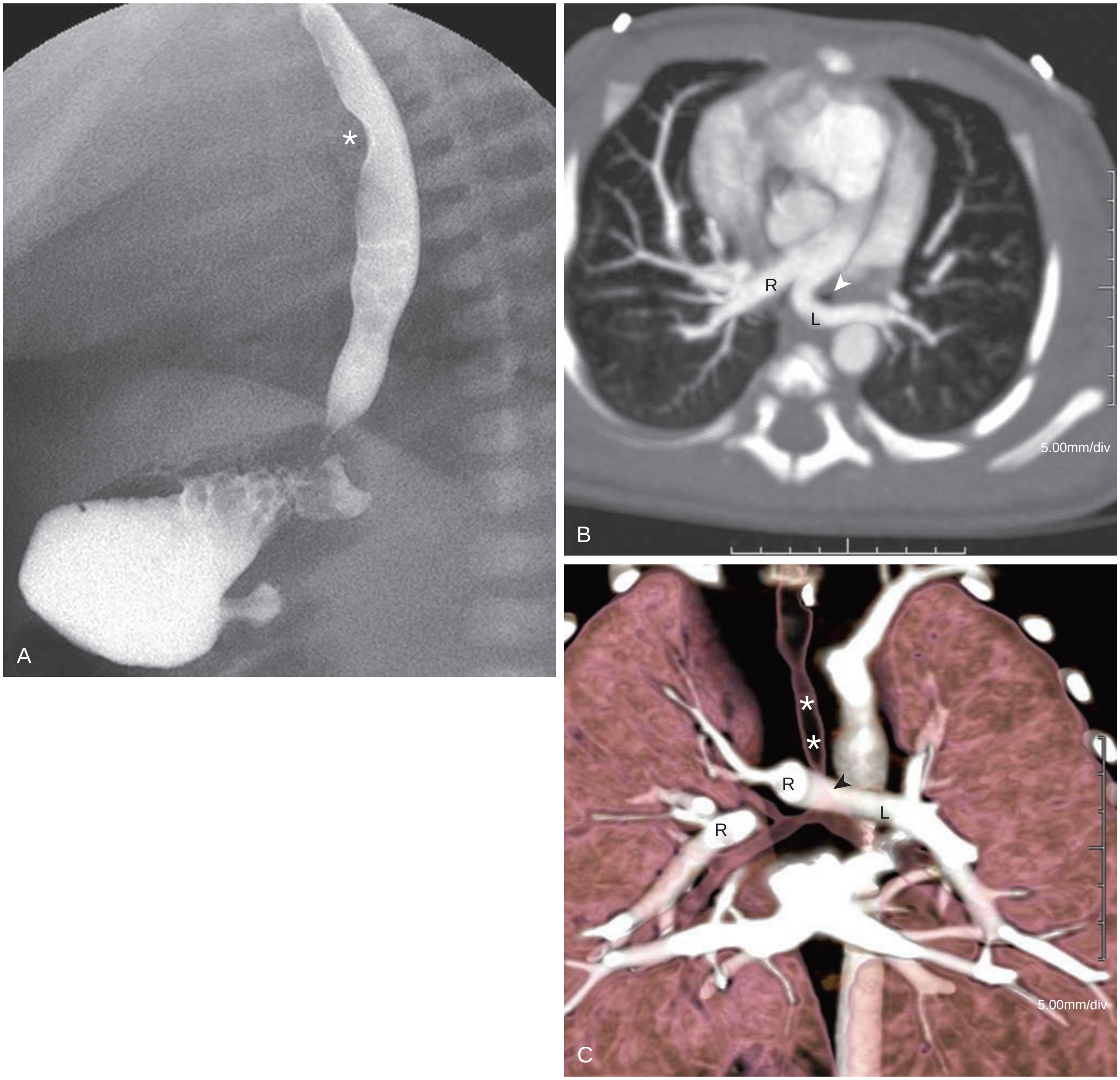

**e-Figure 53.26. Left pulmonary artery sling in a neonate with respiratory distress.** (A) Lateral esophagram shows soft tissue density *(asterisk)* between the trachea and the esophagus, suggesting an LPA sling. (B) Axial maximum intensity projection CTA image shows that the left pulmonary artery *(L)* originates from the proximal right pulmonary *(R)* before crossing behind the trachea *(arrowhead)* to feed the left lung consistent with an LPA sling. (C) Coronal volume-rendered CTA image shows severe distal trachea narrowing *(arrowhead)* at the level of the LPA *(L)* sling. The distal trachea shows long segment narrowing *(asterisks)* from complete tracheal rings. Note the low T-shaped carina.

if the coexisting long-segment tracheal stenosis is not repaired, usually by slide tracheoplasty.[66]

## Anomalies of the Pulmonary Veins

### Pulmonary Vein Atresia/Hypoplasia

***Etiology.*** Pulmonary venous atresia is an uncommon anomaly associated with high morbidity and mortality. The etiology is believed to represent the result of the unsuccessful incorporation of the common pulmonary vein into the left atrium, resulting in the lack of long segments of the central pulmonary veins. If unilateral (most common),[6] the condition may be asymptomatic or may manifest in infancy or childhood with recurrent episodes of pneumonia, hemoptysis (as a result of the systemic collateral supply to the affected lung), exercise intolerance, and pulmonary hypertension. Bilateral involvement without emergent surgical repair is typically fatal.[69,70] Nearly half of the cases are associated with other forms of congenital heart disease.[6,71,72]

***Imaging.*** Chest radiographs typically show a small affected hemithorax and hilum with ipsilateral mediastinal shift. The affected lung is hypoplastic and demonstrates circumferential pleural thickening, diffuse reticular opacities, and septal lines reminiscent of pulmonary edema, which are most pronounced in the lower lung zones.[6,71] On enhanced CT examinations, the margins of the left atrium on the affected side at the expected level of the pulmonary vein ostia appear smooth, and some adjacent enhancing soft tissue density may be present, reflecting collateral pulmonary-to-systemic venous channels. Additional collaterals may be seen in other portions of the mediastinum. The ipsilateral pulmonary artery appears small. On lung windows, diffuse ground-glass attenuation and smooth thickening of the interlobular septa and bronchovascular bundles may be observed.[71] This constellation of findings is believed to represent prominent bronchial veins, dilated lymphatics, and patchy parenchymal fibrosis as a result of pulmonary infarcts (e-Fig. 53.27).[71]

***Treatment and Follow-up.*** In cases of unilateral pulmonary venous atresia, surgical repair usually is not possible, depending on the age at diagnosis. Most patients present late in life once irreversible changes have occurred. Pneumonectomy may be necessary to prevent repeated pulmonary infections, to relieve the left-to-right shunt, and to remove the dead space contributing to exercise intolerance.[72]

### Pulmonary Vein Stenosis

***Etiology.*** Congenital pulmonary vein stenosis (PVS) may be congenital or acquired.[15] Congenital PVS is believed to be the result of an uninhibited myofibroblast-like proliferation causing endoluminal thickening and narrowing of the pulmonary veins.[9,73] However, the term “primary” pulmonary vein stenosis would be more accurate, because increasing evidence exists that the disease is progressive and may not be present at the time of delivery. Association with other congenital heart defects is high, ranging from 30% to 80%.[74,75] A strong association between PVS and prematurity has been recently reported, with a preponderance in premature newborns with cardiac shunt lesions.[76] However, PVS also may occur in isolation, and in these cases PVS usually progresses rapidly.[74]

The age at diagnosis and severity of symptoms are contingent on the number of pulmonary veins involved and the severity of pulmonary venous obstruction to individual pulmonary veins.[69,74] Patients with more than three stenotic pulmonary veins have a poorer prognosis; their mortality rate approaches 85% versus 0% in patients with one or two stenosed pulmonary veins.[75] Most cases of PVS present in infancy with a history of worsening respiratory distress and recurrent pneumonias. With disease progression, pulmonary hypertension develops and becomes progressive. Therefore PVS always should be excluded in young patients with unexplained pulmonary hypertension. Hemoptysis may occur, particularly in older patients.[74] Acquired PVS in pediatric patients typically occurs after anomalous pulmonary vein reimplantation surgery. In approximately 10% of these patients, substantial stenosis develops either at the anastomotic site or within the central portions of the pulmonary veins.[73,77,78]

***Imaging.*** Echocardiography usually can visualize all central pulmonary veins in neonates and infants. Turbulent flow on color Doppler with flow velocities greater than 1.6 m/s indicate hemodynamically significant pulmonary venous obstruction.[79] Findings on chest radiographs include patchy reticular opacities and thickened septa, reflecting the impaired venous drainage in the affected lung. CT shows pulmonary vein thickening and narrowing. Although it typically affects the pulmonary venous-left atrial junction, it may involve more central and peripheral segments, resulting in long-segment narrowing, particularly in cases of advanced disease[1] (Fig. 53.28). In advanced cases of PVS, lung and pleural findings may be indistinguishable from pulmonary venous atresia, with smooth septal thickening, reticular opacities, patchy ground-glass areas, and pleural thickening. MRI may show similar findings, but CT has better spatial resolution. However, MRI may provide additional useful physiologic information.[69]

***Treatment and Follow-up.*** PVS may be amenable to balloon dilatation occasionally followed by stent placement, although restenosis seems universal. Care should be taken, because stent placement before surgery may limit surgical approaches. The restenosis rate after surgery approaches 10%, despite advanced techniques reducing trauma to the veins to avoid any stimulus for regrowth of obstructive tissue. In severe cases with multiple vein involvement, lung transplantation may be necessary.[74]

## Combined Anomalies of the Pulmonary Artery and Vein

### Pulmonary Arteriovenous Malformation

***Etiology.*** Pulmonary AVM is a vascular malformation due to an underlying direct connection between the pulmonary arteries and veins without a normal intervening capillary network.[9] This bypass of the capillary network has two important physiologic consequences. First, the direct communication acts as a right-to-left shunt. Second, blood flowing through a pulmonary AVM circumvents the filter function of the normal pulmonary capillary bed, predisposing patients to paradoxical emboli.

Pulmonary AVMs can be congenital or acquired. Acquired pulmonary AVMs are usually seen in patients with a prior history of congenital heart disease surgeries, chronic liver disease, or infections such as tuberculosis or actinomycosis.[1,9] Congenital pulmonary AVMs may occur sporadically, although characteristically they are seen in 30% to 40% of family members with hereditary hemorrhagic telangiectasia (HHT), also known as Rendu-Osler-Weber syndrome. HHT is an autosomal-dominant condition, which is diagnosed clinically on the basis of Curaçao criteria (cerebral, pulmonary, or hepatic AVMs; epistaxis; family history of HHT; and telangiectasias).[80]

Pediatric patients with small pulmonary AVMs often are asymptomatic. Typical clinical symptoms of patients with larger or multiple pulmonary AVMs include dyspnea on exertion, cyanosis, chest pain, palpitations, and hemoptysis.[9,81] Direct right-to-left shunting through larger or multiple pulmonary AVMs bypassing the pulmonary capillary bed can result in paradoxical emboli to the brain causing a stroke or brain abscess.

***Imaging.*** On chest radiographs, pulmonary AVM may appear as a well-circumscribed serpiginous or lobulated opacity. Occasionally, curvilinear opacities directed toward the hilum representing the feeding artery or draining vein may be observed. Most pulmonary AVMs are located within the lower lobes. Small pulmonary AVMs

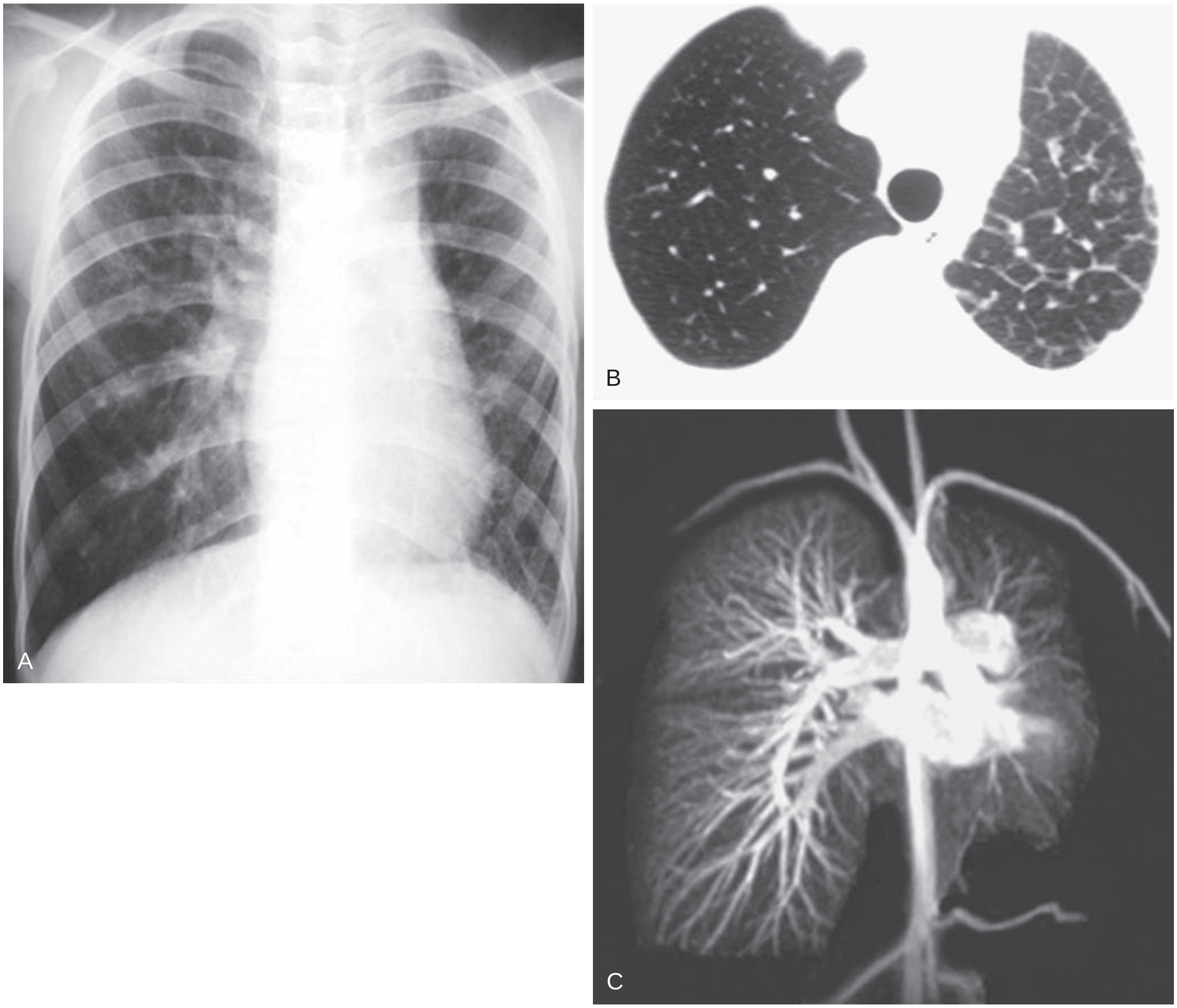

**e-Figure 53.27. Unilateral left pulmonary vein atresia in an asymptomatic 13-year-old girl.** (A) Frontal chest radiograph shows a smaller volume of the left lung, with mediastinal shift to the left. (B) Axial CT image shows thickened interlobular septal lines. (C) Coronal MRA maximum intensity projection image of the chest demonstrates decreased left pulmonary vascularity; however, a left pulmonary artery is present. The left pulmonary veins are not visualized. Note the normal arborization of the right pulmonary vascular bed and the presence of the right pulmonary veins. *(Images reproduced with permission from Gasparetto TD, Daltro P, Marchiori E. Imaging findings of an asymptomatic child with pulmonary vein atresia.* Pediatr Radiol. *2010;40:1458–1459.)*

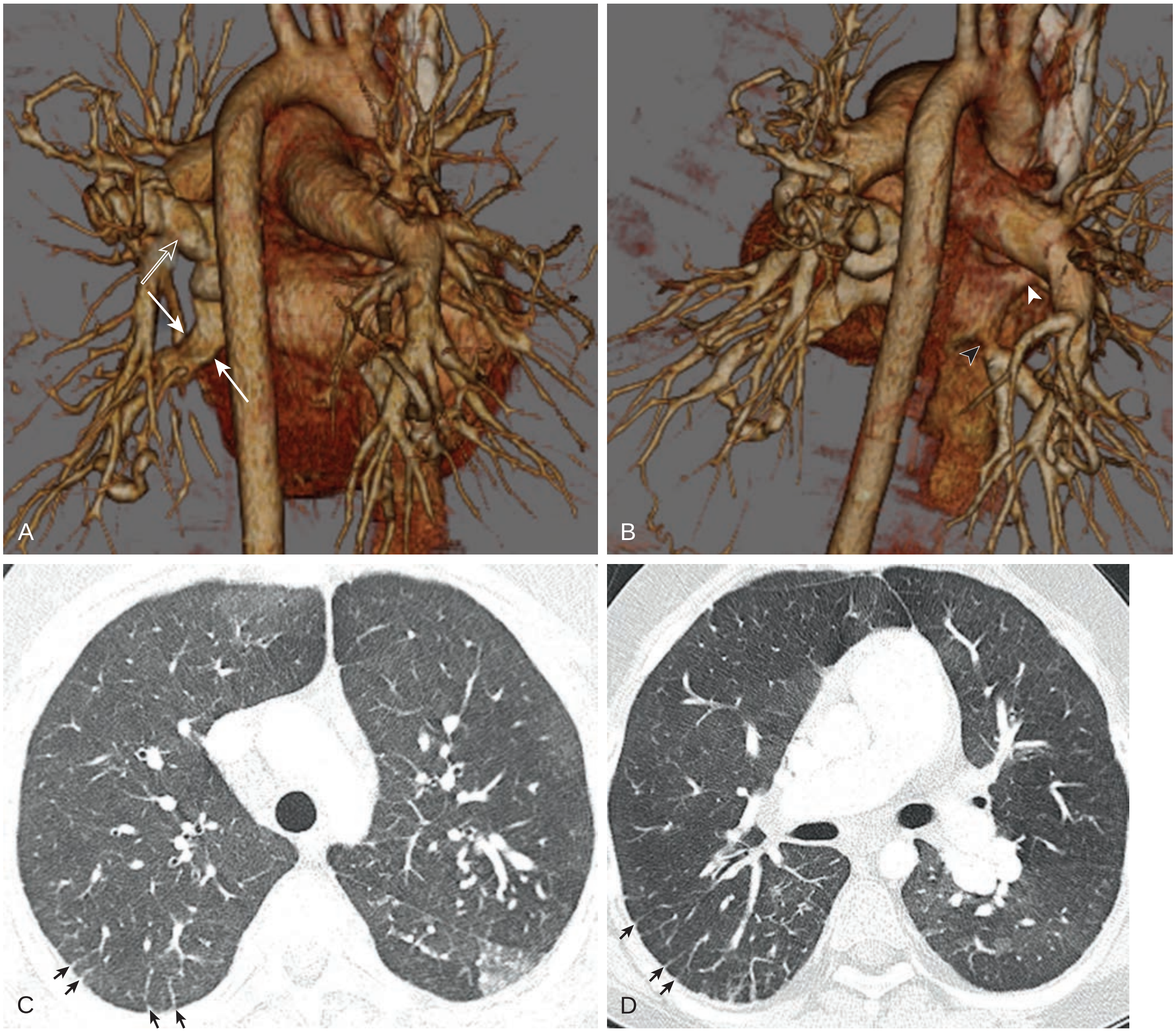

**Figure 53.28. Pulmonary vein stenosis in a 10-year-old boy.** Posterior oblique volume-rendered three-dimensional CT images (A and B) show severe right inferior pulmonary vein narrowing in the anteroposterior dimension resulting in flattening of the vein *(solid arrows)*. Compensatory variceal enlargement of the right superior pulmonary vein is present *(open arrow)*, likely because of the redirection of flow. The left inferior pulmonary vein shows approximately 50% stenosis *(black arrowhead)*, whereas the left superior pulmonary vein *(white arrowhead)* remains patent. Axial CT images in lung windows (C and D) show smooth interlobular septal thickening *(arrows)* and mild patchy areas of ground-glass opacity.

or lesions in areas obscured by normal structures, such as the retrocardiac area or the pulmonary hila, may easily be overlooked.

In the past, pulmonary AVM traditionally was evaluated with conventional pulmonary angiography. Multidetector CT is now the preferred imaging modality for a complete assessment of pulmonary AVMs and can clearly show the often complex angioarchitecture of the pulmonary AVM with its feeding artery and draining vein. This allows preinterventional planning before embolization, which is of outmost importance when managing large or complex lesions[1,81] (Fig. 53.29). Improvements in magnetic resonance angiography (MRA) make it increasingly useful for the assessment of pulmonary AVMs.[82]

Pulmonary AVMs may be simple or complex. Approximately 80% to 90% of pulmonary AVMs have simple angioarchitecture, consisting of single or multiple feeding arteries that all originate from one segmental artery and are connected directly to a single draining vein.[9] Typically, both the artery and vein are dilated and connected by the aneurysmal sac. The remaining 10% to 20% of cases involve complex architecture lesions, with two or more feeding arteries arising from at least two different segmental arteries and connecting with at least two draining veins.[9] Nearly 5% of patients with HHT have multiple pulmonary AVMs.[83]

***Treatment and Follow-up.*** As a general rule, treatment is offered for pulmonary AVMs with feeding arteries larger than 3 mm. However, symptomatic paradoxical emboli have been reported in patients with sub–3-mm feeding arteries. Consequently, many HHT centers currently are treating pulmonary AVMs with feeding arteries of less than 3 mm.[84] Less agreement exists regarding treatment of children who are asymptomatic and younger than 12 years of age[83,85] Developing lungs in this setting may be at

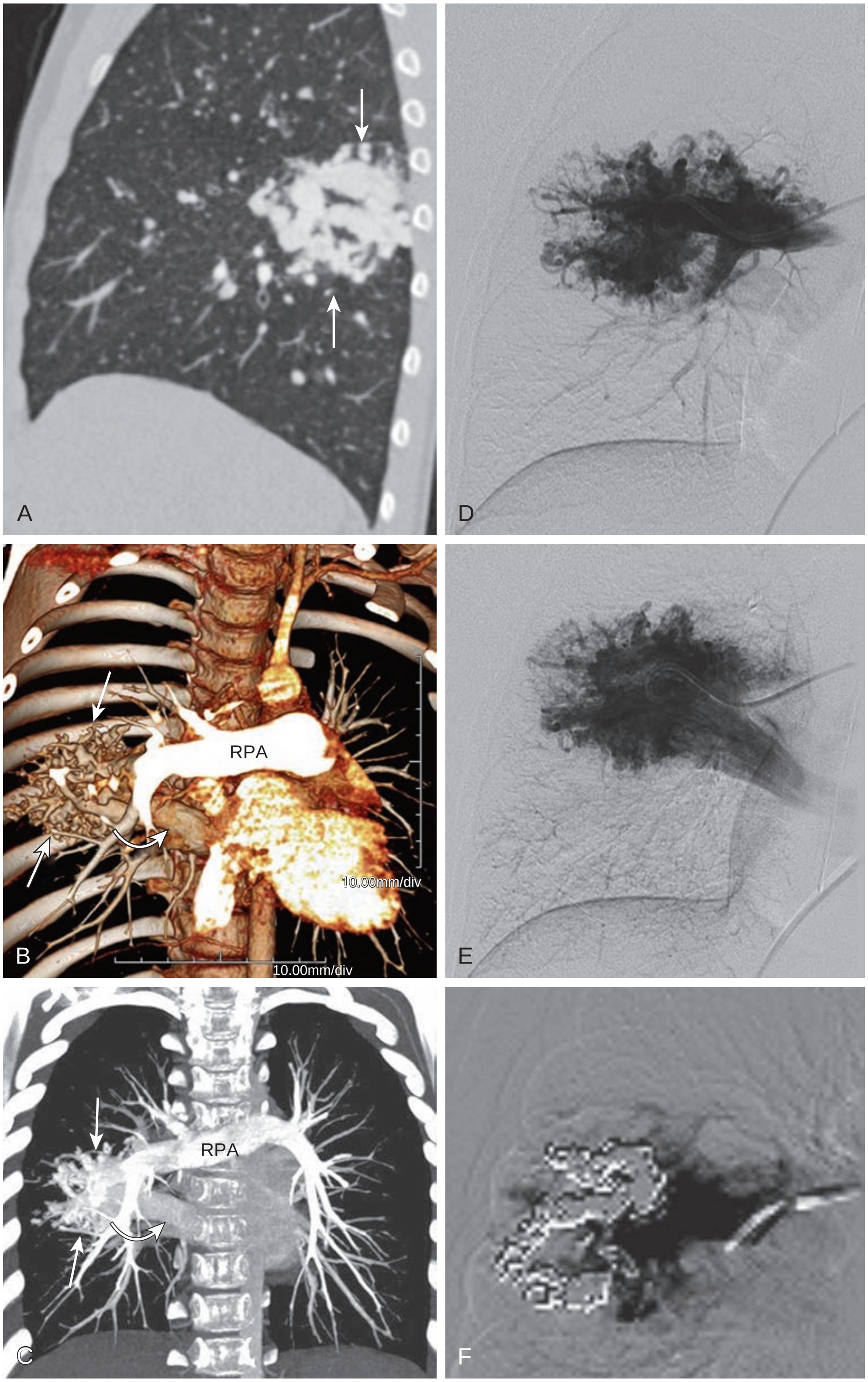

**Figure 53.29. Pulmonary arteriovenous malformation (AVM) in an 8-year-old with a family history of hereditary hemorrhagic telangiectasia and a positive echocardiogram.** (A) Contrast-enhanced sagittal reformatted CT image shows a large AVM *(arrows)* in the superior segment of the right lower lobe. Coronal-oblique volume-rendered (B) and coronal maximum intensity projection (C) CTA images show a large AVM *(straight arrows)* with a feeding artery from the right main pulmonary artery *(RPA)* and a large draining vein into an enlarged right inferior pulmonary vein *(curved arrow)*. Pulmonary angiogram images (D and E) demonstrate a large AVM that correlates well with the CT angiography findings. Postembolization image (F) with platinum coils shows partial obliteration of a large portion of the lesion.

increased risk for reperfusion via pulmonary collaterals, which are even more difficult to treat. Symptomatic pulmonary AVMs should be treated regardless of the age of patients.[81]

The current management choice for pulmonary AVM is transvenous transcatheter embolotherapy, which can be performed using a variety of devices including coils, detachable balloons, and, more recently, the Amplatzer vascular occluder (AGA Medical, Plymouth, MN).[81]

## KEY POINTS

- Congenital lung anomalies can be classified into three groups: predominantly parenchymal abnormalities, combined parenchymal and vascular abnormalities, and predominantly vascular abnormalities, based on morphologic-radiologic-pathologic classification.
- Lung anomalies vary widely in their clinical manifestations, imaging appearance, and pathology, but there is also considerable overlap. Despite advancements in pre- and postnatal imaging that have substantially enhanced our understanding of these lesions, controversy continues to exist regarding nomenclature, classification, pathogenesis, description, and management of congenital lung anomalies. Careful evaluation and thorough understanding of all imaging findings are more important for practical care than trying to categorize the lesions by pathologic terminology.
- Specific imaging findings of congenital lung anomalies that need to be evaluated include (1) location of lesions; (2) vascular supply and drainage of the lesions; (3) internal architecture, presence of cystic components, and degree of aeration; (4) airway abnormality; (5) exclusion of communication with the gastrointestinal tract; (6) integrity of the diaphragm; and (7) an assessment of associated anomalies, such as vertebral anomalies.
- Although radiographs play a role in the detection and initial postnatal imaging evaluation in clinically suspected congenital lung anomalies, cross-sectional imaging such as CT with 2D/3D evaluation often is required for confirmation of diagnosis, further characterization, and preoperative evaluation of surgical lesions.

## SUGGESTED READINGS

Epelman M, Kreiger PA, Servaes S, et al. Current imaging of prenatally diagnosed congenital lung lesions. *Semin Ultrasound CT MR*. 2010;31(2):141–157.

Hellinger JC, Daubert M, Lee EY, et al. Congenital thoracic vascular anomalies: evaluation with state-of-the-art MR imaging and MDCT. *Radiol Clin North Am*. 2011;49(5):969–996.

Langston C. New concepts in the pathology of congenital lung malformations. *Semin Pediatr Surg*. 2003;12:17–37.

Lee EY, Boiselle PM, Cleveland RH. Multidetector CT evaluation of congenital lung anomalies. *Radiology*. 2008;247(3):632–648.

Lee EY, Dorkin H, Vargas SO. Congenital pulmonary malformations in pediatric patients: review and update on etiology, classification, and imaging findings. *Radiol Clin North Am*. 2011;49(5):921–948.

Thacker PG, Schooler GR, Caplan MJ, et al. Developmental lung malformations in children: recent advances in imaging techniques, classification system, and imaging findings. *J Thorac Imaging*. 2015;30:29–43.

Zucker EJ, Epelman M, Newman B. Perinatal thoracic mass lesions: pre- and postnatal imaging. *Semin Ultrasound CT MR*. 2015;36:501–521.

## REFERENCES

Full references for this chapter can be found on www.expertconsult.com.

## REFERENCES

1. Lee EY, Dorkin H, Vargas SO. Congenital pulmonary malformations in pediatric patients: review and update on etiology, classification, and imaging findings. *Radiol Clin North Am*. 2011;49:921–948.
2. Clements BS, Warner JO. Pulmonary sequestration and related congenital bronchopulmonary-vascular malformations: nomenclature and classification based on anatomical and embryological considerations. *Thorax*. 1987;42:401–408.
3. Mata JM, Caceres J. The dysmorphic lung: imaging findings. *Eur Radiol*. 1996;6:403–414.
4. Langston C. New concepts in the pathology of congenital lung malformations. *Semin Pediatr Surg*. 2003;12:17–37.
5. Mata JM, Cáceres J, Lucaya J, et al. CT of congenital malformations of the lung. *Radiographics*. 1990;10:651–674.
6. Newman B. Congenital bronchopulmonary foregut malformations: concepts and controversies. *Pediatr Radiol*. 2006;36:773–791.
7. Alamo L, Gudinchet F, Reinberg O, et al. Prenatal diagnosis of congenital lung malformations. *Pediatr Radiol*. 2012;42:273–283.
8. Epelman M, Kreiger PA, Servaes S, et al. Current imaging of prenatally diagnosed congenital lung lesions. *Semin Ultrasound CT MR*. 2010;31:141–157.
9. Lee EY, Boiselle PM, Cleveland RH. Multidetector CT evaluation of congenital lung anomalies. *Radiology*. 2008;247:632–648.
10. Zucker EJ, Epelman M, Newman B. Perinatal thoracic mass lesions: pre- and postnatal imaging. *Semin Ultrasound CT MR*. 2015;36:501–521.
11. Pacharn P, Kline-Fath B, Calvo-Garcia M, et al. Congenital lung lesions: prenatal MRI and postnatal findings. *Pediatr Radiol*. 2013;43:1136–1143.
12. Alamo L, Vial Y, Gengler C, et al. Imaging findings of bronchial atresia in fetuses, neonates and infants. *Pediatr Radiol*. 2016;46:383–390.
13. Kunisaki SM, Fauza DO, Nemes LP, et al. Bronchial atresia: the hidden pathology within a spectrum of prenatally diagnosed lung masses. *J Pediatr Surg*. 2006;41:61–65, discussion 5.
14. Riedlinger WF, Vargas SO, Jennings RW, et al. Bronchial atresia is common to extralobar sequestration, intralobar sequestration, congenital cystic adenomatoid malformation, and lobar emphysema. *Pediatr Dev Pathol*. 2006;9:361–373.
15. Thacker PG, Schooler GR, Caplan MJ, et al. Developmental lung malformations in children: recent advances in imaging techniques, classification system, and imaging findings. *J Thorac Imaging*. 2015;30:29–43, quiz 4–5.
16. Daltro P, Werner H, Gasparetto TD, et al. Congenital chest malformations: a multimodality approach with emphasis on fetal MR imaging1. *Radiographics*. 2010;30:385–395.
17. Talner LB, Gmelich JT, Liebow AA, et al. The syndrome of bronchial mucocele and regional hyperinflation of the lung. *Am J Roentgenol Radium Ther Nucl Med*. 1970;110:675–686.
18. Zylak CJ, Eyler WR, Spizarny DL, et al. Developmental lung anomalies in the adult: radiologic-pathologic correlation1. *Radiographics*. 2002;22:S25–S43.
19. Abitayeh G, Ruano R, Martinovic J, et al. Prenatal diagnosis of main stem bronchial atresia using 3-dimensional ultrasonographic technologies. *J Ultrasound Med*. 2010;29:633–638.
20. Biyyam DR, Chapman T, Ferguson MR, et al. Congenital lung abnormalities: embryologic features, prenatal diagnosis, and postnatal radiologic-pathologic correlation1. *Radiographics*. 2010;30:1721–1738.
21. Stanton M. The argument for a non-operative approach to asymptomatic lung lesions. *Semin Pediatr Surg*. 2015;24:183–186.
22. Peranteau WH, Merchant AM, Hedrick HL, et al. Prenatal course and postnatal management of peripheral bronchial atresia: association with congenital cystic adenomatoid malformation of the lung. *Fetal Diagn Ther*. 2008;24:190–196.
23. Eber E. Antenatal diagnosis of congenital thoracic malformations: early surgery, late surgery, or no surgery? *Semin Respir Crit Care Med*. 2007;28:355–366.
24. Laje P, Liechty KW. Postnatal management and outcome of prenatally diagnosed lung lesions. *Prenat Diagn*. 2008;28:612–618.
25. Johnston JH, Kline-Fath BM, Bitters C, et al. Congenital overinflation: prenatal MRI and US findings and outcomes. *Prenat Diagn*. 2016;36:568–575.
26. Mani H, Suarez E, Stocker JT. The morphologic spectrum of infantile lobar emphysema: a study of 33 cases. *Paediatr Respir Rev*. 2004;5(supplA):S313–S320.
27. Bulas D, Egloff AM. Fetal chest ultrasound and magnetic resonance imaging: recent advances and current clinical applications. *Radiol Clin North Am*. 2011;49:805–823.
28. Baird R, Puligandla PS, Laberge JM. Congenital lung malformations: informing best practice. *Semin Pediatr Surg*. 2014;23:270–277.
29. Ch'In KY, Tang MY. Congenital adenomatoid malformation of one lobe of a lung with general anasarca. *Arch Pathol (Chic)*. 1949;48:221–229.
30. Rosado-de-Christenson ML, Stocker JT. Congenital cystic adenomatoid malformation. *Radiographics*. 1991;11:865–886.
31. Stocker JT, Madewell JE, Drake RM. Congenital cystic adenomatoid malformation of the lung. Classification and morphologic spectrum. *Hum Pathol*. 1977;8:155–171.
32. Stocker JT. Congenital pulmonary airway malformation—a new name for an expanded classification of congenital cystic adenomatoid malformation of the lung. *Histopathology*. 2002;41(suppl 2):424–431.
33. Stocker JT. Cystic lung disease in infants and children. *Fetal Pediatr Pathol*. 2009;28:155–184.
34. Priest JR, Williams GM, Hill DA, et al. Pulmonary cysts in early childhood and the risk of malignancy. *Pediatr Pulmonol*. 2009;44:14–30.
35. Adzick NS, Harrison MR, Glick PL, et al. Fetal cystic adenomatoid malformation: prenatal diagnosis and natural history. *J Pediatr Surg*. 1985;20:483–488.
36. Azizkhan RG, Crombleholme TM. Congenital cystic lung disease: contemporary antenatal and postnatal management. *Pediatr Surg Int*. 2008;24:643–657.
37. Chetcuti PAJ, Crabbe DCG. CAM lungs: the conservative approach. *Arch Dis Child Fetal Neonatal Ed*. 2006;91:F463–F464.
38. Jaffé A, Chitty LS. Congenital cystic adenomatoid malformations may not require surgical intervention. *Arch Dis Child Fetal Neonatal Ed*. 2006;91:F464.
39. Aziz D, Langer JC, Tuuha SE, et al. Perinatally diagnosed asymptomatic congenital cystic adenomatoid malformation: to resect or not? *J Pediatr Surg*. 2004;39:329–334.
40. Laberge JM, Puligandla P, Flageole H. Asymptomatic congenital lung malformations. *Semin Pediatr Surg*. 2005;14:16–33.
41. Chuang S, Sugo E, Jaffe A. A review of postnatal management of congenital pulmonary airway malformations. *Fetal Matern Med Rev*. 2009;20:179–204.
42. Rosado-de-Christenson ML, Frazier AA, Stocker JT, et al. From the archives of the AFIP. Extralobar sequestration: radiologic-pathologic correlation. *Radiographics*. 1993;13:425–441.
43. Yoon HM, Kim EA, Chung SH, et al. Extralobar pulmonary sequestration in neonates: the natural course and predictive factors associated with spontaneous regression. *Eur Radiol*. 2017;27(6):2489–2496.
44. Conran RM, Stocker JT. Extralobar sequestration with frequently associated congenital cystic adenomatoid malformation, type 2: report of 50 cases. *Pediatr Dev Pathol*. 1999;2:454–463.
45. Cass DL, Crombleholme TM, Howell LJ, et al. Cystic lung lesions with systemic arterial blood supply: a hybrid of congenital cystic adenomatoid malformation and bronchopulmonary sequestration. *J Pediatr Surg*. 1997;32:986–990.
46. Adzick NS. Management of fetal lung lesions. *Clin Perinatol*. 2009;36:363–376, x.
47. Frazier AA, Rosado de Christenson ML, Stocker JT, et al. Intralobar sequestration: radiologic-pathologic correlation. *Radiographics*. 1997;17:725–745.
48. Sauvat F, Michel JL, Benachi A, et al. Management of asymptomatic neonatal cystic adenomatoid malformations. *J Pediatr Surg*. 2003;38:548–552.
49. Konen E, Raviv-Zilka L, Cohen RA, et al. Congenital pulmonary venolobar syndrome: spectrum of helical CT findings with emphasis on computerized reformatting. *Radiographics*. 2003;23:1175–1184.
50. Curros F, Chigot V, Emond S, et al. Role of embolisation in the treatment of bronchopulmonary sequestration. *Pediatr Radiol*. 2000;30:769–773.
51. Lee K-H, Sung K-B, Yoon H-K, et al. Transcatheter arterial embolization of pulmonary sequestration in neonates: long-term follow-up results. *J Vasc Interv Radiol*. 2003;14:363–367.
52. Hellinger JC, Daubert M, Lee EY, et al. Congenital thoracic vascular anomalies: evaluation with state-of-the-art MR imaging and MDCT. *Radiol Clin North Am*. 2011;49:969–996.
53. Epelman WM. Congenital lung anomalies. In: Yoo SJMC, Babyn PS, eds. *Chest Radiographic Interpretation in Pediatric Cardiac Patients*. Thieme Medical Publishers; 2010:206–214.
54. Alsoufi B, Cai S, Van Arsdell GS, et al. Outcomes after surgical treatment of children with partial anomalous pulmonary venous connection. *Ann Thorac Surg*. 2007;84:2020–2026.

55. Vida VL, Padalino MA, Boccuzzo G, et al. Scimitar syndrome: a European Congenital Heart Surgeons Association (ECHSA) multicentric study. *Circulation*. 2010;122:1159–1166.
56. Cicek S, Arslan AH, Ugurlucan M, et al. Scimitar syndrome: the curved Turkish sabre. *Semin Thorac Cardiovasc Surg Pediatr Card Surg Annu*. 2014;17:56–61.
57. Berrocal T, Madrid C, Novo S, et al. Congenital anomalies of the tracheobronchial tree, lung, and mediastinum: embryology, radiology, and pathology. *Radiographics*. 2004;24:e17.
58. Epelman M, Kondrachuk O, Restrepo R, et al. Congenital and acquired mediastinal vascular disorders in children. In: Garcia-Pena P, Guillerman RP, eds. *Pediatric Chest Imaging*. Heidelberg: Springer-Verlag Berlin; 2013:241–264.
59. Cunningham ML, Mann N. Pulmonary agenesis: a predictor of ipsilateral malformations. *Am J Med Genet*. 1997;70:391–398.
60. Gilbert EF, Opitz JM. The pathology of some malformations and hereditary diseases of the respiratory tract. *Birth Defects Orig Artic Ser*. 1976;12:239–270.
61. Eroglu A, Alper F, Turkyilmaz A, et al. Pulmonary agenesis associated with dextrocardia, sternal defects, and ectopic kidney. *Pediatr Pulmonol*. 2005;40:547–549.
62. Trivedi KR, Karamlou T, Yoo SJ, et al. Outcomes in 45 children with ductal origin of the distal pulmonary artery. *Ann Thorac Surg*. 2006;81:950–957.
63. Castañer E, Gallardo X, Rimola J, et al. Congenital and acquired pulmonary artery anomalies in the adult: radiologic overview1. *Radiographics*. 2006;26:349–371.
64. Dillman JR, Sanchez R, Ladino-Torres MF, et al. Expanding upon the unilateral hyperlucent hemithorax in children. *Radiographics*. 2011;31:723–741.
65. Apostolopoulou SC, Kelekis NL, Brountzos EN, et al. "Absent" pulmonary artery in one adult and five pediatric patients: imaging, embryology, and therapeutic implications. *AJR Am J Roentgenol*. 2002;179:1253–1260.
66. Newman B, Cho Y. Left pulmonary artery sling–anatomy and imaging. *Semin Ultrasound CT MR*. 2010;31:158–170.
67. Lee K-H, Yoon CS, Choe KO, et al. Use of imaging for assessing anatomical relationships of tracheobronchial anomalies associated with left pulmonary artery sling. *Pediatr Radiol*. 2001;31:269–278.
68. Lee KS, Boiselle PM. Update on multidetector computed tomography imaging of the airways. *J Thorac Imaging*. 2010;25:112–124.
69. Vyas HV, Greenberg SB, Krishnamurthy R. MR imaging and CT evaluation of congenital pulmonary vein abnormalities in neonates and infants. *Radiographics*. 2012;32:87–98.
70. Dominguez Garcia O, Granados Ruiz MA, Sanchez-Redondo MD, et al. A difficult emergency surgical diagnosis: atresia of the common pulmonary vein. *Pediatr Cardiol*. 2009;30:989–991.
71. Heyneman LE, Nolan RL, Harrison JK, et al. Congenital unilateral pulmonary vein atresia. *AJR Am J Roentgenol*. 2001;177:681–685.
72. Pourmoghadam KK, Moore JW, Khan M, et al. Congenital unilateral pulmonary venous atresia: definitive diagnosis and treatment. *Pediatr Cardiol*. 2003;24:73–79.
73. Riedlinger WF, Juraszek AL, Jenkins KJ, et al. Pulmonary vein stenosis: expression of receptor tyrosine kinases by lesional cells. *Cardiovasc Pathol*. 2006;15:91–99.
74. Latson LA, Prieto LR. Congenital and acquired pulmonary vein stenosis. *Circulation*. 2007;115:103–108.
75. Breinholt JP, Hawkins JA, Minich L, et al. Pulmonary vein stenosis with normal connection: associated cardiac abnormalities and variable outcome. *Ann Thorac Surg*. 1999;68:164–168.
76. Drossner DM, Kim DW, Maher KO, et al. Pulmonary vein stenosis: prematurity and associated conditions. *Pediatrics*. 2008;122:e656–e661.
77. Grosse-Wortmann L, Al-Otay A, Goo HW, et al. Anatomical and functional evaluation of pulmonary veins in children by magnetic resonance imaging. *J Am Coll Cardiol*. 2007;49:993–1002.
78. Caldarone CA, Najm HK, Kadletz M, et al. Relentless pulmonary vein stenosis after repair of total anomalous pulmonary venous drainage. *Ann Thorac Surg*. 1998;66:1514–1520.
79. Smallhorn JF, Pauperio H, Benson L, et al. Pulsed Doppler assessment of pulmonary vein obstruction. *Am Heart J*. 1985;110:483–486.
80. Guttmacher AMD, Pyeritz R. Hereditary hemorrhagic telangiectasia. In: Rimoin DCJ, Pyeritz R, Korf B, eds. *Principles and Practice of Medical Genetics*. 5th ed. Philadelphia, PA: Churchill Livingstone; 2007:1200–1213.
81. Trerotola SO, Pyeritz RE. PAVM embolization: an update. *AJR Am J Roentgenol*. 2010;195:837–845.
82. Schneider G, Uder M, Koehler M, et al. MR angiography for detection of pulmonary arteriovenous malformations in patients with hereditary hemorrhagic telangiectasia. *AJR Am J Roentgenol*. 2008;190:892–901.
83. Faughnan ME, Thabet A, Mei-Zahav M, et al. Pulmonary arteriovenous malformations in children: outcomes of transcatheter embolotherapy. *J Pediatr*. 2004;145:826–831.
84. Faughnan ME, Palda VA, Garcia-Tsao G, et al. International guidelines for the diagnosis and management of hereditary haemorrhagic telangiectasia. *J Med Genet*. 2011;48:73–87.
85. Pollak JS, Saluja S, Thabet A, et al. Clinical and anatomic outcomes after embolotherapy of pulmonary arteriovenous malformations. *J Vasc Interv Radiol*. 2006;17:35–44, quiz 5.

# 54

# Pulmonary Infection

Sjirk J. Westra, Ali Yikilmaz, and Edward Y. Lee

Pneumonia and other pulmonary infections involving the lower respiratory tract continue to be the most common cause of illness in children, affecting over 150 million children under 5 years of age each year worldwide, with 20 million related US hospitalizations annually.[1-5] Despite the decrease in hospitalizations for pediatric pneumonia since the introduction of the pneumococcal conjugate vaccine in 2000, the rates of pneumonia presenting in the ambulatory care setting have not decreased.[6] Because clinical signs and symptoms are poor predictors of pediatric pulmonary infections, and the value of microbial studies is limited, chest radiography with the use of standardized reporting criteria continues to be the best available diagnostic standard.[1,3,7,8] Currently published definitions of pediatric pneumonia do not solely rely on radiographic criteria, but require several additional clinical features to be present.[9] The value of lateral radiographs in diagnosis continues to be debated, but the hyperinflation that is a radiographic hallmark of pulmonary infections in young children is more reliably detected on the lateral radiograph than on the frontal radiograph.[1,10,11]

In experienced hands, ultrasonography of the lung has proven able to diagnose pneumonia, validated in two recent meta-analysis studies.[12,13] In the ambulatory care setting, performing routine chest radiography has not been shown to improve the outcomes of pulmonary infections in young children, and it is not indicated in first-time wheezing episodes presumed to be viral or reactive in etiology.[14-17] The yield of radiography is greater in the presence of a high temperature and in the absence of a family history of asthma.[18] Radiography is most helpful when an inconsistency exists among the data from history, physical examination, and observation.[19] Negative chest radiography provides justification to withhold antibiotics in symptomatic children.[1] Newer evidence-based recommendations suggest that valid indications for chest radiography are severe disease requiring hospitalization, confirmation or exclusion of diagnosis in the presence of an atypical presentation, assessment of complications, and exclusion of other causes of respiratory distress.[20-26] Even in hospitalized individuals in intensive care, chest radiographs should be obtained based on clinical need rather than routine protocols.[27] However, compliance with these, as well as antibiotic use guidelines, is suboptimal.[6,20,24] Follow-up chest radiographs after 4 to 6 weeks are only recommended for children with recurrent pneumonia involving the same lobe, to look for underlying anatomic causes.[22]

Maternal antibodies protect newborns against viral pulmonary infections, and bacterial infections are most common in this age group, usually caused by pathogens acquired during labor and delivery. With dropping maternal antibodies, viral infections become more prevalent between ages 2 months and 2 years. After this, bacterial infections again become more common.[3] Tuberculosis, fungal infections, and parasitic infestations continue to add substantially to the disease burden of children who are immunocompromised or live in endemic areas.[2]

The spectrum of pulmonary infections in childhood is categorized in Table 54.1.[2,28] In young children, the lungs can only respond to insult in a limited number of ways, and this response is more age specific than antigen dependent.[29-33] Viral and bacterial infections frequently coexist, and radiographic criteria alone do not reliably distinguish between them.[34-36] This is compounded by a reported high interobserver variability for interpretation of chest radiographs.[37-41] Use of inexact terminology may hamper communication between radiologists and referring physicians, who agree with radiologists' interpretations in only 78% of cases, and antibiotics are frequently prescribed even when no bacterial agent can be proven.[7,42,43]

## PULMONARY INFECTIONS CAUSED BY VIRUSES

Viral pulmonary infections usually occur after the inhalation of infected air droplets.[2] The clinical presentation depends on the infectious agent, patient age, and immune response (mainly cellular, T-cell–mediated immunity). In young children, degrees of mucosal swelling within the small-caliber terminal airways, which would not compromise air exchange in older individuals with relatively larger-caliber airways, lead to diffuse alveolar air trapping (Fig. 54.1). In addition, more hypersecretion occurs in the inflamed airways in young children, contributing to mucous plugging of the airways; this leads to (sub)segmental atelectasis mimicking alveolar consolidations, which are frequently misinterpreted to represent bacterial pneumonia.[1,43-45]

***Etiology.*** The most common viral agents causing pulmonary infections in childhood are listed in Table 54.2.

*RNA Viruses.* Respiratory syncytial virus (RSV) is the most common cause of pulmonary infections in infants and young children. The disease can be virulent and is fatal in up to 1% of healthy infants, but those with chronic lung disease from prematurity and cardiovascular disease are at much higher risk.[46] Clinical signs range from mild coryza to severe respiratory distress with wheezing, tachypnea, cyanosis, dyspnea, and retractions. Hypoxemia, possibly caused by a ventilation-perfusion imbalance, may be profound and last for several weeks.[47] The diagnosis of RSV infection is made by examining the nasoepithelial cells by using direct fluorescent antibody detection.

Human metapneumovirus (HMV) is the second most common cause of viral pulmonary infections in young children after RSV.[48,49] It affects children who are slightly older than those infected by RSV, and the disease is less severe, except when seen as a coinfection. HMV has a worldwide distribution and causes a disease spectrum indistinguishable from influenza and RSV infection, with the same seasonal variation.

Parainfluenza virus is a common community-acquired virus. Types 1 and 2 fluctuate biannually, typically in the fall, with type 3 common in the late winter or early spring, unlike RSV.

The onset is often more abrupt and intense than that of RSV or parainfluenza. The Asian avian influenza virus (H1N1) spread rapidly over many parts of the world from 2003 to 2007.[48,50,51] Since 2009 a novel H1N1 infection resulting from antigenic shift of the virus has been reported to be associated with a higher rate of shock, acute respiratory distress syndrome (ARDS), and neurologic complications in children compared with seasonal (non-H1N1) infections.[52]

Severe acute respiratory distress syndrome (SARS) is caused by a coronavirus, which was recognized in 2003, and in the following year, it was diagnosed in over 8000 patients, primarily in China, Taiwan, Hong Kong, Vietnam, and Toronto.[48,53] After 2004 the outbreak appeared to have been contained; since then, SARS has only been sporadically reported. SARS typically has a brief prodrome of fever, with or without constitutional symptoms. This quickly progresses to severe respiratory symptoms by day 6 of the fever.[54] It has an overall mortality rate of 10%, but children have constituted only 5% of reported cases; they tend to have a milder

## Abstract:

This chapter reviews the imaging in pulmonary infections in children caused by viruses, bacteria (including mycobacteria), bacteria-like organisms, fungi and parasites. The value and limitations of chest radiography are discussed, supplemented with cross-sectional techniques (ultrasound, CT and MRI) when infections fail to respond to treatment, recur or occur in immunocompromised children. In young children, the imaging findings of viral and bacterial lung infections frequently overlap, making their differentiation difficult. Improved communication of the radiographic findings and their limitations can decrease over-prescription of antibiotics by referring physicians, when no bacterial cause can be proven. CT adds value to radiography only in pulmonary infections that are complicated, recurrent or occur in patients with an impaired immune system. Ultrasound is favored over CT to determine the need and feasibility of percutaneous drainage of parapneumonic effusions and empyemas in children.

## Keywords:

pneumonia
pulmonary infection
acute respiratory illness
radiography
computed tomography
ultrasound
magnetic resonance imaging
evidence-based imaging
cost-effectiveness of diagnostics

course,[55] and no pediatric deaths have been reported.[48,53] Recently, newer coronaviruses (NL63 and HKU1), which cause milder forms of respiratory disease, have been discovered.[48]

Pneumonia as a complication of childhood measles is diminishing in frequency because of vaccination, but it is still occasionally seen in nonimmunized or immunosuppressed children. Atypical measles pneumonia followed exposure to measles or vaccination with the live vaccine and was characterized by a prodromal period of rash and flulike illness.

*DNA Viruses.* Adenovirus pneumonia is responsible for about 5% of respiratory tract disease in infants and children, with a peak age between 6 months and 5 years.[45] Adenovirus has also been associated with a pertussis-like syndrome. Although often relatively benign, adenoviral infection may be severe and even fatal in young infants, particularly when caused by the recently identified serotype Ad14.[48]

**TABLE 54.1** Classification of Pulmonary Infections in Childhood

| By Pathology, Clinical Presentation | By Primary Location | By Radiographic Feature |
|---|---|---|
| Acute focal | Trachea: tracheitis | Alveolar |
| Atypical | Large airways: bronchitis | Interstitial |
| Miliary or nodular | Small airways: bronchiolitis | Volume loss (atelectasis) |
| Progressive or fulminant | Small airways and parenchyma: bronchopneumonia | Pulmonary nodule(s) |
| Aspiration | Parenchyma | Necrosis, cavitation |
| "Pulmonary infiltrates with eosinophilia" | Alveoli ("alveolitis") | Lymphadenopathy |
| Chronic or recurrent | Interstitium | Pleural effusion |

*From Eslamy HK, Newman B. Pneumonia in normal and immunocompromised children: an overview and update.* Radiol Clin North Am. *2011;49:895–920.*

Cytomegalovirus (CMV) is a cause of congenital infection of the lungs, the liver, and the central nervous system, and causes hematologic changes of petechiae, purpura, hemolytic anemia, and atypical lymphocytes. These same systems are involved in acquired disease, but the disease is less severe. Children with a compromised immune status are at lifelong risk for CMV infection, and it is frequently seen in patients with acquired immunodeficiency syndrome (AIDS) and in children treated with cyclosporine.

Varicella (chickenpox) pneumonia is relatively rare, but immunocompromised children are at risk for progressive varicella and more severe pulmonary involvement, as well as for meningoencephalitis and hepatitis. These children are severely ill, with extensive rashes and high fever; chest pain and hemoptysis are frequent.

Epstein–Barr virus (EBV) infects B lymphocytes and pharyngeal and possibly pulmonary epithelial cells. It is associated with infectious mononucleosis, a common disease in older children and young adults, presenting with fever, pharyngitis, and adenopathy. The disease may be suspected if the tonsils and adenoid are markedly enlarged. EBV is frequently associated with posttransplantation lymphoproliferative disorder, lymphomas complicating immune deficiency disorders, and lymphocytic interstitial pneumonitis (with or without associated human immunodeficiency virus [HIV] infection).

***Imaging.*** Bilateral interstitial opacities with peribronchial thickening and hyperinflation (see Fig. 54.1), thought to represent viral bronchiolitis, are nonspecific and are, in fact, indicative of an acute pulmonary infection of any cause (viral or bacterial) in young children.[1,28] Pleural effusions are rare in purely viral lung infections. Radiologic abnormalities often clear slowly and lag behind clinical improvement. Complications are superimposed bacterial infection (often hospital acquired) and postinfectious bronchiolitis obliterans, bronchiectasis, or both.[2] These latter conditions, which frequently follow an adenovirus infection, are characterized by features of chronic air trapping and atelectasis resulting from bronchial dysfunction; mosaic perfusion abnormalities, peribronchial thickening, and bronchiectasis, best seen on

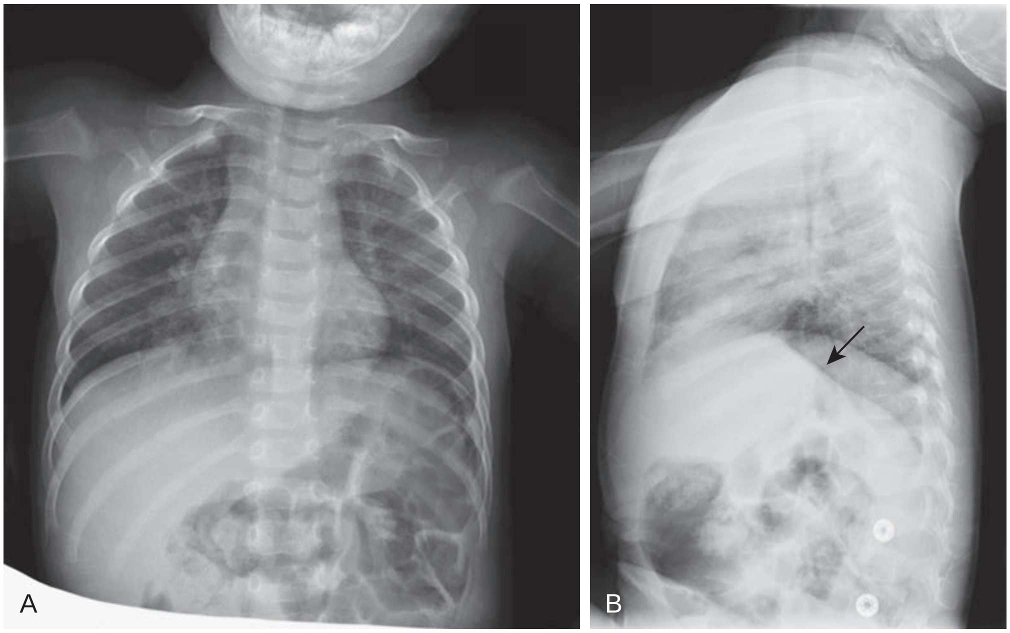

**Figure 54.1. Respiratory syncytial virus pneumonia in a 1.5-year-old boy.** (A) The frontal chest radiograph shows perihilar streaky lung opacities and peribronchial thickening, typical of viral infections, with more focal opacity medially in the right lung base, from superimposed atelectasis. This was mistaken for alveolar consolidation indicative of bacterial pneumonia, and antibiotic treatment was given unnecessarily. (B) The lateral chest radiograph better demonstrates air trapping in the right lung base, with flattening of the right hemidiaphragm *(arrow).*

**TABLE 54.2** Most Common Organisms Causing Pulmonary Infections in Childhood

| Organism | Characteristic Clinical Features | Typical Radiographic Findings and Sequelae |
|---|---|---|
| **VIRUSES** | | |
| **RNA Viruses** | | |
| RSV | Bronchiolitis (winter) | Interstitial pneumonia |
| HMV | Bronchiolitis (winter) | Interstitial pneumonia |
| Parainfluenza | Bronchiolitis (fall, spring) | Interstitial pneumonia |
| Influenza | "Bird flu," pandemic flu | Interstitial pneumonia |
| Corona | SARS | Interstitial pneumonia |
| Measles | Nonimmunized, opportunistic | Atypical pneumonia |
| **DNA Viruses** | | |
| Adenovirus | Necrotizing bronchopneumonia | Bronchiolitis obliterans |
| CMV | Congenital, opportunistic | Ground-glass opacity |
| Varicella | Opportunistic | Pulmonary calcifications |
| EBV | Infectious mononucleosis, PTLD | Lymphadenopathy |
| **BACTERIA** | | |
| **Aerobic/Facultative** | | |
| *Streptococcus pneumoniae* | De novo, postviral | Acute focal pneumonia |
| *Streptococcus* A | Pharyngitis | Bronchopneumonia |
| *Streptococcus* B | Prematurity, neonatal pneumonia | Confusion with hyaline membrane disease |
| *Staphyloccocus aureus* | Postviral, embolic | Bronchopneumonia |
| *Haemophilus influenzae* B | Epiglottitis, vaccination | Atypical pneumonia |
| *Bordetella pertussis* | Whooping cough | Atypical pneumonia, "shaggy heart" |
| *Pseudomonas* | Opportunistic (CF) | Findings of CF, bronchiectasis |
| *Legionella* | Opportunistic | Atypical pneumonia |
| *Anaerobic* | Aspiration, debilitated | Lung necrosis, abscess |
| **BACTERIA-LIKE** | | |
| *Chlamydia trachomatis* | Infancy, conjunctivitis | Interstitial pneumonia |
| *Chlamydia pneumoniae* | School age, bronchitis | Peribronchitis |
| *Mycoplasma* | School age, atypical pneumonia | Interstitial pneumonia, atypical |
| *Mycobacterium tuberculosis* | TB, opportunistic | Primary, miliary, postprimary |
| NTM | NTM disease, opportunistic | Mimics TB |
| **FUNGI** | | |
| *Aspergillus* | Aspergilloma, invasive disease | Halo, air crescent signs |
| *Histoplasma* | Histoplasmosis | Mimics TB, calcified granulomas |
| *Coccidioides* | Coccidioiodomycosis | Mimics TB |
| *Pneumocystis* | Opportunistic | Ground-glass opacities, interstitial pneumonia |
| *Candida* | Opportunistic, debilitated | Nodules |
| **PARASITES** | | |
| *Paragonimus* | Ingestion of uncooked crustaceans | Nodules, ring shadows |
| *Echinococcus* | Contact with infested dogs | Fluid-filled masses, with or without rupture |
| Others | Visceral larva migrans, Löffler syndrome | PIE |

*CF,* Cystic fibrosis; *CMV,* cytomegalovirus; *DNA,* deoxyribonucleic acid; *EBV,* Epstein–Barr virus; *HMV,* human metapneumovirus; *NTM,* nontuberculous mycobacteria; *PIE,* pulmonary infiltrates with eosinophilia; *PTLD,* posttransplantation lymphoproliferative disorder; *RNA,* ribonucleic acid; *RSV,* respiratory syncytial virus; *SARS,* severe acute respiratory syndrome; *TB,* tuberculosis.

computed tomography (CT).[2] Swyer–James–MacLeod syndrome, the result of bronchiolitis obliterans in the growing lung, is characterized by a unilateral small hyperlucent lung, which exhibits hypoperfusion and chronic bronchiectasis (e-Fig. 54.2).

In RSV infection, the lungs are often quite clear, or focal areas of superimposed atelectasis may be noted (see Fig. 54.1); when present, these predict a need for more prolonged mechanical ventilation.[56]

In mild influenza infection, initial chest radiographs are normal or may demonstrate nonspecific prominence of peribronchial markings and hyperinflation. In children with a more severe clinical course, bilateral symmetric and multifocal areas of consolidation, often associated with ground-glass opacities, are seen (e-Fig. 54.3).[57]

The radiographic manifestations of SARS are typically mild, with interstitial thickening, which may progress to focal consolidation.[58,59] In children, unlike in adults, no lymphadenopathy, pleural effusion, or cavitation is reported.[60] However, abnormalities may persist on thin-section CT in older children for up to 12 months after infection.[61]

Measles virus is thought to be the cause of giant cell pneumonia, which produces a diffuse reticulonodular bronchopneumonia-like radiographic pattern (e-Fig. 54.4), with hilar node enlargement and superimposed bacterial infection, usually affecting the lower lobes. Atypical measles pneumonia after vaccination with, or exposure to, live virus was characterized by extensive nonsegmental parenchymal consolidation, with pulmonary nodules, hilar lymph node enlargement, and pleural effusion being common.

Adenovirus may cause necrotizing bronchopneumonia, bronchitis, or bronchiolitis. Radiographic features are nonspecific but usually include bronchial wall thickening, peribronchiolar densities, air trapping, and patchy or confluent consolidations.[44] Adenopathy is more common than in other viral pneumonias. Bronchiectasis or bronchiolitis obliterans may be a permanent sequel (see e-Fig. 54.2).[44,45,62]

In children infected with CMV, a progressive interstitial pneumonitis is seen (e-Fig. 54.5). CT findings are nonspecific, with ground-glass opacities and consolidations in 80% of the cases.[63] Gallium-67 scintigraphy may show abnormal uptake in the lungs of patients who have a normal chest CT.[64]

Findings in varicella are similar to those of measles pneumonia. Multiple focal calcifications frequently develop after severe chickenpox pneumonia (e-Fig. 54.6).

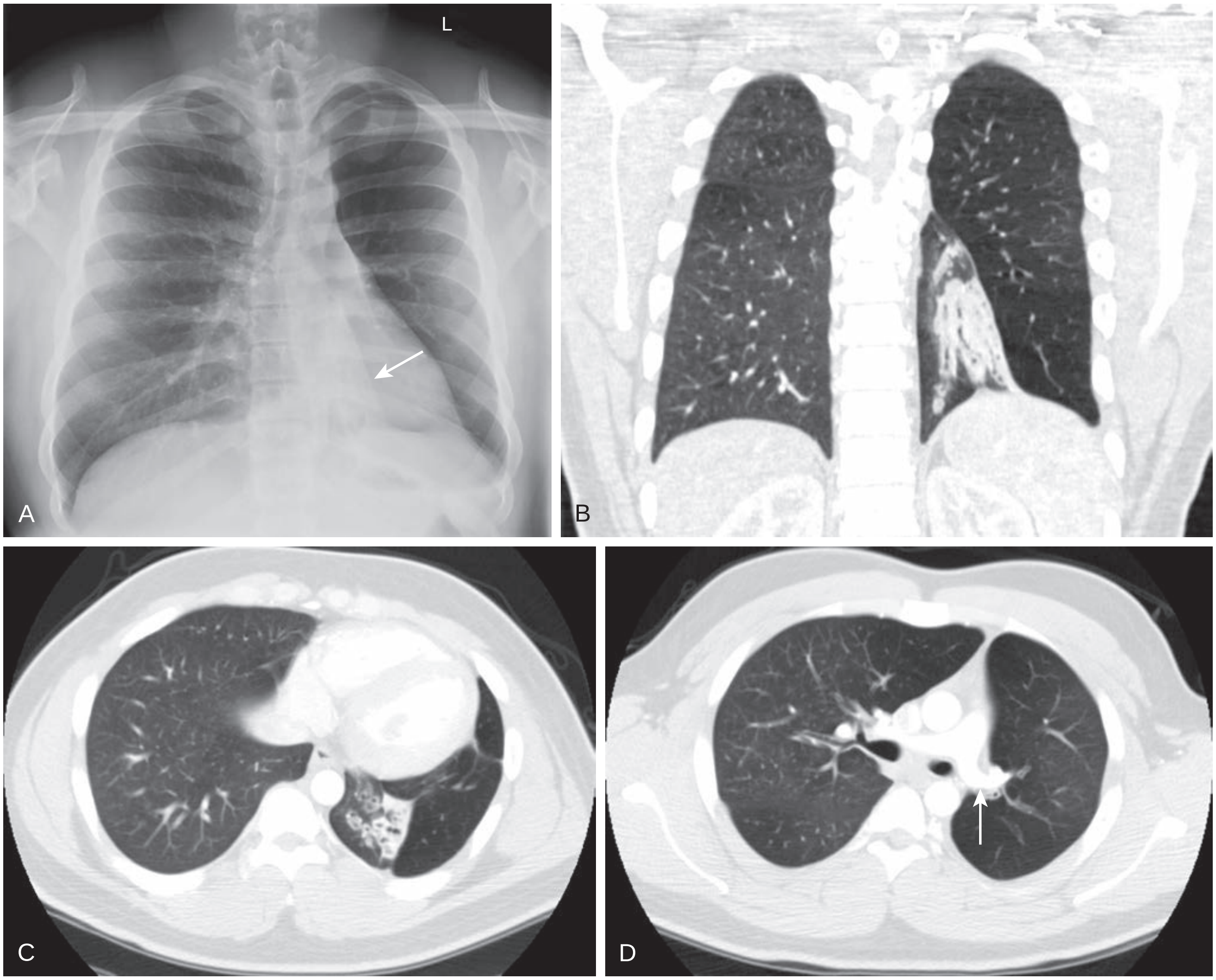

**e-Figure 54.2. Swyer–James–MacLeod syndrome in a 20-year-old man monitored since early childhood; he had chronic left lower lobe collapse and bronchiectasis secondary to bronchiolitis obliterans after an adenovirus infection.** (A) The radiograph shows left lower lobe collapse *(arrow)* and hyperlucency of the left upper lobe. (B–D) Computed tomography images demonstrate a hyperlucent, smaller left lung, cylindric bronchiectasis in the collapsed left lower lobe, and a relatively small left pulmonary artery (*arrow* in D).

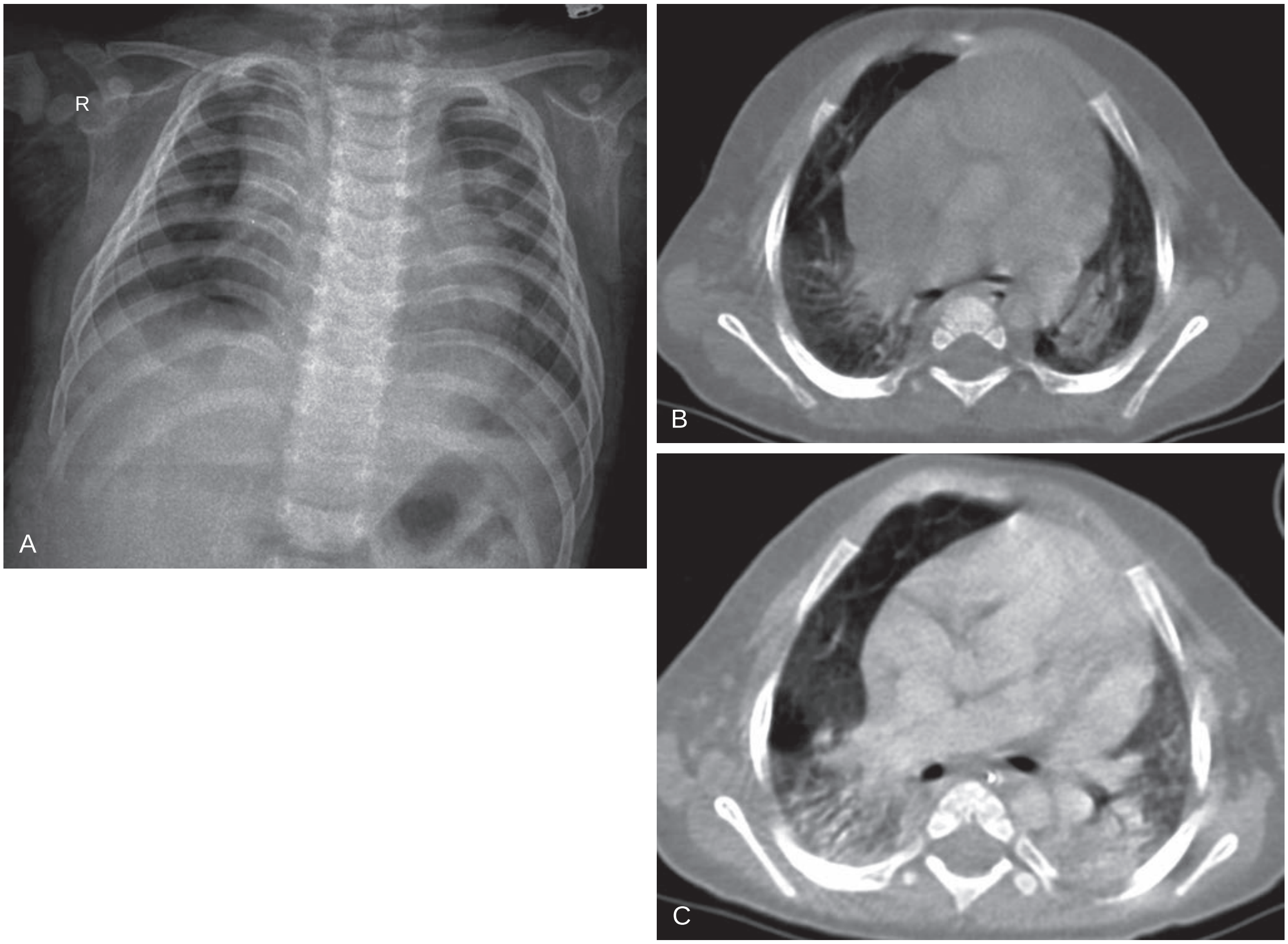

**e-Figure 54.3. Lethal H1N1 influenza in an 8-month-old boy who presented with shortness of breath and fever during an outbreak of epidemic flu.** (A) The radiograph shows nonspecific increased perivascular markings and somewhat low lung volumes. (B) The contrast-enhanced computed tomography (CT) scan demonstrates consolidation in both lower lobes. (C) The follow-up CT scan after 1 month showed progression of the consolidations. Soon after this scan was obtained, the baby died from cardiopulmonary failure.

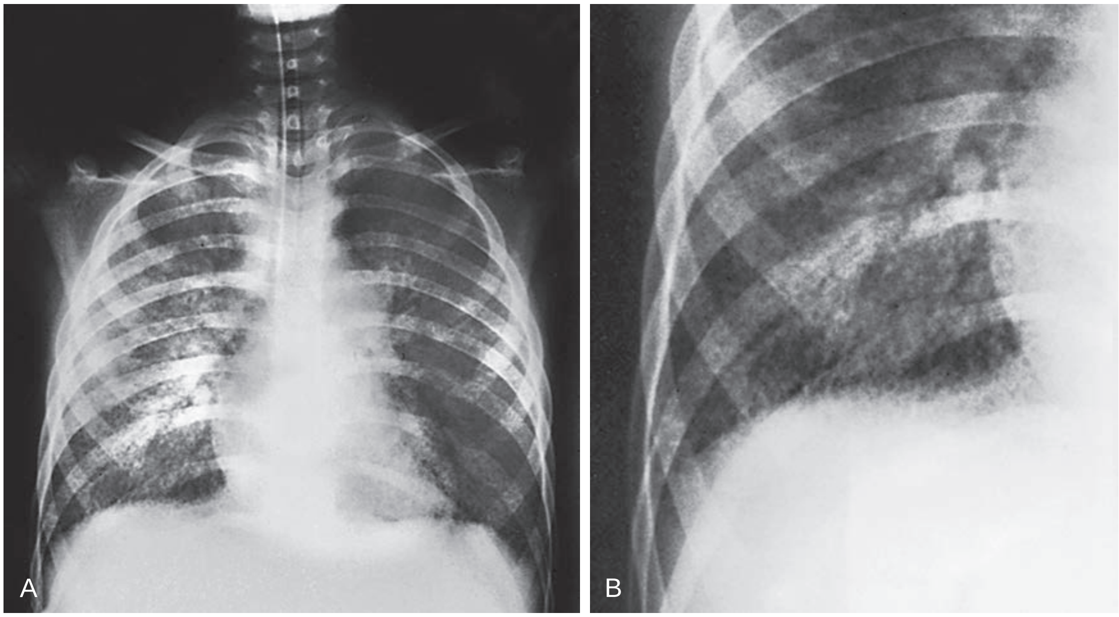

**e-Figure 54.4. A 12-year-old girl with leukemia and measles pneumonia.** (A) Initial radiographic examination showing a diffuse bilateral reticulonodular infiltrate, reflecting the interstitial distribution of the disease. (B) Close-up of the right lower lobe showing the reticulonodular pattern to better advantage.

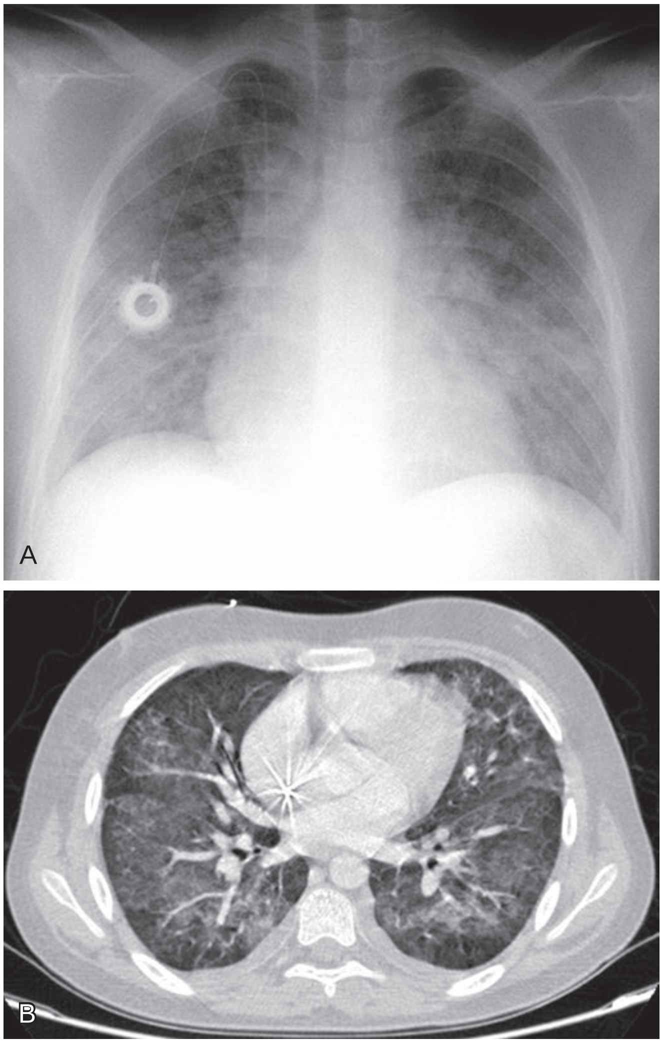

**e-Figure 54.5. Cytomegalic virus infection in a 14-year-old boy with acute lymphoblastic leukemia and immunodeficiency, presenting with dyspnea, fever, cough, and decreased white blood cell counts.** (A) The radiograph shows bilateral ill-defined pulmonary vasculature, more prominent in the lower lung zones. (B) The contrast-enhanced computed tomography scan demonstrates bilateral ground-glass opacities with relative sparing of the peripheral parenchyma.

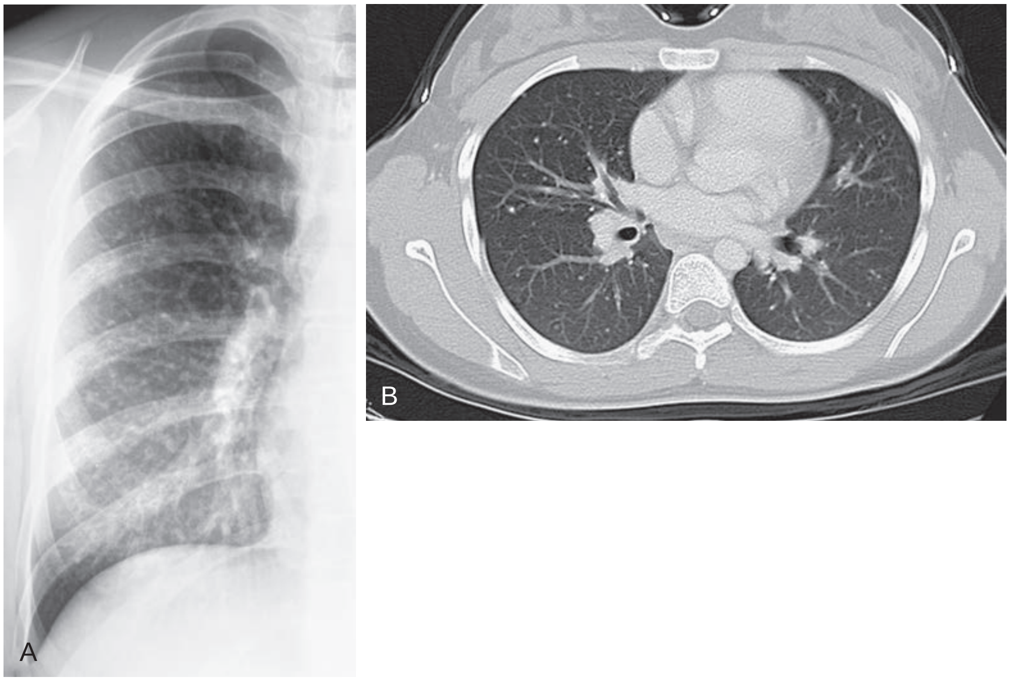

**e-Figure 54.6. Chickenpox pneumonia in a teenager.** (A) The detail from a frontal chest radiograph early in the disease reveals diffuse nodules throughout the right lung. (B) A computed tomography scan done for clarification reveals nodules ranging from 2 to 4 mm, and many are densely calcified.

In EBV infection, hilar and mediastinal lymph node enlargement may be seen (e-Fig. 54.7). Pulmonary involvement is uncommon but is characterized by bilateral reticular perihilar infitrates.[65]

***Treatment and Follow-up.*** Effective antiviral therapies have not been established, and treatment of viral pulmonary infections is mainly supportive. Experimental treatments to correct the acquired surfactant deficiency and dysfunction that occurs in critically ill infants with viral pulmonary infections are actively being investigated.[52] With a few exceptions, the use of extracorporeal membrane oxygenation to treat severe respiratory failure from ARDS, which frequently complicates severe infections, has not led to better outcomes than those of optimal less invasive supportive care.[52] Certain high-risk infants may qualify for prophylactic injection of monoclonal antibodies against the F-glycoprotein of RSV. Because the most important complication of viral pulmonary infection is a superimposed bacterial infection, this should be actively looked for and treated with antibiotics when confirmed.[2]

## PULMONARY INFECTIONS CAUSED BY BACTERIA AND BACTERIA-LIKE ORGANISMS

Bacterial pulmonary infections are acquired through inhalation, aspiration, hematogenously, or rarely by direct extension of chest wall or extrathoracic sites. Their course is determined by the balance between the virulence of the organism and the host immune response (mainly humoral, B-cell–mediated immunity, and macrophageal activity). They are characterized by alveolar airspace consolidation, visible as one or more focal lung opacities that exhibit air bronchograms and obliterate normal air–soft tissue interfaces (the silhouette sign). Pleural effusions are common. The most common bacteria and bacteria-like agents causing pulmonary infections in children are listed in Table 54.2.

In young children, the classic segmental or lobar airspace consolidation is rarely present, and it is nearly absent in neonates. This is reflected by the reported low 30% positive predictive value of radiographic criteria for a bacterial cause of pneumonia, accounting for a widespread overprescription of antibiotics and development of antibiotic-resistant bacteria.[1,34] On the other hand, the high 92% negative predictive value of radiographic criteria for bacterial pneumonia is helpful, allowing clinicians to withhold antibiotics in symptomatic children with a negative chest radiograph and to focus on other potential sources of the fever.[1,34] It is therefore important not to overcall pediatric chest radiographs for the presence of a pulmonary infection, which is the most common interpretation error made by radiologists unfamiliar with pediatric imaging.[66,67]

Clinically occult pneumonia may be diagnosed with radiography in up to 19% of children less than 5 years old with fever of unknown origin and leukocytosis, although a more recent study found a lower incidence (5.3%) and a low utility of radiography when cough was not one of the presenting symptoms in this setting.[68,69]

### Aerobic and Facultative Organisms

#### *Streptococcus pneumoniae*

***Etiology.*** *Streptococcus pneumoniae* is the most common cause of bacterial pneumonia in children less than 5 years of age. It is a gram-positive diplococcus that infects healthy patients but also commonly attacks those with underlying illness, including the hospitalized and immunocompromised, and children with sickle cell anemia.[70] A strong association with a preceding viral infection, in particular influenza, is seen.[71] The virally activated respiratory epithelium has an increased expression of receptors for pneumococcal attachment.[72] In the usual case of an infected but otherwise healthy child, the onset is acute with fever, headache, and abdominal or chest pain with respiratory symptoms and signs. Rapid clinical resolution usually occurs within 24 to 48 hours after treatment with antibiotics in patients with uncomplicated infections. However, a rapid increase has been seen in the incidence of partially or fully penicillin-resistant strains of *S. pneumoniae*.[73] After the institution of conjugate pneumococcal vaccination, the proportion of children younger than 5 years with suspected occult pneumococcal pneumonia confirmed by radiography decreased from 15% to 9%.[74]

***Imaging.*** Pneumococcal pneumonia is usually confined to one lobe, but only rarely is the entire lobe consolidated. A pattern of homogeneous airspace consolidation is usual but not invariable, especially in the presence of underlying lung disease. This pneumonia may initially have a strikingly round appearance in children younger than 8 years (Fig. 54.8), simulating an intrapulmonary mass or abscess, until it spreads further to reach a normal anatomic boundary such as a fissure.[1,75,76] Large pleural effusion, empyema, and lung necrosis are infrequent complications, seen in less than 30% of patients. Resolution on radiographs is usually complete by 6 to 8 weeks.

#### *Streptococcus pyogenes* (Group A Streptococci) and *agalactiae* (Group B Streptococci)

***Etiology.*** Group A streptococcus usually produces tonsillitis or pharyngitis. In the 1990s, *S. pyogenes* pneumonia, often associated with the toxic shock syndrome, was increasingly reported in childhood. It may occur de novo in a healthy child or follow a viral infection. In neonates, group B streptococcus is a leading cause of sepsis, including pneumonia and meningitis.

***Imaging.*** Group A *Streptococcus* produces a bronchopneumonia in a segmental configuration with either homogeneous or patchy consolidation, which frequently affects a lower lobe. It may be bilateral. Pleural effusion and empyema are common in untreated cases. Lung abscess may be a complication. Clinically and on imaging studies, this pneumonia is very similar to staphylococcal pneumonia, although pneumatoceles are less commonly seen. Group B *Streptococcus* may accompany or mimic hyaline membrane disease in neonates and is radiographically difficult to distinguish from it, although the presence of pleural effusion favors (concomitant) infection.

#### *Staphylococcus aureus*

***Etiology.*** This gram-positive, catalase-positive coccus primarily affects infants under 1 year of age (70%). The incidence of "primary" staphylococcal pneumonia has decreased markedly since the early 1950s. However, staphylococcal pneumonia secondary to septicemia rather than inhalation of organisms is increasing and occurs in older children. This form of "embolic" disease may present with multiple nodular masses or abscesses (e-Fig. 54.9). This evolving pulmonary pattern in a child with sepsis should initiate a search for a distant source of infection, often in bones, joints, or skin.[77] Despite extensive pulmonary disease, if recovery occurs it is usually without sequelae. In comparison with methicillin-sensitive strains, methicillin-resistant strains of community-acquired *S. aureus* cause more serious pneumonias in younger children.[78,79]

The more invasive and virulent strains of *S. aureus*, which carry the genetic marker Penton-Valentin leucocydin (PVL), are responsible for the most serious primary or metastatic infections of the lungs that are acquired in community settings.[80]

***Imaging.*** In contrast to pneumococcal pneumonia, staphylococcal pneumonia is a lobular or bronchopneumonia, which begins in the airways rather than in the alveoli (e-Fig. 54.10). Consolidation of peribronchiolar acinar units occurs initially in a segmental distribution. This infectious agent is very virulent, and severe hemorrhagic pulmonary edema may develop rapidly. Pneumatoceles are more common than in any other type (also reported in

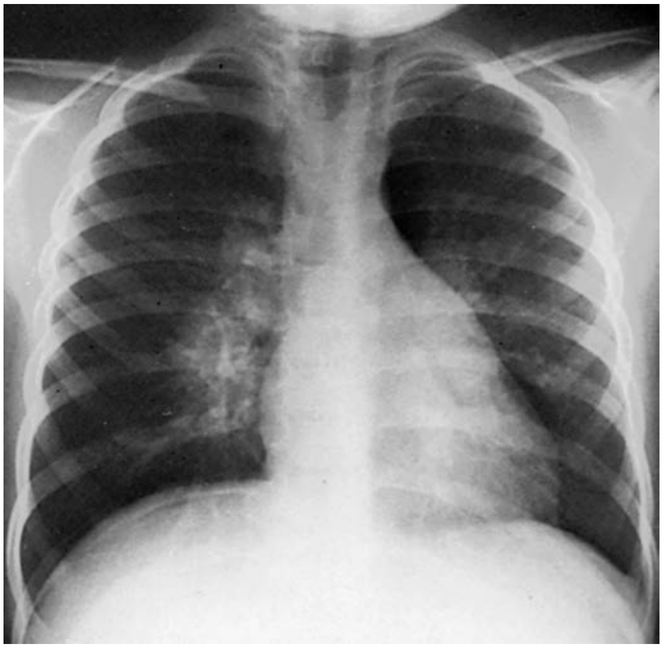

**e-Figure 54.7. Mononucleosis in a teenager with hepatosplenomegaly and lymphadenopathy.** The chest radiograph reveals marked bilateral hilar adenopathy. Lymphoma was considered, but infectious mononucleosis was diagnosed. *(Courtesy of Dr. Jack Sty, Milwaukee, WI.)*

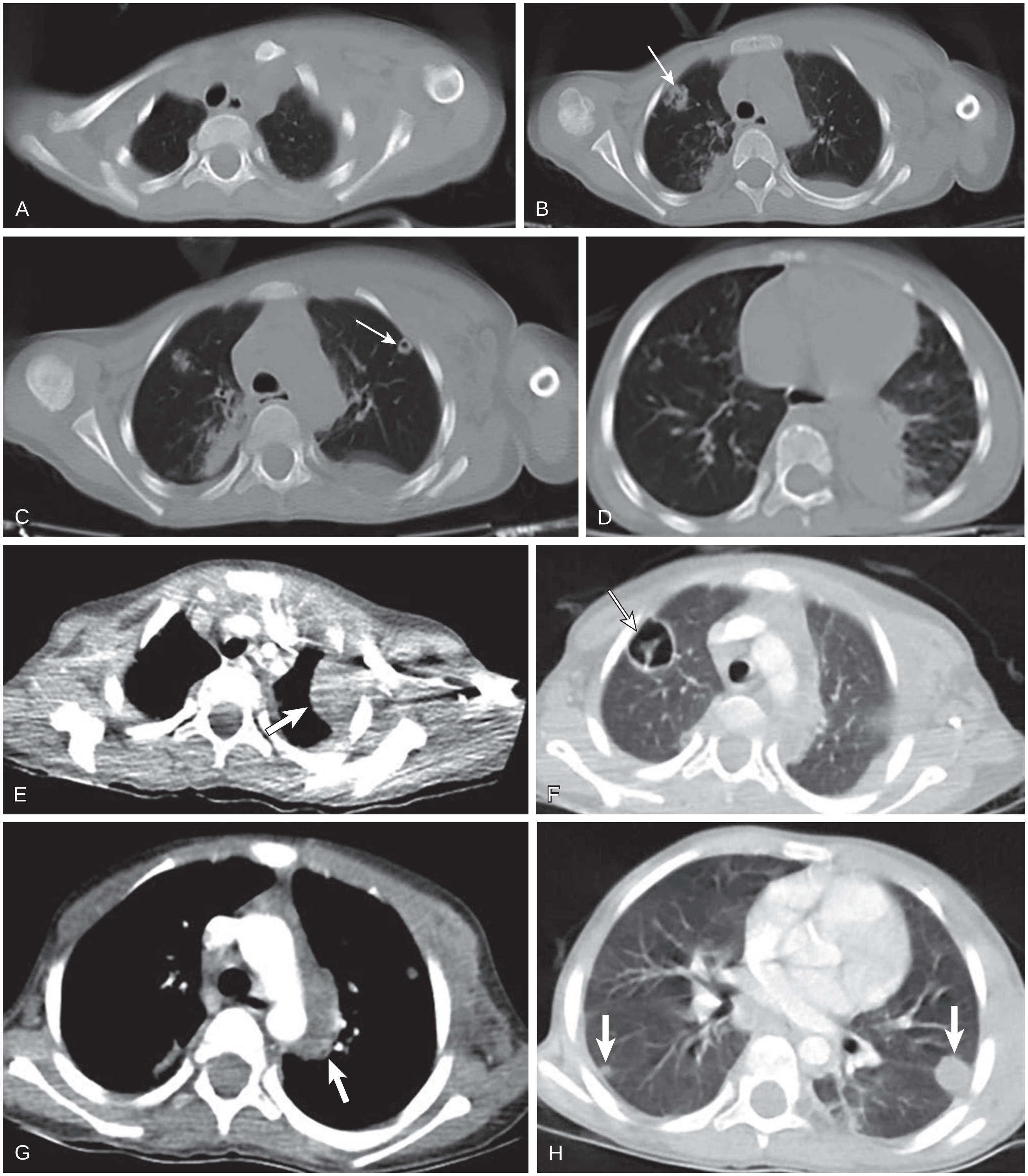

**e-Figure 54.9.** ***Staphylococcus aureus*** **septicemia in 4-year-old male Syrian refugee, who presented with loss of consciousness, dyspnea, fever, and swelling in the left axilla and right forehead. The swelling in the right forehead was punctured and a purulent discharge was observed.** (A–D) A noncontrast enhanced computed tomography (CT) demonstrates soft tissue swelling in the left axilla that extends into the soft tissues along the left hemithorax. There are also multifocal airspace opacities and multiple cavitating nodules involving both lungs. Based on the CT findings *Staphylococcus* sepsis was suspected, and the diagnosis was confirmed by blood cultures and cultures from the wounds. (E–H) Follow-up CT after 16 days demonstrates improvement of the inflammatory soft tissue changes and airspace opacities; however, some parenchymal nodules show progression and cavitation associated with occurrence of new nodules.

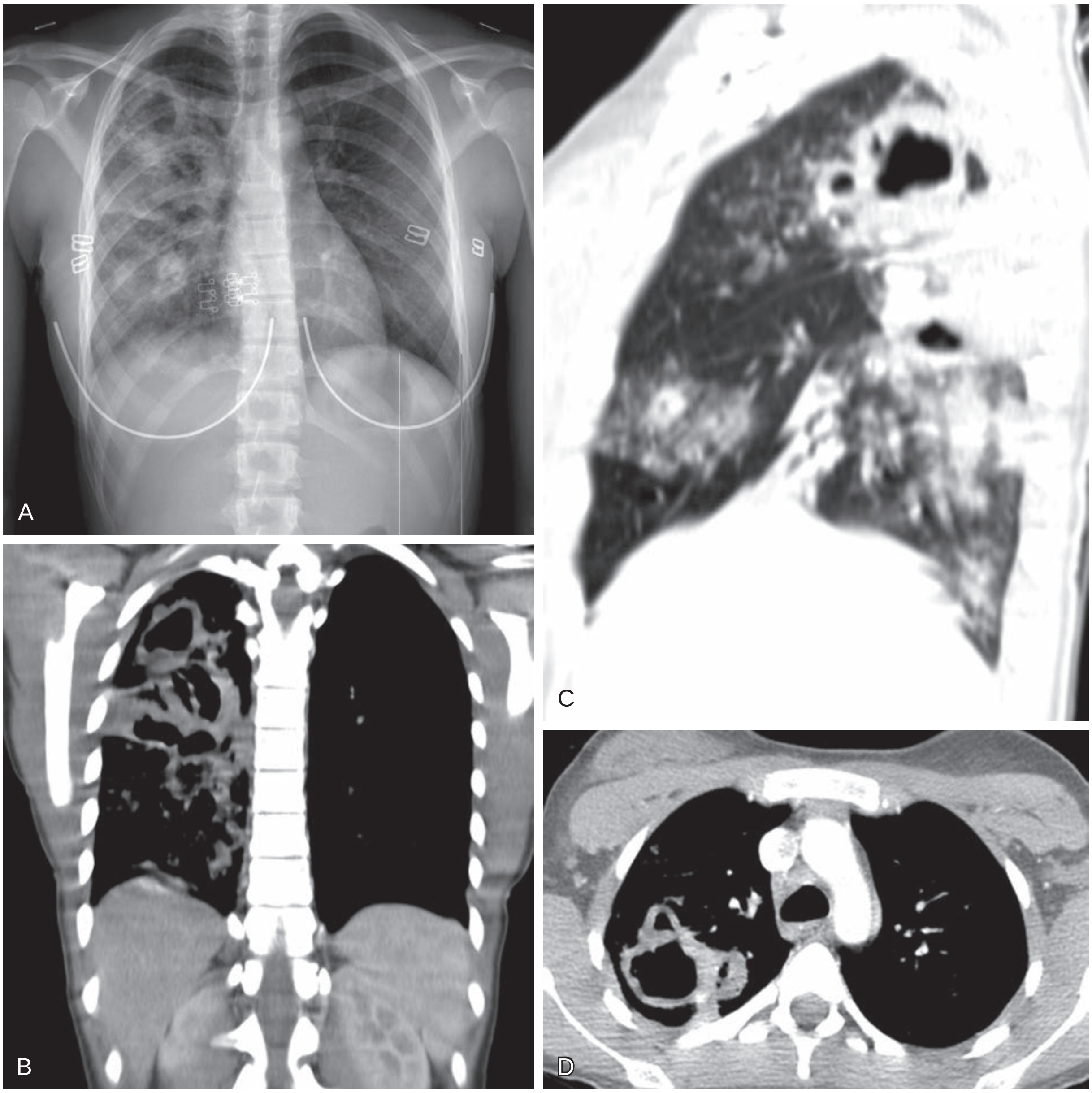

**e-Figure 54.10.** ***Staphylococcus aureus*** **pneumonia in a 15-year-old girl who presented with a 3-day history of fever, cough, fatigue, and vomiting.** (A) Radiograph shows patchy air space opacities and multiple cavitary lesions involving the right lung. (B–D) Contrast-enhanced computed tomography demonstrates diffuse patchy airspace opacities and multiple cavities with thick walls in the right lung. Blood cultures yielded *S. aureus.*

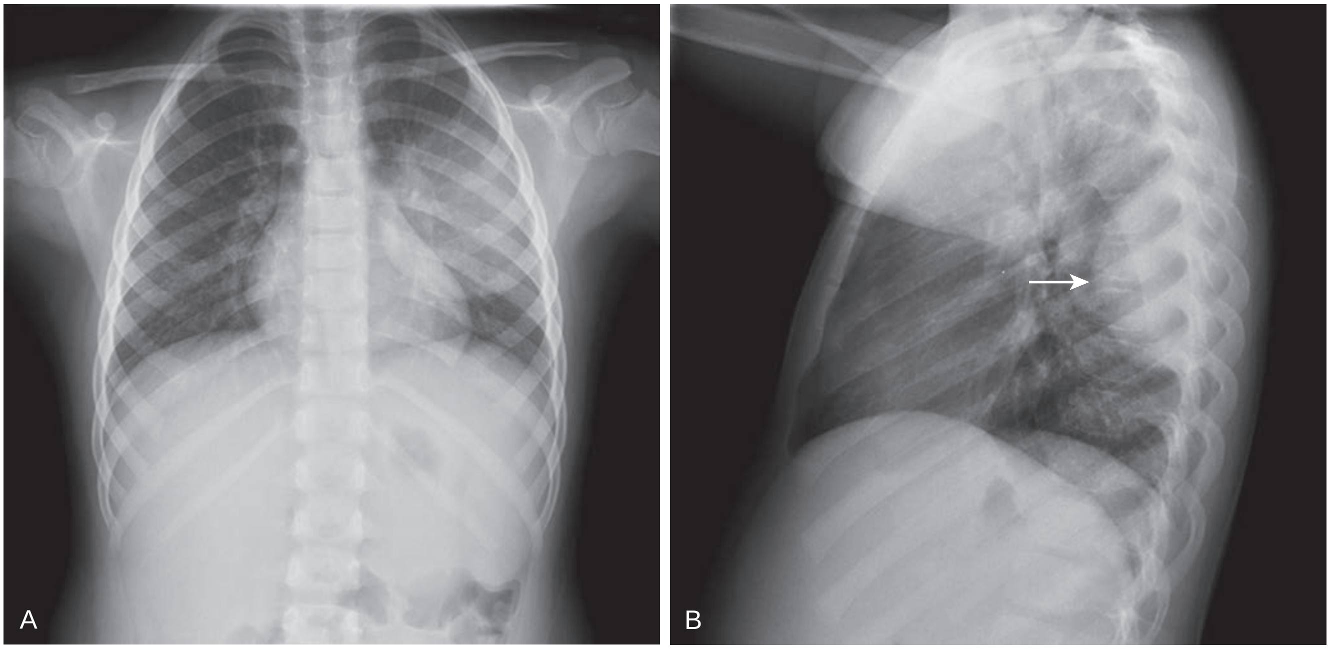

**Figure 54.8. Streptococcal round pneumonia in a 5.5-year-old girl presenting with fever and left-sided back and rib pain.** Frontal (A) and lateral (B) radiographs show alveolar consolidation in the superior segment of the left lower lobe with a rounded appearance (*arrow* in B). Note in (A) the visibility of the left hilar shadow, which is superimposed on the posteriorly located pulmonary pseudomass (hilar overlay sign).

*S. pneumoniae*, *H. influenzae*, and *Escherichia coli* pneumonia) and occur in 40% to 60% of patients.[78,81,82] Ten percent of children with staphylococcal pneumonia have a pneumothorax, which may result from the rupture of a pneumatocele.[78,81,82] Pleural effusion and empyema are also very frequent, occurring in more than 90% of children (Fig. 54.11).[82]

### *Haemophilus influenzae* Type B

***Etiology.*** *Haemophilus influenzae* is a gram-negative, rod-shaped bacterium, which was first discovered in 1892 during an influenza pandemic. In infants and young children, it causes bacteremia, pneumonia, cellulitis, epiglottitis, and meningitis. Since 1990, vaccination has markedly reduced the incidence of this pneumonia (<95%).

***Imaging.*** The radiographic appearance of pneumonia due to *H. influenzae* is nonspecific: pulmonary opacities that often begin as a segmental, interstitial-appearing process progresses to airspace consolidation.[83] Approximately two-thirds of cases have unilateral involvement, but more than one lobe is involved 25% of the time.[83] Empyema is a common complication, occurring in about 40%.[83]

### *Bordetella pertussis*

***Etiology.*** *Bordetella pertussis* is a gram-negative, aerobic, capsulated coccobacillus. The incidence of pertussis (whooping cough) has decreased significantly with immunization, but it is still seen in young infants, particularly in the unimmunized. This agent is spread by airborne droplets. A characteristic clinical sign is the paroxysmal cough (whoop). Even after convalescence, the patient's cough may persist for weeks or months. In China the disease has been called "the cough of 100 days."

***Imaging.*** Abnormal but nonspecific findings are present in most patients with pertussis. Because this is an airways-centered disease, it may mimic viral airways disease and pneumonia. The classic appearance is that of the "shaggy heart" (e-Fig. 54.12). However, nonspecific findings such as hyperaeration, atelectasis, segmental consolidations, and hilar lymphadenopathy are seen more commonly. Bronchiectasis may be a long-term complication.

### *Pseudomonas aeruginosa*

***Etiology.*** *Pseudomonas aeruginosa* is a gram-negative, aerobic, rod-shaped bacterium, which is an opportunistic pathogen in humans. Lungs, urinary tract, and kidneys are the common sites of infection. *P. aeruginosa* usually occurs as a nosocomial infection and is a major problem for patients with cystic fibrosis, in which thick layers of lung mucus and alginate produced by the bacteria may limit the diffusion of oxygen. Diagnosis of this infection depends on the Gram stain of sputum or other bacteriologic specimens (e.g., lung tissue, bronchoscopic aspiration, and bronchoalveolar lavage fluid).

***Imaging.*** When the patient is infected by airway contamination, the process tends to involve both lung bases, with extensive bilateral parenchymal consolidation, patchy areas of disease with small abscess formation, or small regions of lobular emphysema. In the bacteremic form, widespread patchy or nodular shadows may be found throughout both lungs. Lung necrosis may also occur.

### *Legionella pneumophila*

***Etiology.*** *Legionella pneumophila* is an aerobic, pleomorphic, flagellated, gram-negative bacterium. It is the cause of legionnaires' disease, is mainly seen in immunocompromised patients, and is rare in children.[84,85]

***Imaging.*** Typically, initial radiographs show poorly marginated opacities that progress to more widespread consolidation, often accompanied by pleural effusion. Presentation as multiple pulmonary nodules has been reported but is less common.[85] Cavitation and abscess formation are complications.

## Anaerobic Organisms

***Etiology.*** Anaerobic bacteria are uncommonly responsible for pneumonia and lung abscess.[86] Aspiration is the most common

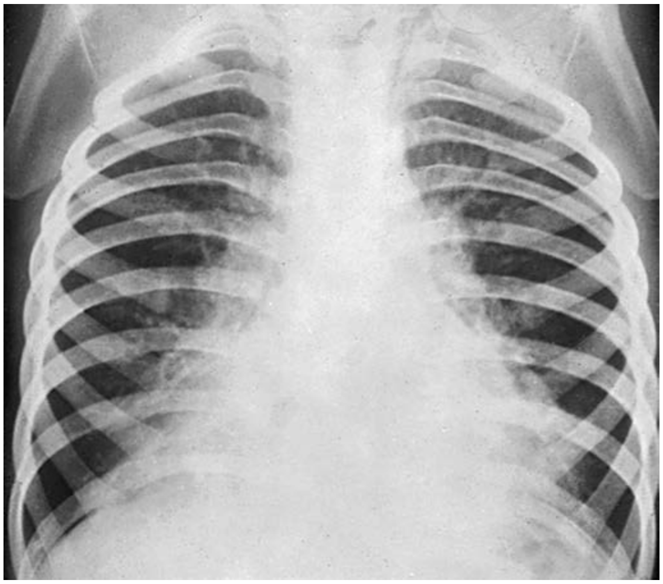

**e-Figure 54.12. Pertussis bronchopneumonia.** Bilateral basilar bronchopneumonia during the active phase of whooping cough. The heart contours are irregular ("shaggy heart").

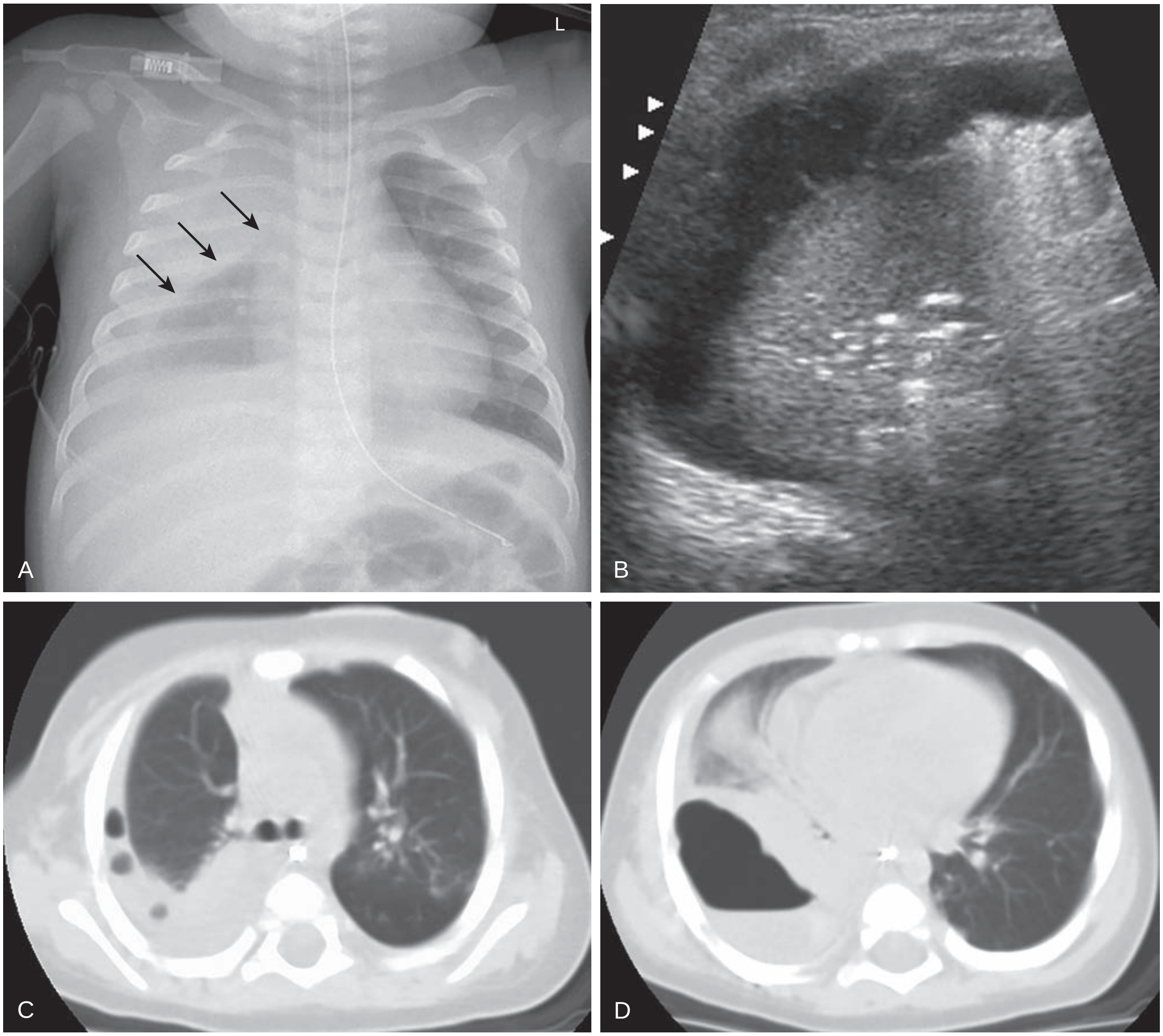

**Figure 54.11. Role of cross-sectional imaging in a 7-month-old girl with staphylococcal pneumonia and empyema.** (A) The radiograph demonstrates right pleural thickening, which has a convex margin toward the lung *(arrows).* (B) The transverse ultrasound image of the right chest shows a complex pleural effusion, containing thin septations. (C and D) Computed tomography confirmed the presence of loculated pleural fluid collections, containing trapped gas bubbles (C) and, more inferiorly, an air-fluid level (D). *(Reprinted with permission granted by Springer-Verlag of Westra SJ, Choy G. What imaging should be performed for the diagnosis and management of pulmonary infections?* Pediatr Radiol. *2009;39[suppl 2]:S178–S183 [Fig. 1, page S179].)*

route of exposure, and *Fusobacterium* species, *Bacteroides* species, *Peptococcus*, and *Peptostreptococcus* may be cultured from the abscess or the pleural fluid.

***Imaging.*** Usually, consolidation occurs in the lower respiratory tract, and the clinical course is slowly progressive (e-Fig. 54.13). Lung abscess (e-Fig. 54.14) and fulminant necrotizing pneumonia may eventually develop.

## Bacteria-like Organisms

### *Chlamydophila trachomatis* and *pneumoniae*

***Etiology.*** *Chlamydia trachomatis* is an intracellular bacterium commonly found in the genital tract, where it causes urethritis in men and cervicitis in women. In neonates, it causes conjunctivitis, which is contracted during passage through an infected birth canal. *Chlamydia* is a common cause of pneumonia in infants between 2 and 14 weeks of age.[87] The infant is affected by a staccato-like cough and may have conjunctivitis and eosinophilia, although these are not invariable findings. Usually, the patient is afebrile, with a radiographic appearance suggesting an illness more severe than the clinical findings indicate. Recently *C. pneumoniae* has been recognized as a common agent causing community-acquired bronchitis and mild atypical pneumonia in school-age children.[3] The clinical response to appropriate therapy is usually rapid.

***Imaging.*** The radiographic findings of *C. trachomatis* infections are nonspecific (e-Fig. 54.15), but when they are analyzed in conjunction with clinical findings, the disease may be suspected. Bilateral involvement is usual.[88] The lungs are usually hyperaerated

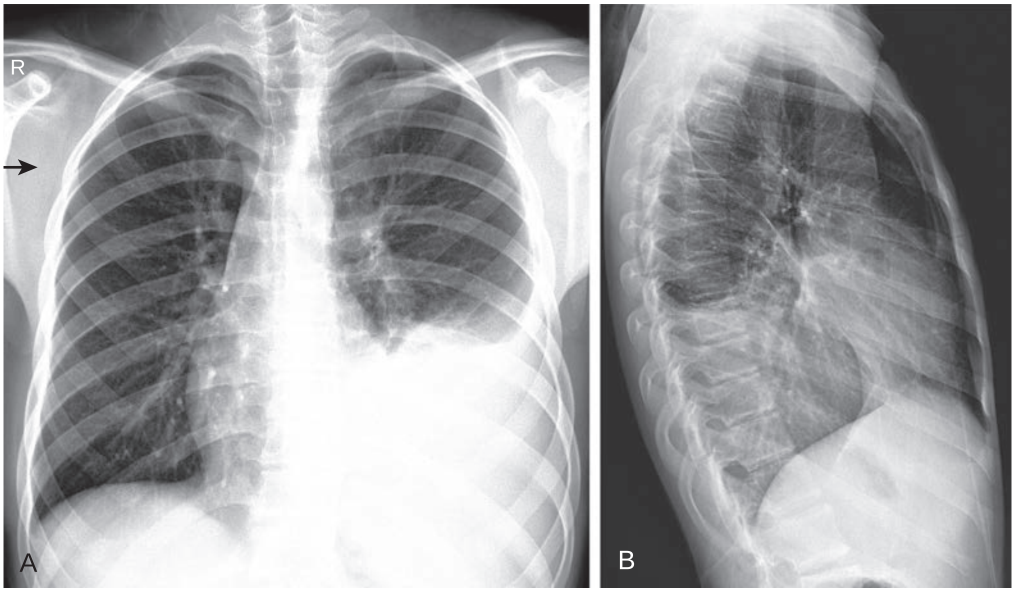

**e-Figure 54.13. Anaerobic pulmonary infection in a 15-year-old boy who presented with chronic cough and chest pain without fever.** Frontal (A) and lateral (B) radiographs show a large opacity in the left lower thorax that obscures the diaphragm, consistent with consolidation with pleural fluid. Polymerase chain reaction on the drainage fluid from the pleural cavity was consistent with *Fusobacterium* infection.

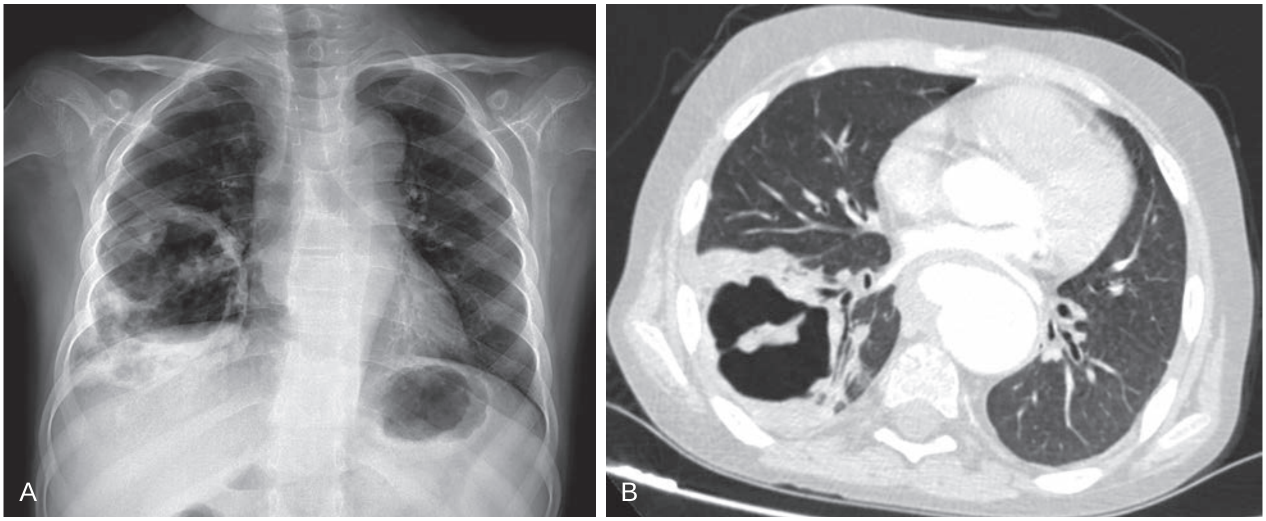

**e-Figure 54.14. Anaerobic pulmonary infection in a 12-year-old boy with Wiskott-Aldrich syndrome presenting with multiple cerebral abscesses, septicemia, cough, and fever.** (A) The radiograph shows a thick-walled air cavity in the right lower lung zone. (B) Contrast-enhanced computed tomography depicts the pulmonary abscess. There is also a pseudoaneurysm in the descending thoracic aorta. Polymerase chain reaction test of the cerebral abscess was consistent with *Peptostreptococcus* infection.

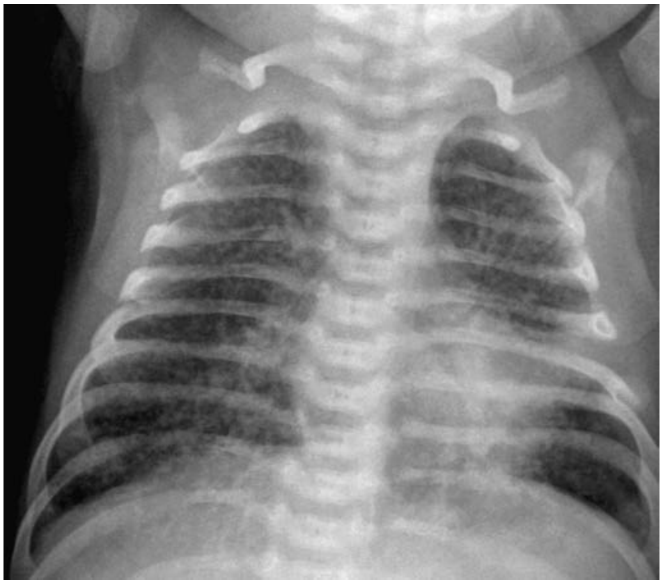

**e-Figure 54.15. Chlamydial pneumonia in a 6-week-old boy with wheezing and a low-grade fever.** The frontal radiograph shows diffuse interstitial infiltrates with hyperinflation. Polymerase chain reaction results confirmed the diagnosis.

with increased linear density and patchy areas of consolidation, probably representing subsegmental atelectasis. Lobar consolidation is rare.[88]

## Mycoplasma pneumoniae

***Etiology.*** *Mycoplasma pneumoniae* is one of the most common causes of pulmonary infection in childhood, accounting for 10% to 30% of pediatric pneumonias.[89] It is most often seen in school-age children and is uncommon in children less than 3 years of age. It is acquired by droplet inhalation, and it is most commonly noted in families, in schools, and among military recruits. The disease is usually mild, with low-grade malaise, headache, fever, and cough. Stevens–Johnson syndrome (erythema multiforme) may complicate the disease. The diagnosis is established by culturing the organisms from sputum or by demonstration of rising specific *Mycoplasma* titers. A rise in the titer of cold agglutinins is seen in about 50% of cases but is nonspecific; of greater diagnostic value are immunofluorescent and complement fixation tests for specific antibodies and the recently developed molecular probes.[90]

***Imaging.*** This classic "atypical pneumonia" has a radiographic appearance that frequently mimics viral pulmonary infection (Fig. 54.16).[1] In early cases, a fine reticular pattern suggestive of interstitial inflammation may be seen.[91] This tends to be in a segmental distribution and in some cases progresses to airspace consolidation suggestive of bacterial pulmonary infection.[92,93] Small pleural effusions are seen in up to 20% of patients. Hilar adenopathy is common. Bilateral involvement occurs in approximately one-third of cases. The radiographic changes are frequently more severe compared with the patient's clinical condition. Resolution is often slow and lags behind clinical improvement.

## Treatment and Follow-up

Treatment of bacterial pulmonary infections is with antibiotics and other chemotherapeutic agents, focused on the causative agent, either presumed (empirical treatment) or preferably directed by the results of culture or immunoassay. Complications of bacterial pulmonary infections are lung necrosis, abscess, empyema, and bronchopleural fistula.[2] Ultrasonography is the most effective initial cross-sectional modality when pleural complications are suspected,[94-96] whereas CT is the preferred modality to diagnose parenchymal complications.[97-103] A review of the diagnostic performance of CT versus radiography confirms the expected higher sensitivity of CT.[99,104-111] CT is more sensitive than radiography to determine the cause of a delayed response to medical and percutaneous treatment of pediatric chest infections, but it is unclear whether this affects the eventual outcomes of treatment.[99,110] An initial trial of image-guided fibrinolytic treatment of empyemas has better outcomes that primary video-assisted thorascopic surgery (VATS).[94] Failure of this regimen and the eventual need for surgery may be expected in those in whom more virulent and antibiotic-resistant bacteria are isolated.[112] Cavitary lung necrosis is demonstrated well by CT.[111] However, most of the affected children recover without permanent sequelae on clinical and imaging follow-up.[1] For this reason, documentation of complete resolution of pneumonia in children who are otherwise healthy is not indicated.[1,35,113] CT and, potentially, magnetic resonance imaging (MRI) are helpful, however, to fully investigate any underlying focal anatomic cause such as anomalous bronchi, bronchogenic cysts, sequestrations, or bronchial atresia (Fig. 54.17), which may underlie recurrent or chronic pneumonia.[1,114-116] Conversely, the value of CT to monitor diffuse processes that predispose to repeated pulmonary infections such as chronic granulomatous disease of childhood and cystic fibrosis remains controversial.[117,118] Children with these chronic conditions will accumulate a substantial radiation burden from repeated examinations during their lifetime, and the theoretical risks of these procedures with regard to the induction of cancer will have to be balanced against the immediate clinical benefits, which remain unproven.[119] MRI has promise as a nonradiating cross-sectional imaging alternative for examination of these conditions.[114,120-122]

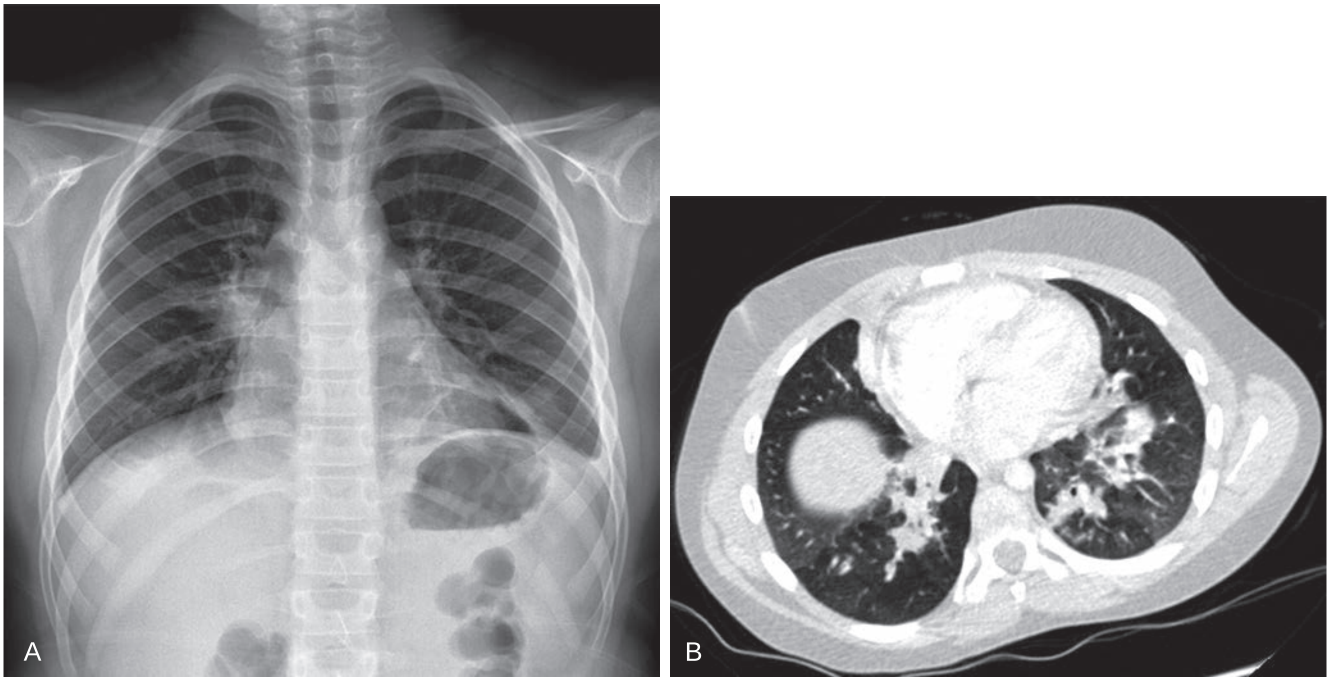

**Figure 54.16. Mycoplasma atypical pneumonia in an 8-year-old girl who presented with fatigue, low-grade fever, and cough.** (A) The chest radiograph shows irregularity of the right hilum and bibasilar infiltration. (B) Contrast-enhanced computed tomography demonstrates bilateral bronchopneumonia in the lower lobes. A direct fluorescent antibody test from nasopharyngeal aspirate confirmed the diagnosis.

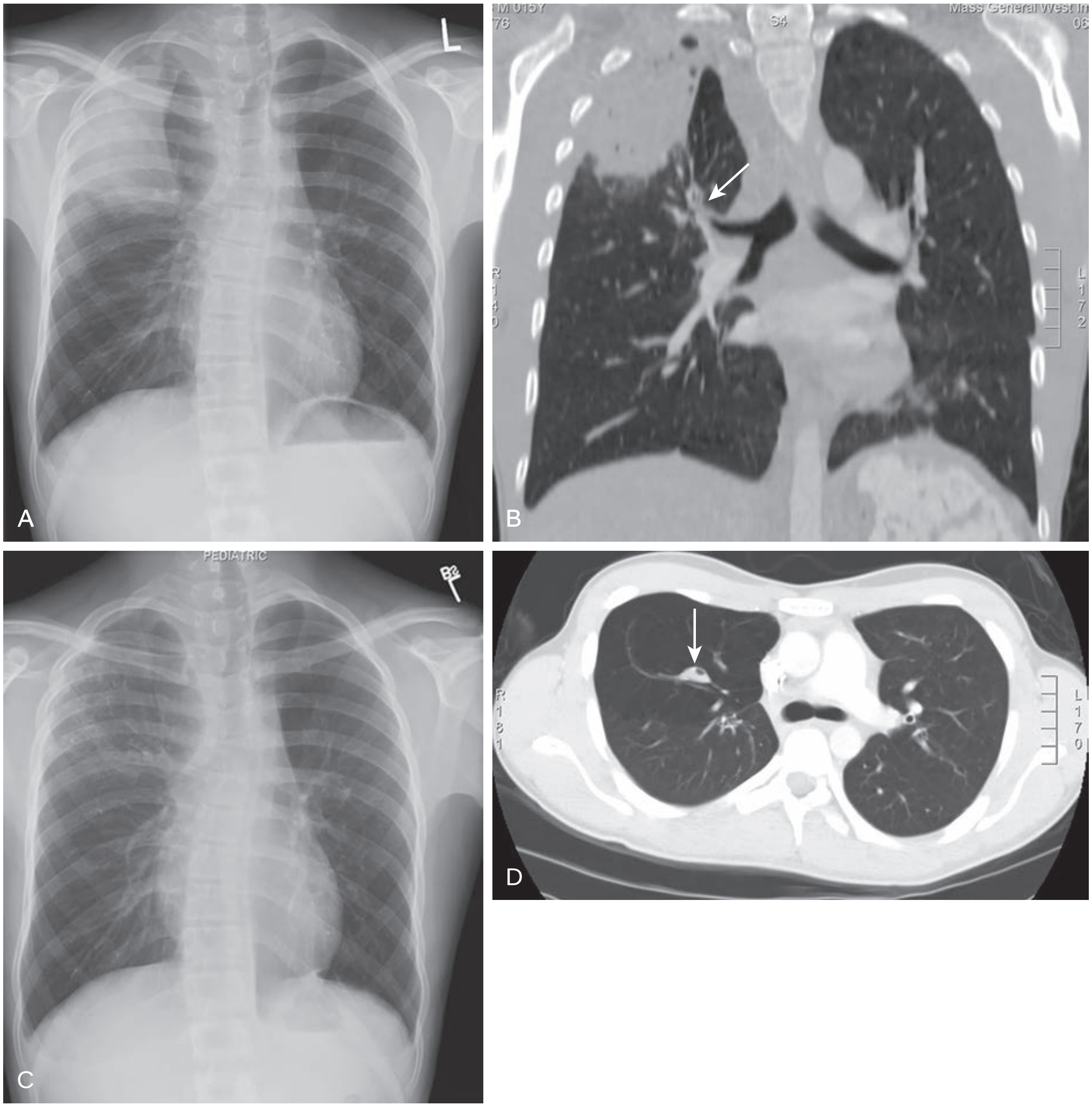

**Figure 54.17. Role of computed tomography (CT) in recurrent pneumonia in a 15-year-old boy with bronchogenic cyst and bronchial atresia.** (A) The chest radiograph shows consolidation in the right upper lobe and right upper mediastinal widening. (B) The CT scan shows atresia in the apical bronchus of the right upper lobe *(arrow)* and right mediastinal widening caused by a bronchogenic cyst. (C and D) The follow-up chest radiograph (C) and CT scan (D) show near-complete resolution of the pneumonia, with persistent architectural distortion of the right upper lobe. The atretic bronchus contains inspissated mucus (*arrow* in D). Right upper lobectomy and resection of the bronchogenic cyst was performed.

## Mycobacterial Infection—Pulmonary Tuberculosis

***Etiology.*** TB is caused by *Mycobacterium tuberculosis*, an aerobic, nonmotile, non–spore-forming rod. Although the resurgence of TB noted in the United States in the 1980s and 1990s has declined, in 2003, 15,000 new cases were reported, and the rate of decline appears to be slowing.[123] A significant number of new cases are diagnosed in foreign-born children, as well as immunocompromised patients (especially HIV).[124-127]

Inhalation of the tubercle bacillus is the most common route of infection in children. Congenital infection is extremely rare and is most often secondary to hematogenous spread across the placenta during pregnancy or from contaminated amniotic fluid. Pulmonary TB infection may be categorized into three groups: (1) primary infection; (2) miliary infection; and (3) reactive or postprimary infection.

The length of the incubation period of TB depends on the size of the initial inhaled inoculum and varies from 2 to 10 weeks; it ends when the patient becomes sensitized (i.e., has a positive skin test). Annual skin testing in high-risk groups is recommended. In the low-risk child, skin testing at 12 to 15 months, at 4 to 6 years, and in adolescence is a reasonable approach.[128] In asymptomatic primary tuberculosis, the disease is detected because of a routine skin test, and chest radiography is most often normal. In endemic areas, radiographs may demonstrate hilar lymphadenopathy only.[129-131] Because children produce little sputum, they do not

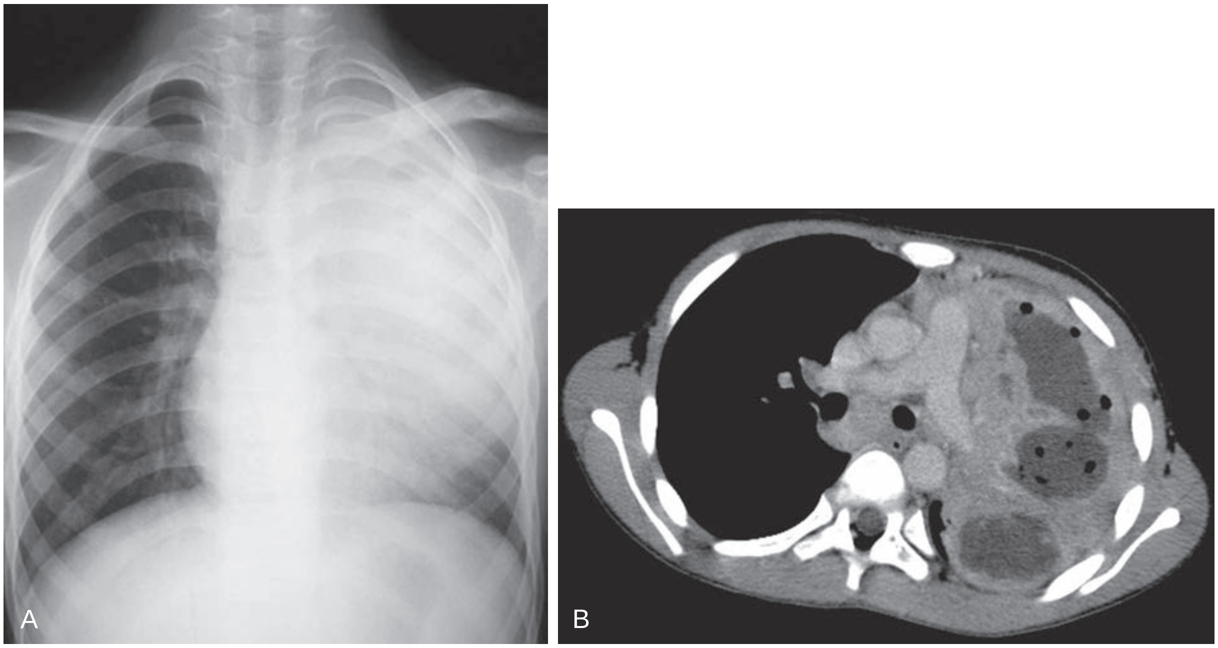

**Figure 54.22. Progressive primary tuberculosis in an older child.** (A) The radiograph shows dense consolidation with expansion in the left upper lobe, which contains an air-filled cavity. (B) Contrast-enhanced computed tomography demonstrates extensive liquefactive parenchymal disease *(Courtesy of Bernard Laya, MD.)*

transmit the disease to one another, and a search for the infected adult must be undertaken. The index child is always treated with antibiotics.

If radiographs are positive, usually a single small primary focus is present (70%), located in the subpleural region. From there, the bacilli spread through the lymphatics to regional hilar and mediastinal lymph nodes (primary complex, e-Fig. 54.18). In postobstructive tuberculosis, large lymph nodes may cause extrinsic bronchial compression, and granuloma formation may cause endobronchial obstruction, leading to segmental air trapping, atelectasis (e-Fig. 54.19), or both. Chronic obstruction may lead to bronchiectasis. Calcification occurs after caseation of the primary lesion and is seen earlier in infants (6 months after infection, e-Fig. 54.20) than in older children (2–3 years after infection, e-Fig. 54.21).

Progressive primary pulmonary tuberculosis is a serious but rare complication.[132] Progressive enlargement of the primary complex occurs, with caseation of the lesion followed by liquefaction (Fig. 54.22). The lesion may rupture into a bronchus, establishing new foci of disease (Fig. 54.23). Affected children are usually quite ill, with weight loss, dyspnea, anorexia, and failure to thrive. Pleural involvement in TB is usually noted in children older than 2 years, who present with fever, chest pain, and symptoms of pneumonia.[133]

The host response to lymphohematogenous spread is varied, with immunosuppressed patients being at greatest risk. A few children present with high spiking fevers, hepatomegaly, and positive blood culture (chronic tuberculous bacteremia, e-Fig. 54.24). Miliary tuberculosis usually occurs within 6 months of the primary infection and results from lymphohematogenous dissemination of *M. tuberculosis* from the primary complex.

Reactivation or postprimary TB infection is the classic adult or adolescent form of the disease. It is the result of growth of previously dormant bacilli in the apices of the lung. Reactivation of tuberculosis is rare in children who were infected with primary tuberculosis before age 2 years. It is much more frequent in children whose primary infection occurred after age 7 years, particularly if they were initially infected near puberty.[123]

***Imaging.*** Primary TB infection of the lung falls under the subcategory of subacute dense focal (atypical) pneumonia (see e-Fig. 54.18).[28,134-136] Chest radiography is insensitive to primary infection.[137,138] With a positive skin test, screening with a frontal radiograph is often sufficient; however, in endemic areas the addition of the lateral radiograph improves detection of hilar lymphadenopathy.[129,139] Almost half (43%) of children diagnosed with tuberculous meningitis have normal chest radiographs.[140] CT typically shows a subtle parenchymal opacity with associated lymph node enlargement. When initial chest radiography is positive, hilar and peritracheal lymphadenopathy is the most common finding, present in 92% of the cases.[124,126] CT studies confirm that infected patients frequently have adenopathy that tends to be low density with rim enhancement and later calcification (see e-Figs. 54.18–54.20), but 50% may not have nodes larger than 1 cm and they may be contralateral to the parenchymal disease.[141] Miliary TB infection (see e-Fig. 54.24) produces a “snowstorm” pattern in the lung, liver, and spleen.[142] Occasionally this may be present before there is overt clinical manifestation of the disease; as expected, CT is more sensitive than chest radiography.[143,144] Regression of abnormalities is slow and may require from 6 months to 2 years to resolve on radiography and up to 15 months on CT evaluation (see e-Fig. 54.20).[126,145]

***Treatment and Follow-up.*** TB is treated with a combination of antibiotics and chemotherapeutic agents to which the organism is sensitive.[146] Multidrug resistance to the regimens is an increasing problem worldwide, but strategies for effective treatment and reinforcing patient adherence have proven successful, even in the developing world.[146] Because of the limited sensitivity of radiography, cross-sectional imaging with CT, when locally available, is frequently helpful for patient management (see e-Figs. 54.18 and 54.20, Figs. 54.22 and 54.23, and e-Fig. 54.24).[125,132,133,142,144,147]

## Nontuberculous Mycobacterial Pulmonary Infection

***Etiology.*** Nontuberculous mycobacteria (NTM) are widely distributed in the environment and may produce infection in patients with normal immunity, although infection is significantly

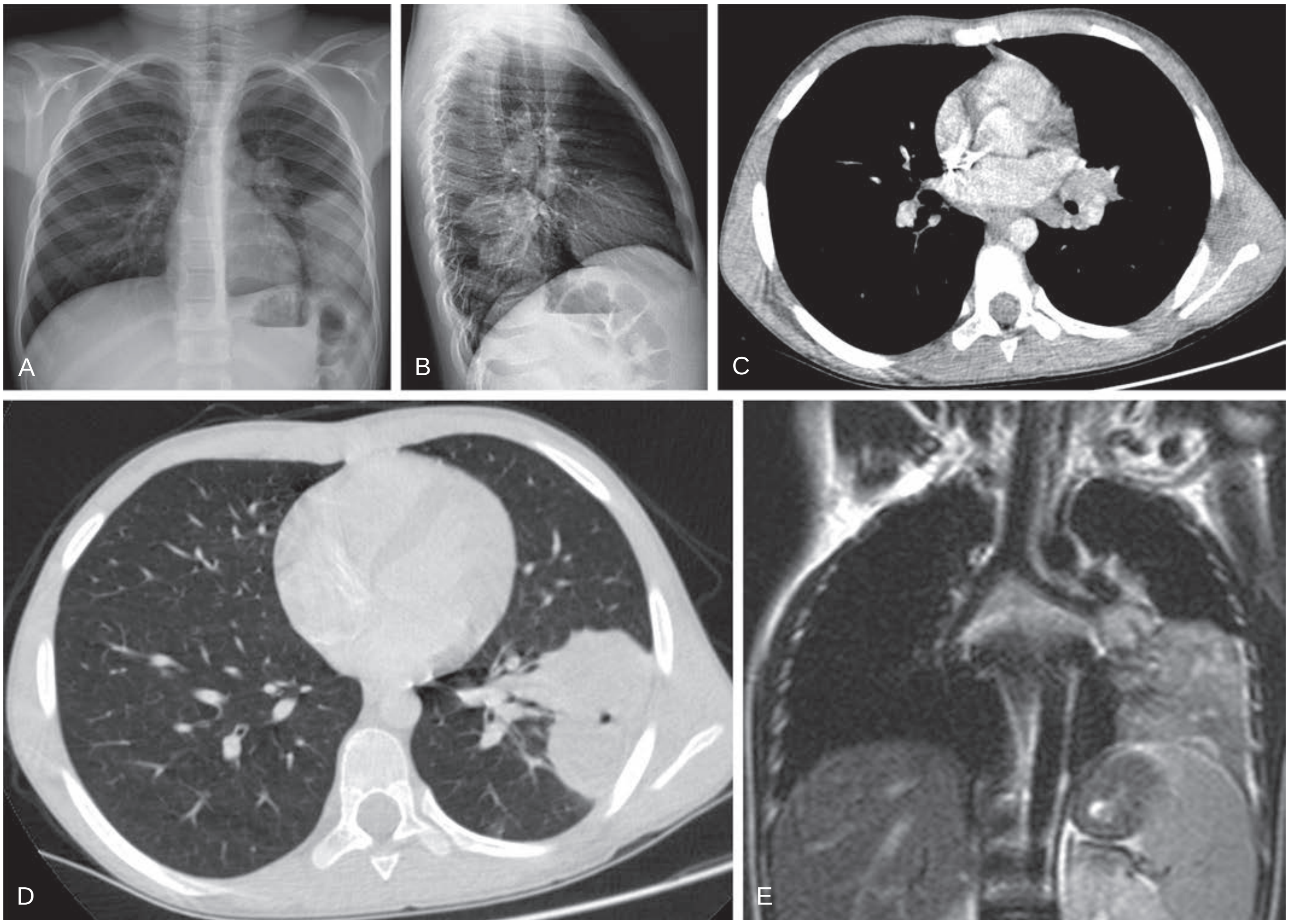

**e-Figure 54.18. Primary tuberculosis (TB) in an 8-year-old boy who presented with cough, abdominal pain, and fatigue.** (A and B) Radiographs show nodular consolidation in the left lower lung zone and an enlarged left hilum. (C and D) Contrast-enhanced computed tomography demonstrates a peripheral consolidation in the left lower lobe, associated with enlarged left hilar lymph nodes. (E) On coronal T2-weighted magnetic resonance imaging, the consolidation and lymph nodes exhibit high signal intensity. The parenchymal consolidation and associated ipsilateral lymph nodes constitute the primary Ghon complex in TB. Culture of bronchial lavage fluid confirmed the diagnosis.

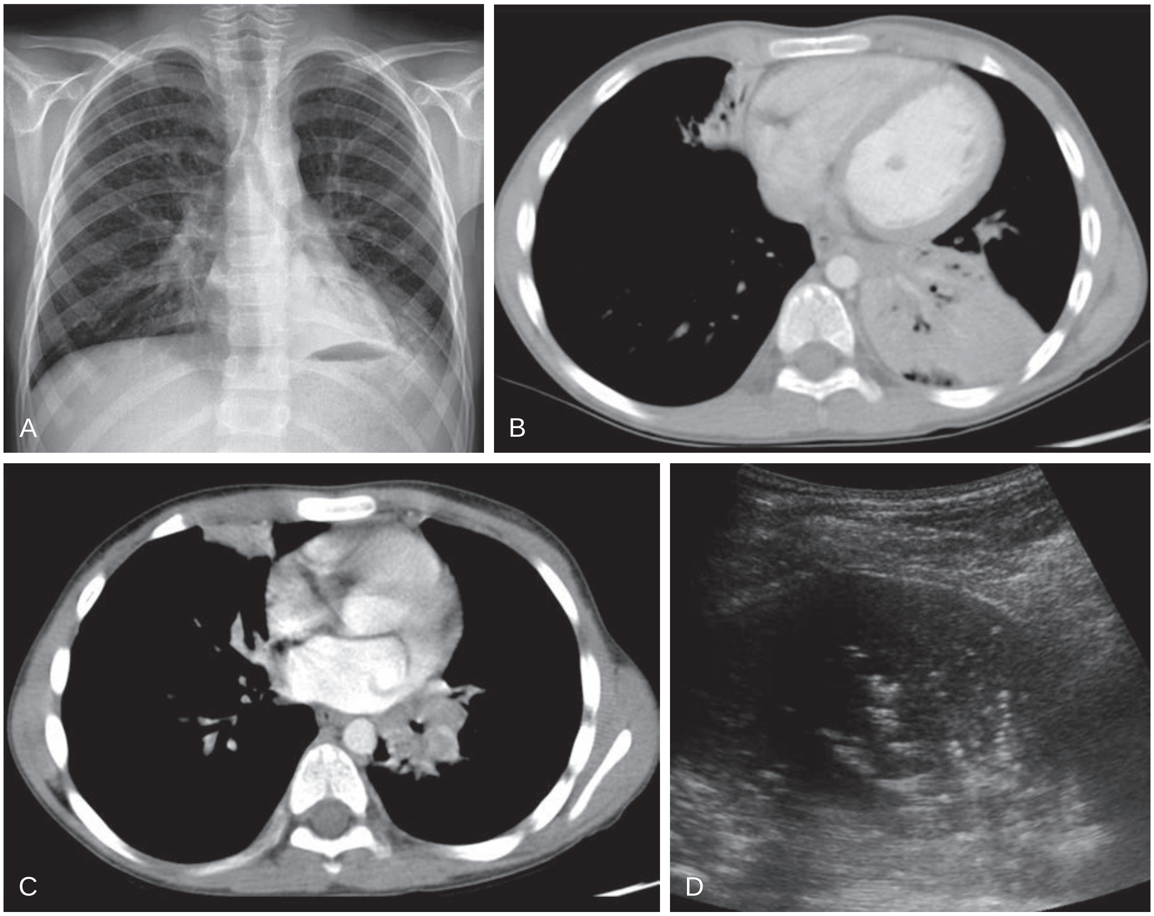

**e-Figure 54.19. Consolidation with atelectasis from pulmonary tuberculosis (TB) in an 8-year-old boy with a history of recurrent lung infections presenting with cough.** (A) The radiograph shows an enlarged left hilum and consolidation in the left retrocardiac area. (B and C) Contrast-enhanced computed tomography demonstrates consolidation with volume loss in the left lower lobe and right middle lobe, with adenopathy in the left pulmonary hilum leading to bronchial compression. (D) Ultrasonography scan shows sonographic air bronchograms within the consolidated left lower lobe. The diagnosis of TB was made on the basis of clinical and radiologic findings, although the organism could not be cultured. The patient responded well to anti-TB treatment.

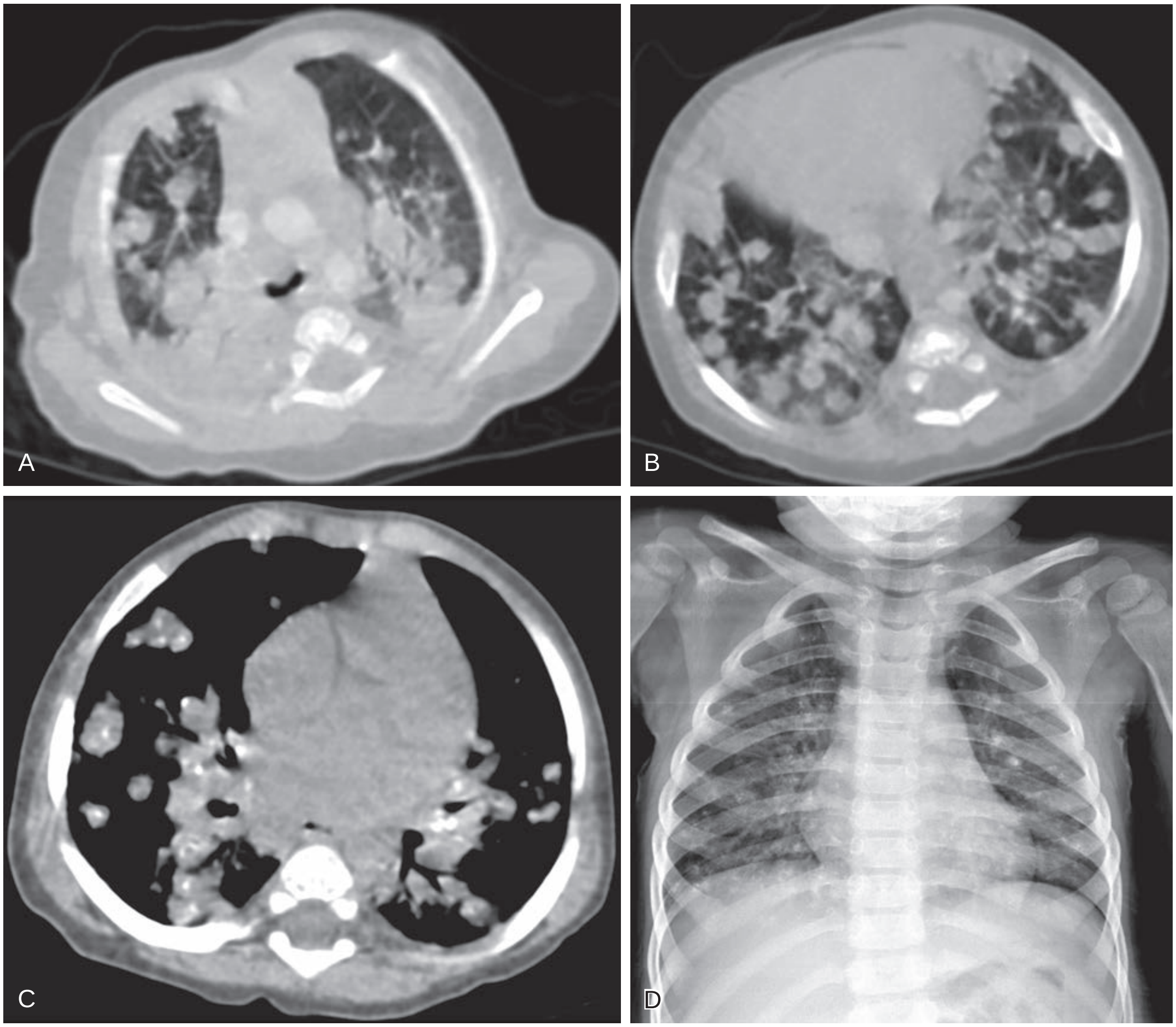

**e-Figure 54.20. Disseminated tuberculosis (TB) in an infant who presented with fever, cough, tachypnea, and intercostal retractions. Her father had TB.** (A and B) Initial contrast-enhanced computed tomography shows multiple bilateral pulmonary nodules (granulomas). Enlarged lymph nodes are present in the mediastinum and hila. (C) After 6 months of anti-TB treatment, the nodules and lymph nodes have decreased in number and size, and several show central calcification. (D) On 2-year follow-up, the nodules and lymph nodes have resolved, leaving calcified foci in the lung, mediastinum, and hila. The diagnosis of TB was made on the basis of clinical and radiologic findings; the microorganism could not be cultured.

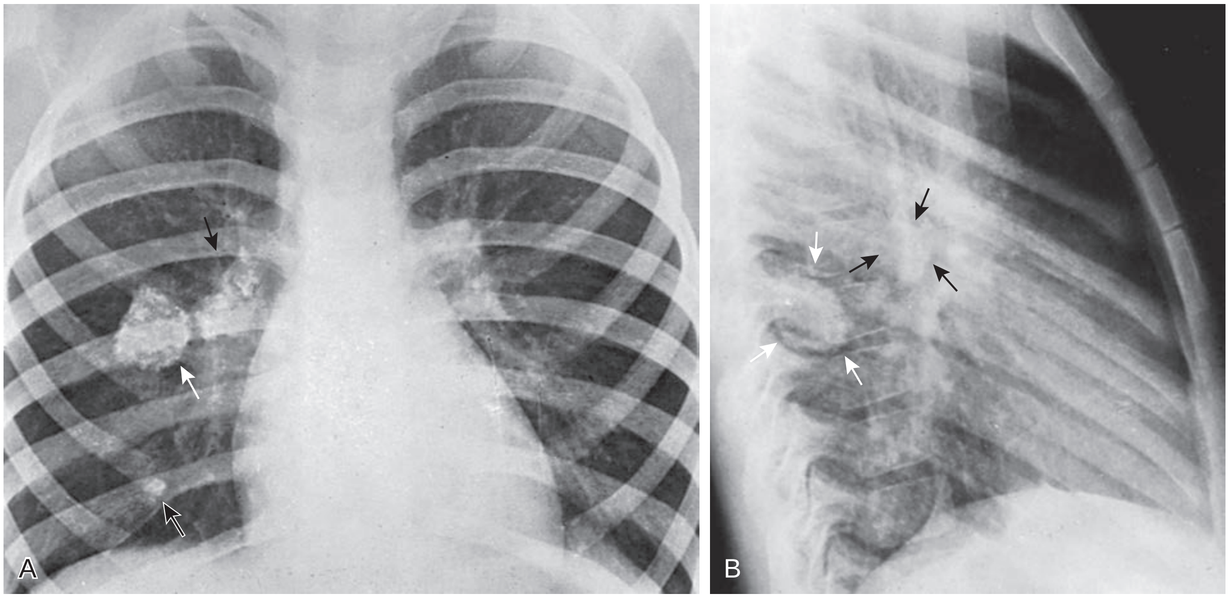

**e-Figure 54.21. Calcified lesions of tuberculosis.** (A) A large calcified primary tuberculous focus in the right lower lobe that dwarfs the rest of the complex in an asymptomatic 6-year-old girl. The healing and calcification of this huge necrotic focus *(white arrow)* without manifest clinical disease at any time shows the often benign clinical aspects of severe structural tuberculous disease. The *black arrow* shows calcified hilar adenopathy. In the frontal projection, the large calcifying focus appears to be perihilar. (B) In the lateral projection, this focus lies posterior to right hilar nodes *(black arrows)* in the apical segment of the right lower lobe *(white arrows)* near the dorsal pleura.

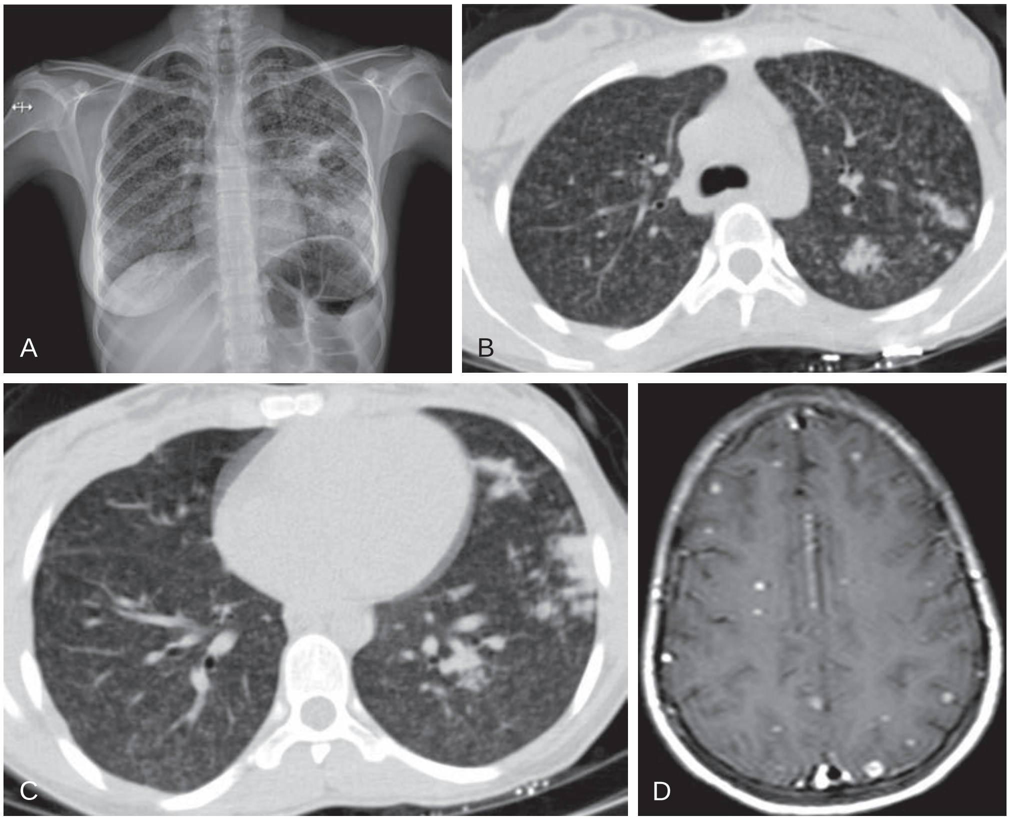

**e-Figure 54.24. Progressive tuberculosis (TB) with tuberculous bacteremia in a 14-year-old girl who presented with a convulsion while on treatment.** (A) The radiograph shows multiple patchy nodules in both lungs and parenchymal consolidations in the left middle and lower lung zones. (B and C) Contrast-enhanced computed tomography shows multiple nodules with a diameter of 1 to 3 mm (miliary) throughout both lungs. (D) Contrast-enhanced T1-weighted cranial magnetic resonance imaging depicts enhancing lesions consistent with TB granulomas. The diagnosis was made on the basis of clinical and radiologic findings, although the organism could not be cultured. The patient responded well to tuberculostatic drug treatment.

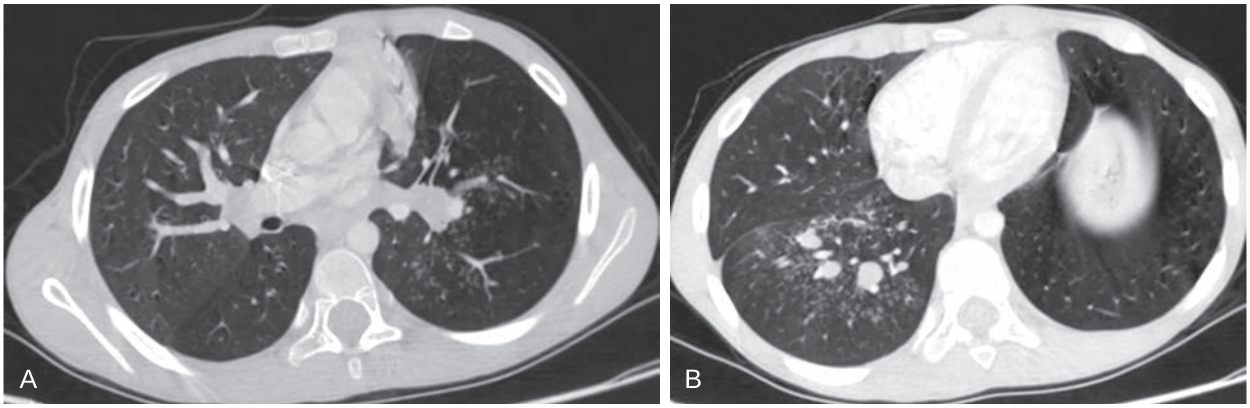

**Figure 54.23. Active pulmonary tuberculosis in a 9-year-old boy who presented with cough and fever.** (A and B) Contrast-enhanced computed tomography demonstrates centrilobular nodules and branching linear opacities ("tree-in-bud" pattern) in both lower lobes. Dilated fluid-filled bronchi are adjacent to areas of parenchymal abnormality. Atelectasis is also present in the paramediastinal parenchyma of the left lung. Culture of bronchial lavage fluid confirmed the diagnosis.

more frequent in patients with immunodeficiencies (particularly HIV infection[26]) or with altered local defenses (e.g., in cystic fibrosis or ciliary dyskinesia). Although the signs and symptoms of NTM pulmonary infection are variable and nonspecific, affected pediatric patients usually present with chronic cough, fever, chills, night sweats, dyspnea on exertion, and weight loss. The diagnosis is based on clinical, radiographic, and bacteriologic criteria.

***Imaging.*** Although the radiologic findings of pulmonary NTM disease are variable, depending on the presence or absence of underlying disease, typical findings include multiple nodules, consolidation, and cavitation. Mediastinal or hilar adenopathy similar to that of TB may be present (e-Fig. 54.25). NTM may also complicate or cause bronchiectasis.

***Treatment and Follow-up.*** Successful treatment depends on tailoring drug treatment to the type of NTM cultured. Because NTM pulmonary infection could be indolent, long-term clinical and radiologic study follow-up (months to years) may be required at relatively short intervals.

## PULMONARY INFECTIONS CAUSED BY FUNGI

Fungal infections of the lung predominantly affect children with a suppressed immune system, mainly those with defective T-cell immunity and granulocyte function, either congenital (DiGeorge syndrome, chronic granulomatous disease of childhood) or acquired (AIDS,[26] those undergoing chemotherapy for malignancies, post-transplant). In immunocompromised children, CT may add both sensitivity and specificity to radiography and should be performed with a low threshold.[105,109] The imaging appearance of fungal infections is typically within the miliary or nodular pneumonia category.[28] The nodules may be surrounded in the acute phase by a ground-glass halo, indicating the angioinvasiveness of the organism, and may eventually calcify.[2,28] Hilar and mediastinal lymphadenopathy is frequently seen, and the lymph nodes often calcify, as in TB. The most common fungal agents causing pulmonary infections in children are listed in Table 54.2.

### Aspergillosis

***Etiology.*** *Aspergillus* species are a group of ubiquitous molds within the environment that may be cultured from a wide variety of soils, water sources, and decaying organic matter. Pulmonary infection is most often caused by *Aspergillus fumigatus*. Although pulmonary infection with *Aspergillus* species may take a variety of clinical courses and imaging appearances, mainly dependent on the affected patients' immune status, it can be grouped into three main categories: (1) fungal ball, (2) allergic bronchopulmonary aspergillosis (ABPA), and (3) invasive aspergillosis.[148] A fungal ball or mycetoma typically grows saprophytically in immunocompetent children with a preexisting cavity, often related to cystic fibrosis or postprimary TB. ABPA, characterized by a hypersensitivity response to *Aspergillus* antigens, typically develops in children with cystic fibrosis or asthma.[149] Invasive aspergillosis almost exclusively occurs in immunocompromised children with underlying neutropenia.[148] The organism may produce a bronchocentric or angiocentric lesion and is associated with a high morbidity and mortality.[150] A semi-invasive, less aggressive form of *Aspergillus* infection may be seen in patients with underlying lung disease or in mildly immunocompromised patients.[151]

***Imaging.*** A fungal ball typically appears on chest radiographs as an intracavitary mass within a thick-walled cavity usually located in an upper lobe, especially the apical segment (e-Fig. 54.26). CT shows a round or oval-shaped cavity containing a freely mobile soft tissue mass surrounded by a crescent of air (Monad sign).[152] The most common features of ABPA are mucoid impaction within bronchiectasis and segmental and lobar atelectasis. Such dilated bronchi filled with inspissated mucus often cause a homogeneous branching opacity referred to as the *finger-in-glove sign*. Invasive aspergillosis characteristically appears as one or a few nodular opacities randomly distributed throughout the lungs. Distinctive but nonspecific characteristics include the halo sign and the air crescent sign. The *halo sign* refers to an irregular ground-glass opacity surrounding a nodule of infection (Fig. 54.27). The indistinct halo probably represents hemorrhage in lung adjacent to the nodule, resulting from vascular invasion. The *air crescent sign* is an air collection that partially outlines a masslike lesion that represents a contracting nodule.[152] This sign is noted in well-established *Aspergillus* infections when the host's defense mechanisms have partially recovered.

***Treatment and Follow-up.*** The main treatment goal in children with pulmonary aspergillosis is to correct any underlying immune deficiency and to control the infection with antifungal medications.

### Histoplasmosis

***Etiology.*** Histoplasmosis, caused by *Histoplasma capsulatum*, is common in many parts of the United States. Initial infection is similar to that of the primary tuberculous complex except that in histoplasmosis, large numbers of pulmonary foci are the rule. Histoplasmosis may be categorized into three phases: (1) acute

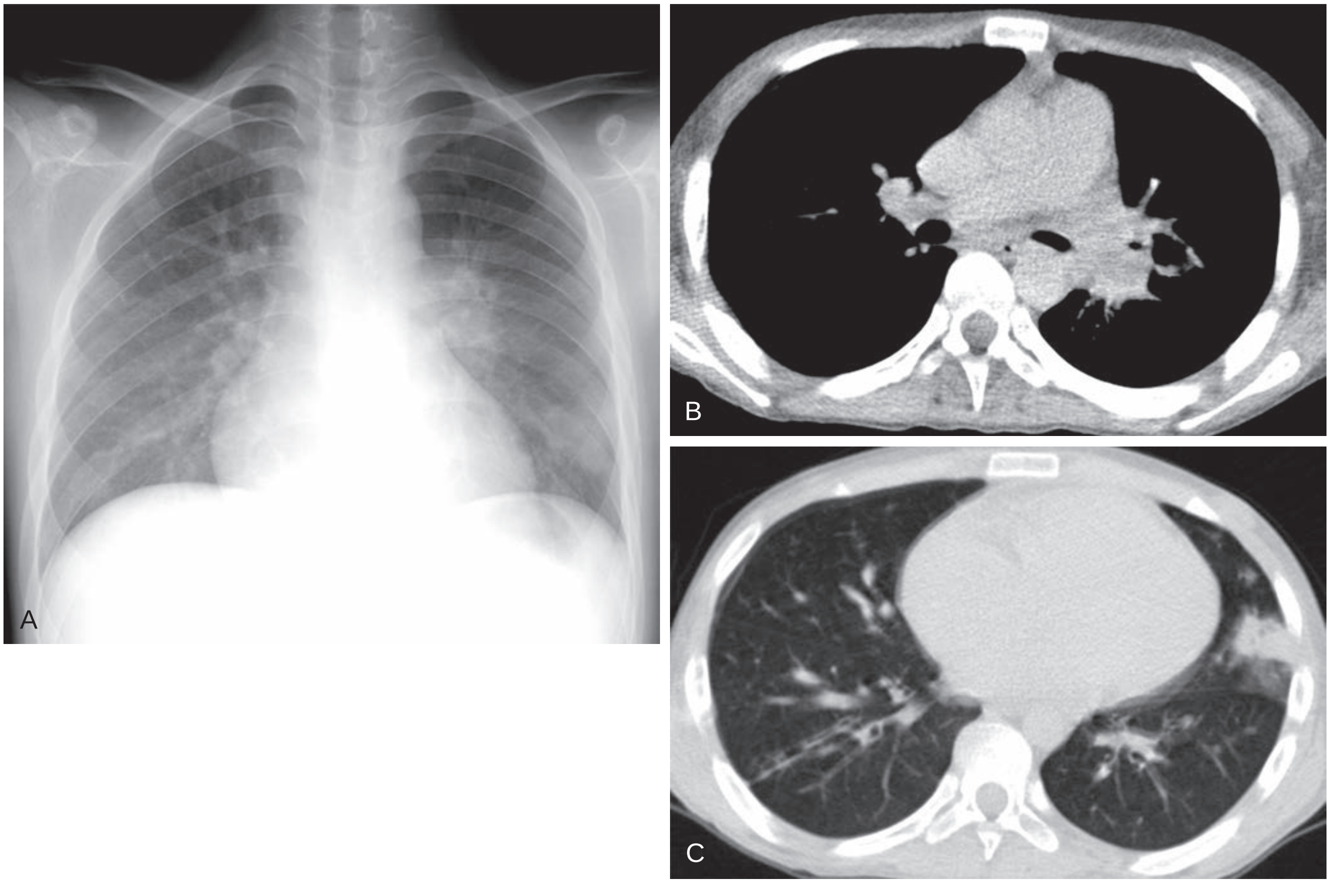

**e-Figure 54.25. Nontuberculous mycobacterial infection in a 15-year-old boy with aplastic anemia who was hospitalized for bone marrow transplantation.** (A) The radiograph shows consolidation in the left lower zone and left hilar lymphadenopathy. (B and C) Noncontrast computed tomography demonstrates consolidation in the inferior lingular segment and lymphadenopathy in the left hilum. Culture of fluid from the pericardial cavity was consistent with nontuberculous mycobacterial infection.

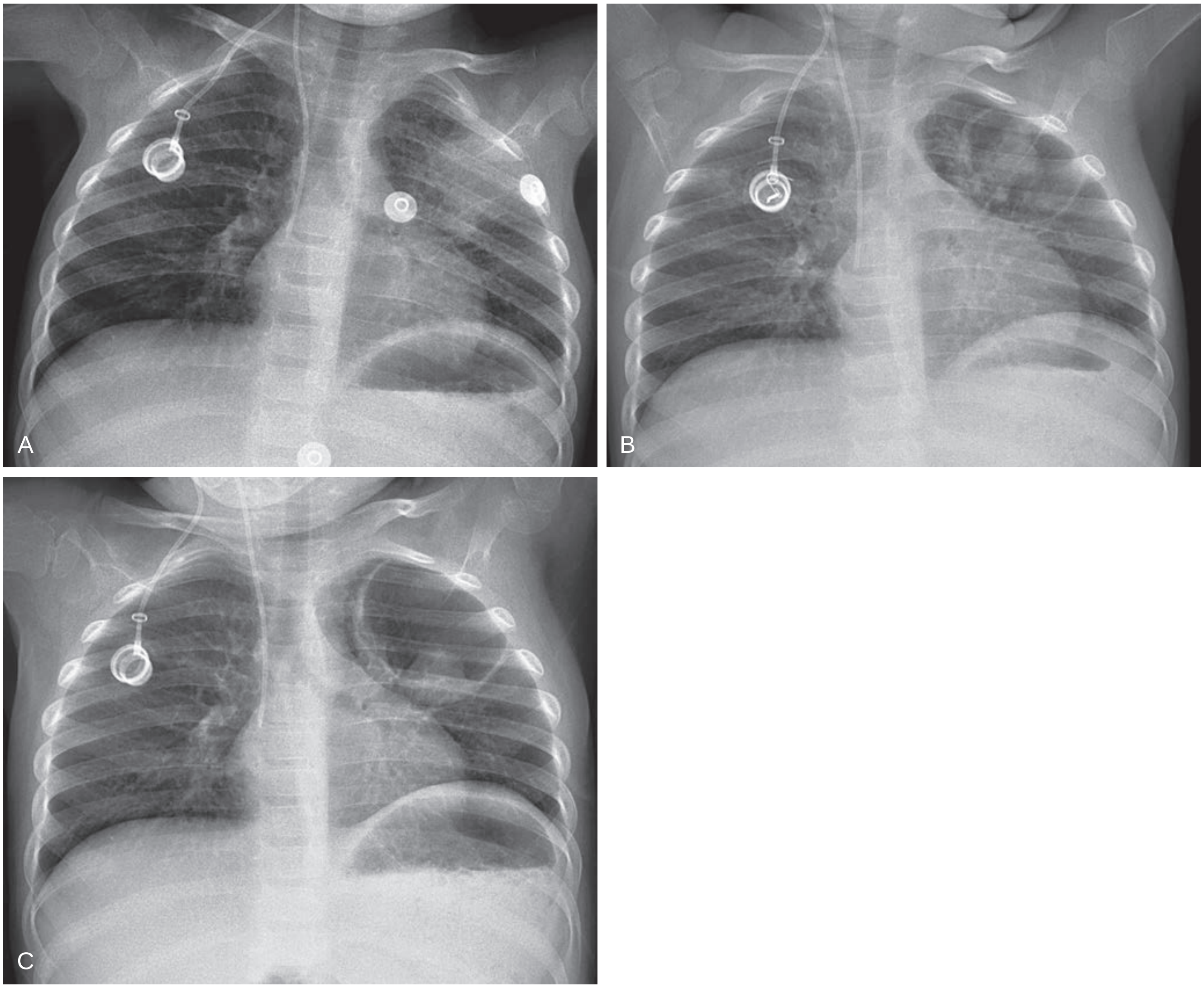

**e-Figure 54.26. Invasive pulmonary aspergillosis in a 30-month-old girl with acute leukemia who presented with neutropenia and fever.** (A) The initial radiograph shows a round consolidation in the left upper lung zone. (B) The follow-up radiograph on day 9 demonstrates cavitation of the consolidation, with an eccentric “fungus ball” attached to the left cavity wall. (C) The radiograph on day 17 shows expansion in the cavity and downward displacement of the “fungus ball,” indicative of its free movement.

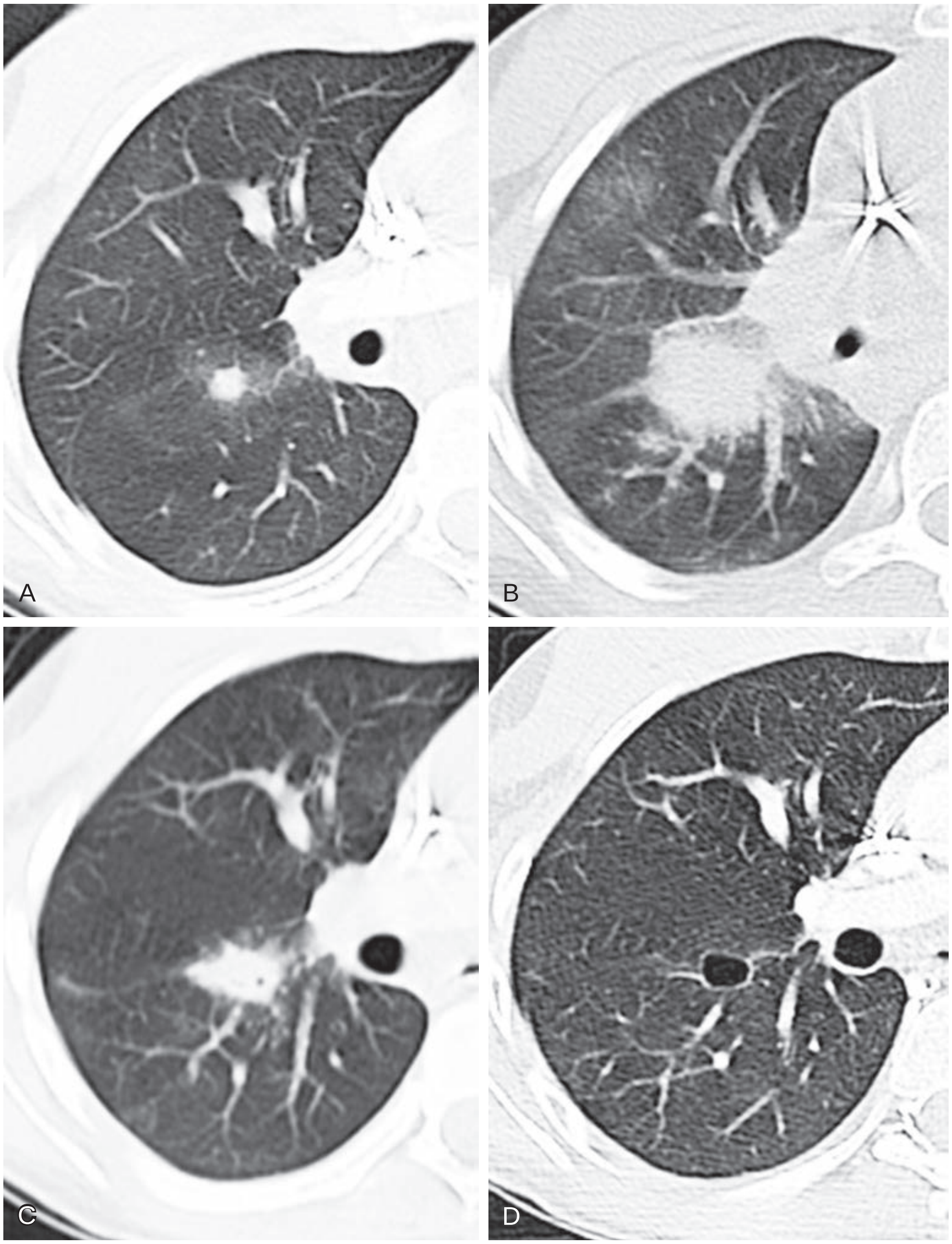

**Figure 54.27. Invasive pulmonary aspergillosis in a 14-year-old girl with non-Hodgkin lymphoma, who presented with fever after chemotherapy. The chest radiograph was normal.** (A–D) Computed tomography scans on days 1, 5, 35, and 75 demonstrate the evolution of the largest nodule after intravenous antifungal therapy. The nodule has spiculated contours surrounded by ground-glass opacity ("halo sign") at presentation, and shows complete resolution with a residual pneumatocele.

infection, characterized by nonspecific respiratory symptoms that usually develop 12 to 14 days after initial exposure; (2) chronic infection, which may resemble TB; and (3) disseminated infection. The diagnosis of pulmonary histoplasmosis rests on the identification of antigen and the demonstration of *Histoplasma*-specific antibodies. Rapid diagnosis may be obtained from biopsy of the granulomas with special fungal stains. *Histoplasma* may be cultured from lavage or blood specimens, but cultures take a long time to grow and have a low sensitivity.

***Imaging.*** Radiographic findings are similar to TB in all phases of these diseases, and in some cases they resemble those in coccidioidomycosis (e-Fig. 54.28).[153] The first phase of the infection is characterized by single or multiple pulmonary nodules that are 1 to 3 cm in size, as well as mediastinal and hilar lymphadenopathy. Pulmonary nodules that have been present for more than a few months usually show central or dystrophic calcification. Calcified mediastinal and hilar lymph nodes are often seen in patients with calcified pulmonary nodules. Sarcoidosis may exhibit similar adenopathy. Because treatment of sarcoidosis involves immunosuppression, histoplasmosis must be excluded, particularly in endemic areas. In children with chronic histoplasmosis, upper lobe consolidations simulating TB infection, sometimes associated with cavitation, may be present. Disseminated histoplasmosis has been observed in infancy, and the imaging findings are similar to those in miliary

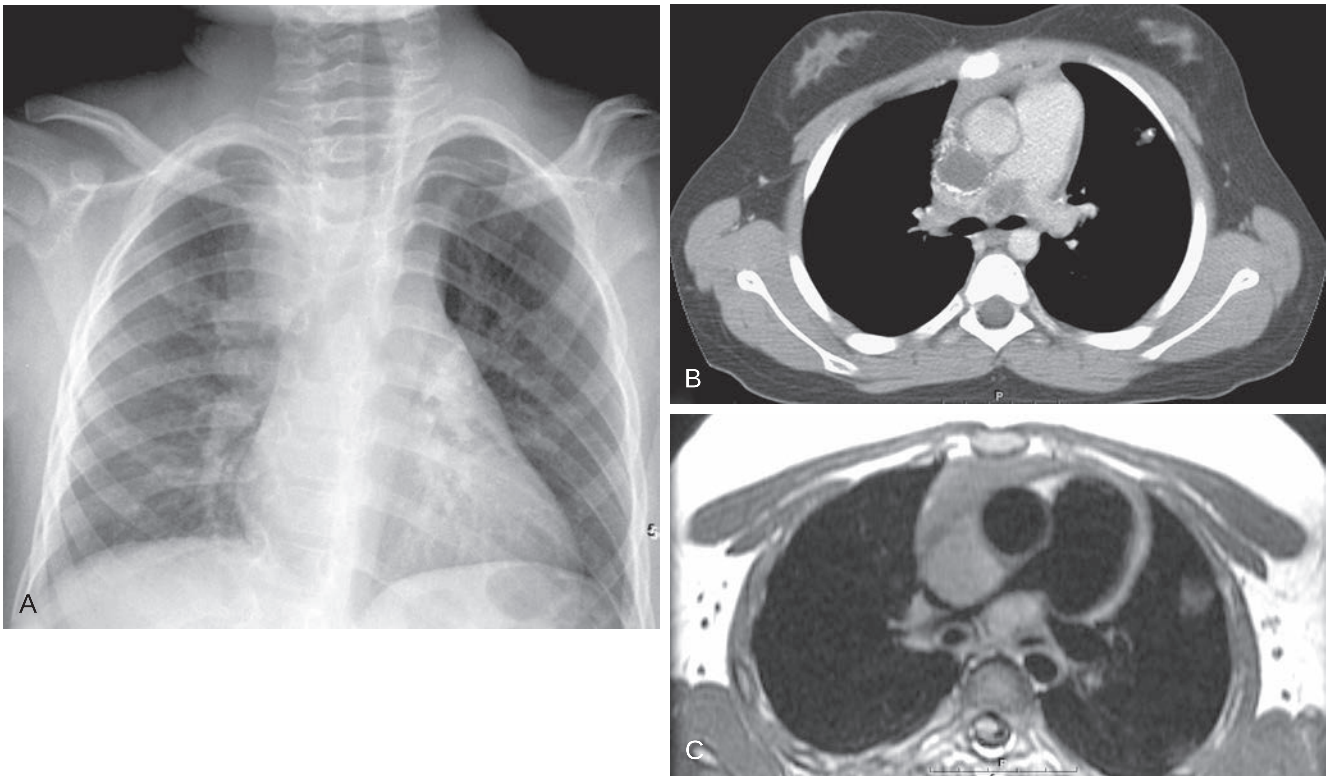

**e-Figure 54.28. Histoplasmosis in a 9-year-old girl who presented with shortness of breath.** (A) The radiograph shows mediastinal adenopathy, particularly in the right paratracheal and right hilar regions. Note the shift of the trachea to the left side. (B) Computed tomography shows a small calcified nodule in the left upper lobe with extensive adenopathy. The mediastinal nodes are centrally low in density, as would be seen in tuberculosis, and are calcifying peripherally. (C) A gated magnetic resonance image shows the marked compression of the right pulmonary artery.

TB. Massive hepatosplenomegaly is common in disseminated cases. Granulomatous or calcified foci in the spleen are a frequent incidental finding in endemic regions and are almost diagnostic of disease exposure in an otherwise healthy patient. A rare but devastating result of chronic pulmonary histoplasmosis is mediastinal fibrosis, which may lead to pulmonary artery compression (see e-Fig. 54.28). It may also result in compression of the superior vena cava, pulmonary veins, esophagus, trachea, and bronchi.

***Treatment and Follow-up.*** Treatment is merely supportive in asymptomatic and mild cases, but when disseminated histoplasmosis is present, a combination therapy of antifungal agents is given.

### Coccidioidomycosis

***Etiology.*** Coccidioidomycosis, caused by *Coccidioides immitis* or *C. posadasi*, is acquired by inhalation. Endemic areas in the United States include the semiarid regions of California, Arizona, New Mexico, and western Texas. The infection is usually self-limiting, and affected children present with mild flulike illness, with fever, cough, headaches, rash, and myalgia. However, severe pulmonary infection may develop in immunocompromised children (particularly those with HIV infection). The diagnosis may be made by positive reaction to the coccidioidin skin test or by positive culture of the sputum or gastric washings.

***Imaging.*** Radiographic examination during the early stages of disease usually shows lobar or segmental airspace consolidation and enlargement of the regional lymph nodes.[154] The pulmonary opacity of primary coccidioidomycosis is similar to that in primary tuberculosis (e-Fig. 54.29). It usually clears after a few weeks—its duration is usually much shorter than in TB—and residual calcified foci appear later within both the lung and lymph nodes. Small localized or large free pleural effusions may be visualized early.[155] Although small, sharply defined, thin-walled pulmonary cavities are commonly noted in adults, they are uncommon in children.

***Treatment and Follow-up.*** Affected children with mild symptoms often do not require treatment. However, immunocompromised children with progressive or disseminated disease are treated with a combination of antifungal agents.

### Pneumocystis jiroveci

***Etiology.*** *Pneumocystis carinii*, a unicellular organism that infects humans, was recently renamed *Pneumocystis jiroveci*. Originally considered a parasite, it is currently categorized as a fungus on the basis of molecular similarities to fungal RNA. This potentially life-threatening opportunistic infection most often affects immunodeficient children, particularly those who are infected with HIV[26] and have CD4 counts of less than 100 cells/mm.[3] The clinical onset is variable but often abrupt, with tachypnea, cough, and cyanosis. A marked decrease in the arterial oxygen saturation is seen, with a normal carbon dioxide level.

***Imaging.*** The characteristic radiographic findings of *P. jiroveci* pneumonia are symmetric bilateral ground-glass opacities (Fig. 54.30). Such opacities may be diffuse but tend to involve predominately the perihilar regions or middle and lower lung zones.[39,156,157] Disease progression may result in more confluent, mainly perihilar or diffuse, bilateral airspace consolidation. Associated interstitial edema or cellular infiltration may present on CT as septal thickening, intralobular thickening, or both.[158] The combination of such interstitial thickening and ground-glass opacities may produce a CT pattern known as “crazy paving.”[159] Terminally, massive consolidation may occur, often complicated by pneumothorax and pneumomediastinum.[160] Pleural effusions are rare.[161]

In 10% to 30% of patient with AIDS who received prophylaxis with aerosolized pentamidine and trimethoprim-sulfamethoxazole, a cystic form of the disease may evolve, characterized by either unilateral or bilateral upper lobe predominant thin-walled cysts.[39,158] Such pulmonary cysts are associated with pneumothoraces.[162] In recent years, in spite of the advances in the prevention and treatment of *P. jiroveci* infection, several atypical presentations have emerged, including multiple pulmonary nodules, mass lesions, pleural effusion, and lymph node enlargement.[163-166]

***Treatment and Follow-up.*** Although imaging findings are not specific for *P. jiroveci* infection, the presence of bilateral ground-glass opacities in immunocompromised children should lead to this diagnosis.[167] Tracheal washings or lung biopsy, when performed, may show the organisms on microscopic examination after silver methenamine staining.

### Candidiasis

***Etiology.*** Pulmonary candidiasis is almost always encountered in immunocompromised children, those with indwelling catheters, those who are undergoing prolonged antibiotic therapy, or those who are on steroids. The organism regularly colonizes the upper respiratory tract and then spreads to the lungs. Pulmonary candidiasis may be either a primary infection (limited to the lungs) or a secondary infection (caused by hematogenous dissemination from other sites of infection).

***Imaging.*** Although radiographs are often normal in the earliest stages of infection, nonspecific features of bronchopneumonia and lung nodules may be noted (e-Fig. 54.31).[168,169] Those nodules may cavitate, and unilateral or bilateral lobar or segmental opacities may also be seen.

***Treatment and Follow-up.*** Children who are severely ill with pulmonary candidiasis receive appropriate antifungal therapy.

## PULMONARY MANIFESTATIONS OF PARASITIC INFESTATIONS

Pulmonary manifestations of parasitic infestations are predominantly encountered in the developing world, in those who have recently traveled to or from these regions, or in immunocompromised patients. A variety of imaging findings are seen, predominantly in the multinodular pneumonia category, as in paragonimiasis and echinococcus (hydatid) disease. However, several types of parasitic infestation may produce clinical and radiographic signs as a consequence of the passage of larval forms through the lung in the course of the parasite’s life cycle. These include *Ascaris lumbricoides*, *Necator americanus*, *Ancylostoma duodenale* (hookworms), *Strongyloides stercoralis*, and *Toxocara cati* and *canis*.[170] *T. cati* and *T. canis* may produce a localized granulomatous reaction, termed *visceral larva migrans*, with resultant opacities in the lungs. The first four mentioned species, as well as a number of rarer parasites, may be associated with Löffler syndrome (acute allergic eosinophilic pneumonia).[2] The most common parasitic agents with pulmonary involvement are listed in Table 54.2.

### Pulmonary Paragonimiasis

***Etiology.*** The lung fluke *Paragonimus westermani* is endemic in parts of Southeast Asia, South America, and Western Africa. In the United States, pulmonary paragonimiasis has affected refugee Indochinese children and Latin American immigrants.[171,172] Children are usually infected after ingestion of undercooked crustaceans, including crabs or crayfish, or by drinking contaminated water. In Southeast Asia, infestation of the lungs by *P. westermani* is said to be a common cause of pediatric lung necrosis and calcification, but it is difficult to differentiate from TB and fungal diseases on the basis of radiographic criteria alone (e-Fig. 54.32). Affected children usually present with fever, pleuritic chest pain, and respiratory symptoms such as chronic cough or hemoptysis. The diagnosis depends on a combination of findings, including history,

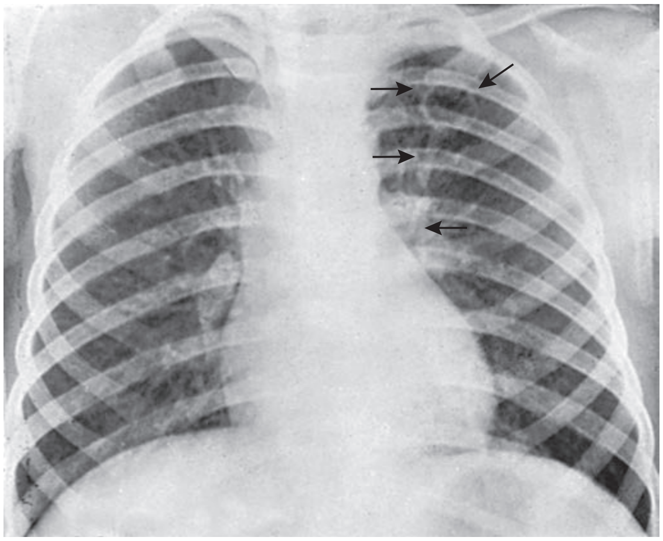

**e-Figure 54.29. Coccidioidomycosis of the lung.** A primary complex in a 4-year-old girl whose skin reaction was positive to coccidioidin. The primary pulmonary focus is excavated into a thin-walled cavity—one of the most distinctive radiologic changes in this disease *(upper arrows).* The strands of increased density between the pulmonary focus and the hilar nodes represent lymphangitis *(lower arrows).* The regional hilar nodes are enlarged. *(Courtesy of Dr. Hugh C. Thompson, Tucson, AZ.).*

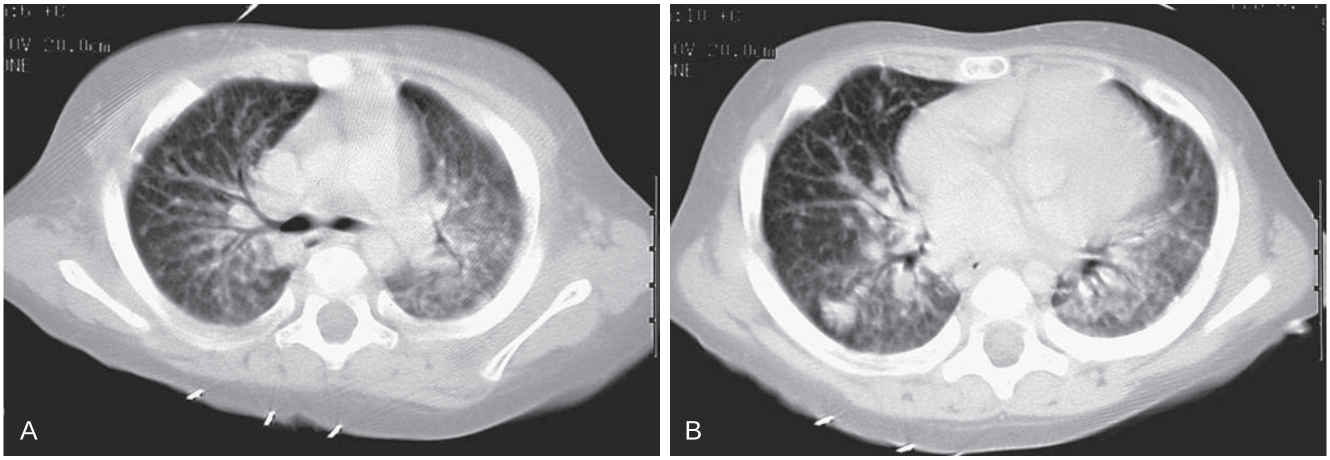

**e-Figure 54.31. Candidiasis in a 10-month-old with acute myelogenous leukemia and fever and hazy opacities in left lung on chest radiograph (not shown).** (A and B) Helical computed tomography (CT) sections at the middle (A) and lower (B) zones show a bilateral pattern of ill-defined nodules and more confluent opacity in the left lung posteriorly.

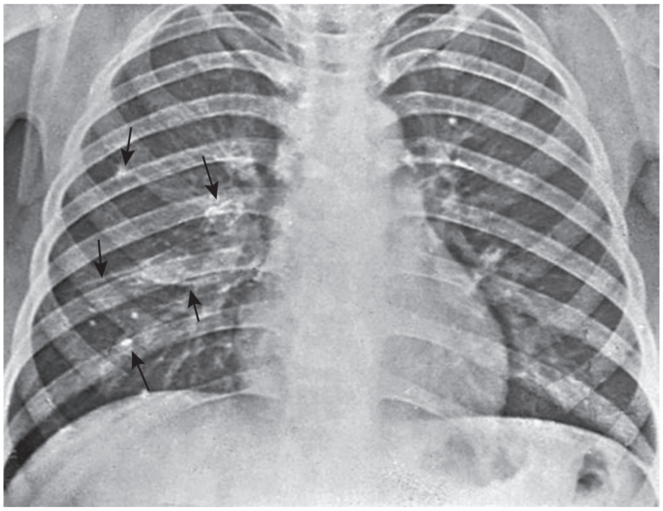

**e-Figure 54.32. Calcifying paragonimiasis in the lungs of a 12-year-old Korean boy, whose sputum had contained *Paragonimus westermani* for 4 years.** The multiple calciferous foci in the right lung and hilum *(arrows)* are identical to the findings in some cases of primary tuberculosis. The clinician found radiographic signs of calcifying paragonimiasis in 60 of 1,000 Korean refugee children examined by him in Poland. *(Courtesy of Dr. Roman Marciniak, Warsaw, Poland.)*

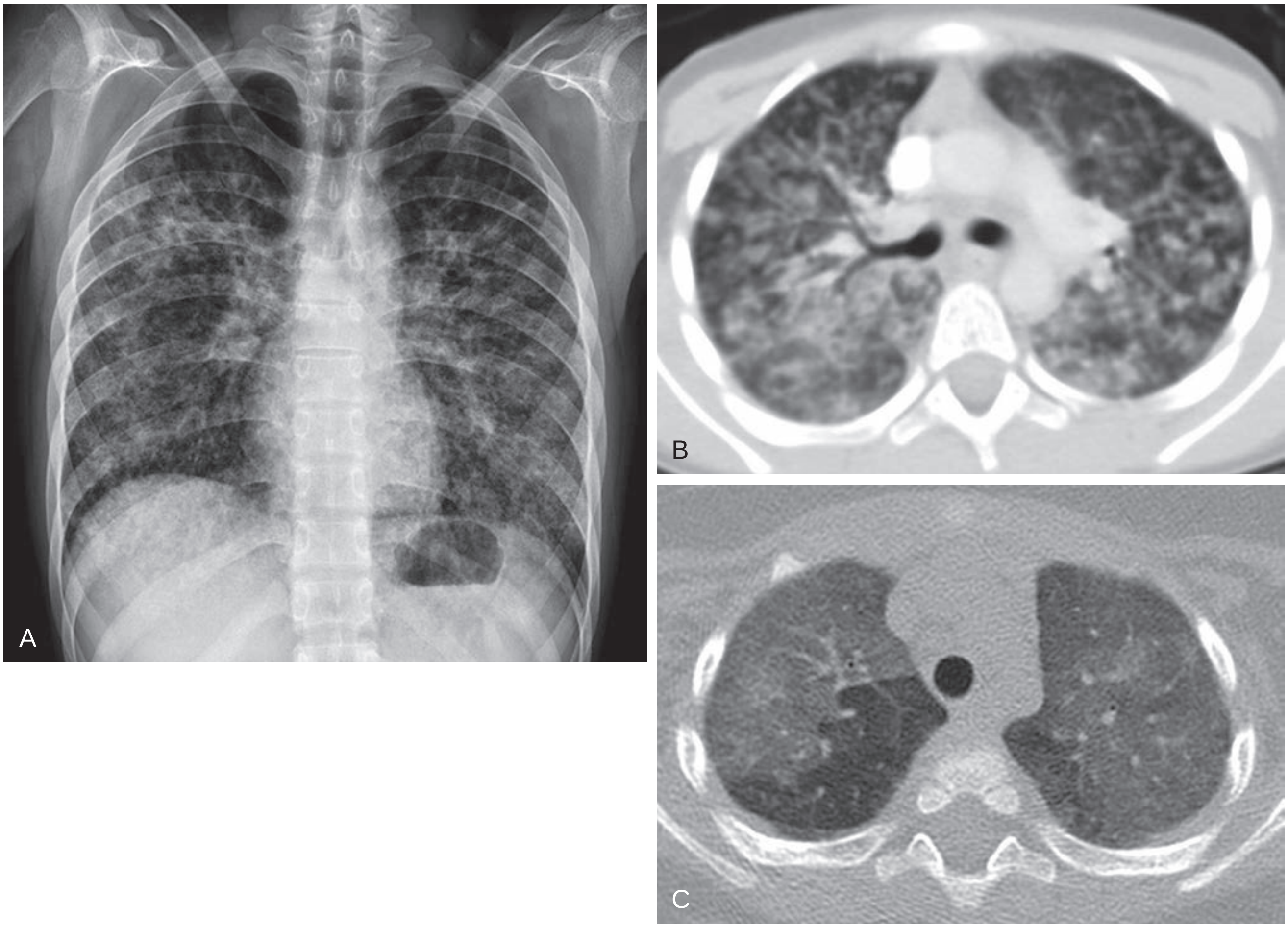

**Figure 54.30.** ***Pneumocystis jiroveci*** **infection in a 17-year-old boy with acute lymphoblastic leukemia and immunodeficiency, who presented with dyspnea, fever, nonproductive cough, and decreased white blood cell counts.** (A) The radiograph shows diffuse bilateral interstitial opacity throughout the lungs. (B) Contrast-enhanced computed tomography (CT) confirms the bilateral patchy and ground-glass opacities in both lungs. The diagnosis was confirmed by a positive polymerase chain reaction test from bronchial lavage fluid. (C) CT in a different patient demonstrates a typical "crazy paving" pattern in both upper lobes.

peripheral blood eosinophilia, identification of ova in the stool or the sputum, and a positive enzyme-linked immunosorbent assay (ELISA) test result.

***Imaging.*** Imaging findings depend on the stage of the disease. The early stage is characterized by (1) linear opacities, which are 2 to 4 mm thick and 3 to 7 cm long, extending inward from the pleura representing the migration of juvenile worms; (2) focal airspace consolidation, representing exudative or hemorrhagic pneumonia caused by the migrating worm; (3) pneumothorax; or (4) hydropneumothorax. Features of the late stage of infection include nodules, thin-walled crescent-shaped worm cysts (the "signet ring" sign), dense masslike consolidation, or bronchiectasis. As the flukes move from the abdomen to the chest, they penetrate the diaphragm and pleural layers, and thus pleural effusions and thickening are commonly noted.

***Treatment and Follow-up.*** Pulmonary paragonimiasis is treated with antiparasitics.

## *Echinococcus Disease of the Lung*

***Etiology.*** Echinococcosis or hydatid disease in humans is caused by infestation with *Echinococcus granulosus* (dog tapeworm). Humans are infected by direct contact with definite hosts (e.g., dogs) or by ingestion of eggs present in infected water, food, or soil. The eggs of *E. granulosus* hatch into larvae in the duodenum and are typically trapped within the liver (approximately 75%) or lungs (approximately 5%–15%). They pass through the portal system in the liver or pulmonary alveolar capillaries, respectively. These larvae eventually develop into round or oval-shaped cysts within the liver or lungs (e-Fig. 54.33). Although most children with pulmonary involvement by hydatid disease are asymptomatic, they may present with fever, shortness of breath, cough, and chest pain, which is usually a sign of cyst rupture. Diagnosis of hydatid disease depends on the combination of imaging and serology.

***Imaging.*** The radiologic findings are characterized by single or multiple (approximately 25%), round or oval-shaped, cystic nodules or masses (1–20 cm in diameter) with well-defined walls, surrounded by normal lung parenchyma (see e-Fig. 54.33). Other findings include an air-crescent sign, when a cyst communicates with a bronchus, or the water-lily sign (Fig. 54.34), when a cyst membrane floats in residual fluid after cyst rupture.[160,161] Pericystic emphysema may be a sign of impending rupture. After rupture of the cysts, cavitation or abscess formation and bronchiectasis may occur.

***Treatment and Follow-up.*** Traditionally, surgical removal of the pulmonary cysts, often with supplemental medication, has been performed. Despite the risk of anaphylactic reactions after

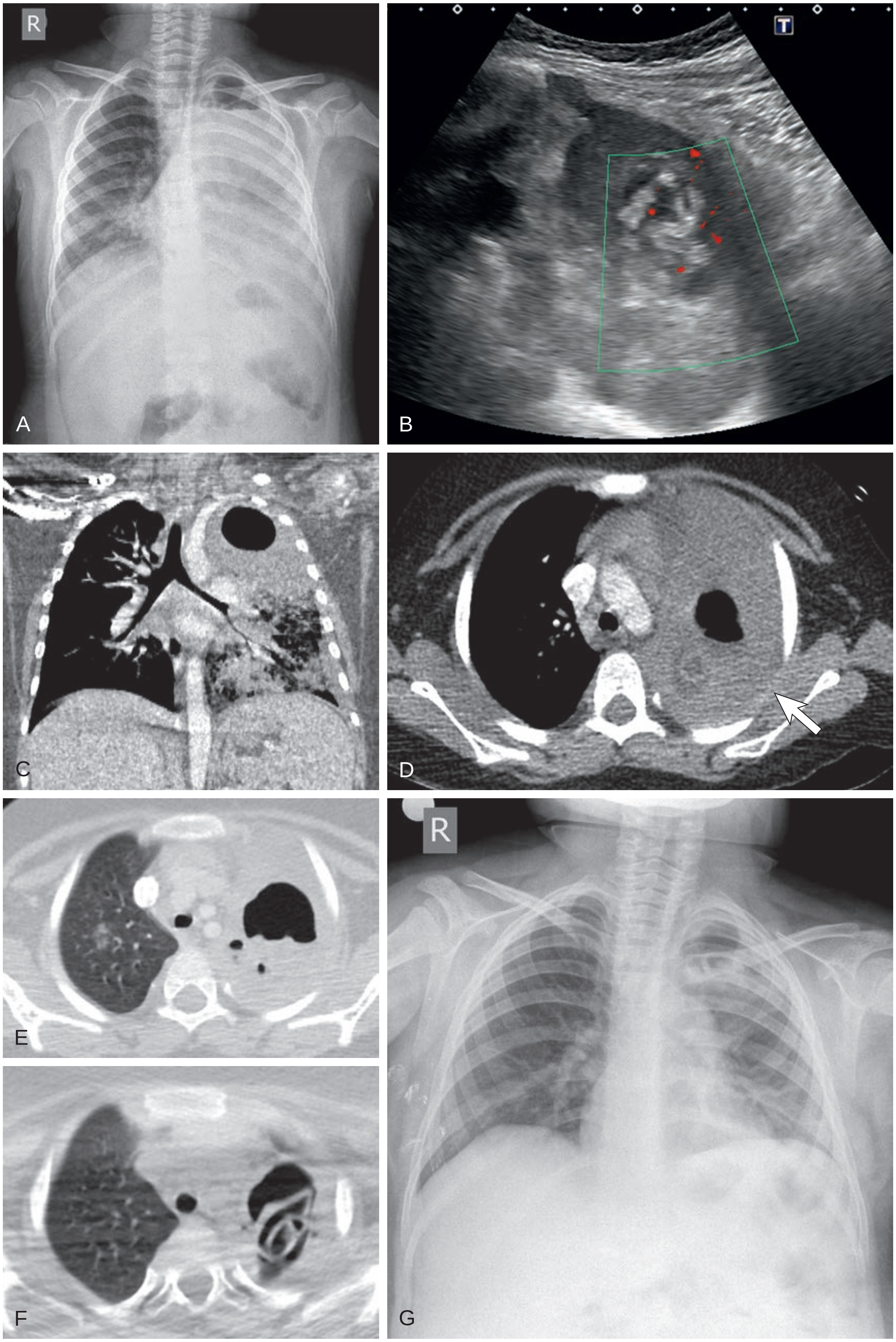

**e-Figure 54.33. Ruptured hydatid disease in a 5-year-old girl, who presented with sudden-onset persistent cough that started 3 days before her admission.** (A) The radiograph shows white-out left lung associated with air-fluid level in the apex. (B) Transverse ultrasonography image obtained by anterior approach through the apex of the left lung demonstrates a nonvascular cyst with internal detached germinative membranes surrounded by consolidated lung. (C–E) Contrast-enhanced computed tomography (CT) on the same day demonstrates a cavity with air-fluid level and floating membranes surrounded by consolidation in the left lung apex. There are also patchy air space opacities in the rest of the lung. (F) Follow-up CT after 12 days shows resolution of the fluid and detached germinative membranes within the cavity. (G) Follow-up radiography on the second month shows marked improvement. Indirect hemagglutination test was positive for echinococcosis.

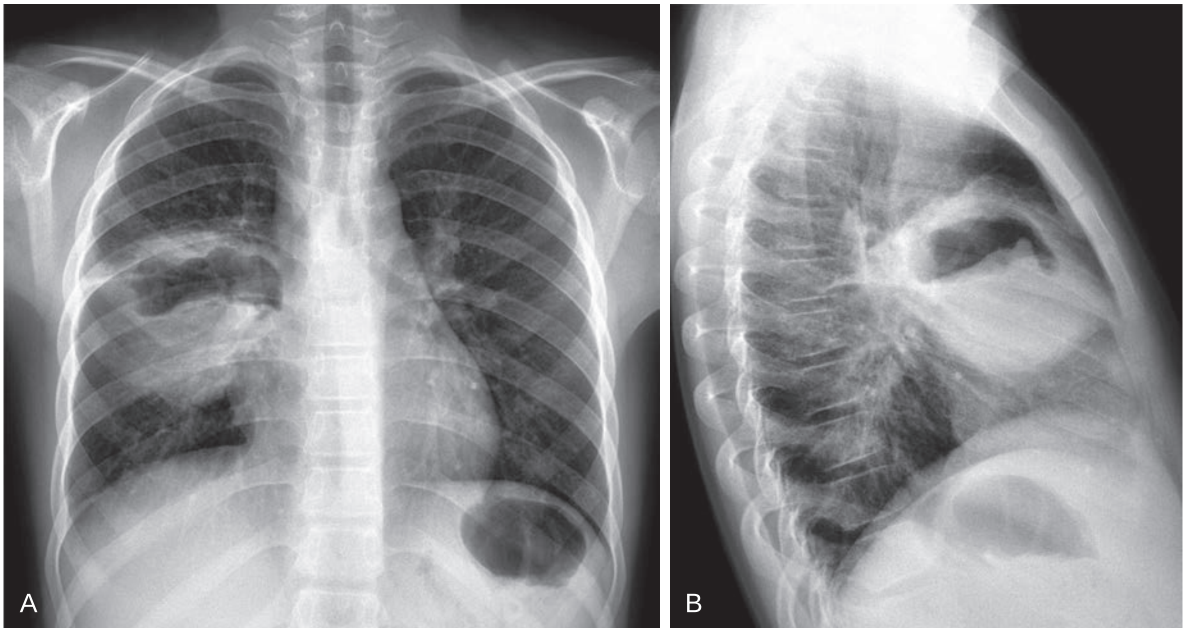

**Figure 54.34. Hydatid disease in a 12-year-old boy who presented with cough.** (A and B) Radiographs show a cavitary lesion with an irregular air-fluid level in the right middle lobe. The floating germinative membranes account for the classic "water lily" sign. Histopathologic diagnosis after surgical resection was consistent with hydatid infection.

cyst aspiration, careful image-guided percutaneous techniques appear to be sufficiently safe.[173]

## KEY POINTS

- Imaging studies have limited value in the differentiation between viral and bacterial pulmonary infections in young children, and these infectious agents frequently coexist.
- Ultrasonography is used as the initial modality to detect and characterize complex effusions from pulmonary infection.
- CT or MRI should be considered when cross-sectional chest imaging is needed for diagnosing unusual pulmonary infections with complications.
- Children who recently tested positive to tuberculin skin testing need to be evaluated with chest radiography for possible acute or chronic pulmonary TB infection.
- CT may improve the diagnosis and management of symptomatic pulmonary TB, fungal infection, and parasite infestation, particularly if an associated immune deficiency exists.

## SUGGESTED READINGS

Bradley JS, Byington CL, Shah SS, et al. The management of community-acquired pneumonia in infants and children older than 3 months of age: clinical practice guidelines by the Pediatric Infectious Diseases Society and the Infectious Diseases Society of America. *Clin Infect Dis*. 2011;53(7):e25–e76.

Daltro P, Santos EN, Gasparetto TD, et al. Pulmonary infections. *Pediatr Radiol*. 2011;41(suppl 1):S69–S82.

Eslamy HK, Newman B. Pneumonia in normal and immunocompromised children: An overview and update. *Radiol Clin North Am*. 2011;49(5):895–920.

McIntosh K. Community-acquired pneumonia in children. *N Engl J Med*. 2002;346:429–437.

Ventre KM, Wolf GK, Arnold JH. Pediatric respiratory diseases: 2011 update for the Rogers' textbook of pediatric intensive care. *Pediatr Crit Care Med*. 2011;12(3):325–338.

Westra SJ, Choy G. What imaging should we perform for the diagnosis and management of pulmonary infections? *Pediatr Radiol*. 2009;39(suppl 2):S178–S183.

## REFERENCES

Full references for this chapter can be found on www.expertconsult.com.

## REFERENCES

1. Donnelly LF. Practical issues concerning imaging of pulmonary infection in children. *J Thorac Imaging*. 2001;16:238–250.
2. Daltro P, Santos EN, Gasparetto TD, et al. Pulmonary infections. *Pediatr Radiol*. 2011;41(suppl 1):S69–S82.
3. McIntosh K. Community-acquired pneumonia in children. *N Engl J Med*. 2002;346:429–437.
4. Selwyn BJ. The epidemiology of acute respiratory tract infection in young children: comparison of findings from several developing countries. Coordinated Data Group of BOSTID Researchers. *Rev Infect Dis*. 1990;12(suppl 8):S870–S888.
5. Rudan I, Boschi-Pinto C, Biloglav Z, et al. Epidemiology and etiology of childhood pneumonia. *Bull World Health Organ*. 2008;86:408–416.
6. Kronman MP, Hersh AL, Feng R, et al. Ambulatory visit rates and antibiotic prescribing for children with pneumonia, 1994-2007. *Pediatrics*. 2011;127(3):411–418.
7. Grossman LK, Caplan SE. Clinical, laboratory, and radiological information in the diagnosis of pneumonia in children. *Ann Emerg Med*. 1988;17:43–46.
8. Cherian T, Mulholland EK, Carlin JB, et al. Standardized interpretation of paediatric chest radiographs for the diagnosis of pneumonia in epidemiological studies. *Bull World Health Organ*. 2005;83:353–359.
9. Langley JM, Bradley JS. Defining pneumonia in critically ill infants and children. *Pediatr Crit Care Med*. 2005;6(3 suppl):S9–S13.
10. Lynch T, Gouin S, Larson C, et al. Should the lateral chest radiograph be routine in the diagnosis of pneumonia in children? A review of the literature. *Paediatr Child Health*. 2003;8:566–568.
11. Manson D. The lateral chest radiograph. *Paediatr Child Health*. 2003;8:564–565.
12. Pereda MA, Chavez MA, Hooper-Miele CC, et al. Lung ultrasound for the diagnosis of pneumonia in children: a meta-analysis. *Pediatrics*. 2015;135(4):714–722.
13. Llamas-Álvarez AM, Tenza-Lozano EM, Latour-Pérez J. Accuracy of lung ultrasound in the diagnosis of pneumonia in adults: systematic review and meta-analysis. *Chest*. 2016.
14. Swingler GH, Hussey GD, Zwarenstein M. Randomised controlled trial of clinical outcome after chest radiograph in ambulatory acute lower-respiratory infection in children. *Lancet*. 1998;351:404–408.
15. Swingler GH, Zwarenstein M. Chest radiograph in acute respiratory infections. *Cochrane Database Syst Rev*. 2008;CD001268.
16. Mathews B, Shah S, Cleveland RH, et al. Clinical predictors of pneumonia among children with wheezing. *Pediatrics*. 2009;124:e29–e36.
17. Perlstein PH, Kotagal UR, Bolling C, et al. Evaluation of an evidence-based guideline for bronchiolitis. *Pediatrics*. 1999;104(6):1334–1341.
18. Roback MG, Dreitlein DA. Chest radiograph in the evaluation of first time wheezing episodes: review of current clinical practice and efficacy. *Pediatr Emerg Care*. 1998;14:181–184.
19. Alario AJ, McCarthy PL, Markowitz R, et al. Usefulness of chest radiographs in children with acute lower respiratory tract disease. *J Pediatr*. 1987;111:187–193.
20. Alak A, Seabrook JA, Rieder MJ. Variations in the management of pneumonia in pediatric emergency departments: compliance with the guidelines. *CJEM*. 2010;12(6):514–519.
21. Barson WJ. *Community-acquired pneumonia in children: clinical features and diagnosis: Wolters Kluwer;* 2016 [updated 6/18/2016]. Available from: https://www.uptodate.com/contents/community-acquired-pneumonia-in-children-clinical-features-and-diagnosis.
22. Bradley JS, Byington CL, Shah SS, et al. Executive summary: the management of community-acquired pneumonia in infants and children older than 3 months of age: clinical practice guidelines by the Pediatric Infectious Diseases Society and the Infectious Diseases Society of America. *Clin Infect Dis*. 2011;53(7):617–630.
23. Iroh Tam PY. Approach to common bacterial infections: community-acquired pneumonia. *Pediatr Clin North Am*. 2013;60(2):437–453.
24. Neuman MI, Hall M, Hersh AL, et al. Influence of hospital guidelines on management of children hospitalized with pneumonia. *Pediatrics*. 2012;130(5):e823–e830.
25. Neuman MI, Shah SS, Shapiro DJ, et al. Emergency department management of childhood pneumonia in the United States prior to publication of national guidelines. *Acad Emerg Med*. 2013;20(3):240–246.
26. Swingler GH, Hussey GD, Zwarenstein M. Randomised controlled trial of clinical outcome after chest radiograph in ambulatory acute lower-respiratory infection in children. *Lancet*. 1998;351(9100):404–408.
27. Graat ME, Hendrikse KA, Spronk PE, et al. Chest radiography practice in critically ill patients: a postal survey in the Netherlands. *BMC Med Imaging*. 2006;6:8.
28. Eslamy HK, Newman B. Pneumonia in normal and immunocompromised children: an overview and update. *Radiol Clin North Am*. 2011;49:895–920.
29. Korppi M, Don M, Valent F, et al. The value of clinical features in differentiating between viral, pneumococcal and atypical bacterial pneumonia in children. *Acta Paediatr*. 2008;97:943–947.
30. Korppi M, Kiekara O, Heiskanen-Kosma T, et al. Comparison of radiological findings and microbial aetiology of childhood pneumonia. *Acta Paediatr*. 1993;82:360–363.
31. Virkki R, Juven T, Rikalainen H, et al. Differentiation of bacterial and viral pneumonia in children. *Thorax*. 2002;57:438–441.
32. Wahlgren H, Mortensson W, Eriksson M, et al. Radiographic patterns and viral studies in childhood pneumonia at various ages. *Pediatr Radiol*. 1995;25:627–630.
33. Wahlgren H, Mortensson W, Eriksson M, et al. Radiological findings in children with acute pneumonia: age more important than infectious agent. *Acta Radiol*. 2005;46:431–436.
34. Bettenay FA, de Campo JF, McCrossin DB. Differentiating bacterial from viral pneumonias in children. *Pediatr Radiol*. 1988;18:453–454.
35. Bradley JS, Byington CL, Shah SS, et al. The management of community-acquired pneumonia in infants and children older than 3 months of age: clinical practice guidelines by the Pediatric Infectious Diseases Society and the Infectious Diseases Society of America. *Clin Infect Dis*. 2011;53:e25–e76.
36. Miller WT Jr, Mickus TJ, Barbosa E Jr, et al. CT of viral lower respiratory tract infections in adults: comparison among viral organisms and between viral and bacterial infections. *AJR Am J Roentgenol*. 2011;197:1088–1095.
37. Bloomfield FH, Teele RL, Voss M, et al. Inter- and intra-observer variability in the assessment of atelectasis and consolidation in neonatal chest radiographs. *Pediatr Radiol*. 1999;29:459–462.
38. Johnson J, Kline JA. Intraobserver and interobserver agreement of the interpretation of pediatric chest radiographs. *Emerg Radiol*. 2010;17:285–290.
39. Stickler GB, Hoffman AD, Taylor WF. Problems in the clinical and roentgenographic diagnosis of pneumonia in young children. *Clin Pediatr (Phila)*. 1984;23:398–399.
40. Davies HD, Wang EE, Manson D, et al. Reliability of the chest radiograph in the diagnosis of lower respiratory infections in young children. *Pediatr Infect Dis J*. 1996;15:600–604.
41. Swingler GH. Observer variation in chest radiography of acute lower respiratory infections in children: a systematic review. *BMC Med Imaging*. 2001;1(1):1.
42. Spottswood SE, Liaw K, Hernanz-Schulman M, et al. The clinical impact of the radiology report in wheezing and nonwheezing febrile children: a survey of clinicians. *Pediatr Radiol*. 2009;39:348–353.
43. Shiley KT, Lautenbach E, Lee I. The use of antimicrobial agents after diagnosis of viral respiratory tract infections in hospitalized adults: antibiotics or anxiolytics? *Infect Control Hosp Epidemiol*. 2010;31:1177–1183.
44. Han BK, Son JA, Yoon HK, et al. Epidemic adenoviral lower respiratory tract infection in pediatric patients: radiographic and clinical characteristics. *AJR Am J Roentgenol*. 1998;170:1077–1080.
45. Osborne D, White P. Radiology of epidemic adenovirus 21 infection of the lower respiratory tract in infants and young children. *AJR Am J Roentgenol*. 1979;133:397–400.
46. Welliver RC Sr, Checchia PA, Bauman JH, et al. Fatality rates in published reports of RSV hospitalizations among high-risk and otherwise healthy children. *Curr Med Res Opin*. 2010;26:2175–2181.
47. Hall CB, Hall WJ, Speers DM. Clinical and physiological manifestations of bronchiolitis and pneumonia. Outcome of respiratory syncytial virus. *Am J Dis Child*. 1979;133:798–802.
48. Brodzinski H, Ruddy RM. Review of new and newly discovered respiratory tract viruses in children. *Pediatr Emerg Care*. 2009;25:352–360.
49. Williams JV, Harris PA, Tollefson SJ, et al. Human metapneumovirus and lower respiratory tract disease in otherwise healthy infants and children. *N Engl J Med*. 2004;350(5):443–450.
50. Qureshi NR, Hien TT, Farrar J, et al. The radiologic manifestations of H5N1 avian influenza. *J Thorac Imaging*. 2006;21:259–264.
51. Jartti A, Rauvala E, Kauma H, et al. Chest imaging findings in hospitalized patients with H1N1 influenza. *Acta Radiol*. 2011;52:297–304.

52. Ventre KM, Wolf GK, Arnold JH. Pediatric respiratory diseases: 2011 update for the Rogers' textbook of pediatric intensive care. *Pediatr Crit Care Med*. 2011;12:325–338.
53. Ng DK, Lau WF, Chan KK, et al. Severe acute respiratory syndrome coronavirus infection in children. *Pediatr Int*. 2005;47:452–455.
54. Antonio GE, Wong KT, Tsui EL, et al. Chest radiograph scores as potential prognostic indicators in severe acute respiratory syndrome (SARS). *AJR Am J Roentgenol*. 2005;184:734–741.
55. Ng DK, Lau WF, Chan KK, et al. Severe acute respiratory syndrome coronavirus infection in children. *Pediatr Int*. 2005;47(4):452–455.
56. Prodhan P, Westra SJ, Lin J, et al. Chest radiological patterns predict the duration of mechanical ventilation in children with RSV infection. *Pediatr Radiol*. 2009;39:117–123.
57. Lee EY, McAdam AJ, Chaudry G, et al. Swine-origin influenza a (H1N1) viral infection in children: initial chest radiographic findings. *Radiology*. 2010;254:934–941.
58. Li AM, So HK, Chu W, et al. Radiological and pulmonary function outcomes of children with SARS. *Pediatr Pulmonol*. 2004;38:427–433.
59. Antonio GE, Wong KT, Chu WC, et al. Imaging in severe acute respiratory syndrome (SARS). *Clin Radiol*. 2003;58:825–832.
60. Babyn PS, Chu WC, Tsou IY, et al. Severe acute respiratory syndrome (SARS): chest radiographic features in children. *Pediatr Radiol*. 2004;34:47–58.
61. Chu WC, Li AM, Ng AW, et al. Thin-section CT 12 months after the diagnosis of severe acute respiratory syndrome in pediatric patients. *AJR Am J Roentgenol*. 2006;186:1707–1714.
62. Gold R, Wilt JC, Adhikari PK, et al. Adenoviral pneumonia and its complications in infancy and childhood. *J Can Assoc Radiol*. 1969;20:218–224.
63. Restrepo-Gualteros SM, Jaramillo-Barberi LE, Gonzalez-Santos M, et al. Characterization of cytomegalovirus lung infection in non-HIV infected children. *Viruses*. 2014;6(5):2038–2051.
64. Chamroonrat W, Cheng G, Servaes S, et al. Cytomegalovirus pneumonitis detected by gallium-67 scintigraphy with a negative diagnostic chest computed tomography. *Clin Nucl Med*. 2010;35:542–544.
65. Pfleger A, Eber E, Popper H, et al. Chronic interstitial lung disease due to Epstein-Barr virus infection in two infants. *Eur Respir J*. 2000;15:803–806.
66. Riggs W. Why radiologists tend to overcall pediatric chest radiographs. *Appl Radiol*. 1996;38–39.
67. Donnelly LF. *Diagnostic Imaging: Pediatrics*. Salt Lake City, UT: Amirsys; 2005.
68. Bachur R, Perry H, Harper MB. Occult pneumonias: empiric chest radiographs in febrile children with leukocytosis. *Ann Emerg Med*. 1999;33:166–173.
69. Murphy CG, van de Pol AC, Harper MB, et al. Clinical predictors of occult pneumonia in the febrile child. *Acad Emerg Med*. 2007;14:243–249.
70. Shah RM, Gupta S, Angeid-Backman E, et al. Pneumococcal pneumonia in patients requiring hospitalization: effects of bacteremia and HIV seropositivity on radiographic appearance. *AJR Am J Roentgenol*. 2000;175:1533–1536.
71. O'Brien KL, Walters MI, Sellman J, et al. Severe pneumococcal pneumonia in previously healthy children: the role of preceding influenza infection. *Clin Infect Dis*. 2000;30:784–789.
72. Tuomanen EI, Austrian R, Masure HR. Pathogenesis of pneumococcal infection. *N Engl J Med*. 1995;332:1280–1284.
73. Minton EJ, Macfarlane JT. Antibiotic resistant *Streptococcus pneumoniae*. *Thorax*. 1996;51(suppl 2):S45–S50.
74. Rutman MS, Bachur R, Harper MB. Radiographic pneumonia in young, highly febrile children with leukocytosis before and after universal conjugate pneumococcal vaccination. *Pediatr Emerg Care*. 2009;25:1–7.
75. Kim YW, Donnelly LF. Round pneumonia: imaging findings in a large series of children. *Pediatr Radiol*. 2007;37:1235–1240.
76. Restrepo R, Palani R, Matapathi UM, et al. Imaging of round pneumonia and mimics in children. *Pediatr Radiol*. 2010;40:1931–1940.
77. Felman AH, Shulman ST. Staphylococcal osteomyelitis, sepsis, and pulmonary disease. Observations of 10 patients with combined osseous and pulmonary infections. *Radiology*. 1975;117:649–655.
78. Erdem G, Bergert L, Len K, et al. Radiological findings of community-acquired methicillin-resistant and methicillin-susceptible *Staphylococcus aureus* pediatric pneumonia in Hawaii. *Pediatr Radiol*. 2010;40:1768–1773.
79. Kefala-Agoropoulou K, Protonotariou E, Vitti D, et al. Life-threatening infection due to community-acquired methicillin-resistant *Staphylococcus aureus:* case report and review. *Eur J Pediatr*. 2010;169:47–53.
80. Gonzalez BE, Hulten KG, Dishop MK, et al. Pulmonary manifestations in children with invasive community-acquired *Staphylococcus aureus* infection. *Clin Infect Dis*. 2005;41(5):583–590.
81. Macfarlane J, Rose D. Radiographic features of staphylococcal pneumonia in adults and children. *Thorax*. 1996;51:539–540.
82. Joosten KF, Hazelzet JA, Tiddens HA, et al. Staphylococcal pneumonia in childhood: will early surgical intervention lower mortality? *Pediatr Pulmonol*. 1995;20:83–88.
83. Asmar BI, Slovis TL, Reed JO, et al. *Hemophilus influenzae* type B pneumonia in 43 children. *J Pediatr*. 1978;93:389–393.
84. Campins M, Ferrer A, Callis L, et al. Nosocomial Legionnaire's disease in a children's hospital. *Pediatr Infect Dis J*. 2000;19:228–234.
85. Quagliano PV, Das Narla L. *Legionella* pneumonia causing multiple cavitating pulmonary nodules in a 7-month-old infant. *AJR Am J Roentgenol*. 1993;161:367–368.
86. Brook I. Anaerobic infections in children. *Microbes Infect*. 2002; 4:1271–1280.
87. Lumicao GG, Heggie AD. Chlamydial infections. *Pediatr Clin North Am*. 1979;26:269–282.
88. Radkowski MA, Kranzler JK, Beem MO, et al. *Chlamydia* pneumonia in infants: radiography in 125 cases. *AJR Am J Roentgenol*. 1981;137:703–706.
89. Guckel C, Benz-Bohm G, Widemann B. Mycoplasmal pneumonias in childhood. Roentgen features, differential diagnosis and review of literature. *Pediatr Radiol*. 1989;19:499–503.
90. Waites KB. New concepts of *Mycoplasma pneumoniae* infections in children. *Pediatr Pulmonol*. 2003;36:267–278.
91. Reittner P, Muller NL, Heyneman L, et al. *Mycoplasma pneumoniae* pneumonia: radiographic and high-resolution CT features in 28 patients. *AJR Am J Roentgenol*. 2000;174:37–41.
92. John SD, Ramanathan J, Swischuk LE. Spectrum of clinical and radiographic findings in pediatric mycoplasma pneumonia. *Radiographics*. 2001;21:121–131.
93. Yang E, Altes T, Anupindi SA. Early mycoplasma pneumoniae infection presenting as multiple pulmonary masses: an unusual presentation in a child. *Pediatr Radiol*. 2008;38:477–480.
94. Islam S, Calkins CM, Goldin AB, et al. The diagnosis and management of empyema in children: a comprehensive review from the APSA Outcomes and Clinical Trials Committee. *J Pediatr Surg*. 2012;47(11):2101–2110.
95. Kurian J, Levin TL, Han BK, et al. Comparison of ultrasound and CT in the evaluation of pneumonia complicated by parapneumonic effusion in children. *AJR Am J Roentgenol*. 2009;193(6):1648–1654.
96. Pillai D, Song X, Pastor W, et al. Implementation and impact of a consensus diagnostic and management algorithm for complicated pneumonia in children. *J Investig Med*. 2011;59(8):1221–1227.
97. Ramnath RR, Heller RM, Ben-Ami T, et al. Implications of early sonographic evaluation of parapneumonic effusions in children with pneumonia. *Pediatrics*. 1998;101:68–71.
98. King S, Thomson A. Radiological perspectives in empyema. *Br Med Bull*. 2002;61:203–214.
99. Donnelly LF, Klosterman LA. CT appearance of parapneumonic effusions in children: findings are not specific for empyema. *AJR Am J Roentgenol*. 1997;169:179–182.
100. Tan Kendrick AP, Ling H, Subramaniam R, et al. The value of early CT in complicated childhood pneumonia. *Pediatr Radiol*. 2002;32:16–21.
101. Donnelly LF. Imaging in immunocompetent children who have pneumonia. *Radiol Clin North Am*. 2005;43:253–265.
102. Kearney SE, Davies CW, Davies RJ, et al. Computed tomography and ultrasound in parapneumonic effusions and empyema. *Clin Radiol*. 2000;55:542–547.
103. Tu CY, Hsu WH, Hsia TC, et al. Pleural effusions in febrile medical ICU patients: chest ultrasound study. *Chest*. 2004;126:1274–1280.
104. Westra SJ, Choy G. What imaging should we perform for the diagnosis and management of pulmonary infections? *Pediatr Radiol*. 2009;39(suppl 2):S178–S183.
105. Heussel CP, Kauczor HU, Heussel G, et al. Early detection of pneumonia in febrile neutropenic patients: use of thin-section CT. *AJR Am J Roentgenol*. 1997;169:1347–1353.
106. Winer-Muram HT, Arheart KL, Jennings SG, et al. Pulmonary complications in children with hematologic malignancies: accuracy of diagnosis with chest radiography and CT. *Radiology*. 1997;204:643–649.

107. Mori M, Galvin JR, Barloon TJ, et al. Fungal pulmonary infections after bone marrow transplantation: evaluation with radiography and CT. *Radiology*. 1991;178:721–726.
108. Janzen DL, Padley SP, Adler BD, et al. Acute pulmonary complications in immunocompromised non-AIDS patients: comparison of diagnostic accuracy of CT and chest radiography. *Clin Radiol*. 1993;47:159–165.
109. Winer-Muram HT, Rubin SA, Fletcher BD, et al. Childhood leukemia: diagnostic accuracy of bedside chest radiography for severe pulmonary complications. *Radiology*. 1994;193:127–133.
110. Donnelly LF, Klosterman LA. The yield of CT of children who have complicated pneumonia and noncontributory chest radiography. *AJR Am J Roentgenol*. 1998;170:1627–1631.
111. Donnelly LF, Losterman LA. Cavitary necrosis complicating pneumonia in children: sequential findings on chest radiography. *AJR Am J Roentgenol*. 1998;171:253–256.
112. Margenthaler JA, Weber TR, Keller MS. Predictors of surgical outcome for complicated pneumonia in children: impact of bacterial virulence. *World J Surg*. 2004;28(1):87–91.
113. Virkki R, Juven T, Mertsola J, et al. Radiographic follow-up of pneumonia in children. *Pediatr Pulmonol*. 2005;40:223–227.
114. Montella S, Santamaria F, Salvatore M, et al. Assessment of chest high-field magnetic resonance imaging in children and young adults with noncystic fibrosis chronic lung disease: comparison to high-resolution computed tomography and correlation with pulmonary function. *Invest Radiol*. 2009;44:532–538.
115. Peltola V, Ruuskanen O, Svedstrom E. Magnetic resonance imaging of lung infections in children. *Pediatr Radiol*. 2008;38:1225–1231.
116. Yikilmaz A, Koc A, Coskun A, et al. Evaluation of pneumonia in children: comparison of MRI with fast imaging sequences at 1.5T with chest radiographs. *Acta Radiol*. 2011;52:914–919.
117. Yin EZ, Frush DP, Donnelly LF, et al. Primary immunodeficiency disorders in pediatric patients: clinical features and imaging findings. *AJR Am J Roentgenol*. 2001;176:1541–1552.
118. Langton Hewer SC. Is limited computed tomography the future for imaging the lungs of children with cystic fibrosis? *Arch Dis Child*. 2006;91:377–378.
119. de Jong PA, Mayo JR, Golmohammadi K, et al. Estimation of cancer mortality associated with repetitive computed tomography scanning. *Am J Respir Crit Care Med*. 2006;173:199–203.
120. Peltola V, Ruuskanen O, Svedstrom E. Magnetic resonance imaging of lung infections in children. *Pediatr Radiol*. 2008;38(11):1225–1231.
121. Yikilmaz A, Koc A, Coskun A, et al. Evaluation of pneumonia in children: comparison of MRI with fast imaging sequences at 1.5T with chest radiographs. *Acta Radiol*. 2011;52(8):914–919.
122. Sodhi KS, Khandelwal N, Saxena AK, et al. Rapid lung MRI - paradigm shift in evaluation of febrile neutropenia in children with leukemia: a pilot study. *Leuk Lymphoma*. 2016;57(1):70–75.
123. Agrons GA, Markowitz RI, Kramer SS. Pulmonary tuberculosis in children. *Semin Roentgenol*. 1993;28:158–172.
124. Bosch-Marcet J, Serres-Creixams X, Zuasnabar-Cotro A, et al. Comparison of ultrasound with plain radiography and CT for the detection of mediastinal lymphadenopathy in children with tuberculosis. *Pediatr Radiol*. 2004;34:895–900.
125. Andreu J, Caceres J, Pallisa E, et al. Radiological manifestations of pulmonary tuberculosis. *Eur J Radiol*. 2004;51:139–149.
126. Leung AN, Muller NL, Pineda PR, et al. Primary tuberculosis in childhood: radiographic manifestations. *Radiology*. 1992;182:87–91.
127. George R, Andronikou S, Theron S, et al. Pulmonary infections in HIV-positive children. *Pediatr Radiol*. 2009;39(6):545–554.
128. Leung AN. Pulmonary tuberculosis: the essentials. *Radiology*. 1999;210:307–322.
129. Smuts NA, Beyers N, Gie RP, et al. Value of the lateral chest radiograph in tuberculosis in children. *Pediatr Radiol*. 1994;24:478–480.
130. Lighter J, Rigaud M. Diagnosing childhood tuberculosis: traditional and innovative modalities. *Curr Probl Pediatr Adolesc Health Care*. 2009;39:61–88.
131. Theart AC, Marais BJ, Gie RP, et al. Criteria used for the diagnosis of childhood tuberculosis at primary health care level in a high-burden, urban setting. *Int J Tuberc Lung Dis*. 2005;9:1210–1214.
132. Jamieson DH, Cremin BJ. High resolution CT of the lungs in acute disseminated tuberculosis and a pediatric radiology perspective of the term “miliary”. *Pediatr Radiol*. 1993;23:380–383.
133. Moon WK, Kim WS, Kim IO, et al. Complicated pleural tuberculosis in children: CT evaluation. *Pediatr Radiol*. 1999;29:153–157.
134. Curvo-Semedo L, Teixeira L, Caseiro-Alves F. Tuberculosis of the chest. *Eur J Radiol*. 2005;55:158–172.
135. Lamont AC, Cremin BJ, Pelteret RM. Radiological patterns of pulmonary tuberculosis in the paediatric age group. *Pediatr Radiol*. 1986;16:2–7.
136. Van Dyck P, Vanhoenacker FM, Van den Brande P, et al. Imaging of pulmonary tuberculosis. *Eur Radiol*. 2003;13:1771–1785.
137. Andronikou S, Wieselthaler N. Modern imaging of tuberculosis in children: thoracic, central nervous system and abdominal tuberculosis. *Pediatr Radiol*. 2004;34:861–875.
138. Swingler GH, du Toit G, Andronikou S, et al. Diagnostic accuracy of chest radiography in detecting mediastinal lymphadenopathy in suspected pulmonary tuberculosis. *Arch Dis Child*. 2005;90:1153–1156.
139. Lee EY, Tracy DA, Eisenberg RL, et al. Screening of asymptomatic children for tuberculosis is a lateral chest radiograph routinely indicated? *Acad Radiol*. 2011;18:184–190.
140. Zarabi M, Sane S, Girdany BR. The chest roentgenogram in the early diagnosis of tuberculous meningitis in children. *Am J Dis Child*. 1971;121:389–392.
141. Delacourt C, Mani TM, Bonnerot V, et al. Computed tomography with normal chest radiograph in tuberculous infection. *Arch Dis Child*. 1993;69:430–432.
142. McGuinness G, Naidich DP, Jagirdar J, et al. High resolution CT findings in miliary lung disease. *J Comput Assist Tomogr*. 1992;16:384–390.
143. Buckner CB, Leithiser RE, Walker CW, et al. The changing epidemiology of tuberculosis and other mycobacterial infections in the United States: implications for the radiologist. *AJR Am J Roentgenol*. 1991;156:255–264.
144. Kim WS, Moon WK, Kim IO, et al. Pulmonary tuberculosis in children: evaluation with CT. *AJR Am J Roentgenol*. 1997;168:1005–1009.
145. Im JG, Itoh H, Shim YS, et al. Pulmonary tuberculosis: CT findings—early active disease and sequential change with antituberculous therapy. *Radiology*. 1993;186:653–660.
146. Vijayasekaran D. Treatment of childhood tuberculosis. *Indian J Pediatr*. 2011;78:443–448.
147. Choe KO, Jeong HJ, Sohn HY. Tuberculous bronchial stenosis: CT findings in 28 cases. *AJR Am J Roentgenol*. 1990;155:971–976.
148. Aquino SL, Kee ST, Warnock ML, et al. Pulmonary aspergillosis: imaging findings with pathologic correlation. *AJR Am J Roentgenol*. 1994;163:811–815.
149. Mintzer RA, Rogers LF, Kruglik GD, et al. The spectrum of radiologic findings in allergic bronchopulmonary aspergillosis. *Radiology*. 1978;127:301–307.
150. Greif Z, Moscuna M, Suprun H, et al. Fatal childhood pulmonary aspergillosis from contact with pigeons. *Clin Pediatr (Phila)*. 1981;20:357–359.
151. Gefter WB, Weingrad TR, Epstein DM, et al. “Semi-invasive” pulmonary aspergillosis: a new look at the spectrum of Aspergillus infections of the lung. *Radiology*. 1981;140:313–321.
152. Abramson S. The air crescent sign. *Radiology*. 2001;218:230–232.
153. Gurney JW, Conces DJ. Pulmonary histoplasmosis. *Radiology*. 1996;199:297–306.
154. Greendyke WH, Resnick DL, Harvey WC. The varied roentgen manifestations of primary coccidioidomycosis. *Am J Roentgenol Radium Ther Nucl Med*. 1970;109:491–499.
155. Pinckney L, Parker BR. Primary coccidioidomycosis in children presenting with massive pleural effusion. *AJR Am J Roentgenol*. 1978;130:247–249.
156. Crans CA Jr, Boiselle PM. Imaging features of *Pneumocystis carinii* pneumonia. *Crit Rev Diagn Imaging*. 1999;40:251–284.
157. Boiselle PM, Tocino I, Hooley RJ, et al. Chest radiograph interpretation of *Pneumocystis carinii* pneumonia, bacterial pneumonia, and pulmonary tuberculosis in HIV-positive patients: accuracy, distinguishing features, and mimics. *J Thorac Imaging*. 1997;12:47–53.
158. Boiselle PM, Crans CA Jr, Kaplan MA. The changing face of *Pneumocystis carinii* pneumonia in AIDS patients. *AJR Am J Roentgenol*. 1999;172:1301–1309.
159. Rossi SE, Erasmus JJ, Volpacchio M, et al. “Crazy-paving” pattern at thin-section CT of the lungs: radiologic-pathologic overview. *Radiographics*. 2003;23:1509–1519.
160. Chow C, Templeton PA, White CS. Lung cysts associated with *Pneumocystis carinii* pneumonia: radiographic characteristics, natural history, and complications. *AJR Am J Roentgenol*. 1993;161:527–531.
161. Kuhlman JE. Pneumocystic infections: the radiologist’s perspective. *Radiology*. 1996;198:623–635.

162. McGuinness G. Changing trends in the pulmonary manifestations of AIDS. *Radiol Clin North Am*. 1997;35:1029–1082.
163. Padley SP, King LJ. Computed tomography of the thorax in HIV disease. *Eur Radiol*. 1999;9:1556–1569.
164. Primack SL, Muller NL. High-resolution computed tomography in acute diffuse lung disease in the immunocompromised patient. *Radiol Clin North Am*. 1994;32:731–744.
165. Hartman TE, Primack SL, Muller NL, et al. Diagnosis of thoracic complications in AIDS: accuracy of CT. *AJR Am J Roentgenol*. 1994;162:547–553.
166. Logan PM, Finnegan MM. Pulmonary complications in AIDS: CT appearances. *Clin Radiol*. 1998;53:567–573.
167. Gruden JF, Huang L, Turner J, et al. High-resolution CT in the evaluation of clinically suspected *Pneumocystis carinii* pneumonia in AIDS patients with normal, equivocal, or nonspecific radiographic findings. *AJR Am J Roentgenol*. 1997;169:967–975.
168. Kassner EG, Kauffman SL, Yoon JJ, et al. Pulmonary candidiasis in infants: clinical, radiologic, and pathologic features. *AJR Am J Roentgenol*. 1981;137:707–716.
169. Buff SJ, McLelland R, Gallis HA, et al. Candida albicans pneumonia: radiographic appearance. *AJR Am J Roentgenol*. 1982;138:645–648.
170. Woodring JH, Halfhill H 2nd, Reed JC. Pulmonary strongyloidiasis: clinical and imaging features. *AJR Am J Roentgenol*. 1994;162:537–542.
171. Burton K, Yogev R, London N, et al. Pulmonary paragonimiasis in Laotian refugee children. *Pediatrics*. 1982;70:246–248.
172. Wall MA, McGhee G. Paragonimiasis. Atypical appearances in two adolescent Asian refugees. *Am J Dis Child*. 1982;136:828–830.
173. Neumayr A, Troia G, de Bernardis C, et al. Justified concern or exaggerated fear: the risk of anaphylaxis in percutaneous treatment of cystic echinococcosis—a systematic literature review. *PLoS Negl Trop Dis*. 2011;5:e1154.

# 55

# Neoplasia

Winnie C. W. Chu, Monica Epelman, and Edward Y. Lee

Pulmonary neoplasm is much less common in children than in adults. Affected children may present clinically with respiratory symptoms, or a pulmonary neoplasm may be detected incidentally on a chest radiograph in an asymptomatic child.[1] In a recent series of 204 pediatric lung tumors, the ratio of primary benign to primary malignant to secondary malignant pulmonary neoplasms (i.e., metastases) is 1.4 : 1 : 11.6.[2] Primary lung tumors represent only 0.19% of all pediatric neoplasms.

## PRIMARY BENIGN PULMONARY NEOPLASMS

Primary benign pulmonary neoplasms are uncommon in children.[3,4] Their imaging characteristics are summarized in Table 55.1.

### Hamartoma

***Etiology.*** Pulmonary hamartoma, originally thought to represent a congenital lesion, is now considered a benign mesenchymal neoplasm. It is slow growing and contains predominantly cartilage, fat, and fibrous tissue. Occasionally, pulmonary hamartoma may also have smooth muscle, bone, and entrapped respiratory epithelium.[5] Pulmonary hamartoma is rare in children; however, it is the most common primary benign pulmonary neoplasm, accounting for 7% to 14% of all solitary pulmonary nodules in children. Ninety percent of pulmonary hamartomas are parenchymal in location. They usually present as incidental findings.

***Imaging.*** The typical radiographic appearance of pulmonary hamartoma is a smooth or slightly lobulated, solitary pulmonary nodule or mass, usually located in the peripheral lung. Characteristic punctate or popcorn-like calcifications may be seen in approximately 10%. On computed tomography (CT), it is typically a well-circumscribed pulmonary nodule that is less than 2.5 cm in diameter and often contains fat or calcification, which, in a solitary pulmonary nodule, is considered diagnostic (Fig. 55.1).[6]

***Treatment and Follow-up.*** No treatment is required unless the lesion grows rapidly or symptoms such as recurrent pneumonia or atelectasis are caused by mass effect from the tumor.[7] In such situations, surgical resection is usually curative.

### Chondroma

***Etiology.*** Pulmonary chondroma is a benign tumor composed of a well-differentiated cartilage with lack of bronchial epithelium.[8] Pulmonary chondroma is associated with the Carney triad,[8,9] which is a rare multitumoral syndrome of unknown etiology affecting the stomach, lungs (pulmonary chondroma), paraganglionic system, adrenal cortex, and esophagus. The syndrome is usually only partially expressed. Seventy-six percent of patients with the Carney triad have one or more pulmonary chondromas.

***Imaging.*** Pulmonary chondroma may be single (51%), multiple unilateral (32%), or bilateral (17%) without predilection for specific lobe or side of lung.[8] Chest radiography usually shows one or more well-demarcated lung masses with central or popcorn-like calcification (Fig. 55.2A). When calcified (45%), the appearance of chondroma is indistinguishable from that of pulmonary hamartoma on imaging studies (Fig. 55.2B).

***Treatment and Follow-up.*** Although surgical resection is sometimes performed, pulmonary chondroma may be left in situ because it is benign and usually indolent. Periodic screening of patients is currently recommended for metachronous development of paragangliomas or gastrointestinal stromal tumors.

### Recurrent Respiratory Papillomatosis

***Etiology.*** Recurrent respiratory papillomatosis (RRP) is characterized by ingrowths of a squamous cell–lined fibrovascular core in the lumen of airways. It is related to human papillomavirus (HPV) infection, most often acquired at birth. The majority of cases are uncomplicated, with lesions remaining localized to the laryngeal and subglottic region.[9] Lung lesions are seen in 1.8% of affected patients, especially if surgical or laser therapy had been provided earlier.[10] The ultimate prognosis is poor when pulmonary involvement occurs. Malignant transformation into squamous cell carcinoma may occur.[11]

***Imaging.*** On chest radiography, RRP typically presents as bilateral, multiple nodular and cystic lesions of varying size containing air or debris. Postobstructive atelectasis, bronchiectasis, or secondary infection presenting as consolidation may also be seen.[12] On CT, scattered nodules are seen in the lungs (e-Fig. 55.3), and these nodules may enlarge, become air-filled cysts, or form large cavities with thin or thick walls.[13] CT virtual bronchoscopy may be useful to evaluate mural nodules within the central airways.

***Treatment and Follow-up.*** A combined concurrent adjunctive therapy including microlaryngeal surgery, pulsed dye laser, and intralesional cidofovir injection is promising as a cure for RRP and restoration of vocal function after treatment.[14-16] It is hoped that the use of HPV vaccination will largely prevent this disease.[17]

### Lymphatic Malformation

***Etiology.*** Lymphatic malformation, previously referred to as lymphangioma,[18,19] is characterized by a benign proliferation of nonfunctional lymphatic tissue that may involve nearly every organ of the body. Only 1% of lymphatic malformations remain confined to the chest. Primary pulmonary lymphatic malformation is even less common.[20] Affected persons are often asymptomatic. Younger patients tend to have lesions that affect the lung.[21,22]

***Imaging.*** On chest radiography, lymphatic malformation typically presents as a masslike opacity. The most common CT finding is a smooth, well-marginated, nonenhancing, cystic mass. In neonates and infants, this may simulate congenital pulmonary airway malformation (CPAM) or diaphragmatic hernia. Older children may have a solid, low-attenuation, masslike lesion that may mimic pneumonia or tumors (e-Fig. 55.4).

***Treatment and Follow-up.*** Early surgical removal or sclerotherapy of lymphatic malformation is currently recommended to prevent local growth and the resultant compression of vital structures.[23]

## BENIGN REACTIVE LYMPHOPROLIFERATIVE DISORDER

Pulmonary lymphoproliferative disorders (LPDs) are characterized by abnormal infiltration of lung parenchyma by lymphoid cells. They encompass a wide spectrum of focal or diffuse abnormalities, which may be classified as reactive or neoplastic (primary or secondary) on the basis of cellular morphology and clonality.[24,25] The

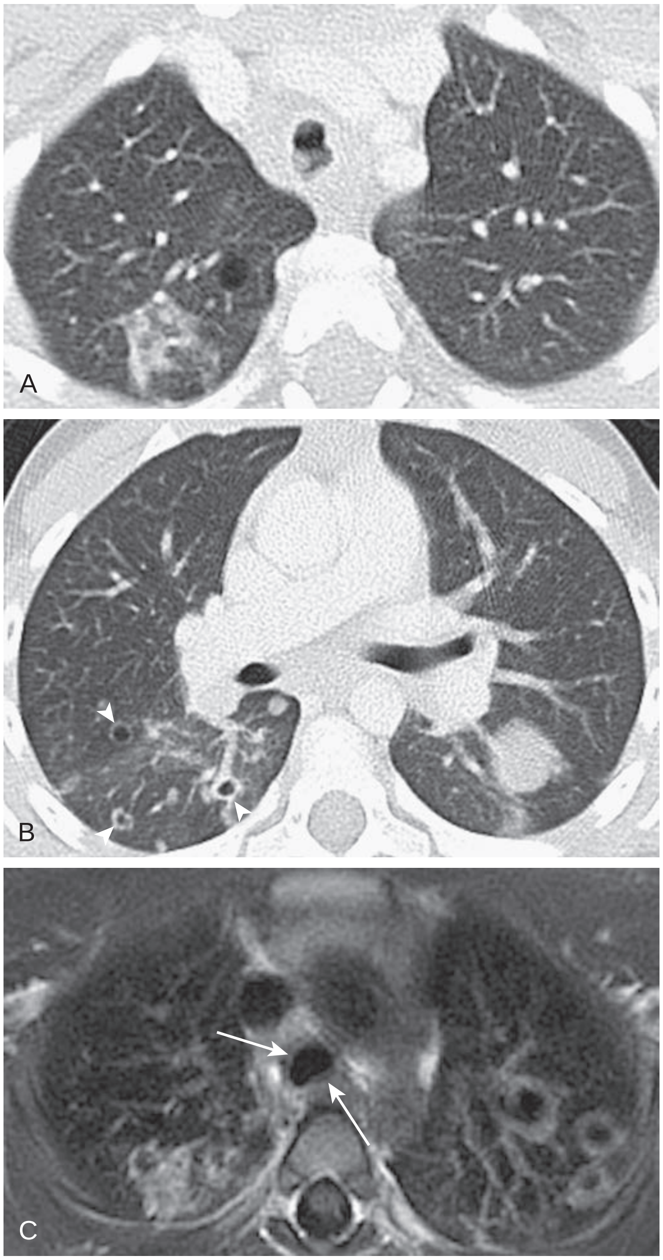

**e-Figure 55.3. Recurrent respiratory papillomatosis.** (A) Axial lung window CT image obtained in a 5-year-old girl with recurrent respiratory papillomatosis shows multiple intratracheal soft tissue nodules. (B) Multiple parenchymal papillomas are also present, some of which show cavitation *(arrowheads).* (C) Axial T1-weighted MRI shows cavitating lesions in both lungs and mildly thickened tracheal walls *(arrows).*

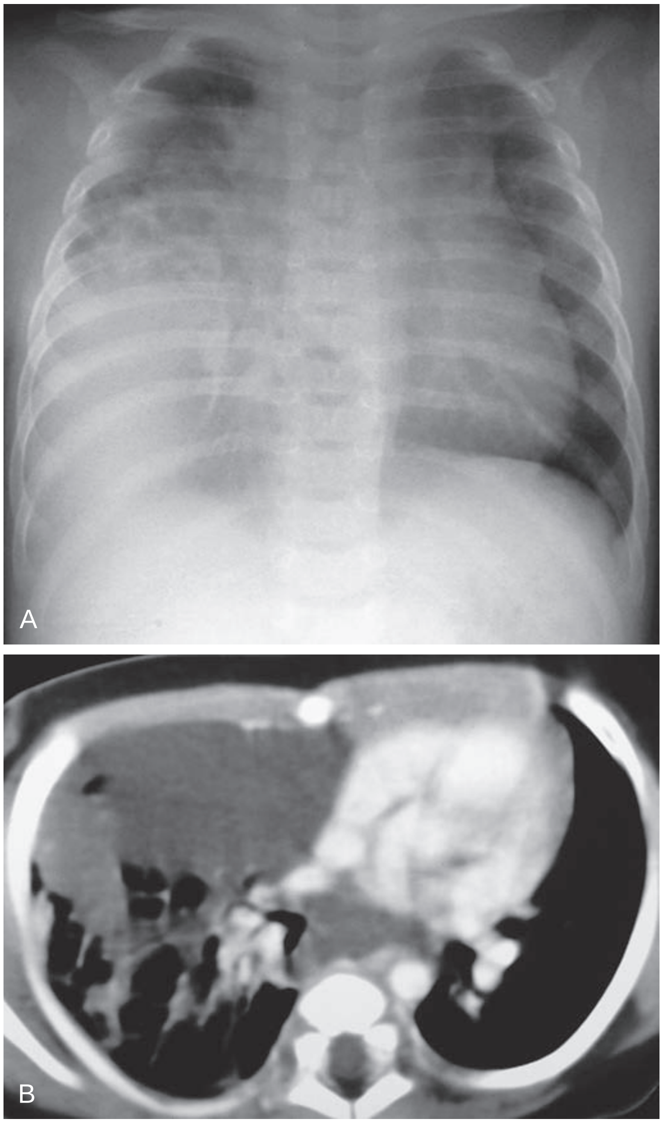

**e-Figure 55.4. Lymphatic malformation.** Biopsy-proven lymphatic malformation in a 4-year-old boy. (A) Chest radiograph demonstrates a mass in the right hemithorax. (B) Axial contrast-enhanced CT image shows a low-attenuation infiltrating mass in the middle mediastinum and right middle lobe.

**TABLE 55.1** Imaging Characteristics of Benign Lung Neoplasm (Nonlymphoproliferative)

| Neoplasm | Imaging Characteristics |
|---|---|
| Hamartoma | Smooth or slightly lobulated, sharply defined mass, occasionally calcified ("popcorn")<br>Fat and calcification in solitary pulmonary mass on computed tomography is diagnostic |
| Chondroma | Solitary or multiple nodules; commonly (45%) calcified; associated with the Carney triad |
| Respiratory papillomatosis | Rarely (<1%) intrapulmonary<br>Bilateral, multiple subpleural solid or cystic nodules; may be associated with bronchiectasis or atelectasis |
| Lymphatic malformation | Rarely intrapulmonary; well-marginated, nonenhancing cystic mass; may simulate congenital pulmonary airway malformation or diaphragmatic hernia in neonates; or solid, low-attenuation mediastinal or pulmonary mass in older children |

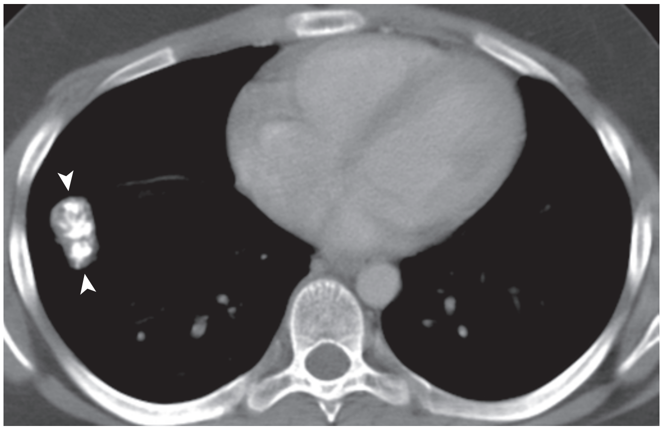

**Figure 55.1. Pulmonary hamartoma.** A 14-year-old boy with incidental calcified lesion noted on chest radiograph (image not shown). Axial contrast-enhanced CT image shows a peripherally located, well-circumscribed, oval shaped smooth mass *(arrowheads)* with popcorn calcifications.

classification and imaging characteristics of lymphoproliferative disorders involving the lungs are listed in Table 55.2.

***Etiology.*** Pulmonary mucosa-associated lymphoid tissue (MALT) and bronchus-associated lymphoid tissue (BALT) is usually inconspicuous in healthy subjects; however, a wide range of antigenic stimulation can induce benign reactive changes of these lymphoid tissues. Primary lymphoid lesions of the lung are increasingly recognized recently due to increases in pediatric organ transplantation, prevalence of human immunodeficiency virus (HIV) infection, and development of potent immunosuppressive therapies. Benign pulmonary lymphoid lesions include reactive lymphoid hyperplasia, nodular lymphoid hyperplasia, follicular bronchiolitis, and lymphoid interstitial pneumonia.[26-28]

Nodular lymphoid hyperplasia (NLH) is relatively rare and represents a benign, localized, reactive polyclonal lymphoproliferative lesion. Follicular bronchiolitis (FB) comprises a benign, polyclonal bronchial MALT hyperplasia in and around the bronchioles. Lymphocytic interstitial pneumonitis (LIP) is characterized by diffuse proliferation of polyclonal lymphocytes and plasma cells in the pulmonary parenchymal interstitium, associated with expansion of the alveolar septa. Because LIP is rarely idiopathic, it is considered an AIDS-defining illness in children younger than 13 years old who are infected with HIV.

***Imaging.*** Features on chest radiography are nonspecific (e-Fig. 55.5A). CT findings are better described,[24,29] though frequently nonspecific, and require correlation with clinical data. Histologic confirmation is required for a definite diagnosis. On CT, NLH usually presents as a discrete nodular mass (2–3 cm in diameter) with mild focal lymphangitic extension. Mediastinal and hilar lymphadenopathy, as well as pleural effusion, are typically absent in NLH (different from malignant lymphoma). FB is limited to the airway without interstitial involvement. It usually presents with bilateral nodules (most commonly 1–3 mm in diameter) of centrilobular/peribronchial distribution, hence having a "tree-in bud" appearance or bilateral patchy ground-glass opacities (e-Fig. 55.5B). There may be bronchial dilation. LIP usually presents as diffuse centrilobular and subpleural nodules[30] (representing local proliferation of lymphoid germinal centers), areas of ground-glass opacity, and bronchovascular and interstitial thickening in both lungs (Fig. 55.6). Peribronchovascular cysts are characteristically distributed in the lower lungs.[24]

***Treatment and Follow-up.*** In general, treatment involves management of underlying disease. NLH is benign and therefore surgical excision is generally curative. The prognosis of FB is generally favorable. Most patients respond to steroids or

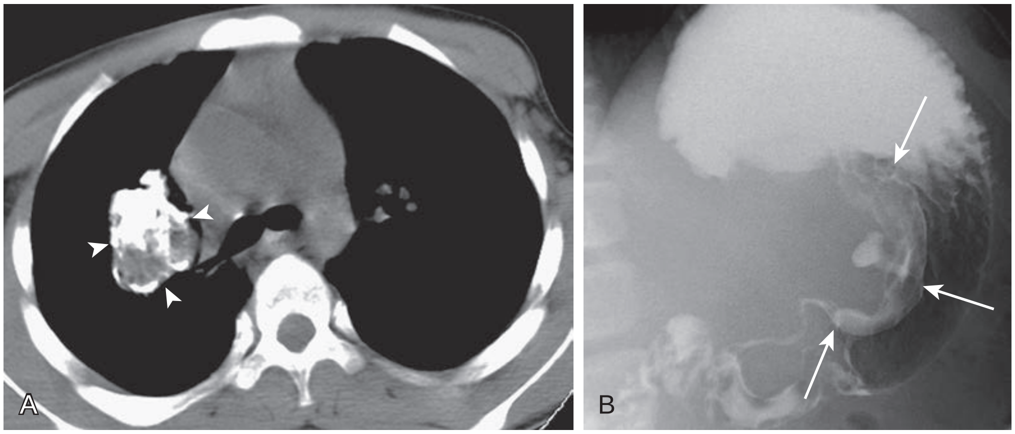

**Figure 55.2. Pulmonary chondroma.** (A) A 14-year-old boy in the setting of the Carney triad. Axial unenhanced CT image shows a large right parahilar mass *(arrowheads)* with extensive calcifications. (B) Upper gastrointestinal study of the same patient demonstrates a large ulcerated exophytic soft tissue mass *(arrows)* in the stomach consistent with gastric leiomyosarcoma.

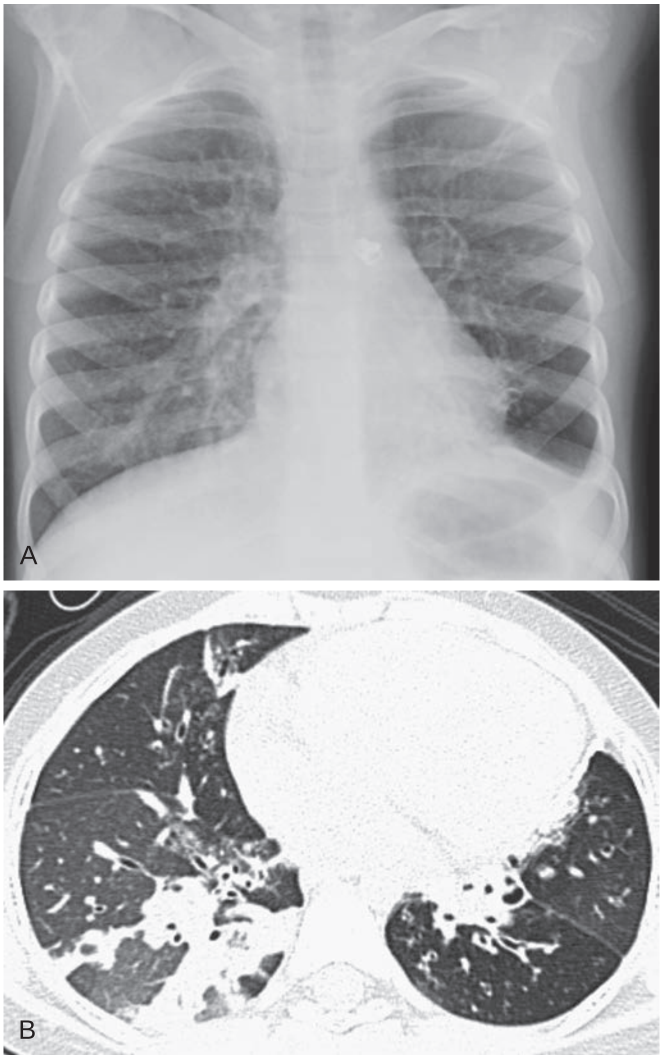

**e-Figure 55.5. Bronchus-associated lymphoid tissue.** A 5-year-old girl who presented with worsening shortness of breath and decreased oxygen saturation. (A) Chest radiograph shows hyperinflation with increased streaky interstitial opacities in both lungs. (B) Axial lung window CT image demonstrates air trappings, mosaic perfusion, and diffuse opacity with cystic bronchiectasis.

**TABLE 55.2** Lymphoproliferative Disorders of the Lungs

| Disorder | Imaging Characteristics |
|---|---|
| **REACTIVE BENIGN PROLIFERATION** | |
| Nodular lymphoid hyperplasia (NLH) | Discrete nodular mass (2–3 cm in diameter) with mild focal lymphangitic extension<br>Rarely mediastinal and hilar lymphadenopathy<br>Absent pleural effusion |
| Follicular bronchiolitis (FB) | Bilateral nodules (most commonly 1–3 mm in diameter) of centrilobular/peribronchial distribution, "tree-in bud" appearance<br>Bilateral patchy ground-glass opacities<br>There may be bronchial dilation |
| Lymphoid interstitial pneumonia (LIP) | Seen in patients with acquired or congenital immunodeficiency<br>Diffuse centrilobular and subpleural nodules<br>Ground-glass opacity<br>Bronchovascular and interstitial thickening<br>Peribronchovascular cysts in the lower lungs |
| **PROLIFERATION IN IMMUNOCOMPROMISED** | |
| Posttransplantation lymphoproliferative disorder (PTLD) | Associated with multiorgan transplant and EBV infection<br>Solitary or multiple lung masses or consolidation<br>Sometimes associated with peripheral ground-glass halo<br>May have associated mediastinal and extrathoracic adenopathy<br>May have air space consolidation, pleural or chest wall masses, pleural or pericardial effusions, and thymic enlargement |
| **PRIMARY MALIGNANT PROLIFERATION** | |
| MALT lymphoma | Single or multiple nodules or areas of consolidation<br>Peribronchovascular distribution<br>Bronchial dilation is common<br>Mediastinal lymphadenopathy |
| Diffuse large B-cell lymphoma (DLBL) | Single or multiple solid pulmonary nodules or masses<br>Cavitation is common (approximately 50%) |
| Lymphomatoid granulomatosis (LYG) | Nodules of peribronchovascular distribution<br>Small thin-walled cysts<br>Conglomerate small nodules |
| **SECONDARY MALIGNANT PROLIFERATION** | |
| Hodgkin lymphoma (HL) and non-Hodgkin lymphoma (NHL) | HL: Almost always have associated with mediastinal and/or hilar lymphadenopathy<br>NHL: Isolated lung disease without mediastinal involvement can occur<br>Three main pulmonary patterns:<br>(1) Nodular: single or multiple pulmonary nodules with irregular borders and sometimes central cavitation<br>(2) Lymphangitic: reticular interstitial opacities<br>(3) Alveolar: lobar or segmental consolidation |

*EBV,* Epstein–Barr virus; *MALT,* mucosa-associated lymphoid tissue.

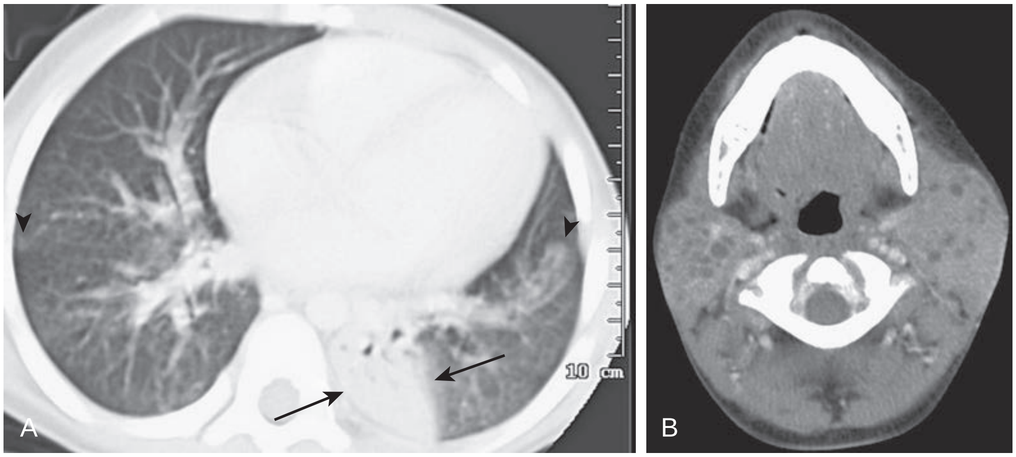

**Figure 55.6. Lymphocytic interstitial pneumonitis.** An 8-year-old girl with human immunodeficiency virus (HIV) infection presenting with increasing shortness of breath. (A) Axial CT image shows bilateral patchy areas of ground-glass attenuation, right greater than left, poorly defined nodules *(arrowheads),* and an area of consolidation in the left lower lobe *(arrows).* (B) Axial, enhanced CT image of neck demonstrates multiple, bilateral parotid lymphoepithelial cysts consistent with HIV parotitis.

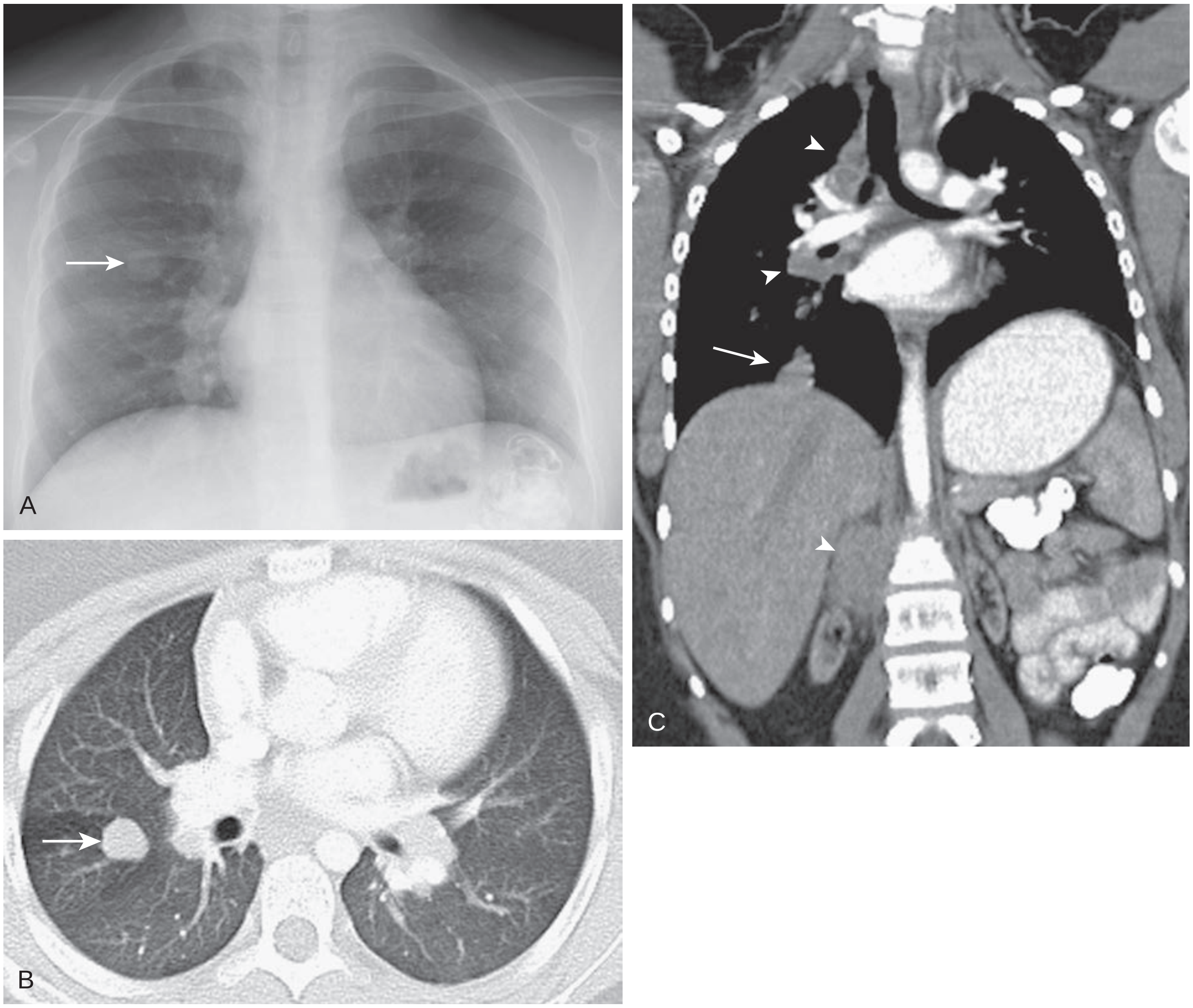

**Figure 55.7. Posttransplantation lymphoproliferative disorder (PTLD).** An 11-year-old girl who presented with PTLD following renal transplantation. (A) Chest radiograph shows a nodular opacity *(arrow)* in the right upper lobe and bilateral hilar lymphadenopathy. (B) Axial lung window CT image demonstrates a right upper lobe lung nodule *(arrow)* corresponding to the opacity noted on chest radiograph. (C) A coronal reformatted CT image shows mediastinal, hilar, and retroperitoneal lymphadenopathy *(arrowheads)* and an additional nodule at the right lung base *(arrow)*. Note the atrophic native kidneys.

azathioprine, although some patients may relapse.[26] Steroid and other immunosuppressive agents are used for treating LIP with variable results. Progressive honeycomb fibrosis or infectious complications may lead to increased mortality in LIP, and low-grade B-cell lymphoma may develop in rare cases.[31]

## Posttransplantation Lymphoproliferative Disorder

***Etiology.*** Posttransplantation lymphoproliferative disorder (PTLD) is a consequence of chronic immunosuppression after solid organ transplantation or, less often, bone marrow transplantation.[32-35] PTLD is intimately associated with Epstein–Barr virus (EBV) infection. The lesions consist of uncontrolled proliferation of B lymphocytes ranging from benign lymphoid hyperplasia to invasive malignant lymphoma. Children are more likely to develop PTLD than adults, most commonly after multiorgan transplant such as heart-lung transplant (up to 33%).[32,36-40] The most common sites for PTLD are the tonsils, cervical nodes, gastrointestinal tract, and chest.[41,42] PTLD tends to occur within the allograft organ itself, as well as in adjacent anatomic regions.[43] Clinical symptoms of PTLD are often vague. Biopsy is typically required to confirm the diagnosis.

***Imaging.*** On chest radiography, the most common finding in PTLD is the presence of multiple well-defined pulmonary nodules with or without mediastinal adenopathy (Fig. 55.7).[40] These are best visualized on CT. These pulmonary nodules may contain air bronchograms, and sometimes have a peripheral ground-glass halo mimicking angioinvasive aspergillosis.[27] Other less frequent patterns of thoracic involvement include air space consolidation, pleural or chest wall masses, pleural or pericardial effusions, and thymic enlargement.[44-46] For a more confident diagnosis, it is helpful to search for extrathoracic PTLD such as thickening of bowel loops, enlarged abdominal lymph nodes, cervical adenopathy, or enlarged oropharyngeal lymphatic tissues.[39,40] Fluorodeoxyglucose positron emission tomography may increase sensitivity and specificity for the diagnosis.[47]

***Treatment and Follow-up.*** Reduction in immunosuppressive therapy remains a primary component of treatment for EBV-positive PTLD.[48] Chemotherapy is used when reduced immunosuppression fails to control disease progression. Newer treatments of PTLD include B-lymphocyte–depleting antibodies and adoptive T-cell immunotherapy using allogeneic or autologous EBV-specific cytotoxic T lymphocytes.[49] EBV vaccination is advocated to be effective prophylaxis against PTLD.

## PRIMARY MALIGNANT PULMONARY NEOPLASMS

Primary malignant pulmonary neoplasms are rare in children and are histologically diverse. The current World Health Organization (WHO) classification system of primary malignant pulmonary neoplasms differs substantially from the prior classification system, particularly with regard to new tumors (e.g., pleuropulmonary blastoma) and reclassification of benign and malignant tumors (e.g., inflammatory myofibroblastic tumor).[50] The most common primary lung malignancies in children are inflammatory myofibroblastic tumor, pleuropulmonary blastoma, and carcinoid tumor.[2,4,51,52] The imaging characteristics of primary malignant lung tumors are listed in Table 55.3.

### Inflammatory Myofibroblastic Tumor

***Etiology.*** Inflammatory myofibroblastic tumor (IMT) is relatively common in children. It is a myofibroblastic spindle cell soft tissue tumor with infiltrative plasma cells, lymphocytes, and eosinophils, defined by the WHO as a low-grade mesenchymal malignancy.[53] Due to the complexity and variable histologic characteristics, it is known by several different terms, including *plasma cell granuloma*, *inflammatory pseudotumor*, *fibroxanthoma*, *myofibroblastic tumor*, *fibrous histiocytoma*, *xanthogranuloma*, or *histiocytoma*.[54,55] A substantial proportion of tumors have *ALK1* gene mutations.[56] The majority of children with IMT are older than 5 years. Approximately 60% of affected children are symptomatic, typically presenting with fever, cough, chest pain, dyspnea, wheezing, or hemoptysis.

***Imaging.*** Radiographically, pulmonary IMT may be seen as solitary (95%) or multiple (5%). IMTs are usually sharply circumscribed, lobulated masses of varying sizes, typically located in the peripheral portion of the lungs. On CT there is usually a soft tissue mass with either homogeneous or heterogeneous attenuation (Fig. 55.8A). Less commonly, there may be both solid and cystic components. IMT may also have an infiltrative pattern simulating an aggressive malignancy (Fig. 55.8B).[57] If the mediastinum is involved or the mass contains calcifications (15%–25%), IMT may mimic a germ cell tumor, neuroblastoma, or metastatic osteosarcoma.

***Treatment and Follow-up.*** Complete surgical resection and close follow-up are necessary for appropriate treatment to avoid recurrences.[58] Sleeve resection is the best option for lesions located in the main-stem bronchus or secondary carina, typically with excellent results.[59]

**TABLE 55.3** Imaging Characteristics of Primary Malignant Lung Tumors

| Neoplasm | Imaging Characteristics |
|---|---|
| Inflammatory myofibroblastic tumor (IMT) | Solitary (95%) or multiple (5%)<br>Usually sharply circumscribed, lobulated mass<br>Typically located in the peripheral portion of the lungs<br>Soft tissue mass with either homogeneous or heterogeneous attenuation, may have both solid and cystic and calcific components |
| Carcinoid or salivary gland tumor | Centrally located lesion: intraluminal soft tissue mass with distal atelectasis or obstructive pneumonitis<br>Peripherally located lesion: oval or lobulated intraluminal or exophytic mass and occasionally calcify |
| Bronchogenic carcinoma | Central mass lesion with bronchial obstruction or, less commonly, small peripheral lesion |
| Pleuropulmonary blastoma | Cystic or mixed cystic and solid lesion adjacent to pleura; can be very large, with mediastinal displacement |
| Epithelioid hemangioendothelioma | Multiple well- or ill-defined nodular opacities up to 3 cm in diameter; very rare in childhood |

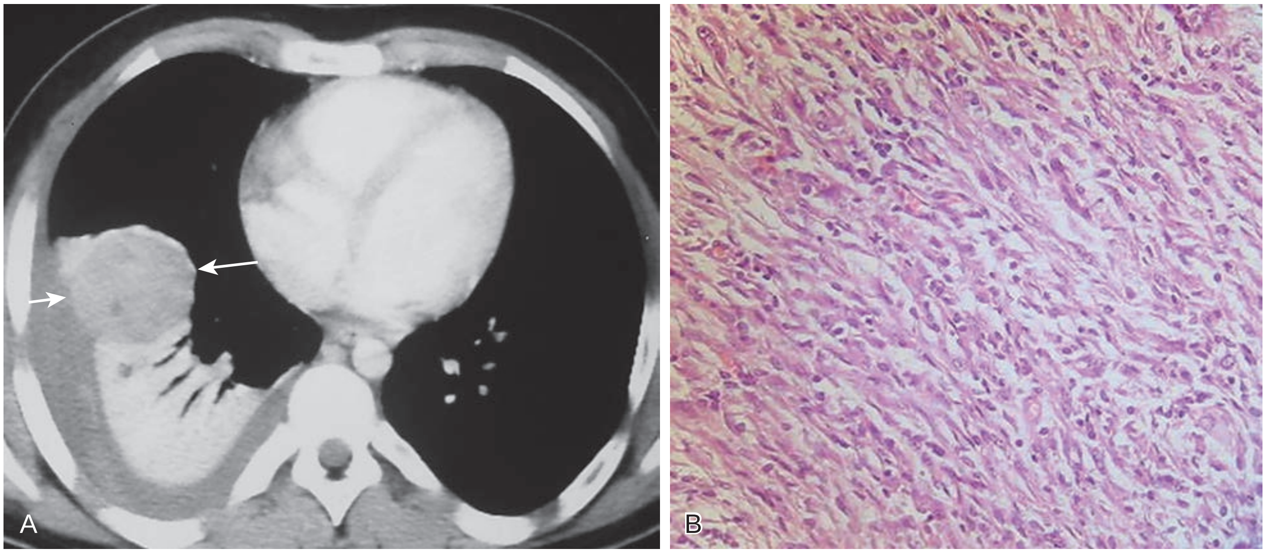

**Figure 55.8. Inflammatory myofibroblastic tumor.** An afebrile 13-year-old boy who presented with increasing dyspnea and right-sided pleuritic chest pain. (A) Axial contrast-enhanced CT of the chest shows a rounded heterogeneously enhancing lesion *(arrows)* located adjacent to an area of atelectatic lung. Pleural fluid at the same level demonstrates increased attenuation consistent with a hemothorax. (B) Photomicrograph (hematoxylin-eosin stain) of the surgical specimen reveals the presence of both spindle-shaped myofibroblasts and inflammatory cells consistent with an inflammatory myofibroblastic tumor of the lung.

## Bronchial Adenoma (Carcinoid Tumor or Salivary Gland Tumor)

***Etiology.*** The term *bronchial adenoma*, which implies a benign disease process, was recently recategorized as either carcinoid or salivary gland tumors by the WHO.[50] The three most common tumors in this group are carcinoid tumor,[60,61] mucoepidermoid tumor, and adenoid cystic carcinoma. Carcinoid tumor accounts for approximately 80% of previously classified pediatric bronchial adenomas, which are low-grade neuroendocrine carcinomas arising in lobar bronchi (75%), main-stem bronchi (10%), or the lung parenchyma (15%).[1,62,63] Mucoepidermoid carcinoma (see Video 55.1, e-Fig. 55.9, and e-Fig. 55.10) and adenoid cystic carcinoma (cylindromas) (Fig. 55.11) arise from the salivary-type mucous cells of the submucosa along the tracheobronchial tree. Adenoid cystic carcinoma is extremely rare in children.[64] Patients with carcinoid tumor and mucoepidermoid carcinoma frequently present with wheezing, cough, hemoptysis, or pneumonia.[62,65,66] Differential diagnosis of these rare tumors includes foreign body aspiration, granulomatous infection, and asthma with mucous plugging.

***Imaging.*** The radiographic presentation depends on the size and location of tumor within the airway or lungs. A centrally located tumor is typically seen as an intraluminal soft tissue attenuation mass with associated distal atelectasis or obstructive pneumonitis. A peripherally located tumor is commonly seen as a sharply marginated, oval, or lobulated intraluminal or exophytic mass.[60,67-70] Associated stippled calcification is seen in up to 30% of carcinoid tumors. CT is particularly helpful for detecting and defining the extrabronchial portion of the tumor and associated adenopathy.

***Treatment and Follow-up.*** The current treatment of choice is surgical resection.[71] Chemotherapy and radiotherapy are reserved for tumors with incomplete surgical resection. Overall survival rate for carcinoid and mucoepidermoid carcinoma is approximately 90%, whereas adenoid cystic carcinoma has a poorer survival rate of 55% because of higher likelihood of distant metastases.[72]

## Bronchogenic Carcinoma

***Etiology.*** Traditionally, the term *bronchogenic carcinoma* has been used to include both small cell and non–small cell lung cancers

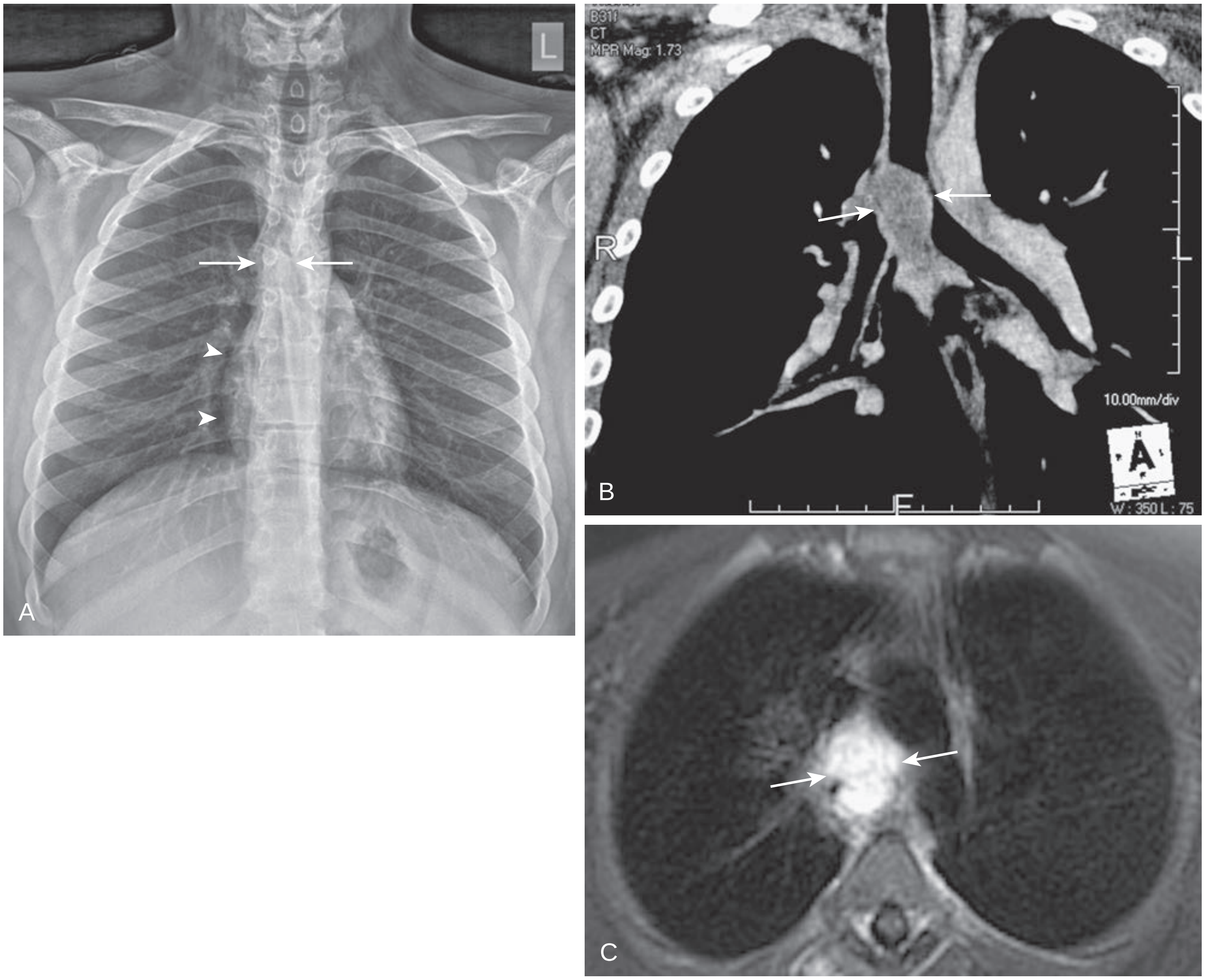

**Figure 55.11. Adenoid cystic carcinoma.** A 14-year-old boy with progressively worsening chronic cough and respiratory difficulty for 1 year who presented with hoarseness and crepitus over the neck. (A) Chest radiograph shows pneumomediastinum *(arrowheads)* and an apparent soft tissue density projecting over the carina *(arrows).* (B) A coronal contrast-enhanced CT image shows a lobulated soft tissue mass *(arrows)* centered near the carina, which results in narrowing of the adjacent airway. (C) Axial contrast-enhanced T1-weighted MRI demonstrates avid enhancement of the mass *(arrows).*

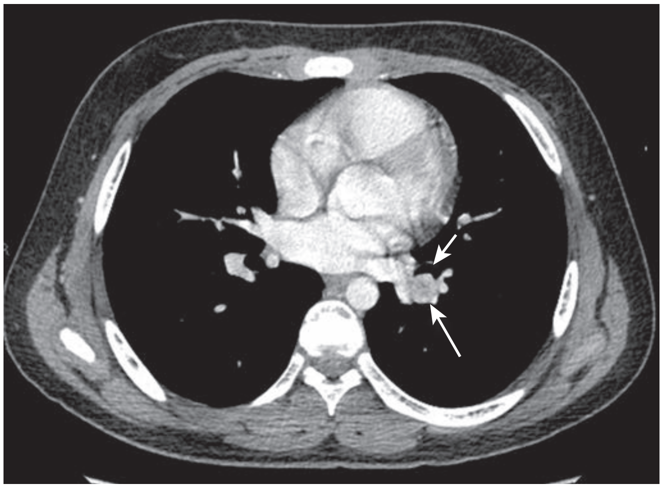

**e-Figure 55.9. Mucoepidermoid carcinoma.** A 9-year-old boy presenting with hemoptysis. Axial contrast-enhanced CT image shows a lobulated soft tissue mass *(long arrow)* centered at the left hilum, which protrudes into the adjacent airway *(short arrow).* CT virtual bronchoscopy demonstrates the protruding mass lesion over the posterior wall of the left main bronchus.

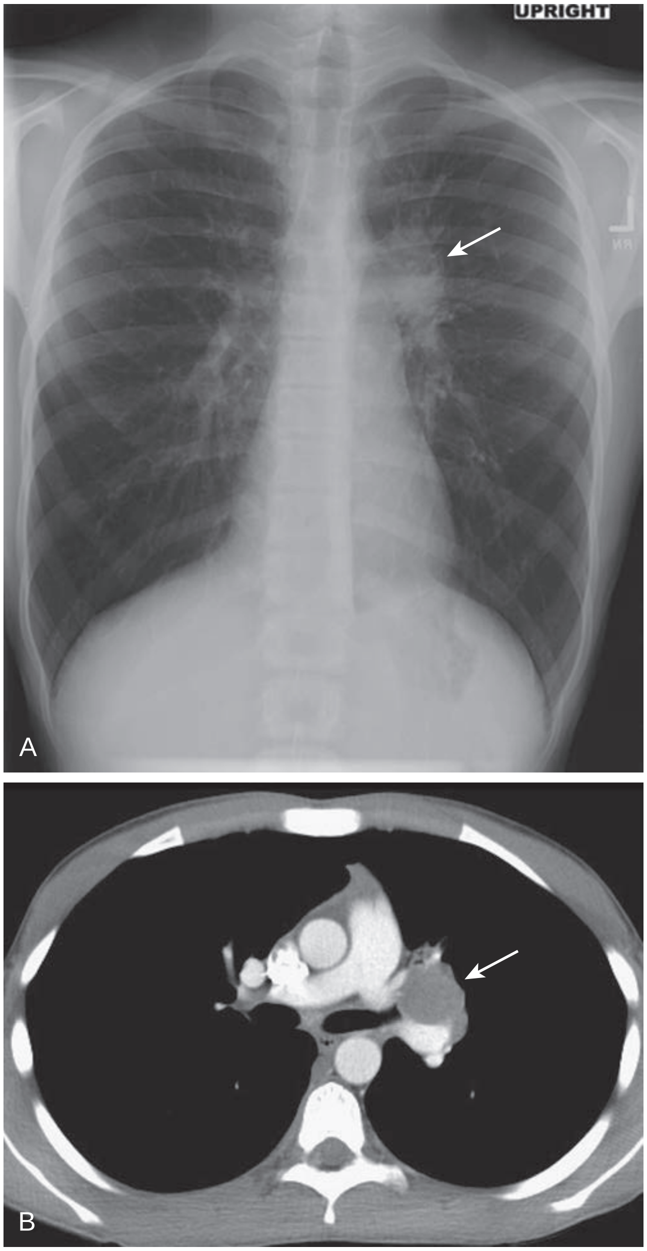

**e-Figure 55.10. Endobronchial mucoepidermoid carcinoma.** A 14-year-old boy presented with cough and fever that had lasted for 1 month. (A) Chest radiograph shows a left hilar mass *(arrow).* (B) Axial contrast-enhanced CT image demonstrates a well-circumscribed, heterogeneously enhancing mass within the left main-stem bronchus *(arrow).* Surgical pathology was consistent with endobronchial mucoepidermoid carcinoma.

(including squamous cell carcinoma, large cell carcinoma, and adenocarcinoma). These tumors are very rare in childhood. In the most recent WHO classification guideline, the term *bronchogenic carcinoma* is not used and each tumor type is listed individually.[50] Among these tumors, adenocarcinoma is the most common in children.[64] Most children with adenocarcinoma present with advanced disease, which results in high mortality rates. Small cell carcinoma, squamous cell carcinoma, and large cell carcinoma are very rare in children.[4,73]

***Imaging.*** On chest radiography, these tumors often present as a solitary pulmonary nodule or central mass, often associated with postobstructive atelectasis or consolidation (e-Fig. 55.12). On CT, the attenuation and enhancement of masses vary substantially among different types of tumors. Concomitant mediastinal or hilar adenopathy, as well as malignant pleural effusion, may also be present. Aggressive tumors may also invade adjacent mediastinal or osseous structures.

***Treatment and Follow-up.*** Surgical resection often combined with subsequent chemotherapy and radiotherapy is the current management of choice. Unfortunately, bronchogenic carcinoma of childhood has been known for its unusually rapid disease course with early metastases.

## Pleuropulmonary Blastoma

***Etiology.*** Pleuropulmonary blastoma (PPB) is an embryonal tumor of the lung; over 90% of affected patients are below 6 years old at diagnosis. It recapitulates the morphogenesis of the fetal lung and may be regarded as a dysontogenetic analog to Wilms tumor, neuroblastoma, and hepatoblastoma. PPB contains primitive mesenchyma and varying degrees of more mature cartilage, skeletal and smooth muscle, and fibrous tissue. A germline mutation in *DICER1* is the genetic cause in the majority of PPB cases, leaving patients at risk for other tumors.[74,75] The three PPB types are (1) type I (purely cystic with primitive mesenchymal cells beneath an intact epithelium), (2) type II (cystic and solid, mesenchymal cells overgrow the septa), and (3) type III (purely solid, complex sarcomatous neoplasm). Cystic type I PPB has a better prognosis than type II, and type II has a better outcome than type III.[75-77] It has been suggested that PPB is probably the same malignant tumor that has been reported in previous studies as mesenchymal sarcoma, malignant mesenchymoma, embryonal sarcoma, primary pulmonary rhabdomyosarcoma, primary pulmonary rhabdomyosarcoma arising in congenital lung cysts, or pulmonary blastoma in children.[78,79] Current data support the assertion that congenital lung cysts do not degenerate to become PPB but that cystic type I PPB may progress to more aggressive type II or type III PPB.[80-84] PPB may metastasize to the central nervous system, bone, and liver.

***Imaging.*** Imaging appearances of PPB depend on the type. PPBs present as solid, cystic, or mixed lesions. On chest radiography, the tumor may appear as a nodule or small mass that rapidly grows or as a large mass occupying the hemithorax. A large PPB may often result in mass effect on mediastinal structures. On CT, type I PPB is typically a cystic lesion often associated with multiple septations (Fig. 55.13), whereas type III PPB is a heterogeneously enhancing solid mass (Fig. 55.14). Type II PPB has a combination of both cystic and solid components (e-Fig. 55.15). Type I PPB is often indistinguishable from CPAM on the basis of radiologic evaluation.[85] Approximately 25% of patients with PPB have other embryonal tumors, most commonly renal cystic nephroma.[86-88]

***Treatment and Follow-up.*** The current treatment of choice for PPB is lobectomy or pneumonectomy.[89] Chemotherapy and local radiotherapy are adjuvant therapies if residual disease is present. Surveillance of *DICER1* mutation carriers may allow the earlier detection of cystic PPB before its progression to type II or III PPB and thereby improve outcomes.[75]

## Epithelioid Hemangioendothelioma

***Etiology.*** Pulmonary epithelioid hemangioendothelioma (PEH) is a rare tumor arising from endothelium with borderline malignant potential. PEH was first described by Dail and Liebow in 1975 as an intravascular bronchoalveolar tumor that may affect bone, soft tissue, liver, and lung. Later studies revealed that intravascular bronchoalveolar tumor and PEH are different manifestations of the same disease.[90,91] Although most of the affected patients are adult women, it may also occur in children.[92] The majority of patients are asymptomatic, and lesions are typically detected incidentally.[93]

***Imaging.*** On chest radiography, PEH typically presents as bilateral multiple pulmonary nodules ranging from 5 mm to 2 cm in diameter. Some patients may present with a solitary lesion

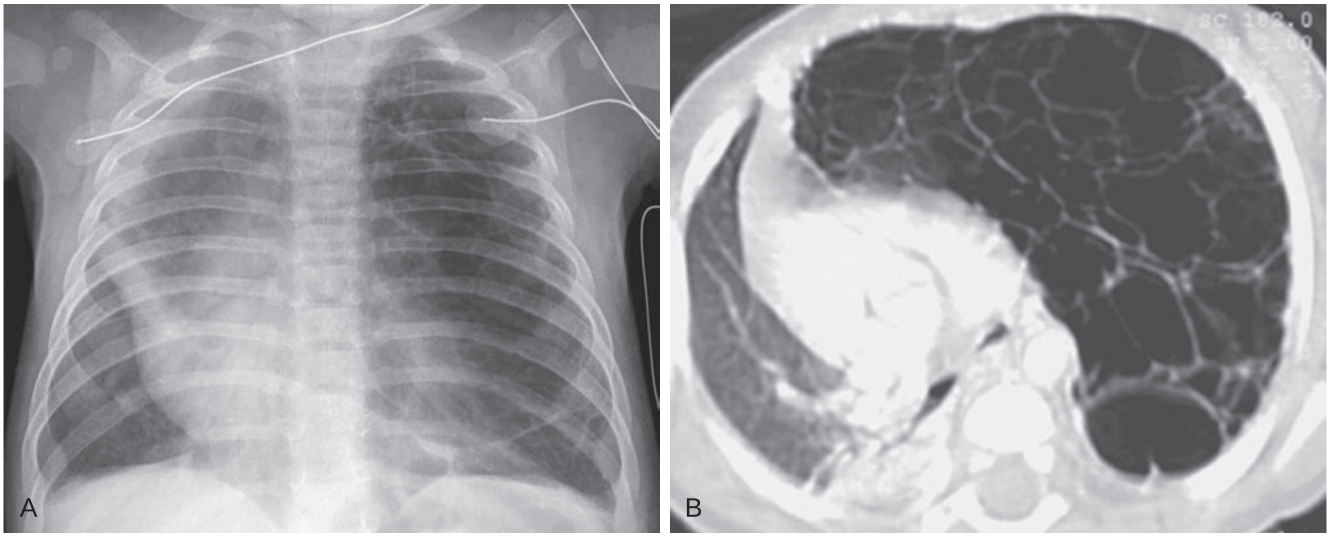

**Figure 55.13. Type 1 Cystic pleuropulmonary blastoma.** A 4-month-old boy with worsening respiratory distress. (A) Chest radiograph demonstrates a large radiolucent lesion with fine septations and multiple cysts within the left lung resulting in mediastinal shift. (B) Axial lung window CT image shows multiple cysts of varying sizes with mass effect on the mediastinum and contralateral right lung.

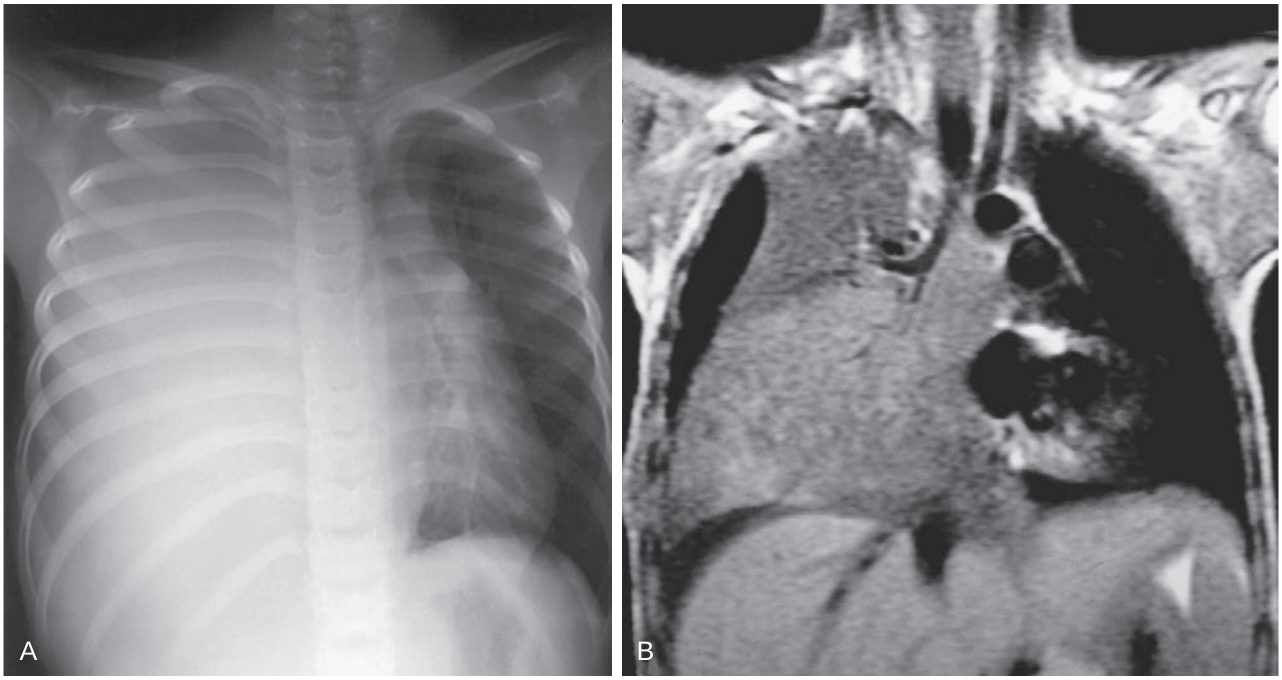

**e-Figure 55.12. Bronchogenic carcinoma.** A 7-year-old girl with cough. (A) Chest radiograph demonstrates a large mass occupying the right hemithorax, with contralateral mediastinal shift. (B) Coronal T1-weighted MRI shows a large right-sided mass encasing the bronchus, abutting the thymus, and extending into the mediastinum. Pathology identified the mass as squamous cell carcinoma.

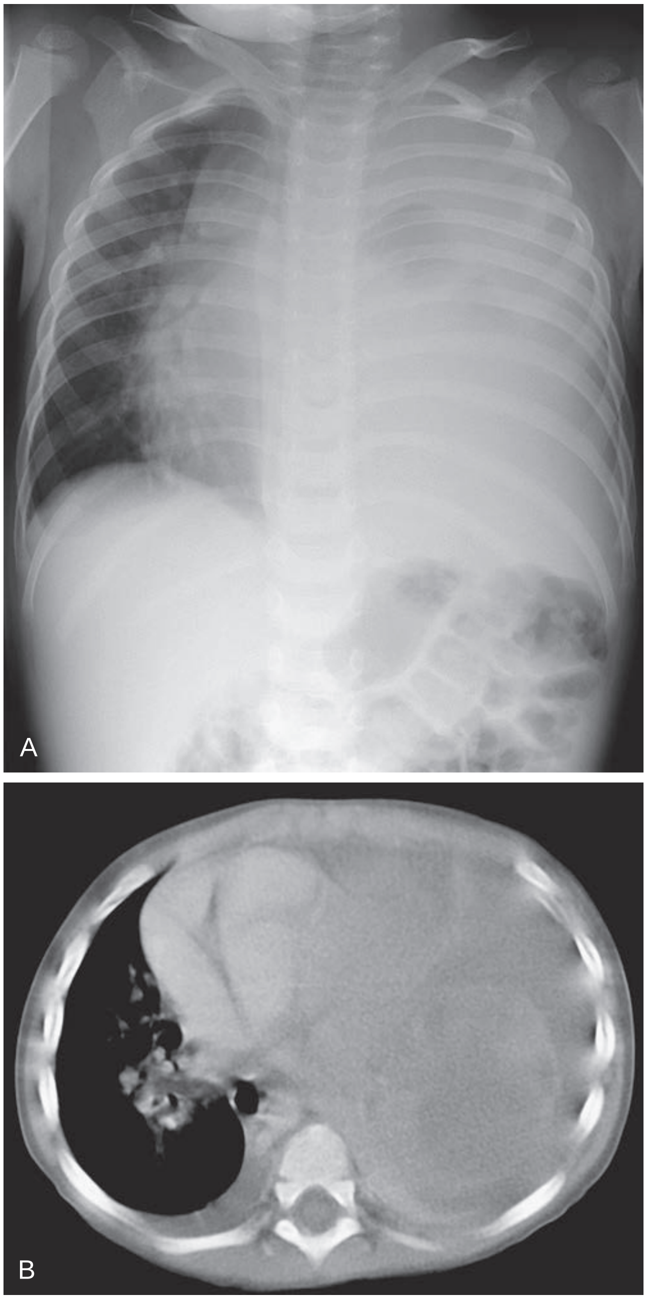

**e-Figure 55.15. Type II mixed cystic and solid pleuropulmonary blastoma in a 2-year-old boy.** (A) Chest radiograph shows a completely opacified left hemithorax with mass effect producing a rightward cardiomediastinal shift. (B) Axial contrast-enhanced CT image demonstrates bilateral pleural effusion and a large, left-sided, predominantly solid, pulmonary and mediastinal heterogeneously enhancing mass.

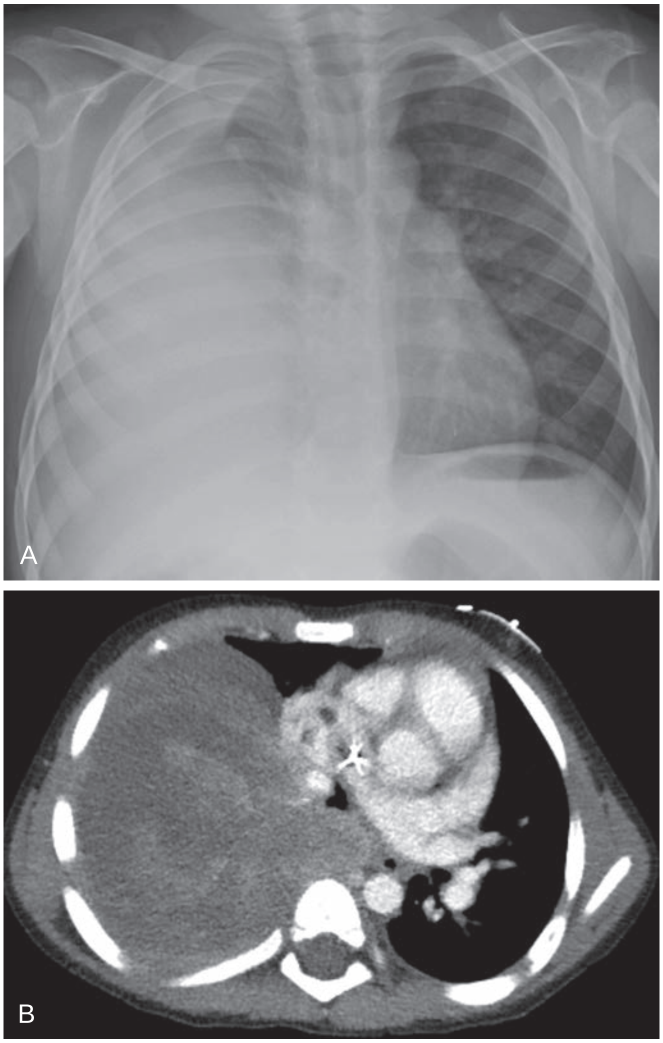

**Figure 55.14. Type III solid pleuropulmonary blastoma.** A 3-year-old boy presenting with tachypnea. (A) Chest radiograph shows near complete opacification of the right hemithorax. (B) An axial contrast-enhanced CT image reveals a large, solid, heterogeneously enhancing mass resulting in leftward mediastinal shift.

(e-Fig. 55.16). Concomitant hilar adenopathy and pleural effusion are seen in less than 10% of cases.[94] On CT, multiple well-defined or ill-defined perivascular nodules located near medium-sized vessels and bronchi are usually seen. Some pulmonary nodules may show calcification.[95,96]

***Treatment and Follow-up.*** Surgical resection is preferred in patients with solitary or a limited number of pulmonary lesions localized within one lobe. Chemotherapy, radiotherapy, and interferon are other treatment choices that are associated with variable results.[97] Close follow-up with no active therapy is usually used for asymptomatic patients with multiple lesions.[93] Recently, vascular endothelium growth factor was proposed as a potential treatment for PEH.

## Primary Malignant Lymphoproliferative Disorder

Primary pulmonary lymphomas are exceedingly rare and represent only 0.5% of all primary lung neoplasms. Malignant forms of lymphoproliferative disorder that, albeit rare, occasionally present with primary lung involvement include (1) extranodal marginal zone lymphoma of MALT origin (MALT lymphoma), (2) diffuse large B-cell lymphoma (DLBCL), and (3) lymphomatoid granulomatosis (LYG). The classification and imaging characteristics of lymphoproliferative disorders involving the lungs are listed in Table 55.2.

***Etiology.*** MALT lymphoma is a form of extranodal marginal zone B-cell lymphoma of MALT origin, characterized by an interstitial infiltrate of small lymphocytes forming a mass-like lesion. MALT lymphomas are frequently associated with autoimmune diseases. DLBCL presents as sheets of medium to large atypical lymphocytes forming a solid lesion. It is characteristically found in immunocompromised patients such as those with transplant or taking cyclosporine. LYG is a rare EBV-associated lymphoproliferative disorder with a propensity for blood vessel destruction, previously considered to be a form of necrotizing vasculitis.[98] The current consensus is that LYG is a distinctive polymorphic form of angiocentric lymphoma[99] with a predilection for extranodal involvement, most frequently of the lung, with a very poor prognosis.[98]

***Imaging.*** On CT, MALT lymphoma usually presents with single or multiple nodules or areas of consolidation of peribronchovascular distribution. Bronchial dilation is common, and mediastinal lymphadenopathy is present in around 30% of cases. DLBCL usually presents as single or multiple solid pulmonary nodules or masses. Cavitation occurs in about 50%.

For LYG, the most common radiographic features are bilateral, poorly defined lung nodules with a basilar predominance (e-Fig. 55.17). The lesions can progress rapidly, coalesce, and commonly cavitate, therefore mimicking Wegener granulomatosis or metastases. Characteristic CT findings of LYG include peribronchovascular distribution of nodules, small thin-walled cysts, and conglomerate small nodules.[29,100]

***Treatment and Follow-up.*** Treatment of MALT lymphoma is usually with chemotherapy or immunotherapy (rituximab).[101] The prognosis of MALT lymphoma is usually good,[102-104] but it tends to recur in the lung and may be complicated by DLBCL.[105] LYG may be resistant to ordinary chemotherapy. Rituximab, combined with other conventional chemotherapy, has been used with promising results.[106-108]

## SECONDARY MALIGNANT CONDITIONS

Secondary malignant conditions of the lungs may be caused by metastatic disease or from systemic diseases such as leukemia or lymphoma. Metastatic disease is by far the most common cause of pulmonary malignancy in childhood. Metastatic tumors accounts for approximately 80% of all lung tumors in children.[2] Osteogenic sarcoma and Wilms tumor are the most common tumors with pulmonary metastasis in children.

### Metastases

***Etiology.*** Pulmonary metastatic disease most often occurs hematogenously via the pulmonary arterial system. However, it may also occur via lymphatics, airways, or direct invasion.

***Imaging.*** On imaging studies, most metastatic lesions are seen as round and sharply marginated and of homogeneous soft tissue attenuation. They tend to be located subpleurally in the outer two-thirds of the lung. Metastatic lesions often appear to be directly contiguous with a pulmonary artery branch, reflecting their hematogenous origin. A greater number of metastatic lesions are located at the lung bases rather than in the upper lobes, likely because of gravity-dependent increased basilar blood flow. Lymphangitic tumors usually present as reticular or reticulonodular opacities on chest radiography. Thickening of interlobular or interlobar septa and bronchovascular bundles are often seen on CT of children with lymphangitic tumor spread.

CT is sensitive but not specific in detecting pulmonary metastasis. No specific CT features (e.g., location, attenuation, size,

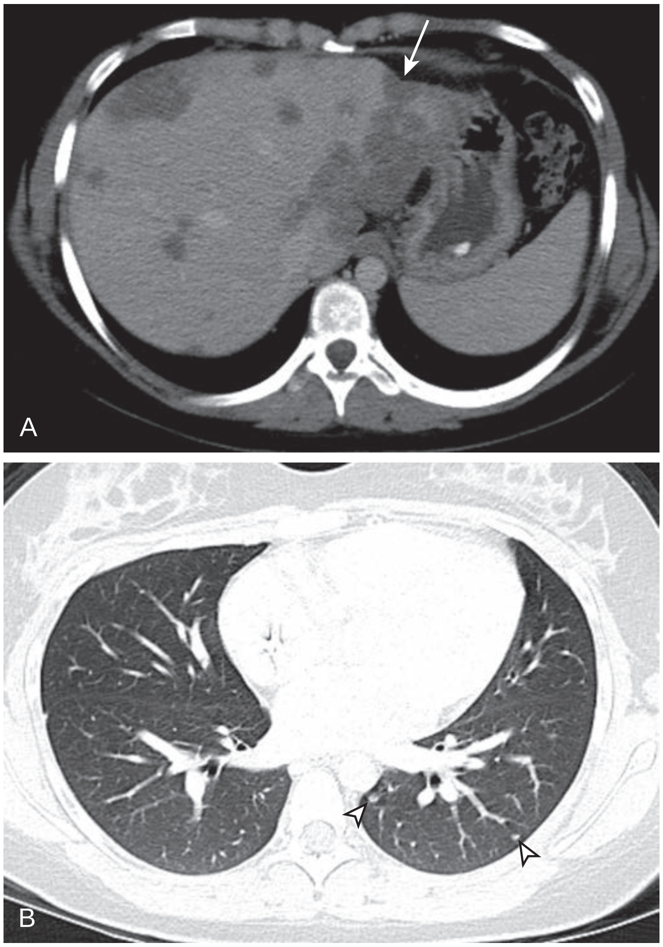

**e-Figure 55.16. Epithelioid hemangioendothelioma.** 13-year-old girl with a history of hepatic epithelioid hemangioendothelioma. (A) Axial enhanced computed tomography image shows numerous hypoattenuating lesions. In the left lobe the lesions coalesce to form a larger confluent mass in a peripheral distribution with capsular retraction *(arrow).* (B) Axial lung window CT image shows two small, subcentimeter noncalcified parenchymal nodules *(arrowheads)* in the left lung.

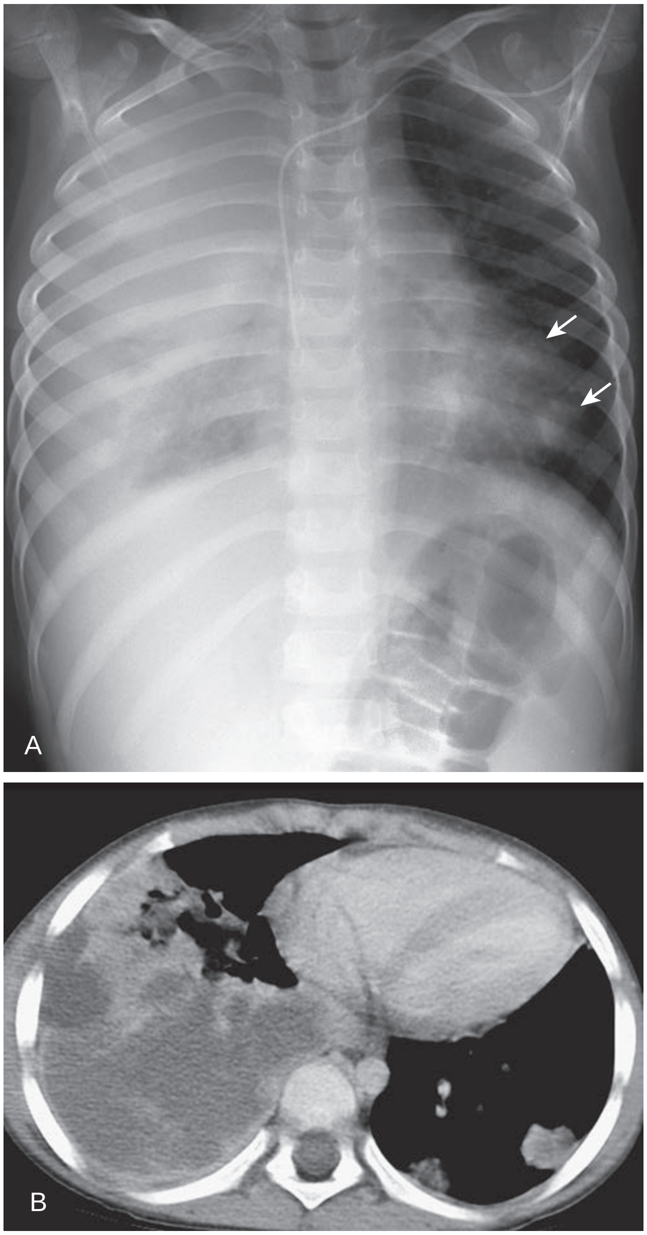

**e-Figure 55.17. Lymphomatoid granulomatosis type III (form of B-cell lymphoma).** A 5-year-old boy with severe combined immunodeficiency who presented with cough and shortness of breath. (A) Chest radiograph demonstrates marked opacity of the right lung and cardiomediastinal shift to the left, with multiple left-sided nodules *(arrows).* (B) Axial contrast-enhanced CT image shows multiple left-sided cavitating nodules in addition to a large heterogeneous, predominantly low-attenuation, and confluent density within the right lung.

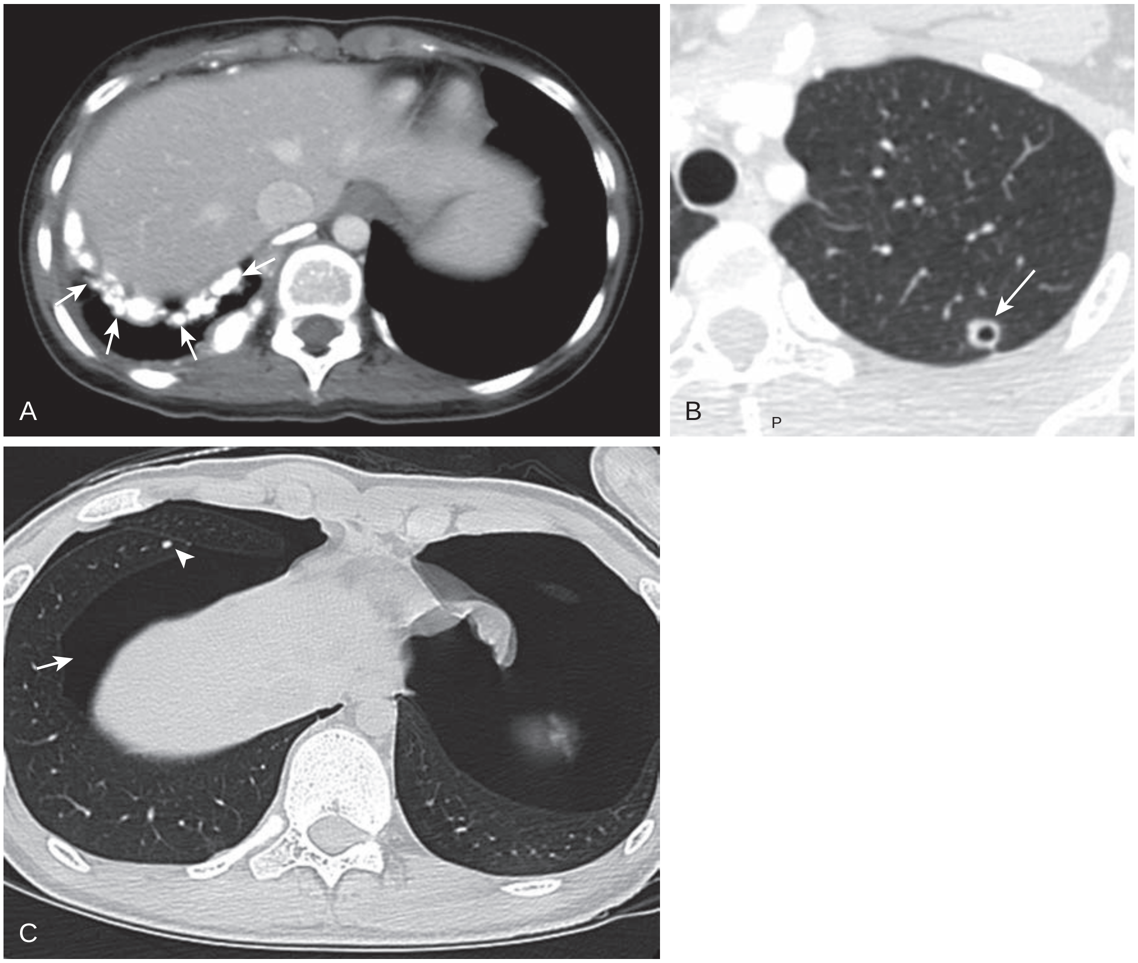

**Figure 55.18. Pulmonary metastases from osteosarcoma.** (A) Axial contrast-enhanced CT image of a 14-year old boy shows numerous calcified nodules of varying sizes, predominantly present at the subpleural lung base *(arrows).* (B) Axial lung window CT image of a 12-year old girl shows a cavitary subpleural nodule *(arrow)* in the left upper lobe. (C) Axial lung window CT image of a 16-year-old boy shows a small metastatic lung nodule *(arrowhead)* associated with a small pneumothorax *(arrow)* at lung base.

margin characteristics) can reliably distinguish benign lesions from malignant pulmonary lesions. However, in general, pulmonary lesions larger than 5 mm in diameter with sharp margins, especially when multiple, are usually malignant.[109] Pulmonary nodules that decrease in size during antineoplastic therapy are usually assumed to be malignant, whereas those that decrease in size without therapy or remain stable during 12 months of follow-up are likely benign.

Although the imaging appearances of the majority of metastatic pulmonary nodules are nonspecific, some primary tumors may produce characteristic pulmonary metastases. Metastatic osteosarcoma may ossify (Fig. 55.18A), cavitate (Fig. 55.18B), or present with pneumothorax (Fig. 55.18C). Lymphangitic spread is most commonly seen in children with rhabdomyosarcoma, neuroblastoma, and lymphoma.

***Treatment and Follow-up.*** Pulmonary metastases have been reported in 10% to 20% of patients with osteogenic sarcoma at initial diagnosis. Approximately 40% to 55% of patients with nonmetastatic osteosarcoma develop lung metastases in the later stages of the disease.[110-114] Number, distribution, and timing, but not the size, of lung metastases are of prognostic value for survival.[115,116] The best treatment for this group of patients is a combination of metastasectomy and adjuvant chemotherapy.[117,118]

The lung is the most common site of metastatic disease in children with Wilms tumor. Traditionally, treatment strategy for metastatic Wilms tumor had been based on lung lesions detectable with chest radiography. Currently, controversy exists over the optimal way for managing small pulmonary lesions that are detected only with CT and are not apparent on chest radiography because of the potential lung toxicity associated with aggressive therapy.[119] Previous studies[120,121] suggested that the majority of these pulmonary lesions represent metastases, and patients with these lesions probably require more aggressive chemotherapy than those children without metastatic disease.[122]

## Leukemia

***Etiology.*** Approximately 20% to 60% of patients with leukemia have histologic evidence of lung involvement at autopsy, but fewer than 5% of these patients present with lung abnormality suggesting leukemic infiltrates on chest radiography.[123] Pulmonary involvement of leukemia is most often seen in patients with acute monocytic and myelogenous leukemia.[124]

***Imaging.*** On chest radiography, leukemic infiltrates usually show a diffuse reticular pattern of opacities (e-Fig. 55.19). Pulmonary nodules and focal homogeneous opacities are also reported in patients with leukemic involvement of lungs. On CT, interstitial thickening in a peribronchial distribution, small pulmonary nodules in a centrilobular or peribronchovascular

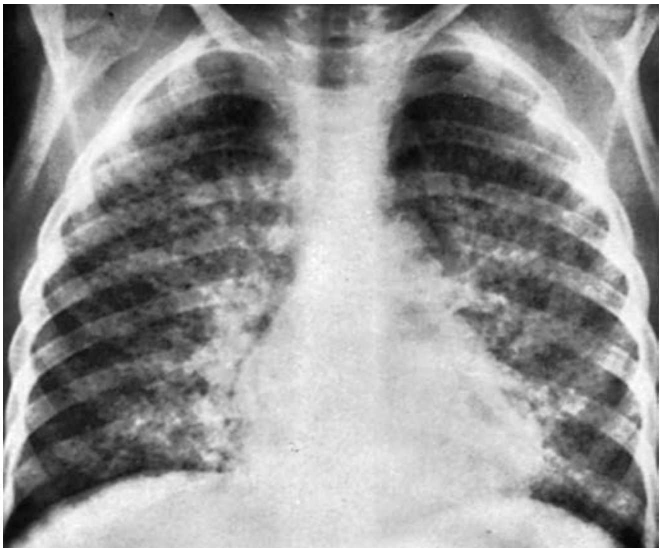

**e-Figure 55.19. Pulmonary leukemia.** A 7-year-old boy with biopsy-proven leukemia of the lungs. Chest radiograph shows a reticulonodular pattern of with central confluence. Relative sparing of the apices and the lateral segments of both lungs is evident. No radiographic evidence for adenopathy is present.

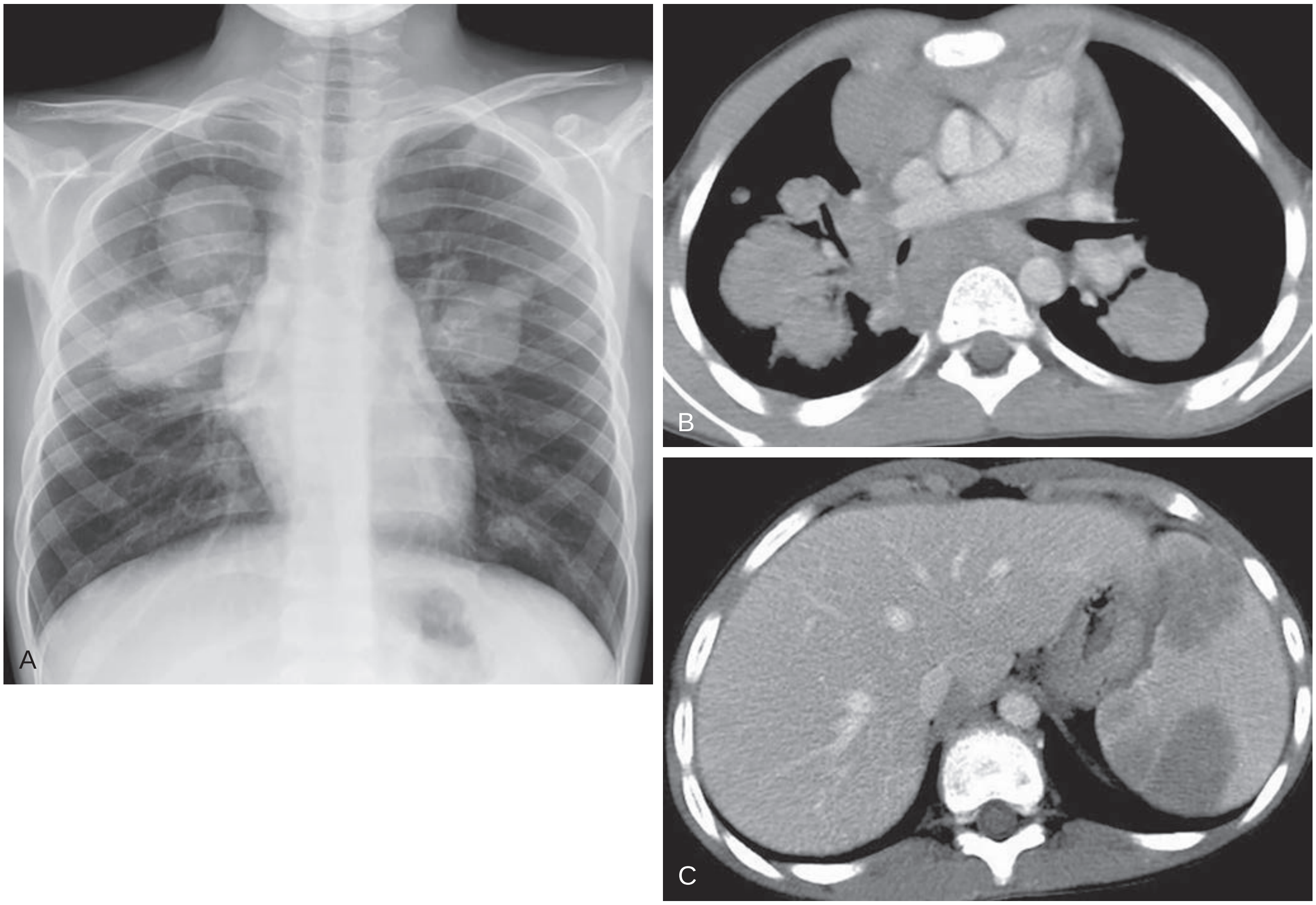

**Figure 55.20. Hodgkin lymphoma.** A 13-year-old boy who presented with cough that had lasted for 6 months. (A) Chest radiograph shows several pulmonary masses in both lungs of varying sizes predominantly in central location. (B) Axial contrast-enhanced CT image demonstrates several, bilateral pulmonary masses of soft tissue density and varying sizes in addition to anterior and posterior mediastinal lymphadenopathy. (C) Axial contrast-enhanced CT image of the upper abdomen shows several hypodense lesions in the spleen likely representing splenic involvement of lymphoma.

distribution, and focal areas of consolidation are common imaging findings.[125,126]

***Treatment and Follow-up.*** Lung biopsy is required for a definitive diagnosis of lung involvement from leukemia. Once the diagnosis is established, multiagent chemotherapy is currently the treatment of choice in pediatric patients with pulmonary leukemic involvement.[127-129]

## Lymphoma

Secondary lymphomatous parenchymal neoplasms are far more prevalent than primary pulmonary lymphoma.[130]

***Etiology.*** Pulmonary parenchymal disease is more prevalent in pediatric lymphoma than that in adults, which is around 12% in Hodgkin disease (HD) and 10% in non-Hodgkin lymphoma (NHL).[131] Lung involvement is almost always seen at initial presentation rather than at disease relapse.[131] In both HD and NHL, the underlying mechanisms of lung involvement are hematogenous spread, lymphangitic dissemination, and, less frequently, direct invasion.

***Imaging.*** Lung involvement of lymphoma in pediatric patients typically presents as one of three patterns[132]: (1) nodular—single or multiple pulmonary nodules with irregular borders and sometimes central cavitation, which is the most common radiographic pattern (Fig. 55.20 and e-Fig. 55.21); (2) lymphangitic—reticular interstitial opacities, which result from venous or lymphatic obstruction caused by hilar or mediastinal adenopathy or from interstitial tumor deposition; and (3) alveolar—lobar or segmental consolidation, which may mimic an infectious process.[133-136] Occasionally, multiple tiny pulmonary nodules in a miliary pattern in children with HD may simulate miliary tuberculosis.[137,138] Pleural effusion is found in less than 5% of children with lymphoma.

Although the imaging appearance of lung involvement in children with HD and NHL is similar on imaging studies, lung involvement is usually concomitantly present with mediastinal or hilar lymphadenopathy in children with HD, whereas lung involvement may occur without associated lymphadenopathy in NHL.[133,139]

***Treatment and Follow-up.*** Chemotherapy is the current treatment of choice. Although infection is more common in pediatric lymphoma patients, especially those undergoing treatment, development of new pulmonary lesions with a poor response to antibiotics may represent lymphoma lesions and therefore should promptly be biopsied for a definitive diagnosis. Pulmonary lesions from lymphoma usually decrease in size, disappear, or leave a parenchymal scar after chemotherapy treatment.[101,140]

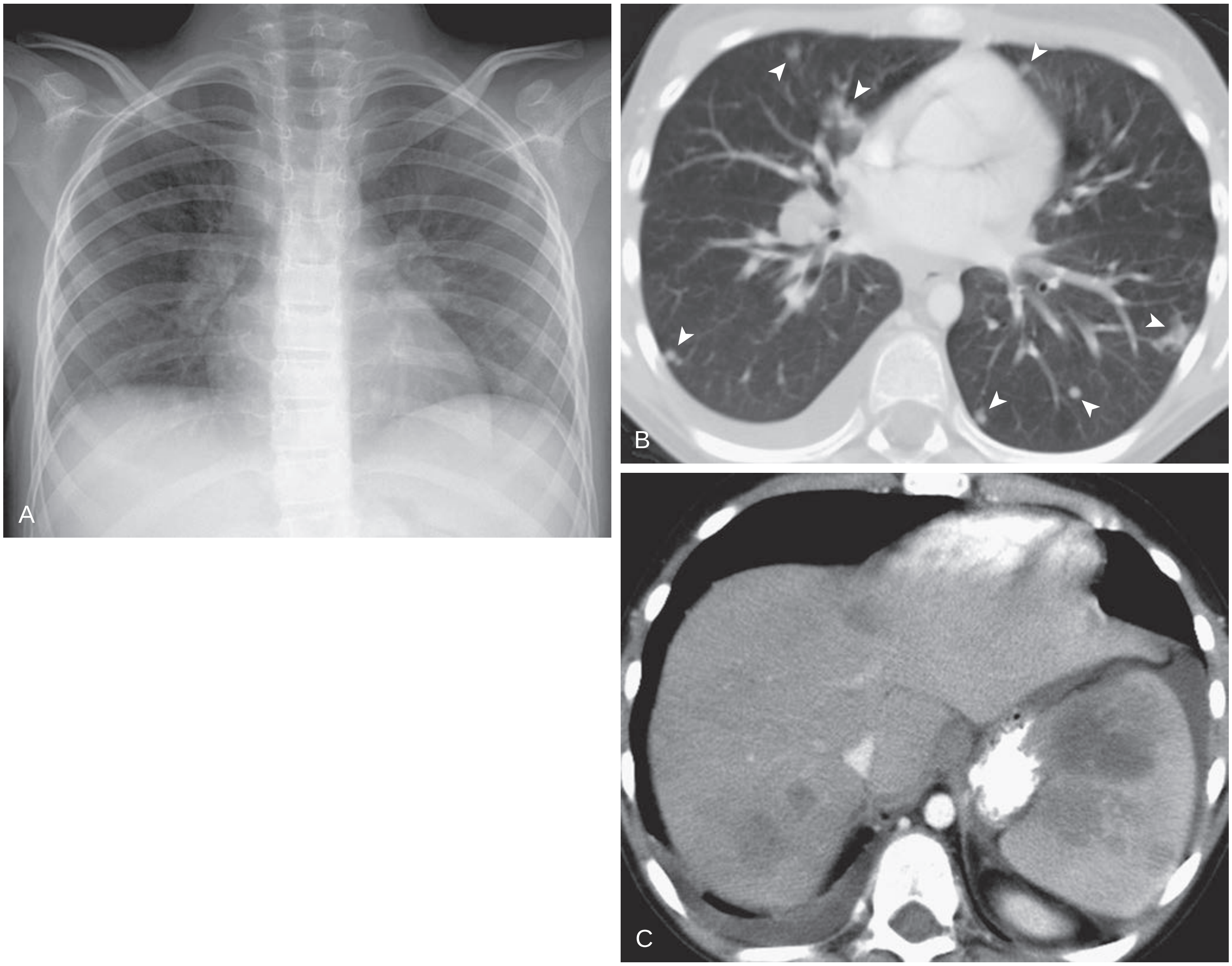

**e-Figure 55.21. Hodgkin lymphoma.** A 12-year-old boy with a history of ataxia telangiectasia, who presented with fevers and intermittent dry cough. He had daily fever with a maximum temperature of 104°F, worse at night, and associated with night sweats. (A) Chest radiograph shows mediastinal and hilar lymphadenopathy. (B) Axial lung window CT image demonstrates multiple, small, bilateral, ill-defined pulmonary nodules *(arrowheads)* and a small right pleural effusion in addition to lymphadenopathy. (C) Axial contrast-enhanced CT image shows numerous low-attenuation lesions in the liver and spleen. Biopsy samples from his liver and pleural fluid confirmed the diagnosis of Hodgkin lymphoma.

## KEY POINTS

- Benign pulmonary neoplasms in children are far less common than malignant lesions. The ratio of primary benign to primary malignant to secondary malignant neoplasms is 1.4 : 1 : 11.6.
- Lymphoproliferative disease is common in immunocompromised children. CT features range from pseudotumor, nodules, reticular interstitial pattern, to cysts. Definitive diagnosis relies on tissue biopsy.
- Metastatic disease is, by far, the most common cause of pulmonary malignancy in childhood. The most frequent causes are osteogenic sarcoma and Wilms tumor.
- Secondary pulmonary involvement in systemic diseases such as leukemia or lymphoma is relatively uncommon in children. CT features are nonspecific and include nodules, reticular interstitial pattern, and consolidation, which mimic infectious lung changes. Lung biopsy is required for definitive diagnosis.

## SUGGESTED READINGS

Dishop MK, Kuruvilla S. Primary and metastatic lung tumors in the pediatric population: a review and 25-year experience at a large children's hospital. *Arch Pathol Lab Med*. 2008;132(7):1079–1103.

Hare SS, Souza CA, Bain G, et al. The radiological spectrum of pulmonary lymphoproliferative disease. *Br J Radiol*. 2012;85(1015):848–864.

Lim GY, Newman B, Kurland G, et al. Posttransplantation lymphoproliferative disorder: manifestations in pediatric thoracic organ recipients. *Radiology*. 2002;222(3):699–708.

Maturen KE, Blane CE, Strouse PJ, et al. Pulmonary involvement in pediatric lymphoma. *Pediatr Radiol*. 2004;34(2):120–124.

McCahon E. Lung tumours in children. *Paediatr Respir Rev*. 2006;7(3): 191–196.

Sirajuddin A, Raparia K, Lewis VA, et al. Primary pulmonary lymphoid lesions: radiologic and pathologic findings. *Radiographics*. 2016;36(1): 53–70.

Yikilmaz A, Lee EY. CT imaging of mass-like nonvascular pulmonary lesions in children. *Pediatr Radiol*. 2007;37(12):1253–1263.

## REFERENCES

Full references for this chapter can be found on www.expertconsult.com.

## REFERENCES

1. McCahon E. Lung tumours in children. *Paediatr Respir Rev*. 2006;7(3):191–196.
2. Dishop MK, Kuruvilla S. Primary and metastatic lung tumors in the pediatric population: a review and 25-year experience at a large children's hospital. *Arch Pathol Lab Med*. 2008;132(7):1079–1103.
3. Weldon CB, Shamberger RC. Pediatric pulmonary tumors: primary and metastatic. *Semin Pediatr Surg*. 2008;17(1):17–29.
4. Yu DC, Grabowski MJ, Kozakewich HP, et al. Primary lung tumors in children and adolescents: a 90-year experience. *J Pediatr Surg*. 2010;45(6):1090–1095.
5. Gjevre JA, Myers JL, Prakash UB. Pulmonary hamartomas. *Mayo Clin Proc*. 1996;71(1):14–20.
6. Siegelman SS, Khouri NF, Scott WW Jr, et al. Pulmonary hamartoma: CT findings. *Radiology*. 1986;160(2):313–317.
7. Fudge TL, Ochsner JL, Mills NL. Clinical spectrum of pulmonary hamartomas. *Ann Thorac Surg*. 1980;30(1):36–39.
8. Rodriguez FJ, Aubry MC, Tazelaar HD, et al. Pulmonary chondroma: a tumor associated with Carney triad and different from pulmonary hamartoma. *Am J Surg Pathol*. 2007;31(12):1844–1853.
9. Carney JA. Endocrine tumor syndromes and their genetics. In: Stratakis CA, ed. *Frontiers of Hormone Research*. Vol. 41. Basel: Karger; 2013:92–110.
10. Soldatski IL, Onufrieva EK, Steklov AM, et al. Tracheal, bronchial, and pulmonary papillomatosis in children. *Laryngoscope*. 2005;115(10):1848–1854.
11. Szyszko T, Gnanasegaran G, Barwick T, et al. Respiratory papillomatosis of lung and F-18 FDG PET-CT. *Clin Nucl Med*. 2009;34(8):521–522.
12. Kramer SS, Wehunt WD, Stocker JT, et al. Pulmonary manifestations of juvenile laryngotracheal papillomatosis. *AJR Am J Roentgenol*. 1985;144(4):687–694.
13. McKay SP, Shinhar SY, Belenky WM. Pulmonary involvement in a case of juvenile-onset recurrent respiratory papillomatosis. *Ear Nose Throat J*. 2003;82(6):447–449.
14. Novakovic D, Cheng AT, Baguley K, et al. Juvenile recurrent respiratory papillomatosis: 10-year audit and Australian prevalence estimates. *Laryngoscope*. 2016.
15. Scott KJ, Greinwald JH Jr, Darrow D, et al. Endobronchial tumors in children: an uncommon clinical entity. *Ann Otol Rhinol Laryngol*. 2001;110(1):63–69.
16. Gelinas JF, Manoukian J, Cote A. Lung involvement in juvenile onset recurrent respiratory papillomatosis: a systematic review of the literature. *Int J Pediatr Otorhinolaryngol*. 2008;72(4):433–452.
17. Wangu Z, Hsu KK. Impact of HPV vaccination on anogenital warts and respiratory papillomatosis. *Hum Vaccin Immunother*. 2016;12(6):1357–1362.
18. Ernemann U, Kramer U, Miller S, et al. Current concepts in the classification, diagnosis and treatment of vascular anomalies. *Eur J Radiol*. 2010;75(1):2–11.
19. Niu ZB. The "lymphangioma": an incorrect and outdated term. *Pediatr Emerg Care*. 2011;27(8):788.
20. Faul JL, Berry GJ, Colby TV, et al. Thoracic lymphangiomas, lymphangiectasis, lymphangiomatosis, and lymphatic dysplasia syndrome. *Am J Respir Crit Care Med*. 2000;161(3 Pt 1):1037–1046.
21. Minato H, Kaji S, Kinoshita E, et al. Solitary intrapulmonary cystic lymphangioma in an infant: a case report with literature review. *Pathol Res Pract*. 2010;206(12):851–856.
22. Green NA, Diaz MC. Pulmonary lymphangioma in a 14-month-old. *Pediatr Emerg Care*. 2011;27(1):52–54.
23. Arbell D, Koplewitz BZ, Udassin R. Anterior mediastinal cystic lesion: excise rather than delay. *Isr Med Assoc J*. 2007;9(8):622–623.
24. Hare SS, Souza CA, Bain G, et al. The radiological spectrum of pulmonary lymphoproliferative disease. *Br J Radiol*. 2012;85(1015):848–864.
25. Poletti V, Ravaglia C, Tomassetti S, et al. Lymphoproliferative lung disorders: clinicopathological aspects. *Eur Respir Rev*. 2013;22(130):427–436.
26. Guinee DG Jr. Update on nonneoplastic pulmonary lymphoproliferative disorders and related entities. *Arch Pathol Lab Med*. 2010;134(5):691–701.
27. Sirajuddin A, Raparia K, Lewis VA, et al. Primary pulmonary lymphoid lesions: radiologic and pathologic findings. *Radiographics*. 2016;36(1):53–70.
28. Varoczy L, Gergely L, Illes A. Diagnostics and treatment of pulmonary BALT lymphoma: a report on four cases. *Ann Hematol*. 2003;82(6):363–366.
29. Do KH, Lee JS, Seo JB, et al. Pulmonary parenchymal involvement of low-grade lymphoproliferative disorders. *J Comput Assist Tomogr*. 2005;29(6):825–830.
30. Swigris JJ, Berry GJ, Raffin TA, et al. Lymphoid interstitial pneumonia: a narrative review. *Chest*. 2002;122(6):2150–2164.
31. Teruya-Feldstein J, Kingma DW, Weiss A, et al. Chemokine gene expression and clonal analysis of B cells in tissues involved by lymphoid interstitial pneumonitis from HIV-infected pediatric patients. *Mod Pathol*. 2001;14(10):929–936.
32. Basgoz N, Preiksaitis JK. Post-transplant lymphoproliferative disorder. *Infect Dis Clin North Am*. 1995;9(4):901–923.
33. Newell KA, Alonso EM, Whitington PF, et al. Posttransplant lymphoproliferative disease in pediatric liver transplantation. Interplay between primary Epstein-Barr virus infection and immunosuppression. *Transplantation*. 1996;62(3):370–375.
34. Shroff R, Rees L. The post-transplant lymphoproliferative disorder—a literature review. *Pediatr Nephrol*. 2004;19(4):369–377.
35. Allen U, Hebert D, Moore D, et al. Epstein-Barr virus-related post-transplant lymphoproliferative disease in solid organ transplant recipients, 1988-97: a Canadian multi-centre experience. *Pediatr Transplant*. 2001;5(3):198–203.
36. Pickhardt PJ, Siegel MJ, Hayashi RJ, et al. Posttransplantation lymphoproliferative disorder in children: clinical, histopathologic, and imaging features. *Radiology*. 2000;217(1):16–25.
37. Montone KT, Litzky LA, Wurster A, et al. Analysis of Epstein-Barr virus-associated posttransplantation lymphoproliferative disorder after lung transplantation. *Surgery*. 1996;119(5):544–551.
38. Nalesnik MA, Makowka L, Starzl TE. The diagnosis and treatment of posttransplant lymphoproliferative disorders. *Curr Probl Surg*. 1988;25(6):367–472.
39. Borhani AA, Hosseinzadeh K, Almusa O, et al. Imaging of posttransplantation lymphoproliferative disorder after solid organ transplantation. *Radiographics*. 2009;29(4):981–1000, discussion 1000-1002.
40. Lim GY, Newman B, Kurland G, et al. Posttransplantation lymphoproliferative disorder: manifestations in pediatric thoracic organ recipients. *Radiology*. 2002;222(3):699–708.
41. Ohta H, Fukushima N, Ozono K. Pediatric post-transplant lymphoproliferative disorder after cardiac transplantation. *Int J Hematol*. 2009;90(2):127–136.
42. Harris KM, Schwartz ML, Slasky BS, et al. Posttransplantation cyclosporine-induced lymphoproliferative disorders: clinical and radiologic manifestations. *Radiology*. 1987;162(3):697–700.
43. Donnelly LF, Frush DP, Marshall KW, et al. Lymphoproliferative disorders: CT findings in immunocompromised children. *AJR Am J Roentgenol*. 1998;171(3):725–731.
44. Siegel MJ, Lee EY, Sweet SC, et al. CT of posttransplantation lymphoproliferative disorder in pediatric recipients of lung allograft. *AJR Am J Roentgenol*. 2003;181(4):1125–1131.
45. Carignan S, Staples CA, Muller NL. Intrathoracic lymphoproliferative disorders in the immunocompromised patient: CT findings. *Radiology*. 1995;197(1):53–58.
46. Scarsbrook AF, Warakaulle DR, Dattani M, et al. Post-transplantation lymphoproliferative disorder: the spectrum of imaging appearances. *Clin Radiol*. 2005;60(1):47–55.
47. McCormack L, Hany TI, Hubner M, et al. How useful is PET/CT imaging in the management of post-transplant lymphoproliferative disease after liver transplantation? *Am J Transplant*. 2006;6(7):1731–1736.
48. Dierickx D, Tousseyn T, De Wolf-Peeters C, et al. Management of posttransplant lymphoproliferative disorders following solid organ transplant: an update. *Leukemia & lymphoma*. 2011;52(6):950–961.
49. Taylor AL, Marcus R, Bradley JA. Post-transplant lymphoproliferative disorders (PTLD) after solid organ transplantation. *Crit Rev Oncol Hematol*. 2005;56(1):155–167.
50. Travis W. *Pathology and genetics of tumours of the lung, pleura, thymus and heart*. Paper presented at: In: World Health Organization, International Agency for Research on Cancer.2004; Lyon.
51. Neville HL, Hogan AR, Zhuge Y, et al. Incidence and outcomes of malignant pediatric lung neoplasms. *J Surg Res*. 2009;156(2):224–230.
52. Giuseppucci C, Reusmann A, Giubergia V, et al. Primary lung tumors in children: 24 years of experience at a referral center. *Pediatr Surg Int*. 2016;32(5):451–457.
53. Coffin CM, Watterson J, Priest JR, et al. Extrapulmonary inflammatory myofibroblastic tumor (inflammatory pseudotumor). A

clinicopathologic and immunohistochemical study of 84 cases. *Am J Surg Pathol*. 1995;19(8):859–872.

54. Cerfolio RJ, Allen MS, Nascimento AG, et al. Inflammatory pseudotumors of the lung. *Ann Thorac Surg*. 1999;67(4):933–936.
55. Narla LD, Newman B, Spottswood SS, et al. Inflammatory pseudotumor. *Radiographics*. 2003;23(3):719–729.
56. Coffin CM, Hornick JL, Fletcher CD. Inflammatory myofibroblastic tumor: comparison of clinicopathologic, histologic, and immunohistochemical features including ALK expression in atypical and aggressive cases. *Am J Surg Pathol*. 2007;31(4):509–520.
57. Rasalkar DD, Chu WC, To KF, et al. Radiological appearance of inflammatory myofibroblastic tumour. *Pediatr Blood Cancer*. 2010;54(7):1029–1031.
58. Karnak I, Senocak ME, Ciftci AO, et al. Inflammatory myofibroblastic tumor in children: diagnosis and treatment. *J Pediatr Surg*. 2001;36(6):908–912.
59. Genchellac H, Kirici MY, Basaran UN, et al. Successful sleeve lobectomy of pediatric inflammatory myofibroblastic tumor. *Pediatr Int*. 2016;58(10):1087–1089.
60. Chong S, Lee KS, Chung MJ, et al. Neuroendocrine tumors of the lung: clinical, pathologic, and imaging findings. *Radiographics*. 2006;26(1):41–57, discussion 57-48.
61. Rizzardi G, Bertolaccini L, Terzi A. Bronchial carcinoid tumours in children - a review. *European Oncology & Haematology*. 2011;7(3): 196–199.
62. McDougall JC, Gorenstein A, Unni K, et al. Carcinoid and mucoepidermoid carcinoma of bronchus in children. *Ann Otol Rhinol Laryngol*. 1980;89(5 Pt 1):425–427.
63. Al-Qahtani AR, Di Lorenzo M, Yazbeck S. Endobronchial tumors in children: institutional experience and literature review. *J Pediatr Surg*. 2003;38(5):733–736.
64. Hartman GE, Shochat SJ. Primary pulmonary neoplasms of childhood: a review. *Ann Thorac Surg*. 1983;36(1):108–119.
65. Broaddus RR, Herzog CE, Hicks MJ. Neuroendocrine tumors (carcinoid and neuroendocrine carcinoma) presenting at extra-appendiceal sites in childhood and adolescence. *Arch Pathol Lab Med*. 2003;127(9):1200–1203.
66. Hause DW, Harvey JC. Endobronchial carcinoid and mucoepidermoid carcinoma in children. *J Surg Oncol*. 1991;46(4):270–272.
67. Yikilmaz A, Lee EY. CT imaging of mass-like nonvascular pulmonary lesions in children. *Pediatr Radiol*. 2007;37(12):1253–1263.
68. Granata C, Battistini E, Toma P, et al. Mucoepidermoid carcinoma of the bronchus: a case report and review of the literature. *Pediatr Pulmonol*. 1997;23(3):226–232.
69. Kim TS, Lee KS, Han J, et al. Mucoepidermoid carcinoma of the tracheobronchial tree: radiographic and CT findings in 12 patients. *Radiology*. 1999;212(3):643–648.
70. Connor GF, Fishman EK. Endobronchial carcinoid in a child: depiction with three-dimensional volume rendering. *Pediatr Radiol*. 2004;34(12):1008–1011.
71. Belak J, Kudlac M, Zak V, et al. Surgical management of bronchopulmonary carcinoid tumors: experience over 8 years and review of the literature. *Tumori*. 2010;96(1):84–89.
72. Molina JR, Aubry MC, Lewis JE, et al. Primary salivary gland-type lung cancer: spectrum of clinical presentation, histopathologic and prognostic factors. *Cancer*. 2007;110(10):2253–2259.
73. Travis WD, Travis LB, Devesa SS. Lung cancer. *Cancer*. 1995;75(1 suppl):191–202.
74. Priest JR, Watterson J, Strong L, et al. Pleuropulmonary blastoma: a marker for familial disease. *J Pediatr*. 1996;128(2):220–224.
75. Messinger YH, Stewart DR, Priest JR, et al. Pleuropulmonary blastoma: a report on 350 central pathology-confirmed pleuropulmonary blastoma cases by the International Pleuropulmonary Blastoma Registry. *Cancer*. 2015;121(2):276–285.
76. Priest JR, Hill DA, Williams GM, et al. Type I pleuropulmonary blastoma: a report from the International Pleuropulmonary Blastoma Registry. *J Clin Oncol*. 2006;24(27):4492–4498.
77. Priest JR, McDermott MB, Bhatia S, et al. Pleuropulmonary blastoma: a clinicopathologic study of 50 cases. *Cancer*. 1997;80(1):147–161.
78. Pai S, Eng HL, Lee SY, et al. Rhabdomyosarcoma arising within congenital cystic adenomatoid malformation. *Pediatr Blood Cancer*. 2005;45(6):841–845.
79. Pai S, Eng HL, Lee SY, et al. Correction: pleuropulmonary blastoma, not rhabdomyosarcoma in a congenital lung cyst. *Pediatr Blood Cancer*. 2007;48(3):370–371.
80. Bagolan P, Nahom A, Giorlandino C, et al. Cystic adenomatoid malformation of the lung: clinical evolution and management. *Eur J Pediatr*. 1999;158(11):879–882.
81. Laberge JM, Puligandla P, Flageole H. Asymptomatic congenital lung malformations. *Semin Pediatr Surg*. 2005;14(1):16–33.
82. Langston C. New concepts in the pathology of congenital lung malformations. *Semin Pediatr Surg*. 2003;12(1):17–37.
83. Wright JR Jr. Pleuropulmonary blastoma. *Cancer*. 2000;88(12): 2853–2858.
84. Miniati DN, Chintagumpala M, Langston C, et al. Prenatal presentation and outcome of children with pleuropulmonary blastoma. *J Pediatr Surg*. 2006;41(1):66–71.
85. Orazi C, Inserra A, Schingo PM, et al. Pleuropulmonary blastoma, a distinctive neoplasm of childhood: report of three cases. *Pediatr Radiol*. 2007;37(4):337–344.
86. Ishida Y, Kato K, Kigasawa H, et al. Synchronous occurrence of pleuropulmonary blastoma and cystic nephroma: possible genetic link in cystic lesions of the lung and the kidney. *Med Pediatr Oncol*. 2000;35(1):85–87.
87. Boman F, Hill DA, Williams GM, et al. Familial association of pleuropulmonary blastoma with cystic nephroma and other renal tumors: a report from the International Pleuropulmonary Blastoma Registry. *J Pediatr*. 2006;149(6):850–854.
88. Lallier M, Bouchard S, Di Lorenzo M, et al. Pleuropulmonary blastoma: a rare pathology with an even rarer presentation. *J Pediatr Surg*. 1999;34(7):1057–1059.
89. Indolfi P, Casale F, Carli M, et al. Pleuropulmonary blastoma: management and prognosis of 11 cases. *Cancer*. 2000;89(6):1396–1401.
90. Dail DH, Liebow AA, Gmelich JT, et al. Intravascular, bronchiolar, and alveolar tumor of the lung (IVBAT). An analysis of twenty cases of a peculiar sclerosing endothelial tumor. *Cancer*. 1983;51(3): 452–464.
91. Weiss SW, Ishak KG, Dail DH, et al. Epithelioid hemangioendothelioma and related lesions. *Semin Diagn Pathol*. 1986;3(4):259–287.
92. Madhusudhan KS, Srivastava DN, Gamanagatti S. Multifocal epithelioid hemangioendothelioma presenting with hemoptysis. *Indian J Pediatr*. 2010;77(6):699–700.
93. Kitaichi M, Nagai S, Nishimura K, et al. Pulmonary epithelioid haemangioendothelioma in 21 patients, including three with partial spontaneous regression. *Eur Respir J*. 1998;12(1):89–96.
94. Ross GJ, Violi L, Friedman AC, et al. Intravascular bronchioloalveolar tumor: CT and pathologic correlation. *J Comput Assist Tomogr*. 1989;13(2):240–243.
95. Luburich P, Ayuso MC, Picado C, et al. CT of pulmonary epithelioid hemangioendothelioma. *J Comput Assist Tomogr*. 1994;18(4):562–565.
96. Mukundan G, Urban BA, Askin FB, et al. Pulmonary epithelioid hemangioendothelioma: atypical radiologic findings of a rare tumor with pathologic correlation. *J Comput Assist Tomogr*. 2000;24(5):719–720.
97. Mehrabi A, Kashfi A, Fonouni H, et al. Primary malignant hepatic epithelioid hemangioendothelioma: a comprehensive review of the literature with emphasis on the surgical therapy. *Cancer*. 2006;107(9):2108–2121.
98. Fauci AS, Haynes BF, Costa J, et al. Lymphomatoid granulomatosis. Prospective clinical and therapeutic experience over 10 years. *N Engl J Med*. 1982;306(2):68–74.
99. Gimenez A, Franquet T, Prats R, et al. Unusual primary lung tumors: a radiologic-pathologic overview. *Radiographics*. 2002;22(3):601–619.
100. Lee JS, Tuder R, Lynch DA. Lymphomatoid granulomatosis: radiologic features and pathologic correlations. *AJR Am J Roentgenol*. 2000;175(5):1335–1339.
101. Plosker GL, Figgitt DP. Rituximab: a review of its use in non-Hodgkin's lymphoma and chronic lymphocytic leukaemia. *Drugs*. 2003;63(8):803–843.
102. Kurtin PJ, Myers JL, Adlakha H, et al. Pathologic and clinical features of primary pulmonary extranodal marginal zone B-cell lymphoma of MALT type. *Am J Surg Pathol*. 2001;25(8):997–1008.
103. Ahmed S, Kussick SJ, Siddiqui AK, et al. Bronchial-associated lymphoid tissue lymphoma: a clinical study of a rare disease. *Eur J Cancer*. 2004;40(9):1320–1326.
104. Arnaoutakis K, Oo TH. Bronchus-associated lymphoid tissue lymphomas. *South Med J*. 2009;102(12):1229–1233.
105. Huang H, Lu ZW, Jiang CG, et al. Clinical and prognostic characteristics of pulmonary mucosa-associated lymphoid tissue lymphoma: a retrospective analysis of 23 cases in a Chinese population. *Chin Med J*. 2011;124(7):1026–1030.

106. Jung KH, Sung HJ, Lee JH, et al. A case of pulmonary lymphomatoid granulomatosis successfully treated by combination chemotherapy with rituximab. *Chemotherapy*. 2009;55(5):386–390.
107. Castrale C, El Haggan W, Chapon F, et al. Lymphomatoid granulomatosis treated successfully with rituximab in a renal transplant patient. *J Transplant.* 2011;2011:865957.
108. Roschewski M, Wilson WH. Lymphomatoid granulomatosis. *Cancer J*. 2012;18(5):469–474.
109. Grampp S, Bankier AA, Zoubek A, et al. Spiral CT of the lung in children with malignant extra-thoracic tumors: distribution of benign vs malignant pulmonary nodules. *Eur Radiol*. 2000;10(8):1318–1322.
110. Link MP, Gebhardt MC, Meyers PA. *Principles and practice of pediatric oncology*. Baltimore: Lippincott Williams and Wilkins; 2002.
111. Ward WG, Mikaelian K, Dorey F, et al. Pulmonary metastases of stage IIB extremity osteosarcoma and subsequent pulmonary metastases. *J Clin Oncol*. 1994;12(9):1849–1858.
112. Saeter G, Hoie J, Stenwig AE, et al. Systemic relapse of patients with osteogenic sarcoma. Prognostic factors for long term survival. *Cancer*. 1995;75(5):1084–1093.
113. Kaste SC, Pratt CB, Cain AM, et al. Metastases detected at the time of diagnosis of primary pediatric extremity osteosarcoma at diagnosis: imaging features. *Cancer*. 1999;86(8):1602–1608.
114. Kager L, Zoubek A, Potschger U, et al. Primary metastatic osteosarcoma: presentation and outcome of patients treated on neoadjuvant Cooperative Osteosarcoma Study Group protocols. *J Clin Oncol*. 2003;21(10):2011–2018.
115. Rasalkar DD, Chu WC, Lee V, et al. Pulmonary metastases in children with osteosarcoma: characteristics and impact on patient survival. *Pediatr Radiol*. 2011;41(2):227–236.
116. Chen F, Miyahara R, Bando T, et al. Prognostic factors of pulmonary metastasectomy for osteosarcomas of the extremities. *Eur J Cardiothorac Surg*. 2008;34(6):1235–1239.
117. Harting MT, Blakely ML, Jaffe N, et al. Long-term survival after aggressive resection of pulmonary metastases among children and adolescents with osteosarcoma. *J Pediatr Surg*. 2006;41(1):194–199.
118. Kayton ML. Pulmonary metastasectomy in pediatric patients. *Thorac Surg Clin*. 2006;16(2):167–183, vi.
119. Meisel JA, Guthrie KA, Breslow NE, et al. Significance and management of computed tomography detected pulmonary nodules: a report from the National Wilms Tumor Study Group. *Int J Radiat Oncol Biol Phys*. 1999;44(3):579–585.
120. Green DM. Use of chest computed tomography for staging and treatment of Wilms' tumor in children. *J Clin Oncol*. 2002;20(12):2763–2764.
121. Green DM, Fernbach DJ, Norkool P, et al. The treatment of Wilms' tumor patients with pulmonary metastases detected only with computed tomography: a report from the National Wilms' Tumor Study. *J Clin Oncol*. 1991;9(10):1776–1781.
122. Brisse HJ, Smets AM, Kaste SC, et al. Imaging in unilateral Wilms tumour. *Pediatr Radiol*. 2008;38(1):18–29.
123. Maile CW, Moore AV, Ulreich S, et al. Chest radiographic-pathologic correlation in adult leukemia patients. *Invest Radiol*. 1983;18(6):495–499.
124. Azoulay É, Fieux F, Moreau D, et al. Acute monocytic leukemia presenting as acute respiratory failure. *Am J Respir Crit Care Med*. 2003;167(10):1329–1333.
125. Sueyoshi E, Uetani M, Hayashi K, et al. Adult T-cell leukemia with multiple pulmonary nodules due to leukemic cell infiltration. *AJR Am J Roentgenol*. 1996;167(2):540–541.
126. Heyneman LE, Johkoh T, Ward S, et al. Pulmonary leukemic infiltrates: high-resolution CT findings in 10 patients. *AJR Am J Roentgenol*. 2000;174(2):517–521.
127. Keating GM. Rituximab: a review of its use in chronic lymphocytic leukaemia, low-grade or follicular lymphoma and diffuse large B-cell lymphoma. *Drugs*. 2010;70(11):1445–1476.
128. Jones L, Carol H, Evans K, et al. A review of new agents evaluated against pediatric acute lymphoblastic leukemia by the Pediatric Preclinical Testing Program. *Leukemia*. 2016;30(11):2133–2141.
129. Darmon M, Thiery G, Ciroldi M, et al. Intensive care in patients with newly diagnosed malignancies and a need for cancer chemotherapy. *Crit Care Med*. 2005;33(11):2488–2493.
130. William J, Variakojis D, Yeldandi A, et al. Lymphoproliferative neoplasms of the lung: a review. *Arch Pathol Lab Med*. 2013;137(3):382–391.
131. Maturen KE, Blane CE, Strouse PJ, et al. Pulmonary involvement in pediatric lymphoma. *Pediatr Radiol*. 2004;34(2):120–124.
132. Mentzer SJ, Reilly JJ, Skarin AT, et al. Patterns of lung involvement by malignant lymphoma. *Surgery*. 1993;113(5):507–514.
133. Au V, Leung AN. Radiologic manifestations of lymphoma in the thorax. *AJR Am J Roentgenol*. 1997;168(1):93–98.
134. Toma P, Granata C, Rossi A, et al. Multimodality imaging of Hodgkin disease and non-Hodgkin lymphomas in children. *Radiographics*. 2007;27(5):1335–1354.
135. Lewis ER, Caskey CI, Fishman EK. Lymphoma of the lung: CT findings in 31 patients. *American Journal of Roentgenology*. 1991;156(4):711–714.
136. Abramson SJ, Price AP. Imaging of pediatric lymphomas. *Radiol Clin North Am*. 2008;46(2):313–338, ix.
137. Kalra M, Dinand V, Sachdeva A, et al. Pediatric Hodgkin lymphoma presenting with pulmonary nodules and leukemoid reaction. *Pediatr Blood Cancer*. 2010;55(1):193–195.
138. Miyake S, Yoshizawa Y, Ohkouchi Y, et al. Non-Hodgkin's lymphoma with pulmonary infiltrates mimicking miliary tuberculosis. *Intern Med*. 1997;36(6):420–423.
139. Bae YA, Lee KS. Cross-sectional evaluation of thoracic lymphoma. *Radiol Clin North Am*. 2008;46(2):253–264, viii.
140. White KS. Thoracic imaging of pediatric lymphomas. *J Thorac Imaging*. 2001;16(4):224–237.

# 56 Diffuse Lung Disease

*Evan J. Zucker and Edward Y. Lee*

The pediatric diffuse lung disorders, also known as childhood interstitial lung diseases (chILDs), comprise a rare and heterogeneous spectrum of progressive and often lethal pulmonary pathology. They are characterized by otherwise unexplained respiratory signs and symptoms, hypoxemia, and widespread pulmonary opacities on imaging.[1] The diseases are not limited to the interstitium and may affect the alveoli, airways, blood vessels, lymphatic channels, and pleural spaces. Although much remains unknown, the revised chILD classification scheme, recognizing disorders distinctly occurring in infants under 2 years of age (Box 56.1), along with advances in imaging and lung biopsy techniques, has greatly improved understanding.[1–20] In this chapter, the diseases of infancy are discussed, followed by an overview of diffuse lung disorders more prevalent in children over 2 years of age. The connective tissue, collagen vascular, and storage diseases are detailed in Chapter 57.

## DISORDERS OF INFANCY

### Diffuse Developmental Disorders

***Etiology.*** Diffuse developmental disorders are characterized by marked alveolar gas exchange impairment and are thought to arise early in prenatal lung development. The three main entities within this category are acinar dysplasia, congenital alveolar dysplasia, and alveolar capillary dysplasia with misalignment of pulmonary veins (ACD/MPV). Acinar dysplasia and congenital alveolar dysplasia are caused by arrest of lung development in the pseudoglandular/early canalicular and late canalicular/early saccular phases, respectively. ACD/MPV results from an abnormal location of pulmonary vein branches next to the pulmonary arteries along with medial hypertrophy of the pulmonary arterioles, reduced alveolar capillary density, and maldevelopment of pulmonary lobules; *FOXF1* gene mutations and 16q24.1 microdeletions are implicated in some cases.[1–27]

***Imaging.*** Chest radiographs, often the only imaging available, may initially appear normal but progress to hazy bilateral pulmonary opacities, resembling surfactant deficiency. Lung volumes are typically normal to decreased but increase with ventilator support. Barotrauma-related air leaks such as pneumothorax and pneumomediastinum develop in about half of patients (Fig. 56.1). With concurrent pulmonary hypertension (PHT), the main pulmonary artery may enlarge. Ultimately, imaging findings are nonspecific; however, the diagnosis should be considered in the term neonate with persistent unexplained respiratory distress.[1–27]

***Treatment and Follow-up.*** Patients develop rapidly progressive and nearly always lethal respiratory failure in the first 2 months of life despite treatment for PHT, intensive ventilation, and extracorporeal membrane oxygenation (ECMO). Serial chest radiographs can monitor the progression of the disease and help identify acute complications that may be seen with prolonged ventilatory support. Patients generally do not survive long enough for lung transplantation, the only viable treatment. More than 80% of patients with ACD/MPV have associated extrapulmonary anomalies (e.g., cardiac, gastrointestinal, or genitourinary), for which screening may be performed. Genetic counseling may be offered to relatives of patients with ACD/MPV, which appears heritable in 10% of cases.[1–27]

### Alveolar Growth Disorders

***Etiology.*** Alveolar growth disorders are the most common form of neonatal interstitial lung disease (ILD), caused by an unprogrammed insult to lung development, resulting in defective alveolar formation, lobular simplification, lack of alveolar septation, and airspace enlargement. Prematurity-related chronic lung disease (bronchopulmonary dysplasia [BPD]) is a frequently encountered subtype. Also included within this group are structural pulmonary changes related to chromosomal abnormalities or congenital heart disease and pulmonary hypoplasia due to oligohydramnios, space-occupying masses, and neuromuscular disease, among other etiologies.[1–20,28–34]

***Imaging.*** Features are variable. Chest radiographs in infants with classic BPD show coarse reticular opacities, cystic appearing lucencies, and disordered lung aeration due to alveolar septal fibrosis and hyperinflation. However, with ever-earlier delivery possible, there has been a shift in the imaging features of BPD. Findings in so-called "new" BPD range from near normal to markedly disordered lung parenchyma, variably sized pulmonary lobules, thick perilobular reticular opacities, linear and triangular subpleural opacities, ground-glass opacities, and hyperlucent areas, some of which resemble cysts or may be mistaken for emphysema (Fig. 56.2). Recently, the pulmonary findings of BPD known by radiography and computed tomography (CT) have been successfully delineated by a novel ultrashort echo time (UTE) magnetic resonance imaging (MRI) technique. In infants with trisomy 21, small subpleural cysts are characteristic (Fig. 56.3). In patients with X-linked filamin A gene mutations causing alveolar growth disturbances, characteristic findings include central pulmonary artery enlargement, atelectasis, progressive severe pulmonary hyperinflation, hyperlucency, and peripheral pulmonary vascular hypoattenuation resembling congenital lobar or acquired emphysema (e-Fig. 56.4).[1–20,28–34]

***Treatment and Follow-up.*** Decreasing respiratory support helps reduce BPD incidence and severity. Low-dose corticosteroids, fluid restriction, vitamin A, and patent ductus arteriosus closure are of equivocal benefit. Linear and subpleural opacities seen on CT correlate with interstitial fibroproliferation but not symptom severity. Lung biopsy may be considered to exclude the not-uncommon coexistence of pulmonary interstitial glycogenosis (PIG) (detailed later), which can be steroid-responsive. Lung transplantation is usually inevitable with filamin A mutations due to severe respiratory decline.[1–20,28–34]

### Surfactant Dysfunction Disorders and Related Abnormalities

***Etiology.*** These disorders are caused by genetic mutations affecting surfactant metabolism, including surfactant proteins B (SpB) and C (SpC) and the adenosine triphosphate–binding cassette transporter protein A3 (ABCA3). Also included in this category are rare genetic disorders that indirectly influence surfactant production, such as thyroid transcription factor-1 (TTF-1)/NK homeobox 1 *(NKX2.1)* abnormalities ("brain-lung-thyroid syndrome"), lysinuric protein intolerance, and granulocyte-macrophage colony-stimulating factor–Rα mutations. Many etiologies remain uncharacterized.[1–20,35–45]

## Abstract:

The pediatric diffuse lung disorders, also known as childhood interstitial lung diseases (chILDs), refer to a rare and heterogeneous spectrum of pulmonary disorders associated with widespread pulmonary opacities and otherwise unexplained respiratory signs and symptoms. They are characteristically progressive and associated with significant morbidity and often mortality. The revised chILD classification scheme, recognizing disorders distinctly occurring in infants less than 2-years-old, combined with advances in imaging and lung biopsy techniques, has greatly improved understanding of these insidious and enigmatic disease. In this chapter, the disorders of infancy are discussed, followed by an overview of diffuse lung disorders more prevalent in children over 2 years of age. Distinctive imaging findings as well as disease pathogenesis and treatment options are highlighted.

## Keywords:

diffuse lung disease
childhood interstitial lung disease
chILD
neuroendocrine cell hyperplasia of infancy
pulmonary interstitial glycogenosis
crazy paving
bronchiolitis obliterans

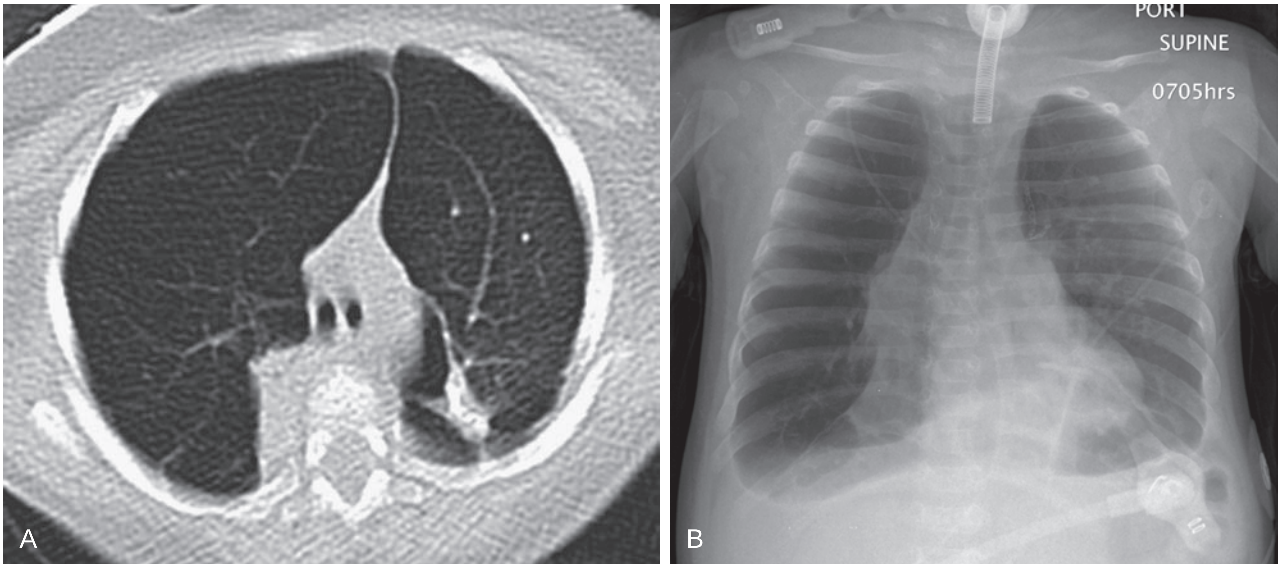

**e-Figure 56.4. Filamin A gene mutation.** Axial computed tomography image at 4 months of age (A) and a chest radiograph at 6 months of age (B) in a female infant with progressive respiratory insufficiency depict severe pulmonary hyperinflation and hyperlucency with pulmonary vascular attenuation and posteromedial atelectasis.

### BOX 56.1 Classification System of Interstitial Lung Diseases in Infants

**DIFFUSE DEVELOPMENTAL DISORDERS**

Acinar dysplasia
Congenital alveolar dysplasia
Alveolar capillary dysplasia with misalignment of pulmonary veins

**ALVEOLAR GROWTH DISORDERS**

Prenatal: secondary pulmonary hypoplasia
Postnatal: chronic lung disease

- Prematurity-related chronic lung disease (bronchopulmonary dysplasia)
- Chronic lung disease in term infant

Associated chromosomal or genetic abnormalities

- Trisomy 21
- Other (e.g., filamin A mutation)

Associated congenital heart disease

**SURFACTANT DYSFUNCTION/RELATED ABNORMALITIES**

Surfactant dysfunction disorders

- *SpB* genetic mutations (pulmonary alveolar proteinosis and variants)
- *SpC* genetic mutations (chronic pneumonitis of infancy; also pulmonary alveolar proteinosis, desquamative interstitial pneumonitis, and nonspecific interstitial pneumonia)
- Adenosine triphosphate–binding cassette transporter protein A3 genetic mutation (pulmonary alveolar proteinosis; also CPI, diffuse interstitial pneumonitis, and nonspecific interstitial pneumonia)
- Congenital GM-CSF receptor deficiency (pulmonary alveolar proteinosis histologic pattern)
- Thyroid transcription factor-1 genetic mutations
- Others: histology consistent with surfactant dysfunction, unrecognized genetic disorder

Lysinuric protein intolerance (pulmonary alveolar proteinosis histologic pattern)

**SPECIFIC CONDITIONS OF UNKNOWN OR POORLY UNDERSTOOD ETIOLOGY**

Neuroendocrine cell hyperplasia of infancy
Pulmonary interstitial glycogenosis

- Primary
- Associated with other pulmonary conditions, especially alveolar growth disorders

Modified with permission from Lee EY, Cleveland RH, Langston C: Interstitial lung disease in infants and children: new classification system with emphasis on clinical, imaging, and pathologic correlation. In: Cleveland RH, ed. *Imaging in Pediatric Pulmonology*, New York: Springer; 2011.

***Imaging.*** Chest radiographs show diffuse or patchy hazy granular pulmonary opacities. CT demonstrates diffuse ground-glass opacity, consolidation, interlobular septal thickening, or a crazy-paving pattern typical of pulmonary alveolar proteinosis (PAP) (detailed in a later section) (Fig. 56.5). With increasing age, ground-glass opacities recede, and progressively larger and more numerous cysts develop (e-Fig. 56.6). Pectus excavatum may develop due to the effects of chronic lung disease on the growing chest wall.[1–20,35–45]

***Treatment and Follow-up.*** The diagnosis can be established by genetic testing, obviating lung biopsy. The mainstays of treatment are chronic ventilator support, nutritional supplementation, and potential lung transplantation, with anecdotal roles for pulse corticosteroids, hydroxychloroquine (Plaquenil), and azithromycin. Targeted gene therapy remains an area of investigation.[1–20,35–45]

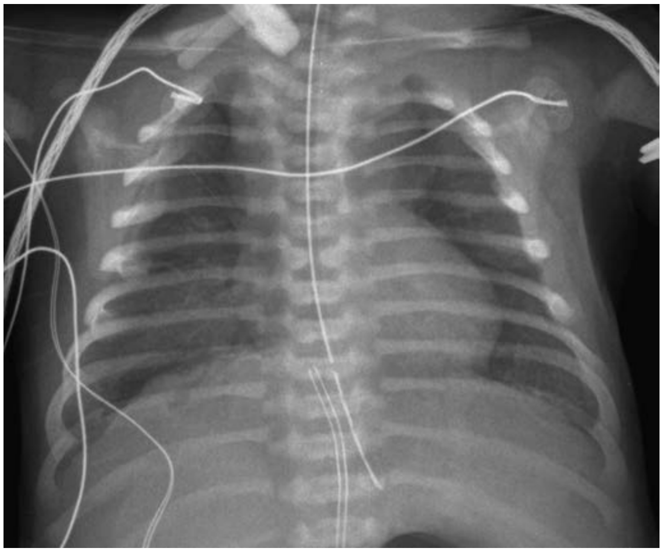

**Figure 56.1. Alveolar capillary dysplasia/misalignment of the pulmonary veins in a full-term newborn.** Chest radiograph demonstrates hazy bilateral pulmonary opacities, pneumomediastinum, and a right pneumothorax.

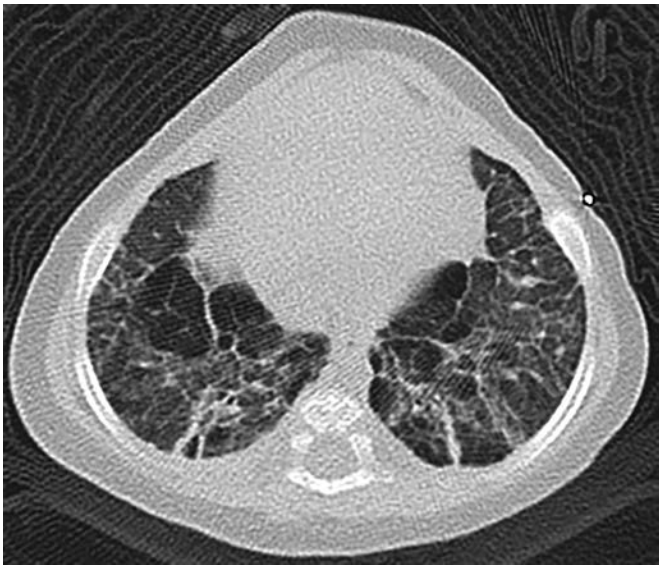

**Figure 56.2. Bronchopulmonary dysplasia (alveolar growth disorder) in a 5-month-old, ex-28-week premature female.** Axial CT image shows diffuse architectural distortion, lobular simplification and hyperlucency resembling emphysema, and thickening of perilobular septae.

## Specific Conditions of Unknown or Poorly Understood Etiology

### Neuroendocrine Cell Hyperplasia of Infancy

***Etiology.*** The etiology of neuroendocrine cell hyperplasia of infancy (NEHI) is unknown. Histopathologically, the disease (previously referred to as persistent tachypnea of infancy) is characterized by increased numbers of pulmonary neuroendocrine cells (PNECs), which function in oxygen sensing and fetal lung development and normally rapidly decline after the neonatal period. Some cases have an identifiable genetic component, including links to *NKX2.1* mutations.[1–20,46–53]

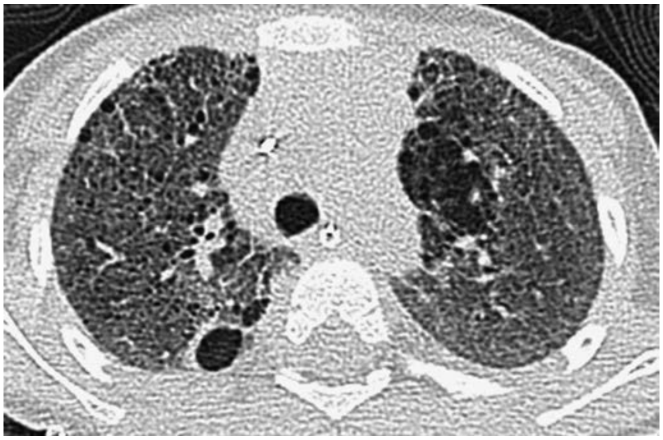

**e-Figure 56.6. Surfactant dysfunction related to ABCA3 gene mutations in a 15-month-old infant.** Axial CT image reveals extensive ground-glass pulmonary opacification and numerous cysts.

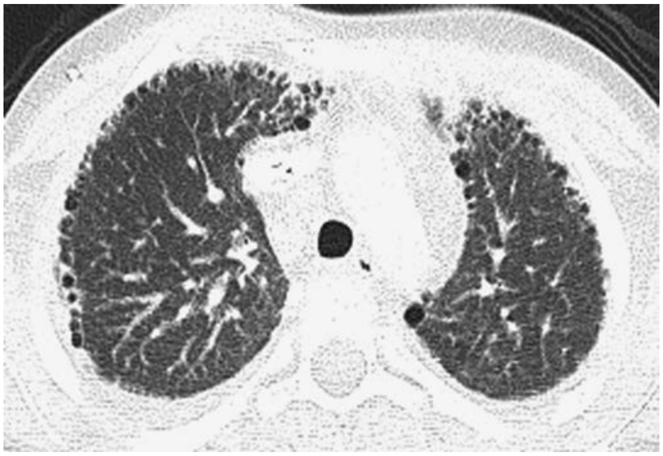

**Figure 56.3. Alveolar growth disorder related to trisomy 21 in a 10-year-old.** Axial CT image reveals numerous bilateral subpleural cysts.

***Imaging.*** Chest radiographs demonstrate hyperinflation and variable increased perihilar opacity resembling bronchiolitis or reactive airways disease (Fig. 56.7). CT characteristically shows a mosaic attenuation pattern indicating air trapping that affects at least four lobes, with geographic ground-glass opacities most prominent in the right middle lobe, lingula, and paramediastinal lung regions (Fig. 56.8). In experienced hands, the sensitivity and specificity of CT for NEHI diagnosis are reported to be 78% to 83% and 100%, respectively; thus CT may obviate the need for lung biopsy.[1–20,46–53]

***Treatment and Follow-up.*** Treatment of NEHI at present is supportive, geared toward preventing hypoxemia and infection and maintaining nutritional support. Although patients may be persistently symptomatic or require long-term oxygen therapy, the prognosis is usually favorable, without progressive respiratory failure or directly attributable death. In later life, acute exacerbations may occur due to intermittent air trapping or infection.[1–20,46–53]

### Pulmonary Interstitial Glycogenosis

***Etiology.*** The etiology of PIG, previously known as infantile cellular interstitial pneumonitis and histiocytoid pneumonia, remains unknown. PIG is characterized histopathologically by infiltration of the interstitium with immature mesenchymal cells containing copious cytoplasmic glycogen and staining positively for vimentin. The lack of PIG in lung biopsies from children older than 10 months suggests that the disorder may be related to lung growth and development. Patchy PIG and alveolar growth abnormalities commonly coexist.[1–20,54–59]

***Imaging.*** Chest radiographs show progressive hyperinflation and evolve from a fine interstitial to a coarse interstitial or alveolar pattern. CT may demonstrate pulmonary architectural distortion, hyperinflated/hyperlucent areas, ground-glass opacities (diffuse, segmental, or subsegmental), interlobular septal thickening, and linear opacities (Fig. 56.9). Because patchy PIG often coexists with alveolar growth abnormalities, the specific imaging features of “pure” PIG are uncertain. In one reported case of PIG, the multiple, small, scattered, air-filled, cystic-appearing changes were most likely attributable to the concomitant alveolar growth abnormality.[1–20,54–59]

***Treatment and Follow-up.*** Most patients require supplemental oxygen. Pulse glucocorticoids, which accelerate lung maturation, may be beneficial and are therefore often recommended. Overall, the prognosis is favorable, with no directly attributable deaths. However, greater mortality and morbidity rates are expected with concomitant growth abnormalities and PHT. During the first several months of life, marked improvement often occurs clinically, radiologically, and histologically, although hyperinflation may persist for years.[1–20,54–59]

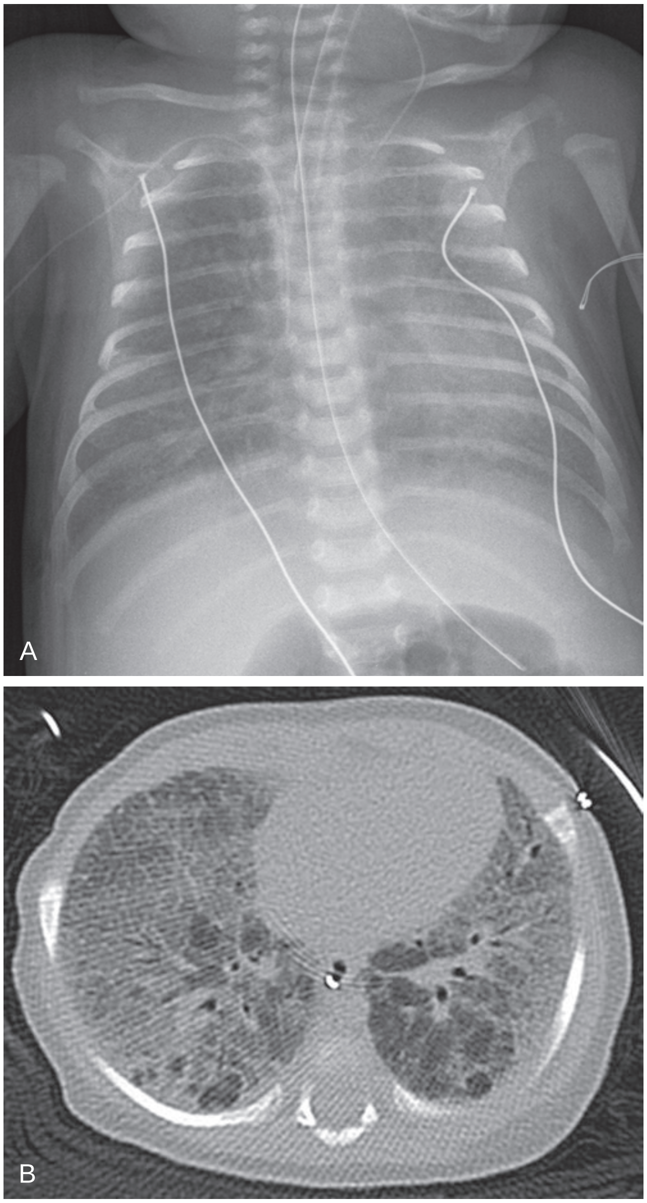

**Figure 56.5. Surfactant dysfunction related to ABCA3 gene mutations in a 4-week-old term female.** (A) Frontal chest radiograph shows diffuse bilateral hazy pulmonary opacities in a pattern resembling neonatal respiratory distress syndrome (RDS). (B) Axial CT image confirms diffuse bilateral ground-glass opacities along with septal thickening and areas of crazy paving.

## DISORDERS OF CHILDHOOD

### Pulmonary Alveolar Proteinosis

***Etiology.*** PAP is characterized by the abnormal accumulation of surfactant, a lipoproteinaceous material, within the alveoli, preventing normal gas exchange. The acquired form of PAP seen in older children and adults is most often caused by autoantibodies to granulocyte macrophage colony-stimulating factor (GM-CSF), impairing surfactant clearance. However, any number of processes that hinder alveolar macrophage function, ranging from leukemia to toxic exposure, can cause the same PAP end result.[1–20,60–67]

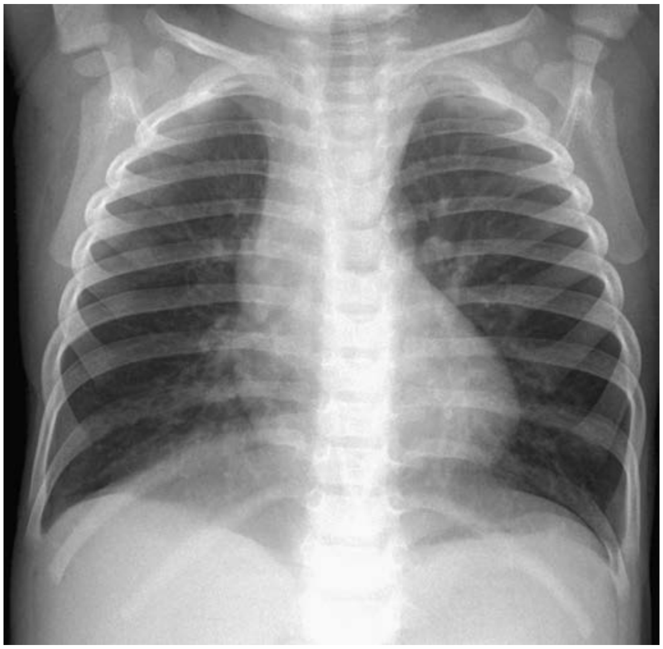

**Figure 56.7. Neuroendocrine cell hyperplasia of infancy in a 15-month-old.** Chest radiograph demonstrates pulmonary hyperinflation and parahilar opacities resembling reactive airways disease or bronchiolitis.

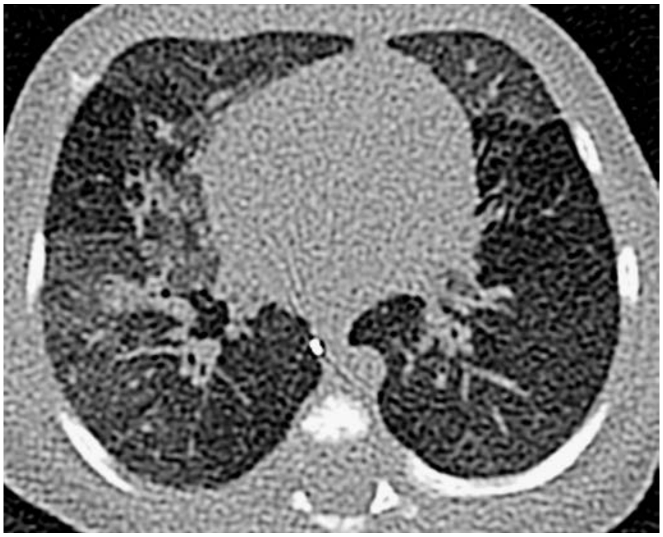

**Figure 56.8. Neuroendocrine cell hyperplasia of infancy in a 13-day-old male.** Axial expiratory CT image shows characteristic geographic ground-glass opacities involving the paramediastinal right middle lobe and lingula, as well the right lower lobe.

*Imaging.* Imaging cannot differentiate the various etiologies of PAP. Chest radiographs demonstrate symmetric perihilar opacities that extend to the periphery but are generally not as densely consolidative as would be expected in bacterial pneumonia. CT shows bilateral ground-glass opacities with smooth intralobular and interlobular septal thickening in polygonal shapes, an appearance known as “crazy-paving”[1–20,60–67] (Fig. 56.10).

*Treatment and Follow-up.* PAP is preferably confirmed by bronchoscopy with bronchoalveolar lavage and transbronchial biopsy rather than surgical lung biopsy. Serologic testing for GM-CSF antibodies should be performed to distinguish between autoimmune and secondary PAP. For secondary PAP, treatment efforts should focus on identifying the underlying cause. For autoimmune PAP, repeated whole-lung lavage is the current treatment of choice, although aerosolized GM-CSF therapy appears promising. Immunosuppression with rituximab or mycophenolate mofetil also has been tried. CT can be used to monitor treatment response.[1–20,60–67]

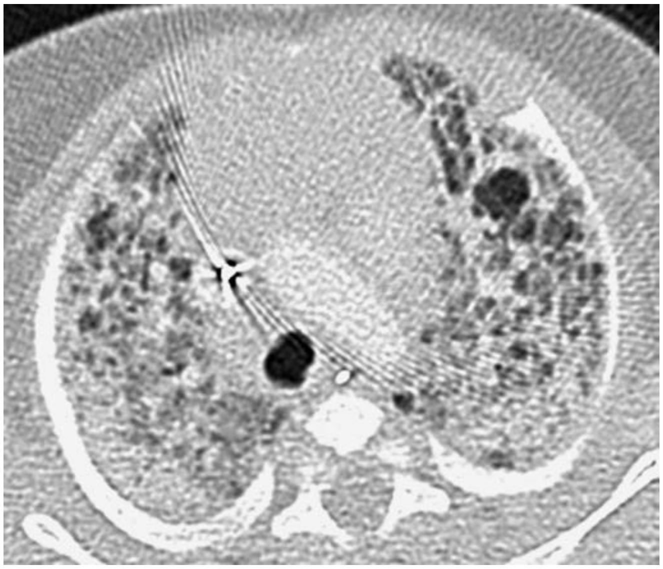

**Figure 56.9. Alveolar growth disorder and pulmonary interstitial glycogenosis in a 5-month-old former 25-week premature infant.** Axial computed tomography image shows cystlike hyperlucent lobules, thick reticular perilobular opacities, and ground-glass opacities.

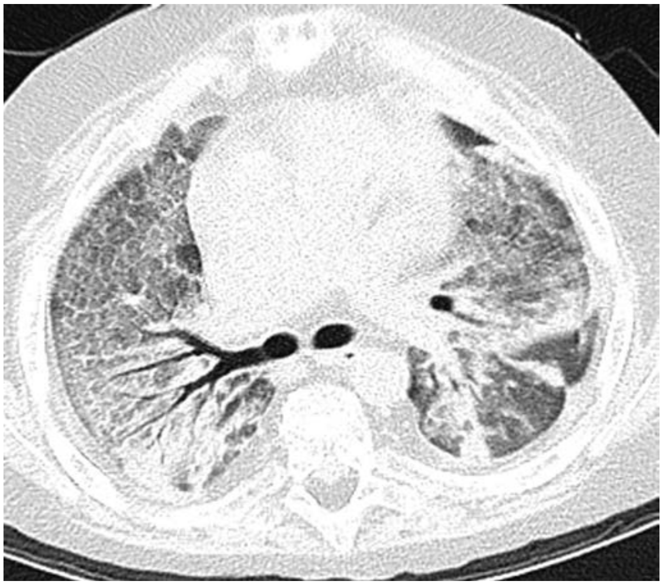

**Figure 56.10. Pulmonary alveolar proteinosis in an 8-year-old male.** Axial CT image shows a characteristic crazy-paving pattern with ground-glass opacities superimposed on inter- and intralobular septal thickening.

## Pulmonary Lymphangiectasia and Lymphangiomatosis

*Etiology.* Pulmonary lymphangiectasia is characterized by congenital or acquired dilation of the lymphatics draining the pulmonary interstitial and subpleural spaces. Pulmonary lymphangiomatosis is caused by proliferation of complex lymphatic channels with secondary lymphatic dilation. In both disorders, the disease may be limited to the lung or involve additional thoracic and/or extrathoracic sites.[1–20,68–73]

***Imaging.*** Chest radiographs demonstrate diffuse hazy opacities and bilateral pleural effusions. CT shows diffuse, smooth thickening of the interlobular septae and peribronchovascular interstitium, patchy ground-glass opacities, and pleural effusions (often chylous) (e-Fig. 56.11). Abnormalities are usually less marked in patients presenting beyond infancy. MRI demonstrates hyperintensity of the pulmonary interstitium on T2-weighted sequences and pleural effusions. Lung findings are very similar in pulmonary lymphangiectasia and lymphangiomatosis. However, lymphangiomatosis more often presents in late childhood and involves extrapulmonary sites, including lytic bone lesions and mediastinal soft tissue edema.[1–20,68–73]

***Treatment and Follow-up.*** Patients with congenital disease may be stillborn or present at birth with severe respiratory distress, leading to death within hours of life. Mechanical ventilation and pleural drainage invariably are required. Patients with long-term survival have variable degrees of respiratory compromise and are managed with supplemental oxygen at home, symptomatic therapy, fluid restriction, and dietary measures. Many other palliative options have been tried with variable success, including propranolol, corticosteroids, interferon-alpha, various chemotherapeutics, and radiotherapy.[1–20,68–73]

## Bronchiolitis Obliterans

***Etiology.*** Bronchiolitis obliterans (BO) is characterized by a fibroblastic reparative response to small airway injury, leading to airway occlusion. While viral infection is the most common precipitant, other etiologies include graft–versus–host disease and chronic allograft rejection postlung transplant. Terminology for BO in the literature is inconsistent, causing confusion. The clinical manifestation may be termed "bronchiolitis obliterans syndrome," whereas the histopathologic correlate is a spectrum termed "constrictive bronchiolitis" or "obliterative bronchiolitis," depending on the degree of airway lumen occlusion that is present.[1–20,74–84]

***Imaging.*** Chest radiographs may be normal. Abnormal findings, most commonly hyperinflation, are nonspecific. A unilateral hyperlucent lung with normal or decreased volume is characteristic of Swyer–James–Macleod syndrome, the result of BO affecting the growing lung. CT findings consist of air trapping accentuated on expiration, parenchymal hyperlucency, mosaic attenuation, bronchial wall thickening, bronchiectasis, and pulmonary vascular hypoattenuation (e-Fig. 56.12), findings are often bilateral and asymmetric. The presence of both hyperlucency and pulmonary vascular hypoattenuation is highly specific for moderate/severe nontransplant BO. With a correlating clinical history and a fixed obstructive pattern on pulmonary function testing, CT is diagnostic, thus avoiding lung biopsy.[1–20,74–84]

***Treatment and Follow-up.*** In the absence of bronchiectasis, BO can be difficult to distinguish from the more common acute viral bronchiolitis. Follow-up imaging thus can be helpful; bronchiolitis will eventually resolve, while BO will persist or worsen. In postinfectious BO, the extent of CT findings correlate with lung function. Postlung transplant, BO is known to increase mortality after the first postoperative year, and thus CT screening is prudent. Recent reports also suggest that serial CT monitoring of airway dimensions after transplant may help predict the presence and severity of BO. For transplant-associated BO, corticosteroids, azithromycin, N-acetyl cysteine, and possibly methotrexate appear beneficial.[1–20,74–84]

## Hypersensitivity Pneumonitis

***Etiology.*** Also known as extrinsic allergic alveolitis, hypersensitivity pneumonitis (HP) is characterized by pulmonary inflammation related to inhalational exposure of organic antigens, usually arising from birds, fungi, or dusts. Other precipitants include spray paints, glues, epoxy resins, insecticides, and drugs such as methotrexate. HP may be subcategorized as acute, subacute, or chronic based on the duration of exposure (hours, weeks to months, or months to years, respectively). Of note, cigarette smoking appears to protect against HP, possibly by inhibiting alveolar macrophage activity.[1–20,85–87]

***Imaging.*** In both acute and subacute HP, chest radiographs characteristically show diffuse micronodular interstitial prominence and opacities in the mid to lower lungs, resembling pulmonary edema or pneumonia. However, radiographs may appear normal, with findings visible only on CT in 40% of cases. CT demonstrates small (1–3 mm) poorly defined centrilobular nodules (reflecting bronchiolitis), ground-glass opacities (reflecting alveolitis), and air trapping, with relative sparing of the upper lungs. The "head-cheese" sign, a conglomerate of ground-glass opacity, mosaic attenuation indicating air trapping, and interspersed normal lung, is classic for subacute HP. On radiography and CT, the chronic form is characterized by volume loss and fibrotic changes with irregular linear/reticular opacities, architectural distortion, and honeycombing (e-Fig. 56.13).[1–20,85–87]

***Treatment and Follow-up.*** The most important aspect of treatment is identifying and eliminating exposure to the inciting antigen. The imaging findings associated with the acute and subacute forms of the disease regress with antigen removal. However, chronic changes persist and may progress. Systemic corticosteroids are the only dependable drug therapy but do not affect the long-term outcome. Irreversible fibrosis may be so severe that lung transplantation is needed.[1–20,85–87]

## Diffuse Pulmonary Hemorrhage Disorders

***Etiology.*** Diffuse pulmonary hemorrhage disorders can be subcategorized according to the presence or absence of capillaritis, which is characterized pathologically by inflammatory disruption of the interstitial capillary network. Disorders with capillaritis include idiopathic pulmonary capillaritis, granulomatosis with polyangiitis (formerly Wegener granulomatosis), microscopic polyangiitis, Goodpasture syndrome, idiopathic pulmonary-renal syndrome, systemic lupus erythematosus, and drug-induced capillaritis. Disorders without capillaritis include idiopathic pulmonary hemosiderosis, acute idiopathic pulmonary hemorrhage of infancy, Heiner syndrome (pulmonary disease caused by food sensitivity, usually to cow's milk), coagulation disorders, and cardiovascular disorders such as pulmonary veno-occlusive disease and pulmonary arteriovenous malformation.[1–20,88–92]

***Imaging.*** The classic radiographic appearance of acute diffuse pulmonary hemorrhage consists of bilateral symmetric airspace opacities in a "butterfly" or "batwing" pattern. However, opacities may be asymmetric or unilateral. CT is more sensitive and shows patchy ground-glass opacities (Fig. 56.14) and consolidation acutely. With organizing or repetitive hemorrhage, findings evolve to interlobular septal thickening, nodular opacities, and potentially a crazy-paving pattern. Multiple bilateral variably-sized pulmonary nodules with cavitation are characteristic of granulomatosis with polyangiitis (e-Fig. 56.15).[1–20,88–92]

***Treatment and Follow-up.*** Distinguishing between pulmonary hemorrhage with capillaritis versus without capillaritis is critical, because pulmonary capillaritis often requires aggressive immunosuppressive therapy. Because imaging findings are similar in the many conditions causing pulmonary hemorrhage, a lung biopsy often is necessary for a definitive diagnosis. With treatment, CT findings typically improve.[1–20,88–92]

## Nonspecific Interstitial Pneumonia

***Etiology.*** Nonspecific interstitial pneumonia (NSIP) can be idiopathic, familial, or the final common pathway of several other disorders, including autoimmune connective tissue and collagen vascular diseases, genetic surfactant disorders, and HP. It has a

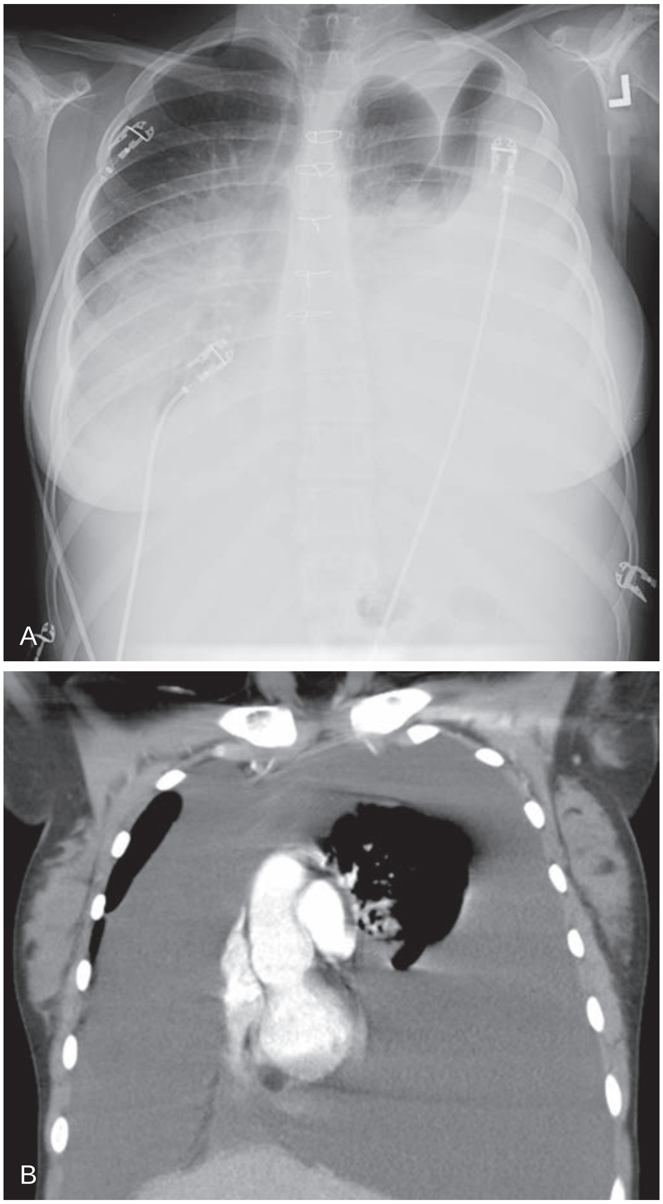

**e-Figure 56.11. Congenital systemic lymphangiectasia in a 16-year-old female.** Frontal chest radiograph (A) and coronal computed tomography (B) image show marked and partially loculated bilateral pleural effusions.

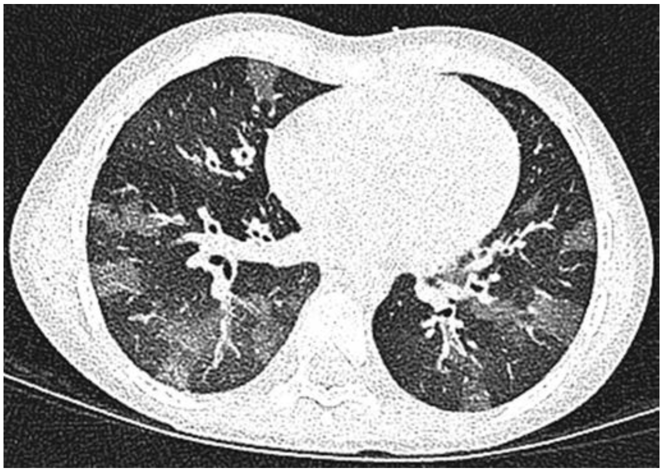

**e-Figure 56.12. Bronchiolitis obliterans in a 3-year-old female.** Axial expiratory CT image shows characteristic findings of mosaic attenuation, parenchymal hyperlucency, bronchial wall thickening, and bronchiectasis.

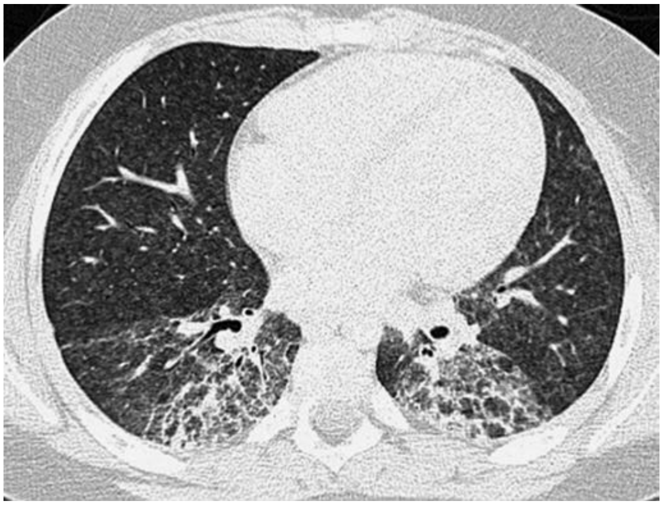

**e-Figure 56.13. Acute-on-chronic hypersensitivity pneumonitis in a 10-year-old.** Axial CT image demonstrates diffusely scattered small centrilobular nodular opacities, as well as lower lobe volume loss and reticular fibrotic opacities.

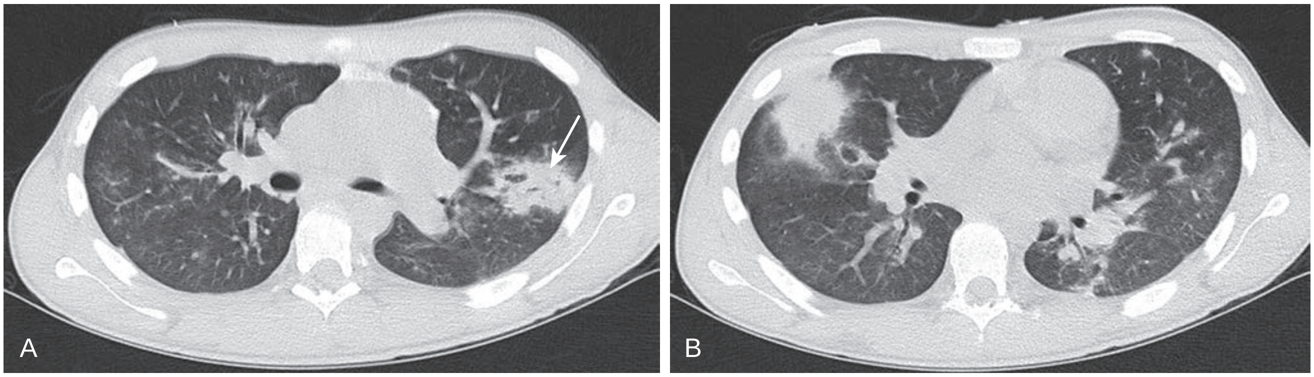

**e-Figure 56.15. Granulomatosis with polyangiitis (formerly Wegener's granulomatosis) in a 15-year-old male.** Axial CT images (A and B) show bilateral irregular pulmonary masses, one with suspected cavitation in the left upper lobe (A, *arrow*). Superimposed ground-glass opacities are present.

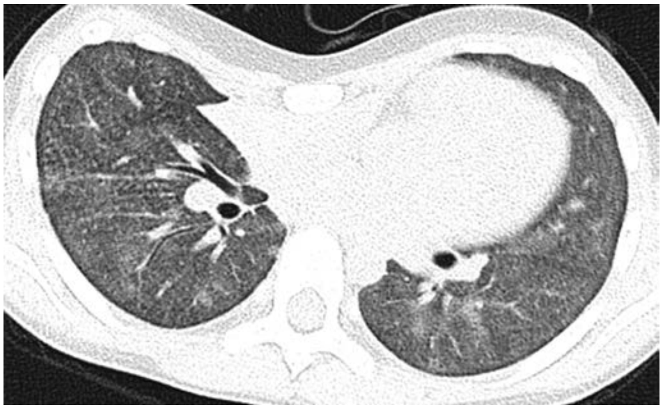

**Figure 56.14. Idiopathic pulmonary hemosiderosis in an 8-year-old female.** Axial CT image shows diffuse bilateral ground-glass nodular opacities.

characteristic histopathologic appearance with temporally and spatially uniform interstitial lymphoplasmacytic inflammation and varying degrees of fibrosis. Cellular and fibrotic subtypes have been described.[1–20,93–95]

***Imaging.*** Best characterized by CT, the typical imaging findings are ground-glass and fine linear or reticular opacities, predominantly at the lung periphery. Traction bronchiectasis, volume loss (predominantly in the lower lobe), and honeycombing may develop over time. Dilation of the esophagus is characteristic of scleroderma, which has an NSIP pattern (e-Fig. 56.16).[1–20,5,93–95]

***Treatment and Follow-up.*** CT findings of NSIP can resolve or persist, depending on the degree of fibrosis. Immunosuppressive therapy often is beneficial. However, patients with progressive disease may require lung transplantation.[1–20,93–95]

## Organizing Pneumonia

***Etiology.*** Organizing pneumonia is characterized histologically by intraluminal organizing fibrosis in the distal airways and airspaces (bronchioles, alveolar ducts, and alveoli). When idiopathic, it may be termed "cryptogenic organizing pneumonia." However, it can result from various causes, including asthma, drug reaction, aspiration pneumonia, autoimmune disease, chemotherapy, bone marrow transplantation, and other conditions stimulating a lung reparative response. The term "bronchiolitis obliterans organizing pneumonia" has been discarded because of its potential confusion with BO, a distinct entity.[1–20,96–100]

***Imaging.*** Imaging findings are variable, with CT most frequently showing peripheral patchy consolidation with or without surrounding ground-glass opacity. Commonly, air bronchograms and mild bronchial dilatation are found within areas of consolidation. Other recognized findings include the atoll or reverse halo sign (central ground-glass opacity surrounded by consolidation) (Fig. 56.17), small pulmonary nodules along bronchovascular bundles, linear and bandlike subpleural opacities, perilobular thickening, and progressive fibrosis.[1–20,96–100]

***Treatment and Follow-up.*** Although organizing pneumonia has many underlying causes, overall, corticosteroids are the best treatment option. Rarely, it may remit spontaneously. The prognosis is generally favorable, with up to an 80% cure rate reported. Imaging findings related to inflammation will improve/resolve on follow-up, whereas irreversible fibrotic changes may persist or worsen.[1–20,96–100]

## Pulmonary Infiltrate With Eosinophilia

***Etiology.*** The eosinophilic lung diseases are a diverse group of disorders characterized by peripheral or tissue eosinophilia, with interstitial and intraalveolar eosinophils at pathology. Three subcategories are recognized: eosinophilic disease of unknown cause, eosinophilic disease of known cause, and eosinophilic vasculitis. Diseases of unknown cause include simple pulmonary eosinophilia (or Löffler syndrome), acute eosinophilic pneumonia (AEP), chronic eosinophilic pneumonia (CEP), and idiopathic hypereosinophilic syndrome. Diseases of known cause include allergic bronchopulmonary aspergillosis (ABPA), bronchocentric granulomatosis, parasitic infections, and drug reactions. Eosinophilic vasculitis includes allergic angiitis and granulomatosis (Churg–Strauss syndrome).[1–20,101–106]

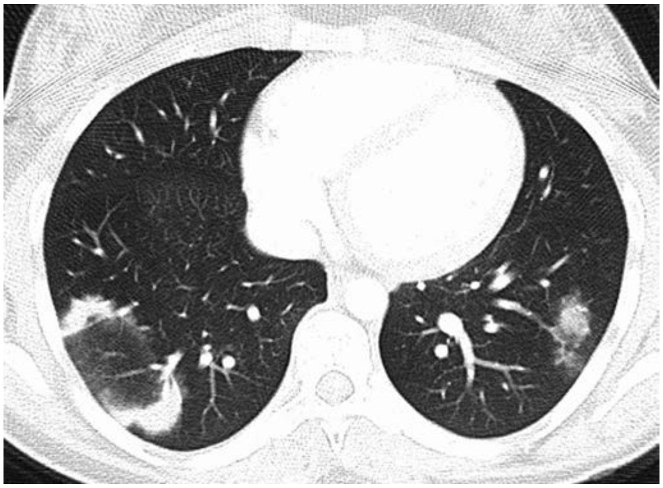

**Figure 56.17. Sjögren syndrome in a 15-year-old.** Axial CT image depicts a patchy consolidation of the peripheral left lower lobe and a ground-glass opacity surrounded by consolidation ("atoll" or "reverse halo" sign) of the peripheral right lower lobe representing sites of organizing pneumonia.

***Imaging.*** Imaging findings of interstitial, alveolar, or mixed interstitial-alveolar opacities are in general nonspecific, but certain key features may suggest the underlying diagnosis. CEP and drug-induced pulmonary infiltrate with eosinophilia (PIE) demonstrate a characteristic pattern of peripheral consolidation with sparing of the central lung zones (a "photographic negative" or "reversed" pulmonary edema pattern), allowing a highly specific diagnosis in the setting of peripheral eosinophilia (Fig. 56.18). AEP presents radiographically with bilateral reticular opacities, possibly with consolidation and pleural effusion. On CT, bilateral patchy ground-glass opacity and often interlobular septal thickening, consolidation, or poorly defined nodules are seen. The imaging findings of AEP mimic those of more common entities such as pulmonary edema and acute respiratory distress syndrome, potentially delaying diagnosis. ABPA demonstrates central bronchiectasis with or without mucoid impaction; the presence of mucoid impaction of the large airways is referred to as the "finger-in-glove" sign. Simple pulmonary eosinophilia and idiopathic hypereosinophilic syndrome characteristically demonstrate pulmonary nodules with ground-glass halos. Bronchocentric granulomatosis demonstrates focal masses and nodules or lobar consolidation with atelectasis. Findings in persons with Churg-Strauss syndrome include subpleural consolidation, centrilobular nodules, bronchial wall thickening, and interlobular septal thickening.[1–20,101–106]

***Treatment and Follow-up.*** Imaging findings, even if nonspecific, can localize potential sites for lung biopsy. Corticosteroids are the treatment of choice, resulting in prompt and complete response. In persons with AEP, relapses do not occur after cessation of corticosteroids, although they can occur with CEP. Therapy may be tailored to the underlying cause; for example, antiparasitic medications may be used in a case of parasite-induced PIE.[1–20,101–106]

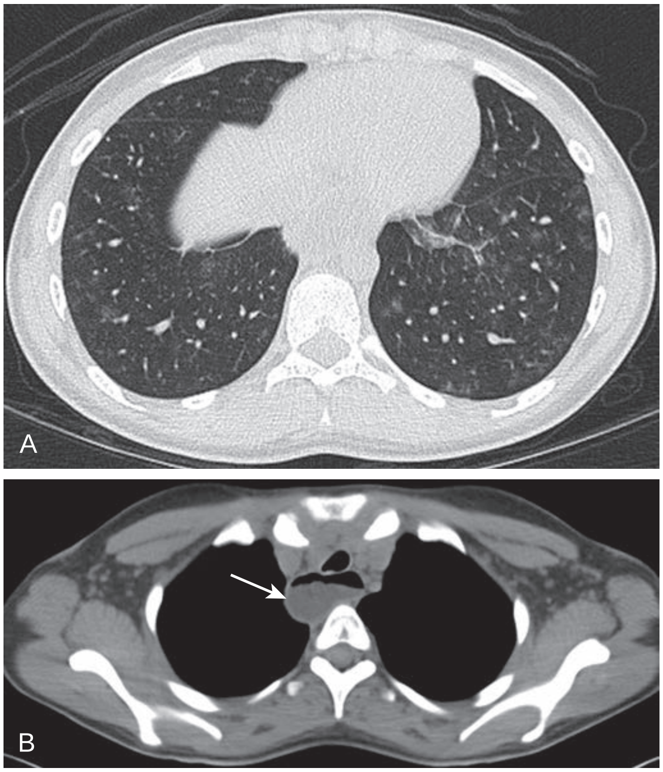

**e-Figure 56.16. Mixed connective tissue disease in a 13-year-old female.** (A) Axial computed tomography (CT) image in lung windows shows basilar-predominant ground-glass nodular opacities with subpleural sparing, findings compatible with nonspecific interstitial pneumonia (NSIP). (B) Axial CT image in mediastinal windows reveals a dilated fluid-filled esophagus (*arrow*), characteristic of a scleroderma-like pattern.

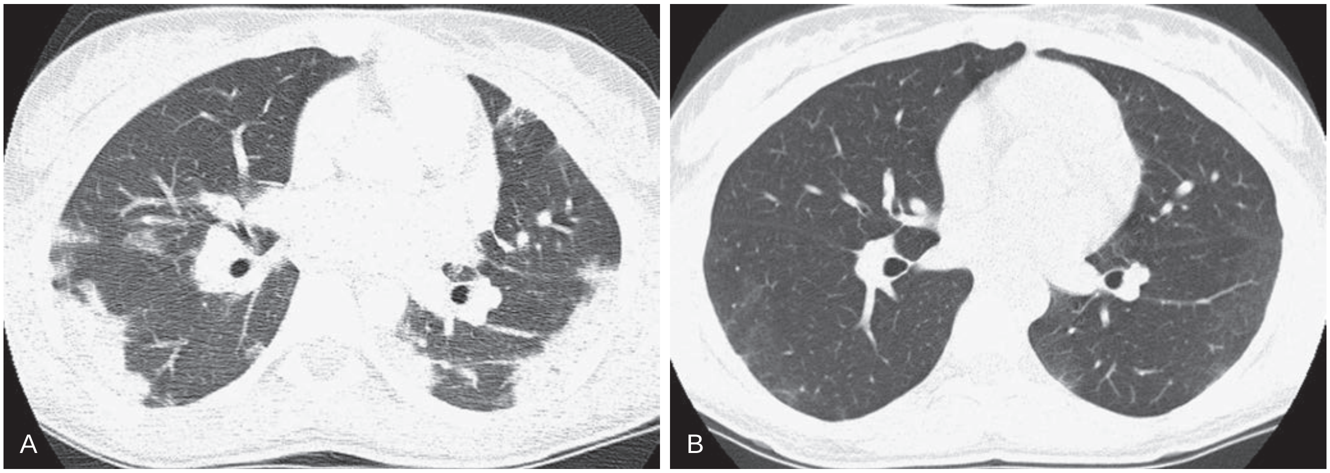

**Figure 56.18. Drug-induced (minocycline) pulmonary infiltrate with eosinophilia in an 18-year-old.** Axial CT images show characteristic peripheral consolidations at the time of diagnosis (A) and marked improvement after 2 weeks of corticosteroid therapy and cessation of the inciting drug (B).

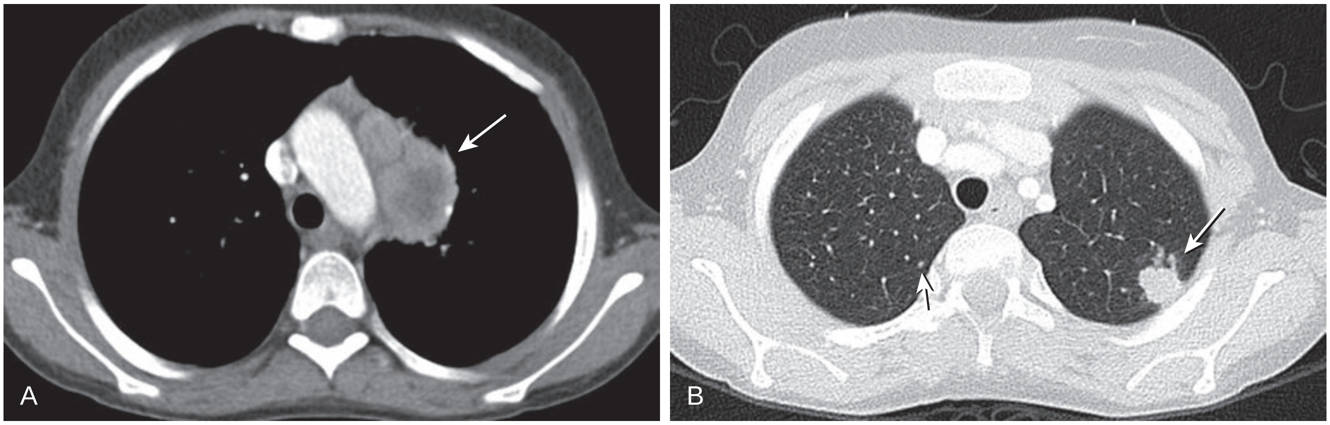

**Figure 56.19. Chronic granulomatous disease in a 16-year-old male.** Axial CT images show necrotic prevascular mediastinal lymphadenopathy (A, *arrow*) and an irregular nodular left upper lobe consolidation (B, *long arrow*). Multiple smaller nodules were also present, one seen in the right upper lobe (B, *short arrow*).

## Chronic Granulomatous Disease

***Etiology.*** Chronic granulomatous disease (CGD) is a rare inherited immunodeficiency disorder that usually is caused by a mutation in one of the four genes encoding subunits of the phagocyte nicotinamide adenine dinucleotide phosphate, impairing superoxide production and oxidative burst mechanisms that normally assist in killing fungal and intracellular catalase-positive bacterial organisms. The lungs are the most common site of infection. Histologically, granulomatous inflammation and often necrosis are present, with surrounding chronic inflammation and fibrosis, hence the name chronic granulomatous disease.[1–20,107–111]

***Imaging.*** A variety of imaging findings may present in patients who have chronic, recurrent infections, including consolidation, ground-glass opacities, tree-in-bud opacities, and centrilobular or random (even miliary) nodules acutely, with bronchiectasis, septal thickening, air trapping, abscess formation, fibrosis, cysts, and honeycombing with long-standing disease. Other common thoracic findings include mediastinal and/or hilar lymphadenopathy, pleural thickening, empyema, vertebral or rib osteomyelitis, and chest wall invasion[1–20,107–111] (Fig. 56.19).

***Treatment and Follow-up.*** CGD is treated with lipophilic antibiotics, antifungal agents, interferon-γ, abscess drainage, surgical resection, and stem cell transplantation. Prophylactic antibiotics and antifungals are beneficial. Fluorine-18 fluorodeoxyglucose positron emission tomography is more reliable than CT for distinguishing between active and dormant disease activity (e-Fig. 56.20). Improved diagnosis and treatment have allowed survival into adulthood.[1–20,107–111]

## Cystic Fibrosis

***Etiology.*** Cystic fibrosis (CF) is caused by autosomal-recessive mutations in the CF transmembrane regulator (CFTR) gene. It is the most common genetic disorder leading to chronic pulmonary disease in children. Recurrent infections develop, in addition to numerous extrapulmonary manifestations such as meconium ileus in infancy. With progressive disease, chronic inflammatory changes occur that lead to alteration of airway walls with epithelial erosion, partial replacement of the mucosa by granulation tissue, progressive airway dilation resulting in bronchiectasis, and fibrotic/obliterative changes involving the small airways.[1–20,112–119]

***Imaging.*** Chest imaging in early CF may be normal or show mild to moderate air trapping and/or bronchiectasis (Fig. 56.21). In more advanced disease, bronchiectasis that is predominant in the upper lobes, bronchial wall thickening, centrilobular nodular and tree-in-bud opacities, and mucus plugging with air trapping

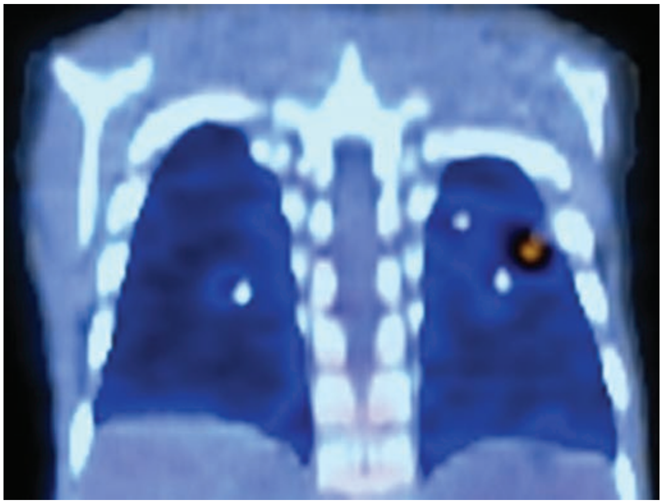

**e-Figure 56.20. Chronic granulomatous disease in a 6-year-old.** Coronal fused fluorodeoxyglucose–positron emission tomography/computed tomography image in this patient undergoing evaluation before bone marrow transplantation demonstrates multiple bilateral pulmonary nodules, only one of which has high fluorodeoxyglucose avidity. A subsequent biopsy of this nodule revealed active fungal infection.

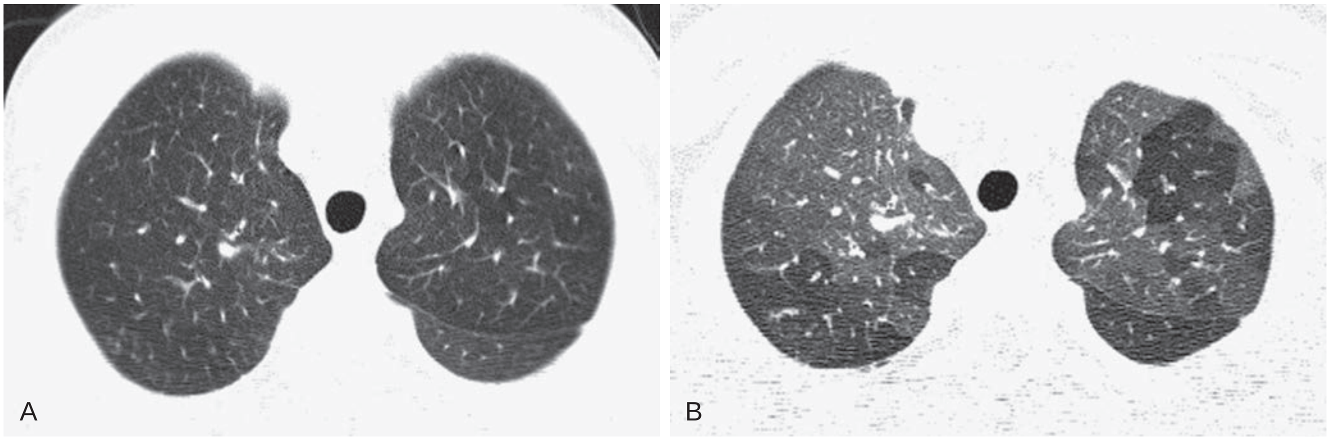

**Figure 56.21. Cystic fibrosis in a 12-year-old.** Paired inspiratory (A) and expiratory (B) phase axial CT images from within this patient with mild pulmonary cystic fibrosis show no bronchiectasis but demonstrate mosaic attenuation from air trapping that is accentuated on the expiratory phase.

occur (Fig. 56.22). A finger-in-glove pattern of mucoid impaction similar to ABPA may be observed. Because of recurrent infections, mediastinal and hilar lymphadenopathy often are present. Bronchial artery hypertrophy and tortuosity may also develop due to chronic airway inflammation. Both radiographic and CT CF scoring systems are available and correlate with lung function although primarily used for research purposes. UTE MR is under investigation as a radiation-free alternative for CF imaging, and the addition of hyperpolarized gas is promising for functional ventilation assessment.[1–20,112–119]

***Treatment and Follow-up.*** Treatment traditionally has focused on the managing/preventing the sequelae of the disease. The standard of care most recently has included oral azithromycin, inhaled tobramycin, hypertonic saline solution, and dornase alfa (Pulmozyme), which functions to break down thick secretions. Additional antibiotics are used depending on the type of infections present and the resistance pattern. Several novel small molecules are now approved for patients with specific mutations: ivacaftor (Kalydeco) with at least one *G551D* mutation and lumacaftor/ivacaftor (Orkambi) for homozygous *F508del* mutations. Targeted gene therapies remain an area of active investigation.[1–20,112–119]

## Pulmonary Disease in Association With Immunosuppression

***Etiology.*** Immunosuppression predisposes to a variety of pulmonary infections that may present as diffuse lung disease. Commonly encountered conditions include medication-related immunosuppression (organ transplant drug maintenance, high-dose steroids, or chemotherapy), human immunodeficiency virus (HIV)/acquired immune deficiency syndrome (AIDS), and congenital immunodeficiency. Patients are at risk for inoculation by both typical organisms and atypical pathogens (e.g., fungal, viral, mycobacterial).[1–20,120–128]

***Imaging.*** Imaging findings are variable depending on the immune status and offending pathogens. However, certain CT patterns are associated with specific infections. For example, ground-glass opacity is seen in pneumocystis and cytomegalovirus; nodules <1 cm are seen in viral pneumonia; nodules >1 cm, potentially cavitary, and the halo sign (ground-glass opacity surrounding a solid nodule) are typical of invasive aspergillosis; tree-in-bud nodules (centrilobular with linear branching) are seen in infectious bronchiolitis, including endobronchial tuberculosis; and consolidation is typical of bacterial pneumonia. Mediastinal/hilar lymphadenopathy and extrathoracic manifestations may also be present (Fig. 56.23). There should be a low threshold to obtain CT even if radiographs are normal to exclude occult abnormalities with potentially dire consequences in these high-risk patients.[1–20,120–128]

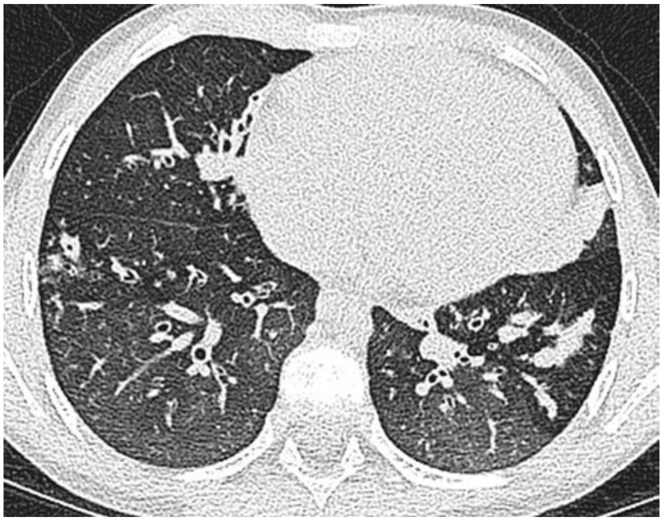

**Figure 56.22. Cystic fibrosis in a 10-year-old female.** Axial expiratory CT image shows multifocal mosaic attenuation indicating air-trapping, bronchiectasis, bronchial wall, thickening, and mucus plugging most marked in the lingula, left lower lobe, and right middle lobe.

***Treatment and Follow-up.*** Broad-spectrum coverage is initially advisable, including antibacterial, antifungal, and antiviral agents, tailored when the specific pathogen(s) are isolated. If feasible, immunosuppressive regimens may be weaned (or antiretroviral therapy increased for HIV). Opportunistic infections can quickly become life-threatening, and thus extreme vigilance is needed. Prophylactic coverage may also be warranted in some circumstances (e.g., for pneumocystis in HIV with low CD4 count). In one series of children with diffuse lung disease, overall mortality in immunocompromised patients was >50% compared with 16.3% for immunocompetent hosts.[1–20,120]

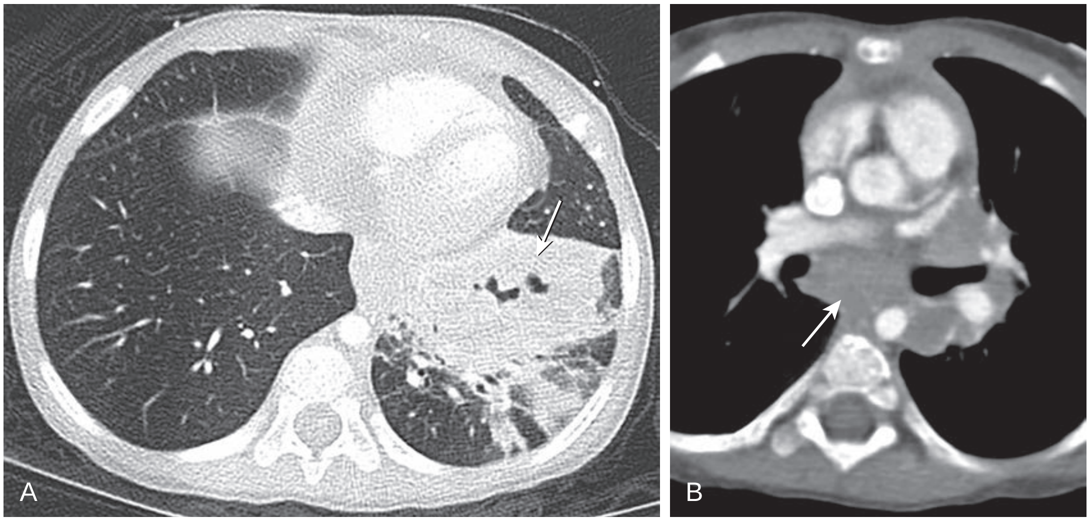

**Figure 56.23. Congenital neutropenia.** Axial CT images in a 2-year-old male who presented with cough and fever shows a cavitary left lower lobe consolidation consistent with necrotizing pneumonia (A, *arrow*) and extensive subcarinal and left hilar lymphadenopathy (B, *arrow*).

## KEY POINTS

- The revised chILD classification scheme, recognizing unique disorders occurring under 2 years of age, has allowed substantial progress in our understanding of pediatric diffuse lung disease. Many of these diseases have a genetic basis and also affect extrapulmonary sites.
- CT findings in NEHI are characteristic with hyperinflation, mosaic attenuation, and geographic ground-glass opacities that are most prominent in the right middle lobe, lingula, and paramediastinal lung regions.
- A crazy-paving pattern (ground-glass opacity superimposed on interlobular septal thickening) is suggestive of but not specific for PAP and also can be observed with diffuse pulmonary hemorrhage, for example. PAP itself is a histopathologic entity with numerous underlying causes including congenital surfactant deficiency in infants.
- Chylous pleural effusions are typical of pulmonary lymphangiectasia and lymphangiomatosis.
- Other important radiologic patterns and signs in pediatric diffuse lung disease include focal diffuse air trapping ± linear scarring or cystic changes in alveolar growth disorders; air trapping, vascular hypoattenuation and bronchiectasis in BO; peripheral-predominant ground-glass, fine reticular opacities, and bronchiectasis with lower-lobe predominance in NSIP; photographic negative or reversed pulmonary edema pattern in CEP and drug-induced PIE; the atoll or reversed halo sign (central ground-glass opacity surrounded by consolidation) in organizing pneumonia; the finger-in-glove sign (mucoid impaction of large airways) in ABPA and CF; and the halo sign (central consolidation surrounded by ground-glass opacity) in invasive aspergillosis.

## SUGGESTED READINGS

Guillerman RP. Imaging of childhood interstitial lung disease. *Pediatr Allergy Immunol Pulmonol*. 2010;23:43–68.

Guillerman RP, Brody AS. Contemporary perspectives on pediatric diffuse lung disease. *Radiol Clin North Am*. 2011;49:847–868.

Kurland G, Deterding RR, Hagood JS, et al. An official American Thoracic Society clinical practice guideline: classification, evaluation, and management of childhood interstitial lung disease in infancy. *Am J Respir Crit Care Med*. 2013;188:376–394.

Lee EY. Interstitial lung disease in infants: new classification system, imaging technique, clinical presentation and imaging findings. *Pediatr Radiol*. 2013;43:3–13.

Thacker PG, Vargas SO, Fishman MP, et al. Current update on interstitial lung disease of infancy: new classification system, diagnostic evaluation, imaging algorithms, imaging findings, and prognosis. *Radiol Clin North Am*. 2016;54:1065–1076.

## REFERENCES

Full references for this chapter can be found on www.expertconsult.com.

## REFERENCES

1. Cazzato S, di Palmo E, Ragazzo V, et al. Interstitial lung disease in children. *Early Hum Dev*. 2013;89(suppl 3):S39–S43.
2. Lee EY, Cleveland RH, Langston C. Interstitial lung disease in infants and children: new classification system with emphasis on clinical, imaging, and pathologic correlation. In: Cleveland RH, ed. *Imaging in Pediatric Pulmonology*. New York: Springer; 2011.
3. Zucker EJ, Lee EY. Pediatric diffuse lung disease. In: Kim I, ed. *Radiology Illustrated: Pediatric Radiology*. Seoul, South Korea: Springer Korea Limited; 2014.
4. Guillerman RP, Brody AS. Contemporary perspectives on pediatric diffuse lung disease. *Radiol Clin North Am*. 2011;49:847–868.
5. Guillerman RP. Imaging of childhood interstitial lung disease. *Pediatr Allergy Immunol Pulmonol*. 2010;23:43–68.
6. Lee EY. Interstitial lung disease in infants: new classification system, imaging technique, clinical presentation and imaging findings. *Pediatr Radiol*. 2013;43(1):3–13.
7. Thacker PG, Vargas SO, Fishman MP, et al. Current update on interstitial lung disease of infancy: new classification system, diagnostic evaluation, imaging algorithms, imaging findings, and prognosis. *Radiol Clin North Am*. 2016;54(6):1065–1076.
8. Kuo CS, Young LR. Interstitial lung disease in children. *Curr Opin Pediatr*. 2014;26(3):320–327.
9. Spagnolo P, Bush A. Interstitial lung disease in children younger than 2 years. *Pediatrics*. 2016;137(6). pii: e20152725.
10. Vece TJ, Fan LL. Interstitial lung disease in children older than 2 years. *Pediatr Allergy Immunol Pulmonol*. 2010;23:33–41.
11. Hines EJ, Walsh M, Armes JE, et al. Interstitial lung disease in infancy: a general approach. *J Paediatr Child Health*. 2016;52(4):370–376.
12. Vece TJ, Young LR. Update on diffuse lung disease in children. Update on diffuse lung disease in children. *Chest*. 2016;149:836–845.
13. Dishop MK. Diagnostic pathology of diffuse lung disease in children. *Pediatr Allergy Immunol Pulmonol*. 2010;23:69–85.
14. Langston C, Dishop MK. Infant lung biopsy: clarifying the pathologic spectrum. *Pathol Int*. 2004;54:s419–s421.
15. Deterding RR. Infants and young children with children's interstitial lung disease. *Pediatr Allergy Immunol Pulmonol*. 2010;23:25–31.
16. Deutsch GH, Young LR, Deterding RR, et al. Diffuse lung disease in young children: application of a novel classification scheme. *Am J Respir Crit Care Med*. 2007;176:1120–1128.
17. O'Reilly R, Kilner D, Ashworth M, et al. Diffuse lung disease in infants less than 1 year of age: histopathological diagnoses and clinical outcome. *Pediatr Pulmonol*. 2015;50:1000–1008.
18. Owens C. Radiology of diffuse interstitial pulmonary disease in children. *Eur Radiol*. 2004;14:L2–L12.
19. Brody AS. Imaging considerations: interstitial lung disease in children. *Radiol Clin North Am*. 2005;43:391–403.
20. Fan LL, Dishop MK, Galambos C, et al. Diffuse lung disease in biopsied children 2 to 18 years of age. Application of the chILD classification scheme. *Ann Am Thorac Soc*. 2015;12:1498–1505.
21. Szafranski P, Herrera C, Proe LA, et al. Narrowing the FOXF1 distant enhancer region on 16q24.1 critical for ACDMPV. *Clin Epigenetics*. 2016;8:112. eCollection 2016.
22. Goel D, Oei JL, Shand AW, et al. FOXF1 gene mutation in alveolar capillary dysplasia associated with Hirschsprung's disease and clinical review. *J Paediatr Child Health*. 2016;52:787–788.
23. Sen P, Thakur N, Stockton DW, et al. Expanding the phenotype of alveolar capillary dysplasia (ACD). *J Pediatr*. 2004;145:646–651.
24. Michalsky MP, Arca MJ, Groenman F, et al. Alveolar capillary dysplasia: a logical approach to a fatal disease. *J Pediatr Surg*. 2005;40:1100–1105.
25. Newman B, Yunis E. Primary alveolar capillary dysplasia. *Pediatr Radiol*. 1990;21:20–22.
26. Hugosson CO, Salama HM, Al-Dayel F, et al. Primary alveolar capillary dysplasia (acinar dysplasia) and surfactant protein B deficiency: a clinical, radiological and pathological study. *Pediatr Radiol*. 2005;35:311–316.
27. Gillespie LM, Fenton AC, Wright C. Acinar dysplasia: a rare cause of neonatal respiratory failure. *Acta Paediatr*. 2004;93:712–713.
28. Mahut B, De Blic J, Emond S, et al. Chest computed tomography findings in bronchopulmonary dysplasia and correlation with lung function. *Arch Dis Child Fetal Neonatal Ed*. 2007;92:F459–F464.
29. Biko DM, Schwartz M, Anupindi SA, et al. Subpleural lung cysts in Down syndrome: prevalence and association with coexisting diagnoses. *Pediatr Radiol*. 2008;38:280–284.
30. Taylor PA, Dishop MK, Lotze TE, et al. Congenital multilobar emphysema: a characteristic lung growth disorder attributable to Filamin A gene mutations. *Pediatr Radiol*. 2009;39(suppl 3):S516.
31. Agrons GA, Courtney SE, Stocker JT, et al. From the archives of the AFIP: lung disease in premature neonates: radiologic-pathologic correlation. *Radiographics*. 2005;25:1047–1073.
32. Mosca F, Colnaghi M, Fumagalli M. BPD: old and new problems. *J Matern Fetal Neonatal Med*. 2011;24(suppl 1):80–82.
33. Kugelman A, Durand M. A comprehensive approach to the prevention of bronchopulmonary dysplasia. *Pediatr Pulmonol*. 2011;46(12):1153–1165.
34. Hahn AD, Higano NS, Walkup LL, et al. Pulmonary MRI of neonates in the intensive care unit using 3D ultrashort echo time and a small footprint MRI system. Pulmonary MRI of neonates in the intensive care unit using 3D ultrashort echo time and a small footprint MRI system. *J Magn Reson Imaging*. 2016;doi:10.1002/jmri.25394. [Epub ahead of print].
35. Devine MS, Garcia CK. Genetic interstitial lung disease. *Clin Chest Med*. 2012;33:95–110.
36. Griese M, Lorenz E, Hengst M, et al. Surfactant proteins in pediatric interstitial lung disease. *Pediatr Res*. 2016;79:34–41.
37. Gower WA, Popler J, Hamvas A, et al. Clinical improvement in infants with ILD due to mutations in the surfactant protein C gene (SFTPC). *Am J Respir Crit Care Med*. 2010;181:A6733.
38. Rosen DM, Waltz DA. Hydroxychloroquine and surfactant protein C deficiency. *N Engl J Med*. 2005;352:207–208.
39. Pachajoa H, Ruiz-Botero F, Meza-Escobar LE. Fatal respiratory disease due to a homozygous intronic ABCA3 mutation: a case report. *J Med Case Rep*. 2016;10(1):266.
40. Clement A, Corvol H, Epaud R, et al. Dramatic improvement by macrolides in surfactant deficiency with ABCA3 mutation. *Am J Respir Crit Care Med*. 2009;179:A3011.
41. Doan ML, Guillerman RP, Dishop MK, et al. Clinical, radiological, and pathological features of ABCA3 mutations in children. *Thorax*. 2008;63:366–373.
42. Guillot L, Carre A, Szinnai G, et al. NKX2-1 mutations leading to surfactant protein promoter dysregulation cause interstitial lung disease in "Brain-Lung-Thyroid Syndrome". *Hum Mutat*. 2010;31:E1146–E1162.
43. Deterding R, Dishop MK, Uchida DA, et al. Thyroid transcription factor 1 gene abnormalities; an under recognized cause of children's interstitial lung disease. *Am J Respir Crit Care Med*. 2010;181:A6725.
44. Thouvenin G, Taam RA, Flamein F, et al. Characteristics of disorders associated with genetic mutations of surfactant protein C. *Arch Dis Child*. 2010;95:449–454.
45. Mechri M, Epaud R, Emond S, et al. Surfactant protein C gene (SFTPC) mutation-associated lung disease: high-resolution computed tomography (HRCT) findings and its relation to histological analysis. *Pediatr Pulmonol*. 2010;45:1021–1029.
46. Caimmi S, Licari A, Caimmi D, et al. Neuroendocrine cell hyperplasia of infancy: an unusual cause of hypoxemia in children. *Ital J Pediatr*. 2016;42(1):84.
47. Carr LL, Kern JA, Deutsch GH. Diffuse idiopathic pulmonary neuroendocrine cell hyperplasia and neuroendocrine hyperplasia of infancy. *Clin Chest Med*. 2016;37(3):579–587.
48. Houin PR, Deterding RR, Young LR. Exacerbations in neuroendocrine cell hyperplasia of infancy are characterized by increased air trapping. *Pediatr Pulmonol*. 2016;51(3):E9–E12.
49. Nevel RJ, Garnett ET, Worrell JA, et al. Persistent lung disease in adults with NKX2.1 mutation and familial neuroendocrine cell hyperplasia of infancy. *Ann Am Thorac Soc*. 2016;13(8):1299–1304.
50. Lee J, Sanchez TR, Zhang Y, et al. The role of high-resolution chest CT in the diagnosis of neuroendocrine cell hyperplasia of infancy - A rare form of pediatric interstitial lung disease. *Respir Med Case Rep*. 2015;16:101–103.
51. Brody AS, Guillerman RP, Hay TC, et al. Neuroendocrine cell hyperplasia of infancy: diagnosis with high-resolution CT. *AJR Am J Roentgenol*. 2010;194:238–244.
52. Bramson RT, Cleveland R, Blickman JG, et al. Radiographic appearance of follicular bronchitis in children. *AJR Am J Roentgenol*. 1996;166:1447–1450.
53. Young LR, Brody AS, Inge TH, et al. Neuroendocrine cell distribution and frequency distinguish neuroendocrine cell hyperplasia of infancy from other pulmonary disorders. *Chest*. 2011;139:1060–1071.
54. Morrison AK, Patel M, Johnson SL, et al. Pulmonary interstitial glycogenosis in a patient with trisomy 21. *J Neonatal Perinatal Med*. 2016;9:227–231.
55. Jiskoot-Ermers ME, Antonius TA, Looijen-Salamon MG, et al. Irreversible respiratory failure in a full-term infant with features of

pulmonary interstitial glycogenosis as well as bronchopulmonary dysplasia. *AJP Rep*. 2015;5:e136–e140.

56. Castillo M, Vade A, Lim-Dunham JE, et al. Pulmonary interstitial glycogenosis in the setting of lung growth abnormality: radiographs and pathologic correlation. *Pediatr Radiol*. 2010;40:1562–1565.
57. Smets K, Dhaene K, Schelstraete P, et al. Neonatal pulmonary interstitial glycogen accumulation disorder. *Eur J Pediatr*. 2004;163:408–409.
58. Deutsch GH, Young LR. Pulmonary interstitial glycogenosis: words of caution. *Pediatr Radiol*. 2010;40:1471–1475.
59. Lanfranchi M, Allbery SM, Wheelock L. Pulmonary interstitial glycogenosis. *Pediatr Radiol*. 2010;40:361–365.
60. Albafouille V, Sayegh N, De Coudenhove S, et al. CT scan patterns of pulmonary alveolar proteinosis in children. *Pediatr Radiol*. 1999;29:147–152.
61. Vrielynck S, Mamou-Mani T, Emond S, et al. Diagnostic value of high-resolution CT in the evaluation of chronic infiltrative lung disease in children. *AJR Am J Roentgenol*. 2008;191:914–920.
62. Copley SJ, Padley SP. High-resolution CT of paediatric lung disease. *Eur Radiol*. 2011;11:2564–2575.
63. Suzuki T, Sakagami T, Rubin BK, et al. Familial pulmonary alveolar proteinosis caused by mutations in CSF2RA. *J Exp Med*. 2008;205: 2703–2710.
64. Martinez-Moczygemba M, Doan ML, Elidemir O, et al. Pulmonary alveolar proteinosis caused by deletion of the GM-CSFRalpha gene in the X chromosome pseudoautosomal region 1. *J Exp Med*. 2008;205:2711–2716.
65. Trukalj M, Perica M, Ferenčić Ž, et al. Successful treatment of autoimmune pulmonary alveolar proteinosis in a pediatric patient. *Am J Case Rep*. 2016;17:641–645.
66. Hadda V, Tiwari P, Madan K, et al. Pulmonary alveolar proteinosis: experience from a tertiary care center and systematic review of Indian literature. *Lung India*. 2016;33(6):626–634.
67. Miller AL, Schissel S, Levy BD, et al. Clinical problem-solving. A crazy cause of dyspnea. *N Engl J Med*. 2011;364:72–77.
68. Esther CR Jr, Barker PM. Pulmonary lymphangiectasia: diagnosis and clinical course. *Pediatr Pulmonol*. 2004;38:308–313.
69. Barker PM, Esther CR Jr, Fordham LA, et al. Primary pulmonary lymphangiectasia in infancy and childhood. *Eur Respir J*. 2004;24: 413–419.
70. Copley SJ, Coren M, Nicholson AG, et al. Diagnostic accuracy of thin-section CT and chest radiography of pediatric interstitial lung disease. *AJR Am J Roentgenol*. 2000;174:549–554.
71. Putta T, Irodi A, Thangakunam B, et al. Young patient with generalized lymphangiomatosis: differentiating the differential. *Indian J Radiol Imaging*. 2016;26(3):411–415.
72. Swenson SJ, Hartman TE, Mayor JR, et al. Diffuse pulmonary lymphangiomatosis: CT findings. *J Comput Assist Tomogr*. 1995;19:348–352.
73. Chung CJ, Fordham LA, Barker P, et al. Children with congenital pulmonary lymphangiectasia: after infancy. *AJR Am J Roentgenol*. 1999;173:1583–1588.
74. Yalçin E, Dog D, Halilog M, et al. Postinfectious bronchiolitis obliterans in children: clinical and radiological profile and prognostic factors. *Respiration*. 2003;70:371–375.
75. Zhang L, Irion K, da Silva Porto N, et al. High-resolution computed tomography in pediatric patients with postinfectious bronchiolitis obliterans. *J Thorac Imaging*. 1999;14:85–89.
76. Smith KJ, Dishop MK, Fan LL, et al. Diagnosis of bronchiolitis obliterans with computed tomography in children. *Pediatr Allergy Immunol Pulmonol*. 2011;23:253–259.
77. Li YN, Liu L, Qiao HM, et al. Post-infectious bronchiolitis obliterans in children: a review of 42 cases. *BMC Pediatr*. 2014;14:238.
78. Mattiello R, Sarria EE, Mallol J, et al. Post-infectious bronchiolitis obliterans: can CT scan findings in early age anticipate lung function? *Pediatr Pulmonol*. 2010;45:315–319.
79. Lucaya J, Gartner S, García-Peña P, et al. Spectrum of manifestations of Swyer-James-Macleod syndrome. *J Comput Assist Tomogr*. 1998;22:592–597.
80. Kim TO, Oh IJ, Kang HW, et al. Temozolomide-associated bronchiolitis obliterans organizing pneumonia successfully treated with high-dose corticosteroid. *J Korean Med Sci*. 2012;27:450–453.
81. Vos R, Vanaudenaerde BM, Verleden SE, et al. Antiinflammatory and immunomodulatory properties of azithromycin involved in treatment and prevention of chronic lung allograft rejection. *Transplantation*. 2012;94(2):101–109.
82. Doellinger F, Weinheimer O, Zwiener I, et al. Differences of airway dimensions between patients with and without bronchiolitis obliterans syndrome after lung transplantation-Computer-assisted quantification of computed tomography. *Eur J Radiol*. 2016;85(8):1414–1420.
83. Abtahi H, Peiman S, Foroumandi M, et al. Long term follow-up of sulfur mustard related bronchiolitis obliterans treatment. *Acta Med Iran*. 2016;54(9):605–609.
84. Sithamparanathan S, Thirugnanasothy L, Morley KE, et al. Observational study of methotrexate in the treatment of bronchiolitis obliterans syndrome. *Transplant Proc*. 2016;48(10):3387–3392.
85. Magee AL, Montner SM, Husain A, et al. Imaging of hypersensitivity pneumonitis. *Radiol Clin North Am*. 2016;54:1033–1046.
86. Torres PP, Moreira MA, Silva DG, et al. High-resolution computed tomography and histopathological findings in hypersensitivity pneumonitis: a pictorial essay. *Radiol Bras*. 2016;49:112–116.
87. Zacharisen MC, Fink JN. Hypersensitivity pneumonitis and related conditions in the work environment. *Immunol Allergy Clin North Am*. 2011;31:769–786.
88. Fullmer JJ, Langston C, Dishop MK, et al. Pulmonary capillaritis in children: a review of eight cases with comparison to other alveolar hemorrhage syndromes. *J Pediatr*. 2005;146:376–381.
89. Susarla SC, Fan LL. Diffuse alveolar hemorrhage syndromes in children. *Curr Opin Pediatr*. 2007;19:314–320.
90. Castellazzi L, Patria MF, Frati G, et al. Idiopathic pulmonary haemosiderosis in paediatric patients: how to make an early diagnosis. *Ital J Pediatr*. 2016;42:86.
91. Feragalli B, Mantini C, Sperandeo M, et al. The lung in systemic vasculitis: radiological patterns and differential diagnosis. *Br J Radiol*. 2016;89:20150992.
92. Connolly B, Manson D, Eberhard A, et al. CT appearance of pulmonary vasculitis in children. *AJR Am J Roentgenol*. 1996;167:901–904.
93. Kligerman SJ, Groshong S, Brown KK, et al. Nonspecific interstitial pneumonia: radiologic, clinical, and pathologic considerations. *Radiographics*. 2009;29:73–87.
94. Flaherty KR, Martinez FJ. Nonspecific interstitial pneumonia. *Semin Respir Crit Care Med*. 2006;27:652–658.
95. Tomassetti S, Ryu JH, Piciucchi S, et al. Nonspecific interstitial pneumonia: what is the optimal approach to management? *Semin Respir Crit Care Med*. 2016;37:378–394.
96. Polverosi R, Maffesanti M, Dalpiaz G. Organizing pneumonia: typical and atypical HRCT patterns. *Radiol Med*. 2006;111:202–212.
97. Epler GR. Bronchiolitis obliterans organizing pneumonia, 25 years: a variety of causes, but what are the treatment options? *Expert Rev Respir Med*. 2011;5:353–361.
98. Long NM, Plodkowski AJ, Schor-Bardach R, et al. Computed tomographic appearance of organizing pneumonia in an oncologic patient population. *J Comput Assist Tomogr*. 2016; [Epub ahead of print].
99. Gupta A, Teo L, Masel P, et al. Transtuzumab induced organizing pneumonia: a case report. *Springerplus*. 2016;5(1):1964. eCollection 2016.
100. Abi-Khalil S, Fadel N, Menassa-Moussa L, et al. Spontaneous resolution of cryptogenic organizing pneumonia in pediatrics: a case report. *Arch Pediatr*. 2016;23:519–522.
101. Jeong YJ, Kim KI, Seo IJ, et al. Eosinophilic lung diseases: a clinical, radiologic, and pathologic overview. *Radiographics*. 2007;27:617–637.
102. Oermann CM, Panesar KS, Langston C, et al. Pulmonary infiltrates with eosinophilia syndromes in children. *J Pediatr*. 2000;136:351–358.
103. Martinez S, Heyneman LE, McAdams HP, et al. Mucoid impactions: finger-in-glove sign and other CT and radiographic features. *Radiographics*. 2008;28:1369–1382.
104. Fernández Pérez ER, Olson AL, Frankel SK. Eosinophilic lung diseases. *Med Clin North Am*. 2011;95:1163–1187.
105. Williams KW, Ware J, Abiodun A, et al. Hypereosinophilia in children and adults: a retrospective comparison. *J Allergy Clin Immunol Pract*. 2016;4(5):941–947.e1.
106. Bayhan GÍ, Batur A, Taylan-Özkan A, et al. A pediatric case of Fascioliasis with eosinophilic pneumonia. *Turk J Pediatr*. 2016;58: 109–112.
107. Towbin AJ, Chaves I. Chronic granulomatous disease. *Pediatr Radiol*. 2010;40:657–668.
108. Khanna G, Kao SC, Kirby P, et al. Imaging of chronic granulomatous disease in children. *Radiographics*. 2005;25:1183–1195.
109. Afrough R, Mohseni SS, Sagheb S. An uncommon feature of chronic granulomatous disease in a neonate. *Case Rep Infect Dis*. 2016;2016:5943783.
110. Bondioni MP, Lougaris V, Di Gaetano G, et al. Early identification of lung fungal infections in chronic granulomatous disease (CGD)

using multidetector computer tomography. *J Clin Immunol*. 2016; [Epub ahead of print].

111. Garg G, DaSilva R, Bhalakia A, et al. Utility of fluorine-18-fluorodeoxyglucose positron emission tomography/computed tomography in a child with chronic granulomatous disease. *Indian J Nucl Med*. 2016;31(1):62–64.
112. Cleveland RH, Stamoulis C, Sawicki G, et al. Brasfield and Wisconsin scoring systems have equal value as outcome assessment tools of cystic fibrosis lung disease. *Pediatr Radiol*. 2014;44:529–534.
113. Calder AD, Bush A, Brody AS, et al. Scoring of chest CT in children with cystic fibrosis: state of the art. *Pediatr Radiol*. 2014;44:1496–1506.
114. Hayes D Jr, Winkler MA, Kirkby S, et al. Preprocedural planning with prospectively triggered multidetector row CT angiography prior to bronchial artery embolization in cystic fibrosis patients with massive hemoptysis. *Lung*. 2012;190(2):221–225.
115. Girón Moreno RM, Caballero P, Friera A. Multidetector computed tomography angiography for pre-embolization assessment in cystic fibrosis patients with massive haemoptysis. *Respir Med*. 2014;108(5):816–817.
116. Dournes G, Menut F, Macey J, et al. Lung morphology assessment of cystic fibrosis using MRI with ultra-short echo time at submillimeter spatial resolution. *Eur Radiol*. 2016;26:3811–3820.
117. Kruger SJ, Nagle SK, Couch MJ, et al. Functional imaging of the lungs with gas agents. *J Magn Reson Imaging*. 2016;43:295–315.
118. Ramsey BW, Davies J, McElvaney NG, et al. A CFTR potentiator in patients with cystic fibrosis and the G551D mutation. *N Engl J Med*. 2011;365:1663–1672.
119. Fajac I, De Boeck K. New horizons for cystic fibrosis treatment. *Pharmacol Ther*. 2016;Dec 1, pii: S0163-7258(16)30235-2.
120. Beigelman-Aubry C, Godet C, Caumes E. Lung infections: the radiologist's perspective. *Diagn Interv Imaging*. 2012;93:431–440.
121. Starlz TE. Infectious pulmonary disease in patients receiving immunosuppressive therapy for organ transplantation. *Rev Med Virol*. 1999;9:3–14.
122. Toma P, Bertaina A, Castagnola E, et al. Fungal infections of the lung in children. *Pediatr Radiol*. 2016;46:1856–1865.
123. Kloth C, Forler S, Gatidis S, et al. Comparison of chest-CT findings of influenza virus-associated pneumonia in immunocompetent vs. immunocompromised patients. *Eur J Radiol*. 2015;84:1177–1183.
124. Jiang T, Xue F, Zheng X, et al. Clinical data and CT findings of pulmonary infection caused by different pathogens after kidney transplantation. *Eur J Radiol*. 2012;81:1347–1352.
125. Wang X, Wang Y, Zhu Q, et al. Pulmonary infection in the renal transplant recipients: analysis of the radiologic manifestations. *Radiology of Infectious Diseases*. 2014;1:3–6.
126. Zheng X, Zhang G. Imaging of pulmonary infectious diseases in immunocompromised patients. *Radiology of Infectious Diseases*. 2014;1: 37-41.
127. Tantisiriwat W, Powderly W. Prophylaxis and treatment of opportunistic infection in patients on HAART. *AIDS Read*. 1999;9:122–130.
128. Lin X, Garg S, Mattson CL, et al. Prescription of pneumocystis jiroveci pneumonia prophylaxis in HIV-infected patients. *J Int Assoc Provid AIDS Care*. 2016;15:455–458.

# 57

# Pulmonary Manifestations of Systemic Disease

*Julie Currie O'Donovan and Beverley Newman*

Many systemic diseases of childhood involve the pulmonary parenchyma. The pulmonary manifestations may in fact prompt the patient or parents to seek medical attention and frequently a chest radiograph is obtained early in the illness. Therefore the radiologist can play an important role in directing the diagnostic workup by recognizing that the pulmonary findings reflect an underlying condition. In some patients, such as those with pulmonary edema or sickle cell disease, the radiograph shows the pulmonary findings adequately to continue appropriate clinical care. In many patients, however, the chest radiograph provides initial clues to the diagnosis but is otherwise nonspecific and prompts further investigation with computed tomography (CT). Techniques such as controlled ventilation inspiratory/expiratory breath-holding (see Chapter 49) and more recently available CT volume scans (mitigating the need for sedation) continue to reduce breathing artifacts and thus improve lung parenchymal assessment.

This chapter will discuss several specific systemic diseases affecting the lung as well as the effects of generalized systemic illness on the lung. In addition, it will detail pulmonary injury that occurs following therapy such as hematopietic stem cell transplantation and extrinsic agents including chemotherapy, radiation therapy, inhalation injury, and ingestion of hydrocarbons and mineral oil. Finally, near drowning events and conditions with pulmonary calcifications will be described.

## SPECIFIC SYSTEMIC DISEASES

### Vasculitis and Collagen Vascular Disease

### Overview

Pediatric patients with pulmonary vasculitis typically present in their teen years. Vasculitides affecting the small vessels are the most likely to cause pulmonary parenchymal disease, and granulomatosis with polyangiitis (GPA, formerly Wegener granulomatosis) and idiopathic pulmonary capillaritis are the most common of these disorders in children. Microscopic polyangiitis (MPA) and eosinophilic granulomatosis with polyangiitis (EGPA, formerly Churg–Strauss syndrome) also involve the lung parenchyma but are rarely seen in children.[1-4]

GPA typically presents with a triad of necrotizing granulomatous lesions in both the upper and lower respiratory tract, as well as glomerulonephritis. MPA is a nongranulomatous necrotizing vasculitis almost always seen with glomerulonephritis. EGPA typically presents with asthma and blood eosinophilia.[1]

Pulmonary involvement is seen less commonly in children than in adults with collagen vascular diseases (CVDs) such as juvenile arthritis, dermatomyositis, systemic sclerosis (scleroderma), systemic lupus erythematosus (SLE), and mixed connective tissue disease. The highest incidence of pulmonary involvement is seen in children with systemic sclerosis (59%–91%) and it is associated with significant morbidity and mortality rates.[5,6] Abnormal pulmonary function tests (PFTs) can act as a monitoring tool to identify children who would benefit from further evaluation with high-resolution CT (HRCT).[6] Symptomatic lung disease is significantly less common in juvenile idiopathic arthritis and SLE, reported in only 5% of patients.[7]

Pulmonary hemorrhage may occur in the vasculitides and in CVDs (e-Fig. 57.1) and has high morbidity and mortality rates (50%–90%).[1,8] Additionally, the vasculitides and CVDs both may cause pulmonary renal syndrome, which is the manifestation of pulmonary hemorrhage and glomerulonephritis. It often occurs in GPA and SLE.[1,2]

***Etiology.*** Most of the pulmonary vasculitides are immunologically mediated although up to half of pediatric capillaritis cases are antibody negative.[4] GPA, MPA, and EGPA are associated with antineutrophil cytoplasmic antibodies (ANCAs) and are sometimes referred to as *ANCA-associated systemic vasculitides*.[1]

Most of the CVDs also have an autoimmune mechanism, SLE being the classic autoimmune condition associated with antinuclear antibody. These disorders are associated with a variable degree of inflammation of multiple organ systems, including the lung. Depending on the specific disorder, patients may present with arthritis, serositis, vasculitis, other soft tissue inflammation, or all of these.

***Imaging.*** The imaging findings of pulmonary vasculitis and CVDs are summarized in Table 57.1. The most frequent imaging findings of GPA are variable sized nodules (seen in up to 70% of patients), followed by ground-glass opacities and airspace consolidation; 17% of the nodules showed cavitation in a pediatric population, and up to 50% of nodules are reported to be cavitary in a general population, with higher incidence of cavitation in nodules larger than 2 cm. The nodules are characteristically surrounded by a halo of ground-glass opacity, which represents hemorrhage[9-11] (Fig. 57.2). Airway wall thickening may also be seen, but airway strictures are significantly less common in children (3%) compared with adults (up to 59%).[9] Diffuse alveolar hemorrhage (occurring in 44% of pediatric GPA) is characterized by lobular or lobar regions of ground-glass opacity or airspace consolidation on CT.[11-13] It may also show the "crazy paving" pattern on CT, especially as it evolves.[14]

In the case of CVDs, pleural and pericardial effusions are the most common findings in the chest. Pulmonary parenchymal abnormalities are significantly less common but follow a similar pattern for most of these disorders and include ground-glass opacity and interstitial septal thickening, which may progress to pulmonary fibrosis. Despite normal chest radiographs or only minimal radiographic abnormalities in children with systemic sclerosis, HRCT demonstrates ground-glass opacities, peripheral areas of pulmonary fibrosis, and subpleural micronodules (Fig. 57.3).[5] Serious and even life-threatening lung disease has been described in some children with systemic juvenile idiopathic arthritis (JIA), including interstitial lung disease, alveolar proteinosis/endogenous lipoid pneumonia, and pulmonary hypertension (e-Fig. 57.4). Pulmonary manifestations may be related to a macrophage activation syndrome.[14,15] "Shrinking lung syndrome" has been described in SLE and represents decrease in lung volume that manifests radiographically by an elevated diaphragm.[8,14,16]

***Treatment and Follow-up.*** Treatment for the vasculitides and CVDs is primarily aimed at suppressing the immune response, typically with corticosteroids and chemotherapeutic agents, as well as newer biologic drugs when appropriate.

Patients who develop diffuse alveolar hemorrhage often show evolving changes on CT follow-up. A more linear and interstitial type of pattern may develop with interlobular septal thickening and the appearance of the crazy paving pattern. If episodes of hemorrhage recur, this may also progress to interstitial fibrosis.[12] Pulmonary involvement with CVD may progress to interstitial

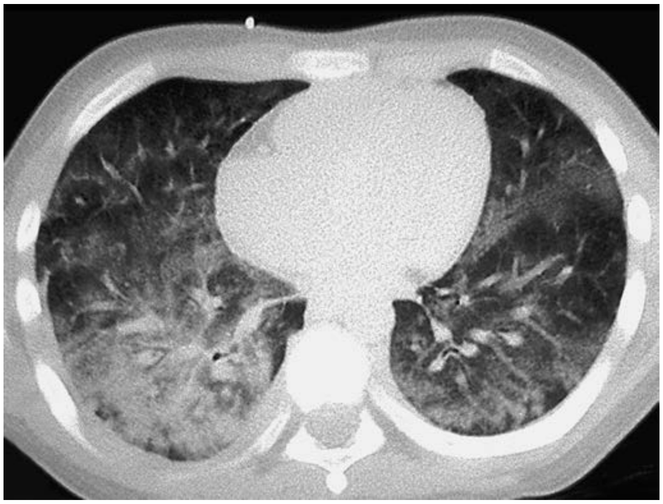

**e-Figure 57.1. Pulmonary hemorrhage in a teenage boy with pulmonary vasculitis resulting from collagen vascular disease.** The patient presented with hemoptysis. CT image shows diffuse but somewhat patchy ground-glass opacification in both lungs.

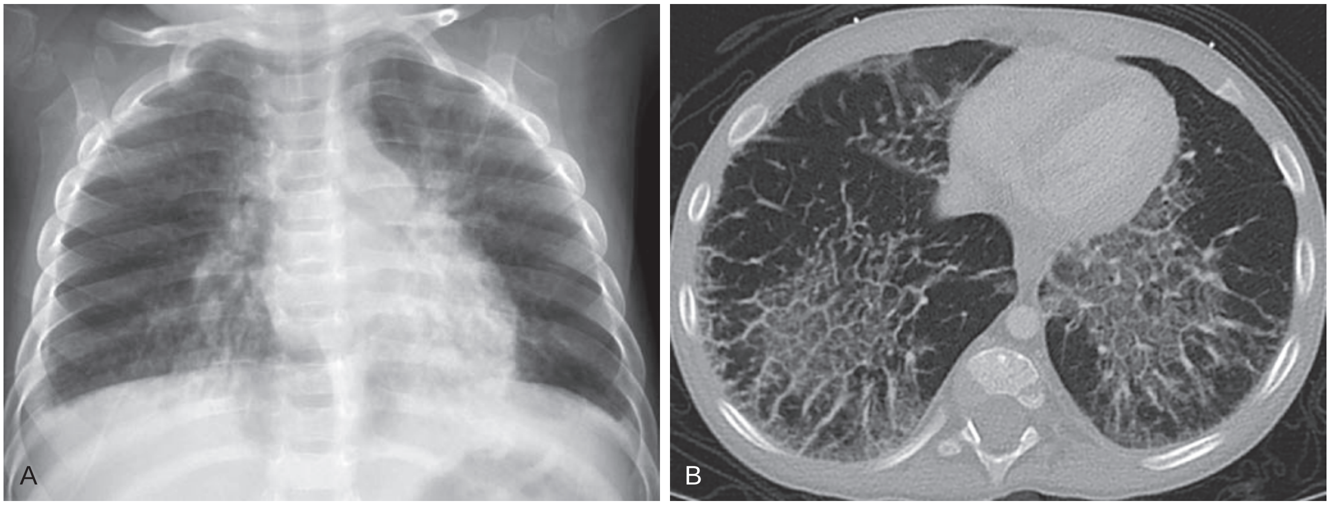

**e-Figure 57.4. Systemic juvenile idiopathic arthritis and acute exacerbation in a 2-year-old.** No clinical evidence of infection. (A) Chest radiograph shows perihilar increased interstitial markings, more confluent right lower lobe opacity and right pleural effusion. (B) Axial CT image (lung window) shows peripheral reticular changes and bilateral basilar interlobular septal thickening with ground-glass opacity suggestive of some fibrosis, as well as alveolar proteinosis (confirmed on bronchoscopy).

**TABLE 57.1** Pulmonary Imaging Findings in Systemic Diseases

| | Nodules (Some Cavitary) | Ground-Glass Opacities | Airspace Opacities | Diffuse Alveolar Hemorrhage[*] | Interstitial Thickening | Pleural/ Pericardial Disease | Lung Cysts |
|---|---|---|---|---|---|---|---|
| Granulomatosis with polyangiitis (Wegener) | ++++<br>90% | ++<br>52% | ++<br>45% | ++<br>44% | — | + | — |
| Microscopic polyangiitis | — | + | + | +++<br>57% | + | + | — |
| Eosinophilic granulomatosis with polyangiitis (Churg–Strauss) | ++<br>38% | +++<br>75% | +++<br>75% | — | — | — | — |
| Juvenile idiopathic arthritis (JIA) | +[†] | ++ | — | — | ++ | +++<br>60% | — |
| Systemic lupus erythematosus | — | ++ | ++ | ++ | + | +++ | — |
| Systemic sclerosis (scleroderma) | ++<br>64%[‡] | +++<br>73% | — | — | ++++<br>91% | + | — |
| Mixed connective tissue disease | — | ++ | — | — | ++ | — | — |
| Dermatomyositis | — | ++ | — | — | + | — | — |
| Acute chest syndrome | — | — | ++++ | — | + | ++ | — |
| Langerhans cell histiocytosis | +++ | — | — | — | — | ++ | ++++ |
| Gaucher/Niemann–Pick disease | + | + | — | — | + | — | — |

[*] Specific imaging findings are a spectrum from ground-glass opacities to airspace consolidation.

[†] Nodules in juvenile arthritis seen in lipoid pneumonia.

[‡] Seen as subpleural micronodules and were not considered a dominant finding.

*Data from references*[1,5,7,8,13]*, and Feng RE, Xu WB, Shi JH, et al. Pathological and high resolution CT findings in Churg-Strauss syndrome.* Chin Med Sci J. *2011;26(1):1–8.*

pulmonary fibrosis regardless of treatment, with advanced stages showing honeycombing. Pulmonary artery hypertension may also develop with advanced lung disease, especially in systemic sclerosis and systemic JIA.

Follow-up imaging is primarily determined by clinical needs, symptoms, or both. Follow-up chest radiograph can be helpful but CT is more likely to show subtle changes. Progression of abnormal PFTs in patients with juvenile systemic sclerosis over time correlate with worsening of changes on CT, suggesting that PFTs could potentially be used as a marker to determine when follow-up CT may be needed.[6]

## Sickle Cell Disease

### Overview

Acute chest syndrome (ACS), an illness that occurs in up to 50% of children with sickle cell disease (SCD), is characterized by chest pain, leukocytosis, fever, and a new pulmonary opacity. It is a primary cause of death and hospitalization in all patients with SCD and in children usually occurs between 2 and 4 years of age.[17] ACS also occurs in patients with other sickle hemoglobinopathies.[18] When not fatal, it may lead to chronic lung disease (4%) and pulmonary hypertension.[19]

***Etiology.*** The etiology of ACS is complex and not always known. In a large multicenter study, established causes were microvascular occlusion and infarction (16%), infection (29%), fat emboli from bone marrow infarcts (9%), and unknown in 46%. *Chlamydia*, *Mycoplasma*, and viral agents were the most common pathogens in cases caused by infection. One-third of patients presented with symptoms of long bone pain caused by vasoocclusive crisis and developed ACS 2 to 3 days later.[20]

***Imaging.*** Radiographic findings of ACS by definition include the presence of a pulmonary opacity (e-Fig. 57.5) but are otherwise nonspecific. Opacities were noted in the lower lobes in about 90%, and pleural effusion was noted in 55% of patients in a large multicenter study (see Table 57.1).[20]

Although CT is not generally used in the setting of ACS, chronic sickle cell lung disease has been studied. Abnormal findings are most pronounced at the lung bases and include parenchymal bands, interlobular septal thickening, architectural distortion, and traction bronchiectasis. Honeycombing is unusual, in contrast to other types of pulmonary fibrosis.[21]

***Treatment and Follow-up.*** Therapy for ACS includes hydration, analgesia, respiratory support (including bronchodilators), broad-spectrum antibiotics, transfusion therapy, and sometimes corticosteroids.[22] Imaging follow-up is primarily dictated by clinical course and usually only requires radiography.

## Langerhans Cell Histiocytosis

### Overview

*Langerhans cell histiocytosis (LCH)* is the preferred term for the condition showing a proliferation of a group of histiocytes known as *Langerhans cells*. Langerhans cells are of myeloid dendritic cell origin and contain characteristic Birbeck bodies on histology.[23] The peak age at initial diagnosis is 1 to 3 years, and most patients present with osseous lesions.[23] LCH is currently classified according to the extent of involvement, whether it involves a single site (better prognosis) or multiple sites (higher risk of long-term problems). The involvement of “risk organs” (bone marrow, liver, or spleen) indicates a poorer prognosis and demands more aggressive treatment.[24]

Pulmonary involvement is reported to be present in 10% of all patients with LCH and 23% to 50% of children with multisystem LCH, with a mean age of 11.9 months in one study.[14,23,24] Disease-free survival in these patients was 69%, with 3 out of 4 deaths occurring when “risk organs” other than the lung were involved. Although lung disease was traditionally considered a poor prognostic indicator in LCH, recent studies have shown that it does not adversely affect outcome. Primary pulmonary LCH (single site) is rare in children and is typically seen in young adult smokers.[24,25]

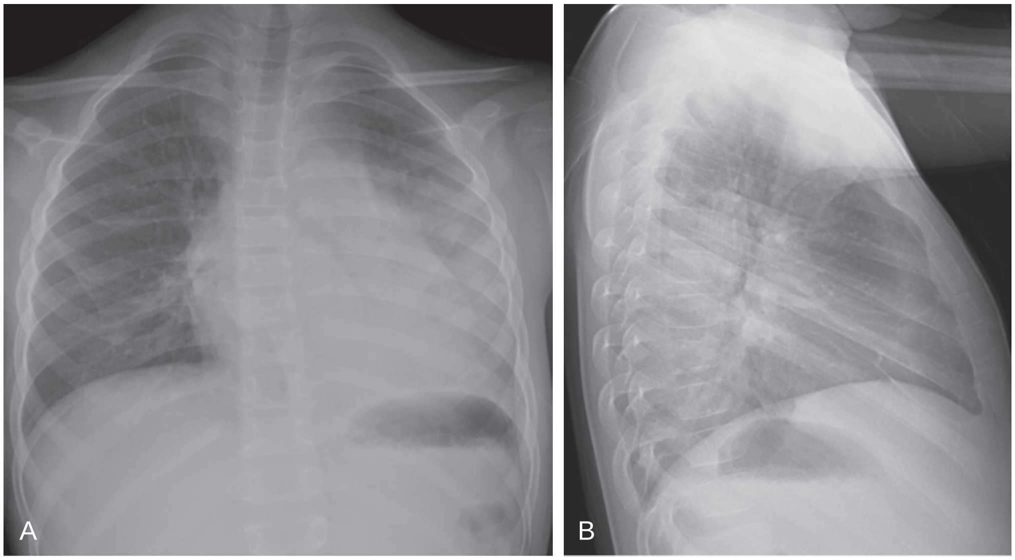

**e-Figure 57.5. Sickle cell disease with acute chest syndrome.** An 8-year-old boy with sickle cell disease who presents with fever. (A and B) Posteroanterior and lateral chest radiographs show dense airspace consolidation in the left lower lobe with a small pleural effusion.

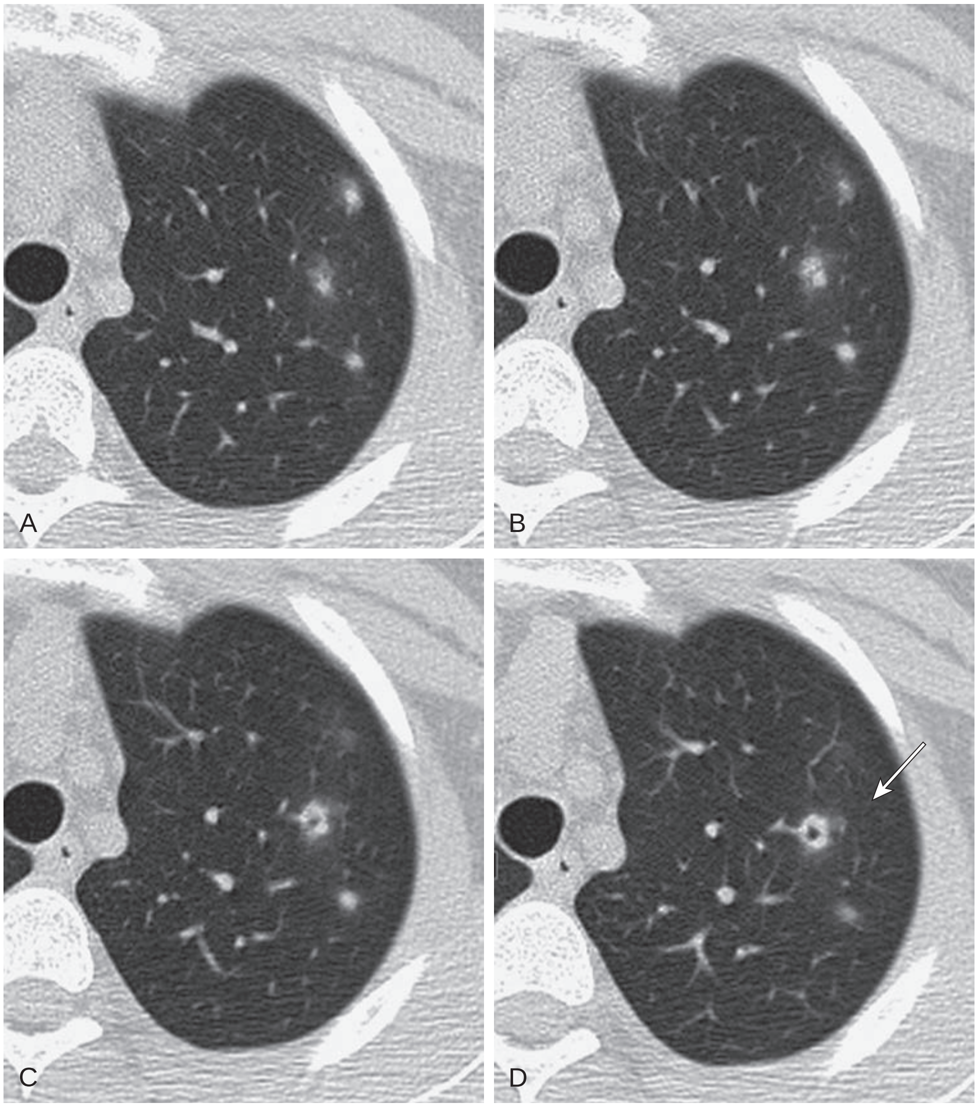

**Figure 57.2. Granulomatosis with polyangiitis (Wegener).** This 16-year-old girl had a history of vasculitic skin lesions and headache. Computed tomography (CT) of the sinuses revealed inflammatory changes *(not shown).* Axial CT images of the chest (A–D) show a left upper lobe cavitary lesion *(D, arrow),* as well as several solid pulmonary nodules (A–C), all with surrounding halos of ground-glass opacity. Lung biopsy was positive for granulomatosis with polyangiitis.

***Etiology.*** The etiology of LCH is not known. Most investigators believe it to be an immune-mediated condition, in which the Langerhans cells accumulate and cause an inflammatory reaction. In the lungs, destructive granulomatous lesions occur in the interstitial tissues, bronchial and bronchiolar epithelium, and subpleural septa and may eventually lead to cystic lesions.[23] Pulmonary fibrosis occurs later in 10% of children.[26]

***Imaging.*** Radiologic findings of LCH vary widely with the extent of the disease and are summarized in Table 57.1. The initial chest radiograph may be normal. Small nodules and cysts may be seen, with upper lobe involvement equal to or more extensive than lower lobe involvement (Fig. 57.6). The reticular appearance noted on a chest radiograph is often from multiple small cysts.[23,27] LCH is the most common cause of acquired extensive cystic lung disease in children (e-Fig. 57.7). Spontaneous pneumothorax is reported to occur in about 11% of patients with pulmonary involvement and may be the first indicator of pulmonary disease.[27] However, it may also be a manifestation of more advanced disease, as in adolescents who more often have large coalescent cysts (see e-Fig. 57.7).[14]

CT is indicated for neonates with LCH and any patient with abnormalities on the chest radiograph.[24] CT findings in LCH are characterized by small nodules (with or without cavitation) with upper and middle lobe predominance (see Fig. 57.6).[14,23,28] The pulmonary late-stage disease shows interstitial thickening and cystic spaces of variable diameter (see e-Fig. 57.7).[23] The pleura may be thickened and sometimes replaced by a thick layer of granulomatous tissue. However, pleural effusions are rare.[29] Mediastinal and hilar adenopathy is also rare in children with pulmonary LCH.[23,27]

***Treatment and Follow-up.*** Treatment of pulmonary LCH depends on the extent of disease and whether "risk" organs are involved. Generally, the first line of treatment is corticosteroids, vinblastine, or both, with duration of therapy being determined by response. Radiation therapy has fallen out of favor except for treating unstable bone lesions.[24] Imaging follow-up for pulmonary LCH depends on clinical symptoms. If abnormalities were present on initial chest radiographs, radiographs can be used for follow-up with CT reserved for progression and/or problem solving.

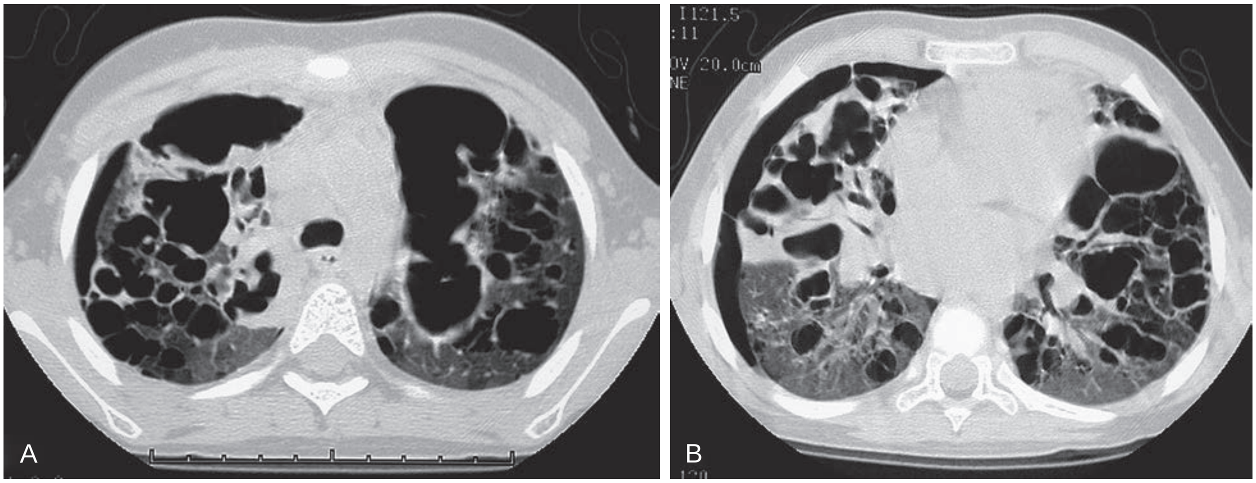

**e-Figure 57.7. Progressive advanced changes in Langerhans cell histiocytosis (LCH) of the lungs.** This child first presented at age 2 years with LCH involving both temporal bones and cystic lung disease. The patient was treated with chemotherapy and returned at age 4 years with increasing respiratory distress. The chest radiograph (not shown) showed a marked interval increase in bilateral cystic lung changes and suggested a possible small right pneumothorax. (A and B) High-resolution computed tomography shows that multiple cysts of varying sizes have largely replaced much of the lung parenchyma; loculated right pneumothorax was confirmed. Within 3 weeks, the patient developed a large left pneumothorax and died of this cystic lung process 1 week later.

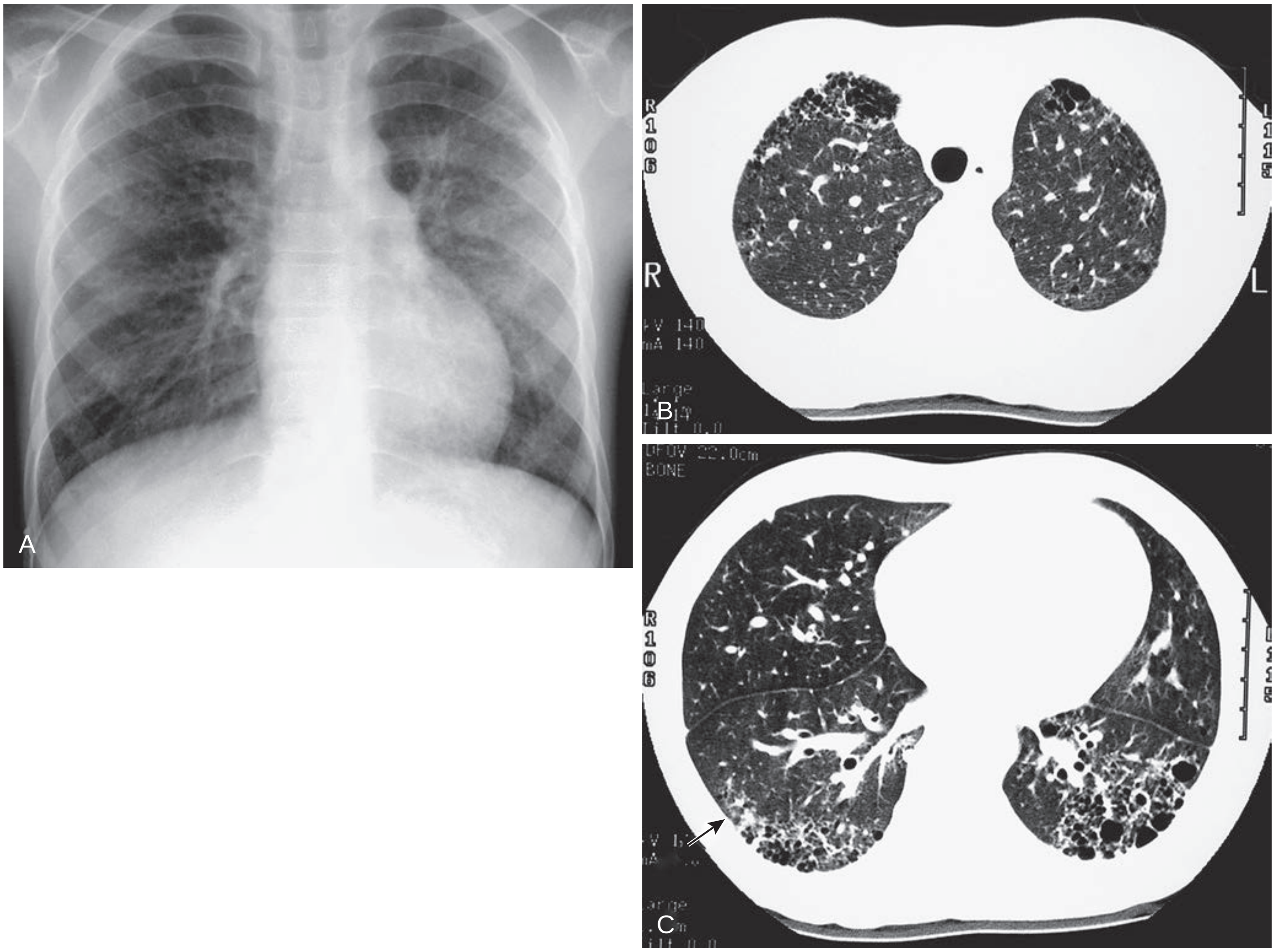

**Figure 57.3. Systemic sclerosis (scleroderma) in an 8-year-old girl diagnosed at age 5 years.** (A) Frontal chest radiograph shows mild increase in perihilar linear opacities. (B) High-resolution computed tomography (HRCT) of upper lung zones shows thin-walled, small cystic areas anteriorly in both lungs and a few small scattered subpleural lucencies and opacities more posteriorly. (C) HRCT through lower lung zones shows honeycomb pattern dependently in both lungs. More lateral area in right lung shows more ground-glass opacity *(arrow)* that may represent active disease.

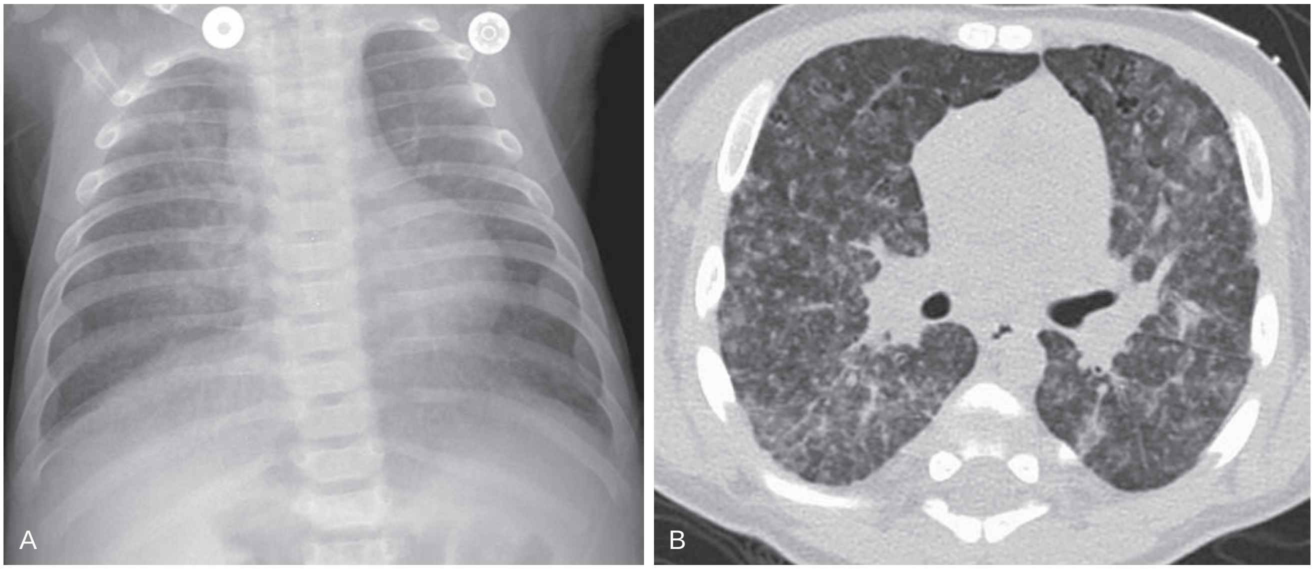

**Figure 57.6. Langerhans cell histiocytosis of the lungs in a 2.5-month-old boy who initially presented with a skin rash.** (A) Anteroposterior chest radiograph shows a coarse reticulonodular interstitial pattern. (B) Axial CT image in a lung window shows the coarse reticulonodular interstitial pattern with some small thin-walled cysts seen in the anterior lung bilaterally.

### Gaucher Disease and Niemann–Pick Disease

#### Overview

These two lysosomal storage disorders have a wide range of pathologic expression in different organ systems most frequently affecting the bone marrow, liver/spleen and/or central nervous system, and rarely affecting the lung parenchyma. Gaucher disease is more common than Niemann–Pick. Gaucher neuronopathic type 3 is more likely to affect the lung than is Niemann–Pick type B.[30-33]

***Etiology.*** Both of these disorders are transmitted by an autosomal recessive inheritance pattern and genetic mutations have been identified for all types. Gaucher disease is caused by a deficiency of the enzyme glucocerebrosidase that results in an accumulation of the lipid glucocerebroside in phagocytic cells, so-called Gaucher cells. Niemann–Pick disease is caused by a deficiency of sphingomyelinase, resulting in accumulation of the lipid sphingomyelin in the Niemann–Pick cells. These lipid-laden "foamy" macrophages deposit in various tissues, and may infiltrate the lung causing pulmonary symptoms.[30-33] Niemann–Pick disease has been associated with endogenous lipoid pneumonia in several patients and was the presenting condition in three adult patients[34,35]

***Imaging.*** Both Gaucher and Niemann–Pick disease cause a diffuse reticulonodular pattern on chest radiographs. CT abnormalities have also been described in both, including ground-glass opacities, areas of consolidation, and interstitial thickening (Fig. 57.8). Mediastinal findings of lymphadenopathy and thymic enlargement are also reported in Gaucher disease.[31-37] Niemann–Pick type C2 occurs in infants and has been reported to cause a crazy paving pattern on CT (e-Fig. 57.9).[32,33]

***Treatment and Follow-up.*** Visceral involvement may improve with enzyme replacement therapy in Gaucher disease, and this therapy may offer an alternative to lung transplantation.[38] The current treatment for Niemann–Pick disease with pulmonary involvement is whole lung lavage.[34,35] Regarding follow-up imaging, chest radiographs have been recommended every 2 years for patients with Gaucher disease to monitor the lungs.[37] In the setting of known pulmonary involvement, CT follow-up would be more sensitive than plain radiography for subtle changes if clinically needed.

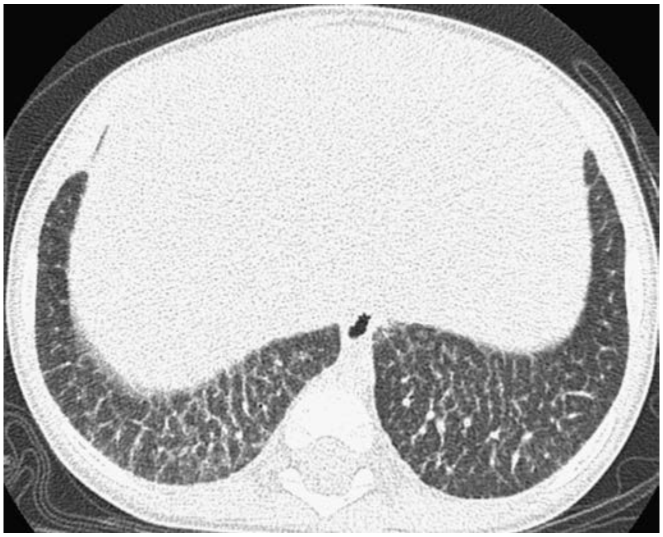

**Figure 57.8. Niemann–Pick disease type B.** Axial CT image from a 22-month-old shows diffuse interstitial septal thickening. *(Courtesy of Paul Guillerman, MD, Houston, Texas.)*

## PULMONARY CONDITIONS OCCURRING WITH GENERALIZED SYSTEMIC ILLNESS

### Pulmonary Edema

#### Overview

Pulmonary edema is the excessive accumulation of water and solute in the lung tissues. Functionally, pulmonary edema is divided into two general categories: (1) those cases having elevated pulmonary venous pressure (cardiogenic or hydrostatic) and (2) those associated with increased capillary permeability with normal microvascular pressure (noncardiogenic). Pulmonary edema may also have mixed etiologies, and sometimes the actual mechanism is unknown. Cardiogenic pulmonary edema is far less common in children than in adults.

#### Cardiogenic Pulmonary Edema

***Etiology.*** In children, cardiogenic edema usually occurs in infants less than 6 months of age as the result of congenital heart disease (CHD) such as left-to-right shunting lesions, left ventricular outlet obstruction, or obstruction of pulmonary venous return (Fig. 57.10).[39] Affected infants often present with nonspecific symptoms, including feeding difficulties, grunting, diaphoresis, wheezing, and retractions.[39] Rarely, pulmonary edema may be the presenting manifestation of CHD. In an older child, cardiomyopathy is the usual cause of cardiogenic edema (e-Fig. 57.11).

***Imaging.*** On the chest radiograph, cardiomegaly is usually found except in instances of pulmonary venous obstruction, in which interstitial edema is present in the absence of cardiac enlargement (see Fig. 57.10).

Early findings in interstitial edema in children with cardiogenic pulmonary edema are indistinct vascular margins and bronchial wall thickening. Interlobular septal thickening (septal lines or Kerley B lines) and interlobar fissural thickening are also seen. In infants and young children, fissural thickening is often more easily recognized than Kerley lines and is therefore an important diagnostic clue in children (see Fig. 57.10). An indirect radiographic finding frequently seen in children with CHD is hyperinflation. This may be a pitfall if the imager attributes the findings of peribronchial thickening and hyperinflation to airways disease and does not recognize them as subtle findings of interstitial edema. Alveolar edema usually occurs after development of interstitial edema and is the most recognizable radiographic finding of pulmonary edema. The classic appearance of acute alveolar edema is a central or "butterfly" distribution of airspace disease, with central edema and sparing of the lung periphery. Pleural effusions are also usually present (see e-Fig. 57.11). In children, pulmonary edema is frequently asymmetric, unilateral, or even lobar in distribution. This can be related to patient position (given the dependent nature of the edema) or more commonly due to the presence of asymmetric pulmonary arterial supply or pulmonary venous drainage in patients with CHD.

Although not commonly used to diagnose pulmonary edema, CT is sensitive for the detection of pulmonary edema of any etiology. CT shows peribronchial cuffing, septal lines, ground-glass opacities, and airspace consolidation in order of increasing severity (e-Fig. 57.12).[40,41]

***Treatment and Follow-up.*** Treatment for cardiogenic pulmonary edema is generally supportive and includes corrective (interventional or surgical) or palliative treatment for CHD. Diuretics and inotropes may be used for cardiac dysfunction. Ventilator support is provided, if needed. Extracorporeal membrane oxygenation and other types of ventricular assist devices are now being used more frequently in the setting of pediatric cardiac failure.[42] Typically, imaging follow-up with chest radiography is adequate, although CT may be used to clarify the vascular anatomy.

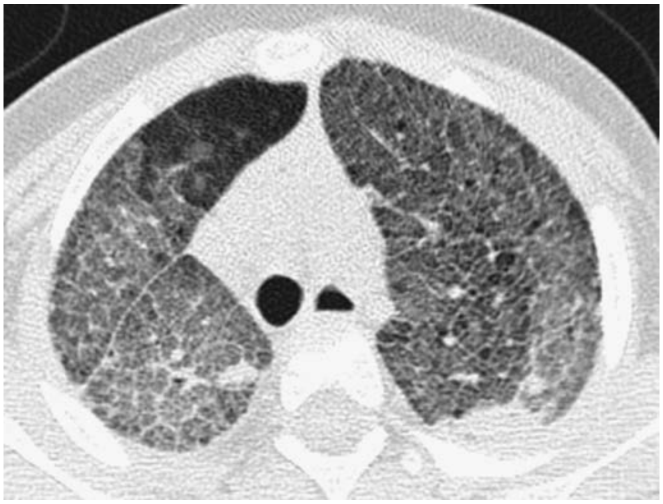

**e-Figure 57.9. Niemann–Pick disease type C2.** Axial CT image from a 23-month-old shows extensive crazy paving with the exception of the spared anterior right upper lobe. *(Courtesy of Paul Guillerman, MD, Houston, Texas.)*

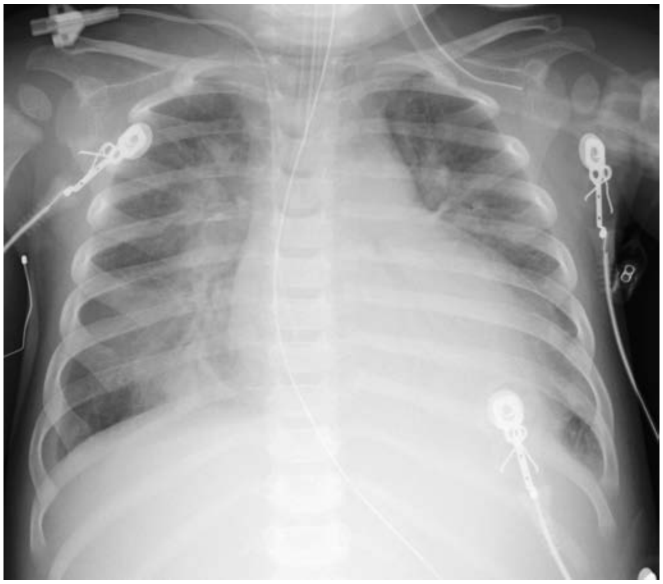

**e-Figure 57.11. Dilated cardiomyopathy.** A 14-month-old girl presented with 24 hours of increased work of breathing and wheezing. Portable chest radiograph shows characteristic cardiomegaly, perihilar and bibasilar distribution of airspace opacity caused by pulmonary edema, and a small right pleural effusion.

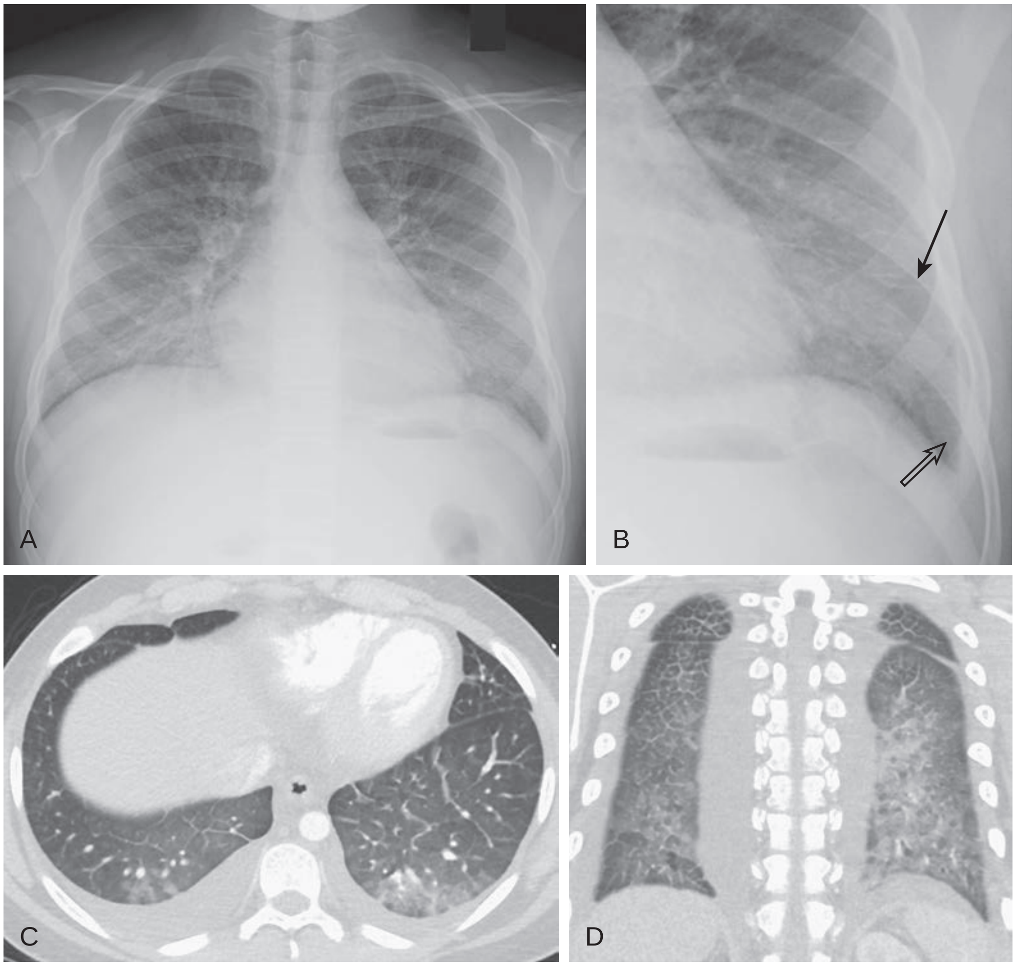

**e-Figure 57.12. Glomerulonephritis.** A 13-year-old boy with history of asthma presented with 5 days of shortness of breath and was found to be hypoxic. (A and B) Posteroanterior chest radiograph and magnified view show pulmonary edema with interstitial septal lines *(arrow)* and tiny left pleural effusion *(open arrow).* (C and D) Axial and coronal CT images depict typical findings of pulmonary edema showing interlobular septal thickening, dependent ground-glass opacity, and bilateral small pleural effusions. The child was diagnosed with postinfectious glomerulonephritis.

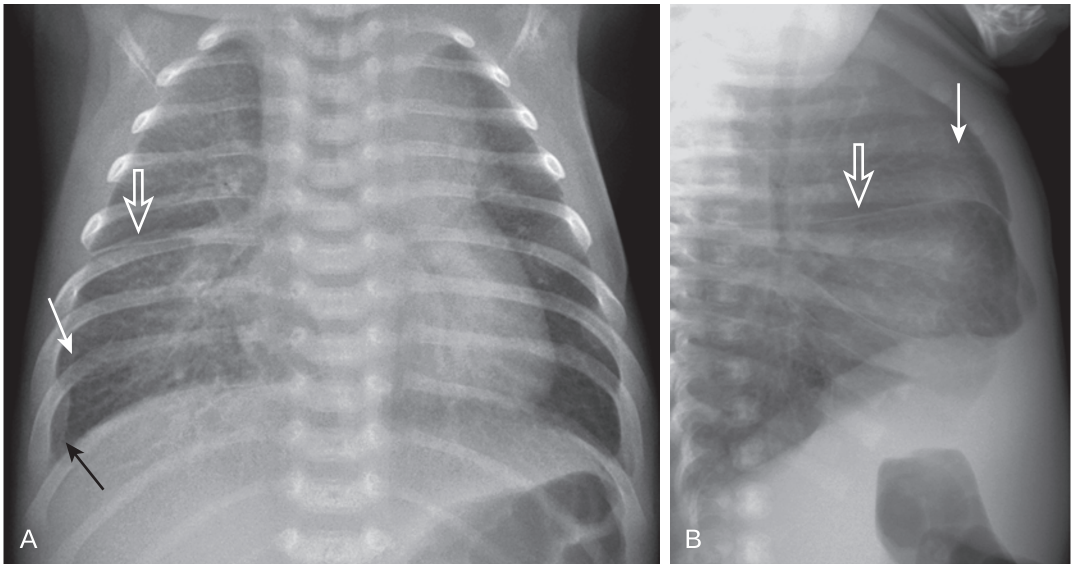

**Figure 57.10. Pulmonary edema caused by obstructed pulmonary venous return (cor triatriatum).** This 6-week-old infant presented to the emergency department with tachypnea and feeding difficulties. (A and B) Anteroposterior and lateral chest radiographs show normal heart size and subtle interstitial edema characterized by hyperinflation, septal lines *(white arrows),* fissural thickening *(open arrows),* and tiny right pleural effusion *(black arrow).* Cor triatriatum was shown by echocardiography.

### Noncardiogenic Pulmonary Edema

***Etiology.*** The frequent causes of noncardiogenic pulmonary edema in children are sepsis, near-drowning, neurogenic pulmonary edema, renal disease (see e-Fig. 57.12), and upper airway obstruction (e-Fig. 57.13). Other less common causes of noncardiogenic pulmonary edema include aspiration pneumonia, hydrocarbon pneumonitis, smoke inhalation, and drug reactions.[43] Pulmonary edema may also develop after inhalation of a variety of noxious fumes or soluble aerosols. Aspiration of hypertonic water-soluble contrast agents may also produce pulmonary edema.

Many episodes of noncardiogenic pulmonary edema progress to acute respiratory distress syndrome (ARDS). ARDS accounts for 1% to 3% of pediatric intensive care admissions, and the mortality rate in various series ranges from 40% to 60%. Sepsis, near-drowning, pneumonia, and smoke inhalation are the most frequent antecedents to pediatric ARDS. The typical course of ARDS progresses through stages of immediate lung injury, exudative alveolitis, fibroproliferative repair, and, in survivors, recovery.[43] A specific definition for pediatric ARDS (PARDS) was recently developed and published by the Pediatric Acute Lung Injury Consensus Conference Group. In brief, the onset of PARDS is defined by hypoxemia and a new chest imaging abnormality occurring within 7 days of a known clinical insult. Additionally, the associated respiratory failure must not be fully explained by cardiac failure or fluid overload.[44]

***Imaging.*** Chest radiographic abnormalities in glomerulonephritis and nephrotic syndrome are often sufficiently characteristic to allow the radiologist to suggest the correct diagnosis. A child or teenager presents without a known cardiac history with a basilar predominant interstitial edema pattern, often with pleural effusions (see e-Fig. 57.12). Glomerulonephritis may reportedly be distinguished from nephrotic syndrome by its tendency to show mild cardiomegaly and increased pulmonary vascularity.[45] Pericardial effusion is also more common in the setting of renal disease.

Like the clinical course, the radiographic pattern for ARDS is a multiple-stage continuum.[46,47] Initially, the radiograph is reflective of the initial insult, or it may be normal. In 12 to 24 hours, bilateral pulmonary opacities develop, consistent with noncardiogenic pulmonary edema, and opacities become progressively more confluent.[47] Subsequent improvement or continued worsening may be seen in the next several days. For patients with progression, the course often is then complicated by air leak phenomena (pneumothorax, pneumomediastinum, pulmonary interstitial emphysema), with or without ventilator-associated infections. Subsequently, further progression to chronic changes of fibrosis may occur.[43,46,47]

***Treatment and Follow-up.*** Treatment of noncardiogenic pulmonary edema is directed toward the primary cause, and is generally supportive. Ventilatory support is often needed. The use of positive end-expiratory pressure with mechanical ventilation has been shown by CT to improve ventilation of dependent regions of the lung in a setting of ARDS.[47,48] Extracorporeal membrane oxygenation is increasingly being used for children with severe respiratory failure. Pulmonary edema from neurogenic causes or upper airway obstruction usually resolves fairly rapidly, often within 12 to 48 hours.[39] Typically, imaging follow-up will be performed with chest radiography, as needed.

Survivors of ARDS may have long-term sequelae, often demonstrable by pulmonary function testing. Follow-up chest radiographs most often show a return to normal (80%) but may demonstrate increased interstitial markings, hyperaeration, or both.[43,47,49]

## LUNG INJURY RELATED TO THERAPY AND CAUSED BY EXTRINSIC AGENTS

### Graft–Versus–Host Disease

### Overview

Pediatric solid organ and hematopoietic stem cell transplant (HSCT) pulmonary complications include edema, hemorrhage, infection (immunosuppression confers susceptibility to unusual organisms; see Chapters 54 and 56), rejection, drug reactions, posttransplant lymphoproliferative disorder (see Chapter 55), and graft–versus–host disease (GVHD). As treatment and prophylaxis have become more precise, noninfectious pulmonary disease has become more important.

***Etiology.*** GVHD is an immune reaction of allogeneic donor cells to host tissues in HSCT. Early acute GVHD most commonly

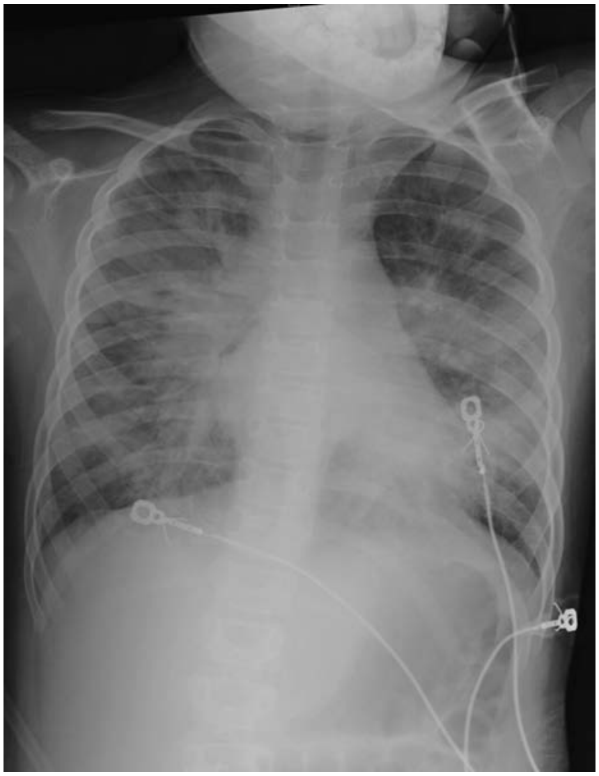

**e-Figure 57.13. Pulmonary edema due to upper airway obstruction.** This 4-year-old girl was admitted to the intensive care unit for asthma with hypoxia and wheezing. She had an acute exacerbation one night and was noted to also have obstructive sleep apnea. The following morning this anteroposterior view of the chest showed pulmonary edema pattern caused by upper airway obstruction, which promptly resolved when her obstructive airway symptoms were addressed more aggressively.

affects the skin, liver, and gastrointestinal tract, and rarely the lung. However, GVHD, especially chronic, represents a major long-term cause of morbidity and mortality in HSCT, and prompt recognition is important.[50] Idiopathic pneumonia syndrome (IPS) (early) and bronchiolitis obliterans (BO) (late) are the most common pulmonary conditions related to GVHD.[51] Acute IPS is defined as manifesting with widespread alveolar damage and pulmonary dysfunction without evidence of infectious, cardiac, and renal abnormality or fluid overload. The classification of IPS now includes other entities such as diffuse alveolar hemorrhage, acute respiratory distress syndrome, and organizing pneumonia. The etiology is likely multifactorial including conditioning toxicity, inflammatory cytokine release, immunologic factors, and occult infection.[50] Pulmonary cytolytic thromboemboli and alveolar proteinosis are less common entities that may be related to GVHD.

***Imaging.*** Chest radiographs are frequently nonspecific. The clinical presentation and time since transplant in conjunction with CT findings are helpful in generating a useful differential diagnosis. Imaging defines the extent of the abnormality and its evolution.

IPS is characterized by rapidly progressive clinical symptoms with nonspecific lobar, multilobar, or diffuse alveolar or reticular opacities that may be indistinguishable from pulmonary edema or infection (Fig. 57.14A).[50] The radiographic findings in organizing pneumonia are described in Chapter 56. BO is characterized on CT by patchy mosaic perfusion, air trapping (expiratory imaging is helpful), and bronchiectasis (Fig. 57.14B and C).

***Treatment.*** Treatment includes steroids and supportive care. Organizing pneumonia related to HSCT has a worse prognosis than other organizing pneumonias.[50] BO is treated with steroids but the disease usually has a slowly progressive course.

## Drug-Induced Pulmonary Disease

### Overview

Although a large number of pharmacologic agents may cause or exacerbate pulmonary disease in adults, the incidence and types of pulmonary effects specific to children are generally unknown.[52] Cause and effect are difficult to establish, and the time between drug administration and reaction is highly variable.

***Etiology.*** Chemotherapeutic agents (such as cyclophosphamide, bleomycin, busulfan, cisplatin, nitrosureas, mitomycin-C, and methotrexate) are the most common drugs associated with pulmonary toxicity (occurring in up to 10% of patients).[53,54] These medications may cause interstitial pneumonitis or fibrosis, hypersensitivity reaction, ARDS, or organizing pneumonia, previously known as bronchiolitis obliterans with organizing pneumonia (BOOP). Amiodarone is used for cardiac arrhythmias and may cause interstitial fibrosis, organizing pneumonia, or both.[53] Airway hyperreactivity has been associated with ingestion of aspirin and nonsteroidal antiinflammatory agents. Hypersensitivity reactions may be produced by methotrexate, sulfonamides, and nitrofurantoin.[53] Noncardiogenic pulmonary edema may result from overdoses of heroin, morphine, methadone, and cocaine.[53,55] Pulmonary hemorrhage may be seen after administration of anticoagulants, surfactants, and penicillamine.[52]

***Imaging.*** Radiographic findings of drug-induced reactions are variable and nonspecific, consisting of heterogeneous pulmonary opacities, homogeneous pulmonary opacities, or both.[52]

CT provides better characterization of pulmonary findings and therefore is more useful for early diagnosis of pulmonary toxicities. The imaging findings depend on the histologic process and may include interstitial disease, alveolar disease, or both.[52,53] Interstitial pneumonitis and fibrosis, typical of bleomycin, produce ground-glass opacities, areas of consolidation, and irregular linear opacities that tend to predominate in the lower lung zones. Methotrexate pulmonary toxicity resembles hypersensitivity pneumonia, showing ground-glass opacities and poorly defined centrilobular nodules.

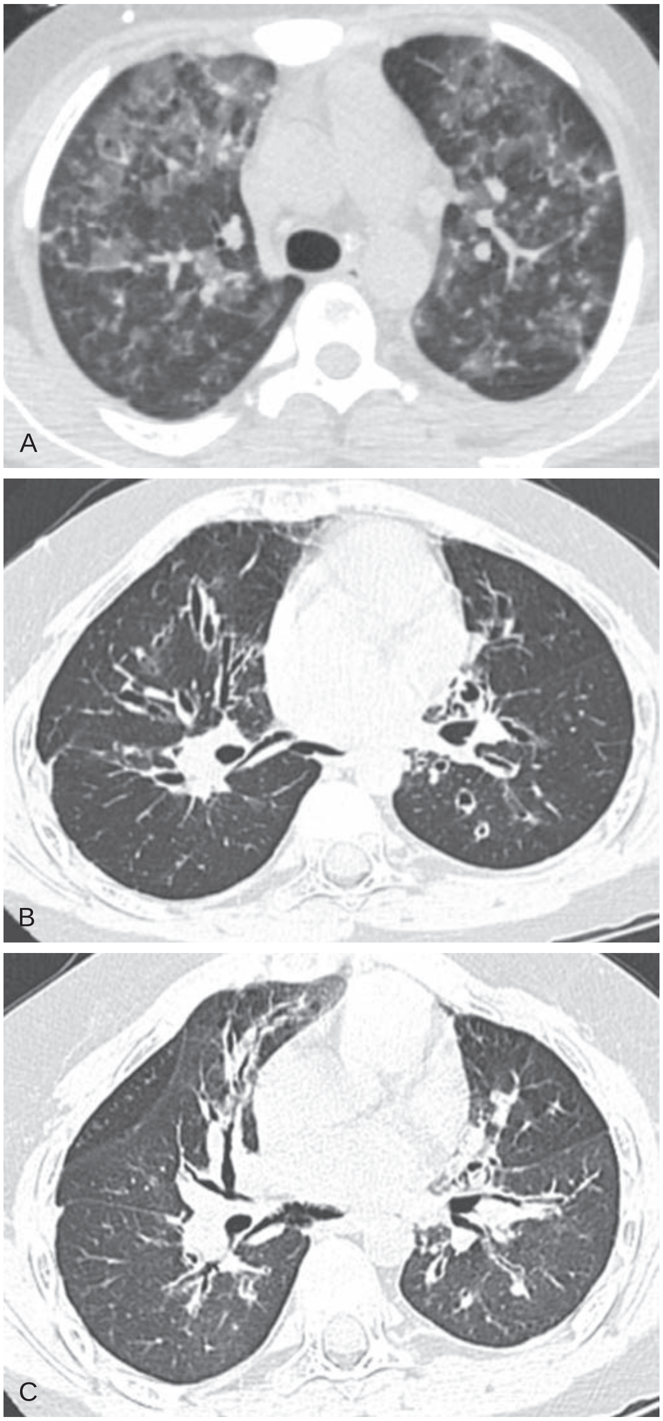

**Figure 57.14. Graft–versus–host disease complicated by idiopathic pneumonia syndrome (IPS) and bronchiolitis obliterans (BO) in two different patients.** (A) A 19-year-old patient 2 months after hematopoietic stem cell transplant (HSCT) with acute respiratory distress. Note patchy bilateral ground-glass opacity and centrilobular nodules. Hemosiderin-laden macrophages were present at bronchoalveolar lavage suggesting IPS with pulmonary hemorrhage. The patient responded promptly to steroids. (B and C) A 10-year-old patient, 2 years after HSCT with BO. Axial inspiratory (B) and expiratory (C) CT images demonstrate mosaic perfusion, scattered peribronchial thickening, bronchiectasis, and exiratory air trapping anteriorly.

ARDS, previously discussed, results in predominantly dependent airspace consolidation. Organizing pneumonia is the least common pattern with chemotherapy and shows peribronchial or subpleural areas of consolidation.[53]

Airway reactivity is associated with air trapping on imaging. The appearance of noncardiogenic pulmonary edema and pulmonary hemorrhage has been discussed earlier in this chapter.

***Treatment and Follow-up.*** Removal of the causative agent is the ideal management for drug-induced pulmonary disease if the toxicity can be recognized and the removal is feasible. Unfortunately, some pulmonary toxicities are irreversible. If symptoms persist, radiography and CT may help in follow-up management.

## Radiation Damage to the Thorax

### Overview

Lung damage may follow radiation therapy given primarily to the lungs, the mediastinum, the chest wall, or the total body. The incidence of radiation damage to the lung in adult patients treated for lung cancer, mediastinal lymphoma, and breast cancer ranges from 5% to 20%.[56] An even larger portion of patients may have changes in pulmonary function tests, although most of these patients remain symptom free.[57]

In pediatric patients, whole-lung irradiation to 12 gray (Gy) was used in the third national Wilms tumor study from 1979 to 1986 and 15 patients (approximately 10%) developed radiation pneumonitis (that may have been exacerbated by chemotherapeutic agents dactinomycin or doxorubicin).[57] Data from the Childhood Cancer Survivor Study showed a 4-times increased risk of lung fibrosis at 5 years or more after diagnosis among children who received chest radiation, total body irradiation, or both. The cumulative incidence of lung fibrosis at 20 years after diagnosis was 3.5%, and the incidence continued to increase from diagnosis up to 25 years. An increased risk for other pulmonary conditions such as supplemental oxygen use, recurrent pneumonia, chronic cough, and pleurisy was also seen in this population.[54]

***Etiology.*** Important factors in determining whether the lungs are damaged include the volume of tissue irradiated, the dosage and its fractionation, the relative biologic effectiveness of the therapy employed, and the use of concomitant chemotherapy. Several chemotherapy agents are known to increase the risk of radiation pneumonitis and/or long-term lung damage.[58,59] Radiation-induced lung injury is typically categorized temporally as early pneumonitis (1–6 months) and late pulmonary fibrosis (>6 months).[60]

***Imaging.*** Radiographic changes, if present, usually appear a few months after the cessation of radiation therapy. The radiographic appearance initially is that of an ill-defined alveolar process. CT typically shows ground-glass opacity in a sharply defined zone not conforming to anatomic boundaries. As the process evolves, it becomes more interstitial in appearance until changes recognized as radiation fibrosis appear. CT is more sensitive than chest radiography in showing these findings. If the mediastinum has been irradiated, a central perimediastinal, sharply delineated area of linear increased opacity corresponding to the radiation portal is typically seen (e-Fig. 57.15).[57,60]

***Treatment and Follow-up.*** Corticosteroids are sometimes used for managing acute radiation-induced pneumonitis, and long-term treatment is aimed at control of symptoms.[60] Choice of follow-up imaging is largely determined by clinical factors. CT is more sensitive to identify subtle findings of fibrosis.

## Inhalation Injuries

### Overview

Children are rarely exposed to the industrial gases, chemicals, and particulates that adult workers may encounter. Secondhand smoke exposure is by far the most common inhalation injury in children, known to cause increased incidence of respiratory illnesses such as asthma, bronchitis, and pneumonia.[61,62] Acute inhalation injury in children is usually secondary to substances encountered in the home, the most common of which is smoke from house fires. Other far less common causes of acute inhalation injury include chlorine gas (pool disinfectant), talcum powder, and household cleaning agents.[43]

***Etiology.*** Pulmonary damage in pediatric fire victims can be related to heat-mediated upper airway injury but is more commonly due to chemical irritation of the peripheral airway and parenchyma from the products of combustion. From 20% to 30% of patients with burn injuries will have concomitant smoke inhalation injury.[63,64] Heat-related airway injury should be suspected in those with burns in the head-and-neck area, blackened sputum, and respiratory symptoms. Inhalation injury with its associated pulmonary complications increases the morbidity and mortality rates from burn injuries at least threefold.[64] Typically, pulmonary burns progress through three distinct clinical stages: (1) bronchospasm (1–12 hours after the burn), (2) pulmonary edema (6–72 hours), and (3) bronchopneumonia (after 60 hours) (Fig. 57.16). Bacterial pneumonia is very frequent (approximately two-thirds of patients) after the third or fourth day of injury and should be anticipated.[43,64]

Inhalation injury from chlorine gas has been reported in children. This irritant gas is found in swimming pool disinfectants and household cleaning agents. It reacts with the water in tissue to produce hydrochloric acid, which leads to mucosal necrosis. Irritation of the upper respiratory tract, cough, and wheezing are early findings.[43,65]

Inhalation injury may occur in infants caused by inhalation of the small (approximately 5 micrometers) particles of hydrous magnesium silicate present in talcum powder. Inhaled talc produces airway obstruction and impairs ciliary action, which leads to inflammation. Symptoms of cough and respiratory distress are rapid after exposure.[66]

Secondhand smoke exposure is associated with an increased rate of respiratory illness in infancy and childhood. The frequency of reactive airways disease is increased in exposed infants.[67,68]

***Imaging.*** Chest radiographs are most often normal or show hyperinflation early after smoke inhalation, but diffuse or focal patchy opacities or pulmonary edema may be noted (see Fig. 57.16). CT at hospital admission has been used to grade lower airway injury in adult patients.[69] Diffuse opacities on radiographs usually appear after a latent period of 12 to 48 hours and may clear slowly. Rapid appearance of total or subtotal lung consolidation has been described in up to 10% of burned children and is associated with high early mortality. ARDS is a serious and common complication of inhalation injuries and burns.[43]

With chlorine gas inhalation, the onset of pulmonary edema is often rapid. The chest radiograph may be normal or may show hyperinflation or pulmonary edema.[65,66] With talcum powder inhalation, the chest radiograph may show hyperinflation and patchy opacities.[66]

***Treatment and Follow-up.*** Treatment, as for noncardiogenic pulmonary edema, is primarily supportive. Late sequelae, including severe bronchiectasis, asthma, and bronchiolitis obliterans, may be noted after smoke inhalation.[43] Follow-up radiographs are adequate if the patient shows clinical improvement. CT may be needed if clinical symptoms persist in a delayed setting.

## Hydrocarbon Pneumonitis

### Overview

Hydrocarbon pneumonitis occurs in 40% of children after ingestion of hydrocarbons such as lamp oil, lighter fluid, cleaning fluid, furniture and floor polishes, kerosene, and gasoline.[70] Because of

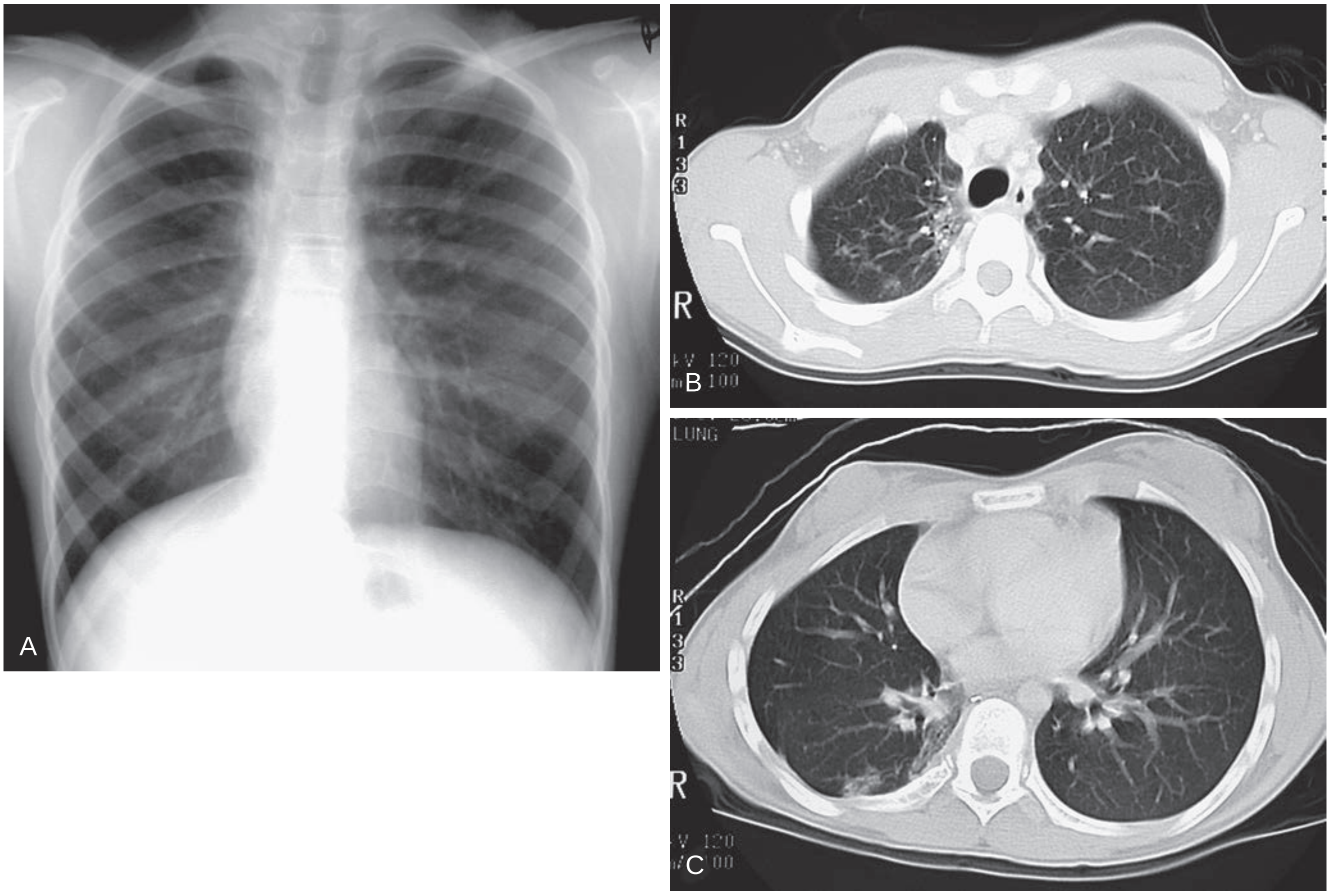

**e-Figure 57.15. Effects of radiation therapy in a 12-year-old girl 2 years after intense radiation therapy for a right paraspinal primitive neuroectodermal tumor.** (A) Chest radiograph shows a smaller right hemithorax and mild rightward mediastinal shift. (B and C) CT images show a smaller right lung, rather sharp-edged changes of lung opacity along the medial aspect of the right upper lobe, and a few scattered peripheral opacities.

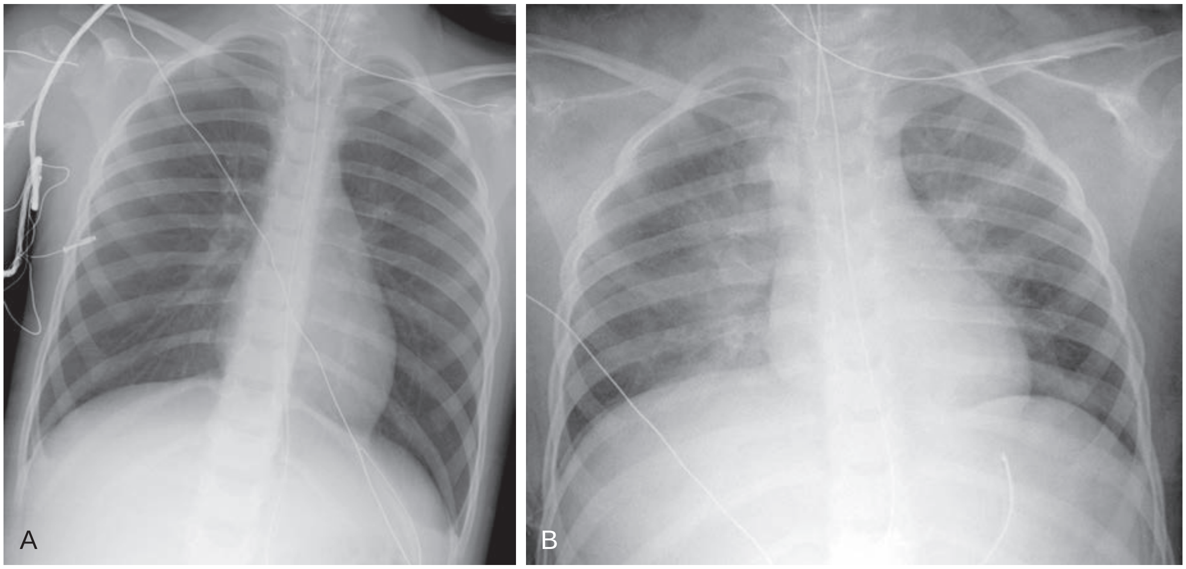

**Figure 57.16. Smoke inhalation injury.** A 4-year-old girl rescued from a house fire. (A) Portable anteroposterior chest radiograph at admission shows clear lungs and hyperinflation. (B) One day later, bilateral pulmonary edema has developed and lung volumes are lower.

their low viscosity, these substances are aspirated when ingested. In the United States, such exposures continue to account for 12% to 25% of lethal poisonings in children less than 5 years old.[43]

***Etiology.*** Aspirated or inhaled material usually results in an intense chemical pneumonitis causing damage to the respiratory epithelium and development of cyanosis through displacement of alveolar gas by the hydrocarbon.[43]

***Imaging.*** Although changes may be evident on the chest radiograph as early as 30 minutes after aspiration, the findings may be delayed several hours; virtually all affected children with lung disease have abnormal chest radiographs by 12 hours (e-Fig. 57.17).[43] The typical pattern of hydrocarbon pneumonitis is one of patchy airspace consolidation and alveolar edema involving predominantly the medial basilar portions of the lungs bilaterally. Pneumatoceles are a well-known complication of hydrocarbon aspiration but reportedly only develop in 10% of children.[70]

***Treatment and Follow-up.*** Treatment is supportive. Resolution of the radiographic changes usually lags behind clinical improvement and may take weeks or months. CT may be performed if improvement does not progress as expected.

### Lipoid Pneumonia

#### Overview

Oral administration of mineral oil for constipation is the most common cause of exogenous lipoid pneumonia. In a study of affected children in Brazil, 79% of patients were less than 24 months of age.[71]

***Etiology.*** Lipids aspirated during oral administration of mineral oil may result in an insidious chronic process that produces an intense lung response and severe lung injury. The current diagnostic method of choice is by analysis of bronchoalveolar lavage fluid, which is reported to show a milky white appearance, sometimes with floating fat globules, and also contains lipid-laden macrophages.[71]

***Imaging.*** The typical radiographic pattern of lipoid pneumonia is perihilar and basilar airspace opacities. CT shows areas of ground-glass opacity or more confluent airspace disease (Fig. 57.18 and e-Fig. 57.19). The airspace consolidation measures as fat attenuation on CT in up to 71% of these children and should alert the radiologist to the diagnosis.[72] However, in some cases the associated inflammation masks the low-density lipid. In adults and children with lipoid pneumonia, the crazy paving pattern has also been noted on thin-section CT.[71-73]

***Treatment and Follow-up.*** Cessation of exposure and clearing of the oil by multiple bronchoalveolar lavages is usually followed by slow clearing of lung opacities and clinical improvement.[72,74] CT and chest radiography are usually used for follow-up.

### Near-Drowning

#### Overview

Drowning is the second most frequent cause of accidental death in children, after motor vehicle accidents. The most common site for a near-drowning episode is the backyard swimming pool. Accidental submersion injuries demonstrate a bimodal age peak of 6 months to 4 years and 18 to 24 years.[43]

***Etiology.*** Submersion time, volume of water aspirated, severity of acidosis, and length of delay in cardiopulmonary resuscitation all correlate directly with morbidity and mortality. Most submersion victims aspirate a small amount of water that may contain vomitus or a variety of contaminants. Laryngospasm then occurs, which may prevent further aspiration.[43]

***Imaging.*** The radiologic pattern of near-drowning is that of pulmonary edema, and the severity depends predominantly on the amount of water aspirated. A significant delay, sometimes as long as 24 to 48 hours after near-drowning, may occur before the appearance of edema (Fig. 57.20). Opacities are usually bilateral and symmetric. Many episodes of near-drowning progress to ARDS.[43]

***Treatment and Follow-up.*** Treatment is primarily supportive with ventilatory support, if needed, in cases of severe respiratory distress. Radiography is usually adequate for imaging follow-up.

## CONDITIONS WITH PULMONARY CALCIFICATIONS

### Pulmonary Alveolar Microlithiasis

#### Overview

Pulmonary alveolar microlithiasis (PAM) is a rare disease characterized by the presence of innumerable calcium phosphate microliths

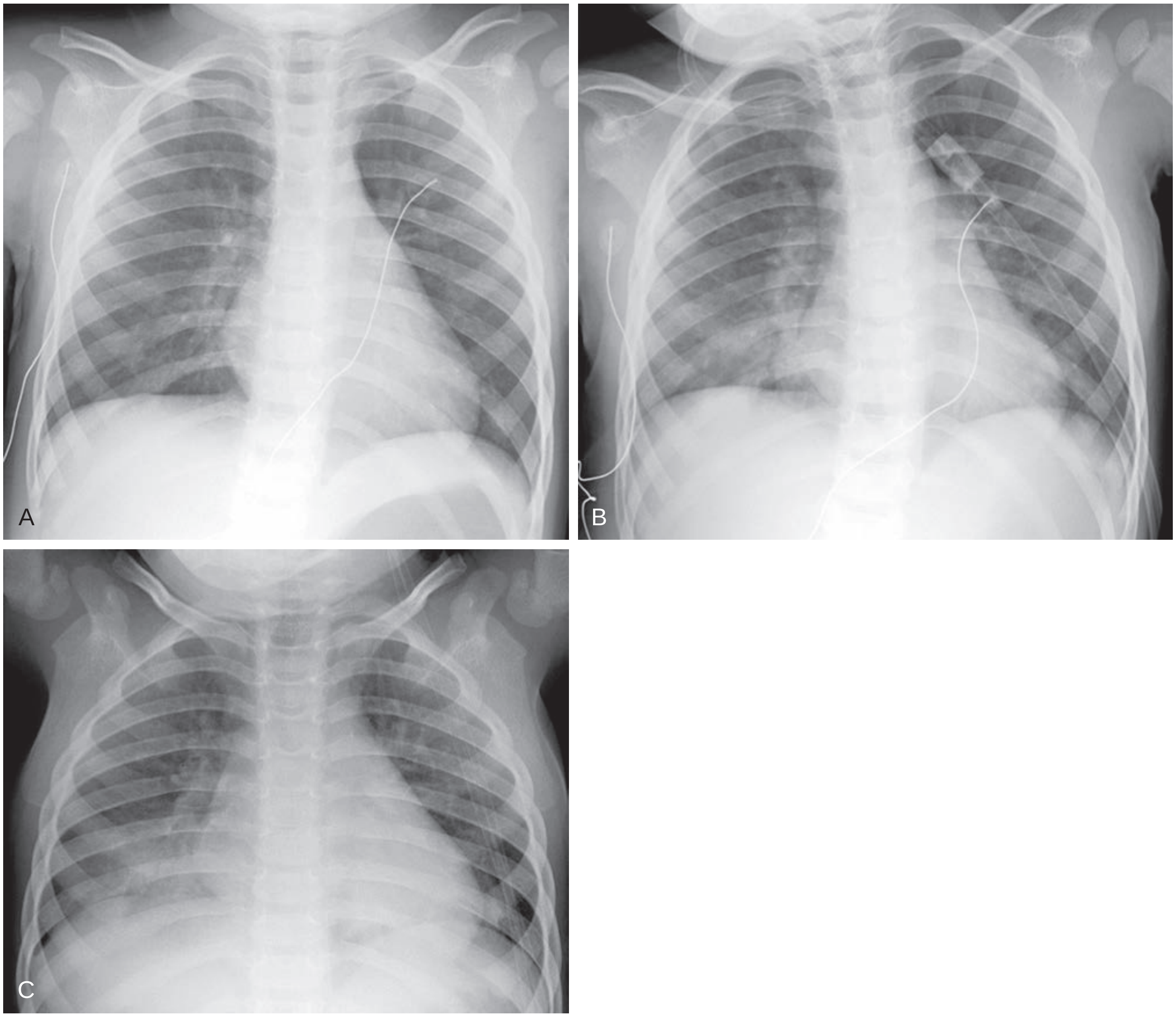

**e-Figure 57.17. Hydrocarbon aspiration in a 23-month-old girl who ingested lighter fluid.** (A–C) Chest radiographs at presentation, 6 hours later, and 2 days later, respectively. The initial radiograph is normal, but subsequent radiographs show delayed development of bibasilar airspace disease.

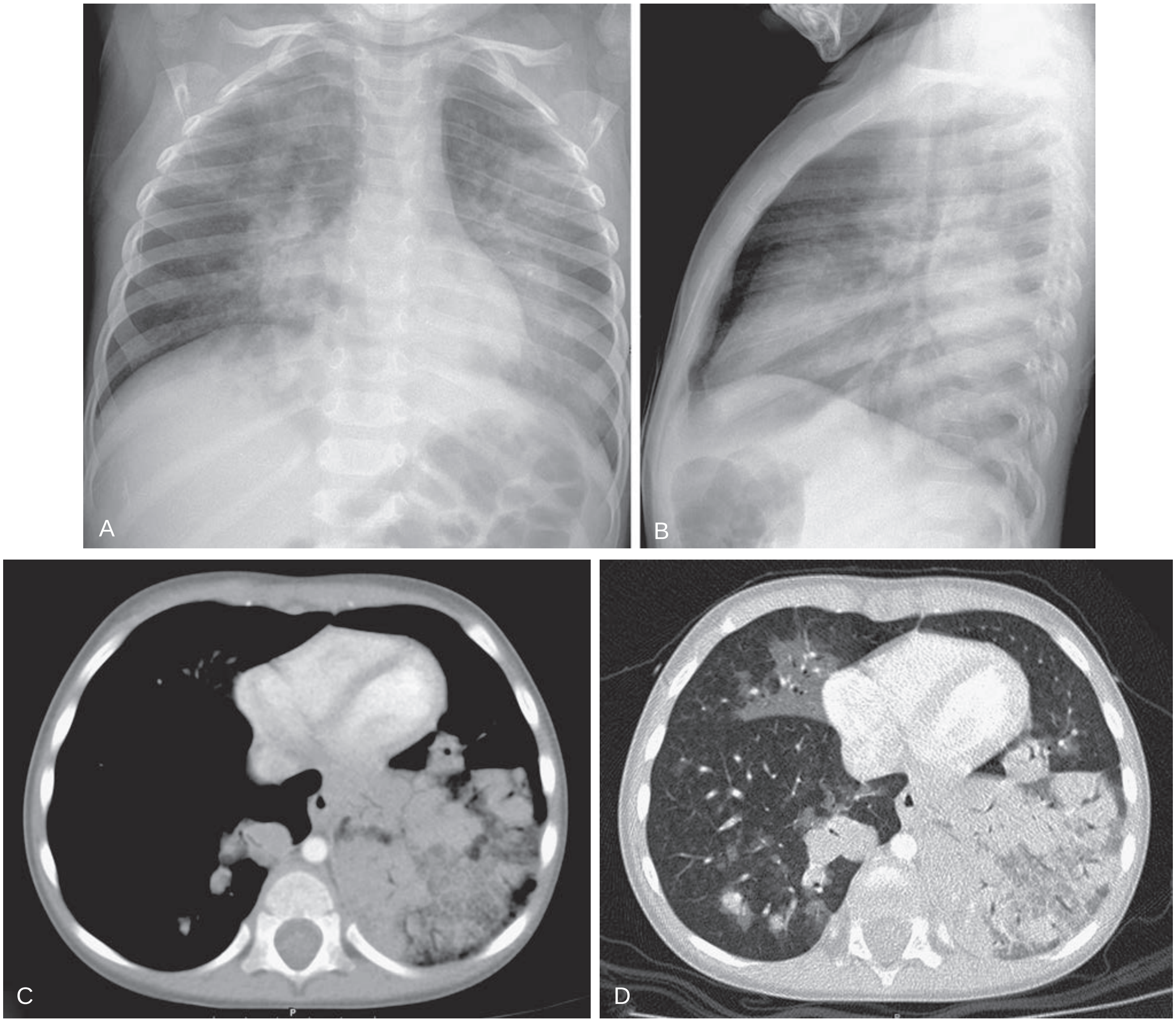

**e-Figure 57.19. Lipoid pneumonia.** This 19-month-old boy had persistent fevers despite antibiotic treatment. He had been ingesting mineral oil as a treatment for constipation. (A) Frontal and (B) lateral chest radiographs show bilateral patchy areas of airspace disease. (C and D) Mediastinal (C) and lung window (D) axial CT images obtained using controlled ventilation technique show partial low-attenuation airspace disease in the left lower lobe with some degree of the crazy paving pattern. Patchy areas of airspace disease, some with ground-glass attenuation, are also seen in the right middle lobe and right lower lobe.

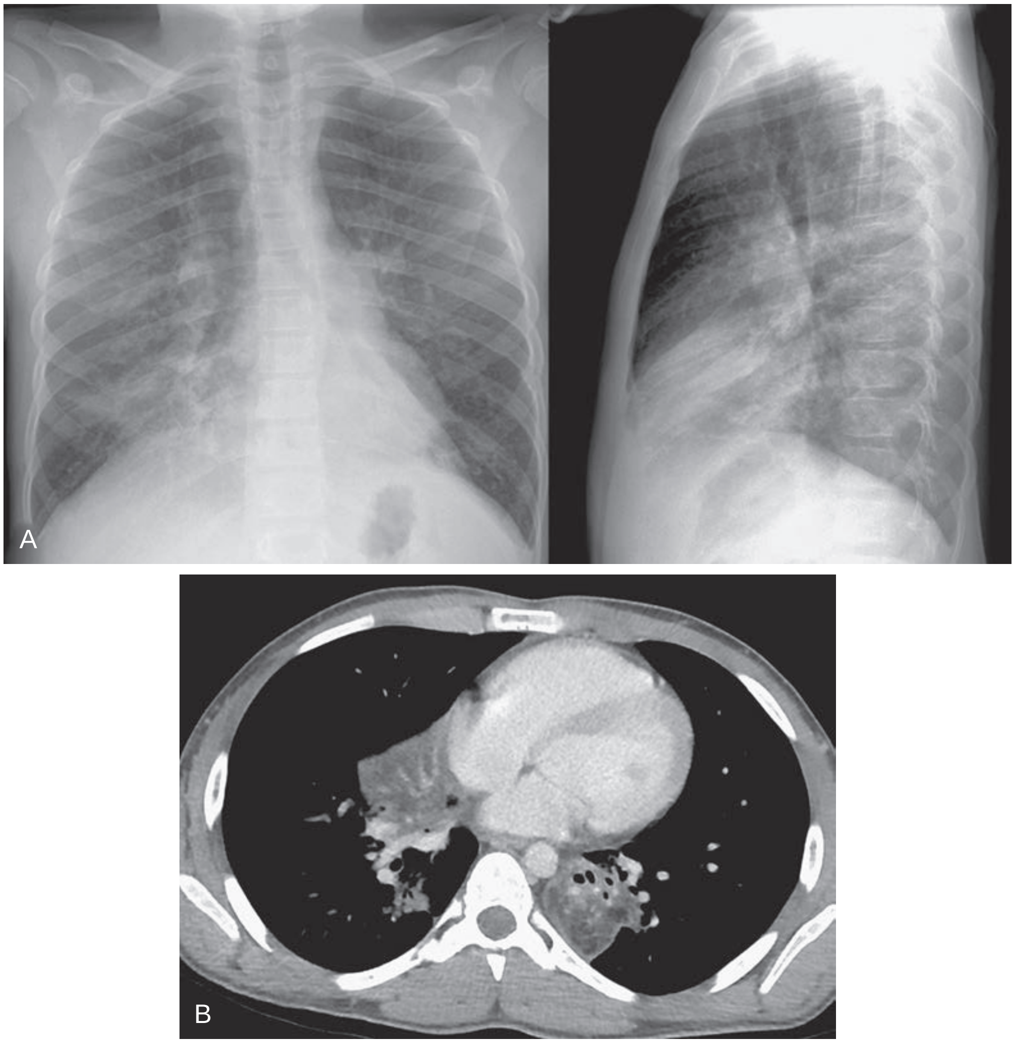

**Figure 57.18. Lipoid pneumonia.** This 11-year-old boy presented with chronic cough and drainage, with recent-onset difficulty breathing. He had a history of being treated for constipation with oral mineral oil. (A) Bilateral airspace opacities are noted predominantly in the lung bases on the initial posteroanterior and lateral chest radiographs. (B) Axial CT image shows focal consolidation with fat attenuation in the left lower lobe and right middle lobe.

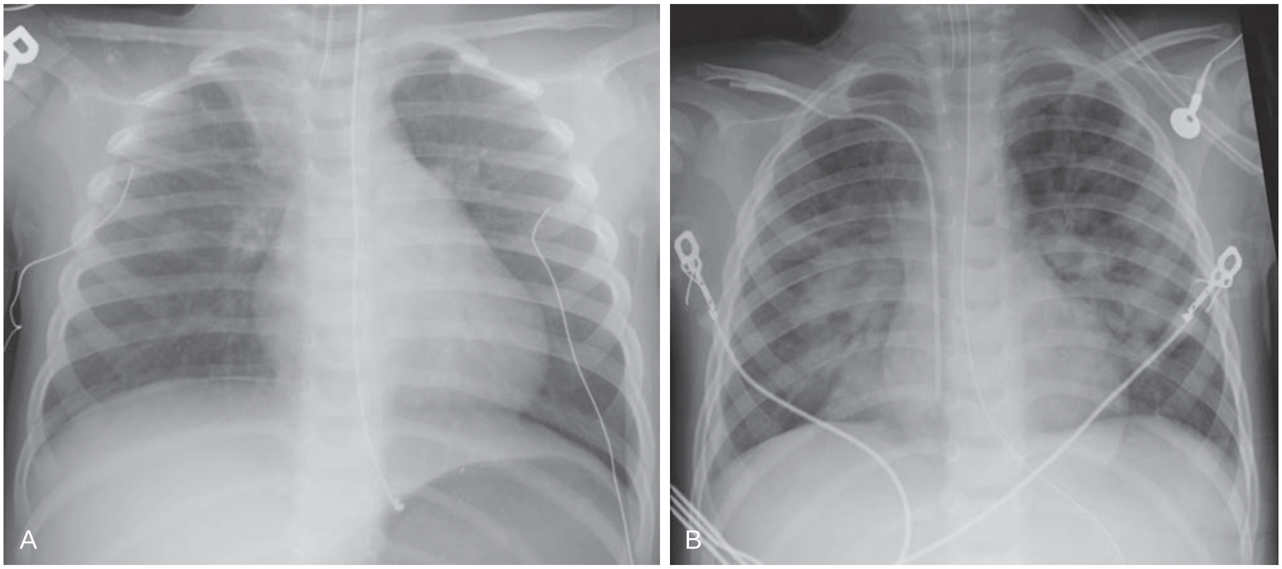

**Figure 57.20. Near-drowning.** This 3-year-old boy suffered a near-drowning episode in a creek. (A) Chest radiograph at presentation is near normal except for atelectasis at the medial right apex. (B) Chest radiograph 2 days later shows development of perihilar airspace disease consistent with noncardiogenic pulmonary edema.

in the alveoli. Many cases are familial and inherited as an autosomal recessive trait.[75] In one review, 17% of affected patients presented at 12 years of age or younger.[76]

***Etiology.*** This disorder is related to a gene mutation associated with a defective cellular phosphate transporter mechanism that leads to the inability of alveolar type II cells to clear phosphorus ions. This then likely causes the accumulation of the characteristic calcium phosphate microliths.[32] The tiny stones in the alveoli consist of concentric calcium rings, which measure from 0.01 to 3 mm in size, and are similar to bone histologically, radiographically, and metabolically. The number and size of the calculi and the amount of interstitial reaction increase with the age of the patient and the duration of the disease.[75,76]

***Imaging.*** On chest radiographs in children with PAM, diffuse ground-glass opacities were more common findings than nodular calcific densities. HRCT shows ground-glass opacities and interstitial septal thickening. Additionally, calcifications are seen in tiny lung nodules, as well as in the pleura and interlobar septae.[77,78] The calcified lung lesions demonstrate an avidity for bone scintigraphy agents.[76]

***Treatment and Follow-up.*** Virtually all types of treatment for PAM have been ineffective except lung transplantation.[76] CT or chest radiography may be used for follow-up, but CT shows the distribution and size of the calcifications more reliably.

## Miscellaneous Pulmonary Calcifications

### Overview

A wide variety of clinical conditions may be associated with pulmonary calcifications.

***Etiology.*** Focal pulmonary calcifications in childhood are usually the result of granulomatous infection, most commonly tuberculosis or histoplasmosis. Diffuse calcifications are probably dystrophic (calcification caused by tissue damage) and are most commonly seen after varicella infection. Metastatic calcification (calcification in normal tissue) is caused by abnormal calcium and phosphorous metabolism, usually in one of the following clinical situations: chronic renal failure with secondary hyperparathyroidism, acute renal failure, after renal transplantation, and after cardiac surgery.[79]

***Imaging.*** Initially, plain radiographs show airspace consolidation or nonspecific nodular opacities, which may demonstrate a progressive increase in density over time. These opacities may not be recognized as representing calcifications and be mistaken for an infectious process such as pneumonia. CT more accurately shows the nature of the opacities as containing calcification.[79]

***Treatment and Follow-up.*** Besides treatment for a discovered active granulomatous process, no treatment or follow-up is needed for the majority of pulmonary calcifications.

### KEY POINTS

- The most common radiologic findings of vasculitis are best delineated by HRCT and include nodules (often cavitary), ground-glass opacities, and airspace opacities.
- Common thoracic findings of CVD are pleural and pericardial effusions. CVD is rarely associated with interstitial lung opacities in children, but this finding would be best demonstrated by HRCT.
- Lung involvement with LCH is virtually always associated with multisystem disease and shows mostly cysts and nodules predominantly in the upper lobes and may progress to honeycombing.
- Subtle radiographic findings of interstitial pulmonary edema in infants and children include peribronchial cuffing, perihilar vascular haziness, fissural thickening, septal lines, hyperinflation, and small pleural effusions. These findings may be mistaken for airway disease.
- Only 10% of pediatric patients with hydrocarbon pneumonitis develop pneumatoceles despite the widely recognized association of this complication.
- Exogenous lipoid pneumonia is usually caused by mineral oil ingestion for constipation and is associated with fat attenuation opacities on CT.

### SUGGESTED READINGS

Garcia-Pena P, Boixadera H, Barber I, et al. Thoracic findings of systemic diseases at high-resolution CT in children. *Radiographics*. 2011;31:465–482.

Guillerman RP. Imaging of childhood interstitial lung disease. *Pediatr Allergy Immunol Pulmonol*. 2010;23(1):43–68.

Schmidt S, Eitch G, Geoffray A, et al. Extraosseous Langerhans cell histiocytosis in children. *Radiographics*. 2008;28:707–726.

Seely JM, Effmann EL. Acute lung injury and acute respiratory distress syndrome in children. *Semin Roentgenol*. 1998;33:163–173.

### REFERENCES

Full references for this chapter can be found on www.expertconsult.com.

## REFERENCES

1. Pesci A, Manganelli P. Respiratory system involvement in antineutrophil cytoplasmic-associated systemic vasculitides: clinical, pathological, radiological and therapeutic considerations. *Drugs R D*. 2007;8(1):25–42.
2. von Vigier RO, et al. Pulmonary renal syndrome in childhood: a report of twenty-one cases and a review of the literature. *Pediatr Pulmonol*. 2000;29(5):382–388.
3. Boyer D, et al. Churg-Strauss syndrome in children: a clinical and pathologic review. *Pediatrics*. 2006;118(3):e914–e920.
4. Susarla SC, Fan LL. Diffuse alveolar hemorrhage syndromes in children. *Curr Opin Pediatr*. 2007;19(3):314–320.
5. Seely JM, et al. Systemic sclerosis: using high-resolution CT to detect lung disease in children. *AJR Am J Roentgenol*. 1998;170(3):691–697.
6. Panigada S, et al. HRCT and pulmonary function tests in monitoring of lung involvement in juvenile systemic sclerosis. *Pediatr Pulmonol*. 2009;44(12):1226–1234.
7. Brody AS. Imaging considerations: interstitial lung disease in children. *Radiol Clin North Am*. 2005;43(2):391–403.
8. Dinwiddie R, Sonnappa S. Systemic diseases and the lung. *Paediatr Respir Rev*. 2005;6(3):181–189.
9. Levine D, et al. Chest CT findings in pediatric Wegener's granulomatosis. *Pediatr Radiol*. 2007;37(1):57–62.
10. Martinez F, et al. Common and uncommon manifestations of Wegener granulomatosis at chest CT: radiologic-pathologic correlation. *Radiographics*. 2012;32(1):51–69.
11. Ananthakrishnan L, Sharma N, Kanne JP. Wegener's granulomatosis in the chest: high-resolution CT findings. *AJR Am J Roentgenol*. 2009;192(3):676–682.
12. Marten K, et al. Pattern-based differential diagnosis in pulmonary vasculitis using volumetric CT. *AJR Am J Roentgenol*. 2005;184(3):720–733.
13. Akikusa JD, et al. Clinical features and outcome of pediatric Wegener's granulomatosis. *Arthritis Rheum*. 2007;57(5):837–844.
14. Garcia-Pena P, et al. Thoracic findings of systemic diseases at high-resolution CT in children. *Radiographics*. 2011;31(2):465–482.
15. Kimura Y, et al. Pulmonary hypertension and other potentially fatal pulmonary complications in systemic juvenile idiopathic arthritis. *Arthritis Care Res (Hoboken)*. 2013;65(5):745–752.
16. Delgado EA, et al. The pulmonary manifestations of childhood onset systemic lupus erythematosus. *Semin Arthritis Rheum*. 1990;19(5):285–293.
17. Vichinsky EP, et al. Acute chest syndrome in sickle cell disease: clinical presentation and course. Cooperative Study of Sickle Cell Disease. *Blood*. 1997;89(5):1787–1792.
18. Martin L, Buonomo C. Acute chest syndrome of sickle cell disease: radiographic and clinical analysis of 70 cases. *Pediatr Radiol*. 1997;27(8):637–641.
19. Lonergan GJ, Cline DB, Abbondanzo SL. Sickle cell anemia. *Radiographics*. 2001;21(4):971–994.
20. Vichinsky EP, et al. Causes and outcomes of the acute chest syndrome in sickle cell disease. National Acute Chest Syndrome Study Group. *N Engl J Med*. 2000;342(25):1855–1865.
21. Aquino SL, et al. Chronic pulmonary disorders in sickle cell disease: findings at thin-section CT. *Radiology*. 1994;193(3):807–811.
22. Heeney MW, Mahoney DH Jr. The acute chest syndrome in children and adolescents with sickle cell disease. In: Post TW, ed. *UpToDate*. Waltham, MA: UpToDate; 2016.
23. Schmidt S, et al. Extraosseous langerhans cell histiocytosis in children. *Radiographics*. 2008;28(3):707–726, quiz 910–911.
24. McClain KL. Clinical manifestations, pathologic features, and diagnosis of Langerhans cell histiocytosis. In: Post TW, ed. *UpToDate*. Waltham, MA: UpToDate; 2016.
25. Odame I, et al. Pulmonary Langerhans cell histiocytosis: a variable disease in childhood. *Pediatr Blood Cancer*. 2006;47(7):889–893.
26. Bernstrand C, et al. Long-term follow-up of Langerhans cell histiocytosis: 39 years' experience at a single centre. *Acta Paediatr*. 2005;94(8):1073–1084.
27. Smets A, et al. Pulmonary and mediastinal lesions in children with Langerhans cell histiocytosis. *Pediatr Radiol*. 1997;27(11):873–876.
28. Brauner MW, et al. Pulmonary histiocytosis X: evaluation with high-resolution CT. *Radiology*. 1989;172(1):255–258.
29. Matlin AH, Young LW, Klemperer MR. Pleural effusion in two children with histiocytosis X. *Chest*. 1972;61(1):33–36.
30. Martins AM, et al. Recommendations on diagnosis, treatment, and monitoring for Gaucher disease. *J Pediatr*. 2009;155(4 suppl):S10–S18.
31. Klusmann M, Owens C. HRCT in paediatric diffuse interstitial lung disease—a review for 2009. *Pediatr Radiol*. 2009;39(suppl 3):471–481.
32. Guillerman RP. Imaging of childhood interstitial lung disease. *Pediatr Allergy Immunol Pulmonol*. 2010;23(1):43–68.
33. Guillerman RP, Brody AS. Contemporary perspectives on pediatric diffuse lung disease. *Radiol Clin North Am*. 2011;49(5):847–868.
34. Nicholson AG, et al. Successful treatment of endogenous lipoid pneumonia due to Niemann-Pick Type B disease with whole-lung lavage. *Am J Respir Crit Care Med*. 2002;165(1):128–131.
35. Nicholson AG, et al. Pulmonary involvement by Niemann-Pick disease. A report of six cases. *Histopathology*. 2006;48(5):596–603.
36. Guillemot N, et al. Lung disease in Niemann-Pick disease. *Pediatr Pulmonol*. 2007;42(12):1207–1214.
37. McHugh K, Olsen EO, Vellodi A. Gaucher disease in children: radiology of non-central nervous system manifestations. *Clin Radiol*. 2004;59(2):117–123.
38. Goitein O, et al. Lung involvement and enzyme replacement therapy in Gaucher's disease. *QJM*. 2001;94(8):407–415.
39. Uejima T. General pediatric emergencies. Acute pulmonary edema. *Anesthesiol Clin North America*. 2001;19(2):383–389, viii.
40. Brasileiro FC, et al. High-resolution CT scan in the evaluation of exercise-induced interstitial pulmonary edema in cardiac patients. *Chest*. 1997;111(6):1577–1582.
41. Lewin S, Goldberg L, Dec GW. The spectrum of pulmonary abnormalities on computed chest tomographic imaging in patients with advanced heart failure. *Am J Cardiol*. 2000;86(1):98–100.
42. Jefferies JL, Price JF, Morales DL. Mechanical support in childhood heart failure. *Heart Fail Clin*. 2010;6(4):559–573, x.
43. Seely JM, Effmann EL. Acute lung injury and acute respiratory distress syndrome in children. *Semin Roentgenol*. 1998;33(2):163–173.
44. Pediatric acute respiratory distress syndrome: consensus recommendations from the Pediatric Acute Lung Injury Consensus Conference. *Pediatr Crit Care Med*. 2015;16(5):428–439.
45. Kirkpatrick JA Jr, Fleisher DS. The roentgen appearance of the chest in acute glomerulonephritis in children. *J Pediatr*. 1964;64:492–498.
46. Terminella L, Sharma G. Diagnostic studies in patients with acute respiratory distress syndrome. *Semin Thorac Cardiovasc Surg*. 2006;18(1):2–7.
47. Goodman PC. Radiographic findings in patients with acute respiratory distress syndrome. *Clin Chest Med*. 2000;21(3):419–433, vii.
48. Gattinoni L, et al. Regional effects and mechanism of positive end-expiratory pressure in early adult respiratory distress syndrome. *JAMA*. 1993;269(16):2122–2127.
49. Fanconi S, et al. Long-term sequelae in children surviving adult respiratory distress syndrome. *J Pediatr*. 1985;106(2):218–222.
50. Pena E, et al. Noninfectious pulmonary complications after hematopoietic stem cell transplantation: practical approach to imaging diagnosis. *Radiographics*. 2014;34(3):663–683.
51. Haddad IY. Stem cell transplantation and lung dysfunction. *Curr Opin Pediatr*. 2013;25(3):350–356.
52. Rossi SE, et al. Pulmonary drug toxicity: radiologic and pathologic manifestations. *Radiographics*. 2000;20(5):1245–1259.
53. Ellis SJ, Cleverley JR, Muller NL. Drug-induced lung disease: high-resolution CT findings. *AJR Am J Roentgenol*. 2000;175(4):1019–1024.
54. Mertens AC, et al. Pulmonary complications in survivors of childhood and adolescent cancer. A report from the Childhood Cancer Survivor Study. *Cancer*. 2002;95(11):2431–2441.
55. McCarroll KA, Roszler MH. Lung disorders due to drug abuse. *J Thorac Imaging*. 1991;6(1):30–35.
56. Marks LB, et al. Radiation-induced lung injury. *Semin Radiat Oncol*. 2003;13(3):333–345.
57. Green DM, et al. Diffuse interstitial pneumonitis after pulmonary irradiation for metastatic Wilms' tumor. A report from the National Wilms' Tumor Study. *Cancer*. 1989;63(3):450–453.
58. Chavhan GB, et al. Imaging of acute and subacute toxicities of cancer therapy in children. *Pediatr Radiol*. 2016;46(1):9–20, quiz 6–8.
59. Huang TT, et al. Pulmonary outcomes in survivors of childhood cancer: a systematic review. *Chest*. 2011;140(4):881–901.
60. Davis SD, Yankelevitz DF, Henschke CI. Radiation effects on the lung: clinical features, pathology, and imaging findings. *AJR Am J Roentgenol*. 1992;159(6):1157–1164.
61. Best D. From the American Academy of Pediatrics: Technical report–Secondhand and prenatal tobacco smoke exposure. *Pediatrics*. 2009;124(5):e1017–e1044.
62. Benjamin RM. Exposure to tobacco smoke causes immediate damage: a report of the Surgeon General. *Public Health Rep*. 2011;126(2):158–159.
63. Enkhbaatar P, et al. Pathophysiology, research challenges, and clinical management of smoke inhalation injury. *Lancet*. 2016;388(10052):1437–1446.

64. Fidkowski CW, et al. Inhalation burn injury in children. *Paediatr Anaesth*. 2009;19(suppl 1):147–154.
65. Ho M, Yang C, Cheung W, et al. Chlorine gas exposure manifesting acute lung injury. *J Intern Med Taiwan*. 2010;21:210–215.
66. Scalzo AJ. Inhalation injuries. In: Barkin RM, ed. *Pediatric emergency medicine: concepts and clinical practice*. 2nd ed. St. Louis, MO.: Mosby; 1997:578.
67. Schwartz J, Timonen KL, Pekkanen J. Respiratory effects of environmental tobacco smoke in a panel study of asthmatic and symptomatic children. *Am J Respir Crit Care Med*. 2000;161(3 Pt 1):802–806.
68. Wright AL, et al. Relationship of parental smoking to wheezing and nonwheezing lower respiratory tract illnesses in infancy. Group Health Medical Associates. *J Pediatr*. 1991;118(2):207–214.
69. Oh JS, et al. Admission chest CT complements fiberoptic bronchoscopy in prediction of adverse outcomes in thermally injured patients. *J Burn Care Res*. 2012;33(4):532–538.
70. Harris VJ, Brown R. Pneumatoceles as a complication of chemical pneumonia after hydrocarbon ingestion. *Am J Roentgenol Radium Ther Nucl Med*. 1975;125(3):531–537.
71. Sias SM, et al. Evolution of exogenous lipoid pneumonia in children: clinical aspects, radiological aspects and the role of bronchoalveolar lavage. *J Bras Pneumol*. 2009;35(9):839–845.
72. Zanetti G, et al. Lipoid pneumonia in children following aspiration of mineral oil used in the treatment of constipation: high-resolution CT findings in 17 patients. *Pediatr Radiol*. 2007;37(11): 1135–1139.
73. Baron SE, Haramati LB, Rivera VT. Radiological and clinical findings in acute and chronic exogenous lipoid pneumonia. *J Thorac Imaging*. 2003;18(4):217–224.
74. Sias SM, et al. Clinic and radiological improvement of lipoid pneumonia with multiple bronchoalveolar lavages. *Pediatr Pulmonol*. 2009;44(4):309–315.
75. Schmidt H, et al. Pulmonary alveolar microlithiasis in children. *Pediatr Radiol*. 1996;26(1):33–36.
76. Castellana G, Lamorgese V. Pulmonary alveolar microlithiasis. World cases and review of the literature. *Respiration*. 2003;70(5): 549–555.
77. Helbich TH, et al. Pulmonary alveolar microlithiasis in children: radiographic and high-resolution CT findings. *AJR Am J Roentgenol*. 1997;168(1):63–65.
78. Deniz O, et al. High resolution computed tomographic features of pulmonary alveolar microlithiasis. *Eur J Radiol*. 2005;55(3):452–460.
79. Brown K, et al. Intrathoracic calcifications: radiographic features and differential diagnoses. *Radiographics*. 1994;14(6):1247–1261.

# PART 4 Mediastinum

# 58

# The Mediastinum

*Gerald G. Behr, Ricardo Restrepo, and Edward Y. Lee*

A variety of congenital and developmental anomalies, inflammatory and infectious diseases, and benign and malignant neoplasms occur in the mediastinum in the pediatric population. Up-to-date knowledge and a practical diagnostic approach combined with a clear understanding of the characteristic imaging appearances of these conditions can facilitate prompt diagnosis and optimal patient management. This chapter reviews the underlying etiology, imaging findings, treatment, and follow-up of commonly encountered congenital and acquired anomalies and abnormalities that occur within the mediastinum in the pediatric population.

## SPECTRUM OF MEDIASTINAL ANOMALIES AND ABNORMALITIES

### Pneumomediastinum

#### Overview

Pneumomediastinum occurs more frequently in infants than in older children.[1,2] Affected pediatric patients may present with a sensation of retrosternal fullness, dysphagia, sore throat, chest pain, or dyspnea.

***Etiology.*** Pneumomediastinum may be spontaneous or iatrogenic. Spontaneous pneumomediastinum results from a sudden forceful increase in intraalveolar pressure such as forceful inhalation or the Valsalva maneuver. In this instance, an alveolus can rupture, allowing gas under pressure into the low-pressure pulmonary interstitial compartment. Subsequently, the air then travels via the peribronchovascular space medially toward the hilum, which opens into the mediastinum.[3,4] Occasionally, the air dissects along the lymphatics as well and extends to the visceral pleura, where a concomitant pneumothorax may occur. Iatrogenic pneumomediastinum may result from chest, abdominal, and cardiac surgery; endotracheal intubation; or cardiac catheterization. Secondary pneumomediastinum can occur after foreign body ingestion, trauma to the neck or chest, or any disruption of the tracheobronchial tree or esophagus (e.g., Boerhaave syndrome).[2]

It is not uncommon for pneumomediastinum and pneumothorax to coexist.[5] This phenomenon sometimes can be attributed to a common mechanism of air leak, or the pneumothorax may arise as a result of a pneumomediastinum. In addition, anatomic communications between the mediastinum and the peritoneal cavity exist. As such, intraabdominal air can dissect superiorly into the mediastinum and vice versa.[6] Rarely, air within the mediastinum can enter the spinal canal, termed *pneumorrhachis*.[7]

***Imaging.*** Air within the mediastinum typically displaces the pleura and lung laterally (Fig. 58.1). It may decompress into the superior mediastinum and dissect along fascial planes into the subcutaneous tissues of the neck and retropharynx (e-Fig. 58.2). In infants and younger children, air within the mediastinum can displace the thymus superiorly to produce the “spinnaker sail” sign (see Fig. 58.1).

Occasionally, only a sliver of curvilinear radiolucency is seen adjacent to the cardiac border, often on the left, outlining the aortic arch and descending aorta. When air is adjacent to the pulmonary artery (typically on the right), the “ring around the artery” sign is seen on the lateral view.[6,8] The “continuous diaphragm sign” results from air interposed between the pericardium and the diaphragm.[8] Although pneumomediastinum is usually anterior in location, posterior mediastinal air collections can also occur, typically toward the right in the infra-azygous space (e-Fig. 58.3). Posterior pneumomediastinum may occur secondary to barotrauma but should raise concern for iatrogenic and especially tracheal or esophageal injury.[9,10]

A large pneumomediastinum may be confused with a pneumothorax, especially when viewed on a supine radiograph. When equivocal, a decubitus radiographic view may be helpful because the mediastinal air does not move, whereas the pneumothorax rises nondependently.[5]

Pneumomediastinum may mimic pneumopericardium. In contrast to pneumomediastinum, pneumopericardium does *not* lift the thymus or outline the aortic arch as the air is contained by pericardium. Pneumopericardium is almost always seen in association with pneumomediastinum except after open-heart surgery.[5]

***Treatment and Follow-up.*** Treatment of pneumomediastinum is aimed at its underlying cause.[11] In most cases, management is supportive.[2] If there is concern for esophageal rupture, an esophagram using water-soluble contrast may be performed, and surgical consultation should be obtained.[12,13] However, esophageal rupture in children is rare and, in most uncomplicated cases of pneumomediastinum, no further imaging beyond the diagnostic chest x-ray is necessary.[13,14] Very rarely, pseudotamponade, laryngeal compression, tension pneumomediastinum, tension pneumothorax, or mediastinitis occur and require surgical intervention.

### Mediastinal Hemorrhage

***Etiology.*** Mediastinal hemorrhage in children may occur as a result of blunt trauma (usually venous bleeding)[5] or iatrogenic causes related to central catheter placement or cardiothoracic procedures. However, mediastinal hemorrhage in children may occur spontaneously in the context of hemophilia, in which case the hemorrhage may be retropharyngeal and dissect into the mediastinum.[5,15] Rare cases of neonatal thymic hemorrhage have been reported, possibly related to vitamin K deficiency.[16,17]

***Imaging.*** Although imaging findings may be nonspecific, the possibility of mediastinal hemorrhage should be considered when mediastinal widening, blurring of the aortic margin, deviation of a nasoenteric tube, and/or left apical “capping” are present on chest radiographs. When evaluating mediastinal widening on chest radiographs, careful attention must be paid to the technique. For example, a portable anteroposterior chest radiograph may exaggerate the size of the mediastinum. Therefore in equivocal cases, confirmation with a posteroanterior view or a cross-sectional imaging study such as computed tomography (CT) may be necessary. On CT, mediastinal fluid with a Hounsfield unit greater than water (approximately 20–80 HU) suggests mediastinal hemorrhage (Fig. 58.4).

***Treatment and Follow-up.*** When mediastinal hemorrhage is considered on chest radiographs, further imaging studies such as echocardiography and/or contrast-enhanced CT using CT angiographic technique with multiplanar and three-dimensional reconstruction is warranted. With rapid clinical deterioration, urgent surgical exploration is an option to avoid delaying proper treatment.

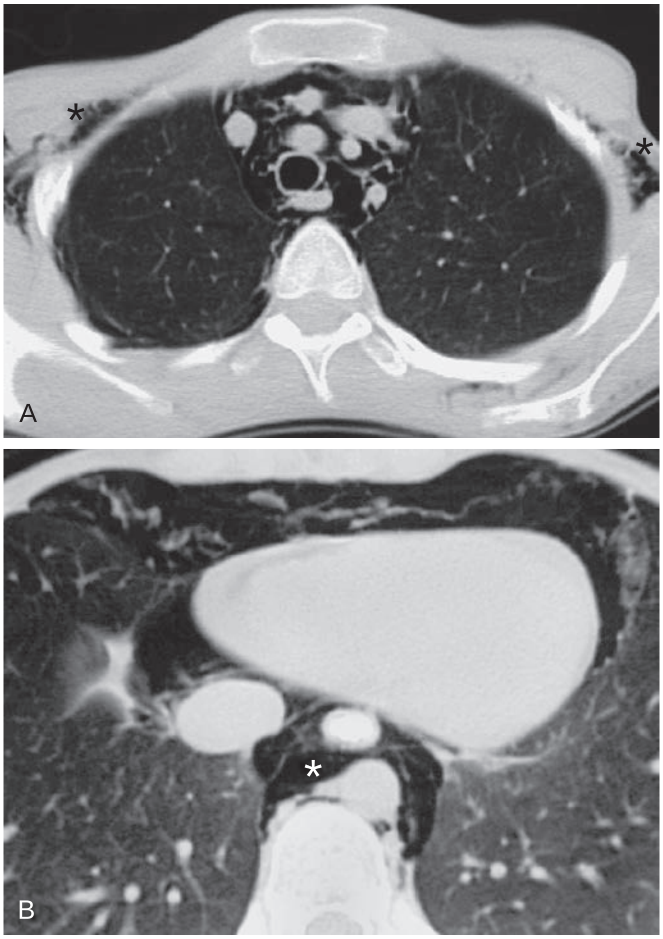

**e-Figure 58.2. Pneumomediastinum in a 2-year-old girl.** (A) Axial lung window CT image at the level of the superior mediastinum shows mediastinal air that outlines major vessels and fascial planes. Air has dissected through the soft tissues and is seen bilaterally in the axilla *(asterisks).* (B) Axial lung window CT image at the level of the lower thorax demonstrates further caudal extent of the mediastinal air *(asterisk).*

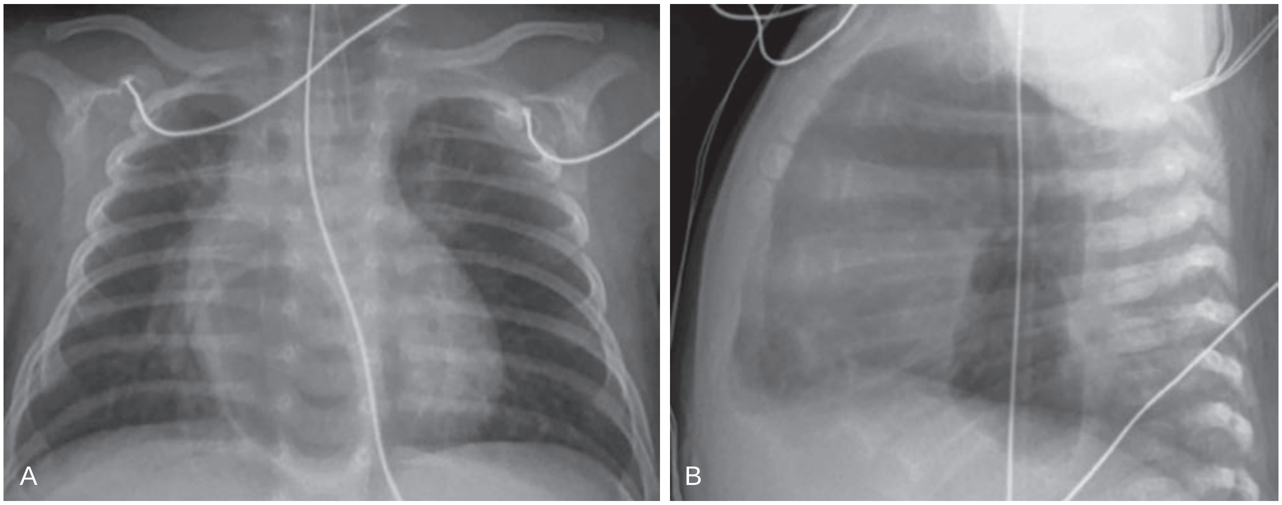

**e-Figure 58.3. Infra-azygos pneumomediastinum in a 5-week-old after repair of an H-type tracheoesophageal fistula.** Frontal (A) and lateral (B) chest radiographs show a large posterior mediastinal lucency due to an infra-azygos pneumomediastinum concerning for an esophageal leak. *(Courtesy of Dr. Beverley Newman, Stanford Children's Hospital, Stanford University. From Pearls and pitfalls in pediatric radiology: variants and other difficult diagnoses, eds Daldrup-Link H, Newman B. Cambridge University Press, 2014. Fig. 20.2.)*

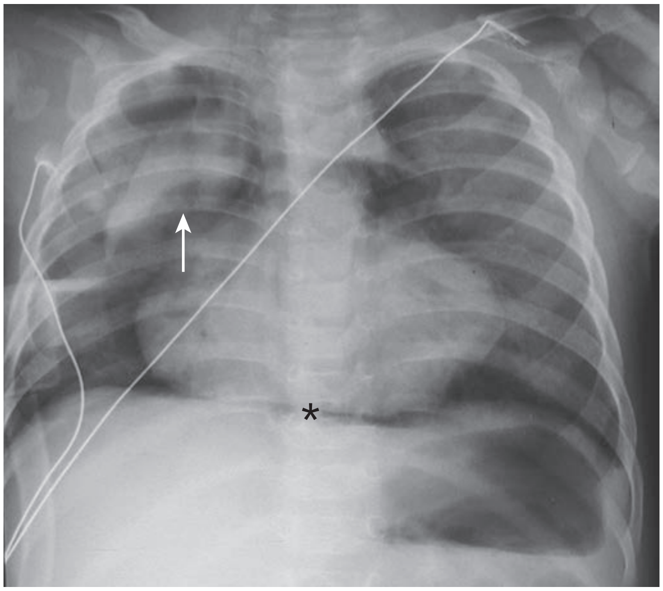

**Figure 58.1. Pneumomediastinum in a 6-month-old boy.** Frontal chest radiograph demonstrates a lifted thymic shadow *(arrow),* the so-called "spinnaker sail sign." Mediastinal air *(asterisk)* also is interposed between the central diaphragm and pericardium, and lucency is seen surrounding the heart.

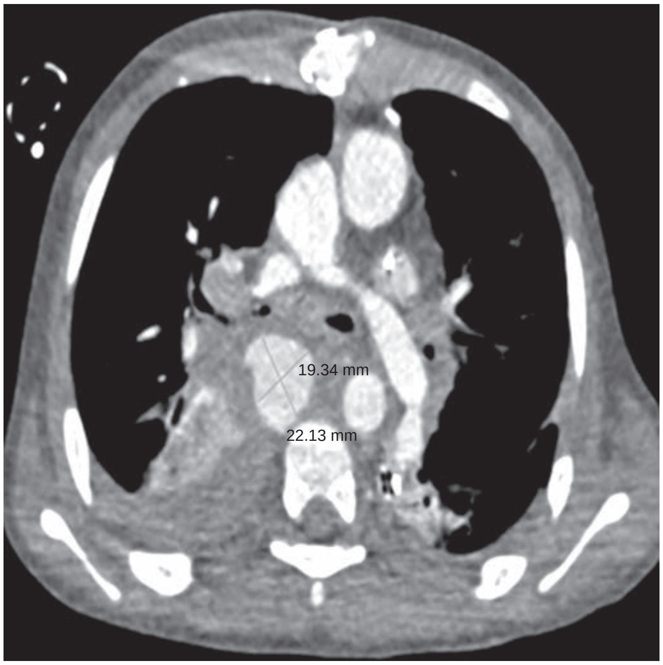

**Figure 58.4. Mediastinal hemorrhage in a 7-year-old boy with congenital heart disease.** Axial contrast-enhanced CT image demonstrates high density fluid in the middle and posterior mediastinum (measurement bars) due to postoperative hemorrhage. *(Courtesy of Dr. Aurelio Secinaro, Bambino Gesù Children's Hospital, Rome, Italy.)*

## Mediastinal Infection

### Overview

Infections arising de novo in the mediastinum are rare in the pediatric population. Mediastinal infections can be classified into acute infection and chronic fibrosing mediastinitis.

### Acute Mediastinitis

***Etiology.*** Acute mediastinal infection in children is most often iatrogenic, related to endoscopic surgery, esophageal instrumentation, and cardiac surgery.[18-20] Chronic fibrosing mediastinitis typically results from tuberculosis or *Histoplasmosis* infections in the pediatric population.[21-23]

In the past, esophageal perforation and spread of infection from other sites into the mediastinum were relatively more common. Affected pediatric patients typically present with chest pain, fever, and an elevated white blood cell count.

***Imaging.*** Plain radiographic findings of acute mediastinitis are nonspecific. However, mediastinal widening, obliteration of normal mediastinal contours, and displaced or narrowed trachea should suggest acute mediastinitis in the appropriate clinical setting. The more specific radiologic imaging finding of acute mediastinitis is the presence of gas within the mediastinum, which can be better evaluated with CT. CT also can show complications from acute mediastinitis such as mediastinal abscess formation or empyema (Fig. 58.5).

***Treatment and Follow-up.*** Acute mediastinitis is treated aggressively with a combination of antibiotics and surgical irrigation. Localized mediastinal abscess formation can be managed with either surgical or percutaneous abscess drainage. Recently, a combination of continuous irrigation and vacuum-assisted postthoracotomy closure has been used and shown to be safe in children.[24-27]

### Chronic Fibrosing Mediastinitis

***Etiology.*** Chronic fibrosing mediastinitis, also known as sclerosing mediastinitis, is rare in the pediatric population. It is a condition characterized by abnormal proliferation of dense acellular collagen and fibrous tissue.[28,29] Although it is most frequently attributed to the sequelae of granulomatous infection such as *Mycobacterium tuberculosis* or *Histoplasmosis* infection, it also can arise as an idiopathic condition or as the sequelae of autoimmune disease, radiotherapy, or drugs such as methysergide and metoprolol.[26,30] Chronic fibrosing mediastinitis is also associated with retroperitoneal fibrosis, sclerosing cholangitis, and Riedel thyroiditis.[31] Affected pediatric patients often present with respiratory distress related to airway narrowing, dysphagia due to esophageal compromise, and/or facial and neck swelling resulting from obstruction of the superior vena cava.

***Imaging.*** Widening of the mediastinum with a lobular paratracheal and/or subcarinal mass that may be calcified is a typical finding on chest radiographs. CT imaging findings of chronic fibrosing mediastinitis can be categorized into two patterns: focal or diffuse.[28,32] The focal form is more likely to calcify (Fig. 58.6). The diffuse type demonstrates a more diffusely infiltrating appearance without calcification.

***Treatment and Follow-up.*** Although no consensus or widely accepted guidelines currently exist for the treatment of chronic fibrosing mediastinitis, systemic antifungal or corticosteroid treatment, surgical resection, and local therapy for complications are the current management options. Surgical resection may be necessary for symptomatic pediatric patients who have extensive chronic fibrosing mediastinitis that results in either obstruction or compression of mediastinal structures such as central airways, the esophagus, or large vessels.

## Mediastinal Masses

### Overview

The mediastinum is the most common location of chest masses in the pediatric population. Mediastinal masses in infants and children can be benign or malignant neoplasms, congenital anomalies, infections, vascular malformations, or pseudomasses. As with adult

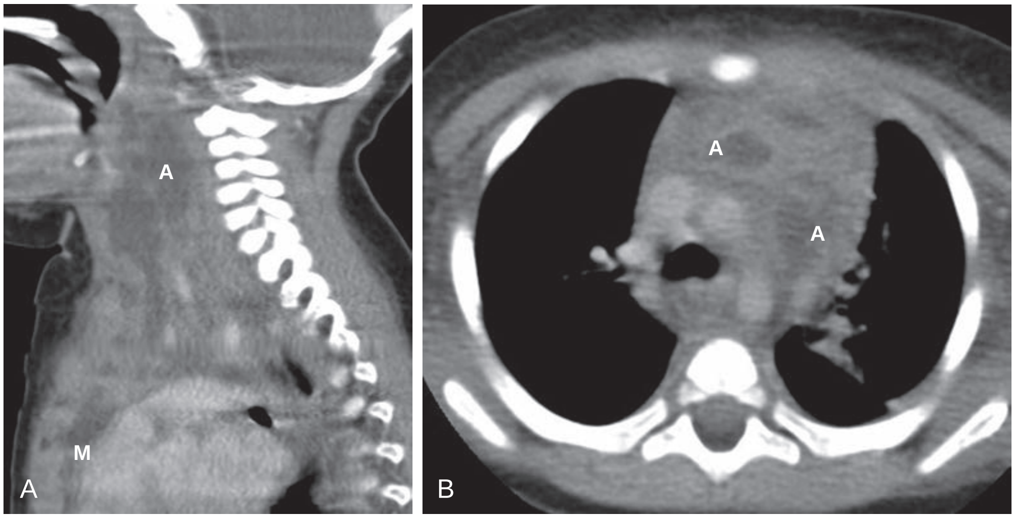

**Figure 58.5. Acute mediastinitis resulting from a retropharyngeal abscess in a 1-year-old boy.** (A) Sagittal reconstruction contrast-enhanced CT image through the neck shows a large, complex fluid collection *(A)* extending caudally into the mediastinum *(M).* (B) Axial contrast-enhanced CT image obtained at the level of the aortic arch demonstrates two of the better defined abscesses *(A)* in the anterior mediastinal compartment embedded in an inflamed and heterogeneous thymus.

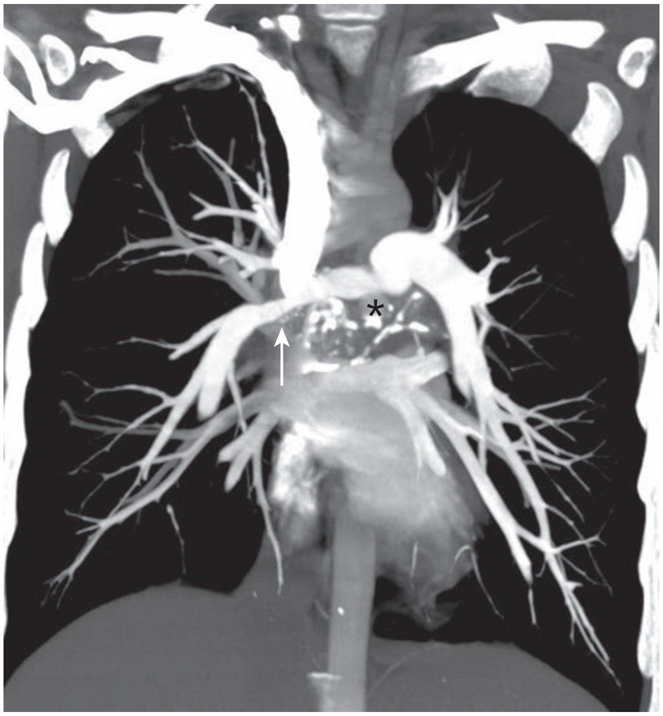

**Figure 58.6. Chronic fibrosing mediastinitis in a 17-year-old girl.** Coronal maximum intensity projection CT image of the chest shows a middle mediastinal ill-defined mass that narrows the right pulmonary artery *(arrow).* Also note the calcifications *(asterisk). (From Daltro PA, Santos EN, Gasparetto TD, et al. Pulmonary infections.* Pediatr Radiol. *2011;41(Suppl 1):S69–S82.)*

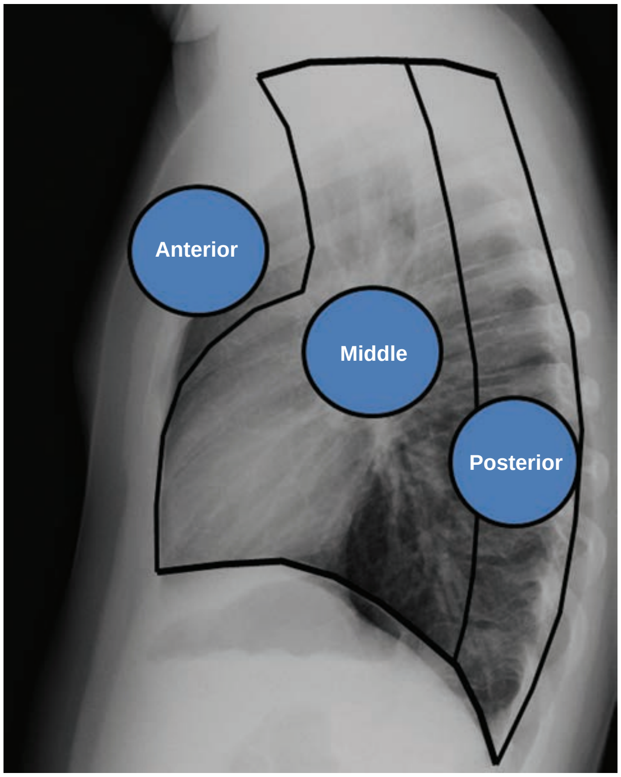

**Figure 58.7. Anatomic landmarks demarcating the anterior, middle, and posterior compartments of the mediastinum on a lateral chest radiograph.** *Anterior* indicates the anterior mediastinal compartment. *Middle* indicates the middle mediastinal compartment. *Posterior* indicates the posterior mediastinal compartment.

patients, it is useful to localize the mediastinal mass to one of three mediastinal compartments (anterior, middle, or posterior) (Fig. 58.7). However, such a system of compartmentalizing the mediastinum may have shortcomings. Specifically, the borders of the anterior, middle, and posterior mediastinum, which are defined by anatomic landmarks as assessed on a lateral radiograph of the chest, do not have true fascial planes. Recently, the International Thymic Malignancy Interest Group has published a similar three compartmental approach but is based on CT anatomy, allowing for anatomic delineation defined, in part, by pericardial and pleural reflections.[33,34] Regardless of the technique or specific classification used, the practice of assigning a mediastinal mass to a specific mediastinal compartment is useful by enabling one to formulate a manageable differential diagnosis, and effectively to direct further imaging workup.

## Anterior Mediastinal Masses

The most common anterior mediastinal masses in children are thymic lesions, lymphoma, lymphatic malformations, and germ cell tumors.

### Congenital Abnormalities of the Thymus

***Etiology.*** Arising from the third pharyngeal pouch, the thymus serves as the site of T-cell maturation. It begins a process of caudal and ventromedial elongation during the seventh and eighth week of gestation whereby the two sides fuse at about the level of the aortic arch. Absence or hypoplasia of the thymus is a component of DiGeorge syndrome,[35] with an incidence of 1 per 2,000 to 4,000.[36-38]

***Imaging.*** The appearance of the thymus on frontal chest radiographs is variable and dependent on the age of the patient (Fig. 58.8).[5,39-41] The thymus is normally prominent, with a quadrilateral shape and convex margins during infancy (e-Fig. 58.9). After approximately the fifth year of life, the thymus becomes more triangular, with straight margins (e-Fig. 58.10). By 15 years, its margins are either straight or concave (e-Fig. 58.11). After puberty, the organ undergoes involution and fatty replacement. Absent thymic tissue in pediatric patients with DiGeorge syndrome is usually evident on chest radiographs in infants and young children. However, an atrophic thymus due to stress response may appear similar.[42,43] The clinical context is often helpful in distinguishing these two conditions. After the stressor is removed, the thymus regains its size, so-called *thymic rebound.*[43,44]

***Treatment and Follow-up.*** Treatment of DiGeorge syndrome is targeted to the associated abnormalities such as hypocalcemia, frequent infections, and conotruncal cardiac defects.

### Normal Variants of the Thymus

***Etiology.*** Partial failure of thymic descent may result in ectopic thymic tissue in the neck or superior mediastinum. The two most common anatomic variants of the thymus are superior and posterior extension. The thymus may extend superiorly to the level of the lower neck[45,46] or posteriorly to the middle or posterior mediastinal compartment.[47,48] The posterior extension of the thymus typically is posterior to the superior vena cava on the right or the aortic arch on the left.

***Imaging.*** An ectopic thymus rarely presents as a mass and is most commonly discovered incidentally as thymic tissue extension on cross-sectional imaging (e-Figs. 58.12 and 58.13). Occasionally, however, ectopic thymus may be mistaken for a mediastinal or neck mass on radiographs. Normal or ectopic thymic tissue can often be identified sonographically, obviating the need for other imaging. The tissue exhibits homogenous echotexture with internal bright specular reflections, similar to the orthotopic thymus and is often in continuity with the rest of the gland.[49]

The appearance of rebound thymus on chest radiographs may be impressive in terms of degree and rapidity of development. Any displacement or compression of adjacent airway or vessels by the thymus should raise suspicion for a neoplasm.

***Treatment.*** Treatment for ectopic thymic tissue or rebound thymus is not necessary. However, its diagnosis is important to avoid unnecessary procedures.

### Thymic Cyst

***Etiology.*** A thymic cyst is a rare, fluid-filled lesion typically representing a remnant of the thymopharyngeal duct.[43,50] Although a thymic cyst can occur anywhere from the pyriform sinus to the anterior mediastinum, it is most commonly found in the lateral infrahyoid neck.[51] When large, affected pediatric patients present with a slowly enlarging neck mass that may be associated with respiratory compromise, dysphagia, or vocal cord paralysis. Although most unilocular thymic cysts are derived from a remnant of the thymopharyngeal duct, multilocular thymic cysts occasionally occur in patients with the human immunodeficiency virus, in various rheumatologic conditions,[52] and in pediatric patients with Langerhans cell histiocytosis.[53,54] Cysts in the latter group may feature small calcifications.[55]

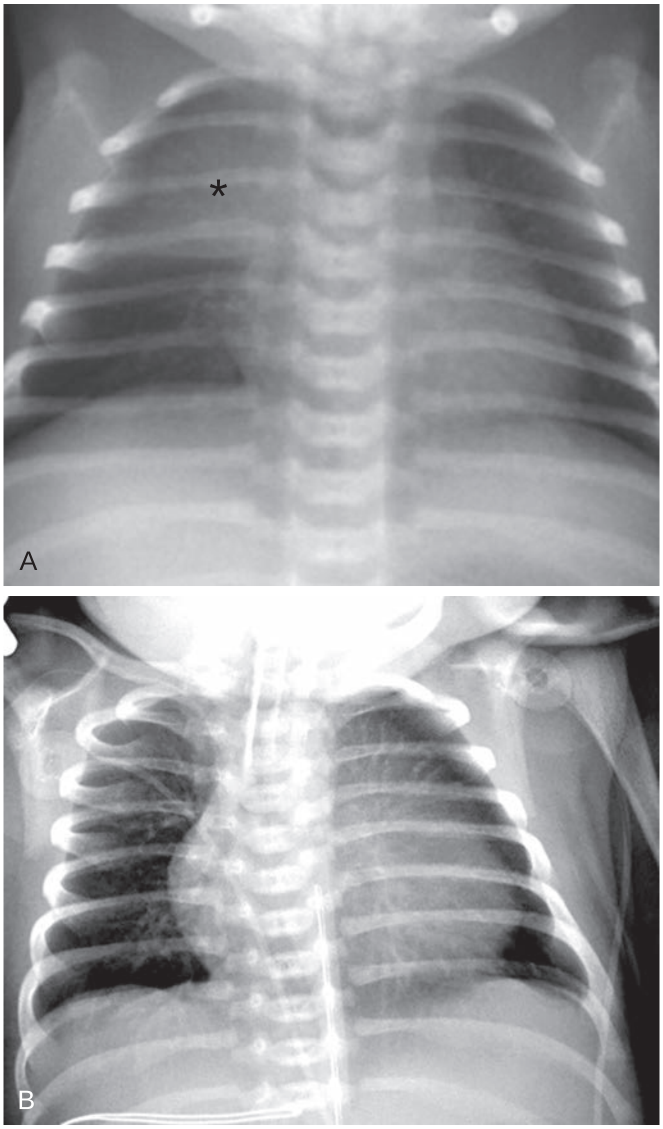

**Figure 58.8. Normal thymus in a female neonate.** (A) Frontal chest radiograph shows a thymic sail sign, which is created by the right lobe of the thymus *(asterisk)* abutting the minor fissure. (B) Frontal chest radiograph in a different neonate depicts a prominent superior mediastinum consistent with a normal thymus. A subtle but sharp contour demarcation—the "thymic notch" is often seen.

***Imaging.*** Thymic cysts appear as a spherical, fluid-filled lesion or as multilocular cystic spaces with a thin wall. They are usually occult on chest radiographs. In infants and young children, ultrasound may confirm the fluid-filled nature of the mass. On CT and magnetic resonance imaging (MRI), thymic cysts typically present as a nonenhancing cystic mass (e-Fig. 58.14). The MRI signal of a thymic cyst is variable depending on whether the contents are proteinaceous and/or hemorrhagic. The differential diagnosis

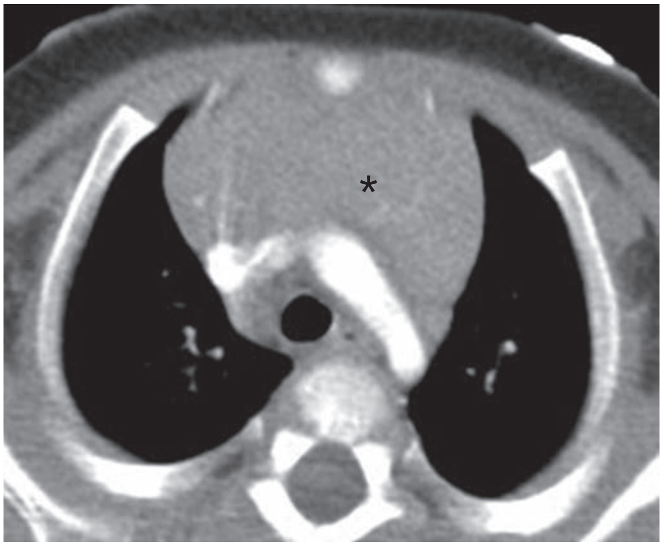

**e-Figure 58.9. Normal thymus in a 5-month-old girl.** Axial contrast-enhanced CT image at the level of the aortic arch shows the expected appearance of the thymus *(asterisk)* in the anterior mediastinal compartment at this age. The thymus has a quadrilateral shape and a convex margin. It is homogeneous in attenuation without any associated cystic, calcific, or fat component.

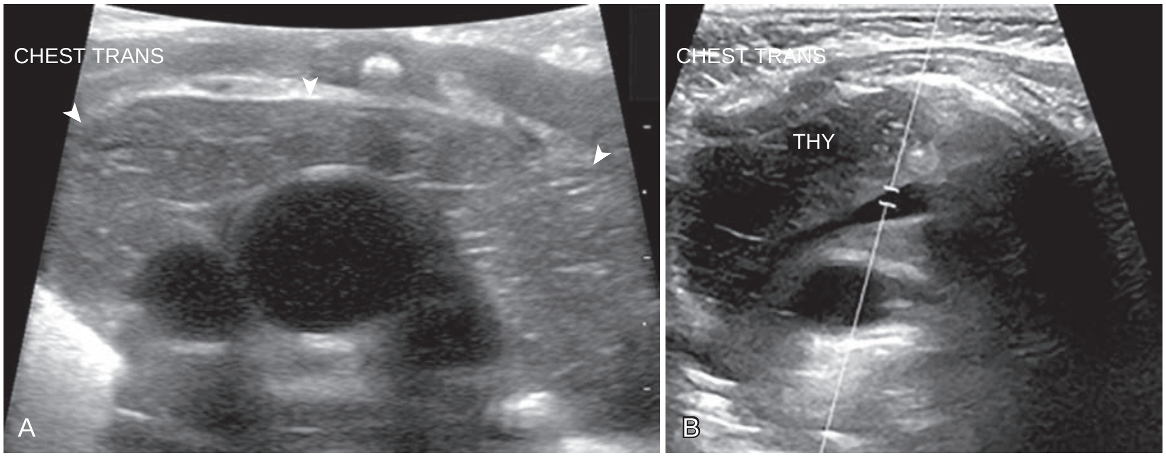

**e-Figure 58.10. Normal thymus in a female neonate.** (A) Ultrasound depicts the superficial structure in the anterior mediastinum with a dot-dash appearance—consistent with normal thymic tissue. (B) The brachiocephalic vein runs deep to the thymus (depicted by the Doppler interrogation gate) and should not be compressed or displaced.

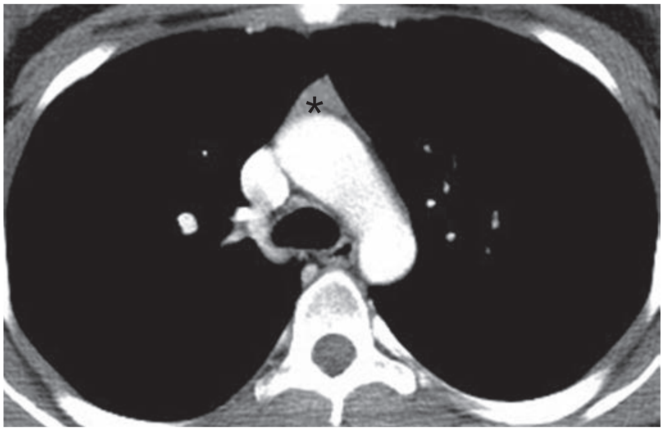

**e-Figure 58.11. Normal thymus in an adolescent boy.** Axial contrast-enhanced CT image at the level of the aortic arch shows the expected appearance of the thymus *(asterisk)* in the anterior mediastinal compartment at this age. The thymus is much smaller with a triangular shape with a straight margin.

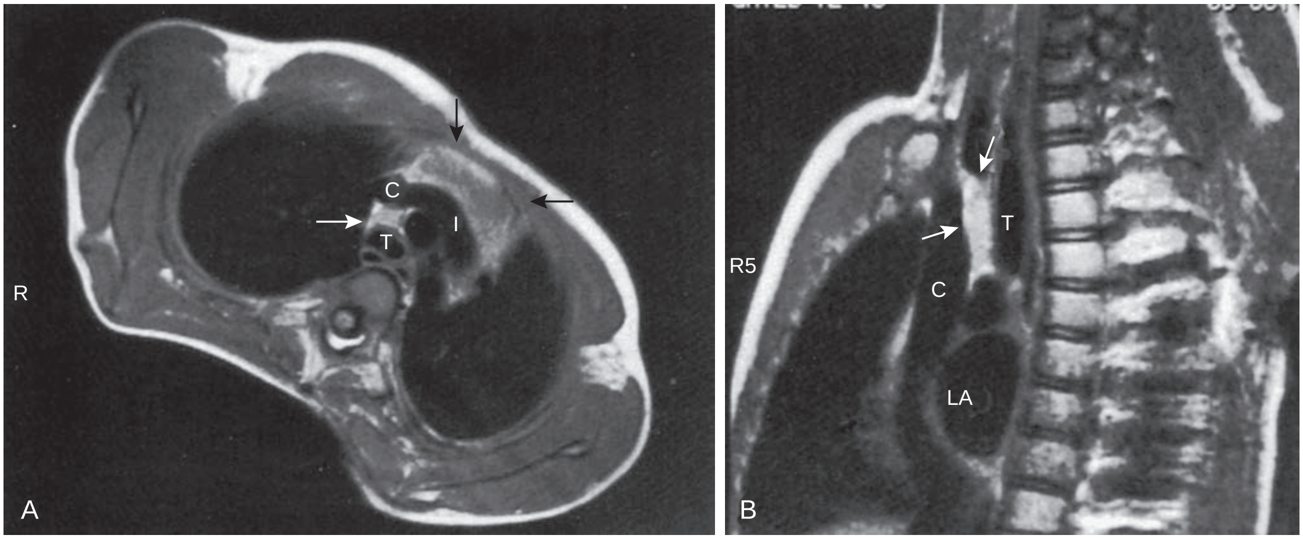

**e-Figure 58.12. Normal superior extension of thymic tissue into the neck.** On this gated axial (A), oblique (B), mildly T1-weighted MRI sequence, the thymus is clearly distinguished from vessels. It is of intermediate signal intensity—less than fat but greater than muscle. Note how far cephalad to the innominate vein *(I)* the thymic tissue extends *(arrows). C,* Superior vena cava; *LA,* left atriu; *T,* trachea;.

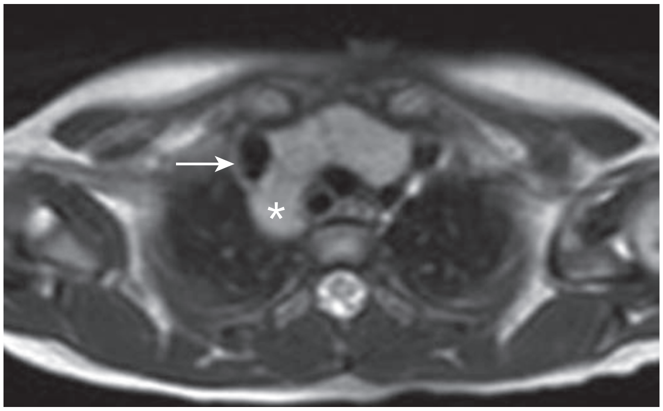

**e-Figure 58.13. Posterior thymic extension as a normal variant in a 1-year-old boy.** Axial T2-weighted MRI at the level of the brachiocephalic vein shows posterior extension *(asterisk)* of the thymus behind the superior vena cava *(arrow).*

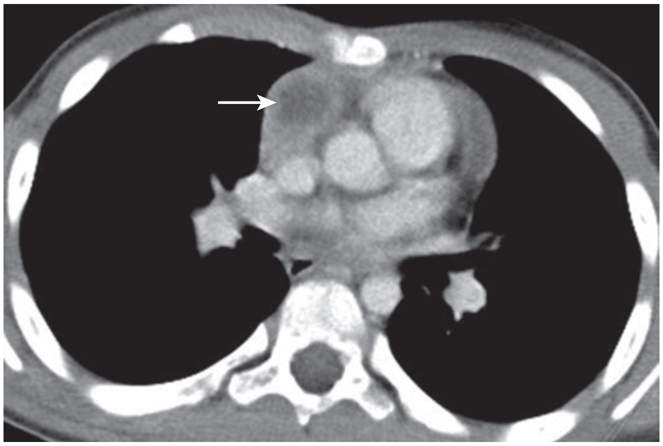

**e-Figure 58.14. Thymic cyst in a 2-year-old girl.** Axial contrast-enhanced CT image at the level of the main pulmonary artery shows a round hypoattenuating lesion *(arrow)* consistent with a cyst in the thymus. Surgical pathology confirmed the diagnosis of a thymic cyst.

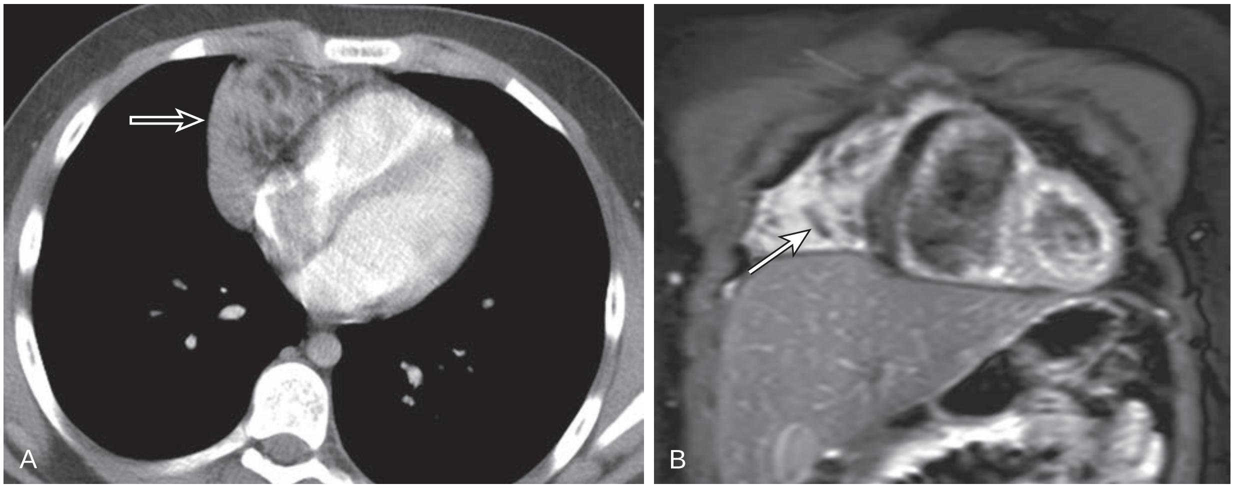

**Figure 58.15. Thymolipoma in an 8-year-old girl.** (A) Axial contrast-enhanced CT image at the level of the mid heart shows an anterior mediastinal mass *(arrow)* with whorls of low attenuating regions consistent with fat. (B) Coronal fluid-sensitive fat-saturated MRI shows the linear low signal fatty striations *(arrow)* through the mass.

includes a branchial cleft cyst, lymphatic malformation, thyroglossal duct cyst, dermoid cyst, bronchogenic cyst, and teratoma.

***Treatment.*** The current choice for managing a thymic cyst, particularly in symptomatic pediatric patients, is surgical resection, which is associated with an excellent prognosis.

### Thymolipoma

***Etiology.*** Thymolipoma is an uncommon benign thymic mass composed of both thymic and adipose tissue. Thymolipomas account for approximately 2% to 9% of all thymic neoplasms.[43,56] The presumed underlying etiologies include a variant of a thymoma, hyperplasia of mediastinal fat, and a neoplasm of mediastinal fat that encases thymic tissue.[56,57] Affected patients typically are asymptomatic.

***Imaging.*** On chest radiographs, a thymolipoma may present as a low-density lesion because of its underlying fatty component. On cross-sectional imaging studies, thymolipomas are characterized by an enlarged thymus with areas of low attenuation on CT, and high signal intensity on T2-weighted MRI, in a whorled pattern representing the underlying fatty component (Fig. 58.15).

***Treatment and Follow-up.*** Although thymolipoma is not malignant, surgical resection often is undertaken because the diagnosis may be uncertain solely on the basis of imaging. Interestingly, there is evidence of association with autoimmune etiologies and paraneoplastic phenomena in adults.[58]

### Thymoma

***Etiology.*** Thymomas arise from the thymic epithelial cells and account for approximately 1% to 2% of anterior mediastinal masses in the pediatric population.[51,59] Thymomas traditionally are classified into two types: noninvasive and invasive, depending on the presence of well-defined margins without extension through its fibrous capsule. Because thymomas may be locally invasive but typically do not metastasize, many authorities prefer the term *invasive thymoma* rather than *malignant thymoma*. From 15% to 30% of affected pediatric patients present with myasthenia gravis.[54,60,61] Other associated autoimmune conditions include pure red cell aplasia and hypogammaglobulinemia.[60,61]

***Imaging.*** On chest radiographs, a thymoma appears as an ovoid anterior mass that occasionally is associated with thin peripheral capsular calcification. Pleural lesions may be seen in patients with invasive thymoma. Cross-sectional imaging studies show an enlarged and homogeneous anterior mediastinal soft tissue mass, sometimes associated with an area of low attenuation representing underlying cystic necrosis (Fig. 58.16).[51] Findings suggestive of invasive-type thymoma include irregular margins, obliterated adjacent mediastinal fat planes, or extension to the pleura or chest wall. A search for these imaging features is particularly important, because the histology between invasive and noninvasive type thymoma overlaps, apart from surgical evidence of capsular extension.

Larger, more coarse-appearing, intralesional calcifications have been rarely encountered in both adults and children with thymomas and have been shown to represent osseous metaplasia. To date, this very rare entity has been exclusively reported in females.[62]

***Treatment and Follow-up.*** All thymomas that are deemed surgically resectable are removed. In addition, most thymomas require radiation therapy and/or chemotherapy.

### Thymic Carcinoma

***Etiology.*** A thymic carcinoma is an aggressive epithelial neoplasm of the thymus, characterized by cellular atypia and are extremely rare in children. Affected pediatric patients most often present with chest pain and constitutional symptoms.[51] Paraneoplastic phenomena such as myasthenia gravis are uncommon with a thymic carcinoma, in contradistinction to a thymoma.[63,64] Metastatic disease or invasion is detected in most new diagnoses.[64,65] Prognosis is poor.

***Imaging.*** Thymic carcinoma typically presents as a large anterior mediastinal mass with irregular margins, heterogeneous contrast enhancement, and local invasion of adjacent mediastinal structures (Fig. 58.17). Calcification and areas of necrosis are common,[66] but their presence has been shown to have limited diagnostic and prognostic value.[67] Although differentiation from a thymoma is difficult, features such as local invasion of adjacent structures, lymphadenopathy, and metastasis favor the diagnosis of a thymic carcinoma.

***Treatment.*** Because of the rarity of such tumors, proposed treatment guidelines are just beginning to emerge.[68] These have included various combinations of neoadjuvant chemotherapy, surgery, and postoperative radiation therapy.[69]

### Lymphoma

***Etiology.*** Lymphoma results from an abnormal proliferation of lymphocytes and is the most common cause of a mediastinal mass in children. It is the third most common group of malignancies after leukemia and central nervous system tumors in the pediatric population[5] and accounts for approximately 46% to 56% of all mediastinal masses.[5] Lymphoma is traditionally classified into non-Hodgkin lymphoma and Hodgkin lymphoma. These two

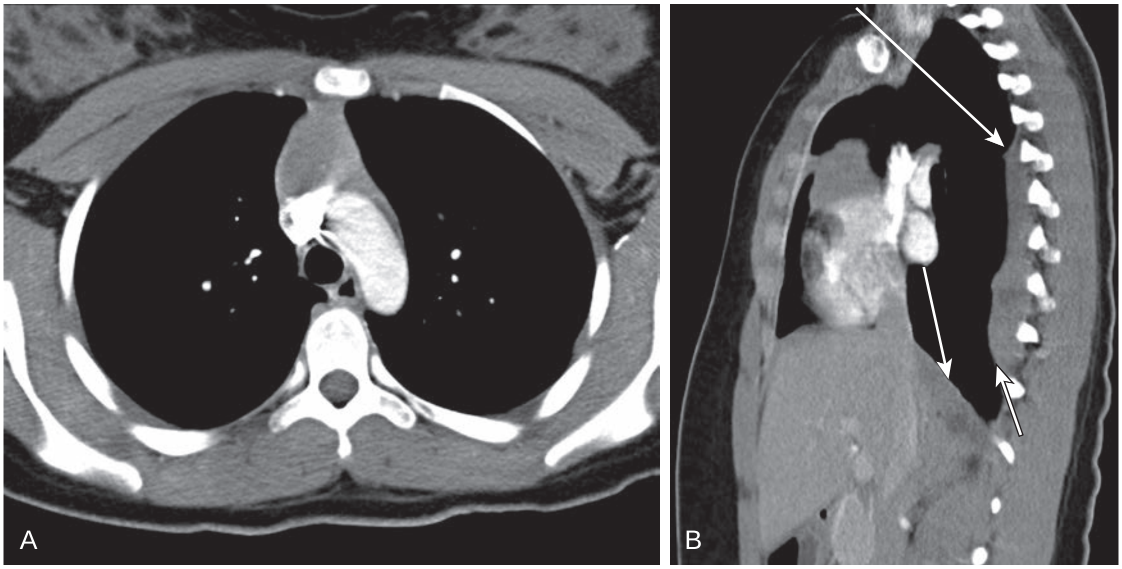

**Figure 58.16. Invasive thymoma in a 15-year-old girl.** Axial (A) and sagittal (B) reformation contrast-enhanced CT images demonstrate an anterior mediastinal mass (in A). It is heterogeneous with lobulated borders unlike normal thymus. There is prominent pleural extension of tumor (*arrows* in B).

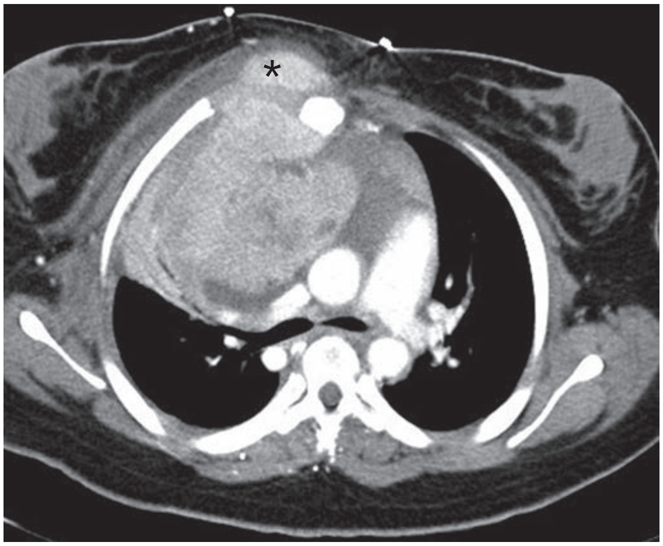

**Figure 58.17. Thymic carcinoma in a 14-year-old girl.** Axial contrast-enhanced CT image at the level of the carina shows an anterior mediastinal mass with poorly defined areas of low attenuation. Note the anterior chest wall invasion by the mass *(asterisk).*

subtypes have many similarities, including their appearance on imaging, but because of their many important differences, especially in clinical behavior, they are discussed separately in the following sections. Pulmonary involvement by lymphoma is discussed in Chapter 55.

Non-Hodgkin lymphoma typically occurs in boys who are younger than 5 years. The four main types of non-Hodgkin lymphoma are (1) lymphoblastic or T cell (the most common); (2) Burkitt; (3) non-Burkitt; and (4) large cell or histiocytic. Pediatric patients with lymphoblastic lymphoma commonly present with a mediastinal mass at initial diagnosis. Large cell or histiocytic types may involve either the thorax or the abdomen, and Burkitt and non-Burkitt types nearly always present in the abdomen. Pediatric patients often present with clinical symptoms related to obstruction or compression of adjacent mediastinal airways and vascular structures.

Hodgkin lymphoma is rare in younger children and occurs with increasing frequency in children older than 5 years.[5] It more frequently affects boys than girls by a ratio of 2 : 1.[5] Hodgkin lymphoma is divided into four main types based on the relative amounts of lymphocytes and Reed-Sternberg cells and the type of connective tissue proliferation: (1) nodular sclerosing; (2) mixed cellularity; (3) lymphocyte depletion; and (4) lymphocyte predominant. Among these four, the nodular sclerosing type (the most common subtype) accounts for approximately 75% of all mediastinal masses in children.[5,70] The majority of affected patients present with chest pain and discomfort. Shortness of breath or wheezing should suggest underlying airway compression. More specific clinical symptoms of Hodgkin lymphoma include weight loss, night sweats, and unexplained fevers.

***Imaging.*** Both Hodgkin and non-Hodgkin lymphoma can arise from or infiltrate the thymus, which may be potentially confused with thymic rebound in young children. Differentiating imaging features include unusually lobular bulky borders, heterogeneity, and displacement of adjacent structures such as airway or vessels—features that are not present with normal thymic tissue.

Hodgkin lymphoma presents as bulky hilar nodes or an anterior mediastinal mass on chest radiographs (Fig. 58.18A and B) in over two-thirds of patients.[71] Contrast-enhanced CT of the chest should be performed to confirm the presence of a mass or enlarged nodes and to characterize its extent for disease staging (Fig. 58.18C).[72,73] Sedation/anesthesia should be avoided and flat supine positioning should be approached with caution because of concern for airway compression. Common nodes involved include the superior prevascular and pretracheal nodes and range from small nodes to large, conglomerate nodal masses. The presence of calcifications before treatment is rare.[51]

On MRI, the signal characteristics of Hodgkin lymphoma are variable but usually are intermediate on T1-weighted images and have increased signal on T2-weighted images. MRI has, to date, added little additional value in the diagnosis or workup of Hodgkin lymphoma, although recent work suggests added benefit in select clinical circumstances. These include follow-up of nodes, assessment of posttreatment fibrosis versus tumor, and the differentiation of thymic rebound from disease recurrence.[74,75] Positron emission

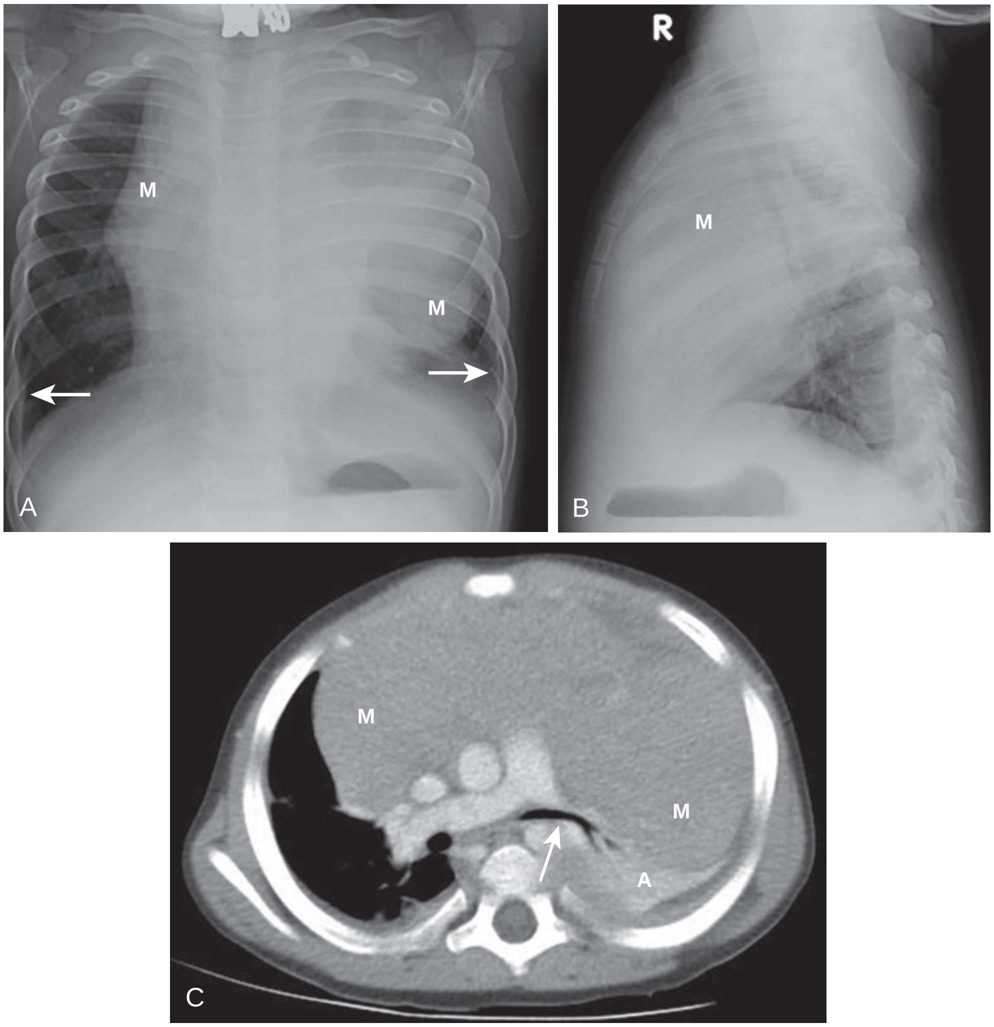

**Figure 58.18. Hodgkin lymphoma in a 2-year-old girl.** (A) Frontal chest radiograph shows a large mediastinal mass *(M)* with lobulated and bulky margins. Small pleural effusions *(arrows)* also are present. (B) Lateral chest radiograph confirms that the location of this mass *(M)* is within the anterior mediastinal compartment. (C) Axial contrast-enhanced CT image at the level of the right pulmonary artery shows a large anterior mediastinal mass *(M)* with compression of the left main-stem bronchus *(arrow)*. Left-sided atelectasis *(A)* is present.

tomography (PET) and/or PET/CT scans have been well validated in the literature in adult patients[76-78] and are now considered to be standard of care in the workup of children with Hodgkin disease.[79,80]

In contradistinction, non-Hodgkin lymphoma may arise in the abdomen, thorax, or head/neck regions. When non-Hodgkin lymphoma occurs in the thorax (in about 50% of cases[51]), its most common appearance is that of a large anterior mediastinal mass (e-Fig. 58.19A). As with any anterior mediastinal mass, such imaging findings should prompt a CT scan, which typically shows discrete or conglomerate mediastinal lymph nodes (e-Fig. 58.19B). After the administration of contrast, areas of heterogeneity and low-density necrosis are a frequent finding. Hilar, subcarinal, and posterior nodal chain involvement is frequent. In contradistinction to Hodgkin lymphoma, pleural disease may be present.[51]

MRI may be useful in the evaluation of sites beyond the anterior mediastinum, including the chest wall.[74] PET/CT can assist in staging; however, its role in children with non-Hodgkin disease has still not been firmly clarified.[81] PET is particularly helpful in discriminating viable tumor from scar, detecting active disease in normal-sized nodes on CT, and searching for extranodal disease. Interpretive pitfalls include increased physiologic metabolic activity in the normal thymus and brown fat.[82,83]

***Treatment and Follow-up.*** The prognosis of lymphoma in pediatric patients depends on two main factors: the type and stage. The prognosis of Hodgkin lymphoma, which has a cure rate of approximately 90%,[51,80,84] is better than that of non-Hodgkin lymphoma, for which the cure rate among pediatric patients is 80%.[85] Currently, multiple chemotherapeutic treatment regimens are used in combination with radiation therapy to treat pediatric patients with lymphoma. In pediatric patients with non-Hodgkin lymphoma, stem cell transplant is an option.

### Lymphatic Malformation

***Etiology.*** Lymphatic malformation represents a nonneoplastic congenital malformation of lymphatic channels, lined by single layer of endothelium.[86] It typically occurs in the cervical region (often posterior to the sternocleidomastoid muscle) but may extend caudally into the superior and/or anterior mediastinum. They can also occur in the middle and posterior mediastinal compartments, as well as the lung. Lymphatic malformations currently are classified into macrocystic and microcystic, although mixed lesions are

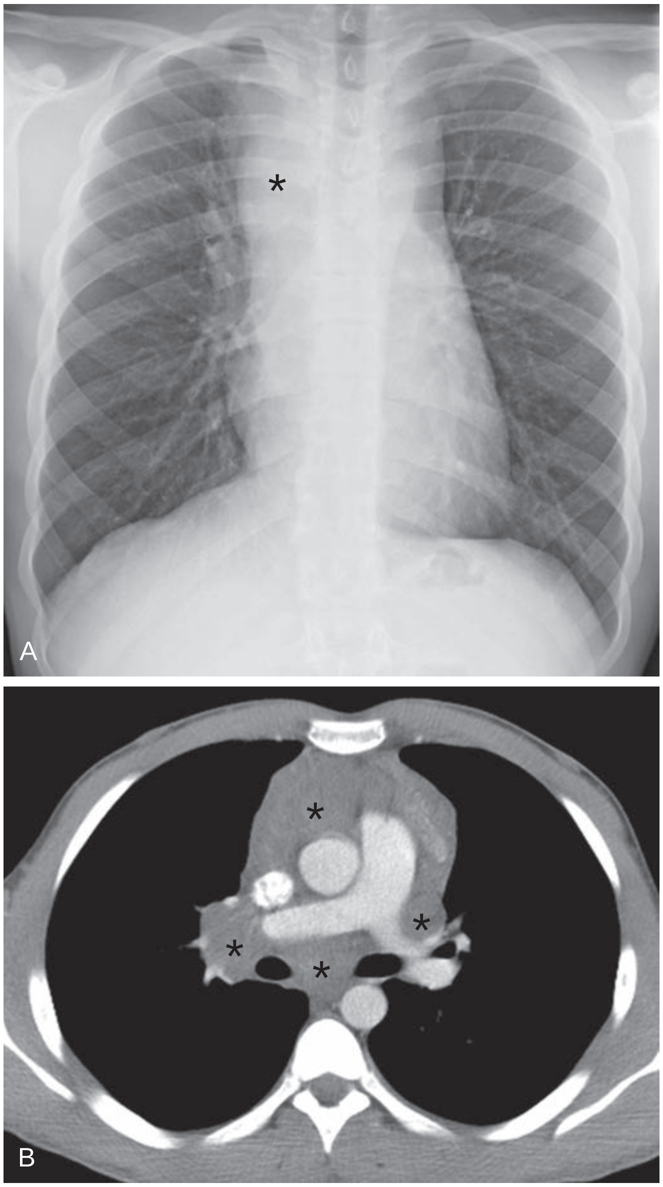

**e-Figure 58.19. Non-Hodgkin lymphoma in an 8-year-old girl.** (A) Frontal chest radiograph shows a mediastinal mass *(asterisk).* (B) Axial contrast-enhanced CT image at the level of the pulmonary artery shows a mediastinal mass *(asterisks)* located within the mediastinum. Note the anterior, subcarinal, and hilar components.

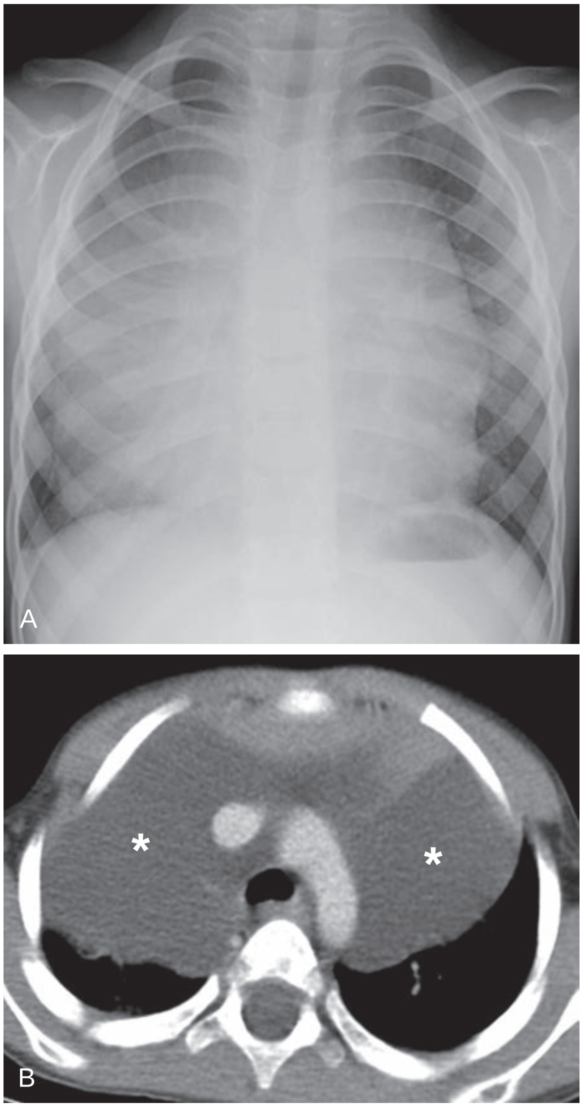

**Figure 58.20. Mediastinal lymphatic malformation in a 1-year-old boy.** (A) Frontal chest radiograph shows a large mediastinal mass. (B) Axial contrast-enhanced CT image at the level of the aortic arch shows a large, predominantly anterior mediastinal mass *(asterisks)* of fluid attenuation that crosses midline and extends laterally, consistent with a macrocystic lymphatic malformation.

common. Outdated terms include *cystic hygroma* and *lymphangioma* that should be avoided.[87] The term *lymphatic malformation* adheres to the nomenclature of the International Society for the Study of Vascular Anomalies (ISSVA).[88] Lymphatic malformations may enlarge as more lymph fills the sacs. They typically present early in life as a palpable, pliable soft tissue mass and grow commensurate with the patient's growth. Sudden enlargement also may occur if they undergo hemorrhage or become infected.

***Imaging.*** Plain radiographs have little role in the evaluation of lymphatic malformations. However, a lymphatic malformation may first be noted as a mediastinal opacity (Fig. 58.20A). CT can suggest the diagnosis but the density may be higher than expected for simple fluid due to internal complexity (Fig. 58.20B). MRI is the best imaging modality for the evaluation of lymphatic malformations because of its excellent capability for soft tissue characterization. The septa are particularly well visualized on MRI and may enhance after the administration of gadolinium. Because of proteinaceous debris and/or blood products, the magnetic resonance signal may be varied on both T1- and T2-weighted sequences. Fluid/fluid levels are common and strongly support the diagnosis of lymphatic malformation, but there should be no solid enhancing components. Calcification in lymphatic malformations is rare.

***Treatment and Follow-up.*** Because there is no known risk of malignant transformation of lymphatic malformation, some controversy exists with regard to treating smaller asymptomatic lesions. If treatment is elected, both percutaneous sclerotherapy and/or surgery currently are used in management.

### Germ Cell Tumor

***Etiology.*** Primitive germ cell rests may reside in the mediastinum and give rise to neoplasms.[89,90] Primary mediastinal germ cell tumors account for 6% to 18% of anterior mediastinal tumors in children,[73,91] and 60% of these tumors are teratomas.[51] Teratomas are divided into mature and immature types (the latter being malignant). Of all mediastinal germ cell tumors, 14% are malignant.[92] Infants with teratomas tend to present with airway compression, whereas older children often are asymptomatic[5] but may experience pain, dyspnea, or cough. The tumor can rupture into the tracheobronchial tree or pleural space with expectoration or deposition of its contents.[5,93]

***Imaging.*** On chest radiographs, germ cell tumors typically appear as round, sharply demarcated anterior mediastinal masses. Calcifications occur in approximately 25% to 53% of teratomas[5,50,51,94] and may be seen on radiographs. As for most anterior mediastinal masses, CT can better characterize their extent and may allow definitive diagnosis. Typically, teratomas (both mature and immature) demonstrate fat, fluid, and calcifications, which, when present, allow a confident diagnosis (Fig. 58.21). However, approximately 15% of mature teratomas display no fat or calcium on imaging.[5] Although calcifications may be difficult to detect on MRI, the intralesional fat and fluid are readily apparent. Invasion of adjacent structures suggests the immature type.

***Treatment and Follow-up.*** Surgical resection is the current management of choice for the benign teratomas with excellent prognosis if complete surgical excision can be achieved. However, immature teratomas generally require chemotherapy and radiation in addition to surgical excision.[95]

## Middle Mediastinal Masses

Masses arising from the middle mediastinum may be mainly categorized into vascular and nonvascular lesions. Most nonvascular middle mediastinal masses in the pediatric population are developmental malformations of the embryonic foregut or adenopathy resulting from underlying infection, primary neoplasm, or metastatic disease.

### Foregut Duplication Cysts

***Etiology.*** Foregut duplication cysts arise from developmental malformations of the embryonic foregut and include bronchogenic, esophageal, and neurenteric cysts. Bronchogenic cysts develop from errors in lung budding during development of the ventral foregut. Errors in development of the posterior division of the embryonic foregut may result in an esophageal duplication cyst. Neurenteric cysts arise from embryologic failure of separation of ectoderm from endoderm. The persistent communication is known as the canal of Kovalevsky and results in a form of spinal dysraphism. The extent of the persistent canal results in a range of abnormalities that includes the neurenteric cyst.[96] The distinction among these three types of foregut duplication cysts can be made histologically. Together, these three account for 11% of all mediastinal masses in children.[73]

***Imaging.*** Chest radiographs often reveal a rounded middle mediastinal mass (e-Fig. 58.22A). In cases of a neurenteric cyst, an accompanying vertebral anomaly also may be present (see also e-Figs. 96.16 and 96.17). The position of the cyst in the

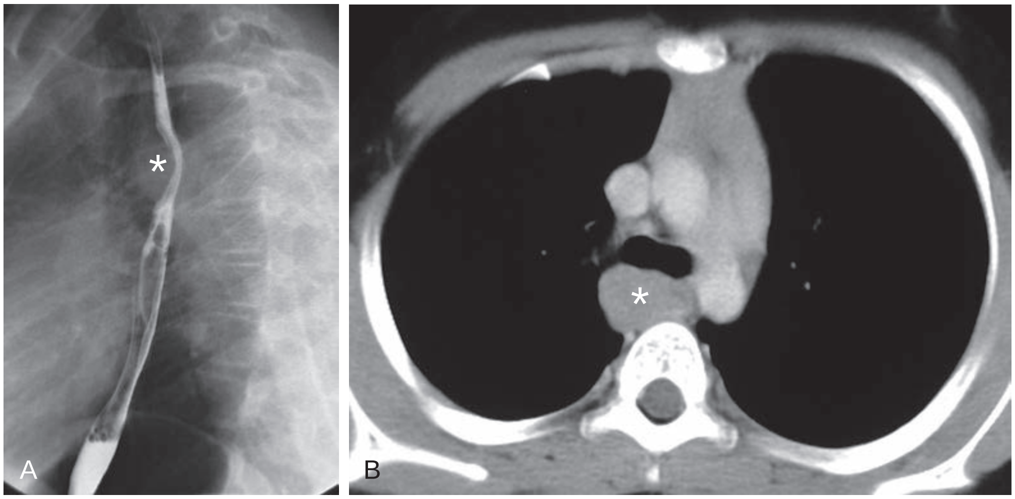

**e-Figure 58.22. Esophageal duplication cyst in a 4-year-old boy.** (A) Lateral view of the esophagus obtained during a barium esophagram study shows a smooth-bordered focal anterior indentation consistent with an extraluminal mass *(asterisk)* centered between the trachea and esophagus. (B) Axial contrast-enhanced CT image at the level of the carina shows a fluid density middle mediastinal mass *(asterisk)*.

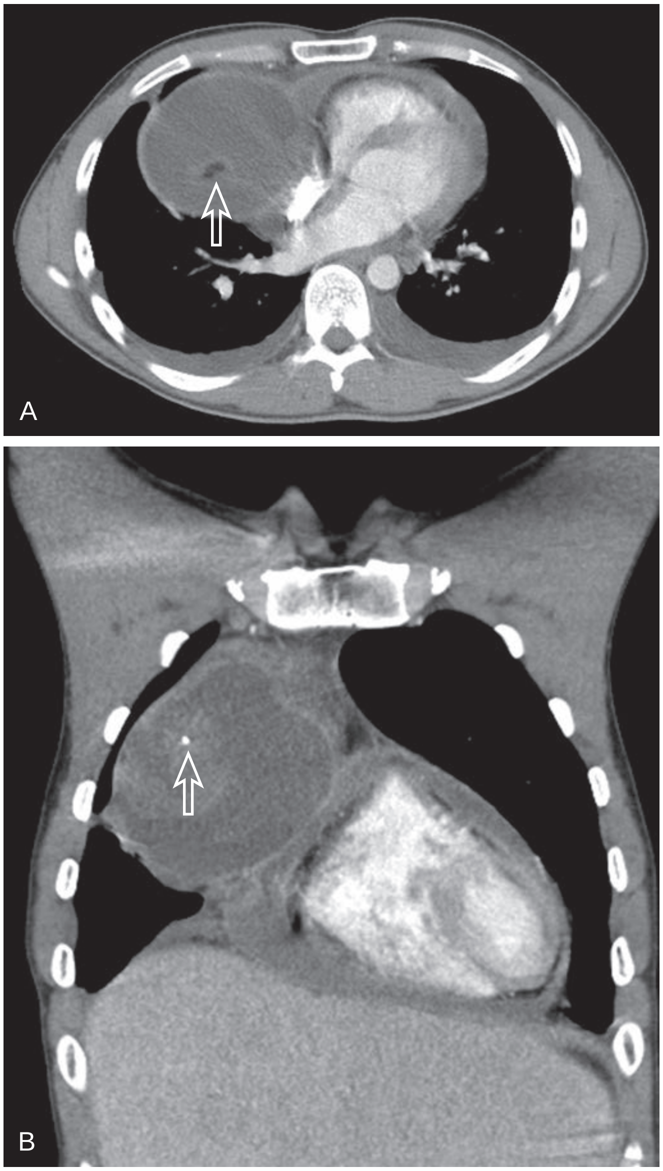

**Figure 58.21. Mediastinal teratoma in a 24-year-old man.** Axial (A) and coronal (B) reformation contrast-enhanced CT images reveal a large low-density mass in the anterior mediastinum. There is a small plug of fat attenuation (*arrow* in A) and punctate calcification (*arrow* in B), findings that are consistent with a teratoma.

mediastinum suggests its type. Bronchial duplication cysts typically are located within the middle mediastinum in close proximity to the airway. Esophageal duplication cysts are in the middle or posterior mediastinum. Neurenteric cysts most often are in the posterior mediastinum but are discussed here because they fall into the same differential. Cross-sectional imaging studies demonstrate a nonenhancing, fluid-filled cystic mass with well-marginated borders (e-Fig. 58.22B). Internal proteinaceous material can increase the Hounsfield units on CT and signal intensity on T1-weighted MRI. The high water content usually results in adequate T2 prolongation to reveal its cystic nature on T2-weighted MRI when CT density is equivocal. On both CT and MRI, foregut duplication cysts lack internal enhancement and appear homogeneous unless superimposed infection is present. Neurenteric cysts are typically associated with a regional vertebral anomaly, allowing differentiation.

***Treatment and Follow-up.*** The current management for a foregut duplication cyst is complete surgical resection, particularly in symptomatic pediatric patients. In some institutions, endoscopic ultrasound-guided fine-needle aspiration is used to preoperatively confirm the diagnosis.[97,98]

### Lymphadenopathy

***Etiology.*** Lymphadenopathy may occur in any mediastinal compartment but is most prevalent in the middle mediastinum. Most enlarged mediastinal lymph nodes in children are reactive and are often seen in children with cystic fibrosis. Particularly prominent hilar lymph nodes may be seen in the setting of granulomatous diseases.

As discussed elsewhere in this chapter, lymphoma is the most common cause of a primary mediastinal neoplastic mass that presents as a conglomeration of lymph nodes. Although nodes commonly are found in the anterior mediastinum, they may extend or arise in the middle mediastinum, particularly in non-Hodgkin lymphoma. Although less common, mediastinal lymphadenopathy also may be seen as a result of metastatic disease from tumors such as Wilms tumor, Ewing tumor, and osteosarcoma.

***Imaging.*** Lymphadenopathy often is first detected on chest radiographs. The presence of hilar involvement, bilaterality, and calcification should be investigated carefully. Unless acute infection is the suspected cause, a CT scan with intravenous contrast material should be obtained for further evaluation after chest radiographs. MRI may be helpful in selected cases but is seldom required. On T1-weighted MRI sequences, nodes are isointense to muscle and are hyperintense on T2-weighted sequences and are easily distinguished from adjacent vessels.

Calcified lymph nodes suggest a history of treated lymphoma or the presence of granulomatous disease. Low-density or centrally necrotic nodes should suggest *Mycobacterium tuberculosis* (Fig. 58.23)[99] or *Mycobacterium avium-intracellulare*.[100,101] Sarcoidosis is rare in children. Large hilar lymphadenopathy also has been described in persons with lymphoma, infectious mononucleosis, and Castleman disease (angiofollicular lymphoid hyperplasia) (e-Fig. 58.24).

## Posterior Mediastinal Masses

### Neurogenic Tumors

***Etiology.*** The vast majority (88%) of masses arising in the posterior mediastinum are of neurogenic origin and together account for about 34% of all mediastinal masses in children.[73] Ganglion cells in the paravertebral sympathetic chain and peripheral nerve sheaths are responsible for most posterior mediastinal neurogenic masses. Sympathetic chain tumors are more common than nerve sheath tumors in the pediatric mediastinum.

Tumors arising from the sympathetic chain include neuroblastoma, ganglioneuroblastoma, and ganglioneuroma, in order of increasing cellular differentiation and increasing age of presentation. These tumors are related by their structure of origin but are distinguished by their underlying histologic cellular differentiation. The least differentiated (and most malignant) and most common of these tumors is neuroblastoma, which usually arises in children younger than 5 years. About 10% to 16% of all neuroblastomas arise in the mediastinum. Clinical manifestations include constitutional symptoms and several paraneoplastic syndromes. Presentations that are unique to the mediastinal location of neuroblastoma include Horner syndrome if the mass involves the superior mediastinum. Still, many children with thoracic neuroblastoma present with incidentally discovered masses on chest or abdominal radiographs. Seventy-six percent of thoracic neuroblastomas are positive for urinary catecholamines.

The two most common nerve sheath masses are neurofibromas and schwannomas, both of which are benign tumors composed of spindle cells and myxoid stroma. Plexiform neurofibromas

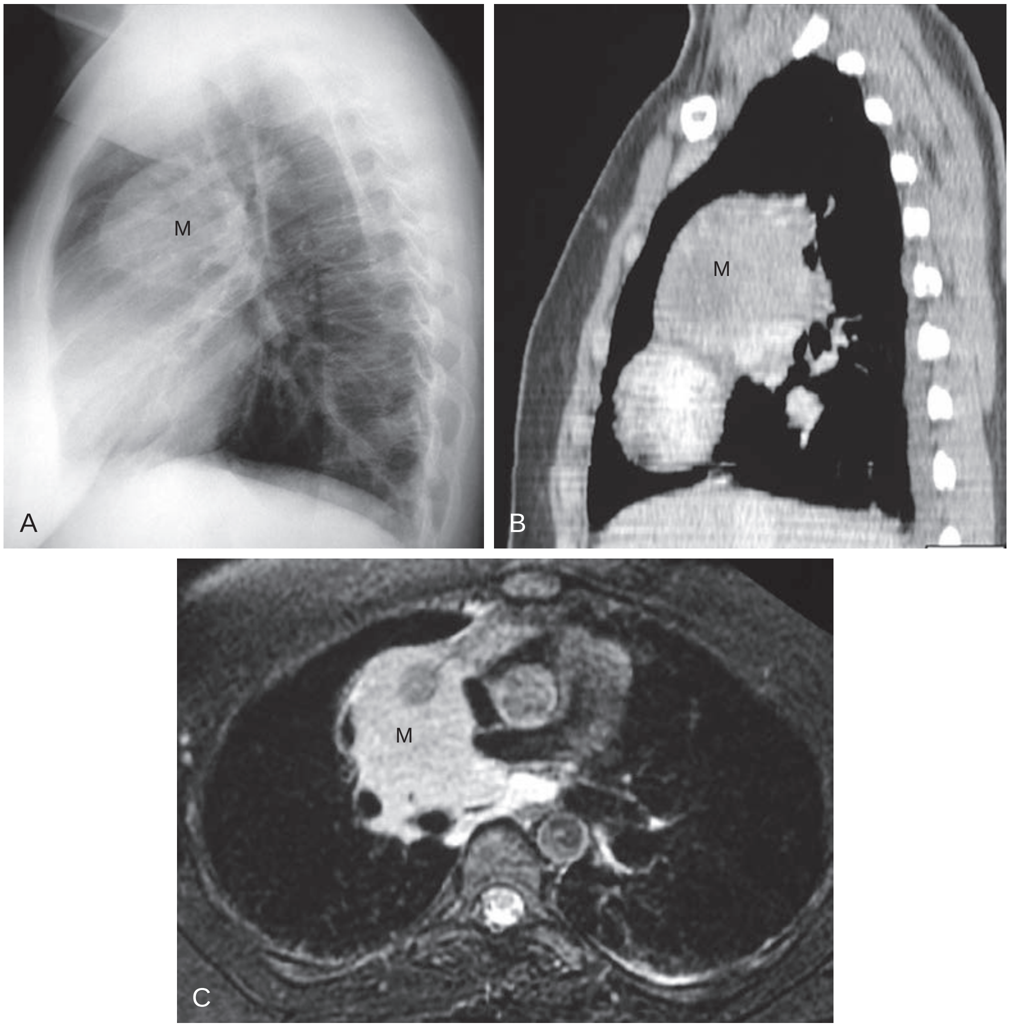

**e-Figure 58.24. Castleman disease in a 17-year-old girl.** (A) Lateral chest radiograph shows a large middle mediastinal mass *(M).* (B) Sagittal contrast-enhanced CT image demonstrates a homogeneously enhancing middle mediastinal mass *(M).* (C) Axial T2-weighted MRI shows a middle mediastinal mass *(M)* with homogeneously high signal intensity.

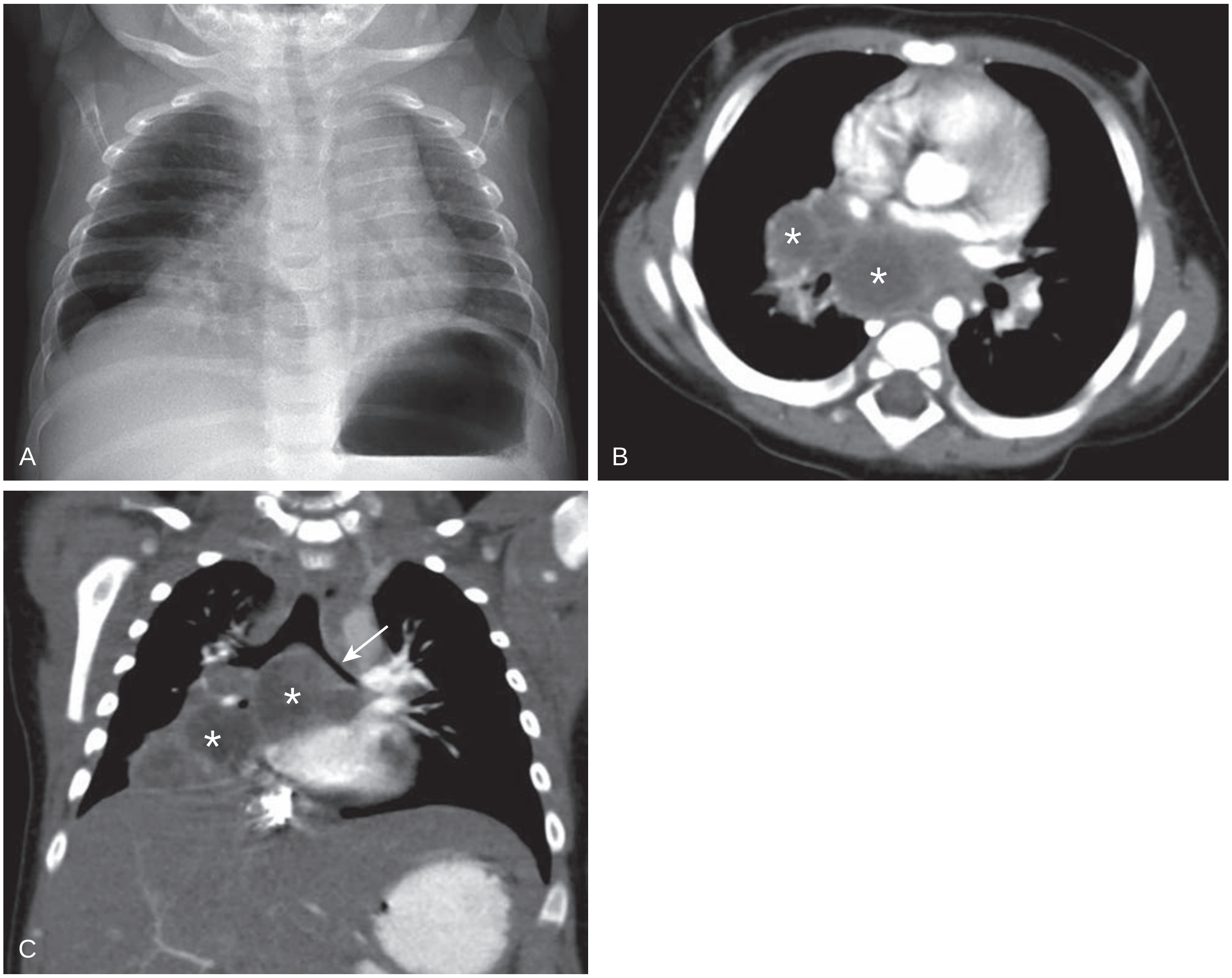

**Figure 58.23. Primary *Mycobacterium tuberculosis* in a 2-year-old boy.** (A) Frontal chest radiograph shows right hilar and infrahilar opacity. In addition, the distal trachea has a slight leftward deviation, suggesting displacement by the mass. (B) Axial contrast-enhanced CT image demonstrates low attenuation hilar, infrahilar, and subcarinal lymphadenopathy *(asterisks).* (C) Coronal contrast-enhanced CT image shows a narrowing of the left main-stem bronchus *(arrow)* as a result of a large mediastinal lymphadenopathy *(asterisks).* The sputum culture confirmed the diagnosis of *Mycobacterium tuberculosis* infection.

commonly are seen in children with neurofibromatosis type 1. These tumors tend to arise in the superior/posterior mediastinum and are usually bilateral. Posterior mediastinal schwannomas are more often seen in adults.

***Imaging.*** Most posterior mediastinal neurogenic tumors are first detected on chest radiographs as a soft tissue opacity (Figs. 58.25 and 58.26). Associated adjacent bone destruction or scalloping and silhouetting of posterior mediastinal structures such as the descending aorta are additional findings. Detection of calcification suggests a sympathetic chain tumor such as a neuroblastoma as opposed to a nerve sheath tumor. Approximately 40% of neuroblastomas in the posterior mediastinum show speckled or curvilinear calcification.[5]

On CT, posterior mediastinal neurogenic tumors typically present as soft tissue masses with a varying degree of contrast enhancement (see Figs. 58.25 and 58.26). Further characterization and differentiation among different types of posterior mediastinal neurogenic tumors with CT is limited.

MRI is currently the best imaging modality for evaluating posterior mediastinal tumors in pediatric patients because of its high sensitivity for detecting the intraspinal (extradural) extension and its lack of ionizing radiation.[73] Moreover, MRI offers exquisite soft tissue contrast resolution, which is an advantage when assessing a region such as the posterior mediastinum with similar soft tissue densities and minimal fat. Finally, MRI is sensitive for assessing bone marrow involvement.

The sympathetic chain tumors have a similar appearance on all imaging studies. These masses appear as T2-hyperintense, well-circumscribed, sausage-shaped structures in a paraspinal distribution along the expected region of the sympathetic chain. Intraspinal extension is common with widening of the neural foramina. After intravenous administration of contrast material, variable, heterogeneous enhancement occurs. A metaiodobenzylguanidine scan can confirm the diagnosis of neuroblastoma and assess for distant sites of disease with a reported sensitivity between 90% and 95%.[102]

Nerve sheath tumors appear as sharply demarcated, rounded, paravertebral masses. Nerve sheath tumors are localized to one or two levels, as opposed to the typically more extensive neuroblastomas. However, plexiform neurofibromas can involve multiple

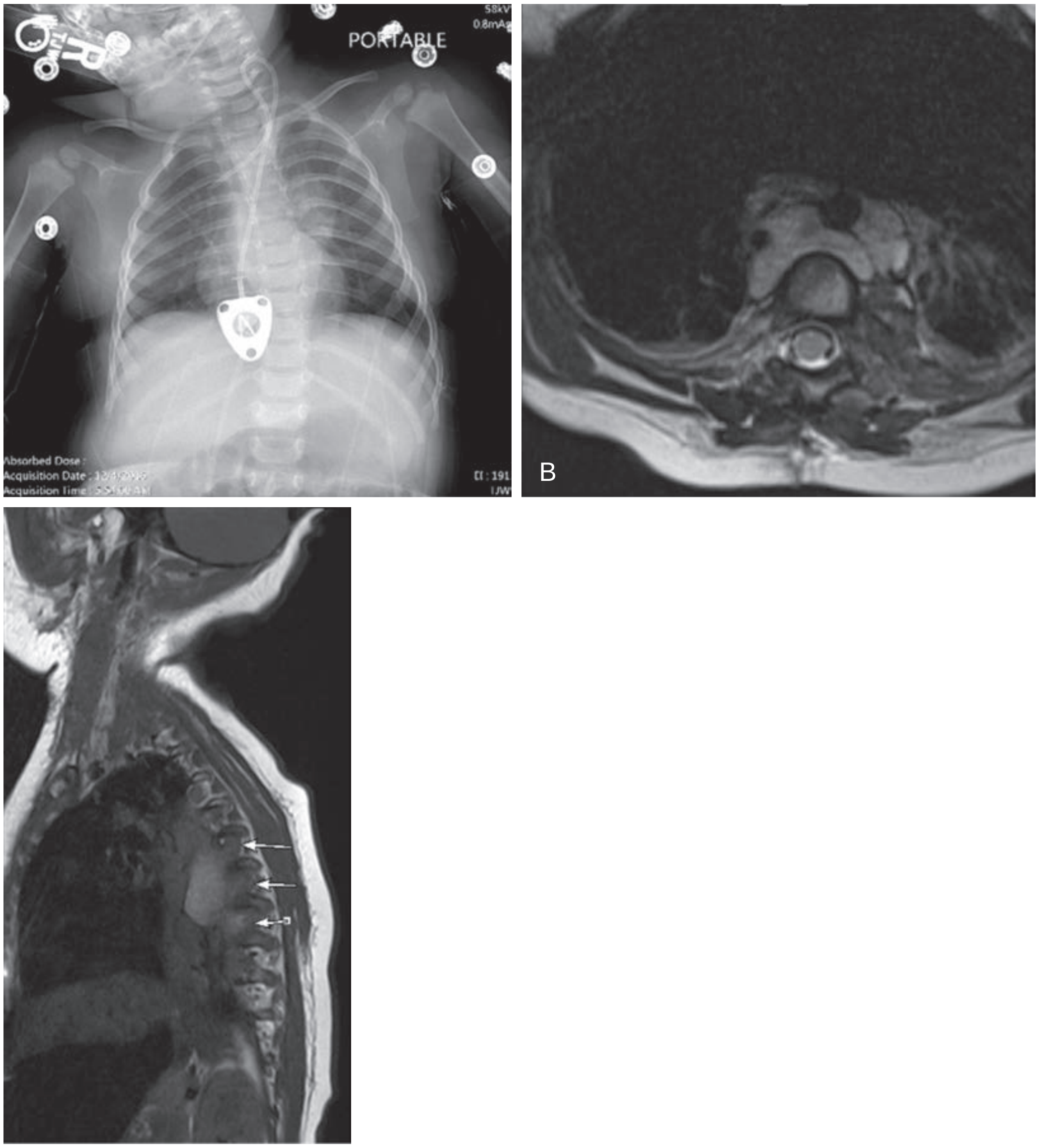

**Figure 58.25. Neuroblastoma in a 10 month old girl.** (A) AP chest radiograph shows a right paraspinal soft tissue convexity *(arrow)*. (B) axial T2 weighted MRI through the thorax shows a posterior mediastinal mass encasing the descending aorta and azygous vein. (C) T1 weighted sagital MRI demonstrates a posterior mediastinal, paraspinal mass with neural foraminal involvement *(arrows)*.

levels and extend into the middle mediastinum. On T2-weighted MRI, plexiform neurofibromas have a distinct high signal periphery with an intermediate signal centrally—the so-called target appearance (Fig. 58.27). Associated findings include thoracic dural ectasia and scalloping of the posterior vertebral bodies.

***Treatment and Follow-up.*** Sympathetic chain neurogenic tumors are treated entirely differently from nerve sheath tumors because the sympathetic chain tumors are considered malignant (although to a varying degree depending on their cellular differentiation). Chemotherapy usually is initiated after a histologic diagnosis is rendered and surgical resection is performed for sympathetic chain neurogenic tumors. Radiation therapy generally has no role.[5] The prognosis depends on the patient's age. Younger patients (particularly infants) have a far better prognosis than older children. Overall, patients with a thoracic neuroblastoma have a better prognosis than patients with retroperitoneal disease.[51] Patients with benign nerve sheath tumors such as neurofibromatosis type 1 do not undergo routine resection of their masses. However, imaging surveillance may be used because of risks of malignant transformation and other tumors arising de novo.

### Other Posterior Mediastinal Lesions and Lesions Simulating Posterior Mediastinal Masses

***Etiology.*** Benign masses and even lung parenchymal processes may mimic more sinister posterior mediastinal masses. For example, extramedullary sites of hematopoiesis include the posterior mediastinal paravertebral space.[103] Rarely, the posterior mediastinum may be the site of herniated bowel loops or kidney relating to diaphragmatic defects. Ectopic thymic extension into the posterior mediastinal compartment was discussed previously. Cystic structures in the posterior mediastinum may be a neurenteric cyst, esophageal duplication cyst (both of which are discussed in the section on middle mediastinal masses), lymphatic malformation (discussed earlier), or meningocele, which usually are associated with

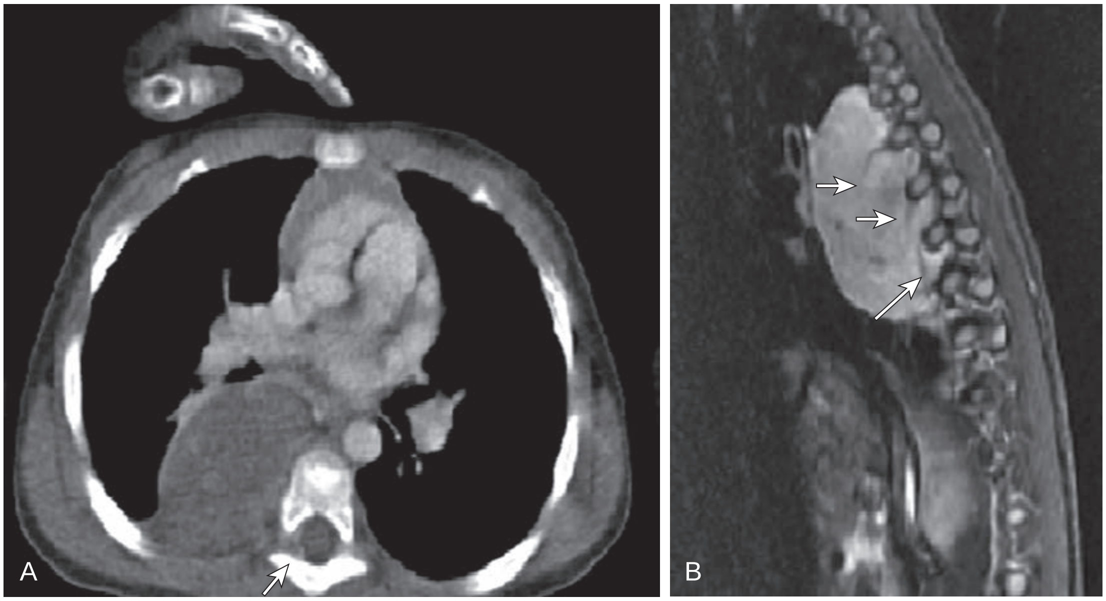

**Figure 58.26. Ganglioneuroma in a 3-year-old.** (A) Axial contrast-enhanced CT image demonstrates a large right paravertebral, posterior mediastinal mass. Neural foraminal extension is present *(arrow).* (B) Sagittal STIR MRI is far superior in its depiction of the neural foraminal extent *(arrows).*

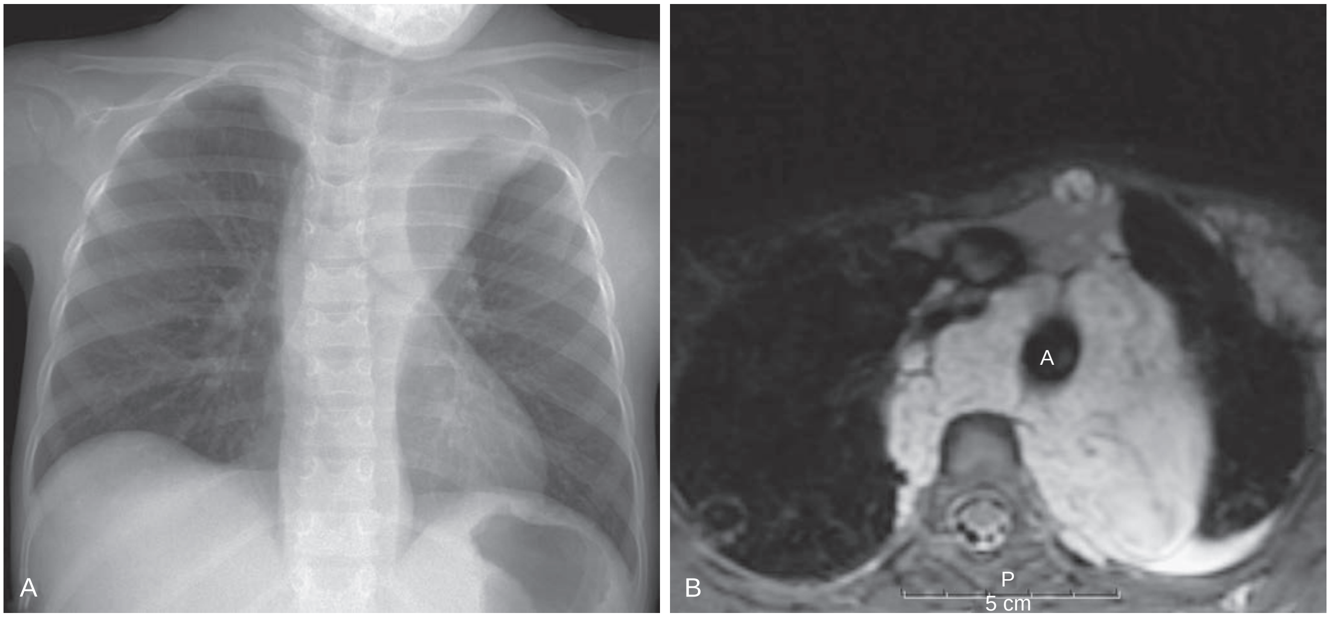

**Figure 58.27. Neurofibromatosis type 1 in a 6-year-old boy who presented with cough.** (A) Frontal chest radiograph shows a large left apical and paraspinal mass that cascades down each side of the spine. (B) Axial T2-weighted MRI demonstrates the "target sign" (central low signal within lesion lobules) and the lobulated shape of the plexiform neurofibromas. *A,* Aorta; *P,* paraspinal muscle.

neurofibromatosis type 1. Finally, pulmonary airspace disease, which is seen through the mediastinal structures on chest radiographs, may mimic a mediastinal mass or vice versa.

***Imaging.*** A focus of hematopoietic tissue is most often seen in a paravertebral position as abnormal smooth or lobulated soft tissue. Other clues such as bone marrow reconversion or evidence of sickle cell disease may suggest the diagnosis. An airspace consolidation such as that seen with pneumonia may mimic a posterior mediastinal mass, particularly when it is in the lower lobe medially and obscures posterior mediastinal structures such as the descending aorta and/or azygoesophageal fissure on a frontal chest radiograph. Conversely, a posterior mediastinal mass such as a neuroblastoma may be confused with lung consolidation, particularly when it is located superiorly. The presence of a diaphragmatic hernia is usually obvious, particularly if air-filled loops of bowel are present. In confusing cases, coronal reformatted CT or MRI that can delineate the entire diaphragm are helpful for confirmation (e-Fig. 58.28).

***Treatment and Follow-up.*** Treatment and follow-up of posterior mediastinal lesions other than neoplasms are dictated entirely by the nature of the underlying lesion. As such, determination of the etiology is essential.

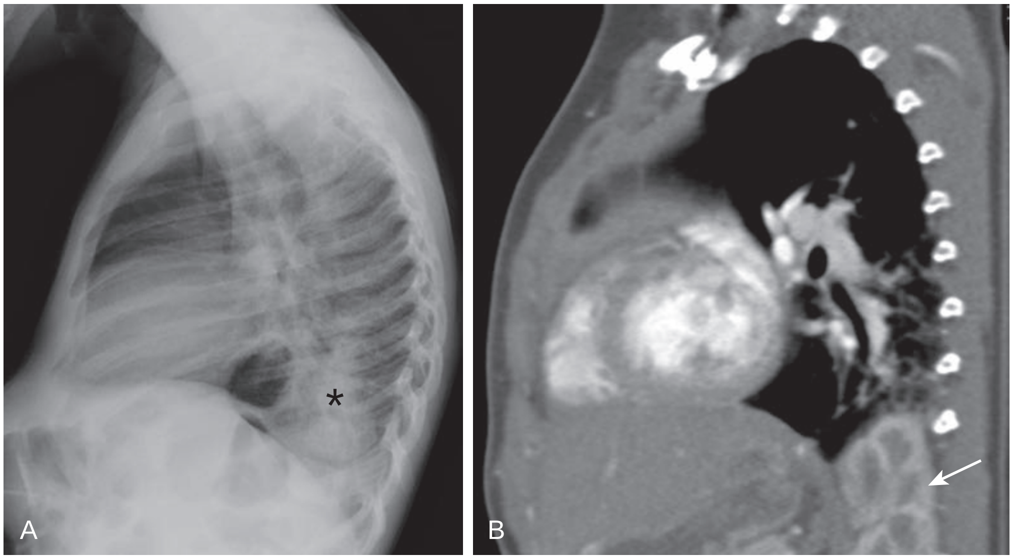

**e-Figure 58.28. Bochdalek hernia with superior herniation of a kidney into the chest in a 1-year-old boy.** (A) Lateral chest radiograph shows an opacity *(asterisk)* with obscuration of the posterior left hemidiaphragm. (B) Sagittal contrast-enhanced CT image demonstrates that the opacity seen on the lateral chest radiograph (A) is caused by upward herniation of the kidney *(arrow)* through a Bochdalek hernia.

## KEY POINTS

- Pneumomediastinum is most often attributed to alveolar rupture. Elevation of the thymus is a very helpful imaging clue for pneumomediastinum in neonates and infants on chest radiographs.
- The mediastinum is the most common location of chest masses in the pediatric population.
- The thymus is variable in size and shape, particularly among pediatric patients, and it changes dramatically over time for each patient. Variations of the thymus should be considered when an anterior mediastinal mass is suspected. Many anterior mediastinal neoplasms arise in or infiltrate the thymus.
- Most nonvascular middle mediastinal masses in the pediatric population are developmental malformations of the embryonic foregut or adenopathy as a result of underlying infection, a primary neoplasm, or metastatic disease.
- Most masses arising in the posterior mediastinum are of neurogenic origin and together account for about 34% of all mediastinal masses in children.

## SUGGESTED READINGS

Lee EY. Evaluation of non-vascular mediastinal masses in infants and children: an evidence-based practical approach. *Pediatr Radiol*. 2009;39(suppl 2):S184–S190.

Nasseri F, Effekhari F. Clinical and radiologic review of the normal and abnormal thymus: pearls and pitfalls. *Radiographics*. 2010;30(2):413–428.

Thacker PG, Mahani MG, Heider A, et al. Evaluation of mediastinal masses in children and adults: practical diagnostic approach based on a new classification system. *J Thorac Imaging*. 2015;30(4):247–267.

Toma P, Granata C, Rossi A, et al. Multimodality imaging of Hodgkin disease and non-Hodgkin lymphomas in children. *Radiographics*. 2007; 27(5):1335–1354.

## REFERENCES

Full references for this chapter can be found on www.expertconsult.com.

## REFERENCES

1. Bejvan SM, Godwin JD. Pneumomediastinum: old signs and new signs. *AJR Am J Roentgenol*. 1996;166(5):1041–1048.
2. Johnson NN, Toledo A, Endom EE. Pneumothorax, pneumomediastinum, and pulmonary embolism. *Pediatr Clin North Am*. 2010;57(6):1357–1383.
3. Macklin MT, Macklin CC. Malignant interstitial emphysema of the lungs and mediastinum as an important occult complication in many respiratory diseases and other conditions: an interpretation of the clinical literature in the light of laboratory experiment. *Medicine (Baltimore)*. 1944;23(4):281–358.
4. Macklin CC. Transport of air along sheaths of pulmonic blood vessels from alveoli to mediastinum: clinical implications. *Arch Intern Med*. 1939;64(5):913–926.
5. Behr GG, Restrepo R, Lee EY. Chap 58. The Mediastinum. In: Coley B, ed. *Caffey's pediatric diagnostic imaging*. 12th ed. Philadelphia: Elsevier; 2013:619–632.
6. Zylak CM, Standen JR, Barnes GR, et al. Pneumomediastinum revisited. *Radiographics*. 2000;20(4):1043–1057.
7. Eesa M, Kandpal H, Sharma R, et al. Spontaneous pneumorrhachis in bronchial asthma. *Acta Radiol*. 2006;47(7):672–674.
8. McLoud TC. *Thoracic Radiology*. St Louis: Mosby–Year Book; 1998.
9. Daldrup-Link HE, Newman B. *Pearls and Pitfalls in Pediatric Imaging: Variants and Other Difficult Diagnoses*. Cambridge University Press; 2014.
10. Newman B. Airleak in the neonate Chapter 20. In: Daldrup-Link HE, Newman B, eds. *Pearls and Pitfalls in Pediatric Imaging Variants and Other Difficult Diagnoses*. Cambridge UK: Cambridge University Press; 2014:72–77.
11. Abbas PI, Akinkuotu AC, Peterson ML, et al. Spontaneous pneumomediastinum in the pediatric patient. *Am J Surg*. 2015;210(6):1031–1035.
12. Gander JW, Berdon WE, Cowles RA. Iatrogenic esophageal perforation in children. *Pediatr Surg Int*. 2009;25(5):395–401.
13. Amodio JB, Berdon WE, Abramson SJ, et al. Retrocardiac pneumomediastinum in association with tracheal and esophageal perforations. *Pediatr Radiol*. 1986;16(5):380–383.
14. Fitzwater JW, Silva NN, Knight CG, et al. Management of spontaneous pneumomediastinum in children. *J Pediatr Surg*. 2015;50(6):983–986.
15. Ylmaz S, Oren H, Irken G, et al. Life-threatening mediastinal-retroperitoneal hemorrhage in a child with moderate hemophilia A and high inhibitor titer: successful management with recombinant activated factor VII. *J Pediatr Hematol Oncol*. 2005;27(7):400–402.
16. Woolley MM, Isaacs H Jr, Lindesmith G, et al. Spontaneous thymic hemorrhage in the neonate: report of two cases. *J Pediatr Surg*. 1974;9(2):231–233.
17. Urvoas E, Pariente D, Rousset A, et al. Ultrasound diagnosis of thymic hemorrhage in an infant with late-onset hemorrhagic disease. *Pediatr Radiol*. 1994;24(2):96–97.
18. Tabari AK, Mirshemirani A, Rouzrokh M, et al. Acute mediastinitis in children: a nine-year experience. *Tanaffos*. 2013;12(2):48–52.
19. Akman C, Kantarci F, Cetinkaya S. Imaging in mediastinitis: a systematic review based on aetiology. *Clin Radiol*. 2004;59(7):573–585.
20. Katabathina VS, Restrepo CS, Martinez-Jimenez S, et al. Nonvascular, nontraumatic mediastinal emergencies in adults: a comprehensive review of imaging findings. *Radiographics*. 2011;31(4):1141–1160.
21. Kirchner SG, Hernanz-Schulman M, Stein SM, et al. Imaging of pediatric mediastinal histoplasmosis. *Radiographics*. 1991;11(3):365–381.
22. David RA, Weiner MA, Rakow JI. Chronic active mediastinitis in a 7-year-old boy: MRI findings. *Pediatr Radiol*. 1996;26(9):669–671.
23. Atasoy C, Fitoz S, Erguvan B, et al. Tuberculous fibrosing mediastinitis: CT and MRI findings. *J Thorac Imaging*. 2001;16(3):191–193.
24. Takahara S, Sai S, Kagatani T, et al. Efficacy and haemodynamic effects of vacuum-assisted closure for post-sternotomy mediastinitis in children. *Interact Cardiovasc Thorac Surg*. 2014;19(4):627–631.
25. Argenta LC, Morykwas MJ, Marks MW, et al. Vacuum-assisted closure: state of clinic art. *Plast Reconstr Surg*. 2006;117(7 suppl):127s–142s.
26. Athanassiadi KA. Infections of the mediastinum. *Thorac Surg Clin*. 2009;19(1):37–45, vi.
27. Mangukia CV, Agarwal S, Satyarthy S, et al. Mediastinitis following pediatric cardiac surgery. *J Card Surg*. 2014;29(1):74–82.
28. Devaraj A, Griffin N, Nicholson AG, et al. Computed tomography findings in fibrosing mediastinitis. *Clin Radiol*. 2007;62(8):781–786.
29. Rodriguez E, Soler R, Pombo F, et al. Fibrosing mediastinitis: CT and MR findings. *Clin Radiol*. 1998;53(12):907–910.
30. Witschi M, Gugger M, Nicod LP. Treatment of mediastinal fibrosis with mycophenolate mofetil. *Respiration*. 2009;78(3):330–333.
31. Mole TM, Glover J, Sheppard MN. Sclerosing mediastinitis: a report on 18 cases. *Thorax*. 1995;50(3):280–283.
32. Sherrick AD, Brown LR, Harms GF, et al. The radiographic findings of fibrosing mediastinitis. *Chest*. 1994;106(2):484–489.
33. Thacker PG, Mahani MG, Heider A, et al. Imaging evaluation of mediastinal masses in children and adults: practical diagnostic approach based on a new classification system. *J Thorac Imaging*. 2015;30(4):247–267.
34. Carter BW, Tomiyama N, Bhora FY, et al. A modern definition of mediastinal compartments. *J Thorac Oncol*. 2014;9(9):S97–S101.
35. Johnson JM, Moonis G, Green GE, et al. Syndromes of the first and second branchial arches, part 2: syndromes. *AJNR Am J Neuroradiol*. 2011;32(2):230–237.
36. Fomin AB, Pastorino AC, Kim CA, et al. DiGeorge syndrome: a not so rare disease. *Clinics*. 2010;65(9):865–869.
37. Shprintzen RJ. Velo-cardio-facial syndrome: 30 years of study. *Dev Disabil Res Rev*. 2008;14(1):3–10.
38. McDonald-McGinn DM, Sullivan KE. Chromosome 22q11.2 deletion syndrome (DiGeorge syndrome/velocardiofacial syndrome). *Medicine (Baltimore)*. 2011;90(1):1–18.
39. Singh AK, Sargar K, Restrepo CS. Pediatric mediastinal tumors and tumor-like lesions. *Semin Ultrasound CT MR*. 2016;37(3):223–237.
40. Silverman FN. A la recherche du temps perdu and the thymus (with apologies to Marcel Proust). *Radiology*. 1993;186(2):310–311.
41. Mandell GA, Bellah RD, Boulden ME, et al. Cervical trachea: dynamics in response to herniation of the normal thymus. *Radiology*. 1993;186(2):383–386.
42. Caffey J, Di Liberti C. Acute atrophy of the thymus induced by adrenocorticosteroids: observed roentgenographically in living infants: a preliminary report. *Am J Roentgenol Radium Ther Nucl Med*. 1959;82:530–540.
43. Nasseri F, Eftekhari F. Clinical and radiologic review of the normal and abnormal thymus: pearls and pitfalls. *Radiographics*. 2010;30(2):413–428.
44. Caffey J, Silbey R. Regrowth and overgrowth of the thymus after atrophy induced by the oral administration of adrenocorticosteroids to human infants. *Pediatrics*. 1960;26:762–770.
45. Castellote A, Vazquez E, Vera J, et al. Cervicothoracic lesions in infants and children. *Radiographics*. 1999;19(3):583–600.
46. Spinner RJ, Moore KL, Gottfried MR, et al. Thoracic intrathymic thyroid. *Ann Surg*. 1994;220(1):91–96.
47. Kuhn JP. Re: Normal thymus extending between the right brachiocephalic vein and the innominate artery. *AJR Am J Roentgenol*. 1996;167(6):1592.
48. Slovis TL, Meza M, Kuhn JP. Aberrant thymus–MR assessment. *Pediatr Radiol*. 1992;22(7):490–492.
49. Song I, Yoo SY, Kim JH, et al. Aberrant cervical thymus: imaging and clinical findings in 13 children. *Clin Radiol*. 2011;66(1):38–42.
50. Jeung MY, Gasser B, Gangi A, et al. Imaging of cystic masses of the mediastinum. *Radiographics*. 2002;22 Spec No:S79–S93.
51. Ranganath SH, Lee EY, Restrepo R, et al. Mediastinal masses in children. *AJR Am J Roentgenol*. 2012;198(3):W197–W216.
52. Nakamura S, Tateyama H, Taniguchi T, et al. Multilocular thymic cyst associated with thymoma a clinicopathologic study of 20 cases with an emphasis on the pathogenesis of cyst formation. *Am J Surg Pathol*. 2012;36(12):1857–1864.
53. Leonidas JC, Berdon WE, Valderrama E, et al. Human immunodeficiency virus infection and multilocular thymic cysts. *Radiology*. 1996;198(2):377–379.
54. Leonidas JC. The thymus: from past misconception to present recognition. *Pediatr Radiol*. 1998;28(5):275–282.
55. Heller GD, Haller JO, Berdon WE, et al. Punctate thymic calcification in infants with untreated Langerhans' cell histiocytosis: report of four new cases. *Pediatr Radiol*. 1999;29(11):813–815.
56. Rosado-de-Christenson ML, Pugatch RD, Moran CA, et al. Thymolipoma: analysis of 27 cases. *Radiology*. 1994;193(1):121–126.
57. Hudacko R, Aviv H, Langenfeld J, et al. Thymolipoma: clues to pathogenesis revealed by cytogenetics. *Ann Diagn Pathol*. 2009;13(3):185–188.
58. Rieker RJ, Schirmacher P, Schnabel PA, et al. Thymolipoma. A report of nine cases, with emphasis on its association with myasthenia gravis. *Surg Today*. 2010;40(2):132–136.
59. Carretto E, Inserra A, Ferrari A, et al. Epithelial thymic tumours in paediatric age: a report from the TREP project. *Orphanet J Rare Dis*. 2011;6:28.

60. Liang X, Lovell MA, Capocelli KE, et al. Thymoma in children: report of 2 cases and review of the literature. *Pediatr Dev Pathol*. 2010;13(3):202–208.
61. Rocha MM, Neves PD, Rodrigues CC, et al. Invasive thymoma in a child: a rare case report. *J Pediatr Surg*. 2012;47(2):e23–e25.
62. Farmakis SG, Herman TE, Siegel MJ. Thymoma with osseous metaplasia in an adolescent. *Pediatr Radiol*. 2014;44(7):888–892.
63. Truong LD, Mody DR, Cagle PT, et al. Thymic carcinoma. A clinicopathologic study of 13 cases. *Am J Surg Pathol*. 1990;14(2): 151–166.
64. Jung KJ, Lee KS, Han J, et al. Malignant thymic epithelial tumors: CT-pathologic correlation. *AJR Am J Roentgenol*. 2001;176(2):433–439.
65. Ogawa K, Toita T, Uno T, et al. Treatment and prognosis of thymic carcinoma: a retrospective analysis of 40 cases. *Cancer*. 2002;94(12): 3115–3119.
66. Eng TY, Fuller CD, Jagirdar J, et al. Thymic carcinoma: state of the art review. *Int J Radiat Oncol Biol Phys*. 2004;59(3):654–664.
67. Harris K, Elsayegh D, Azab B, et al. Thymoma calcification: is it clinically meaningful? *World J Surg Oncol*. 2011;9:95.
68. Stachowicz-Stencel T, Orbach D, Brecht I, et al. Thymoma and thymic carcinoma in children and adolescents: a report from the European Cooperative Study Group for Pediatric Rare Tumors (EXPeRT). *Eur J Cancer*. 2015;51(16):2444–2452.
69. Stachowicz-Stencel T, Bien E, Balcerska A, et al. Thymic carcinoma in children: a report from the Polish Pediatric Rare Tumors Study. *Pediatr Blood Cancer*. 2010;54(7):916–920.
70. Piccaluga PP, Agostinelli C, Gazzola A, et al. Pathobiology of Hodgkin lymphoma. *Adv Hematol*. 2011;2011:920898.
71. Leventaki V, Khoury JD, Voss SD. Tumors of lymphoid and hematopoietic tissues. In: Parham MD, Khoury DJ, McCarville BM, eds. *Pediatric Malignancies: Pathology and Imaging*. New York, NY: Springer New York; 2015:103–149.
72. Tomiyama N, Honda O, Tsubamoto M, et al. Anterior mediastinal tumors: diagnostic accuracy of CT and MRI. *Eur J Radiol*. 2009; 69(2):280–288.
73. Lee EY. Evaluation of non-vascular mediastinal masses in infants and children: an evidence-based practical approach. *Pediatr Radiol*. 2009;39(suppl 2):S184–S190.
74. Manson DE. Magnetic resonance imaging of the mediastinum, chest wall and pleura in children. *Pediatr Radiol*. 2016;46(6):902–915.
75. Takahashi K, Al-Janabi NJ. Computed tomography and magnetic resonance imaging of mediastinal tumors. *J Magn Reson Imaging*. 2010;32(6):1325–1339.
76. Feeney J, Horwitz S, Gonen M, et al. Characterization of T-cell lymphomas by FDG PET/CT. *AJR Am J Roentgenol*. 2010;195(2): 333–340.
77. Rankin S. [(18)F]2-fluoro-2-deoxy-D-glucose PET/CT in mediastinal masses. *Cancer Imaging*. 2010;10(SpecA):S156–S160.
78. Hutchings M. PET imaging in lymphoma. *Expert Rev Hematol*. 2009;2(3):261–276.
79. Kluge R, Kurch L, Montravers F, et al. FDG PET/CT in children and adolescents with lymphoma. *Pediatr Radiol*. 2013;43(4):406–417.
80. Voss SD. Surveillance imaging in pediatric hodgkin lymphoma. *Curr Hematol Malig Rep*. 2013;8(3):218–225.
81. Baka-Kagia MS, Prassopoulos VK, Papaioannou GC. Anaplastic large cell lymphoma in children and adolescents. In: Andreou AJ, Kosmidis AP, Gouliamos DA, eds. *PET/CT in Lymphomas: A Case-Based Atlas*. Cham: Springer International Publishing; 2016:357–362.
82. Hong TS, Shammas A, Charron M, et al. Brown adipose tissue 18F-FDG uptake in pediatric PET/CT imaging. *Pediatr Radiol*. 2011;41(6):759–768.
83. Gawande RS, Khurana A, Messing S, et al. Differentiation of normal thymus from anterior mediastinal lymphoma and lymphoma recurrence at pediatric PET/CT. *Radiology*. 2012;262(2):613–622.
84. Juweid ME, Vose JM. Imaging in early-stage Hodgkin's lymphoma. *N Engl J Med*. 2010;362(10):962.
85. Hamrick-Turner JE, Saif MF, Powers CI, et al. Imaging of childhood non-Hodgkin lymphoma: assessment by histologic subtype. *Radiographics*. 1994;14(1):11–28.
86. Puri P, Höllwarth ME. *Pediatric Surgery*. Springer-Verlag Berlin Heidelberg; 2009.
87. Behr GG, Johnson CM. Vascular anomalies: hemangiomas and beyond–part 2, Slow-flow lesions. *AJR Am J Roentgenol*. 2013;200(2):423–436.
88. Enjolras O, Wassef M, Chapot R. *Color atlas of vascular tumors and vascular malformations*. Cambridge: Cambridge University Press; 2007.
89. Jaggers J, Balsara K. Mediastinal masses in children. *Semin Thorac Cardiovasc Surg*. 2004;16(3):201–208.
90. Moran CA, Suster S. Primary germ cell tumors of the mediastinum: I. Analysis of 322 cases with special emphasis on teratomatous lesions and a proposal for histopathologic classification and clinical staging. *Cancer*. 1997;80(4):681–690.
91. De Pasquale MD, Crocoli A, Conte M, et al. Mediastinal germ cell tumors in pediatric patients: a report from the Italian Association of Pediatric Hematology and Oncology. *Pediatr Blood Cancer*. 2016;63(5):808–812.
92. Billmire D, Vinocur C, Rescorla F, et al. Malignant mediastinal germ cell tumors: an intergroup study. *J Pediatr Surg*. 2001;36(1):18–24.
93. Badar F, Yasmeen S, Afroz N, et al. Benign mediastinal teratoma with intrapulmonary and bronchial rupture presenting with recurrent hemoptysis. *Iran J Radiol*. 2013;10(2):86–89.
94. Totanarungroj K, Watcharaporn C, Muangman N. Helpful CT findings for giving specific diagnosis of anterior mediastinal tumors. *J Med Assoc Thai*. 2010;93(4):489–496.
95. Tsubochi H, Endo S, Nakano T, et al. Extraction of mediastinal teratoma contents for complete thoracoscopic resection. *Asian Cardiovasc Thorac Ann*. 2015;23(1):42–45.
96. Sreedhar M, Menon S, Varma G, et al. Cervico-thoracic neurenteric cyst—a case report. *Indian Journal of Radiology and Imaging*. 2006;16(1):99.
97. Han SE, Kwon WJ, Cha HJ, et al. Mediastinal bronchogenic cysts : demonstration of fluid-fluid level in bronchoscopic US imaging. *J Bronchology Interv Pulmonol*. 2016;Jun 30.
98. Wildi SM, Hoda RS, Fickling W, et al. Diagnosis of benign cysts of the mediastinum: the role and risks of EUS and FNA. *Gastrointest Endosc*. 2003;58(3):362–368.
99. Andreu J, Caceres J, Pallisa E, et al. Radiological manifestations of pulmonary tuberculosis. *Eur J Radiol*. 2004;51(2):139–149.
100. Suwatanapongched T, Gierada DS. CT of thoracic lymph nodes. Part II: diseases and pitfalls. *Br J Radiol*. 2006;79(948):999–1000.
101. Pursner M, Haller JO, Berdon WE. Imaging features of Mycobacterium avium-intracellulare complex (MAC) in children with AIDS. *Pediatr Radiol*. 2000;30(6):426–429.
102. Kushner BH. Neuroblastoma: a disease requiring a multitude of imaging studies. *J Nucl Med*. 2004;45(7):1172–1188.
103. Ejindu VC, Hine AL, Mashayekhi M, et al. Musculoskeletal manifestations of sickle cell disease. *Radiographics*. 2007;27(4):1005–1021.

# PART 5 Chest Wall, Pleura, and Diaphragm

# 59 The Chest Wall

Ricardo Restrepo and Edward Y. Lee

The chest wall provides support and protection to the various thoracic vascular and nonvascular structures. In addition, it allows the important physiologic motion of the lungs and airways. The chest wall is less rigid and more cartilaginous in children than in adults and consists of several fundamental structural components, including bones (ribs, sternum, and vertebrae), nerves, muscles, vessels, and subcutaneous soft tissues.[1] Within these structural components, a wide variety of localized or systemic processes (e.g., congenital and developmental anomalies, inflammatory and infectious diseases, benign and malignant neoplasms, and traumatic lesions) can occur in pediatric patients.[1-3]

## CONGENITAL AND DEVELOPMENTAL ANOMALIES

### Overview

During childhood, congenital and developmental anomalies of the thorax typically manifest as deformities or anterior chest wall defects that can be isolated or part of a syndrome. Most of these anomalies cause only cosmetic problems. However, pediatric patients with severe congenital or developmental anomalies of the chest wall may present with pain, respiratory distress, or cardiovascular compromise. Imaging can provide a road map for the surgeon in evaluating the anatomy and associated anomalies if reconstructive surgery is contemplated.[4]

### Deformities of the Anterior Chest Wall

***Etiology.*** Most asymptomatic palpable anterior chest wall lesions in pediatric patients are normal anatomic osseous or cartilaginous variants, most commonly a prominent anterior convexity of a solitary rib, costal cartilage, or sternal tilt (Fig. 59.1).[5,6] These normal anatomic variations occur in approximately one-third of children.[5] Symptoms that may raise concern and require further evaluation are focal pain and rapid growth of the mass.[3,5]

***Imaging.*** In the case of a palpable but otherwise asymptomatic anterior chest wall lesion in children, a chest radiograph with a BB marker is usually adequate to exclude a potentially aggressive or malignant underlying condition. When chest radiographic findings are equivocal, ultrasound can be performed.[7] To minimize ionizing radiation exposure, computed tomography (CT) should be reserved for situations in which further characterization is still necessary after radiographic and ultrasound evaluation.[3,6] Magnetic resonance imaging (MRI), which is not associated with ionizing radiation exposure, is a particularly helpful imaging modality for confirming and characterizing congenital and developmental chest wall lesions.

***Treatment and Follow-up.*** If the diagnosis of an anterior chest wall developmental variant can be made confidently by imaging studies in asymptomatic infants and children, no further treatment or follow-up is necessary.[5]

### Pectus Deformity

***Etiology.*** Two of the most common abnormalities of the chest wall are pectus excavatum and pectus carinatum, with the former being the most common congenital deformity of the sternum and the most common sternal deformity requiring surgery. The current leading theory for the development of pectus excavatum is a misdirected, rapid growth of the lower costal cartilages. Such abnormal growth of the lower costal cartilages, which often intensifies during growth spurts, displaces the sternum either inward or outward, resulting in pectus deformity.[8] Pectus excavatum occurs in between 1 in 400 and 1 in 1,000 live births.[9] In children with pectus excavatum, the inferior aspect of the sternum is depressed inward, resulting in varying degrees of anterior chest wall concavity and anterior protrusion of the costochondral junctions. Although most cases of pectus excavatum are isolated, approximately 45% of cases are familial.[10,11]

Pectus carinatum is a less common chest wall deformity that occurs in approximately 1 in 1,500 live births and has a familial occurrence of approximately 25%.[9] In children with pectus carinatum, outward displacement of the sternum occurs, with secondary abnormal protrusion of the ribs.

Pectus deformities may occur in association with scoliosis (more frequently with pectus excavatum), Marfan syndrome, Ehlers–Danlos syndrome, Poland syndrome, and congenital heart disease. In addition to cosmetic issues, severe pectus deformities also can cause chest pain, dyspnea, palpitations, and restrictive lung disease.[3]

***Imaging.*** On frontal chest radiographs, the sternal depression of pectus excavatum may cause a pseudoinfiltrate over the right side of the heart and various degrees of leftward cardiac shift. On the lateral chest radiograph, the sternal depression causes narrowing of thoracic anteroposterior (AP) diameter (Fig. 59.2). Pectus carinatum usually is diagnosed on a lateral chest radiograph, which shows an increased AP diameter of the thoracic cavity and an extended retrosternal space (Fig. 59.3).[3,8]

The Haller or pectus index is used to estimate the severity of pectus excavatum. It is calculated from an axial CT image by dividing the maximum transverse dimension of the thorax from the inner aspect of the ribs by the AP dimension of the thoracic cavity at its narrowest point (Fig. 59.4). A pectus index greater than 3.25 in symptomatic pediatric patients typically initiates corrective surgery, whereas an index less than 2.56 is considered normal.[12] Recent studies have advocated the use of chest radiographs instead of CT to preoperatively evaluate the severity of the deformity.[13] In more severe cases, the use of a limited, low-dose CT scan with selective five to seven axial CT images through the deformity can be obtained to generate the pectus index.[14] When the primary purpose of imaging is to assess the Haller index, axial MRI can be used to avoid ionizing radiation.[15]

***Treatment and Follow-up.*** Severe pectus deformity requires surgical correction, particularly in symptomatic pediatric patients. The Ravitch procedure for pectus excavatum includes resection of deformed cartilages and correction of the sternum by a wedge osteotomy in the upper sternal cortex. In the Nuss procedure, a convex metal bar is placed behind the sternum, pulling the sternum anteriorly. The Nuss procedure has a 4% to 11% complication rate (infection and dislocation of the metallic bar are most common),[16-18] and thus follow-up imaging is necessary to monitor the implanted bar and its complications. Corrective surgery for

## Abstract:

The chest wall consists of several fundamental structural components, including bones (ribs, sternum, and vertebrae), nerves, muscles, vessels, and subcutaneous soft tissues. Within these structural components, a wide variety of localized or systemic processes (e.g., congenital and developmental anomalies, inflammatory and infectious diseases, benign and malignant neoplasms, and traumatic lesions) can occur in pediatric patients and will be discussed in this chapter.

## Keywords:

Pectus carinatum
pectus excavatum
Cleidocranial dysostosis
Poland syndrome
actinomycosis
infantile hemangioma
lymphatic malformation
infantile fibrous hamartoma
mesenchymal hamartoma
Ewing sarcoma family of tumors

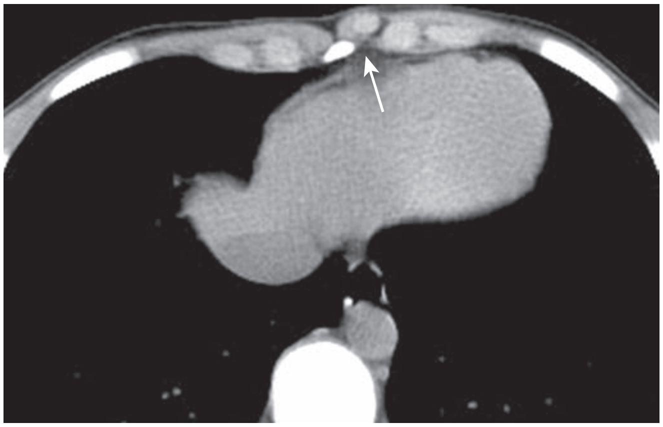

**Figure 59.1. Chondral nodule in an adolescent boy who presented with a focal, palpable, painless lump in the anterior chest wall.** Axial CT image shows a small, round, well-defined structure *(arrow)* protruding anteriorly in the chest wall to the left of the sternum with the same density as the adjacent costochondral junctions.

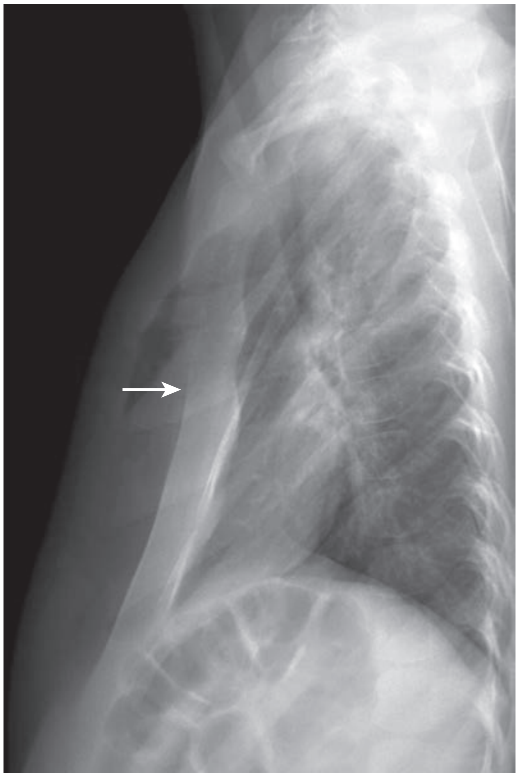

**Figure 59.2. Pectus excavatum in an 8-year-old girl.** Lateral chest radiograph shows the sternal depression *(arrow)* causing narrowing of the anteroposterior diameter of the thorax.

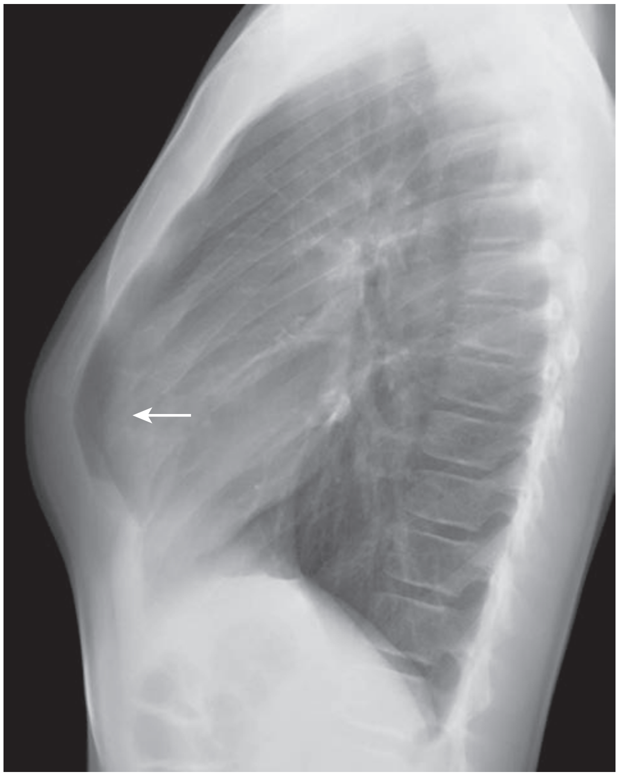

**Figure 59.3. Pectus carinatum in an adolescent boy.** Lateral chest radiograph demonstrates an increased anteroposterior diameter of the thoracic cavity and extended retrosternal space *(arrow).*

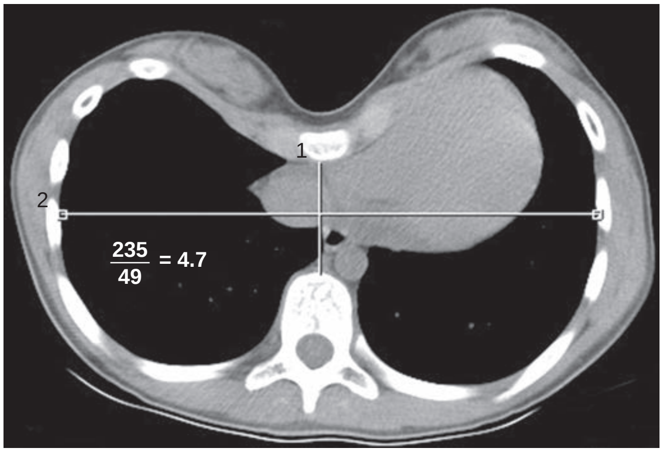

**Figure 59.4. Pectus index.** Axial CT image shows severe anterior depression of the sternum that is compressing and displacing the heart. The pectus index is 4.7.

pectus carinatum also requires costochondral resection and a wedge osteotomy, but the sternum is pushed inward.

## Cleidocranial Dysostosis

***Etiology.*** Cleidocranial dysostosis is a rare syndrome usually caused by an autosomal dominant gene mutation *(CBFA1)* with a high degree of penetrance and variable expression. The triad of partial or complete absence of the clavicles, supernumerary or impacted teeth, and delayed fontanel closure is highly suggestive of this syndrome. Other features include midface hypoplasia, short stature, and pelvic and distal phalangeal hypoplasia that causes brachydactyly.[19-21]

***Imaging.*** Typical chest radiographic findings include a bell-shaped thorax, short ribs, and either complete or partial absence of the clavicles (e-Fig. 59.5). When the clavicle is partially absent, the distal portion of the clavicle usually is involved. Scoliosis may be present. Because many of the characteristic manifestations only become evident during adolescence, early clinical diagnosis may be difficult and often requires a skeletal survey. Other features of the syndrome can support the diagnosis.[19-21]

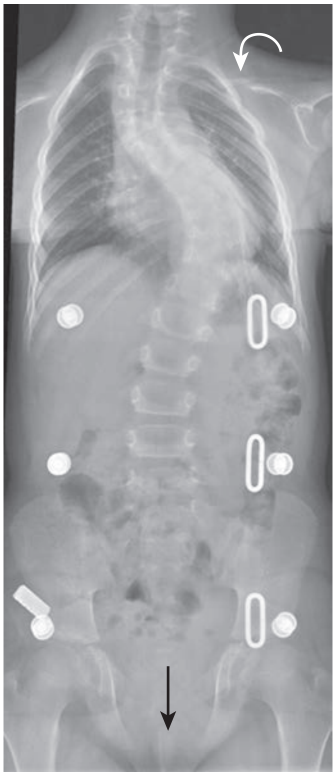

**e-Figure 59.5. Cleidocranial dysostosis in an adolescent boy.** A chest and abdominal radiograph shows absence of the right clavicle and hypoplasia of the distal half of the left clavicle *(curved arrow).* Diastasis *(straight arrow)* of the symphysis pubis also is present. The patient has scoliosis and is wearing a brace.

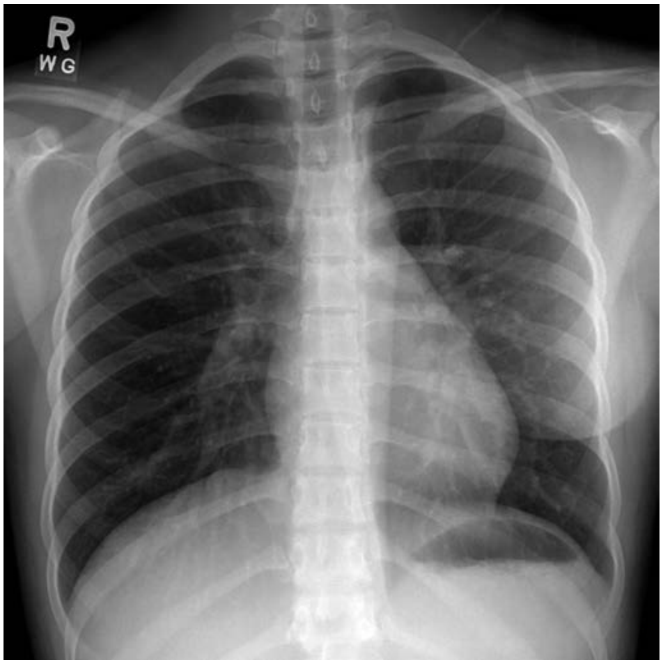

**Figure 59.7. Poland syndrome in an adolescent girl.** Frontal chest radiograph shows a hyperlucent right lung as a result of the absence of right chest wall soft tissues, including the breast.

***Treatment and Follow-up.*** Multidisciplinary management by a team of specialists including pediatricians, geneticists, and orthodontists is the optimal approach for patients with cleidocranial dysostosis. Genetic counseling is recommended. No imaging follow-up is required once the diagnosis has been made.[19]

## Poland Syndrome

***Etiology.*** Poland syndrome is a form of chest wall and breast hypoplasia that occurs in 1 in every 20,000 to 30,000 live births.[22] The syndrome includes absence of the pectoralis muscles and ipsilateral syndactyly. Other associations include rib aplasia, amastia/athelia, and absence of axillary hair. Poland syndrome typically is unilateral and (more often) sporadic and occurs more frequently in boys than in girls, with a ratio of 2 : 1 to 3 : 1.[23] The tendency toward unilaterality (with the right side affected more frequently than the left side) has raised the hypothesis that this anomaly is perhaps a result of interrupted or insufficient blood supply during limb bud development in the sixth week of gestation.[23] Poland syndrome is diagnosed clinically by the apparent asymmetry of the chest wall (e-Fig. 59.6) and syndactyly. Cardiopulmonary impairment and functional deficiency of the shoulder, although rare, also can be present.[3,22,23]

***Imaging.*** On chest radiographs, hyperlucency of the affected hemithorax is usually apparent in unilateral cases because of the absent pectoralis muscle and breast (Fig. 59.7). Because the extent of involvement is difficult to assess with clinical examination or chest radiographs, cross-sectional imaging with CT or MRI is useful (Fig. 59.8). Furthermore, it is imperative to preoperatively assess the presence of all of the chest wall and anterior abdominal wall muscles, because muscle flaps are used in surgical reconstruction.[2,22]

***Treatment and Follow-up.*** Corrective surgery often is performed for cosmetic reasons, particularly in girls. Such surgery includes (1) restoration of the structural integrity of the rib cage and (2) improvement in the appearance of the chest by performing transposition of musculocutaneous flaps (most commonly with latissimus dorsi and rectus abdominis muscles), as well as concomitant breast implants in female patients.[8,22,23]

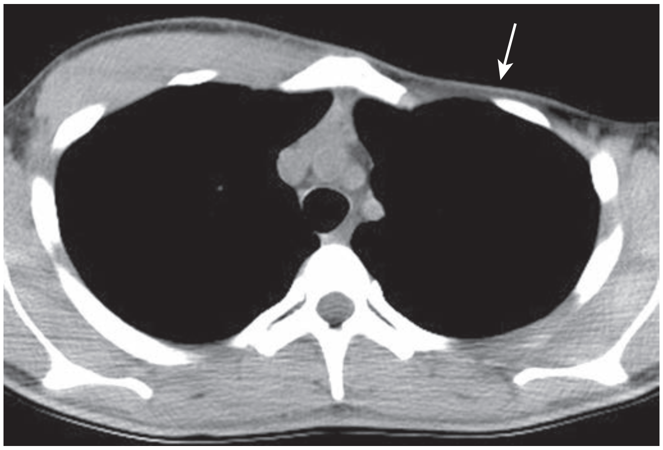

**Figure 59.8. Poland syndrome in an adolescent boy.** Axial CT image demonstrates complete absence of the left pectoralis muscles *(arrow)*, causing asymmetry of the anterior chest wall.

# INFECTIOUS DISEASES

## Overview

Chest wall infections are relatively rare in children. Chest wall infections occur either by direct extension or, less frequently, by hematogenous spread. Such infectious processes can involve the soft tissues, cartilage, and osseous structures. Chest wall infections can be the result of bacterial, mycobacterial, or fungal infections. They range from superficial cellulitis to deeper infections, which include myositis, abscess, necrotizing fasciitis, and osteomyelitis.[24,25]

## Bacterial Infection

***Etiology.*** Bacterial infections of the chest wall are rare in children. The common organisms that cause bacterial infections of the chest wall are *Staphylococcus aureus* and *Salmonella* species in persons with sickle cell disease. Sternal osteomyelitis may occur in patients with an underlying disease, such as immunodeficiency and hemoglobinopathies.[11] Rib osteomyelitis is most commonly acquired by direct spread from an adjacent pneumonia or empyema. Empyema necessitans is a rare complication of empyema characterized by the extension of the infection from the pleural space into the chest wall. Pediatric patients with a bacterial chest wall infection often present with focal soft tissue erythema, edema, and pain. Additionally, other signs of infection, such as leukocytosis and elevated erythrocyte sedimentation rate, often are present.[3,11,26,27]

***Imaging.*** Chest radiographs may reveal localized soft tissue edema in cases of cellulitis or fasciitis. Bone changes such as periosteal reaction or lytic or sclerotic lesions can be present, particularly in the late stage of disease. Concomitant pulmonary consolidation, empyema, and subcutaneous emphysema also may be present. Ultrasound, CT, and MRI are more sensitive than chest radiographs in detecting and characterizing chest wall infections. Ultrasound should be reserved for superficial and more localized chest wall infections because of the limited field of view (Fig. 59.9A). The extent of the chest wall infection is best demonstrated on CT or MRI. For evaluation of chest wall abscess and bone marrow edema in the earlier stage of osteomyelitis, MRI is the most sensitive imaging modality (Fig. 59.9B). CT is the imaging modality of choice for evaluating concomitant pulmonary parenchymal infection.[2,11,26-28]

***Treatment and Follow-up.*** Antibiotics are administered to treat bacterial chest wall infections. In cases of abscesses localized to the chest wall or empyema, drainage may be necessary to relieve the focus of infection and avoid further spread. Prolonged antibiotic

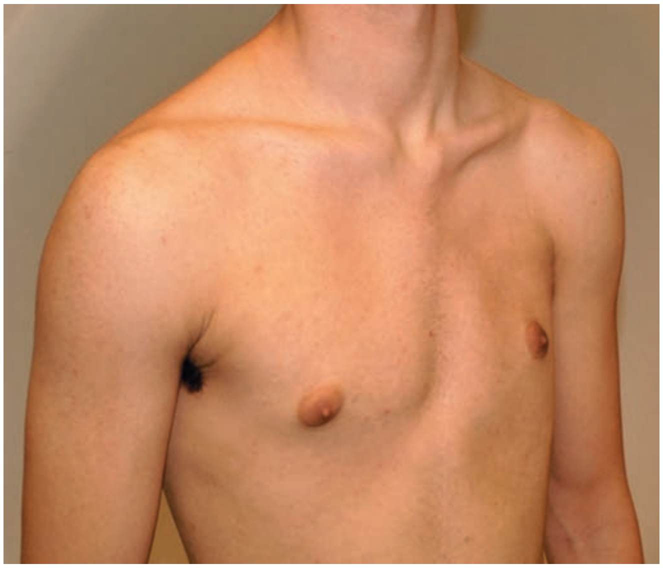

**e-Figure 59.6. Poland syndrome in an adolescent boy.** Asymmetry of the chest wall is apparent because of a lack of soft tissue on the left side.

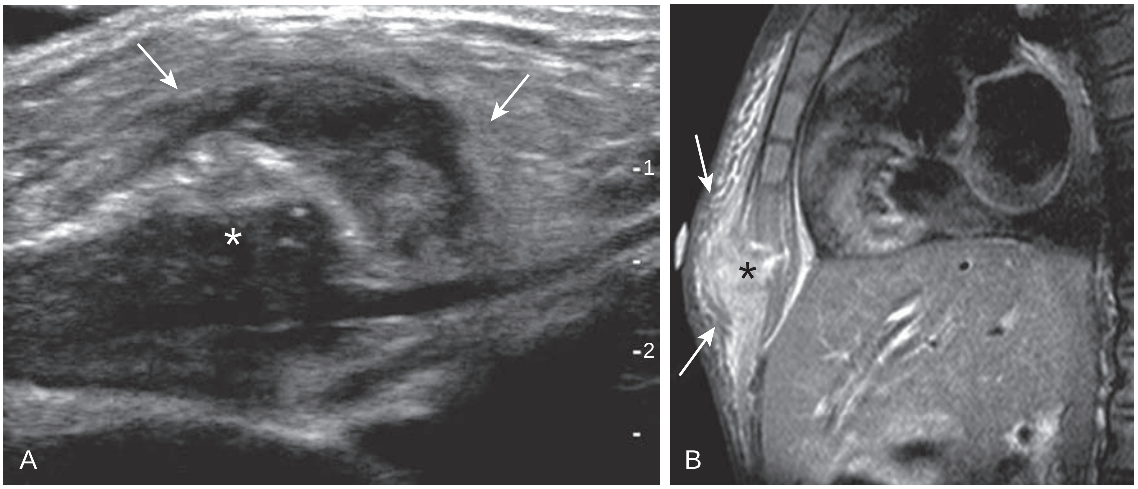

**Figure 59.9. Sternal osteomyelitis in a 6-year-old girl who presented with prolonged fever and a painful, palpable, and erythematous sternal lump.** (A) Longitudinal sonogram of the inferior aspect of the sternum *(asterisk)* shows marked surrounding soft tissue edema and swelling *(arrows).* (B) Sagittal contrast T1-weighted MRI of the chest with fat saturation demonstrates focal destruction of the distal ossification center of the sternum *(asterisk)* with contrast enhancement and edema of the adjacent soft tissues *(arrows).*

therapy is necessary for cases of osteomyelitis.[27,29] Evaluation of response to treatment by monitoring C-reactive protein in pediatric patients with osteomyelitis has dramatically decreased both the average duration of therapy and the need for follow-up imaging.[30]

## Tuberculosis

***Etiology.*** Tuberculosis (TB) is a potentially deadly infectious disease caused by various strains of mycobacteria, usually *Mycobacterium tuberculosis* in humans. Tuberculosis infection of the chest wall often is a result of the hematogenous spread of pulmonary TB infection.[31] However, tuberculosis of the chest wall also can occur as an isolated primary infection with no evidence of pulmonary disease, although this presentation is rare.[32] Skeletal TB infection accounts for 10% to 20% of extrapulmonary cases and 1% to 2% of all TB infection cases.[33] Affected patients present with a slow-growing soft tissue chest wall mass, often without associated pain or fever. Respiratory symptoms may be present in cases of lung involvement.[32,34]

***Imaging.*** TB infection can involve any bone of the chest wall; however, the ribs are most commonly affected. On radiographs, osseous TB infections are usually lytic and sharply marginated. Associated periosteal reaction is a relatively rare finding.[35] On CT or MRI, TB chest wall infections usually present as a rim-enhancing chest wall mass. CT and MRI can play an important role in demonstrating bone involvement from a chest wall TB infection that may not be seen on radiographs.[32] Expansion and destruction of the bone with an adjacent soft tissue mass from a TB infection of the chest wall may mimic an underlying malignancy.[31,33,34]

***Treatment and Follow-up.*** Treatment of chest wall TB infection currently is not well established. Some advocate at least 6 months of antituberculous medication, whereas others suggest more aggressive management consisting of surgical excision of affected bones and soft tissues, in addition to preoperative and postoperative antituberculous medication regimens.[32,36]

## Actinomycosis

***Etiology.*** In humans, actinomycosis is most commonly caused by *Actinomyces israelii*, a branching gram-positive, facultative anaerobe. Actinomycosis infection typically affects the cervicofacial region in patients with dental caries. Pulmonary and chest wall involvement of actinomycosis in children is less frequent without underlying predisposing pulmonary conditions. Actinomycosis infection initially involves the lungs and then usually spreads to the adjacent soft tissues. Clinically, affected patients present with cough, intermittent fever, and weight loss. Pain develops once the microorganism invades the pleura and chest wall.[37,38]

***Imaging.*** On a chest radiograph, the classic radiologic appearance of actinomycosis infection is a chronic lung consolidation that crosses the fissures with a pleural effusion. Because actinomycosis infection does not respect tissue boundaries, it tends to invade the surrounding tissues with fistulous tracts and abscess formation that are best seen on CT or MRI. Rib periostitis, pulmonary cavitation, and diaphragmatic invasion also may occur in more advanced cases and are very suggestive of actinomycosis infection.[38,39] Advanced actinomycosis infection of the chest wall may mimic TB or a malignancy of the Ewing sarcoma family of tumors (ESFT).[37]

***Treatment and Follow-up.*** A definite diagnosis of actinomycosis of the chest wall requires either microscopic visualization of the typical sulfur granules representing the colonies of the microorganism or recovery of the *Actinomyces* organisms in an anaerobic culture. The standard treatment of actinomycosis is long-term, high-dose penicillin. In cases with an abscess, image-guided percutaneous drainage may help expedite recovery and isolate the organism.[37,38]

# TUMORS OF THE CHEST WALL

## Overview

Because the chest wall is composed of several different types of tissues, a wide variety of both benign and malignant tumors may occur, including vascular, cartilaginous, osseous, muscular, or adipose tumors. Imaging evaluation plays a pivotal role in (1) initial detection, (2) assessment of the extent of disease, (3) guidance for tissue sampling, (4) evaluation of the response to treatment, and (5) surveillance for recurrence.[7,25]

## Benign Tumors

### Soft Tissue Tumors

#### Infantile Hemangioma

***Etiology.*** Infantile hemangiomas are benign vascular tumors of abnormally proliferating endothelial cells that follow a predictable course. Infantile hemangiomas are the most common tumor of childhood, with a reported incidence of approximately 10% in the general population.[40-42] The etiology of hemangiomas currently is unknown. Several proposed theories include placental emboli, somatic mutation, and clonal expansion of progenitor stem cells.[43,44] Infantile hemangiomas are more common in premature white children, with female predominance ratios ranging from 1.4 : 1 to 3 : 1.[41] Hemangiomas can involve any part of the body, including the chest wall and breast bud. At birth, these lesions frequently are underdeveloped, with only a macule or discoloration representing a "precursor" lesion. Soon after birth, infantile hemangiomas grow during the so-called proliferative phase and become raised and red in color. Around the first year of life, they begin to involute, eventually leaving a fibro-fatty scar. Multiple lesions are found in 15% to 30% of patients.[41,44,45]

***Imaging.*** Ultrasound is the first imaging modality of choice, especially for evaluating localized, superficial hemangiomas. For large and extensive lesions with a deep soft tissue component, MRI often is necessary for a complete evaluation. Although CT can be used when MRI is not available, it is less preferable because of the associated radiation and inferior soft tissue characterization. The imaging appearance of infantile hemangiomas may change according to the stage of disease. On ultrasound, hemangiomas are well-defined, lobulated, hyperechoic masses that become more heterogeneous during the involuting phase. Increased vascularity, containing arteries, veins, and even evidence of shunting, often is seen on color Doppler, especially during the proliferative phase (e-Fig. 59.10). On MRI, infantile hemangiomas are isointense or slightly hyperintense compared with muscle on T1-weighted images, and hyperintense on T2-weighted images, containing flow voids that represent arteries or rapid venous flow. Hyperintense fatty elements may be seen on T1-weighted images. The pattern of contrast enhancement also varies according to the stage of disease. Marked contrast enhancement usually is seen during the proliferative phase, whereas heterogeneous contrast enhancement is observed during the involuting phase. On CT, hemangiomas present as well-defined soft tissue masses that are isodense to muscle with marked postcontrast enhancement.[44,46-49]

***Treatment and Follow-up.*** Most infantile hemangiomas require no treatment because they typically involute. A pulsed dye laser can be used for the cosmetic management of superficial lesions.[30] Propranolol is the drug of choice in the treatment of hemangiomas with minor complications, such as hypoglycemia and hypotension.[50-52]

### Lymphatic Malformation

***Etiology.*** Lymphatic malformations are a subtype of slow-flow vascular malformations.[42] These lesions are fully developed at birth and grow commensurate to the patient's growth. Lymphatic malformations, although congenital and not true neoplasms, are discussed in the tumor section. Lymphatic malformations consist of dilated lymphatic channels and spaces, with walls lined by mature endothelium that have normal rates of endothelial cell turnover. These lesions occur anywhere in the body, but the cervicofacial, axillary, and chest regions are the most common locations. Lymphatic malformations have no sex predilection. Except for very small lesions, these lesions present as a mass that usually is discovered at birth. The lesions have normal overlying skin and often display transillumination. With superimposed hemorrhage or infection, a sudden increase in the lesion size is typical.[3,53]

***Imaging.*** Plain radiography plays no role in the evaluation of lymphatic malformations in the chest wall of pediatric patients. The imaging workup of lymphatic malformations includes ultrasound and MRI, with the former more commonly used for localized and superficial lesions. More extensive lesions are better evaluated with contrast-enhanced MRI, with CT as an alternative imaging modality. On ultrasound, lymphatic malformations appear as multiloculated cystic lesions that are macrocystic or microcystic, depending on the size of the locules. No internal blood flow is seen on color Doppler imaging. With associated bleeding or superimposed infection, echogenic material, low-level echoes, or fluid-fluid levels can be observed (Fig. 59.11A). On MRI, the cystic lesions are hyperintense on T2-weighted images (Fig. 59.11B) and hypointense on T1-weighted images. Lymphatic malformations display no solid components and have minimal, if any, peripheral and septal enhancement, unless superimposed infection is present. Hyperintense elements on T1-weighted images suggest proteinaceous material, bleeding, or infection. Because of their pliable nature, lymphatic malformations typically insinuate and displace, rather than invade, adjacent structures.[3,46-48]

***Treatment and Follow-up.*** The treatment for lymphatic malformation is percutaneous sclerosis, surgical resection, or a

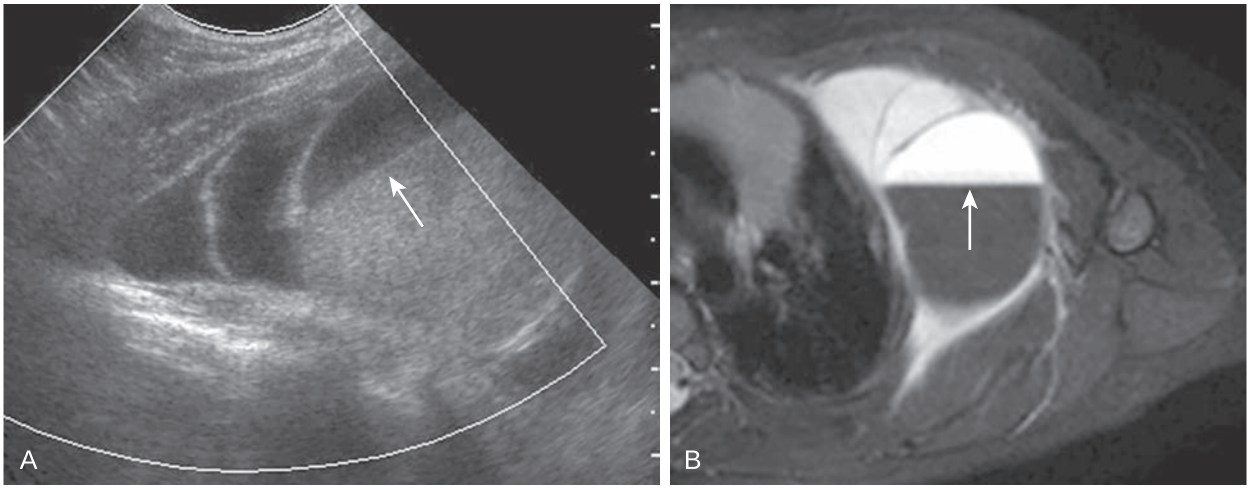

**Figure 59.11. Lymphatic malformation in a 2-year-old boy who presented with an enlarging chest wall lump after a fall.** (A) Longitudinal color Doppler sonogram shows a multiloculated avascular cystic mass in the anterolateral chest wall. Some of the locules are anechoic, but a fluid-fluid level *(arrow)* is present in the most dominant one, likely indicating recent bleeding. (B) Axial T2-weighted MRI of the chest demonstrates the multiseptated mass with hyperintense elements representing lymphatic fluid and hypointense elements with a fluid-fluid level *(arrow)* indicating recent bleeding. The patient has minimal, if any, adjacent soft tissue edema, and no soft tissue component is seen in the lesion.

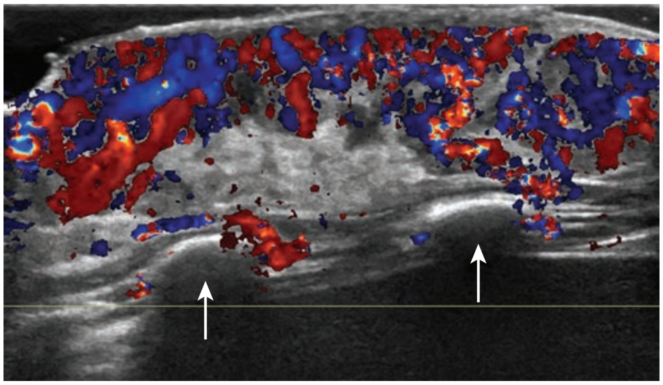

**e-Figure 59.10. Infantile hemangioma in a 6-week-old girl in whom a raised red cutaneous lesion developed in the anterior chest wall 3 weeks after birth.** Color Doppler sonogram shows a well-defined soft tissue mass confined to the subcutaneous soft tissues that insinuates along the ribs *(arrows)* and involves the dermis. The lesion has a hyperechoic and markedly vascular soft tissue component containing arteries and veins.

combination of both. Sclerotherapy is the preferred method for macrocystic lymphatic malformations. The treatment of microcystic lesions is more difficult and can include observation, sclerotherapy, and/or surgical resection.[46,48,53]

### Infantile Fibrous Hamartoma

***Etiology.*** An infantile fibrous hamartoma is a tumor of neonates, infants, and young children, with approximately 90% occurring in the first year of life.[54] They are more common in boys than in girls. The most common location is around the shoulder girdle. The tumor usually presents as a painless, mobile soft tissue mass. Histologically, an infantile fibrous hamartoma contains fibrocollagenous tissue, primitive mesenchyma, and mature fat.[54-56]

***Imaging.*** An infantile fibrous hamartoma is a well-defined lesion with a heterogeneous echotexture on ultrasound, attenuation on CT, and signal intensity on MRI because of different underlying tissue components. Hyperechoic elements seen on ultrasound and T1 hyperintensities seen on MRI represent the fatty elements, which is an important clue in the diagnosis. On MRI, the fibrous component of infantile fibrous hamartoma is seen as hypointense areas on T1- and T2-weighted images.[54,57]

***Treatment and Follow-up.*** Local surgical resection of infantile fibrous hamartoma is usually curative, with a low risk of recurrence. No metastatic disease from infantile fibrous hamartoma has been reported.[56,58]

## Osseous Tumors

### Fibrous Dysplasia

***Etiology.*** Fibrous dysplasia is a benign, intramedullary, fibro-osseous lesion thought to occur as a result of a developmental failure in the remodeling of primitive bone to mature lamellar bone, and failure of the bone to realign in response to mechanical stress.[59] The true incidence of fibrous dysplasia is difficult to estimate, but the lesions are not rare and typically are discovered before age 30 years. Fibrous dysplasia has been reported to represent 20% to 30% of chest wall masses, with the rib being the most commonly affected bone.[3,60] Fibrous dysplasia can be monostotic or polyostotic; however, monostotic disease does not progress to polyostotic disease. Although a focal mass or chest wall deformity can be seen, most cases of monostotic fibrous dysplasia are discovered incidentally when radiographs of the area are obtained for different reasons. Localized pain may be the presenting symptom in cases with pathologic fractures or mass effect on adjacent thoracic structures.[59,60]

***Imaging.*** The diagnosis of fibrous dysplasia usually is made with plain radiographs. Radiographic characteristics include a focal, well-defined, expansile, intramedullary lytic lesion with a lucent, ground-glass, or sclerotic matrix, causing cortical thinning and loss of trabecular definition (e-Fig. 59.12). Rarely, fibrous dysplasia can be cystic with fluid-fluid levels. Fibrous dysplasia is usually a radiographic diagnosis that requires no further imaging.[3,61] When seen on CT, amorphous calcification inside the lesion with bone expansion is usually present. MRI is helpful in assessing the extent of the disease. The lesions are isointense to muscle on T1-weighted images. On fluid-sensitive sequences, the lesions are predominantly hyperintense, with focal hypointense, isointense, or markedly hyperintense foci. The heterogeneous MRI signal is due to the presence of calcifications, fat, cystic changes, or septations. Fibrous dysplasia displays various contrast enhancement patterns that can be patchy, peripheral, or homogeneous.[61,62]

***Treatment and Follow-up.*** Fibrous dysplasia of the chest wall usually requires no treatment unless symptoms such as nerve or vascular compression develop. In such cases, resection of the affected bone can alleviate the symptoms.[63,64] In symptomatic polyostotic cases, bisphosphonates can be used because of their inhibitory effect on bone resorption. When the lesions are discovered incidentally and the radiographic features are characteristic, no biopsy is indicated; a follow-up study every 6 months to ensure stability currently is advised.[59]

### Osteochondroma

***Etiology.*** An osteochondroma is a benign cartilage-capped developmental lesion rather than a true neoplasm. It affects bones with epiphyses and apophyses. These lesions result from the separation of a fragment of epiphyseal growth plate cartilage, which subsequently herniates through the periosteal bone cuff normally surrounding the physis. An osteochondroma usually is diagnosed in the first 3 decades of life and may be inherited as a multifocal, familial, autosomal dominant disease. Solitary lesions have a male predilection; they occur in approximately 1% to 2% of persons undergoing radiographic evaluations and constitute 10% to 15% of all bone tumors.[65] Osteochondromas are the most common benign osseous neoplasm involving the chest wall.[3] Most solitary osteochondromas are asymptomatic. Symptomatic lesions tend to occur in younger patients, with 75% to 80% of those cases discovered before age 20 years.[65] Lesions in the chest wall usually present with a palpable, painless mass or focal deformity. Pain may occur as a result of mechanical irritation, fracture, and nerve or vascular compression.[3,61,66]

***Imaging.*** Osteochondromas are usually diagnosed on plain radiographs. In patients with multiple osteochondromatosis, a skeletal survey usually is obtained to assess the overall extent of disease. In the chest wall, the lesions arise most frequently from the ribs or scapula (Fig. 59.13). They can be sessile or pedunculated, depending on whether a narrow or broad pedicle is located at the base. Corticomedullary continuity is the characteristic imaging

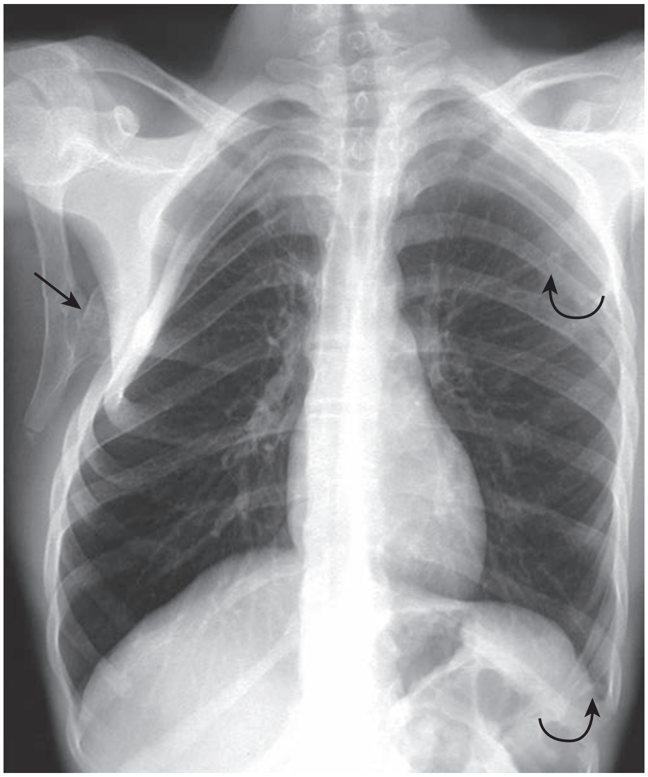

**Figure 59.13. Multiple osteochondromas in an adolescent boy with hereditary exostosis.** Frontal chest radiograph shows a large pedunculated osteochondroma *(straight arrow)* arising from the undersurface of the right scapula that is causing remodeling of the underlying right ribs and chest wall deformity. Smaller lesions *(curved arrows)* are seen in the left scapula and the tenth left rib at the mid axillary line, producing focal rib deformity.

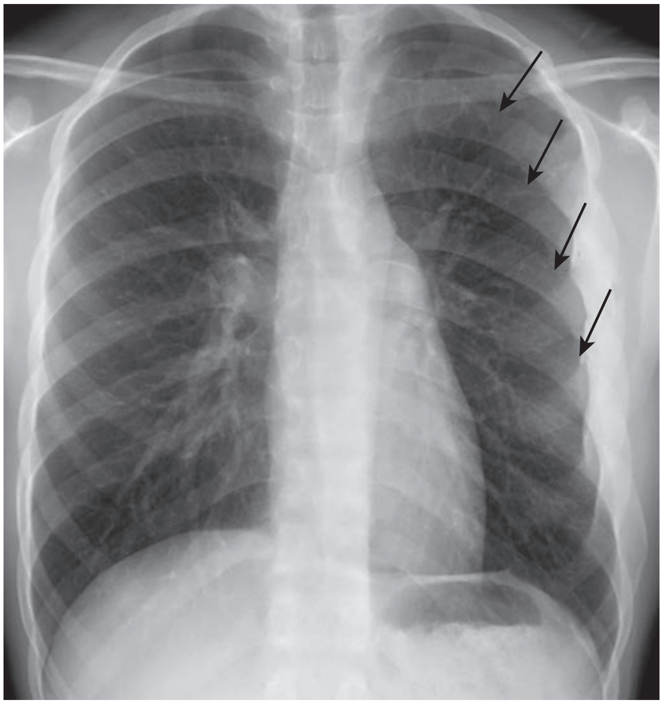

**e-Figure 59.12. Polyostotic fibrous dysplasia in an adolescent.** Frontal chest radiograph shows diffuse thickening of multiple left ribs *(arrows)* with a ground-glass matrix and an indistinct cortex.

finding of an osteochondroma, but this finding may be difficult to completely assess on radiographs. Although both CT and MRI demonstrate the corticomedullary continuity, MRI has an advantage over CT in evaluating the thickness of the cartilaginous cap that should be thin, uniform, and hyperintense on fluid-sensitive sequences. Additionally, MRI can be helpful in assessing the adjacent soft tissue edema and bursa formation that are indicative of the irritation often resulting from osteochondromas. It has been reported that CT with three-dimensional reconstructions can be valuable in preoperative planning.[27,61,65,66]

***Treatment and Follow-up.*** Indications for surgical resection of solitary osteochondromas include pain, cosmetic deformity, and nerve impingement. The treatment choice for multiple hereditary exostoses is more complicated and often is directed to correct bone deformity.[65,66] Malignant transformation of the cartilaginous cap into a chondrosarcoma occurs in fewer than 1% of solitary cases and in up to 25% of multiple hereditary exostoses.[65] The risk of malignant transformation is proportional to the size and number of lesions and only occurs in adulthood. Solitary osteochondromas in children do not require routine follow-up unless symptoms or rapid growth occur.[66] In cases of multiple lesions, close clinical and radiographic monitoring is required to evaluate the progression of deformities and the development of complications.[65]

### Mesenchymal Hamartoma

***Etiology.*** A mesenchymal hamartoma of the chest wall is a rare, benign lesion. It typically presents at birth as a large, extrapleural mass arising from a rib that causes chest wall deformity or respiratory distress because of mass effect. Mesenchymal hamartomas, which are not considered true neoplasms, are composed of maturing, proliferating normal skeletal elements with a prominent cartilaginous component and hemorrhagic cavities as a result of aneurysmal bone cyst (ABC) formation. To date, no instances of malignant degeneration of mesenchymal hamartoma of the chest wall have been reported.[67-69]

***Imaging.*** A mesenchymal hamartoma may have an ominous imaging appearance, despite its benign nature. On chest radiographs, it usually presents as a partially calcified extrapleural mass causing erosion of one or more ribs. A mass effect on the adjacent lungs and mediastinum often is present.[70] CT or MRI scans show a well-circumscribed lesion with solid and cystic components, the latter representing ABC, a feature specific to this lesion (Fig. 59.14). Cortical bone partially surrounding the lesion and mineralization also can be seen. In one series, mineralization was present in 100% of cases and hemorrhagic cystic areas of aneurysmal bone cyst were present in more than half of patients.[67] On MRI, the signal intensity of mesenchymal hamartoma is variable. Hyperintense areas on fluid-sensitive sequences represent ABC formation and chondroid elements, whereas areas of low signal on T1 and fluid-sensitive sequences represent areas of mineralization.[67,71] Multifocal cases of mesenchymal hamartoma also have been reported.[67,71]

***Treatment and Follow-up.*** Surgical excision of a mesenchymal hamartoma with rib resection and chest wall reconstruction is recommended if cardiorespiratory symptoms from mass effect or chest wall deformity are present. Smaller lesions can be monitored with chest radiographs and ultrasound because spontaneous regression of the lesion has been reported, and the lesions typically stop growing after age 1 year.[67,68,72]

### Other Osseous Tumors (Langerhans Cell Histiocytosis, Enchondroma, and Aneurysmal Bone Cyst)

***Etiology.*** Several other benign tumors can involve the chest wall in the pediatric population, including Langerhans cell histiocytosis (LCH), enchondroma, and ABC. These tumors can arise from any bone in the chest wall, including the ribs, scapula, and (less frequently) the sternum.

Langerhans cells are a type of histiocyte that originates from the bone marrow and play a role in the immune system. Abnormal clonal proliferation causes LCH, the most common form of which is a localized bone lesion (formerly called eosinophilic granuloma). In the chest wall, LCH most commonly affects the thoracic vertebral bodies causing vertebrae plana, but it can involve any bone. Bone destruction, pain, localized swelling, and a palpable mass often are present.[73,74]

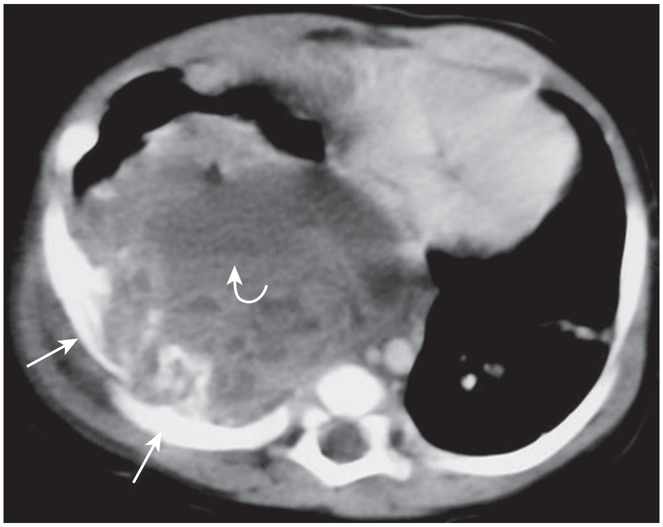

**Figure 59.14. Mesenchymal hamartoma in a newborn girl with respiratory distress and a palpable mass in the right chest wall.** Axial contrast-enhanced CT image shows a very large, round mass in the posterior right hemithorax with erosion of two consecutive ribs *(straight arrows).* The lesion has a heterogeneous parenchyma with a fluid-fluid level *(curved arrow)* corresponding to the aneurysmal bone cyst component.

Enchondromas occur less frequently in children than osteochondromas and represent benign, mainly hyaline cartilage tumors arising from the medullary canal of a bone. Most enchondromas are solitary and usually are found incidentally; they also may be multiple, such as in patients with Ollier or Maffucci syndromes.[3,26,61,75]

ABCs are benign, expansile, osteolytic lesions that contain multiple blood-filled spaces of different sizes and are lined by fibroblasts and giant cells of the osteoclast type (see also Chapter 138). An ABC is a hyperplastic lesion reactive to a subperiosteal or intraosseous hemorrhage. Although they are benign, these lesions can grow rapidly, causing bone destruction and pathologic fractures that produce pain and a palpable mass. ABCs may be found either as primary osteolytic lesions or as a reactive process as part of another lesion. The primary ABC is found mostly in the second decade of life and more frequently in females, with a ratio of 2 : 1.[61,76] In the chest wall, the most common sites of involvement from ABCs are the posterior elements of the spine and the ribs.[61]

***Imaging.*** The classic imaging finding of an LCH lesion when it involves the thoracic spine is vertebrae plana, characterized by flattening of vertebral bodies. When it involves other bones of the chest wall, the radiographic appearance of LCH varies. In the acute phase of the disease, the lesion develops rapidly and has a more aggressive appearance. In this phase, the lesions typically are lytic with poorly defined borders (Fig. 59.15). Periosteal reaction occurs when the lesion involves the cortex. A soft tissue component of an LCH often is present and is best seen on CT or MRI. In the later phase of disease, the lesions can be lytic and sclerotic, and they may adopt a bubbly appearance and have sharp, sclerotic borders.[3,73,74]

Enchondromas arise from the medullary portion of bone with well-defined, lobulated borders and endosteal scalloping. Localized bone expansion and a chondroid matrix frequently are present in enchondromas (e-Fig. 59.16).[3,61,75] ABCs are well-defined, lytic, expansile, intramedullary lesions. In the short and flat bones, such

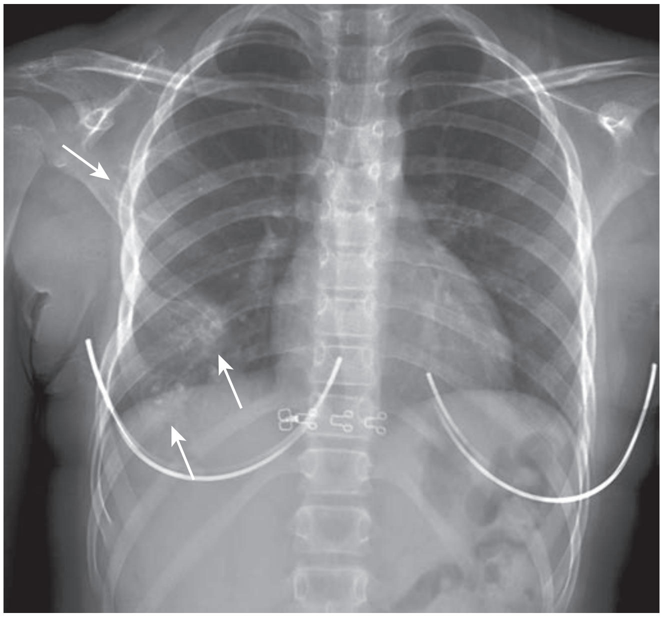

**e-Figure 59.16. Chest wall enchondromas in an adolescent girl with Ollier disease.** Frontal chest radiograph shows several well-defined lytic lesions involving the costochondral junction of the right sixth and seventh ribs and the mid aspect and superior border of the right scapular wing *(arrows).* Chondroid matrix is better identified in the rib lesions.

as the ribs, the cyst usually appears as an eccentric osteolytic area extending into the cancellous bone with overlying cortical thinning. Because of the rapid growth, a more aggressive appearance with cortical disruption also can be seen (Fig. 59.17A). On CT or MRI, ABCs are typically cystic, with multiple locules and fluid-fluid levels representing the underlying hemorrhagic nature of the lesion (Fig. 59.17B). ABCs do not have an associated soft tissue component.[61,76]

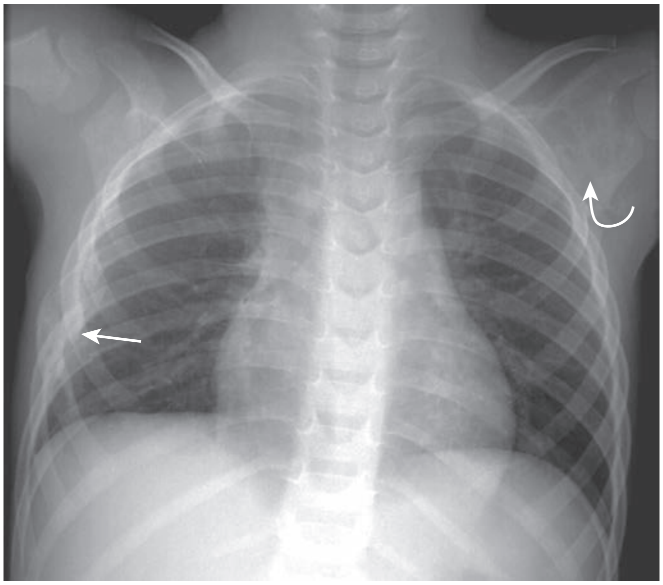

**Figure 59.15. Langerhans cell histiocytosis of a rib and left scapula in a young boy who presented with chest pain.** Frontal chest radiograph shows a lytic, slightly expansile lesion involving a segment of the right sixth rib *(straight arrow)* with cortical disruption. A second lytic lesion *(curved arrow)* with rather defined borders involves the left scapular neck.

***Treatment and Follow-up.*** LCH treatment is not standardized. Solitary LCH lesions initially can be managed conservatively with close radiographic follow-up, because some of these lesions may heal spontaneously with bone remodeling. Alternatively, the lesion can be treated with curettage and bone grafting. More disseminated disease may require systemic chemotherapy.[73,74] Incidental enchondromas, especially the solitary ones, require no treatment. For symptomatic lesions that often are associated with pathologic fractures, curettage and bone grafting usually are curative.[77] ABCs can be treated with selective arterial embolization, percutaneous sclerotherapy, or excision with bone grafting.[78,79] En bloc resection of ABC is recommended for small lesions located in the ribs. For large lesions, excision with bone grafting may be necessary.[76]

## Malignant Tumors

### Soft Tissue Tumors

**Rhabdomyosarcoma**

***Etiology.*** Rhabdomyosarcoma (RMS) tumors are the second most common primary malignancy that occurs in the chest wall in children.[80] RMS arises from primitive mesenchymal cells committed to develop into striated muscles. It can arise from any tissue anywhere in the body, except from cortical bone.[80] Tumors of the trunk account for 7% of all RMS tumors.[81] In children, the age-standardized annual incidence rate for RMS is 4 to 7 per million. In a study of 15 chest wall tumors out of 303 RMS tumors, the mean age of diagnosis was 16 years.[82] Affected children typically present with a painful and rapidly enlarging chest wall mass.[82,83]

***Imaging.*** On ultrasound, RMS presents as a heterogeneous soft tissue mass with increased internal vascularity. The outer margin of the tumor may be either well defined or ill defined. For a complete assessment of tumor extension, CT or MRI is necessary. Although CT is more sensitive than MRI for the evaluation of osseous abnormality and pulmonary metastatic disease, MRI is better than CT for assessment of the local extension of the tumor. On CT and MRI, chest wall RMS usually presents as

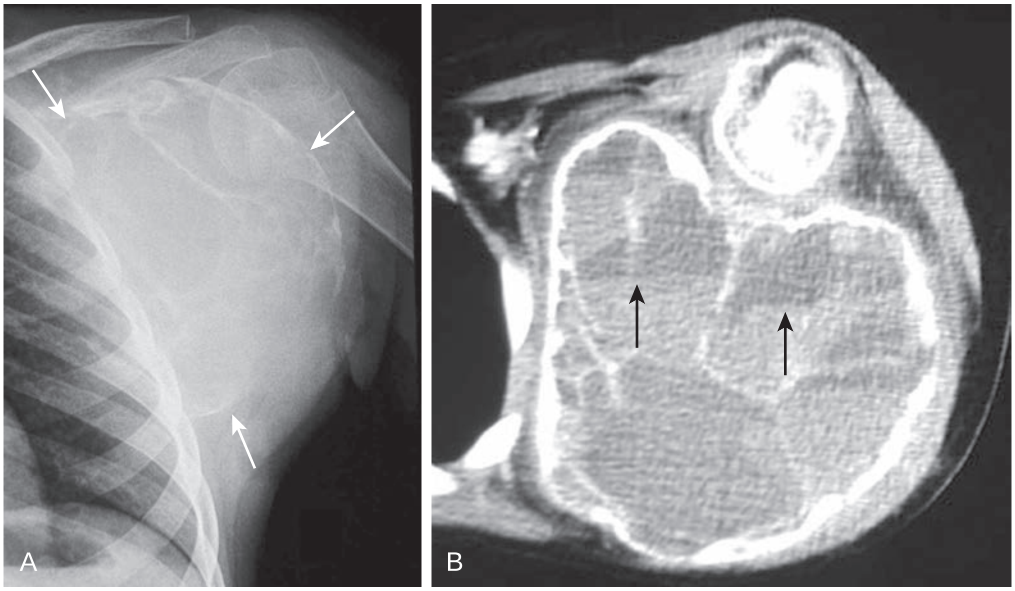

**Figure 59.17. Aneurysmal bone cyst in a patient with a slowly growing left shoulder mass.** (A) Frontal radiograph of the left shoulder demonstrates a very large expansile lytic lesion *(arrows)* arising from the left scapular wing. Thin bony septations are seen inside the lesion. The inferior margin of the lesion is indistinct. (B) Axial contrast-enhanced CT image clearly shows the expansile lytic lesion containing multiple bony septae arising from the left scapular wing and its relationship with the rib cage and humerus. Several slightly hyperintense fluid-fluid levels are seen in some of the internal locules *(arrows).*

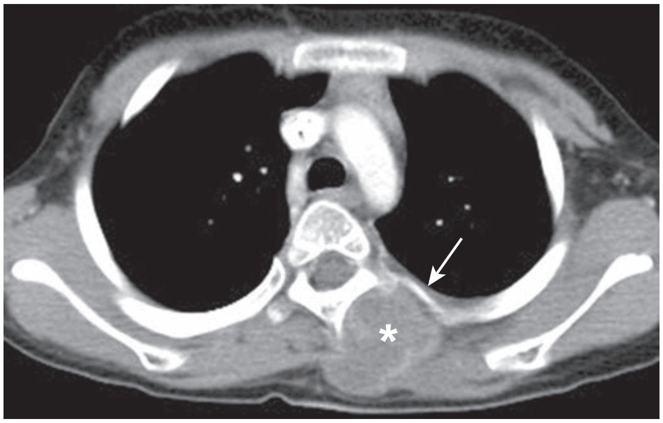

**Figure 59.18. Rhabdomyosarcoma of the left paraspinal musculature in a 14-year-old girl who presented with a painful, palpable, soft tissue lump.** Axial contrast-enhanced CT image shows a well-defined, slightly hypodense mass in the left paraspinal region *(asterisk).* The mass causes mild remodeling of the underlying bone but no destruction *(arrow).*

a large, heterogeneous, soft tissue mass with intrathoracic extension. The tumor tends to show a heterogeneously increased signal on T1 and fluid-sensitive MRI sequences. RMS mass typically displays enhancement that is heterogeneous contrast enhancement in cases of underlying tumor necrosis.[5,84-86] In comparison with Ewing sarcoma family of tumors (ESFT), bone involvement is much less frequent in children with an RMS, and if present, it tends to occur later in the course of the disease (Fig. 59.18).[84]

***Treatment and Follow-up.*** The current treatment of RMS tumors of the chest wall is chemotherapy to control local disease and reduce the size of the mass before surgical resection. Radiotherapy often is used if surgical resection margins are positive.[80,83] Because of its higher sensitivity in detecting residual, recurrent, or metastatic disease, CT positron emission tomography (PET) in conjunction with MRI currently is recommended as the follow-up imaging modality of choice.[87-89]

## Osseous Tumors

### Ewing Sarcoma Family of Tumors

***Etiology.*** The Ewing sarcoma family of tumors (ESFT) represent the most common primary chest wall malignancies in children and young adults.[90] They comprise the classic Ewing sarcoma, atypical Ewing sarcoma, primitive neuroectodermal tumor, and Askin tumor. These tumors belong to the small, round, blue cell tumors that originate from unique mesenchymal cells capable of multilineage differentiation. Based on their varied but similar underlying neural differentiation, their immunohistochemical, cytogenetic, and molecular uniformity, and their identical response to Ewing-based chemotherapy regimens, tumors such as ESFT are regarded as being related to sarcomas. A common chromosomal translocation (t11; 22) (q24; q12) has been implicated in 80% to 95% of cases. ESFT lesions have been reported in all age groups, but most cases are diagnosed in the second decade of life, with a median age of 15 years.[91] It is more common in males, with a ratio of 1.3 : 1 to 1.5 : 1, and has a predilection for white persons.[91] Affected children usually present with a rapidly growing palpable chest wall mass that often is painful. In cases with pleural effusions and substantial mass effect on the lung, dyspnea can be the predominant symptom. Pediatric patients with a paraspinal ESFT may present with symptoms related to neurologic impairment. Systemic symptoms such as fever, and laboratory test abnormalities, including leukocytosis and an elevated erythrocyte sedimentation rate, may simulate infectious processes such as osteomyelitis.[83,91]

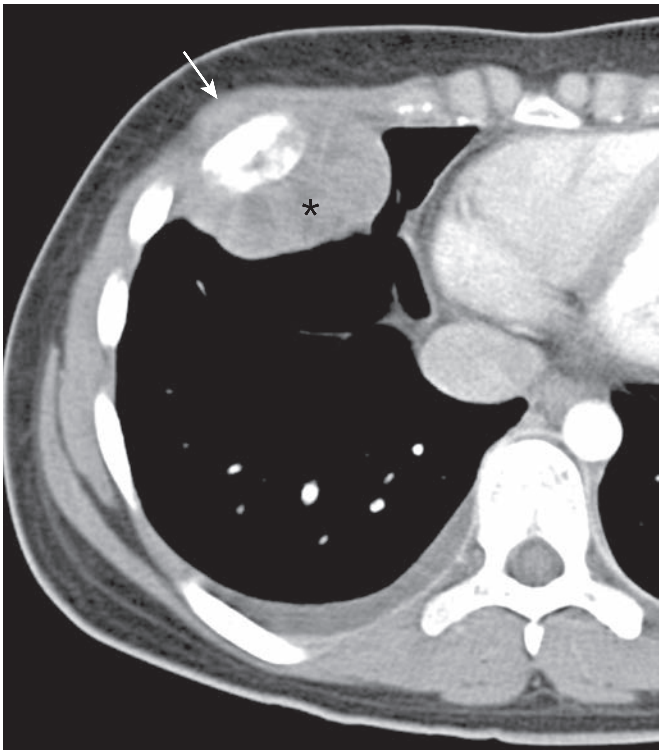

**Figure 59.19. Ewing sarcoma of a rib in an 11-year-old boy who presented with a painful, palpable lump in the anterior chest wall.** Axial contrast-enhanced CT image shows focal thickening of the anterior aspect of a right rib *(arrow)* surrounded by a soft tissue mass *(asterisk).*

***Imaging.*** On chest radiographs, ESFT usually presents as an extraparenchymal and lytic osseous mass with associated bone destruction and aggressive periosteal reaction. An associated soft tissue component can be suggested on plain radiographs but is best seen on CT or MRI (Fig. 59.19).[91-93] Calcifications within the mass may be present in approximately 10% of cases.[93] On CT and MRI, an ESFT mass typically presents as a lytic and destructive osseous lesion associated with aggressive periosteal reaction and heterogeneous soft tissue components (e-Fig. 59.20). On MRI, the soft tissue component is isointense or slightly hyperintense to muscle and hyperintense on fluid-sensitive sequences. Heterogeneous contrast enhancement is seen frequently, except in areas of necrosis. Pleural effusions that obscure the soft tissue mass can be present. Regional lymphadenopathy in patients with ESFT is unusual.[91-94]

***Treatment and Follow-up.*** Chest wall ESFT is currently treated with chemotherapy to reduce the size of the tumor and achieve optimal local control, as well as to treat distant microscopic metastatic lesions, followed by surgical resection.[80,83,90,91] Currently, CT-PET is used to stage the tumor and monitor patients. CT in the follow-up of these patients plays an important role in detecting pulmonary metastasis, because surgical resection of the pulmonary metastasis and radiotherapy may be curative.[87,95]

### Osteosarcoma

***Etiology.*** Chest wall osteosarcoma is rare. Osteosarcomas that do present in this location occur more frequently in younger children. It can arise from a rib, scapula, or clavicle or can be a focus of metastatic disease.[83] The incidence of osteosarcomas is 4.8 per 1 million children, with about 1% located in the chest wall and spine.[83] The peak incidence of osteosarcoma lesions occurs in the second decade of life.[96] Much like the other malignant chest

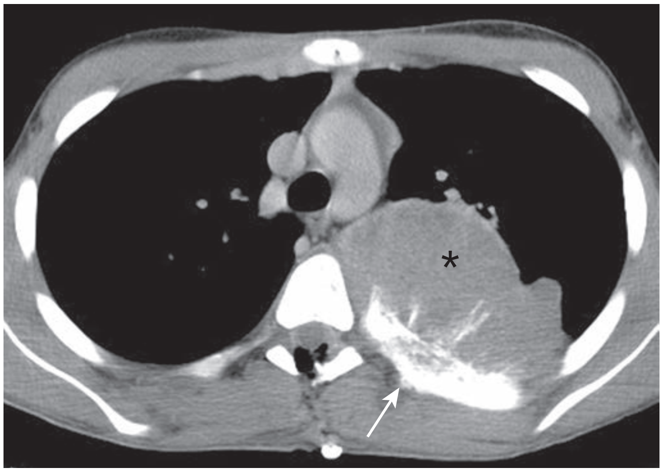

**e-Figure 59.20. Primitive neuroectodermal tumor of a rib in a 10-year-old boy with back pain.** Axial contrast-enhanced CT image shows a large, extrapleural, soft tissue mass arising from the medial aspect of a left rib *(asterisk).* The patient has aggressive associated periosteal reaction, sclerosis, and thickening of the rib *(arrow).*

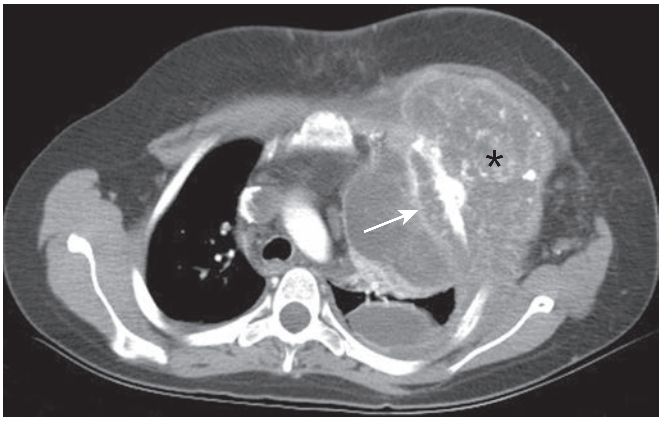

**Figure 59.21. Osteosarcoma in an adolescent boy who presented with a painful asymmetry of the anterior chest wall.** Axial contrast-enhanced CT image shows destruction of a left rib with aggressive periosteal reaction *(arrow)* and a large, partially calcified soft tissue mass *(asterisk)* that is causing deformity of the anterior left chest wall.

wall tumors, osteosarcomas typically present as rapidly growing and usually painful chest wall masses.

***Imaging.*** An osteosarcoma typically demonstrates prominent new bone formation on all imaging modalities. Chest radiographs show a lytic or blastic osseous lesion with a soft tissue mass containing calcifications. On CT, areas of bone formation characteristically are seen at the center, rather than the periphery, of the lesion (Fig. 59.21). On MRI, the areas of bone formation are seen as hypointense relative to muscle on T1-weighted images. A mixed but predominantly hyperintense mass is seen on fluid-sensitive sequences. Heterogeneous contrast enhancement of the soft tissue component of an osteosarcoma indicates necrosis.[86]

***Treatment and Follow-up.*** Chemotherapy and surgical resection constitute the current treatment of choice for chest wall osteosarcoma; this lesion is relative insensitivity to radiotherapy. The possibility of complete surgical resection is the primary factor in determining the ultimate outcome of affected patients.[80]

## TRAUMA OF THE CHEST WALL

### Overview

The chest wall in children is more elastic and flexible than in adults because of its larger cartilaginous component, and thus less force is absorbed by the chest wall with impact and proportionally more force is transmitted to intrathoracic organs. Thus intrathoracic injury may occur without visible damage to the chest wall. Although death from a chest injury is uncommon, after head injury, chest trauma is the second most common cause of death in pediatric patients. In children younger than 12 years, 60% to 80% of chest injuries are the result of blunt trauma, and more than half are accounted for by impact with motor vehicles.[97-99] However, among infants and young children, it is important to recognize that rib fractures occur most commonly as the result of nonaccidental trauma.[100-103]

***Etiology.*** Rib fractures constitute the majority of chest wall injuries in children. In a prospective study of 80 children after thoracic trauma, 28 (35%) had rib fractures, and one (1%) had a sternal fracture.[100] Rib fractures occur as a result of blunt trauma, such as falls or motor vehicle accidents. In pediatric trauma, the location of rib fractures is more a function of the mechanism of injury than the magnitude of the force that is transferred, although the number of fractured ribs is proportional to the severity of the trauma and the likelihood of associated multisystemic injury.[103]

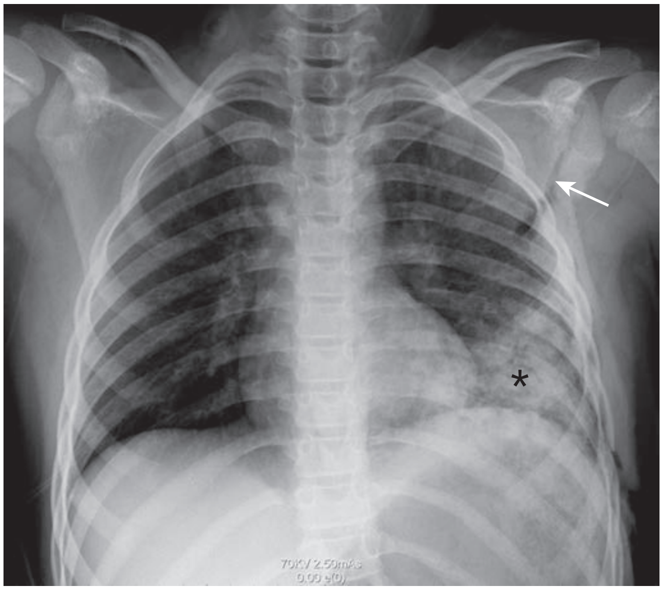

**Figure 59.22. Multiple fractures of the left ribs and a left scapular fracture in a young boy involved in a high-speed jet ski accident.** Frontal chest radiograph shows fractures of the seventh through ninth left ribs posterolaterally and more subtle fractures of the left tenth and eleventh ribs. A minimally diastatic fracture *(arrow)* is seen through the neck and body of the left scapula. Subcutaneous emphysema is seen along the lateral side of the left chest wall, as well as a fluffy consolidation *(asterisk)* in the left lower lobe consistent with a pulmonary contusion.

In infants or young children (<3 years) without underlying metabolic bone disease, rib fractures are very unusual and highly suggest nonaccidental trauma as a result of abuse.[104] Although fractures related to abuse can occur along any part of the ribs, when they are posterior in location they are highly specific for nonaccidental trauma (see also Chapter 143). This specificity occurs because of the substantial posterior levering force that the transverse processes exert over the posterior aspect of the ribs, resulting in fracture during a tight squeeze by the perpetrator.[26,104] In addition to abuse, birth trauma and diseases associated with underlying bone fragility, such as rickets and osteogenesis imperfecta, are other rare causes of rib fractures in infants and young children.[105]

***Imaging.*** In the acute setting, the initial assessment of possible traumatic chest wall injury usually requires chest radiographs. Once the diagnosis of rib fractures is established, careful attention to exclude associated intrathoracic injury must be provided. The most commonly associated nonosseous abnormality with chest wall injury is pulmonary contusion (Fig. 59.22), followed by pneumothorax. In the case of unconscious and hemodynamically unstable pediatric patients, a CT of the chest with contrast using CT angiography technique can be performed to evaluate intrathoracic vascular and nonvascular structures.[99,100] First rib fractures are uncommon but suggest severe trauma and increased risk of intrathoracic vascular injury.[106] Flail chest occurs when a segment of the rib cage fractures and becomes detached from the rest of the chest wall, but is rare in the pediatric population compared with adults.[107] Lower rib fractures can be associated with traumatic injury to the upper abdominal organs, such as the liver, spleen, and kidneys.[108]

In cases of suspected child abuse, a skeletal survey must be obtained. Acute nondisplaced rib fractures can be difficult to detect on radiographs in infants and young children. These fractures become more apparent during healing, when callus is present (Fig. 59.23). Fractures involving the anterior and posterior ends

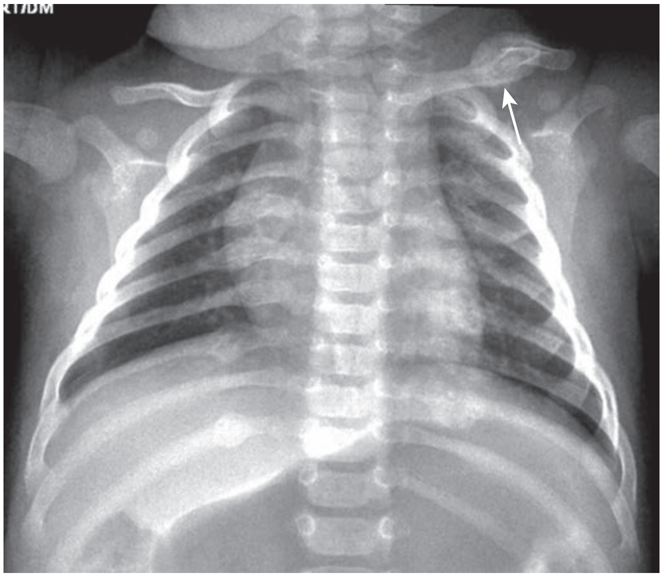

**Figure 59.23. Multiple bilateral rib fractures in a young girl who sustained nonaccidental trauma.** Frontal chest radiograph shows multiple, consecutive, bilateral, posterior rib fractures in the stage of healing. A healing fracture of the left clavicle is also present *(arrow).*

of a rib can be seen better on oblique radiographic views. The presence of acute and healing rib fractures is highly suggestive of abuse.[26,104,105] First rib fractures can be seen in the setting of child abuse.[109] Because not all chest wall fractures are detected on radiographs, a bone scintigraphy or follow-up radiographs may be necessary.[26,104] Assessment of the chest wall musculature and soft tissue injury can be performed with ultrasound or MRI. Ultrasound also allows dynamic evaluation of muscle function.[110]

***Treatment and Follow-up.*** The treatment of rib fractures is supportive, with pain medications and aggressive respiratory therapy to prevent atelectasis and pneumonia. In cases of flail chest, ventilatory support during the healing phase may be necessary.[99,102] Because nondisplaced acute rib fractures can be difficult to identify on plain radiographs, follow-up chest radiographs or bone scintigraphy can be obtained approximately 1 week later to increase the detection of fractures in cases of suspected child abuse.[26,104] Nonoperative, conservative treatment currently is advocated for the low-grade muscular and musculotendinous injury of the chest wall. Early surgical intervention is recommended for patients who have complete tears or avulsion of tendon from the bone.[110]

## KEY POINTS

- Palpable but otherwise asymptomatic chest wall masses in children usually are congenital or developmental osseous or cartilaginous normal anatomic variants.
- Congenital malformations of the chest wall can be isolated or part of a syndrome. These malformations usually cause cosmetic rather than physiologic problems. The two most common chest wall deformities are pectus excavatum and pectus carinatum.
- Chest wall infections in children are rare and usually occur as a result of hematogenous dissemination or local spread. Unusual organisms causing chest wall infections in children include actinomycosis and tuberculosis, and the imaging manifestations may be confused with malignancies.
- Malignant chest wall tumors in children are uncommon and usually present with a rapidly growing, painful mass. Malignant chest wall tumors include rhabdomyosarcomas, which usually involves the soft tissues; the Ewing sarcoma family of tumors; and osteosarcomas, which most commonly involve a rib.
- The chest wall in children is more elastic and flexible than in adults; therefore the chest wall absorbs less impact force, and more force is transmitted to intrathoracic organs. This mechanism allows intrathoracic injury to occur without visible chest wall injury. The presence of rib fractures in pediatric patients indicates a significant traumatic force, and associated internal injuries must be suspected and investigated.

## SUGGESTED READINGS

Donnelly LF, Taylor CN, Emery K, et al. Asymptomatic, palpable, anterior chest wall lesions in children: is cross-sectional imaging necessary? *Radiology*. 1997;202:829–831.

Fefferman NR, Pinkney LP. Evaluation of chest wall disorders in children. *Radiol Clin North Am*. 2005;43:355–370.

Glass RB, Norton KI, Mitre SA, et al. Pediatric ribs: a spectrum of abnormalities. *Radiographics*. 2002;22:87–104.

Groom KR, Murphey MD, Lonergan GJ, et al. Mesenchymal hamartoma of the chest wall: radiologic manifestations with emphasis on cross-sectional imaging and histopathologic comparison. *Radiology*. 2002;222:205–211.

La Quaglia MP. Chest wall tumors in childhood and adolescence. *Semin Pediatr Surg*. 2008;17:173–180.

Laffan EE, Ngan BY, Navarro OM. Pediatric soft tissue tumors and pseudotumors: MR imaging features with pathologic correlation. Part 2. Tumors of fibroblastic/myofibroblastic, so called fibrohistiocytic, muscular, lymphomatous, neurogenic, hair matrix and uncertain origin. *Radiographics*. 2009;29(4):e36.

## REFERENCES

Full references for this chapter can be found on www.expertconsult.com.

## REFERENCES

1. Netscher DT, Peterson R. Normal and abnormal development of the extremities and trunk. *Clin Plast Surg*. 1990;17(1):13–21.
2. Donnelly LF, Frush DP. Abnormalities of the chest wall in pediatric patients. *AJR Am J Roentgenol*. 1999;173(6):1595–1601.
3. Fefferman NR, Pinkney LP. Imaging evaluation of chest wall disorders in children. *Radiol Clin North Am*. 2005;43(2):355–370.
4. Williams AM, Crabbe DC. Pectus deformities of the anterior chest wall. *Paediatr Respir Rev*. 2003;4(3):237–242.
5. Donnelly LF, Frush DP, Foss JN, et al. Anterior chest wall: frequency of anatomic variations in children. *Radiology*. 1999;212(3):837–840.
6. Donnelly LF, Taylor CN, Emery KH, et al. Asymptomatic, palpable, anterior chest wall lesions in children: is cross-sectional imaging necessary? *Radiology*. 1997;202(3):829–831.
7. Coley BD. Pediatric chest ultrasound. *Radiol Clin North Am*. 2005;43(2):405–418.
8. Fokin AA, Steuerwald NM, Ahrens WA, et al. Anatomical, histologic, and genetic characteristics of congenital chest wall deformities. *Semin Thorac Cardiovasc Surg*. 2009;21(1):44–57.
9. Creswick HA, et al. Family study of the inheritance of pectus excavatum. *J Pediatr Surg*. 2006;41(10):1699–1703.
10. Goretsky MJ, Kelly RE, Croitoru D, et al. Chest wall anomalies: pectus excavatum and pectus carinatum. *Adolesc Med Clin*. 2004;15(3):455–471.
11. Restrepo CS, et al. Imaging appearances of the sternum and sternoclavicular joints. *Radiographics*. 2009;29(3):839–859.
12. Haller JA, Kramer SS, Lietman SA. Use of CT scans in selection of patients for pectus excavatum surgery: a preliminary report. *J Pediatr Surg*. 1987;22(10):904–906.
13. Mueller C, Saint-Vil D, Bouchard S. Chest x-ray as a primary modality for preoperative imaging of pectus excavatum. *J Pediatr Surg*. 2008;43(1):71–73.
14. Rattan AS, Laor T, Ryckman FC, et al. Pectus excavatum imaging: enough but not too much. *Pediatr Radiol*. 2010;40(2):168–172.
15. Marcovici PA, LoSasso BE, Kruk P, et al. MRI for the evaluation of pectus excavatum. *Pediatr Radiol*. 2011;41(6):757–758.
16. Iida H. Surgical repair of pectus excavatum. *Gen Thorac Cardiovasc Surg*. 2010;58(2):55–61.
17. Robicsek F, Watts LT, Fokin AA. Surgical repair of pectus excavatum and carinatum. *Semin Thorac Cardiovasc Surg*. 2009;21(1):64–75.
18. Fonkalsrud EW, Beanes S. Surgical management of pectus carinatum: 30 years' experience. *World J Surg*. 2001;25(7):898–903.
19. Cooper SC, Flaitz CM, Johnston DA, et al. A natural history of cleidocranial dysplasia. *Am J Med Genet*. 2001;104(1):1–6.
20. Tanaka JL, Ono E, Filho EM, et al. Cleidocranial dysplasia: importance of radiographic images in diagnosis of the condition. *J Oral Sci*. 2006;48(3):161–166.
21. Mundlos S. Cleidocranial dysplasia: clinical and molecular genetics. *J Med Genet*. 1999;36(3):177–182.
22. van Aalst JA, Phillips JD, Sadove AM. Pediatric chest wall and breast deformities. *Plast Reconstr Surg*. 2009;124(1 suppl):38e–49e.
23. Borschel GH, Costantino DA, Cederna PS. Individualized implant-based reconstruction of Poland syndrome breast and soft tissue deformities. *Ann Plast Surg*. 2007;59(5):507–514.
24. Garcia-Pena P, Barber I. Pathology of the thoracic wall: congenital and acquired. *Pediatr Radiol*. 2010;40(6):859–868.
25. Lee TJ, Collins J. MR imaging evaluation of disorders of the chest wall. *Magn Reson Imaging Clin N Am*. 2008;16(2):355–379.
26. Glass RB, Norton KI, Mitre SA, et al. Pediatric ribs: a spectrum of abnormalities. *Radiographics*. 2002;22(1):87–104.
27. Bishara J, Gartman-Israel D, Weinberger M, et al. Osteomyelitis of the ribs in the antibiotic era. *Scand J Infect Dis*. 2000;32(3):223–227.
28. Komolafe F. Pyogenic osteomyelitis of the rib in children. *Pediatr Radiol*. 1982;12(5):245–248.
29. Basa NR, Si M, Ndiforchu F. Staphylococcal rib osteomyelitis in a pediatric patient. *J Pediatr Surg*. 2004;39(10):1576–1577.
30. Song KM, Sloboda JF. Acute hematogenous osteomyelitis in children. *J Am Acad Orthop Surg*. 2001;9(3):166–175.
31. De Vuyst D, Vanhoenacker F, Gielen J, et al. Imaging features of musculoskeletal tuberculosis. *Eur Radiol*. 2003;13(8):1809–1819.
32. Teo HE, Peh WC. Skeletal tuberculosis in children. *Pediatr Radiol*. 2004;34(11):853–860.
33. Gaude GS, Reyas A. Tuberculosis of the chest wall without pulmonary involvement. *Lung India*. 2008;25(3):135–137.
34. Watt AJ. Chest wall lesions. *Paediatr Respir Rev*. 2002;3(4):328–338.
35. Lee G, Im JG, Kim JS, et al. Tuberculosis of the ribs: CT appearance. *J Comput Assist Tomogr*. 1993;17(3):363–366.
36. Hsu HS, Wang LS, Wu YC, et al. Management of primary chest wall tuberculosis. *Scand J Thorac Cardiovasc Surg*. 1995;29(3):119–123.
37. Yeung VH, Wong QH, Chao NS, et al. Thoracic actinomycosis in an adolescent mimicking chest wall tumor or pulmonary tuberculosis. *Pediatr Surg Int*. 2008;24(6):751–754.
38. Snape PS. Thoracic actinomycosis: an unusual childhood infection. *South Med J*. 1993;86(2):222–224.
39. Thompson AJ, Carty H. Pulmonary actinomycosis in children. *Pediatr Radiol*. 1979;8(1):7–9.
40. Bruckner AL, Frieden IJ. Infantile hemangiomas. *J Am Acad Dermatol*. 2006;55(4):671–682.
41. Haggstrom AN, et al. Prospective study of infantile hemangiomas: demographic, prenatal, and perinatal characteristics. *J Pediatr*. 2007;150(3):291–294.
42. Wassef M, et al. Vascular anomalies classification: recommendations from the International Society for the Study of Vascular Anomalies. *Pediatrics*. 2015;136(1):e203–e214.
43. Ritter MR, Butschek RA, Friedlander M, et al. Pathogenesis of infantile haemangioma: new molecular and cellular insights. *Expert Rev Mol Med*. 2007;9(32):1–19.
44. Restrepo R, Palani R, Cervantes LF, et al. Hemangiomas revisited: the useful, the unusual and the new. Part 1: overview and clinical and imaging characteristics. *Pediatr Radiol*. 2011;41(7):895–904.
45. Liang MG, Frieden IJ. Infantile and congenital hemangiomas. *Semin Pediatr Surg*. 2014;23(4):162–167.
46. Burrows PE, Laor T, Paltiel H, et al. Diagnostic imaging in the evaluation of vascular birthmarks. *Dermatol Clin*. 1998;16(3):455–488.
47. Restrepo R. Multimodality imaging of vascular anomalies. *Pediatr Radiol*. 2013;43(suppl 1):S141–S154.
48. Dubois J, Alison M. Vascular anomalies: what a radiologist needs to know. *Pediatr Radiol*. 2010;40(6):895–905.
49. Kollipara R, Odhav A, Rentas KE, et al. Vascular anomalies in pediatric patients: updated classification, imaging, and therapy. *Radiol Clin North Am*. 2013;51(4):659–672.
50. Leaute-Labreze C, Dumas de la Roque E, Hubiche T, et al. Propranolol for severe hemangiomas of infancy. *N Engl J Med*. 2008;358(24):2649–2651.
51. Restrepo R, Palani R, Cervantes LF, et al. Hemangiomas revisited: the useful, the unusual and the new. Part 2: endangering hemangiomas and treatment. *Pediatr Radiol*. 2011;41(7):905–915.
52. Drolet BA, et al. Initiation and use of propranolol for infantile hemangioma: report of a consensus conference. *Pediatrics*. 2013;131(1):128–140.
53. Garzon MC, Huang JT, Enjolras O, et al. Vascular malformations: Part I. *J Am Acad Dermatol*. 2007;56(3):353–370.
54. Laffan EE, Ngan BY, Navarro OM. Pediatric soft-tissue tumors and pseudotumors: MR imaging features with pathologic correlation: part 2. Tumors of fibroblastic/myofibroblastic, so-called fibrohistiocytic, muscular, lymphomatous, neurogenic, hair matrix, and uncertain origin. *Radiographics*. 2009;29(4):e36.
55. Dickey GE, Sotelo-Avila C. Fibrous hamartoma of infancy: current review. *Pediatr Dev Pathol*. 1999;2(3):236–243.
56. Eich GF, Hoeffel JC, Tschappeler H, et al. Fibrous tumours in children: imaging features of a heterogeneous group of disorders. *Pediatr Radiol*. 1998;28(7):500–509.
57. Sargar KM, Sheybani EF, Shenoy A, et al. Pediatric fibroblastic and myofibroblastic tumors: a pictorial review. *Radiographics*. 2016;36(4):1195–1214.
58. Seguier-Lipszyc E, Hermann G, Kaplinski C, et al. Fibrous hamartoma of infancy. *J Pediatr Surg*. 2011;46(4):753–755.
59. DiCaprio MR, Enneking WF. Fibrous dysplasia. Pathophysiology, evaluation, and treatment. *J Bone Joint Surg Am*. 2005;87(8):1848–1864.
60. Stelzer P, Gay WA. Tumors of the chest wall. *Surg Clin North Am*. 1980;60(4):779–791.
61. Tateishi U, et al. Chest wall tumors: radiologic findings and pathologic correlation: part 1. Benign tumors. *Radiographics*. 2003;23(6):1477–1490.
62. Shah ZK, Peh WC, Koh WL, et al. Magnetic resonance imaging appearances of fibrous dysplasia. *Br J Radiol*. 2005;78(936):1104–1115.
63. Payne-James JJ, Walesby RK. Symptomatic fibrous dysplasia of the right first rib excised via a posterolateral thoracotomy. *Thorax*. 1986;41(7):575–576.
64. Andrisano A, Soncini G, Calderoni PP, et al. Critical review of infantile fibrous dysplasia: surgical treatment. *J Pediatr Orthop*. 1991;11(4):478–481.

65. Murphey MD, Choi JJ, Kransdorf MJ, et al. Imaging of osteochondroma: variants and complications with radiologic-pathologic correlation. *Radiographics*. 2000;20(5):1407–1434.
66. Brien EW, Mirra JM, Luck JV. Benign and malignant cartilage tumors of bone and joint: their anatomic and theoretical basis with an emphasis on radiology, pathology and clinical biology. II. Juxtacortical cartilage tumors. *Skeletal Radiol*. 1999;28(1):1–20.
67. Groom KR, Murphey MD, Howard LM, et al. Mesenchymal hamartoma of the chest wall: radiologic manifestations with emphasis on cross-sectional imaging and histopathologic comparison. *Radiology*. 2002;222(1):205–211.
68. Jung AL, Johnson DG, Condon VR, et al. Congenital chest wall mesenchymal hamartoma. *J Perinatol*. 1994;14(6):487–491.
69. Shamberger RC, Grier HE. Chest wall tumors in infants and children. *Semin Pediatr Surg*. 1994;3(4):267–276.
70. Cohen MC, Drut R, Garcia C, et al. Mesenchymal hamartoma of the chest wall: a cooperative study with review of the literature. *Pediatr Pathol*. 1992;12(4):525–534.
71. Sodhi KS, Aiyappan SK, Menon P, et al. Unilateral multifocal mesenchymal hamartoma of the chest wall: a case report and review of literature. *J Pediatr Surg*. 2009;44(2):464–467.
72. Blumenthal BI, Capitanio MA, Queloz JM, et al. Intrathoracic mesenchymoma. Observations in two infants. *Radiology*. 1972;104(1): 107–109.
73. Azouz EM, Saigal G, Rodriguez MM, et al. Langerhans' cell histiocytosis: pathology, imaging and treatment of skeletal involvement. *Pediatr Radiol*. 2005;35(2):103–115.
74. Hoover KB, Rosenthal DI, Mankin H. Langerhans cell histiocytosis. *Skeletal Radiol*. 2007;36(2):95–104.
75. Brien EW, Mirra JM, Kerr R. Benign and malignant cartilage tumors of bone and joint: their anatomic and theoretical basis with an emphasis on radiology, pathology and clinical biology. I. The intramedullary cartilage tumors. *Skeletal Radiol*. 1997;26(6):325–353.
76. Capanna R, Campanacci DA, Manfrini M. Unicameral and aneurysmal bone cysts. *Orthop Clin North Am*. 1996;27(3):605–614.
77. Matysiakiewicz J, et al. Manifestations, diagnosis and surgical treatment of enchondroma–own experience. *Ortop Traumatol Rehabil*. 2010;12(2):155–159.
78. De Cristofaro R, et al. Selective arterial embolization in the treatment of aneurysmal bone cyst and angioma of bone. *Skeletal Radiol*. 1992;21(8):523–527.
79. Varshney MK, Rastogi S, Khan SA, et al. Is sclerotherapy better than intralesional excision for treating aneurysmal bone cysts? *Clin Orthop Relat Res*. 2010;468(6):1649–1659.
80. van den Berg H, van Rijn RR, Merks JH. Management of tumors of the chest wall in childhood: a review. *J Pediatr Hematol Oncol*. 2008;30(3):214–221.
81. Maurer HM, et al. The Intergroup Rhabdomyosarcoma Study-I. A final report. *Cancer*. 1988;61(2):209–220.
82. Saenz NC, Ghavimi F, Gerald W, et al. Chest wall rhabdomyosarcoma. *Cancer*. 1997;80(8):1513–1517.
83. La Quaglia MP. Chest wall tumors in childhood and adolescence. *Semin Pediatr Surg*. 2008;17(3):173–180.
84. Wyttenbach R, Vock P, Tschappeler H. Cross-sectional imaging with CT and/or MRI of pediatric chest tumors. *Eur Radiol*. 1998;8(6):1040–1046.
85. Kim EE, Valenzuela RF, Kumar AJ, et al. Imaging and clinical spectrum of rhabdomyosarcoma in children. *Clin Imaging*. 2000;24(5):257–262.
86. Tateishi U, et al. Chest wall tumors: radiologic findings and pathologic correlation: part 2. Malignant tumors. *Radiographics*. 2003;23(6):1491–1508.
87. Daldrup-Link HE, et al. Whole-body MR imaging for detection of bone metastases in children and young adults: comparison with skeletal scintigraphy and FDG PET. *AJR Am J Roentgenol*. 2001;177(1):229–236.
88. Baum SH, Fruhwald M, Rahbar K, et al. Contribution of PET/CT to prediction of outcome in children and young adults with rhabdomyosarcoma. *J Nucl Med*. 2011;52(10):1535–1540.
89. Norman G, et al. An emerging evidence base for PET-CT in the management of childhood rhabdomyosarcoma: systematic review. *BMJ Open*. 2015;5(1):e006030.
90. Dang NC, Siegel SE, Phillips JD. Malignant chest wall tumors in children and young adults. *J Pediatr Surg*. 1999;34(12):1773–1778.
91. Maheshwari AV, Cheng EY. Ewing sarcoma family of tumors. *J Am Acad Orthop Surg*. 2010;18(2):94–107.
92. Sallustio G, Pirronti T, Lasorella A, et al. Diagnostic imaging of primitive neuroectodermal tumour of the chest wall (Askin tumour). *Pediatr Radiol*. 1998;28(9):697–702.
93. Dick EA, McHugh K, Kimber C, et al. Imaging of non-central nervous system primitive neuroectodermal tumours: diagnostic features and correlation with outcome. *Clin Radiol*. 2001;56(3):206–215.
94. Murphey MD, Senchak LT, Mambalam PK, et al. From the radiologic pathology archives: Ewing sarcoma family of tumors: radiologic-pathologic correlation. *Radiographics*. 2013;33(3):803–831.
95. Bestic JM, Peterson JJ, Bancroft LW. Pediatric FDG PET/CT: physiologic uptake, normal variants, and benign conditions [corrected]. *Radiographics*. 2009;29(5):1487–1500.
96. Lim W, Ahmad Sarji S, Yik Y, et al. Osteosarcoma of the rib. *Biomed Imaging Interv J*. 2008;4(1):e7.
97. Samarasekera SP, Mikocka-Walus A, Butt W, et al. Epidemiology of major paediatric chest trauma. *J Paediatr Child Health*. 2009;45(11):676–680.
98. Peterson RJ, Tepas JJ, Edwards FH, et al. Pediatric and adult thoracic trauma: age-related impact on presentation and outcome. *Ann Thorac Surg*. 1994;58(1):14–18.
99. Bliss D, Silen M. Pediatric thoracic trauma. *Crit Care Med*. 2002;30(11 suppl):S409–S415.
100. Holmes JF, Sokolove PE, Brant WE, et al. A clinical decision rule for identifying children with thoracic injuries after blunt torso trauma. *Ann Emerg Med*. 2002;39(5):492–499.
101. Peclet MH, Newman KD, Eichelberger MR, et al. Thoracic trauma in children: an indicator of increased mortality. *J Pediatr Surg*. 1990;25(9):961–965.
102. Schweich P, Fleisher G. Rib fractures in children. *Pediatr Emerg Care*. 1985;1(4):187–189.
103. Garcia VF, Gotschall CS, Eichelberger MR, et al. Rib fractures in children: a marker of severe trauma. *J Trauma*. 1990;30(6):695–700.
104. Lonergan GJ, Baker AM, Morey MK, et al. From the archives of the AFIP. Child abuse: radiologic-pathologic correlation. *Radiographics*. 2003;23(4):811–845.
105. Bulloch B, Schubert CJ, Brophy PD, et al. Cause and clinical characteristics of rib fractures in infants. *Pediatrics*. 2000;105(4):E48.
106. Hamilton NA, Bucher BT, Keller MS. The significance of first rib fractures in children. *J Pediatr Surg*. 2011;46(1):169–172.
107. Moore MA, Wallace EC, Westra SJ. The imaging of paediatric thoracic trauma. *Pediatr Radiol*. 2009;39(5):485–496.
108. Nakayama DK, Ramenofsky ML, Rowe MI. Chest injuries in childhood. *Ann Surg*. 1989;210(6):770–775.
109. Strouse PJ, Owings CL. Fractures of the first rib in child abuse. *Radiology*. 1995;197(3):763–765.
110. Hopper MA, Tirman P, Robinson P. Muscle injury of the chest wall and upper extremity. *Semin Musculoskelet Radiol*. 2010;14(2):122–130.

# 60

# The Pleura

Ricardo Restrepo and Edward Y. Lee

The pleura is a serous membrane consisting of two layers, the visceral and the parietal pleura. The parietal pleura covers the inner aspect of the chest wall and the diaphragm. The visceral pleura is strongly adherent to the surface of the lungs and interlobar fissures. In normal conditions, no imaging study can visualize the pleural space because pleural membranes are only 0.2 to 0.4 mm thick, and the physiologic volume of pleural fluid forms a thin 5- to 10-micron layer. However, in children, various pathologic processes can occur within this space that require imaging evaluation. In this chapter, etiologies, imaging characteristics, treatment, and follow-up of pathologic processes involving the pleura are discussed.[1-4]

## PLEURAL EFFUSION

***Etiology.*** The lymphatic system plays an important role in the homeostasis of pleural fluid. Excess production or decreased absorption of lymphatic fluid can result in an increased volume of pleural fluid.[1-5]

Causes of pleural effusion in pediatric patients differ substantially from those in adults. Whereas the most frequent cause of pleural effusions in adults is congestive heart failure, pleural effusions in children are most commonly a result of underlying pleuropulmonary infection (Table 60.1).[3] Although pediatric patients with small pleural effusions are usually asymptomatic, large pleural effusions can result in symptomatic respiratory distress or inspiratory pleuritic chest pain as a result of stretching or irritation of the parietal pleura.[3] When infection is the underlying cause, the predominant symptoms are cough, dyspnea, fever, and elevated white blood cell counts.[1,3]

***Imaging.*** Chest radiography plays an important first-line role in the initial diagnosis of pleural effusions in children. The radiographic appearance depends on the volume and consistency of the pleural fluid, the patient's position, and the presence of septations and/or loculations. On chest radiographs, a free-flowing effusion forms an internally concave meniscus paralleling the chest wall that changes in position on lateral decubitus radiographs. On supine radiographs, mobile fluid may layer over the hemithorax, resulting in diffuse opacity. The presence of a lentiform-shaped effusion with internal convex margins is suggestive of a loculated pleural effusion.[2,6]

The most common indication of chest ultrasound in children is to characterize an opaque hemithorax seen on a chest radiograph (Fig. 60.1).[6,7] Ultrasound is the best imaging modality for diagnosing and characterizing pleural fluid.[7] Ultrasound is more sensitive than radiographs in detecting pleural fluid, particularly when the amount is small (approximately 5 mL).[2,8]

The internal echogenicity of pleural effusions on ultrasound can be categorized into four types (Table 60.2): (1) homogeneously anechoic (see Fig. 60.1B); (2) nonseptated with internal low-level echoes (e-Fig. 60.2); (3) septated (e-Fig. 60.3A); and (4) homogeneously echogenic (Fig. 60.4A).[7,9] Anechoic and free-flowing effusions are called simple pleural effusions, and the remainder are classified as complex pleural effusions.

Computed tomography (CT) also is more sensitive than chest radiographs in detecting small pleural effusions. The advantage of CT is that it provides an unobstructed view of the entire underlying lung parenchyma, mediastinum, and chest wall; however, it is associated with ionizing radiation exposure. Intravenous administration of contrast material is necessary to optimally visualize and assess the pleura and lung parenchyma (Fig. 60.4B). In comparison to ultrasound, CT is limited in characterizing pleural effusions and demonstrating internal septations (see e-Fig. 60.3).[2]

***Treatment and Follow-up.*** Thoracentesis is useful in evaluating the underlying cause of a pleural effusion and also in relieving symptoms. Indications for thoracentesis in children with pleural effusions are persistent fever, respiratory compromise, mediastinal shift, pleuritic pain, and underlying lung disease.[3]

## PARAPNEUMONIC EFFUSION AND EMPYEMA

***Etiology.*** A parapneumonic pleural effusion refers to a pleural fluid collection in association with an underlying pneumonia, whereas empyema is the presence of pus in the pleural space.[1,10] *Streptococcus pneumoniae* is still the main etiologic agent in parapneumonic effusions in children, although the number of cases caused by *Staphylococcus aureus* has increased.[1,10,11] More recently, the *Streptococcus milleri* group, typically found in the oropharynx and upper respiratory and gastrointestinal tracts, has been recognized as an important pathogen causing purulent pleuropulmonary infections, especially in immunocompromised patients.[12]

Pleural infection can be classified into three phases based on the progression of infection: exudative, fibrinopurulent, and organizing (Box 60.1). During the exudative phase, the inflammatory process associated with the underlying pneumonia leads to the accumulation of free-flowing clear fluid within the pleural cavity. During the fibrinopurulent phase, deposition of fibrin and white blood cells in the pleural space results in septations and loculations, limiting the flow of pleural fluid. The organizing phase begins when fibroblasts infiltrate the pleural cavity, forming a thick rigid pleural rind. This pleural rind may prevent lung reexpansion, impair lung function, and create a persistent pleural space with ongoing potential for infection.[1,6,13]

***Imaging.*** A chest radiograph is the initial imaging modality for assessing the presence of parapneumonic effusions. Ultrasound subsequently can be obtained for characterization of the parapneumonic effusion. As the underlying infection progresses, parapneumonic effusions may develop low-level internal echoes and floating debris (see e-Fig. 60.2) followed by septations and loculations (see e-Fig. 60.3A), preventing free motion of the fluid. The internal echoes indicate increased underlying cellularity of fluid; these pleural effusions are usually exudates but not necessarily empyemas.[1,6,7,9,14] The parapneumonic effusion eventually may become semisolid in appearance on ultrasound (see Fig. 60.4A). The development of pleural thickening indicates the presence of a fibrous capsule.

The routine use of CT is not necessary to evaluate parapneumonic pleural effusions.[1,6,15] However, CT with intravenous contrast may aid in the evaluation of the lung parenchyma when a complication such as a bronchopleural fistula is suspected (Fig. 60.5) or in the differentiation of a parapneumonic effusion from a lung abscess.[2] An imaging finding suggestive of empyema on CT is a lentiform-shaped fluid collection with pleural thickening and/or enhancement.[16] In contrast, lung abscesses tend to be round and are embedded within the lung parenchyma rather than displacing it.[2] Loculations in parapneumonic effusions, which are best visualized by ultrasound, can be suggested on CT indirectly when the surface of the underlying lung shows smooth indentations due to fibrin

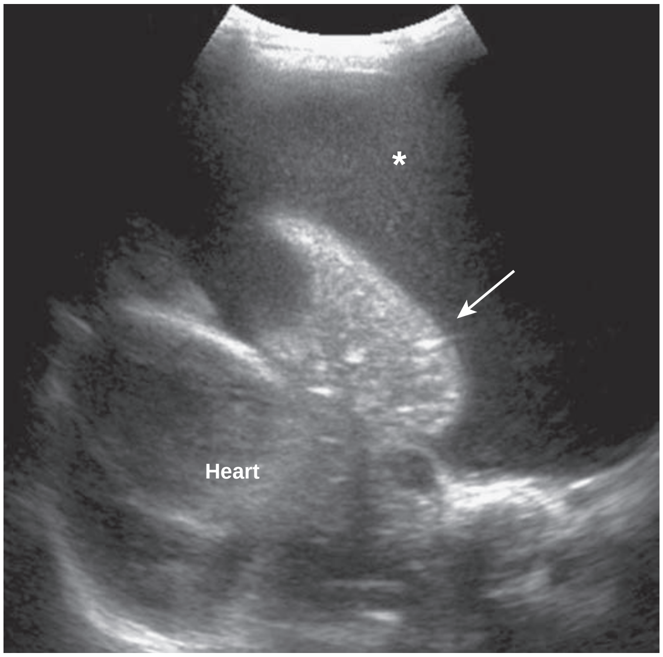

**e-Figure 60.2. Complex effusion with low-level echoes in a 9-year-old girl with bacterial pneumonia.** An ultrasound image of the left hemithorax reveals a large parapneumonic pleural effusion with floating low-level echoes indicating debris *(asterisk)* and the consolidated underlying lung *(arrow).*

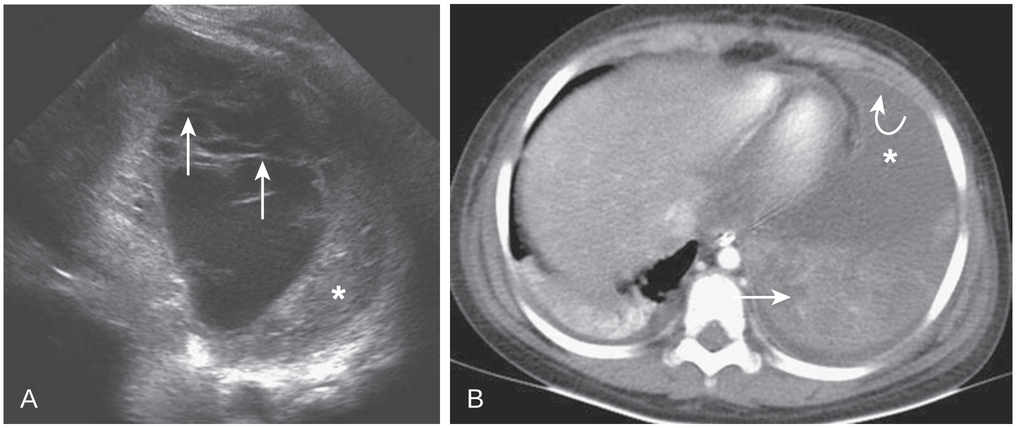

**e-Figure 60.3. Complex septated effusion in a 6-year-old patient with bacterial pneumonia.** (A) Ultrasound image of the left hemithorax shows a large parapneumonic effusion with multiple septations *(arrows).* Consolidation of the adjacent lung also is present *(asterisk).* (B) Axial contrast-enhanced CT image shows the pleural effusion *(asterisk)* in the anterior aspect of the left base. The septations seen on the ultrasound are not clearly visualized on CT. Pleural enhancement is present *(curved arrow)* adjacent to consolidated lung *(straight arrow).*

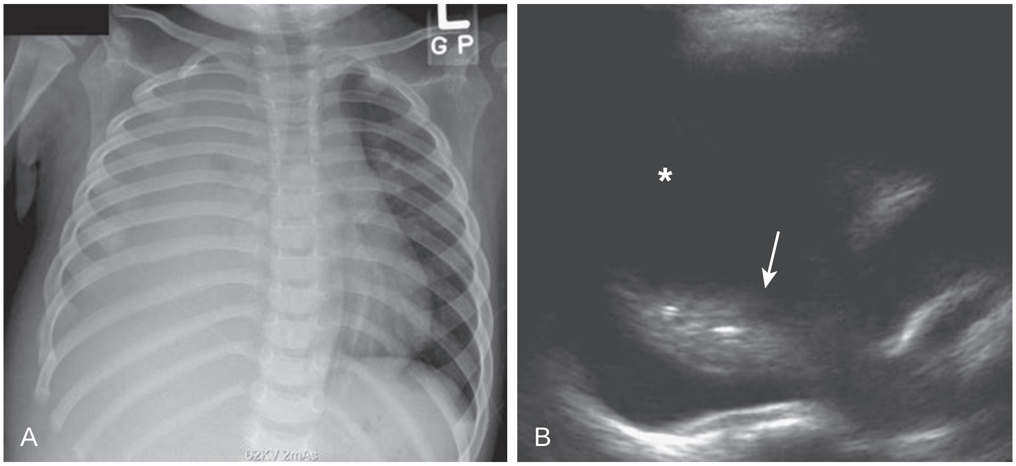

**Figure 60.1. Simple effusion in a 2-year-old boy.** (A) Chest radiograph shows complete opacification of the right hemithorax with obliteration of the right side of the mediastinum and hemidiaphragm. The cardiac and tracheal deviations to the left are imaging findings suggestive of a pleural effusion. (B) Ultrasound of the right hemithorax confirms the presence of a large simple pleural effusion *(asterisk)*. Consolidation *(arrow)* of the underlying lung also is seen.

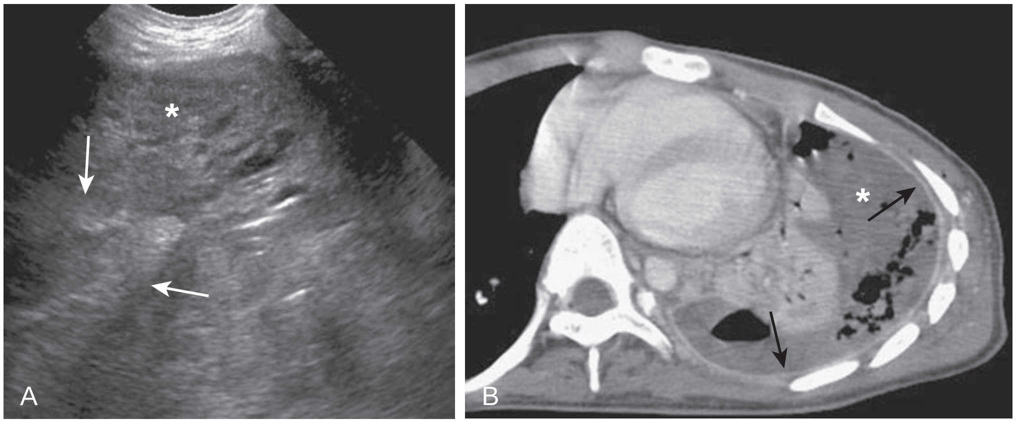

**Figure 60.4. Complex effusion in a 6-year-old patient with bacterial pneumonia.** (A) Ultrasound image shows a mostly solid-appearing parapneumonic effusion *(arrows)*. The consolidated underlying lung *(asterisk)* also is seen. (B) Axial contrast-enhanced CT image shows the large pleural effusion *(asterisk)* with pleural enhancement *(arrows)*.

**TABLE 60.1** Phases of Pleural Infection

| Phase | Description |
|---|---|
| Exudative | Pleural inflammation leads to accumulation of free-flowing clear liquid |
| Fibrinopurulent | Deposition of fibrin in the pleural space results in septation/loculations limiting the flow of fluid; pus accumulates in the pleural cavity |
| Organizing phase | Fibroblasts infiltrate the pleura, forming a rigid pleura and preventing lung expansion |

**BOX 60.1** Common Causes of Pleural Effusions in Children

- Bacterial pneumonia
- Renal disease
- Trauma
- Viral infection
- Malignancy
- Congenital heart disease
- Liver failure
- Sickle cell disease

**TABLE 60.2** Pleural Effusions on Ultrasound Based on Internal Echogenicity

| Type of Effusion | Description |
|---|---|
| Simple | Homogeneously anechoic |
| Complex | Nonseptated with internal low-level echoes<br>Multiseptated<br>Homogenously echogenic |

strands that produce intrapleural adhesions, or in the presence of a lentiform-shaped pleural fluid collection.[2] The presence of air or gas in the dependent portion of the effusion also suggests loculation (see Fig. 60.4B). In the absence of a previous thoracentesis or thoracostomy tube placement, the presence of air/gas or an air-fluid level in the pleural cavity in a patient with pneumonia is diagnostic of a bronchopleural fistula (see Fig. 60.5).[1,2,6,17,18]

***Treatment and Follow-up.*** Anechoic simple pleural effusions can be managed by thoracentesis or percutaneous placement of a chest tube. Because 50% of parapneumonic effusions recur after aspiration in children, the routine placement of a drainage catheter currently is recommended after aspiration.[7] Distinction between parapneumonic pleural effusions and empyema in children is less

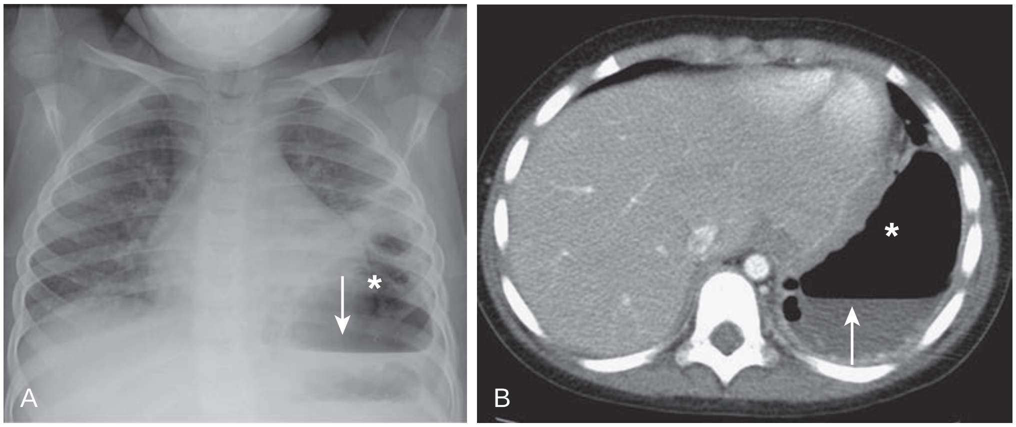

**Figure 60.5. Bronchopleural fistula in a 4-year-old boy with necrotizing pneumonia.** (A) Frontal chest radiograph shows a collection of air in the left pleural space superior to the gastric bubble *(asterisk),* with an air-fluid level *(arrow)* indicating a hydropneumothorax. (B) Axial contrast-enhanced CT image of the same patient confirms the presence of air in the pleural space *(asterisk)* and the air-fluid level *(arrow).*

important than in adults because diagnostic thoracentesis is rarely performed before definitive treatment in children with clinically suspected pleuropulmonary infection.[1,6]

The management choice for complex pleural effusions in children, particularly in the presence of septations, is currently somewhat controversial. Some investigators advocate the use of percutaneous insertion of a chest tube combined with instillation of a fibrinolytic agent, whereas others support the use of video-assisted thoracoscopy (VATS).[1,19-24] The presence of septations or complex effusions is not necessarily a contraindication for percutaneous drainage. However, concomitant fibrinolytic therapy typically is required and should be started promptly to maximize the benefit of the procedure.[25,26] In a retrospective study consisting of 54 pediatric patients with parapneumonic effusions, chest tube insertion with intrapleural instillation of a fibrinolytic agent was successful, safe, and less costly as the first therapeutic option compared with VATS.[27] A recent cost-effective analysis study of the management of empyema in children that was conducted with a Bayesian tree approach showed that chest tube insertion with instillation of a fibrinolytic agent was the most cost-effective strategy for treating pediatric empyema based on the length of hospital stay.[28] The management of bronchopleural fistulas is initially medical, including pleural space decompression with a thoracostomy tube and nutritional support. When conservative management is ineffective, closure of the fistula must be considered through VATS for peripheral fistulas and through an open thoracotomy for central fistulas.[17,29]

In children with parapneumonic effusions or empyema that is successfully treated, most chest radiographs return to the baseline in 3 to 6 months. The British Thoracic Society currently recommends follow-up chest radiographs 4 to 6 weeks after treatment of parapneumonic effusion or empyema.[1] In cases of no improvement on follow-up chest radiographs, a subsequent ultrasound or CT scan may be beneficial to exclude underlying complications.[1,6,30]

## PNEUMOTHORAX

***Etiology.*** Pneumothorax is the presence of air in the potential space between the parietal and visceral pleura. Pneumothorax is classified as spontaneous or traumatic depending on the underlying etiology. Spontaneous pneumothorax can be further subdivided into primary and secondary. Primary spontaneous pneumothorax occurs in an otherwise healthy child and often is attributed to a ruptured preexisting apical bleb or bulla. Secondary spontaneous pneumothorax occurs as a complication of an underlying pulmonary disease, most commonly asthma and cystic fibrosis in children.[31,32] In the United States, the incidence of spontaneous pneumothorax is approximately 1.8 to 7.4 per 100,000 in boys and 1.2 to 6 per 100,000 in girls. The mean age at presentation is 14 to 15.9 years.[31,33] The classic phenotype is a thin, tall male with a low body mass index. Children with primary spontaneous pneumothorax typically present with a sudden onset of unilateral chest pain and dyspnea at rest. Patients with secondary spontaneous pneumothorax often present with cardiopulmonary distress.[31,33] Traumatic pneumothorax occurs as a result of blunt or penetrating mechanisms, with iatrogenic pneumothorax being a subset resulting from medical procedures. The most concerning outcome of traumatic pneumothorax is progression to tension pneumothorax. Tension phenomenon occurs when the lung or airway defect acts as a check-valve mechanism, allowing flow of air into, but not out from, the pleural cavity. The diagnosis of tension pneumothorax is based on both radiologic and clinical findings. Hemodynamic and ventilatory compromise may be present with rapid cardiorespiratory collapse. On physical examination, signs of tension include neck vein distension, tracheal deviation away from the affected side, and cyanosis (Beck triad).[31] Tension pneumothorax in the absence of trauma is rare in pediatric patients, occurring in 1% to 3% of cases.[34]

***Imaging.*** Chest radiography is the initial test in the diagnosis of a pneumothorax by visualizing the visceral pleural with absence of pulmonary markings beyond the pleural margin (Fig. 60.6A). For evaluation of pneumothorax, an upright chest radiograph is the procedure of choice, with a lateral decubitus as an alternative.[31,33] Inspiratory and expiratory views are reported to be equally sensitive in the detection of pneumothorax, and thus the expiratory view does not need to be obtained routinely.[35] On chest radiographs, a tension pneumothorax is characterized by a large pneumothorax, resulting in collapse of the ipsilateral lung and shifting of the mediastinum, including the trachea, to the contralateral side.[31] Widened ipsilateral rib spaces and flattening or eversion of the diaphragm are also often seen in patients with a tension pneumothorax.

Ultrasound is increasingly used for evaluating pneumothorax, particularly in point-of-care applications, and it may be encountered during ultrasound evaluation of the pediatric chest performed for other reasons. Without a pneumothorax, the strong acoustic interface between the pleura and aerated lung produces posterior reverberations (so-called A lines). The normal sliding motion of the lung during respiration also is visualized. When air is introduced into the pleural space, the normal tension between the pleural layers is lost and a gap is created between the parietal and visceral

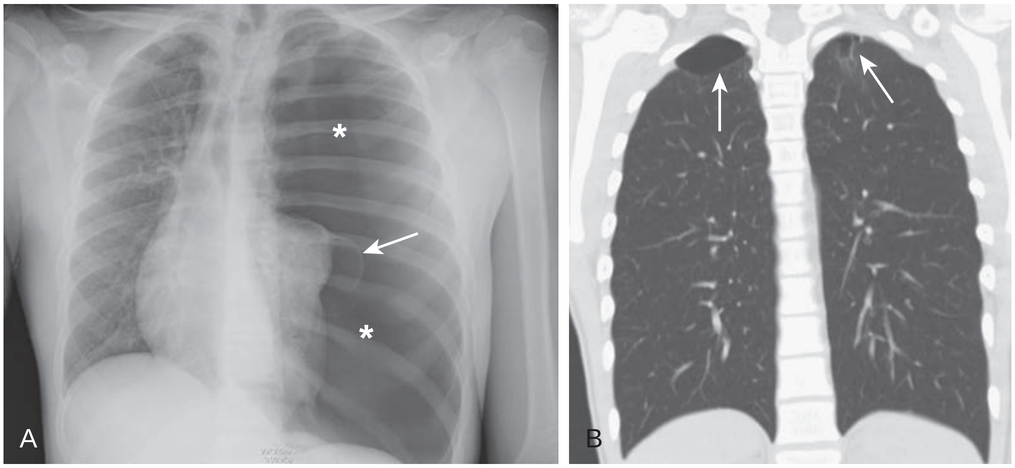

**Figure 60.6. Spontaneous pneumothorax in a tall, thin teenager presenting with tachypnea, tachycardia, and normal blood pressure.** (A) Frontal chest radiograph shows a large pneumothorax occupying the entire left hemithorax *(asterisks),* with a mild cardiomediastinal shift to the right. A bleb is noted along the surface of the collapsed left lung *(arrow).* (B) Coronal CT image obtained 1 month after thoracostomy tube removal shows biapical blebs *(arrows),* which are larger on the right. The right apical bleb was not seen on the chest radiographs.

pleura, disrupting the normal acoustic interface. The sliding of the underlying lung no longer can be seen, and the normal reverberation is replaced by a static homogeneous acoustic shadowing.[7,31] A literature review published in 2010 reported a sensitivity between 86% and 98% and a specificity between 97% and 100% for ultrasound compared with a sensitivity between 28% and 75% for supine chest radiographs in detecting pneumothorax.[36]

In cases of primary spontaneous pneumothorax, a CT scan may play a role in identifying preexisting subpleural blebs and bullae (Fig. 60.6B). The exact relationship between blebs and primary spontaneous pneumothorax is not clear. However, with CT there is an increased recognition of subpleural blebs in patients with primary spontaneous pneumothorax and, in particular, in patients presenting with recurrent pneumothoraces.[37-42]

***Treatment and Follow-up.*** No pediatric-specific management guidelines for primary spontaneous pneumothorax have been developed to date. Pediatric patients have not been addressed separately in the available international guidelines.[32,33] In the setting of primary spontaneous pneumothorax, observation should be the initial management of choice for small closed pneumothoraces separated less than 2 cm from the chest wall in asymptomatic patients. Administration of oxygen should be considered because it may increase the rate of reabsorption of the pneumothorax. Symptomatic pneumothoraces, whether primary or secondary, require active intervention with a simple aspiration or placement of a thoracostomy tube in cases of a large pneumothorax.[31,32] When a tension pneumothorax is present, urgent insertion of a large-bore needle or angiocatheter should be inserted in the affected side at the second intercostal space to decompress the tension pneumothorax.[31]

The risk of recurrence after a single episode of spontaneous pneumothorax with conservative treatment ranges from 16% to 52%.[42] Patients with a primary spontaneous pneumothorax that is treated successfully by a simple aspiration should be observed before discharge. Patients with a spontaneous pneumothorax who are discharged without intervention should have a follow-up chest radiograph after 2 weeks. Patients who have a secondary pneumothorax that is treated with simple aspiration should be admitted for 24 hours for a repeat chest radiograph to ensure no recurrence.[32] A recent study advocates for a CT scan of the chest in children with recurrent primary spontaneous pneumothorax or first episode of a large pneumothorax to evaluate for apical blebs or bullae.[43] It has been advocated that a limited CT scan of the lung apices with coronal reconstruction may suffice in children because most blebs and bullae occur in this location, thus allowing a decrease in radiation exposure.[33,40]

## PLEURAL NEOPLASMS

***Etiology.*** Pleural tumors in children are rare and much less common than in adults. Secondary neoplasms (i.e., metastasis or direct invasion) are more common than are primary tumors.[7] Metastatic neoplasms involving the pleura include lymphoma, neuroblastoma, Wilms tumors, rhabdomyosarcoma, and other sarcomas.[7] A metastatic Wilms tumor may involve the peritoneal, pleural, and pericardial cavities and is one of the most common causes of malignant effusions in children.[44]

Primary malignant tumors of the pleura include desmoplastic small round cell tumors and mesotheliomas. The former more commonly occur in the peritoneal cavity but may arise primarily from the pleura.[45,46] Mesotheliomas are regarded as adult-type neoplasms that rarely occur in children in the second decade. Clinicopathologic features of mesothelioma are similar to those in adults, with a predilection for the pleura, a male predominance, and a poor prognosis.[47] Malignant pleural tumors typically present with chest pain and respiratory distress, especially in the presence of a large pleural effusion.

The most common benign lesions of the pleura include a calcifying fibrous tumor, myofibromatosis, and lipomas.[45] Calcifying fibrous tumors usually are found in subcutaneous and deep soft tissues, but on rare occasions have been reported in the pleura.[45]

***Imaging.*** Malignant pleural neoplasms, whether primary or secondary, usually manifest with pleural effusions that initially are identified on chest radiographs. Ultrasound subsequently can be used for the confirmation and characterization of pleural neoplasms. Pleural metastases tend to produce large effusions with hemorrhage presenting as increased cellularity and low-level echoes on ultrasound. The presence of pleural fluid aids in the detection of nodules or masses adherent to the parietal or visceral pleura on ultrasound (Fig. 60.7).[7] CT and magnetic resonance imaging are helpful imaging modalities for evaluating the tumor, its extent, and its relationship with adjacent organs. Because of the markedly overlapping imaging findings among different types of primary and secondary pleural neoplasms, definitive diagnosis is based on histopathologic analysis. If the neoplasm is visible on ultrasound, biopsy under ultrasound guidance can be performed for the diagnosis.[7]

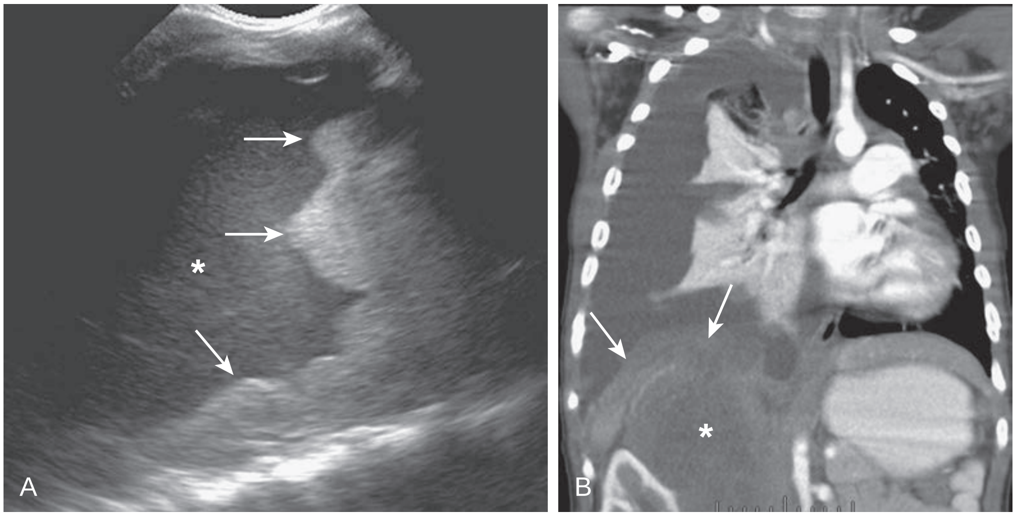

**Figure 60.7. Primary retroperitoneal rhabdomyosarcoma with metastasis to the pleura in a 3-year-old girl.** (A) Ultrasound of the right hemithorax shows a large complex effusion with low-level echoes *(asterisk)* and nodularity of the pleura *(arrows).* (B) A coronal contrast-enhanced CT image shows the large right suprarenal rhabdomyosarcoma *(asterisk).* The soft tissue along the right diaphragm and pleura indicate metastasis *(arrows).* A secondary large right pleural effusion causing collapse of the right lung also is seen.

***Treatment and Follow-up.*** The current treatment of primary malignant pleural neoplasms is surgical resection, often combined with chemotherapy. When pleural metastasis is discovered, it usually indicates advanced disease, and the treatment is aimed at treating the primary tumor. In cases of recurrent intractable pleural effusions, pleurodesis as a palliative treatment can be performed.[48]

## KEY POINTS

- Pleural effusions are best characterized on ultrasound as simple and complex. Simple effusions are anechoic, whereas complex effusions contain floating low-level echoes, septations, and/or semisolid components.
- Parapneumonic effusions and empyema are part of a spectrum of pleural infection.
- The three phases of pleural infection include exudative, fibrinopurulent, and organizing.
- The diagnosis of a tension pneumothorax is both clinical and radiologic, based on cardiorespiratory deterioration in the presence of a large pneumothorax.
- Primary spontaneous pneumothorax occurs in an otherwise healthy child and often is attributed to ruptured preexisting apical blebs or bullae.

## SUGGESTED READINGS

Balfour-Lynn IM, Abrahamson E, Cohen G, et al. BTS guidelines for the management of pleural infection in children. *Thorax*. 2005;60:i1–i21.
Calder A, Owens CM. Imaging of parapneumonic effusions and empyema in children. *Pediatr Radiol*. 2009;39:527–537.
Chen HJ, Tu CY, Ling SJ, et al. Sonographic appearances in transudative pleural effusions: not always an anechoic pattern. *Ultrasound Med Biol*. 2008;34:362–369.
Coley BD. Chest sonography in children: current indications, techniques, and imaging findings. *Radiol Clin North Am*. 2011;49(5):825–849.
Johnson NN, Toledo A, Endon EE. Pneumothorax, pneumomediastinum and pulmonary embolism. *Pediatr Clin North Am*. 2010;57:1357–1383.

## REFERENCES

Full references for this chapter can be found on www.expertconsult.com.

## REFERENCES

1. Balfour-Lynn IM, et al. BTS guidelines for the management of pleural infection in children. *Thorax*. 2005;60(suppl 1):1–21.
2. Heffner JE, Klein JS, Hampson C. Diagnostic utility and clinical application of imaging for pleural space infections. *Chest*. 2010;137(2):467–479.
3. Efrati O, Barak A. Pleural effusions in the pediatric population. *Pediatr Rev*. 2002;23(12):417–426.
4. Beers SL, Abramo TJ. Pleural effusions. *Pediatr Emerg Care*. 2007;23(5):330–334.
5. English JC, Leslie KO. Pathology of the pleura. *Clin Chest Med*. 2006;27(2):157–180.
6. Calder A, Owens CM. Imaging of parapneumonic pleural effusions and empyema in children. *Pediatr Radiol*. 2009;39(6):527–537.
7. Coley BD. Pediatric chest ultrasound. *Radiol Clin North Am*. 2005;43(2):405–418.
8. Kocijancic I, Vidmar K, Ivanovi-Herceg Z. Chest sonography versus lateral decubitus radiography in the diagnosis of small pleural effusions. *J Clin Ultrasound*. 2003;31(2):69–74.
9. Chen HJ, et al. Sonographic appearances in transudative pleural effusions: not always an anechoic pattern. *Ultrasound Med Biol*. 2008;34(3):362–369.
10. Hernandez-Bou S, Garcia-Garcia JJ, Esteva C, et al. Pediatric parapneumonic pleural effusion: epidemiology, clinical characteristics, and microbiological diagnosis. *Pediatr Pulmonol*. 2009;44(12):1192–1200.
11. Krenke K, Urbankowska E, Urbankowski T, et al. Clinical characteristics of 323 children with parapneumonic pleural effusion and pleural empyema due to community acquired pneumonia. *J Infect Chemother*. 2016;22(5):292–297.
12. Lee EY, et al. Streptococcus milleri group pleuropulmonary infection in children: computed tomographic findings and clinical features. *J Comput Assist Tomogr*. 2010;34(6):927–932.
13. Hamm H, Light RW. Parapneumonic effusion and empyema. *Eur Respir J*. 1997;10(5):1150–1156.
14. Yang PC, Luh KT, Chang DB, et al. Value of sonography in determining the nature of pleural effusion: analysis of 320 cases. *AJR Am J Roentgenol*. 1992;159(1):29–33.
15. Kurian J, Levin TL, Han BK, et al. Comparison of ultrasound and CT in the evaluation of pneumonia complicated by parapneumonic effusion in children. *AJR Am J Roentgenol*. 2009;193(6):1648–1654.
16. Stark DD, Federle MP, Goodman PC, et al. Differentiating lung abscess and empyema: radiography and computed tomography. *AJR Am J Roentgenol*. 1983;141(1):163–167.
17. Sarkar P, Patel N, Chusid J, et al. The role of computed tomography bronchography in the management of bronchopleural fistulas. *J Thorac Imaging*. 2010;25(1):W10–W13.
18. Seo H, Kim TJ, Jin KN, et al. Multi-detector row computed tomographic evaluation of bronchopleural fistula: correlation with clinical, bronchoscopic, and surgical findings. *J Comput Assist Tomogr*. 2010;34(1):13–18.
19. Levinson GM, Pennington DW. Intrapleural fibrinolytics combined with image-guided chest tube drainage for pleural infection. *Mayo Clin Proc*. 2007;82(4):407–413.
20. Ampofo K, Byington C. Management of parapneumonic empyema. *Pediatr Infect Dis J*. 2007;26(5):445–446.
21. Kurt BA, Winterhalter KM, Connors RH, et al. Therapy of parapneumonic effusions in children: video-assisted thoracoscopic surgery versus conventional thoracostomy drainage. *Pediatrics*. 2006;118(3):e547–e553.
22. St Peter SD, et al. Thoracoscopic decortication vs tube thoracostomy with fibrinolysis for empyema in children: a prospective, randomized trial. *J Pediatr Surg*. 2009;44(1):106–111.
23. Sonnappa S, et al. Comparison of urokinase and video-assisted thoracoscopic surgery for treatment of childhood empyema. *Am J Respir Crit Care Med*. 2006;174(2):221–227.
24. Shirota C, Uchida H. Initial treatment of septated parapneumonic empyema with drainage plus fibrinolytic agents is equally effective as video-assisted thoracoscopic surgery, and is suitable as first-line therapy. *Transl Pediatr*. 2015;4(1):41–44.
25. Wells RG, Havens PL. Intrapleural fibrinolysis for parapneumonic effusion and empyema in children. *Radiology*. 2003;228(2):370–378.
26. Weinstein M, Restrepo R, Chait PG, et al. Effectiveness and safety of tissue plasminogen activator in the management of complicated parapneumonic effusions. *Pediatrics*. 2004;113(3 Pt 1):e182–e185.
27. Gates RL, Hogan M, Weinstein S, et al. Drainage, fibrinolytics, or surgery: a comparison of treatment options in pediatric empyema. *J Pediatr Surg*. 2004;39(11):1638–1642.
28. Cohen E, Weinstein M, Fisman DN. Cost-effectiveness of competing strategies for the treatment of pediatric empyema. *Pediatrics*. 2008;121(5):e1250–e1257.
29. Sarkar P, Chandak T, Shah R, et al. Diagnosis and management bronchopleural fistula. *Indian J Chest Dis Allied Sci*. 2010;52(2):97–104.
30. Chan PW, Crawford O, Wallis C, et al. Treatment of pleural empyema. *J Paediatr Child Health*. 2000;36(4):375–377.
31. Johnson NN, Toledo A, Endom EE. Pneumothorax, pneumomediastinum, and pulmonary embolism. *Pediatr Clin North Am*. 2010;57(6):1357–1383.
32. Henry M, Arnold T, Harvey J. BTS guidelines for the management of spontaneous pneumothorax. *Thorax*. 2003;58(suppl 2):39–52.
33. Robinson PD, Cooper P, Ranganathan SC. Evidence-based management of paediatric primary spontaneous pneumothorax. *Paediatr Respir Rev*. 2009;10(3):110–117.
34. Weissberg D, Refaely Y. Pneumothorax: experience with 1,199 patients. *Chest*. 2000;117(5):1279–1285.
35. Seow A, Kazerooni EA, Pernicano PG, et al. Comparison of upright inspiratory and expiratory chest radiographs for detecting pneumothoraces. *AJR Am J Roentgenol*. 1996;166(2):313–316.
36. Wilkerson RG, Stone MB. Sensitivity of bedside ultrasound and supine anteroposterior chest radiographs for the identification of pneumothorax after blunt trauma. *Acad Emerg Med*. 2010;17(1):11–17.
37. Mitlehner W, Friedrich M, Dissmann W. Value of computer tomography in the detection of bullae and blebs in patients with primary spontaneous pneumothorax. *Respiration*. 1992;59(4):221–227.
38. Smit HJ, Wienk MA, Schreurs AJ, et al. Do bullae indicate a predisposition to recurrent pneumothorax? *Br J Radiol*. 2000;73(868):356–359.
39. Warner BW, Bailey WW, Shipley RT. Value of computed tomography of the lung in the management of primary spontaneous pneumothorax. *Am J Surg*. 1991;162(1):39–42.
40. Guimaraes CV, Donnelly LF, Warner BW. CT findings for blebs and bullae in children with spontaneous pneumothorax and comparison with findings in normal age-matched controls. *Pediatr Radiol*. 2007;37(9):879–884.
41. Choudhary AK, Sellars ME, Wallis C, et al. Primary spontaneous pneumothorax in children: the role of CT in guiding management. *Clin Radiol*. 2005;60(4):508–511.
42. Sihoe AD, et al. Can CT scanning be used to select patients with unilateral primary spontaneous pneumothorax for bilateral surgery? *Chest*. 2000;118(2):380–383.
43. Soccorso G, Anbarasan R, Singh M, et al. Management of large primary spontaneous pneumothorax in children: radiological guidance, surgical intervention and proposed guideline. *Pediatr Surg Int*. 2015;31(12):1139–1144.
44. Schinstine M, Abati A, Tsokos M, et al. Cytological identification of metastatic epithelial nephroblastoma in pleural fluid: report of a case and review of literature. *Diagn Cytopathol*. 2006;34(9):621–625.
45. Granville L, et al. Review and update of uncommon primary pleural tumors: a practical approach to diagnosis. *Arch Pathol Lab Med*. 2005;129(11):1428–1443.
46. Karavitakis EM, et al. Desmoplastic small round cell tumor of the pleura. *Pediatr Blood Cancer*. 2007;49(3):335–338.
47. Coffin CM, Dehner LP. Mesothelial and related neoplasms in children and adolescents: a clinicopathologic and immunohistochemical analysis of eight cases. *Pediatr Pathol*. 1992;12(3):333–347.
48. Hoffer FA, Hancock ML, Hinds PS, et al. Pleurodesis for effusions in pediatric oncology patients at end of life. *Pediatr Radiol*. 2007;37(3):269–273.

# 61

# The Diaphragm

*Ricardo Restrepo and Edward Y. Lee*

## OVERVIEW

The diaphragm is a dome-shaped musculofibrous membrane that separates the thoracic and abdominal cavities and performs an important respiratory function. The diaphragm has a fibrous portion centrally (i.e., a central tendon) surrounded by a peripheral muscular portion. Major structures pass through three openings: caval (inferior vena cava and some right phrenic nerve branches), esophageal (esophagus, vagal nerves, and small esophageal arteries), and aortic (aorta, azygous vein, and thoracic duct). The diaphragm is innervated by the phrenic nerve, which is formed from the central nerves of C3, C4, and C5.[1,2] Diaphragmatic lesions can arise from a variety of congenital, traumatic, infectious, and neoplastic conditions.

## CONGENITAL ANOMALIES

### Duplication of the Diaphragm (Accessory Diaphragm)

***Etiology.*** Duplication of the diaphragm, also known as an accessory diaphragm, is a rare congenital anomaly. It is almost always located on the right side and frequently is associated with lobar agenesis-aplasia complex.[3,4] Although the precise pathogenesis of duplication of the diaphragm is currently unknown, it is suggested that this anomaly is the result of a defect of synchronization between the caudal migration of the septum transversum and the development of the bronchial system.[3,5] In gross pathology, the accessory diaphragm is a fine fibromuscular membrane with a serosal lining that is connected to the anterior part of the diaphragm.[3] It follows a posterosuperior direction to join the posterior chest wall, separating the right hemithorax into two parts.[3,4] It is crescentic in form and usually has an opening (i.e., central hiatus) medially, through which vessels and bronchial structures pass. Affected patients may be asymptomatic, but most present with respiratory difficulties of varying degrees.[5]

***Imaging.*** On chest radiographs or computed tomography (CT), the accessory diaphragm may have two different appearances.[3] When the central hiatus is markedly narrowed and the trapped lung is not aerated, it appears like a mass. However, when the trapped lung is aerated, the accessory diaphragm is seen as a fissure-like structure in the right base extending from the anterior aspect of the hemidiaphragm cephalad toward the posterior chest wall. On CT, it is seen as a bandlike structure with crowding of pulmonary structures as the bronchi and vessels traverse the central hiatus (Fig. 61.1).[4,5]

***Treatment and Follow-up.*** Most duplicated diaphragms require no surgical intervention or other treatment. Surgical repair should be performed only when dyspnea or recurrent respiratory infections occur.[3,5]

### Congenital Diaphragmatic Hernia

#### Overview

Traditionally, congenital diaphragmatic hernias (CDHs) have been classified according to their anatomic location. Almost 90% of CDHs are reported to involve the posterolateral aspect of the diaphragm and are referred as to Bochdalek hernias.[6] Nonposterolateral CDHs occur most often in the anterior portion of the diaphragm and are known as Morgagni hernias. However, diaphragmatic defects do not exclusively localize to these two areas, and thus some defects do not follow this classification. In addition, some diaphragmatic hernias have a sac, which is thought to represent focal thinning of the diaphragmatic musculature. Thus the terms *sac hernia* and *eventration* currently are poorly defined. Despite its limitations, an anatomic-based classification system continues to be used (Box 61.1).[6]

#### Congenital Diaphragmatic Hernia: Bochdalek

***Etiology.*** The prevalence of CDH has been reported as ranging from 1.6 to 2.3 per 10,000 births, including isolated cases and those associated with other malformations.[7,8] CDH of the Bochdalek type is associated with significant morbidity and mortality, and accounts for 90% to 95% of CDH.[6,7] Approximately 85% of these hernias occur on the left side, whereas right-sided and bilateral hernias represent only 13% and 2% of cases, respectively.[9]

The diaphragm initially develops as a septum between the heart and the liver, progresses posterolaterally, and closes at the Bochdalek foramen at approximately 8 to 10 weeks of gestation.[9,10] The primary abnormality resulting in a Bochdalek hernia is failure or delay of the pleuroperitoneal fold and transverse septum to properly fuse with the intercostal muscles around the eighth week of gestation.[10] Diaphragmatic hernia and lung hypoplasia can occur concomitantly, possibly a polygenic association.[9,11]

***Imaging.*** Many cases of CDH are initially found prenatally by ultrasound (US) or magnetic resonance imaging (MRI) (see Chapter 50). On a newborn chest radiograph a Bochdalek hernia may appear as an opacified hemithorax with contralateral cardiomediastinal shift. As the infant swallows air, the air-filled bowel located within the hemithorax may become apparent (Fig. 61.2). In the case of intraabdominal solid organ herniation, the hemithorax can remain homogeneously opacified. When the bowel-containing hernia is large, a paucity of abdominal contents causes the so-called "scaphoid abdomen" and can be seen on abdominal radiographs.[10] The position of catheters and tubes is helpful in confirming the presence of a Bochdalek hernia. The nasogastric (NG) tube deviates to the side opposite to the hernia in the chest. If the stomach is herniated within the hemithorax, the tip of the NG tube can project in the chest. The position of umbilical venous catheters is affected by the location of the liver, which is shifted either in the abdomen or chest. In contrast, the position of umbilical arterial catheters is rarely affected because of their retroperitoneal location.[12] Ultrasound with color Doppler may help delineate the venae cavae and the hepatic vasculature, and it may identify the presence of herniated solid organs before surgery. CT and MRI may play an occasional role in excluding a congenital lung anomaly such as congenital pulmonary airway malformation or pulmonary sequestration.[10]

After hernia repair, an ipsilateral pneumothorax is a common finding and should not be rapidly evacuated as this may cause mediastinal rotation and subsequent venae cavae obstruction because of the increased mobility of the neonatal mediastinum.[10] The pleural air typically reabsorbs by itself and sometimes is replaced by fluid.

***Treatment and Follow-up.*** Treatment of all types of CDH includes medical and surgical management. The medical management of CDH focuses on addressing the underlying major causes of neonatal death as a result of CDH, such as pulmonary

## Abstract:

The diaphragm is an organ that in the pediatric population, can be affected primarily by congenital, traumatic and neoplastic diseases; of these, congenital processes being the most common. On this chapter, we discuss the etiology, imaging, treatment and follow up of the different pathology affecting this organ in the pediatric population.

## Keywords:

Diaphragm
Diaphragmatic hernia
Diaphragmatic eventration
Diaphragmatic paralysis

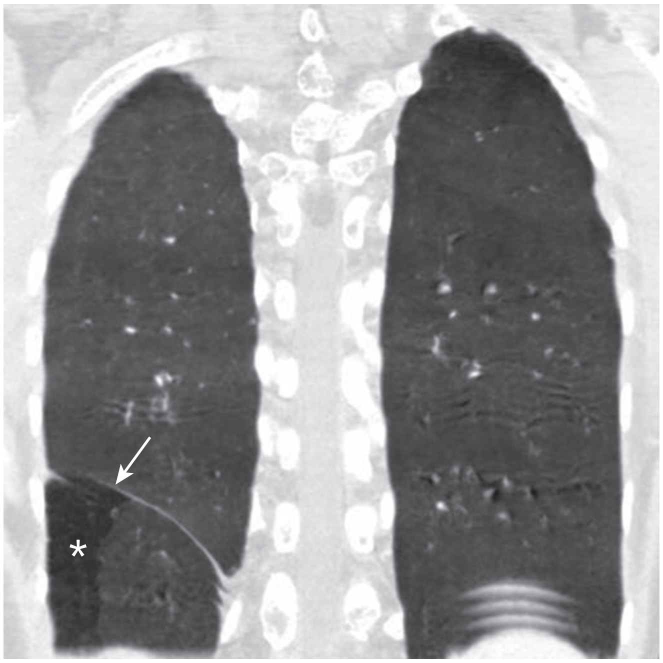

**Figure 61.1. Duplicated diaphragm in a 12-year-old girl presenting with cough.** Coronal lung window CT image shows a bandlike structure *(arrow)* in the right base with the hyperlucent *(asterisk)* lateral aspect of the right lower lobe, indicating air trapping.

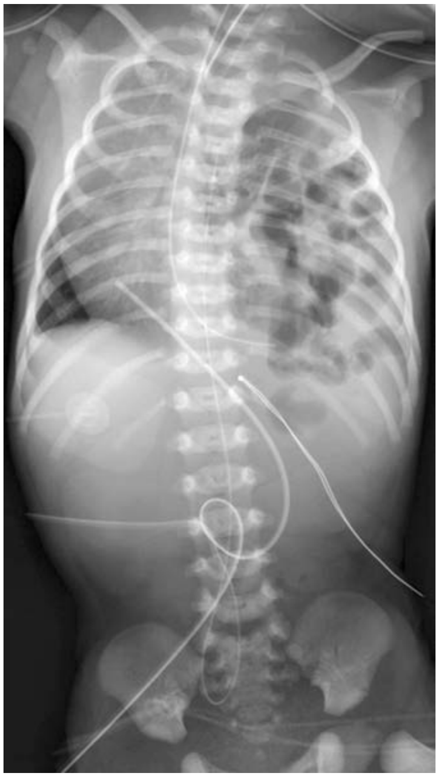

**Figure 61.2. Bochdalek hernia in a newborn.** Radiograph of the chest and abdomen shows multiple air-filled bowel loops in the left hemithorax with cardiomediastinal and umbilical venous line shift to the right and a paucity of bowel gas in the abdomen and a scaphoid abdomen.

**BOX 61.1** Anatomic Classification of Congenital Diaphragmatic Hernias

Posterolateral (Bochdalek)
Parasternal (Morgagni)
Central
Posteromedial
Anterolateral

hypoplasia and pulmonary hypertension. It includes the use of extracorporeal membrane oxygenation, high-frequency ventilation, and inhaled nitric oxide.[13-16] Surgical repair of CDH is performed with a transabdominal or transthoracic approach, and more recently, laparoscopic or thoracoscopic techniques have evolved. The herniated abdominal viscera are removed from the chest and repositioned in the abdomen. The posterolateral diaphragmatic defect is usually closed with nonabsorbable sutures if the defect is small or with a prosthetic patch if the defect is larger than 5 cm.[17,18] Currently no specific guideline exists for following up on children with a repaired CDH. However, chest radiographs often are obtained routinely for confirmation of an intact diaphragm and early detection of a possible CDH recurrence. On follow-up chest radiographs, abnormalities including persistent lung hypoplasia, decreased pulmonary vascularity, and mediastinal shift may be observed.

## Congenital Diaphragmatic Hernia: Morgagni

***Etiology.*** The foramen of Morgagni is an anterior opening in the diaphragm that extends between the sternum medially and the eighth rib laterally. In Morgagni hernias, also known as retrosternal hernias, the underlying congenital defect results from developmental failure of the fibrotendinous elements of the sternal part of the diaphragm to fuse with the costal part.[19-21] They account for 9% to 12% of the diaphragmatic defects in infancy. These hernias usually are unilateral and are right sided in 90% of cases.[10] A Morgagni hernia may occur as one of the components of the pentalogy of Cantrell, which is characterized by omphalocele, anterior diaphragmatic hernia, sternal cleft, ectopia cordis, and intracardiac defect such as a ventricular septal defect or a diverticulum of the left ventricle.[10,21] A Morgagni hernia can be seen in association with congenital heart disease, intestinal malrotation, and chromosomal abnormalities, most frequently Down syndrome.[10,21]

***Imaging.*** Most cases of Morgagni hernias are discovered incidentally on chest radiographs that are obtained for evaluation of other conditions in older children and adults. On chest radiographs, the diagnosis is made when anterior herniation of bowel loops is identified on the lateral chest radiograph (Fig. 61.3). When solid organs such as the liver or spleen are involved, the appearance may not be specific and can resemble focal diaphragmatic eventration, lymphadenopathy, or a foregut duplication cyst. Ultrasound, CT, or MRI can be helpful in the diagnosis when solid organs are herniated.[10,20,21]

***Treatment and Follow-up.*** The current treatment of choice for a Morgagni hernia is surgical repair at the initial diagnosis, even in the absence of symptoms, because of the increased risk of developing bowel obstruction and subsequent incarceration. Most Morgagni hernias can be repaired laparoscopically.[1,10,20,22]

## Delayed Presentation of Congenital Diaphragmatic Hernia

***Etiology.*** Approximately 5% to 20% of pediatric patients may present with a delayed CDH.[23] Although currently it is not clear whether the diaphragmatic defect in these patients is congenital

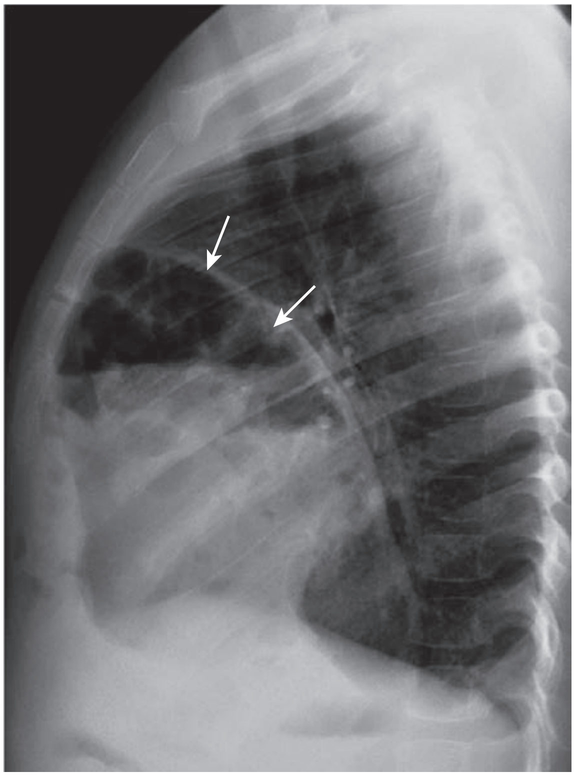

**Figure 61.3. Morgagni hernia in an 8-year-old boy who presented with cough and fever.** Lateral chest radiograph shows multiple bowel loops *(arrows)* projecting in the anterior aspect of the chest.

or acquired, it has been assumed that the defect may have been present prenatally but was either small or temporarily occluded by solid organs such as the liver or spleen.[23,24] In a multicenter retrospective study by the Congenital Diaphragmatic Hernia Study Group,[24] the location, male/female ratio, birth weight, and gestational age all were similar between children with neonatal CDH and infants or children with delayed presentation of CDH. These findings support the assumption that the defect of late-presenting CDH is most likely congenital in nature.[25,26]

Infants with delayed presentation of CDH usually become symptomatic in the first few months of life, often in association with right-sided pneumonia caused by group B streptococcal infection. Initially the hernia may be obscured by consolidative changes. In contrast, the larger group of older children presenting later in life have symptoms of abdominal pain or recurrent vomiting. Approximately two-thirds of this delayed presentation of CDH occurs on the posterolateral right side (i.e., Bochdalek). Asymptomatic cases discovered incidentally also occur.[23-26]

***Imaging.*** Several studies have shown that delayed presentation of a CDH often can be missed on initial chest radiographs.[23,25] The chest radiograph of a neonate with this type of hernia may be normal in the neonatal period. When only solid organs are herniated, a homogeneous opacity may be seen that can be confused with pneumonia or a pleural effusion (Fig. 61.4). In the case of herniated bowel, tubular air-filled, radiolucent structures projecting into the chest may mimic pneumatoceles or a pneumothorax. Such situations may cause mismanagement such as insertion of a chest tube, which is associated with a potential risk of gastrointestinal perforation or bleeding. A gas-filled herniated stomach may mimic a pneumothorax or a lung abscess. A delayed presentation of an anteriorly located Morgagni hernia, if it is not gas filled, may simulate cardiomegaly or a mediastinal mass.[23-26] A chest radiograph

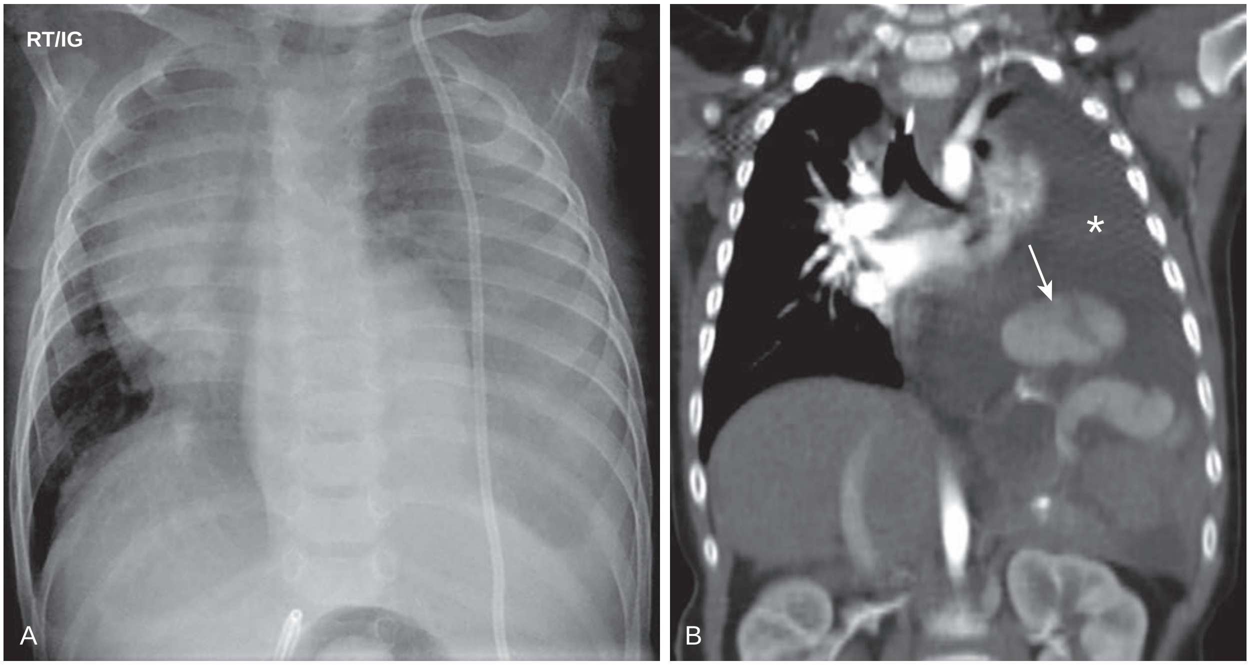

**Figure 61.4. Late-presenting congenital diaphragmatic hernia in a 16-month-old boy with shunted hydrocephalus and vomiting.** (A) Frontal chest radiograph shows an opacity in the left hemithorax without clear visualization of the left hemidiaphragm. Cardiomediastinal shift to the right side is also present. Note a left shunt catheter. (B) Coronal soft tissue window CT image shows a left pleural effusion *(asterisk)* and herniated spleen *(arrow)* into the left hemithorax and poor visualization of the left hemidiaphragm. The left pleural effusion was attributed to a malfunctioning shunt catheter.

after insertion of an NG tube can confirm a late-presenting hernia.[27] An upper gastrointestinal study can be useful if it demonstrates the presence of bowel in the chest; however, it may yield false-negative results in cases of exclusive solid organ herniation. To correctly diagnose a hernia containing only large bowel, it is important to obtain a delayed image during an upper gastrointestinal study. Ultrasound is particularly useful for patients with intrathoracic herniation of only solid organs, or when the hernia mimics a pleural effusion. CT or MRI has the advantage of demonstrating the diaphragmatic defect and herniating mesentery and bowel.[23,26]

***Treatment and Follow-up.*** The treatment of delayed diaphragmatic hernia is surgical, with repositioning of the herniated organs in the abdomen and primary closure of the defect or placement of mesh to patch the defect when it is large. The outcome is generally favorable, but misdiagnosis may result in significant morbidity or death. Gastrointestinal obstruction or volvulus with visceral incarceration is a possible presentation beyond the neonatal period. The role of routine follow-up chest radiographs after surgical repair currently is unclear; however, it may be beneficial for assessing possible recurrence rather than evaluating underlying pulmonary hypoplasia.[25,28,29]

### Eventration

***Etiology.*** *Diaphragmatic eventration* is defined as an abnormal elevation of all or a portion of an attenuated but otherwise intact diaphragmatic leaf. It may be congenital or may develop as a result of paralysis, with the former situation being more common. Congenital diaphragmatic eventration occurs when the fetal diaphragm fails to muscularize, leaving a layer of pleura and peritoneum in that region.[1,30] The focal type of diaphragmatic eventration is more common, most often anteromedially on the right side, whereas the diffuse type tends to be on the left side.[20] Pediatric patients with focal diaphragmatic eventration usually are asymptomatic. With diffuse eventration, an early presentation with respiratory insufficiency due to pulmonary and venous compression by the elevated viscera can be seen.[20,21,31]

***Imaging.*** Focal diaphragmatic eventration, which is a common incidental finding on a chest radiograph, appears as a focal diaphragmatic bulge in the anteromedial side of the right hemithorax (Fig. 61.5).[20,21] Radiographs may show the elevated diaphragm, allowing distinction in some cases from CDH, in which the diaphragm is in a normal position but the intestinal contents have herniated through an opening in the diaphragm.[20,25] After chest radiographs are obtained, ultrasound can be used to exclude a possible underlying mass and also to evaluate the diaphragmatic mobility using M-mode.[21] Total eventration of the diaphragm in older children and adults often is indistinguishable from diaphragmatic paralysis on chest radiographs. A helpful differentiating sign is that an eventration typically will not have adjacent areas of atelectasis, whereas paralysis of the diaphragm will have such areas. During fluoroscopy, an eventrated diaphragm typically displays an inspiratory lag followed by delayed downward motion. However, slight paradoxic movement, little movement, or no movement may occur in cases of an eventrated diaphragm, which sometimes makes the distinction from paralysis challenging.[20,21]

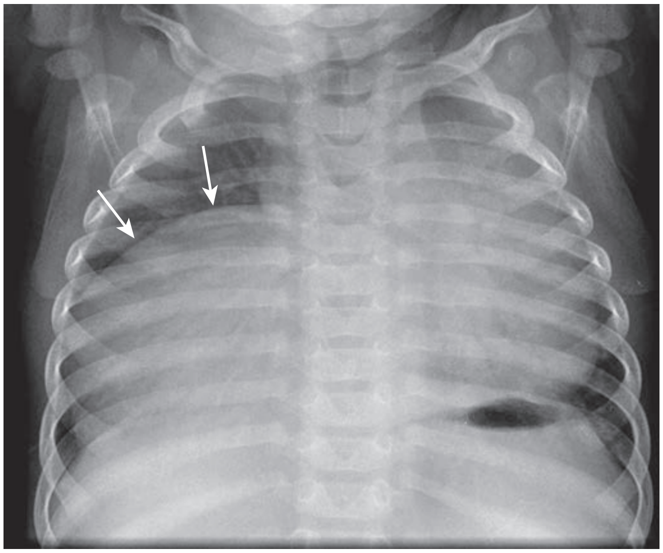

**Figure 61.5. Diaphragmatic eventration in a 2-year-old boy who presented with a cough and fever.** Frontal chest radiograph shows an elevation of the right hemidiaphragm *(arrows).*

***Treatment and Follow-up.*** A focal diaphragmatic eventration generally requires no treatment or follow-up because it is usually of no clinical significance. In pediatric patients with a focal or complete diaphragmatic eventration that causes respiratory distress, the eventration is plicated. Plication involves a folding and subsequent suturing of the eventrated diaphragm to reduce the excess diaphragmatic tissue. The indication for and the timing of surgery are still somewhat controversial.[1,31]

## DIAPHRAGMATIC INJURIES

### Diaphragmatic Paralysis

***Etiology.*** Injury or abnormality of the phrenic nerve leading to diaphragmatic motion abnormalities may occur unilaterally or bilaterally as a result of birth trauma or after surgical interventions, most commonly cardiac surgery.[2] The prevalence of diaphragmatic paralysis is 0.03% to 0.5%.[2] The prevalence after thoracic surgery in children has been reported to range between 0.5% and 10%.[2,32-34] In infants, diaphragmatic paralysis may result in life-threatening respiratory insufficiency and ventilatory failure. Unexplained difficulty in weaning a patient from mechanical ventilation or an increasing oxygen requirement should raise the suspicion of diaphragmatic paralysis.[21,33]

***Imaging.*** Diaphragmatic paralysis usually is suggested on chest radiographs when they show persistent elevation of the affected hemidiaphragm. However, the position of the diaphragm may not be reliable in the newborn period. Fluoroscopic assessment of diaphragmatic motion, which previously was commonly obtained, largely has been replaced by ultrasound. Ultrasound with the use of M-mode is superior to fluoroscopy in the evaluation of the diaphragm because of its portability, lack of ionizing radiation, and ability to visualize the entire diaphragm (Fig. 61.6).[33,35] Diaphragmatic movement is considered normal if the diaphragm moves toward the transducer during inspiration, with excursion of greater than 4 mm and a difference in excursion between the domes of less than 50%.[20,21,32-34]

***Treatment and Follow-up.*** The initial treatment of patients with diaphragmatic paralysis is supportive, which includes positioning the affected patients ipsilateral to the affected side and providing oxygen and mechanical ventilation in cases of respiratory failure.[2,36] After 30 days of unsuccessful noninvasive treatment, plication usually is needed, especially in patients younger than 1 year and those with iatrogenic injuries of the phrenic nerve.[1,2,21,37]

### Diaphragmatic Rupture

***Etiology.*** Diaphragmatic rupture, which is rare in children, typically occurs after a blunt or penetrating trauma. In one large study, the incidence of traumatic diaphragmatic rupture was found to be 0.07%, with a mean age of 7.5 years.[38] It was slightly more frequent in boys and occurred more commonly as a result of blunt, rather than penetrating, trauma.[38] Associated injuries such as a

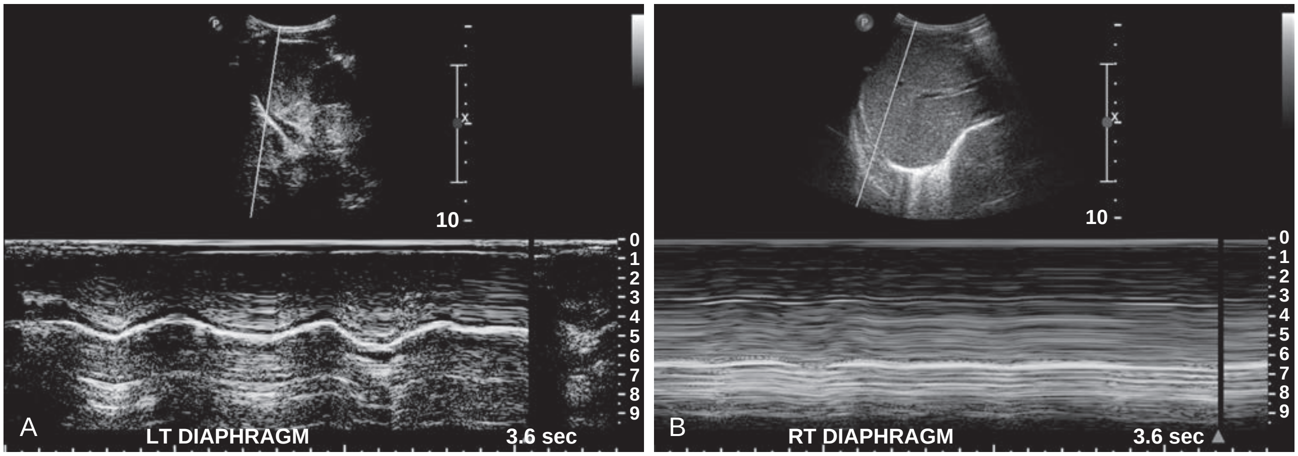

**Figure 61.6. Diaphragmatic paralysis in a 10-month-old boy after tetralogy of Fallot repair who was unable to be weaned from the ventilator.** (A) Longitudinal M-mode sonogram of the left hemidiaphragm reveals a normal diaphragmatic motion. (B) Longitudinal M-mode sonogram of the right hemidiaphragm reveals a flat waveform, indicating no diaphragmatic motion.

head injury, pelvic fractures, and splenic and renal injuries are common. However, isolated diaphragmatic injuries have been reported more often in children than in adults. Diaphragmatic rupture is more common on the left than on the right. The left-sided predominance probably is the result of a protective effect by the liver on the right diaphragm.[39] Because of its rarity, the correct diagnosis of diaphragmatic rupture often is delayed or missed; this may lead to bowel herniation, obstruction, and ischemia.[38]

***Imaging.*** Diaphragmatic rupture in children is difficult to detect clinically and on imaging, and it requires a high index of suspicion.[38-40] Several studies show that chest radiographs have suggestive findings in 64% to 77% of cases; however, they are diagnostic in only 25% to 50% of cases.[40] Nonspecific but suggestive imaging findings of diaphragmatic rupture on chest radiographs include (1) an archlike soft tissue opacity in the lower chest; (2) unusual densities or gas bubbles resulting from bowel herniation; and (3) atelectasis, pleural effusions, and a mediastinal shift to the nonaffected side.[40] Imaging findings considered diagnostic of a diaphragmatic rupture after trauma are the presence of herniated abdominal organs (e.g., bowel loops or solid organs) and an NG tube in the chest (Fig. 61.7).[40] CT, especially coronal reformations, may confirm the diagnosis of diaphragmatic rupture by showing irregularity and thickening of the diaphragmatic leaflet and herniated abdominal organs.[39,40] Fluoroscopy and contrast studies have limited use in the acute setting.[41]

***Treatment and Follow-up.*** The treatment of diaphragmatic rupture is surgical, whether the patient presents in the acute or delayed setting. Repair of the acute traumatic diaphragmatic rupture is directed by the concomitant injuries. Small defects are repaired by direct suturing, whereas larger defects are patched with mesh.[1,39] Although fluoroscopy plays little role in the preoperative diagnosis of diaphragmatic rupture, it can be useful in assessing the diaphragm after repair to evaluate diaphragmatic motion and hernia recurrence.

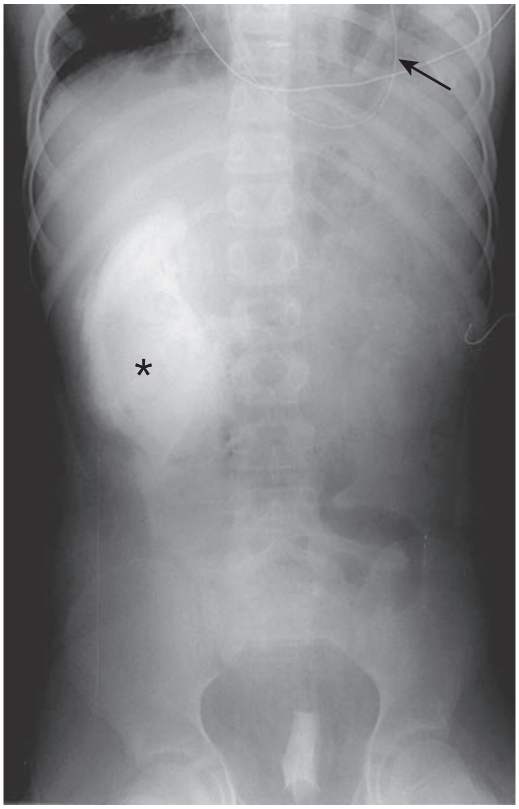

**Figure 61.7. Diaphragmatic rupture in a 5-year-old boy who fell from playground equipment.** Abdominal radiograph shows obliteration of the left hemidiaphragm with soft tissue and lucencies projecting in the left base. The tip *(arrow)* of a nasogastric tube projects in the chest, confirming a left diaphragmatic rupture. The hyperdensity in the right flank is due to perinephric intravenous contrast extravasation as a result of a shattered kidney *(asterisk)*.

## DIAPHRAGMATIC NEOPLASMS

***Etiology.*** Primary diaphragmatic tumors are very rare.[21] In a study by Cada and colleagues,[41] 41 cases were found in patients younger than 18 years with equal gender frequency and a mean age at diagnosis of 10 years. Most diaphragmatic tumors are malignant, with rhabdomyosarcoma being the most common tumor found in the diaphragm.[21,42] Other primary diaphragmatic malignant tumors in children are undifferentiated sarcomas, germ cell tumors, and the Ewing sarcoma family of tumors.[21,42-44] Secondary involvement of the diaphragm by adjacent malignant tumors also can occur.[21,42] Benign tumors include neurofibromas, lipomas, myofibroblastic tumors, and hemangiomas.[21] Cystic lesions (not necessarily neoplasms) involving the diaphragm include mesothelial cysts, bronchogenic cysts, cystic teratomas, and hydatid cysts.[21,45]

Affected patients, especially those with benign lesions, usually are asymptomatic and the diagnosis of diaphragmatic neoplasm is made incidentally as part of unrelated imaging, at surgery, or even at autopsy. Patients with a large or malignant diaphragmatic tumor usually present with symptoms such as chest pain, cough, dyspnea, nausea, vomiting, and dysphagia.[21,42,44] An exophytic, large diaphragmatic tumor also may be palpable on physical examination.

***Imaging.*** The greatest challenge in assessing a diaphragmatic tumor is determining its exact site of origin. Especially with right-sided lesions, the site of origin frequently has been mistakenly assigned to the liver. No single imaging modality has demonstrated superiority in diagnosing diaphragmatic tumors, and frequently a combination of ultrasound, CT, and MRI is necessary for a correct diagnosis.[21,42] The majority of malignant tumors present as large masses with advanced local disease or metastasis to the pleura and lung.[43] The claw sign, the pattern of organ displacement, and the presence of an obtuse angle between the tumor and the diaphragm may help determine diaphragmatic origin (Fig. 61.8).[42] Not infrequently, the diaphragmatic origin of the tumor becomes more evident after size reduction after chemotherapy. In cases of a palpable mass or a mass seen on chest or abdominal radiographs, ultrasound may be the initial study of choice to begin the investigation.

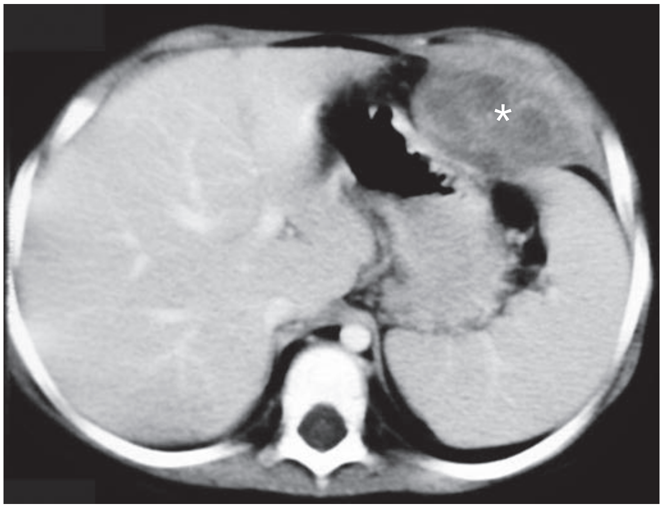

**Figure 61.8. Germ cell tumor of the diaphragm in a 7-year-old boy with a palpable mass.** Axial CT image at the thoracoabdominal junction shows a heterogeneous anteriorly located mass *(asterisk)* with obtuse angles in relation to the diaphragm.

***Treatment and Follow-up.*** After imaging studies, a definitive diagnosis of diaphragmatic tumors can be made on the basis of histopathologic evaluation of a biopsy specimen. Once a histopathologic diagnosis is made, chemotherapy usually is instituted to reduce the size before surgical resection. Adjuvant preoperative radiation therapy may help in cases of infiltrative tumors. Germ cell tumors may go into remission after chemotherapy because of their high chemosensitivity.[21,42,43]

## KEY POINTS

- The Bochdalek hernia, which involves the posterolateral aspect of the diaphragm, is the most common subtype, accounting for approximately 90% to 95% of all CDHs.
- The clinical presentation of late-onset CDH is varied and may require multiple imaging modalities to reach a diagnosis.
- Ultrasound with M-mode is the imaging modality of choice to evaluate diaphragmatic paralysis and motion.
- The diagnosis of diaphragmatic rupture is usually delayed because of its rarity and multiple associated injuries, and it requires a high index of suspicion.
- Primary diaphragmatic tumors are very rare in children. Most diaphragmatic tumors are malignant, with rhabdomyosarcoma being the most common diaphragmatic tumor.

## SUGGESTED READINGS

Baglaj M, Dorobisz U. Late presenting congenital diaphragmatic hernia in children: a literature review. *Pediatr Radiol*. 2005;35:478–488.

Chavhan GB, Babyn PS, Chohen RA, et al. Multimodality imaging of the pediatric diaphragm: anatomy and pathologic conditions. *Radiographics*. 2010;30:1797–1817.

Ramos CT, Koplewitz BZ, Babyn PS, et al. What have we learned about traumatic diaphragmatic hernias in children? *J Pediatr Surg*. 2000;35:601–604.

Schumpelick V, Steinau G, Schluper I, et al. Surgical embryology and anatomy of the diaphragm with surgical applications. *Surg Clin North Am*. 2000;80:213–239.

## REFERENCES

Full references for this chapter can be found on www.expertconsult.com.

## REFERENCES

1. Maish MS. The diaphragm. *Surg Clin North Am*. 2010;90(5):955–968.
2. Schumpelick V, Steinau G, Schluper I, et al. Surgical embryology and anatomy of the diaphragm with surgical applications. *Surg Clin North Am*. 2000;80(1):213–239.
3. Hidalgo A, Franquet T, Gimenez A. 16-MDCT and MR angiography of accessory diaphragm. *AJR Am J Roentgenol*. 2006;187(1):149–152.
4. Mata JM, Caceres J. The dysmorphic lung: imaging findings. *Eur Radiol*. 1996;6(4):403–414.
5. Pober BR. Overview of epidemiology, genetics, birth defects, and chromosome abnormalities associated with CDH. *Am J Med Genet C Semin Med Genet*. 2007;145C(2):158–171.
6. Skari H, Bjornland K, Haugen G, et al. Congenital diaphragmatic hernia: a meta-analysis of mortality factors. *J Pediatr Surg*. 2000;35(8):1187–1197.
7. Keijzer R, Puri P. Congenital diaphragmatic hernia. *Semin Pediatr Surg*. 2010;19(3):180–185.
8. McGivern MR, et al. Epidemiology of congenital diaphragmatic hernia in Europe: a register-based study. *Arch Dis Child Fetal Neonatal Ed*. 2015;100(2):F137–F144.
9. Taylor GA, Atalabi OM, Estroff JA. Imaging of congenital diaphragmatic hernias. *Pediatr Radiol*. 2009;39(1):1–16.
10. Sakurai M, Donnelly LF, Klosterman LA, et al. Congenital diaphragmatic hernia in neonates: variations in umbilical catheter and enteric tube position. *Radiology*. 2000;216(1):112–116.
11. Donahoe PK, Longoni M, High FA. Polygenic causes of congenital diaphragmatic hernia produce common lung pathologies. *Am J Pathol*. 2016;186(10):2532–2543.
12. Holt PD, Arkovitz MS, Berdon WE, et al. Newborns with diaphragmatic hernia: initial chest radiography does not have a role in predicting clinical outcome. *Pediatr Radiol*. 2004;34(6):462–464.
13. Morini F, Goldman A, Pierro A. Extracorporeal membrane oxygenation in infants with congenital diaphragmatic hernia: a systematic review of the evidence. *Eur J Pediatr Surg*. 2006;16(6):385–391.
14. Chao PH, et al. Congenital diaphragmatic hernia in the neonatal period: review of 21 years' experience. *Pediatr Neonatol*. 2010;51(2):97–102.
15. Shah SR, et al. Minimally invasive congenital diaphragmatic hernia repair: a 7-year review of one institution's experience. *Surg Endosc*. 2009;23(6):1265–1271.
16. Puligandla PS, et al. Management of congenital diaphragmatic hernia: a systematic review from the APSA outcomes and evidence based practice committee. *J Pediatr Surg*. 2015;50(11):1958–1970.
17. Bagolan P, Morini F. Long-term follow up of infants with congenital diaphragmatic hernia. *Semin Pediatr Surg*. 2007;16(2):134–144.
18. Zhu Y, Wu Y, Pu Q, et al. Minimally invasive surgery for congenital diaphragmatic hernia: a meta-analysis. *Hernia*. 2016;20(2):297–302.
19. Roberts HC. Imaging the diaphragm. *Thorac Surg Clin*. 2009;19(4):431–450.
20. Chavhan GB, Babyn PS, Cohen RA, et al. Multimodality imaging of the pediatric diaphragm: anatomy and pathologic conditions. *Radiographics*. 2010;30(7):1797–1817.
21. Baglaj M, Dorobisz U. Late-presenting congenital diaphragmatic hernia in children: a literature review. *Pediatr Radiol*. 2005;35(5):478–488.
22. Al-Salem AH, Zamakhshary M, Al Mohaidly M, et al. Congenital Morgagni's hernia: a national multicenter study. *J Pediatr Surg*. 2014;49(4):503–507.
23. Kitano Y, Lally KP, Lally PA. Late-presenting congenital diaphragmatic hernia. *J Pediatr Surg*. 2005;40(12):1839–1843.
24. Elhalaby EA, Abo Sikeena MH. Delayed presentation of congenital diaphragmatic hernia. *Pediatr Surg Int*. 2002;18(5–6):480–485.
25. Cigdem MK, Onen A, Otcu S, et al. Late presentation of bochdalek-type congenital diaphragmatic hernia in children: a 23-year experience at a single center. *Surg Today*. 2007;37(8):642–645.
26. Berman L, Stringer D, Ein SH, et al. The late-presenting pediatric Bochdalek hernia: a 20-year review. *J Pediatr Surg*. 1988;23(8):735–739.
27. Ayala JA, Naik-Mathuria B, Olutoye OO. Delayed presentation of congenital diaphragmatic hernia manifesting as combined-type acute gastric volvulus: a case report and review of the literature. *J Pediatr Surg*. 2008;43(3):E35–E39.
28. Groth SS, Andrade RS. Diaphragmatic eventration. *Thorac Surg Clin*. 2009;19(4):511–519.
29. Kim DJ, Chung JH. Late-presenting congenital diaphragmatic hernia in children: the experience of single institution in Korea. *Yonsei Med J*. 2013;54(5):1143–1148.
30. Yazici M, et al. Congenital eventration of the diaphragm in children: 25 years' experience in three pediatric surgery centers. *Eur J Pediatr Surg*. 2003;13(5):298–301.
31. Oh A, Gulati G, Sherman ML, et al. Bilateral eventration of the diaphragm with perforated gastric volvulus in an adolescent. *J Pediatr Surg*. 2000;35(12):1824–1826.
32. Epelman M, Navarro OM, Daneman A, et al. M-mode sonography of diaphragmatic motion: description of technique and experience in 278 pediatric patients. *Pediatr Radiol*. 2005;35(7):661–667.
33. Urvoas E, Pariente D, Fausser C, et al. Diaphragmatic paralysis in children: diagnosis by TM-mode ultrasound. *Pediatr Radiol*. 1994;24(8):564–568.
34. Celli BR. Respiratory management of diaphragm paralysis. *Semin Respir Crit Care Med*. 2002;23(3):275–281.
35. Kharma N. Dysfunction of the diaphragm: imaging as a diagnostic tool. *Curr Opin Pulm Med*. 2013;19(4):394–398.
36. Tonz M, von Segesser LK, Mihaljevic T, et al. Clinical implications of phrenic nerve injury after pediatric cardiac surgery. *J Pediatr Surg*. 1996;31(9):1265–1267.
37. Ramos CT, Koplewitz BZ, Babyn PS, et al. What have we learned about traumatic diaphragmatic hernias in children? *J Pediatr Surg*. 2000;35(4):601–604.
38. Shehata SM, Shabaan BS. Diaphragmatic injuries in children after blunt abdominal trauma. *J Pediatr Surg*. 2006;41(10):1727–1731.
39. Koplewitz BZ, Ramos C, Manson DE, et al. Traumatic diaphragmatic injuries in infants and children: imaging findings. *Pediatr Radiol*. 2000;30(7):471–479.
40. Iochum S, Ludig T, Walter F, et al. Imaging of diaphragmatic injury: a diagnostic challenge? *Radiographics*. 2002;22:Spec No, pp. S103–116.
41. Cada M, Gerstle JT, Traubici J, et al. Approach to diagnosis and treatment of pediatric primary tumors of the diaphragm. *J Pediatr Surg*. 2006;41(10):1722–1726.
42. Raney RB, Anderson JR, Andrassy RJ, et al. Soft-tissue sarcomas of the diaphragm: a report from the Intergroup Rhabdomyosarcoma Study Group from 1972 to 1997. *J Pediatr Hematol Oncol*. 2000;22(6):510–514.
43. Traubici J, Daneman A, Hayes-Jordan A, et al. Primary germ cell tumor of the diaphragm. *J Pediatr Surg*. 2004;39(10):1578–1580.
44. Esparza Estaun J, Gonzalez Alfageme A, Saenz Banuelos J. Radiological appearance of diaphragmatic mesothelial cysts. *Pediatr Radiol*. 2003;33(12):855–858.
45. Akinci D, Akhan O, Ozmen M, et al. Diaphragmatic mesothelial cysts in children: radiologic findings and percutaneous ethanol sclerotherapy. *AJR Am J Roentgenol*. 2005;185(4):873–877.

## PART 1 Overview

# 62 Introductory Embryology

James René Herlong

## CARDIAC DEVELOPMENT

The major task in cardiac development is to form a four-chambered heart that functions in a coordinated fashion from a straight tube that functions merely by peristalsis. Cardiac development can be thought of as proceeding along various phases: fusion of myocardium and endocardium in the ventral midline to form a simple tube, onset of function, looping to the right side, specification and formation of chambers, development of specialized conduction tissue, formation of the coronary circulation, innervation of the heart, and formation of mature valves. The approximate times at which these various events occur in human development are shown in Table 62.1.

Three main groups of cells contribute to the morphogenesis of the heart. These main groups are the mesoderm of the primary heart fields (located in the splanchnic layer of lateral plate mesoderm bilaterally), the secondary heart fields (located in the pharyngeal mesenchyme), and the cardiac neural crest (a subdivision of the cranial portion of the neural crest). These tissues and their roles in the developing heart are illustrated in e-Fig. 62.1, along with the two important extracardiac populations of cells described later in this chapter.

The first stage in the development of the heart is the formation of a single midline heart tube from the bilateral cardiogenic fields (e-Fig. 62.2). The heart begins to beat even at this single tubular stage. Cells are then added to each end of the heart tube, and the tube begins to loop to the right. During looping, the tube is further lengthened by the addition of cells from the secondary heart field to the outflow pole. Looping and convergence bring the inflow and outflow poles of the heart into proximity (Fig. 62.3), setting the stage for septation and definitive chamber formation. The traditional names of the various segments of the recently looped heart are illustrated in e-Fig. 62.4. Note that the heart in this configuration is set up to become a double-inlet left ventricle and a double-outlet right ventricle; if septation proceeds properly, these forms of congenital heart disease are avoided. Formation of a four-chamber heart requires the right ventricle to obtain an inlet and the left ventricle to obtain an outlet.

The atrioventricular canal of the heart is divided into right and left sides by endocardial cushions that develop at the atrioventricular junction and ultimately form the septum of the atrioventricular canal and the atrioventricular valves (Fig. 62.5). The right atrioventricular canal and right ventricle expand to the right, and the atria are septated from one another. Septum primum, the primary atrial septum, is led by the spina vestibuli (vestibular spine) and ultimately fuses with the endocardial cushions to close the first interatrial communication or ostium primum. As the septum primum is growing, fenestrations begin to develop within it. These fenestrations coalesce to form the secondary interatrial communication, or ostium secundum (see Fig. 62.5). A second septum, or septum secundum, forms to the right of the septum primum much later, and postnatal fusion of the two septa obliterates any interatrial communication. Note that septum primum is ultimately a left atrial structure and that septum secundum is considered a right atrial structure, even though it expresses left-sided molecular markers. Note further that, in the common parlance of naming atrial septal defects, the defect is named for the embryonic ostium that persists, not for the embryonic tissue in which the defect exists. Thus, for example, a secundum atrial septal defect is persistence of the embryonic ostium secundum, even though the defect itself is most often in the septum primum. This naming practice is one of the more confusing points in the nomenclature of congenital heart disease.

Just as the atria and the atrioventricular canal portions of the heart are septated, so are the ventricles. The muscular ventricular septum arises from the deepest convexity of the cardiac loop and grows toward the atrioventricular septum. The membranous septum ultimately will bridge the gap between these two portions of the septum. The outlet, conal, or infundibular septum (i.e., the portion of the septum that ultimately will lie just below the semilunar valves and between the outflow tracts) forms from the conal cushions. Initially it is mesenchymal and only later muscularizes. Ventricular septal defects tend to occur at the locations where these various primordia of the ventricular septum fuse.

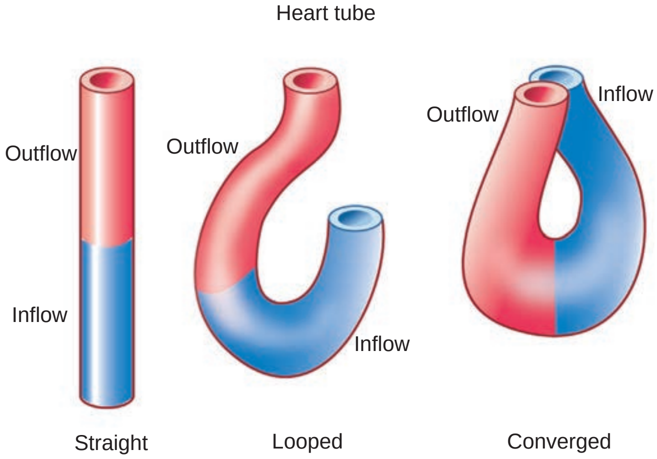

**Figure 62.3.** The heart tube begins as a straight midline tube with blood entering caudally via the inflow tract and exiting cranially via the outflow tract. Under normal circumstances, the tube loops to the right, creating an inflow limb *(blue)* and an outflow limb *(red)*. The distal extremities of the inflow and outflow limbs grow toward each other in a process called *convergence*. Convergence is necessary before septation can create a four-chambered heart. *(From Kirby ML.* Cardiac development. *New York: Oxford University Press; 2006.)*

## Abstract:

This chapter describes the development of the heart from straight tube to fully differentiated heart. Embryonic tissues and mechanisms responsible for heart development are detailed. The chapter then describes development of the vascular system. Remodeling of embryonic vascular networks into definitive vasculature is demonstrated.

## Keywords:

Cardiac Development
Cardiac Embryology
Vascular Development
Vascular Embryology
Cardiac Looping
Proepicardium
Neural Crest

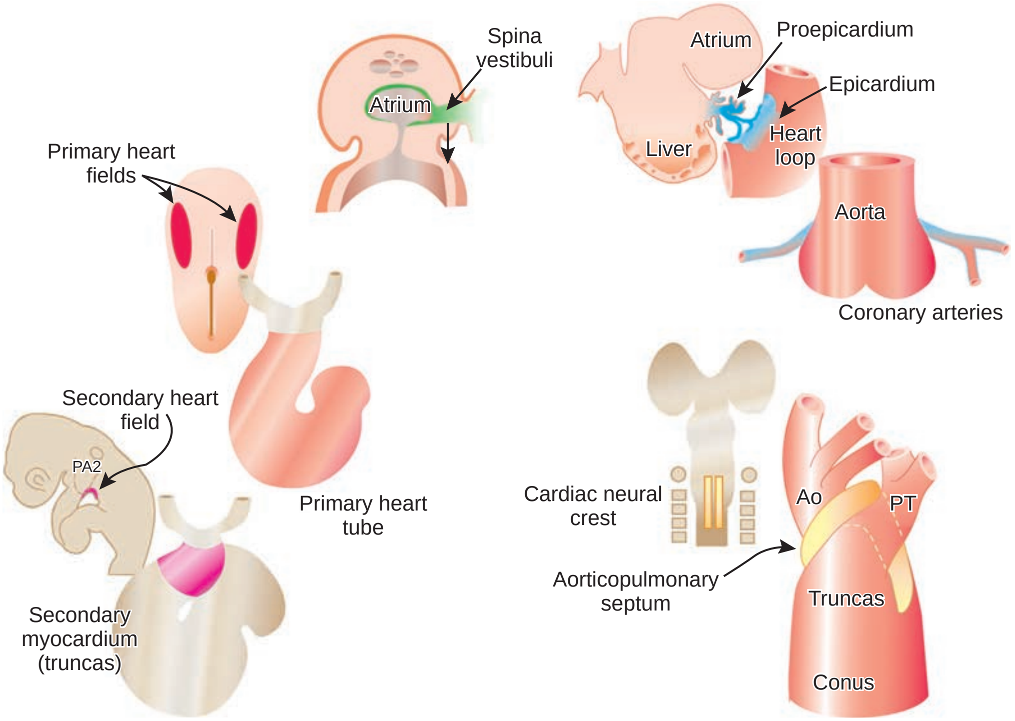

**e-Figure 62.1.** The main groups of cells that contribute to morphogenesis of the heart and their roles. *Ao,* Aorta; *PT,* pulmonary trunk. *(From Kirby ML.* Cardiac development*. New York: Oxford University Press; 2006.)*

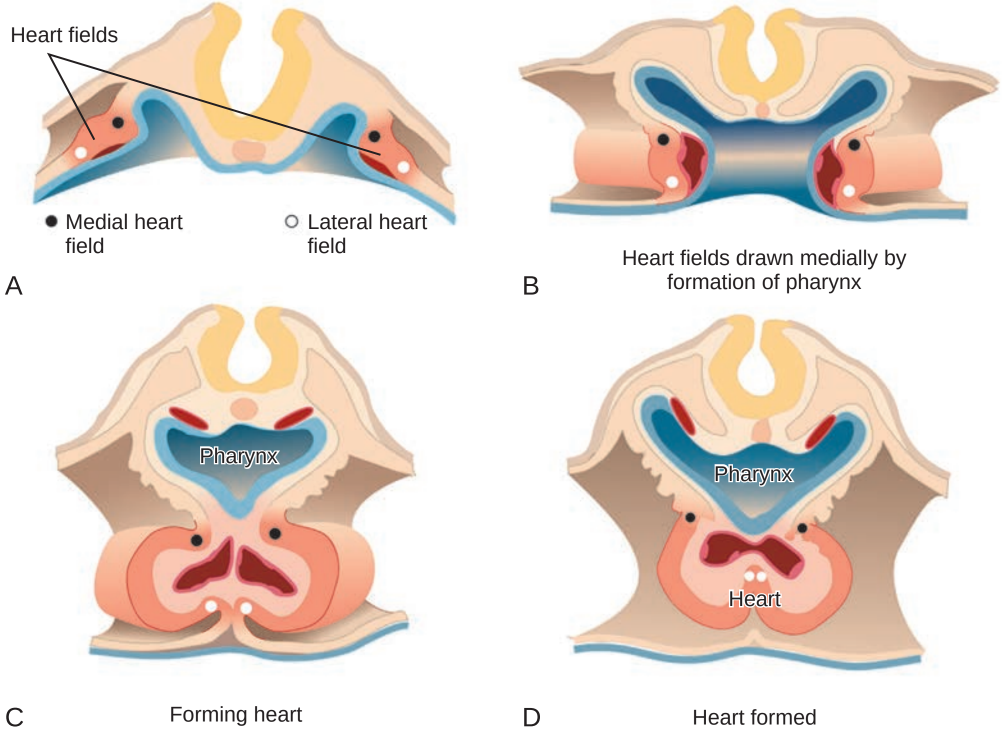

**e-Figure 62.2.** Steps in development of the bilateral cardiogenic fields in the splanchnic mesoderm into a single midline heart tube (A–D). Formation of the midline heart tube depends on formation of the foregut pocket that forms the pharynx. The myocardial trough (C and D) already shows three layers: cellular endocardial and myocardial layers with an acellular layer of cardiac jelly in between. *(From Kirby ML.* Cardiac development*. New York: Oxford University Press; 2006.)*

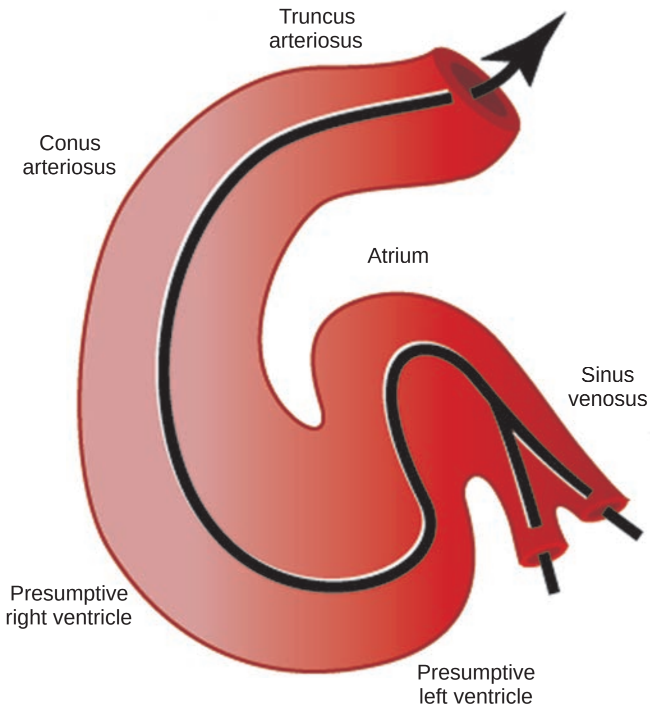

**e-Figure 62.4.** Traditional names of the various parts of the tubular heart. *(From Kirby ML.* Cardiac development*. New York: Oxford University Press; 2006.)*

The aorticopulmonary septum is derived from the cardiac neural crest and functions to separate the aortic sac into the aorta and pulmonary artery and to separate the truncus into the aortic and pulmonic valve orifices. This septum is contiguous proximally with the conal septum. The aorticopulmonary septation complex segregates the ventricular outflows from one another just as the septation of the atrioventricular canal segregates the ventricular inflows.

**TABLE 62.1** Timing of the Onset of Various Events in Human Cardiovascular Development

| Event | Gestational Age (wk) |
|---|---|
| Formation of a heart tube | 3 |
| Aortic arches form | 3 |
| Onset of function | 4 |
| Looping | 4 |
| Onset of chamber septation | 5 |
| Development of specialized conduction tissue | 5 |
| Formation of the coronary circulation | 5–6 |
| Onset of innervation of the heart | 7–8 |
| Formation of mature valves | 10 |
| Definitive venous system established | 12 |

The cardiac electrical system, which is composed of pacemaking cells and a specialized conduction system, develops from regions of specialized myocardial cells that are set aside from working myocardium for this purpose. One of the most important processes involved in the electrical coordination of cardiac function is the electrical isolation of the atria from the ventricles by the fibrous skeleton of the heart. Only the penetrating bundle of His normally electrically connects (via muscle to muscle) the atria and the ventricles. This atrioventricular discontinuity is established by the incorporation of nonmyocardial tissue into the atrioventricular junction.

The epicardium of the heart is derived from an extracardiac population of cells known as the proepicardium. These cells come from the mesenchyme of the septum transversum or liver and literally jump across the coelomic cavity to reach the heart (see e-Fig. 62.1). The proepicardium not only forms the definitive epicardium of the heart but also the endothelium and smooth muscles of the coronary arteries, as well as the connective tissue of the heart. The formation of the coronary arteries and the connective tissue of the heart is made possible by a process known

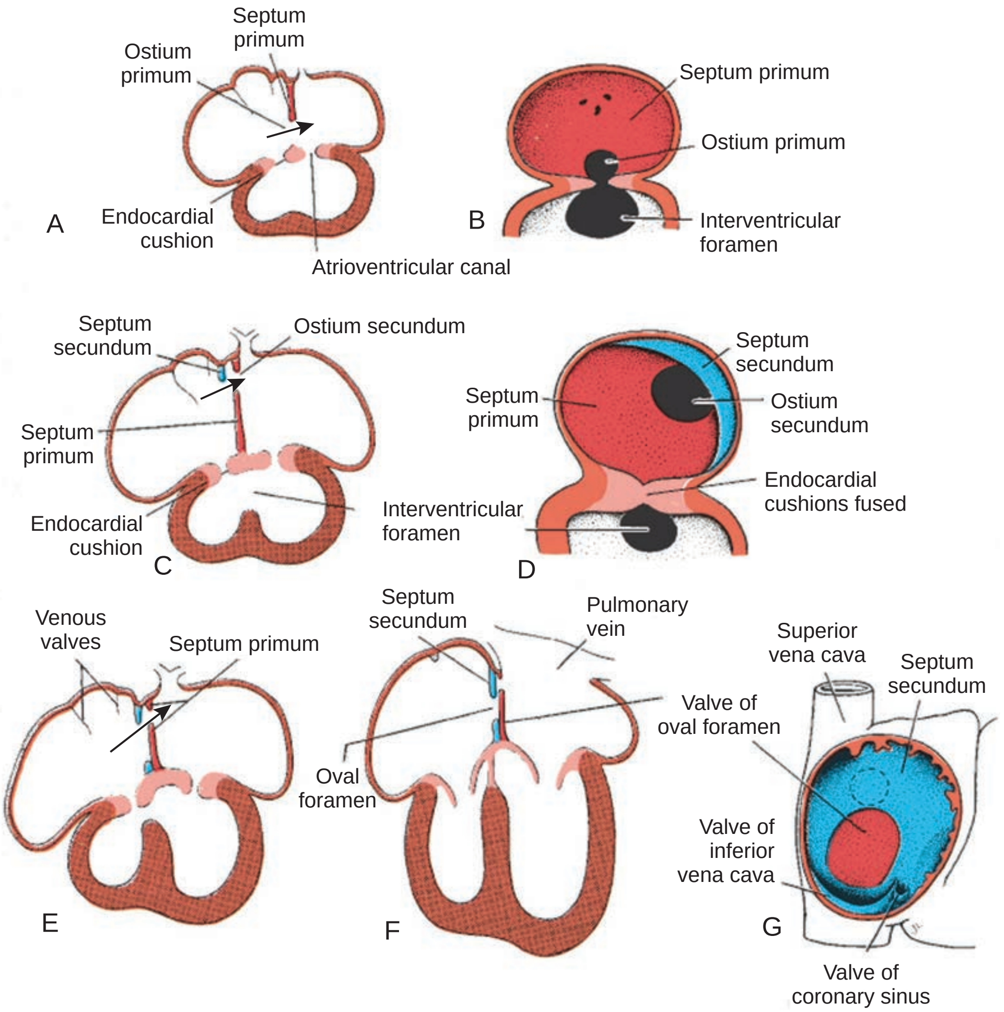

**Figure 62.5. Development of the atrial septum.** (A) Cross-sectional and (B) en face from the right atrium show the atrial septum at 30 days of gestation. (C) Cross-sectional and (D) en face from the right atrium show the atrial septum at 33 days of gestation. (E) The atrial septum at 37 days of gestation. (F) Cross-sectional and (G) en face from the right atrium show the atrial septum immediately after birth. *(From Sadler T.* Langman's medical embryology*. 10th ed. Philadelphia: Lippincott Williams & Wilkins; 2004.)*

as epithelial to mesenchymal transformation. The epicardium of the outflow tract is distinct from that of the remainder of the heart and is derived from the splanchnic mesoderm of the ventral pharynx. Because of the diversity of cells that the proepicardium provides, many investigators consider the proepicardium to be an important potential source of cardiac stem cells.

Before the development of the coronary arteries, the loosely packed myocardium of the embryonic heart is nourished from the cavities by sinusoids. As the myocardium becomes more compact, arteries and veins develop within the epicardial layer, with the intramyocardial circulation developing within the myocardium itself. The arterial channels then grow into the developing aortic valvar sinuses to form true coronary arteries arising from the aorta.

Innervation of the heart is a late development and is not complete until well after birth. Parasympathetic ganglia are intrinsic to the heart and develop from the cardiac neural crest. Sympathetic ganglia are paravertebral and develop from the truncal neural crest. All postganglionic neurons develop from the cardiac neural crest.

The final step in cardiac development is sculpting of the endocardial cushions at the ventricular inflow and outflow to form functional valves. This process occurs at the atrioventricular junction by undermining of the cell layers just underneath the luminal cells to free the leaflets from the myocardium and to create the support apparatus (papillary muscles and chordae tendineae) of the valves. At the ventriculoarterial junction, the sculpting occurs distal to the cushions themselves, and no such support apparatus is formed.

## VASCULAR DEVELOPMENT

The arteries and veins are developed by a combination of vasculogenesis and angiogenesis. Vasculogenesis occurs first to form the major arteries and veins, and vessels sprout from these larger vessels by angiogenesis. The vasculature of the embryo begins as a bilaterally symmetric system of arteries and veins. This symmetry is maintained in the head and limbs as well as in the derivatives of the somites and spinal cord.

The central vessels, however, lose their symmetry and are extensively remodeled. The great arteries begin as bilaterally symmetric, paired arch arteries that connect the ventral aortic sac to the bilateral dorsal aortae. These symmetrical arch arteries undergo involution and remodeling to form the aortic arch, arch vessels, main and branch pulmonary arteries, and the ductus arteriosus (e-Fig. 62.6). This patterning is supported by cells from the cardiac neural crest. Abnormal arterial remodeling leads to aberrant origins of arch arteries and to vascular rings. To understand the embryonic origin of various arch anomalies, it is useful to consider a “totipotential arch” that includes all the relevant arch arteries and imagine how this arch may be “cut” to produce each anomaly. The “totipotential arch” is a theoretic construct. Such an arch never exists in fetal life; because of involution and remodeling, all of the represented components never exist simultaneously. However, the concept (illustrated in Fig. 62.7) is quite useful in understanding how various arch anomalies occur and which of them produce vascular rings.

The embryonic venous system is also extensively remodeled. Originally there are bilaterally symmetric vitelline, umbilical, and cardinal systems. The original systems drain to ipsilateral horns of the sinus venosus portion of the developing heart. Because the left sinus horn regresses and systemic venous return is directed solely to the right atrium, the left system of veins must involute or form anastomotic connections with the right system. The inferior vena cava is composed of elements of four separate systems (e-Fig. 62.8). When the inferior vena cava is interrupted, as in cases of the polysplenic form of heterotaxy, bilateral symmetry of all but the intrahepatic portion is largely maintained. The inferior venous drainage then proceeds to one or both superior venae cavae via azygous or hemiazygous veins.

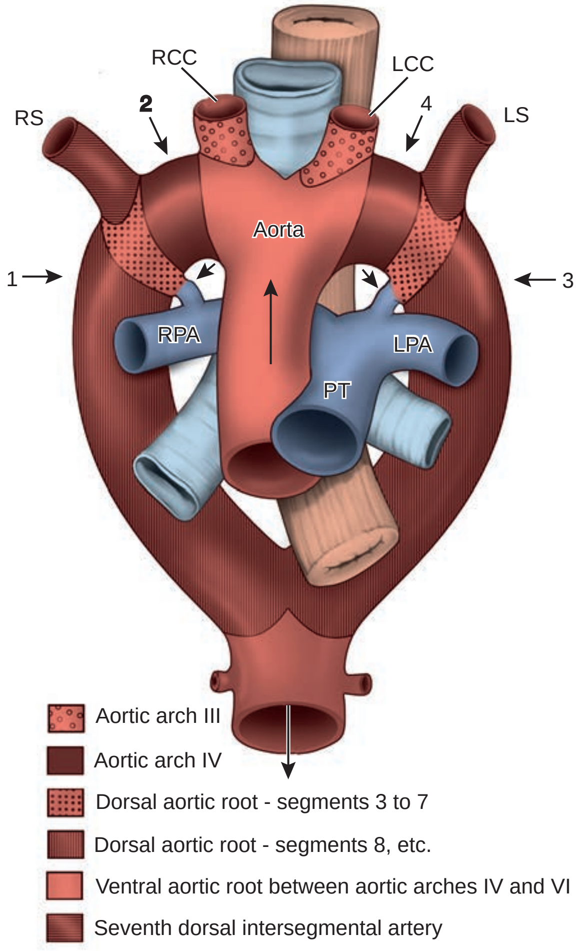
RCC
LCC
2
4
RS
LS
Aorta
1
3
RPA
LPA
PT
Aortic arch III
Aortic arch IV
Dorsal aortic root - segments 3 to 7
Dorsal aortic root - segments 8, etc.
Ventral aortic root between aortic arches IV and VI
Seventh dorsal intersegmental artery

**Figure 62.7. Totipotential arch.** Ventral view of Dr. Jesse Edward’s “totipotential arch” or hypothetic double aortic arch and bilateral ductus arteriosi. The *numbered arrows* point to the four key locations where regression occurs in various anomalies. *Arrow 1* indicates the eighth segment of the right dorsal aortic root; *arrow 2,* the right fourth arch; and *arrows 3 and 4,* the corresponding two positions on the left. The *small black arrows* point to the ductus arteriosi bilaterally, and the *larger black arrows* indicate the direction of blood flow. *LCC,* Left subclavian artery; *LPA,* left pulmonary artery; *LS,* left subclavian artery; *PT,* pulmonary trunk; *RCC,* right common carotid artery; *RPA,* right pulmonary artery; *RS,* right subclavian artery. *(From Stewart JR, Kincaid OW, Edwards JE.* An atlas of vascular rings and related malformations of the aortic arch system*. Springfield, IL: Charles C. Thomas; 1964.)*

The head and neck veins derive from the anterior cardinal veins. The left anterior cardinal vein involutes, and anastomotic channels drain the left head, neck, and arm to the remnants of the right anterior cardinal system and ultimately to the heart by the right superior vena cava. A persistent left superior vena cava is a common variant of normal. This vein drains into the coronary sinus, which is a remnant of the left horn of the sinus venosus.

The pulmonary veins form from fusion of the veins developing in the mesoderm surrounding the bronchial buds with the common pulmonary vein that develops as an evagination of the developing left atrium. Before this fusion, connections of the developing pulmonary veins to the systemic venous system are formed. These connections persist as “vertical veins” when atresia of the common pulmonary vein occurs, a condition known more commonly as totally anomalous pulmonary venous connection.

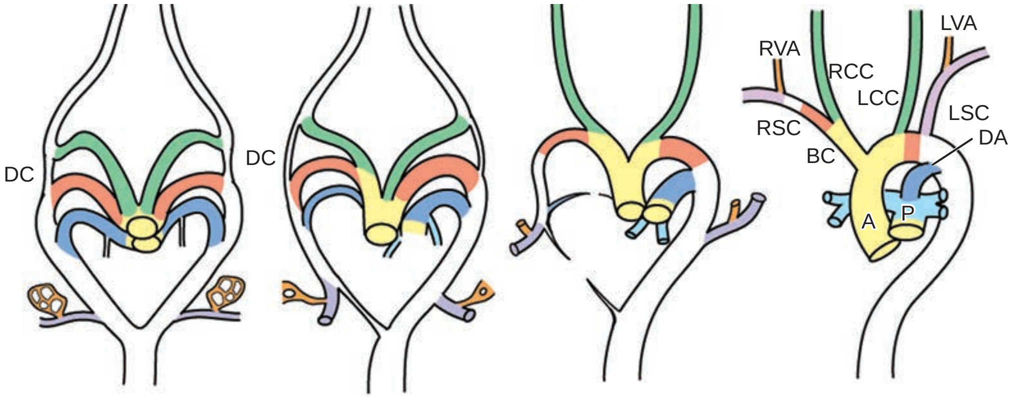

**e-Figure 62.6.** Diagram of the bilaterally symmetrical aortic arch arteries that carry the early cardiac output to the dorsal aorta, which then distributes blood to the embryo. The early symmetry is lost when these vessels are remodeled to be the adult great arteries of the thorax. *Green,* Aortic arch artery 3; *red,* aortic arch artery 4; *blue,* aortic arch artery 6; *A,* aorta; *BC,* brachiocephalic; *DA,* ductus arteriosus; *DC,* ductus caroticus; *LCC,* left common carotid artery; *LSC,* left subclavian artery; *LVA,* left vertebral artery; *P,* pulmonary trunk; *RCC,* right common carotid artery; *RSC,* right subclavian artery; *RVA,* right vertebral artery. *(From Kirby ML.* Cardiac development*. New York: Oxford University Press; 2006.)*

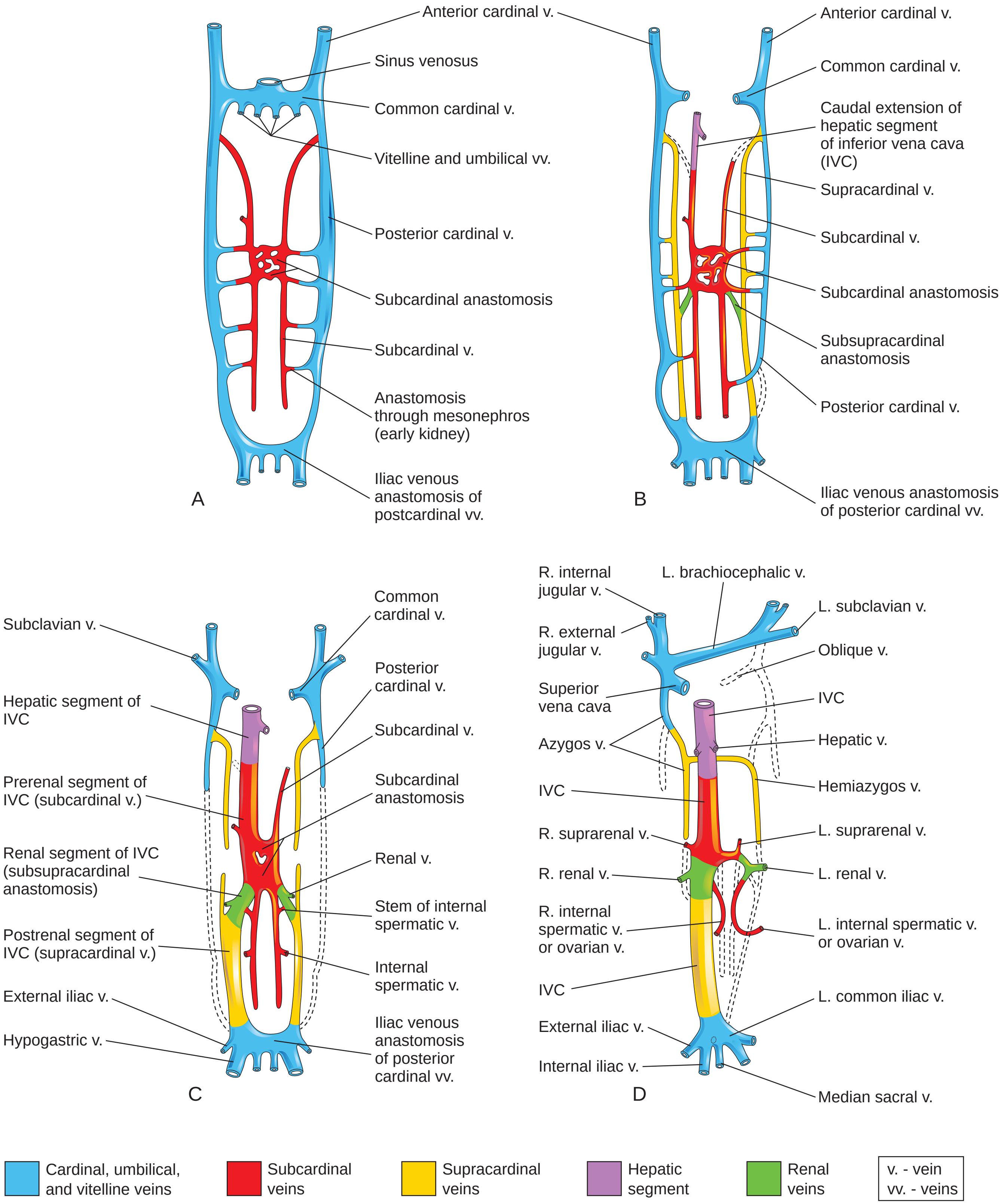

**e-Figure 62.8. The primordial veins of the trunk in the human embryo (ventral views).** Initially, three systems of veins are present: the umbilical veins from the chorion, the vitelline veins from the umbilical vesicle (yolk sac), and the cardinal veins from the body of the embryo. Next, the subcardinal veins appear, and finally the supracardinal veins develop. (A) At 6 weeks. (B) At 7 weeks. (C) At 8 weeks. (D) Adult. This drawing illustrates the transformation that produces the adult venous pattern. *(From Moore KL, Persaid TVN.* The developing human: clinically oriented embryology. *8th ed. Philadelphia: Saunders Elsevier; 2008. Fig. 13.4; as modified from Arey LB.* Developmental anatomy. *7th ed revised. Philadelphia: WB Saunders; 1974.)*

To understand common associations in congenital malformations, it is important to realize that the heart develops in close juxtaposition to the forebrain, face, and anterior neck as part of what has been called the cardiocraniofacial field. The simultaneous occurrence of defects in these other organ systems with congenital heart defects therefore is not surprising.

### Acknowledgment

I thank Dr. Margaret L. Kirby for her lucid teaching, her patience with this clinician, her sharing of figures, her review of this manuscript, and her enormous contributions to the field of cardiovascular development.

### KEY POINTS

- Looping and convergence of the primitive heart tube set the stage for cardiac septation and definitive chamber formation.
- Atrial septal defects are named for the embryonic ostium that persists, not for the embryonic tissue in which the defect exists.
- The proepicardium gives rise to a very diverse population of cells and is an important potential source of cardiac stem cells.
- The vasculature of the head, limbs, and derivatives of the somites maintains its embryonic symmetry, whereas the central vessels are remodeled extensively.

### SUGGESTED READINGS

Bogers AJJC, Gittenberger-de Groot AC, Poelmann RE, et al. Development of the origin of the coronary arteries, a matter of ingrowth or outgrowth. *Anat Embryol (Berl)*. 1989;180:437–441.

Harvey RP, Rosenthal N, eds. *Heart Development*. San Diego, CA: Academic Press; 1998.

Horsthuis T, Christoffels VM, Anderson RH, et al. Can recent insights into cardiac development improve our understanding of congenitally malformed hearts? *Clin Anat*. 2009;22:4–20.

Hutson MR, Kirby ML. Neural crest and cardiovascular development: a 20-year perspective. *Birth Defects Res C Embryo Today*. 2003;69:2–13.

Kirby ML. *Cardiac Development*. New York: Oxford University Press; 2007.

Moorman AFM, Christoffels VM. Cardiac chamber formation: development, genes and evolution. *Physiol Rev*. 2003;83:1223–1267.

Wessels A, Pérez-Pomares JM. The epicardium and epicardially derived cells (EPDCs) as cardiac stem cells. *Anat Rec A Discov Mol Cell Evol Biol*. 2004;276(1):43–57.

# 63

# Cardiovascular Anatomy and Segmental Approach to Imaging of Congenital Heart Disease

*Rajesh Krishnamurthy*

Because of the large variety of human hearts in nature, a standardized approach and nomenclature is needed to understand and describe cardiac anatomy and physiology in the setting of congenital heart disease. The most widely used approach is called the segmental approach to heart disease, first proposed by Richard Van Praagh in 1972 and later modified by others. It is strongly rooted in embryologic principles, and follows a logical sequence from evaluation of morphology and physiology of the heart to decision making regarding treatment.

## EMBRYOLOGIC BASIS FOR THE SEGMENTAL APPROACH TO HEART DISEASE

Embryology of the heart is covered in a separate chapter (see Chapter 62). In this section, some embryologic events that are fundamental to understanding the segmental approach to heart disease are reiterated.

The heart develops from two simple epithelial tubes that fuse to form a single tube (Fig. 63.1) with the following components:

**Sinus venosus:** Consists of right and left horns. Each horn receives blood from three important veins: the umbilical vein, the common cardinal vein, and the vitelline vein.

**Paired primitive atria:** Will later fuse together to form a common atrium.

**Atrioventricular sulcus:** Divides the common atrium and the primitive ventricle.

**Primitive ventricle:** Becomes the left ventricle, and the inflow portion of the right ventricle.

**Interventricular sulcus:** Divides the left and right ventricles.

**Bulbus cordis:** This may be divided as follows: the proximal one-third contributes to the body of the right ventricle; the distal one-third is called the truncus arteriosus, which develops into the aortic root and part of the pulmonary artery (PA); and the middle third is called the conus cordis and connects the primitive right ventricle to the truncus arteriosus. The conus cordis partitions to form the outflow tracts of the right and left ventricles.

Although the two ends of the heart tube remain relatively fixed, rapid growth of the middle section results in the development of a large S-shaped curve called the *bulboventricular loop* (see Fig. 63.1). As the heart tube grows and becomes longer, it usually bends to the right, termed by Van Praagh as D-looping. D-looping is responsible for the proximal bulbus cordis (RV) lying anterior and to the right of the primitive ventricle (LV). If the heart tube loops to the left, termed L-looping, the RV will lie anterior and to the left of the LV.

In the heart tube stage, the primitive LV and the proximal bulbus cordis (primitive RV) are separated from the truncus arteriosus (which gives rise to both great arteries) by the conus or infundibulum. The conus consists of the subpulmonary and subaortic conus cushions. Normally, there is expansile growth of the subpulmonary conus, causing it to protrude anteriorly on the left, carrying the pulmonary valve anteriorly, superiorly, and to the left of the aortic valve. There is resorption of the subaortic conus. Hence, the aortic valve lies posterior, inferior, and right-sided, in direct fibrous contiguity with the mitral valve (Fig. 63.2). The anterior PA arises above the anterior ventricle (RV) and leads to the posterior sixth arterial arch, which forms the branch pulmonary arteries. The posterior aorta originates above the posterior LV, and leads to the anterior fourth arterial arch (which forms the aortic arch).

The segmental approach involves the analysis of the three major cardiac segments: atria, ventricles and great arteries, and the two connecting segments: the atrioventricular canal and the conotruncus. These segments of the heart can be distinguished in the very early embryo. There are some important embryologic concepts that underlie the segmental approach to heart disease:

1. The development of the suprahepatic portion of the inferior vena cava (IVC) is closely linked to the growth of the liver, so that the anatomic right atrium and the liver almost invariably develop on the same side of the body. This concept of visceroatrial situs is fundamental to the segmental approach.
2. Another important concept underlying the segmental approach is the recognition that the ventricular looping is independent of the visceroatrial situs. This gives rise to the concept of concordance (RA-RV and LA-LV) and discordance (RA-LV and LA-RV).
3. Similarly, ventricular looping and great arterial relationship are independent entities. The direction of bulboventricular looping, and the development of the conotruncus is responsible for the ultimate relationship of the great arteries to each other, and to the underlying ventricles and atrioventricular valves.

## THE SEGMENTAL APPROACH TO DIAGNOSIS OF CONGENITAL HEART DISEASE

Any imaginable combination of visceral, atrial, ventricular, and great vessel morphology can and does occur in congenital heart disease. A simple, logical, step-by-step approach to diagnosis and decision-making and a standardized nomenclature go a long way in advancing patient care by ensuring that different caregivers have similar understanding of the disease, and are speaking the same language. This approach is known as the segmental approach to heart disease, first described by Richard Van Praagh in 1972.

One can think of the heart as a three-level house (Fig. 63.3). The first level is the visceroatrial situs, the middle level is the ventricular loop, and the third level is the conotruncus. To describe it simply, the three levels are the atria, ventricles, and great arteries. There are two staircases: the atrioventricular junction and the ventriculoarterial junction. The levels represent the major cardiac segments. The staircases represent the connecting segments.

The segmental approach to heart disease comprises the following steps:

1. What is the anatomic type of each of the three major cardiac segments: the atria, the ventricles, and great arteries?
2. How is each segment connected to the adjacent segment?

## Abstract:

Because of the large variety of human hearts in nature, a standardized approach and nomenclature is needed to understand and describe cardiac anatomy and physiology in the setting of congenital heart disease. The most widely used approach is called the segmental approach to heart disease, first proposed by Richard Van Praagh in 1972 and later modified by others. It is strongly rooted in embryological principles, and follows a logical sequence from evaluation of morphology and physiology of the heart to decision making regarding treatment.

## Keywords:

congenital heart disease
embryology
segmental approach
visceroatrial situs

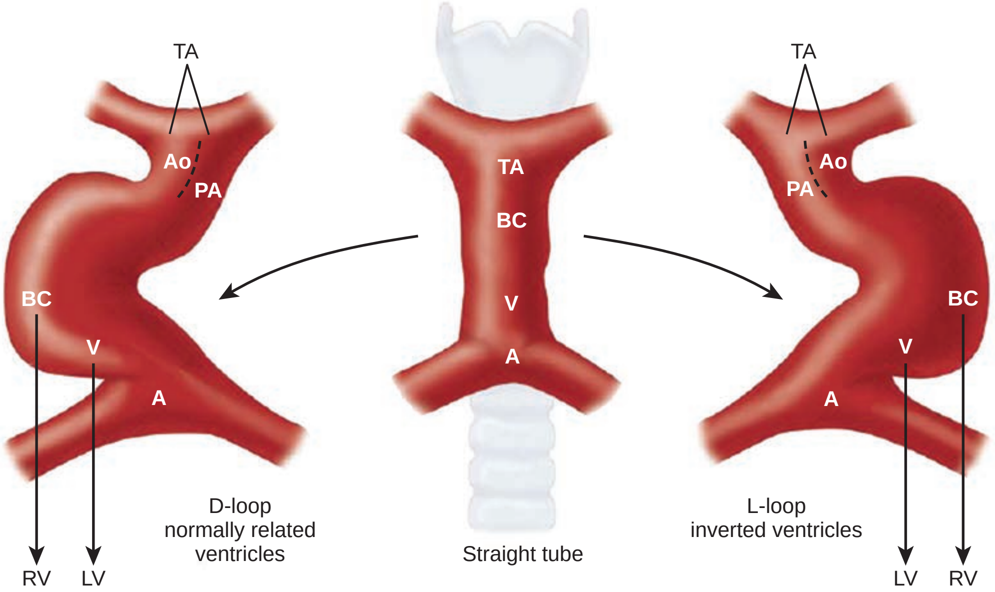

**Figure 63.1. Bulboventricular looping of the primitive heart tube may occur to the right (D-looping) or to the left (L-looping).** *Ao,* Aorta; *BC,* bulbus cordis; *LV,* left ventricle; *PA,* pulmonary artery; *RV,* right ventricle. *(Modified from Van Praagh R, Weinberg PM, Matsuoka R, et al. Malposition of the heart and the segmental approach to diagnosis. In: Adams FH, Emmanouilides GC, eds.* Moss' Heart Diseases in Infants, Children and Adolescents. *3rd ed. Baltimore: Williams & Wilkins; 1983.)*

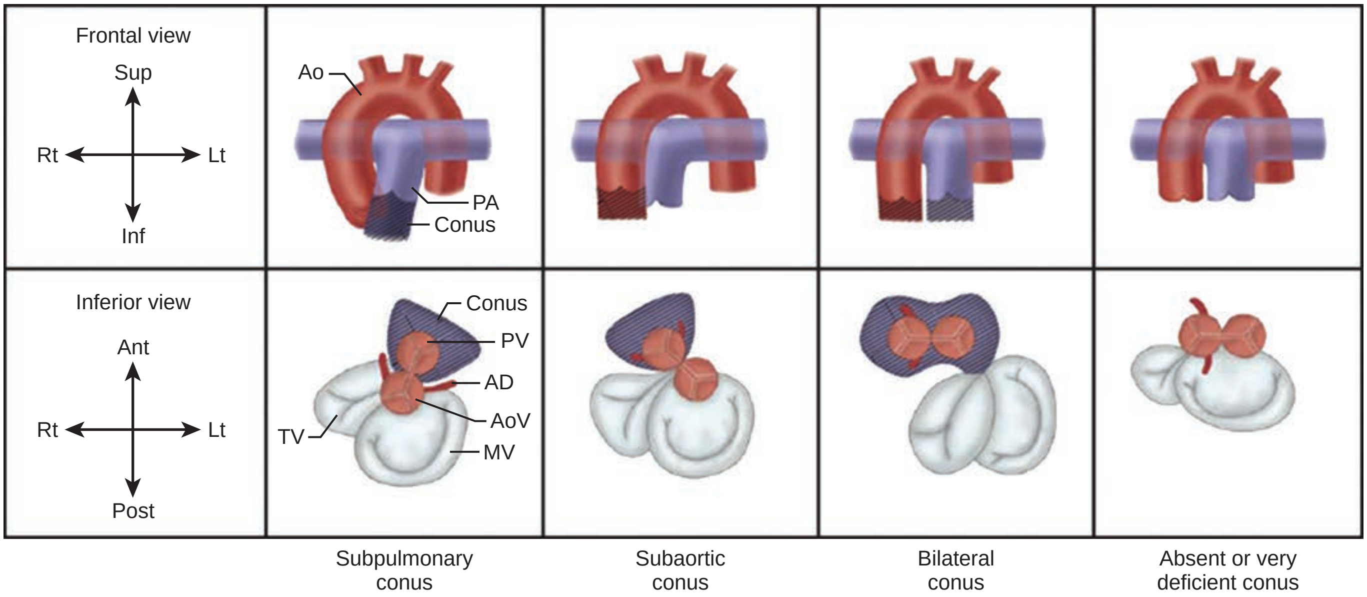

**Figure 63.2. Normal and abnormal conal development.** (A) Subpulmonary conus seen in normally related great arteries. (B) Subaortic conus in typical transposition of the great arteries. (C) Bilateral conus, as in double-outlet right ventricle. (D) Absent or deficient conus, as in double-outlet left ventricle. On the side of the conus, the semilunar valve sits atop the muscular infundibulum, and no direct fibrous contiguity exists between the semilunar valve and the atrioventricular (AV) valve. On the side of the deficient conus, direct fibrous contiguity usually exists between the AV valve and the semilunar valve. *Ant,* Anterior; *Ao,* aorta; *AoV,* aortic valve; *Inf,* inferior; *Lt,* left; *MV,* mitral valve; *PA,* pulmonary artery; *Post,* posterior; *PV,* pulmonary valve; *Rt,* right; *Sup,* superior; *TV,* tricuspid valve. *(Modified from Van Praagh R, Weinberg PM, Matsuoka R, et al. Malposition of the heart and the segmental approach to diagnosis. In: Adams FH, Emmanouilides GC, eds.* Moss' Heart Diseases in Infants, Children and Adolescents. *3rd ed. Baltimore: Williams & Wilkins; 1983.)*

3. What are the associated anomalies involving the valves, atrial and ventricular septum, the great vessels, and the systemic and pulmonary veins?
4. How do the segmental combinations and connections function, with or without the associated malformations?

The first three steps in the segmental approach are concerned with morphology, while the last step determines physiology.

Van Praagh used a segmental set to provide a shorthand description of the floorplan of the heart. The first letter stands for the visceroatrial situs, the second for the ventricular loop, and the third for the great arterial relationship. In a person with situs solitus of the viscera and atria, D-looping of the ventricles, and solitus relationship of the great arteries, the segmental set is {S,D,S}.

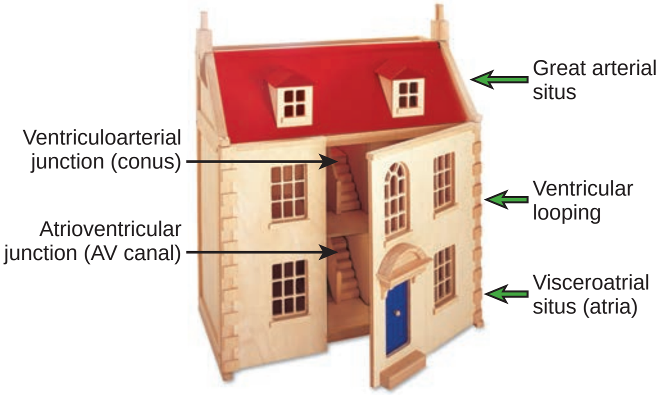
Great arterial situs
Ventriculoarterial junction (conus)
Ventricular looping
Atrioventricular junction (AV canal)
Visceroatrial situs (atria)

**Figure 63.3. The "house" model of the heart.** The three levels (major cardiac segments) are the atria, ventricles, and great arteries. The house has two connecting walls with doors (connecting segments): the atrioventricular junction and the ventriculoarterial junction. The house has two entrances: the systemic veins and the pulmonary veins.

## IDENTIFICATION OF THE MAJOR CARDIAC SEGMENTS

Reliable identification of the cardiac chambers based on specific morphologic features is the first step in the segmental approach to heart disease. It is important to remember that right and left do not refer to the side of the body on which the chamber lies but to specific morphologic criteria that identify each component of the heart. For instance, right atrium does not refer to the atrium that is on the right side of the body but to the atrium that receives the insertion of the IVC and the coronary sinus, and has a triangular appendage with a broad base. Hence, the morphologic right atrium will be on the right side of the body in situs solitus and on the left side in situs inversus.

### Atrial Identification

The defining features of the morphologic right atrium (systemic venous atrium) and left atrium (pulmonary venous atrium) are based on their venous connections as well as their appendage and pectinate muscle morphology. Using venoatrial connections for atrial identification is based on the fact that the sinus venosus, which carries the systemic venous return, is an integral part of the morphologic right atrium. Hence, the morphologic right atrium receives the inferior and superior vena cavae, and orifice of coronary sinus. However, the superior vena cava (SVC) and coronary sinus have a high incidence of variation, which can be a source of diagnostic confusion. These variations include left SVC to an unroofed coronary sinus, and bilateral SVCs with the left SVC draining to an unroofed coronary sinus. In these cases, the SVC would appear to drain into the left atrium. In rare instances, even the IVC may drain into the coronary sinus, which may be unroofed, or the coronary sinus septum may be absent. In spite of this rare exception, the most reliable means of identifying the morphologic right atrium by cross-sectional imaging is by recognizing its connection to the IVC (Fig. 63.4). Even in the setting of an interrupted IVC, a suprahepatic segment of the IVC is present entering the right atrium, allowing accurate identification.

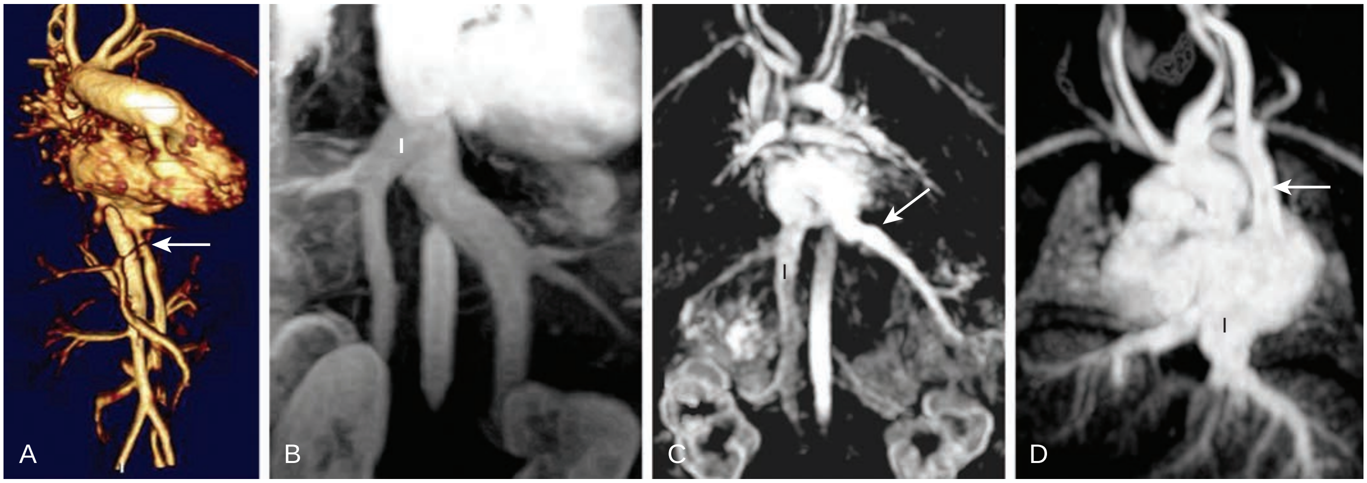

**Figure 63.4. The inferior vena cava (IVC) as a marker of the morphologic right atrium (RA).** (A) The IVC *(arrow)* and aorta are on the left and the IVC enters the left-sided atrium, which represents the morphologic RA. (B) Bilateral IVC that fuse *(I)* prior to entering the right atrium. (C) The right hepatic vein enters the IVC *(I)*, which drains into the RA, while the remaining hepatic veins *(arrow)* drain separately into the left atrium. (D) Left sided-interrupted IVC with azygos continuation. A suprahepatic segment of the IVC *(I)* drains into the left-sided right atrium in this patient with atrial situs inversus. A left superior vena cava also is present *(arrow)*.

The morphologic left atrium is defined as the atrium that receives all or half of the pulmonary veins and none of the systemic veins (except an SVC to an unroofed coronary sinus). The left atrium is also the chamber that may receive no veins at all (in the setting of total anomalous pulmonary venous return). When all systemic veins and part or all of the pulmonary veins drain into one atrium, this atrium represents the morphologic right atrium.

Robert Anderson has described the morphologic right atrium (systemic atrium) as being characterized by the presence of a triangular appendage with a broad junction and by the recognition of pectinate muscles extending to the atrioventricular junction. The morphologic left atrium is characterized by a tubular narrow-based appendage and lack of pectinate muscle extension to the atrioventricular junction. Because determination of pectinate muscle morphology is beyond the resolution of MRI or CT, atrial identification is performed by recognition of venoatrial connections and morphology of the appendages. If this analysis fails to yield a confident identification of the right and left atrium, then a diagnosis of atrial situs ambiguous is made. Even in the setting of visceral situs ambiguous, reliable identification of atrial situs may be made in more than 80% of the cases.

## Ventricular Identification

Ventricles are defined by their morphologic features, not by their spatial relationships. The morphologic right ventricle is defined by the following features:

1. Muscular connection between the free wall and the interventricular septum (moderator band) (Fig. 63.5A).
2. The septal attachment of the AV valve of the RV (tricuspid valve) is more apically placed relative to that of the LV (Fig. 63.5B).
3. Presence of a conus/infundibulum. The infundibulum is identified as a muscular cone of tissue that separates the atrioventricular valve from the semilunar valve on the same side, resulting in lack of fibrous contiguity between the two valves (Fig. 63.5C).

The morphologic LV is identified by the following features:

1. Smooth surface of the interventricular septum without any muscular attachments to the free wall (Fig. 63.6).
2. The septal attachment of the AV valve of the LV (mitral valve) is more cranially located relative to that of the RV (Fig. 63.6B).
3. Absence of a conus/infundibulum, resulting in fibrous contiguity between the atrioventricular valve and the semilunar valve on that side (see Fig. 63.6).

The atrioventricular valves follow the ventricle, rather than the atrium. Thus, the tricuspid valve is related to the morphologic right ventricle, and the mitral valve to the morphologic left ventricle. The tricuspid valve typically has papillary muscle attachments to the right ventricular septal surface (septophilic valve) while the mitral valve is septophobic and only attaches to the free wall of the left ventricle.

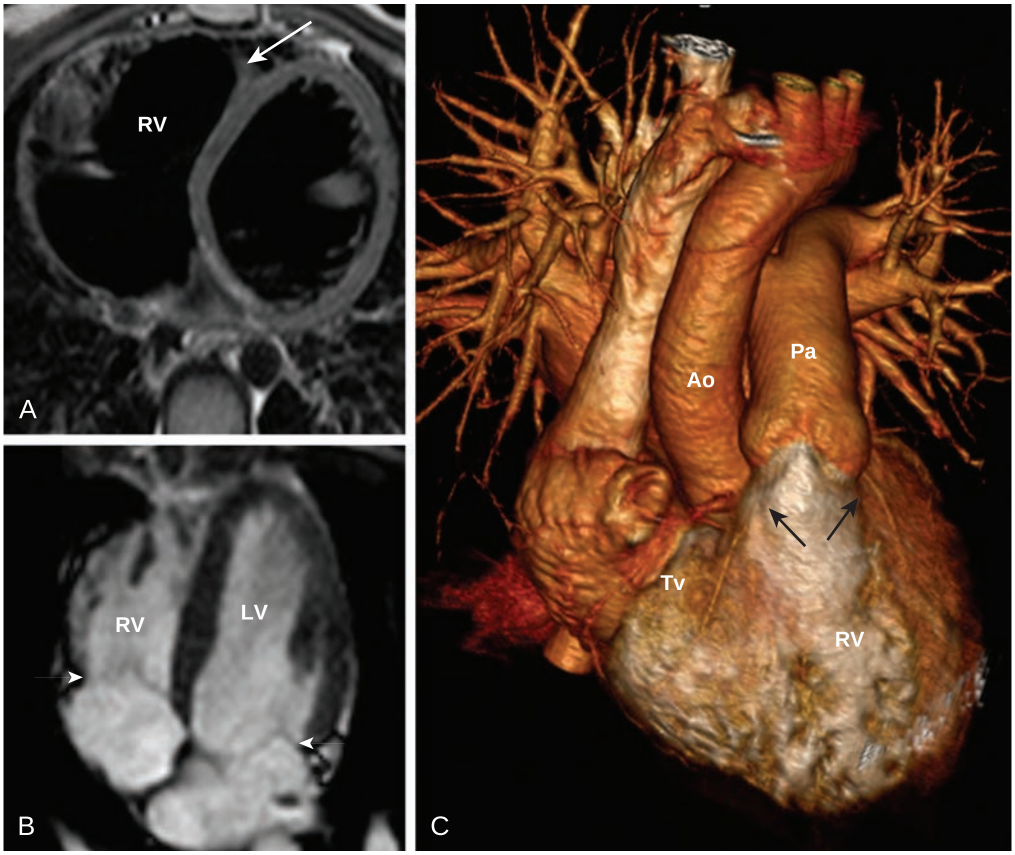

**Figure 63.5. Right ventricular identification.** (A) Moderator band of the right ventricle *(RV) (arrow)*. (B) The atrioventricular (AV) valve of the *RV* (tricuspid valve) is more apically displaced *(long arrow)* than the AV valve of the left ventricle *(LV)* (mitral valve) *(short arrow)*. (C) The conus *(arrows)* is a marker of the *RV*. It is a muscular cone of tissue that separates the AV valve *(Tv)* from the semilunar (pulmonary) valve on the same side. *Ao,* Aorta; *Pa,* pulmonary artery.

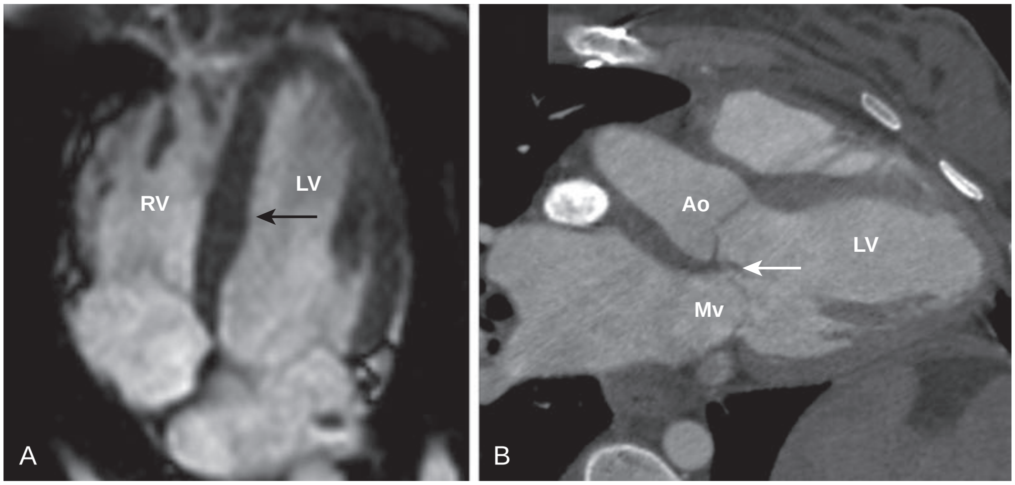

**Figure 63.6. Left ventricular identification.** (A) Smooth septal surface of the left ventricle *(LV) (arrow)*. (B) The *LV* does not have a conus, resulting in mitral *(Mv)* to aortic *(Ao)* fibrous contiguity *(arrow)*. *RV,* Right ventricle.

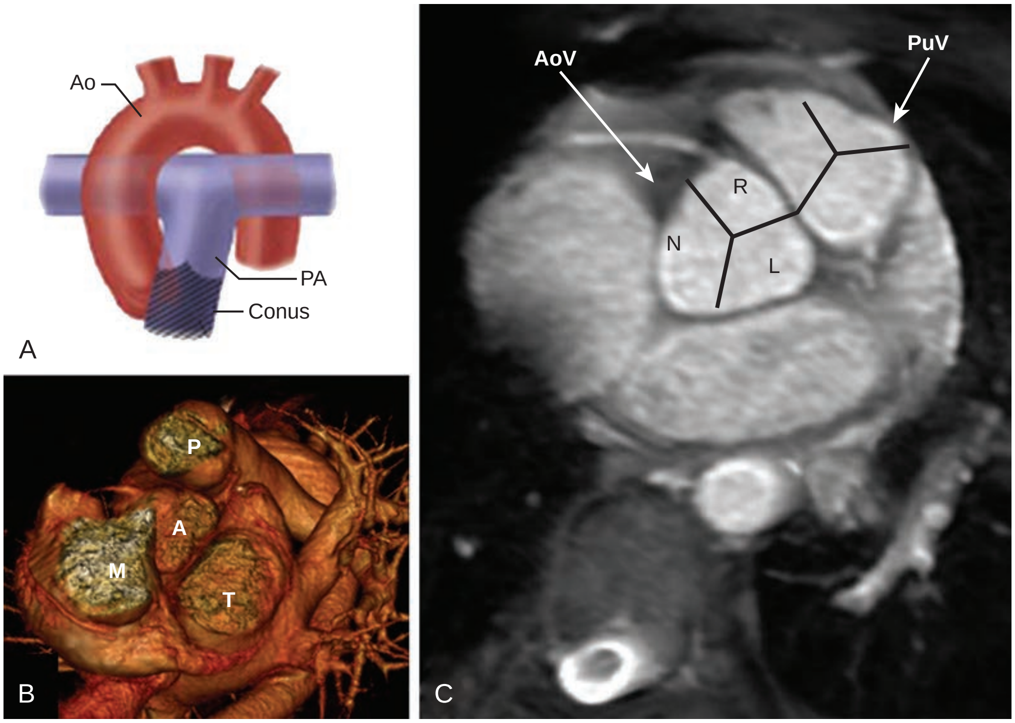

**Figure 63.7.** (A) Solitus (normal) relationship of the great arteries. (B) Three-dimensional view of the heart from above. The aortic valve *(A)* has direct fibrous contiguity with the mitral *(M)* and tricuspid *(T)* valves, whereas the pulmonary valve *(P)* lies ventrally, and is separated from the atrioventricular valves by the conus. (C) The aortic valve annulus *(AoV)* lies posterior and to the right of the pulmonary valve annulus *(PuV)*. The intercoronary commissure of the aortic valve is pointed toward the right-left commissure of the pulmonary valve. *Ao,* Aorta; *L,* left sinus of Valsalva; *N,* noncoronary sinus of Valsalva; *PA,* pulmonary artery; *R,* right sinus of Valsalva.

Neither the shape of the ventricle nor the degree of trabeculation or hypertrophy is considered a reliable marker for ventricular identification, as they are frequently affected by pressure or volume changes in the ventricle.

## Great Arterial Identification

The PA gives rise to branches to the lungs and no branches to the body. The aorta gives rise to branches to the body as well as the coronary arteries. A common vessel arising from the ventricles that gives rise to the coronaries and branches to the body as well the lungs is termed a common arterial trunk or truncus, and a segmental relationship is not assigned (labeled X for undetermined). On transverse cross-sectional imaging at the level of the outflow tract, the coronary artery origin is used to identify the aortic annulus. The intercoronary commissure of the aortic valve is pointed toward the right-left commissure of the pulmonary valve and is an important landmark for determining great arterial relationship (Fig. 63.7). In solitus relationship of the great arteries, the aortic valve annulus lies posterior and to the right of the pulmonary valve annulus.

## ANALYSIS OF THE THREE MAJOR CARDIAC SEGMENTS

### First Major Segment: Visceroatrial Situs

Situs refers to the position of the atria and viscera relative to the midline. There are three types of situs: solitus (S), inversus (I), and ambiguous (A) (Fig. 63.8). Heterotaxy is synonymous with situs ambiguous, and is simply defined as “situs other than solitus or inversus.”

Visceral situs solitus is characterized by the presence of a right-sided liver, a single or dominant left-sided spleen, three-lobed right lung with an eparterial bronchus, and a two-lobed left lung with a hyparterial bronchus. Atrial situs solitus is characterized by the presence of the systemic venous atrium on the right and the pulmonary venous atrium on the left. Situs inversus is defined as the “mirror image” of situs solitus. Hence, visceral situs inversus is characterized by a left-sided liver, a single or dominant right-sided spleen, three-lobed left lung with an eparterial bronchus, and a two-lobed right lung with a hyparterial bronchus. Atrial situs inversus is characterized by the presence of the systemic venous atrium on the left and the pulmonary venous atrium on the right. Although the location of the cardiac apex and the stomach is usually on the left in situs solitus and on the right in situs inversus, they are not considered reliable markers of visceral situs due to the high incidence of variation in the setting of normal situs.

Because heterotaxy is defined as “situs other than solitus or inversus,” it is not a specific disease but a constellation of cardiac, vascular, and visceral abnormalities, including situs ambiguous of the viscera, lung symmetry, atrial appendage symmetry, anomalous

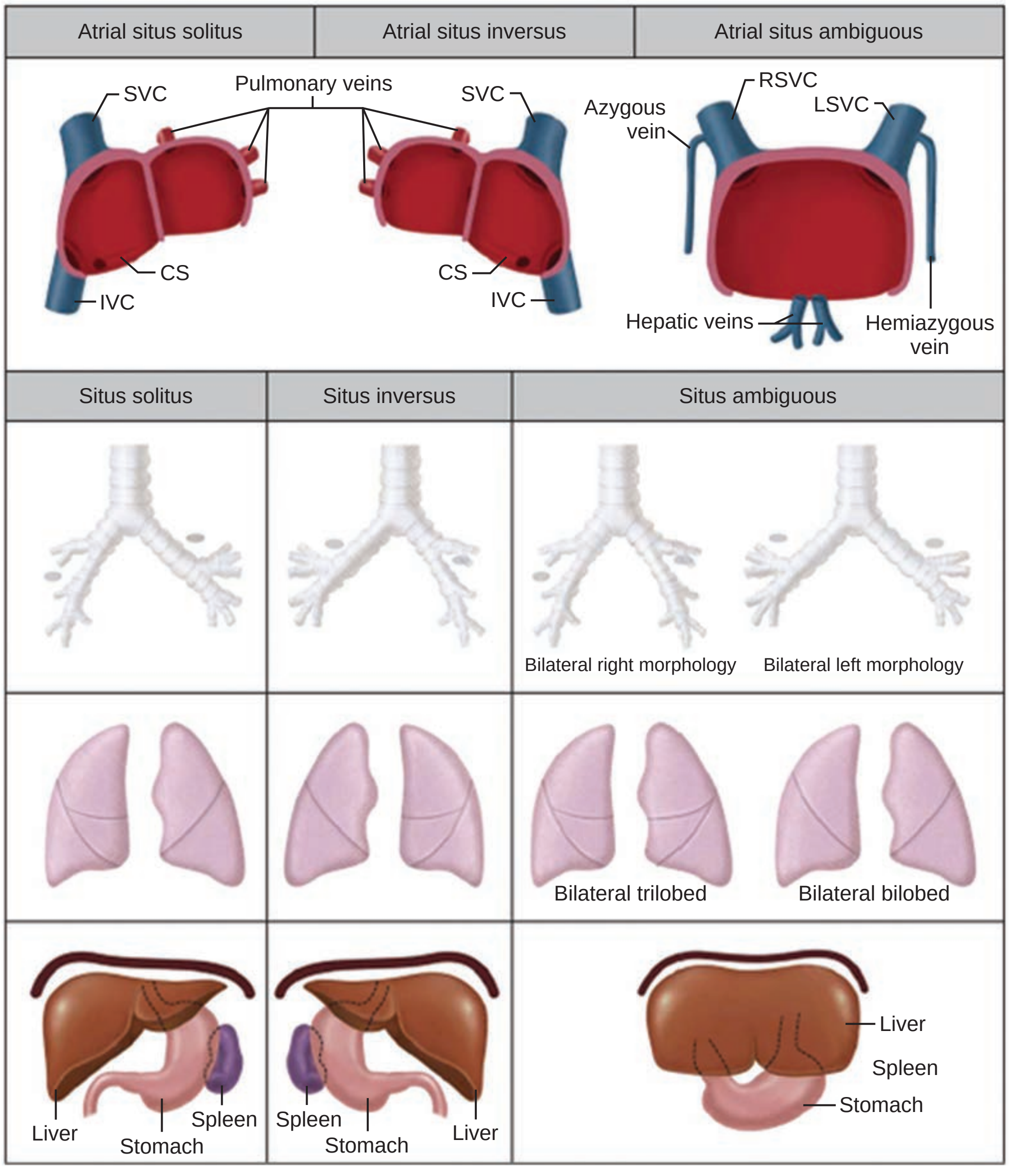

**Figure 63.8. First major cardiac segment: visceroatrial situs.** The three types of visceroatrial situs: situs solitus, situs inversus, and situs ambiguous. *CS,* Coronary sinus; *IVC,* inferior vena cava; *LSVC,* left-sided vena cava; *RSCV,* right-sided vena cava; *SVC,* superior vena cava. *(Modified from Van Praagh R, Weinberg PM, Matsuoka R, et al. Malposition of the heart and the segmental approach to diagnosis. In: Adams FH, Emmanouilides GC, eds.* Moss’ Heart Diseases in Infants, Children and Adolescents. *3rd ed. Baltimore: Williams & Wilkins; 1983.)*

systemic venous return, anomalous pulmonary venous return, and associated intracardiac defects. No single finding is pathognomonic. There is a tendency toward clustering of defects into two syndromes based on the predominance of right-sided or left-sided structures:

1. Asplenia complex—Manifestations include bilateral three-lobed lungs with eparterial bronchi, a transverse or symmetric liver, bilateral SVCs, and bilateral triangular broad-based atrial appendages. The spleen is absent.
2. Polysplenia complex—Manifestations include bilateral two-lobed lungs with hyparterial bronchi, a transverse liver, multiple splenic fragments, and bilateral tubular atrial appendages. The renal to hepatic segment of the IVC is frequently absent, with associated azygos continuation.
3. Van Praagh has added a third syndrome of heterotaxy manifested by levocardia with a single right-sided spleen. Features of this syndrome are similar to that of right isomerism.

The use of the terms *atrial isomerism*, *bilateral right-sidedness*, or *bilateral left-sidedness* as substitutes for the syndromes of situs ambiguous is discouraged because they are semantically inaccurate representations of the anatomy found in these patients.

### Second Major Segment: Ventricular Loop

Depending on the direction of ventricular looping during development, the right ventricle may be located spatially on the right or left side of the heart (Fig. 63.9). If the bulboventricular loop occurs to the right, it is termed a D-loop, and the morphologic RV lies anterior and to the right of the morphologic LV. If the bulboventricular loop occurs to the left, it is termed an L-loop, and the morphologic RV lies anterior and to the left of the morphologic LV.

### Third Major Segment: Great Arterial Relationship

Normally, the aortic annulus lies posterior, inferior, and to the right of the pulmonary valve annulus. This position is called solitus (S) (Fig. 63.10A). In situs inversus, the aorta lies posterior and to the left of the pulmonary valve, termed inversus (I) (Fig. 63.10B). Any other position of the aorta and PA other than solitus or inversus is termed malposition. If the aorta lies to the right of the PA, it is called D-malposition (Fig. 63.10C). If the aorta lies to the left of the PA, it is termed L-malposition (Fig. 63.10D).

## DIFFERENT TYPES OF HUMAN HEARTS

The segmental possibilities at each level are as follows:

Atria: Solitus (S), inversus (I), and ambiguous (A)
Ventricles: D and L
Great arteries: Solitus (S), inversus (I), D-malposition, and L-malposition

Based on the various permutations and combinations of atrial, ventricular, and great arterial relationships, as well as on the anatomy of the conus, Van Praagh provided an overview of the diversity that exists in human hearts (Fig. 63.11). It becomes immediately apparent that a pattern-based approach or an approach based on connections or the direction of flow of blood will not do justice to the complexity of the disease processes. The segmental approach not only takes into account the morphologic variations at each level but also provides structural landmarks to distinguish the variations from each other, determine their impact on physiology, and thereby allows informed decision making regarding management.

## ANALYSIS OF THE CONNECTING SEGMENTS

### First Connecting Segment: Atrioventricular Junction

The anatomic possibilities at the atrioventricular junction level may be classified based on the number of ventricles as follows:

1. Biventricular AV connections
2. Univentricular AV connections

The types of biventricular AV connections (Fig. 63.12) include

1. Concordant AV connections (RA-RV and LA-LV)
2. Discordant AV connections (RA-LV and LA-RV)
3. Straddling AV valve, in which there is abnormal attachment of the tensor apparatus of the valve to the opposite ventricle
4. Overriding AV valve, in which the AV valve annulus crosses the interventricular septum and partly overlies the opposite ventricle
5. Overriding and straddling AV valve
6. Balanced common AV canal with two symmetric sized ventricles

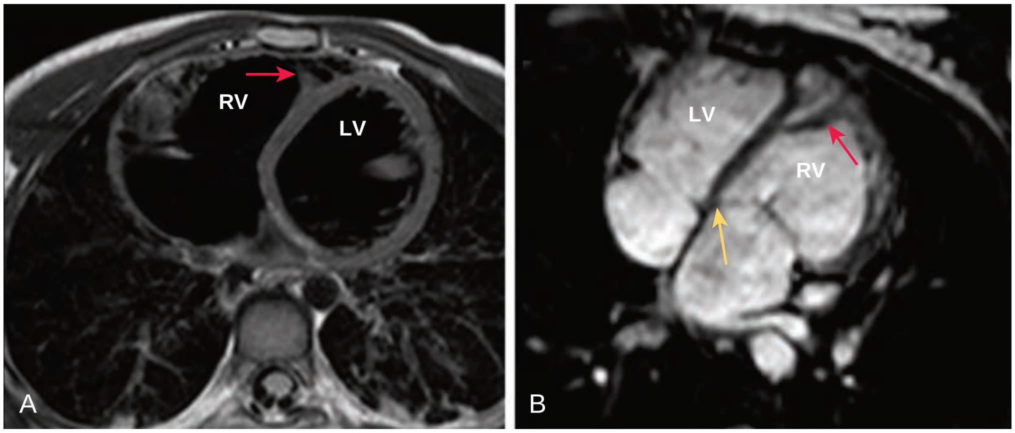

**Figure 63.9. The second major cardiac segment: ventricular looping.** (A) D-looping with the right ventricle *(RV)* lying anterior and to the right of the left ventricle *(LV)*. (B) L-looping, with the RV lying anterior and to the left of the LV. The RV is identified by the moderator band *(red arrow)*, apical displacement of the AV valve *(yellow arrow)*, and the conus *(not shown)*.

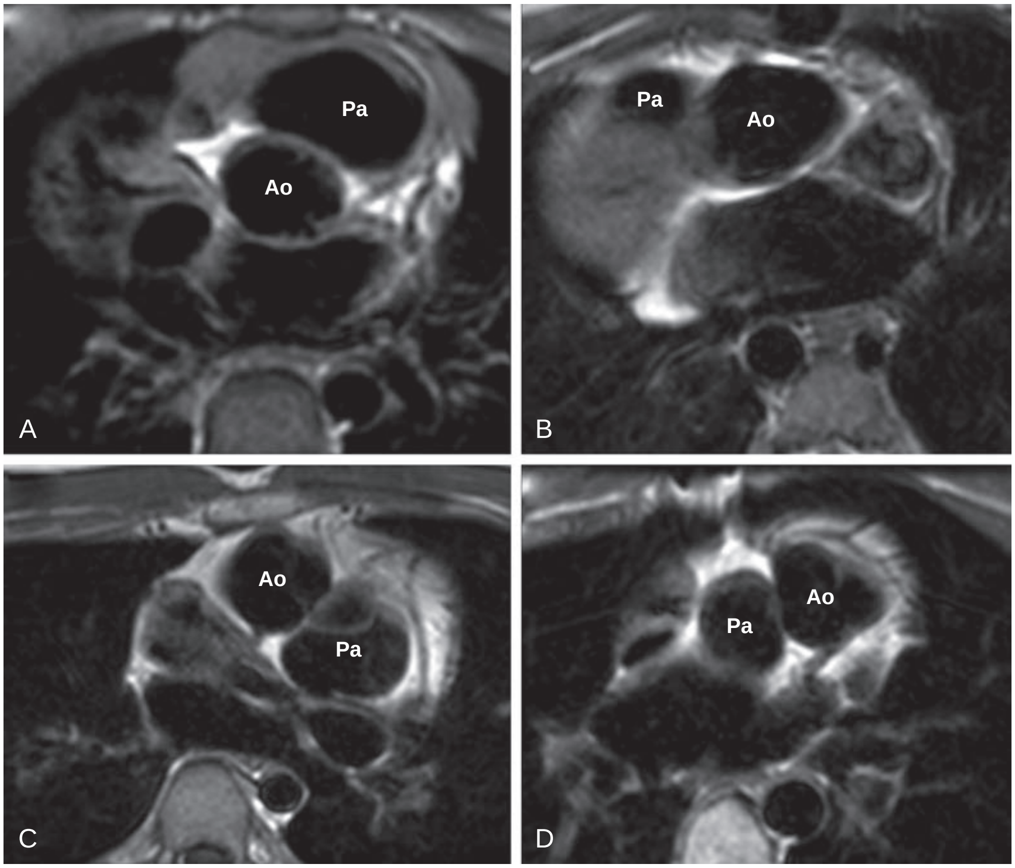

**Figure 63.10. The third major cardiac segment: arterial relationship.** (A) Solitus: the aortic annulus *(Ao)* lies posterior, inferior, and to the right of the pulmonary valve annulus *(Pa)*. (B) Inversus: the aorta lies posterior and to the left of the pulmonary valve. (C) D-malposition: the aorta lies anterior and to the right of the pulmonary artery. (D) L-malposition: the aorta lies anterior and to the left of the pulmonary artery.

The types of univentricular AV connections (Fig. 63.13) include:

1. Unilateral left AV valve atresia (mitral atresia)
2. Unilateral right AV valve atresia (tricuspid atresia)
3. Double inlet LV
4. Double inlet RV
5. Left dominant unbalanced common AV canal
6. Right dominant unbalanced common AV canal

In the setting of univentricular AV connections, one of the AV valves is atretic or both AV valves open partly or wholly into the same ventricle. The second ventricular chamber is subsequently very small or just an outflow chamber and is of little functional use, apart from serving as a conduit for one of the great arteries. Single ventricles may be of a left ventricular, right ventricular, or indeterminate morphology. The functional single LV is characterized by the presence of a bulboventricular foramen, which connects the LV chamber to the small anteriorly located infundibular outlet chamber of the RV. The RV sinus (inflow portion) is typically absent. A functional single RV is characterized by the presence of a septal band, and in most cases, by a rudimentary posterolaterally located LV chamber.

## Second Connecting Segment: Conotruncus or Ventriculoarterial Junction

The development of the conotruncus is the most important variable in the genesis of outflow tract anomalies. The differential growth of the subpulmonary and subaortic conus cushions largely determines the relationship between the semilunar valves, between the semilunar valves and the ventricles, and between the semilunar valves and the atrioventricular valves. It also determines the presence of distal infundibular stenosis and the location of the ventricular septal defect (VSD) in outflow tract anomalies. Based on conal development, the following anatomic types of conus (Fig. 63.14) may be recognized:

1. Development of subpulmonary conus and resorption of the subaortic conus results in ventriculoarterial concordance and normal relationship of great arteries. The aorta lies posterior and to the right in a D-loop heart (solitus) and posterior and to the left in an L-looped heart (inversus).
2. Development of the subaortic conus and resorption of the subpulmonary conus results in ventriculoarterial discordance and transposition of the great arteries. Transposition means that the left ventricle is connected to the main PA and the right ventricle to the aorta. The aorta lies anterior and to the right in a D-looped heart (D-malposition) (Fig. 63.15) and anterior and to the left in an L-looped heart (L-malposition).
3. Persistence and development of both the subaortic and subpulmonary conus leads to double outlet RV. Double outlet right ventricle means that both great vessels arise predominantly from the RV (Fig. 63.16). There may be variable development of the pulmonary and aortic conus resulting in variable location of the VSD in relation to the great arteries.

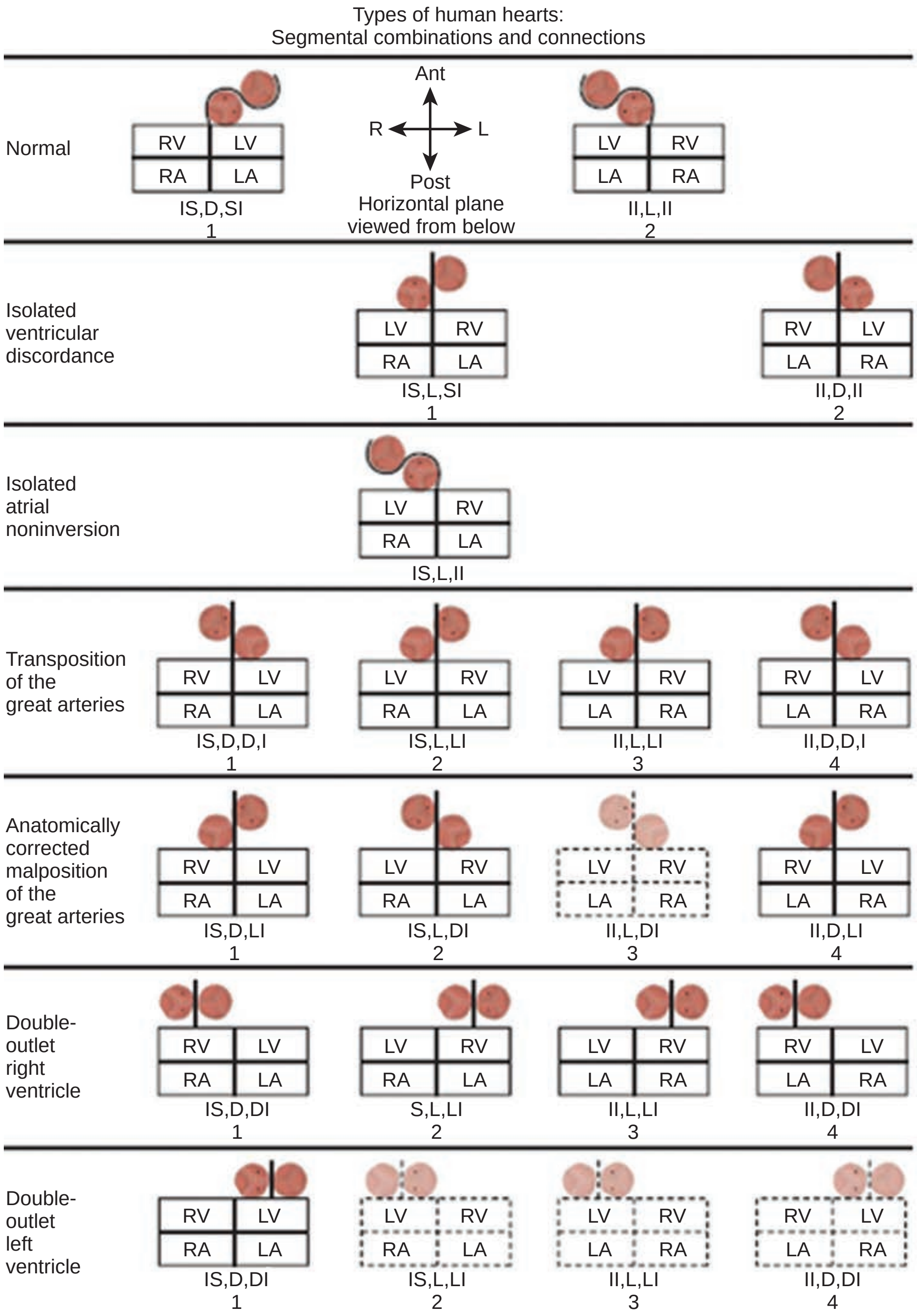

**Figure 63.11. Van Praagh's types of human hearts, based on segmental combinations of visceroatrial situs, ventricular looping, and great arterial situs.** The segmental combination is expressed as a set, within braces. For instance, a normal heart would be expressed as {S,D,S} for visceroatrial situs solitus, D-looping of the ventricles, and solitus relationship of the great arteries. The segmental connections and associated anomalies are expressed outside the braces. For instance, physiologically corrected transposition would be expressed as {S,L,L} transposition of the great arteries for solitus atria, L-looped ventricles, and L-malposition of the great arteries. If this patient also had straddling atrioventricular valve and an inlet ventricular septal defect (VSD), it would be expressed as {S,L,L} transposition of great arteries, straddling tricuspid valve, and inlet VSD. *Ant,* Anterior; *LA,* left atrium; *LV,* left ventricle; *Post,* posterior; *R,* right; *RA,* right atrium; *RV,* right ventricle. *(Modified from Van Praagh R, Weinberg PM, Matsuoka R, et al. Malposition of the heart and the segmental approach to diagnosis. In: Adams FH, Emmanouilides GC, eds.* Moss' Heart Diseases in Infants, Children and Adolescents. *3rd ed. Baltimore: Williams & Wilkins; 1983.)*

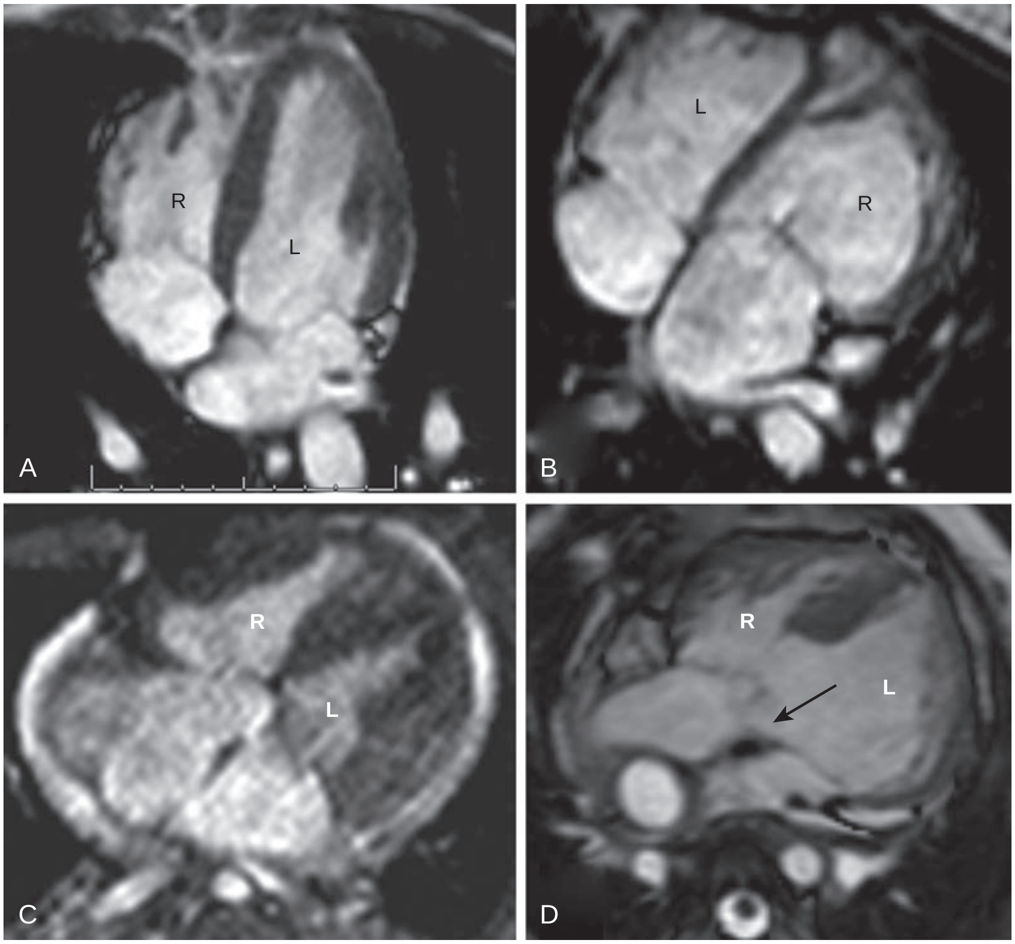

**Figure 63.12. Types of biventricular atrioventricular (AV) connections.** (A) Concordant AV connections (right atrium-right ventricle [RA-RV] and left atrium-left ventricle [LA-LV]) (B) Discordant AV connections (RA-LV and LA-RV). (C) Balanced common AV canal with two symmetric sized ventricles. (D) Straddling and overriding tricuspid valve *(arrow)* in a patient with D-looped ventricles. *L,* Left ventricle; *R,* right ventricle.

4. Resorption of both the subpulmonary and subaortic conus results in double outlet LV. Double outlet LV means that both vessels arise predominantly from the LV.

A rare form of conal maldevelopment is anatomically corrected malposition of the great arteries in which there is origin of the malposed aorta above the LV and origin of the malposed PA above the RV. Malalignment of the conal septum is the cause of infundibular obstruction in tetralogy of Fallot (anterior malalignment) and subaortic stenosis with interrupted aortic arch (posterior malalignment).

## EVALUATION OF ASSOCIATED ANOMALIES

The presence of associated anomalies involving the atrial and ventricular septum, the atrioventricular and semilunar valves, aorta, pulmonary arteries, pulmonary veins, and systemic veins plays an important part in the functional outcome of the patient, and screening for these conditions is an integral part of the segmental approach to heart disease.

## EVALUATION OF FUNCTION

The final step in the segmental approach to heart disease is to determine how the segmental combinations and connections function. Broadly, abnormal function of the congenitally malformed heart may be classified into the following subgroups:

1. Pressure overload related to phenomena such as valvular stenosis, coarctation, and branch PA stenosis
2. Volume overload related to phenomena such as valvular regurgitation and left to right shunts
3. Intermixing, in which there is mixing of oxygenated blood with deoxygenated blood before entering the systemic circulation; this phenomenon typically occurs in the setting of a common chamber, vessel, valve, or in a right-left shunt
4. Poor contractility of the myocardium related to conditions such as cardiomyopathy or ischemia

When all relevant information regarding morphology and function has been collected, decisions regarding management may be made, which may be in the form of medical therapy, surgical therapy, or both.

## ILLUSTRATED CASE DISCUSSION

A case study of a segmental approach to imaging of congenital heart disease is illustrated in Fig. 63.17.

- Situs solitus of the atria (S): The coronary sinus and IVC enter the right-sided atrium, which therefore represents the morphologic RA. The pulmonary veins enter the

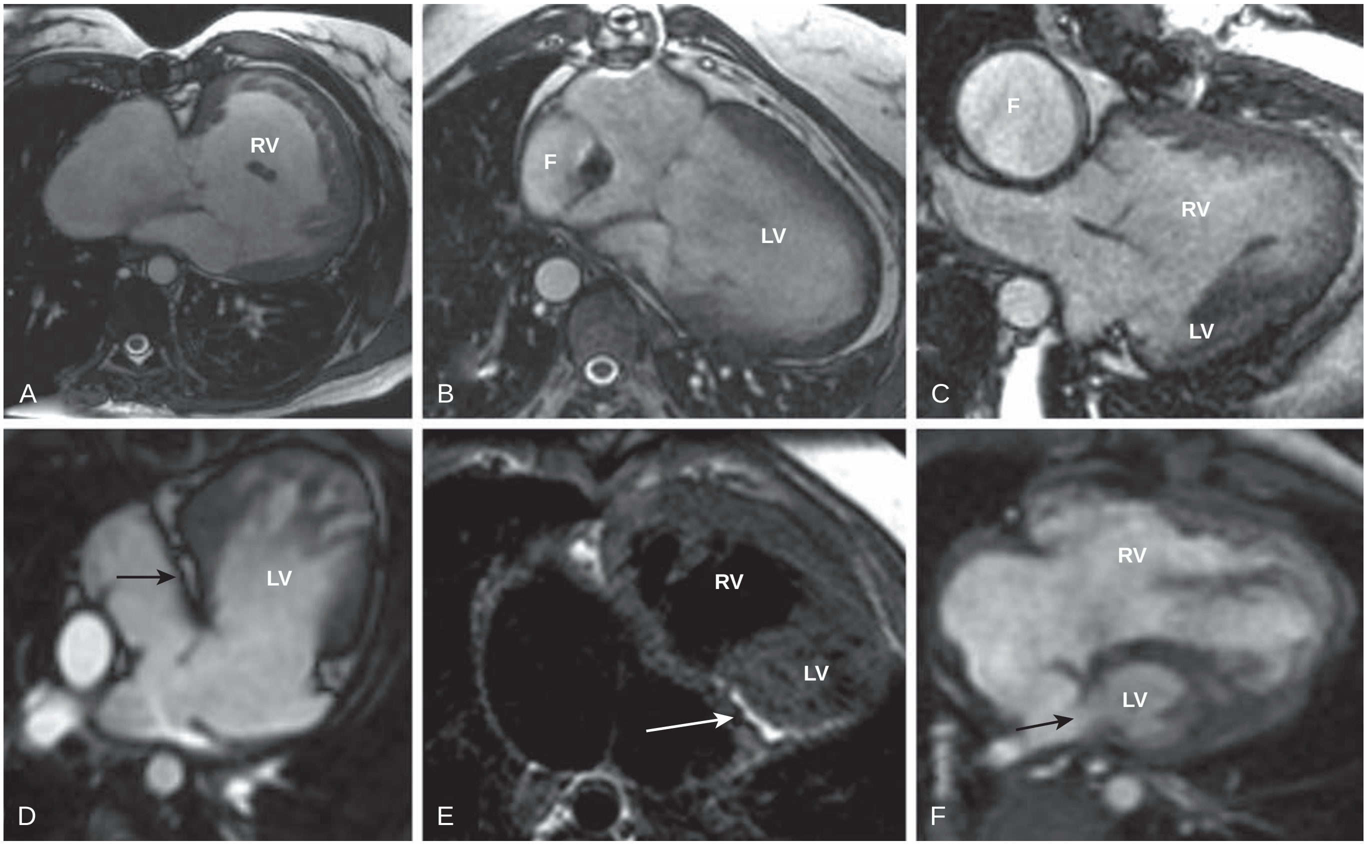

**Figure 63.13. Types of univentricular atrioventricular (AV) connections.** (A) Double inlet right ventricle *(RV)*. (B) Double inlet left ventricle *(LV)*. (C) Right dominant unbalanced common AV canal. (D) Tricuspid atresia (*arrow* shows atretic tricuspid valve plane). (E) Mitral atresia (*arrow* shows atretic fatty mitral valve plane). (F) Severe mitral stenosis *(arrow)* in hypoplastic left heart syndrome. *F,* Fontan.

morphologic LA. The RA connects to the right PA via an atriopulmonary anastomosis. The SVC also connects to the right PA.

- AV connection: The right AV valve (tricuspid valve) is atretic and fatty replaced. The left AV valve (mitral valve) is normal.
- D-looping of the ventricles: The large left-sided ventricle has a smooth septal surface consistent with a morphologic LV. The small blind-ending chamber to the right is the infundibular outlet chamber of the RV, which fills via a bulboventricular foramen.
- Ventriculoarterial connection: RV-PA outflow is atretic. Aortic outflow from the LV is normal.
- Solitus relationship of the great arteries (S): The aortic valve lies posterior and to the right of the atretic pulmonary valve.

The final diagnosis is {S,D,S} tricuspid atresia, pulmonary atresia, status postoperative Fontan completion.

## CONCLUSION

The segmental approach to heart disease provides an elegantly simple method to break down the complexity of congenital heart disease on cross-sectional imaging. It creates a template for standardizing nomenclature, thereby ensuring that caregivers from different specialties understand each other. It is firmly rooted in embryologic principles and is, therefore, intuitive to the beginner in the field. MRI and CT almost rival pathologic evaluation of specimens in the detail that they provide on cardiovascular morphology. Additionally, MRI provides unique information regarding function, flow and tissue characterization that decreases the need for more invasive means of diagnosis. Thus they are ideal vehicles for the segmental approach to heart disease.

### KEY POINTS

- The segmental approach is a simple, logical, step-by-step approach to diagnosis and decision making in congenital heart disease and is rooted in sound embryologic concepts.
- The segmental approach involves the analysis of the three major cardiac segments (atria, ventricles, and great arteries), the two connecting segments (the AV canal and the conotruncus), and associated anomalies involving the atrial and ventricular septum, great arteries, and systemic and pulmonary veins. The final step is evaluation of physiology and function, which paves the way for decision making regarding management.
- Reliable identification of the cardiac chambers based on specific morphologic features is the first step in the segmental approach to heart disease. These features may be appreciated easily on cross-sectional imaging.
- Characterizing the specific type of visceroatrial situs, ventricular looping, and great arterial situs is the next step. Based on the various permutations and combinations of atrial, ventricular, and great arterial relationships, Van Praagh created a chart that outlines the diversity that exists in human hearts.

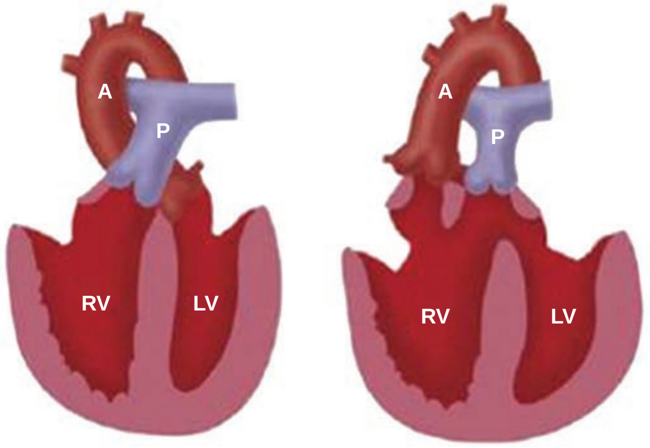

A Concordant connection B Double-outlet right ventricle

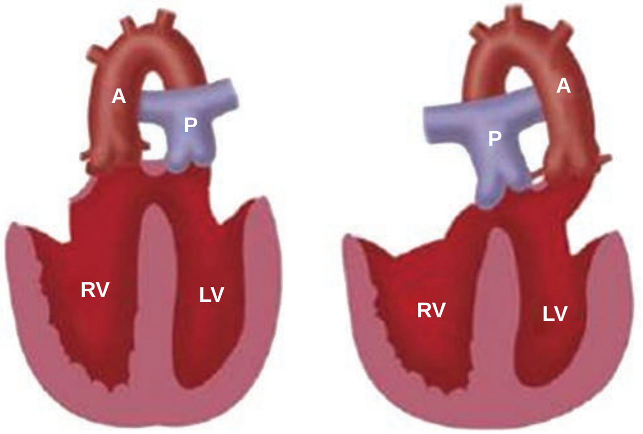

C Discordant connection D Double-outlet left ventricle

**Figure 63.14. Types of ventriculoarterial connections based on conal development.** (A) Concordant ventriculoarterial connection: solitus great arteries with subpulmonary conus. (B) Double-outlet right ventricle *(RV)* with bilateral conus. (C) Discordant ventriculoarterial connection: dextra-posed transposition of the great arteries with subaortic conus. (D) Double-outlet left ventricle *(LV)* with absent conus. *A,* Aorta; *P,* pulmonary artery. *(From Krishnamurthy R. Embryologic basis and segmental approach to imaging of congenital heart disease. In: Ho V, Reddy GP, eds.* Cardiovascular Imaging. *1st ed. Philadelphia: Saunders Elsevier; 2010.)*

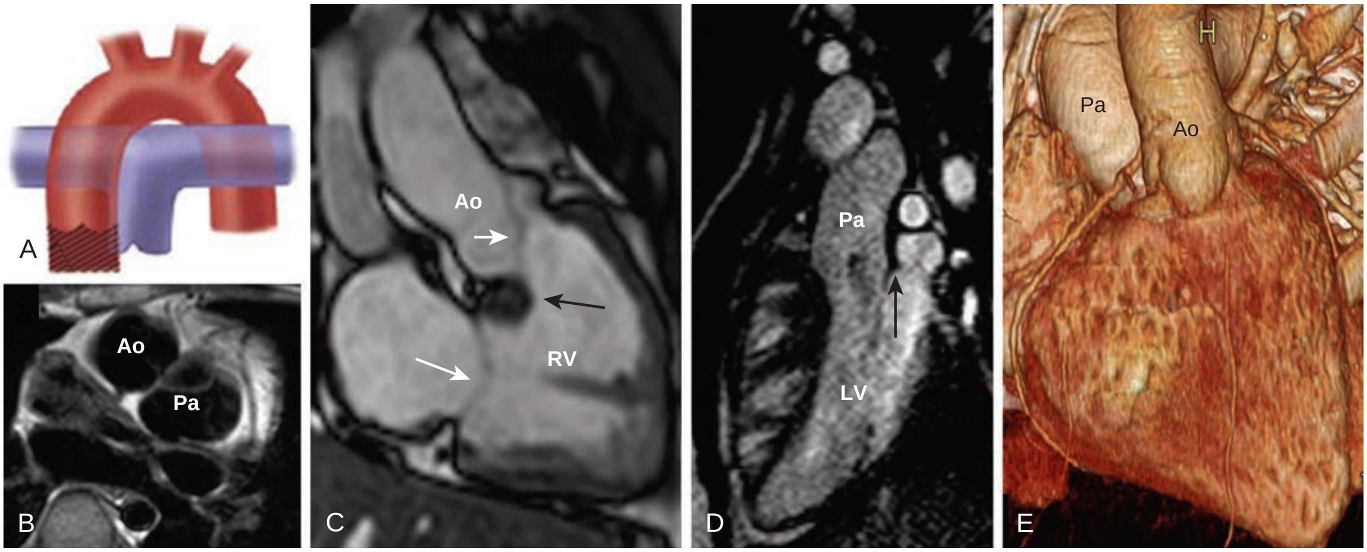

**Figure 63.15. Conus in dextroposed transposition of the great arteries (D-TGA).** (A) and (B) The aorta *(Ao)* lies anterior and to the right of the pulmonary artery (D-malposition). (C) The right ventricle *(RV)* is connected to the aorta by a muscular infundibulum *(black arrow)*, resulting in lack of fibrous contiguity between the tricuspid valve *(long white arrow)* and the aortic valve *(short white arrow)*. (D) The left ventricle *(LV)* is connected to the main pulmonary artery *(Pa)* with absence of an intervening conus, resulting in direct fibrous contiguity between the aortic and pulmonary valves *(arrow)*. (E) Three-dimensional volume rendering of a patient with D-TGA. *H,* Heart.

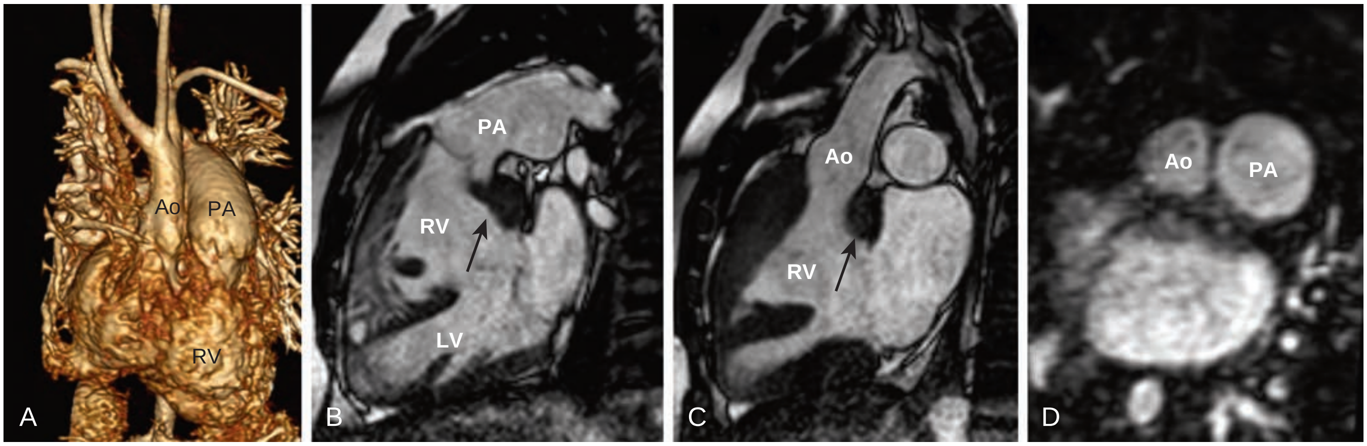

**Figure 63.16. Double outlet right ventricle *(RV)* with bilateral conus and side-by-side great arteries.** (A) Three-dimensional volume rendering of double outlet *RV* showing both great arteries arising from the *RV*. (B) and (C) Presence of a subpulmonary and subaortic conus *(arrows)*. (D) Side-by-side great arteries. *Ao,* Aorta; *LV,* left ventricle; *PA,* pulmonary artery.

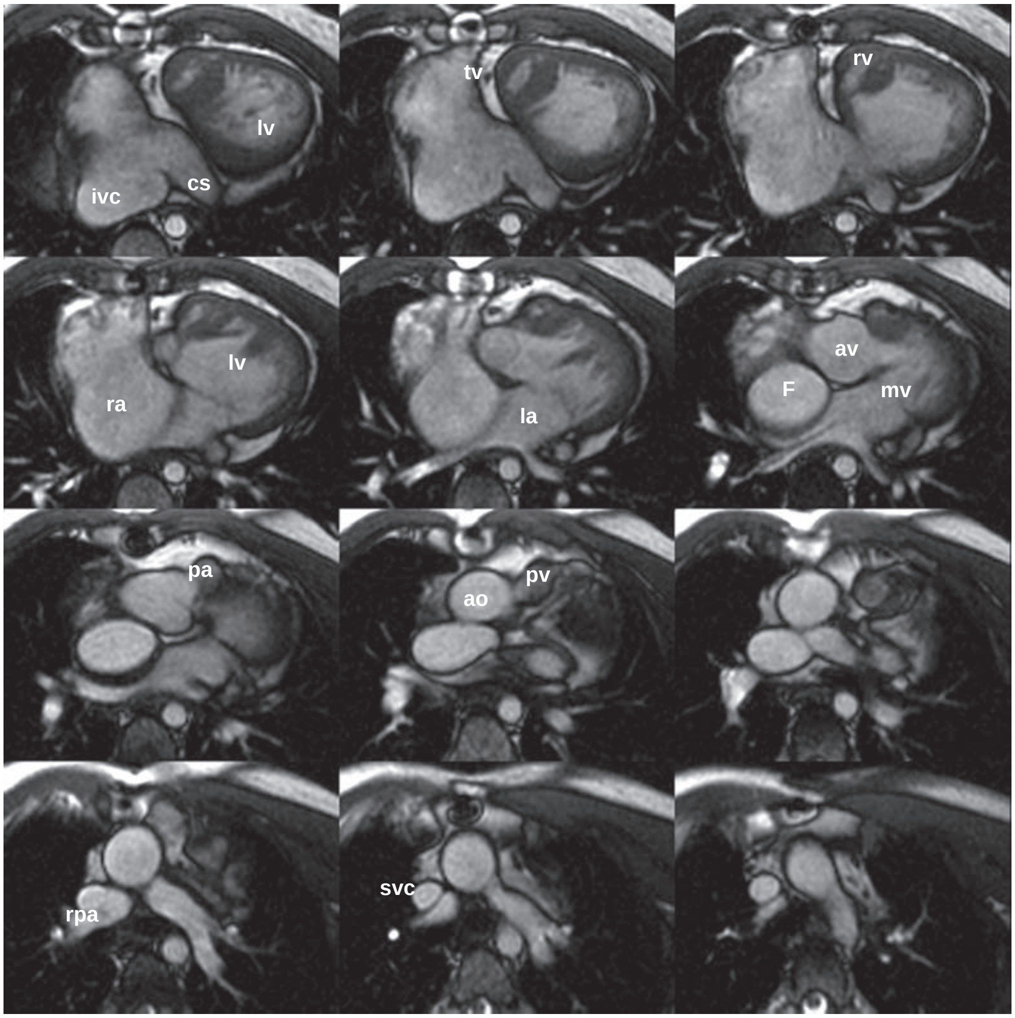

**Figure 63.17. Illustrative case study of segmental approach to imaging of congenital heart disease.** *ao,* Aortic outflow; *av,* aortic valve; *cs,* coronary sinus; *F,* Fontan; *ivc,* inferior vena cava; *la,* left atrium; *lv,* left ventricle; *mv,* mitral valve; *pa,* pulmonary artery; *pv,* pulmonary veins; *ra,* right atrium; *rpa,* right pulmonary artery; *svc,* superior vena cava; *tv,* tricuspid valve.

## SUGGESTED READINGS

Krishnamurthy R. Embryologic basis and segmental approach to imaging of congenital heart disease. In: Ho V, Reddy GP, eds. *Cardiovascular Imaging*. 1st ed. Philadelphia: Saunders/Elsevier; 2010.

Shinebourne EA, Macartney FJ, Anderson RH. Sequential chamber localization-logical approach to diagnosis in congenital heart disease. *Br Heart J*. 1976;38:327–340.

Van Praagh R. The segmental approach to diagnosis in congenital heart disease. *Birth Defects*. 1972;8:4–23.

Van Praagh R. Diagnosis of complex congenital heart disease: morphologic-anatomic method and terminology. *Cardiovasc Intervent Radiol*. 1984;7:115–120.

Van Praagh S, Kreutzer J, Alday L, et al. Systemic and pulmonary venous connections in visceral heterotaxy, with emphasis on the diagnosis of the atrial situs: a study of 109 postmortem cases. In: Clark E, Takao A, eds. *Developmental Cardiology, Morphogenesis and Function*. Mt. Kisco, NY: Futura; 1990.

# 64

# Pediatric Echocardiography

*James René Herlong*

Echocardiography is the primary imaging modality used to assess the heart and extracardiac thoracic vasculature in children. Echocardiography is sufficiently robust to be used as the sole imaging modality in assessing cardiac anatomy before surgical repair in most pediatric patients with congenital heart disease, so familiarity with echocardiography is important for anyone involved in diagnostic imaging in these patients.

## TECHNIQUE

Transthoracic echocardiography is an ultrasound technique that is optimized for imaging the moving heart. Standard imaging windows that are free of interference from the lungs are illustrated in Fig. 64.1. These windows allow imaging of the heart in multiple planes. These planes are based on the axes of the heart and not on the axes of the body (Fig. 64.2).

In each acoustic window, the heart is imaged in orthogonal planes. Because the heart is a three-dimensional structure and because ultrasonography is a tomographic imaging technique, slow sweeps in each view are necessary to understand the complex relationships between various segments of the heart. Three- and four-dimensional echocardiography are becoming ever more robust, but they are not yet capable of high-resolution imaging of the entire heart. Currently, the utility of these techniques is largely in the assessment of the cardiac valves, particularly the atrioventricular valves.

Assessment of ventricular systolic function is performed in every echocardiographic examination. Among the various techniques of quantifying left ventricular systolic function, the left ventricular shortening fraction is the most easily accomplished and universally used. Standards for left ventricular dimensions and shortening fraction according to body surface area are available in standard references. Assessment of left ventricular diastolic function is less exact, and techniques continue to be developed to evaluate this rather elusive entity. The method with the most promise is tissue Doppler imaging, which uses the Doppler principle to measure the high amplitude but low velocity signals derived from myocardial motion.

Doppler echocardiography uses color and spectral Doppler in the same manner as in vascular ultrasound imaging. One important difference is that when using color Doppler, the color map is always set so that flow toward the transducer is red, whereas flow away from the transducer is blue. Color Doppler imaging is useful for screening for valvar stenosis or regurgitation, septal defects, and arterial and venous stenoses. Color Doppler should be used to complement two-dimensional imaging, not to replace it, because color Doppler obscures anatomy.

In a typical echocardiographic examination, all cardiac valves are assessed by spectral Doppler, as are the aortic arch at the isthmus and any identified septal defects. As with all Doppler applications, the most accurate assessment is obtained by aligning the angle of interrogation exactly along the direction of flow. The simplified Bernoulli equation states that the pressure gradient across an area is approximately equal to four times the measured Doppler velocity squared ($4v^2$). By using this equation, gradients are estimated in each of the locations that are assessed by spectral Doppler. In general, peak instantaneous pressure gradients across semilunar valves and in the arterial system should be less than 15 mm Hg, and mean gradients in veins and across atrioventricular valves should be less than 3 mm Hg.

Other differences from noncardiac ultrasound involve sedation and image archiving. Because accurate assessment of anatomy and

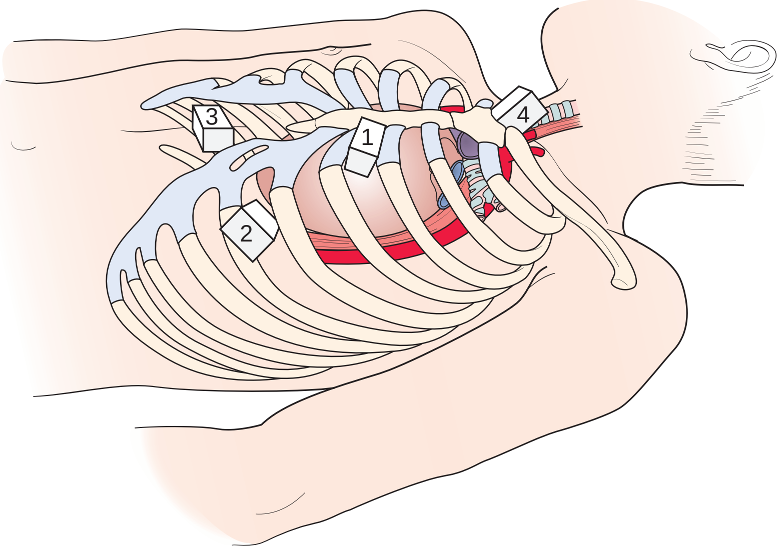

**Figure 64.1. Probe positions for the four standard windows used in transthoracic echocardiography.** Position *1,* parasternal; position *2,* apical; position *3,* subcostal; position *4,* suprasternal. *(From Snider AR, Serwer GA, Ritter SB.* Echocardiography In Pediatric Heart Disease*, 2nd ed, St. Louis: Mosby–Year Book; 1997.)*

## Abstract:

This chapter discusses the technique, interpretation and reporting of the normal pediatric echocardiographic examination. It compares and contrasts echocardiography with other ultrasound imaging techniques and points out differences between the pediatric echocardiogram and the adult echocardiogram. Schema for formulating a diagnosis and for formatting a report are presented, as well.

## Keywords

Pediatric Echocardiogram
Pediatric Transthoracic Echocardiogram
Pediatric Transesophageal Echocardiogram
Pediatric Doppler Echocardiography
Diagnostic Imaging of Congenital Heart Disease

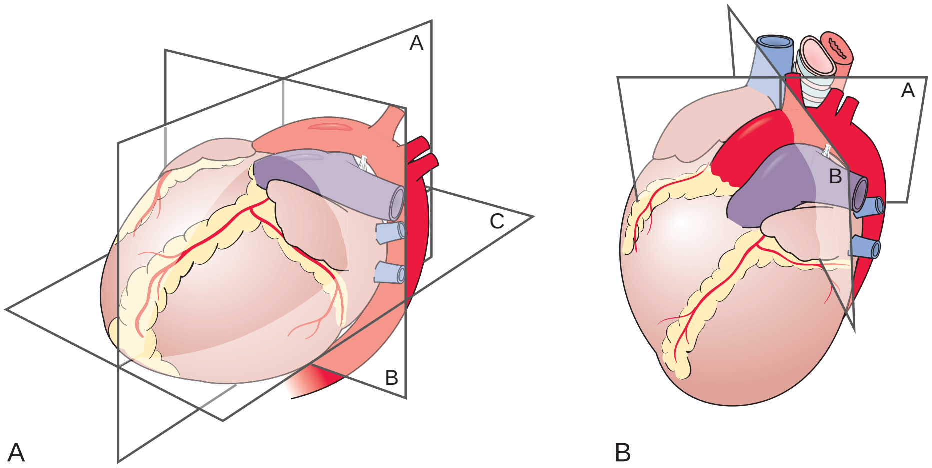

**Figure 64.2.** (A) Three standard cardiac imaging planes. Plane *A* is a long-axis plane parallel to the major axis of the left ventricle. Plane *B* is a short-axis plane perpendicular to the major axis of the left ventricle. Plane *C* is a coronal plane of the heart through the cardiac apex that produces a standard four-chamber view. (B) Two standard suprasternal notch imaging planes. Plane *A* is a long-axis plane parallel to the major axis of the aortic arch. Plane *B* is a short-axis plane perpendicular to the major axis of the aortic arch. *(From Snider AR, Serwer GA, Ritter SB.* Echocardiography in Pediatric Heart Disease*, 2nd ed, St. Louis: Mosby–Year Book; 1997.)*

**BOX 64.1** Format for Organizing the Report of an Echocardiogram

Cardiac position
Description of venoatrial segment
Description of atrioventricular canal, including atrioventricular valves
Description of ventricles
Description of conotruncus
Description of semilunar valves
Description of coronary arteries
Description of aorta, including arch sidedness and branching as well as presence or absence of coarctation
Description of main and branch pulmonary arteries
Description of ductus arteriosus
Description of ventricular function
Description of pericardium and pericardial effusion
Description of any masses, vegetations, or thrombi
Presence or absence of pleural effusions
Comment upon diaphragm motion

function requires images free of patient movement and because accurate assessment of pressure gradients requires the patient to be in a resting state, sedation may be necessary in patients younger than 3 years. Because assessment of function and complex anatomy requires viewing moving images, echocardiograms are archived as video clips rather than as still-frame images.

Transesophageal echocardiography in the pediatric population is used primarily in the operating room during surgery for congenital heart disease and in the interventional cardiac catheterization laboratory. Techniques are similar to those previously described.

## FORMULATING A DIAGNOSIS

Once the images have been obtained, a comprehensive diagnosis must be constructed; this is accomplished by using the segmental approach to cardiac anatomy (see Chapter 63). A common template for reporting the findings of an echocardiogram is presented in Box 64.1. Note that the scheme is logical and largely follows the blood flow through the various segments of the heart.

### KEY POINTS

- Most pediatric patients with congenital heart disease are taken to the operating room on the basis of an echocardiographic diagnosis alone.
- Standard imaging planes for echocardiography relate to the axes of the heart, not to the axes of the body.
- The heart is best understood by considering its anatomy segmentally.

## SUGGESTED READINGS

Ayers NA, Miller-Hance W, Fyfe DA, et al. Indications and guidelines for performance of transesophageal echocardiography in the patient with pediatric acquired or congenital heart disease: a report from the Task Force of the Pediatric Council of the American Society of Echocardiography. *J Am Soc Echocardiogr*. 2005;18:91–98.

Eidem BW, Cetta F, O'Leary PW, eds. *Echocardiography in Pediatric and Adult Congenital Heart Disease*. 2nd ed. Philadelphia: Lippincott Williams & Wilkins; 2014.

Lai WW, Geva T, Shirali GS. Guidelines and standards for the performance of a pediatric echocardiogram: a report from the Task Force of the Pediatric Council of the American Society of Echocardiography. *J Am Soc Echocardiogr*. 2006;19:1413–1430.

Lai WW, Mertens L, Cohen MS, et al. *Echocardiography in Pediatric and Congenital Heart Disease: From Fetus to Adult*. 2nd ed. Hoboken, NJ: Wiley-Blackwell; 2015.

Lopez L, Colan SD, Frommelt PC, et al. Recommendations for quantification methods during the performance of a pediatric echocardiogram: a report from the Pediatric Measurements Writing Group of the American Society of Echocardiography Pediatric and Congenital Heart Disease Council. *J Am Soc Echocardiogr*. 2010;23:465–495.

Simpson J, Lopez L, Acar P, et al. Three-dimensional echocardiography in congenital heart disease: an expert consensus document from the European Association of Cardiovascular Imaging and the American Society of Echocardiography. *J Am Soc Echocardiogr*. 2017;30:1–27.

# 65

# Chest Radiography in Pediatric Cardiovascular Disease

*J. A. Gordon Culham and John B. Mawson*

The role of chest radiography in the diagnosis and evaluation of congenital cardiovascular disease continues to evolve. At one time a major tool in the assessment of heart disease, radiography now occupies an ancillary role, with echocardiography serving as the major primary investigation after physical examination, especially in the neonatal period. However, the chest radiograph still may provide the first indication of unsuspected cardiovascular disease, and in infants and children with known cardiac disease radiography offers an important overview of the heart and pulmonary circulation. Moreover, chest radiography is a vital tool in the early postoperative period and is useful in the follow-up of heart disease. These latter topics are beyond the scope of this chapter.

The major chest radiographic findings in patients with cardiac disease are cardiomegaly, pulmonary vascular changes (predominantly overcirculation or undercirculation), and signs of pulmonary venous hypertension and edema. However, several caveats need to be emphasized. First, children with relatively mild structural defects and even some children with severe or complex disease may have normal chest radiographs. This situation is particularly true in newborns. In addition, the chest radiograph usually does not provide useful information about specific chamber size, hypertrophy, or intracardiac connections or malformations. Echocardiography, magnetic resonance imaging, computed tomography, or angiography is needed for precise evaluation of intracardiac structure and function. Furthermore, findings such as a boot-shaped or egg-shaped heart are nonspecific for tetralogy of Fallot or transposition of the great arteries, respectively. On the other hand, plain radiographic findings may be specific for some extracardiac lesions, such as supracardiac total anomalous pulmonary venous return, pulmonary stenosis, aortic arch anomalies, and coarctation of the aorta.

A systematic approach to evaluation of the chest radiograph consists of an assessment of heart size, shape, and position; pulmonary vasculature; the airway and mediastinum; visceral situs; and skeletal abnormalities. Applying such an approach often results in the recognition of a cardiovascular disease category, which in turn leads to a differential diagnosis and the identification of the likely etiology of nonspecific clinical findings, such as congestive heart failure or cyanosis.

## TECHNIQUE

Proper exposure, centering, collimation, patient positioning, and inspiration are necessary to optimize the examination and its interpretation (e-Fig. 65.1). Many infant radiographs are obtained using the anteroposterior projection and supine position. Because of the small size of the chest, this technique results in little magnification of the heart, as can be seen in larger children. Beam angulation also may affect the appearance of the heart and great vessels. With lordotic positioning or low centering for a combined chest and abdomen radiograph, the heart may appear more globular, with an uplifted apex and accentuation of the pulmonary outflow tract; with reverse lordosis, much of the heart may be obscured by the hemidiaphragms. Oblique views are not useful for cardiac evaluation. Chest fluoroscopy is rarely used except to evaluate prosthetic valve function, the diaphragm, or airway dynamics.

## SYSTEMATIC INTERPRETATION

### Normal Anatomy and Physiology

One of the challenges in evaluating the chest radiographs of younger children is their variable anatomy and physiology. For example, the thymus is variable in size and position and may mimic cardiomegaly, abnormally positioned vessels, pericardial fluid, or a mediastinal mass (e-Fig. 65.2). It is rare for the thymus to extend posteriorly. The thymus usually causes few problems in the interpretation of chest radiographs in children older than 6 years.

Newborn infants have physiologic pulmonary hypertension, and as a result, large shunt lesions do not become apparent until the pulmonary vascular resistance falls, which usually manifests by 4 to 6 weeks (Fig. 65.3). Similarly, newborn infants may not show the expected changes of severe pulmonary stenosis or atresia if the ductus arteriosus is patent.

The physiology of small airways in infants and children up to approximately 2 years of age results in unique manifestations of pulmonary edema. Specifically, infants show hyperinflation as a response to interstitial edema, as happens in airway inflammation with bronchiolitis (see Figs. 65.3 and 65.4). The hyperinflation occurs as an adaptive response to the interstitial edema to prevent small airway closure. In the absence of clinical signs of a respiratory infection or aspiration, hyperinflation is an important sign of early pulmonary edema.

### Heart Size

The size of the heart can be difficult to assess in the frontal projection of infants and young children because of the presence of the relatively large thymus and poor inspiration (see e-Figs. 65.1 and 65.2). Measurement of the cardiothoracic ratio is of little use. The lateral view provides a more reliable indication of true heart size by permitting an assessment of the anteroposterior dimension without interference from the thymus. However, the thymus does fill in the retrosternal space, obscuring the right ventricular outflow tract. Posterior displacement of the trachea can be indicative of cardiac enlargement. In older children, the frontal radiograph is more useful; however, the radiologist should evaluate both views to assess the three-dimensional volume of the heart. In a child with pectus excavatum, the heart may appear large in the frontal view but compressed on the lateral view. Marked cardiomegaly is seen in children with severe valve regurgitation, especially tricuspid valve disease (Ebstein anomaly), pericardial effusion, and cardiomyopathy, and it is rarely seen in children with cardiac tumors. Mediastinal masses may mimic cardiomegaly (Box 65.1, e-Fig. 65.5).

### Pulmonary Vasculature

Chest radiography provides a window into the pulmonary circulation, which is the main area in which chest radiography supplements the information gained from echocardiography. The pulmonary vasculature may show evidence of increased flow, decreased flow, normal flow, or pulmonary venous hypertension. The assessment

## Abstract:

In this chapter we review the role and limitations of conventional chest radiography in the detection and evaluation of congenital cardiovascular disease in children. An approach to the interpretation is suggested. Cases illustrate the common findings as well as the unique anatomy, physiology and cardiovascular pathology of infants and young children.

## Keywords:

Chest Radiography
Chest X-ray
Congenital Heart Disease
Congenital Cardiovascular Disease

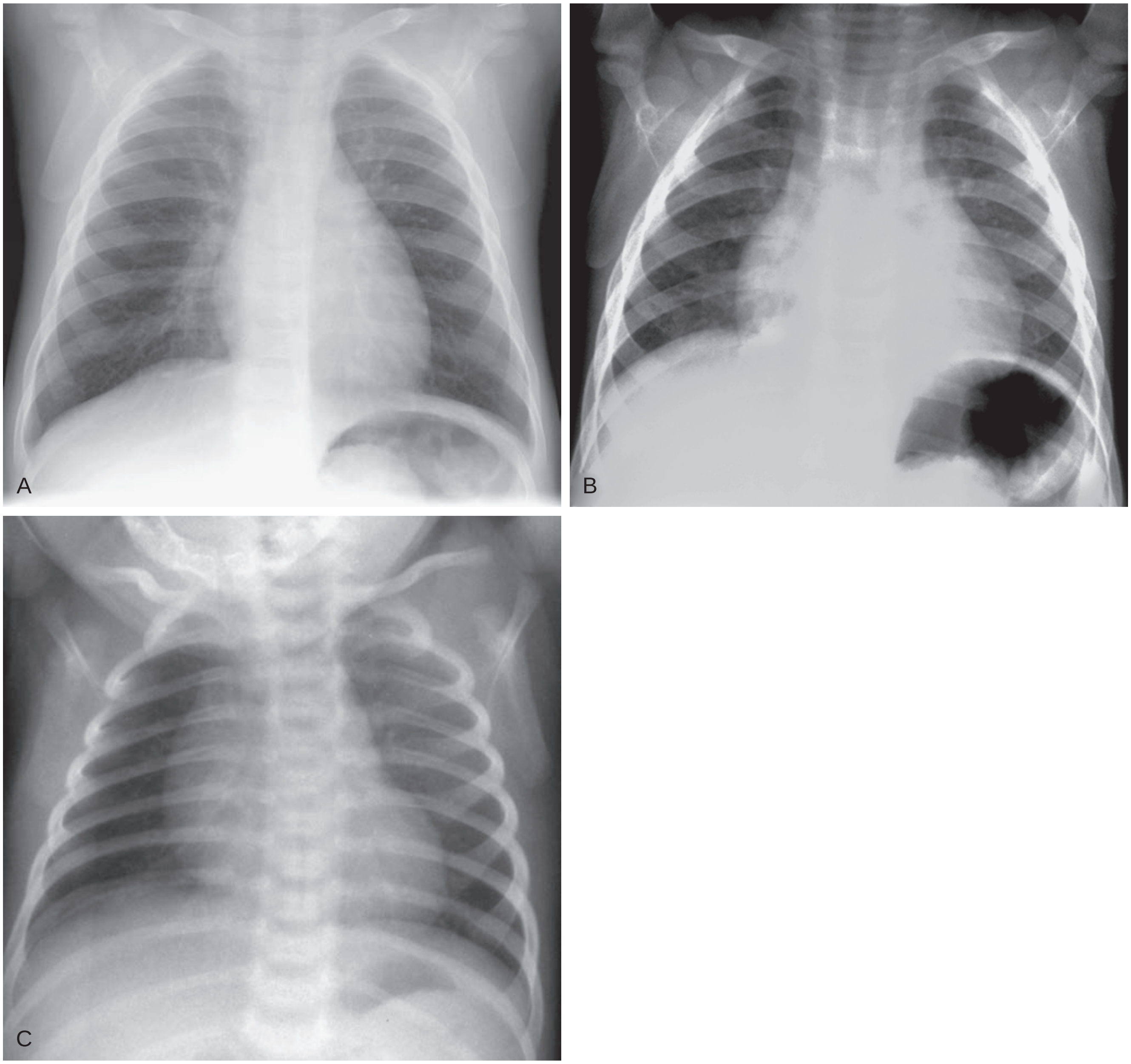

**e-Figure 65.1. Normal chest examination in an infant.** Frontal radiographs in inspiration (A) and expiration (B) show the profound impact of an expiratory radiograph on the appearance of the heart and lungs. In another example (C), a lucent right lung reflects patient rotation to the right rather than asymmetric pulmonary blood flow.

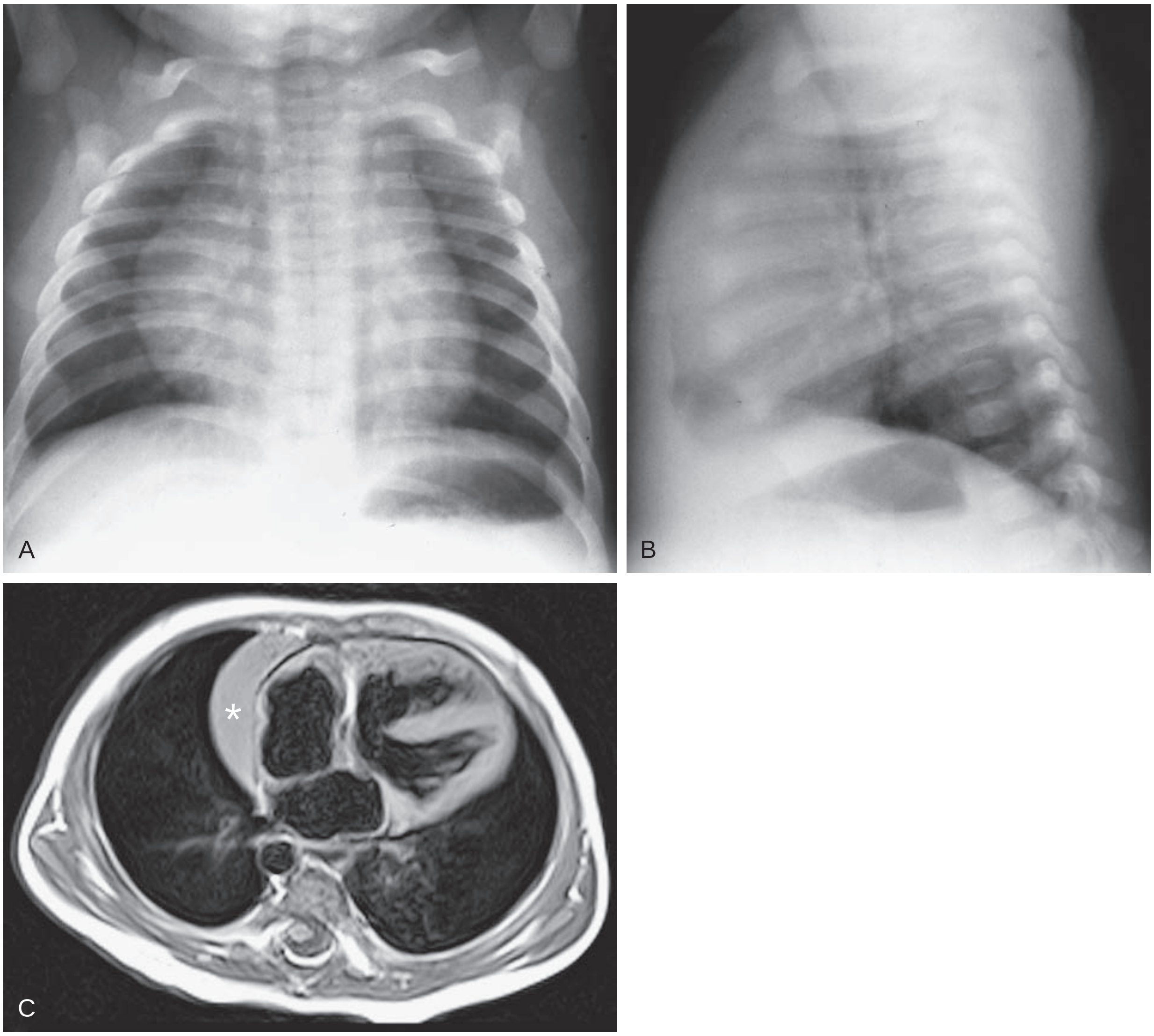

**e-Figure 65.2. Normal chest examination in an infant.** A frontal chest radiograph (A) shows a large cardiomediastinal silhouette, which on the lateral view (B) reflects a normal heart and a large retrosternal thymus. In another child, T1-weighted axial MRI of the chest (C) shows the right lobe of the thymus *(star)* beside the right atrium. Note also the ventricular septal defect, right ventricular hypertrophy, and right-sided descending aorta in this child with tetralogy of Fallot.

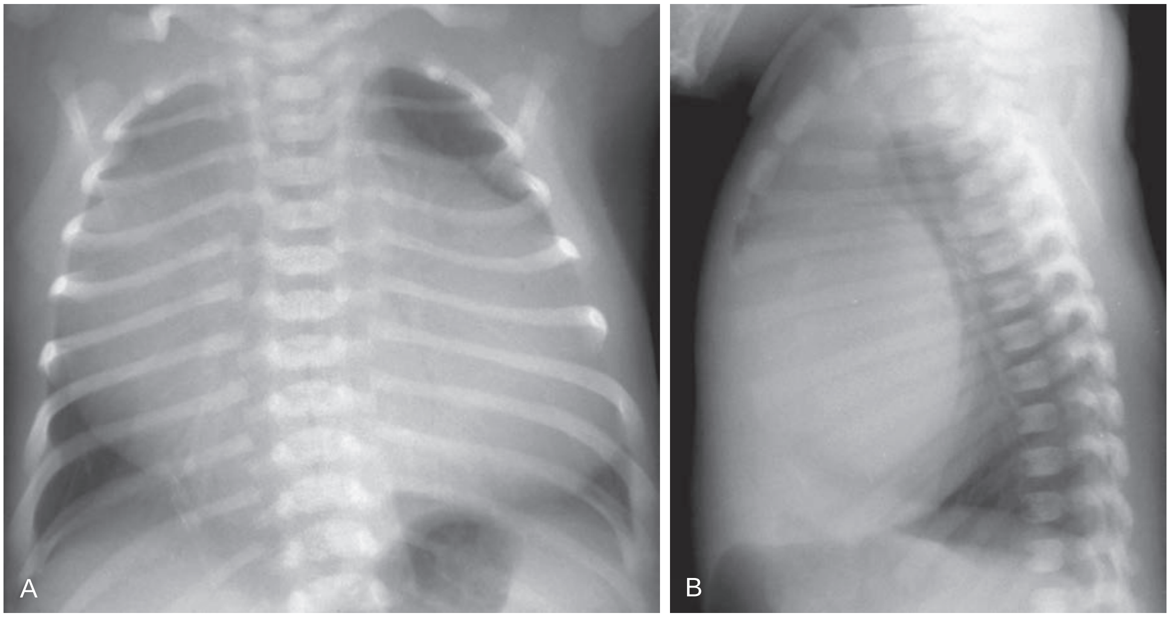

**e-Figure 65.5. Ebstein anomaly in an infant.** Frontal (A) and lateral (B) chest radiographs show severe cardiac enlargement. Volume loading of the right atrium and the atrialized portion of the right ventricle account for the cardiac enlargement.

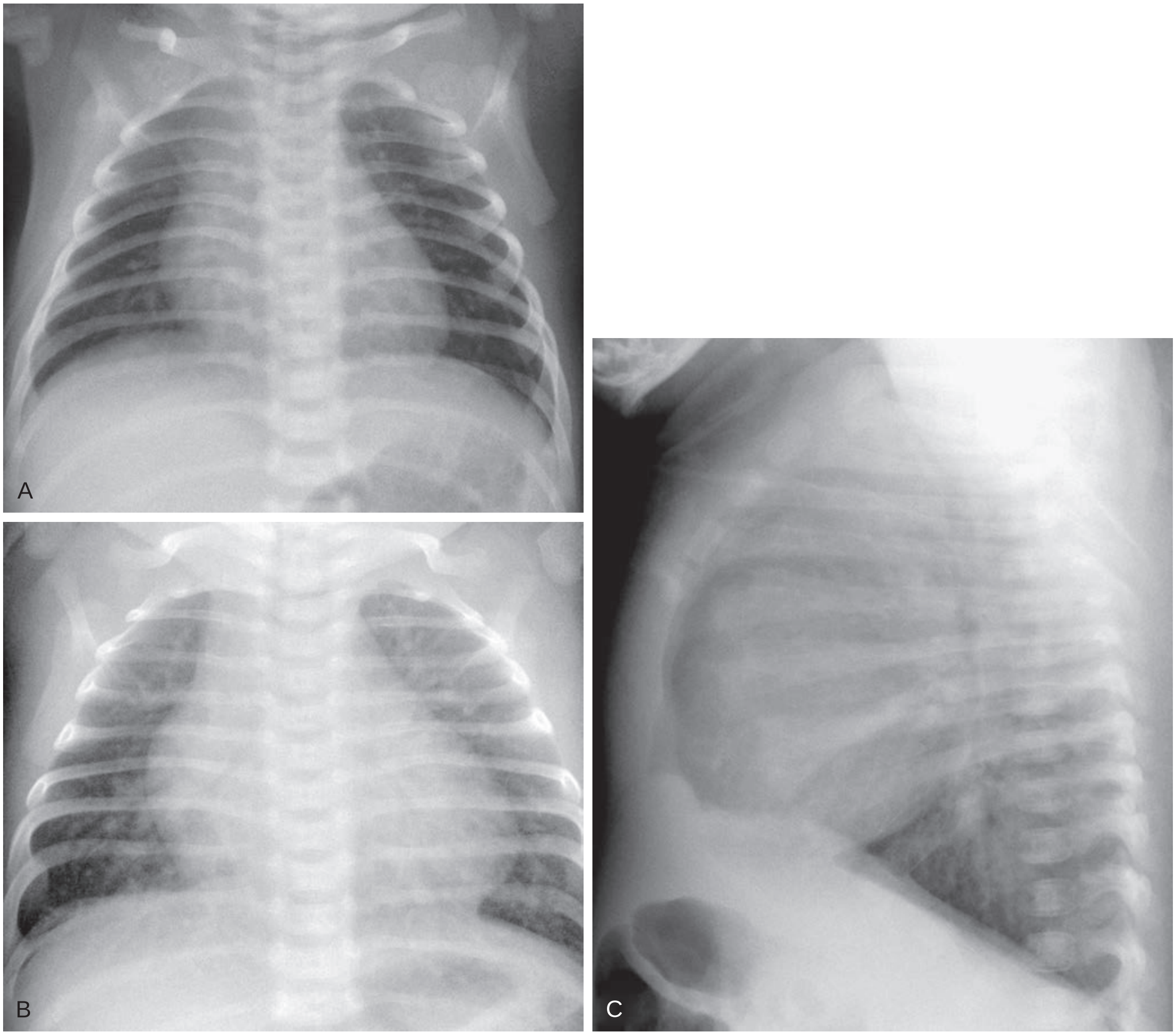

**Figure 65.3. Complete transposition of the great arteries in a neonate.** A frontal radiograph (A) on day 1 of life shows a heart that is within normal limits in size and shows normal pulmonary vascularity. Frontal and lateral radiographs of the same child at 7 weeks of age (B and C) show an enlarged heart and increased pulmonary vascularity. Volume loading of the heart and pulmonary circulation has occurred as pulmonary vascular resistance has dropped.

of the pulmonary vasculature is both important and difficult. Poor-quality images that are rotated or obtained during expiration are difficult to interpret (see e-Fig. 65.1). Many radiographs in younger children are obtained in the supine position, and therefore flow is symmetric from base to apex.

**BOX 65.1** Differential Diagnosis of Severe Cardiomegaly

- Volume loading, as seen with severe valve regurgitation (e.g., Ebstein anomaly or pulmonary atresia with intact ventricular septum), large shunts, or both
- Pump failure, as seen with cardiomyopathy (including anomalous origin of the left coronary artery from the pulmonary artery)
- Pericardial disease
- Cardiac or mediastinal mass

## Increased Pulmonary Vascularity

The size of the pulmonary vessels is noticeably larger only when the amount of flow doubles (thus when the pulmonary to systemic flow ratio is 2 : 1 or greater) (e-Figs. 65.6 and 65.7). Smaller shunts are not detectable. Increased vascularity occurs in large left-to-right shunts, admixture lesions without obstruction to pulmonary blood flow, and in high-output states such as severe anemia. To evaluate pulmonary vascularity, the size of the end-on pulmonary artery

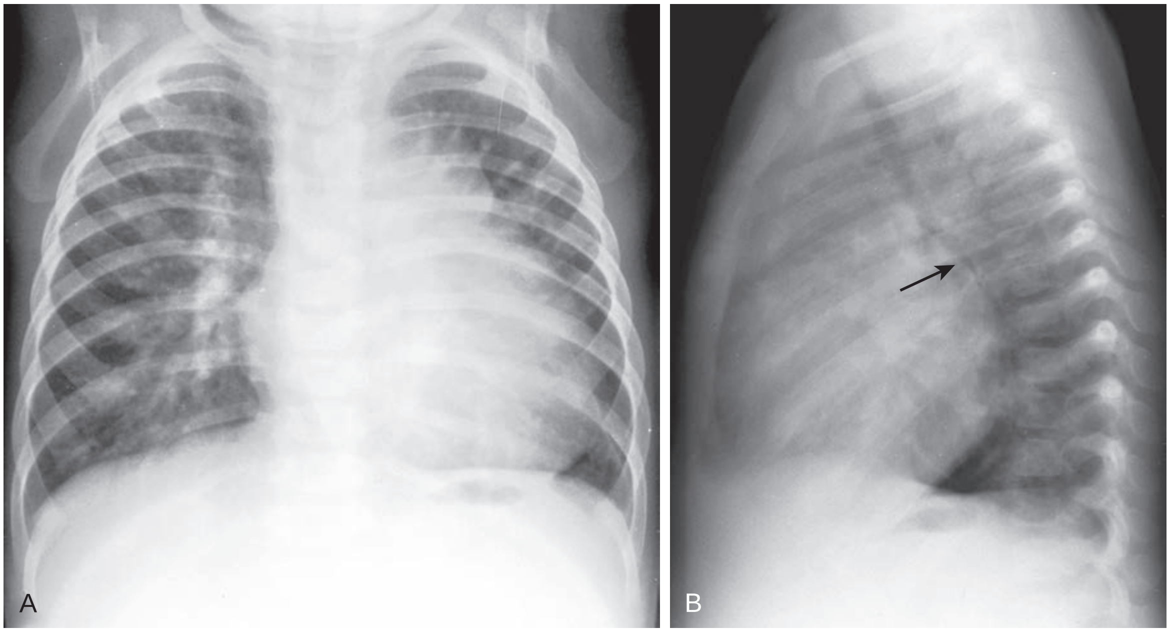

**e-Figure 65.6. Ventricular septal defect in an infant.** Frontal (A) and lateral (B) chest radiographs show cardiomegaly with increased pulmonary vascularity. The pulmonary vessels are prominent in the hilar regions and taper in a normal fashion, extending into the periphery of the lung. On the lateral radiograph (B), the left bronchus is displaced posteriorly by the enlarged left atrium *(arrow).* The lungs are hyperinflated and mild interstitial thickening is present, representing congestive heart failure.

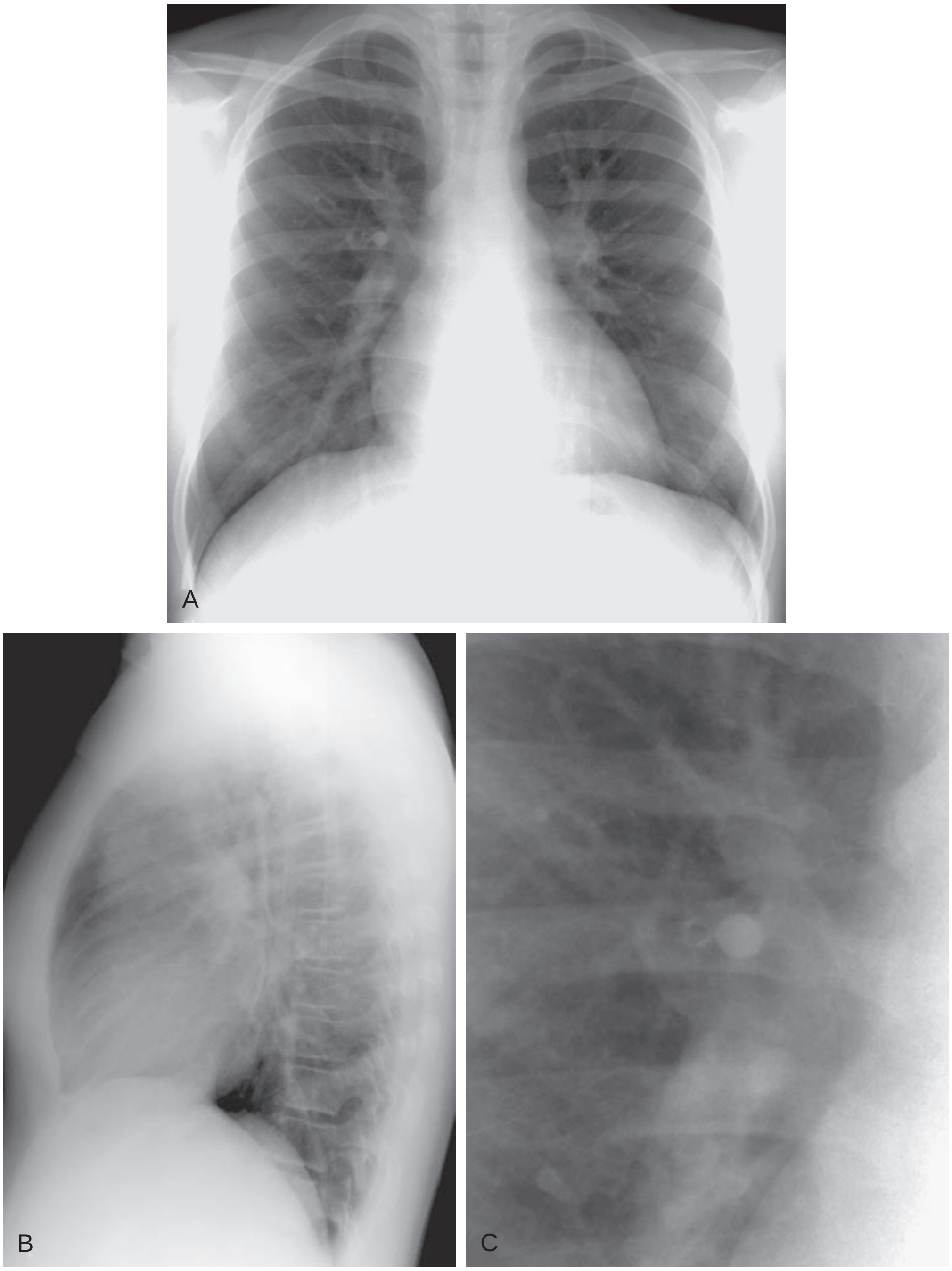

**e-Figure 65.7. Ventricular septal defect in an older child.** Frontal (A) and lateral (B) chest radiographs show mild cardiac enlargement and increased vascularity. A magnified view of the right hilum (C) shows that the pulmonary artery is larger than its accompanying bronchus.

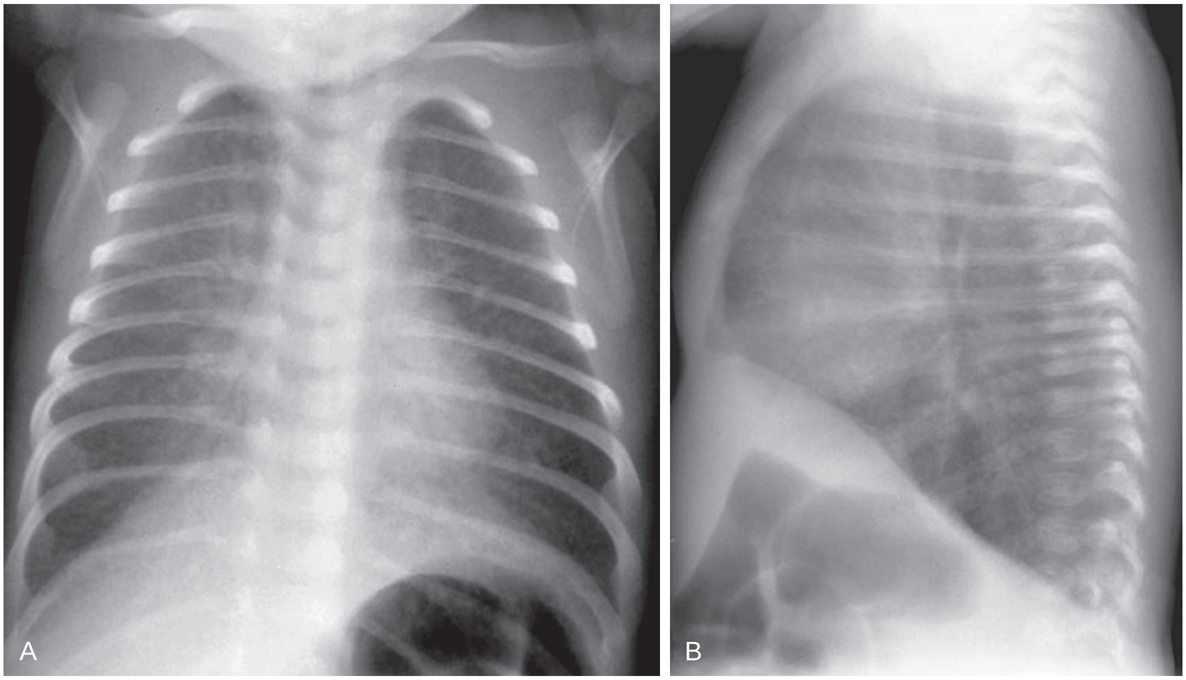

**Figure 65.4. Total anomalous pulmonary venous return with obstruction in an infant.** Frontal (A) and lateral (B) radiographs show a normal heart size, marked hyperinflation, and interstitial thickening consistent with pulmonary edema.

### BOX 65.2 Differential Diagnosis for the Radiographic Appearance of Decreased Pulmonary Vascularity With Cyanosis

Tetralogy of Fallot
Tricuspid atresia
Ebstein anomaly
Critical pulmonary stenosis or pulmonary atresia with an intact ventricular septum
Complex cardiac anomalies associated with significant pulmonary stenosis or atresia

### BOX 65.3 Differential Diagnosis for the Radiographic Appearance of Pulmonary Venous Congestion

Total anomalous pulmonary venous connection with obstruction
Pulmonary vein atresia
Severe pulmonary vein hypoplasia or stenosis
Cor triatriatum
Mitral atresia
Hypoplastic left heart syndrome
Cardiomyopathy
Critical aortic stenosis
Severe aortic coarctation
Large shunts with congestive heart failure
Combined shunts with left-sided obstruction

to the adjacent bronchus can be compared. An arterial dimension greater than that of the bronchus is suggestive of increased flow. However, a slightly larger dimension can be seen normally. The larger vessels extend more peripherally into the lung. Increases in pulmonary blood flow should be accompanied by a proportional increase in heart size because of volume loading.

## Decreased Pulmonary Vascularity

Identifying decreased vascularity is more difficult than identifying increased flow (e-Fig. 65.8). A cyanotic child beyond the newborn period whose flow appears to be within normal limits very likely has a right-to-left shunt Box 65.2.

## Normal Pulmonary Vascularity

The pulmonary vascularity is normal in the presence of valve lesions without shunting or congestive heart failure, in small to moderate shunts, and even in certain cases of balanced complex congenital heart disease. For example, in a patient with a functionally single ventricle and moderate pulmonary stenosis, the flow to the lungs is neither increased nor decreased.

## Pulmonary Venous Hypertension and Pulmonary Edema

Early pulmonary venous hypertension often manifests as hyperinflation in infants and children younger than 2 years (see Fig. 65.4 and e-Fig. 65.6). As interstitial fluid accumulates, the perihilar bronchi and vessels become poorly defined. Septal (i.e., Kerley) lines are uncommon in children. Eventually, frank alveolar pulmonary edema is seen. In a supine patient, pleural fluid will layer posteriorly creating hazy opacity over the entire thorax. In the presence of severe heart failure, it can be difficult to determine whether the cause is pulmonary venous hypertension alone or is associated with an underlying large left-to-right shunt (e-Fig. 65.9) (Box 65.3). Pulmonary edema can obscure vessel detail, and left-sided heart failure can distend the vessels. The detection of heart disease can be difficult in the child who presents with an acute viral respiratory illness because the inflammation can produce ill-defined vascular markings and hyperinflation similar to the findings in congestive heart failure. Unlike in children with large shunts in whom the heart size is proportional to the increased

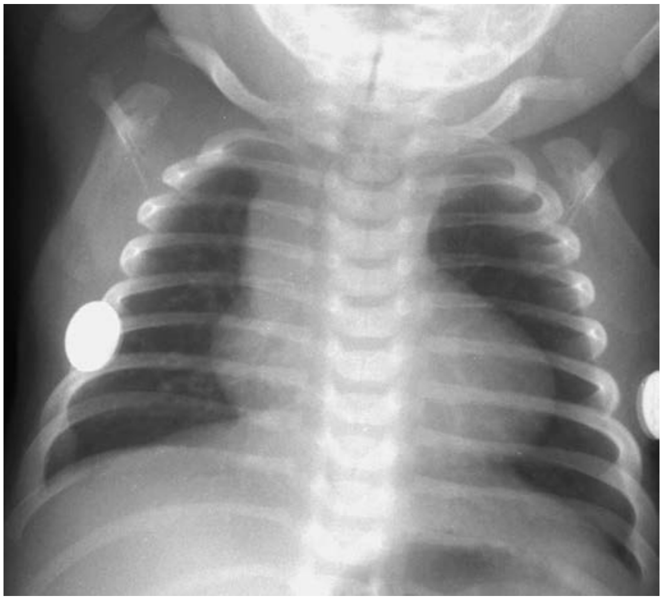

**e-Figure 65.8. Tetralogy of Fallot in an infant.** A frontal radiograph of the chest shows a mildly enlarged heart and decreased pulmonary vascularity. The aortic arch is left sided.

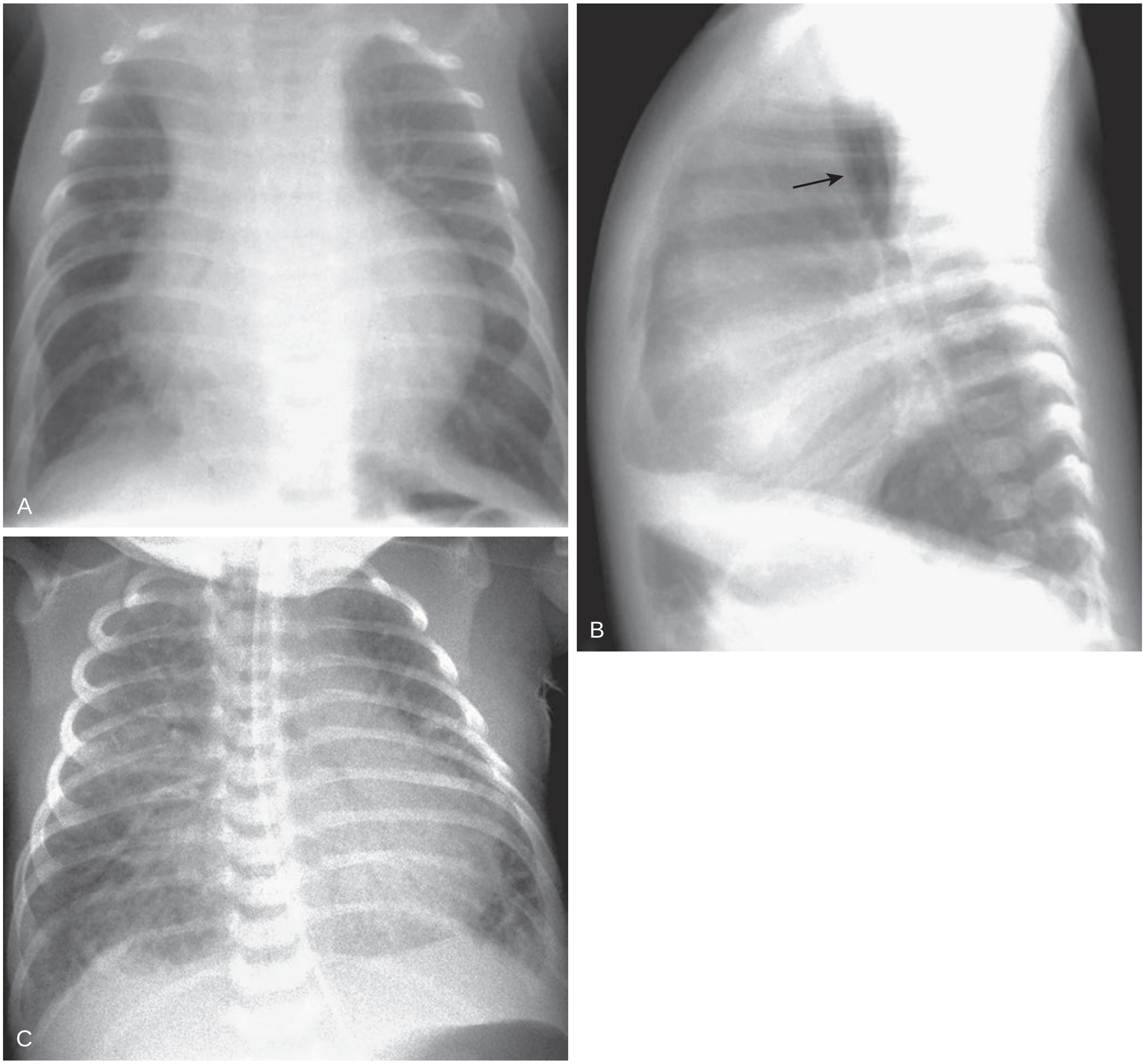

**e-Figure 65.9. Coarctation of the aorta.** Frontal (A) and lateral (B) chest radiographs in a 2-month-old show cardiomegaly, normal pulmonary blood flow, and evidence of congestive heart failure as shown by mild interstitial thickening and obvious hyperinflation. Note the posterior displacement of the trachea *(arrow)* by the enlarged heart on the lateral projection. In another child (C) who presented in the first week of life with severe congestive heart failure due to coarctation of the aorta, it is difficult to determine from the chest radiograph whether there is increased vascularity caused by a shunt, severe pulmonary venous hypertension, or a combination of the two. This child had no associated left-to-right shunt.

vascularity, children with left-sided obstruction or pump failure have a disproportionately large heart relative to the degree of increased vascularity (see e-Fig. 65.9A and B).

### Centralized Pulmonary Vascularity

Prominence of the perihilar vessels with rapid tapering as a sign of pulmonary arterial hypertension is rarely seen in children. In a rare variation of tetralogy of Fallot with absent pulmonary valve, large hilar vessels may be seen even during the newborn period due to severe pulmonary regurgitation and are not caused by pulmonary arterial hypertension (e-Fig. 65.10).

### Asymmetric Pulmonary Flow

The chest radiograph must be carefully evaluated for asymmetric flow, which can occur as a result of pulmonary arterial stenosis, hypoplasia or proximal absence, pulmonary venous obstruction, or disturbances in ventilation with secondary vasoconstriction, as well as postoperatively. Care must be taken to avoid misinterpretation of the rotated radiograph (see e-Fig. 65.1). In children with decreased pulmonary blood flow as a result of tetralogy of Fallot or pulmonary atresia, stenosis of the pulmonary artery (at the site of ductal insertion) is a common problem (e-Fig. 65.11).

## Airway and Mediastinum

The chest radiograph is evaluated for the presence of the thymus, a mediastinal mass, the side of the aortic arch, and the presence of a vascular ring. The size and position of the trachea is an important indicator of arch abnormalities. A careful search should be made on both frontal and lateral radiographs for displacement or narrowing of the trachea (e-Fig. 65.12).

Mechanical displacement or obstruction of large airways occurs in anomalies of the aortic arch, pulmonary arteries, and more severe forms of cardiomegaly (e-Fig. 65.13; also see e-Figs. 65.5–65.7, 65.9, 65.10, and 65.12). The position and contour of the descending aorta should be carefully examined. In coarctation of the aorta, the only sign in younger children may be a leftward convexity to the descending aorta (e-Fig. 65.14). Such a contour is seen often in older adults as a result of age-related tortuosity or ectasia, but it is abnormal in children.

## Situs

The chest radiographic assessment is incomplete unless abnormalities of abdominal and thoracic situs (the anatomic location of organs that are asymmetrically positioned in the body) are sought and the cardiac position relative to visceral situs is determined. Abnormal situs can be subtle, with a normal-appearing liver and stomach. Airway anatomy and lung morphology are valuable indicators of visceral situs. Dextrocardia in situs solitus is strongly associated with complex cardiac abnormalities (e-Fig. 65.15). Situs inversus has a small but increased risk of associated congenital heart disease. Symmetric bronchi are seen in most patients with right isomerism (asplenia) (e-Fig. 65.16) and in 68% of patients with left isomerism (polysplenia). Splenic dysfunction and intestinal malrotation occur in children with both right and left isomerism and should be investigated.

## Bony Abnormalities

A complete evaluation of the chest radiograph must include the bony thorax. Few skeletal abnormalities are strongly associated with congenital heart disease, but abnormalities of the spine (e.g., scoliosis, segmentation anomalies, and rib anomalies) and sternum (e.g., an abnormal number of ossification centers and caudal deficiency) occur. Rib notching is rarely seen in younger children with aortic coarctation, but may be present in adolescents and teenagers in whom intercostal artery collaterals have developed (e-Fig. 65.17). Bony changes are common after a thoracotomy, particularly when the surgery was performed in a neonate.

## CONCLUSION

The role of chest radiography has changed with the development of echocardiography. Previous texts and articles have either overstated or understated the utility of the chest radiograph. The carefully performed and thoughtfully interpreted chest radiograph continues to play a useful role in the care of children with congenital cardiovascular disease.

### KEY POINTS

- Changes in pulmonary vascular resistance influence the manifestations of cardiovascular disease in the newborn.
- Hyperinflation is a sign of congestive heart failure in infants.
- Chest radiographs may appear normal in children with serious heart disease.

### SUGGESTED READINGS

Donnelly LF, Gelfand KJ, Schwartz DC, et al. The “wall to wall” heart: massive cardiothymic silhouette in newborns. *Appl Radiol*. 1997;26:23–28.
Kellenberger CJ. Aortic arch malformations. *Pediatr Radiol*. 2010;40:876–884.
Laya BF, Goske MJ, Morrison S, et al. The accuracy of chest radiographs in the detection of congenital heart disease and in the diagnosis of specific congenital cardiac lesions. *Pediatr Radiol*. 2006;36:677–681.
Markowitz RI, Fellows KE. The effects of congenital heart disease on the lungs. *Semin Roentgenol*. 1998;33:126–135.
Strife JL, Sze RW. Radiographic evaluation of the neonate with congenital heart disease. *Radiol Clin North Am*. 1999;37:1093–1107.

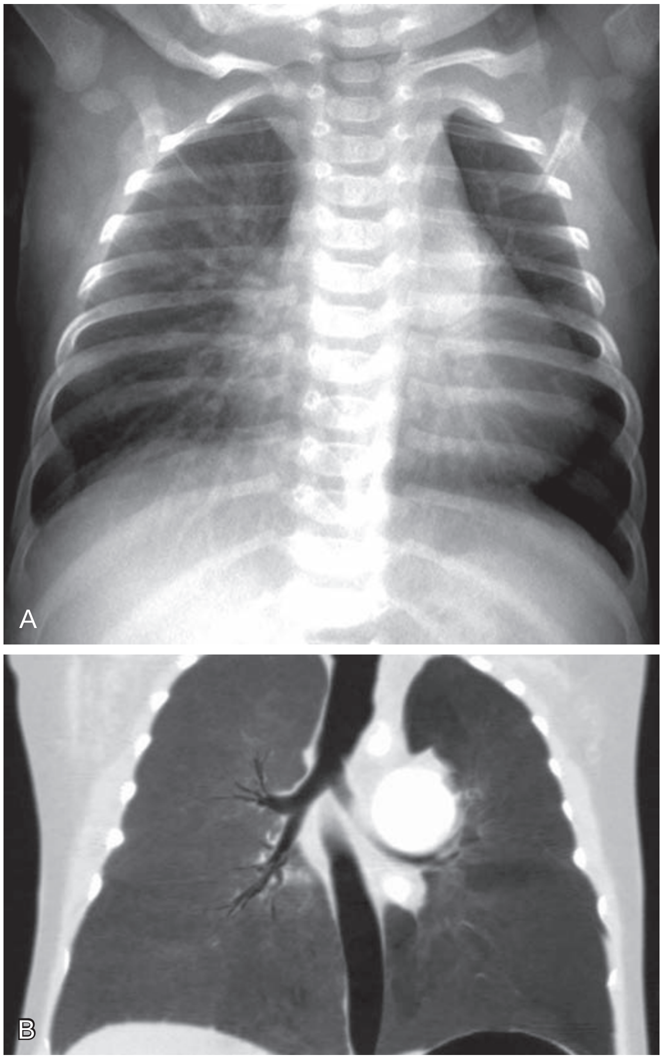

**e-Figure 65.10. Tetralogy of Fallot with an absent pulmonary valve.** A frontal chest radiograph (A) shows a significantly enlarged proximal left pulmonary artery in a 2-month-old. A coronal minimum intensity projection CT image (B) shows the marked dilation of the central left pulmonary artery and left bronchial compression.

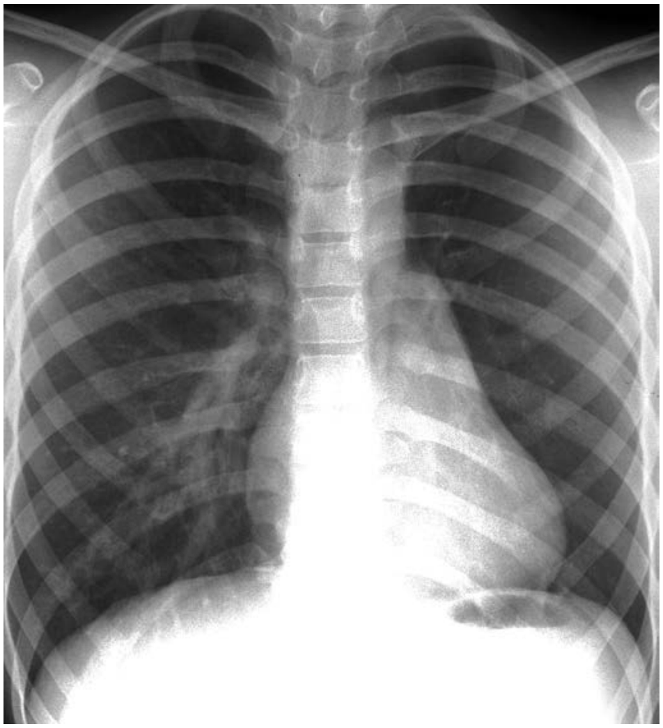

**e-Figure 65.11. Tetralogy of Fallot with left pulmonary artery stenosis in a 7-year-old girl.** A frontal chest radiograph shows decreased left lung vascularity as a result of pulmonary artery stenosis and hypoplasia. As a consequence of chronic underperfusion, the left lung and hemithorax are underdeveloped.

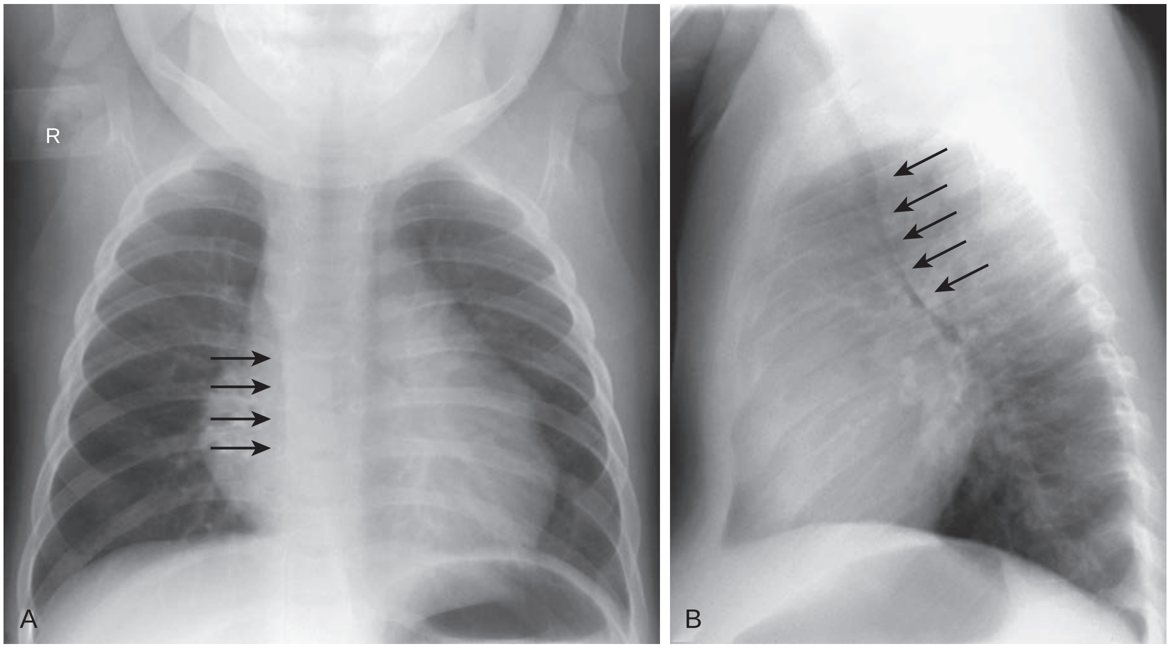

**e-Figure 65.12. Double aortic arch.** Frontal radiograph of the chest in an infant (A) shows a right-sided aortic arch and a right-sided descending aorta *(arrows).* The trachea is in the midline and the air column appears narrow on the frontal projection. The lateral view (B) shows anterior displacement and narrowing *(arrows)* of the air column as a result of the vascular ring.

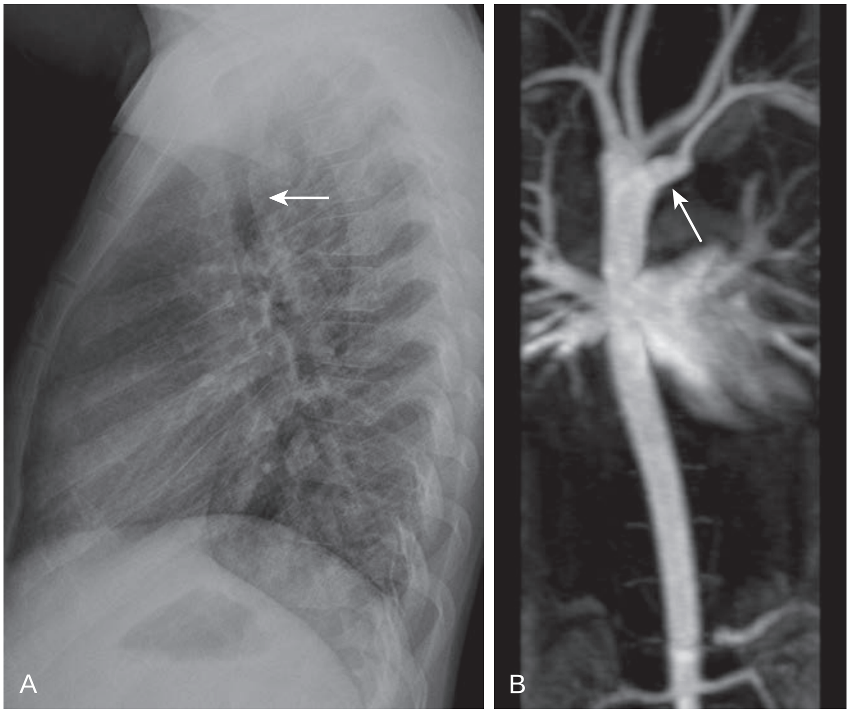

**e-Figure 65.13. Vascular ring in a teenage boy.** Lateral view of the chest (A) shows that the trachea *(arrow)* does not parallel the thoracic spine indicative of a vascular ring. A magnetic resonance angiogram (B) in this patient shows the ring consisting of a right aortic arch with an aberrant left subclavian artery arising from a diverticulum *(arrow)* with a posterior left-sided ligamentum arteriosum (not patent so not visualized) that connects the diverticulum to the left pulmonary artery (not shown).

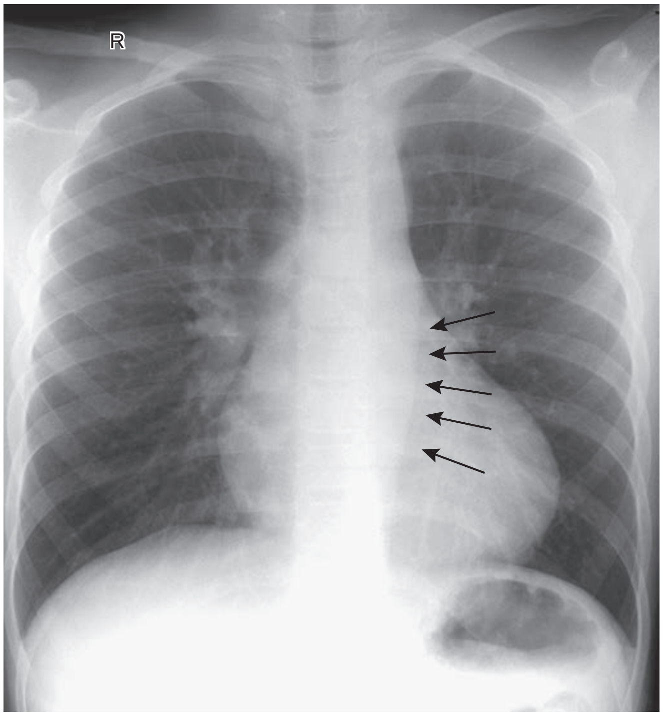

**e-Figure 65.14. Coarctation of the aorta in a 10-year-old girl.** A frontal radiograph of the chest shows an outward convexity to the descending thoracic aorta *(arrows)* caused by poststenotic dilation. The poststenotic dilation is more prominent than the arch above the coarctation.

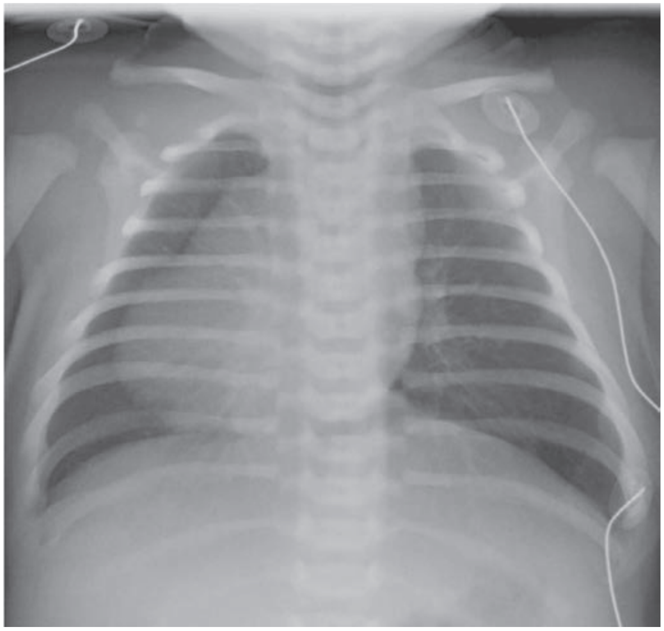

**e-Figure 65.15. Newborn with complex congenital heart disease and dextrocardia in situs solitus.** Discordance between the right-sided cardiac apex and the left-sided gastric air shadow is shown on a frontal chest radiograph. Note that the right hemidiaphragm is lower than the left due to the heart position.

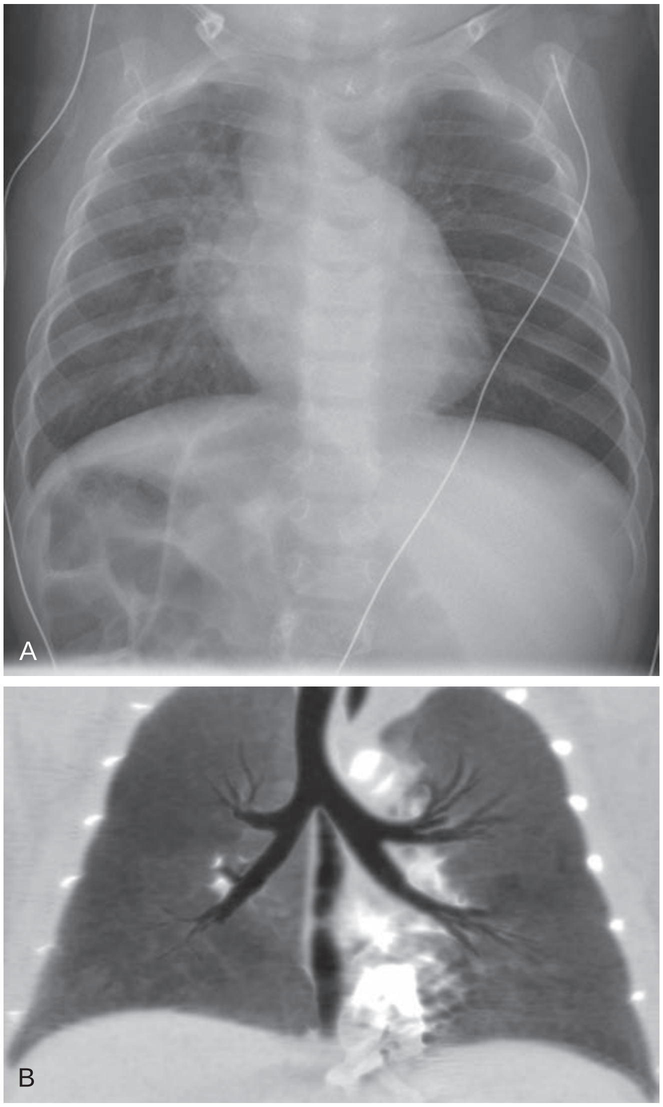

**e-Figure 65.16. A 7-month-old child with complex congenital heart disease and asymmetric pulmonary blood flow.** Discordance between the left-sided cardiac apex and the right-sided gastric air shadow is shown on a frontal chest radiograph (A). A coronal minimum intensity projection image from a computed tomography scan (B) confirms right isomerism with bilateral morphologic right bronchi.

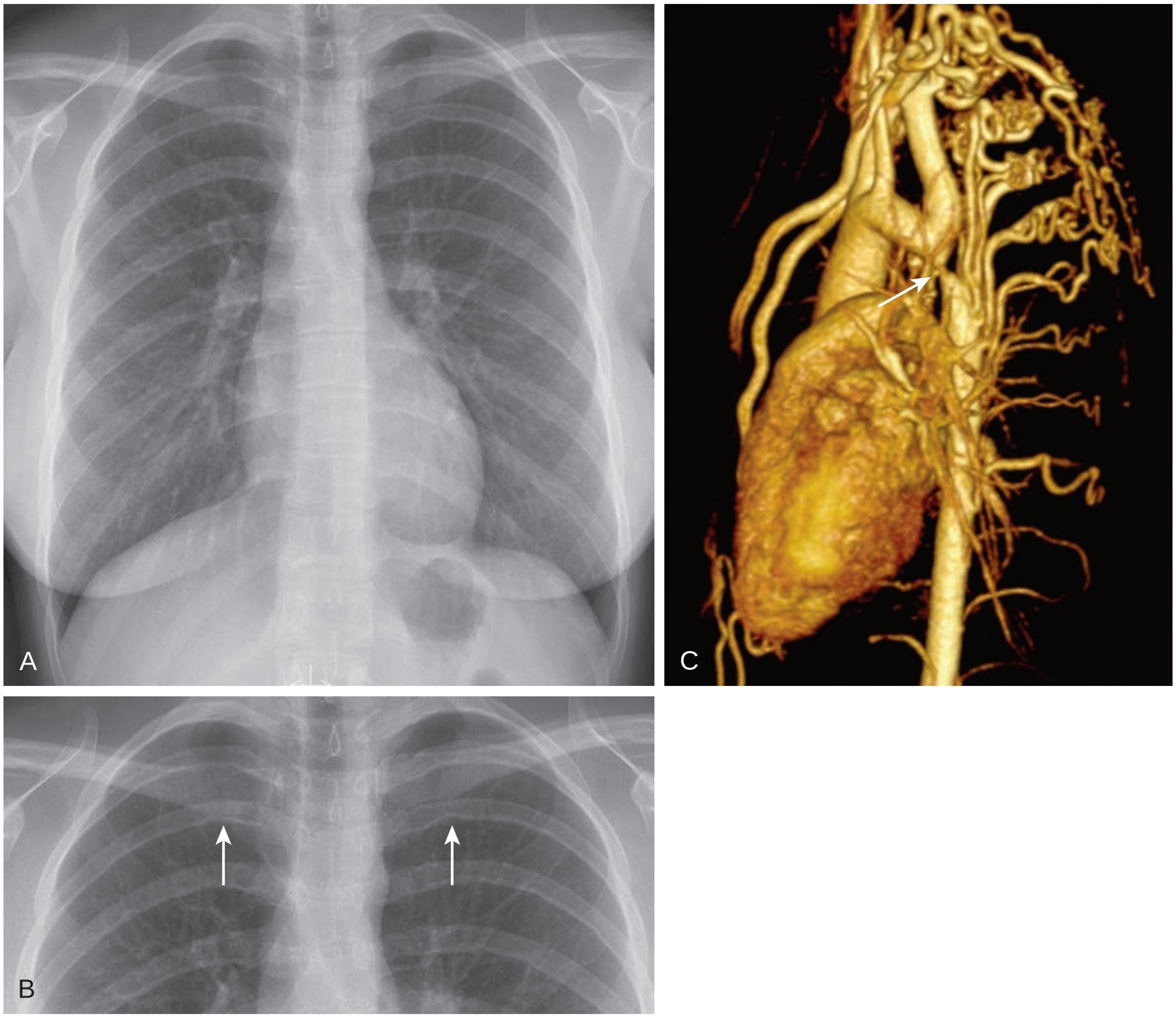

**e-Figure 65.17. Teenage girl with severe coarctation.** Frontal radiograph (A) shows bilateral posterior rib notching, which is better shown *(arrows)* on the radiograph highlighting the upper thorax (B). A volume-rendered three-dimensional image from a magnetic resonance angiogram (C) shows the severe narrowing of the aorta *(arrow)* and extensive collateral vessels.

# 66

# Pediatric Cardiothoracic Computed Tomographic Angiography

Elizabeth F. Sheybani and Donald P. Frush

Remarkable advances have occurred in noninvasive imaging evaluation of pediatric cardiothoracic vascular disorders. One such technologic advancement is multidetector array computed tomography angiography (CTA). CTA has become a primary imaging consideration for structural cardiovascular evaluation beginning as early as the newborn period.[1-7] Attention to technique is fundamental for pediatric CTA.[8-10] Without optimal or at least sufficient technical performance, diagnostic capabilities may be limited. This technical aspect (in addition to the diagnostic interpretation and communication of results) is the responsibility of the imaging expert. This chapter provides technical guidelines for performing pediatric thoracic CTA. The clinical examples provided illustrate these technical considerations.

## COSTS AND BENEFITS

Although echocardiography is generally the first-line imaging modality in evaluation of structural congenital cardiovascular disease, pediatric CTA offers several advantages over echocardiography and other imaging modalities.

The primary advantage of CTA is speed. With newer technology, such as wide detector multidetector computed tomography (MDCT) (e.g., 320 detector array single rotation acquisition)[2] or dual-source MDCT (Fig. 66.1),[11,12] an examination of the entire chest of an infant can be completed in less than 1 second. With echocardiography, magnetic resonance (MR) vascular imaging, or angiography, imaging times typically exceed 20 minutes and may last 1 to 2 hours. Its rapid examination time means that CTA is frequently performed without sedation, an important consideration given the potential risks posed by anesthesia to the developing brains of very young children,[13] as well as the frequently tenuous conditions of critical care patients undergoing imaging evaluation.

CTA is particularly useful in evaluation of extracardiac vascular structures and may be used for preoperative evaluation of pulmonary arteries, pulmonary veins, and/or aortic arch and other systemic arteries (such as aortopulmonary collaterals) in children with known congenital heart disease or for investigation of postoperative complications.[14,15] Computed tomography (CT) provides the best global assessment of the lungs and airways (e-Fig. 66.2 and Fig. 66.3).[5] Congenital cardiovascular disorders may cause tracheal compression or deviation (e.g., from vascular rings or pulmonary slings) with resulting obstructive effects or air trapping at the parenchymal level. In addition, CT can suggest or demonstrate associated primary abnormalities of the respiratory system, such as pulmonary hypoplasia or tracheomalacia.

The excellent spatial and temporal resolutions of CTA allow for high-quality off-line multiplanar and three-dimensional (3D) volumetric reconstructions and printed models, a major benefit over both echocardiography and direct angiography. The technical quality is also more consistent with CT compared with echocardiography, a more operator-dependent examination, and compared with magnetic resonance imaging (MRI), where parameter and sequence selection may result in variable study quality. In addition, many of the contraindications of MRI (e.g., pacemakers, internal support apparatus, and some surgical devices) are not contraindications to CTA and produce less image artifact than with MR angiography. The cost of CT is comparable with that of Doppler echocardiography, in general is less than that of MR, and is much less than that of conventional angiography.

CTA has some disadvantages. Similar to catheter angiography, CTA involves the use of ionizing radiation, which is not an issue with MRI or echocardiography. CT radiation doses can vary greatly depending on examination parameters and can be managed with utilization of dose optimization techniques. In general, CTA should be performed with a radiation dose similar to or lower than that of a routine chest CT. CTA dose estimates in young children can be less than 1.0 mSv.[1,11,16] When using electrocardiographic (ECG) synchronization, prospective triggering and smaller volume scanning substantially lower radiation dose when compared with retrospective gating.[17,18] With rare exceptions, properly performed pediatric CTA results in a lower radiation dose than conventional diagnostic angiographic evaluation. ECG-synchronized CTA may involve a greater radiation dosage than limited diagnostic conventional angiography or a nongated CTA. Intravenous (IV) contrast material is required for CTA but also is required for conventional angiography and for MR angiography. The risk of major adverse effects (e.g., airway spasm and cardiovascular collapse) from iodinated IV contrast material is extremely low in children.[19,20] In addition, there is no long-term deposition of components of iodinated contrast media as with gadolinium-based contrast agents. Unlike with echocardiography, MRI, and conventional angiography, pediatric thoracic CTA typically is used for morphologic assessment. Although cardiac function and other hemodynamic information can be obtained from CTA, this requires retrospective cardiac gating with a potential radiation dose penalty and thus is reserved for select circumstances.[18]

Various factors must be taken into consideration in choosing an appropriate imaging algorithm. Individual expertise is a strong consideration, as is the availability of the desired modality. Personnel must be able to perform these examinations, and imaging experts, such as radiologists, may have preferences. In general, echocardiography should be the first examination considered, followed by MRI or CT. Performing CTA on an MDCT system that is less than 64 slice is problematic, and image quality (both contrast enhancement and multiplanar reformations) is more limited. A CT study that can be performed relatively quickly may be preferred over waiting several days for an MR evaluation.

## TECHNIQUE

Box 66.1 shows the steps taken to perform a pediatric CTA study (see e-Fig. 66.2).[21,22]

Pediatric cardiovascular CT evaluation is less protocol driven than is cardiovascular CT evaluation in adults. The examination should be constructed to obtain the appropriate diagnostic information while minimizing radiation dosage. The imager should understand the clinical indications for the examination and the anatomy in question. Familiarity of abnormal congenital anatomy and understanding palliative and corrective cardiovascular anatomy is critical to optimal vascular opacification and minimization of streak artifacts.

Patient motion needs to be controlled (e-Fig. 66.4), which may require swaddling of infants or sedation of younger children. Breath holding is preferred during CTA but is not required, especially

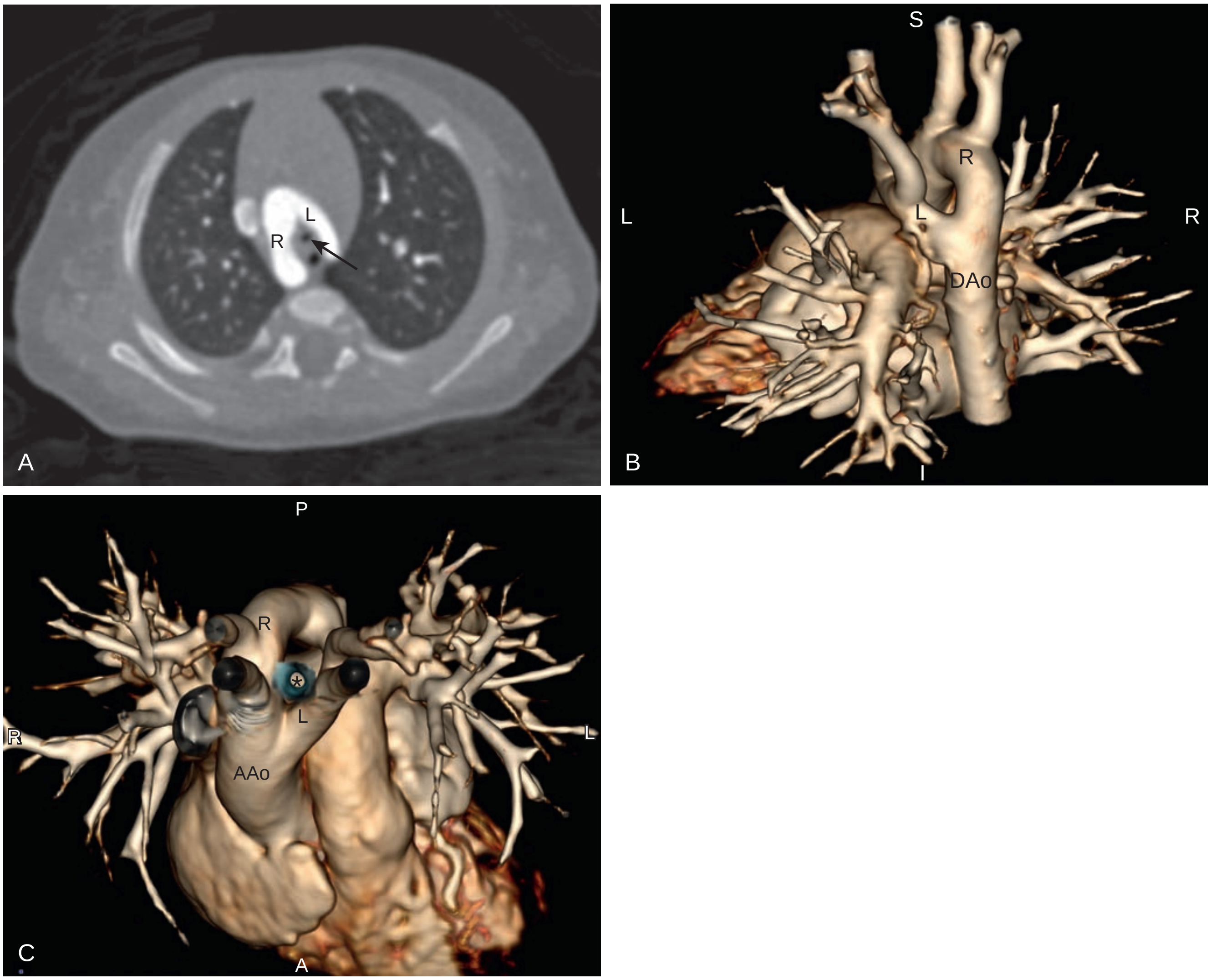

**e-Figure 66.2. Vascular ring in a 4-month-old boy with stridor.** (A) Axial contrast-enhanced image from a CTA study in the upper chest shows the right *(R)* and left *(L)* arches. There is associated tracheal narrowing *(arrow)* at the level of the vascular ring. The mildly dilated esophagus is seen posterior to the trachea. (B) Three-dimensional reformation from the posterolateral projection shows the double arch with the larger and higher right-sided arch *(R)* and the smaller and lower left-sided arch *(L)*. *DAo,* Descending aorta. (C) Three-dimensional reformation from the superior projection including the trachea shows significant tracheal narrowing *(*)* at the level of the ring. *AAo,* Ascending aorta; *L,* left arch; *R,* right arch.

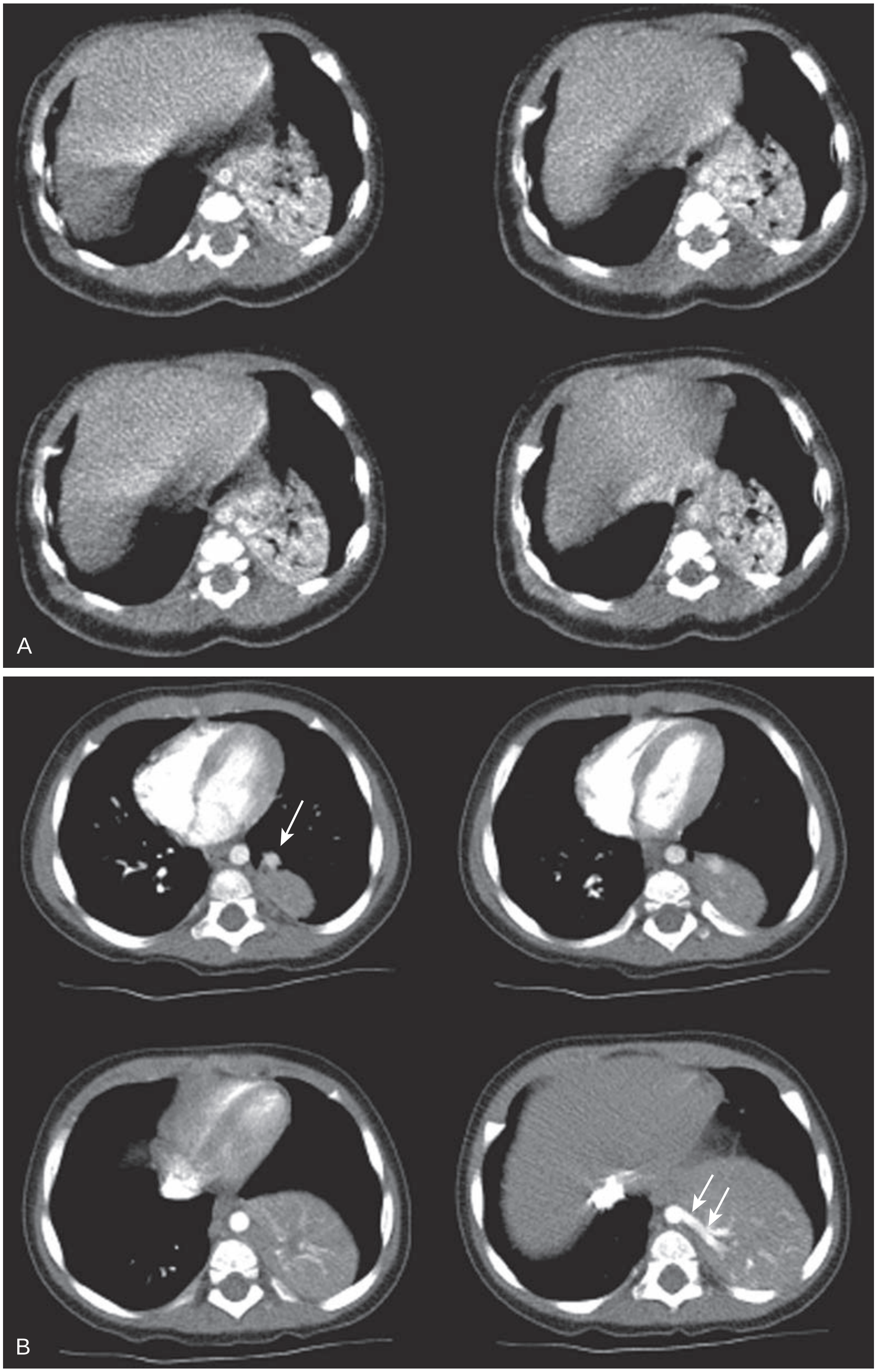

**e-Figure 66.4. Effect of motion on image quality in an infant with pulmonary sequestration.** (A) Four basilar axial images from the initial CTA performed without sedation were inadequate because of movement and poor arterial bolus. (B) A subsequent examination performed after adequate sedation and improved contrast administration shows pulmonary venous drainage (*arrow* in upper left image) and systemic arterial supply (*arrows* in lower right image).

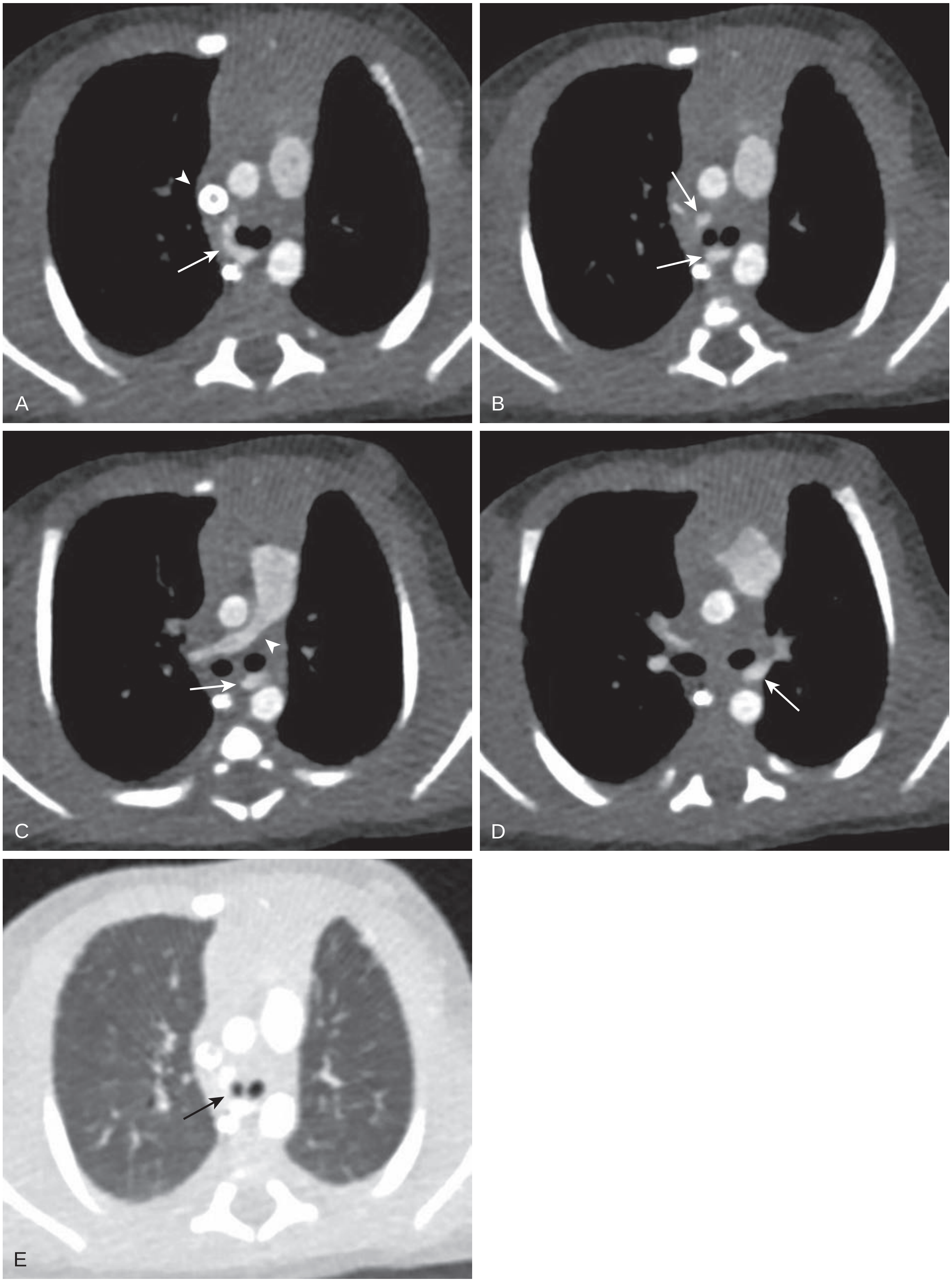

**Figure 66.1. Two-day-old boy on extracorporeal membrane oxygenation (ECMO) for pulmonary hypertension with structural cardiac disease, including a pulmonary artery sling.** Non–ECG-synchronized CTA examination was performed using a total of 3.0 mL of 370 mg/dL nonionic iodinated contrast media through an angiocatheter at 3.0 mL/sec while the ECMO circuit was briefly discontinued. (A–D) The course of the small, aberrant left pulmonary artery originating from the right pulmonary is denoted by the *white arrows* in these axial images. Note the venous ECMO cannula (*arrowhead* in A) and the small right pulmonary artery (*arrowhead* in C). E, The proximal right bronchus is mildly narrowed by the left pulmonary artery (*black arrow* in E).

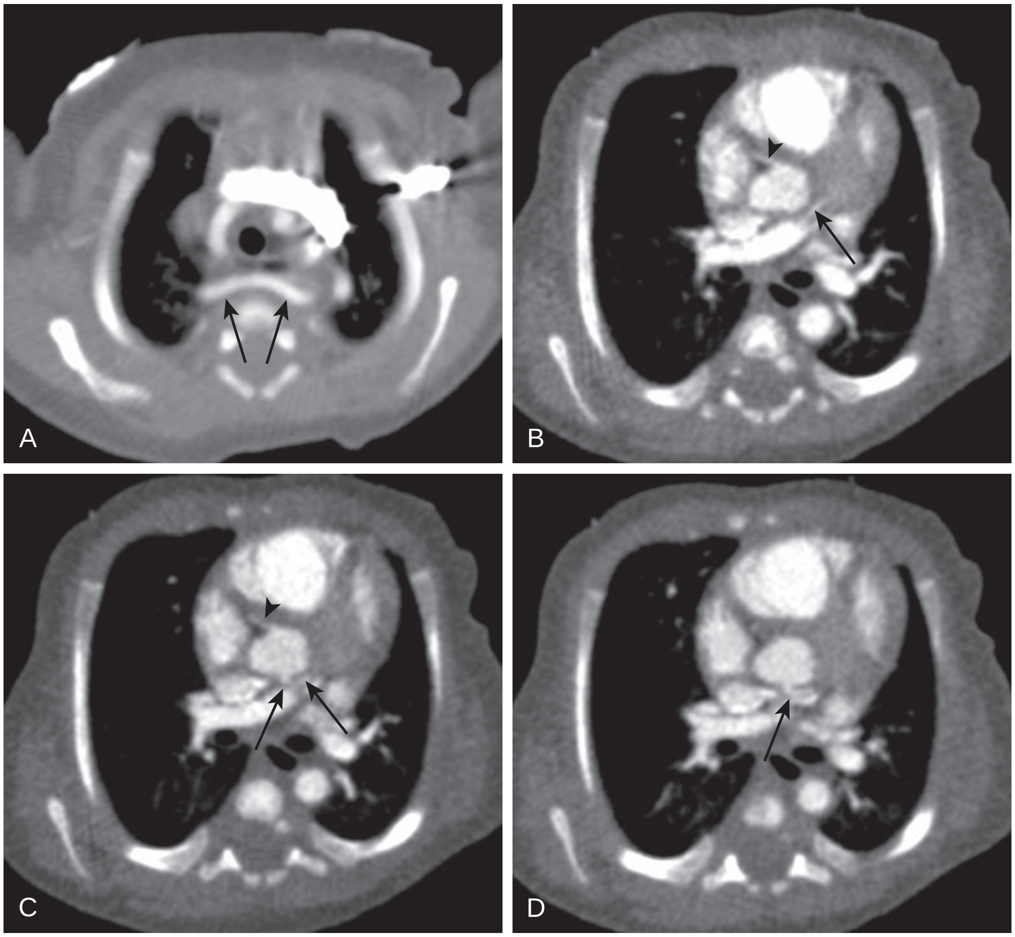

**Figure 66.3. Newborn boy with labored stridor.** Aortic arch anatomy was incompletely assessed on echocardiography. Nongated dual-source cardiac computed tomography angiography was performed using high-pitch (3.2), 80 kVp, 60 effective mA, and 6.0 mL of 300 mg/mL iodine. The scan was performed in about 0.6 seconds. (A) An aberrant right subclavian artery *(arrows)* is seen to pass behind a normal-caliber trachea. No cause for respiratory difficulty was identified. (B–D) Note excellent depiction of small structures as a result of high-pitch scanning, demonstrating the normal origin of the right coronary artery (B and C) *(arrowheads)* and the relatively posterior origin and course of the left main coronary artery, probably from the left coronary cusp in B–D *(arrows).*

with wide detector scanning and other fast scanning technology (e.g., dual-source, high-pitch). If the child is intubated, an inspiratory hold during the CTA evaluation is recommended. Metal (e.g., pacemakers, intracardiac leads, sternal wires, stents, clips, and valves) and arms may cause streak artifacts (Fig. 66.5). Monitors and associated leads should be positioned outside the scan field if possible to minimize streak artifact across the chest. The location and caliber of angiocatheters will determine the rate of intravenous contrast administration and the time it takes contrast material to reach the heart and extracardiac vasculature.[23] Finally, because patients undergoing cardiac CTA may have left-to-right shunts or admixture lesions, extreme care must be taken to avoid injection of air or a thrombus when contrast is administered.

Technical considerations regarding the IV contrast material include type and concentration, dosage, rate of administration, and timing of scan onset after administration.[24] In general, low-osmolar, nonionic contrast media are recommended for contrast-enhanced CT scanning in children. The iodine concentration varies but usually is around 300 mg/mL. For newborns and small children, higher concentrations such as 370 mg/mL may afford better enhancement of smaller vessels with less contrast. A dosage of 1.0 to 1.5 mL/kg is generally adequate, with a maximum total volume of 125 mL. If another CT study must be performed while the patient remains on the scanner, 1.5 to 2.0 mL/kg of additional contrast can be administered. In such cases the maximal dosage would be 3.0 mL/kg, which is still reasonable for a single examination.

The rate of contrast administration depends on whether a manual injection or a power injector is used and also on the size of the angiocatheter. Suggested maximal rates of administration are 1.5 to 2.0 mL/sec for a 24-gauge angiocatheter, 2.5 to 3.0 mL/sec for a 22-gauge angiocatheter, and 4.0 mL/sec for a 20-gauge angiocatheter at a maximum pressure of 300 psi. When possible, contrast should be administered by a power injector, which gives a more predictable and consistent enhancement curve. However, performing manual administration as quickly as possible can provide adequate enhancement when power injection is not appropriate. Use of central venous catheters for power administration varies based on individual practice and catheter suitability.

The timing of contrast administration with respect to scanning initiation is a critical factor in CTA. In general, scanning is started either during or immediately after completion of administration of the contrast. Timing depends on the structures that need to be evaluated. Later scan initiation is used for opacification of the thoracic aorta and major branches or systemic venous structures,

### BOX 66.1 Steps in Performing Pediatric Computed Tomography Angiography

The subject is an otherwise healthy, 4-week-old, 4.0-kg male infant with congenital stridor. Findings of an echocardiogram suggest the presence of a vascular ring.

**PLANNING THE COMPUTED TOMOGRAPHY ANGIOGRAM (CTA)**

1. **Determine that CTA is the appropriate examination.** Echocardiography was inconclusive. Magnetic resonance imaging would require sedation and a 1- to 2-week wait for a sedation slot. CTA has a 1-day turnaround and requires no sedation.
2. **Define the question to be answered.** Aortic arch and airway. A high-detail examination (e.g., for small vessels) is not necessary. It is not necessary to image below the mid to lower thoracic aorta (thus the radiation dose can be lower).
3. **Understand the anatomy.** Vascular rings, including innominate compression; a pulmonary sling is not exhibited with true stridor.
4. **Patient limitations.** Essentially none. The patient will be fed immediately before the CTA but after the intravenous line is in place.

**PERFORMING THE CTA**

1. **Intravenous contrast material**
   **Type:** Low-osmolar, nonionic iodinated contrast, 300 mg/mL
   **Dose:** Total volume of 6.0 mL (4.0 kg at 1.5 mL/kg)
   **Rate and route:** 24-gauge angiocatheter in hand vein; administration via power injector at 2.0 mL/sec or manual injection as quickly as possible
   **Onset of scanning:** Determined with a test bolus of 1.0 mL contrast followed by a flush adequate to clear contrast from the line. Start monitoring images at 2-second intervals and begin push of the test bolus when the first monitoring image appears. Contrast reaches the right ventricle in 5 seconds and the left ventricle in 6 to 7 seconds. Add 3 seconds, so the scan onset for the diagnostic study will be 9 to 10 seconds after starting administration of contrast.
2. **Select scan parameters:**
   **Tube current:** Adjusted for image quality using automatic exposure control
   **Peak kilovoltage:** 80 kVp (or 70 kVp if available)
   **Gantry cycle time:** Fastest available
   **Pitch:** Highest pitch available
   **ECG synchronization:** Not necessary for vascular ring evaluation
   **Data reconstruction:** 2.0 mm at 2.0-mm interval axial, coronal, and sagittal; 0.6 at 0.4-mm interval for three-dimensional reformations
   **Iterative reconstruction:** On

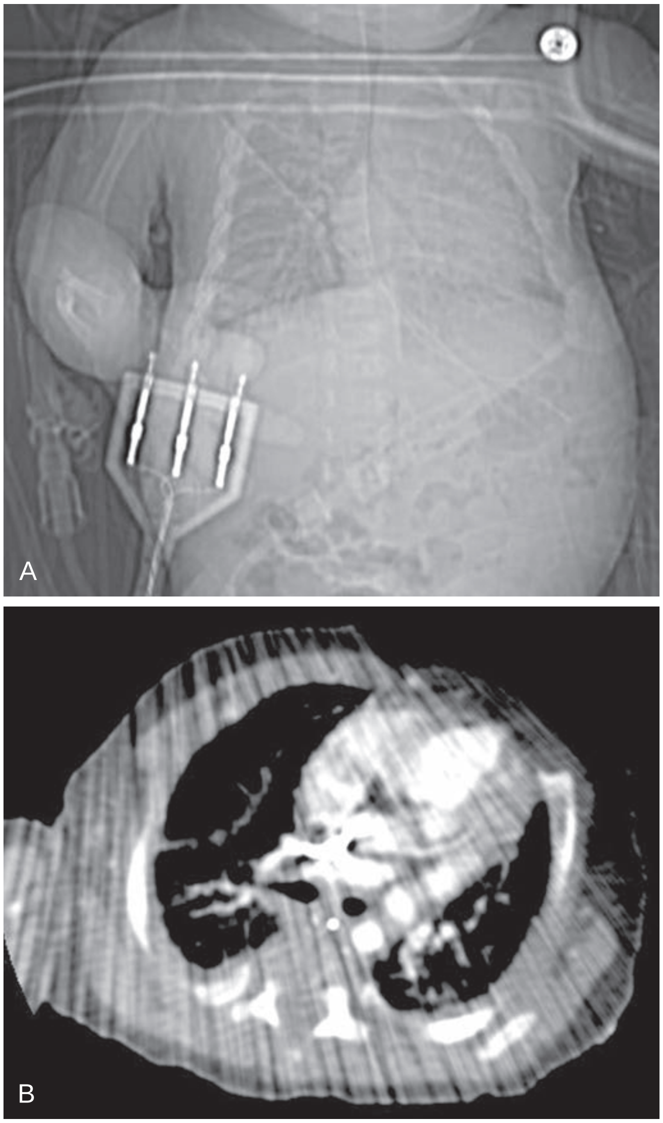

**Figure 66.5. Artifact from leads.** (A) Topogram demonstrates the leads that were in the scan range. (B) Note substantial streak artifact. *(From Frush DP. Thoracic cardiovascular CT: technique and applications.* Pediatr Radiol*. 2009;39(3):464–470. Reprinted with permission.)*

whereas earlier scan initiation is appropriate for right-sided structures, especially pulmonary arteries. An empiric delay can be used, but because of the wide range of sizes and heart rates encountered in pediatric CTA (i.e., 1–100 kg), a single recommendation for an empiric delay is not possible. A range of delays could be determined depending on the rate of administration.

One of two methods is generally used for individualized determination of the scan delay in pediatric CTA: test injection or bolus tracking. Bolus tracking is used more commonly and is straightforward. A region of interest is placed over the desired structure, and the examination triggers when this region reaches 100 to 150 HU (or by initiation of scanning based on visual appearance of enhancement during tracking), usually with a 7-second delay when the child is able to breath hold to allow for breath-hold instructions. The monitoring scan onset should be set to start shortly before the expected time of opacification of the structure of interest to minimize unnecessary radiation during monitoring. The monitoring CT parameters can be very low (e.g., 80–100 kVp and 10 mA) to further minimize dose.

Alternatively, a test bolus can be administered, and the arrival of contrast to the desired location (for cardiac CT, the right side versus the left side of the heart) can be used (Fig. 66.6). A test bolus of 10% of the total expected volume is administered. The arrival of the test bolus at the appropriate structure is timed, and this time is used to set the delay for the start of scanning after full-contrast bolus injection. In neonates, usually about 2 to 3 seconds is added to the arrival time of the test bolus for optimal enhancement, and up to 8 seconds may be added for teenagers.

Scan techniques include adjustment of technical parameters such as the number of detector rows, the thickness of detectors, the gantry cycle time, tube current (milliamperes [mA]), and peak kilovoltage (kVp). Parameters such as scan thickness and interval are adjustable after the scan volume is obtained.[5]

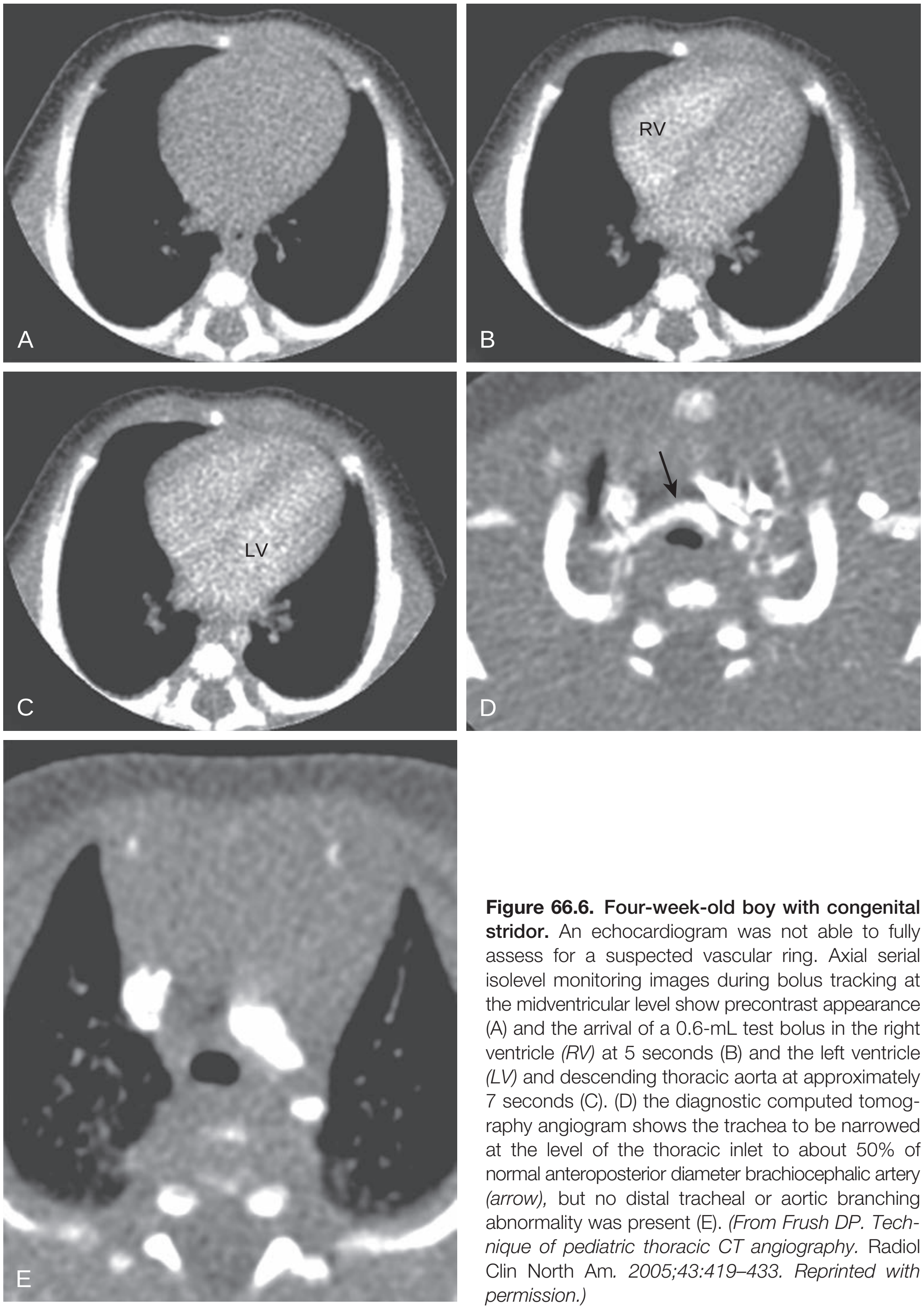

**Figure 66.6. Four-week-old boy with congenital stridor.** An echocardiogram was not able to fully assess for a suspected vascular ring. Axial serial isolevel monitoring images during bolus tracking at the midventricular level show precontrast appearance (A) and the arrival of a 0.6-mL test bolus in the right ventricle *(RV)* at 5 seconds (B) and the left ventricle *(LV)* and descending thoracic aorta at approximately 7 seconds (C). (D) the diagnostic computed tomography angiogram shows the trachea to be narrowed at the level of the thoracic inlet to about 50% of normal anteroposterior diameter brachiocephalic artery *(arrow),* but no distal tracheal or aortic branching abnormality was present (E). *(From Frush DP. Technique of pediatric thoracic CT angiography.* Radiol Clin North Am*. 2005;43:419–433. Reprinted with permission.)*

The isotropic images obtained with 64-slice and higher MDCT scanners provide excellent multiplanar reformations and three-dimensional evaluation, which show complicated anatomy in a way to which clinical care providers (e.g., cardiac surgeons) are accustomed (e-Figs. 66.7–66.9). The thinnest detector option should be chosen for pediatric CTA, because thinner slices improve the quality of reformations. The fastest gantry cycle time is recommended to minimize motion artifact and to obtain the fastest scanning time possible, which is important in children who may be anxious or otherwise fidgety. Pitch, essentially representing table speed (mm/sec) divided by effective collimation (mm), generally is in the range of 1.5 for nongated, single-source CTA.

Tube current, including tube current modulation technology,[25] varies depending on patient size. Automatic radiation dose modulation (either automatic exposure control or automatic tube current modulation, and newer kVp modulation) are features of all modern MDCT scanners. Although the features differ among vendors, the principle of dose modulation is to dynamically control the tube current throughout the scan based on the patient's body habitus and user settings, and with kVp modulation to include desired contrast quality. Although it is possible to reduce radiation dose using these features, pediatric-specific dose modulation is not widely available and reference data are lacking. Therefore dose modulation techniques should be used with caution in children.[24]

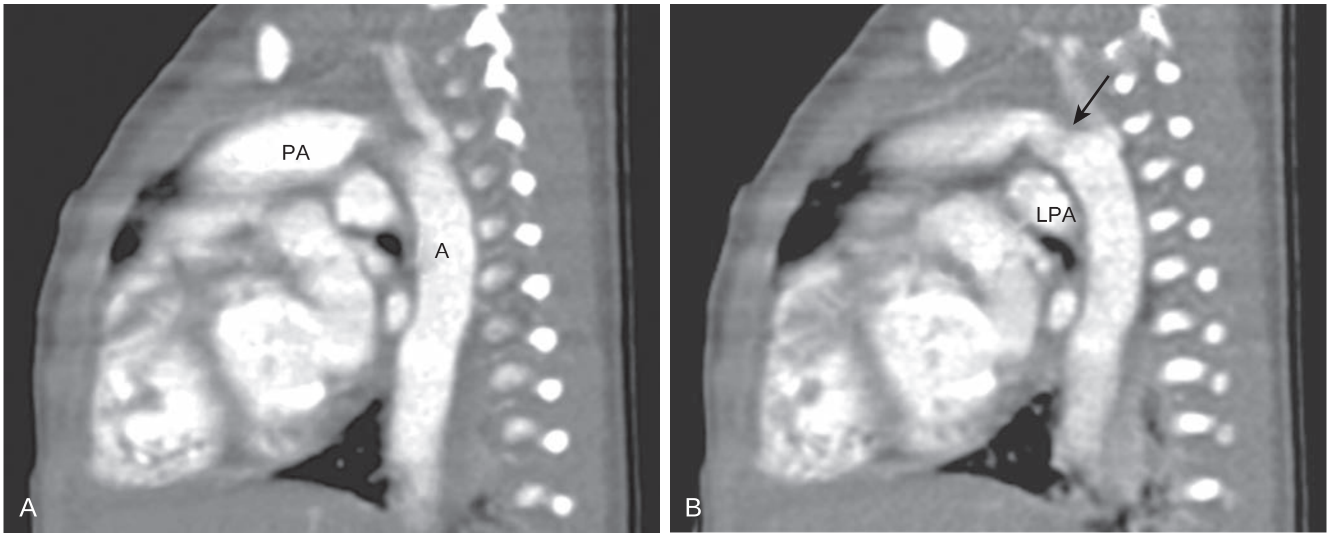

**e-Figure 66.7. Two-day-old infant boy with interrupted aortic arch identified by echocardiography.** Because the aortic branch anatomy was not well visualized, CTA was performed. The examination was performed at 80 kVp. (A and B) With sagittal reformation, the relationship between the large ductus arteriosus *(arrow)* connecting the main pulmonary artery *(PA)* and the aorta *(A)* is seen. *LPA,* Left pulmonary artery. *(From Frush DP, Herlong RJ. Pediatric thoracic CT angiography.* Pediatr Radiol. *2005;35:11–25. Reprinted with permission.)*

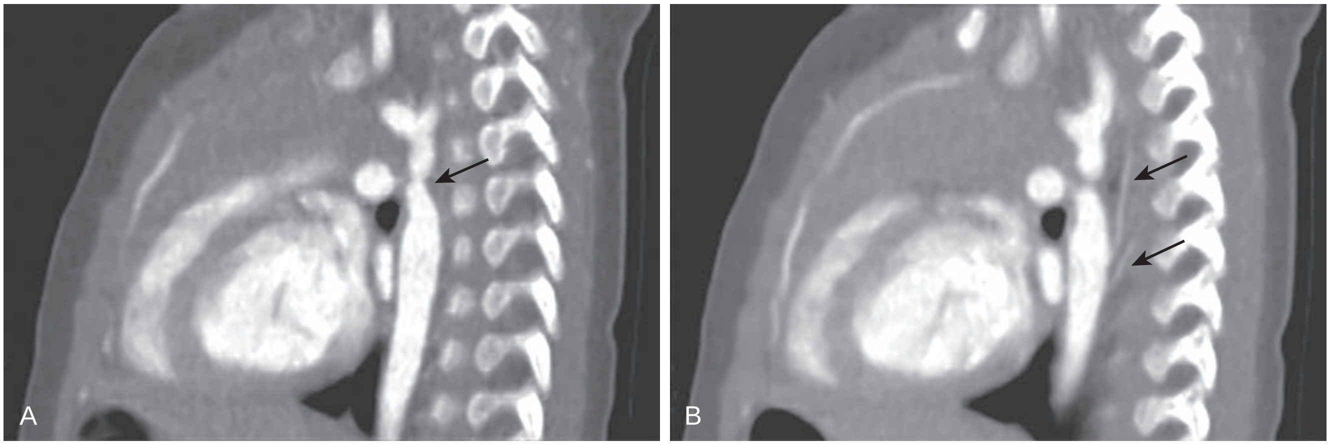

**e-Figure 66.8. Sagittal reformations of aortic coarctation in a 4-month-old infant boy.** (A) The location of the coarctation is well demonstrated *(arrow).* (B) Collaterals *(arrows)* are seen feeding the descending aorta distal to the coarctation. *(From Frush DP. Technique of pediatric thoracic CT angiography.* Radiol Clin North Am. *2005;43:419–433. Reprinted with permission.)*

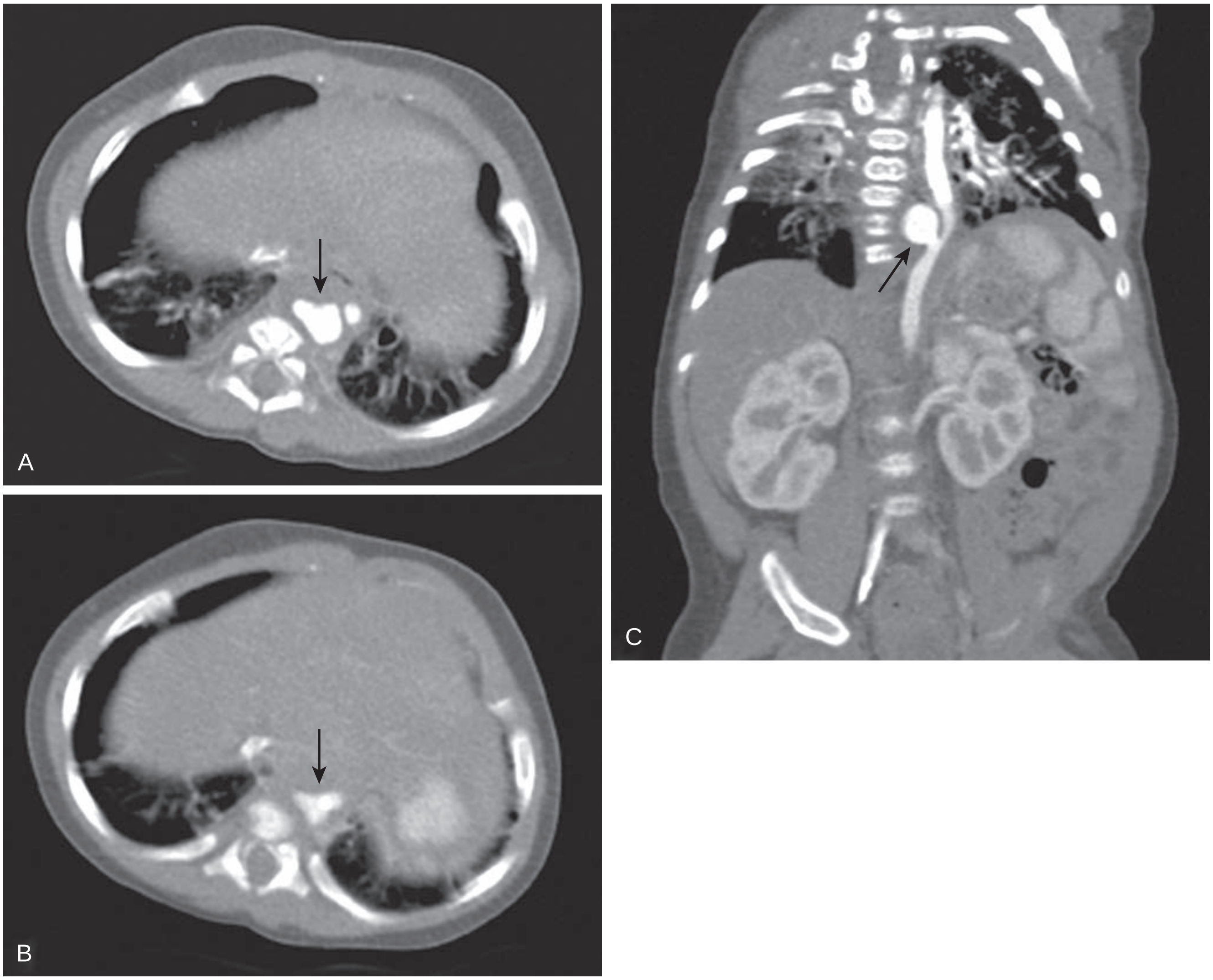

**e-Figure 66.9. Descending thoracic aortic aneurysm in an infant, probably from an infected umbilical arterial catheter in the neonatal period.** Axial images (A and B, slightly inferior to A) show an irregularity of the aorta *(arrows).* (C) Coronal reconstruction shows an aneurysm *(arrow),* neck, and displacement of the adjacent aorta. The aneurysm was successfully occluded with a coil. *(From Frush DP, Yoshizumi T. Conventional and CT angiography in children: dosimetry and dose comparisons.* Pediatr Radiol. *2006;36:154–158. Reprinted with permission.)*

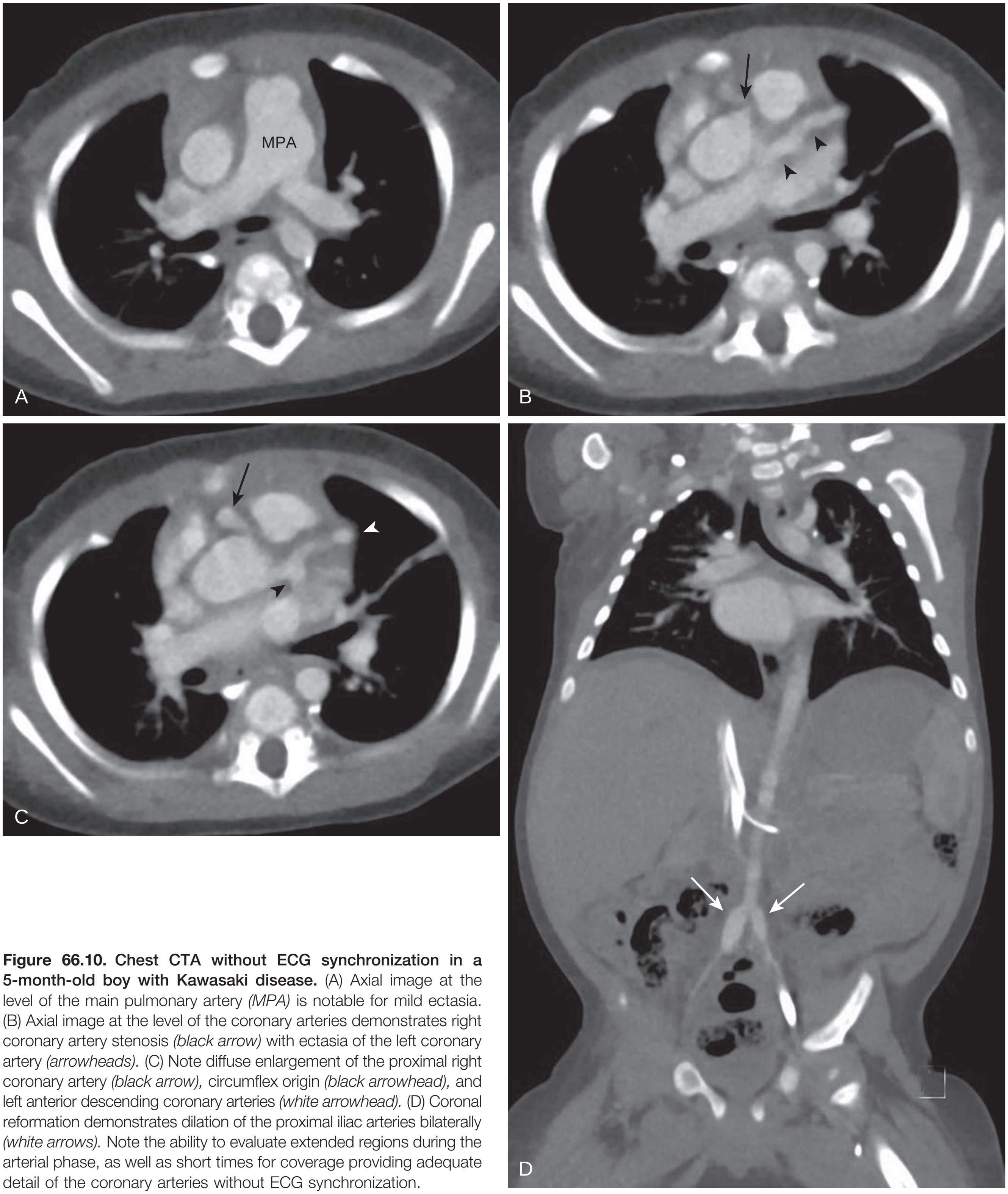

**Figure 66.10. Chest CTA without ECG synchronization in a 5-month-old boy with Kawasaki disease.** (A) Axial image at the level of the main pulmonary artery *(MPA)* is notable for mild ectasia. (B) Axial image at the level of the coronary arteries demonstrates right coronary artery stenosis *(black arrow)* with ectasia of the left coronary artery *(arrowheads).* (C) Note diffuse enlargement of the proximal right coronary artery *(black arrow),* circumflex origin *(black arrowhead),* and left anterior descending coronary arteries *(white arrowhead).* (D) Coronal reformation demonstrates dilation of the proximal iliac arteries bilaterally *(white arrows).* Note the ability to evaluate extended regions during the arterial phase, as well as short times for coverage providing adequate detail of the coronary arteries without ECG synchronization.

Because image contrast is relatively high in cardiothoracic CTA, consideration should be given to lowering the peak kilovoltage.[26] This step will improve image contrast and, although some increased noise occurs, the increase in contrast is greater than the increase in noise in small children, which produces an improved contrast-to-noise ratio and better image quality. Therefore 80 kVp (or 70 kVp, if available) (Fig. 66.10) should be used for newborns, infants, and young children, and 100 kVp for older children is acceptable. A value of 120 kVp can be used for larger children and adolescents. With advances in image processing time and storage and the availability of off-line workstations, evaluation of the pediatric heart and great vessels in multiple perspectives is now performed rapidly. Images should be reconstructed at the narrowest slice thickness possible (submillimeter) and at intervals

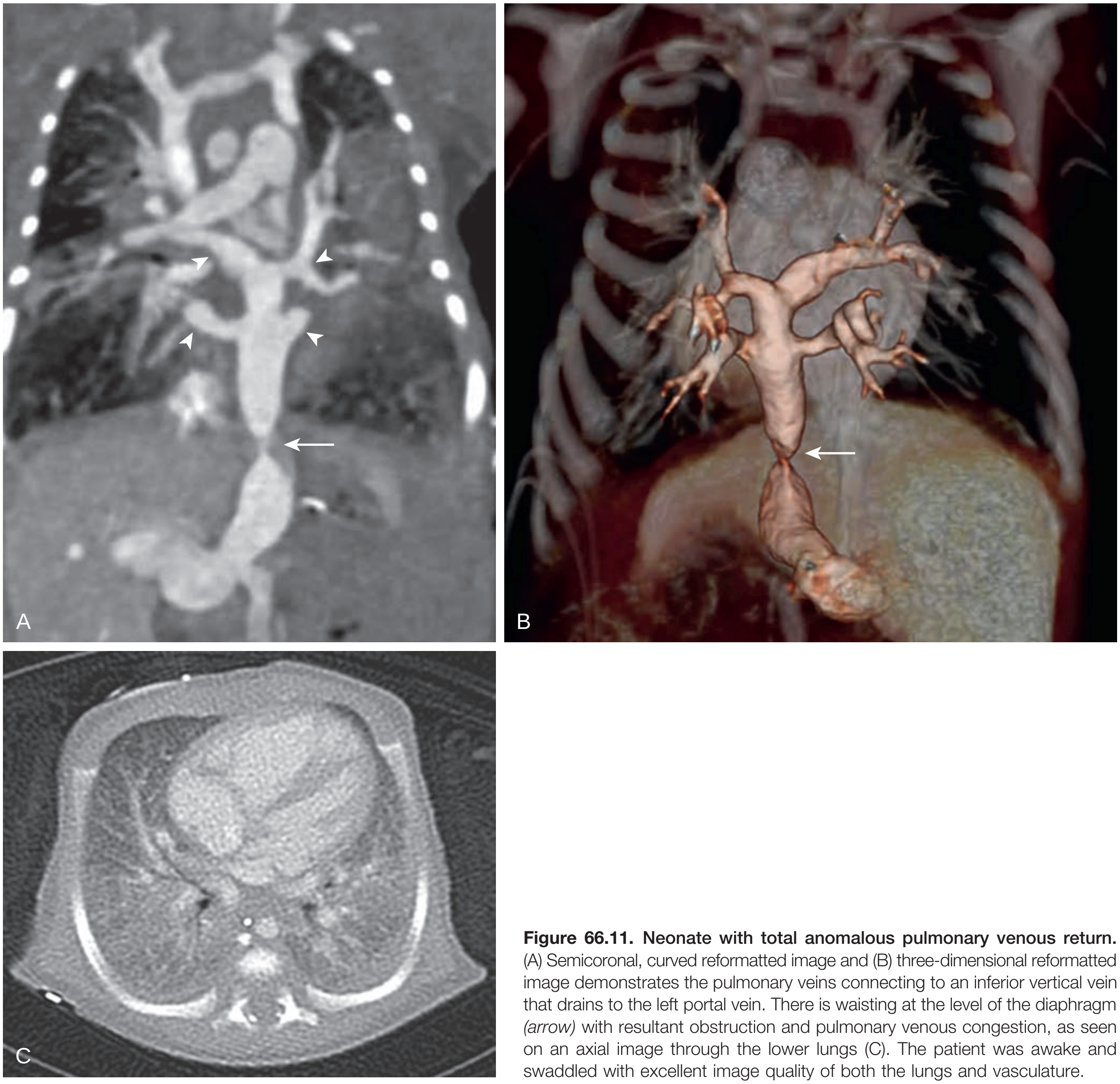

**Figure 66.11. Neonate with total anomalous pulmonary venous return.** (A) Semicoronal, curved reformatted image and (B) three-dimensional reformatted image demonstrates the pulmonary veins connecting to an inferior vertical vein that drains to the left portal vein. There is waisting at the level of the diaphragm *(arrow)* with resultant obstruction and pulmonary venous congestion, as seen on an axial image through the lower lungs (C). The patient was awake and swaddled with excellent image quality of both the lungs and vasculature.

just under the slice thickness. Iterative reconstruction techniques should be used routinely to improve image noise.[11,27]

The speed of modern CT scanners has obviated the need for cardiac gating in much of pediatric cardiovascular CT. As with adults, intracardiac anatomy is better displayed with use of ECG synchronization, although dual-source high-pitch and wide detector scanners can provide improved intracardiac detail compared with non–high-pitch and single-source scanners. However, ECG synchronization is still generally recommended for evaluation of the coronary arteries. As previously noted, when compared with retrospective ECG gating, prospective ECG gating reduces radiation dose. Limiting the z-axis coverage to the area of interest (i.e., the aortic root in evaluation of anomalous coronary origins) further decreases radiation dose. Technical considerations have been reviewed[18,28]; a detailed description of ECG-synchronized techniques is beyond the intent of this chapter. Even more than with the nongated angiographic technique, presence at the scanner by the imaging expert usually is necessary to determine contrast details, particularly with the timing bolus, and scan parameters (e.g., scan range, tube current, and peak kilovoltage), as well as performance of postacquisition processing. Dual-source design (i.e., two x-ray tubes) has improved temporal resolution (lessening the need for β-blockade to decrease heart rate, even to heart rates around 120 beats/min) (see Figs. 66.10 and 66.11).[29] Applying adult techniques to pediatric scanning can result in excessively high radiation dosages—reported to be as high as 30 millisieverts (mSv)—which is approximately 10 to 20 times the dose of a normal chest CT examination in a child. Dose and image quality for ECG-synchronized cardiac evaluation should reflect reduced-dosage techniques for other body applications in infants and children, with consideration of lower tube current and kilovoltage (see Fig. 66.6).

The use of bismuth breast shields to reduce breast dose has lowered radiation dose and maintained image quality for pediatric chest CT, although the benefit of shielding is debated given the availability of other techniques for dose reduction. The use of organ-based dose modulation, where the tube current is reduced over an arc to reduce surface dose such as for the breasts, has yet to be systematically studied in pediatric chest CT.

## CONCLUSION

CT evaluation of intrathoracic cardiovascular anatomy has increased dramatically in both adults and children during the past decade. In certain pediatric populations, including very young children, technical challenges need to be considered before and during performance of cardiac CT angiography. Considerations include proper patient preparation and individualization of scanning techniques to address the specific clinical questions, as well as considerations unique to that child (such as size). These considerations also will minimize radiation exposure. Despite these challenges, excellent cardiac angiographic evaluation can be obtained even in the most challenging cases.

### KEY POINTS

- Technique is critical for optimizing pediatric cardiovascular CTA.
- Pediatric CTA is less protocol driven than with adults.
- If performed properly, nongated and ECG-synchronized CT angiography in children can result in dose estimates at or below 1.0 mSv.
- Familiarity with clinical questions and anatomy with congenital disorders will afford the greatest potential for safe and high-quality pediatric examinations.
- Lower peak kilovoltage (e.g., 70, 80, and 100 kVp) can be used in CTA compared with other body imaging because of high-contrast vascular enhancement.

### SUGGESTED READINGS

Frush DP. Thoracic cardiovascular CT: technique and applications. *Pediatr Radiol*. 2009;39(3):464–470.

Goo HW. Coronary artery imaging in children. *Korean J Radiol*. 2015;16(2):239–250.

Hellinger J, Pena A, Poon M, et al. Pediatric computed tomographic angiography: imaging the cardiovascular system gently. *Radiol Clin North Am*. 2010;48:439–467.

Young C, Taylor A, Owens C. Paediatric cardiac computed tomography: a review of imaging techniques and radiation dose consideration. *Eur Radiol*. 2011;21:518–529.

### REFERENCES

Full references for this chapter can be found on www.expertconsult.com.

## REFERENCES

1. Young C, Taylor AM, Owens CM. Paediatric cardiac computed tomography: a review of imaging techniques and radiation dose consideration. *Eur Radiol*. 2011;21:518–529.
2. Al-Mousily F, Shifrin RY, Fricker FJ, et al. Use of 320-detector computed tomographic angiography for infants and young children with congenital heart disease. *Pediatr Cardiol*. 2011;32:426–432.
3. Siegel MJ. Computed tomography of pediatric cardiovascular disease. *J Thorac Imaging*. 2010;25:256–266.
4. Dillman JR, Hernandez RJ. Role of CT in the evaluation of congenital cardiovascular disease in children. *AJR Am J Roentgenol*. 2009;192:1219–1231. doi:10.2214/AJR.09.2382.
5. Hellinger JC, Pena A, Poon M, et al. Pediatric computed tomographic angiography: imaging the cardiovascular system gently. *Radiol Clin North Am*. 2010;48:439–467, x. doi:10.1016/j.rcl.2010.03.005.
6. Goo HW. Cardiac MDCT in children: CT technology overview and interpretation. *Radiol Clin North Am*. 2011;49:997–1010. doi:10.1016/j.rcl.2011.06.001.
7. Siripornpitak S, Pornkul R, Khowsathit P, et al. Cardiac CT angiography in children with congenital heart disease. *Eur J Radiol*. 2013;82:1067–1082. doi:10.1016/j.ejrad.2011.11.042.
8. Goo HW. Coronary artery imaging in children. *Korean J Radiol*. 2015;16:239–250.
9. Lederlin M, Thambo JB, Latrabe V, et al. Coronary imaging techniques with emphasis on CT and MRI. *Pediatr Radiol*. 2011;1516–1525.
10. Han BK, Lesser AM, Vezmar M, et al. Cardiovascular imaging trends in congenital heart disease: a single center experience. *J Cardiovasc Comput Tomogr*. 2013;7:361–366.
11. Zheng M, Zhao H, Xu J, et al. Image quality of ultra-low-dose dual-source CT angiography using high-pitch spiral acquisition and iterative reconstruction in young children with congenital heart disease. *J Cardiovasc Comput Tomogr*. 2013;7:376–382.
12. Long CM, Long SS, Johnson PT, et al. Utility of low-dose high-pitch scanning for pediatric cardiac computed tomographic imaging. *J Thorac Imaging*. 2015;0:1–5. doi:10.1097/RTI.0000000000000131.
13. Rappaport BA, Suresh S, Hertz S, et al. Anesthetic neurotoxicity–clinical implications of animal models. *N Engl J Med*. 2015;372:796–797. doi:10.1056/NEJMp1414786.
14. Vyas H V, Greenberg SB, Krishnamurthy R. MR imaging and CT evaluation of congenital pulmonary vein abnormalities in neonates and infants. *Radiographics*. 2012;32:87–98.
15. Haramati LB, Glickstein JS, Issenberg HJ, et al. MR imaging and CT of vascular anomalies and connections in patients with congenital heart disease: significance in surgical planning. *Radiographics*. 2002;22:337-347-349.
16. Frush DP, Yoshizumi T. Conventional and CT angiography in children: dosimetry and dose comparisons. *Pediatr Radiol*. 2006;36:154–158. doi:10.1007/s00247-006-0190-6.
17. Xu J, Zhao H, Wang X, et al. Accuracy, image quality, and radiation dose of prospectively ECG-triggered high-pitch dual-source CT angiography in infants and children with complex coarctation of the aorta. *Acad Radiol*. 2014;21:1248–1254.
18. Podberesky DJ, Angel E, Yoshizumi TT, et al. Radiation dose estimation for prospective and retrospective ECG-gated cardiac CT angiography in infants and small children using a 320-MDCT volume scanner. *AJR Am J Roentgenol*. 2012;199:1129–1135. doi:10.2214/AJR.12.8480.
19. Callahan MJ, Poznauskis L, Zurakowski D, et al. Nonionic iodinated intravenous contrast material–related reactions: incidence in large urban children's hospital—retrospective analysis of data in 12 494 patients. *Radiology*. 2009;250:674–681.
20. Dillman JR, Ellis JH, Cohan RH, et al. Frequency and severity of acute allergic-like reactions to gadolinium-containing IV contrast media in children and adults. *AJR Am J Roentgenol*. 2007;189:1533–1538.
21. Frush DP. Technique of pediatric thoracic CT angiography. *Radiol Clin North Am*. 2005;43:419–433.
22. Nievelstein RA, van Dam IM, van der Molen AJ. Multidetector CT in children: current concepts and dose reduction strategies. *Pediatr Radiol*. 2010;40:1324–1344. doi:10.1007/s00247-010-1714-7.
23. Yang M, Mo XM, Jin JY, et al. Image quality and radiation exposure in pediatric cardiovascular CT angiography from different injection sites. *AJR Am J Roentgenol*. 2011;196.
24. Herzog C, Mulvihill DM, Nguyen SA, et al. Pediatric cardiovascular CT angiography: radiation dose reduction using automatic anatomic tube current modulation. *AJR Am J Roentgenol*. 2008;190:1232–1240.
25. Yu L, Bruesewitz MR, Thomas KB, et al. Optimal tube potential for radiation dose reduction in pediatric CT: principles, clinical implementations, and pitfalls. *Radiographics*. 2011;31:835–848.
26. Siegel MJ, Hildebolt C, Bradley D. Effects of automated kilovoltage selection technology on contrast-enhanced pediatric CT and CT angiography. *Radiology*. 2013;268:1–8.
27. Son SS, Choo KS, Jeon UB, et al. Image quality of CT angiography with model-based iterative reconstruction in young children with congenital heart disease: comparison with filtered back projection and adaptive statistical iterative reconstruction. *Int J Cardiovasc Imaging*. 2015;31:31–38. doi:10.1007/s10554-014-0570-1.
28. Hollingsworth CL, Yoshizumi TT, Frush DP, et al. Pediatric cardiac-gated CT angiography: assessment of radiation dose. *AJR Am J Roentgenol*. 2007;189:12–18.
29. Sriharan M, Lazoura O, Pavitt CW, et al. Evaluation of high-pitch ungated pediatric cardiovascular computed tomography for the assessment of cardiac structures in neonates. *J Thorac Imaging*. 2016;31:177–182.

# 67

# Magnetic Resonance Imaging for Congenital Heart Disease

*Elizabeth F. Sheybani*

Cardiac magnetic resonance imaging (MRI) has become integral in the evaluation, treatment planning, and posttreatment surveillance of congenital and acquired heart disease. Although echocardiography remains the primary mode of evaluation for these children, cardiac MRI has the unique ability to accurately assess multidimensional anatomic, functional, volumetric, and flow data in even the youngest patients with congenital heart disease, and thus can be an invaluable supplement. The mainstays of cardiac MRI in congenital heart disease are electrocardiographic (ECG) gated balanced steady-state free-precession (b-SSFP) cine sequences for anatomic and functional evaluation and phase-contrast cine sequences for velocity and flow measurements. ECG and respiratory navigated magnetic resonance angiography (MRA) acquisitions, with or without gadolinium contrast, have become commonplace, as they allow offline reformats in any plane and three-dimensional (3D) image or model production.

## PULSE SEQUENCES

ECG-gated spin echo and gradient echo sequences are used for cardiac evaluation. Spin echo, or "black blood," imaging gives excellent contrast resolution between the endocardium or vessel wall and the blood-filled lumen (Fig. 67.1). Alternatively, on gradient echo (GRE) images, or "bright blood" images, the blood pool has high signal intensity. The GRE sequence balanced SSFP (b-SSFP) is the current mainstay of cardiac imaging. Balanced SSFP sequences are faster than (GRE) sequences and yield better contrast between myocardium and blood. By obtaining data during set phases of the cardiac cycle, b-SSFP cine images can be used for analysis of myocardial or valvular motion throughout the cardiac cycle. Although b-SSFP is ideally performed with the patient holding his or her breath, respiratory motion artifacts are minimized in sedated or uncooperative children by increasing the number of excitations. This technique is the preferred sequence for evaluating cardiac motion and quantifying cardiac function (Fig. 67.2).

## FUNCTIONAL EVALUATION

MRI is the reference standard for noninvasive cardiac functional assessment and is superior to echocardiography in assessing right ventricular function, particularly in patients with congenital heart disease.[1] This is an important consideration in evaluation of these children as they generally need serial and reproducible measurements of ventricular function to determine optimal timing of potential interventions.[2] A stack of short-axis cine images through the ventricles is obtained to measure ventricular volumes. Using postprocessing software, the operator defines the endocardial border on each slice, and the software then multiplies the resultant cross-sectional area by the slice thickness to obtain the ventricular volume. There is no consensus on inclusion or exclusion of the papillary muscles in the left ventricular volume or trabeculation in the right ventricular volume, so either method should be used with knowledge that the volumes can be affected by differences in postprocessing technique and similar methodology should be used when comparing studies.[3] End-diastolic and end-systolic phases are identified for calculation of ejection fraction and stroke volume. The additional application of pericardial contours allows determination of myocardial mass.

Because children vary in size, cardiac MRI measurements are reported as indexed values. These are obtained by dividing each measurement by the patient's body surface area. This allows more standardized comparisons as patients grow and across patient populations. There are reported normal values for left and right ventricular volumes in children, and these can be used for general reference but are based on small sample sizes.[3]

The right and left ventricular stroke volumes are the same in the structurally normal heart. Differences in stroke volumes are caused by shunts and/or valvular regurgitation. Using MRI, both shunt volumes and regurgitant fractions can be calculated from stroke volumes or flow data if there is an isolated single shunt lesion or regurgitation involving a single valve. If there are multiple abnormalities, more detailed evaluation is needed. Shunt fraction, or the pulmonary to systemic flow ratio (Qp:Qs), is determined by dividing the larger stroke volume by the smaller. The valvular regurgitant fraction is determined by dividing the regurgitant volume, which is the difference of ventricular stroke volumes, by the larger ventricle stroke volume (Fig. 67.3). The regurgitant volume may result from atrioventricular valve or semilunar valve insufficiency, or a combination of both.

$$\begin{aligned}&\mathrm{Qp} : \mathrm{Qs} =\\&\text{Ventricular stroke volume}_1/\text{Ventricular stroke volume}_2\end{aligned}$$

$$\begin{aligned}&\text{Valvular regurgitant fraction} =\\&(\text{Ventricular stroke volume}_1 - \text{Ventricular}\\&\text{stroke volume}_2)/\text{Ventricular stroke volume}_1\end{aligned}$$

where Ventricular stroke volume$_1$ is the larger of the two ventricular stroke volumes.

Phase-contrast imaging uses a GRE sequence to measure phase shift and produces both magnitude and directional information (Fig. 67.4). By setting an acquisition plane perpendicular to a vessel or valve of interest, phase-contrast imaging allows for accurate quantification of blood flow velocity. The pressure gradient across a stenosis can then be calculated from the blood flow velocity using the modified Bernoulli equation:

$$\Delta P = 4v^2$$

where $\Delta P$ is the peak instantaneous pressure gradient across the stenosis and $v$ is the velocity across the stenosis measured by flow analysis. Using postprocessing software, the velocity within each pixel of the targeted vessel can be multiplied by the vessel area and then summed across the cross section of the vessel across the cardiac cycle to generate the flow per beat within the vessel. Given the limitless scan plans of cardiac MRI, this method has proved superior to echocardiography for flow determinations and is used extensively in congenital heart disease to evaluate stenoses, shunt fractions, and collateral vessel burden.[4] More recently, 3D phase-contrast imaging (four-dimensional [4D] flow) has allowed

---

Acknowledgment: The editors and the publisher would like to thank Drs. Sadaf T. Bhutta and S. Bruce Greenberg for contributing a chapter on this topic to the prior edition of this work. It has served as the foundation for the current chapter.

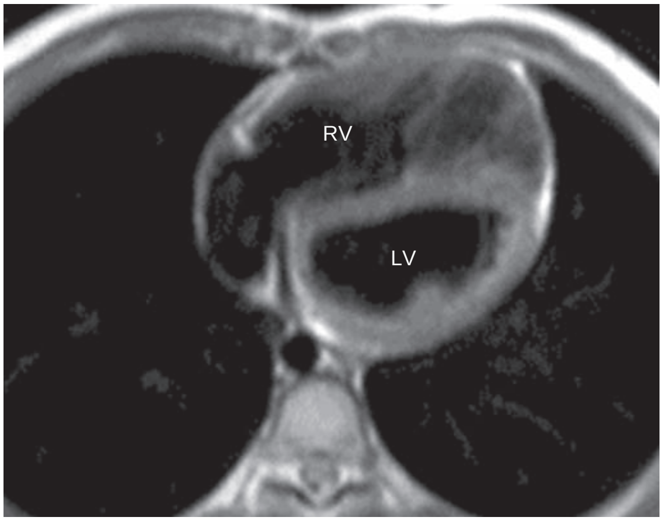

**Figure 67.1. Black blood imaging.** Axial double inversion recovery fast spin echo MRI shows both ventricles. The nulled blood signal provides excellent visualization of the static myocardial tissue. *LV,* Left ventricle; *RV,* right ventricle.

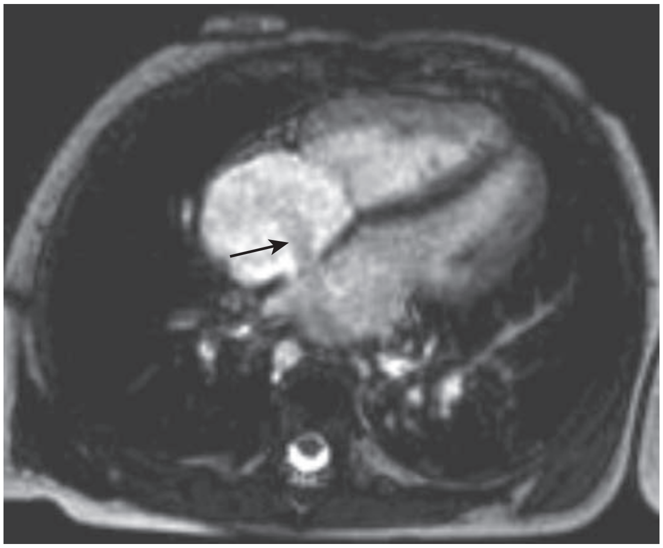

**Figure 67.2. Atrial septal defect.** Four-chamber steady-state free-precession MRI shows mild right atrial and right ventricular enlargement. A small atrial septal defect is seen with a jet of blood passing from the left atrium to the right atrium, indicating a left-to-right shunt *(arrow).*

acquisition of a volumetric 3D flow dataset over the cardiac cycle, which can be postprocessed in any plane to yield velocity and flow data throughout the acquired volume.[5]

## MAGNETIC RESONANCE ANGIOGRAPHY

Contrast-enhanced magnetic resonance angiography (CE-MRA) is performed after injection of a gadolinium chelate bolus. The technique relies on T1 shortening of blood and requires rapid imaging. A spoiled gradient sequence with a short echo time is used. Conventionally, CE-MRA has high spatial and low temporal resolution and is performed during suspended respiration. More recently, high-temporal resolution, free-breathing, time-resolved CE-MRA has proved to be feasible in children with higher heart rates by using k-space undersampling techniques and parallel imaging.[6] In contrast to conventional CE-MRA, time-resolved MRA achieves greater temporal resolution but lower spatial resolution by oversampling the center of k-space (contrast) compared with the periphery (edge detail). Portions of k-space are shared across measurements with resulting high temporal resolution. Before contrast material is injected, a mask volume is obtained. The contrast material is then injected and the scan is initiated. The precontrast mask is subtracted from each subsequent volume to obtain a series of maximum-intensity projection images over time (Video 67.1). CE-MRA datasets can be used to create 3D volume renderings and multiplanar reformations (Fig. 67.5).

Balanced steady-state free-precession imaging (b-SSFP) is a respiratory- and cardiac-gated, fat-suppressed, 3D MRA sequence used for cardiac and extracardiac anatomy imaging. It provides high resolution because it is ECG gated, and there is excellent delineation of intracardiac anatomy and the coronary arteries (Fig. 67.6 and Video 67.2).[7] Given its high spatial resolution, this technique is used in children with complex congenital heart disease where 3D assessment, either with multiplanar or volumetric reformatted images or printed models, is critical for treatment planning. Because this technique can be performed without contrast, it can be useful in evaluating patients with severe renal dysfunction who cannot undergo testing with gadolinium-based contrast agents because of the risk of developing nephrogenic systemic fibrosis and to minimize gadolinium-based contrast agent exposure to decrease gadolinium deposition in the brain.[8,9,10]

## PERFUSION AND LATE GADOLINIUM ENHANCEMENT

First-pass contrast-enhanced perfusion images, with or without the concomitant administration of vasodilators, provide assessment of myocardial perfusion reserve. Myocardial perfusion is acquired by rapid imaging during multiple cardiac cycles over time, which allows visualization of a contrast bolus through the heart. A perfusion defect is suggestive of a stenosed arterial supply to that territory. Recent studies in children have shown that stress perfusion imaging is feasible and has reasonable sensitivity, specificity, and positive and negative predictive values for coronary disease when compared with coronary angiography.[11-13]

Late gadolinium enhancement of the myocardium is assessed 10 to 20 minutes after administration of an intravenous gadolinium-based contrast agent. An inversion pulse nulls the signal from normal myocardium, and abnormal myocardium appears bright on the black background of normal myocardium. Late gadolinium enhanced images provide information about abnormal myocardium in both ischemic and nonischemic cardiomyopathies, including myocarditis, and may help characterize cardiac masses and infiltrative diseases. Late gadolinium enhancement is seen due to increased extracellular distribution of contrast in abnormal tissues, whether from scarring (infarction), fibrosis (cardiomyopathy), inflammation (myocarditis), or infiltrative disease (amyloid, sarcoid). Regardless of the etiology, the presence of extensive late gadolinium enhancement portends a poor prognosis.[14]

### Preoperative and Postoperative Imaging

MRI is performed as a complement to echocardiography for preoperative evaluation of cardiovascular anomalies and function. Most intrinsic cardiac anomalies do not require MRI for initial diagnosis or treatment, although patients with complex anatomy can be difficult to fully evaluate with echocardiography, so these patients may benefit from cardiac MRI. However, cardiac MRI is performed more commonly in children after surgical repair or palliation than before surgery for preoperative diagnosis.

To assess cardiac anatomy and morphology, a combination of multiplanar spin echo and b-SSFP imaging usually is performed. Long- and short-axis b-SSFP cine imaging of the ventricles and

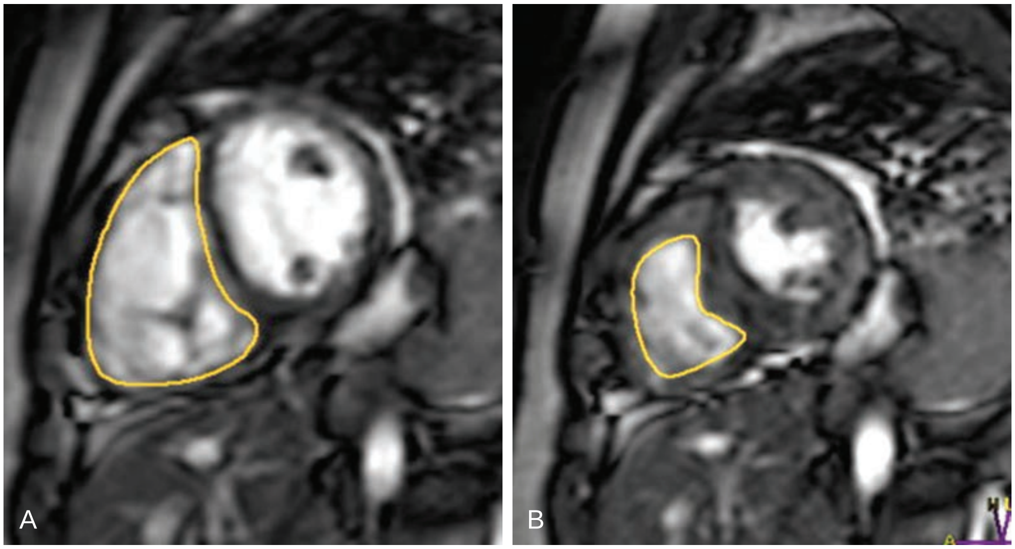

**Figure 67.3. Pulmonary regurgitation.** Endocardial right ventricular contours are drawn on a short-axis steady-state free-precession MRI in end-diastole (A) and end-systole (B) in a patient with a history of pulmonary stenosis after a pulmonary valvectomy and now with pulmonary regurgitation. The calculated pulmonary regurgitant fraction was calculated to be 37% by right and left ventricular stroke volume differences.

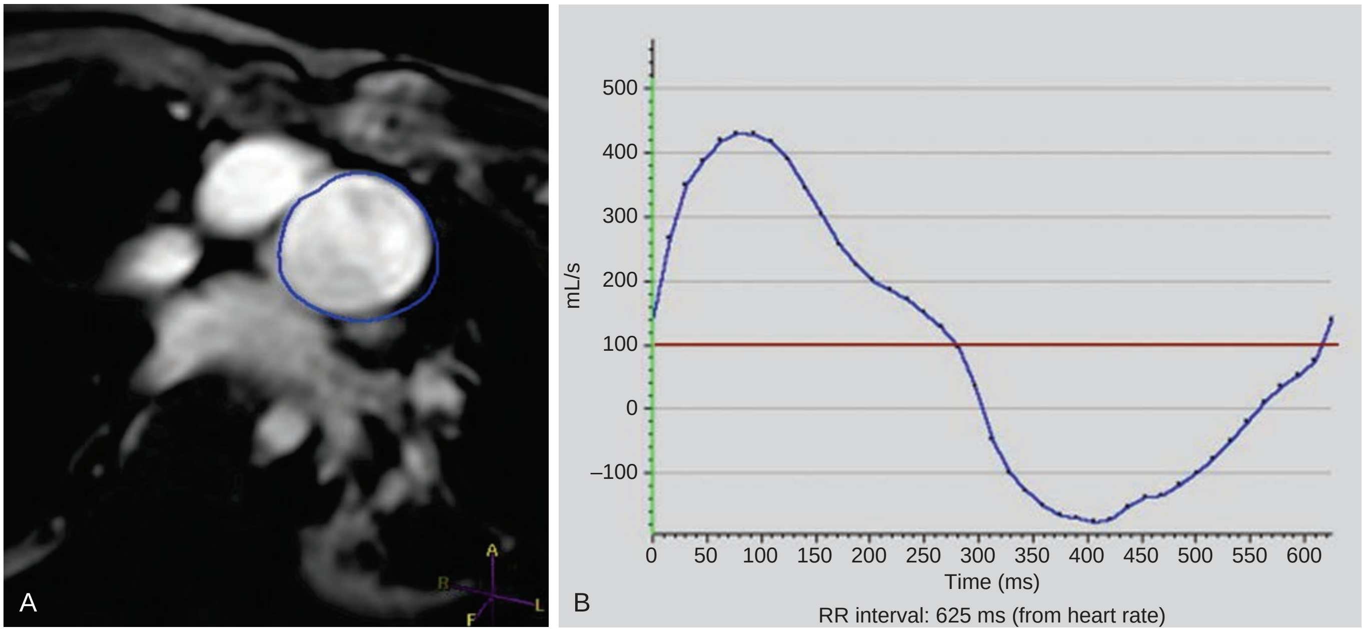

**Figure 67.4. Tetralogy of Fallot.** Phase-contrast velocity mapping of the pulmonary artery in a 15-year-old with a history of tetralogy of Fallot after patch augmentation of the subpulmonary outflow tract obstruction. The blue region of interest is around the pulmonary outflow tract (A). The flow curve demonstrates moderate pulmonary regurgitation with a calculated regurgitant fraction of 34% (B).

outflow tracts should be obtained for ventricular functional and volumetric analysis and to detect flow disturbances associated with septal defects or regurgitant valves. Phase-contrast imaging of the valves and pertinent vessels allows for blood flow velocity and vascular blood flow assessment. Extracardiac vascular evaluation is generally performed with CE-MRA. A spin echo dark blood sequence complements CE-MRA by allowing visualization of vessel walls. Vascular rings are well delineated by CE-MRA but require additional spin echo imaging to identify the degree of associated airway compression.

Because children with congenital heart disease often have complex anatomy, an organized segmental approach is necessary for image acquisition and interpretation. This includes determination of visceral situs and cardiac position, atrial relationship, atrioventricular and ventriculoarterial connections, and great arterial relationship (see Chapter 63). Potential abnormalities at each level should be assessed, including the number and connections of pulmonary veins, septal defects or additional shunt lesions, pulmonary artery or aortic anomalies, valvular abnormalities, and vascular dilation and stenoses.

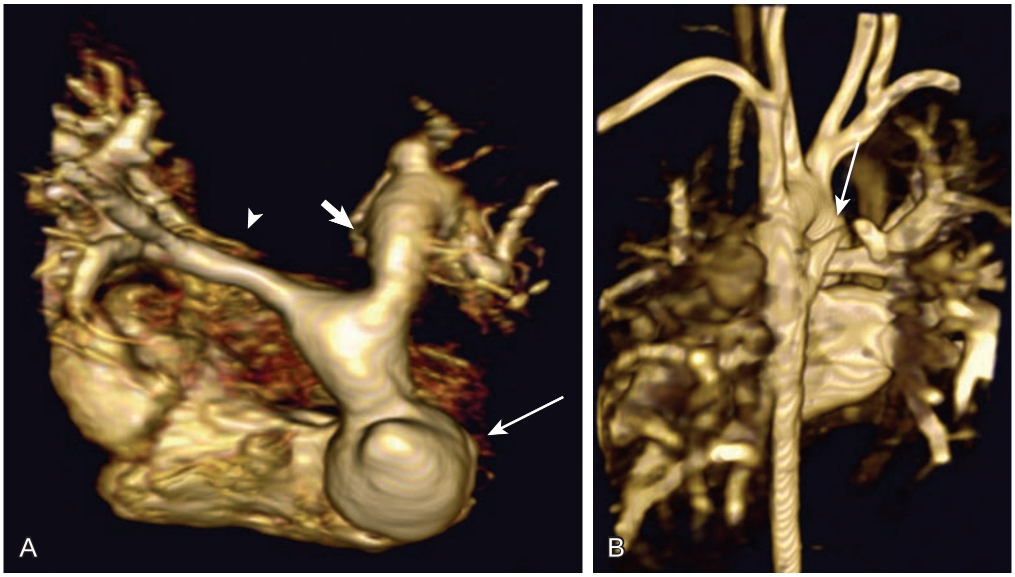

**Figure 67.5. Tetralogy of Fallot after patch augmentation for right ventricular outflow tract obstruction.** Three-dimensional volume-rendered MRI of the pulmonary artery and branches (A) from a superior-to-inferior view. A pseudoaneurysm of the right ventricular outflow tract is seen *(long arrow).* Hypoplasia of the right pulmonary artery is present *(arrowhead),* along with ectasia of the left pulmonary artery *(short bold arrow).* A posterior image of the chest (B) in the same patient shows a major aortopulmonary collateral artery to the upper lobe segment of the right lung *(arrow).*

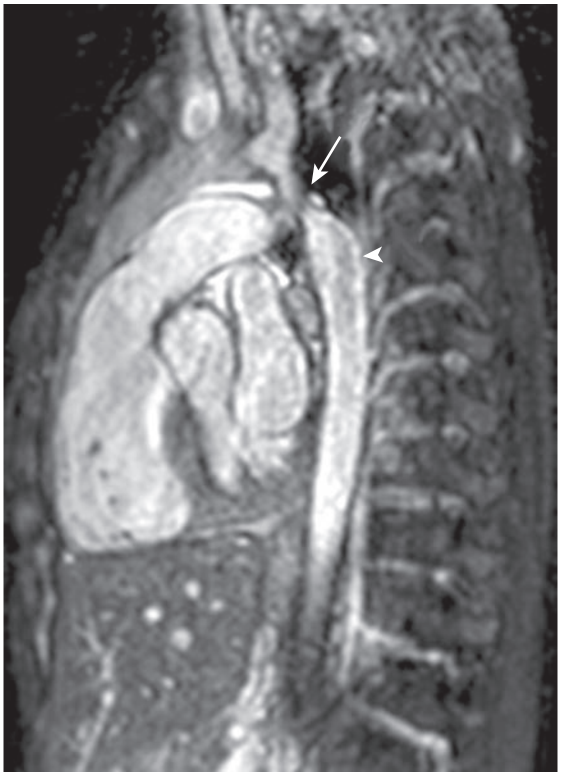

**Figure 67.6. Aortic coarctation in a 3-year-old.** A three-dimensional noncontrast b-SSPP 3D MRA of the chest was performed. The *arrow* points to a focal area of high-grade stenosis in the postductal aorta, and the *arrowhead* shows the turbulent flow distal to the coarctation (see Video 67.3).

### KEY POINTS

- Cardiac MRI is an excellent supplement to echocardiography in congenital and acquired heart disease given its ability to produce 3D images and accurately assess volumetrics, function, and flow.
- Time-resolved MRA produces better temporal resolution than conventional contrast-enhanced MRA. The shorter acquisition time makes it an ideal choice for pediatric cardiovascular imaging.
- The b-SSFP noncontrast 3D MRA technique gives excellent intracardiac and coronary artery detail and avoids exposure to gadolinium-based contrast agents.

## SUGGESTED READINGS

Fratz S, Chung T, Greil G, et al. Guidelines and protocols for cardiovascular magnetic resonance in children and adults with congenital heart disease: SCMR expert consensus group on congenital heart disease. *J of Cardiovasc Magn Reson*. 2013;15:51.

Krishnamurthy R, Slesnick T, Taylor M, et al. Free breathing high temporal resolution time resolved contrast enhanced MRA (4D MRA) at high heart rates using keyhole SENSE CENTRA in congenital heart disease. *J Cardiovasc Magn Reson*. 2011;i12(suppl 1):O31.

Lim R, Srichai M, Lee V. Non-ischemic causes of delayed myocardial hyperenhancement on MRI. *AJR Am J Roentgenol*. 2007;188:1675–1681.

Varaprasathan GA, Araoz PA, Higgins CB, et al. Quantification of flow dynamics in congenital heart disease: applications of velocity-encoded cine MR imaging. *Radiographics*. 2002;22(4):895–905.

Vasanawala SS, Chan FP, Newman B, et al. Combined respiratory and cardiac triggering improves blood pool contrast-enhanced pediatric cardiovascular MRI. *Pediatr Radiol*. 2011;41(12):1536–1544.

## REFERENCES

Full references for this chapter can be found on www.expertconsult.com.

## REFERENCES

1. Warnes CA, Williams RG, Bashore TM, et al. ACC/AHA 2008 guidelines for the management of adults with congenital heart disease. Vol. 52. *J Am Coll Cardiol*. 2008;1890–1947.
2. Helbing WA, Ouhlous M. Cardiac magnetic resonance imaging in children. Vol. 45. *Pediatr Radiol*. 2015;20–26.
3. Kawel-Boehm N, Maceira A, Valsangiacomo-Buechel ER, et al. Normal values for cardiovascular magnetic resonance in adults and children. *J Cardiovasc Magn Reson [Internet]*. 2015;17(1):29. Available from:: http://jcmr-online.com/content/17/1/29.
4. Srichai MB, Lim RP, Wong S, et al. Cardiovascular applications of phase-contrast MRI. *AJR Am J Roentgenol*. 2009;192:662–675.
5. Vasanawala SS, Hanneman K, Alley MT, et al. Congenital heart disease assessment with 4D flow MRI. Vol. 42. *J Magn Reson Imaging*. 2015;870–886.
6. Steeden JA, Pandya B, Tann O, et al. Free breathing contrast-enhanced time-resolved magnetic resonance angiography in pediatric and adult congenital heart disease. *J Cardiovasc Magn Reson [Internet]*. 2015;17:38. Available from: http://www.ncbi.nlm.nih.gov/pubmed/25997552%5Cnhttp://www.pubmedcentral.nih.gov/articlerender.fcgi?artid=PMC4490694.
7. Kato S, Kitagawa K, Ishida N, et al. Assessment of coronary artery disease using magnetic resonance coronary angiography: a national multicenter trial. *J Am Coll Cardiol*. 2010;56(12):983–991.
8. Weinreb JC, Abu-Alfa AK. Gadolinium-based contrast agents and nephrogenic systemic fibrosis: why did it happen and what have we learned? In. *J Magn Reson Imaging*. 2009;1236–1239.
9. Kanda T, Ishii K, Kawaguchi H, et al. High signal intensity in the dentate nucleus and globus pallidus on unenhanced T1-weighted MR images: relationship with increasing cumulative dose of a gadolinium-based contrast material. *Radiology*. 2014;270:834–841.
10. Miller JH, Hu HH, Pokorney A, et al. MRI brain signal intensity changes of a child during the course of 35 gadolinium contrast examinations. *Pediatrics*. 2015;136:e1637–e1640.
11. Buechel ER, Balmer C, Bauersfeld U, et al. Feasibility of perfusion cardiovascular magnetic resonance in paediatric patients. *J Cardiovasc Magn Reson*. 2009;11:51.
12. Noel CV, Krishnamurthy R, Moffett B, et al. Myocardial stress perfusion magnetic resonance: initial experience in a pediatric and young adult population using regadenoson. *Pediatr Radiol*. 2016.
13. Vijarnsorn C, Noga M, Schantz D, et al. Stress perfusion magnetic resonance imaging to detect coronary artery lesions in children. *Int J Cardiovasc Imaging*. 2016.
14. Etesami M, Gilkeson RC, Rajiah P. Utility of late gadolinium enhancement in pediatric cardiac MRI. Vol. 46. *Pediatr Radiol*. 2016;1096–1113.

# 68

# Pediatric Cardiac Catheterization and Electrophysiology

*John F. Rhodes and Ronald J. Kanter*

## PEDIATRIC CARDIAC CATHETERIZATION

### Introduction

Pediatric cardiovascular catheterization laboratories today involve a variety of complex diagnostic and interventional procedures for congenital abnormalities using multiple imaging tools to improve procedural outcome and patient safety. Preprocedure imaging to map the complex anatomy is more routinely performed, including modalities such as computed tomography (CT), cardiac magnetic resonance imaging (cardiac MRI), and three-dimensional (3D) model creation to plan the interventional procedure. Many centers are also using 3D rotational angiography to outline anatomy and important stenoses in the laboratory. In addition, intracardiac echocardiography remains a frequently used modality to guide septal closures, assess paravalvar leaks during transcatheter valve implantation, and assess mitral valve anatomy or appendage anatomy during structural interventions. Consequently, the pediatric cardiovascular catheterization laboratory has evolved to diagnostic procedures using an assortment of imaging modalities to assess complex congenital abnormalities before surgery and interventional procedures that permit therapeutic options that often preclude surgery.[1]

### Procedural Techniques

Catheterizations are performed with the Seldinger technique in the femoral vein and/or artery. Alternative venous access includes the internal jugular, subclavian, or transhepatic approaches. Arterial access also may be obtained via the arteries of the upper extremities or the carotid artery, but these approaches typically are either emergent conditions, secondary to occluded standard vessels, or anatomy deemed inadequate due to a small vessel diameter relative to the sheath required for the procedure. Anticoagulation is managed with heparin, 80 to 100 U/kg or 5000 U in patients greater than 50 kg, for an activated clotting time goal of 200 to 280 seconds, depending on the procedure to be performed. Antibiotics are administered to patients who receive an implanted device or are at risk for endocarditis based on the American Heart Association guidelines. Baseline hemodynamics (including pressures and oxygen saturations) and angiography are obtained in room air. Subsequently, relative blood flows and vascular resistances are calculated. The ratio of pulmonary blood flow (Qp) to systemic blood flow (Qs) is calculated according to the following formula: $Qp/Qs = [(AO_2 - MVO_2)/(PVO_2 - PaO_2)]$, where $AO_2$ is the aortic oxygen saturation, $MVO_2$ is the mixed venous oxygen saturation, $PaO_2$ is the pulmonary arterial saturation, and $PVO_2$ is the pulmonary venous saturation. These data then determine whether additional information or interventions are necessary, as well as whether the patient is a future surgical or transplant candidate.

## CONGENITAL ABNORMALITIES OF THE RIGHT SIDE OF THE HEART

### Pulmonary Valve Stenosis

Valvar pulmonary stenosis is found in 8% to 10% of patients with congenital heart disease (see Chapter 74). Balloon pulmonary valvuloplasty has supplanted surgical valvotomy as the treatment of choice. The recommended balloon-to-annulus ratio is between 100% and 140%.[2] The reported success rate is greater than 90% with complications occurring in less than 1%.[3] Hemodynamic measurements include the right ventricular (RV) pressure compared with systemic arterial pressure and the peak-to-peak systolic pressure gradient across the pulmonary valve. The guideline recommendations for balloon pulmonary valvuloplasty is the presence of at least moderate pulmonary valve stenosis defined as peak instantaneous pressure gradient of ≥36 mm Hg by echocardiography.[4] We use as a guideline the “rule of 50,” which is defined as a peak RV systolic pressure of more than 50 mm Hg, a peak RV systolic pressure more than 50% of the systemic systolic pressure, or a peak-to-peak systolic gradient across the pulmonary valve of more than 50 mm Hg. An end-hole catheter is used to obtain a pressure from the pulmonary artery to the body of the right ventricle to assess the severity and location of any stenoses.

RV angiography in the anteroposterior view angled cephalad and in the lateral view is performed to provide information about location and severity of pulmonary valve stenosis. The valve annulus is measured digitally. The angiographic diagnosis of dysplastic pulmonary valve stenosis is confirmed when the valve leaflets are markedly thickened and severely immobile. For patients who meet the hemodynamic criteria, balloon pulmonary valvuloplasty is performed using a standard technique and deemed successful if the estimated peak RV pressure is less than 50 mm Hg, less than 50% of the peak systemic pressure, and less than 50 mm Hg peak-to-peak gradient across the pulmonary valve (guidelines state less than 40 mm Hg). Also, procedures are deemed successful only if there is a stable saturation with a closed ductus arteriosus and no immediate operative intervention is necessary before discharge from the hospital.

### Tricuspid Valve Stenosis

Bioprosthetic valves in the tricuspid position are amenable to transcatheter valve implantation.[5] Data are limited, but limited experience using the internal jugular approach has shown promising results (e-Fig. 68.1). Further data and clinical studies are necessary.

### Postoperative Right Ventricular Outflow Tract Derangements

Nearly 5,000 babies are born each year in the United States with some form of RV outflow tract derangement, and many of these patients require surgery early in life.[1] As these patients return with either hemodynamically significant RV outflow stenosis, regurgitation, or a combination, they are now candidates for a transcatheter pulmonary valve replacement.

Currently there are two Food and Drug Administration (FDA)–approved transcatheter pulmonary valves available for patients with hemodynamically abnormal RV outflow tracts, including either free pulmonary insufficiency and RV volume overload or RV outflow obstruction with RV hypertension and RV systolic or diastolic failure. The two valves are the Sapien XT[6] (Edwards Lifesciences, Irvine, CA) and the Melody valve[7] (Medtronic, Minneapolis, MN). The transcatheter pulmonary valve has replaced many patients’

## Abstract:

Pediatric cardiovascular catheterization laboratories involve a variety of complex diagnostic and interventional procedures for congenital abnormalities using multiple imaging tools to improve procedural outcome and patient safety. Preprocedure imaging to map the complex anatomy is more routinely performed, including modalities such as computed tomography (CT), cardiac magnetic resonance imaging (cardiac MRI), and three-dimensional (3D) model creation to plan the interventional procedure. Many centers are also using 3D rotational angiography to outline anatomy and important stenoses in the laboratory.

The pediatric cardiovascular catheterization laboratory has evolved to diagnostic procedures using an assortment of imaging modalities to assess complex congenital abnormalities before surgery and interventional procedures that permit therapeutic options that often preclude surgery.

## Keywords:

Cardiac catheterization
balloon angioplasty
transcatheter valve implantation
closure devices
catheter ablation
cardiac implantable electronic devices
electromagnetic interference

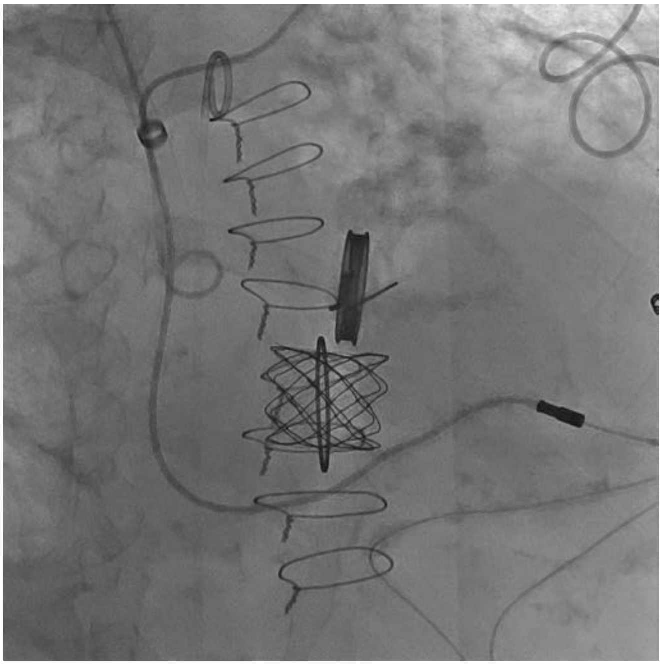

**e-Figure 68.1. Melody valve.** Anterior-posterior projection fluoroscopy demonstrating a Melody valve successfully deployed in the bioprosthetic ring in the tricuspid position via the right internal jugular vein.

need for a reoperation. Consequently, patients who often required two to four surgeries before an adult age can be treated with a nonsurgical valve technique (e-Fig. 68.2).

## Pulmonary Artery Stenosis

Since the introduction of high-pressure balloons (>30 atmospheres), pulmonary artery angioplasty has a success rate of more than 70%. Patients with severely hypoplastic pulmonary arteries with multiple stenoses that are refractory to high-pressure angioplasty may be amenable to cutting balloon angioplasty.[8] Cutting balloons are now FDA approved for pulmonary artery angioplasty with balloons 4 to 8 mm in diameter going to 7 to 8 atmospheres. Cutting balloon angioplasty often is followed by standard angioplasty (8–12 atm) for the best final result. Balloon-expandable stents have improved results in proximal vessels, eliminating the need for surgery in most patients (e-Fig. 68.3), but they are of limited value in distal pulmonary vessels. Furthermore, stents are contraindicated in noncompliant vessels that cannot be expanded using high-pressure balloons. Although balloon catheters, as well as stents, have not specifically been approved by the FDA as a treatment for pulmonary artery stenoses, these techniques have become the mainstay of treatment for distal vessel obstruction.

# CONGENITAL ABNORMALITIES OF THE LEFT SIDE OF THE HEART

## Aortic Valve Stenosis

Valvar aortic stenosis results from fusion of the aortic valve leaflets, creating either a unicuspid or bicuspid apparatus with functionally a one- or two-leaflet aortic valve. This is the most common congenital heart lesion, occurring in 1% to 2% of the population (see Chapter 73). Valvar aortic stenosis can be classified into two groups: group 1 has disease that is severe enough that it presents at birth or within 1 to 2 years of age (10%–15%), and group 2 has disease that is not diagnosed until after age 2 years and will progress much more slowly.[9,10] Morbidity, mortality, and the need for intervention are significantly skewed toward group 1. As with pulmonary stenosis, noninvasive imaging techniques have advanced to the point that nearly all anatomic and functional information about the valve may be obtained without catheterization. Fusion of the right and left coronary cusps is more significantly associated with coarctation of the aorta[11] compared with fusion of the right and noncoronary cusp. All bicuspid aortic valve patients are at risk for aortic root enlargement, and 8% to 10% may have a cerebral aneurysm. Catheterization is performed for valves that clearly merit intervention or when symptoms and imaging findings are incomplete or confounding.[12]

Aortic valve stenosis is classified into the following categories: trivial, mild, moderate, severe, and critical. Critical aortic stenosis is not defined by a specific pressure gradient or valve orifice size but on the basis of physiologic manifestations. If the stenosis is such that the patient is unable to produce and maintain an adequate cardiac output, the stenosis is critical. Patients in this group may have a low valve gradient due to decreased cardiac function and low cardiac output. Although controversy may exist with regard to the most beneficial treatment method for this patient population, most centers have adopted balloon valvuloplasty as the initial treatment of choice. Balloon valvuloplasty has demonstrated a reduction in gradient and resultant valve regurgitation with a shorter course in the cardiac intensive care unit and a shorter hospital stay compared with surgical valvotomy.

However, balloon valvuloplasty has been associated with an increased rate of reintervention compared with surgical valvotomy as a result of recurrent stenosis or worsening regurgitation. Given that residual aortic valve disease, especially regurgitation, may progress over time, the recommendation for the valvuloplasty technique is more conservative, with a smaller maximal balloon diameter (80% to <100% of the annulus) than that recommended for the pulmonary valve (100%–140%). The valve may be approached retrograde from the aorta, with arterial access usually from the femoral or carotid via a surgical cutdown. Our preference is to approach the aortic valve prograde by crossing an existing atrial communication or by performing a transseptal puncture to access the left side of the heart. Once in the left ventricle, angiography is performed to measure the valve annulus and identify landmarks for valvuloplasty. Many centers have adopted rapid right or left ventricular pacing at the time of balloon inflation. This rapid pacing transiently reduces cardiac output and the shearing force transmitted to the balloon as it is inflated across the valve annulus. The goal is to reduce the balloon shear force motion on the fragile valve leaflets and prevent excessive damage and subsequent regurgitation. Repeat angiography and echocardiography after inflation are essential to evaluate the success of the valvuloplasty and monitor for regurgitation or other complications. The differentiation between noncritical stenosis categories is made by noninvasive echocardiographic measurements of valve area and Doppler gradient. A normal valve area is 2 $cm^2/m^2$. Mild obstruction is consistent with valve areas less than 2 $cm^2/m^2$ but greater than 0.7 $cm^2/m^2$, and severe obstruction is consistent with valve areas less than 0.5 $cm^2/m^2$. Mean echocardiographic Doppler gradients are good predictors of the peak-to-peak pressure gradient measured at catheterization. Gradients less than 25 mm Hg are considered trivial, those 25 to 50 mm Hg are mild, those 50 to 75 mm Hg are moderate, and those greater than 75 mm Hg are severe.[12] These measurements are made with the understanding that the cardiac function and cardiac output are normal. Catheterization is not recommended for trivial or mild stenosis. Moderate and severe stenoses are approached with primary balloon valvuloplasty using the techniques previously described.

## Coarctation of the Aorta—Angioplasty and Stent Placement

Often, aortic obstruction after an end-to-end surgical repair at the isthmus is a result of aortic narrowing within the transverse arch. These obstructive lesions are further defined as either the proximal transverse arch between the innominate artery and left carotid artery or the distal transverse arch, defined as the region between the left carotid artery and the left subclavian artery. Although few data exist regarding stent angioplasty within the distal transverse aortic arch, general experience has been that this procedure is safe and effective. A sheath is placed in the femoral artery and an arterial monitoring catheter is placed in the right upper extremity. A 4-Fr sheath is used to advance a 4-Fr pigtail catheter from the right radial artery to the proximal transverse aortic arch. This catheter is used to monitor pressures during stent angioplasty of the distal transverse arch from the femoral artery and to perform cine angiograms to determine appropriate stent placement distal to the takeoff of the left carotid artery.

Transcatheter stent angioplasty for postoperative recoarctation of the aorta at the isthmus has been demonstrated to be safe and effective.[14] The technique usually involves a femoral arterial approach. Recently, the coarctation of the aorta stent trial (COAST) resulted in an FDA approval for a bare metal stent (CP stent, NuMED, Hopkinton, NY) for coarctation of the aorta and COAST II resulted in FDA approval of a Gore-Tex–covered stent (CP Covered Stent, NuMED, Hopkinton, NY) for coarctation of the aorta (Fig. 68.4).

An exchange length wire is placed in the ascending aorta or right subclavian artery. An angioplasty balloon is used with a maximum diameter that is equal to or less than the diameter of the normal aortic segments adjacent to the stenotic region and/or the diameter of the descending thoracic aorta at the diaphragm. The stent is mounted on the angioplasty balloon and passed through

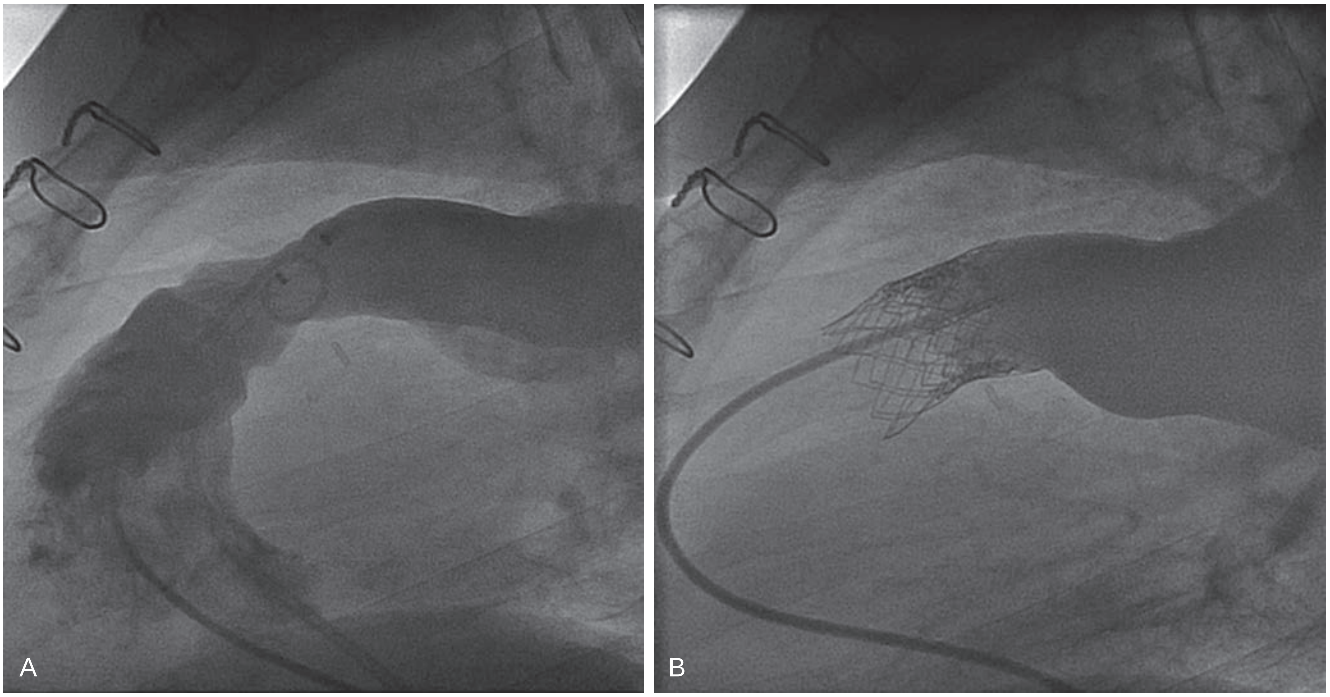

**e-Figure 68.2. Right ventricular outflow tract evaluation.** (A) Lateral projection fluoroscopy and cine angiography of a patient with truncus arteriosus post–right ventricular outflow tract reconstruction. Angiography shows free pulmonary insufficiency and supravalvar narrowing. (B) Lateral projection fluoroscopy and cine angiography of a patient with tetralogy of Fallot post–right ventricular outflow tract revision with a 26-mm Sapien XT valve. Angiography in the main pulmonary artery demonstrates no pulmonary insufficiency or stenosis.

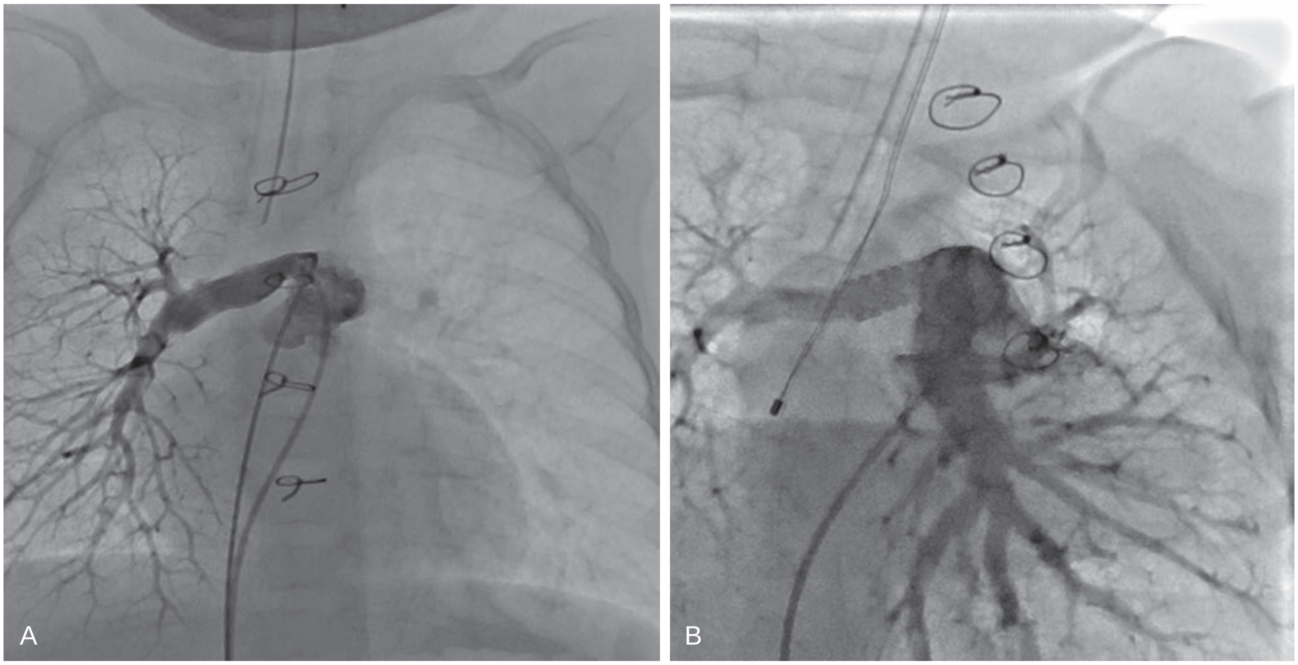

**e-Figure 68.3. Pulmonary artery stenosis.** (A) Anterior-posterior projection fluoroscopy and cine angiography demonstrating a proximal right pulmonary artery stenosis. (B) Caudal right anterior oblique projection fluoroscopy and cine angiography demonstrating a successful balloon stent angioplasty of the right pulmonary artery.

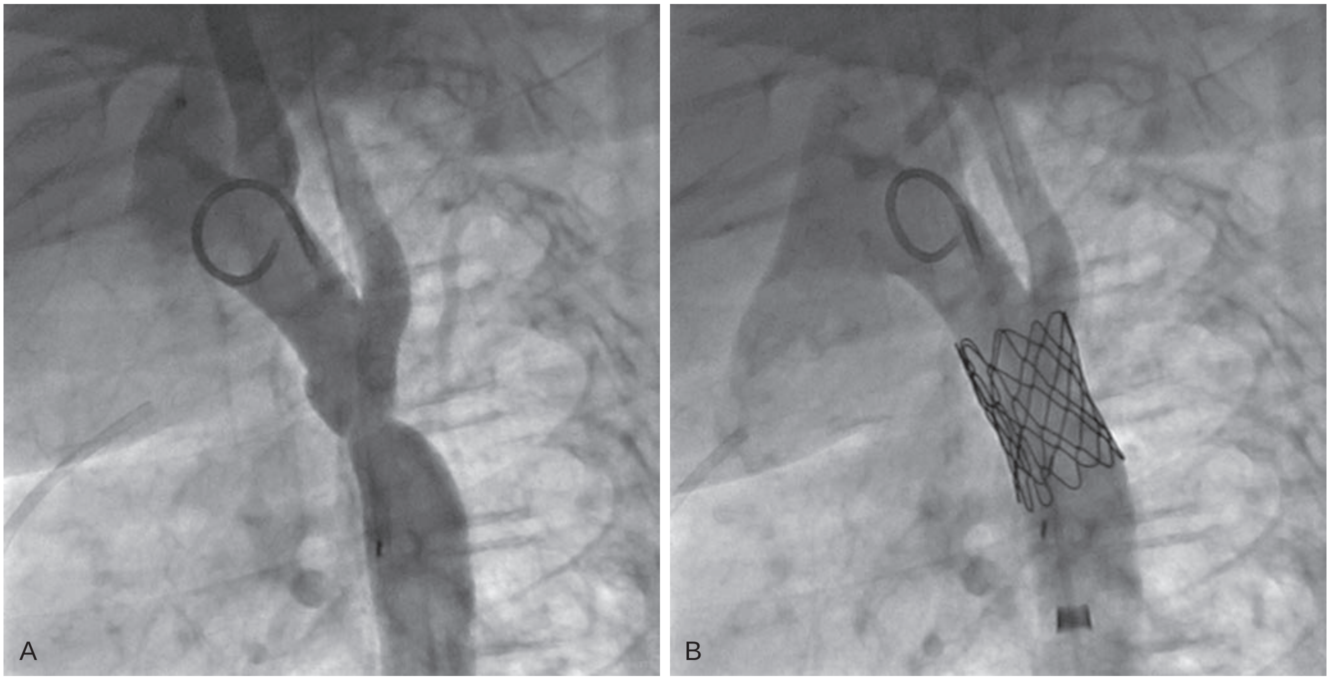

**Figure 68.4. Aortic coarctation.** (A) Lateral projection fluoroscopy and cine angiography of a patient with Turner's syndrome, bicuspid aortic valve, and coarctation of the aorta demonstrates severe native stenosis of the aorta at the isthmus. (B) Lateral projection fluoroscopy and cine angiography after CP covered stent angioplasty for coarctation of the aorta demonstrates improved flow through the isthmus.

a sheath at least 1 to 2 Fr larger than that required by the balloon. The stent length is dependent on the lesion length but is usually 28 to 45 mm. The stent is fully dilated in most cases, but at times it is deemed safer to serially dilate the lesion over two procedures.

## SEPTAL AND VASCULAR CLOSURE DEVICES

### Secundum Atrial Septal Defect

Although atrial septal defect (ASD) diagnosis rarely requires cardiac catheterization, today many patients undergo cardiac catheterization for therapeutic device closure.[14] These patients require assessment of associated anomalies such as abnormalities of pulmonary venous connections. A step-up in oxygen saturations in the right atrium and pulmonary arteries is characteristic for an ASD, and the degree of left-to-right shunting or the pulmonary to systemic blood flow ratio (Qp:Qs) can be determined. The ideal age or timing for elective ASD closure is 2 to 5 years of age or within 6 to 12 months of diagnosis. Rarely, a child with an ASD presents with severe congestive heart failure and requires intervention in the first year of life.

Percutaneous ASD closure has been established as a safe and effective alternative to operative repair. The technique involves transcatheter delivery of a device in its retracted state via the femoral vein under fluoroscopic and echocardiographic guidance. Echocardiographic guidance can be transthoracic in young children and transesophageal, intracardiac, or even 3D in older children and adults. The most commonly available devices today consist of a double-disc design made of nickel and titanium (Nitinol) with deployment of the first disc on the left atrial aspect of the septum followed by deployment of the second opposing disc on the right atrial wall. The expanded discs are tightly approximated, thus closing the defect. The device becomes endothelialized during the next 3 to 6 months while the patient is treated with antiplatelet medications. Relative contraindications include some defect diameters too large in relation to body weight; the absence of adequate septal tissue margins, especially the posterior inferior septum near the atrioventricular valves; and close proximity to vital cardiac structures.

The world experience of transcatheter ASD closure using the FDA-approved Amplatzer Septal Occluder (St. Jude Medical, St. Paul, MN) has been reported with a greater than 97% immediate success rate.[15] The occlusion rate reached 100% by 3 years. An overall 2.8% adverse event rate was found, and no procedural deaths occurred. Several studies regarding comparisons of device occlusion versus surgical closure have been performed prospectively. These reports include the Amplatzer (St. Jude Medical, St. Paul, MN) and Helex (W. L. Gore & Associates, Flagstaff, AZ) devices. Findings include shorter hospital stays, less discomfort, and shorter convalescence in patients undergoing successful device closure. Hospital costs are similar. Regression of right ventricular dilation was similar for both groups of patients; however, it was dependent on the patient's age at the time of closure, with greater regression after earlier intervention and before puberty. Most recently, the Gore Septal Occluder (GSO) device (W. L. Gore & Associates, Flagstaff, AZ) reached FDA approval and is routinely use to close ASD with diameters up to 17 to 18 mm (e-Fig. 68.5).[16]

Procedural adverse events are uncommon but include embolization into the right or left atrium, pulmonary artery, left ventricle, and aorta; stroke as a result of a clot or air embolization; and bleeding complications.[14] Both acute and late embolization have been reported, and thus it is critical for the radiologist to be familiar with the location of the interatrial septum on radiography to ascertain correct device position in the anteroposterior and lateral chest radiograph.

### Patent Ductus Arteriosus

The first transcatheter closure of a persistently patent ductus arteriosus (PDA) was performed by Portsmann in 1967. Since that time a number of different PDA closure devices have been studied, some of which

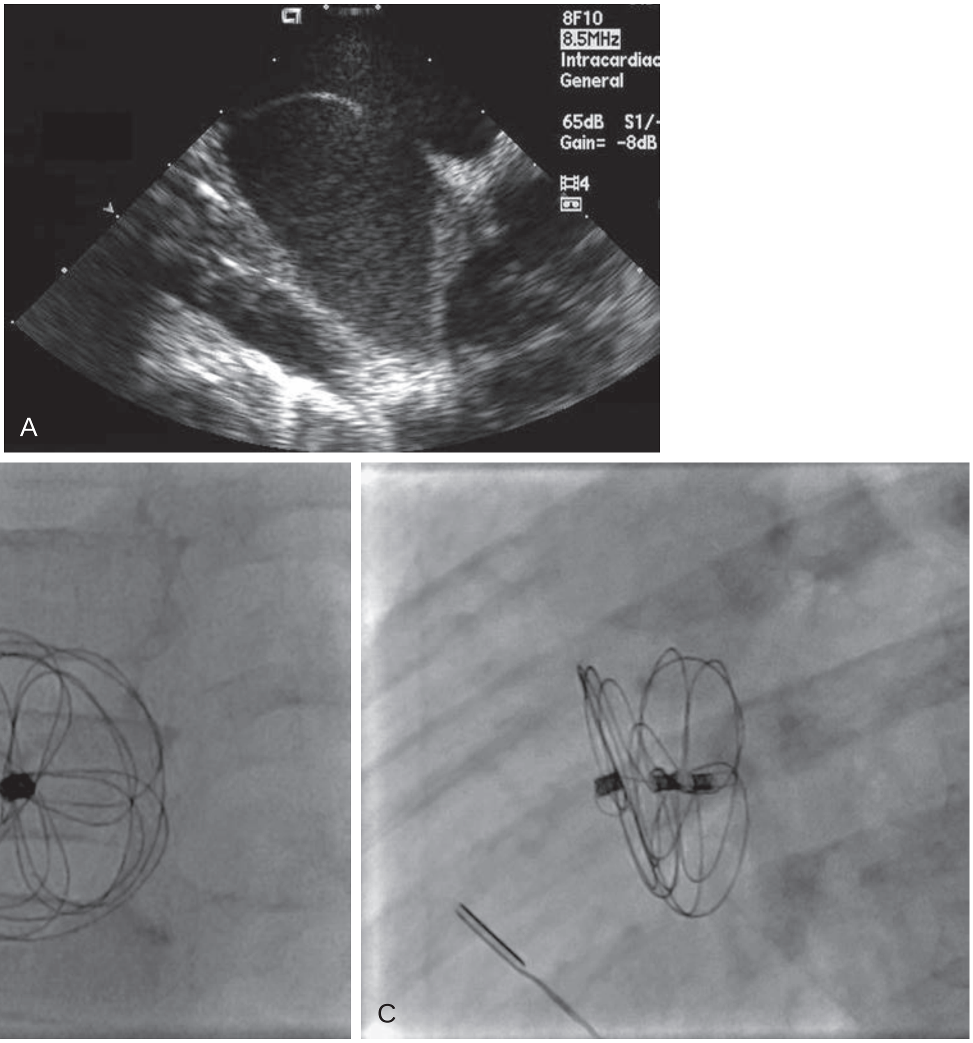

**e-Figure 68.5. Atrial septal defect.** (A) Intracardiac echocardiography (Biosense Webster, Diamond Bar, CA) from the right atrium demonstrates a secundum atrial septal defect in a 4-year-old child. (B) Anterior-posterior projection fluoroscopy demonstrates a well-positioned 30-mm Gore Septal Occluder device in a secundum atrial septal defect. (C) Lateral projection fluoroscopy demonstrates a well-positioned 30-mm Gore Septal Occluder device in a secundum atrial septal defect.

are no longer available. The goal of the procedure has always been to achieve 100% closure of the PDA without obstruction of either adjoining blood vessel (i.e., the aorta and the left pulmonary artery) with minimal risk of complications. The difficulty is that the PDA exhibits extreme variability in size and shape. Krichenko and colleagues[17] classified the PDA into five anatomic types based on the lateral aortic angiogram. The most common (type A) ductus is conical with a narrowed pulmonary arterial end and large aortic ampulla. Other types include those with a narrowed aortic end, narrowing at both ends, and a tubular configuration.

There has been great success since the first coil closure of a PDA in 1992. As expected, the recommended technique for coil embolization is variable, depending on the size and shape of the PDA. The vessel can be approached from the venous or arterial side, and the coils may be deployed "free hand" or secured with a bioptome or modified catheter. Smaller coils, such as the Flipper coil (Cook Medical, Bloomington, IN), are attached to a delivery system and are released once they are verified to be in the proper position.

A more recent addition to the interventional cardiologist's armamentarium for PDA closure is the Amplatzer Duct Occluder and the Amplatzer Duct Occluder II (St. Jude Medical, St. Paul, MN).[18] Both devices are self-expanding wire mesh devices attached to a delivery cable and deployed through a long sheath from the venous system (e-Fig. 68.6). The device has a retention skirt to occupy the aortic ampulla and tapers slightly to the pulmonary artery end. The device is filled with a polyester mesh that stimulates thrombus formation within the lumen of the PDA. The shape of the device and self-expanding properties exert radial force on the walls of the PDA, holding the device in place until endothelialization occurs. The device has excellent closure rates approaching 100% at 1 month after the procedure. The main limitation is the size and bulky nature of the device. The PDA must have an aortic ampulla adequate to accommodate the retention skirt without creating aortic obstruction. Furthermore, the device can create left pulmonary artery stenosis by compressing adjoining structures once it is released.

More recently, the Nit Occlude (pfm medical, Carlsbad, CA) reached FDA approval for PDA closure.[19] This device is deployed through a 4-Fr system making it a preferred technique in smaller children (e-Fig. 68.7).

### Other Abnormal Vessels

Accessory blood vessels are of concern for the interventional radiologist and interventional cardiologist. These accessory blood vessels may include aortopulmonary or venovenous collaterals, arteriovenous fistulae and malformations, surgically placed shunts, and transhepatic access tracts. Techniques for closure are similar to those described for the PDA, predominately involving Gianturco (Cook Medical, Bloomington, IN) and similar coils, the Amplatzer Duct Occluder (St. Jude Medical, St. Paul, MN), or the Amplatzer Vascular Plug (St. Jude Medical, St. Paul, MN). The vascular plug is similar to the duct occluder in that it is a self-expanding wire mesh design. It differs in that it is cylindrical in shape with no retention skirt, no tapering through its length, and no polyester mesh interior fabric. The device has excellent occlusion results but has been unsuccessful in short arterial vessels, such as aortopulmonary collaterals and the PDA. It is thought that the lack of occlusive material through the center of the device does not provide enough restriction to arterial blood flow to stimulate thrombosis and occlude the vessel.

## PEDIATRIC ELECTROPHYSIOLOGY

### Introduction

With regard to imaging, the clinical practices of the pediatric radiologist and pediatric electrophysiologist intersect in two ways: Both subspecialists are interested in detailed internal anatomy, and both subspecialties have evolved toward performing therapeutic procedures. In particular, advances in imaging have helped improve outcomes of catheter ablation for nearly every tachyarrhythmia.

This section is divided into two parts: (1) items of interest to the radiologist pertaining to activities in the electrophysiology laboratory, especially newer imaging technologies to guide catheter ablation and radiation exposure risks during catheter ablation; and (2) cardiac rhythm device therapy and special concerns in the radiology department.

### Catheter Ablation in Children

#### History and Indications

Curative therapies for pathologic tachyarrhythmias began with open-chest surgery for Wolff–Parkinson–White syndrome in 1968 followed by transvascular catheter delivery of alternating current in the radiofrequency range (about 550 kHz) in 1987 in adults[20] and in 1994 in children[21] for common forms of supraventricular tachycardia (SVT). The importance of complex electroanatomic correlation within the cardiac chamber walls was first applied to atrial and ventricular tachycardias post–congenital heart surgery in the late 1990s[22] and in adults having paroxysmal atrial fibrillation starting with the seminal discovery by Haissaguerre in 1998 that repetitive pulmonary vein discharges are its source.[23] Since 2000, technical advances in catheter design have enabled the creation of larger lesions—necessary for transmural arrhythmia substrates—and have brought about the use of cryoenergy, with its greater safety profile when substrates are proximate to vital structures such as the coronary arteries and atrioventricular node. Owing to improved outcomes and safety profiles, almost no tachyarrhythmia substrate is now considered exempt from catheter ablation. Accordingly, current indications to perform catheter ablation in children and after congenital heart surgery are more liberal[24] (e-Box 68.1) compared with those from 2002.[25]

#### Technical Considerations

The guiding principle of electrophysiologic testing and catheter ablation involves coupling of anatomic structures to electrical phenomena. As a result of improvements in electroanatomic mapping systems, the anatomic shell of the structurally normal heart may now be accurately created with minimal or no fluoroscopy.[26,27] In patients with normal cardiac anatomy and SVT, multielectrode catheters are typically positioned in the right ventricle, right atrium, coronary sinus, and His bundle region of the tricuspid valve annulus, with one for mapping and ablation (e-Fig. 68.8). These anatomic sites are accessed from a combination of femoral, internal jugular, and subclavian venous approaches. However, in some patients with complex congenital cardiovascular anomalies (e.g., interrupted inferior vena cava in some patients with heterotaxy), in those whose surgical procedure segregated the systemic venous return from the heart (e.g., cavopulmonary connection or extracardiac conduit in patients having single ventricle physiology), and in those who have lost venous access due to multiple prior procedures, some or all of these venous sites will not allow access to the heart. In these instances, alternate approaches may include transhepatic venous,[28] transthoracic,[29] or transbaffle.[30] Furthermore, occasional arrhythmia substrates are primarily epicardial, requiring transpericardial access. Transthoracic or intracardiac echocardiography[31] may aid in understanding anatomic details and in the positioning of catheters.

Electroanatomic mapping systems currently use a combination of magnetic field–based and impedance-based technologies to derive accurate 3D reconstructions of the cardiac chambers and associated structures. Simultaneous acquisition of local electrical signals provides a rapid display of tachycardia substrates in real

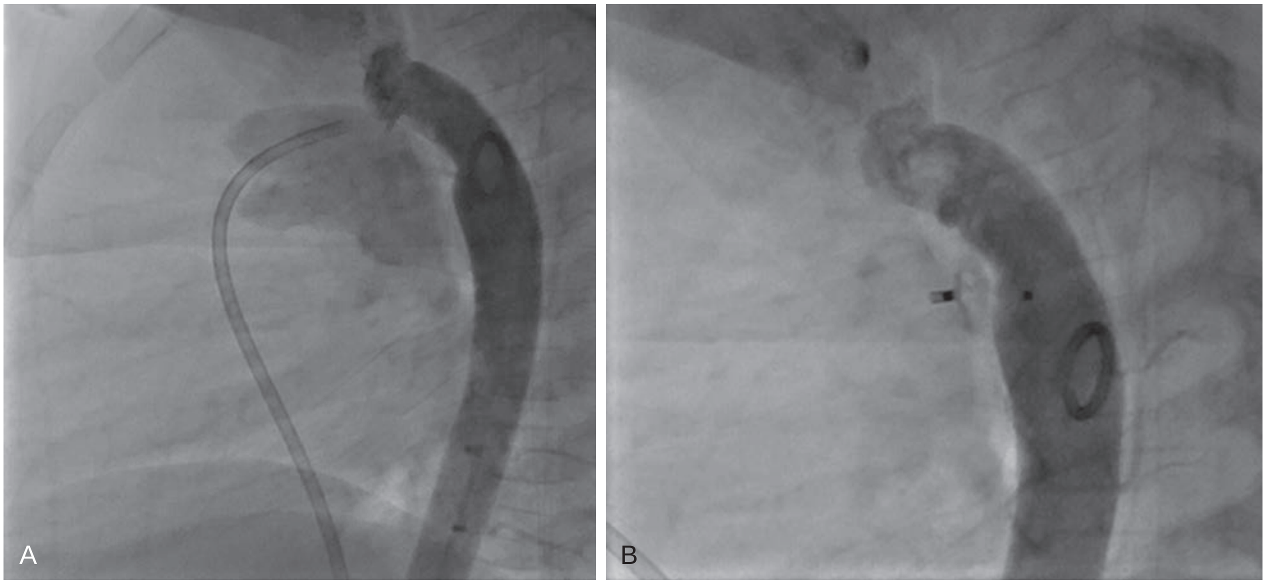

**e-Figure 68.6. Patent ductus arteriosus.** (A) Lateral projection fluoroscopy and cine angiography of a child with patent ductus arteriosus. (B) Lateral projection fluoroscopy and cine angiography after successful Amplatzer Duct Occluder II (AGA Medical Corporation, Golden Valley, MN) closure of the patent ductus arteriosus.

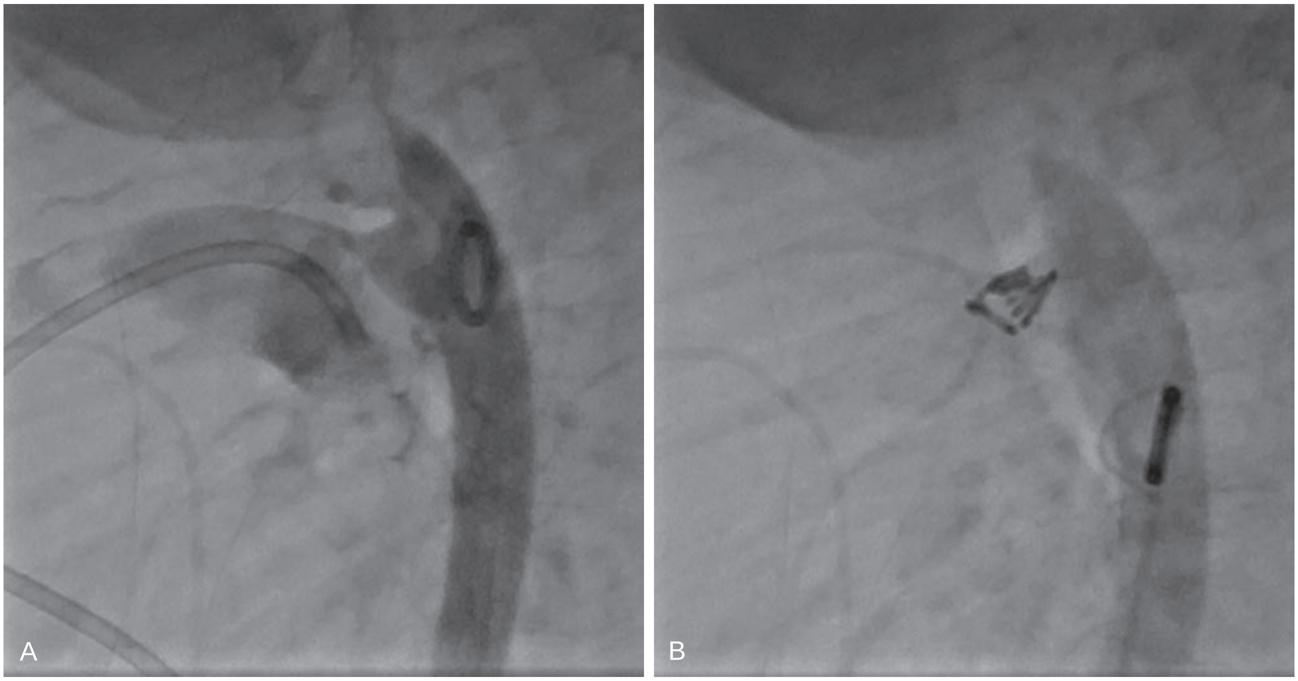

**e-Figure 68.7. Patent ductus arteriosus.** (A) Lateral projection fluoroscopy and cine angiography of an infant with patent ductus arteriosus. (B) Lateral projection fluoroscopy and cine angiography after successful closure of the patent ductus arteriosus using the pfm Nit Occlud device (pfm medical, Carlsbad, CA).

## e-BOX 68.1 Indications for Ablation Procedures in Pediatric and Adolescent Patients

### INDICATIONS FOR ABLATION PROCEDURES IN PEDIATRIC PATIENTS WITH NARROW-COMPLEX SVT (AVNRT/AVRT/AET/NAFAT/ATRIAL FLUTTER) WITHOUT CONGENITAL HEART DISEASE

**Class I**

1. Ablation is recommended for documented SVT, recurrent or persistent, associated with ventricular dysfunction in larger* patients (LOE: C).
2. Ablation is recommended for documented SVT, recurrent or persistent, when medical therapy is either not effective or is associated with intolerable side effects (medical therapy used before ablation depends on patient size)† (LOE: C).
3. Ablation is recommended for documented SVT, recurrent or persistent, when the family wishes to avoid chronic antiarrhythmic medications in larger* patients (LOE: C).
4. Ablation is recommended for recurrent acute hemodynamic compromise (hypotension or syncope) from SVT in larger* patients (level of evidence [LOE]: E).
5. Ablation is effective for recurrent SVT requiring emergency medical care or electrical cardioversion for termination in larger* patients (LOE: C).

**Class IIa Ablation Can Be Useful for the Following:**

1. Recurrent clinical symptoms clearly consistent with paroxysmal SVT in larger* patients, and one of the following: evidence for involvement of an atrioventricular (AV) accessory pathway; inducible SVT (LOE: C).
2. Slow pathway modification in larger* patients with a history of documented SVT, when SVT is not inducible at electrophysiologic testing but evidence for dual AV nodal physiology with or without single AV nodal echos is demonstrated (LOE: C). Cryotherapy should be considered for slow pathway modification (LOE: B).

**Class IIb Ablation May Be Reasonable for the Following:**

1. Slow pathway modification in larger* patients with clinical symptoms clearly consistent with paroxysmal SVT but not documented, when SVT is not inducible at electrophysiologic testing but evidence for dual AV nodal physiology with or without single AV nodal echos is demonstrated (LOE: C). Cryotherapy should be considered for slow pathway modification (LOE: B).
2. Recurrent clinical symptoms clearly consistent with paroxysmal SVT in smaller* patients, and one of the following at electrophysiology study: evidence for involvement of an AV accessory pathway; inducible SVT (LOE: C). Medical therapy should be considered before ablation (LOE: C). Cryotherapy should be considered for slow pathway modification (LOE: B).
3. Recurrent acute hemodynamic compromise (hypotension or syncope) from SVT in smaller* patients (LOE: C).
4. Intermittent symptomatic SVT that is nonsustained (<30 seconds) in larger* patients (LOE: C).

### INDICATIONS FOR ABLATION PROCEDURES IN PEDIATRIC PATIENTS WITH INAPPROPRIATE SINUS TACHYCARDIA

**Class IIb Ablation May Rarely Be Reasonable for the Following:**

1. Inappropriate sinus tachycardia when autonomic causes such as postural orthostatic tachycardia syndrome have been ruled out, and medical therapy is either not effective or is associated with intolerable side effects (LOE: C).

### INDICATIONS FOR ABLATION PROCEDURES IN PEDIATRIC PATIENTS WITH WPW PATTERN (SEE SVT INDICATIONS FOR PATIENTS WITH WPW PATTERN AND AVRT; SEE CHD INDICATIONS FOR PATIENTS WITH WPW AND CHD)

Predictors of high risk for cardiac arrest in WPW pattern include the following:

- A shortest preexcited RR interval during atrial fibrillation, or during incremental atrial pacing ≤250 msec
- Multiple accessory pathways

**Class I Ablation Is Recommended for the Following:**

1. WPW pattern after resuscitated cardiac arrest (LOE: B).
2. WPW pattern with syncope when there are predictors of high risk for cardiac arrest (LOE: B).

**Class IIa Ablation Can Be Useful for the Following:**

1. WPW pattern with ventricular dysfunction presumed due to dyssynchrony in larger* patients, or when medical therapy is either not effective or is associated with intolerable side effects† in smaller* patients (LOE: B). (Note: This indication was Class IIb in the prior guidelines for asymptomatic WPW.)
2. WPW pattern without symptoms, when there are predictors of high risk for cardiac arrest in larger patients* (LOE: C).
3. WPW pattern with syncope, without predictors* of high risk for cardiac arrest in larger* patients (LOE: C).
4. WPW pattern without symptoms in larger* patients when the absence of WPW pattern is a prerequisite for participation in personal or professional activities (LOE: E).

**Class IIb Ablation May Be Reasonable for the Following:**

1. WPW pattern without symptoms in larger* patients with predictors of low risk for cardiac arrest, as patient/family choice (LOE: E).

### INDICATIONS FOR ABLATION PROCEDURES IN ADOLESCENT PATIENTS WITH ATRIAL FIBRILLATION (AF), WITH OR WITHOUT CHD

**Class I**

None

**Class IIa Ablation Can Be Useful For the Following:**

1. An SVT substrate identified as the initiating event for AF, using either ambulatory ECG monitoring or invasive electrophysiologic evaluation. It is reasonable to ablate possible provocative SVT substrates, including a single ectopic focus within a larger pulmonary vein, or isolation of a single pulmonary vein orifice for an ectopic focus/foci initiating AF (LOE: C).

**Class IIb Ablation May Rarely Be Considered for the Following:**

1. Empiric wide area circumferential isolation of all pulmonary veins in the absence of a documented triggering focus or arrhythmia, as is performed in adults with paroxysmal AF, in adolescent pediatric patients when AF is recurrent; requires repeated DC cardioversion; and medical therapy is either not effective or is associated with intolerable side effects.† The procedure should be undertaken by or with the direct assistance of a clinician experienced in the technique (LOE: C).

### INDICATIONS FOR ABLATION PROCEDURES IN PEDIATRIC PATIENTS WITH JUNCTIONAL ECTOPIC TACHYCARDIA (JET)

**Class I**

1. Ablation is recommended for persistent or recurrent idiopathic JET, or congenital JET associated with ventricular dysfunction, when medical therapy is either not effective or is associated with intolerable side effects† (LOE: C).

## e-BOX 68.1 Indications for Ablation Procedures in Pediatric and Adolescent Patients—cont'd

2. When ablation of JET is being performed, cryotherapy is the preferred first choice due to the high risk of AV block. Radiofrequency energy should be used with extreme caution, after a detailed discussion with the family/patient concerning the high risk of AV block and potential need for permanent pacing (LOE: C).

**Class IIa Ablation Can Be Useful for the Following:**

1. Persistent or symptomatic recurrent idiopathic JET, or congenital JET in larger* patients, when medical therapy is either not effective or is associated with intolerable side effects† (LOE: C).

**Class IIb Ablation May Be Reasonable for the Following:**

1. Persistent or symptomatic recurrent idiopathic JET, or congenital JET in larger* patients, as an alternative to chronic antiarrhythmic therapy that has been effectively controlling the arrhythmia (LOE: C).
2. Persistent or symptomatic recurrent idiopathic JET, or congenital JET in smaller* patients, when medical therapy is either not effective or is associated with intolerable side effects† (LOE: C).

### INDICATIONS FOR ABLATION PROCEDURES IN PEDIATRIC PATIENTS WITH VENTRICULAR ARRHYTHMIAS WITHOUT CONGENITAL HEART DISEASE

**Class I**

1. Ablation is recommended for frequently ventricular ectopy or tachycardia, predominantly from a single focus, thought to be causing ventricular dysfunction, when medical therapy is either not effective or is associated with intolerable side effects (medical therapy used depends on patient size†), or as an alternative to medical therapy in larger* patients (LOE: C).
2. Ablation is effective for recurrent or persistent symptomatic intrafascicular verapamil-sensitive reentrant VT, idiopathic outflow tract VT, or VT with hemodynamic compromise, when medical therapy is either not effective or is associated with intolerable side effects (medical therapy used depends on patient size†), or as an alternative to medical therapy in larger* patients (LOE: C). (Notes: Additional consideration should be used for tachycardia origins in proximity to a coronary artery, e.g., aortic sinus; outflow tract VT was a Class IIa indication in the prior pediatric guidelines for ventricular arrhythmias.)

**Class IIa Ablation Can Be Useful for the Following:**

1. Frequent ventricular ectopy with correlated symptoms in larger* patients (LOE: C).

**Class IIb Ablation May Be Reasonable for the Following:**

1. Accelerated idioventricular rhythm with correlated symptoms in larger* patients (LOE: C). (Note: This indication was Class IIa in the prior pediatric guidelines for ventricular arrhythmias.)
2. Recurrent/frequent polymorphic ventricular arrhythmia when there is a suspected triggering focus, arrhythmia, or substrate that can be targeted (LOE: C).

### INDICATIONS FOR ABLATION PROCEDURES IN PATIENTS WITH CONGENITAL HEART DISEASE

**Class I**

1. Ablation is recommended for recurrent or persistent SVT related to accessory AV connections or twin AV nodes in CHD patients, when medical therapy is either not effective or is associated with intolerable side effects (medical therapy used depends on patient size†), or as an alternative to medical therapy, in larger* patients (LOE: B).
2. Ablation is effective for patients with WPW pattern and high-risk or multiple accessory pathways, as commonly encountered in Ebstein's anomaly, in larger* patients with CHD (LOE: C).
3. Ablation is effective for recurrent symptomatic atrial tachycardia in patients with CHD presenting outside the early postoperative phase (>3–6 months), when medical therapy is either not effective or is associated with intolerable side effects (medical therapy used depends on patient size†), or as an alternative to medical therapy in larger* patients (LOE: B).
4. Ablation is recommended for adjunctive therapy to an ICD in patients with CHD and recurrent monomorphic VT, a VT storm, or multiple appropriate shocks that are not manageable by device reprogramming or drug therapy (LOE: C).

**Class IIa Ablation Can Be Useful for the Following:**

1. Sustained monomorphic VT in patients with CHD causing symptoms or hypotension, when medical therapy is either not effective or is associated with intolerable side effects (medical therapy used depends on patient size†), or as an alternative to medical therapy in larger* patients. The decision whether or not to have an ICD as adjunctive therapy should follow the ACHD guidelines (LOE: B).
2. Recurrent or persistent AVNRT, when medical therapy is either not effective or is associated with intolerable side effects in larger* patients with moderate or complex CHD (mild CHD can be managed as narrow [usual] complex SVT) (LOE: C).
3. Substrates that have a reasonable likelihood of contributing to tachyarrhythmias in the postoperative period, in the absence of other indications, when impending congenital heart surgery will result in restriction of vascular or chamber access following surgery (LOE: C).
4. Substrates that have a reasonable likelihood of contributing to tachyarrhythmias in the postoperative period, in the absence of other indications in larger* patients with Ebstein's anomaly before anticipated cardiac surgery (LOE: C). (Note: This was a Class IIb indication in the prior ACHD guidelines.)
5. Recurrent asymptomatic atrial tachycardia presenting outside the early postoperative phase (>3–6 months), in larger* patients with CHD who are at increased risk of thromboembolic events or worsening heart failure, or in smaller* patients when medical therapy is either not effective or is associated with intolerable side effects (LOE: C).
6. Frequent ventricular ectopy, predominantly from a single focus, thought to be contributing to deteriorating ventricular function in larger* patients with CHD, or in smaller* patients when medical therapy is either not effective or is associated with intolerable side effects (LOE: C). (Note: This was a Class IIb indication in the prior ACHD guidelines.)

**Class IIb Ablation May Be Reasonable for the Following:**

1. SVT with acute hemodynamic compromise in smaller* patients with CHD (LOE: E).
2. Creation of complete AV block with permanent pacing in patients with atrial tachyarrhythmias refractory to all medications and substrate targeted catheter ablation, who are not candidates for surgical therapy (LOE: B).

### INDICATIONS FOR CATHETER ABLATION IN SMALLER CHILDREN*

**Class I Ablation is Recommended for the Following:**

1. Documented SVT, recurrent or persistent, when medical therapy is either not effective or is associated with intolerable side effects (LOE: C).

Continued

### e-BOX 68.1 Indications for Ablation Procedures in Pediatric and Adolescent Patients—cont'd

2. WPW pattern after resuscitated cardiac arrest (LOE: B).
3. WPW pattern with syncope when there are predictors of high risk for cardiac arrest (LOE: B).
4. Persistent or recurrent idiopathic JET, or congenital JET associated with ventricular dysfunction, when medical therapy is either not effective or is associated with intolerable side effects† (LOE: C).

When ablation of JET is being performed, cryotherapy is the preferred first choice due to the high risk of AV block. Radiofrequency energy should be used with extreme caution, after a detailed discussion with the family/patient concerning the high risk of AV block and potential need for permanent pacing (LOE: C).

5. Ventricular ectopy or tachycardia with ventricular dysfunction, when medical therapy is either not effective or is associated with intolerable side effects (LOE: C).
6. Recurrent or persistent SVT related to accessory AV connections or twin AV nodes in patients with CHD, when medical therapy is either not effective or is associated with intolerable side effects (LOE B).
7. Ablation is effective for recurrent symptomatic atrial tachycardia presenting outside the early postoperative phase (>3–6 months) in patients with CHD, when medical therapy is either not effective or is associated with intolerable side effects (LOE B).
8. Pediatric cardiovascular surgical support should be available in-house during ablation procedures for smaller patients* (LOE: E).

**Class IIa Ablation Can Be Useful for the Following:**

1. WPW pattern with ventricular dysfunction presumed due to dyssynchrony when medical therapy is either not effective or is associated with intolerable side effects† (LOE: B).
2. Recurrent sustained monomorphic VT causing symptoms or hypotension despite antiarrhythmic drug therapy in patients with CHD (LOE: B).
3. Recurrent asymptomatic atrial tachycardia presenting outside the early postoperative phase (>3–6 months), in patients with CHD who are at increased risk of thromboembolic events or worsening heart failure, when medical therapy is either not effective or is associated with intolerable side effects (LOE: C).
4. Substrates that have a reasonable likelihood of contributing to tachyarrhythmias in the postoperative period in the absence of other indications, when impending congenital heart surgery will result in restriction of vascular or chamber access after surgery (LOE: C).
5. Frequent ventricular ectopy thought to be contributing to deteriorating ventricular function in patients with CHD, when medical therapy is either not effective or is associated with intolerable side effects (LOE: C).

**Class IIb**

1. Recurrent clinical symptoms clearly consistent with paroxysmal SVT, and one of the following at electrophysiology study: evidence for involvement of an AV accessory pathway; inducible SVT (LOE: C). Medical therapy should be considered before ablation (LOE: C). Cryotherapy should be considered for slow pathway modification (LOE: B).
2. When ablation is indicated, cryoablation can be useful to avoid the higher risks of complications with RF ablation (LOE: C).
3. Recurrent acute hemodynamic compromise (hypotension or syncope) from SVT (LOE: C).
4. Persistent or symptomatic recurrent idiopathic JET, or congenital JET, when medical therapy is either not effective or is associated with intolerable side effects† (LOE: C).
5. Polymorphic ventricular arrhythmia when there is a suspected triggering focus, arrhythmia, or substrate that can be targeted (LOE: C).
6. Creation of complete AV block with permanent pacing in patients with atrial tachyarrhythmias refractory to all medications and substrate targeted catheter ablation, who are not candidates for surgical therapy (LOE: B).

---

*In general, smaller patients are less than approximately 15 kg, and larger patients are greater than approximately 15 kg.

†The precise definition of "medical therapy that is either not effective or is associated with intolerable side effects" is left up to the practitioner and family to decide. However, in general, the threshold for ineffectiveness and intolerability should be higher in smaller patients. For example, failure or intolerability of a beta-blocker alone might be adequate in the larger patient, but not in the smaller patient, unless there were additional circumstances. In the smallest patients, failure or intolerability of drug combinations from multiple classes, including membrane-stabilizing agents, with adequate loading time, would be required before the decision for ablation.

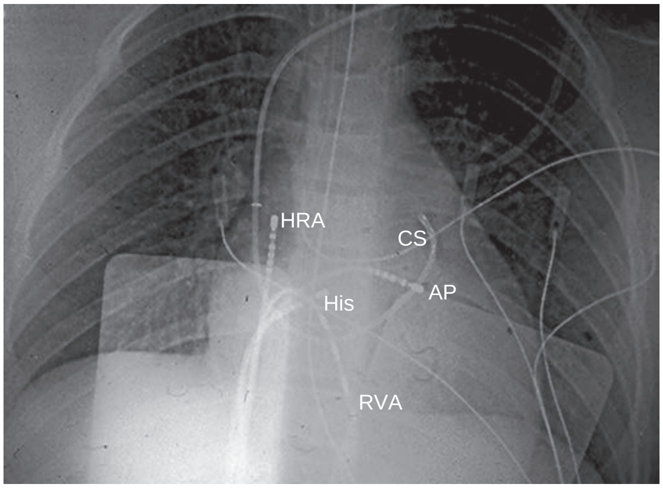

**e-Figure 68.8. Electrophysiology testing.** Anterior-posterior projection of a chest fluorograph during a radiofrequency catheter ablation procedure in a teenager with Wolff–Parkinson–White syndrome and a left lateral accessory pathway. Standard multipole electrode catheters are positioned in the high right atrium *(HRA),* across the tricuspid valve in the His bundle region *(His),* in the right ventricular apex *(RVA),* in the coronary sinus *(CS),* and at the mapped location of the accessory pathway *(AP)* along the mitral valve.

time. Isochronal activation maps, isopotential (voltage) maps, and customized rendering of derived electrophysiologic features are afforded by these systems.

The CARTO system (Biosense Webster, Diamond Bar, CA) was originally only a magnetic field–based system, wherein a low-energy, triple-source transmitter located on a position pad mounted beneath the patient identified the receiver, which was mounted in the tip of the specialized mapping/ablation catheter using a global positioning system technology (e-Fig. 68.9). This system was handicapped by the necessity that only proprietary catheters be used. The Ensite system (St. Jude Medical, St. Paul, MN) was originally only an impedance-based system, wherein three pairs of skin surface patches served as low-energy transmitters in the x-y-z axes. Using continuous impedance measurements, the electrodes from any nonproprietary electrode catheters were the receivers. This system suffered from impedance drift, with spatial inaccuracies introduced by long procedure durations and changes in chest and lung water. Both systems have adopted technologies from the other, and both now use both magnetic field– and impedance-based features. These companies have also evolved catheter designs that enable simultaneous acquisition of multiple endocardial sites. Finally, both of these systems have the capacity to merge previously obtained CT or MRI scans of the patient's heart chambers with the real-time anatomic renderings.

This technology has been of greatest value in the mapping and ablation of atrial or ventricular muscle reentrant tachycardias whose substrates are within the wall of a chamber and are defined by areas of slow conduction related to scar or structural conduction boundaries, such as venous ostia or valve annuli. Nonreentrant tachycardias are mapped and ablated by identifying sites of earliest activation.

## Radiation Exposure

As electroanatomic mapping system technology has become the workhorse for electrophysiologic procedures, fluoroscopy has taken on an adjunctive role. In published series of children undergoing these procedures, fluoroscopy duration fell from 61.5 minutes in 1994 to 38.3 minutes in 2004.[32] In the modern era, groups using either the CARTO or Ensite systems now report mean fluoroscopy times less than 5 minutes and total absorbed radiation doses less than 60 mGy.[26,27] Complete elimination of fluoroscopy has been reported for 31% to 54% of cases.[26,27] When fluoroscopy is necessary, adherence to the ALARA (As Low As Reasonably Achievable) principle is paramount. Most operators limit x-ray exposure by reducing frame rates to 15 and even 7.5 frames/sec and by minimizing the use of magnification.

Data on actual x-ray exposure during catheter ablation procedures comes largely from adult series, in which thermoluminescent dosimeters and/or anthropomorphic radiologic phantoms were used.[33-37] Considering fluoroscopy times ranging from 41 to 60 minutes, a single procedure has been estimated to carry a risk of fatal malignancy in 0.03% to 0.13% of individuals and to result in birth defects in 0.00012%.[34,35,37] These figures are approximately equivalent to 1% and 0.1% of the spontaneous incidences, respectively. Geise and colleagues[38] reported that radiation doses to exposed skin were 6.2 to 49 mGy/min in nine children, which calculated to total doses of 0.09 to 2.35 Gy.

# DEVICE THERAPY IN CHILDREN

## Fundamentals of Pacing Hardware

Bradycardia devices (i.e., pacemakers) and antitachycardia devices (i.e., implantable cardioverter-defibrillators [ICDs]) require two basic hardware components, the pulse generator and conductors (primarily, "leads"). The pulse generator consists of an energy source (battery), microcircuitry, titanium alloy housing, and a plastic connector block for conductor attachment. In addition, the ICD contains capacitors to store deliverable energy. The lead consists of one (unipolar) or two (bipolar) wires, a nonconducting insulation, one or more connector pins that insert into the pulse generator connector block, and a fixation end that attaches to myocardium (via a tiny screw, fish hook, plaque, or other device). Transvenous bipolar leads generally have a radiodense distal electrode and a slightly more proximal "ring" electrode, whereas the unipolar lead has only a distal electrode. Epicardial leads are mostly unipolar, but bifurcated plaque electrodes and in-line bipolar leads also exist. In addition, the ventricular lead for an ICD may have one or two additional insulated conductors that are exposed on the outer surface of the lead (so-called coils) and participate in the shock field. Arrays and patches may be necessary to optimize cardioversion or defibrillation and are inserted in subcutaneous or intrapericardial sites. Figs. 68.10 and 68.11 illustrate the radiographic appearance of this hardware. Entirely subcutaneous cardioverter-defibrillators are now available for larger patients (at least 40 kg) not requiring bradycardia pacing (e-Fig. 68.12), and transvenous leadless pacemakers are being inserted into older adults requiring only ventricular bradycardia pacing.

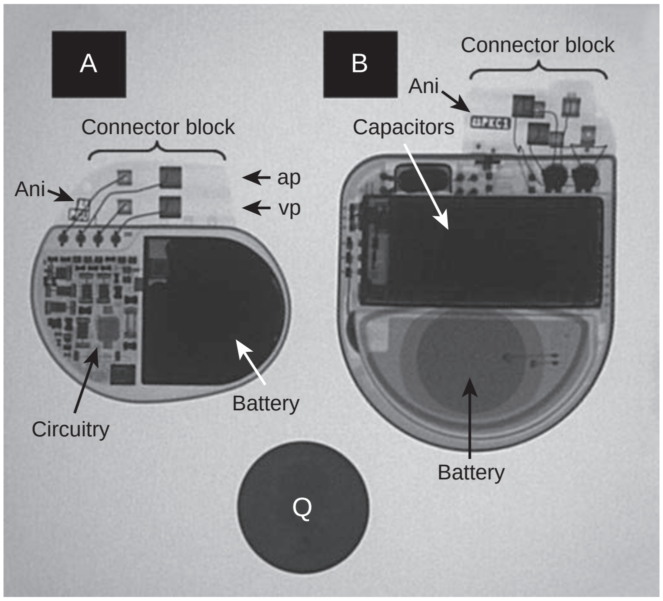

**Figure 68.10. Pacemaker components.** (A) Fluoroscopic image of a modern dual-chamber pacemaker and implantable cardioverter-defibrillator. (B) *Ani,* Alphanumeric identifier; *ap,* atrial port (the portion of the connector block that accepts the connector pin of the atrial lead); *Q,* quarter (for size comparison); *vp,* ventricular port (the portion of the connector block that accepts the connector pin of the ventricular lead).

## Radiography of Pacing Systems

The radiologist will be called on to interpret radiographs from children with devices immediately after device implantation, during routine follow-up, and when component failure is suspected.

A systematic approach will enable the radiologist to interpret the appearance of the hardware. The first step is to identify the location of the pulse generator. When the device is infraclavicular, the conductors usually are transvenous. Epicardial leads are generally tunneled to a subcutaneous abdominal device, but subcostal and flank locations (especially in premature infants) also may be used. Hybrid systems use a combination of transvenous, epicardial, and/or subcutaneous conductors, configured to accommodate restricted venous access, and/or a preexisting lead that is considered valuable, and/or an optimized shock vector in the case of ICDs. The pulse generator will be positioned in a location optimal to

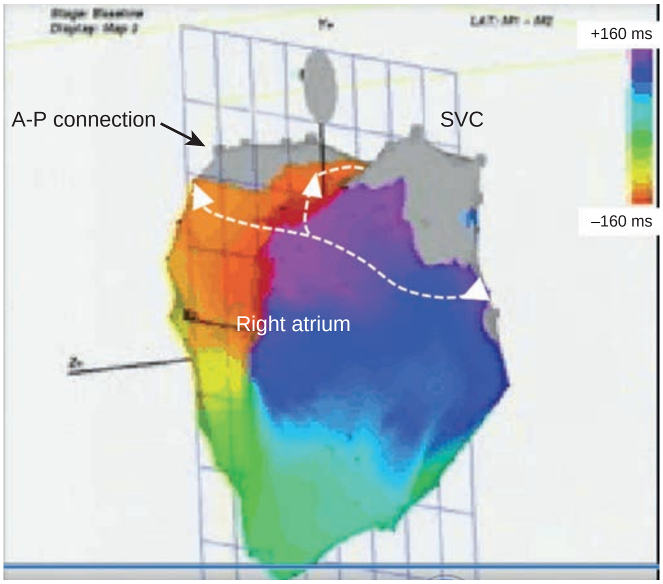

**e-Figure 68.9. Electrophysiology mapping.** Left posterior oblique projection of an electroanatomic map of the right atrium following atriopulmonary-style Fontan operation in a 34-year-old man who was born with tricuspid atresia. This is an isochronal depiction of atrial flutter in which slow conduction is identified by color-coded local activation timing (*broken line* and *arrowheads*) defined by endocardial electrograms that were obtained by point-to-point contact registration using the CARTO system. Areas of scar are *gray*. *A-P,* Atriopulmonary connection; *SVC,* superior vena cava.

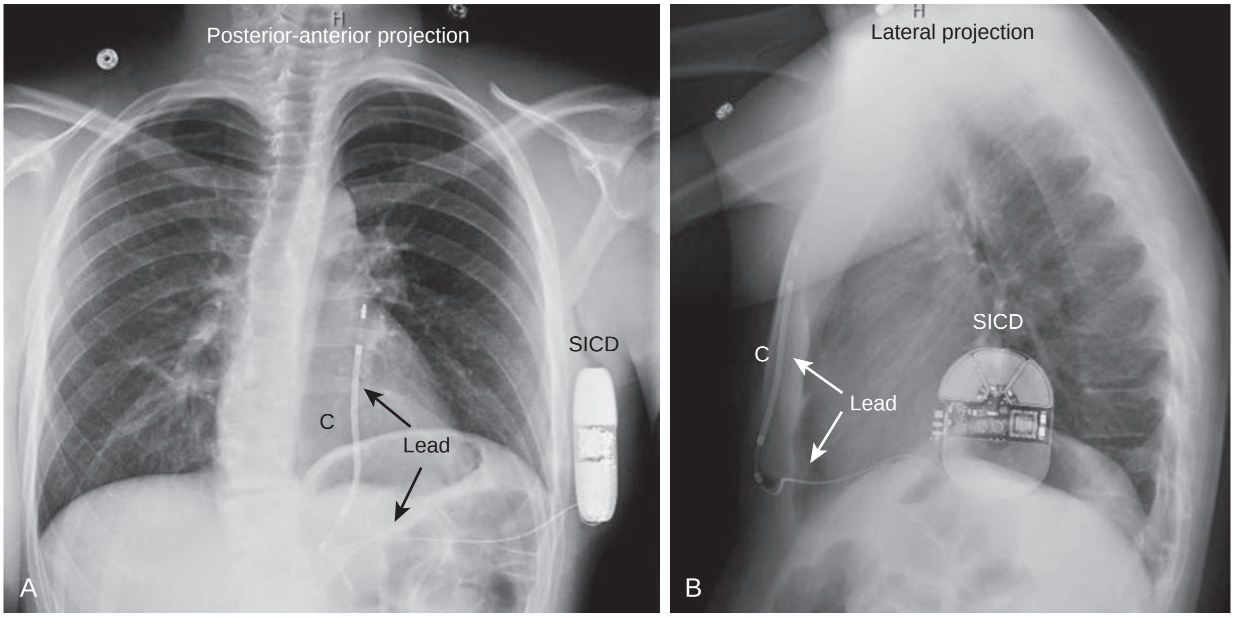

**e-Figure 68.12.** Posterior-anterior and lateral chest radiographs from a 17-year-old boy who suffered idiopathic ventricular fibrillation during cross-country competition. Visualized is a completely subcutaneous implantable cardioverter-defibrillator *(SICD)* and lead. The shock coil *(C)* is parasternal, and the device is slightly posterior to straight lateral. Precise location of all hardware is paramount.

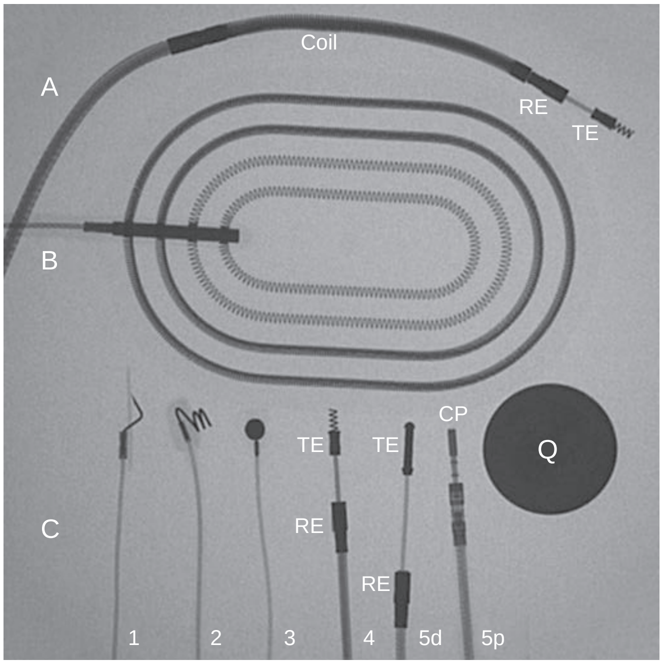

**Figure 68.11. Fluoroscopic images of several types of conductors used for cardiac device therapy in children and teenagers.** (A) A transvenous, active fixation, bipolar, ventricular lead used with implantable cardioverter-defibrillators (ICDs) and containing a coil for participation in shock delivery. (B) A patch, which is placed in the subcutaneous location, and is used with ICDs for participation in shock delivery. (C) A variety of leads used with either pacemakers or ICDs. *1,* The distal (cardiac) end of a unipolar, epicardial active fixation (stab-on or fish hook) lead. *2,* The distal end of a unipolar, epicardial active fixation (screw-in) lead. *3,* The distal end of a unipolar, epicardial passive fixation (plaque, suture-on) lead. *4,* The distal end of a bipolar, transvenous active fixation lead (with a retractable screw). *5d* and *5p* illustrate the distal (cardiac) and proximal (connector block of pacemaker) ends of a bipolar, passive fixation lead, respectively. *CP,* Connector pin; *Q,* quarter (for size comparison); *RE,* ring electrode; *S,* screw; *TE,* tip electrode.

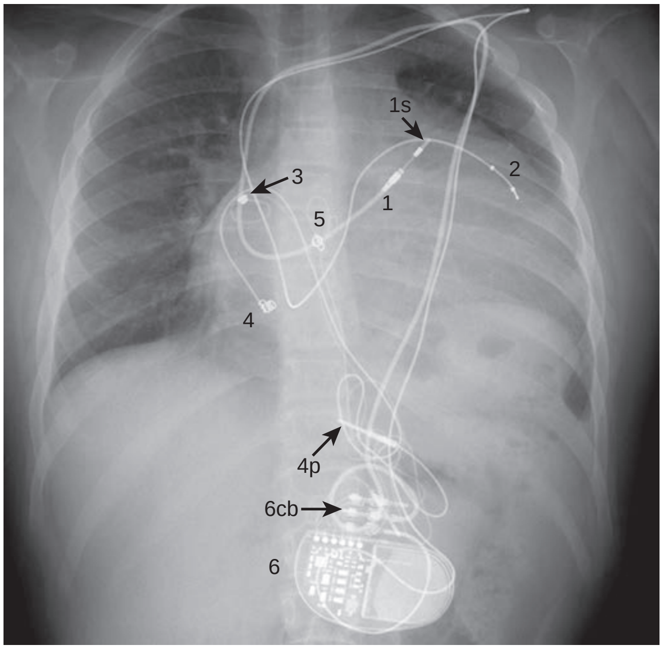

**Figure 68.13.** Posterior-anterior chest radiograph from an 11-year-old girl who underwent repair of an atrioventricular septal defect and who has postoperative heart block, severe mitral regurgitation, and left ventricular dysfunction. *1,* A transvenous, bipolar, active fixation (*1s,* screw) lead positioned in the right ventricular outflow tract. *2,* A transvenous, bipolar, passive fixation lead positioned in the posterolateral cardiac vein via the coronary sinus for the purpose of synchronizing ventricular activation. *3,* An epicardial, unipolar, passive fixation (plaque electrode) lead positioned on the right atrium. *4,* An epicardial, unipolar, active fixation (screw-in) lead positioned on the right atrium, abandoned, with the proximal end (*4p,* connector pin) in the abdominal pacemaker pocket. *5,* An epicardial, unipolar screw fragment positioned on the right ventricle. *6,* Pacemaker (*6cb,* pacemaker connector block).

the complex configuration of the conductors. The second step is to describe each conductor, including the type (e.g., lead, lead with coils, array, or patch), its course from the pulse generator to the heart or other thoracic site, its form of attachment to the heart in the case of leads, and whether the lead is unipolar or bipolar. Magnification of the lead tip may be required. The third step is to correlate the congenital and surgical anatomy with lead locations and courses. Understanding the appropriateness of the course of each lead often requires some knowledge of the surgical anatomy. Figs. 68.13 and 68.14 and e-Fig. 68.15 illustrate the radiographic appearance of patients who have complex cardiac device therapy. Finally, leads attached to both right and left ventricles suggest an attempt at ventricular resynchronization as a result of ventricular dysfunction. The left ventricular lead may be transvenous to the cardiac venous system or epicardial surface of the heart.

In children undergoing chronic device therapy, symptoms suggestive of device malfunction may develop, such as syncope, skeletal muscle twitching, hiccoughs, new onset of fatigue, palpitations, and, in the case of ICDs, inappropriate shocks. Radiographic abnormalities that may suggest the etiology include lead conduction fracture, lead dislodgement (especially if symptoms occur soon after implantation), lead stretch as a result of somatic growth, and connector pin separation from pulse generator. Transvenous leads usually fracture beneath the clavicle, but epicardial leads may fracture anywhere along their length. A caveat: The Medtronic model 4968 (Medtronic, Minneapolis, MN) bifurcated, epicardial, double-plaque lead always has the appearance of near-fracture at the union of the two conductors (Fig. 68.16). Finally, the radiologist may be called on to identify the type of implanted device (i.e., the manufacturer and model number) that is in a patient. Each pulse generator has a radiodense alphanumeric identifier (often its model number) that can be referenced in any of the major companies' device encyclopedias (see Fig. 68.10).

## Caring for Children With Devices While in the Radiology Department

Cardiac devices became interactive with the first inclusion of demand circuitry, which was developed in 1965 to allow sensing of intrinsic electrical activity. We now communicate with these devices for purposes of reprogramming, functional testing, and telemetry using a computerized programmer and radiofrequency signals. Despite various forms of protective shielding and electronic filters, all devices may be affected by certain sources of electromagnetic interference (EMI) that may be present in the radiology department. It should be emphasized that ionizing radiation used for diagnostic procedures usually is not a source of EMI. High-dose x-rays during CT, only when applied directly to the device, can rarely result in oversensing.[39] This effect theoretically can inhibit a device, resulting in loss of output. However, the effect is transient and reverses as the beam moves away from the devices.

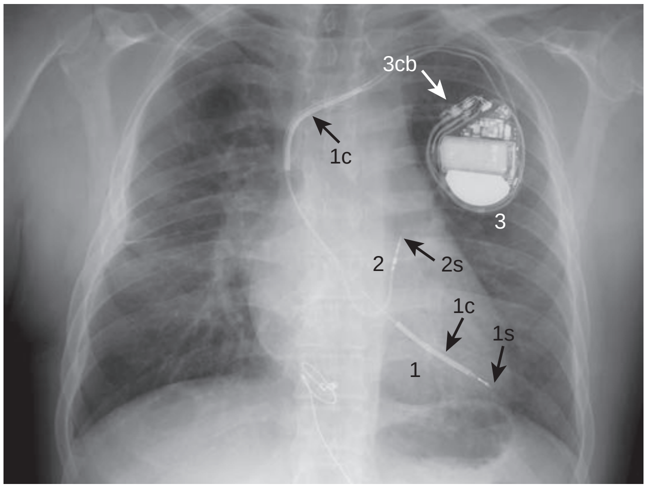

**e-Figure 68.15.** A posterior-anterior chest radiograph from a 19-year-old who had a Senning operation for d-transposition of the great arteries, sinus node dysfunction, and a history of ventricular tachycardia. *1,* A transvenous, active fixation lead that is attached to the left ventricular apex (systemic venous ventricle) by a retractable screw *(1s).* The lead contains two coils *(1c)* that will participate in possible shock delivery. *2,* A transvenous, bipolar, active fixation lead that is attached to the roof of the left atrium (systemic venous atrium) by a retractable screw *(2s).* *3,* An implantable cardioverter-defibrillator (ICD) (*3cb,* ICD connector block).

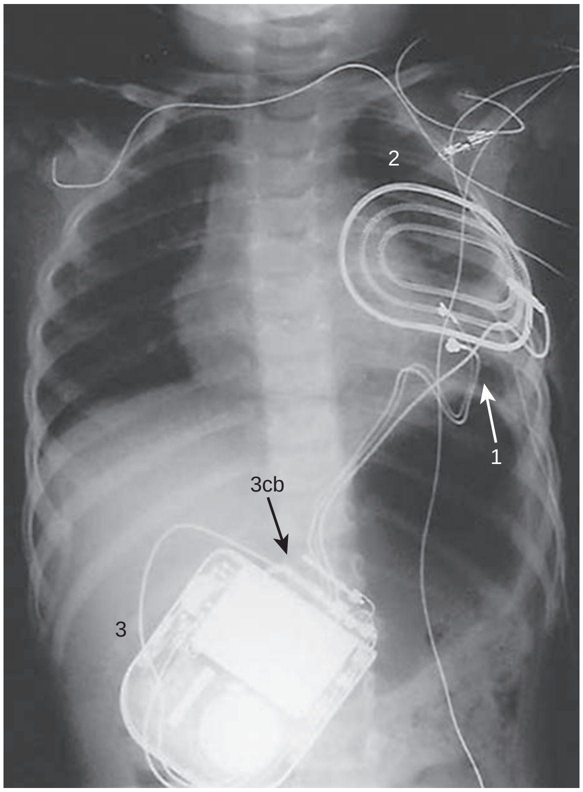

**Figure 68.14.** A posterior-anterior chest radiograph from a 3-month-old male infant with ventricular tachycardia associated with Brugada syndrome. *1,* An epicardial, bifurcated (hence, bipolar), passive fixation (plaque electrodes) lead positioned on the left ventricle for purposes of ventricular pacing and sensing. *2,* A patch placed posteriorly and in a subcutaneous location for participation in possible shock delivery. *3,* An implantable cardioverter-defibrillator (ICD) in a subcutaneous pocket over the left abdomen (*3cb,* ICD connector block).

Repeated high-dose radiation therapy may damage the silicone and silicone oxide insulation necessary for the complementary metal oxide semiconductor chip technology of cardiac devices. Device manufacturers have provided guidelines to minimize risk of damage to ICDs resulting from radiotherapy.[40] Occasionally, the device may even have to be repositioned away from the treatment field. EMI-device interactions may result from MRI, defibrillation, electrocautery, peripheral nerve stimulation, transcutaneous electrical nerve stimulation, diathermy, radiofrequency ablation, and lithotripsy. Untoward responses by the device may include oversensing, noise reversion, power-on reset, permanent circuit failure, and damage to the lead-tissue interface, causing a permanent rise in the stimulation threshold. A glossary of these terms appears in e-Box 68.2. Some of these potentially harmful medical procedures, specific responses to EMI, and ways to prevent these responses appear in e-Table 68.1.[41] For older devices, MRI theoretically may cause device malfunction as a result of static magnetic, gradient, and radiofrequency fields and may cause tissue heating at the conductor-cardiac interface. MRI conditional devices and conductors are now available from all of the major manufacturers for up to 1.5-T field strength.

## SUMMARY

Cardiac catheterization for congenital heart disease has evolved from its early days when it was exclusively a diagnostic tool to a dynamic and continuously growing field of therapeutic interventional procedures for children and adults with cardiac abnormalities. Clinicians and industry have a history of working together to push the field forward and find novel solutions to difficult problems while making the products to accomplish these goals smaller and safer. The interventional cardiologist and cardiothoracic surgeon have truly become an organized team in the treatment of once uniformly fatal conditions to offer longer and better quality of life to a diverse group of medically complex and rewarding patients.

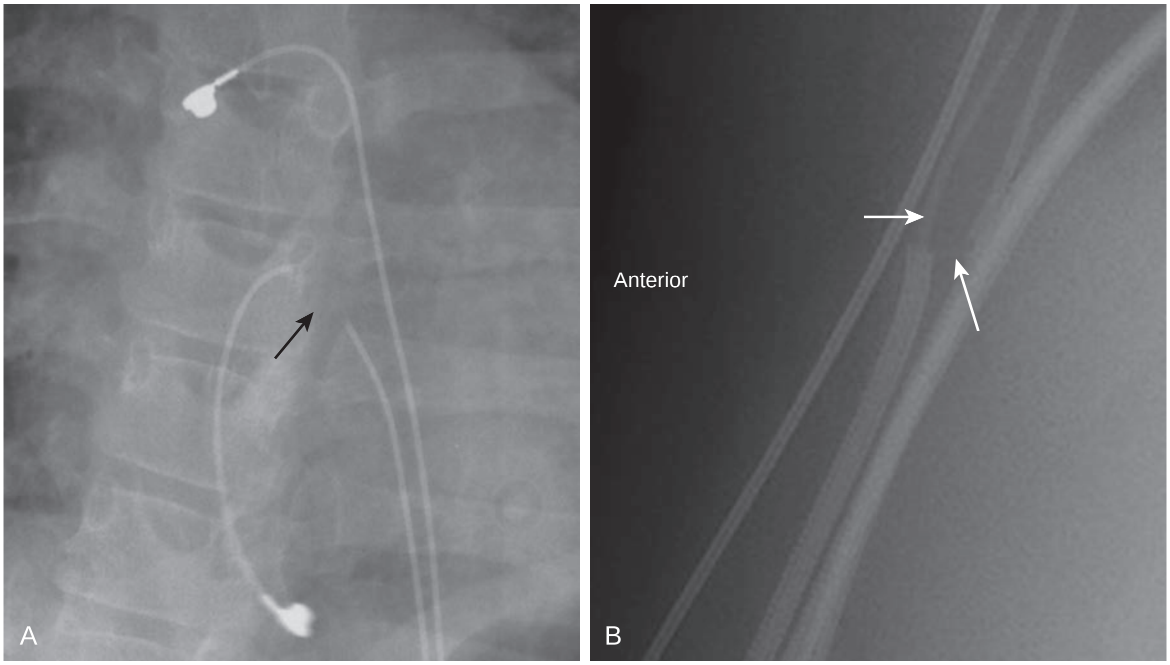

**Figure 68.16.** (A) Posterior-anterior projection of the chest showing an epicardial lead fracture *(arrow).* (B) Lateral projection of the upper abdomen in a different child showing a pseudofracture in the Medtronic 4968 epicardial lead. The proximal conductors are identified by *white arrows* just superior to their union at the bifurcation. The *lower arrow* identifies the smallest caliber component of the conductor. This image shows the normal appearance of this lead.

### e-BOX 68.2 Glossary of Terms Applicable to Electromagnetic Interference–Cardiac Device Interactions

**Activity sensor:** A pacing device component that responds to a physiologic or nonphysiologic patient parameter (e.g., motion or minute ventilation) to provide a faster pacing rate.

**Asynchronous mode:** A mode of operation in which the pacemaker is insensitive to incoming signals from the chamber being paced.

**Backup mode:** A pacing mode typically similar to that observed when the device battery has reached critical depletion; usually VVI (see below).

**DDD mode:** Dual-chamber mode of operation in which pacing and sensing occur in both the atrium and ventricle; atrioventricular synchrony is thus maintained from the lower programmed rate to the upper P-wave tracking (sensing) rate.

**Inhibition:** A pacemaker response in which a stimulus is withheld in response to a sensed event.

**Noise reversion mode:** A pacing mode that is activated when electrical noise is sensed. The mode usually consists of fixed-rate pacing for one pacing cycle, but in some devices this mode may continue as long as the electrical noise is sensed, and normal pacemaker function resumes when the noise is no longer sensed.

**OOO mode:** A programmable mode in some devices in which no chambers are sensed and no chambers can be paced; in essence, the device is off.

**Oversensing:** When the sensing circuitry of a pacemaker senses noncardiac electrical activity (such as electromagnetic interference) and interprets it as cardiac activity; this may result in inappropriate inhibition (see above) or inappropriate pacing, depending on the underlying programmed pacing mode.

**Pacing mode:** A programmable feature of all cardiac devices that defines the cardiac chamber or chambers that can be paced and sensed from and how the device will respond to a sensed intrinsic electrical event; the mode is abbreviated using an internationally recognized three- to five-letter code.

**Pacing threshold:** The minimum programmable energy output required to result in a propagated response by the cardiac chamber of interest; this value is dependent on complex lead, tissue, and metabolic interactions.

**Power-on reset:** The phenomenon in which older bradycardia pacemakers may change from an asynchronous mode to inhibition of pacing as a consequence of electromagnetic interference during MRI scanning.

**Reed switch:** A magnetically activated component of most pacemakers that "closes" when exposed to certain magnetic fields. This action typically results in asynchronous pacing (see above), thus ensuring pacemaker output in the presence of possible electromagnetic interference–induced oversensing (see above) and inappropriate inhibition.

**Sensing threshold:** The minimum cardiac chamber electrogram amplitude that can still be identified by the pacemaker circuitry as an intrinsic electrical event; this value depends on complex lead orientation, tissue, and metabolic interactions.

**VDD mode:** A dual-chamber mode of operation in which pacing can only occur in the ventricle but sensing can occur in both chambers.

**VOO mode:** A single-chamber mode of operation that is asynchronous, and only pacing occurs in the ventricle at the programmed rate, irrespective of the intrinsic ventricular rate.

**VVI mode:** A single-chamber mode of operation in which both pacing and sensing occur in the ventricle; intrinsic ventricular beats are sensed by the pacemaker, resetting the lower-rate timing circuitry and thus avoiding competitive pacing.

**e-TABLE 68.1** Potential Sources, Effects, and Prevention of Electromagnetic Interference During Medical Procedures That May Be Performed in the Radiology Department

| Procedure | Possible Effects | Prevention of Untoward Effects |
|---|---|---|
| Cardioversion/ defibrillation | Reprogramming to backup mode; local tissue-lead damage (increasing pacing and sensing thresholds) | Paddles should be greater than 4–6 inches from the device; patches should be placed in the anterior-posterior orientation; cardiologist should reevaluate the device afterward |
| Diathermy | Oversensing and inhibition; heating and destruction of device components (if placed directly over the device) | Avoid application directly over the device |
| Electrocautery | Oversensing and inhibition (if brief); noise reversion mode (if prolonged); reprogramming to backup mode; inappropriate tachycardia recognition (ICD) | Place a ground patch distant from the device; use bipolar cautery; never apply cautery within 4–6 inches of device; program to asynchronous mode during duration of procedure (or tape a magnet over the device); program tachycardia recognition "off" (ICDs) |
| Extracorporeal shock wave lithotripsy | Oversensing and inhibition; noise reversion mode; malfunction of reed switch; activity sensor-driven pacing; inappropriate tachycardia recognition (ICDs) | Synchronize lithotripter to patient's R wave; maintain focal point of lithotripter greater than 6 inches from device; program pacemaker to VVI or VOO modes for duration of procedure; program tachycardia recognition "off" (ICDs); cardiologist should reevaluate device afterward |
| Magnetic resonance imaging (MRI nonconditional) | Reed switch closure and reversion to asynchronous mode; theoretical (from RF scanning):<br>• Rapid pacing (>300)<br>• Heating of conductors with local lead tissue damage<br>• Oversensing and inhibition (pacers)<br>• Inappropriate tachycardia recognition (ICDs)<br>• Backup mode<br>Power-on reset | If not pacemaker dependent:<br>• Program output to less than pacing threshold<br>• Program to OOO mode<br>• Avoid procedure, if possible; explant device first<br>If pacemaker-dependent:<br>• Continuous rhythm monitoring during procedure with transcutaneous backup pacing available |
| Transcutaneous electrical nerve stimulators | Oversensing and inhibition; reprogramming; rapid ventricular pacing if VDD or DDD modes; inappropriate tachycardia recognition (ICDs) (all rare) | Probably safe, if a bipolar cardiac device; avoid stimulation using vector parallel to leads; program tachycardia recognition "off" (ICDs) |

*ICD,* Implantable cardioverter-defibrillator; *RF,* radiofrequency.

## KEY POINTS

- Electrophysiologic testing in children has benefitted greatly from magnetic field- and impedance-based technologies to aid in mapping of tachycardia substrates. This has reduced the duration of ionizing radiation required to image electrode catheters in the heart. Uncomplicated electrophysiologic studies that include catheter ablation are now commonly performed with less than 5 minutes of fluoroscopy time and, in some institutions, using no fluoroscopy at all.
- Cardiac implantable electronic devices remain an important treatment option for young patients with serious bradycardic conditions, patients at high risk for sudden cardiac arrest from ventricular tachyarrhythmia, and occasional patients with severely reduced ventricular systolic function. The weak link in these systems remains the electrical conductors, so-called “leads”. Periodic radiographic analysis is required for all such systems, and this is even more important in very young patients and those having congenital heart disease, because the incidence of lead malfunction is higher in those groups. An understanding of the radiographic appearance of this equipment as well as a working knowledge of any associated congenital heart disease, especially post-operative anatomy, is important.
- Cardiac implantable electronic devices (CIEDs) are variably affected by large electromagnetic fields as may be required during certain diagnostic and therapeutic procedures, especially diathermy, electrocautery, extracorporeal shock wave lithotripsy, transcutaneous electrical nerve stimulation, and magnetic resonance imaging. Effects may include suppression of electrical output, inappropriate identification of tacharrhythmias, thermal heating of myocardium, and actual reprogramming. The radiologist in concert with the electrophysiology team should carefully plan these procedures, sometimes with on site involvement of the cardiologist. These issues are becoming more common, since all of the newest CIEDs are MRI conditional.

## SUGGESTED READINGS

### Pediatric Cardiac Catheterization

1. Hijazi ZM, Ruiz CE, Zahn E, et al. SCAI/AATS/ACC/STS operator and institutional requirements for transcatheter valve repair and replacement, part III: Pulmonic valve. *J Thorac Cardiovasc Surg*. 2015;149(5):e71–e78.
2. McElhinney DB, Cabalka AK, Aboulhosn JA, et al. Valve-in-valve international database (VIVID) registry. Transcatheter tricuspid valve-in-valve implantation for the treatment of dysfunctional surgical bioprosthetic valves: an international, multicenter registry study. *Circulation*. 2016;133(16):1582–1593.
3. Holzer RJ, Gauvreau K, Kreutzer J, et al. Balloon angioplasty and stenting of branch pulmonary arteries: adverse events and procedural characteristics: results of a multi-institutional registry. *Circ Cardiovasc Interv*. 2011;4(3):287–296.
4. Rhodes JF Jr, Goble J. Combined prospective United States clinical study data for the GORE(®) HELEX(®) septal occluder device. *Catheter Cardiovasc Interv*. 2014;83(6):944–952.
5. Holzer R, Qureshi S, Ghasemi A, et al. Stenting of aortic coarctation: acute, intermediate, and long-term results of a prospective multi-institutional registry–Congenital Cardiovascular Interventional Study Consortium (CCISC). *Catheter Cardiovasc Interv*. 2010;76(4): 553–563.
6. Perez KM, Laughon MM. What is new for patent ductus arteriosus management in premature infants in 2015? *Curr Opin Pediatr*. 2015;27(2):158–164.
7. Zellers TM, Hijazi ZM, Sandhu S, et al. Catheter closure of patent ductus arteriosus using the Amplatzer device: interim report on US phase I and II clinical trial. *Circulation*. 2000;102:II587.

### Pediatric Electrophysiology

1. Khairy P, Van Hare GF, Balaji S, et al. PACES/HRS expert consensus statement on the recognition and management of arrhythmias in adult congenital heart disease: developed in partnership between the Pediatric and Congenital Electrophysiology Society (PACES) and the Heart Rhythm Society (HRS). Endorsed by the governing bodies of PACES, HRS, the American College of Cardiology (ACC), the American Heart Association (AHA), the European Heart Rhythm Association (EHRA), the Canadian Heart Rhythm Society (CHRS), and the International Society for Adult Congenital Heart Disease (ISACHD). *Can J Cardiol*. 2014;30(10):e1–e63.
2. Crosson JE, Callans DJ, Bradley DJ, et al. PACES/HRS expert consensus statement on the evaluation and management of ventricular arrhythmias in the child with a structurally normal heart. *Heart Rhythm*. 2014;11(9):e55–e78.
3. Pediatric and Congenital Electrophysiology Society (PACES). Heart Rhythm Society (HRS); American College of Cardiology Foundation (ACCF); American Heart Association (AHA); American Academy of Pediatrics (AAP); Canadian Heart Rhythm Society (CHRS), Cohen MI, Triedman JK, et al. PACES/HRS expert consensus statement on the management of the asymptomatic young patient with a Wolff-Parkinson-White (WPW, ventricular preexcitation) electrocardiographic pattern: developed in partnership between the Pediatric and Congenital Electrophysiology Society (PACES) and the Heart Rhythm Society (HRS). Endorsed by the governing bodies of PACES, HRS, the American College of Cardiology Foundation (ACCF), the American Heart Association (AHA), the American Academy of Pediatrics (AAP), and the Canadian Heart Rhythm Society (CHRS). *Heart Rhythm*. 2012;9(6): 1006–1024.
4. Stephenson EA, Kaltman JR. Current state of the art for use of pacemakers and defibrillators in patients with congenital cardiac malformations. *Cardiol Young*. 2006;16(3):151–156.

## REFERENCES

Full references for this chapter can be found on www.expertconsult.com.

## REFERENCES

1. Mullins CE. History of pediatric interventional catheterization: pediatric therapeutic cardiac catheterization. *Pediatr Cardiol*. 1998;19(1):3–7.
2. Harrild DM, Powell AJ, Tran TX, et al. Long-term pulmonary regurgitation following balloon valvuloplasty for pulmonary stenosis risk factors and relationship to exercise capacity and ventricular volume and function. *J Am Coll Cardiol*. 2010;55(10):1041–1047.
3. Pathak SJ, Pockett CR, Moore JW, et al. Effect of balloon: annulus ratio on incidence of pulmonary insufficiency following valvuloplasty. *Congenit Heart Dis*. 2016;11(5):415–419.
4. Baumgartner H, Hung J, Bermejo J, et al. Echocardiographic assessment of valve stenosis: European Association of Echocardiography/American Society of Echocardiography recommendations for clinical practice. *J Am Soc Echocardiogr*. 2009;22(1):1–23.
5. Taramasso M, Pozzoli A, Guidotti A, et al. Percutaneous tricuspid valve therapies: the new frontier. *Eur Heart J*. 2016;[Epub ahead of print]; Pii: ehv766.
6. Kenny D, Hijazi ZM, Kar S, et al. Percutaneous implantation of the Edwards SAPIEN transcatheter heart valve for conduit failure in the pulmonary position: early phase 1 results from an international multicenter clinical trial. *J Am Coll Cardiol*. 2011;58(21): 2248–2256.
7. Armstrong AK, Balzer DT, Cabalka AK, et al. One-year follow-up of the Melody transcatheter pulmonary valve multicenter post-approval study. *JACC Cardiovasc Interv*. 2014;7(11):1254–1262.
8. Bergersen L, Gauvreau K, Justino H, et al. Randomized trial of cutting balloon compared with high-pressure angioplasty for the treatment of resistant pulmonary artery stenosis. *Circulation*. 2011;124(22): 2388–2396.
9. Weber HS. Catheter management of aortic valve stenosis in neonates and children. *Catheter Cardiovasc Interv*. 2006;67(6):947–955. Review.
10. Vlahos AP, Marx GR, McElhinney D, et al. Clinical utility of Doppler echocardiography in assessing aortic stenosis severity and predicting need for intervention in children. *Pediatr Cardiol*. 2008;29(3): 507–514.
11. Bissell MM, Hess AT, Glaze SJ, et al. Cusp fusion pattern in bicuspid aortic valve disease predicts severity of aortic flow abnormalities. *J CV Magnetic Resonance*. 2013;15(suppl 1):069.
12. Nishimura RA, Otto CM, Sorajja P, et al. 2014 AHA/ACC guideline for the management of patients with valvular heart disease. *J Am Coll Cardiol*. 2014;63(22):e57–e185.
13. [deleted in review]
14. Jalal Z, Hascoet S, Baruteau AE, et al. Long-term complications after transcatheter atrial septal defect closure: a review of the medical literature. *Can J Cardiol*. 2016;32(11):1315.e11–1315.e18. doi:10.1016/j.cjca.2016.02.068. Review.
15. Du ZD, Hijazi ZM, Kleinman CS, et al. Amplatzer Investigator (2002) comparison between transcatheter and surgical closure of atrial septal defect in children and adults: results of a multicenter nonrandomized trial. *J Am Coll Cardiol*. 2002;39:1836–1844.
16. Sondergaard L, Loh PH, Franzen O, et al. The first clinical experience with the new gore septal occluder (GSO). *EuroIntervention*. 2013;9:959–963.
17. Krichenko A, Benson LN, Burrows P, et al. Angiographic classification of the isolated, persistently patent ductus arteriosus and implications for percutaneous catheter occlusion. *Am J Cardiol*. 1989;63:877–880.
18. Matsura J, Walsh KP, Thanpoulous B, et al. Catheter closure of moderate to large sized patent ductus arteriosus using the new Amplatzer duct occluder: immediate and short-term results. *J Am Coll Cardiol*. 1998;31:878–882.
19. Moore JW, Greene J, Palomares S, et al. For pivotal and continued access studies of the nit occlud PDA investigators. *JACC Cardiovasc Interv*. 2014;7(12):1430–1436.
20. Budde T, Breithardt G, Borggrefe M, et al. Initial experiences with high–frequency electric ablation of the AV conduction system in the human. *Z Kardiol*. 1987;76:204–210.
21. Kugler JD, Danford DA, Deal BJ, et al. Radiofrequency catheter ablation for tachyarrhythmias in children and adolescents, The Pediatric Electrophysiology Society. *N Engl J Med*. 1994;330:1481–1487.
22. Van Hare GF, Lesh MD, Stanger P. Radiofrequency catheter ablation of supraventricular arrhythmias in patients with congenital heart disease: results and technical considerations. *J Am Coll Cardiol*. 1993;22:883–890.
23. Haïssaguerre M, Jaïs P, Shah DC, et al. Spontaneous initiation of atrial fibrillation by ectopic beats originating in the pulmonary veins. *N Engl J Med*. 1998;339:659–666.
24. Saul JP, Kanter RJ, Abrams D, et al. PACES/HRS expert consensus statement on the use of catheter ablation in children and patients with congenital heart disease: developed in partnership with the Pediatric and Congenital Electrophysiology Society (PACES) and Heart Rhythm Society (HRS). Endorsed by the governing bodies of PACES, HRS, the American Academy of Pediatrics (AAP), the American Heart Association (AHA), and the Association for European Pediatric and Congenital Cardiology (AEPC). *Heart Rhythm*. 2016;13:e251–e289.
25. Friedman RA, Walsh EP, Silka MJ, et al. NASPE Expert Consensus Conference: Radiofrequency catheter ablation in children with and without congenital heart disease. Report of the writing committee. North American Society of Pacing and Electrophysiology. *Pacing Clin Electrophysiol*. 2002;25:1000–1017.
26. Nagaraju L, Menon D, Aziz PF. Use of 3D electroanatomical navigation (CARTO-3) to minimize fluoroscopy use in the ablation of pediatric supraventricular tachyarrhythmias. *Pacing Clin Electrophysiol*. 2016;39:574–580.
27. Clark BC, Sumihara K, McCarter R, et al. Getting to zero: impact of electroanatomical mapping on fluoroscopy use in pediatric catheter ablation. *J Interv Card Electrophysiol*. 2016;46:183–189.
28. Fischbach P, Campbell RM, Hulse E, et al. Transhepatic access to the atrioventricular ring for delivery of radiofrequency energy. *J Cardiovasc Electrophysiol*. 1997;8:512–516.
29. Nehgme RA, Carboni MP, Care J, et al. Transthoracic percutaneous access for electroanatomic mapping and catheter ablation of atrial tachycardia in patients with a lateral tunnel Fontan. *Heart Rhythm*. 2006;3:37–43.
30. Jones DG, Jarman JW, Lyne JC, et al. The safety and efficacy of trans-baffle puncture to enable catheter ablation of atrial tachycardias following the Mustard procedure: a single centre experience and literature review. *Int J Cardiol*. 2013;168:1115–1120.
31. Peichl P, Kautzner J, Gebauer R. Ablation of atrial tachycardias after correction of complex congenital heart diseases: utility of intracardiac echocardiography. *Europace*. 2009;11:48–53.
32. Van Hare GF, Javitz H, Carmelli D, et al. Prospective assessment after pediatric cardiac ablation: demographics, medical profiles, and initial outcomes. *J Cardiovasc Electrophysiol*. 2004;15:759–770.
33. Lickfett L, Mahesh M, Vasamreddy C, et al. Radiation exposure during catheter ablation of atrial fibrillation. *Circulation*. 2004;110:3003–3010.
34. Lindsay BD, Eichling JO, Ambos HD, et al. Radiation exposure to patients and medical personnel during radiofrequency catheter ablation for supraventricular tachycardia. *Am J Cardiol*. 1992;70:218–223.
35. Perisinakis K, Damilakis J, Theocharopoulos N, et al. Accurate assessment of patient effective radiation dose and associated detriment risk from radiofrequency catheter ablation procedures. *Circulation*. 2001;104:58–62.
36. Kovoor P, Ricciardello M, Collins L, et al. Radiation exposure to patient and operator during radiofrequency ablation for supraventricular tachycardia. *Aust N Z J Med*. 1995;25:490–495.
37. Kovoor P, Ricciardello M, Collins L, et al. Risk to patients from radiation associated with radiofrequency ablation for supraventricular tachycardia. *Circulation*. 1998;98:1534–1540.
38. Geise RA, Peters NE, Dunnigan A, et al. Radiation doses during pediatric radiofrequency catheter ablation procedures. *Pacing Clin Electrophysiol*. 1996;19:1605–1611.
39. McCollough CH, Zhang J, Primak AN, et al. Effects of CT irradiation on implantable cardiac rhythm management devices. *Radiology*. 2007;243:766–774.
40. Solan AN, Solan MJ, Bednarz G, et al. Treatment of patients with cardiac pacemakers and implantable cardioverter-defibrillators during radiotherapy. *Int J Radiat Oncol Biol Phys*. 2004;59:897–904.
41. Sweesy MW, Holland JL, Smith KW. Electromagnetic interference in cardiac rhythm management devices. *AACN Clin Issues*. 2004;15:391–403.

# 69

# Surgical Considerations for Congenital Heart Disease

*Asvin M. Ganapathi and Andrew J. Lodge*

Congenital cardiac defects may be categorized in a variety of ways. One approach is to separate them based on the presence or absence of cyanosis at the time of presentation. Cyanotic lesions are either associated with shunting of deoxygenated blood into the systemic arterial circulation or with severely reduced pulmonary blood flow. These lesions include transposition of the great arteries, tetralogy of Fallot (TOF), truncus arteriosus, total anomalous pulmonary venous connection, and hypoplastic left heart syndrome (HLHS). Acyanotic lesions include obstructions to left ventricular outflow, such as aortic stenosis or coarctation of the aorta, and defects with shunting of blood from the systemic circulation to the pulmonary circulation, including atrial, ventricular, and atrioventricular (AV) septal defects and patent ductus arteriosus (PDA). Often a combination of lesions exists, and associated anomalies must be thoroughly identified by preoperative imaging studies. This chapter will review the pathophysiology and clinical and imaging evaluation of patients with congenital heart disease as they relate to surgical planning. Discussion will reference treatments, particularly with regard to choice of surgical approach, along with intraoperative and postoperative considerations pertinent for radiologists.

## GENERAL CONSIDERATIONS

Many congenital heart defects are fatal or can lead to long-term complications or a shortened life expectancy if not corrected surgically. Due to advances in congenital heart surgery, anesthesia, critical care, and diagnostic imaging, many defects can be treated effectively with consistently improving results. Although some congenital heart defects are effectively and permanently treated with one operation, many require subsequent interventions and long-term follow-up, including the use of different imaging modalities.

## SURGICAL APPROACHES

Surgery for congenital heart disease is most commonly performed via a median sternotomy with an anterior midline thoracic incision. After exposure of the sternum, a sternal saw is used to split the sternum and a retractor is placed to expose the operative field within which the pericardial sac is contained (Fig. 69.1). This incision offers excellent access to all of the structures of the heart, which is useful when multiple lesions are present or if a complicated repair must be performed.

Less invasive incisions such as a partial median sternotomy or a minithoracotomy can also be utilized. In the case of a partial median sternotomy, the skin incision is kept small and only the upper or lower sternum is divided (e-Fig. 69.2). Depending on the necessary exposure, thoracotomy incisions can be anterior, lateral, or posterior (e-Fig. 69.3) and, in the current era, these incisions are performed by dividing the intercostal muscles and leaving the ribs intact.

The type of lesion being repaired determines the choice of surgical incision. Straightforward repair of extracardiac lesions such as aortic coarctation, vascular rings, or PDA generally can be performed through a left thoracotomy. With refined techniques, even intracardiac repairs requiring cardiopulmonary bypass (CPB) such as an atrial septal defect (ASD) or mitral, tricuspid, and aortic valve operations can be done through minimally invasive incisions. In addition, interest has developed in performing relatively straightforward operations, including some heart valve surgery, using thoracoscopic or robotic techniques. In these cases, several very small incisions and specially designed instruments are used to perform the procedure (e-Fig. 69.4). Advantages touted include an improved cosmetic result and potentially shorter recovery times inside and outside the hospital.

For most complex congenital heart defects, such as repair of an AV septal defect or a cyanotic defect, a median sternotomy is used. This allows better exposure of both intracardiac and extracardiac structures that need to be repaired. For example, the repair of TOF might involve incisions in both the right atrium and the pulmonary artery to close the ventricular septal defect (VSD) and relieve the right ventricular outflow obstruction. In some cases in which a very small pulmonary annulus or significant infundibular stenosis is present, the incision might even need to be extended to the right ventricular cavity (Fig. 69.5).

The choice of surgical approach also is important in the case of staged operations. Lesions that commonly require multiple operations include HLHS, TOF, and truncus arteriosus. A patient with HLHS generally will undergo three operations for complete palliation, and the need for a repeat sternotomy carries both operative and radiographic implications. Imaging of the chest can help with operative planning because redo median sternotomy incisions carry a risk of damage to the thoracic contents as a result of the formation of postoperative adhesions. For example, the aorta or other structures can be found very close to the sternum (e-Fig. 69.6) and might be damaged upon entry to the chest during the sternotomy. This sometimes necessitates the emergent institution of CPB or alternative, peripheral cannulation (discussed later).

Other scenarios influencing operative planning and the choice of incision include the presence of multiple lesions or when a palliative procedure, instead of complete repair, is indicated. For example, many congenital heart defects can occur together, such as coarctation of the aorta and VSD. In this case, a surgical procedure that might have been accomplished through a thoracotomy incision for isolated coarctation (e-Fig. 69.7) would necessitate a median sternotomy to address both lesions.

The incision used for surgery has a variety of clinical and radiographic consequences. Patients who have had median sternotomy incisions often will have steel wires re-approximating the sternum, although in children, sutures that are not radio-opaque often are used. Occasionally, chest wall deformities may develop in children who have sternotomy incisions as the children grow. Children who have had surgery for congenital heart disease also are at higher risk for developing scoliosis than the general population (e-Fig. 69.8). Thoracotomy incisions can produce distortion of the ribs on the side that has been operated upon and also can lead to scoliosis.[1] In the current era, ribs usually are not cut or sectioned during thoracotomy procedures, but sometimes inadvertent rib

## Abstract:

Congenital cardiac defects may be categorized in a variety of ways. One approach is to separate them based on the presence or absence of cyanosis at the time of presentation. Cyanotic lesions are either associated with shunting of deoxygenated blood into the systemic arterial circulation or with severely reduced pulmonary blood flow. These lesions include transposition of the great arteries, tetralogy of Fallot (TOF), truncus arteriosus, total anomalous pulmonary venous connection, and hypoplastic left heart syndrome (HLHS). Acyanotic lesions include obstructions to left ventricular outflow, such as aortic stenosis or coarctation of the aorta, and defects with shunting of blood from the systemic circulation to the pulmonary circulation, including atrial, ventricular, and atrioventricular (AV) septal defects and patent ductus arteriosus (PDA).

Congenital cardiac defects may be categorized in a variety of ways. One approach is to separate them based on the presence or absence of cyanosis at the time of presentation. Cyanotic lesions are either associated with shunting of deoxygenated blood into the systemic arterial circulation or with severely reduced pulmonary blood flow. These lesions include transposition of the great arteries, tetralogy of Fallot (TOF), truncus arteriosus, total anomalous pulmonary venous connection, and hypoplastic left heart syndrome (HLHS). Acyanotic lesions include obstructions to left ventricular outflow, such as aortic stenosis or coarctation of the aorta, and defects with shunting of blood from the systemic circulation to the pulmonary circulation, including atrial, ventricular, and atrioventricular (AV) septal defects and patent ductus arteriosus (PDA). Often a combination of lesions exists, and associated anomalies must be thoroughly identified by preoperative imaging studies. This chapter will review the pathophysiology and clinical and imaging evaluation of patients with congenital heart disease as they relate to surgical planning. Discussion will reference treatments, particularly with regard to choice of surgical approach, along with intraoperative.

## Keywords:

congenital heart disease
cardiac surgery

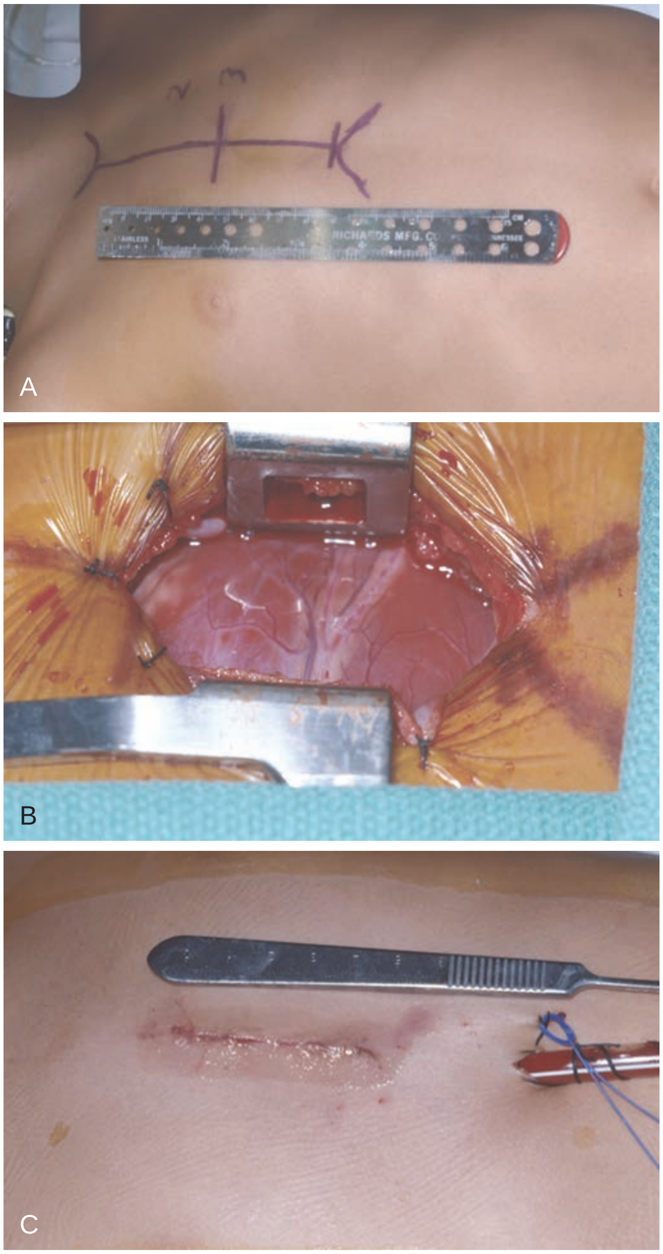

**e-Figure 69.2. Partial lower median sternotomy.** (A) With the patient supine and the head to the left of the picture, the skin is marked preoperatively to show the length of the entire sternum, the second and third intercostal spaces (2 and 3), and the planned incision between the horizontal lines. In small children, a skin incision approximately 4 cm long can be used. (B) The exposure created with this incision is shown. Compared with Fig. 69.1, less of the pericardial contents are immediately obvious. (C) The closed incision after repair of an atrial septal defect. A chest tube and pacing wires are seen exiting the skin caudal to the incision.

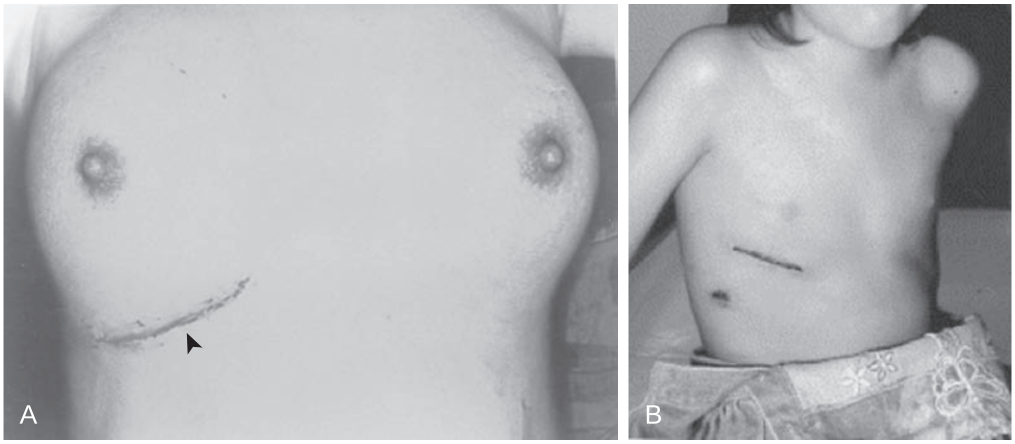

**e-Figure 69.3. Anterior right thoracotomy incisions for minimally invasive heart surgery.** (A) Frontal and (B) Right oblique views of the thorax. The incisions are generally made in the inframammary crease. These incisions sometimes are preferred, particularly for female patients.

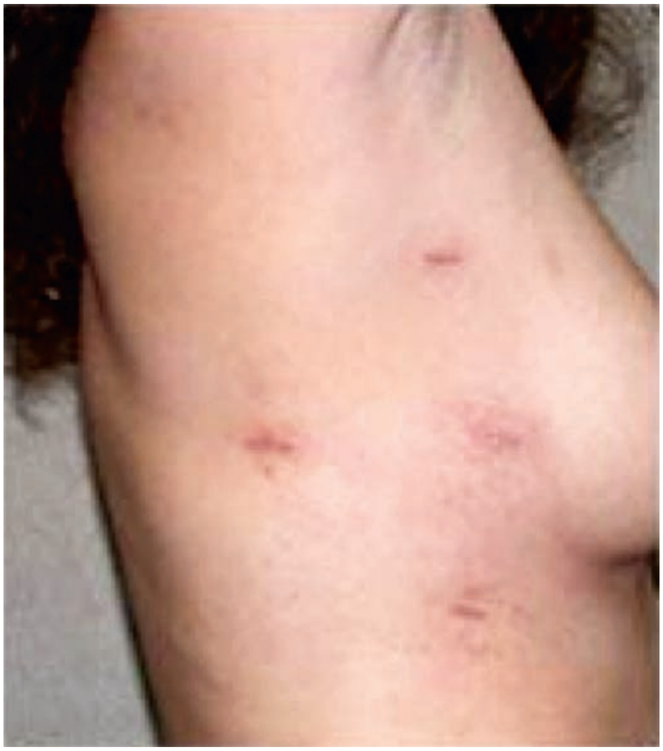

**e-Figure 69.4.** Incision sites for robotic ports used in atrial septal defect repair.

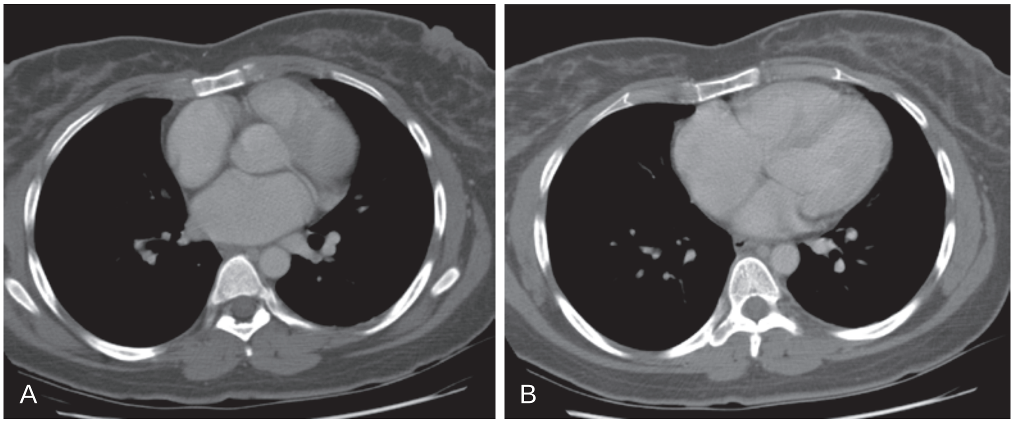

**e-Figure 69.6. Axial computed tomography images of a patient with previously repaired tetralogy of Fallot.** (A) The right atrium and right ventricular outflow tract are in close proximity to the anterior chest wall. (B) A more caudal image showing close proximity of the right atrium and ventricle to the anterior chest wall.

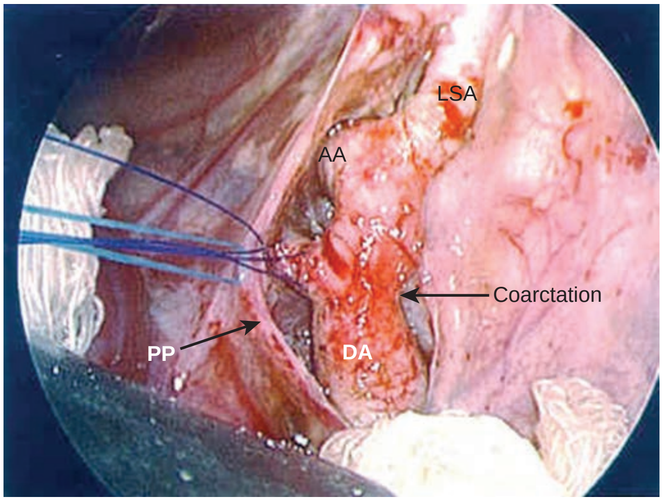

**e-Figure 69.7. Intraoperative photograph during repair of aortic coarctation.** The parietal pleura *(PP)* has been opened to expose the aorta. This flap of tissue contains the vagus and recurrent laryngeal nerves. The sutures are around the ductus arteriosus. The coarctation is visible as a subtle indentation externally. The internal diameter will be substantially smaller. *AA,* Aortic arch; *DA,* descending aorta; *LSA,* left subclavian artery.

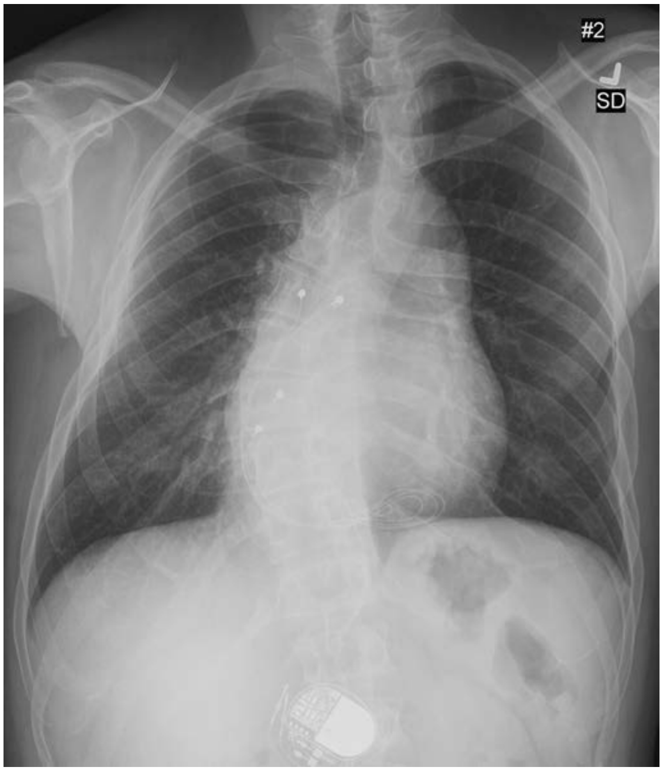

**e-Figure 69.8. Scoliosis after CHD.** Frontal chest radiograph shows significant scoliosis in a patient with complex CHD who underwent multiple cardiac surgeries as a child.

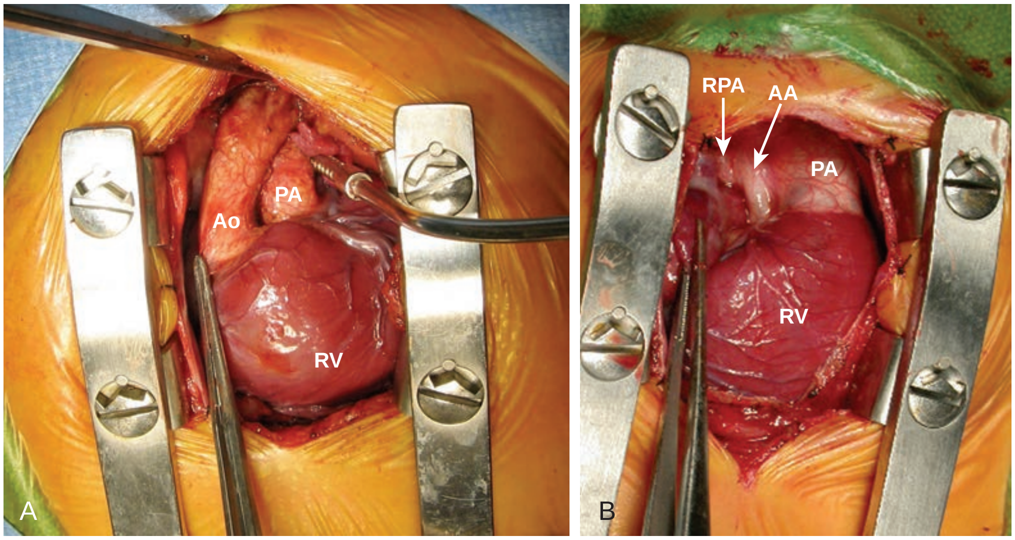

**Figure 69.1. Median sternotomy.** (A) A sternal retractor is in place in a patient with transposition of the great arteries. The pericardium has been opened and sutured to the margins of the incision to expose the heart. The aorta *(Ao)* arises from the right ventricle *(RV)* and the pulmonary artery *(PA)* from the left ventricle. The left coronary artery and some of its branches also are seen. Note that the left ventricle, which is a posterior structure, is not well exposed. (B) Similar exposure in a patient with hypoplastic left heart syndrome. The main *PA* is large and the ascending aorta *(AA)* is diminutive. The right pulmonary artery *(RPA)* is visible emerging from behind the aorta. The right atrial appendage is being grasped with a forceps. The right ventricle *(RV)* is also exposed. The cut pericardial edge, which is sutured to the skin edge, is more easily seen in this picture.

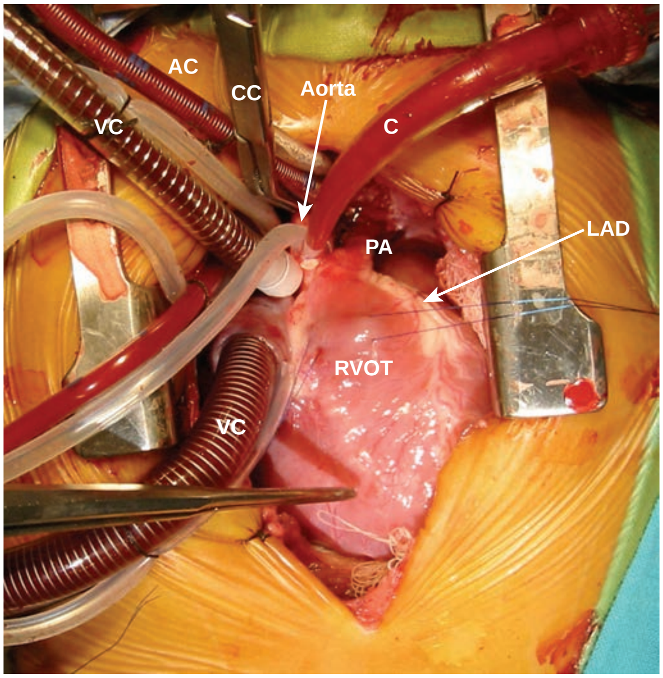

**Figure 69.5. An intraoperative photograph of an infant with tetralogy of Fallot (TOF) demonstrates a typical setup for cardiopulmonary bypass.** The patient's head is toward the top of the picture. A cross-clamp *(CC)* has been applied to the aorta between the arterial cannula *(AC)* and the cardioplegia catheter *(C)*. Venous cannulae *(VC)* are positioned in the superior vena cava and right atrium. The surface of the right ventricle is visible, and sutures are present in the right ventricular infundibulum *(RVOT)*. The diminutive main pulmonary artery *(PA)*, which is typical of patients with TOF, is seen. The left anterior descending coronary artery *(LAD)* is seen at the left lateral margin of the field. The left ventricle typically is not visible without retraction through a median sternotomy because it is a posterior structure.

fractures can occur, which would be noted on the postoperative chest radiograph.

## CARDIOPULMONARY BYPASS AND EXTRACORPOREAL MEMBRANE OXYGENATION

Most congenital heart operations are performed using CPB to support the circulation. The principal components of the system are a blood pump (commonly a roller or centrifugal pump) and an artificial lung (oxygenator) (Fig. 69.9). CPB is established by the placement of arterial and venous cannulae (e-Fig. 69.10), usually in the ascending aorta and right atrium, however, the femoral, iliac, or axillary arteries can serve as alternatives for arterial cannulation, and in surgeries necessitating opening of the heart, venous cannulation is accomplished by separate superior and inferior vena cavae cannulae. CPB facilitates cardiac surgery by emptying the heart of blood, allowing ventilation to be stopped, and, if necessary, arresting the heart with cardioplegia, a potassium-rich solution circulated through the coronary vasculature after clamping the aorta between the coronary arteries and the CPB arterial inflow. The evolution of this technology has reduced CPB-related complications and morbidity such as the systemic inflammatory response, catastrophic air embolism, myocardial injury, and pulmonary dysfunction.[2,3]

Some surgery on extracardiac structures, such as modified Blalock-Taussig shunts and pulmonary artery banding, can be performed without CPB if the patient remains hemodynamically stable. In these cases, CPB generally is readily available should circumstances change. Sometimes extracorporeal circulatory support is necessary after surgery to allow for recovery of the heart over an extended period or as a bridge to transplant in the case of an unsuccessful repair. In these cases, a modified CPB circuit is used for extracorporeal membrane oxygenation (ECMO) (Fig. 69.11). Chest radiography can be used to assess the position of ECMO cannulas (Fig. 69.12). ECMO can be continued for days to weeks if necessary. However, a recent registry study demonstrated that the majority of survivors were on ECMO for 8 days or less.[4]

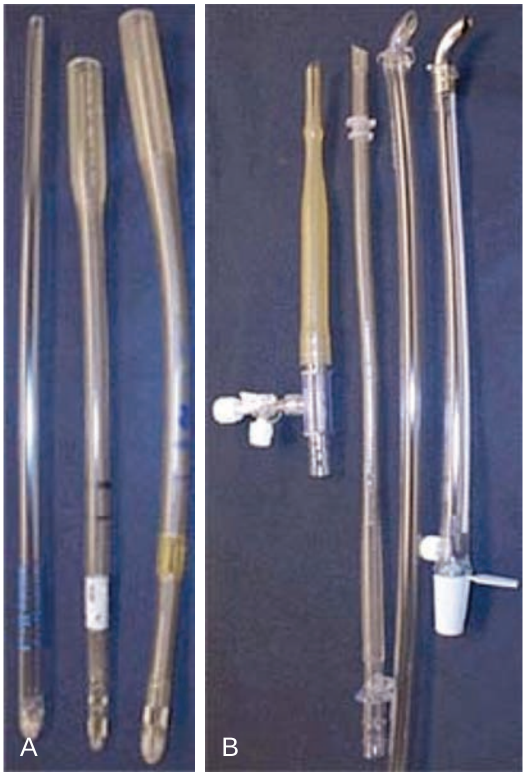

**e-Figure 69.10. Cannulae used for cardiopulmonary bypass.** (A) Examples of venous cannulae. (B) Examples of arterial cannulae.

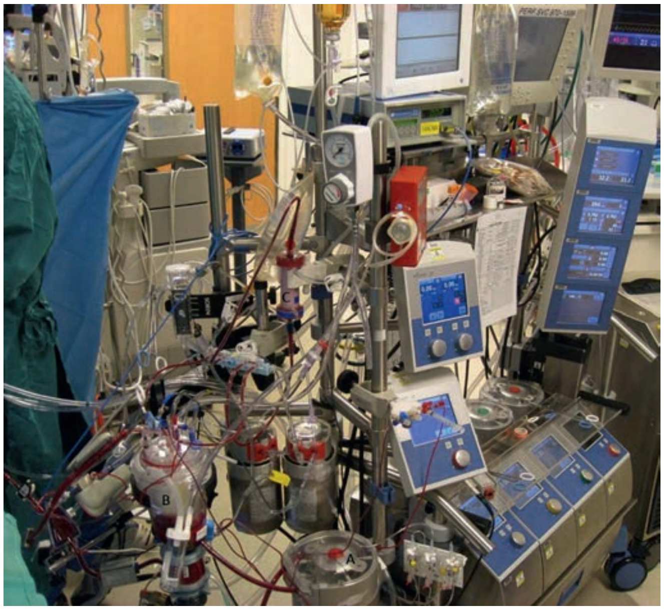

**Figure 69.9. Pediatric cardiopulmonary bypass (heart-lung) machine.** The roller pump, the reservoir with oxygenator below, and hemofilter are visible. The blood tubing connecting the components can be seen. Below the oxygenator is a temperature coil to which water lines are attached, allowing control of the patient's body temperature. Some of the monitoring equipment for the apparatus can be seen to the right of the image.

Survival rates in patients who require ECMO after surgery range from 38% to 53%.[5]

## CIRCULATORY ARREST AND REGIONAL CEREBRAL PERFUSION

In very complex cases such as those involving small neonates or complex aortic arch reconstruction, it occasionally is desirable to temporarily stop the entire circulation for a period. This technique, termed "deep hypothermic circulatory arrest" (DHCA), uses total body cooling to approximately 18°C, thus allowing the circulation to be safely suspended for up to 30 to 45 minutes. The safety of circulatory arrest and its effect on long-term neurologic outcome are controversial. The landmark Boston Circulatory Arrest Study suggested that neurodevelopmental abnormalities became significantly more prevalent after 41 minutes of DHCA.[6] However, it should be noted that data from other studies suggest that DHCA has little or no effect.[7–9] One limitation of all of these studies is the relatively small sample size.

Examples of operations in which patients possibly may be subjected to DHCA include the Norwood procedure for HLHS or repair of total anomalous pulmonary venous connection. As techniques have evolved, the use of DHCA has decreased, and many surgeons prefer to use regional cerebral perfusion, a technique that uses selective arterial inflow at a lower rate to the innominate or carotid artery and thereby limits periods of total ischemia. One advantage of this technique is blood flow not only to the brain but also to subdiaphragmatic organs.[10] There is wide variation in the use and technique of regional cerebral perfusion.[11]

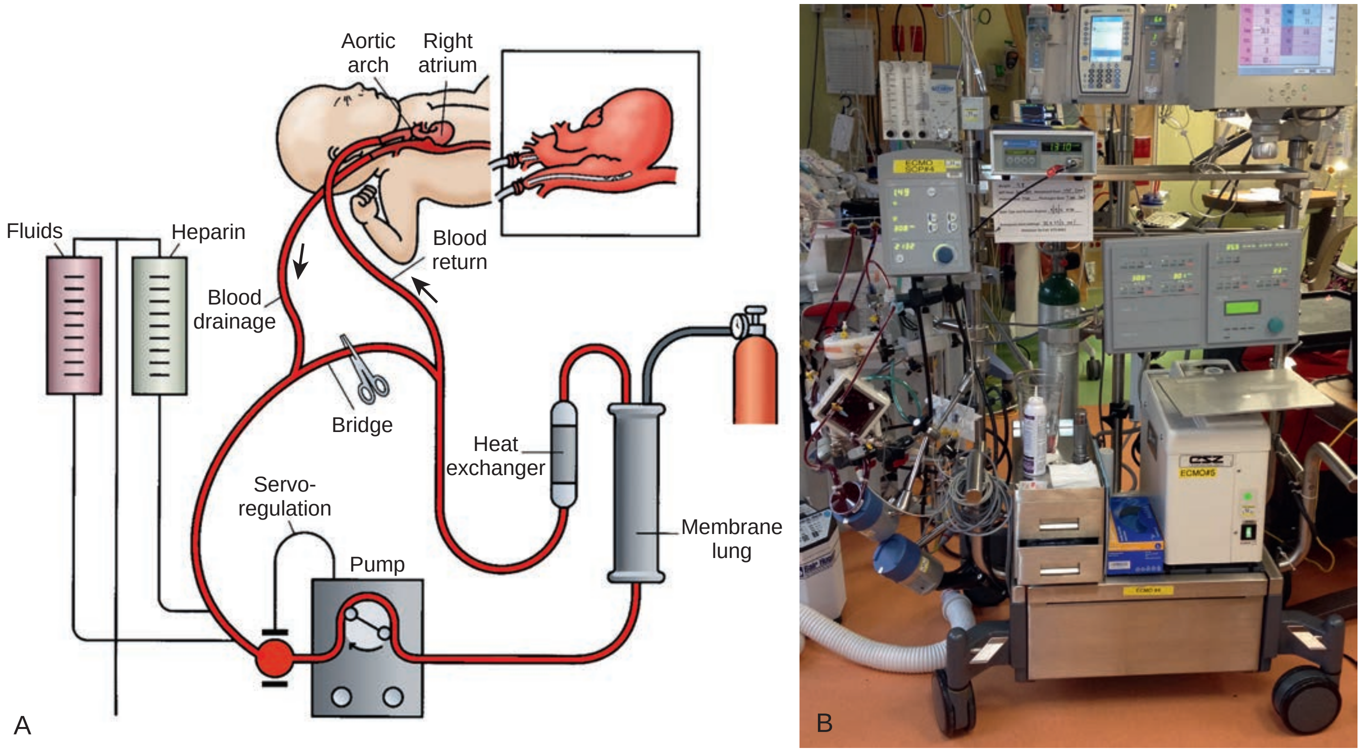

**Figure 69.11. Extracorporeal membrane oxygenation (ECMO).** (A) A schematic diagram of an ECMO circuit. (B) An actual ECMO circuit in clinical use. *(A, from* http://www.nichd.nih.gov/publications/pubs/images/Efig1p26.gif*. Accessed April 2, 2012.)*

## CHEST RADIOGRAPHY

Chest radiographs are useful both before and after cardiac surgery. From a preoperative standpoint, the chest radiograph can be used for diagnostic purposes, because many lesions have characteristic findings, as well as a means to determine the severity of disease by indicating evidence of congestive heart failure, pulmonary edema, or atrial/generalized cardiac enlargement. These findings may influence medical management before surgery or help to predict the postoperative course. In addition, a chest radiograph provides an important baseline to which to compare postoperative films. However, in some centers, the use of preoperative chest radiography in otherwise healthy children is being questioned as it may not be cost effective.

Chest radiographs are the most common radiographic study obtained after heart surgery, and are obtained immediately upon arrival at the recovery room or intensive care unit (e-Fig. 69.13). These images are used to verify the positioning of central venous lines, chest tubes, the endotracheal tube, sternal wires, and prostheses, as well as to assess the degree of lung expansion and to rule out unsuspected pleural effusions or pneumothoraces. In small children with limited percutaneous vascular access, pressure monitoring lines sometimes are inserted directly into the cardiac chamber (and later removed at the bedside). The most common points of insertion, in decreasing order of frequency, are the right atrium, left atrium (usually via the right superior pulmonary vein; less often via the left atrial appendage), and pulmonary artery.

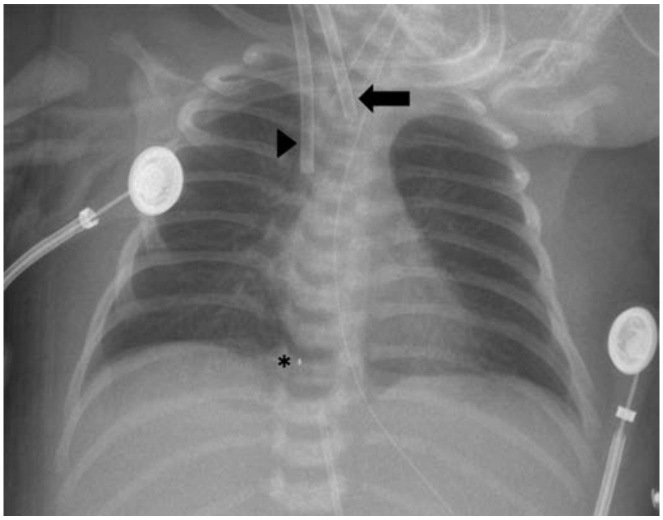

**Figure 69.12. Positioning of ECMO cannulas in infant.** ECMO cannulas (arterial and venous marked by *arrow* and *arrowhead* respectively) in a child. A radiopaque marker *(asterisk)* is noted at the bottom of the venous cannula indicating its depth.

Obtaining and interpreting the immediate postoperative film in a timely fashion is critical because delays can be life-threatening. For instance, mediastinal widening—a new or enlarging opacity in the vicinity of the aorta after the repair of coarctation of the aorta—may represent postoperative bleeding. An unsuspected pneumothorax can be life threatening if it is not detected early. A pneumothorax may arise in the case of a patient who undergoes PDA ligation via a left thoracotomy but does not have a pleural drain left in at the end of the operation (a common scenario). If a patient has undergone a left thoracotomy, one might observe asymmetry of the lung fields because of congestion or atelectasis of the right lung paired with hyperinflation of the left lung (e-Fig. 69.14). This asymmetry occurs because the patient is positioned with the right side down for an extended period and the left lung is partially or completely collapsed during the procedure for surgical exposure purposes. Many patients have mild pulmonary edema or small pleural effusions related to the inflammatory response to CPB. These findings generally resolve with diuretic treatment. Many current valve prostheses also are visible on a chest radiograph because of the presence of radiopaque material in the sewing ring, stent, or the valve itself. However, some bioprosthetic valves, including homografts and autografts, will not be apparent on radiographs (Table 69.1).

Daily chest radiographs frequently are obtained for patients after cardiac surgery. Posterior-anterior and lateral films generally are preferred for patients who are stable enough to travel to the radiology department, including patients with indwelling appliances such as chest tubes. However, it is common practice to obtain daily portable films while the patient requires intensive care unit monitoring. Neonates and infants who remain intubated with small bore endotracheal tubes are at risk for the development of atelectasis, which can be a major impediment to clinical care. The presence, extent, and distribution of atelectasis and the position of the endotracheal tube are critically important elements of the chest radiograph that may require daily assessment. Follow-up radiographs generally are obtained immediately after the removal of pleural chest tubes, but they are not routinely necessary after the removal of intracardiac lines, pacing wires, and pericardial (mediastinal) drains. Although these radiographs primarily are used to observe if a pneumothorax is present after removal of the chest tube, they also can help identify other conditions such as pleural or pericardial effusions.

## OTHER CONSIDERATIONS

Imaging studies performed or interpreted by radiologists are important in many other situations in the evaluation and surgical management of congenital heart disease. Many patients with complex congenital heart disease, particularly patients requiring intervention as neonates or infants, may have associated syndromes

**TABLE 69.1** Cardiac Valve Prostheses

| Prosthesis Type | Synonym | Definition | Characteristics |
|---|---|---|---|
| Bioprosthetic | Xenograft, heterograft | Manufactured valve; uses tissue from other species such as pig or cow | Does not require long-term anticoagulation; subject to structural deterioration |
| Mechanical | — | Manufactured valve, generally composed of metal and pyrolytic carbon | Requires long-term anticoagulation; the most durable prosthesis; magnetic resonance imaging compatible |
| Homograft | Allograft | Cryopreserved human valve or valved conduit | Included segment of aorta or pulmonary artery offers greater reconstructive potential; subject to structural deterioration; aortic valve particularly prone to calcification |
| Autograft | — | Patient's own tissue | Pulmonary autograft used to replace aortic valve in Ross procedure |
| Stentless | — | Bioprosthetic valve that does not have a rigid plastic or metal stent built in | Technically more difficult to implant; may have greater effective orifice area |

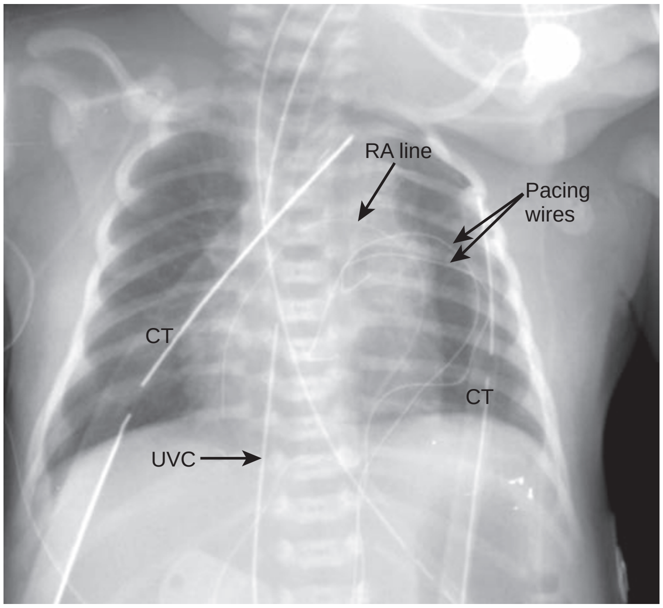

**e-Figure 69.13. Typical chest radiograph of a postoperative infant.** The tip of the endotracheal tube can be seen above the carina. A variety of other support equipment is labeled. The pacing wires can appear similar to the transthoracic pressure lines. The wires can be identified by their typical termination in a "J" configuration, whereas the pressure lines will be straight. Typically some redundant length of each is seen in the pericardial space. The right chest tube *(CT)* traverses the right pleural space and terminates in the pericardium/mediastinum. The right atrial *(RA)* line tip is near the RA-inferior vena cava junction. *UVC,* Umbilical vein catheter.

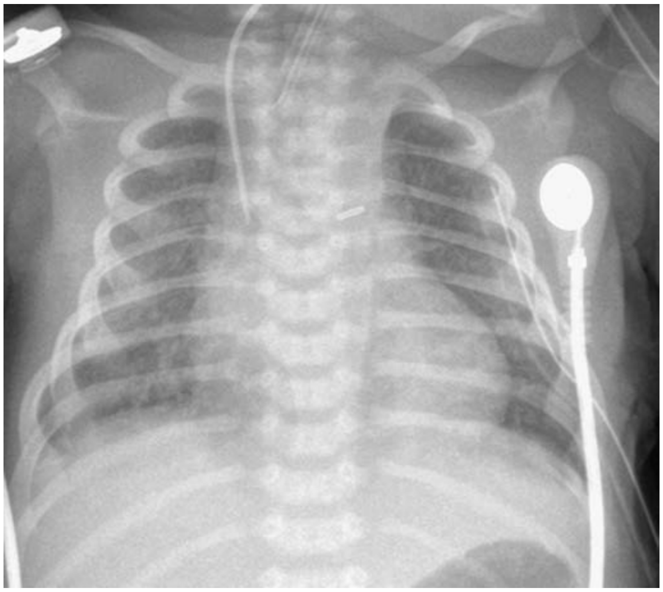

**e-Figure 69.14. Postoperative chest radiograph after aortic coarctation repair.** Hyperinflation of the left lung is observed with a central line noted in the right internal jugular vein and patchy opacities in the right lung likely related to atelectasis.

or anomalies. In these cases, it is common practice to obtain imaging studies such as an ultrasound of the brain and/or kidneys before surgery to establish baseline diagnoses. It has been increasingly recognized that neonates with complex congenital heart disease have brain pathology that exists even before neonatal surgical correction, and at some centers, preoperative magnetic resonance imaging (MRI) studies of the brain have become routine (e-Fig. 69.15). Brain imaging becomes important when considering ECMO or during the use of ECMO because findings of a severe neurologic insult may affect decision making.

Feeding problems in infants who undergo congenital heart surgery are common and involve the use of radiology services. In certain subsets of patients, such as those with HLHS, gastroesophageal reflux is particularly common. These patients may require diagnostic tests such as upper gastrointestinal series and gastric emptying studies to help establish a diagnosis or to plan for antireflux surgery. They also may require placement or repositioning of feeding tubes with fluoroscopic guidance.

Other studies may be required to aid in the assessment of postoperative complications. Renal insufficiency is relatively common in the postoperative period. Renal ultrasound with Doppler assessment of renal artery and vein flow may be helpful. Many patients who require prolonged ventilation have a confusing combination of lung and pleural space disease, and chest ultrasound can be very helpful in differentiating pathologic processes in the chest. Occasionally, image-guided drainage using ultrasound can be helpful in treating more complicated effusions. Infants who require ECMO and are at risk for ongoing coagulopathy require serial cranial ultrasound imaging procedures to assess for bleeding.

Imaging studies also have become increasingly useful for preoperative planning in complicated cases. CT and MRI play an increasingly important role in these situations. In patients who have had previous cardiac surgery and are at risk for injury to the heart with a repeat sternotomy, CT scans can be very helpful in risk assessment or surgical planning by showing the relationship of the heart and great vessels to the sternum. CT angiography also can be helpful in patients with aortic coarctation who have complex anatomy or late diagnosis, both for operative planning and assessing candidacy for stent placement. CT or CT angiography also are useful in the diagnoses or characterization of complicated pulmonary artery or vein anatomy, such as in patients who have had repair of anomalous pulmonary venous connections, TOF, or transposition of the great arteries. Cardiac MRI is being used more commonly for many of these same indications (e-Fig. 69.16). In addition, cardiac MRI can be used to evaluate intracardiac shunts and plan therapy, such as in the case of transcatheter device closure of ASD. MRI also has become quite useful for evaluating right ventricular function and pulmonary insufficiency in patients who have had repair of TOF (Videos 69.1 and 69.2). CT and MRI are the best imaging modalities for most vascular rings (e-Fig. 69.17). Some patients require cannulation of peripheral vessels for the institution of CPB but also may have had multiple heart catheterizations or cutdowns. In these cases, ultrasound imaging with Doppler can help establish the patency of peripheral vessels such as the femoral artery and vein.

## SUMMARY

Congenital heart disease can present with a variety of symptoms in patients at any age. Surgical and catheter-based techniques, as well as pediatric cardiac anesthesiology, have evolved during the past 30 years. Interventions are being performed at an earlier age and through smaller incisions, with improving short- and long-term survival. Diagnosis is established by echocardiography in most circumstances, although MRI and CT may be useful in a number of preoperative and postoperative circumstances. Management decisions are based on the overall clinical picture, which takes into consideration patient symptoms, physical findings, and results of imaging studies. Imaging studies performed and interpreted by radiologists during the preoperative and postoperative phases are critical for the successful treatment of these patients.

### KEY POINTS

- Incisions for pediatric cardiac surgery range from minimally invasive options such as small incisions for robotic procedures and thoracotomies to large midline, sternal incisions requiring splitting of the sternum.
- Radiographic studies are extremely important for both the diagnosis and operative planning of congenital heart disease. These studies consist primarily of chest radiographs, CT scans, and MRI. Echocardiography also plays a significant role in diagnosis.
- Chest radiographs are perhaps the most important study utilized in patients undergoing congenital heart surgery. They provide important diagnostic, preoperative, and postoperative information. Additionally, they serve to verify correct positioning of intraoperatively placed lines, chest tubes, and endotracheal tubes.
- Because many children with congenital heart disease have comorbidities involving other organ systems, radiographic studies for diagnosis and management of these processes are essential, such as renal and vascular ultrasound, brain imaging, and a variety of gastrointestinal studies.

### SUGGESTED READINGS

Jonas RA. *Comprehensive Surgical Management of Congenital Heart Disease*. London: Hodder Arnold; 2004.

Mavroudis C, Backer C. *Pediatric Cardiac Surgery*. 3rd ed. St. Louis: Mosby; 2003.

Stark JF, de Laval MR, Tsang VT, eds. *Surgery for Congenital Heart Defects*. 3rd ed. Hoboken, NJ: John Wiley & Sons; 2006.

### REFERENCES

Full references for this chapter can be found on www.expertconsult.com.

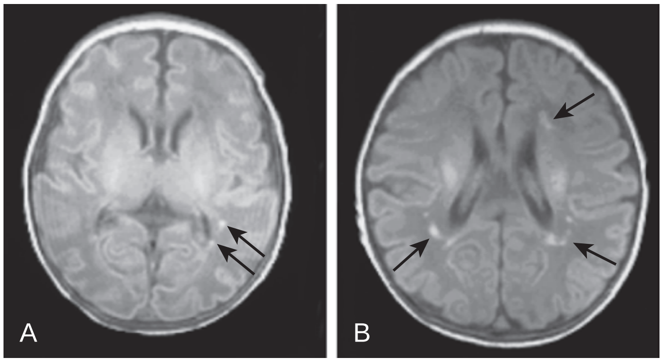

**e-Figure 69.15. Periventricular leukomalacia.** (A) Axial T1-weighted magnetic resonance (MR) image demonstrates two small areas of increased signal intensity *(arrows)* in periventricular white matter consistent with mild periventricular leukomalacia. (B) Axial T1-weighted MR image shows multiple large areas of increased signal density *(arrows)* consistent with moderate periventricular leukomalacia. *(From Galli KK, Zimmerman RA, Jarvik GP, et al. Periventricular leukomalacia is common after neonatal cardiac surgery,* J Thorac Cardiovasc Surg. *2004;127:692–694.)*

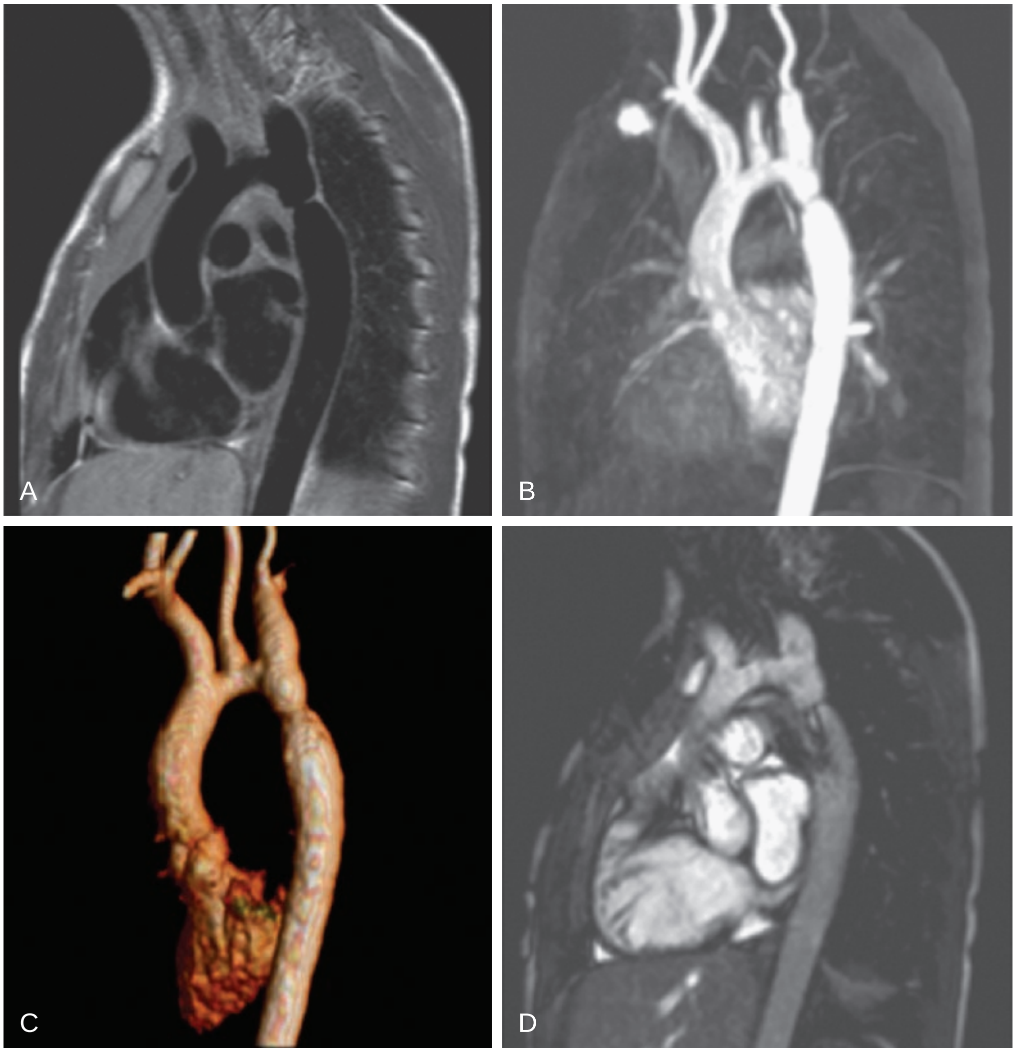

**e-Figure 69.16. Aortic coarctation.** MR images showing the relationship of the coarctation to the brachiocephalic vessels and aortic arch. Oblique sagittal images. (A) Black blood (B) Contrast enhanced magnetic resonance angiography (MRA) (C) 3D MRA (D) Cine gradient echo. Images such as these are helpful for planning the surgical approach or stenting. *(From Atilli AK, Parish V, Valverde I, et al. Cardiovascular MRI in childhood,* Arch Dis Child. *2011;96:1147–1155.)*

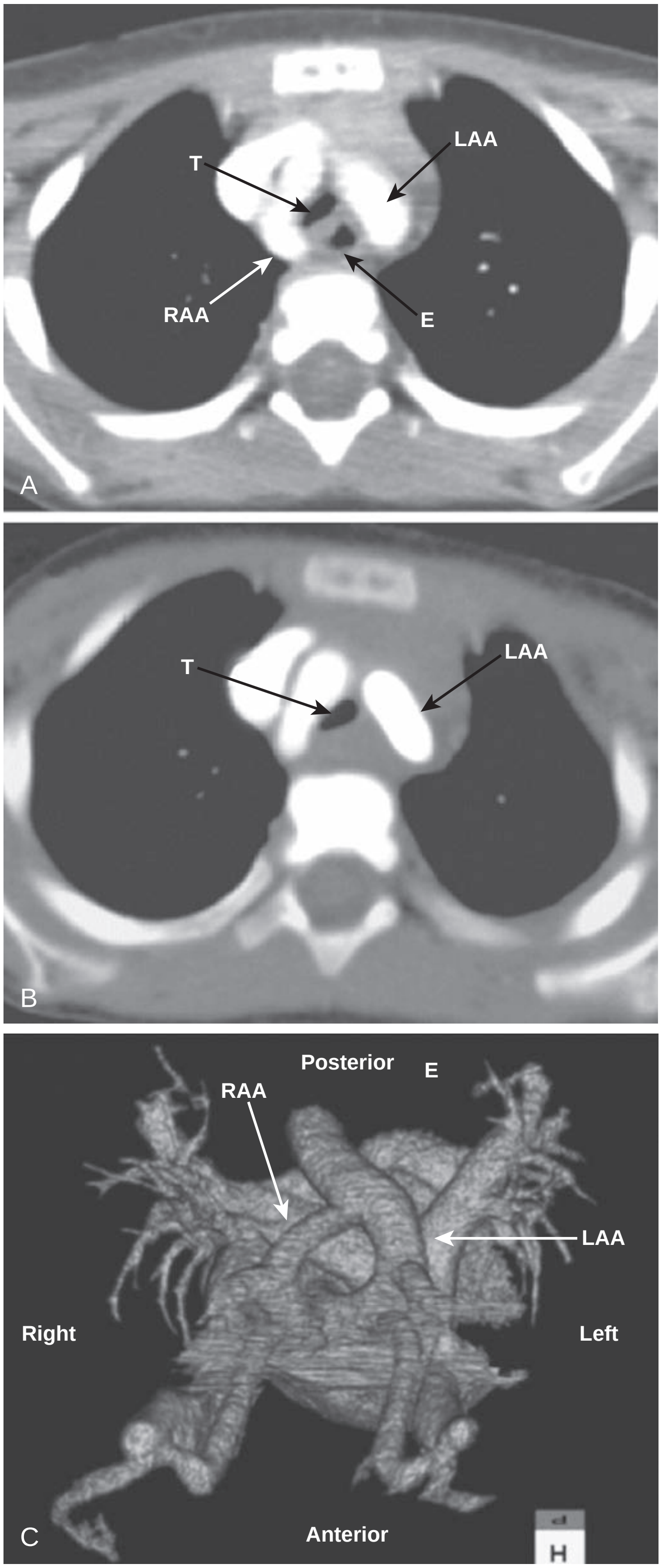

**e-Figure 69.17.** Contrast-enhanced CT images (A and B) and three-dimensional reconstruction (C) showing a vascular ring, in this case a double aortic arch. The right and left arches encircle the esophagus *(E)* and trachea *(T)*, potentially compressing them. *LAA,* Left aortic arch; *RAA,* right aortic arch. *(From Iida C, Shiota M, Hata Daisuke. Dying spell caused by vascular ring,* Emerg Med J. *2011;28[7]:628.)*

## REFERENCES

1. Roclawski M, Sabiniewicz R, Potaz P, et al. Scoliosis in patients with aortic coarctation and patent ductus arteriosus: does standard posterolateral thoracotomy play a role in the development of the lateral curve of the spine? *Pediatr Cardiol*. 2009;30:941–945.
2. Levy JH, Tanaka KA. Inflammatory response to cardiopulmonary bypass. *Ann Thorac Surg*. 2003;75:S715–S720.
3. Landis RC, Brown JR, Fitzgerald D, et al. Attenuating the systemic inflammatory response to adult cardiopulmonary bypass: a critical review of the evidence base. *J Extra Corpor Technol*. 2014;46:197–211.
4. Ford MA, Gauvreau K, McMullan DM, et al. Factors associated with mortality in neonates requiring extracorporeal membrane oxygenation for cardiac indications: analysis of the extracorporeal life support organization registry data. *Pediatr Crit Care Med*. 2016;17:860–870.
5. Coskun KO, Coskun ST, Popov AF, et al. Extracorporeal life support in pediatric cardiac dysfunction. *J Cardiothorac Surg*. 2010;5:112.
6. Wypij D, Newburger JW, Rappaport LA, et al. The effect of duration of deep hypothermic circulatory arrest in infant heart surgery on late neurodevelopment: the Boston Circulatory Arrest Trial. *J Thorac Cardiovasc Surg*. 2003;126:1397–1403.
7. Baum M, Freier MC, Freeman K, et al. Neuropsychological outcome of infant heart transplant recipients. *J Pediatr*. 2004;145:365–372.
8. Mahle WT, Clancy RR, Moss EM, et al. Neurodevelopmental outcome and lifestyle assessment in school-aged and adolescent children with hypoplastic left heart syndrome. *Pediatrics*. 2000;105:1082–1089.
9. Kirshbom PM, Flynn TB, Clancy RR, et al. Late neurodevelopmental outcome after repair of total anomalous pulmonary venous connection. *J Thorac Cardiovasc Surg*. 2005;129:1091–1097.
10. Pigula FA, Nemoto EM, Griffith BP, et al. Regional low-flow perfusion provides cerebral circulatory support during neonatal aortic arch reconstruction. *J Thorac Cardiovasc Surg*. 2000;119:331–339.
11. Meyer DB, Jacobs JP, Hill K, et al. Variation in perfusion strategies for neonatal and infant aortic arch repair: contemporary practice in the STS congenital heart database. *World J Pediatr Congenit Heart Surg*. 2016;7:638–644.

# 70

# Prenatal Imaging and Therapy of Congenital Heart Disease

*David N. Schidlow and Mary T. Donofrio*

## INTRODUCTION

Congenital abnormalities of the heart are the most common birth defects, occurring in approximately 8 of every 1,000 newborns.[1] Approximately 25% of those in whom an abnormality is identified have critical congenital heart disease (CHD) with risk for significant perinatal compromise or death.[2,3] Despite advances in imaging technology and technique, much CHD remains undetected until after birth.[4–8] Fortunately, routine prenatal cardiac screening has evolved from single-frame acquisition imaging of the four-chamber heart view to include delineation of the outflow tracts, an addition which significantly improves CHD detection.[9,10] Appropriate screening, when combined with fetal echocardiography when indicated, can readily identify and guide management for most cardiac abnormalities.

The complete fetal echocardiogram includes two-dimensional imaging, pulsed-wave and color Doppler interrogation, and M-mode imaging to completely assess fetal cardiac structure, function, and rhythm. Newer techniques may supplement the standard fetal echocardiogram and include tissue Doppler imaging, strain analysis, and three-dimensional imaging.[11,12] This chapter reviews (1) normal fetal cardiac anatomy, physiology, and rhythm assessment; (2) common congenital cardiovascular lesions and heart rhythm abnormalities; and (3) indications for interventions for fetal heart disease and outcomes.

## FETAL PHYSIOLOGY AND FLOW

An understanding of normal fetal cardiovascular anatomy and physiology is essential to interpretation of the fetal echocardiogram. The following are important differences between the fetal and postnatal circulation:

1. The right ventricular output exceeds that of the left ventricle, resulting in a slightly larger right atrium, tricuspid valve, right ventricle, pulmonary valve, and main pulmonary artery when compared with their left-sided counterparts.
2. The ductus venosus and foramen ovale are present; the ductus venosus shunts placental venous return to the right atrium and the foramen ovale directs this blood to the left atrium.
3. The ductus arteriosus is present, allowing deoxygenated systemic venous return to bypass the branch pulmonary arteries and be directed to the descending aorta and placenta.
4. The pulmonary vascular resistance is high, resulting in a relatively small proportion (approximately 10%) of the fetal cardiac output being directed toward the lungs.

## FETAL ANATOMIC AND FUNCTION ASSESSMENT

A complete fetal echocardiogram includes imaging of the atria, ventricles, atrioventricular and semilunar valves, foramen ovale, pulmonary veins, ductal and aortic arches, main and branch pulmonary arteries, and assessment of cardiac rhythm and function. Quantitative assessments of valve and vessel size should be compared with gestation-matched normative data. Pulsed-wave and color Doppler interrogation of each structure should be performed.

### Visceral/Atrial Situs and Cardiac Position

Proper identification of situs at the beginning of a fetal echocardiogram is of paramount importance for framing the rest of the examination. The positions of the viscera within the abdomen and the heart within the thorax should be identified. In normal abdominal situs, the liver is right-sided and the stomach is left-sided. The normal position of the heart within the thorax is on the left (levocardia); additional possibilities are dextrocardia and mesocardia, wherein the majority of the cardiac mass is rightward or midline, respectively. The direction of the cardiac apex should also be identified. The apex normally points leftward, but rightward or posterior-anterior orientations are possible.

Once abdominal situs and cardiac position have been determined, delineation of atrial morphology should follow (Fig. 70.1). The right atrium receives the coronary sinus and inferior vena cava, and its appendage is broad-based and triangular. The left atrium is characterized by the presence of septum primum, the "valve" of the foramen ovale and its appendage, which is slender and finger-like. The pulmonary veins usually connect to the left atrium, but there is significant variability of the pulmonary venous connections in CHD. Although "right" and "left" atria are typically in their usual right- and left-sided locations respectively, it is important to note that they may be inverted or ambiguous in nature.

### Right and Left Ventricles

The right and left ventricles should be identified by their distinguishing morphologic features. The right ventricle has a moderator band, attachments of its atrioventricular (tricuspid) valve to the ventricular septum (septophilic), an atrioventricular valve annulus apical to its left ventricular counterpart, and coarse trabeculations. The left ventricle, in contrast, has an atrioventricular (mitral) valve without attachments to the septum (septophobic), and appears smooth due to its fine trabeculations (see Fig. 70.1). As with the atria, although "right" and "left" ventricles are typically in their usual right- and left-sided locations, it is critical to note that other anatomic arrangements are possible, and ventricles may be left-right inverted (ventricular inversion) and, rarely, may assume a superior-inferior relationship. Ventricular function may be qualitatively assessed in both a four-chamber transverse view and a short-axis view. Calculation of left ventricular shortening fraction (left ventricular end diastolic—systolic/end diastolic diameter) and ejection fraction (left ventricular end diastolic—systolic/end diastolic volume) is possible with meticulous attention to imaging technique and precise measurements.

### Atrioventricular and Semilunar Valves

The tricuspid and pulmonary valve annuli measure slightly larger than the mitral and aortic valves. Valves should be measured when they are maximally open: in diastole for the atrioventricular valves and systole for the semilunar valves. Significant size discrepancy between the two semilunar and/or atrioventricular valves should prompt careful evaluation for CHD.[13] The mitral valve should be supported by two well-spaced ventricular papillary muscles easily

## Abstract:

Congenital abnormalities of the heart are common, occurring in approximately 8 of every 1000 newborns, and approximately 25% of those in whom an abnormality is identified have critical congenital heart disease (CHD) with risk for significant perinatal compromise or death. With appropriate technique, fetal echocardiography may reveal virtually all in-utero cardiovascular abnormalities, including congenital and acquired fetal heart disease and arrhythmias. Accurate and timely diagnosis affords the opportunity to guide in-utero therapy and planning for the perinatal period. This chapter reviews indications for fetal echocardiography, imaging technique, and several cardiovascular abnormalities.

## Keywords:

prenatal cardiac assessment
fetal echocardiography
fetal heart
fetal arrhythmia
congenital heart disease

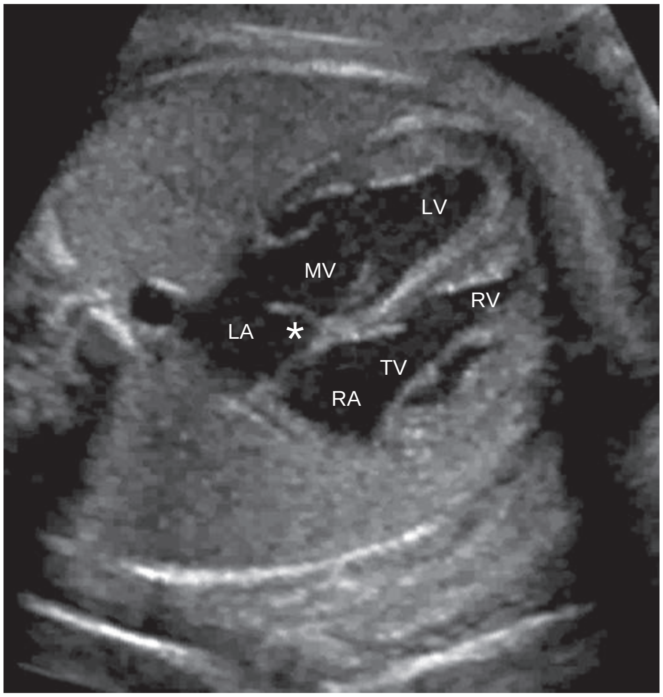

**Figure 70.1. Normal atrial and ventricular morphology on four-chamber view.** *LA,* Left atrium; *LV,* left ventricle; *MV,* mitral valve; *RA,* right atrium; *RV,* right ventricle; *TV,* tricuspid valve; * denotes septum primum. The systemic venous connections and atrial appendages are not visible in this projection.

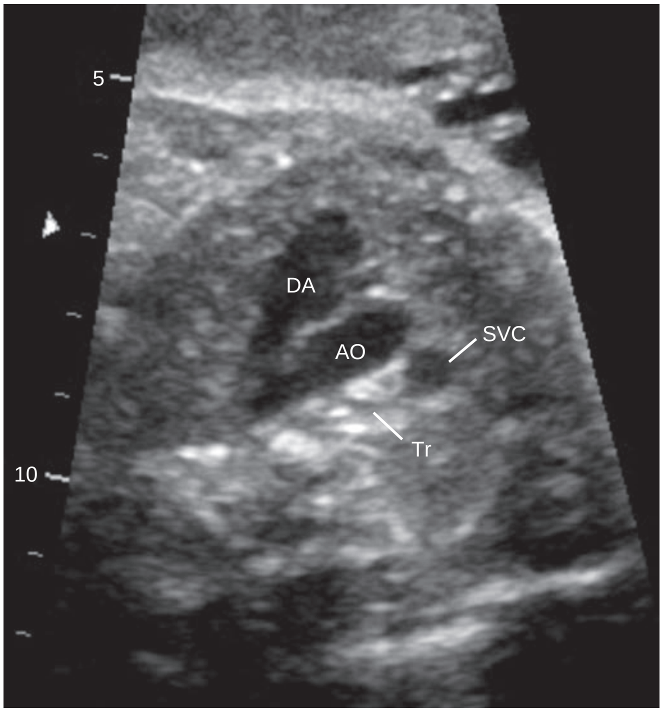

**Figure 70.2. Normal three-vessel trachea view.** The aorta and ductus arteriosus course away from the right-sided superior vena cava and to the left of the trachea. *Ao,* Aorta; *DA,* ductus arteriosus; *SVC,* superior vena cava; *Tr,* trachea.

identifiable on short-axis imaging. Color Doppler should readily identify any atrioventricular or semilunar valve regurgitation. Pulsed-wave Doppler assessment of all valves should be performed. Both atrioventricular valves should have biphasic flow patterns, and both semilunar valves should have a brisk upstroke with a narrow spectrum of normal velocities and no aliasing or increased velocity to suggest stenosis.

## Aorta, Pulmonary Artery, and the Aortic and Ductal Arches

The relationship of the aorta and pulmonary outflow to the ventricles should be determined. The aorta and pulmonary artery arise from the left and right ventricles, respectively, and should cross over one another. Any relationship where the great vessels do not cross should prompt consideration of transposed great arteries and significant CHD.

The aortic arch, main and branch pulmonary arteries, and ductal arch should be assessed in multiple planes. In addition to the sagittal view, where the entirety of the aortic and ductal arches can be assessed, the three-vessel trachea view is particularly useful in assessing location, size, and flow pattern of the aortic and ductal arches.[14] Arch sidedness can be determined from the three-vessel view; the usual arrangement being the aorta and ductus arteriosus coursing to the left as they pass in front of the trachea (Fig. 70.2). Additionally, the three-vessel-trachea view is of particular utility in diagnosing aortic arch hypoplasia and/or ductus arteriosus abnormalities.

# PRENATAL IMAGING: TIMING AND INDICATIONS

The optimal period for transabdominal imaging is 20 to 28 weeks' gestation, although transabdominal imaging at earlier gestations ages has been reported.[15] Transvaginal transducers can be used to image the fetal heart as early as 8 weeks, with successful diagnosis of heart defects possible at 11 weeks.[16,17] Although some particularly nuanced anatomic features are not detectable with early scanning, identification of single ventricle CHD and significant outflow abnormalities is feasible. Third-trimester imaging is frequently limited by less amniotic fluid relative to the size of the fetus, and the diminished likelihood of significant changes in fetal position further restricts available imaging planes.

Indications for fetal echocardiography based on maternal or fetal risk factors are extensive and expanding (Box 70.1).[18] The most common reasons for referral are a family history of CHD, fetal arrhythmia, maternal diabetes, and extracardiac abnormalities. The indication most predictive of cardiac disease is an abnormal four-chamber view on routine obstetric ultrasound, underscoring the importance of high-quality obstetric screening. Fetal arrhythmia, hydrops, and polyhydramnios are also important predictors of CHD. Equally important is an understanding of indications for which fetal echocardiography is not recommended (Box 70.2); fetal echocardiography is a highly specialized examination and should be reserved for appropriate circumstances, as unnecessary fetal cardiac evaluations may generate family anxiety.[19]

# EVALUATION FOR SPECIFIC CARDIAC DEFECTS

## Septation Defects

### Atrial Septal Defects

Atrial septal defects are the second most common form of CHD; however, detection of most atrial septal defects during fetal life is challenging due to the presence of the normal fetal foramen ovale (see Chapter 72). The most common atrial septal defect, the somewhat confusingly named "secundum" type, is actually a deficiency in septum primum, the flap valve of the foramen ovale. As such, secundum defects are in close proximity to a normal and large fetal shunt, making prenatal detection virtually impossible.

### **BOX 70.1** Indications for Fetal Echocardiography

**INDICATIONS WITH HIGHER RISK PROFILE (ESTIMATED >2% ABSOLUTE RISK)**

- Maternal pregestational diabetes mellitus
- Diabetes mellitus diagnosed in the first trimester
- Maternal phenylketonuria (uncontrolled)
- Maternal autoantibodies (SSA/SSB+)
- Maternal medications
- ACE inhibitors
- Retinoic acid
- NSAIDs in third trimester
- Maternal first trimester rubella infection
- Maternal infection with suspicion of fetal myocarditis
- Assisted reproduction technology
- CHD in first degree relative of fetus (maternal, paternal, or sibling with CHD)
- First- or second-degree relative with disorder with Mendelian inheritance with CHD association
- Fetal cardiac abnormality suspected on obstetrical ultrasound
- Fetal extracardiac abnormality suspected on obstetrical ultrasound
- Fetal karyotype abnormality
- Fetal tachycardia or bradycardia, or frequent or persistent irregular heart rhythm
- Fetal increased nuchal thickness >95% (≥3 mm)
- Monochorionic twinning
- Fetal hydrops or effusions

**INDICATIONS WITH LOWER RISK PROFILE (ESTIMATED >1% BUT <2% ABSOLUTE RISK)**

- Maternal medications
    - Anticonvulsants
    - Lithium
    - Vitamin A
    - Selective serotonin reuptake inhibitors (only paroxetine)
    - NSAIDs in first/second trimester
- CHD in second-degree relative of fetus
- Fetal abnormality of the umbilical cord or placenta
- Fetal intraabdominal venous anomaly

### **BOX 70.2** Fetal Echocardiography Not Indicated (≤1% Risk)

- Maternal gestational diabetes mellitus with HbA1c <6%
- Maternal medications
    - Selective serotonin reuptake inhibitors (other than paroxetine)
    - Vitamin K agonists (Coumadin), although fetal survey is recommended
- Maternal infection other than rubella with seroconversion only
- Isolated CHD in a relative other than first or second degree

Similarly, superior and inferior type sinus venosus defects, which represent a deficiency in a wall shared between a pulmonary vein and either the superior or inferior vena cava, are difficult to detect. Coronary sinus septal defect, a deficiency in the wall of the coronary sinus, is also difficult to detect. Primum atrial septal defects, a form of endocardial cushion defect and one that is often associated with Down syndrome, may be more readily detectable (Fig. 70.3).

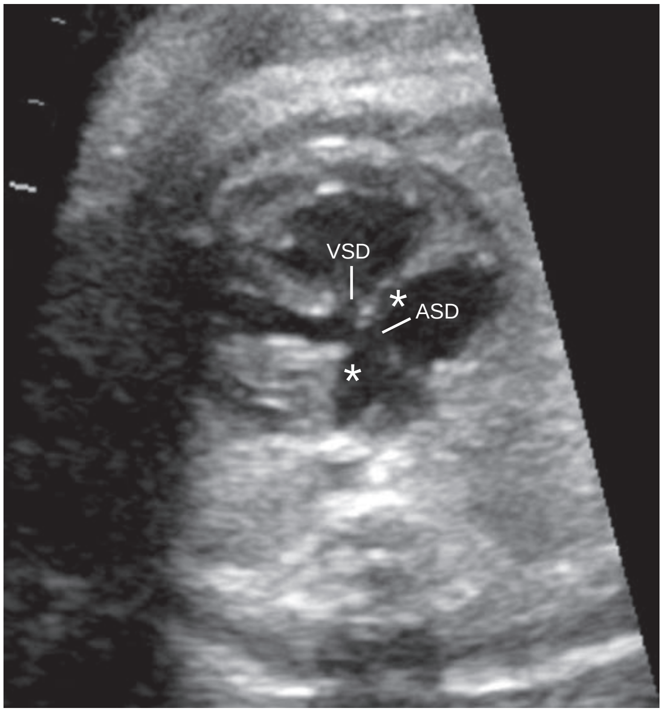

**Figure 70.3.** Balanced atrioventricular canal defect comprising a primum type atrial septal defect, an atrioventricular (inlet) type ventricular septal defect, and a common atrioventricular valve. *ASD,* Atrial septal defect; *VSD,* ventricular septal defect; * denotes common atrioventricular valve.

## Ventricular Septal Defects

Ventricular septal defects are the most common form of CHD. There are several nomenclature systems for describing their location. One relatively simple and effective way of grouping them is (1) perimembranous (or membranous), (2) atrioventricular (AV) canal (or inlet), (3) conoventricular (or outlet), and (4) muscular (see Chapter 72). Perimembranous defects are the most common but, due to the presence of the nearby tricuspid and aortic valves and their often being partially occluded with tricuspid valve tissue, they are relatively difficult to detect. AV canal type defects are posterior and located next to the atrioventricular valves. Conoventricular defects are generally readily visible with close attention to the ventriculoarterial junction and are often associated with other abnormalities (tetralogy of Fallot, truncus arteriosus). Muscular defects can be found anywhere in the muscular septum. Moderate to large defects require surgical intervention in infancy for patients with congestive heart failure, whereas small defects often close on their own. Conoventricular defects with or without other associated lesions frequently require surgical intervention in infancy.

Proper imaging technique for evaluation of the ventricular septum is essential. As some defects are more readily detectable by color Doppler, side-by-side two-dimensional and color Doppler imaging is often helpful. Sweeps through the septum in multiple planes, beginning at the level of the fetal stomach and continuing throughout the outflows are often helpful. Narrowed sector width, a color box over the region of interest, and a scale low enough to detect flow across the pressure-equalized fetal ventricles also facilitate detection (Fig. 70.4).

## Atrioventricular Canal Defects

Atrioventricular canal (endocardial cushion) defects comprise a spectrum of abnormalities. In their complete form, there is a primum type atrial septal defect, an atrioventricular canal type ventricular septal defect, and a common atrioventricular valve (see Chapter 72). Other forms of atrioventricular defects may include virtually any combination of the above noted defects. Repair for the complete form is required in infancy.

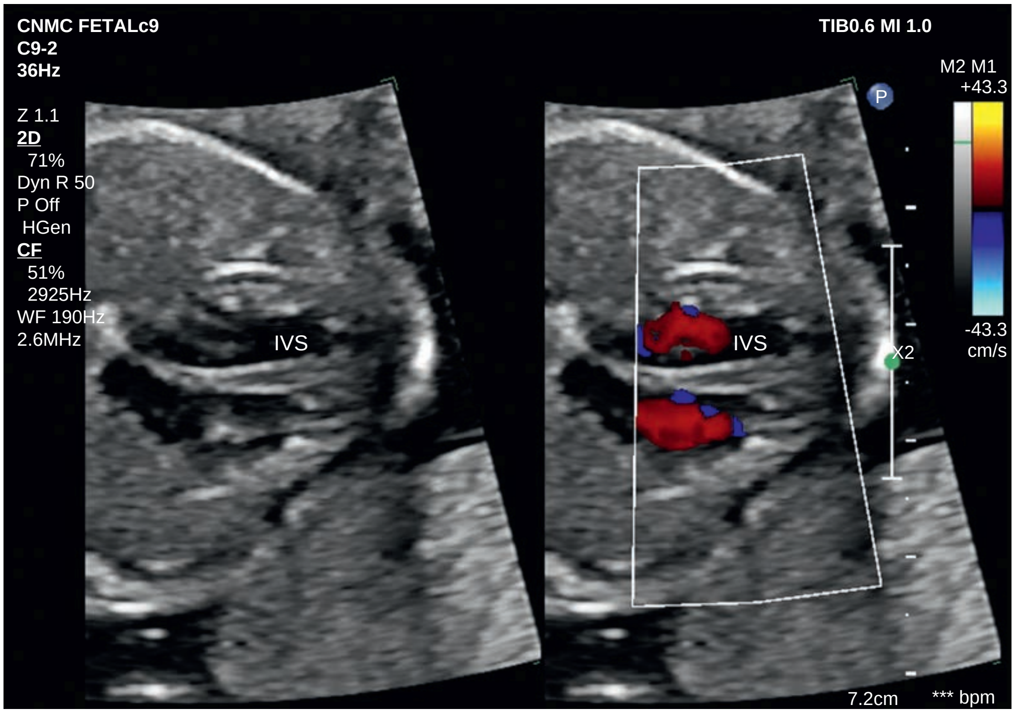

**Figure 70.4. Proper technique for imaging the ventricular septum.** The ventricular septum is perpendicular to the ultrasound beam, the *color scale* is relatively low, the *color box* covers the entire region of interest, and the frame rate is adequate (>30 Hz), all increasing the likelihood that abnormal flow across the ventricular septum will be detected. Imaging should be performed with sweeps in multiple planes. *IVS,* Interventricular septum.

## Inflow/Outflow Abnormalities

### Right-sided Inflow Lesions

Right-sided inflow lesions include abnormalities of the tricuspid valve and right ventricular development. These include Ebstein anomaly, tricuspid valve dysplasia, and tricuspid stenosis or atresia (see Chapter 74). In Ebstein anomaly, there is incomplete delamination of the septal leaflet of the tricuspid valve during development, resulting in poor leaflet coaptation and regurgitation (Fig. 70.5). There is a wide spectrum of outcomes of fetal Ebstein abnormality, ranging from in-utero hydrops and fetal demise to those requiring no intervention.[20] The distinction between tricuspid valve dysplasia and Ebstein anomaly is somewhat academic, but the term tricuspid valve dysplasia typically refers to incomplete delamination but with maintenance of the usual annular level and perhaps more functional myocardium, whereas in Ebstein anomaly, the valve annulus is displaced apically into the ventricle.

Tricuspid atresia or stenosis can be associated with hypoplasia of the right ventricle and pulmonary outflow obstruction. Tricuspid atresia may be associated with ductal-dependent systemic or pulmonary blood flow requiring prostaglandin, depending on whether a ventricular septal defect is present and the relationship of the great arteries. In all cases of tricuspid atresia, single-ventricle palliation is required.

### Right-sided Outflow Lesions

Pulmonary outflow obstruction can be subvalvar, valvar, or supravalvar (see Chapter 74). The disease spectrum ranges from newborns with severe cyanosis and single ventricle CHD to infants with normal oxygen saturation and a near normal pulmonary outflow tract. Isolated pulmonary valve stenosis is diagnosed by

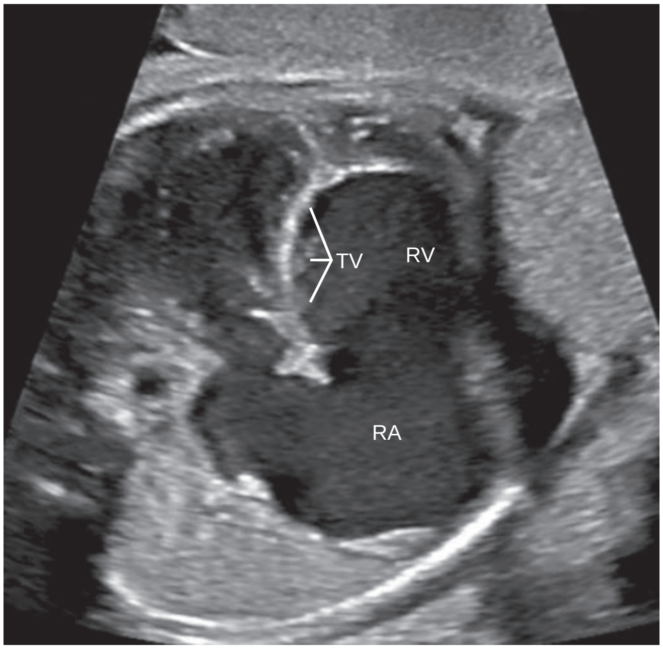

**Figure 70.5. Ebstein anomaly of the tricuspid valve.** The septal leaflet of the tricuspid valve is apically displaced with multiple tethering attachments to the ventricular septum, resulting in tricuspid insufficiency and right atrial and ventricular enlargement. *RA,* Right atrium; *RV,* right ventricle; *TV,* tricuspid valve.

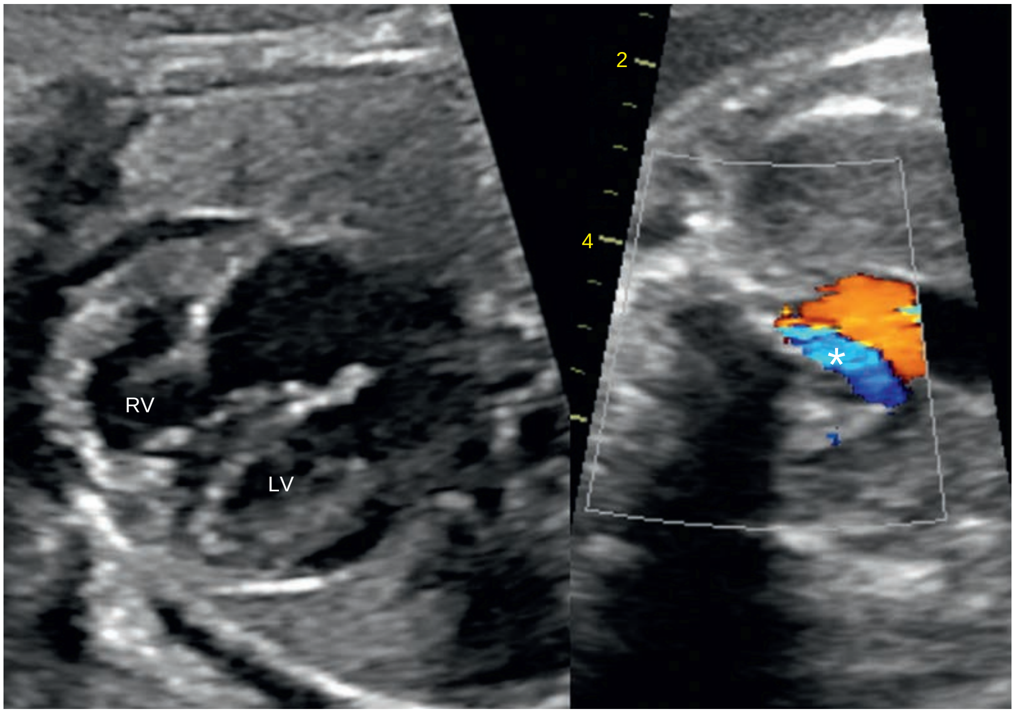

**Figure 70.6. Fetus with coarctation of the aorta.** There is significant ventricular size discrepancy, with the tricuspid valve and right ventricle larger than the mitral valve and left ventricle. Color Doppler imaging in the three-vessel trachea view demonstrates a narrow and retrograde jet of flow in the transverse aortic arch. *LV,* Left ventricle; *RV*, right ventricle, * on color Doppler image denotes retrograde transverse aortic arch flow.

identifying doming and thickened pulmonary valve leaflets, but this lesion can be very difficult to diagnose in utero due to the normally high fetal pulmonary vascular resistance. Supravalvar and branch pulmonary artery stenosis is difficult to detect in utero, but when recognized in the absence of a conotruncal defect, the possibility of Williams syndrome should be entertained. Subvalvar obstruction is usually seen in combination with other defects, such as tetralogy of Fallot, discussed later.

### Left-sided Inflow Lesions

Left ventricular inflow abnormalities include cor triatriatum, congenital mitral stenosis, and congenital mitral insufficiency (see Chapter 73). Cor triatriatum implies incomplete incorporation of the pulmonary veins into the posterior aspect of the left atrium and is rarely detected in utero. Congenital mitral valve anomalies may occur in isolation or in combination with left ventricle, aortic valve, and aortic arch abnormalities, an association sometimes referred to as Shone syndrome.[21] A mitral valve abnormality should be suspected when there is a small mitral valve annulus, an abnormal subvalvar apparatus, or mitral regurgitation.

### Left-sided Outflow Lesions

Left sided outflow tract obstruction can occur at the subvalvar, valvar, or supravalvar level (see Chapter 73). Infants of diabetic mothers, especially mothers with poor glucose control, are at risk for hypertrophic cardiomyopathy, with or without significant obstruction.[22] Even in severe cases, the hypertrophy usually regresses by 3 months of age. Valvar aortic stenosis, identified by a thick and doming aortic valve and increased flow velocity across the valve, can be seen in utero and can be associated with left ventricular dysfunction and progressive hypoplasia.

Coarctation of the aorta can be particularly difficult to diagnosis in utero, as imaging of the fetal aortic arch is often limited. Suspicion for coarctation should be raised in the presence of right-left size discrepancy, including a significantly larger tricuspid or pulmonary valve when compared with the mitral or aortic valves, respectively. Aortic isthmus hypoplasia, antegrade diastolic flow in the transverse aortic arch, or retrograde flow in the transverse aortic arch are also important indicators of fetal coarctation (Fig. 70.6). Importantly, any left-sided obstructive lesions in the presence of a female fetus should prompt consideration of Turner syndrome.[23]

## Conotruncal Defects

Conotruncal defects comprise a wide spectrum of abnormalities involving the connection between the ventricles and great arteries (see Chapter 75). Together these lesions comprise a large percentage of significant CHD, some of which are lethal if not detected promptly after birth and underscore the importance of careful interrogation of the outflow tracts on screening cardiac ultrasound. Lesions in this group include transposition of the great arteries (TGA), tetralogy of Fallot, truncus arteriosus, interrupted aortic arch, and double outlet right ventricle; a common unifying factor is typically a conoventricular (outlet) septal defect. With the exception of TGA, any conotruncal defect should raise suspicion for chromosome 22q11 microdeletion (DiGeorge syndrome), a possibility that should be incorporated into prenatal counseling.[24]

Tetralogy of Fallot is the most common form of cyanotic CHD and represents a failure of the conal septum to align properly with the remainder of the ventricular septum. This single embryologic aberration is responsible for the other typical findings, including an overriding aorta, subpulmonary and valvar pulmonary stenosis, and right ventricular hypertrophy (Fig. 70.7).

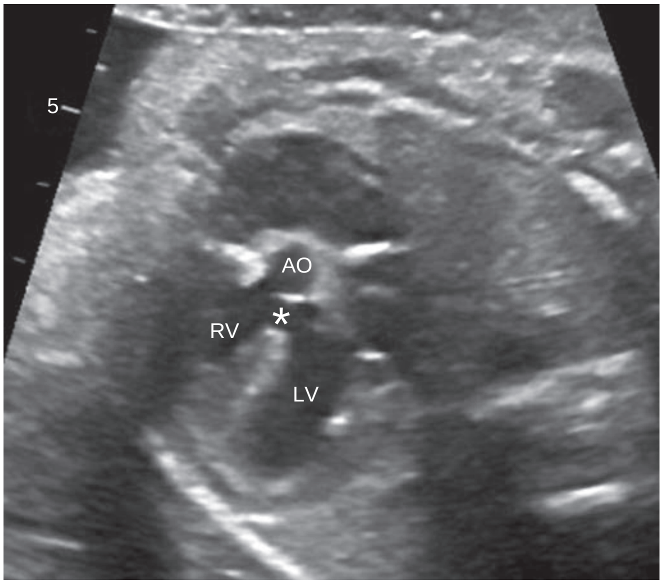

**Figure 70.7. Tetralogy of fallot.** Typical appearance of tetralogy of Fallot and many other conotruncal defects. There is a conoventricular septal defect and an over-riding semilunar valve. *AO,* Aorta; *RV,* right ventricle; *LV,* Left ventricle; * denotes ventricular septal defect.

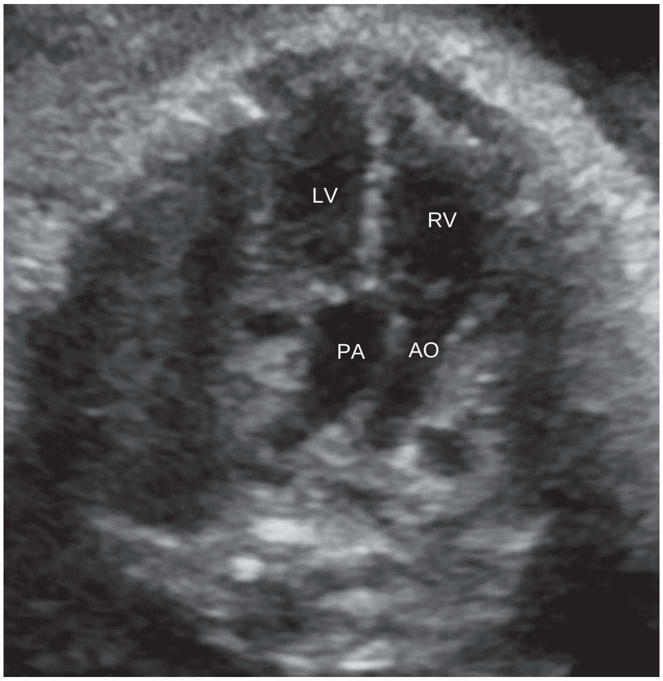

**Figure 70.8. Transposition of the great arteries.** The main pulmonary artery arises from the left ventricle and bifurcates. The aorta arises from the right ventricle. The great vessels appear parallel as they arise from the ventricles. *AO,* Aorta; *LV,* left ventricle; *PA,* pulmonary artery; *RV,* right ventricle.

TGA is the second most common form of cyanotic CHD. In TGA the aorta originates from the right ventricle, and the pulmonary artery arises from the left ventricle. Echocardiography shows parallel great vessels with the aorta located anterior and rightward of the pulmonary artery. The bifurcation of the pulmonary artery can by readily identified as it arises from the left ventricle (Fig. 70.8). Additional abnormalities, such as ventricular septal defects, multilevel pulmonary stenosis, or coarctation of the aorta, may also be identified. It is critically important to recognize that the four-chamber view is normal in TGA, as it is in most conotruncal defects, again underscoring the importance of outflow tract views.

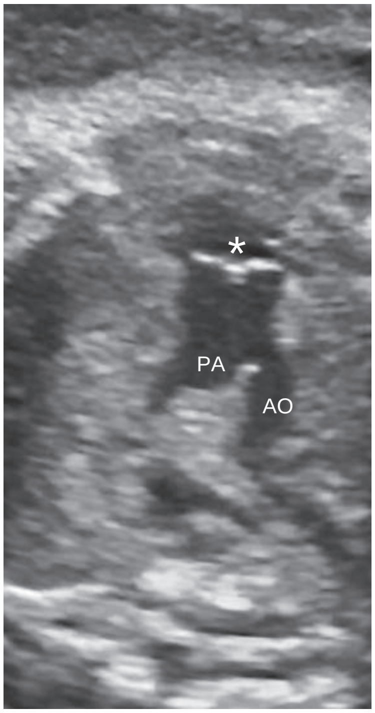

**Figure 70.9. Truncus arteriosus.** This view demonstrates the truncal valve, which gives rise to a vessel that bifurcates into a pulmonary vessel and an aortic vessel. *AO,* Aorta; *PA,* pulmonary artery; * denotes the truncal valve.

In truncus arteriosus, a single outflow tract originates from the heart and bifurcates into aortic and pulmonary branches; there is usually an associated conoventricular septal defect (Fig. 70.9). The truncal (outflow) valve is often abnormal, with significant stenosis or insufficiency possible.

## Ventricular Hypoplasia

Significant underdevelopment of either ventricle can result in single-ventricle CHD, broadly referred to as hypoplastic right or left heart syndromes (HRHS or HLHS) (Fig. 70.10 and Chapter 75). Single-ventricle CHD is usually recognizable on transverse (four-chamber) views of the fetal heart. After birth, patients require staged surgical palliation ultimately resulting in a Fontan-type circulation, wherein the systemic venous blood is rerouted directly into the pulmonary arteries, and the single functional ventricle ejects exclusively into the systemic circulation.

Hypoplastic right heart syndrome can result from tricuspid atresia or pulmonary atresia with an intact ventricular septum (see Chapter 74). Hypoplastic left heart syndrome may have severe aortic and mitral stenosis or atresia and requires complex surgery (Norwood palliation) in the newborn period. While single-ventricle abnormalities represent significant and severe forms of CHD, it is important to recognize that outcomes for infants diagnosed with single-ventricle CHD continue to improve as therapies evolve. Many infants survive well into adulthood with an excellent quality of life.

## Systemic and Pulmonary Venous Abnormalities

Abnormalities of the systemic and pulmonary veins comprise a vast array of entities (see Chapter 71). In isolation, systemic venous

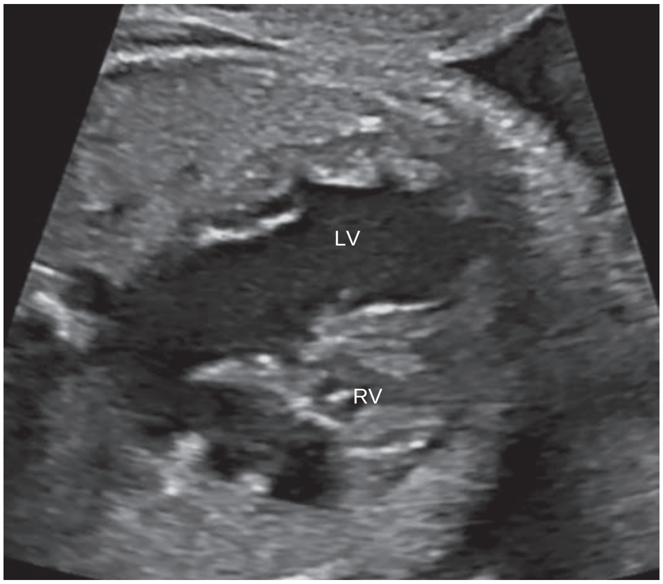

**Figure 70.10. Hypoplastic right heart syndrome (pulmonary atresia with intact ventricular septum).** The right ventricle has severely diminished intracavity volume and is not capable of sustaining the pulmonary circulation. *LV,* Left ventricle; *RV,* right ventricle.

abnormalities often have no clinical consequences, although their presence should prompt a thorough investigation for associated defects. Bilateral superior vena cavae, including persistent left superior vena cava into the coronary sinus is one such common normal variant with no clinical consequence. This should be suspected when there is an abnormal "extra" vessel in the three-vessel trachea view and a dilated coronary sinus. It can also readily be visualized in a short-axis view (e-Fig. 70.11). Postnatal imaging is warranted, however, to evaluate for any subtle abnormalities such as coronary sinus septal defect or bicuspid aortic valve.

Abnormalities of pulmonary veins are often difficult to detect prenatally due to the relatively small amount of flow, approximately 10% of the cardiac output, coursing to the lungs in utero. Usually, two left and two right pulmonary veins connect to the left atrium. Fetal echocardiographic imaging is considered sufficient when one right and one left pulmonary vein is visualized connecting normally to the left atrium with a normal pulsed-wave Doppler pattern (Fig. 70.12). Some or all of the pulmonary veins can drain anomalously to the systemic circulation, called partial or total anomalous pulmonary venous connection (PAPVC or TAPVC), respectively. While PAPVC is difficult to diagnose prenatally, TAPVC should be identifiable with proper technique. Multiple sonographic signs have been identified suggesting TAPVC including a "bald" left atrium, a "twig" sign, and increased left atrium to descending aorta distance (e-Fig. 70.13). In addition, abnormalities in pulmonary venous Doppler have been shown to be diagnostic for abnormal pulmonary venous connection.[25] Although most forms of TAPVC are not associated with perinatal compromise, the infradiaphragmatic form is associated with obstruction to pulmonary venous egress, low cardiac output, and severe perinatal compromise.

## AORTIC ARCH ANOMALIES

Abnormalities of the aortic arch (apart from coarctation of the aorta, discussed earlier) include the relatively benign and normal variant of right aortic arch with mirror image branching but also include vascular rings, including double aortic arch, which can cause aerodigestive difficulties in infancy and childhood (see Chapter 76). Detection of these abnormalities is most readily achieved by utilizing the three-vessel trachea view (Fig. 70.14).

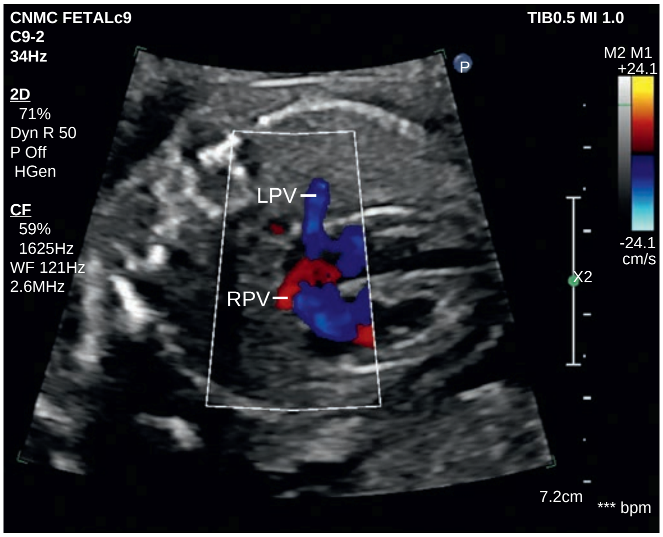

**Figure 70.12. Proper technique for imaging the pulmonary veins.** The pulmonary veins are most easily imaged in a transverse (four-chamber) view of the heart. A relatively narrow color box is placed over the left atrium, and the color scale is decreased. One right and one left pulmonary vein are clearly identified connecting to the left atrium. Pulsed-wave Doppler interrogation should follow. *LPV,* Left pulmonary vein; *RPV,* right pulmonary vein.

Delineation between right aortic arch and double aortic arch in utero, while possible, may be difficult due to the presence of the fetal ductus arteriosus. Nevertheless, detection of a right aortic arch should raise suspicion for a vascular ring and should prompt evaluation with postnatal echocardiogram and possibly cardiovascular magnetic resonance imaging or computed tomography to accurately assess the aortic arch and related structures. Perhaps most importantly, abnormalities of arch sidedness, including when found in isolation, can be associated with chromosome 22q11 microdeletion syndrome (DiGeorge syndrome).[26] Therefore family counseling as well as prenatal and/or postnatal genetic testing should strongly be considered when such an abnormality is detected.

The patent ductus arteriosus is a normal fetal structure; its premature closure can lead to right-sided heart failure in utero. Indomethacin and other nonsteroidal anti-inflammatory drugs predispose to this condition. Another rare abnormality is aneurysm of the ductus arteriosus in utero. In both cases, the heart typically normalizes at delivery, although postnatal evaluation is warranted.[27,28]

### Heterotaxy Syndrome

Heterotaxy syndrome comprises a broad spectrum of abnormalities, the underlying abnormality of which is derangement of the usual laterality of thoracic and abdominal organs.[29] Although often quite complex, the CHD in heterotaxy syndrome is readily delineated with the usual structured fetal echocardiographic examination with meticulous attention to systemic and pulmonary venous abnormalities, atrial and ventricular morphology, and outflow tracts. While often classified into asplenia (bilateral "right-sidedness") or polysplenia (bilateral "left-sidedness") subtypes to accompany the presence or absence of an identifiable spleen, this designation is of limited clinical utility as both subtypes may have splenic dysfunction. More important is the correct identification of the CHD and appropriate subspecialty consultations before and after birth (Fig. 70.15). Of note, polysplenia subtypes may be associated with heart block, which can affect prenatal and perinatal outcomes.[30]

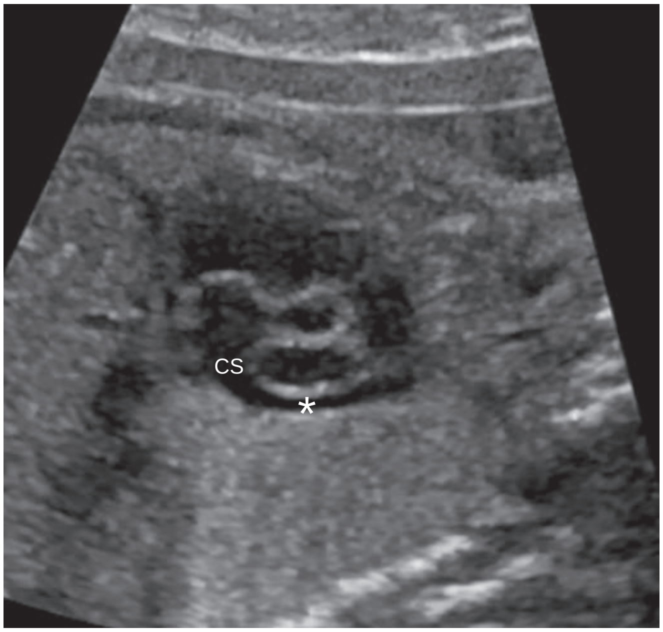

**e-Figure 70.11.** Left superior vena cava to coronary sinus. *CS,* Coronary sinus; * denotes left superior vena cava.

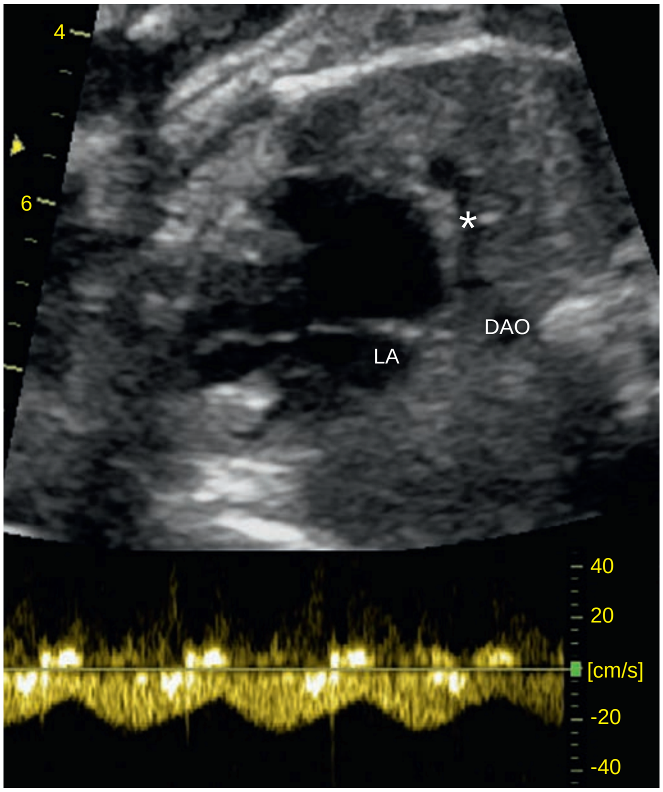

**e-Figure 70.13. Sonographic signs consistent with total anomalous pulmonary venous connection.** The left atrium is "bald" (no pulmonary venous connection), there is increased left atrium-to-descending aorta distance, and there is a "twig" sign, indicating the presence of a pulmonary venous confluence posterior to the left atrium. There is an abnormal pulmonary venous spectral Doppler pattern with a monophasic pulsatile pattern. *DAO,* Descending aorta; *LA,* left atrium; * denotes "twig" sign (pulmonary venous confluence).

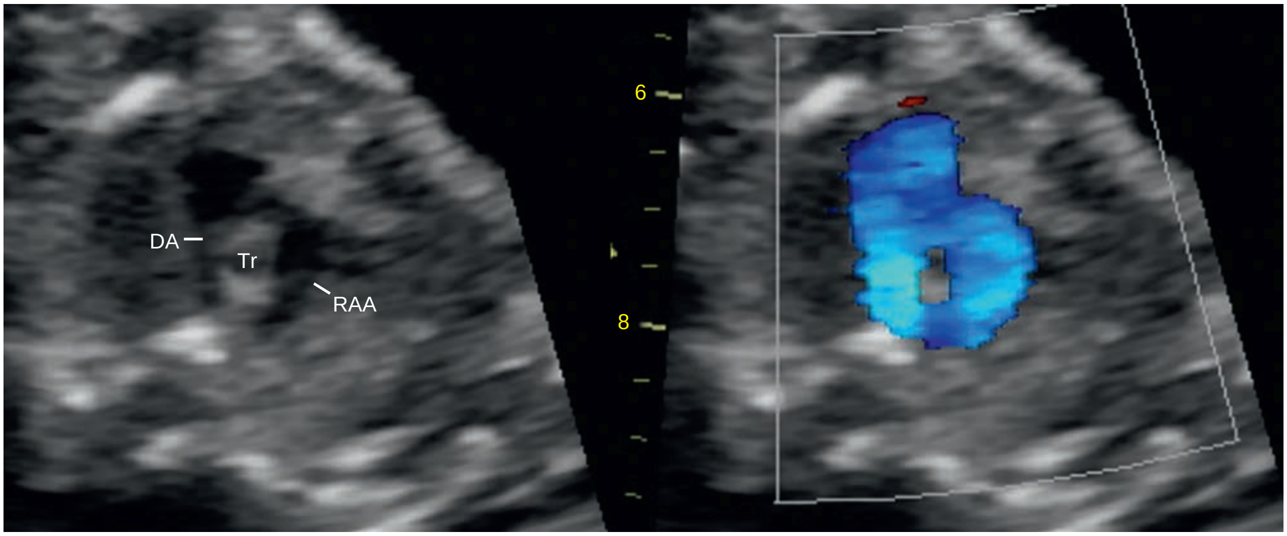

**Figure 70.14. Right aortic arch.** The right aortic arch courses to the right of the trachea, whereas the ductus arteriosus courses to the left of the trachea. Similar findings are likely in the presence of a double aortic arch. *DA,* Ductus arteriosus; *RAA,* right aortic arch; *Tr,* trachea.

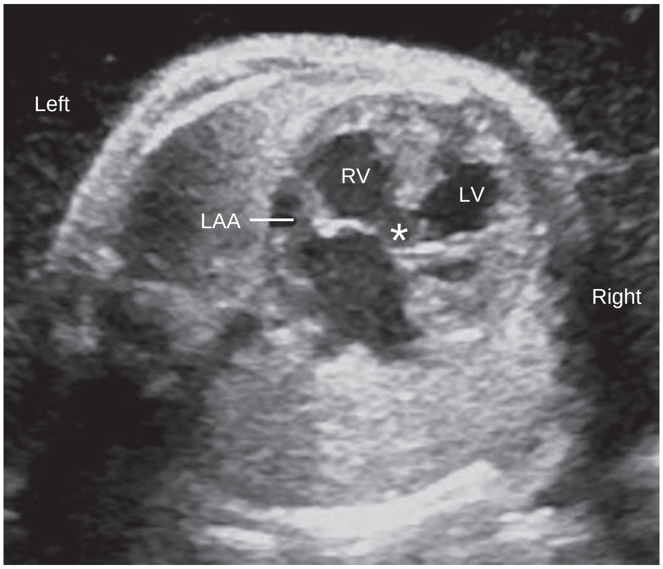

**Figure 70.15. Heterotaxy.** Fetal left and right are labeled. Ventricular inversion is present. There is a balanced atrioventricular canal defect. Bilateral left atrial appendages are present, consistent with polysplenia. *LAA,* Left atrial appendage, *LV*, left ventricle; *RV,* right ventricle; * denotes atrioventricular canal defect.

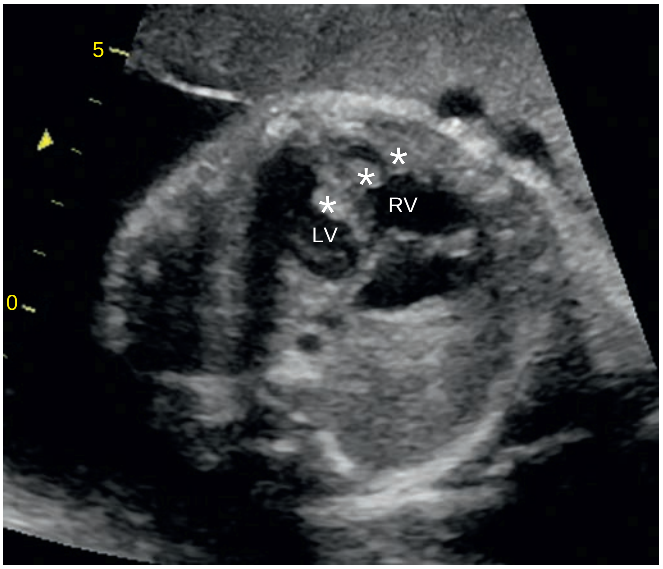

**Figure 70.16. Rhabdomyoma.** Multiple cardiac masses (*) are seen within the right and left ventricular myocardium consistent with rhabdomyomas. Genetic testing revealed the presence of tuberous sclerosis. *LV,* Left ventricle; *RV,* right ventricle.

## Cardiac Masses

Echogenic foci associated with the mitral valve chordae and papillary muscles are frequently noted on fetal heart imaging and are of no clinical consequence. Their presence is benign and does not require additional follow-up.[31] Larger or more numerous masses, particularly those found adherent to the atrial wall or embedded in the ventricular myocardium, suggest the presence of cardiac tumors. The most common prenatally identified cardiac tumors are rhabdomyomas (Fig. 70.16 and Chapter 80). These tumors are typically benign and regress in childhood, although they can rarely cause obstruction to inflow or outflow. While the tumors regress, it is important to note that rhabdomyomas have a strong association with tuberous sclerosis.[32,33]

## FETAL ARRHYTHMIAS

Echocardiography can provide accurate diagnosis of fetal arrhythmias.[34,35] Premature atrial contractions (e-Fig. 70.17) are common and usually benign. Supraventricular tachycardia comprises a spectrum of heart rhythm abnormalities, including inappropriate sinus tachycardia, reentrant accessory pathway-mediated tachycardias, atrial flutter and fibrillation, or ectopic atrial tachycardia. M-mode and pulsed-wave Doppler imaging is particularly useful in identifying these arrhythmias (e-Fig. 70.18). Ventricular tachycardia, while less common, can be a sign of fetal compromise or inherited arrhythmia, such as long QT syndrome.

Fetal bradycardia may be benign and is often caused by blocked premature atrial contractions. Complete heart block, a rare

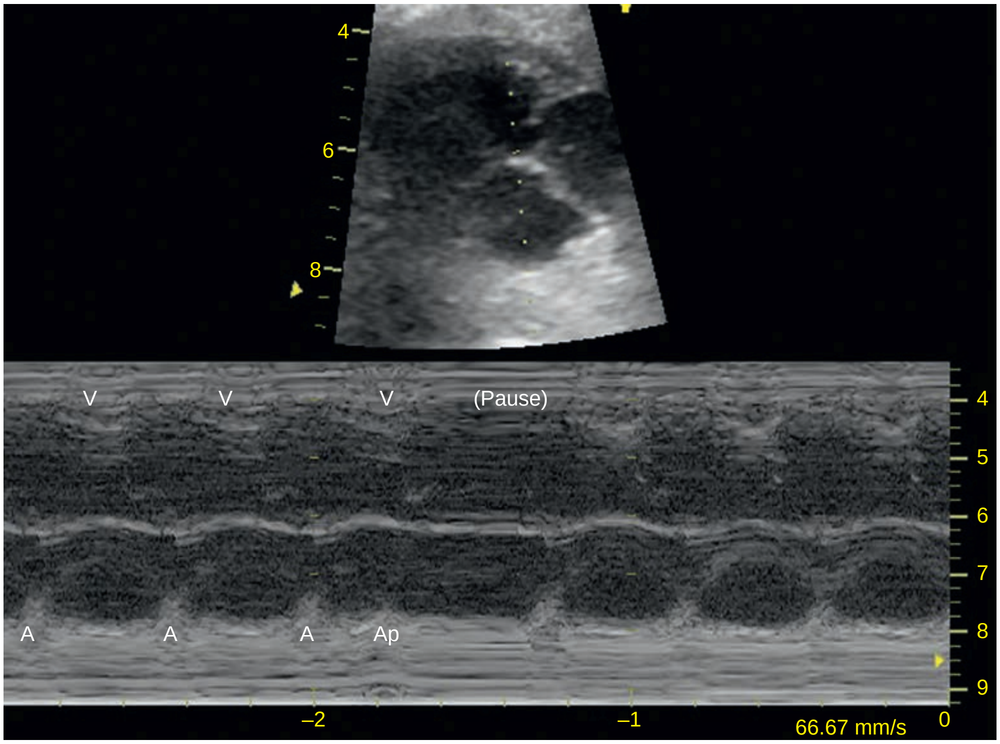

**e-Figure 70.17. Premature atrial contractions as detected by M-mode interrogation.** Three sinus beats are followed by a premature atrial contraction, which is not conducted to the ventricles, resulting in a compensatory pause. *A,* Atrial contractions; *Ap,* premature atrial contraction; *V,* ventricular contraction.

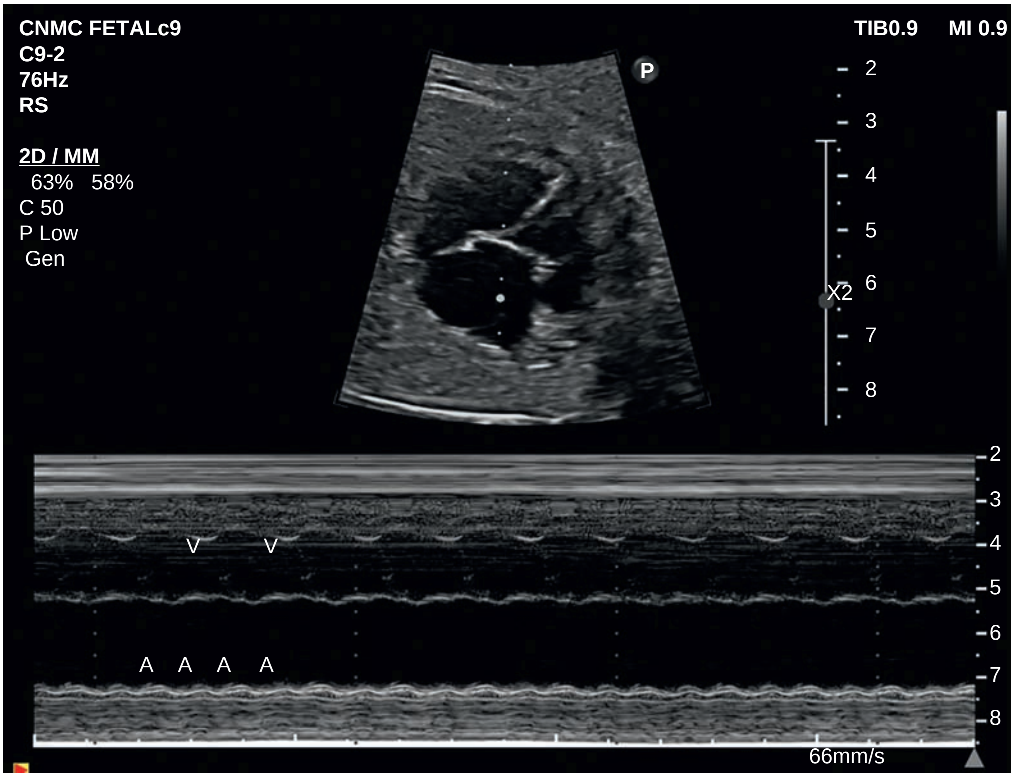

**e-Figure 70.18. Atrial flutter with 2 : 1 atrial to ventricular conduction.** For every two atrial contractions, there is one ventricular contraction. The atrial rate is approximately 440 beats per minute, and the ventricular rate is approximately 220 beats per minute. *A,* Atrial contractions; *V,* ventricular contractions.

complication of fetal exposure to maternal SSA autoantibodies,[36] can be diagnosed by M-mode or pulsed-wave Doppler (e-Fig. 70.19). Serial Doppler assessment of the time between atrial and ventricular contraction is used in maternal SSA antibody carriers to follow the fetal conduction system (e-Fig. 70.20).[37] Sinus bradycardia is also important and may be associated with maternal medication administration (beta-blocker) or possibly an inherited or de-novo genetic predisposition to arrhythmia (long QT syndrome).

## MANAGEMENT OF FETAL CARDIAC DISEASE

### Delivery Planning for Fetuses With Heart Disease

Fetal echocardiography is an exceptionally useful tool for informing families and planning for the delivery of a fetus with a cardiovascular abnormality. Somewhat reassuringly, most forms of structural CHD do not progress in utero and, with thoughtful management, the fetus with heart disease may deliver safely at term in a controlled fashion, even in the presence of ductal-dependent CHD. Some lesions, such as TGA or HLHS with restrictive or intact atrial septum, TAPVC with obstruction, or complete heart block, may merit additional resources in the delivery room and/or highly specialized delivery planning involving multiple subspecialists. Many centers utilize an acuity-level-based system for assessing and planning for the delivery of infants with congenital abnormalities, an approach that has been shown to be both accurate and effective (e-Table 70.1).[18,38]

### Treatment of Fetal Arrhythmias

Fetal arrhythmias in which there is potential for or evidence of compromise are amenable to in utero treatment. Persistent arrhythmias can result in cardiac dysfunction and hydrops if left untreated. Maternal administration of digoxin or flecainide is often successful as a first-line drug in fetuses with many forms of supraventricular tachycardia, although some reports suggest sotalol may be preferable in the treatment of atrial flutter.[39,40] Multidrug therapy or other agents such as amiodarone can be used in refractory cases. Close monitoring of the mother for drug toxicity and the fetus for arrhythmia control is mandatory, and initiation of drug therapy may necessitate hospitalization. Complete heart block is difficult to manage if the rate is low or if there is associated cardiac dysfunction. Screening of a mother with SSA antibodies beginning at approximately 16 weeks is recommended, and if heart block is identified, prompt maternal steroid administration and in some instances intravenous immune globin have been used with some success; however, early delivery if feasible and pacemaker placement may be required if hydrops and fetal compromise is present.

## FETAL INTERVENTIONS FOR STRUCTURAL HEART DISEASE

As previously noted, most CHD changes little throughout gestation. Rarely, however, some lesions progress throughout gestation and may be amenable to percutaneous in-utero intervention. Specifically, fetuses with aortic or pulmonary valve stenosis identified early in the second trimester may have progressive right- or left-heart hypoplasia, ultimately resulting in single-ventricle CHD. For a highly select group of patients, fetal catheter-based intervention to relieve aortic stenosis or pulmonary atresia/stenosis can be considered (Fig. 70.21).[41] The most robust experience with percutaneous fetal cardiac intervention has been for aortic stenosis with evolving HLHS. There is evidence to suggest that progression of left ventricular hypoplasia can be interrupted with appropriately timed intervention in well-selected patients. Among the first 100 patients undergoing fetal aortic valvuloplasty for evolving HLHS, 38 were able to achieve a biventricular circulation, although virtually all patients required multiple catheter-based and/or surgical interventions for left-sided heart disease.[42] Results have also been reported for intervention on HLHS with intact or restrictive atrial septum, pulmonary atresia with intact ventricular septum with evolving HRHS, and dysplastic mitral valve complex.[43,44] Fetal cardiac intervention requires a highly specialized center with multiple care providers for the fetus and mother as well as a thorough understanding of the risks and benefits of such procedures.

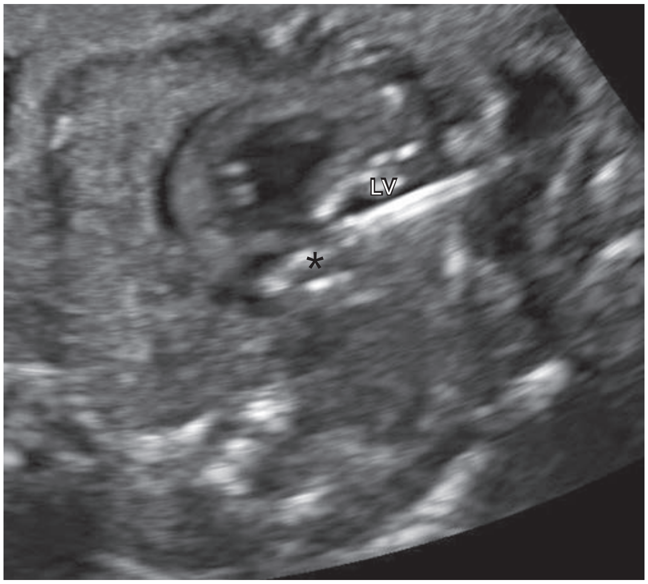

**Figure 70.21. Fetal cardiac intervention for aortic stenosis with evolving hypoplastic left heart syndrome.** Under sonographic guidance, a coronary angioplasty balloon is guided through the maternal abdomen, fetal thoracic wall, and left ventricular myocardium and advanced into the stenotic aortic valve and inflated, relieving aortic stenosis. *LV,* Left ventricle; * denotes coronary angioplasty balloon.

## LIMITATIONS OF FETAL ECHOCARDIOGRAPHY

Fetal echocardiography is a highly sensitive and specific diagnostic test; nevertheless, it is important for providers and families that its limitations be well understood. Due to the presence of the foramen ovale, most atrial septal defects are virtually undetectable in the fetal heart. Similarly, subtle abnormalities of pulmonary venous connections, such as PAPVC, are extremely difficult to detect in the fetus. While large ventricular septal defects, particularly in the conotruncal region, should be readily detectable, more subtle perimembranous and muscular ventricular septal defects are difficult or impossible to detect. Similarly, isolated coarctation of the aorta can be difficult to detect given the presence of the fetal ductus arteriosus. Despite these limitations, prenatal detection of significant or critical CHD likely to affect the newborn or young infant is virtually always possible. This realistic framing of the capabilities and limitations of fetal echocardiography will help families understand the results of their diagnostic testing.

## CONCLUSION

Fetal echocardiography is used as an adjunct to other prenatal evaluations, including radiology, genetics, high-risk perinatology, and subspecialty services, to provide a multidisciplinary treatment and counseling approach for fetuses with cardiovascular disease. Detection of most forms of CHD is possible, allowing delivery planning to optimize outcomes. Therapies are available for many arrhythmias, and prenatal intervention is possible for a select group of structural abnormalities.

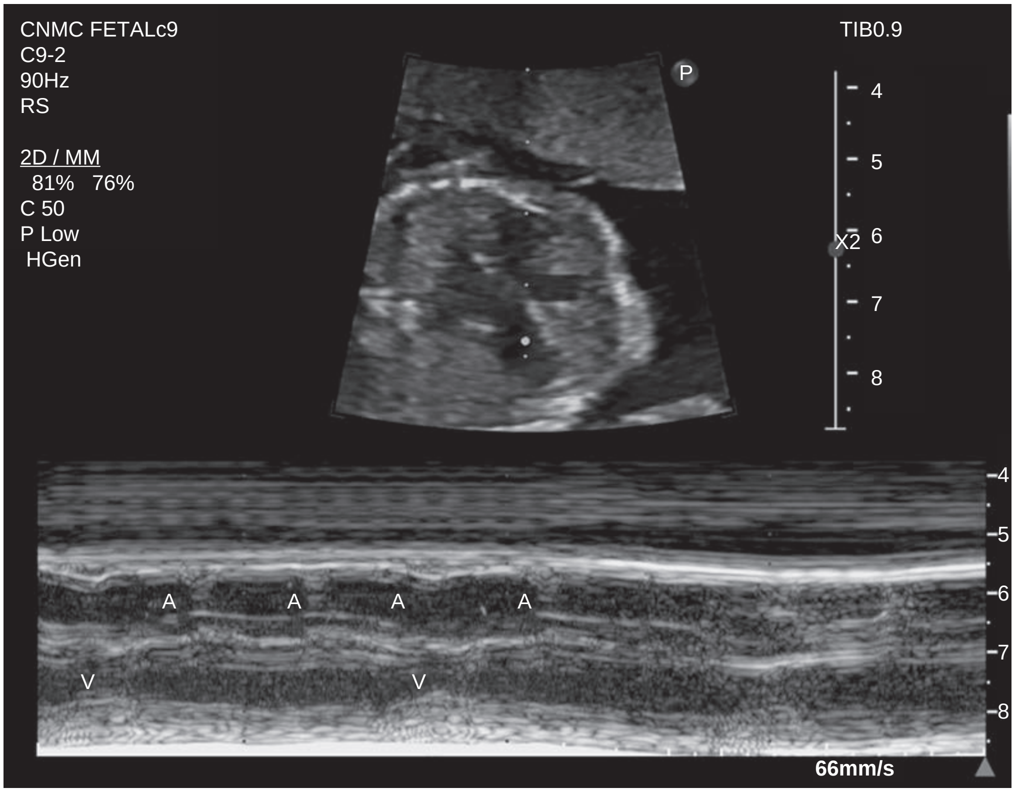

**e-Figure 70.19. Complete heart block.** There is complete dissociation between atrial and ventricular activity. The atrial rate is approximately 130 beats per minute, and the ventricular rate is approximately 50 beats per minute. *A,* Atrial contractions; *V,* ventricular contractions.

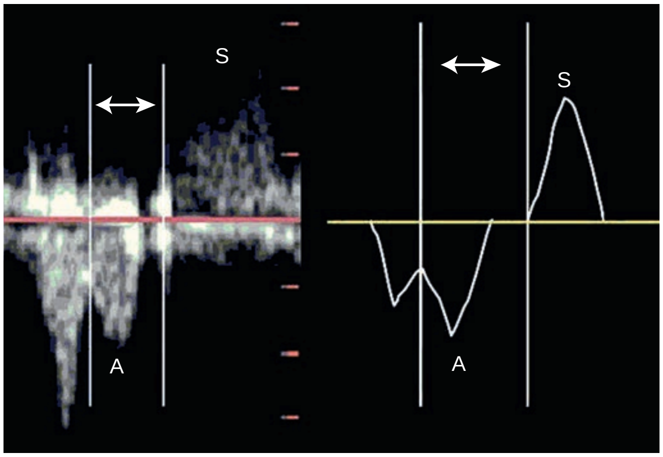

**e-Figure 70.20. Mechanical atrioventricular ("PR") interval.** The interval is calculated by determining the time between atrial systole (the mitral a wave) and ventricular systole, typically delineated by the aortic outflow Doppler. *A,* Atrial systole; *S,* ventricular systole.

**e-TABLE 70.1** Level of Care Assignment and Coordinating Action Plan

| Loc | Definition | Example CHD | Delivery Recommendations | DR Recommendations |
|---|---|---|---|---|
| P | CHD in which palliative care is planned | CHD with severe/fatal chromosome abnormality or multisystem disease | Arrange for family support/ palliative care services<br>Normal delivery at local hospital | |
| 1 | CHD without predicted risk of hemodynamic instability in the DR or first days of life | VSD, AVSD, mild TOF | Arrange cardiology consultation or outpatient evaluation<br>Normal delivery at local hospital | Routine DR care<br>Neonatal evaluation |
| 2 | CHD with minimal risk of hemodynamic instability in DR but requiring postnatal catheterization/surgery | Ductal-dependent lesions, including HLHS, critical coarctation, severe AS, IAA, PA/IVS, severe TOF | Consider planned induction usually near term<br>Delivery at hospital with neonatologist and accessible cardiology consultation | Neonatalogist in DR<br>Routine DR care, initiate PGE if indicated<br>Transport for catheterization/ surgery |
| 3 | CHD with likely hemodynamic instability in DR requiring immediate specialty care for stabilization | d-TGA with concerning atrial septum primum (note: it is reasonable to consider all d-TGA fetuses without an ASD at risk)<br>Uncontrolled arrhythmias<br>CHB with heart failure | Planned induction at 38–39 wk; consider C/S if necessary to coordinate services<br>Delivery at hospital that can execute rapid care, including necessary stabilizing/lifesaving procedures | Neonatologist and cardiac specialist in DR, including all necessary equipment<br>Plan for intervention as indicated by diagnosis<br>Plan for urgent transport if indicated |
| 4 | CHD with expected hemodynamic instability with placental separation requiring immediate catheterization/surgery in DR to improve chance of survival | HLHS/severely RFO or IAS<br>d-TGA/severely RFO or IAS and abnormal DA<br>Obstructed TAPVR<br>Ebstein anomaly with hydrops<br>TOF with APV and severe airway obstruction<br>Uncontrolled arrhythmias with hydrops<br>CHB with low ventricular rate, EFE, and/or hydrops | C/S in cardiac facility with necessary specialists in the DR usually at 38–39 wk | Specialized cardiac care team in DR<br>Plan for intervention as indicated by diagnosis; may include catheterization, surgery, or ECMO |

*APV,* Absent pulmonary valve; *AS,* aortic stenosis; *ASD,* atrial septal defect; *AVSD,* atrioventricular septal defect; *CHB,* complete heart block; *CHD,* congenital heart disease; *C/S,* cesarean section*; d-TGA,* transposition of the great arteries, *DA,* ductus arteriosus; *DR,* delivery room; *ECMO,* extracorporeal membrane oxygenation; *EFE,* endocardial fibroelastosis; *HLHS,* hypoplastic left heart syndrome; *IAA,* interrupted aortic arch; *IAS,* intact atrial septum; *LOC,* level of care; *PA/IVS,* pulmonary atresia/intact ventricular septum; *PGE,* prostaglandin; *RFO,* restrictive foramen ovale; *TAPVR,* total anomalous pulmonary venous return; *TOF,* tetralogy of Fallot; *VSD,* ventricular septal defect.

*Modified from the* Children's National Level of Care Protocol, *Donofrio et al with permission from Elsevier. Copyright © 2012, Elsevier, Inc.*

## KEY POINTS

- Congenital abnormalities of the heart are the most common birth defects, occurring in approximately 8 of every 1,000 newborns. Approximately 25% of those in whom a cardiac abnormality is identified have critical CHD, with risk for serious morbidity or mortality in the perinatal period.
- A structured examination of the fetal cardiac anatomy and physiology allows identification of most forms of CHD, providing the opportunity to plan proper perinatal cardiac care to optimize outcomes.
- The optimal timing for imaging the fetal heart is 20 to 28 weeks' gestation, although imaging before and after this window is possible.
- Therapies are available for many fetal arrhythmias, and prenatal intervention is possible for a select group of structural abnormalities. With proper medical and surgical care, outcomes for the overwhelming majority infants and children with heart defects, including those with single-ventricle CHD, are excellent.

## SUGGESTED READINGS

American Institute of Ultrasound in Medicine. AIUM practice guideline for the performance of fetal echocardiography. *J Ultrasound Med*. 2013;32:1067–1082.

Donofrio MT, Moon-Grady AJ, Hornberger LK, et al. Diagnosis and treatment of fetal cardiac disease: a scientific statement from the American Heart Association. *Circulation*. 2014;129:2183–2242.

## REFERENCES

Full references for this chapter can be found on www.expertconsult.com.

## REFERENCES

1. Hoffman JI, Kaplan S. The incidence of congenital heart disease. *J Am Coll Cardiol*. 2002;39:1890–1900.
2. Ferencz C, Rubin JD, Mccarter RJ, et al. Congenital heart disease: prevalence at livebirth. The Baltimore-Washington Infant Study. *Am J Epidemiol*. 1985;121:31–36.
3. Hoffman JIE. Incidence of congenital heart disease: I. Postnatal incidence. *Pediatr Cardiol*. 1995;16:103–113.
4. Sharland GK, Allan LD. Screening for congenital heart disease prenatally. Results of a 2 1/2-year study in the South East Thames Region. *Br J Obstet Gynaecol*. 1992;99:220–225.
5. Meyer-Wittkopf M, Cooper S, Sholler G. Correlation between fetal cardiac diagnosis by obstetric and pediatric cardiologist sonographers and comparison with postnatal findings. *Ultrasound Obstet Gynecol*. 2001;17:392–397.
6. Skeels M, Taylor D, Park J, et al. Test characteristics of a level I or II fetal ultrasound in detecting structural heart disease. *Pediatr Cardiol*. 2002;23:594–597.
7. Friedberg MK, Silverman NH, Moon-Grady AJ, et al. Prenatal detection of congenital heart disease. *J Pediatr*. 2009;155:26–31, 31 e1.
8. Escobar-Diaz MC, Freud LR, Bueno A, et al. Prenatal diagnosis of transposition of the great arteries over a 20-year period: improved but imperfect. *Ultrasound Obstet Gynecol*. 2014.
9. Wigton TR, Sabbagha RE, Tamura RK, et al. Sonographic diagnosis of congenital heart disease: comparison between the four-chamber view and multiple cardiac views. *Obstet Gynecol*. 1993;82:219–224.
10. Guideline AP. AIUM practice guideline for the performance of fetal echocardiography. *J Ultrasound Med*. 2013;32:1067–1082.
11. Chan LY, Fok WY, Wong JT, et al. Reference charts of gestation-specific tissue Doppler imaging indices of systolic and diastolic functions in the normal fetal heart. *Am Heart J*. 2005;150:750–755.
12. Araujo Júnior E, Rolo LC, Rocha LA, et al. The value of 3D and 4D assessments of the fetal heart. *Int. J Womens Health*. 2014;6:501–507.
13. Quartermain MD, Cohen MS, Dominguez TE, et al. Left ventricle to right ventricle size discrepancy in the fetus: the presence of critical congenital heart disease can be reliably predicted. *J Am Soc Echocardiogr*. 2009;22:1296–1301.
14. Gardiner H, Chaoui R. The fetal three-vessel and tracheal view revisited. *Semin Fetal Neonatal Med*. 2013;18:261–268.
15. Pike JI, Krishnan A, Donofrio MT. Early fetal echocardiography: congenital heart disease detection and diagnostic accuracy in the hands of an experienced fetal cardiology program. *Prenat Diagn*. 2014;34:790–796.
16. Dolkart LA, Reimers FT. Transvaginal fetal echocardiography in early pregnancy: normative data. *Am J Obstet Gynecol*. 1991;165:688–691.
17. Persico N, Moratalla J, Lombardi CM, et al. Fetal echocardiography at 11-13 weeks by transabdominal high-frequency ultrasound. *Ultrasound Obstet Gynecol*. 2011;37:296–301.
18. Donofrio MT, Moon-Grady AJ, Hornberger LK, et al. Diagnosis and treatment of fetal cardiac disease: a scientific statement from the American Heart Association. *Circulation*. 2014;129:2183–2242.
19. Sklansky M, Tang A, Levy D, et al. Maternal psychological impact of fetal echocardiography. *J Am Soc Echocardiogr*. 2002;15:159–166.
20. Freud LR, Escobar-Diaz MC, Kalish BT, et al. Outcomes and predictors of perinatal mortality in fetuses with ebstein anomaly or tricuspid valve dysplasia in the current EraCLINICAL PERSPECTIVE. *Circulation*. 2015;132:481–489.
21. Shone J, Seller R, Anderson R, et al. The developmental complex of “parachute mitral valve, supravalvular ring of left atrium, subaortic stenosis aorta*, and coarctation of the aorta. *Am J Cardiol*. 1963;714–725.
22. Abu-Sulaiman RM, Subaih B. Congenital heart disease in infants of diabetic mothers: echocardiographic study. *Pediatr Cardiol*. 2004;25: 137–140.
23. Surerus E, Huggon IC, Allan LD. Turner’s syndrome in fetal life. *Ultrasound Obstet Gynecol*. 2003;22:264–267.
24. Marino B, Digilio MC, Toscano A, et al. Anatomic patterns of conotruncal defects associated with deletion 22q11. *Genet Med*. 2001;3: 45–48.
25. Ganesan S, Brook MM, Silverman NH, et al. Prenatal findings in total anomalous pulmonary venous return: a diagnostic road map starts with obstetric screening views. *J Ultrasound Med*. 2014;33:1193–1207.
26. Mcelhinney DB, Clark BJ, Weinberg PM, et al. Association of chromosome 22q11 deletion with isolated anomalies of aortic arch laterality and branching. *J Am Coll Cardiol*. 2001;37.
27. Dyamenahalli U, Smallhorn JF, Geva T, et al. Isolated ductus arteriosus aneurysm in the fetus and infant: a multi-institutional experience. *J Am Coll Cardiol*. 2000;36:262–269.
28. Huhta JC, Moise KJ, Fisher DJ, et al. Detection and quantitation of constriction of the fetal ductus arteriosus by Doppler echocardiography. *Circulation*. 1987;75:406–412.
29. Escobar-Diaz MC, Friedman K, Salem Y, et al. Perinatal and infant outcomes of prenatal diagnosis of heterotaxy syndrome (asplenia and polysplenia). *Am J Cardiol*. 2014;114:612–617.
30. Escobar-Diaz MC, Tworetzky W, Friedman K, et al. Perinatal outcome in fetuses with heterotaxy syndrome and atrioventricular block or bradycardia. *Pediatr Cardiol*. 2014;35:906–913.
31. Petrikovsky BM, Challenger M, Wyse LJ. Natural history of echogenic foci within ventricles of the fetal heart. *Ultrasound Obs Gynecol*. 1995;5:92–94.
32. D’Addario V, Pinto V, Di Naro E, et al. Prenatal diagnosis and postnatal outcome of cardiac rhabdomyomas. *J Perinat Med*. 2002;30: 170–175.
33. Tworetzky W, McElhinney DB, Margossian R, et al. Association between cardiac tumors and tuberous sclerosis in the fetus and neonate. *Am J Cardiol*. 2003;92:487–489.
34. van Engelen AD, Weijtens O, Brenner JI, et al. Management outcome and follow-up of fetal tachycardia. *J Am Coll Cardiol*. 1994;24:1371–1375.
35. Simpson LL. Fetal supraventricular tachycardias: diagnosis and management. *Semin Perinatol*. 2000;24:360–372.
36. Buyon JP, Clancy RM. Neonatal lupus: basic research and clinical perspectives. *Rheum Dis Clin North Am*. 2005;31:299–313, vii.
37. Glickstein JS, Buyon J, Friedman D. Pulsed Doppler echocardiographic assessment of the fetal PR interval. *Am J Cardiol*. 2000;86:236–239.
38. Donofrio MT, Levy RJ, Schuette JJ, et al. Specialized delivery room planning for fetuses with critical congenital heart disease. *Am J Cardiol*. 2013;111:737–747.
39. Van Der Heijden LB, Oudijk MA, Manten GTR, et al. Sotalol as first-line treatment for fetal tachycardia and neonatal follow-up. *Ultrasound Obstet Gynecol*. 2013;42:285–293.
40. Jaeggi ET, Carvalho JS, De Groot E, et al. Comparison of transplacental treatment of fetal supraventricular tachyarrhythmias with digoxin, flecainide, and sotalol: results of a nonrandomized multicenter study. *Circulation*. 2011;124:1747–1754.
41. Schidlow DN, Tworetzky W, Wilkins-Haug LE. Percutaneous fetal cardiac interventions for structural heart disease. *Am J Perinatol*. 2014;31:629–636.
42. Freud LR, McElhinney DB, Marshall AC, et al. Fetal aortic valvuloplasty for evolving hypoplastic left heart syndrome: postnatal outcomes of the first 100 patients. *Circulation*. 2014;638–645.
43. Tworetzky W, McElhinney DB, Marx GR, et al. In utero valvuloplasty for pulmonary atresia with hypoplastic right ventricle: techniques and outcomes. *Pediatrics*. 2009;124:e510–e518.
44. Marshall AC, Velde ME, Van Der Tworetzky W, et al. Creation of an atrial septal defect in utero for fetuses with hypoplastic left heart syndrome and intact or highly restrictive atrial septum. *Circulation*. 2004;110(3):253–258.

## PART 3 Congenital and Cardiovascular Abnormalities

# 71

# Abnormal Pulmonary and Systemic Venous Connections

*Joyce T. Johnson, Angira Patel, Brian Reilly, and Cynthia K. Rigsby*

## PARTIAL ANOMALOUS PULMONARY VENOUS CONNECTION AND SCIMITAR SYNDROME

***Overview.*** Partial anomalous pulmonary venous connection (PAPVC) is present when one or more pulmonary veins drain into a systemic vein. Because a single anomalous connection may be unrecognized, the incidence is difficult to establish, but it has been reported to be present in 1 in 200 postmortem examinations.[1,2]

***Etiology, Pathophysiology, and Clinical Presentation.*** All pulmonary veins from one lung may have anomalous drainage or parts of the lung may have anomalous drainage to the same or different systemic veins. Anomalous drainage of the left pulmonary veins is most often to the brachiocephalic vein or coronary sinus.[3] On the right, anomalous drainage is most often to the superior vena cava (SVC), right atrium, or inferior vena cava (IVC).[4] When there is anomalous pulmonary venous drainage of all the right pulmonary veins or just the middle and lower lobe veins to the IVC, scimitar syndrome is present. Other anomalies associated with scimitar syndrome include hypoplasia of the right lung and bronchial system, hypoplasia of the right pulmonary artery, systemic arterial supply to the right lower lung, and pulmonary sequestration.[5–8]

Approximately 67% of patients with partial anomalous pulmonary venous return also have atrial-level defects, most commonly a sinus venosus defect (see Chapter 72).[9] Sinus venosus defects are not true atrial septal defects (ASDs) but occur as a result of deficiency of the wall between the SVC and the right upper pulmonary veins or of the wall between the right atrium and the right upper or lower pulmonary veins. Thus a superior sinus venosus defect is associated with anomalous drainage of the right pulmonary veins to the SVC or to the right atrium.

Anomalous connection of one pulmonary vein usually is not clinically apparent in childhood, but these patients may present in the third and fourth decades with cyanosis resulting from increased pulmonary vascular resistance.[10] If all but one of the pulmonary veins drains anomalously, the clinical manifestations may be similar to total anomalous pulmonary venous connection. If an anomalous pulmonary venous connection is associated with a sinus venosus defect, signs and symptoms usually are related to the amount of shunting through the defect. Patients with scimitar syndrome may present in infancy with pulmonary hypertension from the arterial supply to the right lower lung, stenosis of the anomalous pulmonary veins, or pulmonary infections. Otherwise, this syndrome may be detected in adulthood in patients who do not have significant symptoms.[11]

***Imaging.*** With anomalous drainage of multiple veins, cardiomegaly with right heart enlargement and increased pulmonary flow are seen on chest radiography. Findings with scimitar syndrome include a crescent-shaped anomalous pulmonary vein (resembling a Turkish sword or scimitar) paralleling the lower right heart border (Fig. 71.1). Patients generally have associated hypoplasia of the right lung, a small right pulmonary artery, and varying degrees of cardiac dextroposition.

Cross-sectional imaging goals include identifying the anomalous pulmonary to systemic venous connection, locating each pulmonary vein and its drainage relative to the left atrium, and determining the location of venous obstruction, if present (e-Fig. 71.2). Evaluation for the presence and size of either an ASD or sinus venosus defect is necessary (e-Figs. 71.3 and 71.4). The heart and great vessels are evaluated for other abnormalities, and when scimitar syndrome is present, the upper abdomen should be assessed for anomalous venous drainage and systemic arterial supply to the lung (Fig. 71.5). Both computed tomography (CT) and magnetic resonance imaging (MRI) are highly sensitive and specific for evaluation of anomalous pulmonary venous drainage, and three-dimensional CT or magnetic resonance angiography (MRA) is very useful for identifying the relationship between the anomalous pulmonary veins and the left atrium.[12,13] MRI also is useful for ASD evaluation and for quantification of systemic to pulmonary shunting. CT and MRI are accurate in assessing for postoperative pulmonary vein obstruction or narrowing (e-Fig. 71.6).[13–15]

***Treatment.*** Surgical correction is indicated when the ratio of pulmonary to systemic arterial flow is greater than 1.5 : 1; outcomes generally are excellent.[4] In patients with scimitar syndrome, pulmonary resection or catheter occlusion of the anomalous arterial blood supply may be necessary. The anomalous vein in patients with scimitar syndrome may be anastomosed directly to the left atrium.

Superior sinus venosus defects may be closed with a patch at the junction of the SVC and right atrium, with baffling of the pulmonary venous return to the left atrium. Alternatively, the SVC is divided above the pulmonary veins, with implantation of the SVC to the right atrial appendage and baffling of the SVC orifice with the right pulmonary venous return to the left atrium. The incidence of postoperative SVC or pulmonary vein stenosis is less than 10%.[16]

## TOTAL ANOMALOUS PULMONARY VENOUS CONNECTION

***Overview.*** Total anomalous pulmonary venous connection (TAPVC) is a congenital anomaly in which all of the pulmonary veins connect to the systemic venous circulation rather than to the left atrium. TAPVC accounts for approximately 1% to 5% of all congenital heart disease.[17,18] TAPVC often is present in patients with visceral heterotaxy and asplenia and single-ventricle physiology.[18]

***Etiology, Pathophysiology, and Clinical Presentation.*** The cause of TAPVC is thought to be lack of incorporation of the common pulmonary vein into the left atrium. In type I or supracardiac TAPVC (49% of cases), all four pulmonary veins join to form a confluence posterior to the left atrium and then most commonly connect to a persistent left vertical vein, which drains to the left brachiocephalic vein and to the right SVC or via the right vertical vein to the right SVC. In type II or cardiac TAPVC (16% of cases), the pulmonary veins form a confluence that drains either

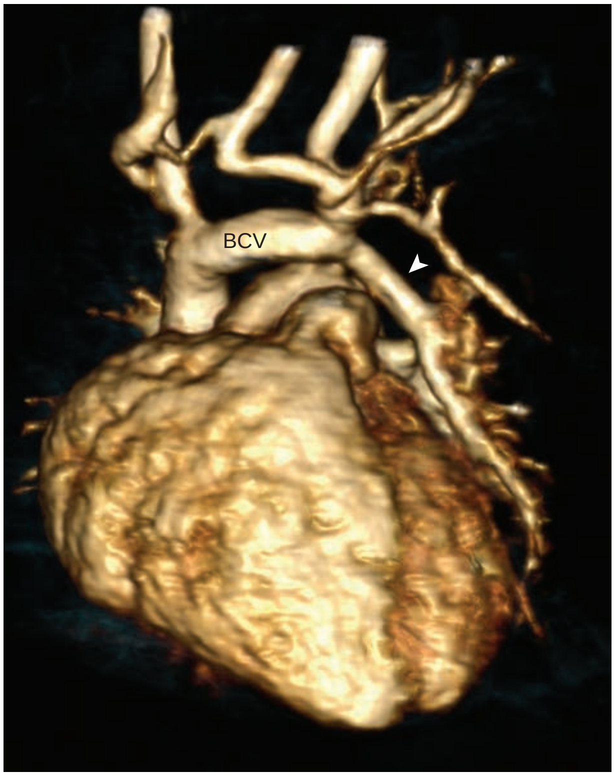

**e-Figure 71.2. Partial anomalous pulmonary venous connection (PAPVC).** A three-dimensional magnetic resonance angiogram viewed from the left anterior oblique projection shows the PAPVC *(arrowhead)* from the left upper lobe with drainage to the left brachiocephalic vein *(BCV)*.

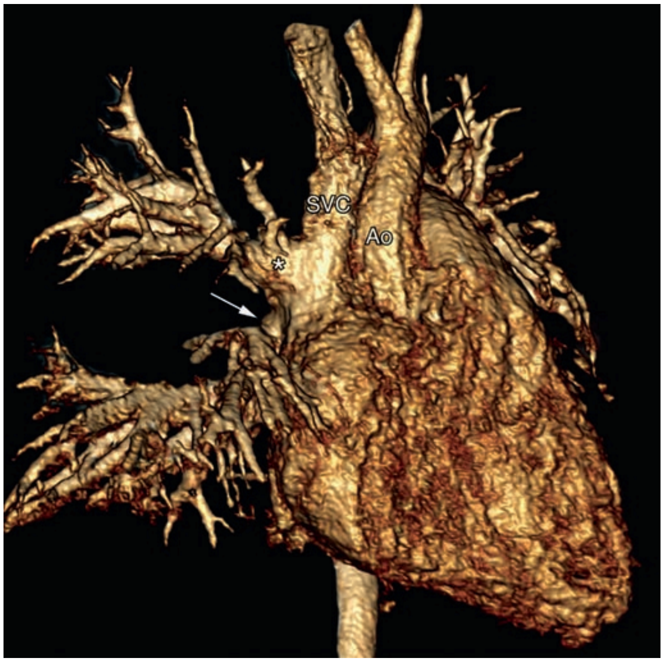

**e-Figure 71.3. Partial anomalous pulmonary venous return in the setting of a superior sinus venosus defect.** A right anterior oblique three-dimensional magnetic resonance angiogram shows the right upper pulmonary veins *(asterisk)* draining to the SVC and the right middle lobe pulmonary veins *(arrow)* draining to the SVC at the level of the sinus venosus defect. *Ao,* Aorta; *SVC,* superior vena cava.

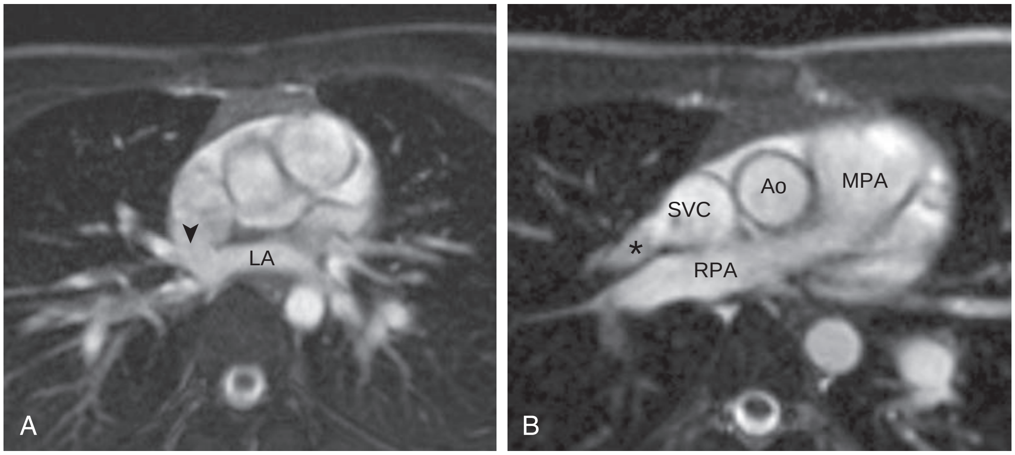

**e-Figure 71.4. Sinus venosus defect with partial anomalous pulmonary venous return.** (A) An axial cine steady-state free-precession (SSFP) image shows the sinus venosus defect *(arrowhead)* located superior to the expected location of the oval fossa, consistent with a superior sinus venosus defect. (B) Oblique axial SSFP located superior to (A) showing the right upper pulmonary vein *(asterisk)* draining to the superior vena cava. *Ao,* Aorta; *LA,* left atrium; *MPA,* main pulmonary artery; *RPA,* right pulmonary artery; *SVC,* superior vena cava.

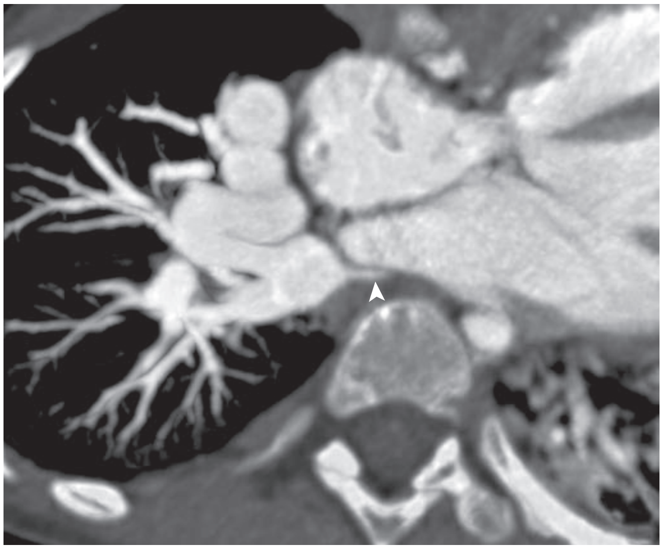

**e-Figure 71.6. Severe right pulmonary vein stenosis.** A computed tomography axial oblique reformat performed 5 years after repair of obstructed supracardiac total anomalous pulmonary venous connection with separate anastomoses of the right and left pulmonary veins to the left atrium. Severe right pulmonary vein stenosis *(arrowhead)* is present at the anastomotic site.

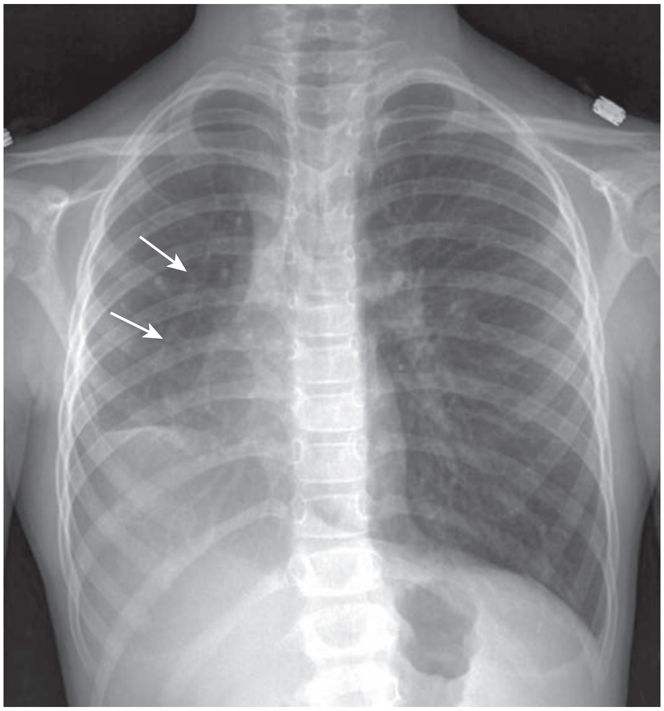

**Figure 71.1. Scimitar syndrome.** A frontal chest radiograph shows the rightward shift of the mediastinum as a result of right lung hypoplasia. In the right side of the chest, a linear density indicative of the anomalous draining "scimitar" vein is seen *(arrows)*.

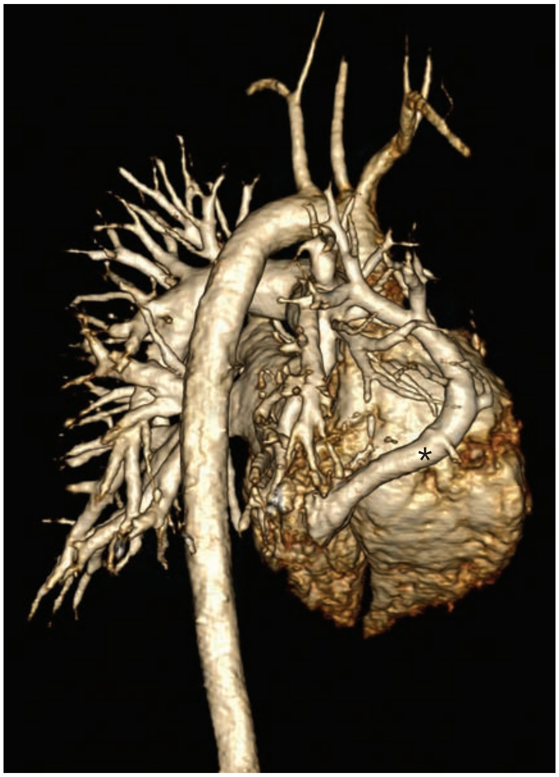

**Figure 71.5. Scimitar syndrome.** A three-dimensional magnetic resonance angiogram viewed from right posterior oblique shows the anomalously draining right pulmonary "scimitar" vein *(asterisk)* draining to the inferior vena cava.

directly into the right atrium or to the coronary sinus, which then drains normally into the right atrium. In type III or infracardiac TAPVC (26% of cases), the pulmonary veins converge as a common pulmonary vein that extends below the diaphragm and drains to the portal vein, ductus venosus, hepatic vein, or IVC. Type IV TAPVC (9% of cases) is a mixed type in which the pulmonary veins drain separately to at least two different systemic sites, most commonly supracardiac and cardiac sites (e-Fig. 71.7 and Fig. 71.8).[20]

Obstruction occurs in 46% of patients with supracardiac TAPVC as the left vertical vein passes between the left pulmonary artery and left mainstem bronchus or as the right vertical vein crosses between the right pulmonary artery and right mainstem bronchus or at its entrance into the right SVC.[17,20] With cardiac TAPVC, obstruction is not nearly as frequent (20%).[20] With infracardiac TAPVC, obstruction is common (87%) and can occur at the level of the diaphragm and/or at the site of anomalous systemic venous insertion, including the ductus venosus or the hepatic sinusoids.[17,20]

Pulmonary venous obstruction dictates the clinical presentation and physiology.[17] Patients without pulmonary venous obstruction generally present with symptoms later in the newborn period or in infancy or childhood.[18,20] Symptoms can be nonspecific and include tachypnea, feeding difficulties, repeated respiratory infections, and failure to thrive.[10] The anomalous venous connection acts as a large left-to-right shunt with a marked increase in pulmonary blood flow, especially after the pulmonary vascular resistance drops normally after birth. All patients with TAPVC have either a patent foramen ovale or an ASD. The atrial connection can be small and can contribute to venous obstruction. When pulmonary venous flow is obstructed, pulmonary blood flow is limited, leading to pulmonary venous hypertension and congestion. Because the amount of blood flowing through the pulmonary circuit is not increased, inadequate oxygenation occurs. Patients with this disorder typically present in the neonatal period, often shortly after birth, with marked cyanosis and cardiorespiratory failure.

***Imaging.*** Chest radiographic findings in TAPVC without obstruction include increased pulmonary vascularity because of the marked left-to-right shunt, along with main pulmonary artery and right heart enlargement. Occasionally, the anomalous course of a pulmonary vein or the vertical course of a dilated left vertical vein may be seen (Fig. 71.9). In patients with obstructed pulmonary venous flow, the chest radiograph shows pulmonary venous congestion, and because of the decreased inflow to the left heart, the heart often is not enlarged (Fig. 71.10). Cross-sectional imaging goals are as listed in the PAPVC imaging section.

***Treatment.*** Patients with obstructed TAPVC and unstable hemodynamics must undergo urgent repair because no effective medical management options are available. Timing of repair for patients without venous obstruction can be more elective. The surgical objective is to redirect pulmonary venous flow to the left atrium, remove the anomalous connection or connections, and close the ASD. Long-term outcome is excellent after repair, with 5-year survival rates of up to 97%.[21] The major postoperative complication is persistent or progressive pulmonary venous obstruction in 15% to 19% of patients.[18,20]

## COR TRIATRIATUM AND OTHER ANOMALIES OF THE PULMONARY VEINS

***Overview.*** Cor triatriatum sinister is rare, representing only 0.1% to 0.4% of congenital heart disease cases.[22,23] It is associated with other cardiac anomalies in 12% to 50% of cases.[24]

***Etiology, Pathophysiology, and Clinical Presentation.*** In cor triatriatum, the pulmonary veins connect to an accessory left atrial chamber, which is separated from the true left atrium by a fibromuscular membrane with a typically small, obstructed opening (e-Fig. 71.11).[23] An ASD may be present. The embryology is

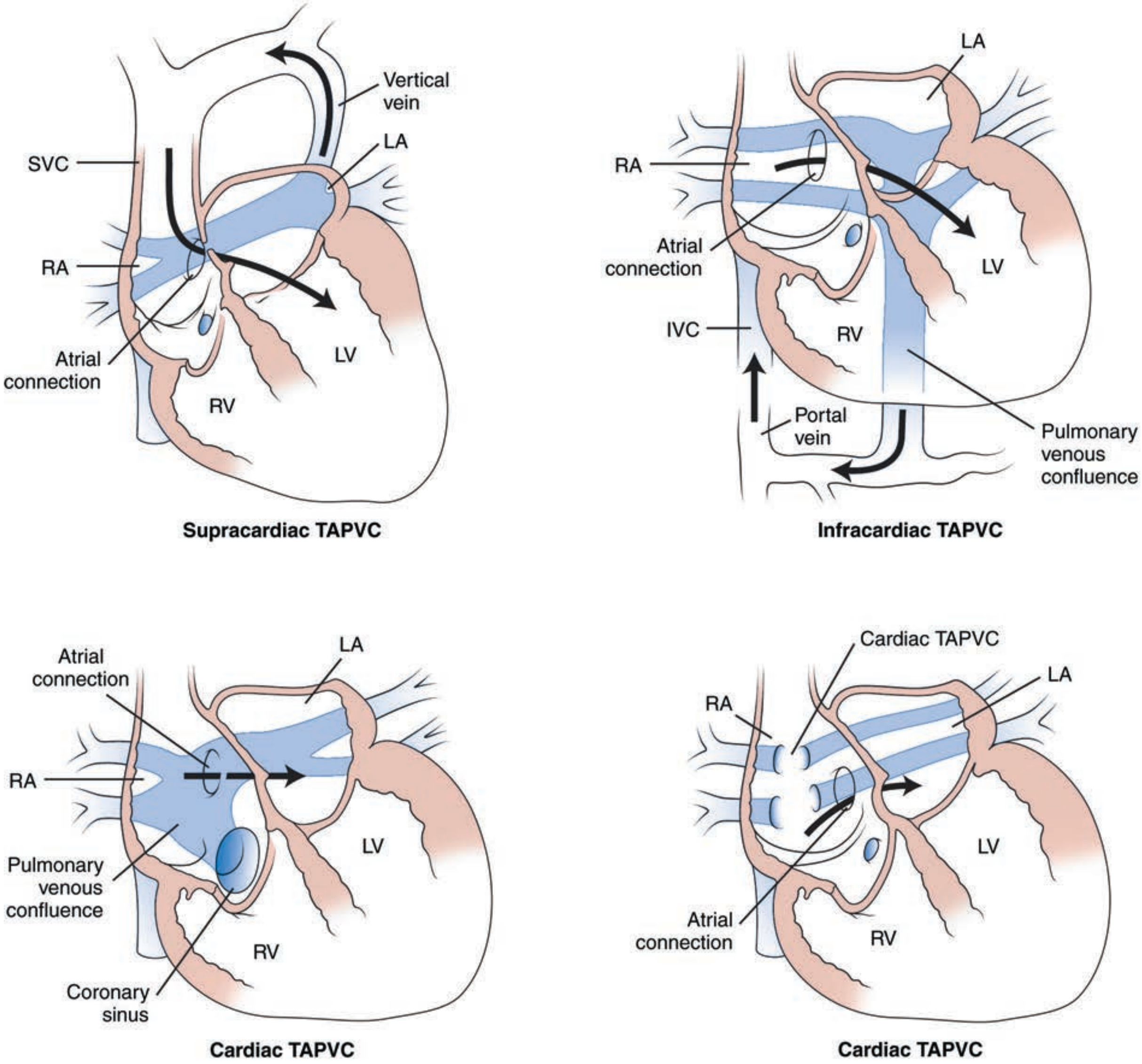

**Supracardiac TAPVC** **Infracardiac TAPVC**

**Cardiac TAPVC** **Cardiac TAPVC**

**e-Figure 71.7. Darling classification of total anomalous pulmonary venous connection (TAPVC).** With supracardiac TAPVC, pulmonary venous connection is to a vertical vein, draining to the left brachiocephalic vein and superior vena cava *(SVC)*. With infracardiac TAPVC, the pulmonary veins connect to a systemic venous vessel below the diaphragm (the portal vein in this diagram). With cardiac TAPVC, the pulmonary veins connect either to the coronary sinus or directly to the right atrium *(RA)*. The direction of systemic blood flow *(dark arrows)* is shown. Note that blood must flow through an atrial connection to reach the left side of the heart. *IVC,* Inferior vena cava; *LA,* left atrium; *LV,* left ventricle; *RV,* right ventricle. *(From Wilson A. Total anomalous pulmonary venous connection,* E-Medicine, *March 28, 2006.)*

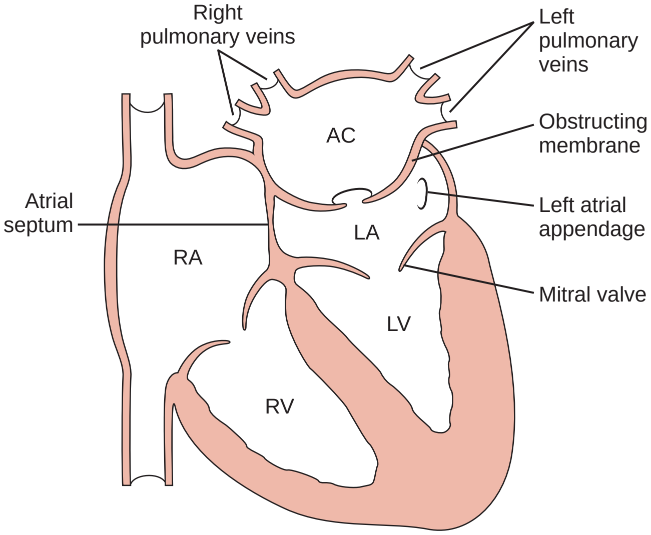

**e-Figure 71.11. Diagram of cor triatriatum.** An accessory chamber *(AC)* of the left atrium *(LA)* is present, with an obstructing membrane in between. Note that the mitral valve and the left atrial appendage are part of the true LA. *LV,* Left ventricle; *RA,* right atrium; *RV,* right ventricle.

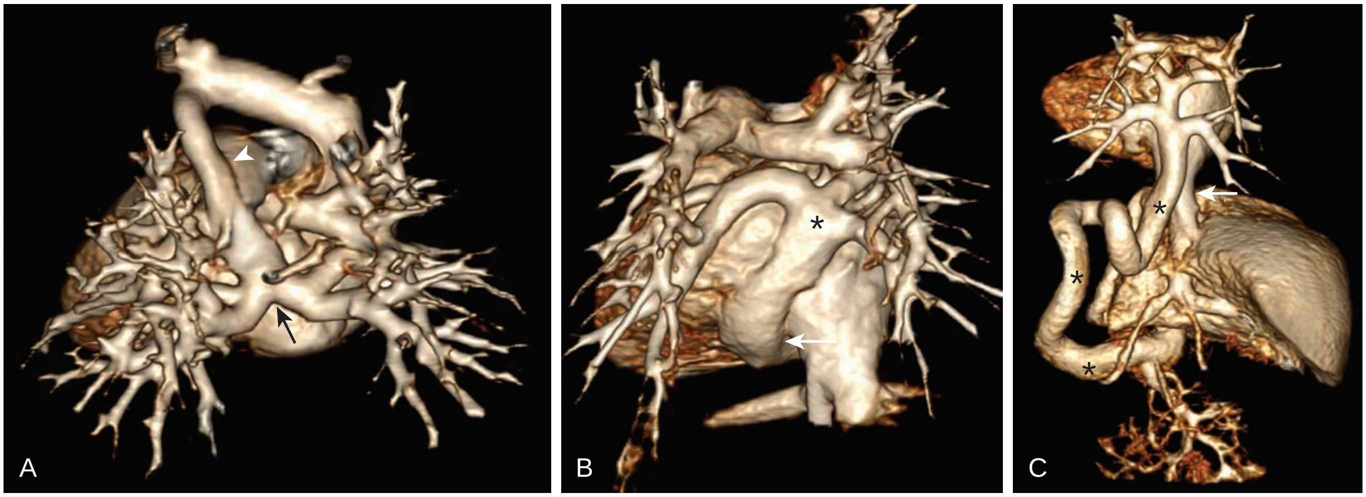

**Figure 71.8. Three-dimensional computed tomography angiogram posterior views of different types of total anomalous pulmonary venous connection (TAPVC).** (A) Supracardiac TAPVC. The pulmonary venous confluence *(arrow)* connects to the ascending vertical vein, the enlarged left brachiocephalic vein, and the enlarged superior vena cava. (B) Cardiac TAPVC. The pulmonary venous confluence *(asterisk)* connects to the coronary sinus *(arrow)*. (C) Infracardiac TAPVC. The pulmonary venous confluence extends below the diaphragm via a tortuous descending vertical vein *(asterisks)* to drain to the portal vein and inferior vena cava *(arrow)*.

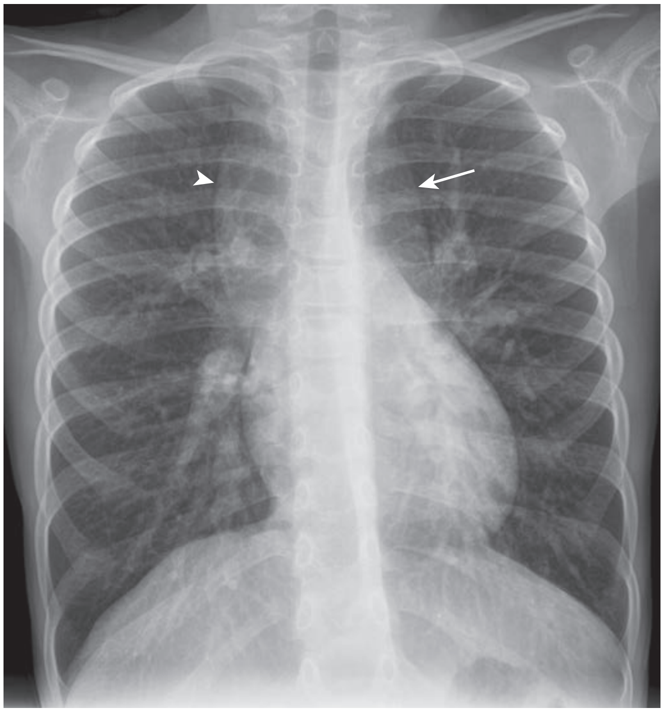

**Figure 71.9. Total anomalous pulmonary venous connection (TAPVC).** A chest radiograph in a 12-year-old with nonobstructed supracardiac TAPVC shows a "snowman" heart as a result of an enlarged left vertical vein *(arrow)* and superior vena cava *(arrowhead)*.

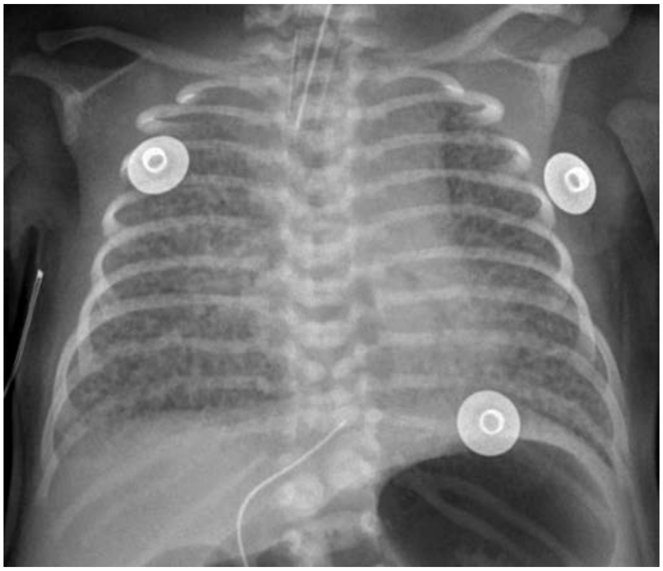

**Figure 71.10. Obstructed total anomalous pulmonary venous connection (TAPVC).** A chest radiograph in a newborn with obstructed TAPVC shows a normal heart size and pulmonary edema pattern as a result of venous obstruction.

thought to result from incomplete incorporation of the common pulmonary vein into the left atrium, and the accessory chamber represents the embryologic common pulmonary vein.[25] Localized stenosis, hypoplasia, or atresia of individual or all pulmonary veins also can occur, with abnormal absorption of the common pulmonary vein into the left atrium.[26] With these variants, an accessory left atrial chamber does not exist, but there is either focal stenosis of pulmonary veins near the left atrial junction, diffuse long-segment hypoplasia or narrowing of individual pulmonary veins, or unilateral or bilateral atresia of the common pulmonary vein or of individual pulmonary veins in extreme cases.[27]

Because of the typically obstructed opening between the accessory left atrium and the true left atrium, the predominant physiology is that of pulmonary venous obstruction. With small openings and more severe obstruction, patients tend to present in the neonatal period with low cardiac output and right heart failure.[28] With larger, less obstructed openings, patients may not present with symptoms until older childhood or even adulthood. Complete atresia of all the individual pulmonary veins is not compatible with life unless significant bronchopulmonary venous collaterals are present (e-Fig. 71.12).[29]

***Imaging.*** The chest radiograph may show evidence of right ventricular enlargement and pulmonary edema related to the pulmonary venous obstruction. Enlargement of the left atrial region, representing both left atrial chambers, also may be present.

Cross-sectional imaging goals include evaluation of the two left atrial chambers and the intervening membrane and complete evaluation of the pulmonary veins and the relationship of the veins to the membrane (Fig. 71.13). CT is ideal for evaluation of pulmonary vein stenosis and for evaluation of the lung.[30,31]

***Treatment.*** Surgery for cor triatriatum is generally performed as soon as the diagnosis is made. The intervening septum of the left atrium is resected and, if an ASD is present, it is closed. The prognosis is good for patients who survive the perioperative period and who have no associated cardiac anomalies.[28] Operative management of individual pulmonary vein hypoplasia, stenosis, or atresia is variable, and balloon angioplasty has led to disappointing results.[32,33] Atresia of the common pulmonary vein with a sizable pulmonary venous confluence may be repaired, similar to TAPVC.[34,35]

## ANOMALIES OF SYSTEMIC VENOUS CONNECTIONS

Abnormal systemic venous connections represent a heterogeneous group of malformations with clinical manifestations that can range from none to severe desaturation.

### Anomalies of the Superior Vena Cava

Persistence of the left SVC results from failure of the left anterior and left common cardinal veins to involute.[36] In patients with congenital heart disease, the incidence varies from 11% to 34%.[37,38] Bilateral SVCs usually have normal drainage, with the right SVC into the right atrium and the left SVC to the coronary sinus and the right atrium (92%); however, abnormal drainage to the left atrium via an unroofed coronary sinus occurs in 8% of cases (e-Fig. 71.14).[39] Although bilateral SVCs with normal drainage have no hemodynamic consequences, they can have technical implications for cardiac catheterization or surgery. Abnormal SVC drainage into the left atrium can result in cyanosis. A left SVC may be suspected based on a shadow in the left upper border of the mediastinum on a chest radiograph. Imaging will show an associated dilated coronary sinus, and the caliber of the brachiocephalic vein is inversely proportional to the size of the left SVC (Fig. 71.15). In some cases, the brachiocephalic vein is absent when a left SVC is present.

### Anomalies of the Inferior Vena Cava and Hepatic Veins

IVC anomalies include interrupted IVC, which is defined by the absence of the hepatic or suprahepatic segment of the IVC with azygous or hemiazygous continuation into the right or left SVC (e-Fig. 71.16)[40] and is seen in up to 86% of patients with visceral heterotaxy and polysplenia.[41] Patients with asplenia usually have a normal IVC but can have a prominent azygous vein and separate drainage of the hepatic veins into the right atrium (e-Fig. 71.17).[42,43]

### Anomalies of the Brachiocephalic Veins

The normal course of the left brachiocephalic vein is obliquely downward to the right, passing anterior to the aortic arch. A retroaortic brachiocephalic vein is characterized by an abnormal position behind the ascending aorta (e-Fig. 71.18).[44] An anomalous retroesophageal brachiocephalic vein is characterized by an abnormal course posterior to the trachea and esophagus, and joining the azygous vein before draining to the SVC (e-Fig. 71.19).[45]

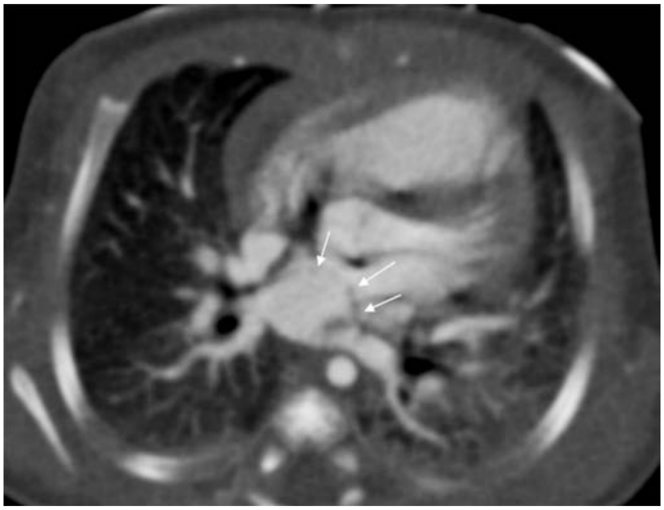

**Figure 71.13. Cor triatriatum.** Axial contrast-enhanced computed tomography (CT) image showing a linear membrane in the left atrium upstream from the mitral valve *(arrows)*. The pulmonary veins enter the left atrium proximal to the membrane are separated from the true left atrium by the membrane.

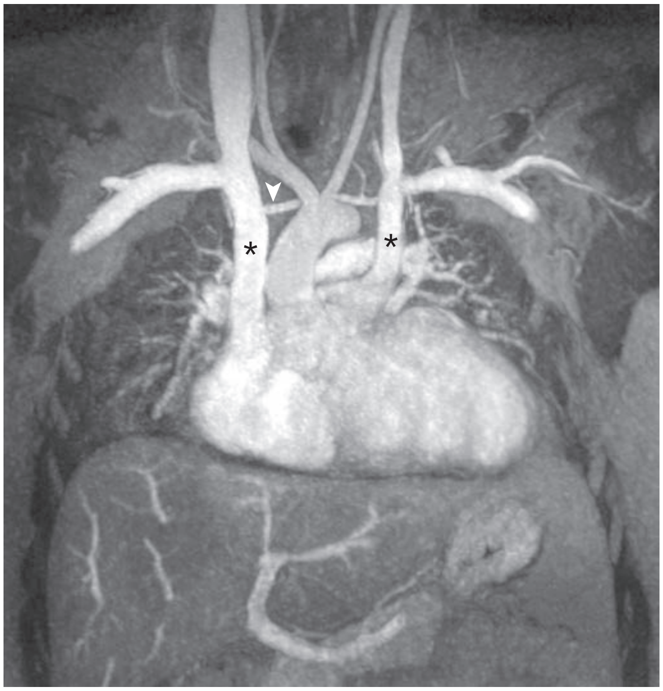

**Figure 71.15. Left superior vena cava.** A coronal thick maximum intensity projection MRA showing bilateral superior vena cavae (SVCs) *(asterisks)*. A small bridging vein is present *(arrowhead)*.

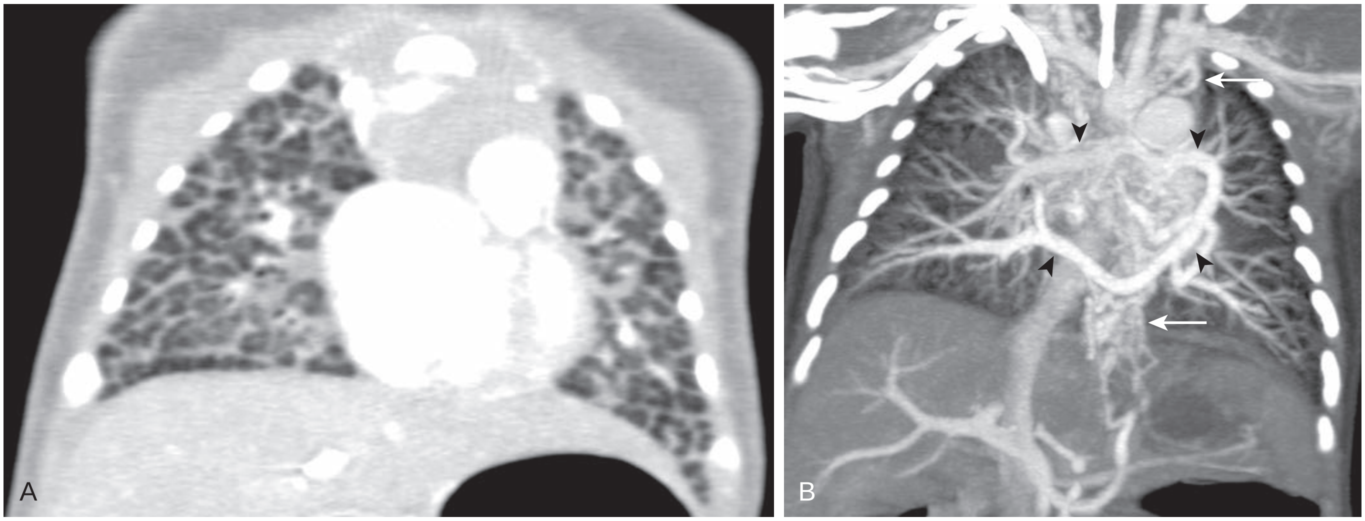

**e-Figure 71.12. Newborn with total anomalous pulmonary venous connection and pulmonary vein atresia.** (A) Coronal computed tomography (CT) lung window shows severe interstitial edema and septal thickening. (B) Coronal CT maximum intensity projection image shows that the anomalous pulmonary veins *(arrowheads)* join but the common pulmonary vein is atretic, and thus the venous drainage is via multiple small collateral vessels to the systemic system *(arrows)*.

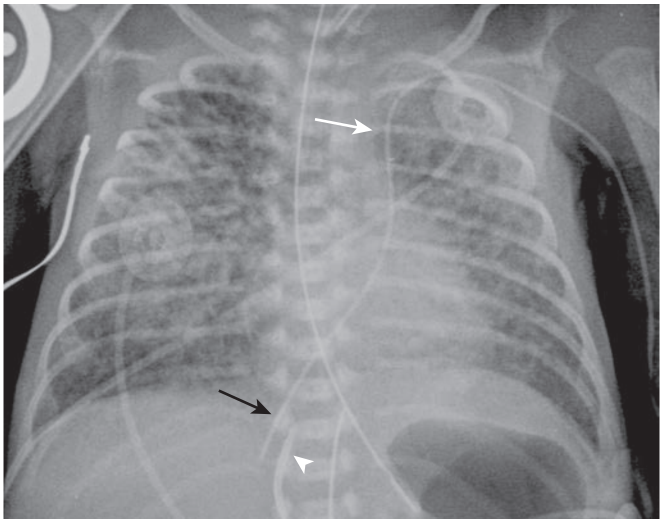

**e-Figure 71.14. Chest radiograph with left superior vena cava.** A frontal chest radiograph in a newborn showing a left-sided central venous catheter extending into the left SVC *(white arrow)*, the coronary sinus, and through the right atrium with its tip in the inferior vena cava, hepatic vein, or ductus venosus *(black arrow)*. An umbilical venous catheter also is shown *(arrowhead)*.

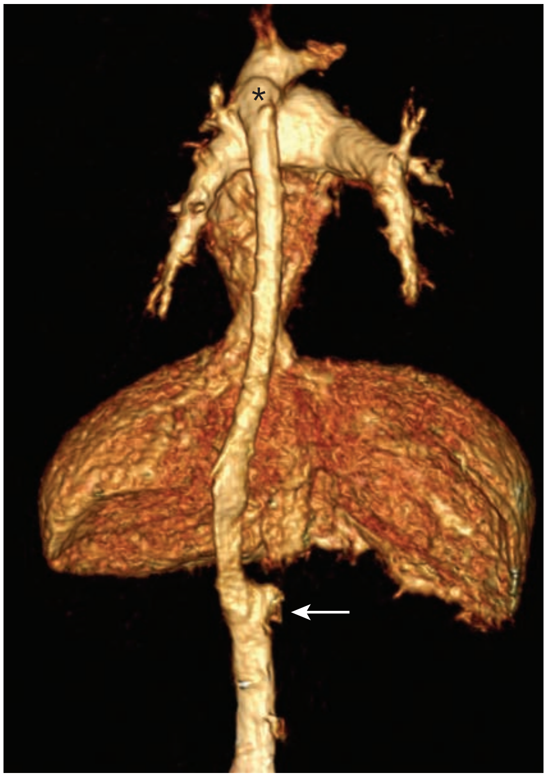

**e-Figure 71.16. Interrupted inferior vena cava with azygous continuation.** Posterior view three-dimensional magnetic resonance angiogram showing interrupted IVC *(arrow)* with azygous continuation coursing posterior to the liver, draining into the left superior vena cava *(asterisk)*.

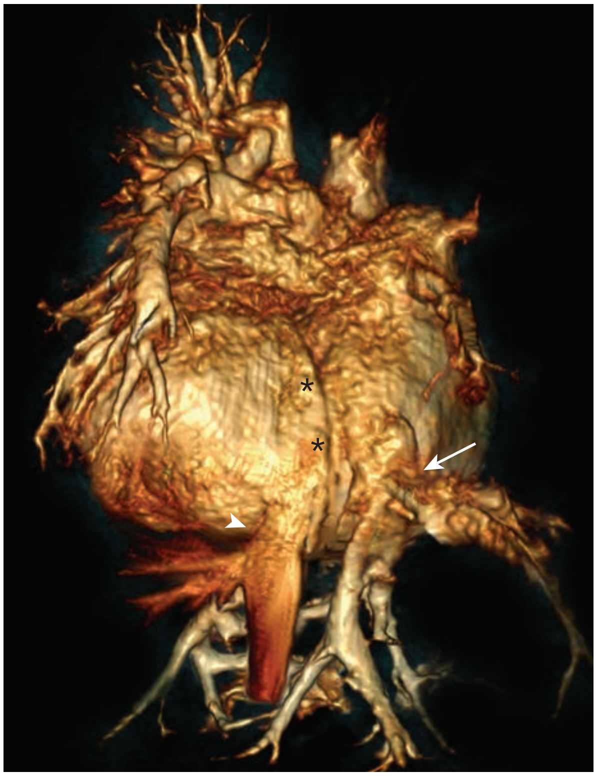

**e-Figure 71.17. Systemic venous abnormality in heterotaxy.** A three-dimensional magnetic resonance angiogram posterior view showing abnormal hepatic venous drainage with the right-sided hepatic veins *(arrow)* draining directly to the right-sided atrium and the left-sided hepatic veins *(arrowhead)* draining to the left-sided atrium. *Asterisks* mark the atrial septum.

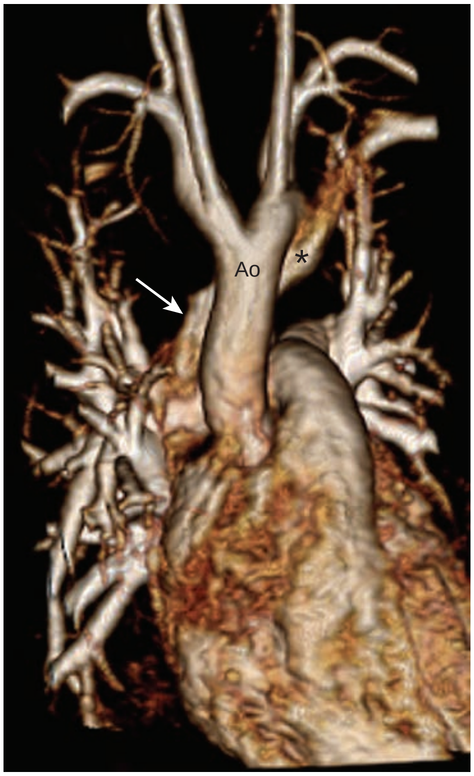

**e-Figure 71.18. Retroaortic left brachiocephalic vein.** A three-dimensional magnetic resonance angiogram showing the left brachiocephalic vein *(asterisk)* coursing posterior and inferior to the aortic arch *(Ao)* draining to the superior vena cava *(arrow)*. *(Courtesy Rajesh Krishnamurthy, Nationwide Children's Hospital, Columbus, Ohio.)*

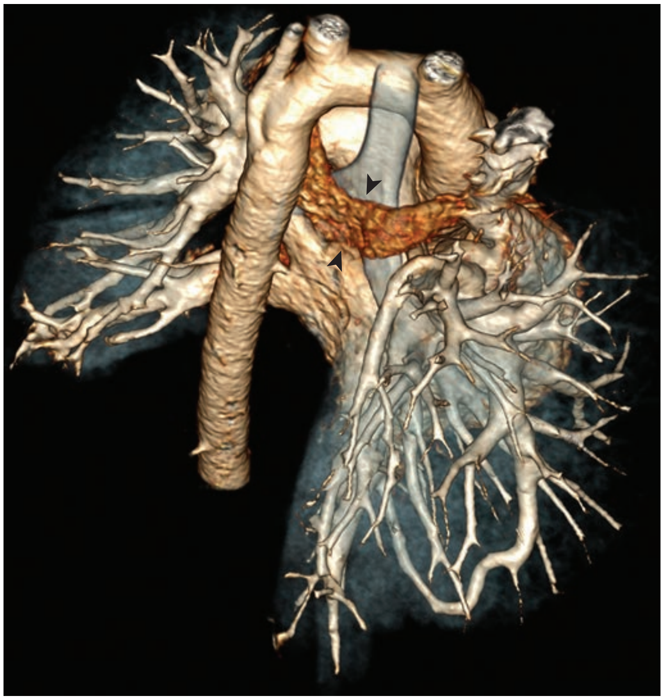

**e-Figure 71.19. Retrotracheal and retroesophageal left brachiocephalic vein.** A three-dimensional computed tomography angiography posterior oblique view showing the retroaortic and retrotracheal left brachiocephalic vein *(arrowheads)*. The esophagus is collapsed and not seen. An anomalous right pulmonary arterial to venous communication is present.

## KEY POINTS

- PAPVC and partial anomalous pulmonary venous return present with right side volume overload similar to an ASD. Assessment of the degree of left-to-right shunting and associated cardiovascular defects is important.
- TAPVC presents in early infancy with variable cyanosis and pulmonary edema on a chest radiograph. The ascending or descending vein course must be accurately described, with assessment for any obstruction to the pulmonary venous drainage.
- Anomalous systemic venous connections can present with no clinical manifestations or cyanosis depending on the route of drainage. Diagnosis can be important for surgical planning such as placement of central lines and/or cannulation for cardiopulmonary bypass.

## SUGGESTED READINGS

Dillman JR, Yarram SG, Hernandez RJ. Imaging of pulmonary venous developmental anomalies. *AJR Am J Roentgenol*. 2009;192(5):1272–1285.

Kafka H, Mohiaddin RH. Cardiac MRI and pulmonary MR angiography of sinus venosus defect and partial anomalous pulmonary venous connection in cause of right undiagnosed ventricular enlargement. *AJR Am J Roentgenol*. 2009;192(1):259–266.

Martinez-Jimenez S, Heyneman LE, McAdams HP, et al. Nonsurgical extracardiac vascular shunts in the thorax: clinical and imaging characteristics. *Radiographics*. 2010;30(5):e41.

## REFERENCES

Full references for this chapter can be found on www.expertconsult.com.

## REFERENCES

1. Brody H. Drainage of the pulmonary veins into the right side of the heart. *Arch Pathol*. 1942;33:221–240.
2. Healey JE Jr. An anatomic survey of anomalous pulmonary veins: their clinical significance. *J Thorac Surg*. 1952;23(5):433–444.
3. Van Meter C Jr, LeBlanc JG, Culpepper WS 3rd, et al. Partial anomalous pulmonary venous return. *Circulation*. 1990;82(5 suppl):IV195–IV198.
4. Alsoufi B, Cai S, Van Arsdell GS, et al. Outcomes after surgical treatment of children with partial anomalous pulmonary venous connection. *Ann Thorac Surg*. 2007;84(6):2020–2026.
5. Chassinat R. Observation d'anomalies anatomiques remarquables d l'appariel circulatoire. *Arch Gen Med*. 1836;11:80–91.
6. Cooper G. Case of malformation of thoracic viscera. *London Med Gaz*. 1836;18:600–602.
7. Gao YA, Burrows PE, Benson LN, et al. Scimitar syndrome in infancy. *J Am Coll Cardiol*. 1993;22(3):873–882.
8. Midyat L, Demir E, Askin M, et al. Eponym. Scimitar syndrome. *Eur J Pediatr*. 2010;169(10):1171–1177.
9. Kafka H, Mohiaddin RH. Cardiac MRI and pulmonary MR angiography of sinus venosus defect and partial anomalous pulmonary venous connection in cause of right undiagnosed ventricular enlargement. *AJR Am J Roentgenol*. 2009;192(1):259–266.
10. Geva T, Van Praagh S. Anomalies of the pulmonary veins. In: Moss A, Allen H, eds. *Moss and Adams' Heart Disease in Infants, Children, and Adolescents: Including the Fetus and Young Adult*. Vol. 2. 7th ed. Philadelphia: Lippincott Williams & Wilkins; 2008.
11. Dupuis C, Charaf LA, Breviere GM, et al. The "adult" form of the scimitar syndrome. *Am J Cardiol*. 1992;70(4):502–507.
12. Oh KH, Choo KS, Lim SJ, et al. Multidetector CT evaluation of total anomalous pulmonary venous connections: comparison with echocardiography. *Pediatr Radiol*. 2009;39(9):950–954.
13. Valsangiacomo ER, Levasseur S, McCrindle BW, et al. Contrast-enhanced MR angiography of pulmonary venous abnormalities in children. *Pediatr Radiol*. 2003;33(2):92–98.
14. Ou P, Marini D, Celermajer DS, et al. Non-invasive assessment of congenital pulmonary vein stenosis in children using cardiac-non-gated CT with 64-slice technology. *Eur J Radiol*. 2009;70(3):595–599.
15. Grosse-Wortmann L, Al-Otay A, Goo HW, et al. Anatomical and functional evaluation of pulmonary veins in children by magnetic resonance imaging. *J Am Coll Cardiol*. 2007;49(9):993–1002.
16. Backer CL, Mavroudis C. Atrial septal defect, partial anomalous pulmonary venous connection, and scimitar syndrome. In: Mavroudis C, Backer CL, eds. *Pediatric Cardiac Surgery*. 3rd ed. Philadelphia: Mosby; 2003.
17. Herlong J, Jaggers J, Ungerleider R. Congenital Heart Surgery Nomenclature and Database Project: pulmonary venous anomalies. *Ann Thorac Surg*. 2000;69(4 suppl):S56–S69.
18. Kelle A, Backer C, Gossett J, et al. Total anomalous pulmonary venous connection: results of surgical repair of 100 patients at a single institution. *J Thorac Cardiovasc Surg*. 2010;139(6):1387–1394.
19. Deleted in review.
20. Seale AN, Uemura H, Webber SA, et al. Total anomalous pulmonary venous connection: morphology and outcome from an international population-based study. *Circulation*. 2010;122(25):2718–2726.
21. Karamlou T, Gurofsky R, Al Sukhni E, et al. Factors associated with mortality and reoperation in 377 children with total anomalous pulmonary venous connection. *Circulation*. 2007;115(12):1591–1598.
22. Jorgensen CR, Ferlic RM, Varco RL, et al. Cor triatriatum. Review of the surgical aspects with a follow-up report on the first patient successfully treated with surgery. *Circulation*. 1967;36(1):101–107.
23. Niwayama G. Cor triatriatum. *Am Heart J*. 1960;59:291–317.
24. Brown JW, Hanish SI. Cor triatriatum sinister, atresia of the common pulmonary vein, pulmonary vein stenosis, and cor triatriatum dexter. In: Mavroudis C, Backer CL, eds. *Pediatric Cardiac Surgery*. 3rd ed. Philadelphia: Mosby; 2003.
25. Parsons CG. Cor triatriatum; concerning the nature of an anomalous septum in the left auricle. *Br Heart J*. 1950;12(4):327–338.
26. Reye RD. Congenital stenosis of the pulmonary veins in their extrapulmonary course. *Med J Aust*. 1951;1(22):801–802.
27. Shone JD, Amplatz K, Anderson RC, et al. Congenital stenosis of individual pulmonary veins. *Circulation*. 1962;26:574–581.
28. van Son JA, Danielson GK, Schaff HV, et al. Cor triatriatum: diagnosis, operative approach, and late results. *Mayo Clin Proc*. 1993;68(9):854–859.
29. Deshpande JR, Kinare SG. Atresia of the common pulmonary vein. *Int J Cardiol*. 1991;30(2):221–226.
30. Gahide G, Barde S, Francis-Sicre N. Cor triatriatum sinister: a comprehensive anatomical study on computed tomography scan. *J Am Coll Cardiol*. 2009;54(5):487.
31. Saremi F, Gurudevan SV, Narula J, et al. Multidetector computed tomography (MDCT) in diagnosis of "cor triatriatum sinister." *J Cardiovasc Comput Tomogr*. 2007;1(3):172–174.
32. Driscoll DJ, Hesslein PS, Mullins CE. Congenital stenosis of individual pulmonary veins: clinical spectrum and unsuccessful treatment by transvenous balloon dilation. *Am J Cardiol*. 1982;49(7):1767–1772.
33. Mendelsohn AM, Bove EL, Lupinetti FM, et al. Intraoperative and percutaneous stenting of congenital pulmonary artery and vein stenosis. *Circulation*. 1993;88(5 Pt 2):II210–II217.
34. Shimazaki Y, Yagihara T, Nakada T, et al. Common pulmonary vein atresia: a successfully corrected case. *J Cardiovasc Surg (Torino)*. 1987;28(4):395–397.
35. Suzuki T, Sato M, Murai T, et al. Successful surgical repair of common pulmonary vein atresia in a newborn. *Pediatr Cardiol*. 2001;22(3):255–257.
36. Sanders JM. Bilateral superior vena cavae. *Anat Rec*. 1946;94:657–662.
37. Nsah EN, Moore GW, Hutchins GM. Pathogenesis of persistent left superior vena cava with a coronary sinus connection. *Pediatr Pathol*. 1991;11(2):261–269.
38. Van Praagh S, O'Sullivan J, Brili S, et al. Juxtaposition of the morphologically right atrial appendage in solitus and inversus atria: a study of 35 postmortem cases. *Am Heart J*. 1996;132(2 Pt 1):382–390.
39. Meadows WR, Sharp JT. Persistent left superior vena cava draining into the left atrium without arterial oxygen unsaturation. *Am J Cardiol*. 1965;16:273–279.
40. Walters HL. Anomalous systemic venous connections. In: Mavroudis C, Backer CL, eds. *Pediatric Cardiac Surgery*. 3rd ed. Philadelphia: Mosby; 2003.
41. Bengur AR, Jaggers J, Ungerleider RM. Intraoperative transesophageal echocardiography in congenital heart disease. In: Mavroudis C, Backer CL, eds. *Pediatric Cardiac Surgery*. 3rd ed. Philadelphia: Mosby; 2003.
42. Geva T, Van Praagh S. Abnormal systemic venous connections. In: Moss A, Allen H, eds. *Moss and Adams' Heart Disease in Infants, Children, and Adolescents: Including the Fetus and Young Adult*. Vol. 2. 7th ed. Philadelphia: Lippincott Williams & Wilkins; 2008.
43. Rubino M, Van Praagh S, Kadoba K, et al. Systemic and pulmonary venous connections in visceral heterotaxy with asplenia. Diagnostic and surgical considerations based on seventy-two autopsied cases. *J Thorac Cardiovasc Surg*. 1995;110(3):641–650.
44. Choi JY, Jung MJ, Kim YH, et al. Anomalous subaortic position of the brachiocephalic vein (innominate vein): an echocardiographic study. *Br Heart J*. 1990;64(6):385–387.
45. Ming Z, Aimin S, Rui H. Evaluation of the anomalous retroesophageal left brachiocephalic vein in Chinese children using multidetector CT. *Pediatr Radiol*. 2009;39(4):343–347.

# 72

# Systemic to Pulmonary Arterial Shunts

*Joseph A. Camarda, Joshua D. Robinson, and Cynthia K. Rigsby*

## ATRIAL SEPTAL DEFECT

***Overview.*** An atrial septal defect (ASD) is a defect in the atrial septum that allows communication between the right atrium (RA) and left atrium (LA). Isolated ASDs account for 6% to 10% of all congenital heart disease.

***Etiology.*** Two primary types of ASDs occur and are classified by their relationship to the fossa ovalis (Fig. 72.1). Secundum-type defects (80%–90% of all ASDs) occur in the region of the fossa ovalis. Although a patent foramen ovale is similar in location, it usually is not considered a true defect as it is a persistence of the normal interatrial communication from fetal life and is present in 27% to 34% of the general population (Fig. 72.2).[1,2] Ostium primum defects occur anterior to the fossa ovalis at the base of the atrial septum, are usually larger defects, and are almost always associated with other structural heart defects. Additionally, two defects—sinus venosus defects and unroofed coronary sinus—do not involve the atrial septum but are physiologically equivalent to an ASD as they allow blood to shunt from the LA to RA.[3,4] Sinus venosus defects are typically located posterior and superior to the fossa ovalis but may sometimes be posterior and inferior. These occur as a result of abnormal resorption of the right horn of the sinus venosus during embryologic development leading to a defect in the wall that separates the right pulmonary veins from the superior vena cava and the RA, typically resulting in anomalous drainage of the right upper, middle, or lower pulmonary veins to either the RA or superior vena cava (see Chapter 71).[5] An unroofed coronary sinus is rare and occurs as a result of a partial or complete absence of the wall between the inferior LA and the roof of the coronary sinus. An unroofed coronary sinus generally is associated with drainage of a left superior vena cava to the coronary sinus or LA.[6]

***Pathophysiology and Clinical Presentation.*** Small secundum ASDs may close spontaneously[7]; however, primum ASDs, sinus venosus defects, and coronary sinus defects generally do not decrease in size. Shunt volume is related to the size of the defect, right and left heart compliance, and pulmonary vascular resistance. Larger shunt volumes lead to right atrial, right ventricular, and pulmonary artery enlargement. Over time, pulmonary hypertension may develop.

Most infants and young children with ASDs are asymptomatic. ASDs usually are detected at about 6 months of age,[8] often during evaluation for a murmur or as an incidental finding on a chest radiograph. Older children with moderate to large ASDs may have symptoms of fatigue and dyspnea. In addition to pulmonary hypertension, older children and adults with ASDs may have atrial tachyarrhythmias or paradoxical strokes, a risk that increases with age.[9–12]

***Imaging.*** Chest radiography in the neonate usually shows that the heart is normal in size and pulmonary flow is normal. Findings in infancy and childhood include mild cardiomegaly related to right atrial and ventricular enlargement (Fig. 72.3). The LA is not enlarged, which distinguishes an ASD from other left-to-right shunt lesions. Usually main pulmonary artery enlargement and increased pulmonary vascularity is found if the pulmonary to systemic flow ratio is greater than two to one. If the patient has significant pulmonary hypertension, enlarged central pulmonary arteries and peripheral pulmonary arterial vessel tapering may be seen (e-Fig. 72.4).

Echocardiography is the imaging modality of choice to evaluate the location, size, direction of flow across the defect, atrial and ventricular chamber size, ventricular function, right ventricular systolic pressure, and to assess for associated cardiovascular abnormalities. Magnetic resonance imaging (MRI) or computed tomography (CT) may also be used for evaluation of the atrial septum in cases of poor acoustic windows[13] or to evaluate the pulmonary veins in patients with suspected sinus venosus defects (Videos 72.1 to 72.3).[14] Left and right ventricular size and quantitative systolic function can be assessed. Right ventricular volume overload is detected as diastolic septal flattening or diastolic bowing of the septum from right to left with severe volume overload. Comparison of right and left ventricular stroke volumes can be used to calculate the ratio of pulmonary to systemic arterial flow (Qp:Qs). Right ventricular pressure is assessed by evaluating the degree of tricuspid regurgitation and septal systolic position. Systolic septal flattening is indicative of elevated right ventricular pressure. Phase contrast MRI can be used to estimate the size of the ASD and to determine the direction and amount of atrial shunting by calculation of Qp:Qs (e-Fig. 72.5).[15]

***Treatment.*** Closure should be performed in childhood to avoid complications of arrhythmia, right ventricular dysfunction, pulmonary hypertension, and paradoxical embolus.[16] ASD closure can be performed surgically or via transcatheter closure; the latter procedure has become the primary therapy for anatomically favorable secundum defects. After closure, children with ASDs have an excellent prognosis.

## ATRIOVENTRICULAR SEPTAL DEFECT

***Overview.*** Atrioventricular septal defects (AVSDs) account for 4% of all cases of congenital heart disease.[17] Most patients with complete AVSD have Down syndrome.[18] AVSD is also associated with visceral heterotaxy syndromes.[19,20]

***Etiology.*** AVSD results from abnormal development of the embryologic endocardial cushions and produces a spectrum of disease (Fig. 72.6). In its mild form, partial AVSD, a crescent-shaped primum ASD is found in the inferior portion of the atrial septum immediately adjacent to the atrioventricular (AV) valves, along with an associated "cleft" mitral valve with separate mitral and tricuspid valve orifices. Persons with the complete form have an ostium primum defect, an inlet ventricular septal defect (VSD) beneath the plane of the AV valves, and a single or common AV valve, with variable leaflet size, location, and morphology. Most importantly, the common valve has two components that "bridge" the ventricular septum and may form attachments to the septal surface and/or both the right and left sides of the heart.[21] In most cases, the common AV valve is shared equally between the right and left ventricles, but the valve orifice may be unequally shared favoring either the right or left ventricle.[20] Components of common AV valves are referred to as left- or right-sided valves rather than mitral or tricuspid as there is a single valve annulus.

***Pathophysiology and Clinical Presentation.*** In complete AVSD, the amount of left-to-right shunting is generally large and related to the size of the ASD and VSD, right and left heart compliance, and pulmonary vascular resistance. The shunting may be interatrial, interventricular, or typically both. Significant left AV valve insufficiency can exacerbate congestive heart failure.

## Abstract:

Systemic to pulmonary arterial shunts refers to any physiologic shunting in which fully oxygenated blood intended for systemic circulation is diverted to the pulmonary circulation after return of systemic venous blood to the heart. This results in the mixing of fully oxygenated blood with deoxygenated blood. The result of this shunting leads to increased pulmonary blood flow and is not associated with clinical cyanosis. The clinical presentations, pathologic features and characteristic imaging findings are dependent on the location of such a shunt as well as the degree of shunting that occurs. These shunts include atrial septal defects, atrioventricular septal defects, ventricular septal defects, patent ductus arteriosus and aortopulmonary windows. This chapter is a concise review of the etiologies, pathophysiology, clinical presentations, imaging findings and treatment of these defects.

## Keywords:

atrial septal defect
ventricular septal defect
patent ductus arteriosus
AP window
atrioventricular septal defect

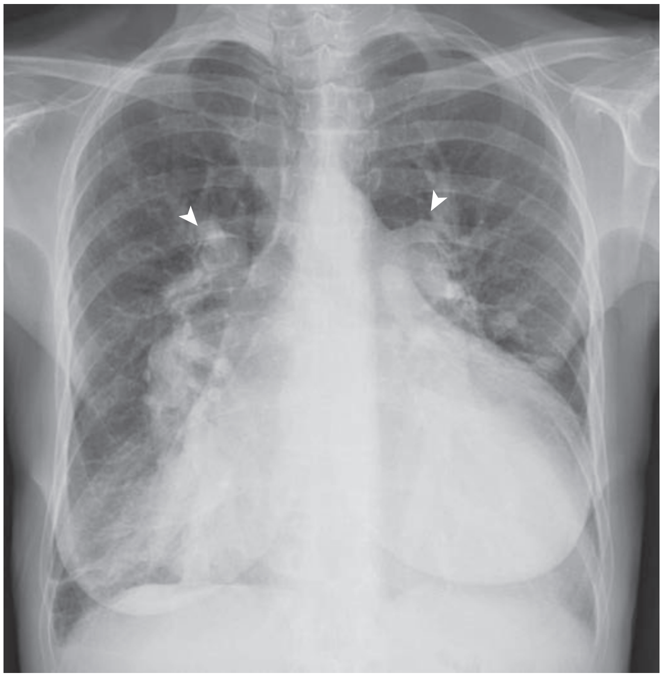

**e-Figure 72.4. Atrial septal defect and pulmonary hypertension.** Frontal chest radiograph of an adult with an atrial septal defect and Eisenmenger syndrome shows moderate to severe cardiomegaly with enlarged central pulmonary arteries *(arrowheads)* and peripheral tapering of pulmonary vessels.

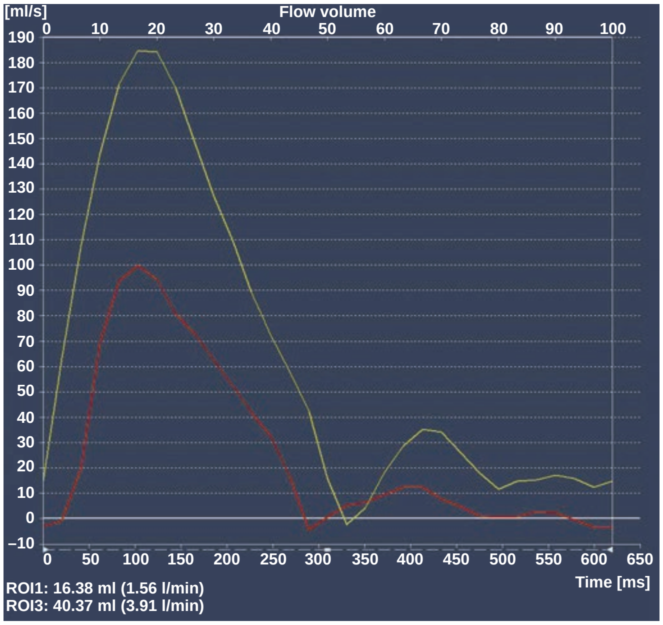

**e-Figure 72.5.** Curves representing blood flow in the aorta *(red)* and pulmonary artery *(yellow)* obtained by phase contrast magnetic resonance imaging in a child with an atrial septal defect. The pulmonary flow is 3.9 L/min, the systemic flow is 1.6 L/min, and the pulmonary-to-systemic flow ratio is 2.5 : 1, indicating a significant left-to-right shunt.

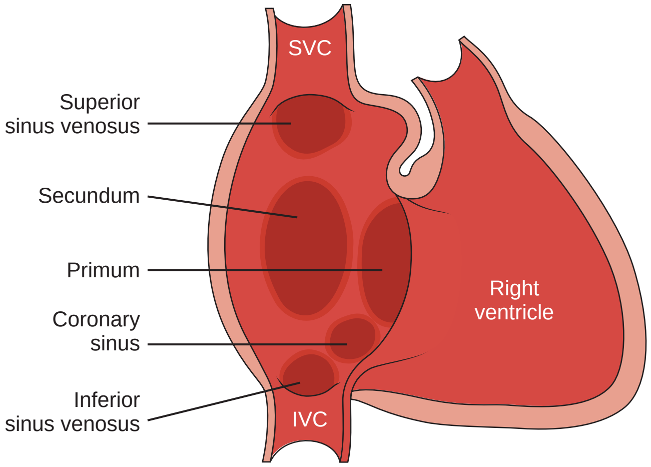

**Figure 72.1.** Diagram showing the types of atrial septal defects as viewed from the right atrium. *IVC,* Inferior vena cava; *SVC,* superior vena cava. *(Modified from Rigsby ML. Atrial septal defect. In Gatzoulis MA, Webb GD, Daubeney PEF, eds.* Diagnosis and Management of Adult Congenital Heart Disease, *Edinburgh: Churchill Livingstone; 2003.)*

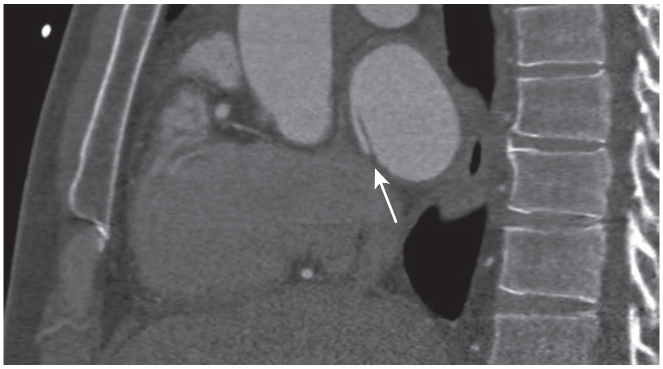

**Figure 72.2. Patent foramen ovale in a teenage boy.** Short-axis CT angiography image of the heart at the level of the atria shows the flap valve of a patent foramen ovale *(arrow)*. *(Courtesy B. Kelly Han, Minneapolis Heart Institute/Children's Hospitals and Clinics of Minnesota.)*

Infants with complete AVSD present with tachypnea, tachycardia, and signs of congestive heart failure as pulmonary resistance falls during the newborn period. Patients with partial AVSD may be asymptomatic as infants and young children, although symptoms may develop early in life if significant associated mitral valve regurgitation is present.[22]

***Imaging.*** The amount of left-to-right shunting is reflected on the chest radiograph and may reflect the physiology of either the ASD, VSD, or both. In complete AVSD, findings include moderate to marked cardiomegaly with right atrial and right ventricular enlargement and increased pulmonary vascularity (Fig. 72.7). Left atrial enlargement may be seen in large VSDs or, if significant, associated left AV valve insufficiency is present. Children with large left-to-right shunts commonly have lung hyperinflation, which may be related to an increase in airway resistance from enlarged pulmonary arteries and veins or to an increase in lung volume related to the increase in blood volume.

Echocardiography is the primary modality for evaluation of AVSD, but MRI can be used as an adjunct in complex cases, especially when an accurate assessment of right and left ventricular size is needed.[23,24] Components to evaluate include the ostium primum portion of the atrial septum and the inlet portion of the ventricular septum, the AV valve leaflet morphology and attachments, the papillary muscle architecture, the level and direction of shunting, ventricle size and systolic function, and the presence of outflow tract obstruction or other cardiovascular anomalies (Fig. 72.8).

***Treatment.*** Patients with partial AVSD generally undergo complete surgical repair between 1 and 4 years of age. For patients with complete AVSD, early repair between 2 and 4 months of life is recommended to avoid the development of significant pulmonary hypertension.[20] Surgical goals include ASD and VSD closure with creation of two patent and competent AV valves, and preservation of the conduction system. Long-term survival after repair for partial and complete AVSD is excellent.[18,25–27]

## VENTRICULAR SEPTAL DEFECT

***Overview.*** Isolated VSD accounts for approximately 20% of all cases of congenital heart disease, with an incidence of approximately 2 per 1000 live births.[28] Isolated VSDs are slightly more common in girls than in boys.[29,30] VSD may be isolated or part of a complex congenital heart malformation.[31–33]

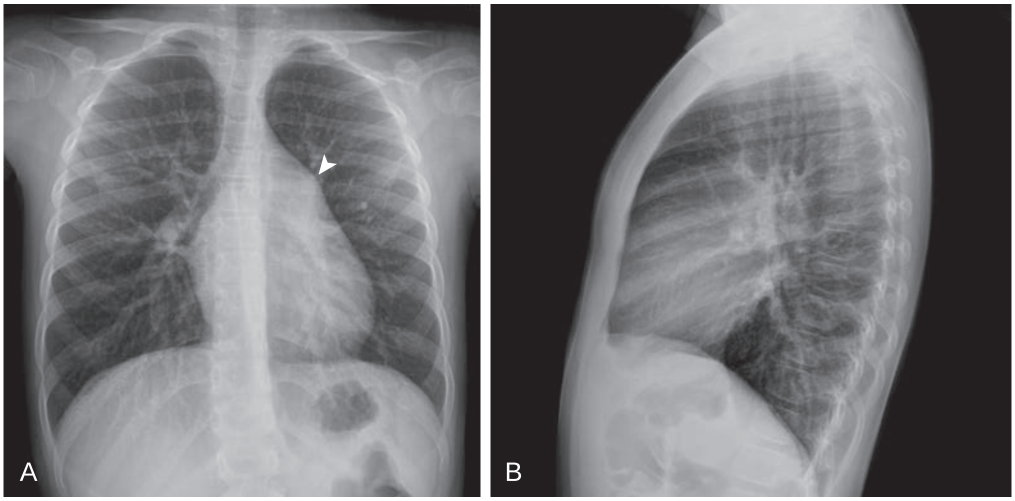

**Figure 72.3. Atrial septal defect, secundum type, in a 7-year-old.** Frontal (A) and lateral (B) views of the chest show mild cardiomegaly, a prominent pulmonary artery *(arrowhead)*, and increased pulmonary vascularity without left atrial dilation.

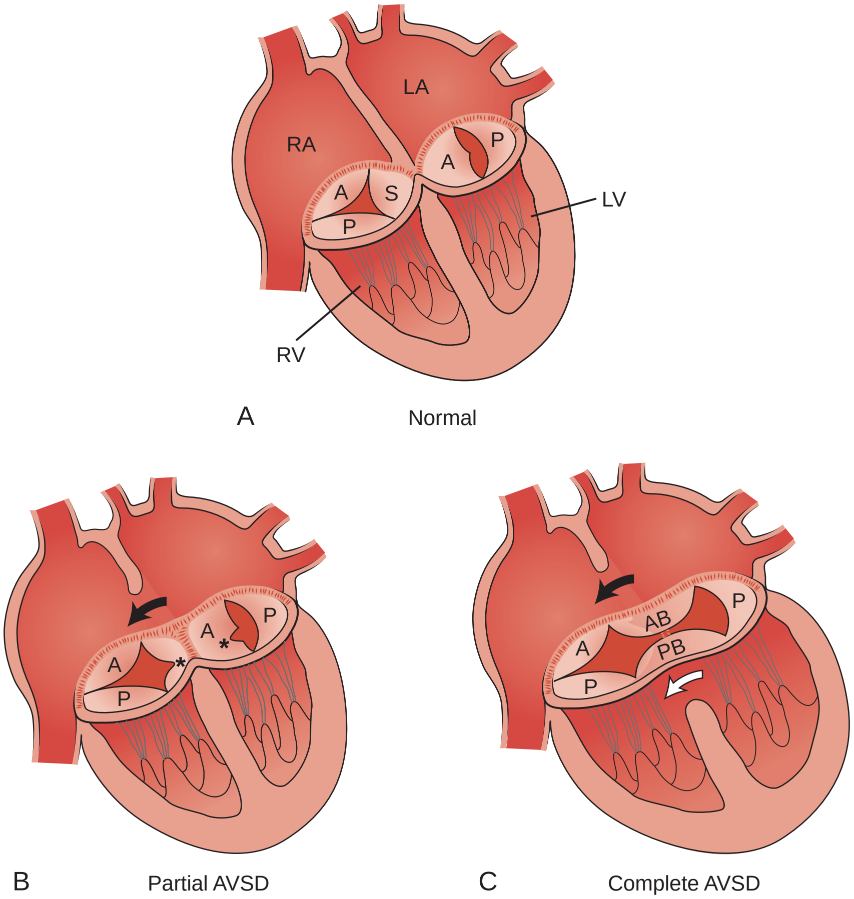

**Figure 72.6. Diagrams illustrating the spectrum of atrioventricular septal defect (AVSD).** (A) The normal tricuspid valve has three leaflets, anterior *(A)*, posterior *(P)*, and septal *(S)*, and the normal mitral valve has two leaflets, anterior *(A)* and posterior *(P)*. (B) Partial AVSD showing the clefts *(asterisks)* in the septal leaflet of the tricuspid valve, the anterior leaflet of the mitral valve, and the ostium primum atrial septal defect (ASD) *(arrow)*. (C) Complete AVSD showing the common atrioventricular valve with the anterior bridging *(AB)* and posterior bridging *(PB)* leaflets, the ostium primum ASD *(black arrow)*, and the inlet ventricular septal defect *(white arrow)*. *LA,* Left atrium; *LV,* left ventricle; *RA,* right atrium; *RV,* right ventricle. *(Modified from Park MK. Left-to-right shunt lesions. In Park MK, ed.* Pediatric Cardiology for Practitioners, *St Louis: Mosby Elsevier; 2002.)*

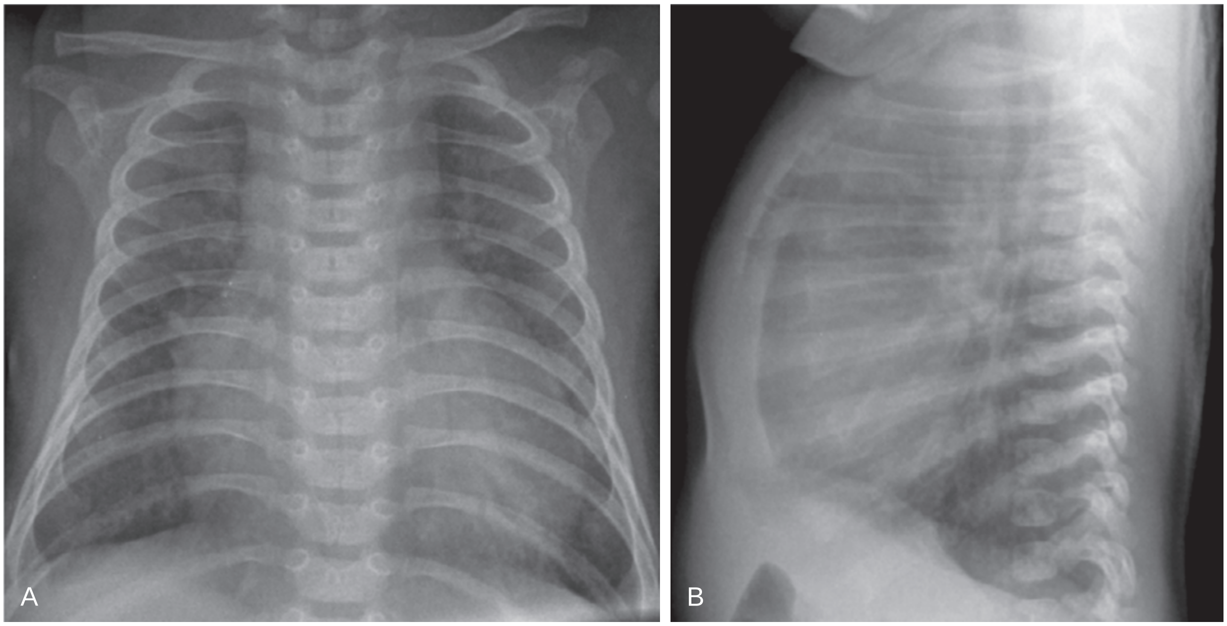

**Figure 72.7. Atrioventricular septal defect in a 6-week-old.** Frontal (A) and lateral (B) views of the chest show moderate cardiomegaly with enlargement of the right atrium and ventricle, increased pulmonary vascularity, and lung hyperinflation.

***Etiology.*** The ventricular septum can be divided into four components, and VSDs may involve one or more of these components (Table 72.1). The inlet septum extends from the tricuspid annulus to the septal attachments of the tensor apparatus of the tricuspid valve. AVSD is associated with a defect in this portion of the septum. The muscular septum involves the trabeculated portion of the right ventricle and extends from the tricuspid valve attachments to the apex of the ventricle and up to the septal band. Single or multiple muscular defects can be present in this portion of the septum. The outlet or conal portion of the ventricular septum separates the ventricular outflow tracts and, when viewed from the right ventricle, extends from the septal band to the pulmonary valve. The thin, membranous septum lies adjacent to the anteroseptal commissure of the tricuspid valve on the right side of the heart and to the right and noncoronary cusps of the aortic valve on the left side. Approximately 80% of VSDs involve the area around the membranous septum (Fig. 72.9).[34,35]

***Pathophysiology and Clinical Presentation.*** The physiologic effect of a VSD is determined by its size, right and left heart compliance, and pulmonary vascular resistance. Small defects offer high resistance to flow, and large defects offer low resistance to flow. Large defects subject the pulmonary vasculature to high flow and high pressure, which frequently results in pulmonary hypertension.

Symptoms vary depending on the size of the VSD and the degree of left-to-right shunting. At birth, pulmonary resistance is high, limiting left-to-right shunting. As pulmonary resistance falls during early infancy, left-to-right shunting increases. When shunting becomes significant, failure to thrive, dyspnea, and congestive heart failure may be seen. Irreversible pulmonary hypertension can develop within 2 to 3 years and frequently is seen in young adults.[32]

***Imaging.*** Chest radiograph findings vary depending on the size of the VSD and are normal in a person with a small VSD. Findings

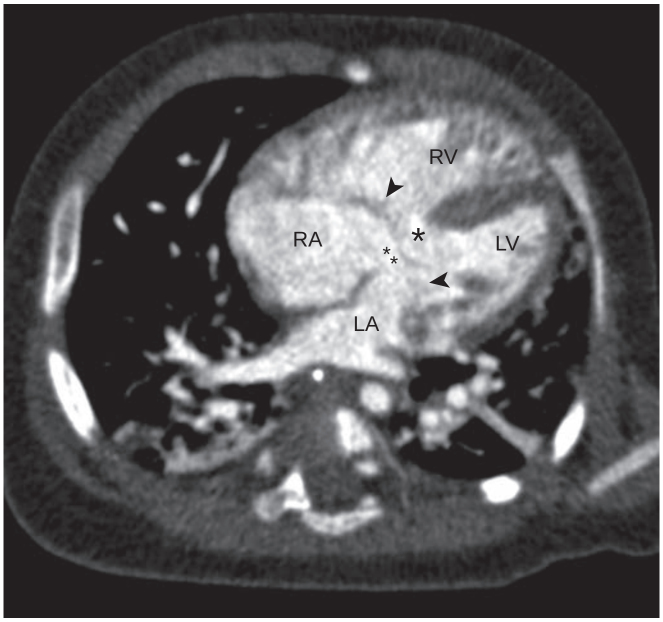

**Figure 72.8. Complete atrioventricular septal defect (AVSD).** Four-chamber view from a contrast enhanced CT angiography study in an infant with a balanced AVSD shows the ostium primum defect *(double asterisks)*, inlet ventricular septal defect *(single asterisk)*, and common atrioventricular valve *(arrowheads)* that bridges the right and left sides of the heart. *LA,* Left atrium; *LV,* left ventricle; *RA,* right atrium; *RV,* right ventricle.

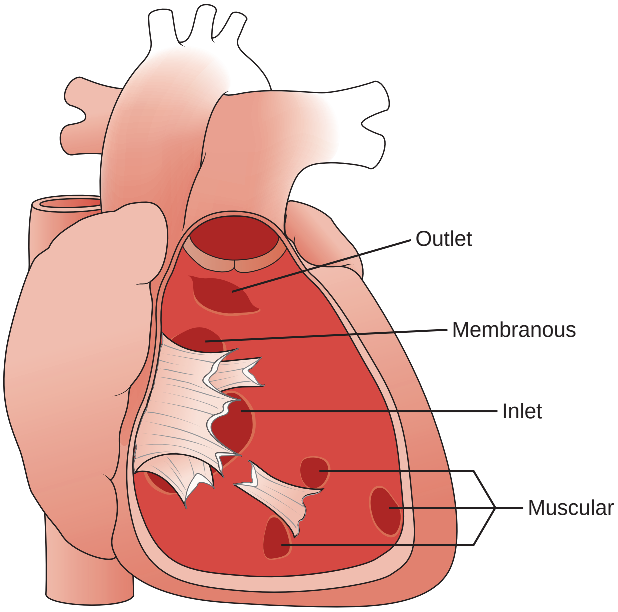

**Figure 72.9.** Diagram showing ventricular septal defect locations as viewed from the right ventricle. *(Modified from Fyler DC. Ventricular septal defects. In Fyler DC, ed.* Nadas' Pediatric Cardiology, *Philadelphia: Hanley & Belfus; 1992.)*

**TABLE 72.1** Classification of Ventricular Septal Defects

| Type | Synonym | Frequency | Associated Features |
|---|---|---|---|
| Membranous | Perimembranous<br>Paramembranous<br>Conoventricular<br>Infracristal | 80% | Adherence of tricuspid valve tissue to defect with left ventricle–right atrial shunt<br>Extension to muscular, inlet, or outlet septum<br>Anterior malalignment of the infundibular septum causing aortic override<br>Posterior malalignment of the ventricular septum causing subaortic stenosis<br>Small defects may spontaneously close |
| Inlet | Atrioventricular septal defect<br>Atrioventricular canal type | 5%-8% | — |
| Outlet | Conal<br>Subpulmonary<br>Doubly committed juxtaarterial<br>Supracristal<br>Infundibular | 5%-7% | Right coronary leaflet prolapse through defect<br>Aortic regurgitation<br>Dilation of the right sinus of Valsalva |
| Muscular | Trabecular<br>Marginal | 5%-20% | Small defects may spontaneously close<br>Defects may be multiple |

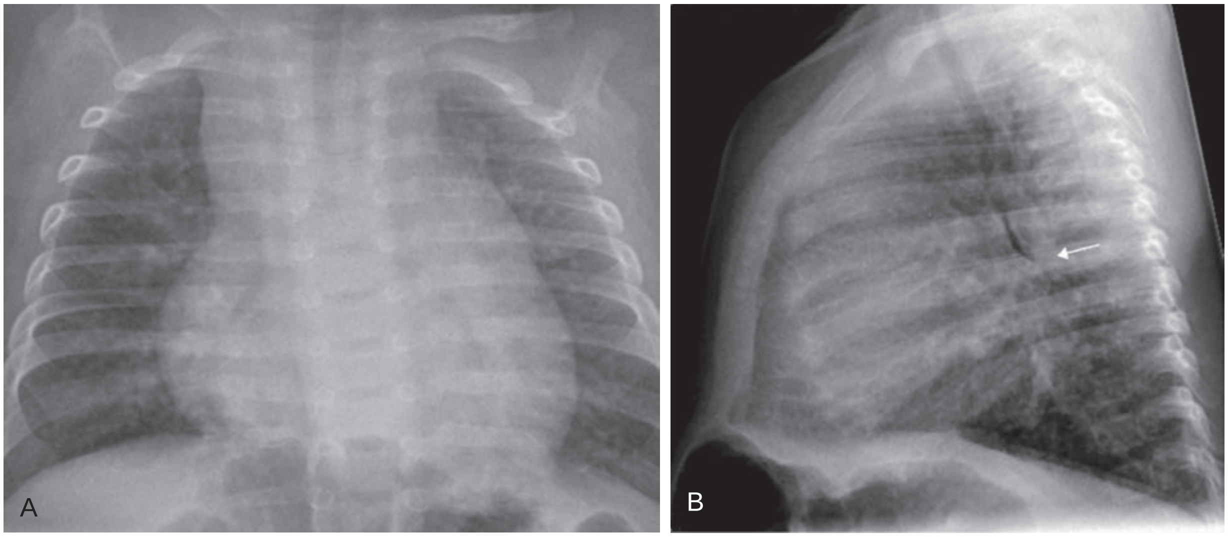

**Figure 72.10. Ventricular septal defect in a 3-month-old.** Frontal (A) and lateral (B) views of the chest show right atrial, right ventricular, and left atrial enlargement with posterior displacement of the left main stem bronchus (*arrow* in B) and increased pulmonary vascularity.

with moderate to large VSDs include cardiomegaly with enlargement of the LA, left ventricle, and pulmonary arteries and increased pulmonary blood flow (Fig. 72.10). Congestive heart failure occurs frequently in infants with a moderate or large defect. Pulmonary hypertension may be evident in older children or young adults.

Echocardiography is the imaging method of choice for evaluation of VSDs. Imaging goals include addressing the size, number, and location of VSDs and the degree of left-to-right or right-to-left shunting. Estimates of right ventricular and pulmonary artery pressures and right and left heart volumes are obtained. The tricuspid and aortic valves are evaluated for possible tethering of valve tissue into the borders of the defect. MRI and CT are useful for noninvasive evaluation of VSDs and hemodynamic consequences, with a reported 90% accuracy in detection (Fig. 72.11).[36,37] Phase contrast MRI measurements in the aorta and pulmonary artery or a comparison of right and left ventricular stroke volumes can be used to evaluate Qp:Qs, and qualitative assessment of the septal position can be used as a measure of ventricular volume and/or pressure overload.

***Treatment.*** During the first year of life, 80% to 90% of small (<0.5 cm) VSDs become smaller or completely close.[30] Operative correction is preferable before 6 months of age in patients with large VSDs to decrease the risk of developing irreversible pulmonary hypertension. Consideration for early closure of outlet defects is recommended to prevent development of aortic sinus prolapse and progressive valve regurgitation. The results of operative closure are excellent, with a very low risk of morbidity or mortality. VSDs are closed most frequently via a right atrial approach, but transpulmonary artery and transaortic approaches also are used. Transcatheter device closure is an alternative to surgery for selected single or multiple VSDs, usually in the muscular septum, and also has been used intraoperatively (e-Fig. 72.12).

## PATENT DUCTUS ARTERIOSUS

***Overview.*** Patent ductus arteriosus (PDA) accounts for approximately 10% of all congenital heart disease.[38] Approximately 20% to 30% of premature infants have a PDA, and the incidence increases with increased prematurity.[39] Complex congenital heart disease may include PDA with ductal dependent pulmonary or systemic blood flow.

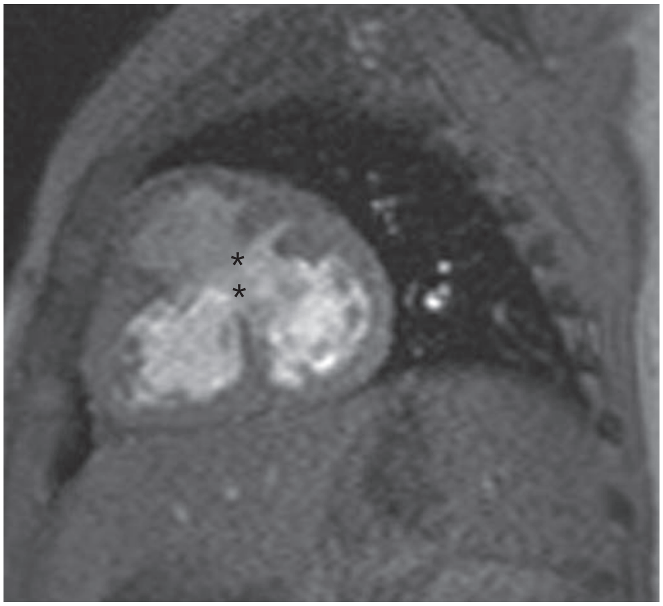

**Figure 72.11. A ventricular septal defect in a 2-year-old.** A short-axis steady-state free-precession magnetic resonance (MR) image shows a large muscular ventricular septal defect *(asterisks)*.

***Etiology and Pathophysiology.*** PDA represents the persistence of the embryologic sixth aortic arch, which most commonly connects the left pulmonary artery with the descending aorta just beyond the origin of the left subclavian artery (see Chapter 62). With a right arch, the ductus arteriosus may be on the right. Prostaglandins maintain ductal patency during fetal life. At birth, increased blood oxygen concentration causes constriction of the duct, usually within hours after birth. Ductal closure is delayed in premature infants with respiratory distress and hypoxia because the immature ductal tissue is less sensitive to oxygen-mediated constriction. In a majority of cases of PDA in term infants, the etiology is unknown.[40–42]

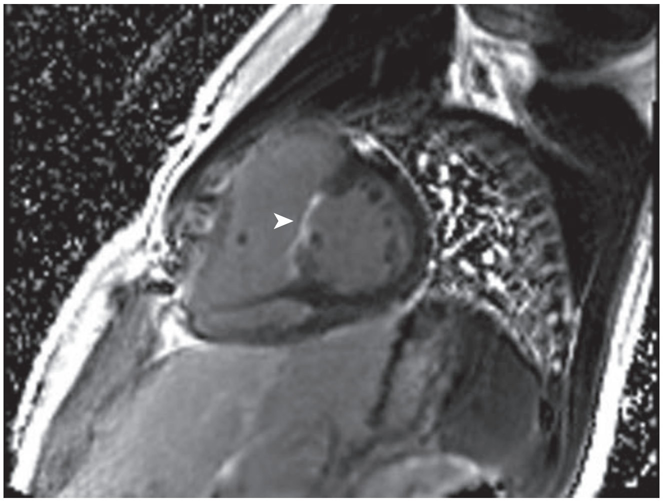

**e-Figure 72.12. Patch repair of a ventricular septal defect.** A short-axis delayed-enhancement MR image shows late enhancement corresponding to the location of the ventricular septal defect patch *(arrowhead)*. The patch is significantly thinner than the adjacent normal myocardium.

***Clinical Presentation.*** The amount of left-to-right shunting depends on the length and diameter of the duct and the degree of pulmonary hypertension. Pulmonary hypertension may develop if a large PDA is left untreated. In premature infants without significant lung disease, a PDA may become clinically apparent 24 to 72 hours after birth. Congestive heart failure occurs if the shunt is large. In premature infants with significant lung disease, the prevalence of PDA is greater than 80%. Screening echocardiography may detect a PDA in these infants before clinical manifestations occur. A term infant with a small PDA is generally asymptomatic, and the PDA often is detected because of the presence of a murmur. Term infants with moderate to large PDAs may display poor feeding, irritability, and failure to thrive and may have congestive heart failure.[43]

***Imaging.*** Pulmonary edema and cardiomegaly may be seen as signs of a PDA on a chest radiograph. In premature infants who exhibit lung infiltrates after the first few days of life, particularly with an increase in heart size, PDA should be considered. Chest radiographs of term infants with significant shunting show increased pulmonary blood flow and cardiomegaly (e-Fig. 72.13).

Echocardiography is the standard imaging technique for evaluating a PDA. Goals of imaging are to measure the PDA size and diameter, assess the amount of left-to-right or right-to-left shunting and the degree of pulmonary hypertension, and identify possible complicating factors such as a ductal aneurysm. CT or MRI may be used in conjunction with echocardiography to define anatomy in complicated cases and to determine Qp:Qs (Fig. 72.14).[44,45]

***Treatment.*** Indomethacin or ibuprofen therapy often are successful in achieving PDA closure in premature infants, followed by surgical ligation if medical therapy fails. Nonsurgical transcatheter closure is the method of choice for small to moderate PDAs in most term infants.[46,47] Larger PDAs in term infants generally are managed surgically. Patient prognosis is excellent if ductal closure is performed between 6 and 24 months of age.[48]

## AORTOPULMONARY WINDOW

Aortopulmonary (AP) window is rare and accounts for 0.2% cases of congenital heart disease.[49–52] AP window is the result of incomplete aortopulmonary septation resulting in communication between the ascending aorta and pulmonary artery. This defect creates a large, high-pressure, left-to-right shunt that usually is apparent clinically in the first weeks of life and is similar to a large PDA in pathophysiology.

***Imaging.*** Chest radiographic findings include cardiomegaly with left atrial and left ventricular enlargement, increased pulmonary blood flow, and prominence of the ascending aorta and pulmonary artery related to the left-to-right shunt at the level of the great vessels. Imaging is performed to evaluate the anatomy of the aortopulmonary window and its relationship to the aortic and pulmonary valves, to define the coronary anatomy, to estimate pulmonary pressure and ventricular function, to assess Qp:Qs, and to evaluate for other cardiovascular defects. Differentiation from truncus arteriosus is critical and is accomplished by the identification of two separate semilunar valves (Fig. 72.15).

***Treatment.*** Early surgical patch repair for large defects or suture repair for small defects to separate the great vessels should be performed before the development of pulmonary hypertension. The outcome following surgery generally is excellent.

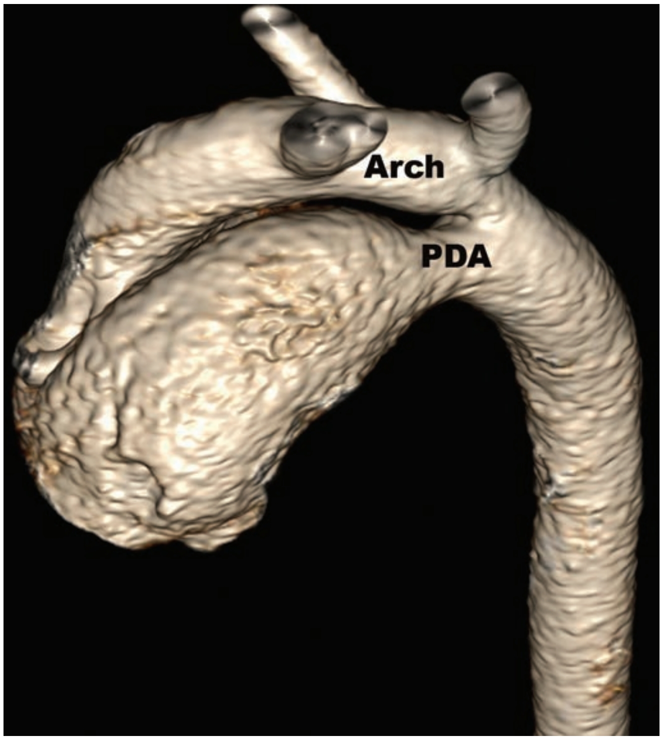

**Figure 72.14. Patent ductus arteriosus.** An anterior oblique volume-rendered CT angiogram shows near-parallel configuration between the aortic arch *(arch)* and the PDA.

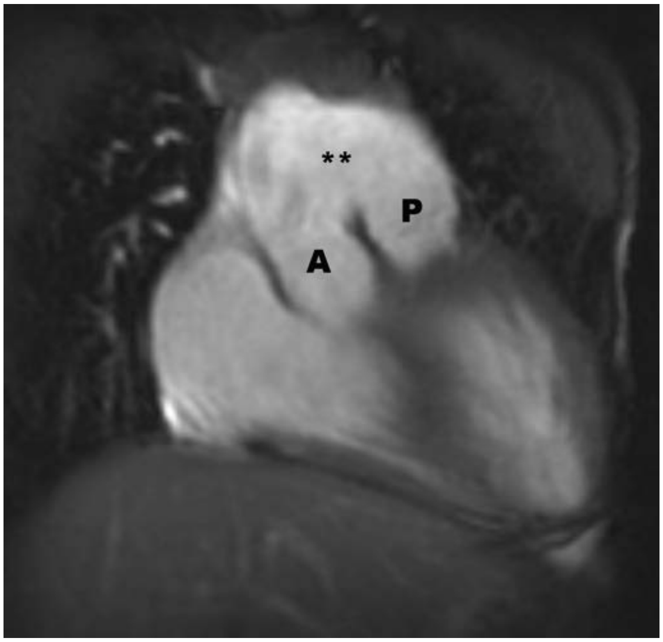

**Figure 72.15. Aortopulmonary window.** A coronal steady-state free-precession MR image shows separate origins of the aortic root *(A)* and pulmonary trunk *(P)* with a large communication *(asterisks)* between the ascending aorta and the pulmonary trunk. *(Courtesy Deborah L. Thompson, MD, Dalhousie University.)*

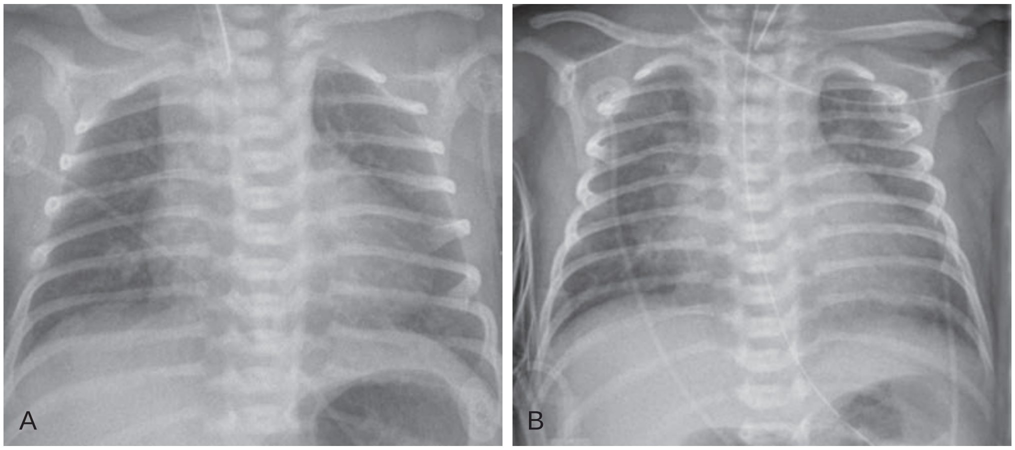

**e-Figure 72.13. Sequential chest radiographs in a newborn with a patent ductus arteriosus (PDA).** (A) Frontal chest radiograph on day 2 of life shows top normal heart size and normal pulmonary vascularity. (B) A chest radiograph on day 8 of life shows an increase in heart size and increased pulmonary vascularity consistent with a PDA diagnosed by echocardiography.

## KEY POINTS

- The most common cause of cardiomegaly in an acyanotic patient with increased pulmonary vascularity is VSD. Differential diagnosis includes ASD, AVSD, PDA, and aortopulmonary window.
- ASD does not cause left atrial enlargement, which distinguishes ASD from other left-to-right shunts.
- Phase contrast MRI can be used to assess the direction of flow and to determine the amount of shunting by calculation of the ratio of pulmonary to systemic flow (Qp:Qs).

## SUGGESTED READINGS

Rojas CA, El-Sherief A, Medina HM, et al. Embryology and developmental defects of the interatrial septum. *AJR Am J Roentgenol*. 2010;195(5):1100–1104.

Van Praagh R, Geva T, Kreutzer J. Ventricular septal defects: how shall we describe, name and classify them? *J Am Coll Cardiol*. 1989;14(5):1298–1299.

Wang ZJ, Reddy GP, Gotway MB, et al. Cardiovascular shunts: MR imaging evaluation. *Radiographics*. 2003;23(Spec No):S181–S194.

## REFERENCES

Full references for this chapter can be found on www.expertconsult.com.

## REFERENCES

1. Hagen PT, Scholz DG, Edwards WD. Incidence and size of patent foramen ovale during the first 10 decades of life: an autopsy study of 965 normal hearts. *Mayo Clin Proc*. 1984;59(1):17–20.
2. Schneider B, Zienkiewicz T, Jansen V, et al. Diagnosis of patent foramen ovale by transesophageal echocardiography and correlation with autopsy findings. *Am J Cardiol*. 1996;77(14):1202–1209.
3. Attenhofer Jost CH, Connolly HM, Danielson GK, et al. Sinus venosus atrial septal defect: long-term postoperative outcome for 115 patients. *Circulation*. 2005;112(13):1953–1958.
4. Rojas CA, El-Sherief A, Medina HM, et al. Embryology and developmental defects of the interatrial septum. *AJR Am J Roentgenol*. 2010;195(5):1100–1104.
5. Van Praagh S, Carrera ME, Sanders SP, et al. Sinus venosus defects: unroofing of the right pulmonary veins—anatomic and echocardiographic findings and surgical treatment. *Am Heart J*. 1994;128(2):365–379.
6. Raghib G, Ruttenberg HD, Anderson RC, et al. Termination of left superior vena cava in left atrium, atrial septal defect, and absence of coronary sinus; a developmental complex. *Circulation*. 1965;31:906–918.
7. Hanslik A, Pospisil U, Salzer-Muhar U, et al. Predictors of spontaneous closure of isolated secundum atrial septal defect in children: a longitudinal study. *Pediatrics*. 2006;118(4):1560–1565.
8. Porter C-BJ, Edwards JE. Atrial septal defects. In: Moss A, Allen H, eds. *Moss and Adams' Heart Disease in Infants, Children, and Adolescents: Including the Fetus and Young Adult*. Vol. 2. 7th ed. Philadelphia: Lippincott Williams & Wilkins; 2008.
9. Berger F, Vogel M, Kramer A, et al. Incidence of atrial flutter/fibrillation in adults with atrial septal defect before and after surgery. *Ann Thorac Surg*. 1999;68(1):75–78.
10. Gatzoulis MA, Freeman MA, Siu SC, et al. Atrial arrhythmia after surgical closure of atrial septal defects in adults. *N Engl J Med*. 1999;340(11):839–846.
11. Shah D, Azhar M, Oakley CM, et al. Natural history of secundum atrial septal defect in adults after medical or surgical treatment: a historical prospective study. *Br Heart J*. 1994;71(3):224–227, discussion 228.
12. Tikoff G, Schmidt AM, Hecht HH. Atrial fibrillation in atrial septal defect. *Arch Intern Med*. 1968;121(5):402–405.
13. Holmvang G, Palacios IF, Vlahakes GJ, et al. Imaging and sizing of atrial septal defects by magnetic resonance. *Circulation*. 1995;92(12):3473–3480.
14. Valente AM, Sena L, Powell AJ, et al. Cardiac magnetic resonance imaging evaluation of sinus vensosus defects. *Pediatr Cardiol*. 2007;28:51–56.
15. Powell AJ, Tsai-Goodman B, Prakash A, et al. Comparison between phase-velocity cine magnetic resonance imaging and invasive oximetry for quantification of atrial shunts. *Am J Cardiol*. 2003;91(12):1523–1525, A1529.
16. Backer CL, Mavroudis C. Atrial septal defect, partial anomalous pulmonary venous connection, and scimitar syndrome. In: Mavroudis C, Backer CL, eds. *Pediatric Cardiac Surgery*. 3rd ed. Philadelphia: Mosby; 2003.
17. Backer CL, Mavroudis C. Atrioventricular canal defects. In: Mavroudis C, Backer CL, eds. *Pediatric Cardiac Surgery*. 3rd ed. Philadelphia: Mosby; 2003.
18. Backer CL, Mavroudis C, Alboliras ET, et al. Repair of complete atrioventricular canal defects: results with the two-patch technique. *Ann Thorac Surg*. 1995;60(3):530–537.
19. Digilio MC, Marino B, Toscano A, et al. Atrioventricular canal defect without Down syndrome: a heterogeneous malformation. *Am J Med Genet*. 1999;85(2):140–146.
20. Shuhaiber JH, Ho SY, Rigby M, et al. Current options and outcomes for the management of atrioventricular septal defect. *Eur J Cardiothorac Surg*. 2009;35(5):891–900.
21. Rastelli GC, Ongley PA, Kirklin JW, et al. Surgical repair of the complete form of persistent common atrioventricular canal. *J Thorac Cardiovasc Surg*. 1968;55(3):299–308.
22. Clapp S, Perry BL, Farooki ZQ, et al. Down's syndrome, complete atrioventricular canal, and pulmonary vascular obstructive disease. *J Thorac Cardiovasc Surg*. 1990;100(1):115–121.
23. Grosse-Wortmann L, Yun TJ, Al-Radi O, et al. Borderline hypoplasia of the left ventricle in neonates: insights for decision-making from functional assessment with magnetic resonance imaging. *J Thorac Cardiovasc Surg*. 2008;136(6):1429–1436.
24. Banka P, Schaetzle B, Komarlu R, et al. Cardiovascular magnetic resonance parameters associated with early transplant-free survival in children with small left hearts following conversion of a univentricular to a biventricular circulation. *J Cardiovasc Magn Reson*. 2014;16(1):1.
25. Bogers AJ, Akkersdijk GP, de Jong PL, et al. Results of primary two-patch repair of complete atrioventricular septal defect. *Eur J Cardiothorac Surg*. 2000;18(4):473–479.
26. El-Najdawi EK, Driscoll DJ, Puga FJ, et al. Operation for partial atrioventricular septal defect: a forty-year review. *J Thorac Cardiovasc Surg*. 2000;119(5):880–889, discussion 889-890.
27. Stellin G, Vida VL, Milanesi O, et al. Surgical treatment of complete A-V canal defects in children before 3 months of age. *Eur J Cardiothorac Surg*. 2003;23(2):187–193.
28. Wells WJ, Lindesmith GG. Ventricular septal defect. In: Arciniegas E, ed. *Pediatric Cardiac Surgery*. Chicago: Year Book Medical Publishers; 1985.
29. Mavroudis C, Backer CL, Jacobs JP. Ventricular septal defect. In: Mavroudis C, Backer CL, eds. *Pediatric Cardiac Surgery*. 3rd ed. Philadelphia: Mosby; 2003.
30. Garne E. Atrial and ventricular septal defects—epidemiology and spontaneous closure. *J Matern Fetal Neonatal Med*. 2006;19(5):271–276.
31. Marino B, Papa M, Guccione P, et al. Ventricular septal defect in Down syndrome. Anatomic types and associated malformations. *Am J Dis Child*. 1990;144(5):544–545.
32. McDaniel NL, Gutgesell HP. Ventricular septal defects. In: Moss A, Allen H, eds. *Moss and Adams' Heart Disease in Infants, Children, and Adolescents: Including the Fetus and Young Adult*. Vol. 2. 7th ed. Philadelphia: Lippincott Williams & Wilkins; 2008.
33. Musewe NN, Alexander DJ, Teshima I, et al. Echocardiographic evaluation of the spectrum of cardiac anomalies associated with trisomy 13 and trisomy 18. *J Am Coll Cardiol*. 1990;15(3):673–677.
34. Soto B, Ceballos R, Kirklin JW. Ventricular septal defects: a surgical viewpoint. *J Am Coll Cardiol*. 1989;14(5):1291–1297.
35. Van Praagh R, Geva T, Kreutzer J. Ventricular septal defects: how shall we describe, name and classify them? *J Am Coll Cardiol*. 1989;14(5):1298–1299.
36. Didier D, Higgins CB. Identification and localization of ventricular septal defect by gated magnetic resonance imaging. *Am J Cardiol*. 1986;57(15):1363–1368.
37. Rajiah P, Kanne JP. Computed tomography of septal defects. *J Cardiovasc Comput Tomogr*. 2010;4(4):231–245.
38. Mitchell SC, Korones SB, Berendes HW. Congenital heart disease in 56,109 births. Incidence and natural history. *Circulation*. 1971;43(3):323–332.
39. Siassi B, Blanco C, Cabal LA, et al. Incidence and clinical features of patent ductus arteriosus in low-birthweight infants: a prospective analysis of 150 consecutively born infants. *Pediatrics*. 1976;57(3):347–351.
40. Gittenberger-de Groot AC. Persistent ductus arteriosus: most probably a primary congenital malformation. *Br Heart J*. 1977;39(6):610–618.
41. Gittenberger-de Groot AC, Strengers JL. Histopathology of the arterial duct (ductus arteriosus) with and without treatment with prostaglandin E1. *Int J Cardiol*. 1988;19(2):153–166.
42. Gittenberger-de Groot AC, Strengers JL, Mentink M, et al. Histologic studies on normal and persistent ductus arteriosus in the dog. *J Am Coll Cardiol*. 1985;6(2):394–404.
43. Moore P, Brook MM, Heymann MA. Patent ductus arteriosus and aortopulmonary window. In: Moss A, Allen H, eds. *Moss and Adams' Heart Disease in Infants, Children, and Adolescents: Including the Fetus and Young Adult*. Vol. 2. 7th ed. Philadelphia: Lippincott Williams & Wilkins; 2008.
44. Goitein O, Fuhrman CR, Lacomis JM. Incidental finding on MDCT of patent ductus arteriosus: use of CT and MRI to assess clinical importance. *AJR Am J Roentgenol*. 2005;184(6):1924–1931.
45. Wang ZJ, Reddy GP, Gotway MB, et al. Cardiovascular shunts: MR imaging evaluation. *Radiographics*. 2003;23(Spec No):S181–S194.
46. Dyamenahalli U, Smallhorn JF, Geva T, et al. Isolated ductus arteriosus aneurysm in the fetus and infant: a multi-institutional experience. *J Am Coll Cardiol*. 2000;36(1):262–269.
47. Butera G, De Rosa G, Chessa M, et al. Transcatheter closure of persistent ductus arteriosus with the Amplatzer duct occluder in very young symptomatic children. *Heart*. 2004;90(12):1467–1470.
48. Hillman ND, Mavroudis C, Backer CL. Patent ductus arterious. In: Mavroudis C, Backer CL, eds. *Pediatric Cardiac Surgery*. 3rd ed. Philadelphia: Mosby; 2003.

49. Backer CL, Mavroudis C. Surgical management of aortopulmonary window: a 40-year experience. *Eur J Cardiothorac Surg*. 2002;21(5):773–779.
50. Hew CC, Bacha EA, Zurakowski D, et al. Optimal surgical approach for repair of aortopulmonary window. *Cardiol Young*. 2001;11(4):385–390.
51. Tkebuchava T, von Segesser LK, Vogt PR, et al. Congenital aortopulumonary window: diagnosis, surgical technique and long-term results. *Eur J Cardiothorac Surg*. 1997;11(2):293–297.
52. van Son JA, Puga FJ, Danielson GK, et al. Aortopulmonary window: factors associated with early and late success after surgical treatment. *Mayo Clin Proc*. 1993;68(2):128–133.

# 73

# Left Heart Lesions

*Amanda M. Perak, Brian Reilly, Joshua D. Robinson, and Cynthia K. Rigsby*

## HYPOPLASTIC LEFT HEART SYNDROME

***Overview.*** Hypoplastic left heart syndrome (HLHS) is a spectrum of disease characterized by underdevelopment of the left ventricle with obstruction or atresia of ventricular inflow and outflow. HLHS accounts for approximately 2% to 3% of all cases of congenital heart disease, with a slight male predominance.[1,2] HLHS is most commonly isolated, but extracardiac anomalies occur in up to 30%[3] and a variety of genes and syndromes may be associated.

***Etiology and Pathophysiology.*** The structural defects of HLHS include varying degrees of hypoplasia of left heart structures: hypoplastic ascending aorta and arch (often with discrete coarctation), aortic valve atresia or stenosis, hypoplastic left ventricle, and mitral atresia or stenosis (Fig. 73.1). Patent ductus arteriosus (PDA) and patent foramen ovale or atrial septal defect (ASD) are essential for survival. The ventricular septum is intact, and endocardial fibroelastosis or thickening of the left ventricular endocardium may be present.[4] Right heart structures are typically enlarged,[5] and the tricuspid valve may be abnormal and regurgitant.[6]

Both the pulmonary and systemic circulations depend on the right ventricle. Oxygenated pulmonary venous blood returns to the left atrium, and because of the significant left ventricular inflow obstruction and decreased compliance, an obligatory left-to-right shunt is present at the atrial level through a patent foramen ovale or ASD. In the right atrium, the oxygenated pulmonary venous blood mixes with deoxygenated systemic venous blood and flows into the right ventricle. Blood is pumped to the pulmonary artery, with systemic blood then flowing from right to left through the PDA. The brachiocephalic vessels and coronary arteries are perfused through retrograde flow from the PDA into the arch and ascending aorta. The descending aorta is perfused from antegrade flow through the PDA.

***Clinical Presentation.*** Cyanosis and tachypnea generally are apparent within hours to 2 days after birth.[7] With the normal postnatal drop in pulmonary vascular resistance, pulmonary blood flow increases and systemic blood flow decreases, leading to respiratory distress and poor systemic perfusion. As the PDA constricts, perfusion of the ductal-dependent systemic and coronary circulations further declines, with resulting myocardial ischemia, shock, and death. In the setting of poor arteriovenous mixing as a result of inadequate interatrial communication, shock and death may occur almost immediately after birth without intervention.

***Imaging.*** HLHS is readily identified in utero by the obstetric ultrasound four-chamber cardiac view, with approximately 60% of cases diagnosed prenatally.[8,9] Chest radiographic findings are variable. If the interatrial communication is unrestrictive, there is progressively increasing pulmonary overcirculation with increased vascularity and cardiomegaly after the first hours of life (e-Fig. 73.2). With a restrictive atrial septum, the heart size may be normal with pulmonary venous congestion that may be misinterpreted as primary lung disease.

Echocardiography is the imaging method of choice and generally delineates all relevant presurgical anatomy. Cross-sectional imaging can be performed as an adjunct to echocardiography in complex cases.[10] Magnetic resonance imaging (MRI) may be especially useful when the left ventricle is marginally hypoplastic and the possibility exists of a two-ventricle surgical repair, whether in the neonatal period or after initial single-ventricle palliation (Fig. 73.3 and Video 73.1).[4,11] In these cases, MRI quantifies left ventricular volume, left versus right ventricular stroke volumes, and mitral versus tricuspid valve inflows to help plan the most appropriate surgical repair. MRI is also increasingly being used after the first stage of the palliative single ventricle surgery to quantify systemic right ventricular systolic function and tricuspid regurgitation and to evaluate for residual or recurrent coarctation and pulmonary artery stenosis or hypoplasia before the second-stage bidirectional cavopulmonary anastomosis.[12–14] Less frequently, cardiac computed tomography angiography (CTA) may be used for preoperative vascular evaluation.[15] After the third-stage Fontan completion procedure, MRI (Fig. 73.4) is complementary to echocardiography, particularly in older patients with poor acoustic windows, and can improve risk stratification for transplant-free survival in this population.[16,17]

***Treatment.*** Initial medical management includes intravenous prostaglandin $E_1$ (PGE$_1$) to maintain ductal patency. Ventilatory strategies and medications may be required to maintain adequate systemic perfusion and minimize pulmonary edema by optimizing the ratio of pulmonary to systemic blood flow.[18]

Surgical treatment consists of a three-stage reconstruction procedure (Fig. 73.5). The goal is to create in-series pulmonary and systemic circulations, with right ventricular support of the systemic circulation and passive flow through the pulmonary circulation. This allows for normal arterial oxygen saturation and decreases the volume load on the systemic right ventricle, but the reconstruction must be staged to account for the high neonatal pulmonary vascular resistance and subsequent decrease over the first year of life.

Stage I of the reconstruction—the Norwood procedure—often is performed in the first week of life.[19] The goals of this procedure are to relieve any obstruction to atrial mixing, provide unobstructed systemic and coronary blood flow, and create a stable but restrictive source of pulmonary blood flow. A complete atrial septectomy is performed. The PDA is ligated, and the neo-aortic outflow is created by transecting the main pulmonary artery and anastomosing it to the hypoplastic ascending aorta (Damus-Kaye-Stansel anastomosis), with use of a homograft patch to augment the hypoplastic ascending aorta and aortic arch. Blood flow to the lungs is reestablished either via a right ventricle to pulmonary artery (RV-PA) conduit (Sano shunt)[20] or via a modified Blalock-Taussig shunt (BT shunt) from the subclavian or brachiocephalic artery to the branch pulmonary arteries (Fig. 73.6). If a BT shunt is used, there is diastolic runoff through the shunt that may lead to excessive pulmonary blood flow and "steal" from the coronary and systemic circulation. Conversely, the RV-PA conduit is associated with pulmonary regurgitation and potential right ventricular volume overload, a need for ventriculotomy and potential right ventricular dysfunction, and potential aneurysm formation or pulmonary artery distortion at the site of the conduit insertion.[1,20]

By approximately 3 to 6 months of age, pulmonary vascular resistance has physiologically dropped, and stage II of the reconstruction—the bidirectional cavopulmonary anastomosis (Glenn) or hemi-Fontan procedure—is performed to redirect the upper body systemic venous return directly to the lungs. The superior vena cava (SVC) is anastomosed to the right pulmonary artery, and the SVC is either transected from the right atrium

## Abstract:

This chapter addresses obstructive left heart lesions, including hypoplastic left heart syndrome (HLHS), sub-valvar, valvar, and supravalvar aortic stenosis, and coarctation of the aorta. All have the physiologic similarity of obstruction to systemic outflow, and they often coexist. On the other hand, they vary widely in their prevalence, associations, presentation, and management. Aortic stenosis is most common, accounting for 10% of congenital heart disease cases, and is most often (95%) associated with bicuspid aortic valve, which is found in 1–2% of the general population. HLHS is most rare, accounting for 2–3% of congenital heart disease cases. While HLHS is associated with extracardiac anomalies in up to 30%, valvar aortic stenosis is most commonly isolated, and supravalvar aortic stenosis and coarctation are sometimes associated with typical genetic syndromes. The initial presentation of left heart obstructive lesions ranges from in utero or the first days of life for HLHS, to as late as adulthood for the mildest forms of aortic stenosis. Management varies from staged surgical palliation starting in the neonatal period for HLHS, to the possibility for prolonged medical management in cases of aortic stenosis.

## Keywords:

aortic stenosis
hypoplastic left heart syndrome
coarctation
bicuspid aortic valve

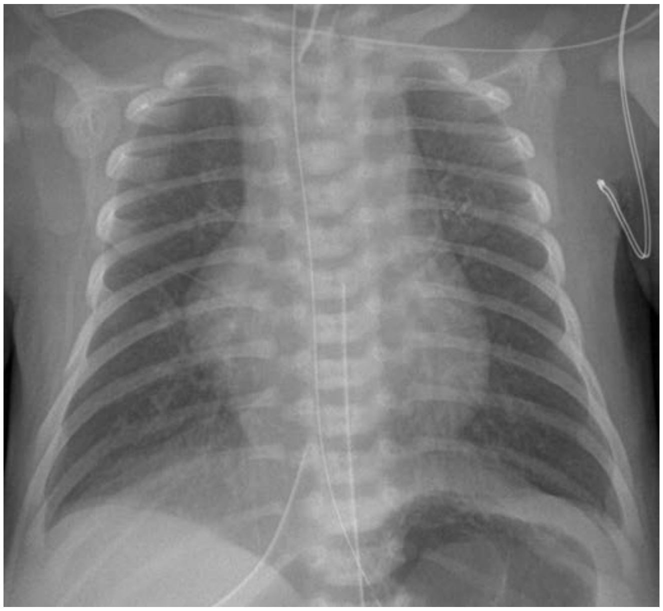

**e-Figure 73.2. Newborn with hypoplastic left heart syndrome.** A frontal view of the chest shows a globular cardiac silhouette, consistent with multichamber enlargement. Mild perihilar haziness also is present, indicative of mild venous congestion.

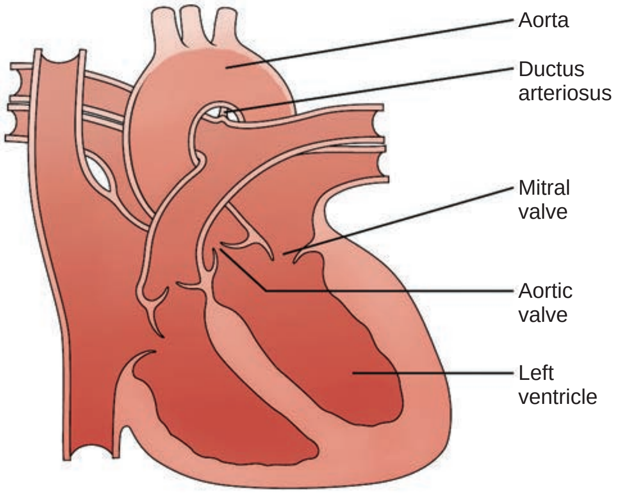

Normal

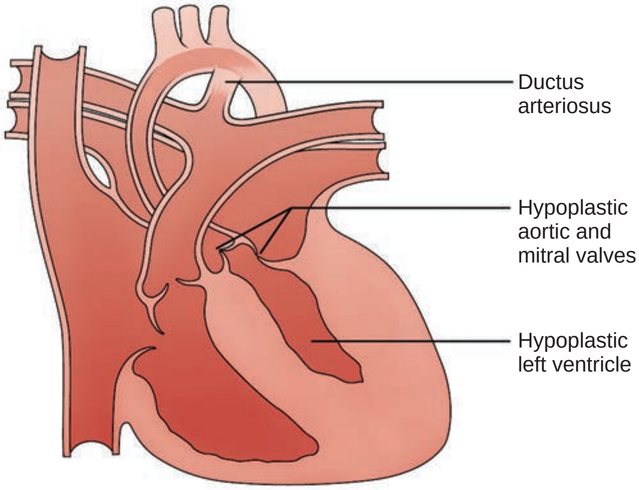
Ductus arteriosus
Hypoplastic aortic and mitral valves
Hypoplastic left ventricle

Hypoplastic left heart syndrome

**Figure 73.1. Diagram of hypoplastic left heart syndrome.** Compared with the normal heart, the mitral and aortic valves are severely hypoplastic or atretic, the left ventricular cavity and aorta are hypoplastic, and systemic blood flow is supplied by the patent ductus arteriosus. *(From American Heart Association. Hypoplastic left heart syndrome. www.americanheart.org. © 2006, American Heart Association, Inc.)*

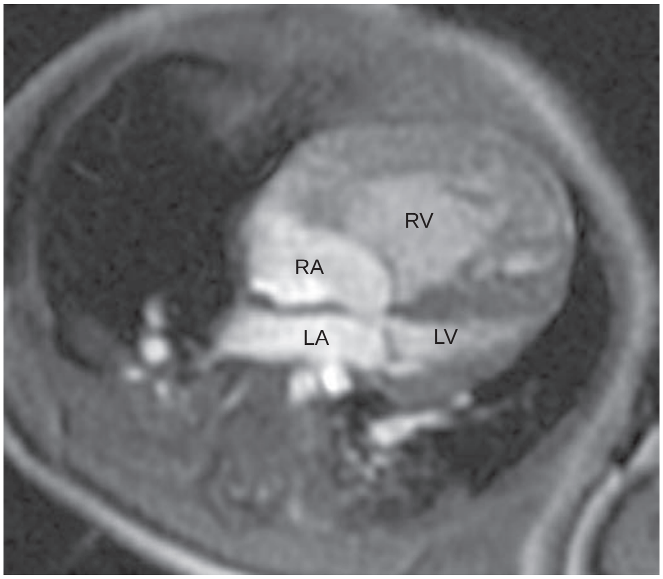

**Figure 73.3. Hypoplastic left heart syndrome.** Four-chamber steady-state free-precession (SSFP) magnetic resonance (MR) image of a 12-week-old with a marginally hypoplastic left ventricle to evaluate for a two-ventricle versus single-ventricle repair. The left atrium *(LA)* and left ventricle *(LV)* are small, with the left ventricular volume calculated at 24.2 mL/m$^2$. The study also showed adequate mitral and aortic valve dimensions. Based on the MRI measurements, the patient underwent a successful two-ventricle repair. See Video 73.1 for a four-chamber cine SSFP MRI of the same patient. *RA,* Right atrium; *RV,* right ventricle.

(Glenn procedure) or isolated from the right atrium with a patch (hemi-Fontan procedure). The BT shunt is divided or the RV-PA conduit is obliterated, and, if necessary, tricuspid valve repair and pulmonary artery angioplasty are performed.

As an alternative to the typical stage I and II procedures previously described, a "hybrid" approach may be undertaken to avoid cardiopulmonary bypass in the fragile neonatal period, particularly when mortality risk is high (e.g., low birth weight or cerebrovascular accident).[1,21] The hybrid stage I procedure combines transcatheter ductus arteriosus stenting to provide systemic flow and surgical branch pulmonary artery banding to limit pulmonary blood flow (e-Fig. 73.7). The comprehensive stage II procedure then must involve creation of the Damus-Kaye-Stansel anastomosis and reconstruction of the aortic arch, removal of the PDA stent and pulmonary artery bands, repair of the pulmonary arteries, atrial septectomy, and the Glenn or hemi-Fontan procedure.[1,21]

Stage III of the reconstruction—the Fontan completion procedure—is generally performed at 18 to 36 months of age (see Fig. 73.4). Inferior vena cava blood flow is directed to the pulmonary arteries either via an extracardiac conduit or an intracardiac right atrial baffle (lateral tunnel). If the stage II procedure was a hemi-Fontan, the lateral tunnel is created and the SVC patch is removed. The Fontan procedure achieves complete separation of the systemic and pulmonary circulations. A fenestration may be left in the Fontan circuit as a "pop-off" into the heart if Fontan pressures are high, and this may lead to a more stable postoperative course.[22,23] Many fenestrations close spontaneously, or they can be closed with a device at later cardiac catheterization.

Survival after the three-stage palliative procedure has improved steadily and now approaches 70%.[9] The stage I Norwood procedure carries the highest mortality, ranging from 7% to 19%.[20] Cardiac transplantation had been considered an alternative to staged Norwood palliation in the past, but because of limited donor availability and the recent improvement in survival after Norwood palliation, transplantation now generally is reserved for patients in whom staged palliation has failed.[1,24]

## AORTIC STENOSIS

***Overview.*** Left ventricular outflow tract (LVOT) obstruction can occur at the level of the aortic valve or in the subvalvar or supravalvar regions. This spectrum of disease represents approximately 10% of cases of congenital heart disease.[25] Valvar aortic stenosis (AS) is by far the most common form of LVOT obstruction and has a male predominance of nearly 80%.[26] Supravalvar AS accounts for 1% to 2% of AS in childhood and is a manifestation of elastin-related arteriopathy; it may occur spontaneously, via autosomal dominant transmission, or in up to 50% as part of Williams syndrome.[27] Subvalvar AS is more common than supravalvar AS[28]; it also has a male predominance and may be associated with more complex disease such as double-outlet right ventricle and transposition of the great arteries.

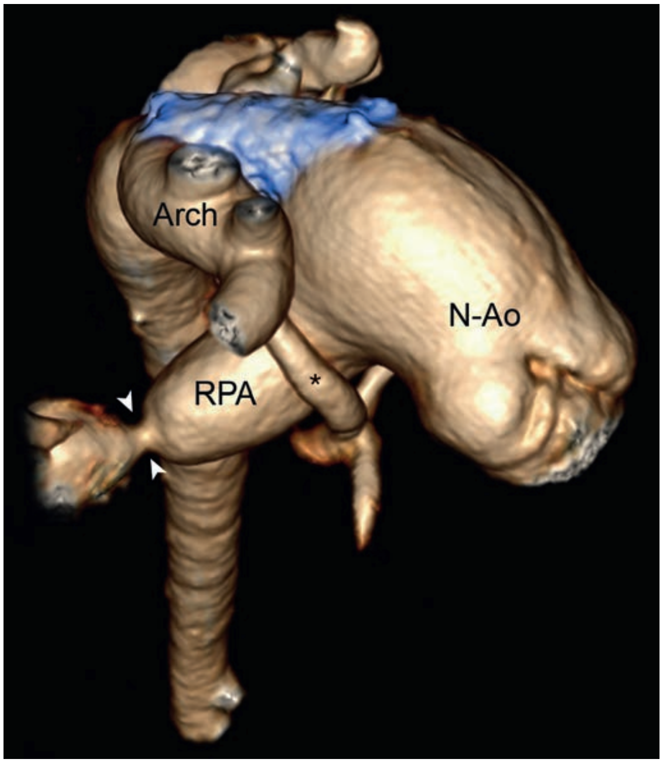

**e-Figure 73.7. A 5-month-old with hypoplastic left heart syndrome after the hybrid procedure.** Anterior oblique volume-rendered computed tomographic angiography shows the hypoplastic native aorta *(asterisk)*. A stent *(blue)* has been placed to keep the large patent ductus arteriosus open and bilateral branch pulmonary artery bands have been placed to limit pulmonary blood flow (*arrowheads* denote the right pulmonary artery band). *Arch,* Transverse aortic arch; *N-Ao,* neo-aorta; *RPA,* right pulmonary artery.

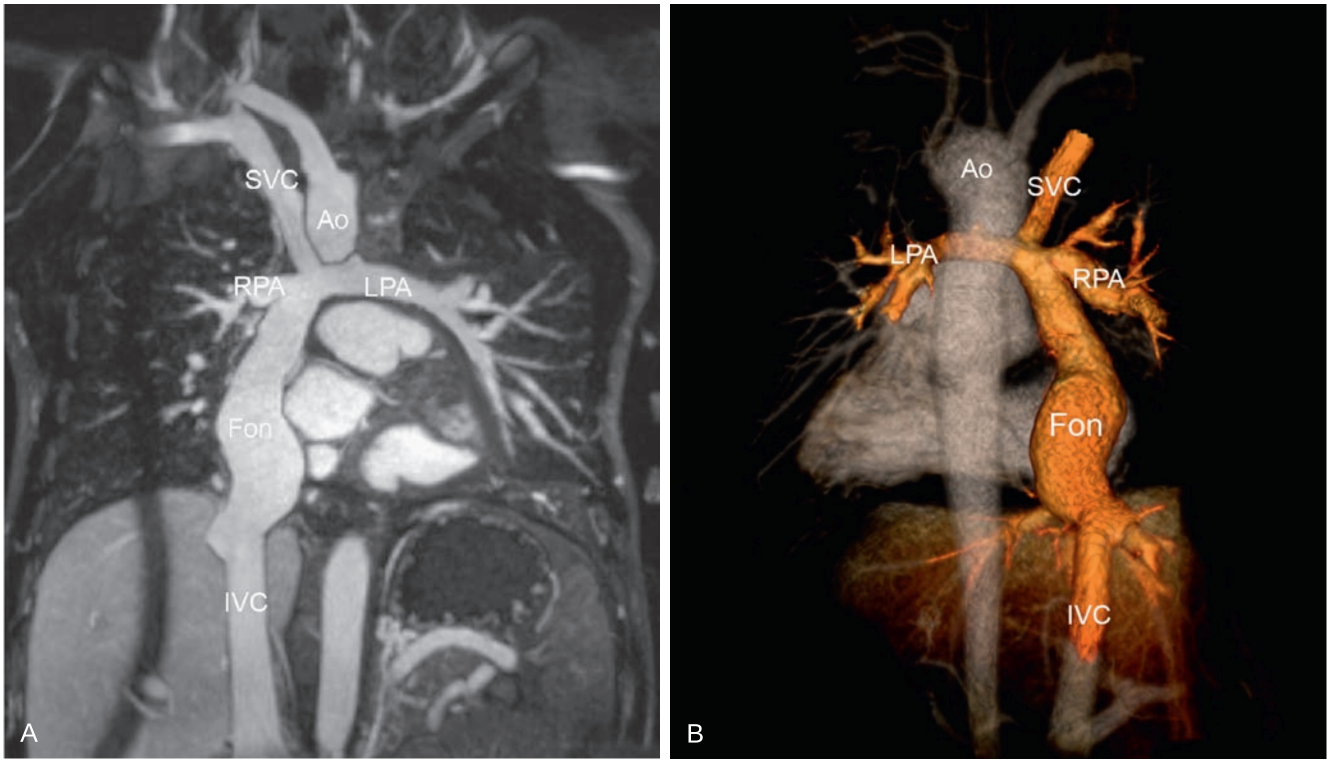

**Figure 73.4. Completed Fontan palliation.** (A) Oblique coronal MR angiography image demonstrating the Fontan connections. (B) Posterior projection of a three-dimensional MR angiography reconstruction demonstrating the Fontan connections. *Ao,* Aorta; *Fon,* Fontan conduit; *IVC,* inferior vena cava; *LPA,* left pulmonary artery; *RPA,* right pulmonary artery; *SVC,* superior vena cava.

***Etiology and Pathophysiology.*** Congenital aortic valve stenosis results from abnormal valve development rather than the degenerative disease commonly seen in adults. The stenotic valve has variable anatomy, with annular hypoplasia, thickened or tethered leaflets, and/or incompletely developed commissures. Valve morphology may predict clinical severity or associated disease.[29,30] Whereas neonatal critical AS often is associated with a unicuspid valve and a small eccentric orifice, bicuspid morphology accounts for up to 95% of cases of congenital valvar AS and is present in up to 85% of patients with coarctation.[31–33] Bicuspid aortic valve is associated with abnormal aortic tissue histologically similar to the medial disease of Marfan syndrome, and aortic dilation can occur even in the absence of significant valvar dysfunction.[34,35]

The narrowing in supravalvar AS most commonly is hourglass in shape and occurs immediately above the sinuses of Valsalva at the sinotubular junction. It may be associated with poststenotic dilatation of the aorta, diffuse aortic arch hypoplasia, aortic valve abnormalities, or coronary artery ostial stenosis.[36,37] Supravalvar AS often is part of a widespread elastin-related arteriopathy.

Subvalvar AS can be discrete or diffuse. The discrete form, which represents the majority of cases, consists of a circumferential thin fibrous membrane just below the valve or less commonly a fibromuscular ridge. In the more severe diffuse form, muscular hypertrophy produces tunnel-like narrowing along the length of the LVOT; this form is usually associated with other cardiac lesions, including multiple left-sided obstructions (Shone complex: supramitral ring, parachute mitral valve with stenosis, coarctation of the aorta),[38] double outlet right ventricle, or interrupted aortic arch.

***Clinical Presentation.*** Critical or severe AS may be diagnosed prenatally or present early in infancy with severe left heart obstruction, congestive heart failure, dyspnea, and poor peripheral circulation. In critical AS, systemic flow is ductal dependent. In severe AS, the left ventricle may be dilated, dysfunctional, or hypoplastic. The clinical manifestations of AS in infancy depend on the degree of valvar obstruction and left ventricular dysfunction, as well as other associated left-sided obstructive lesions and the amount of shunted atrial and ductal flow.

AS in children usually is the result of a bicuspid aortic valve, and the obstruction generally is not severe but progresses gradually with age. Children with mild to moderate AS generally are asymptomatic and present with a characteristic systolic ejection murmur. With more severe AS, symptoms include chest pain, dyspnea, decreased exercise tolerance, and syncope, and sudden death may occur.

Patients with supravalvar AS may also experience left heart failure, dyspnea, angina, and syncope related to the degree of LVOT obstruction. Sudden death is a particular risk and may be related to associated coronary ostial obstruction and/or peripheral pulmonary arterial stenosis with biventricular hypertrophy. Patients may also present with systemic hypertension related to diffuse arteriopathy with reduced vascular elasticity.

Subvalvar AS is rarely detected in infancy but may be detected in childhood and is generally progressive. Children may have an asymptomatic systolic ejection murmur. A diastolic murmur of aortic insufficiency may be found in older children, as the turbulent subaortic jet damages the aortic valve over time.[39] In older patients with moderate to severe obstruction, signs of left ventricular failure with dyspnea, chest pain, syncope, and tachypnea may occur.

***Imaging.*** The chest radiograph in infants with critical AS shows cardiomegaly and pulmonary venous congestion. In older children with mild stenosis, the radiograph generally is normal. With more severe stenosis, left atrial enlargement and left ventricular hypertrophy, indicated by depression of the cardiac apex inferiorly toward the diaphragm and posteriorly to the inferior vena cava, may be seen. Poststenotic dilation of the ascending aorta is rare in young children (e-Fig. 73.8).

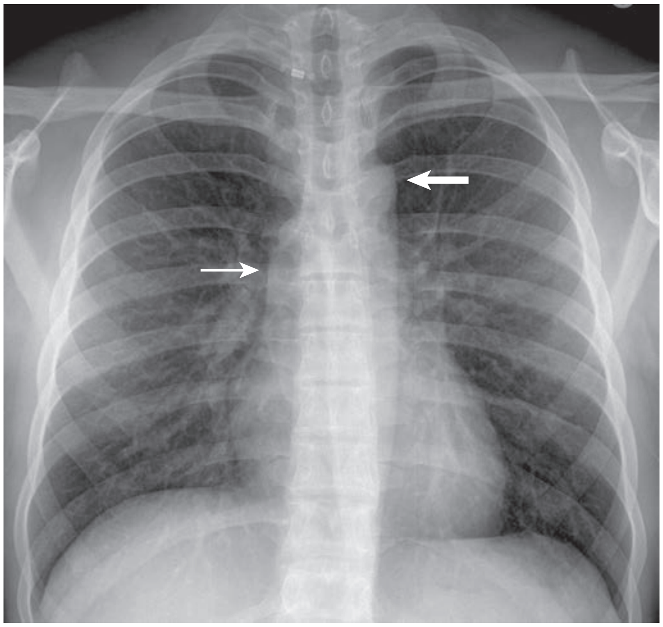

**e-Figure 73.8. Aortic valve stenosis.** A frontal view of the chest in an 18-year-old shows poststenotic dilation of the ascending aorta *(thin arrow)* and aortic arch *(thick arrow)*.

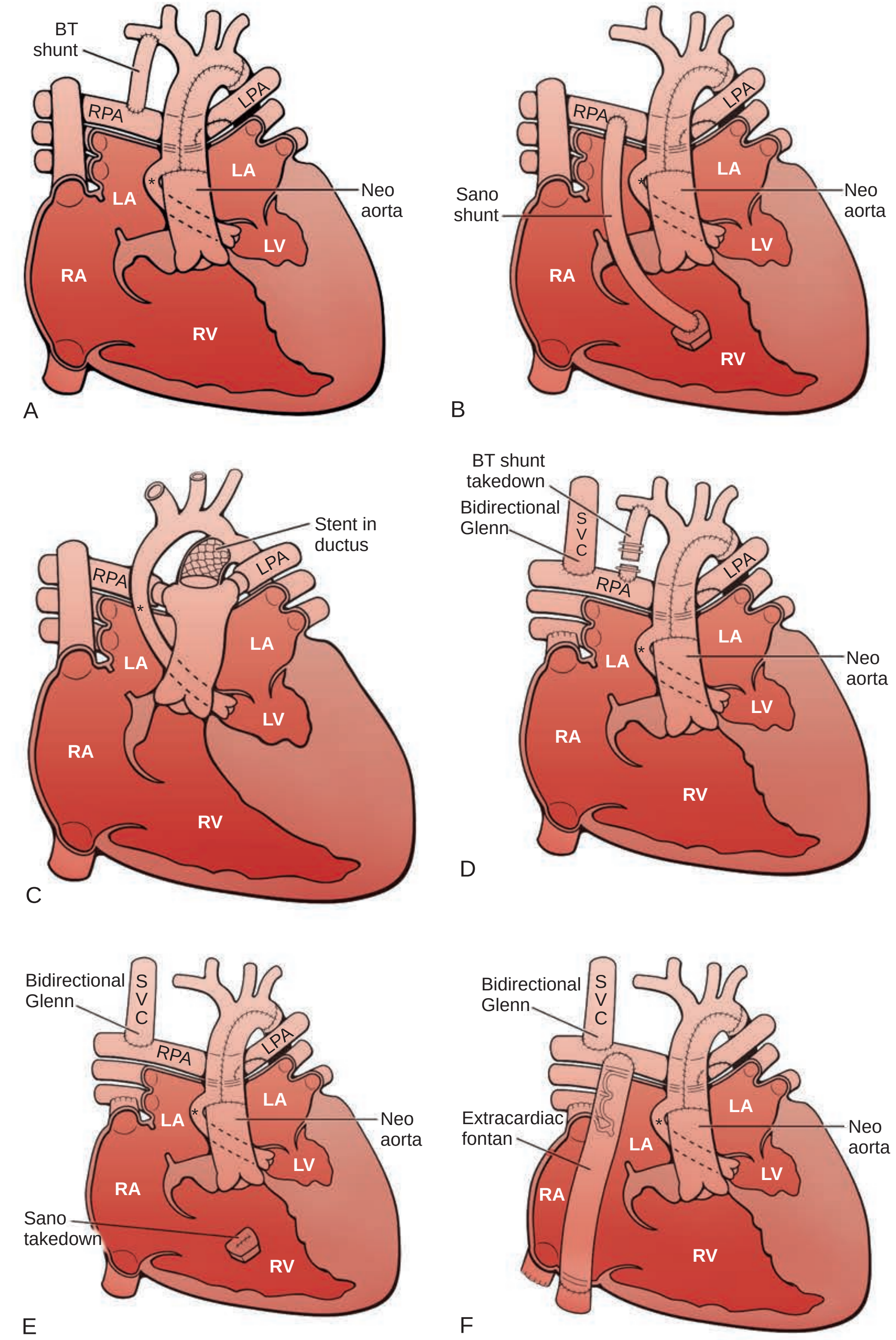

**Figure 73.5. Staged reconstruction for hypoplastic left heart syndrome.** (A) Stage I Norwood reconstruction using a modified Blalock-Taussig *(BT)* shunt. (B) Stage I Norwood reconstruction using the Sano modification. (C) Hybrid procedure. (D) Stage II or bidirectional Glenn anastomosis. (E) Stage II or bidirectional Glenn anastomosis after the Sano modification. (F) Stage III or Fontan procedure. *Asterisk,* Native ascending aorta; *LA,* left atrium; *LPA,* left pulmonary artery; *LV,* left ventricle; *RA,* right atrium; *RPA,* right pulmonary artery; *RV,* right ventricle; *SVC,* superior vena cava.

Echocardiography is the imaging procedure of choice for the evaluation of valvar AS, but cardiac MRI can complement echocardiography if acoustic windows are poor or larger field of view is needed. Goals of imaging include demonstration of the degree and location of obstruction, valve morphology, leaflet mobility, and effective valve orifice area. The valve typically appears thickened and doming, with asymmetric or restricted leaflet excursion (e-Fig. 73.9 and Video 73.2). Systolic valve area calculated by MRI planimetry correlates well with transesophageal echocardiography and cardiac catheterization measurements (Fig. 73.10 and Video 73.3).[40] Phase-contrast MRI is used to measure transvalvar velocity and regurgitant fraction (e-Fig. 73.11), and the gradient across the aortic valve in millimeters of mercury is calculated using the modified Bernoulli equation ($4V^2$, where $V$ is peak velocity beyond the aortic valve in meters per second). Left ventricular size and function are assessed, and delayed enhancement imaging may demonstrate endocardial fibroelastosis in severe cases (e-Fig. 73.12). Assessment of aortic root, ascending aorta, and arch size is crucial in infants with critical AS, and ongoing surveillance of the thoracic aorta for dilation is indicated in all patients with aortic valve disease.[35]

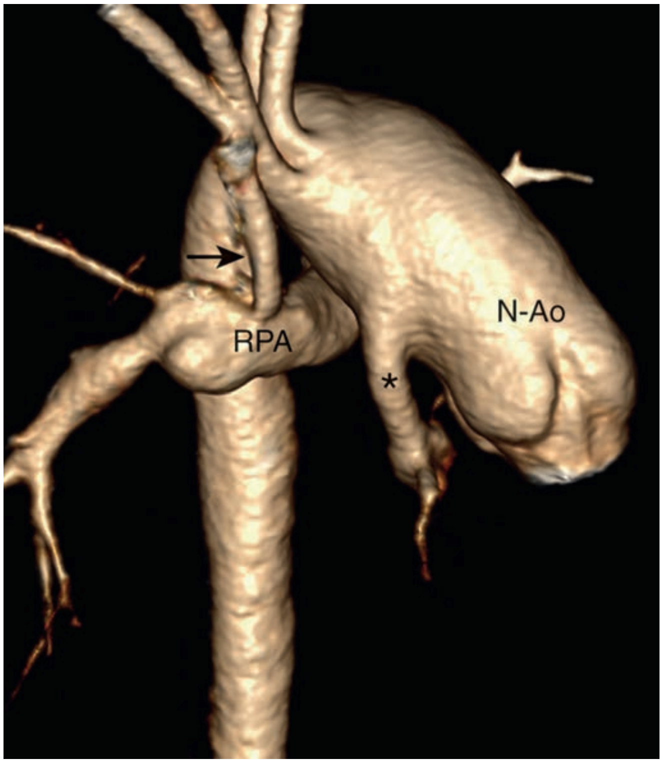

**Figure 73.6. A 6-month-old with hypoplastic left heart syndrome after Stage I Norwood procedure.** Anterior oblique volume-rendered CT angiography shows the hypoplastic native aorta *(asterisk)* anastomosed with the native pulmonary artery (now neo-aorta) and a Blalock-Taussig shunt *(arrow)* extending from the right brachiocephalic artery to the right pulmonary artery. *N-Ao,* Neo-aorta; *RPA,* right pulmonary artery.

In supravalvar AS, cardiac MRI or CTA may complement echocardiography to evaluate the type of stenosis (discrete or diffuse), the coronary ostia, ventricular mass and function, and other sites of vasculopathy (e.g., supravalvar pulmonary stenosis) (Fig. 73.13). In subvalvar AS, echocardiography and sometimes MRI are used to define the discrete subaortic membrane or ridge (Fig. 73.14) or the extent of the tunnel-type subaortic lesion and to quantify effects on ventricular mass and function.

***Treatment.*** Infants with severe or critical AS need urgent treatment. Patients are supported with $PGE_1$ infusion to maintain ductal patency, mechanical ventilation, and inotropic medications. Urgent percutaneous balloon valvuloplasty is the treatment of choice. During the era of aggressive transcatheter intervention, early mortality for infants with severe or critical AS has fallen from as high as 43% to 4% to 13%.[41,42] A neonatal Ross procedure (i.e., transplant of the pulmonary valve to the aortic position with coronary reimplantation and replacement of the pulmonary valve with a homograft conduit) may be considered for dysplastic valves or small aortic annuli[43,44] but is limited by higher rates of autograft deterioration in children compared with adults.[45,46]

Balloon valvotomy is considered in older children with a peak gradient of 50 mm Hg or greater at catheterization, for patients with angina, syncope, or ischemia, and for persons who want to play competitive sports or become pregnant.[47–49] Routine follow-up is necessary to evaluate for aortic insufficiency and recurrent stenosis. Late surgical valve repair or replacement is necessary in approximately 25% to 35% of patients.[42,50] For patients who require valve replacement, a bioprosthetic or mechanical valve may be placed or a Ross procedure may be performed.

Indications for interventions related to supravalvar AS are less clear, and outcomes are less favorable.[51,52] Aortoplasty is performed to enlarge the aortic sinuses, and additional patching of the ascending aorta and transverse aorta may be necessary. Associated coronary ostial stenoses are addressed. Complications include aortic aneurysms and aortic valve dysfunction.[51] Given the recurrent

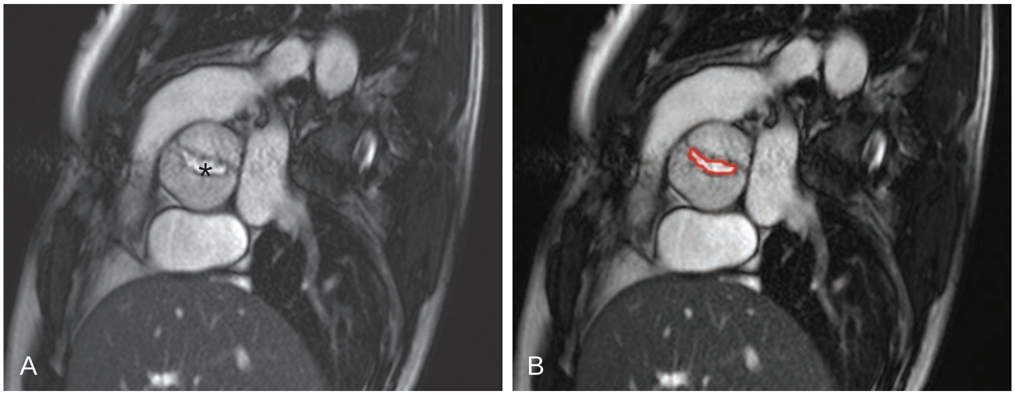

**Figure 73.10. Bicuspid aortic valve in a 25-year-old with history of aortic coarctation.** (A) A cross-sectional steady-state free-precession (SSFP) systolic MR image of a severely stenotic bicuspid aortic valve *(asterisk)* with fusion of the right and noncoronary commissures, giving a "fish-mouth" appearance. See Video 73.3 for a cine SSFP image of the same. (B) The aortic valve area (outlined in red) as measured by planimetry is 1.18 $cm^2$.

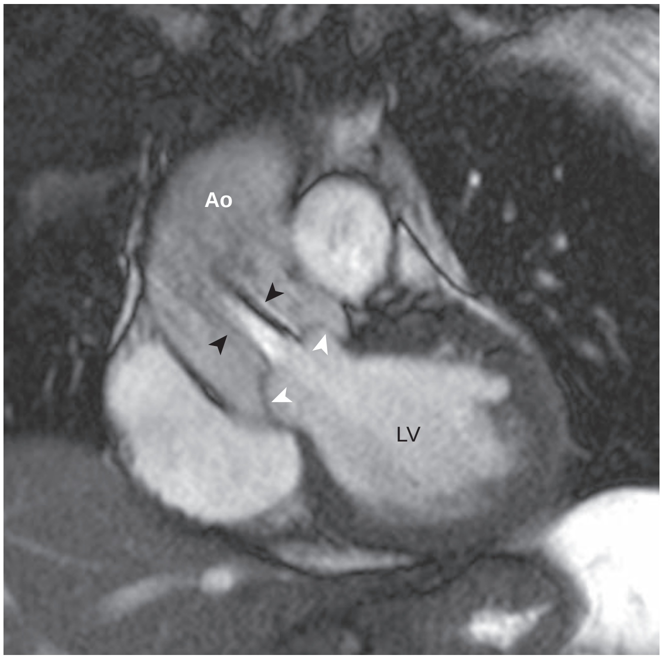

**e-Figure 73.9. Bicuspid aortic valve in a 25-year-old with history of aortic coarctation.** Steady-state free-precession (SSFP) MR image perpendicular to the plane of the bicuspid aortic valve shows upward ballooning of the aortic valve leaflets *(white arrowheads)* and a turbulent poststenotic jet *(black arrowheads)* into the dilated ascending aorta *(Ao)*. See Video 73.2 for cine SSFP MRI of the same case with a regurgitant jet visible. *LV,* Left ventricle.

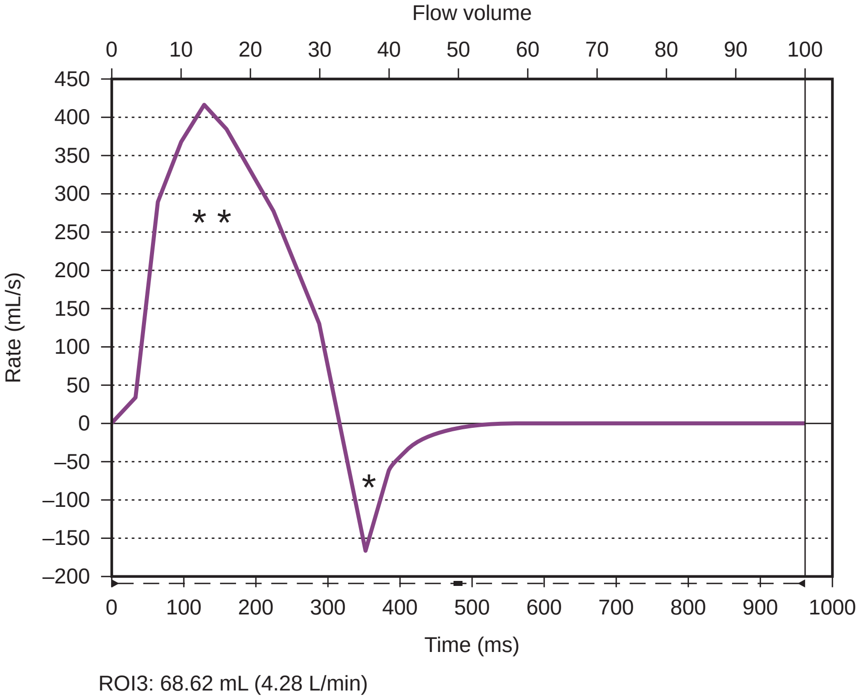

**e-Figure 73.11. Aortic valve flow curve.** A flow curve obtained by MR phase-contrast imaging acquired just above the aortic valve shows forward *(two asterisks)* and regurgitant *(single asterisk)* flow. The regurgitant fraction (regurgitant flow volume/forward flow volume) was calculated to be 18%.

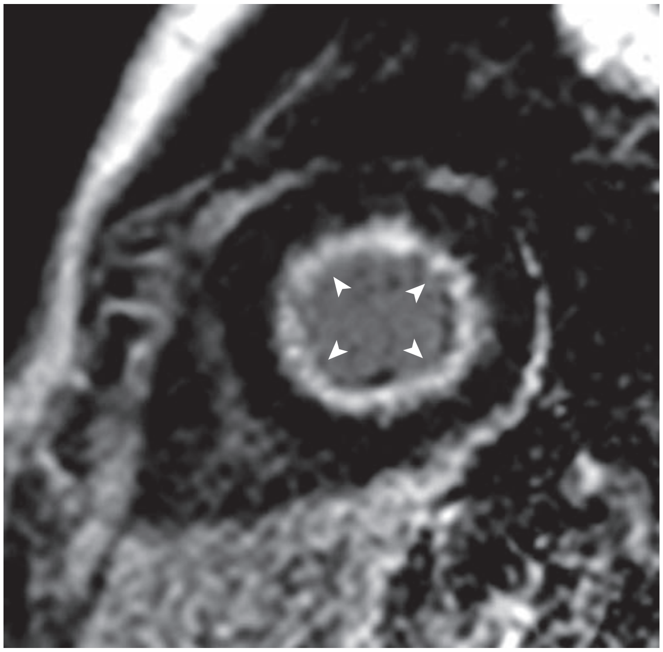

**e-Figure 73.12. Endocardial fibroelastosis.** Short-axis MRI delayed enhancement image in a 14-year-old with bicuspid aortic valve after multiple balloon aortic valvuloplasty procedures who, in his teenage years, experienced progressive heart failure symptoms, including dyspnea on exertion, increasing fatigue, and decreased exercise tolerance in the setting of normal systolic function. Delayed enhancement inversion recovery images show diffuse subendocardial late enhancement *(arrowheads)*. He underwent a high-risk, but ultimately successful, cardiac transplantation approximately 1 year after he became symptomatic. Pathology of the explanted heart revealed a bicommissural aortic valve, biventricular hypertrophy, hypertrophic subendocardial thebesian veins with prominent intimal thickening, and diffuse endocardial fibroelastosis. *(Modified from Robinson JD, Del Nido PJ, Geggel RL, et al. Left ventricular diastolic heart failure in teenagers who underwent balloon aortic valvuloplasty in early infancy.* Am J Cardiol. *2010;106[3]:426–429.)*

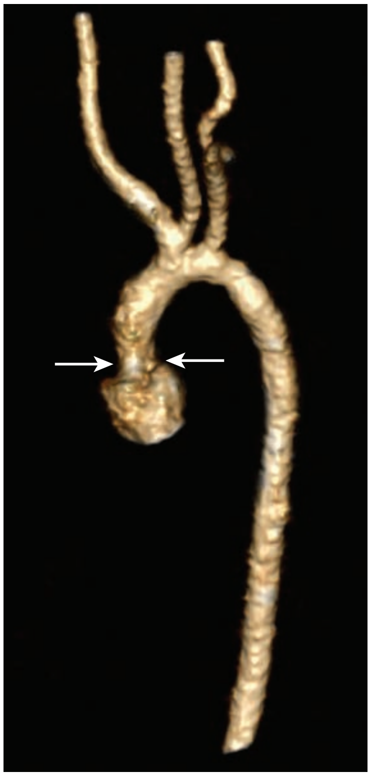

**Figure 73.13. Supravalvar aortic stenosis (AS).** An oblique volume-rendered three-dimensional CT angiographic image shows supravalvar AS with an abrupt caliber change in the proximal ascending aorta *(arrows)*.

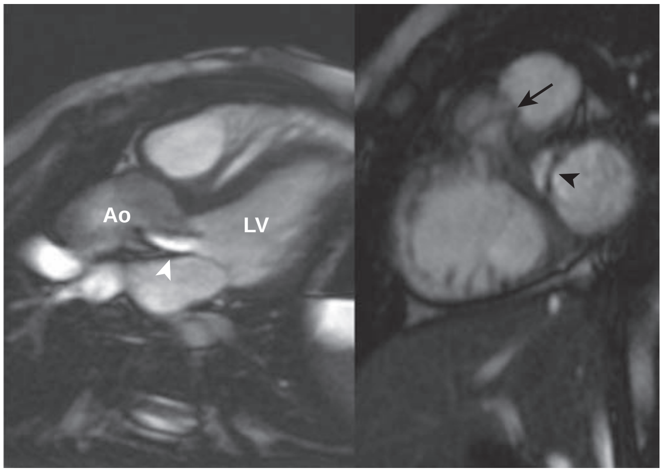

**Figure 73.14. Subaortic stenosis.** Steady-state free-precession MRI long-axis *(left)* and short-axis *(right)* images of the left ventricular outflow tract (LVOT) show a subaortic membrane *(black arrowhead)* causing a jet of flow acceleration across the LVOT *(white arrowhead)* beginning just below the aortic valve plane *(arrow)*. *Ao,* Aorta; *LV,* left ventricle.

and progressive nature of diffuse arteriopathy, long-term follow-up is warranted.

In asymptomatic patients, the timing of surgical intervention for subvalvar AS is controversial and is related to the degree and progression of LVOT obstruction and other associated heart disease.[53–55] Discrete subvalvar obstruction is treated with membrane resection with or without septal myectomy, while treatment for the tunnel-like obstruction varies with aortic valve size and function. The Konno procedure (i.e., aortoventriculoplasty, including replacement of the aortic valve) and modifications including valve repair or the Ross procedure may be performed (e-Fig. 73.15). Stenosis recurrence and aortic regurgitation are more common after repair of tunnel-like stenosis but occur with both types of subvalvar AS.

## COARCTATION OF THE AORTA

***Overview.*** Coarctation of the aorta accounts for approximately 7% of cases of congenital heart disease,[56] with a male-to-female ratio of approximately 1.5 : 1.[35] A bicuspid aortic valve is seen in up to 80% of patients,[33] and ventricular septal defect (VSD) is seen in 11% to 18% of patients.[57,58] Other associated lesions include ASD, left-sided obstructive lesions, transposition of the great arteries, double-outlet right ventricle, and atrioventricular septal defect.[57] Berry aneurysms are seen in up to 10% of patients.[59] Approximately 5% of girls presenting with aortic coarctation have Turner syndrome,[60] and up to 15% of girls with Turner syndrome have coarctation.[61,62] Atypical, complex aortic coarctation (e.g., long-segment, with aneurysmal segments) is present in 15% of patients with PHACES syndrome (posterior fossa defects, hemangiomas, arterial anomalies, cardiac defects and coarctation, eye anomalies, and sternal defects or supraumbilical raphe).[63]

***Etiology and Pathophysiology.*** Coarctation of the aorta is a narrowing of the thoracic aorta that generally occurs adjacent to the insertion site of the ductus arteriosus just distal to the left subclavian artery. The coarctation is almost always juxtaductal and discrete, but varying degrees of tubular hypoplasia of the transverse arch and isthmus may be present and are more commonly seen in infancy.[64] The embryology of aortic coarctation is not known, but two theories have been proposed. The ductal sling theory suggests that contractile ductal tissue abnormally extends around the aortic lumen, leading to a shelflike aortic narrowing in the juxtaductal region with ductal closure.[64] The flow theory postulates that aortic coarctation develops as a result of decreased blood flow through the aortic isthmus with left-sided obstructive lesions. In fetal life, the isthmus normally receives a relatively low volume of blood flow from the left ventricle, while most of the flow to the descending aorta arises from the right ventricle through the PDA; isthmic flow is even lower with left-sided obstructive lesions.[64,65]

The pathophysiology of coarctation of the aorta is related to the severity of the arch obstruction, the presence of collateral vessels, and associated cardiac lesions.[57] Initially, the neonate with coarctation will have a PDA, allowing blood flow to bypass the obstruction. However, associated left-sided obstructive lesions may further increase left ventricular afterload, and the presence of a VSD may increase left ventricular volume load, leading to early pulmonary venous and arterial hypertension and heart failure. With severe coarctation, closure of the PDA acutely increases left ventricular afterload, resulting in acute heart failure and shock. With less severe obstruction, collateral blood vessels develop to bypass the obstruction, and this may mask the presence of the coarctation until later in childhood or adulthood. Upper extremity hypertension is present in 90% of children, with three proposed mechanisms: mechanical aortic obstruction, abnormal baroreceptor function and altered vascular reactivity proximal to the obstruction, and hyperactivation of the renin-angiotensin system caused by the underperfused kidneys.[57,66,67]

***Clinical Presentation.*** Infants with critical coarctation of the aorta, especially when it is associated with other cardiac defects, typically present by 7 to 14 days of life as the PDA begins to close and they have dramatic signs of congestive heart failure and poor systemic perfusion. In fact, congestive heart failure presenting between the first and fourth weeks of life strongly suggests

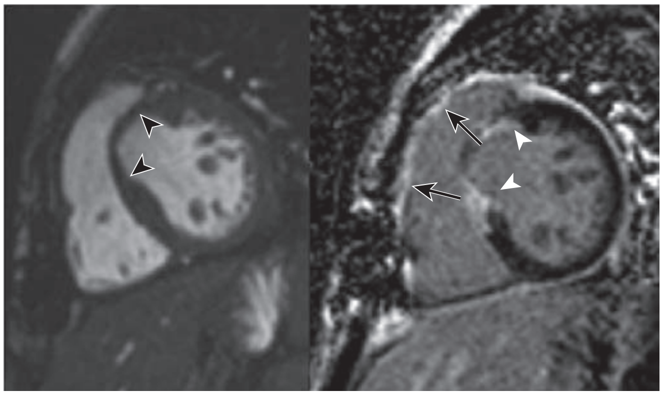

**e-Figure 73.15. Ross-Konno procedure for aortic and subaortic stenosis in a 17-year-old.** MRI short-axis steady-state free-precession *(left)* and postcontrast phase-sensitive inversion recovery delayed enhancement *(right)* views show thinning of the myocardium in the region of the left ventricular outflow tract *(black arrowheads)* with corresponding late enhancement *(white arrowheads)* consistent with the Konno ventriculoplasty and Ross procedure. Also, note the postoperative late enhancement in the region of the right ventricular outflow tract related to placement of the pulmonary homograft *(arrows)*.

coarctation. Clinical symptoms include dyspnea, poor feeding, tachycardia, and signs of shock, including oliguria, anuria, and severe acidemia. Femoral pulses are weak or absent, and differential blood pressures generally show a gradient between the upper and lower limbs.[57]

Coarctation of the aorta also may be diagnosed from infancy to adulthood in asymptomatic or mildly symptomatic patients, with a reported median age of 10 years (range, 1–36 years).[68] These patients present later because the coarctation is not significant or because adequate collateral circulation has developed. The diagnosis usually is made on the basis of routine physical examination findings such as an incidental murmur, hypertension, or absent or diminished lower extremity pulses.[68]

***Imaging.*** Infants with severe coarctation demonstrate evidence of congestive heart failure, including cardiomegaly and increased pulmonary vascular markings (e-Fig. 73.16). Chest radiographs in children older than 1 year and younger than 5 years usually show a normal heart size, but cardiomegaly due to left ventricular hypertrophy can be seen. The hallmark of aortic coarctation is rib notching, grooves on the undersurfaces of the posterior ribs (typically fourth through eighth) formed by dilated intercostal collateral arteries, which is usually seen after 5 years of age.[69] Rib notching is bilateral unless one subclavian artery arises distal to the coarctation or is stenotic. A "figure three" sign frequently is seen along the left upper mediastinal border, representing the prominent aortic knob and left subclavian artery proximally, the indentation from the coarctation, and the poststenotic aortic segment (Fig. 73.17). The imprint of the aorta on the adjacent barium-filled esophagus, which is known as the "E" sign or "reversed three" sign, is caused by dilation of the aorta proximal and distal to the coarctation.

Echocardiography is the method of choice for imaging coarctation in infancy. CTA and MRI can provide detailed anatomic imaging of the coarctation in older children or adults with limited acoustic windows (Figs. 73.18 and 73.19). MRI also can be used

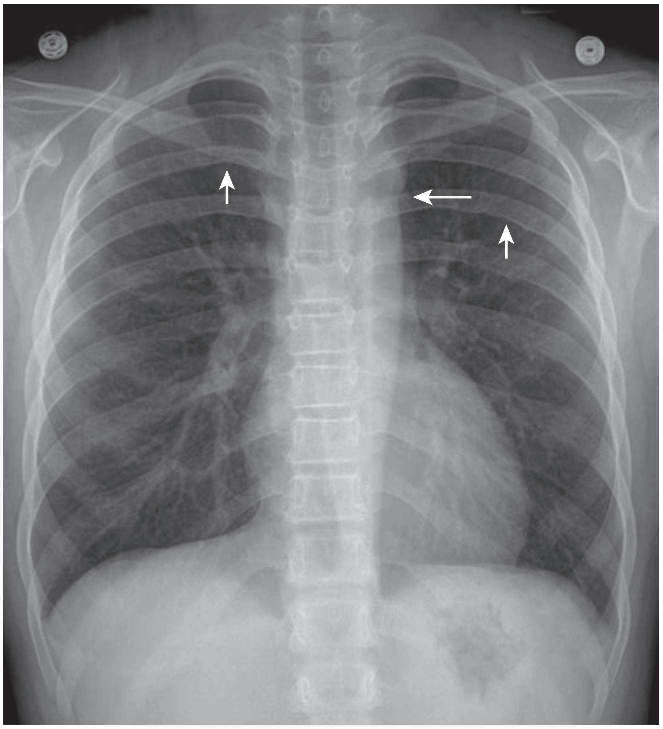

**Figure 73.17. Coarctation of the aorta in a 10-year-old.** A frontal view of the chest shows the "figure three" sign *(long arrow)*, which is indicative of aortic coarctation, and bilateral posterior rib notching *(short arrows)*, which is indicative of collateral vessels.

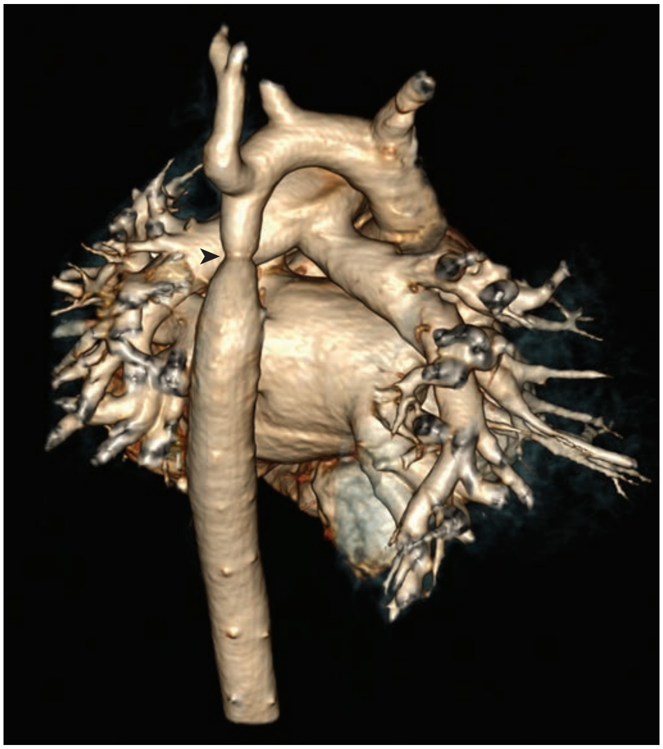

**Figure 73.18. Aortic coarctation in a 3-year-old.** Posterior projection from a volume-rendered MR angiography image shows a discrete aortic coarctation *(arrowhead)* distal to the left subclavian artery.

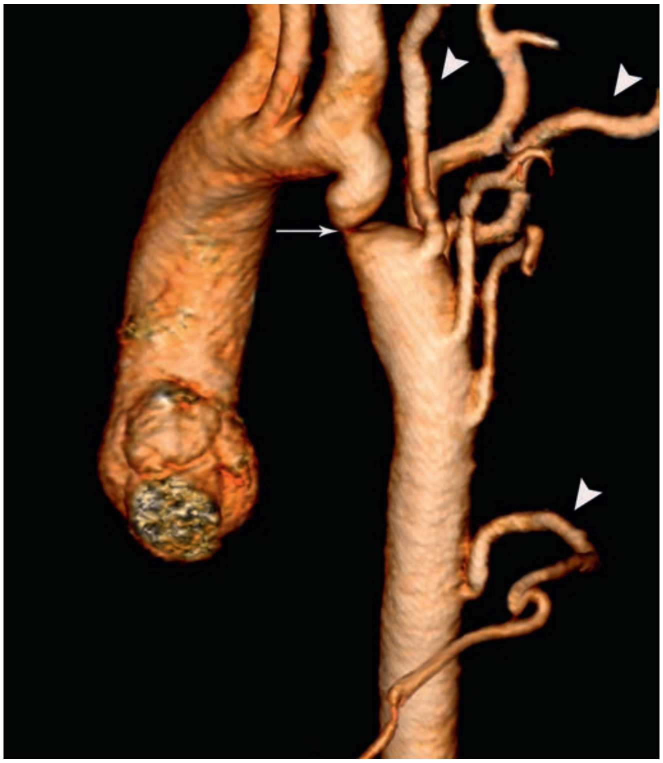

**Figure 73.19. Aortic coarctation in an 11-year-old.** A three-dimensional CT angiography reconstruction lateral view shows a discrete aortic coarctation *(long arrow)* distal to the left subclavian artery, with multiple dilated tortuous collateral vessels *(arrowheads)* arising from head and neck arteries proximal to the coarctation and feeding the descending aorta distal to the coarctation.

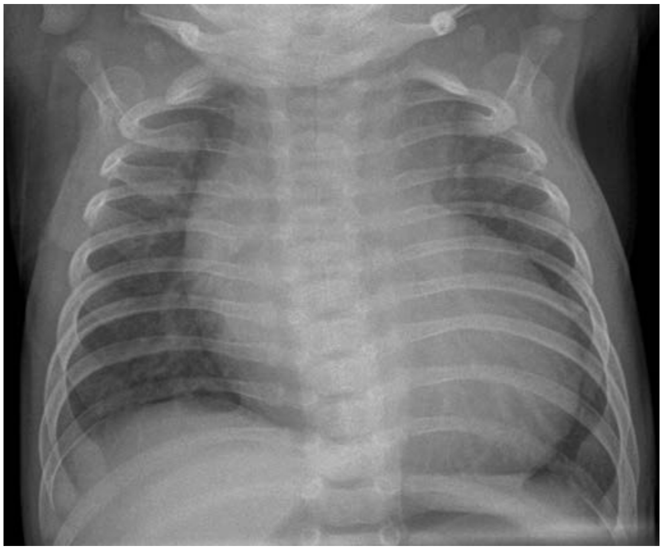

**e-Figure 73.16. Critical aortic coarctation in a 2-week-old.** Frontal view of the chest shows cardiomegaly with mild pulmonary vascular congestion.

to assess the hemodynamic significance of the coarctation. A complete examination involves imaging for ventricular systolic function, volume and mass; atrioventricular and semilunar valve assessment with particular attention to the aortic valve; and imaging of the aortic root, ascending aorta, arch, coarctation, and descending aorta to the renal arteries. Maximum blood flow velocity, blood flow volume, and flow pattern in the aorta just distal to the coarctation can be assessed using phase-contrast MRI sequences (e-Fig. 73.20 and Video 73.4). The maximal flow velocity obtained across the coarctation can be used in the Bernoulli equation (see aortic stenosis imaging section) to estimate the pressure gradient.[70] Aortic flow volume at the diaphragm also can be assessed and may be increased relative to flow volume just distal to the coarctation as a result of recruitment of collateral flow through the intercostal arteries; this can be an indicator of the significance of the coarctation.[71–73]

***Treatment.*** Neonates presenting with congestive heart failure due to aortic coarctation are initially stabilized with inotropic drugs and $PGE_1$ to maintain ductal patency and improve blood flow to the descending aorta. After stabilization, urgent surgical repair is the treatment of choice.[74,75] Balloon angioplasty can be considered as an initial procedure for neonates at high surgical risk.[74]

Repair is performed on a more elective basis in patients who present in infancy or childhood with a murmur or upper extremity hypertension. Conventional therapy for aortic coarctation is surgical, most typically resection of the coarctation with end-to-end or extended end-to-end anastomosis.[57,74,75] Other surgical procedures, including patch aortoplasty and subclavian flap repair, are less commonly performed because of the risk of aneurysm formation at the patch site with patch aortoplasty and left arm complications and remnant residual ductal tissue with the subclavian flap repair.[57,74] The use of balloon angioplasty for native aortic coarctation in infants and children is controversial because rates of aneurysm formation,[76] iliofemoral artery injury,[76] and reintervention for recurrent stenosis[74] may be higher than for conventional surgical therapy. Larger children may be candidates for stenting of native coarctation, using a stent with diameter potential sufficient for the adult-sized aorta.[77] For recoarctation, the transcatheter approach is accepted therapy in all age groups.[74] Late complications after surgical or endovascular treatment include recurrent coarctation, aneurysm or pseudoaneurysm formation, aortic dissection, and hypertension.[57,74,78]

## KEY POINTS

- Surgical palliation of HLHS is a staged reconstruction that involves three surgical procedures, with the ultimate goal of creating in-series pulmonary and systemic circulations supported by the right ventricle.
- A bicuspid aortic valve is the most common cause of congenital aortic stenosis and is associated with aortic root dilation and aortic wall abnormalities.
- Aortic coarctation morphology, collateral circulation, and associated lesions have important implications for presentation, management, and prognosis.

## SUGGESTED READINGS

Etnel JR, Takkenberg JJ, Spaans LG, et al. Paediatric subvalvular aortic stenosis: a systematic review and meta-analysis of natural history and surgical outcome. *Eur J Cardiothorac Surg*. 2015;48(2):212–220.

Feinstein JA, Benson DW, Dubin AM, et al. Hypoplastic left heart syndrome: current considerations and expectations. *J Am Coll Cardiol*. 2012;59(1 suppl):S1–S42.

Holloway BJ, Rosewarne D, Jones RG. Imaging of thoracic aortic disease. *Br J Radiol*. 2011;84(Spec Iss 3):S338–S354.

Merla G, Brunetti-Pierri N, Piccolo P, et al. Supravalvar aortic stenosis: elastin arteriopathy. *Circ Cardiovasc Genet*. 2012;5(6):692–696.

Michelena HI, Prakash SK, Della Corte A, et al. Bicuspid aortic valve: identifying knowledge gaps and rising to the challenge from the International Bicuspid Aortic Valve Consortium (BAVCon). *Circulation*. 2014;129(25):2691–2704.

## REFERENCES

Full references for this chapter can be found on www.expertconsult.com.

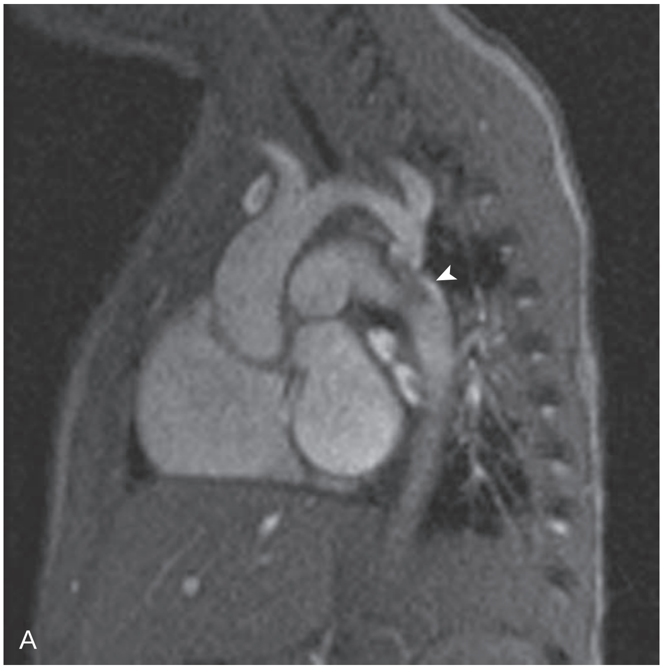

**e-Figure 73.20. Aortic coarctation in a 16-month old.** (A) Oblique sagittal still image from a cine MRI gradient echo image series shows a systolic flow void distal to the coarctation *(arrowhead)* indicative of turbulent flow across the coarctation. The transverse aortic arch is mildly hypoplastic.

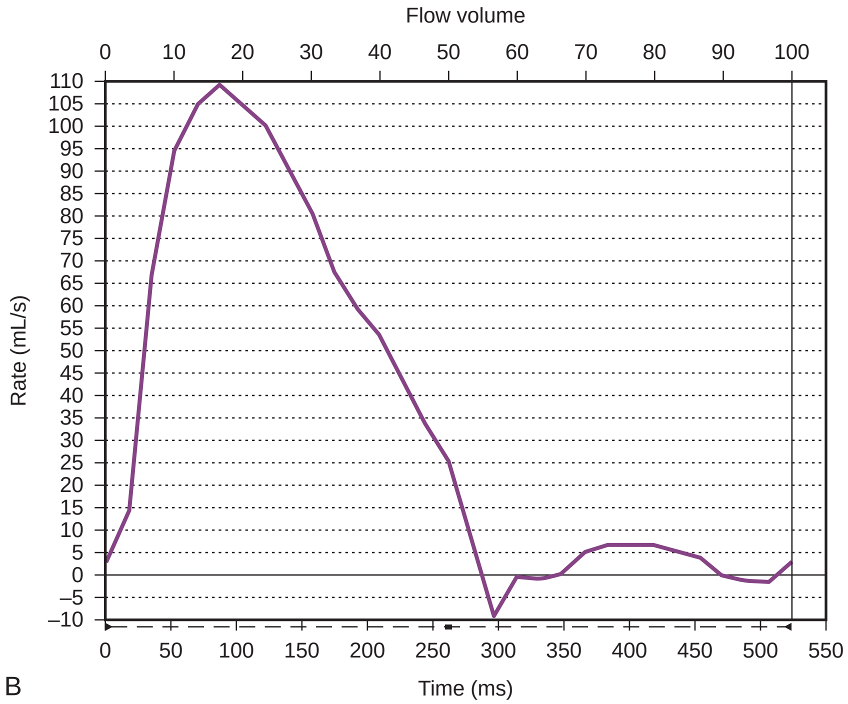

ROI3: 18.95 mL (2.17 L/min)

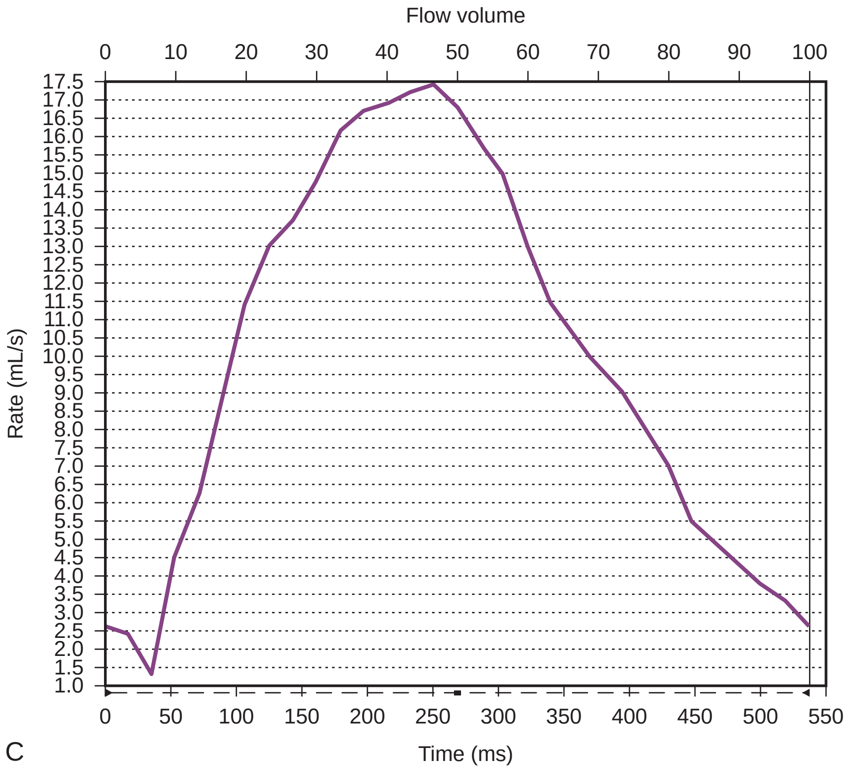

ROI3: 5.40 mL (603.81 L/min)

**e-Figure 73.20, cont'd.** (B) A flow curve obtained by phase-contrast imaging in the aortic arch proximal to the coarctation shows a normal arterial flow pattern. (C) A flow curve obtained by phase-contrast imaging in the descending aorta distal to the coarctation shows a slow upstroke, lower stroke volume, slow downstroke, and forward flow throughout ventricular diastole. See Video 73.4 for oblique sagittal cine gradient echo images showing systolic flow void beyond the coarctation consistent with turbulent flow across the coarctation.

## REFERENCES

1. Barron DJ, Kilby MD, Davies B, et al. Hypoplastic left heart syndrome. *Lancet*. 2009;374(9689):551–564.
2. Morris CD, Outcalt J, Menashe VD. Hypoplastic left heart syndrome: natural history in a geographically defined population. *Pediatrics*. 1990;85(6):977–983.
3. Glauser TA, Rorke LB, Weinberg PM, et al. Congenital brain anomalies associated with the hypoplastic left heart syndrome. *Pediatrics*. 1990;85(6):984–990.
4. Grosse-Wortmann L, Yun TJ, Al-Radi O, et al. Borderline hypoplasia of the left ventricle in neonates: insights for decision-making from functional assessment with magnetic resonance imaging. *J Thorac Cardiovasc Surg*. 2008;136(6):1429–1436.
5. Hawkins JA, Doty DB. Aortic atresia: morphologic characteristics affecting survival and operative palliation. *J Thorac Cardiovasc Surg*. 1984;88(4):620–626.
6. Stamm C, Anderson RH, Ho SY. The morphologically tricuspid valve in hypoplastic left heart syndrome. *Eur J Cardiothorac Surg*. 1997;12(4):587–592.
7. Abu-Harb M, Wyllie J, Hey E, et al. Presentation of obstructive left heart malformations in infancy. *Arch Dis Child Fetal Neonatal Ed*. 1994;71(3):F179–F183.
8. Perolo A, Prandstraller D, Ghi T, et al. Diagnosis and management of fetal cardiac anomalies: 10 years of experience at a single institution. *Ultrasound Obstet Gynecol*. 2001;18(6):615–618.
9. Stumper O. Hypoplastic left heart syndrome. *Heart*. 2010;96(3):231–236.
10. Dillman JR, Yarram SG, Hernandez RJ. Imaging of pulmonary venous developmental anomalies. *AJR Am J Roentgenol*. 2009;192(5):1272–1285.
11. Banka P, Schaetzle B, Komarlu R, et al. Cardiovascular magnetic resonance parameters associated with early transplant-free survival in children with small left hearts following conversion from a univentricular to biventricular circulation. *J Cardiovasc Magn Reson*. 2014;16:73.
12. Jones BO, Ditchfield MR, Cahoon GD, et al. Cardiac magnetic resonance imaging prior to bidirectional cavopulmonary connection in hypoplastic left heart syndrome. *Heart Lung Circ*. 2010;19(9):535–540.
13. Muthurangu V, Taylor AM, Hegde SR, et al. Cardiac magnetic resonance imaging after stage I Norwood operation for hypoplastic left heart syndrome. *Circulation*. 2005;112(21):3256–3263.
14. Brown DW, Gauvreau K, Powell AJ, et al. Cardiac magnetic resonance versus routine cardiac catheterization before bidirectional glenn anastomosis in infants with functional single ventricle: a prospective randomized trial. *Circulation*. 2007;116(23):2718–2725.
15. Han BK, Vezmar M, Lesser JR, et al. Selective use of cardiac computed tomography angiography: an alternative diagnostic modality before second-stage single ventricle palliation. *J Thorac Cardiovasc Surg*. 2014;148(4):1548–1554.
16. Rathod RH, Prakash A, Kim YY, et al. Cardiac magnetic resonance parameters predict transplantation-free survival in patients with fontan circulation. *Circ Cardiovasc Imaging*. 2014;7(3):502–509.
17. Kutty S, Rathod RH, Danford DA, et al. Role of imaging in the evaluation of single ventricle with the Fontan palliation. *Heart*. 2016;102(3):174–183.
18. Reddy VM, Liddicoat JR, Fineman JR, et al. Fetal model of single ventricle physiology: hemodynamic effects of oxygen, nitric oxide, carbon dioxide, and hypoxia in the early postnatal period. *J Thorac Cardiovasc Surg*. 1996;112(2):437–449.
19. Norwood WI, Lang P, Hansen DD. Physiologic repair of aortic atresia-hypoplastic left heart syndrome. *N Engl J Med*. 1983;308(1):23–26.
20. Ohye RG, Sleeper LA, Mahony L, et al. Comparison of shunt types in the Norwood procedure for single-ventricle lesions. *N Engl J Med*. 2010;362(21):1980–1992.
21. Galantowicz M, Cheatham JP. Lessons learned from the development of a new hybrid strategy for the management of hypoplastic left heart syndrome. *Pediatr Cardiol*. 2005;26(3):190–199.
22. Bridges ND, Lock JE, Castaneda AR. Baffle fenestration with subsequent transcatheter closure. Modification of the Fontan operation for patients at increased risk. *Circulation*. 1990;82(5):1681–1689.
23. Salazar JD, Zafar F, Siddiqui K, et al. Fenestration during Fontan palliation: now the exception instead of the rule. *J Thorac Cardiovasc Surg*. 2010;140(1):129–136.
24. Backer CL, Idriss FS, Zales VR, et al. Cardiac transplantation for hypoplastic left heart syndrome: a modified technique [see comment]. *Ann Thorac Surg*. 1990;50(6):894–898.
25. Samanek M, Slavik Z, Zborilova B, et al. Prevalence, treatment, and outcome of heart disease in live-born children: a prospective analysis of 91,823 live-born children. *Pediatr Cardiol*. 1989;10(4):205–211.
26. Wagner HR, Ellison RC, Keane JF, et al. Clinical course in aortic stenosis. *Circulation*. 1977;56(1 suppl):I47–I56.
27. Metcalfe K, Rucka AK, Smoot L, et al. Elastin: mutational spectrum in supravalvular aortic stenosis. *Eur J Hum Genet*. 2000;8(12):955–963.
28. Kitchiner D, Jackson M, Malaiya N, et al. Incidence and prognosis of obstruction of the left ventricular outflow tract in Liverpool (1960-91): a study of 313 patients. *Br Heart J*. 1994;71(6):588–595.
29. Fernandes SM, Sanders SP, Khairy P, et al. Morphology of bicuspid aortic valve in children and adolescents. *J Am Coll Cardiol*. 2004;44(8):1648–1651.
30. Roberts WC, Ko JM. Frequency by decades of unicuspid, bicuspid, and tricuspid aortic valves in adults having isolated aortic valve replacement for aortic stenosis, with or without associated aortic regurgitation. *Circulation*. 2005;111(7):920–925.
31. Becker AE, Becker MJ, Edwards JE. Anomalies associated with coarctation of aorta: particular reference to infancy. *Circulation*. 1970;41(6):1067–1075.
32. Teo LL, Cannell T, Babu-Narayan SV, et al. Prevalence of associated cardiovascular abnormalities in 500 patients with aortic coarctation referred for cardiovascular magnetic resonance imaging to a tertiary center. *Pediatr Cardiol*. 2011.
33. Ward C. Clinical significance of the bicuspid aortic valve. *Heart*. 2000;83(1):81–85.
34. Biner S, Rafique AM, Ray I, et al. Aortopathy is prevalent in relatives of bicuspid aortic valve patients. *J Am Coll Cardiol*. 2009;53(24):2288–2295.
35. Aboulhosn J, Child JS. Left ventricular outflow obstruction: subaortic stenosis, bicuspid aortic valve, supravalvar aortic stenosis, and coarctation of the aorta. *Circulation*. 2006;114(22):2412–2422.
36. Stamm C, Li J, Ho SY, et al. The aortic root in supravalvular aortic stenosis: the potential surgical relevance of morphologic findings. *J Thorac Cardiovasc Surg*. 1997;114(1):16–24.
37. Vaideeswar P, Shankar V, Deshpande JR, et al. Pathology of the diffuse variant of supravalvar aortic stenosis. *Cardiovasc Pathol*. 2001;10(1):33–37.
38. Shone JD, Sellers RD, Anderson RC, et al. The developmental complex of "parachute mitral valve," supravalvular ring of left atrium, subaortic stenosis, and coarctation of aorta. *Am J Cardiol*. 1963;11:714–725.
39. McMahon CJ, Gauvreau K, Edwards JC, et al. Risk factors for aortic valve dysfunction in children with discrete subvalvar aortic stenosis. *Am J Cardiol*. 2004;94(4):459–464.
40. John AS, Dill T, Brandt RR, et al. Magnetic resonance to assess the aortic valve area in aortic stenosis: how does it compare to current diagnostic standards? *J Am Coll Cardiol*. 2003;42(3):519–526.
41. McCrindle BW. Independent predictors of immediate results of percutaneous balloon aortic valvotomy in children. Valvuloplasty and Angioplasty of Congenital Anomalies (VACA) Registry Investigators. *Am J Cardiol*. 1996;77(4):286–293.
42. McElhinney DB, Lock JE, Keane JF, et al. Left heart growth, function, and reintervention after balloon aortic valvuloplasty for neonatal aortic stenosis. *Circulation*. 2005;111(4):451–458.
43. Ohye RG, Gomez CA, Ohye BJ, et al. The Ross/Konno procedure in neonates and infants: intermediate-term survival and autograft function. *Ann Thorac Surg*. 2001;72(3):823–830.
44. Schoof PH, Cromme-Dijkhuis AH, Bogers JJ, et al. Aortic root replacement with pulmonary autograft in children. *J Thorac Cardiovasc Surg*. 1994;107(2):367–373.
45. Laudito A, Brook MM, Suleman S, et al. The Ross procedure in children and young adults: a word of caution. *J Thorac Cardiovasc Surg*. 2001;122(1):147–153.
46. Takkenberg JJ, Klieverik LM, Schoof PH, et al. The Ross procedure: a systematic review and meta-analysis. *Circulation*. 2009;119(2):222–228.
47. Feltes TF, Bacha E, Beekman RH 3rd, et al. Indications for cardiac catheterization and intervention in pediatric cardiac disease: a scientific statement from the American Heart Association. *Circulation*. 2011;123(22):2607–2652.
48. Keane JF, Driscoll DJ, Gersony WM, et al. Second natural history study of congenital heart defects. Results of treatment of patients with aortic valvar stenosis. *Circulation*. 1993;87(2 suppl):I16–I27.
49. Bonow RO, Carabello BA, Chatterjee K, et al. 2008 Focused update incorporated into the ACC/AHA 2006 guidelines for the management of patients with valvular heart disease: a report of the American College

of Cardiology/American Heart Association Task Force on Practice Guidelines (Writing Committee to Revise the 1998 Guidelines for the Management of Patients With Valvular Heart Disease): endorsed by the Society of Cardiovascular Anesthesiologists, Society for Cardiovascular Angiography and Interventions, and Society of Thoracic Surgeons. *Circulation*. 2008;118(15):e523–e661.

50. Hawkins JA, Minich LL, Shaddy RE, et al. Aortic valve repair and replacement after balloon aortic valvuloplasty in children. *Ann Thorac Surg*. 1996;61(5):1355–1358.
51. Stamm C, Kreutzer C, Zurakowski D, et al. Forty-one years of surgical experience with congenital supravalvular aortic stenosis. *J Thorac Cardiovasc Surg*. 1999;118(5):874–885.
52. Scott DJ, Campbell DN, Clarke DR, et al. Twenty-year surgical experience with congenital supravalvar aortic stenosis. *Ann Thorac Surg*. 2009;87(5):1501–1507, discussion 1507-1508.
53. Douville EC, Sade RM, Crawford FA Jr, et al. Subvalvar aortic stenosis: timing of operation. *Ann Thorac Surg*. 1990;50(1):29–33, discussion 33-24.
54. Gersony WM. Natural history of discrete subvalvar aortic stenosis: management implications. *J Am Coll Cardiol*. 2001;38(3):843–845.
55. Karamlou T, Gurofsky R, Bojcevski A, et al. Prevalence and associated risk factors for intervention in 313 children with subaortic stenosis. *Ann Thorac Surg*. 2007;84(3):900–906, discussion 906.
56. Report of the New England Regional Infant Cardiac Program. *Pediatrics*. 1980;65(2 Pt 2):375–461.
57. Abbruzzese PA, Aidala E. Aortic coarctation: an overview. *J Cardiovasc Med (Hagerstown)*. 2007;8(2):123–128.
58. Keane JF, Fyler DC. Coarctation of the aorta. In: Keane JF, Lock JE, Fyler DC, eds. *Nadas' Pediatric Cardiology*. 2nd ed. Philadelphia: Saunders Elsevier; 2006:627.
59. Connolly HM, Huston J 3rd, Brown RD Jr, et al. Intracranial aneurysms in patients with coarctation of the aorta: a prospective magnetic resonance angiographic study of 100 patients. *Mayo Clin Proc*. 2003;78(12):1491–1499.
60. Wong SC, Burgess T, Cheung M, et al. The prevalence of turner syndrome in girls presenting with coarctation of the aorta. *J Pediatr*. 2014;164(2):259–263.
61. Dulac Y, Pienkowski C, Abadir S, et al. Cardiovascular abnormalities in Turner's syndrome: what prevention? *Arch Cardiovasc Dis*. 2008;101(7–8):485–490.
62. Kim HK, Gottliebson W, Hor K, et al. Cardiovascular anomalies in Turner syndrome: spectrum, prevalence, and cardiac MRI findings in a pediatric and young adult population. *AJR Am J Roentgenol*. 2011;196(2):454–460.
63. Metry D, Heyer G, Hess C, et al. Consensus statement on diagnostic criteria for PHACE Syndrome. *Pediatrics*. 2009;124(5):1447–1456.
64. Allan LD, Crawford DC, Tynan M. Evolution of coarctation of the aorta in intrauterine life. *Br Heart J*. 1984;52(4):471–473.
65. Rudolph AM, Heymann MA, Spitznas U. Hemodynamic considerations in the development of narrowing of the aorta. *Am J Cardiol*. 1972;30(5):514–525.
66. de Divitiis M, Pilla C, Kattenhorn M, et al. Vascular dysfunction after repair of coarctation of the aorta: impact of early surgery. *Circulation*. 2001;104(12 suppl 1):I165–I170.
67. de Divitiis M, Rubba P, Calabro R. Arterial hypertension and cardiovascular prognosis after successful repair of aortic coarctation: a clinical model for the study of vascular function. *Nutr Metab Cardiovasc Dis*. 2005;15(5):382–394.
68. Strafford MA, Griffiths SP, Gersony WM. Coarctation of the aorta: a study in delayed detection. *Pediatrics*. 1982;69(2):159–163.
69. Ferguson EC, Krishnamurthy R, Oldham SA. Classic imaging signs of congenital cardiovascular abnormalities. *Radiographics*. 2007;27(5):1323–1334.
70. Konen E, Merchant N, Provost Y, et al. Coarctation of the aorta before and after correction: the role of cardiovascular MRI. *AJR Am J Roentgenol*. 2004;182(5):1333–1339.
71. Araoz PA, Reddy GP, Tarnoff H, et al. MR findings of collateral circulation are more accurate measures of hemodynamic significance than arm-leg blood pressure gradient after repair of coarctation of the aorta. *J Magn Reson Imaging*. 2003;17(2):177–183.
72. Steffens JC, Bourne MW, Sakuma H, et al. Quantification of collateral blood flow in coarctation of the aorta by velocity encoded cine magnetic resonance imaging. *Circulation*. 1994;90(2):937–943.
73. Varaprasathan GA, Araoz PA, Higgins CB, et al. Quantification of flow dynamics in congenital heart disease: applications of velocity-encoded cine MR imaging. *Radiographics*. 2002;22(4):895–905, discussion 905-896.
74. Egan M, Holzer RJ. Comparing balloon angioplasty, stenting and surgery in the treatment of aortic coarctation. *Expert Rev Cardiovasc Ther*. 2009;7(11):1401–1412.
75. Kaushal S, Backer CL, Patel JN, et al. Coarctation of the aorta: midterm outcomes of resection with extended end-to-end anastomosis. *Ann Thorac Surg*. 2009;88(6):1932–1938.
76. Cowley CG, Orsmond GS, Feola P, et al. Long-term, randomized comparison of balloon angioplasty and surgery for native coarctation of the aorta in childhood. *Circulation*. 2005;111(25):3453–3456.
77. Holzer R, Qureshi S, Ghasemi A, et al. Stenting of aortic coarctation: acute, intermediate, and long-term results of a prospective multi-institutional registry–Congenital Cardiovascular Interventional Study Consortium (CCISC). *Catheter Cardiovasc Interv*. 2010;76(4):553–563.
78. Vriend JW, Mulder BJ. Late complications in patients after repair of aortic coarctation: implications for management. *Int J Cardiol*. 2005;101(3):399–406.

# 74

# Right Heart Lesions

Nazia Husain, R. Andrew deFreitas, Cynthia K. Rigsby, and Andrada R. Popescu

## IMAGING OF THE RIGHT HEART

The algorithms used for left ventricular assessment cannot always be applied to the right ventricle (RV), which differs in morphology, shape, and function. The RV has a complex geometrical shape with a thinner and more trabeculated myocardium than the left ventricle (LV).[1] The chest x-ray is a preliminary imaging tool, with the lateral view best suited to detect RV enlargement. Echocardiography is the mainstay for assessment of the RV, with published adult[2] and pediatric guidelines.[3] Cardiac magnetic resonance imaging (CMR) is the current gold standard for RV assessment and tissue characterization. Gated cardiac computed tomography angiography (CTA) is an alternative when CMR is contraindicated.[4]

The retrosternal location of the right ventricular outflow tract (RVOT) and pulmonary valve (PV) makes echocardiography difficult, especially in adolescents and adults. CMR and CTA allow detailed assessment of anatomy, valve mobility, presence of poststenotic dilation, and associated condition of the branch pulmonary arteries (PAs).[5] With current CT scanners, image acquisition can be completed within seconds or less and with a short breath hold. CTA is excellent for assessment of proximal and distal PAs. CMR is excellent for sequential assessment of the PV. Anatomy and function of the RVOT and PV can be assessed by balanced steady state free precession (SSFP) CMR imaging. Turbo spin-echo with blood suppression technique is very useful for imaging RVOT and branch PAs especially in patients with metallic implants causing artifacts. Through-plane and in-plane phase contrast quantification of flow across the PV and branch PAs provides comprehensive functional assessment including valve stenosis or regurgitation, and differential pulmonary blood flow. Magnetic resonance angiography (MRA) is an alternative to CTA for assessment of extracardiac structures.[5]

## EBSTEIN ANOMALY

***Overview.*** Ebstein anomaly accounts for fewer than 1% of all cases of congenital heart disease.[6] Associated malformations include atrial septal defect (ASD), ventricular septal defect (VSD), pulmonary stenosis and atresia, tetralogy of Fallot, congenitally corrected transposition of the great arteries, and patent ductus arteriosus (PDA).[6] Conduction system abnormalities and arrhythmias, including Wolff–Parkinson–White syndrome, have been seen in 22% to 42% of patients.[7]

***Etiology, Pathophysiology, and Clinical Presentation.*** Wilhelm Ebstein provided the first description of this abnormality in 1866.[8] It is characterized by abnormal development and positioning of the tricuspid valve (TV) leaflets, with apical displacement of the septal and posterior leaflets. This phenomenon leads to partitioning of the RV into an atrialized basal inlet segment and an apical outflow chamber. The displaced valve leaflets may be adherent to the RV wall. The anterior valve leaflet tends to be normally positioned, however, it is frequently large and redundant, and sometimes adherent to the RV free wall with a "sail-like" appearance.[9]

The pathophysiology of Ebstein anomaly varies, depending on the degree of dysplasia and displacement of the TV leaflets and the presence and severity of associated defects. With greater degrees of dysplasia and displacement, the severity of tricuspid insufficiency increases, resulting in elevated right atrial pressures and thus right-to-left shunting at the atrial level. Patients with mild forms of Ebstein anomaly may be asymptomatic in childhood and present with symptoms of cyanosis, right heart failure, or arrhythmia in adulthood. Patients with severe forms present in early neonatal life with severe combined cyanosis and acidosis, and a ductal-dependent circulation.[10]

***Imaging.*** Classically, the chest radiographic appearance includes a globular or box-shaped heart as a result of right atrial enlargement associated with normal to diminished pulmonary vascularity (Fig. 74.1).[11] Findings can vary by clinical presentation. Patients with significant valvar dysplasia and severe tricuspid insufficiency have marked right heart enlargement and decreased antegrade pulmonary blood flow. With less marked valve displacement and tricuspid insufficiency, only mild right heart enlargement may be present (e-Fig. 74.2).

Ebstein anomaly can be readily diagnosed by both prenatal and postnatal echocardiography.[10] Echocardiography and CMR allow for detailed anatomic and functional evaluation. The characteristic features include displacement and tethering of the septal and posterior leaflets of the TV, dilation of the right atrium, and atrialization of the RV (Fig. 74.3). Imaging goals include evaluation of the TV and severity of tricuspid regurgitation; evaluation of right-to-left shunting through the ASD or patent foramen ovale, evaluating volume and function of the RV including the atrialized portion; delayed enhancement in the thin atrialized ventricular wall and septum; PV and branch PA stenoses; left ventricular size and systolic function; and aortic arch anomalies.[7,12–14] Axial imaging provides reliable information about the atrialized RV.[15] A total right/left ventricular volume index obtained by CMR has been found to correlate with heart failure markers and disease severity.[16]

***Treatment.*** Patients with mild forms of Ebstein anomaly may not require surgical treatment, or the need for surgery may not arise until later in life until right heart dysfunction develops. Indications for surgical intervention/reintervention and/or medical therapy include limited exercise capacity (greater than New York Heart Association class II), increasing heart size (cardiothoracic ratio >65%), cyanosis (resting oxygen saturations <90%), severe tricuspid regurgitation with symptoms, progressive right ventricular dilation or dysfunction, transient ischemic attack, or stroke.[17,18]

Surgery includes valvuloplasty with either the Carpentier or Da Silva's cone procedures. The Carpentier procedure involves reimplantation of the anterior and posterior TV leaflets at the level of the neotricuspid annulus, resulting in a monocuspid or bicuspid valve configuration.[19] More recently described "cone reconstruction" includes mobilization and re-anastomosis of the TV leaflets and subvalvar apparatus to form a cone-shaped valve with improved competence.[9] Other possible treatments include TV replacement or, rarely, oversewing of the TV and creation of a central shunt in infancy with an ultimate single ventricle type palliation. Transcatheter closure of the ASD may be considered if severe cyanosis is present without tricuspid insufficiency necessitating valve repair.[20] Rarely, cardiac transplantation may be indicated.[10] Clinically significant arrhythmias develop in some patients and require transcatheter or surgical ablation procedures.[7]

## Abstract:

Cardiovascular magnetic resonance (CMR) and computed tomography angiography (CTA) allow detailed assessment of right ventricular anatomy, pulmonary valve mobility, presence of post-stenotic dilation and associated condition of the branch pulmonary arteries. For Ebstein anomaly, CMR provides detailed evaluation of the atrialized and functional segments of the right ventricle. For tricuspid atresia, cross-sectional imaging after the Glenn or Fontan procedures includes assessment of anatomy and flow through the cavopulmonary and Fontan pathways, atrioventricular valve function, and quantification of ventricular size and systolic function and the presence of collaterals. For pulmonary atresia with intact ventricular septum, preoperative imaging goals include evaluation of associated coronary artery anomalies. For pulmonary valve stenosis, the peak velocity obtained by either echocardiography or phase contrast MRI can be used to calculate the peak pulmonary valve pressure gradient in mmHg.

## Keywords:

Cardiovascular magnetic resonance
computed tomography angiography
Fontan pathways
atrioventricular valve function
pulmonary valve stenosis

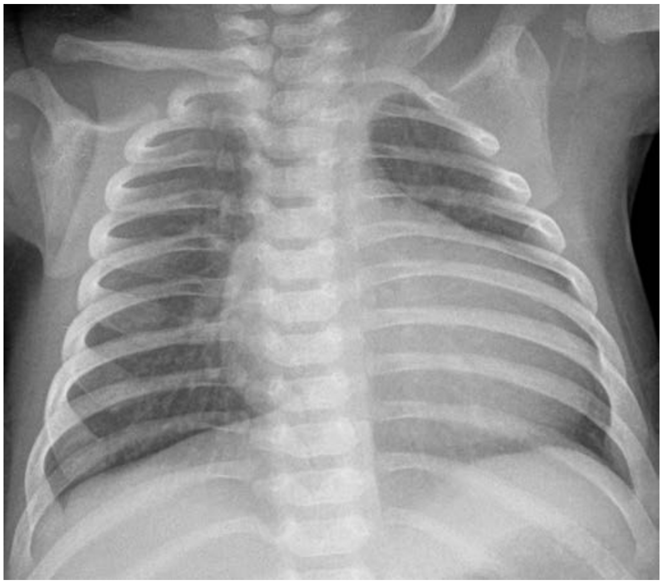

**e-Figure 74.2. Ebstein anomaly.** Frontal chest radiograph in a mildly cyanotic 7-day-old girl with mild Ebstein anomaly reveals mild to moderate enlargement of the heart and normal to decreased pulmonary vascularity.

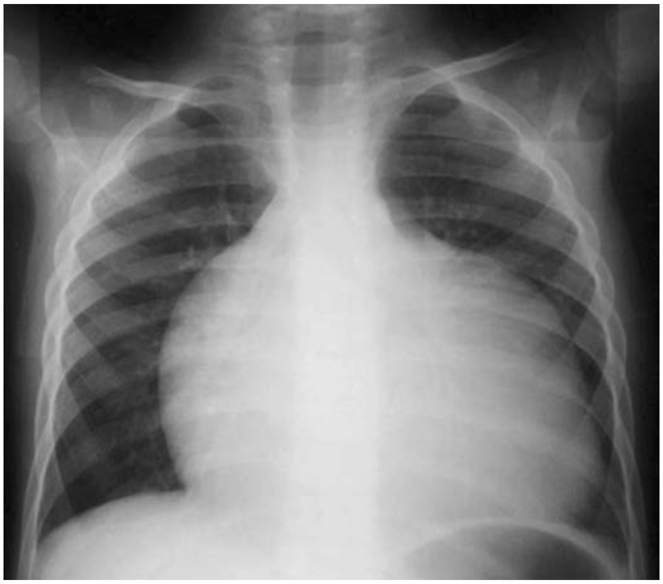

**Figure 74.1. Classic radiographic appearance of Ebstein anomaly.** Frontal chest radiograph shows globular box-shaped heart enlargement and diminished pulmonary vascularity.

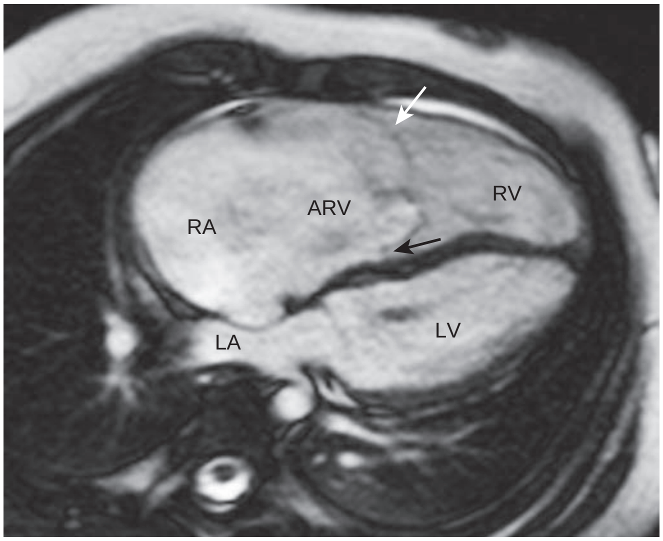

**Figure 74.3. Ebstein anomaly.** Axial steady-state free-precession MRI demonstrates right heart enlargement with redundancy of the anterior tricuspid valve leaflet *(white arrow)* and displacement of the septal tricuspid valve leaflet *(black arrow)* into the right ventricle *(RV)*. As a result, a large atrialized portion of the right ventricle *(ARV)* is present. *LA,* Left atrium; *LV,* left ventricle; *RA,* right atrium.

## TRICUSPID ATRESIA

***Overview.*** Tricuspid atresia features an absence of the TV with a resultant lack of a direct connection between the right atrium and RV. It accounts for approximately 3% to 4% of congenital heart disease.[21] Most cases are sporadic, but familial cases and association with 22q11 microdeletions have been reported.[22]

***Pathophysiology and Clinical Presentation.*** The TV is usually absent; instead, muscular tissue or, less commonly, fibrous tissue is present on the floor of the right atrium. An interatrial communication is present to allow blood to reach the left side of the heart from the right, and a VSD is usually present. The degree of RV development is related to the size of the VSD.[21] In tricuspid atresia, there is complete mixing of systemic venous and pulmonary venous return and a variable degree of cyanosis. The severity of cyanosis is related to the degree of RV outflow obstruction, the size of the VSD, the origins of the great arteries (ventriculo-arterial connections are concordant in 70% of cases and discordant or transposed in 30% of the cases), the presence or absence of a PDA, pulmonary vascular resistance (associated variable degree of pulmonary or subpulmonary stenosis), and LV outflow obstruction. The most commonly used classification system was developed by Tandon and Edwards in 1974 describing tricuspid atresia as types I, II, and III (Table 74.1).[23] An unrestrictive VSD with no pulmonary outflow obstruction leads to greater pulmonary than systemic blood flow, resulting in mild cyanosis with overcirculated, congested lungs. In contrast, restricted pulmonary blood flow results in more severe cyanosis.[21]

***Imaging.*** The heart usually appears normal or may be mildly enlarged on chest radiography. With pulmonary outflow obstruction, normal to decreased pulmonary vascularity is noted. With no obstruction, there is cardiomegaly and increased pulmonary vascularity (e-Fig. 74.4).

The characteristic imaging feature of tricuspid atresia is replacement of the TV with a ridge of muscular and fatty tissue positioned between the enlarged right atrium and the hypoplastic RV (e-Fig. 74.5). The size of the VSD and the relationship of the great arteries should be characterized. Echocardiography is the imaging modality of choice in infancy, but CMR and CTA can be used to determine anatomy in more complex cases. These modalities are playing an increasing role in preoperative evaluation in this disease, sometimes obviating the need for cardiac catheterization (see Treatment section).[24] Important components of cross-sectional imaging after Glenn or Fontan procedures include assessment of anatomy and flow through the cavopulmonary and Fontan pathways, atrioventricular valve function, quantification of ventricular size and systolic function, and the presence of collaterals. New MR techniques like 4D flow can be used to evaluate the vascular geometry and complex blood flow patterns in Fontan patients.[25]

***Treatment.*** Ultimately, patients with tricuspid atresia require univentricular palliation because the hypoplastic RV is not capable of handling the entire cardiac output. The goal of univentricular repair is to have the single LV support the systemic circulation and for the systemic venous return to directly enter the PAs, thus bypassing the nonfunctional RV. The first stage of single ventricle palliation is performed in early infancy. Those with cyanosis may

**TABLE 74.1** Anatomic Classification of Tricuspid Atresia

| Type | A | B | C |
|---|---|---|---|
| I, normally positioned great arteries (70%) | Pulmonary atresia | Small ventricular septal defect, pulmonary artery hypoplasia | Large ventricular septal defect, normal pulmonary artery |
| II, dextro-transposition of the great vessels (25%) | Pulmonary atresia/stenosis | Pulmonary or subpulmonary stenosis | Large pulmonary artery |
| III, levo-transposition of the great vessels (5%) | Pulmonary or subpulmonary stenosis | Subaortic stenosis | |

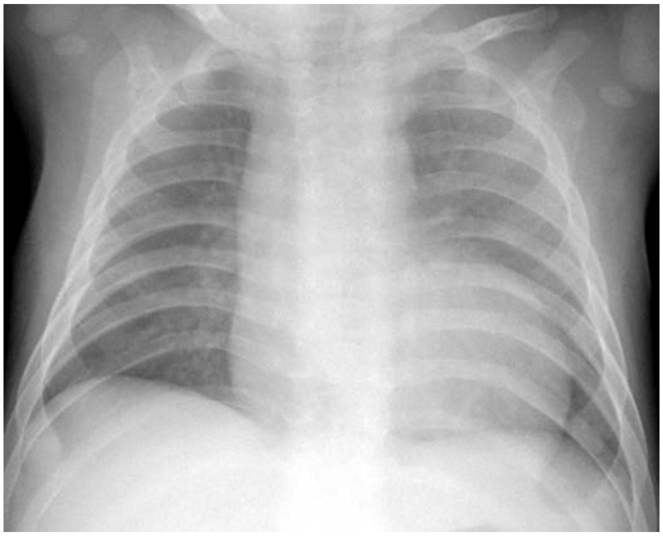

**e-Figure 74.4. Tricuspid atresia in a 4-month-old boy.** A frontal chest radiograph shows mild cardiac enlargement with a rounded apex and a concave left upper heart margin as a result of pulmonary atresia.

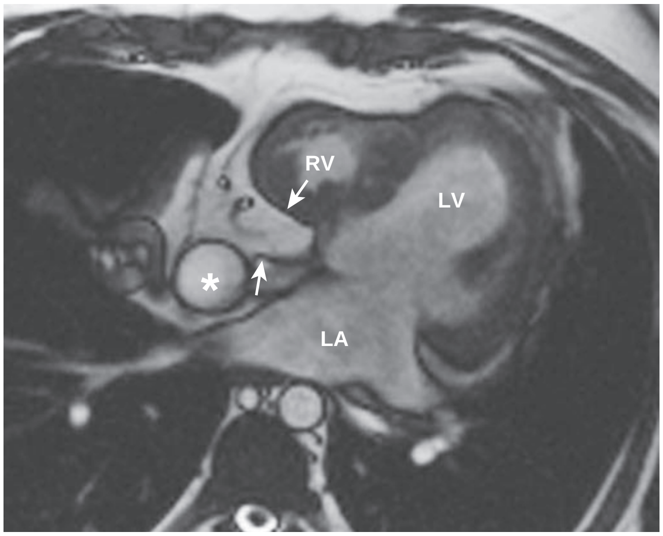

**e-Figure 74.5. Tricuspid atresia after extracardiac Fontan palliation *(asterisk)* in a 27-year-old.** An axial steady-state free-precession image shows a ridge of fatty tissue *(arrows)* in the floor of the right atrium at the site of the atretic tricuspid valve. A small caliber right ventricle *(RV)* also is present. *LA,* Left atrium; *LV,* left ventricle.

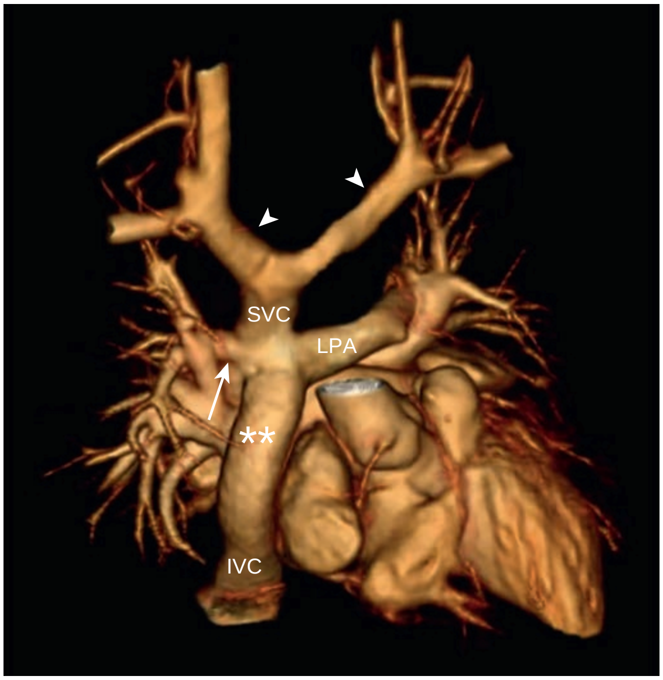

**Figure 74.6. Fontan palliation in an adult.** An extracardiac Fontan baffle *(asterisks)* extends from the inferior vena cava *(IVC)* to the right pulmonary artery *(arrow)*. A bidirectional Glenn anastomosis is seen between the superior vena cava *(SVC)* and right and left pulmonary arteries. *LPA*, Left pulmonary artery; *arrowheads* right and left innominate veins.

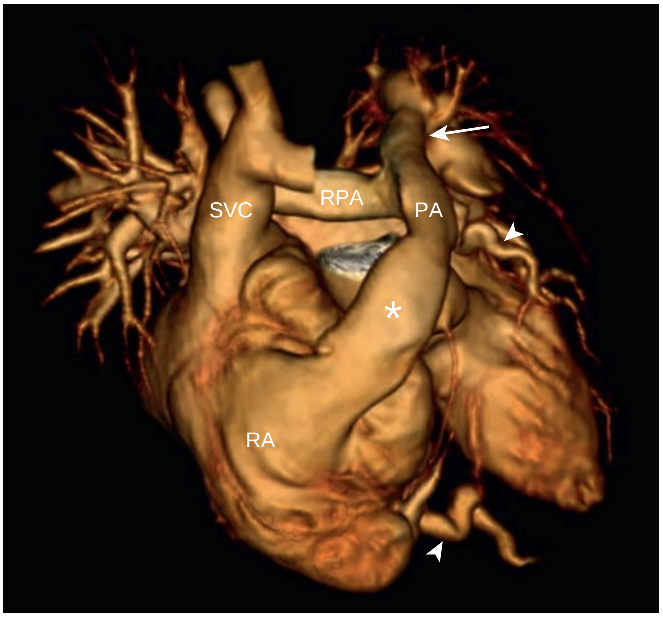

**Figure 74.7. Right atrial** ***(RA)*** **to pulmonary artery** ***(PA)*** **Fontan conduit anastomosis for palliation of tricuspid atresia.** *Asterisk* indicates the conduit that extends from the *RA* to the main pulmonary artery *(PA)*; *RPA*, right pulmonary artery; *LPA*, *white arrow; SVC*, superior vena cava. Venovenous collaterals to the coronary venous circulation *(white arrowheads)*.

require a prostaglandin infusion to keep the PDA open until a surgical aorto-pulmonary shunt (like the modified Blalock–Taussig shunt) is placed. In overcirculated infants with no pulmonary stenosis, diuretics and a surgical PA band are needed.

The second stage of the palliation is generally performed between 3 and 9 months of age in the form of a bidirectional Glenn shunt, anastomosing the superior vena cava to the right PA. The aorto-pulmonary shunt is taken down. Completion of the total cavopulmonary anastomosis with the Fontan procedure, performed between 1 and 5 years of age, involves anastomosing the inferior vena cava to the PAs via an extracardiac conduit or an intracardiac "lateral tunnel" (current Fontan pathway modifications) (Fig. 74.6).[26] This procedure completes the separation of the systemic and pulmonary circulations and eliminates cyanosis. Other approaches to creating a cavopulmonary connection, including direct anastomosis of the right atrium to the PA, have been used in the past (Fig. 74.7).[27]

Surgical mortality rates for the modified Fontan procedure range between 1.1% and 2.7%.[26] Acute complications after the Fontan procedure include pleural effusions and ascites that may be slow to resolve.[28] Long-term complications of Fontan palliation include thrombosis within the cavopulmonary pathway, especially in a dilated right atrium; stenoses within the cavopulmonary pathway; cyanosis due to the development of pulmonary arteriovenous malformations or systemic venous to pulmonary venous collateral shunts; arrhythmias; congestive hepatopathy or cirrhosis; and protein-losing enteropathy (Fig. 74.8).[28] Cardiac transplantation remains the only definitive treatment for patients with failing Fontan procedure circulation.[28]

## PULMONARY ATRESIA WITH INTACT VENTRICULAR SEPTUM

***Overview.*** Pulmonary atresia (PA) with intact ventricular septum (PA/IVS), a rare cardiac disorder that is highly variable in its appearance and presentation, represents approximately 1% to 3% of all cases of congenital heart disease.[29] RV outflow tract obstruction is present because of atresia of the PV or the pulmonary infundibulum with an intact ventricular septum. Obstruction of the outflow from the right heart necessitates an interatrial communication or PDA to allow for pulmonary blood flow.[30]

***Etiology, Pathophysiology, and Clinical Presentation.*** In contrast to patients with PA with VSD, patients with PA/IVS generally have well-developed, confluent central PAs.[31] Morphology of the TV however is highly variable, with both severe stenosis and marked insufficiency seen. The spectrum of RV development is also variable, with varying degrees of hypoplasia (hypoplastic right heart syndrome). The RV is less hypoplastic in the setting of severe tricuspid regurgitation. Significant RV hypertrophy is common. Associated coronary artery anomalies may include RV to coronary connections. Some may exhibit an RV-dependent coronary circulation.[32] In this condition, blood from the hypertensive RV perfuses the coronary arteries with possible associated coronary stenosis or even atresia. Significant drop in RV pressure (after pulmonary valvotomy) may result in myocardial ischemia and hemodynamic collapse in those cases. RV-dependent coronary circulation is typically seen in patients with small RVs and no significant tricuspid regurgitation.[33] The major clinical manifestation of PA/IVS is cyanosis, which is typically seen shortly after birth when the PDA begins to close.

***Imaging.*** In infancy, the size of the heart on a chest radiograph correlates with the degree of tricuspid insufficiency, with larger cardiac size correlating with increasing tricuspid regurgitation. Severe cardiomegaly producing the "wall-to-wall" heart may be present with severe tricuspid regurgitation (Fig. 74.9).[34]

Echocardiography yields diagnostic imaging in infancy, and CMR may be used in complex cases.[35] Imaging features include atresia of the PV or infundibulum, hypoplastic RV and TV, an interatrial communication, and a PDA. Preoperative imaging goals include a comprehensive evaluation of the right heart structures. Attention to the anatomy and function of the hypoplastic TV

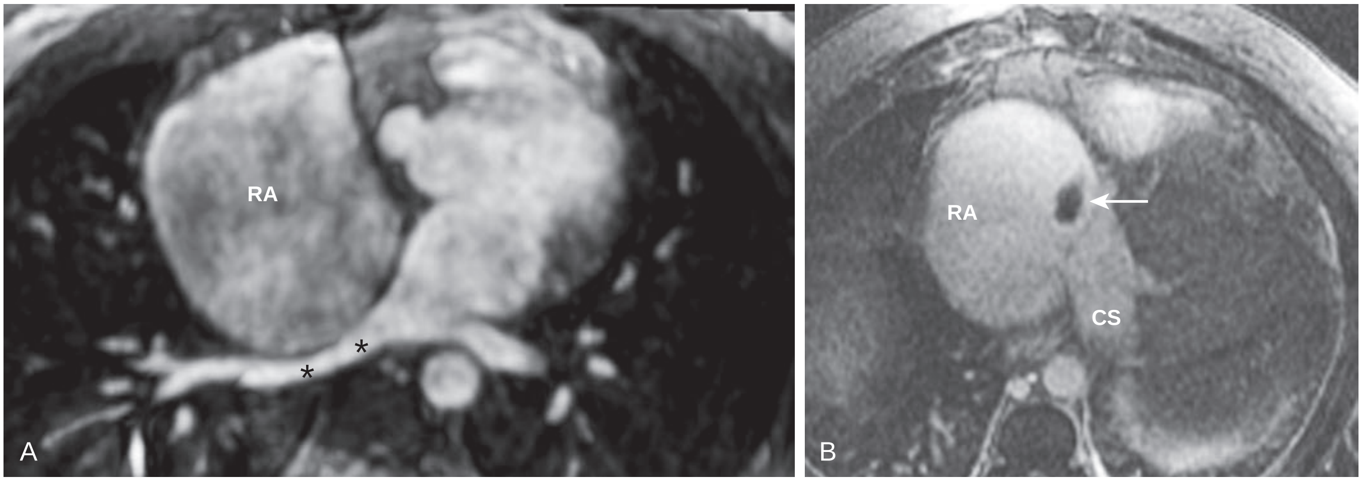

**Figure 74.8. Fontan complications.** (A) A 25-year-old with tricuspid atresia after right atrial to pulmonary artery Fontan palliation. A four-chamber MR steady-state free-precession image shows a markedly dilated right atrium *(RA)* compressing the right inferior pulmonary vein *(asterisks).* (B) A 27-year-old with tricuspid atresia after *RA* to right ventricle Fontan palliation. A four-chamber MR late gadolinium enhancement image shows a markedly dilated *RA* and coronary sinus *(CS)* with a thrombus *(arrow)* in the *RA.*

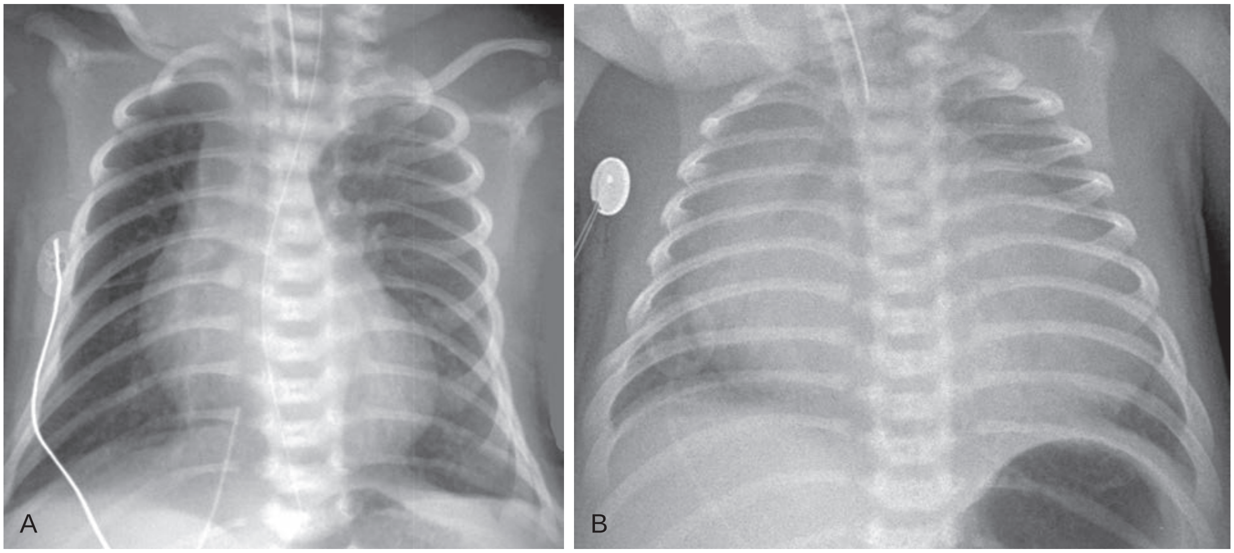

**Figure 74.9. Pulmonary atresia with intact ventricular septum (PA/IVS).** (A) Frontal chest radiograph demonstrates mild cardiac enlargement in a cyanotic newborn boy. Additionally, asymmetric pulmonary vascularity is present with decreased pulmonary blood flow on the right compared with the left related to stenosis of the right pulmonary artery just proximal to the insertion of the patent ductus arteriosus. (B) Frontal chest radiograph in a cyanotic newborn boy showing severe cardiomegaly because of significant tricuspid regurgitation producing severe cardiomegaly with a "wall-to-wall" appearance of the heart.

and RV is necessary (Fig. 74.10). Coronary artery anatomy and ventriculo-coronary communications may not be well visualized on echocardiography, and thus additional evaluation with angiocardiography, CTA, or MRA may be necessary. Postoperatively, the type of imaging that is used will depend on the type of repair that has been performed. CMR may be important in these postoperative patients since RV evaluation is limited with echocardiography.

***Treatment.*** Initial management of a neonate with PA/IVS includes the administration of prostaglandins to prevent PDA closure and maintenance of pulmonary blood flow. Interventions depend on the degree of RV and PA development and the coronary circulation pattern. A pulmonary valvotomy is contraindicated in the presence of an RV-dependent coronary circulation.[32] A transcatheter pulmonary valvotomy and balloon dilation is performed if the morphology of the imperforate PV is favorable.[36] When the pulmonary anatomy is not favorable for a transcatheter intervention, a surgical valvotomy may be performed.[37] In the setting of significant RV hypoplasia, a one-and-one-half ventricular repair may be considered.[38] This repair uses a bidirectional Glenn shunt to partially unload the right heart so that it receives venous return only from the inferior vena cava. Univentricular repair or cardiac transplantation may be considered with significant coronary anomalies.[39]

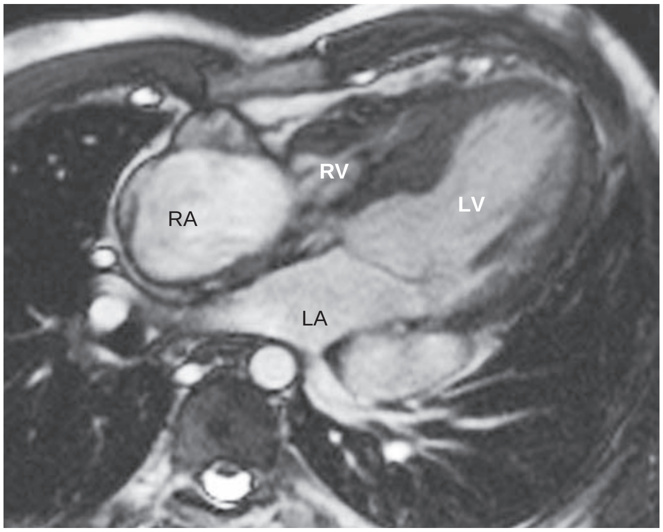

**Figure 74.10. Pulmonary atresia with intact ventricular septum after undergoing right classic Glenn and right atrium *(RA)* to pulmonary artery Fontan procedures in a 21-year-old.** A four-chamber steady-state free-precession MR image shows the hypoplastic right ventricle *(RV)*. The *RA* is mildly dilated. *LA,* Left atrium; *LV,* left ventricle.

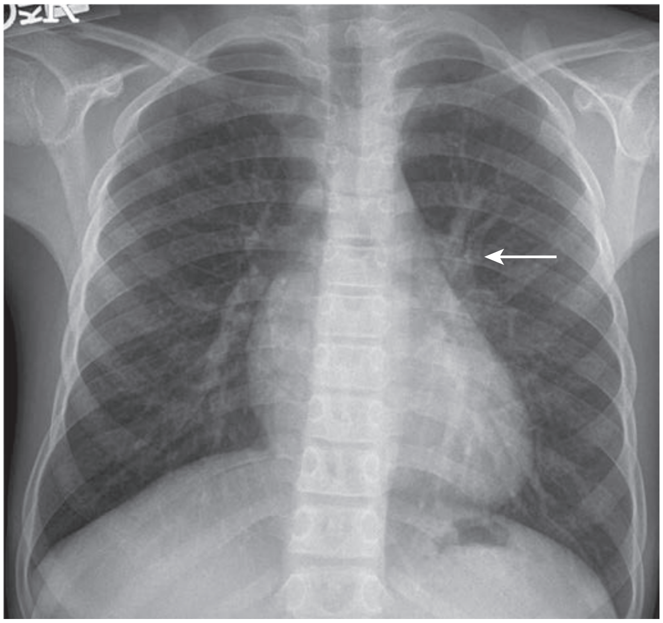

**Figure 74.11. Pulmonary valve stenosis.** Frontal chest radiograph in a 10-year-old shows a normal heart size and pulmonary vascularity. Mild enlargement of the pulmonary trunk and left pulmonary artery is present *(arrow)*.

## PULMONARY VALVE STENOSIS

***Overview.*** Pulmonary valve stenosis (PVS) accounts for approximately 8% to 10% of all cases of congenital heart disease[40] and 80% to 90% of cases of RV outflow obstruction.[41] Less commonly, pulmonary outflow stenosis occurs at the subvalvular, supravalvular, or peripheral PA levels. Peripheral pulmonary stenosis can be seen after maternal rubella infection and in Noonan, Alagille, and Williams syndromes (see Chapter 78).[42–44]

***Etiology, Pathophysiology, and Clinical Presentation.*** In most cases of PVS, the valve leaflets are thickened, and fusion of the leaflets produces a domelike PV with a small central or eccentric opening. The stenotic valve may be trileaflet, bicuspid, unicuspid, or dysplastic. In severe forms (10%–20% of cases) and when associated with syndromes, the PV is dysplastic, with markedly thickened, nonfused cusps and a hypoplastic annulus.[45] The peripheral pulmonary stenoses seen in Williams and Alagille syndromes may be single or multiple.[42,43]

When severe or critical PVS manifests in infancy, the stenosis leads to decreased right ventricular output.[46] The RV and TV may be hypoplastic because limited forward flow through these structures during embryonic life decreases the stimulus for their development. Right atrial pressures are increased, resulting in cyanosis caused by right-to-left shunting through an atrial level shunt. Pulmonary blood flow may depend on the PDA. Closure of the PDA can lead to decreased pulmonary blood flow, cyanosis, hypoxemia, and death.[46]

Clinical presentation in childhood depends on the degree of RV outflow obstruction. Most children with mild to moderate PVS are asymptomatic and only have a systolic murmur. In cases of severely stenotic and dysplastic valves, symptoms include dyspnea, fatigue, and chest pain with right heart failure.[47]

***Imaging.*** Significant cardiomegaly due to right atrial and left heart enlargement may be seen in infants with critical PVS. In cases of moderate to severe PVS, poststenotic dilation of the PAs may be seen (Fig. 74.11). The chest radiograph of patients with mild PVS may appear normal. Enlargement of the main and left PAs may be seen as a result of the extension of the flow jet from the pulmonary trunk directly posterior into the left PA.[48] The pulmonary vascularity is normal if adequate RV output is present. RV hypertrophy with elevation of the cardiac apex and associated filling in of the upper retrosternal space can be seen.

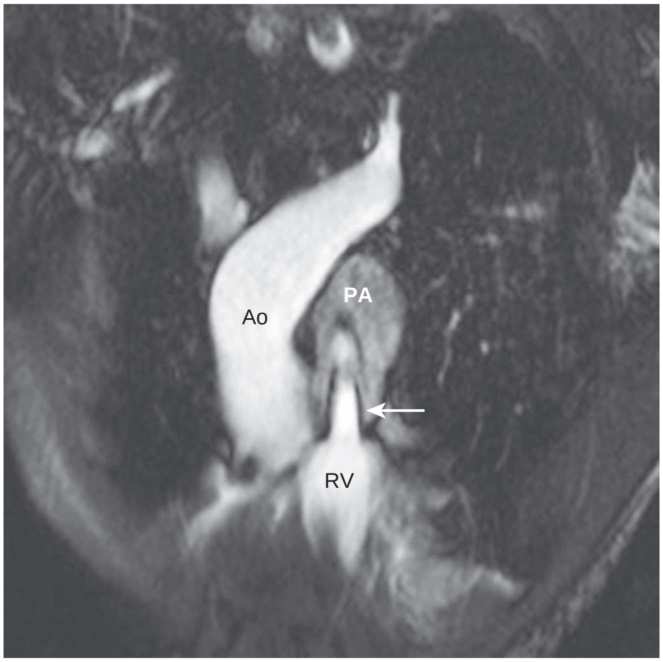

**Figure 74.12. Pulmonary valve stenosis.** A steady-state free-precession MR image coronal to the right ventricular outflow tract *(RV)* shows a poststenotic jet of turbulent flow *(arrow)* across the pulmonary valve. *Ao,* Aorta; *PA,* pulmonary artery.

Echocardiography is the initial imaging method of choice. The role of CMR has increased and is particularly important in adult patients with limited echocardiographic windows.[49] Imaging findings include valve thickening and systolic doming with poststenotic enlargement of the PAs (Fig. 74.12). With a dysplastic valve, the pulmonary annulus is small. Imaging goals include evaluation of the level of the obstruction, valve anatomy, and determination of the peak systolic velocity and pressure gradient across the obstruction. The pressure gradient can be estimated from the flow velocity obtained by echocardiography or CMR phase contrast imaging using the modified Bernoulli equation, $\Delta P = 4V^2$ (where $\Delta P$ is the pressure gradient and $V$ is the peak velocity across the PV in m/sec). Lower peak velocities may be obtained on CMR relative to echocardiography.[50,51] Quantitative assessment of the RV size and systolic function is necessary, as is assessment of the left heart.[45] MRA or CTA allows determination of peripheral PA stenosis. After intervention, imaging is used to determine the degree of residual pulmonary stenosis and the severity of pulmonary regurgitation, and to evaluate RV size and systolic function.

***Treatment.*** Infants with critical PVS are treated medically with prostaglandin $E_1$ infusion to maintain ductal patency; inotropic support and intubation may be needed.[46,47] Balloon valvuloplasty is the treatment of choice for isolated PVS in a nondysplastic valve, with excellent outcomes.[46,52–54] A systemic-to-pulmonary artery shunt is rarely indicated for continued cyanosis.[55] Balloon valvuloplasty often is used as the initial treatment for "dysplastic" PVs, but surgery is frequently needed because of the lower response rate.[40,56] Peripheral pulmonary stenoses often require repeat angioplasties and/or stent placement.[57,58]

Indications for catheter reintervention or surgery include residual RV outflow obstruction from severe infundibular hypertrophy, residual PVS, or peripheral arterial stenosis. PV replacement is indicated for symptomatic severe pulmonary insufficiency, RV dysfunction and dilation, or significant ventricular arrhythmia.[59–62]

## KEY POINTS

- CMR and CTA allow detailed assessment of right heart anatomy, PV mobility, presence of poststenotic dilation, and associated conditions of the branch PAs.
- Ebstein Anomaly: Assessment of atrialized and functional segments of the RV is key.
- Tricuspid Atresia: Studies should focus on anatomic and flow evaluation of the Glenn and Fontan pathways, atrioventricular valve function, ventricular size and systolic function, and presence of collateral vasculature.
- PA with intact ventricular septum: In addition to right and left heart assessment, evaluation for associated coronary artery anomalies and RV-dependent coronary circulation should be undertaken.

## SUGGESTED READINGS

Attenhofer Jost CH, Connolly HM, Dearani JA, et al. Ebstein's anomaly. *Circulation*. 2007;115(2):277–285.

Fredenburg TB, Johnson TR, Cohen MD. The Fontan procedure: anatomy, complications, and manifestations of failure. *Radiographics*. 2011;31(2):453–463.

Kawel N, Valsangiacomo-Buechel E, Hoop R, et al. Preoperative evaluation of pulmonary artery morphology and pulmonary circulation in neonates with pulmonary atresia—usefulness of MR angiography in clinical routine. *J Cardiovasc Magn Reson*. 2010;12:52.

Valsangiacomo Buechel ER, Mertens LL. Imaging the right heart: the use of integrated multimodality imaging. *Eur Heart J*. 2012;33(8):949–960.

## REFERENCES

Full references for this chapter can be found on www.expertconsult.com.

## REFERENCES

1. Valsangiacomo Buechel ER, Mertens LL. Imaging the right heart: the use of integrated multimodality imaging. *Eur Heart J*. 2012;33(8):949–960.
2. Lang RM, Badano LP, Mor-Avi V, et al. Recommendations for cardiac chamber quantification by echocardiography in adults: an update from the American Society of Echocardiography and the European Association of Cardiovascular Imaging. *Eur Heart J Cardiovasc Imaging*. 2015;16(3):233–270.
3. Lopez L, Colan SD, Frommelt PC, et al. Recommendations for quantification methods during the performance of a pediatric echocardiogram: a report from the Pediatric Measurements Writing Group of the American Society of Echocardiography Pediatric and Congenital Heart Disease Council. *J Am Soc Echocardiogr*. 2010;23:465–495.
4. Sanz J, Conroy J, Narula J. Imaging of the right ventricle. *Cardiol Clin*. 2012;30(2):189–203.
5. Saremi F, Gera A, Ho SY, et al. CT and MR imaging of the pulmonary valve. *Radiographics*. 2014;34(1):51–71.
6. Legius B, Van De Bruaene A, Van Deyk K, et al. Behavior of Ebstein's anomaly: single-center experience and midterm follow-up. *Cardiology*. 2010;117(2):90–95.
7. Delhaas T, Sarvaas GJ, Rijlaarsdam ME, et al. A multicenter, long-term study on arrhythmias in children with Ebstein anomaly. *Pediatr Cardiol*. 2010;31(2):229–233.
8. Ebstein W. Ueber einen sehr seltenen Fall von Insufficienz der Valvula tricuspidalis, bedingt durch eine angeborene hochgradige Missbildung derselben. *Arch Anat Physiol*. 1866;7:238–254.
9. Boston US, Goldberg SP, Ward KE, et al. Complete repair of Ebstein anomaly in neonates and young infants: a 16-year follow-up. *J Thorac Cardiovasc Surg*. 2011;141(5):1163–1169.
10. Attenhofer Jost CH, Connolly HM, Dearani JA, et al. Ebstein's anomaly. *Circulation*. 2007;115(2):277–285.
11. Ferguson EC, Krishnamurthy R, Oldham SA. Classic imaging signs of congenital cardiovascular abnormalities. *Radiographics*. 2007;27(5):1323–1334.
12. Irwin RB, Luckie M, Khattar RS. Tricuspid regurgitation: contemporary management of a neglected valvular lesion. *Postgrad Med J*. 2010;86(1021):648–655.
13. Yalonetsky S, Tobler D, Greutmann M, et al. Cardiac magnetic resonance imaging and the assessment of Ebstein anomaly in adults. *Am J Cardiol*. 2011;107(5):767–773.
14. Nakamura I, Kotooka N, Komori Y, et al. Ebstein anomaly by cardiac magnetic resonance imaging. *J Am Coll Cardiol*. 2009;53(17):1568.
15. Dearani JA, Mora BN, Nelson TJ, et al. Ebstein anomaly review: what's now, what's next? *Expert Rev Cardiovasc Ther*. 2015;13(10):1101–1109.
16. Hösch O, Sohns JM, Nguyen TT, et al. The total right/left-volume index: a new and simplified cardiac magnetic resonance measure to evaluate the severity of Ebstein anomaly of the tricuspid valve: a comparison with heart failure markers from various modalities. *Circ Cardiovasc Imaging*. 2014;7(4):601–609.
17. ACC/AHA 2008 guidelines for the management of adults with congenital heart disease: a report of the American College of Cardiology/American Heart Association Task Force on Practice Guidelines (Writing Committee to Develop Guidelines on the Management of Adults With Congenital Heart Disease). Developed in Collaboration With the American Society of Echocardiography, Heart Rhythm Society, International Society for Adult Congenital Heart Disease, Society for Cardiovascular Angiography and Interventions, and Society of Thoracic Surgeons. *J Am Coll Cardiol*. 2008;52(23):e143–e263.
18. Silversides CK, Kiess M, Beauchesne L, et al. Canadian Cardiovascular Society 2009 Consensus Conference on the management of adults with congenital heart disease: outflow tract obstruction, coarctation of the aorta, tetralogy of Fallot, Ebstein anomaly and Marfan's syndrome. *Can J Cardiol*. 2010;26(3):e80–e97.
19. da Silva JP, Baumgratz JF, da Fonseca L, et al. The cone reconstruction of the tricuspid valve in Ebstein's anomaly. The operation: early and midterm results. *J Thorac Cardiovasc Surg*. 2007;133(1):215–223.
20. Paranon S, Acar P. Ebstein's anomaly of the tricuspid valve: from fetus to adult: congenital heart disease. *Heart*. 2008;94(2):237–243.
21. Berg C, Lachmann R, Kaiser C, et al. Prenatal diagnosis of tricuspid atresia: intrauterine course and outcome. *Ultrasound Obstet Gynecol*. 2010;35(2):183–190.
22. Hu P, Ji X, Yang C, et al. 22q11.2 microduplication in a family with recurrent fetal congenital heart disease. *Eur J Med Genet*. 2011;54(4):e433–e436.
23. Jacobs ML, Mayer JE Jr. Congenital heart surgery nomenclature and database project: single ventricle. *Ann Thorac Surg*. 2000;69:197–204.
24. Brown DW, Gauvreau K, Powell AJ, et al. Cardiac magnetic resonance versus routine cardiac catheterization before bidirectional Glenn anastomosis in infants with functional single ventricle: a prospective randomized trial. *Circulation*. 2007;116(23):2718–2725.
25. Jarvis K, Schnell S, Barker AJ, et al. Evaluation of blood flow distribution asymmetry and vascular geometry in patients with Fontan circulation using 4-D flow MRI. *Pediatr Radiol*. 2016;46(11):1507–1519.
26. Backer CL, Deal BJ, Kaushal S, et al. Extracardiac versus intra-atrial lateral tunnel Fontan: extracardiac is better. *Semin Thorac Cardiovasc Surg Pediatr Card Surg Annu*. 2011;14(1):4–10.
27. de Leval MR, Deanfield JE. Four decades of Fontan palliation. *Nat Rev Cardiol*. 2010;7(9):520–527.
28. Fredenburg TB, Johnson TR, Cohen MD. The Fontan procedure: anatomy, complications, and manifestations of failure. *Radiographics*. 2011;31(2):453–463.
29. Santos MA, Azevedo VM. Angiographic morphologic characteristics in pulmonary atresia with intact ventricular septum. *Arq Bras Cardiol*. 2004;82(5):420–425, 413-429.
30. Gutgesell HP. Pulmonary valve atresia with intact ventricular septum. *Cardiovasc Dis*. 1975;2(2):148–155.
31. Buckley LP, Dooley KJ, Flyer DC. Pulmonary atresia with intact ventricular septum in New England. *Am J Cardiol*. 1976;37:124.
32. Giglia TM, Mandell VS, Connor AR, et al. Diagnosis and management of right ventricle-dependent coronary circulation in pulmonary atresia with intact ventricular septum. *Circulation*. 1992;86(5):1516–1528.
33. Patel RG, Freedom RM, Moes CA, et al. Right ventricular volume determinations in 18 patients with pulmonary atresia and intact ventricular septum. Analysis of factors influencing right ventricular growth. *Circulation*. 1980;61(2):428–440.
34. Freedom RM, Jaeggi E, Perrin D, et al. The "wall-to-wall" heart in the patient with pulmonary atresia and intact ventricular septum. *Cardiol Young*. 2006;16(1):18–29.
35. Liang XC, Lam WW, Cheung EW, et al. Restrictive right ventricular physiology and right ventricular fibrosis as assessed by cardiac magnetic resonance and exercise capacity after biventricular repair of pulmonary atresia and intact ventricular septum. *Clin Cardiol*. 2010;33(2):104–110.
36. Lee ML, Tsao LY, Chiu HY, et al. Outcomes in neonates with pulmonary atresia and intact ventricular septum underwent pulmonary valvulotomy and valvuloplasty using a flexible 2-French radiofrequency catheter. *Yonsei Med J*. 2009;50(2):245–251.
37. El Louali F, Villacampa C, Aldebert P, et al. Pulmonary stenosis and atresia with intact ventricular septum. *Arch Pediatr*. 2011;18(3):331–337.
38. Yoshimura N, Yamaguchi M. Surgical strategy for pulmonary atresia with intact ventricular septum: initial management and definitive surgery. *Gen Thorac Cardiovasc Surg*. 2009;57(7):338–346.
39. Guleserian KJ, Armsby LB, Thiagarajan RR, et al. Natural history of pulmonary atresia with intact ventricular septum and right-ventricle-dependent coronary circulation managed by the single-ventricle approach. *Ann Thorac Surg*. 2006;81(6):2250–2257, discussion 2258.
40. Voet A, Rega F, de Bruaene AV, et al. Long-term outcome after treatment of isolated pulmonary valve stenosis. *Int J Cardiol*. 2012;156(1):11–15.
41. Davlouros PA, Niwa K, Webb G, et al. The right ventricle in congenital heart disease. *Heart*. 2006;92(suppl 1):i27–i38.
42. Kamath BM, Spinner NB, Emerick KM, et al. Vascular anomalies in Alagille syndrome: a significant cause of morbidity and mortality. *Circulation*. 2004;109(11):1354–1358.
43. Zalzstein E, Moes CA, Musewe NN, et al. Spectrum of cardiovascular anomalies in Williams-Beuren syndrome. *Pediatr Cardiol*. 1991;12(4):219–223.
44. Zenker M, Buheitel G, Rauch R, et al. Genotype-phenotype correlations in Noonan syndrome. *J Pediatr*. 2004;144(3):368–374.
45. Sato Y, Komatsu S, Matsuo S, et al. Isolated subvalvular pulmonary stenosis: depiction at whole heart magnetic resonance imaging. *Int J Cardiovasc Imaging*. 2007;23(1):49–52.
46. Sommer RJ, Rhodes JF, Parness IA. Physiology of critical pulmonary valve obstruction in the neonate. *Catheter Cardiovasc Interv*. 2000;50(4):473–479.
47. Tynan M. Clinical presentation of heart disease in infants and children. In: Anderson RH, Baker E, McCartney FJ, et al, eds. *Pediatric Cardiology*. Vol. 2. 2nd ed. London: Churchill Livingstone; 2002.
48. Guntheroth WG. Causes and effects of poststenotic dilation of the pulmonary trunk. *Am J Cardiol*. 2002;89(6):774–776.
49. Myerson SG. Valvular and hemodynamic assessment with CMR. *Heart Fail Clin*. 2009;5(3):389–400, vi-vii.

50. Baumgartner H, Hung J, Bermejo J, et al. Echocardiographic assessment of valve stenosis: EAE/ASE recommendations for clinical practice. *J Am Soc Echocardiogr*. 2009;22(1):1–23, quiz 101-102.
51. Lotz J, Meier C, Leppert A, et al. Cardiovascular flow measurement with phase-contrast MR imaging: basic facts and implementation. *Radiographics*. 2002;22(3):651–671.
52. Garty Y, Veldtman G, Lee K, et al. Late outcomes after pulmonary valve balloon dilatation in neonates, infants and children. *J Invasive Cardiol*. 2005;17(6):318–322.
53. Hanley FL, Sade RM, Freedom RM, et al. Outcomes in critically ill neonates with pulmonary stenosis and intact ventricular septum: a multiinstitutional study, Congenital Heart Surgeons Society. *J Am Coll Cardiol*. 1993;22(1):183–192.
54. Rao PS. Diagnosis and management of cyanotic congenital heart disease: part I. *Indian J Pediatr*. 2009;76(1):57–70.
55. Mitchell MB, Clarke DR. Isolated right ventricular outflow tract obstruction. In: Mavroudis C, Backer CL, eds. *Pediatric Cardiac Surgery*. 3rd ed. Philadelphia: Mosby; 2003.
56. Moguillansky D, Schneider HE, Rome JJ, et al. Role of high-pressure balloon valvotomy for resistant pulmonary valve stenosis. *Congenit Heart Dis*. 2010;5(2):134–140.
57. Geggel RL, Gauvreau K, Lock JE. Balloon dilation angioplasty of peripheral pulmonary stenosis associated with Williams syndrome. *Circulation*. 2001;103(17):2165–2170.
58. Rosales AM, Lock JE, Perry SB, et al. Interventional catheterization management of perioperative peripheral pulmonary stenosis: balloon angioplasty or endovascular stenting. *Catheter Cardiovasc Interv*. 2002;56(2):272–277.
59. Gaynor JW. Severe pulmonary insufficiency should be conservatively treated. *Cardiol Young*. 2005;15(suppl 1):68–71.
60. Rao PS. Balloon pulmonary valvuloplasty in children. *J Invasive Cardiol*. 2005;17(6):323–325.
61. Masura J, Burch M, Deanfield JE, et al. Five-year follow-up after balloon pulmonary valvuloplasty. *J Am Coll Cardiol*. 1993;21(1):132–136.
62. McCrindle BW. Independent predictors of long-term results after balloon pulmonary valvuloplasty. Valvuloplasty and Angioplasty of Congenital Anomalies (VACA) Registry Investigators. *Circulation*. 1994;89(4):1751–1759.

## 75

# Conotruncal Anomalies

Maryam Ghadimi Mahani, Prachi P. Agarwal, Jimmy C. Lu, and
Adam L. Dorfman

Conotruncal anomalies are a group of congenital heart defects involving the outflow tracts of the heart. The conotruncal anomalies include tetralogy of Fallot (TOF), transposition of the great arteries (TGA), double-outlet ventricles, truncus arteriosus, and interrupted aortic arch (IAA) type B.

Conotruncal abnormalities are the result of abnormal division or rotation of the primitive truncus during embryologic development.[1,2] The common outlet of the embryonic univentricular heart normally undergoes a complex sequence of events to separate into the right ventricular outflow tract (RVOT) and left ventricular outflow tract (LVOT), the aorta, and the main pulmonary artery (see Chapter 62).[3] Control by numerous genes and migration of the mesenchymal cells from the embryonic neural crest are required for this development.[1] Mutations in a number of genes have been associated with conotruncal anomalies in humans and animal models.[4]

Echocardiography is the mainstay of clinical diagnosis. Conventional angiography is used primarily to evaluate coronary artery anatomy and aortopulmonary collaterals. Magnetic resonance imaging (MRI) and computed tomography (CT) occasionally are used to clarify anatomic details that are not fully delineated by echocardiography in the preoperative patient; these details often are related to the aortic arch, pulmonary arteries and their supply, and pulmonary veins. MRI and CT more often are requested for routine follow-up of patients with conotruncal anomalies, particularly as they reach their teenage and adult years.

## TETRALOGY OF FALLOT

***Overview.*** TOF is the most common cyanotic congenital heart defect. The median described incidence of TOF is 356 per 1 million live births in the United States.[5] Classic manifestations include RVOT obstruction, ventricular septal defect (VSD), overriding of the aortic root above the VSD, and right ventricular (RV) hypertrophy (Fig. 75.1A). These findings are a result of underdevelopment of the subpulmonary infundibulum,[6] which is associated with anterior deviation of the conal septum. Rather than sitting between the anterior and posterior limbs of the trabecula septomarginalis (a Y-shaped bundle of muscle along the right side of the ventricular septum), the conal septum in TOF typically is fused with the anterior limb, bringing the aorta over the ventricular septum and leading to the malalignment VSD.[7,8] The septal malalignment and hypertrophy of the trabeculations of the infundibular free wall result in RVOT obstruction (Fig. 75.1B). The VSD in TOF is located between the malaligned conal septum superiorly and the muscular septum inferiorly,[9] and typically is large, nonrestrictive, and subaortic.

TOF can include pulmonary atresia or dysplastic (absent) pulmonary valve syndrome, in addition to the more common pulmonary stenosis. The extent of RVOT obstruction is variable, ranging from minimal to complete atresia.[10] The pulmonary valve is often thickened with doming leaflets and a hypoplastic annulus causing valvular stenosis. The size of the main and branch pulmonary arteries also varies. Patients with pulmonary valve atresia have pulmonary blood flow supplied by a patent ductus arteriosus, aortopulmonary collateral arteries, or both (e-Fig. 75.2). The central pulmonary arteries can be absent, discontinuous, or diminutive. In TOF with a dysplastic pulmonary valve, congenital severe pulmonary regurgitation occurs, which often is associated with severe dilatation of the central pulmonary arteries and resultant airway compression (e-Fig. 75.3A and B).[11]

***Etiology, Pathophysiology, and Clinical Presentation.*** Genetic abnormalities such as chromosome 22q11 deletion, which also leads to DiGeorge or velocardiofacial syndrome, may play an important role in some patients with TOF.[12] Many cases are sporadic, without any specific genetic abnormality identified.

Clinical manifestations are variable. Most patients have adequate pulmonary blood flow at birth, and increasing cyanosis develops early in life.[13] If RVOT obstruction is severe, right-to-left shunting occurs, resulting in cyanosis. When the obstruction is less severe, the shunting is predominantly left to right; patients with this condition can present with congestive heart failure. If patients who have TOF with pulmonary atresia are dependent on the patent ductus arteriosus, an infusion of prostaglandin $E_1$ is necessary to maintain ductal patency until a more stable pulmonary blood flow can be established. In patients who have TOF with dysplastic pulmonary valve syndrome, presentation may be with tracheobronchomalacia and air trapping, as well as cyanosis.

Other congenital heart anomalies can accompany TOF, including right aortic arch (25%) and coronary artery anomalies such as abnormal origin of the left anterior descending (LAD) coronary artery arising from the right coronary artery (5%–6%) or dual LAD coronary arteries.[14] When the LAD coronary artery arises from the right coronary artery, it passes over the RVOT before supplying its usual territory (e-Fig. 75.4).

***Imaging.*** RV hypertrophy causes uplifting of the cardiac apex. Concavity is present at the location of the main pulmonary artery because of underdevelopment, causing a “wooden shoe “or “boot shape” appearance of the heart (in French, *Coeur en sabot)* on frontal chest radiographs, a classic sign for TOF (Fig. 75.5). The shadow of the main pulmonary artery is absent, and pulmonary vascularity is decreased.[15] Rarely, dilatation of the pulmonary artery occurs as a result of an aneurysm, or asymmetric pulmonary vascularity is present as a result of differential pulmonary artery stenosis and collateralization. In the absence of a thymus, the possibility of DiGeorge syndrome should be considered. A right-sided aortic arch also can be seen on the frontal chest radiograph (see Fig. 75.5).

Complete anatomic diagnosis in a neonate with TOF usually is made by echocardiography, with an infrequent need for cross-sectional imaging. CT or MRI typically is requested to determine pulmonary artery anatomy and sources of pulmonary blood flow, including the central pulmonary arteries, patent ductus arteriosus, and aortopulmonary collaterals. CT angiography is an effective modality for delineating pulmonary artery and collateral anatomy in these patients but has the disadvantage of using ionizing radiation.[16] MRI also can accurately describe these anatomic details without the risks of ionizing radiation. Turbo spin echo techniques can display vessels clearly and demonstrate airway anatomy. The mainstay of MRI for these anatomic questions is three-dimensional, gadolinium contrast-enhanced magnetic resonance angiography (MRA), which is highly accurate compared with diagnostic catheterization.[17]

***Treatment and Follow-up.*** Current management of TOF in most large centers is early single-stage reconstructive surgery, typically performed at 3 to 6 months of age.[18] Staged reconstruction can be required if significant hypoplasia of the central pulmonary arteries is present; a palliative shunt is placed from the systemic to the

## Abstract:

Conotruncal anomalies are a group of congenital heart defects involving the outflow tract of the heart and great vessels. The conotruncal anomalies described in this chapter include tetralogy of Fallot (TOF), transposition of the great arteries (TGA), double-outlet ventricles, truncus arteriosus and interrupted aortic arch (IAA) type B. An overview of each disease is presented, along with clinical course and treatment. Focus is on imaging characteristics, particularly for indications and findings of MRI and CT.

## Keywords:

Conotruncal anomalies
Tetralogy of Fallot
Transposition of the great arteries
Double outlet right ventricle
Truncus arteriosus
Interrupted aortic arch type B

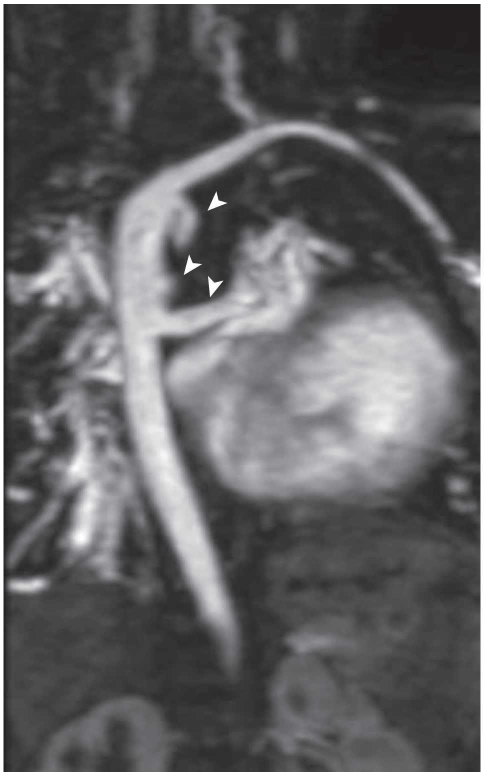

**e-Figure 75.2. Tetralogy of Fallot and pulmonary atresia in a 2-month-old girl.** Coronal-oblique maximum intensity projection from a contrast-enhanced MRA demonstrates aortopulmonary collaterals *(arrowheads)*. This patient also had a right aortic arch with aberrant left subclavian artery.

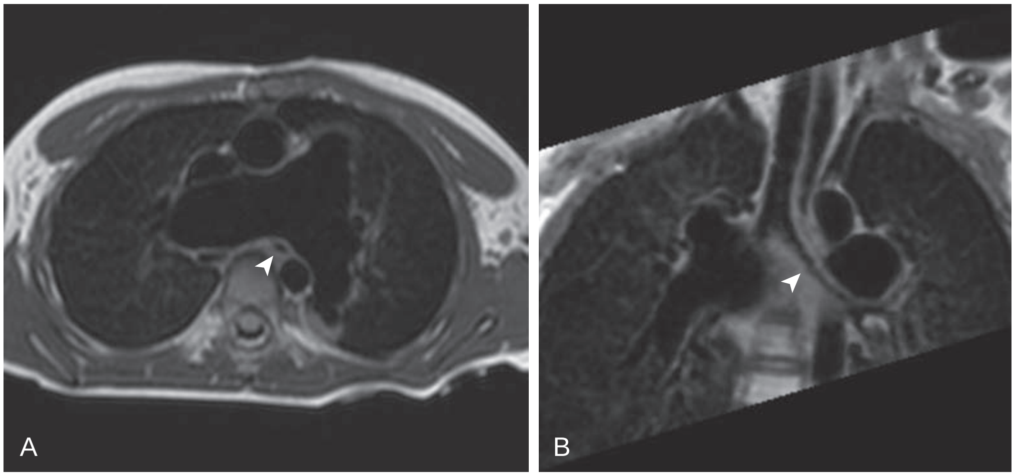

**e-Figure 75.3. Tetralogy of Fallot and an absent pulmonary valve after repair with a transannular patch in a 5-year-old boy.** (A) Axial black blood turbo spin echo MR image demonstrating markedly dilated branch pulmonary arteries. Note the caliber and position of the left mainstem bronchus *(arrowhead)* relative to the right pulmonary artery. (B) Coronal oblique minimum intensity projection demonstrates a narrowed left mainstem bronchus *(arrowhead)* as it passes posterior to the proximal right pulmonary artery.

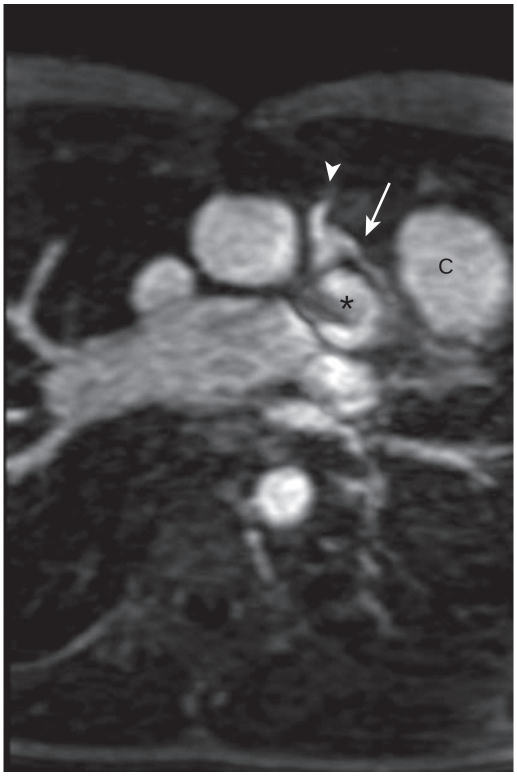

**e-Figure 75.4. Tetralogy of Fallot in a 14-year-old boy.** Axial oblique maximum intensity projection from a contrast-enhanced MRA shows a left anterior descending (LAD) coronary artery *(arrow)* arising from the right coronary artery *(arrowhead)* and traveling anterior to the right ventricular outflow tract *(asterisk)*, preventing use of a transannular patch. A right ventricle to pulmonary artery conduit *(C)* was placed instead, anterior to the LAD coronary artery.

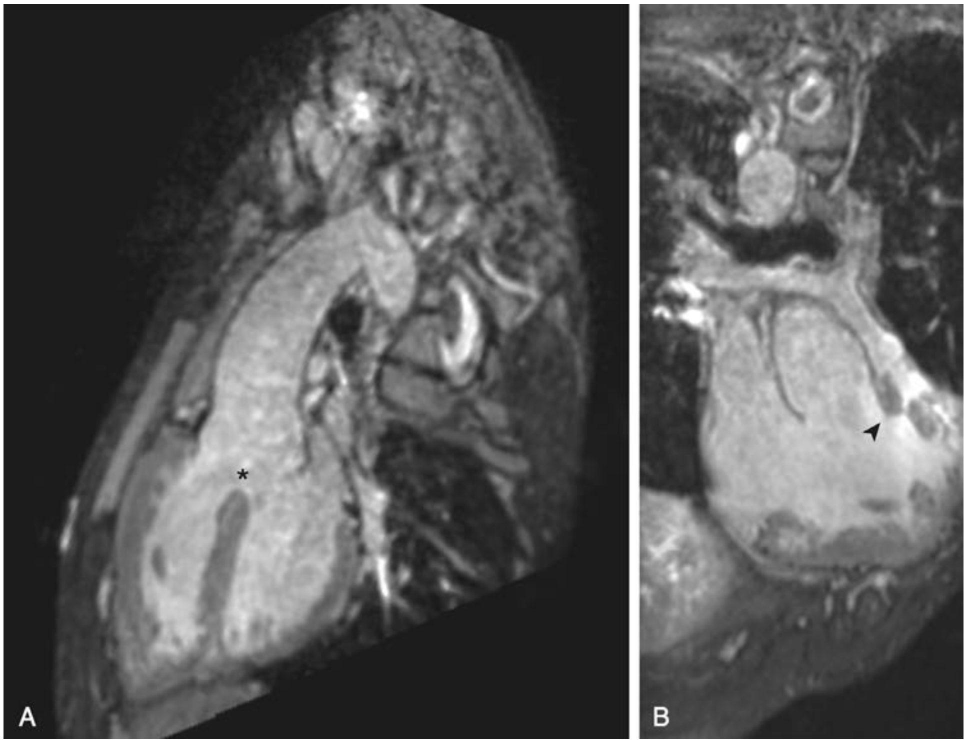

**Figure 75.1. Unrepaired tetralogy of Fallot in an 18-year-old.** (A) Sagittal oblique MRI balanced steady-state free-precession imaging demonstrates the aorta overriding an anterior malalignment ventricular septal defect *(asterisk)*. (B) Coronal oblique projection demonstrates the anterior deviation of the conal septum *(arrowhead)*, leading to subvalvar and valvar pulmonary stenosis.

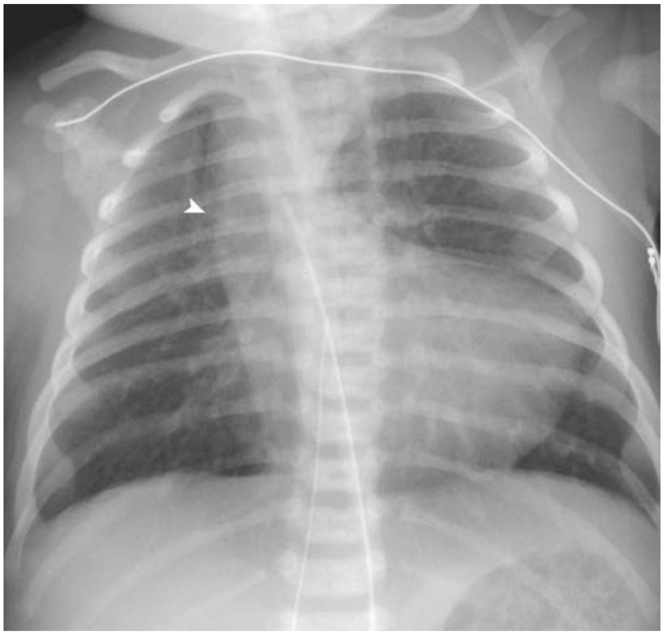

**Figure 75.5. Tetralogy of Fallot and pulmonary atresia in a 1-day-old girl.** Anteroposterior chest radiograph demonstrates the upturned apex and concavity in the region of the pulmonary artery (a boot-shaped heart). Note the shadow to the right of the trachea *(arrowhead)*, which is indicative of a right aortic arch.

pulmonary circulation to provide pulmonary blood flow. When pulmonary supply is from multiple aortopulmonary collaterals, a staged approach of unifocalization of collaterals to either a shunt or the central pulmonary arteries is utilized, eventually bringing the major vessels into continuity with the RV. VSD closure often is not tolerated until later in life in this subgroup of patients.[18]

The goal of surgical repair of TOF is to close the VSD and relieve the RVOT obstruction, thus providing unobstructed flow to the pulmonary vessels from the RV. The approach depends on the severity of the anatomy. The entire repair can be performed transatrially, including VSD closure and division of muscle bundles within the RVOT to relieve obstruction, with no right ventriculotomy. If the pulmonary valve annulus is hypoplastic, a limited transannular patch may be needed to relieve the obstruction.[18] This procedure inevitably results in severe pulmonary regurgitation. In the past, this operation was performed with a large right ventriculotomy, which now usually is avoided. In patients who have TOF with pulmonary atresia, a limited transannular patch may be sufficient to relieve RVOT obstruction. With a longer segment atresia, an RV to pulmonary artery conduit may be required. In patients with an LAD coronary artery arising from the right coronary artery and crossing the RVOT, an RV to pulmonary artery conduit occasionally is necessary to avoid damaging the vessel (see e-Fig. 75.4).[11]

In patients with a transannular patch, a pulmonary valve replacement may be indicated later in life to remove the volume load of pulmonary regurgitation from the RV (Video 75.1). The appropriate timing of this valve replacement is the subject of intense interest.[19] In patients who require an RV to pulmonary artery conduit, a conduit replacement will be needed in time because of somatic growth of the patient. A percutaneous pulmonary valve is also available for placement within a conduit to relieve both stenosis and regurgitation (Video 75.2).

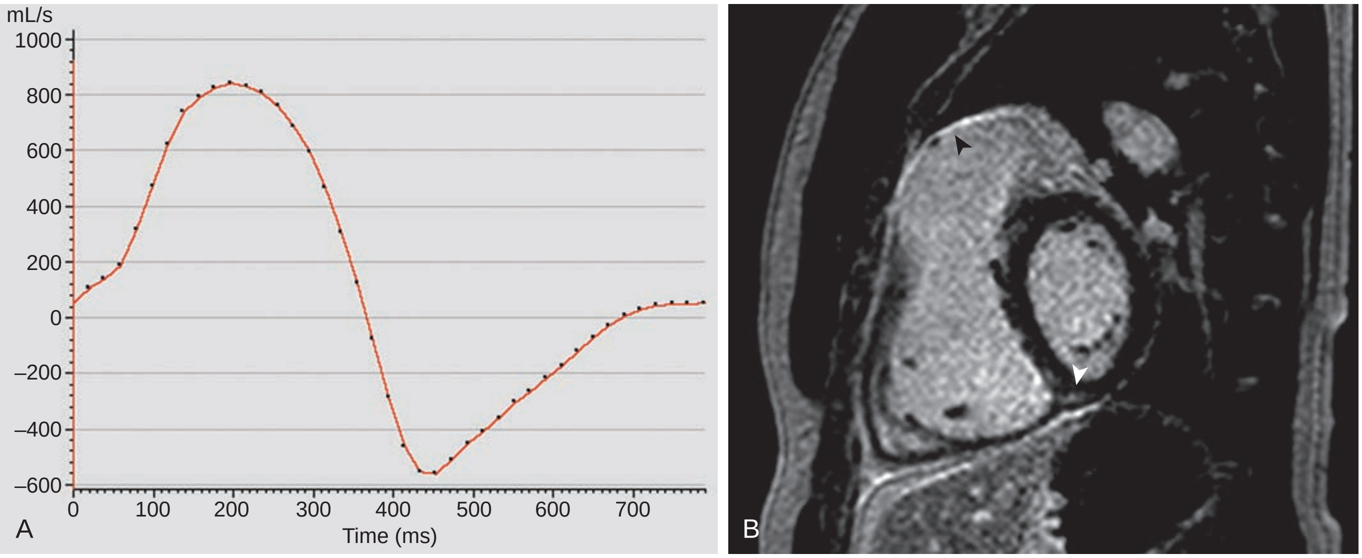

**Figure 75.6. Repaired tetralogy of Fallot in a 31-year-old man.** (A) Graphic representation of quantification of MR phase contrast imaging (flux vs. time) showing antegrade and retrograde flow in the main pulmonary artery. There is severe pulmonary insufficiency, with a regurgitant fraction of 57%. (B) Late gadolinium enhancement MRI in the short axis demonstrates enhancement *(arrowheads)* along the right ventricular outflow tract and at the inferior insertion point of the interventricular septum. See Videos 75.3, 75.4, and 75.5.

Repaired TOF is a frequent referral diagnosis for cardiac MRI. Chronic, severe pulmonary regurgitation can lead to RV pathology. Cardiac MRI is widely considered the gold standard for assessment of RV size and function, making it particularly useful in this patient population (Video 75.3). Other questions in this patient population include anatomy of the RVOT (Video 75.4), quantification of pulmonary regurgitation (Video 75.5 and Fig. 75.6A), assessment of branch and segmental pulmonary artery anatomy, measurement of branch pulmonary artery flow, anatomy of aortopulmonary collaterals, assessment of the left ventricle (LV), and aortic valve and root pathology.

These studies typically are performed with balanced steady-state free-precession (bSSFP) imaging in the vertical and horizontal long-axis planes and short axis of the ventricles, as well as parallel to the RVOT. Gadolinium-enhanced three-dimensional MRA offers high-resolution assessment of the distal pulmonary arteries and can evaluate for aortopulmonary collaterals. Velocity-encoded phase-contrast imaging assesses the ratio of pulmonary to systemic flow, differential pulmonary blood flow, and valve regurgitation. Late gadolinium enhancement imaging reveals scarring or fibrosis in the heart (Fig. 75.6B).[1,11]

CT for patients with repaired TOF is used for evaluation of pulmonary artery anatomy and aortic size, particularly in patients in whom MRI is contraindicated (e.g., patients with an internal defibrillator). Electrocardiographic-gated multidetector array CT can provide RV size and systolic function, although with less temporal resolution than MRI.

## TRANSPOSITION OF THE GREAT ARTERIES

***Overview.*** TGA is defined by discordant ventriculoarterial relations; the aorta is connected to the RV and the pulmonary artery is connected to the LV. The most common type of TGA has {S,D,D} cardiac segmental anatomy—that is, visceral and atrial situs solitus (S), ventricular D loop (D), and dextroposition of the aortic valve (D) (see Chapter 63). The aortic valve is side-by-side or anterior and rightward of the pulmonary valve (Fig. 75.7A) and usually is separated from the tricuspid valve by conal tissue. "D-looped TGA" also is acceptable terminology.[1] {S,D,D} TGA is the second most common cyanotic congenital heart disease.[11] The median described incidence of {S,D,D} TGA is 303 per 1 million live births.[5]

***Etiology, Pathophysiology, and Clinical Presentation.*** TGA usually is not associated with extracardiac anomalies or syndromes.[15] It is associated with VSD in approximately 40% to 45% of cases. Other anomalies that can be seen in patients with TGA are LVOT obstruction, aortic coarctation or interrupted aortic arch, tricuspid valve abnormalities, or, less commonly, mitral valve abnormalities, leftward juxtaposition of the atrial appendages, and RV hypoplasia.[20]

Patients present with cyanosis as a result of parallel systemic and pulmonary circulations. Deoxygenated blood returns to the right side of the heart via systemic veins, then circulates back to the aorta. Pulmonary venous blood returns to the left atrium and LV, then back to the pulmonary artery. Survival depends on communication between the systemic and pulmonary circulations, typically via an atrial septal defect, patent ductus arteriosus, and/or VSD.

***Imaging.*** The radiographic appearance is variable. The classic finding of TGA by chest radiography is the "egg on a string" sign (Fig. 75.7B), which is caused by a narrow mediastinum and the cardiac shadow. The narrow mediastinum is a result of stress-related thymic atrophy and the parallel position of the great vessels, with the pulmonary artery obscured by the aorta. The heart size varies from normal to enlarged.[15]

Cross-sectional imaging is seldom used for preoperative evaluation of TGA, but it can be helpful for specific questions that are unanswered by echocardiography, typically complex associated abnormalities of the aorta or pulmonary arteries. MRI often is preferred instead of CT to avoid the risks of ionizing radiation. In some centers, CT may be preferred because it offers greater accessibility and decreases the need for anesthesia or sedation as a result of shorter scanning times. CT scans should be performed with parameters optimized to minimize exposure of the patient to ionizing radiation.

***Treatment and Follow-up.*** In newborn infants with {S,D,D} TGA, adequate communication between the pulmonary and

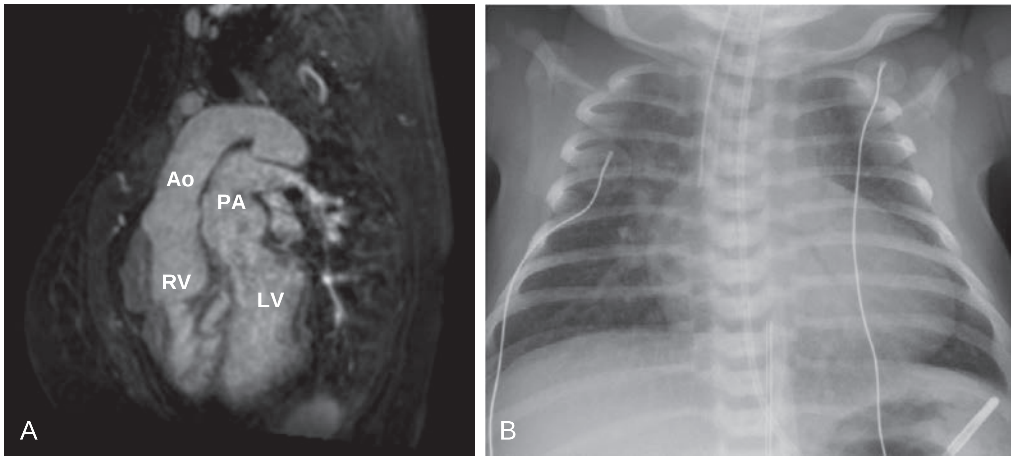

**Figure 75.7. {S,D,D} transposition of the great arteries (TGA).** (A) Sagittal oblique projection from three-dimensional balanced steady-state free-precession MRI in a 29-year old woman after the atrial switch procedure demonstrates parallel outflow tracts, with the aorta *(Ao)* arising from the right ventricle *(RV)* and the pulmonary artery *(PA)* arising from the left ventricle *(LV)*. (B) Chest radiograph of a neonate with {S,D,D} TGA before repair. As a result of the parallel, anterior-posterior relationship of the great arteries, there is a narrow mediastinum that combined with cardiomegaly and increased vascular flow, produces the classic "egg on a string" appearance.

systemic circulations is critical. Infusion of prostaglandin $E_1$ maintains ductal patency. If the atrial septum is restrictive, urgent cardiac catheterization for balloon atrial septostomy is often required.[21] In this procedure, a catheter is passed across the atrial septum into the left atrium. The balloon is inflated, and the catheter is sharply pulled back, fracturing the septum and enlarging the opening, allowing for greater mixing of oxygenated and deoxygenated blood.

In the first decades of surgical repair of TGA, the atrial switch was used (i.e., "Mustard" or "Senning" procedures). In these procedures, an intraatrial baffle is created with use of pericardium or native atrial tissue, which directs systemic venous return to the morphologic LV and pulmonary artery, and pulmonary venous return to the morphologic RV and aorta (Fig. 75.8A and B).

The atrial switch has been replaced by the arterial switch operation, which has been used widely in the United States since the mid to late 1980s. In this operation, the ascending aorta and pulmonary artery are transected at the sinotubular junction and anastomosed to the concordant ventricle, after the pulmonary artery is relocated anterior to the aorta (the "Lecompte maneuver") (Fig. 75.9A). The coronary arteries are relocated from the native aorta to the neoaorta (Fig. 75.9B).[22]

In the presence of a VSD and LVOT obstruction, a Rastelli repair can be performed,[23] with baffling of the LV through the VSD to the native aortic valve, along with placement of an RV to pulmonary artery conduit (e-Fig. 75.10).

Each of these procedures can be associated with early and late complications. For the atrial switch procedure, important early and mid-term complications include systemic baffle obstruction, most commonly affecting the superior limb of the baffle at the junction of the right atrium with the superior vena cava,[24] baffle leaks (in approximately 20% of patients) (e-Fig. 75.11),[25] and pulmonary venous obstruction (less common) (e-Fig. 75.12). The most important complication after the atrial switch procedure, early or late, is failure of the systemic RV and tricuspid regurgitation. Less common complications include conduction and rhythm disturbances, which can require mechanical pacing or cause sudden death.[11]

MRI is frequently used for assessment after the atrial switch procedure and is tailored for assessment of the aforementioned complications.[1,11] Specifically, MRI is useful for the following assessments:

1. Evaluation of the size and function of the ventricles (Video 75.6)
2. Evaluation of the systemic and pulmonary venous pathways (e-Fig. 75.13)
3. Assessment of tricuspid valve regurgitation
4. Evaluation of the LVOT and RVOT
5. Late gadolinium enhancement for evaluation of fibrosis in the RV[26]

The arterial switch procedure uses the LV as the systemic ventricle and therefore is favored. Potential complications after the arterial switch procedure is performed can include RVOT obstruction, stenosis at the arterial anastomotic sites (most commonly pulmonary stenosis), branch pulmonary artery obstruction (see Fig. 75.9C), aortic root dilatation, neoaortic valve regurgitation, and coronary artery ostial stenosis.[27]

MRI is used frequently for assessment of patients who have undergone an arterial switch procedure, with clinical questions dictated by the aforementioned potential complications[1,11]:

1. RV and LV size and function
2. Evaluation of the RVOT and LVOT
3. Evaluation of the great arteries
4. Evaluation of the semilunar valves
5. Evaluation of the coronary arteries

The Rastelli repair includes a conduit that can become stenotic and/or regurgitant. In addition, the baffle from the LV to the aorta can become obstructed, often at the level of the VSD, resulting in subaortic stenosis. After a Rastelli-type repair, answers to the following primary questions may be sought with MRI:

1. LV and RV size and systolic function
2. Anatomy and potential obstruction of the LV to aorta pathway
3. Stenosis and regurgitation of the RV to pulmonary artery conduit

MRI protocols are similar to those previously described for TOF, although additional sequences often are needed. For example, an axial bSSFP image stack can help define post-Lecompte pulmonary artery anatomy and the venous baffles of the atrial switch.

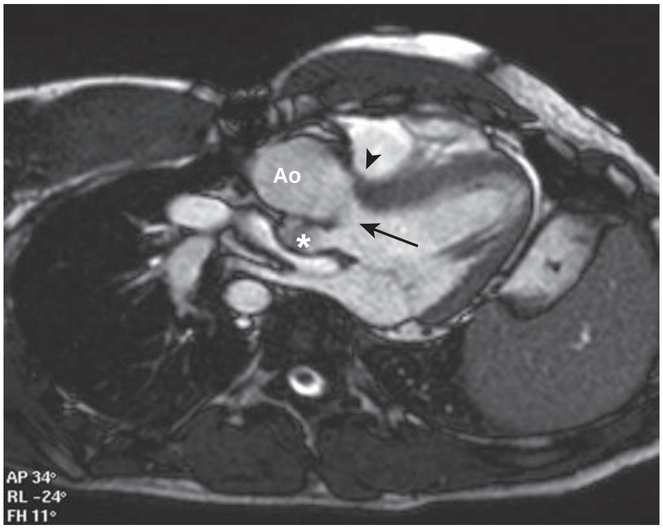

**e-Figure 75.10. {S,D,D} transposition of the great arteries, a ventricular septal defect, and pulmonary stenosis after the Rastelli procedure in a 22-year-old man.** Transverse oblique balanced steady-state free-precession MR image shows flow from the left ventricle being redirected via the ventricular septal defect *(arrow)* to the aorta *(Ao)* via a baffle; arrowhead denotes the lateral aspect of the baffle, which has closed the ventricular septal defect. Note the hypoplastic native pulmonary valve *(asterisk)*, which ends in a blind pouch. A right ventricle to pulmonary artery conduit was placed to reconstitute pulmonary blood flow (not shown in this image).

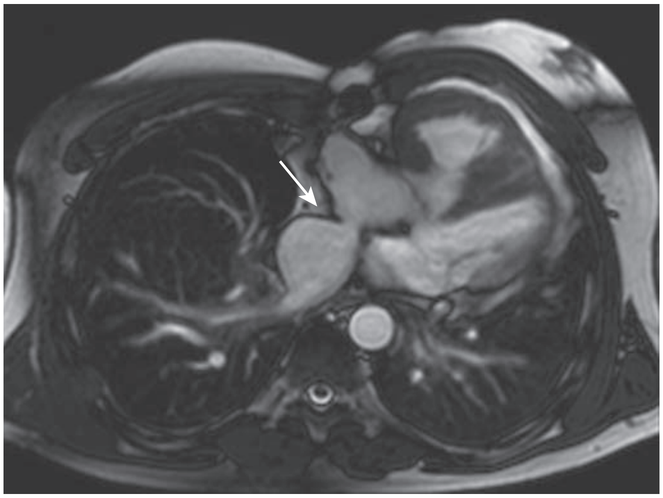

**e-Figure 75.12. {S,D,D} transposition of the great arteries after the atrial switch procedure in a 36-year-old man.** Axial balanced steady-state free-precession MR image demonstrates narrowing of the pulmonary venous pathway *(arrow)* to the tricuspid valve.

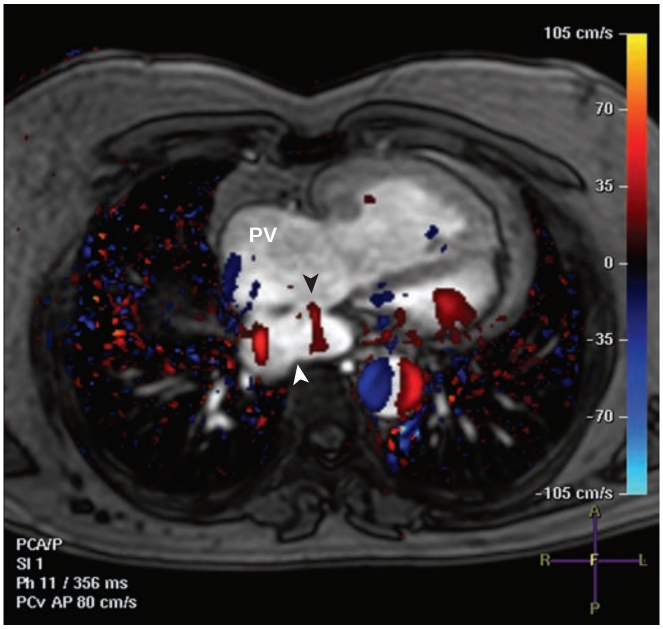

**e-Figure 75.11. {S,D,D} transposition of the great arteries after the Mustard procedure in a 40-year-old man.** Axial phase contrast MRI with in-plane velocity encoding demonstrates a baffle leak, with flow from the pulmonary venous pathway to the systemic venous pathway *(black arrowhead)*. Red denotes flow from anterior to posterior from the pulmonary venous pathway *(PV)* into the inferior vena cava portion of the systemic venous pathway *(white arrowhead)*.

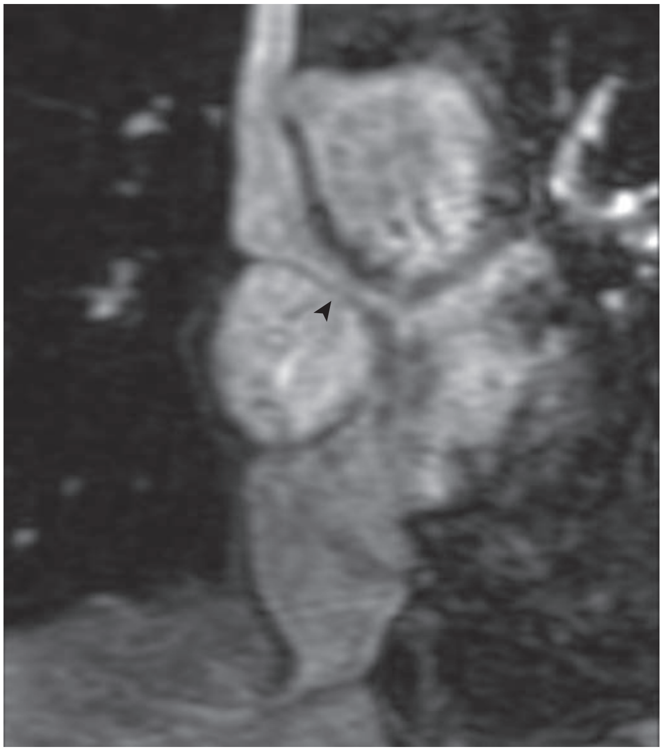

**e-Figure 75.13. {S,D,D} transposition of the great arteries after the atrial switch procedure in a 42-year-old man.** Coronal oblique projection from a contrast-enhanced MRA demonstrates the typical location of narrowing of the superior vena cava pathway *(arrowhead)* to the mitral valve.

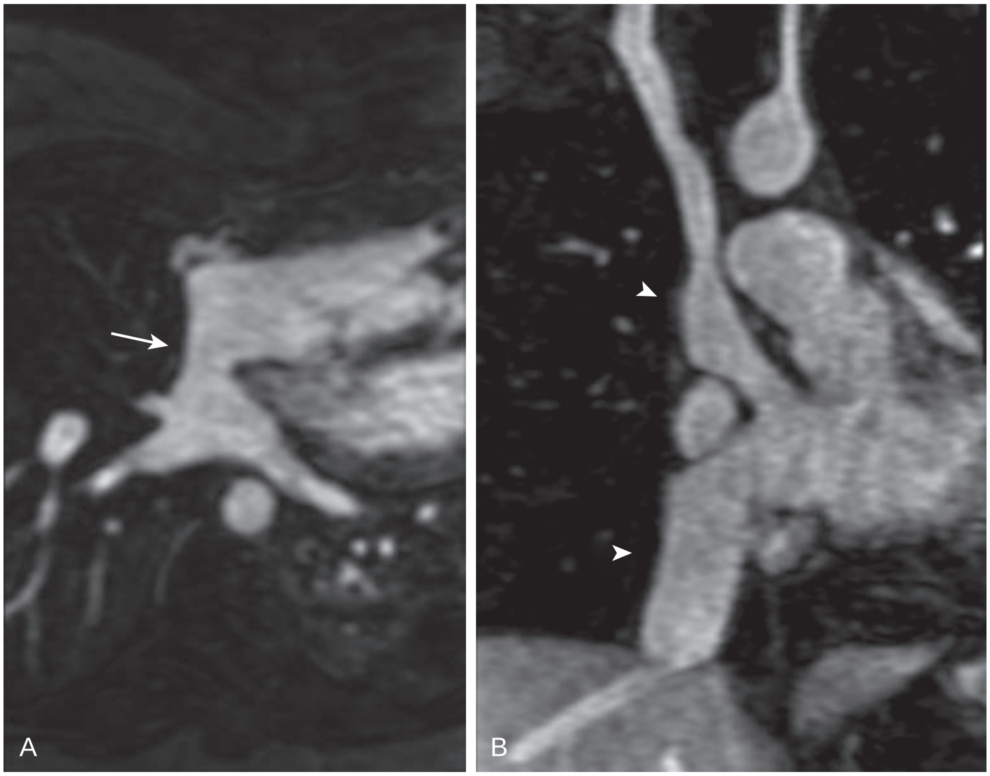

**Figure 75.8. {S,D,D} transposition of the great arteries, after the atrial switch in a 29-year-old woman.** (A) Transverse oblique projection from a contrast enhanced MRA demonstrates an unobstructed pulmonary venous baffle *(arrow)* to the tricuspid valve. (B) Coronal oblique projection demonstrating unobstructed pathways from the superior and inferior vena cavae *(arrowheads)* to the mitral valve. See Video 75.6.

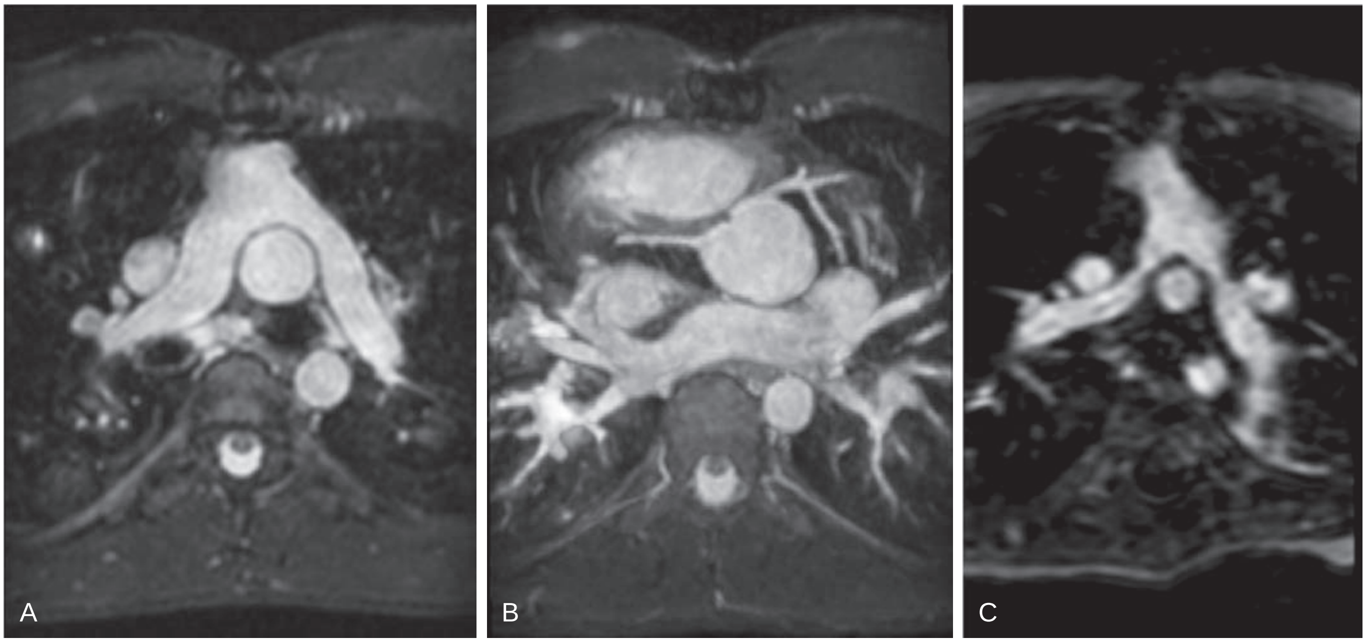

**Figure 75.9. Cardiovascular MR evaluation after the arterial switch operation.** (A) Transverse projection demonstrating the pulmonary artery bifurcation anterior to the ascending aorta, with no narrowing of the proximal branch pulmonary arteries. (B) Maximum intensity projection in the transverse oblique plane from three-dimensional steady-state free precession in a 16-year-old boy with {S,D,D} transposition of the great arteries (TGA), after the arterial switch operation, demonstrates unobstructed proximal coronary arteries that have been translocated to the facing sinuses of the native pulmonary (neoaortic) root. (C) Transverse oblique projection of a contrast-enhanced MRA in a 19-month-old boy with {S,D,D} TGA after an arterial switch operation demonstrates proximal narrowing of both left and right branch pulmonary arteries.

Oblique bSSFP imaging along the LVOT is performed to rule out obstruction of the Rastelli pathway.

CT is used postoperatively in selected cases to answer anatomic questions, particularly when MRI is contraindicated. CT is particularly useful for assessment of extracardiac anatomy such as repaired aortic coarctation, arterial anastomotic sites, and branch pulmonary arteries after an arterial switch procedure is performed (e-Fig. 75.14) and venous baffles after an atrial switch procedure is performed. Functional evaluation of the heart is limited compared with MRI.

## PHYSIOLOGICALLY CORRECTED TRANSPOSITION OF THE GREAT ARTERIES

***Overview.*** Physiologically corrected or {S,L,L} TGA is rare, with an estimated incidence of 30 per 1 million live births.[28] The segmental anatomy of this lesion includes visceral and atrial situs solitus, L-ventricular loop, and levo-transposition of the aortic valve (see Chapter 63). In L-looped TGA, atrioventricular and ventriculoarterial discordance occurs. The morphologic RV receives the pulmonary venous blood via the left atrium and connects to the aorta (Fig. 75.15A and Video 75.7). The LV receives systemic venous blood via the right atrium and connects to the pulmonary artery. The outflow tracts are parallel and the aorta is leftward and anterior to the pulmonary artery.

***Etiology, Pathophysiology, and Clinical Presentation.*** Physiologically corrected TGA is attributed to abnormal cardiac looping during embryologic development. It can be characterized as ventricular inversion, with the systemic and pulmonary circulations in series. If no associated lesions are present, the patient is acyanotic and typically is asymptomatic in early life. Patients with this lesion can present for the first time in adulthood, although this presentation is atypical.

More than 90% of patients with physiologically corrected TGA have additional anatomic abnormalities. Associated anomalies include dextrocardia, tricuspid valve abnormalities such as Ebstein anomaly, VSD (e-Fig. 75.16), RV hypoplasia, subvalvar and valvar pulmonary stenosis (Video 75.8), and conduction abnormalities, including complete heart block.[1]

***Imaging.*** The ascending aorta is not visible on the right, and the descending aorta and pulmonary artery may not be visible on the left. The vascular pedicle looks narrow, and straightening of the left heart border occurs as a result of the anterior and leftward position of the aorta. The cardiac silhouette has a "humped" appearance and is more vertical than usual (Fig. 75.15B).[29] In the presence of systemic atrioventricular valve regurgitation and ventricular dysfunction, the heart may be enlarged. Dextrocardia or mesocardia also occurs with {S,L,L} TGA; if the chest radiograph reveals the gastric bubble on the left (abdominal situs solitus) and the apex of the heart on the right, this lesion should be suspected. Associated cardiac lesions such as VSD and pulmonary atresia also can be detected.

MRI is useful in preoperative assessment of systemic RV function and tricuspid regurgitation. MRI can evaluate RV size and assess the morphology of the cardiac chambers, particularly in relationship to a VSD and the great arteries if a complex intraventricular baffle repair is planned.

CT can evaluate coronary artery and extracardiac anatomy. In patients who undergo pacing because of a complete heart block, electrocardiographic-gated multidetector array CT study can be used to assess RV size and systolic function.

***Treatment and Follow-up.*** The early management of patients with physiologically corrected TGA who have no associated structural anomalies is controversial. Because this lesion is acyanotic and usually asymptomatic, it can be managed medically.[11,30] However, some physicians believe that earlier surgery should be performed, particularly in the presence of tricuspid valve (systemic) regurgitation.[31]

Until the early to mid 1990s, repair of physiologically corrected TGA was intended only to repair the pertinent associated anomalies, including VSD, pulmonary stenosis or atresia, and tricuspid valve abnormalities,[22] leaving the RV as the systemic ventricle. However, in many patients, systemic (RV) ventricular failure develops over time.[32] Tricuspid (systemic atrioventricular) valve regurgitation also is associated with RV dysfunction and heart failure. In addition to RV failure and tricuspid regurgitation, complete heart block develops in many patients. These complications become more prevalent with increasing patient age and have led to greater interest

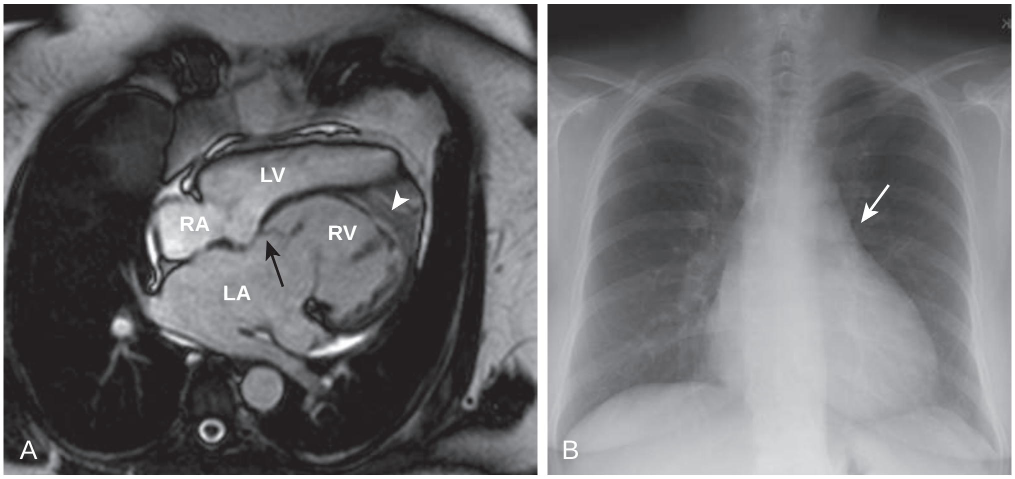

**Figure 75.15. {S,L,L} congenitally corrected transposition of the great arteries in a 56-year-old woman with no previous intervention.** (A) Balanced steady-state free-precession MR image in the four-chamber view demonstrates apical displacement of the septal insertion of the left-sided atrioventricular valve *(black arrow)*, a moderator band *(white arrowhead)*, and coarse trabeculation of the left-sided ventricle, consistent with a left-sided morphologic right ventricle *(RV)*. Note the bowing of the septum into the right-sided, morphologic left (subpulmonary) ventricle *(LV)*. (B) Posterior-anterior chest radiograph demonstrates a straightened upper left heart border *(arrow)* as a result of leftward malposition of the aorta. *LA,* Left atrium; *RA,* right atrium. See Video 75.7.

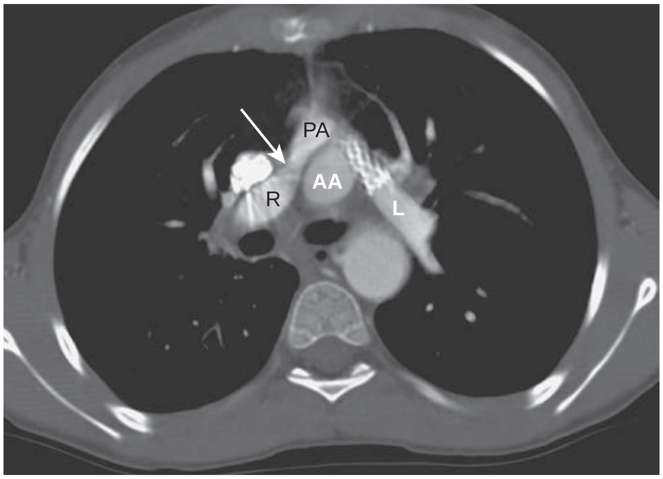

**e-Figure 75.14. {S,D,D} transposition of the great arteries after the arterial switch procedure complicated by pulmonary stenoses.** Axial contrast-enhanced CT image showing mild right pulmonary artery *(R)* narrowing *(arrow)* developed in this patient in between the superior vena cava and the ascending aorta *(AA)*. Previous left pulmonary artery *(L)* narrowing has been alleviated with a stent. *PA,* Pulmonary artery.

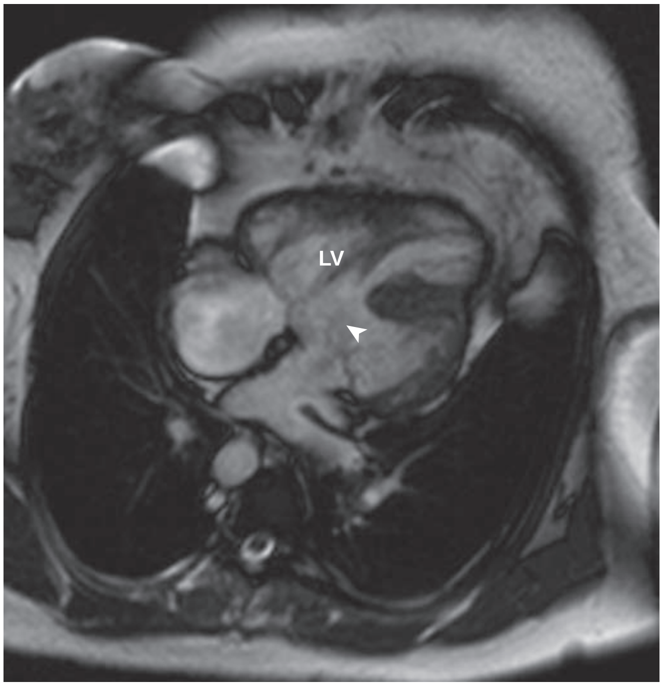

**e-Figure 75.16. {S,L,L} congenitally corrected transposition of the great arteries, ventricular septal defect and pulmonary stenosis, after prior subpulmonic resection in a 52-year-old woman.** Four-chamber balanced steady-state free-precession MR image demonstrates ventricular inversion, with a right-sided morphologic left ventricle *(LV)* and a large inlet ventricular septal defect *(arrowhead)*. See Video 75.8.

in performing early surgery for an anatomic correction with a systemic LV. Depending on the individual anatomy, this correction can be accomplished with a combination of an atrial switch with an arterial switch (a "double switch"), or, in the presence of LVOT obstruction and a VSD, with a Rastelli procedure.[22] In the absence of significant LVOT obstruction, the LV is not prepared to function at systemic pressure. A pulmonary artery band is first placed to "train" the LV to pump at higher pressures. After approximately 6 months, the complete repair is undertaken.

The complications associated with these operations are the same as those associated with the individual procedures, previously described in detail. MRI and CT can assess the atrial switch and arterial switch or intraventricular baffle (Rastelli repair), as previously delineated.

## DOUBLE-OUTLET RIGHT VENTRICLE

***Overview.*** According to the Congenital Heart Surgery Nomenclature and Database Project, double-outlet right ventricle (DORV) is "a type of ventriculoarterial connection in which both great vessels arise entirely or predominantly from the right ventricle."[33] DORV has been defined by some investigators as the degree of aortic override, with diagnosis if the aorta is more than 50% over the RV.[34] However, this definition can be difficult to apply practically, because the degree of override may appear different from various anatomic planes, which can lead to lack of clarity, for example, in differentiating DORV from TOF. The absence of fibrous continuity between the aortic and mitral valve also has been referred to as a criterion for diagnosis of DORV; however, according to the Congenital Heart Surgery Nomenclature and Database Project, this finding should not be used as an absolute prerequisite for the diagnosis of DORV.[33,35] Although the definition may be problematic, the median described incidence of DORV is 127 per 1 million live births.[5]

The anatomy and consequent physiology of a person with DORV is differentiated by the position of the VSD, the conal morphology, and the relationship of the great vessels. An understanding of these anatomic-physiologic variants is important to the surgical approach and management of the patients.[1] The VSD usually is found between the limbs of the trabecula septomarginalis (Fig. 75.17). The aorta can be located rightward and posterior, directly rightward, anterior and rightward, directly anterior, or anterior and leftward of the pulmonary artery (Fig. 75.18A). Because both vessels arise from one ventricle, abnormal positioning of the great arteries is termed "malposition" rather than "transposition."[36]

The relationship of the VSD to the conal septum and great arteries has been used as the basis for a widely used clinical classification, in which DORV is classified into four anatomic subtypes (Fig. 75.17):[35,37]

1. DORV with subaortic VSD (most common): the conal septum (outlet septum) is attached to the anterior limbus of the trabecula septomarginalis
2. DORV with subpulmonary VSD: the conal septum is attached to the posterior limbus of the trabecula septomarginalis
3. DORV with doubly committed VSD: the conal septum is hypoplastic or absent
4. DORV with noncommitted VSD: the defect is located at the inlet or at the trabecular zone of the interventricular septum, usually as an atrioventricular canal–type or apical muscular defect

***Etiology, Pathophysiology, and Clinical Presentation.*** In one review, chromosomal abnormalities, including trisomies 13 and 18 and deletion of chromosome 22q11, were the most commonly associated cytogenetic lesions[35].

DORV also can be classified by physiologic subtypes, which dictate clinical presentation[1]:

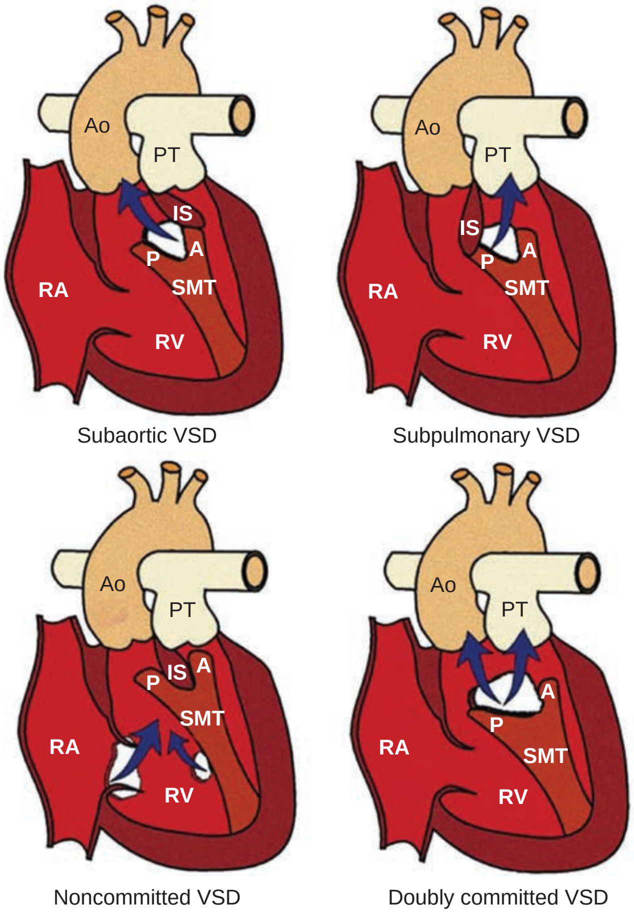

**Figure 75.17.** Types of double-outlet right ventricle, classified by relationship of the ventricular septal defect and great arteries. *A,* Anterior limb; *Ao,* aorta; *IS,* infundibular septum; *P,* posterior limb; *PT,* pulmonary trunk; *RA,* right atrium; *RV,* right ventricle; *SMT,* trabecula septomarginalis; *VSD,* ventricular septal defect. *(From Peixoto LB, Leal SMB, Silva CES, et al. Double outlet right ventricle with anterior and left-sided aorta and subpulmonary ventricular septal defect.* Arq Bras Cardiol. *1999;73:446–450.)*

1. VSD physiology: Subaortic VSD and no pulmonary stenosis
2. TOF physiology: Subaortic VSD and pulmonary stenosis
3. TGA physiology: Subpulmonary VSD, with or without systemic outflow obstruction
4. Single-ventricle physiology: DORV with mitral atresia, unbalanced atrioventricular canal, or severe hypoplasia of one of the ventricular sinuses (often in association with heterotaxy syndrome)

DORV is associated with several cardiac anomalies. VSD is almost ubiquitous. Obstruction to either pulmonary or systemic outflow is common. Coarctation of the aorta is common in patients with a subpulmonary VSD, particularly when aortic outflow is obstructed. Coronary artery anomalies often follow the physiology. For example, in TOF-type DORV physiology, supply of the LAD coronary artery from the right coronary artery can occur. In TGA-type DORV physiology, anomalies can vary, such as the circumflex coronary artery supplied from the right coronary artery.[11]

***Imaging.*** Given the many anatomic and physiologic variants of DORV, no specific pattern is described in the chest radiograph. Chest radiograph findings follow the anatomic-physiologic type of DORV, such as an enlarged heart and increased pulmonary

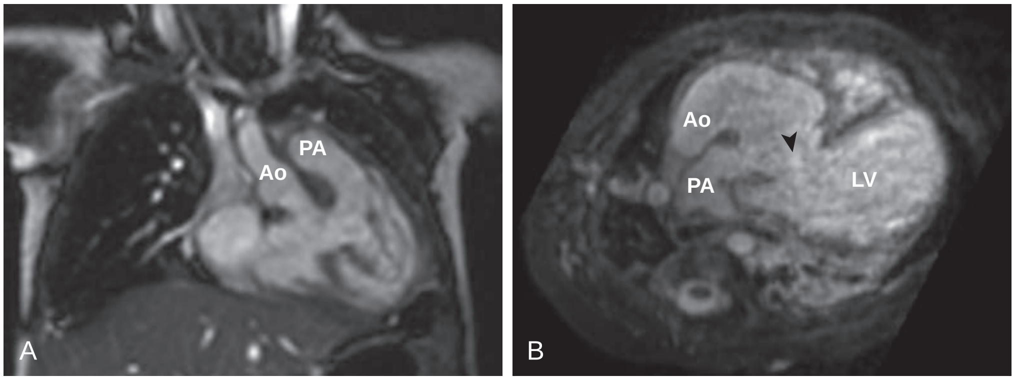

**Figure 75.18. Double-outlet right ventricle (DORV) variations.** (A) Coronal oblique SSFP MR image in a 5-month-old girl with DORV, side-by-side great arteries (aorta to the right), with no subaortic or subpulmonary stenosis, requiring previous pulmonary artery banding. (B) Transverse oblique three-dimensional balanced steady-state free-precession MR image in a 4-month-old boy with DORV, shows anterior-posterior great arteries (aorta anterior to the pulmonary artery), subpulmonary ventricular septal defect (VSD) *(arrowhead)*, and subvalvar and valvar pulmonary stenosis. This patient subsequently underwent a Rastelli procedure, with complicated baffle of the VSD to the anterior aortic valve and a right ventricle to the pulmonary artery conduit. *Ao,* Aorta; *LV,* left ventricle; *PA,* pulmonary artery.

vascular markings with a VSD, decreased pulmonary vascularity, a concave main pulmonary artery shadow and upward lifted heart apex in the TOF type, or varied findings with the TGA type, sometimes including cardiomegaly and increased pulmonary vascularity.

Echocardiography is adequate for diagnosis and surgical planning in most newborns or infants with DORV. Cardiac MRI or CT is helpful in the evaluation of complex anomalies of the aortic arch, pulmonary arteries, aortopulmonary collaterals, and systemic or pulmonary venous anomalies that are not completely delineated by echocardiography. Considerations for CT versus MRI have been discussed previously. Assessment of the relationship between the VSD and the position of the great vessels in relation to the conal septum also can be answered by cardiac MRI (Fig. 75.18B)[1] and can be helpful in planning complex surgical baffling of the LV to the aorta. In addition, MRI can accurately assess the size of the RV when its adequacy for a two-ventricle repair is in question.

***Treatment and Follow-up.*** The goal of surgical treatment of DORV is the connection of the LV to the systemic circulation and the RV to the pulmonary circulation. The preferred approach is to use an intraventricular tunnel repair, but such a repair may not be possible because of anatomic barriers, which may preclude a two-ventricle circulation. Alternative surgical procedures have been applied in these situations.[33]

With a subaortic VSD, an intraventricular patch directing LV outflow to the aorta is the usual approach. Resection of RVOT obstruction may be necessary. With a subpulmonary VSD, an intraventricular patch can be used to direct LV outflow to the pulmonary artery, which is accompanied by an arterial switch operation. Alternatively, the pulmonary artery can be closed proximally, the LV baffled through the VSD to the aorta, and a valved conduit placed between the RV and distal pulmonary artery (Rastelli procedure).[36] More complex forms of DORV with heterotaxy syndrome, severe hypoplasia or absence of one of the ventricular sinuses, major straddling of an AV valve, or mitral atresia are palliated as a functional single ventricle.[1]

MRI is an important modality in the assessment of patients with repaired DORV. Questions for MRI depend on the anatomic-physiologic subtype of DORV and follow the descriptions in the previous sections for MRI of TOF and {S,D,D} TGA. In addition, assessment of the LV to aortic pathway for potential obstruction is crucial, similar to the aforementioned description for a Rastelli repair. Imaging for patients with single ventricle physiology can be found under the section regarding Fontan imaging in Chapter 74.

Similarly, CT is useful in assessing patients with repaired DORV, with questions analogous to those previously described for TOF and {S,D,D} TGA.

## TRUNCUS ARTERIOSUS

***Overview.*** Truncus arteriosus is defined as a single vessel arising from the heart that has a single semilunar valve, giving rise to the coronary arteries, aorta, and at least one branch of the pulmonary artery. Truncus arteriosus is uncommon, with a reported incidence of 94 per 1 million live births.[5]

The classification of truncus arteriosus is based on the branching pattern of the pulmonary arteries[1,38]:

- Type I: The branch pulmonary arteries arise from a short main pulmonary artery
- Type II: The branch pulmonary arteries arise directly from the arterial trunk through separate orifices (Fig. 75.19A and B)
- Type III: One branch pulmonary artery arises from the ascending segment of the trunk; collateral vessels usually supply the contralateral lung
- Type IV: Truncus arteriosus with aortic arch hypoplasia, coarctation, or interruption (usually type B, between the common carotid and subclavian arteries)

***Etiology, Pathophysiology, and Clinical Presentation.*** Truncus arteriosus results from failure of septation of the conotruncus into a separate aorta and pulmonary artery. It is associated with DiGeorge syndrome and chromosome 22q11 deletion.[39]

The semilunar valve of the truncus is most often tricommissural. A bicommissural or quadricommissural truncal valve occurs less frequently. The truncal valve often is thickened with deformed leaflets, causing stenosis or insufficiency. The conal septum is usually absent, and a malalignment VSD is present in almost all patients (>80%). An IAA is a commonly associated lesion (occurring in 11%–14% of patients). Abnormalities of the mitral valve, coronary arteries, and pulmonary venous connections also are among the associated cardiac abnormalities.[11,38]

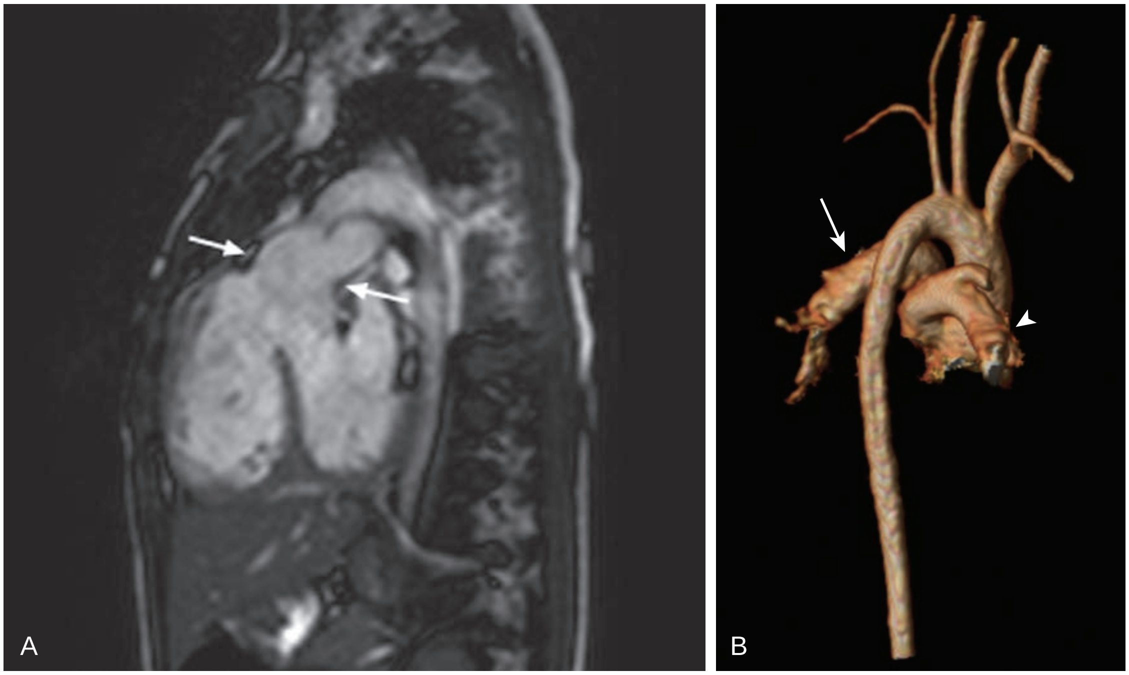

**Figure 75.19. Unrepaired truncus arteriosus type II in a 3-year-old girl.** (A) Sagittal oblique balanced steady-state free-precession MR image demonstrates the truncal root *(arrows)* overriding a conoventricular ventricular septal defect, with the origin of the pulmonary arteries from the truncal root. (B) Three-dimensional reconstruction (viewed posteriorly) from a contrast-enhanced MRA demonstrates the origin of the left *(arrow)* and right *(arrowhead)* branch pulmonary arteries from the truncal root.

Neonates with truncus arteriosus generally are asymptomatic while pulmonary vascular resistance remains elevated. As pulmonary vascular resistance decreases in early life, excessive pulmonary blood flow and symptoms of congestive heart failure develop. These children are at high risk for pulmonary vascular disease if they are not treated in the first 3 to 6 months of life.[18]

***Imaging.*** Cardiomegaly, increased pulmonary vascularity, and right-sided aortic arch (in 30% of cases) are consistent with truncus arteriosus (e-Fig. 75.20). A depressed diaphragm and thymic atrophy may also be noted.

In most neonates with this diagnosis, echocardiography is sufficient for anatomic diagnosis and surgical planning. Evaluation with MRI or CT is helpful for extracardiac anatomy that is difficult to fully delineate by echocardiography, such as complex aortic arch or pulmonary arterial anomalies.

***Treatment and Follow-up.*** Surgical repair is undertaken within the first few weeks of life. In 1968, McGoon et al.[40] described the first surgical repair of truncus arteriosus; the pulmonary arteries were separated from the aorta, and a valved homograft was placed from the RV to the pulmonary arteries. The VSD was closed with a patch to align the truncal valve with the LV. This technique remains the predominant method of repair.[18] Aortic arch interruption or coarctation is repaired at the same time. A severe valve abnormality can be addressed at the time of repair as well.[41]

In the absence of associated lesions, repair can be accomplished with very good survival rates in the neonatal and early infancy period.[42] Newborns with truncus arteriosus and associated IAA have a poorer prognosis.[43]

Important complications after truncal repair are RV–pulmonary artery conduit stenosis or regurgitation, branch pulmonary artery stenosis, neoaortic valve (truncal) insufficiency or stenosis, residual VSD, and aortic arch obstruction. Conduits require replacement over time.[18,43] As previously discussed, a percutaneously placed pulmonary valve is available for relief of conduit obstruction and regurgitation.

The anatomic and functional issues in patients who have undergone this repair are similar to those in patients with repaired TOF, specifically those with an RV to pulmonary artery conduit. Neoaortic valve dysfunction and aortic arch obstruction may require additional investigation. The postoperative MRI should address the following questions (e-Fig. 75.21)[1]:

1. Quantitative assessment of LV and RV volumes, function, and mass
2. Measurements of pulmonary (conduit) and neoaortic valve regurgitation
3. Imaging of the RVOT, conduit, and pulmonary arteries
4. Assessment of residual shunts
5. Imaging of the aortic arch and isthmus

## INTERRUPTED AORTIC ARCH TYPE B

***Overview.*** IAA is a rare congenital abnormality, with estimated incidence of 19 per 1 million live births.[44] IAA type B, the most common type of IAA, is a luminal interruption of the aorta (Fig. 75.22) between the left common carotid and left subclavian arteries, which accounts for approximately two-thirds of the cases of IAA.[44] IAA is distinguished from aortic arch atresia, in which a fibrous band is present at the area of the arch defect. Type B IAA is usually associated with VSD with posterior malalignment of the conal septum and is often categorized with other conotruncal anomalies.

***Etiology, Pathology, and Clinical Presentation.*** IAA type B results from an early regression of the fourth arch before migration of the left subclavian artery. Chromosome 22q11.2 deletion is

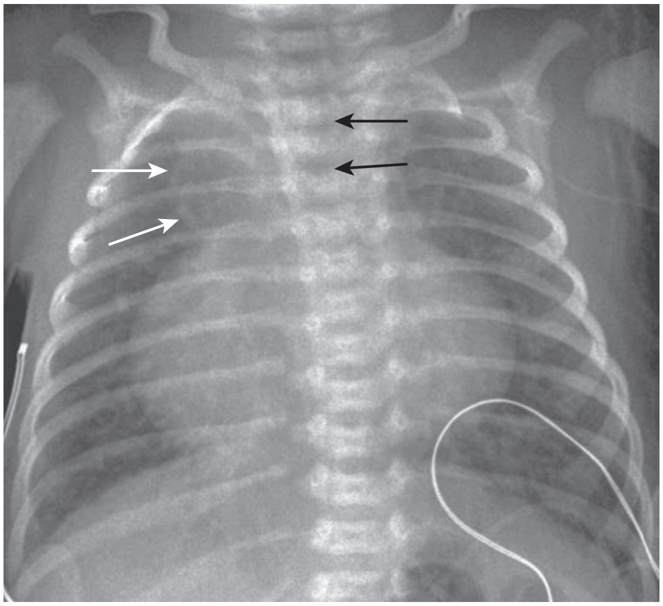

**e-Figure 75.20. Truncus arteriosus in a neonate.** Frontal chest radiograph shows an enlarged heart with right heart predominance and increased pulmonary vascularity. The trachea is deviated to the left *(black arrows)* by the large, right-sided truncal arch *(white arrows)*.

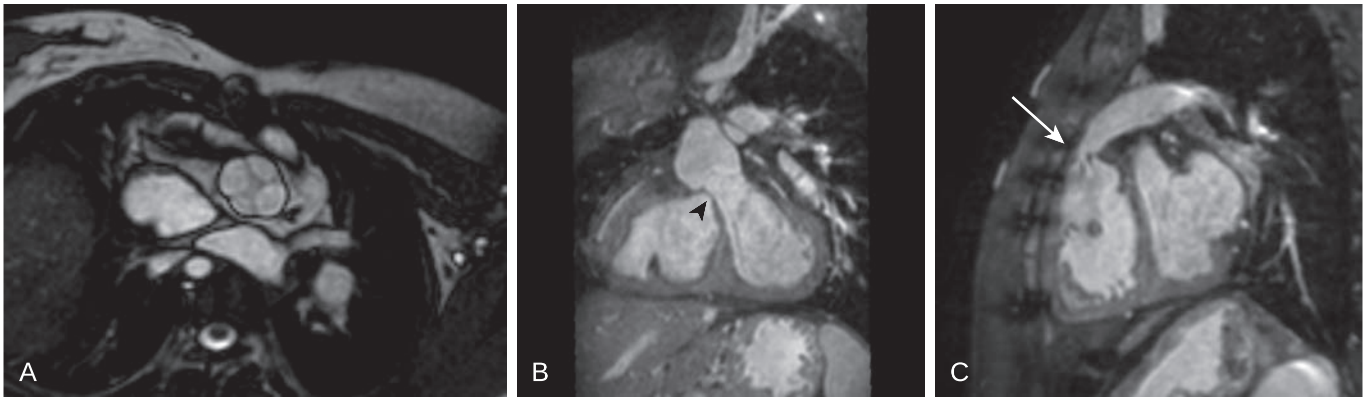

**e-Figure 75.21. Repaired truncus arteriosus in a 13-year-old girl.** (A) Short axis balanced steady-state free-precession (bSSFP) MR image of the truncal root demonstrates a quadricommissural valve. (B) Coronal oblique three-dimensional bSSFP MR image demonstrates a patch *(arrowhead)* closing the ventricular septal defect, connecting the left ventricle to the truncal (neoaortic) valve. (C) Sagittal oblique bSSFP MR image demonstrates the right ventricle to pulmonary artery conduit, which is narrowed proximally *(arrow)*.

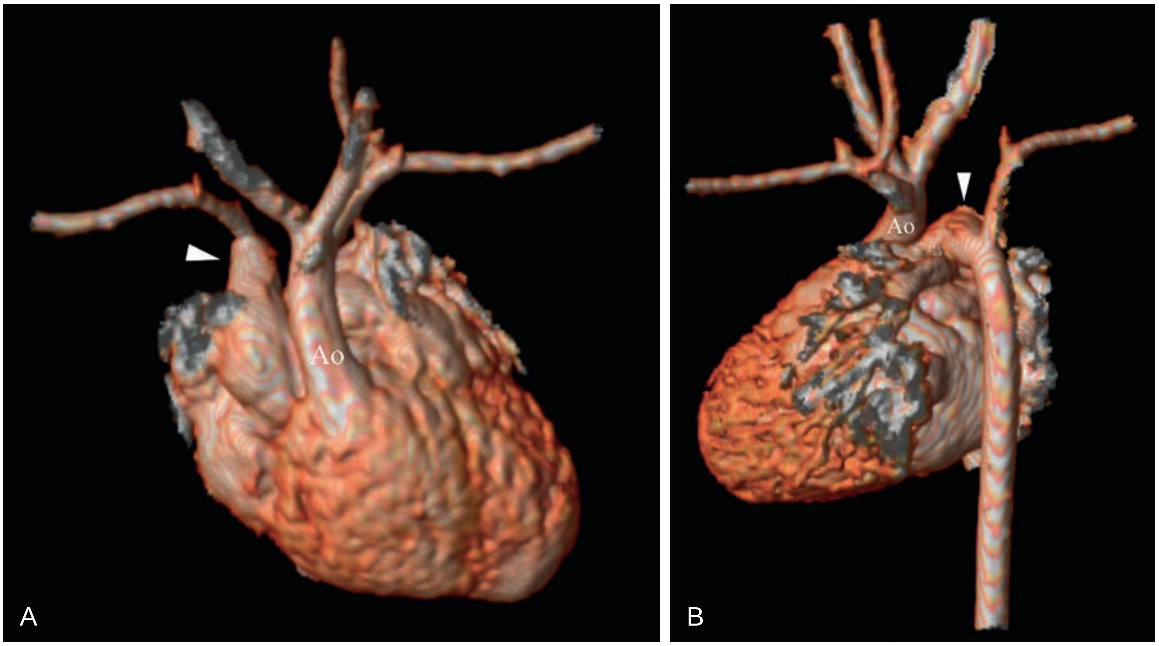

**Figure 75.22. Unrepaired interrupted aortic arch in a 13-day-old girl with D-looped transposition of the great arteries.** Three-dimensional reconstructions from a contrast-enhanced MRA study. (A) Viewed from anterosuperior, the ascending aorta *(Ao)* supplies the common carotid arteries and left subclavian artery, while the patent ductus arteriosus *(arrowhead)* supplies the right subclavian artery and descending aorta. (B) Viewed from posteriorly, the descending aorta descends on the right, supplied by the patent ductus arteriosus *(arrowhead)*.

commonly seen in these patients. Associated congenital cardiac lesions include VSD, atrial septal defect, truncus arteriosus, and bicuspid aortic valve.[44] Aberrant origin of the contralateral subclavian artery from the proximal descending aorta is also seen in 50% of cases of type B IAA.[1] If not recognized prenatally or perinatally, the natural history of IAA is typically development of shock or severe heart failure in the first 2 weeks of life.[45]

***Imaging.*** Echocardiography, including prenatal imaging, is usually sufficient to diagnose IAA and associated defects before surgical repair. CT or MRI is rarely requested but may be used if the arch anatomy is not clearly defined or to evaluate additional cardiac anomalies. Anatomic features that must be defined include the location of the defect, aortic arch sidedness and branching pattern, distance between the proximal and distal ends of the arch, diameter of the aorta proximal and distal to the defect, and location of the patent ductus arteriosus, as well as evaluation of the LVOT and for additional cardiac abnormalities.[46]

***Treatment and Follow-up.*** IAA and associated congenital cardiac anomalies require urgent neonatal repair.[44] Survival of patients with IAA depends on patency of the ductus arteriosus. Prostaglandin $E_1$ infusion begins soon after birth to maintain ductal patency and is followed by surgery, typically in the first week of life. Repair is typically via direct end-to-end anastomosis between the proximal and distal ends of the aortic arch. If the length of the defect prevents direct anastomosis, patch augmentation or reconstruction of the arch can be performed. Modifications of the type of surgery are performed according to additional congenital cardiac lesions and on an individual basis.

Important indications for imaging after repair include evaluation for postoperative complications such as restenosis and pseudoaneurysm at the area of repair (Fig. 75.23), as well as effects on the LV such as hypertrophy or diminished systolic function. Pseudoaneurysms and collaterals are best seen on three-dimensional MRA images. Residual narrowing can be assessed by a combination of findings, similar to the assessment of repaired coarctation of the aorta. These include the smallest cross-sectional area or diameter of the aorta, indexed to body surface area or compared with the aortic size at the diaphragmatic hiatus, the presence of spin dephasing jets on cine imaging, the presence of increased flow velocity at the site of narrowing by phase contrast magnetic resonance (MR), and the pattern of flow in the descending aorta assessed by phase contrast MR.

## KEY POINTS

- In neonates with conotruncal defects, echocardiography is the principal imaging modality for preoperative diagnosis. Cross-sectional imaging is used to clarify anatomy that is not adequately imaged by echocardiography, usually extracardiac vascular structures.
- Cardiac MRI plays a crucial role in the routine follow-up of postoperative patients with conotruncal defects, particularly as they reach their teens and adulthood.
- Assessment of the RV is an important part of follow-up imaging, whether there is a systemic RV (e.g., {S,D,D} TGA after an atrial switch procedure or uncorrected {S,L,L} TGA) or a pulmonary RV with abnormal pressure and/or volume loading conditions (e.g., free pulmonary regurgitation, conduit stenosis and regurgitation, and residual outflow tract obstruction).

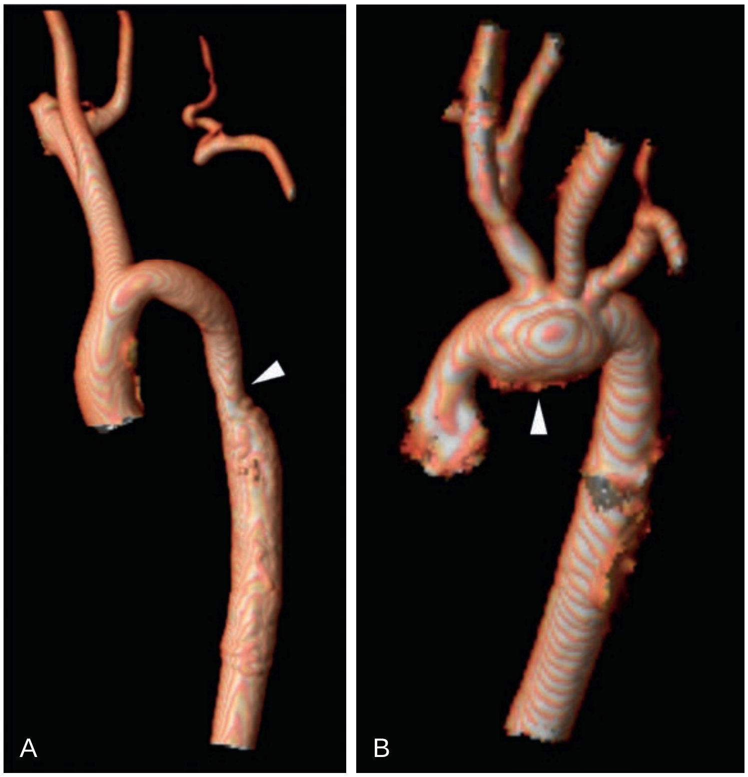

**Figure 75.23. Complications after repair of interrupted aortic arch.** (A) Three-dimensional reconstruction from a contrast-enhanced MRA in a 31-year-old man with interrupted aortic arch (IAA) status postrepair shows discrete narrowing at the repair site *(arrow)*. Note that the left subclavian artery is no longer in continuity with the aortic arch, as it may be divided at the time of repair to facilitate mobilization of the descending aorta. (B) Three-dimensional reconstruction from a contrast-enhanced MRA in a 17-day-old boy postrepair of IAA type B with aneurysmal dilatation of the aortic arch repair.

## SUGGESTED READINGS

Jonas RA. *Comprehensive Surgical Management of Congenital Heart Disease*. London: Arnold; 2004.

Lai WW, Mertens LL, Cohen MS, et al, eds. *Echocardiography in Pediatric and Congenital Heart Disease: From Fetus to Adult*. Chichester, UK: Wiley-Blackwell; 2009.

Lewin MB, Salerno JC. Truncus arteriosus. In: *Echocardiography in Pediatric and Congenital Heart Disease: From Fetus to Adult*. Chichester, UK: Wiley-Blackwell; 2009.

Lopez L. Double outlet ventricle. In: *Echocardiography in Pediatric and Congenital Heart Disease: From Fetus to Adult*. Chichester, UK: Wiley-Blackwell; 2009.

Mertens LL, Otto Vogt M, Marek J, et al. Transposition of the great arteries. In: *Echocardiography in Pediatric and Congenital Heart Disease: From Fetus to Adult*. Chichester, UK: Wiley-Blackwell; 2009.

Oechslin E. Physiologically "corrected" transposition of the great arteries. In: *Echocardiography in Pediatric and Congenital Heart Disease: From Fetus to Adult*. Chichester, UK: Wiley-Blackwell; 2009.

Srivastava S, Parness IA. Tetralogy of Fallot. In: *Echocardiography in Pediatric and Congenital Heart Disease: From Fetus to Adult*. Chichester, UK: Wiley-Blackwell; 2009.

## REFERENCES

Full references for this chapter can be found on www.expertconsult.com.

## REFERENCES

1. Dorfman AL, Geva T. Magnetic resonance imaging evaluation of congenital heart disease: conotruncal anomalies. *J Cardiovasc Magn Reson*. 2006;8(4):645–659.
2. Donnelly LF, Higgins CB. MR imaging of conotruncal abnormalities. *AJR Am J Roentgenol*. 1996;166(4):925–928.
3. Restivo A, Piacentini G, Placidi S, et al. Cardiac outflow tract: a review of some embryogenetic aspects of the conotruncal region of the heart. *Anat Rec A Discov Mol Cell Evol Biol*. 2006;288(9):936–943.
4. De Luca A, Sarkozy A, Ferese R, et al. New mutations in zfpm2/fog2 gene in tetralogy of Fallot and double outlet right ventricle. *Clin Genet*. 2011;80(2):184–190.
5. Hoffman JI, Kaplan S. The incidence of congenital heart disease. *J Am Coll Cardiol*. 2002;39(12):1890–1900.
6. Van Praagh R, Van Praagh S, Nebesar RA, et al. Tetralogy of Fallot: underdevelopment of the pulmonary infundibulum and its sequelae. *Am J Cardiol*. 1970;26(1):25–33.
7. Sommer RJ, Hijazi ZM, Rhodes JF. Pathophysiology of congenital heart disease in the adult: part iii: complex congenital heart disease. *Circulation*. 2008;117(10):1340–1350.
8. Shinebourne EA, Babu-Narayan SV, Carvalho JS. Tetralogy of Fallot: from fetus to adult. *Heart*. 2006;92(9):1353–1359.
9. Van Praagh R, Geva T, Kreutzer J. Ventricular septal defects: how shall we describe, name and classify them? *J Am Coll Cardiol*. 1989;14(5):1298–1299.
10. Fox D, Devendra GP, Hart SA, et al. When 'blue babies' grow up: what you need to know about tetralogy of Fallot. *Cleve Clin J Med*. 2010;77(11):821–828.
11. Frank L, Dillman JR, Parish V, et al. Cardiovascular MR imaging of conotruncal anomalies. *Radiographics*. 2010;30(4):1069–1094.
12. Lu JH, Chung MY, Betau H, et al. Molecular characterization of tetralogy of Fallot within DiGeorge critical region of the chromosome 22. *Pediatr Cardiol*. 2001;22(4):279–284.
13. Apitz C, Webb GD, Redington AN. Tetralogy of Fallot. *Lancet*. 2009;374(9699):1462–1471.
14. Need LR, Powell AJ, del Nido P, et al. Coronary echocardiography in tetralogy of Fallot: diagnostic accuracy, resource utilization and surgical implications over 13 years. *J Am Coll Cardiol*. 2000;36(4):1371–1377.
15. Ferguson EC, Krishnamurthy R, Oldham SA. Classic imaging signs of congenital cardiovascular abnormalities. *Radiographics*. 2007;27(5):1323–1334.
16. Brenner D, Elliston C, Hall E, et al. Estimated risks of radiation-induced fatal cancer from pediatric CT. *AJR Am J Roentgenol*. 2001;175(2):289–296.
17. Geva T, Greil GF, Marshall AC, et al. Gadolinium-enhanced 3-dimensional magnetic resonance angiography of pulmonary blood supply in patients with complex pulmonary stenosis or atresia: comparison with x-ray angiography. *Circulation*. 2002;106(4):473–478.
18. Gaca AM, Jaggers JJ, Dudley LT, et al. Repair of congenital heart disease: a primer—part 2. *Radiology*. 2008;248(1):44–60.
19. Geva T. Repaired tetralogy of Fallot: the roles of cardiovascular magnetic resonance in evaluating pathophysiology and for pulmonary valve replacement decision support. *J Cardiovasc Magn Reson*. 2011;13:9.
20. Wernovsky G. Transposition of the great arteries. In: Allen HD, Gutgesell HP, Clark EB, et al, eds. *Moss and Adams' Heart Disease in Infants, Children, and Adolescents*. 6th ed. Philadelphia: Lippincott; 2001.
21. Fulton DR, Fyler DC. D-Transposition of the great arteries. In: Keane JF, Lock JE, Fyler DC, eds. *Nadas' Pediatric Cardiology*. 2nd ed. Philadelphia: Saunders; 2006.
22. Gaca AM, Jaggers JJ, Dudley LT, et al. Repair of congenital heart disease: a primer—part 1. *Radiology*. 2008;247(3):617–631.
23. Rastelli GC, Wallace RB, Ongley PA. Complete repair of transposition of the great arteries with pulmonary stenosis. A review and report of a case corrected by using a new surgical technique. *Circulation*. 1969;39(1):83–95.
24. Bottega NA, Silversides CK, Oechslin EN, et al. Stenosis of the superior limb of the systemic venous baffle following a mustard procedure: an under-recognized problem. *Int J Cardiol*. 2012;154(1):32–37.
25. Chin AJ, Sanders SP, Norwood WI, et al. Two-dimensional echocardiographic localization of residual atrial shunts after the Senning procedure. *Am J Cardiol*. 1985;55(9):1238–1289.
26. Giardini A, Lovato L, Donti A, et al. Relation between right ventricular structural alterations and markers of adverse clinical outcome in adults with systemic right ventricle and either congenital complete (after Senning operation) or congenitally corrected transposition of the great arteries. *Am J Cardiol*. 2006;98(9):1277–1282.
27. Warnes CA, Williams RG, Bashore TM, et al. ACC/AHA 2008 guidelines for the management of adults with congenital heart disease: a report of the American College of Cardiology/American Heart Association Task Force on Practice Guidelines (Writing Committee to Develop Guidelines on the Management of Adults with Congenital Heart Disease). *Circulation*. 2008;118(23):e714–e833.
28. Wallis GA, Debich-Spicer D, Anderson RH. Congenitally corrected transposition. *Orphanet J Rare Dis*. 2011;6(1):22.
29. Warnes CA. Transposition of the great arteries. *Circulation*. 2006;114(24):2699–2709.
30. Graham TP Jr, Bernard YD, Mellen BG, et al. Long-term outcome in congenitally corrected transposition of the great arteries: a multi-institutional study. *J Am Coll Cardiol*. 2000;36(1):255–261.
31. Bacha E. Patients with congenitally corrected transposition of the great arteries and systemic tricuspid valve regurgitation should be referred for surgical consultation as soon as the diagnosis of regurgitation is made. *J Am Coll Cardiol*. 2011;57(20):2018–2019.
32. Silversides CK, Salehian O, Oechslin E, et al. Canadian Cardiovascular Society 2009 Consensus conference on the management of adults with congenital heart disease: complex congenital cardiac lesions. *Can J Cardiol*. 2009;26(3):e98–e117.
33. Walters HL 3rd, Mavroudis C, Tchervenkov CI, et al. Congenital heart surgery nomenclature and database project: double outlet right ventricle. *Ann Thorac Surg*. 2000;69(4 suppl):S249–S263.
34. Kirklin JW, Pacifico AD, Bargeron LM Jr, et al. Cardiac repair in anatomically corrected malposition of the great arteries. *Circulation*. 1973;48(1):153–159.
35. Obler D, Juraszek AL, Smoot LB, et al. Double outlet right ventricle: aetiologies and associations. *J Med Genet*. 2008;45(8):481–497.
36. Weir EK, Joffe HS, Barnard CN, et al. Double outlet right ventricle: clinical and anatomical spectrum. *Thorax*. 1978;33(3):283–289.
37. Lev M, Bharati S, Meng CC, et al. A concept of double-outlet right ventricle. *J Thorac Cardiovasc Surg*. 1972;64(2):271–281.
38. Van Praagh R, Van Praagh S. The anatomy of common aorticopulmonary trunk (truncus arteriosus communis) and its embryologic implications. A study of 57 necropsy cases. *Am J Cardiol*. 1965;16(3):406–425.
39. Goldmuntz E, Clark BJ, Mitchell LE, et al. Frequency of 22q11 deletions in patients with conotruncal defects. *J Am Coll Cardiol*. 1998;32(2):492–498.
40. McGoon DC, Rastelli GC, Ongley PA. An operation for the correction of truncus arteriosus. *JAMA*. 1968;205(2):69–73.
41. Mavroudis C, Backer CL. Surgical management of severe truncal insufficiency: experience with truncal valve remodeling techniques. *Ann Thorac Surg*. 2001;72(2):396–400.
42. Brown JW, Ruzmetov M, Okada Y, et al. Truncus arteriosus repair: outcomes, risk factors, reoperation and management. *Eur J Cardiothorac Surg*. 2001;20(2):221–227.
43. Sinzobahamvya N, Boscheinen M, Blaschczok HC, et al. Survival and reintervention after neonatal repair of truncus arteriosus with valved conduit. *Eur J Cardiothorac Surg*. 2008;34(4):732–737.
44. Reardon MF, Hallman GL, Cooley DA. Interrupted aortic arch: brief review and summary of an eighteen-year experience. *Tex Heart Inst J*. 1984;11(3):250–259.
45. Gruber PJ, Epstein JA. Development gone awry: congenital heart disease. *Circ Res*. 2004;94:273–283.
46. Dillman JR, Yarram SG, D'Amico AR, et al. Interrupted aortic arch: spectrum of MRI findings. *AJR Am J Roentgenol*. 2008;190:1467–1474.

# 76

# Congenital Anomalies of the Thoracic Great Arteries

Simon Lee

This chapter covers congenital anomalies of the great arteries that result in a vascular ring or sling. Overall, anomalies of the aortic arch and the cervical vessels are relatively common, with an estimated prevalence of 0.5% to 3%.[1] They can be understood as the result of abnormal persistence and/or regression of branches in the totipotential arch, which is derived from the theoretical double aortic arch proposed by Jesse Edwards (Fig. 76.1).[2] The most common variations in arch branching are the common brachiocephalic trunk (common origin of the right subclavian and both carotids) and the arch origin of the left vertebral artery, estimated to occur in 8% and 4% of the population, respectively.[3] These are of minimal clinical consequence and are considered normal variants.

## VASCULAR RINGS

***Overview.*** *Vascular ring* is a term that refers to encirclement of the trachea and esophagus caused by the abnormal embryologic development of the aortic arch. This can be caused by the vascular structures of the aorta, the fibrous remnant of a ductus, the ligamentum arteriosum, or an atretic aortic arch. Only a small subset of aortic arch developmental anomalies leads to a vascular ring, accounting for less than 1% of all congenital cardiovascular defects. Although about a dozen different types of vascular rings exist, the most common are a double aortic arch and a right aortic arch with a retroesophageal left subclavian with left ligamentum arteriosum.[4] They can occasionally be associated with other congenital heart defects.

Chromosome 22q11 deletion causes abnormalities in aortic arch and conotruncal development, and has been reported in 24% of patients with isolated arch anomalies.[5,6] Testing for this chromosomal abnormality should be considered if there are other congenital heart defects or dysmorphic features.

***Clinical Manifestations.*** The severity of symptoms and the age of onset depend on the extent of the compression of the esophagus and trachea. Patients may be completely asymptomatic or may present with significant respiratory distress.[7] A high index of suspicion is necessary due to the nonspecific symptoms and rarity of a vascular ring compared with other diagnoses. It is not uncommon for the diagnosis of vascular ring to be preceded by a history of reactive airway disease or recurrent croup.

The clinical presentation most commonly includes respiratory symptoms like stridor, “barky” cough, wheezing, and frequent upper respiratory infections. Symptoms related to constriction of the esophagus are dysphagia, recurrent emesis, and failure to thrive. Esophageal symptoms are more commonly seen in older infants as they start taking solid foods. Because the trachea and esophagus share the same space within the ring, respiratory symptoms can worsen during feedings. Patients with double aortic arch tend to present earlier with more severe symptoms compared with other vascular ring types.[8]

***Imaging.*** Chest radiography may show tracheal compression by a vascular ring, but by itself a chest radiograph cannot confirm or exclude a vascular ring. Because a vascular ring is more likely in the presence of a right aortic arch, symptoms of tracheal compression in the presence of a right aortic arch should raise the possibility of a vascular ring.

Historically a barium esophagram was considered the initial test of choice in the evaluation for a vascular ring.[9] Other imaging modalities are now utilized in lieu of an esophagram, although occasionally a vascular ring can be discovered incidentally when an esophagram is ordered to evaluate for other diagnoses such as gastroesophageal reflux, aspiration, or tracheoesophageal fistula (Fig. 76.2).

Echocardiography with gray scale and color Doppler imaging may visualize the vascular ring directly in neonates and infants because these patients have excellent sonographic windows, particularly if the ductus is patent.[10] Generally echocardiography is not as useful for diagnosing a vascular ring in older children and adolescents due to limited acoustic windows. Its main utility is in the assessment for concomitant congenital heart disease. The presence of a vascular ring has been diagnosed accurately in utero with fetal echocardiography, where the airways are seen reasonably well and the ductus arteriosus remains patent.[11]

Patients with a high suspicion for a vascular ring should undergo vascular imaging to confirm the vascular abnormalities and to gather information for surgical planning. Contrast-enhanced computed tomographic angiography (CTA) or magnetic resonance angiography (MRA) are the preferred modalities. Both can visualize the course and morphology of the intrathoracic vessels well. The advantage of MRA is the absence of ionizing radiation, although sedation or general anesthesia is often necessary before the age of 8 years.[12,13] CTA provides superior spatial resolution and visualization of the airway compared with MRA, and newer multidetector scanners can typically obtain this imaging without sedation.

***Treatment.*** The definitive treatment is surgical division of the ring via a lateral thoracotomy.[14] A double aortic arch is repaired by dividing the nondominant (smaller) arch between its last cervical artery and the point where it joins the descending aorta. Whether the arch is patent or atretic should be noted. If the ductus arteriosus or the ligamentum arteriosum forms a border of the ring, it is ligated. Persistent stenosis or tracheomalacia may develop in the constricted trachea, requiring additional repair.[15]

### Double Aortic Arch

Double aortic arch is the most common vascular ring. The head and neck branches arise symmetrically from the two arches, and their parallel orientation in axial imaging can serve as an imaging hint that a double aortic arch is present. Embryologically, the persistence of both the right and the left fourth aortic arches and distal dorsal aortic segments results in the double aortic arch. Two vessels, the right and left carotid arteries and right and left subclavian arteries, arise symmetrically from the ascending aorta and course dorsally, one on each side of the trachea and esophagus, to join the thoracic descending aorta. The descending aorta is on the left in 80% of cases. The larger aortic arch is considered the dominant arch, with the right being dominant in 75% of cases. The ductus arteriosus is usually left-sided but can be right-sided

## Abstract:

Overall, aortic arch and arch branching anomalies are relatively common. They result from the abnormal persistence and/or regression of branches in the totipotential arch. This can result in clinically significant encirclement of the trachea and esophagus, termed a vascular ring. Cross-sectional imaging is often necessary to make the diagnosis, as a part of the ring may be formed by fibrous tissue or ligaments. Genetic abnormalities, particularly chromosome 22q11 deletion syndrome, are commonly reported in association with aortic arch anomalies. Additional abnormalities, such as bronchotracheomalacia, may require further diagnostic studies and interventions.

## Keywords:

Vascular ring
aortic arch anomalies
right aortic arch
double aortic arch
diverticulum of Kommerell

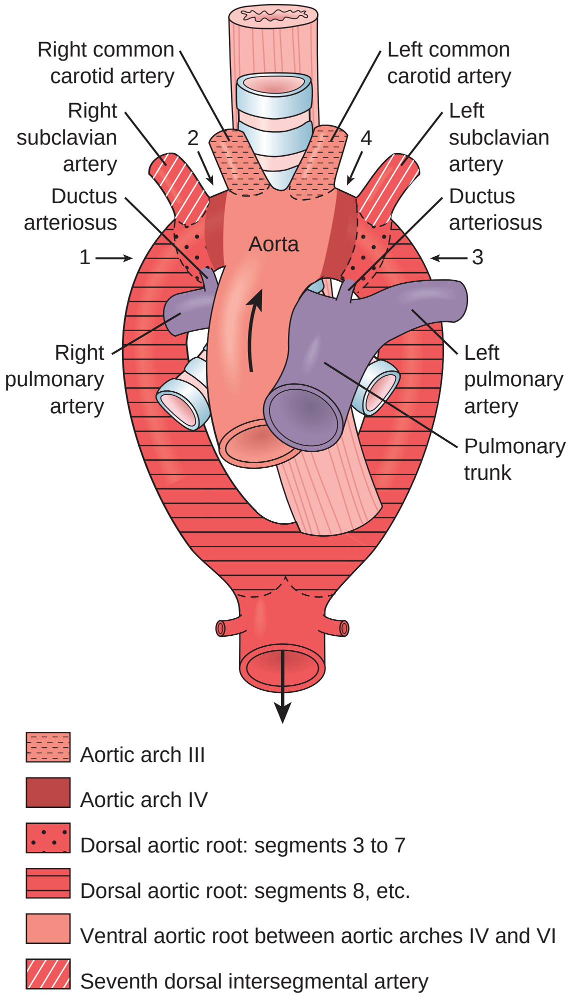
Right common carotid artery
Left common carotid artery
Right subclavian artery
2
4
Left subclavian artery
Ductus arteriosus
Ductus arteriosus
Aorta
1
3
Right pulmonary artery
Left pulmonary artery
Pulmonary trunk
Aortic arch III
Aortic arch IV
Dorsal aortic root: segments 3 to 7
Dorsal aortic root: segments 8, etc.
Ventral aortic root between aortic arches IV and VI
Seventh dorsal intersegmental artery

**Figure 76.1. Ventral view of Dr. Jesse Edward's "totipotential arch" or hypothetic double aortic arch and bilateral ducti arteriosi.** The *numbered arrows* point to the four key locations where regression occurs in various anomalies. *Arrow 1* indicates the eighth segment of the right dorsal aortic root; *arrow 2,* the right fourth arch; and *arrows 3* and *4,* the corresponding two positions on the left. The *shortest black arrows* point to the ducti arteriosi bilaterally, and the *longest black arrow* indicates the direction of blood flow. *(From Stewart JR, Kincaid OW, Edwards JE.* An Atlas of Vascular Rings and Related Malformations of the Aortic Arch System. *Springfield, IL: Charles C Thomas; 1964.)*

or bilaterally present. Bilateral patent arterial ducts can increase the severity of the tracheal and esophageal compression.

One portion of one aortic arch may be atretic, almost always occurring on the left. Double aortic arches with left arch atresia develop from regression of varying segments of the left aortic arch, with fibrous continuity of the segments completing the vascular ring.[16] The atretic segment may lie between the left subclavian artery and the descending aorta (Fig. 76.3) or between the left common carotid artery and the left subclavian artery. The former configuration is similar to a right aortic arch with a mirror-image branching pattern, and the latter configuration is similar to a right aortic arch with an aberrant left subclavian artery. However, a right aortic arch with mirror-image branching is almost always associated with significant congenital heart disease, and its absence should raise suspicion for a double aortic arch. An aortic diverticulum may be present posterior to the esophagus, which is part of the distal left aortic arch, before connecting to the aberrant left subclavian artery. Patients with atresia of a portion of one of the arches tend to have more severe tracheal and esophageal compression (see Fig. 76.2). Echocardiography does not provide optimal imaging for a double aortic arch, particularly if there is an atretic segment. Although it is recommended to screen for congenital heart defects, double aortic arch is not usually associated with significant abnormalities. CTA and MRA can readily visualize the atretic segment that appears to tether adjacent vascular structures and can be used to identify the associated aortic diverticulum.

## Right Aortic Arch With Aberrant Left Subclavian Artery

A right aortic arch with an aberrant or retroesophageal left subclavian artery is the second most common cause of a vascular ring. With an aberrant left subclavian artery, the left-sided ductus arteriosus/ligamentum arteriosum completes the vascular ring. Although the ligamentum is not seen on cross-sectional imaging, a diverticulum of Kommerell indicates the presence and location of the prior ductus (Fig. 76.4). In some cases, the diverticulum itself may cause symptoms, and a diverticulum resection and subclavian reimplantation may be necessary (e-Fig. 76.5). In 10% of cases, the ligamentum arteriosum is on the right side, and thus there would be no vascular ring. Unlike double aortic arches, this vascular ring typically is loose, and many patients are asymptomatic or present with mild symptoms later in life. There is a significant association with chromosome 22q11 deletion reported, even in the absence of congenital heart disease.[5]

## Left Aortic Arch With Aberrant Right Subclavian Artery

Compared with a right aortic arch, vascular ring formation in a left aortic arch is rare because the ductus arteriosus and ligamentum arteriosum are usually left-sided. In the specific case of a left aortic arch with an aberrant right subclavian artery, very few proven cases of vascular ring have been reported. Occasionally the retroesophageal course of the right subclavian artery can cause difficulty swallowing, in the absence of a vascular ring; this association has been termed *dysphagia lusoria* (Fig. 76.6).

## Right Aortic Arch With Mirror-Image Branching

The right aortic arch with mirror-image branching pattern is associated with congenital heart disease in 98% of cases, most commonly tetralogy of Fallot and truncus arteriosus. In most instances, the aorta descends on the right. If the ductus is left-sided, it usually connects between the anteriorly located innominate artery and the pulmonary artery, which does not form a vascular ring. In rare cases, a true ring forms when a ligamentum arteriosum extends from the left pulmonary artery to an aortic diverticulum.[17]

## Right Aortic Arch With Circumflex Aorta

Unlike the typical right aortic arch, in which the descending aorta is right-sided, a circumflex aorta descends on the left. To do so, the distal aortic arch travels from right to left, posterior to the esophagus, before turning downward (Fig. 76.7). A left ligamentum arteriosum arises posteriorly from a diverticulum of Kommerell and connects the pulmonary artery to the descending aorta, forming a vascular ring. An aberrant left subclavian artery frequently arises from an aortic diverticulum with stenosis at its origin.

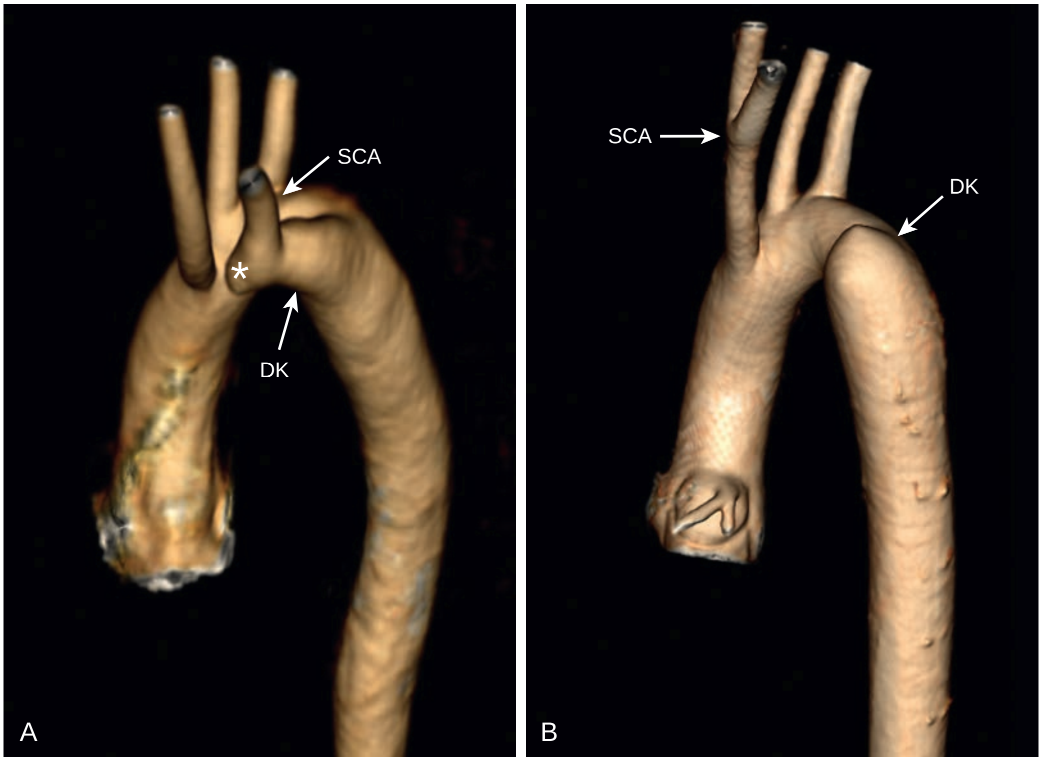

**e-Figure 76.5. Right aortic arch with an aberrant left subclavian artery in a 12-year-old boy.** (A) Volume-rendered view of the aortic arch reconstructed from the preoperative MRA examination. The aberrant left subclavian artery *(SCA)* arises from the diverticulum of Kommerell *(DK)* which has an anterior outpouching *(asterisk)* indicating the attachment of the ligamentum arteriosum. (B) Volume-rendered view of the aortic arch reconstructed from a post-operative CTA examination. The left subclavian artery *(SCA)* has been reimplanted into the left carotid artery and the diverticulum of Kommerell *(DK)* has been resected.

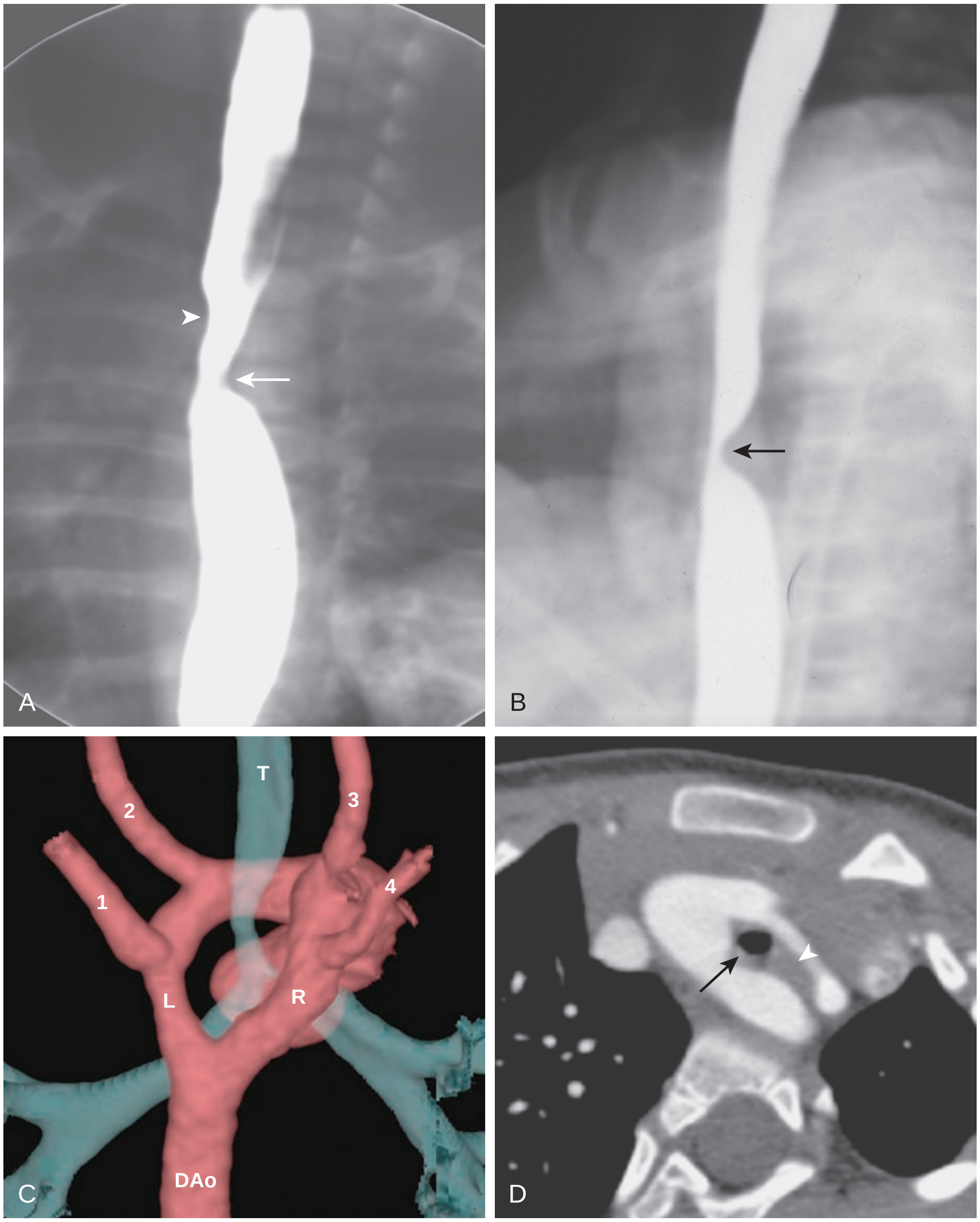

**Figure 76.2. Bilaterally patent double aortic arches in a 7-year-old boy.** (A) Frontal view of a barium esophagram shows bilateral indentations of the barium column. The right arch indention *(arrowhead)* is higher than the left *(arrow)*. (B) Lateral view of a barium esophagram shows a posterior indentation *(arrow)* corresponding to the posterior right arch. (C) Volume-rendered posterior projection CTA image shows the dominant right arch *(R)* and a nondominant left arch *(L)*, both feeding into the descending aorta *(DAo)*. Four cervical arteries arise from the arch: left subclavian artery *(1)*, left common carotid artery *(2)*, right common carotid artery *(3)*, and right subclavian artery *(4)*. The ring encloses the trachea *(T)*, causing tracheal narrowing just above the carina. (D) Axial CT image shows a complete double aortic arch constricting the trachea *(black arrow)* and the esophagus *(white arrowhead)*.

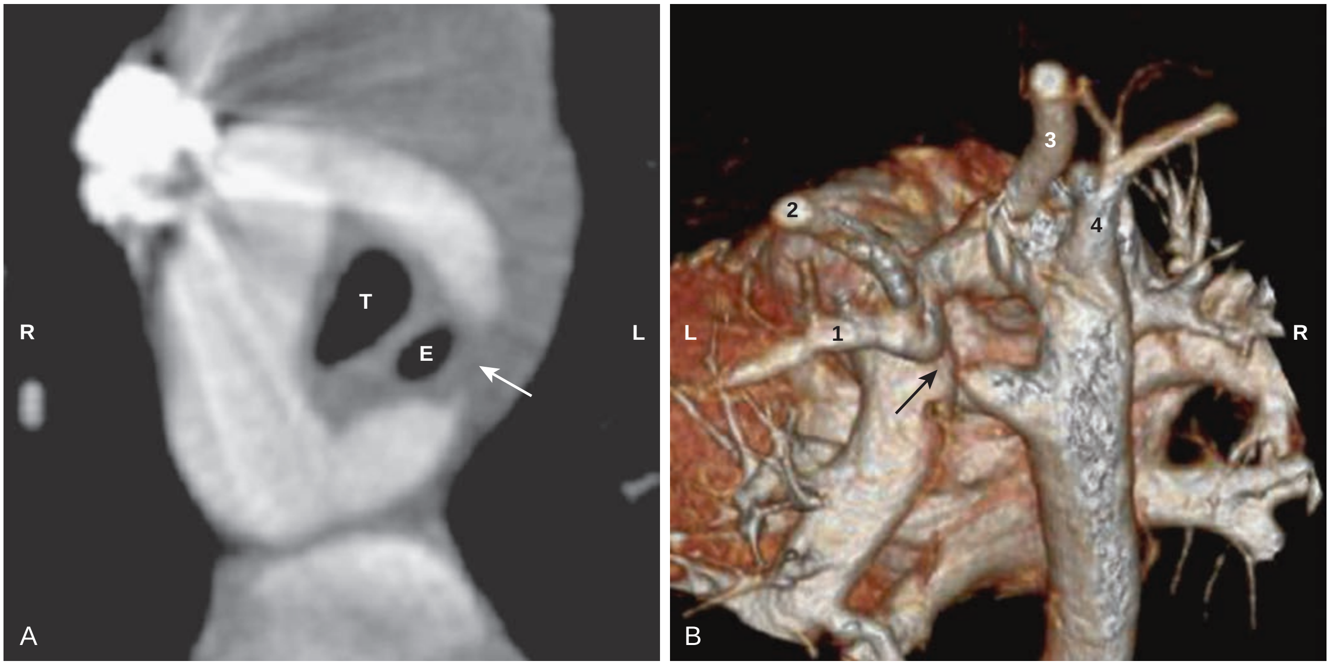

**Figure 76.3. Double aortic arch with an atretic left arch in a 2-year-old girl.** (A) Axial CTA image shows a patent right arch and an incomplete left arch. A ligamentous connection *(arrow)* can be inferred from the tapered contour of the left arch, forming the left border of the vascular ring and constricting the trachea *(T)* and esophagus *(E)*. (B) Volume-rendered view from the CTA shows the atretic left arch segment *(arrow)*. The left subclavian artery *(1)* and the left common carotid artery *(2)* are supplied by the proximal portion of the left arch. The right arch gives off the right common carotid artery *(3)* and the right subclavian artery *(4)*. The patient's right *(R)* and left *(L)* are labeled for reference.

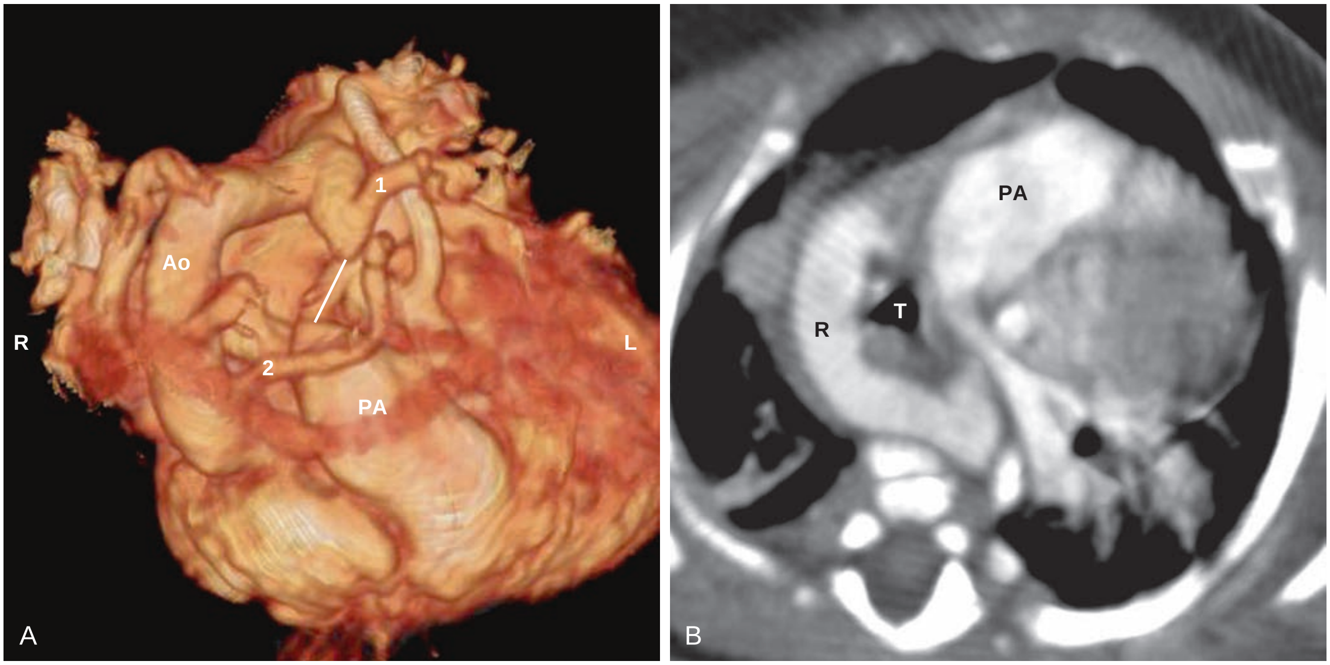

**Figure 76.4. Right aortic arch with an aberrant left subclavian artery in a 1-year-old girl.** (A) Volume-rendered anterior and superior view reconstructed from a CTA study. The right aortic arch *(Ao)* gives off the left common carotid artery *(2)* as the first branch and the left subclavian artery *(1)* as the last branch. A kink is seen between the diverticulum of Kommerell and the left subclavian artery, suggesting the attachment of a tight ligamentum arteriosum. The probable connection of the ligamentum arteriosum is drawn as a white line, which forms the left border of the vascular ring. The patient's right *(R)* and left *(L)* are labeled for reference. (B) Axial CT angiogram of the same patient. The right aortic arch *(R)* forms the right and posterior border of the vascular ring; the ligamentum arteriosum forms the left border, enclosing the trachea *(T)*. *PA,* Pulmonary artery.

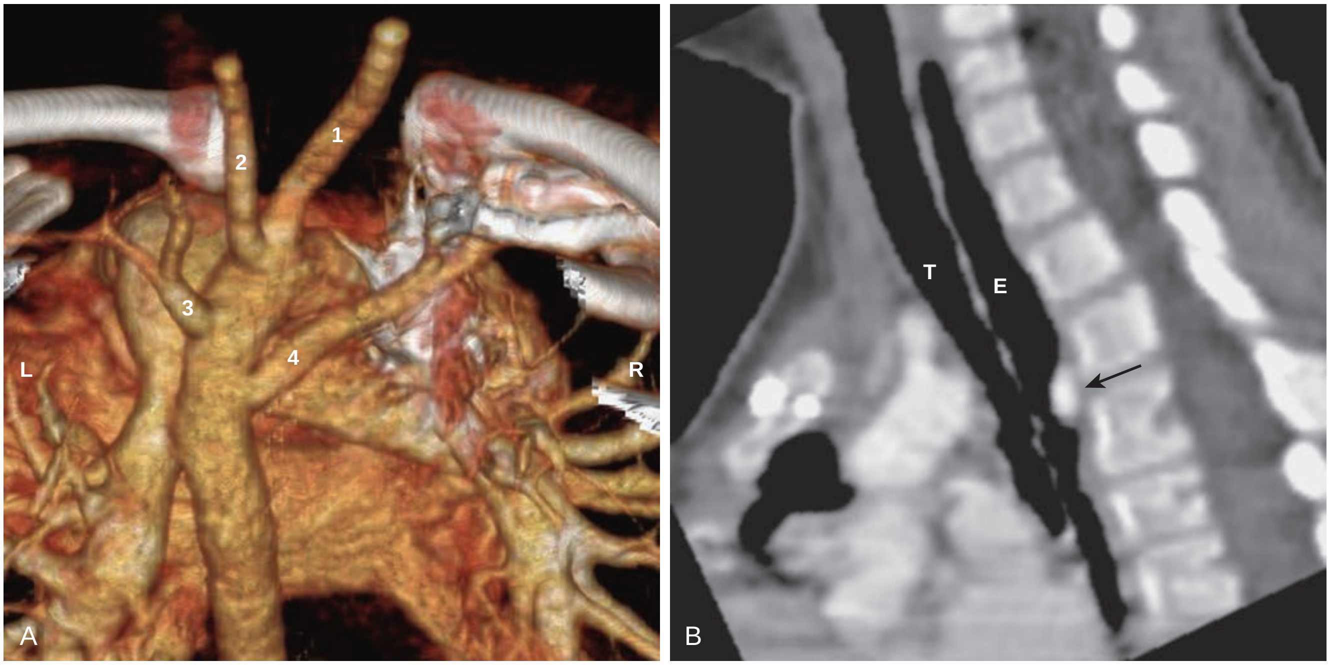

**Figure 76.6. Left aortic arch with an aberrant right subclavian artery in a 4-year-old boy.** (A) Posterior view volume-rendered CTA shows the arch vessels: right common carotid artery *(1)*, left common carotid artery *(2)*, left subclavian artery *(3)*, and aberrant right subclavian artery *(4)*. The patient's right *(R)* and left *(L)* are labeled for reference. (B) Sagittal reformation shows the air-filled trachea *(T)* and the esophagus *(E)*. The esophagus is indented posteriorly by the aberrant subclavian artery *(arrow)*.

## Left Aortic Arch With Circumflex Aorta

A left aortic arch with a circumflex aorta is analogous to a right aortic arch with a circumflex aorta, in that the distal arch travels from left to right behind the esophagus before turning downward to become a right descending aorta. To complete a vascular ring, a right ligamentum arteriosum must connect the pulmonary artery to the descending aorta.[18]

## Right Cervical Aortic Arch

A right cervical aortic arch is a rare anomaly that occurs when there is abnormal cephalic migration of the aortic arch into the supraclavicular and neck region. Embryologically, the cervical aortic arch forms from the third arch rather than the normal fourth arch. The aortic arch branching pattern varies, and separate origins of the internal and external carotid arteries may arise from the cervical aortic arch. The right cervical aortic arch is often associated with an aberrant left subclavian and may cause a vascular ring when associated with a left ligamentum arteriosum. Clinically, a pulsatile mass may be present in the supraclavicular region. Radiographic findings include right superior mediastinal widening, tracheal displacement to the left and anteriorly, a large oblique impression on the esophagram from cephalic right to caudal left, and a left descending aorta (Fig. 76.8).

## Left Cervical Aortic Arch

Although a left cervical aortic arch is much less common than the right-sided version, it similarly extends abnormally high in the upper mediastinal–low cervical region on the left side of the trachea. Aortic arch branching anomalies are similar to those mentioned previously. A vascular ring is formed when a right ligamentum arteriosum is present. Clinical and radiographic findings are similar to those previously mentioned.

## PULMONARY ARTERY SLING

***Overview.*** Pulmonary artery sling is a congenital anomaly that produces tracheal compression between the main and left pulmonary arteries. Instead of the normal bifurcation of the main pulmonary artery into the right and left pulmonary arteries (Fig. 76.9A), the left pulmonary artery arises from the posterior aspect of the right pulmonary artery and courses leftward between the trachea and esophagus, at or near the level of the carina (Fig. 76.9B).

The incidence of pulmonary artery sling is not known, with one study suggesting an incidence of 1 in 17,000, with a slight male predilection.[19] Patients present with clinical symptoms in childhood, and 90% of patients present with symptoms before the first year of life.[20] Nonspecific respiratory symptoms include an asthmatic cough and acute and recurrent bronchopulmonary infections. Symptom severity depends on the degree of airway compression and coexisting airway abnormalities. Coexisting airway abnormalities are present in more than 50% of patients, including abnormal branching of the airways, complete tracheal rings, and tracheal stenosis.[21] The vertical position of the left pulmonary artery origin, along with the branching pattern of the airways, has been used to classify pulmonary artery sling.[22] In type 1 pulmonary artery sling, the left pulmonary artery originates at T4–T5 vertebral levels, just above the normal level of the carina. Subtype 1A has normal branching pattern of the airways; subtype 1B has a tracheal bronchus. In type 2 pulmonary artery sling, the left pulmonary artery originates below the T5 vertebral level, below the normal carina. Subtype 2A has a right main bronchus connecting to the right upper lobe only. A separate "bridging" airway arises from the left main bronchus, below the aberrant left pulmonary artery, that supplies the right middle and right lower lobes (e-Fig. 76.10A). In subtype 2B, the right main bronchus is absent and the bridging airway defined in 2A supplies the entire right lung. Except for the level of the left pulmonary artery, the right main bronchus in type 2A superficially resembles the tracheal

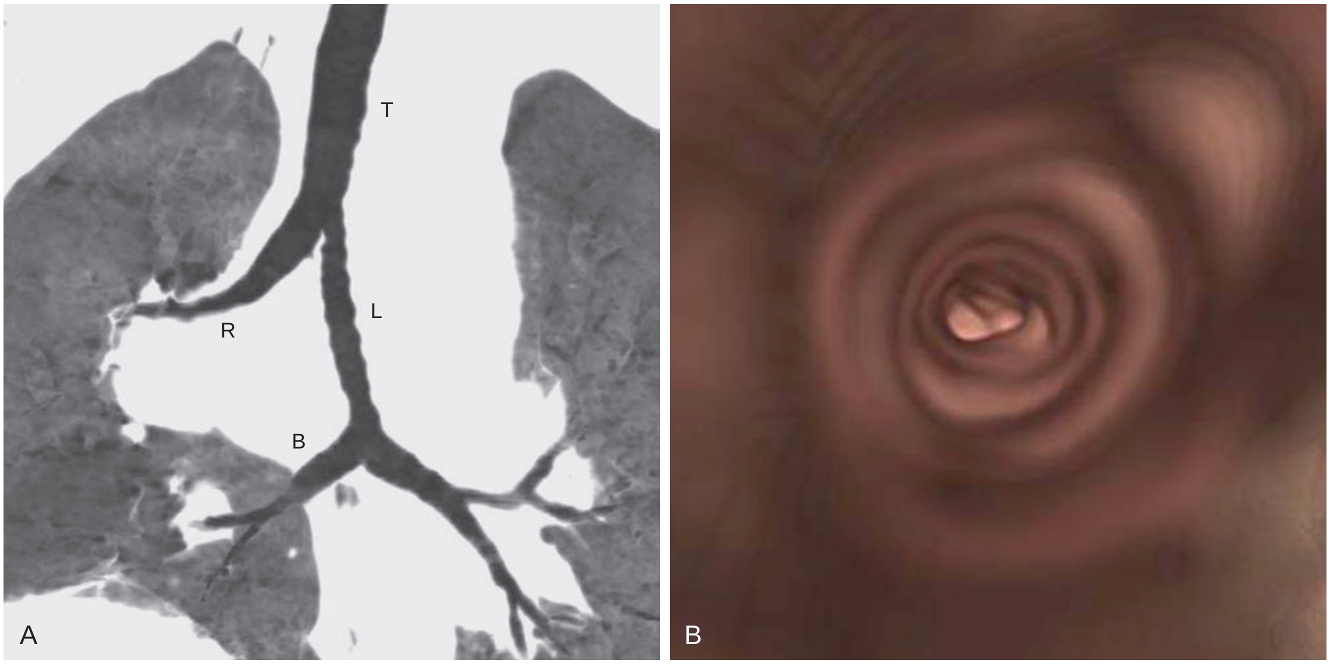

**e-Figure 76.10. Abnormal central airways of a 40-year-old woman with a pulmonary artery sling.** (A) Coronal reformation with minimum intensity projection shows type 2A configuration where the trachea *(T)* bifurcates into a right main bronchus *(R)* and a left main bronchus *(L)*. The right main bronchus supplies the right upper lobe airways only. A bridging bronchus *(B)* supplies the rest of the right lung. Superficially, the right main bronchus resembles a tracheal bronchus, except that it arises at the expected location of the carina, instead of high up from the trachea. (B) The endoscopic view in the trachea shows complete tracheal rings.

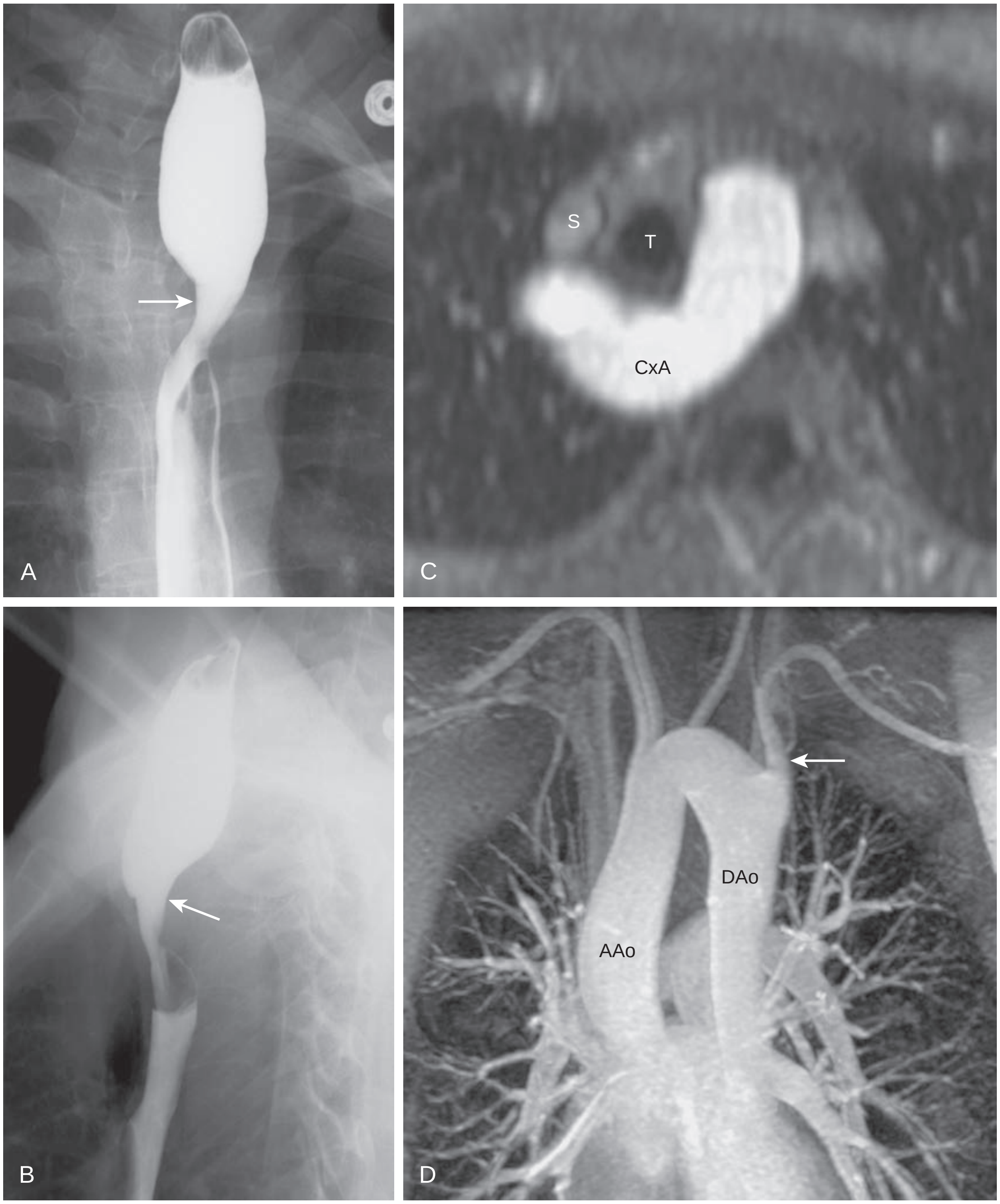

**Figure 76.7. Circumflex aortic arch.** (A) Frontal esophagram of an 18-year-old female shows a large right indentation on the esophagus *(arrow)* corresponding to a right aortic arch. (B) Lateral esophagram shows a posterior indentation *(arrow)* larger than expected for an aberrant left subclavian artery. (C) Axial MRA reconstruction shows that the aorta *(CxA)* passes behind the trachea *(T)* and the esophagus. The superior vena cava *(S)* is labeled for reference. (D) Maximal intensity projection MRA shows a right ascending aorta *(AAo)* and a left descending aorta *(DDo)*. There is an aberrant left subclavian artery *(arrow)* as the last branch off the arch.

bronchus in type 1B. Regardless of the type, complete tracheal rings and stenosis frequently are present (e-Fig. 76.10B).

Unlike with a vascular ring, the obstructive symptoms of the esophagus tend to be mild or absent in pulmonary artery sling. About a third of pulmonary artery sling cases are associated with other cardiovascular anomalies, including ventricular septal defect, atrial septal defect, patent ductus arteriosus, tetralogy of Fallot, single ventricle, and coarctation.[20] Genetic associations include trisomy 18 and 21.[23]

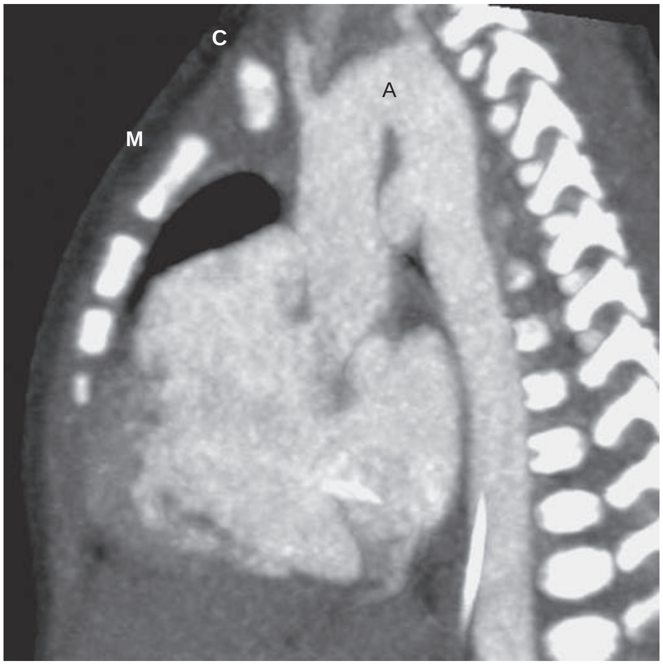

**Figure 76.8. Cervical aortic arch in a 1-month-old boy.** Sagittal chest CTA reformation shows a high aortic arch *(A)* with its apex above the level of the manubrium *(M)* at vertebral level T3–T4. *C,* Clavicle.

***Imaging.*** As the left pulmonary artery wraps around the right side of the trachea, the right main bronchus or the bridging airway can be obstructed. In the newborn, this phenomenon may manifest as retained fluid in the right lung. In older children, this phenomenon may present as a hyperinflated right lung from air trapping. The most specific finding is the abnormal architecture of the central airways, often described as a low carina and an inverted T shape of the central airways (see e-Fig. 76.10A). This finding is a result of the abnormal airway structure found in type 2 pulmonary artery sling. The apparent low carina is the result of the low origin of the bridging bronchus. The horizontal course of the bridging bronchus gives the carina a flattened look, hence the inverted T shape.

Barium esophagography demonstrates an anterior indentation of the esophagus at the level of the carina (Fig. 76.11), unlike the posterior indentation seen with a vascular ring. In addition, on the lateral projection, the trachea is separated from the esophagus by the left main pulmonary artery.

Direct visualization of the anomalous left pulmonary artery can be performed with CTA or MRA.[24] Because assessment of the tracheobronchial tree and lungs is important for pulmonary artery sling, CTA is the preferred imaging modality. CTA images can be postprocessed to provide virtual endoscopic views to evaluate for focal versus diffuse airway stenosis, extrinsic vascular compression, and tracheal rings (see e-Fig. 76.10B). Endoscopic bronchoscopy is recommended to evaluate dynamic airway obstruction from tracheobronchomalacia and to confirm the extent of complete tracheal rings or stenosis for surgical planning.

***Treatment.*** The definite treatment is surgical reimplantation or relocation of the left pulmonary artery and release of the entrapped trachea. In many of these patients, stenosis of the trachea requires a sliding tracheoplasty or pericardial patch to augment the narrowed segment. A diameter of the trachea less than 3 mm is associated with the need for tracheoplasty or a poor outcome.[25] Airway narrowing that involves the carina or the bronchi is particularly difficult to repair.[26]

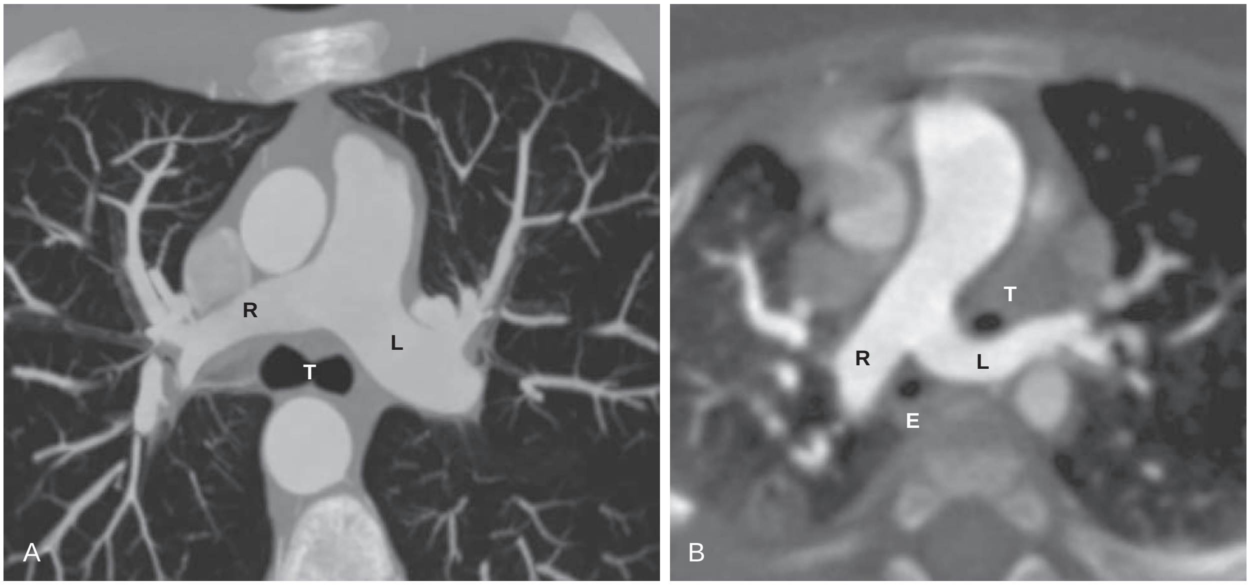

**Figure 76.9. Pulmonary artery sling in a 6-month-old girl.** (A) Axial CTA image showing the normal pulmonary artery branching pattern. The main pulmonary artery bifurcates into the left pulmonary artery *(L)* and right pulmonary artery *(LR)*. The trachea *(T)* is seen posterior to the bifurcation. (B) Axial CTA image shows the anomalous left pulmonary artery *(L)* arising from the right pulmonary artery *(R)*. It courses between the trachea *(T)* and the esophagus *(E)*. The trachea is entrapped between the left and right pulmonary arteries.

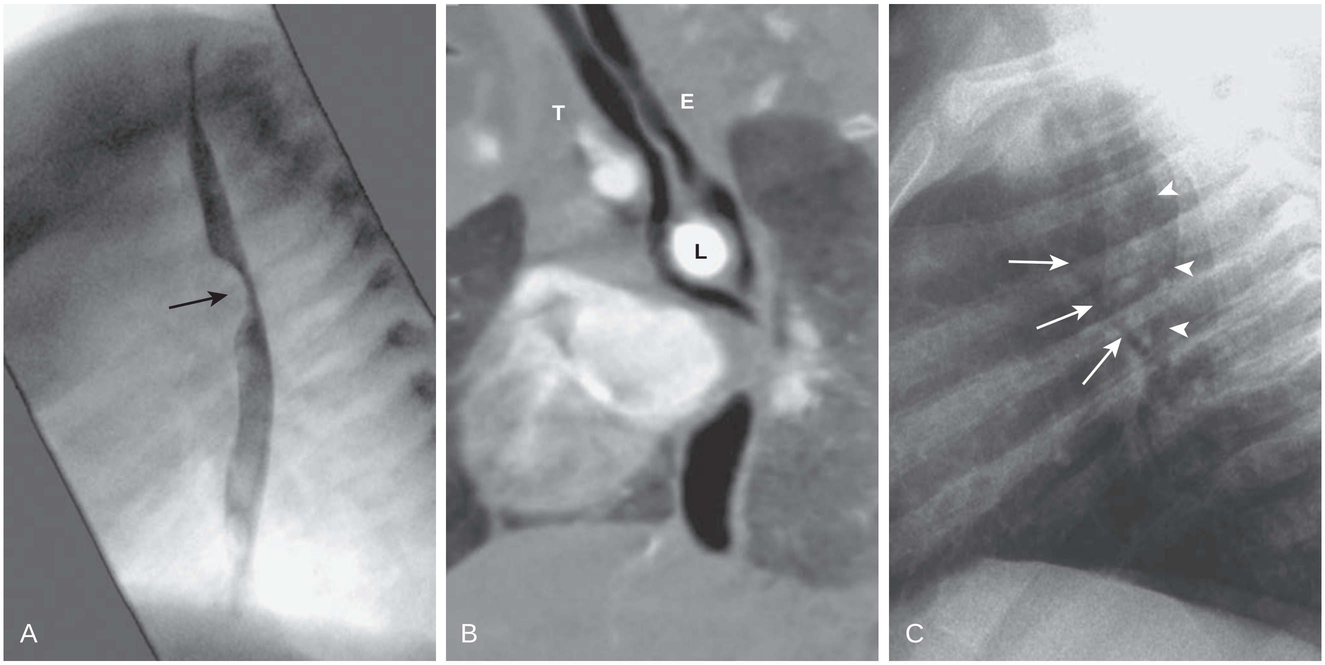

**Figure 76.11. Pulmonary artery sling in a 6-month-old girl.** (A) Lateral esophagram shows an anterior indentation *(arrow)*. (B) Reformatted CTA in the same plane shows the left pulmonary artery *(L)* separating the trachea *(T)* from the esophagus *(E)* at the carina level. The anterior indentation seen in the esophagram is caused by compression by the left pulmonary artery. (C) Lateral chest radiograph shows the same separation of the trachea *(arrows)* and the air-filled esophagus *(arrowheads)*.

## KEY POINTS

- Barium esophagography has historically been performed for the evaluation of a vascular ring, but CTA and MRA are now the studies of choice for diagnosis.
- Vascular rings involving a right aortic arch include these variations:
  - Aberrant left subclavian artery, left ductus arteriosus/ligamentum arteriosum
  - Mirror-imaging branching, left ductus arteriosus/ligamentum arteriosum
  - Circumflex aorta with a left descending thoracic aorta, left ductus arteriosus/ligamentum arteriosum
  - Cervical aortic arch, aberrant left subclavian artery, left ductus arteriosus/ligamentum arteriosum
- Vascular rings involving a left aortic arch includes these variations:
  - Aberrant right subclavian artery, right ductus arteriosus/ligamentum arteriosum
  - Circumflex aorta with a right descending thoracic aorta, right ductus arteriosus/ligamentum arteriosum
  - Cervical aortic arch, aberrant right subclavian artery, right ductus arteriosus/ligamentum arteriosum
- Imaging evaluation of a pulmonary artery sling must include the central airways because of the frequent associations with abnormal branching of the airways, complete tracheal rings, and tracheobronchial stenosis.

## Acknowledgment

The author would like to acknowledge Frandics Chan, MD, for his contributions to prior editions of this chapter.

## SUGGESTED READINGS

Hellinger JC, Daubert M, Lee EY, et al. Congenital thoracic vascular anomalies: evaluation with state-of-the-art MR imaging and MDCT. *Radiol Clin North Am*. 2011;49:969–996.
Hernanz-Schulman M. Vascular rings: a practical approach to imaging diagnosis. *Pediatr Radiol*. 2005;35:961–979.
Momma K, Matsuoka R, Takao A. Aortic arch anomalies associated with chromosome 22q11 deletion (CATCH 22). *Pediatr Cardiol*. 1999;20:97–102.
Newman B, Cho Y. Left pulmonary artery sling-anatomy and imaging. *Semin Ultrasound CT MR*. 2010;31:158–170.
Oddone M, Granata C, Vercellino N, et al. Multi-modality evaluation of the abnormalities of the aortic arches in children: techniques and imaging spectrum with emphasis on MRI. *Pediatr Radiol*. 2005;35:947–960.

## REFERENCES

Full references for this chapter can be found on www.expertconsult.com.

## REFERENCES

1. Marmon LM, Bye MR, Haas JM, et al. Vascular rings and slings: long-term follow-up of pulmonary function. *J Pediatr Surg*. 1984;19(6):683–692.
2. *Development of the Cardiovascular and Lymphatic Systems*. 39th ed. Elsevier; 2005.
3. Muller M, Schmitz BL, Pauls S, et al. Variations of the aortic arch - a study on the most common branching patterns. *Acta Radiol*. 2011;52(7):738–742.
4. Bonnard A, Auber F, Fourcade L, et al. Vascular ring abnormalities: a retrospective study of 62 cases. *J Pediatr Surg*. 2003;38(4):539–543.
5. McElhinney DB, Clark BJ III, Weinberg PM, et al. Association of chromosome 22q11 deletion with isolated anomalies of aortic arch laterality and branching. *J Am Coll Cardiol*. 2001;37(8):2114–2119.
6. Momma K, Matsuoka R, Takao A. Aortic arch anomalies associated with chromosome 22q11 deletion (CATCH 22). *Pediatr Cardiol*. 1999;20(2):97–102.
7. Woods RK, Sharp RJ, Holcomb GW, et al. Vascular anomalies and tracheoesophageal compression: a single institution's 25-year experience. *Ann Thorac Surg*. 2001;72:434–439.
8. Alsenaidi K, Gurofsky R, Karamlou T, et al. Management and outcomes of double aortic arch in 81 patients. *Pediatrics*. 2006;118(5):e1336–e1341.
9. Hernanz-Schulman M. Vascular rings: a practical approach to imaging diagnosis. *Pediatr Radiol*. 2005;35(10):961–979.
10. Murdison KA. Ultrasonic imaging of vascular rings and other anomalies causing tracheobronchial compression. *Echocardiography*. 1996;13(3):337–355.
11. Patel CR, Lane JR, Spector ML, et al. Fetal echocardiographic diagnosis of vascular rings. *J Ultrasound Med*. 2006;25(2):251–257.
12. Malik TH, Bruce IA, Kaushik V, et al. The role of magnetic resonance imaging in the assessment of suspected extrinsic tracheobronchial compression due to vascular anomalies. *Arch Dis Child*. 2005;91(1):52.
13. Oddone M, Granata C, Vercellino N, et al. Multi-modality evaluation of the abnormalities of the aortic arches in children: techniques and imaging spectrum with emphasis on MRI. *Pediatr Radiol*. 2005;35(10):947–960.
14. Chun K, Colombani PM, Dudgeon DL, et al. Diagnosis and management of congenital vascular rings: a 22-year experience. *Ann Thorac Surg*. 1992;53(4):597–603.
15. Backer CL, Monge MC, Popescu AR, et al. Vascular rings. *Semin Pediatr Surg*. 2016;25(3):165–175.
16. Holmes KW, Bluemke DA, Vricella LA, et al. Magnetic resonance imaging of a distorted left subclavian artery course: an important clue to an unusual type of double aortic arch. *Pediatr Cardiol*. 2006;27(3):316–320.
17. Zachary CH, Myers JL, Eggli KD. Vascular ring due to right aortic arch with mirror-image branching and left ligamentum arteriosus: complete preoperative diagnosis by magnetic resonance imaging. *Pediatr Cardiol*. 2001;22(1):71–73.
18. McLeary MS, Frye LL, Young LW. Magnetic resonance imaging of a left circumflex aortic arch and aberrant right subclavian artery: the other vascular ring. *Pediatr Radiol*. 1998;28(4):263–265.
19. Yu J-M, Liao C-P, Ge S, et al. The prevalence and clinical impact of pulmonary artery sling on school-aged children: a large-scale screening study. *Pediatr Pulmonol*. 2008;43(7):656–661.
20. Gikonyo BM, Jue KL, Edwards JE. Pulmonary vascular sling: report of seven cases and review of the literature. *Pediatr Cardiol*. 1989;10(2):81–88.
21. Berdon WE, Baker DH, Wung JT, et al. Complete cartilage-ring tracheal stenosis associated with anomalous left pulmonary artery: the ring-sling complex. *Radiology*. 1984;152(1):57–64.
22. Wells TR, Gwinn JL, Landing BH, et al. Reconsideration of the anatomy of sling left pulmonary artery: the association of one form with bridging bronchus and imperforate anus. Anatomic and diagnostic aspects. *J Pediatr Surg*. 1988;23(10):892–898.
23. Newman B, Cho YA. Left pulmonary artery sling–anatomy and imaging. *Semin. Ultrasound CT MR*. 2010;31(2):158–170.
24. Hodina M, Wicky S, Payot M, et al. Non-invasive imaging of the ring–sling complex in children. *Pediatr Cardiol*. 2001;22(4):333–337.
25. Huang S-C, Wu E-T, Wang C-C, et al. Surgical management of pulmonary artery sling: trachea diameter and outcomes with or without tracheoplasty. *Pediatr Pulmonol*. 2012;47(9):903–908.
26. Oshima Y, Yamaguchi M, Yoshimura N, et al. Management of pulmonary artery sling associated with tracheal stenosis. *Ann Thorac Surg*. 2008;86(4):1334–1338.

# 77

# Coronary Artery Disease in Children

*Simon Lee*

Coronary artery disease in children can be acquired, but the majority of anomalies are congenital.[1,2] Among acquired coronary abnormalities, Kawasaki disease (KD) is the most common. Other causes include sequelae from trauma, vasculitides, radiation injury after oncologic treatment, and rare cases of familial hyperlipidemia and idiopathic infantile arterial calcification. Congenital coronary anomalies can be characterized as abnormalities in origin, abnormalities associated with the coronary vessel, and abnormalities associated with congenital heart disease. Boxes 77.1 and 77.2 outline the common acquired and congenital coronary anomalies seen in children.

## IMAGING CONSIDERATIONS

Transthoracic echocardiography (TTE) remains the first-line imaging tool for evaluating children with suspected coronary anomalies. In experienced hands, the coronary origins and proximal coronary courses are reliably imaged. When further anatomic detail of luminal dimensions, ostial morphology, or evaluation of more distal portions of the coronary anatomy is necessary, other imaging modalities are necessary. Catheter angiography is the reference standard for the determination of coronary luminal abnormalities, such as coronary stenosis.[3] Additional techniques that further characterize the arterial wall and myocardial perfusion can be performed during catheterization, such as intravascular ultrasound (IVUS) and fractional flow reserve measurement.[4,5] However given the invasive nature of catheter angiography, electrocardiographic (ECG)-gated coronary computed tomography angiography (CCTA) and cardiac magnetic resonance angiography (CMRA) are the main diagnostic modalities utilized.[6,7] Both techniques yield three-dimensional images of the heart, with the coronary vessels shown in the context of adjacent cardiac structures. Visualization is facilitated by various postprocessing techniques, such as curved multiplanar reformatting and endoluminal views via virtual angioscopy. CCTA has excellent diagnostic accuracy in detecting coronary stenosis, and several studies show that it is now comparable to catheter angiography.[8,9] These capabilities have made CCTA and CMRA the preferred method for the diagnosis and characterization of coronary anomalies.

CCTA provides excellent visualization of coronary anatomy, including the distal coronary branches. Images synchronized to the cardiac cycle can be acquired with prospective or retrospective ECG synchronization. Prospective ECG-triggering yields a snapshot of the heart at a predetermined portion of the cardiac cycle, whereas with retrospective ECG-gating, data is acquired throughout the cardiac cycle and can therefore be reconstructed at multiple time-points in the cardiac cycle and can be used to produce cine images of the heart. However, because data is acquired throughout the cardiac cycle, images obtained with retrospective ECG-gating generally incur a greater radiation dose compared with prospective ECG-triggering. With 64-slice scanners, the typical scan time in either mode is less than 10 seconds. Newer generation dual source and volumetric computed tomography (CT) scanners provide full anatomic coverage of a pediatric thorax in less than a second or in a single heartbeat, freezing respiratory and cardiac motion, and obviating the need for sedation in many cases. As CCTA uses ionizing radiation to produce images, measures should be taken to minimize the dose of ionizing radiation delivered while maintaining image quality. Strategies for CCTA dose optimization are listed in Box 77.3 and have been detailed in Chapter 66.[9–12]

The lack of ionizing radiation makes CMRA an attractive alternative to CCTA. CMRA can also provide information regarding ventricular size, systolic function, and tissue characterization (such as perfusion imaging, myocardial delayed enhancement, and T1 mapping). CMRA for assessment of the heart and great arteries is often performed using a three-dimensional, cardiac-gated, navigated echo, T2-prepared, steady-state, free-precession sequence (see Chapter 67).[13] Coronary vessel visualization with this sequence is based on the intrinsic long-T2 value of blood, so no gadolinium contrast administration is required.[14]

One of the main drawbacks of CMRA is that it lags in spatial resolution compared with CCTA, which can provide isotropic submillimeter resolution. Additionally, despite the lack of ionizing radiation, CMRA often requires anesthesia in patients younger than 8 years of age, and the risks of anesthesia versus radiation exposure must be weighed.[14a]

## NORMAL CORONARY ARTERY ANATOMY

Embryologically, the spatial configuration of the aortic sinuses adjacent to the pulmonary trunk act as a stimulus for coronary bud development. In a structurally normal heart with normal coronary artery anatomy, the left main coronary artery (LMCA) and right coronary artery (RCA) arise from the left and right sinuses of Valsalva, respectively. The LMCA then divides into the left anterior descending (LAD) and circumflex (Cx) coronary arteries. Many anatomic variations of the coronary arteries exist, with normal variants typically having no clinical significance (Fig. 77.1).

In cases where there is associated congenital heart disease, nomenclature of the coronary arteries should refer to the coronary dependent territory as opposed to the site of coronary origin. For example, in congenitally corrected transposition of the great arteries (L-transposition of the great arteries) where the morphologic left ventricle lies to the right, the coronary artery in the right-sided atrioventricular groove is named the left circumflex artery (see Chapter 75). When derangement of the ventricles is so severe that the ventricular morphology cannot be clearly identified, then the coronary arteries should be described relative to physical landmarks—for example, left-sided atrioventricular branch instead of left Cx, right-sided atrioventricular branch instead of RCA, anterior interventricular septal branch instead of LAD, and posterior interventricular septal branch instead of posterior descending artery (PDA).

### Right Coronary Artery

After its takeoff from the right sinus of Valsalva, the RCA courses anteriorly into the right atrioventricular groove and gives rise to several branches. The right conal artery arises as the first branch of the right coronary artery 50% to 60% of the time, arising directly from the right sinus of Valsalva in 40% to 50% of cases. The sinoatrial nodal artery arises from the proximal RCA in the majority of cases and from the proximal left Cx in the other (Fig.

---

The author would like to acknowledge Frandics Chan, MD, PhD, for his contributions to prior editions of this chapter.

## Abstract:

Coronary artery disease in children can be divided into acquired versus congenital etiologies, with congenital anomalies being far more prevalent. The breadth of coronary anomalies seen in children and young adults is wide. For most children, particularly pre-school age, transthoracic echocardiography is the first-line imaging modality. Further coronary imaging with computed tomography (CT) or magnetic resonance (MR) for diagnosis of a coronary anomaly, confirmation and clarification of echocardiographic findings, mapping out the coronary arteries for surgical planning, and evaluation for a coronary aneurysm or stenosis is often necessary. Dose-optimization strategies for CT should be utilized in all cases. In patients with congenital coronary anomalies that require surgical manipulation, follow up imaging with coronary CT angiography or stress MR perfusion imaging may be necessary.

## Keywords:

Coronary computed tomography angiography
cardiac magnetic resonance angiography
coronary anomalies
coronary imaging
pediatric coronary imaging

**BOX 77.1** Acquired Coronary Artery Diseases

**CORONARY ANEURYSM OR ECTASIA**

- Kawasaki disease
- Behçet disease
- Polyarteritis nodosa
- Trauma (pseudoaneurysm)

**CORONARY STENOSIS**

- Kawasaki disease
- Heart transplant-associated coronary artery vasculopathy
- Radiation
- Behçet disease
- Polyarteritis nodosa
- Trauma (dissection)
- Homozygous familial hypercholesterolemia
- Idiopathic infantile arterial calcification

**BOX 77.2** Congenital Coronary Artery Diseases

**ABNORMALITIES IN CORONARY ORIGIN**

- Anomalous aortic origin of the left coronary artery (AAOLCA)
- Anomalous aortic origin of the right coronary artery (AAORCA)
- Anomalous coronary artery origin from the pulmonary artery (ALCAPA)

**ABNORMALITIES OF THE CORONARY ARTERY ANATOMY/VESSEL**

- Coronary fistulae
- Congenital coronary stenosis
- Congenital coronary aneurysms
- Myocardial bridging

**ABNORMALITIES ASSOCIATED WITH CONGENITAL HEART DISEASE**

- Tetralogy of Fallot
- Transposition of the great arteries
- Truncus arteriosus
- Pulmonary atresia with intact ventricular septum

**BOX 77.3** Computed Tomography Radiation Dose Optimization Strategies

- Limit scan range to anatomy of clinical interest.
- Center the patient within the gantry.
- Lower tube potential and tube current to account for patient size. Consider automated algorithms.
- Technique should be adjusted to the lowest practical radiation dose that will yield diagnostic image quality based on the clinical indication.
- Prospective ECG-triggering should be used when possible.
- For coronary imaging, the narrowest temporal acquisition window possible should be used.
- Iterative reconstruction should be used on all scans.
- Heart rate lowering medications should be considered.

77.2A). The midportion of the RCA gives rise to the acute marginal branches, which supply the RV free wall (Fig. 77.2B). The distal portion of the RCA wraps around the inferior surface of the heart. An atrioventricular node branch often arises from the RCA near the crux of the heart (Fig. 77.2D). In 70% to 85% of the population, the RCA gives rise to a PDA that courses within the posterior interventricular sulcus to supply the basilar inferior wall of the left ventricle (Fig. 77.2C). This pattern is called a *right-dominant coronary system*. There can be codominance, where the RCA supplies the PDA and the Cx supplies additional posterior left ventricular branches. The least common pattern is left-dominance, where the PDA arises from the Cx.

### Left Coronary Artery

The LMCA originates from the left sinus of Valsalva and courses to the left for a short distance before it bifurcates into the LAD and Cx coronary arteries. Occasionally, the LMCA trifurcates into an LAD coronary artery, a Cx coronary artery, and a ramus intermedius branch (Fig. 77.3A). This ramus intermedius branch supplies the anterior left ventricular wall. The LAD artery gives rise to two sets of vessels: an epicardial set called the *diagonal branches* and an intramuscular set called the *anterior septal perforator branches*. The diagonal branches are responsible for perfusing the anterior left ventricular wall, whereas the septal perforator branches are responsible for the anterior septum. The distal LAD artery typically wraps around the cardiac apex and terminates at the inferior wall of the apex (Fig. 77.3B). In a minority of cases, the Cx artery gives off a sinoatrial nodal branch (Fig. 77.3C) before it enters the left atrioventricular groove. The Cx artery then gives rise to a number of obtuse marginal branches, which supply the lateral left ventricular wall (see Fig. 77.3B).

## CONGENITAL CORONARY ARTERY ANOMALIES

### Epidemiology

The true prevalence of congenital coronary artery anomalies is unknown. According to adult catheter angiographic data, 0.6% to 1.5% of patients were found to have coronary artery anomalies.[15,16] The largest study of this type reviewed more than 126,000 coronary studies and revealed a prevalence of 1.3%, with the majority (80%) felt to have no clinical significance.[15,16] The two most common anomalies are separate origins of the LAD and Cx arteries arising from the left sinus of Valsalva (0.41%) (e-Fig. 77.4A) and a retroaortic Cx artery arising from the right sinus or the RCA (0.37%) (e-Fig. 77.4B). Both configurations are clinically benign. Other examples of benign anomalies are an absent Cx artery with a superdominant RCA that reaches the anterior atrioventricular groove and a high takeoff of either coronary (>1 cm above the sinotubular junction).

### Anomalous Aortic Origin of a Coronary Artery

***Overview.*** An anomalous aortic origin of the LMCA (AAOLCA) may originate from the right sinus of Valsalva or may arise as a single coronary artery with the RCA. Before bifurcating into the LAD and Cx arteries, the LMCA must travel toward the left by one of four routes: anterior to the right ventricular outflow tract (RVOT), within the interventricular septum beneath the RVOT (intraseptal), between the aorta and the pulmonary artery (interarterial), or posterior to the aorta.[17,18] Similarly, an anomalous aortic origin of the RCA (AAORCA) may originate from the left sinus of Valsalva or as a single coronary with the LMCA. It typically has an interarterial course toward the right atrioventricular groove, although other routes are possible.[18] While the anterior and posterior courses are considered clinically benign, the interarterial course (Fig. 77.5) is associated with sudden cardiac death.[19] This association was originally described in several autopsy series, with AAOLCA found more frequently than AAORCA.[20–22] Several studies and case reports have subsequently established this association, with congenital coronary anomalies reported as the

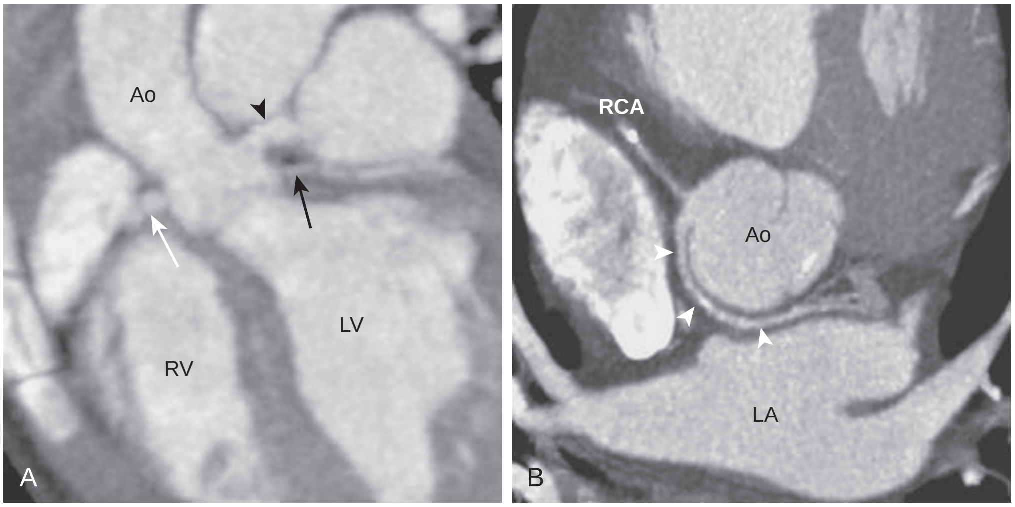

**e-Figure 77.4. Common benign variants of the coronary arteries.** (A) Horizontal long-axis view reconstructed from a CCTA of a 1-year-old boy shows separate origins for the left anterior descending *(arrowhead)* and the left circumflex (LCx) *(black arrow)* arteries. The right coronary artery (RCA) *(white arrow)* is in normal position. This variant occurs in 0.41% of the population. (B) Short-axis view from a 40-year-old man shows the LCx artery and the *RCA* arising separately from the right sinus. The LCx artery *(white arrowheads)* wraps around posterior to the aorta *(Ao)* and then enters the left atrioventricular groove. This variant occurs in 0.37% of the population. *LA,* Left atrium; *LV,* left ventricle; *RV,* right ventricle.

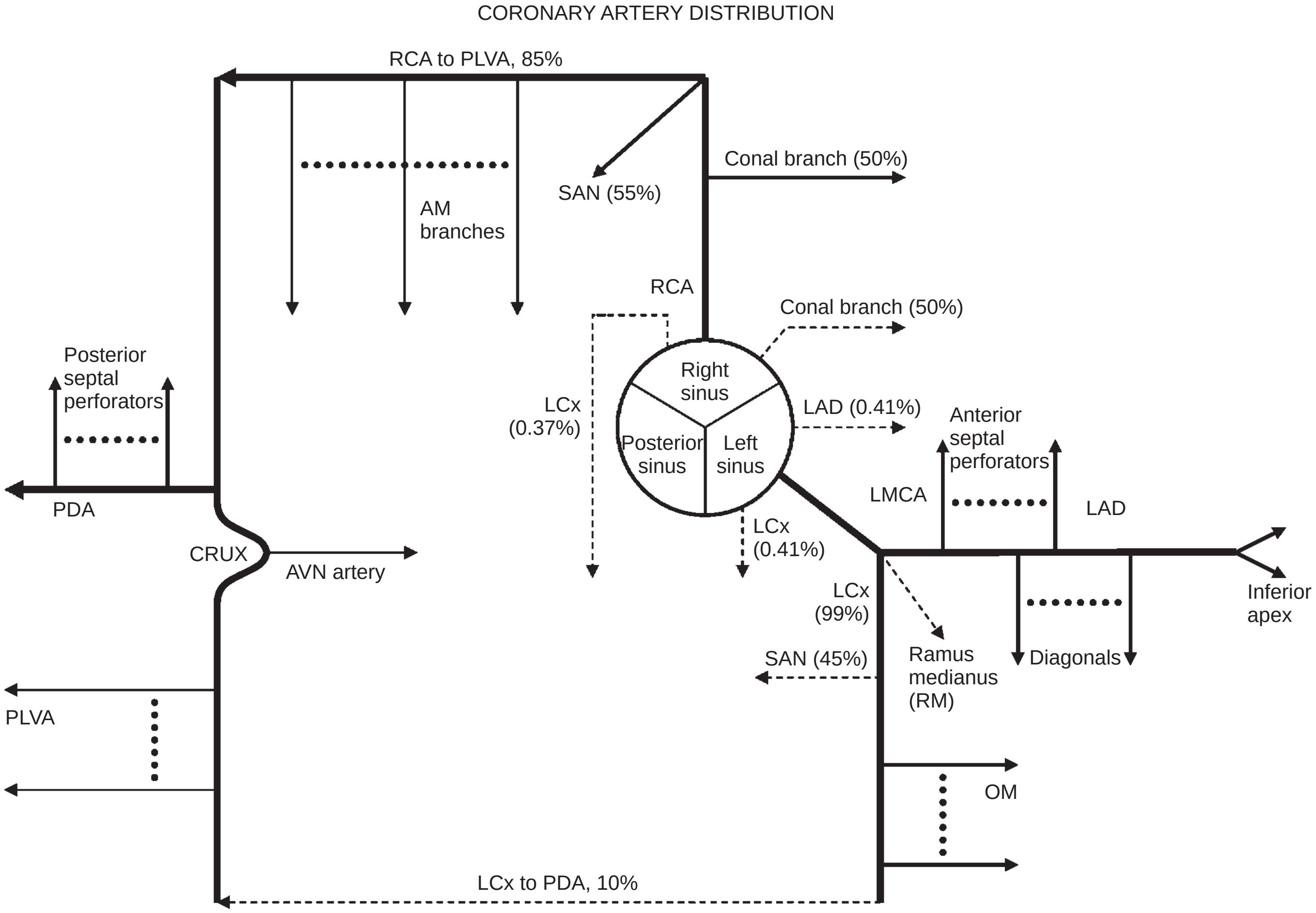

**Figure 77.1. Coronary artery distribution diagram.** *Solid lines* represent the most common coronary artery pattern. *Dashed lines* represent common variants (prevalences in percentages). *AM,* Acute marginal; *AVN,* atrioventricular nodal; *LAD,* left anterior descending; *LCx,* left circumflex; *LMCA,* left main coronary artery; *OM,* obtuse marginal; *PDA,* posterior descending artery; *PLVA,* posterior left ventricular artery; *RCA,* right coronary artery; *RM,* ramus medianus; *SAN,* sinoatrial nodal.

second-most common cause for sudden cardiac death in adolescent athletes.[23]

The true prevalence of anomalous aortic origin of the coronary arteries is unknown. The majority of patients are asymptomatic and a major adverse cardiac event is often the initial presentation. Based on prior angiographic studies, the prevalence of AAOLCA with an interarterial course is estimated at 0.02% to 0.05% of the population, and the prevalence of AAORCA is estimated at 0.1%.[24] Given that AAORCA appears to be three to five times more common than AAOLCA in the general population, the prior autopsy studies suggest that AAOLCA is a higher risk lesion.

The pathophysiology of sudden cardiac death has not been conclusively determined. Most patients with sudden cardiac death had no significant clinical findings or known premonitory symptoms.[25] In about 30% of the cases, syncope or chest pain occurred within 2 years of death, but resting ECG and stress ECG have been reported as normal. The prevailing thought is that the risk of sudden cardiac death is increased with significant physical exertion, such as strenuous athletic activity. Presumed risk factors for a lethal arrhythmia are transient ischemia caused by inadequate coronary flow through a narrowed “intramural” lumen compressed by the aorta and pulmonary artery, a slitlike opening caused by an acute takeoff (<45 degrees) of the anomalous coronary artery, and the presence of an ostial ridge or flap that also occludes the ostium.[26] An intramural lumen refers to a portion of the coronary artery where the tunica media is shared with the aortic wall and there is no interposed adventitial layer.

In addition to interarterial coronary arteries, sudden death has rarely been reported with AAOLCA arising from the noncoronary sinus without an interarterial course.[27] In this configuration, the alignment of the LMCA origin and the anterior interventricular groove is such that the LMCA may have a more acute takeoff angle from the noncoronary sinus (e-Fig. 77.6). This acute takeoff angle creates a narrowing at the ostium that is thought to be a factor leading to ischemia and sudden death.

***Imaging.*** In neonates and young children, echocardiography can delineate the coronary origins to suggest the anomalous coronary types previously discussed. In adolescents and young adults, the coronary arteries may not be adequately assessed with echocardiography. Confirmation of the diagnosis and detailed characterization of the high-risk features previously mentioned is better performed by CMRA and CCTA.[28] In particular, the presence of an intramural course should be evaluated by cross-sectional imaging, as this is poorly characterized by echocardiography.[29] Current data suggests the risk of sudden cardiac death is low before 10 years of age, and so many centers defer surgical intervention until after this age.[30] Further cross-sectional imaging can likely be deferred in most routine cases until around 10 years of age. This has the benefit of avoiding sedation or anesthesia in the majority of cases. Depending on the expertise and equipment

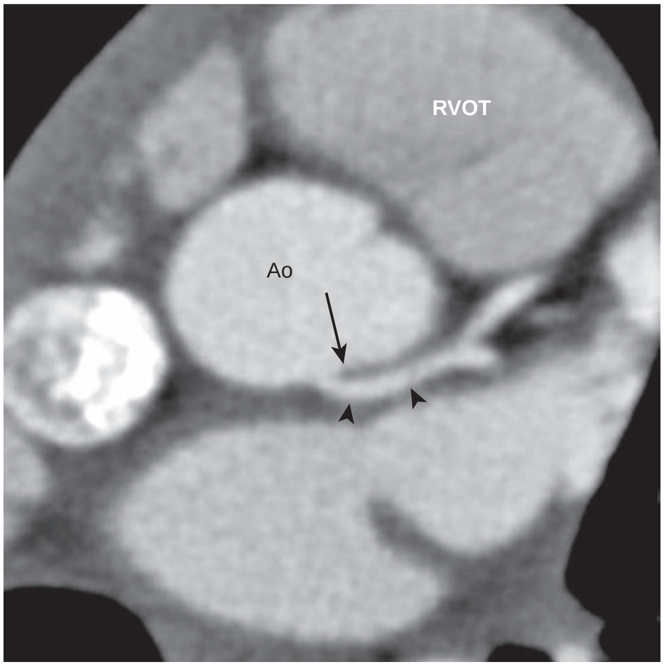

**e-Figure 77.6. CCTA of an anomalous left main coronary artery (LMCA) from the noncoronary sinus.** Short-axis view from a CCTA of a 3-year-old girl shows the LMCA *(arrowheads)* arising from the noncoronary sinus just to the left of the commissure *(arrow)*. *Ao,* Aorta; *RVOT,* right ventricular outflow tract.

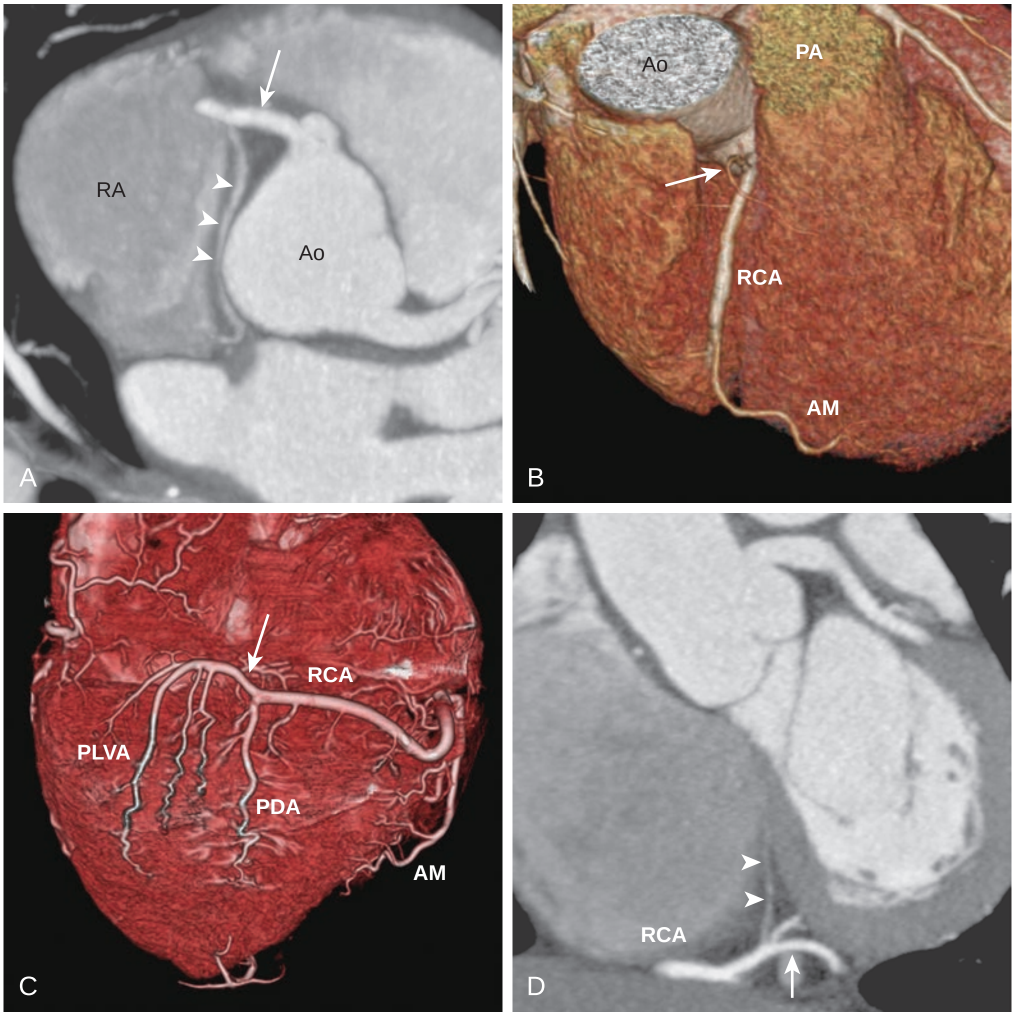

**Figure 77.2. Major branches of the normal right coronary artery *(RCA)*.** (A) Axial ECG-gated CCTA image shows the RCA *(arrow)* originating from the aorta *(Ao)* and extending toward the right atrioventricular groove. It gives off a sinoatrial nodal branch *(arrowheads)* that terminates at the right atrium *(RA)* near the atrial septum. (B) Volume-rendered image shows an acute marginal *(AM)* branch arising from the *RCA* at the right ventricular free wall. The conal branch *(arrow)* is the first branch of the *RCA. PA,* Pulmonary artery. (C) Volume-rendered image shows the inferior surface of a heart. The *RCA* gives off in succession of the *AM* branch, the posterior descending artery *(PDA)*, and the posterior left ventricular arteries *(PLVA)*, which lie on the left side of the crux *(arrow)*. (D) Short-axis view shows the *RCA* at the crux *(arrow)* giving off an atrioventricular nodal branch *(arrowheads)*.

available to individual centers, CMRA can be considered the first test of choice to avoid radiation exposure. If CMRA is not feasible due to technical or diagnostic reasons, then CCTA presents an excellent choice. Diagnostic catheter angiography does not have much of a role for this indication.

Morphologic features considered clinically relevant are: ostial size/morphology (including the presence of an acute angle takeoff from the aorta, a slitlike origin, and the presence of an ostial ridge), interarterial narrowing suggestive of an intramural course, length of the intramural portion, location in relation to the sinotubular junction and aortic commissures, and coronary dominance.[30] Determination of the intramural course can be difficult with CCTA and CMRA. Correlation with surgical pathology suggests that CCTA findings of a slitlike origin, an acute angle at vessel takeoff, and an elliptical cross-section with parallel course along the aortic root are related to an intramural coronary segment (Fig. 77.7).[31] Endoluminal views and volume rendered reconstructions are helpful for ostial characterization and surgical planning.

***Treatment.*** Although there is a strong association with sudden cardiac death, the absolute risk among individuals, particularly in the absence of participation in competitive sports, is unknown. There is marked practice variation among congenital heart surgery centers due to this uncertainty.[31] Recent data from a multicenter registry by the Congenital Heart Surgeons Society involving 23 pediatric centers reported 52% of AAORCA and 67% of AAOLCA had undergone surgery at a median age of 12.6 years.[32,33] The type of surgical repair is dependent on the coronary anatomy. In those with an intramural course, an unroofing procedure is the technique of choice. This involves incising the common wall between the aorta and intramural coronary. Aortic valve commissural resuspension may be necessary in cases where the intramural coronary courses behind the commissure. Direct reimplantation or creation of a neo-ostium and ostioplasty is performed when there are separate ostia and no significant intramural course. A pulmonary artery translocation can be performed in the case of a single coronary with evidence of coronary compression and/or

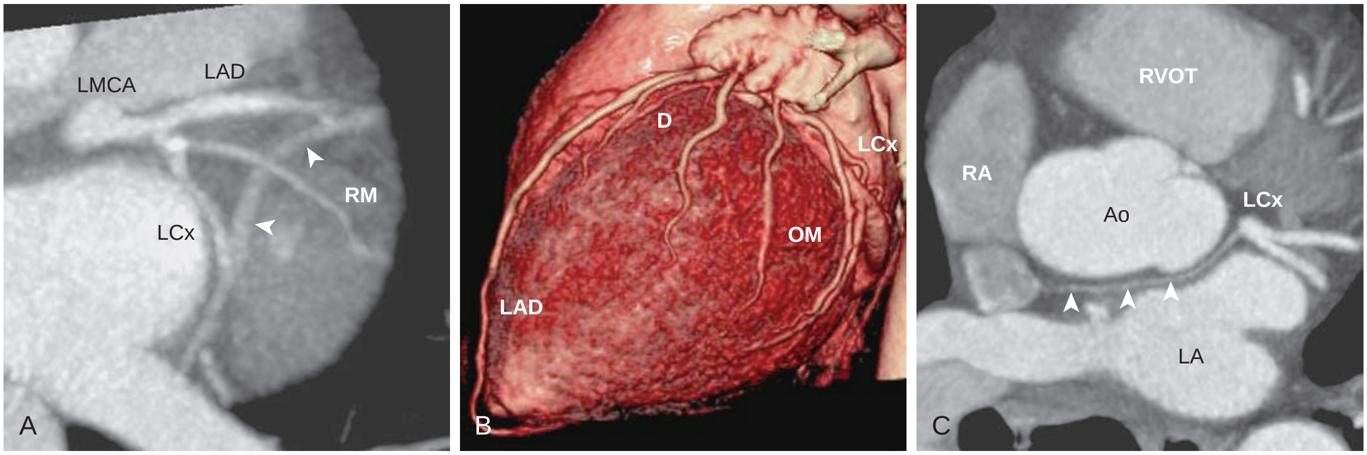

**Figure 77.3. Major branches of the normal left main coronary artery *(LMCA)*.** (A) Oblique axial ECG-gated CCTA image shows the trifurcation of the *LMCA* into a left anterior descending *(LAD)* artery, a ramus medianus *(RM)* branch, and a left circumflex *(LCx)* artery. The crossing vessel *(arrowheads)* is the greater cardiac vein. (B) Volume-rendered image shows the *LAD* and several diagonal *(D)* branches. The *LAD* wraps around the apex to reach the apical inferior surface. The *LCx* artery gives off several obtuse marginal *(OM)* branches. (C) Axial image shows the *LCx* giving off a sinoatrial nodal branch *(arrowheads)* that travels behind the aorta *(Ao)* and terminates at the right atrium *(RA)* near the atrial septum. *LA,* Left atrium; *RVOT,* right ventricular outflow tract.

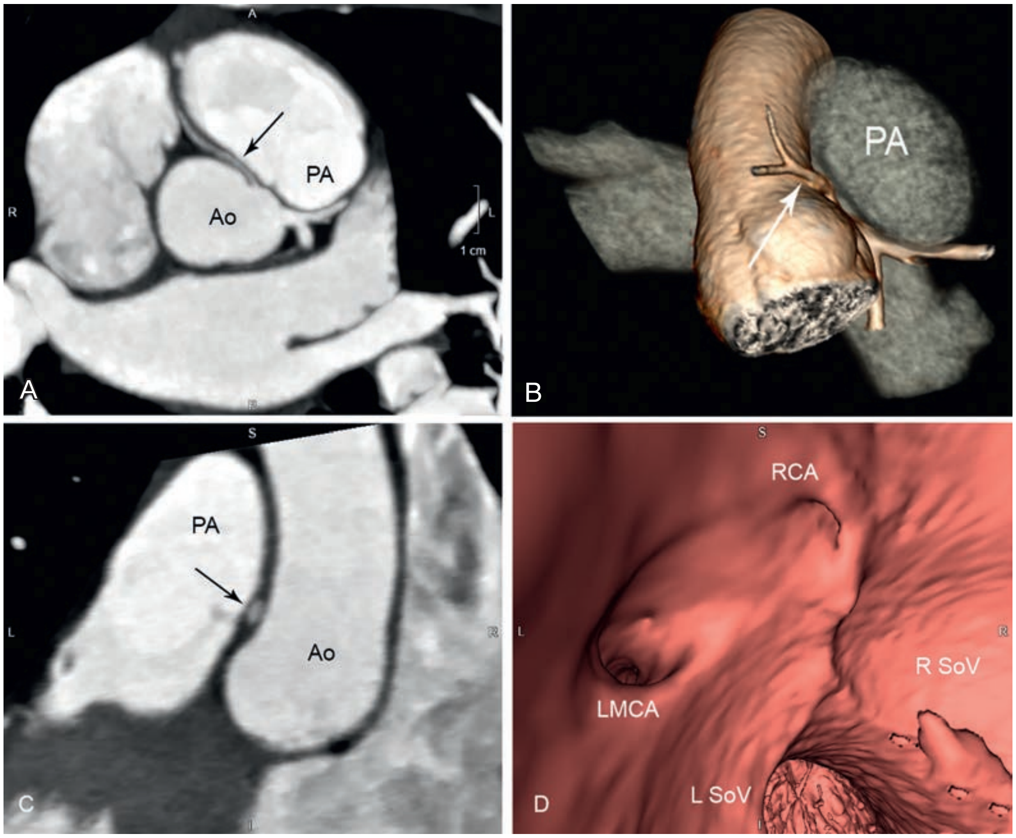

**Figure 77.5. Anomalous right coronary artery with an interarterial course.** (A) Short-axis view of the aortic root from a CCTA shows an anomalous aortic origin of the right coronary artery from the left sinus of Valsalva (AAORCA) with an interarterial course *(arrow)*. Note the acute angle of origin and interarterial narrowing, suggestive of an intramural course. (B) 3D volume rendered reconstruction demonstrating the RCA *(arrow)* as it courses from the left sinus of Valsalva between the aortic root and main pulmonary artery. (C) Multiplanar reformatted image of an interarterial segment of the coronary *(arrow)* demonstrating the elliptical shape and A-P narrowing. (D) Endoluminal reconstruction demonstrating the separate orifices of the left and right coronary arteries. The AAORCA orifice appears slitlike and narrowed, and arises adjacent to the intercoronary commissure (juxtacommissural). *L SoV,* Left sinus of Valsalva; *R SoV*, right sinus of Valsalva.

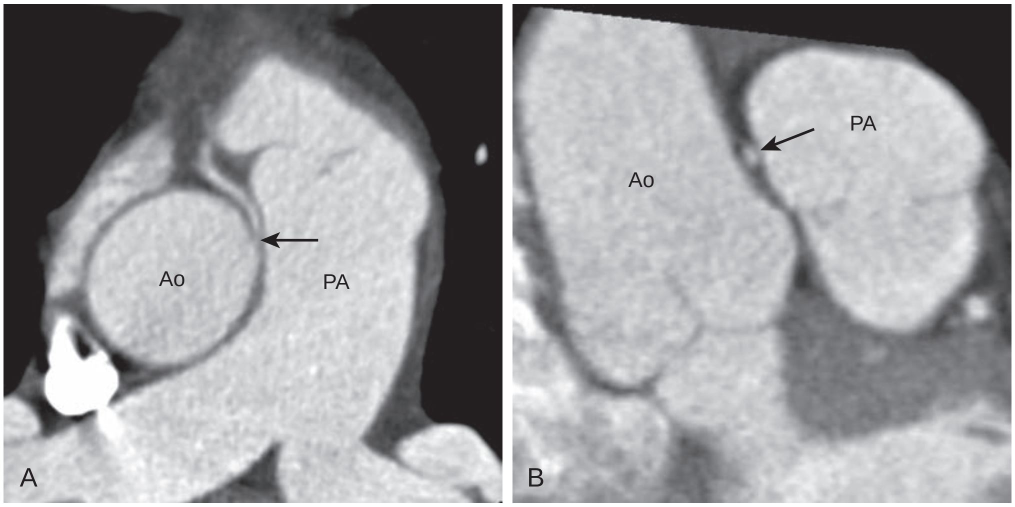

**Figure 77.7. CCTA of an intramural right coronary artery (RCA) arising from the left sinus of Valsalva in an 8-year-old girl.** (A) Short-axis view shows an interarterial RCA *(arrow)* arising from the aorta *(Ao)* in an acute angle. The proximal RCA tapers to a slitlike opening at the ostium. (B) Longitudinal view shows the RCA compressed *(arrow)* by the *Ao* and the pulmonary artery *(PA)*. The cross-section of the RCA is elliptical in shape.

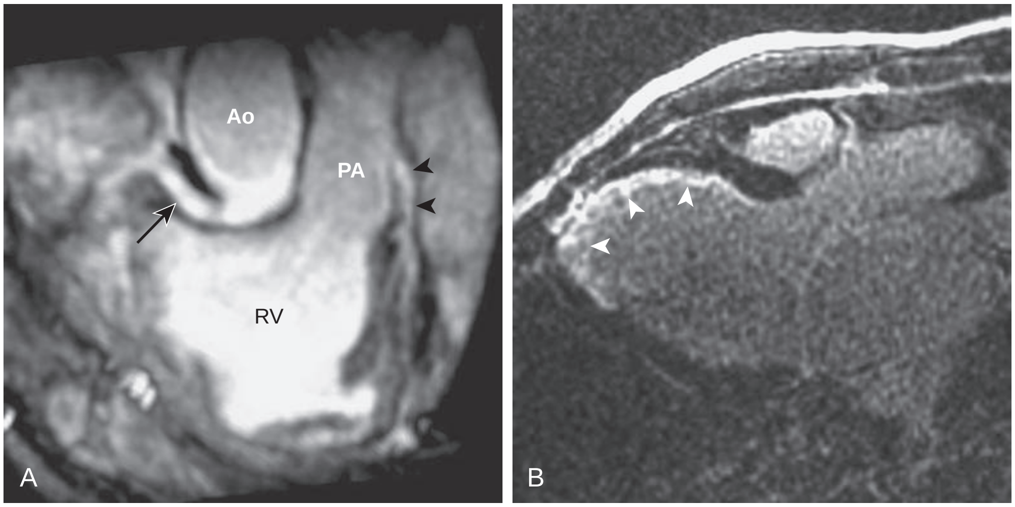

**Figure 77.8. CMRA of a 12-year-old boy with an anomalous left coronary artery from the pulmonary artery *(PA)*.** (A) Oblique image reformatted from a noncontrast coronary CMRA shows the right coronary artery *(arrow)* arising from the aorta *(Ao)* at the normal location and the left main coronary artery (LMCA) *(arrowheads)* originating from the *PA.* (B) Three-chamber view from a delayed-enhancement study shows endocardial infarction at the left ventricular anteroseptal wall and the apex *(arrowheads)* caused by inadequate myocardial perfusion from the LMCA. *RV,* Right ventricle.

ischemia. A bypass graft can be performed but has a very limited role due to concerns with competitive flow from the native coronary.

## Coronary Artery From Pulmonary Artery

***Overview.*** Origination of a coronary artery from a pulmonary artery includes anomalous origin of the LMCA, LAD artery, left circumflex (LCx) artery, or RCA from the pulmonary trunk or the branch pulmonary arteries. The most common type is the anomalous left coronary artery from the pulmonary artery (ALCAPA) (Fig. 77.8). The incidence is approximately 1 in 300,000 live births, accounting for 0.24% to 0.5% of congenital cardiac anomalies.[34] The clinical presentation depends on how much of the coronary flow to the left ventricle is compromised.

In the fetal circulation, ALCAPA does not cause significant abnormalities due to the relatively small difference between the pulmonary artery and aortic pressures and oxygen saturations. After birth, the pulmonary resistance decreases, the ductus arteriosus closes, and the pulmonary pressure and LMCA flow decrease. As the pulmonary resistance reaches its nadir, blood flows retrograde into the pulmonary artery causing coronary "steal." Retrograde flow from the RCA and collaterals supplies the left ventricle, but in the majority of patients (90%) there is inadequate collateralization to sustain myocardial viability. Myocardial ischemia, ventricular dilation, mitral regurgitation, and subsequent congestive heart failure and pulmonary edema develop around the sixth to eighth week of life, representing the infantile form of ALCAPA, also known as *Bland-White-Garland syndrome*. Without intervention, mortality can be as high as 90%.

Clinical symptoms are classically described as episodes of inconsolable crying and discomfort associated with feeding, which represent angina. In 10% of patients with ALCAPA, collateral flow from RCA to LMCA is large enough to sustain myocardial viability, and patients survive into adulthood with few or no significant clinical symptoms. As a result of the high shunt flow, the coronary arteries can be abnormally large. ALCAPA usually is an isolated lesion, but it can be associated with ventricular septal defect, atrioventricular canal, tetralogy of Fallot, truncus arteriosus, and aortic stenosis.

An anomalous right coronary artery from the pulmonary artery (ARCAPA) is four times less common than ALCAPA.[35] The clinical course of ARCAPA is more benign, with most patients being asymptomatic in the first 2 years of life and presenting with exertional chest pain later in adolescence or adulthood.

***Imaging.*** Chest radiographs for patients with the infantile form of ALCAPA usually show an enlarged cardiac silhouette and signs of pulmonary venous congestion or pulmonary edema. Echocardiography is the primary modality for diagnosis. The anomalous coronary connection and the reversed coronary flow by color Doppler imaging are usually well seen. In more complex cases, the connection between the anomalous coronary artery and the pulmonary artery can be seen readily with CCTA or CMRA.[36] Typically diagnostic catheter angiography is not necessary.

***Management.*** The definitive treatment is surgery. The most straightforward approach is to reimplant the anomalous coronary artery from the pulmonary artery to the aorta.[37] With ALCAPA, reimplantation of the LMCA can be difficult because the LMCA may be too short to reach the centrally located aorta. This problem can be solved with the Takeuchi operation,[38] in which an aortopulmonary window is created first. Then a baffled tunnel is created inside the pulmonary trunk to connect the aortopulmonary window to the ostium of the anomalous LMCA. Blood flows from the aorta, through the aortopulmonary window, into the baffled tunnel, and then into the anomalous LMCA ostium.

## Coronary Artery Fistula

***Overview.*** A coronary artery fistula is a common coronary abnormality seen in 0.3% to 0.8% of patients referred for cardiac catheterization.[39] It is an abnormal communication between a normal coronary artery and another cardiovascular structure. Although it usually is congenital, it can form after trauma or after a surgical procedure such as a myomectomy. Anatomically, a coronary fistula most frequently originates from the RCA system (55%), followed in frequency by the LMCA system (35%), both arteries (5%), and others (5%). A coronary fistula terminates in the right side of the heart far more often than in the left side of the heart. Recent echocardiography-based studies have shown the most common sites of termination are the pulmonary artery (58%–75%) (e-Fig. 77.9), followed by the right ventricle (11%–29%) (Fig. 77.10), the right atrium (6%–12%), left ventricle (6%), and left atrium (2%).[40,41] Coronary artery fistulae usually are isolated without associated cardiac anomalies. However, in pulmonary atresia with intact ventricular septum, coronary fistulae to the right ventricle are an integral part of the disease, with important consequences for treatment options. Coronary fistulae in pulmonary atresia with intact ventricular septum are discussed later in the context of complex congenital heart disease.

The clinical significance of a coronary artery fistula depends on the size of the fistulous communication, as well as its termination site. Most fistulae are small, and recent reports suggest a higher incidence of spontaneous closure than previously reported. Patients with small fistulae usually are asymptomatic and may have a continuous murmur. A large fistula can result in left heart volume overload, with resultant left ventricular dilation, coronary steal, and a risk of endocarditis, aneurysm formation, thrombosis, or rupture. Some studies have also noted significant coronary ectasia proximal to the fistula, with residual dilation and a risk of thrombosis even after closure.

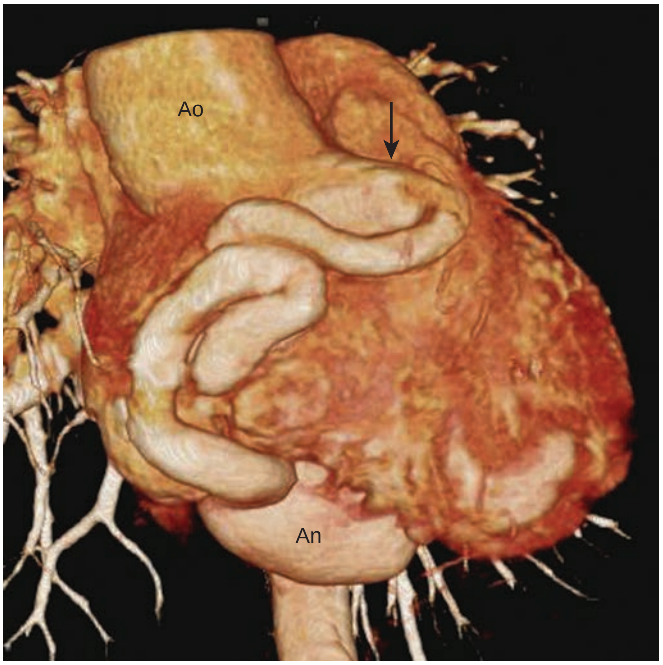

**Figure 77.10. Coronary fistula to the right ventricle.** Volume-rendered image from a CCTA of a 22-year-old woman shows a large and extremely tortuous right coronary artery arising *(arrow)* from the aorta *(Ao)*. At the inferior surface of the heart, this coronary fistula connects to a giant aneurysm *(An)*, which empties into the right ventricle *(not shown)*.

***Imaging.*** A small coronary artery fistula may be detected incidentally when a screening echocardiography is ordered for an unexplained murmur or for unrelated symptoms. If the fistula is large, the course and connections of the fistula, as well as aneurysmal or stenotic segments, should be defined with catheter angiography, CCTA, or CMRA. In addition, MRI can quantify the shunt flow, shunt ratio, and assess myocardial perfusion.

***Management.*** In patients with a small coronary artery fistula without a murmur and no evidence of coronary ectasia, there is no evidence of adverse clinical outcomes in childhood and adolescence. Some groups recommend continued follow up due to the unknown risk of endocarditis, coronary ectasia, aneurysm formation, and rupture. For patients with a small fistula and a murmur or those with a large fistula, closure is typically recommended to prevent myocardial ischemia, endocarditis, and aneurysm formation. Fistulae with favorable connections and shapes can be closed with catheter embolization. Otherwise, they can be closed with surgical ligation.[42,43] Aneurysmal segments should be surgically reduced to prevent rupture. There is some evidence of an increased risk of coronary stenosis and/or thrombosis after transcatheter fistula closure, and close monitoring with anticoagulation may be necessary.[44]

## Anomalous Coronary Artery in Structural Heart Disease

The prevalence of anomalous coronary arteries is much greater in the presence of underlying cardiac malformations, especially conotruncal anomalies, such as truncus arteriosus, transposition of the great arteries (TGA), tetralogy of Fallot (TOF), and pulmonary atresia with intact ventricular septum (PA/IVS). The origins and courses of the anomalous coronary arteries can affect important surgical decisions. The role of the imager is to map out the coronary

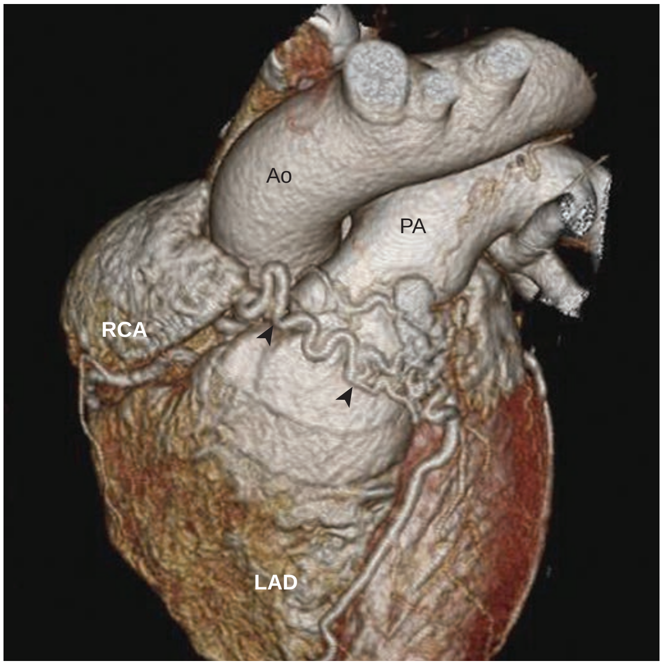

**e-Figure 77.9. Coronary fistulae to the pulmonary artery.** Volume-rendered image from a CCTA of a 30-year-old man shows multiple, small, tortuous coronary fistulae *(arrowheads)* arising from both the right coronary artery *(RCA)* and the left anterior descending *(LAD)* artery, feeding into the pulmonary artery *(PA)*. *Ao,* Aorta.

pattern in relationship to other cardiovascular structures to help a surgeon plan the surgical approach. Instead of describing all the possible coronary variations associated with cardiac malformations, the importance of certain coronary anomalies in the surgical repair of TOF, TGA, and PA/IVS will be explained.

## Tetralogy of Fallot

***Overview.*** TOF is the most common cyanotic congenital heart disease, accounting for up to 10% of all congenital heart defects (see Chapter 75). The majority of centers today perform a complete repair as a neonate for symptomatic patients, and semielectively between 3 and 12 months of age. The surgical repair has two components: a patch closure of the ventricular septal defect (VSD) through which the aorta is overriding, and a transannular patch augmentation of the RVOT and the pulmonary trunk. In 4% of patients with TOF, an anomalous LAD artery arises from the RCA and crosses anterior to the RVOT before entering the anterior interventricular septal groove (Fig. 77.11).[45] This LAD artery lies in the path of the transannular incision and can prevent adequate relief of RVOT obstruction. If it cannot be adequately mobilized, it may necessitate conduit placement.[46]

***Imaging.*** Diagnosis of TOF is made with TTE. Coronary branching pattern can usually be delineated by echocardiography in the neonatal period. In those with poor acoustic windows or inadequate delineation, CCTA or catheter angiography are performed.

## Transposition of the Great Arteries

***Overview.*** TGA accounts for 5% of all congenital heart defects (see Chapter 75). Most patients with TGA have normal ventricular positioning (D-looping), atrioventricular concordance, and ventriculoarterial discordance with the aorta anterior and to the right of the pulmonary trunk.

***Imaging and Treatment.*** The preferred surgical treatment for TGA is the arterial switch, or Jatene operation. This surgery is a definitive operation in which the aorta and the pulmonary trunk are surgically transposed, thereby returning the circulatory anatomy to a "normal" state. In this operation, the coronary arteries also must be reimplanted from the aortic sinuses to the pulmonary sinuses. In normal truncal anatomy, the left and right coronary arteries arise from the facing sinuses. This relationship usually is preserved even when the aorta and the pulmonary trunk are congenitally transposed. The close proximity of the coronary origins from both great arteries makes surgical translocation of the coronary arteries technically uncomplicated. However, frequent variations of coronary origins and course occur that make this operation difficult or even impossible (Fig. 77.12).[47] By mapping out the coronary anatomy, CCTA or CMRA can be very useful for surgical planning.[48]

After the arterial switch operation, the surgically manipulated coronary arteries are at risk for stenosis or even occlusion. In the past, patients who had this operation underwent regular catheter coronary angiography to assess this complication. Today, CCTA and CMRA are useful noninvasive alternatives, and catheter angiography is reserved for patients in whom signs and symptoms of myocardial ischemia develop.

## Pulmonary Atresia With Intact Ventricular Septum

***Overview.*** PA/IVS is believed to be caused by the in-utero obstruction of the pulmonary valve after the formation of the pulmonary infundibulum and the central pulmonary arteries (see Chapter 74). The reduced right ventricular flow prevents the normal growth of the right ventricle and the tricuspid valve, causing hypoplasia of both structures. Without an outlet, the right ventricular systolic pressure can rise above the left ventricular systolic

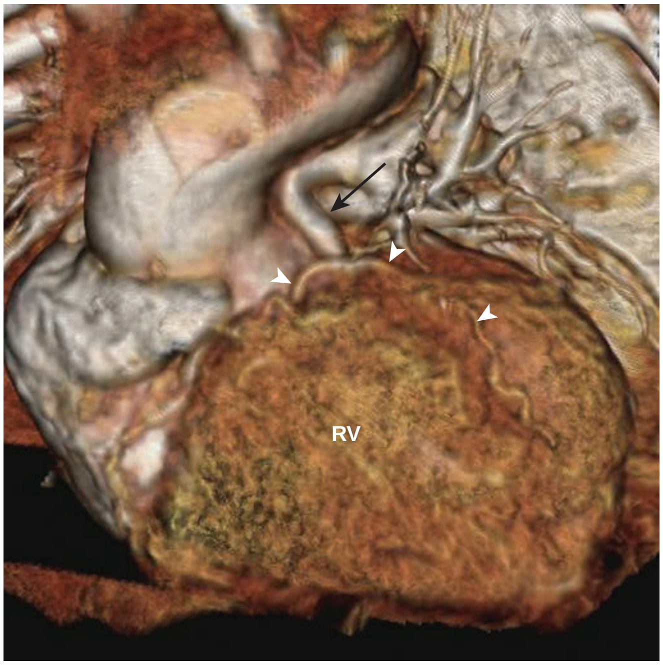

**Figure 77.11. Aberrant left anterior descending (LAD) artery in a child with tetralogy of Fallot.** Volume-rendered CCTA image from a 1-year-old boy viewed from the front shows an LAD artery *(arrowheads)* that travels in front of the stenotic pulmonary trunk *(black arrow)*. The position of this LAD artery may complicate the surgical repair. *RV,* Right ventricle.

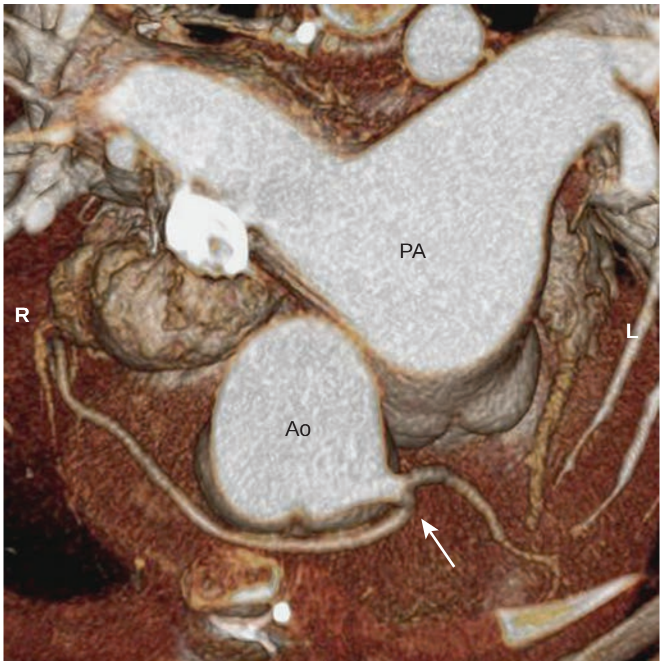

**Figure 77.12. Coronary artery arrangement in d-transposition of the great arteries (d-TGA).** Volume-rendered image from a CCTA of a 12-year-old girl shows an aorta *(Ao)* that is situated in front and to the right of the pulmonary artery *(PA)*, consistent with a d-TGA. A single coronary ostium is present *(arrow)*, and the right coronary artery courses in front of the *Ao.* This coronary pattern is not favorable for the arterial switch operation.

pressure and the coronary arterial pressure. This mechanism, in turn, disrupts the normal regression of embryologic communications between epicardial coronary arteries and the right ventricle, resulting in coronary fistulae between the two in 75% of the patients at birth. This can also result in areas of coronary stenosis and, in some cases, coronary ostial atresia. This is considered a “right ventricular-dependent coronary circulation.”[49]

After birth, the right ventricular pressure remains high and blood flows from the right ventricle into the coronary system. If there is a right ventricular dependent coronary circulation and the right ventricle is decompressed by surgically relieving the pulmonary obstruction, blood flow in the coronary fistulae abruptly reverses, leading to “coronary steal” and myocardial ischemia and infarction. Myocardial perfusion, then, depends on a pressurized right ventricle and precludes a biventricular repair. These patients undergo the staged Fontan palliation. In the absence of a right ventricular dependent coronary circulation, a biventricular repair can be considered.

***Imaging and Management.*** Catheter coronary angiography is the standard imaging study to detect PA/IVS-related coronary fistulae. Classic findings on coronary angiography include systolic retrograde filling of the RCA and the LAD artery during right ventriculography (Fig. 77.13) and end-diastolic filling of the right ventricle during coronary angiography. Due to the need for dynamic imaging, CCTA and CMRA are often not indicated in the initial management.

## Coronary Artery Hypoplasia

***Overview.*** Coronary artery hypoplasia (CAH) is a rare condition characterized by a diffusely narrowed, underdeveloped major coronary segment or branch.[50] The prevalence of CAH is estimated to be 0.03% based on adult coronary angiography, and it represents 6% of all coronary anomalies. Most reported cases involve the left coronary system (Fig. 77.14). The pathogenesis of this lesion is unknown, but an in-utero embolic event affecting a coronary artery may be a cause. The clinical significance of CAH also is unknown. In a few cases, it was related to sudden death, but other persons with this anomaly led normal lives, with the diagnosis being made at autopsy after they died from unrelated causes.

***Imaging and Management.*** CCTA can be used to visualize the threadlike epicardial coronary artery. However, catheter angiography is required to delineate all collateral vessels. The optimal treatment has not been determined, but in patients who have CAH along with documented arrhythmia or syncope, implantation of a defibrillator would be a prudent choice.

# ACQUIRED CORONARY ARTERY DISEASES

## Kawasaki Disease

KD, or mucocutaneous lymph node syndrome, was first described by Tomisaku Kawasaki in 1967. KD is the most common acquired coronary artery disease in children. It is an acute, febrile, multisystem vasculitis of unknown etiology that affects primarily children younger than 5 years of age, with a slight male predominance. Clinical features consist of prolonged high fever, conjunctivitis, red cracked lips, a red oral mucous membrane, a strawberry tongue, a multiform rash, cervical lymphadenopathy, and swollen hands and feet.[51] The clinical findings are self-limiting, but the main concern is the development of coronary aneurysms and thrombosis. Multiple studies have demonstrated the efficacy of treatment during the acute phase in preventing coronary artery abnormalities.

***Imaging.*** The most important complication of KD is the development of coronary artery aneurysms. Coronary artery aneurysms develop in 15% to 30% of patients who do not receive gamma globulin therapy, usually 1 to 4 weeks after disease onset. Thromboembolism of coronary artery aneurysms (Fig. 77.15) and coronary artery stenosis are the causes of myocardial ischemia,

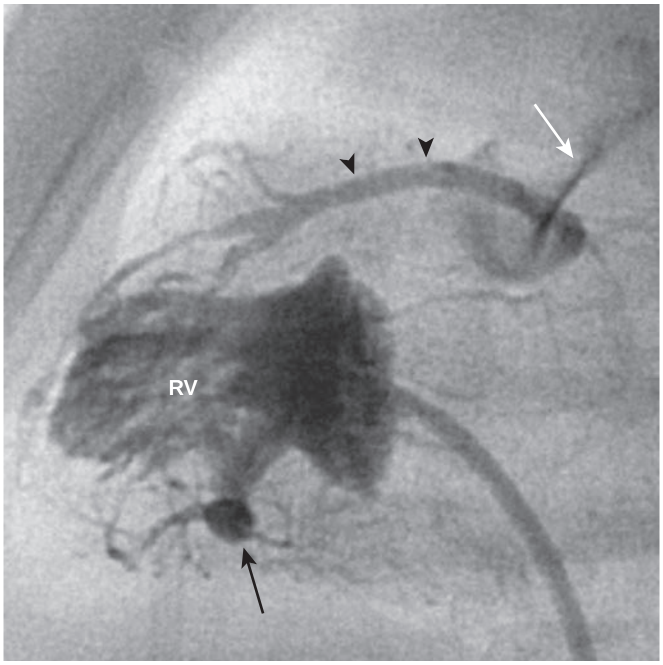

**Figure 77.13. Catheter angiography of the right ventricle of a 1-year-old boy with pulmonary atresia and an intact ventricular septum.** Contrast material injected into the right ventricle *(RV)* flows through the sinusoids *(black arrow)* into the coronary arterial system *(arrowheads)* and then flows retrograde out of the pulmonary artery *(white arrow)*. This coronary circulation is judged right-ventricular dependent.

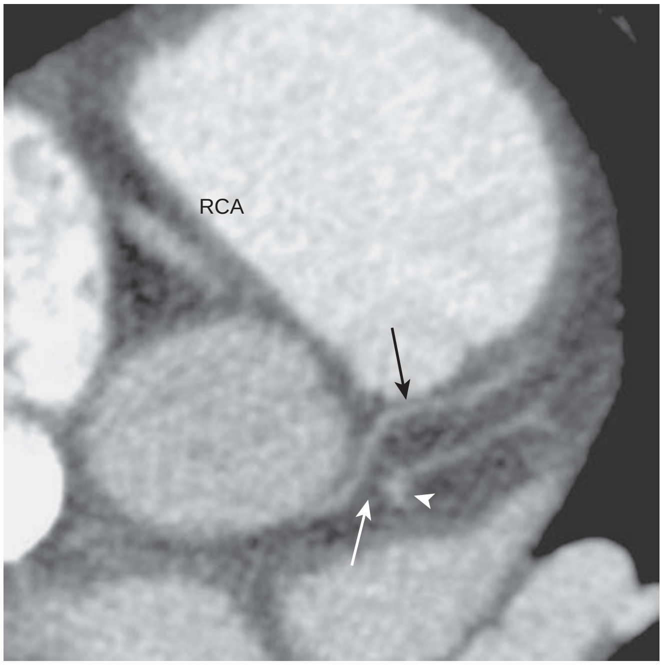

**Figure 77.14. Coronary artery hypoplasia in a 15-year-old girl with exertional angina.** Axial view from a CCTA shows diffusely small left coronary arteries compared with the right coronary artery *(RCA)*. The left circumflex artery *(arrowhead)* is occluded *(white arrow)* from the left main coronary artery *(black arrow)*.

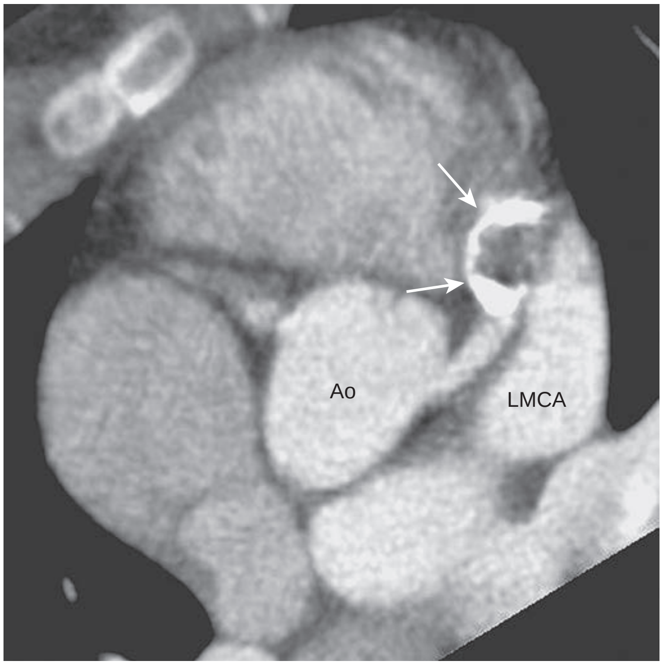

**Figure 77.15. Kawasaki disease.** Axial CCTA image shows chronic changes of Kawasaki disease, which include a calcified, thrombosed aneurysm *(arrows)* involving the left main coronary artery *(LMCA)*. *Ao,* Aorta.

infarction, heart failure, and sudden death in these patients. Expanding aneurysms may rupture. Echocardiography is the primary imaging tool in children with KD. In young children, echocardiography is quite effective in detecting coronary aneurysms. Giant aneurysms (>8 mm in diameter) are associated with increased risk of myocardial infarction and sudden death. However, the sensitivity and specificity of echocardiography for detection of thrombi is unclear. Assessment of thrombus in the infant and young child should be performed with CCTA. Although catheterization angiography can be performed, it has been associated with greater risk of adverse vascular events. Echocardiography is less effective in following older children and young adults with coronary aneurysms, and serial angiography is needed to monitor progression of aneurysms and the development of stenosis. Both CCTA and CMRA are useful noninvasive alternatives for this purpose.[52,53] In addition, CMRA is useful in the assessment of myocardial ischemia, infarction, and ventricular function.

## Trauma

***Overview.*** The most common cause of pediatric trauma is blunt trauma from motor vehicle accidents, although in urban areas, penetrating injuries from assaults and other violence occur not infrequently. Blunt injury to the coronary artery can cause an intimal tear, dissection, and acute thrombosis, leading to myocardial infarction and arrhythmia.[54,55] Both blunt and penetrating injury can cause rupture of the coronary arteries, resulting in hemorrhage, tamponade, and myocardial infarction. The infarcted or contused myocardium can become aneurysmal (e-Fig. 77.16), and if the injury to myocardium is extensive, heart failure can result. Over time, weakened or ruptured coronary vessel walls can form a pseudoaneurysm.

***Imaging and Management.*** The initial management of chest trauma focuses on more common lethal injuries such as airway compromise, pneumothorax, aortic rupture, and tamponade. Conventional non ECG-gated computed tomography angiography is routinely performed to evaluate for these findings. If signs of cardiac injury such as an abnormal ECG, hemodynamic instability, and elevated myocardial enzymes are found, echocardiography can be performed to evaluate ventricular function and pericardial effusion or blood. To assess for acute coronary injury, catheter angiography is the imaging modality of choice. Less acutely, CCTA or MRI can be used to assess structural damages in the heart, such as traumatic VSD and myocardial aneurysm. In addition, MRI is useful for the evaluation of myocardial infarction and ventricular functions.

Management of traumatic coronary artery injuries depends on the type of injury and the degree and extent of myocardial compromise. Imaging should assess for areas of dissection, intimal flap formation, and stenosis of the coronary artery, which can be treated with a stent to maintain coronary patency. Coronary aneurysms, traumatic coronary fistulae, and secondary cardiac abnormalities such as ventricular aneurysm, VSD, and injured valves require surgical repair.

## TREATMENT COMPLICATIONS INVOLVING CORONARY ARTERIES

Surgical manipulation of the coronary arteries always carries the risk of postsurgical stenosis or occlusion of the arteries. Indeed, this risk was a concern during the early surgical experience with the arterial switch operation. Other pediatric cardiac operations that affect the coronary arteries are reimplantation of an anomalous coronary artery, the Takeuchi operation for ALCAPA, surgical augmentation for supravalvular aortic stenosis, the aortic translocation or Nikaidoh procedure for TGA with a ventricular septal defect and severe pulmonary stenosis, composite valve-graft repair (the Bentall procedure) for a Marfan aortic aneurysm, and aortic valve replacement with an autologous pulmonary valve (the Ross procedure). Aneurysms of the coronary ostia after aortic root replacement can be seen in patients with connective tissue diseases, such as Marfan syndrome. Finally, radiation therapy that includes the aortic root in the radiation mantle causes accelerated atherosclerosis and stenoses of the proximal coronary arteries and the coronary ostia. Symptoms typically occur a decade or more after treatment.

## METABOLIC DISEASES AFFECTING THE CORONARY ARTERY

### Familial Hypercholesterolemia

Familial hypercholesterolemia is an autosomal dominant disorder that causes a severe elevation in total cholesterol and low-density lipoprotein (LDL) levels. It is caused by mutations in the LDL receptor gene in chromosome 19. The prevalence of the heterozygous form of familial hypercholesterolemia is 1 in 500 people, and the prevalence of homozygous familial hypercholesterolemia is 1 in 1 million people.[56] Children with the heterozygous form usually are asymptomatic. Children with the rare but clinically much more severe homozygous form present with early atherosclerosis of the coronary arteries, leading to acute myocardial infarction and sudden death at as young as 1 to 2 years of age. These patients also experience peripheral vascular disease, cerebrovascular disease, aortic stenosis, cutaneous xanthomas, corneal arcus, and an LDL level of greater than 600 mg/dL. The role of imaging, except for echocardiography screening for aortic stenosis, has not been defined for this rare disease.

### Coronary Calcinosis

Although coronary calcification is rare in children, it can occur in children with chronic vasculitis, which is seen with KD, radiation, end-stage renal disease, and type I diabetes mellitus. Coronary calcification can be seen as part of idiopathic infantile arterial calcification, a very rare disease characterized by extensive

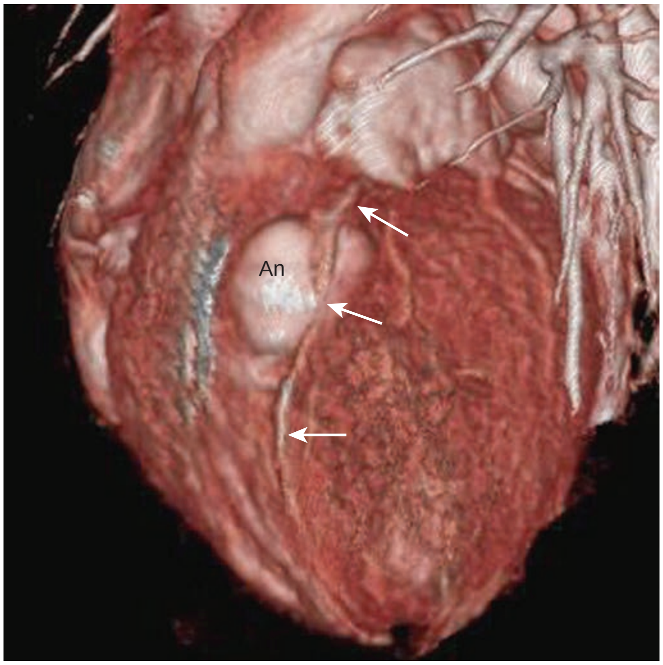

**e-Figure 77.16. Ventricular aneurysm *(An)* after blunt trauma to the chest of a 13-year-old boy after a motor vehicle accident.** An aneurysm developed at the anterior interventricular septum in close proximity to the left anterior descending artery *(arrows)*.

depositions of hydroxyapatite in the elastic layer of the large- and medium-sized muscular arteries, including the coronary arteries.[57] Coronary stenosis is caused by intimal proliferation, and patients with idiopathic infantile arterial calcification experience myocardial infarction in infancy. Similarly, renal artery stenosis causes hypertension, and carotid stenosis causes cerebral infarction. Patients rarely survive beyond infancy, and many die prenatally. Diagnosis is made by radiologic demonstration of diffuse arterial calcification, arterial biopsy, or prenatal ultrasound demonstrating dilated cardiac ventricles, hydrops fetalis, and hyperechogenic large vessels.

## KEY POINTS

- Patients usually are referred for coronary imaging with CT or MR for diagnosis of a coronary anomaly, confirmation and clarification of echocardiographic findings of coronary anomalies, mapping out the coronary arteries for surgical planning, and evaluation for a coronary aneurysm or stenosis.
- Evaluation of the following congenital heart diseases should include the coronary arteries: tetralogy of Fallot, preoperative; transposition of the great arteries; arterial switch procedure, postoperative; pulmonary atresia with intact ventricular septum; and Williams syndrome.

## SUGGESTED READINGS

Basso C, Maron BJ, Corrado D, et al. Clinical profile of congenital coronary artery anomalies with origin from the wrong aortic sinus leading to sudden death in young competitive athletes. *J Am Coll Cardiol*. 2000;35:1493–1501.

Frommelt PC, Frommelt MA. Congenital coronary artery anomalies. *Pediatr Clin North Am*. 2004;51:1273–1288.

Hill KD, Frush DP, Han BK, et al. Radiation safety in children with congenital and acquired heart disease: a scientific position statement on multimodality dose optimization from the image gently alliance. *JACC Cardiovasc Imaging*. 2017;10(7):797–818.

Stuber M, Weiss RG. Coronary magnetic resonance angiography. *J Magn Reson Imaging*. 2007;26:219–234.

Tacke CE, Kuipers IM, Groenink M, et al. Cardiac magnetic resonance imaging for noninvasive assessment of cardiovascular disease during the follow-up of patients with Kawasaki disease. *Circ Cardiovasc Imaging*. 2011;4:712–720.

## REFERENCES

Full references for this chapter can be found on www.expertconsult.com.

## REFERENCES

1. De WD, Vercruysse T, Suys B, et al. Major coronary anomalies in childhood. *Eur J Pediatr*. 2002;161:637–642.
2. Frommelt PC, Frommelt MA. Congenital coronary artery anomalies. *Pediatr Clin North Am*. 2004;51:1273–1288.
3. Levin DC, Fellows KE, Abrams HL. Hemodynamically significant primary anomalies of the coronary arteries: angiographic aspects. *Circulation*. 1978;58:25–34.
4. Sugimura T, Kato H, Inoue O, et al. Intravascular ultrasound of coronary arteries in children. Assessment of the wall morphology and the lumen after Kawasaki disease. *Circulation*. 1994;89:258–265.
5. De Bruyne B, Sarma J. Fractional flow reserve: a review. *Heart*. 2008;94:949–959.
6. Chan FP. MR and CT imaging of the pediatric patient with structural heart disease. *Semin Thorac Cardiovasc Surg*. 2008;20:393–399.
7. Dweck MR, Williams MC, Moss AJ, et al. Computed tomography and cardiac magnetic resonance in ischemic heart disease. *J Am Coll Cardiol*. 2016;68(20):2201–2216.
8. Budoff MJ, Dowe D, Jollis JG, et al. Diagnostic performance of 64-multidetector row coronary computed tomographic angiography for evaluation of coronary artery stenosis in individuals without known coronary artery disease: results from the prospective multicenter ACCURACY (Assessment by Coronary Computed Tomographic Angiography of Individuals Undergoing Invasive Coronary Angiography) trial. *J Am Coll Cardiol*. 2008;52(21):1724–1732.
9. Stehli J, Fuchs TA, Bull S, et al. Accuracy of coronary CT angiography using a submillisievert fraction of radiation exposure: comparison with invasive coronary angiography. *J Am Coll Cardiol*. 2014;64(8):772–780.
10. Hill KD, Frush DP, Han BK, et al. Radiation safety in children with congenital and acquired heart disease: a scientific position statement on multimodality dose optimization from the image gently alliance. *JACC Cardiovasc Imaging*. 2017;10(7):797–818.
11. Hellinger JC, Pena A, Poon M, et al. Pediatric computed tomographic angiography: imaging the cardiovascular system gently. *Radiol Clin North Am*. 2010;48(2):439–467.
12. Moscariello A, Takx RA, Schoepf UJ, et al. Coronary CT angiography: image quality, diagnostic accuracy, and potential for radiation dose reduction using a novel iterative image reconstruction technique-comparison with traditional filtered back projection. *Eur Radiol*. 2011;21(10):2130–2138.
13. Stuber M, Weiss RG. Coronary magnetic resonance angiography. *J Magn Reson Imaging*. 2007;26(2):219–234.
14. Hellman RN. Gadolinium-induced nephrogenic systemic fibrosis. *Semin Nephrol*. 2011;31:310–316.

14a. https://www.fda.gov/Drugs/ DrugSafety/ucm532356.htm.

15. Rigatelli G, Docali G, Rossi P, et al. Congenital coronary artery anomalies: angiographic classification revisited. *Int J Cardiovasc Imaging*. 2003;19:361–366.
16. Engel HJ, Torres C, Page HL. Major variations in anatomical origin of the coronary arteries: angiographic observations in 4,250 patients without associated congenital heart disease. *Cathet Cardiovasc Diagn*. 1975;1:157.
17. Roberts WC, Shirani J. The four subtypes of anomalous origin of the left main coronary artery from the right aortic sinus (or from the right coronary artery). *Am J Cardiol*. 1992;70(1):119–121.
18. Cheezum MK, Ghoshhajra B, Bittencourt MS, et al. Anomalous origin of the coronary artery arising from the opposite sinus: prevalence and outcomes in patients undergoing coronary CTA. *Eur Heart J Cardiovasc Imaging*. 2017;18(2):224–235.
19. Frommelt PC, Frommelt MA, Tweddell JS, et al. Prospective echocardiographic diagnosis and surgical repair of anomalous origin of a coronary artery from the opposite sinus with an interarterial course. *J Am Coll Cardiol*. 2003;42:148–154.
20. Kragel AH, Roberts WC. Anomalous origin of either the right or left main coronary artery from the aorta with subsequent coursing between aorta and pulmonary trunk: analysis of 32 necropsy cases. *Am J Cardiol*. 1988;62:771–777.
21. Frescura C, Basso C, Thiene G, et al. Anomalous origin of coronary arteries and risk of sudden death: a study based on an autopsy population of congenital heart disease. *Hum Pathol*. 1998;29:689–695.
22. Roberts WC, Siegel RJ, Zipes DP. Origin of the right coronary artery from the left sinus of Valsalva and its functional consequences: analysis of 10 necropsy patients. *Am J Cardiol*. 1982;49:863–868.
23. Maron BJ, Haas TS, Ahluwalia A, et al. Demographics and epidemiology of sudden deaths in young competitive athletes: from the United States national registry. *Am J Med*. 2016;129(11):1170–1177.
24. Yamanaka O, Hobbs RE. Coronary artery anomalies in 126,595 patients undergoing coronary arteriography. *Cathet Cardiovasc Diagn*. 1990;21(1):28–40.
25. Liberthson RR. Sudden death from cardiac causes in children and young adults. *N Engl J Med*. 1996;334:1039–1044.
26. Angelini P. Coronary artery anomalies: an entity in search of an identity. *Circulation*. 2007;115(10):1296–1305.
27. Hamamichi Y, Okada E, Ichida F. Anomalous origin of the main stem of the left coronary artery from the non-facing sinus of Valsalva associated with sudden death in a young athlete. *Cardiol Young*. 2000;10:147–149.
28. Lee S, Uppu SC, Lytrivi ID, et al. Utility of multimodality imaging in the morphologic characterization of anomalous aortic origin of a coronary artery. *World J Pediatr Congenit Heart Surg*. 2016;7(3):308–317.
29. Lorber R, Srivastava S, Wilder TJ, et al. Anomalous aortic origin of coronary arteries in the young: echocardiographic evaluation with surgical correlation. *JACC Cardiovasc Imaging*. 2015;8(11):1239–1249.
30. Brothers JA, Frommelt MA, Jaquiss RDB, et al. Expert consensus guidelines: anomalous aortic origin of a coronary artery. *J Thorac Cardiovasc Surg*. 2017;153(6):1440–1457.
31. Miller JA, Anavekar NS, El Yaman MM, et al. Computed tomographic angiography identification of intramural segments in anomalous coronary arteries with interarterial course [published online ahead of print September 3, 2011]. *Int J Cardiovasc Imaging*. 2013;30(2):225–233.
32. Jacobs ML. Anomalous aortic origin of a coronary artery: the gaps and the guidelines. *J Thorac Cardiovasc Surg*. 2017;153(6):1462–1465.
33. Poynter JA, Williams WG, McIntyre S, et al. Anomalous aortic origin of a coronary artery. *World J Pediatr Congenit Heart Surg*. 2014;5(1):22–30.
34. Lee AC, Foster E, Yeghiazarians Y. Anomalous origin of the left coronary artery from the pulmonary artery: a case series and brief review. *Congenit Heart Dis*. 2006;1:111–115.
35. William IA, Gersony WM, Hellenbrand WE. Anomalous right coronary artery arising from the pulmonary artery: a report of 7 cases and a review of the literature. *Am Heart J*. 2006;152:1004.e9–1004.e17.
36. Ten. Kate GJ, Weustink AC, de Feyter PJ. Coronary artery anomalies detected by MSCT-coronary angiography in the adult. *Neth Heart J*. 2008;16:369–375.
37. Alexi-Meskishvili V, Nasseri BA, Nordmeyer S, et al. Repair of anomalous origin of the left coronary artery from the pulmonary artery in infants and children. *J Thorac Cardiovasc Surg*. 2011;142:868–874.
38. Ginde S, Earing MG, Bartz PJ, et al. Late complications after Takeuchi repair of anomalous left coronary artery from the pulmonary artery: case series and review of literature. *Pediatr Cardiol*. 2012;33(7):1115–1123.
39. Vavuranakis M, Bush CA, Boudoulas H. Coronary artery fistulas in adults: incidence, angiographic characteristics, natural history. *Cathet Cardiovasc Diagn*. 1995;35:116–120.
40. Vinograd CA, Ostermayer S, Lytrivi ID, et al. Prevalence and outcomes of coronary artery ectasia associated with isolated congenital coronary artery fistula. *Am J Cardiol*. 2014;114(1):111–116.
41. Sherwood MC, Rockenmacher S, Colan SD, et al. Prognostic significance of clinically silent coronary artery fistulas. *Am J Cardiol*. 1999;83(3):407–411.
42. Carrel T, Tkebuchava T, Jenni R, et al. Congenital coronary fistulas in children and adults: diagnosis, surgical technique and results. *Cardiology*. 1996;87:325–330.
43. Said SA, Landman GH. Coronary-pulmonary fistula: long-term follow-up in operated and non-operated patients. *Int J Cardiol*. 1990;27:203–210.
44. Gowda ST, Forbes TJ, Singh H, et al. Remodeling and thrombosis following closure of coronary artery fistula with review of management: large distal coronary artery fistula–to close or not to close? *Catheter Cardiovasc Interv*. 2013;82(1):132–142.
45. Dabizzi RP, Caprioli G, Aiazzi L, et al. Distribution and anomalies of coronary arteries in tetralogy of Fallot. *Circulation*. 1980;61:95–102.
46. Ruzmetov M, Jimenez MA, Pruitt A, et al. Repair of tetralogy of Fallot with anomalous coronary arteries coursing across the obstructed right ventricular outflow tract. *Pediatr Cardiol*. 2005;26:537–542.
47. Sim EK, van Son JA, Edwards WD, et al. Coronary artery anatomy in complete transposition of the great arteries. *Ann Thorac Surg*. 1994;57:890–894.
48. McMahon CJ, el Said HG, Feltes TF, et al. Preoperative identification of coronary arterial anatomy in complete transposition, and outcome after the arterial switch operation. *Cardiol Young*. 2002;12:240–247.

49. Giglia TM, Mandell VS, Connor AR, et al. Diagnosis and management of right ventricle-dependent coronary circulation in pulmonary atresia with intact ventricular septum. *Circulation*. 1992;86:1516–1528.
50. Amabile N, Fraisse A, Quilici J. Hypoplastic coronary artery disease: report of one case. *Heart*. 2005;91:e12.
51. Freeman AF, Shulman ST. Kawasaki disease: summary of the American Heart Association guidelines. *Am Fam Physician*. 2006;74:1141–1148.
52. Peng Y, Zeng J, Du Z, et al. Usefulness of 64-slice MDCT for follow-up of young children with coronary artery aneurysm due to Kawasaki disease: initial experience. *Eur J Radiol*. 2009;69:500–509.
53. Tacke CE, Kuipers IM, Groenink M, et al. Cardiac magnetic resonance imaging for noninvasive assessment of cardiovascular disease during the follow-up of patients with Kawasaki disease. *Circ Cardiovasc Imaging*. 2011;4:712–720.
54. Cizmarova E, Simkovic I, Zelenay J, et al. Post-traumatic coronary occlusion and its consequences in a young child. *Pediatr Cardiol*. 1988;9:117–120.
55. Harada H, Honma Y, Hachiro Y, et al. Traumatic coronary artery dissection. *Ann Thorac Surg*. 2002;74:236–237.
56. Marais AD, Firth JC, Blom DJ. Homozygous familial hypercholesterolemia and its management. *Semin Vasc Med*. 2004;4:43–50.
57. van de Sluis I, Boot AM, Vernooij M, et al. Idiopathic infantile arterial calcification: clinical presentation, therapy and long-term follow-up. *Eur J Pediatr*. 2006;165:590–593.

# 78

# Syndromes and Chromosomal Anomalies

*Beverley Newman, Alexander J. Towbin, and Frandics P. Chan*

A large number of syndromes, dysplasias, and chromosomal anomalies are associated with congenital or acquired cardiac and vascular disease. This chapter discusses the cardiovascular features of some of the more commonly encountered lesions. A more extensive list is provided in Tables 78.1 to 78.3 later in this chapter.

## SYNDROMES

### Situs and Cardiosplenic (Heterotaxy) Syndromes

***Overview.*** The heterotaxy syndromes, comprising right and left isomerism, feature abnormalities of visceral/atrial laterality. These syndromes have an estimated incidence of 1 in 6,000 to 1 in 20,000 live births and account for 1% to 3% of all congenital heart defects. Although heterotaxy usually occurs sporadically, familial cases have been described, particularly an X-linked form.[1] There is also an association between heterotaxy and gestational diabetes.

Body situs generally is divided into three types: solitus, inversus, and ambiguus. Situs solitus is the normal arrangement of the atria and viscera in the body (see Chapter 63). Situs inversus is the mirror image of normal; it is seen in 0.01% of the population and is associated with a slightly higher incidence of congenital heart disease (3%–5%) compared with the solitus population (0.6%–0.8%). Situs ambiguus, or heterotaxy, encompasses all other visceroatrial arrangements. By definition, in situs ambiguus, visceral malposition and dysmorphism associated with an indeterminate atrial arrangement is present.[2] Abnormal body situs occurs frequently in association with ciliary dyskinesia, as these entities are thought to be linked by underlying fetal cilial dysfunction.[3,4]

Heterotaxy syndrome with right isomerism or bilateral right-sidedness is usually, but not invariably, accompanied by asplenia.[5] The condition is more common in males and is characterized by bilateral systemic atria with broad trabeculated appendages (Fig. 78.1), bilateral trilobed lungs with bilateral minor fissures and short eparterial bronchi, a central horizontal liver, abnormal bowel rotation, and the stomach in an indeterminate position (see Fig. 78.1).[1,3,6] The abdominal aorta and inferior vena cava often are located on the same side of the spine, frequently in a posterior-anterior orientation. Other occasional anomalies include tracheoesophageal fistula, imperforate anus, absent gallbladder, pancreatic anomalies, fused adrenal glands, and genitourinary abnormalities.[3,4] The prognosis for right isomerism is often poor because of an abnormal immune status (asplenia) and the typically complex cardiac anomalies.

Cardiac anomalies are almost invariable and present with cyanosis and severe respiratory distress. The “right isomerism heart” often consists of a common atrioventricular canal, a single ventricle, a large ventricular septal defect (VSD), and a double-outlet right ventricle and/or transposition of the great vessels, along with pulmonary outflow obstruction or atresia and total anomalous pulmonary venous drainage (frequently obstructed) (see Fig. 78.1). The spectrum of cardiovascular anomalies also can include cardiac malposition (dextrocardia or mesocardia), tricuspid atresia, truncus arteriosus, right aortic arch, anomalous systemic venous return, and bilateral superior vena cavae.[5,6]

Heterotaxy syndrome with left isomerism or bilateral left-sidedness most often accompanies polysplenia. It is characterized by bilateral pulmonary atria with narrow finger-like appendages, bilateral bilobed lungs, bilateral long hyparterial bronchi, a centrally located liver, the stomach in an indeterminate position, abnormal bowel rotation, and multiclefted or multiple spleens (either right sided or left sided) (Fig. 78.2).[2,6] An interrupted inferior vena cava with azygos continuation is the most consistent abdominal finding in left isomerism (see Fig. 78.2). Left isomerism is slightly more common in females and generally has a better prognosis than right isomerism with less complex cardiovascular disease. Other associated anomalies include ciliary dyskinesia, biliary atresia, pancreatic and other gastrointestinal abnormalities, and congenital portosystemic shunts (see Fig. 78.2).[1,4,5,7]

Cardiac anomalies are seen in more than 50% of patients who have heterotaxy syndrome with left isomerism. The common cardiovascular anomalies include abnormalities of the inferior and superior vena cavae, cardiac malposition, atrial septal defect (ASD), VSD, common atrioventricular canal, double-outlet right ventricle, and anomalous pulmonary venous return (usually partial).[3,4]

***Imaging.*** Eight major structures are appraised to evaluate situs in heterotaxy syndromes[2]:

- Atrial morphology
- Cardiac apex
- Aortic position
- Stomach and bowel position
- Liver and gallbladder position
- Spleen location and morphology
- Abdominal venous drainage
- Bronchial and pulmonary anatomy

Decreased pulmonary vascularity related to pulmonary outflow obstruction or pulmonary edema as a result of pulmonary venous obstruction is the most typical pattern seen on chest radiographs in persons with right isomerism. Cardiomegaly and increased vascularity on chest radiographs as a result of left-to-right shunting is the most common appearance in persons with left isomerism (see Fig. 78.2). Other chest radiographic features of the heterotaxy syndromes are related to duplicated structures, such as fissures and bronchi, as well as abnormal cardiac and visceral situs.

Echocardiography is the main imaging modality used to evaluate disordered intracardiac anatomy associated with heterotaxy. Both magnetic resonance imaging (MRI) and computed tomography (CT) have a role in fully defining this often complex anatomy. MRI, magnetic resonance angiography (MRA), and functional MRI assessment have partially replaced catheter-based angiography in evaluating these anomalies, especially the extracardiac vascular, airway, and visceral abnormalities (see Figs. 78.1 and 78.2).[2]

Ultrasound is often the first step in evaluating the abdominal anatomy. An upper gastrointestinal study should be performed to evaluate for malrotation. A small bowel follow-through in conjunction with the upper gastrointestinal study may be helpful to determine the relative locations of the small and large bowel and to separate nonrotation from malrotation.[3]

Ultrasound, CT, MRI, or liver-spleen scans using technetium-99m sulfur colloid or p-isopropylacetanilidoimidodiacetic acid are used to evaluate the presence and location of splenic tissue, to assess other organs/anomalies, and to help diagnose biliary atresia (associated with polysplenia). Multimodality imaging may be needed to elucidate other less common anomalies associated with heterotaxy such as a congenital portosystemic shunt and a hypoplastic or

## Abstract:

This chapter highlights the cardiovascular lesions and complications associated with a broad spectrum of syndromes and chromosomal anomalies. More common or important entities are described in the text with a more comprehensive list in tabular form. Imaging features are emphasized and illustrated. Lesions covered include: heterotaxy syndromes, inherited connective tissue disorders, neurocutaneous syndromes and chromosome anomalies.

## Keywords:

cardiac
vasculopathy
syndrome
chromosome anomaly

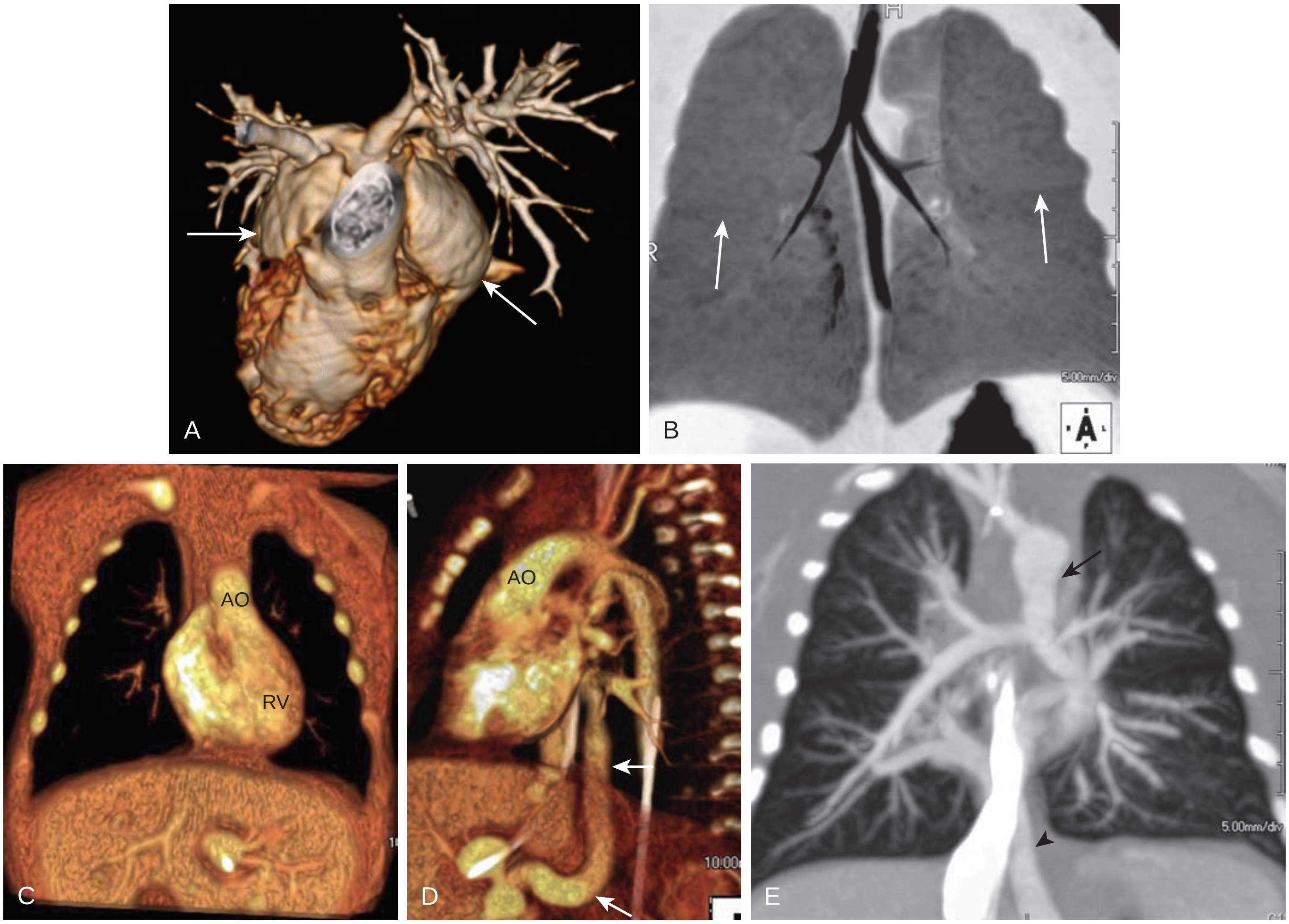

**Figure 78.1. Heterotaxy and right isomerism.** (A) Volumetric left anterior oblique, 3D CTA in a 3-year-old girl demonstrates bilateral symmetric broad atrial appendages *(arrows)* consistent with right atrial morphology. Note also the anteriorly transposed ascending aorta. (B–E) A newborn infant with complex congenital heart disease and heterotaxy with right isomerism. (B) Coronal CT minimum intensity projection reconstruction demonstrates symmetric short main-stem bronchi consistent with bilateral right-sided bronchial branching. Bilateral minor fissures also are visible *(arrows).* (C) Coronal volumetric reconstruction demonstrates a horizontal liver with no spleen. The patient has complex congenital heart disease consisting of an atrioventricular septal defect (not shown), L-transposition and pulmonary atresia, and total anomalous pulmonary venous return. On this image the left-sided ascending aorta *(AO)* is seen arising from the left-sided morphologic right ventricle *(RV).* (D) Sagittal volumetric reconstruction demonstrates the anteriorly positioned transposed ascending aorta *(AO),* absent pulmonary artery, and an anomalously draining confluence of pulmonary veins *(arrows)* extending below the diaphragm to the portal vein. (E) Coronal maximum intensity projection demonstrates a large patent ductus arteriosus *(arrow)* as the sole source of flow to the branch pulmonary arteries (the main pulmonary artery is absent). The anomalous inferiorly draining pulmonary veins *(arrowhead)* also are seen, partially obscured by dense contrast in the inferior vena cava.

absent portal vein (Abernethy malformation) with consequent hyperammonemic encephalopathy or hepatopulmonary syndrome (associated with left isomerism; see Fig. 78.2).[4,7]

## Inherited Connective Tissue Disorders

### Ehlers–Danlos Syndrome

***Overview.*** Ehlers–Danlos syndrome (EDS) is an inherited group of connective tissue disorders affecting the skin, ligaments, joints, vasculature, and visceral organs. It is characterized by joint and skin hyperextensibility, excessive bruisability, blood vessel fragility, and poor wound healing.[8] It occurs in as many as 1 in 5,000 individuals. Although EDS is incompletely understood, multiple distinct varieties of EDS have been recognized based on genetics, biochemical structure, and clinical presentation.[8,9] The vascular or arterial ecchymotic type of EDS is the most clinically severe form. Mitral valve prolapse (MVP) is the most common cardiovascular anomaly; others include a dilated aortic root, aneurysm, and aortic dissection or rupture (Fig. 78.3). Papillary muscle dysfunction or rupture and left ventricular rupture also can occur.[8]

EDS is an autosomal dominant disorder caused by heterozygous mutations in the *COL3A1* gene encoding type III collagen. More than 250 *COL3A1* mutations have been identified.[8] Patients are subject to spontaneous rupture of the bowel and other viscera. Vascular complications can occur either spontaneously or after minor trauma and include arteriovenous fistulas and aneurysms of the aorta and medium-sized arteries, with degeneration and subsequent rupture or dissection (see Fig. 78.3). The thoracic and abdominal arteries are involved in half of the cases, with extremity and head and neck vessels each contributing 25%. Neurovascular complications include carotid-cavernous fistula formation, carotid dissection, aneurysm formation, and rupture.[8-10]

***Imaging, Treatment, and Follow-up.*** Echocardiography is the mainstay for evaluation of the heart and valvular function. Ultrasound, CT, and MRI are geared toward defining areas of aneurysm, dissection, and rupture. The size and the rate of growth of each aneurysm should be quantified. Because the neurovascular system may be involved, imaging of the cerebral circulation and the carotid arteries may be necessary.

The pattern of aneurysm distribution in persons with EDS differs from that in persons with Marfan syndrome. Whereas Marfan syndrome typically results in dilation of the aortic root and the sinuses of Valsalva, EDS produces discrete, fusiform aneurysms at different locations of the aorta, the iliac arteries, the cervical arteries, and their branches. Dissection in persons with EDS often has a complex morphology (see Fig. 78.3). The abnormal vessels usually are well characterized by noninvasive computed

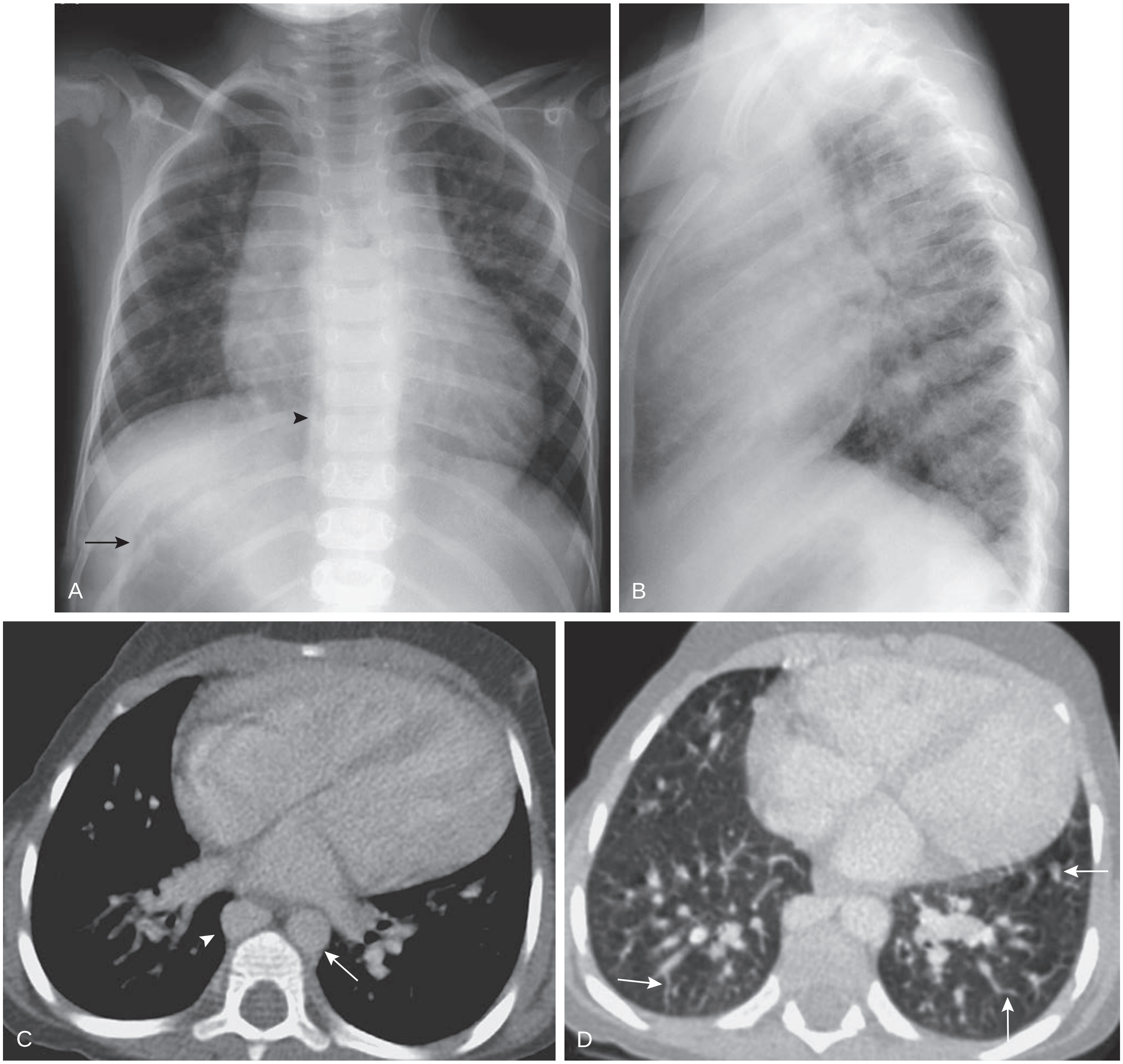

**Figure 78.2. Heterotaxy and left isomerism.** This 3-year-old girl, infant of a diabetic mother, has polysplenia and Abernethy malformation with hepatopulmonary syndrome. (A) Posteroanterior radiograph of the chest shows heterotaxy with a left-sided cardiac apex, right-sided stomach *(arrow),* and left-sided liver. Cardiomegaly and increased pulmonary vascularity (a small atrial septal defect and pulmonary arteriovenous shunting) are present. It is difficult to see the bilateral left-sided bronchi. A prominent right paraspinal line is present as a result of an enlarged azygos vein *(arrowhead).* (B) Lateral view of the chest is notable for the absence of the inferior vena cava shadow. (C) Contrast-enhanced CT of the chest shows cardiomegaly, a left-sided aorta *(arrow),* prominent pulmonary veins, and an enlarged azygos vein *(arrowhead).* (D) A contrast-enhanced CT scan of the chest displayed in the lung window shows the presence of multiple dilated peripheral pulmonary vessels *(arrows).*

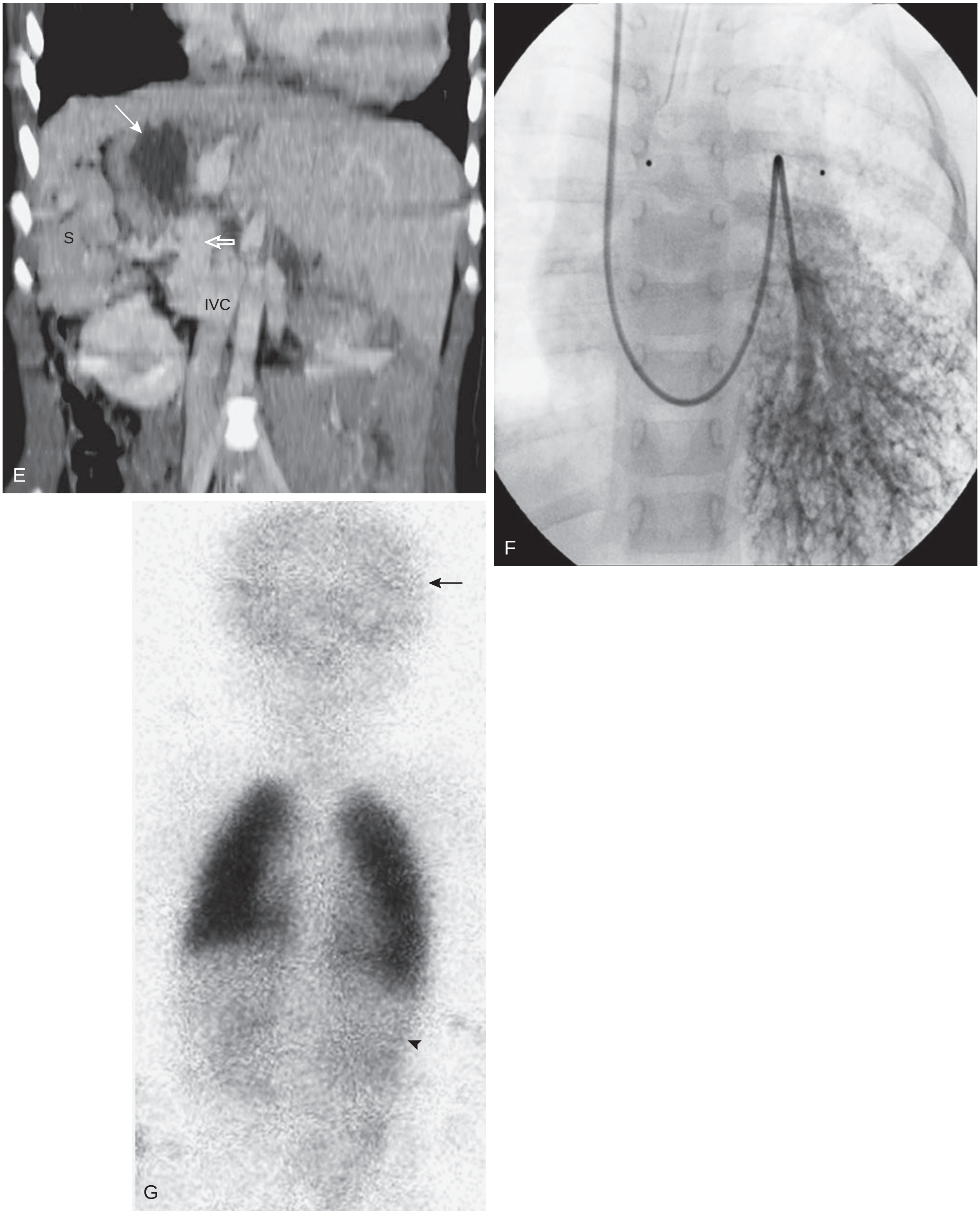

**Figure 78.2, cont'd** (E) Coronal reconstruction from a contrast-enhanced CT scan of the upper abdomen shows right-sided polysplenia *(S),* a right-sided stomach *(white arrow),* and a left-sided liver. A large right-sided portosystemic shunt (splenic vein to renal vein) is present *(open arrow).* Superiorly, there is interruption of the inferior vena cava *(IVC)* with azygos continuation (not shown). (F) Left pulmonary artery angiogram from a right jugular approach shows dilated peripheral pulmonary arteries and microarteriovenous connections, consistent with hepatopulmonary syndrome as a result of the congenital portosystemic shunt. This child does not have liver disease, and the intrahepatic portal veins are present but small (Abernethy malformation type II). (G) Perfusion portion of a ventilation-perfusion scan using technetium-99m macroaggregated albumin performed after closure of the patient's atrial septal defect shows normal perfusion of the lungs. There is abnormal radiotracer uptake within the brain *(arrow)* and kidneys *(arrowhead).* The percentage of systemic tracer uptake was calculated at 44.7%. These findings are typical of a right-to-left arteriovenous shunt and confirm the presence of hepatopulmonary syndrome.

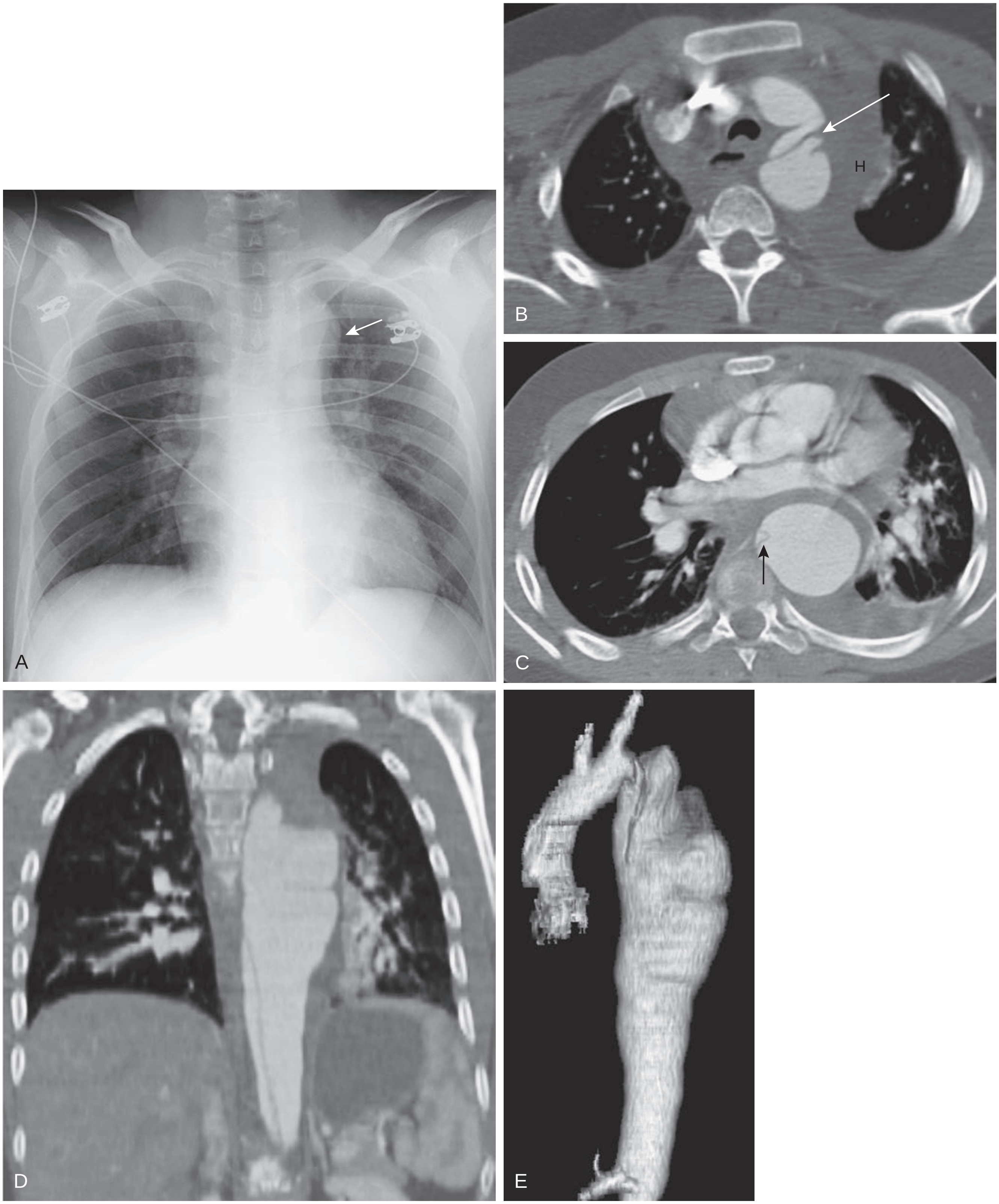

**Figure 78.3. Ehlers–Danlos syndrome.** This 14-year-old boy presented to the emergency department with chest pain and a family history of dissecting aortic aneurysm. (A) Posteroanterior radiograph of the chest shows a widened mediastinum and prominent aortic knob *(arrow).* (B) CTA of the upper chest shows an intimal flap within the aortic arch *(arrow),* representing a dissection. Other findings include a mediastinal hematoma *(H)* and a left-sided pleural effusion. (C) CTA of the chest at the level of the descending aorta shows a dilated descending aorta with a small intimal flap *(arrow),* a moderate amount of periaortic hematoma, and a small left pleural effusion. Coronal reconstruction (D) and three-dimensional reconstruction from the CTA (E) show a dissecting aortic aneurysm and an irregular severely dilated aorta.

tomography angiography (CTA) and MRA.[9,10] Catheter-based angiography carries significant hazards in these patients, with a reported complication rate of 67%.[10] Because of the fragility of the vascular wall, elective surgery is generally discouraged with conservative management favored.[8,10] Treatment with the beta-blocker celiprolol has been shown to reduce the risk of vascular events in patients with EDS.[8]

### Marfan Syndrome

***Overview.*** Marfan syndrome is an autosomal dominant disorder of connective tissue caused by mutations in the *FBN1* gene that codes for the extracellular matrix protein fibrillin-1.[11,12] Marfan syndrome is present in 1 in 3,000 to 1 in 5,000 persons and is associated with skeletal, ocular, and cardiovascular manifestations.[12] The diagnosis of Marfan syndrome is based on clinical criteria—the 2011 revised Ghent nosology.[13]

Common cardiovascular features of Marfan syndrome include mitral valve prolapse (MVP), mitral regurgitation, aortic regurgitation, aortic root dilation, and ascending aortic aneurysm (Fig. 78.4). Aortic dissection and aortic rupture are life-threatening complications.

MVP affects 35% to 100% of patients with Marfan syndrome and is more common in women and children.[14] More than 80% of children with Marfan syndrome have aortic root dilation, MVP, or both before age 18 years; aneurysms can be present even in young children.[14] Symptoms of heart failure, usually related to valvular insufficiency, can develop in childhood or young adulthood.

***Imaging.*** On chest radiographs, a pectus deformity, kyphoscoliosis, and occasionally cystic lung disease may be present in addition to cardiomegaly and a dilated ascending aorta (see Fig. 78.4). Both MRI and transthoracic echocardiography are used for initial evaluation of the heart and aorta. Both have the advantage of being relatively noninvasive without exposing the patient to ionizing radiation. In Marfan syndrome, the dilated aorta/aneurysm typically is pear shaped because the most marked area of dilation is at the level of the sinuses of Valsalva (see Fig. 78.4).

Long-term surveillance of the aortic root is performed via MRA or CTA, which have the advantage of providing a global view of the entire aorta. Reformatted and three-dimensional techniques provide excellent visualization of the anatomy and accurate long-term measurements (see Fig. 78.4).[15]

***Treatment and Follow-up.*** Measurement of the aortic root and assessment of aortic regurgitation are diagnostic criteria for Marfan syndrome. Affected individuals require long-term follow-up to identify progressive aortic root dilation and the appropriate timing for surgical intervention. In older children and adolescents, the incidence of complications such as dissection or rupture increases once the aortic root is larger than 5 cm in diameter.[14,15] Cystic medial necrosis is the underlying pathologic abnormality of the aortic wall. A composite aortic valve graft replacement or aortic graft with a surgically resuspended native aortic valve are the most common surgical procedures. The latter has the advantage of avoiding the need for anticoagulation.

It is now recognized that fibrillin-1 is involved in regulating transforming growth factor–β (TGF-β), a cytokine pathway that affects cell performance; its increased activity is thought to cause many of the manifestations of Marfan syndrome. Several other TGF-β signalopathy vascular syndromes have been identified, including Loeys–Dietz syndrome and related disorders and autosomal recessive cutis laxa.[16] Therapy using TGF-β antagonists (angiotensin receptor blockers) appears to offer promise.[11,15-17]

### Loeys–Dietz Syndrome

***Overview.*** Loeys–Dietz syndrome (LDS) is a rare connective tissue disorder associated with the dysregulation of TGF-β caused by mutations in the TGF-β receptor gene.[18] Recently, mutations in the genes coding for the ligand TGFB2 and the first downstream effector SMAD3 were also associated with an LDS-like presentation.[17] LDS is divided into two types. Type 1 patients have both craniofacial anomalies (e.g., bifid uvula, cleft palate, hypertelorism, craniosynostosis, and cervical spine instability) and widespread vascular anomalies. Type 2 patients generally have less severe manifestations; they may have a bifid uvula but usually do not have other craniofacial anomalies.[18,19]

Vascular manifestations of LDS include elongated and tortuous large arteries, aneurysm formation, and stenoses (Fig. 78.5 and Videos 78.1 and 78.2).[20] Abnormalities may be manifested in infancy. Dissection and aneurysm rupture occur commonly in persons with LDS at an earlier age and are associated with smaller-sized aneurysms than are typical for persons with Marfan syndrome.[16,18,19] Although spontaneous visceral perforation may occur in patients with LDS (similar to patients with the vascular form of EDS), both the vascular and visceral lesions tend to do well with surgical intervention (unlike in patients with EDS).[19]

## Neurocutaneous Syndromes

Neurocutaneous diseases affecting the cardiovascular system in children include neurofibromatosis type 1, tuberous sclerosis complex, and PHACES syndrome. Although not typically included in the neurocutaneous diseases, Noonan syndrome will be grouped here because of its genetic and phenotypic overlap with neurofibromatosis type 1.

### Neurofibromatosis Type 1

***Overview.*** Neurofibromatosis type 1 (NF1) is an autosomal dominant disorder with variable multisystem involvement. The incidence is 1 in 3,500 newborns; about 50% of cases are nonfamilial.[21] The classic clinical presentation of NF1 includes café-au-lait spots, axillary freckling, dermal and plexiform neurofibromas, and learning disabilities.

NF1 is associated with a broad spectrum of heterozygous germline mutations in the NF1 gene encoding a protein called neurofibrin.[21] This is a negative regulator of the retrovirus associated DNA sequence (RAS) proto-oncogene pathway; loss of function can produce disturbances in cell development and migration and increased cellular proliferation.[21,22] RASopathies are a group of germline mutation conditions that affect the RAS/mitogen activated protein kinase (MAPK) pathway that controls cellular differentiation, migration, proliferation, and apoptosis.[23] In addition to NF1, RASopathies include Noonan, LEOPARD, Costello, and cardiofaciocutaneous syndromes.[23] These all have distinct phenotypic features with some overlap that includes craniofacial, cutaneous, and cardiovascular lesions and an increased propensity for malignant tumors.[23]

Congenital heart defects are present in 2% to 4.3% of persons with NF1. Pulmonic stenosis is the most common abnormality. Other lesions include tetralogy of Fallot (TOF), aortic stenosis, aortic coarctation, ASD, VSD, patent ductus arteriosus (PDA), MVP, and occasionally hypertrophic cardiomyopathy.[24-26] Neurofibromas can develop within the heart and obstruct blood flow by compression or invasion, or erode a vessel and cause hemorrhage.

Vascular manifestations include stenosis, aneurysms, fistulas, arteriovenous malformations, and spontaneous rupture of systemic arteries and veins (Fig. 78.6). Cerebrovascular disease is of particular concern, including stenosis, aneurysms, and moyamoya. Hypertension with or without renovascular stenosis is also common. Another vascular manifestation known as middle aortic syndrome is caused by the narrowing of the distal thoracic or abdominal aorta, leading to renal vascular hypertension and ischemia of the visceral organs and lower extremities (see Fig. 78.6).[26]

***Imaging and Treatment.*** In addition to cardiovascular findings, chest imaging in persons with NF1 can show rib deformities

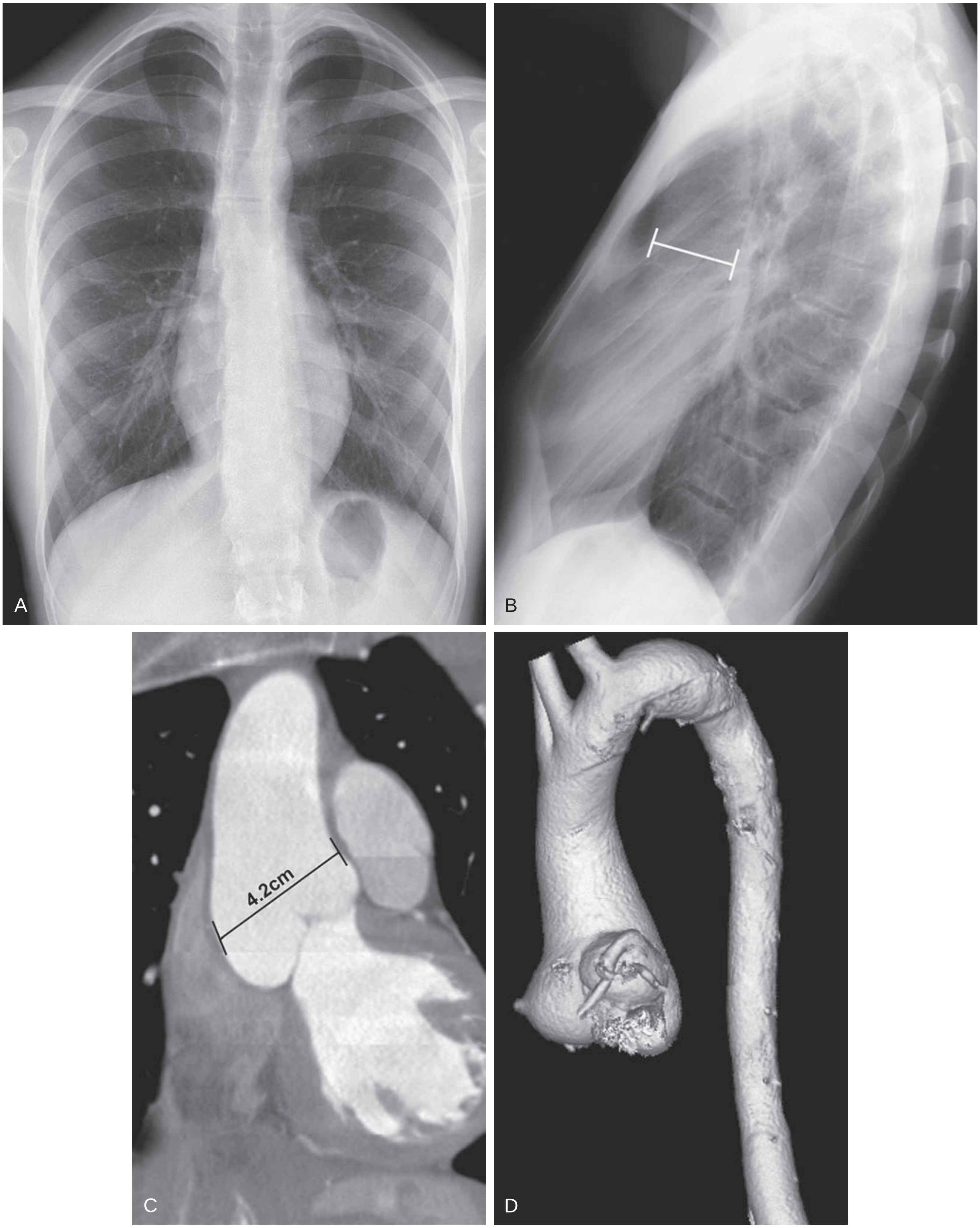

**Figure 78.4. Marfan syndrome in an 18-year-old boy.** (A) Posteroanterior chest radiograph demonstrates a marfanoid appearance, with an elongated chest and little subcutaneous tissue. The anterior ribs are vertically oriented, suggesting a pectus deformity. (B) Lateral view of the chest confirms the pectus excavatum and shows a dilated ascending aorta *(line)*. Coronal reconstruction (C) and oblique sagittal three-dimensional reconstruction (D) from CTA of the chest demonstrate the dilated aortic root, which is largest at the level of the sinuses of Valsalva (measurement in C).

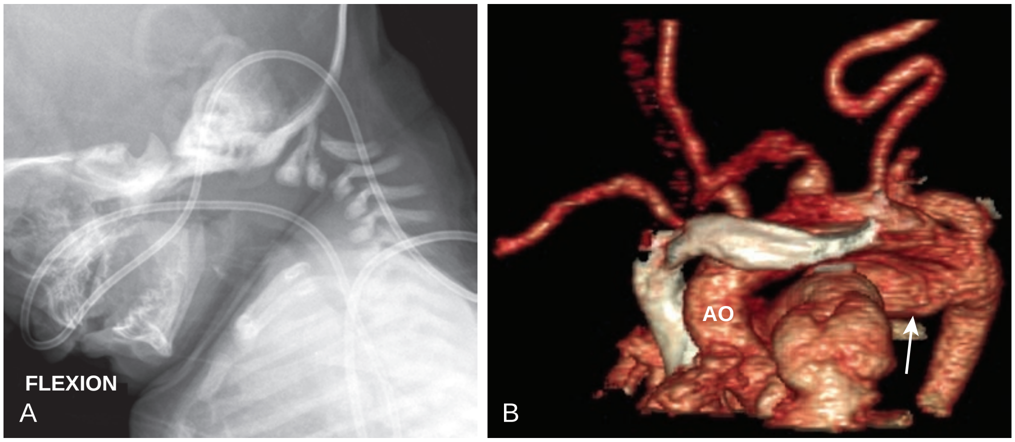

**Figure 78.5. Infant with Loeys–Dietz syndrome.** (A) Flexion lateral view of the cervical spine demonstrates instability with marked subluxation, posterior hypoplasia, and kyphosis at C2–C3. (B) Oblique coronal volumetric CTA reconstruction shows a very tortuous aortic *(AO)* arch and all cervical branches as well as an aneurysmal patent ductus arteriosus *(arrow).* See Video 78.1 for markedly tortuous aorta and iliac arteries with multiple stenoses and Video 78.2 for diffuse arterial tortuosity and multiple stenoses. *(Courtesy of Ron Cohen, Oakland Children's Hospital.)*

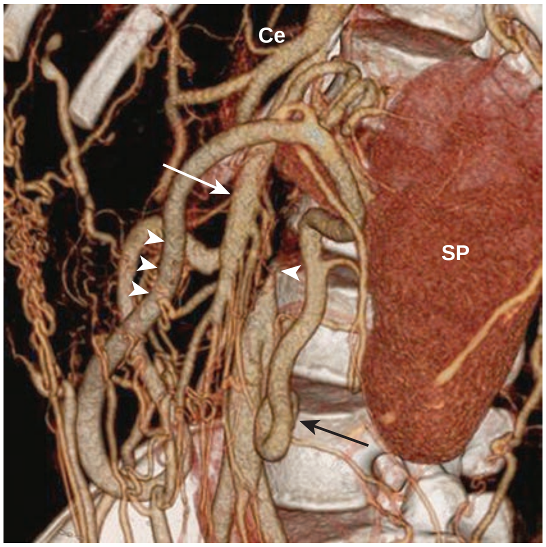

**Figure 78.6. Aortic obstruction from neurofibromatosis type 1 in a 14-year-old boy.** Volume rendering of an abdominal CTA shows a complete obstruction of the aorta beyond the origins of the celiac trunk *(Ce)* and the superior mesenteric artery *(white arrow).* The distal aorta *(single arrowhead)* is reconstituted through the superior mesenteric artery, the marginal artery of Drummond *(three arrowheads),* and the inferior mesenteric artery *(black arrow). SP,* Spleen.

("penciling" and "twisted ribbon"); enlargement of the neural foramina; intercostal, mediastinal, pleural, and soft tissue neurofibromas; and pulmonary cysts, nodules, and fibrosing alveolitis.

NF1 patients are screened with frequent blood pressure measurements and undergo arterial imaging (i.e., CTA or MRA) if hypertension or other symptoms develop.[26] Vascular lesions may be treated with drug therapy, angioplasty, or surgery. Development of additional lesions, including aneurysms, has been reported after surgery or stenting, consistent with underlying vascular fragility. Elucidation of the genetic and cellular pathophysiology of NF1 and other related diseases shows promise in the development of targeted cellular pathway therapies.[21]

## Tuberous Sclerosis

***Overview.*** Tuberous sclerosis is an autosomal dominant inherited disease occurring in 1 in 6,000 live births and is characterized by hamartomas of multiple organs, including cerebral cortical tubers, subependymal giant cell astrocytomas, and renal angiomyolipomas.[27,28] The classic clinical triad is seizures, cognitive impairment, and skin lesions.[29] The presentation and manifestations of tuberous sclerosis are quite varied, and the diagnosis can be missed for a prolonged period.[28] Mutations of *TSC1* and *TSC2*, tumor suppressor genes that encode hamartin and tuberlin proteins, have been identified as the cause of tuberous sclerosis. *TSC2* mutations tend to produce more severe clinical manifestations.[27,29]

Cardiac rhabdomyomas are the most common pediatric cardiac tumors, and 70% to 90% are associated with tuberous sclerosis (Fig. 78.7) (see Chapter 80).[29]

Other cardiovascular manifestations of tuberous sclerosis can include CNS, central and peripheral arterial aneurysms, aortic coarctation, and vascular stenotic–occlusive disease including renal artery stenosis.[30] Aneurysms may form due to medial atrophy and disruption, with abdominal aneurysms appearing at an earlier age than those in the thorax.[31]

***Imaging, Treatment, and Follow-up.*** Rhabdomyoma is the earliest finding of tuberous sclerosis in utero and can be diagnosed with ultrasound. The presence of multiple cardiac tumors in utero is sufficient to establish the diagnosis.[32] On ultrasound, rhabdomyomas appear as rounded, homogeneous, hyperechoic areas within the myocardium (see Fig. 78.7).

The signal characteristics of rhabdomyomas on MRI are variable. They often are isointense or minimally hyperintense to the myocardium on T1-weighted images (see Fig. 78.7) and hyperintense on T2-weighted images. Rhabdomyomas may be hypointense to the myocardium after administration of intravenous gadolinium contrast. They usually appear as low-density masses on contrast-enhanced CT (see Fig. 78.7).

Rhabdomyomas can cause obstruction of ventricular blood flow, arrhythmias, and loss of functional myocardium, which can lead to low cardiac output, congestive heart failure, and even myocardial infarction. Rhabdomyomas can arise anywhere in the myocardium, most commonly in the ventricles. They often are multiple and can invade the pericardium. Areas of central necrosis may be present.

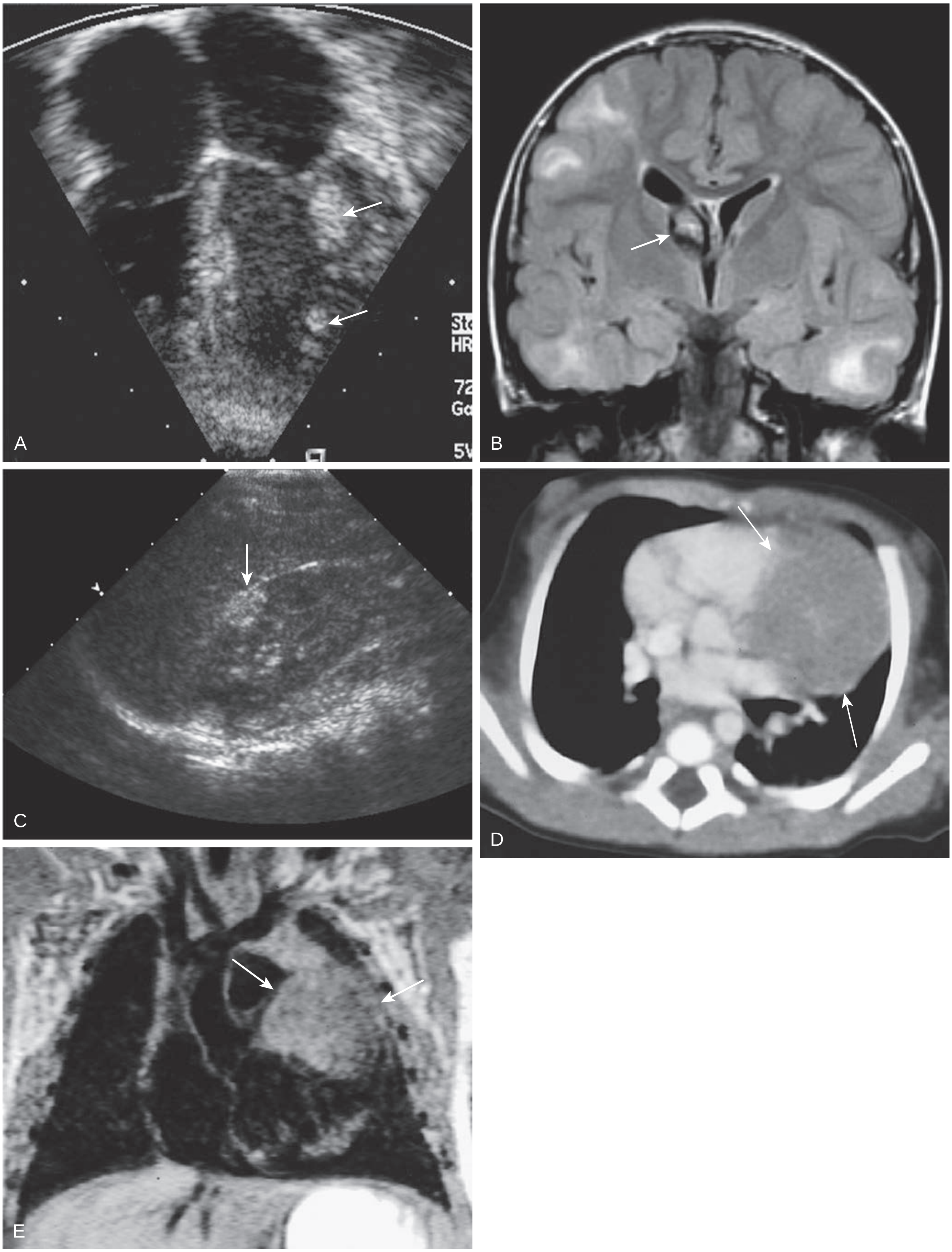

**Figure 78.7. Tuberous sclerosis.** (A) Four-chamber view from an echocardiogram shows multiple echogenic masses within the free wall of the left ventricle *(arrows).* The cardiac tumors, representing rhabdomyomas, resolved spontaneously. (B) Coronal fluid-attenuated inversion recovery MRI of the brain from the same child 2 years later shows multiple hyperintense subcortical tubers and a mixed-signal giant cell astrocytoma *(arrow)* at the foramen of Monro. (C) Sagittal ultrasonography of the right kidney shows a hyperechoic lesion in the anterior mid kidney *(arrow)* indicating an angiomyolipoma. (D and E) Different 3-day-old boy with an abnormal chest radiograph. (D) Contrast-enhanced CT demonstrates a large, hypodense, soft tissue density mass of the left ventricular wall *(arrows).* (E) Coronal T1-weighted MRI demonstrates the large, isointense-to-muscle rhabdomyoma in the left ventricular free wall *(arrows). (A, Courtesy of Lizabeth Lanford, MD, Children's Hospital, Pittsburgh, PA.)*

Rhabdomyomas tend to increase in size until 32 weeks of gestation and then progressively regress, especially during the first year of life.[32] Children can be monitored with serial echocardiograms; complete regression is observed in most patients by age 6 years and surgery is rarely required. Patients should continue to be monitored for bradyarrhythmias and tachyarrhythmias.[29]

Screening for aortic aneurysms (via ultrasound, MRA, or CTA) is recommended both at the time of diagnosis and at frequent regular intervals thereafter.[31] Open elective repair of an identified aneurysm is important because one-third of patients with tuberous sclerosis complex and aortic aneurysm present with rupture.[31]

### PHACES Syndrome

***Overview.*** PHACES syndrome, consisting of *P*osterior fossa malformations, *H*emangiomas, *A*rterial anomalies, *C*ardiac defects, *E*ye abnormalities, and *S*ternal clefting or a *S*upraumbilical raphe, is a neurocutaneous complex with a strong female predominance.[33-36] Specific major and minor criteria have been established for more accurate diagnosis of PHACES syndrome.[36,37]

The hemangioma is typically large and segmental, located on the face and/or cervical region, and behaves like an infantile hemangioma: barely visible at birth, markedly proliferating in infancy, with subsequent slow regression. It also appears to respond to propranolol therapy.[37]

Vascular lesions predominantly affect the arterial system and include dysplasia, tortuosity, dilation, narrowing, occlusion, aberrant origin or course, and persistent embryonic vessels.[36] More than 30% of patients with PHACES syndrome have coarctation of the aorta, which is often unusually complex with irregular areas of narrowing and ectasia.[36,37] Other congenital aortic abnormalities include arch interruption, atresia, aberrant subclavian origins, hypoplasia of the descending thoracic aorta, and right or double aortic arch.[34,36] Progressive abnormalities such as stenosis of and aneurysm formation in the aorta and the cervical arteries are of particular concern. Patients with PHACES syndrome are at an unusually high risk of stroke (as a result of a progressive arterial vasculopathy) and cerebrovascular abnormalities.[33,36] Currently the imaging strategy is geared toward identification of vascular lesions, treatment planning, and monitoring of disease progression.

### Noonan Syndrome

***Overview.*** Noonan syndrome is an autosomal dominant RASopathy that occurs in both male and female infants with an incidence of 1 in 1,000 to 1 in 2,000. It has been associated with advanced paternal age and linked to a large number of underlying familial or spontaneous genetic mutations; the most common, in 50% of cases, is in the *PTPN11* gene.[38] Noonan syndrome is typified by characteristic facies and a webbed neck, short stature, cardiac anomalies, deafness, motor delays, and mild cognitive impairment.

Cardiac defects are common in Noonan syndrome; the most prevalent is pulmonary stenosis (57%), frequently with a dysplastic pulmonary valve.[38,39] Hypertrophic cardiomyopathy occurs in 20% to 50% of cases, often presents in infancy, is highly associated with concomitant cardiac anomalies, and may resolve spontaneously.[39] Other abnormalities include ASD, VSD, PDA, TOF, anomalous pulmonary venous return, aortic coarctation, partial atrioventricular septal defect, mitral valve abnormalities, coronary anomalies, and electrocardiographic abnormalities.[38] Lymphatic system abnormalities are particularly common and include lymphedema, lymphangiectasia, lymphatic malformation, and chylothorax.[40] Coagulation and platelet defects with easy bruising and a propensity to develop hematologic malignancies are also notable.[23,38]

The term *neurofibromatosis–Noonan syndrome* has been used for cases of NF1 with Noonan features such as pectus excavatum, broad neck, and congenital heart disease.[6] Noonan syndrome with multiple lentigenes was formerly known as LEOPARD syndrome (lentigines, electrocardiogram abnormalities, ocular hypertelorism, pulmonary stenosis, abnormalities of genitalia, retardation of growth, and deafness) (e-Fig. 78.8 and Video 78.3).[6,38]

## Other Syndromes

Other syndromes and their associated cardiovascular components are listed in Table 78.1 (e-Figs. 78.9–78.14 and Video 78.4; also see e-Fig. 78.8). The most common associated cardiac lesions are listed first, vascular lesions after. Many other rare syndromes have associated cardiac malformations; however, these syndromes are too numerous to mention specifically. Table 78.2 outlines syndromes that have cardiovascular manifestations almost exclusively (e-Figs. 78.15 and 78.16). This list is not exhaustive but includes the more common, important, and interesting entities.

# SPECIFIC CHROMOSOMAL ANOMALIES

## 22Q11 Deletion—DiGeorge Syndrome

***Overview.*** The 22q11 deletion is the most common chromosome deletion in DiGeorge syndrome, as well as the velocardiofacial syndrome.[6] DiGeorge syndrome often is remembered by the acronym CATCH 22, which refers to the major manifestations: *C*ardiac defects, *A*bnormal facies, *T*hymic hypoplasia, *C*left palate, *H*ypocalcemia (absent parathyroid), and *22*q11 chromosome deletions. The defects seen in the DiGeorge syndrome reflect field defects of the third and fourth pharyngeal pouches. The most commonly associated cardiac anomalies are truncus arteriosus (40% of truncus arteriosus cases have DiGeorge syndrome) (e-Fig. 78.17) and interruption of the aortic arch (usually type B) (see Chapter 75), as well as TOF and aberrant or isolated subclavian artery.[41]

DiGeorge syndrome is associated with other syndromes, including fetal alcohol syndrome, Noonan syndrome, and Zellweger syndrome. It also is associated with infants of diabetic mothers.[6]

The absence of the thymic shadow on radiographs in the first week of life in association with heart disease should raise strong consideration of DiGeorge syndrome. However, the thymus is not necessarily entirely absent and may just be hypoplastic.

Imaging and management depends on the severity of cardiac and other anomalies. Increased susceptibility to infections, especially respiratory infections, including unusual organisms seen in immunocompromised hosts (such as acid-fast bacilli and pneumocystis), is a significant management concern.

## Fragile X Syndrome

***Overview.*** Fragile X syndrome is the most common inherited form of intellectual disability. Approximately 1 in 850 people carry the gene for this X-linked disorder; however, about 20% of males with the gene are unaffected. Affected individuals may have large heads and facial abnormalities along with learning disabilities and behavioral problems. Associated cardiac abnormalities include MVP, mitral regurgitation, aortic regurgitation, tricuspid regurgitation, a dilated aortic root, and coarctation.[6]

## Trisomy 21 (Down Syndrome)

***Overview.*** Down syndrome, the most common chromosomal anomaly, is seen in 1 in 600 to 1 in 800 live births.[6a] Down syndrome is the most frequent genetic anomaly associated with congenital heart disease. Approximately 40% to 45% of patients with Down

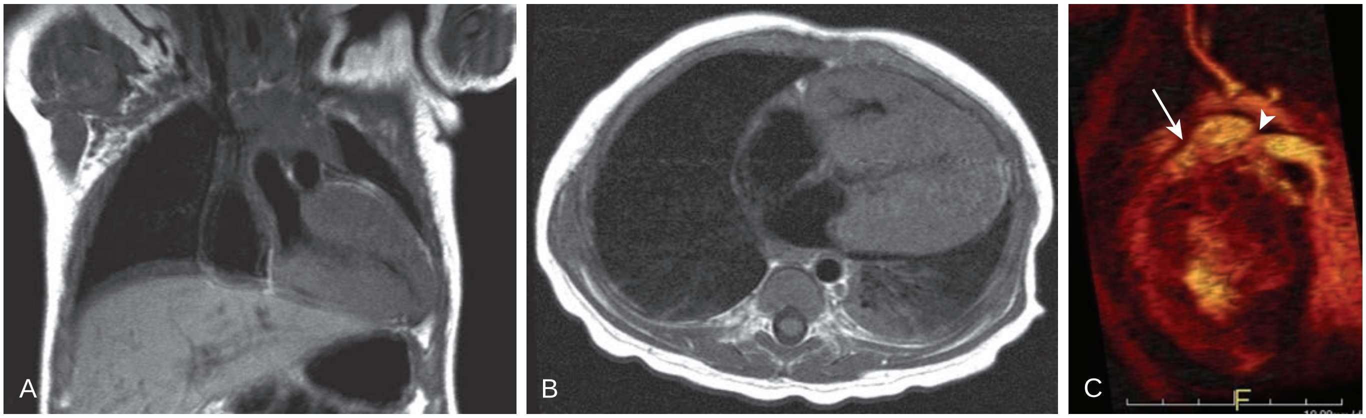

**e-Figure 78.8. A 6-month-old girl with a hypertrophic cardiomyopathy and features of LEOPARD variant of Noonan syndrome.** Coronal (A) and axial T1-weighted (B) MRI demonstrates marked thickening of the right and left ventricular myocardium with small ventricular cavities. See also Video 78.3. (C) Oblique sagittal three-dimensional MRA reconstruction demonstrates moderate pulmonic stenosis with poststenotic dilation of the pulmonary artery *(arrow)* and mild stenosis at the origin of the left pulmonary artery *(arrowhead).*

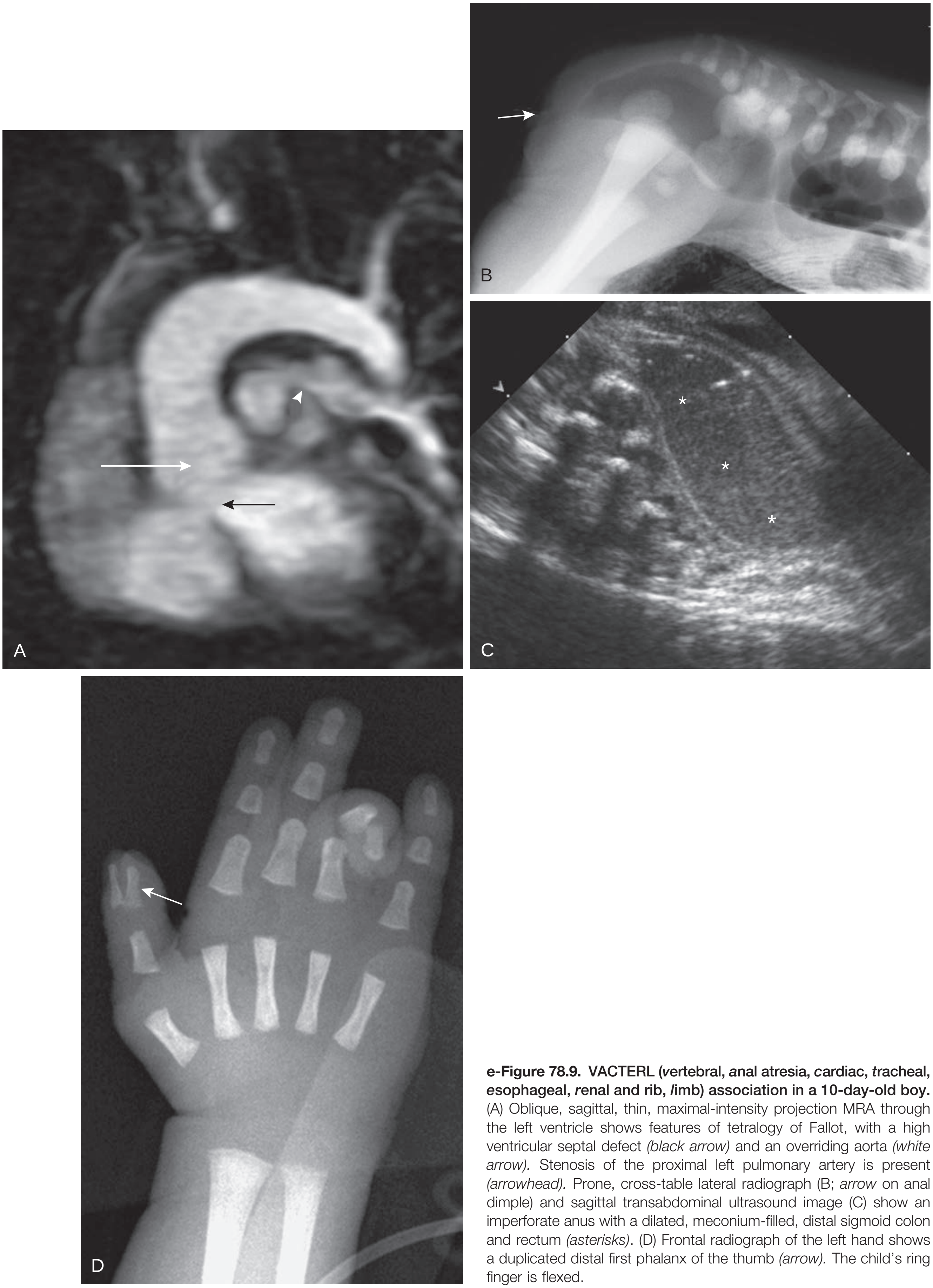

**e-Figure 78.9. VACTERL (*v*ertebral, *a*nal atresia, *c*ardiac, *t*racheal, *e*sophageal, *r*enal and rib, *l*imb) association in a 10-day-old boy.** (A) Oblique, sagittal, thin, maximal-intensity projection MRA through the left ventricle shows features of tetralogy of Fallot, with a high ventricular septal defect *(black arrow)* and an overriding aorta *(white arrow).* Stenosis of the proximal left pulmonary artery is present *(arrowhead).* Prone, cross-table lateral radiograph (B; *arrow* on anal dimple) and sagittal transabdominal ultrasound image (C) show an imperforate anus with a dilated, meconium-filled, distal sigmoid colon and rectum *(asterisks)*. (D) Frontal radiograph of the left hand shows a duplicated distal first phalanx of the thumb *(arrow).* The child's ring finger is flexed.

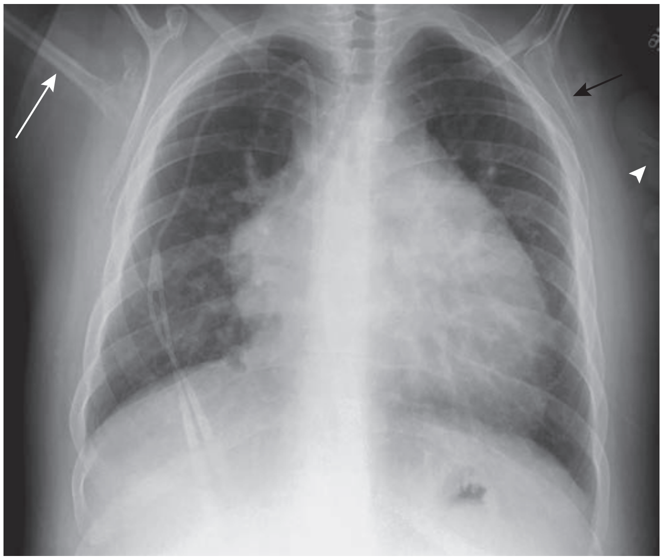

**e-Figure 78.10. Holt–Oram syndrome in a 35-year-old man with a history of atrial and ventricular septal defect repairs, as well as pulmonary arterial hypertension.** Chest radiograph shows cardiomegaly, prominent pulmonary vessels, hypoplastic scapulae (left scapula, *black arrow*), a hypoplastic right humerus *(white arrow),* and an absent left humerus with a rudimentary digit *(arrowhead).*

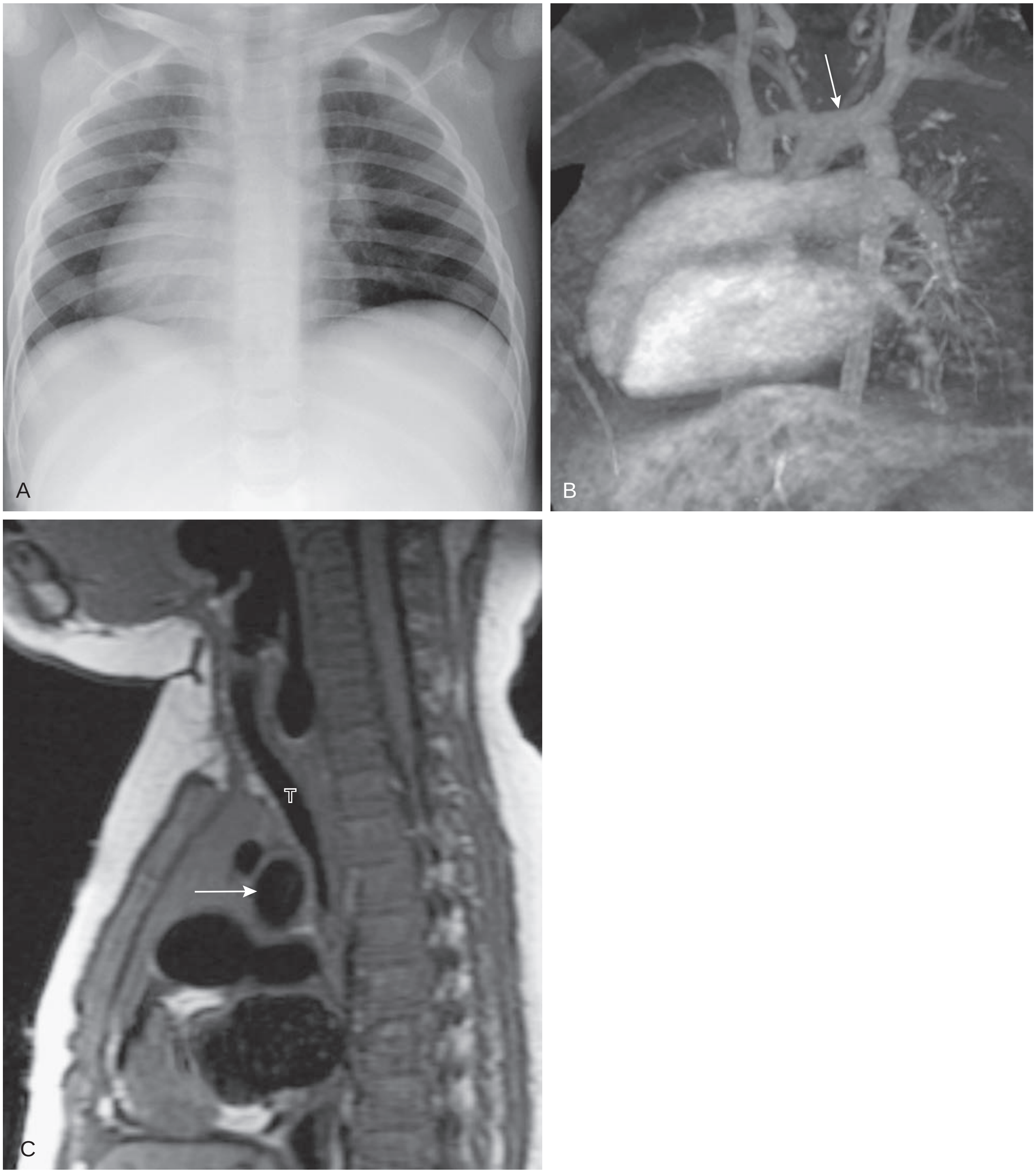

**e-Figure 78.11. A 1-year-old boy with Kartagener syndrome and stridor.** (A) Chest radiograph shows dextrocardia. The left lung is mildly hyperlucent. The abdominal situs was normal. (B) Coronal, three-dimensional, maximum-intensity projection MRA shows dextrocardia and a right-to-left course of the aorta, with a left-sided aortic arch *(arrow).* (C) Sagittal, T1-weighted MRI shows compression of the distal trachea *(T)* by the crossing aortic arch *(arrow).*

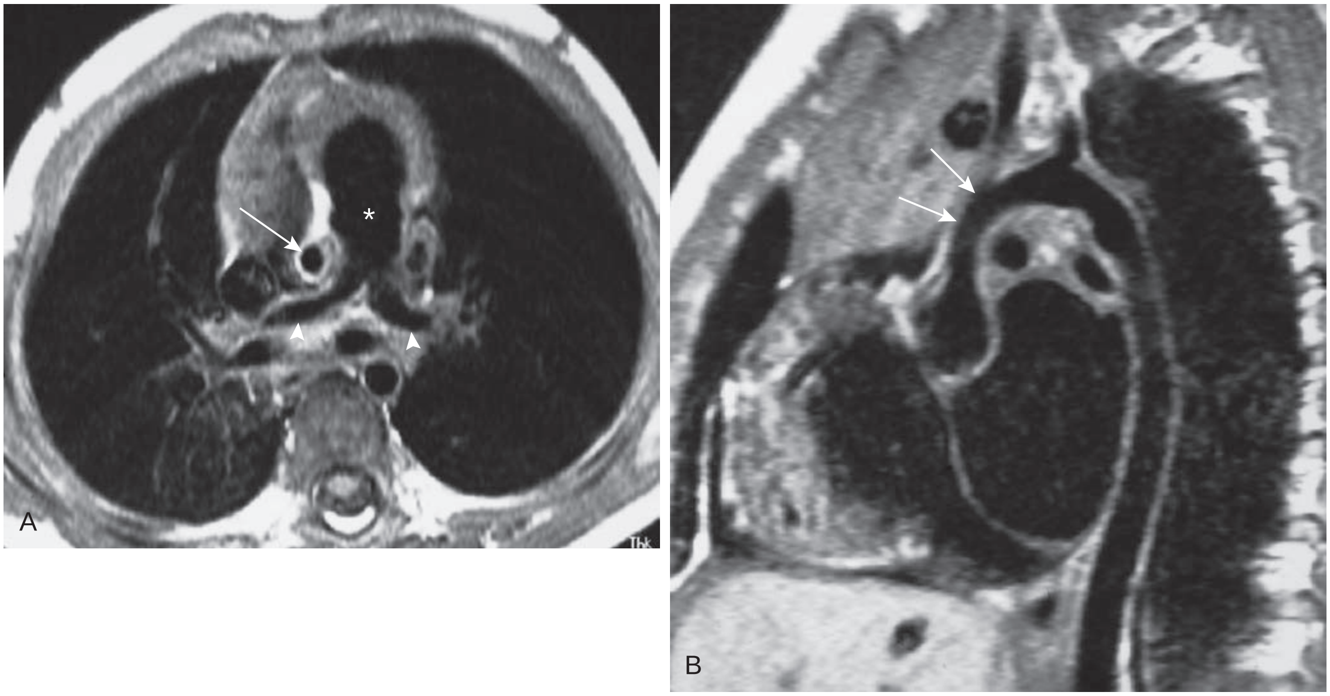

**e-Figure 78.12. Williams syndrome in a 3-year-old boy.** (A) Axial, T1-weighted MRI of the chest shows an enlarged main pulmonary artery *(asterisk),* with narrowing of the branch pulmonary arteries *(arrowheads).* Note the very small ascending aorta *(arrow).* (B) Oblique, sagittal, T1-weighted MRI shows hypoplasia of the supravalvar aorta *(arrows).*

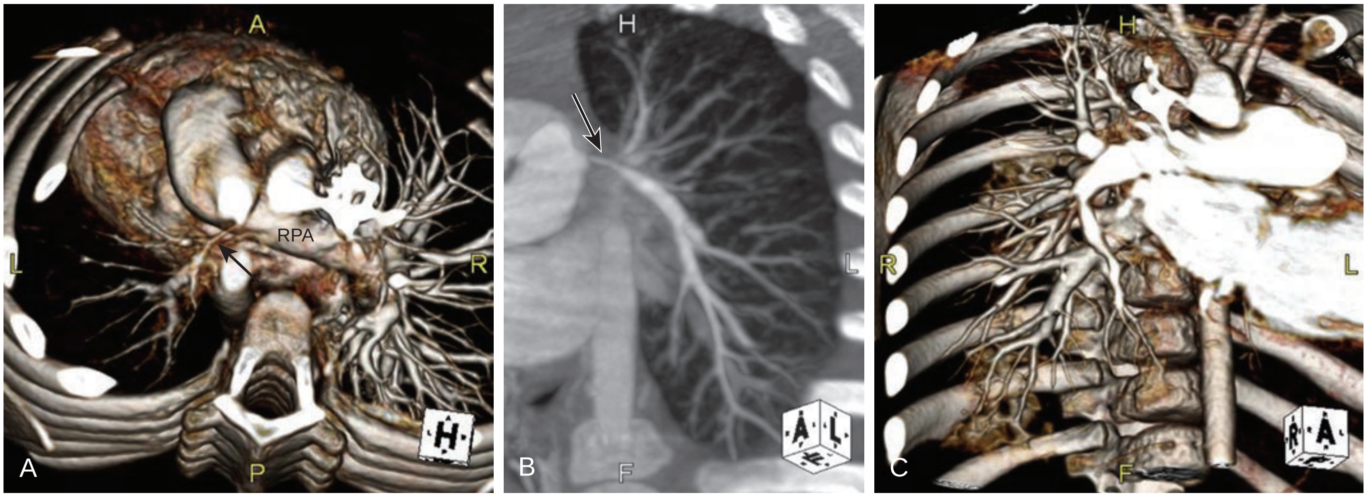

**e-Figure 78.13. Alagille syndrome (arteriohepatic dysplasia) in a 3-year-old child.** (A) Volumetric reconstruction from a CTA (viewed from above) demonstrates marked stenosis and hypoplasia of the left pulmonary artery and branches *(arrow).* The central right pulmonary artery *(RPA)* is patent, but numerous peripheral branch stenoses are present (see C). On a nuclear perfusion scan (not shown), the distribution of pulmonary flow was 86% right and 14% left. (B) Coronal maximum-intensity projection reconstruction demonstrates the very stenotic central left pulmonary artery *(arrow)* with much improved caliber more peripherally. Note additional peripheral stenosis of the origin of the left upper lobe branch. (C) Coronal volume-rendered reconstruction. Multiple peripheral RPA stenoses are present.

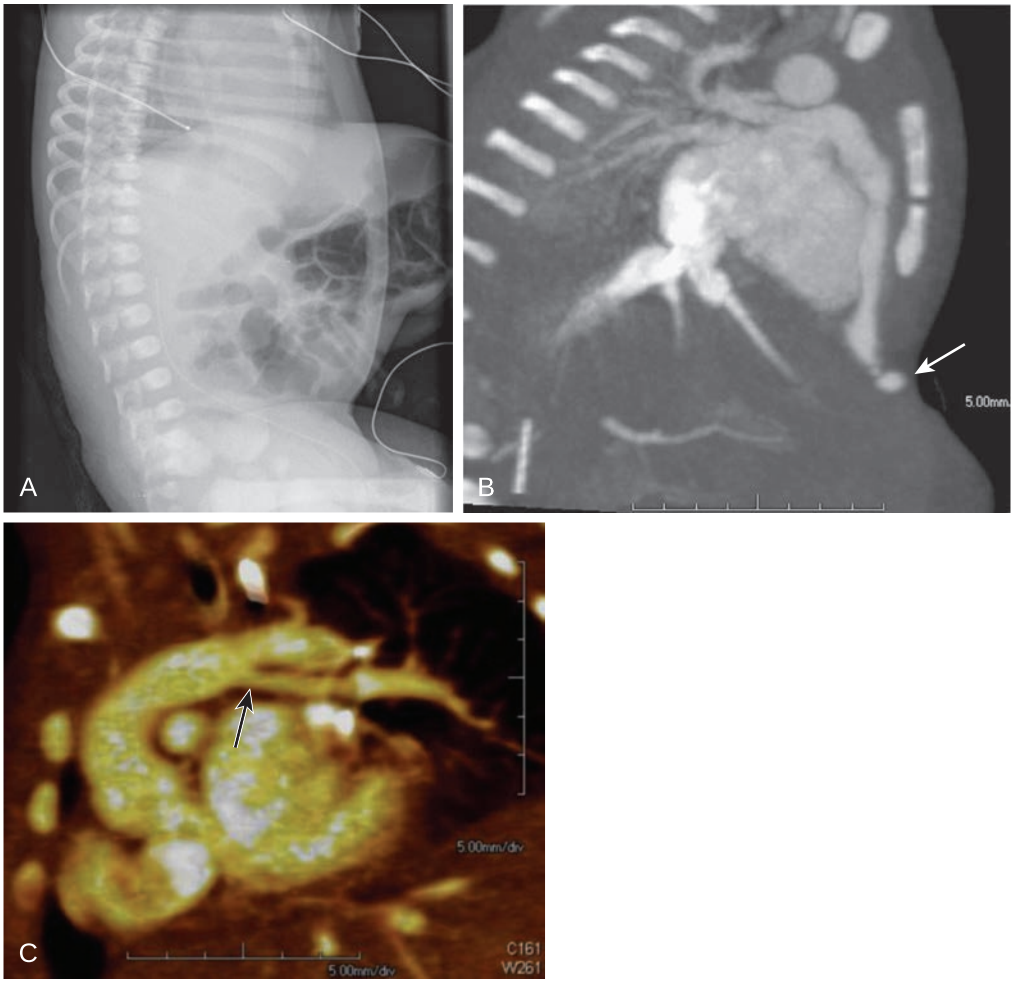

**e-Figure 78.14. Cantrell syndrome (pentalogy of Cantrell: abnormalities of the anterior abdominal wall, diaphragm sternum, pericardium, and heart) in a 2-day-old girl.** (A) Lateral chest radiograph showing a large, high omphalocele. (B) Sagittal maximum intensity projection CTA showing an absent lower sternum and hypoplastic right ventricle with an aneurysm of the right ventricular apex *(arrow)* extending into the omphalocele, probably through pericardial and diaphragmatic defects. (C) Oblique three-dimensional volumetric reconstruction shows the left pulmonary artery *(arrow)* originating from the proximal portion of the patent ductus arteriosus. The main and right pulmonary arteries were normal (not shown). Also see Video 78.4.

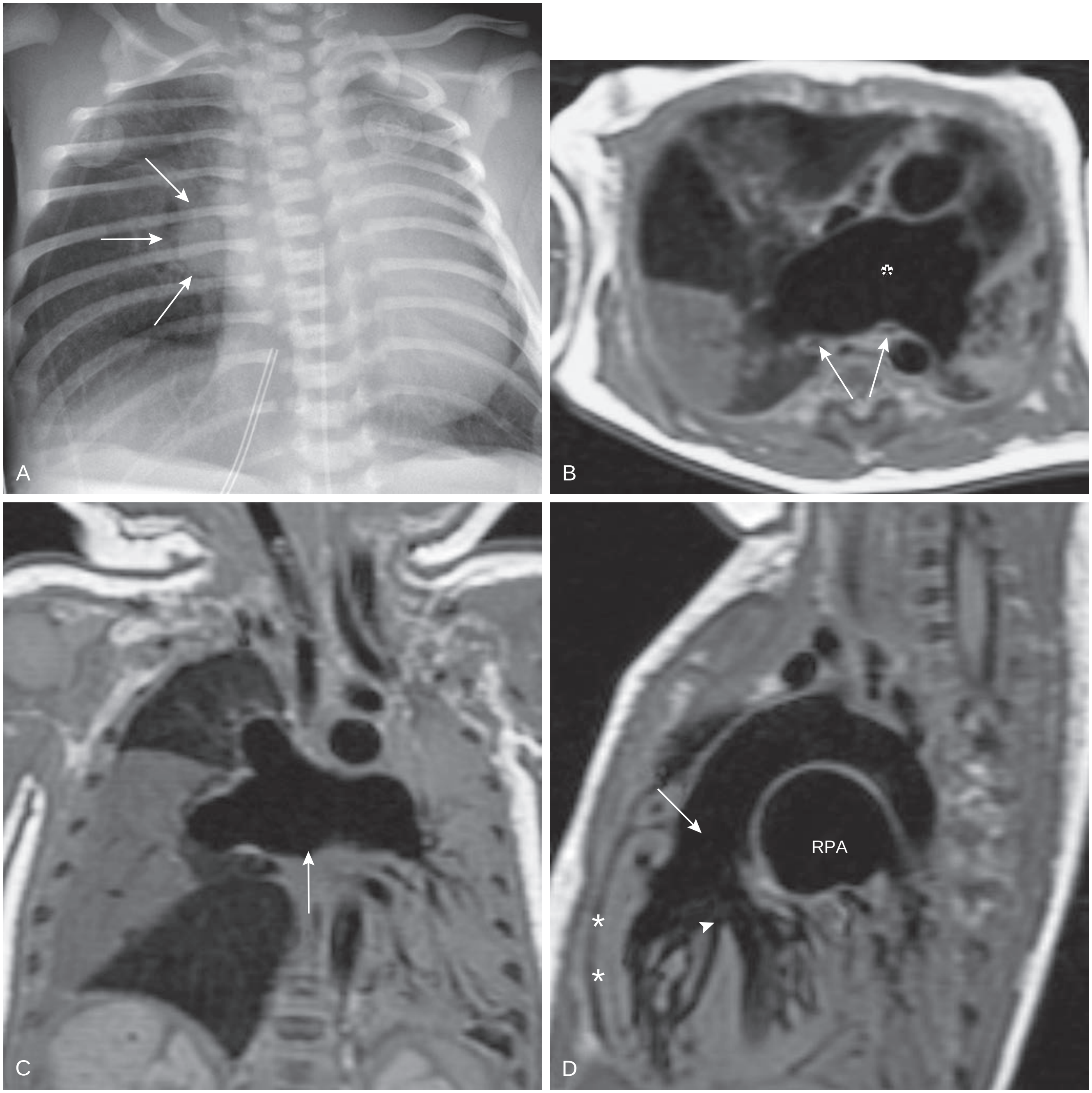

**e-Figure 78.15. Tetralogy of Fallot–absent pulmonary valve syndrome in a 3-day-old boy with respiratory distress.** (A) Frontal chest radiograph shows a right perihilar “mass” *(arrows)* and a hyperinflated right lung with associated leftward mediastinal shift and atelectasis. (B) Axial T1-weighted MRI obtained to evaluate the perihilar mass shows markedly dilated central pulmonary arteries *(asterisk)* compressing the bilateral bronchi *(arrows)* and causing atelectasis. (C) Coronal T1-weighted MRI shows markedly dilated central pulmonary arteries *(arrow)* with aberrant branching. There is complete atelectasis of the right middle lobe and much of the left lung. (D) Sagittal T1-weighted MRI shows features of tetralogy of Fallot with right ventricular hypertrophy *(asterisks),* a ventricular septal defect *(arrowhead),* and an overriding aorta *(arrow).* The right pulmonary artery *(RPA)* is markedly dilated.

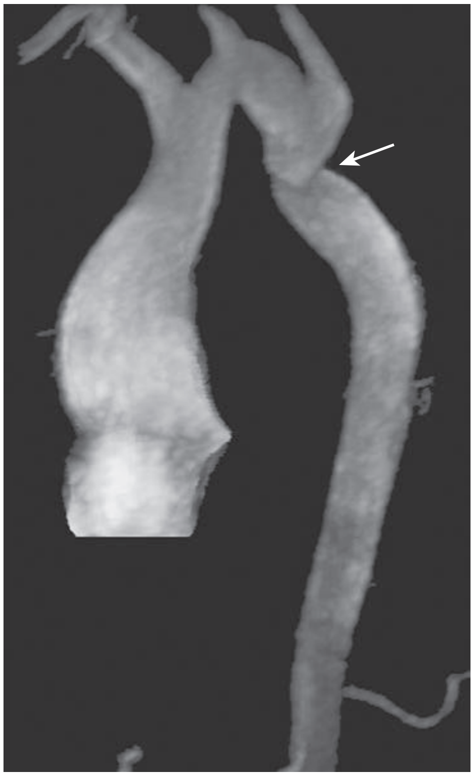

**e-Figure 78.16. Shone syndrome with mitral and aortic valve stenosis and prior coarctation repair in a 15-year-old boy.** Oblique, sagittal, volumetric, three-dimensional MRA shows a dilated ascending aorta, tortuous cervical aortic arch, and residual aortic coarctation *(arrow).*

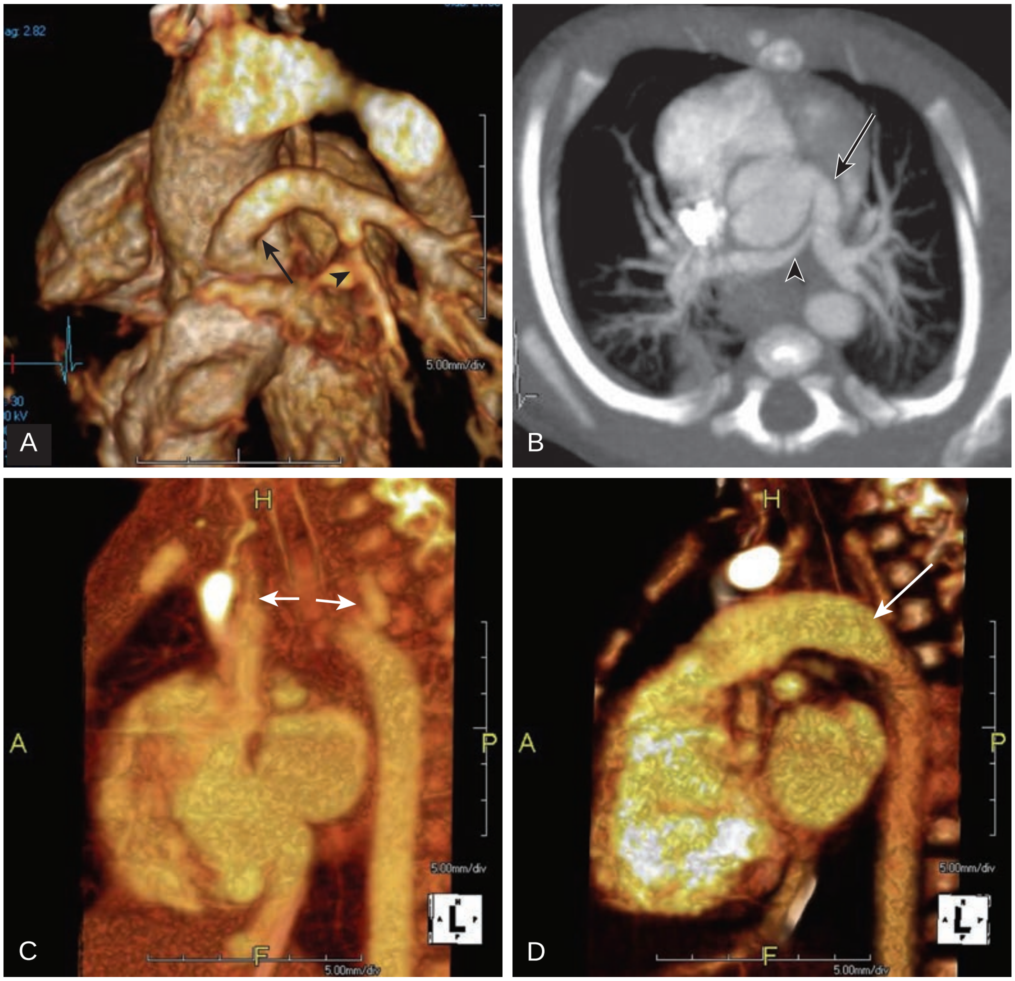

**e-Figure 78.17. 22q11 deletion (DiGeorge syndrome) in two newborn infants.** (A and B) Truncus arteriosus type 1. Volume-rendered, three-dimensional reconstruction, posterior oblique view (A) and axial thin maximum-intensity projection CTA (B) demonstrate a single great artery arising from the heart. The main pulmonary artery *(arrow)* arises from this vessel, which continues as the ascending aorta. Note branch pulmonary arteries with narrowing of the right pulmonary artery *(arrowhead).* (C and D) Sagittal three-dimensional volumetric CTA reconstructions show interruption of the aortic arch (type B). A marked gap exists between the ascending and descending aorta, with interruption between the left common carotid and left subclavian arteries (*arrows* in C). A large patent ductus arteriosus extends from the pulmonary artery centrally and supplies the descending aorta (*arrow* in D).

**TABLE 78.1** Syndromes, Dysplasias, and Their Associated Cardiovascular Anomalies

| Syndrome | Cardiovascular Anomalies |
|---|---|
| Achondrogenesis | PDA, ASD, VSD, COA |
| Alagille syndrome (arteriohepatic dysplasia) (see e-Fig. 78.13) | PS, PPS, ASD, VSD, TOF, PDA, PAT, PAPVR, dysplastic AV valves, COA |
| Apert syndrome (acrocephalosyndactyly) | ASD, PDA, VSD, PS, TOF, EFE, DEXTRO, COA |
| Arthrogryposis | CMY |
| Beckwith–Wiedemann syndrome (EMG syndrome) | CM, CMY, ASD, PDA, TOF, HPLH, subvalvular AS, cardiac fibromas |
| Cardioauditory syndromes | LVH, RVH |
| Cantrell syndrome (pentalogy of Cantrell) (see e-Fig. 78.14) | Combined sternal, pericardial, intracardiac, diaphragmatic, and anterior abdominal wall defects<br>Radiographic findings: sternal defect, ectopia cordis, CHD, ASD, VSD, PS, TOF, APVR, DEXTRO, ventricular diverticulum, intrapericardial herniation of abdominal organs; associated with Turner, trisomy 18, sirenomelia, and amniotic band syndromes |
| Cardiofaciocutaneous syndrome | PS, ASD, VSD, hypertrophic cardiomyopathy, heart valve abnormalities |
| Cardiosplenic (heterotaxy) syndromes (see Figs. 78.1 and 78.2) | |
| Right atrial isomerism (see Fig. 78.1) | Cardiac malposition, TAPVR, AVSD, pulmonary outflow obstruction or PAT, DORV, TGA, single atrium (R), single common ventricle, TAT, TRU (rare), AO-IVC juxtaposition, bilateral right PAs, RAA, bilateral SVC, interrupted IVC |
| Left atrial isomerism (see Fig. 78.2) | Cardiac malposition, single atrium (L), single ventricle, ASD,VSD, AVSD, DORV, APVR, interrupted IVC, bilateral left PAs, bilateral SVC |
| Cayler syndrome (cardiofacial syndrome) | ASD, PDA, VSD, AVSD, TOF, RAA, COA |
| CHARGE association | ASD, VSD, conotruncal malformations, PDA, TOF, parachute mitral valve |
| Costello syndrome | Hypertrophic cardiomyopathy, PS, Ao dilation, arrhythmia |
| Cutis laxa syndrome (autosomal recessive type) | Arteriopathy, dilation, stenosis, tortuosity, dissection |
| Degos syndrome (malignant atrophic papulosis) | MI, pericarditis, constrictive pericarditis, myocardial fibrosis, renal, cerebral, coronary, visceral and peripheral arteriopathy |
| Diamond–Blackfan syndrome (congenital red cell aplasia) | VSD, ASD, mitral valve dysplasia |
| Ehlers–Danlos syndrome (see Fig. 78.3) | MVP, dilated AO root, coronary, and aortic, carotid, and large-branch aneurysms, dissection or rupture, AS, AR, TR, PS, ASD, VSD, TOF, DEXTRO, LV rupture, arteriovenous fistula |
| Ellis–van Creveld syndrome (chondroectodermal dysplasia) | Common atrium, ASD, AVSD |
| Fryns syndrome | Septal defects, arch anomalies, TOF, cystic hygroma |
| Hallermann–Streiff syndrome (oculomandibulofacial syndrome) | PS, TOF, ASD, VSD |
| Holt–Oram syndrome (heart-hand syndrome) (see e-Fig. 78.10) | ASD, VSD, MVP, PDA, HPLH, TAPVR, TRU, conduction disorder, hypoplastic peripheral vessels |
| Jeune syndrome (asphyxiating thoracic dystrophy) | CHF |
| Kartagener syndrome (primary ciliary dyskinesia) (see e-Fig. 78.11) | DEXTRO, CHD |
| Klippel–Trénaunay–Weber syndrome (angioosteohypertrophy syndrome) | CHF, pericardial effusion, superficial varices, telangiectatic nevi, organ hemangiomas, lymphatic obstruction |
| LEOPARD syndrome (cardiomyopathic lentiginosis) aka Noonan syndrome with multiple lentigenes (see e-Fig. 78.8) | CMY, conduction defect, PS, sub-AS |
| Loeys–Dietz syndrome (see Fig. 78.5) | Congenital heart defects include PDA, bicuspid aortic valve, bicuspid pulmonary valve, MVP and ASD; arterial tortuosity, stenoses, aneurysms, dissection, diffuse arterial involvement; spontaneous rupture of viscera |
| Marfan syndrome (see Fig. 78.4) | MVP, MR, dilation of AO root, AR, CHF, aneurysms (AO, pulmonary, ductus), AO dissection, MI, arrhythmia, TR, ASD, TOF |
| MELAS syndrome | CMY, CHF, conduction abnormalities |
| Mucolipidosis III | AR |
| Mucopolysaccharidoses | |
| IH (Hurler syndrome) | Acute CMY associated with EFE, AR, MR, MS, arteriopathy (coronary, renal, AO, mesenteric) |
| IS (Scheie syndrome) | AS, MS |
| II (Hunter syndrome) | AR, CHF, valve thickening, CMY |
| III (Sanfilippo syndrome) | CMY, MR, AR |
| IV (Morquio syndrome) | AR, CMY, AS, MR, CAD |
| VI (Maroteaux–Lamy syndrome) | AS, MS, CMY |
| Neurofibromatosis type 1 (see Fig. 78.6) | PS, COA, ASD, VSD, CMY, MVP, AS, TOF, PDA, hypertrophic cardiomyopathy, vasculopathy (coronary, pulmonary, renal, systemic), cardiac neurofibroma, systemic and intracranial vascular stenosis, aneurysms, arteriovenous fistula, spontaneous vascular rupture, lymphatic abnormality |

**TABLE 78.1** Syndromes, Dysplasias, and Their Associated Cardiovascular Anomalies—cont'd

| Syndrome | Cardiovascular Anomalies |
|---|---|
| Noonan syndrome (Turner phenotype with normal karyotype) | PS, dysplastic pulmonic valve, hypertrophic CMY, lymphatic abnormalities, PDA, ASD, VSD, AVSD, TOF, COA, mitral valve abnormalities, AS, pericarditis, APVR, coronary anomalies, arrhythmias, coagulopathy, platelet defects |
| Oculoauriculovertebral dysplasia (Goldenhar syndrome) | TOF, VSD, DORV, PAT, TAPVR, RAA, COA, asplenia |
| PHACES | Large segmental facial/cervical hemangioma, COA, aortic arch atresia/ interruption, aberrant subclavian origins, hypoplasia of the descending thoracic aorta, RAA, double aortic arch, COA arterial tortuosity, stenosis, occlusion, and aneurysm, aberrant origin/course formation of the aorta and the cervical, intracranial arteries, stroke |
| Progeria (Hutchinson–Gilford syndrome) | Accelerated atherosclerosis, CM, MI, CHF, stroke |
| Proteus syndrome | CHD, CMY, myocardial mass, conduction abnormality, venous dilation, hemangioma, lymphangioma |
| Ravitch syndrome (thoracoabdominal wall defect) | Ectopia cordis, pentalogy of Cantrell, TGA, PDA, ASD, VSD, PS, TOF |
| Robinow syndrome (fetal face syndrome) | CHD (right-sided heart lesions) |
| Rubinstein–Taybi syndrome | ASD, VSD, PDA, COA, PS, bicuspid AO valve |
| Silver–Russell syndrome | CHD |
| Smith–Lemli–Opitz syndrome | ASD, complex cardiac anomalies |
| Thrombocytopenia–absent radius (TAR) syndrome | COA, ASD, VSD, PDA, AVSD, TOF |
| Tuberous sclerosis (Bourneville–Pringle syndrome) (see Fig. 78.7) | Rhabdomyoma, other hamartoma, CHF, CMY, COA, arrhythmia, arterial aneurysm and stenosis (AO, cerebral, renal, peripheral) |
| VATER/VACTERL association (see e-Fig. 78.9) | VSD, ASD, PDA, TOF, TGA, COA, DEXTRO, single ventricle; associated with infants of diabetic mothers and trisomy 18 |
| Velocardiofacial syndrome (Shprintzen syndrome) | TOF, TRU, PA, VSD, absent pulmonary valve, TGA, AS, interrupted AO arch, RAA |
| Williams syndrome (see e-Fig. 78.12) | Supravalvar AS, PPS, MR, ASD, VSD, TOF, MI, COA, interrupted arch, hypoplastic AO, aneurysm or stenosis (AO, systemic, coronary, renal, cerebral arteries) |
| Zellweger syndrome (cerebrohepatorenal syndrome) | CHD, PDA, VSD, DiGeorge |

*AO,* Aorta or aortic; *APVR,* anomalous pulmonary venous return; *AR,* aortic regurgitation; *AS,* aortic stenosis; *ASD,* atrial septal defect; *AV,* atrioventricular; *AVSD,* atrioventricular septal defect; *CAD,* coronary artery disease; *CHARGE,* coloboma, heart defects, atresia choanae, retardation of growth and development, genitourinary problems, ear abnormalities; *CHD,* congenital heart disease; *CHF,* congestive heart failure; *CM,* cardiomegaly; *CMY,* cardiomyopathy; *COA,* coarctation of the aorta; *DEXTRO,* dextrocardia; *DORV,* double-outlet right ventricle; *EFE,* endocardial fibroelastosis; *EMG,* exomphalos, macroglossia, gigantism; *HPLH,* hypoplastic left heart; *IVC,* inferior vena cava; *L,* left; *LEOPARD,* lentigines, electrocardiographic conduction abnormalities, ocular hypertelorism, pulmonary stenosis, abnormal genitalia, retardation of growth, deafness; *LV,* left ventricle; *LVH,* left ventricular hypertrophy; *MELAS,* mitochondrial myopathy, encephalopathy, lactic acidosis, stroke; *MI,* myocardial infarction; *MR,* mitral regurgitation; *MS,* mitral stenosis; *MVP,* mitral valve prolapse; *PA,* pulmonary artery; *PAPVR,* partial anomalous pulmonary venous return; *PAT,* pulmonary atresia; *PDA,* patent ductus arteriosus; *PHACES,* posterior fossa brain malformations, hemangiomas of the face, arterial anomalies, cardiac anomalies, eye abnormalities, sternal clefting or supraumbilical raphe; *PPS,* peripheral pulmonary stenosis; *PS,* pulmonary stenosis; *R,* right; *RAA,* right aortic arch; *RVH,* right ventricular hypertrophy; *SVC,* superior vena cava; *TAPVR,* total anomalous pulmonary venous return; *TAT,* tricuspid atresia; *TGA,* transposition of the great arteries; *TOF,* tetralogy of Fallot; *TR,* tricuspid regurgitation; *TRU,* truncus arteriosus; *VACTERL,* vertebral, anal atresia, cardiac, tracheal, esophageal, renal, limb; *VATER,* vertebral defects, VSD, imperforate anus, tracheoesophageal fistula, radial and renal dysplasia; *VSD,* ventricular septal defect.

syndrome have congenital cardiac malformations, which represent the leading cause of death in the first 2 years of life.[42]

The most characteristic abnormality in Down syndrome is an atrioventricular septal defect (AVSD), also known as a common atrioventricular canal or endocardial cushion defect (e-Fig. 78.18) (see Chapter 72). Almost 70% of AVSDs are associated with Down syndrome. Other common cardiac defects include VSD, PDA, TOF, and pulmonary stenosis.[6,42] Arterial and lymphatic abnormalities also occur, the latter especially in utero.[6] Because persons with Down syndrome have decreased muscular tone, a relatively large tongue, a small pharynx, and laryngotracheomalacia, chronic upper airway obstruction may be a significant clinical problem and can result in congestive heart failure.

***Imaging.*** A combination of plain chest radiographs, ultrasound, and CT or MRI is used most often to evaluate and manage cardiovascular lesions in persons with Down syndrome, supplemented by catheter angiography as needed (see Chapter 72 and e-Fig. 78.18).

Noncardiac chest imaging findings include the presence of 11 ribs and hypersegmentation of the manubrium, as well as multiple small peripheral and parafissural cysts thought to represent hypoplastic/dysplastic lung changes. Recurrent infection, follicular bronchiolitis, and increased tumor propensity, especially leukemia and lymphoma, are additional features related to immune dysfunction in persons with Down syndrome. Abdominal findings include a characteristic configuration of the pelvis (flattened acetabula and flared iliac wings), duodenal stenosis or atresia, annular pancreas, and Hirschsprung disease.[6a]

## Trisomy 13 (Patau Syndrome)

***Overview.*** Trisomy 13 is the least common and the most severe of the viable trisomies. It occurs in 1 in 29,000 live births.

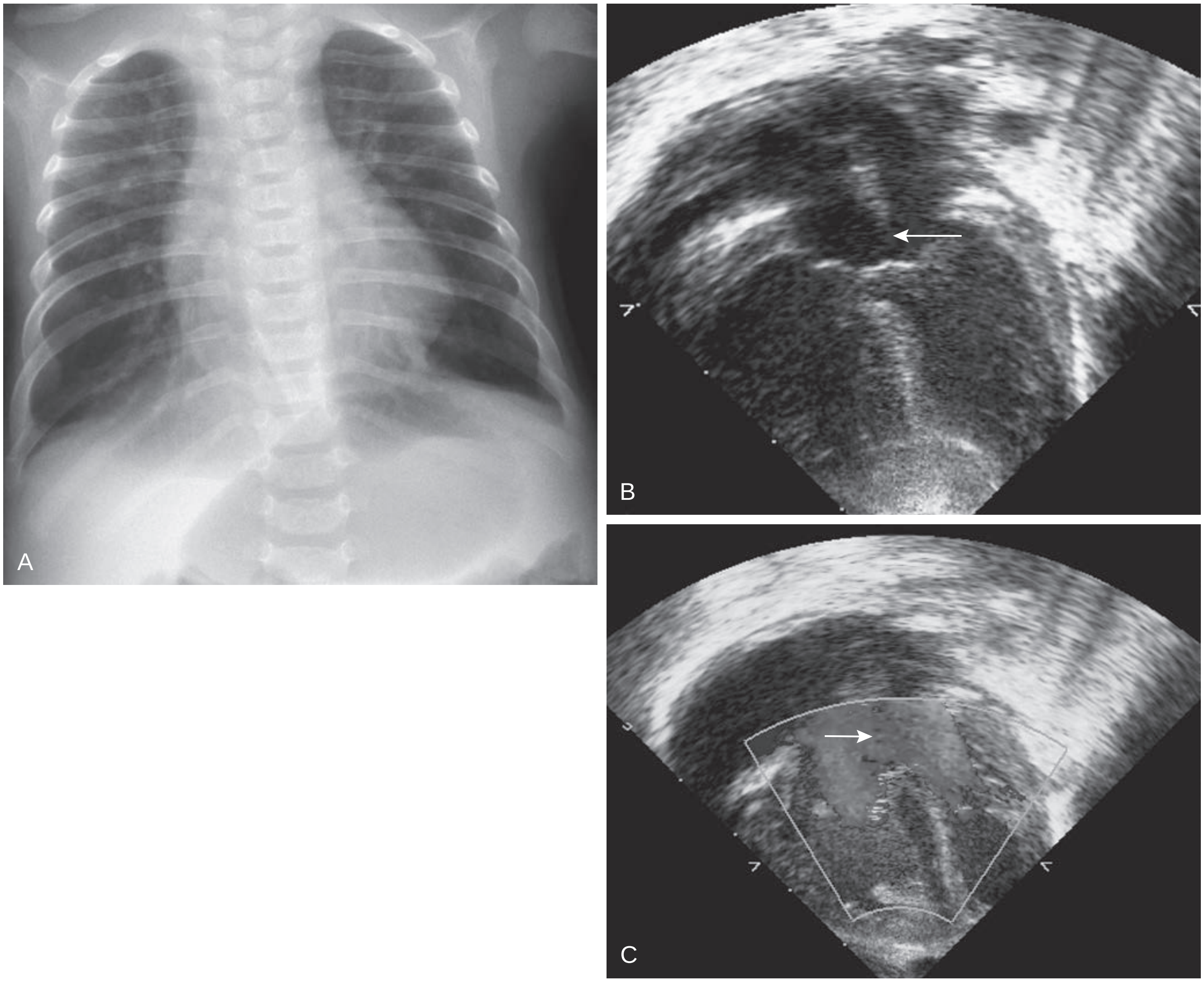

**e-Figure 78.18. Down syndrome and an atrioventricular septal defect in a 3-month-old girl.** (A) Frontal chest radiograph shows increased vascularity, mild congestion, and accompanying hyperinflation of the lungs. Eleven ribs are present bilaterally. (B) Four-chamber view from an echocardiogram shows a large atrioventricular septal defect *(arrow).* (C) Left-to-right Doppler flow is shown across the atrial defect *(arrow). (*B *and* C, *Courtesy of Lizabeth Lanford, MD, Children's Hospital, Pittsburgh, PA.)*

**TABLE 78.2** Syndromes That Predominantly Affect the Cardiovascular System

| Syndrome | Cardiovascular Defects |
|---|---|
| Absent pulmonary valve leaflet syndrome (see e-Fig. 78.15) | Maldeveloped nodular myxoid pulmonary valve cusps with aneurysmal dilation of central PAs associated with TOF, airway compression, lobar emphysema and abnormal PA branching, CM, RAA, ASD, VSD, PDA, DORV, AVSD, Marfan syndrome, 18q deletion |
| Berry syndrome | Distal AP window with AO origin of the right PA and arch interruption |
| Bland–White–Garland syndrome | Anomalous origin of left coronary artery from PA |
| Congenital cardiomyopathy: hypertrophic cardiomyopathy | Asymmetric septal hypertrophy, systolic anterior motion of mitral valve, LVOT obstruction, myocardial scar, arrhythmias |
| Arrhythmogenic right ventricular dysplasia | Fibrofatty infiltration of right ventricular myocardium, RV dyskinesia/aneurysms, arrhythmias |
| Eisenmenger syndrome | Pulmonary hypertension with bidirectional or reversed shunt at atrial, ventricular, or AP level; cyanosis; dyspnea; sudden death; peripartum CMY radiographic findings: dilated central PAs with tapering, PA calcification |
| Floppy valve syndrome | MVP, prolapse of other valves, CAD, congestive or hypertrophic CMY, ASD, MR, AR, papillary muscle or chordae tendineae rupture |
| Hypoplastic left heart syndrome | Combined mitral and AO obstruction (stenosis or atresia), underdeveloped LA and LV, hypoplastic ascending AO ± COA or AO interruption; may be associated with right diaphragmatic hernia, omphalocele, brain anomalies; radiographic findings: CM and pulmonary edema |
| Lutembacher syndrome | ASD associated with MS |
| Postmyocardial infarction syndrome (Dressler syndrome) | Chest pain, fever, polyserositis—several weeks postinfarction; radiographic findings: pericardial or pleural effusion, noncardiogenic edema |
| Postpericardiotomy syndrome | Chest pain, fever, joint pain—weeks or months after closed or open heart surgery; radiographic findings: pericardial or pleural effusion, noncardiogenic pulmonary edema, constrictive pericarditis |
| Romano–Ward syndrome | Familial Q-T prolongation, arrhythmias, syncope |
| Shone syndrome (or complex) (see e-Fig. 78.16) | Complex of multiple left-sided obstructions, parachute mitral valve, supravalvar ring of LA, sub-AS, COA |
| Sick sinus syndrome | Arrhythmias |
| Tetralogy of Fallot (see e-Figs. 78.9 and 78.15) | Combination of VSD, overriding AO, RVH, RV outflow obstruction; may be PS and PPS |
| Trilogy of Fallot | PS, ASD (or PFO), right-to-left shunting |
| Uhl syndrome (anomaly) | Congenital aplasia of RV myocardium, RV CMY |
| Wolff–Parkinson–White syndrome | Aberrant intracardiac ECG pathway producing arrhythmias; associated with Ebstein anomaly, IHSS, levo-TGA, giant RA diverticulum |

*AO,* Aorta or aortic; *AP,* aorticopulmonary; *AR,* aortic regurgitation; *AS,* aortic stenosis; *ASD,* atrial septal defect; *AVSD,* atrioventricular septal defect; *CAD,* coronary artery disease; *CM,* cardiomegaly; *CMY,* cardiomyopathy; *COA,* coarctation of the aorta; *DORV,* double-outlet right ventricle; *ECG,* electrocardiogram; *IHSS,* idiopathic hypertrophic subaortic stenosis; *LA,* left atrium; *LV,* left ventricle; *LVOT,* left ventricular outflow tract; *MR,* mitral regurgitation; *MS,* mitral stenosis; *MVP,* mitral valve prolapse; *PA,* pulmonary artery; *PDA,* patent ductus arteriosus; *PFO,* patent foramen ovale; *PPS,* peripheral pulmonary stenosis; *PS,* pulmonary stenosis; *RA,* right atrium; *RAA*, right aortic arch; *RV,* right ventricle; *RVH,* right ventricular hypertrophy; *TGA,* transposition of the great arteries; *TOF,* tetralogy of Fallot; *VSD,* ventricular septal defect.

Eighty-two percent of patients die within the first month of life. Congenital heart defects are seen in approximately 80% of patients. The most common defects include ASD, VSD, PDA, dextrocardia, and a double-outlet right ventricle.[6,43]

## Trisomy 18 (Edwards Syndrome)

***Overview.*** Trisomy 18 is the second most common autosomal trisomy, with prevalence at birth of about 1 in 7,000. It is characterized by severe psychomotor and growth retardation, microcephaly, microphthalmia, micrognathia or retrognathia, microstomia, malformed ears, distinctively clenched fingers, and other congenital malformations.

Cardiac anomalies are seen in 90% to 100% of cases. The most common cardiac anomalies are VSD and valvular heart disease.[6] The pulmonary and aortic valves usually are affected. Other cardiac anomalies include ASD, PDA, aortic coarctation, TOF, transposition of the great arteries, and a hypoplastic left heart. Anomalies of the VACTERL spectrum also are associated with trisomy 18.

## Turner Syndrome

***Overview.*** Turner syndrome (XO, monosomy X) is one of the most frequent chromosomal aberrations in females. It affects approximately 1 in 2,000 live female births, but it has been estimated that only 1% of fetuses survive to term and that as many as 10% of spontaneous miscarriages have the 45,XO karyotype.[44] The characteristic clinical findings include a webbed neck, a shield chest with widely spaced nipples, short stature, gonadal insufficiency, and infertility.[45]

A congenital heart defect occurs in 20% to 40% of patients with Turner syndrome. The most common are coarctation of the aorta (30%) (e-Fig. 78.19) and bicuspid aortic valve (30%–50%) (see Chapter 73). Dilation of the aortic root is not as common (3%–8%) but can have devastating consequences such as dissection and rupture.[44] Other less common malformations include MVP, aortic stenosis, aortic regurgitation, partial anomalous pulmonary venous drainage, and hypoplastic left heart syndrome. Lymphangiectasia, lymphedema, hemangiomas, and systemic venous anomalies also can occur.[45]

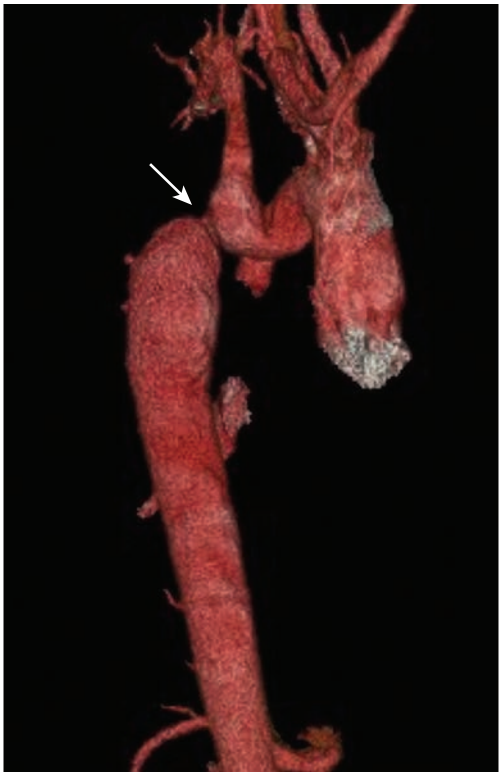

**e-Figure 78.19. Turner syndrome in a 10-year-old girl.** This sagittal oblique three-dimensional volumetric reconstruction of the aortic arch demonstrates marked tortuosity of the transverse arch along with focal coarctation immediately distal to the left subclavian artery *(arrow).*

**TABLE 78.3** Chromosomal Anomalies and Their Associated Cardiovascular Defects

| Chromosomal Anomaly | Cardiovascular Defects |
|---|---|
| Fragile X | MVP, MR, AR, TR, dilated AO root, COA |
| Trisomy 13 (Patau syndrome) | PDA, VSD, ASD, DEXTRO, capillary hemangioma, cervical cystic hygroma |
| Trisomy 18 (Edwards syndrome) | VSD, polyvalvular heart disease (pulmonary and AO valves), ASD, PDA, COA, TOF, TGA, HPLH, VACTERL, pentalogy of Cantrell |
| Trisomy 21 (Down syndrome) (see e-Fig. 78.18) | AVSD, VSD, ASD, TOF, PDA, PS, MVP, aberrant right SCA, intimal arterial fibrodysplasia, lymphatic abnormality, upper airway obstruction and CHF |
| Cat-eye syndrome (trisomy or tetrasomy 22) | TAPVR, TOF |
| Monosomy X, XO (Turner syndrome) (see e-Fig. 78.19) | COA, bicuspid AO valve, AO aneurysm, dissection, septal defects, abnormal mitral valve, sub-AS, PS, APVR, HPLH, pentalogy of Cantrell, DEXTRO, RAA, hemangioma, lymphangiectasia, venous anomalies |
| XXY (Klinefelter syndrome) | MVP, Takayasu arteritis, cerebral aneurysms, varicose veins |
| **DELETION SYNDROMES** | |
| Monosomy 1p36 syndrome | Dilated CMY, PDA |
| 22q11 (predominantly DiGeorge syndrome (CATCH 22), also velocardiofacial syndrome) (see e-Fig. 78.17) | Type B interrupted arch, RAA, VSD, TOF, TRU, COA, aberrant right SCA, isolated SCA |
| 5p: Cri du chat syndrome | CHD |
| 4p: Wolf–Hirschhorn syndrome | ASD, VSD, valve anomalies, complex CHD, persistent left SVC |
| 17p: Miller–Dieker syndrome (lissencephaly type 1) | ASD, CHD, conduction abnormalities |
| 18q syndrome | Absent pulmonary valve, PDA, AS, dilated ascending AO |

*AO,* Aorta or aortic; *APVR,* anomalous pulmonary venous return; *AR,* aortic regurgitation; *AS,* aortic stenosis; *ASD*, atrial septal defect; *AVSD,* atrioventricular septal defect; *CATCH 22,* cardiac defects, abnormal facies, thymic hypoplasia, cleft palate, hypocalcemia, 22q11 deletions; *CHD,* congenital heart disease; *CHF,* congestive heart failure; *CMY,* cardiomyopathy; *COA,* coarctation of the aorta; *DEXTRO,* dextrocardia; *HPLH,* hypoplastic left heart; *L,* left; *MR,* mitral regurgitation; *MVP,* mitral valve prolapse; *PDA,* patent ductus arteriosus; *PS,* pulmonary stenosis; *RAA,* right aortic arch; *SCA,* subclavian artery; *SVC,* superior vena cava; *TAPVR,* total anomalous pulmonary venous return; *TGA,* transposition of the great arteries; *TOF,* tetralogy of Fallot; *TR,* tricuspid regurgitation; *TRU,* truncus arteriosus; *VACTERL,* vertebral, anal atresia, cardiac, tracheal fistula, esophageal atresia, renal, limb; *VSD,* ventricular septal defect.

***Imaging.*** The approach to imaging of the cardiovascular system in Turner syndrome varies with the clinical scenario and is similar to other diseases with widespread cardiovascular manifestations.

## Klinefelter Syndrome

***Overview.*** Klinefelter (47,XXY) syndrome is present in 1 in 500 to 1 in 1,000 live male births.[46] The clinical findings of Klinefelter syndrome include infertility, gynecomastia, hypogonadotropic hypogonadism, cognitive impairment, and predisposition to malignancy.[46]

MVP, the most common cardiac anomaly, occurs in 55% of patients. Other uncommon defects include TOF, ASD, VSD, tricuspid atresia, and aortic coarctation. Vascular abnormalities include cerebral aneurysms, varicose veins, venous thromboemboli, and arteritis.[47]

## Other Chromosomal Anomalies

Less common chromosomal anomalies and their associated cardiovascular lesions are listed in Table 78.3. The most commonly associated defects are listed first, and cardiac lesions generally are listed before vascular malformations.

### KEY POINTS

- The typical right atrial isomerism often includes AVSD, single ventricle, DORV or TGA with pulmonary atresia, and TAPVR (often obstructed).
- Left atrial isomerism is more commonly associated with less complex CHD. The most consistent vascular anomaly is absence of the intrahepatic inferior vena cava with azygos continuation.
- Conservative management is favored where possible in the vasculopathy associated with Ehlers–Danlos syndrome. Marked vascular fragility makes both catheter and surgical interventions hazardous.
- Elucidation of the genetic and cellular pathophysiology of many of the syndromes discussed in this chapter has shed new light on the spectrum of related disorders and shows promise in the development of targeted cellular pathway therapies.
- Several hereditary vascular lesions have been linked to altered regulation of TGF-β, a cytokine pathway that affects cell performance. These TGF-β signalopathies include Marfan syndrome, Loeys–Dietz syndrome, and autosomal recessive cutis laxa. Treatment with TGF-β antagonists appears to be promising.
- RASopathies are a group of lesions with germline mutations that affect the RAS/MAPK pathway, which controls cell development, growth, and proliferation. These include NF1 and Noonan, Costello, and cardiofaciocutaneous syndromes. These lesions have distinct but overlapping features with craniofacial, cutaneous, and cardiovascular lesions and an increased propensity for malignant tumors.
- Truncus arteriosus and type B interruption of the aortic arch are often associated with a 22q11 deletion (DiGeorge syndrome).
- Trisomy 21 (Down syndrome) is the most common chromosomal disorder associated with congenital heart disease; atrioventricular septal defect is especially common.
- Monosomy X (Turners syndrome) is most strongly associated with bicuspid aortic valve and aortic coarctation. There is also a specific association with ascending aortic aneurysm and venolymphatic abnormalities.

## SUGGESTED READINGS

Allanson JE, Roberts AE. Noonan syndrome. In: Pagon RA, Adam MP, Ardinger HH, et al, eds. *GeneReviews (R)*. Seattle (WA): University of Washington, Seattle; 2016. https://www.ncbi.nlm.nih.gov/pubmed/20301303.

Applegate KE, Goske MJ, Pierce G, et al. Situs revisited: imaging of the heterotaxy syndrome. *Radiographics*. 1999;19:837–852.

De Paepe A, Malfait F. The Ehlers-Danlos syndrome, a disorder with many faces. *Clin Genet*. 2012;82:1–11.

Morisaki T, Morisaki H. Genetics of hereditary large vessel diseases. *J Hum Genet*. 2016;61:21–26.

Taybi H, Lachman RS. *Radiology of Syndromes, Metabolic Disorders, and Skeletal Dysplasias*. 5th ed. St. Louis: Mosby; 2007.

## REFERENCES

Full references for this chapter can be found on www.expertconsult.com.

## REFERENCES

1. Lambert TE, Kuller J, Small M, et al. Abnormalities of fetal situs: an overview and literature review. *Obstet Gynecol Surv*. 2016;71(1):33–38.
2. Applegate KE, Goske MJ, Pierce G, et al. Situs revisited: imaging of the heterotaxy syndrome. *Radiographics*. 1999;19(4):837–852.
3. Newman B, Koppolu R, Murphy D, et al. Heterotaxy syndromes and abnormal bowel rotation. *Pediatr Radiol*. 2014;44(5):542–551.
4. Harrison MJ, Shapiro AJ, Kennedy MP. Congenital heart disease and primary ciliary dyskinesia. *Paediatr Respir Rev*. 2016;18:25–32.
5. Bartram U, Wirbelauer J, Speer CP. Heterotaxy syndrome – asplenia and polysplenia as indicators of visceral malposition and complex congenital heart disease. *Biol Neonate*. 2005;88(4):278–290.
6. Taybi H, Lachman RS. *Radiology of Syndromes, Metabolic Disorders and Skeletal Dysplasias*. 5th ed. St. Louis: Mosby; 2007.

6a. Radhakrishnan R, Towbin AJ. Imaging findings in Down syndrome. *Pediatr Radiol*. 2014;44(5):506–521. doi:10.1007/s00247-013-2859-y. [Epub 2014 Apr 16].

7. Newman B, Feinstein JA, Cohen RA, et al. Congenital extrahepatic portosystemic shunt associated with heterotaxy and polysplenia. *Pediatr Radiol*. 2010;40(7):1222–1230.
8. De Paepe A, Malfait F. The Ehlers-Danlos syndrome, a disorder with many faces. *Clin Genet*. 2012;82(1):1–11.
9. Beighton P, De Paepe A, Steinmann B, et al. Ehlers-Danlos syndromes: revised nosology, Villefranche, 1997. Ehlers-Danlos National Foundation (USA) and Ehlers-Danlos Support Group (UK). *Am J Med Genet*. 1998;77(1):31–37.
10. Germain DP. The vascular Ehlers-Danlos syndrome. *Curr Treat Options Cardiovasc Med*. 2006;8(2):121–127.
11. Judge DP, Dietz HC. Marfan's syndrome. *Lancet*. 2005;366(9501): 1965–1976.
12. Milewicz DM, Dietz HC, Miller DC. Treatment of aortic disease in patients with Marfan syndrome. *Circulation*. 2005;111(11):e150–e157.
13. Radonic T, de Witte P, Groenink M, et al. Critical appraisal of the revised Ghent criteria for diagnosis of Marfan syndrome. *Clin Genet*. 2011;80(4):346–353.
14. van Karnebeek CD, Naeff MS, Mulder BJ, et al. Natural history of cardiovascular manifestations in Marfan syndrome. *Arch Dis Child*. 2001;84(2):129–137.
15. Gao LG, Luo F, Hui RT, et al. Recent molecular biological progress in Marfan syndrome and Marfan-associated disorders. *Ageing Res Rev*. 2010;9(3):363–368.
16. Morisaki T, Morisaki H. Genetics of hereditary large vessel diseases. *J Hum Genet*. 2016;61(1):21–26.
17. Loeys BL. Angiotensin receptor blockers: a panacea for Marfan syndrome and related disorders? *Drug Discov Today*. 2015;20(2): 262–266.
18. Van Hemelrijk C, Renard M, Loeys B. The Loeys-Dietz syndrome: an update for the clinician. *Curr Opin Cardiol*. 2010;25(6):546–551.
19. Johnson PT, Chen JK, Loeys BL, et al. Loeys-Dietz syndrome: MDCT angiography findings. *AJR Am J Roentgenol*. 2007;189(1): W29–W35.
20. Kalra VB, Gilbert JW, Malhotra A. Loeys-Dietz syndrome: cardiovascular, neuroradiological and musculoskeletal imaging findings. *Pediatr Radiol*. 2011;41(12):1495–1504, quiz 1616.
21. Hirbe AC, Gutmann DH. Neurofibromatosis type 1: a multidisciplinary approach to care. *Lancet Neurol*. 2014;13(8):834–843.
22. Jett K, Friedman JM. Clinical and genetic aspects of neurofibromatosis 1. *Genet Med*. 2010;12(1):1–11.
23. Bezniakow N, Gos M, Obersztyn E. The RASopathies as an example of RAS/MAPK pathway disturbances - clinical presentation and molecular pathogenesis of selected syndromes. *Dev Period Med*. 2014;18(3):285–296.
24. Lin AE, Birch PH, Korf BR, et al. Cardiovascular malformations and other cardiovascular abnormalities in neurofibromatosis 1. *Am J Med Genet*. 2000;95(2):108–117.
25. Friedman JM, Arbiser J, Epstein JA, et al. Cardiovascular disease in neurofibromatosis 1: report of the NF1 Cardiovascular Task Force. *Genet Med*. 2002;4(3):105–111.
26. Lama G, Graziano L, Calabrese E, et al. Blood pressure and cardiovascular involvement in children with neurofibromatosis type1. *Pediatr Nephrol*. 2004;19(4):413–418.
27. Lendvay TS, Marshall FF. The tuberous sclerosis complex and its highly variable manifestations. *J Urol*. 2003;169(5):1635–1642.
28. Staley BA, Vail EA, Thiele EA. Tuberous sclerosis complex: diagnostic challenges, presenting symptoms, and commonly missed signs. *Pediatrics*. 2011;127(1):e117–e125.
29. Hinton RB, Prakash A, Romp RL, et al. Cardiovascular manifestations of tuberous sclerosis complex and summary of the revised diagnostic criteria and surveillance and management recommendations from the International Tuberous Sclerosis Consensus Group. *J Am Heart Assoc*. 2014;3(6):e001493.
30. Salerno AE, Marsenic O, Meyers KE, et al. Vascular involvement in tuberous sclerosis. *Pediatr Nephrol*. 2010;25(8):1555–1561.
31. Jost CJ, Gloviczki P, Edwards WD, et al. Aortic aneurysms in children and young adults with tuberous sclerosis: report of two cases and review of the literature. *J Vasc Surg*. 2001;33(3):639–642.
32. Tworetzky W, McElhinney DB, Margossian R, et al. Association between cardiac tumors and tuberous sclerosis in the fetus and neonate. *Am J Cardiol*. 2003;92(4):487–489.
33. Drolet BA, Dohil M, Golomb MR, et al. Early stroke and cerebral vasculopathy in children with facial hemangiomas and PHACE association. *Pediatrics*. 2006;117(3):959–964.
34. Frieden IJ, Reese V, Cohen D. PHACE syndrome. The association of posterior fossa brain malformations, hemangiomas, arterial anomalies, coarctation of the aorta and cardiac defects, and eye abnormalities. *Arch Dermatol*. 1996;132(3):307–311.
35. Wendelin G, Kitzmuller E, Salzer-Muhar U. PHACES: a neurocutaneous syndrome with anomalies of the aorta and supraaortic vessels. *Cardiol Young*. 2004;14(2):206–209.
36. Metry D, Heyer G, Hess C, et al. Consensus statement on diagnostic criteria for PHACE syndrome. *Pediatrics*. 2009;124(5):1447–1456.
37. Rao RP, Drolet BA, Holland KE, et al. PHACES association: a vasculocutaneous syndrome. *Pediatr Cardiol*. 2008;29(4):793–799.
38. Allanson JE, Roberts AE. Noonan syndrome. In: Pagon RA, Adam MP, Ardinger HH, et al, eds. *GeneReviews (R)*. Seattle (WA): University of Washington, Seattle; 2016. https://www.ncbi.nlm.nih.gov/pubmed/20301303.
39. Prendiville TW, Gauvreau K, Tworog-Dube E, et al. Cardiovascular disease in Noonan syndrome. *Arch Dis Child*. 2014;99(7):629–634.
40. Tartaglia M, Gelb BD, Zenker M. Noonan syndrome and clinically related disorders. *Best Pract Res Clin Endocrinol Metab*. 2011;25(1):161–179.
41. Chan FP. Truncus arteriosus. In: Ho H, Reddy GP, eds. *Cardiovascular Imaging - Expert Radiology Series*. St. Louis: Mosby; 2011.
42. Vida VL, Barnoya J, Larrazabal LA, et al. Congenital cardiac disease in children with Down's syndrome in Guatemala. *Cardiol Young*. 2005;15(3):286–290.
43. Duarte AC, Menezes AI, Devens ES, et al. Patau syndrome with a long survival. A case report. *Genet Mol Res*. 2004;3(2):288–292.
44. Elsheikh M, Dunger DB, Conway GS, et al. Turner's syndrome in adulthood. *Endocr Rev*. 2002;23(1):120–140.
45. Frias JL, Davenport ML, Committee on Genetics, Section on Endocrinology. Health supervision for children with Turner syndrome. *Pediatrics*. 2003;111(3):692–702.
46. Smyth CM, Bremner WJ. Klinefelter syndrome. *Arch Intern Med*. 1998;158(12):1309–1314.
47. Wattendorf DJ, Muenke M. Klinefelter syndrome. *Am Fam Physician*. 2005;72:2259–2262.

# 79

# Myocardial, Endocardial, and Pericardial Diseases

*Randolph Otto, A. Luana Stanescu, and Mark Ferguson*

## MYOCARDIAL DISEASES

Cardiomyopathies include various diseases of the myocardium, often chronic or progressive, and associated with cardiac dysfunction. These are rare but serious disorders; only 25% of children survive more than 5 years after the onset of symptoms. Although our understanding of the causes of pediatric cardiomyopathy has advanced, the prognosis has not changed considerably in the past 30 years and is the same in developing and industrialized nations.[1,2]

Cardiomyopathies may be classified according to the dominant pathophysiology (e-Box 79.1). Four major physiologic forms of cardiomyopathy are described: dilated, hypertrophic, restrictive, and arrhythmogenic. While often discussed as distinct entities, occasionally there is considerable overlap in pathophysiologic features. Dilated and hypertrophic cardiomyopathies are the most common forms in children.[2]

Cardiomyopathy may also be classified according to etiology. Inflammatory and isolated familial cardiomyopathies account for the majority of pediatric cases with a known cause.[3] Other specific cardiomyopathies that are less common in the pediatric population include those resulting from metabolic disorders, general systemic diseases, muscular dystrophies, neuromuscular disorders, and sensitivity or toxic reactions (e.g., radiation and chemotherapy). In two-thirds of children with cardiomyopathy, no specific etiology is found.[2,3]

Because of its availability, lack of radiation use, and portability, echocardiography is the most common method used to classify cardiomyopathy and evaluate cardiac function. With improvements in technology, cardiovascular magnetic resonance imaging (MRI) has become an increasingly powerful tool.[4,5] With the multiple techniques available, cardiac MRI can be used to assess myocardial morphology and function (cine sequences), with expanding techniques for myocardial tissue characterization, including perfusion, delayed myocardial enhancement, and T1 mapping.[4]

### Hypertrophic Cardiomyopathy

Hypertrophic cardiomyopathy (HCM) is the most common genetic cardiovascular disease and has autosomal dominant inheritance. HCM demonstrates quite variable penetrance and expression, but significant disability and even sudden death can occur at any age.[6]

The cellular myocardial architecture in HCM is disorganized, while the characteristic gross morphologic feature is that of hypertrophy. Myocardial wall thickening most commonly manifests in an asymmetric distribution involving the anterior septum, but some patients show symmetric (concentric) involvement of the left ventricle (Video 79.1). Furthermore, there can be associated obstruction of the left ventricular outflow tract secondary to septal hypertrophy and systolic anterior motion of the mitral valve.[6,7]

Echocardiography is the primary imaging study used to diagnose and characterize HCM. MRI can provide a more comprehensive evaluation of regions of wall thickening as well as offer more advanced techniques such as assessing for late myocardial enhancement within regions of scarring (Fig. 79.1), perform native T1 mapping of the myocardium, and even analyze cardiac strain parameters.[7–9]

### Dilated Cardiomyopathy

Dilated cardiomyopathy is the most common form of cardiomyopathy and currently the most frequent indication for heart transplantation.[1] Characterized by dilation and impaired systolic function of the left or occasionally both ventricles, patients typically present with progressive heart failure (Fig. 79.2), up to 75% succumbing or undergoing transplantation within 5 years.[1] While the majority of pediatric cases (66%) are idiopathic, common specific etiologies may include infectious myocarditis, familial disease, and neuromuscular disorders (most commonly Duchenne and Becker muscular dystrophies).[10] Although a frequent cause of dilated cardiomyopathy in adults, coronary artery disease is uncommon in childhood. Children with sickle cell disease may develop ischemic cardiomyopathy related to “sludging microinfarctions” with resulting focal myocardial fibrosis.[11] Most children with dilated cardiomyopathy are diagnosed in the first year of life. Late presentation in childhood, reduced left ventricular shortening fraction or ejection fraction, severe mitral regurgitation, right ventricular failure, and mural thrombus were found to be associated with a worsened prognosis, while those with infectious myocarditis generally fare better.[12]

Cardiac MRI can be helpful in characterizing the presence of myocardial edema, late enhancement, ventricular function, myocardial mass, and valvular regurgitation.[13,14]

### Arrhythmogenic Right Ventricular Cardiomyopathy

Arrhythmogenic right ventricular cardiomyopathy (ARVC) is the most arrhythmogenic form of human heart disease,[15] characterized by progressive fibrofatty replacement of myocardium, most commonly involving the right ventricle (RV). Approximately 50% of affected individuals have one or more identified mutations encoding desmosomal proteins,[16] with substantial variation in genetic penetrance and clinical manifestations. ARVC is also related to the rare autosomal recessive cardiocutaneous disorders Naxos disease and Carvajal syndrome. Remodeling of intercellular gap junctions is found diffusely in ARVC, including areas not exhibiting myocyte degeneration and fibrofatty replacement. These changes may play a role in the onset of ventricular arrhythmias and sudden death, with symptoms often manifesting earlier in athletic adolescents and young adults.[17] Fibrofatty myocardial infiltration and wall thinning of ARVC can be visualized on T1-weighted spin echo magnetic resonance (MR) sequences but has low sensitivity and specificity compared with right ventricular volumes and function.[18] Additional reliable MR findings include abnormal right ventricular regional or global wall motion and aneurysms, most frequently involving the RV free wall, inflow, and outflow tracts.[19] Late gadolinium enhancement may also be present.[20–22] Biventricular involvement has been identified on MRI in more than half of ARVC cases, and while less common, left dominant forms of the disease are increasingly recognized, with involvement of the left ventricle

**e-BOX 79.1** Classification of Cardiomyopathies According to the World Health Organization

**DILATED CARDIOMYOPATHY**

- Congestive cardiomyopathy

**HYPERTROPHIC CARDIOMYOPATHY**

- Hypertrophic obstructive cardiomyopathy
- Idiopathic hypertrophic subaortic stenosis
- Asymmetrical septal hypertrophy
- Nonobstructive hypertrophic cardiomyopathy

**RESTRICTIVE CARDIOMYOPATHY**

- Arrhythmogenic right ventricular cardiomyopathy
- Arrhythmogenic right ventricular dysplasia
- Right ventricular dysplasia
- Right ventricular cardiomyopathy

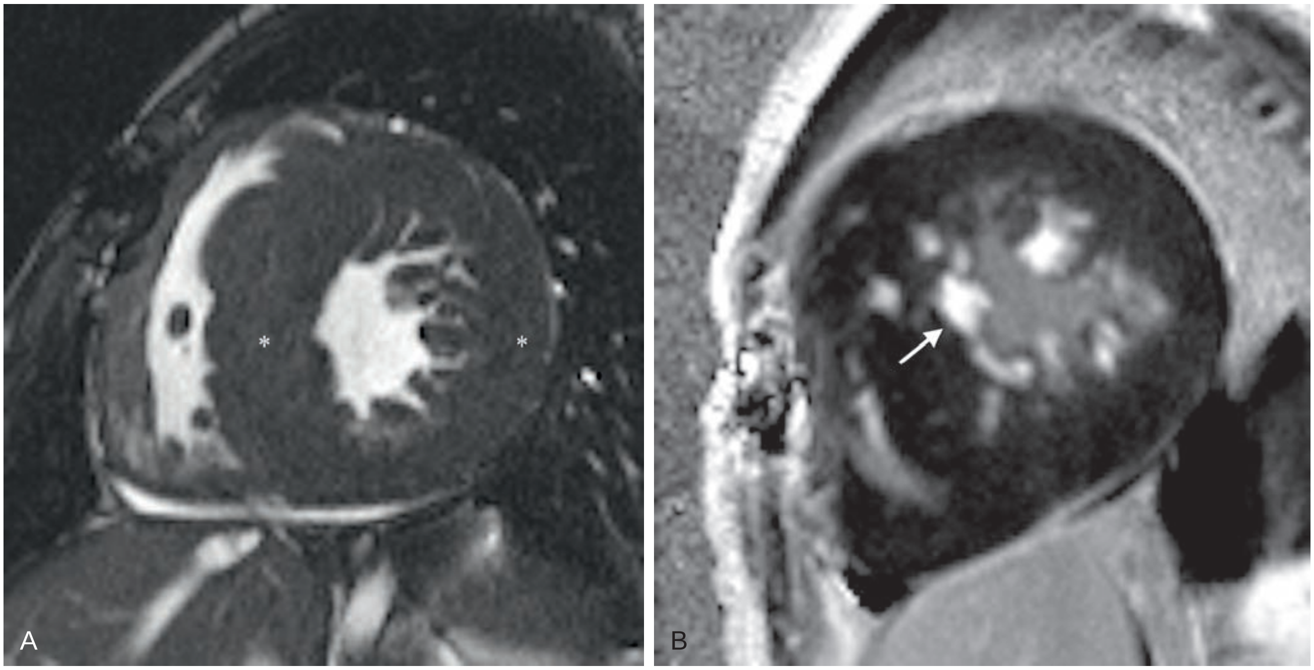

**Figure 79.1. Hypertrophic cardiomyopathy.** (A) Bright blood short axis MR image at end-diastole shows marked concentric LV wall thickening *(asterisk)*. (B) Postcontrast short axis MR image at end-diastole shows patchy late gadolinium enhancement in the LV myocardium including some trabeculations *(arrow)*.

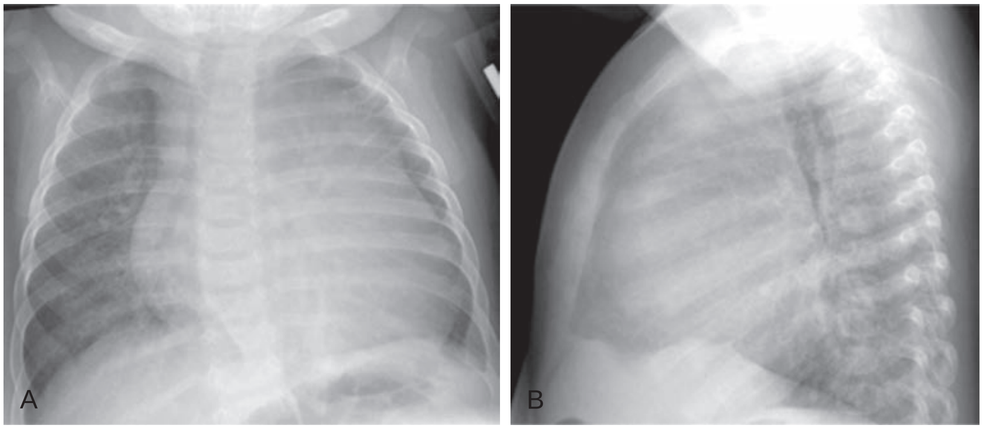

**Figure 79.2. Dilated cardiomyopathy.** (A) Antero-posterior (AP) and (B) lateral chest radiographs in an 11-month-old infant with dilated cardiomyopathy and glutamic aciduria type II show moderate enlargement of the cardiothymic silhouette.

(LV) posterolateral wall most frequent, where the changes can be potentially mistaken for myocarditis.

## Restrictive Cardiomyopathy

Restrictive cardiomyopathy (RCM) is the least common pediatric cardiomyopathy[3] and continues to carry the worst prognosis and transplant-free survival despite advances in therapy.[23,24] RCM is characterized by increased myocardial or endomyocardial stiffness leading to incomplete ventricular relaxation with decreased diastolic filling, while preserving normal or near-normal systolic function.[25,26] Endomyocardial fibrosis is one of the most common etiologies of restrictive cardiomyopathy in children and adolescents. A wide variety of genetic or acquired causes of infiltrative as well as noninfiltrative myocardial diseases may also be involved in restrictive cardiomyopathy pathogenesis. However, the majority of pediatric cases remain idiopathic.[23] Marked atrial dilation contrasting with the normal or small-sized ventricles is pathognomonic on imaging. Chest radiographs demonstrate cardiomegaly with pulmonary venous congestion in up to 90% of the cases.[23] Cardiac MRI will reflect the same anatomic findings, while additionally allowing real-time evaluation of regional and global ventricular function, calculation of ventricular volumes, and quantitative assessment of blood flow across the atrioventricular valves.

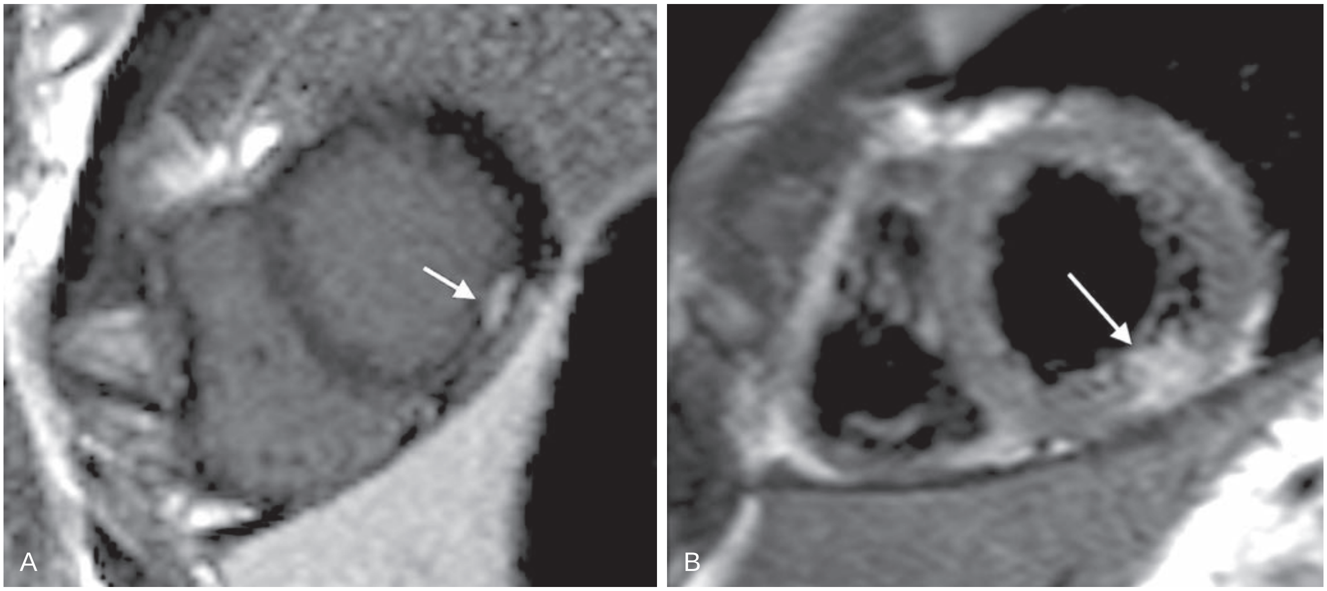

**Figure 79.3. Inflammatory cardiomyopathy.** (A) T2-weighted short axis MR image at end-diastole shows a focal region of hyperintense signal *(arrow)* within the LV inferolateral wall. (B) Postcontrast short axis MR image shows focal late gadolinium enhancement at the same site *(arrow)*. Findings are consistent with viral myocarditis.

Structural myocardial abnormalities, usually fibrosis, can be detected on delayed postcontrast inversion recovery MRI or T1 mapping. A variable degree of increased LV myocardial thickness is present in up to 34% of patients indicating a "mixed" restrictive/hypertrophic phenotype, which has been found to be associated with a better prognosis than "pure" restrictive cardiomyopathy.[24]

Constrictive pericarditis presents with similar restrictive physiology and should be differentiated from restrictive cardiomyopathy given the different management and prognosis. Increased pericardial thickness (>4 mm) with calcifications with or without contrast enhancement on computed tomography (CT) or MRI as well as a tubular configuration of the compressed ventricles are usually present in constrictive pericarditis, in contradistinction to restrictive cardiomyopathy.

## SPECIFIC CARDIOMYOPATHIES

### Inflammatory Cardiomyopathy

Inflammatory cardiomyopathy (myocarditis) is primarily caused by infectious agents, but can also be secondary to autoimmune diseases, hypersensitivity reactions, and toxic insults. While the infectious agent can be bacterial, fungal, or parasitic, in developed countries the most common etiology is viral (enterovirus, adenovirus, parvovirus, herpesvirus, etc.).[27]

Myocarditis can present with diverse manifestations ranging from nonspecific systemic symptoms (exertional dyspnea, fever, myalgia, etc.) to hemodynamic collapse and death.[28] Myocarditis has been involved in 8.6% to 12% of cases of sudden death in young adults.[29]

Echocardiography remains the initial imaging modality of choice and may demonstrate dilated cardiomyopathy, reduced ejection fraction, wall motion abnormalities, and even transient left ventricular hypertrophy.[30] However, MRI can provide a more complete and extensive evaluation of both cardiac function and myocardial tissue characterization (Fig. 79.3). The Lake Louise Criteria for diagnosing myocarditis by MRI include: hyperintense T2 signal (myocardial edema), early gadolinium enhancement of myocardium (hyperemia), and late gadolinium enhancement (fibrosis). If two of the three findings are present, the diagnostic accuracy is 78%.[31] Furthermore, T1 mapping may provide for greater diagnostic accuracy, perhaps even without the need for an intravenous contrast agent.[32,33]

### Neuromuscular Cardiomyopathy

Neuromuscular cardiomyopathy occurs in a variety of inherited neuromuscular disorders. Duchenne muscular dystrophy (DMD) is the most common of the muscular dystrophies and is caused by a defective gene on the X chromosome responsible for dystrophin production. Cardiac involvement by DMD results in myocardial fibrosis, degeneration, and fatty infiltration with associated compromise of left ventricular function.[34]

While changes associated with DMD related cardiomyopathy can be appreciated by electrocardiography and echocardiography, MRI is the superior modality for assessment.[35] Specifically, MRI offers the most comprehensive and accurate assessment of cardiac function as well as the ability to detect regions of myocardial fibrosis with late gadolinium enhancement (typically in the inferolateral wall, Fig. 79.4) and to evaluate myocardial strain metrics.[36,37] T1 mapping of the myocardium has the potential for additional quantitative assessment and detection of cardiac involvement in DMD.[38]

Becker muscular dystrophy (BMD) is another X-linked disorder that involves the dystrophin gene. While the overall clinical manifestations demonstrate a later onset and slower progression than those of DMD, the cardiac involvement in BMD can be more severe.[39]

Friedreich ataxia is an autosomal recessive trait related to mutations in the frataxin gene characterized by progressive ataxia and musculoskeletal abnormalities. The specific cardiac manifestations include hypertrophic cardiomyopathy (HCM) with systolic function impairment and associated arrhythmic complications. Heart failure is the primary cause of death in about 60% of patients.[40]

Cardiomyopathy related to BMD and Friederich ataxia can be best assessed by MRI similar to DMD.

### Metabolic Cardiomyopathy

Inborn errors of metabolism account for approximately 5% to 26% of cases of pediatric cardiomyopathy. There is a wide spectrum

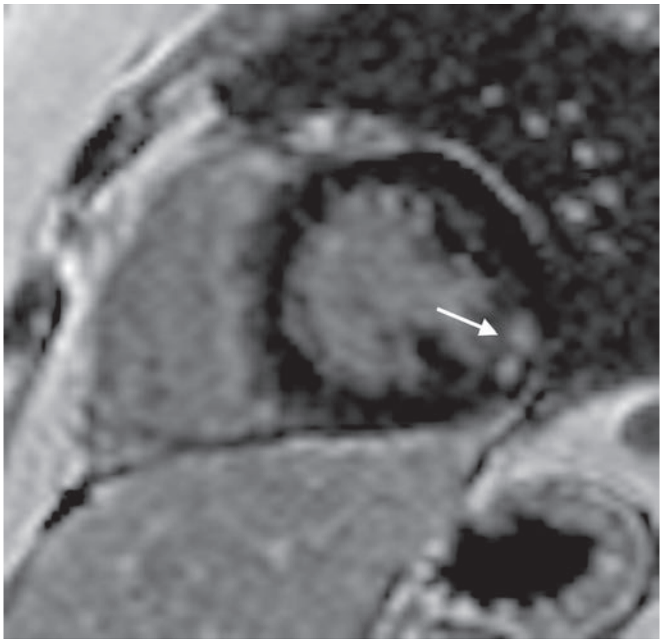

**Figure 79.4. Duchenne muscular dystrophy.** Postcontrast short axis MR image at end-diastole shows patchy late gadolinium enhancement within the LV inferolateral wall *(arrow)*.

of underlying pathophysiologies most commonly including storage disorders, fatty acid oxidation disorders, and organic acidurias, but mitochondrial and glycosylation disorders have also been implicated.[41,42]

Lysosomal storage disorders are characterized by accumulation of waste material within lysosomes. The mucopolysaccharidoses (Hurler syndrome and Hunter syndrome) are the most well known to be associated with cardiovascular disease with manifestations including thickened valves with shortened/thickened chordae tendineae resulting in valvular dysfunction as well as rigid and thickened coronary arteries. Fabry disease, a deficiency of lysosomal α-galactosidase A, can result in myocardial hypertrophy and dilation as well as conduction abnormalities and valvular dysfunction.[43]

Glycogen storage diseases are caused by deficiencies in glycogen metabolism. Types II (Pompe disease), III, and IV are the most common to involve the heart.[43]

Glycogen storage disease II is secondary to a deficiency in acid α-glucosidase and presents with two traditionally described phenotypes: classic infantile onset (<1 year of age) and late onset. Infantile onset disease classically manifests with cardiomegaly, HCM, and heart failure, with 75% of patients dying before 12 months of age.[44] However, some cases of early onset disease without cardiomyopathy have been described. Later onset disease (juvenile or adult) is often more mild in nature.[43] Cardiomyopathy tends to be rare in glycogen storage disease III; however, electrophysiologic evidence of heart dysfunction is typical. Patients with glycogen storage disease IV often die of liver disease before their cardiomyopathy becomes clinically evident.[43]

## Myocardial Iron Overload

Hemochromatosis is a disease in which there is abnormal iron deposition (iron overload) within multiple organs and can be classified as primary or secondary. Primary disease results from abnormal regulation of iron absorption. Secondary hemochromatosis is secondary to another disorder typically requiring chronic red blood cell transfusions.

Neonatal hemochromatosis is a condition in which severe liver disease is also accompanied by extrahepatic siderosis. Gestational alloimmune liver disease is typically the underlying process in which maternal antibodies bind to fetal liver antigens and result in hepatocyte injury and death.[45] While iron deposition is most notable in the liver, extrahepatic siderosis involves the heart, pancreas, exocrine and endocrine organs, and intestines, as well as the gastric and salivary glands. The reticuloendothelial elements are typically spared.[46]

Juvenile hereditary hemochromatosis is a characterized by severe iron overload occurring in the first to third decade of life. Two underlying gene mutations have been identified, *HJV* and *HAMP*. Typical clinical features include liver fibrosis/cirrhosis, hypogonadotropic hypogonadism, cardiomyopathy, and arthropathy. The primary cause of death is cardiac disease.[47]

Transfusion-related iron overload (a form of secondary hemochromatosis) is the most frequently encountered type of hemochromatosis in pediatric patients referred for imaging. Patients with refractory anemias, such as thalassemia, sickle cell anemia, myelodysplastic syndrome, or aplastic anemia, receive chronic transfusions resulting in overload of total body iron. While the liver remains the primary organ affected by iron deposition, cardiotoxicity related to iron deposition is largely accountable for patient's morbidity and mortality. Chelation therapy is critical and is guided by assessment of total body iron.

MRI has proven to be an effective method to determine total body iron (via liver assessment) as well as more specifically cardiac iron deposition. Increasing tissue iron concentrations result in an accelerated loss of T2 and T2* signal on multi-echo imaging from which tissue values can be derived (Fig. 79.5). The liver and heart can be routinely directly evaluated. However, assessment of pancreatic iron concentration has also been proposed as a simple stratification method to determine which patients are at risk for cardiac iron overload.[48]

## Toxic Cardiomyopathy

Survival rates for childhood cancers have significantly improved over the past few decades, often related to the use of anthracycline chemotherapeutic agents. However, the leading noncancer-related cause of morbidity and mortality amongst these cancer survivors is cardiovascular related disease. Anthracyclines, such as doxorubicin, are the underlying cause of many of these cardiovascular complications including decreased left ventricular mass, wall thickness, and contractility with associated heart failure.[49]

Conventional cardiac MRI offers a comprehensive evaluation of the cardiac function, whereas advanced MRI techniques include quantitative assessment of myocardial strain parameters as well as tissue characterization with T1 mapping.[50,51]

## Left Ventricular Noncompaction

Left ventricular noncompaction, also known as persistence of the spongy myocardium or left ventricular hypertrabeculation, is characterized by prominent left ventricular trabeculae, a thin compacted myocardial layer, and deep intertrabecular recesses. This appearance may be observed in healthy subjects with normal ventricular size and function, can be acquired, and can even be reversible. With more than 30 known associated genetic mutations, it remains uncertain if these features represent a distinct entity or merely a phenotypic manifestation of various cardiomyopathies. Patients with this condition may be at risk for systolic and diastolic dysfunction, arrhythmias, and embolic events.[52] Echocardiography and MRI can be useful in the identification of the thickened left ventricular trabeculae, bilayered myocardium, and deep recesses within the myocardial wall. The areas of left ventricular noncompaction may be focal or diffuse, and the diagnosis is suggested on CT or MRI by a noncompacted to compacted wall ratio of greater than 2.3 in diastole (Fig. 79.6).[53] Delayed contrast enhancement is associated with more advanced disease and is rare in infants and young children.

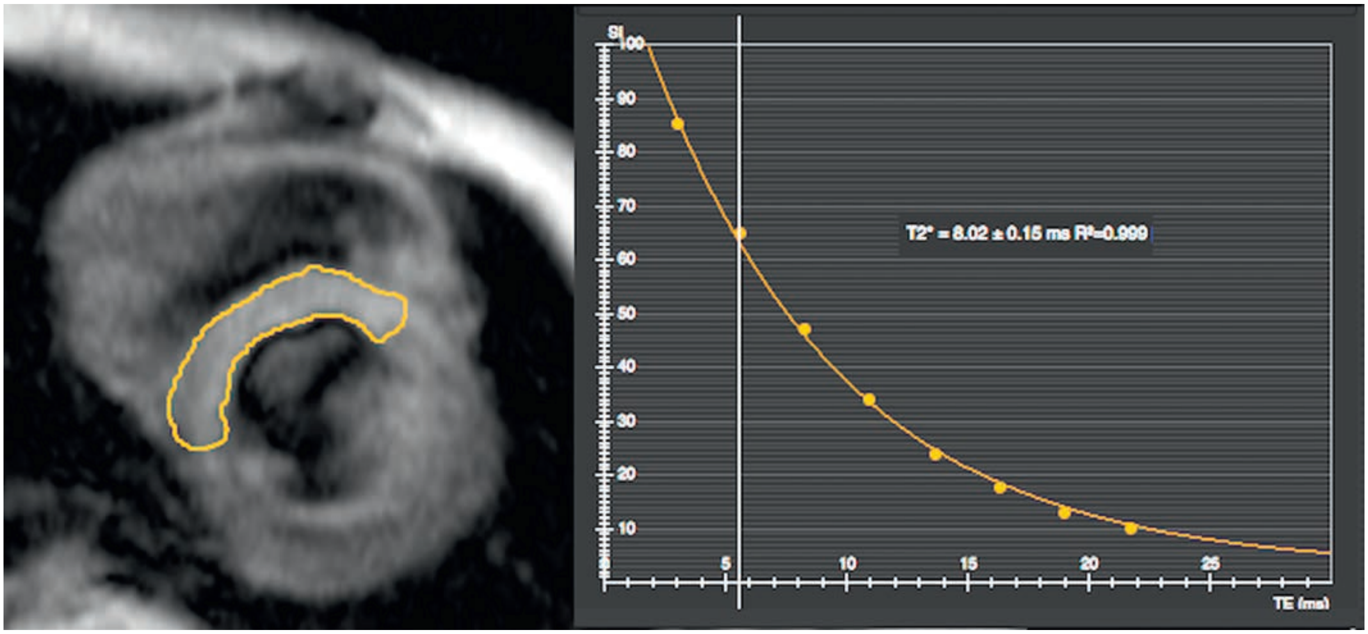

**Figure 79.5. Iron overload.** Representative image from a multiecho gradient echo MR acquisition in short axis orientation with a region of interest drawn to include the interventricular septum. Corresponding signal intensity curve over progressively increasing echo times with calculated T2* value is shown on right (Created in CVI42).

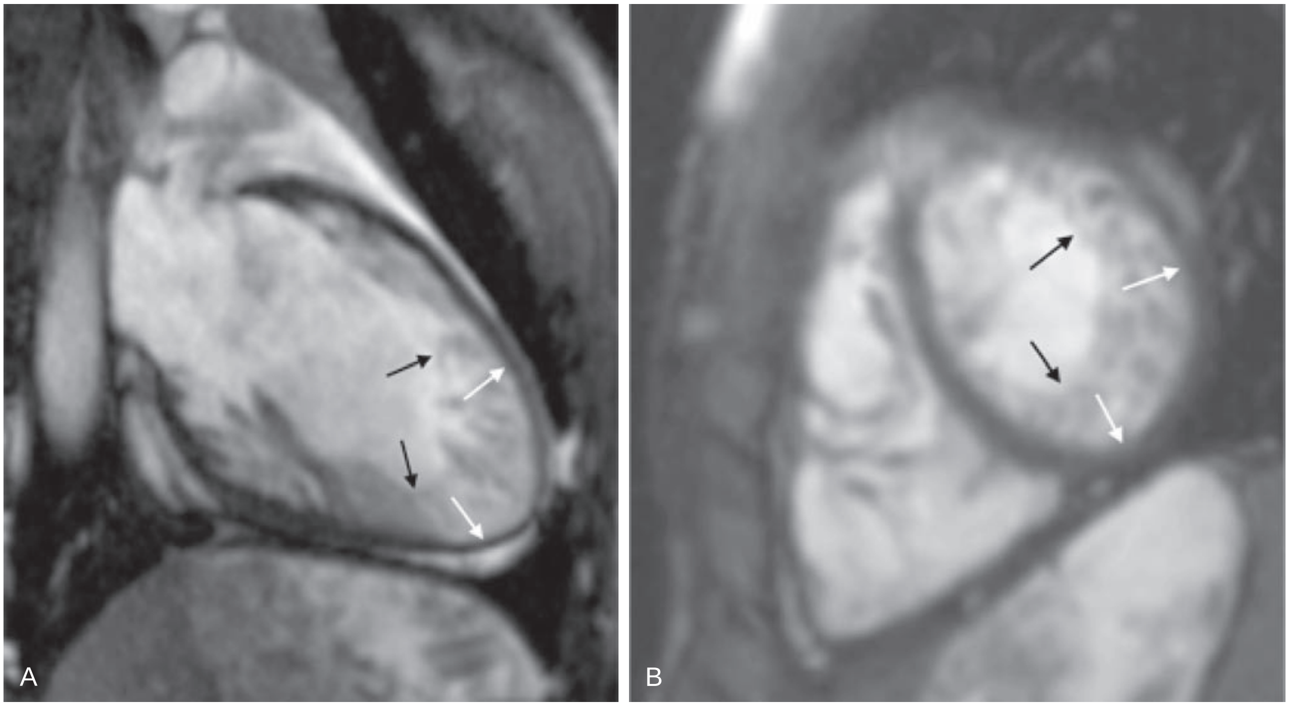

**Figure 79.6. Left ventricular noncompaction.** Left ventricular vertical long axis (A) and short axis (B) end-diastolic steady state free precession (SSFP) MR images demonstrate thickening of noncompacted myocardium *(black arrows),* compacted myocardium *(white arrows),* with noncompacted to compacted ratio greater than 2.3.

## VALVES

### Infectious Endocarditis

Before 1970, infectious endocarditis was common in children with underlying rheumatic heart disease. In the current era, endocarditis is most commonly associated with underlying congenital heart disease, whether untreated or after palliative or corrective surgery, where prosthetic patches, conduits, and valves can increase this risk. The incidence of catheter-associated infectious endocarditis involving the right heart has also risen among neonates and children receiving intensive care.[54] In recent years, an increase in infectious endocarditis in children without preexisting congenital heart disease has also been described. These cases are believed to be a result of valve infection from *Staphylococcus bacteremia*.[55,56]

Although children with infectious endocarditis may present acutely with high spiking fevers, the presentation typically is more indolent, with prolonged low-grade fever and nonspecific complaints including lethargy, weakness, arthralgia, myalgia, and weight loss.[56] In neonates, the symptoms may be more difficult to recognize and may include feeding difficulties and neurologic signs and symptoms, including seizures, hemiparesis, and apnea. Over the past 80 years, the leading bacteriologic agent responsible for infectious endocarditis has changed from viridans streptococci to staphylococci.[57]

The diagnosis of infectious endocarditis is based on the modified Duke criteria.[58] These criteria involve a combination of major criteria, including positive blood cultures or evidence of endocardial or valve involvement by echocardiography (e.g., vegetations and valve dysfunction), and minor criteria, including fever, predisposing factors (e.g., a heart condition or intravenous drug use), and evidence of embolic disease (e.g., septic pulmonary emboli, intracranial hemorrhage, conjunctival hemorrhage, and Janeway lesions).[58]

Radiographic findings of infectious endocarditis may include cardiomegaly and congestive heart failure. In the setting of right heart involvement, septic emboli may result in poorly marginated, cavitary, and nodular pulmonary parenchymal opacities with a basilar predilection. Diagnostic imaging also is beneficial in assessing for sequelae of endocarditis. Mycotic aneurysms may develop when infections involve the great arteries or a patent ductus arteriosus. Prompt diagnosis of these life-threatening aneurysms by echocardiography, CT, MRI (Fig. 79.7), or angiography is critical. The valves themselves are best assessed with echocardiography from both a morphologic and a functional standpoint.

Clinical settings increasing the risk for complications include prosthetic valves, left-sided endocarditis, infection with *Staphylococcus aureus* or fungal organisms, recurrent or prolonged course, cyanotic heart disease, and systemic to pulmonary shunts. Surgery is indicated in patients with recurrent systemic embolization, unresponsive congestive heart failure, acute valvular insufficiency, conduction abnormalities such as complete heart block, or persistent sepsis despite adequate antibiotic therapy. Surgery may also be useful in patients with fungal endocarditis, large or enlarging abscesses, mycotic aneurysms, or fistulous tracts (into the pericardium, between the cardiac chambers or vascular structures).[59]

### Rheumatic Fever

Rheumatic heart disease was once the leading cause of childhood-acquired heart disease in the United States and remains preeminent within disadvantaged populations across the globe. Rheumatic heart disease is the most serious manifestation of rheumatic fever, an autoimmune disease seen after pharyngitis with group A beta-hemolytic Streptococcus. The incidence of rheumatic fever and rheumatic heart disease has decreased dramatically with improved living conditions and the prompt use of antibiotics in the developed world.[60]

Diagnosis of rheumatic fever is based on the Jones criteria.[61] Rheumatic fever is diagnosed if the child has two major criteria or one major and two minor criteria, plus evidence of recent streptococcal infection. Major criteria include migratory arthritis, carditis, Sydenham chorea, erythema marginatum, and subcutaneous nodules. Minor criteria for diagnosis include aseptic arthralgias or monoarthritis, fever, elevated erythrocyte sedimentation rate, presence of C-reactive protein, prolonged PR interval on the electrocardiogram, and leukocytosis.[62]

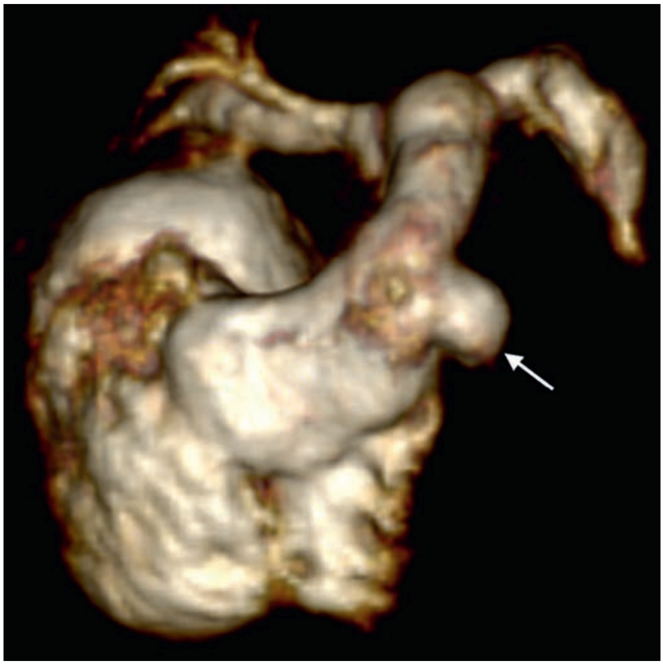
**Figure 79.7. Infectious endocarditis.** Contrast-enhanced MR angiography of the right heart and pulmonary arteries in a 3-year-old child with palliated complex congenital heart disease. Volume rendered image demonstrates a saccular mycotic pseudoaneurysm arising at the proximal right ventricle to pulmonary artery conduit anastomosis *(arrow)*.

Although all four cardiac valves may be affected by rheumatic heart disease, it is predominantly the mitral valve that is involved.[60] Acute valvular insufficiency develops, which, if severe, can result in congestive heart failure and death.[60] Noninfectious vegetations can be present on the valve leaflets, and the diagnosis of subclinical carditis is increasing with the use of echocardiography.[62] Other abnormalities that can be seen in patients with rheumatic heart disease include pericardial effusion and left atrial enlargement, characteristically involving the atrial appendage (Fig. 79.8). In chronic disease, affected valves may become stenotic in addition to the regurgitation that develops acutely.

## PERICARDIUM

### Normal Pericardium

The pericardium is a thin double-layered serous and fibrous structure that covers the heart and the origin of the great vessels.[63] The pericardial cavity is delineated by the visceral and parietal components of the inner serosal layer. Up to 50 mL of physiologic serous fluid can fill the pericardial cavity in adults. The pericardial fluid usually accumulates in the two main pericardial sinuses, transverse and oblique, and their multiple recesses (Fig. 79.9), which may be confused on CT with mediastinal lymphadenopathy, bronchogenic cysts or aortic dissection.[64,65]

Given that normal pericardial thickness measures less than 2 mm, radiologic visualization is possible only when facilitated by adjacent epicardial fat (more prominent along the right ventricle), mediastinal fat, and/or pericardial fluid.[65] Limited visualization

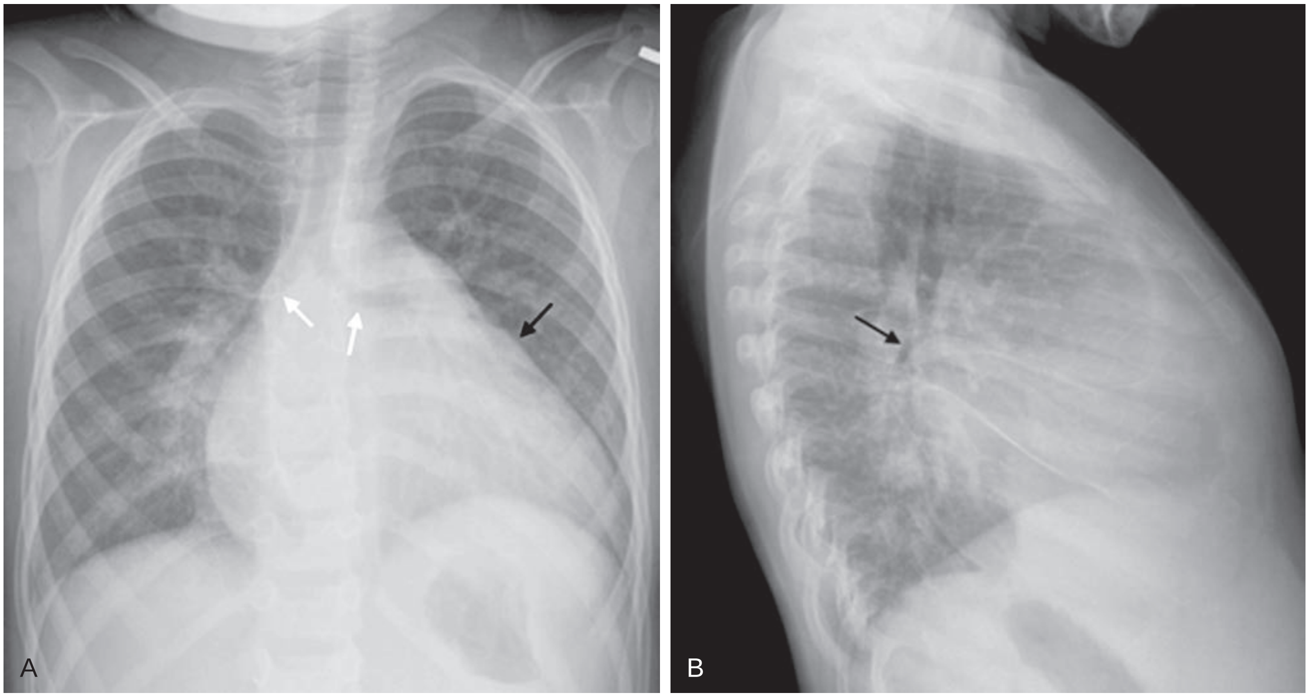

**Figure 79.8. Rheumatic heart disease.** PA (A) and lateral (B) chest radiographs demonstrating typical findings of generalized cardiac enlargement, with splaying of the carina *(white arrows)* and posterior displacement of the left lower lobe bronchus *(black arrow)* on (B) as evidence of left atrial enlargement, with prominent left atrial appendage *(black arrow)* on (A). Interstitial pulmonary edema and pleural fluid reflect elevated pulmonary venous pressure.

of the pericardium along the left ventricular wall due to minimal epicardial fat should not be confused with a pericardial defect in the absence of additional imaging signs.

Similar to adults, echocardiography has an important initial role in evaluating pericardial disease in pediatric patients, but is limited at times by difficulties in detecting mildly increased pericardial thickness or loculated pericardial effusions.[65,66] MR and CT provide a more complete evaluation of the pericardium and can be utilized as problem-solving tools in complicated cases.[65] MR is becoming the imaging modality of choice in children, allowing morphologic as well as functional cardiac evaluation with a large field of view, high soft tissue contrast, and characterization of inflammatory pericardial disease with late gadolinium enhancement.[13]

Normal pericardium is indirectly visualized as an echogenic line on echocardiography. On CT, the pericardium is best appreciated in systole as a hyperdense linear structure outlined by adjacent fat, while on MRI, the normal pericardium is characterized by intermediate to low signal on both T1 and T2 sequences given the fibrous composition.[67]

## Congenital Absence of the Pericardium

Pericardial defects are rare, found in less than 1/10,000 autopsies, and can be partial or complete.[67]

Partial pericardial defects involve the left heart in the majority of cases.[68] Partial pericardial defects, particularly the so-called foramen types, were found to cause herniation of cardiac structures that may lead to left atrial appendage strangulation or coronary artery compression with acute myocardial necrosis.[66,67,69] A focal bulge is typically present along the left heart border on imaging, corresponding to the herniated region.[67]

Complete absence of the pericardium usually involves the left side more frequently than the right, or may be bilateral. Complete pericardial absence is usually asymptomatic. Incidental imaging findings in complete bilateral as well as left-sided pericardial absence include levorotation of the heart with effacement of the right heart border and abnormal lucent bands on radiographs and CT due to lung tissue interposition in the aortopulmonary window and between the heart base and the diaphragm.[67,70] Excessive apical mobility may be present on cardiovascular magnetic resonance (CMR) imaging.[71]

## Pneumopericardium

In infants and neonates, pneumopericardium associated with other air leaks can occur in the setting of resuscitation or severe lung disease requiring utilization of positive end-expiratory pressure (PEEP) and continuous positive airway pressure (CPAP).[72] In older children with obstructive airway disease like asthma, pneumopericardium may present with pneumomediastinum and subcutaneous emphysema as part of air leak syndrome.[73]

On chest radiographs and CT, the hallmark of pneumopericardium is a lucent band that surrounds the cardiac silhouette up to the origin of the great vessels (Fig. 79.10). Pneumopericardium should be differentiated from pneumomediastinum that may also surround the heart but usually extends more superiorly in the upper thorax above the great vessels root, potentially dissecting into the cervical region soft tissues. Tension pneumopericardium in neonates is associated with high mortality and should be recognized and treated promptly.[74,75]

## Infectious/Inflammatory Pericarditis

In children, pericarditis most often occurs after cardiac surgery. In the absence of a surgical history, idiopathic or viral pericarditis accounts for up to 68% of cases, while bacterial etiology is found

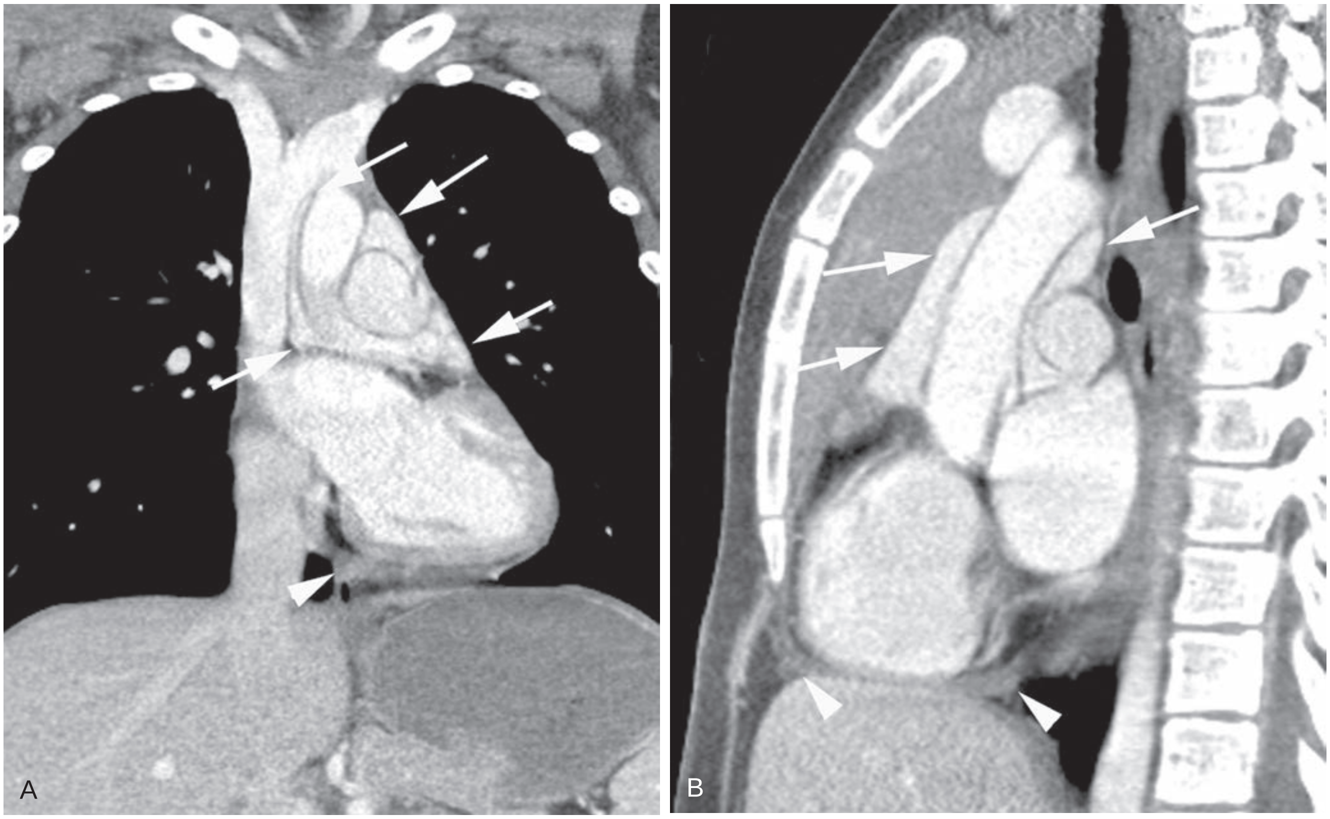

**Figure 79.9. Hemorrhagic pericarditis.** Coronal (A) and sagittal (B) contrast-enhanced chest CT images in an 11-year old with recurrent hemorrhagic pericarditis show active extravasation within the antero-superior aspect of the transverse pericardial sinus *(arrows)*. No hemorrhagic source was clearly identified. Slightly hyperdense pericardial fluid is also noted along the inferior aspect of the ventricles *(arrowheads)*. The patient was eventually diagnosed with pulmonary capillaritis and familial factor X deficiency.

in approximately 5% of cases (Fig. 79.11).[76,77] Chest trauma or connective tissue disorders such as lupus may also cause pericarditis in pediatric patients.

Cardiac MR plays an increasing role in the diagnosis and management of pericarditis in children, similar to adults. In the acute phase, inflammatory changes will cause pericardial thickening greater than 4 mm, with effusion and focal or diffuse pericardial enhancement on late gadolinium enhancement sequences (see Fig. 79.11).[13] Chronic inflammatory pericarditis is characterized by irregular thickening of the pericardium with variable contrast enhancement and occasionally increased adjacent epicardial fat.[66] In constrictive pericarditis, the fibrotic and/or calcified pericardium will demonstrate low signal on all MR sequences. Pericardial calcifications are best depicted on CT. The presence of late gadolinium enhancement may indicate potential reversibility with medical therapy.[78] Functional MRI will demonstrate diastolic interventricular septal flattening while phase contrast imaging of the tricuspid valve will show a restrictive filling pattern.[79]

## Pericardial Effusion

The etiologic spectrum of pericardial effusions in children has dramatically changed over the last decades. Neoplastic disease has become the leading cause, since the use of vaccines and antibiotic therapy has significantly decreased the incidence of pericardial effusion associated with bacterial pericarditis.[80] Idiopathic or viral pericardial effusions are more common in adolescents, particularly males.[77]

Accumulation of pericardial fluid follows a sequential pattern, with early collection seen along the posterolateral left or inferolateral right ventricular walls, followed by filling of the superior pericardial recess. Moderate to large pericardial effusions eventually accumulate anterior to the right ventricle and right atrium (Fig. 79.12).[66,79] Echocardiography remains the first-line imaging method of choice. CT and MRI can help differentiate pericardial effusion from pericardial thickening as well as characterize the pericardial fluid based on attenuation values (CT) and signal intensity (MRI). Chest radiographs have a limited utility in the diagnosis of pericardial effusion.[65,79]

Cardiac tamponade is the result of rapid accumulation of a relatively small amount of pericardial fluid or air (150–200 mL) that causes increased pericardial pressure, limiting the ventricular filling and cardiac output and eventually leading to cardiogenic shock and cardiac arrest.[79,81] Although the diagnosis is mostly clinical, if patients are evaluated with CT or MRI the imaging signs would include a large pericardial effusion with dilation of the superior vena cava (SVC), inferior vena cava (IVC), and hepatic veins, as well as flattening or inversion of the anterior right atrial and right ventricle walls during early systole and diastole.[66,79]

Pericardial tamponade in neonates after central venous catheter placement with vessel wall perforation is rare but associated with high mortality. A recent study suggests that this may be prevented if the tip of the catheter remains above the superior pericardial reflection, projected on chest radiographs just below the posterior right third intercostal space.[82]

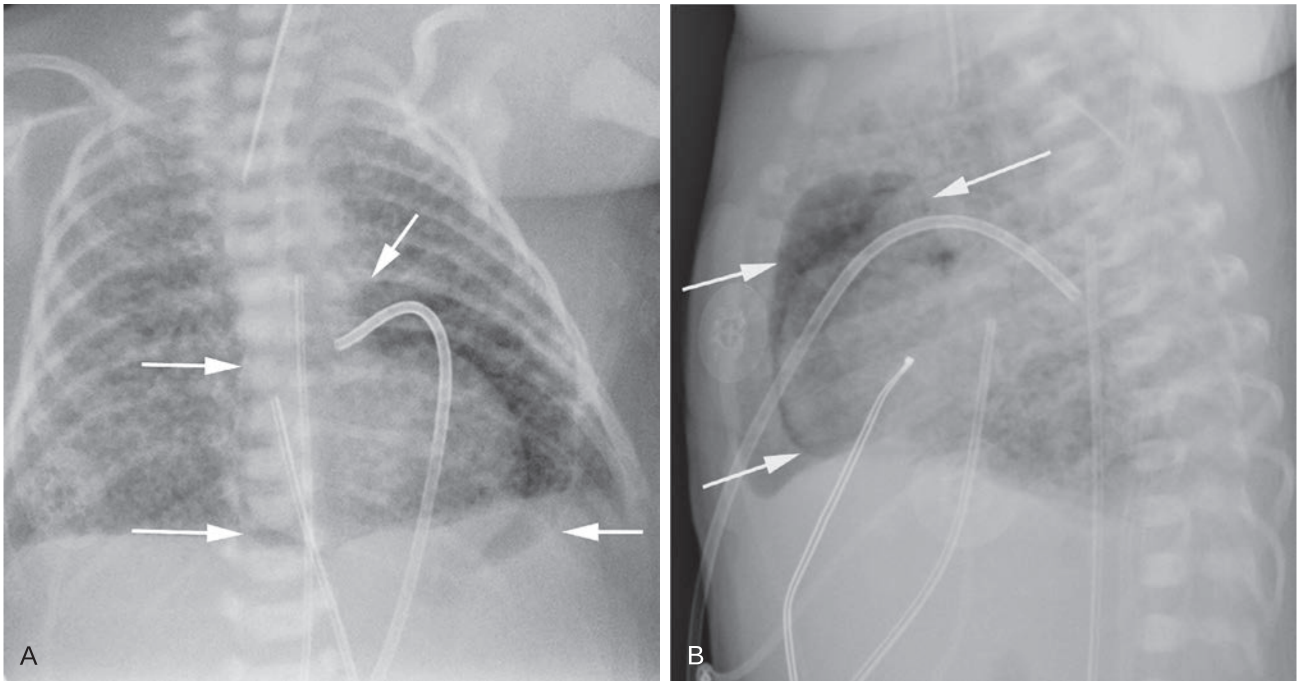

**Figure 79.10. Pneumopericardium.** Frontal (A) and lateral (B) chest radiographs in a ventilated premature newborn female with a large neck mass demonstrate air outlining the cardiac silhouette and the origin of the great vessels *(arrows)*. Diffuse granular and patchy pulmonary opacities are also noted consistent with infantile respiratory distress syndrome.

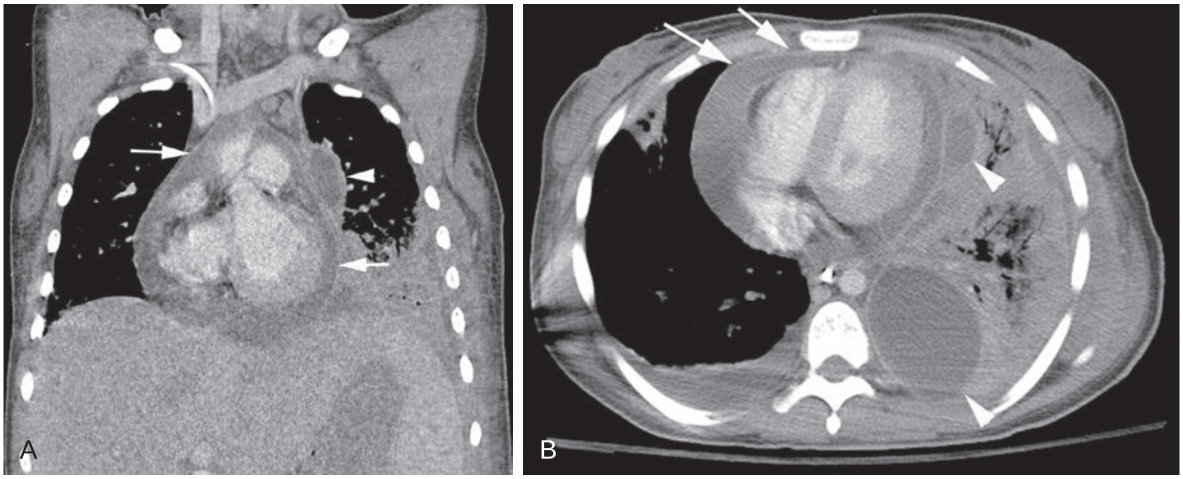

**Figure 79.11. Infectious pericarditis.** Contrast-enhanced coronal (A) and axial (B) CT images of the chest show a large pericardial effusion with pericardial enhancement *(arrows)* suggestive of pericarditis in this 16-year-old with severe pneumonia. Loculated left empyema *(arrowheads)* is also noted.

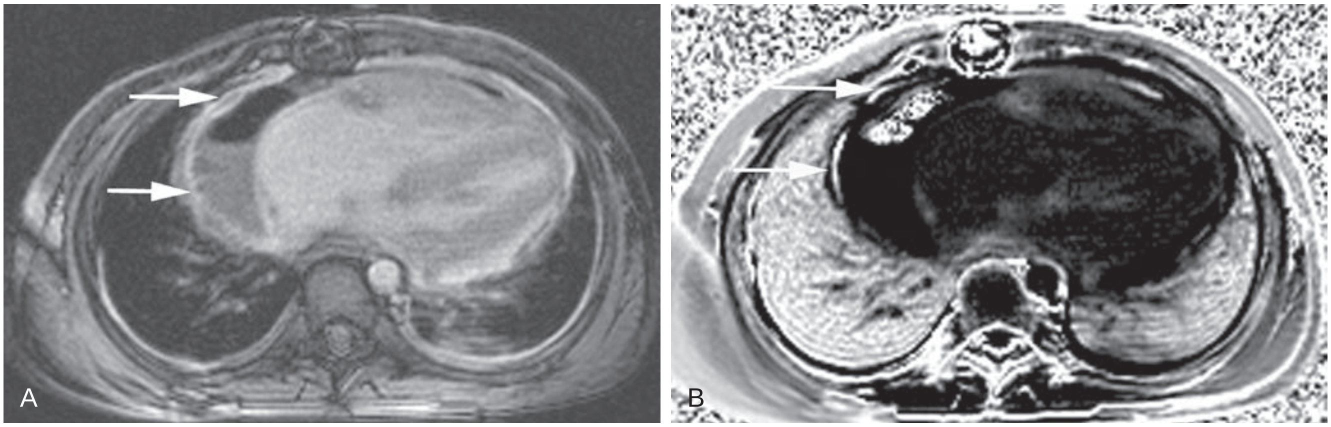

**Figure 79.12. Pericardial effusion.** Magnitude (A) and phase sensitive (B) axial LGE (late gadolinium enhancement) PSIR (phase-sensitive inversion recovery) images with optimized TI at 170 msec in a 14-year-old 3 weeks post heart transplant with recurrent hemorrhagic pericardial effusion status postdrainage. There is evidence for a large pericardial collection with air and complex fluid along the right atrium. Mild pericardial thickening and enhancement is also noted *(arrows),* likely reactive. No evidence of infection on microbiology exams.

## KEY POINTS

- Nearly two-thirds of pediatric cardiomyopathy cases are idiopathic. Of the cases of cardiomyopathy with an identified cause, 30% are infectious and 20% to 25% are familial.
- HCM is the most common genetic cardiovascular disease.
- Idiopathic dilated cardiomyopathy is the most common cause of congestive heart failure in children and the most frequent indication for heart transplantation.
- ARVC is a genetic desmosomal disorder with variable penetrance and characteristic MRI findings.
- Increased pericardial thickness (>4 mm) with calcifications, contrast enhancement on CT/MRI, and a tubular configuration of the compressed ventricles can help in differentiating constrictive pericarditis from restrictive cardiomyopathy.
- DMD is the most common of the muscular dystrophies affecting the heart.
- Iron deposition related cardiomyopathy is a potential serious consequence of repeated red blood cell transfusions.
- The radiologic visualization of the normal pericardium (<2 mm) depends on adjacent epicardial fat, usually more prominent along the right ventricle, and minimal along the left ventricular wall. Nonvisualization of the left pericardium should not be confused with pericardial absence/defect in the absence of additional imaging signs.
- Pneumopericardium should be differentiated from pneumomediastinum that may also surround the heart but usually extends more superiorly in the upper thorax above the roots of the great arteries.

## SUGGESTED READINGS

Chun EJ, Choi SI, Jin KN, et al. Hypertrophic cardiomyopathy: assessment with MR imaging and multidetector CT. *Radiographics*. 2010;30(5):1309–1328.

Etesami M, Gilkeson RC, Rajiah P. Utility of late gadolinium enhancement in pediatric cardiac MRI. *Pediatr Radiol*. 2016;46(8):1096–1113.

Ferreira VM, Piechnik SK, Dall'Armellina E, et al. T(1) mapping for the diagnosis of acute myocarditis using CMR: comparison to T2-weighted and late gadolinium enhanced imaging. *JACC Cardiovasc Imaging*. 2013;6(10):1048–1058.

Price JF, Jeewa A, Denfield SW. Clinical characteristics and treatment of cardiomyopathies in children. *Curr Cardiol Rev*. 2016;12(2):85–98.

## REFERENCES

Full references for this chapter can be found on www.expertconsult.com.

## REFERENCES

1. Lipshultz SE. Ventricular dysfunction clinical research in infants, children and adolescents. *Prog Pediatr Cardiol*. 2000;12(1):1–28.
2. Lipshultz SE, Sleeper LA, Towbin JA, et al. The incidence of pediatric cardiomyopathy in two regions of the United States. *N Engl J Med*. 2003;348(17):1647–1655.
3. Cox GF, Sleeper LA, Lowe AM, et al. Factors associated with establishing a causal diagnosis for children with cardiomyopathy. *Pediatrics*. 2006;118(4):1519–1531.
4. Macedo R, Schmidt A, Rochitte CE, et al. MRI to assess arrhythmia and cardiomyopathies. *J Magn Reson Imaging*. 2006;24(6):1197–1206.
5. Schulz-Menger J, Friedrich MG. Magnetic resonance imaging in patients with cardiomyopathies: when and why. *Herz*. 2000;25(4):384–391.
6. Maron BJ. Hypertrophic cardiomyopathy: a systematic review. *JAMA*. 2002;287(10):1308–1320.
7. Chun EJ, Choi SI, Jin KN, et al. Hypertrophic cardiomyopathy: assessment with MR imaging and multidetector CT. *Radiographics*. 2010;30(5):1309–1328.
8. Puntmann VO, Voigt T, Chen Z, et al. Native T1 mapping in differentiation of normal myocardium from diffuse disease in hypertrophic and dilated cardiomyopathy. *JACC Cardiovasc Imaging*. 2013;6(4):475–484.
9. To AC, Dhillon A, Desai MY. Cardiac magnetic resonance in hypertrophic cardiomyopathy. *JACC Cardiovasc Imaging*. 2011;4(10):1123–1137.
10. Towbin JA, Lowe AM, Colan SD, et al. Incidence, causes, and outcomes of dilated cardiomyopathy in children. *JAMA*. 2006;296(15):1867–1876.
11. Westwood MA, Shah F, Anderson LJ, et al. Myocardial tissue characterization and the role of chronic anemia in sickle cell cardiomyopathy. *J Magn Reson Imaging*. 2007;26(3):564–568.
12. Alvarez JA, Wilkinson JD, Lipshultz SE. Outcome predictors for pediatric dilated cardiomyopathy: a systematic review. *Prog Pediatr Cardiol*. 2007;23(1):25–32.
13. Etesami M, Gilkeson RC, Rajiah P. Utility of late gadolinium enhancement in pediatric cardiac MRI. *Pediatr Radiol*. 2016;46(8):1096–1113.
14. Latus H, Gummel K, Klingel K, et al. Focal myocardial fibrosis assessed by late gadolinium enhancement cardiovascular magnetic resonance in children and adolescents with dilated cardiomyopathy. *J Cardiovasc Magn Reson*. 2015;17:34.
15. Saffitz JE. The pathobiology of arrhythmogenic cardiomyopathy. *Annu Rev Pathol*. 2011;6:299–321.
16. Calkins H. Arrhythmogenic right ventricular dysplasia. *Curr Probl Cardiol*. 2013;38(3):103–123.
17. Hughes SE, McKenna WJ. New insights into the pathology of inherited cardiomyopathy. *Heart*. 2005;91(2):257–264.
18. Tandri H, Macedo R, Calkins H, et al. Role of magnetic resonance imaging in arrhythmogenic right ventricular dysplasia: insights from the North American arrhythmogenic right ventricular dysplasia (ARVD/C) study. *Am Heart J*. 2008;155(1):147–153.
19. Marcus FI, McKenna WJ, Sherrill D, et al. Diagnosis of arrhythmogenic right ventricular cardiomyopathy/dysplasia: proposed modification of the task force criteria. *Circulation*. 2010;121(13):1533–1541.
20. Hunold P, Wieneke H, Bruder O, et al. Late enhancement: a new feature in MRI of arrhythmogenic right ventricular cardiomyopathy? *J Cardiovasc Magn Reson*. 2005;7(4):649–655.
21. Tandri H, Saranathan M, Rodriguez ER, et al. Noninvasive detection of myocardial fibrosis in arrhythmogenic right ventricular cardiomyopathy using delayed-enhancement magnetic resonance imaging. *J Am Coll Cardiol*. 2005;45(1):98–103.
22. Te Riele AS, Tandri H, Sanborn DM, et al. Noninvasive multimodality imaging in ARVD/C. *JACC Cardiovasc Imaging*. 2015;8(5):597–611.
23. Price JF, Jeewa A, Denfield SW. Clinical characteristics and treatment of cardiomyopathies in children. *Curr Cardiol Rev*. 2016;12(2):85–98.
24. Webber SA, Lipshultz SE, Sleeper LA, et al. Outcomes of restrictive cardiomyopathy in childhood and the influence of phenotype: a report from the Pediatric Cardiomyopathy Registry. *Circulation*. 2012;126(10):1237–1244.
25. Gupta A, Singh Gulati G, Seth S, et al. Cardiac MRI in restrictive cardiomyopathy. *Clin Radiol*. 2012;67(2):95–105.
26. Maron BJ, Towbin JA, Thiene G, et al. Contemporary definitions and classification of the cardiomyopathies: an American Heart Association Scientific Statement from the Council on Clinical Cardiology, Heart Failure and Transplantation Committee; Quality of Care and Outcomes Research and Functional Genomics and Translational Biology Interdisciplinary Working Groups; and Council on Epidemiology and Prevention. *Circulation*. 2006;113(14):1807–1816.
27. Canter CE, Simpson KE. Diagnosis and treatment of myocarditis in children in the current era. *Circulation*. 2014;129(1):115–128.
28. Magnani JW, Dec GW. Myocarditis: current trends in diagnosis and treatment. *Circulation*. 2006;113(6):876–890.
29. Doolan A, Langlois N, Semsarian C. Causes of sudden cardiac death in young Australians. *Med J Aust*. 2004;180(3):110–112.
30. Felker GM, Boehmer JP, Hruban RH, et al. Echocardiographic findings in fulminant and acute myocarditis. *J Am Coll Cardiol*. 2000;36(1):227–232.
31. Friedrich MG, Sechtem U, Schulz-Menger J, et al. Cardiovascular magnetic resonance in myocarditis: a JACC White Paper. *J Am Coll Cardiol*. 2009;53(17):1475–1487.
32. Ferreira VM, Piechnik SK, Dall'Armellina E, et al. T(1) mapping for the diagnosis of acute myocarditis using CMR: comparison to T2-weighted and late gadolinium enhanced imaging. *JACC Cardiovasc Imaging*. 2013;6(10):1048–1058.
33. Ferreira VM, Piechnik SK, Dall'Armellina E, et al. Native T1-mapping detects the location, extent and patterns of acute myocarditis without the need for gadolinium contrast agents. *J Cardiovasc Magn Reson*. 2014;16:36.
34. Muntoni F. Cardiac complications of childhood myopathies. *J Child Neurol*. 2003;18(3):191–202.
35. Buddhe S, Lewin M, Olson A, et al. Comparison of left ventricular function assessment between echocardiography and MRI in Duchenne muscular dystrophy. *Pediatr Radiol*. 2016;46(10):1399–1408.
36. Lang SM, Shugh S, Mazur W, et al. Myocardial fibrosis and left ventricular dysfunction in duchenne muscular dystrophy carriers using cardiac magnetic resonance imaging. *Pediatr Cardiol*. 2015;36(7):1495–1501.
37. Otto RK, Ferguson MR, Friedman SD. Cardiac MRI in muscular dystrophy: an overview and future directions. *Phys Med Rehabil Clin N Am*. 2012;23(1):123–132, xi-xii.
38. Florian A, Ludwig A, Rosch S, et al. Myocardial fibrosis imaging based on T1-mapping and extracellular volume fraction (ECV) measurement in muscular dystrophy patients: diagnostic value compared with conventional late gadolinium enhancement (LGE) imaging. *Eur Heart J Cardiovasc Imaging*. 2014;15(9):1004–1012.
39. Melacini P, Fanin M, Danieli GA, et al. Myocardial involvement is very frequent among patients affected with subclinical Becker's muscular dystrophy. *Circulation*. 1996;94(12):3168–3175.
40. Payne RM, Wagner GR. Cardiomyopathy in Friedreich ataxia: clinical findings and research. *J Child Neurol*. 2012;27(9):1179–1186.
41. Byers SL, Ficicioglu C. Infant with cardiomyopathy: when to suspect inborn errors of metabolism? *World J Cardiol*. 2014;6(11):1149–1155.
42. Cox GF. Diagnostic approaches to pediatric cardiomyopathy of metabolic genetic etiologies and their relation to therapy. *Prog Pediatr Cardiol*. 2007;24(1):15–25.
43. Gilbert-Barness E. Review: metabolic cardiomyopathy and conduction system defects in children. *Ann Clin Lab Sci*. 2004;34(1):15–34.
44. Lee DH, Qiu WJ, Lee J, et al. Hypertrophic cardiomyopathy in pompe disease is not limited to the classic infantile-onset phenotype. *JIMD Rep*. 2014;17:71–75.
45. Feldman AG, Whitington PF. Neonatal hemochromatosis. *J Clin Exp Hepatol*. 2013;3(4):313–320.
46. Murray KF, Kowdley KV. Neonatal hemochromatosis. *Pediatrics*. 2001;108(4):960–964.
47. Goldberg YP. Juvenile hereditary hemochromatosis. In: Pagon RAAM, Ardinger HH, et al, eds. *Authors. GeneReviews® [Internet]*. Seattle (WA): University of Washington; 2005:1993–2017. Available from:: https://www.ncbi.nlm.nih.gov/books/NBK1170/. [Updated 2011 Aug 11].
48. Wood JC. Estimating tissue iron burden: current status and future prospects. *Br J Haematol*. 2015;170(1):15–28.
49. Franco VI, Henkel JM, Miller TL, et al. Cardiovascular effects in childhood cancer survivors treated with anthracyclines. *Cardiol Res Pract*. 2011;2011:134679.
50. Tham EB, Haykowsky MJ, Chow K, et al. Diffuse myocardial fibrosis by T1-mapping in children with subclinical anthracycline cardiotoxicity: relationship to exercise capacity, cumulative dose and remodeling. *J Cardiovasc Magn Reson*. 2013;15:48.
51. Toro-Salazar OH, Gillan E, O'Loughlin MT, et al. Occult cardiotoxicity in childhood cancer survivors exposed to anthracycline therapy. *Circ Cardiovasc Imaging*. 2013;6(6):873–880.
52. Arbustini E, Favalli V, Narula N, et al. Left ventricular noncompaction: a distinct genetic cardiomyopathy? *J Am Coll Cardiol*. 2016;68(9):949–966.

53. Zuccarino F, Vollmer I, Sanchez G, et al. Left ventricular noncompaction: imaging findings and diagnostic criteria. *AJR Am J Roentgenol*. 2015;204(5):W519–W530.
54. Baltimore RS, Gewitz M, Baddour LM, et al. Infective endocarditis in childhood: 2015 update: a scientific statement from the American Heart Association. *Circulation*. 2015;132(15):1487–1515.
55. Day MD, Gauvreau K, Shulman S, et al. Characteristics of children hospitalized with infective endocarditis. *Circulation*. 2009;119(6):865–870.
56. Ferrieri P, Gewitz MH, Gerber MA, et al. Unique features of infective endocarditis in childhood. *Circulation*. 2002;105(17):2115–2126.
57. Elder RW, Baltimore RS. The changing epidemiology of pediatric endocarditis. *Infect Dis Clin North Am*. 2015;29(3):513–524.
58. Durack DT, Lukes AS, Bright DK. New criteria for diagnosis of infective endocarditis: utilization of specific echocardiographic findings. Duke Endocarditis Service. *Am J Med*. 1994;96(3):200–209.
59. Baddour LM, Wilson WR, Bayer AS, et al. Infective endocarditis: diagnosis, antimicrobial therapy, and management of complications: a statement for healthcare professionals from the Committee on Rheumatic Fever, Endocarditis, and Kawasaki Disease, Council on Cardiovascular Disease in the Young, and the Councils on Clinical Cardiology, Stroke, and Cardiovascular Surgery and Anesthesia, American Heart Association: endorsed by the Infectious Diseases Society of America. *Circulation*. 2005;111(23):e394–e434.
60. Seckeler MD, Hoke TR. The worldwide epidemiology of acute rheumatic fever and rheumatic heart disease. *Clin Epidemiol*. 2011;3:67–84.
61. Jones TD. The diagnosis of rheumatic fever. *JAMA*. 1944;26(8):481–484.
62. Gewitz MH, Baltimore RS, Tani LY, et al. Revision of the Jones Criteria for the diagnosis of acute rheumatic fever in the era of Doppler echocardiography: a scientific statement from the American Heart Association. *Circulation*. 2015;131(20):1806–1818.
63. Lewis WH. The pericardium. In: Gray H, ed. *eAothbP*. PA: Lea & Febiger; 1918.
64. Edwards ED. Applied anatomy of the heart. In: Giuliani ERFV, ed. *Cardiology: Fundamentals and Practice*. 2nd ed. St. Louis, MO: Mosby–Year Book; 1991:47–51.
65. Wang ZJ, Reddy GP, Gotway MB, et al. CT and MR imaging of pericardial disease. *Radiographics*. 2003;23(Spec No):S167–S180.
66. Rajiah P, Cardiac MRI. Part 2, pericardial diseases. *AJR Am J Roentgenol*. 2011;197(4):W621–W634.
67. Shah AB, Kronzon I. Congenital defects of the pericardium: a review. *Eur Heart J Cardiovasc Imaging*. 2015;16(8):821–827.
68. Rajiah P, Kanne JP. Computed tomography of the pericardium and pericardial disease. *J Cardiovasc Comput Tomogr*. 2010;4(1):3–18.
69. Brulotte S, Roy L, Larose E. Congenital absence of the pericardium presenting as acute myocardial necrosis. *Can J Cardiol*. 2007;23(11):909–912.
70. Kim HJ, Cho YS, Cho GY, et al. Congenital absence of the pericardium. *J Cardiovasc Ultrasound*. 2014;22(1):36–39.
71. Psychidis-Papakyritsis P, de Roos A, Kroft LJ. Functional MRI of congenital absence of the pericardium. *AJR Am J Roentgenol*. 2007;189(6):W312–W314.
72. Mansfield PB, Graham CB, Beckwith JB, et al. Pneumopericardium and pneumomediastinum in infants and children. *J Pediatr Surg*. 1973;8(5):691–699.
73. Giuliani S, Franklin A, Pierce J, et al. Massive subcutaneous emphysema, pneumomediastinum, and pneumopericardium in children. *J Pediatr Surg*. 2010;45(3):647–649.
74. Auden SM, Lapin SL, Joseph-Reynolds AM. Cardiac arrest from tension pneumopericardium in a premature infant. *Anesth Analg*. 2002;95(5):1245–1247, table of contents.
75. Heckmann M, Lindner W, Pohlandt F. Tension pneumopericardium in a preterm infant without mechanical ventilation: a rare cause of cardiac arrest. *Acta Paediatr*. 1998;87(3):346–348.
76. Ratnapalan S, Brown K, Benson L. Children presenting with acute pericarditis to the emergency department. *Pediatr Emerg Care*. 2011;27(7):581–585.
77. Shakti D, Hehn R, Gauvreau K, et al. Idiopathic pericarditis and pericardial effusion in children: contemporary epidemiology and management. *J Am Heart Assoc*. 2014;3(6):e001483.
78. Feng D, Glockner J, Kim K, et al. Cardiac magnetic resonance imaging pericardial late gadolinium enhancement and elevated inflammatory markers can predict the reversibility of constrictive pericarditis after antiinflammatory medical therapy: a pilot study. *Circulation*. 2011;124(17):1830–1837.
79. Bogaert J, Francone M. Pericardial disease: value of CT and MR imaging. *Radiology*. 2013;267(2):340–356.
80. Kuhn B, Peters J, Marx GR, et al. Etiology, management, and outcome of pediatric pericardial effusions. *Pediatr Cardiol*. 2008;29(1):90–94.
81. Cummings KW, Green D, Johnson WR, et al. Imaging of pericardial diseases. *Semin Ultrasound CT MR*. 2016;37(3):238–254.
82. Eifinger F, Vierzig A, Roth B, et al. The pericardial reflection and the tip of the central venous catheter - topographical analysis in stillborn babies. *Pediatr Radiol*. 2016;46(11):1528–1531.

# 80

# Cardiac and Pericardial Tumors

*Karen Lyons and S. Bruce Greenberg*

Primary cardiac tumors are rare in children, with a reported prevalence of up to 0.32%.[1] Use of echocardiography has resulted in more frequent detection of cardiac tumors in the fetus and neonate.[2] More than 90% of pediatric cardiac tumors are benign.[1] Symptoms are variable and usually depend on tumor location and size. Intracavitary cardiac tumors can cause cardiac valve obstruction or spread of tumor emboli, and present with heart failure, dyspnea, or neurologic symptoms. Myocardial tumors compress the cardiac lumen, leading to obstruction or heart failure, and can be associated with arrhythmias. Pericardial tumors are associated with pericardial effusions. Conventional radiographs may show cardiomegaly, an abnormal cardiac silhouette, or pulmonary edema (e-Fig. 80.1). Cardiac tumors in children can be associated with several syndromes (e-Table 80.1). Computed tomography (CT) and magnetic resonance imaging (MRI) findings help differentiate tumor types (Table 80.2).

## RHABDOMYOMA

***Pathophysiology and Clinical Presentation.*** Rhabdomyoma, the most common primary cardiac tumor of childhood, accounts for 60% to 79% of all cardiac tumors in infancy.[1,3] Rhabdomyomas are hamartomas that regress and have no potential for malignancy. Although greater than half of patients with rhabdomyoma are asymptomatic, presentations include nonimmune fetal hydrops, outflow tract obstruction, or arrhythmia. At least 50% of patients with rhabdomyoma have tuberous sclerosis, and rhabdomyomas can be the first manifestation.[3]

***Imaging.*** Rhabdomyomas are round, hyperechoic, solid masses on echocardiography (e-Fig. 80.2). They usually are multiple and occur most commonly in the ventricular tissue but also can arise from atrial walls.[4,5] Signal characteristics on T1- and T2-weighted MRI are similar to those of myocardium, making noncontrast MRI less sensitive than echocardiography.[6] They have increased attenuation compared with myocardium on noncontrast-enhanced CT scans, and decreased perfusion and variable postcontrast enhancement on MRI (Figs. 80.3 and 80.4).[7–9] Small fat globules may be detected.

## FIBROMA

***Pathophysiology and Clinical Presentation.*** Cardiac fibroma is the second most common and the most commonly resected primary cardiac tumor of childhood.[9–11] The tumors are frequently detected in infancy but can present throughout childhood. Fibromas are solitary tumors arising from myocardium composed of fibroblasts and collagen, and can be associated with Gorlin (basal cell nevus) syndrome.[10,11] Children can present with heart failure and arrhythmia.

***Imaging.*** Echocardiography reveals a heterogeneous, echogenic, solitary mass.[11] Cardiac fibromas are isointense to hypointense on T1-weighted MRI with variable T2 signal.[9,10,12] Classically, MRI shows decreased first pass perfusion and characteristic rim enhancement with decreased central enhancement on delayed imaging[9,13] (Video 80.1 and e-Fig. 80.5).[7,14] Calcifications are a frequent and differentiating finding compared with rhabdomyoma (e-Fig. 80.6).[1,11,15]

## MYXOMA

***Pathophysiology and Clinical Presentation.*** Myxoma, the most common cardiac tumor in adults, is rare in children.[1,3,10,11] Most myxomas are pedunculated, exophytic irregular masses attached to the atrial septum but can originate from other endocardial locations. Myxomas in children frequently are associated with Carney syndrome.[16] Compared with adults, they are more likely to be multiple and to recur. Clinical symptoms include obstructive cardiac symptoms, embolic phenomena, and constitutional symptoms.

***Imaging.*** Echocardiography identifies a pedunculated mass that often prolapses across the mitral or tricuspid valve.[6,11] On MRI, myxomas demonstrate heterogeneous signal and myxoid

**TABLE 80.2** Cardiac Tumors: Computed Tomographic and Magnetic Resonance Imaging Findings

| Tumor | Location | Number | CT | MRI Signal Intensity |
|---|---|---|---|---|
| Rhabdomyoma | Myocardium | Multiple | – Calcification<br>↑ Attenuation[*]<br>Mild contrast enhancement | Isointense T1- and T2-weighted images<br>Decreased signal on FPP<br>Variable contrast enhancement |
| Fibroma | Myocardium | Solitary | + Calcification<br>Heterogeneous enhancement | Variable T2-weighted signal<br>Decreased signal on FPP<br>Early rim enhancement<br>↑ Delayed enhancement |
| Myxoma | Intracavitary | Solitary[†] | + Calcification<br>↓ Attenuation, outlined by intracavitary contrast | ↑ T2-weighted images<br>Heterogeneous contrast enhancement |
| Teratoma | Pericardium | Solitary | + Calcification<br>+ Fat<br>Heterogeneous attenuation | ↑ T2-weighted images<br>↑ T1-weighted images |

*CT,* Computed tomography; *MRI,* magnetic resonance imaging; *FPP,* first pass perfusion.

[*] Relative to myocardium.

[†] Multiple and recurrent tumors associated with familial forms.

## Abstract:

Primary pediatric cardiac tumors are rare. Use of echocardiography has resulted in more frequent detection of cardiac tumors in the fetus and neonate. More than 90% of pediatric cardiac tumors are benign. Symptoms are variable and usually depend on tumor location and size. Intracavitary cardiac tumors can cause cardiac valve obstruction or spread of tumor emboli, and present with heart failure, dyspnea, or neurologic symptoms. Myocardial tumors compress the cardiac lumen, leading to obstruction or heart failure, and can be associated with arrhythmias. Pericardial tumors are associated with pericardial effusions. Conventional radiographs may show cardiomegaly, an abnormal cardiac silhouette, or pulmonary edema. Cardiac tumors in children can be associated with several syndromes. Computed tomography (CT) and magnetic resonance imaging (MRI) findings help differentiate tumor types.

## Keywords:

pediatric cardiac tumors
rhabdomyoma
fibroma
myxoma
cardiac teratoma

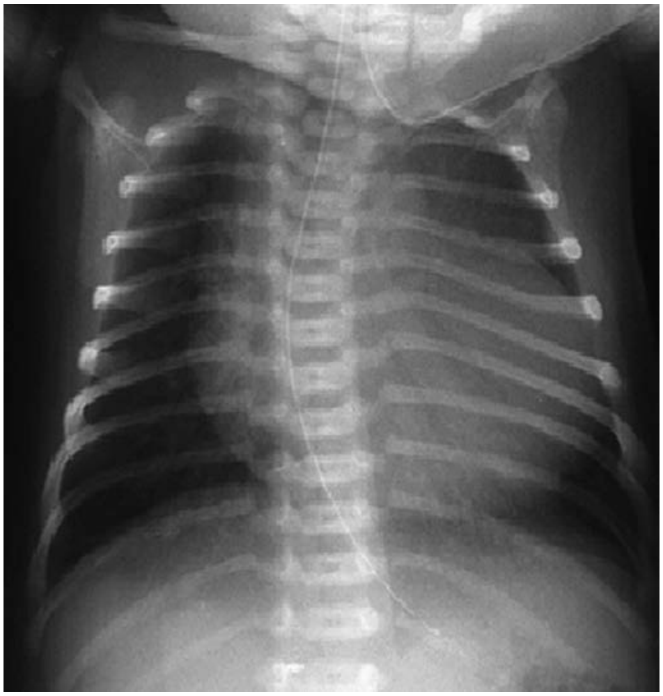

**e-Figure 80.1. Cardiomegaly in a child with a cardiac fibroma.**

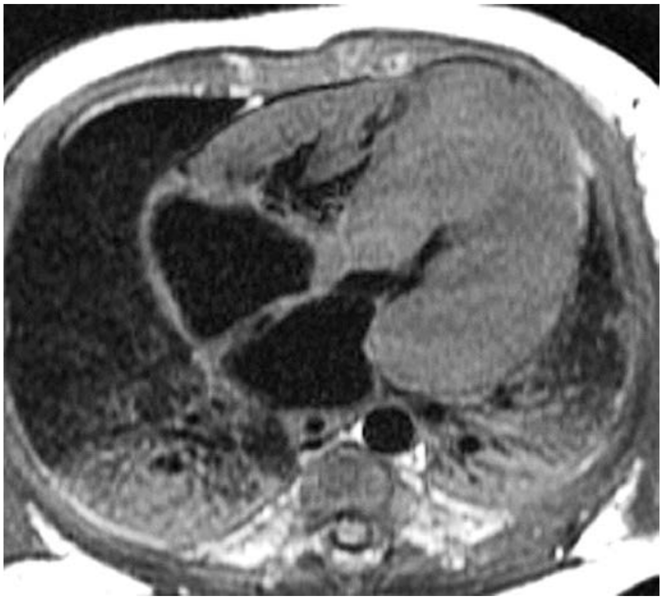

**e-Figure 80.2. Rhabdomyomatosis.** Axial T1-weighted MR image in an infant shows multiple bulging tumors with isointense signal to the left ventricular myocardium.

**e-TABLE 80.1** Cardiac Tumors Associated With Syndromes

| Tumor | Association |
|---|---|
| Rhabdomyoma | Tuberous sclerosis |
| Fibroma | Gorlin (basal cell nevus) syndrome |
| Myxoma | Carney syndrome |

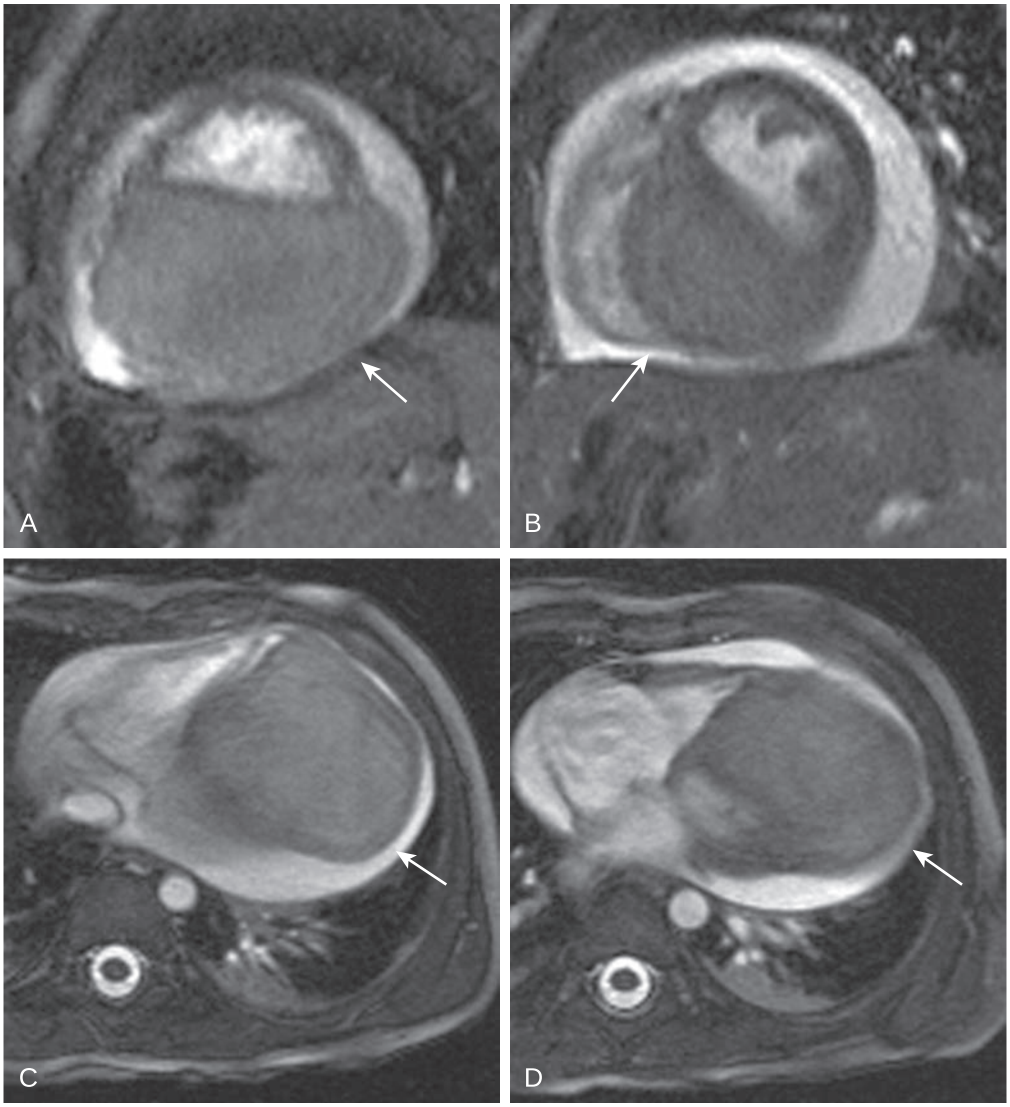

**e-Figure 80.5. Cardiac fibroma in a newborn.** Short axis (A and B) and axial (C and D) MR gradient echo imaging shows a large, well-defined, hypointense mass *(arrows)* arising from the left ventricle associated with a pericardial effusion.

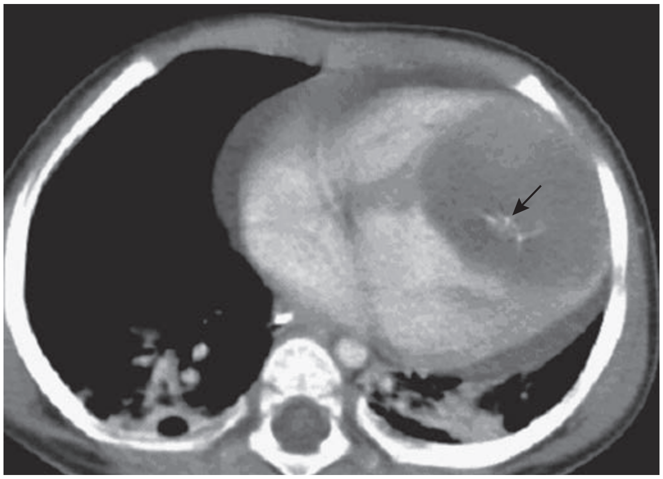

**e-Figure 80.6. Cardiac fibroma.** Contrast-enhanced CT shows calcification *(arrow)* in the low-attenuation mass in the left ventricular apex.

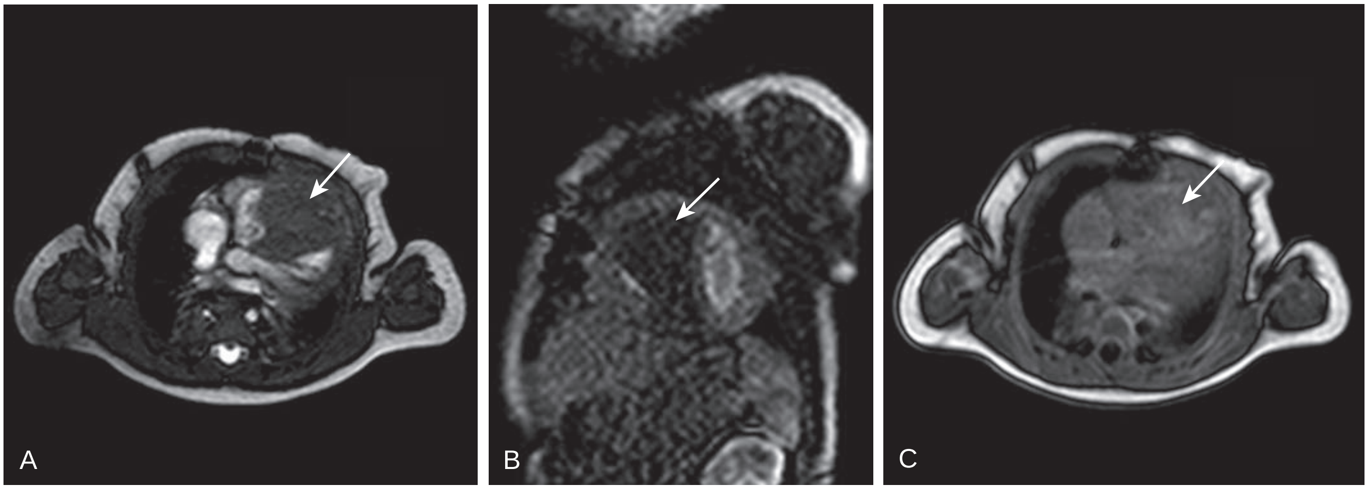

**Figure 80.3. Rhabdomyoma in an infant with neurostigmata of tuberous sclerosis.** A broad-based ovoid mass *(arrow)* extends from the interventricular septum on four chamber steady state free precession MR imaging (A), demonstrating decreased short axis first pass perfusion (B) and no significant delayed enhancement on four chamber phase sensitive inversion recovery (C) imaging.

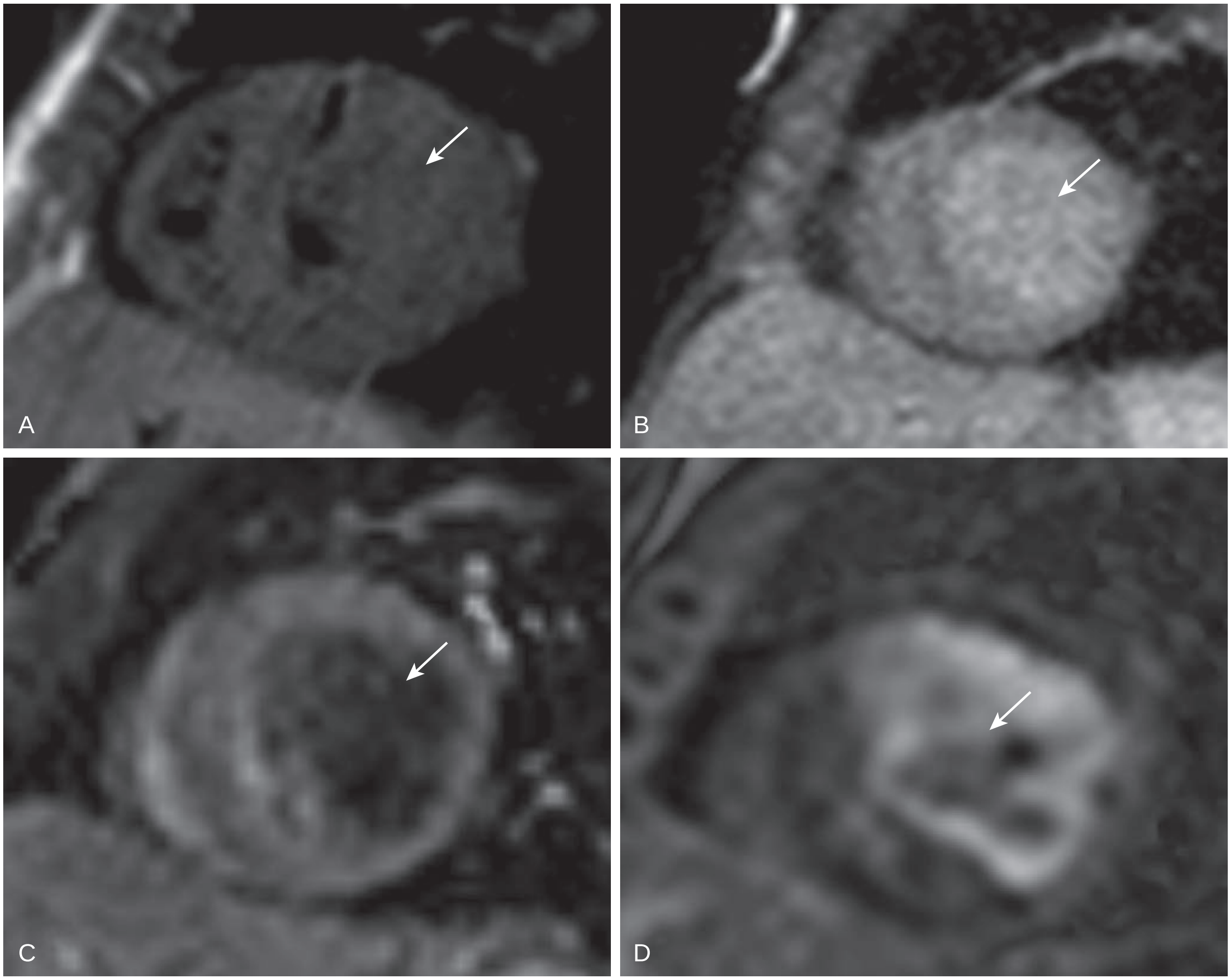

**Figure 80.4. Cardiac fibroma in a 1-year-old boy with ventricular tachycardia.** A mass arising from the mid posterolateral left ventricular wall *(arrow)* is isointense with normal myocardium on T1-weighted MR imaging (A), hyperintense on STIR imaging *(arrow)* (B), has decreased first pass perfusion *(arrow)* (C), and characteristic rim delayed enhancement on phase sensitive recovery imaging *(arrow)* (D).

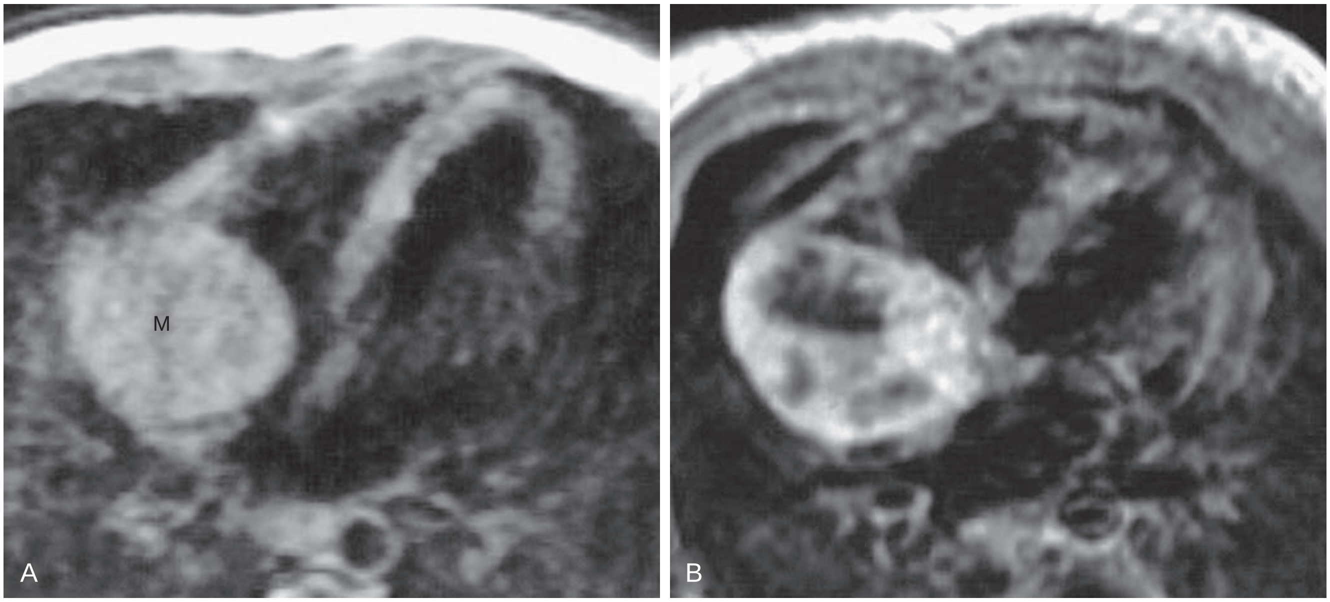

**Figure 80.7. Right atrial myxoma in a child.** (A) Axial T1-weighted MR image shows an intraluminal right atrial mass *(M)*. (B) The mass enhances heterogeneously with gadolinium.

regions, with low signal on T1-weighted imaging, high signal on T2-weighted imaging,[6,7,9,10,12] and postcontrast enhancement (Fig. 80.7). Tumor attenuation is lower than nonopacified blood on CT, and they are often calcified.[10,15]

## TERATOMA

***Pathophysiology and Clinical Presentation.*** Cardiac teratomas, although rare, are the most common pericardial tumors in infants.[3,10,17,18] Teratomas typically are attached to the pulmonary artery and aortic root, and extend into the pericardium;[3,17] rarely, they originate from the myocardium.[19] Pericardial effusions are frequent. Fetal hydrops from caval obstruction can lead to spontaneous fetal loss.

***Imaging.*** Echocardiography shows a heterogeneous, multilocular, cystic mass that may be associated with cardiac chamber compression and pericardial effusion.[3,11] MRI with both T1- and T2-weighted sequences can show high signal within a well-defined pericardial mass (e-Fig. 80.8).[20] Calcifications and fat within these tumors are well defined by CT.[17]

## OTHER CARDIAC TUMORS

Other benign tumors, such as fibroelastomas, hemangiomas, and lipomas, are extremely rare in children. A fibroelastoma is an intracavitary tumor usually attached to a cardiac valve.[21,22] Hemangiomas can occur in the heart and pericardium and are associated with pericardial effusion.[3] Hemangiomas enhance intensely on MRI and CT (e-Fig. 80.9) and are T2 hyperintense (Fig. 80.10).[9,11,23] CT and MRI demonstration of fat allows specific diagnosis of lipoma[20,24] (e-Fig. 80.11).

## MALIGNANT TUMORS

Primary malignant tumors are so rare that they are frequently absent from a series of cardiac tumors in children, appearing only in case reports.[1,2,25,26] Sarcomas have a variable imaging appearance. The presence of infiltration is the most helpful finding (e-Fig. 80.12).[27] Primary cardiac lymphoma is typically restricted to the heart and pericardium (e-Fig. 80.13).[28] Kaposiform hemangioendothelioma can occur antenatally and is associated with pericardial effusion.[29] MRI shows high signal on T2-weighted images. Contrast uptake is similar to hemangiomas with early fill-in on perfusion and postcontrast imaging (e-Fig. 80.14). Metastatic tumors are more common than primary malignancies[20] and may be the result of leukemia, lymphoma, Wilms tumor, hepatoblastoma, neuroblastoma, Ewing sarcoma, and osteosarcoma. Spread may be from direct extension, by extension through the inferior vena cava (e-Fig. 80.15), or via hematogenous metastases.

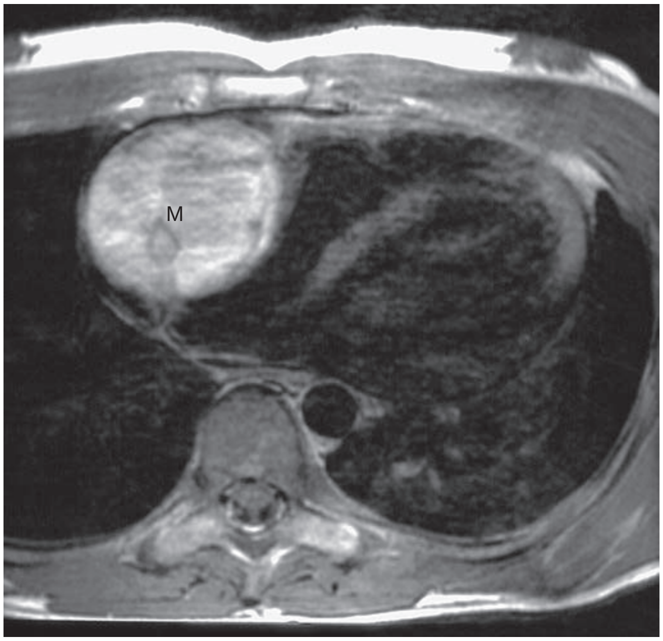

**Figure 80.10. Pericardial hemangioma in an 8-year-old child.** MRI shows a high-signal mass *(M)* on T1-weighted imaging. The mass impinges on the right atrium and ventricle.

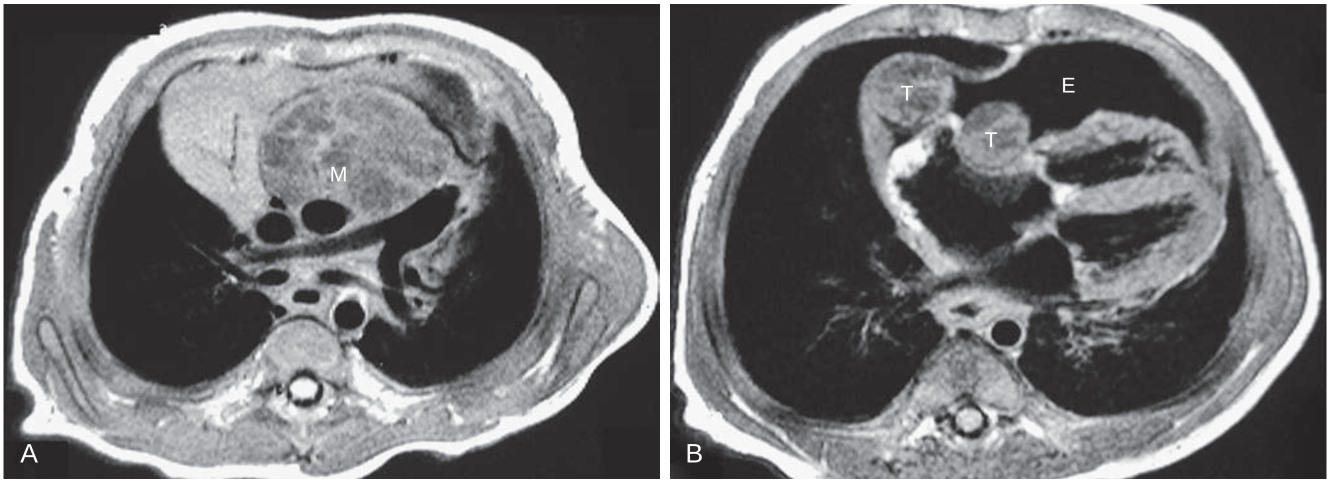

**e-Figure 80.8. Pericardial teratoma in a child.** (A) Axial T1-weighted MR image shows a pericardial mass *(M)* with low-signal cystic components. (B) Daughter tumors *(T)* are present in the pericardial space. Note the large pericardial effusion *(E)*.

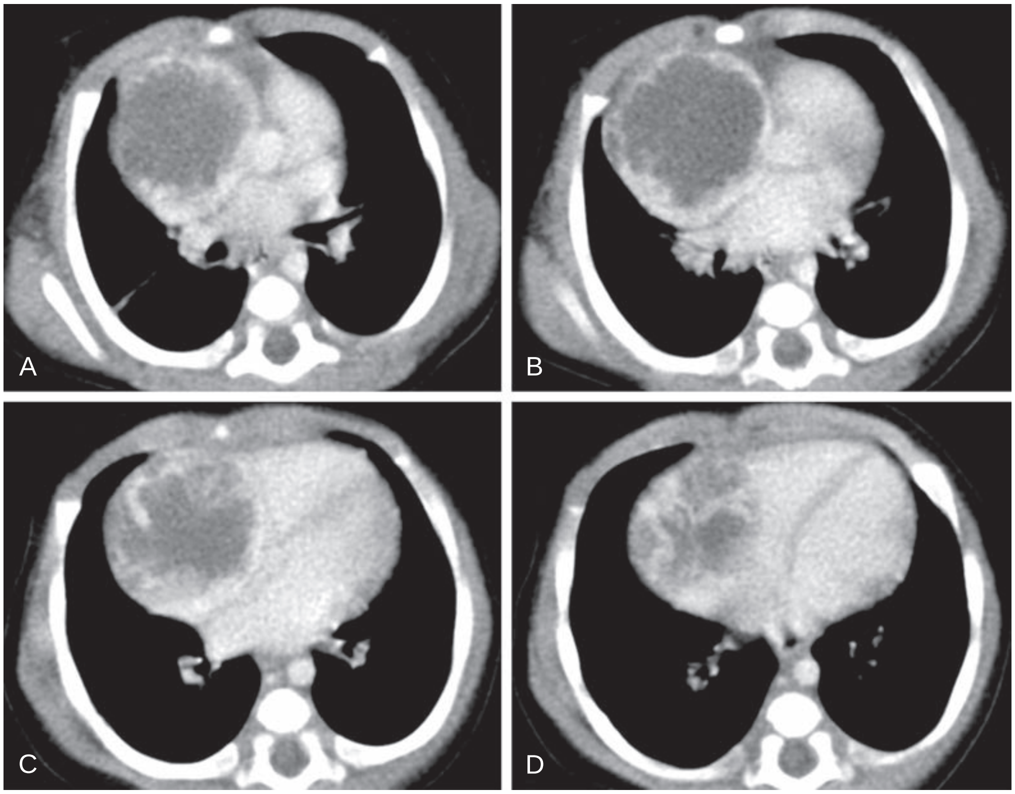

**e-Figure 80.9. Pericardial hemangioma in a newborn.** (A–D) Contrast-enhanced CT images from superior to inferior show a hypodense pericardial mass arising from the right atrial wall that compresses the right atrium. Dense peripheral contrast enhancement is present.

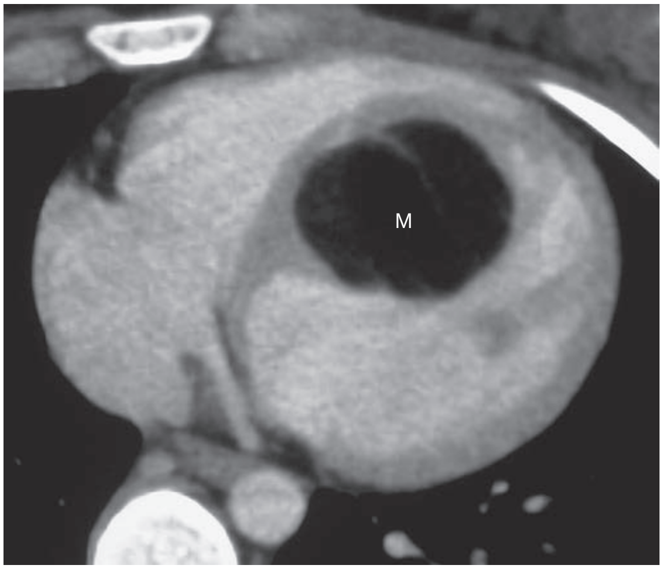

**e-Figure 80.11. Intracardiac lipoma in a teenager.** Contrast-enhanced CT shows a fatty, low-attenuation mass *(M)* extending into the left ventricular lumen from the ventricular septum.

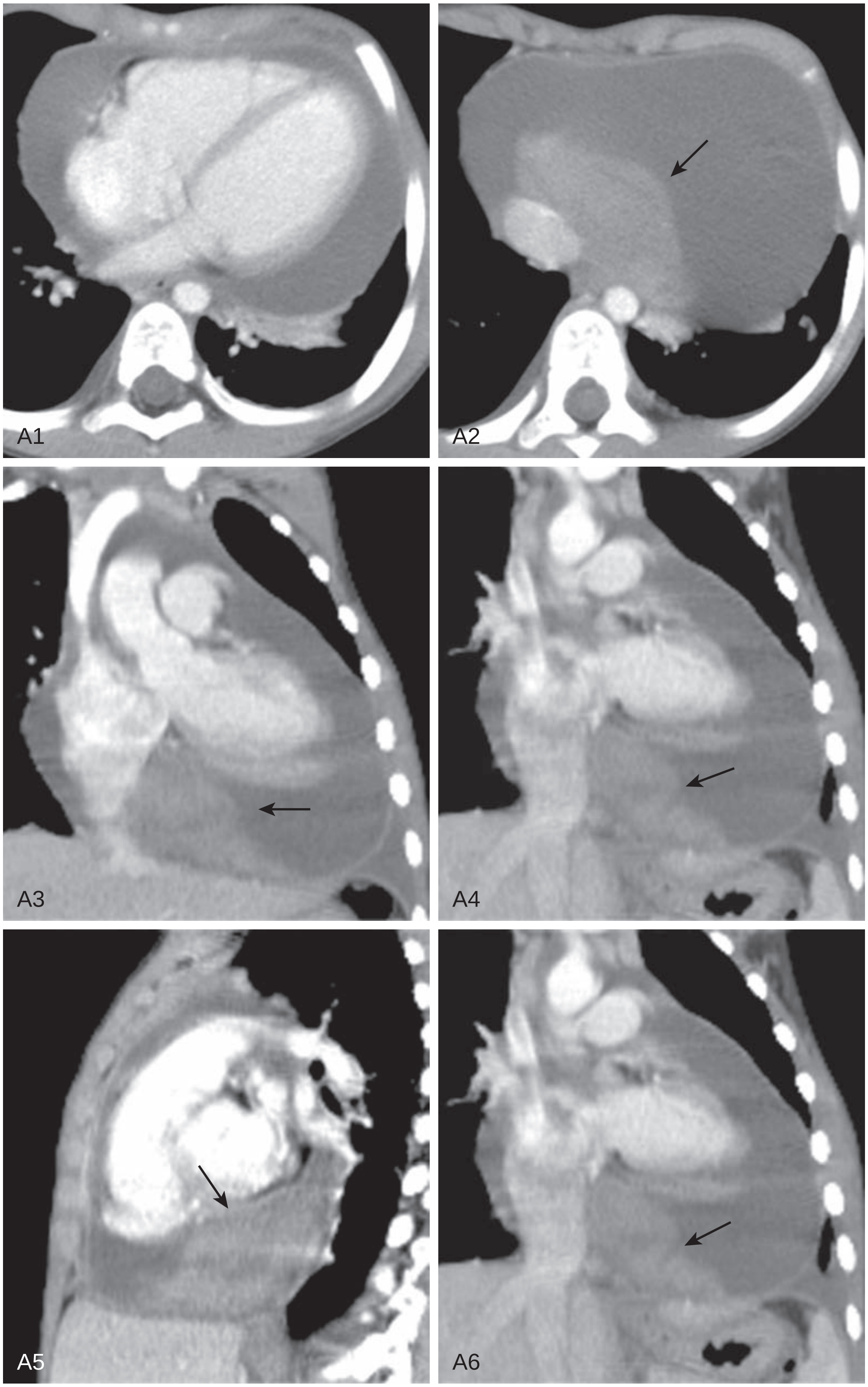

**e-Figure 80.12. Pericardial synovial sarcoma in a 6-year-old child who presented with chest pain.** (A) Contrast-enhanced CT images (A1–A6) show a large pericardial effusion with a focal soft tissue density mass *(arrows)* at the base of the pericardium adjacent to the right atrium. *Continued*

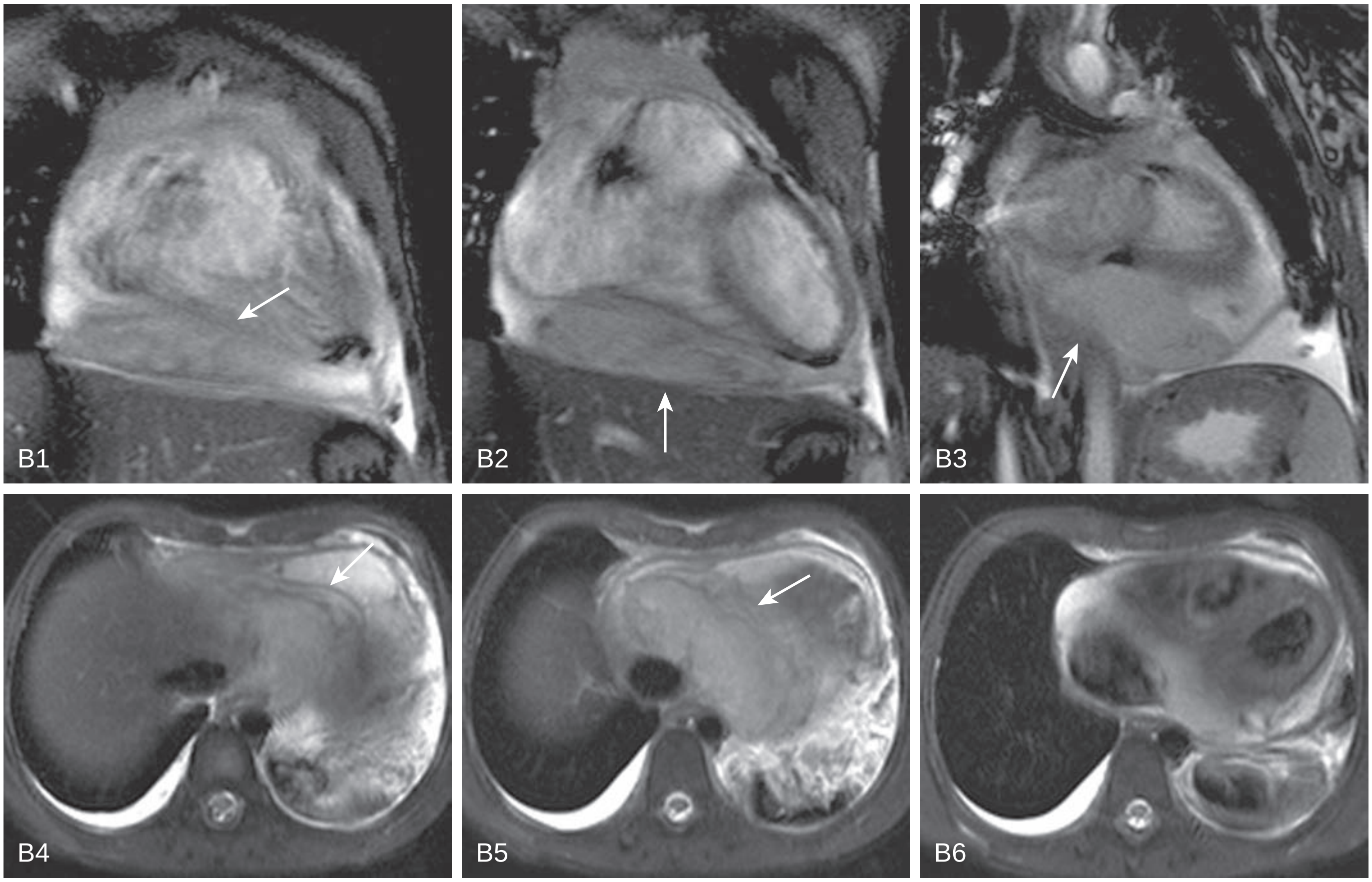

**e-Figure 80.12, cont'd.** (B) Coronal fast spin echo (B1–B3) and axial T2-weighted MR images (B4–B6) show the pericardial effusion and a slightly hyperintense mass *(arrows)* on T2-weighted images.

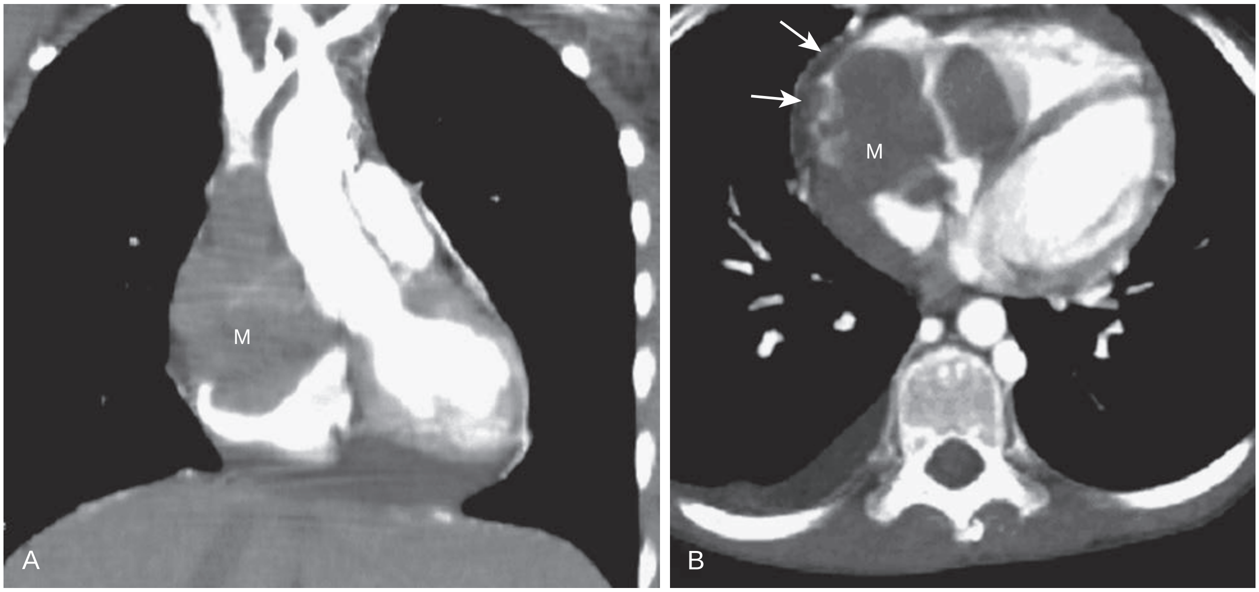

**e-Figure 80.13. Primary cardiac lymphoma in a child.** Coronal (A) and axial (B) contrast-enhanced CT images show a low-attenuation mass *(M)* involving the pericardium (*arrows* in B) and right heart.

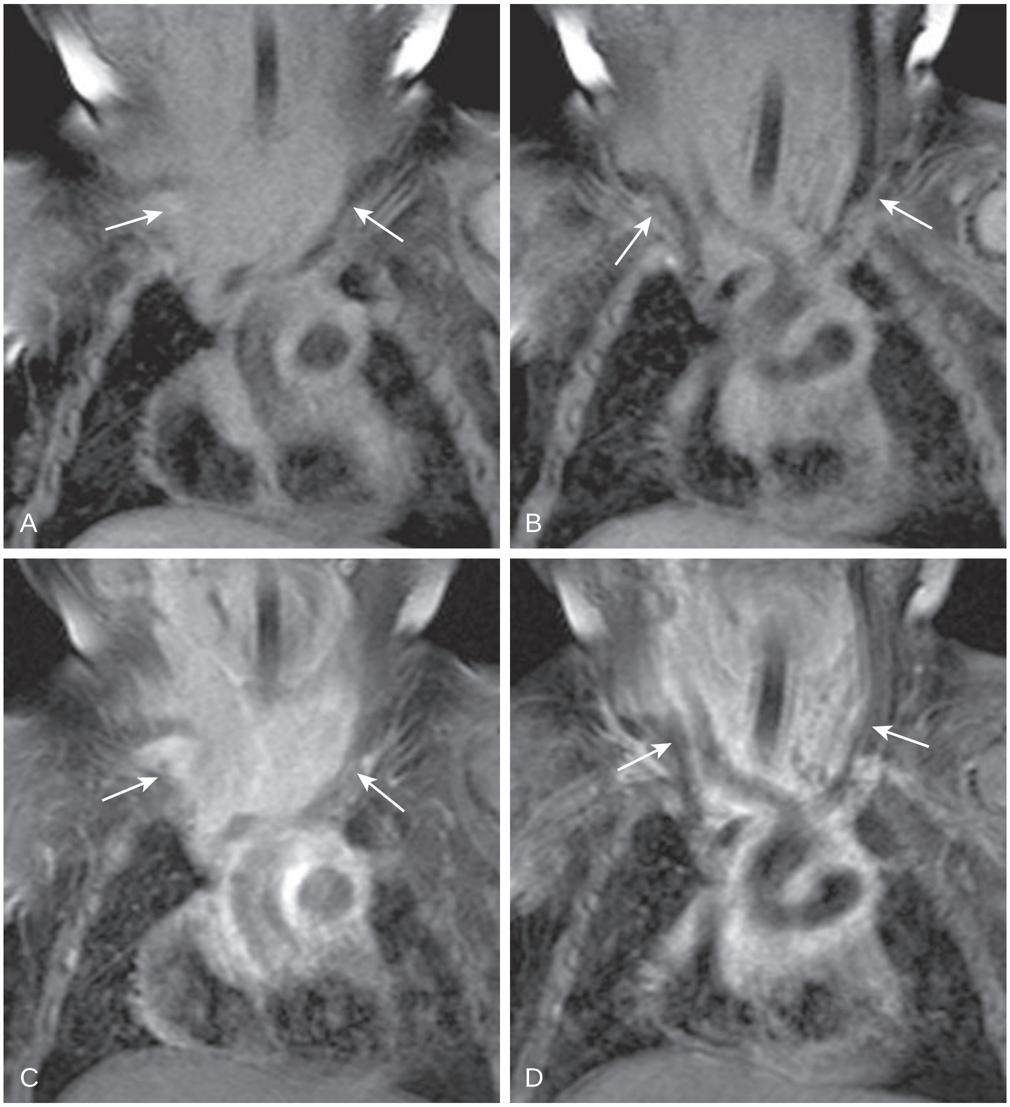

**e-Figure 80.14. Kaposiform hemangioendothelioma in a 1-month-old child who presented initially with a pericardial effusion.** Coronal T1-weighted precontrast (A, B) and postcontrast (C, D) MR images show an infiltrative enhancing vascular mass encasing the great vessels and airway *(arrows)*.

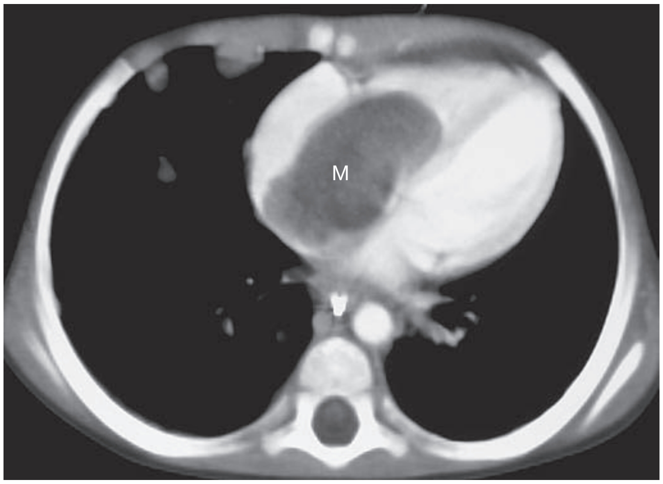

**e-Figure 80.15. Wilms tumor thrombus extending into the heart in a child.** Contrast-enhanced CT image shows a right atrial mass *(M)* that prolapses across the tricuspid valve in a child with Wilms tumor. Lung metastases also are evident in the right lung.

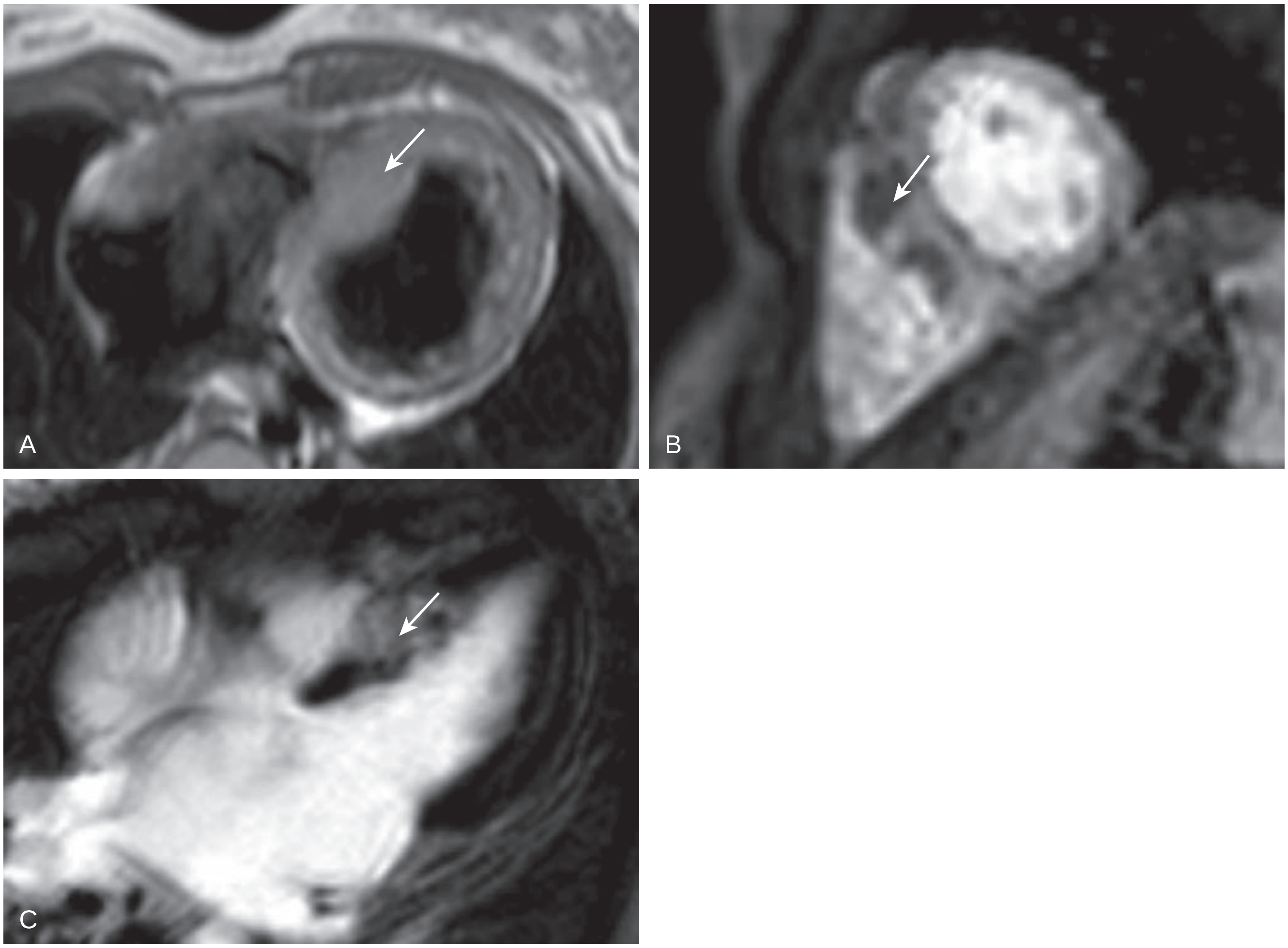

**Figure 80.16. Masslike hypertrophic cardiomyopathy in a 16-year-old girl who presented with cardiac arrest.** MRI shows an interventricular mass *(arrow),* which is (A) isointense to myocardium on T1-weighted imaging, (B) has patchy decreased first pass perfusion, and (C) shows patchy delayed enhancement on phase sensitive inversion recovery imaging.

## NON-NEOPLASTIC MIMICS OF CARDIAC TUMORS

Several entities may be mistaken for a cardiac tumor on echocardiography and on cross-sectional imaging. Masslike hypertrophic cardiomyopathy typically occurs in an older child and may present with or have a family history of cardiac arrest.[30] MRI may show patchy perfusion and delayed enhancement (Fig. 80.16). Adherent thrombus can be mistaken for myxoma on echocardiography. Absence of delayed enhancement on MRI (using standard and prolonged inversion times) is a helpful differentiator.[31] The crista terminalis is a common mimic of a cardiac tumor on CT and can be mistaken for right atrial mass or thrombus.[32] It can be distinguished on CT as a focal low-density attenuation structure.

### KEY POINTS

- Cardiac tumors are rare in children.
- Rhabdomyomas are the most common tumor in children and frequently are associated with tuberous sclerosis.
- Fibromas have a characteristic appearance on postcontrast-delayed imaging.
- Metastatic tumors in children are more common than primary cardiac malignancies.

### SUGGESTED READINGS

Bruce CJ. Cardiac tumours: diagnosis and management. *Heart*. 2011; 97:151–160.
Isaacs H. Fetal and neonatal cardiac tumors. *Pediatr Cardiol*. 2004;25:252–273.
Mahani MG, Lu JC, Rigsby CK, et al. MRI of pediatric cardiac masses. *AJR*. 2014;202:971–981.
Marx GR, Moran AM. Cardiac tumors. In: Allen HD, Driscoll DJ, Shaddy RE, et al, eds. *Moss and Adam's Heart Disease in Infants, Children, and Adolescents: Including the Fetus and Young Adult*. 8th ed. Philadelphia: Lippincott Williams and Wilkins; 2013:[Chapter 72] pp 1549–1564.
Salanitri J, Lisle D, Rigsby C, et al. Benign cardiac tumours: cardiac CT and MRI imaging appearances. *J Med Imaging Radiat Oncol*. 2008;52(6):550–558.
Van Beek EJR, Stolpen AH, Khanna G, et al. CT and MRI of pericardial and cardiac neoplastic disease. *Cancer Imaging*. 2007;7:19–26.

### REFERENCES

Full references for this chapter can be found on www.expertconsult.com.

## REFERENCES

1. Freedom RM, Lee KJ, Macdonald C, et al. Selected aspects of cardiac tumors in infancy and childhood. *Pediatr Cardiol*. 2000;21:299–316.
2. Yinon Y, Chitayat D, Blaser S, et al. Fetal cardiac tumors: a single-center experience of 40 years. *Prenat Diagn*. 2010;30:941–949.
3. Isaacs H. Fetal and neonatal cardiac tumors. *Pedatr Cardiol*. 2004;25:252–273.
4. Tworetzky W, McElhinney DB, Margossian R, et al. Association between cardiac tumors and tuberous sclerosis in the fetus and neonate. *Am J Cardiol*. 2003;92:487–489.
5. Pipitone S, Mongiovi M, Grillo R, et al. Cardiac rhabdomyoma in intrauterine life: clinical features and natural history. A case series and review of published reports. *Ital Heart J*. 2002;3:48–52.
6. Kaminaga T, Takeshita T, Kimura I. Role of magnetic resonance imaging for evaluation of tumors in the cardiac region. *Eur Radiol*. 2003;13(suppl 4):L1–L10.
7. Syed IS, Feng D, Harris SR, et al. MR imaging of cardiac masses. *Magn Reson Imaging Clin N Am*. 2008;16:137–164.
8. Sugiyama H, Naito H, Tsukano S, et al. Evaluation of cardiac tumors I children by electron-beam computed tomography: rhabdomyoma and fibroma. *Circ J*. 2005;69:1352–1356.
9. Beroukhim RS, Prakash A, Valsangiacomo Buechel ER, et al. Characterization of cardiac tumors in children by cardiovascular magnetic resonance imaging. *J Am Coll Cardiol*. 2011;58:1044–1054.
10. Salanitri J, Lisle D, Rigsby C, et al. Benign cardiac tumours: cardiac CT and MRI imaging appearances. *M Med Imaging Radiat Oncol*. 2008;52:550–558.
11. Grebenc ML, Rosado de Christenson ML, Burke AP, et al. Primary cardiac and pericardial neoplasms: radiologic-pathologic correlation. *Radiographics*. 2000;20:1073–1103.
12. Grizzard JD, Ang GB. Magnetic resonance imaging of pericardial disease and cardiac masses. *Magn Reson Imaging Clin N Am*. 2007;15:579–607.
13. Kiaffas MG, Powell AJ, Geva T. Magnetic resonance imaging evaluation of cardiac tumor characteristics in infants and children. *Am J Cardiol*. 2002;15:1229–1233.
14. De Cobelli F, Esposito A, Mellone R, et al. Images I cardiovascular medicine. Late enhancement of a left ventricular cardiac fibroma assessed with gadolinium-enhanced cardiovascular magnetic resonance. *Circulation*. 2005;112:e242–e243.
15. Schvartzman PR, White RD. Imaging of cardiac and paracardiac masses. *J Thorac Imaging*. 2000;15:265–273.
16. Mahilmaran A, Seshadri M, Nayar PG, et al. Familial cardiac myxoma: Carney's complex. *Tex Heart Inst J*. 2003;30:80–82.
17. Taori K, Jawale R, Sanyal R, et al. Intrapericardial teratoma diagnosed on CT. *J Thorac Imaging*. 2007;22:185–187.
18. Reddy SC, Fenton KM, Gandhi SK, et al. Intrapericardial teratoma in a neonate. *Ann Thorac Surg*. 2003;76:626.
19. Patel A, Rigsby C, Young L. Cardiac teratoma of the interventricular septum with congenital aortic stenosis in a newborn. *Pedatr Cardiol*. 2008;29:1126–1128.
20. Van Beek EJR, Stolpen AH, Khanna G, et al. CT and MRI of pericardial and cardiac neoplastic disease. *Cancer Imaging*. 2007;7:19–26.
21. Gowda RM, Khan IA, Nair CK, et al. Cardiac papillary fibroelastoma: a comprehensive analysis of 725 cases. *Am Heart J*. 2003;146:404–410.
22. Sridar AV, Bulock F, Hickey MS, et al. Papillary fibroelastoma of the tricuspid valve presenting as neonatal pulmonary haemorrhage. *Acta Paediatr*. 2004;93:1254–1256.
23. Sparrow PJ, Kurian JB, Jones TR, et al. MR imaging of cardiac tumors. *Radiographics*. 2005;25:1255–1276.
24. Gan C, An Q, Tao K, et al. An asymptomatic lipoma of the right atrium in a neonate. *J Pediatr Surg*. 2008;43:1920–1922.
25. Sánchez Andrés A, Insa Albert B, Carrasco Moreno JI, et al. Primary cardiac tumours in infancy. *An Pediatr (Barc)*. 2008;69:15–22.
26. Barnes WS, Craft AW, Hunter AS, et al. Primary malignant cardiac tumors in children. *Pediatr Hematol Oncol*. 1986;3:347–351.
27. Romanos-Sirakis EC, Meyer DB, Chun A, et al. A primary cardiac sarcoma with features of a desmosplastic small round cell tumor in an adolescent male. *J Pedatr Hematol Oncol*. 2010;32:236–239.
28. Patel J, Melly L, Sheppard MN. Primary cardiac lymphoma: B- and T-cell cases at a specialist UK centre. *Ann Oncol*. 2010;21:1041–1045.
29. Walsh MA, Carcao M, Pope E, et al. Kaposiform hemangioendothelioma presenting antenatally with pericardial effusion. *J Pediatr Hematol Oncol*. 2008;30:761–763.
30. Hansen MW, Merchant N. MRI of hypertrophic cardiomyopathy: part I, MRI appearances. *AJR*. 2007;189:1335–1348.
31. Barkhausen J, Hunold P, Eggebrecht H, et al. Detection and characterization of intracardiac thrombi on MR imaging. *AJR*. 2002; 179:1539–1544.
32. Broderick LS, Brooks GN, Kuhlman JE. Anatomic pitfalls of the heart and pericardium. *Radiographics*. 2005;25:441–453.

# 81

# Cardiovascular Involvement by Systemic Diseases

Beverley Newman, Alexander J. Towbin, and Frandics P. Chan

Numerous systemic diseases can affect the heart and great vessels and are important causes of cardiac dysfunction. These systemic diseases include both prenatal and postnatal toxic and infectious exposures (e-Fig. 81.1); adverse effects of therapeutic agents; and various nutritional, metabolic, inflammatory, granulomatous, and autoimmune entities. Endocrine, circulatory, and blood disorders frequently have secondary cardiac effects. Primary cardiac tumors can occur in association with underlying systemic disorders; although rare, neoplasms elsewhere can metastasize to the heart or locally invade the great vessels or pericardium. Congenital and acquired neurologic and musculoskeletal conditions that affect the chest are associated with structural and functional cardiac abnormalities.

These entities and the spectrum of their cardiac effects are outlined in Table 81.1. We have included both common diseases that have cardiovascular features and uncommon lesions in which cardiovascular manifestations are prominent. A small number of selected entities are discussed in the following sections. Many of the lesions outlined in Table 81.1 overlap with other chapters and thus are not specifically discussed here.

## INFECTIOUS, INFLAMMATORY, AND AUTOIMMUNE DISORDERS

### Infectious Aortitis

***Overview.*** Acute infectious aortitis in children is usually caused by bacterial septicemia originating from infected lines and intravascular devices and from valvular endocarditis or occasionally by direct spread from an adjacent infection or abscess.[1] Staphylococci and streptococci are the organisms most frequently responsible for acute infectious aortitis.[1,2] Predisposing conditions include congenital heart disease and an immunocompromised state. Once they are in the bloodstream, virulent organisms may adhere to and invade the aortic wall. The resulting inflammation leads to suppurative necrosis that weakens the aortic wall and forms an aneurysm (Fig. 81.2A). A contained leak may lead to pseudoaneurysm formation (Fig. 81.2B). Staphylococcal aortitis is particularly prone to aneurysm or pseudoaneurysm rupture and is the most serious complication of infectious aortitis. Fungi, especially Aspergillus or Candida, also may be the cause of infectious aortitis, especially in immune-compromised individuals.[3] Syphilitic and tuberculous aortic aneurysms are rare complications of chronic infection by those organisms and are very uncommon in children.

Diagnosis of infectious aortitis is difficult because presenting symptoms are often minor or nonspecific, such as fever and abdominal or back pain. Common laboratory markers of infection can be normal. One adult study showed that blood cultures were negative in 28% of cases and white blood cell counts were normal in 42% of cases; however, an elevated erythrocyte sedimentation rate, a nonspecific finding of inflammation, was found in 92% of patients.[2]

***Imaging.*** Few clinical studies have evaluated the imaging appearance and distribution of infected aortic aneurysms in children. Experience from adult patients suggests that these aneurysms are more often saccular (93%) than fusiform (7%) and can be distributed throughout the course of the aorta: 6% in the ascending aorta, 23% in the descending thoracic aorta, 19% in the thoracoabdominal aorta, 10% in the juxtarenal aorta, and 32% in the infrarenal aorta.[4] Periaortic fluid, stranding, or a soft tissue mass was present in 48% of patients with infectious aortitis. Periaortic gas, a specific sign, was present in only 7%. Rapid progression of aneurysm size was found in infected aneurysms in both adults and children.[4] Computed tomography angiography (CTA) and magnetic resonance angiography (MRA) imaging have largely supplanted conventional angiography in the diagnosis of aortic aneurysms and their complications (see Fig. 81.2). Ultrasound may be an initial screening examination but usually is not definitive enough to support management decisions.

***Treatment.*** Antibiotic treatment with the goal of eradicating the offending organism is the first step in the treatment of infectious aortitis.[2] At the same time, imaging to document stability of the aortic lumen is necessary. If an aneurysm has formed, it should be surgically repaired after an adequate period of antibiotic treatment.[1,2] Deployment of endovascular stent grafts in infected aortic aneurysms has been attempted.[5] Although this is not considered a treatment of choice, it may be useful to act as a bridge to open surgical repair, especially in the presence of low-virulence organisms or rapidly expanding aneurysms.

### Takayasu Arteritis

***Overview.*** Takayasu arteritis, also known as pulseless arteritis, is a chronic inflammatory arteritis of large vessels.[6] The aorta is most commonly involved: 59% to 75% of cases affect the abdominal aorta and branches, and 40% to 56% of cases involve the thoracic aorta. Pulmonary and coronary arteries can also be involved.[7] Takayasu arteritis is a rare disease, occurring in 2.6 per 1 million people in North America.[8] It is more common in patients of Asian descent, and females make up 80% to 90% of patients.

The diagnosis of Takayasu arteritis is based on patient symptoms, physical findings, clinical laboratory values, serologic markers, and vascular findings.[6] The American College of Rheumatology criteria include arm or leg claudication, age less than 40 years, a blood pressure difference between extremities of greater than 10 mm Hg, a subclavian or aortic bruit, a decreased brachial artery pulse, and aortic or branch narrowing.[9] Three of these criteria provide a diagnosis of Takayasu arteritis with a sensitivity of 90.5% and a specificity of 97.8%.[8] Other clinical manifestations of Takayasu arteritis that are not specific diagnostic criteria include fever, headache, stroke, postural dizziness, arthralgias, weight loss, myalgias, and systemic or pulmonary hypertension.[8,10]

Takayasu arteritis has a triphasic pattern: a systemic nonvascular phase, a vascular inflammatory phase, and a quiescent “burnt-out” phase, although the inflammatory and fibrotic changes often overlap.[7,8] In children, the correct diagnosis is frequently delayed, especially when systemic symptoms predominate.[8,10,11]

The lesions of Takayasu arteritis are segmental with a patchy distribution. The vasculitis can lead to stenosis, occlusion, and aneurysm formation.[7] Severe stenosis or occlusive thrombosis of the pulmonary vasculature may lead to pulmonary infarction and pulmonary hypertension.[12] Cardiac symptoms include aortic regurgitation, dilated cardiomyopathy, myocarditis, pericarditis, congestive heart failure, and myocardial ischemia.

***Etiology and Classification.*** The specific cause of Takayasu arteritis is unknown, but it is probably a T-cell–mediated autoimmune

## Abstract:

Cardiovascular disease accompanies many systemic conditions. These include the adverse effects of toxins/drugs, metabolic, infectious/inflammatory and autoimmune diseases as well as nutritional, endocrine, circulatory, neoplastic and neuro/musculoskeletal conditions. A select number of these diseases are discussed and their imaging manifestations illustrated in this chapter. Many other entities with associated cardiovascular manifestations are summarized in tabular form.

## Keywords:

Systemic disease
cardiovascular disease
vasculitis
cardiomyopathy
MR
CT

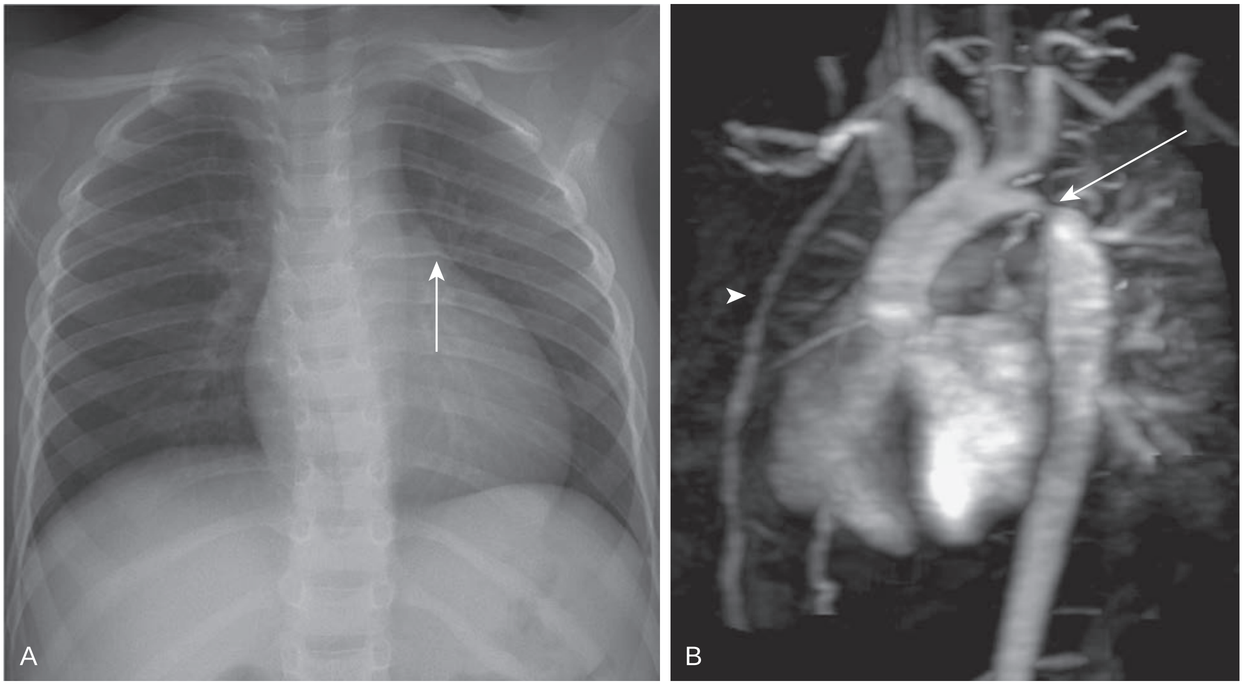

**e-Figure 81.1. Fetal alcohol syndrome and aortic coarctation in a 4-year-old boy.** (A) Chest radiograph shows a prominent aortic arch and descending aorta. Notching of the posterior left sixth rib *(arrow)* from an intercostal aortic collateral vessel is present. (B) Oblique sagittal three-dimansional MRA image demonstrates marked coarctation of the aorta *(arrow)* distal to the left subclavian artery. Multiple large intercostal collateral vessels are present, as well as enlarged internal mammary collaterals *(arrowhead).*

**TABLE 81.1** Cardiovascular Manifestations of Systemic Diseases or Disorders

| Disease or Disorder Category | Cardiovascular Manifestations |
|---|---|
| **TOXINS/DRUGS** | |
| Carbon monoxide | Tachycardia, noncardiogenic pulmonary edema |
| Doxorubicin (Adriamycin) | Cardiomyopathy, CHF |
| Fetal alcohol exposure (e-Fig. 81.1) | ASD, VSD, PDA, COA, arch interruption, PA hypoplasia, DORV, DEXTRO, TOF |
| HAART (used to treat HIV) | Cardiomyopathy, CHF |
| Iron | Cardiomyopathy, CHF |
| Lead | Myocarditis, atherosclerosis |
| Radiation | Cardiomyopathy, MI, pericarditis, valvular disease, especially aortic |
| Steroids (chronic) | Cardiomyopathy, CHF, cardiomegaly |
| Theophylline | Arrhythmias |
| **METABOLIC** | |
| Alkaptonuria | CAD, aortic and mitral valvulitis |
| Amyloidosis | Cardiomyopathy, CHF, arrhythmias |
| Carnitine deficiency | Dilated cardiomyopathy, CHF, endocardial fibroelastosis |
| Fabry disease | Cardiomyopathy, mitral valve disease, thromboembolism, arrhythmias, coronary aneurysm |
| Glycogen storage disease | |
| Type II (Pompe disease) | Cardiomyopathy, CHF, outflow tract obstruction |
| Type III | Hypertrophic cardiomyopathy |
| Type IV | Dilated cardiomyopathy |
| Danon disease (lysosomal glycogen-storage disease) | Hypertrophic cardiomyopathy |
| Hemochromatosis | Cardiomyopathy, arrhythmia, CHF |
| Gaucher disease (cerebroside lipidosis) | Cardiomyopathy, MR, MS, AS, coagulopathy |
| GM1 gangliosidosis | Infantile cardiomyopathy |
| Homocystinuria | Vascular stenoses and occlusions, aneurysms, thromboembolic episodes |
| Long-chain acetyl CoA dehydrogenase deficiency | Cardiomyopathy |
| Mucolipidosis III | AR, cardiomyopathy |
| Mucopolysaccharidosis | |
| IH (Hurler syndrome) | Acute cardiomyopathy associated with endocardial fibroelastosis, AR, MR, coronary narrowing |
| IS (Scheie) | AS, MS |
| II (Hunter syndrome) | AR |
| III (Sanfilippo syndrome) | Functional and morphologic mitral valve deterioration |
| IV (Morquio syndrome) | AR, MR, CAD |
| VI (Maroteaux–Lamy syndrome) | AS, MS |
| Oncocytic (histiocytoid) cardiomyopathy (infantile histiocytic cardiomyopathy, Purkinje cell tumor, focal lipid cardiomyopathy, idiopathic infantile cardiomyopathy) | Cardiomyopathy, ASD, VSD, nodular deposits on the ventricular endocardium or valves |
| Pseudoxanthoma elasticum | Premature atherosclerosis, MI, restrictive cardiomyopathy, mitral valve disease, AO dilation, vascular, coronary occlusions |
| Refsum disease (phytanic acid $\alpha$-oxidase deficiency) | CHF, cardiomyopathy, conduction abnormality |
| Sitosterolemia (inherited plant sterol storage disease) | CAD, MI, CHF |
| Uremia | Pericardial effusion, constrictive pericarditis, CHF, cardiomyopathy |
| **GRANULOMATOUS** | |
| Histoplasmosis | Pericardial effusion, tamponade, AR, endocarditis, fibrosing mediastinitis |
| Sarcoid | Infiltrative cardiomyopathy, pericardial effusion, papillary muscle dysfunction, valvular disease, fibrosing mediastinitis, large-vessel vasculitis |
| Tuberculosis | Myocarditis, ventricular aneurysms, calcific/constrictive pericarditis, fibrosing mediastinitis, vasculitis |
| Wegener granulomatosis | Pulmonary vasculitis, pericarditis, coronary arteritis, MI |
| **INFECTIOUS/INFLAMMATORY/AUTOIMMUNE/CONNECTIVE TISSUE DISORDERS** | |
| Aortitis (infectious) (Fig. 81.2) | Abscess, aneurysm, leak, pseudoaneurysm, rupture |
| Behçet syndrome | Aortic, pulmonary and coronary vasculitis and aneurysms, cardiac valvular vegetations |
| Chagas disease *(Trypanosoma cruzi)* | Myocarditis, CHF, apical aneurysm |
| Dermatomyositis | Cardiomyopathy |
| Diphtheria | Cardiomyopathy, myocarditis |
| Enterovirus (Coxsackie B) | Myocarditis |
| Fetal rubella infection | PDA, pulmonary artery stenosis, COA, ASD, VSD, myocarditis, cardiomyopathy |
| HIV | Cardiomyopathy, CHF |
| Juvenile rheumatoid arthritis | Pericarditis, myocarditis, CHF |
| Kawasaki disease | Coronary artery aneurysm, coronary thrombosis, MR, papillary muscle dysfunction, MI, myocarditis, CHF, pericarditis, AR, systemic vasculitis |
| Polyarteritis nodosa | Cardiomyopathy, pericarditis, coronary artery aneurysms, MI, systemic vasculitis |
| Relapsing polychondritis | CM, AO dilation/aneurysm, AR, TR, MR |
| Rheumatic fever | Pancarditis, valve insufficiency, CHF, valvular stenosis (MS, AS, TS), atrial dilation, left atrial thrombus, constrictive pericarditis |
| Scleroderma | CM, pericarditis, myocarditis, conduction abnormality, cor pulmonale |

**TABLE 81.1** Cardiovascular Manifestations of Systemic Diseases or Disorders—cont'd

| Disease or Disorder Category | Cardiovascular Manifestations |
|---|---|
| Systemic lupus erythematosus | Pericarditis, cardiomyopathy, Libman-Sacks endocarditis, heart block, endocardial fibroelastosis, systemic/coronary vasculitis |
| Takayasu arteritis (Fig. 81.3, e-Fig. 81.4, and Fig. 81.5) | Widened mediastinum, AR, CHF, myocarditis, aortitis, pulmonary/coronary vasculitis, aneurysms, stenoses |
| Toxoplasmosis | Myocarditis |
| **MALNUTRITION** | |
| Anorexia | Decreased ventricular mass, MVP |
| Bulimia | Arrest, cardiac rupture, pneumomediastinum |
| Marasmus | Thinning of cardiac muscle, CHF, CHD |
| Obesity | CM, pulmonary hypertension, early atherosclerotic disease |
| Selenium deficiency (Keshan disease) | Congestive cardiomyopathy, cardiogenic shock, CHF |
| Vitamin $B_1$ (thiamine) deficiency (beriberi) | Cardiomyopathy, CHF |
| **CARDIAC TUMORS ASSOCIATED WITH SYSTEMIC DISEASE** | |
| Fibromas (in Beckwith–Wiedemann syndrome, nevoid basal cell carcinoma syndrome, or Gorlin syndrome) | Cardiomyopathy, CHF, mass most commonly originates at the intraventricular septum, occasional calcification in the tumor |
| Myxomas (in Carney complex, LAMB/NAME syndrome) (e-Fig. 81.9) | Attached to atrial septum and mitral apparatus in LA, can prolapse or embolize, multiple, can occur in any cardiac chamber, can recur at distant intracardiac and extracardiac sites, intracardiac valvular obstruction leading to CHF |
| Rhabdomyomas (in tuberous sclerosis) | Multiple intramural hamartomas, present in utero, abnormal valve function, outflow obstruction, cardiomyopathy, spontaneously regress |
| **METASTASES** | |
| Lymphoma | Great vessel obstruction, SVC syndrome, CHF, pericardial infiltration |
| Wilms tumor (hepatoblastoma less commonly) (e-Fig. 81.10) | IVC extension, CHF, cardiomyopathy |
| **ENDOCRINE** | |
| Cushing disease | Cardiomyopathy, blood vessel fragility |
| Diabetes (acquired) | Early CAD |
| Diabetes, gestational (infant of a diabetic mother) (Fig. 81.6) | Cardiomyopathy, cardiovisceral or atrioventricular discordance, outflow tract anomalies, TGA, AVSD, DiGeorge complex |
| Gigantism/acromegaly | Cardiac hypertrophy, LVH |
| Hyperthyroidism | CHF, cardiomyopathy |
| Hypothyroidism | Pericardial effusion, CHF |
| **CIRCULATORY/BLOOD DISORDERS** | |
| Arteriovenous fistula (especially vein of Galen malformation, HHT, and infantile hepatic hemangioma) (e-Fig. 81.11) | CHF, high output; HHT: skin, visceral, single or multiple pulmonary AVM, angiodysplasia, coronary ectasia, Kasabach–Merritt syndrome (platelet trapping and consumptive coagulopathy) |
| Fanconi anemia | PDA, VSD, peripheral PS, cardiomyopathy, ASD, TOF, AS, COA, AO atheromas, hypoplastic AO, double AO arch |
| Hepatopulmonary syndrome (chronic liver disease, hypoxemia, clubbing) | Pulmonary capillary microshunts, vasodilation, CHF—high output |
| Portopulmonary syndrome (Abernethy malformation): hepatopulmonary syndrome with no liver disease, portosystemic shunting | Type I abnormal portal-systemic connection; absent intrahepatic portal vein; associated with VSD, AO arch anomalies<br>Type II abnormal portal-systemic connection; intrahepatic portal vein present |
| Leukemia | SVC syndrome, cardiomyopathy, CHF, pericardial effusion |
| Polycythemia vera | MI, arterial and venous clots, CHF |
| Sickle cell disease (Fig. 81.7) | Cardiomyopathy, MI, acute chest syndrome, CHF, vascular thromboses |
| Thalassemia (Fig. 81.8) | CHF, cardiomyopathy, iron overload |
| Twin-to-twin transfusion | Shared placental circulation leads to unbalanced flow; CM and CHF may develop in both the anemic and the polycythemic twin |
| **MUSCULOSKELETAL/NEUROLOGIC** | |
| Abetalipoproteinemia | Arrhythmia, cardiomyopathy, CHF |
| Duchenne muscular dystrophy | Cardiomegaly, progressive cardiomyopathy, conduction abnormalities, CHF, MVP |
| Friedreich ataxia (spinocerebellar degeneration) | CM, cardiomyopathy, CHF, cardiac thrombus |
| Kyphoscoliosis | Cardiac, vascular, and airway displacement and compression |
| Osteogenesis imperfecta | MVP, AR, enlarged AO root |
| Pectus excavatum | Cardiac displacement, MVP, anterior compression of right ventricle |

*AO,* Aorta/aortic; *AR,* aortic regurgitation; *AS,* aortic stenosis; *ASD,* atrial septal defect; *AVM,* arteriovenous malformation; *AVSD,* atrioventricular septal defect; *CAD,* coronary artery disease; *CHD*, congenital heart disease; *CHF,* congestive heart failure; *CM,* cardiomegaly; *CoA,* coenzyme A; *COA,* aorta coarctation; *DEXTRO,* dextrocardia; *DORV,* double-outlet right ventricle; *HAART,* highly active antiretroviral therapy; *HHT,* hereditary hemorrhagic telangiectasia; *HIV,* human immunodeficiency virus; *IVC,* inferior vena cava; *LA,* left atrium; *LAMB,* lentigines, atrial myxoma, mucocutaneous myxomas, blue nevi; *LVH,* left ventricular hypertrophy; *MI,* myocardial infarction; *MR,* mitral regurgitation; *MS,* mitral stenosis; *MVP,* mitral valve prolapse; *NAME,* nevi, atrial myxoma, myxoid neurofibromas, ephelides; *PA,* pulmonary artery; *PDA,* patent ductus arteriosus; *PS,* pulmonary stenosis; *SVC,* superior vena cava; *TGA,* transposition of great arteries; *TOF,* tetralogy of Fallot; *TR,* tricuspid regurgitation; *TS,* tricuspid stenosis; *VSD,* ventricular septal defect.

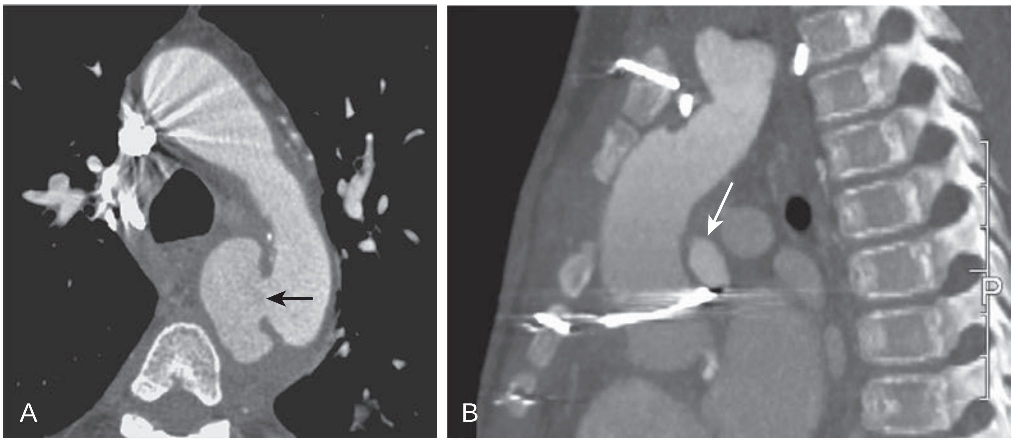

**Figure 81.2. Infectious aortitis.** (A) Axial CTA image shows a thick-walled saccular aneurysm communicating with the aortic arch through a narrow opening *(arrow).* (B) An 8-year-old child after repair of aortic coarctation and aortic stenosis with prosthetic aortic valve replacement whose postoperative course was complicated by *Staphylococcus aureus* mediastinitis. Sagittal maximal-intensity projection image from a gated CTA demonstrates a small posterior aortic pseudoaneurysm *(arrow)* adjacent to the aortic valve. Note diffuse anterior soft tissue edema/inflammation.

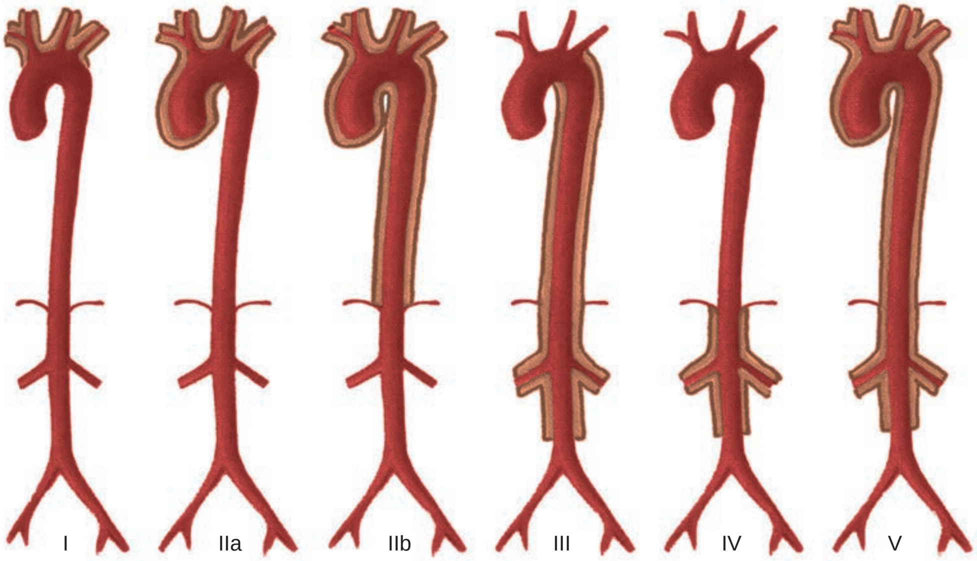

**Figure 81.3. Classification schema of Takayasu arteritis.** Coronary (C+) and/or pulmonary (P+) involvement can occur in all types. Type I involves aortic arch branches only; type IIa involves the ascending aorta, arch, and branches; type IIb involves the descending thoracic aorta, with or without involvement of the ascending aorta, arch, and branches; type III involves the descending thoracic aorta, abdominal aorta, and the renal arteries; type IV involves the abdominal vessels only; and type V is generalized. *(From Nastri MV, Baptista LPS, Baroni RH, et al. Gadolinium-enhanced three-dimensional MR angiography of Takayasu arteritis.* Radiographics*. 2004;24:773–786.)*

process. Infection, particularly tuberculosis, has been linked to the development of Takayasu arteritis, especially in children.[10] The diseased vessel wall is thickened and shows granulomatous changes from the adventitia to the media. Giant cell (or temporal) arteritis has an identical pathologic appearance to Takayasu arteritis but affects an older population and typically involves the temporal artery.[13]

Takayasu arteritis currently is divided into six types depending on the location of aortic involvement. Coronary (C+) or pulmonary (P+) involvement may occur in all types (Fig. 81.3).[7]

***Imaging.*** Vascular stenosis and aneurysm are the primary causes of mortality and morbidity and therefore should be evaluated with angiographic techniques. Conventional angiography has been the gold standard for diagnosis, but it is being supplanted by MRA (e-Fig. 81.4 and Fig. 81.5).[7,8] MRA has several advantages, including its lack of ionizing radiation, its noninvasive nature, and its ability to show abnormal vascular wall signal and thickening before luminal narrowing becomes apparent.[6] Active inflammation is suggested when a high T2 signal is noted within the vessel wall (Fig. 81.5). Vessel wall enhancement can be seen with the administration of gadolinium and also is used to gauge the activity of the inflammatory process (e-Fig. 81.4).[7,8,11] Inversion recovery delayed enhancement of the vessel wall also may be seen; the significance of this phenomenon is uncertain.[8]

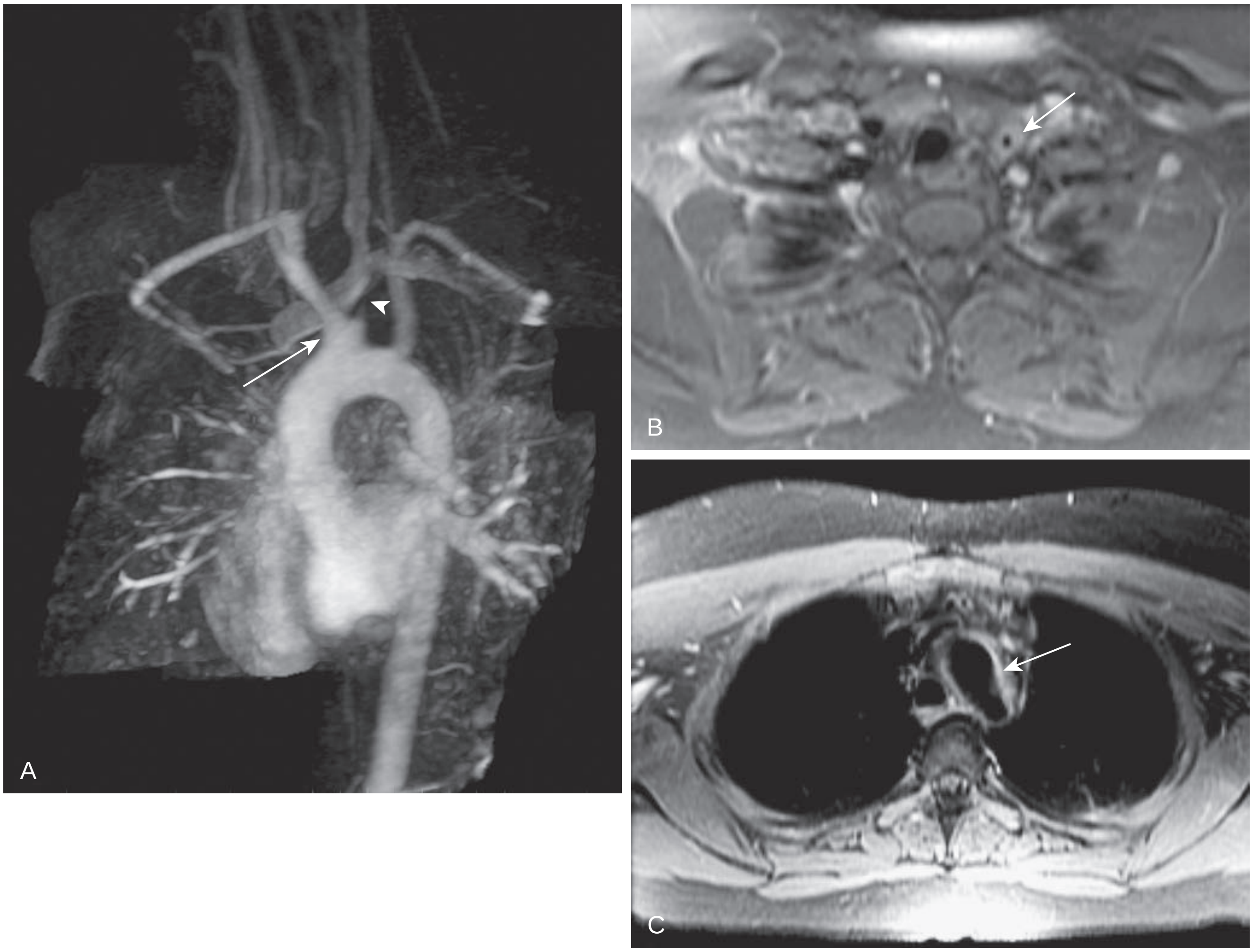

**e-Figure 81.4. Takayasu arteritis type IIa in a 14-year-old girl with active disease.** (A) Oblique sagittal, thin, maximal-intensity projection MRA image shows a common origin of the left common carotid artery and the brachiocephalic artery *(arrow).* Severe stenosis of the left common carotid artery is present at its origin *(arrowhead),* with only a small amount of flow extending superiorly. (B) T1-weighted axial MRI with contrast shows thickening and enhancement of the wall of the left common carotid artery *(arrow).* (C) T1-weighted axial MRI with contrast shows thickening and enhancement of the wall of the aortic arch *(arrow),* suggestive of active inflammation.

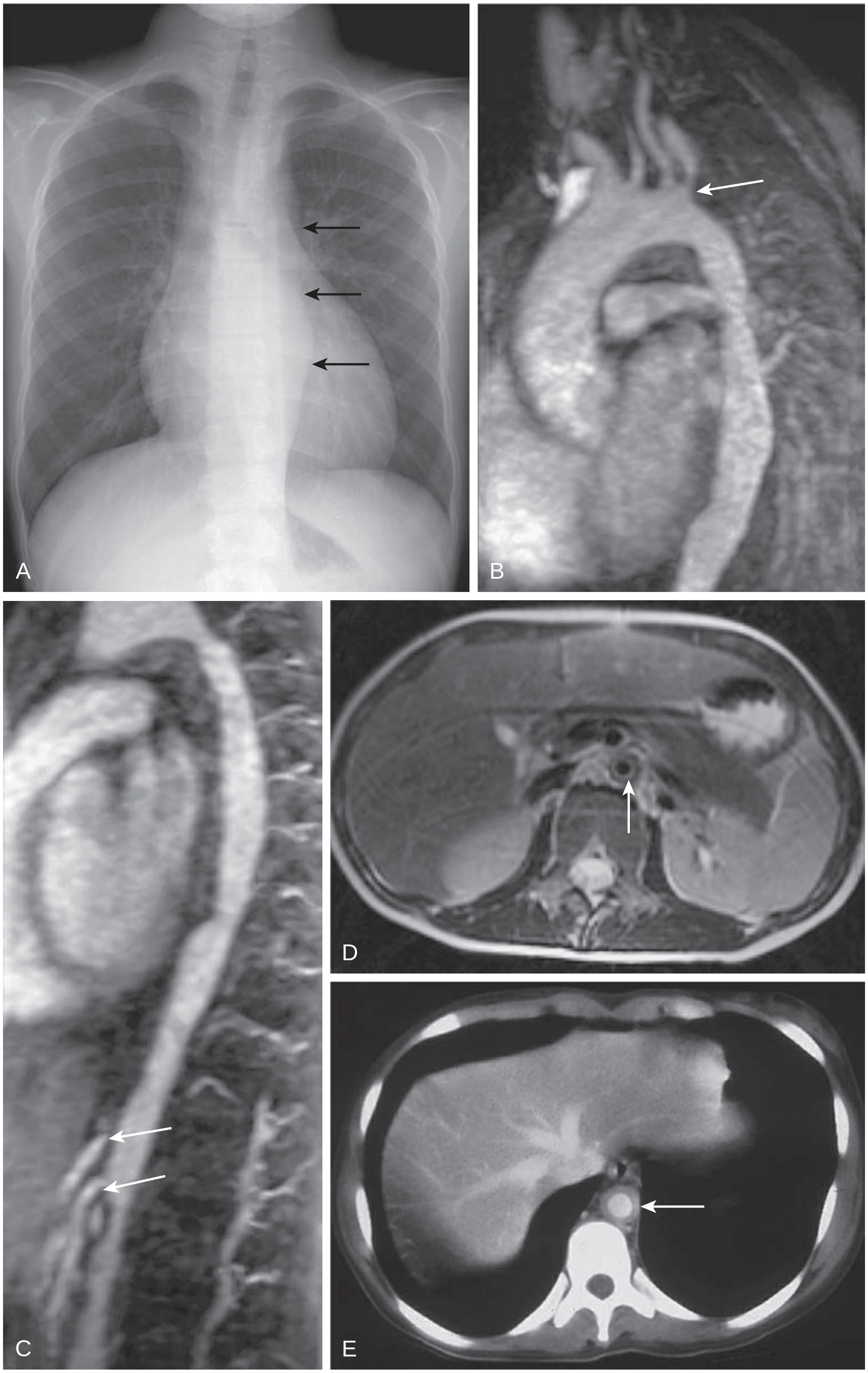

**Figure 81.5. Takayasu arteritis type V in a 11-year-old girl.** (A) Chest radiograph shows a heart that is top-normal in size and there is an abnormal wavy contour to the descending thoracic aorta *(arrows).* (B) Oblique sagittal thin maximal-intensity projection (MIP) MRA image shows four vessels arising from the aortic arch: the right brachiocephalic artery, left common carotid artery, left vertebral artery, and left subclavian artery. Stenosis is present at the origin of the left subclavian artery *(arrow)* along with areas of stenosis and aneurysmal dilation of the visible portions of the descending aorta. (C) Thin sagittal MIP MRA image shows an irregular contour and narrowing of the descending aorta, as well as at the origins of the celiac and the superior mesenteric arteries *(arrows).* (D) T2-weighted axial MRI shows increased signal and thickening of the wall with a narrowed lumen *(arrow)* of the inframesenteric abdominal aorta. (E) A contrast-enhanced CT image of a different patient shows wall thickening and enhancement *(arrow)* of the abdominal aorta.

Ultrasound can show vessel wall thickening and CTA may demonstrate mural thickening and wall enhancement, as well as luminal dilation, narrowing, or occlusion (Fig. 81.5).[6] Fluorodeoxyglucose positron emission tomography uptake also may be useful in evaluating active inflammation.[6,8]

***Treatment and Follow-up.*** Medical therapy of Takayasu arteritis initially focuses on the suppression of the immunologic responses with corticosteroids, methotrexate, azathioprine, and cyclophosphamide. In refractory Takayasu arteritis, the anti–tumor necrosis factor–α agents etanercept and infliximab have been used to achieve sustained remission.[14] Follow-up with MRA or CTA helps document stability or progression of the vascular abnormalities and their complications.[6,11]

Patients with renovascular hypertension, severe coarctation of the aorta, claudication, progressive aneurysm enlargement, coronary artery disease, or cervicocranial vessel stenosis may benefit from surgical revascularization.[10] Bypass grafts, either synthetic or autologous, can be used, but restenosis is common: up to one-third of synthetic graft cases and approximately 10% of autologous vessel cases. Other postoperative complications include heart failure, intractable hypertension, and graft deterioration with pseudoaneurysm formation. Postsurgical anastomotic aneurysm formation is seen in up to 34% of patients. Angioplasty of Takayasu vascular stenoses has an initial success rate of 92% and a restenosis rate of 22%. Surgical options preferably are performed during disease remission.[10]

### Other Vasculitides

Aneurysmal disease of the aorta, which generally afflicts older patients, is a rare complication of systemic lupus erythematosus. The exact pathophysiology of the aortic aneurysm is unknown. It may be caused directly by the systemic lupus erythematosus–related inflammation of the vessel wall or as a result of chronic steroid treatment and the resultant accelerated aortic atherosclerosis.[15] Sarcoidosis has been reported as a rare cause of large-vessel vascular stenosis, and it has been recommended that children with early-onset sarcoidosis be evaluated for occlusive arterial disease.[16]

Other rare causes of vasculitis, especially of the pulmonary artery, include Behçet syndrome and Wegener granulomatosis.[9,17] Behçet syndrome is a multisystem inflammatory disease of unknown cause. Classically, Behçet syndrome describes a combination of recurrent aphthous ulcers, genital ulceration, and uveitis. It also involves the central nervous system in 10% to 30% of cases and the vascular system (including systemic, pulmonary, and coronary vessels) in 10% to 40% of cases. Its prevalence in the United States is probably less than 5 cases per 100,000 people, but it is much more common in Turkey, with an estimated prevalence of 100 cases per 100,000 people. Although Behçet syndrome typically is an adult disease, onset in childhood is well recognized. When the pulmonary artery is affected, the most common lesion is pulmonary artery aneurysm. Other findings include pulmonary artery stenosis and thrombosis, pulmonary infarct, and hemorrhage.[18] These lesions are readily evaluated with pulmonary CTA.[17] Treatment is focused on immunosuppression, and resolution of aneurysms has been observed after remission of Behçet syndrome.[18]

## MALNUTRITION

### Anorexia

Anorexia is a common eating disorder characterized by an intense fear of gaining weight, undue influence of body shape or weight on self-image, the refusal to maintain a body weight of greater than 85% of that predicted, and the absence of at least three consecutive menstrual periods. It is 10 times more common in girls and occurs mostly during adolescence.

Cardiovascular complications occur in up to 80% of patients and are the cause of approximately one-third of deaths in this disorder. The most common cardiac abnormality is decreased ventricular wall thickness caused by a loss of cardiac muscle. Other cardiac manifestations include sinus bradycardia, hypotension, arrhythmias, QT-interval prolongation, and even sudden death.[19] These abnormalities are reversible in the early stages of disease.[19,20]

### Obesity

A worldwide epidemic of obesity is occurring among people of all ages.[21] The Obesity Consensus Working Group reported that the prevalence of overweight status has doubled among children 6 to 11 years of age and tripled in those 12 to 17 years of age from 1980 to 2000. Approximately 15% of all 15-year-olds in the United States can be classified as obese (defined as a body mass index greater than the 95th percentile).

Obesity in children has led to an increase in type 2 diabetes mellitus, hypertension, fatty-related liver disease, and possibly asthma. Heart disease is a significant cause of morbidity in obese persons.[21] Excessive adipose accumulation induces increased blood volume and cardiac output, leading to cardiomegaly. Decreased alveolar ventilation and sleep apnea may contribute to both cardiomegaly and pulmonary hypertension (Pickwickian syndrome). Obesity and type 2 diabetes lead to the development of early atherosclerotic disease. It is uncertain whether childhood obesity increases the risk of myocardial infarction or stroke in adulthood.

The high incidence of obesity has led to a corresponding increase in the number of bariatric procedures used to treat patients, including children. Rapid loss of a large amount of weight and decreased absorption of nutrients postoperatively puts individuals at risk for nutritional deficiencies. Beriberi, a disorder of thiamine deficiency, has been reported after gastric bypass surgery.[22] The wet form of beriberi is associated with cardiac failure and edema.

## ENDOCRINE DISORDERS

### Type 1 Diabetes Mellitus

***Overview.*** Type 1 insulin-dependent diabetes mellitus occurs relatively frequently in the United States, developing in an estimated 3 of 1,000 children by age 20 years. Cardiovascular complications are the most common causes of morbidity and mortality in persons with diabetes in childhood and are mainly the result of atherosclerotic disease.[23] Persons with diabetes are more likely than nondiabetic individuals to have severe narrowing of the coronary arteries, stenosis in all three major coronary vessels, and disease in more distal segments.

***Etiology.*** The precise etiology of diabetes is unknown, but it is thought to be an autoimmune disorder of islet cells, possibly related to a prior viral infection. Most children present with polyuria, polydipsia, polyphagia, and weight loss with hyperglycemia, glycosuria, ketonemia, and ketonuria.

### Gestational Diabetes

Gestational diabetes is associated with congenital abnormalities in infants born to affected mothers. The Baltimore-Washington Infant Study found that maternal diabetes was strongly associated with early cardiovascular malformations and with cardiomyopathy.[24] These malformations include defects in early cardiac development such as laterality and cardiac looping defects, outflow tract anomalies with or without transposed great vessels, and atrioventricular septal defects. Maternal diabetes was not associated with obstructive and simple shunt defects.[24]

Visceromegaly, hypoglycemia, and cardiomegaly occur commonly in neonates born to diabetic mothers (Fig. 81.6). The severity of these findings and of congenital heart defects may be related

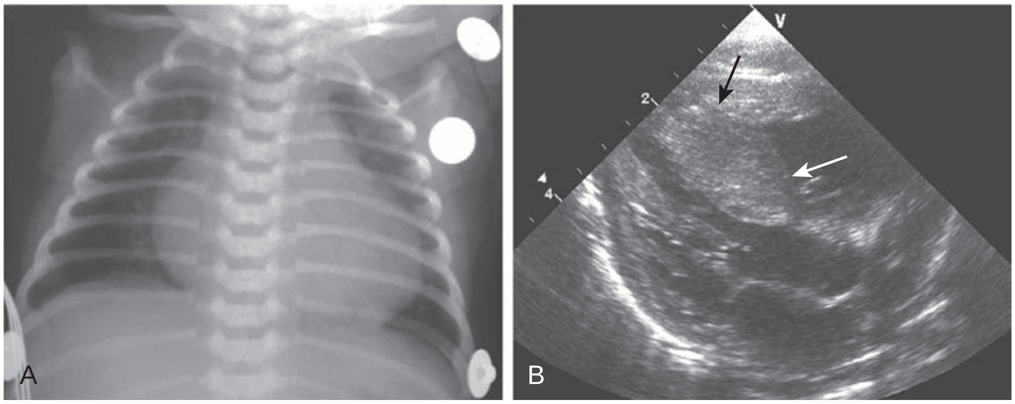

**Figure 81.6. Newborn boy with a diabetic mother.** (A) Chest radiograph shows an enlarged heart and mild congestive heart failure. A hypoplastic left-sided heart malformation was diagnosed on echocardiography. (B) Long-axis echocardiogram from another patient with neonatal diabetic cardiomyopathy shows septal hypertrophy *(arrows),* which partially impinges on the left ventricular outflow tract. *(*B, *Courtesy of Fred Sherman, MD, Children's Hospital of Pittsburgh.)*

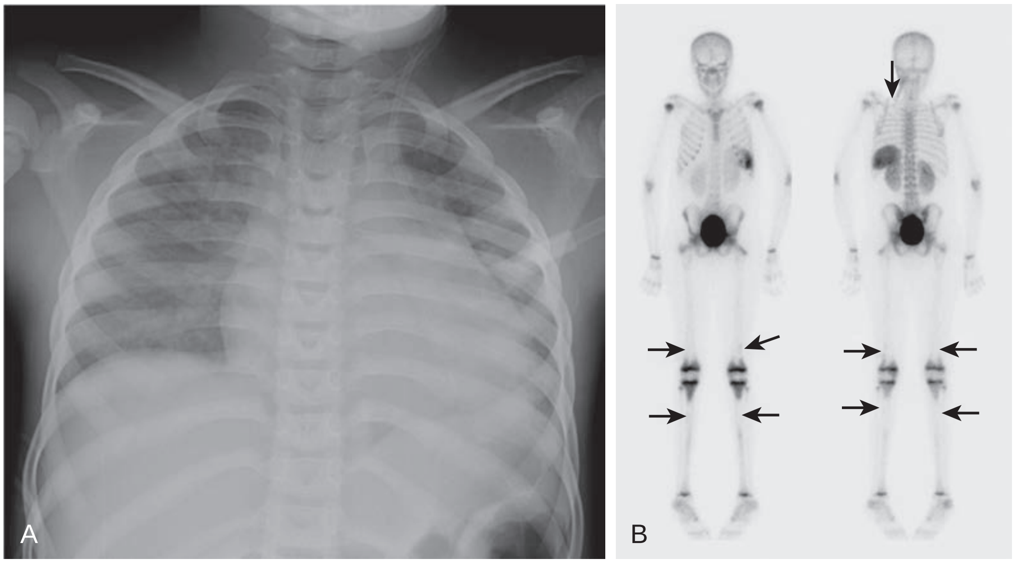

**Figure 81.7. Acute chest syndrome in a patient with sickle cell disease.** (A) Frontal view of the chest in a patient with sickle cell disease shows a new opacity in the left lower lobe and a mildly enlarged heart. (B) Anterior and posterior projection from a technetium-99m methylene-diphosponate bone scan in a different patient shows multiple areas of decreased uptake due to infarcts *(arrows)* in the distal femurs, proximal tibias, and left posterior third rib.

to how well the maternal blood sugar was controlled during pregnancy.[25] Left ventricular septal wall thickening and hypertrophic subaortic stenosis are characteristic and often transient features in affected neonates (Fig. 81.6).

## BLOOD DISORDERS

### Sickle Cell Disease

***Overview.*** Sickle cell disease is the most common single gene disorder of African Americans. Almost 1 in 12 African Americans are heterozygous for the sickle trait. Children with sickle cell disease constitute the largest subgroup of patients with chronic anemia in the United States. Cardiac enlargement is the most common cardiac feature related to the chronic anemia.[26] Cardiomyopathy also may develop from coronary sickling and ischemia, along with cardiac dysfunction resulting from chronic transfusion and myocardial iron deposition.[26,27]

***Imaging.*** Acute chest syndrome is a common cause of hospitalization, morbidity, and mortality in children with sickle cell disease (Fig. 81.7). Clinical presentation includes chest pain, leukocytosis, and fever. Typical chest radiographic manifestations include cardiomegaly, venous congestion, new radiographic opacity (atelectasis or consolidation), and pleural effusion. The inciting etiology is not always apparent, but possibilities include infection, pulmonary sickling and infarction, and fat emboli from marrow infarction. Infection appears to be a more common underlying factor in younger children, whereas infarction is more common in older persons.

Imaging of the chest in children with sickle cell disease depends on the clinical scenario. Plain chest radiographs are the mainstay but can be supplemented with echocardiography, computed

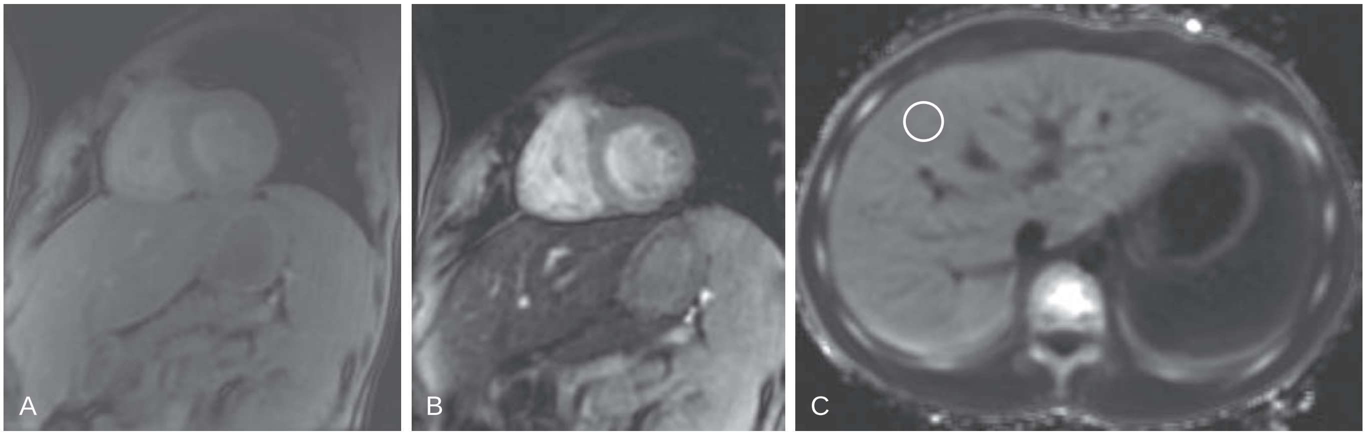

**Figure 81.8. β-Thalassemia in a 14-year-old boy with who has received multiple transfusions.** MRI of the liver and heart was done to evaluate iron deposition. (A and B) Short axis gated, multiecho gradient echo sequence with increasing echo time shows progressive darkening of the liver but not the myocardium. (A) Echo time (TE) 2.2. (B) TE 13.4. (C) An axial R2* map of the liver that was reconstructed from multiple gradient echo images. A region of interest in the liver as shown gave an R2* reading in the liver parenchyma of 124 Hertz. T2* can be calculated as the inverse of R2*, 8.1 msec. This T2* number reflects moderate iron deposition within the liver. Note the absence of iron in the spleen (dark on this image). T2* in the myocardium was similarly calculated (not shown) to be 30 msec (within normal limits).

tomography (CT), magnetic resonance imaging (MRI), or a nuclear scan for such concerns as bone infarcts or osteomyelitis, pulmonary emboli, complicated pulmonary infection, myocardial ischemia or dysfunction, and liver/myocardial iron overload related to repeated transfusion.[27]

Children with sickle cell disease and specific risk factors have been shown to be at risk for myocardial ischemia.[28] Consequences of ischemia include chest pain, heart failure, or a ventricular arrhythmia. Thallium-201 single-photon emission CT scans show that almost one-third of symptomatic children have a fixed perfusion defect. These perfusion defects may not have a specific vascular pattern, suggesting involvement of the cardiac microcirculation.[28]

### Thalassemia

Cardiac manifestations of thalassemia are primarily due to chronic anemia and vary with the severity of the disease.[29] Thalassemia major (homozygous) has more marked hematologic, cardiac, and bone changes than thalassemia minor (heterozygous) and intermedia (the homozygous, milder form). A hyperdynamic circulation and congestive heart failure are the most common clinical cardiac findings.

Cardiomyopathy may develop as a result of ischemia or myocardial iron overload related to chronic transfusion. Widened and coarsely trabeculated rib changes are common in association with red marrow conversion. Extramedullary hematopoiesis occurs commonly in the liver and spleen, as well as paraspinal soft tissues, most often in the lower thoracic region, with resultant visceromegaly and paraspinal soft tissue masses. MRI is useful for serial follow-up of children who undergo chronic transfusion to assess their visceral and myocardial iron burden and cardiac function (Fig. 81.8).

## OTHER SYSTEMIC DISORDERS

Many other systemic disorders affect the cardiovascular system. These disorders are listed in Table 81.1 and e-Figs. 81.9–81.11.

### KEY POINTS

- The diagnosis of infectious and inflammatory vasculitides is often delayed due to nonspecific symptoms.
- MRA and CTA have become the major modalities in evaluating large- and medium-vessel disease.
- Eating disorders and diabetes are increasingly important causes of cardiovascular disease in both the pediatric and adult populations.

### SUGGESTED READINGS

Lisowski LA, Verheijen PM, Copel JA, et al. Congenital heart disease in pregnancies complicated by maternal diabetes mellitus. An international clinical collaboration, literature review, and meta-analysis. *Herz*. 2010;35(1):19–26.

Lopes RJ, Almeida J, Dias PJ, et al. Infectious thoracic aortitis: a literature review. *Clin Cardiol*. 2009;32(9):488–490.

Nastri MV, Baptista LP, Baroni RH, et al. Gadolinium-enhanced three-dimensional MR angiography of Takayasu arteritis. *Radiographics*. 2004;24(3):773–786.

Speiser PW, Rudolf MC, Anhalt H, et al. Childhood obesity. *J Clin Endocrinol Metab*. 2005;90(3):1871–1887.

### REFERENCES

Full references for this chapter can be found on www.expertconsult.com.

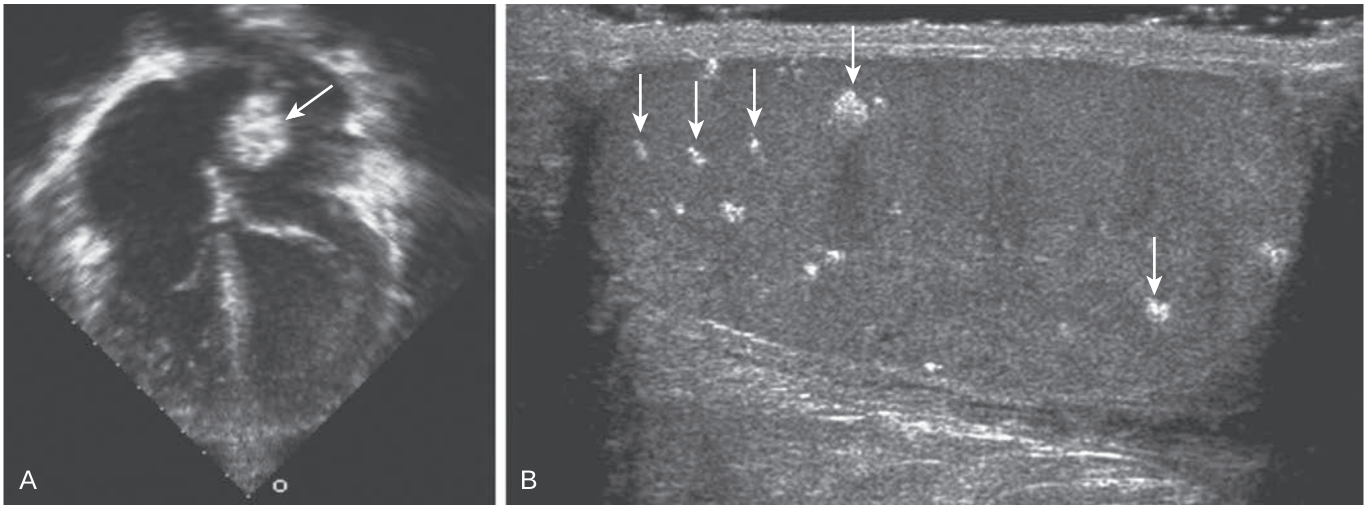

**e-Figure 81.9. 12-year-old boy with a family history of cardiac myxomas and a diagnosis of Carney complex.** (A) Four-chamber view from an echocardiogram shows an echogenic mass in the left atrium *(arrow)* that on resection was a cardiac myxoma. (B) Ultrasound of the right testis shows multiple echogenic foci with posterior acoustic shadowing *(arrows).* Similar findings were present on the left (not shown). Carney complex is a rare autosomal dominant disorder that has a constellation of findings, including spotty skin pigmentation, endocrine hyperactivity, and cardiac myxomas. Common endocrine gland manifestations are acromegaly, thyroid and testicular tumors, and adrenocorticotropic hormone–independent Cushing syndrome. The large-cell calcifying Sertoli cell tumor is the most common testicular tumor and can have macrocalcifications. *(A, Courtesy of Lizabeth Lanford, MD, Children's Hospital of Pittsburgh.)*

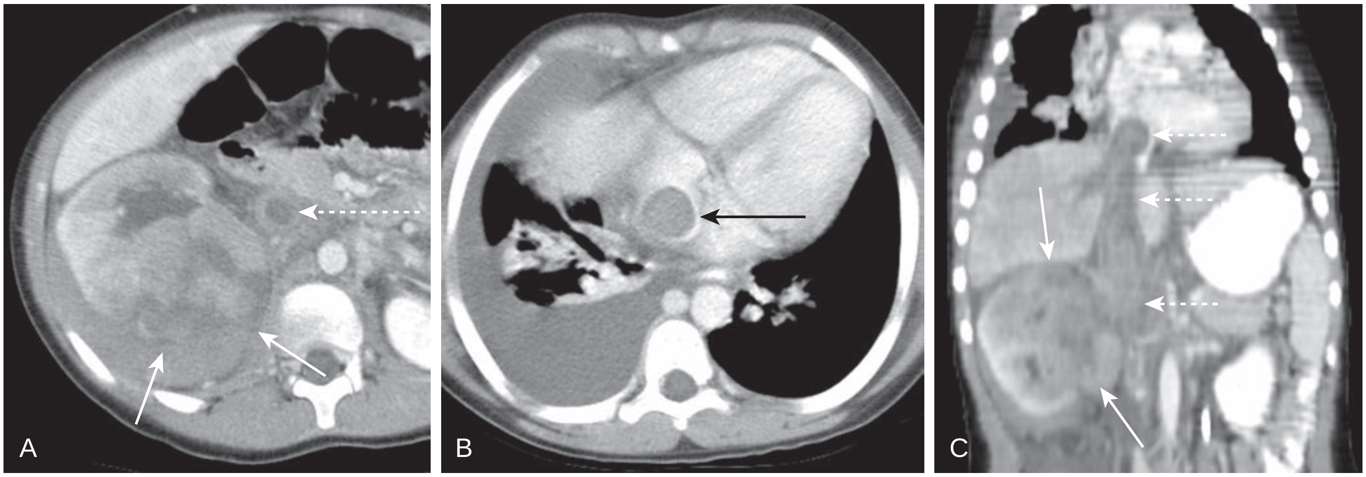

**e-Figure 81.10. Wilms tumor with inferior vena cava thrombus.** (A) Axial contrast-enhanced CT image of the abdomen shows a large infiltrative mass *(arrows)* of the right kidney. The inferior vena cava is enlarged and thrombosed *(dashed arrow).* (B) Axial contrast-enhanced CT of the chest at the level of the heart shows extension of the tumor thrombus *(arrow)* into the right atrium. (C) Coronal contrast-enhanced CT shows the infiltrative Wilms tumor *(arrows)* of the right kidney. The tumor thrombus *(dashed arrows)* extends from the insertion of the renal vein to the right atrium.

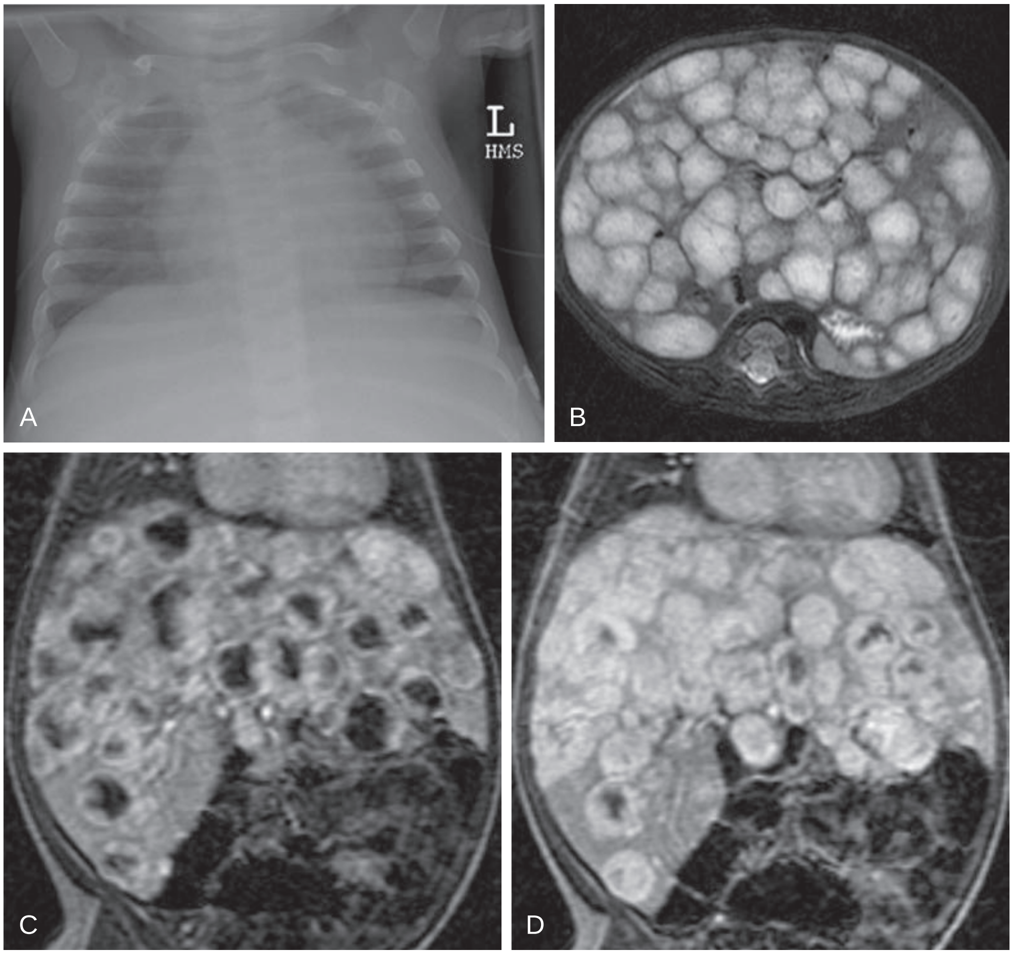

**e-Figure 81.11. Infantile hepatic hemangioma.** (A) Frontal radiograph of the chest shows an enlarged heart and increased pulmonary vascularity. The abdomen is not completely imaged but hepatomegaly appears to be present. (B) Axial T2-weighted MRI of the liver shows multiple hyperintense lesions replacing the enlarged liver. (C) Coronal liver acquisition with volume acceleration (LAVA) in the arterial phase of imaging shows multiple lesions with peripheral nodular enhancement. (D) Coronal LAVA image in the portal venous phase of imaging shows that the multiple hepatic lesions have filled in with time, consistent with infantile hepatic hemangiomas.

## REFERENCES

1. Barth H, Moosdorf R, Bauer J, et al. Mycotic pseudoaneurysm of the aorta in children. *Pediatr Cardiol*. 2000;21(3):263–266.
2. Lopes RJ, Almeida J, Dias PJ, et al. Infectious thoracic aortitis: a literature review. *Clin Cardiol*. 2009;32(9):488–490.
3. Knirsch W, Cavigelli-Brunner A, Dodge-Khatami A, et al. Candida mediastinitis with aortic rupture after congenital heart surgery. *Int J Cardiol*. 2009;134(2):e76–e78.
4. Macedo TA, Stanson AW, Oderich GS, et al. Infected aortic aneurysms: imaging findings. *Radiology*. 2004;231(1):250–257.
5. Gonzalez-Fajardo JA, Gutierrez V, Martin-Pedrosa M, et al. Endovascular repair in the presence of aortic infection. *Ann Vasc Surg*. 2005;19(1):94–98.
6. Mason JC. Takayasu arteritis—advances in diagnosis and management. *Nat Rev Rheumatol*. 2010;6(7):406–415.
7. Nastri MV, Baptista LP, Baroni RH, et al. Gadolinium-enhanced three-dimensional MR angiography of Takayasu arteritis. *Radiographics*. 2004;24(3):773–786.
8. Tann OR, Tulloh RM, Hamilton MC. Takayasu's disease: a review. *Cardiol Young*. 2008;18(3):250–259.
9. Ozen S, Ruperto N, Dillon MJ, et al. EULAR/PReS endorsed consensus criteria for the classification of childhood vasculitides. *Ann Rheum Dis*. 2006;65(7):936–941.
10. Jain S, Sharma N, Singh S, et al. Takayasu arteritis in children and young indians. *Int J Cardiol*. 2000;75(suppl 1):S153–S157.
11. Aluquin VP, Albano SA, Chan F, et al. Magnetic resonance imaging in the diagnosis and follow up of Takayasu's arteritis in children. *Ann Rheum Dis*. 2002;61(6):526–529.
12. Nakamura T, Hayashi S, Fukuoka M, et al. Pulmonary infarction as the initial manifestation of Takayasu's arteritis. *Intern Med*. 2006;45(11):725–728.
13. Weyand CM, Goronzy JJ. Medium- and large-vessel vasculitis. *N Engl J Med*. 2003;349(2):160–169.
14. Liang P, Hoffman GS. Advances in the medical and surgical treatment of Takayasu arteritis. *Curr Opin Rheumatol*. 2005;17(1):16–24.
15. Ohara N, Miyata T, Kurata A, et al. Ten years' experience of aortic aneurysm associated with systemic lupus erythematosus. *Eur J Vasc Endovasc Surg*. 2000;19(3):288–293.
16. Fauroux B, Clement A. Paediatric sarcoidosis. *Paediatr Respir Rev*. 2005;6(2):128–133.
17. Hiller N, Lieberman S, Chajek-Shaul T, et al. Thoracic manifestations of Behcet disease at CT. *Radiographics*. 2004;24(3):801–808.
18. Uzun O, Akpolat T, Erkan L. Pulmonary vasculitis in Behcet disease: a cumulative analysis. *Chest*. 2005;127(6):2243–2253.
19. Mont L, Castro J, Herreros B, et al. Reversibility of cardiac abnormalities in adolescents with anorexia nervosa after weight recovery. *J Am Acad Child Adolesc Psychiatry*. 2003;42(7):808–813.
20. Olivares JL, Vazquez M, Fleta J, et al. Cardiac findings in adolescents with anorexia nervosa at diagnosis and after weight restoration. *Eur J Pediatr*. 2005;164(6):383–386.
21. Speiser PW, Rudolf MC, Anhalt H, et al. Childhood obesity. *J Clin Endocrinol Metab*. 2005;90(3):1871–1887.
22. Towbin A, Inge TH, Garcia VF, et al. Beriberi after gastric bypass surgery in adolescence. *J Pediatr*. 2004;145(2):263–267.
23. Dahl-Jorgensen K, Larsen JR, Hanssen KF. Atherosclerosis in childhood and adolescent type 1 diabetes: early disease, early treatment? *Diabetologia*. 2005;48(8):1445–1453.
24. Loffredo CA, Wilson PD, Ferencz C. Maternal diabetes: an independent risk factor for major cardiovascular malformations with increased mortality of affected infants. *Teratology*. 2001;64(2):98–106.
25. Lisowski LA, Verheijen PM, Copel JA, et al. Congenital heart disease in pregnancies complicated by maternal diabetes mellitus. An international clinical collaboration, literature review, and meta-analysis. *Herz*. 2010;35(1):19–26.
26. Batra AS, Acherman RJ, Wong WY, et al. Cardiac abnormalities in children with sickle cell anemia. *Am J Hematol*. 2002;70(4):306–312.
27. Lonergan GJ, Cline DB, Abbondanzo SL. Sickle cell anemia. *Radiographics*. 2001;21(4):971–994.
28. de Montalembert M, Maunoury C, Acar P, et al. Myocardial ischaemia in children with sickle cell disease. *Arch Dis Child*. 2004;89(4):359–362.
29. Ferrara M, Matarese SM, Borrelli B, et al. Cardiac involvement in beta-thalassemia major and beta-thalassemia intermedia. *Hemoglobin*. 2004;28(2):123–129.

# 82 Acquired Diseases of the Thoracic Great Vessels

Cynthia K. Rigsby and Frandics P. Chan

This chapter reviews acquired diseases of the thoracic aorta, venae cavae, pulmonary arteries, and pulmonary veins seen in childhood. Acquired pediatric aortic disease is uncommon, but radiologists and imagers play an important role in the care of these patients. Pulmonary embolism (PE) is the most common acquired disease of the pulmonary artery. The most common acquired abnormalities of the pulmonary veins and venae cavae are obstruction or stenosis caused by luminal occlusion or extrinsic compression from mediastinal pathologies.

## ACQUIRED DISEASES OF THE THORACIC AORTA

Acquired pediatric aortic pathology can be categorized into valvar aortic stenosis (see Chapter 73), aortic aneurysm, aortic dissection, and vasculitis such as Takayasu disease (see Chapter 81).[1] Although aortic diseases may present with one or more of these manifestations, it is the clinical consequences of the abnormalities that determine morbidity and mortality (Table 82.1).

Normally, the caliber of the aorta gradually decreases in size from the sinotubular junction to the aortic hiatus at the level of the diaphragm. An aortic aneurysm is defined as an abnormal dilation of the aorta, which may undergo progressive expansion. An aortic aneurysm may form if aortic wall stress increases, as in the case of systemic hypertension; if the aortic wall is structurally abnormal, as in connective tissue diseases; or due to infection and resultant wall weakening (see Chapter 81). Aortic dissection can occur in children as a complication of trauma or may be related to a connective tissue disease (Fig. 82.1). A dissection is created when blood forces through a tear in the aortic intima and progressively separates the intimal layer from the aortic media, creating a true lumen that originally was connected to the aortic root and a false lumen that was not connected to the aortic root. Dissection can cause end-organ ischemia if the branch arteries supplying the organ are obstructed by the dissection flap. Dissection can weaken the aortic wall sufficiently to cause aortic rupture.

### Trauma

***Overview.*** Trauma is a major cause of death in children and results primarily from motor vehicle accidents, pedestrian versus auto accidents, and falls, although penetrating injuries (Fig. 82.2) and child abuse are other important causes of traumatic death. Survival of a child with a traumatic aortic injury until arrival at the emergency department is rare, accounting for one to two cases per year at large metropolitan level I pediatric trauma centers. Operative treatment involves less than 0.14% of all trauma patients, and only 6% of all traumatic ruptures of the aorta occur in patients younger than 16 years.[2,3] The outcome of traumatic aortic injury in the pediatric population is directly related to timely diagnosis, proper treatment, and hemodynamic status at the time of presentation.

***Imaging.*** Chest radiographic findings such as pleural capping at the left lung apex, obscuration of the aortic arch, mediastinal widening, pleural effusion, pneumothorax, pulmonary contusion, tracheal and nasogastric tube deviation, and upper rib and clavicle fracture in the setting of blunt trauma should raise clinical suspicion for an aortic injury (Fig. 82.3). Historically, the definitive diagnosis of traumatic aortic injury was made by conventional catheter angiography. Today, computed tomographic angiography (CTA) has supplanted catheter angiography as the diagnostic method of choice.[4,5] Care should be taken to identify the location of aortic transection, active extravasation of arterial contrast, a dissection flap extending to major aortic branches, pseudoaneurysm, hemothorax and hemopericardium, and other organ and musculoskeletal injuries.

***Treatment and Imaging Follow-up.*** The goals of treatment of pediatric traumatic aortic rupture are identical to those in adults. The mainstay of treatment is operative repair of the aorta.[6] Patients for whom surgery poses a high risk have been treated successfully with endovascular stent grafts. CTA should be performed immediately after stent placement, with a follow-up study in 48 hours to document the stability of the repair. Observational management has also been utilized in patients with comorbidities too severe to allow intervention.

## ACQUIRED DISEASES OF THE PULMONARY ARTERY

### Pulmonary Embolism

***Overview.*** PE is an uncommon but potentially fatal disease in children.[7] In pediatric patients with deep venous thrombosis and PE, the mortality rate from all causes has been reported to be as high as 16%, whereas the mortality rate directly attributable to deep venous thrombosis or PE is 2.2%.[8] The most common risk factor for PE in children is catheter thrombosis, which develops in as many as 50% of patients with central venous catheters.[9] Other risk factors include peripartum asphyxia, dehydration, septicemia, trauma and burns, surgery, hemolysis, malignancy, immobility, and renal disease such as nephrotic syndrome. Two or more risk factors are often seen in children with PE.[10] Abnormal coagulation factors associated with PE in adults that also have been reported in children are antiphospholipid antibodies, factor V Leiden mutation, and deficiencies in protein S, protein C, and antithrombin III.[11]

The clinical diagnosis of PE is often difficult because, in many cases of venous thrombosis, younger children present with subtle symptoms related to their good cardiopulmonary reserve. Older children most commonly present with pleuritic chest pain. Symptoms of PE may be masked by intrinsic lung disease or other underlying illness. Unlike in adults, a negative D-dimer assay in pediatric patients has not been proven useful to exclude PE. Also, children may have other concomitant illnesses that can raise D-dimer levels, so the specificity of this assay in children is low.[10] A high level of clinical suspicion for PE in the presence of risk factors is imperative.

***Imaging.*** Chest radiographs may show cardiac enlargement, pleural effusions, or peripheral lung opacities, but these findings are not specific for PE. Traditionally, catheter pulmonary angiography was considered the diagnostic gold standard.[12] In current clinical practice, catheter pulmonary angiography has been replaced by noninvasive CT pulmonary angiography (CTPA). The accuracy of the detection of PE by CTPA in an adult population has been studied in the Prospective Investigation of Pulmonary Embolism Diagnosis II trial.[13] With use of CT technology available before 2003, the sensitivity and specificity in this trial were reported as 83% and 96%, respectively.

CTPA is the primary modality used to diagnose PE in children (Fig. 82.4), although its accuracy in children has not been studied by rigorous clinical trials. CTPA in children can be technically

## Abstract:

This chapter reviews acquired diseases of the thoracic aorta, venae cavae, pulmonary arteries, and pulmonary veins seen in childhood. Acquired pediatric aortic disease is uncommon, but radiologists and imagers play an important role in the care of these patients. Pulmonary embolism (PE) is the most common acquired disease of the pulmonary artery. The most common acquired abnormalities of the pulmonary veins and venae cavae are obstruction or stenosis caused by luminal occlusion or extrinsic compression from mediastinal pathologies.

## Keywords:

Pulmonary embolism
aortic trauma
superior vena cava syndrome
acquired pulmonary vein stenosis

**TABLE 82.1** Principal Etiologies of Acquired Aortic Diseases

| Manifestation | Causes |
|---|---|
| Aortic aneurysm | Infectious aortitis |
| | Inflammatory aortitis |
| | Takayasu syndrome (acute, chronic) |
| | Systemic lupus erythematosus |
| | Sarcoid |
| | Connective tissue disease |
| | Marfan syndrome |
| | Ehlers–Danlos syndrome (vascular type) |
| | Loeys–Dietz syndrome |
| | Arterial tortuosity syndrome |
| | Neurocutaneous disease |
| | Tuberous sclerosis |
| | Trauma or postsurgical (pseudoaneurysm) |
| Aortic dissection | Connective tissue disease |
| | Marfan syndrome |
| | Ehlers–Danlos syndrome (vascular type) |
| | Trauma |
| Aortic stenosis | Inflammatory aortitis |
| | Takayasu syndrome (chronic) |
| | Congenital rubella syndrome |
| | Radiation |
| | Neurocutaneous disease |
| | Neurofibromatosis (type I) |
| | *PHACES* syndrome |
| | Postsurgical |
| | Coarctation repair |
| | Aortopulmonary shunts |

*PHACES,* Posterior fossa malformations, hemangiomas, arterial anomalies, cardiac defects, eye abnormalities, sternal cleft and supraumbilical raphe.

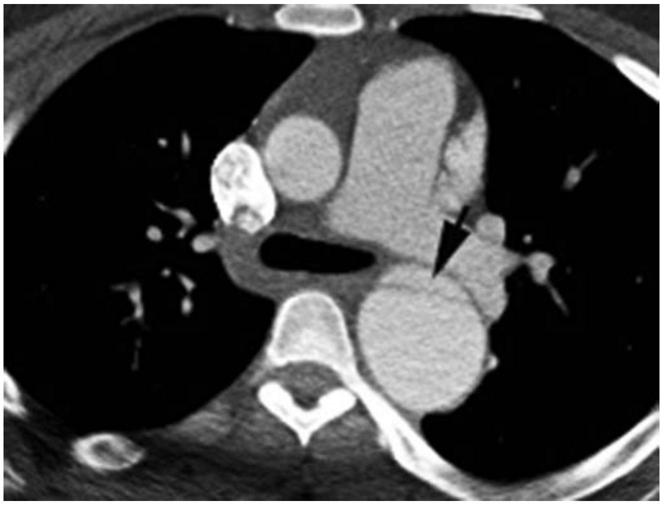

**Figure 82.1. Aortic dissection in a 16-year-old male with Marfan syndrome who presented with chest pain.** Axial CTA image shows the dissection flap *(arrow)* in the dilated proximal descending aorta. The dissection involved the descending aorta from the level of the left subclavian artery through the diaphragm.

challenging because of the size of the pulmonary arteries in small children, their inability to cooperate with breath-holding, and concerns about radiation exposure. The principal strategy for reducing radiation dose is to lower exposure factors such as x-ray tube voltage and tube current. Both maneuvers increase image noise and can confound visual detection of PE. As a result, the CTPA protocol for children requires meticulous attention to optimize spatial resolution, scan speed, and exposure factors.

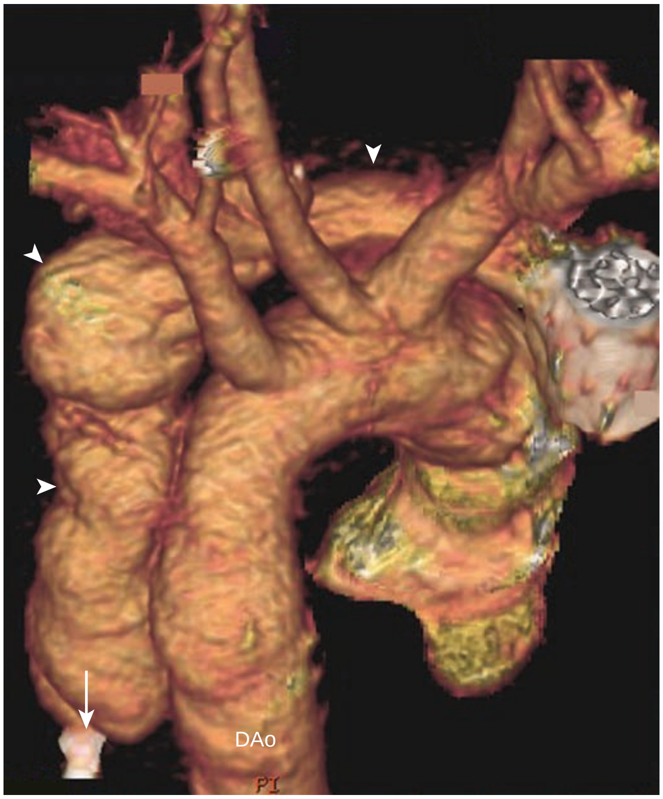

**Figure 82.2. False aortic aneurysm from a gunshot wound in an 18-year-old male.** Volume rendering of a CTA study shows a false aneurysm *(arrowheads)* that follows the track of a bullet. The bullet first entered the chest horizontally, parallel to the aortic arch, rupturing the aorta. Then it was deflected downward and came to rest *(arrow)* adjacent to the descending aorta *(DAo)*.

Dual-energy CT has been recently introduced for evaluation of lung perfusion. This technique involves acquisition of CT data with two different kilovolt potentials and allows for post-acquisition analysis of lung tissue components. For imaging of pulmonary embolism, lung perfusion can be quantified by mapping the injected iodine contrast medium distribution throughout the lungs to assess for perfusion defects. This technique is complimentary to standard CTPA as peripheral perfusion defects can be seen with dual-energy CT that locate smaller peripheral thrombi that may not be seen on standard CTPA. Dual-energy image data can also be selectively analyzed for central pulmonary arteries tissue characterization for the presence of thrombus.[14] MRA has been performed for assessment of PE, but has lower sensitivity (88% relative to CT in adults) for its detection.[15] Scintigraphic ventilation-perfusion scanning was historically used for PE detection, but its use has been supplanted by CTPA.

***Treatment and Follow-up.*** Anticoagulation is the mainstay of medical therapy for PE. Thrombolytic therapy is reserved for patients with hemodynamic instability. Surgical or interventional pulmonary thrombectomy has been successful for treating central or saddle emboli.

PE can also be caused by materials other than bland thrombus. Septic emboli can be the result of endocarditis and of thrombophlebitis. Lemierre syndrome describes jugular vein thrombosis associated with anaerobic infection of the head and neck (classically by *Fusobacterium necrophorum*), and more than 50% of these cases are complicated by septic emboli to the lungs.[16] Tumor emboli may be seen in patients with Wilms tumor, neuroblastoma, osteosarcoma, and hepatocellular carcinoma, because occasionally

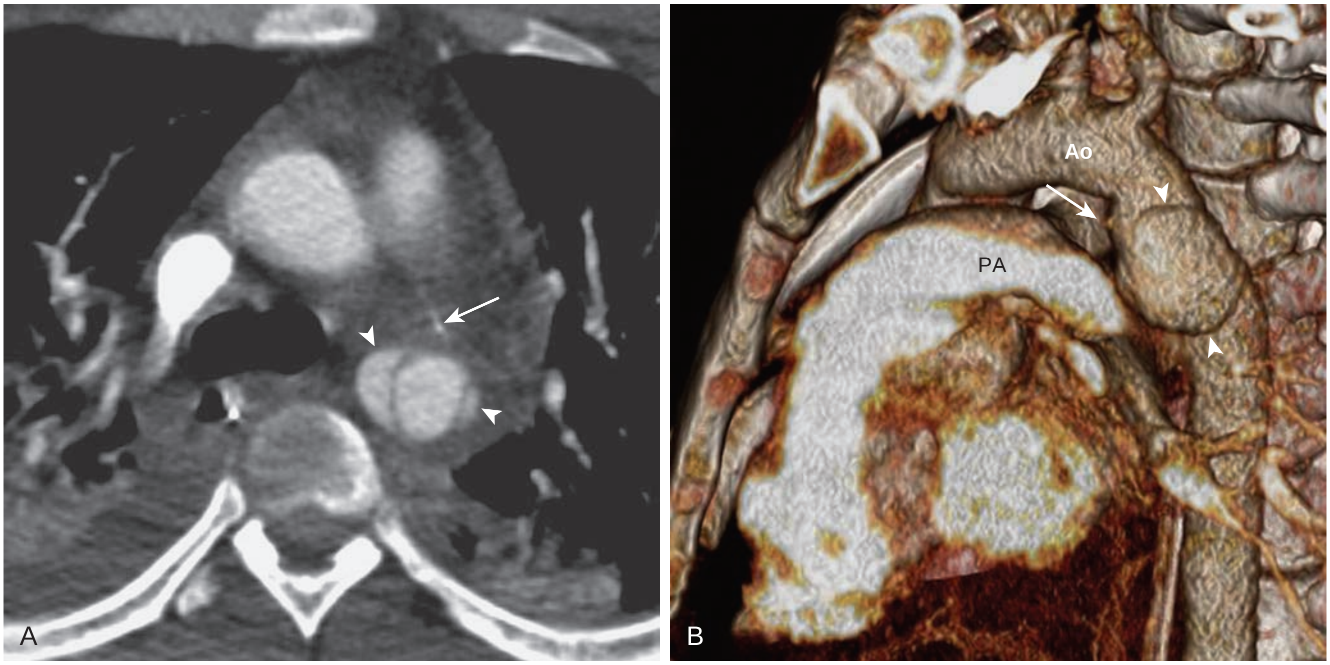

**Figure 82.3. Aortic rupture in a 16-year-old boy as a result of a motor vehicle accident.** (A) Axial CTA image shows a ruptured descending aorta at the level of the ligamentum arteriosum *(arrow)* and two pseudoaneurysms *(arrowheads)* extending beyond the aortic wall. (B) Volume-rendered image from the CTA study shows the relationship between one of the pseudoaneurysms *(arrowheads)* and the ligamentum arteriosum *(arrow)* between the aorta *(Ao)* and the pulmonary trunk *(PA)*.

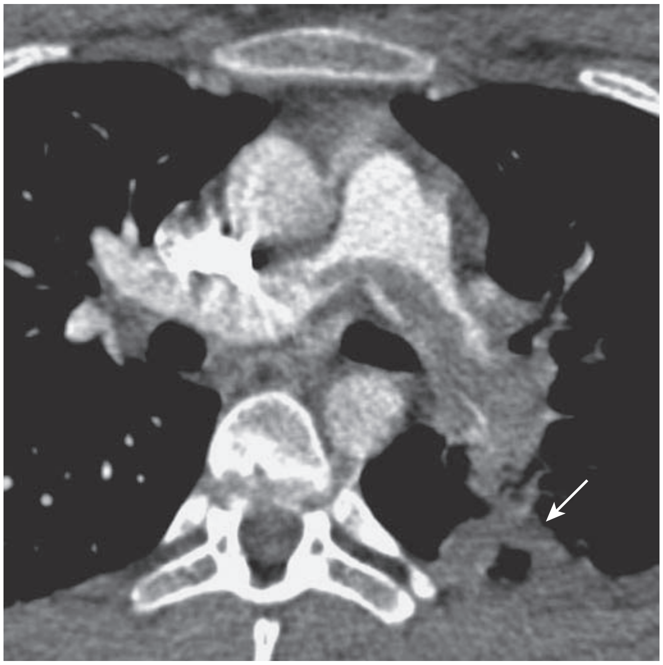

**Figure 82.4. Saddle pulmonary embolus in a 15-year-old girl who recently started taking oral contraceptive pills.** Computed tomography pulmonary angiography (CTPA) image shows a large saddle pulmonary embolism as a filling defect spanning the left and right pulmonary arteries. A peripheral consolidation *(arrow)* is a pulmonary infarction.

these tumors invade the inferior vena cava (IVC) or embolize to the lungs. Rarely, tumor emboli originate from primary cardiac tumors, such as atrial myxomas. Foreign bodies that embolize to the lungs include broken catheter tips and guide wires, misplaced embolization coils, and other endovascular devices. Finally, fat emboli may occur after major orthopedic trauma or surgery.

## ACQUIRED DISEASES OF THE VENAE CAVAE

### Superior Vena Cava Syndrome

***Overview.*** Superior vena cava (SVC) syndrome is a clinical manifestation of gradual obstruction of SVC flow, leading to elevated central venous pressure of the upper extremities and the head, interstitial edema and swelling of the upper body, and development of venous collaterals to the IVC. In children, SVC syndrome is a medical emergency because swelling of the neck can compress and obstruct their small airway more easily than in adults. The most common pediatric cause of SVC syndrome is extrinsic compression of the SVC by non-Hodgkin lymphoma.[17] The SVC can be compressed by other mediastinal masses, infectious lymphadenopathy, aortic aneurysm, and mediastinal fibrosis.[18] Intrinsic stenosis of the SVC can be caused by scarring from a chronic indwelling catheter and by infusion of caustic agents. Luminal occlusion (Fig. 82.5) can be the result of a thrombus forming around a central venous catheter or pacemaker wires, of venous thrombosis secondary to a hypercoagulable state, or with a vasculitis involving the venous system as can be seen in Behçet syndrome (see Chapter 81). Finally, SVC flow may be obstructed within the atrial baffle after the atrial switch or the Mustard/Senning procedure (see Chapter 75).[19] Obstruction of the SVC above the azygos return precludes decompression by retrograde flow into the azygos vein and leads to more severe symptoms.

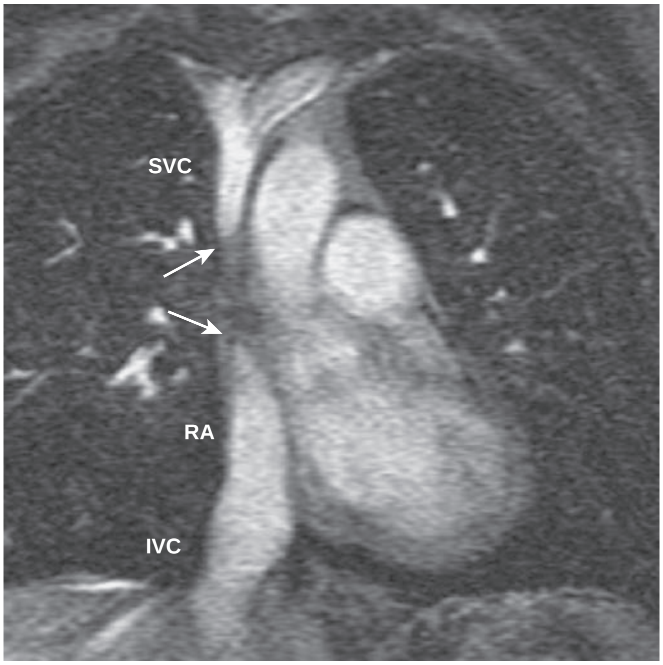

**Figure 82.5. Superior vena cava occlusion in a 14-year-old girl who had a long-term central venous catheter placed in the SVC.** Coronal MRA reconstruction shows a complete obstruction *(arrows)* between the SVC and the right atrium *(RA)*, whereas the inferior vena cava *(IVC)* drains freely into the RA.

***Imaging and Treatment.*** The gold standard for the diagnosis of SVC syndrome is catheter venography, with which the level of SVC obstruction, the presence of venous collaterals, and the central venous pressure can be assessed. Noninvasive tomographic techniques such as CT and magnetic resonance (MR) venography can define the SVC stenosis and are helpful in evaluating for an extrinsic mass.[20] An advantage of MRI is that venography can be done without use of a contrast agent through use of phase-contrast or time-of-flight inflow enhancement techniques. Treatment of SVC syndrome depends on the underlying cause. Radiation or chemotherapy that reduces tumor size may relieve SVC obstruction due to tumor. Central venous catheters causing venous thrombosis may be removed and residual thrombosis or stenosis treated with selective thrombolysis and venous stenting as needed.

### Inferior Vena Cava Obstruction

***Overview.*** Reasons for acquired obstruction of the IVC are similar to those of the SVC. Thrombosis of the IVC can be the result of catheter access, placement of a caval filter, severe illness including sepsis and dehydration, and other hypercoagulopathy. The IVC can be obstructed at its entrance to the right atrium by direct extension from abdominal tumors, such as Wilms tumor, neuroblastoma, hepatoblastoma, and hepatocellular carcinoma. Obstruction can be caused by thrombus or an IVC web. The Budd–Chiari syndrome classically is attributed to hepatic venous obstruction, but the intrahepatic portion of the IVC can be involved, resulting in symptoms of hepatomegaly, ascites, and abdominal pain (Fig. 82.6).[21]

***Imaging and Treatment.*** Imaging evaluation can be performed with abdominal ultrasound, CT, and MRI, with the investigation focused on the location and severity of the obstruction and on the presence of a thrombus or extrinsic mass. Treatment is directed to correcting the underlying conditions. In the short term, patency of the IVC can be maintained with an endovascular stent.

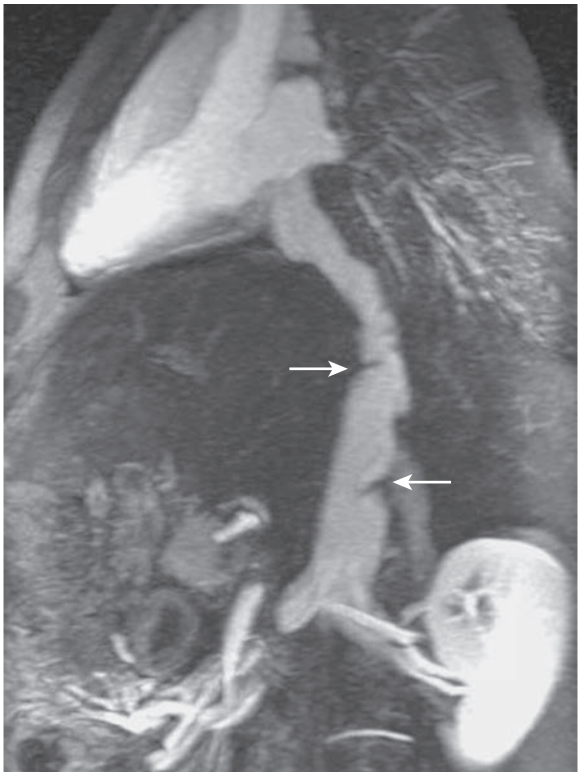

**Figure 82.6. Inferior vena cava (IVC) stenosis in a 13-year-old boy who developed Budd–Chiari syndrome after trauma.** Sagittal MRA reconstruction shows a narrowed IVC with multiple webs *(arrows)* protruding into the caval lumen.

### Superior Vena Cava Aneurysm

***Overview.*** Although a true SVC aneurysm is very rare, dilation of the SVC is more commonly seen with elevated central venous pressure as a result of right heart failure or severe tricuspid valve regurgitation.[22] Dilation of the SVC also is associated with mediastinal lymphatic malformation, although the pathophysiology is not known.[23] Patients with saccular SVC aneurysms may be at risk for SVC thrombosis and PE.

***Imaging and Treatment.*** Surgical resection of an SVC aneurysm has been performed successfully. CT and MRI can help aid surgical planning by defining the extent of the aneurysm and detecting involvement of other draining veins.

## ACQUIRED DISEASE OF THE PULMONARY VEINS

### Pulmonary Vein Stenosis

***Overview.*** Acquired pulmonary vein stenosis in children is uncommon but can be seen in children with complications of surgical repair of congenital pulmonary vein anomalies. Children who undergo repair of total anomalous pulmonary venous connection (Fig. 82.7) and scimitar syndrome are at increased risk for acquired pulmonary vein stenosis. Pulmonary vein stenosis develops in up to 10% of infants who undergo repair of total anomalous pulmonary venous connection.[24] These patients are often ill from pulmonary edema and poor oxygen saturation, with a mortality rate as high as 50%. The prognosis is worse for patients who have coexisting complex cardiac anomalies, often as part of the heterotaxy syndrome. Other acquired causes of pulmonary vein stenosis include mediastinal fibrosis and extrinsic compression by mediastinal tumors.

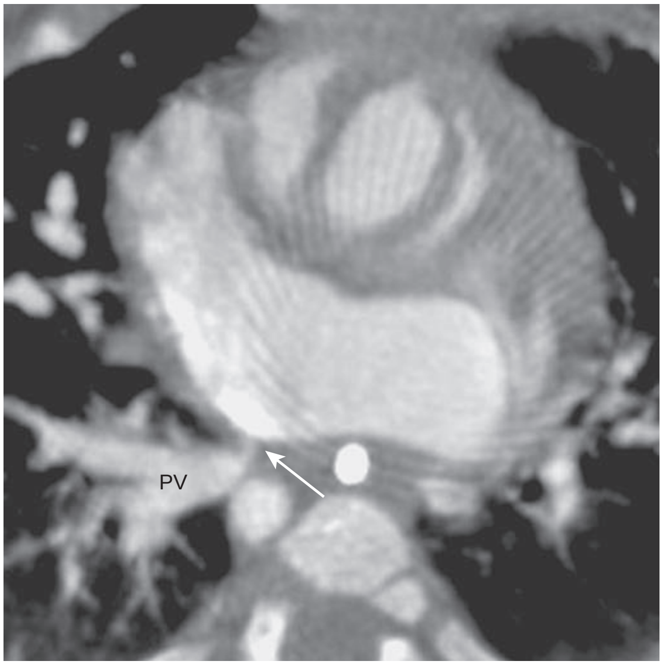

**Figure 82.7. Pulmonary venous stenosis after surgical repair for total anomalous pulmonary venous connection in a 6-month-old girl.** Axial CTA image shows a tight stenosis *(arrow)* at the origin of a right pulmonary vein *(PV)*.

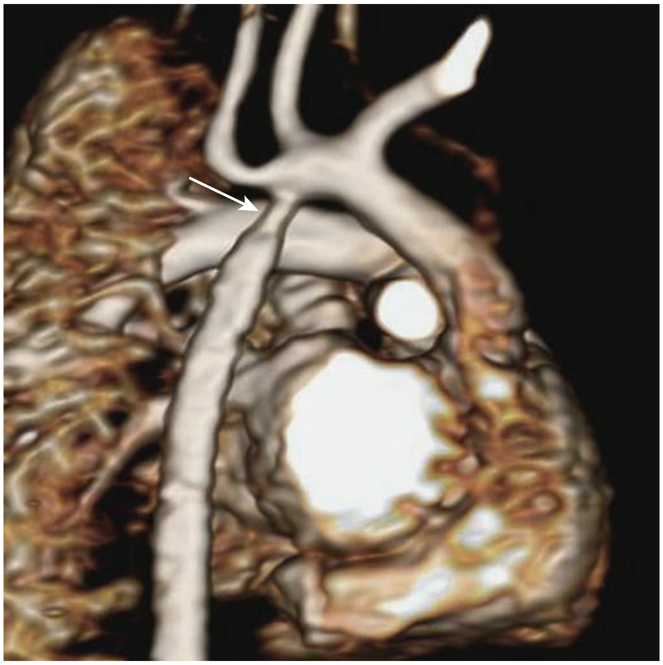

**Figure 82.8. Aortic restenosis 5 months after a surgical repair for coarctation in a 6-month-old boy.** Volume CTA rendering shows a segmental, circumferential narrowing *(arrow)* at the surgical site.

***Imaging and Treatment.*** CTA and MRA can define the anatomy of the venous obstruction. CTA has the added advantage of evaluating the pulmonary parenchyma and related complications. Catheter angiography is used in anticipation of an intervention to define the location of the pulmonary venous obstruction and to evaluate the severity of the stenosis by measuring the pressure gradient across the stenosis.

Pulmonary vein stenosis has been treated with angioplasty, endovascular stent placement, and surgical repair.[24,25] Despite immediate postprocedural or postoperative success, restenosis often occurs, and mortality is not substantially improved. The pathophysiology of pulmonary vein restenosis is not well understood. Medial fibrosis of the injured pulmonary veins, endothelial ingrowth into the stent, and abnormal reactivity of the pulmonary vascular bed have been proposed as possible mechanisms of restenosis.

## Pulmonary Vein Varix

***Overview.*** Pulmonary varices are rare aneurysmal dilations of the pulmonary veins and may be congenital or acquired.[26] Acquired pulmonary varices usually are the result of pulmonary venous hypertension caused by central pulmonary vein stenosis, mitral regurgitation, mitral stenosis, and coarctation. Pulmonary varices generally are benign and require no specific treatment. They usually regress with correction of the underlying abnormality. However, it is important to distinguish pulmonary varices from pulmonary arteriovenous malformations, which can have a similar appearance. Pulmonary arteriovenous malformations carry the risk of stroke and other embolic events and require surgical removal or catheter embolization.

***Imaging.*** Both CTA and magnetic resonance angiography (MRA) can detect pulmonary varices. In difficult cases, catheter angiography may be needed to differentiate varices from arteriovenous malformations.

## Neoplasms of the Great Vessels

***Overview.*** Primary tumors of the great arteries are rare.[27] Secondary involvement of the great vessels by metastatic disease, invasion or compression from a nearby tumor or by radiation vasculitis from radiation treatment can occur.[28,29]

***Imaging and Treatment.*** Because most great vessel tumors occur as a result of metastatic disease or infiltration due to adjacent disease, the tumor cell types and origins usually are known. The primary roles of imaging are to determine favorable sites for tumor biopsy, evaluate the extent and the degree of vascular obstruction in preparation for vascular intervention, and monitor changes in vascular involvement after treatment. In most cases, either CT or MRI is used for evaluating the disease process.[30]

## Postoperative Complications

***Overview.*** Pseudoaneurysm and stenosis can develop as complications of surgical repair or interventional treatment of pediatric thoracic great vessels, of which coarctation is the best studied. The average restenosis rates are 15% and 2% for balloon angioplasty and surgical repair of coarctation, respectively (Fig. 82.8).[31] Other surgical procedures that can be complicated by aneurysm or stenosis are surgical aortopulmonary and central shunts.[32] The Blalock-Taussig shunt, which classically connects the right subclavian artery to the right pulmonary artery, can lead to stenosis or obstruction of the right pulmonary artery (Fig. 82.9). The Potts shunt, which connects the descending aorta to the left pulmonary artery, often results in left pulmonary artery stenosis. The Waterston shunt connects the ascending aorta to the pulmonary trunk. Excessive shunt flow can create aneurysms of the pulmonary artery.[32]

***Imaging and Treatment.*** Noninvasive imaging by CTA or MRA has largely supplanted catheter angiography for the purpose of detecting and characterizing these thoracic vascular lesions before surgical or interventional treatment. Catheterization is reserved for angioplasty and stenting of stenotic lesions and for stent graft deployment to exclude an aneurysm.

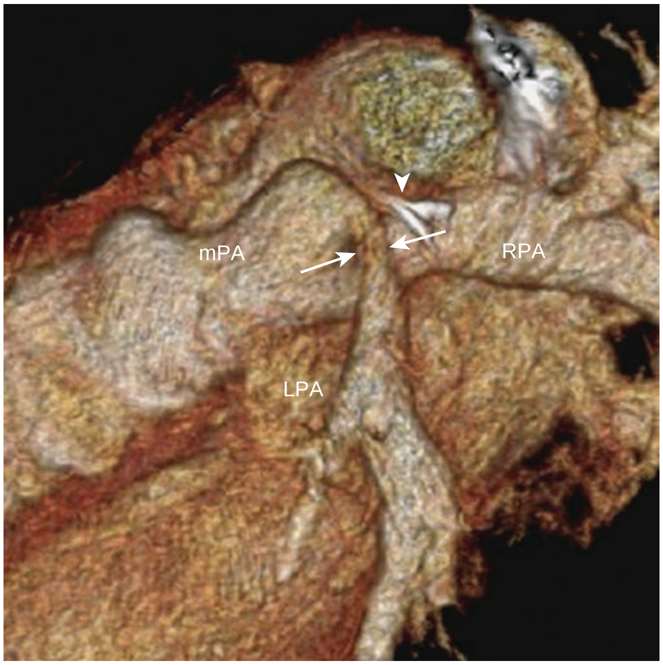

**Figure 82.9. Postsurgical pulmonary artery stenosis in a 10-year-old boy.** Volume CTA rendering shows evidence of an arteriopulmonary shunt, now closed, identified by a surgical clip *(arrowhead)*. Adjacent to this clip is a kink and a focal narrowing *(arrows)* of the left pulmonary artery *(LPA)*. *mPA,* Main pulmonary artery; *RPA,* right pulmonary artery.

## KEY POINTS

- Acquired aortic pathology can be categorized as aortic aneurysm, aortic dissection, or aortic stenosis, and the clinical consequences of these three diagnostic entities directly determine mortality and morbidity.
- The most common risk factor for PE in children is catheter thrombosis, which develops in as many as half of patients with central venous catheters.
- A negative D-dimer assay in pediatric patients does not exclude PE.
- SVC syndrome is a medical emergency in children because swelling of the neck can cause compression and obstruction of the airway.
- Restenosis of the pulmonary vein(s) in children is common after surgical or interventional treatment and can be diagnosed with CTA or MRA.

## SUGGESTED READINGS

Bendel EC, Maleszewski JJ, Araoz PA. Imaging sarcomas of the great vessels and heart. *Semin Ultrasound CT MR*. 2011;32:377–404.

Lowe LH, Bulas DI, Eichelberger MD, et al. Traumatic aortic injuries in children: radiologic evaluation. *AJR Am J Roentgenol*. 1998;170:39–42.

Stein PD, Fowler SE, Goodman LR, et al. Multidetector computed tomography for acute pulmonary embolism. *N Engl J Med*. 2006;354:2317–2327.

Thacker PG, Lee EY. Pulmonary embolism in children. *AJR Am J Roentgenol*. 2015;204:1278–1288.

Williams BJ, Mulvihill DM, Pettus BJ, et al. Pediatric superior vena cava syndrome: assessment at low radiation dose 64-slice CT angiography. *J Thorac Imaging*. 2006;21:71–72.

## REFERENCES

Full references for this chapter can be found on www.expertconsult.com.

## REFERENCES

1. Coady MA, Rizzo JA, Goldstein LJ, Elefteriades JA. Natural history, pathogenesis, and etiology of thoracic aortic aneurysms and dissections. *Cardiol Clin* 1999;17:615-635; vii.
2. Cox CS Jr, Black CT, Duke JH, et al. Operative treatment of truncal vascular injuries in children and adolescents. *J Pediatr Surg*. 1998;33:462–467.
3. Takach TJ, Anstadt MP, Moore HV. Pediatric aortic disruption. *Tex Heart Inst J*. 2005;32:16–20.
4. Lowe LH, Bulas DI, Eichelberger MD, et al. Traumatic aortic injuries in children: radiologic evaluation. *AJR Am J Roentgenol*. 1998;170:39–42.
5. Spouge AR, Burrows PE, Armstrong D, et al. Traumatic aortic rupture in the pediatric population. Role of plain film, CT and angiography in the diagnosis. *Pediatr Radiol*. 1991;21:324–328.
6. Karmy-Jones R, Hoffer E, Meissner M, et al. Management of traumatic rupture of the thoracic aorta in pediatric patients. *Ann Thorac Surg*. 2003;75:1513–1517.
7. Van Ommen CH, Peters M. Acute pulmonary embolism in childhood. *Thromb Res*. 2006;118:13–25.
8. Monagle P, Adams M, Mahoney M, et al. Outcome of pediatric thromboembolic disease: a report from the Canadian Childhood Thrombophilia Registry. *Pediatr Res*. 2000;47:763–766.
9. Journeycake JM, Buchanan GR. Thrombotic complications of central venous catheters in children. *Curr Opin Hematol*. 2003;10:369–374.
10. Thacker PG, Lee EY. Pulmonary embolism in children. *AJR Am J Roentgenol*. 2015;204:1278–1288.
11. Nuss R, Hays T, Chudgar U, et al. Antiphospholipid antibodies and coagulation regulatory protein abnormalities in children with pulmonary emboli. *J Pediatr Hematol Oncol*. 1997;19:202–207.
12. Babyn PS, Gahunia HK, Massicotte P. Pulmonary thromboembolism in children. *Pediatr Radiol*. 2005;35:258–274.
13. Stein PD, Fowler SE, Goodman LR, et al. Multidetector computed tomography for acute pulmonary embolism. *N Engl J Med*. 2006;354:2317–2327.
14. Lu GM, Wu SY, Yeh BM, et al. Dual-energy computed tomography in pulmonary embolism. *Br J Radiol*. 2010;83:707–718.
15. Kalb B, Sharma P, Tigges S, et al. MR imaging of pulmonary embolism: diagnostic accuracy of contrast-enhanced 3D MR pulmonary angiography, contrast-enhanced low-flip angle 3D GRE, and nonenhanced free-induction FISP sequences. *Radiology*. 2012;263:271–278.
16. Goldenberg NA, Knapp-Clevenger R, Hays T, et al. Lemierre's and Lemierre's-like syndromes in children: survival and thromboembolic outcomes. *Pediatrics*. 2005;116:e543–e548.
17. Yellin A, Mandel M, Rechavi G, et al. Superior vena cava syndrome associated with lymphoma. *Am J Dis Child*. 1992;146:1060–1063.
18. Robertson BD, Bautista MA, Russell TS, et al. Fibrosing mediastinitis secondary to zygomycosis in a twenty-two-month-old child. *Pediatr Infect Dis J*. 2002;21:441–442.
19. Santoro G, Ballerini L, Bialkowski J, et al. Stent implantation for post-Mustard systemic venous obstruction. *Eur J Cardiothorac Surg*. 1998;14:332–334.
20. Williams BJ, Mulvihill DM, Pettus BJ, et al. Pediatric superior vena cava syndrome: assessment at low radiation dose 64-slice CT angiography. *J Thorac Imaging*. 2006;21:71–72.
21. Kamath PS. Budd-Chiari syndrome: radiologic findings. *Liver Transpl*. 2006;12:S21–S22.
22. Pasic M, Schopke W, Vogt P, et al. Aneurysm of the superior mediastinal veins. *J Vasc Surg*. 1995;21:505–509.
23. Joseph AE, Donaldson JS, Reynolds M. Neck and thorax venous aneurysm: association with cystic hygroma. *Radiology*. 1989;170:109–112.
24. Devaney EJ, Ohye RG, Bove EL. Pulmonary vein stenosis following repair of total anomalous pulmonary venous connection. *Semin Thorac Cardiovasc Surg Pediatr Card Surg Annu*. 2006;51–55.
25. Wax DF, Rocchini AP. Transcatheter management of venous stenosis. *Pediatr Cardiol*. 1998;19:59–65, discussion 66.
26. Platzker J, Goldhammer E, Simon J, et al. Pulmonary varices, benign congenital anomalies simulating perihilar masses of various etiologies. *Clin Cardiol*. 1984;7:295–298.
27. Chiche L, Mongredien B, Brocheriou I, et al. Primary tumors of the thoracoabdominal aorta: surgical treatment of 5 patients and review of the literature. *Ann Vasc Surg*. 2003;17:354–364.
28. Bagatell R, Morgan E, Cosentino C, et al. Two cases of pediatric neuroblastoma with tumor thrombus in the inferior vena cava. *J Pediatr Hematol Oncol*. 2002;24:397–400.
29. Upadhyaya M, Jaffar Sajwany M, Tomas-Smigura E. Recurrent immature mediastinal teratoma with life-threatening respiratory distress in a neonate. *Eur J Pediatr Surg*. 2003;13:403–406.
30. Bendel EC, Maleszewski JJ, Araoz PA. Imaging sarcomas of the great vessels and heart. *Semin Ultrasound CT MR*. 2011;32:377–404.
31. Brown ML, Burkhart HM, Connolly HM, et al. Late outcomes of reintervention on the descending aorta after repair of aortic coarctation. *Circulation*. 2010;122:S81–S84.
32. Sachweh J, Dabritz S, Didilis V, et al. Pulmonary artery stenosis after systemic-to-pulmonary shunt operations. *Eur J Cardiothorac Surg*. 1998;14:229–234.

SECTION
6

# Gastrointestinal System

## PART 1 Overview

# 83

# Embryology, Anatomy, and Normal Findings

*Amie M. McPherson and Evelyn Y. Anthony*

## ABDOMINAL WALL AND PERITONEAL CAVITY

During the third week of gestation, the intraembryonic mesoderm differentiates, forming the lateral plates.[1,2] Mesoderm from paravertebral myotomes invades the lateral plates during the sixth week. The leading edges of the lateral plates will differentiate into the right and left rectus abdominis muscles. The main portion of the mesoderm splits into three layers and forms the external oblique, internal oblique, and transverse abdominis muscles. Approximation of the right and left recti is complete by the 12th week except for the umbilical ring.

The aponeurosis of the external oblique muscles forms the anterior and posterior rectus sheaths.[1] These sheaths join in the midline to form the linea alba. The lowest portion of the aponeurosis ends in the inguinal ligament. The external inguinal ring is an opening in the aponeurosis between the inguinal ligament inferiorly and the tendinous portion superiorly. The spermatic cord in males and the round ligament in females pass through the inguinal canal.

Closure of the cephalic, caudal, and lateral folds leads to the formation of the intraembryonic coelom.[3,4] The mesoderm surrounding the coelom splits into two layers, the somatic mesoderm and the splanchnic mesoderm. The somatic layer forms the parietal peritoneum, which lines the inner abdominal wall, and the splanchnic layer forms the visceral peritoneum, which covers the abdominal organs. The space between the parietal and visceral peritoneum is the peritoneal cavity.

## HEPATIC AND BILIARY SYSTEM

The liver, gallbladder, and biliary duct system arise as a ventral outgrowth from the caudal end of the foregut early in the fourth week of development (Fig. 83.1).[5,6] This outgrowth, known as the *hepatic diverticulum*, extends into the septum transversum, which is the future diaphragm. The hepatic diverticulum grows rapidly and divides into cranial and caudal portions. The larger cranial portion forms the primordium of the liver parenchyma. Proliferating endodermal cells develop into cords of hepatocytes and into the epithelial lining of the biliary system. The connective tissue, hematopoietic cells, and Kupffer cells are derived from the mesoderm of the septum transversum. The caudal portion expands to form the gallbladder, and its stalk becomes the cystic duct. The two major intrahepatic ducts join to form the common hepatic duct. The stalk connecting the hepatic and cystic ducts to the duodenum becomes the common bile duct.

The liver grows rapidly, with the right lobe growing faster than the left lobe. Intrahepatic ducts appear in the region of the hilus and grow peripherally. This ductal system is complete by the 10th week of gestation, and bile formation is seen in the 12th week. The extrahepatic biliary tree initially is formed as a solid cord that canalizes by the 10th to 12th week of gestation. Bile is excreted into the duodenum via the common bile duct and is responsible for the characteristic dark green color of meconium.

The superior portion of the liver is in direct contact with the diaphragm and is termed the *bare area* because it is not covered by the peritoneum. The inferior vena cava, distal esophagus, and right adrenal gland abut the posterior margin of the liver, which inferiorly is bordered by the right and transverse colon, right kidney, and gallbladder. The visceral surface of the liver contains the biliary and vascular structures of the porta hepatis. Hepatic segmental anatomy has been defined by several nomenclature systems. The Couinaud system is most frequently used today as it is based on biliary vascular anatomy and surgically resectable segments (Fig. 83.2).[7] The middle hepatic vein and the Cantlie line, a plane between the inferior vena cava and the gallbladder fossa, split the liver anatomically into right and left lobes. Each lobe is further divided into four segments based on a vertical plane through the hepatic vein to that lobe and a horizontal plane through the corresponding portal vein branch. Hence, the left hepatic lobe has lateral segments designated II cranially and III caudally with the medial segments labelled IVA and IVB. The right hepatic lobe segments are numbered in a clockwise fashion starting at the gallbladder fossa as VIII, V, VI, and VII. The caudate lobe is named segment I. It lies between the main portal vein and the inferior vena cava and has its own unique vascular supply, separate from the remainder of the liver.

## SPLEEN

The spleen begins to develop during the fifth week of gestation.[8,9] It is derived from a mass of mesenchymal cells in the dorsal mesogastrium that coalesce to form the spleen. Failure of these cells to fuse completely gives rise to accessory spleens, which are quite common. As the stomach's greater curvature rotates to the left, the spleen is carried with it into the left upper quadrant. It lies in a niche formed by the diaphragm, the stomach, the left kidney and adrenal gland, the phrenicocolic ligament, and the chest wall. The splenic hilum is a depression along the medial surface through which the splenic artery, vein, and nerves pass. The two major ligaments that hold the spleen in place are the gastrosplenic and the splenorenal ligaments. Other ligaments that support the spleen are the splenophrenic, splenocolic, splenopancreatic, colophrenic, and pancreaticocolic ligaments.

The spleen is an important lymphatic organ and plays a role in providing protection from infection caused by encapsulated organisms. The spleen also filters damaged red blood cells and foreign particles and acts as a reservoir for platelets. Lymphocytes begin to appear in the spleen around 11 weeks of gestation.

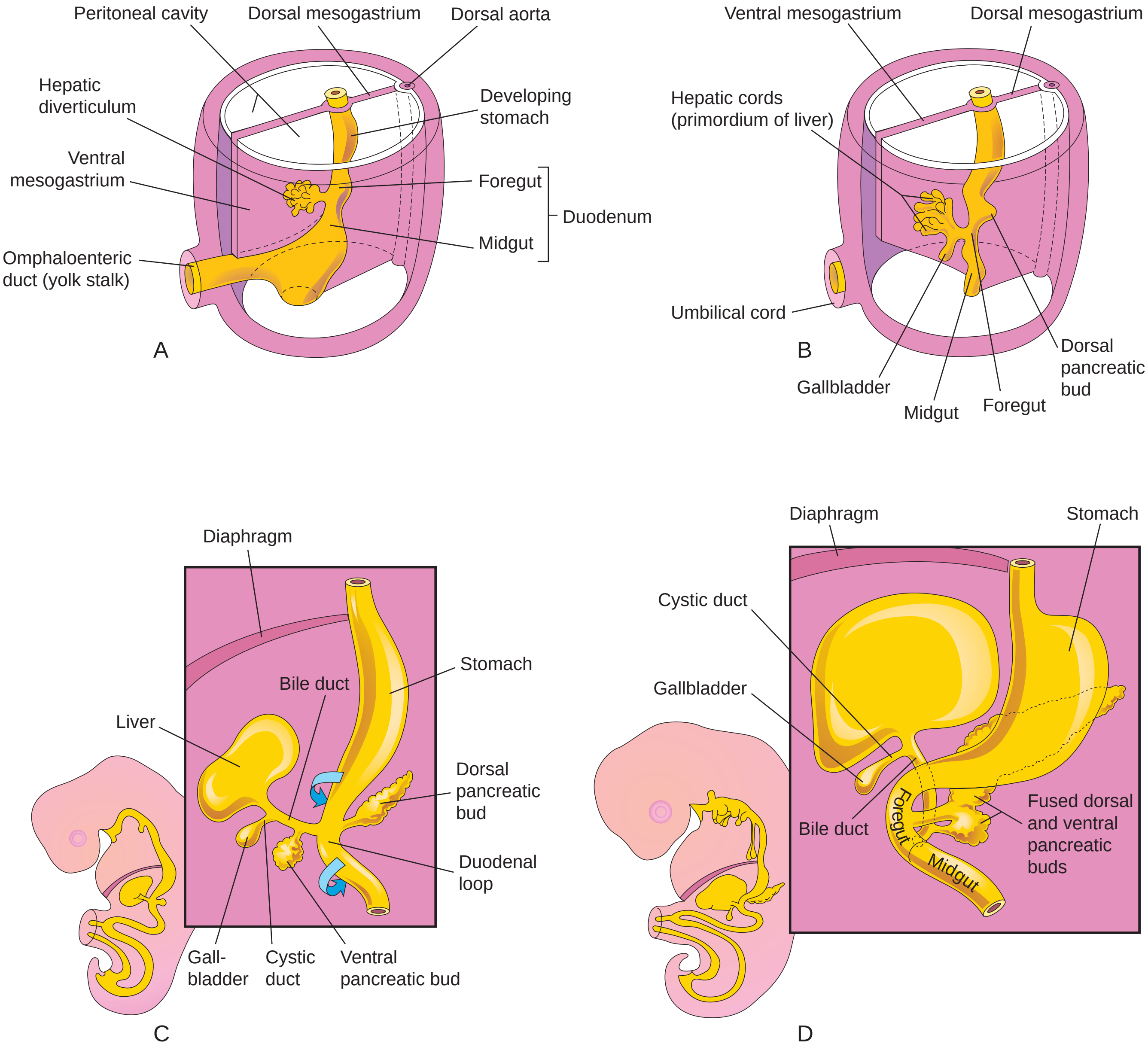

**Figure 83.1. Schematic illustrations of hepatic embryology.** (A) Hepatic embryology at 4 weeks. (B and C) Hepatic embryology at 5 weeks. (D) Hepatic embryology at 6 weeks. Note hepatic diverticulum extending into the ventral mesentery and dividing into cranial (liver primordium) and caudal (gallbladder and common bile duct) buds. Also note that the entrance of the bile duct into the duodenum shifts gradually to a posterior position, which explains why the bile duct passes posterior to the duodenum. *(From Moore KL, Persaud TVN. The digestive system. In: Moore KL, Persaud TVN, eds.* The Developing Human: Clinically Oriented Embryology. *8th ed. Philadelphia: WB Saunders; 2007.)*

## PANCREAS

The development of the pancreas is closely related to duodenal development. The dorsal pancreatic bud arises from the dorsal side of the duodenum, and the ventral pancreatic bud arises from the hepatic diverticulum (Fig. 83.3).[10–12] The larger dorsal bud appears first and arises cranial to the smaller ventral bud. It will form the tail, body, and part of the head of the pancreas. The ventral bud develops at the site of entry of the common bile duct and forms part of the pancreatic head and the uncinate process. As the duodenal loop rotates, the ventral bud is carried dorsally to lie in a position posterior to the dorsal bud, with which it fuses. After fusion of the pancreatic buds, the duct systems anastomose. Thus the proximal portion of the main pancreatic duct is formed from the ventral bud and the distal portion is formed from the dorsal pancreatic bud. The proximal portion of the dorsal duct either disappears or persists as the accessory pancreatic duct. Islet cells appear at the end of the second month of gestation, and acinar cells develop during the third month. The islet cells secrete insulin, glucagon, somatostatin, and pancreatic polypeptide. Acinar cells produce digestive enzymes that are secreted into the second portion of the duodenum.

The pancreas lies horizontally in the retroperitoneum. The body of the pancreas is in contact with the stomach anteriorly; the splenic artery and vein run along the superior and dorsal margin of the pancreas, and serve as markers on cross-sectional imaging.

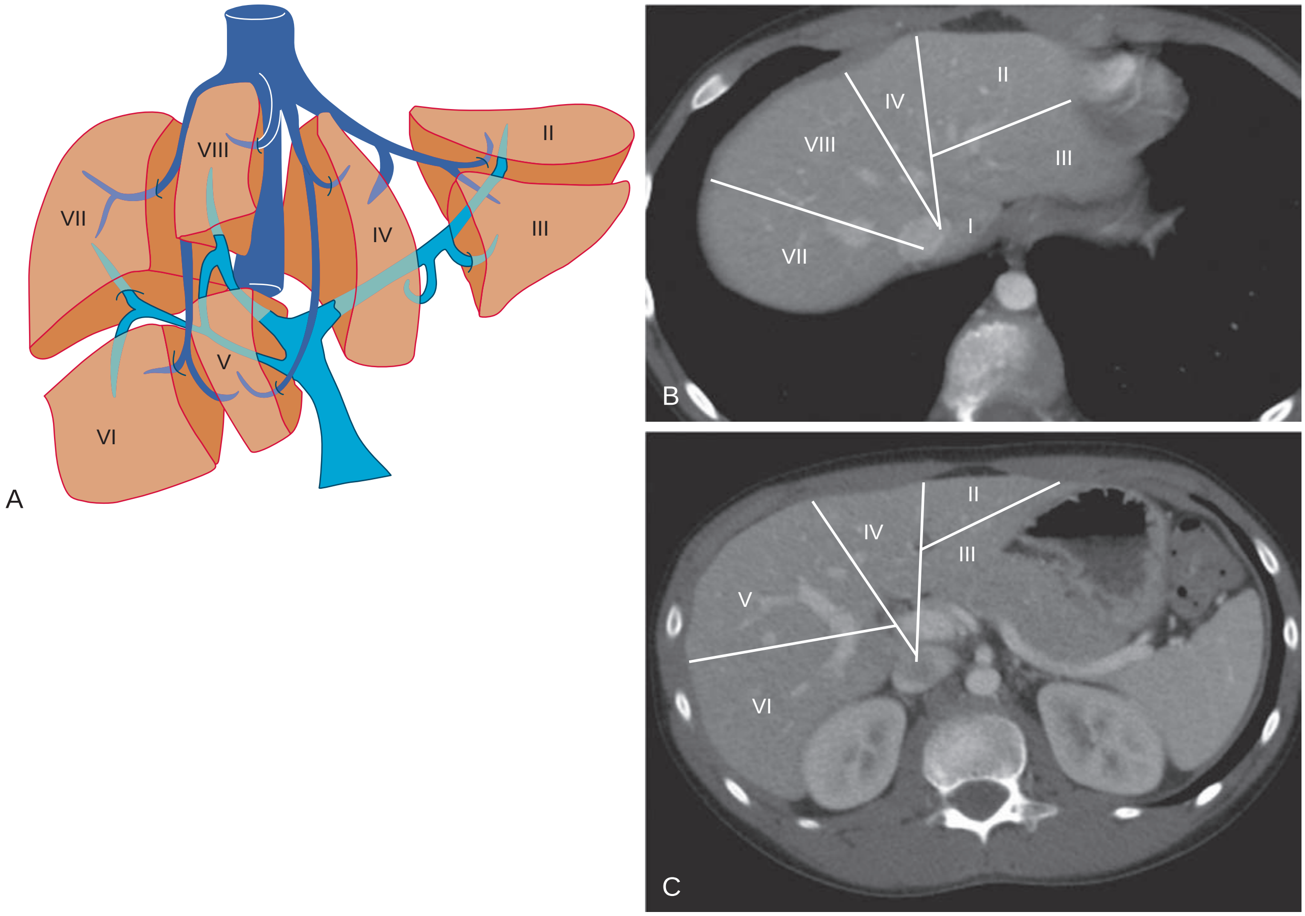

**Figure 83.2. Schematic illustration of hepatic segmental anatomy according to Couinaud.** (A) The portal venous supply to each segment is in light blue, and the hepatic veins draining each segment are in dark blue. Not shown are the bile ducts, which follow the course of the portal veins. (B and C) Segmental anatomy as seen on computed tomography. *(A, Modified from Gazelle GS, Lee MJ, Mueller PR. Cholangiographic segmental anatomy of the liver.* Radiographics. *1994;14:1005. Reprinted with permission;* B *and* C, *Courtesy of Marta Hernanz-Schulman, Nashville, TN.)*

The head of the pancreas lies to the right of the midline in the curve of the duodenum, whereas the tail is in contact with the gastric surface of the spleen and the splenic surface of the colon. The uncinate process is an extension of gland substance at the junction of the inferior and left margins of the pancreatic head.

## GASTROINTESTINAL TRACT

The primitive gastrointestinal tract forms during the third to fourth week of gestation.[13–16] It is marked by the oropharyngeal membrane at the cranial end and the cloacal membrane caudally (Fig. 83.4). It is divided into three parts: the foregut, midgut, and hindgut. The foregut includes the esophagus, stomach, and proximal duodenum, and receives most of its arterial supply from the celiac axis, with the exception of the esophagus that is proximal to the lower esophageal sphincter. The midgut is supplied by the superior mesenteric artery and includes the distal duodenum, jejunum, ileum, cecum, appendix, ascending colon, and approximately two-thirds of the transverse colon. The hindgut is supplied by the inferior mesenteric artery and comprises the remainder of the transverse colon, the descending and sigmoid colon, and the upper two-thirds of the rectum.

### Esophagus

The esophagus begins as a ventral diverticulum from the primitive foregut that will give rise to the trachea and the esophagus.[15–18] As this diverticulum elongates, a partition forms, the tracheoesophageal septum, which ultimately leads to separation of the esophagus from the trachea at 34 to 36 days of gestation. Elongation of the esophagus initially occurs cranially, and the final proportionate length of the esophagus is reached at 7 weeks. Epithelial proliferation with partial to complete obliteration of the esophageal lumen occurs, which normally recanalizes by the 10th week. The muscular coat of the esophagus is derived from the surrounding splanchnic mesenchyme. In the upper third of the esophagus, striated muscle innervated by the vagus nerve is present, whereas the lower two-thirds contains smooth muscle innervated by the splanchnic plexus.

The esophagus begins at the level of C7 and ends at the esophagogastric junction, which is usually at the T10–11 vertebral body level (Fig. 83.5). The caliber varies with peristaltic activity but is slightly narrower at both ends than along its intrathoracic course. Extrinsic impressions are caused by the aorta, the left mainstem bronchus, and the diaphragm (Fig. 83.6).

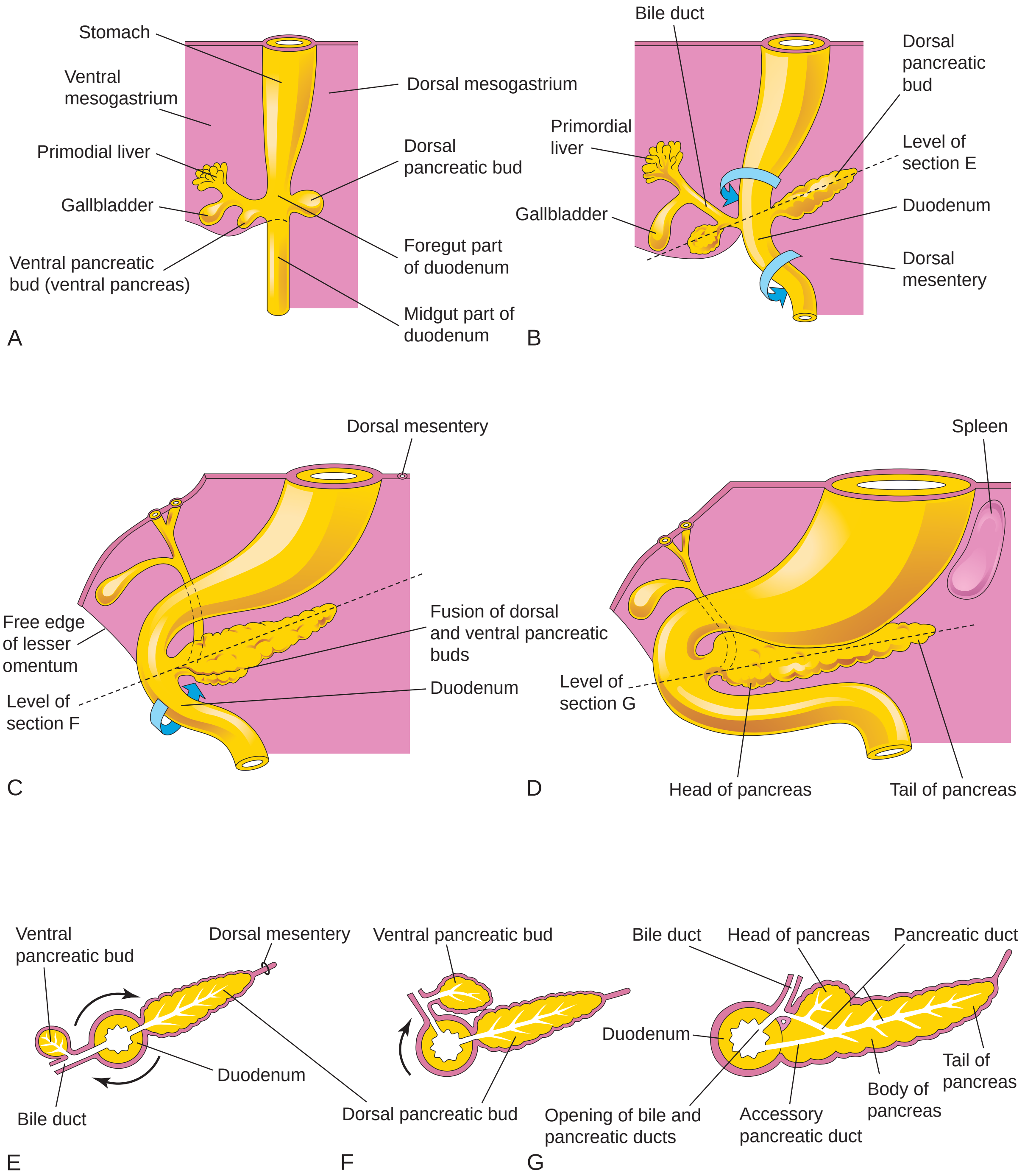

**Figure 83.3. Development of the pancreas.** (A–C) Illustrations of successive stages in the development of the pancreas from the fifth to the eighth weeks. (D–G) Transverse sections through the duodenum and the developing pancreas. Growth and rotation *(arrows)* of the duodenum bring the ventral pancreatic bud toward the dorsal bud; these two structures subsequently fuse. Note that the bile duct initially attaches to the ventral aspect of the duodenum and is carried around to the dorsal aspect as the duodenum rotates. The pancreatic duct is formed by the union of the distal part of the dorsal pancreatic duct (duct of Santorini) and the entire ventral pancreatic duct (duct of Wirsung). The proximal part of the dorsal pancreatic duct usually is obliterated, but it may persist as an accessory pancreatic duct, as labeled in the figure. *(From Moore KL, Persaud TVN. The alimentary or digestive system. In: Moore KL, Persaud TVN, eds.* Before We Are Born: Essentials of Embryology and Birth Defects. *7th ed. Philadelphia: Saunders Elsevier; 2008.)*

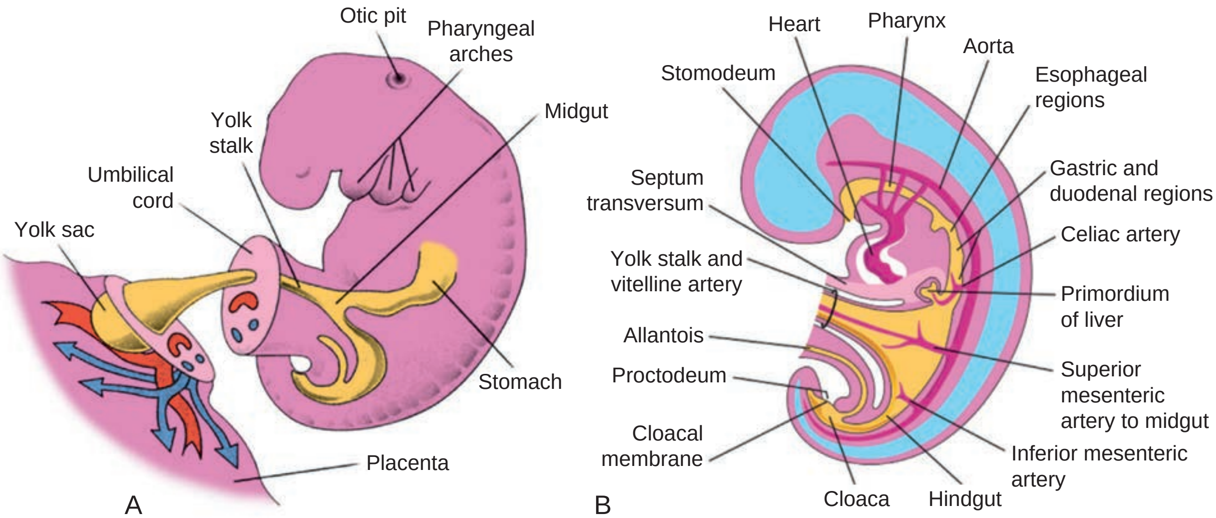

**Figure 83.4. Early digestive tract.** (A) A drawing of a median section of the embryo showing the early digestive system and its blood supply. The primordial gut is a long tube extending the length of the embryo. Its blood vessels are derived from the vessels that supplied the yolk sac. (B) The primordial gut is a long tube extending the length of the embryo from the stomodeum to the cloaca. Note again the blood supply from the vitelline artery via the yolk stalk and the relationship of the developing celiac axis, superior mesenteric artery, and inferior mesenteric artery to the primordial gut segments. *(From Moore KL, Persaud TVN, eds.* Before We Are Born: Essentials of Embryology and Birth Defects. *7th ed. Philadelphia: Saunders Elsevier; 2007.)*

The esophageal mucosa normally has thin, smooth longitudinal folds that flatten when the esophagus is distended by gas or barium. When fully distended, the distal esophagus enlarges and forms a fusiform shape commonly termed the *esophageal vestibule* or *phrenic ampulla*. The upper margin of the vestibule is radiographically delineated by a transient contractile area that forms bilateral, semilunar indentations termed the *A ring*, *inferior esophageal sphincter*, or *Wolf ring*. The lower margin is also delineated by a transient contractile region termed the *B ring*, *transverse mucosal fold*, *lower esophageal ring*, *Schatzki ring*, or *lower esophageal diaphragm*. In young infants, the vestibule spans the diaphragmatic hiatus so that the upper part lies within the thorax and the lower part lies within the abdomen.

## Stomach

The stomach arises as a tubular dilatation at the distal end of the foregut at 4 to 5 weeks of gestation.[13,15,16,19] The dorsal border grows more rapidly than the ventral border, leading to a 90-degree clockwise rotation on its longitudinal axis. As a result, the dorsal border rotates to the left and becomes the greater curvature, whereas the ventral border rotates to the right and becomes the lesser curvature of the stomach. The left and right vagal nerve branches rotate with the stomach, such that the left vagal nerve innervates the anterior gastric wall and the right vagal nerve innervates the posterior wall.

The stomach lies below the left hemidiaphragm with its long axis transverse to the long axis of the body.[19] The stomach is relatively fixed proximally by the esophagogastric junction and distally by the fixed retroperitoneal position of the first portion of the duodenum. The stomach also is fixed to neighboring structures by four major peritoneal folds or ligaments: gastrophrenic, gastrohepatic, gastrosplenic, and gastrocolic ligaments.

The stomach is divided into four major regions. The cardia is a small, ill-defined area immediately adjacent to the esophagogastric junction and just to the left of the midline. The fundus is the most bulbous portion of the stomach. It projects upward, above the cardia and gastroesophageal junction, and is in contact with the left hemidiaphragm and the spleen. The body is the largest part of the stomach and is bounded by the greater and lesser curvatures. The incisura angularis, a sharp indentation two-thirds of the distance down the lesser curvature, marks the beginning of the gastric antrum. The antrum in turn is divided by the sulcus intermedius into the pyloric vestibule more proximally, and the pyloric antrum, which extends to the junction with the duodenum.[20] The normal size, shape, and position of the stomach vary with the volume of gastric content and the age of the individual. In infancy, the stomach is high and transverse, whereas in older children and adults it is more longitudinal and J-shaped.

## Duodenum

The duodenum is derived from the caudal portion of the foregut and the cranial portion of the midgut.[13,15,16] The junction of these two parts is just distal to the common bile duct. The duodenal segment elongates rapidly, forming a C-shaped loop. As the stomach rotates, the duodenal loop rotates to the right, causing the duodenum to be pressed against the posterior abdominal wall, which leads to fusion and resorption of peritoneal layers such that the duodenum becomes a retroperitoneal structure. Because it is derived from both foregut and midgut, the duodenum receives its blood supply from both the celiac and superior mesenteric arteries. Unlike the rest of the midgut, the duodenum does not herniate into the extraembryonic coelom.

The duodenum is the most proximal portion of the small intestine.[19] The first portion of the duodenum begins at the pylorus and ends at the neck of the gallbladder. It is loosely attached to the liver by the hepatoduodenal portion of the lesser omentum; the second, third, and fourth portions are retroperitoneal. The second or descending portion extends from the neck of the gallbladder and is in contact with the head of the pancreas. The common bile duct enters in its midportion. The third portion is horizontal and courses to the left across the midline, anterior to the spine, aorta, and inferior vena cava. Anteriorly, the third portion is covered by peritoneum and is crossed by the superior mesenteric artery and vein. The fourth portion ascends along the left side of the aorta and turns ventrally to become the jejunum at the level of the duodenojejunal flexure. The duodenojejunal flexure is retroperitoneal and is also fixed by the ligament of Treitz.

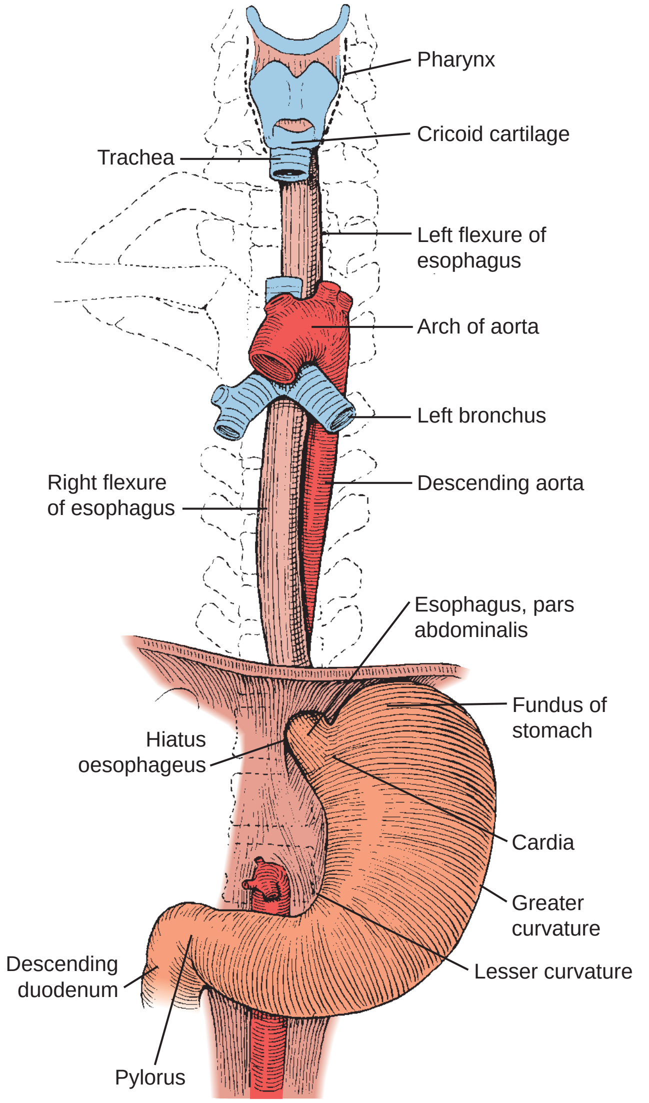

**Figure 83.5. Normal esophagus.** Semi-schematic drawing of the normal esophagus depicting its relation to the trachea, aorta, diaphragm, and stomach. *(Modified from Schaegger JP.* Morris' Human Anatomy. *10th ed. New York: McGraw-Hill; 1943. Reprinted with permission.)*

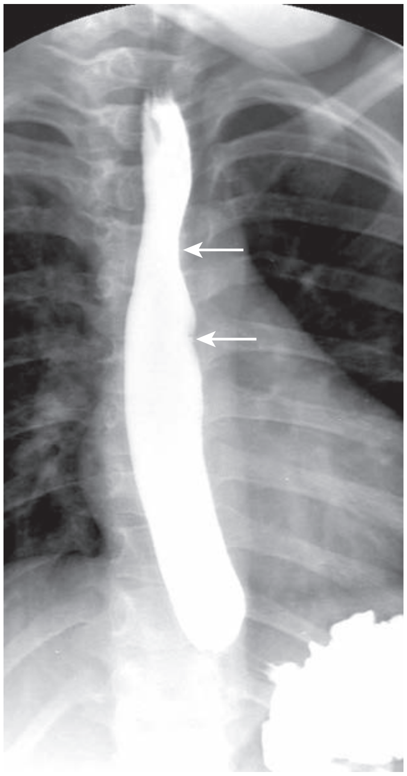

**Figure 83.6. Normal esophageal impressions.** Barium swallow study demonstrates the impression of the aortic knob *(upper arrow)* and the left main stem bronchus *(lower arrow)* on the barium-filled esophagus. These impressions are normal and are not to be confused with mediastinal abnormalities.

## Midgut

The midgut is the portion of the gut that opens ventrally into the yolk sac and undergoes a 270-degree counterclockwise rotation (see also Chapter 102).[13,16,18] It elongates rapidly so that, by the beginning of the sixth week, it forms a U-shaped ventral loop that projects into the extraembryonic coelom, herniating into the umbilical cord. The stalk at the apex of the loop is the omphalomesenteric duct (Fig. 83.7). The midgut proximal to the apex of the loop is small bowel and the midgut distal to the apex is colon. A Meckel diverticulum is the result of persistence of the proximal portion of the omphalomesenteric duct, which is the most common congenital malformation of the gastrointestinal tract. During the sixth week of gestation, a diverticulum forms on the antimesenteric border of the distal portion of the midgut, which will give rise to the cecum and appendix.

While the bowel is in the extraembryonic coelom, it undergoes a 90-degree counterclockwise rotation around the superior mesenteric artery (see Fig. 83.7B). During this rotation, the jejunum and ileum grow more rapidly than the colon; this rotation brings the proximal midgut (jejunum and ileum) to the right and the distal portion (large intestine) to the left. The bowel abruptly returns to the abdominal cavity at about 10 weeks of development (see Fig. 83.7C and D). The forces responsible for this sudden return are unknown. The small bowel enters first, passes posterior to the superior mesenteric artery, and ultimately occupies the central part of the abdomen. As the large intestine returns to the abdominal cavity, it undergoes a 180-degree counterclockwise rotation, with the cecum ending up below the liver. Further growth of the ascending colon forces the cecum down into the right lower quadrant (see Fig. 83.7E).

Fixation of the midgut begins during the twelfth week of gestation. The mesenteries of the ascending and descending colon fuse with the posterior abdominal wall and become retroperitoneal. As a result of the fusion of the mesenteries of the ascending and descending colon and of the duodenum to the posterior abdominal wall, the small bowel mesentery becomes fan-shaped, with a broad-based attachment extending from the left upper quadrant to the right lower quadrant (Fig. 83.8). This broad attachment limits the mobility of the mesentery and prevents a midgut volvulus around the superior mesenteric artery. Failure to complete this rotation, which is known as *malrotation*, leads to a narrow mesenteric pedicle, which, in conjunction with the lack of mesenteric attachments, may result in midgut volvulus (see Chapter 102).

## Hindgut

The hindgut is supplied by the inferior mesenteric artery, begins in the mid to distal transverse colon and terminates at the cloaca.[13,16,21] The watershed region between the superior and inferior mesenteric arteries is located in the mid to distal transverse colon.

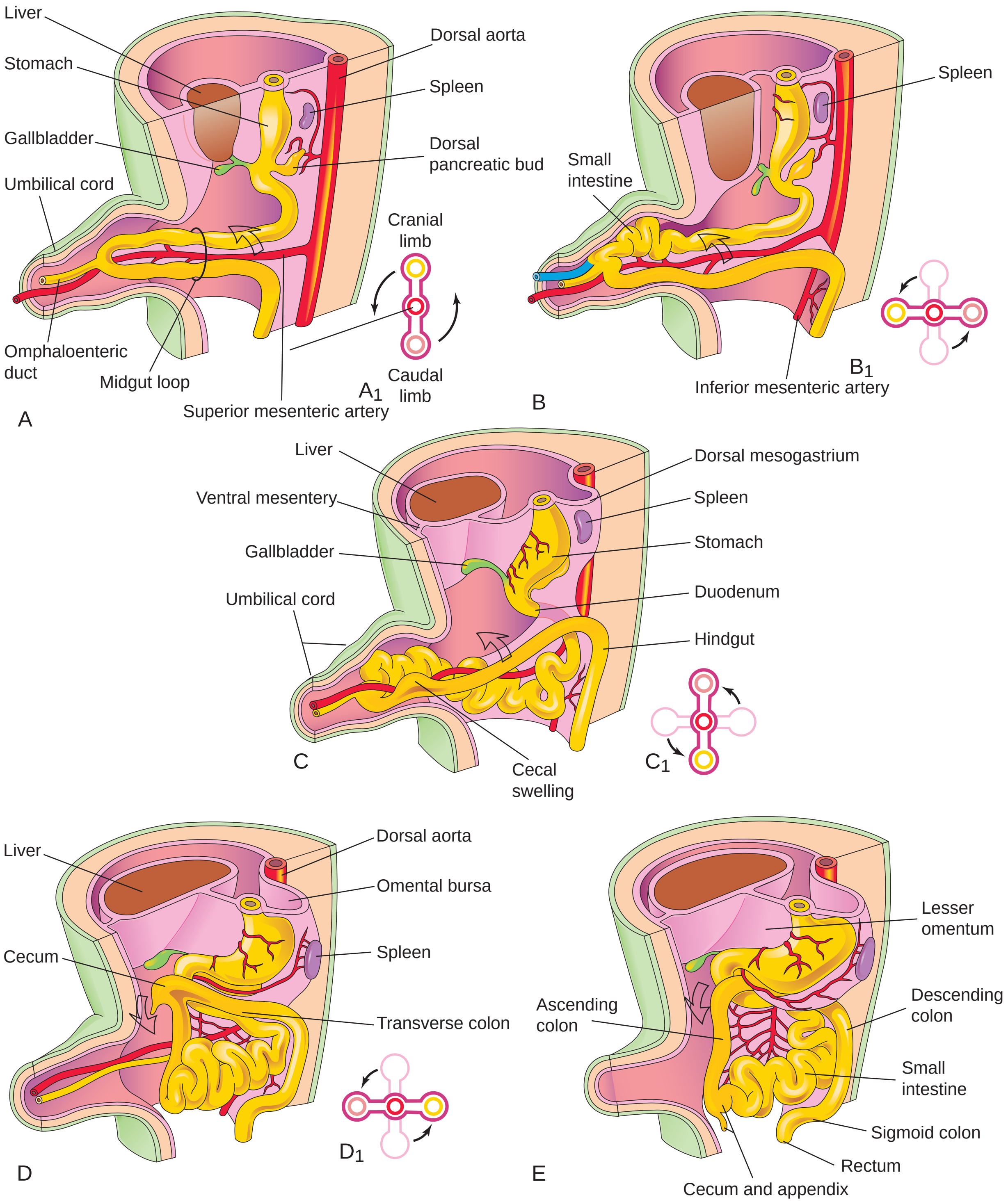

**Figure 83.7. Illustrations of the rotation of the midgut, as seen from the left.** (A) During the sixth week, the midgut loop is situated in the proximal part of the umbilical cord. ($A_1$) Transverse section through the midgut loop, showing the initial relationship of the limbs of the midgut loop to the superior mesenteric artery. (B) A later stage, showing the beginning of midgut rotation. ($B_1$) Illustration of the 90-degree counterclockwise rotation that carries the cranial limb of the midgut to the right. (C) At approximately 10 weeks, the intestines return to the abdomen. ($C_1$) Illustration of a further rotation of 90 degrees. (D) By approximately 11 weeks, all of the intestines return to the abdomen. ($D_1$) A further 90-degree rotation of the gut, for a total of 270 degrees. (E) The later fetal period showing the cecum rotating to its normal position in the lower right quadrant of the abdomen. *(From Moore KL, Persaud TVN. The alimentary or digestive system. In: Moore KL, Persaud TVN, eds.* Before We Are Born: Essentials Of Embryology and Birth Defects. *7th ed. Philadelphia: Saunders Elsevier; 2008.)*

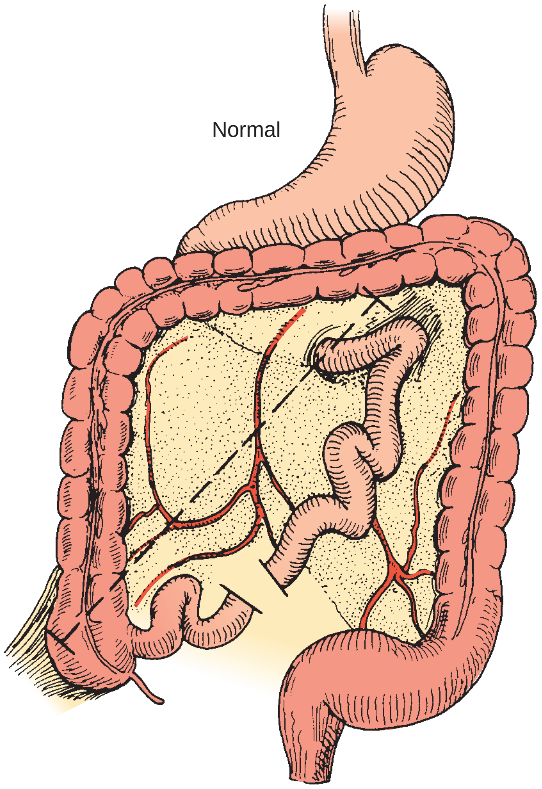

**Figure 83.8. Normal rotation and fixation of the midgut.** Note the broad-based fixation between the left upper and right lower quadrants, which fixes the superior mesenteric artery and prevents volvulus of the vascular pedicle. *(From Ross AJ III. Organogenesis, innervation, and histologic development of the gastrointestinal tract. In: Polin RA, Fox WW, eds.* Fetal and Neonatal Physiology. *2nd ed. Philadelphia: WB Saunders; 1998.)*

Around day 13 of gestation, a ventral diverticulum of the hindgut, the allantois, forms. The hindgut distal to the allantois disappears around the sixth week of gestation (Fig. 83.9). The junction of the allantoic stalk and the hindgut is the site of the cloaca. The cloaca, which is lined with endoderm, is in direct contact with the ectodermally lined proctodeum (anal pit). The area of contact between these two surfaces is the cloacal membrane. A wedge of mesenchyme, the urorectal septum, develops in the angle between the allantois and the hindgut (see Fig. 83.9C and 83.9D). As the urorectal septum grows toward the cloacal membrane, it produces infoldings of the lateral walls of the cloaca. These folds grow toward each other and fuse, forming a partition that divides the cloaca into two parts: the rectum and upper anal canal dorsally and the urogenital sinus ventrally. The area of fusion of the urorectal septum with the cloacal membrane forms the perineal body. The anal membrane ruptures at the end of the eighth week, allowing the intestinal tract to communicate with the amniotic cavity.

## NORMAL ANATOMY OF THE SMALL INTESTINE

The small intestine is a tubular structure within the abdominal cavity that is located between the stomach and the colon,[23] and consists of the duodenum, jejunum, and ileum. The length of the small intestine increases from approximately 200 cm at birth to 6 m in the adult.

The anatomy of the duodenum is discussed earlier in this chapter. Jejunum comprises the proximal two-fifths of the small bowel; the remainder is ileum. No morphologic demarcation exists between the two segments. The jejunum and ileum are suspended by a broad-based mesentery attached to the posterior peritoneal wall and thus are freely mobile within the abdominal cavity, although secured at both ends. Generally, the proximal third of the small bowel occupies the left upper quadrant; the middle third is in the midportion of the abdomen and right upper quadrant; and the distal third lies on the right side of the abdomen and pelvis. The location of any portion of the small bowel from the duodenojejunal junction to the cecum can vary over time due to the broad, fanlike mesentery and bowel peristalsis. The caliber of the small intestine tapers as it progresses distally, with the diameter of the terminal ileum being about one-third smaller than the first portion of the jejunum. The external surface is smooth while the internal surface has transverse and spiral folds that are covered by villi. The jejunum has more visible folds than the ileum (Fig. 83.10).

## NORMAL ANATOMY OF THE COLON

The colon extends from the ileocecal valve to the anus and is divided into the ascending, transverse, descending, and sigmoid portions as well as the rectum and anus.[23,24] In the newborn, it is 30 to 40 cm long, and it reaches 1.5 m in length in the adult. The cecum is the beginning of the ascending colon; it lies in the right lower quadrant, although it often is higher in infants, even above the iliac crest. The appendix is a blind outpouching of the cecum.

The retroperitoneal ascending colon extends upward along the right side of the peritoneal cavity to the underside of the liver. The colon turns medially at the hepatic flexure and emerges into the peritoneal cavity as the transverse colon. It courses right to left to reach its highest point in the left upper quadrant at the splenic flexure. The transverse colon is suspended by the mesocolon and is freely mobile. At the splenic flexure, the colon again becomes retroperitoneal and turns caudally to become the descending colon, running along the left lateral abdominal wall to the pelvic brim. At this point, it emerges into the peritoneal cavity as the sigmoid colon. The sigmoid colon is an S-shaped, redundant segment of variable length. The narrowest portion of the colon is in the sigmoid segment. In children, the redundancy of the sigmoid may cause the apex to extend to the right upper quadrant and the distal portion to loop into the right lower quadrant. The rectum begins at the peritoneal reflection and follows the curve of the sacrum, ending at the anal canal. The distal one-third of the rectum is retroperitoneal.

### KEY POINTS

- The liver and gallbladder arise during the fourth week of gestation from a ventral outgrowth of the caudal end of the foregut.
- The gastrointestinal tract begins to form during the third week of gestation.
- The foregut receives blood supply from the celiac axis, the midgut from the superior mesenteric artery, and the hindgut from the inferior mesenteric artery.
- The midgut returns to the abdominal cavity from the extraembryonic coelom between the 10th and 11th weeks of gestation.
- Normal rotation of the bowel leads to a broad-based mesentery with proximal and distal attachments; incomplete rotation (malrotation) leads to a narrow mesentery without attachments, a situation conducive to midgut volvulus.
- The urorectal septum divides the cloaca into the urogenital sinus anteriorly and the anorectal canal posteriorly. The cloacal membrane ruptures into the amniotic cavity in the seventh week of gestation.

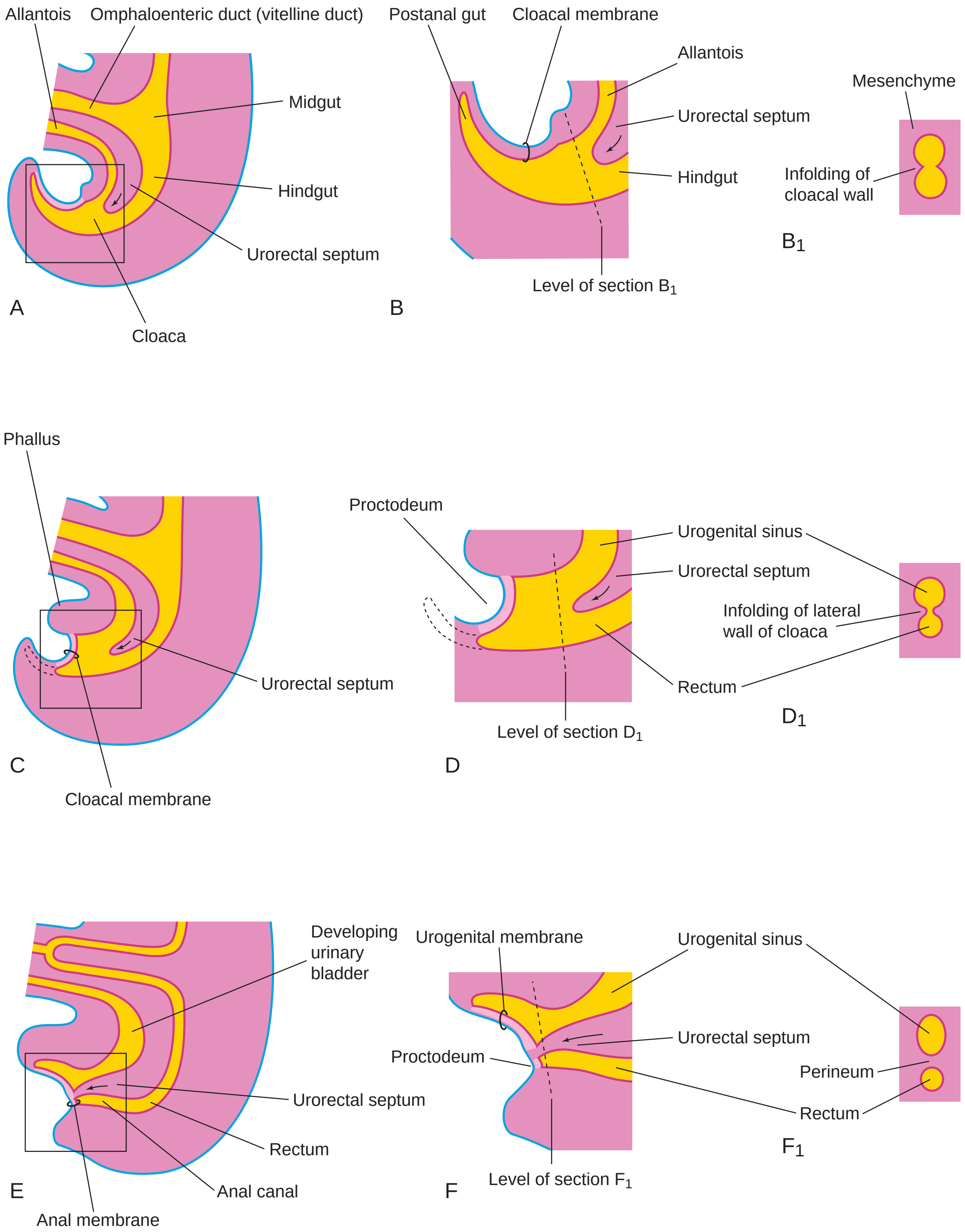

**Figure 83.9. Illustrations of successive stages in the partitioning of the cloaca into the urogenital sinus and the rectum by the urorectal septum.** (A, C, and E) Views from the left side at 4, 6, and 7 weeks, respectively. (B, D, and F) Enlargements of the cloacal region. ($B_1$, $D_1$, and $F_1$) Transverse sections of the cloaca at the levels shown in (B, D, and F), respectively. Note that the postanal gut, or tailgut (shown in B), degenerates and disappears as the rectum forms from the dorsal part of the cloaca (shown in C). The *arrows* indicate the growth of the urorectal septum. *(From Moore KL, Persaud TVN. The alimentary or digestive system. In: Moore KL, Persaud TVN, eds.* Before We Are Born: Essentials of Embryology and Birth Defects. *7th ed. Philadelphia: Saunders Elsevier; 2008.)*

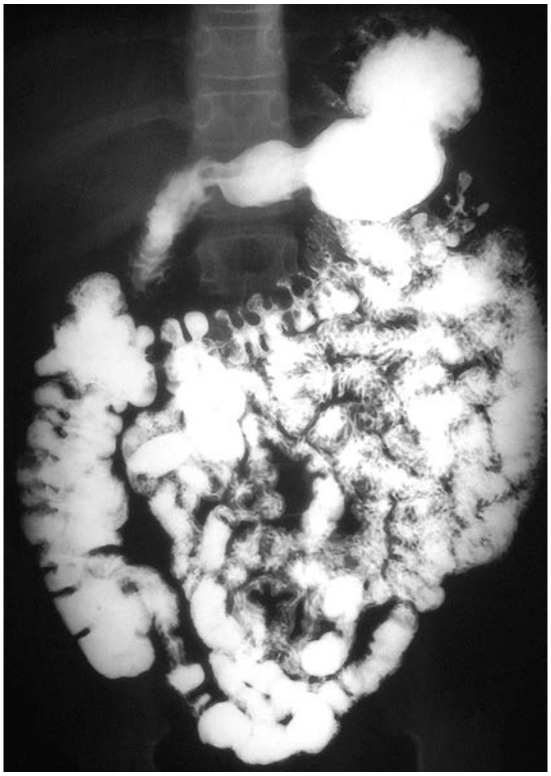

**Figure 83.10. Normal small intestine.** Frontal radiograph from an upper gastrointestinal series with small bowel follow-through shows contrast in the stomach, duodenum, jejunum, ileum, and ascending portion of the colon. The jejunal loops in the left upper quadrant have a feather-like fold pattern, while the ileum is relatively featureless.

## SUGGESTED READINGS

Moore KL, Persaud TVN, Torchia MG. *Before We Are Born: Essentials of Embryology and Birth Defects*. 9th ed. Philadelphia: Elsevier/Saunders; 2016.
O'Rahilly R, Müller F. *Human Embryology & Teratology*. 3rd ed. New York: Wiley-Liss; 2001.
Polin RA, Fox WW, Abman SH, eds. *Fetal and Neonatal Physiology*. 3rd ed. Philadelphia: Saunders; 2004.
Sadler TW, Langman J. *Langman's Medical Embryology*. 12th ed. Philadelphia: Wolters Kluwer Health/Lippincott Williams & Wilkins; 2012.

## REFERENCES

Full references for this chapter can be found on www.expertconsult.com.

## REFERENCES

1. Skandalakis JE, Gray SW, Ricketts R, et al. The anterior body wall. In: Skandalis JE, Gray SW, eds. *Embryology for Surgeons*. 2nd ed. Baltimore: Williams & Wilkins; 1994.
2. O'Rahilly R, Müller F. The digestive system. In: O'Rahilly R, Müller F, eds. *Human Embryology & Teratology*. 2nd ed. New York: Wiley-Liss; 1996.
3. Skandalakis JE, Gray SW, Ricketts R, et al. The peritoneum. In: Skandalis JE, Gray SW, eds. *Embryology for Surgeons*. 2nd ed. Baltimore: Williams & Wilkins; 1994.
4. Moore KL, Persaud TVN. Body cavities and mesenteries. In: Moore KL, Persaud TVN, eds. *Before We Are Born: Essentials of Embryology and Birth Defects*. 7th ed. Philadelphia: Saunders; 2008.
5. Moore KL, Persaud TVN. The alimentary or digestive system. In: Moore KL, Persaud TVN, eds. *Before We Are Born: Essentials of Embryology and Birth Defects*. 7th ed. Philadelphia: Saunders; 2008.
6. Sadler TW. The digestive system. In: Sadler TW, ed. *Langman's Medical Embryology*. 8th ed. Philadelphia: Lippincott Williams & Wilkins; 2000.
7. Dodd GD 3rd. An American's guide to Couinaud's numbering system. *Am J Roentgenol*. 1993;161(3):574–575.
8. O'Rahilly R, Müller F. The cardiovascular and lymphatic systems. In: O'Rahilly R, Müller F, eds. *Human Embryology & Teratology*. 2nd ed. New York: Wiley-Liss; 1996.
9. Skandalakis LJ, Gray SW, Ricketts R, et al. The spleen. In: Skandalis JE, Gray SW, eds. *Embryology for Surgeons*. 2nd ed. Baltimore: Williams & Wilkins; 1994.
10. Skandalakis JE, Gray SW, Ricketts R, et al. The pancreas. In: Skandalis JE, Gray SW, eds. *Embryology for Surgeons*. 2nd ed. Baltimore: Williams & Wilkins; 1994.
11. Moore KL, Persaud TVN. The alimentary or digestive system. In: Moore KL, Persaud TVN, eds. *Before We Are Born: Essentials of Embryology and Birth Defects*. 7th ed. Philadelphia: Saunders; 2008.
12. Werlin SL, Lee PC. Development of the exocrine pancreas. In: Polin RA, Fox WW, Abman SG, eds. *Fetal and Neonatal Physiology*. 3rd ed. Philadelphia: Saunders; 2004.
13. Moore KL, Persaud TVN. The alimentary or digestive system. In: Moore KL, Persaud TVN, eds. *Before We Are Born: Essentials of Embryology and Birth Defects*. 7th ed. Philadelphia: Saunders; 2008.
14. O'Rahilly R, Müller F. The digestive system. In: O'Rahilly R, Müller F, eds. *Human Embryology & Teratology*. 2nd ed. New York: Wiley-Liss; 1996.
15. Sadler TW. The digestive system. In: Sadler TW, ed. *Langman's Medical Embryology*. 8th ed. Philadelphia: Lippincott Williams & Wilkins; 2000.
16. Ross AJIII. Organogenesis of the gastrointestinal tract. In: Polin RA, Fox WW, Abman SG, eds. *Fetal and Neonatal Physiology*. 3rd ed. Philadelphia: Saunders; 2004.
17. Long JD, Orlando RC. Anatomy and developmental and acquired anomalies of the esophagus. In: Feldman L, Scharschmidt BF, Sleisenger MH, eds. *Gastrointestinal and Liver Disease*. 6th ed. Philadelphia: WB Saunders; 1998.
18. Skandalakis JE, Gray SW, Ricketts R. The esophagus. In: Skandalis JE, Gray SW, eds. *Embryology for Surgeons*. 2nd ed. Baltimore: Williams & Wilkins; 1994.
19. Redel CA, Zwiener RJ. Anatomy and anomalies of the stomach and duodenum. In: Feldman L, Scharschmidt BF, Sleisenger MH, eds. *Gastrointestinal and Liver Disease*. 6th ed. Philadelphia: WB Saunders; 1998.
20. Hernanz-Schulman M. Infantile hypertrophic pyloric stenosis. *Radiology*. 2003;227(2):319–331.
21. Skandalakis JE, Gray SW, Ricketts R, et al. The small intestines. In: Skandalis JE, Gray SW, eds. *Embryology for Surgeons*. 2nd ed. Baltimore: Williams & Wilkins; 1994.
22. [deleted in review]
23. Keljo DJ, Squires RH Jr. Anatomy and anomalies of the small and large intestines. In: Feldman L, Scharschmidt BF, Sleisenger MH, eds. *Gastrointestinal and Liver Disease*. 6th ed. Philadelphia: WB Saunders; 1998.
24. Skandalakis JE, Gray SW, Ricketts R. The colon and rectum. In: Skandalis JE, Gray SW, eds. *Embryology for Surgeons*. 2nd ed. Baltimore: Williams & Wilkins; 1994.

# 84

# Imaging Techniques

Marta Hernanz-Schulman, Lisa States, and Shreyas Vasanawala

## OVERVIEW

When the first edition of this textbook was published in 1945, its title was *Caffey's Pediatric X-ray Diagnosis*, denoting the single modality available at the time. In the intervening seven decades, there have been twelve additional editions of the book, and the title has changed to *Caffey's Pediatric Diagnostic Imaging* to reflect the diversity of tools now available to the pediatric radiologist. This expansion has been coupled with increasing awareness of radiation safety (as exemplified by the Image Gently Alliance) and concern for safety profiles of contrast agents and anesthetics, further adding to the complexity of choosing and implementing optimal pediatric imaging. This chapter is an overview of the various modalities available to image the pediatric gastrointestinal (GI) tract, with detailed applications addressed in the organ-specific chapters.

## RADIOGRAPHY AND FLUOROSCOPY

### Overview

Evaluation of the GI system includes the hollow viscera: from esophagus to rectum; solid viscera: liver, spleen, and pancreas; and the peritoneal cavity and retroperitoneal spaces in which all are contained. Although there can be considerable overlap among various modalities and newer applications continue to be defined, radiography and fluoroscopy are often used for initial imaging of the GI system.

Air is the inherent contrast medium in plain film diagnosis, and the abdominal series is based on distribution and movement of gas. The basic radiographic evaluation typically consists of supine and horizontal-beam images. Left-side-down decubitus and upright views evaluate for free intraperitoneal air and air-fluid levels. The left-side-down decubitus further directs air toward the right colon for evaluation of the right lower quadrant and into the rectum for evaluation of obstruction. Prone positioning is more effective in directing gas to the rectum when there is concern for bowel obstruction, with a horizontal-beam film (cross-table lateral) of the rectum often particularly helpful.

Fluoroscopy remains an important tool in further assessment of suspected pathology of the hollow viscera. Pulsed fluoroscopy can substantially decrease radiation dose while enhancing image sharpness and detectability of moving objects.[1,2] Capture and storage of the fluoroscopic images (fluorostore) can document such findings as viscus distension, course of contrast, and peristaltic activity, with spot films reserved for areas in which greater anatomic detail is of diagnostic importance, such as mucosal abnormalities and potential leaks.

### Contrast Media

In most GI fluoroscopic studies, enteric contrast is required for diagnosis, and it is important to choose the correct contrast medium for the clinical setting. Choices are usually barium or water-soluble iodinated media, which in turn are subdivided into high and low osmolality agents.[3,4] Barium, an inert substance that is not absorbed and has physical properties well suited to the roentgen ray, remains the major fluoroscopic contrast medium, particularly in older children. Barium is administered orally in evaluation of the esophagus and upper GI tract, or rectally for contrast enema. Several barium preparations are available: barium sulfate powder (96% w/w) can be diluted with sterile water for infant UGI examinations to the desired concentration of 40% to 60% w/v. Premixed suspensions (60% w/v) can be used in older children and adolescents as well as in adults. Enema kits containing 97% barium w/w can be mixed with water to a final concentration of 15% to 33% barium w/v for infants, older children, and adolescents. Adverse reactions to barium products are rare, typically related to any one of several additives such as methylparaben and carboxymethylcellulose, or even latex allergy to the enema tip.[5–7] Reaction rates are reportedly 2 per million or less,[5] but they do occur and may present as a rash, loss of consciousness, and anaphylaxis. Aspiration of barium in small quantities is tolerated but can be fatal if aspirated in a large volume.[8–10]

Barium is not indicated in cases in which viscus perforation is possible or suspected. In such cases, low-osmolality, nonionic water-soluble iodinated media are indicated (Table 84.1).

It is important that hypertonic media, such as ionic or high-osmolality media (diatrizoate, iothalamate), not be used orally due to the risk of aspiration and consequent pulmonary edema and chemical pneumonitis.[11–13] Further, such hypertonic media have been associated with risk of mucosal injury and with large fluid shifts, which are potentially dangerous, particularly in young infants, patients with obstruction, or those with tenuous cardiac or renal function,[14] as major fluid shifts into the bowel lumen can lead to a decrease in intravascular volume, an increase in serum osmolarity, and a decrease in cardiac output. The intraluminal contrast dilution generated by these fluid shifts also renders them generally unsuitable for small bowel evaluation, particularly in patients with suspected obstruction.[15,16]

Iohexol is a nonionic, water-soluble, iodinated contrast medium, which is available in concentrations of 140, 180, 240, 300, and 350 mg/mL of iodine. It is poorly absorbed from the intact GI tract, with renal excretion of 0.1% to 0.5% of administered dose. Iopamidol (Isovue) has also been used in the evaluation of the pediatric GI tract, but currently only iohexol is officially approved for this purpose. It must be emphasized that the osmolality of both of these media is greater than that of blood, and no agent is safe in the tracheobronchial tree. Therefore great care and close fluoroscopic monitoring is necessary in all patients in whom aspiration is a potential complication.[17]

Barium is the standard agent in evaluation of the colon. However, in cases of potential perforation, water-soluble agents are used and can be diluted to approximate the tonicity of serum. For example, iothalamate meglumine 30% with an osmolality of 600 can be diluted 1:1 with water to achieve a nearly iso-osmolal solution, with an iodine concentration that remains diagnostic for most purposes. Higher osmolality contrast media are used rectally for therapeutic purposes in cases of uncomplicated meconium ileus, after diagnosis with a low osmolarity agent. Gastrografin™ (diatrizoate meglumine and diatrizoate sodium) was the original agent described for this purpose.[18] However, this can be associated with large fluid shifts and systemic complications in severely ill infants.[15] Full-strength iothalamate meglumine 30% can also be used successfully for this purpose. Close attention to water and electrolyte balance, and surgical standby, are mandatory.

Air can also be used as a contrast during fluoroscopic procedures. For example, it is an excellent way to distend a viscus during

## Abstract:

To describe the various modalities available in Pediatric Imaging. Review of the relevant current literature, and include relevant illustrations and examples. Radiography, Fluoroscopy and the various fluoroscopic imaging examinations, CT are described, discussing appropriate use, technique and radiation optimization. Ultrasound and its various uses in abdominal imaging is also described and illustrated. Magnetic resonance imaging, indications, protocols, patient preparation, pulse sequences, contrast media are described and illustrated. Finally nuclear medicine examinations are described as an overview and individually

## Keywords:

Fluoroscopy
Radiography
contrast enema
Upper GI
ultrasound
appendicitis
intussusception
MRI
MRA
MR contrast media
radiopharmaceuticals
scintigraphy
pediatrics
PET

**TABLE 84.1** Commonly Used Types of Contrast Media in Fluoroscopy of the Gastrointestinal Tract

| Contrast | mg Organically Bound Iodine/mL | Osmolality (mOsm/kg) | Viscosity (37°C) | Comments |
|---|---|---|---|---|
| **HIGH OSMOLAR, IONIC** | | | | |
| Gastrografin (diatrizoate meglumine and diatrizoate sodium) | 367 | 1600 | | Potential for aspiration, dehydration, precarious electrolyte balance<br>May cause problems if underlying bowel injury |
| Conray 30 (iothalamate meglumine) | 141 | 600 | 1.5 | Lower GI tract |
| **LOW OSMOLAR, NONIONIC** | | | | |
| Omnipaque (Iohexol) | | | | |
| 140 | 140 | 322 | 1.5 | Young infants |
| 180 | 180 | 408 | 2 | Infants and young children |
| 240 | 240 | 520 | 3.4 | Young children or ostomy evaluations |
| 300 | 300 | 672 | 6.3 | Not used |
| 350 | 350 | 844 | 10.4 | Not used |

*Source: Package inserts.*
*GI,* Gastrointestinal.

fluoroscopic transpyloric tube placement without obscuring the tube or adjacent bowel loops, and it is the preferred agent in reduction of intussusception.

## Specific Procedures, Indications, and Imaging Techniques

### Esophagram and Upper Gastrointestinal Examination

These two procedures are usually performed in conjunction and include evaluation of swallowing, the esophagus, stomach, and duodenum to the duodenojejunal junction.

The examination is begun with the child lying on his/her left side to maintain the ingested contrast agent within the fundus of the stomach. Images of the esophagus include from the nasopharynx to the esophagogastric junction, with special attention paid to nasopharyngeal aspiration, tracheal aspiration, masses, fistulas, and esophageal peristalsis and distensibility. The child is then placed supine, and the esophagus is examined in the anteroposterior projection. When the evaluation of the esophagus is completed, the barium in the fundus will be directed into the duodenum by laying the child in the prone right anterior oblique (RAO) position. Gastric emptying is assessed, along with distensibility of the antrum, the pylorus, duodenal bulb, and descending duodenum. Once the contrast has reached the junction of second and third portions of the duodenum, the infant is rapidly placed in the supine position for assessment of the duodenojejunal junction, visible through the air-filled antrum. This should lie to the left of the spine at approximately the same level as the duodenal bulb. Once this is accomplished, the child is again quickly turned, this time into a lateral projection, for documentation of the posterior course of ascending and descending limbs of the normally rotated retroperitoneal duodenum. Presence or absence of gastroesophageal reflux (GER) is assessed throughout the procedure, although the upper GI is not the optimal procedure to diagnose or exclude reflux. A final image documents gastric emptying (Fig. 84.1). Most of the findings in this examination are documented with fluorostore images, with exposures reserved for patients in whom abnormalities necessitating particularly high detail are evaluated.

Small bowel follow-through studies usually require ingestion of a larger amount of contrast agent, typically barium, although in premature infants a nonionic water-soluble contrast agent can be used. Radiographs are obtained at regular intervals based on the course of the contrast media through the bowel, with fluoroscopic evaluation when indicated. Images of the terminal ileum with and without compression are obtained if necessary once the contrast has reached the cecum. In ill infants in the neonatal intensive care unit who do not require visualization of the ligament of Treitz, a small bowel follow-through can be done with the contrast administered at the bedside, and portable radiographs obtained at the appropriate intervals.

### Contrast Enema

Although for many prior indications such as inflammatory bowel disease and colonic polyps, the contrast enema has been superseded by other procedures, such as endoscopy, computed tomography (CT), and magnetic resonance imaging (MRI) this examination remains extremely useful in many pediatric clinical settings. These include evaluation of distal bowel obstruction in the neonate, evaluation of surgical complications, sequela of disease such as necrotizing enterocolitis, and reduction of ileocolic intussusception.

The choice of contrast medium and the technique used for the contrast enema vary with the clinical indication and are discussed in the general fluoroscopy section above. Barium is the mainstay contrast medium used unless perforation is suspected, in which case near iso-osmolal water-soluble media is employed. In newborns suspected of distal bowel obstruction, near-iso-osmolal concentration water-soluble media is used with a change to hyperosmolal media if meconium ileus is encountered. Air is the contrast of choice for fluoroscopic intussusception reduction because of the rapidity of reduction, the decreased complications compared with liquid media in cases of perforation, and the lower radiation exposure.[19–22]

To perform an enema, a small tip catheter is placed in the rectum, and secured with tape to both buttocks, which are then taped together using manual pressure. Use of a balloon-tipped catheter is usually unnecessary, and some believe that it is inadvisable in young infants due to the potential for rectal injury. Fluorostore images can be recorded liberally to document the progression of the contrast medium and to document any findings dependent upon temporal change; spot filming is needed in areas requiring greater definition, such as mucosal detail, or if a subtle leak or perforation is suspected.

## ULTRASOUND

### Overview

Ultrasound (US) has become an extremely useful modality for evaluating patients with GI symptoms. It is particularly useful in children, because their small body size allows the use of higher frequency transducers leading to extraordinary resolution and detail in many clinical circumstances; harmonic imaging allows improved resolution with decreased artifacts. Beyond real-time gray-scale imaging, US includes spectral and color Doppler information on vascularity, ability to capture fleeting information via cine loops and to document motion such as peristalsis and diaphragmatic

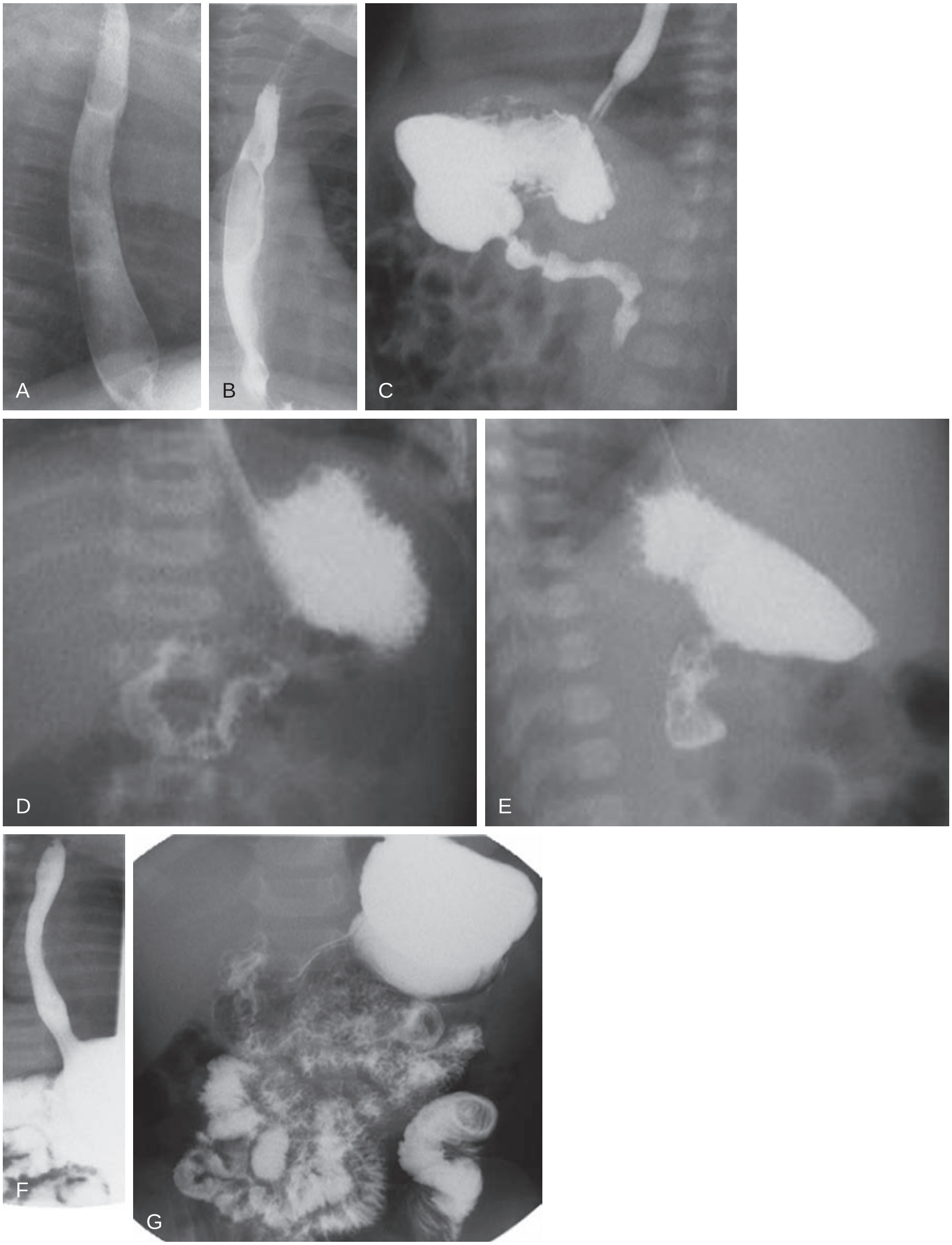

**Figure 84.1. (A–G) Typical UGI showing reflux in otherwise normal infant.** All are fluorostore images. (A and B) Lateral and anteroposterior views of esophagus during drinking show full distensibility without intrinsic or extrinsic mass lesions. (C) Oblique imaging (right anterior oblique) directs barium to gastric outlet and shows prompt emptying, normal pylorus, and first and second portions of the duodenum. (D) Anteroposterior image immediately following (C) shows progress of contrast to normally located gastroduodenal junction at the ligament of Treitz. (E) Subsequent lateral view of duodenum shows its posterior location anterior to the spine. (F) After further drinking and gastric filling, an episode of reflux to the cervical esophagus is documented. Note the wide-open gastroesophageal junction, a typical appearance during reflux. (G) Image recorded at the completion of the study shows good progress of contrast through the small bowel.

excursion. Extended field-of-view or panoramic imaging can outline large structures and masses on a single image, helpful in assessing pathology in context, or entirely. Newer technologies include ability to assess organ stiffness with elastography. US elastography has been found useful in pediatric patients as a marker for liver fibrosis[23] and in specific entities including biliary atresia,[24,25] liver transplantation,[26] and liver pathology developing after Fontan palliation of single ventricle anatomy,[27] with normal pediatric values available.[28] Elastography should be performed with the child NPO for at least 2 to 4 hours, without sedation, as both eating and anesthesia can transiently increase liver stiffness. More recently, the United States Food and Drug Administration (FDA) has approved intravenous US contrast media for pediatric liver imaging. Because of the very high temporal resolution of real-time US, use of intravenous contrast agents allows remarkable evaluation of perfusion dynamics not available with other modalities. The safety profile of the sonographic contrast agents compares favorably with that of CT and magnetic resonance (MR) contrast agents, and their utility has been documented in several areas, including characterization of liver masses and detection of complications of liver transplantation.[29–33]

## Indications

The utility and application of US in the pediatric patient is extensive and increasing (Box 84.1). Application of US to pediatric patients suspected of pyloric stenosis and appendicitis occurs daily in pediatric radiology practices (e-Fig. 84.2).[34–37] US is also useful in evaluation of mesenteric adenopathy (e-Fig. 84.3), assessment of the bowel (Fig. 84.4) and bowel wall,[38] small and large bowel intussusception (e-Fig. 84.5),[39] and coupled with Doppler allows accurate estimation of disease activity in Crohn disease.[40–43]

**BOX 84.1** Common Indications for Abdominal Ultrasound

- Bowel: pyloric stenosis, appendicitis, inflammatory bowel disease, intussusception
- Liver: masses, infection, biliary disease, congenital anomalies
- Spleen: heterotaxy, splenic masses, wandering spleen
- Pancreas: pancreatic ductal dilatation, pancreatic masses, pseudocysts
- Peritoneum: ascites, loculated collections
- Doppler: portal hypertension, portosystemic shunts, vascular congenital malformations, tumors
- Elastography: hepatic fibrosis
- Intravenous contrast: liver masses, vascular anomalies

The role of US in diagnosis of solid organ pathology is also extensive and can be the final diagnostic tool in many abnormalities. Indications include evaluation of hepatic, biliary, splenic, and pancreatic abnormalities. Liver masses are often first diagnosed and evaluated by US, allowing refinement of any subsequent CT or MRI protocol.

Although vascular structures are easily seen with contrast-enhanced CT, the direction and velocity of flow can be evaluated with Doppler sonography, often rendering the findings in these modalities complementary. Analysis of waveform pattern can identify hepatofugal flow in collateral vessels in patients with portal hypertension or vascular stenoses. In patients with heterotaxy, US is helpful in assessing splenic mass (located along the greater curvature of the stomach) and the associated vascular anomalies, such as interruption of the inferior vena cava, preduodenal portal vein, and infradiaphragmatic total anomalous pulmonary venous connection.[44,45]

## Practical Technical Points

The type and frequency of the transducer used is particularly important in pediatric imaging, as patient size can vary from 500 grams to 150 kilograms or larger. In general, the patient should be scanned with the highest frequency transducer that will penetrate the anatomy to be imaged; linear transducers are preferred if the access window will allow it. We typically image the bowel in neonates with a linear transducer operating at frequencies of 10 to 18 MHz. If overview and detail are both needed, more than one type of transducer may be necessary in many patients; for example, imaging of the abdomen in a 3-year-old child may be accomplished with a curved transducer operating at 6 MHz for overview, but additional images of detailed hepatic parenchyma or of the bowel can be performed with a linear transducer operating at higher frequency.

# COMPUTED TOMOGRAPHY

## Overview

CT is a particularly useful modality in pediatric abdominal imaging and has become a surrogate for many exploratory laparotomies

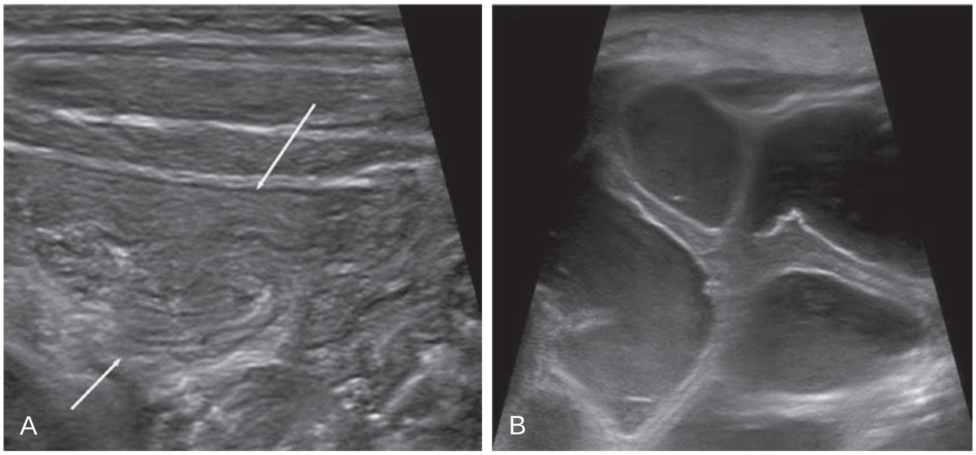

**Figure 84.4. Bowel ultrasound.** (A) Abdominal sonogram in 3-month-old demonstrates normal, collapsed loops of small bowel *(arrows)*. (B) Abdominal sonogram in 2-month-old ex-premature infant status-post bowel perforation and complex surgical history reveals dilated fluid-filled loops of bowel.

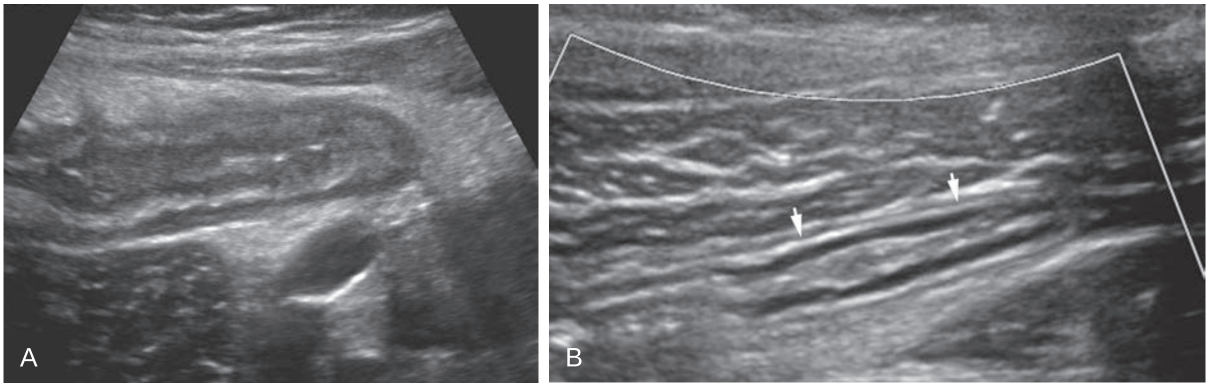

**e-Figure 84.2. Appendicitis and normal appendix.** (A) Longitudinal sonogram of acute appendicitis shows that the appendix measures 8 mm in diameter, is fluid-filled, and is surrounded by hyperechoic material consistent with periappendiceal edema. (B) Longitudinal sonogram of a normal appendix *(arrow)*.

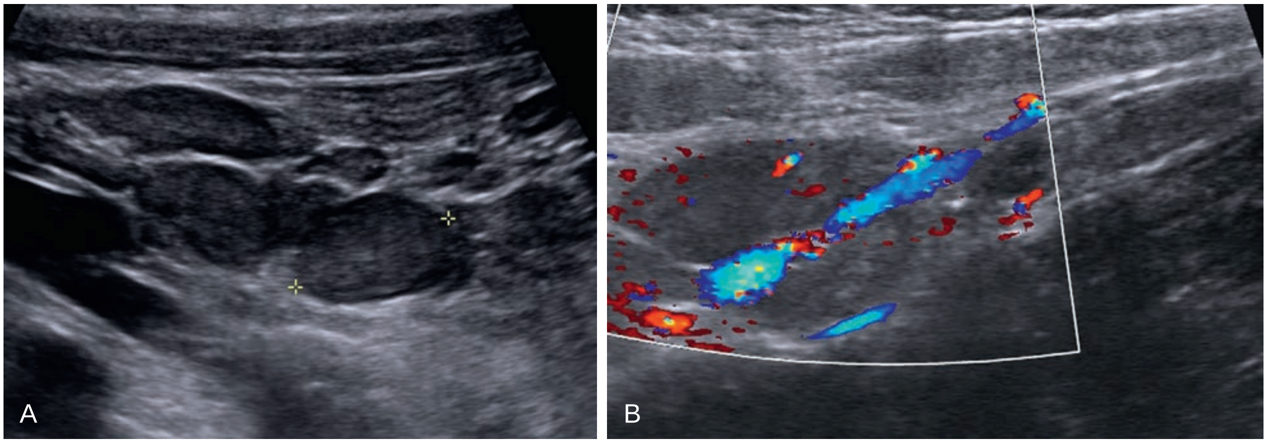

**e-Figure 84.3. Mesenteric adenopathy.** (A) Transverse sonogram through right lower quadrant with linear transducer demonstrates multiple enlarged mesenteric nodes in 8-month-old child with gastroenteritis. (B) Doppler interrogation reveals flow into the nodal hilum.

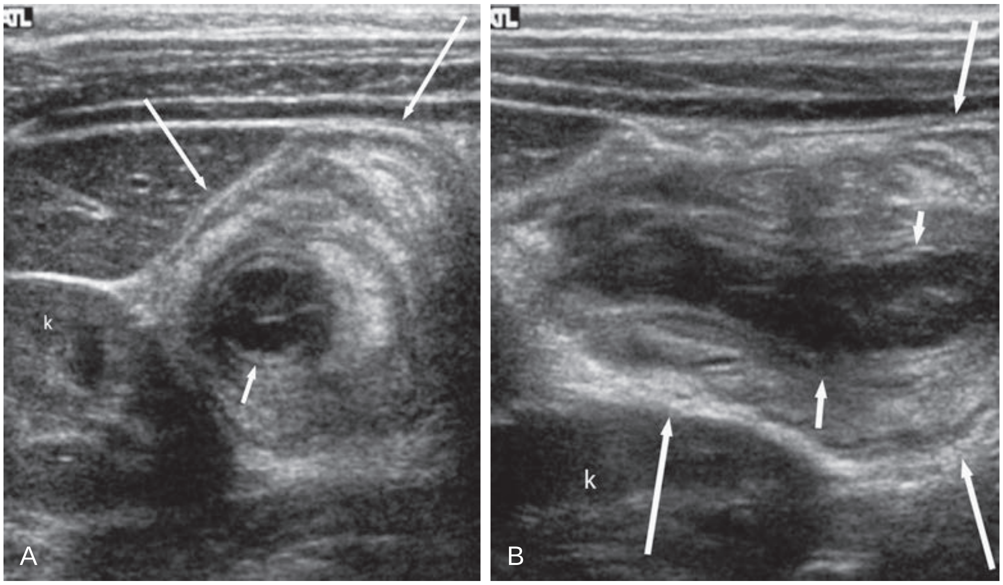

**e-Figure 84.5. Intussusception of the appendix.** Three-year-old girl with 3-day history of abdominal pain and bloody stools. (A) Transverse and (B) longitudinal image through right lower quadrant reveal the appendix *(short arrows)* within the intussusceptum complex *(long arrows)*. Air reduction was only partly successful; at surgery, reduction was completed and appendix removed, which showed gross lymphoid hyperplasia obliterating the lumen. *k*, Right kidney.

of the past. Current scanners with multidetector technology and volumetric acquisition permit very rapid examinations with isotropic reconstructions and new applications in areas such as angiography. Further developments in reconstruction techniques and temporal resolution have enabled subsecond examinations, with greatly reduced radiation dose and very limited need for sedation.[46–51]

These new capabilities are both an opportunity and a challenge,[52,53] with the need for newer protocols to accommodate more complex and sophisticated diagnostic demands. The timing and rate of contrast administration, with the ability to scan during a specific phase of intravascular contrast distribution, demand particular attention to technical details and new approaches to image interpretation. Dual energy examinations offer the ability to generate virtual precontrast images as well as iodine maps, and to perform tissue characterization.[54–57] The pediatric radiologist is further challenged by the need to balance image detail with radiation dose and implementation of the "as low as reasonably achievable" (ALARA) concept. The Image Gently Alliance sponsors the concept of justification and optimization, simply stated as the Right Study, for the Right Patient, at the Right Time, done the Right Way (www.imagegently.org).[58–61]

## Indications

Unlike US, CT images are sequential, standardized, and much less operator dependent. CT is particularly useful in patients with complex disease affecting multiple organ systems, such as malignancies, with reliable monitoring of change in extent of disease during therapy and follow-up (Box 84.2). CT is helpful as a problem-solving technique in patients with unusual multicompartment abnormalities (e-Fig. 84.6). Evaluation of solid organ pathology, such as hepatic portal hypertension, trauma, pancreatitis, and tumors, is rapidly accomplished with great anatomic detail and physiologic information. CT is also widely and successful applied to pathology of the hollow viscera and peritoneal cavity. The lack of operator dependence and high sensitivity and specificity of CT in the imaging diagnosis of appendicitis has led to its increasing use when this diagnosis is clinically equivocal, with documented reduction in negative appendectomy.[62] However, this success led to overuse in patients with abdominal pain; therefore physical examination, followed by US when the diagnosis is clinically uncertain, is recommended by most pediatric radiologists.[34,35] More recently, MRI has been shown to be an accurate substitute for CT scanning in many pediatric patients.[63–65] In the acute and chronic evaluation of inflammatory bowel disease, there is a role for US, contrast-enhanced US, CT, and particularly MR; MR is preferred for surveillance monitoring of disease activity and evaluation of perianal disease.[66,67]

## Protocols

Protocols for various pediatric abdominopelvic CT examinations vary and undergo change with the ongoing introduction of new applications and advances in equipment capability; generalizable protocols applicable to pediatric patients can be downloaded at www.imagegently.org. However, some underlying principles underscore most successful pediatric examinations. Administration of intravenous contrast is extremely important for diagnostic images, particularly in pediatric patients, in whom paucity of intraabdominal fat decreases intrinsic intraabdominal contrast.[56,68] CT angiography requires rapid contrast bolus injection, which in pediatrics can be challenging due to the caliber of possible intravenous access, but this limitation is countered by the smaller volume of contrast needed. Lowering kVp is important in patients in whom high contrast structures are of interest, such as those undergoing angiography or bone examinations. In neonates, the kVp can be decreased to as low as 80 or 70, with some adjustment of the mAs to produce acceptable image quality.[58] Precontrast images are rarely necessary, which decreases radiation dose. The use of oral contrast material is usually important when outlining intraperitoneal pathology, such as abscess or masses. In the evaluation of the bowel, its use is more controversial[69]; positive oral contrast material will mask mucosal enhancement, and water-density contrast may be more appropriate in such cases. We review images at 3 mm collimation in most patients and at 2 mm collimation in infants. Coronal and sagittal reformatted images are often diagnostically helpful.

CT is a life-saving, important modality in pediatric diagnosis. As with any imaging tool, it must be used judiciously, according to the principles of appropriateness, justification, and optimization.[70]

### BOX 84.2 Common Indications for Computed Tomography of the Gastrointestinal Tract

- Trauma
- Masses and malignancy
- Peritoneal disease: abscess, tumor, loculated collections
- Inflammatory conditions
- Liver disease: portal hypertension, liver transplantation
- Congenital anomalies: bowel rotation and fixation, duplication cysts, complications of Meckel/omphalomesenteric duct remnants

# MAGNETIC RESONANCE IMAGING

## Overview

MRI is increasingly used for pediatric GI applications. In this section, we review hepatic, biliary, pancreatic, and enteric MRI, including the most common indications and goals of MRI for these indications, followed by patient preparation concerns and a brief overview on preferred hardware. We also discuss the most commonly used sequences as well as combinations of these sequences to form protocols.

## Indications

### Hepatic Tumors

Hepatic tumors are well evaluated by MRI relative to CT in both adult and pediatric situations,[71] with the goal of imaging being tumor characterization, staging, and assessment of resectability. For characterization of these lesions, determination of T2 signal and enhancement characteristics is essential.[72] Tumor staging and determination of resectability requires delineation of anatomic boundaries, lymph node involvement, vascular invasion, and delineation of the biliary tree. In patients with hepatoblastoma, PRETEXT (PRETreatment tumor EXTension) staging dictates features that must be delineated, outlined by the International Childhood Liver Tumor Strategy Group (SIOPEL).[73,74] The same features are helpful in assessment of other malignant hepatic tumors.

### Biliary and Pancreatic Diseases

These are also well assessed by MRI.[75,76] Common indications include cholelithiasis, pancreatitis, sclerosing cholangitis,[77,78] ductal plate malformations, as well as choledochal cysts[79–81] and biliary complications of liver transplantation. Goals of imaging include (1) delineation of anatomy for strictures, stones, and anomalies; (2) assessment of inflammatory findings; and (3) assessment of obstruction. In the case of liver transplantation, assessment of vascular complications is often essential.

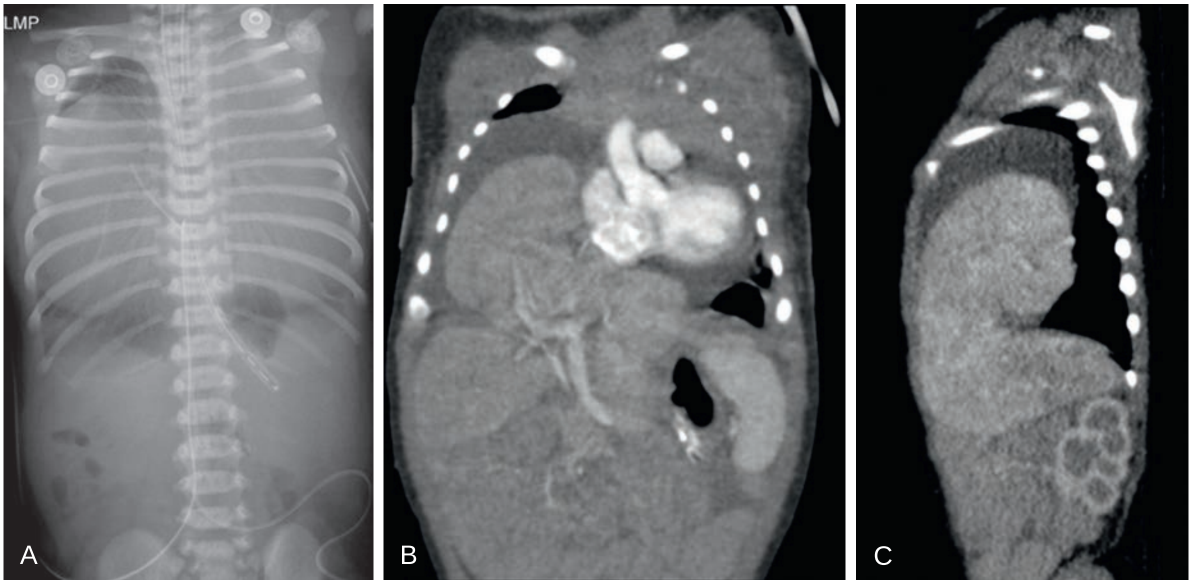

**e-Figure 84.6. Unusual presentation of Morgagni hernia.** (A) Abdominopelvic radiograph of newborn infant with prenatal diagnosis of hydrothorax. The radiographs suggest absence of most of the liver shadow from the right upper quadrant. The posterior costophrenic sulci are well outlined, indicating that chest density is not related to bilateral hydrothorax. (B) Coronal and (C) sagittal reformats of contrast-enhanced CT examination outline herniation of the liver into the pericardial sac with large pericardial effusion.

### Diffuse Liver Disease

These include conditions such as fibrosis, steatosis,[82–84] and iron deposition. Fibrosis can be assessed qualitatively[85] by T2-weighted imaging and delayed contrast enhancement.[86] More recently, MR elastography offers an accurate method to assess liver stiffness as a correlate to liver fibrosis. Other conditions that can lead to increased liver stiffness include acute liver inflammation and increased bloodflow in the postprandial state in patients with chronic liver disease; therefore the procedure should be performed with fasting.[87–91] Although steatosis can be assessed by spectroscopic methods,[92] more commonly steatosis, as well as iron deposition, are assessed by multiecho gradient echo imaging.[84,93–98]

### Enterography

MR enterography is most commonly performed for evaluation of inflammatory bowel disease.[99–101] The goals of MR include detection of bowel inflammation, distinction of active inflammation from chronic fibrosing disease, detection of fistulae and abscesses, characterization of disease, and response to therapy.[41,102–109]

### Fistulography

Fistulography, particularly for fistula in ano, is well performed by MRI.[104,110,111] The goals of the examination include detection of fistulae, classification (intersphincteric, transphincteric, suprasphincteric, or extrasphincteric), and abscess detection.

## Patient Preparation

### Sedation

Preparation begins with assessment of the needed sedation/anesthesia. Generally, children younger than 6 years of age who cannot perform a 20-second breath-hold will need sedation/anesthesia. This breath-holding requirement can be relaxed for MR cholangiopancreatography (MRCP), as will be detailed later, as well as in facilities with a distracting MRI-compatible goggle system. Sedation is avoided in patients undergoing enterography examinations due to the need for oral contrast. Finally, once the patient is on the MR table, a respiratory monitoring pillow or belt should be carefully placed. Often this is challenging and time-consuming in young children but is well worth the aggravation.

### Fasting Requirements

Patients should refrain from oral intake for 4 hours before the examination to minimize artifacts from bowel peristalsis as well as ensure full gallbladder distension in examinations of the biliary tree.

### Contrast

For all cases requiring vascular assessment, power injection of contrast is optimal, which requires adequate peripheral venous access. Oral contrast is essential for enterography examinations. A number of choices for oral contrast medium is acceptable, although most regimens consist of a biphasic agent (i.e., one that gives the bowel lumen a long T2 and T1 relaxation time). Agents include VoLumen (E-Z-Em, New York, NY), Breeza (Beekley Medical, Bristol, CT), mannitol solution, polyethylene glycol, locust bean gum solutions, and some fruit juices. The difference in efficacy of these choices is relatively small, though patient tolerance may vary.[112] The most important aspect of the regimen is rapid consumption of a large volume; 25 mL per kilogram of body weight over an hour is adequate. Placing the patient in right decubitus for the last 15 minutes before the start of imaging aids in emptying of the stomach.

### Antiperistaltic Agents

Spasmolytic agents that can be used during MR enterography include glucagon and hyoscine-N-butylbromide. Glucagon, the more commonly used intravenous agent, can be employed with either of two strategies: (1) half of the dose at the beginning of the examination and half just before intravenous contrast or (2) entire dose just before intravenous contrast. The dose varies between facilities from 0.5 mg to 1 mg. Although glucagon causes nausea and vomiting, it is well tolerated by the vast majority of patients if it is given as a slow intravenous push over 1 minute and if before administration the patient is instructed to expect a brief period of nausea.

## Hardware Requirements

Although the literature to date remains relatively sparse on pediatric abdominal imaging at 3 Tesla (T),[113–118] existing literature and experience suggest that most children will benefit from the higher signal provided by the higher field strength. In smaller patients, such as children younger than 8 years, the improvement in image quality is striking. Phased array surface coils are now standard, typically with 8 to 32 channels. For almost all children, cardiac arrays are optimal. For the largest patients, a torso array may be necessary. Situations in which 1.5 T often provides improved image quality over 3 T include very large patients, ascites, enterography examinations (fewer banding artifacts in steady-state imaging), and hepatic iron quantification in children with severe iron overload.

## Protocols

Suggested protocols are given in Table 84.2, with examples in Figs. 84.7 and 84.8 and e-Figs. 84.9 and 84.10, and details to follow. In general, matrix, field of view, and slice thickness should be adjusted to the patient size and are thus not emphasized in this chapter.

### Localizers

At 1.5 T, three-plane single-shot fast spin echo with low bandwidth (20 kHz), matrix, and repetition time (TR) are performed. If diagnostic single-shot images are required, the matrix (320 × 256), slice thickness (4–5 mm), and echo time (200 ms) can be adjusted appropriately and images acquired with respiratory triggering.[119] At 3 T, if diagnostic single-shot images are not required, localizers may be more efficiently achieved with balanced steady state imaging to conserve SAR (specific absorption rate), especially for small patients. All localizer sequences should employ parallel imaging.

### Conventional T2 Imaging

Conventional T2 imaging can be performed with fast spin echo in coronal and axial planes. In this instance, parallel imaging should not be employed, as the primary emphasis is on tissue characterization with high signal-noise ratio (SNR). Sequences should be respiratory-triggered or navigated, and performed at least in the axial plane.[120,121] Typical echo times are 80 to 90 msec at 1.5 T and 70 to 80 msec at 3 T. Fast recovery may be employed to improve SNR. As the literature is mixed on the ability of single-shot images with T2 weighting to provide an equivalent alternative to longer conventional T2 imaging,[122] our protocols almost always include conventional T2-weighted imaging.

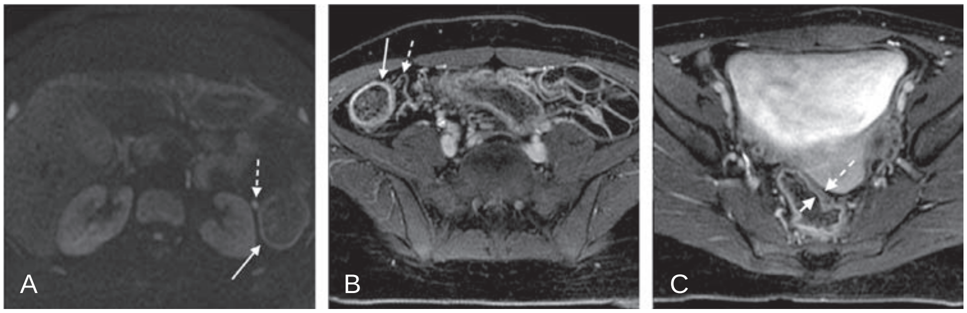

**e-Figure 84.9. MR enterography of a 16-year-old girl with ulcerative colitis.** (A) Diffusion-weighted image highlights the colonic wall *(arrow)* as well as a small pericolonic lymph node *(dashed arrow)*. (B) Contrast-enhanced SPGR image shows cecal mucosal enhancement *(arrow)* and prominent adjacent vessels *(dashed arrow)*. (C) Enhancement is pancolonic and mucosal as seen by the signal intensity difference between the luminal *(arrow)* and serosal *(dashed arrow)* side of the bowel.

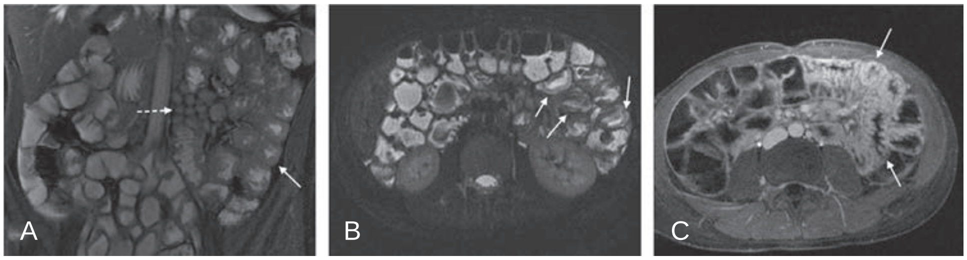

**e-Figure 84.10. MR enterography of a 14-year-old boy with Crohn disease and jejunitis.** (A) Coronal balanced steady state imaging shows jejunal wall thickening *(arrow)* and prominent mesenteric lymph nodes *(dashed arrow)*. (B) Axial single-shot T2-weighted image shows submucosal edema *(arrows)*. (C) Axial contrast-enhanced spoiled gradient echo with fat suppression immediately after intravenous glucagon administration shows hyperemic bowel and again demonstrates thickened folds *(arrows)*.

**TABLE 84.2** Common Pulse Sequences for Hepatobiliary and Bowel Magnetic Resonance Imaging

| | | Indication | | | | | |
|---|---|---|---|---|---|---|---|
| **Pulse Sequence** | **Scan Time** | **Tumors** | **MRCP** | **Transplant** | **Liver Iron/Fat** | **Enterography** | **Fistulography** |
| Localizer (1.5 T: SSFSE, HASTE, SSH-TSE; 3 T: FIESTA, TrueFISP, Balanced FFE) | 20 sec-3 min | x | x | x | x | x | x |
| Two dimensional T2 (FSE, TSE, TSE) | 3-4 min | x | x | x | Optional | | Two planes |
| Volumetric T2 (CUBE, SPACE, VISTA) | 4-5 min | Optional | x | x | | | x |
| Single-shot (SSFSE, HASTE, SSH-TSE) | 2-3 min | | x | x | | x | |
| Balanced steady state (FIESTA, True-FISP, balanced FFE) | | | | | | x | |
| Diffusion | 1-3 min | x | | Optional | | Optional | Optional |
| Dual echo (LAVA-Flex, VIBE-Dixon) | 30 sec | x | | x | x | | |
| Multi-echo gradient echo | 30 sec | | | | x | | |
| Noncontrast MRA | 4-5 min | | | x | | | |
| SPGR (LAVA, VIBE, THRIVE) | 30 sec | Full echo | Optional with gadoxetate | Partial echo | | x | x |

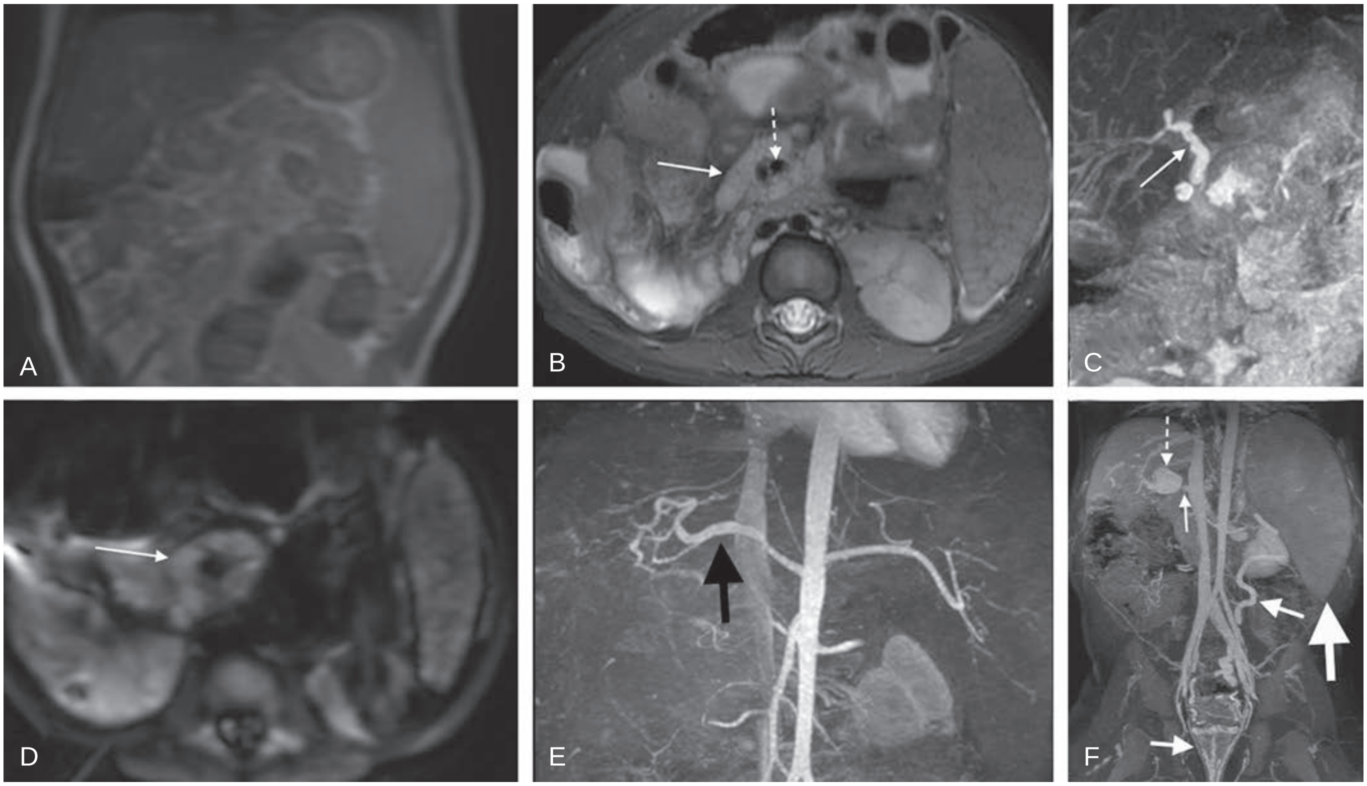

**Figure 84.7. MRI of a 1-year-old girl with a left lobe lateral segment liver transplant.** (A) Localizer is performed quickly. (B) Axial fat-suppressed T2-weighted image shows lymph nodes *(arrow)* surrounding mesenteric vessels *(dashed arrow)*, suggesting posttransplant lymphoproliferative disorder. (C) Maximum intensity projection of volumetric T2-weighted images showing patent bile ducts *(arrow)*. (D) Axial diffusion imaging again showing lymph nodes *(arrow)*. (E) Contrast-enhanced angiogram (SPGR with fat-suppression) showing patent hepatic artery *(black arrow)*. (F) Venous phase imaging shows proximal portal vein *(small arrow)*, poststenotic dilation of intrahepatic portal vein *(dashed arrow)*, hemorrhoidal varices *(medium arrow)*, and splenomegaly *(large arrow)*.

## Volumetric T2 Imaging

Volumetric T2-weighted sequences have been mostly described for musculoskeletal and neuroimaging.[123–125] These pulse sequences are similar to fast spin echo in that a 90-degree excitation is required, although it excites a slab rather than a slice. This excitation is followed by a train of refocusing pulses, and the flip angle is varied to maintain signal uniformity despite a long train (typically 60–100 echoes). This variation of the flip angle is set by the various vendors and does not require the user to prescribe it. These sequences

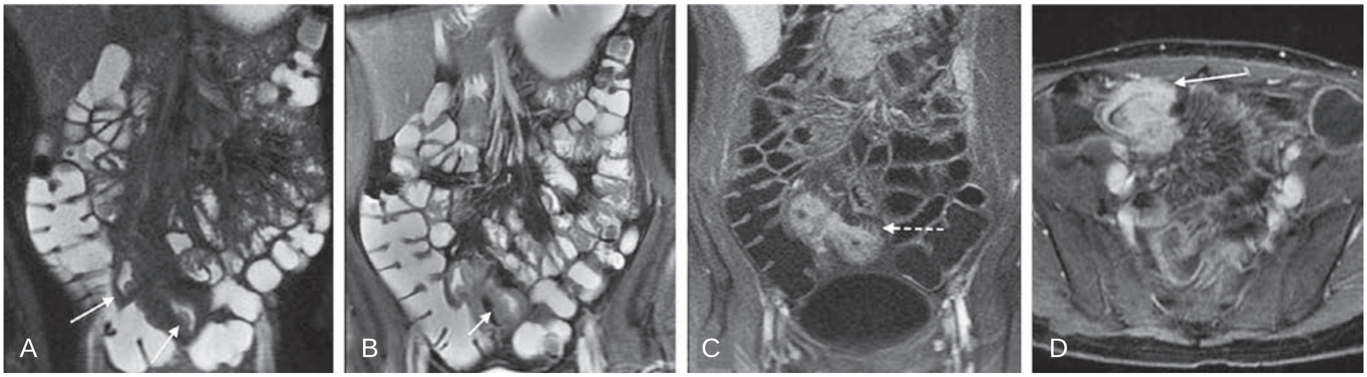

**Figure 84.8. MR enterography of a 20-year-old woman with typical manifestations of Crohn disease.** (A) Single-shot T2-weighted imaging shows thickened terminal ileum with submucosal edema *(arrows)*. (B) Balanced steady-state imaging shows wall thickening *(arrow)*. (C) Hyperemia and early transmural enhancement is seen after contrast administration *(dashed arrow)*. (D) Delayed imaging shows persistent enhancement of the terminal ileum *(arrow)*.

permit thin slices (1–2 mm) and reformatting in arbitrary planes. Parallel imaging is essential to maintain a reasonable scan time of 4 to 5 minutes. Navigation or respiratory triggering should be used along with a high bandwidth (e.g., 62 kHz). For dedicated MRCP examinations, a high TE (>500 msec) can be used to permit excellent maximum intensity reformation of the biliary tree and pancreatic duct. For other examinations, a TE of 70 to 90 msec can be used, which permits delineation of all anatomy, including a good assessment of the bile ducts on individual slices.

## Single-Shot Imaging

Although volumetric imaging usually displays the bile ducts well,[126] image quality will likely be suboptimal in patients with irregular breathing, peristalsis, and voluntary motion. Thus single-shot imaging is complementary[127] for biliary imaging and essential for bowel imaging.[116,128] In patients with irregular breathing, the user can hand-trigger acquisition of each slice by observing the respiratory belt tracing, enabling reasonable assessment of bile ducts in even the most challenging patients.

## T1-weighted Imaging

Dual echo imaging (SPGR with both in-phase and opposed-phase echoes) offers volumetric images at high spatial resolution along with fat-water separation. These sequences can be performed in a breath-hold, and data can be processed to yield four image sets from one acquisition: water, in-phase, opposed-phase, and fat. Typical parameters are high bandwidth (100 kHz), 4-mm slice thickness, and 12- to 15-degree flip angle.

## Contrast Agents

For assessment of contrast enhancement, several gadolinium-based agents are available. In the setting of renal insufficiency, macrocyclic agents have an enhanced safety profile.[129] If the primary clinical concern is evaluation of the vascular structures, gadobenate dimeglumine (MultiHance) is a reasonable option given its higher relaxivity and longer intravascular residence time. Gadofosveset trisodium (Ablavar) has been approved by the FDA for assessment of aortoiliac disease in adults and became an option in vascular evaluation; however, as of this writing, it is no longer available. More recently, ferumoxytol has become available for prolonged intravascular enhancement.[130–132] Finally, gadoxetate disodium (Eovist) is a good option in hepatic and biliary imaging.[133–141] This agent is taken up by hepatocytes and has 50% hepatobiliary excretion in the setting of normal hepatic and renal function and thus provides a functional as well as anatomic MRCP examination.[142] However, the user should note that gadoxetate dose is 0.025 mmol/kg (i.e., only a quarter of the gadolinium of other agents). As the T1 relaxivity of this agent is higher than that of conventional agents, adequate first-pass imaging of the liver can still be performed. For all agents, rate of single-dose administration at 1 mL/sec, followed by a saline flush is acceptable.

## Dynamic Gadolinium-Enhanced Imaging

In dynamic studies, a three-dimensional (3D) SPGR sequence with intermittent fat suppression can be used (minimum TR, 15-degree flip angle, 62 kHz bandwidth). Generally, if a patient can perform a breath-hold, the matrix and number of slices are adjusted to make the scan time match the patient's ability. If the patient cannot breath-hold sufficiently, quiet breathing can be used, along with motion-tolerant techniques, such as navigation,[143] radial,[144] or other noncartesian k-space trajectories.[145] Additionally, these techniques can be combined with parallel imaging,[146,147] view sharing,[148,149] and compressed sensing.[150,151]

There are two significant differences in technique of dynamic gadolinium studies, depending on the goal of the examination. If tumor characterization or detection of bowel wall enhancement is the primary goal, a scan delay should be set to ensure that the center of k-space is acquired at 30 seconds after half the contrast is administered: The scan delay to achieve this is calculated as follows: Scan delay = 30 seconds – (scan duration + bolus duration)/2. For example, with a 30-second scan and a 10-mL bolus infused at 1 mL/sec, the scan delay is 30 – (30+10)/2 = 10 sec. If vascular assessment is a primary goal, a timing run can be performed with fluoroscopic triggering and centric k-space acquisition, or sequential k-space acquisition and calculation of the scan delay substituting the time to abdominal aortic peak enhancement for 30 seconds in the previous equation.

The second difference in technique is the choice of echo time. For tumor characterization, the minimum full echo time should be chosen to maximize SNR. However, for vascular or bowel enhancement, the minimum echo time (i.e., a fractional echo) should be used to minimize spin dephasing artifacts from flowing blood, or field inhomogeneity near the bowel wall from enteric gas, as well as to minimize scan time.

## Noncontrast MRA and Alternatives to Gadolinium

Although contrast-enhanced MR angiography (MRA) has become the dominant MR method of vascular assessment, the administration of gadolinium contrast may be contraindicated in some patients with renal insufficiency. Additionally, the technique has little room for error as intravenous contrast can only be given once; an injection-scan timing mismatch or patient motion during the scan cannot be rectified. Thus noncontrast-enhanced techniques improve the reliability of MRI as a modality for assessment of abdominal vasculature.

Although time-of-flight-based approaches have been used, these sequences produce limited image quality in the abdomen. Noncontrast-enhanced techniques based on balanced-steady state approaches are useful, such as in the context of adult renal artery stenosis.[152] A variation of this method is based on a respiratory-triggered inversion pulse covering the imaged volume as well as a region inferior to it.[153] This is followed by a balanced steady-state echo train, similar to that used for noncontrast-enhanced coronary artery imaging but without cardiac gating. Thus blood flowing from superior to the inverted region is bright, producing an MR angiogram. These sequences have pitfalls similar to time-of-flight-based techniques, including flow-related dephasing, slow-flow related signal dropout, and intrinsically high T1 signal, but on the whole provide a nice complement to contrast-enhanced MR angiography.

Another option for vascular studies is the use of iron oxide–based contrast agents.[154,155] These agents have high relaxivity and prolonged residence time in the blood pool, which is particularly advantageous for pediatric applications.[156,157] However, these agents may have a higher rate of severe adverse reactions compared with gadolinium and thus should be administered with caution.[158–160]

### Iron/Fat Quantification

Although MRI methods of hepatic iron quantification based on T2 signal and a composite of signals (proton density, T2, T2*, and T1: see[161]) have been used, the most common approach is based solely on T2* measurement. T2* value depends on field strength, and measurement can be done on any scanner with a multiecho gradient-echo sequence. These examinations are generally done on 1.5 T scanners, but the calibration of iron concentration based on T2* has been reported at both 1.5 T[93] and 3 T.[162,163]

T2* may be calculated by running a gradient echo sequence multiple times at different TE values but with a fixed TR of approximately 150 msec. Typical normal values should range from approximately 1 to 20 msec, and the user should avoid prescanning between sequences (or the transmit and receiver gains may change). A region of interest can then be drawn in the same area of the liver on each of the resulting series of images. Thus mean signal at each echo time is known and will demonstrate an exponential decay relationship (Signal = $Ae^{-R_2^*TE} + B$, where $R_2^* = 1/T_2^*$). $R_2^*$ and hence $T_2^*$ can be determined by various software packages using logarithms and linear regression.

The previously described process for determining $T_2^*$ is time-consuming for data acquisition as a breath-hold for each echo time is required. Additionally, regression must be performed and is disruptive to workflow. An alternative is multiecho gradient echo sequences, in which a series of gradient echoes is obtained at various echo times after each excitation. The multiecho approach can be performed with two-dimensional (2D) acquisition of a single slice of the liver or a 3D volume acquisition. Whether 2D or 3D, the acquisition is a single breath-hold, which has the advantage of avoiding slice misregistration, is easier on the patient, and facilitates patient throughput. When coupled with an image reconstruction algorithm that performs a fit to determine $R_2^*$, image maps are obtained and workflow is improved. These pulse sequences and reconstruction programs are now widely available on all major MRI vendor platforms.

One of the challenges of pediatric hepatic iron determination is the wide range of $T_2^*$ values that are acquired in practice. Obtaining accurate $T_2^*$ over such a wide range can be challenging. A long series of echoes with long echo times in a patient with a short $T_2^*$ will have mean signal over region of interest dominated by noise, giving an overestimation of $T_2^*$. Conversely, a series of echoes with short echo times to address this situation will yield minimal signal decay in a patient with a long $T_2^*$, again resulting in poor estimation of $T_2^*$. Thus the longest echo time used to determine $T_2^*$ should be based in part on the $T_2^*$. One approach is to acquire two datasets (one with long echo times and one with short), and use the appropriate one.

For assessment of steatosis, qualitative evaluation may be performed by dual echo imaging (in phase/opposed phase gradient echo). For quantitative assessment, low flip angle multiecho imaging may be used to generate a proton density fat fraction map, or alternatively spectroscopy can be performed.[164–166] In general, the gradient echo methods are faster and easier, although considerable care has to be taken for quantitative accuracy to be maintained.

# NUCLEAR MEDICINE

## Overview

Nuclear scintigraphy plays an important role in the evaluation of hepatobiliary dysfunction and disorders of the GI tract in infants, children, and adolescents. The unique diagnostic information provided is often complementary to that obtained with other modalities. Radionuclide imaging of the GI system will be divided into two major categories: imaging of the hepatobiliary system and spleen (Table 84.3) and imaging of the GI tract (Table 84.4).

Hepatobiliary scintigraphy provides an anatomic and dynamic physiologic evaluation of biliary function. Splenic scintigraphy is useful in the evaluation of splenic sequestration, accessory spleens, posttraumatic splenosis, postsurgical residual splenic tissue, and wandering spleen with torsion. GI scintigraphy allows the dynamic assessment of swallowing, gastric emptying, GER,

**TABLE 84.3** Radionuclide Imaging of the Liver, Biliary System, and Spleen

| Study | Radiopharmaceutical | Indication |
|---|---|---|
| Hepatobiliary scan | $^{99m}$Tc–IDA | Hepatitis<br>Biliary atresia<br>Choledochal cyst<br>Acute cholecystitis<br>Bile plug syndrome<br>Caroli disease<br>Trauma—bile leak<br>Liver transplantation<br>Assess vascularity<br>Assess parenchymal function<br>Evaluate bile drainage<br>Evaluate possible bile leak<br>Evaluate possible obstruction |
| Liver-spleen scan | $^{99m}$Tc sulfur colloid | Hepatitis<br>Hepatic mass (e.g., FNH)<br>Diffuse hepatic disease<br>Abnormal LFTs<br>Hepatitis<br>Congenital abnormalities<br>Diaphragmatic hernia<br>Splenogonadal fusion<br>Wandering spleen<br>Ectopic/accessory spleen<br>Functional asplenia |
| Hemangioma scan | $^{99m}$Tc-labeled RBCs | Liver hemangioma |
| Splenic sequestration scan | $^{99m}$Tc-labeled, heat-damaged RBCs | Hypersplenism |

*99mTC,* Technetium-99m; *FNH,* focal nodular hyperplasia; *IDA,* iminodiacetic acid; *LFTs,* liver function tests; *RBCs,* red blood cells.

**TABLE 84.4** Radionuclide Imaging of the Gastrointestinal Tract

| Study | Radiopharmaceutical | Indication |
|---|---|---|
| Milk Scan | $^{99m}$Tc Sulfur colloid | Gastroesophageal regurgitation<br>Gastroesophageal reflux<br>Pulmonary aspiration |
| Solid emptying study | $^{99m}$Tc Sulfur colloid (radiolabeled eggs) | Early satiety<br>Nausea<br>Pre-op Nissen/ G-tube |
| Salivagram | $^{99m}$Tc Sulfur colloid | Pulmonary aspiration |
| Meckel Scan | $^{99m}$ Tc Sulfur colloid | GI bleeding |
| GI Bleeding Scan | $^{99m}$Tc pertechnetate (labeled RBCs) | GI bleeding |
| Infection | $^{99m}$TcHMPAO (labeled WBCs)<br>$^{18}$F-FDG | Inflammatory bowel disease<br>Abscess |

*99mTC,* Technetium-99m; *F-FDG,* fluorodeoxyglucose; *G-tube,* gastrostomy tube; *HMPAO,* hexamethylpropyleneamine oxime; *RBCs,* red blood cells; *WBCs,* white blood cells.

esophageal transit, colonic transit, and tracheobronchial aspiration. Red blood cell labeling allows the anatomic localization of intestinal bleeding, and white blood cell (WBC) labeling can be used for the localization of sites of abdominal infection and inflammation. Finally, gastric mucosa scintigraphy is used for evaluation of suspected Meckel diverticulum. Tumor imaging will not be addressed in this chapter.

## Patient Preparation and Technical Aspects

Sedation usually is not required for GI radionuclide examinations. However, correct anatomic positioning beneath the camera is essential, and some type of restraint is usually required, even with cooperative children. Distraction techniques using videos or listening to music can be helpful in lengthy examinations, but rarely sedation may be necessary.

Many of the studies discussed in this section require a period of fasting before imaging. Prolonged fasting greater than 24 hours is not recommended. Medications can be used to enhance imaging in specific conditions. Standard imaging parameters vary, but imaging usually is performed with the child in the supine position with either a single-head or dual-head gamma camera, preferably using a low-energy high-resolution collimator. The photopeak and window settings should be predetermined for technetium-99m ($^{99m}$Tc) (140 keV, 20%). Imaging typically is performed using a dynamic acquisition framed at intervals for optimal viewing and interpretation depending on the study and institutional preference. Suggested protocols will be described. In our practice, we require that no barium studies be performed 24 to 48 hours before radionuclide imaging of the abdomen and pelvis.

## Radiopharmaceuticals

The radionuclide used for most of the indications discussed in this chapter is $^{99m}$Tc, which is administered either intravenously or orally, usually combined with a nonradioactive compound (pharmaceutical agent). The clinical information sought by the clinician dictates the specific radiopharmaceutical agent used, which is taken up by the target tissue and allows imaging. Ionizing radiation from the internalized radiopharmaceutical agent emanates in the form of gamma rays that deposit energy into the imaging detector.

The dose of a radiopharmaceutical agent used in a child should be determined by the minimal dose required to yield a high-quality diagnostic examination. Appropriate dose recommendations can be found in the recent publication *2016 Update of the North American Consensus Guidelines for Pediatric Administered Radiopharmaceutical Activities*.[167]

## Indications and Specific Examinations

### Hepatobiliary Scintigraphy

Hepatobiliary scintigraphy is a useful adjunct to sonography in the evaluation of infants with jaundice and cholestasis, as well as in children with hyperbilirubinemia and/or chronic abdominal pain. Its value in jaundiced neonates is the timely differentiation of neonatal hepatitis and biliary atresia, because surgical intervention with the Kasai procedure in patients with biliary atresia is most successful when performed in patients less than 3 months of age. Post-Kasai procedure, a hepatobiliary scan, can be used to confirm patency of the bilioenteric anastomosis. Imaging with sonography, CT, or MRI is frequently diagnostic for choledochal cysts. Hepatobiliary scintigraphy adds value in the diagnosis of the rare association of choledochal cyst with biliary atresia.[168] Similarly, the evaluation of Caroli disease is often facilitated with hepatobiliary imaging. Cystic duct patency can be assessed in children with suspected acute cholecystitis. Hepatobiliary scintigraphy remains the test of choice for detection of postoperative or posttraumatic biliary leaks, or for the identification of spontaneous neonatal bile duct perforation.[169] Other clinical indications are listed in Table 84.3.

Currently, $^{99m}$Tc mebrofenin is widely used for hepatobiliary imaging due to its high hepatic extraction. It is transported into the hepatocytes, then excreted into the bile ducts; $^{99m}$Tc Disofenin is also used. The radiopharmaceutical agent is administered intravenously, and an anterior dynamic acquisition is acquired at 5 minutes/frame during the first 60 minutes in the supine position. Static images are usually obtained at 60 minutes in the anterior, RAO, and right lateral views. Delayed images may be obtained at 2 to 4 hours and up to 24 hours, as necessary, to visualize the gallbladder and biliary tree and excretion into the duodenum. A normal scan demonstrates radiopharmaceutical uptake in the liver by 5 minutes, the biliary tree by 15 minutes, and the small bowel by 15 to 45 minutes. In patients with neonatal hepatitis, delayed and diminished uptake by the liver occurs, but the radiopharmaceutical agent eventually reaches the small bowel. In patients with biliary atresia, radiopharmaceutical uptake by the liver is usually adequate, but the radiotracer never reaches the small bowel, even on the 24-hour images (Fig. 84.11). When the differentiation between biliary atresia and neonatal hepatitis is required, premedication with phenobarbital (5 mg/kg per day for 3–5 days) can be considered due to improved hepatic extraction of radiotracer.[170] An alternative is ursodeoxycholic acid 20 mg/kg given every 12 hours over 2 to 3 days.[171] In addition, infants should fast for 2 to 4 hours. Diminished extraction of radiotracer can be seen in the setting of chronic cholestasis from long-term total parenteral nutrition administration, bile plug syndrome, Alagille syndrome, other forms of hepatocellular dysfunction, and delayed diagnosis of biliary atresia.

Acute cholecystitis is characterized by prompt hepatic extraction and excretion into the biliary system and bowel but lack of gallbladder visualization. Fasting of 4 to 6 hours is required, and the same imaging protocol is utilized with dynamic imaging acquired at 5 minutes/frame for 1 hour. When the gallbladder is visualized, an RAO and/or right lateral view is acquired. If the gallbladder is not visualized at 60 minutes delayed images at 4 hours may be necessary. Alternatively, if the gallbladder is not visualized at 45 to 60 minutes, in lieu of further delayed imaging, intravenous morphine sulfate (0.04 mg/kg) may be administered, followed by dynamic 1 minute imaging for 30 minutes. Morphine should not be given if the small intestine is not visualized or in setting of acute pancreatitis. If gallbladder dyskinesia is of concern, cholecystokinin (Sincalide or Kinevac) is administered (0.02 mcg/kg) as a slow infusion over 30 minutes after the gallbladder is visualized. A normal gallbladder ejection fraction is greater than 35%[172] (e-Fig.

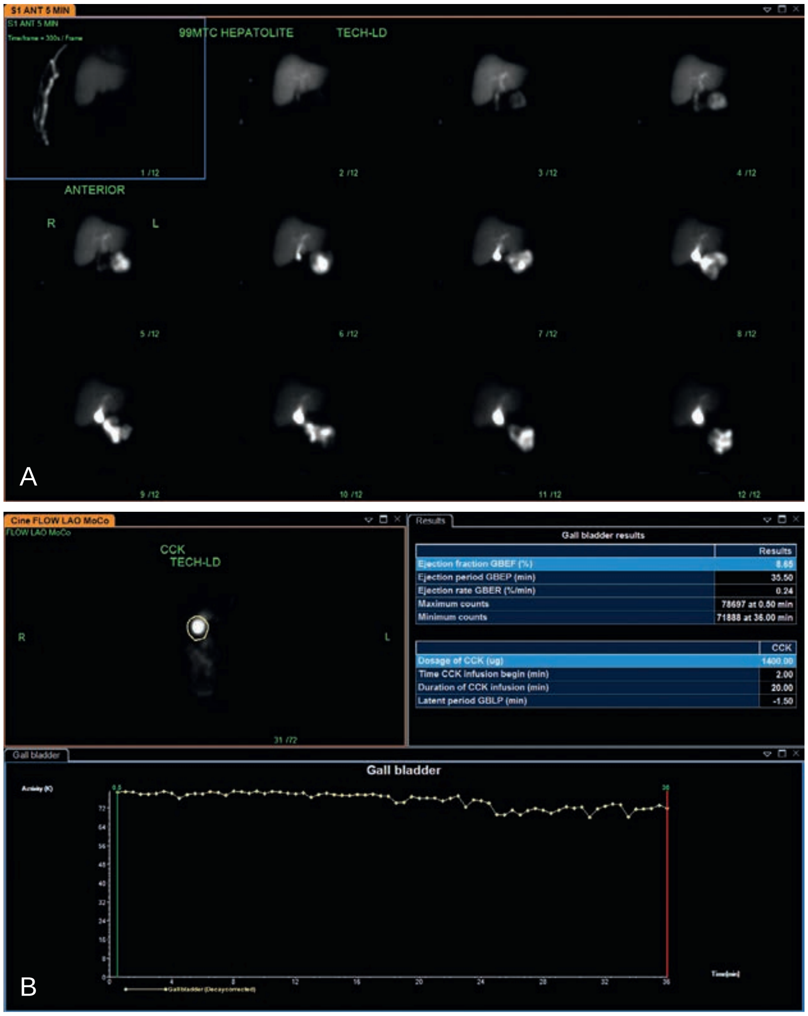

Gall bladder results

| | Results |
|---|---|
| Ejection fraction GBEF (%) | 8.65 |
| Ejection period GBEP (min) | 35.50 |
| Ejection rate GBER (%/min) | 0.24 |
| Maximum counts | 78697 at 0.50 min |
| Minimum counts | 71888 at 36.00 min |

| | CCK |
|---|---|
| Dosage of CCK (ug) | 1400.00 |
| Time CCK infusion begin (min) | 2.00 |
| Duration of CCK infusion (min) | 20.00 |
| Latent period GBLP (min) | -1.50 |

**e-Figure 84.12. Hepatobiliary scan with delayed gall bladder emptying.** Hepatobiliary study in a 15-year-old with right upper abdominal pain. (A) Anterior static images of the abdomen were obtained every 5 minutes for 60 minutes after the administration of $^{99m}$Tc disofenin. There is homogeneous radiotracer accumulation throughout the liver, with prompt visualization of the intrahepatic ducts and common bile duct by 10 minutes, small bowel by 15 minutes, and gallbladder by 30 minutes. These findings are normal. (B) Next, a Sincalide infusion was given over 30 minutes. Dynamic imaging revealed a decreased gallbladder ejection fraction of 8.65%.

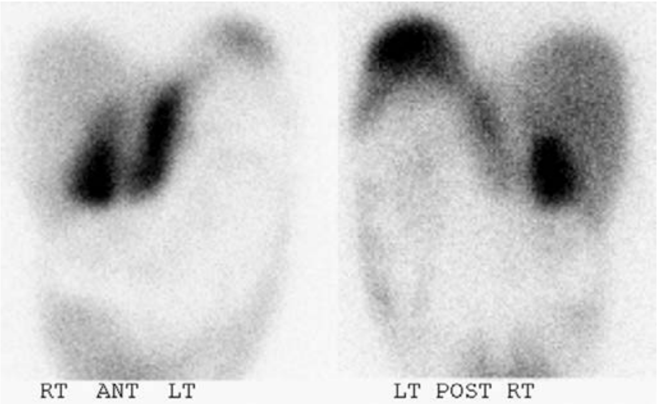

**e-Figure 84.13. Hepatobiliary scan with bile leak.** A 12-year-old girl with persistent abdominal pain and jaundice after laparoscopic choledochal cyst resection and cholecystectomy. Images obtained in the anterior and posterior projection at 30 minutes show pooling of radiotracer in the midabdomen and the left subdiaphragmatic recess. Faint radiotracer activity is also seen in both paracolic gutters and in the upper pelvis consistent with radiotracer in the peritoneal cavity.

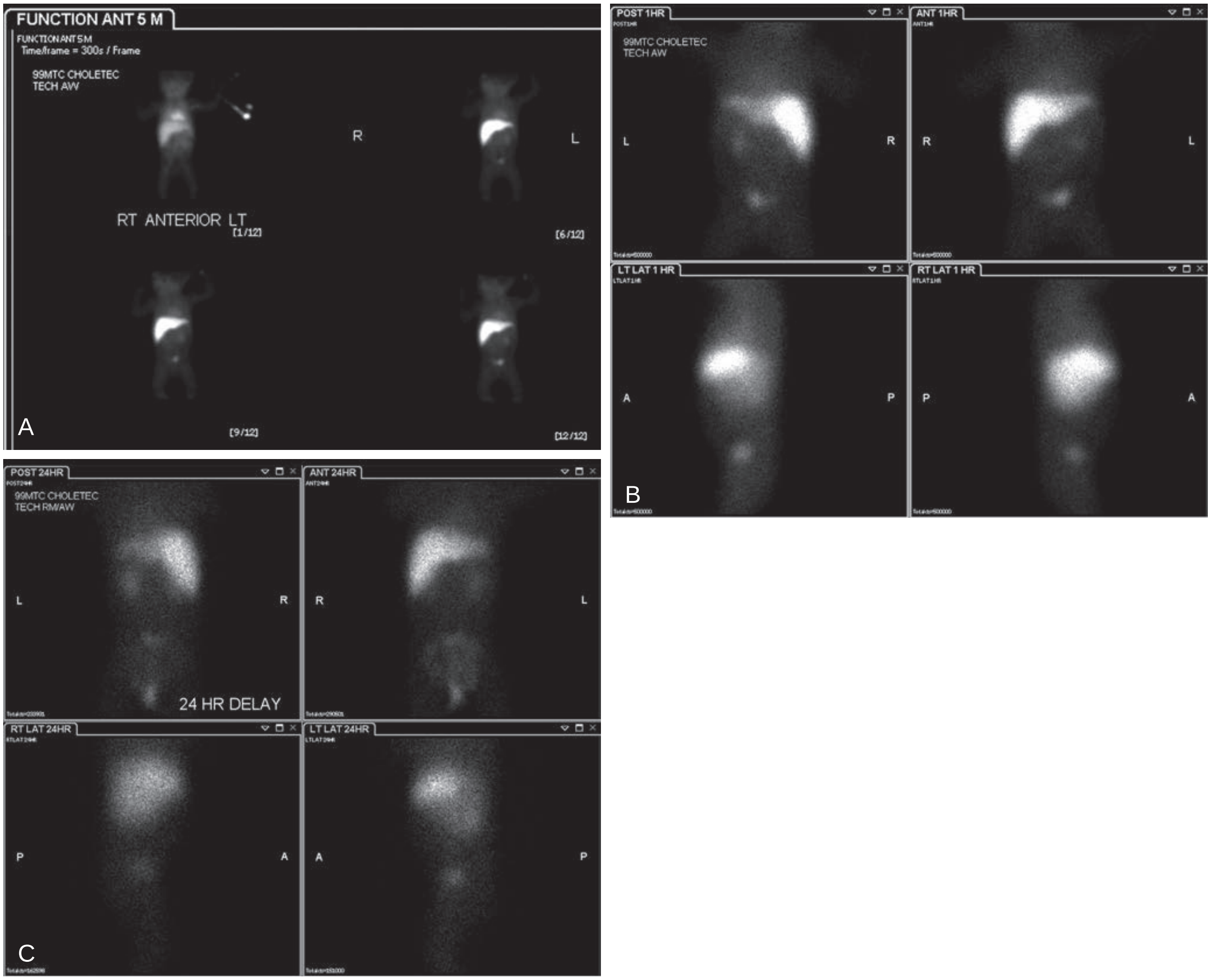

**Figure 84.11. Hepatobiliary scan in biliary atresia.** Eight-week-old infant presents with persistent jaundice and conjugated hyperbilirubinemia. $^{99m}$Tc mebrofenin biliary scintigraphy demonstrates good hepatic extraction of the radiotracer, nonvisualization of the biliary system, and no evidence of radiotracer passage into the bowel. (A) 0- to 60-minute, (B) 4-hour, and (C) 24-hour anterior projection images are shown. All images reveal normal, faint radiopharmaceutical accumulation in the urinary bladder.

84.12). Duodenal gastric reflux should be documented, as bile reflux gastritis may be the cause of symptoms. In patients in whom there is concern for bile leak, the cholecystitis protocol is utilized and fasting is not necessary. Delayed static images with patient in different positions may be helpful for detection or confirmation of a bile leak. A positive study demonstrates quite dramatic radiopharmaceutical accumulation around the liver, in the right paracolic gutter, and sometimes the pelvis (e-Fig. 84.13).

## Liver-Spleen Scintigraphy

The traditional liver spleen scan is seldom used today due to the advances in sonography, CT, and MRI, which provide far greater spatial and contrast resolution and provide more precise anatomic details. However, several important indications for the liver-spleen scan still exist, such as the location of accessory or ectopic spleens. The physiologic basis of the liver-spleen scan is the phagocytosis of radioactive colloid particles by the reticuloendothelial cells of the liver, spleen, and bone marrow. Normal images reveal homogeneous distribution of the radiopharmaceutical in the liver and spleen, which can be evaluated for size, position, configuration, and any focal areas of radiotracer deficit.

No patient preparation is necessary for the liver-spleen scan. The child receives an intravenous injection of $^{99m}$Tc sulfur colloid, and static images are obtained from multiple projections approximately 15 minutes after injection, with the child lying supine. Dynamic images may also be acquired, depending on the clinical indication. Single-photon emission computed tomography (SPECT) imaging can be performed to aid in the detection of small foci of splenic tissue.

In children with hepatitis, the liver-spleen scan may be normal. In the setting of severe hepatic disease, there is a redistribution of the colloidal radiotracer, with diminished uptake by the liver, greater than normal uptake by the spleen, and colloid shift with visualization of the bone marrow.

## Splenic Scintigraphy

Spleen scintigraphy can also be used to identify accessory spleens, posttraumatic “splenosis,” and to evaluate splenic uptake in a wandering spleen, as well as in splenic sequestration where there is acceleration of the sequestration and phagocytosis of abnormal erythrocytes, neutrophils, and platelets. Splenic function and functional asplenia is better documented with $^{99m}$Tc–labeled, heat-damaged red blood cell imaging. No patient preparation is necessary. Red blood cells are withdrawn from the patient, labeled with $^{99m}$Tc pertechnetate, and then denatured (in a warm temperature bath at 49.5°C for 12–15 min) to improve splenic localization. The child receives an intravenous injection of the $^{99m}$Tc–labeled, heat-damaged red blood cells, and static images are obtained from multiple projections approximately 15 minutes after injection. Images diagnostic of hypersplenism reveal rapid clearance of the radiolabeled red blood cells from the blood pool and greater than normal splenic uptake.

## Scintigraphy of the Gastrointestinal Tract

Radionuclide imaging of the GI tract is a sophisticated, systematic technique that allows anatomic and functional imaging of the esophagus and stomach, small bowel, and colon. Anatomic location of GI bleeding or infection can be accomplished with dynamic imaging of the entire GI tract.

These studies are usually more sensitive than conventional radiographic and fluoroscopic studies because dynamic, uninterrupted imaging can be performed for longer periods and with less radiation exposure. The physiologic information obtained with GI scintigraphy complements the anatomic information provided by other imaging studies.

## Gastroesophageal Reflux and Scintigraphy of Liquid Gastric Emptying

GER in infants and young children, when severe, manifests clinically with vomiting and failure to thrive; it can be associated with recurrent bronchitis and pneumonia, peripheral airway disease, esophagitis, and GI bleeding. Radionuclide imaging can detect GER and associated pulmonary aspiration as well as quantify gastric emptying. The sensitivity for detection of GER is greater than with conventional barium fluoroscopy because the chest and abdomen can be monitored continuously over a longer period of time without additional radiation exposure. The only disadvantage is the lack of resolution compared with conventional radiography. Patient preparation requires fasting for 2 to 4 hours. In neonates and infants, a liquid meal radiolabeled with $^{99m}$Tc sulfur colloid is administered with formula or saved breast milk to replace a scheduled feed. If the child is on continuous feeds, these should be stopped 2 to 4 hours before the examination. Older children should be fasted for 4 to 6 hours, and an age-appropriate volume up to 8 ounces of whole milk, whole chocolate milk, or Pediasure is administered. If the liquid meal is given via nasogastric tube, appropriate position of the tube should be verified with radiography. If the liquid meal is being introduced with a gastrostomy tube, the connector tubing should be removed before imaging, because residual activity in the tubing could skew gastric emptying calculations.

The meal should be introduced into the stomach quickly, preferably within 10 minutes. The radiolabeled meal should be followed with nonlabeled liquid; approximately two-thirds is labeled. Posterior images are acquired at 5 sec/frame for 60 minutes. If a longer frame rate of 30 sec/frame is used, up to 25% of GER episodes can be missed.[173] A radioactive marker is placed at the sternal notch or shoulders for anatomic localization. At the end of 1 hour, a 5-minute static image over the lungs is obtained to evaluate for possible aspiration. If gastric emptying is delayed, a 2-hour image can be performed for an additional time point to determine delayed vs. normal emptying.[173]

A study with normal findings shows the radiopharmaceutical agent in the stomach but no activity in the esophagus or lungs. If reflux is detected, the number of episodes and proximal extent is noted (e-Fig. 84.14). Quantification of gastric emptying is expressed as either the percent residual or the percent amount emptied at 1 hour. A study performed on normal infants who were fed radiolabeled milk demonstrated a T1/2 of 87 ± 29 minutes. Extrapolation of the data provides a normal 1-hour gastric residual range of 48% to 71%.[174] Feeds performed using a nasogastric tube bypasses the fundus and results in an increased rate of gastric emptying.[175] Gastric emptying data are particularly useful in the preoperative assessment of children with reflux undergoing fundoplication and gastrostomy tube placement.

## Gastric Emptying Scintigraphy of Solids

Gastric emptying imaging performed with a solid meal is useful in the evaluation of nausea, early satiety, bloating, or abdominal pain, and for evaluation of accelerated gastric emptying. The advantage of the gastric emptying study over fluoroscopic studies is that a real solid meal is used and it is quantitative. The disadvantages are that meal content and volume vary depending on the child's intake and food preference, imaging techniques vary, and precise normal pediatric gastric emptying standards are not established.

In children and adolescents, the typical standard solid meal-based $^{99m}$Tc sulfur colloid labeled egg whites followed by two pieces of toast, jam, and 8 ounces of radiopharmaceutical-free liquid, such as water, juice, or milk. Images are obtained with a dual-head camera in the anterior and posterior projections in the supine position for 30 seconds every 10 minutes for 120 minutes; delayed images at 3 and 4 hours can be performed. Patient preparation requires fasting for 4 hours. An ambulatory child can move between images, but walking about is discouraged. Fractional emptying is expressed in percent emptied or percent residual. In normal studies, the time-activity curve should exhibit a continuous decline in activity over time. Pediatric standards have not been developed.[173] Normal values for gastric retention in adults are 30% to 90% at 1 hour, less than 60% at 2 hours, less than 30% at 3 hours, and less than 10% at 4 hours.[176] Alternatives to the standard solid meal include $^{99m}$Tc labeled chocolate "Technecrispy cake," with a T1/2 of 107 minutes[174] or cheddar cheese on macaroni or pizza.[177,178]

## Esophageal Transit Scintigraphy

Esophageal transit scintigraphy may be used to evaluate esophageal motility disorders such as achalasia, diffuse esophageal spasm, and impaired motility from esophagitis and esophageal atresia/tracheoesophageal fistula. Patient preparation requires fasting for 2 to 4 hours. The child is placed in the supine position with the mouth and stomach in the field of view. A small radioactive marker may be placed over the cricoid cartilage to localize the upper esophagus. The child is instructed to swallow a $^{99m}$Tc sulfur colloid radiolabeled bolus of liquid (water or milk) as the computer acquisition begins. Posterior images are acquired dynamically at 0.25 to 1 sec/frame for 1 to 3 minutes. Regions of interest are drawn around the upper, middle, and lower thirds of the esophagus and stomach, and a time-activity curve is generated. Comparison of swallowing curves can be used to identify normal peristaltic waves, dysmotility, and functional obstruction. The normal transit time through the esophagus is generally less than 10 seconds.[179]

## Colonic Transit Scintigraphy

Colonic transit scintigraphy is useful in patients with chronic constipation to establish whether the cause is slow colonic transit or functional fecal retention, because the treatment strategy is different for each. Patient preparation requires discontinuation of laxatives for 5 days, and 4 hours of patient fasting is recommended.

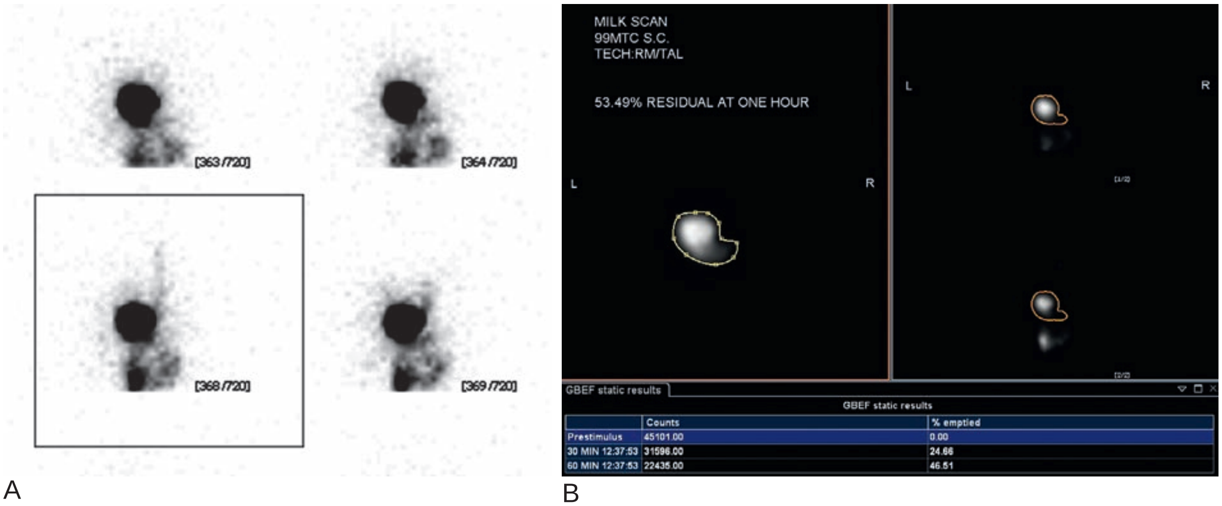

MILK SCAN
99MTC S.C.
TECH:RM/TAL

53.49% RESIDUAL AT ONE HOUR

GBEF static results

| | Counts | % emptied |
|---|---|---|
| Prestimulus | 45101.00 | 0.00 |
| 30 MIN 12:37:53 | 31596.00 | 24.66 |
| 60 MIN 12:37:53 | 22435.00 | 46.51 |

**e-Figure 84.14. Milk scan with gastroesophageal reflux and normal gastric emptying in a 6-month-old boy with persistent emesis.** (A) Dynamic images acquired at 5 seconds/frame reveal gastroesophageal reflux to the upper esophagus *(box)*. Other frames demonstrated 11 more episodes to the upper esophagus. (B) Quantitative analysis of gastric emptying reveals normal emptying with a residual of 53.5% at 1 hour, which is within the normal range at the institution where the study was performed.

A $^{99m}$Tc sulfur colloid radiolabeled liquid or solid meal is administered orally. Anterior and posterior static images are obtained in the supine position at 0 to 2, 6, 24, 30, and 48 hours. Radioactivity is measured in six regions (precolonic, ascending, transverse, descending, rectosigmoid colon, and evacuated feces). A normal examination shows radioactivity in the cecum by 6 hours and evacuation by 30 to 58 hours. Retention in the proximal colon at 48 hours indicates "slow colonic transit," while retention in the rectum at 48 hours indicates "functional fecal retention."[180–182]

## Salivagram

The salivagram allows the dynamic assessment of swallowing in patients suspected of having primary aspiration with feeding or in patients with neurologic deficits fed only by g-tube and suspected of aspirating saliva. Fasting is not required. A small dose of $^{99m}$Tc sulfur colloid mixed in 0.1 to 0.5 mL of water or saline is delivered as a drop under the tongue and allowed to mix with oral secretions. Dynamic images of the neck, chest, and upper abdomen are acquired for 1 hour. If there is no transit into the esophagus within 10 minutes, a small volume of water (1–2 cc) can be administered. At 1 hour, a posterior static image is acquired for 5 minutes. Detection of any radiopharmaceutical in the tracheobronchial tree is abnormal (Fig. 84.15).

## Meckel Scintigraphy

Meckel diverticulum is a congenital anomaly resulting from incomplete closure of the ileal attachment of the omphalomesenteric duct; it is present in approximately 2% of the population. Most of these diverticula are asymptomatic and lined by ileal mucosa. However, those that contain ectopic gastric mucosa are capable of producing hydrochloric acid and pepsin, thereby inducing ulceration of the gastric and adjacent ileal mucosa. Peptic ulceration causes acute GI hemorrhage in children, usually in the first 2 years of life. The Meckel scan is the study of choice for unexplained painless GI bleeding in children. Duplication cysts with ectopic gastric mucosa can also be detected with scintigraphy. Pharmacologic pretreatment is not considered a prerequisite to produce a high quality Meckel scan; however, histamine H2 blockers (cimetidine, ranitidine, famotidine) block secretions and increase gastric mucosa uptake that can increase diagnostic sensitivity.[183]

After the intravenous injection of $^{99m}$Tc pertechnetate, dynamic images are obtained at 1 to 5 sec/frame for 1 minute followed by 60 sec/frame for 30 minutes, and static images are obtained in anterior, posterior, right lateral, and left lateral projections. A normal study reveals radiotracer accumulation in the stomach as well as the urinary bladder and faint uptake by the kidneys due to excretion. An abnormal study demonstrates accumulation of radiotracer in ectopic tissue simultaneously with the appearance of gastric mucosa, usually between 6 and 10 minutes after injection (Fig. 84.16). SPECT imaging coregistered with simultaneously acquired low-dose CT (SPECT/CT) on a hybrid scanner has proven useful in discriminating between a Meckel diverticulum and artifact from the urinary tract or other visualized activity.[184,185]

## Gastrointestinal Bleeding Scintigraphy

Lower GI bleeding has many causes in infants and children, and the causes are largely age specific. When entities such as volvulus or intussusception are excluded, radionuclide imaging is useful for the localization of a bleeding source. Radiolabeled red blood cells are useful in patients who are bleeding slowly or intermittently.

No patient preparation is necessary. Simultaneously, intravenous injection of $^{99m}$Tc–labeled red blood cells and a dynamic flow study is performed for 1 minute, followed by a dynamic scan framed every 5 minutes for 30 minutes. If the images do not immediately reveal bleeding, delayed images are obtained at 45 minutes and 60 minutes and can be obtained up to 24 hours after injection. A positive study reveals activity in a location and configuration consistent with bowel, displays progressively increased intensity, and exhibits movement through the GI tract over time (Fig. 84.17). A cinematic display is often the most helpful method for localizing the abnormal bleeding site as determination of small bowel versus colon determines the next test (endoscopy, colonoscopy, or angiography).

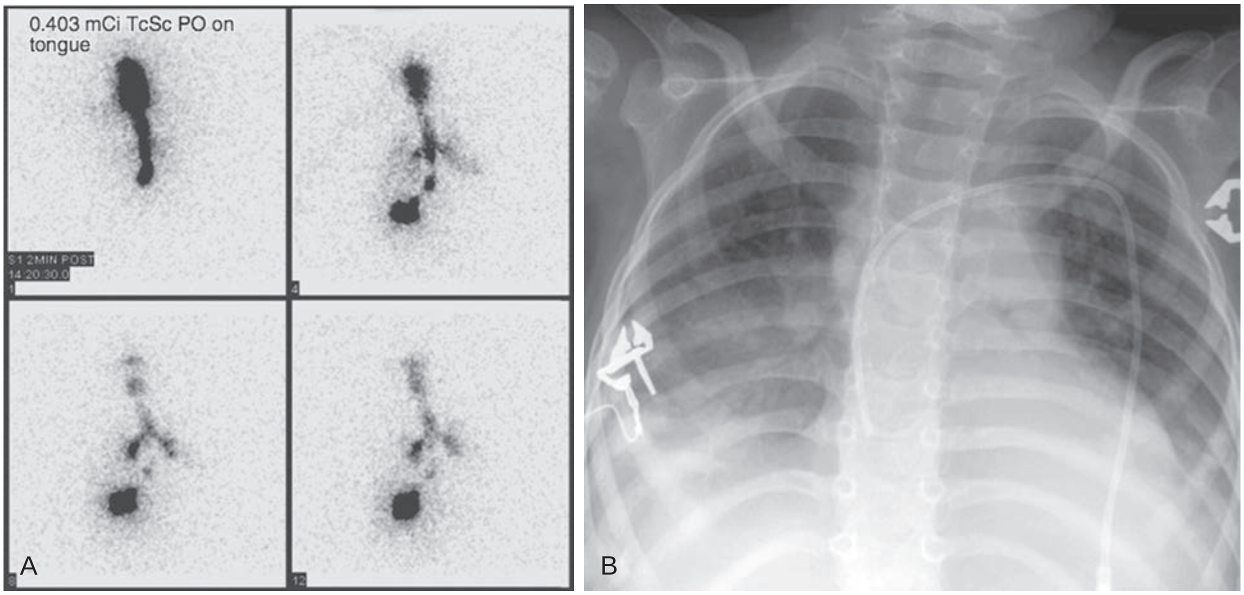

**Figure 84.15. Salivagram with pulmonary aspiration.** (A) Radionuclide salivagram (posterior images) obtained in a child with recurrent pneumonia and neuromuscular incoordination demonstrates $^{99m}$Tc sulfur colloid outlining the tracheobronchial tree. Some swallowed radiopharmaceutical is seen in the stomach. (B) Chest radiograph obtained the same day reveals bibasilar lung opacity, consistent with aspiration pneumonitis.

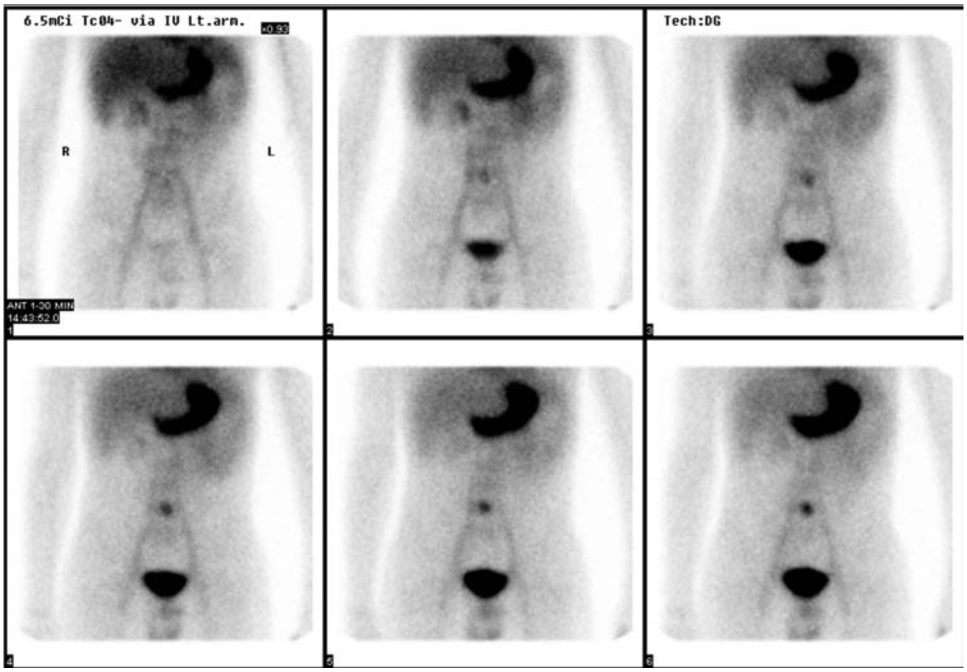

**Figure 84.16. Meckel scan with Meckel diverticulum.** Meckel scan in an 11-year-old with lower gastrointestinal bleeding reveals ectopic gastric mucosa in the midline of the lower abdomen. The timing coincides with the appearance of the stomach, with increasing conspicuity over time. Lateral views (not shown) revealed the abnormal uptake anteriorly in the lower abdomen.

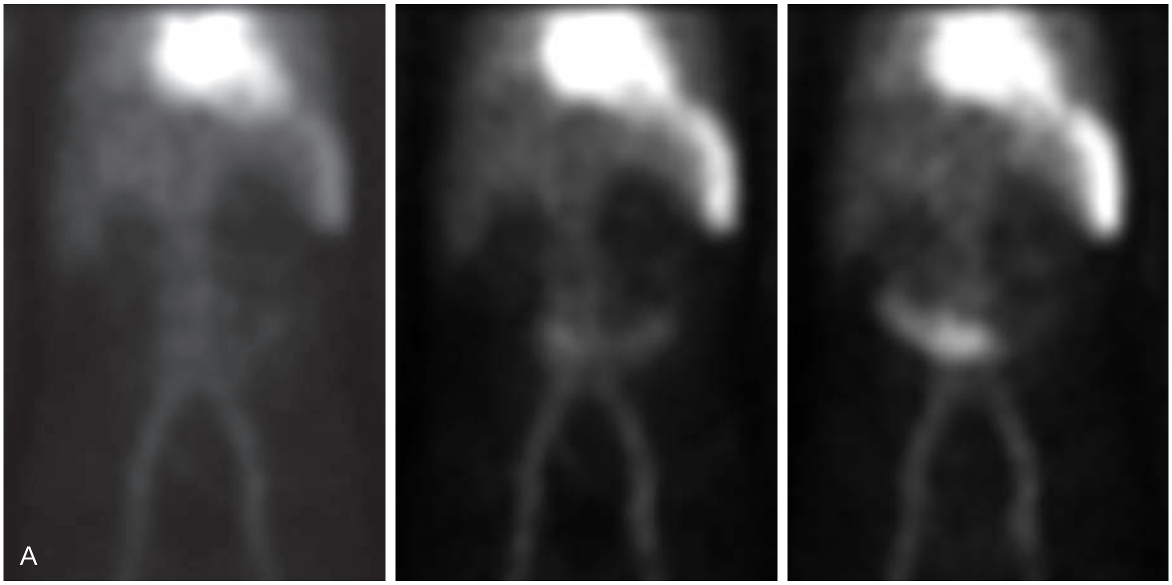

**Figure 84.17. Jejunal venous malformation in a 14-year-old with gastrointestinal bleeding.** (A) $^{99m}$Tc-labeled red blood cell scan performed dynamically at 1 minute per frame reveals an oblong region of radiotracer in the left upper quadrant. Selected successive frames at 1, 3, and 6 minutes show progression of radiotracer into the right lower quadrant.

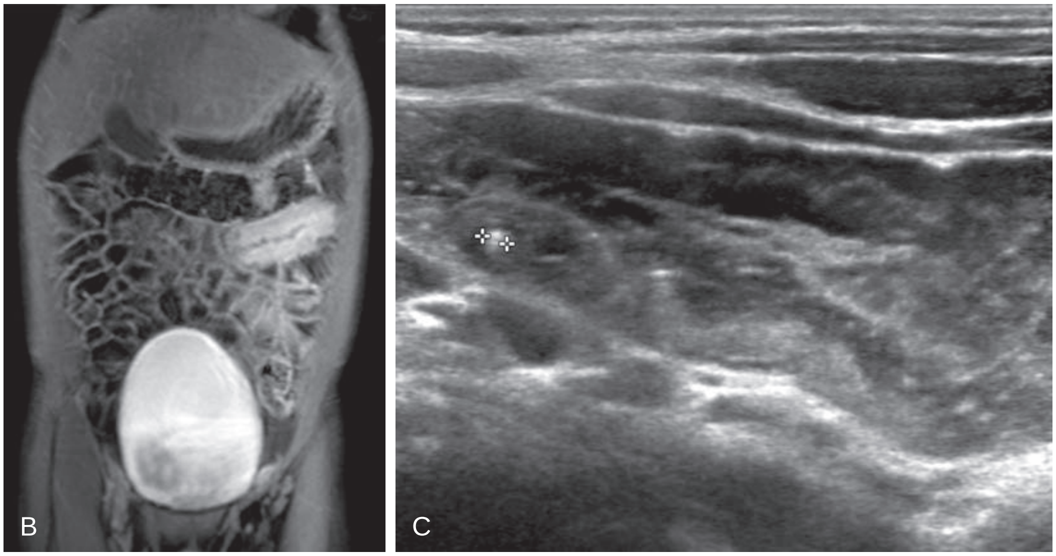

**Figure 84.17, cont'd.** (B) Coronal T1-weighted contrast-enhanced VIBE MR image shows an enhancing thick-walled loop of jejunum. (C) Ultrasound image reveals a hyperechoic focus (phlebolith) in the wall of a markedly thick-walled small bowel loop in the left upper quadrant. Superior mesenteric arteriogram (not shown) confirmed a low-flow jejunal venous malformation.

## Gastrointestinal Inflammation and Infection Scintigraphy

The radionuclide labeling of WBCs can be used for the localization of sites of abdominal infection, bowel inflammation,[186] and suspected intraabdominal abscess in critically ill patients with complex medical histories.

The radiopharmaceutical agent used is $^{99m}$Tc hexamethylpropyleneamine oxime (HMPAO). In children, the minimal amount of blood needed for labeling depends on the lab used and can range between 10 to 15 mL, depending on the child's size and circulating leukocyte count. Images are acquired at 30 minutes and 2 to 3 hours after the injection of the labeled WBCs. The patient should void before each image acquisition. A study with normal findings reveals uptake of the radiolabeled leukocytes by the liver, spleen, bone marrow, kidneys, and urinary bladder (e-Fig. 84.18). Normal bowel activity due to hepatobiliary excretion is seen in 20% to 30% of children by 1 hour. Abnormal bowel activity may be seen in 15 to 30 minutes and usually increases in intensity over the next 2 to 3 hours. Focal abdominal activity identified outside of the liver, spleen, and bowel may indicate focal infection or an abscess. SPECT imaging and SPECT/CT can be useful for localizing a collection.[187]

## Molecular Imaging

Positron emission tomography (PET) using $^{18}$F-fluorodeoxyglucose (FDG) is a sensitive alternative to conventional studies in the identification and localization of intestinal inflammatory and infectious processes in children. Specific inflammatory conditions described using $^{18}$F-FDG PET imaging include: inflammatory bowel disease,[188–190] chronic granulomatous disease, and fever of unknown origin.[191] PET/MR may have a role in the evaluation of inflammatory bowel disease, in the assessment of strictures, in determining the degree of active inflammation vs. fibrosis, and in detecting extraluminal disease.[192]

PET imaging using $^{18}$F-dihydroxyphenylalanine ($^{18}$F-DOPA, currently used under an investigational drug license supported by the FDA) is used to detect and localize the focal form of congenital hyperinsulinism in infants and neonates who are not responsive to medical therapy or have genetic defects associated with focal disease (Fig. 84.19). Histopathologic diagnosis is essential in the treatment of these infants. Diffuse disease is described as diffuse islet nuclear enlargement, and focal disease is described as focal beta cell adenomatosis. The term nesidioblastosis is no longer recommended for diffuse disease. Beta cell adenomatosis has a distinct histopathologic appearance different from insulinoma.[193] Resection of focal disease results in a greater than 95% cure rate. Patients found to have diffuse disease by biopsy may be treated with octreotide or undergo subtotal pancreatectomy, depending on the severity of the disease.

### KEY POINTS

- Hypertonic contrast media should not be used in the setting of possible aspiration.
- When hypertonic contrast media are used in contrast enema, fluid and electrolyte balance should be closely monitored and corrected.
- Pulsed fluoroscopy, removal of grid on small patients, and use of flurostore images can reduce radiation exposure by over 80%.
- Ultrasound should be performed with the highest frequency transducer that will penetrate to the area of interest.
- Protocols for pediatric CT imaging can be downloaded from the image gently website http://www.imagegently.org.
- Pediatric body MRI benefits from 3T fields strength and multi-channel receive arrays.
- Core pediatric MRI protocols consist of T2-weighted imaging, DWI, and contrast-enhanced T1-weighted imaging.
- Nuclear medicine studies provide a unique opportunity to utilize physiology in diagnosis.
- Most nuclear medicine studies can be performed with immobilization and distraction techniques, without sedation.

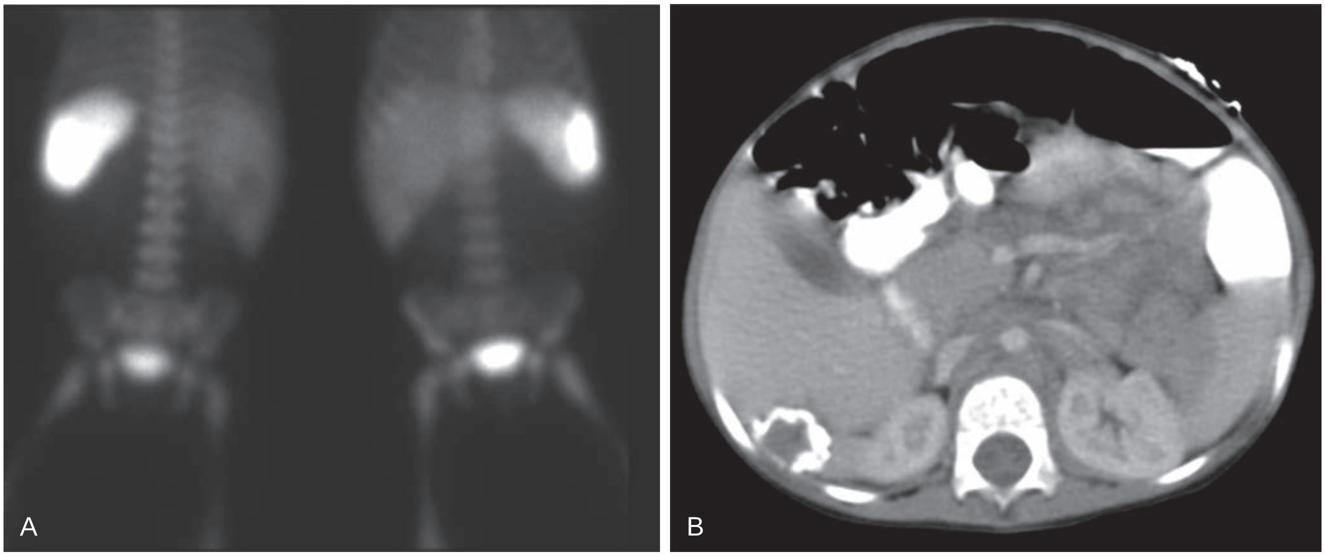

**e-Figure 84.18. White blood cell scan confirms successful treatment of liver abscess.** A 3-year-old with chronic granulomatous disease and liver abscess treated with interventional radiology drain placement and 6 week course of antibiotic therapy. (A) Coronal planar static images performed at 2 hours reveal a round, photopenic defect in the inferior right lobe. Nonuniform uptake is seen in the spleen. (B) Axial contrast-enhanced CT performed on the same day reveals a nonenhancing round focus in the right lobe with a rim of calcification that corresponds to the photopenic defect consistent with resolution of infection.

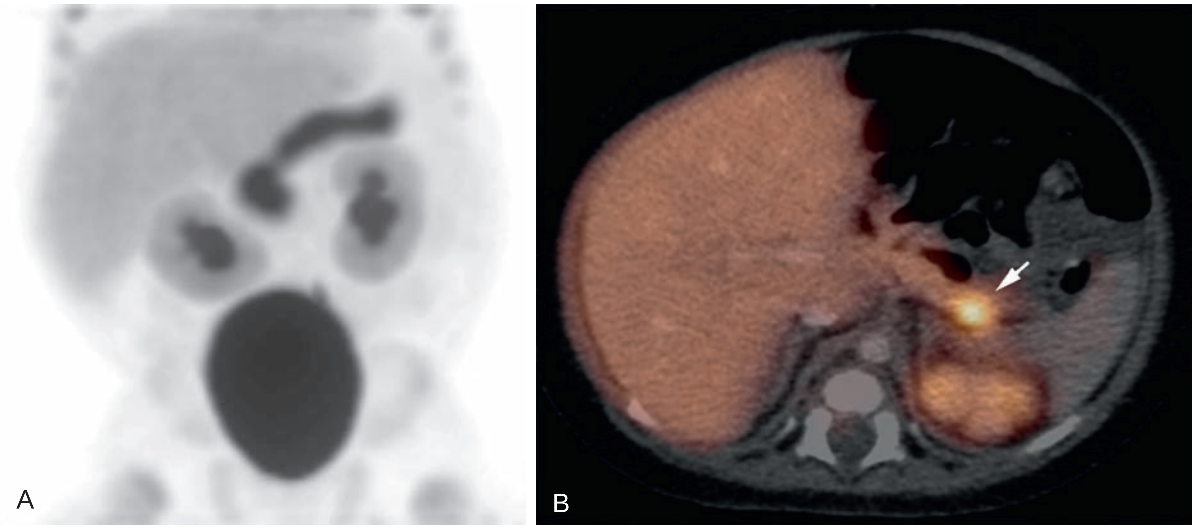

**Figure 84.19. PET/CT $^{18}$F-DOPA in congenital hyperinsulinism.** (A) Diffuse disease. Static MIP image in a 2-month-old reveals diffuse uptake throughout the pancreas. Note the normal uptake by the liver and kidneys and excretion into the urinary tract. Histopathology revealed diffuse islet cell nucleomegaly consistent with diffuse disease. The patient underwent a 98% subtotal pancreatectomy. (B) Focal disease. Fused axial CT and 18F-DOPA scan in a 5-week-old shows a round focus of increased radiotracer uptake in the pancreatic tail *(arrow)*. A 5% pancreatectomy was performed and confirmed a focal lesion of beta cell adenomatosis. Biopsies from the rest of the pancreas were normal.

## SUGGESTED READINGS

ACR Manual on Contrast Media. Version 10.3, 2017. *ACR Committee on Drugs and Contrast Media* https://www.acr.org/~/media/ACR/Documents/PDF/QualitySafety/Resources/Contrast-Manual/Contrast_Media.pdf?la=en.

Andersen SB, et al. Ultrasound elastography is useful for evaluation of liver fibrosis in children-a systematic review. *J Pediatr Gastroenterol Nutr*. 2016;63(4):389–399.

Chavhan GB, et al. MR imaging at 3.0 T in children: technical differences, safety issues, and initial experience. *Radiographics*. 2009;29(5):1451–1466.

Hernanz-Schulman M, et al. Pause and pulse: ten steps that help manage radiation dose during pediatric fluoroscopy. *AJR Am J Roentgenol*. 2011;197(2):475–481.

Mollard BJ, Smith EA, Dillman JR. Pediatric MR enterography: technique and approach to interpretation-how we do it. *Radiology*. 2015;274(1):29–43.

Smith EA, et al. Model-based iterative reconstruction: effect on patient radiation dose and image quality in pediatric body CT. *Radiology*. 2014;270(2):526–534.

Strauss KJ, et al. Image gently: ten steps you can take to optimize image quality and lower CT dose for pediatric patients. *AJR Am J Roentgenol*. 2010;194(4):868–873.

Treves ST, et al. 2016 Update of the North American Consensus Guidelines for pediatric administered radiopharmaceutical activities. *J Nucl Med*. 2016;57(12):15N–18N.

Vasanawala SS, et al. Navigated abdominal T1-W MRI permits free-breathing image acquisition with less motion artifact. *Pediatr Radiol*. 2010;40(3):340–344.

Vasanawala SS, et al. Safety and technique of ferumoxytol administration for MRI. *Magn Reson Med*. 2016;75(5);2107-2111.

## REFERENCES

Full references for this chapter can be found on www.expertconsult.com.

## REFERENCES

1. Hernanz-Schulman M, et al. Pause and pulse: ten steps that help manage radiation dose during pediatric fluoroscopy. *AJR Am J Roentgenol*. 2011;197(2):475–481.
2. Newman B, et al. Pause and pulse: radiation dose in pediatric fluoroscopy. *Pediatr Rev*. 2011;32(9):e83–e90.
3. Cohen MD. Choosing contrast media for the evaluation of the gastrointestinal tract of neonates and infants. *Radiology*. 1987;162(2):447–456.
4. Cohen MD. Choosing contrast media for pediatric gastrointestinal examinations. *Crit Rev Diagn Imaging*. 1990;30(4):317–340.
5. Muroi N, et al. Anaphylaxis from the carboxymethylcellulose component of barium sulfate suspension. *N Engl J Med*. 1997;337(18):1275–1277.
6. Janower ML. Hypersensitivity reactions after barium studies of the upper and lower gastrointestinal tract. *Radiology*. 1986;161(1):139–140.
7. Skucas J. Anaphylactoid reactions with gastrointestinal contrast media. *AJR Am J Roentgenol*. 1997;168(4):962–964.
8. Katsanoulas C, et al. Severe barium sulphage aspiration: a report of two cases and review of the literature. *Signa Vitae*. 2007;2(1):25–28.
9. Tamm I, Kortsik C. Severe barium sulfate aspiration into the lung: clinical presentation, prognosis and therapy. *Respiration*. 1999;66(1):81–84.
10. Zhang L, et al. Barium sulfate aspiration: severe chemical pneumonia induced by a massive reflux of contrast medium during small bowel barium enema. *Forensic Sci Int*. 2015;253:e16–e19.
11. Trulzsch DV, et al. Gastrografin-induced aspiration pneumonia: a lethal complication of computed tomography. *South Med J*. 1992;85(12):1255–1256.
12. Reich SB. Production of pulmonary edema by aspiration of water-soluble nonabsorbable contrast media. *Radiology*. 1969;92(2):367–370.
13. Tuladhar R, Patole S, Whitehall J. Gastrografin aspiration in a neonate with tracheoesophageal fistula. *J Paediatr Child Health*. 2000;36(1):94–95.
14. ACR. *ACR Manual on Contrast Media, Version 10.2*. 2016.
15. Rowe MI, et al. The neonatal response to gastrografin enema. *Pediatrics*. 1971;48(1):29–35.
16. Tuladhar R, et al. Oral gastrografin in neonates: a note of caution. *Int J Clin Pract*. 1999;53(7):565.
17. Moore DE, et al. Comparison of nonionic and ionic contrast agents in the rabbit lung. *Invest Radiol*. 1991;26(2):134–142.
18. Noblett HR. Treatment of uncomplicated meconium ileus by Gastrografin enema: a preliminary report. *J Pediatr Surg*. 1969;4(2):190–197.
19. Hernanz-Schulman M, et al. Experimental study of mortality and morbidity of contrast media and standardized fecal dose in the peritoneal cavity. *Pediatr Radiol*. 2000;30(6):369–378.
20. Hernanz-Schulman M, et al. Effect of radiographic contrast agents on leukocyte metabolic response. *Pediatr Radiol*. 2000;30(6):361–368.
21. Sadigh G, et al. Meta-analysis of air versus liquid enema for intussusception reduction in children. *AJR Am J Roentgenol*. 2015;205(5):W542–W549.
22. Persliden J, Schuwert P, Mortensson W. Comparison of absorbed radiation doses in barium and air enema reduction of intussusception: a phantom study. *Pediatr Radiol*. 1996;26(5):329–332.
23. Andersen SB, et al. Ultrasound elastography is useful for evaluation of liver fibrosis in children-a systematic review. *J Pediatr Gastroenterol Nutr*. 2016;63(4):389–399.
24. Leschied JR, et al. Shear wave elastography helps differentiate biliary atresia from other neonatal/infantile liver diseases. *Pediatr Radiol*. 2015;45(3):366–375.
25. Hanquinet S, et al. Contribution of acoustic radiation force impulse (ARFI) elastography to the ultrasound diagnosis of biliary atresia. *Pediatr Radiol*. 2015;45(10):1489–1495.
26. Pinto J, et al. Comparison of acoustic radiation force impulse/serum noninvasive markers for fibrosis prediction in liver transplant. *J Pediatr Gastroenterol Nutr*. 2014;58(3):382–386.
27. DiPaola FW, et al. Effect of Fontan operation on liver stiffness in children with single ventricle physiology. *Eur Radiol*. 2017;27(6):2434–2442.
28. Matos H, Trindade A, Noruegas MJ. Acoustic radiation force impulse imaging in paediatric patients: normal liver values. *J Pediatr Gastroenterol Nutr*. 2014;59(6):684–688.
29. Sidhu PS, et al. Role of Contrast-Enhanced Ultrasound (CEUS) in Paediatric Practice: An EFSUMB Position Statement. *Ultraschall Med*. 2017;38(1):33–43.
30. Rennert J, et al. Identification of early complications following liver transplantation using contrast enhanced ultrasound (CEUS). First results. *J Gastrointestin Liver Dis*. 2012;21(4):407–412.
31. Jacob J, et al. Contrast enhanced ultrasound (CEUS) characterization of grey-scale sonographic indeterminate focal liver lesions in pediatric practice. *Ultraschall Med*. 2013;34(6):529–540.
32. Rafailidis V, et al. Enhancing the role of paediatric ultrasound with microbubbles: a review of intravenous applications. *Br J Radiol*. 2017;90(1069):20160556.
33. Coleman JL, et al. Safety of ultrasound contrast agents in the pediatric oncologic population: a single-institution experience. *AJR Am J Roentgenol*. 2014;202(5):966–970.
34. Hernanz-Schulman M. CT and US in the diagnosis of appendicitis: an argument for CT. *Radiology*. 2010;255(1):3–7.
35. Strouse PJ. Pediatric appendicitis: an argument for US. *Radiology*. 2010;255(1):8–13.
36. Trout AT, et al. A critical evaluation of US for the diagnosis of pediatric acute appendicitis in a real-life setting: How can we improve the diagnostic value of sonography? *Pediatr Radiol*. 2012;42:813.
37. Binkovitz LA, et al. Pediatric appendiceal ultrasound: accuracy, determinacy and clinical outcomes. *Pediatr Radiol*. 2015;45(13):1934–1944.
38. Ledermann HP, et al. Bowel wall thickening on transabdominal sonography. *AJR Am J Roentgenol*. 2000;174(1):107–117.
39. Verschelden P, et al. Intussusception in children: reliability of US in diagnosis–a prospective study. *Radiology*. 1992;184(3):741–744.
40. Spalinger J, et al. Doppler US in patients with Crohn disease: vessel density in the diseased bowel reflects disease activity. *Radiology*. 2000;217(3):787–791.
41. Anupindi SA, et al. Pediatric inflammatory bowel disease: imaging issues with targeted solutions. *Abdom Imaging*. 2015;40(5):975–992.
42. Darge K, et al. Ultrasound of the bowel in children: how we do it. *Pediatr Radiol*. 2010;40(4):528–536.
43. Dillman JR, et al. Pediatric small bowel Crohn disease: correlation of US and MR enterography. *Radiographics*. 2015;35(3):835–848.
44. Applegate KE, et al. Situs revisited: imaging of the heterotaxy syndrome. *Radiographics*. 1999;19(4):837–852, discussion 853-4.
45. Hernanz-Schulman M, et al. Pictorial essay. Current evaluation of the patient with abnormal visceroatrial situs. *AJR Am J Roentgenol*. 1990;154(4):797–802.
46. Deak Z, et al. Submillisievert computed tomography of the chest using model-based iterative algorithm: optimization of tube voltage with regard to patient size. *J Comput Assist Tomogr*. 2017;41(2):254–262.
47. Martine RJ, et al. Radiation dose levels in pediatric chest CT: experience in 499 children evaluated with dual-source single-energy CT. *Pediatr Radiol*. 2017;47(2):161–168.
48. Park CH, et al. The feasibility of sub-millisievert coronary CT angiography with low tube voltage, prospective ECG gating, and a knowledge-based iterative model reconstruction algorithm. *Int J Cardiovasc Imaging*. 2015;31(suppl 2):197–203.
49. Smith EA, et al. Model-based iterative reconstruction: effect on patient radiation dose and image quality in pediatric body CT. *Radiology*. 2014;270(2):526–534.
50. Rompel O, et al. Third-generation dual-source 70-kVp chest CT angiography with advanced iterative reconstruction in young children: image quality and radiation dose reduction. *Pediatr Radiol*. 2016;46(4):462–472.
51. Lell MM, et al. High-pitch spiral computed tomography: effect on image quality and radiation dose in pediatric chest computed tomography. *Invest Radiol*. 2011;46(2):116–123.
52. Pappas JN, Donnelly LF, Frush DP. Reduced frequency of sedation of young children with multisection helical CT. *Radiology*. 2000;215(3):897–899.
53. Lemos AA, et al. Single-versus multidetector-row CT: comparison of sedation rates, conventional angiograms and motion artefacts in young children following liver transplantation. *Radiol Med*. 2006;111(7):911–920.
54. Lestra T, et al. Applications of dual energy computed tomography in abdominal imaging. *Diagn Interv Imaging*. 2016;97(6):593–603.
55. Silva AC, et al. Dual-energy (spectral) CT: applications in abdominal imaging. *Radiographics*. 2011;31(4):1031–1046, discussion 1047-50.
56. Frush DP. Pediatric abdominal CT angiography. *Pediatr Radiol*. 2008;38(suppl 2):S259–S266.
57. Siegel MJ. Computed tomography of pediatric cardiovascular disease. *J Thorac Imaging*. 2010;25(3):256–266.
58. Strauss KJ, et al. Image gently: ten steps you can take to optimize image quality and lower CT dose for pediatric patients. *AJR Am J Roentgenol*. 2010;194(4):868–873.

59. Frush DP, Yoshizumi T. Conventional and CT angiography in children: dosimetry and dose comparisons. *Pediatr Radiol*. 2006;36(suppl 2):154–158.
60. Goske MJ, et al. Image Gently: progress and challenges in CT education and advocacy. *Pediatr Radiol*. 2011;41(suppl 2):461–466.
61. Frush DP, Goske MJ. Image Gently: toward optimizing the practice of pediatric CT through resources and dialogue. *Pediatr Radiol*. 2015;45(4):471–475.
62. Applegate KE, et al. Effect of cross-sectional imaging on negative appendectomy and perforation rates in children. *Radiology*. 2001;220(1):103–107.
63. Imler D, et al. Magnetic resonance imaging versus ultrasound as the initial imaging modality for pediatric and young adult patients with suspected appendicitis. *Acad Emerg Med*. 2017;24(5): 569–577.
64. Kinner S, et al. Diagnostic accuracy of MRI Versus CT for the evaluation of acute appendicitis in children and young adults. *AJR Am J Roentgenol*. 2017;209:911–919.
65. Johnson AK, et al. Ultrafast 3-T MRI in the evaluation of children with acute lower abdominal pain for the detection of appendicitis. *AJR Am J Roentgenol*. 2012;198(6):1424–1430.
66. Kilcoyne A, Kaplan JL, Gee MS. Inflammatory bowel disease imaging: current practice and future directions. *World J Gastroenterol*. 2016;22(3):917–932.
67. Duigenan S, Gee MS. Imaging of pediatric patients with inflammatory bowel disease. *AJR Am J Roentgenol*. 2012;199(4):907–915.
68. Frush DP. Technique of pediatric thoracic CT angiography. *Radiol Clin North Am*. 2005;43(2):419–433.
69. Donnelly LF. Commentary: oral contrast medium administration for abdominal CT - reevaluating the benefits and disadvantages in the pediatric patient. *Pediatr Radiol*. 1997;27(9):770–772.
70. Brody AS, et al. Radiation risk to children from computed tomography. *Pediatrics*. 2007;120(3):677–682.
71. Weinreb JC, et al. Imaging the pediatric liver: MRI and CT. *AJR Am J Roentgenol*. 1986;147(4):785–790.
72. Finn JP, et al. Primary malignant liver tumors in childhood: assessment of resectability with high-field MR and comparison with CT. *Pediatr Radiol*. 1990;21(1):34–38.
73. Roebuck DJ, et al. 2005 PRETEXT: a revised staging system for primary malignant liver tumours of childhood developed by the SIOPEL group. *Pediatr Radiol*. 2007;37(2):123–132, quiz 249-50.
74. Roebuck DJ, Olsen O, Pariente D. Radiological staging in children with hepatoblastoma. *Pediatr Radiol*. 2006;36(3):176–182.
75. Arcement CM, et al. MRCP in the evaluation of pancreaticobiliary disease in children. *Pediatr Radiol*. 2001;31(2):92–97.
76. Delaney L, et al. MR cholangiopancreatography in children: feasibility, safety, and initial experience. *Pediatr Radiol*. 2008;38(1):64–75.
77. Ferrara C, et al. Magnetic resonance cholangiopancreatography in primary sclerosing cholangitis in children. *Pediatr Radiol*. 2002;32(6):413–417.
78. Chavhan GB, et al. Primary sclerosing cholangitis in children: utility of magnetic resonance cholangiopancreatography. *Pediatr Radiol*. 2008;38(8):868–873.
79. Hamada Y, et al. Magnetic resonance cholangiopancreatography on postoperative work-up in children with choledochal cysts. *Pediatr Surg Int*. 2004;20(1):43–46.
80. Irie H, et al. Value of MR cholangiopancreatography in evaluating choledochal cysts. *AJR Am J Roentgenol*. 1998;171(5):1381–1385.
81. Kim MJ, et al. Using MR cholangiopancreatography to reveal anomalous pancreaticobiliary ductal union in infants and children with choledochal cysts. *AJR Am J Roentgenol*. 2002;179(1):209–214.
82. Fishbein M, et al. Hepatic MRI for fat quantitation: its relationship to fat morphology, diagnosis, and ultrasound. *J Clin Gastroenterol*. 2005;39(7):619–625.
83. Fishbein MH, et al. Introduction of fast MR imaging in the assessment of hepatic steatosis. *Magn Reson Imaging*. 1997;15(3):287–293.
84. Qayyum A, et al. Accuracy of liver fat quantification at MR imaging: comparison of out-of-phase gradient-echo and fat-saturated fast spin-echo techniques–initial experience. *Radiology*. 2005;237(2):507–511.
85. Dietrich O, et al. Measurement of signal-to-noise ratios in MR images: influence of multichannel coils, parallel imaging, and reconstruction filters. *J Magn Reson Imaging*. 2007;26(2):375–385.
86. Fujita T, et al. Hepatic parenchymal enhancement in the cirrhotic liver: evaluation by triple-phase dynamic MRI. *Abdom Imaging*. 2002;27(1):29–33.
87. Asrani SK, et al. Role of magnetic resonance elastography in compensated and decompensated liver disease. *J Hepatol*. 2014;60(5):934–939.
88. Low G, Kruse SA, Lomas DJ. General review of magnetic resonance elastography. *World J Radiol*. 2016;8(1):59–72.
89. Serai SD, Towbin AJ, Podberesky DJ. Pediatric liver MR elastography. *Dig Dis Sci*. 2012;57(10):2713–2719.
90. Tan CH, Venkatesh SK. Magnetic resonance elastography and other magnetic resonance imaging techniques in chronic liver disease: current status and future directions. *Gut Liver*. 2016;10(5):672–686.
91. Venkatesh SK, Yin M, Ehman RL. Magnetic resonance elastography of liver: technique, analysis, and clinical applications. *J Magn Reson Imaging*. 2013;37(3):544–555.
92. Lee JK, et al. Fatty infiltration of the liver: demonstration by proton spectroscopic imaging. Preliminary observations. *Radiology*. 1984;153(1):195–201.
93. Wood JC, et al. MRI R2 and R2* mapping accurately estimates hepatic iron concentration in transfusion-dependent thalassemia and sickle cell disease patients. *Blood*. 2005;106(4):1460–1465.
94. Rehm JL, et al. Proton density fat-fraction is an accurate biomarker of hepatic steatosis in adolescent girls and young women. *Eur Radiol*. 2015;25(10):2921–2930.
95. Wells SA. Quantification of hepatic fat and iron with magnetic resonance imaging. *Magn Reson Imaging Clin N Am*. 2014;22(3):397–416.
96. Hernando D, et al. Quantification of liver iron with MRI: state of the art and remaining challenges. *J Magn Reson Imaging*. 2014;40(5):1003–1021.
97. Meisamy S, et al. Quantification of hepatic steatosis with T1-independent, T2-corrected MR imaging with spectral modeling of fat: blinded comparison with MR spectroscopy. *Radiology*. 2011;258(3):767–775.
98. Idilman IS, et al. A comparison of liver fat content as determined by magnetic resonance imaging-proton density fat fraction and MRS versus liver histology in non-alcoholic fatty liver disease. *Acta Radiol*. 2016;57(3):271–278.
99. Chalian M, et al. MR enterography findings of inflammatory bowel disease in pediatric patients. *AJR Am J Roentgenol*. 2011;196(6):W810–W816.
100. Darge K, Anupindi SA, Jaramillo D. MR imaging of the bowel: pediatric applications. *Magn Reson Imaging Clin N Am*. 2008;16(3):467–478, vi.
101. Gee MS, et al. Prospective evaluation of MR enterography as the primary imaging modality for pediatric Crohn disease assessment. *AJR Am J Roentgenol*. 2011;197(1):224–231.
102. Braithwaite KA, Alazraki AL. Use of the star sign to diagnose internal fistulas in pediatric patients with penetrating Crohn disease by MR enterography. *Pediatr Radiol*. 2014;44(8):926–931.
103. Quencer KB, et al. Detecting active inflammation and fibrosis in pediatric Crohn's disease: prospective evaluation of MR-E and CT-E. *Abdom Imaging*. 2013;38(4):705–713.
104. Essary B, et al. Pelvic MRI in children with Crohn disease and suspected perianal involvement. *Pediatr Radiol*. 2007;37(2):201–208.
105. Ahmad TM, et al. Bowel Sonography and MR Enterography in Children. *AJR Am J Roentgenol*. 2016;206(1):173–181.
106. Mollard BJ, Smith EA, Dillman JR. Pediatric MR enterography: technique and approach to interpretation-how we do it. *Radiology*. 2015;274(1):29–43.
107. Mollard BJ, et al. MR enterography under the age of 10 years: a single institutional experience. *Pediatr Radiol*. 2016;46(1):43–49.
108. Anupindi SA, Terreblanche O, Courtier J. Magnetic resonance enterography: inflammatory bowel disease and beyond. *Magn Reson Imaging Clin N Am*. 2013;21(4):731–750.
109. Towbin AJ, et al. CT and MR enterography in children and adolescents with inflammatory bowel disease. *Radiographics*. 2013;33(7):1843–1860.
110. Sheedy SP, et al. MR Imaging of perianal Crohn disease. *Radiology*. 2017;282(3):628–645.
111. Hammer MR, et al. Magnetic resonance imaging of perianal and perineal crohn disease in children and adolescents. *Magn Reson Imaging Clin N Am*. 2013;21(4):813–828.
112. Kuehle CA, et al. Hydro-MRI of the small bowel: effect of contrast volume, timing of contrast administration, and data acquisition on bowel distention. *AJR Am J Roentgenol*. 2006;187(4):W375–W385.
113. Dagia C, Ditchfield M. 3T MRI in paediatrics: challenges and clinical applications. *Eur J Radiol*. 2008;68(2):309–319.
114. Schindera ST, et al. Abdominal magnetic resonance imaging at 3.0 T what is the ultimate gain in signal-to-noise ratio? *Acad Radiol*. 2006;13(10):1236–1243.

115. Chavhan GB, et al. MR imaging at 3.0 T in children: technical differences, safety issues, and initial experience. *Radiographics*. 2009;29(5):1451–1466.
116. Ruangwattanapaisarn N, et al. Faster pediatric 3-T abdominal magnetic resonance imaging: comparison between conventional and variable refocusing flip-angle single-shot fast spin-echo sequences. *Pediatr Radiol*. 2015;45(6):847–854.
117. Chavhan GB, Babyn PS, Vasanawala SS. Abdominal MR imaging in children: motion compensation, sequence optimization, and protocol organization. *Radiographics*. 2013;33(3):703–719.
118. Herrmann KA, et al. Benefits and challenges in bowel MR imaging at 3.0 T. *Top Magn Reson Imaging*. 2010;21(3):165–175.
119. Runge VM, et al. Respiratory gating in magnetic resonance imaging at 0.5 Tesla. *Radiology*. 1984;151(2):521–523.
120. Kim YK, et al. Comparison of gadobenate dimeglumine-enhanced dynamic MRI and 16-MDCT for the detection of hepatocellular carcinoma. *AJR Am J Roentgenol*. 2006;186(1):149–157.
121. Klessen C, et al. Magnetic resonance imaging of the upper abdomen using a free-breathing T2-weighted turbo spin echo sequence with navigator triggered prospective acquisition correction. *J Magn Reson Imaging*. 2005;21(5):576–582.
122. Lee SS, et al. Image quality and focal lesion detection on T2-weighted MR imaging of the liver: comparison of two high-resolution free-breathing imaging techniques with two breath-hold imaging techniques. *J Magn Reson Imaging*. 2007;26(2):323–330.
123. Busse RF, et al. Fast spin echo sequences with very long echo trains: design of variable refocusing flip angle schedules and generation of clinical T2 contrast. *Magn Reson Med*. 2006;55(5):1030–1037.
124. Hennig J, Weigel M, Scheffler K. Multiecho sequences with variable refocusing flip angles: optimization of signal behavior using smooth transitions between pseudo steady states (TRAPS). *Magn Reson Med*. 2003;49(3):527–535.
125. Kijowski R, et al. Knee joint: comprehensive assessment with 3D isotropic resolution fast spin-echo MR imaging–diagnostic performance compared with that of conventional MR imaging at 3.0 T. *Radiology*. 2009;252(2):486–495.
126. Nandalur KR, et al. Possible biliary disease: diagnostic performance of high-spatial-resolution isotropic 3D T2-weighted MRCP. *Radiology*. 2008;249(3):883–890.
127. Miyazaki T, et al. Single-shot MR cholangiopancreatography of neonates, infants, and young children. *AJR Am J Roentgenol*. 1998;170(1):33–37.
128. Loening AM, et al. Increased speed and image quality in single-shot fast spin echo imaging via variable refocusing flip angles. *J Magn Reson Imaging*. 2015;42(6):1747–1758.
129. Media, A.C.o.D.a.C. *ACR Manual on Contrast Media*, *version 10.3*. 2017.
130. Hope MD, et al. Vascular imaging with ferumoxytol as a contrast agent. *AJR Am J Roentgenol*. 2015;205(3):W366–W373.
131. Bashir MR, et al. Emerging applications for ferumoxytol as a contrast agent in MRI. *J Magn Reson Imaging*. 2015;41(4):884–898.
132. Stabi KL, Bendz LM. Ferumoxytol use as an intravenous contrast agent for magnetic resonance angiography. *Ann Pharmacother*. 2011;45(12):1571–1575.
133. O'Connor OJ, O'Neill S, Maher MM. Imaging of biliary tract disease. *AJR Am J Roentgenol*. 2011;197(4):W551–W558.
134. Keup CP, et al. Magnetic resonance imaging of the pediatric liver: benign and malignant masses. *Magn Reson Imaging Clin N Am*. 2013;21(4):645–667.
135. Carlos RC, et al. Biliary imaging with Gd-EOB-DTPA: Is a 20-minute delay sufficient? *Acad Radiol*. 2002;9(11):1322–1325.
136. Koelblinger C, et al. Gadoxate-enhanced T 1-weighted MR cholangiography: comparison of 1.5 T and 3.0 T. *Rofo*. 2009;181(6):587–592.
137. Lee NK, et al. Biliary MR imaging with Gd-EOB-DTPA and its clinical applications. *Radiographics*. 2009;29(6):1707–1724.
138. Seale MK, et al. Hepatobiliary-specific MR contrast agents: role in imaging the liver and biliary tree. *Radiographics*. 2009;29(6):1725–1748.
139. Takao H, et al. MR imaging of the biliary tract with Gd-EOB-DTPA: effect of liver function on signal intensity. *Eur J Radiol*. 2011;77(2):325–329.
140. Tamrazi A, Vasanawala SS. Functional hepatobiliary MR imaging in children. *Pediatr Radiol*. 2011;41(10):1250–1258.
141. Meyers AB, et al. Characterization of pediatric liver lesions with gadoxetate disodium. *Pediatr Radiol*. 2011;41(9):1183–1197.
142. Ringe KI, et al. Gadoxetate disodium-enhanced MRI of the liver: part 1, protocol optimization and lesion appearance in the noncirrhotic liver. *AJR Am J Roentgenol*. 2010;195(1):13–28.
143. Vasanawala SS, et al. Navigated abdominal T1-W MRI permits free-breathing image acquisition with less motion artifact. *Pediatr Radiol*. 2010;40(3):340–344.
144. Chandarana H, et al. Free-breathing radial 3D fat-suppressed T1-weighted gradient echo sequence: a viable alternative for contrast-enhanced liver imaging in patients unable to suspend respiration. *Invest Radiol*. 2011;46(10):648–653.
145. Zucker EJ, et al. Free-breathing pediatric chest MRI: performance of self-navigated golden-angle ordered conical ultrashort echo time acquisition. *J Magn Reson Imaging*. 2017.
146. Griswold MA, et al. Generalized autocalibrating partially parallel acquisitions (GRAPPA). *Magn Reson Med*. 2002;47(6):1202–1210.
147. Pruessmann KP, et al. SENSE: sensitivity encoding for fast MRI. *Magn Reson Med*. 1999;42(5):952–962.
148. Saranathan M, et al. Differential Subsampling with Cartesian Ordering (DISCO): a high spatio-temporal resolution Dixon imaging sequence for multiphasic contrast enhanced abdominal imaging. *J Magn Reson Imaging*. 2012;35(6):1484–1492.
149. Korosec FR, et al. Time-resolved contrast-enhanced 3D MR angiography. *Magn Reson Med*. 1996;36(3):345–351.
150. Vasanawala SS, et al. Improved pediatric MR imaging with compressed sensing. *Radiology*. 2010;256(2):607–616.
151. Lustig M, Donoho D, Pauly JM. Sparse MRI: the application of compressed sensing for rapid MR imaging. *Magn Reson Med*. 2007;58(6):1182–1195.
152. Maki JH, et al. Steady-state free precession MRA of the renal arteries: breath-hold and navigator-gated techniques vs. CE-MRA. *J Magn Reson Imaging*. 2007;26(4):966–973.
153. Katoh M, et al. Free-breathing renal MR angiography with steady-state free-precession (SSFP) and slab-selective spin inversion: initial results. *Kidney Int*. 2004;66(3):1272–1278.
154. Prince MR, et al. A pilot investigation of new superparamagnetic iron oxide (ferumoxytol) as a contrast agent for cardiovascular MRI. *J Xray Sci Technol*. 2003;11(4):231–240.
155. Li W, et al. First-pass contrast-enhanced magnetic resonance angiography in humans using ferumoxytol, a novel ultrasmall superparamagnetic iron oxide (USPIO)-based blood pool agent. *J Magn Reson Imaging*. 2005;21(1):46–52.
156. Lai LM, et al. Feasibility of ferumoxytol-enhanced neonatal and young infant cardiac MRI without general anesthesia. *J Magn Reson Imaging*. 2017;45(5):1407–1418.
157. Ruangwattanapaisarn N, Hsiao A, Vasanawala SS. Ferumoxytol as an off-label contrast agent in body 3T MR angiography: a pilot study in children. *Pediatr Radiol*. 2015;45(6):831–839.
158. Muehe AM, et al. Safety report of ferumoxytol for magnetic resonance imaging in children and young adults. *Invest Radiol*. 2016;51(4):221–227.
159. Ning P, et al. Hemodynamic safety and efficacy of ferumoxytol as an intravenous contrast agents in pediatric patients and young adults. *Magn Reson Imaging*. 2016;34(2):152–158.
160. Vasanawala SS, et al. Safety and technique of ferumoxytol administration for MRI. *Magn Reson Med*. 2016;75(5):2107–2111.
161. Kreeftenberg HG, Mooyaart EL, Huizenga JR, et al. Quantification of liver iron concentration with magnetic resonance imaging by combining T1-, T2-weighted spin echo sequences and a gradient echo sequence. *Neth J Med*. 2000;56(4):133–137.
162. Sharma SD, et al. MRI-based quantitative susceptibility mapping (QSM) and R2* mapping of liver iron overload: comparison with SQUID-based biomagnetic liver susceptometry. *Magn Reson Med*. 2017;78(1):264–270.
163. Storey P, et al. R2* imaging of transfusional iron burden at 3T and comparison with 1.5T. *J Magn Reson Imaging*. 2007;25(3):540–547.
164. Reeder SB, et al. Quantitative assessment of liver fat with magnetic resonance imaging and spectroscopy. *J Magn Reson Imaging*. 2011;34(4):p. spcone.
165. Yokoo T, et al. Estimation of hepatic proton-density fat fraction by using MR imaging at 3.0 T. *Radiology*. 2011;258(3):749–759.
166. van Werven JR, et al. Assessment of hepatic steatosis in patients undergoing liver resection: comparison of US, CT, T1-weighted dual-echo MR imaging, and point-resolved 1H MR spectroscopy. *Radiology*. 2010;256(1):159–168.

167. Treves ST, et al. 2016 Update of the North American Consensus Guidelines for Pediatric Administered Radiopharmaceutical Activities. *J Nucl Med*. 2016;57(12):15N–18N.
168. Muise AM, et al. Biliary atresia with choledochal cyst: implications for classification. *Clin Gastroenterol Hepatol*. 2006;4(11):1411–1414.
169. Vijay BB, et al. Spontaneous biliary perforation in an infant: an unusual chronic presentation. *Clin Nucl Med*. 2008;33(4):273–275.
170. Majd M. Radionuclide imaging in clinical pediatrics. *Pediatr Ann*. 1986;15(5):396–402, 407-8.
171. Poddar U, et al. Ursodeoxycholic acid-augmented hepatobiliary scintigraphy in the evaluation of neonatal jaundice. *J Nucl Med*. 2004;45(9):1488–1492.
172. Lugo-Vicente HL. Trends in management of gallbladder disorders in children. *Pediatr Surg Int*. 1997;12(5–6):348–352.
173. Zvi B. Gastroesophageal reflux, gastric emptying, esophageal transit and pulmonary aspiration. In: Treves ST, ed. *Pediatric Nuclear Medicine and Molecular Imaging*. New York: Springer Verlag; 2014.
174. Singh SJ, et al. Gastric emptying of solids in normal children–a preliminary report. *J Pediatr Surg*. 2006;41(2):413–417.
175. Chen W, et al. Tube feeding increases the gastric-emptying rate determined by gastroesophageal scintigraphy. *Clin Nucl Med*. 2013;38(12):962–965.
176. Donohoe KJ, et al. Procedure guideline for adult solid-meal gastric-emptying study 3.0. *J Nucl Med Technol*. 2009;37(3):196–200.
177. Piepsz A, et al. Gastro-oesophageal scintiscanning in children. *Pediatr Radiol*. 1981;11(2):71–74.
178. Drubach LA, Kourmouzi V, Fahey FH. Cheese is a reliable alternative meal for solid-phase gastric emptying study. *Nucl Med Commun*. 2010;31(5):430–433.
179. Heyman S. Assessment of gastro-esophageal dysfunction in children. *Q J Nucl Med*. 1997;41(4):269–280.
180. Cook BJ, et al. Radionuclear transit to assess sites of delay in large bowel transit in children with chronic idiopathic constipation. *J Pediatr Surg*. 2005;40(3):478–483.
181. Shin YM, et al. Signs and symptoms of slow-transit constipation versus functional retention. *J Pediatr Surg*. 2002;37(12):1762–1765.
182. Notghi A, et al. Use of geometric center and parametric images in scintigraphic colonic transit studies. *Gastroenterology*. 1994;107(5):1270–1277.
183. Spottswood SE, et al. SNMMI and EANM practice guideline for meckel diverticulum scintigraphy 2.0. *J Nucl Med Technol*. 2014;42(3):163–169.
184. Papathanassiou D, et al. SPECT-CT of Meckel diverticulum. *Clin Nucl Med*. 2007;32(3):218–220.
185. Schneider P, Duren C, Reiners C. SPECT-CT image fusion could enhance Meckel scan. *World J Pediatr*. 2010;6(3):281.
186. Stathaki MI, et al. Role of scintigraphy in inflammatory bowel disease. *World J Gastroenterol*. 2009;15(22):2693–2700.
187. Rypins EB, Kipper SL. 99mTc-hexamethylpropyleneamine oxime (Tc-WBC) scan for diagnosing acute appendicitis in children. *Am Surg*. 1997;63(10):878–881.
188. Skehan SJ, et al. 18F-fluorodeoxyglucose positron tomography in diagnosis of paediatric inflammatory bowel disease. *Lancet*. 1999;354(9181):836–837.
189. Lemberg DA, et al. Positron emission tomography in the investigation of pediatric inflammatory bowel disease. *Inflamm Bowel Dis*. 2005;11(8):733–738.
190. Loffler M, et al. High diagnostic value of 18F-FDG-PET in pediatric patients with chronic inflammatory bowel disease. *Ann N Y Acad Sci*. 2006;1072:379–385.
191. Jasper N, et al. Diagnostic value of [(18)F]-FDG PET/CT in children with fever of unknown origin or unexplained signs of inflammation. *Eur J Nucl Med Mol Imaging*. 2010;37(1):136–145.
192. Pellino G, et al. PET/MR Versus PET/CT Imaging: impact on the clinical management of small-bowel Crohn's disease. *J Crohns Colitis*. 2016;10(3):277–285.
193. Gopal-Kothandapani JS, Hussain K. Congenital hyperinsulinism: role of fluorine-18L-3, 4 hydroxyphenylalanine positron emission tomography scanning. *World J Radiol*. 2014;6(6):252–260.

# 85

# Prenatal Gastrointestinal and Hepatobiliary Imaging

*Christopher I. Cassady*

## OVERVIEW

Fetal abdominal abnormalities evaluated on prenatal imaging can be grouped into one of several general categories: obstructions, ventral wall defects, echogenic bowel and peritoneal abnormalities, and finally masses and solid organ abnormalities.

In circumstances when ultrasound (US) cannot accurately determine the extent or nature of an abnormality, fetal magnetic resonance imaging (MRI) can be useful. Sequence selection includes standard single-shot fast spin echo (SSFSE) T2-weighted images at 3- to 5-mm slice thickness and steady-state free-precession (SSFP) imaging at overlapping intervals. Echo-time lengths range from 80 to 250 ms; longer lengths are advantageous for delineation of cystic abnormalities. T1-weighted fast gradient echo (GRE) sequences may be useful in the fetal abdomen, specifically for identification of the liver, which is mildly hyperintense, and very bright signal meconium.[1] Imaging modalities using ionizing radiation have no present role in the evaluation of a fetus with a gastrointestinal (GI) tract abnormality.

## INTESTINAL OBSTRUCTIONS

***Etiology.*** Interruption of the fetal GI tract can occur at any point from the esophagus to the anus, and the etiology for the loss of continuity is not the same at each site. The cause of esophageal atresia (EA) with or without a fistula to the trachea is not known but is believed to be a result of failure of the "system of folds" in the cranial and caudal ends of the tracheoesophageal space (see Chapter 96).[2–4] EA occurs in approximately 1 in 4,000 live births and can be associated with a number of additional abnormalities in the fetus. Most commonly, these abnormalities include those comprising the VACTERL complex (*V*ertebral, *A*nal, *C*ardiac, *T*racheo*E*sophageal, *R*enal, and *L*imb anomalies) and those seen in Down syndrome, such as common atrioventricular canal, absent or hypoplastic nasal bone, and nuchal thickening. EA occurs most commonly with a distal fistula (84%).[5]

Gastric atresia is the rarest atresia and is almost always pyloric with a distended proximal stomach. It likely results from vascular impairment during fetal development and is associated with epidermolysis bullosa, as well as multiple hereditary atresia and other conditions.[6]

In contrast to pyloric atresia, duodenal atresia (DA) is relatively common and, along with EA, is associated with Down syndrome. The etiology of DA has been thought to be related to failure of recanalization of the lumen of this segment of the proximal small bowel; more recent work implicates potential disruptions in fibroblast growth factor receptor 2 (FGFR2) and retinoic acid signaling pathways[7,8] (see Chapter 102).

Atresias distal to the duodenum are thought to be the result of ischemia or other focal insult to the bowel and may be multiple. Small bowel atresias are the most common cause of fetal and neonatal bowel obstructions, with colonic segments affected much more rarely (in 10% of all atresias).[9,10] Although most atresias are sporadic, some populations are prone to multiple atresia syndromes.[11,12] Meconium ileus in persons with cystic fibrosis also can have small bowel atresia, and colonic atresia can be seen in persons with Hirschsprung disease.[13,14] Anorectal atresia/malformation deserves special consideration because it often is seen in combination with other malformations, such as VACTERL, caudal regression, cloacal malformation, or the Currarino association (see Chapter 105).

***Imaging of the Esophagus.*** Despite the likelihood of a distal fistula that might allow for flow of fluid into the gut, the most consistent clues to the diagnosis of EA on US are a persistently small-volume stomach and polyhydramnios. Distension of a proximal esophageal pouch typically is intermittent and therefore unreliably witnessed either on US or MRI, although in the rare cases where it is vital to make a prenatal diagnosis, serial midline sagittal MRI with cine T2-weighted sequences may prove useful (Fig. 85.1).[15]

***Imaging of the Stomach.*** A lack of visualization of the stomach is most likely EA, with or without a distal fistula. Other considerations in the differential diagnosis of a small fetal stomach include congenital microgastria; oligohydramnios/anhydramnios; diminished swallowing function (e.g., in arthrogryposis, with little to no fetal movement); or obstruction to normal swallowing, including from increased intrathoracic pressure (Fig. 85.2). A markedly distended stomach, on the other hand, might raise concern for outlet obstruction, as with pyloric atresia. Gastric volvulus rarely has been reported in utero and is more of a risk when the stomach is not in its normal location.[16] A right-sided stomach in situs ambiguous or inversus should be evident as long as one is careful to establish the orientation of the fetus to the mother during the examination.

***Imaging of the Duodenum.*** DA appears on fetal imaging as the classic fluid-filled double bubble of dilated stomach and duodenal bulb (Fig. 85.3). Duodenal stenosis sometimes can be distinguished by hyperperistalsis of the dilated proximal duodenum as seen on US whereas, in DA, no peristalsis may exist at all. DA can be associated with malrotation of the bowel. Other causes for proximal obstruction include annular pancreas or an adhesive Ladd band in a patient with primary midgut malrotation. As with other obstructions to the GI tract, the more proximal the atresia, the earlier and the more frequent presentation with polyhydramnios; therefore polyhydramnios is typical in duodenal and proximal jejunal atresias.[17]

***Imaging of the Small Bowel.*** On T2-weighted sequences, high signal in liquid small bowel content should be evident on both sides of the abdomen; location of the small bowel primarily on the right may be an indication of a rotational abnormality (Fig. 85.4). The small bowel is considered to be dilated if it is larger than 7 mm; the colon is usually up to 15 mm in the third trimester, while the normal rectum, which should be the largest segment, can be larger[18–20] (Fig. 85.5). In proximal jejunal atresia, more loops will be dilated than just the double bubble seen with DA ("triple bubble" in very proximal jejunal atresia) (Fig. 85.6); distal jejunal atresia and ileal atresia, on the other hand, may be more difficult to distinguish prospectively because multiple dilated, fluid-filled loops are seen in both conditions, and typically a normal amniotic fluid volume is present.

The differential diagnosis for multiple dilated loops signifying a distal obstruction parallels that in newborn imaging and, in addition to atresia, includes meconium ileus, midgut volvulus, volvulus around a residual of the omphalomesenteric duct, and total colonic aganglionosis (Hirschsprung disease). One clue to the diagnosis of meconium ileus might be the presence of hyperechoic debris filling distended loops near the point of obstruction in the distal small bowel on US; MRI shows that the

## Abstract:

To detail the etiologies, imaging appearances, and treatment plan and follow up for gastrointestinal and hepatobiliary pathologies in the fetus. Fetal abdominal abnormalities evaluated on prenatal imaging can be grouped into one of several general categories: obstructions, ventral wall defects, echogenic bowel and peritoneal abnormalities, and masses and solid organ abnormalities. In circumstances when ultrasound (US) cannot accurately determine the extent or nature of an abnormality, fetal magnetic resonance imaging (MRI) can be useful.

## Keywords:

Fetal imaging review
Fetal MRI
Fetal ultrasound
Gastrointestinal
Hepatobiliary
Fetal abdomen

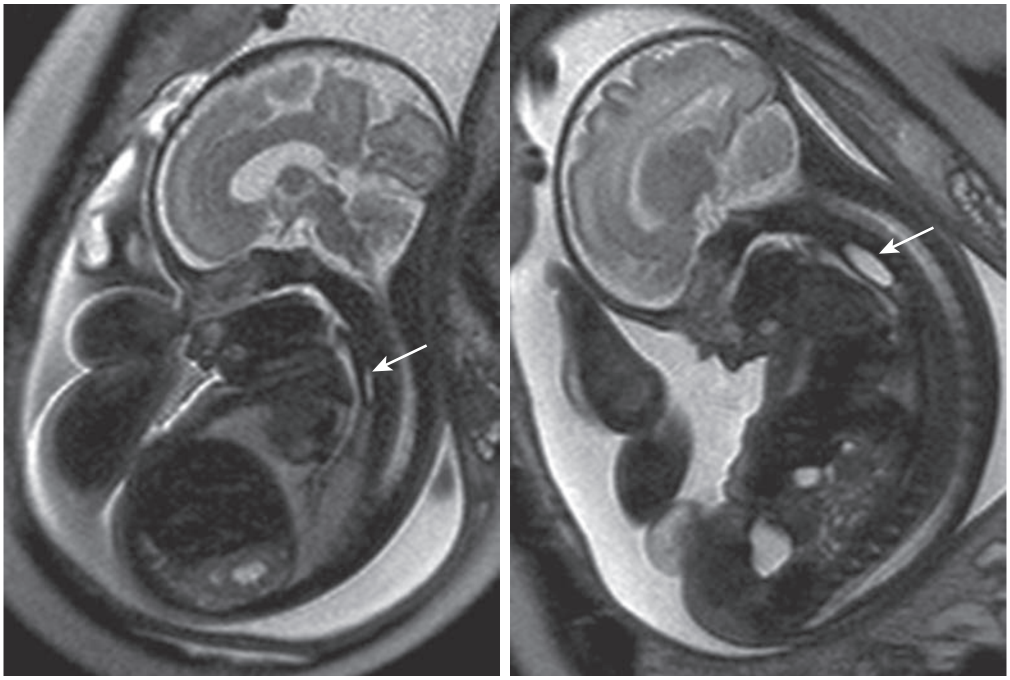

**Figure 85.1. Esophageal atresia.** Serial imaging may show intermittent phenomena: A sagittal SSFSE MR image in the neck and chest shows a small amount of fluid in the proximal esophagus that distends to a pouch on a later sequence *(arrows)*. Cine steady-state free-precession sequences are especially useful for serial imaging because of their fast acquisition times.

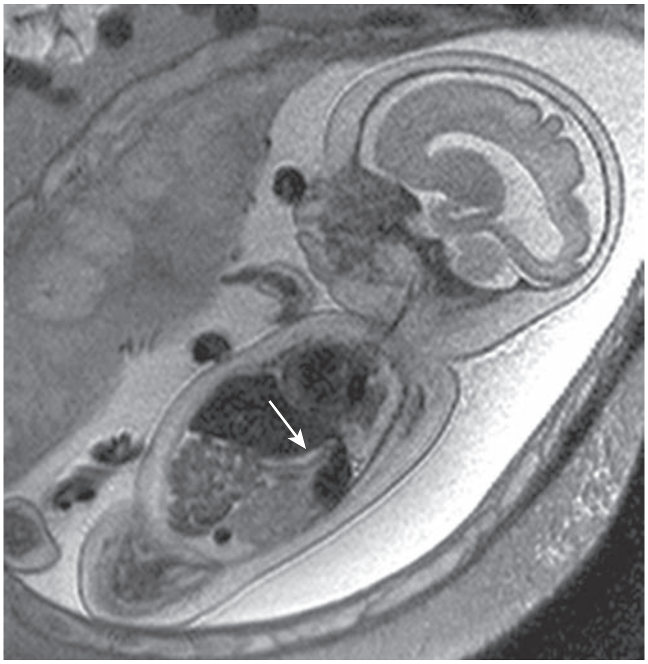

**Figure 85.2. Small stomach.** A small collapsed stomach *(arrow)* in a fetus with hydrops, hypotonia, and limited swallowing. Note the fetal edema, and the lack of any motion artifact in the amniotic fluid.

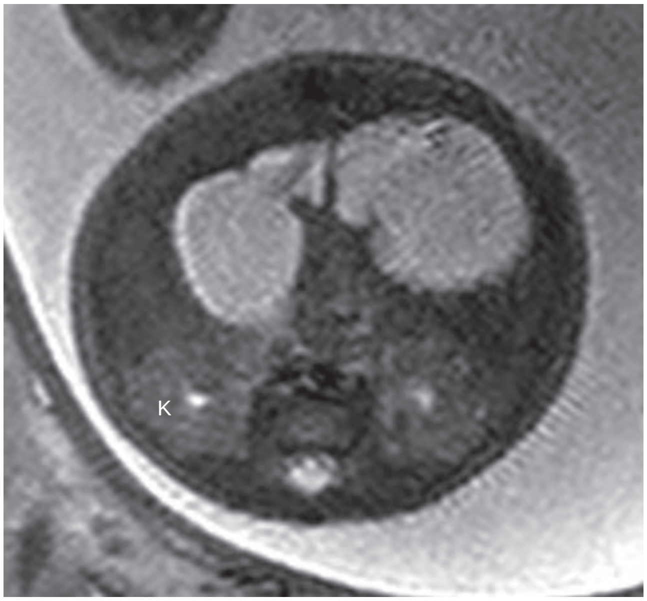

**Figure 85.3. Duodenal atresia.** Axial single-shot fast spin echo MR image of the stomach, pylorus, and dilated duodenum ("double bubble"). The right kidney is marked for reference *(K)*.

internal contents are hyperintense on T1-weighted images and intermediate on T2 imaging, consistent with meconium.[21–23] However, practically speaking, the MR pattern of dilated bowel containing meconium-typical signal characteristics is nonspecific, and both small bowel and colonic obstructions can show a pattern similar to that described for meconium ileus (Fig. 85.7). Vigorous hyperperistalsis of the bowel is indicative of obstruction (Fig. 85.8 and Video 85.1). Cases of in utero volvulus, although uncommon, have been prospectively identified either with a classic "whirlpool" twisting of the bowel or when the dilated ischemic segments are thick-walled, nonperistaltic, and have internal echogenicity from hemorrhage.[24,25] High-grade mechanical and functional obstructions of the distal small bowel are associated with congenitally small

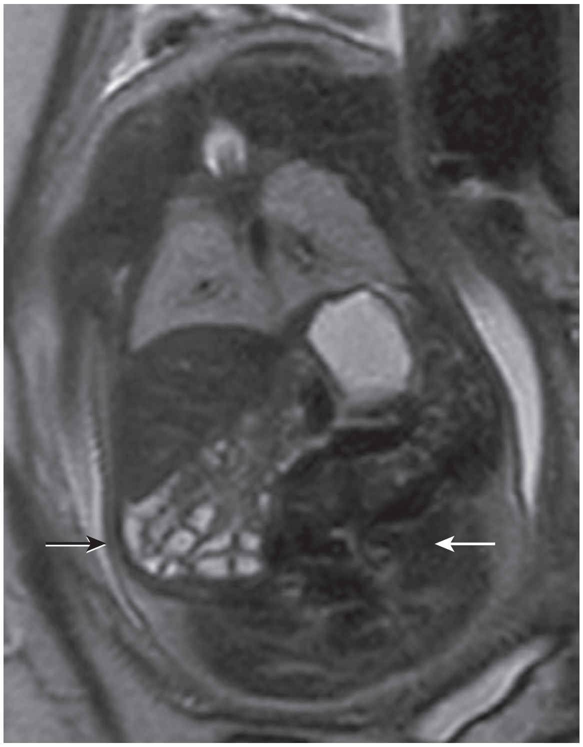

**Figure 85.4. Nonrotation.** All of the T2 high-signal small bowel is in the right abdomen *(black arrow),* and the low-signal meconium-filled distal ileum and colon are in the left abdomen *(white arrow)*.

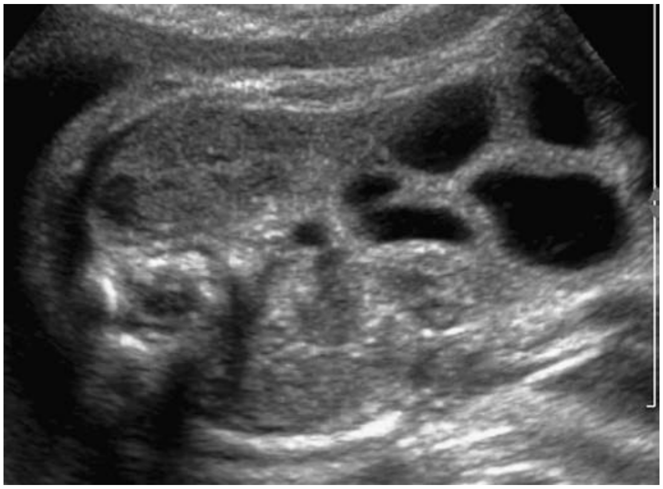

**Figure 85.5. Ileal atresia.** A coronal sonogram of the abdomen shows multiple dilated small bowel loops.

colons (“microcolon”), typically detectable on MR beginning in the late second trimester.

***Imaging of the Colon.*** Colonic atresias are difficult to diagnose specifically unless the obstructed segment can be identified with certainty in the expected location of the colon or interhaustral notches can be separated from valvulae conniventes on US. Meconium typically is seen in the rectum by 20 weeks’ gestation, in the left colon by 24 weeks’ gestation, and in the right colon by 31 weeks’ gestation, but this pattern may be altered by the pathology that is present.[26] On FSE T2-weighted sequences, meconium has a very low signal, whereas it shows a high signal on T1 weighting.

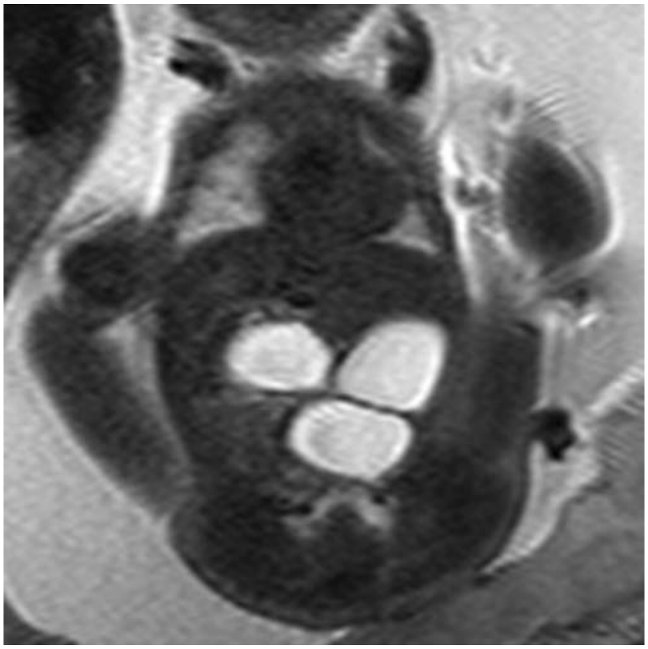

**Figure 85.6. Proximal jejunal atresia.** A single-shot fast spin echo coronal image with a dilated stomach, duodenal bulb, and proximal jejunum (“triple bubble”).

**BOX 85.1** Absent or Abnormal Signal in the Colon on Fetal Magnetic Resonance Imaging

Distal bowel obstruction
Bowel perforation (meconium peritonitis/pseudocyst)
Megacystis–microcolon–hypoperistalsis syndrome
Cloacal exstrophy
Cloacal malformation
Congenital diarrhea syndromes

In general, when dilated loops are discovered, US is sufficient to diagnose the level of obstruction as proximal versus distal and to generate a focused differential diagnosis. Fetal MRI is reserved for complex cases or for those in which other abnormalities are suspected and might be confirmed by additional imaging.[27] The advantage of MRI is in its larger field of view and reproducible multiplanar capability, showing the anatomy relative to other landmarks.[28] This advantage usually is demonstrated well with single-shot T2-weighted sequences in multiple planes, whereas the addition of GRE T1-weighted sequences to show the distribution of high-signal meconium can provide useful additional information (Fig. 85.9). It is crucial to understand that meconium is not exclusively restricted to the colon, can normally be seen in the distal ileum, and meconium signal may be present in dilated loops proximal to distal obstructions.[29] Box 85.1 lists causes of absent or abnormal meconium signal in the colon.

Although one might anticipate that bowel loops would be dilated in cases of anorectal atresia, such dilation is uncommon, and the diagnosis often is made on the basis of a high level of suspicion because of associated features.[30] On US, the diagnosis may be suspected if the characteristic hypoechoic configuration of the anal musculature with a central focus of echogenic mucosa (Fig. 85.10) is absent.[31,32] Also, a cord or ridge of abnormal fibrous tissue at the perineum may be imaged by US or MRI (e-Fig. 85.11). If a fistula between the colon and the urinary tract allows

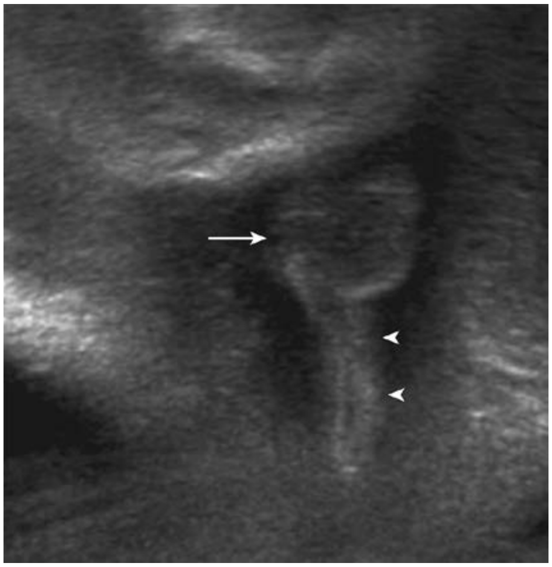

**e-Figure 85.11. Typical configuration of the perineal cord (*arrowheads*) that may be seen from the genitalia toward the level of anal atresia.** The arrow indicates the scrotum in this male fetus.

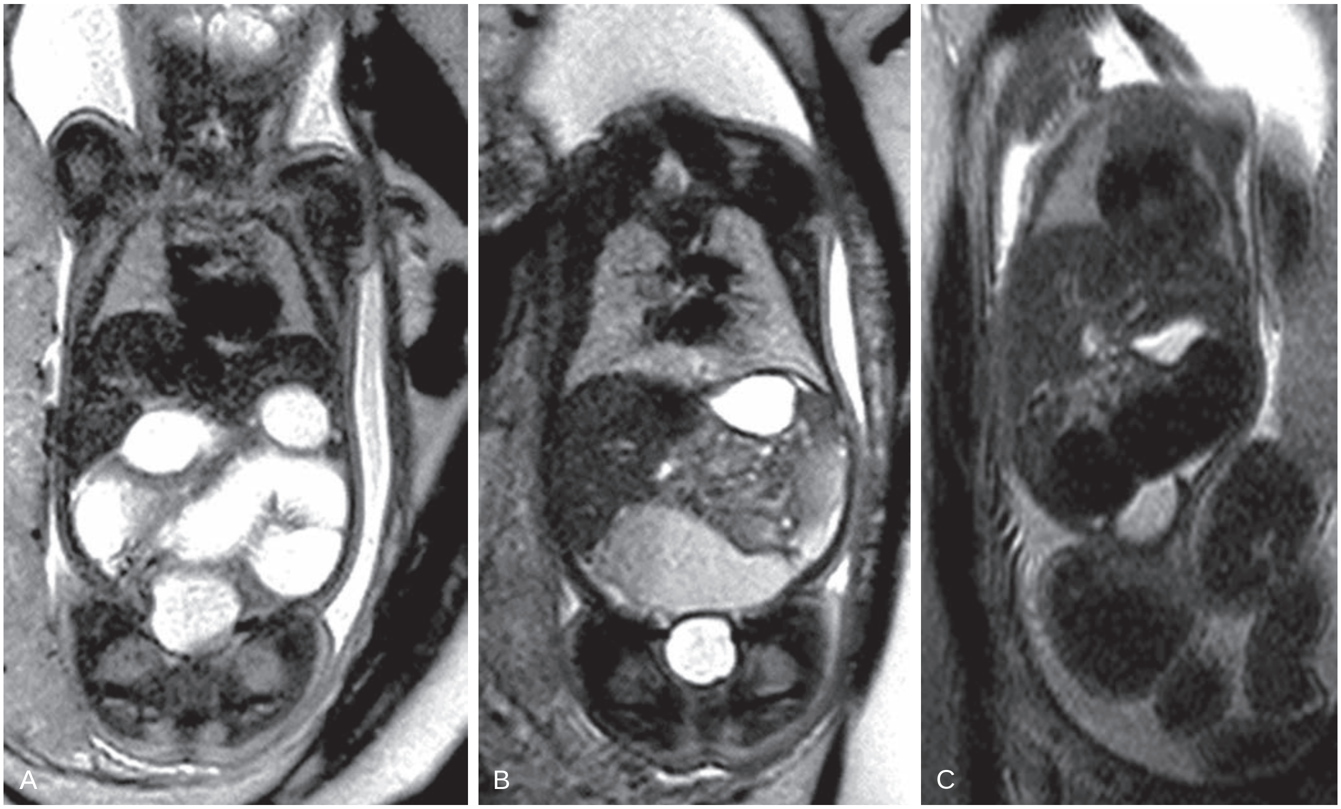

**Figure 85.7. Distal small bowel atresias, varying appearance.** Coronal MR imaging. On T2-weighted SSFSE imaging, these can have a variety of signal patterns. (A) Jejunal atresia with simple high signal in dilated loops. (B) Ileal atresia with medium intensity signal in focally dilated loops in the low abdomen. (C) Jejunal atresia with low signal from meconium in obstructed loops.

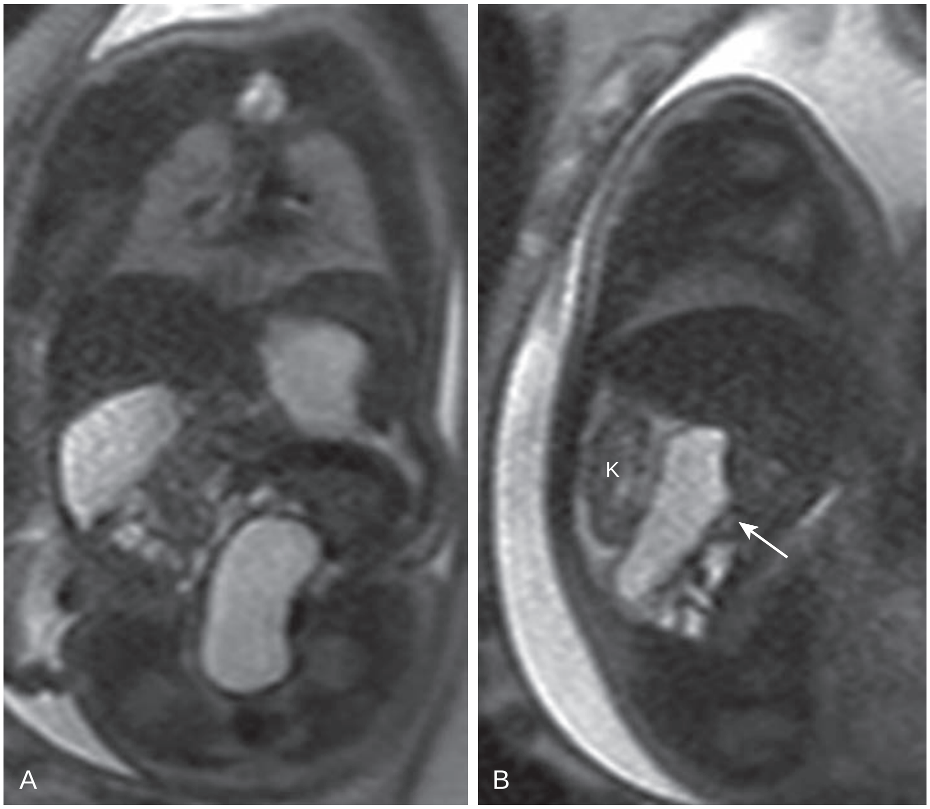

**Figure 85.8. Duodenal obstruction due to Ladd's band in malrotation.** (A) Coronal and (B) sagittal SSFSE MR images show the stomach in the left upper quadrant and a dilated segment of bowel in the right upper quadrant *(arrow)* ventral to the right kidney *(K),* representing the duodenum. The bladder is seen in the pelvis. The ultrasound clip shown in Video 85.1 is remarkable for hyperperistalsis of this segment.

mixing of meconium and urine, intraluminal precipitant calcifications may be detected (Fig. 85.12).

Hirschsprung aganglionosis only very rarely is identified by bowel dilatation antenatally in the third trimester, although it is among the most common causes of neonatal intestinal obstruction, and therefore this diagnosis is more often made postnatally.[33,34] Intestinal neuronal dysplasia type B, a malformation of the parasympathetic plexus, has been identified retrospectively in a fetus as a cause of bowel obstruction but is extraordinarily unusual.[35] Another rare form of functional obstruction that can be seen in the neonate, congenital segmental dilation of the bowel, has been described with both short segment or more extensive antenatal bowel enlargement, the latter indistinguishable from a pattern of mechanical obstruction.[36]

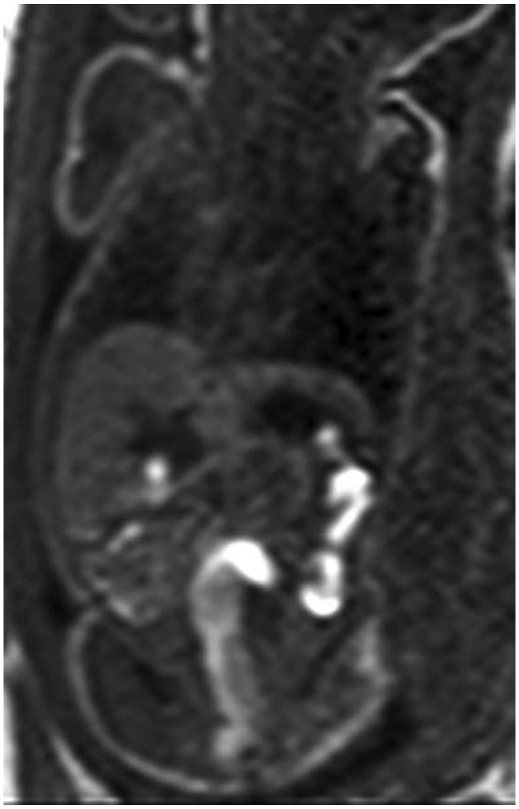

**Figure 85.9. Meconium.** A coronal T1-weighted gradient echo MR image showing T1 high-signal meconium in the colon.

Congenital diarrhea syndromes have been reported as showing dilation of the bowel to the rectum but without meconium signal on T1-weighted imaging, reflecting the loss of normal meconium.[37] Therefore lack of colonic meconium is not exclusive to mechanical small bowel obstructions. Differential considerations include secretory sodium or chloride diarrheas, megacystis-microcolon-hypoperistalsis syndrome, pseudoobstruction, and total colonic aganglionosis (Hirschsprung disease).[26,29,38,39]

***Treatment and Follow-up.*** At this time, no criteria have been established for intervention in the fetus based on bowel obstruction unrelated to ventral wall defects, aside from amnioreduction for polyhydramnios. Selected patients may have amniocentesis to evaluate for the possibility of chromosomal abnormalities or cystic fibrosis. Follow-up is performed with ultrasonography, with a plan to have the newborn evaluated at birth by the appropriate pediatric specialists.

## VENTRAL WALL DEFECTS

***Overview.*** Ventral wall defects include all abnormalities in which extrusion of internal anatomic structures to the outside of the fetal abdomen and/or pelvis occurs. The major abnormalities under this category include Pentalogy of Cantrell, omphalocele, bladder and cloacal exstrophy, and gastroschisis.

***Etiology.*** Normal herniation of the midgut into the proximal umbilical cord occurs in the eighth gestational week, and 270 degrees of midgut rotation, return of the bowel, and fixation are completed by the end of the twelfth week. Visualization of either the liver or bowel in the umbilical cord after 12 weeks is abnormal. In general, these abnormalities are thought to occur from a failure

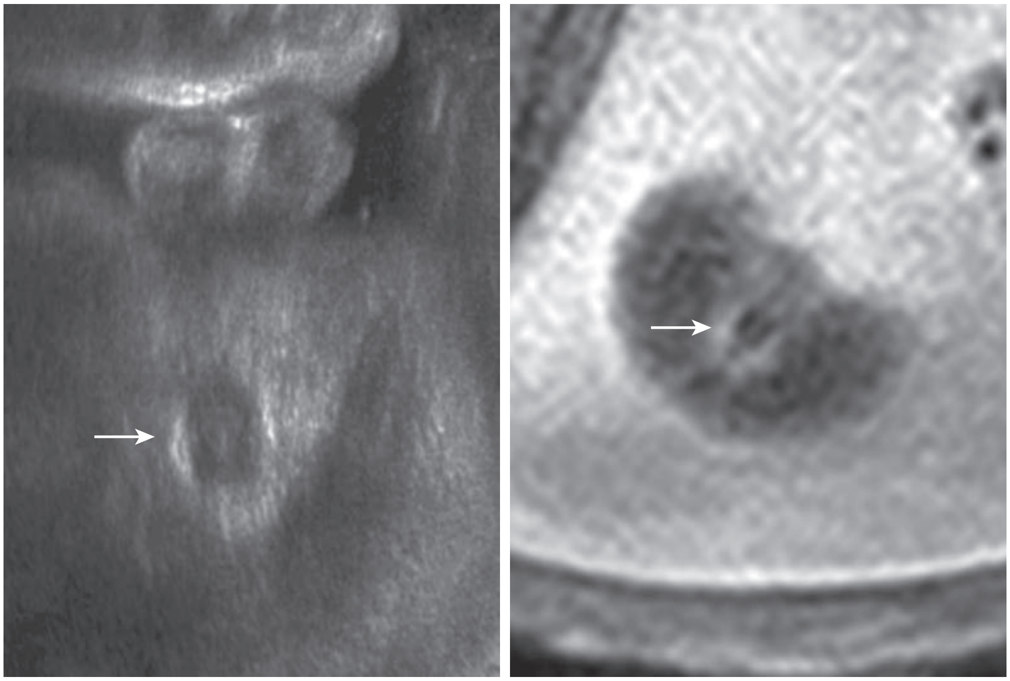

**Figure 85.10. Normal perineum.** The normal hypoechoic configuration of the anal musculature at the perineum *(arrows)* on ultrasound *(left)* and axial SSFSE T2-weighted MR *(right)*.

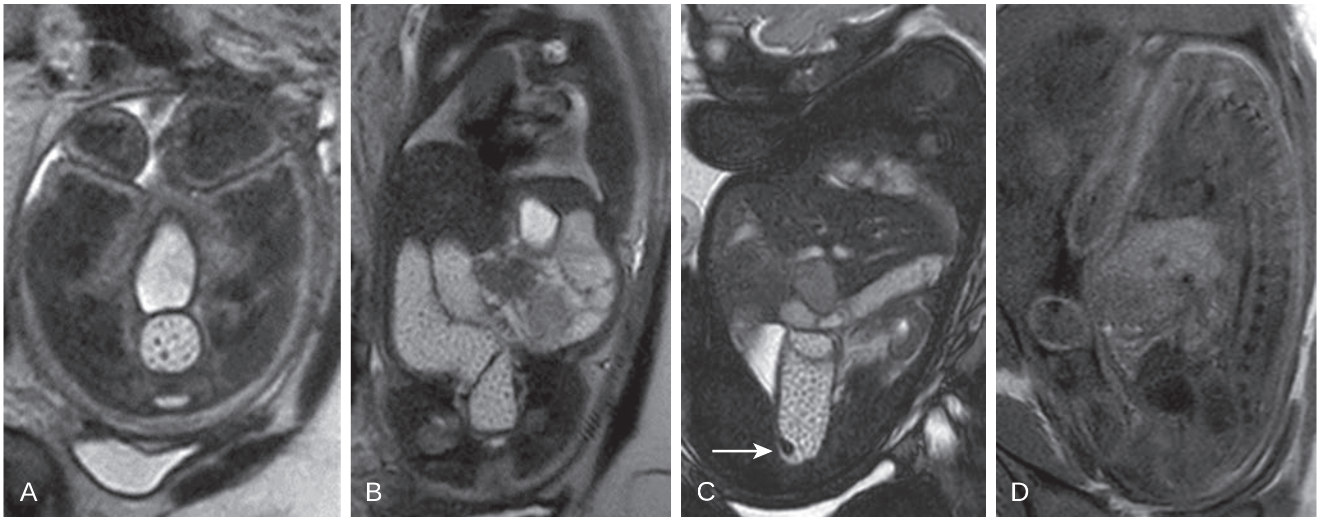

**Figure 85.12. Anal atresia with fistula.** (A) Axial, (B) coronal, and (C) sagittal SSFSE MR images demonstrate abnormal medium-high signal, containing multiple intraluminal punctate low-signal calcifications in the distal colon. (D) Sagittal T1-weighted GRE image confirms the lack of normal high signal meconium in the rectum. There is a fistula directed toward the expected level of the urethra on the sagittal image *(arrow)*.

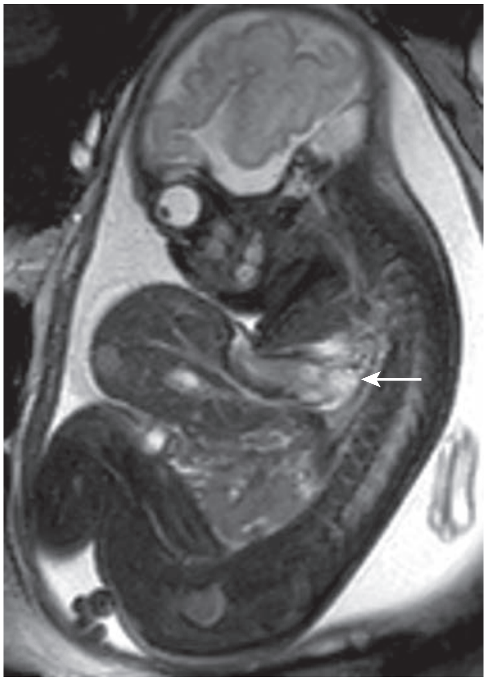

**Figure 85.13. Pentalogy of Cantrell.** Sagittal SSFP MR image through the chest shows herniation of low-signal liver and high-signal flowing blood within the heart *(arrow)* through a ventral wall defect.

of the normal infolding and fusion of the embryonic disc.[40] If craniad infolding fails, the resulting defect would be to the abdominal wall and lower chest, resulting in findings in the spectrum of the pentalogy of Cantrell (omphalocele, sternal defect, ventral mediastinal diaphragmatic hernia, pericardial defect, and ectopia cordis) (Fig. 85.13). Lateral fold defects lead to an omphalocele, which is the most common isolated ventral wall defect and is contained by a membrane (parietal peritoneum and amnion) unless ruptured (e-Fig. 85.14).[41] Caudal fold failure results in bladder or cloacal exstrophy, which primarily affects the genitourinary tract.

In bladder exstrophy, the ventral wall of the bladder, inferior rectus musculature, and skin are absent, and the residual dorsal wall of the bladder is continuous with the abdominal wall ("opened bladder") (e-Fig. 85.15). Imperforate anus with fistula is rarely associated. Cloacal exstrophy is more complex; persistence of the infraumbilical cloacal membrane is thought to prevent normal anterior abdominal wall closure and separation of the urogenital system from the rectum; as a result, two open hemibladders are separated by bowel. There is always an associated anorectal malformation. Both bladder and cloacal exstrophy include diastasis of the pubic symphysis and may have more complex pelvic bone deformities. OEIS complex describes the particular association of *O*mphalocele, bladder *E*xstrophy, *I*mperforate anus, and *S*pinal defect,[42] but this complex is believed by most to be a synonym for cloacal exstrophy.[43]

Limb-body wall complex is a severe form of ventral wall defect that results from failure of folding along multiple planes and is not compatible with extrauterine life (Fig. 85.16).[44]

Gastroschisis is a type of ventral wall defect that may be unrelated to embryonic disc folding. It is possible that a vascular insult results in a through-and-through defect in the layers of the abdominal wall adjacent to the umbilicus, almost universally on the right, through which the bowel herniates without a covering membrane; other hypotheses have been proposed, but the cause is not yet known (e-Fig. 85.17).[45,46] The risk of bearing a fetus with gastroschisis is reportedly increased in young primigravida women and also has been associated with the use of agents that may cause vasoconstriction, such as tobacco and salicylates.[47,48]

Because of the lack of skin covering in this constellation of defects, the maternal alpha-fetoprotein levels can be elevated, and further subsequent screening with US leads to the prenatal diagnosis.

***Imaging.*** Visualization of liver or bowel within the umbilical cord beyond the twelfth week of gestation is evidence of an omphalocele. There is a spectrum, however: small lesions may just indicate an umbilical cord hernia, which has normal skin over it when the baby is born. Larger lesions should be considered likely true omphaloceles, and genetic evaluation should be strongly considered. A giant omphalocele is defined when more than 50% of the liver is extracorporeal or the defect is greater than 5 cm wide.[49,50] Wharton's jelly pseudocysts may be found in association with the defect, located near the cord insertion site on the omphalocele.[51]

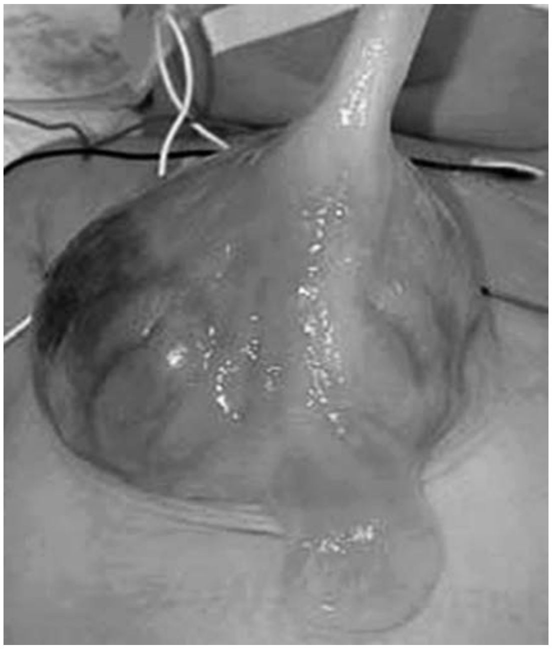

**e-Figure 85.14. Omphalocele.** Photograph of a newborn shows a large anterior wall defect with a surrounding membrane. The umbilical cord is inserting at the apex.

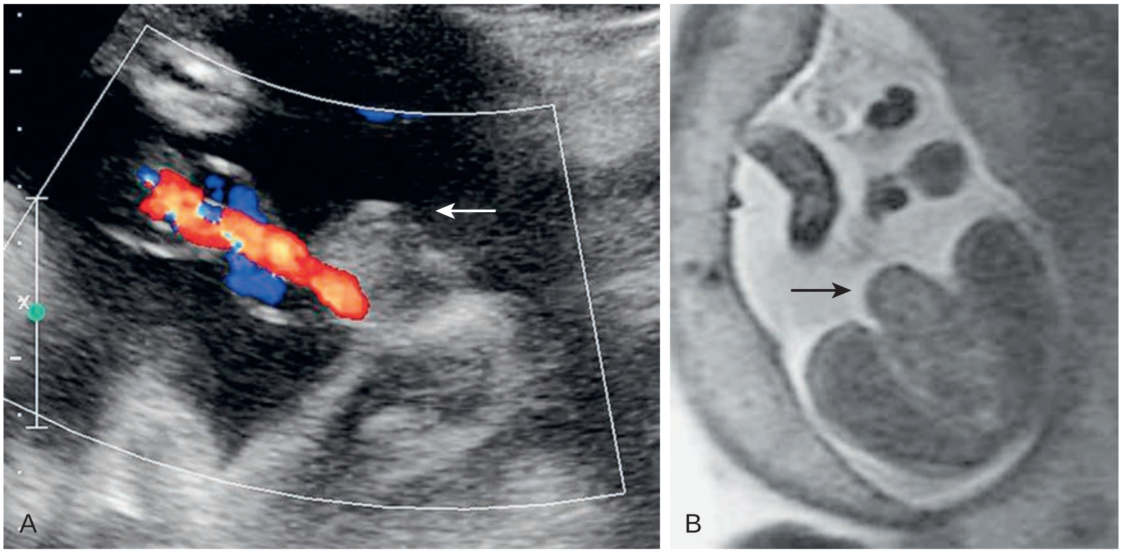

**e-Figure 85.15. Bladder exstrophy.** (A) Longitudinal sonogram of the anterior pelvis shows a small outpouching just below the low-lying umbilical cord insertion *(arrow)*. No bladder is noted. (B) Axial SSFSE T2-weighted MR image of the pelvis confirms the presence of a soft tissue outpouching below the cord insertion *(arrow)*. No bladder is present.

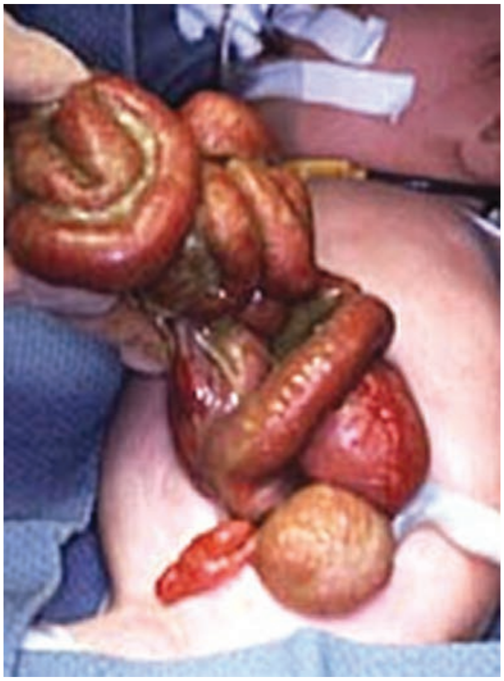

**e-Figure 85.17. Gastroschisis.** This newborn has a large amount of dilated bowel protruding outside the abdominal cavity at the level of the umbilicus. No covering membrane is present.

Although, as noted earlier, the differentiation of a small, skin-covered umbilical hernia from omphalocele is difficult, US typically can diagnose these defects readily and accurately define the extruded anatomy (Fig. 85.18). When US fails to reveal the pertinent details, MRI can be useful and relies on standard single-shot FSE T2-weighted imaging; the liver tends to have a higher signal than other abdominal structures on T1-weighted sequences, which is useful for identification of the position of the liver in questionable cases. Characteristically, however, when fetal MRI is requested in cases of omphalocele, it is because of an interest in assessing for additional abnormalities or a need to calculate MR-derived lung volumes. Newborns with giant omphalocele have a tendency to need long-term ventilatory support and may have pulmonary hypoplasia.[50,52,53] Echocardiography is indicated, because 50% of fetuses with omphalocele have congenital heart disease. Ascites may be present but tends to decrease through gestation. Note that if a normal bladder is not seen over time or in repeated studies, exstrophy must be considered.

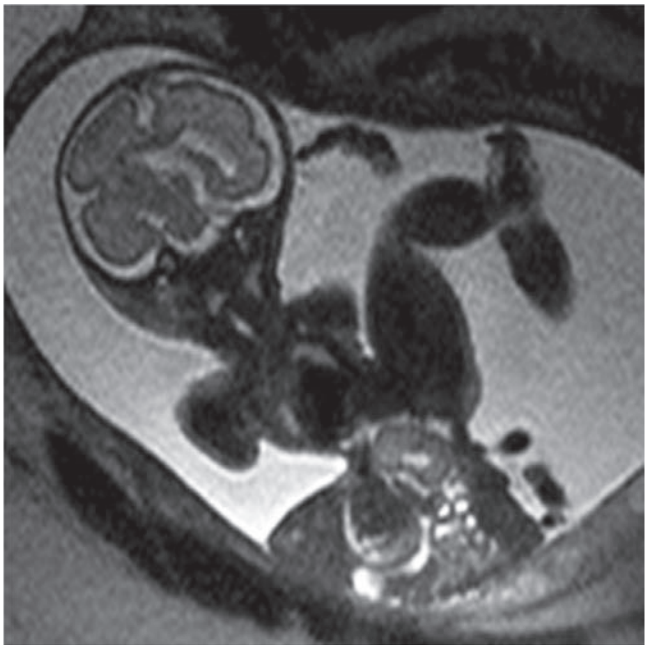

**Figure 85.16. Limb-body wall complex.** Extrusion of all abdominal contents in limb-body wall complex is seen on this T2-weighted MR image. Typically a very short umbilical cord and significant fetal contortion are present.

Gastroschisis is differentiated from omphalocele by the lack of a covering membrane of the herniated viscera and the normal insertion of the umbilical vessels at the abdominal wall (Fig. 85.19). MRI generally is not necessary for evaluation of this diagnosis because gastroschisis almost always is an isolated defect without additional fetal malformations or lung hypoplasia.[40] Closure of the abdominal wall defect in utero with subsequent severing of the extruded bowel, thus leading to extensive atresia/congenital short-gut syndrome, has been reported.[54] Additionally, on rare occasions, the membrane covering an omphalocele may rupture, thus simulating gastroschisis on imaging because of the free-floating appearance of the bowel. Differentiation is made by examining the relationship of the umbilical vessels to the extruded bowel and liver. Liver extrusion strongly favors ruptured omphalocele, though up to 6% of gastroschisis cases can have extracorporeal liver[55] (Fig. 85.20).

More complex ventral wall defects may benefit from combined US and MR evaluations, given their complementary attributes. MRI can provide a confident diagnosis of cloacal exstrophy in the appropriate setting.[56]

***Treatment and Follow-up.*** Fetuses in whom omphalocele is diagnosed are tested for chromosomal abnormalities because the incidence of aneuploidy is 40% to 60%, especially if only bowel is herniated.[57] The outcome for patients with omphalocele is usually dependent on the severity of other anomalies, including cardiac defects.[58] Repair of omphaloceles in the newborn period has a high rate of success, especially with surgical techniques emphasizing gradual reduction for larger lesions.[41,59,60]

Gastroschisis, unlike omphalocele, is not associated with chromosomal abnormalities, although the occurrence of extraintestinal abnormalities is approximately 6%.[61] Fetuses with gastroschisis experience complications that occur in the part of the bowel directly exposed to amniotic fluid during pregnancy; perforation or atresia occurs in up to 20% of cases.[61] Although dilation of the herniated loops is poorly correlated to worsened prognosis, sustained distension of intraabdominal bowel loops is of concern.[62] Postnatally, these patients may require resection of portions of their

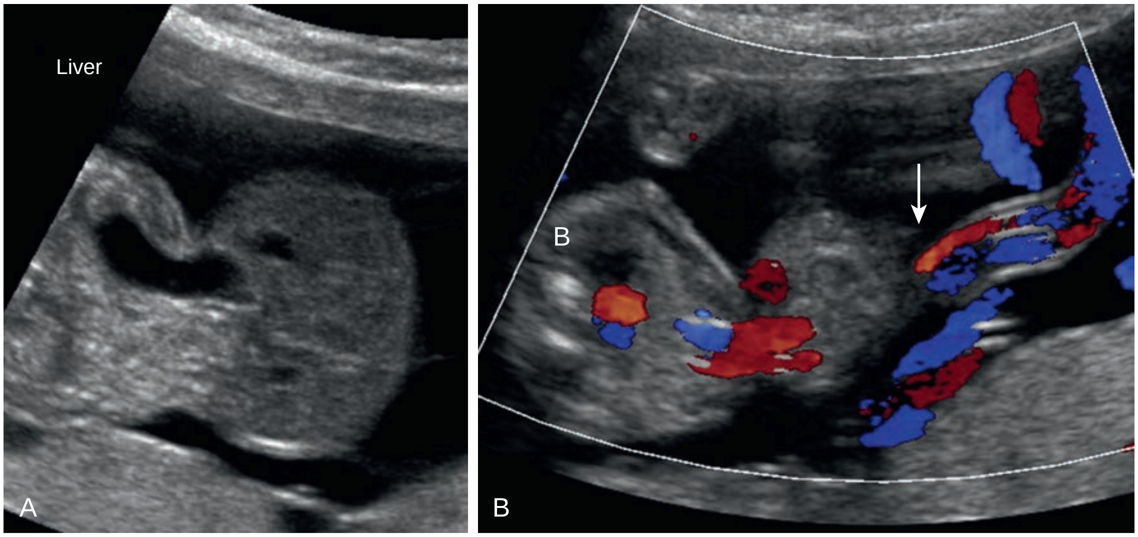

**Figure 85.18. Omphalocele containing liver and distal stomach.** (A) Gray-scale and (B) color Doppler sonogram shows the umbilical cord inserting into the omphalocele sac *(arrow);* see also Fig. 85.14. The spine is on the *left.*

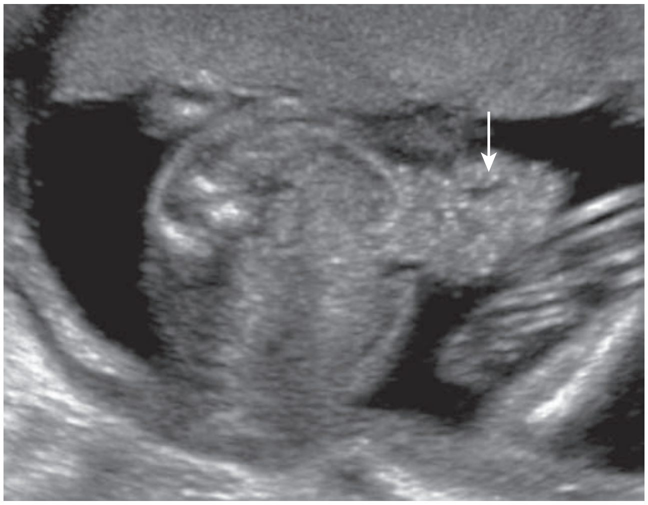

**Figure 85.19. Gastroschisis.** Transverse sonogram shows a right paraumbilical defect with herniation of small bowel loops *(arrow)* into the amniotic cavity with no surrounding membrane.

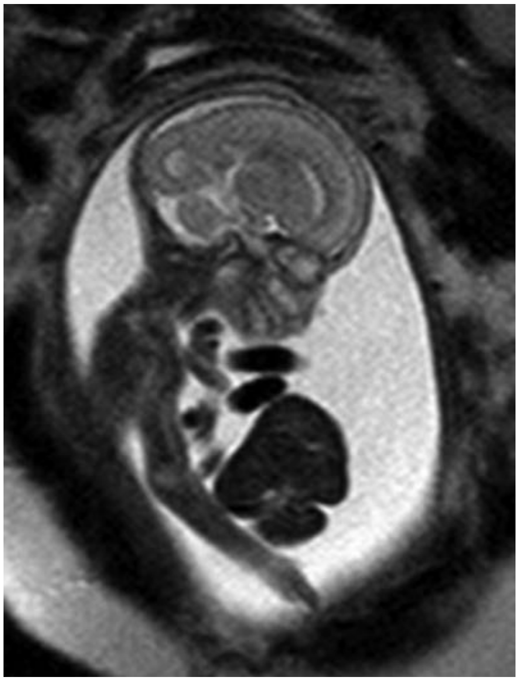

**Figure 85.20. Ruptured omphalocele.** Sagittal SSFSE MR image shows liver outside the fetal abdomen without a covering membrane.

bowel, and short-gut syndrome may develop. These children are at risk for presentation with necrotizing enterocolitis and perforation even months after undergoing repair.[63,64]

In fetuses with either omphalocele or gastroschisis, bowel rotation does not occur, and these patients, by definition, have malrotation of the midgut.

## ECHOGENIC BOWEL AND PERITONEAL ABNORMALITIES

***Overview.*** Echogenic bowel is a nonspecific US finding that should not be ignored, as it could be a marker for an underlying abnormality, although, in most cases, no subsequent fetal or neonatal problem develops.[65] Abnormalities of the peritoneum in the fetus include ascites and calcifications.

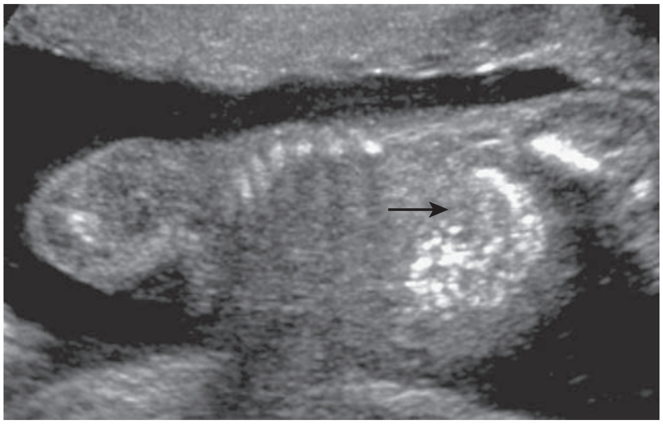

**Figure 85.21. Echogenic bowel.** Longitudinal sonogram of a 20-week fetus with echogenic bowel *(arrow)* that is as hyperechoic as the adjacent bone. Intrauterine growth retardation was present.

**BOX 85.2** Causes of Fetal Ascites

**SEROUS**

Bowel perforation (fluid may be complex)
Hydrops: immune and nonimmune (most common cause)
Ruptured or torted ovarian cyst
Cardiac decompensation
Hypoproteinemia
Hepatic dysfunction (storage disorders, mass, infection)

**BILIOUS**

Perforation of a choledochal cyst

**CHYLOUS**

Thoracic duct obstruction, increased intrathoracic pressure
Lymphatic malformation (e.g., Klippel–Trenaunay syndrome)
Mesenteric lymphangiomatosis

**HEMORRHAGIC**

Rupture of a vascular tumor
Trauma

**URINIFEROUS**

Perforation of the collecting system or bladder
Cloacal malformation, urogenital sinus

***Etiology.*** The underlying conditions in fetuses with echogenic bowel are as varied in etiology as infection (e.g., cytomegalovirus or parvovirus), intrauterine growth retardation, or aneuploidy (e.g., trisomy 21); alternatively, the direct cause of the increased conspicuity of the bowel might remain unclear. In other cases, the etiology may be more obvious; for example, in persons with cystic fibrosis, the meconium is more viscous and may present as hyperechoic contents within the bowel lumen. If bleeding has occurred into either the amniotic fluid or GI tract, intraluminal fluid can appear bright on US.

The etiology of fetal ascites can be classified under five general categories, ranging from serous through chylous, hemorrhagic, bilious, and related to the urinary tract (Box 85.2).[66–75]

***Imaging.*** When the echogenicity of the fetal bowel equals that of the fetal skeleton, it is considered abnormal (Fig. 85.21).[76] It has been recommended that transducer frequencies of 5 MHz or less be used for confirmation, because higher frequencies may make the bowel appear unnecessarily bright.[77] Although most of these patients are healthy, the finding of abnormally bright bowel in the fetus should prompt a careful US search for additional abnormalities, with consideration of further imaging by MRI for evaluation of the neural axis if infection is suspected.

Imaging of fetal ascites should be directed toward determining whether the fluid can be related to a particular organ system. Anatomy should be examined carefully, whether on US or MRI, for abnormalities of the urinary or reproductive tracts, biliary system, chest, and bowel. The presence of septations or loculations might suggest protein contamination from blood products, bowel pathology, or abdominal lymphangiomatosis. In some cases, ascites may be a physiologic consequence of a condition (e.g., hypoproteinemia, hydrops, or infection) not directly related to an anatomic abnormality. It is important to look for any evidence of calcifications in the peritoneum, especially along the liver capsule, that would indicate meconium peritonitis and the implied disruption of bowel integrity, as from perforations secondary to obstruction or ischemia. Calcifications in the parenchyma of the liver or spleen might be a clue to the presence of aneuploidy or infection, or rarely may be related to portal emboli.[78,79] Calcification inside the bowel lumen is an indication of GI-genitourinary fistula (see Fig. 85.12).[80]

***Treatment and Follow-up.*** Treatment and follow-up are directed toward the cause of the finding and could include in utero intervention (e.g., intrauterine transfusion) and postnatal surgery, depending on the etiology. Fetuses who have isolated fetal ascites with a normal karyotype and a negative infection screen have a good prognosis.[81,82]

## MASSES AND OTHER VISCERAL ABNORMALITIES

***Overview.*** The category of fetal abdominal mass includes visceral enlargement and neoplasia. Cystic and solid mass lesions can also occur in the peritoneal cavity. Moreover, absence of structures, such as the spleen, should also be considered.

***Etiology.*** Visceromegaly includes hepatosplenomegaly, which may be the result of viral infection, fetal hydrops, glycogen or lysosomal storage disorders, Beckwith–Wiedemann syndrome, or the presentation in utero of anemia or hematologic malignancy (particularly for trisomy 21), and amniotic fluid testing may be necessary.[67,69,83–85] Isolated hepatomegaly may be secondary to increased right heart pressure; the liver also might appear enlarged if it lies transversely across the abdomen, as in heterotaxy. Neoplasia also may present with visceromegaly, with the organ being either a repository for metastatic disease, such as neuroblastoma diffusely metastatic to the liver,[86,87] or the site of a primary intraperitoneal mass, most frequently in the fetal liver, such as a hemangioma or hepatoblastoma (Fig. 85.22). Intrauterine torsion also can present with visceromegaly secondary to edema.[88–90] A special note should be made of megacystis-microcolon-hypoperistalsis syndrome, which can be considered in patients, more commonly female, with gross bladder enlargement and no colonic meconium on T1-weighted MRI (Fig. 85.23).[26,91]

The category of abnormal structures presenting as mass lesions includes intraperitoneal cysts or fluid collections, such as meconium cyst as a result of perforation of the bowel and meconium peritonitis (Figs. 85.24 and 85.25), or, as recently reported, as a result of reflux of meconium into the peritoneum through the uterus in a fetus with cloacal malformation.[92] Box 85.3 lists the origins of cystic masses in the abdomen and pelvis, and Box 85.4 describes solid masses that have been reported. Occasionally, a “pseudomass” is described inside of a bowel lumen, such as the stomach; in this particular case, it is thought to represent debris such as blood products and may be seen after a history of intervention (e.g., amniocentesis).[93] Note that, most commonly, masses in the fetal abdomen are related to the genitourinary tract.

Some abnormalities are related to the absence of expected structures. For example, the spleen may be absent, and the gallbladder may be in abnormal position or absent; these findings suggest heterotaxy, which would mandate careful evaluation of the cardiac axis and configuration and other viscerovascular structures. The gallbladder usually can be detected on serial US[94] and is identified consistently on MRI.[95] Its absence would suggest biliary atresia and polysplenia if found within the heterotaxy complex. A gallbladder also may be indistinguishable in a fetus with cystic fibrosis.

Calcifications and/or debris in the gallbladder can be a sign of fetal hemolysis, but most are incidental and do not cause

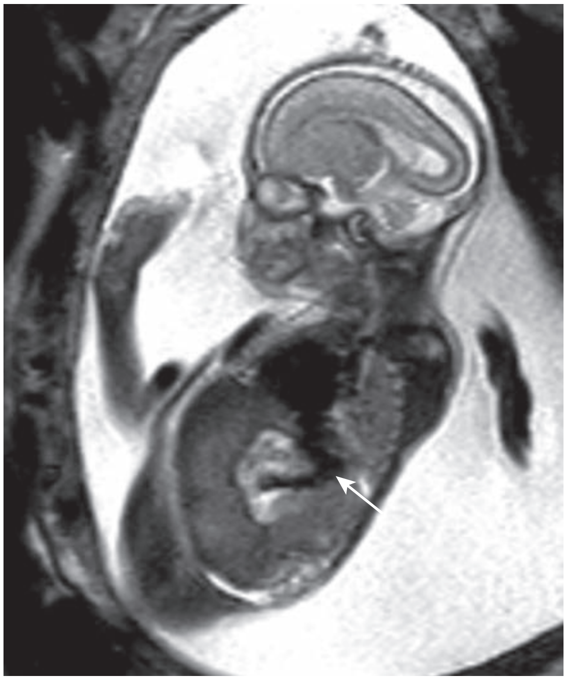

**Figure 85.22. Rapidly involuting congenital hemangioma (RICH).** Sagittal T2-weighted MR image of a high-signal mass lesion in the liver with large flow-void draining vein *(arrow)*.

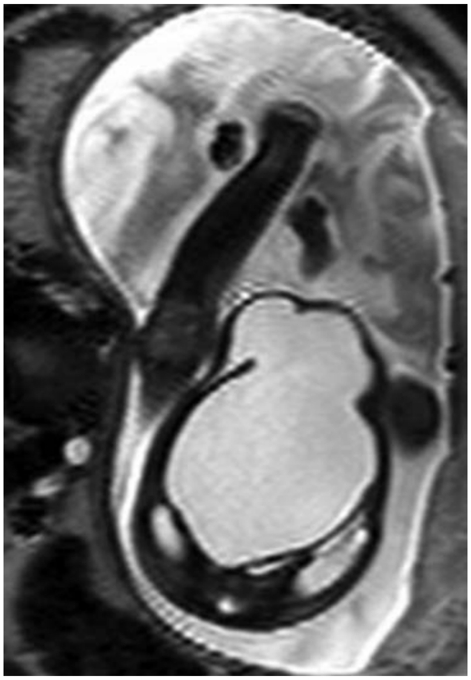

**Figure 85.23. Megacystis-microcolon-hypoperistalsis syndrome.** Axial SSFSE MR image in a female fetus with hydronephrosis and marked bladder distension. Normal amniotic fluid volume was present. No meconium could be identified in the bowel on T1-weighted imaging.

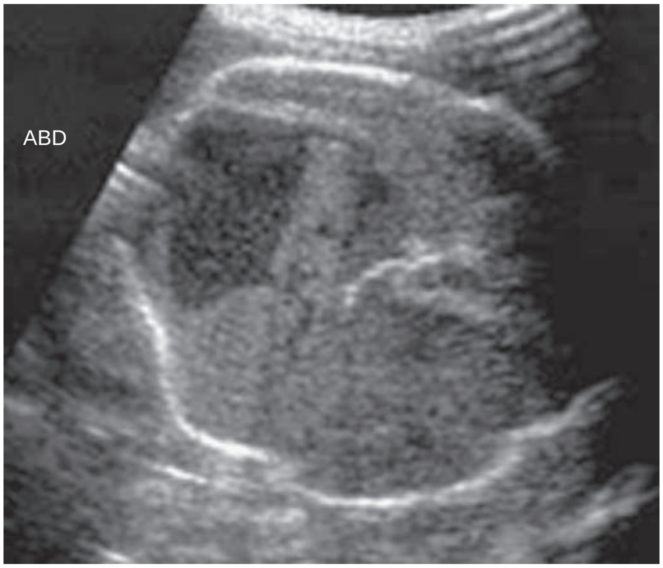

**Figure 85.24. Meconium pseudocyst.** Transverse sonogram shows a large loculated heterogeneous collection with a calcified rim within the abdomen. A sigmoid perforation was identified after delivery.

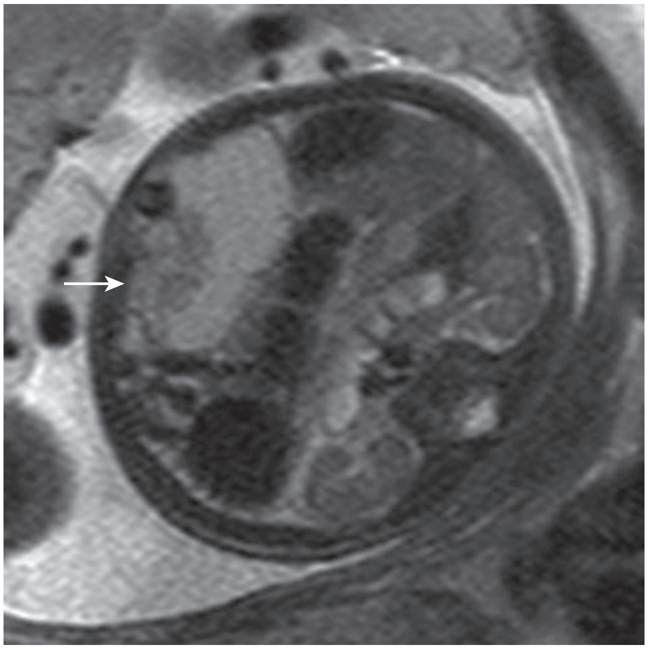

**Figure 85.25. Meconium pseudocyst.** T2-weighted MR image shows a medium to moderately high signal collection containing debris *(arrow),* consistent with meconium mixing.

### BOX 85.3 Intraperitoneal Cystic Masses in the Fetus*

Gastrointestinal tract: duplication, meconium pseudocyst, segmental dilatation of the ileum (ileal dysgenesis)
Biliary: choledochal cyst
Hepatic: epithelial cyst, mesenchymal hamartoma, vascular malformation
Splenic: congenital epithelial cyst, epidermoid
Lymphatic: mesenteric cyst, mesenteric lymphangiomatosis
Ovarian†: follicular cyst, torsion (late), teratoma

*Most cystic masses in the fetal abdomen are related to the genitourinary tract.

†Technically retroperitoneal, but may seem to present as an intraperitoneal mass. Note that other retroperitoneal masses, such as cystic neuroblastoma in the adrenal, may seem to be intraperitoneal depending on size.

### BOX 85.4 Intraperitoneal Solid Masses in the Fetus

Hepatic: hepatoblastoma, leukemic infiltration, rapidly involuting congenital hemangioma, torsion of accessory lobe, mesenchymal hamartoma, infarction
Splenic: torsion, leukemic infiltration
Gonadal*: torsion (early), teratoma, endometrioma
Pulmonary*: infradiaphragmatic sequestration

*Technically retroperitoneal, but may seem to present as an intraperitoneal mass.

complications.[96] Small stones typically resolve without intervention. Finally, organs may be displaced from their normal position in persons with splenogonadal fusion, the so-called *wandering spleen* or *liver*, and of course with diaphragmatic hernias and ventral wall defects.

***Imaging.*** Careful delineation of the organ of involvement and of the pertinent anatomy can suggest the correct diagnosis (Fig. 85.26). When calcifications are identified, infection should be considered, as discussed earlier.[97] The use of a high-resolution linear transducer in the appropriate patient can be extremely advantageous in delineating fine detail, such as subtle calcifications, the presence of a daughter cyst within a large cyst, indicative of ovarian origin, or the characteristic bowel signature of a duplication cyst. For all abnormalities, in addition to identifying the organ of origin, Doppler evaluation will help to understand whether a primary vascular lesion (increased flow) or torsion/ischemia (decreased flow) should be advanced in the differential diagnosis (Fig. 85.27).

US generally delineates well the origin of fetal abdominal masses from solid organs. Masses are investigated by MRI when the organ of origin or the extent of involvement is imprecisely detailed by ultrasonography. In addition to the use of GRE T1-weighted and FSE T2-weighted sequences, SSFP T2-weighted sequences are useful because of their ability to delineate adjacent structures and high-signal blood flow. This effect can be very helpful in identifying primary vascular lesions (e-Fig. 85.28) or enlarged vessels supplying tumors. In addition, fetal MRI may be indicated in the evaluation of the liver in conditions of potential iron overload, in which the signal from the liver is abnormally low.[98,99]

Umbilical venous varix is a vascular lesion that is variably associated with in utero complications.[100] Other vascular anomalies of the venous system, such as absence of the ductus venosus or agenesis of the portal vein, have been described and require meticulous delineation of the associated portosystemic shunt pathway by US Doppler or bright-blood (SSFP) MRI for accurate diagnosis.[101,102]

***Treatment and Follow-up.*** Depending on the diagnosis, alterations in planning and timing of delivery may be indicated; amniocentesis and in utero therapies may be considered (e.g., intrauterine transfusion for fetal anemia). In general, therapy is targeted at providing the safest environment in which appropriate treatment can be directed for the fetus or neonate. To date, there are no clear indications for fetal surgery for GI anomalies, although imaging evaluation can alter both the timing and mode of delivery. Open fetal surgery has been reserved for conditions determined to be terminal without intervention in a previable fetus, and has been limited to excisions of malformations and tumors of the chest, head and neck, and coccyx (e.g., sacrococcygeal teratoma).[103–105]

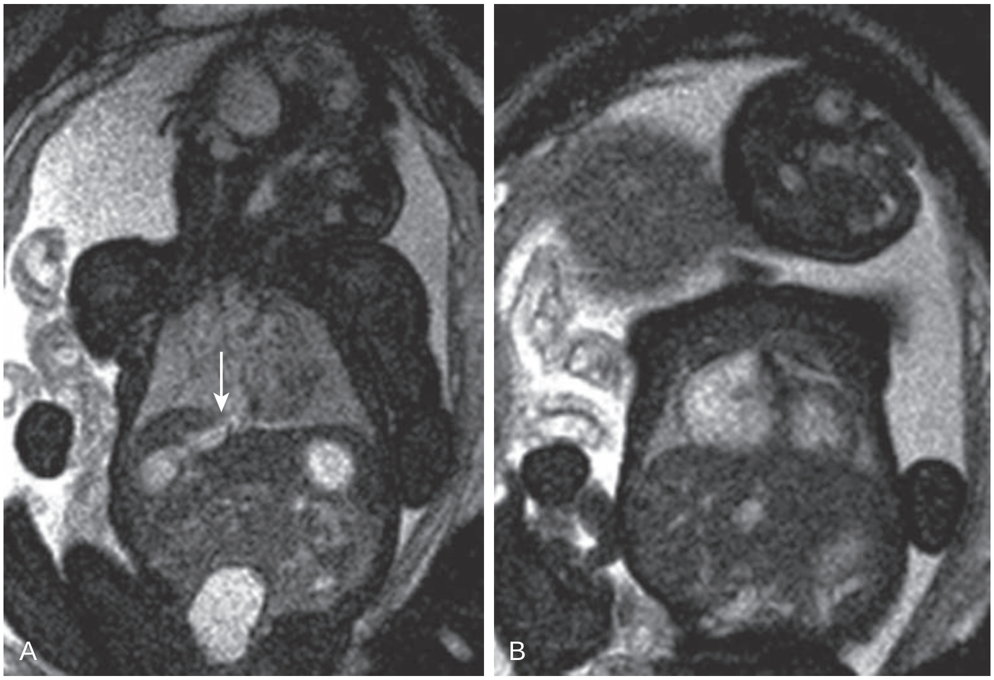

**e-Figure 85.28. Hepatic vascular malformation.** Balanced coronal SSFP MR images show an enlarged draining vein *(arrow*, (A)*)* and enlarged right atrium (B) as a result of congenital vascular malformation in the liver.

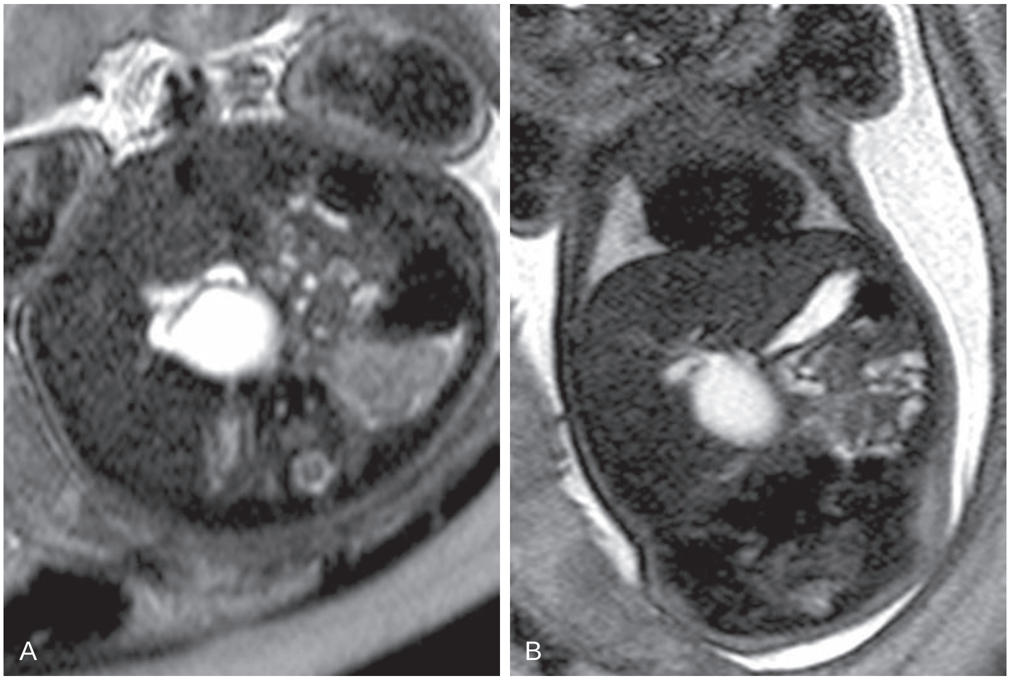

**Figure 85.26. Choledochal cyst.** (A) Axial and (B) coronal T2-weighted SSFSE MR images of a cystic mass at the margin of the liver demonstrate a connection to the biliary system.

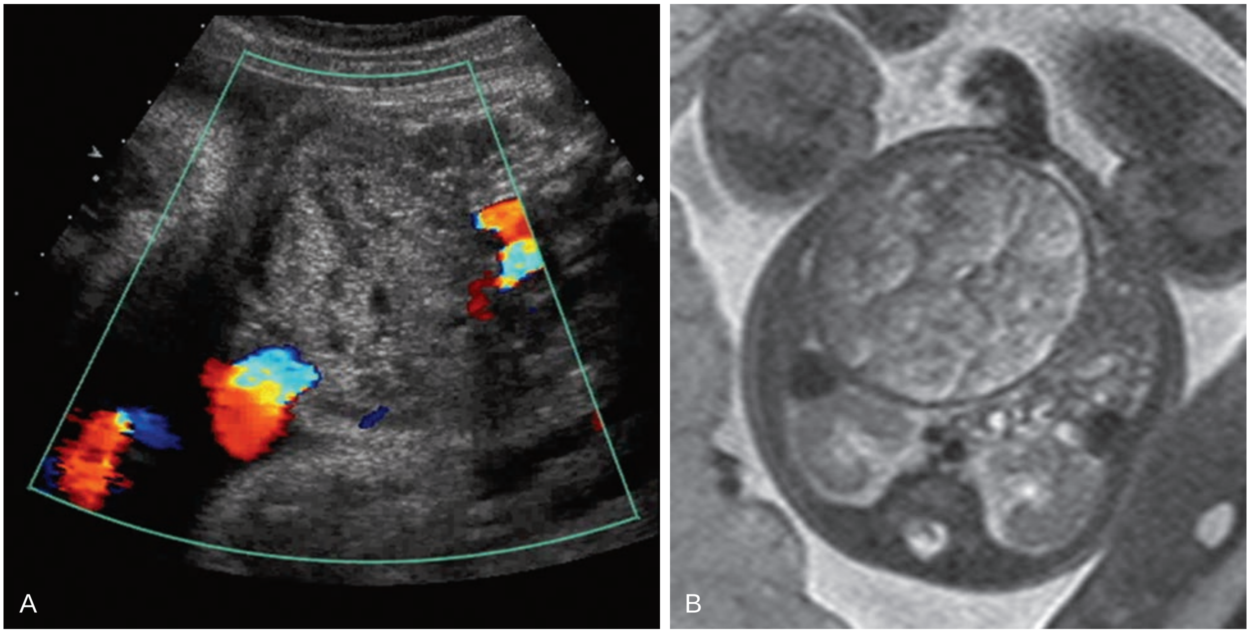

**Figure 85.27. Ovarian torsion.** A solid-appearing but avascular mass is delineated in this female fetus with both color Doppler ultrasound (A) and MRI (B).

## KEY POINTS

- US is for screening of fetal bowel abnormalities and will answer almost all questions. MRI can be useful for targeted questions unanswered by ultrasonography, including evaluation of microcolon and abnormal meconium signal distribution.
- Ventral wall defects are distinguished by what is herniated from the fetal abdomen, the presence of a covering membrane, and the relationship of the umbilical vessels to the herniated viscera.
- When fetal ascites are encountered, a careful search for an anatomic abnormality to the cardiac, pulmonary, biliary, genitourinary, and GI systems is indicated.
- Precise identification of the organ(s) of origin will determine an appropriate differential diagnosis for fetal abdominal masses.

## SUGGESTED READINGS

Birkemeier KL. Abdominal masses. In: Kline-Fath BM, ed. *Fundamental and Advanced Fetal Imaging*. Philadelphia: Wolters Kluwer Health; 2015:651–667.

Brugger PC. MRI of the fetal abdomen. In: Prayer D, ed. *Fetal MRI*. Berlin: Springer-Verlag; 2011:377–402.

Bulas DI. Bowel abnormalities. In: Kline-Fath BM, ed. *Fundamental and Advanced Fetal Imaging*. Philadelphia: Wolters Kluwer Health; 2015:617–634.

Linam LE. Ventral Wall Defects. In: Kline-Fath BM, ed. *Fundamental and Advanced Fetal Imaging*. Philadelphia: Wolters Kluwer Health; 2015:635–650.

## REFERENCES

Full references for this chapter can be found on www.expertconsult.com.

## REFERENCES

1. Brugger PC, et al. Methods of fetal MR: beyond T2-weighted imaging. *Eur J Radiol*. 2006;57(2):172–181.
2. Spilde TL, et al. Fibroblast growth factor signaling in the developing tracheoesophageal fistula. *J Pediatr Surg*. 2003;38(3):474–477, discussion 474-477.
3. Hryhorczuk AL, Lee EY, Eisenberg RL. Esophageal abnormalities in pediatric patients. *AJR Am J Roentgenol*. 2013;201(4):W519–W532.
4. Oddsberg J, et al. Influence of maternal parity, age, and ethnicity on risk of esophageal atresia in the infant in a population-based study. *J Pediatr Surg*. 2008;43(9):1660–1665.
5. El-Gohary Y, Gittes GK, Tovar JA. Congenital anomalies of the esophagus. *Semin Pediatr Surg*. 2010;19(3):186–193.
6. Al-Salem AH. Congenital pyloric atresia and associated anomalies. *Pediatr Surg Int*. 2007;23(6):559–563.
7. Botham RA, et al. Formation of duodenal atresias in fibroblast growth factor receptor 2IIIb-/- mouse embryos occurs in the absence of an endodermal plug. *J Pediatr Surg*. 2012;47(7):1369–1379.
8. Celli J. Genetics of gastrointestinal atresias. *Eur J Med Genet*. 2014;57(8):424–439.
9. Dalla Vecchia LK, et al. Intestinal atresia and stenosis: a 25-year experience with 277 cases. *Arch Surg*. 1998;133(5):490–496, discussion 496-497.
10. Touloukian RJ. Diagnosis and treatment of jejunoileal atresia. *World J Surg*. 1993;17(3):310–317.
11. Bilodeau A, et al. Hereditary multiple intestinal atresia: thirty years later. *J Pediatr Surg*. 2004;39(5):726–730.
12. Gahukamble DB, Adnan AR, Al-Gadi M. Atresias of the gastrointestinal tract in an inbred, previously unstudied population. *Pediatr Surg Int*. 2002;18(1):40–42.
13. Seo T, et al. Colonic atresia and Hirschsprung's disease: importance of histologic examination of the distal bowel. *J Pediatr Surg*. 2002;37(8):E19.
14. Sweeney B, Surana R, Puri P. Jejunoileal atresia and associated malformations: correlation with the timing of in utero insult. *J Pediatr Surg*. 2001;36(5):774–776.
15. Brugger PC. Methods of fetal MRI. In: Prayer D, ed. *Fetal MRI*. Berlin: Springer-Verlag; 2011.
16. Al-Assiri A, Wiseman N, Bunge M. Prenatal diagnosis of intrathoracic stomach (gastric herniation). *J Pediatr Surg*. 2005;40(2):E15–E17.
17. Kimble RM, Harding JE, Kolbe A. Does gut atresia cause polyhydramnios? *Pediatr Surg Int*. 1998;13(2–3):115–117.
18. Brugger PC, Prayer D. Fetal abdominal magnetic resonance imaging. *Eur J Radiol*. 2006;57(2):278–293.
19. Malas MA, et al. The development of large intestine during the fetal period. *Early Hum Dev*. 2004;78(1):1–13.
20. Zalel Y, et al. In-utero development of the fetal colon and rectum: sonographic evaluation. *Ultrasound Obstet Gynecol*. 2003;21(2):161–164.
21. Carcopino X, et al. Foetal magnetic resonance imaging and echogenic bowel. *Prenat Diagn*. 2007;27(3):272–278.
22. Muller F, et al. Prenatal diagnosis of cystic fibrosis. II. Meconium ileus in affected fetuses. *Prenat Diagn*. 1985;5(2):109–117.
23. Zizka J, et al. Liver, meconium, haemorrhage: the value of T1-weighted images in fetal MRI. *Pediatr Radiol*. 2006;36(8):792–801.
24. Miyakoshi K, et al. Prenatal diagnosis of midgut volvulus by sonography and magnetic resonance imaging. *Am J Perinatol*. 2001;18(8):447–450.
25. Sciarrone A, et al. Fetal midgut volvulus: report of eight cases. *J Matern Fetal Neonatal Med*. 2016;29(8):1322–1327.
26. Veyrac C, et al. MRI of fetal GI tract abnormalities. *Abdom Imaging*. 2004;29(4):411–420.
27. Benachi A, et al. Determination of the anatomical location of an antenatal intestinal occlusion by magnetic resonance imaging. *Ultrasound Obstet Gynecol*. 2001;18(2):163–165.
28. Biyyam DR, Dighe M, Siebert JR. Antenatal diagnosis of intestinal malrotation on fetal MRI. *Pediatr Radiol*. 2009;39(8):847–849.
29. Colombani M, et al. Fetal gastrointestinal MRI: all that glitters in T1 is not necessarily colon. *Pediatr Radiol*. 2010;40(7):1215–1221.
30. Harris RD, et al. Anorectal atresia: prenatal sonographic diagnosis. *AJR Am J Roentgenol*. 1987;149(2):395–400.
31. Lee MY, et al. Sonographic determination of type in a fetal imperforate anus. *J Ultrasound Med*. 2016;35(6):1285–1291.
32. Perlman S, et al. More than a gut feeling - sonographic prenatal diagnosis of imperforate anus in a high-risk population. *Prenat Diagn*. 2014;34(13):1307–1311.
33. Eliyahu S, et al. Sonographic presentation of Hirschsprung's disease. A case of an entirely aganglionic colon and ileum. *Prenat Diagn*. 1994;14(12):1170–1172.
34. Jakobson-Setton A, et al. Retrospective analysis of prenatal ultrasound of children with Hirschsprung disease. *Prenat Diagn*. 2015;35(7):699–702.
35. Akdag A, et al. *Fetal Bowel Dilatation Due to Intestinal Neuronal Dysplasia: a Rarity*. *APSP J Case Rep*. 2016;7(2):14.
36. Paradiso FV, et al. Antenatal ultrasonographic features associated with segmental small bowel dilatation: an unusual neonatal condition mimicking congenital small bowel obstruction. *Pediatr Neonatol*. 2013;54(5):339–343.
37. Colombani M, et al. Magnetic resonance imaging in the prenatal diagnosis of congenital diarrhea. *Ultrasound Obstet Gynecol*. 2010;35(5):560–565.
38. Samuel N, et al. Ultrasound diagnosis and management of fetal intestinal obstruction and volvulus in utero. *J Perinat Med*. 1984;12(6):333–337.
39. Shen O, et al. Prenatal diagnosis of intestinal pseudo-obstruction. *Ultrasound Obstet Gynecol*. 2007;29(2):229–231.
40. Vermeij-Keers C, Hartwig NG, van der Werff JF. Embryonic development of the ventral body wall and its congenital malformations. *Semin Pediatr Surg*. 1996;5(2):82–89.
41. Langer JC. Gastroschisis and omphalocele. *Semin Pediatr Surg*. 1996;5(2):124–128.
42. El-Hattab AW, et al. OEIS complex associated with chromosome 1p36 deletion: a case report and review. *Am J Med Genet A*. 2010;152A(2):504–511.
43. Bohring A. OEIS complex, VATER, and the ongoing difficulties in terminology and delineation. *Am J Med Genet*. 2002;107(1):72–76.
44. Aguirre-Pascual E, et al. Prenatal MRI evaluation of limb-body wall complex. *Pediatr Radiol*. 2014;44(11):1412–1420.
45. Feldkamp ML, Carey JC, Sadler TW. Development of gastroschisis: review of hypotheses, a novel hypothesis, and implications for research. *Am J Med Genet A*. 2007;143A(7):639–652.
46. Stevenson RE, et al. Escape of the yolk sac: a hypothesis to explain the embryogenesis of gastroschisis. *Clin Genet*. 2009;75(4):326–333.
47. Haddow JE, Palomaki GE, Holman MS. Young maternal age and smoking during pregnancy as risk factors for gastroschisis. *Teratology*. 1993;47(3):225–228.
48. Loane M, et al. Maternal age-specific risk of non-chromosomal anomalies. *BJOG*. 2009;116(8):1111–1119.
49. Lee SL, et al. Initial nonoperative management and delayed closure for treatment of giant omphaloceles. *J Pediatr Surg*. 2006;41(11):1846–1849.
50. Wilson RD, Johnson MP. Congenital abdominal wall defects: an update. *Fetal Diagn Ther*. 2004;19(5):385–398.
51. Sepulveda W, et al. Pseudocyst of the umbilical cord: prenatal sonographic appearance and clinical significance. *Obstet Gynecol*. 1999;93(3):377–381.
52. Argyle JC. Pulmonary hypoplasia in infants with giant abdominal wall defects. *Pediatr Pathol*. 1989;9(1):43–55.
53. Edwards EA, et al. Long-term respiratory support in children with giant omphalocele. *Anaesth Intensive Care*. 2007;35(1):94–98.
54. Bhatia AM, Musemeche CA, Crino JP. Gastroschisis complicated by midgut atresia and closure of the defect in utero. *J Pediatr Surg*. 1996;31(9):1288–1289.
55. McClellan EB, et al. Liver herniation in gastroschisis: incidence and prognosis. *J Pediatr Surg*. 2011;46(11):2115–2118.
56. Calvo-Garcia MA, et al. Fetal MRI of cloacal exstrophy. *Pediatr Radiol*. 2013;43(5):593–604.
57. Nyberg DA, et al. Chromosomal abnormalities in fetuses with omphalocele. Significance of omphalocele contents. *J Ultrasound Med*. 1989;8(6):299–308.
58. Mayer T, et al. Gastroschisis and omphalocele. An eight-year review. *Ann Surg*. 1980;192(6):783–787.
59. Pacilli M, et al. Staged repair of giant omphalocele in the neonatal period. *J Pediatr Surg*. 2005;40(5):785–788.
60. Schlatter M, et al. Improved outcomes in the treatment of gastroschisis using a preformed silo and delayed repair approach. *J Pediatr Surg*. 2003;38(3):459–464, discussion 459-464.
61. Brantberg A, et al. Surveillance and outcome of fetuses with gastroschisis. *Ultrasound Obstet Gynecol*. 2004;23(1):4–13.
62. Huh NG, Hirose S, Goldstein RB. Prenatal intraabdominal bowel dilation is associated with postnatal gastrointestinal complications in fetuses with gastroschisis. *Am J Obstet Gynecol*. 2010;202(4):396 e1–396 e6.

63. Benamar A, et al. [Necrotizing enterocolitis in two infants with gastroschisis]. *Arch Pediatr*. 2008;15(2):149–152.
64. Oldham KT, et al. The development of necrotizing enterocolitis following repair of gastroschisis: a surprisingly high incidence. *J Pediatr Surg*. 1988;23(10):945–949.
65. Kesrouani AK, et al. Etiology and outcome of fetal echogenic bowel. Ten years of experience. *Fetal Diagn Ther*. 2003;18(4):240–246.
66. Alkan M, et al. Fetal urinary ascites in a neonate without detectable obstructive uropathy or neurogenic bladder etiology. *J Pediatr Urol*. 2009;5(2):151–153.
67. Camanni D, et al. Isolated fetal ascites secondary to persistent urogenital sinus. *Obstet Gynecol Int*. 2009;2009:219010.
68. Casaccia G, et al. Prenatal rectal perforation: an unsuspected cause of isolated ascites. *J Perinatol*. 2006;26(11):717–719.
69. Chen CP, et al. Prenatal sonographic findings of Klippel-Trenaunay-Weber syndrome. *J Clin Ultrasound*. 2007;35(7):409–412.
70. Degani S. Sonographic findings in fetal viral infections: a systematic review. *Obstet Gynecol Surv*. 2006;61(5):329–336.
71. Degani S, Lewinsky RM. Transient ascites associated with a fetal ovarian cyst. Case report. *Fetal Diagn Ther*. 1995;10(3):200–203.
72. Nitta A, et al. Fetal hemophagocytic lymphohistiocytosis in a premature infant. *J Pediatr*. 2007;151(1):98.
73. Piersigilli F, et al. Isolated fetal ascites due to Budd-Chiari syndrome. *Ultrasound Obstet Gynecol*. 2008;31(2):222–223.
74. Spiegel R, et al. The clinical spectrum of fetal Niemann-Pick type C. *Am J Med Genet A*. 2009;149A(3):446–450.
75. Truin G, et al. Pericardial and abdominal fluid accumulation in congenital disorder of glycosylation type Ia. *Mol Genet Metab*. 2008;94(4):481–484.
76. Al-Kouatly HB, et al. The clinical significance of fetal echogenic bowel. *Am J Obstet Gynecol*. 2001;185(5):1035–1038.
77. Vincoff NS, et al. Effect of ultrasound transducer frequency on the appearance of the fetal bowel. *J Ultrasound Med*. 1999;18(12):799–803, quiz 805-806.
78. Achiron R, et al. Prenatal ultrasonographic diagnosis of fetal hepatic hyperechogenicities: clinical significance and implications for management. *Ultrasound Obstet Gynecol*. 1996;7(4):251–255.
79. Simchen MJ, et al. Fetal hepatic calcifications: prenatal diagnosis and outcome. *Am J Obstet Gynecol*. 2002;187(6):1617–1622.
80. Lubusky M, et al. Fetal enterolithiasis: prenatal sonographic and MRI diagnosis in two cases of urorectal septum malformation (URSM) sequence. *Prenat Diagn*. 2006;26(4):345–349.
81. El Bishry G. The outcome of isolated fetal ascites. *Eur J Obstet Gynecol Reprod Biol*. 2008;137(1):43–46.
82. Zelop C, Benacerraf BR. The causes and natural history of fetal ascites. *Prenat Diagn*. 1994;14(10):941–946.
83. Ghidini A, et al. Hepatosplenomegaly as the only prenatal finding in a fetus with pyruvate kinase deficiency anemia. *Am J Perinatol*. 1991;8(1):44–46.
84. Lipitz S, et al. Prenatal diagnosis of fetal primary cytomegalovirus infection. *Obstet Gynecol*. 1997;89(5 Pt 1):763–767.
85. Smrcek JM, et al. Fetal hydrops and hepatosplenomegaly in the second half of pregnancy: a sign of myeloproliferative disorder in fetuses with trisomy 21. *Ultrasound Obstet Gynecol*. 2001;17(5):403–409.
86. Jaffa AJ, et al. Prenatal sonographic diagnosis of metastatic neuroblastoma: report of a case and review of the literature. *Prenat Diagn*. 1993;13(1):73–77.
87. Jennings RW, et al. Fetal neuroblastoma: prenatal diagnosis and natural history. *J Pediatr Surg*. 1993;28(9):1168–1174.
88. Applegate KE, Ghei M, Perez-Atayde AR. Prenatal detection of a solitary liver adenoma. *Pediatr Radiol*. 1999;29(2):92–94.
89. Catanzarite V, et al. Prenatal diagnosis of fetal hepatoblastoma: case report and review of the literature. *J Ultrasound Med*. 2008;27(7):1095–1098.
90. Woodward PJ, et al. From the archives of the AFIP: a comprehensive review of fetal tumors with pathologic correlation. *Radiographics*. 2005;25(1):215–242.
91. Garel C, et al. Contribution of fetal magnetic resonance imaging and amniotic fluid digestive enzyme assays to the evaluation of gastrointestinal tract abnormalities. *Ultrasound Obstet Gynecol*. 2006; 28(3):282–291.
92. Hamada T, et al. Giant cystic meconium peritonitis associated with a cloacal anomaly: case report. *J Pediatr Surg*. 2008;43(3):E21–E23.
93. McNamara A, Levine D. Intraabdominal fetal echogenic masses: a practical guide to diagnosis and management. *Radiographics*. 2005;25(3):633–645.
94. Shen O, et al. Absent gallbladder on fetal ultrasound: prenatal findings and postnatal outcome. *Ultrasound Obstet Gynecol*. 2011;37(6):673–677.
95. Brugger PC, Weber M, Prayer D. Magnetic resonance imaging of the fetal gallbladder and bile. *Eur Radiol*. 2010;20(12):2862–2869.
96. Brown DL, et al. Echogenic material in the fetal gallbladder: sonographic and clinical observations. *Radiology*. 1992;182(1):73–76.
97. Imbar T, et al. Diagnosis, surveillance, and treatment of the anemic fetus using middle cerebral artery peak systolic velocity measurement. *Prenat Diagn*. 2006;26(1):45–51.
98. Cassart M, et al. Fetal liver iron overload: the role of MR imaging. *Eur Radiol*. 2011;21(2):295–300.
99. Marti-Bonmati L, et al. Prenatal diagnosis of idiopathic neonatal hemochromatosis with MRI. *Abdom Imaging*. 1994;19(1):55–56.
100. Zalel Y, et al. Varix of the fetal intra-abdominal umbilical vein: prenatal sonographic diagnosis and suggested in utero management. *Ultrasound Obstet Gynecol*. 2000;16(5):476–478.
101. Achiron R, et al. Prenatal diagnosis of congenital agenesis of the fetal portal venous system. *Ultrasound Obstet Gynecol*. 2009;34(6):643–652.
102. Perles Z, et al. Absent ductus venosus in the fetus: review of the literature and first report of direct umbilical venous drainage to the coronary sinus. *Fetal Diagn Ther*. 2003;18(4):247–251.
103. Adzick NS, et al. Fetal surgery for cystic adenomatoid malformation of the lung. *J Pediatr Surg*. 1993;28(6):806–812.
104. Hirose S, Farmer DL. Fetal surgery for sacrococcygeal teratoma. *Clin Perinatol*. 2003;30(3):493–506.
105. Hirose S, et al. Spectrum of intrapartum management strategies for giant fetal cervical teratoma. *J Pediatr Surg*. 2003;38(3):446–450, discussion 446-450.

# 86

# The Abdominal Wall and Peritoneal Cavity

*Katrina F. Chu and Michael S. Gee*

## PERITONEAL CAVITY

***Overview.*** The peritoneum is a thin serosal membrane of mesodermal origin that comprises a single layer of mesothelial cells resting on a basement membrane.[1] It is divided into visceral and parietal components, and the space between the two components constitutes the peritoneal cavity. The layer covering the abdominal viscera, omentum, and the mesenteries is designated *visceral*, whereas the layer covering the abdominal walls, undersurface of the diaphragm, anterior surface of the retroperitoneal viscera, and the pelvis is designated as *parietal*. The peritoneum is continuous in males, whereas in females it is discontinuous at the ostia of the oviducts to allow communication between the peritoneal cavity and extraperitoneal pelvis.

The layers of peritoneum that invest blood vessels, lymphatics, nerves, adipose tissue, and connective tissue within the abdomen and the pelvis form the various peritoneal ligaments, omentum, and mesenteries. A ligament usually supports a structure within the cavity, whereas a mesentery usually suspends the structure to the retroperitoneum. Omentum is a specialized ligament that connects the stomach to another structure. These ligaments and mesenteries not only serve to suspend and support the visceral organs but also divide the peritoneal cavity into multiple compartments that dictate the location and routes of spread of malignancies and infection.

The mesothelial cells produce a small amount of sterile fluid within the peritoneal cavity that is continuously circulated by the movement of the diaphragm and peristalsis of bowel, and the fluid provides a frictionless surface over which the viscera can move, a site for fluid transport, and local bacterial defense.[1] Peritoneal fluid predominantly flows up the right paracolic gutter into the right supramesocolic compartment, and 90% of the fluid is cleared by the subphrenic lymphatics to the supradiaphragmatic nodes.[2] Areas of relative stasis include (1) the rectouterine pouch or cul-de-sac (pouch of Douglas) in females, (2) the rectovesical region in males, (3) the right lower abdomen at the end of the small bowel mesentery, (4) the left lower abdomen along the sigmoid mesocolon, (5) the right paracolic gutter, and (6) the right subhepatic/subdiaphragmatic space (Morison pouch).[2]

## ENTITIES AFFECTING THE PERITONEUM

### Pneumoperitoneum

***Overview.*** The term *pneumoperitoneum* refers to the presence of air within the peritoneal cavity. Benign postoperative pneumoperitoneum is a separate entity that results from accumulation of free air after abdominal surgery. Usually, free intraperitoneal air clears more rapidly in children than in adults, but the timing can be variable. Timing of clearance usually depends upon the amount of air initially trapped after surgery, which in most cases is related to patient body habitus; obese patients trap less air than thin patients.[3] Several studies have demonstrated clearing of free air in 68% to 90% of children postoperatively by 24 hours, but free air can be seen for as long as 6 to 7 days postoperatively in 2% to 3% of cases.[3]

***Etiology.*** Free intraperitoneal air is most commonly a consequence of gastrointestinal (GI) tract perforation.[4] In the neonate, this usually results from intestinal obstruction, necrotizing enterocolitis, or spontaneous gastric or bowel perforation, usually at the ileocecal region (Box 86.1).[5] Necrotizing enterocolitis is the most common cause of pneumoperitoneum in the neonatal intensive care unit.[6]

Free intraperitoneal air sometimes results from mediastinal extension in newborns supported by mechanical ventilation. Rarely, nasogastric or nasoduodenal tubes may perforate the bowel. The position of the tube is often a clue to the perforation (e-Fig. 86.1).

In children beyond the neonatal period, perforated peptic ulcers and inflammatory bowel disease (IBD) are other causes of pneumoperitoneum; it should be noted that pneumoperitoneum is rarely found with appendiceal perforation, because the omentum usually seals off the perforation very quickly.[7] Trauma, both accidental and nonaccidental, may also result in pneumoperitoneum.

***Clinical Presentation.*** Pneumoperitoneum may be suspected clinically because of the history of an underlying condition that predisposes to bowel perforation, detection of acute abdominal distension with increased tympany on physical examination, and clinical deterioration of the patient. Occasionally it is incidentally discovered on imaging of the chest or abdomen.

***Imaging.*** A single supine abdominal radiograph is usually the most common imaging study requested for patients with suspected abdominal pathology. The cited overall detection rate of free intraperitoneal air on supine imaging ranges from 56% to 59%; detection rates as high as 80% have been quoted on supine abdominal radiographs and 78.7% on supine chest radiographs.[4] It is important to be familiar with the various signs of intraperitoneal free air on supine radiographs, because this may be the only initial study requested by the patient's primary caregiver.

Once suspected, the diagnosis can be confirmed on upright or decubitus films. Upright radiographs will show air collecting between the diaphragm and the liver on the right and between

**BOX 86.1** Causes of Pneumoperitoneum in Newborns

**WITH PERFORATION OF THE GASTROINTESTINAL TRACT**

- Gastric perforation, spontaneous or iatrogenic (nasogastric tubes)
- Duodenal ulcer with perforation
- Isolated perforation of the small bowel or colon in the absence of associated abnormality
- Perforation of Meckel diverticulum (ectopic gastric mucosa with ulceration)
- Necrotizing enterocolitis
- Colonic perforation (secondary to instrumentation, enema tip, thermometer)
- Perforation secondary to intestinal obstruction (atresia, meconium ileus, Hirschsprung disease, neonatal small left colon)
- Secondary to postsurgical anastomotic leak

**WITHOUT PERFORATION OF THE GASTROINTESTINAL TRACT**

- Pulmonary air leaks (pneumomediastinum) with or without other manifestations of alveolar leaks
- Idiopathic (extremely rare)

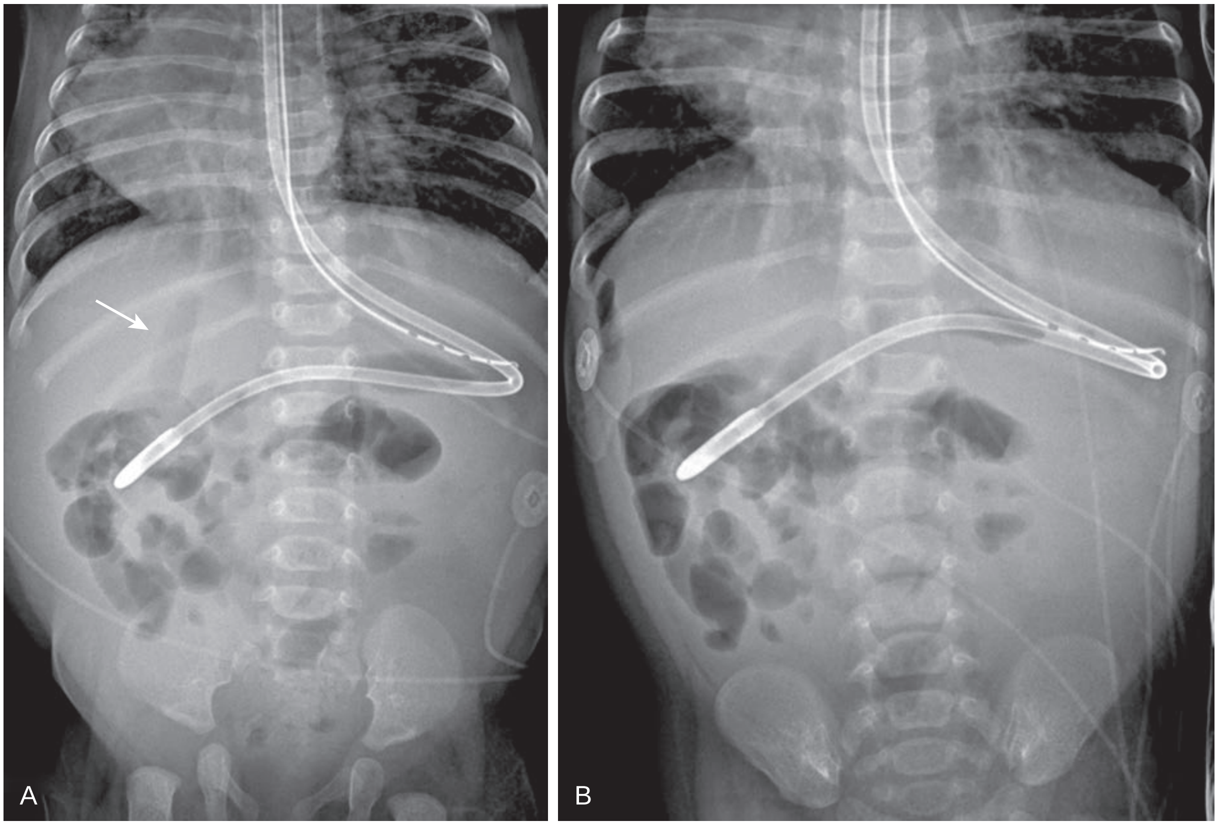

**e-Figure 86.1. Perforation by enteric tube.** (A) This 3-month-old infant with dextrocardia and heterotaxy underwent imaging for abdominal distension. The feeding tube is more lateral than expected, and a concerning lucency overlies the liver (*arrow*). (B) The left-side-down decubitus view shows gas collecting adjacent to the liver. The patient was found to have a duodenal perforation at surgery.

the diaphragm and the liver, spleen, stomach, or colon on the left (Figs. 86.2 and 86.3). Young children and those too ill to sit or stand can be examined in the decubitus position. The decubitus view should be obtained with the right side up to allow the liver to fall away from the wall of the peritoneal cavity to allow visualization of free air between the liver and the abdominal wall. Both techniques are considered equally effective.[4]

If decubitus or upright imaging is difficult to obtain, a supine view using a horizontal-beam technique can be utilized. On the horizontal-beam supine radiograph, free peritoneal air may collect between the anterior surface of the liver and the anterior abdominal wall (Fig. 86.4), but small amounts of free air may be more difficult to detect, particularly if located over loops of bowel.

Multiple signs related to pneumoperitoneum are described on plain radiographs (Table 86.1) based on the location and volume of air and its relationship to adjacent structures. The lucency caused by the free air rising to an anterior position in the abdomen

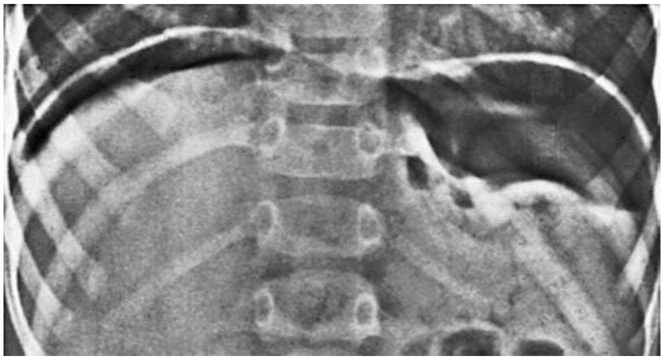

**Figure 86.2. Free intraperitoneal air.** Upright abdominal radiograph in a 2-year-old boy with perforated gastric ulcer. Air is easily demonstrated between the diaphragm and the liver on the right side and between the diaphragm and the spleen and stomach on the left.

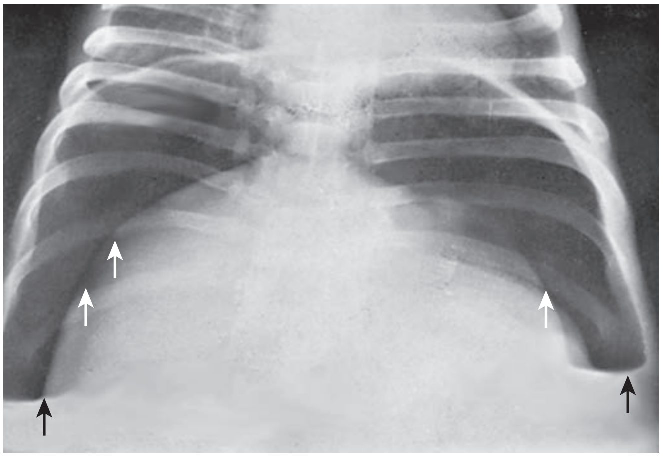

**Figure 86.3. Hydropneumoperitoneum.** Upright abdominal radiograph shows a massive amount of free air below the diaphragm *(white arrows)* with air-fluid levels *(black arrows)*.

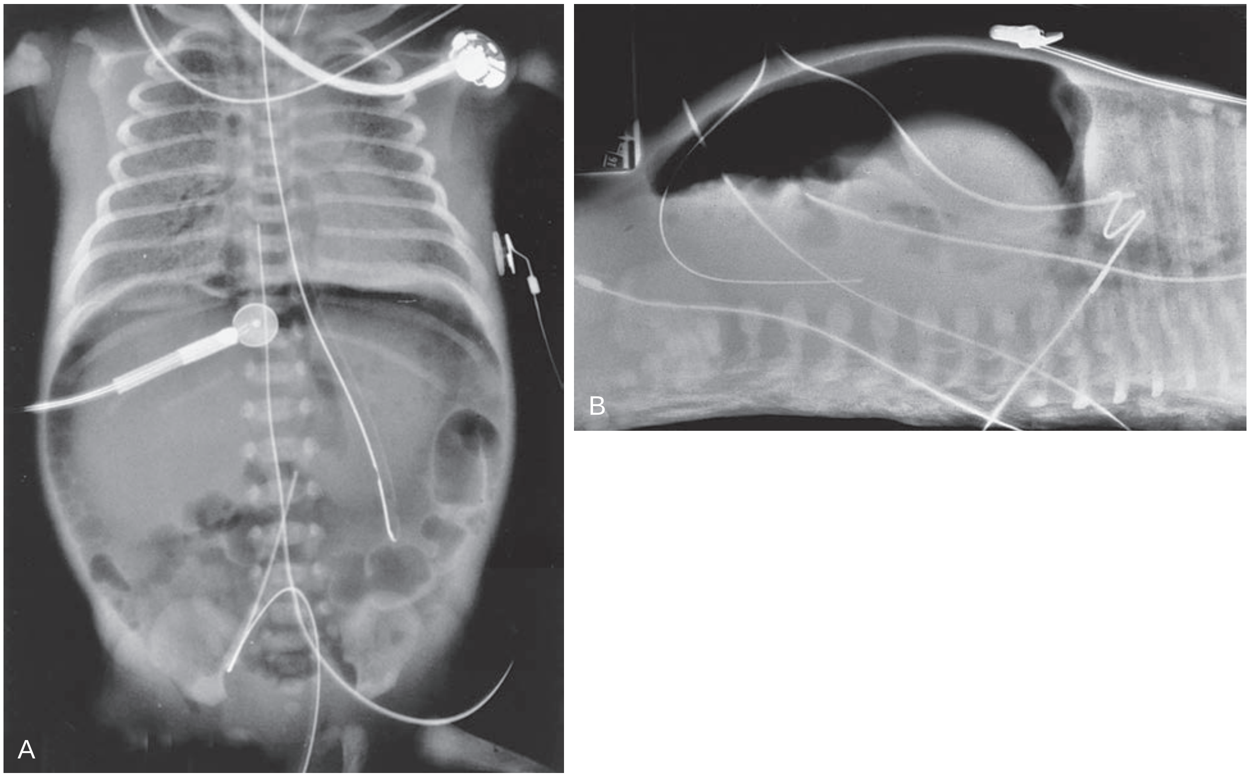

**Figure 86.4. Pneumoperitoneum.** (A) Anteroposterior view of the chest and abdomen in a newborn with pulmonary interstitial emphysema, pneumomediastinum, and pneumoperitoneum. A large amount of gas is in the peritoneal cavity, there is a Rigler sign and the density of the liver is decreased compared with the extraperitoneal soft tissues. The falciform ligament per se is not visualized because of the obscuring umbilical venous catheter. (B) Cross-table lateral view of the same patient demonstrates large pneumoperitoneum without air-fluid levels, suggesting that the air has dissected into the peritoneum from the chest.

is most easily detected when it projects over the liver, thus many right upper quadrant signs of free air are described.[8] The normal density of liver is uniform and typically denser than the heart. Air overlying the liver on a supine radiograph decreases the radiodensity of that portion of the liver.

Small amounts of free air may appear as subtle, localized collections in the right upper quadrant. Linear accumulation of air in the right subhepatic space is known as the *hepatic edge sign*, whereas triangular collections seen with air in the Morison pouch is known as the *Doge cap sign*, because it resembles the cap worn by the Venetian Doge.[9,10] A linear collection of air may also be located in the fissure of the ligamentum teres.[11]

*Rigler sign* refers to visualization of the bowel wall caused by the presence of air on both sides of the wall (e-Fig. 86.5). The telltale *triangle sign* is a triangular focus of extraluminal air seen on the cross-table lateral view of the abdomen, created by the external surface walls of adjacent bowel loops and the anterior abdominal wall, as the air collects at the highest point in the peritoneal space.[12]

**TABLE 86.1** Radiographic Signs of Pneumoperitoneum

| Bowel-Related Signs | Right Upper Quadrant Signs | Peritoneal Ligament–Related Signs | Miscellaneous Signs |
|---|---|---|---|
| Rigler sign | Hyperlucent liver sign | Falciform ligament sign | Football sign |
| Triangle sign | Anterior-superior oval sign | Inverted V sign | Cupola sign |
| | Fissure for ligamentum teres sign | Urachus sign | Left-sided anterior-superior oval sign |
| | Doge cap sign | | Subphrenic radiolucency |
| | Hepatic edge sign | | Focal radiolucency |
| | Dolphin sign | | |

A sufficiently large amount of free air can be seen as a large, ovoid lucency overlying the abdominal contents (Fig. 86.6). In the supine position, the liver falls away from the anterior peritoneal surface and free air can dissect along both sides of the falciform ligament, which attaches the liver to the anterior abdominal wall. When outlined by free air, the ligament appears as a thin, vertical, opaque line. The distension of the flanks caused by the free intraperitoneal air and the outline of the falciform ligament centrally are the elements of the well-known *football sign*, so termed because of its similarity to an American football; the falciform ligament represents the central thread in the ball (see Fig. 86.6). A less commonly encountered sign of pneumoperitoneum is the *inverted V sign*, caused by air outlining the medial umbilical folds in the pelvis.[13]

Causes of pneumoperitoneum can sometimes be inferred by certain signs. For example, a ruptured viscus permits both air and fluid to escape into the peritoneal cavity, causing abnormal extraluminal air-fluid levels (compare Figs. 86.3 and 86.4). On the other hand, tension pneumomediastinum is an entity in which air dissects along the retroperitoneum and subadventitial layer of the mesenteric vessels and sometimes ruptures into the peritoneal cavity; this will not demonstrate significant extraluminal air-fluid levels unless the patient has underlying ascites from an unrelated cause. The latter is also usually suspected from a history of assisted ventilation and the presence of pneumomediastinum on the chest radiograph.

Apart from plain radiographs, ultrasound (US) can also be used in the detection of pneumoperitoneum by detecting gas over the liver, with a reported sensitivity of 93%, specificity of 64%, and accuracy of 90%.[14] However, US should not be considered definitive

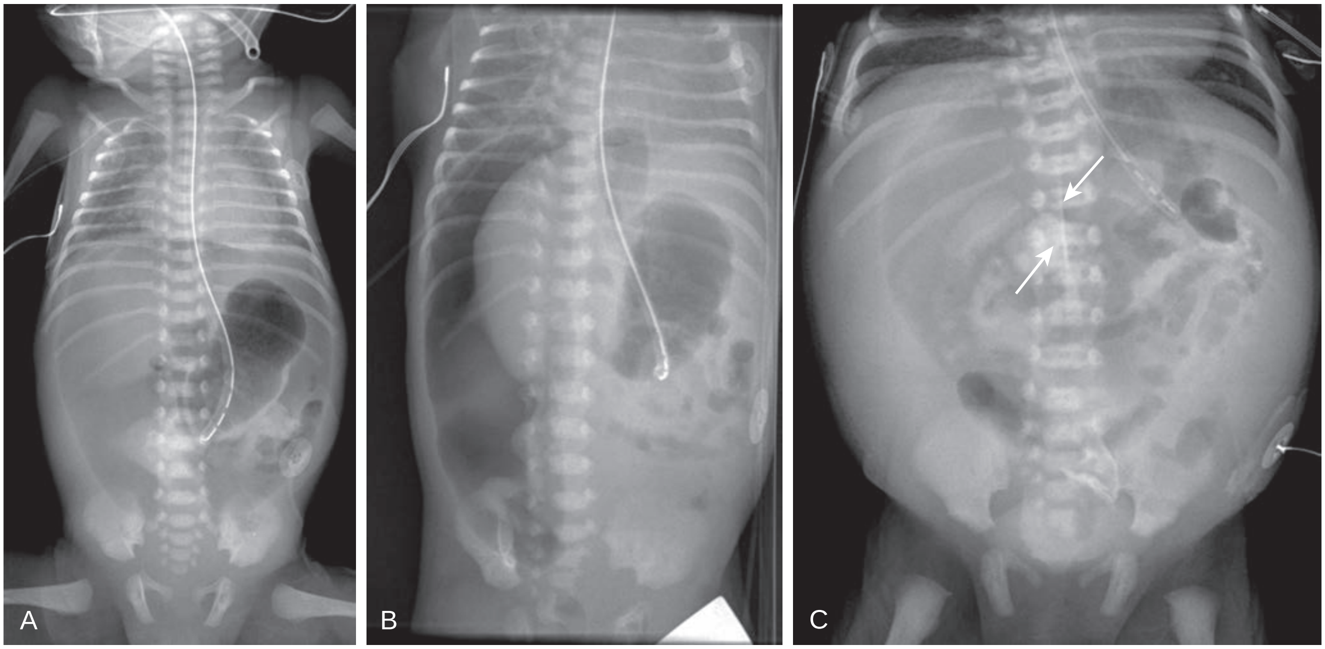

**Figure 86.6. Pneumoperitoneum with "football sign."** (A) Supine radiograph in a 5-day-old, 30-week-gestation premature infant shows a large lucency over the entire abdomen. (B) Decubitus view in the same infant confirms the large pneumoperitoneum. Multiple intestinal perforations were found at surgery. (C) Another patient with pneumoperitoneum demonstrates the classic football sign on abdominal imaging. Gas outlines the falciform ligament *(arrows),* and a large lucency overlies the upper abdomen centrally as the gas accumulates anteriorly. At surgery, this patient was found to have a colonic perforation.

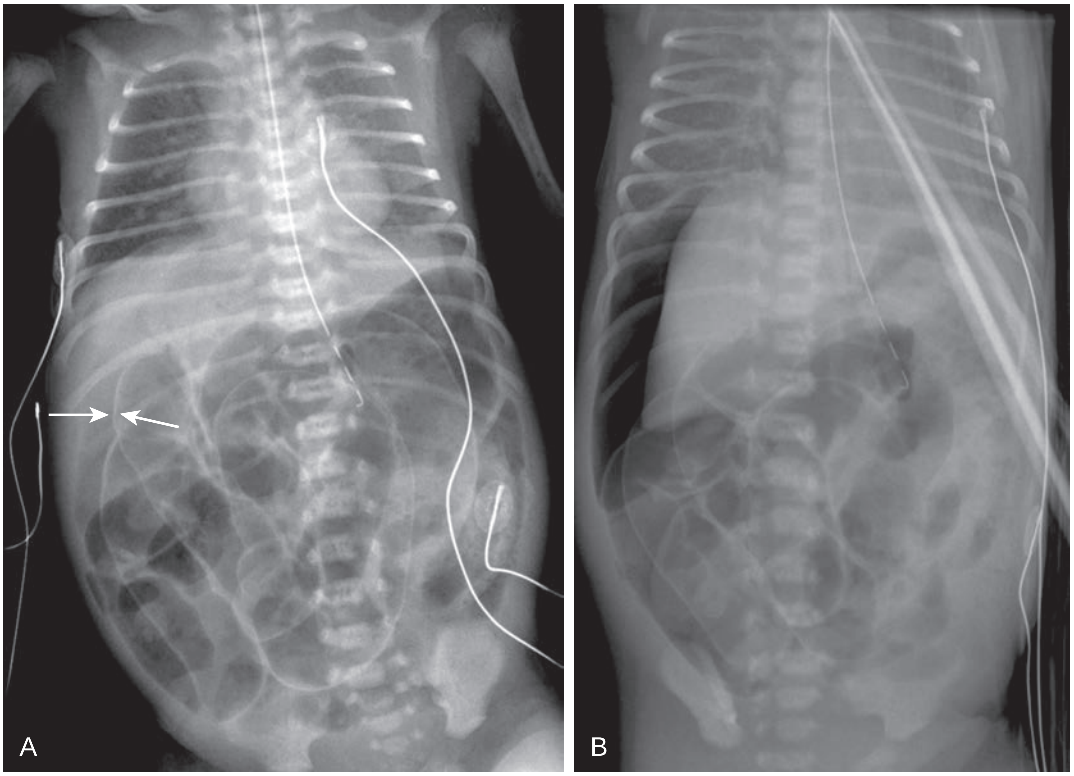

**e-Figure 86.5. Pneumoperitoneum with Rigler sign.** (A) Supine radiograph in a 6-day-old, 33-week-gestation premature infant shows a large amount of free intraperitoneal gas with right upper quadrant lucency. Rigler sign is present, and air outlines both sides of the bowel loops *(arrows);* subtle signs of portal venous gas are also present. (B) Left-side-down decubitus view of the same infant shows a large amount of free intraperitoneal gas rising to outline the liver. Rigler sign is again evident.

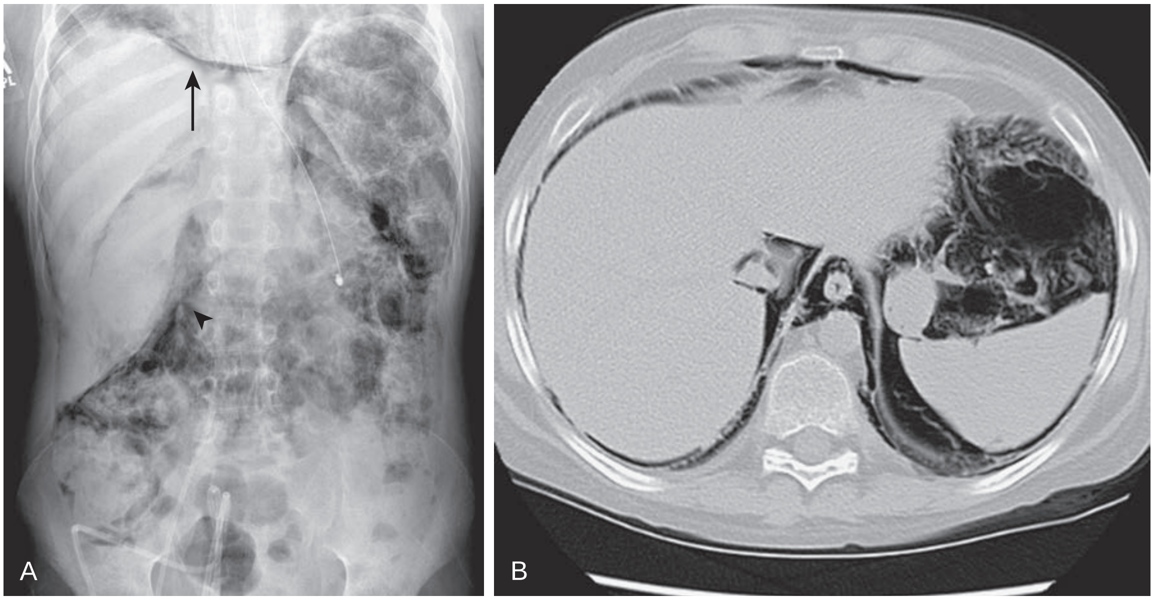

**Figure 86.8. Pneumatosis intestinalis.** (A) Radiograph of the abdomen and pelvis in a patient who underwent bone marrow transplantation for refractory recurrent neuroblastoma. Abundant pneumatosis intestinalis has resulted in pneumoperitoneum *(arrow)* and pneumoretroperitoneum *(arrowhead)*. (B) CT image through the upper abdomen viewed with lung windows confirms the pneumoperitoneum, pneumoretroperitoneum, and pneumomediastinum. Note absence of air-fluid levels.

in diagnosing or excluding a pneumoperitoneum without extensive expertise and experience, and US findings should be confirmed by appropriate radiographic evaluation.

Although not typically performed for assessment of pneumoperitoneum, computed tomography (CT) is an extremely sensitive method to identify small amounts of intra- or retroperitoneal air, intraperitoneal air-fluid levels, and often the underlying cause of pneumoperitoneum.[15] It can be optimized by reviewing abdominal images using lung-window parameters (e-Fig. 86.7 and Fig. 86.8).

## Mimics and Potential Pitfalls

A *pseudo-Rigler sign* occurs when two loops of dilated air-filled bowel lie adjacent to one another. The line seen in the pseudo-Rigler sign is thicker than with free peritoneal air, because it represents a double thickness of bowel wall (from the two adjacent bowel loops), whereas the line in patients with free peritoneal air—a true Rigler sign—represents a single bowel wall. However, this is not always a reliable differentiation, because the underlying disease-causing perforation may lead to a thickened bowel wall. In equivocal cases, a left lateral decubitus radiograph can be obtained for clarification.[16]

## Ascites

***Overview.*** A small amount of fluid in the peritoneal cavity is normal. This is more common in females and is often seen incidentally on cross-sectional imaging. *Ascites* refers to abnormal or pathologic accumulation of fluid within the peritoneal cavity.

***Etiology.*** Pathologic intraperitoneal fluid collections stem from a variety of causes and most commonly result from sequestration of fluid from the splanchnic vascular bed. Other causes of pathologic intraperitoneal fluid include hemoperitoneum, urinary ascites, bile, pancreatic juices, chylous fluid, and cerebrospinal fluid (CSF). *Transudative ascites* is most commonly found in patients with hepatobiliary disease, especially cirrhosis; heart failure; hyponatremia; renal failure; peritonitis; and Budd-Chiari syndrome. *Exudative ascites* can occur secondary to peritoneal infections and peritoneal metastases. Perforation of the GI tract results in the escape of both air and fluid into the peritoneal cavity. In children, the most common causes for ascites are hepatic, renal, and cardiac disease.[17]

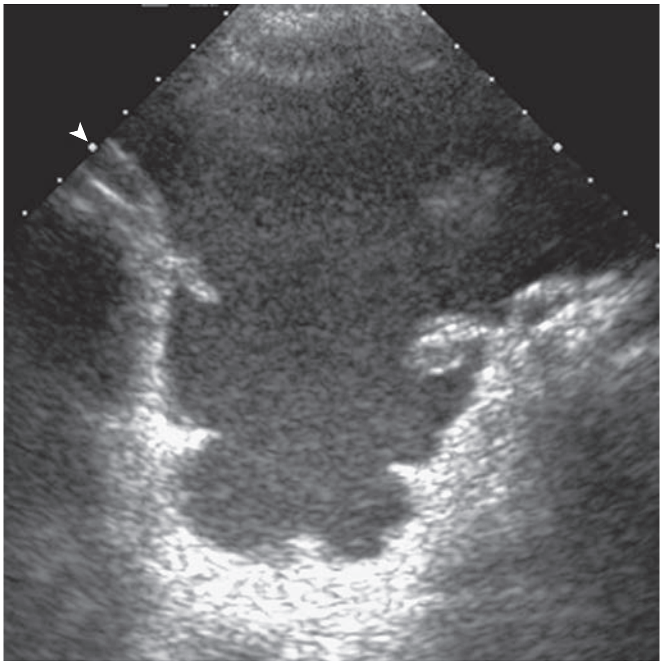

**Figure 86.9. Complex ascites.** Transverse ultrasound image through the deep pelvis in a 6-year-old patient with epithelioid sarcoma demonstrates abundant complex ascites. The thickening of the lateral peritoneal surface indicates peritoneal disease.

The lesser sac, Morison pouch, paracolic gutters, pelvis, and recesses formed by many of the peritoneal ligaments are all sites where fluid can collect (Fig. 86.9). Typically, small amounts of

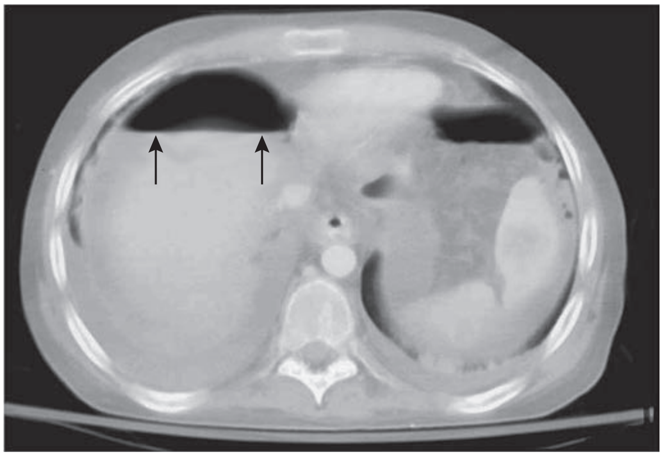

**e-Figure 86.7. Hydropneumoperitoneum.** Axial contrast-enhanced CT image at lung-window settings shows hydropneumoperitoneum in a 19-year-old man with relapsed Hodgkin disease who presented with severe abdominal pain. Note air-fluid levels *(arrows)*.

ascites collect in the pelvis when the patient is supine. As the amount of fluid increases, it moves cephalad along the paracolic gutters into the subhepatic spaces and Morison pouch, and it can sometimes be identified in the fossa of the ligamentum teres (e-Fig. 86.10). Ascites eventually spreads through the peritoneal cavity and into the mesenteric recesses (e-Fig. 86.11); in cases of inflammation, loculations may occur. Encysted collections of CSF may be seen adjacent to the tip of a ventriculoperitoneal shunt tube ("CSF pseudocyst"), usually as a result of an inflammatory response around the shunt tube tip entrapping fluid (Fig. 86.12).

***Clinical Presentation.*** The clinical hallmark of ascites is abdominal distension, which in itself is a nonspecific sign. The clinical findings are in part governed by the underlying etiology. Early satiety and dyspnea can be seen with increasing accumulation of fluid within the abdominal cavity.[17]

*Abdominal compartment syndrome* is an uncommon sequela of acute accumulation of large-volume ascites or other material that leads to intraabdominal hypertension. Increased pressure in a confined space leads to progressive organ failure with significant associated mortality. It is most commonly described after trauma but can also be seen in the setting of surgery and other entities, such as pancreatitis. The diagnosis is usually made at the bedside with measurement of intravesical pressure.[18] The criteria for diagnosis of abdominal compartment syndrome include elevation of intraabdominal pressure to 20 mm Hg or higher, coupled with impaired function of at least one organ; typically, it affects respiratory or renal function.[19]

***Imaging.*** Diagnosis of ascites is usually made based on clinical history, physical examination, and aspirated fluid analysis. Imaging is usually performed to confirm clinical ascites; estimate its volume; identify loculations, septations, or internal echoes; or to assist in sampling or draining of ascitic fluid.

Abdominal radiographs are only sensitive to large amounts of intraperitoneal fluid. In such cases, the gas-filled bowel loops will appear centrally located within the abdomen (Fig. 86.13). Separation of bowel loops may also occur as a result of ascites, but this appearance can be simulated by large amounts of intraluminal fluid or thick-walled bowel loops (e-Fig. 86.14).[20]

US is an extremely sensitive imaging modality for ascites.[21] Simple ascites appears as anechoic fluid and can be seen in the various peritoneal recesses.[22,23] Septations, loculations, and internal echoes usually suggest complex fluid, which can be seen in the setting of blood, chyle, inflammatory cells, or peritoneal metastases (see e-Fig. 86.14). Ascites occasionally will pass through the esophageal hiatus or patent pleuroperitoneal canals to present as intrathoracic fluid.[24]

CT is equally sensitive to detect ascites, although it does not visualize internal septations, which are easily seen on US. Because of radiation exposure, CT is not the first-line modality in the evaluation of ascites.

*Abdominal compartment syndrome* is suggested on CT by a ratio of anteroposterior to transverse diameters of the abdomen exceeding 0.81 (e-Fig. 86.15).[19] However, abdominal measurements on a single CT scan may be nonspecific, because an increased anteroposterior abdominal dimension may be seen with chronic ascites. Other telling findings include an elevated diaphragm, the presence of hemoperitoneum, increasing girth on serial examinations, attenuated inferior vena cava or renal veins, and shock bowel. Although not specific, a combination of these findings in the appropriate clinical setting or worsening on sequential imaging studies should raise the possibility of abdominal compartment syndrome.[18]

***Treatment.*** The course, prognosis, and treatment of ascites depend entirely on the cause. Drainage of the ascitic fluid can usually provide symptomatic relief; however, in most cases treatment is aimed at the underlying disorder. The treatment for abdominal compartment syndrome includes emergent drainage or decompressive laparotomy. The mortality rate in abdominal compartment syndrome remains high, at approximately 60% to 70%.[18]

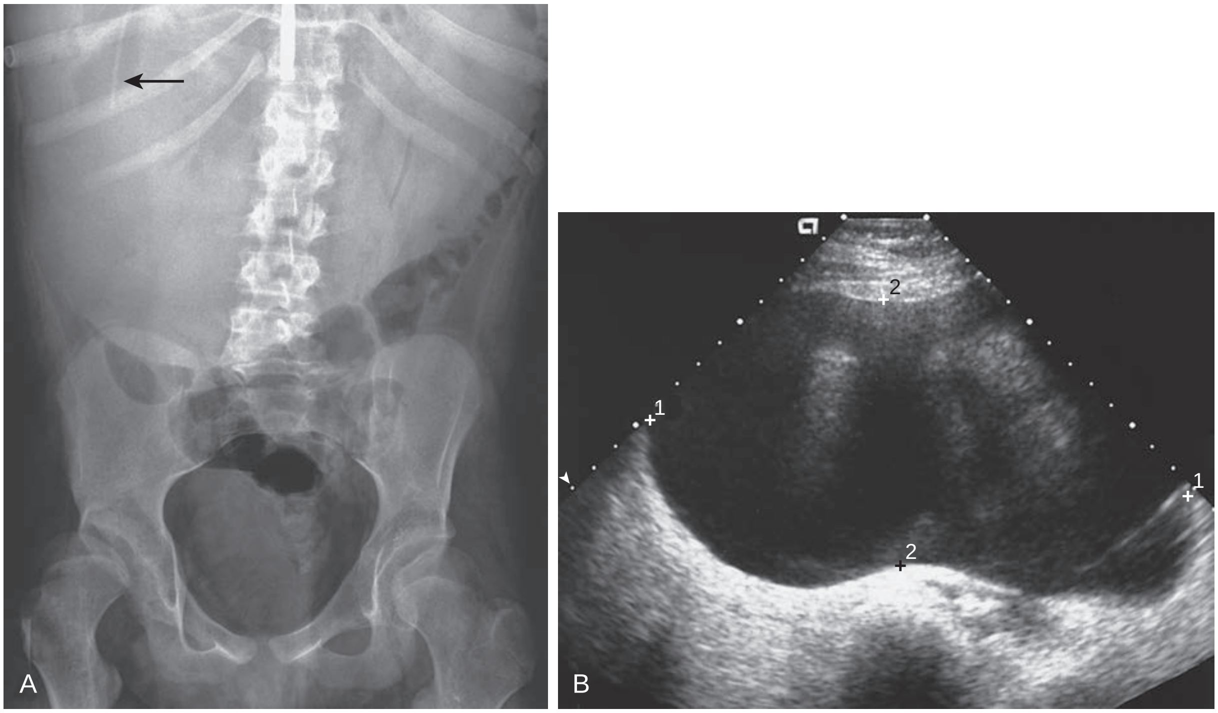

**Figure 86.12. Cerebrospinal fluid pseudocyst.** (A) Abdominal radiograph demonstrates a large soft tissue mass that occupies the entire upper abdomen, especially the right abdomen. The tip of a ventriculoperitoneal shunt is seen in the right upper quadrant *(arrow).* (B) Transverse sonogram through the upper abdomen confirms a large cystic mass surrounding the tip of the shunt.

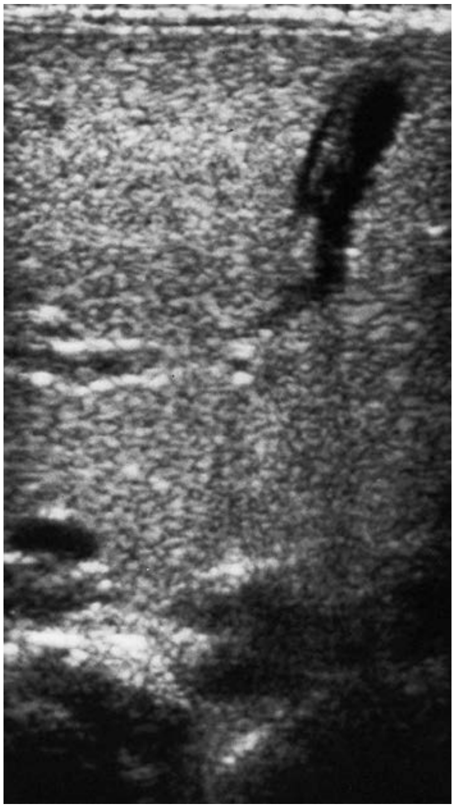

**e-Figure 86.10. Ascites.** Oblique sonogram through the liver demonstrates ascitic fluid in the fissure of the ligamentum teres. The ligament and the obliterated umbilical vein can be seen within the fluid collection.

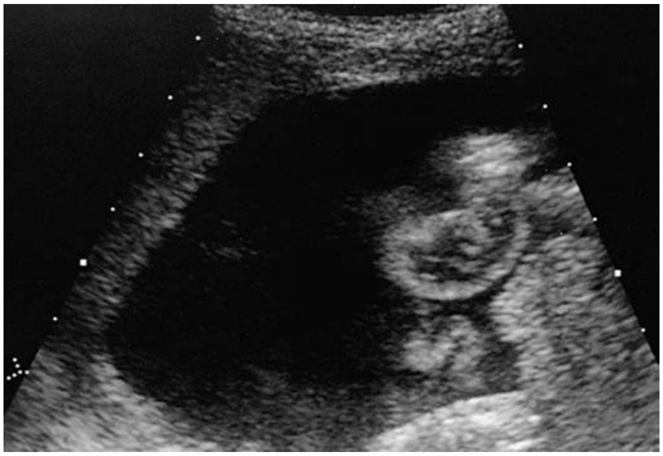

**e-Figure 86.11. Ascites.** Transverse sonogram through the left lower quadrant demonstrates anechoic ascitic fluid that outlines thick-walled loops of intestine in a patient with graft-versus-host disease after bone marrow transplantation.

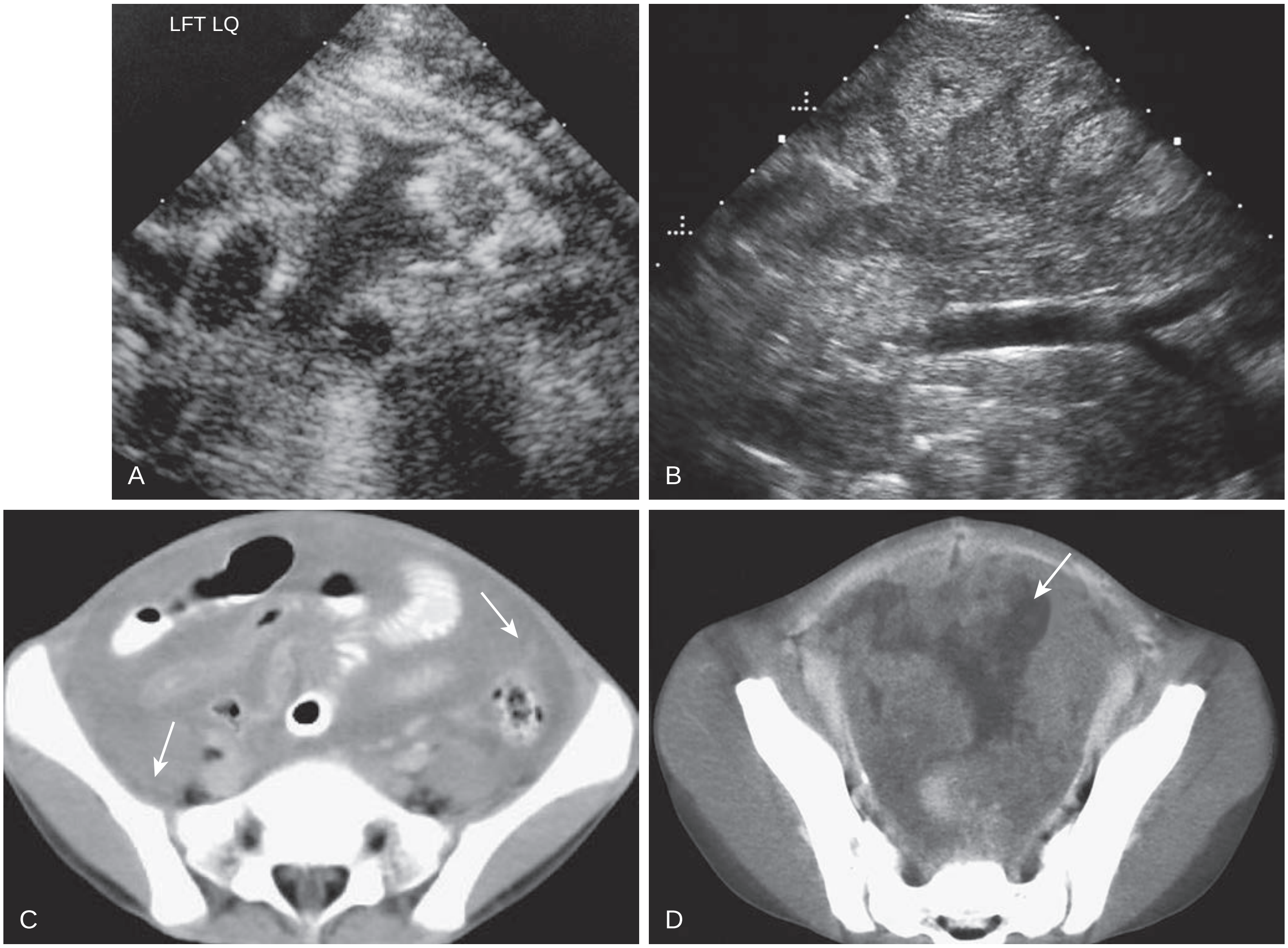

**e-Figure 86.14. Complex peritoneal fluid.** (A) Transverse sonogram through the left lower quadrant of a 1-year-old boy with disseminated intravascular coagulation and thrombocytopenia after surgery for congenital heart disease. Fluid separates multiple loops of bowel and is not completely anechoic as in simple ascites. Rather, it contains some internal echoes. Paracentesis confirmed hemorrhage. (B) Peritoneal mesothelioma in a 7-year-old boy who had been treated with whole-abdomen radiation therapy at age 3 for non-Hodgkin lymphoma. Coronal ultrasound through the midabdomen shows echogenic material surrounding and displacing small bowel loops, which are also hyperechoic. (C) Axial contrast-enhanced CT image through the same area shows ascites and peritoneal soft tissue densities and masses *(arrows)*. (D) Axial contrast-enhanced CT through the pelvis shows intense peritoneal enhancement and numerous soft tissue masses *(arrow)*.

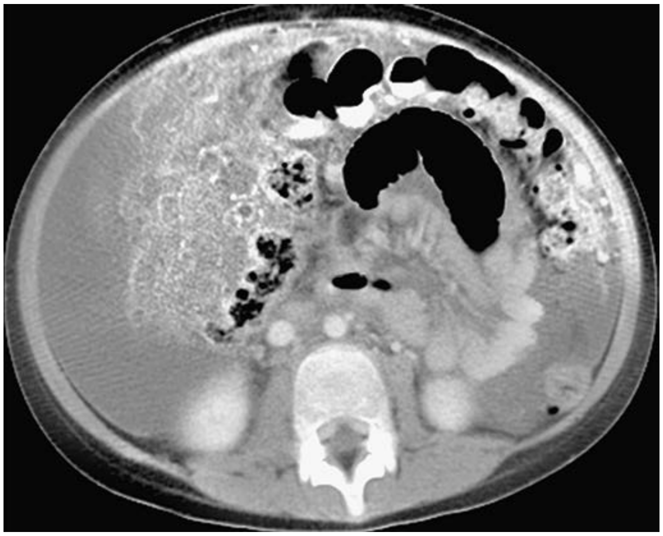

**e-Figure 86.15. Abdominal compartment syndrome.** Axial contrast-enhanced CT image in a 6-year-old with abdominal epithelioid sarcoma has an increased ratio of the anteroposterior to transverse diameters of the midabdomen measuring 0.84, consistent with abdominal compartment syndrome.

## Peritonitis

***Overview.*** Peritonitis is a generalized or localized inflammatory process that affects the peritoneum. Acute generalized peritonitis is usually of infectious etiology and can be further subclassified as primary and secondary. *Primary peritonitis*, also called *spontaneous bacterial peritonitis*, is a primary infection of the peritoneal cavity that does not result from spread from the visceral organs. *Secondary peritonitis* results from secondary infection of the peritoneum, usually from urogenital or GI sources, particularly perforation.[25] Abscesses may develop locally and at sites where fluid is likely to accumulate. The subhepatic and subphrenic spaces are common distant sites for abscess formation.

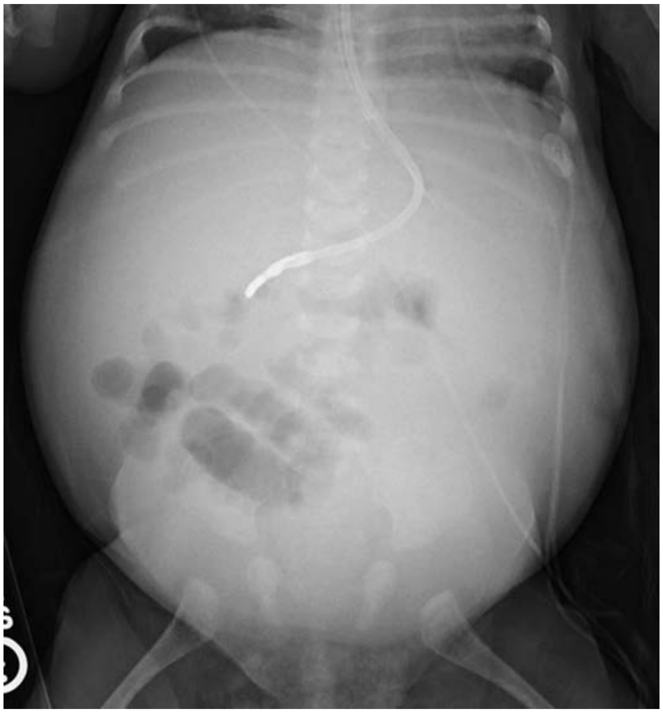

**Figure 86.13. Ascites on plain radiograph.** Anteroposterior views of the abdomen in a neonate with severe nephrotic syndrome. Abdominal distension is noted with bulging flanks, and loops of gas-containing intestine are seen floating in the center of the abdomen.

***Etiology.*** *Primary peritonitis* may occur spontaneously in patients without underlying pathology, and it is usually seen in association with postnecrotic cirrhosis and nephrotic syndrome.[25] Access of organisms to the peritoneal cavity through the fallopian tubes is another putative cause of this condition, supported by the increased occurrence in patients with intrauterine contraceptive devices.[25]

*Secondary peritonitis* in children is most commonly caused by a perforated appendix. Other causes of bowel perforation that could potentially result in secondary peritonitis include IBD, incarcerated hernias, complications of Meckel diverticulum, midgut volvulus, intussusception, hemolytic uremic syndrome, necrotizing enterocolitis, typhlitis, and traumatic perforation.[17] Peritoneal dialysis is another cause of peritonitis in children and is the most common cause of dialysis failure.[26]

*Granulomatous peritonitis* is usually associated with infectious etiologies such as tuberculosis, histoplasmosis, or pneumocystosis, most often in immunocompromised hosts. Involvement of the peritoneum occurs in approximately 4% of patients with tuberculosis[27] but is reported to occur in 10% of children aged less than 10 years.[28] Noninfectious causes for granulomatous peritonitis include foreign material, such as talc and barium, meconium, bowel contents, bile, or gallstones.[2] *Meconium peritonitis* is a sterile peritonitis that results from prenatal perforation of the bowel; this is discussed in Chapter 102.

***Clinical Presentation.*** Patients usually come to medical attention with fever (≥39.5°C), diffuse abdominal pain, nausea, and vomiting. Signs of peritoneal inflammation on physical examination include rebound tenderness, abdominal wall rigidity, and decreased or absent bowel sounds from a paralytic ileus.[17] Patients with infectious granulomatous peritonitis secondary to histoplasmosis or pneumocystosis are nearly always immunocompromised.[2]

***Imaging.*** Abdominal radiographs in patients with peritonitis often show a nonspecific, adynamic ileus pattern with dilated bowel, multiple intraluminal air-fluid levels, and evidence of ascites; in addition, the properitoneal fat plane may be obliterated (e-Fig. 86.16). US may demonstrate intraperitoneal fluid with internal echoes and septations, and abscesses are identified as focal collections of mixed echogenicity.

CT demonstrates enhancement of the peritoneal lining with associated dense ascites (Fig. 86.17). Abscesses appear as focal fluid collections with relatively high attenuation values and densely enhancing walls (Fig. 86.18). On magnetic resonance imaging

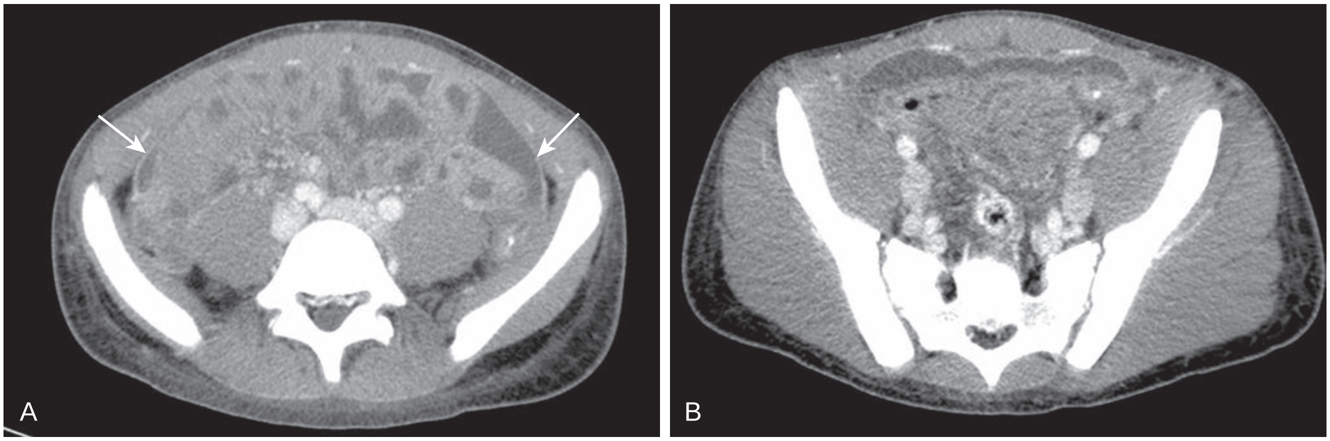

**Figure 86.17. Peritonitis.** (A) Axial contrast-enhanced CT image in a 14-year-old boy with perforation occurring after severe retching after a Heller myotomy shows low-attenuation fluid within the pelvis and between bowel loops. The peritoneal lining is enhancing *(arrows)* consistent with a clinical diagnosis of peritonitis. (B) Image caudal to (A) shows similar findings.

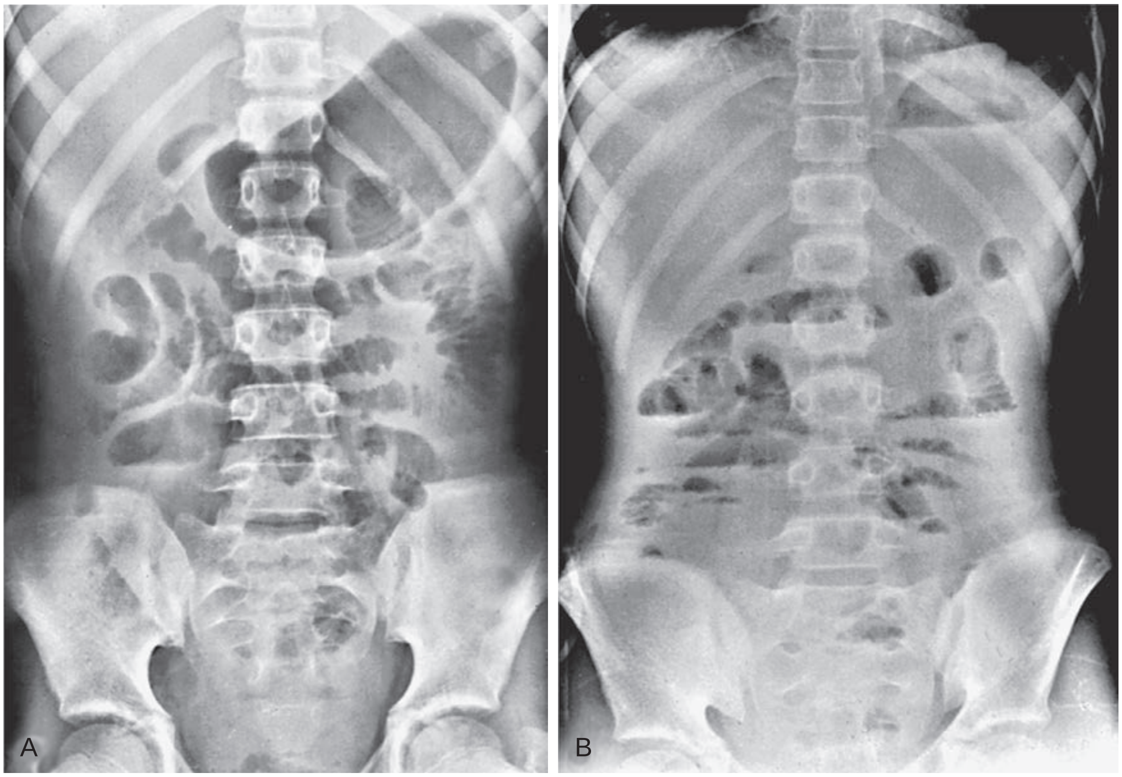

**e-Figure 86.16. Peritonitis.** (A) Supine abdominal radiograph in a teenage patient with purulent peritonitis shows gas-filled loops of small intestine that are mildly dilated and separated from one another, suggestive of ascites. (B) Upright view of the same patient shows multiple scattered air-fluid levels throughout the peritoneal cavity in a pattern concerning for ileus.

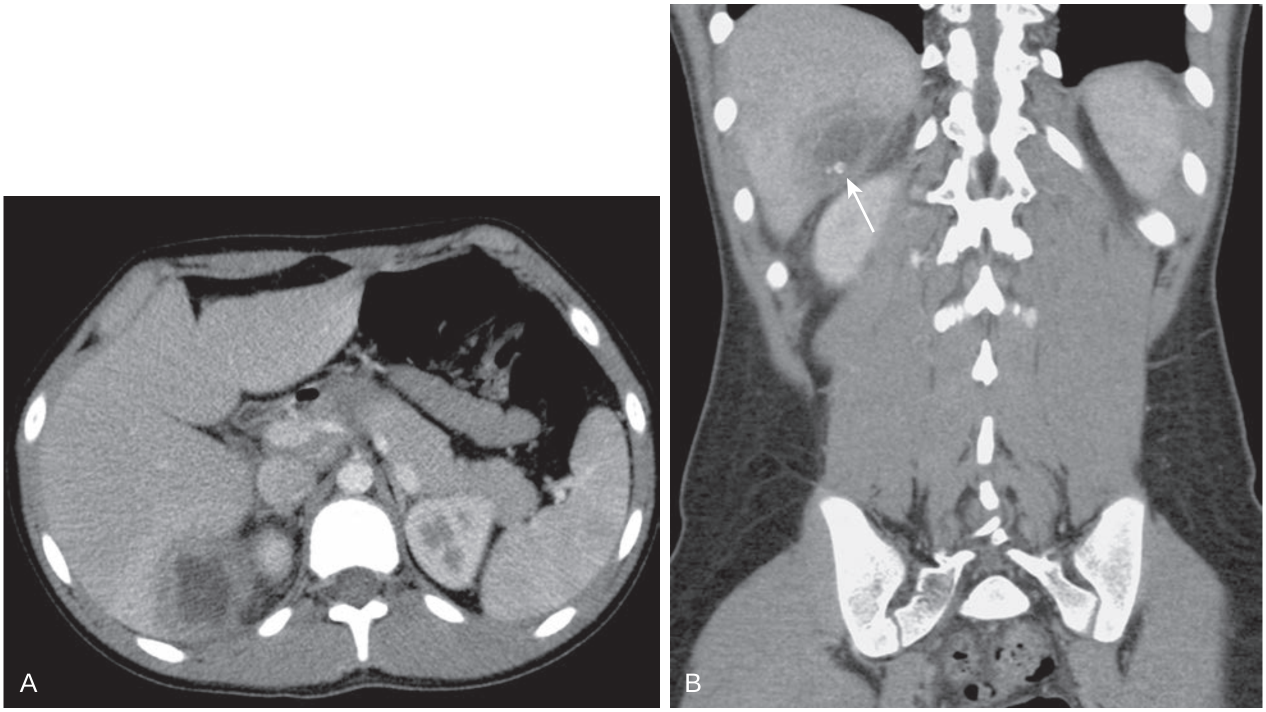

**Figure 86.18. Ruptured appendicitis with intraabdominal abscess.** (A) Axial contrast-enhanced CT image in a patient with perforated appendicitis shows an irregular, thick-walled, peripherally enhancing abscess adjacent to the right lobe of the liver. (B) Coronal reformat reveals the location of the mass in the subhepatic/parahepatic region. In addition, two hyperdense foci are seen *(arrow)* within the mass, most consistent with appendicoliths.

(MRI), abscesses in the peritoneum show similar findings as elsewhere, with high internal T2 signal and dense peripheral enhancement. Both gallium citrate- and indium-labeled white blood cells have been used as scintigraphic agents in the diagnosis of abscesses, although these are rarely used.

*Granulomatous peritonitis* is secondary to a spectrum of lesions, as previously discussed. *Peritoneal tuberculosis* has been subdivided into three overlapping subtypes—a wet type; a fibrotic type; and a dry, plastic type—with decreasing ascites and increasing soft tissue components along the spectrum.[2,28] The wet type is the most common and is characterized by ascites, which on CT is often (but not always) of high density[2,28,29] with free or localized fluid collections (Fig. 86.19). Dry plastic or fibrotic fixed patterns are characterized by a relative lack of ascites and a variable amount of peritoneal and omental nodules and masses, peritoneal adhesions, and fibrotic fixation of the small bowel and mesentery as the predominant features.[2] Omental involvement is usually seen as diffuse, infiltrating, ill-defined enhancing lesions that produce a "smudged" appearance of the omentum (see Fig. 86.19). The findings in tuberculosis are indistinguishable from those in histoplasmosis.[2] Although no single CT feature is diagnostic of peritoneal tuberculosis, additional imaging features that help in diagnosis include concomitant central, low-attenuation lymph node enlargement, miliary microabscesses in the liver or spleen, splenic or lymph node calcification, and inflammation that involves the terminal ileum and cecum.[29,30]

***Treatment.*** The treatment of peritonitis includes correction of the underlying etiology and supportive therapy. General supportive measures include vigorous intravenous rehydration, correction of electrolyte disturbances, and infection control. Early control of the infection can be achieved medically, operatively, and through image-guided percutaneous interventions.

## Abdominal Wall and Peritoneal Calcification

***Overview.*** Abdominal wall calcification is uncommon in infants and children. The etiology depends upon the location of the calcification (skin, muscles, soft tissue, or peritoneum) and on the age of the patient. Most causes of intraabdominal calcification are related to specific organs, and these are discussed in the appropriate chapters.

***Etiology.*** Fat necrosis is one of the causes of abdominal wall calcification in neonates and infants.[31] Although there are many causes of fat necrosis, the majority are associated with neonatal asphyxia, sepsis, gestational diabetes, and hypothermia.[32] Older children with hypothermia, hepatic failure, and renal failure may also experience subcutaneous fat necrosis.[31]

Abdominal wall calcification may be seen in fibrodysplasia ossificans progressiva and in myositis ossificans, but are more common in the thoracic wall. Calcifications secondary to dermatomyositis are more likely to be in the extremities than in the trunk, but calcifications can be found in the abdominal wall. Subcutaneous hemangiomas may contain phleboliths. Abdominal wall calcification in infants has also been described after subcutaneous emphysema and in prune-belly syndrome.[33]

The most common cause of peritoneal calcification in the neonate is meconium peritonitis,[34] discussed in Chapter 102. Peritoneal calcification in older children is rare. Intestinal perforation with subsequent peritonitis may cause calcification. Other causes include granulomatous peritonitis, peritoneal dialysis (Fig. 86.20), calcification along surgical scars, hyperparathyroidism, and peritoneal malignancies such as ovarian adenocarcinoma.[34]

***Clinical Presentation.*** Clinical presentation is strongly dependent on the underlying cause. Subcutaneous fat necrosis appears clinically as firm, erythematous plaques. Patients may develop hypercalcemia, particularly when involvement is extensive.[35]

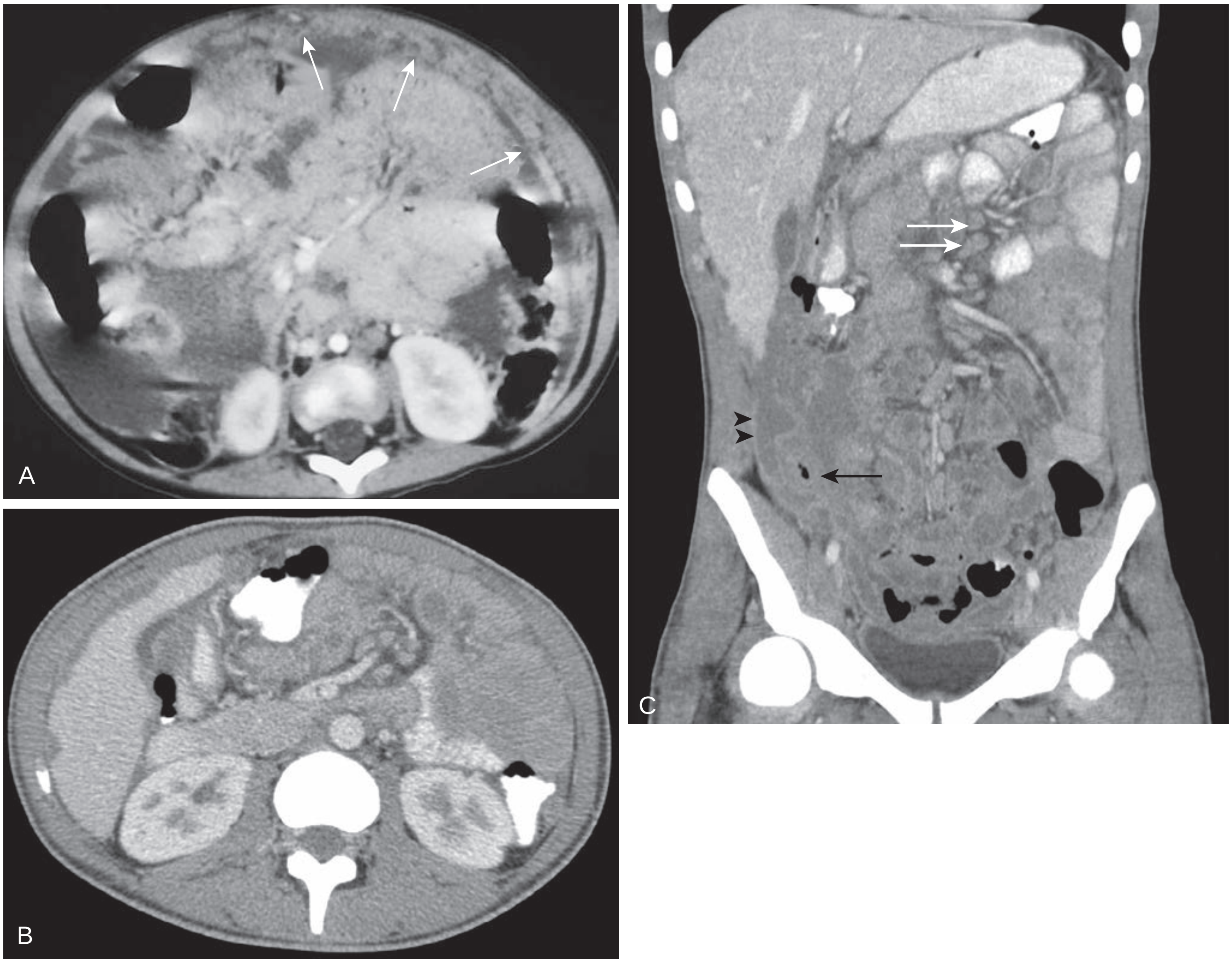

**Figure 86.19. Peritoneal tuberculosis subtypes.** (A) Contrast-enhanced CT image shows a 14-month-old girl with a large amount of ascites displacing bowel loops centrally, and studding of the peritoneal surface *(arrows)*. This is an example of wet type peritoneal tuberculosis. (B and C) Axial and coronal contrast-enhanced CT images demonstrate dry plastic or fixed fibrotic manifestation of peritoneal tuberculosis in a different patient. Note the relative lack of free fluid, with loculated fluid collections scalloping the anterior liver surface and along the right peritoneal cavity *(arrowheads)* causing adhesions of the bowel *(black arrow)*. Omental and mesenteric nodules *(white arrows)* were biopsied laparoscopically and demonstrated necrotizing caseating granulomas.

***Imaging.*** Most abdominal wall and peritoneal calcifications are detected incidentally on plain radiographs and/or CT scans obtained for other clinical indications. Shape of calcifications, location, and correlation with any predisposing condition may help identify the underlying etiology. Peritoneal calcification associated with calcified lymph nodes is significantly more likely to be associated with malignancy, whereas a sheetlike appearance of peritoneal calcification is associated more frequently with benign disease (see Fig. 86.20).[34]

## ANTERIOR ABDOMINAL WALL ABNORMALITIES

***Overview.*** Anterior abdominal wall defects encompass a variety of conditions, most commonly omphalocele and gastroschisis. *Omphalocele* refers to a midline defect larger than 4 cm that typically contains both gut and the liver and may or may not include other abdominal organs. It has a covering bilayer membrane consisting of the peritoneum as the inner layer and the amnion as the outer layer, with Wharton jelly in between (Fig. 86.21A).[36] It is differentiated from the less common *umbilical cord hernia* in that the latter is less than 4 cm, does not contain liver, has a normal abdominal wall, and has few associated anomalies. *Gastroschisis* is a defect located lateral to the umbilical cord insertion, most commonly to the right, with no covering membrane (Fig. 86.21B), and typically containing gut without abdominal organs although a gonad may occasionally protrude. Unlike all of the previously mentioned defects, an umbilical hernia is not associated with gut malrotation, is covered by skin, and usually becomes apparent several weeks after birth.[37]

### Omphalocele

***Overview.*** Omphaloceles are the second most common anterior abdominal wall defect (gastroschisis is the first), with a prevalence of approximately 1 to 5 in 10,000 live births. It is more common in boys.[36,37]

***Etiology.*** An omphalocele forms when fusion fails in the lateral folds of the body wall, the rectus muscles fail to meet in the

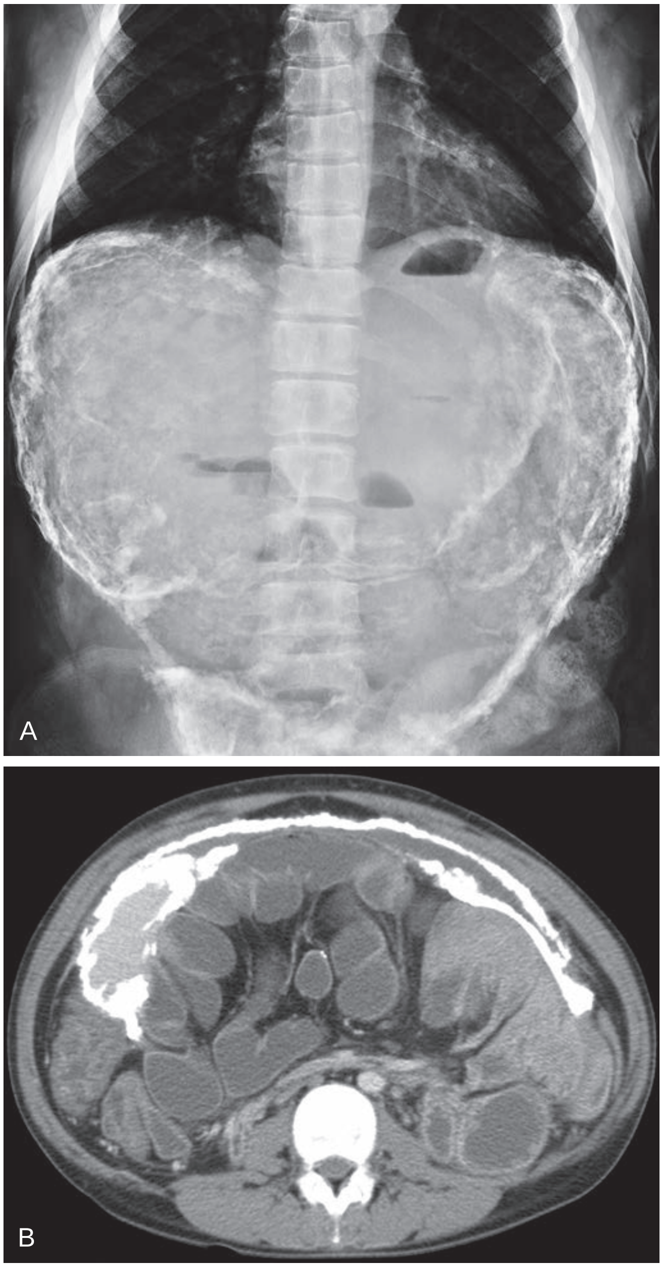

**Figure 86.20. Peritoneal calcifications from dialysis.** (A) Abdominal radiograph in a patient with a history of peritoneal dialysis shows diffuse peritoneal calcifications. Sheetlike calcifications tend to be benign. (B) Axial contrast-enhanced CT image is a patient with chronic peritoneal dialysis causing adhesions and small bowel obstruction, also known as *sclerosing peritonitis*. Notice the dilated bowel loops and the calcified, loculated effusion.

midline, and the herniated bowel fails to return into the peritoneal cavity, with the umbilical cord inserting into the covering membrane (see Figs. 86.21 and 86.22).[36,37] Involvement of the cephalic folds results in the spectrum of pentalogy of Cantrell: midline supraumbilical abdominal wall defect, defect in the diaphragmatic pericardium, deficiency of the anterior diaphragm resulting in herniation of the heart, congenital intracardiac abnormalities, and sternal clefts (e-Fig. 86.23).[36,38] Failure of caudal fold development results in cloacal exstrophy.

***Clinical Presentation.*** Associated anomalies are present in 50% to 70% of cases. Chromosomal anomalies, primarily trisomies, occur in 40% to 60%.[39] Smaller defects, absence of liver in the sac, and abnormal amounts of amniotic fluid are associated with an increased incidence of other anomalies, and 50% of these patients have congenital heart disease. Omphaloceles are also associated with Beckwith-Wiedemann syndrome and omphalocele–bladder exstrophy–imperforate anus–spinal defect complex.[39] Intrauterine growth retardation and prematurity commonly coexist.[36]

***Imaging.*** Diagnosis is usually made on antenatal US. Antenatal evaluation includes assessment of umbilical cord insertion, presence or absence of a covering membrane, contents of the omphalocele, and coexisting anomalies.[40] Multiple associated anomalies indicate a poorer prognosis, as do oligohydramnios and polyhydramnios.

***Treatment.*** Definitive treatment is surgical and may consist of primary closure or a staged procedure. If primary closure is not possible, the sac may be covered with nonadherent dressings to prevent trauma to the sac and exposure of the underlying bowel until delayed closure is possible.[36,37]

## Gastroschisis

***Overview.*** For unclear reasons, the prevalence of gastroschisis has been rising over the past three decades, particularly in infants born to young mothers,[36,37,41] with a prevalence of approximately 2 to 5 per 10,000 live births.[42] Gastroschisis is not usually associated with chromosomal abnormalities or congenital anomalies outside of the GI tract. Complex gastroschisis results when associated GI complications are present.[43]

***Etiology.*** The etiology of gastroschisis remains uncertain, but it is postulated to result from ischemia to the paraumbilical abdominal wall causing its involution. The defect occurs much more commonly on the right. This may be related to mistiming of the involution of the right omphalomesenteric artery and right umbilical vein, with herniation of the bowel through the defect.[36] A vascular genesis of the defect is supported by reported incidence of cases of maternal use of vasoactive compounds, such as cocaine and cigarettes.[44]

***Clinical Presentation.*** Infants with gastroschisis are typically born prematurely. At birth, the bowel may appear normal, but soon after, it may be covered with fibrinous exudates.[37] The maternal α-fetoprotein level is elevated because lack of a covering membrane allows the bowel loops to be exposed to the amniotic fluid. The incidence of associated anomalies is approximately 10% to 20%. Most involve the GI tract[45] and include antenatal perforation, necrosis, atresia, and volvulus.[37,46]

***Imaging.*** On prenatal US, gastroschisis is characterized by a normal umbilical insertion, a defect located adjacent to the umbilicus, most commonly on the right, and absence of a covering sac, which can result in an apparent lobulated contour of the herniated bowel loops (e-Fig. 86.24 and see Figs. 86.21B and 86.25). Dilatation of the bowel loops on prenatal imaging has been found to correlate with complex gastroschisis, with poorer survival and increased morbidity.

***Treatment.*** In the immediate postnatal period, close attention to heat preservation and fluid balance is important, because the large surface area of the exposed bowel leads to heat and fluid loss. Rapid coverage of the exposed bowel is a priority and may be accomplished with a silastic silo bag. The defect itself may need to be surgically enlarged if the bowel is at risk of vascular compromise.[36] Whenever possible, surgery as soon as possible after delivery is advocated.[37]

## Omphalomesenteric Duct and Urachal Remnants

### Omphalomesenteric Duct Remnant

***Overview.*** *Omphalomesenteric duct remnant* refers to a variety of conditions that range from a Meckel diverticulum to ligamentous and umbilical abnormalities (Fig. 86.26).

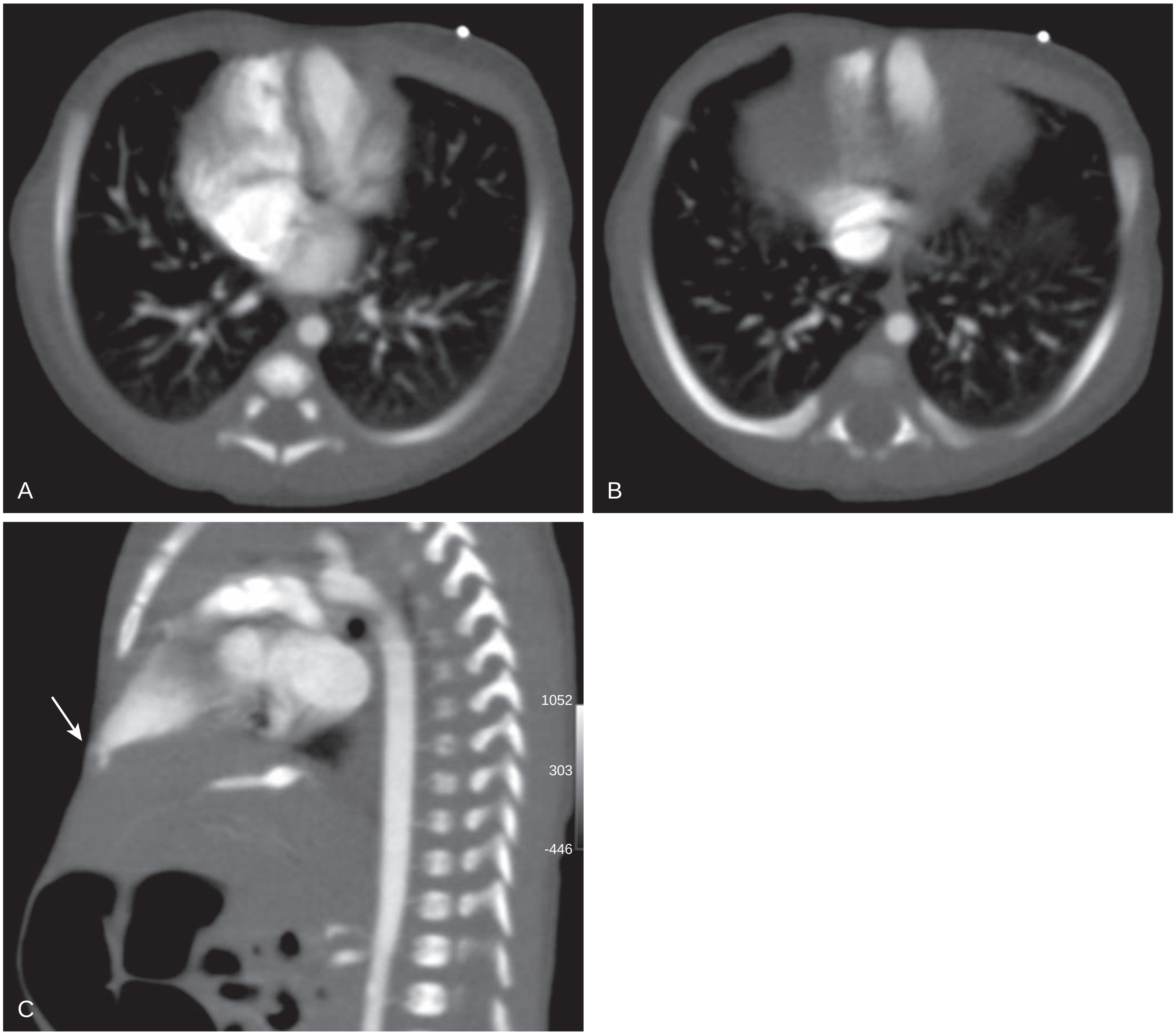

**e-Figure 86.23. Pentalogy of cantrell.** Neonate with an inferior sternal defect and protrusion of anterior abdominal wall with deficient epigastric abdominal wall musculature. (A and B) Axial contrast-enhanced CT images show a midline heart with a left ventricular diverticulum. (C) Sagittal reformat demonstrates the herniating left ventricular diverticulum to better advantage *(arrow)*. *(Courtesy of Marta Hernanz-Schulman, MD, Nashville, TN.)*

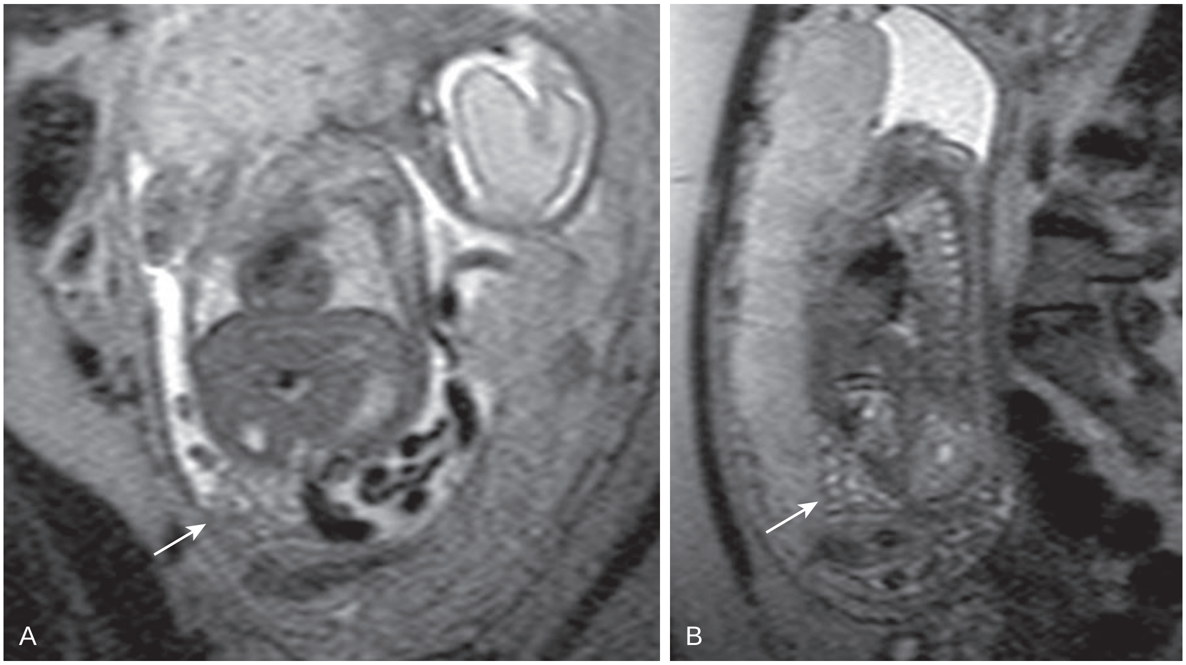

**e-Figure 86.24. Gastroschisis.** Coronal (A) and sagittal (B) images from a fetal MRI examination show meconium-filled bowel loops *(arrows)* freely floating in the amniotic fluid outside the abdominal cavity in a 26-week fetus with gastroschisis.

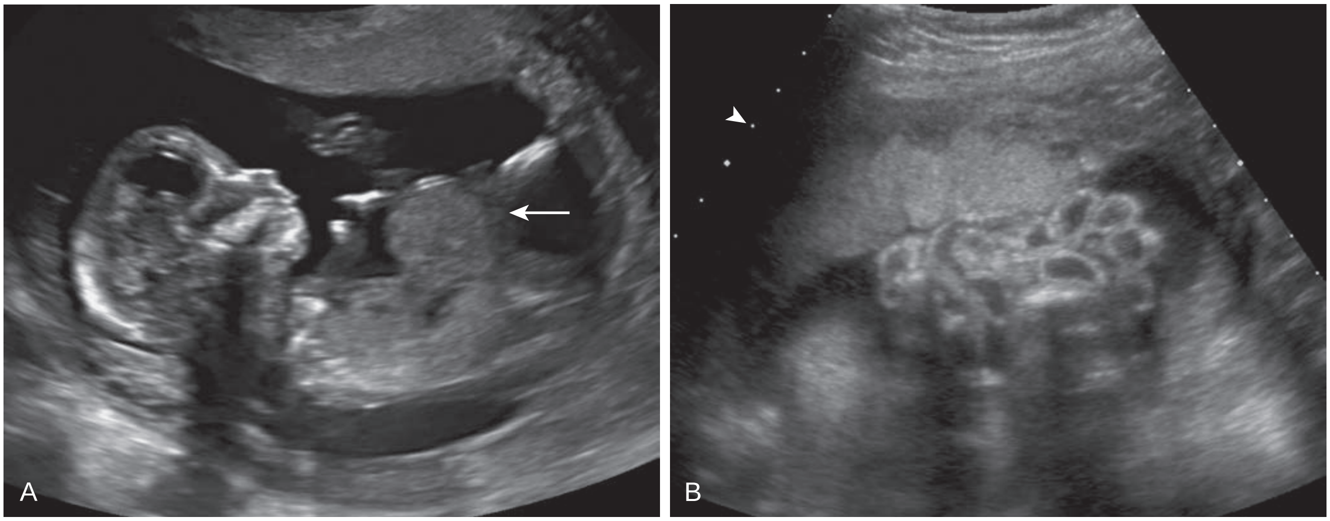

**Figure 86.21. Omphalocele versus gastroschisis.** (A) Prenatal sonogram of an omphalocele demonstrates a covered midline abdominal wall defect at the base of the umbilical cord insertion *(arrow)*. The herniated defect contains liver and bowel loops. (B) Prenatal sonogram of gastroschisis show mildly dilated bowel loops free-floating in the amniotic cavity. Besides the location adjacent to the umbilical insertion, the lobulated contour of the herniated bowel contents (versus smooth contours in omphalocele) is another clue.

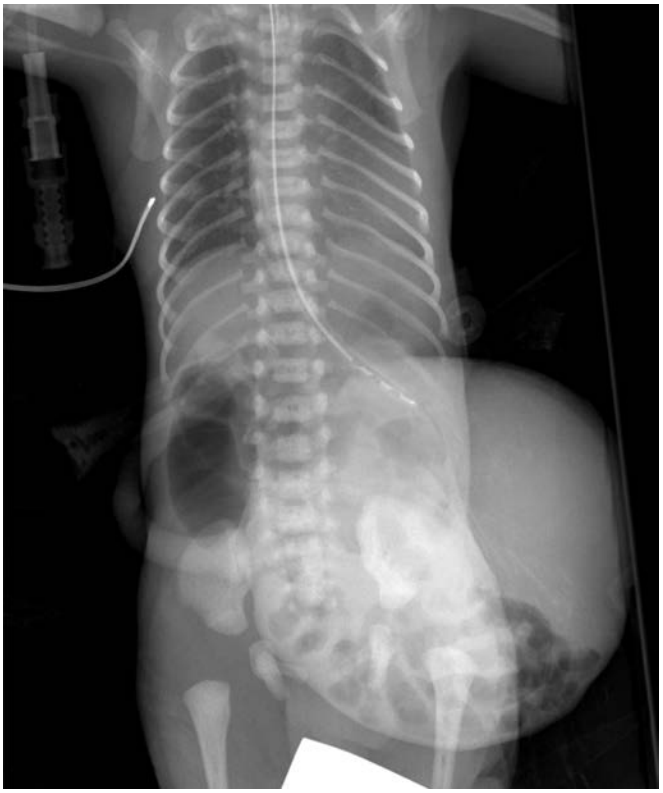

**Figure 86.22. Omphalocele.** Frontal radiograph of the chest and abdomen in a neonate shows a large anterior wall defect covered by a membrane and containing the liver, which is well visualized adjacent to air-filled and mildly distended bowel loops. The umbilical cord inserts on the omphalocele.

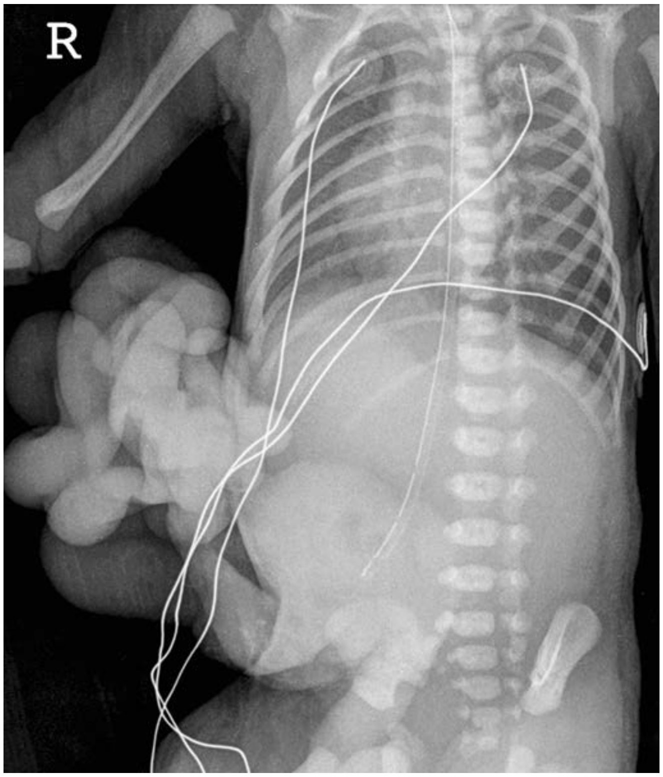

**Figure 86.25. Gastroschisis.** Frontal radiograph of the chest and abdomen of a newborn shows bowel loops outside the abdominal cavity. The bowel loops are not covered by a membrane, and the defect is to the right of the insertion of the umbilical cord into the anterior abdominal wall.

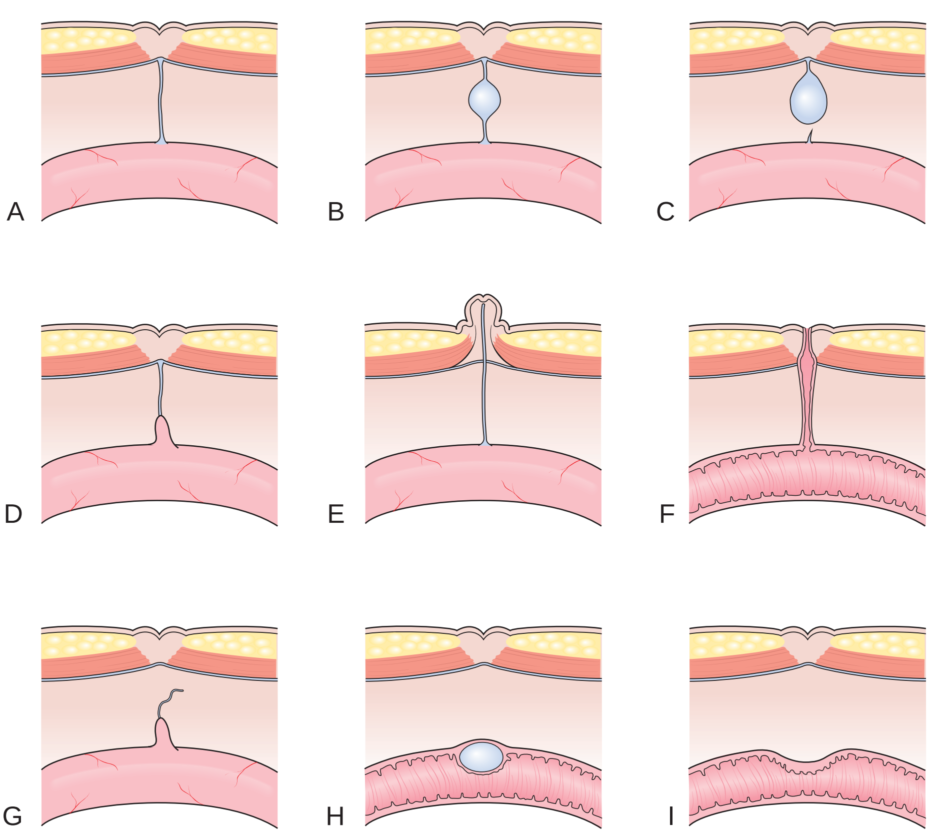

**Figure 86.26. Variants of omphalomesenteric duct remnants.** (A) Persistent cord between the ileal wall and the closed umbilicus. (B) Cyst in the same cord. (C) Cyst anchored at the umbilical end of the cord but free at the ileal end. (D) Meckel diverticulum attached to the closed umbilicus by a closed cord. (E) Everted mucocele of the umbilicus with the cord attached to the ileal wall. (F) Fecal fistula open at both the umbilical and ileal ends. (G) Meckel diverticulum open at the ileal end but blind at the umbilical end, which is unattached. (H) Intramural cystic diverticulum. (I) Local stenosis of the ileum at the site of the mouth of the omphalomesenteric duct. *(From Cullen TS.* Embryology, anatomy and diseases of the umbilicus, *Philadelphia: Saunders; 1916.)*

***Etiology.*** The *omphalomesenteric duct*, also called the *vitelline duct*, connects the primitive midgut, the future ileum, to the yolk sac remnant; normally, it obliterates during the fifth to seventh week of embryonic development. However, if this process does not proceed normally, a spectrum of abnormalities may ensue. Closure of the duct with failure of complete involution results in a ligamentous remnant. Failure of duct closure has been subdivided into three general categories.[47] In a *type 1 abnormality*, the entire duct is open. A *type 2 abnormality* refers to a duct that is open at one end but ends blindly at the other; when open at the ileal end, it represents a *Meckel diverticulum* (see Chapter 102). A *type 3 abnormality* refers to a focal patency along the duct that becomes a cyst.

***Clinical Presentation.*** Patients with a type 1 abnormality present with fecal material draining from the umbilicus. Patients in whom the duct is open only along the umbilical end are seen with discharge from the umbilicus that consists of secretions produced by the lining of the tract. A type 3 abnormality, or *vitelline duct cyst*, is often asymptomatic but may become infected, in which case it can manifest with acute symptoms. Omphalomesenteric duct remnants or attachments may also lead to mechanical bowel obstruction.

***Imaging.*** In a type 1 abnormality, contrast injected through the umbilicus passes directly into the ileum (Fig. 86.27). In a type 2 defect, contrast injection reveals a blind-ending sinus tract of varying length. Imaging over the palpable abnormality in a type 3 defect may demonstrate a simple or complex cystic mass on US or other cross-sectional imaging. These may also be discovered as incidental findings.

***Treatment.*** Management depends on the clinical presentation. Definitive treatment is surgical with resection of the omphalomesenteric duct remnant.[48]

## Urachal Remnant

***Overview.*** The urachus connects the bladder to the allantois; when normally obliterated, it becomes the median umbilical ligament. In a manner analogous to the omphalomesenteric duct, the urachus can be open throughout its course from the bladder to the skin surface at the umbilicus. Alternatively, a portion of the urachus can be open as a blind-ending sinus, from either the dome of the bladder, as a vesicourachal diverticulum, or from the umbilicus, as an umbilicourachal sinus, which is seen in approximately 15% of cases. If only the midportion remains patent, it is known as a *urachal cyst*, seen in approximately 30% of cases.[49]

***Etiology.*** Urachal remnants result from failure of obliteration of a portion of or the entire embryonic urachus.

***Clinical Presentation.*** Periumbilical discharge is the most common presenting complaint, whether due to leaking urine in a fully patent urachus or intermittent discharge from an umbilicourachal sinus.[50,51] Patients may also present with symptoms of an infected urachal remnant. Vesicourachal diverticula, although

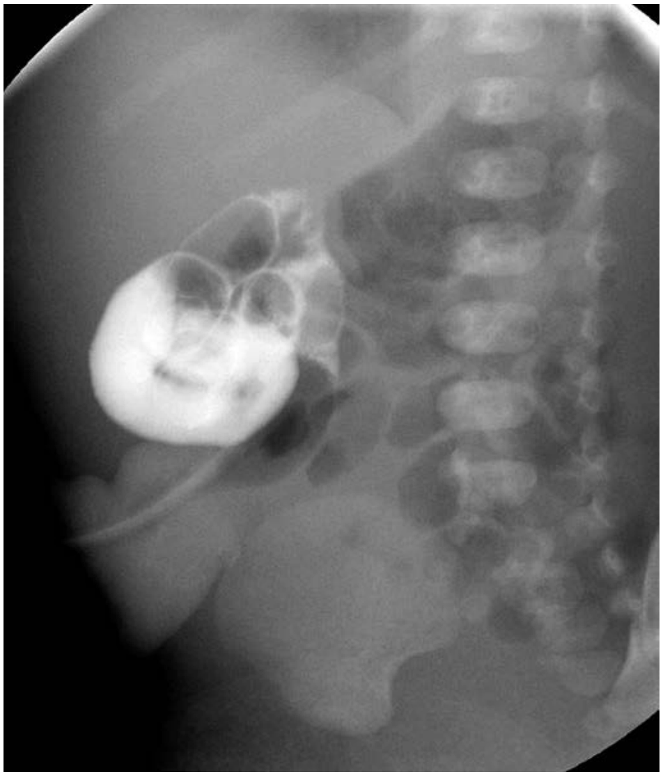

**Figure 86.27. Patent omphalomesenteric duct remnant.** Neonate with history of discharge from umbilicus and bowel loops prolapsed into umbilicus. Oblique view of the abdomen from a gastrointestinal study demonstrates contrast flowing from patent omphalomesenteric remnant into small bowel loops. *(Image courtesy of Geetika Khanna, MD, MS.)*

typically asymptomatic, may serve as a reservoir for stone formation or for development of malignancy in adulthood.[49,52] Other urologic abnormalities—such as hypospadias, posterior urethral valves, or urethral atresia—have been reported in a few cases.[49,53]

***Imaging.*** US is a good initial diagnostic test of choice, followed by CT if unsuccessful.[50,51] The patent urachus may be seen as a fluid-filled tubular structure that extends from the anterosuperior aspect of the bladder to the umbilicus (e-Fig. 86.28). The vesicourachal diverticulum appears as an extension of the anterosuperior bladder, often found in patients being imaged for prune-belly syndrome.[49] An urachal cyst is seen as a well-circumscribed cyst in the anterior abdominal wall, with mural thickening and increased enhancement if complicated by infection (Fig. 86.29).[54] Voiding cystourethrograms may also be used to demonstrate a patent connection to the umbilicus or fistulogram to demonstrate an umbilical sinus tract.

***Treatment.*** Definitive treatment is surgical, using either an open or laparoscopic technique with complete resection of the urachal remnants. If infection has supervened, this is treated before surgical resection.

## Groin and Pelvic Hernias

***Overview.*** Inguinal hernias may be direct or indirect, depending on their relationship to the inferior epigastric vessels. Direct inguinal hernias, with the hernia sac medial to the epigastric vessels, are acquired rather than congenital, and are uncommon in children. Indirect inguinal hernias, with the hernia sac lateral to the epigastric vessels, are the most common form of inferior abdominal wall herniation. The true incidence of inguinal hernias is difficult to determine, but it ranges from 0.8% to 4.4% in children and is more common in boys.[55] Premature infants are at increased risk of developing inguinal hernia, with an approximate 30% incidence.[56] Patients with bladder exstrophy, Ehlers-Danlos syndrome, or prune-belly syndrome also have an increased incidence.[55]

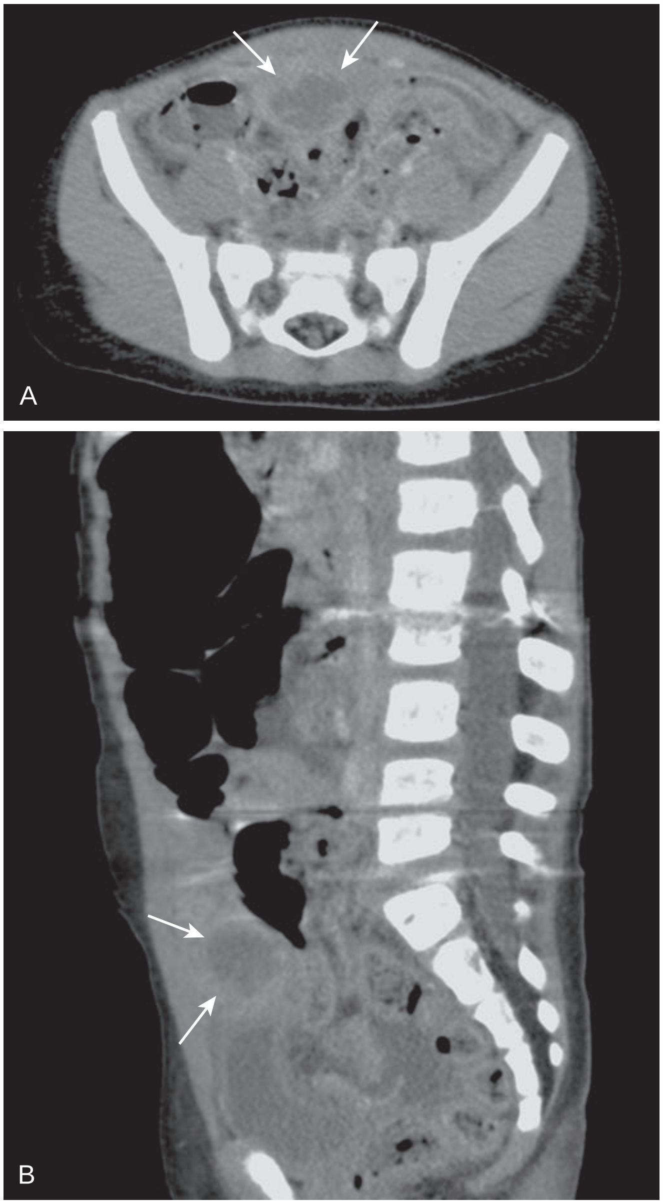

**Figure 86.29. Infected urachal cyst.** (A) Axial contrast-enhanced CT image shows a thick-walled cyst *(arrows)* with surrounding inflammation just superior to the urinary bladder. (B) Midline sagittal reformat shows its location with respect to the bladder and umbilicus to better advantage.

***Etiology.*** The processus vaginalis normally closes between the 36th and 40th weeks of gestation. However, if it remains open, as in indirect inguinal hernias, abdominal contents can herniate through the inguinal ring into the scrotum in boys (e-Fig. 86.30). In girls, abdominal contents or ovaries can herniate through the canal of Nuck into the labia majora (Fig. 86.31).

Although rare in children, femoral hernias, obturator hernias, sciatic hernias, and perineal hernias need to be included in the differential diagnosis of pelvic masses that extend into the buttock or perineum.

***Clinical Presentation.*** Patients usually come to medical attention with an intermittent painless bulge in the inguinal region, scrota,

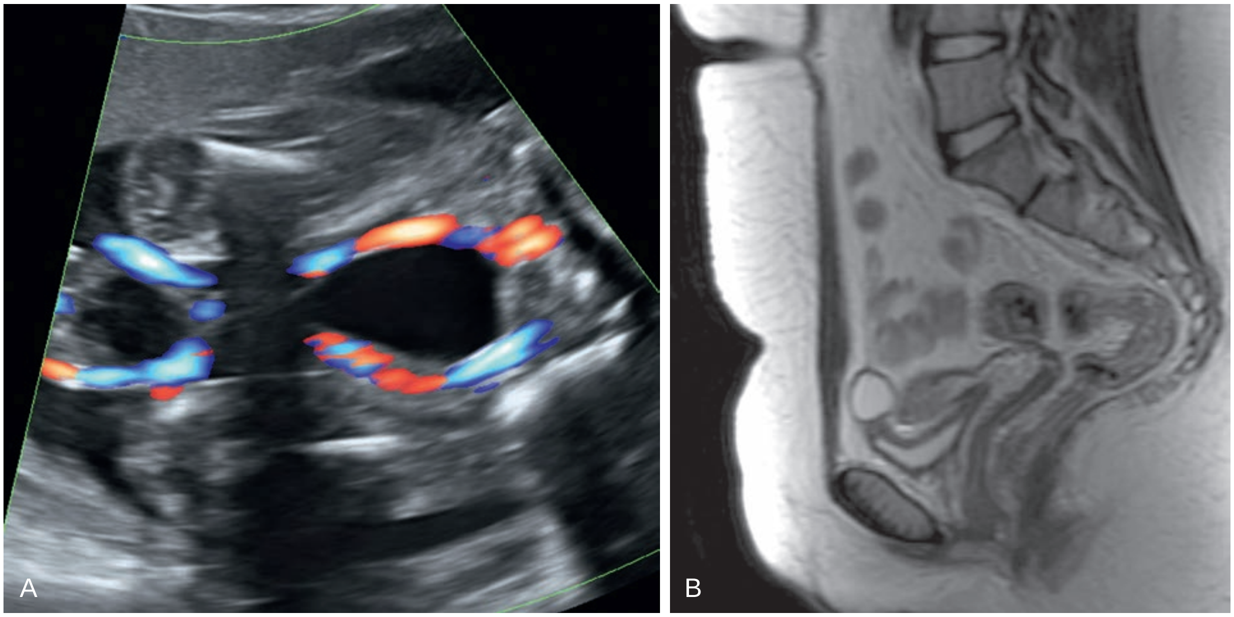

**e-Figure 86.28. Urachal remnants.** (A) Fetal sonogram demonstrates a large incidental urachal remnant in a 22-week gestational age fetus. The paired umbilical arteries surround the urachal remnant as well as the bladder. (B) Incidental urachal cyst seen on a T2-weighted sagittal MR image. Note the positioning anterior and superior to the bladder in the expected location of the urachus.

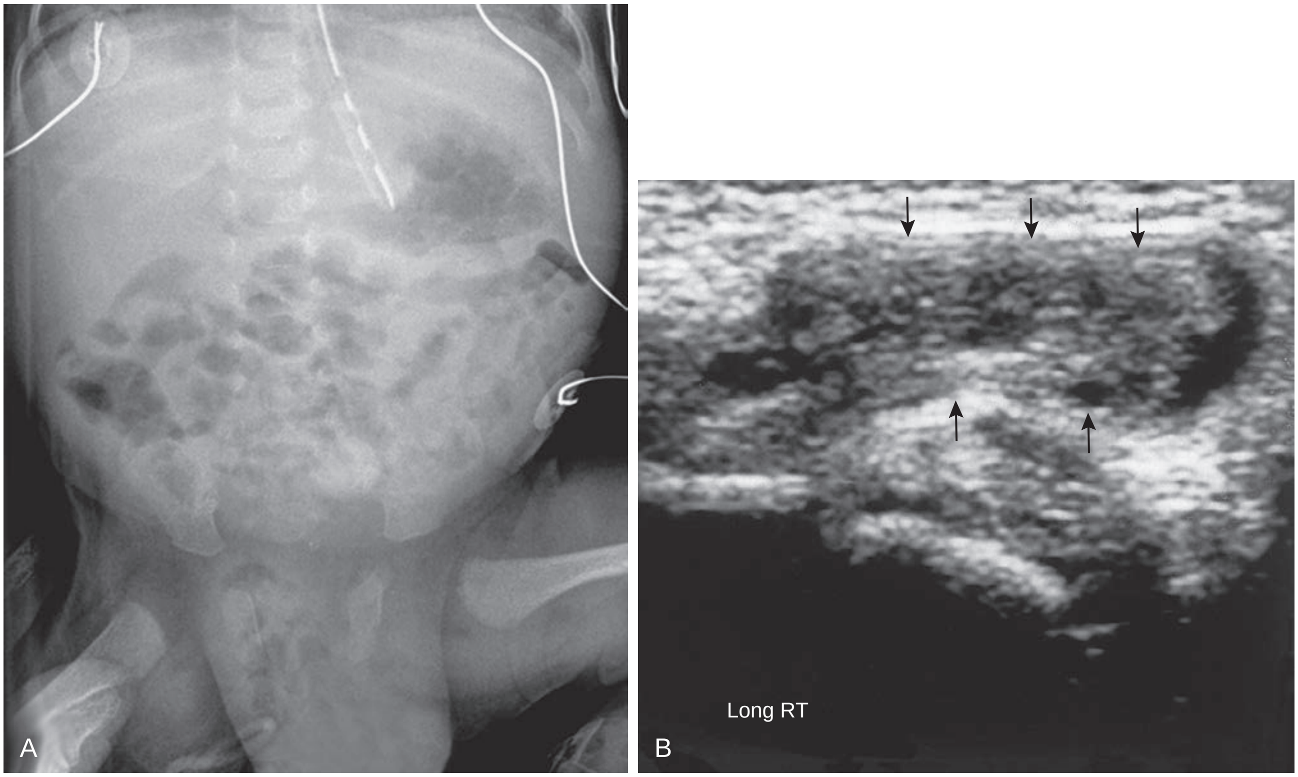

**e-Figure 86.30. Inguinal hernia.** (A) Anteroposterior view of the abdomen and pelvis in a newborn boy shows an enlarged scrotum, with multiple air-filled loops of intestine within it, secondary to indirect right inguinal hernia. (B) Ultrasound in the inguinal region of an infant girl with a labial mass confirms a herniated ovary *(arrows)* in the canal of Nuck.

or labia that is noticed when the abdominal pressure rises, such as during crying, straining, or coughing.[55,56] If the bowel loop becomes entrapped or incarcerated in the hernia (e-Fig. 86.32), the patient may exhibit signs and symptoms of bowel obstruction, such as abdominal distension or vomiting. If the hernia is not reduced, the blood supply to the trapped bowel loops may be compromised, leading to bowel necrosis and perforation. Incarceration occurs most frequently in the first 6 months of life.[56]

***Imaging.*** In patients with equivocal clinical findings, US is highly accurate (95%) in demonstrating an inguinal hernia (Fig. 86.33).[57] US can identify the intestinal wall surrounding fluid-filled loops of bowel or may show bubbles of air or peristalsis. Color Doppler US can show blood flow in the wall of the herniated bowel loop. These findings help differentiate a hernia from a hydrocele.

Inguinal hernias may be seen on radiographs as an air-filled loop of bowel in the scrotum (see e-Fig. 86.30), but this is often obscured by gonadal shielding. Herniating bowel loops may be an incidental finding on small bowel series. In contrast enemas for infants with intestinal obstruction, reflux into the small intestine may show a pinched-off loop at the entrance to the inguinal canal.

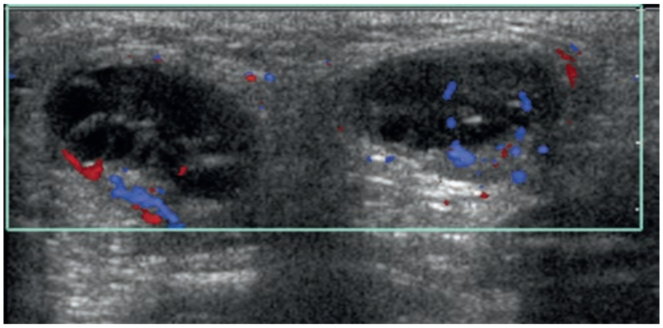

**Figure 86.31. Canal of Nuck hernia.** Transverse ultrasound image through labia majora in a newborn with bilateral palpable labial masses demonstrates ovaries herniated through the canal of Nuck into the labia.

Hernias are well seen on CT (see e-Fig. 86.32) and MRI,[58,59] though these studies are rarely indicated as first-line modalities for diagnosing hernias.

***Treatment.*** The treatment of inguinal hernia is surgery using open or laparoscopic technique.[60]

## BENIGN AND MALIGNANT NEOPLASMS

### Cystic Neoplasms

***Overview.*** Abdominal cystic lesions include lymphatic malformations, lesions related to the bowel such as duplication cysts, and those related to the urogenital system including urachal cysts. The term *mesenteric cyst* has been previously applied to cysts of variable histopathologic origin.[61,62] More recent literature classifies such "mesenteric cysts" based on their histopathologic features, such as lymphatic, mesothelial, enteric, urogenital, or dermoid cysts; mature cystic teratomas; or pseudocysts.[63,64] This section will discuss lymphatic and mesothelial cystic peritoneal lesions.

### Lymphatic Malformations

***Overview.*** *Lymphatic malformations*, formerly known as *lymphangiomas*, are the most common type of vasculolymphatic malformation to affect the peritoneal cavity and mesentery, although they are rare in this region and most commonly occur in the head and neck.[65] Lymphatic malformations have an endothelial lining with walls that contain smooth muscle and lymphatic spaces.[63,66]

***Etiology.*** Lymphatic malformations do not have a clear origin and have been variously postulated to be developmental, congenital, or neoplastic.[67–69] A prevalent hypotheses suggests that they result from the proliferation of abnormal lymphatic channels that do not communicate with the systemic lymphatics.[70]

***Clinical Presentation.*** Lymphatic malformations may be encountered as a palpable abdominal mass—which, if sufficiently large, could be mistaken for ascites—or incidentally during imaging for another reason. They may manifest with small bowel obstruction secondary to acute enlargement of the cyst or segmental volvulus

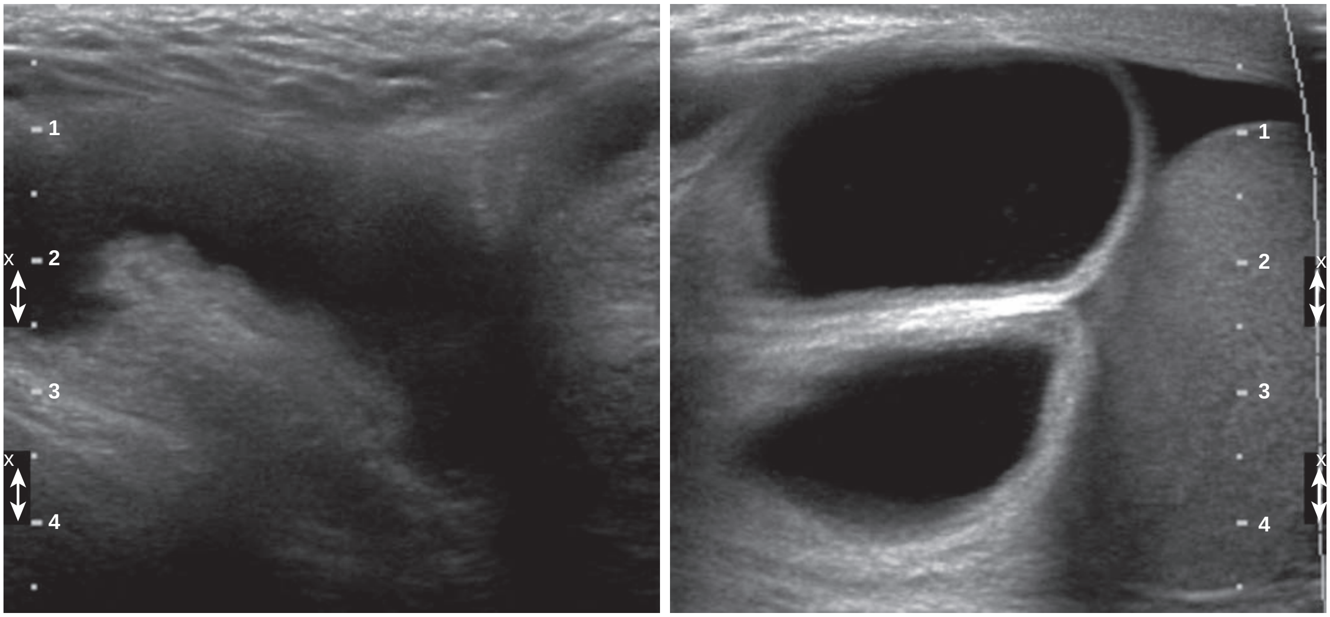

**Figure 86.33. Inguinal hernia.** Composite oblique ultrasound image along the inguinal canal from a scrotal sonogram demonstrates an inguinal hernia that contains moderately distended fluid-filled bowel loops. During real time imaging, the herniated bowel loops demonstrated peristalsis. The normal right testis is seen lower in the scrotal sac.

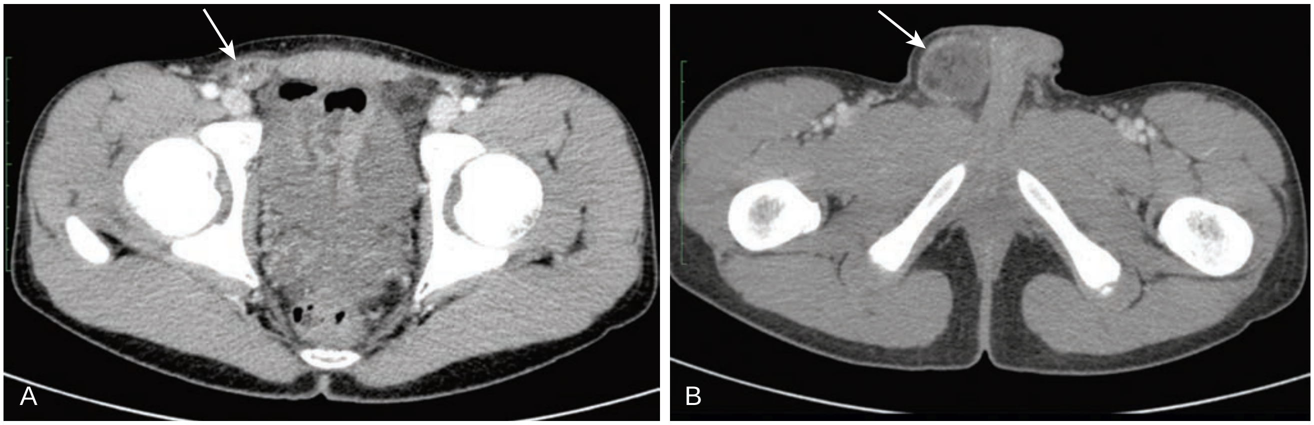

**e-Figure 86.32. Incarcerated inguinal hernia.** (A and B) Sequential axial images from a contrast-enhanced CT demonstrates an incarcerated right inguinal hernia *(arrows)* that contains omentum, with adjacent inflammatory changes *(arrows)*.

of adjacent bowel loops, with symptoms that include abdominal distension, pain, vomiting, and peritonitis or septic shock.[62,65,70,71]

***Imaging.*** On US, lymphatic malformations are typically seen as thin-walled, fluid-filled, single or multiple cysts, often with thin septations.[11] In the presence of hemorrhage or infection, internal echoes may be detected. Ascites, often chylous, can also be present.[65] Despite the internal echoes, Doppler interrogation will reveal no internal flow within the echogenic but cystic component, differentiating it from a solid mass. On real time visualization, movement of the internal echoes can be seen.

CT shows cystic or multicystic lesions with thin or imperceptible walls, and internal septations may enhance as a result of the presence of vascular structures (Fig. 86.34). The CT attenuation of the cyst contents may be lower than water because of their chylous nature.[65,67]

On MRI, lymphatic malformations typically demonstrate low signal intensity on T1-weighted sequences and high signal intensity on T2-weighted sequences.[72] Internal hemorrhage can manifest as increased signal intensity on both T1- and T2-weighted sequences.[72] The peripheral rim and internal septations may enhance, but the majority of the lesion does not enhance and should not enhance centrally.[72] MRI may aid in distinguishing large lymphangiomatous masses that have hemorrhaged from complex intraperitoneal fluid (Fig. 86.35). Cross-sectional imaging

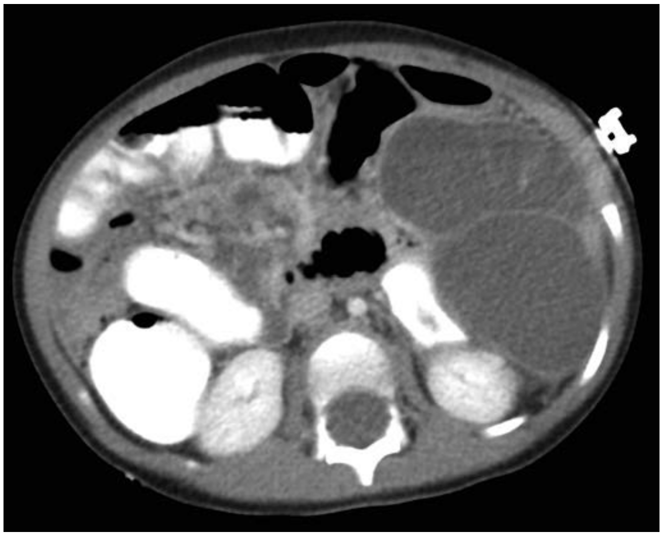

**Figure 86.34. Peritoneal lymphatic malformation.** Axial contrast-enhanced CT image demonstrates a large multiloculated lymphatic malformation in the peritoneal cavity.

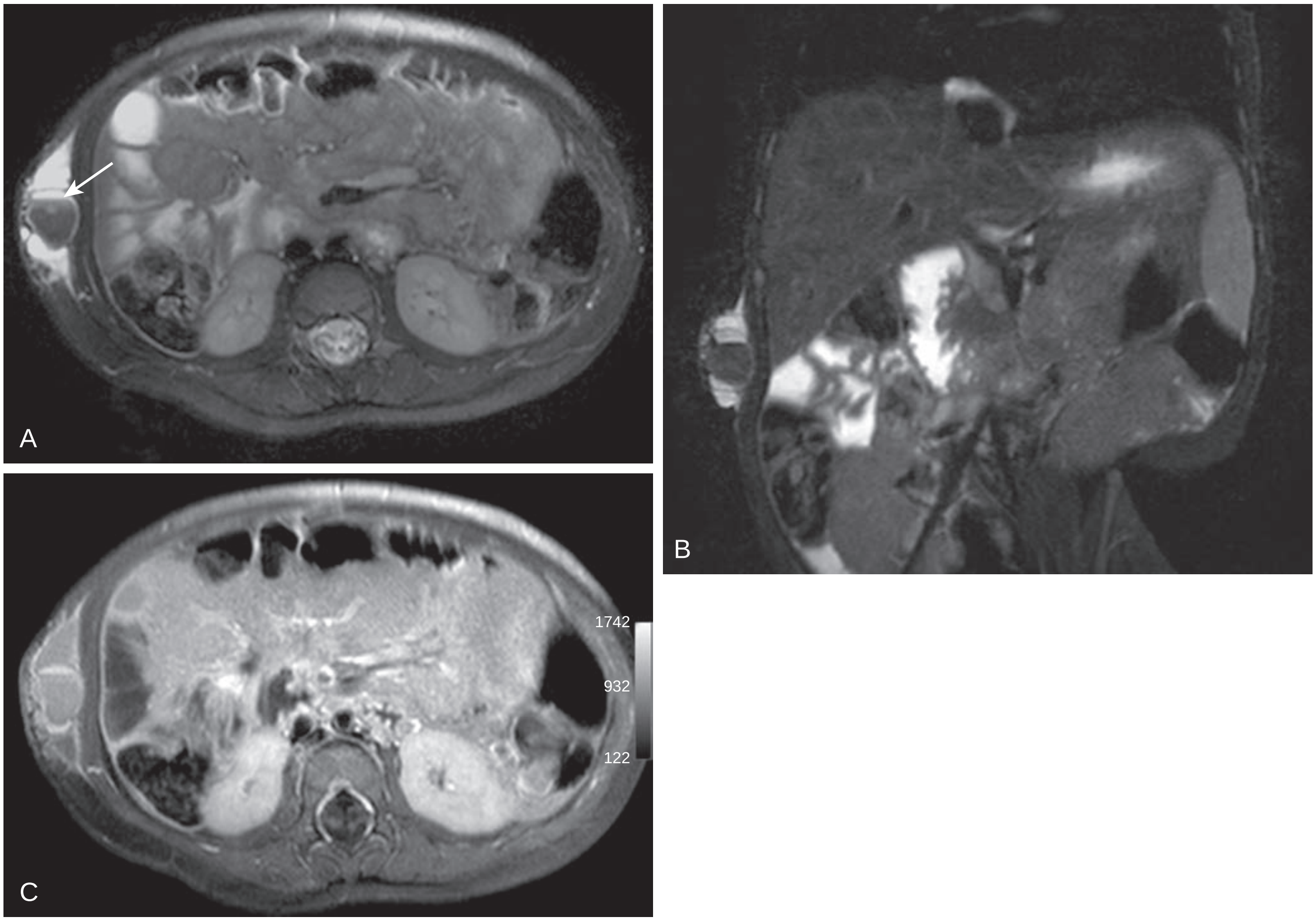

**Figure 86.35. Abdominal wall lymphatic malformation.** (A and B) Axial and coronal T2-weighted MR images with fat saturation in a 16-month-old girl with 2 weeks of localized swelling in the right flank show a multiloculated cystic lesion within the subcutaneous tissues of the abdominal wall with some mass effect upon the underlying musculature. Most of the locules are hyperintense on T2, with a large T2 hypointensity within and a fluid level *(arrow)* consistent with a hematocrit level. (C) After the administration of contrast, T1-weighted, fat-suppressed MR image shows that the septations enhance, but the internal contents do not, which is typical of a lymphatic malformation. No solid components were detected.

is useful to assess the entire extent of the lesion and to define the relationship with adjacent structures.

***Treatment.*** Lymphatic malformations may be treated with sclerotherapy or surgical resection. The decision largely depends on the location and size of the lesion. Staged sclerotherapy and/or surgical resection may be required, particularly with multicentric lesions or lesions that extend into the retroperitoneum. The prognosis is generally good, with a low recurrence rate.[70]

## Cysts of Mesothelial Origin

***Overview.*** Cysts of mesothelial origin include simple mesothelial cysts, benign cystic mesotheliomas, and malignant cystic mesothelioma. Simple cysts are unilocular and are usually 1 to 5 cm in size, whereas benign cystic mesotheliomas are large and multilocular.[63] Mesothelial cysts are lined by flat cuboidal or columnar cells without lymphatic structures; this distinguishes these lesions from lymphatic malformations.[63,66]

Benign cystic mesotheliomas are rare, most commonly arising from the peritoneal surface of the pelvis. This lesion has many alternative names that include *peritoneal inclusion cyst*, *multilocular inclusion cyst*, and *benign multicystic mesothelioma*.[1] Although most commonly found in middle-aged women, it can also occur in children.[1,73–75] Malignant degeneration to peritoneal cystic mesotheliomas has been infrequently described in adult patients.[73,76]

***Etiology.*** The cause of mesothelial cysts remains unclear, although theories postulate developmental, neoplastic, and reactive etiologies. The reactive hypothesis suggests that a stimulus produces chronic irritation that can lead to reactive and loculated proliferation of mesothelial cells, resulting in a cystic fluid collection with mesothelial lining.[72]

***Clinical Presentation.*** Similar to lymphatic malformations, mesothelial cysts can be detected as masses,[66,71] ascites,[76] or they may present with acute abdominal symptoms that can mimic appendicitis.[61,62,77]

***Imaging.*** Because differentiation from cystic lymphatic malformations is based on histologic elements, imaging findings in these lesions are very similar to those in lymphatic malformations.[73]

***Treatment.*** The goal is complete surgical resection[70] because these tumors recur in as many as 75% of cases and because malignant degeneration has been reported.[73]

## Other Benign Lesions

### Lipoblastoma

***Overview.*** Lipoblastoma is a rare, benign, mesenchymal fat-containing tumor seen almost exclusively in infants and children, with a slight male predilection. Multiple series support that 70% to 90% of these tumors occur in children under 3 years of age.[78–83] The most common sites involved are the subcutaneous and superficial soft tissue of the neck and extremities[78,80,81]; approximately 7% of lipoblastomas occur in the abdomen.[84] Lipoblastoma differs from lipoma in that it contains both mature and immature adipocytes and is almost exclusively found in young children.[85] Lipoblastoma differs from lipoblastomatosis in that it is a well-circumscribed, encapsulated lesion, whereas lipoblastomatosis is a diffuse infiltrating process.[78,84]

***Etiology.*** Lipoblastomas arise from embryonal white fat, in contradistinction to hibernomas, which arise from brown fat.[83] The etiology of the lesions is not known, but lipoblastomas demonstrate chromosomal abnormalities with deletions or abnormal sequencing. The vast majority of cases have characteristic cytogenetic abnormality containing a 8q11-13 clonal chromosomal rearrangement that affects *PLAG1*.[86–88] Distinction from liposarcoma, particularly the myxoid variety, may be difficult: histologic criteria are based on a uniform growth pattern, absence of nuclear atypia, and cytogenetics; clinical criteria include patient age, because liposarcomas in children younger than 10 years are very rare.[82,88]

***Clinical Presentation.*** Clinical manifestations depend upon mass size and location and its effect on adjacent structures. Lipoblastomas frequently manifest as rapidly growing painless masses. Abdominal lipoblastomas may result in symptoms of vomiting, anorexia, abdominal pain, and diarrhea secondary to mass effect upon adjacent structures.[84]

***Imaging.*** Imaging features of lipoblastoma reflect the underlying pathology and vary depending upon the extent of underlying myxoid stroma versus adipose tissue.[88] Abdominal radiographs may demonstrate radiolucency,[89] although US may be the initial modality to confirm the presence of a mass and to assess its characteristics and location. A lipoblastoma is seen as a homogenously hyperechoic solid lesion, but mixed echogenicity and fluid-filled spaces can be present.[88,90] On CT and MRI, lipoblastoma appears as a lobular, fat-containing, well-circumscribed mass, often with internal septations (Fig. 86.36). The amount of fat will depend on the maturity of the cells that make up the tumor, with the proportion of mature adipocytes correlating with fat attenuation and signal characteristics respectively on CT and MRI.[88] If fat is the predominant component, the lipoblastoma is usually indistinguishable from a lipoma, with the diagnosis suggested based on patient age. If myxoid stroma is the predominant component, as seen in very young children, imaging will reflect decreased fat[85] and a variable amount of contrast enhancement.[88]

Differential diagnosis includes liposarcoma, which may be difficult to distinguish based solely on imaging findings.[82,88] Benign cystic teratomas also contain fat, but these may be distinguished from lipoblastoma by calcification or ossification.[88]

***Treatment and Follow-up.*** Treatment for lipoblastoma is complete surgical resection. Lesions may locally recur in up to 9% to 25% of cases. Recurrences are more often seen with lipoblastomatosis, likely related to incomplete resection. Current management suggests that extensive surgery to achieve complete resection is not required, because the lesions have no malignant potential and spontaneous regression and maturation into lipoma may occur.[88,91,92]

### Desmoid Tumors

***Overview.*** Desmoid tumors are histologically benign but locally aggressive, nonmetastasizing tumors that belong to a group of disorders known as *fibromatoses*.[93,94] Approximately 37% to 50% of desmoids arise in the abdominal region.[95] In the abdominal wall, desmoid tumors arise from the aponeuroses of fascia and near surgical scars.[89]

These tumors can occur sporadically or in association with familial adenomatous polyposis (FAP) and Gardner syndrome, and they occur in as many as 20% of affected patients.[89,96] They can also occur in FAP patients after prophylactic colectomy and are one of the leading causes of death after colectomy in these patients.[97,98]

***Etiology.*** The etiology of desmoid tumors is unknown but is thought to be multifactorial.[95] Their development within the setting of the polyposis syndromes suggests a genetic correlation. Desmoid tumors tend to develop after trauma and often arise 6 to 30 months after colectomy in FAP patients[96] or after chemotherapy or radiation treatment.[88] There is also evidence of hormonal influence, and some tumors express estrogen receptors.[88] These lesions are more common in women, with a ratio as high as 4:1.[95]

***Clinical Presentation.*** Abdominal desmoids may be asymptomatic. However, as they enlarge, they may infiltrate adjacent structures and lead to symptoms related to compression of bowel, vascular, or other retroperitoneal structures.[95]

***Imaging.*** Desmoid tumors vary in imaging characteristics, depending upon the amounts of collagen, proliferating fibroblasts,

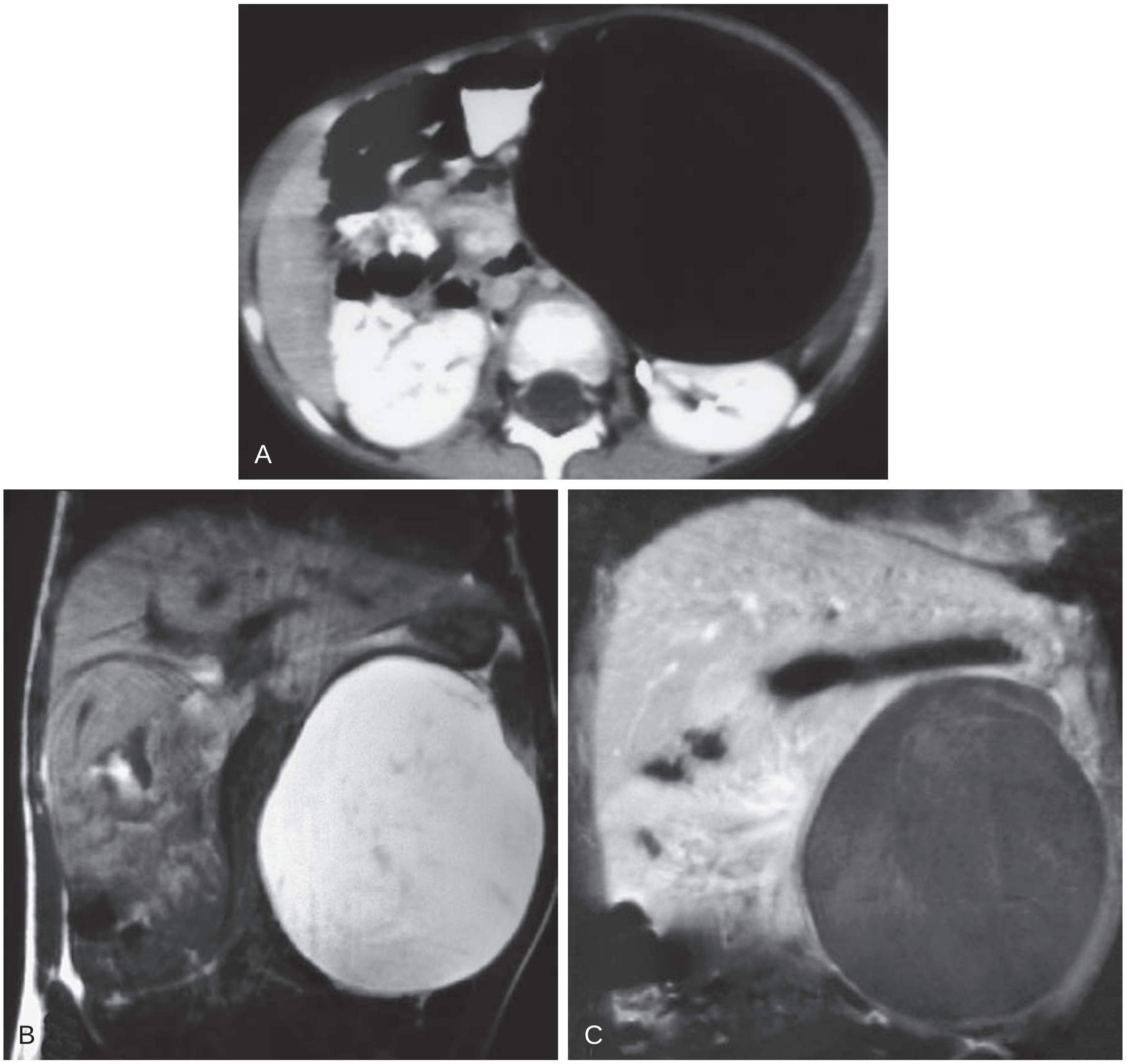

**Figure 86.36. Lipoblastoma.** Encapsulated left upper quadrant lipoblastoma attached to the pancreatic tail of a 2-year-old girl. (A) Axial contrast-enhanced CT image through the midabdomen shows a large fatty mass. Coronal MR T1-weighted sequences without (B) and with (C) fat saturation depict the fatty nature of the entire mass as well as some internal septations.

fibrosis, and vascularity. The fibrous and cellular composition of desmoid tumors varies with the stage of their evaluation.

On US, the margins may be ill-defined or irregular, and echogenicity is variable. CT density and margins likewise vary. On magnetic resonance (MR), desmoid tumors typically demonstrate decreased signal intensity on T1- and variable signal intensity on T2-weighted sequences compared with muscle. An association has been found between increased tumor cellularity, as shown on T2-weighted images, and tendency for rapid tumor growth.[89] Enhancement patterns are variable (Fig. 86.37). MRI is a useful method for staging desmoid tumors and detecting recurrence.

***Treatment.*** Surgical resection has been the mainstay of treatment; however, many abdominal desmoids are discovered when they are no longer easily resectable, particularly with sufficiently wide margins to prevent recurrence, thus risking significant morbidity and mortality.[93] The goal of resection is negative margins; positive margins or incomplete resection are treated with adjuvant radiotherapy.[77,96,99] Other systemic therapies have been tried, including steroids, antiestrogen agents, nonsteroidal antiinflammatory agents, and chemotherapeutic agents.[91,94]

## Pseudomyxoma Peritonei

***Overview.*** Pseudomyxoma peritonei occurs when the omental and peritoneal surfaces are caked with copious amounts of mucinous or gelatinous material.[2]

***Etiology.*** Pseudomyxoma peritonei arises from most commonly from rupture of an appendiceal mucinous adenoma into the peritoneal cavity. Pseudomyxoma peritonei may also originate from, or may secondarily involve, the ovary.[95] Abundant amounts of mucus, which may or may not contain epithelial cells, spreads through peritoneal pathways and accumulates in spaces such as the cul-de-sac, Morison pouch, and paracolic gutters.[2,100]

***Clinical Presentation.*** Pseudomyxoma peritonei is more common in adults and affects women more than men.[95] Patients typically present with abdominal pain and weight loss, despite increasing abdominal size.[2]

***Imaging.*** Imaging findings are generally similar to those seen in massive ascites. US reveals ascitic fluid that demonstrates nonmobile internal echoes.[2] Septations and occasionally solid-appearing masses can be seen. On CT, the mucinous material is

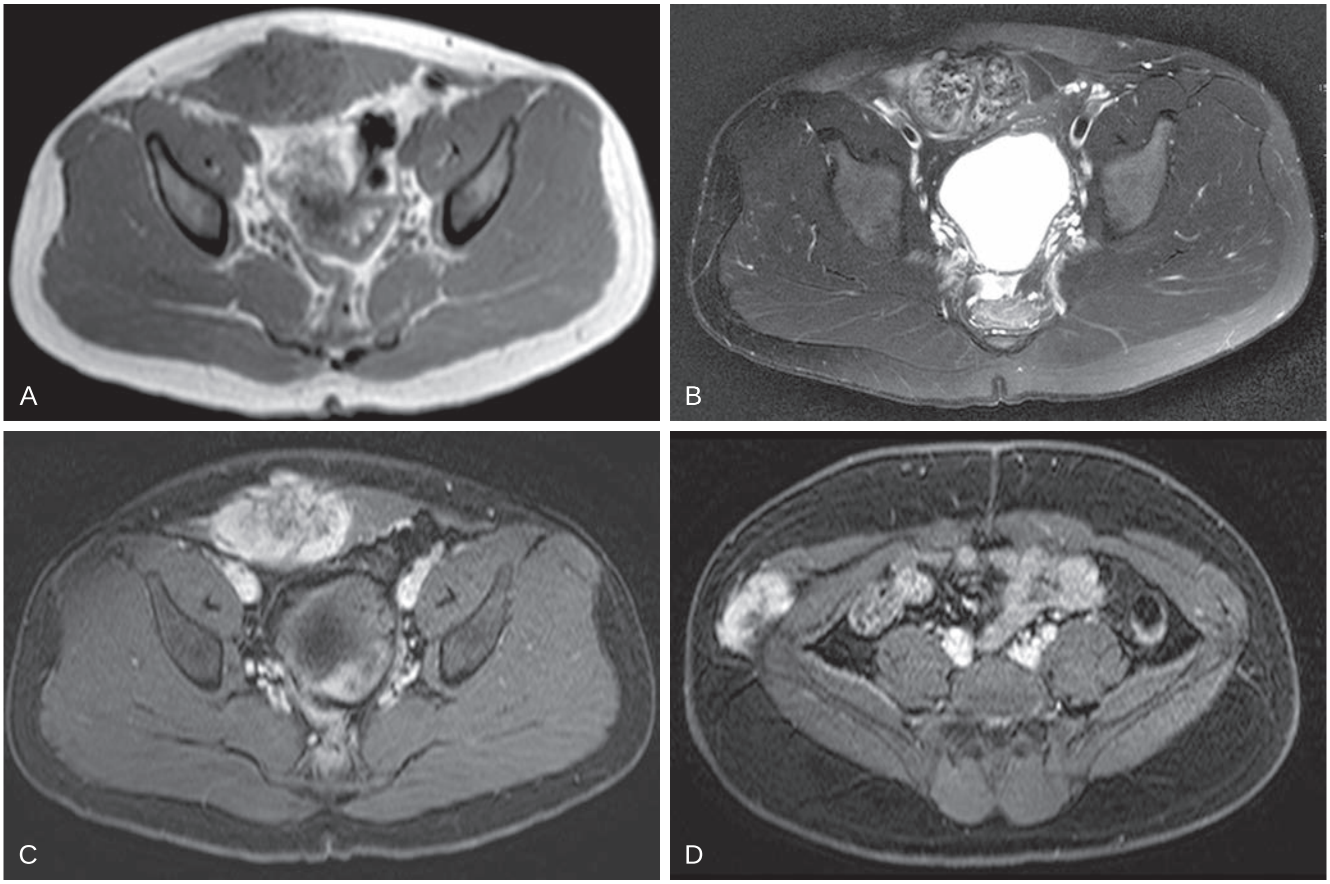

**Figure 86.37. Desmoid tumor.** (A) Axial T1-weighted MR image in a 16-year-old girl with an abdominal wall mass for 1 year shows a relatively well-defined rounded mass within the right rectus muscle. (B) Axial T2-weighted image with fat saturation shows a heterogeneous appearance to the mass. (C) T1-weighted fat saturation MR image after administration of contrast shows avid enhancement, especially when compared with adjacent muscle. (D) An additional lesion with similar imaging characteristics is also identified more laterally in the abdominal wall.

typically low density and accumulates in dependent areas as previously discussed. Scalloping of visceral surfaces, particularly the liver, is an important imaging sign to differentiate pseudomyxoma peritonei from ascites.[2] On imaging it is difficult to differentiate the benign form of pseudomyxoma peritonei from peritoneal mucinous carcinomatosis. Adenopathy, pleural involvement, enhancing masses, and invasion of visceral organs favors a malignant process.[2]

***Treatment.*** The treatment for the benign forms of pseudomyxoma peritonei consists mainly of surgical evacuation and appendectomy, with the potential need for resection of other involved structures. Malignant causes need additional treatment, such as intraperitoneal instillation of chemotherapeutic agents and radiotherapy.[101,102]

## MALIGNANT LESIONS

### Peritoneal Metastases and Carcinomatosis

***Overview.*** Peritoneal metastatic spread is rare in pediatric patients. Germ cell tumors or carcinoma of the colon account for up to 47% of cases of peritoneal carcinomatosis in children.[103] Other tumors that can be seen with diffuse peritoneal dissemination include Wilms tumors, neuroblastoma, melanoma, teratoma, leiomyosarcoma, epithelioid carcinoma, desmoplastic small round cell tumor (DSRCT), and non-Hodgkin lymphoma.[103,104]

***Etiology.*** Malignancy disseminates throughout the peritoneum by intraperitoneal seeding, direct invasion, hematogenous spread, or lymphatic dissemination.[2] Peritoneal metastases frequently occur in the presence of other sites of metastatic disease. Seeding may occur at the time of operative intervention through tumor rupture and intraperitoneal spillage, with rare instances of intraabdominal spread of intracranial disease via ventriculoperitoneal shunt.

Malignant cells migrate through the normal circulation of the peritoneal fluid. The adhesion of tumor cells to mesothelial cells is believed to be mediated through the expression of intercellular adhesion molecules.[2,105] Ascites results when disseminated disease interferes with the absorptive capacity of the mesothelial lining of the peritoneum.[105]

***Clinical Presentation.*** Peritoneal metastases may initially be asymptomatic; with progression of disease, patients may present with abdominal enlargement, ascites, nausea, and abdominal pain.[103,104] Approximately 20% are seen with bowel obstruction and 50% with ascites.[105,106] CT may demonstrate solitary or multiple masses, diffuse peritoneal thickening, peritoneal enhancement, and tumor studding of the peritoneal surfaces.[98] Diffuse caking is a feature of peritoneal metastases from rhabdomyosarcoma, non-Hodgkin lymphoma, and germ cell tumors (e-Figs. 86.38 and 86.39).[98]

MRI detection of peritoneal implants may be improved over CT because of the inherent tissue contrast and multiplanar capabilities.[2] Peritoneal implants tend to be hypointense on T1- and

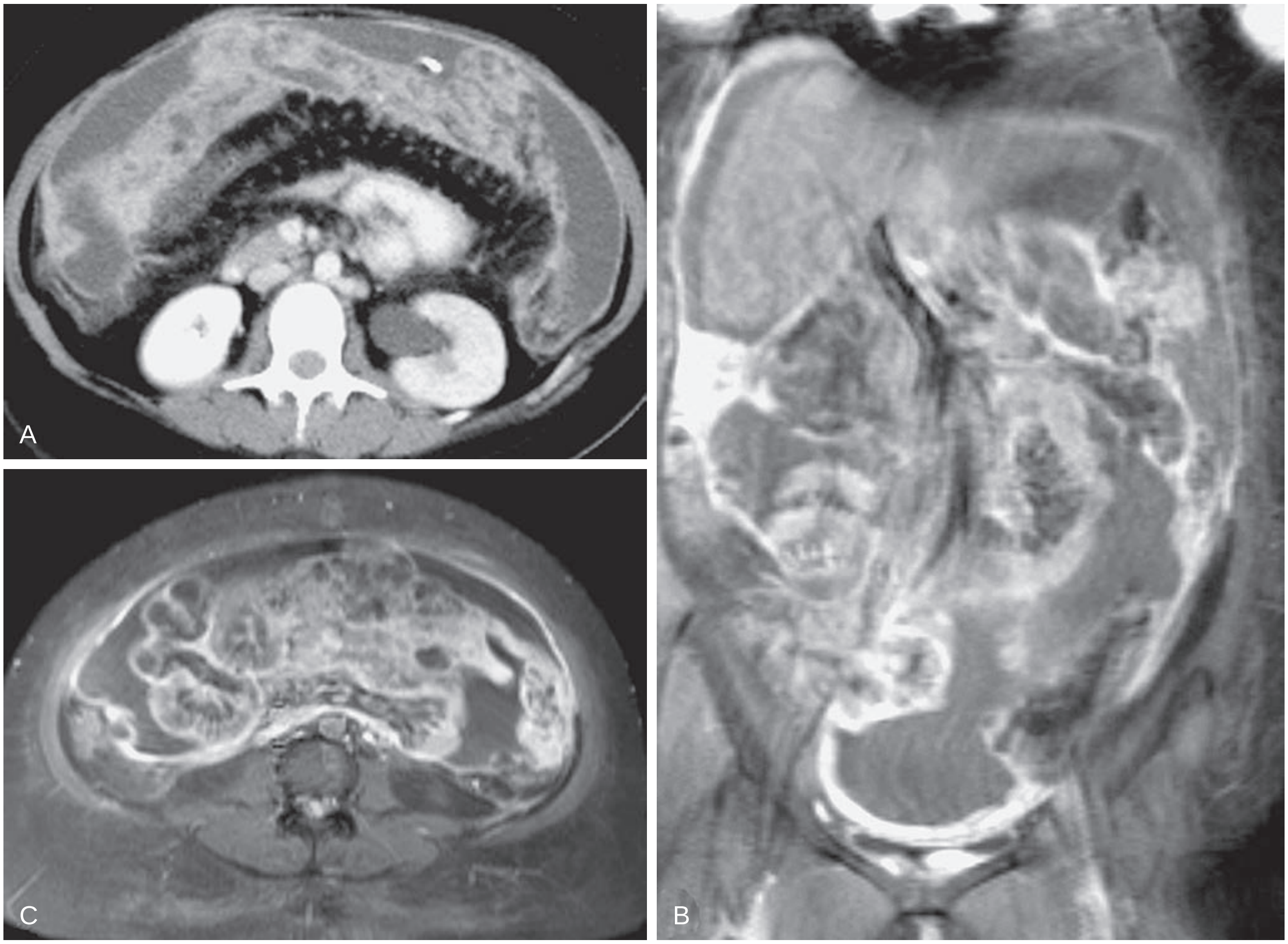

**e-Figure 86.38. Peritoneal mesothelioma.** An 18-year-old patient with a history of posterior fossa medulloblastoma is seen with new onset of hemorrhagic ascites. (A) Axial contrast-enhanced CT image through the midabdomen demonstrates abundant ascites and abnormal enhancement of the peritoneal surfaces. Note diffuse, enhancing omental caking. Coronal (B) and axial (C) contrast-enhanced T1-weighted magnetic resonance images of the abdomen and pelvis demonstrate the thickened, intensely enhancing peritoneal surfaces and abundant ascites.

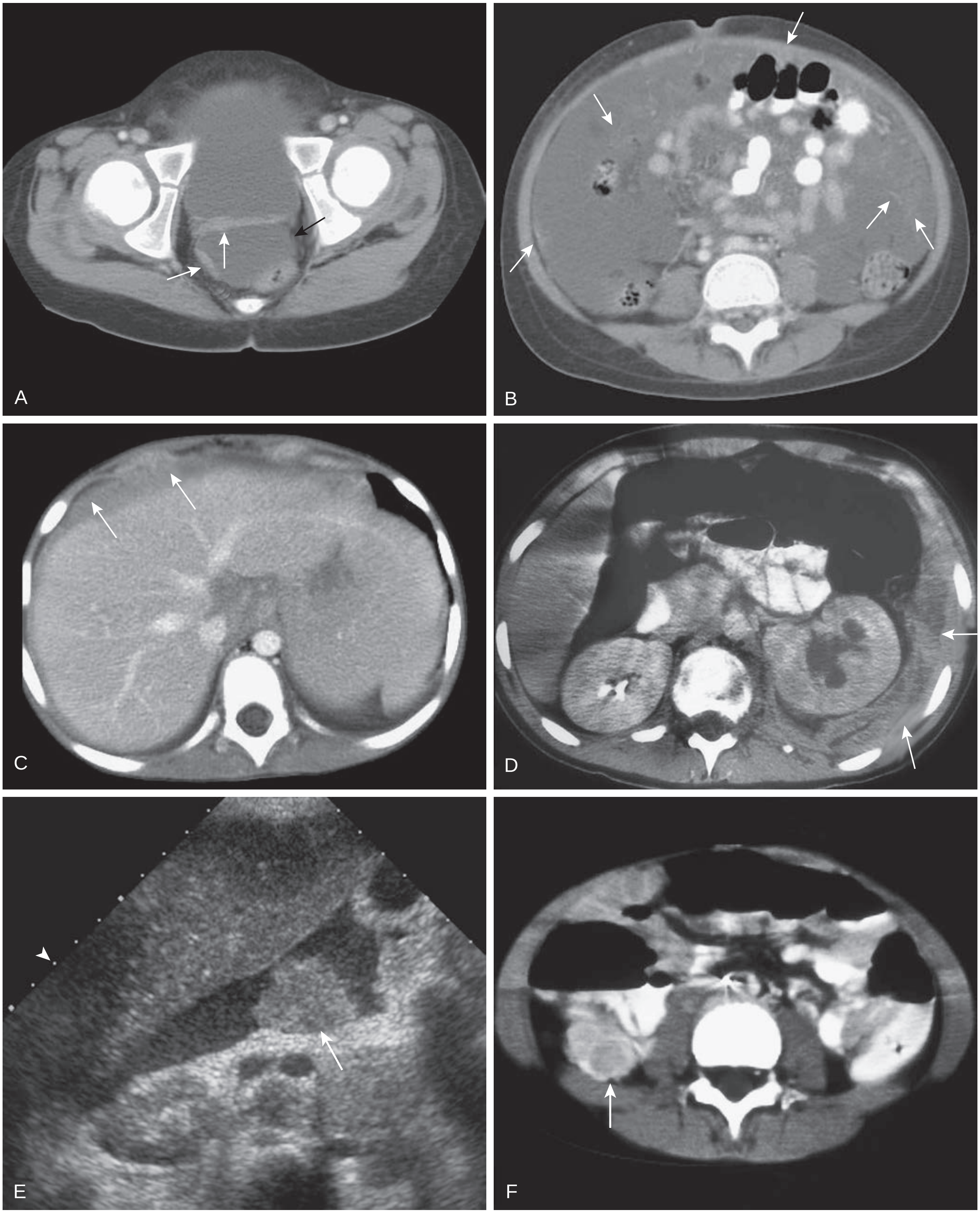

**e-Figure 86.39. Peritoneal metastases may have a varied appearance.** (A) Axial contrast-enhanced CT image of the deep pelvis shows a moderate amount of pelvic ascites *(black arrow),* resulting from the peritoneal metastases evidenced by abnormal thickening and enhancement of the peritoneal surface *(white arrows)* in a patient with history of desmoplastic small round cell tumor (DSRCT) and recurrent ascites. (B) Contrast-enhanced CT through the midabdomen in a patient with epithelioid sarcoma shows more extensive peritoneal disease and complex ascites. Note tiny masses studding the peritoneum *(arrows)* and numerous strands of solid disease throughout the ascites *(arrows)*. Contrast-enhanced CT images in a patient with Burkitt lymphoma. (C) Patient with metastatic melanoma. (D) Diffuse thickening of the peritoneal surface (*arrows* in C and D). (E) Transverse ultrasound image shows metastatic disease manifested as a discrete mass *(arrow)* surrounded by ascitic fluid. (F) Contrast-enhanced CT image shows a cystic peritoneal metastasis *(arrow)* in a patient with neuroblastoma.

hyperintense on T2-weighted sequences, with variable enhancement.[105] Delayed images obtained 10 to 15 minutes after gadolinium administration may show lesions better, because they are slow to enhance.[2,105] However, respiratory and bowel motion may degrade identification of peritoneal and serosal lesions. Positron emission tomography (PET) or CT scan may also help to identify peritoneal carcinomatosis with greater confidence, depending on the size of the lesions.[2]

***Treatment.*** Surgical cytoreductive procedures are employed to remove gross or bulky disease, followed by hyperthermic intraperitoneal chemotherapy. However, tumor recurrence rates as high as 70% are reported.[105]

## Desmoplastic Small Round Cell Tumor

***Overview.*** DSRCT is a rare and aggressive abdominal malignancy.[106–108] Intraperitoneal involvement is most common, and less common sites include paratesticular, pleural, lung, ovary, sinus, central nervous system, kidney, and stomach.[102,109,110]

***Etiology.*** The etiology of DSRCT is unknown; it has been hypothesized that the tumor originates from the mesothelial, submesothelial, or subserosal mesenchyma.[105] Pathologically DSRCTs are part of the small round blue cell family that includes Ewing sarcoma, neuroblastoma, Wilms tumor, rhabdomyosarcoma, and primitive neuroectodermal tumors. Immunocytochemical staining is usually required to distinguish DSRCTs from other small round cell tumors.[111]

***Clinical Presentation.*** DSCRTs typically affect adolescents and young adults aged 15 to 25 years, and there is a strong male predilection with ratios that range from 3 : 1 to 9 : 1. Patients generally come to medical attention with vague abdominal pain and/or distension, and palpable abdominal masses may be present on physical examination.[106,109]

***Imaging.*** On CT imaging, DSRCT is usually seen as multiple, scattered peritoneal masses without an apparent primary parenchymal source. The masses are generally of low attenuation and have a variable degree of central necrosis or hemorrhage with mild to moderate contrast enhancement.[102,112] US and MRI findings for DSRCT are variable and nonspecific (e-Fig. 86.40). The utility of fluorodeoxyglucose PET/CT is still evolving and is currently used to evaluate metastatic progression and response to systemic therapy.[113,114]

Tumor spread by direct peritoneal seeding results in multiple omental and mesenteric masses. Liver metastases, both intrahepatic (hematogenous) and serosal (direct spread), are seen in up to 50% of patients (Fig. 86.41).[104,112] Other hematogenous metastatic lesions are less common. In addition, hydronephrosis and small bowel obstruction may result from mass effect. Multiple studies have found a correlation between retroperitoneal lymphadenopathy and ascites with a large pelvic mass (see Fig. 86.41).[1,104,115] Although imaging features are usually nonspecific, the combination of scattered small peritoneal masses, a dominant pelvic mass, retroperitoneal lymphadenopathy, and ascites is somewhat characteristic for this entity. Primary differential diagnostic considerations include

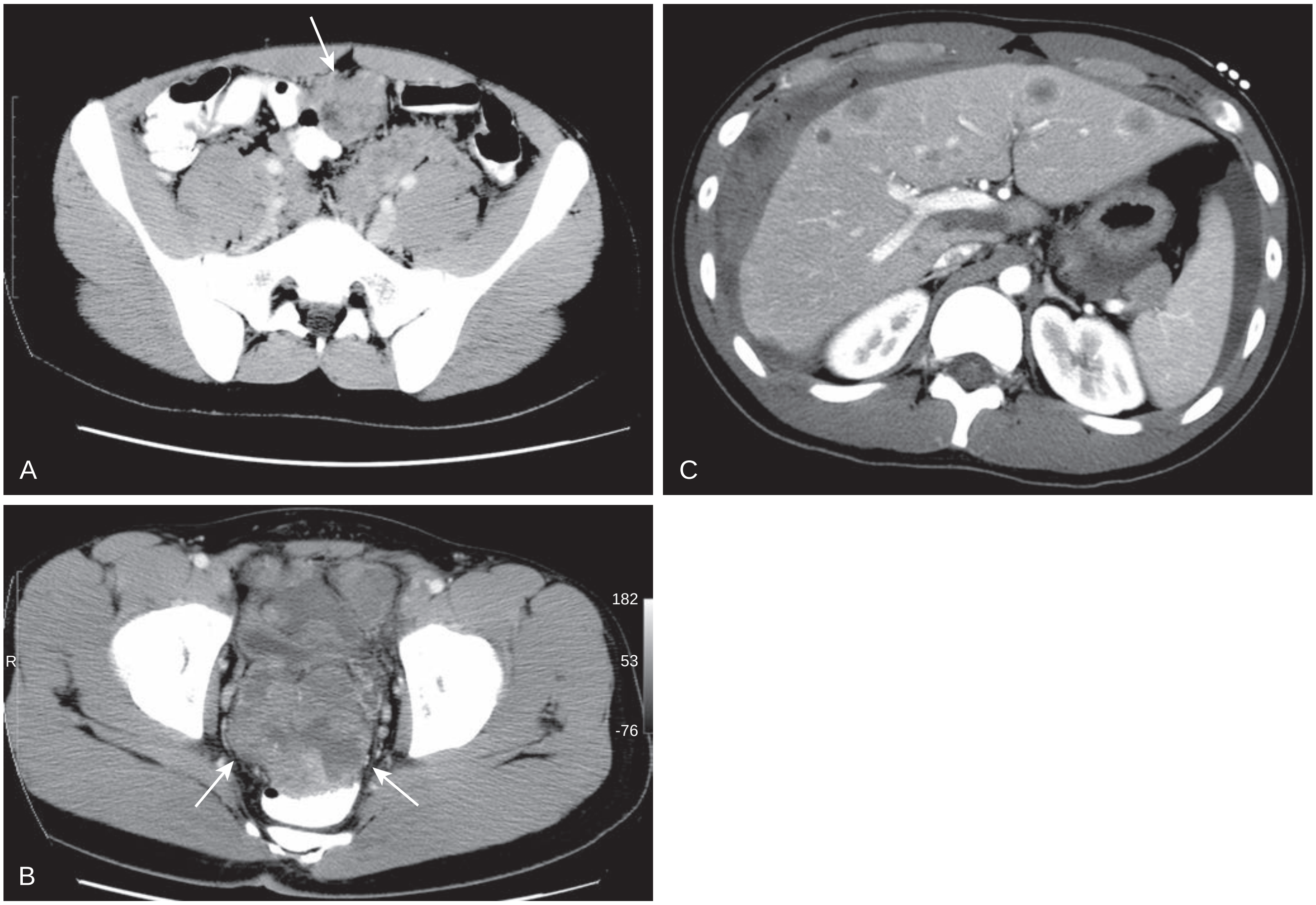

**Figure 86.41. Desmoplastic small round cell tumor.** (A and B) Axial contrast-enhanced CT images in a 17-year-old boy show multiple heterogeneously enhancing pelvic masses *(arrows)* with a dominant mass seen within the rectovesical pouch. (C) Metastatic spread and peritoneal seeding are evident as multiple enhancing nodules within the liver with a large, heterogeneous, peritoneal subcapsular mass indenting the hepatic surface.

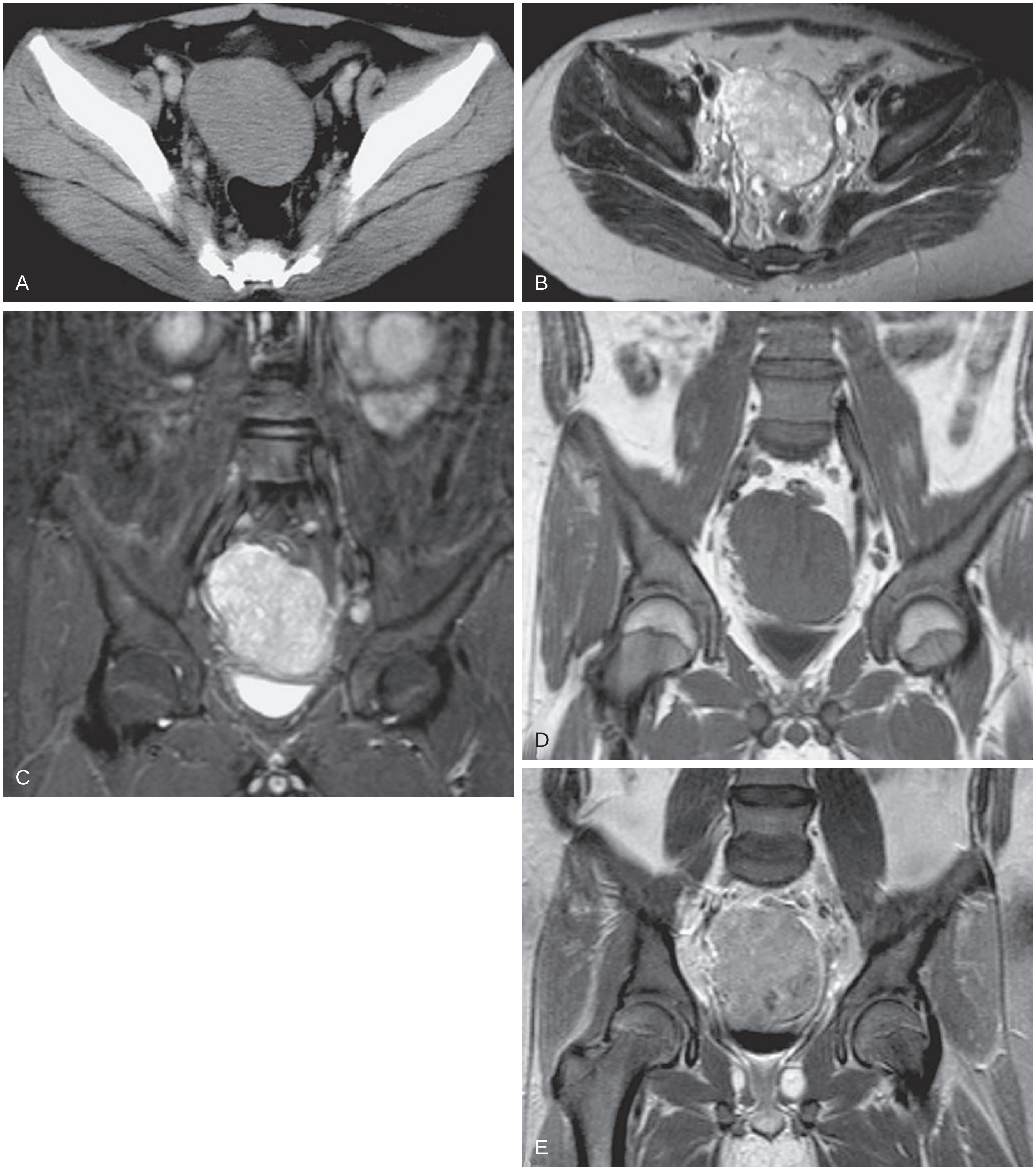

**e-Figure 86.40. Desmoplastic small round cell tumor in a 14-year-old boy with 2-month history of fatigue, poor appetite, and anemia.** (A) Axial contrast-enhanced pelvic CT image shows a well-defined midline pelvic mass that is of homogenous intermediate density. (B) Corresponding axial T2-weighted MR image shows the mass to have diffusely increased signal with mild heterogeneity. (C) The appearance in a short-tau inversion recovery sequence is similar to (B). (D) Coronal T1-weighted MR image shows the mass to be isointense with muscle. (E) Coronal T1-weighted contrast-enhanced fat-saturated MR image demonstrates mild heterogeneous enhancement of the lesion.

peritoneal carcinomatosis, rhabdomyosarcoma, neuroblastoma, lymphoma, and germ cell tumors.[104,115,116]

***Treatment.*** Treatment generally includes a combination of chemotherapy and surgical resection. Chemotherapy may be useful to reduce tumor bulk before surgery, because improved outcomes have been reported in patients with complete resection.[102,103,117] However, DSRCT is an aggressive malignancy that has poor prognosis despite treatment, with a reported 29% survival at 3 years.[117]

## Miscellaneous Tumors

*Rhabdomyosarcoma* comprises about half of pediatric soft tissue sarcomas but is less common in the trunk (Fig. 86.42).[118] Abdominal wall and other truncal rhabdomyosarcomas have a poorer prognosis when compared with other sites.[118] Truncal tumors are more likely to be of the embryonal than the alveolar type, are more likely to be greater than 5 cm at presentation, and tend to present with advanced disease. The ability to undergo gross total resection

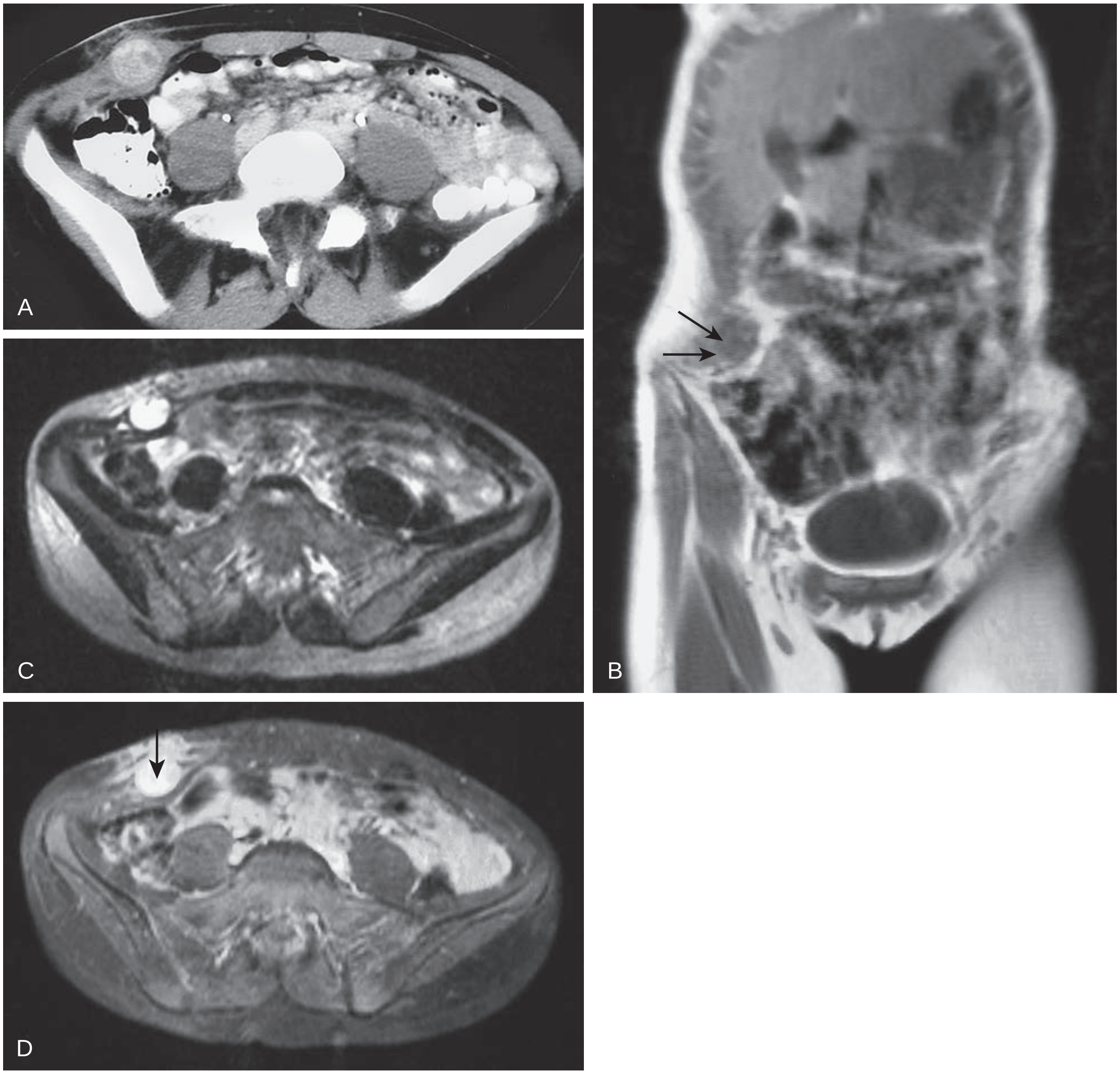

**Figure 86.42. Embryonal rhabdomyosarcoma.** (A) Axial contrast-enhanced image of the lower abdomen in a 13-year-old girl with a firm subcutaneous mass in the right lower abdominal wall shows a heterogeneously enhancing mass that causes focal enlargement of the right lateral oblique muscles. Edema is evident within the subcutaneous fat overlying the mass. Local infiltration by tumor cannot be excluded on this image. (B) Oblique, coronal, noncontrast T1-weighted MR image shows the 3-cm round tissue mass within the right lateral oblique muscles *(arrows)*. (C) On an axial T2-weighted MR image, the mass exhibits intense signal (as it did on short-tau inversion recovery sequence, *not shown*). (D) Intense enhancement is seen with intravenous contrast administration in the soft tissue mass and in the overlying subcutaneous fat *(arrow)*. This finding warrants concern about tumor infiltration.

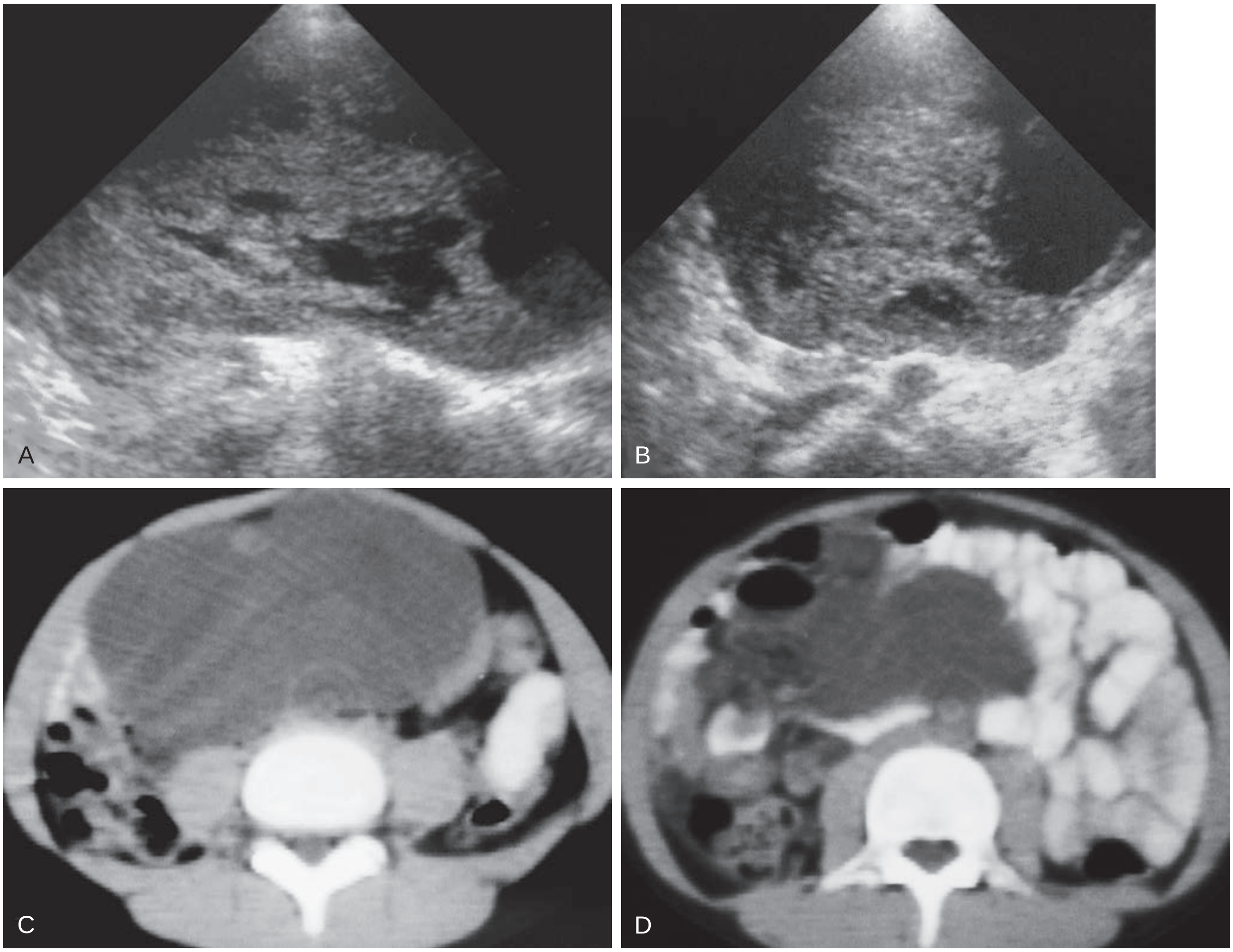

**Figure 86.43. Leiomyosarcoma.** Longitudinal (A) and transverse (B) sonograms through the midabdomen in a 10-year-old boy show a large, heterogeneous, solid and cystic mass. (C and D) CT images without intravenous contrast show a large, homogenous, low-density, midline soft tissue mass displacing bowel.

influences the prognosis, and gross total resection should be the goal of therapy.

*Synovial sarcoma* is a rare malignancy constituting 5% to 6% of pediatric soft tissue sarcomas. It most often originates in the extremities and near large joints, but it may rarely affect the anterior abdominal wall.[119]

*Leiomyosarcoma* often originates in the retroperitoneum, genitourinary or GI tract, and lower extremity.[120] Rarely, such a lesion may arise in the omentum (Fig. 86.43 and e-Fig. 86.44).

*Liposarcoma* has been briefly discussed; the presence of fat may help to distinguish this tumor from other sarcomas unless it is dedifferentiated. It is more commonly seen in the retroperitoneum. It is the least frequent soft tissue sarcoma to occur in childhood.[121]

*Fibrosarcoma* has two forms in children: the *congenital* or *infantile form* occurs in children up to 2 years of age, and the *childhood form* affects the 10- to 15-year-old age group (Fig. 86.45). The histology of the two forms is similar, but the infantile form has a distinct chromosomal translocation. Infantile fibrosarcoma has been reported to involve the trunk and retroperitoneum in children.[120,122] After complete surgical resection, prognosis is better for the infantile form than for the childhood form.[122]

*Malignant mesenchymomas* are very rare soft tissue tumors seen predominantly in adults. These tumors contain at least two distinct

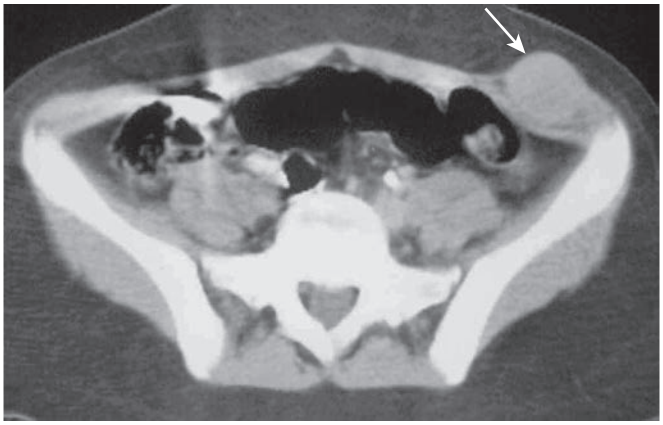

**Figure 86.45. Fibrosarcoma.** Axial contrast-enhanced CT image through the upper pelvis in a 14-year-old girl shows a well defined, round 3-cm mass in the left anterior abdominal wall. The mass expands and is isointense with the left lateral oblique muscles *(arrow).*

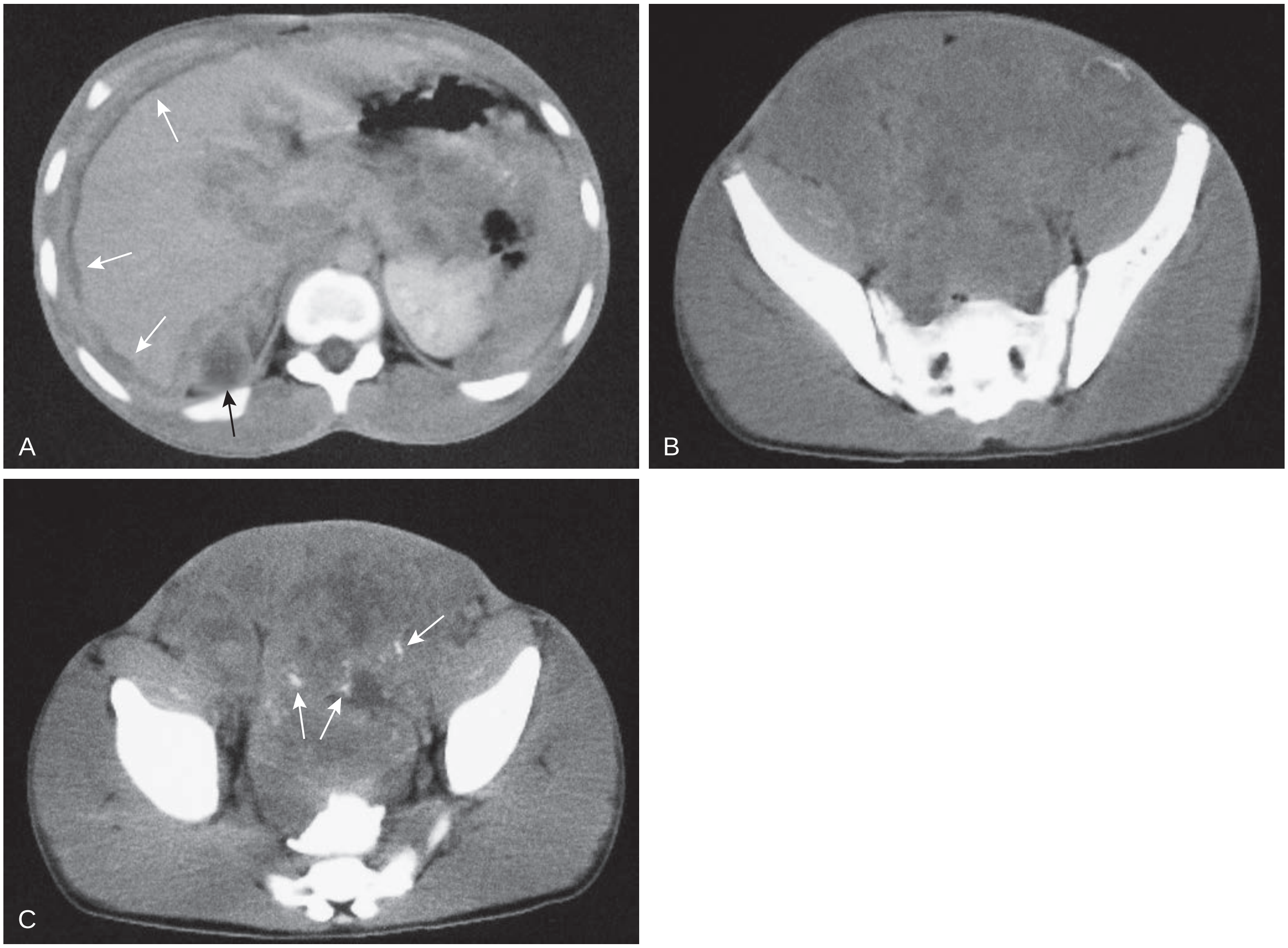

**e-Figure 86.44. Leiomyosarcoma.** (A) Contrast-enhanced CT image in a 16-year-old boy shows extensive peritoneal metastases around the liver *(white arrows)* and surrounding the pancreas in addition to a cystic peritoneal metastasis *(black arrow)*. (B) Lower image in the upper pelvis shows that the mass occupies most of the lower abdomen and pelvis. (C) Another image lower in the pelvis shows scattered calcifications *(arrows)*. Bowel contrast is present in the rectum.

histologic sarcoma subtypes and are considered to be high-grade tumors with an overall poor prognosis. The most common sites of primary malignant mesenchymoma are the retroperitoneum or the thigh, though various locations have been reported.[123] CT demonstrates a soft tissue mass with mixed attenuation often containing areas of necrosis and calcification, with heterogeneous enhancement and moderate vascularity (e-Fig. 86.46). On MR, these lesions are typically heterogeneous on T2-weighted images.[124] Treatment includes a combination of surgical incision, radiation, and chemotherapy.

*Malignant mesothelioma* of the peritoneum is rare in children and does not seem to be related to radiation or asbestos exposure.[1,125] Children with peritoneal malignant mesothelioma come to medical attention with ascites and multiple tumor nodules along the peritoneal surface (see e-Fig. 86.38).[120] Treatment with cytoreduction and hyperthermic intraperitoneal chemotherapy improves median survival to between 2.5 and 9 years.[126]

## KEY POINTS

- Upright radiographs and decubitus abdominal radiographs for detection of free air have similar sensitivity.
- Abdominal compartment syndrome is a clinical diagnosis that includes elevation of intraabdominal pressure to 20 mm Hg or greater, coupled with impaired function of at least one organ.
- Fat necrosis is one of the causes of abdominal wall calcification in neonates and infants. The majority of such calcifications are associated with neonatal asphyxia, sepsis, gestational diabetes, and hypothermia.
- Peritoneal calcification associated with calcified intraabdominal lymph nodes is more likely to be associated with a malignant process.
- Lipoblastomas can have a variable amount of macroscopic fat and may not appear completely fatty on imaging.
- MRI is preferred for detection of peritoneal implants given the inherent tissue contrast and multiplanar capabilities.
- Scalloping of visceral surfaces, particularly the liver, is one of the most important imaging signs to differentiate pseudomyxoma peritonei from ascites.
- DSRCTs usually are seen as multiple, scattered peritoneal masses without an apparent primary parenchymal source.

## SUGGESTED READINGS

Agarwal A, et al. Peritoneal calcification: causes and distinguishing features on CT. *AJR Am J Roentgenol*. 2004;182(2):441–445.

Bellah R, et al. Desmoplastic small round cell tumor in the abdomen and pelvis: report of CT findings in 11 affected children and young adults. *AJR Am J Roentgenol*. 2005;184(6):1910–1914.

Chiu YH, et al. Reappraisal of radiographic signs of pneumoperitoneum at emergency department. *Am J Emerg Med*. 2009;27(3):320–327.

Ledbetter DJ. Gastroschisis and omphalocele. *Surg Clin North Am*. 2006;86(2):249–260, vii.

Patel A, et al. Abdominal compartment syndrome. *AJR Am J Roentgenol*. 2007;189(5):1037–1043.

## REFERENCES

Full references for this chapter can be found on www.expertconsult.com.

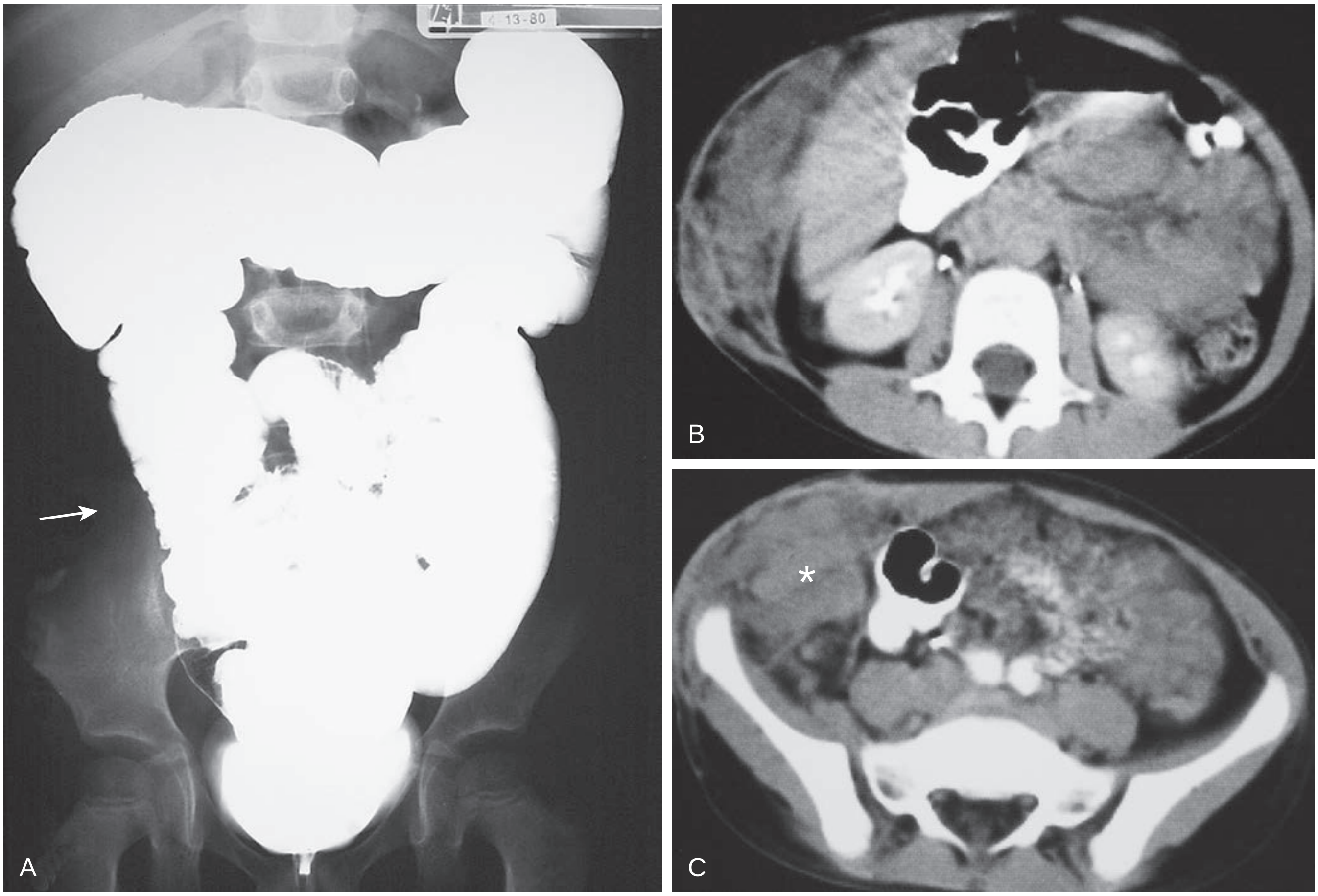

**e-Figure 86.46. Recurrent mesenchymoma.** Recurrent mass in a 5-year-old girl originally diagnosed at 3 years of age. (A) Abdominal radiograph from a barium enema demonstrates a normal colon with displacement of the right colon *(arrow)* from the adjacent abdominal wall mesenchymoma. (B and C) Axial contrast-enhanced CT images show expansion of the anterolateral abdominal wall by heterogeneous infiltrative soft tissue *(asterisk)*. Extension from the subcutaneous location (B and C) infiltrates the abdomen, with mass effect on adjacent structures, most notably the right colon, as depicted in (A).

## REFERENCES

1. Levy AD, Arnaiz J, Shaw JC, Sobin LH. From the archives of the AFIP: primary peritoneal tumors: imaging features with pathologic correlation. *Radiographics*. 2008;28(2):583–607.
2. Levy AD, Shaw JC, Sobin LH. Secondary tumors and tumorlike lesions of the peritoneal cavity: imaging features with pathologic correlation. *Radiographics*. 2009;29(2):347–373.
3. Wiot J, Benton C, McAlister W, et al. Postoperative pneumoperitoneum in children. *Radiology*. 1967;89:285.
4. Chiu YH, Chen JD, Tiu CM, et al. Reappraisal of radiographic signs of pneumoperitoneum at emergency department. *Am J Emerg Med*. 2009;27(3):320–327.
5. Miller RE. Perforated viscus in infants: a new roentgen sign. *Radiology*. 1960;74:65–67.
6. Leonidas JC, Hall RT, Rhodes PG, Amoury RA. Pneumoperitoneum in ventilated newborns: a medical or a surgical problem? *Am J Dis Child*. 1974;128(5):677–680.
7. Greenberg BE. Spontaneous pneumoperitoneum in appendicitis. *Radiology*. 1961;77:248–251.
8. Menuck L, Siemers PT. Pneumoperitoneum: importance of right upper quadrant features. *AJR Am J Roentgenol*. 1976;127(5):753–756.
9. Levine MS, Scheiner JD, Rubesin SE, Laufer I, Herlinger H. Diagnosis of pneumoperitoneum on supine abdominal radiographs. *AJR Am J Roentgenol*. 1991;156(4):731–735.
10. Brill PW, Olson SR, Winchester P. Neonatal necrotizing enterocolitis: air in Morison pouch. *Radiology*. 1990;174(2):469–471.
11. Cho KC, Baker SR. Air in the fissure for the ligamentum teres: new sign of intraperitoneal air on plain radiographs. *Radiology*. 1991;178(2):489–492.
12. Seibert JJ, Parvey LS. The telltale triangle: use of the supine cross table lateral radiograph of the abdomen in early detection of pneumoperitoneum. *Pediatr Radiol*. 1977;5(4):209–210.
13. Bray JF. The "inverted V" sign of pneumoperitoneum. *Radiology*. 1984;151(1):45–46.
14. Chen SC, Wang HP, Chen WJ, et al. Selective use of ultrasonography for the detection of pneumoperitoneum. *Acad Emerg Med*. 2002;9(6):643–645.
15. Stapakis JC, Thickman D. Diagnosis of pneumoperitoneum: abdominal CT vs. upright chest film. *J Comput Assist Tomogr*. 1992;16(5):713–716.
16. Ly JQ. The Rigler sign. *Radiology*. 2003;228(3):706–707.
17. Kliegman RM, Stanton B. *Nelson Textbook of Pediatrics*. 19th ed. Philadelphia, PA: Elsevier Saunders; 2011.
18. Patel A, Lall CG, Jennings SG, Sandrasegaran K. Abdominal compartment syndrome. *AJR Am J Roentgenol*. 2007;189(5):1037–1043.
19. Hendrick JM, Kaste SC, Tamburro RF, et al. Abdominal compartment syndrome in a newly diagnosed patient with Burkitt lymphoma. *Pediatr Radiol*. 2006;36(3):254–257.
20. Hoffman RB, Wankmuller R, Rigler LG. Pseudoseparation of bowel loops: a fallacious sign of intraperitoneal fluid. *Radiology*. 1966;87(5):845–847.
21. Thoeni RF. The role of imaging in patients with ascites. *AJR Am J Roentgenol*. 1995;165(1):16–18.
22. Colli A, Cocciolo M, Buccino G, et al. Thickening of the gallbladder wall in ascites. *J Clin Ultrasound*. 1991;19(6):357–359.
23. Dinkel E, Lehnart R, Troger J, Peters H, Dittrich M. Sonographic evidence of intraperitoneal fluid. An experimental study and its clinical implications. *Pediatr Radiol*. 1984;14(5):299–303.
24. Pandolfo I, Gaeta M, Scribano E, et al. Mediastinal pseudotumor due to passage of ascites through the esophageal hiatus. *Gastrointest Radiol*. 1989;14(3):209–211.
25. Johnson CC, Baldessarre J, Levison ME. Peritonitis: update on pathophysiology, clinical manifestations, and management. *Clin Infect Dis*. 1997;24(6):1035–1045.
26. Chadha V, Schaefer FS, Warady BA. Dialysis-associated peritonitis in children. *Pediatr Nephrol*. 2010;25(3):425–440.
27. Na-ChiangMai W, Pojchamarnwiputh S, Lertprasertsuke N, Chitapanarux T. CT findings of tuberculous peritonitis. *Singapore Med J*. 2008;49(6):488–491.
28. Andronikou S, Welman CJ, Kader E. The CT features of abdominal tuberculosis in children. *Pediatr Radiol*. 2002;32(2):75–81.
29. Burrill J, Williams CJ, Bain G, et al. Tuberculosis: a radiologic review. *Radiographics*. 2007;27(5):1255–1273.
30. Ha HK, Jung JI, Lee MS, et al. CT differentiation of tuberculous peritonitis and peritoneal carcinomatosis. *AJR Am J Roentgenol*. 1996;167(3):743–748.
31. Duhn R, Schoen EJ, Siu M. Subcutaneous fat necrosis with extensive calcification after hypothermia in two newborn infants. *Pediatrics*. 1968;41(3):661–664.
32. Hogeling M, Meddles K, Berk DR, et al. Extensive subcutaneous fat necrosis of the newborn associated with therapeutic hypothermia. *Pediatr Dermatol*. 2012;29(1):59–63.
33. Naidech HJ, Chawla HS. Soft-tissue calcification after subcutaneous emphysema in a neonate. *AJR Am J Roentgenol*. 1982;139(2):374–376.
34. Agarwal A, Yeh BM, Breiman RS, Qayyum A, Coakley FV. Peritoneal calcification: causes and distinguishing features on CT. *AJR Am J Roentgenol*. 2004;182(2):441–445.
35. Scales JW, Krowchuk DP, Schwartz RP, Jorizzo JL. An infant with firm, fixed plaques. *Arch Dermatol*. 1998;134(4):425–426.
36. Ledbetter DJ. Gastroschisis and omphalocele. *Surg Clin North Am*. 2006;86(2):249–260, vii.
37. Klein M. Congenital defects of the abdominal wall. In: Coran A, Caldamone A, Adzick N, et al, eds. *Coran: Pediatric Surgery*. 7th ed. Philadelphia: CV Mosby, an imprint of Elsevier; 2012.
38. Cantrell JR, Haller JA, Ravitch MM. A syndrome of congenital defects involving the abdominal wall, sternum, diaphragm, pericardium, and heart. *Surg Gynecol Obstet*. 1958;107(5):602–614.
39. Nicolaides KH, Snijders RJ, Cheng HH, Gosden C. Fetal gastro-intestinal and abdominal wall defects: associated malformations and chromosomal abnormalities. *Fetal Diagn Ther*. 1992;7(2):102–115.
40. Bair JH, Russ PD, Pretorius DH, Manchester D, Manco-Johnson ML. Fetal omphalocele and gastroschisis: a review of 24 cases. *AJR Am J Roentgenol*. 1986;147(5):1047–1051.
41. Salihu HM, Pierre-Louis BJ, Druschel CM, Kirby RS. Omphalocele and gastroschisis in the State of New York, 1992–1999. *Birth Defects Res A Clin Mol Teratol*. 2003;67(9):630–636.
42. Laughon M, Meyer R, Bose C, et al. Rising birth prevalence of gastroschisis. *J Perinatol*. 2003;23(4):291–293.
43. Kuleva M, Khen-Dunlop N, Dumez Y, Ville Y, Salomon LJ. Is complex gastroschisis predictable by prenatal ultrasound? *BJOG*. 2012;119(1):102–109.
44. Fogata ML, Collins HB 2nd, Wagner CW, Angtuaco TL. Prenatal diagnosis of complicated abdominal wall defects. *Curr Probl Diagn Radiol*. 1999;28(4):101–128.
45. Molik KA, Gingalewski CA, West KW, et al. Gastroschisis: a plea for risk categorization. *J Pediatr Surg*. 2001;36(1):51–55.
46. Snyder CL, Miller KA, Sharp RJ, et al. Management of intestinal atresia in patients with gastroschisis. *J Pediatr Surg*. 2001;36(10):1542–1545.
47. DiSantis DJ, Siegel MJ, Katz ME. Simplified approach to umbilical remnant abnormalities. *Radiographics*. 1991;11(1):59–66.
48. Clley R. Disorders of the umbilicus. In: Coran A, Caldamone A, Adzick N, et al, eds. *Coran: Pediatric Surgery*. 7th ed. Philadelphia: CV Mosby, an imprint of Elsevier; 2012.
49. Yu JS, Kim KW, Lee HJ, et al. Urachal remnant diseases: spectrum of CT and US findings. *Radiographics*. 2001;21(2):451–461.
50. Yiee JH, Garcia N, Baker LA, et al. A diagnostic algorithm for urachal anomalies. *J Pediatr Urol*. 2007;3(6):500–504.
51. Choi YJ, Kim JM, Ahn SY, et al. Urachal anomalies in children: a single center experience. *Yonsei Med J*. 2006;47(6):782–786.
52. Snyder CL. Current management of umbilical abnormalities and related anomalies. *Semin Pediatr Surg*. 2007;16(1):41–49.
53. McCollum MO, Macneily AE, Blair GK. Surgical implications of urachal remnants: presentation and management. *J Pediatr Surg*. 2003;38(5):798–803.
54. Nagasaki A, Handa N, Kawanami T. Diagnosis of urachal anomalies in infancy and childhood by contrast fistulography, ultrasound and CT. *Pediatr Radiol*. 1991;21(5):321–323.
55. Kapur P, Caty MG, Glick PL. Pediatric hernias and hydroceles. *Pediatr Clin North Am*. 1998;45(4):773–789.
56. Glick PL, Boulanger S. Inguinal hernias and hydroceles. In: Coran A, Caldamone A, Adzick N, et al, eds. *Coran: Pediatric Surgery*. 7th ed. Philadelphia: CV Mosby, an imprint of Elsevier; 2012.
57. Chou TY, Chu CC, Diau GY, Wu CJ, Gueng MK. Inguinal hernia in children: US versus exploratory surgery and intraoperative contralateral laparoscopy. *Radiology*. 1996;201(2):385–388.
58. Burkhardt JH, Arshanskiy Y, Munson JL, Scholz FJ. Diagnosis of inguinal region hernias with axial CT: the lateral crescent sign and other key findings. *Radiographics*. 2011;31(2):E1–E12.
59. van den Berg JC. Inguinal hernias: MRI and ultrasound. *Semin Ultrasound CT MR*. 2002;23(2):156–173.

60. Brandt ML. Pediatric hernias. *Surg Clin North Am*. 2008;88(1):27–43, vii–viii.
61. Hebra A, Brown MF, McGeehin KM, Ross AJ 3rd. Mesenteric, omental, and retroperitoneal cysts in children: a clinical study of 22 cases. *South Med J*. 1993;86(2):173–176.
62. Bliss DP Jr, Coffin CM, Bower RJ, Stockmann PT, Ternberg JL. Mesenteric cysts in children. *Surgery*. 1994;115(5):571–577.
63. de Perrot M, Brundler M, Totsch M, Mentha G, Morel P. Mesenteric cysts. Toward less confusion? *Dig Surg*. 2000;17(4):323–328.
64. Tan JJ, Tan KK, Chew SP. Mesenteric cysts: an institution experience over 14 years and review of literature. *World J Surg*. 2009;33(9):1961–1965.
65. Konen O, Rathaus V, Dlugy E, et al. Childhood abdominal cystic lymphangioma. *Pediatr Radiol*. 2002;32(2):88–94.
66. Takiff H, Calabria R, Yin L, Stabile BE. Mesenteric cysts and intra-abdominal cystic lymphangiomas. *Arch Surg*. 1985;120(11):1266–1269.
67. Pickhardt PJ, Bhalla S. Primary neoplasms of peritoneal and sub-peritoneal origin: CT findings. *Radiographics*. 2005;25(4):983–995.
68. Levine C. Primary disorders of the lymphatic vessels—a unified concept. *J Pediatr Surg*. 1989;24(3):233–240.
69. de Perrot M, Rostan O, Morel P, Le Coultre C. Abdominal lymphangioma in adults and children. *Br J Surg*. 1998;85(3):395–397.
70. Ricketts RR. Mesenteric and omental cysts. In: Coran AG, ed. *Pediatric Surgery*. Vol. 2. 7th ed. Philadelphia, PA: Elsevier; 2012: 1165–1170.
71. Kosir MA, Sonnino RE, Gauderer MW. Pediatric abdominal lymphangiomas: a plea for early recognition. *J Pediatr Surg*. 1991; 26(11):1309–1313.
72. Kim JS, Chandler A, Borzykowski R, Thornhill B, Taragin BH. Maximizing time-resolved MRA for differentiation of hemangiomas, vascular malformations and vascularized tumors. *Pediatr Radiol*. 2012;42(7):775–784.
73. Terry NE, Fowler CL. Benign cystic mesothelioma in a child. *J Pediatr Surg*. 2009;44(5):e9–e11.
74. Stojsic Z, Jankovic R, Jovanovic B, Vujovic D, Vucinic B. Bacetic D. Benign cystic mesothelioma of the peritoneum in a male child. *J Pediatr Surg*. 2012;47(10):e45–e49.
75. Shakya VC, Agrawal CS, Karki S, et al. Benign cystic mesothelioma of the peritoneum in a child—case report and review of the literature. *J Pediatr Surg*. 2011;46(4):e23–e26.
76. Gonzalez-Moreno S, Yan H, Alcorn KW, Sugarbaker PH. Malignant transformation of "benign" cystic mesothelioma of the peritoneum. *J Surg Oncol*. 2002;79(4):243–251.
77. Coran AG, Adzick NS. *Pediatric surgery*. 7th ed. Philadelphia, PA: Elsevier Mosby; 2012.
78. Chung EB, Enzinger FM. Benign lipoblastomatosis. An analysis of 35 cases. *Cancer*. 1973;32(2):482–492.
79. Collins MH, Chatten J. Lipoblastoma/lipoblastomatosis: a clinicopathologic study of 25 tumors. *Am J Surg Pathol*. 1997;21(10):1131–1137.
80. Stringel G, Shandling B, Mancer K, Ein SH. Lipoblastoma in infants and children. *J Pediatr Surg*. 1982;17(3):277–280.
81. Jung SM, Chang PY, Luo CC, et al. Lipoblastoma/lipoblastomatosis: a clinicopathologic study of 16 cases in Taiwan. *Pediatr Surg Int*. 2005;21(10):809–812.
82. Mentzel T, Calonje E, Fletcher CD. Lipoblastoma and lipoblastomatosis: a clinicopathological study of 14 cases. *Histopathology*. 1993;23(6):527–533.
83. Hicks J, Dilley A, Patel D, et al. Lipoblastoma and lipoblastomatosis in infancy and childhood: histopathologic, ultrastructural, and cytogenetic features. *Ultrastruct Pathol*. 2001;25(4):321–333.
84. Cudnik R, Efron PA, Chen MK, Reith JD, Beierle EA. Mesenteric lipoblastoma: a rare location in children. *J Pediatr Surg*. 2008;43(12):e5–e7.
85. Sheybani EF, Eutsler EP, Navarro OM. Fat-containing soft-tissue masses in children. *Pediatr Radiol*. 2016;46(13):1760–1773.
86. Hibbard MK, Kozakewich HP, Dal Cin P, et al. PLAG1 fusion oncogenes in lipoblastoma. *Cancer Res*. 2000;60(17):4869–4872.
87. Brandal P, Bjerkehagen B, Heim S. Rearrangement of chromosomal region 8q11-13 in lipomatous tumours: correlation with lipoblastoma morphology. *J Pathol*. 2006;208(3):388–394.
88. Moholkar S, Sebire NJ, Roebuck DJ. Radiological-pathological correlation in lipoblastoma and lipoblastomatosis. *Pediatr Radiol*. 2006;36(8):851–856.
89. Murphey MD, Carroll JF, Flemming DJ, et al. From the archives of the AFIP: benign musculoskeletal lipomatous lesions. *Radiographics*. 2004;24(5):1433–1466.
90. Mo YH, Peng SS, Li YW, Shun CT. Mesenteric lipoblastoma: case report. *Pediatr Radiol*. 2003;33(1):37–40.
91. Jones KB, Morcuende JA, DeYoung BR, et al. Unusual presentation of lipoblastoma as a skin dimple of the thigh. A report of three cases. *J Bone Joint Surg Am*. 2004;86.A(5):1040–1046.
92. Mognato G, Cecchetto G, Carli M, et al. Is surgical treatment of lipoblastoma always necessary? *J Pediatr Surg*. 2000;35(10):1511–1513.
93. Rosoff PM, Larrier N, Rice HE. Intra-abdominal desmoid tumor after successful treatment for Hodgkin disease. *Pediatr Blood Cancer*. 2005;45(5):728–731.
94. Healy JC, Reznek RH, Clark SK, Phillips RK, Armstrong P. MR appearances of desmoid tumors in familial adenomatous polyposis. *AJR Am J Roentgenol*. 1997;169(2):465–472.
95. Shields CJ, Winter DC, Kirwan WO, Redmond HP. Desmoid tumours. *Eur J Surg Oncol*. 2001;27(8):701–706.
96. Lelli J. Polypoid diseases of the gastrointestinal tract. In: Coran AG, ed. *Pediatric Surgery*. 7th ed. Philadelphia, PA: Elsevier; 2012.
97. Arvanitis ML, Jagelman DG, Fazio VW, Lavery IC, McGannon E. Mortality in patients with familial adenomatous polyposis. *Dis Colon Rectum*. 1990;33(8):639–642.
98. Quintini C, Ward G, Shatnawei A, et al. Mortality of intra-abdominal desmoid tumors in patients with familial adenomatous polyposis: a single center review of 154 patients. *Ann Surg*. 2012;255(3):511–516.
99. Jordan A. Other soft tissue tumors. In: Coran AG, ed. *Pediatric Surgery*. 7th ed. Philadelphia, PA: Elsevier; 2012.
100. van Ruth S, Acherman YI, van de Vijver MJ, et al. Pseudomyxoma peritonei: a review of 62 cases. *Eur J Surg Oncol*. 2003;29(8):682–688.
101. Jurgeleit HC. Pseudomyxoma peritonei. A localized, benign variant of appendiceal origin. *Dis Colon Rectum*. 1986;29(7):469–470.
102. Qu ZB, Liu LX. Management of pseudomyxoma peritonei. *World J Gastroenterol*. 2006;12(38):6124–6127.
103. Kaste SC, Marina N, Fryrear R, et al. Peritoneal metastases in children with cancer. *Cancer*. 1998;83(2):385–390.
104. Andronikou S, Moon A, Ussher R. Peritoneal metastatic disease in a child after excision of a solid pseudopapillary tumour of the pancreas: a unique case. *Pediatr Radiol*. 2003;33(4):269–271.
105. Huh WW, Fitzgerald NE, Mahajan A, Hayes-Jordan A. Peritoneal sarcomatosis in pediatric malignancies. *Pediatr Blood Cancer*. 2013;60(1):12–17.
106. Gerald WL, Rosai J. Case 2. Desmoplastic small cell tumor with divergent differentiation. *Pediatr Pathol*. 1989;9(2):177–183.
107. Kim YS, Cha SJ, Choi YS, et al. Retroperitoneal desmoplastic small round cell tumor: pediatric patient treated with multimodal therapy. *World J Gastroenterol*. 2009;15(33):4212–4214.
108. Mingo L, Seguel F, Rollan V. Intraabdominal desmoplastic small round cell tumour. *Pediatr Surg Int*. 2005;21(4):279–281.
109. Bellah R, Suzuki-Bordalo L, Brecher E, et al. Desmoplastic small round cell tumor in the abdomen and pelvis: report of CT findings in 11 affected children and young adults. *AJR Am J Roentgenol*. 2005;184(6):1910–1914.
110. Egloff AM, Lee EY, Dillon JE, Callahan MJ. Desmoplastic small round cell tumor of the kidney in a pediatric patient: sonographic and multiphase CT findings. *AJR Am J Roentgenol*. 2005;185(5):1347–1349.
111. Leuschner I, Radig K, Harms D. Desmoplastic small round cell tumor. *Semin Diagn Pathol*. 1996;13(3):204–212.
112. Pickhardt PJ, Fisher AJ, Balfe DM, Dehner LP, Huettner PC. Desmoplastic small round cell tumor of the abdomen: radiologic-histopathologic correlation. *Radiology*. 1999;210(3):633–638.
113. Kushner BH, Laquaglia MP, Gerald WL, et al. Solitary relapse of desmoplastic small round cell tumor detected by positron emission tomography/computed tomography. *J Clin Oncol*. 2008;26(30): 4995–4996.
114. Ben-Sellem D, Liu KL, Cimarelli S, Constantinesco A, Imperiale A. Desmoplastic small round cell tumor: impact of F-FDG PET induced treatment strategy in a patient with long-term outcome. *Rare Tumors*. 2009;1(1):e19.
115. Jeong YJ, Kim S, Kwak SW, et al. Neoplastic and nonneoplastic conditions of serosal membrane origin: CT findings. *Radiographics*. 2008;28(3):801–817.
116. Hiralal, Gamanagatti S, Thulkar S, Rao SK. Desmoplastic round cell tumour of the abdomen. *Singapore Med J*. 2007;48(1):e19–e21.
117. Quaglia MP, Brennan MF. The clinical approach to desmoplastic small round cell tumor. *Surg Oncol*. 2000;9(2):77–81.
118. Chui CH, Billups CA, Pappo AS, Rao BN, Spunt SL. Predictors of outcome in children and adolescents with rhabdomyosarcoma of

the trunk—the St Jude Children's Research Hospital experience. *J Pediatr Surg*. 2005;40(11):1691–1695.
119. Fetsch JF, Meis JM. Synovial sarcoma of the abdominal wall. *Cancer*. 1993;72(2):469–477.
120. Kransdorf MJ. Malignant soft-tissue tumors in a large referral population: distribution of diagnoses by age, sex, and location. *AJR Am J Roentgenol*. 1995;164(1):129–134.
121. Marcus KC, Grier HE, Shamberger RC, et al. Childhood soft tissue sarcoma: a 20-year experience. *J Pediatr*. 1997;131(4):603–607.
122. Stein-Wexler R. Pediatric soft tissue sarcomas. *Semin Ultrasound CT MR*. 2011;32(5):470–488.
123. Brady MS, Perino G, Tallini G, Russo P, Woodruff JM. Malignant mesenchymoma. *Cancer*. 1996;77(3):467–473.
124. Suzuki S, Furui S, Kokubo T, et al. Retroperitoneal malignant mesenchymoma: imaging findings in five cases. *Abdom Imaging*. 1999;24(1):92–97.
125. Moran CA, Albores-Saavedra J, Suster S. Primary peritoneal mesotheliomas in children: a clinicopathological and immunohistochemical study of eight cases. *Histopathology*. 2008;52(7):824–830.
126. Raza A, Huang WC, Takabe K. Advances in the management of peritoneal mesothelioma. *World J Gastroenterol*. 2014;20(33):11700–11712.

# 87

# Congenital Hepatobiliary Anomalies

*Govind B. Chavhan*

## INTRODUCTION

Hepatorenal fibrocystic disorders are a group of associated congenital anomalies of the liver and kidney caused by malformation of the embryonic ductal plates formed by bipotential progenitor hepatoblasts surrounding portal venous ramifications (Fig. 87.1).[1,2] They include choledochal cysts, Caroli disease, hepatic fibrosis, biliary hamartomas, and cystic liver disease. The specific type of fibrocystic disorder depends on the size of the embryonic duct with faulty development (Table 87.1) and may be associated with renal cystic disease.

## CHOLEDOCHAL CYST

***Overview.*** Choledochal cysts, which are among the most frequent of congenital hepatobiliary anomalies, are a fusiform or saccular dilation of the bile ducts. The Todani classification system is commonly used to categorize these anomalies into five general types (with several subtypes) that differ based on etiology, pathogenesis, appearance, and presentation[3] (Fig. 87.2).

The most common choledochal cyst is the Todani type I, found in 80% to 90% of cases.[4] It involves variable lengths and degrees of common bile duct dilatation and is further classified into subtypes IA, IB, and IC.[4] Todani types IA, B, and C describe cystic dilation of the entire extrahepatic bile duct, segmental dilation below the cystic duct, and fusiform/cylindrical dilation of entire extrahepatic bile duct, respectively. Type I choledochal cysts are more common in girls than boys in Western countries, but the sex ratio is equal in Asia.[4,5] About 65% of all reported cases are from Japan.[4] Todani type II choledochal cysts are rare, found in only 2% of cases, and consist of one or more diverticula of the common bile duct.[5] Todani type III occurs in 1.5% to 5% of cases and involves dilation of the intraduodenal portion of the duct forming a cystlike mass termed a *choledochocele* with both the common bile and pancreatic ducts emptying into it. Todani type IVA consists of multiple intrahepatic and extrahepatic biliary dilatations and occurs in 10% of patients with choledochal cysts.[3,5] Type IVB involves multiple extrahepatic biliary cysts, without intrahepatic involvement, and it is extremely rare. Todani type V is synonymous with Caroli disease.[3] It may be difficult to differentiate between a type I cyst with intrahepatic dilatation from stagnation and the true type IV A cyst. This differentiation, however, is not necessary for treatment.[6] Intrahepatic dilation will improve postoperatively in type I cysts.

***Etiology.*** Several theories for the pathogenesis of type I choledochal cysts exist. In addition to the ductal plate malformation described previously, other theories suggest cyst formation due to obstruction of the distal biliary duct and/or reflux of pancreatic enzymes into the biliary tree, due to anomalous pancreaticobiliary junction (PBJ).[7,8]

When the junction of a common bile duct and pancreatic duct form a common channel outside the sphincter of Oddi, it is considered anomalous.[9] The anomalous junction outside the sphincter mechanism is thought to allow reflux of pancreatic secretions into the biliary tree and vice versa, and likely plays a role in pathogenesis of choledochal cysts and predisposes to pancreatitis[10] as well as the formation of stones, polyps, and cancer.[11]

Type II choledochal cysts, have been theorized to result from prenatal rupture of the common bile duct with subsequent healing.[5] Type III choledochal cysts may be the sequelae of ampullary obstruction or congenital duplication of the duodenum at the ampulla. The intrahepatic cysts seen in types IV and V are thought to be due to primary ductal ectasia resulting from ductal plate malformation.

***Clinical Presentation.*** Choledochal cysts may present in infancy with cholestatic jaundice, clinically inseparable from neonatal hepatitis or biliary atresia.[4] In older children and young adults, the clinical presentation is variable. The characteristic triad of abdominal pain, obstructive jaundice, and fever is seen in a minority of patients present. Abdominal pain is the most characteristic presentation, followed by obstructive jaundice, fever, pale stools, splenomegaly, hepatomegaly, and a palpable mass.[12] Pancreatitis can be a presentation in older children, particularly in type IV A.[13] The most common complication of a choledochal cyst is ascending cholangitis.[14] Long-term complications, such as hepatic cirrhosis with subsequent portal hypertension, can occur.[12] Carcinoma of the biliary tree has a 20-fold increased incidence in patients with choledochal cysts. This risk is low in the first decade but increases with advancing age.[15,16] Spontaneous cyst rupture has also been reported.[12]

***Imaging.*** Sonography is usually the initial imaging study. The markedly dilated common bile duct in types I and IV choledochal cyst is readily discernible. The gallbladder can usually be identified adjacent to the dilated common duct (Fig. 87.3). Sludge or stones may be identified within the dilated ducts. Type III cysts may cause mass effect at the Ampulla of Vater (e-Fig. 87.4).

Abdominal magnetic resonance imaging (MRI) with cholangiopancreatography (MRCP) is the modality of choice to delineate the type of cyst, the length of the involved duct, the presence and location of protein plugs or calculi, the PBJ, and the length of the common channel[9,17,18] (Figs. 87.5 and 87.6). A common pancreaticobiliary channel of more than 15 mm in length is considered abnormal in adults.[10] However, there is limited data on normal length of common channel in children, with one recent study using 5 mm as a cut-off value[19] while another found an average length of 9.25 mm.[9]

MRI is also useful for evaluation of any associated abnormalities such as masses, portal hypertension, and renal abnormalities. Contrast-enhanced MRCP with hepatocyte specific contrast media such as gadobenate and gadoxetate can be used to demonstrate communication between choledochal cyst and the biliary tree and to evaluate postoperative bile leak,[20] as can hepatobiliary scintigraphy. Computed tomography (CT) may have a limited role in evaluation of choledochal cyst when MRCP is not available.

With improved diagnostic imaging, the role of percutaneous transhepatic cholangiography (PTC) and endoscopic retrograde cholangiopancreatography (ERCP) is usually reserved for therapeutic intervention.

***Treatment.*** Due to the potential long-term sequelae, surgical excision and hepatojejunostomy are performed as definitive treatments. Patients with intrahepatic cysts are closely monitored for cholangitis, cholestasis, and stone formation. Antibiotics are administered in the setting of acute cholangitis. Medical therapy

## Abstract:

Congenital biliary hepatobiliary anomalies include hepatorenal fibrocystic disorders, biliary atresia and Alagille syndrome. Hepatorenal fibrocystic disorders are a group of associated congenital anomalies of the liver and kidney caused by malformation of the embryonic ductal plates that form intrahepatic bile ducts. These disorders include choledochal cysts, Caroli disease, hepatic fibrosis, biliary hamartomas and cystic liver disease. The anomalous pancreatobiliary junction outside the sphincter mechanism is thought to allow reflux of pancreatic secretions into biliary tree and vice versa and likely plays a role in pathogenesis of choledochal cysts and one of the predispositions for pancreatitis. Imaging plays important role in the assessment of fibrocystic disorders. In utero biliary inflammation is thought to be the cause of biliary atresia for which ultrasound is 98% accurate when a combination of the triangular cord sign and gallbladder size <15mm is used. Alagille syndrome is a multisystem disorder including cholestasis from bile duct paucity and multiorgan vasculopathy.

## Keywords:

hepatorenal fibrocystic disorders
choledochal cyst
caroli disease
congenital hepatic fibrosis
biliary hamartoma
biliary atresia
Alagille syndrome
pancreatobiliary junction

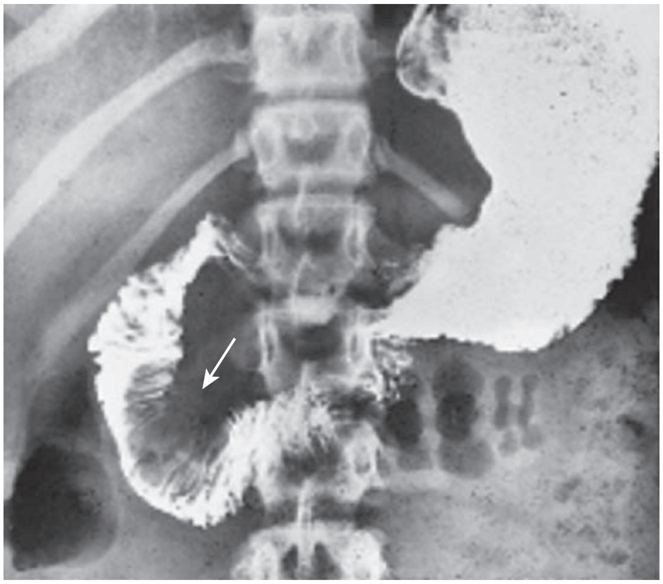

**e-Figure 87.4. Choledochocele (Todani type III) in a 12-year-old girl with abdominal pain.** Upper gastrointestinal tract image shows a large filling defect *(arrow)* coincident with the site of the Ampulla of Vater.

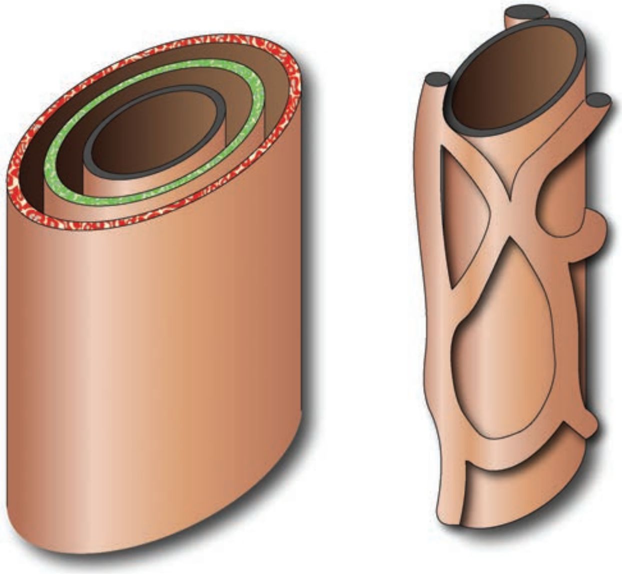

**Figure 87.1. Schematic model of ductal plate malformations.** A bilayer of hepatocytes surrounds the portal vascular structures, forming the lumina of primitive bile ducts *(left)*. A process of organized resorption leads to the normal organization of biliary ducts within the portal triads. Failure of this process leads to ductal plate malformations.

**TABLE 87.1** Hepatorenal Fibrocystic Liver Disorders and Size of Ducts With Faulty Embryogenesis

| Disorder | Duct Size | Renal Association |
|---|---|---|
| Congenital hepatic fibrosis | Small | ARPKD |
| Biliary hamartoma | Small | |
| Polycystic liver disease | Medium | ADPKD |
| Caroli disease | Large Intrahepatic | ARPKD |
| Choledochal cyst | Large extrahepatic | |

*ADPKD,* Autosomal dominant polycystic kidney disease; *ARPKD,* autosomal recessive polycystic kidney disease.

can be instituted to reduce the risk of cholestasis and promote bile flow.

## CAROLI DISEASE

***Overview.*** Caroli disease, also classified as Todani type V choledochal cyst, is a segmental nonobstructive dilation of the intrahepatic bile ducts. It is characterized by multifocal saccular dilation of intrahepatic ducts.[14] It can be associated with stone formation, cholangitis, hepatic abscesses, and cholangiocarcinoma later in life.[16]

***Etiology.*** Leading theories on the etiology of Caroli disease include maldevelopment of the large intrahepatic ductal plates. Other postulated mechanisms include: occlusion of the hepatic artery in the neonatal period with associated ischemia of the bile ducts versus abnormal growth rate of the biliary epithelium and supporting connective tissues with lack of the normal involution of ductal plates. This process leads to ectatic biliary ducts surrounding the portal triads. In *Caroli syndrome*, which involves large and small ductal plate abnormalities, there is associated hepatic fibrosis. Caroli hepatic ductal ectasia may also be associated with extrahepatic ductal plate abnormalities and choledochal cysts (Todani IVA choledochal cyst) as discussed previously. An association also exists with renal disorders including autosomal recessive polycystic kidney disease (ARPKD), medullary sponge kidney, and nephronopthisis.[14] Although typically a diffuse process, monolobar Caroli disease has been reported, with 88% involving the left lobe.[21]

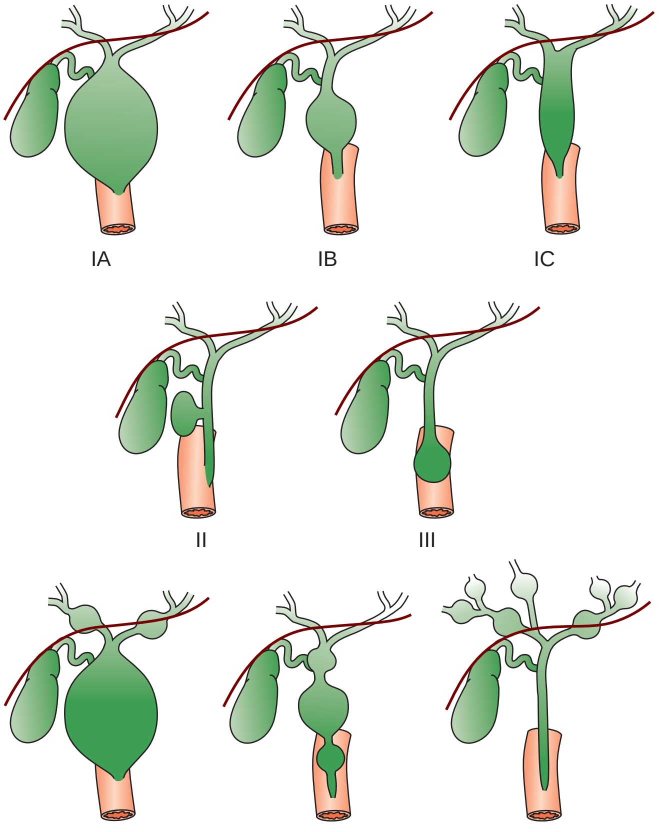

**Figure 87.2. Todani classification of choledochal cysts based on cholangiographic morphology.** Type *IA* and *IB* involve cystic dilatation of the common duct, with *IB* limited to the area below the insertion of the cystic duct; *IC* is cylindrical dilatation of the duct. Type *II* is a saccular diverticulum from the common bile duct. Type *III* is a choledochocele at the ampulla of Vater. Types *IVA* and *IVB* are multiple cystic dilatations of the both intra- and extrahepatic ducts and extrahepatic biliary tree only, respectively. Type *V* is equivalent to Caroli disease with numerous intrahepatic cystic dilatations throughout the biliary tree and liver. *(From Kim OH, Chung HJ, Choi BG. Imaging of the choledochal cyst.* Radiographics. *1995;15:69–88.)*

***Clinical Presentation.*** Although the disease is present from birth, most patients do not present until later in life when abdominal pain secondary to cholangitis and cholestasis leads them to seek medical attention. The abdominal pain may also be related to hepatic abscesses (secondary to cholangitis) or to biliary stones (secondary to cholestasis). Patients with associated hepatic fibrosis may present with symptoms and signs of portal hypertension.[22]

***Imaging.*** In most patients, sonography reveals large and irregular ectatic ducts.[14,23] Recognition that the ectatic ducts connect with one another and with the ductal system is important to distinguish Caroli disease from hepatic cysts (Fig. 87.7). The ectatic ducts surround portal vein radicles and hepatic arterial branches producing the "central dot" sign, which has been considered pathognomonic for Caroli disease.[24] Biliary sludge and calculi are common findings within the dilated bile ducts.[14] If an abscess develops, one or more cysts will show mixed echogenicity.

MRI and CT show the extent of disease well. An enhancing central dot may be seen that corresponds to the portal vein radicles seen sonographically.[25] If an abscess is present, the affected cyst may show higher attenuation or peripheral enhancement compared with adjacent uninfected cysts.[14] Contrast-enhanced MRCP can be used to demonstrate connection to the biliary tree.

In all patients with Caroli disease, the kidneys should be examined. Kidneys may appear normal, polycystic, or have increased medullary echogenicity with loss of corticomedullary differentiation (Fig. 87.8).

***Treatment.*** Ursodeoxycholic acid can decrease cholelithiasis and its complications. Broad-spectrum antibiotic coverage can be used to prevent and treat cholangitis. Supplementation of fat-soluble vitamins may help alleviate symptoms of cholestasis. In addition, serologic screening for carbohydrate antigen (CA) 19-9 and carcinoembryonic antigen (CEA) are helpful. PTC may be used for abscess drainage or to alleviate obstructed biliary ducts. Surgical resection has been used successfully in patients with monolobar disease. For patients with diffuse involvement and progression beyond medical management, orthotopic liver transplant is the definitive treatment.[26]

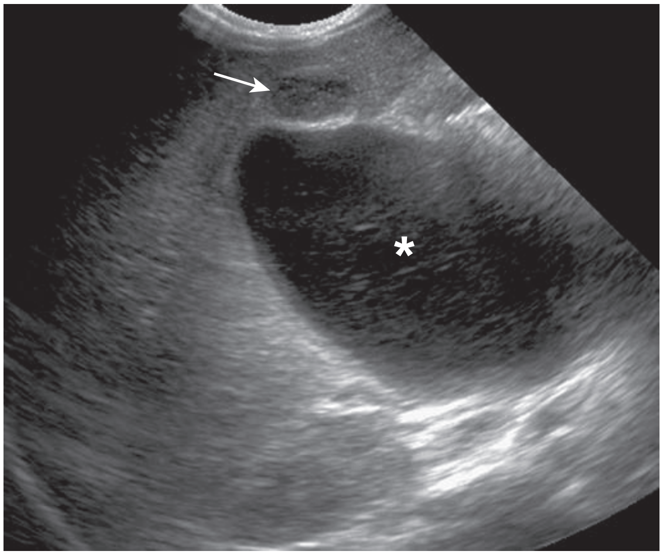

**Figure 87.3. Choledochal cyst (Todani type I) in an 8-day-old girl with jaundice.** Transverse sonogram shows a large fusiform cyst at the porta hepatis *(asterisk)* just beneath a small, contracted sludge-filled gallbladder *(arrow)*.

## CONGENITAL HEPATIC FIBROSIS

***Overview.*** Congenital hepatic fibrosis is a ductal plate malformation involving the small interlobular ducts.[27] Periportal fibrosis occurs from scarring between adjacent biliary tracts and ductal plate remnants. It is a progressive condition that leads to portal hypertension. ARPKD and congenital hepatic fibrosis are part of a fibrocystic disease mainly caused by mutation of the *PKHD1* gene, which encodes firbocystin/polycystin.[28] Hepatic fibrosis can be associated with Caroli disease, which is a large ductal plate anomaly; this association is known as Caroli syndrome.[29]

***Clinical Presentation.*** The onset of congenital hepatic fibrosis is variable with less severe disease presenting later in childhood or in adulthood, frequently with splenomegaly and portal hypertension.[14,27,30] Major complications include ascending cholangitis, hepatic failure, and an increased risk of cholangiocarcinoma[28] and hepatocellular carcinoma.[14,31]

***Imaging.*** Ultrasound (US) is the initial imaging modality. Increased hepatic echogenicity and poorly defined portal vessels are seen, with increased echogenicity of the portal triads (e-Fig. 87.9A). If associated with Caroli syndrome, large ectatic biliary cysts are seen encircling irregular portal vein radicals. When portal hypertension supervenes splenomegaly, multiple collaterals bypassing the hepatic sinusoids can be seen with US but are more easily and completely revealed with contrast-enhanced CT or MRI. CT and MRI reveal areas of hepatic parenchymal heterogeneity with variable CT attenuation (e-Fig. 87.9B) and T1 and T2 MRI parenchymal signal.[14] MR angiography can demonstrate the vascular sequelae of portal hypertension, and MRCP is useful to ascertain the anatomy of the biliary tree.[27,30] MR elastography can be used to detect the presence of fibrosis and quantify it.[32]

***Treatment.*** Medical management of hepatic fibrosis and portal hypertension consists of diuretics as first-line pharmacotherapy used to reduce ascites and increase glomerular filtration. When hepatic cirrhosis and portal hypertension become severe, hepatic transplantation may be required.

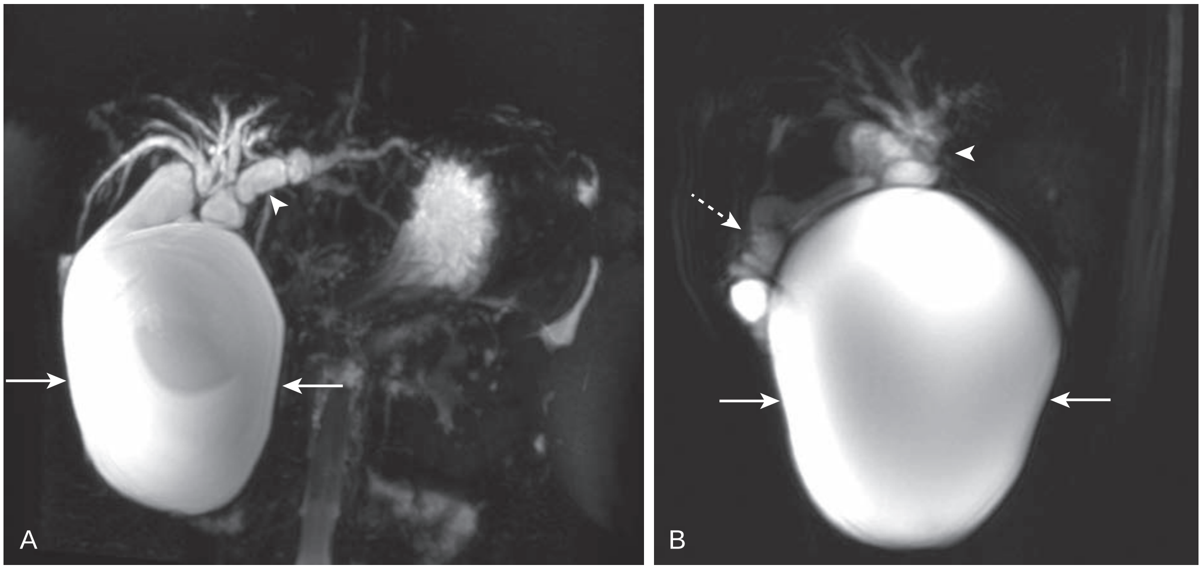

**Figure 87.5. Choledochal cyst type I in a 13-year-old girl with abdominal pain.** Frontal (A) and lateral (B) maximum intensity projection (MIP) images from 3D MRCP demonstrate a large choledochal cyst involving almost entire extrahepatic bile duct *(arrows)*. There is mild dilatation of central intra-hepatic ducts *(arrowhead)* from stasis related to the cyst. *Dashed arrow* on (B) = gallbladder.

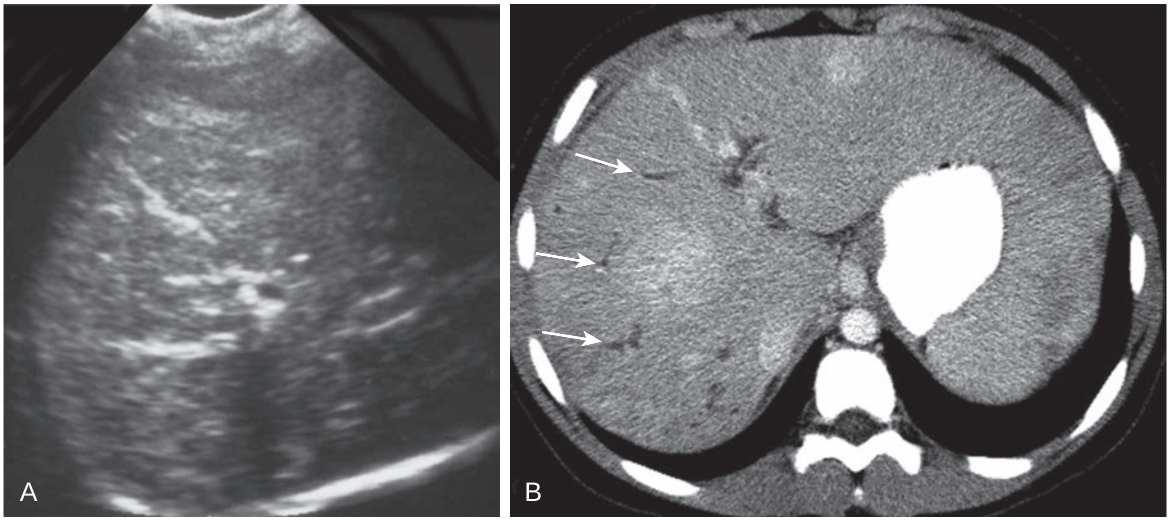

**e-Figure 87.9. Congenital hepatic fibrosis complicated by portal hypertension in a 12-year-old girl.** (A) Transverse sonogram shows heterogeneous increased periportal echogenicity of the liver due to advanced fibrosis. (B) Axial contrast enhanced CT images show heterogeneous hepatic enhancement and linear branching hypoattenuating tubular structures indicating ductal dilatation *(arrows)*. Extensive collateral vessels caused by portal hypertension were also present *(not shown)*.

## BILIARY HAMARTOMAS

***Overview.*** Biliary hamartomas, also known as microhamartomas and Von Meyenburg complex,[33] are rare and result from ductal plate malformations of the small bile ducts. They are usually multiple and typically without associated abnormalities, although they can at times coexist with simple hepatic cysts, Caroli disease, or polycystic kidney and congenital hepatic fibrosis.[31,34] Patients usually have many well-defined, similar-sized lesions measuring less than 15 mm; their uniform size helps distinguish these lesions from metastatic disease, although biopsy is required in some cases.[14,35] Because microhamartomas are small in size, they are usually asymptomatic. There is a small increased risk of hepatobiliary carcinomas.[14]

***Imaging.*** Biliary hamartomas are seen sonographically as multiple tiny hypo- or hyperechoic foci with some showing comet tail artifact scattered throughout the liver.[36,37] There is often increased heterogeneity of the hepatic architecture.[35] On CT, the lesions are of low attenuation, and of decreased signal on T1- and increased signal on T2-weighting on MRI[14] (e-Fig. 87.10).

***Treatment.*** The majority of biliary hamartomas are asymptomatic, so no treatment is required. However, monitoring with periodic imaging may be useful due to the rare possibility of malignancy.

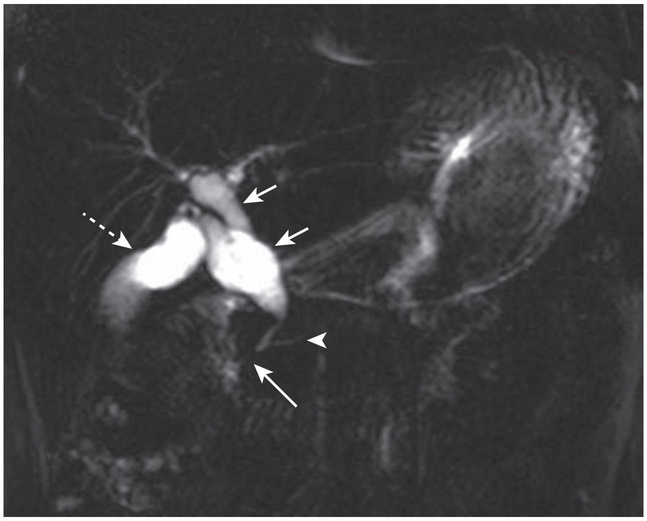

**Figure 87.6. Choledochal cyst with common channel in a 7-year-old girl.** Frontal projection of radial slab MRCP image demonstrates dilatation of extrahepatic bile ducts involving common hepatic, common bile duct, and cystic duct *(short thick arrows)*. The pancreaticobiliary junction is anomalous and away from the duodenal wall with a long common channel *(long thin arrow)*. *Arrowhead* = pancreatic duct; *dashed arrow* = gallbladder.

## BILIARY ATRESIA

***Overview.*** Biliary atresia is the most common cause of neonatal cholestasis and the most common indication for pediatric liver transplantation. Biliary atresia is more common in Asian populations, in particular Chinese and Japanese infants.[38] Biliary atresia is characterized by obliteration or discontinuity of the extrahepatic ducts. The obliteration can involve a segment or entire common bile duct only, but more commonly it also involves right and left hepatic ducts apart from extrahepatic biliary tree. A rare variant of biliary atresia with cyst formation at porta is termed cystic biliary atresia.[39] Biliary atresia can be isolated (neonatal form) accounting for 65% to 90% of cases or associated with congenital anomalies such as situs inversus or polysplenia (fetal/embryonic form) accounting for 10% to 35% cases.

***Etiology.*** The etiology of biliary atresia remains unknown with viral, genetic, toxic, and autoimmune origins suggested as possibilities. Recent theories suggest that biliary atresia and hepatitis are inflammatory cholangiopathies on two ends of a spectrum.[4] With severe inflammation, bile ducts are obliterated and the patient develops biliary atresia. Less severe inflammatory cholangiopathy does not cause duct obliteration, thus hepatitis ensues. Distinguishing between biliary atresia and hepatitis is important to determine therapy.[40]

***Clinical Presentation.*** Biliary atresia usually presents in the first month of life with jaundice, light colored stools, and direct hyperbilirubinemia.[4] Untreated, it progresses to end-stage liver disease and death within the first 3 years of life.[38] The majority

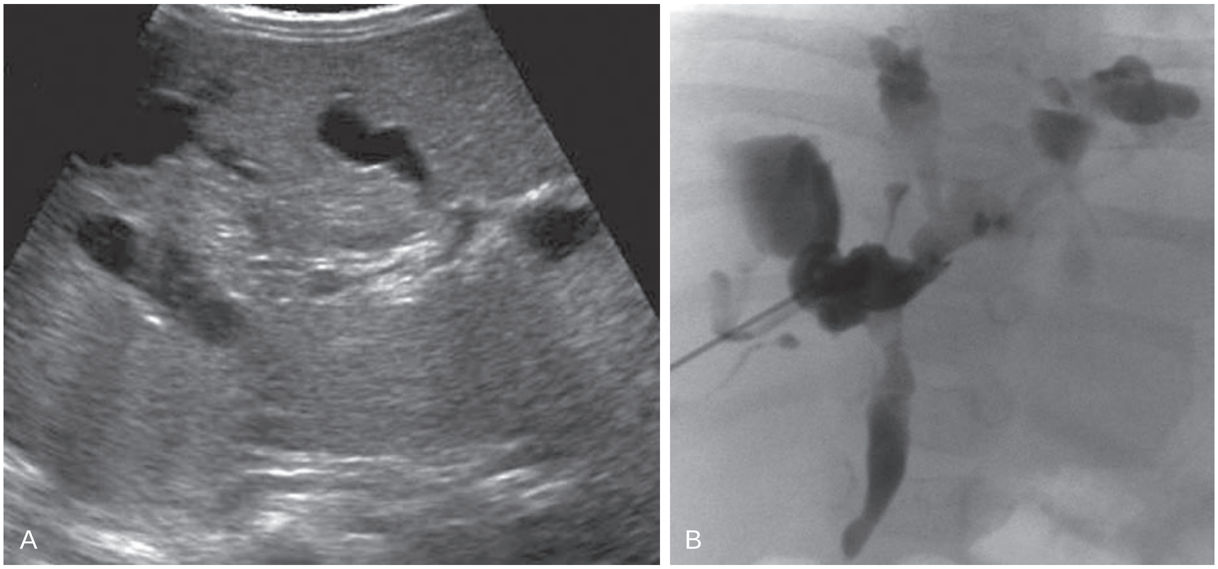

**Figure 87.7. Caroli disease (type V choledochal cyst) in a 6-month-old girl with failure to thrive.** (A) Transverse hepatic sonogram shows multiple large hypoechoic well-defined variably shaped dilatations scattered throughout the liver. (B) Percutaneous transhepatic cholangiogram confirms variable shaped patulous bile lakes connected to the biliary tree.

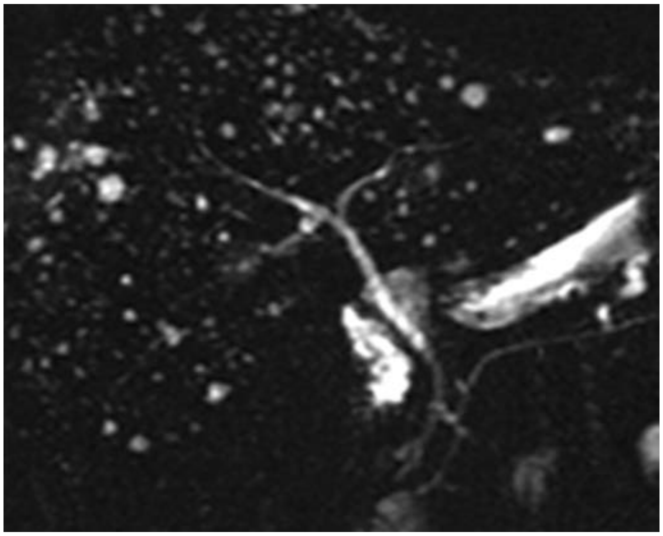

**e-Figure 87.10. Biliary hamartomas.** MRCP demonstrates innumerable small, well-defined hyperintense foci throughout the liver. Note the normal-sized ductal system. *(Image reproduced with permission from Brancatelli G, et al. Fibropolycystic liver disease: CT and MR imaging findings.* Radiographics*. 2005;25(3):659–670.)*

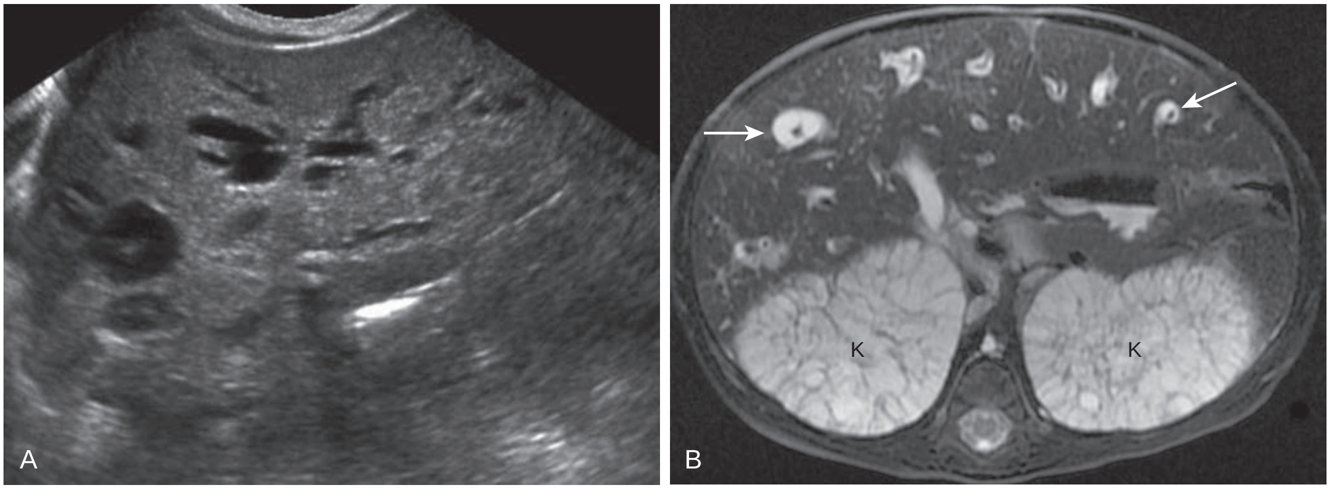

**Figure 87.8. Caroli disease (type V choledochal cyst) in a 3-day-old girl with organomegaly and associated autosomal recessive polycystic kidney disease.** (A) Longitudinal sonogram through the liver shows focal dilatation of the biliary ducts throughout the liver. (B) Axial T2-weighted MR image shows the central dot sign, seen as numerous T2 bright distended bile ducts each surrounding a portal vessel *(arrows)*. Associated enlarged polycystic kidneys *(K)* are also seen.

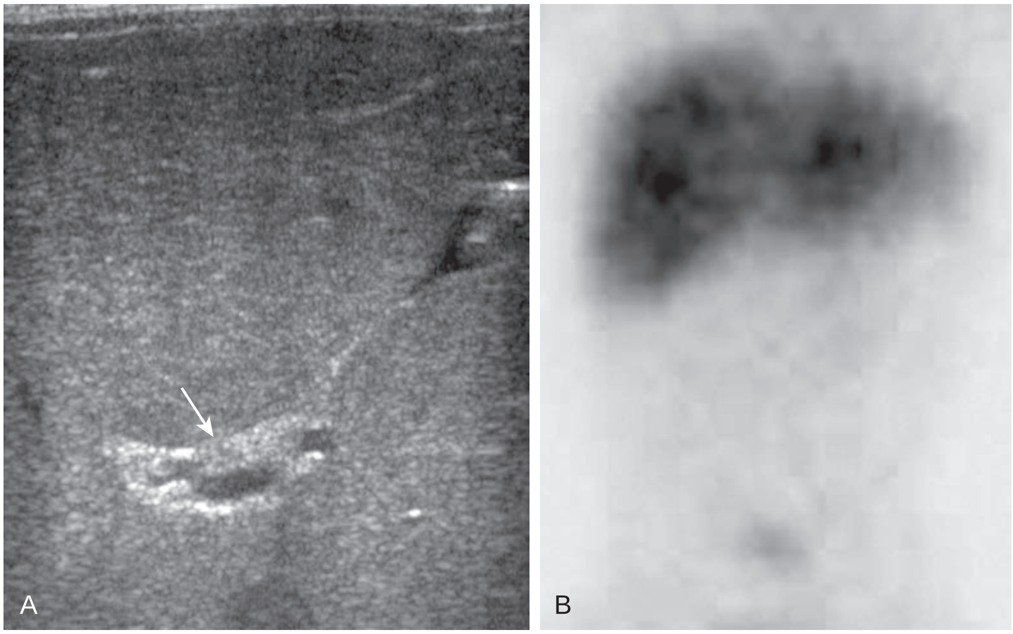

**Figure 87.11. Biliary atresia in a 2-month-old boy with persistent jaundice.** (A) Transverse image at the porta hepatis shows increased echogenicity along the expected course of the common bile duct and common hepatic ducts indicating the "triangular cord sign" *(arrow)*. Small (9 mm) gallbladder was present *(not shown)*. (B) Delayed image from a technetium-99m–labeled hepatoiminodiacetic acid shows normal radiotracer uptake in the liver, but lack of excretion into the biliary tree. This finding persisted on all images.

of patients develop portal hypertension. Benign and malignant liver tumors can develop in about 8% of children.[41]

***Imaging.*** US is the initial study for neonatal jaundice. Key findings include absent or abnormal morphology of the gallbladder including a small gallbladder (length <15 mm) and presence of a triangular cord sign (>4 mm echogenic tissue anterior to the right portal vein) (Fig. 87.11A).[42] Identification of a triangular cord sign has been cited as 96% accurate for a diagnosis of biliary atresia. Similarly, a small or absent gallbladder has been cited as 73% accurate compared with neonatal hepatitis, where 90% of infants will have a normal gallbladder.[43] Enlargement of the hepatic artery (>1.5 mm in diameter at the porta)[44] and presence of hepatic subcapsular flow[45] have been described as important findings to differentiate biliary atresia from neonatal hepatitis. Accuracy can be improved to 98% when US findings are combined, and most infants with biliary atresia could be identified using US.[46–48] Shear wave elastography has also been shown to have the potential for differentiating biliary atresia from neonatal hepatitis, as neonates with biliary atresia have higher shear wave velocity.[49]

Biliary scintigraphy using $^{99m}$Tc iminodiacetic acid with phenobarbital pretreatment has been used to distinguish biliary atresia and neonatal hepatitis (Fig. 87.11B), although this examination is not necessary in all patients.[50,51] A study without excretion is difficult to interpret, but if there is excretion of radiopharmaceutical into

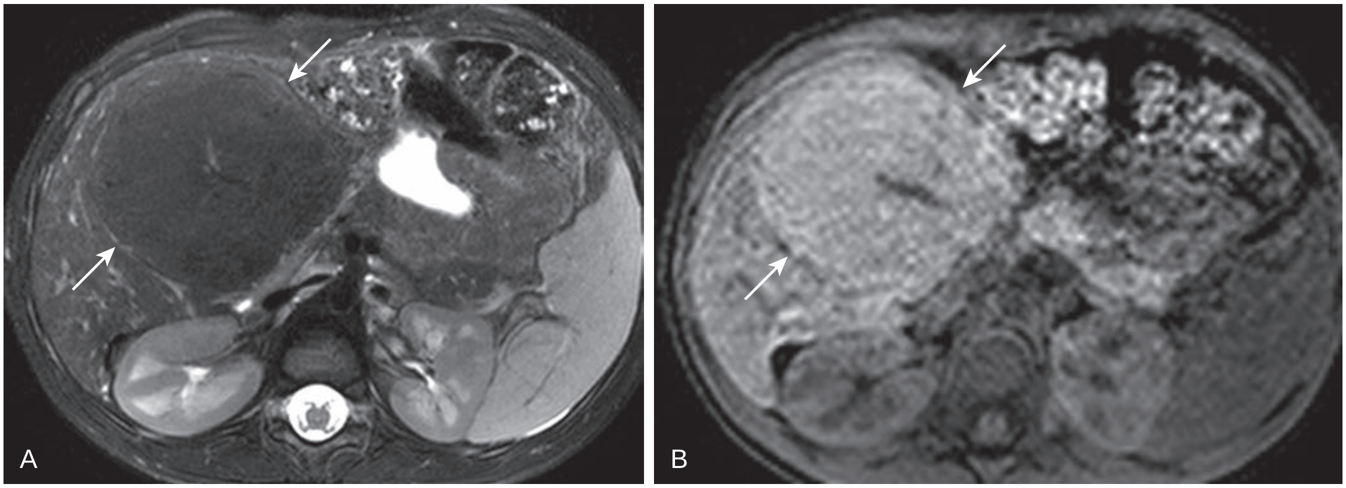

**Figure 87.12. A large regenerative nodule in a 4-year-old child with Alagille syndrome.** (A) Axial T2-weighted and (B) T1-weighted MR images demonstrate a large nodular mass *(arrows)* with vessels running through it. The nodule is hypointense on T2-weighted and hyperintense on T1-weighted images in keeping with regenerative nodule. This nodule is near right portal vein, typical for Alagille syndrome.

the bowel, biliary atresia is excluded. Diagnostic sensitivity and specificity of scintigraphy is reported to be 98.7% and 70%, respectively.[52] Currently, MRCP is limited in evaluation of biliary atresia because of poor visualization of the biliary tree in infants less than 3 months of age[53] and the need for anesthesia. Despite all of the aforementioned imaging techniques, making a definitive diagnosis of biliary atresia can be challenging. In some cases, even biopsy is nondiagnostic and diagnosis is confirmed via intraoperative cholangiogram.[54,55] US-guided percutaneous cholecystocholangiography has been used for the exclusion of biliary atresia and for determining its type.[56] Liver biopsy can be performed under the same anesthesia.

***Treatment.*** Biliary atresia is managed surgically with the Kasai procedure (hepatic portoenterostomy)[57] and neonatal hepatitis is managed medically. It is important to diagnose biliary atresia early because infants less than 2 months of age treated with the Kasai procedure tend to have a good long-term prognosis compared with infants over 2 months of age who often require future liver transplantation.[47]

## ALAGILLE SYNDROME

***Overview.*** Alagille syndrome (arteriohepatic dysplasia) is a multisystem autosomal dominant condition that produces cholestasis from bile duct paucity.[58] It is defined by pathologically proven paucity of intrahepatic biliary ducts, cardiac disease, and involvement of the face, skeleton (usually butterfly vertebrae), and eyes with variable expression of these features.[59,60] Some form of renal anomaly is seen in almost 40% of children with Alagille syndrome.[61]

***Etiology.*** Alagille syndrome is an autosomal dominant genetic disorder primarily caused by *JAGGED 1* gene mutation at the short arm of chromosome 20.[62] In some cases, it is caused by *NOTCH 2* mutation.[62]

***Clinical Presentation.*** Most children with Alagille syndrome present in early infancy with jaundice or cardiac murmur.

***Imaging.*** Imaging plays an important role in excluding structural abnormalities of hepatobiliary system causing cholestasis, showing butterfly vertebrae, and assessing the cardiac anomalies including pulmonary artery stenosis. Spine radiographs and US of the abdomen are the initial imaging methods. The common bile duct and gallbladder are normal in the majority of cases. US may show heterogeneity and coarsening of parenchyma suggesting fibrosis/cirrhosis with or without signs of portal hypertension.[63] Focal hepatic lesions can be seen in older children, with the most common being large regenerative nodules adjacent to right portal vein[63,64] (Fig. 87.12). These patients are predisposed to multisystemic vascular anomalies including aortic coarctation, renal artery stenosis, aneurysms, and moyamoya disease; vascular disease can account for up to 34% of mortality in these patients.

***Treatment.*** Medications such as ursodiol can be used to promote bile flow. Bile duct paucity and hepatic fibrosis increase with age in Alagille syndrome, and approximately 21% cases ultimately require liver transplantation.[60]

### KEY POINTS

- Fibropolycystic liver diseases are caused by mutation of the *PKHD1* gene and are associated with faulty development of the embryonic ductal plates and renal disorders including ARPKD.
- Anomalous union of the pancreatic and biliary ducts results in a common channel. Reflux of pancreatic enzymes into the biliary system and bile into the pancreatic duct through this common channel predisposes to formation of choledochal cysts and pancreatitis.
- In utero biliary ductal inflammation causes a spectrum of cholangiopathic injury ranging from mild, self-limited hepatitis up to complete ductal obliteration and biliary atresia.
- US diagnosis of biliary atresia is 98% accurate when using a combination of the triangular cord sign and gallbladder size of less than 15 mm, which individually are 96% and 73% accurate, respectively.
- Alagille syndrome is a multisystem condition that includes cholestasis from bile duct paucity and has an association of multiorgan vasculopathy.

### SUGGESTED READING

Almehdar A, Chavhan GB. MR cholangiopancreatography at 3.0 T in children: diagnostic quality and ability in assessment of common paediatric pancreatobiliary pathology. *Br J Radiol*. 2013;86(1025):20130036.

Nievelstein RAJ, Robben SGF, Blickman JG. Hepatobiliary and pancreatic imaging in children—techniques and an overview of non-neoplastic disease entities. *Pediatr Radiol*. 2011;41:55–75.

### REFERENCES

Full references for this chapter can be found on www.expertconsult.com.

## REFERENCES

1. Turkbey B, et al. Autosomal recessive polycystic kidney disease and congenital hepatic fibrosis (ARPKD/CHF). *Pediatr Radiol*. 2009; 39(2):100–111.
2. Desmet VJ. Ludwig symposium on biliary disorders–part I. Pathogenesis of ductal plate abnormalities. *Mayo Clin Proc*. 1998;73(1):80–89.
3. Todani T, et al. Congenital bile duct cysts: classification, operative procedures, and review of thirty-seven cases including cancer arising from choledochal cyst. *Am J Surg*. 1977;134(2):263–269.
4. Gubernick JA, et al. US approach to jaundice in infants and children. *Radiographics*. 2000;20(1):173–195.
5. Carneiro RC, Fordham LA, Semelka RC. MR imaging of the pediatric liver. *Magn Reson Imaging Clin N Am*. 2002;10(1):137–164.
6. Acker SN, et al. Preoperative imaging does not predict intrahepatic involvement in choledochal cysts. *J Pediatr Surg*. 2013;48(12):2378–2382.
7. Kim OH, Chung HJ, Choi BG. Imaging of the choledochal cyst. *Radiographics*. 1995;15(1):69–88.
8. Wiedmeyer DA, et al. Choledochal cyst: findings on cholangiopancreatography with emphasis on ectasia of the common channel. *AJR Am J Roentgenol*. 1989;153(5):969–972.
9. Almehdar A, Chavhan GB. MR cholangiopancreatography at 3.0 T in children: diagnostic quality and ability in assessment of common paediatric pancreatobiliary pathology. *Br J Radiol*. 2013;86(1025):20130036.
10. Mortelé KJ, et al. Multimodality imaging of pancreatic and biliary congenital anomalies. *Radiographics*. 2006;26(3):715–731.
11. Nagi B, et al. Endoscopic retrograde cholangiopancreatography in the evaluation of anomalous junction of the pancreaticobiliary duct and related disorders. *Abdom Imaging*. 2003;28(6):847–852.
12. de Vries JS, et al. Choledochal cysts: age of presentation, symptoms, and late complications related to Todani's classification. *J Pediatr Surg*. 2002;37(11):1568–1573.
13. Muthucumaru M, et al. Acute pancreatitis complicating choledochal cysts in children. *J Paediatr Child Health*. 2016.
14. Brancatelli G, et al. Fibropolycystic liver disease: CT and MR imaging findings. *Radiographics*. 2005;25(3):659–670.
15. Yoshida H, et al. Biliary malignancies occurring in choledochal cysts. *Radiology*. 1989;173(2):389–392.
16. Moslim MA, et al. Choledochal cyst disease in a western center: a 30-year experience. *J Gastrointest Surg*. 2016;20(8):1453–1463.
17. Irie H, et al. Value of MR cholangiopancreatography in evaluating choledochal cysts. *AJR Am J Roentgenol*. 1998;171(5):1381–1385.
18. Chavhan GB, et al. Pediatric MR cholangiopancreatography: principles, technique, and clinical applications. *Radiographics*. 2008;28(7):1951–1962.
19. Guo WL, et al. Imaging findings in 75 pediatric patients with pancreaticobiliary maljunction: a retrospective case study. *Pediatr Surg Int*. 2012;28(10):983–988.
20. Chavhan GB, et al. Diagnosis of postoperative bile leak and accurate localization of the site of leak by gadobenate dimeglumine-enhanced MR cholangiography in a child. *Pediatr Radiol*. 2013;43(6): 763–766.
21. Terada T, Moriki T. Monolobar ductal plate malformation disease of the liver. *Pathol Int*. 2010;60(5):407–412.
22. Dodd GD 3rd, et al. End-stage primary sclerosing cholangitis: CT findings of hepatic morphology in 36 patients. *Radiology*. 1999; 211(2):357–362.
23. Marchal GJ, et al. Caroli disease: high-frequency US and pathologic findings. *Radiology*. 1986;158(2):507–511.
24. Toma P, Lucigrai G, Pelizza A. Sonographic patterns of Caroli's disease: report of 5 new cases. *J Clin Ultrasound*. 1991;19(3):155–161.
25. Choi BI, et al. Caroli disease: central dot sign in CT. *Radiology*. 1990;174(1):161–163.
26. Bockhorn M, et al. The role of surgery in Caroli's disease. *J Am Coll Surg*. 2006;202(6):928–932.
27. Akhan O, Karaosmanoglu AD, Ergen B. Imaging findings in congenital hepatic fibrosis. *Eur J Radiol*. 2007;61(1):18–24.
28. Srinath A, Shneider BL. Congenital hepatic fibrosis and autosomal recessive polycystic kidney disease. *J Pediatr Gastroenterol Nutr*. 2012;54(5):580–587.
29. Lowe LH. Imaging hepatobiliary disease in children. *Semin Roentgenol*. 2008;43(1):39–49.
30. Ernst O, et al. Congenital hepatic fibrosis: findings at MR cholangiopancreatography. *AJR Am J Roentgenol*. 1998;170(2):409–412.
31. Veigel MC, et al. Fibropolycystic liver disease in children. *Pediatr Radiol*. 2009;39(4):317–327, quiz 420-421.
32. Serai SD, Dillman JR, Trout AT. Spin-echo Echo-planar Imaging MR Elastography versus Gradient-echo MR Elastography for Assessment of Liver Stiffness in Children and Young Adults Suspected of Having Liver Disease. *Radiology*. 2016;160589.
33. Karahan OI, et al. Hepatic von Meyenburg complex simulating biliary cystadenocarcinoma. *Clin Imaging*. 2007;31(1):50–53.
34. Yonem O, et al. Is congenital hepatic fibrosis a pure liver disease? *Am J Gastroenterol*. 2006;101(6):1253–1259.
35. Zheng RQ, et al. Imaging findings of biliary hamartomas. *World J Gastroenterol*. 2005;11(40):6354–6359.
36. Markhardt BK, et al. Sonographic features of biliary hamartomas with histopathologic correlation. *J Ultrasound Med*. 2006;25(12):1631–1633.
37. Lung PF, et al. Appearances of von Meyenburg complex on cross sectional imaging. *J Clin Imaging Sci*. 2013;3:22.
38. Superina R, et al. The anatomic pattern of biliary atresia identified at time of Kasai hepatoportoenterostomy and early postoperative clearance of jaundice are significant predictors of transplant-free survival. *Ann Surg*. 2011;254(4):577–585.
39. Pariente D, Franchi-Abella S. Cystic biliary atresia is different from choledochal cyst. *Pediatr Radiol*. 2009;39(9):1019.
40. Kirks DR, et al. An imaging approach to persistent neonatal jaundice. *AJR Am J Roentgenol*. 1984;142(3):461–465.
41. Yoon HJ, et al. Hepatic tumours in children with biliary atresia: single-centre experience in 13 cases and review of the literature. *Clin Radiol*. 2014;69(3):e113–e119.
42. Lee HJ, et al. Objective criteria of triangular cord sign in biliary atresia on US scans. *Radiology*. 2003;229(2):395–400.
43. Kanegawa K, et al. Sonographic diagnosis of biliary atresia in pediatric patients using the "triangular cord" sign versus gallbladder length and contraction. *AJR Am J Roentgenol*. 2003;181(5):1387–1390.
44. Kim WS, et al. Hepatic arterial diameter measured with US: adjunct for US diagnosis of biliary atresia. *Radiology*. 2007;245(2):549–555.
45. Lee MS, et al. Biliary atresia: color Doppler US findings in neonates and infants. *Radiology*. 2009;252(1):282–289.
46. Humphrey TM, Stringer MD. Biliary atresia: US diagnosis. *Radiology*. 2007;244(3):845–851.
47. Sun Y, Zheng S, Qian Q. Ultrasonographic evaluation in the differential diagnosis of biliary atresia and infantile hepatitis syndrome. *Pediatr Surg Int*. 2011;27(7):675–679.
48. Zhou LY, et al. Optimizing the US diagnosis of biliary atresia with a modified triangular cord thickness and gallbladder classification. *Radiology*. 2015;277(1):181–191.
49. Leschied JR, et al. *Pediatr Radiol*. 2015;45(3):366–375. doi:10.1007/s00247-014-3149-z.
50. Majd M, Reba RC, Altman RP. Hepatobiliary scintigraphy with 99mTc-PIPIDA in the evaluation of neonatal jaundice. *Pediatrics*. 1981;67(1):140–145.
51. Park WH, et al. A new diagnostic approach to biliary atresia with emphasis on the ultrasonographic triangular cord sign: comparison of ultrasonography, hepatobiliary scintigraphy, and liver needle biopsy in the evaluation of infantile cholestasis. *J Pediatr Surg*. 1997;32(11):1555–1559.
52. Kianifar HR, et al. Accuracy of hepatobiliary scintigraphy for differentiation of neonatal hepatitis from biliary atresia: systematic review and meta-analysis of the literature. *Pediatr Radiol*. 2013;43(8): 905–919.
53. Siles P, et al. A prospective pilot study: can the biliary tree be visualized in children younger than 3 months on magnetic resonance cholangiopancreatography? *Pediatr Radiol*. 2014;44(9):1077–1084.
54. Sokol RJ, et al. Pathogenesis and outcome of biliary atresia: current concepts. *J Pediatr Gastroenterol Nutr*. 2003;37(1):4–21.
55. Schwartz MZ. An alternate method for intraoperative cholangiography in infants with severe obstructive jaundice. *J Pediatr Surg*. 1985;20(4):440–442.
56. Lee SY, et al. Efficacy of US-guided percutaneous cholecystocholangiography for the early exclusion and type determination of biliary atresia. *Radiology*. 2011;261(3):916–922.
57. Kasai M, et al. Technique and results of operative management of biliary atresia. *World J Surg*. 1978;2(5):571–579.
58. Alagille D, et al. Syndromic paucity of interlobular bile ducts (Alagille syndrome or arteriohepatic dysplasia): review of 80 cases. *J Pediatr*. 1987;110(2):195–200.
59. Krantz ID, et al. Deletions of 20p12 in Alagille syndrome: frequency and molecular characterization. *Am J Med Genet*. 1997;70(1):80–86.

60. Emerick KM, et al. Features of Alagille syndrome in 92 patients: frequency and relation to prognosis. *Hepatology*. 1999;29(3):822–829.
61. Kamath BM, et al. Renal anomalies in Alagille syndrome: a disease-defining feature. *Am J Med Genet A*. 2012;158A(1):85–89.
62. Kamath BM, et al. NOTCH2 mutations in Alagille syndrome. *J Med Genet*. 2012;49(2):138–144.
63. Alhammad A, et al. Solitary hepatic nodule adjacent to the right portal vein: a common finding of alagille syndrome? *J Pediatr Gastroenterol Nutr*. 2016;62(2):226–232.
64. Rapp JB, Bellah RD, Maya C, et al. Giant hepatic regenerative nodules in Alagille syndrome. *Pediatr Radiol*. 2016 Oct 28; [Epub ahead of print], PubMed PMID: 27796468.

# 88

# Acquired Biliary Tract Disease

Govind B. Chavhan

## CHOLELITHIASIS AND CHOLEDOCHOLITHIASIS

***Overview.*** Cholelithiasis, previously thought rare in children without hemolytic anemia, is diagnosed with increasing frequency since the increased ultrasound use. Gallstones have been reported in the fetus, although most resolve spontaneously.[1]

Development of gallstones in infants may be related to immature physiologic regulation of bile salt secretion. Chronic cholestasis likely plays a role in the pathophysiology of cholelithiasis. Although infantile gallstones are often discovered incidentally, many predisposing conditions have been described (Box 88.1). Infantile gallstones resolve spontaneously less often than in the fetus and are rarely complicated by biliary tract perforation and peritonitis.[2]

Although most gallstones seen in older children are idiopathic, a number of underlying states are associated (Box 88.2). Prominent among these are sickle cell disease and intestinal problems that interfere with normal enterohepatic circulation.[3] Patients with sickle cell disease have an increased incidence of gallstones with advancing age. Gallstones have also been reported after surgery and antibiotic therapy.[4]

***Clinical Presentation.*** Cholelithiasis is usually asymptomatic in most infants and young children with an increased incidence of symptoms in older children. When symptoms occur in older children and adolescents, they are similar to those seen in adults and include bloating, nausea, vomiting, and postprandial right upper quadrant colicky pain radiating to the shoulder. Younger children may present with nonspecific symptoms such as irritability and may be unable to verbalize or relate their discomfort to the right upper quadrant or to a recent meal.[5]

Choledocholithiasis results from migration of stones from the gallbladder into the common duct. Stones are more likely to be symptomatic when they pass into the cystic duct or the common bile duct. The most common complication of gallstones in children is pancreatitis,[5] although the most common cause of pancreatitis is idiopathic or posttraumatic.[6]

***Imaging.*** While radiolucent cholesterol stones are the most common type overall, they are rare in children and many pediatric gallstones are visible radiographically. Even so, sonography remains the primary imaging modality for the evaluation of cholelithiasis. Gallstones are seen as echogenic focus with posterior acoustic shadowing (Fig. 88.1), and most demonstrate twinkling artifact on color Doppler images.[7] Most stones move with change in patient position, which should be a routine maneuver during hepatobiliary sonography (Fig. 88.2). Four general sonographic patterns of cholelithiasis are described here.

The first is the simple echogenic, shadowing, mobile stone, which may be single or multiple. The second describes collections of very tiny, sandlike stones, termed *milk of calcium*, which may mimic gallbladder sludge. Acoustic shadowing may be seen only in the aggregate (see Fig. 88.2).[8] Third, if bile within the gallbladder is of high density, stones may seem to float on the surface, giving an apparent fluid-fluid level. The fourth pattern of cholelithiasis relates to stones within a contracted gallbladder when the stones produce an echogenic double arc known as the wall echo shadow (WES) complex. This pattern may also be seen in patients who have not fasted sufficiently (Fig. 88.3). Careful scrutiny must be employed so as not to confuse the WES complex with emphysematous cholecystitis, which is far more common in adults than in children.[9]

Sonography is less successful detecting choledocholithiasis than cholelithiasis due to interference from adjacent bowel gas. Dilated bile ducts (Fig. 88.4) may be the only sonographic sign of a more distal obstructing stone. If no stone is seen on sonography, yet there is evidence of biliary ductal dilation, magnetic resonance cholangiopancreatography (MRCP) is the next modality of choice. With MRCP, most stones are seen as hypointense filling defects within the gallbladder and the biliary tree[10] (Fig. 88.5). Some stones, such as pigment stones, are hyperintense on T1-weighted 3D gradient echo sequences.[11,12]

***Treatment and Follow-up.*** Treatment of infantile gallstones is generally conservative and includes addressing the underlying cause of disease. Surgery, particularly laparoscopic surgery, is the usual treatment of choice for symptomatic patients and patients with choledocholithiasis.[13] Obstructive stones in the distal common bile duct (CBD) may be treated via endoscopic retrograde cholangiopancreatography (ERCP).

## BILIARY SLUDGE

***Overview.*** Biliary sludge, particulate matter within the bile produced by cholestasis, is of debated clinical significance. Although the majority of biliary sludge is a transient finding, particularly if associated with a transient predisposing condition, it may evolve into gallstones.[14] Occasionally, the sludge itself may cause obstructive jaundice, which is termed as inspissated bile syndrome.

Sludge is formed predominantly of calcium bilirubinate particles and, depending on the underlying process, cholesterol crystals. Predisposing conditions that share the common pathway of biliary stasis include biliary outflow obstruction, intravenous hyperalimentation, hemolysis, treatment with ceftriaxone, and prolonged fasting.[15,16]

***Clinical Presentation.*** Biliary sludge is usually asymptomatic; however, it may cause symptoms if associated with microlithiasis or if "bile balls" course into the biliary ducts. When this happens, symptoms are similar to those produced by cholelithiasis.[14]

***Imaging.*** On sonography, sludge is echogenic without acoustic shadowing; it typically layers in the dependent portion of the gallbladder or other part of the biliary tree, such as a choledochal cyst, and demonstrates a fluid-sludge level (e-Fig. 88.6). Inspissated bile may be slightly more echogenic than regular sludge, but it does not cause any posterior acoustic shadowing.[2] Occasionally, sludge coalesces within the gallbladder lumen, forming a tumefactive "sludge ball" that, when fixed, may mimic a polyp or mass.[9] Differential considerations include uncommon conditions such as hemobilia, biliary mucus, and parasitic infection.

***Treatment and Follow-up.*** Because biliary sludge is generally asymptomatic and resolves spontaneously with resolution of the underlying condition, it does not require separate treatment. However, follow-up in patients in whom the underlying condition does not remit is important, particularly if the patient becomes symptomatic.[14] Inspissated bile syndrome may resolve with removal of predisposing factors but has also been treated with mucolytic agents and laparoscopic surgery.[16,17]

## ACUTE CHOLECYSTITIS

***Overview.*** Acute cholecystitis is uncommon in infants and children compared with adults. However, it has a mortality rate

## Abstract:

In this chapter, some acquired biliary tract diseases affecting children are discussed. These include cholelithiasis and choledocholithiasis, biliary sludge, acute cholecystitis, acute cholangitis, primary sclerosing cholangitis and gallbladder hydrops.

## Keywords:

cholelithiasis
choledocholithiasis
biliary sludge
acute cholecystitis
acute cholangitis
primary sclerosing cholangitis
gallbladder hydrops

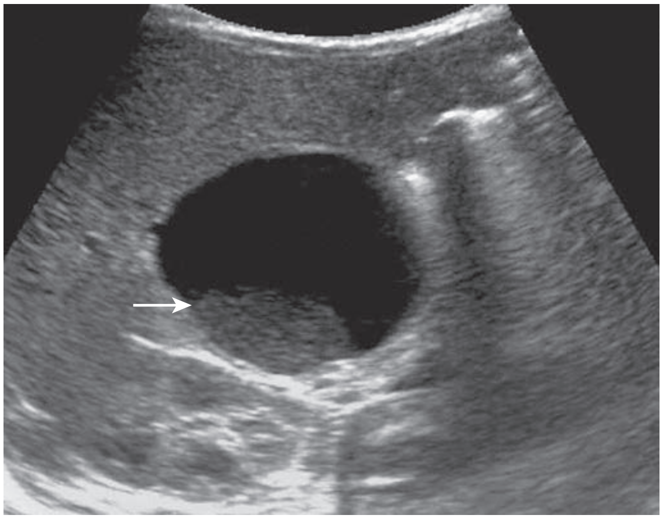

**e-Figure 88.6. Biliary sludge in a 1-year-old boy with a choledochal cyst.** Transverse sonogram shows layering echogenic material within the cyst *(arrow)*; its echogenicity, which is less than that of a stone, and lack of shadowing, distinguish it from a calculus.

### BOX 88.1 Conditions Associated With Development of Gallstones in Infants

- Obstructive congenital biliary tree anomalies
- Total parenteral nutrition
- Diuretics (furosemide)
- Gastrointestinal dysfunction (short-gut syndrome or terminal ileal disease)
- Prolonged fasting
- Phototherapy
- Dehydration
- Infection
- Hemolytic anemia
- Umbilical venous catheterization
- Antibiotics

### BOX 88.2 Conditions Associated With Development of Gallstones in Children

- Sickle cell disease
- Cystic fibrosis or other pancreatic disease
- Malabsorption
- Total parenteral nutrition
- Inflammatory bowel disease (Crohn disease)
- Short-gut syndrome (intestinal resection)
- Hemolytic anemia
- Choledochal cyst
- Antibiotics

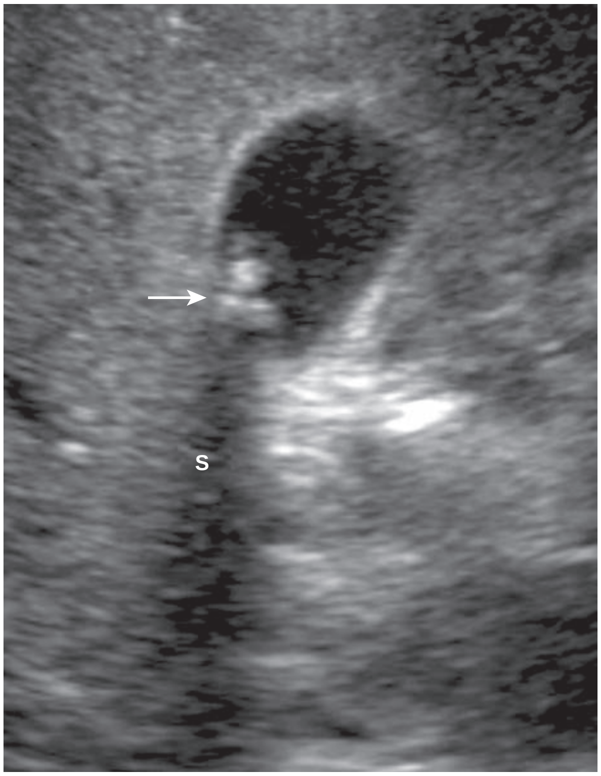

**Figure 88.1. Cholelithiasis in a 17-year-old girl with abdominal pain.** Transverse sonogram of the gallbladder shows cholelithiasis *(arrow)* with associated posterior acoustic shadowing *(S)*.

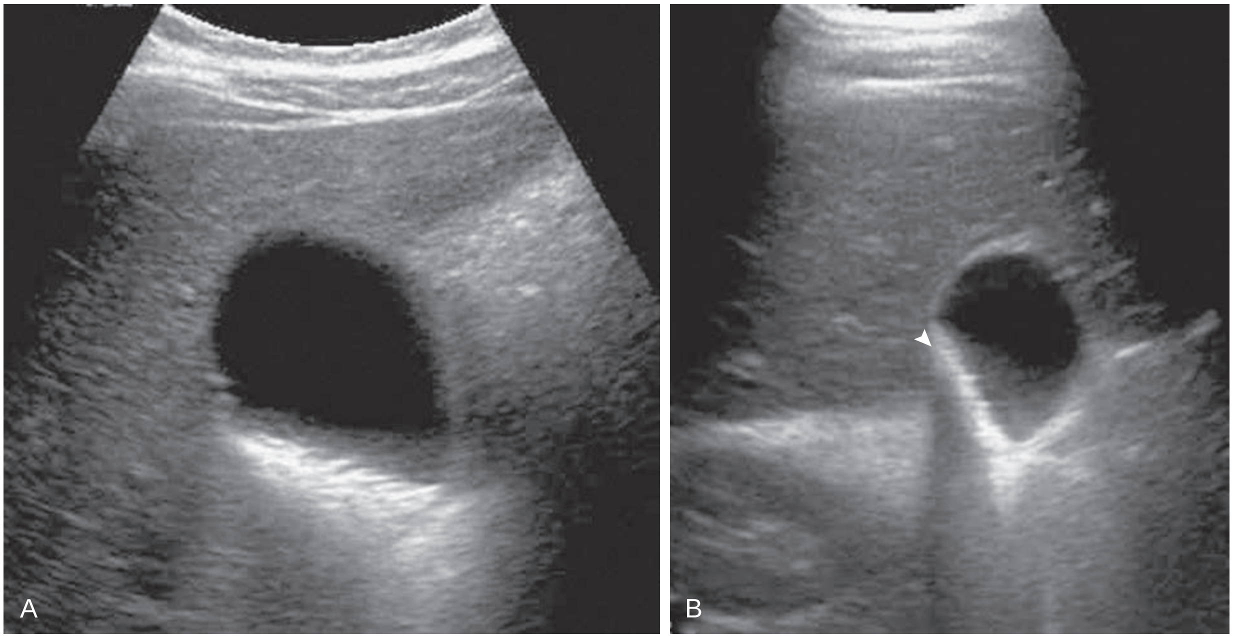

**Figure 88.2. Cholelithiasis in a 16-year-old girl with right upper quadrant pain.** Transverse sonograms in the supine (A) and decubitus (B) positions reveal echogenic layering of tiny stones. Note the change in stones with change in patient position, as well as diffuse shadowing of the stone aggregate (*arrowhead* in B).

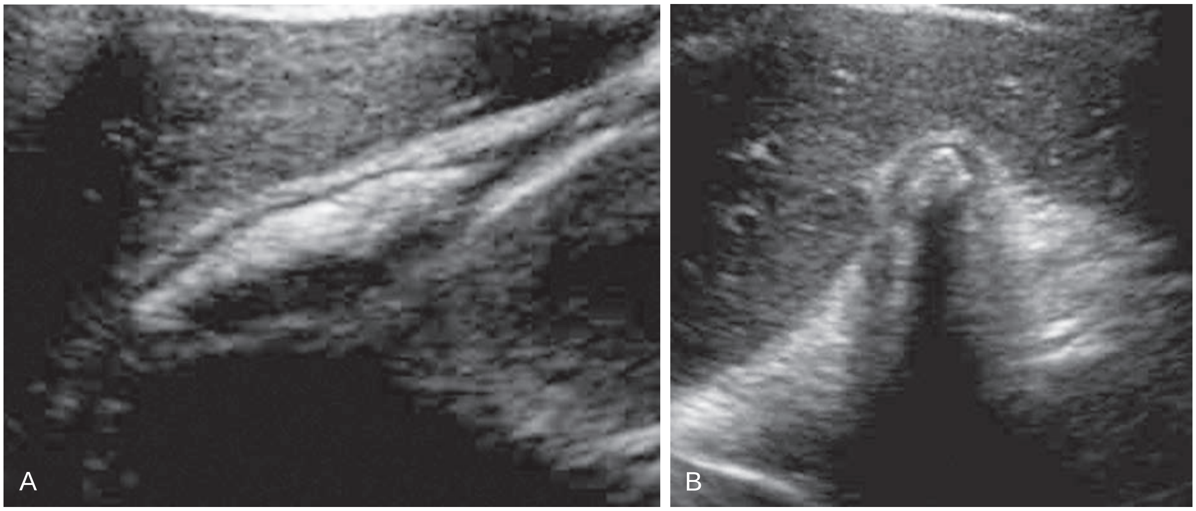

**Figure 88.3. Cholelithiasis in a 16-year-old girl with abdominal pain.** Longitudinal (A) and transverse (B) sonograms performed without fasting show the anterior gallbladder wall and multiple echogenic stones with posterior acoustic shadowing (wall-echo-shadow [WES] triad).

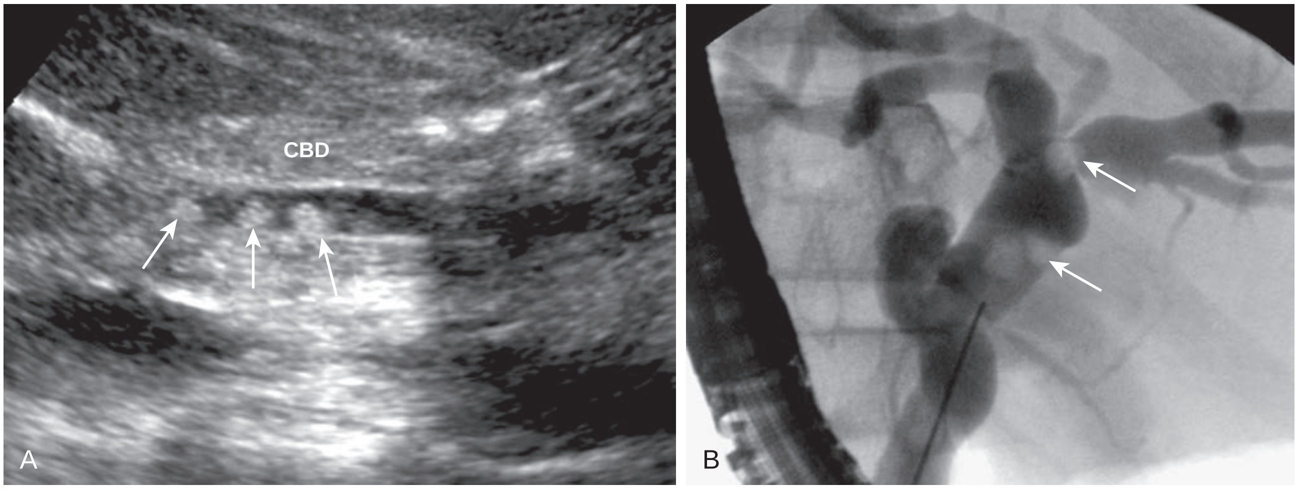

**Figure 88.4. Choledocholithiasis in a 15-year-old girl with sickle cell disease and abdominal pain.** (A) A sonogram of the common bile duct *(CBD)* reveals three stones *(arrows)*. (B) Subsequent ERCP shows dilated bile ducts and intraluminal filling defects *(arrows)*.

of at least 30% due to the potential for rapid progression with gangrene occurring in greater than 50% and perforation in greater than 10% of cases.[18]

***Etiology.*** A small percentage of children with cholelithiasis develop cholecystitis, and acute acalculous cholecystitis represents 50% to 70% of all cases of cholecystitis in children.[19] In most cases, the pathophysiology of acute cholecystitis involves obstruction of the cystic duct, which leads to gallbladder distension, followed successively by edema, ischemia, mural necrosis, and, in severe cases, perforation. The pathophysiology of acalculous cholecystitis is thought to involve biliary stasis, dehydration, gallbladder ischemia, and elevated ampullary pressures as contributing factors.[18] In neonates with acute cholecystitis, the diagnosis may not be suspected, leading to a high mortality rate. Acute acalculous cholecystitis in children can be caused by systemic infectious diseases and a variety of noninfectious systemic diseases including Kawasaki disease.[20] The majority of infectious causes are viral and include hepatitis A and Epstein–Barr.[21,22]

***Clinical Presentation.*** Diagnosing acalculous cholecystitis can be difficult. The condition is most dangerous when it occurs during a serious illness, as the underlying illness may mask clinical symptoms and laboratory abnormalities. Patients who may develop acalculous cholecystitis include patients with septicemia, postoperative patients, and patients who have sustained severe trauma or burns. Systemic infection may be more common in pediatric patients. Symptoms include jaundice, nausea, vomiting, and tenderness to palpation, and there may be fever and leukocytosis.[14,18,19,23]

***Imaging.*** The sonographic findings of calculous and acalculous cholecystitis are identical except for the lack of gallstones in the latter condition. Sonographic findings of cholecystitis when viewed individually are nonspecific, but when combined, they may indicate a specific diagnosis.[24] Ultrasound, in general, has low sensitivity and positive predictive value for the diagnosis of cholecystitis, which, according to some authors, is related to a higher prevalence of chronic cholecystitis.[25] The best indicators of acute cholecystitis include cholelithiasis, a sonographic Murphy sign (tenderness when the gallbladder is compressed with the ultrasound probe), and gallbladder wall edema with wall thickening >3.5 mm[18,26] (Fig. 88.7). Intramural edema related to acute cholecystitis is usually striated, with multiple interrupted bands of hypoechogenicity. This

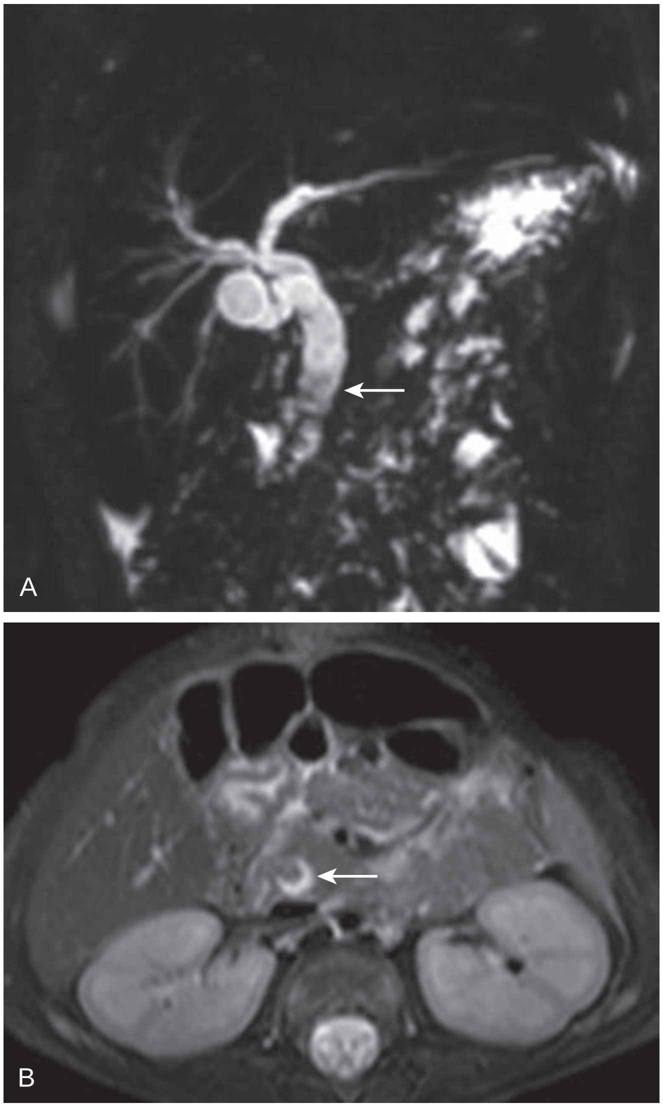

**Figure 88.5. Choledocholithiasis in a 3-month-old baby with prior history of congenital diaphragmatic hernia.** 3D reformatted T2-weighted sequence from an MRCP (A) shows subtle filling defect consistent with a stone *(arrow)* in the distal common bile duct. Axial T2-weighted thin section (B) confirms a hypointense filling defect in the distal CBD *(arrow)*.

appearance has also been associated with gangrenous cholecystitis. This should not be confused with homogeneous gallbladder wall thickening, a common nonspecific finding seen in a variety of disorders such as ascites, hypoalbuminemia, congestive heart failure, hepatitis, portal hypertension, and gallbladder wall varices. Other sonographic findings of acute cholecystitis include gallbladder distension, pericholecystic fluid (especially with perforation), adjacent rim of hypoechogenicity or hypervascularity in the liver, biliary sludge, and rarely dirty shadowing due to air-producing infection (found most often in adults with diabetes). Computed tomography (CT) is not the modality of choice in most pediatric patients with cholecystitis, but if performed for other reasons, it shows similar findings (e-Fig. 88.8).

Hepatobiliary scintigraphy with technetium-99m–labeled iminodiacetic acid derivatives is highly sensitive for the diagnosis of acute cholecystitis. Normally, radiopharmaceutical appears in the gallbladder in the first 30 minutes of the study or in the first hour with slow injection of intravenous (IV) morphine. In acute cholecystitis, gallbladder filling does not occur in the first 30 minutes or within 1 hour after IV morphine. Occasionally, a rim of increased activity is seen in the liver surrounding the gallbladder (the rim sign), and peritoneal activity may be seen with perforation[27] (Fig. 88.9).

***Treatment and Follow-up.*** Treatment for acute acalculous cholecystitis may differ depending on patient's clinical status and underlying conditions. Children may be treated medically and observed before surgery.[23,28] Percutaneous cholecystostomy is increasingly a lifesaving, minimally invasive alternative. Gallbladder perforation is a surgical emergency that occurs in 3% to 15% of patients with acute cholecystitis.[29]

## CHOLANGITIS

***Overview and Etiology.*** Cholangitis refers to acute or chronic inflammation of bile ducts. Acute cholangitis is a potentially life-threatening infection of the biliary tract associated with some form of biliary obstruction and presents with fever, chills, right upper quadrant pain, and jaundice.[30] Causes of obstruction include gallstones, benign and malignant strictures, structural abnormalities of the biliary tree, and iatrogenic causes such as sphincterotomy and choledochoenterostomy.[31] Cholangitis can be seen in endemic areas from parasitic infestations such as ascariasis,[32] liver fluke (fasciola),[33] clonorchiasis,[34] and schistosomiasis.[35] Acute bacterial cholangitis is rare in children.

***Imaging.*** Imaging demonstrates biliary dilatation and may demonstrate the cause of obstruction and complications such as cholangitic abscesses. A syndrome of recurrent bacterial cholangitis (Oriental cholangitis) is typically seen in Asia and is characterized by biliary dilatation, strictures, and intraductal stone formation.[36]

***Treatment.*** Appropriate therapy is directed toward relief of the underlying cause of obstruction, whether congenital or acquired, and any associated infection.

## PRIMARY SCLEROSING CHOLANGITIS

***Overview.*** Primary sclerosing cholangitis (PSC) is a chronic fibrosing inflammation of the bile ducts leading to obliteration of the bile duct lumen and cholestasis.[37,38] It involves both intra- and extrahepatic ducts that can show multifocal strictures. Even though uncommon in children as compared with adults, PSC is one of the common indications for pediatric liver transplantation.[37] It is a progressive disorder that eventually leads to cirrhosis, portal hypertension, and hepatic decompensation in most patients. Development of cholangiocarcinoma in long-standing cases of PSC is rare in children as compared with adults but can be occasionally seen.[39]

***Etiology.*** PSC is likely an immune-mediated disorder.[37] It may overlap with other autoimmune conditions such as autoimmune hepatitis in 35% to 58% of cases.[40,41] It is associated with inflammatory bowel disease (IBD) in 60% to 80% of children,[37,40,41] mainly those with ulcerative colitis. Approximately 10% of children with ulcerative colitis develop PSC.[39] Sclerosing cholangitis associated with immune deficiency states, Cryptosporidium infection, Langerhans cell histiocytosis, sickle cell anemia, Hodgkin disease, and cystic fibrosis is generally regarded as being "secondary sclerosing cholangitis."[42]

***Clinical Presentation.*** Boys are affected more often than girls and typically present in the second decade of life. Presentation is with jaundice, abdominal pain, and hepatomegaly. Alkaline phosphatase levels may be normal or elevated. Gamma glutamyltranspeptidase (GGT), alanine aminotransferase (ALT), and aspartate aminotransferase (AST) enzyme levels are elevated. In many instances, elevation of liver function tests in asymptomatic children with IBD leads to the diagnosis of PSC.

***Imaging.*** Sonography is usually the initial imaging method in evaluation of suspected PSC. It excludes other obstructive causes such as stones and choledochal cyst. It may show mild dilatation

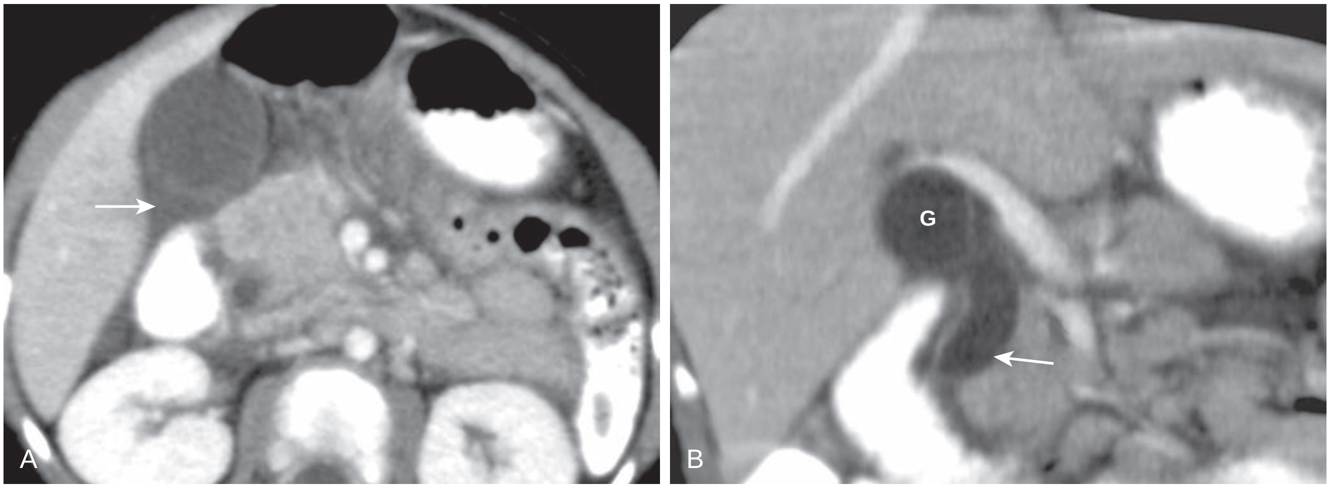

**e-Figure 88.8. Cholecystitis and ascending cholangitis in a 25-month-old boy with subsequent confirmed passage of a gallstone.** (A) Axial contrast-enhanced CT image demonstrates pericholecystic edema *(arrow)* on the axial image. (B) Coronal reformatted image demonstrates a distended gallbladder *(G)* and dilation of the common bile duct *(arrow)*.

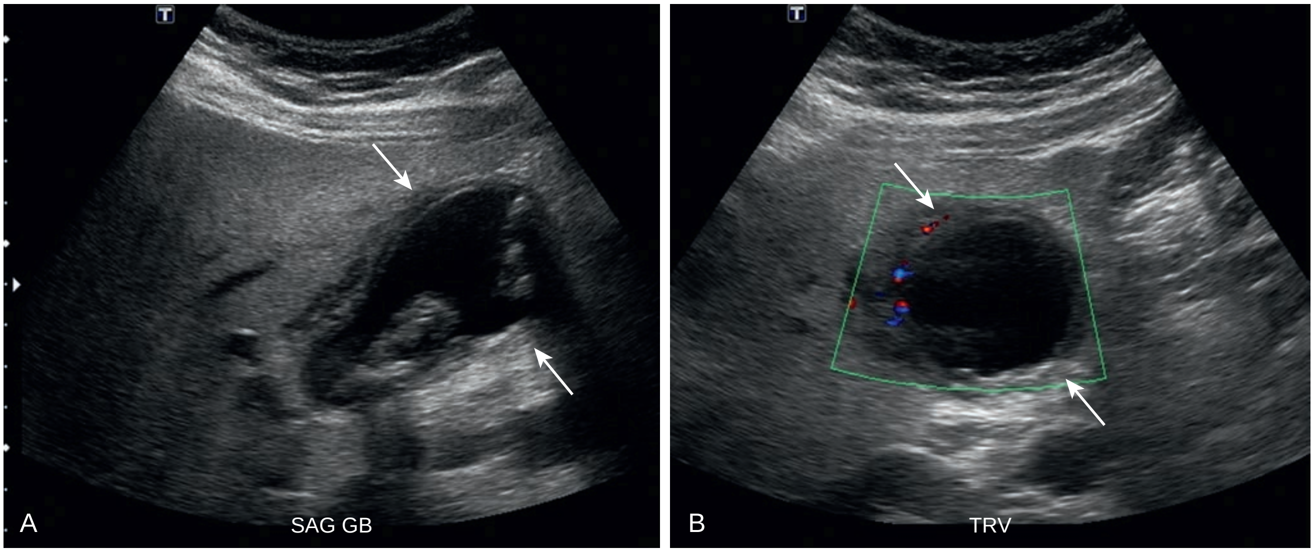

**Figure 88.7. Acute cholecystitis in a 17-year-old girl with a history of cholelithiasis.** Longitudinal (A) and transverse (B) sonogram through the gallbladder reveals a thickened, edematous gallbladder wall with multiple stones in the lumen *(arrows)*. Color Doppler image (B) demonstrates hyperemia of the thickened gallbladder wall.

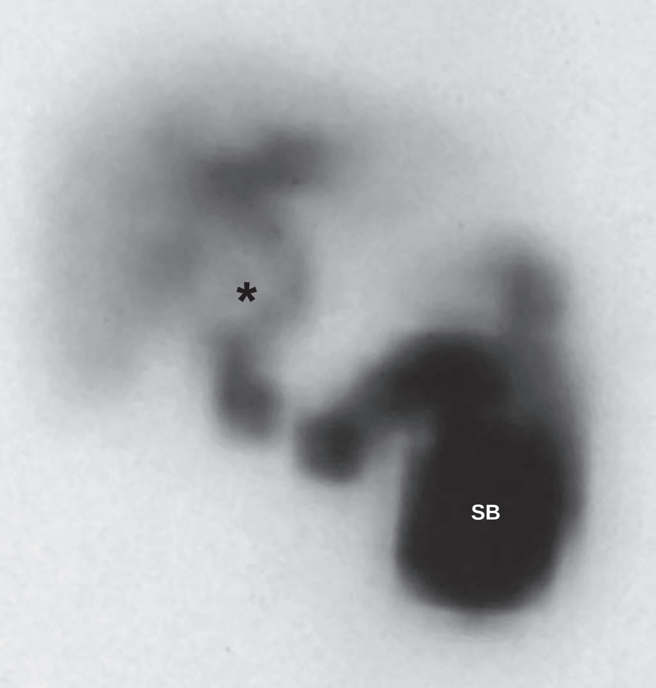

**Figure 88.9. Acute cholecystitis in a 15-year-old girl with a history of cholelithiasis.** Four-hour image from a biliary patency scan shows hepatic uptake and excretion of technetium-99m–labeled iminodiacetic acid into the biliary tree and small bowel *(SB)* without gallbladder *(asterisk)* opacification. A halo of increased activity surrounds the gallbladder fossa known as the rim sign is suggestive of hyperemia.

of ducts. Thickening of wall of the CBD is a very specific finding for PSC but may have limited sensitivity. MRCP is the modality of choice for the diagnosis of PSC in children and has replaced ERCP.[38] MRCP has been found to be 84% sensitive and accurate in the diagnosis of PSC.[38] Findings in early stages include mild diffuse dilation of the entire biliary tree with subtle irregularity of the duct outline, portal lymphadenopathy, and increased periportal signal abnormality on T2-weighted images (Fig. 88.10). As the disease progresses, irregularity of the duct wall increases with intermittent ductal dilation and narrowing. In advanced stage, there is severe structuring of the ducts with a “beaded appearance” (Fig. 88.11). Sacculations and pseudodiverticula formation is usually not seen in children. It is important to identify any dominant stricture on MRCP that can be treated. Liver parenchymal changes also progress from nonspecific increased periportal signal abnormality and heterogeneity of the parenchyma to frank imaging features of fibrosis/cirrhosis of the liver with portal hypertension. Although cholangitis is occasionally segmental, the entire biliary tract is usually involved. The intrahepatic ducts are involved in 100% of cases while the extrahepatic ducts are involved in 60%.[43] The gallbladder is rarely involved.

A variant of PSC with typical cholestatic and histologic features of PSC but without any cholangiographic abnormalities is called “small duct PSC.”[37] It accounts for about 6% to 10% of cases in children.[44]

***Treatment and Follow-up.*** PSC is a progressive disease ultimately resulting in cirrhosis and portal hypertension and may be complicated by superimposed infective cholangitis and cholangiocarcinoma. Treatment includes medical therapy (ursodeoxycholic acid), interventional dilation of dominant strictures, and drainage of infected obstructed ducts. Most patients eventually require liver transplantation. The median reported time until liver transplantation is approximately 12.7 years.[40,45] Recurrence of PSC can be seen in 10% of liver grafts.[46]

## HYDROPS OF THE GALLBLADDER

***Overview.*** Gallbladder hydrops refers to marked dilatation of gallbladder from accumulation of the sterile nonpigmented mucin. It is a rare cause of right upper quadrant mass in children.

***Etiology.*** Thought to be related to transient cholestasis and obstruction of the biliary tree, gallbladder hydrops is associated with preceding infectious disorders elsewhere in the body (Box 88.3), most notably mucocutaneous lymph node syndrome (Kawasaki disease) and parenteral hyperalimentation. It can also result from chronic obstruction of cystic duct.

***Clinical Presentation.*** Hydrops of the gallbladder is more frequent in boys and most commonly presents from ages 17 months

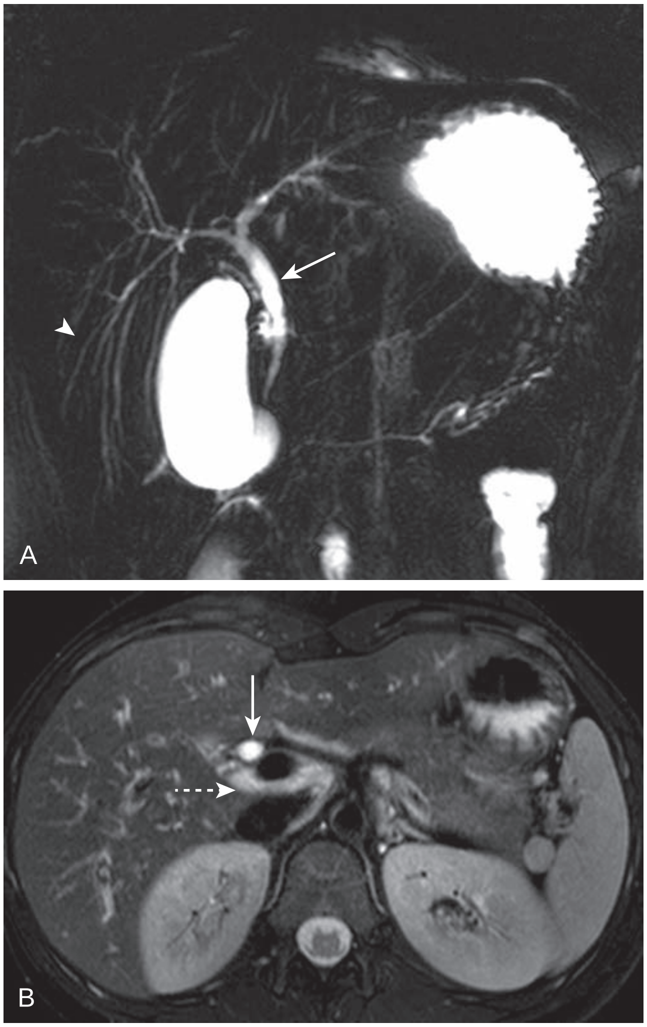

**Figure 88.10. Early primary sclerosing cholangitis (PSC) in an adolescent boy with ulcerative colitis.** Radial slab MRCP (A) demonstrates diffuse mild dilatation of intrahepatic (*arrowhead*) as well as extrahepatic bile ducts (*arrow*) with subtle irregularity of the outline. T2-weighted axial MR image (B) demonstrates a dilated CBD (*arrow*) and enlarged portal lymph nodes (*dashed arrow*).

**BOX 88.3** Causes of Gallbladder Hydrops

Mucocutaneous lymph node syndrome (Kawasaki disease)
Obstruction
Familial Mediterranean fever
Scarlet fever
Leptospirosis
Ascariasis
Typhoid fever
Sepsis
Total parenteral nutrition

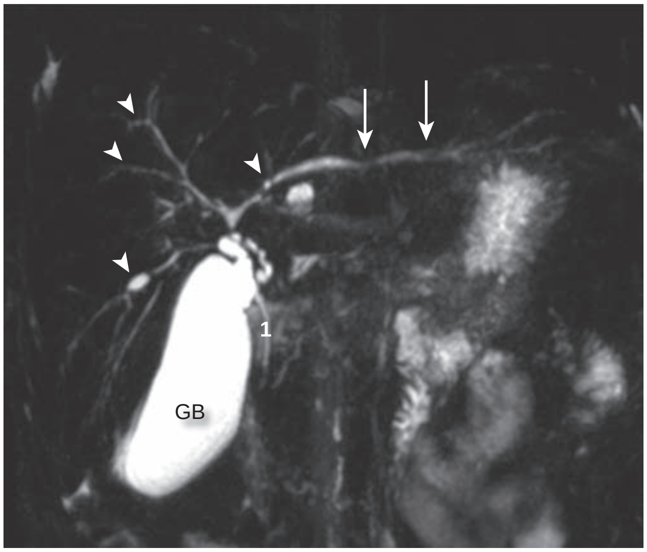

**Figure 88.11. Primary sclerosing cholangitis in a 13-year-old boy with Crohn disease.** A 5-mm-thick maximum intensity projection (MIP) image from 3D MRCP shows multiple areas of beading in the intrahepatic ducts *(arrowheads)*. Areas of low grade narrowing are seen in the left duct *(arrows)*. *1* = common bile duct; *GB* = gallbladder.

to 7 years. Presentation may include jaundice, abdominal pain, right upper quadrant tenderness, vomiting, or a palpable mass.[47]

***Imaging.*** Sonography shows gallbladder dilation without gallbladder wall thickening. The gallbladder may resemble a balloon in which normal contours are lost (e-Fig. 88.12). A normal gallbladder length is 1.5 to 3 cm in infants (<1 year old) and 3 to 7 cm in older children.[48] Maximum gallbladder transverse dimension of greater than 4 cm in adults is diagnostic of hydrops, but there is no data on this in children. Sludge is seen in some cases, and the biliary tree is otherwise normal. Serial sonographic studies may demonstrate resolution of gallbladder hydrops.[49]

***Treatment and Follow-up.*** Hydrops generally responds to conservative therapy, although gallbladder perforation has been reported in Kawasaki disease.[50]

## KEY POINTS

- Cholelithiasis and choledocholithiasis is a significant disease seen with increasing frequency in infants and children with several predisposing causes.
- Acute acalculous cholecystitis is more common in children as compared with calculous cholecystitis. There is a higher mortality in children than adults due to frequent and rapid progression to gangrene and perforation.
- Primary sclerosing cholangitis is a chronic fibrosing inflammation of the bile ducts leading to cholestasis and eventually liver failure.
- MRCP is the current modality of choice for the diagnosis of PSC with an accuracy of 84%, demonstrating mild dilatation of the biliary tree, irregularity of outline in early stage, and severe structuring with beaded appearance in advanced stages.

## SUGGESTED READINGS

Albuquerque PA, Morales Ramos DA, Faingold R. Magnetic resonance imaging of the liver and biliary tree in children. *Curr Probl Diagn Radiol*. 2009;38(3):126–134.
Chavhan GB, Babyn PS, Manson D, et al. Pediatric MR cholangiopancreatography: principles, technique, and clinical application. *Radiographics*. 2008;28:1951–1962.
Lowe LH. Hepatobiliary disease in children. *Seminar Roentgenol*. 2008; 43(1):39–49.

## REFERENCES

Full references for this chapter can be found on www.expertconsult.com.

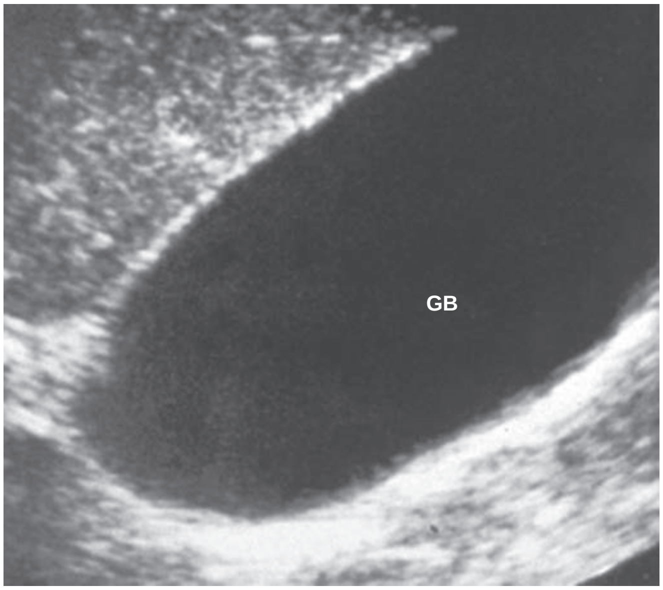

**e-Figure 88.12. Hydrops of the gallbladder in a child with Kawasaki disease.** Longitudinal sonogram shows a markedly enlarged, balloon-shaped gallbladder *(GB)*. Hydrops resolved spontaneously as the patient's condition improved.

## REFERENCES

1. Suma V, et al. Fetal gallstones: sonographic and clinical observations. *Ultrasound Obstet Gynecol*. 1998;12(6):439–441.
2. Gubernick JA, et al. US approach to jaundice in infants and children. *Radiographics*. 2000;20(1):173–195.
3. Darge K, Anupindi S. Pancreatitis and the role of US, MRCP and ERCP. *Pediatr Radiol*. 2009;39(suppl 2):S153–S157.
4. Bogue CO, et al. Risk factors, complications, and outcomes of gallstones in children: a single-center review. *J Pediatr Gastroenterol Nutr*. 2010;50(3):303–308.
5. Reif S, Sloven DG, Lebenthal E. Gallstones in children. Characterization by age, etiology, and outcome. *Am J Dis Child*. 1991;145(1):105–108.
6. Shanbhogue AK, et al. A clinical and radiologic review of uncommon types and causes of pancreatitis. *Radiographics*. 2009;29(4):1003–1026.
7. Kim HJ, et al. Color Doppler twinkling artifacts from gallstones: in vitro analysis regarding their compositions and architectures. *Ultrasound Med Biol*. 2010;36(12):2117–2122.
8. Wu SS, et al. Milk of calcium cholelithiasis in children. *J Pediatr Surg*. 2001;36(4):644–647.
9. Rosenthal SJ, et al. Pitfalls and differential diagnosis in biliary sonography. *Radiographics*. 1990;10(2):285–311.
10. Anupindi SA, Victoria T. Magnetic resonance cholangiopancreatography: techniques and applications. *Magn Reson Imaging Clin N Am*. 2008;16(3):453–466, v.
11. Tsai HM, et al. MRI of gallstones with different compositions. *AJR Am J Roentgenol*. 2004;182(6):1513–1519.
12. Almehdar A, Chavhan GB. MR cholangiopancreatography at 3.0 T in children: diagnostic quality and ability in assessment of common paediatric pancreatobiliary pathology. *Br J Radiol*. 2013;86(1025):20130036.
13. Chan S, et al. Paediatric cholecystectomy: shifting goalposts in the laparoscopic era. *Surg Endosc*. 2008;22(5):1392–1395.
14. Jungst C, Kullak-Ublick GA, Jungst D. Gallstone disease: microlithiasis and sludge. *Best Pract Res Clin Gastroenterol*. 2006;20(6):1053–1062.
15. Mitchell CL, Vasanawala SS. An approach to pediatric liver MRI. *AJR Am J Roentgenol*. 2011;196(5):W519–W526.
16. Miloh T, et al. Inspissated bile syndrome in a neonate treated with cefotaxime: sonographic aid to diagnosis, management, and follow-up. *J Ultrasound Med*. 2009;28(4):541–544.
17. Berger S, et al. One-stage laparoscopic surgery for inspissated bile syndrome: case report and review of surgical techniques. *Springerplus*. 2013;2:648.
18. Barie PS, Fischer E. Acute acalculous cholecystitis. *J Am Coll Surg*. 1995;180(2):232–244.
19. Tsakayannis DE, Kozakewich HP, Lillehei CW. Acalculous cholecystitis in children. *J Pediatr Surg*. 1996;31(1):127–130, discussion 130-131.
20. Yi DY, et al. Age, predisposing diseases, and ultrasonographic findings in determining clinical outcome of acute acalculous inflammatory gallbladder diseases in children. *J Korean Med Sci*. 2016;31(10):1617–1623.
21. Poddighe D, et al. Acalculous acute cholecystitis in previously healthy children: general overview and analysis of pediatric infectious cases. *Int J Hepatol*. 2015;2015:459608.
22. Alkhoury F, Diaz D, Hidalgo J. Acute acalculous cholecystitis (AAC) in the pediatric population associated with Epstein-Barr Virus (EBV) infection. Case report and review of the literature. *Int J Surg Case Rep*. 2015;11:50–52.
23. Imamoglu M, et al. Acute acalculous cholecystitis in children: diagnosis and treatment. *J Pediatr Surg*. 2002;37(1):36–39.
24. Imamoğlu M, et al. Acute acalculous cholecystitis in children: diagnosis and treatment. *J Pediatr Surg*. 2002;37(1):36–39.
25. Tsai J, et al. Sensitivity and predictive value of ultrasound in pediatric cholecystitis. *J Surg Res*. 2013;184(1):378–382.
26. Deitch EA, Engel JM. Acute acalculous cholecystitis. Ultrasonic diagnosis. *Am J Surg*. 1981;142(2):290–292.
27. Mariat G, et al. Contribution of ultrasonography and cholescintigraphy to the diagnosis of acute acalculous cholecystitis in intensive care unit patients. *Intensive Care Med*. 2000;26(11):1658–1663.
28. Glenn F, Becker CG. Acute acalculous cholecystitis. An increasing entity. *Ann Surg*. 1982;195(2):131–136.
29. Granlund A, et al. Ultrasound-guided percutaneous cholecystostomy in high-risk surgical patients. *Langenbecks Arch Surg*. 2001;386(3):212–217.
30. Schneider J, et al. Mortality risk for acute cholangitis (MAC): a risk prediction model for in-hospital mortality in patients with acute cholangitis. *BMC Gastroenterol*. 2016;16:15.
31. Mosler P. Diagnosis and management of acute cholangitis. *Curr Gastroenterol Rep*. 2011;13(2):166–172.
32. Javid G, et al. Etiology and outcome of acute pancreatitis in children in Kashmir (India). An endemic area of hepatobiliary ascariasis. *World J Surg*. 2013;37(5):1133–1140.
33. Xia J, Jiang SC, Peng HJ. Association between liver fluke infection and hepatobiliary pathological changes: a systematic review and meta-analysis. *PLoS ONE*. 2015;10(7):e0132673.
34. Choi MS, et al. Correlation between sonographic findings and infection intensity in clonorchiasis. *Am J Trop Med Hyg*. 2005;73(6):1139–1144.
35. Richter J, et al. Ultrasonography of gallbladder abnormalities due to schistosomiasis. *Parasitol Res*. 2016;115(8):2917–2924.
36. Heffernan EJ, et al. Recurrent pyogenic cholangitis: from imaging to intervention. *AJR Am J Roentgenol*. 2009;192(1):W28–W35.
37. Chapman R, et al. Diagnosis and management of primary sclerosing cholangitis. *Hepatology*. 2010;51(2):660–678.
38. Chavhan GB, et al. Primary sclerosing cholangitis in children: utility of magnetic resonance cholangiopancreatography. *Pediatr Radiol*. 2008;38(8):868–873.
39. Deneau M, et al. Primary sclerosing cholangitis, autoimmune hepatitis, and overlap in Utah children: epidemiology and natural history. *Hepatology*. 2013;58(4):1392–1400.
40. Feldstein AE, et al. Primary sclerosing cholangitis in children: a long-term follow-up study. *Hepatology*. 2003;38(1):210–217.
41. Tenca A, et al. Clinical course and prognosis of pediatric-onset primary sclerosing cholangitis. *United European Gastroenterol J*. 2016;4(4):562–569.
42. Wilschanski M, et al. Primary sclerosing cholangitis in 32 children: clinical, laboratory, and radiographic features, with survival analysis. *Hepatology*. 1995;22(5):1415–1422.
43. Debray D, et al. Sclerosing cholangitis in children. *J Pediatr*. 1994;124(1):49–56.
44. Angulo P, Maor-Kendler Y, Lindor KD. Small-duct primary sclerosing cholangitis: a long-term follow-up study. *Hepatology*. 2002;35(6):1494–1500.
45. Ibrahim SH, Lindor KD. Current management of primary sclerosing cholangitis in pediatric patients. *Paediatr Drugs*. 2011;13(2):87–95.
46. Miloh T, et al. Pediatric liver transplantation for primary sclerosing cholangitis. *Liver Transpl*. 2011;17(8):925–933.
47. Egritas O, et al. Early but prolonged gallbladder hydrops in a 7-month-old girl with Kawasaki syndrome: report of a case. *Surg Today*. 2007;37(2):162–164.
48. Rozel C, et al. Imaging of biliary disorders in children. *Pediatr Radiol*. 2011;41(2):208–220.
49. Neu J, Arvin A, Ariagno RL. Hydrops of the gallbladder. *Am J Dis Child*. 1980;134(9):891–893.
50. Suddleson EA, et al. Hydrops of the gallbladder associated with Kawasaki syndrome. *J Pediatr Surg*. 1987;22(10):956–959.

# 89

# Parenchymal Liver Disease

Mougnyan Cox, Monica Epelman, and Daniel J. Podberesky

## INTRODUCTION

Imaging plays a central role in the initial assessment and serial monitoring of chronic pediatric liver disease. While liver biopsy remains the accepted gold standard test for diffuse parenchymal liver disease, a single biopsy specimen only samples 1/50,000 or 0.002% of the liver,[1] and heterogeneity in severity and distribution of disease can result in sampling errors.[2] Liver biopsy is invasive even when done percutaneously, and up to 3% of patients require hospitalization after the procedure.[1] There is also significant variability in interpretation of liver biopsy specimens by pathologists with discordance in up to 33% of cases.[3] For these reasons, noninvasive methods, mainly ultrasound (e-Fig. 89.1) and magnetic resonance imaging (MRI), of assessing response to therapy and disease progression have come to play a prominent role in the management of chronic pediatric liver disease.

## HEPATIC STEATOSIS

***Overview.*** Nonalcoholic fatty liver disease (NAFLD) is the most common cause of chronic pediatric liver disease, with some series listing a prevalence of approximately 10%.[4] NAFLD is defined as the presence of microvesicular/macrovesicular fat in more than 5% of the hepatocytes after the exclusion of significant alcohol consumption, drug use, or other recognizable secondary causes that may result in fatty liver.[5] The prevalence of pediatric fatty liver increases with age and is seen in up to 17% of adolescents.[4] NAFLD is usually diagnosed between 10 and 13 years of age. The majority of patients with NAFLD also have insulin resistance or obesity.[6] NAFLD can range in severity from simple steatosis and nonalchoholic steatohepatitis (NASH), through fibrosis and cirrhosis,[7] but it also may be associated with a number of metabolic processes and toxins (Box 89.1). In addition to fat deposition, NASH patients show hepatic cell injury and inflammation. NASH significantly increases the risks of cirrhosis, hepatic failure, and hepatocellular carcinoma (HCC). At the time of diagnosis, 25% to 50% of children will have NASH, while 10% to 25% will have advanced fibrosis.[8]

***Clinical Presentation.*** Many pediatric patients with NAFLD are either asymptomatic or present with vague clinical complaints (abdominal pain, fatigue). On physical exam, hepatomegaly and acanthosis nigricans are seen in up to 40% of patients.[9] Elevation of liver enzymes is common in NAFLD patients, particularly alanine aminotransferase (ALT) and aspartate aminotransferase (AST). Some NAFLD patients also come to clinical attention after incidental detection of a fatty liver on abdominal ultrasounds performed for other reasons.

***Imaging Findings.*** Diagnostic confidence for fatty liver on ultrasound improves with increasing severity of fatty infiltration, with a sensitivity and specificity of over 90% for moderate steatosis.[10] Deposition of fat in hepatocytes causes increased echogenicity of the liver, manifested as difficulty visualizing the portal triads (Fig. 89.2). There is increased attenuation of the sound beam as it propagates through the liver, causing loss of signal in the posterior portions of the liver and inability to visualize the hemidiaphragm. The liver may be substantially more echogenic than the adjacent right kidney (see Fig. 89.2). Areas of focal fatty sparing manifest as hypoechoic foci within the fatty liver, without mass effect, which could potentially be misdiagnosed as a mass. Ultrasound elastography is a noninvasive method of assessing liver stiffness, which is a correlate for fibrosis.[11] This method has shown promise for severe fibrosis and advanced cirrhosis but is limited in whole liver assessment due to the small acoustic window used for scanning.[12]

Computed tomography (CT) is not routinely used for the primary diagnosis of fatty liver, but this finding may be seen incidentally. Normally, the liver attenuation is at least the same as the spleen. This relationship is reversed in hepatic steatosis, and the liver is of lower attenuation than the spleen on noncontrast CT (e-Fig. 89.3).

Fat deposition in hepatocytes can readily be detected on conventional MR, with a high degree of sensitivity and specificity.[13] More specifically, the amount of fat in the liver can also be quantified using either MR spectroscopy or chemical shift imaging. MR spectroscopy is the most accurate method of hepatic fat quantification and is very sensitive to small changes in hepatic fat concentration.[14] However, the complexity of analysis and lack of reproducibility are barriers to its widespread clinical adoption.

Chemical shift imaging is the mainstay of hepatic fat quantification on MR because it is quick and easy to perform. Chemical shift imaging takes advantage of the different precession frequencies of hydrogen protons in fat and water.[14] When fat and water are present within the same voxel, there is signal loss on the opposed-phase images. Comparing the signal intensity on the opposed-phase image (short TE image) with the in-phase image (long TE image) allows for calculation of the hepatic fat fraction[15] (Fig. 89.4). Hepatic iron deposition may limit evaluation for steatosis on opposed-phase images, as signal loss also occurs from iron-related susceptibility effects. Chemical shift imaging can help resolve confusing patterns of focal fat deposition or fatty sparing in the liver when present in atypical locations. Focal fat deposition commonly occurs in specific locations, usually around the gallbladder, adjacent to the falciform ligament, and in subcapsular regions. Unlike a mass, vessels course through regions of fatty deposition unperturbed.

MR elastography (MRE) measures hepatic parenchymal stiffness using special hardware that generates shear waves and measures their propagation through the liver.[16] The hardware used in pediatric MRE is the same type used in adults, except the driver is set to lower power/amplitude settings.[17] An active driver outside the scanner transmits vibrations at 60 Hz to a passive driver on the patient's right upper quadrant.[13] Four magnitude and four phase images are obtained at four different levels in the liver, and these images are then used to generate qualitative and quantitative stiffness maps using specific postprocessing software.[13] For MRE, liver stiffness values greater than 2.74 kiloPascal (kPa) are suggestive of steatohepatitis and greater than 2.93 kPa is diagnostic for liver fibrosis.[18] Compared with ultrasound elastography, MRE has been shown to be more accurate, samples a larger portion of the liver, has greater reliability, and is less limited by ascites or obesity.[19–21]

***Treatment.*** Lifestyle modification aimed at weight loss is the first-line therapy for NAFLD, and even mild reduction in weight can improve histologic findings of steatosis and steatohepatitis.[22,23] Drugs being investigated include antioxidants such as vitamin E, metformin, and thiazolidinediones.[5] The need for accurate and reliable noninvasive monitoring of NAFLD is imperative given the recent discovery that fibrosis and early cirrhosis may be reversible in some patients.[24–26]

## Abstract:

There are myriad causes of pediatric parenchymal liver disease, of which hepatic steatosis is the most common. The major concern with diffuse parenchymal liver disease is progression to end-stage fibrosis and cirrhosis. As such, early detection and treatment of pediatric liver disease can improve patient outcomes and prolong survival. Liver biopsy remains the gold standard for diagnosis of parenchymal liver disease, but it is not without several shortcomings (sampling error and invasiveness being most prominent). Various imaging modalities can provide important information on the extent of liver involvement and development of complications without the invasiveness of a liver biopsy. Of these noninvasive modalities, MRI provides the most comprehensive evaluation of liver parenchyma. Liver MRI, including advanced MR modalities like spectroscopy and elastography, can provide noninvasive monitoring of disease distribution within the liver, as well as disease progression and response to therapy. In end-stage liver disease, MRI can also monitor for the development of hepatocellular carcinoma, and can help determine eligibility for transplantation when indicated. In this review, we summarize the more common pediatric parenchymal liver diseases encountered at any busy children's hospital, with an emphasis on the imaging appearance of the various diseases. A summary of MR applications in diffuse parenchymal liver disease is also provided.

## Keywords:

Pediatric liver disease
parenchymal liver disease
pediatric fatty liver
hepatic steatosis
steatohepatitis
hepatic fibrosis
MRI
MR spectroscopy
MR elastography

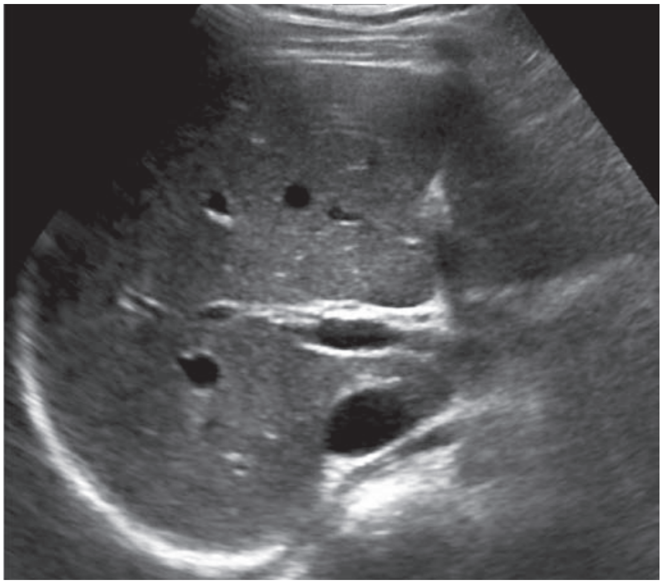

**e-Figure 89.1. Normal liver ultrasound in an 11-year-old girl.** Transverse ultrasound image of the liver shows the normal sonographic appearance of the hepatic parenchyma with visualization of the normal echogenic portal triads. The liver is homogeneous in echotexture with good sound transmission, and the posterior portions of the liver as well as the posterior right hemidiaphragm are well seen.

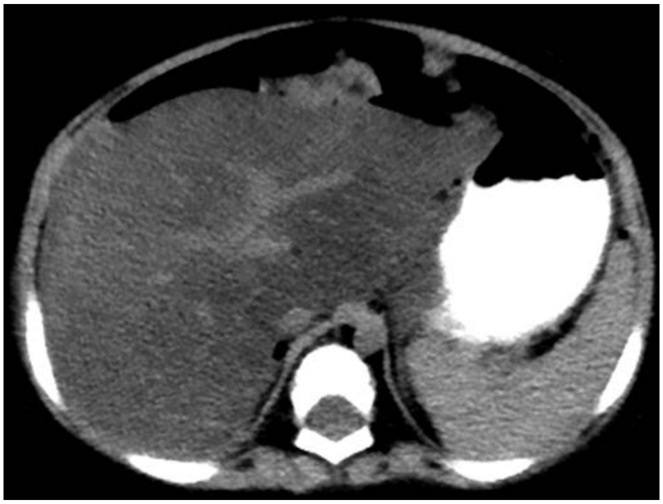

**e-Figure 89.3. Fatty liver.** This image shows the CT appearance of a fatty liver, with the liver being substantially less dense than the spleen due to the presence of fat in hepatocytes. Note that the liver parenchyma is even less dense than the intrahepatic blood vessels, consistent with severe fatty deposition.

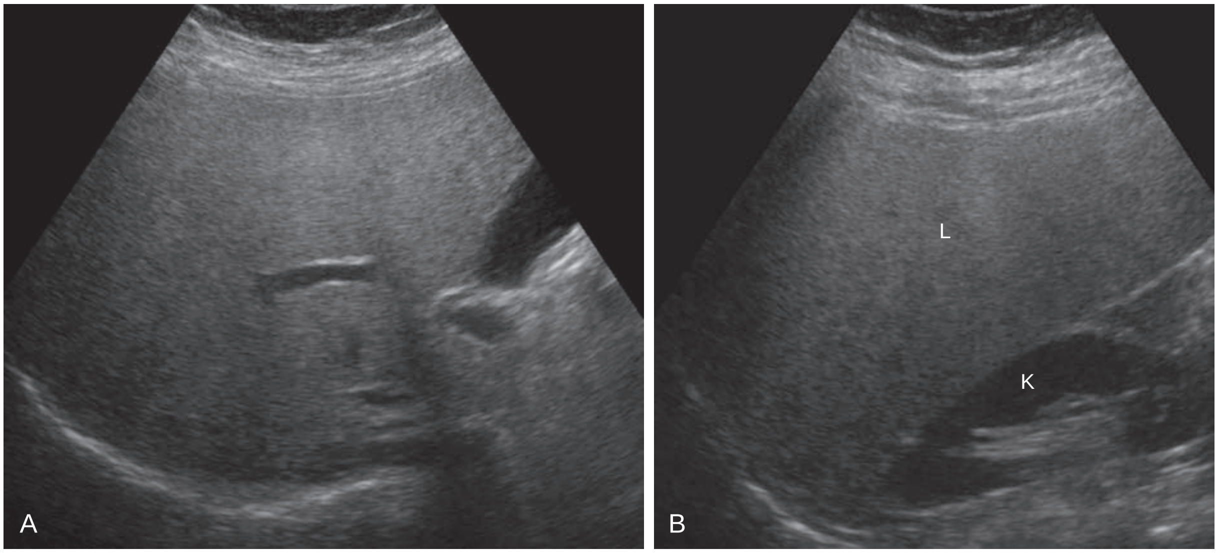

**Figure 89.2. Fatty liver in an 11-year-old girl with NAFLD.** (A) Transverse and (B) longitudinal ultrasound images show diffuse increased echogenicity of the liver *(L)* compared with the kidney *(K)* parenchyma. There is poor visualization of the portal triads. The posterior portions of the liver are less well seen when compared with e-Fig. 89.1, due to decreased sound transmission.

**BOX 89.1** Causes of Hepatic Steatosis

**METABOLIC AND GENETIC DISORDERS**

- Obesity
- Extreme malnutrition
- Total parenteral nutrition
- Cystic fibrosis

**STEROIDS (EXOGENOUS AND ENDOGENOUS; E.G., CUSHING SYNDROME)**

- Familial hyperlipoproteinemia
- Glycogen storage disease
- Wilson disease
- Galactosemia
- Reye syndrome
- Severe hepatitis
- Poorly controlled diabetes mellitus
- Chronic tuberculosis
- Chronic congestive heart failure

**HEPATOTOXINS (MOSTLY ADULTS)**

- Alcohol
- Chemotherapy
- Carbon toxins
- Phosphorus
- Amiodarone

## IRON DEPOSITION IN THE LIVER

***Overview.*** Hepatic iron overload is the result of abnormal intracellular accumulation of iron within the hepatocytes. Normally, excess iron is stored bound to intracellular ferritin. In cases of increased and sustained iron overload, the capacity of ferritin to collect and store iron is surpassed, resulting in deposition of unbound iron primarily in the liver, pancreas, spleen, and bone marrow. Unbound iron may result in cellular injury by reacting with hydrogen and lipids to produce free radicals. In the liver, this can lead to fibrosis and cirrhosis.[13]

There are two main patterns of iron deposition: parenchymal and reticuloendothelial.[27] Parenchymal iron deposition occurs in hereditary hemochromatosis (HH), an autosomal recessive disorder with a gene locus *(HFE)* on the short arm of chromosome 6. There is increased gastrointestinal absorption of iron with eventual pathologic deposition in the liver, pancreas, heart, pituitary, synovium, and other parenchymal organs. Abnormal parenchymal iron deposition results in oxidative injury and organ dysfunction over time, with patients developing liver fibrosis/cirrhosis, cardiomyopathy, and endocrinopathies including diabetes mellitus. Iron deposition in the pancreas is specific for HH, whereas splenic and bone marrow involvement is usually seen with transfusional/reticuloendothelial iron deposition. A neonatal form of primary hemochromatosis exists in which newborns present with fulminant hepatic failure, along with pancreatic and cardiac involvement.

Reticuloendothelial iron deposition occurs mainly after multiple blood transfusions. This form of iron deposition is also referred to as secondary hemochromatosis, and it is more common than the hereditary form. Iron in transfused red blood cells is taken up by reticuloendothelial cells in the liver, spleen, and bone marrow after phagocytosis. Unlike HH, organs other than the liver, spleen, and bone marrow are affected relatively late in the disease. The pancreas is usually spared in patients with reticuloendothelial iron deposition.

***Clinical Presentation.*** Men with HH become symptomatic at least a decade earlier than women (as a result of the protective effect of menstruation) after total body accumulation of approximately 20 g of iron. The most common presenting symptoms are weakness, lethargy, and elevated liver function tests, occurring in 75% of patients.[28] Patients with transfusional iron overload become symptomatic much earlier than in HH because each blood transfusion provides approximately 200 mg of iron, and there is no mechanism for iron excretion in the body other than through sweat, shedding of skin cells, and menstruation (an iron loss rate of approximately 1 mg per day for men and 2 mg per day for premenopausal women).[29] Elevated serum ferritin levels are seen in patients with iron overload, but this finding may also be seen with any inflammatory process, as ferritin is an acute phase reactant. Transferrin saturation levels can also be performed, and levels greater than 60% are over 90% accurate for identifying HH.[30,31] These tests are less helpful for transfusional iron overload. Iron overload occurs in virtually all patients requiring life-long blood transfusions, necessitating careful monitoring and

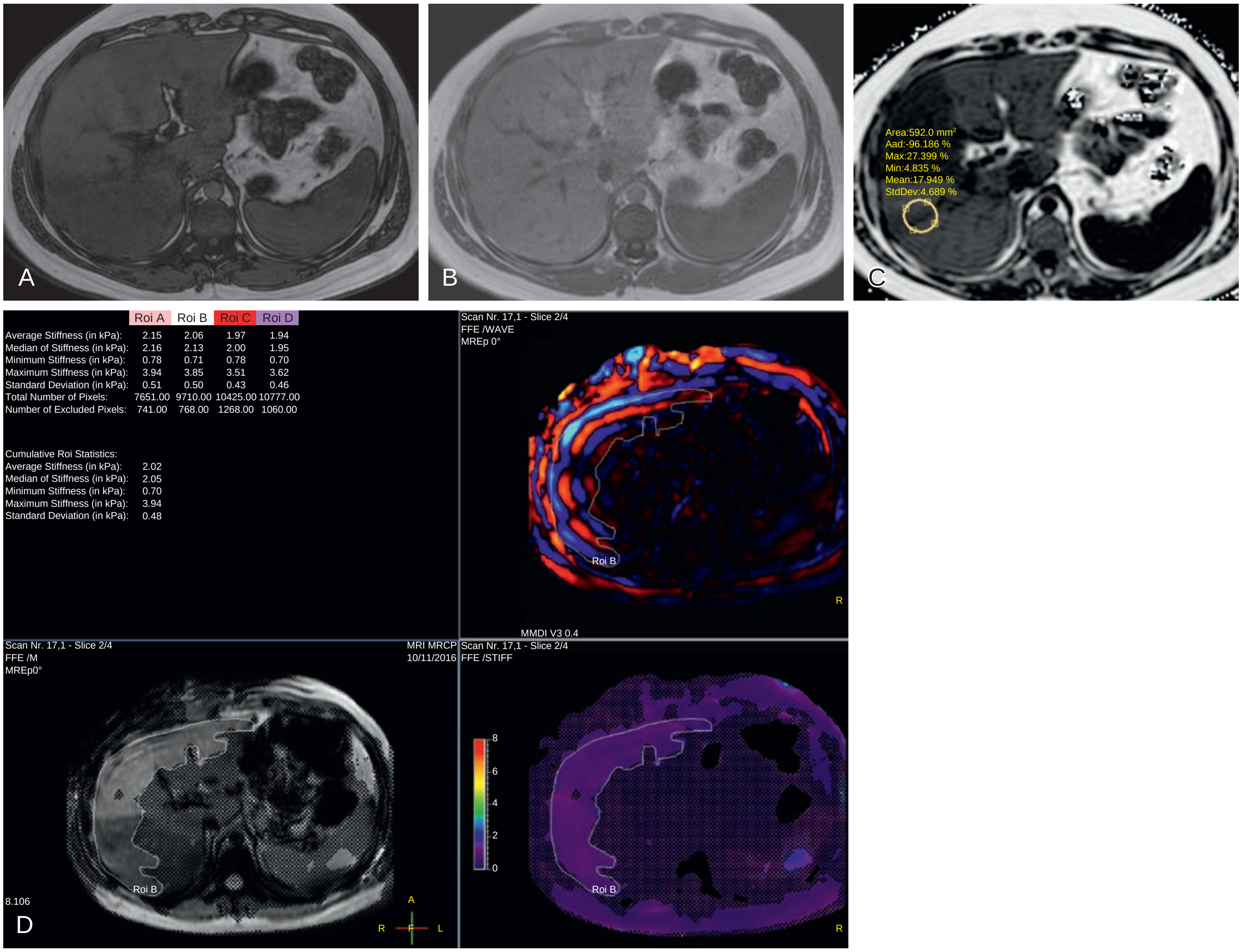

| | Roi A | Roi B | Roi C | Roi D |
|---|---|---|---|---|
| Average Stiffness (in kPa): | 2.15 | 2.06 | 1.97 | 1.94 |
| Median of Stiffness (in kPa): | 2.16 | 2.13 | 2.00 | 1.95 |
| Minimum Stiffness (in kPa): | 0.78 | 0.71 | 0.78 | 0.70 |
| Maximum Stiffness (in kPa): | 3.94 | 3.85 | 3.51 | 3.62 |
| Standard Deviation (in kPa): | 0.51 | 0.50 | 0.43 | 0.46 |
| Total Number of Pixels: | 7651.00 | 9710.00 | 10425.00 | 10777.00 |
| Number of Excluded Pixels: | 741.00 | 768.00 | 1268.00 | 1060.00 |

| Cumulative Roi Statistics: | |
|---|---|
| Average Stiffness (in kPa): | 2.02 |
| Median of Stiffness (in kPa): | 2.05 |
| Minimum Stiffness (in kPa): | 0.70 |
| Maximum Stiffness (in kPa): | 3.94 |
| Standard Deviation (in kPa): | 0.48 |

**Figure 89.4. Fatty liver in an 18-year-old boy with elevated BMI and abnormal liver function tests.** (A) Out-of-phase and (B) in-phase MR images of a fatty liver show extensive fatty infiltration evidenced by loss of signal on the opposed phase image compared with the in-phase image. Notice a large wedge-shaped region of focal fatty sparing involving segments 5 and 8 within the right hepatic lobe. (C) Liver fat fraction was estimated at 17.9% (normal is <5%). (D) MR elastography in this patient shows a mean shear stiffness value of 2.02 kPa (range 1.94–2.15 kPa), which is within normal limits.

treatment of parenchymal iron deposition to limit toxicity and avoid complications.

***Imaging Findings.*** Ultrasound is not helpful for the detection of iron deposition but may show findings of cirrhosis, portal venous hypertension, or HCC late in the disease. Noncontrast CT may show increased attenuation of the liver (>72 HU), but this is a late finding with a sensitivity of approximately 60% and may be seen with other conditions such as amiodarone therapy or glycogen storage disease (GSD).[32]

MR is the imaging modality of choice for confirming the diagnosis, determining severity, and monitoring therapy in persons with hemochromatosis. Excess iron deposition causes a proportional decrease in signal intensity on T1- and T2-weighted sequences and is most pronounced on gradient echo sequences. Skeletal muscle is relatively unaffected by iron deposition and serves as a good internal reference to compare the signal intensity of affected abdominal organs and bone marrow, which will be hypointense to skeletal muscle. On in-phase and out-of-phase imaging, decreased signal intensity is seen in the affected organs on the in-phase sequence (an opposite finding from steatosis). The key findings in HH are low signal intensity within the liver and pancreas on T2-weighted images (Fig. 89.5). Patients with reticuloendothelial iron deposition demonstrate low signal in the liver, spleen, and bone marrow (Fig. 89.6) with sparing of the pancreas.[27]

There are two main methods of MRI liver iron quantification: signal intensity ratio and relaxometry.[33] Signal intensity ratio is widely used because it is accurate and easy to perform. This method takes advantage of the effect of iron on adjacent proton spins; iron causes rapid dephasing of spins/loss of coherence with resultant loss of signal on long TE images (T2- or T2*-weighted). This effect is more pronounced on gradient echo images due to the lack of a 180-degree refocusing pulse. Signal intensity ratio is obtained by comparing the signal intensity of the liver with skeletal muscle on gradient echo imaging at varying TE and flip angles, and the values obtained are used to quantify iron deposition.[34] An online calculator is available.[35] The main limitation of this technique is that high levels of iron cannot be measured and are reported as greater than 350 umol/g.[35]

Relaxometry estimates iron content by measuring the loss of transverse magnetization caused by iron susceptibility over increasing values of TE.[36] Signal loss occurs in the liver with increasing TE values, and the rate of signal decay is measured as a constant

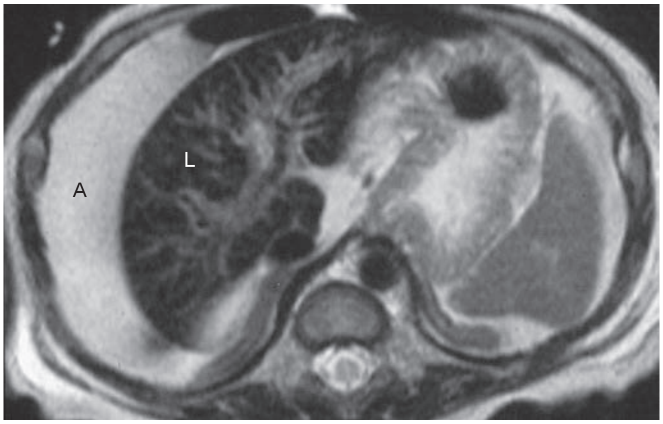

**Figure 89.5. Primary hemochromatosis in an infant with multiorgan system failure.** Axial T2-weighted MR image reveals extensive ascites *(A)* surrounding a liver *(L)* of low signal intensity. *(Courtesy of Lynn Fordham, MD, University of North Carolina–Chapel Hill.)*

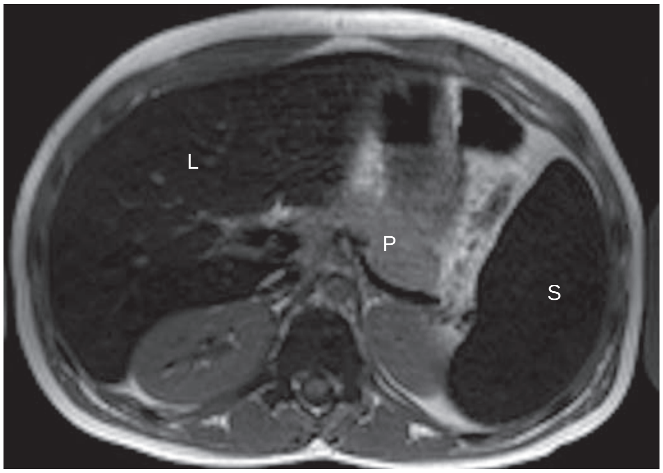

**Figure 89.6. Transfusional iron overload.** T1-weighted MR image of the abdomen in a 13-year-old male with sickle cell disease on chronic transfusional therapy shows marked hypointensity of the liver *(L),* spleen *(S),* and vertebral bone marrow with sparing of the pancreas *(P),* consistent with transfusional iron overload.

(T2 or T2* depending on whether spin echo or gradient echo techniques are used). Reciprocal values of the signal decay constant, R2 or R2*, have also been used as they provide direct correlation with liver iron content (LIC).[33] In general, R2* values are more sensitive for low levels of iron and are faster to acquire (performed with GRE techniques) but are inaccurate at higher iron levels, while R2 values are less susceptible to artifact or hardware/scanner differences but take longer to perform.[33] R2 and R2* methods of estimating LIC are statistically equivalent in children when LIC is less than 20 mg/g.[37]

***Treatment.*** Treatment aims to reduce iron levels and relies on either scheduled phlebotomy or chelation therapy, depending on the etiology.[38] MR quantification of liver iron concentration may be used to follow treatment regimes, obviating the need for liver biopsies.

## GLYCOGEN STORAGE DISEASE

***Overview.*** The GSDs are autosomal recessive disorders with abnormal storage or utilization of glycogen.[39] In the postprandial period, glucose is stored in the liver and muscle in the form of glycogen, which can then be released for energy during periods of starvation or high energy demand. Mutations in genes resulting in deficiencies of the enzymes involved in glycogen synthesis, degradation, or regulation result in GSDs.[40] GSDs are a heterogeneous group of disorders with varying time of onset, severity of disease, and pattern of organ involvement. Fifteen types of GSD have been identified. The most common forms of GSD are types I (von Gierke), type III (Cori), and type IV (Andersen disease or amylopectinosis).

***Clinical Presentation.*** Enzyme deficiencies that affect the liver impair hepatic gluconeogenesis and glycogenolysis and cause hypoglycemia. Of these, type I GSD (von Gierke disease) is the most common. Patients with type I GSD have a deficiency of the enzyme glucose-6-phosphatase and usually present with hypoglycemia around 3 months of age.[41] While hypoglycemia is the dominant clinical finding in liver-related GSDs, these patients may also present with hepatomegaly, lethargy, and seizures related to hypoglycemia. GSDs affect muscles causing exercise intolerance, with weakness, cramps, and rhabdomyolysis.

Complications of GSD affecting the liver include steatosis and the development of hepatic adenomas,[42] which may be associated with poor metabolic control.[39] Hepatic adenomas in patients with GSD-I may be multiple and can be seen in 25% to 50% of patients.[42] Spontaneous intraperitoneal bleeding is a known complication due to rupture of a hepatic adenoma. Malignant transformation of hepatic adenomas to HCCs has been described but is rare.[43]

***Imaging Findings.*** Hepatic ultrasound surveillance is recommended every 12 to 24 months until age 16 years. If adenomas are detected, contrast-enhanced hepatic CT or MRI every 3 to 6 months are recommended.[44]

Ultrasound of the liver in patients with GSD-I usually show hepatomegaly and diffusely increased parenchymal echogenicity, which may be related to steatosis or glycogen deposition[45] (e-Fig. 89.7). Likewise, adenomas with varying degrees of echogenicity may also be present (e-Fig. 89.8).[46] It is difficult to distinguish adenomas from HCCs on ultrasound, but rapid enlargement of masses and elevated serum alpha-fetoprotein are worrisome for carcinoma.

CT shows similar features, with hepatomegaly from glycogen deposition in hepatocytes and low-attenuation related to steatosis. Because hepatic attenuation is increased by glycogen but decreased by fat, the CT findings are variable depending on which factor predominates. In younger patients without steatosis, the liver may actually be hyperdense due to the presence of excess glycogen in liver cells.[47] Masses may be relatively hyperdense on noncontrast CT compared with the background liver parenchyma. Adenomas may contain fat or hemorrhage, and a small number will show areas of coarse internal calcification, presumably related to necrosis. Arterial enhancement and washout on portal venous phases is diagnostic of HCC in the cirrhotic liver on dynamic contrast-enhanced CT but may be seen in some patients with GSD and hepatic adenomas.[48]

On MRI, diffuse hepatic steatosis is readily demonstrable on chemical shift images. Adenomas are of hepatocellular origin, and are usually T1 isointense to mildly hyperintense and hyperintense on T2-weighted images. After Gadoxetate disodium (Gd-EOB-DTPA) administration, adenomas usually enhance during the arterial phase with washout on later phases. During the hepatocyte phase of enhancement, adenomas are typically hypointense to the surrounding liver (Fig. 89.9).[49,50] An enhancing pseudocapsule can be seen in up to a third of hepatic adenomas, and some lesions show heterogeneous internal enhancement with areas of increased T1 signal resulting from hemorrhage or fat.[50]

***Treatment.*** Management of liver-related GSD centers on prevention of severe hypoglycemic episodes with frequent oral glucose polymer/cornstarch administration.[39] Infants may also require continuous feeds overnight via a nasogastric or gastrostomy

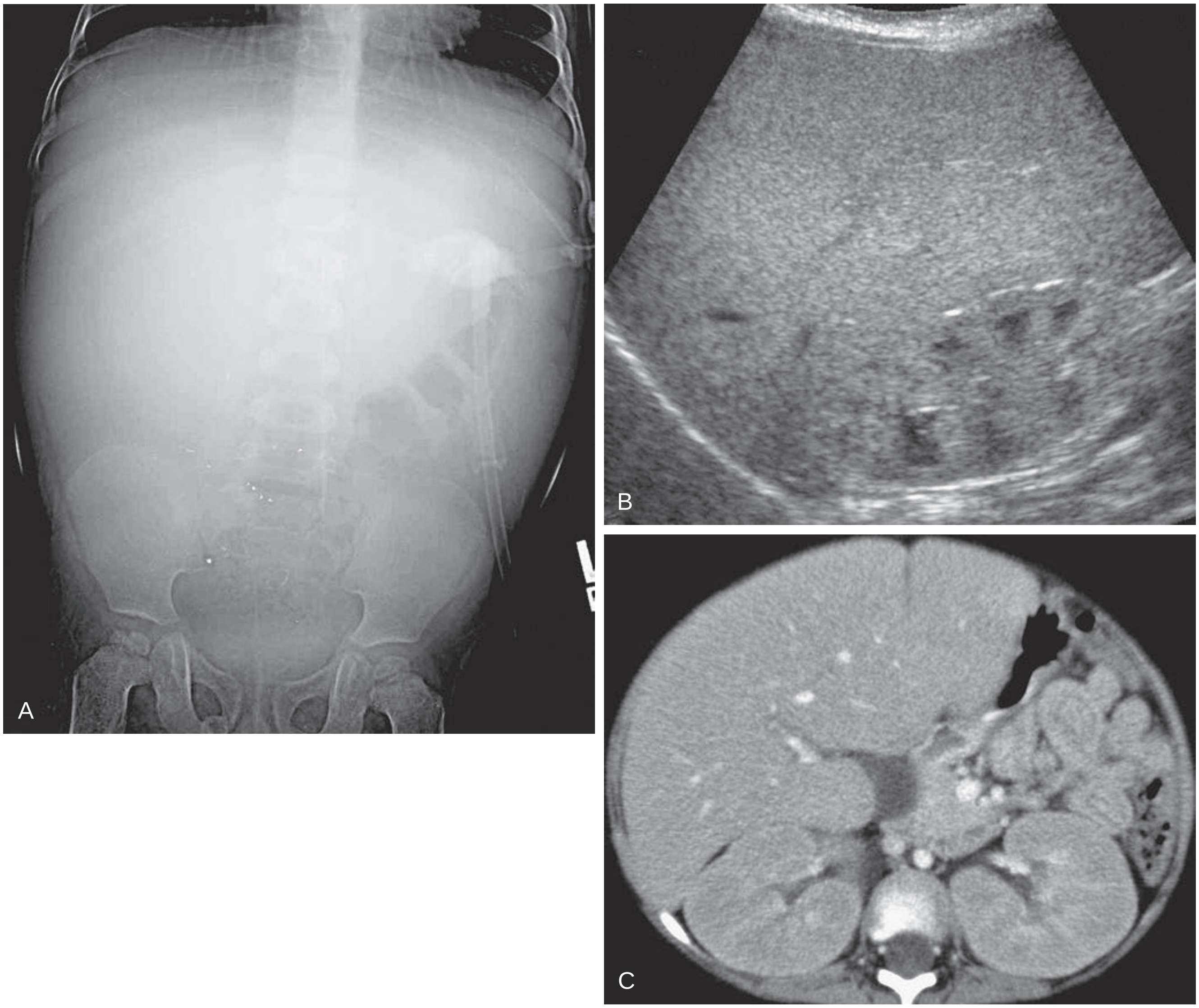

**e-Figure 89.7. Glycogen storage disease in a 3-year-old boy with abdominal distension and elevated liver function enzymes.** (A) Abdominal radiograph shows mass effect from diffuse hepatomegaly. Punctate radiodense foci over the lower abdomen were artifactual. (B) Longitudinal ultrasound of the right upper quadrant shows hepatomegaly and diffusely increased hepatic echogenicity. The renal cortex also is hyperechoic. (C) Axial contrast-enhanced CT reveals hepatomegaly and nephromegaly.

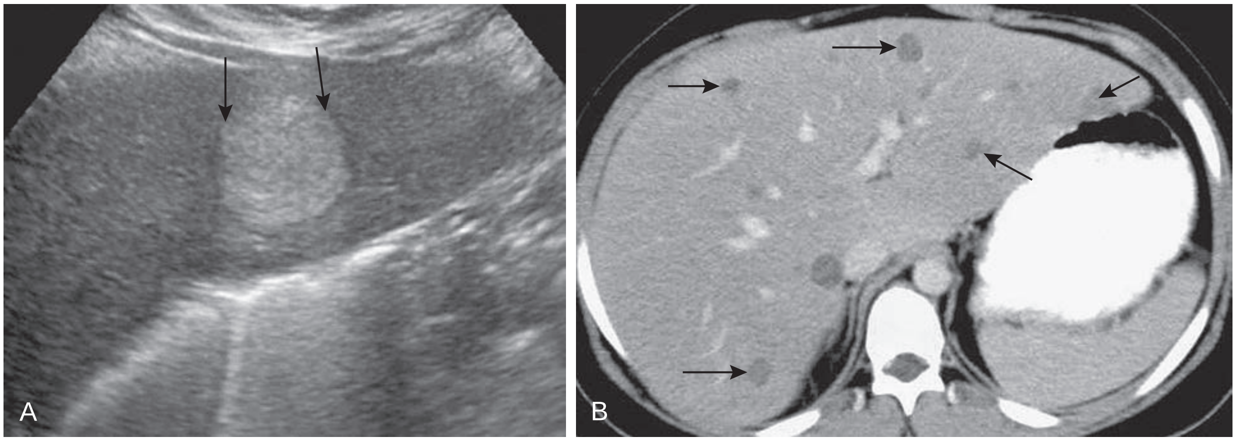

**e-Figure 89.8. Glycogen storage disease in a 9-year-old boy with hepatic adenomas.** (A) Longitudinal ultrasound reveals a hyperechoic mass with enhanced through-transmission and refractory shadowing at the margins *(arrows),* typical of a hepatic adenoma. (B) Enhanced axial computed tomography demonstrates numerous scattered, low-attenuation, well-defined hepatic adenomas *(arrows).*

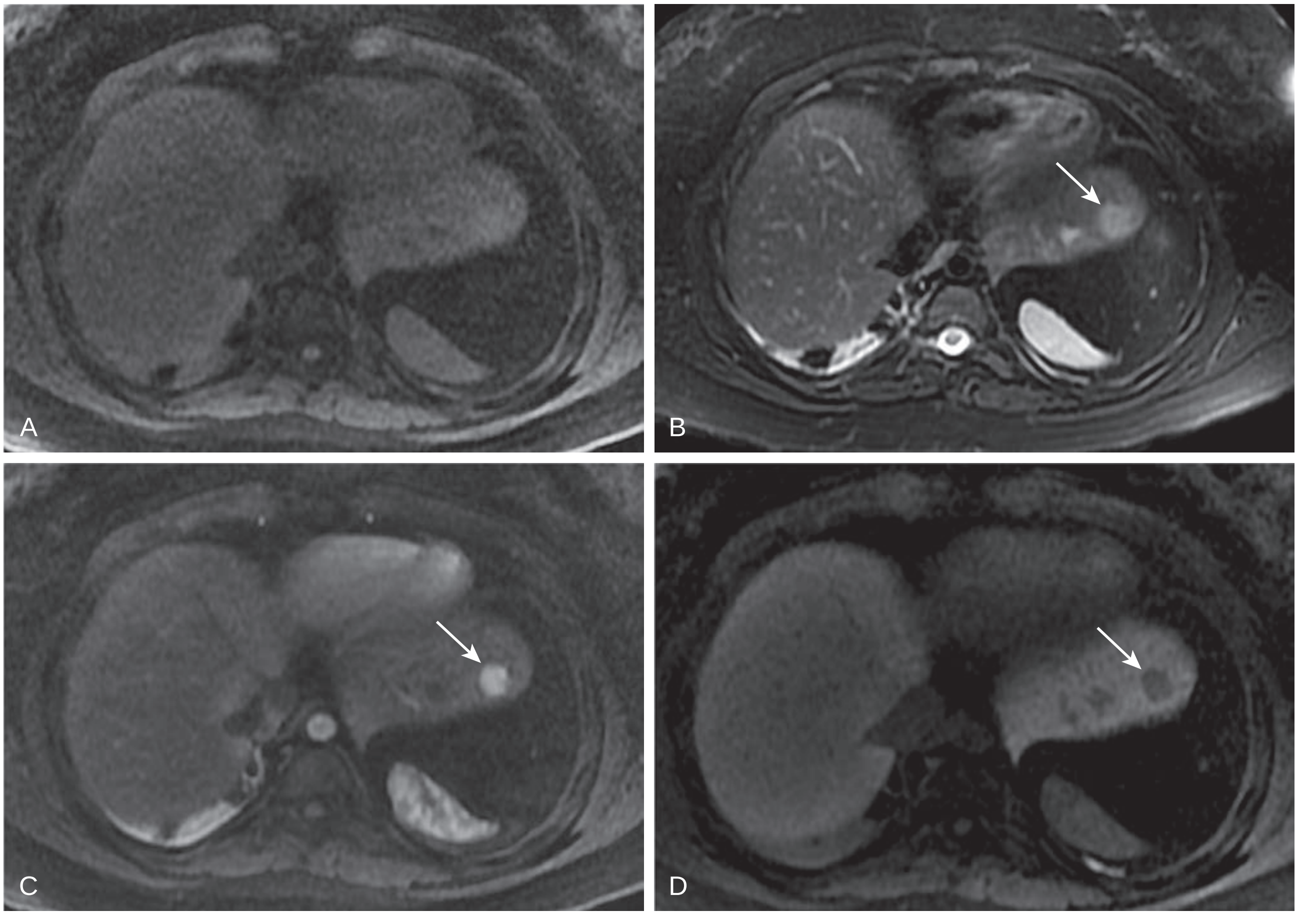

**Figure 89.9. Hepatic adenoma in an adolescent patient.** (A) Axial T1-weighted fat suppressed MR image, (B) axial T2-weighted fat suppressed MR image, (C) axial T1-weighted MR image obtained in the early arterial phase, and (D) axial T1-weighted MR image obtained during the delayed hepatocyte phase after Gd-EOB-DTPA administration show the typical appearance of a hepatic adenoma. There is a T1-isointense, T2-hyperintense round lesion (*arrow* in B, C and D) in the superior left hepatic lobe, which is arterially hyperenhancing compared with the background liver. This lesion shows washout or portal venous hypoenhancement on the delayed images. In a normal noncirrhotic liver, these findings are compatible with a hepatic adenoma.

tube to prevent hypoglycemia.[51] Liver transplantation has been performed for some patients with HCC, liver failure, or poor metabolic control. Transplantation improves glucose homeostasis in some patients.[52]

## GAUCHER DISEASE

***Overview.*** Gaucher disease (GD) is an autosomal recessive lysosomal storage disorder resulting from deficiency of the lysosomal enzyme glucocerebrosidase. GD is more common in patients of Ashkenazi-Jewish descent but is seen in other populations as well. There are three main types of GD, but the type I form (nonneuronopathic) accounts for over 90% of cases. Deficiency of glucocerebrosidase results in accumulation of undegraded glucosylceramide in the reticuloendothelial system of the bone marrow, spleen, and liver causing cellular and organ dysfunction.[53,54]

***Clinical Presentation.*** The clinical manifestations of GD include hepatosplenomegaly, anemia, thrombocytopenia, and bone disease. Thrombocytopenia and clinically significant bleeding may result from splenic sequestration of platelets. Bone disease is the most important cause of long-term morbidity, and poorly controlled disease is characterized by episodes of acute crises with bone infarcts and avascular necrosis. Patients also have low bone mineral density, which puts them at risk for fractures. Over 90% of patients have radiographic evidence of bone disease, and bone crises are more common in patients under 10 years of age.[55] The diagnosis of GD can be made by detecting decreased levels of glucocerebrosidase activity in peripheral leukocytes. Lipid-laden macrophages (Gaucher cells) may also be seen in bone marrow or liver biopsy specimens.

***Imaging Findings.*** Abdominal imaging of GD is nonspecific. Hepatomegaly and splenomegaly are seen in the majority of patients. Liver volumes in GD type 1 patients are usually approximately two times normal.[54] The Gaucher cells may accumulate and form nodules that may be seen with ultrasound or MRI. These nodules may show a variable sonographic appearance. On MRI, these nodules are usually hypointense on T1-weighted and hyperintense on T2-weighted imaging.[54] Areas of fibrosis and fibrous septa are seen in the enlarged liver.

In many cases, the splenic enlargement is out of proportion to hepatic enlargement and dominates the clinical presentation. Splenic volumes in type 1 GD may be enlarged 5 to 50 times (e-Fig. 89.10). Focal splenic lesions are not uncommon and may reflect clusters of Gaucher cells or extramedullary hematopoiesis.[54] Splenic infarcts may occur as a result of the massive splenomegaly and can be seen in up to a third of patients on MRI.[56] Abnormal marrow infiltration by Gaucher cells can be seen on MRI and are usually hypointense on T1-weighted images with corresponding hyperintensity on T2-weighted images and fat-suppressed

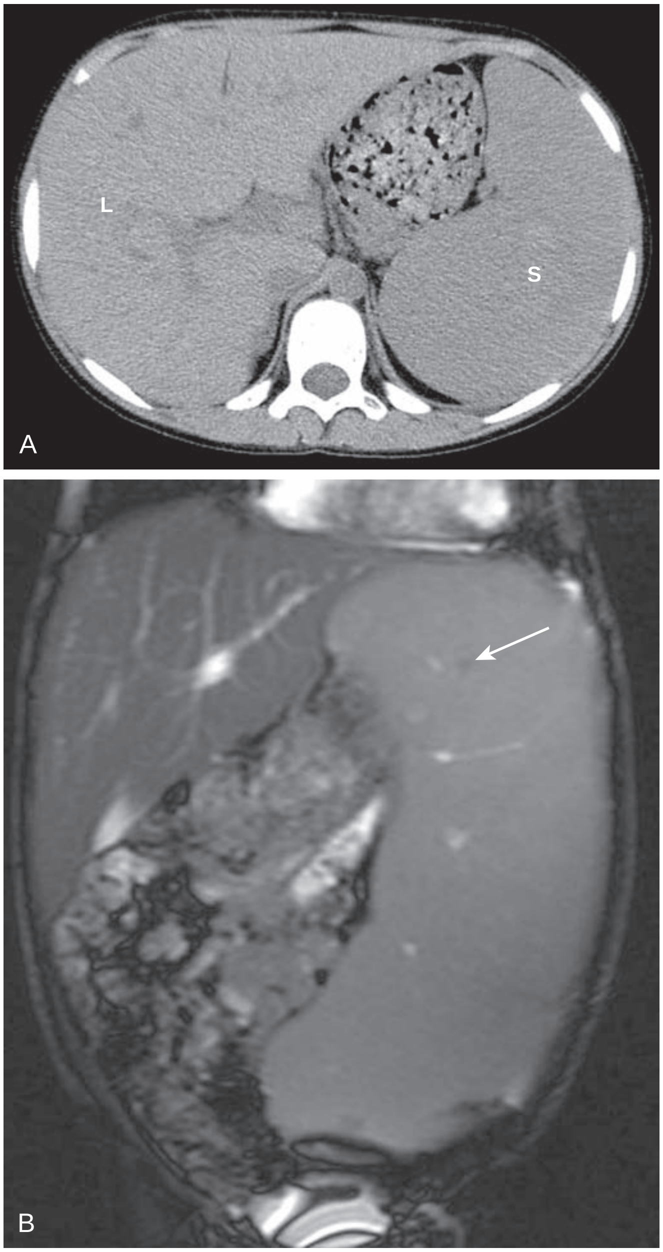

**e-Figure 89.10. Gaucher disease in a 10-year-old boy.** (A) CT of the abdomen without contrast demonstrates hepatosplenomegaly. (B) Coronal T2-weighted MR image demonstrates hepatosplenomegaly with small hypointense foci in the spleen suggestive of infarcts or Gaucher cells *(arrow)*. *L,* Liver; *S,* spleen.

fluid-sensitive sequences.[57] Bone marrow edema from acute crises can also be seen, and poor disease control in some patients can cause progression to avascular necrosis.[57]

***Treatment.*** Early treatment of GD with enzyme replacement therapy can improve outcomes.[58] Liver and spleen volumes correlate with disease severity and are used in the initial phenotyping of GD.[59] The abnormal T1 hypointense marrow signal related to marrow infiltration also resolves after enzyme therapy, with conversion back to fatty marrow signal.[60]

## ALPHA-1 ANTITRYPSIN DEFICIENCY

***Overview.*** Alpha-1 antitrypsin (AAT) deficiency is an autosomal recessive disorder caused by abnormal protein folding and accumulation of AAT in hepatocytes. AAT is caused by mutations in the *SERPINA1* gene located in the long arm of chromosome 14.[61] AAT is a protease inhibitor that degrades elastase and other proteolytic enzymes in the body. Uninhibited elastase activity in the lungs causes early-onset emphysema in a basilar-predominant distribution. Accumulation of polymerized AAT in hepatocytes causes liver inflammation, fibrosis, and organ dysfunction. Necrotizing panniculitis is a documented but rare manifestation of AAT deficiency.[62]

***Clinical Presentation.*** Liver manifestations of AAT are more common in the first 3 decades of life, with pulmonary airflow limitation occurring later in the disease course.[63] The disease can present early, with neonatal hepatitis and cholestasis, findings that can be initially concerning for biliary atresia.[64] Hepatomegaly, elevated liver function tests, and conjugated hyperbilirubinemia may be present. Clinically, infants may have dark stools and pale urine. Low serum levels of AAT can suggest the disease, and genetic testing can identify the mutated alleles. Both children and adults can progress to end-stage liver disease and cirrhosis related to AAT deficiency, and some patients develop HCC.

***Imaging Findings.*** Infants presenting in the first months of life with neonatal cholestasis and elevated direct bilirubin levels may undergo scintigraphy with the intention of excluding biliary atresia.[65] However, hepatobiliary scans are not helpful in distinguishing AAT from biliary atresia, as both entities can have radiotracer uptake in the liver without excretion into the bile ducts and bowel as a result of a paucity of intralobular bile ducts in some cases of AAT deficiency (e-Fig. 89.11). Abdominal ultrasound may show hepatomegaly and a normal gallbladder in AAT, but a small number of patients with biliary atresia may also have a gallbladder. Complications of AAT such as cirrhosis and HCC can be seen on ultrasound, CT, or MR.

***Treatment.*** There is no specific treatment for AAT deficiency liver disease, but obesity can contribute to disease severity. The prognosis is extremely variable, depending on disease severity, age at diagnosis, and therapeutic interventions. Liver transplantation has a 5-year survival rate of 85% in patients with AAT associated end-stage liver disease.[66]

## WILSON DISEASE

***Overview.*** Wilson disease or hepatolenticular degeneration is an autosomal recessive disorder localized to chromosome 13 that results in impaired biliary excretion of copper. Copper accumulation leads to chronic liver disease ranging from steatosis, hepatitis, and eventually cirrhosis eventually in untreated patients.[67] The brain is also affected, particularly the basal ganglia and midbrain, with neuropsychiatric and parkinsonian syndromes seen in older patients.

***Clinical Presentation.*** Patients with Wilson disease can present acutely with fulminant liver failure (encephalopathy, coagulopathy) or Coombs-negative hemolysis, or chronically with neuropsychiatric symptoms and chronic liver disease. Movement disorders are common due to involvement of the extrapyramidal pathway. Laboratory tests can suggest the diagnosis, with many patients having low serum ceruloplasmin levels and elevated serum and 24-hour urinary copper. Slit-lamp examination of the eyes may reveal Kayser–Fleischer rings or sunflower cataracts. Kayser–Fleischer rings are seen in over 90% of patients with neurologic disease, but only about half of patients with liver disease. Biopsy allows for measurement of hepatic copper concentration, which is considered the single most important test for diagnosing hepatolenticular degeneration.[67] Hepatic copper levels over 250 ug/mg dry weight of liver are diagnostic.[67]

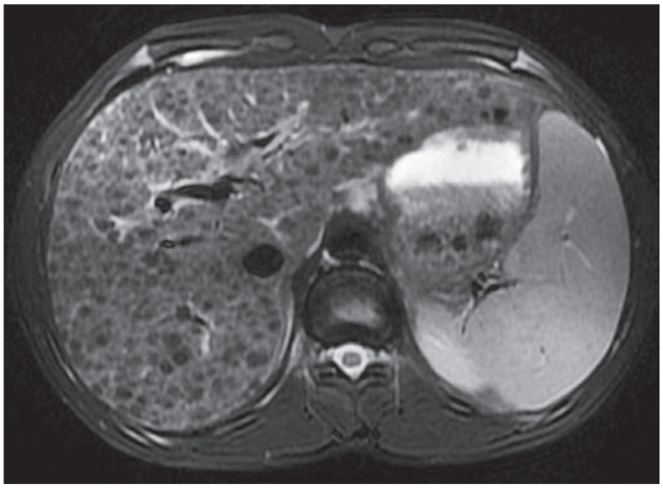

**Figure 89.12. Wilson disease in a 17-year-old male.** Axial T2-weighted MR image shows a cirrhotic liver with innumerable, subcentimeter, hypointense nodules, which are typical of cirrhotic regenerative nodules. Imaging findings of the liver in patients with Wilson disease are typically nonspecific and only show the sequelae of liver inflammation caused by copper deposition.

***Imaging Findings.*** Imaging findings in patients with liver-predominant Wilson disease are nonspecific and range from fatty deposition to inflammation and fibrosis/cirrhosis (Fig. 89.12). Noncontrast CT may show increased attenuation of the liver, which has been attributed to copper deposition in hepatocytes.[68] However, this finding is infrequent and nonspecific. On occasions, focal liver lesions may be seen.[69] In patients with neurologic symptoms, brain MRI may show abnormal hyperintensity in the basal ganglia and midbrain on T2-weighted images.[70] Intrinsic T1-weighted hyperintensity may be seen in these areas as well in other patients with Wilson disease, but this finding has been attributed to the hyperammonemia/encephalopathy syndrome which sometimes accompanies liver-predominant Wilson disease.

***Treatment.*** The introduction of copper chelators into clinical practice radically changed medical therapy for Wilson disease. Many patients today can be medically managed with copper chelators (penicillamine, trientine) and zinc.[67] Patients with fulminant liver failure or medically-resistant disease are candidates for liver transplantation.

## CIRRHOSIS

***Overview.*** Cirrhosis is end-stage liver disease resulting from repeated liver injury and inflammation. It is characterized by parenchymal fibrosis and the development of regenerative nodules which distort the normal liver architecture. Once considered an irreversible process, it is now known that early fibrosis and cirrhosis are potentially reversible. While cirrhosis represents the end result of any chronic liver injury, a specific cause or etiology can be found in over 85% of cases, which has implications for treatment and screening of family members.[71] Some imaging patterns of cirrhosis are suggestive of an underlying etiology (for example, marked caudate hypertrophy in patients with Budd–Chiari syndromes), but are not specific enough to serve as stand-alone

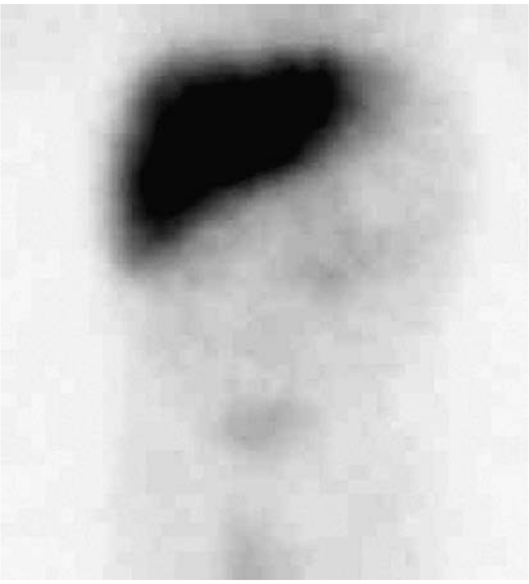

**e-Figure 89.11. AAT deficiency in a 6-week-old girl with poor weight gain and hyperbilirubinemia.** Biliary scintigraphy shows liver uptake of radiopharmaceutical without excretion into the biliary tree.

**BOX 89.2** Causes of Cirrhosis in Children

- Viral hepatitis
- Hepatic fibrosis
- Biliary atresia
- Primary biliary cirrhosis
- Cystic fibrosis
- Budd–Chiari syndrome
- Iron overload
- Chronic biliary obstruction
- $\alpha_1$-antitrypsin deficiency
- Glycogen storage disease
- Tyrosinemia
- Wilson disease
- Galactosemia
- Autosomal recessive polycystic kidney disease (hepatic fibrosis)
- Hereditary hemorrhagic telangiectasia

diagnostic criteria. Cirrhosis traditionally has been classified into three main categories depending on the size of the regenerative nodules: micronodular (Laënnec), with equal-sized nodules up to 3 mm; macronodular (postnecrotic), with variable-sized nodules ranging from 3 mm to 3 cm; and mixed cirrhosis.[72,73]

***Clinical Presentation.*** In children, cirrhosis is the result of many different disease processes, including biliary, postnecrotic, and metabolic causes (Box 89.2). Many patients with cirrhosis are asymptomatic, other than vague nonspecific complaints. When acutely symptomatic, the clinical presentation is determined by the complications of portal hypertension (encephalopathy, ascites, spontaneous bacterial peritonitis, variceal bleeding, HCC). On physical examination, the liver may be enlarged with a nodular edge. Other signs of portal hypertension and altered metabolic homeostasis may be seen including jaundice, spider nevi, palmar erythema, hypogonadism, gynecomastia, caput medusa, and esophageal varices on upper endoscopy.

***Imaging Findings.*** Ultrasound of the cirrhotic liver shows a heterogeneous echotexture with surface irregularity. Contrast-enhanced CT and MR show heterogeneous enhancement of the liver parenchyma and a nodular surface (Fig. 89.13). Fibrous bands may also be seen, which can be striking in some patients. Other morphologic changes include right lobe atrophy, with caudate and left lateral segment hypertrophy. There may also be widening of the gallbladder fossa. In patients with decompensated cirrhosis and portal hypertension, ascites, splenomegaly, and portosystemic collaterals are also seen.

Regenerative nodules are common in cirrhotic livers and represent a reparative process in the liver in response to chronic injury.[74] Regenerative nodules reiterate normal hepatic parenchymal signal and enhancement characteristics. Regenerative nodules are usually hypointense to background cirrhotic liver parenchyma on T2-weighted MR images, without arterial hyperenhancement (Fig. 89.14). Dysplastic nodules (low-grade and high-grade) and siderotic nodules are also common findings in cirrhotic livers. Dysplastic nodules harbor hisologically abnormal cells. Low-grade dysplastic nodules are isointense to hyperintense on T1-weighted images when compared with the background liver, without arterial hyperenhancement. Low-grade nodules are usually isointense to the liver on T2-weighted images but may be hypointense in the case of iron accumulation.[74] High-grade nodules are hyperintense to liver on T2-weighted images and may be difficult to distinguish from HCC on imaging alone. The term *siderotic nodule* refers to iron deposition in regenerative or dysplastic nodules. The Liver Imaging-Reporting and Data System (LI-RADS) is used in cross-sectional imaging of cirrhotic livers in an attempt to standardize the degree of certainty regarding findings seen on imaging, however, it is not categorically used for pediatric liver lesion characterization at this time.[74] Lesions are classified from LI-RADS 1 to 5, with LI-RADS 1 being definitely benign and LI-RADS 5 representing definite HCC. Findings concerning for HCC include masslike configuration, arterial hyperenhancement, portal venous washout, tumor thrombus, and growth by more than 1 cm over a 12-month interval. Focal iron sparing in a siderotic liver or nodule is also concerning for the development of HCC. MRE is useful in patients with chronic liver disease. Early identification of at-risk patients can result in earlier treatment, potentially averting progression to late-stage fibrosis and cirrhosis (e-Fig. 89.15).

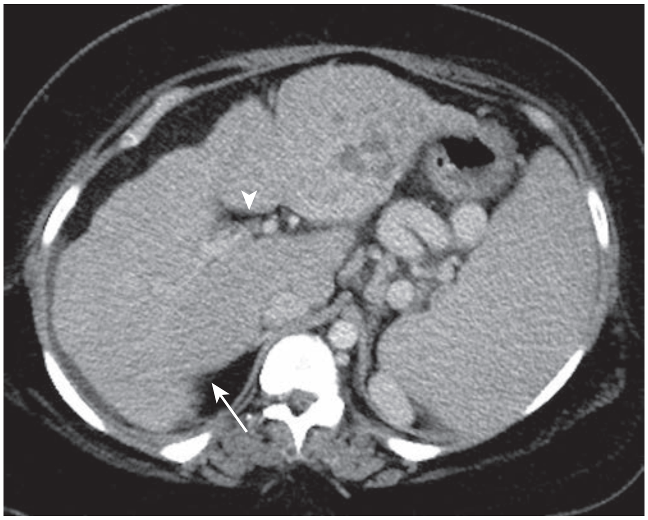

**Figure 89.13. Cirrhosis in a 16-year-old male.** Contrast-enhanced CT of the liver shows a shrunken, nodular liver, consistent with cirrhosis. Linear hypoattenuating lesions in the left hepatic lobe reflect mild intrahepatic biliary ductal dilatation. There is evidence of portal hypertension, with splenomegaly and perisplenic collaterals. Notice the "hepatic-notch" sign *(arrow),* the result of right lobe atrophy, and the relative prominence of the hilar periportal space *(arrowhead)* due to medial segment atrophy.

***Treatment.*** Treatment for cirrhosis depends on the cause and extent of liver damage. The goals of treatment are to slow the progression and to prevent or treat symptoms and complications of cirrhosis. Chemotherapy and ablative therapies can be used as a bridge to transplant or in patients who are not candidates for liver transplantation.

## KEY POINTS

- NAFLD is the most common cause of chronic liver disease in childhood.
- MR can be used to quantify hepatic steatosis and MRE is useful for monitoring the development of hepatic fibrosis in patients with NAFLD.
- Pancreatic iron deposition is a characteristic feature of primary or hereditary hemochromatosis. Splenic iron deposition is seen in transfusional iron overload.
- Patients with alpha-1 antitrypsin deficiency (AAT) may present in a fashion similar to patients with biliary atresia, with similar findings on hepatobiliary scans. Abdominal ultrasound performed in patients with AAT usually shows a normal gallbladder.
- Arterial hyperenhancement and portal venous phase washout of a mass in a cirrhotic liver is HCC until proven otherwise.
- Focal iron sparing in a siderotic liver or siderotic nodule should be viewed with suspicion for HCC, as tumor cells do not usually take up iron to any significant degree.

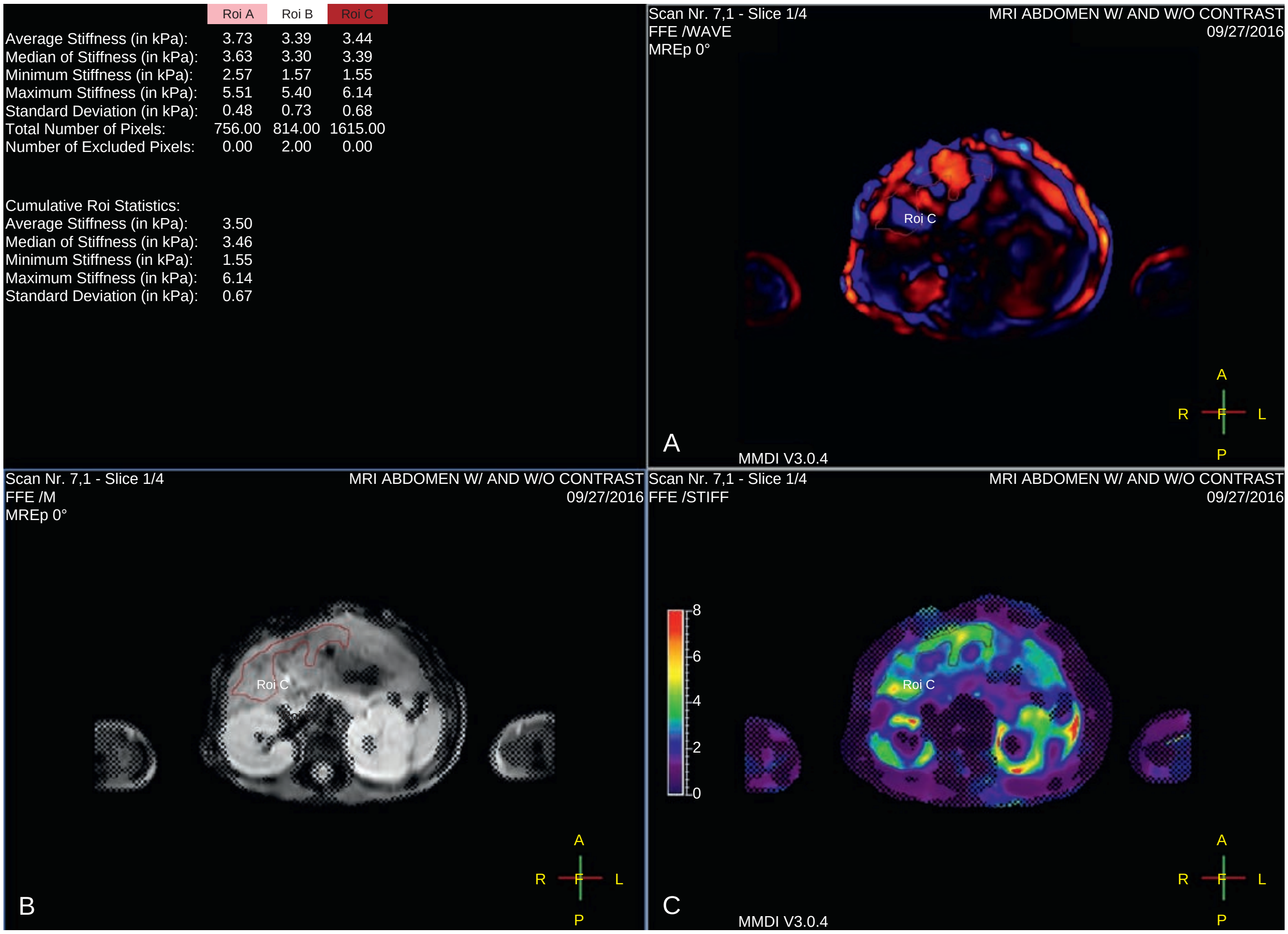

| | Roi A | Roi B | Roi C |
|---|---|---|---|
| Average Stiffness (in kPa): | 3.73 | 3.39 | 3.44 |
| Median of Stiffness (in kPa): | 3.63 | 3.30 | 3.39 |
| Minimum Stiffness (in kPa): | 2.57 | 1.57 | 1.55 |
| Maximum Stiffness (in kPa): | 5.51 | 5.40 | 6.14 |
| Standard Deviation (in kPa): | 0.48 | 0.73 | 0.68 |
| Total Number of Pixels: | 756.00 | 814.00 | 1615.00 |
| Number of Excluded Pixels: | 0.00 | 2.00 | 0.00 |

| Cumulative Roi Statistics: | |
|---|---|
| Average Stiffness (in kPa): | 3.50 |
| Median of Stiffness (in kPa): | 3.46 |
| Minimum Stiffness (in kPa): | 1.55 |
| Maximum Stiffness (in kPa): | 6.14 |
| Standard Deviation (in kPa): | 0.67 |

**e-Figure 89.15. MR elastography performed in a 3 year-old male with autosomal recessive polycystic kidney disease.** (A) The cinegraphic image shows the propagation of the shear waves into the liver. (B) This image shows the ROI measurements obtained in kilopascals (kPAs). In this case, stiffness measurements average 3.5 kPAs consistent with mild to moderate fibrosis. (C) The elastogram depicts a tissue stiffness map displaying pixel intensity proportionally to stiffness.

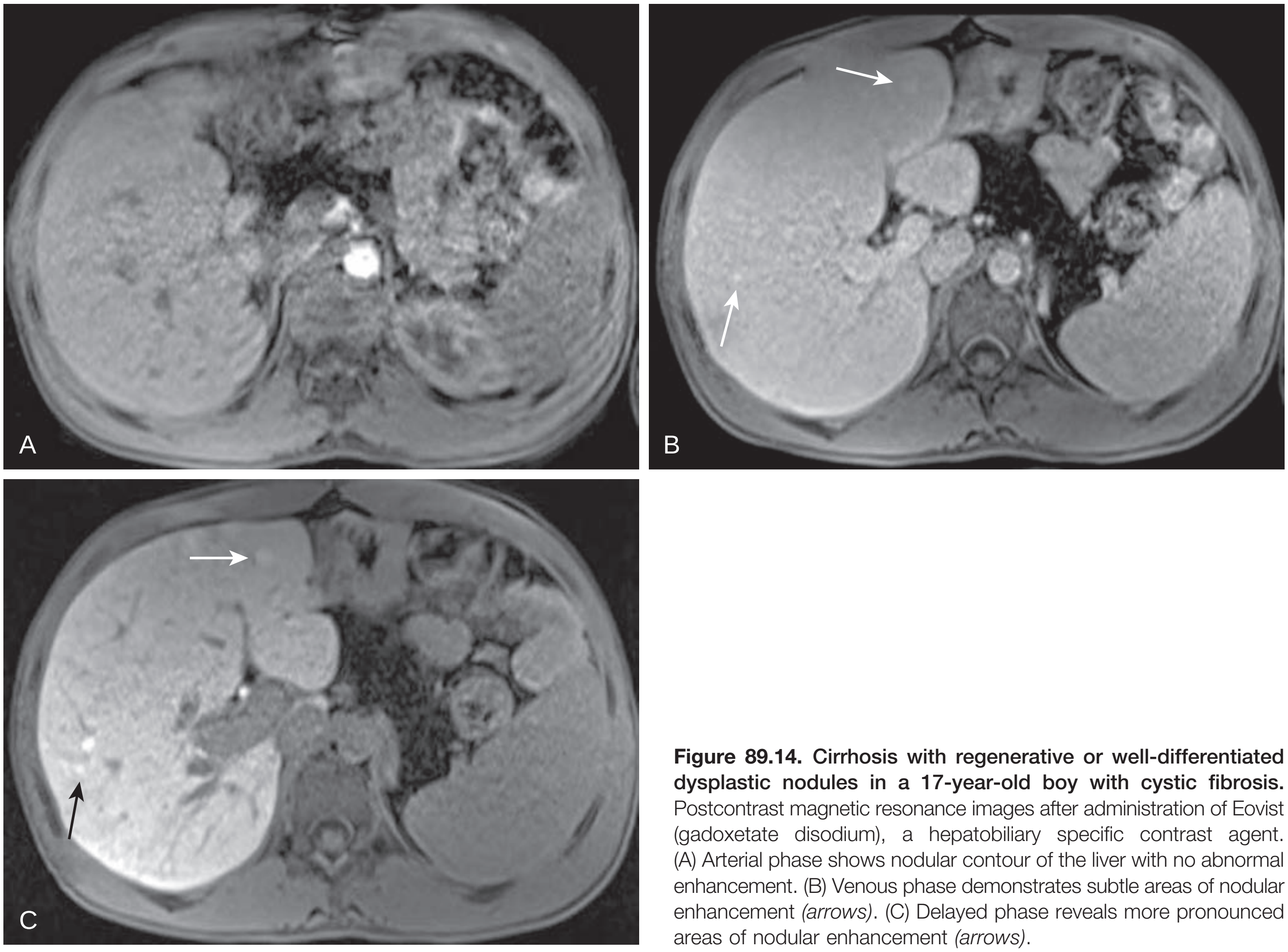

**Figure 89.14. Cirrhosis with regenerative or well-differentiated dysplastic nodules in a 17-year-old boy with cystic fibrosis.** Postcontrast magnetic resonance images after administration of Eovist (gadoxetate disodium), a hepatobiliary specific contrast agent. (A) Arterial phase shows nodular contour of the liver with no abnormal enhancement. (B) Venous phase demonstrates subtle areas of nodular enhancement *(arrows)*. (C) Delayed phase reveals more pronounced areas of nodular enhancement *(arrows)*.

## SUGGESTED READINGS

Binkovitz LA, El-Youssef M, Glaser KJ, et al. Pediatric MR elastography of hepatic fibrosis: principles, technique and early clinical experience. *Pediatr Radiol*. 2012;42:402–409.

Boll DT, Merkle EM. Diffuse liver disease: strategies for hepatic CT and MR imaging. *Radiographics*. 2009;29:1591–1614.

Chavhan GB, Shelmerdine S, Jhaveri K, et al. Liver MR imaging in children: current concepts and technique. *Radiographics*. 2016;36:1517–1532.

Ma X, Holalkere NS, Kambadakone RA, et al. Imaging-based quantification of hepatic fat: methods and clinical applications. *Radiographics*. 2009;29:1253–1277.

Purysko AS, Remer EM, Coppa CP, et al. LI-RADS: a case-based review of the new categorization of liver findings in patients with end-stage liver disease. *Radiographics*. 2012;32:1977–1995.

Seigelman ES, Mitchell DG, Rubin R, et al. Parenchymal versus reticuloendothelial iron overload in the liver: distinction with MR imaging. *Radiology*. 1991;179:361–366.

Towbin AJ, Serai SD, Podberesky DJ. Magnetic resonance imaging of the pediatric liver: imaging of steatosis, iron deposition, and fibrosis. *Magn Reson Imaging Clin N Am*. 2013;21:669–680.

## REFERENCES

Full references for this chapter can be found on www.expertconsult.com.

## REFERENCES

1. Bravo AA, Sheth SG, Chopra S. Liver biopsy. *N Engl J Med*. 2001;344:495–500.
2. Ratziu V, Charlotte F, Heurtier A, et al. Sampling variability of liver biopsy in nonalcoholic fatty liver disease. *Gastroenterology*. 2005;128:1898–1906.
3. Regev A, Berho M, Jeffers LJ, et al. Sampling error and intraobserver variation in liver biopsy in patients with chronic HCV infection. *Am J Gastroenterol*. 2002;97:2614–2618.
4. Schwimmer JB, Deutsch R, Kahen T, et al. Prevalence of fatty liver in children and adolescents. *Pediatrics*. 2006;118:1388–1393.
5. Mencin AA, Lavine JE. Advances in pediatric nonalcoholic fatty liver disease. *Pediatr Clin North Am*. 2011;58:1375–1392, x.
6. Schwimmer JB, Deutsch R, Rauch JB, et al. Obesity, insulin resistance, and other clinicopathological correlates of pediatric nonalcoholic fatty liver disease. *J Pediatr*. 2003;143:500–505.
7. Schwimmer JB, Behling C, Newbury R, et al. Histopathology of pediatric nonalcoholic fatty liver disease. *Hepatology*. 2005;42:641–649.
8. Goyal NP, Schwimmer JB. The progression and natural history of pediatric nonalcoholic fatty liver disease. *Clin Liver Dis*. 2016;20:325–338.
9. Rashid M, Roberts EA. Nonalcoholic steatohepatitis in children. *J Pediatr Gastroenterol Nutr*. 2000;30:48–53.
10. Joseph AE, Saverymuttu SH, al-Sam S, et al. Comparison of liver histology with ultrasonography in assessing diffuse parenchymal liver disease. *Clin Radiol*. 1991;43:26–31.
11. Friedrich-Rust M, Ong MF, Herrmann E, et al. Real-time elastography for noninvasive assessment of liver fibrosis in chronic viral hepatitis. *AJR Am J Roentgenol*. 2007;188:758–764.
12. Barr RG, Ferraioli G, Palmeri ML, et al. Elastography assessment of liver fibrosis: society of radiologists in ultrasound consensus conference statement. *Radiology*. 2015;276:845–861.
13. Towbin AJ, Serai SD, Podberesky DJ. Magnetic resonance imaging of the pediatric liver: imaging of steatosis, iron deposition, and fibrosis. *Magn Reson Imaging Clin N Am*. 2013;21:669–680.
14. Ma X, Holalkere NS, Kambadakone RA, et al. Imaging-based quantification of hepatic fat: methods and clinical applications. *Radiographics*. 2009;29:1253–1277.
15. Liu CY, McKenzie CA, Yu H, et al. Fat quantification with IDEAL gradient echo imaging: correction of bias from T(1) and noise. *Magn Reson Med*. 2007;58:354–364.
16. Talwalkar JA, Yin M, Fidler JL, et al. Magnetic resonance imaging of hepatic fibrosis: emerging clinical applications. *Hepatology*. 2008;47:332–342.
17. Serai SD, Towbin AJ, Podberesky DJ. Pediatric liver MR elastography. *Dig Dis Sci*. 2012;57:2713–2719.
18. Chen J, Talwalkar JA, Yin M, et al. Early detection of nonalcoholic steatohepatitis in patients with nonalcoholic fatty liver disease by using MR elastography. *Radiology*. 2011;259:749–756.
19. Huwart L, Sempoux C, Vicaut E, et al. Magnetic resonance elastography for the noninvasive staging of liver fibrosis. *Gastroenterology*. 2008;135:32–40.
20. Binkovitz LA, El-Youssef M, Glaser KJ, et al. Pediatric MR elastography of hepatic fibrosis: principles, technique and early clinical experience. *Pediatr Radiol*. 2012;42:402–409.
21. Xanthakos SA, Podberesky DJ, Serai SD, et al. Use of magnetic resonance elastography to assess hepatic fibrosis in children with chronic liver disease. *J Pediatr*. 2014;164:186–188.
22. Pozzato C, Verduci E, Scaglioni S, et al. Liver fat change in obese children after a 1-year nutrition-behavior intervention. *J Pediatr Gastroenterol Nutr*. 2010;51:331–335.
23. Huang MA, Greenson JK, Chao C, et al. One-year intense nutritional counseling results in histological improvement in patients with non-alcoholic steatohepatitis: a pilot study. *Am J Gastroenterol*. 2005;100:1072–1081.
24. Bonis PA, Friedman SL, Kaplan MM. Is liver fibrosis reversible? *N Engl J Med*. 2001;344:452–454.
25. Hammel P, Couvelard A, O'Toole D, et al. Regression of liver fibrosis after biliary drainage in patients with chronic pancreatitis and stenosis of the common bile duct. *N Engl J Med*. 2001;344:418–423.
26. Falize L, Guillygomarc'h A, Perrin M, et al. Reversibility of hepatic fibrosis in treated genetic hemochromatosis: a study of 36 cases. *Hepatology*. 2006;44:472–477.
27. Siegelman ES, Mitchell DG, Rubin R, et al. Parenchymal versus reticuloendothelial iron overload in the liver: distinction with MR imaging. *Radiology*. 1991;179:361–366.
28. Niederau C, Strohmeyer G, Stremmel W. Epidemiology, clinical spectrum and prognosis of hemochromatosis. *Adv Exp Med Biol*. 1994;356:293–302.
29. Ware HM, Kwiatkowski JL. Evaluation and treatment of transfusional iron overload in children. *Pediatr Clin North Am*. 2013;60:1393–1406.
30. Edwards CQ, Kushner JP. Screening for hemochromatosis. *N Engl J Med*. 1993;328:1616–1620.
31. Pippard MJ. Detection of iron overload. *Lancet*. 1997;349:73–74.
32. Guyader D, Gandon Y, Deugnier Y, et al. Evaluation of computed tomography in the assessment of liver iron overload. A study of 46 cases of idiopathic hemochromatosis. *Gastroenterology*. 1989;97:737–743.
33. Sirlin CB, Reeder SB. Magnetic resonance imaging quantification of liver iron. *Magn Reson Imaging Clin N Am*. 2010;18:359–381, ix.
34. Gandon Y, Olivie D, Guyader D, et al. Non-invasive assessment of hepatic iron stores by MRI. *Lancet*. 2004;363:357–362.
35. *Liver iron quantification by MRI (1.5 Tesla)*. http://radio.univ-rennes1.fr/Sources/EN/HemoCalc15.html.
36. Alustiza Echeverria JM, Castiella A, Emparanza JI. Quantification of iron concentration in the liver by MRI. *Insights Imaging*. 2012;3:173–180.
37. Serai SD, Fleck RJ, Quinn CT, et al. Retrospective comparison of gradient recalled echo R2* and spin-echo R2 magnetic resonance analysis methods for estimating liver iron content in children and adolescents. *Pediatr Radiol*. 2015;45:1629–1634.
38. Brissot P. Optimizing the diagnosis and the treatment of iron overload diseases. *Expert Rev Gastroenterol Hepatol*. 2016;10:359–370.
39. Burda P, Hochuli M. Hepatic glycogen storage disorders: what have we learned in recent years? *Curr Opin Clin Nutr Metab Care*. 2015;18:415–421.
40. Wolfsdorf JI, Weinstein DA. Glycogen storage diseases. *Rev Endocr Metab Disord*. 2003;4:95–102.
41. Rake JP, Visser G, Labrune P, et al. Glycogen storage disease type I: diagnosis, management, clinical course and outcome. Results of the European Study on Glycogen Storage Disease Type I (ESGSD I). *Eur J Pediatr*. 2002;161(suppl 1):S20–S34.
42. Labrune P, Trioche P, Duvaltier I, et al. Hepatocellular adenomas in glycogen storage disease type I and III: a series of 43 patients and review of the literature. *J Pediatr Gastroenterol Nutr*. 1997;24:276–279.
43. Lee PJ. Glycogen storage disease type I: pathophysiology of liver adenomas. *Eur J Pediatr*. 2002;161(suppl 1):S46–S49.
44. Bali DS, Chen YT, Austin S, et al. Glycogen storage disease type I. In: Pagon RA, Adam MP, Ardinger HH, et al, eds. *GeneReviews(R)*. Seattle: University of Washington, Seattle University of Washington; 1993. GeneReviews is a registered trademark of the University of Washington, Seattle. All rights reserved, Seattle (WA).
45. Grossman H, Ram PC, Coleman RA, et al. Hepatic ultrasonography in type I glycogen storage disease (von Gierke disease). Detection of hepatic adenoma and carcinoma. *Radiology*. 1981;141:753–756.
46. Boll DT, Merkle EM. Diffuse liver disease: strategies for hepatic CT and MR imaging. *Radiographics*. 2009;29:1591–1614.
47. Doppman JL, Cornblath M, Dwyer AJ, et al. Computed tomography of the liver and kidneys in glycogen storage disease. *J Comput Assist Tomogr*. 1982;6:67–71.
48. Ichikawa T, Federle MP, Grazioli L, et al. Hepatocellular adenoma: multiphasic CT and histopathologic findings in 25 patients. *Radiology*. 2000;214:861–868.
49. Arrive L, Flejou JF, Vilgrain V, et al. Hepatic adenoma: MR findings in 51 pathologically proved lesions. *Radiology*. 1994;193:507–512.
50. Meyers AB, Towbin AJ, Serai S, et al. Characterization of pediatric liver lesions with gadoxetate disodium. *Pediatr Radiol*. 2011;41:1183–1197.
51. Greene HL, Slonim AE, O'Neill JA Jr, et al. Continuous nocturnal intragastric feeding for management of type 1 glycogen-storage disease. *N Engl J Med*. 1976;294:423–425.
52. Muraca M, Gerunda G, Neri D, et al. Hepatocyte transplantation as a treatment for glycogen storage disease type 1a. *Lancet*. 2002;359:317–318.
53. Grabowski GA, Andria G, Baldellou A, et al. Pediatric non-neuronopathic Gaucher disease: presentation, diagnosis and assessment. Consensus statements. *Eur J Pediatr*. 2004;163:58–66.
54. Simpson WL, Hermann G, Balwani M. Imaging of Gaucher disease. *World J Radiol*. 2014;6:657–668.
55. Charrow J, Andersson HC, Kaplan P, et al. The Gaucher registry: demographics and disease characteristics of 1698 patients with Gaucher disease. *Arch Intern Med*. 2000;160:2835–2843.
56. Hill SC, Damaska BM, Ling A, et al. Gaucher disease: abdominal MR imaging findings in 46 patients. *Radiology*. 1992;184:561–566.

57. Wenstrup RJ, Roca-Espiau M, Weinreb NJ, et al. Skeletal aspects of Gaucher disease: a review. *Br J Radiol*. 2002;75(suppl 1):A2–A12.
58. Mistry PK, Deegan P, Vellodi A, et al. Timing of initiation of enzyme replacement therapy after diagnosis of type 1 Gaucher disease: effect on incidence of avascular necrosis. *Br J Haematol*. 2009;147:561–570.
59. Di Rocco M, Giona F, Carubbi F, et al. A new severity score index for phenotypic classification and evaluation of responses to treatment in type I Gaucher disease. *Haematologica*. 2008;93:1211–1218.
60. Maas M, Poll LW, Terk MR. Imaging and quantifying skeletal involvement in Gaucher disease. *Br J Radiol*. 2002;75(suppl 1):A13–A24.
61. Stoller JK. Alpha-1 antitrypsin deficiency: an underrecognized, treatable cause of COPD. *Cleve Clin J Med*. 2016;83:507–514.
62. Stoller JK, Lacbawan FL, Aboussouan LS. Alpha-1 antitrypsin deficiency. In: Pagon RA, Adam MP, Ardinger HH, et al, eds. *GeneReviews(R)*. Seattle: University of Washington, Seattle University of Washington; 1993. All rights reserved, Seattle (WA).
63. Wall M, Moe E, Eisenberg J, et al. Long-term follow-up of a cohort of children with alpha-1-antitrypsin deficiency. *J Pediatr*. 1990;116:248–251.
64. Kelly DA, McKiernan PJ. Metabolic liver disease in the pediatric patient. *Clin Liver Dis*. 1998;2:1–30, v.
65. McKiernan PJ. Neonatal cholestasis. *Semin Neonatol*. 2002;7:153–165.
66. Kemmer N, Kaiser T, Zacharias V, et al. Alpha-1-antitrypsin deficiency: outcomes after liver transplantation. *Transplant Proc*. 2008;40:1492–1494.
67. Ala A, Walker AP, Ashkan K, et al. Wilson's disease. *Lancet*. 2007;369:397–408.
68. Mergo PJ, Ros PR, Buetow PC, et al. Diffuse disease of the liver: radiologic-pathologic correlation. *Radiographics*. 1994;14:1291–1307.
69. Dohan A, Vargas O, Dautry R, et al. MR imaging features of focal liver lesions in Wilson disease. *Abdom Radiol (NY)*. 2016;41:1811–1824.
70. Kim TJ, Kim IO, Kim WS, et al. MR imaging of the brain in Wilson disease of childhood: findings before and after treatment with clinical correlation. *AJNR Am J Neuroradiol*. 2006;27:1373–1378.
71. Charlton MR, Kondo M, Roberts SK, et al. Liver transplantation for cryptogenic cirrhosis. *Liver Transpl Surg*. 1997;3:359–364.
72. Lefton HB, Rosa A, Cohen M. Diagnosis and epidemiology of cirrhosis. *Med Clin North Am*. 2009;93:787–799, vii.
73. Pariente D, Franchi-Abella S. Paediatric chronic liver diseases: how to investigate and follow up? Role of imaging in the diagnosis of fibrosis. *Pediatr Radiol*. 2010;40:906–919.
74. Purysko AS, Remer EM, Coppa CP, et al. LI-RADS: a case-based review of the new categorization of liver findings in patients with end-stage liver disease. *Radiographics*. 2012;32:1977–1995.

# 90

# Infectious Causes of Liver Disease

Melissa A. Hilmes

## INTRODUCTION

A wide range of viruses, bacteria, fungi, and parasites can infect the liver. The liver can be the primary organ of infection (as seen with viral hepatitis), or the liver can be secondarily involved as part of a systemic infection (such as with bacterial or fungal infections). The agents can cause a wide range of disease, ranging from subclinical infection, jaundice and cholestasis, diffuse hepatitis, microabscesses, focal abscess, or necrosis. Immunocompromised patients are affected differently than immunocompetent patients.

## VIRAL INFECTIONS OF THE LIVER

***Overview.*** Viral hepatitis presents a spectrum of clinical severity, which can range from subclinical infections to fulminant hepatitis with further evolution to cirrhosis.

***Etiology.*** In the neonatal period and in early infancy, patients are more likely to show signs and symptoms from viruses that cause perinatal and congenital infections, such as cytomegalovirus (CMV), herpes simplex virus (HSV), rubella virus, and parvovirus rather than the hepatotropic viruses.[1] They can become seriously ill with hepatitis and present with massive hepatocellular necrosis. It is important in these infants to exclude biliary atresia as a cause for cholestasis.

In childhood, viral hepatitis is most commonly caused by the hepatitis A, hepatitis B, and hepatitis C viruses, which are viruses that target the liver.[2] A number of other viruses have been implicated in childhood hepatitis, including mumps, measles, varicella-zoster virus, HSV, CMV, adenovirus, Coxsackie virus, and Epstein–Barr virus (EBV). These viruses cause systemic or disseminated illness, with hepatitis a part of the illness.[3]

Most affected patients have a short-lived acute disease with complete recovery. Complications include subacute and chronic active hepatitis, evolution into cirrhosis, and development of hepatocellular carcinoma. Chronic hepatitis B and C viral infections are linked directly to hepatocellular carcinoma development.[4,5]

***Imaging.*** Nuclear scintigraphy may be performed in infants with cholestasis to differentiate biliary atresia from other causes, collectively known as neonatal hepatitis. In neonatal hepatitis, liver function is decreased, and there is poor uptake of radiopharmaceutical with delayed excretion through the biliary tree into the small bowel and vicarious excretion through the kidneys (Fig. 90.1). The test has high sensitivity (98%–99%) but lower specificity (70%).[6] More accurate specificity is obtained when using premedication with phenobarbital to induce the hepatocytes, radiotracers with higher hepatic extraction (such as trimethylbromo-iminodiacetic acid [BrIDA] and diethyl iodophenyl-carbamoylmethyl-iminodiacetic acid [IODIDA]), dosing by body weight, and use of booster doses.[6]

In children and adults, diagnosis of a viral hepatitis infection is made clinically and on the basis of laboratory data. If imaging is performed during the acute phase of the illness, the liver may be enlarged or normal in size. On ultrasound (US), the liver echotexture may be normal or sonography may demonstrate increased parenchymal echogenicity and heterogeneity.[7] The "starry sky" pattern describes an edematous liver that is diffusely hypoechoic, allowing the portal triads and portal venous walls to appear bright; this imaging finding has limited sensitivity and specificity, and may be present in other forms of liver disease other than viral hepatitis[8] (Fig. 90.2). Computed tomography (CT) scans may show heterogeneous changes in attenuation but more commonly show hepatomegaly, gallbladder wall thickening, and periportal low attenuation (Fig. 90.3).

If the course of the viral infection progresses to hepatocellular necrosis, the areas of necrosis can mimic pyogenic microabscesses or diffuse hypoattenuating nodules on contrast-enhanced CT, as in reported cases of fulminant herpes-simplex virus hepatitis.[9,10]

In patients with fulminant hepatitis and subsequent hepatic regeneration, imaging differences have been described between necrotic areas and regenerating nodules. Regions of necrosis have central low attenuation on precontrast CT relative to regions of regeneration. After intravenous contrast administration, areas of necrosis and regeneration may enhance similarly such that they become indistinguishable, or the regenerating nodules may show hyperenhancement, which can simulate a neoplastic lesion. Similarly, magnetic resonance (MR) imaging may show nonspecific periportal high intensity on T2-weighted images and hepatomegaly.[7] On MR, areas of nodular regeneration show high signal on T1- and low signal on T2-weighted images relative to adjacent necrotic parenchyma.[11]

Measuring liver stiffness with US and MR elastography techniques is proving useful for detecting development of liver fibrosis and cirrhosis associated with hepatitis B and C infection.[12–14] Children have special considerations, as the liver stiffness changes over normal development from childhood to adolescence to adulthood, as demonstrated on MR elastography.[15]

***Treatment and Follow-up.*** Treatment of viral hepatitis varies from symptomatic treatment to antiviral medication or transplant depending on the type and severity of the disease. Fulminant hepatitis may be fatal without hepatic transplant.[11]

## BACTERIAL INFECTIONS OF THE LIVER

***Overview.*** Bacterial infections of the liver have a wide range of manifestations, including cholestatic jaundice, hepatitis, hepatomegaly, abscess formation, and fulminant hepatic necrosis. Many of the bacterial infections that have liver involvement do not require the aid of imaging for diagnosis and treatment, and lack specific imaging findings. Patients with prolonged fever without a source or patients with unexplained hepatomegaly often come to imaging for assistance in identifying the source of infection, and liver findings, such as identification of complications such as abscess, can aid in the diagnosis.

***Etiology.*** Because of the wide range of bacteria that can cause infection with liver involvement, identification of the specific organism causing the patients' symptoms is the key to diagnosis and treatment. Table 90.1 lists prominent bacterial infections that involve the liver, including spirochetes, rickettsial organisms, and tuberculosis.

Neonates are at risk for sepsis, jaundice with a urinary tract infection, and disseminated listeriosis and syphilis.[19–22] Patients with immune deficiency such as chronic granulomatous disease have special considerations such as infections with actinomycosis and nocardiosis.[23] Important to note is a history of animal exposure, especially in the case of bartonellosis, leptospirosis, and Q fever, or tick exposure with Lyme disease or Rocky Mountain spotted fever.

## Abstract:

A wide range of viruses, bacteria, fungi, and parasites can infect the liver. The liver can be the primary organ of infection (as seen with viral hepatitis), or the liver can be secondarily involved as part of a systemic infection (such as with bacterial or fungal infections). Patients can be affected at any age, from the newborn period to adulthood. The agents can cause a wide range of disease, ranging from subclinical infection, jaundice and cholestasis, diffuse hepatitis, microabscesses, focal abscess, or necrosis. Immunocompromised patients are affected differently than immunocompetent patients. Diagnostic imaging can help differentiate infectious conditions from other causes of liver inflammation, such as biliary atresia, identify abscesses that would be amenable to therapeutic interventions, and identify the source of fever and infection in immunocompromised patients.

## Keywords:

Viral hepatitis
Liver abscess
Hepatic abscess
Hepatic microabscesses
Schistosomiasis
Amebiasis
Echinococcosis

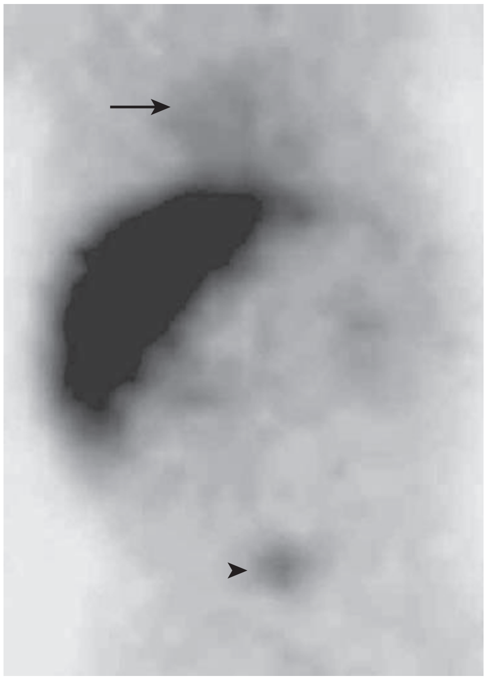

**Figure 90.1. Hepatitis in a 7-week-old boy with persistent jaundice.** Technetium-99m-labeled hepatoiminodiacetic (HIDA) scan shows poor uptake within the liver with large amount of background activity in the heart *(arrow)* and vicarious excretion through the genitourinary tract *(arrowhead)*.

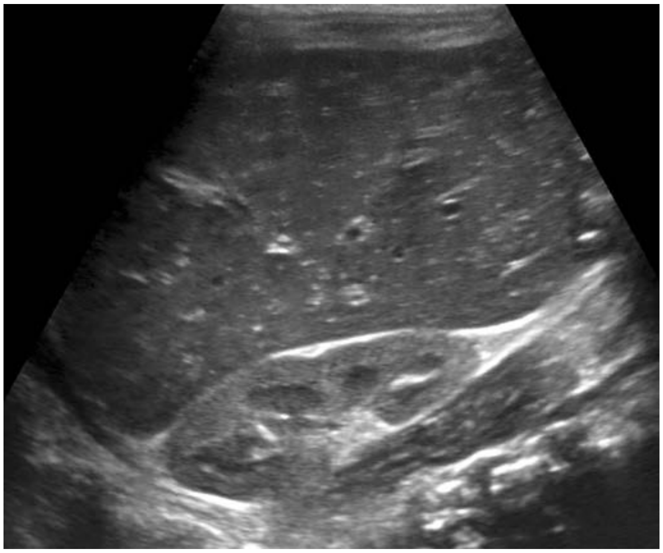

**Figure 90.2. Hepatitis B in a 5-month-old boy with persistent elevation of liver function tests.** Longitudinal sonogram of the liver shows an enlarged, diffusely hypoechoic liver which is decreased in echogenicity when compared with the kidney. The liver shows a “starry sky” appearance, as the portal venous triads and portal venous walls appear bright against the edematous liver. (Image courtesy of Dr. Gabriella Crane, Nashville, TN.)

**TABLE 90.1** Bacterial Pathogens and Their Manifestations in the Liver

| Disease | Causative Organism | Patient Population | Liver Disease Manifestations |
|---|---|---|---|
| Sepsis syndrome with cholestatic jaundice[1,21,59] | Gram positive organisms *(Staphylococcus aureus, Group B Streptococcus, pneumococcus)*<br>Gram negative bacteria (such as *Pseudomonas*, *E. coli, Klebsiella*) | Infants, children, adults | Immune response to bacterial endotoxins create cholestasis and jaundice; hepatomegaly |
| Urinary tract infection in neonates[1,22,60] | mainly *Escherichia coli;* also *Enterobacter, Klebsiella, Enterococcus* | Neonates | Prolonged jaundice and indirect hyperbilirubinemia |
| Actinomycosis[23,61] | *Actinomyces israelii* and other species | Mostly reported in immunocompetent adults; children with chronic granulomatous disease | Hepatic abscess formation |
| Bacille Calmette-Guerin (BCG) vaccination[62] | Live attenuated vaccine against tuberculosis disease | Immunodeficiency disorders such as severe combined immunodeficiency (SCID) | Multiple liver lesions; enlarged lymph nodes |
| Bacillus cereus[63] | *Bacillus cereus* | Immunocompetent patient; food borne illness | Fulminant hepatic failure from emetic toxin |
| Bartonellosis[64-66] | *B. henselae* and *B. quintana* | Children more so than adults; bite or scratch from infected cat or infected fleas | Granulomatous lesions with microabscesses; can calcify late |
| Brucellosis[67] | *Brucella* | Humans in contact with infected animals or their products | Hepatic abscess (necrotizing granuloma), possible calcification |
| Listeriosis[21,68,69] | *Listeria monocytogenes* | Fetal infection; immunocompetent and immunocompromised | Abscesses or granulomas in fetal infections (part of granulomatosis infantiseptica)<br>Hepatitis; solitary abscess; multiple liver abscesses (in adults) |
| Leptospirosis (spirochete)[70,71] | *Leptospira* species | Children exposed to infected animals, contaminated soil or water | Fever and jaundice; can lead to liver failure (Weil disease) |
| Lyme disease (spirochete)[72] | *Borrelia burgdorferi* | Tick bite | Subclinical hepatitis, abnormal liver function tests, hepatomegaly |

*Continued*

**TABLE 90.1** Bacterial Pathogens and Their Manifestations in the Liver—cont'd

| Disease | Causative Organism | Patient Population | Liver Disease Manifestations |
|---|---|---|---|
| Nocardiosis[23,73] | *Nocardia* species | Immunocompromised patients especially with chronic granulomatous disease; some immunocompetent patients | Mainly pulmonary and CNS disease; hematogenously disseminated disease affects liver |
| Q fever (Rickettsia)[74,75] | *Coxiella burnetii* | Children and adults exposed to infected animals and drinking raw milk | Hepatomegaly, jaundice and granulomatous hepatitis; fibrosis and cirrhosis in chronic form |
| Rocky Mountain spotted fever[72] | *Rickettsia rickettsia* | Tick bite | Jaundice, elevation of liver function tests |
| Syphillis (spirochete)[1,76] | *Treponema pallidum* | Fetal infection; neonatal and congenital infection | Cholestasis, hepatosplenomegaly, ascites, intrahepatic calcifications |
| Tuberculosis[25,26,77] | *Mycobacterium tuberculosis* | | Miliary dissemination with caseating granulomas and hepatomegaly; focal or nodular tuberculosis; hepatic abscess; enlarged lymph nodes |

*CNS,* Central nervous system.

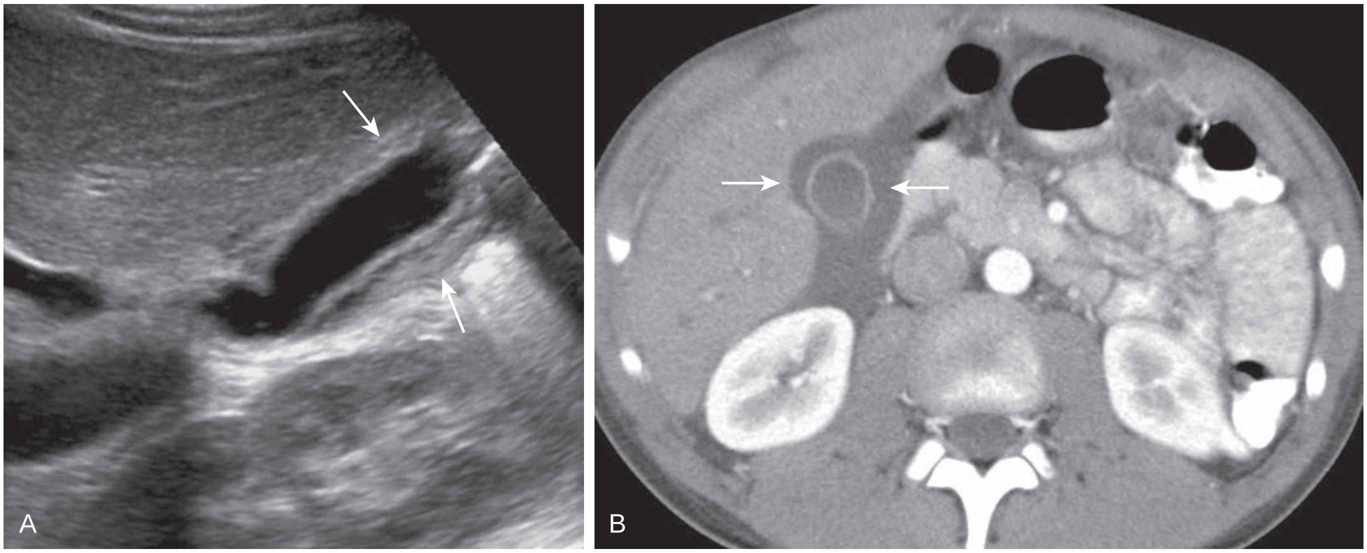

**Figure 90.3. Gallbladder wall thickening in a 10-year-old boy with viral hepatitis.** (A) Longitudinal sonogram shows a thick, hyperechoic gallbladder wall *(arrows)*. (B) Contrast-enhanced CT image confirms gallbladder wall thickening *(arrows)* and periportal edema.

## LIVER ABSCESS

In neonates, common bacterial pathogens causing liver abscess are *Staphylococcus aureus*, *Streptococcus pyogenes*, and *Escherichia coli*. Other organisms such as *Klebsiella* and *Pseudomonas* have been identified, as well as fungal species like *Candida albicans*. Up to half of the reported abscesses are polymicrobial.[24]

***Hepatic Abscess Formation.*** In neonates, hepatic abscess are rarely reported, but risk factors include prematurity, umbilical vein catheterization, sepsis, total parenteral nutrition, and necrotizing enterocolitis (Fig. 90.4).[16] Worldwide, liver abscess in children is more frequent in developing countries than in developed countries.[17] Risk factors include intraabdominal infection such as perforated appendicitis and inflammatory bowel disease such as ulcerative colitis.[17,18] Immunocompromised patients are at particularly high risk for liver abscesses, and the risks include acquired immunodeficiency such as with chemotherapy and bone marrow transplantation, and congenital immunodeficiency like chronic granulomatous disease.[17]

The most common bacterial cause of liver abscess in children is *S. aureus;* the most common parasitic cause is *Entamoeba histolytica*.[17] In endemic areas, tuberculosis is a significant cause of liver abscess, regardless of the presence or absence of active disease elsewhere.[25] The occurrence of multiple hepatic abscesses in a child should raise concern for underlying immunodeficiency.

***Imaging.*** The identification of an hepatic abscess or multiple microabscesses are specific imaging findings in bacterial infection, often found while working up abdominal pain, prolonged illness, or unexplained fever. Other imaging findings of hepatitis or hepatomegaly are nonspecific.

The hepatic abscess can take on multiple appearances. They can appear as multiple microabscesses less than 2 cm scattered throughout the liver. These lesions can appear on US as discrete hypoechoic foci in the liver with little or no posterior acoustic enhancement. On contrast-enhanced CT, they appear as hypoattenuating lesions. Rim enhancement help to differentiate from simple cysts.[26]

The lesions in hepatosplenic cat-scratch disease are an example of a granulomatous infection common in children and adolescents that produces microabscesses/granulomata with multiple lesions in the liver and spleen in association with enlarged abdominal lymph nodes and organomegaly[26,27] (Fig. 90.5). The disease mimics malignancy such as lymphoma, and the lesions are FDG avid at 18F-FDG PET imaging.[28] Calcifications can occur with healing, especially in granulomatous disease such as hepatosplenic catscratch disease or in children with chronic granulomatous disease.[29,30]

Larger abscesses on US range from hypoechoic to hyperechoic and can have internal debris and gas, which causes strong shadowing (Fig. 90.4). With CT, they are largely hypoattenuating, with or without septations, and may be unilocular or multilocular. The variable protein content of a hepatic abscess gives them a variable appearance on MR. There may be perilesional edema with increased signal on T2-weighted imaging.[26]

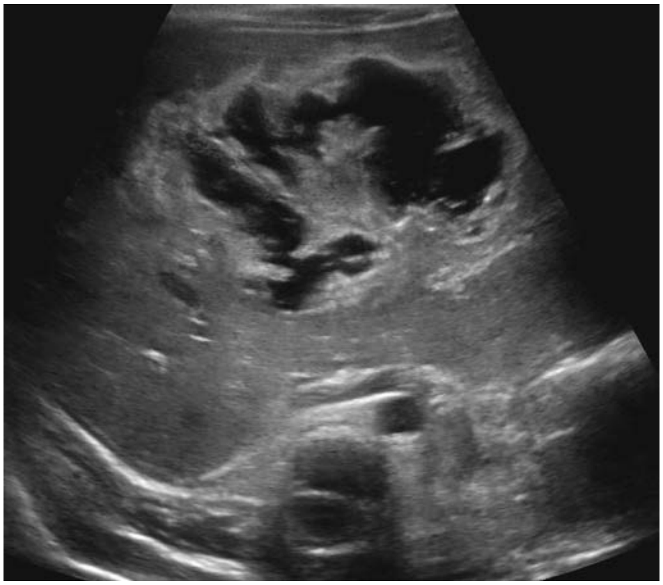

**Figure 90.4. Liver abscess.** Liver sonogram in an 8-day-old girl born prematurely who had an umbilical line placement and persistent fevers shows an irregularly shaped fluid collection with echogenic rim. Patient was treated with percutaneous drainage and antimicrobials. *(Image courtesy of Dr. Gabriella Crane, Nashville, Tennessee.)*

***Treatment and Follow-up.*** Treatment of bacterial infections is the appropriate antimicrobial therapy targeted to the specific organisms causing disease.

Hepatic abscess, if left untreated, can be fatal due to sepsis and rupture into pleural, peritoneal, and retroperitoneal spaces. Treatment of small pyogenic abscesses, less than 5 cm, is usually successfully managed with appropriate antimicrobials alone. Lesions that appear liquefied on imaging can be managed with percutaneous needle aspiration in combination with antimicrobials. Percutaneous catheter drainage may be required for larger lesions. Open surgical drainage is a less common management approach but may be required for patients with peritonitis or peritoneal rupture, or failure of percutaneous drainage.[17,31]

Diffuse liver microabscesses can be successfully treated with appropriate antimicrobial therapy, such as a combination of doxycycline and rifampin for hepatosplenic cat-scratch disease.[32] The occurrence of multiple hepatic abscesses in a child should raise concern for underlying immunodeficiency.

## FUNGAL INFECTIONS OF THE LIVER

***Overview.*** Fungal infection of the liver is often from dissemination of systemic disease and occurs frequently in the setting of immune compromise, such as neutropenia with hematologic malignancies, or stem cell or solid organ transplants; patients with AIDS and chronic granulomatous disease are at an increased risk.[33,34] In vulnerable patient populations, such as those listed, a high index of suspicion in patients with prolonged fever is essential, as is early detection. Mortality rates are approximately 30%.[34]

***Etiology.*** The majority of disseminated hepatic fungal infections are caused by *Candida* species, *Aspergillus* species, and *Cryptococcus neoformans*, with *Candida* species predominating.[34] Other possible fungal species include *Histoplasma* and *Mucor*. Emerging pathogens include *Trichosporon*, *Blastoschizomyces*, and *Fusarium*.[34] The specific cause can be hard to detect, as blood cultures are often only positive 50% of the time.[34]

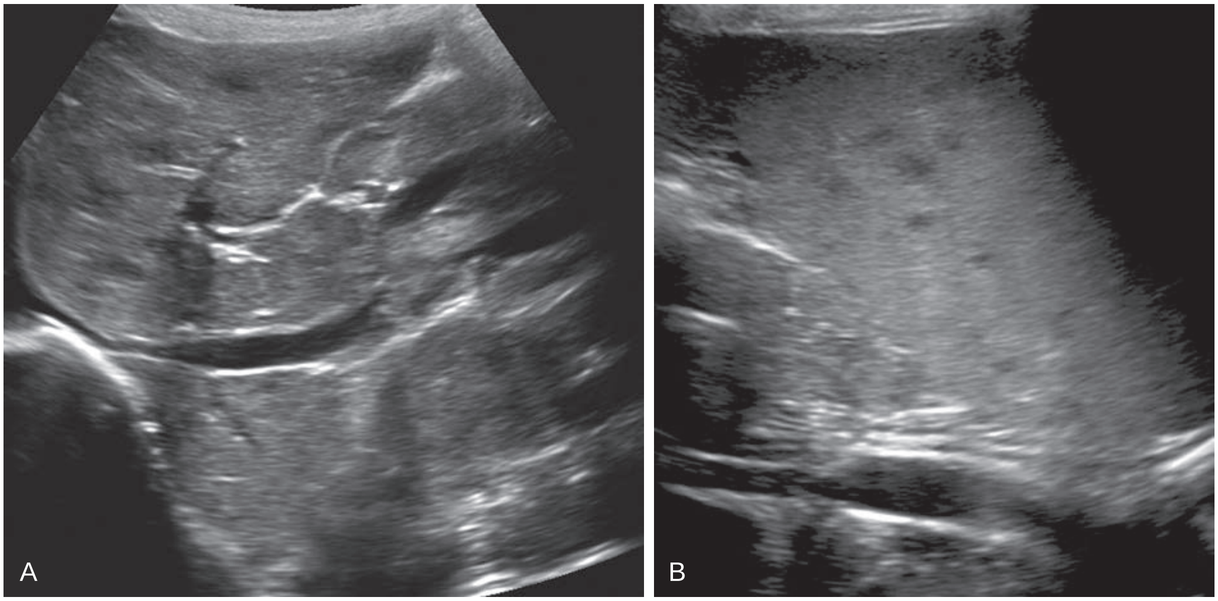

**Figure 90.5. Cat-scratch disease in a 6-year-old girl with 3 weeks of fevers, organomegaly, and diffusely enlarged lymph nodes.** (A) Sagittal sonogram of the liver show ill-defined hypoechoic lesions. (B) Sagittal sonogram of the spleen shows splenomegaly and multiple hypoechoic lesions. *(Images courtesy of Dr. Gabriella Crane, Nashville, Tennessee.)*

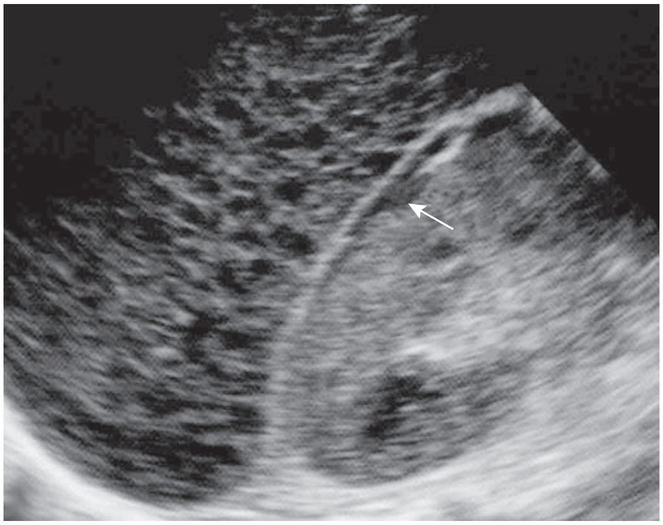

**Figure 90.6. Hepatic candidiasis in a 7-month-old immunodeficient boy.** Longitudinal sonogram shows diffuse, homogeneous, hypoechoic foci consistent with microabscesses throughout the liver. Tiny amount of fluid in Morrison pouch is noted *(arrow)* adjacent to the right kidney.

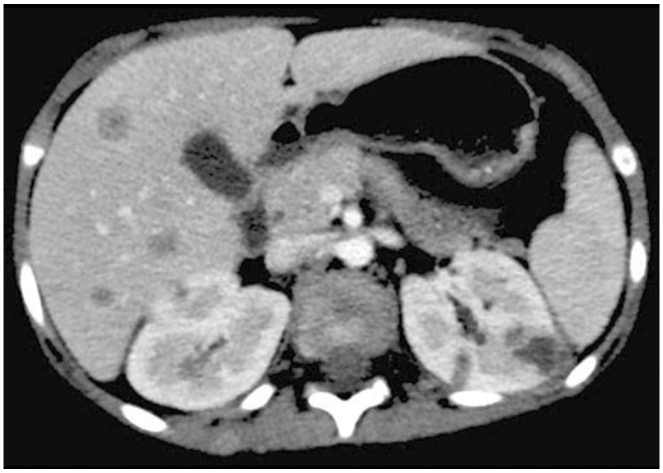

**Figure 90.7. Disseminated candidiasis in a 6-year-old boy undergoing treatment for acute lymphocytic leukemia.** Contrast-enhanced CT image shows multiple lesions in the liver, as well as disease in the kidneys. *(Image courtesy of Dr. Gabriella Crane, Nashville, Tennessee.)*

*Histoplasma capsulatum* is a dimorphic fungus with two varieties, one commonly found in the eastern United States and Latin America, and another in sub-Saharan Africa.[35] Histoplasmosis is a common infection in immunocompetent patients. Most often it is an asymptomatic, self-limiting infection, but the infection can disseminate and can cause life-threatening infection, including hepatitis.[36] Histoplasmosis can also infect immunocompromised patients, such as those receiving solid organ transplant[37] and individuals with AIDS; it is now considered an AIDS-defining illness.[35]

***Imaging.*** Imaging may be useful to detect the typical presence of disseminated fungal disease with diffuse microabscesses. Sometimes only hepatomegaly with or without splenomegaly without focal lesions may occur. Imaging findings generally cannot distinguish among causative organisms. The imaging features are similar across US, CT, and MR.[34]

MRI is the modality of choice when evaluating suspected fungal infection of the solid organs in pediatric patients, as the sensitivity is high and no ionizing radiation is involved.[35,38,39] Disseminated disease usually manifests are diffuse microabscesses. The lesions are hyperintense on T2-weighted imaging and minimally hypointense on T1-weighted imaging. With diffusion-weighted imaging, the lesions may show restriction.[40]

These numerous microabscesses have multiple patterns described on US, including wheel-within-a-wheel, bull's eye, hypoechoic nodule, and echogenic focus of calcification that occurs with resolution[41] (Fig. 90.6). CT may show multiple small low attenuation lesions throughout the liver and spleen, with peripheral enhancement possible as well as calcifications, especially in the healing stage[33] (Fig. 90.7). Arterial phase CT is more sensitive for lesion detection.[42]

Invasive aspergillosis has been reported manifesting as liver abscesses, with multiple large hypoechoic lesions, easily identified on imaging.[43]

***Treatment and Follow-up.*** Clinical practice guidelines exist for invasive candidiasis and invasive aspergillosis in neutropenic and nonneutropenic patients.[44,45] Various antifungal treatments include echinocandins, a group of antifungal drugs that include caspofungin, micafungin, and anidulafungin.[46] These drugs are more expensive but have lower infusion related effects and nephrotoxicity compared with amphotericin B. Hepatotoxicity is their main adverse effect.[46] Other options include fluconazole and amphotericin B. Recommendations for chronic disseminated hepatosplenic candidiasis include amphotericin B, followed by oral fluconazole.[44] For hepatic aspergillosis, voriconazole or the lipid formulation of amphotericin B is recommended.[45] For severe histoplasmosis, amphotericin B is preferred; itraconazole is used for moderate disease.[34]

## PARASITIC INFECTIONS OF THE LIVER

Parasitic infections are a worldwide problem, usually affecting the less developed regions of the world. With travel and immigration, these diseases may be encountered unexpectedly. Major groups of parasites that infect or involve the liver include protozoans and flatworms of the phylum *Platyhelminthes*. The flatworms can be divided into the cestodes, tapeworms such as *Echinococcus* species, and trematodes, flukes such as *Schistosoma*.[47]

Malaria is caused by plasmodium protozoa, and is one of the most devastating diseases in the world. A WHO report in 2014 estimated 200 million people were infected in 2013, with nearly 1 million deaths.[47] The infection can cause hepatosplenomegaly and other nonspecific abdominal findings such as periportal edema, ascites, and gallbladder wall thickening.[47]

Other parasitic infections preferentially involve the biliary tree, such as ascariasis, clonorchiasis, and fascioliasis, and are not covered in this section.

### Amebiasis

***Overview.*** Amebiasis is widespread worldwide but is more common in tropical areas with poor sanitation. In a study from 2007 to 2011, most travelers diagnosed with *Entamoeba histolytica* had returned from touring India, Indonesia, Mexico, and Thailand.[48]

***Etiology.*** *Entamoeba histolytica* is the main amebic protozoan that infects the gastrointestinal tract. Infection occurs after drinking contaminated water or eating contaminated food. The most common extraintestinal complication is a liver abscess.[47] Studies suggest that amebic abscess is rare in children.[17]

***Imaging.*** Amebic liver abscesses are usually unilocular; septa are present less commonly. The majority of lesions are solitary and in the right lobe of the liver, near the liver capsule. They appear similar to pyogenic abscesses (discussed earlier) and appear as a hypoechoic mass on US. The lesion appears as a

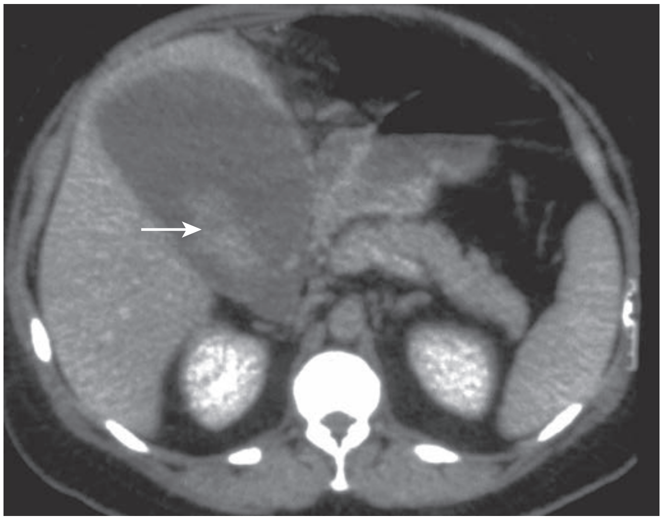

**Figure 90.8. Amebic abscess.** Axial contrast-enhanced CT image shows a large, exophytic low-attenuation cyst with hyperdense central debris *(arrow)*.

well-defined lesion with rim enhancement on a contrast-enhanced CT (Fig. 90.8). At MR, the abscesses appear as low-signal intensity on T1-weighted imaging and high-signal intensity on T2-weighted imaging.[34] Diaphragmatic disruption and direct extension into the thorax is highly suggestive of this disease and may manifest as a pleural effusion.[47]

***Treatment and Follow-up.*** Once the infection is confirmed with culture, serology, or immunofluorescence on biopsy specimens, treatment with metronidazole or ketoconazole is recommended.[47] Most studies suggest that amebic abscess can be managed with medical therapy without aspiration.[17] If a secondary bacterial infection occurs, addition of antibiotics should be considered as well as abscess drainage.[17]

## Echinococcosis or Hydatid Disease

***Overview.*** Echinococcosis is a worldwide infection. Affected areas are slightly different for the cystic and alveolar forms, but affected areas are mostly where herding and grazing are prevalent, as dogs are the definitive hosts and sheep and goats are intermediate hosts. Affected areas include the Mediterranean, central Europe, Russia, central Asia, China, southern South America, Australia, northwest Canada, western Alaska, and parts of Africa.[49]

***Etiology.*** These infections are mainly caused by the tapeworm *Echinococcus granulosus*, which causes cystic echinococcosis. *E. multilocularis* causes alveolar echinococcosis, a much less common infection. After ingesting the worm eggs in contaminated food, water, or soil, humans become accidental intermediate hosts. The embryonic form of the worms, onchospheres, settle into the liver and lungs, and then progress into the larval stage, forming hydatid cysts.[47]

***Imaging.*** There are several classification systems of hepatic hydatid cysts and the appearance on US, including a radiologic classification,[50,51] WHO classification of 2003,[52] and the oldest system, the Gharbi classification of 1981.[53] The WHO classification can also apply to MR. The classifications describe degeneration of the hydatid cysts from unilocular cysts, confused with other simple cysts, to lesions with daughter cysts, to chronic hydatid cysts with complete calcification[47] (Figs. 90.9 and 90.10). Some unique imaging features of this disease include "falling snowflakes," a description of denser material inside the unilocular cyst on US or higher attenuation material on CT. The "rosette" describes a cyst that contains daughter cysts; the mother cyst has more dense content and has higher attenuation on CT than the daughter cysts. The "water lily" sign describes a rupture of the cyst with internal floating membranes.[34]

The lesions of *E. multilocularis* are multiloculated and mimic large tumors, infiltrating surrounding tissues and displacing intrahepatic structures. Central necrosis and calcifications are common.[54]

***Treatment and Follow-up.*** Traditionally, the standard treatment is removal of the cysts and antiparasitic treatment such as albendazole or mebendazole.[47]

## Schistosomiasis

***Overview and Etiology.*** Schistosomiasis is a blood fluke parasitic disease endemic to tropical and subtropical regions.[34] These waterborne parasitic flatworms are found in freshwater and aquatic snails that serve as the intermediate hosts. Worldwide, there are 252 million cases, and 90% are in Africa.[55] Schistosomiasis takes on two main forms: the genitourinary form caused by *S. hematobium*, (representing two-thirds of cases worldwide) and the intestinal form caused by *S. mansoni* (one-third of cases worldwide) and *S. japonicum* (1% of cases worldwide, mainly East Asia).[55]

The secondary larvae of these blood flukes leave the intermediate hosts, aquatic snails, and swim to invade final hosts, human beings. They penetrate skin, enter blood and lymphatics, and then lodge into liver sinusoids to copulate. The adult worms then migrate into venous plexus and venules where they live and produce eggs. In intestinal schistosomiasis, rectal and mesenteric venules are involved; in the genitourinary form, the pelvic and paravesical plexus is infested. The eggs migrate through bowel or bladder wall, and then are passed in stool or urine.[47,55]

Chronic infection in children can lead to anemia, chronic pain, malnutrition, growth failure, and cognitive deficits.[55]

***Imaging.*** Acute infection, known as Katayama fever, is sometimes observed in travelers. Although rarely imaged, imaging can demonstrate hepatosplenomegaly, hypoechoic liver lesions corresponding to granulomata, and enlarged portal nodes.[47,56]

Chronic infection is a result of egg deposition in tissues causing fibrosis, inflammation, bleeding, and end organ damage.[55] Imaging findings of chronic hepatic infection include fibrosis and signs of portal hypertension, such as hepatofugal flow and splenomegaly. Other findings include periportal fibrosis, irregular or nodular liver surface, heterogeneous parenchyma, atrophy of right lobe, and hypertrophy of caudate of left lobe.[47]

The differences in egg size and distribution accounts for the different appearances on imaging. The larger *S. mansoni* eggs are deposited along the large portal branches from the liver hilum, producing a central distribution of periportal fibrosis. The smaller eggs of *S. japonicum* are deposited along the small portal radicles at the periphery of the liver, producing periportal fibrosis along the peripheral part of the liver.[57] Fibrotic tracts in patients with *S. japonicum* form a "polygonal network" with a honeycomb or tortoise shell appearance and are likely to calcify. Fibrotic tracts in patients with *S. mansoni* do not tend to calcify and form a "Symmers' pipe-stem" fibrosis.[57] Sonography reveals hyperechoic septa outlining polygonal areas which may resemble a "fish scale network." On CT, dense fibrous and calcific septa distributed at right angles to the hepatic surface produce the classic CT appearance of "turtle back calcification" in *S. japonicum* infection. MR imaging may show isointense periportal bands on T1-weighted images, which are bright on T2-weighted images and enhance after gadolinium contrast administration.[26,58]

***Treatment and Follow-up.*** Schistosomiasis is treated with praziquantel, although up to 20% of patients will develop fibrosis even with treatment. Current control strategies include mass drug administrations of praziquantel, although most children do not receive their needed regular treatment. Vaccine development is underway.[55]

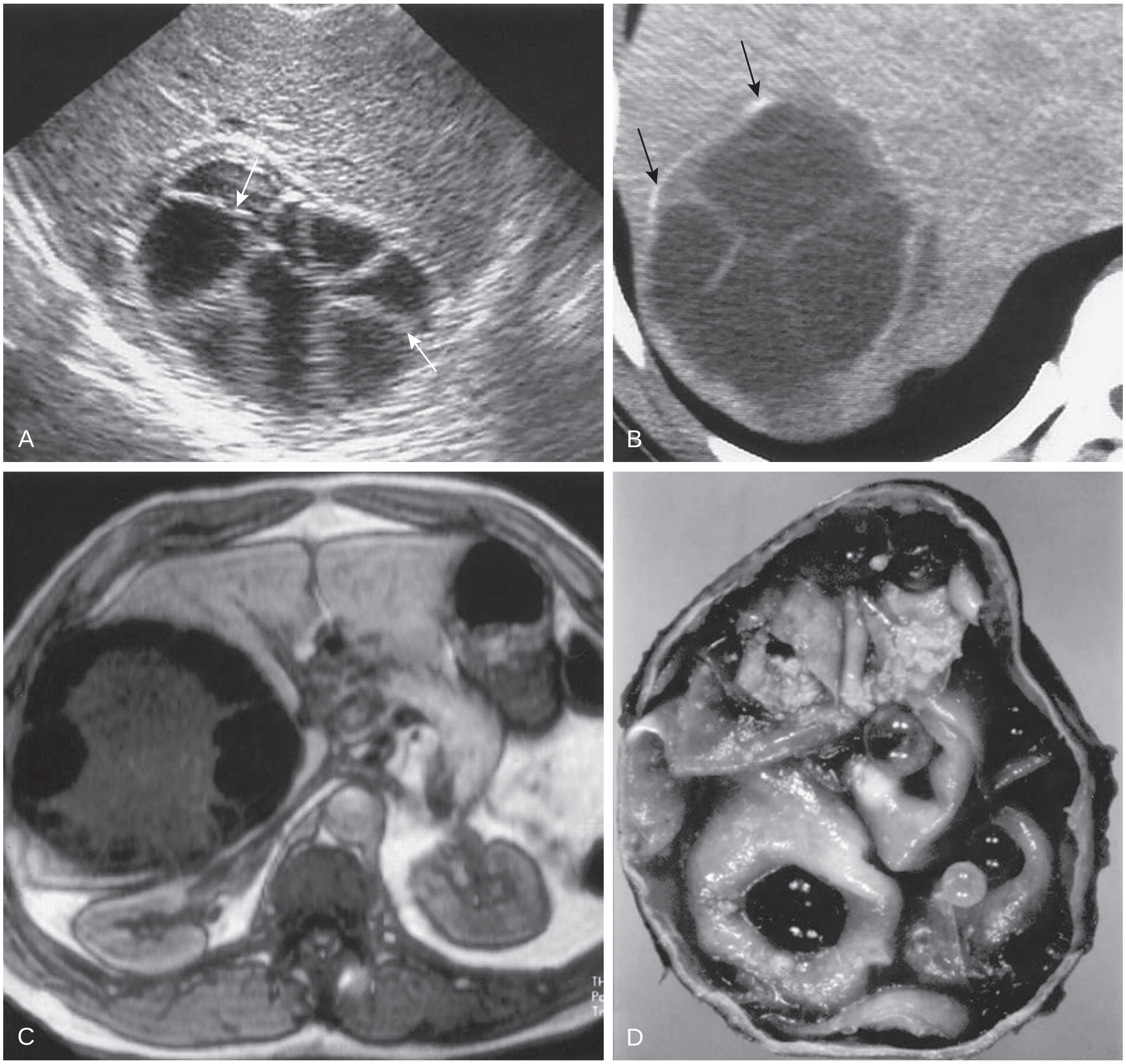

**Figure 90.9. Echinococcal (hydatid) cyst.** (A) Longitudinal hepatic sonogram shows a type II well-defined *(arrows),* multilocular lesion with a “spoke wheel” appearance. (B) Axial unenhanced CT image confirms a mass with multiple septations and peripheral daughter cysts. (C) Axial T1-weighted gradient echo MR image shows a hepatic hydatid cyst with a hypointense fibrous pericyst and extensive peripheral low-signal-intensity daughter cysts surrounding central intermediate-signal-intensity matrix that was bright on T2-weighted images *(not shown)*. (D) Gross specimen of resected hydatid cyst reveals numerous daughter cysts. *(From Mortele KJ, Segatto E, Ros PR. The infected liver: radiologic-pathologic correlation.* Radiographics *2004;24:937–955.)*

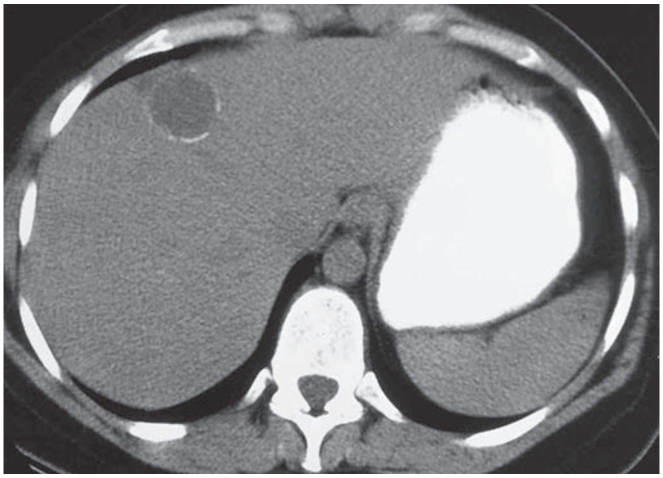

**Figure 90.10. Echinococcal (hydatid) cyst.** Axial unenhanced CT images show peripheral calcification in a hepatic echinococcal cyst.

## KEY POINTS

- Imaging of hepatitis can be nonspecific, no matter the causal pathogen. Imaging can help to find complications of disseminated infections, such as diffuse microabscesses or focal abscesses.
- Viruses that cause neonatal hepatitis are from congenital or perinatal infection, rather than the heterotropic viruses of childhood and beyond. Biliary atresia should be excluded as a cause in neonatal cholestasis.
- Fungal infections involving the liver tend to occur in immunocompromised patients, with *Candida* and *Aspergillus* as the main pathogens.
- Parasitic infections that involve the liver are prevalent worldwide and may be seen in tourists who have traveled to endemic areas. Chronic parasitic infections negatively affect the health of children worldwide.

## REFERENCES

Full references for this chapter can be found on www.expertconsult.com.

## REFERENCES

1. Gottesman LE, Del Vecchio MT, Aronoff SC. Etiologies of conjugated hyperbilirubinemia in infancy: a systematic review of 1692 subjects. *BMC Pediatr*. 2015;15:192.
2. Gubernick JA, et al. US approach to jaundice in infants and children. *Radiographics*. 2000;20(1):173–195.
3. Leung DH, Chen LL. *Hepatitis in Feigin and Cherry's Textbook of Pediatric Infectious Diseases*. M. James D. Cherry MD, Author. Philadelphia, PA.: Saunders; 2014:648–658.
4. El-Guindi MA. Hepatitis C viral infection in children: updated review. *Pediatr Gastroenterol Hepatol Nutr*. 2016;19(2):83–95.
5. Tan YJ. Hepatitis B virus infection and the risk of hepatocellular carcinoma. *World J Gastroenterol*. 2011;17(44):4853–4857.
6. Kianifar HR, et al. Accuracy of hepatobiliary scintigraphy for differentiation of neonatal hepatitis from biliary atresia: systematic review and meta-analysis of the literature. *Pediatr Radiol*. 2013;43(8):905–919.
7. Itoh H, et al. Periportal high intensity on T2-weighted MR images in acute viral hepatitis. *J Comput Assist Tomogr*. 1992;16(4):564–567.
8. Patel NJ, Caserta MP, DiSantis DJ. The "starry sky" liver. *Abdom Radiol*. 2016;NY.
9. Down C, et al. Herpes simplex virus hepatitis in an immunocompetent host resembling hepatic pyogenic abscesses. *Case Reports Hepatol*. 2016;2016:8348172.
10. Tripuraneni V, et al. Fulminant herpes simplex viral hepatitis: ultrasound and CT imaging appearance and a review of the imaging literature. *Clin Imaging*. 2014;38(2):191–194.
11. Murakami T, Baron RL, Peterson MS. Liver necrosis and regeneration after fulminant hepatitis: pathologic correlation with CT and MR findings. *Radiology*. 1996;198(1):239–242.
12. Ying HY, et al. Accuracy of transient elastography in the assessment of chronic hepatitis C-related liver cirrhosis. *Clin Invest Med*. 2016;39(5):E150–E160.
13. Xu X, et al. Performance of transient elastography assessing fibrosis of single hepatitis B virus infection: a systematic review and meta-analysis of a diagnostic test. *Hepatol Int*. 2015;9(4):558–566.
14. Lu Q, et al. Stiffness value and serum biomarkers in liver fibrosis staging: study in large surgical specimens in patients with chronic hepatitis B. *Radiology*. 2016;280(1):290–299.
15. Etchell E, et al. Liver stiffness values are lower in pediatric subjects than in adults and increase with age: a multifrequency MR elastography study. *Radiology*. 2016;160252.
16. Tan NW, et al. Neonatal hepatic abscess in preterm infants: a rare entity? *Ann Acad Med Singapore*. 2005;34(9):558–564.
17. Mishra K, et al. Liver abscess in children: an overview. *World J Pediatr*. 2010;6(3):210–216.
18. Albuquerque A, et al. Liver abscess of the caudate lobe due to Staphylococcus aureus in an ulcerative colitis patient: first case report. *J Crohns Colitis*. 2011;5(4):360–363.
19. Newman L, et al. Global estimates of syphilis in pregnancy and associated adverse outcomes: analysis of multinational antenatal surveillance data. *PLoS Med*. 2013;10(2):e1001396.
20. Tappero JW, et al. Reduction in the incidence of human listeriosis in the United States. Effectiveness of prevention efforts? The Listeriosis Study Group. *JAMA*. 1995;273(14):1118–1122.
21. Shah BA, Padbury JF. Neonatal sepsis: an old problem with new insights. *Virulence*. 2014;5(1):170–178.
22. Omar C, et al. Urinary tract infection and indirect hyperbilirubinemia in newborns. *N Am J Med Sci*. 2011;3(12):544–547.
23. Bassiri-Jahromi S, Doostkam A. Actinomyces and nocardia infections in chronic granulomatous disease. *J Glob Infect Dis*. 2011;3(4):348–352.
24. Bosnali O, et al. Liver abscess: increasing occurrence in premature newborns. *J Neonatal Surg*. 2013;2(2):23.
25. Dey J, et al. Tuberculosis as an etiological factor in liver abscess in adults. *Tuberc Res Treat*. 2016;2016:8479456.
26. Mortele KJ, Segatto E, Ros PR. The infected liver: radiologic-pathologic correlation. *Radiographics*. 2004;24(4):937–955.
27. Hopkins KL, et al. Imaging manifestations of cat-scratch disease. *AJR Am J Roentgenol*. 1996;166(2):435–438.
28. Kraft KE, Doedens RA, Slart RH. Hepatosplenic cat-scratch disease in children and the positive contribution of 18F-FDG imaging. *Clin Nucl Med*. 2015;40(9):746–747.
29. Talenti E, et al. Disseminated hepatic and splenic calcifications following cat-scratch disease. *Pediatr Radiol*. 1994;24(5):342–343.
30. Khanna G, Kao SC, Kirby P, et al. Imaging of chronic granulomatous disease in children. *Radiographics*. 2005;25(5):1183–1195. Review. PubMed PMID: 16160105.
31. Roy Choudhury S, et al. Protocol-based management of 154 cases of pediatric liver abscess. *Pediatr Surg Int*. 2016.
32. Rolain JM, et al. Recommendations for treatment of human infections caused by Bartonella species. *Antimicrob Agents Chemother*. 2004;48(6):1921–1933.
33. Adeyiga AO, Lee EY, Eisenberg RL. Focal hepatic masses in pediatric patients. *AJR Am J Roentgenol*. 2012;199(4):W422–W440.
34. Bachler P, et al. Multimodality Imaging of Liver Infections: Differential Diagnosis and Potential Pitfalls. *Radiographics*. 2016;36(4):1001–1023.
35. Tyagi R, et al. Disseminated histoplasmosis: a fatal opportunistic infection in disguise. *J Lab Physicians*. 2016;8(2):129–131.
36. Gill D, et al. Unusual presentation of disseminated histoplasmosis. *Am J Emerg Med*. 2016.
37. Assi M, et al. Histoplasmosis after solid organ transplant. *Clin Infect Dis*. 2013;57(11):1542–1549.
38. Semelka RC, et al. Hepatosplenic fungal disease: diagnostic accuracy and spectrum of appearances on MR imaging. *AJR Am J Roentgenol*. 1997;169(5):1311–1316.
39. Semelka RC, et al. Detection of acute and treated lesions of hepatosplenic candidiasis: comparison of dynamic contrast-enhanced CT and MR imaging. *J Magn Reson Imaging*. 1992;2(3):341–345.
40. Chan JH, et al. Diffusion-weighted MR imaging of the liver: distinguishing hepatic abscess from cystic or necrotic tumor. *Abdom Imaging*. 2001;26(2):161–165.
41. Pastakia B, et al. Hepatosplenic candidiasis: wheels within wheels. *Radiology*. 1988;166(2):417–421.
42. Metser U, et al. Fungal liver infection in immunocompromised patients: depiction with multiphasic contrast-enhanced helical CT. *Radiology*. 2005;235(1):97–105.
43. Thomas KE, et al. The radiological spectrum of invasive aspergillosis in children: a 10-year review. *Pediatr Radiol*. 2003;33(7):453–460.
44. Pappas PG, et al. Executive summary: clinical practice guideline for the management of candidiasis: 2016 update by the infectious diseases society of America. *Clin Infect Dis*. 2016;62(4):409–417.
45. Patterson TF, et al. Executive summary: practice guidelines for the diagnosis and management of aspergillosis: 2016 update by the infectious diseases society of America. *Clin Infect Dis*. 2016;63(4):433–442.
46. Grover ND. Echinocandins: a ray of hope in antifungal drug therapy. *Indian J Pharmacol*. 2010;42(6):422.
47. Rodriguez Carnero P, et al. Unexpected hosts: imaging parasitic diseases. *Insights Imaging*. 2016.
48. Roy SL. Infectious diseases related to travel: ambebiasis. In: *CDC Health Information for International Travel 2016*. M. Gary W. Brunette, MS, Author. New York: Oxford University Press; 2016.
49. Moro P, Schantz PM. Echinococcosis: a review. *Int J Infect Dis*. 2009;13(2):125–133.
50. Polat P, et al. Hydatid disease from head to toe. *Radiographics*. 2003; 23(2):475–494, quiz 536-537.
51. von Sinner W, et al. MR imaging in hydatid disease. *AJR Am J Roentgenol*. 1991;157(4):741–745.
52. Group WHOIW. International classification of ultrasound images in cystic echinococcosis for application in clinical and field epidemiological settings. *Acta Trop*. 2003;85(2):253–261.
53. Gharbi HA, et al. Ultrasound examination of the hydatic liver. *Radiology*. 1981;139(2):459–463.
54. Etlik O, et al. Contrast-enhanced CT and MRI findings of atypical hepatic Echinococcus alveolaris infestation. *Pediatr Radiol*. 2005; 35(5):546–549.
55. Merrifield M, et al. Advancing a vaccine to prevent human schistosomiasis. *Vaccine*. 2016;34(26):2988–2991.
56. Passos MC, et al. Ultrasound and CT findings in hepatic and pancreatic parenchyma in acute schistosomiasis. *Br J Radiol*. 2009;82(979):e145–e147.
57. Manzella A, et al. Schistosomiasis of the liver. *Abdom Imaging*. 2008.
58. Palmer PE. Schistosomiasis. *Semin Roentgenol*. 1998;33(1):6–25.
59. Minemura M, Tajiri K, Shimizu Y. Liver involvement in systemic infection. *World J Hepatol*. 2014;6(9):632–642.
60. Bilgen H, et al. Urinary tract infection and hyperbilirubinemia. *Turk J Pediatr*. 2006;48(1):51–55.
61. Valour F, et al. Actinomycosis: etiology, clinical features, diagnosis, treatment, and management. *Infect Drug Resist*. 2014;7:183–197.
62. Shrot S, et al. BCGitis and BCGosis in children with primary immunodeficiency - imaging characteristics. *Pediatr Radiol*. 2016;46(2):237–245.
63. Mahler H, et al. Fulminant liver failure in association with the emetic toxin of Bacillus cereus. *N Engl J Med*. 1997;336(16):1142–1148.

64. Garcia JC, et al. Hepatosplenic cat scratch disease in immunocompetent adults: report of 3 cases and review of the literature. *Medicine (Baltimore)*. 2014;93(17):267–279.
65. Nelson CA, Saha S, Mead PS. Cat-scratch disease in the United States, 2005-2013. *Emerg Infect Dis*. 2016;22(10):1741–1746.
66. Arisoy ES, et al. Hepatosplenic cat-scratch disease in children: selected clinical features and treatment. *Clin Infect Dis*. 1999;28(4):778–784.
67. Sisteron O, et al. Hepatic abscess caused by Brucella US, CT and MRI findings: case report and review of the literature. *Clin Imaging*. 2002;26(6):414–417.
68. Yu VL, et al. Disseminated listeriosis presenting as acute hepatitis. Case reports and review of hepatic involvement in listeriosis. *Am J Med*. 1982;73(5):773–777.
69. Scholing M, et al. Clinical features of liver involvement in adult patients with listeriosis. Review of the literature. *Infection*. 2007;35(4):212–218.
70. Lokida D, et al. Case report: Weil's disease with multiple organ failure in a child living in dengue endemic area. *BMC Res Notes*. 2016;9(1):407.
71. Narayanan R, et al. Paediatric leptospirosis: a population based case-control study from Chennai, India. *Indian J Med Microbiol*. 2016;34(2):228–232.
72. Zaidi SA, Singer C. Gastrointestinal and hepatic manifestations of tickborne diseases in the United States. *Clin Infect Dis*. 2002;34(9):1206–1212.
73. Wilson JW. Nocardiosis: updates and clinical overview. *Mayo Clin Proc*. 2012;87(4):403–407.
74. Baquero-Artigao F, del Castillo F, Tellez A. Acute Q fever pericarditis followed by chronic hepatitis in a two-year-old girl. *Pediatr Infect Dis J*. 2002;21(7):705–707.
75. Honarmand H, Fever Q. an old but still a poorly understood disease. *Interdiscip Perspect Infect Dis*. 2012;2012:131932.
76. Araujo Junior E, et al. Prenatal diagnosis of congenital syphilis using two- and three-dimensional ultrasonography: case report. *Case Rep Infect Dis*. 2012;2012:478436.
77. Karaosmanoglu AD, et al. Hepatobiliary tuberculosis: imaging findings. *AJR Am J Roentgenol*. 2016;1–11.

# 91 Neoplasia

*Josée Dubois and Michael Ditchfield*

## OVERVIEW

Hepatic neoplasms constitute approximately 2% of all childhood tumors, approximately 6% of pediatric abdominal neoplasms, and are the third most common intra-abdominal tumors in children after Wilms tumor and neuroblastoma. Two-thirds of liver tumors in children are malignant and most of these are hepatoblastomas. The remaining malignant tumors in order of frequency are: hepatocellular carcinoma (HCC) including the fibrolamellar variant, undifferentiated embryonal sarcoma (UES), and angiosarcoma.[1] The benign hepatic tumors in pediatrics include those specific to children, such as vascular tumors and mesenchymal hamartomas, as well as entities that are also seen in adults, such as focal nodular hyperplasia (FNH), hepatocellular adenoma (HCA), and nodular regenerative hyperplasia (NRH). The most common benign pediatric tumors are infantile hemangiomas and FNH.

Some pediatric hepatic tumors may be discovered incidentally, however, the majority present with abdominal pain or a mass.

A differential diagnosis of liver tumors can be obtained based on the age of the patient, clinical setting, laboratory findings such as serum alpha fetoprotein (AFP) levels, and some characteristic imaging findings in some tumors as illustrated in Table 91.1. However, serum AFP levels can be confusing in the first few months of life, being normally elevated at birth (25,000–50,000 ng/mL) and do not reach the normal adult level (<25 ng/mL) until 6 months of age.[2,3]

All standard imaging modalities are used in the evaluation of liver masses, including plain radiographs, ultrasonography (US), computed tomography (CT), magnetic resonance imaging (MRI), radionuclide scintigraphy, and positron emission tomography (PET). US is the initial study of choice to confirm the organ of origin, characterize the lesion, and decide on the most appropriate subsequent imaging. Additional imaging with CT, MRI, nuclear scintigraphy, and, rarely, angiography, may be required to fully characterize a hepatic lesion before biopsy and treatment.

New developments in US and MR contrast have improved the diagnostic capabilities of these modalities in the investigation of focal liver masses; however, there is little data available of their use in pediatrics and their use remains off-label in children.[4,5]

Currently, the most commonly used liver specific contrast agents in adult practice are gadobenate dimeglumine (MultiHance, Bracco) and gadoxetate disodium (Gd-EOB-DTPA, gadoxetic acid, Eovist or Primovist, Bayer HealthCare). Gadobenate dimeglumine demonstrates weak and transient binding with serum albumin in the intravascular space and therefore remains within the intravascular space for a longer time than do other gadolinium chelates. This improves evaluation of vascular structures. In addition, up to 5% of the administered dose has hepatobiliary excretion. Gadoxetate disodium has 50% hepatobiliary excretion in the setting of normal renal and hepatic function and can therefore provide both a functional and anatomic magnetic resonance cholangiopancreatography (MRCP) examination. Gadoxetate disodium has higher T1 relaxivity and allows adequate first-pass hepatic imaging, and delayed phase postcontrast imaging can demonstrate the relationship of the tumor with the portal and hepatic veins and identify intrahepatic satellite lesions.[6]

## MALIGNANT HEPATOBILIARY TUMORS

### Hepatoblastoma

Hepatoblastoma is the most common primary malignant liver tumor in infants and children. Sixty-eight percent of cases are seen in the first year of life and 90% in patients younger than 5 years of age, with a male predominance of 2 : 1.[3] Four percent of cases are congenital.[1,3,7–9] Predisposing conditions include Beckwith–Wiedemann syndrome, familial adenomatous polyposis, type 1A glycogen storage disease, Gardner syndrome, fetal alcohol syndrome, Wilms tumor, and trisomy 18. It is also reported in premature and low birth weight infants and in infants born of mothers taking oral contraceptives. There is a strong association with low birth weight, raising the issue of a potential contribution by a variety of iatrogenic exposures in the neonatal intensive care unit.[10]

Hepatoblastoma usually presents as a palpable mass. Infrequently, it can present with jaundice and precocious puberty related to the secretion of chorionic gonadotropins. Serum AFP is markedly elevated in approximately 90% of patients and can be used to monitor therapy and detect recurrence.

***Pathology.*** Hepatoblastoma is classified into two histologic types: the more common epithelial type and the mixed epithelial mesenchymal type.[1–3] Hepatoblastoma is usually solitary and is most commonly located in the right hepatic lobe (60%).[11] It may also be multifocal or, less commonly, diffusely infiltrating. Multifocal disease may consist of a dominant mass with satellite nodules or multiple small masses. Vascular compression or invasion is important to identify. The portal vein is most commonly affected. When the hepatic veins are involved, extension to the inferior vena cava and right atrium can also occur.

Distant metastases are present in less than 10% of cases at diagnosis, most commonly to the lungs, followed by lymph nodes, bone, brain, eye, and ovary.

***Imaging.*** Sonographically, hepatoblastomas are most often well-defined and hyperechoic relative to adjacent liver (Fig. 91.1). Epithelial type hepatoblastomas are more homogeneous, whereas mixed tumors are more heterogeneous often containing areas of calcifications, necrosis, or hemorrhage.[12–14] Infiltrative hepatoblastomas show diffuse heterogeneous echogenicity.[12–14] Intravascular tumor thrombus may be seen within the hepatic or portal veins. Flow within the thrombus on color Doppler imaging aids in differentiating neoplastic from nonneoplastic thrombus.

Unenhanced CT typically shows a well-circumscribed low density mass with speckled or amorphous calcifications (50%).[12] It enhances heterogeneously with contrast and may be hyperdense compared with liver parenchyma in the early arterial postcontrast phase and usually iso- or hypodense on delayed images. Peripheral enhancement can be seen. The routine use of multiphase CT imaging is, however, not recommended in suspected hepatoblastomas.

On MRI, epithelial type hepatoblastomas are homogeneously hypointense on T1- and hyperintense on T2-weighted images relative to adjacent liver and enhance with intravenous gadolinium contrast.[12] Mixed-type tumors show more heterogeneous signal intensity with areas of calcifications, necrosis, hemorrhage, and septation.[12–14] Vascular invasion is demonstrated with gradient-echo sequences; tumor thrombus appears as high signal on T1-weighted

## Abstract:

Hepatic neoplasms constitute approximately 2% of all childhood tumors, approximately 6% of pediatric abdominal neoplasms, and are the third most common intraabdominal tumor in children after Wilms tumor and neuroblastoma. Two-thirds of liver tumors in children are malignant and most of these are hepatoblastomas. The remaining malignant tumors in order of frequency are: hepatocellular carcinoma (HCC) including the fibrolamellar variant, undifferentiated embryonal sarcoma, and angiosarcoma. The benign hepatic tumors in pediatrics include those specific to children, such as vascular tumors and mesenchymal hamartomas, as well as entities that are also seen in adults, such as focal nodular hyperplasia (FNH), hepatocellular adenoma, and nodular regenerative hyperplasia. The most common benign pediatric tumors are infantile hemangiomas and FNH.

All standard imaging modalities are used in the evaluation of liver masses. Ultrasound (US) is the initial study of choice to confirm the organ of origin, characterize the lesion, and decide on the most appropriate subsequent imaging. Additional imaging with computed tomography, magnetic resonance imaging (MRI), nuclear scintigraphy, and, rarely, angiography, may be required to fully characterize a hepatic lesion before biopsy and treatment.

New developments in US and MRI contrast have improved the diagnostic capabilities of these modalities in the investigation of focal liver masses. Currently, the most commonly used liver specific MR contrast agents in adult practice are gadobenate dimeglumine and gadoxetate disodium; however, there is little data available of their use in pediatrics and their use remains off-label in children.

## Keywords:

pediatric
hepatic tumor
hepatoblastoma
hepatocellular carcinoma
focal nodular hyperplasia
hemangioma

**TABLE 91.1** Summary for Differential Diagnosis of Liver Tumor

| Tumor | Age Group | Clinical Features | Imaging Features |
|---|---|---|---|
| Hepatoblastoma | <5 y | AFP levels: elevated | Calcifications: coarse, chunky<br>Solid mass<br>Invasion veins<br>Enhancement: less than adjacent liver |
| Hepatocellular carcinoma | 10–14 y | AFP levels: elevated<br>Underlying liver disease | Solid, focal, multifocal<br>Heterogeneous, hemorrhage, necrosis<br>Invasion veins |
| Fibrolamellar carcinoma | Adolescent | AFP levels: normal<br>No liver disease | Fibrous scar: hypointense T2-weighted imaging, no enhancement<br>Homogeneous<br>Solitary mass |
| Undifferentiated embryonal sarcoma | 6–10 y | AFP levels: normal | Cystic on CT and MRI<br>Solid on ultrasound<br>Enhancement: solid portion and septa |
| Embryonal rhabdomyosarcoma | <5 y | AFP levels: normal | Often located near porta hepatis with intraductal growth pattern |
| Liver hemangioma | <1 y | AFP levels: normal<br>Cardiac heart failure<br>Coagulopathy<br>Hypothyroidism | Calcifications (50%): fine, granular<br>Enhancement: more than adjacent liver |
| Mesenchymal hamartoma | <5 y | AFP levels: normal | Cystic lesion<br>Enhancement: septa and solid portion enhancement<br>No calcification |
| Focal nodular hyperplasia | Young children<br>Adolescents | AFP levels: normal<br>Strong predilection girls | Vascular, myxoid scar: hyperintense T2-weighted imaging, delayed enhancement<br>Homogeneous lesion enhancement |
| Adenoma | >10 y | AFP levels: normal<br>Oral contraceptive or androgenic steroid use<br>Glycogen storage disease | No central scar<br>Heterogeneous: fat/hemorrhage<br>Opposed-phase T1-weighted gradient echo or fat suppressed: evidence of fat and glycogen |
| Metastases | | | Multifocal |
| Hydatid cyst | | History travel | Cystic lesion |
| Simple cyst | | | No enhancement |
| Choledochal cyst | | | Location in porta hepatis with communication with biliary tree |

*AFP,* Alpha fetoprotein; *CT,* computed tomography; *MRI,* magnetic resonance imaging.

images and signal void on gradient-echo images. On postgadolinium arterial and venous phase images, the tumor thrombus respectively enhances and then becomes a filling defect.

Hepatic scintigraphy may demonstrate increased activity on the initial angiographic phase due to tumor vascularity, and photopenia on the delayed images. Rarely, increased uptake of the radiopharmaceutical may be seen on delayed images, a finding more typical of FNH. Catheter angiography is currently rarely performed but usually shows tumor hypervascularity except in avascular areas of necrosis.[12–14]

The International Childhood Liver Tumor Strategy Group (SIOPEL) created the PRETEXT staging system for primary malignant liver tumors in children and is primarily used in hepatoblastoma. It has good interobserver reliability. It divides the liver into four sections (left lateral, left medial, right anterior, and right posterior). A PRETEXT number is designated by subtracting the highest number of contiguous sections not involved by tumor from 4. This system assists with surgical planning and prognosis, and predicts expected surgical difficulty.[15]

***Treatment.*** Where possible, hepatoblastomas are treated with surgical resection. However, about 40% to 60% of cases are unresectable at diagnosis.[16] Treatment with chemotherapy permits up to 85% of these to become resectable.[3] Imaging is crucial in assessing surgical resectability at presentation and after chemotherapy. Disseminated tumors have been successfully treated with chemotherapy and multiple resections of metastases. Radiofrequency ablation may be a promising treatment for recurrence.[17] Liver transplantation is an alternative for lesions that are considered unresectable. The presence of pulmonary metastases is not considered an absolute contraindication to liver transplantation due to their sensitivity to chemotherapy.[12] However, there should be no residual evidence of pulmonary metastasis postchemotherapy and before liver transplantation. The overall survival rate is reported at 65% to 70%.[1,12–14] Poor prognostic factors include AFP levels less than 100 ng/mL or more than 1,000,000 ng/mL, vascular invasion, and aneuploid nuclear content. Factors associated with favorable prognosis include single lobe involvement, pure fetal histologic composition, and AFP levels between 100 and 1,000,000 ng/mL.[12]

## Hepatocellular Carcinoma

HCC, the second most common liver tumor in children after hepatoblastoma, accounts for 35% of primary pediatric hepatic malignancies.[18] It affects two age peaks in childhood: 4 to 5 years, and, more commonly, 12 to 14 years.

In non-endomic areas of the world, approximately half of HCC arise in patients with underlying liver disease. Predisposing conditions

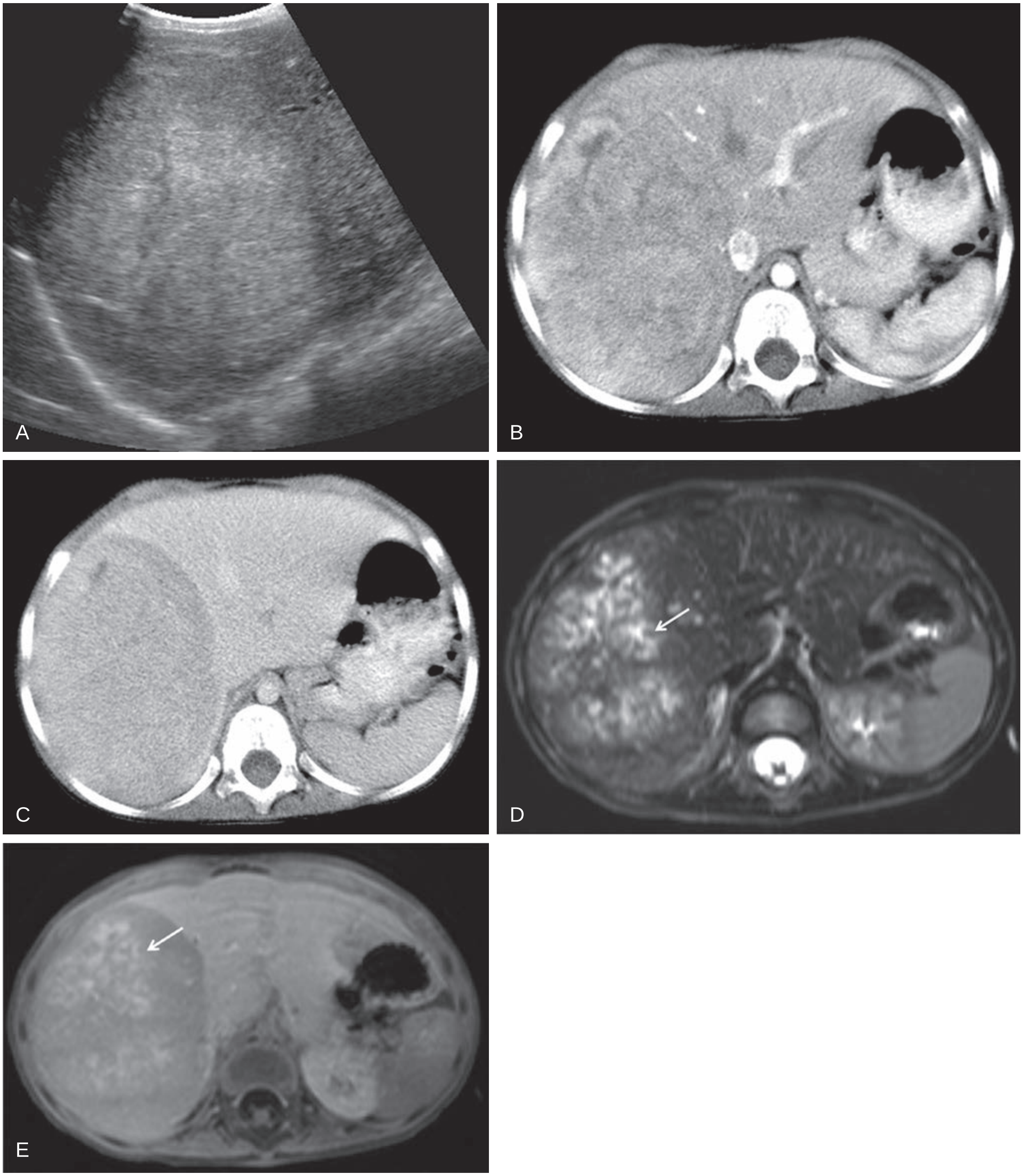

**Figure 91.1. Hepatoblastoma.** (A) Transverse abdominal sonogram in a 3-year-old boy shows a well-defined hyperechoic lesion relative to the liver. (B) CT-scan in early arterial postcontrast phase demonstrates a heterogeneous mass, hyperdense compared with the liver. (C) CT scan in delayed contrast phase shows a hypodense lesion. (D) Axial T2-weighted MR image shows hyperintense nodules with hypointense septa in between *(arrow)*. (E) Axial T1-weighted MR image after intravenous administration of gadolinium demonstrates enhancement of septa and capsule *(arrow)*.

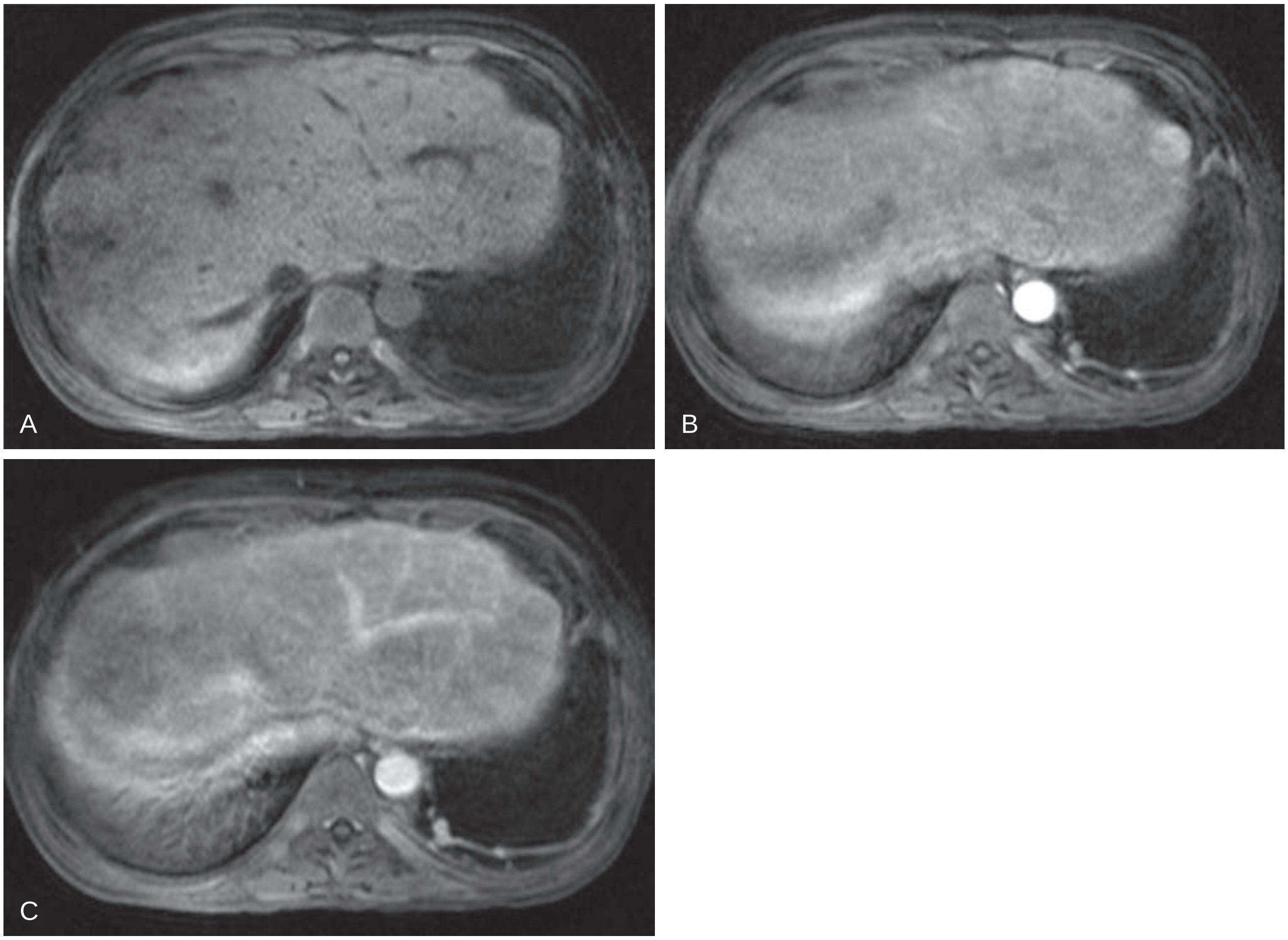

**Figure 91.2. Hepatocellular carcinoma in a 16-year-old male with cardiac cirrhosis secondary to hypoplastic left heart and Fontan circuit.** (A) Axial T1-weighted gradient echo MR image shows a nodular contour to the liver secondary to cardiac cirrhosis. (B) Postcontrast arterial phase image shows an arterial enhancing 2 cm lesion in segment 4a. (C) The lesion demonstrates washout with a peripheral enhancing pseudocapsule seen on portal venous phase images leading to a diagnosis of hepatocellular carcinoma.

include entities leading to cirrhosis such as biliary atresia, infantile cholestasis, Alagille syndrome, hemochromatosis, hereditary tyrosinemia, glycogen storage disorder, $\alpha_1$-antitrypsin deficiency, Wilson disease, galactosemia, and viral hepatitis B and C.

Serum AFP levels, like hepatoblastomas, is markedly elevated in 70% of patients.[18,19]

***Pathology.*** Neoplastic cells vary from very well to poorly differentiated. The most helpful histologic feature in distinguishing HCCs from metastases is the presence of bile canaliculi or bile pigment.[1] Kupffer cells may also be present.[12] HCCs, like hepatoblastomas, have three main growth patterns: solitary, multifocal, and diffuse/infiltrative.[12] The solitary pattern occurs most often in the right lobe of the liver. HCC demonstrates a high propensity for vascular invasion, which is present in approximately 75% of cases. Metastatic disease occurs in the lungs, brain, and skeleton.

***Imaging.*** The US findings of HCC are variable. With respect to liver parenchyma, most are hypoechoic, however, smaller lesions may be iso- or hyperechoic[12–14]; larger lesions are heterogeneous. Internal areas of increased echogenicity may represent acute hemorrhage, fat, or calcifications (less common than in hepatoblastoma), whereas areas of decreased echogenicity may represent necrosis. If a capsule is present, this may be detected as a thin halo of decreased echogenicity. Doppler demonstrates high-velocity arterial flow and is useful to identify vascular invasion by showing blood flow within the substance of the tumoral thrombus.[12]

On unenhanced CT, HCC appears as a solitary mass or as multiple well or poorly defined, hypo- to isodense masses.[14] The tumor shows variable contrast enhancement and may contain low attenuation regions of necrosis. The tumor capsule may also show a rim of low attenuation on unenhanced images that enhances on the delayed phase after contrast injection.[14] Vascular tumor thrombi may be seen as intraluminal filling defects with a surrounding meniscus of contrast. When the tumor arises in a cirrhotic liver, differentiation from regenerating nodules may be difficult.

With MR imaging, the tumor is typically slightly hyperintense on T2-weighted and hypointense on T1-weighted images, although the latter tends to be more variable because fat or hemorrhage may produce regions of hyperintensity. If a fibrous pseudocapsule is present, MR shows low signal intensity on T1- and T2-weighted pulse sequences.[20] After gadolinium, in the early arterial phase, the lesion demonstrates enhancement and washes out during the portal venous phase. The presence of a delayed enhancing pseudocapsule favors the diagnosis of HCC (Fig. 91.2). The presence of "washout" and delayed enhancing pseudocapsule are highly specific features of HCC when using extracellular contrast agents. Though the liver imaging and reporting data system (LI-RADS) is often applied in children for suspected HCC, its use has not been validated in the pediatric population. Vascular invasion appears as lack of a signal on spin-echo images and as an intravascular arterial enhancing mass with a delayed filling defect on dynamic gadolinium-enhanced images.[21]

Nuclear scintigraphy is rarely performed in patients with HCC, and usually shows decreased uptake. Fluorodeoxyglucose (FDG) PET is useful in evaluating the degree of tumor differentiation. Although the uptake of FDG is variable in HCCs, markedly elevated uptake is usually seen in poorly differentiated tumors, and well-differentiated tumors may have normal uptake.

***Treatment.*** The treatment for HCC is complete surgical resection when possible. However, approximately two-thirds of children present with unresectable disease due to multifocal or massive involvement of the liver, major vascular involvement, or metastases. HCC is relatively insensitive to systemic chemotherapy.[22] The impact of chemotherapy is unclear with no evidence that it offers additional benefit in children with resectable localized HCC. Liver transplantation is reported for unresectable tumor but remains controversial.[18]

Radiofrequency and intra-arterial chemotherapy have been reported, but the benefits need further investigation.[23,24] The prognosis is variable and directly related to the resectability and histology of the lesion. In tumors with favorable histology and complete resection, the 2-year survival rate may exceed 97%. However, without complete resection and with unfavorable histology, the 2-year survival rate may be less than 20%.[18] In places where the prevalence of tyrosinemia is especially high, routine neonatal screening and immediate treatment of positive cases by NTBC (2-[2-nitro-4-trifluoromethylbenzoyl]-1,3-cyclohexanedione) has resulted in a marked decrease in the prevalence of HCC in this population.[25]

## Fibrolamellar Carcinoma

***Overview.*** Fibrolamellar carcinoma (FLC) is a variant of HCC representing approximately 5% to 8% of all cases of HCC. It occurs in patients without underlying hepatic disease and has distinctive clinical and pathologic features. It occurs in younger patients; approximately 85% of patients are less than 35 years of age and can occur in children as young as 10 years.[26]

It has been associated with syndromes including Wilms, Carney, Fanconi anemia, and familial adenomatous polyposis; these associations have been implicated in shared molecular pathways.

Patients present with abdominal symptoms or pain, and sometimes a palpable mass. Uncommon presentations are gynecomastia, jaundice, and venous compression or thrombosis. AFP levels are generally normal.[12,20]

***Pathology.*** In 80% to 90% of patients, FLC is a large, circumscribed, and nonencapsulated mass.[20] Uncommonly, it is multifocal. A central fibrous scar is common and may contain calcifications. Metastatic lymphadenopathy is seen in 70% of cases.[27]

***Imaging.*** US shows a well-defined mass with heterogeneous echotexture containing iso- or hyperechoic areas.[28] The central scar is visualized in 50% of patients, is hyperechoic, and may contain calcifications.

CT shows a low-density, well-defined lobulated mass with calcifications in 30% to 55% of cases and a central scar in 45% to 60% of cases. The central scar is hypoattenuating with little

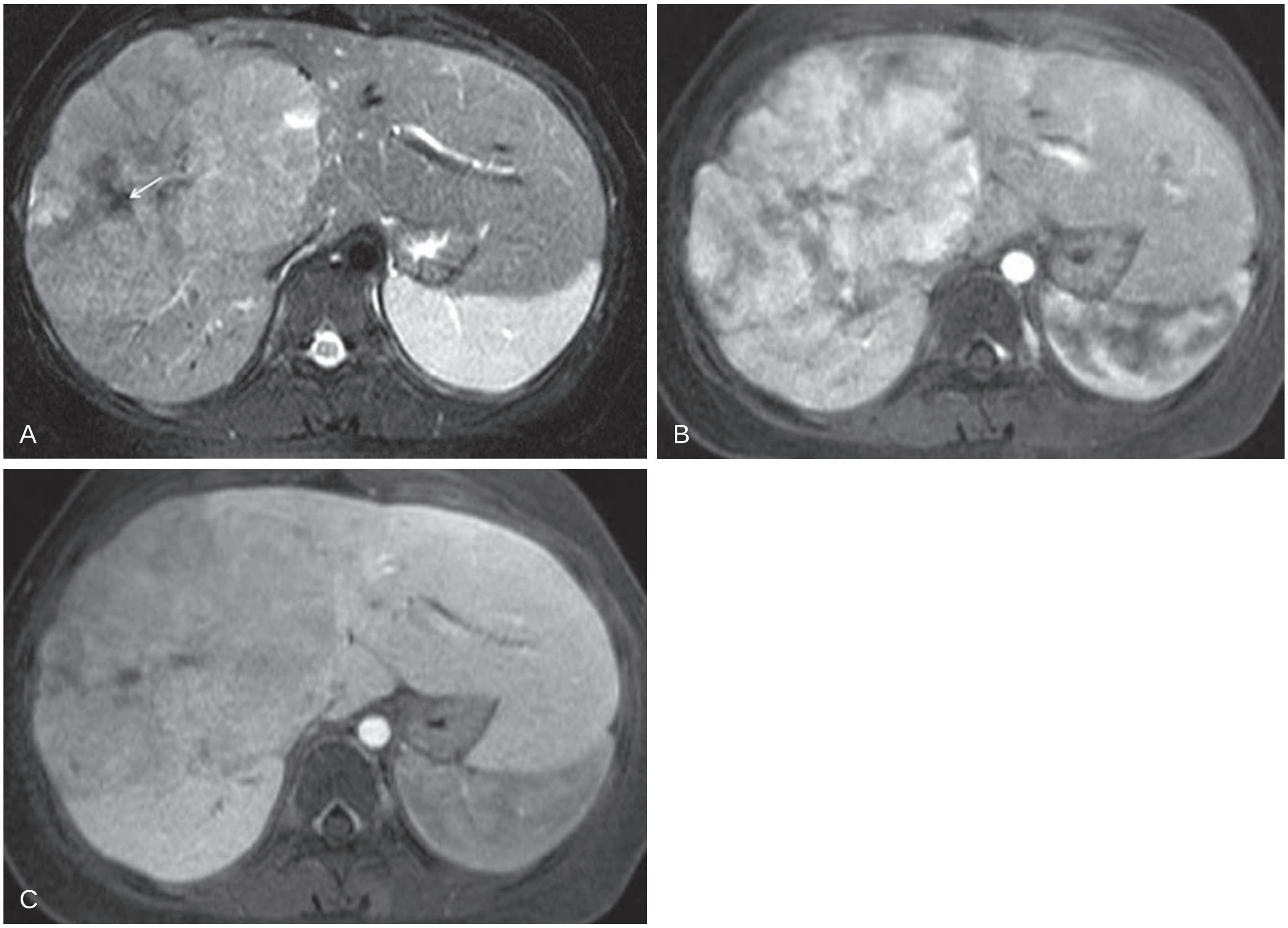

**Figure 91.3. Fibrolamellar carcinoma in a 16-year-old girl.** (A) Axial T2-weighted MR image shows a large mass in the right lobe of the liver with a hypointense *(arrow)* central scar. (B) The mass enhances avidly in the early arterial phase. (C) Portal venous phase demonstrates washout of contrast with the lesion becoming hypointense compared with the normal liver parenchyma.

or no enhancement. Adjacent lymphadenopathy is often present in the hepatic hilum at diagnosis.

On T1-weighted MRI, the tumor is hypo- (86%) to isointense (14%), and slightly hyper- (85%) to isointense (15%) on T2-weighted images (Fig. 91.3).[12–14,16–24,26–29] The fibrous scar is hypointense on T1 and T2 imaging. The hypointensity of the central scar and lack of contrast retention in the mass on hepatocyte phase imaging helps differentiate FLC from FNH.

***Treatment.*** The treatment of FLC is primarily surgical resection, and surgical resectability is therefore the most important prognostic factor.[28] When the tumor is not resectable, liver transplantation, systemic chemotherapy, or hepatic intra-arterial chemoembolization are considered. Recent literature reports no significant difference in the prognosis of FLC compared with HCC in patients without underlying hepatic disease.[26,27] Normal hepatic function, younger age, absence of vascular invasion or thrombosis, lack of lymphadenopathy, and negative surgical margins are favorable prognostic indicators. The 5-year survival rate ranges from 30% to 67%.[23,24,26,27]

## Undifferentiated Embryonal Sarcoma

UES, previously called malignant mesenchymoma, embryonal sarcoma, or fibromyxosarcoma, is a rare, aggressive tumor of mesenchymal origin.

Most commonly, the tumor affects children between 6 to 10 years of age with a slight male predominance.[30] It is the third most common malignant pediatric liver tumor.[3,19,31]

***Pathology.*** On histology, UES shows primitive spindle-shaped, sarcomatous satellite cells, closely packed in sheets or whorls, and scattered throughout a background of loose myxoid tissue, which contains foci of hematopoiesis in 50% of cases.[30] It is usually large at presentation, solitary, and is predominantly solid with occasional cystic, necrotic or hemorrhagic areas and involves the right lobe of the liver (75%).[30] Metastases are usually to the lung and bone. AFP levels are normal.[19]

***Imaging.*** On sonography, the tumor is solid and iso- to hyperechoic relative to normal liver with small anechoic spaces, which correspond to necrosis, hemorrhage, or cystic degeneration.[30,32]

On CT, the tumor reveals predominantly water attenuation correlating with myxoid stroma (88% of tumor volume).[12,30] After IV contrast, a dense enhancing peripheral rim can be seen in relation to the pseudocapsule. Uncommon hyperattenuated regions may indicate hemorrhage and calcifications.

At MR, the tumor is of low intensity on T1- and increased intensity on T2-weighted sequences (Fig. 91.4). A hypointense rim on T1- and T2-weighted images indicates a pseudocapsule. Bright areas on T1-weighted images correspond to regions of hemorrhage. Fluid levels, internal debris, and septa may be seen on T2-weighted images.[30,32] Heterogeneous enhancement of the tumor is seen after intravenous gadolinium contrast.[33]

***Treatment.*** The treatment is complete tumor resection. As late as three decades ago, the prognosis was poor with death occurring within 12 months in many cases.[31] However, more recent reports of multimodal treatment show markedly improved survival. Patients with unresectable tumors, which are not responsive to chemotherapy, can be treated with liver transplantation.[12]

## Rhabdomyosarcoma of the Biliary Tree

Although rhabdomyosarcoma can be found throughout the body, involvement of the biliary ducts is one of the rarest forms of this mesenchymal tumor. It occurs almost exclusively in the pediatric age group and under the age of 5 years (75% of cases).[12] Jaundice is the most frequent presentation, and it may resemble hepatitis, which can cause a delay in diagnosis.[34] Elevated serum conjugated bilirubin and alkaline phosphatase occur with normal levels of AFP.

***Pathology.*** The tumor arises from beneath the biliary epithelium[35] and grows as a polypoid mass within the biliary tree. It most frequently occurs in the common bile duct but can arise within the intrahepatic bile ducts, gallbladder, and cystic duct. Only the embryonal subtype of rhabdomyosarcoma arises in the biliary tree.[12] Histologically, rhabdomyosarcoma demonstrates undifferentiated blue cells with scant cytoplasm and primitive nuclei that form a firm, lobulated mass with infiltrative margins and a well-defined pseudocapsule.[9,12,16,36]

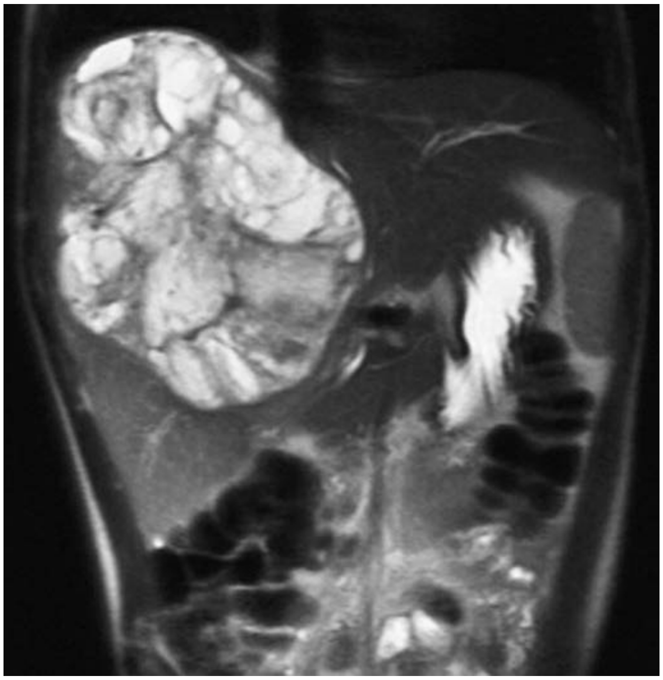

**Figure 91.4. Undifferentiated embryonal sarcoma in a 13-year-old girl.** Coronal T2-weighted MR image shows a multiloculated mass of heterogeneous signal intensity in the right lobe of the liver. *(Courtesy of Lynn Fordham, MD.)*

At diagnosis, metastases are present in 30% of cases,[12] typically to the lung, skeleton, and pericardium, although the tumor has a greater propensity to invade contiguous structures.[35]

***Imaging.*** US usually demonstrates a solitary, heterogeneous, relatively hypoechoic mass or multiple hypoechoic nodules associated with biliary duct dilatation and intraductal extension.[12,37] Portal vein displacement without thrombosis is common.[37]

CT shows a homo- or heterogeneous hypo- or hyperattenuating intraductal mass with variable contrast enhancement associated with biliary dilatation (Fig. 91.5).[37,38] MRI usually shows low-signal intensity on T1- and high-signal intensity on T2-weighted sequences, with intense, heterogeneous enhancement after IV contrast administration.[12,37] MR cholangiopancreatography often demonstrates a partially cystic lesion in the common bile duct and a mass adjacent to the duct causing mural irregularity. Percutaneous cholangiography displays an intraluminal polypoid mass.[37–39] Gallium uptake can help localize metastatic disease.[37]

***Treatment.*** Multimodal therapy, including surgical resection, radiation, and chemotherapy, has improved outcome with 78% survival in local disease.[40] Concurrent internal or external biliary drainage is essential because some chemotherapeutic agents depend on hepatobiliary excretion, and an inability to excrete them may result in significant systemic toxicity.[40]

## Angiosarcoma

Angiosarcoma is a rare, aggressive, malignant vascular tumor. It typically presents in adults with a history of exposure to thorium dioxide (Thorotrast), arsenic, and vinyl chloride[12,41]; however,

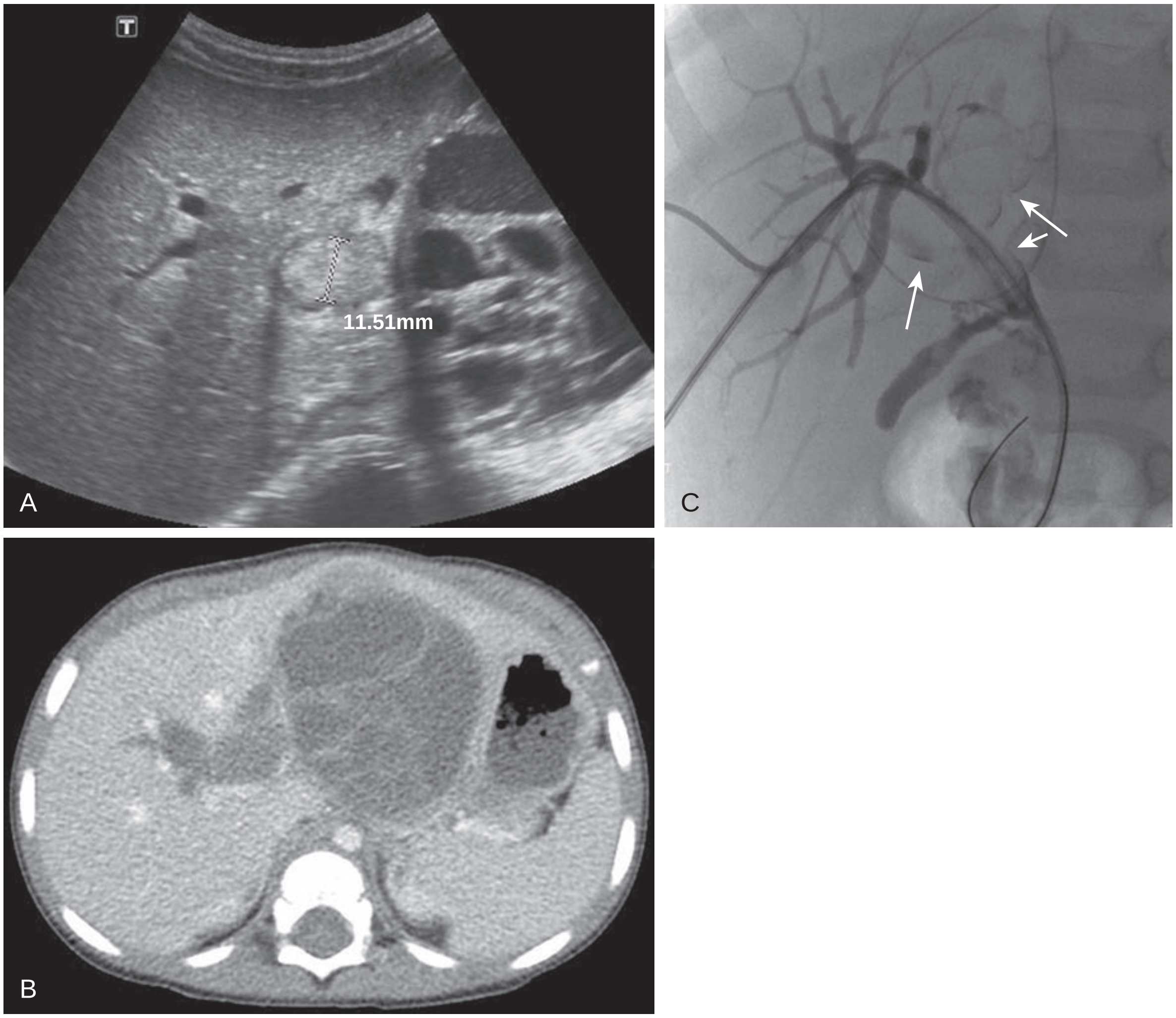

**Figure 91.5. Embryonal rhabdomyosarcoma in a 20-month-old boy.** (A) Transverse sonogram shows a multicystic lesion with a hyperechoic mass in the common biliary tree. (B) CT-scan shows the hypoattenuating tumor in the common bile duct that extends into the intrahepatic and extrahepatic bile ducts. (C) Percutaneous cholangiography reveals multiple filling defect of the common bile duct with extension in the intrahepatic bile ducts *(arrows)*.

exposure to these toxins is now rare. It can arise de novo in adults, in a cirrhotic background, or associated with hemochromatosis and use of anabolic steroids, leading to this tumor being considered the "quintessential example of malignant transformation secondary to environmental exposures."[42,43]

In children, the tumors are very rare, occurring after the age of 1 year. They typically arise without prior history of exposure, with cases reported arising in children with previously diagnosed infantile hemangioendotheliomas.[41,44] Clinical symptoms include hepatomegaly associated with pain, anorexia, and weight loss, as well as thrombocytopenia and consumptive coagulopathy.[43]

***Pathology.*** Histologically, the spindle cell form (hypercellular whorls with intermingled bile ducts and vessels) is especially common in children.[36,41] At the time of diagnosis, 60% of cases have metastatic disease, most commonly to the lungs and spleen.[42,43]

Immunohistochemical studies demonstrate reactivity of tumor cells to factor VIII-related antigen, CD31, and CD34 confirming the vascular nature of the tumor.[45]

***Imaging.*** Imaging findings are variable. It can be solitary, multifocal, or diffuse.

On US, the lesion is heterogeneous, and the echogenicity varies depending on the amount of hemorrhage or necrosis. At CT, nodules are hypoattenuating and may contain foci of hemorrhage. Contrast enhancement is variable.[42,46] At MR imaging, the masses show low-signal intensity on T1-weighted images with hyperintense foci (related to hemorrhage), and heterogeneous-signal intensity on T2-weighted images (e-Fig. 91.6). Dynamic MR imaging with contrast reveals a heterogeneous pattern of enhancement.[43] FDG PET/CT displays marked uptake in the tumors and is helpful for the detection of metastases.

***Treatment.*** The prognosis is dismal with a rapid deterioration of patients within six months from the diagnosis regardless of treatment.[12,42,45]

## Cholangiocarcinoma

Cholangiocarcinoma is a rare hepatic neoplasm accounting for less than 1% of all carcinomas. It may complicate disorders that affect children, such as choledochal cysts and sclerosing cholangitis, but it usually occurs late in the disease process and thus presents mainly in adults.

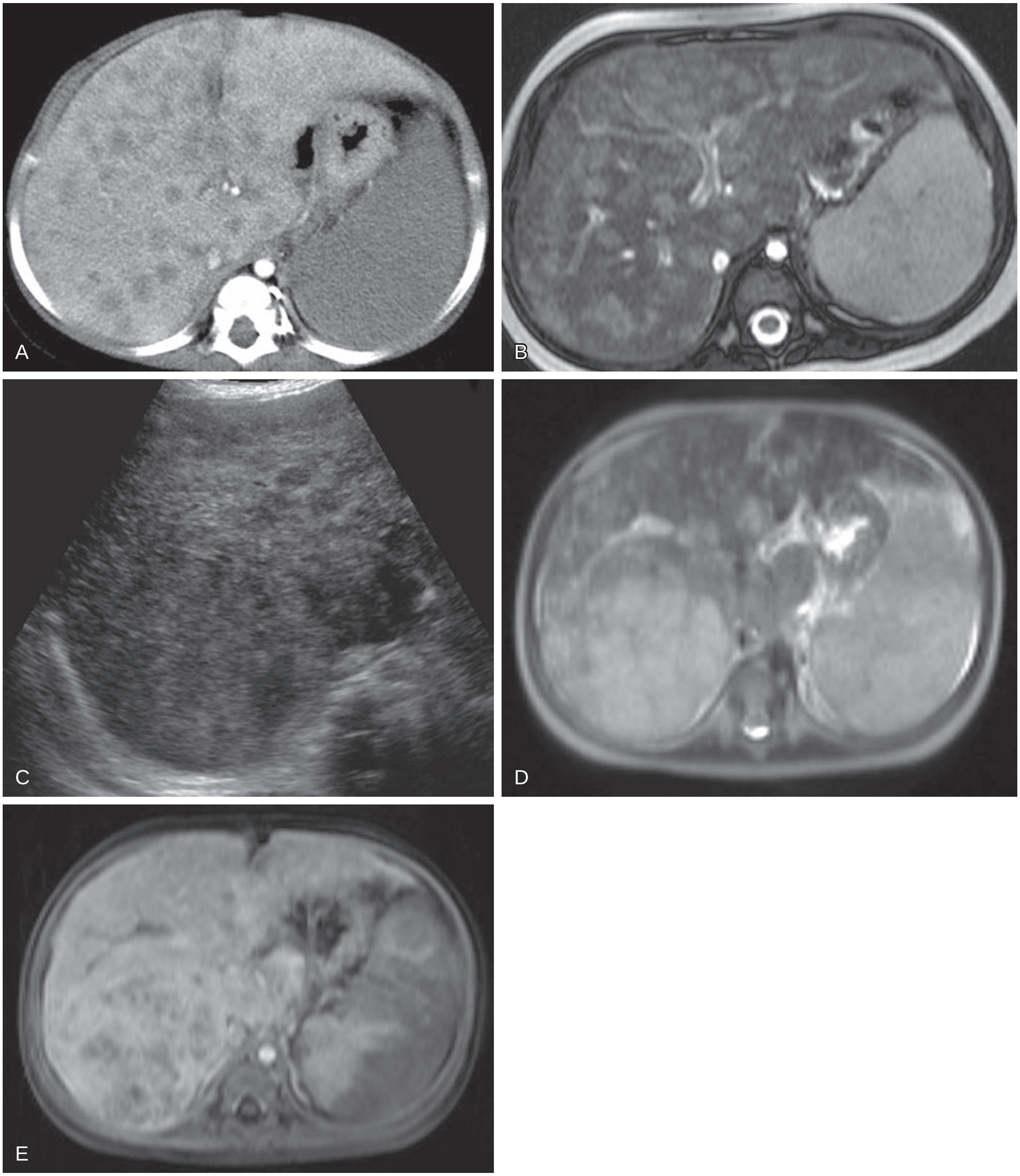

**e-Figure 91.6. Angiosarcoma.** (A) A 9-month-old girl with normal US liver at 3 days of life shows numerous hypodense lesions in the liver on CT-scan with contrast enhancement. (B) Axial T2-weighted MR image demonstrates multiple hyperintense nodules diagnosed as infantile hemangioma. Under steroid and interferon, a complete regression of lesions was seen. Eight months later, the patient presented a coagulopathy and abdominal mass. (C) US shows multiple infiltrating nodules associated with a significant lesion in the right lobe. (D) Axial T2-weighted MR image shows a heterogeneous signal intensity. (E) Dynamic MR at 5 minutes demonstrates a heterogeneous pattern of enhancement. *(Courtesy of Lise H. Lowe, MD.)*

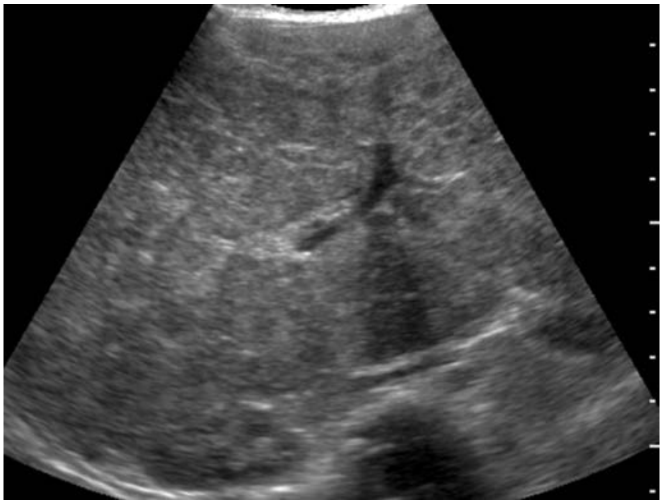

**Figure 91.7. Metastatic infiltrative neuroblastoma in an 8-month-old boy with hepatomegaly.** Transverse sonogram reveals numerous discrete lesions of variable echogenicity and loss of normal architecture.

## Hepatic Metastases

Hepatic metastases in children most often arise from neuroblastoma, lymphoma, and Wilms tumor. The appearance of metastatic disease is highly variable, ranging from one or more focal lesions to a diffuse infiltrative pattern, which is most often seen in neuroblastoma. Most discrete hepatic metastases are multiple; hypoechoic on sonography; low attenuation on CT, with a tendency toward peripheral enhancement; and hypointense on T1- and hyperintense on T2-weighted MRI. Hepatic metastases demonstrate diffusion restriction and lack of contrast retention on hepatocyte phase imaging with hepatobiliary contrast agents. These imaging findings however have to be interpreted in conjunction with patient history and signal intensity on T1- and T2-weighted imaging as benign lesions such as FNH can also demonstrate diffusion restriction.

Metastatic neuroblastoma to the liver has two typical patterns: (1) numerous discrete lesions of variable echogenicity, attenuation, and enhancement; and (2) diffuse infiltration with distortion of the normal hepatic architecture, leading to hepatomegaly (Fig. 91.7). The latter pattern is especially common with stage IV-S disease (primary lesion limited to the organ of origin or primary lesion with regional spread but without extension across the midline, and involvement of the liver, skin, or bone marrow).

Both Hodgkin disease and non-Hodgkin lymphoma involve the liver in more than one-half of patients. Primary hepatic lymphoma is rare. Lymphoma may present with multiple discrete lesions or an infiltrative pattern similar to that of neuroblastoma. In addition, lymphoma is often associated with lymphadenopathy and splenic lesions.

## BENIGN HEPATIC NEOPLASMS

### Liver Hemangioma

Hepatic hemangiomas (HHs) are true benign vascular tumors and can be divided into infantile and congenital hemangiomas. Congenital hemangiomas are divided into rapidly involuting congenital hemangiomas (RICH) and noninvoluting congenital hemangiomas (NICH). These must be differentiated from misnamed adult HHs, which are venous malformations. The literature reports three patterns of presentation of HHs: focal, multifocal, and diffuse.

Usually, focal HHs are RICH diagnosed during in utero. RICH has an equal sex distribution, negative GLUT-1 immunoexpression, and no association with cutaneous infantile hemangiomas. RICH is a significant hypervascular tumor with shunting that may lead to cardiac insufficiency at birth. It may be associated with transient thrombocytopenia and anemia.

Multifocal and diffuse HHs are true infantile hemangiomas with the female:male ratio of 3–5 : 1. Most are associated with cutaneous infantile hemangioma with a positive GLUT-1 immunoexpression.

Most liver hemangiomas are clinically silent and remain undetected. However, they can also present with life-threatening complications, especially in the setting of multifocal lesions with congestive heart failure related to an intralesional shunt, hypothyroidism secondary to overproduction of type III iodothyronine deiodinase, fulminant hepatic failure and/or abdominal compartment syndrome, consumptive coagulopathy related to intralesional thrombosis, hemorrhage, and hemolysis.

***Pathology.*** The differentiation between infantile and congenital hemangiomas (NICH or RICH) is often impossible because: (1) usually there is no biopsy to look for GLUT-1 marker present in infantile hemangioma; and (2) unlike skin lesions, it is usually not known whether or not the hepatic lesion is present at birth.

***Imaging***

*(1) Solitary Lesions.* On US, a well-defined hypo- or hyperechoic lesion is seen. The echotexture is sometimes heterogeneous, related to central hemorrhage or necrosis. Color Doppler US demonstrates a variety of flow patterns depending on the presence of microshunt, portosystemic, or arteriovenous shunt. These shunts are clinically significant only when associated with cardiac failure.

HHs typically appear on CT as low-attenuation masses that may contain calcifications. After IV contrast, there is usually early peripheral and nodular enhancement with variable delayed central enhancement.

On MRI, they are typically hypointense on T1-weighted images and hyperintense on T2-weighted images. The contrast enhancement pattern on MRI is similar to that seen on CT (Fig. 91.8).[47] Heterogeneous signal on all sequences is seen if hemorrhage, thrombosis, and/or necrosis are present. Calcification occurs in approximately 16% of cases.

*(2) Multifocal Lesions.* On US, small multifocal lesions are homogeneous and most are hypoechoic, although hyperechoic nodules may occur. The hepatic arteries and veins generally appear enlarged. Large feeding arteries and draining veins are seen in and around the vascular tumors (Fig. 91.9).

On MR, multiple nodular tumors are T1 hypointense and T2 hyperintense, and demonstrate homogeneous enhancement after gadolinium injection. Flow voids are seen within and/or adjacent to the lesions due to large hepatic arteries or veins. Aortic tapering distal to the celiac trunk is a good indicator of increased hepatic flow, and accordingly is a predictor of cardiac overload risk.[48]

*(3) Diffuse Lesions.* Diffuse lesions present with extensive hepatic involvement, the numerous small lesions in the liver leading to severe hepatomegaly.[49] Despite the size of the lesions, most diffuse liver hemangiomas show no cardiac failure in relation to the shunt. The enlarged infiltrated liver reveals numerous hypoechoic lesions. MR imaging findings are similar to the focal and multifocal lesions.

***Treatment.*** No treatment is required for asymptomatic focal, multifocal, or diffuse HH.

RICH characteristically regresses in an accelerated fashion by 12 to 14 months.[50–53]

Medical treatment can be attempted even though the benefit of medical treatment is unknown.

Patients with multifocal or diffuse infantile HH associated with compartment syndrome, cardiac failure, or hypothyroidism are treated with propranolol (a nonselective beta blocker) and/or systemic glucocorticoid, and control of hypothyroidism. Catheter embolization is recommended for patients with cardiac failure

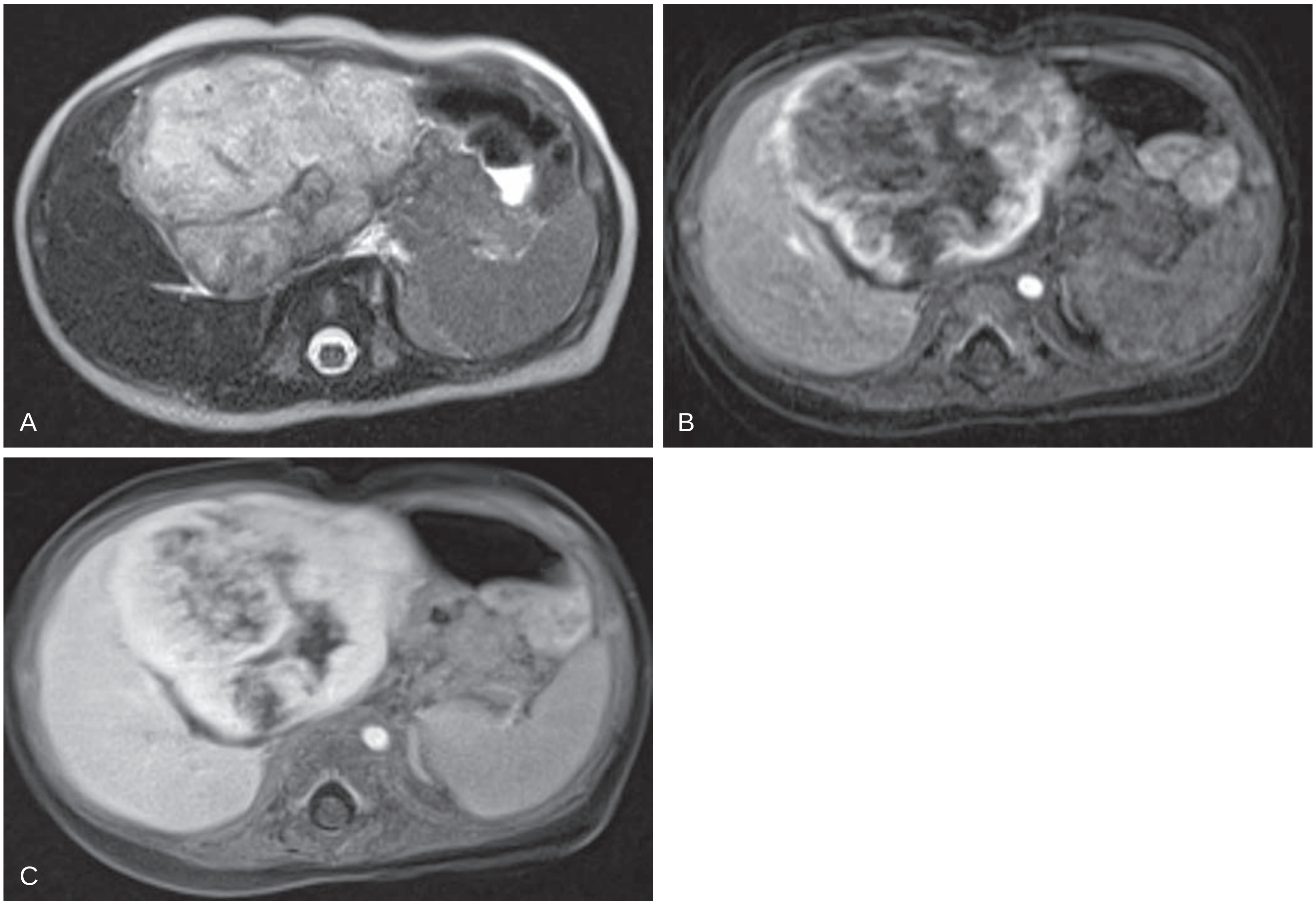

**Figure 91.8. Focal liver hemangioma in a 4-month-old boy.** (A) Axial T2-weighted MR image shows a fairly well-circumscribed T2 hyperintense mass in the left lobe of the liver. (B) Dynamic postcontrast arterial phase image shows peripheral puddling enhancement in the mass. (C) Equilibrium phase image obtained at five minutes postcontrast demonstrates gradual fill in. Note that the intensity of enhancement follows the blood pool closely.

related to arteriovenous or portosystemic shunts when medical treatment has failed.[54] Vincristine is an alternative for patients refractory to beta blockers or steroid treatment.[55] In selected instances, liver transplant may be contemplated.

## Mesenchymal Hamartoma

Mesenchymal hamartoma is the second most common benign liver mass in children after vascular tumors. Most of them are discovered by 5 years of age.[3,56,57] Mesenchymal hamartomas affect boys slightly more often than girls and have been diagnosed on prenatal US. The most common clinical presentation is painless abdominal distension. AFP levels are normal.

***Pathology.*** Histologically, it is composed of disordered, primitive, fluid-filled mesenchyme, hepatic parenchyma, and bile ducts, in addition to stromal cysts of variable size without a capsule. The mass may be pedunculated and attached to the inferior surface of the liver.

***Imaging.*** On US and CT, mesenchymal hamartomas are typically multicystic, heterogeneous masses with septa (Fig. 91.10). They are not typically associated with calcifications or hemorrhage. The cysts are anechoic with thin or thick septa. When the cysts are tiny, the lesion appears as a solid echogenic lesion. Low-level echoes may be seen within the fluid related to gelatinous contents or hemorrhage. On CT, mesenchymal hamartomas are complex cystic masses. Their septations and solid components enhance after IV contrast. On MRI, the cystic regions are hypointense on T1- and hyperintense on T2-weighted images. The signal intensity varies, depending on the stromal content, the amount of protein, and the presence or absence of hemorrhage within the cyst. Septa and solid portions of the lesion are usually of decreased signal on T1- and T2-weighted images.[13,14,58–60] Enhancement occurs within septa and the solid components of hamartomas.

***Treatment.*** The treatment for mesenchymal hamartoma is surgical resection. Observation of mesenchymal hamartoma is not recommended due to rare reports of malignant transformation to UES.[61,62] Long-term survival is 90% even with incomplete resection.[3,57]

## Focal Nodular Hyperplasia

FNH accounts for 2% of all primary pediatric hepatic tumors. It is most commonly diagnosed incidentally in children with a mean age at diagnosis between 8 and 11 years and has a marked female predominance.[3]

Although the exact cause of this lesion is often uncertain, it is generally thought to be due to an underlying hepatic vascular disturbance.[63] Long-term survivors of pediatric malignancy have a higher incidence of FNH believed to be a manifestation of injury sustained to the vascular endothelium secondary to chemotherapy and/or radiotherapy.[64,65] This represents about one-third of children with FNH. Most patients have a history of malignancy or

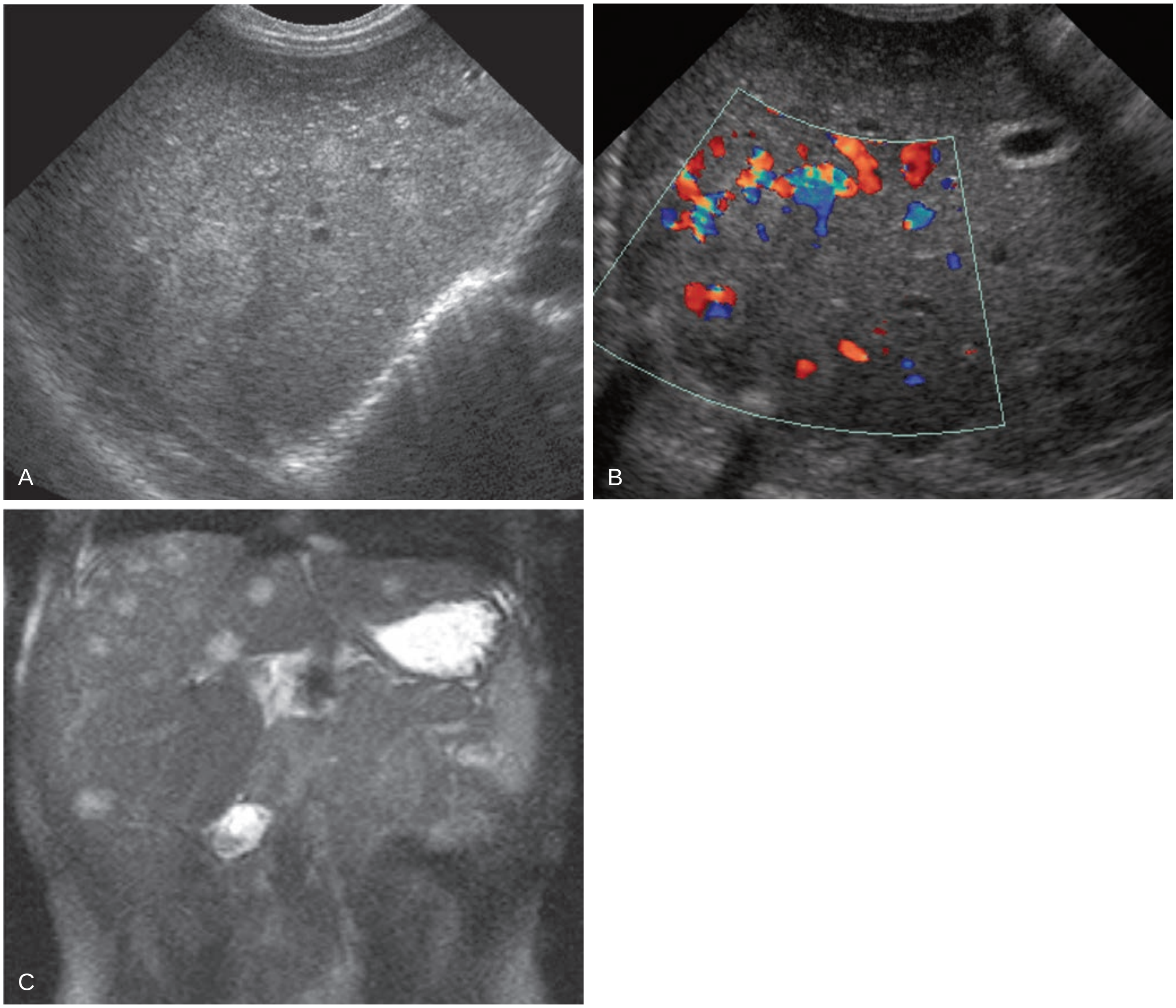

**Figure 91.9. 14-day-old girl with multiple skin infantile hemangiomas with liver hemangioma.** (A) Transverse sonogram shows hyperechoic multiple lesions. (B) Color Doppler US reveals hypervascular nodules. (C) Coronal T2-weighted MR image shows multiple hyperintense lesions.

hematologic disorder requiring stem cell or bone marrow transplant, high doses of alkylating agents that are very hepatotoxic and associated with hepatic veno-occlusive disease and radiotherapy. Oral contraceptives and pregnancy are no longer considered risk factors for the FNH development,[66] however the discontinuation of oral contraceptives is recommended. FNH is also seen in patients with portosystemic shunts and most of them regress after the closure of the shunt.

***Pathology.*** Histologically, FNH is composed of hepatocytes (filled with fat, triglyceride, and glycogen), Kupffer cells, malformed blood vessels, and radial fibrous septa with bile ducts unconnected to the biliary tree. Foci of necrosis and hemorrhage are rare compared with HCA.[66] It usually contains a central vascular scar. FNH is most common in the right hepatic lobe and is multiple in 20% of cases.

***Imaging.*** On imaging, FNH is composed of a single, well-defined, often subcapsular mass with a characteristic vascular myxomatous central scar. However, atypical imaging features are common and necessitate multiple studies to obtain the diagnosis. FNH in pediatric cancer survivors tend to be multiple as opposed to the solitary lesions seen in healthy individuals.

On US, FNH is a well-defined homogeneous mass.[67] The central scar, seen in approximately 33% of cases on US, appears hyperechoic relative to the remaining mass.[66,67] On color Doppler US, increased blood flow is seen in the central scar extending to the periphery in a spoke-wheel pattern.[68,69] The flow is arterial compared with intratumoral venous flow seen in an adenoma.

On unenhanced CT, the mass and central scar are hypo- to isodense in comparison with liver. A central scar is found in up to 60% of cases. After the administration of contrast material, the mass enhances brightly, with delayed enhancement and washout of the central scar.[70]

On MRI, FNH is iso- to slightly hypointense to liver on T1- and iso- to slightly hyperintense on T2-weighted images. The scar is hypointense on T1- and hyperintense on T2-weighted images. Dynamic intravenous contrast imaging shows uniform enhancement, during the arterial phase and mild to absent enhancement on delayed images.[67,71,72] When using a MRI hepatobiliary contrast

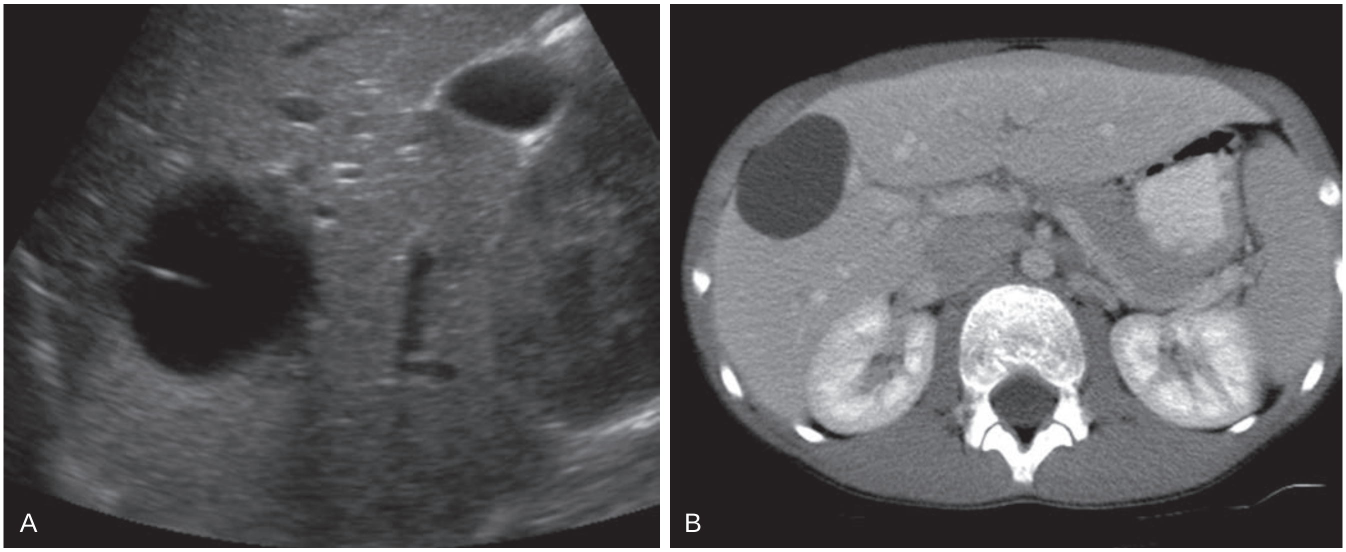

**Figure 91.10. Mesenchymal hamartoma in an 11-year-old male with an abdominal pain.** (A) Transverse sonogram demonstrates a well-defined, lobulated anechoic mass with a septation. (B) Axial contrast-enhanced CT image confirms the well-defined fluid attenuation lesion.

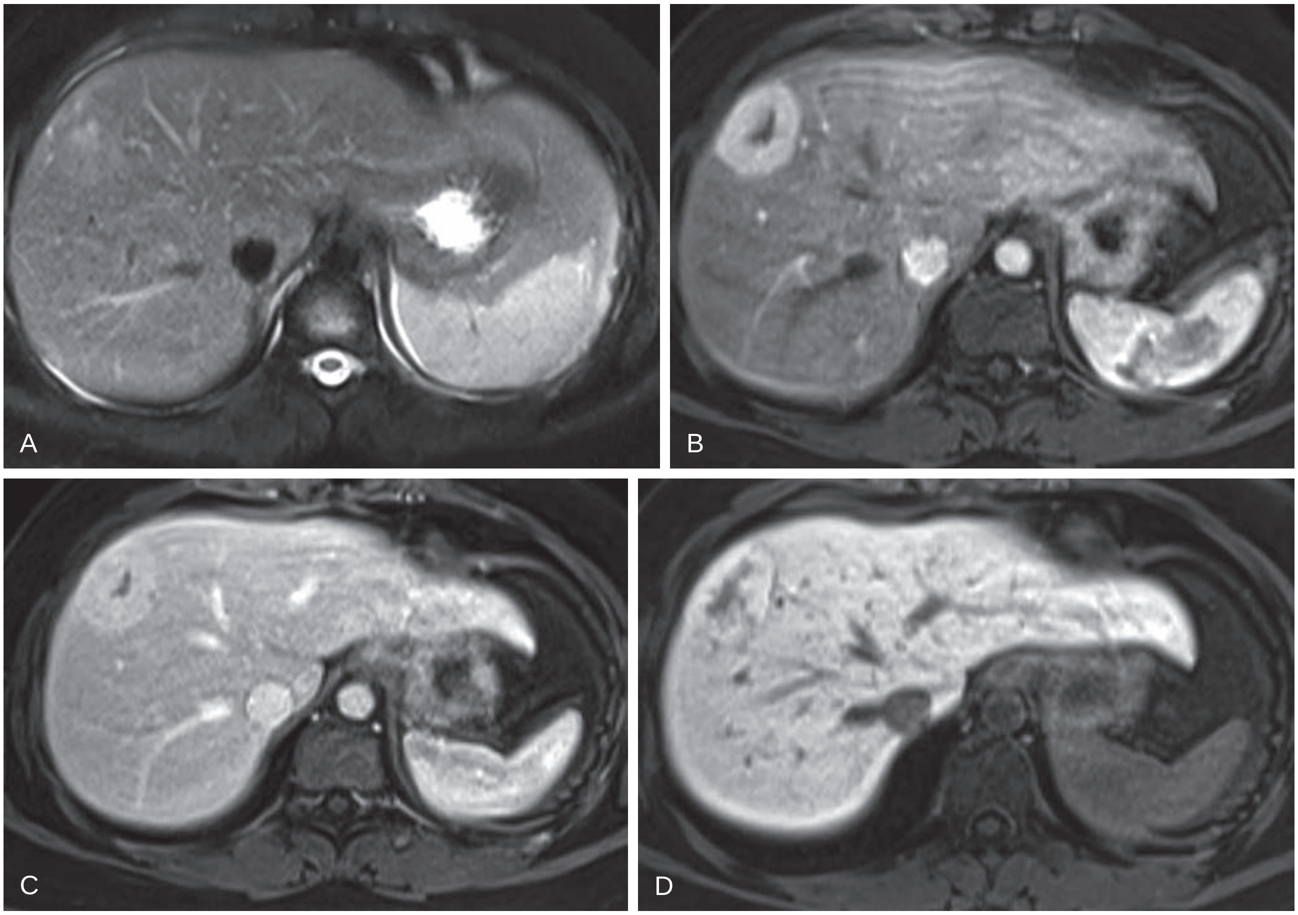

**Figure 91.11. 14-year-old girl with incidentally detected focal nodular hyperplasia.** (A) Axial T2-weighted MR demonstrates a lesion in segment 8 of the liver. The lesion is essentially isointense to the liver parenchyma and has a central T2 hyperintense scar. Dynamic postcontrast imaging was performed with hepatobiliary contrast agent. (B) The lesion demonstrates intense peripheral enhancement on arterial phase imaging. (C) Portal venous phase image shows the lesion is becoming isointense to the liver parenchyma. (D) Hepatocyte phase imaging demonstrates retention of contrast within the lesion leading to a diagnosis of FNH.

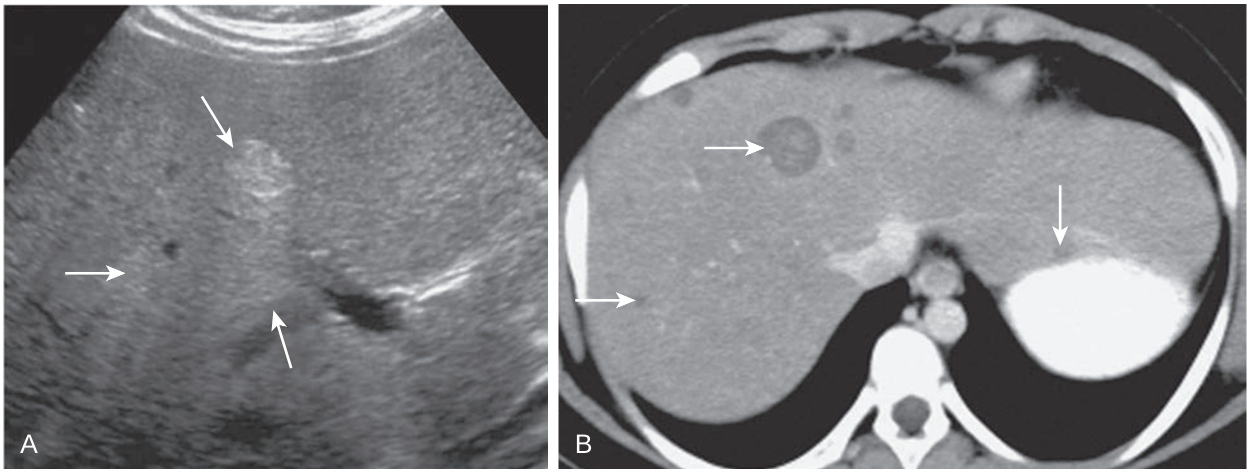

**Figure 91.12. Hepatocellular adenoma in a 9-year-old girl with glycogen storage disease.** (A) Axial sonogram reveals hyperechoic foci within the liver *(arrows)*. (B) Axial contrast-enhanced CT confirms multiple well-defined, hypoattenuating masses of varied size throughout the liver *(arrows)*. *(Courtesy of Dr. Lisa Hutchison.)*

agent, which is currently off-label in the pediatric population (e.g., Eovist; gadoxetate disodium), FNHs demonstrate retention of contrast on delayed images obtained 20 minutes after contrast material injection (hepatobiliary phase) (Fig. 91.11). The enhancement is often vivid resembling a spoked wheel because of the central scar and radiating fibrous septa. On hepatocyte phase images after Gd-EOB-DTPA, it usually appears iso- or hyperintense relative to the surrounding liver parenchyma, showing the classic popcorn like enhancement pattern because of the accumulation of Gd-EOB-DTPA and poor biliary drainage unlike an adenoma that typically appears hypointense because of the lack of biliary canaliculi.

Only FNH contains sufficient Kupffer cells to cause normal to increased uptake on technetium-99m TC sulfur colloid scintigraphy, a finding that is nearly pathognomonic. Sulfur colloid scans may be utilized to distinguish between FNH and HCA.[9,67–69]

In the group of children with a history of chemo- and/or radiotherapy, FNH can be confused with tumor recurrence. Strong enhancement at the arterial or early portal phase is important to differentiate FNH from metastases that usually remain hypointense on arterial or early portal phase when compared with the surrounding liver. Even if not presenting the typical diagnostic criteria for FNH, multiple liver lesions strongly enhancing at the arterial phase in a long-term cancer survivor are highly suggestive of the diagnosis.

***Treatment.*** FNH has no malignant potential and rarely hemorrhages or ruptures. Conservative management with serial hepatic US examination is recommended for asymptomatic patients. Recommendations for symptomatic patients include discontinuation of oral contraceptives, surgical resection, ablative therapy, or embolization.[9]

## Hepatocellular Adenoma

HCAs are extremely rare during childhood and occur more often in adult women. Girls over 10 years of age using oral contraceptives are the most frequent pediatric patients with liver adenomas.[19,57] HCAs are also associated with anabolic steroid therapy in men (e.g., Fanconi anemia),[73,74] glycogen storage disease types I and III, galactosemia, and familial diabetes mellitus. An association between hypervascular liver neoplasms, such as HCA and FNH, and patients with congenital or acquired abnormal hepatic vasculature (portal vein absence or occlusion, and congenital portosystemic shunts) has been reported. Malignant transformation of HCA into HCC is rare. Patients are commonly asymptomatic. Liver function is normal with no elevation of AFP levels.[75–76]

***Pathology.*** On histology, HCA consists of a solitary, spherical growth of hepatocytes within a pseudocapsule. The hepatocytes contain an increased amount of fat and glycogen, and are organized in sheets, along with thin-walled vessels, bile ducts, and dysfunctional Kupffer cells. Intratumoral hemorrhage occurs in approximately 10% of patients and results rarely in intraperitoneal hemorrhage and hypovolemic shock.[74] Adenomas are multiple in 20% of cases and are called adenomatosis when four or more are present.

***Imaging.*** Making the diagnosis of HCA by imaging can be challenging. When sporadic, HCA are frequently large solitary masses. In predisposed children, multiple HCA are more frequently observed.

The US appearance of HCA depends on the tumor content, which consists of lipid or hemorrhage. The hyperechoic component can be related to the lipid content or hemorrhage; they may have a surrounding hypoechoic rim, and some may lack a well-defined wall (Fig. 91.12). The lesion may appear hypoechoic especially in the setting of diffuse fatty infiltration and/or glycogen storage.[77] Color Doppler US shows central venous flow, which is different from FNH with a central arterial scar.[78]

On unenhanced CT, HCAs are usually hypodense with a low-attenuation capsule (25%) and a well-defined border; the presence of hemorrhage or fat can result in heterogeneous attenuation (7%). Homogeneous enhancement is seen during the arterial phase of contrast injection, and the mass becomes isodense on delayed CT images.[76–79]

On MRI, most HCAs are mildly hyperintense to liver on T1- and on T2-weighted images.[76,80–82] On fat suppressed or opposed-phase images, the signal drops out relative to the fat content.[76] This finding is not specific to adenomas and can also be seen in HCC. The pseudocapsule is hypointense on T1- and variable signal on T2-weighted images, and may enhance. Experience with hepatocyte-specific agents suggests that the lack of bile ducts can be used to distinguish between HCA and FNH. HCAs lack biliary ducts and therefore do not enhance, and are typically hypointense to liver parenchyma on hepatocyte phase imaging, while FNHs often demonstrate hyperenhancement during that phase.

Common features that distinguish HCA from FNH include: lack of a central scar, T1-weighted gradient recalled echo (GRE), out-of-phase signal loss due to the presence of intracellular lipid, and lack of contrast material retention on delayed imaging when using a hepatobiliary contrast agent.

Gallium uptake in HCAs is decreased, and they do not usually take up sulfur colloid, appearing as photopenic defects on both studies. Rarely, a HCA contains enough Kupffer cells to show uptake of sulfur colloid on scintigraphy, a finding typically associated with FNH.[78] With hepatobiliary scintigraphic agents, HCAs usually have early uptake, which persists on delayed images.[83]

***Treatment.*** Treatment options include discontinuation of oral contraceptives, dietary therapy in patients with glycogen storage, or surgery. Some authors recommend surgery due to the risks of hemorrhage and the fact that HCC has been reported in solitary or multiple adenomas over 4 cm in size.[84] Radiofrequency ablation is an alternative to surgical resection.[85]

## INFLAMMATORY PSEUDOTUMOR OF THE LIVER

Inflammatory pseudotumor of the liver occurs in adults and children. Patients have a typical clinical presentation of low-grade fever, abdominal pain, and weight loss. Single or multiple well-defined hepatic masses occur.

***Imaging.*** The lesion is hypoechoic on sonography and of low attenuation on CT. It is not possible to reliably distinguish inflammatory pseudotumor from hepatic malignancy with imaging (e-Fig. 91.13).

***Treatment.*** In some cases, the lesion may be resected based on a high preoperative probability of neoplasm, although a percutaneous biopsy may be diagnostic. Inflammatory pseudotumor is generally a self-limited condition with an excellent prognosis. Therefore it is important for clinicians, surgeons, and radiologists to be familiar with this diagnosis and consider it in the appropriate clinical setting.[86]

## NODULAR REGENERATIVE HYPERPLASIA

NRH of the liver is a lesion of unknown cause that develops in noncirrhotic livers, rarely in children.[66] It is characterized by regenerative nodules surrounded by atrophic liver in the absence of fibrosis. This entity has been associated with vasculitis, collagen vascular diseases, hematologic disorders, cardiovascular diseases, neoplasms, metabolic disorders, and some drugs. Histologically, regenerative nodules are composed of focal proliferation of cells resembling hepatocytes within a supporting stroma.[66]

***Imaging.*** On imaging, NRH may be confused with FNH, HCA, or metastases. Imaging findings are variable and depend on the size of the nodules. The nodules may bleed or lead to portal hypertension from pressure on portal radicals, and the liver may or may not be enlarged.

On US, the nodules are difficult to detect because they are made of hepatocyte-like cells. Regenerative nodules may show heterogeneous echotexture with distortion of normal architecture. When detected, most nodules are hypoechoic, but they can be hyperechoic.[87,88] On CT, lesions are hypoattenuated compared with normal liver and do not enhance significantly.[87,88] On MRI, regenerative nodules are slightly hyperintense to adjacent liver on T1- and variable on T2-weighted images. A T1 hyper- or hypointense or T2 hyperintense rim can be seen.[89] Due to the presence of fat in the lesion, decreased signal intensity on fat-suppressed T1-weighted images may be seen. After gadolinium injection, enhancement occurs during the portal phase similar to the signal intensity of normal liver.[87]

***Treatment.*** No specific treatment is recommended other than discontinuation of drugs associated with the NRH. Malignant transformation to HCC has been reported.

### KEY POINTS

- The most common liver masses in children <5 years of age are hemangiomas, metastases, and hepatoblastoma. After 5 years, HCC and FNH are more common.
- Hepatic hemangiomas have a characteristic appearance of hypervascular tumors.
- Mesenchymal hamartomas are typically multicystic, heterogeneous masses with septa.
- The typical central scar in FNH has increased T2 signal unlike the scar in FLC, which is hypointense on T1- and T2-weighted MR imaging.
- Only FNH contains sufficient Kupffer cells to cause normal to increased uptake on technetium-99m TC sulfur colloid scintigraphy, and retention of hepatobiliary MR contrast agents in hepatocyte phase imaging.
- Hepatic metastases in children are most often due to neuroblastoma, lymphoma, and Wilms tumor.
- There is an increased incidence of regenerative nodules in pediatric cancer survivors.

### SUGGESTED READINGS

Adeyiga AO, Lee EY, Eisenberg RL. Focal hepatic masses in pediatric patients. *AJR Am J Roentgenol*. 2012;199:W422–W440.

Christison-Lagay ER, Burrows PE, Alomari A, et al. Hepatic hemangiomas: subtype classification and development of a clinical practice algorithm and registry. *J Pediatr Surg*. 2007;42:62–68.

Chung EM, Cube R, Lewis RB, et al. From the archives of the AFIP. Pediatric liver masses: radiologic-pathologic correlation. Part 1. Benign tumors. *Radiographics*. 2010;30:801–826.

Chung EM, Lattin GE Jr, Cube R, et al. From the archives of the AFIP. Pediatric liver masses: radiologic-pathologic correlation. Part 2. Malignant tumors. *Radiographics*. 2011;31:483–507.

### REFERENCES

Full references for this chapter can be found on www.expertconsult.com.

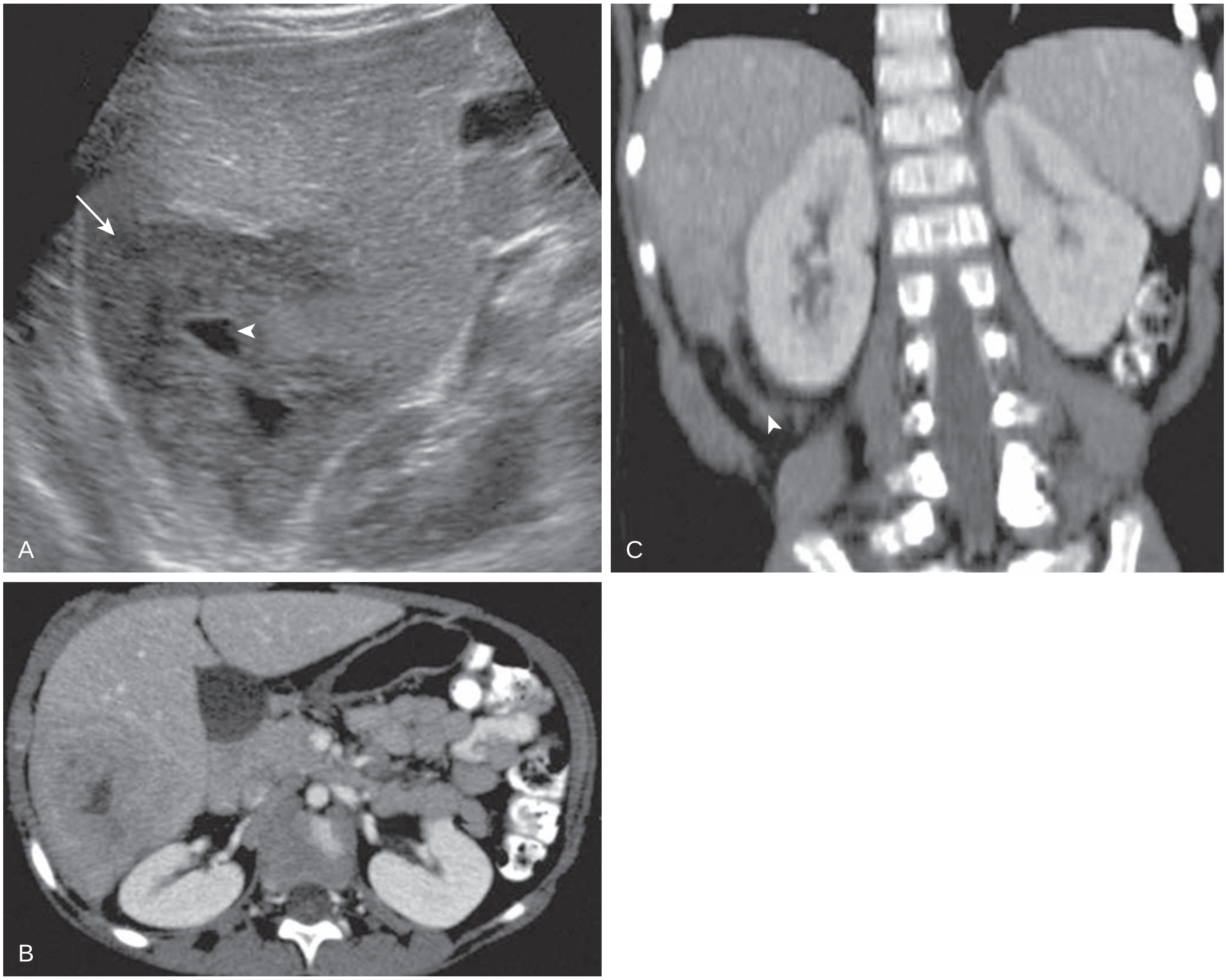

**e-Figure 91.13. Inflammatory pseudotumor in a 5-year-old girl with a 1-week history of abdominal pain and low-grade fever.** (A) Longitudinal sonogram of the right lobe of the liver reveals a hypoechoic mass *(arrow)* with small focus of central necrosis *(arrowhead)*. (B and C) Axial postcontrast (B) and reconstructed coronal (C) CT images confirm the mass and show inflammatory extension into the adjacent perirenal space *(arrowhead)*. *(Courtesy of Lisa H. Lowe, MD.)*

## REFERENCES

1. Ishak KG, Goodman ZD, Stocker JT. *Tumors of the Liver and Intrahepatic Bile Ducts*. Washington, DC: Armed Forces Institute of Pathology; 2001.
2. Koklu E, et al. Alpha-fetoprotein levels in the neonatal period. *Eur J Pediatr*. 2008;167(8):961–962, author reply 963.
3. Stocker JT. Hepatic tumors in children. *Clin Liver Dis*. 2001;5(1):259–281, viii-ix.
4. Mitchell CL, Vasanawala SS. An approach to pediatric liver MRI. *AJR Am J Roentgenol*. 2011;196(5):W519–W526.
5. Ringe KI, Husarik DB, Sirlin CB, et al. Gadoxetate disodium-enhanced MRI of the liver: part 1, protocol optimization and lesion appearance in the noncirrhotic liver. *AJR Am J Roentgenol*. 2010;195(1):13–28.
6. Meyers AB, Towbin AJ, Geller JI, et al. Hepatoblastoma imaging with gadoxetate disodium-enhanced MRI–typical, atypical, pre- and post-treatment evaluation. *Pediatr Radiol*. 2012;42(7):859–866.
7. Stocker JT, Schmidt D. Hepatoblastoma. In: Hamilton SR, Aatonen LA, eds. *Pathology and Genetics of Tumours of the Digestive System*. Lyon, France: IARC Press; 2000:184–189.
8. Woodward PJ, et al. From the archives of the AFIP: a comprehensive review of fetal tumors with pathologic correlation. *Radiographics*. 2005;25(1):215–242.
9. Meyers RL. Tumors of the liver in children. *Surg Oncol*. 2007;16(3):195–203.
10. Slovis TL, Roebuck DJ. Hepatoblastoma: why so many low-birth-weight infants? *Pediatr Radiol*. 2006;36(3):173–174.
11. Dachman AH, Pakter RL, Ros PR, et al. Hepatoblastoma: radiologic-pathologic correlation in 50 cases. *Radiology*. 1987;164(1):15–19.
12. Chung EM, et al. From the archives of the AFIP: pediatric liver masses: radiologic-pathologic correlation. Part 2. Malignant tumors. *Radiographics*. 2011;31(2):483–507.
13. Powers C, et al. Primary liver neoplasms: MR imaging with pathologic correlation. *Radiographics*. 1994;14(3):459–482.
14. Helmberger TK, et al. Pediatric liver neoplasms: a radiologic-pathologic correlation. *Eur Radiol*. 1999;9(7):1339–1347.
15. Roebuck DJ, Aronson D, Clapuyt P, et al. 2005 PRETEXT: a revised staging system for primary malignant liver tumors of childhood developed by the SIOPEL group. *Pediatr Radiol*. 2007;37(2):123–132.
16. Roebuck DJ, Perilongo G. Hepatoblastoma: an oncological review. *Pediatr Radiol*. 2006;36(3):183–186.
17. Ye J, et al. Percutaneous radiofrequency ablation for treatment of hepatoblastoma recurrence. *Pediatr Radiol*. 2008;38(9):1021–1023.
18. Yu SB, et al. Clinical characteristics and prognosis of pediatric hepatocellular carcinoma. *World J Surg*. 2006;30(1):43–50.
19. Siegel MJ, Chung EM, Conran RM. Pediatric liver: focal masses. *Magn Reson Imaging Clin N Am*. 2008;16(3):437–452, v.
20. Levy AD. Malignant liver tumors. *Clin Liver Dis*. 2002;6(1):147–164.
21. Hussain SM, et al. Benign versus malignant hepatic nodules: MR imaging findings with pathologic correlation. *Radiographics*. 2002;22(5):1023–1036, discussion 1037-1039.
22. Czauderna P, et al. Hepatocellular carcinoma in children: results of the first prospective study of the International Society of Pediatric Oncology group. *J Clin Oncol*. 2002;20(12):2798–2804.
23. Katzenstein HM, et al. Hepatocellular carcinoma in children and adolescents: results from the Pediatric Oncology Group and the Children's Cancer Group intergroup study. *J Clin Oncol*. 2002;20(12):2789–2797.
24. Gerber DA, et al. Use of intrahepatic chemotherapy to treat advanced pediatric hepatic malignancies. *J Pediatr Gastroenterol Nutr*. 2000;30(2):137–144.
25. Van Spronsen FJ, Bijleveld CM, van Maldegem BT, et al. Hepatocellular carcinoma in hereditary tyrosinemia type I despite 2-(2 nitro-4-3 trifluoromethylbenzoyl)-1, 3-cyclohexanedione treatment. *J Pediatr Gastroenterol Nutr*. 2005;40(1):90–93.
26. Torbenson M. Review of the clinicopathologic features of fibrolamellar carcinoma. *Adv Anat Pathol*. 2007;14(3):217–223.
27. Liu S, et al. Fibrolamellar hepatocellular carcinoma. *Am J Gastroenterol*. 2009;104(10):2617–2624, quiz 2625.
28. McLarney JK, et al. Fibrolamellar carcinoma of the liver: radiologic-pathologic correlation. *Radiographics*. 1999;19(2):453–471.
29. Mody RJ, et al. FDG PET for the study of primary hepatic malignancies in children. *Pediatr Blood Cancer*. 2006;47(1):51–55.
30. Buetow PC, et al. Undifferentiated (embryonal) sarcoma of the liver: pathologic basis of imaging findings in 28 cases. *Radiology*. 1997;203(3):779–783.
31. Stocker JT, Ishak KG. Undifferentiated (embryonal) sarcoma of the liver: report of 31 cases. *Cancer*. 1978;42(1):336–348.
32. Ros PR, et al. Undifferentiated (embryonal) sarcoma of the liver: radiologic-pathologic correlation. *Radiology*. 1986;161(1):141–145.
33. Psatha EA, et al. Undifferentiated (embryonal) sarcoma of the liver (USL): MRI findings including dynamic gadolinium enhancement. *Magn Reson Imaging*. 2004;22(6):897–900.
34. Ruymann FB, et al. Rhabdomyosarcoma of the biliary tree in childhood. A report from the Intergroup Rhabdomyosarcoma Study. *Cancer*. 1985;56(3):575–581.
35. Davis GL, Kissane JM, Ishak KG. Embryonal rhabdomyosarcoma (sarcoma botryoides) of the biliary tree. Report of five cases and a review of the literature. *Cancer*. 1969;24(2):333–342.
36. Suriawinata AA, Thung SN. Malignant liver tumors. *Clin Liver Dis*. 2002;6(2):527–554, ix.
37. Roebuck DJ, et al. Hepatobiliary rhabdomyosarcoma in children: diagnostic radiology. *Pediatr Radiol*. 1998;28(2):101–108.
38. Donnelly LF, Bisset GS 3rd, Frush DP. Diagnosis please. Case 2: Embryonal rhabdomyosarcoma of the biliary tree. *Radiology*. 1998;208(3):621–623.
39. Miller JH, Greenspan BS. Integrated imaging of hepatic tumors in childhood. Part I: Malignant lesions (primary and metastatic). *Radiology*. 1985;154(1):83–90.
40. Spunt SL, et al. Aggressive surgery is unwarranted for biliary tract rhabdomyosarcoma. *J Pediatr Surg*. 2000;35(2):309–316.
41. Awan S, et al. Angiosarcoma of the liver in children. *J Pediatr Surg*. 1996;31(12):1729–1732.
42. Buetow PC, et al. Malignant vascular tumors of the liver: radiologic-pathologic correlation. *Radiographics*. 1994;14(1):153–166, quiz 167-168.
43. Koyama T, et al. Primary hepatic angiosarcoma: findings at CT and MR imaging. *Radiology*. 2002;222(3):667–673.
44. Burrows PE, Dubois J, Kassarjian A. Pediatric hepatic vascular anomalies. *Pediatr Radiol*. 2001;31(8):533–545.
45. Ishak KG, et al. Mesenchymal tumours of the liver. In: Hamilton SR, Aatonen LA, eds. *Pathology and Genetics of Tumours of the Digestive System*. Lyon, France: IARC Press; 2000.
46. Peterson MS, Baron RL, Rankin SC. Hepatic angiosarcoma: findings on multiphasic contrast-enhanced helical CT do not mimic hepatic hemangioma. *AJR Am J Roentgenol*. 2000;175(1):165–170.
47. Mulliken JB, Glowacki J. Hemangiomas and vascular malformations in infants and children: a classification based on endothelial characteristics. *Plast Reconstr Surg*. 1982;69(3):412–422.
48. Christison-Lagay ER, et al. Hepatic hemangiomas: subtype classification and development of a clinical practice algorithm and registry. *J Pediatr Surg*. 2007;42(1):62–67, discussion 67-68.
49. Huang SA, et al. Severe hypothyroidism caused by type 3 iodothyronine deiodinase in infantile hemangiomas. *N Engl J Med*. 2000;343(3):185–189.
50. Drut RM, Drut R. Extracutaneous infantile haemangioma is also Glut1 positive. *J Clin Pathol*. 2004;57(11):1197–1200.
51. Mo JQ, Dimashkieh HH, Bove KE. GLUT1 endothelial reactivity distinguishes hepatic infantile hemangioma from congenital hepatic vascular malformation with associated capillary proliferation. *Hum Pathol*. 2004;35(2):200–209.
52. Hernandez F, et al. The role of GLUT1 immunostaining in the diagnosis and classification of liver vascular tumors in children. *J Pediatr Surg*. 2005;40(5):801–804.
53. North PE, et al. GLUT1 immunoreaction patterns reliably distinguish hemangioblastoma from metastatic renal cell carcinoma. *Clin Neuropathol*. 2000;19(3):131–137.
54. Kassarjian A, et al. Infantile hepatic hemangiomas: clinical and imaging findings and their correlation with therapy. *AJR Am J Roentgenol*. 2004;182(3):785–795.
55. Wasserman JD, Mahant S, Carcao M, et al. Vincristine for successful treatment of steroid-dependent infantile hemangiomas. *Pediatrics*. 2015;135(6):e1501–e1505.
56. Ishak KG, Goodman ZD, Stocker JT. Benign mesenchymal tumors and pseudotumors. In: Rosai J, Sobin L, eds. *Atlas of Tumor Pathology*. Washington, DC: Armed Forces Institute of Pathology; 2001:71–157.
57. Stocker JT, Ishak KG. Mesenchymal hamartoma of the liver: report of 30 cases and review of the literature. *Pediatr Pathol*. 1983;1(3):245–267.
58. Mortele KJ, Ros PR. Benign liver neoplasms. *Clin Liver Dis*. 2002;6(1):119–145.
59. Ros PR, et al. Mesenchymal hamartoma of the liver: radiologic-pathologic correlation. *Radiology*. 1986;158(3):619–624.

60. Ye BB, et al. Mesenchymal hamartoma of liver: magnetic resonance imaging and histopathologic correlation. *World J Gastroenterol*. 2005;11(37):5807–5810.
61. Stringer MD, Alizai NK. Mesenchymal hamartoma of the liver: a systematic review. *J Pediatr Surg*. 2005;40(11):1681–1690.
62. Lauwers GY, et al. Hepatic undifferentiated (embryonal) sarcoma arising in a mesenchymal hamartoma. *Am J Surg Pathol*. 1997;21(10):1248–1254.
63. Franchi-Abella S, Branchereau S. Benign hepatocellular tumors in children: focal nodular hyperplasia and hepatocellular adenoma. *Int J Hepatol*. 2013;2013:215064.
64. Ishak KG, Goodman ZD, Stocker JT. Benign hepatocellular tumors. In: Rosai J, Sobin L, eds. *Atlas of Tumor Pathology*. Washington, DC: Armed Forces Institute of Pathology; 2001:9–48.
65. Smith EA, Salisbury S, Martin R, et al. Incidence and etiology of new liver lesions in pediatric patients previously treated for malignancy. *AJR Am J Roentgenol*. 2012;199(1):186–191.
66. Bouyn CI, et al. Hepatic focal nodular hyperplasia in children previously treated for a solid tumor. Incidence, risk factors, and outcome. *Cancer*. 2003;97(12):3107–3113.
67. Shamsi K, et al. Focal nodular hyperplasia of the liver: radiologic findings. *Abdom Imaging*. 1993;18(1):32–38.
68. Bartolozzi C, et al. Differentiation of hepatocellular adenoma and focal nodular hyperplasia of the liver: comparison of power Doppler imaging and conventional color Doppler sonography. *Eur Radiol*. 1997;7(9):1410–1415.
69. Kehagias D, et al. Focal nodular hyperplasia: imaging findings. *Eur Radiol*. 2001;11(2):202–212.
70. Choi CS, Freeny PC. Triphasic helical CT of hepatic focal nodular hyperplasia: incidence of atypical findings. *AJR Am J Roentgenol*. 1998;170(2):391–395.
71. Marti-Bonmati L, Casillas C, Dosda R. Enhancement characteristics of hepatic focal nodular hyperplasia and its scar by dynamic magnetic resonance imaging. *MAGMA*. 2000;10(3):200–204.
72. Vilgrain V, et al. Focal nodular hyperplasia of the liver: MR imaging and pathologic correlation in 37 patients. *Radiology*. 1992;184(3):699–703.
73. Tajada M, et al. Liver adenoma and focal nodular hyperplasia associated with oral contraceptives. *Eur J Contracept Reprod Health Care*. 2001;6(4):227–230.
74. Resnick MB, Kozakewich HP, Perez-Atayde AR. Hepatic adenoma in the pediatric age group. Clinicopathological observations and assessment of cell proliferative activity. *Am J Surg Pathol*. 1995;19(10):1181–1190.
75. Brancatelli G, et al. CT and MR imaging evaluation of hepatic adenoma. *J Comput Assist Tomogr*. 2006;30(5):745–750.
76. Grazioli L, et al. Hepatic adenomas: imaging and pathologic findings. *Radiographics*. 2001;21(4):877–892, discussion 892-894.
77. Hussain SM, et al. Hepatocellular adenoma: findings at state-of-the-art magnetic resonance imaging, ultrasound, computed tomography and pathologic analysis. *Eur Radiol*. 2006;16(9):1873–1886.
78. Golli M, et al. Hepatocellular adenoma: color Doppler US and pathologic correlations. *Radiology*. 1994;190(3):741–744.
79. Ichikawa T, et al. Hepatocellular adenoma: multiphasic CT and histopathologic findings in 25 patients. *Radiology*. 2000;214(3):861–868.
80. Arrive L, et al. Hepatic adenoma: MR findings in 51 pathologically proved lesions. *Radiology*. 1994;193(2):507–512.
81. Chung KY, et al. Hepatocellular adenoma: MR imaging features with pathologic correlation. *AJR Am J Roentgenol*. 1995;165(2):303–308.
82. Paulson EK, et al. Hepatic adenoma: MR characteristics and correlation with pathologic findings. *AJR Am J Roentgenol*. 1994;163(1): 113–116.
83. Chaib E, et al. Hepatic adenoma. Timing for surgery. *Hepatogastroenterology*. 2007;54(77):1382–1387.
84. Micchelli ST, et al. Malignant transformation of hepatic adenomas. *Mod Pathol*. 2008;21(4):491–497.
85. Rocourt DV, et al. Contemporary management of benign hepatic adenoma using percutaneous radiofrequency ablation. *J Pediatr Surg*. 2006;41(6):1149–1152.
86. Lee SL, DuBois JJ. Hepatic inflammatory pseudotumor: case report, review of the literature, and a proposal for morphologic classification. *Pediatr Surg Int*. 2001;17(7):555–559.
87. Casillas C, Marti-Bonmati L, Galant J. Pseudotumoral presentation of nodular regenerative hyperplasia of the liver: imaging in five patients including MR imaging. *Eur Radiol*. 1997;7(5):654–658.
88. Dachman AH, et al. Nodular regenerative hyperplasia of the liver: clinical and radiologic observations. *AJR Am J Roentgenol*. 1987;148(4):717–722.
89. Siegelman ES, et al. MR imaging of hepatic nodular regenerative hyperplasia. *J Magn Reson Imaging*. 1995;5(6):730–732.

# 92

# Vascular Abnormalities of the Liver

*Douglas C. Rivard and Patrick N. Bacon*

Vascular abnormalities of the liver discussed in this chapter are divided into the following broad categories: portal hypertension, hepatopulmonary syndrome (HPS), Budd–Chiari syndrome, sinusoidal obstructive syndrome, and congenital vascular anomalies of the liver.

## PORTAL HYPERTENSION

***Overview.*** Portal hypertension is defined as a rise in pressure within the splanchnic venous system above 10 mm Hg. This increase in pressure may result from either increased resistance to hepatic venous drainage (presinusoidal and postsinusoidal) or increase in inflow pressure, such as is seen in persons with an arterioportal fistula.[1] The pathophysiology and clinical presentation of portal hypertension depend on the underlying hepatic disorder.

***Etiology.*** Cirrhosis, the most common cause of portal hypertension, is due to hepatic scarring resulting from chronic liver injury. In pediatric patients, cirrhosis can result from a variety of conditions, including biliary atresia, cystic fibrosis, hemochromatosis, and Wilson disease[2] (Box 92.1).

Extrahepatic portal vein occlusion is a relatively frequent cause of presinusoidal portal hypertension in children. Incidence is increased in cases of complicated umbilical vein catheterization, sepsis, dehydration, hyperviscosity, shock, coagulopathy, portal vein thrombosis, hypercoagulable syndromes, and congenital portal venous webs, but it may occur without an identifiable cause.[2,3] Cavernous transformation of the portal vein is a result of portoportal collaterals that develop along the thrombosed portal vein and that have been observed to occur in as little as 1 to 3 weeks after acute occlusion.[4]

Postsinusoidal obstruction includes primary liver disease with cirrhosis or hepatic vein obstruction, such as Budd–Chiari syndrome or hepatic veno-occlusive disease/sinusoidal obstructive syndrome, as seen in patients who have had bone marrow transplantation.[2]

***Clinical Presentation.*** Children may present with the consequences of portal hypertension, such as gastrointestinal bleeding, unexplained splenomegaly, and hypersplenism without jaundice, ascites, or cholestasis.[5,6] The Child–Turcotte–Pugh classification system provides a severity score that plays a part in treatment decisions.[3] Patients are stratified into grades A through C based on bilirubin elevation, albumin level, prothrombin time, ascites, and severity of encephalopathy.[7,8]

***Imaging.*** Splenic enlargement may be the earliest imaging finding of portal hypertension. As resistance to portal flow increases, portal venous flow slows down, portal vein diameter decreases, and, with high resistance, portal venous flow may become reversed or even arterialized. In persons with a normal liver, the portal vein has a larger cross-sectional area than the splenic vein.[6,9] If instead the portal vein is smaller than the splenic vein, the presence of collaterals diverting portal flow away from the liver must be assumed (Fig. 92.1). Reversal of venous flow in the superior mesenteric and splenic veins also is suggestive of collaterals and spontaneous portosystemic shunting. Hepatopetal flow in the main portal vein (MPV) does not exclude severe portal hypertension when collaterals are present or when lobe-to-lobe shunting occurs; hepatofugal flow is a late finding in persons with portal hypertension.[6,9] Recently, evaluation of liver stiffness by shear wave elastography has shown promise in predicting clinically significant portal hypertension as well as noninvasive monitoring of fibrosis.[10]

The presence of a paraumbilical varix allows decompression of portal venous flow via the left portal vein, thus allowing hepatopetal flow in the MPV even in the presence of extreme portal hypertension. Because the paraumbilical varices are supplied by the left portal vein, intrahepatic portal flow may be directed toward them, causing reversal of flow in the right portal vein despite hepatopetal flow in the MPV. The paraumbilical varices are well seen in the falciform fossa by color and power Doppler imaging, as well as by computed tomography angiography (CTA) and magnetic resonance angiography (MRA). Hepatic decompression by those veins may serve as relative protection against esophageal varices and variceal hemorrhage.

When portal venous pressure increases in the setting of portal hypertension, splanchnic venous return finds alternative drainage pathways connecting the portal circulation to the systemic circulation. Left gastric and splenic vein branches drain into the azygos system through esophageal and gastric varices, which in turn drain into the inferior vena cava (IVC) via the left renal vein. Paraumbilical varices (e-Fig. 92.2) communicate with inferior epigastric and internal mammary abdominal wall venous networks to drain into the inferior and superior vena cava, respectively. These collateral pathways can be examined with cross-sectional imaging.[4]

Additional collateral pathways develop with portal hypertension. Retroperitoneal and peripancreatic collaterals drain through renal and gonadal veins into the IVC and into paraspinal veins, which drain into the azygos system (Fig. 92.3). Inferior mesenteric branches drain into superior, middle, and inferior hemorrhoidal veins that lead to the iliac veins. Portosystemic collaterals also may form at enterocutaneous junctions in fistulas and enterostomies. Surgical anastomoses, such as a Roux-en-Y biliary-enteric anastomosis, may serve as sites of portoportal collaterals (e-Fig. 92.4). Finally, intercostal and phrenic veins also may serve as a means of portosystemic communication across the diaphragm.[4]

In patients with cavernous transformation of the portal vein, key cross-sectional imaging features include a tangle of venous channels in the liver hilum with no identifiable normal portal vein (Fig. 92.5). In most patients (76%), portoportal collaterals extend over a variable distance along the course of the intrahepatic portal branches. In extreme cases, no portal vein branches are demonstrated (e-Fig. 92.6). Preserved intrahepatic portal vein branches may be identified, some of which may demonstrate hepatofugal flow toward the cavernous vessels. Collateral veins may traverse the liver parenchyma to enter hepatic and capsular veins (e-Fig. 92.7). Doppler ultrasound imaging can be used to interrogate flow characteristics within the cavernous collaterals, revealing abnormal flow.[11]

***Treatment and Prognosis.*** Multiple therapeutic options exist for children with portal hypertension, depending on the underlying cause and severity of liver disease. Treatments range from percutaneous transjugular intrahepatic portosystemic shunts to sclerotherapy and variceal ligation to surgical portosystemic shunts.[2,12] Endovascular therapies have become more refined and are used with increasing frequency.[13,14]

Surgical portosystemic shunts include splenorenal shunts, mesocaval shunts, and the mesoportal (Rex) bypass. In the splenorenal shunt, the distal splenic vein is connected end-to-side to the left renal vein (Fig. 92.8), leaving the superior mesenteric vein connected to the liver. The Rex bypass is used in patients with extrahepatic portal vein obstruction.[15] In this bypass procedure,

## Abstract:

Vascular abnormalities of the liver can be congenital, acquired, or iatrogenic in nature. Knowledge of pertinent anatomy is essential for timely diagnosis. Medical imaging techniques play an integral role in evaluation of these entities and can help guide surgical or minimally invasive image guided therapies.

## Keywords:

liver vascular abnormalities pediatric imaging congenital treatment

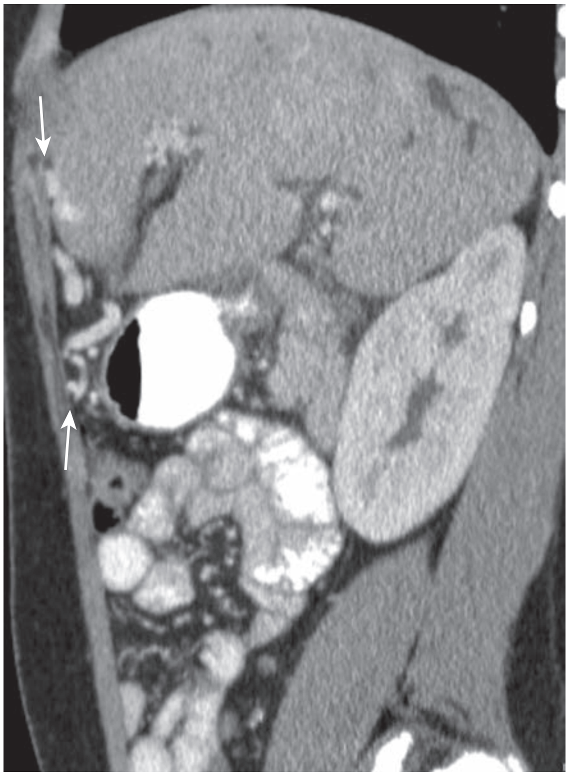

**e-Figure 92.2. Paraumbilical collaterals in a 12-year-old girl with hepatic fibrosis, cirrhosis, and portal hypertension.** Sagittal contrast-enhanced CT image shows enhancing paraumbilical venous collaterals and enhancing internal mammary collateral vessels anterior to the liver *(arrows)*.

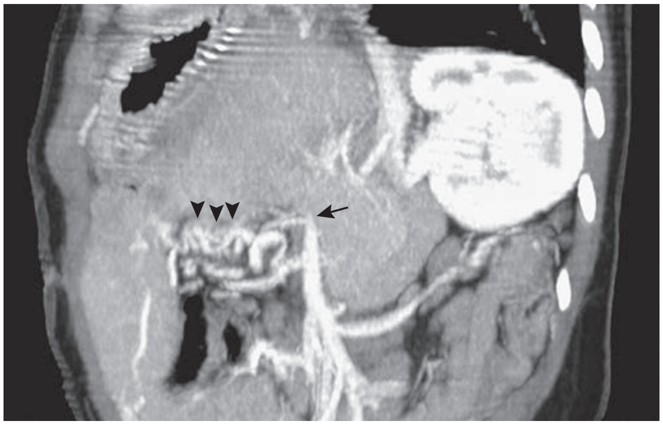

**e-Figure 92.4. Nonacute portal vein thrombosis in an 11-year-old boy with a left lateral segment liver transplant.** Oblique sagittal reformat of contrast-enhanced CT image shows an occluded extrahepatic portal vein *(arrow),* and multiple corkscrew collaterals from jejunal branches of the superior mesenteric vein are seen at the Roux-en-Y loop *(arrowheads)* used for the biliary anastomosis. Capsular collaterals are seen at the inferior edge of the liver.

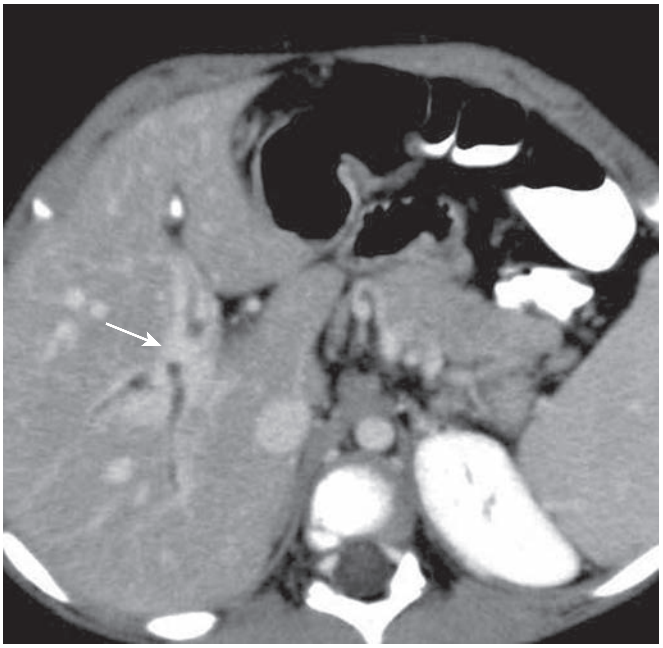

**e-Figure 92.6. Cavernous transformation of the portal vein in a 3-year-old girl with biliary atresia and cirrhosis.** Axial contrast-enhanced CT image shows no visible intrahepatic portal vein branches. Tangles of intrahepatic collaterals *(arrow)* follow the expected course of the entire intrahepatic portal system.

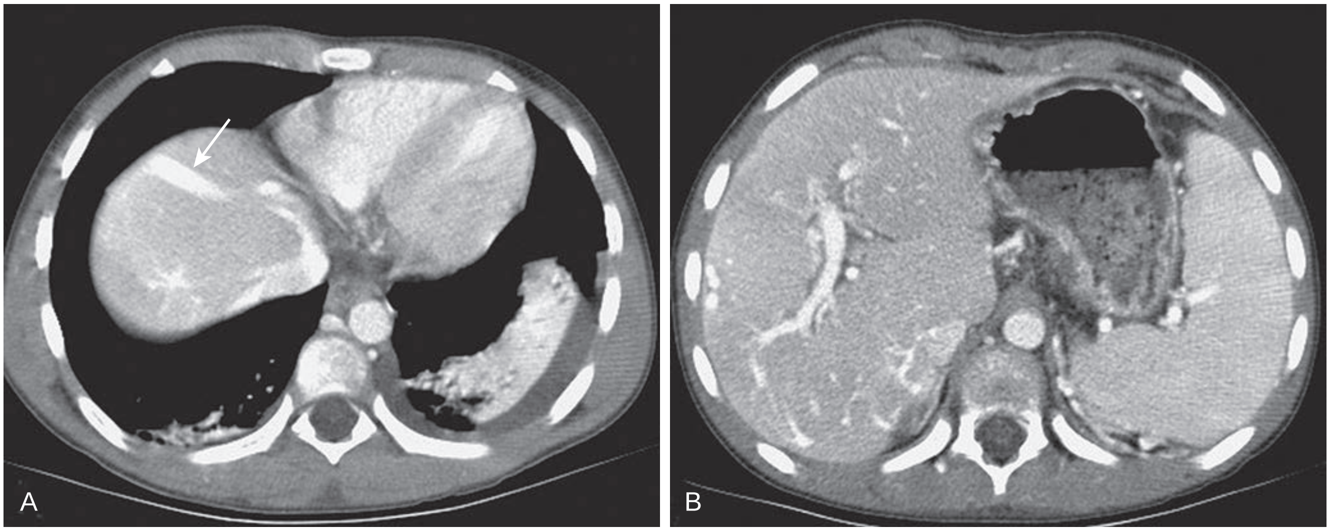

**e-Figure 92.7. Portovenous and transcapsular collaterals in a patient with extrahepatic portal vein obstruction. Portovenous and transcapsular connections are present across the liver parenchyma.** (A) Axial contrast-enhanced CT image at the liver dome shows a large peripheral collateral vein *(arrow)* communicating with the left hepatic vein. (B) A more inferior image shows numerous transcapsular venous collaterals that communicate with the intrahepatic portal vein branches.

**BOX 92.1** Causes of Portal Hypertension in Children

**INCREASED INFLOW PRESSURE OR VOLUME**

- Hepatic artery to portal vein fistula
- Total anomalous pulmonary venous return below the diaphragm
- Pulmonary sequestration with portal venous drainage

**PRESINUSOIDAL VENOUS OBSTRUCTION**

- Splenic vein occlusion (sinistral portal hypertension)
- Extrahepatic portal vein thrombosis/cavernous transformation of portal vein
- Posttransplantation portal vein stenosis, thrombosis, and occlusion
- Congenital hepatic fibrosis
- Schistosomiasis

**INCREASED SINUSOIDAL RESISTANCE**

- Biliary atresia
- Cirrhosis
- Hepatitis: C, non-A, non-B, autoimmune, neonatal
- Sclerosing cholangitis

**POSTSINUSOIDAL OBSTRUCTION**

- Budd–Chiari syndrome
- Glenn, Fontan systemic to pulmonary venous shunts
- Medications: 6-thioguanine

**IDIOPATHIC PORTAL HYPERTENSION**

a venous graft is interposed between the superior mesenteric vein (inferior to the pancreas) and the left portal vein, restoring portal venous flow into the liver (Fig. 92.9). The Rex shunt may be definitive therapy for children with extrahepatic portal vein obstruction.[16] The collapsed intrahepatic portal system, which may be difficult to image before surgery because of exuberant intrahepatic collaterals that dominate portal flow, has been shown to distend rapidly and accommodate the large volume of flow from the shunt. The shunt can be seen by all vascular imaging modalities and should demonstrate hepatopetal flow.[17]

Because the Rex shunt is a bypass graft, portal flow is hepatopetal. Portal vein flow is hepatofugal in patent mesocaval and proximal splenorenal shunts; it may be hepatopetal in the more selective distal splenorenal shunts, which are designed to decompress esophageal varices and preserve some portal venous flow. These shunts provide short- and long-term palliation in children with portal hypertension to prevent gastrointestinal hemorrhages and improve hypersplenism. In children with severe underlying liver disease, these shunts are temporizing procedures before liver transplantation.[18]

## HEPATOPULMONARY SYNDROME

***Overview.*** HPS is defined as an elevated age-adjusted alveolar-arterial oxygen gradient that often leads to hypoxemia and pulmonary vascular dilation in patients with liver disease.[19] It can be acute or chronic and can occur with or without portal hypertension.[20]

***Etiology.*** HPS is associated with hepatic vascular abnormalities (such as portal hypertension or Abernethy malformation) that alter the normal portosystemic circulation, leading to right to left intrapulmonary shunting. The pathophysiology of HPS has not been fully elucidated but is thought to involve increased pulmonary expression of endothelin B receptor, leading to nitric oxide overproduction. Endothelial and arterial wall changes produce either (1) ventilation-perfusion mismatch through vasodilatation and arteriovenous shunting or (2) pulmonary hypertension.[21]

***Clinical Presentation.*** The characteristic clinical features of HPS are orthodeoxia and platypnea in the presence of liver disease. The clinical presentation can range from relatively asymptomatic to the presence of cyanosis and clubbing.[19] Pulmonary manifestations may precede the clinical presentation of the liver disease.

***Imaging.*** Plain radiographs may demonstrate increased vascular markings and cardiomegaly (Fig. 92.10). Computed tomography (CT) may outline enlarged vessels, predominantly in the lung bases. Contrast echocardiography may show microbubbles in the left atrium in three to five cardiac cycles as a result of intrapulmonary arteriovenous shunting and is considered the gold standard for diagnosis of HPS.

***Treatment and Prognosis.*** The treatment of HPS is aimed at the underlying disease, which affects prognosis. In patients in whom the syndrome is a consequence of a portovenous shunt, occlusion of the shunt can lead to regression of the intrapulmonary shunts and resolution of symptoms.[13,19,22]

## BUDD–CHIARI SYNDROME

***Overview.*** Budd–Chiari syndrome is characterized by obstruction of hepatic venous outflow in the absence of constrictive pericarditis or right heart failure, by occlusion of the hepatic veins and/or suprahepatic IVC. This results in severe liver congestion, ascites, and portal hypertension.[23] As sinusoidal pressure increases, the pressure gradient between the portal venous system and the sinusoidal system is reversed, causing the portal vein to become a draining system for the hepatic artery. In complete Budd–Chiari syndrome, blood supply to the liver is solely from the hepatic artery. Because the caudate lobe has separate venous drainage, it is spared in most patients with Budd–Chiari syndrome.

***Etiology.*** The causes of Budd–Chiari syndrome include a caval web, thrombosis in hypercoagulable states, tumor extension into the IVC, external compression, or liver transplantation; the syndrome also may be idiopathic.[23–25]

***Clinical Presentation.*** Clinically, collateral venous drainage develops in some patients, and they may be relatively asymptomatic. Other patients present with intractable ascites, liver failure, or gastrointestinal hemorrhage. Children who experience hepatic vein or IVC obstruction after liver transplantation may experience recurrence of portal hypertension.[26]

***Imaging.*** On cross-sectional imaging, hepatomegaly with ascites and poorly or nonvisible hepatic veins are characteristic.[24,27] Reversal of portal venous flow usually is found in complete cases; however, in patients with partial hepatic vein occlusion, the flow may shunt from higher resistance segments into lower resistance segments, such as the caudate lobe. Intrahepatic portal-to-systemic collaterals may occur via transcapsular and paraumbilical veins, and extrahepatic collaterals occur via esophageal and gastric varices. These hemodynamic changes can be well demonstrated by Doppler ultrasound, CTA, and magnetic resonance imaging (MRI).[9,24,27]

On CT and CTA (Fig. 92.11), the liver parenchyma may demonstrate patchy, abnormal, wedge-shaped areas of attenuation with the apex pointing to the IVC. A heterogeneous, reticular, or mosaic pattern in the hepatic arterial phase that persists during the portal phase also may be observed. The caudate lobe retains a normal appearance and may be hypertrophied. The portal vein may fill before its tributaries as a result of intrahepatic flow reversal. Similar findings are visible on MRI and MRA.

***Treatment and Prognosis.*** Treatment consists of medical control of ascites, percutaneous angioplasty when feasible, surgical creation of a diverting shunt, and liver transplantation in severe cases.[25,28] Prognosis of Budd–Chiari syndrome is highly variable depending on the timeliness of diagnosis and the ability to treat the underlying causes.[23]

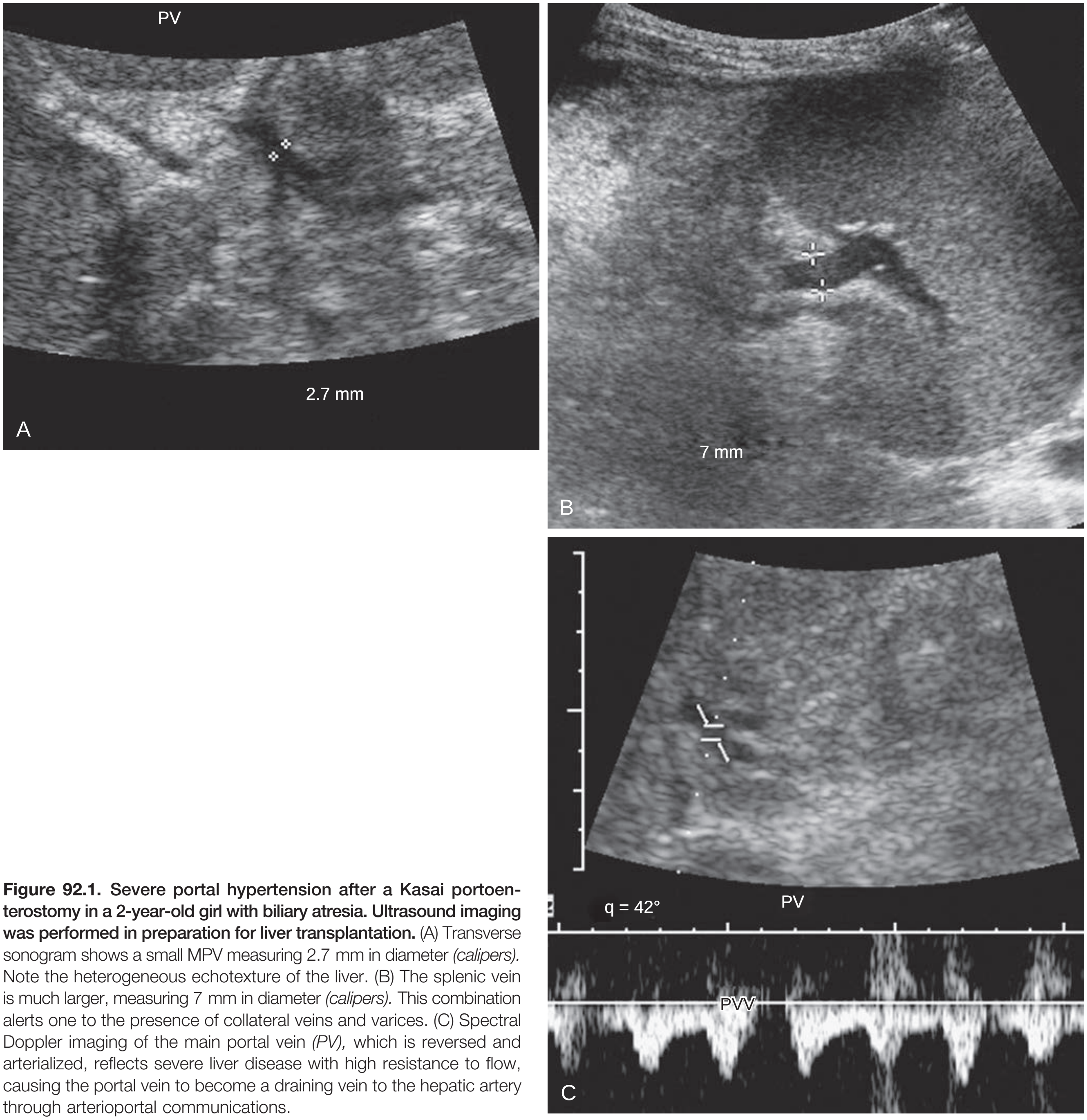

**Figure 92.1. Severe portal hypertension after a Kasai portoenterostomy in a 2-year-old girl with biliary atresia. Ultrasound imaging was performed in preparation for liver transplantation.** (A) Transverse sonogram shows a small MPV measuring 2.7 mm in diameter *(calipers).* Note the heterogeneous echotexture of the liver. (B) The splenic vein is much larger, measuring 7 mm in diameter *(calipers).* This combination alerts one to the presence of collateral veins and varices. (C) Spectral Doppler imaging of the main portal vein *(PV),* which is reversed and arterialized, reflects severe liver disease with high resistance to flow, causing the portal vein to become a draining vein to the hepatic artery through arterioportal communications.

## SINUSOIDAL OBSTRUCTION SYNDROME

***Overview.*** Sinusoidal obstruction syndrome (SOS), previously known as hepatic veno-occlusive disease, is a life-threatening complication that typically occurs within the first 35 to 40 days after myeloablative preparation regimen. It is a primary circulatory disorder characterized by obstruction at the sinusoidal level, which leads to liver dysfunction.

***Etiology.*** Hepatic SOS develops most frequently in patients undergoing myeloablative therapy for hematopoietic stem cell transplantation. The reported frequency in patients who undergo bone marrow transplantation varies wildly (5% to 60%) but has been shown to be higher in patients who are younger (under 1 to 2 years of age), underweight, and treated with actinomycin D.[29–31] Additional risk factors include the presence of previous liver disease or other preexistent conditions such as osteopetrosis, repeat myeloablative procedure beyond second relapse, and specific chemotherapeutic regimens, such as the use of cyclophosphamide in combination with busulfan or total body irradiation.[32] In patients who have not undergone bone marrow transplantation, the entity can occur when the patient has received hepatic radiation or after liver transplantation.

***Clinical Presentation.*** Patients present with fluid retention, abdominal pain, jaundice, and hepatomegaly. SOS is a clinical diagnosis. The Baltimore criteria used for the diagnosis of SOS after hematopoietic cell transplantation are hyperbilirubinemia >2 mg/dL and at least two of the following: hepatomegaly, weight gain ≥5%, and ascites.[33] Based on the course of disease, it can be

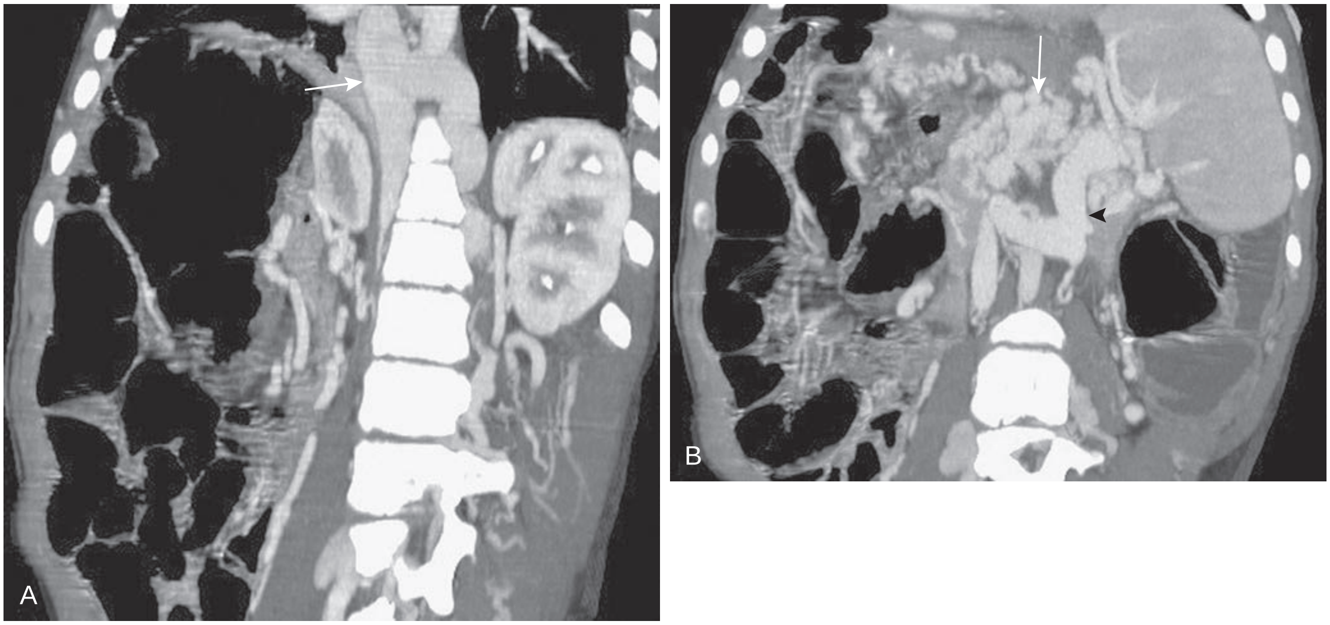

**Figure 92.3. Occluded portal vein and IVC in a liver transplant patient.** (A) Coronal contrast-enhanced CT image shows retroperitoneal, paraspinal, and intraspinal venous collaterals. The azygos and hemiazygos veins are massively enlarged *(arrow)*. (B) Extensive pancreatic *(arrow)* and perisplenic collaterals are present, along with a splenorenal shunt *(arrowhead)*.

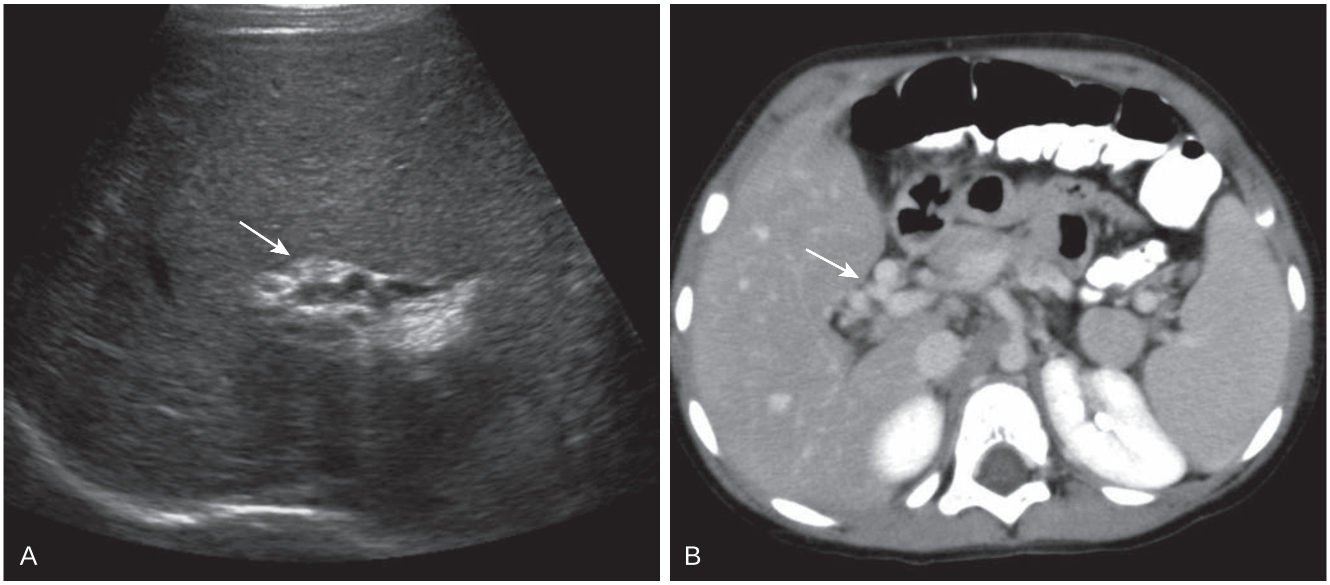

**Figure 92.5. Cavernous transformation of the portal vein in a 3-year-old boy with cirrhosis.** (A) Transverse sonogram shows a tangle of periportal vessels without an identifiable normal portal vein *(arrow)*. (B) Axial contrast-enhanced CT image confirms multiple collateral vessels in the porta hepatis *(arrow)*.

classified as mild (self-limiting), moderate (requiring intervention for fluid excess and pain management), and severe (not resolving by day 100 or leading to death).[34]

***Imaging.*** On ultrasound imaging, hepatomegaly, ascites, and thickening of the gallbladder wall are common findings. On Doppler imaging, decreased or reversed flow in the portal vein, increased resistive index of the hepatic artery, attenuation of hepatic venous flow, and the appearance of hepatofugal flow in paraumbilical varices have been described (Fig. 92.12). In some early cases, partial hemodynamic involvement may be present, resulting in flow reversal in only one segmental or lobar portal vein branch.[35] The full gamut of findings is seldom present, and in many patients, no specific ultrasound findings may be observed.[36]

MRI findings include hepatomegaly, abnormal periportal cuffing, and gallbladder wall thickening with intense wall signal on T2-weighted sequences, ascites, and pleural effusion. Since these findings are nonspecific, they do not necessarily aid in the differential diagnosis.[37] The gold standard for diagnosis is measurement of wedged hepatic venous pressure and transjugular liver biopsy. A hepatic venous pressure gradient of ≥10 mm Hg in a patient without previous liver disease allows an exact diagnosis with a high specificity.[38]

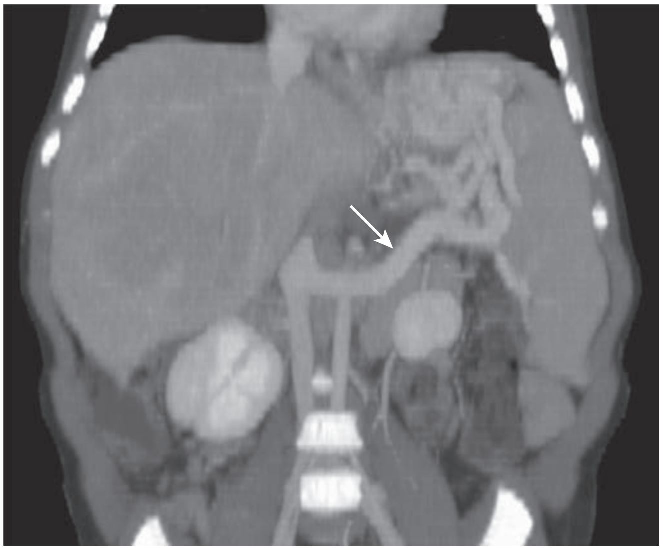

**Figure 92.8. Distal splenorenal shunt in an 8-year-old boy.** Coronal reconstructed CTA image shows the splenic vein connected end to side *(arrow)* to the left renal vein draining into the IVC.

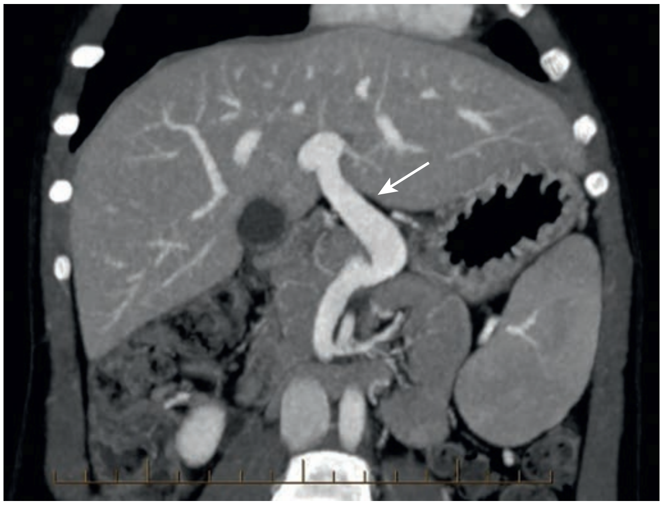

**Figure 92.9. Rex bypass (superior mesenteric to left portal vein).** Angled coronal maximum intensity projection (MIP) image from a contrast-enhanced CT shows the patent Rex shunt *(arrow)* connecting the superior mesenteric vein to the left portal vein.

***Treatment.*** Treatment consists of supportive care and controlling the inflammation and the deposition of fibrin. Agents that have been used include antithrombotic agents such as prostaglandin E1 and heparin, which are of limited value. More promising is defibrotide, which is derived from porcine tissue and has antithrombotic and antiischemic properties, with complete resolution seen in 35% to 55% of patients in reported uncontrolled clinical trials.[32,39,40]

## CONGENITAL ANOMALIES OF LIVER VASCULATURE

### Anomalies of the Portal Vein

#### Preduodenal Portal Vein

***Overview.*** Preduodenal portal vein is a rare anomaly in which the portal vein courses ventral to the duodenum and pancreatic head.

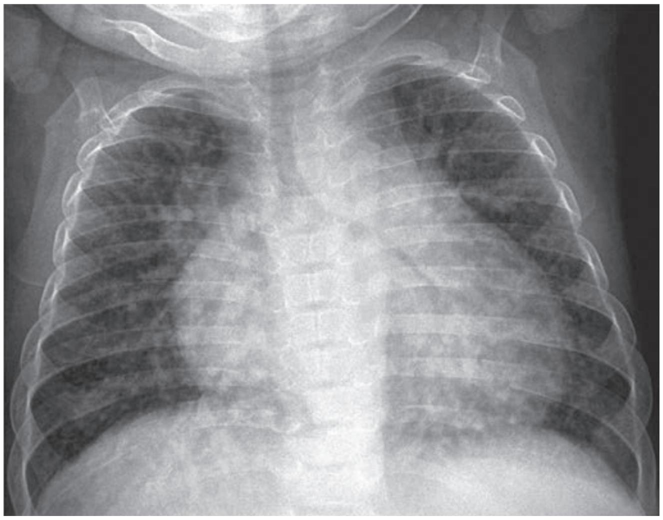

**Figure 92.10. Hepatopulmonary syndrome in an 8-month-old boy with portal vein occlusion and cyanosis.** Chest radiograph shows cardiomegaly and extensively increased pulmonary vascularity, representing diffuse pulmonary arteriovenous shunts.

***Etiology.*** The proposed embryology is nonregression of the caudal anastomotic vein that connects the two vitelline veins ventral to the duodenum, where it then contributes to the formation of the portal vein.[41,42]

***Clinical Presentation.*** The anomaly is closely associated with the heterotaxy syndromes, particularly polysplenia[43] and malrotation, as well as splenic, pancreatic, cardiac, and duodenal anomalies. In approximately 50% of patients, an associated duodenal obstruction is present; however, the anomaly may be asymptomatic and discovered incidentally, particularly during workup of patients with heterotaxy or biliary atresia. Approximately 10% of patients with biliary atresia have associated heterotaxy/polysplenia.[42–45]

***Imaging.*** The preduodenal portal vein is seen as a vein anterior to the duodenum and pancreas, which is visible on cross-section imaging including ultrasound, CT, and MRI; it is particularly well seen on sagittal images (e-Fig. 92.13).[42,43]

***Treatment.*** Treatment addresses correction of the underlying duodenal obstruction, if present. Awareness of this anatomic abnormality is necessary because it can pose a surgical hazard during other hepatobiliary or proximal intestinal surgical procedures, particularly in patients with concomitant heterotaxy/polysplenia and biliary atresia.[41,45]

#### Extrahepatic Congenital Portosystemic Shunts

***Overview.*** Abernethy[46] first described an extrahepatic portosystemic connection in 1793, and this malformation is now known as the Abernethy malformation. These malformations are classified as type 1 or 2.[47] Type 1 involves a complete shunt; no portal blood reaches the liver, as in congenital absence of the portal vein. In type 1a, the superior mesenteric and splenic veins do not join, and in type 1b, the superior mesenteric and splenic veins join before draining into the systemic circulation. Type 2 involves a partial shunt to the hepatic vein or IVC.[47,48]

***Etiology.*** Extrahepatic portosystemic shunts result from maldevelopment of the coordinated preservation and atresia of the left and right vitelline veins in the abdomen. Such maldevelopment could arise de novo, such as in patients with heterotaxy in whom orderly right-left processes are affected, with secondary hypoplasia of the portal venous system, or they may be a result of hypoplasia of the portal venous system with redirection of portal venous flow through extrahepatic channels.[49]

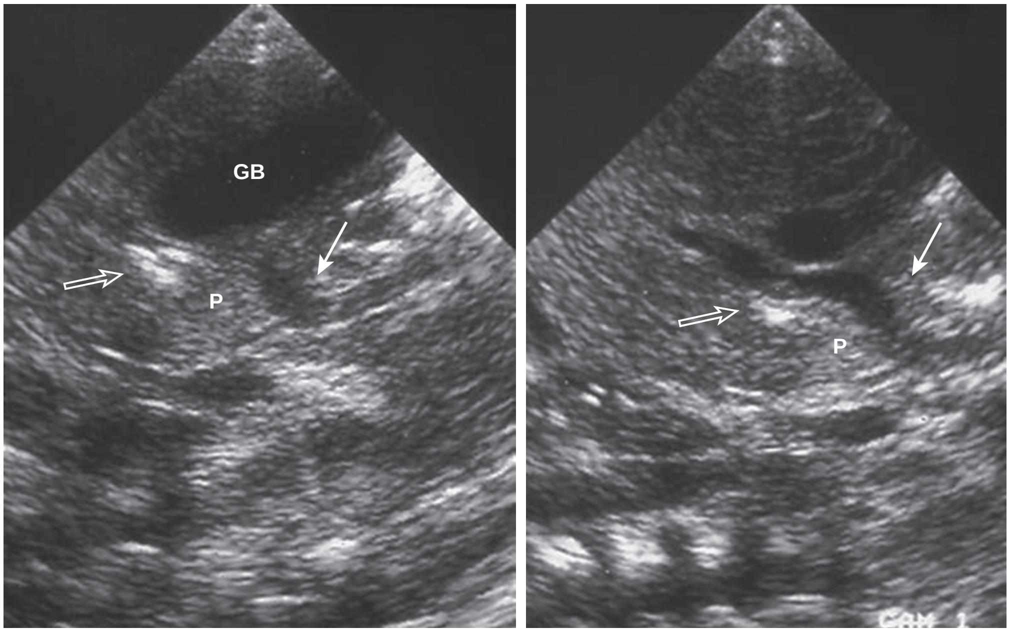

**e-Figure 92.13. Preduodenal portal vein in an infant with polysplenia.** Transverse sonograms show the superior mesenteric vein *(solid arrow)* courses anterior to pancreas *(P)* and duodenum *(open arrow)* to enter the liver. *GB,* Midline gallbladder. *(Courtesy of Marta Hernanz-Schulman, MD, Nashville, TN.)*

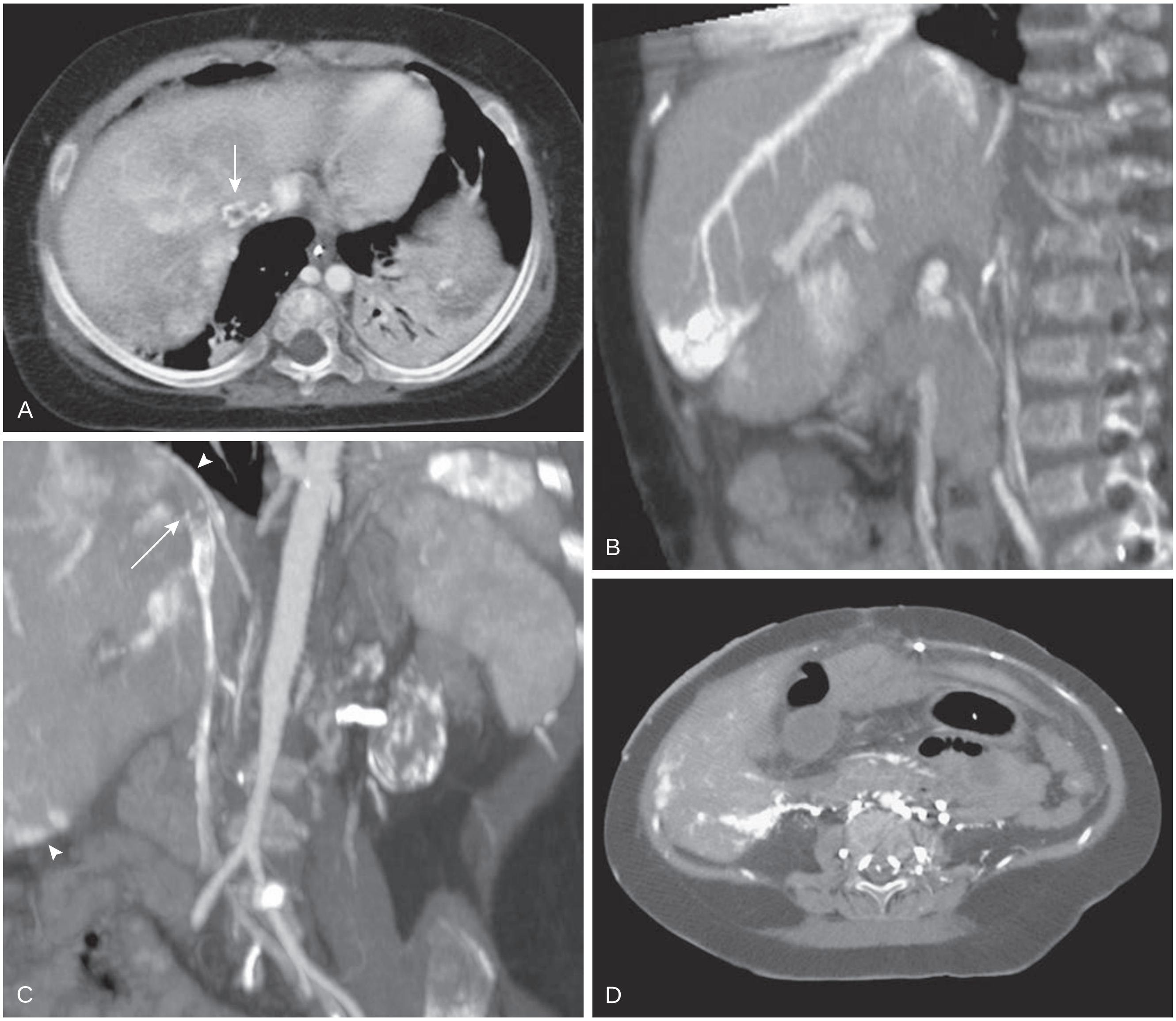

**Figure 92.11. Budd–Chiari syndrome due to IVC thrombosis.** (A) Axial CTA image shows a filling defect within the intrahepatic IVC *(arrow)*. Note the patchy, inhomogeneous enhancement of the liver. (B) Sagittal reformatted CTA shows intense contrast retention peripherally in the territory of the obstructed hepatic vein and transcapsular collateral. (C) Thrombus is visible in the intrahepatic IVC *(arrow)* with transcapsular collaterals at the liver dome and lower lateral edge *(arrowheads)* in this coronal reconstruction. (D) Axial CT image more inferiorly shows extensive retroperitoneal, paraspinal, and transcapsular collaterals enhancing brightly.

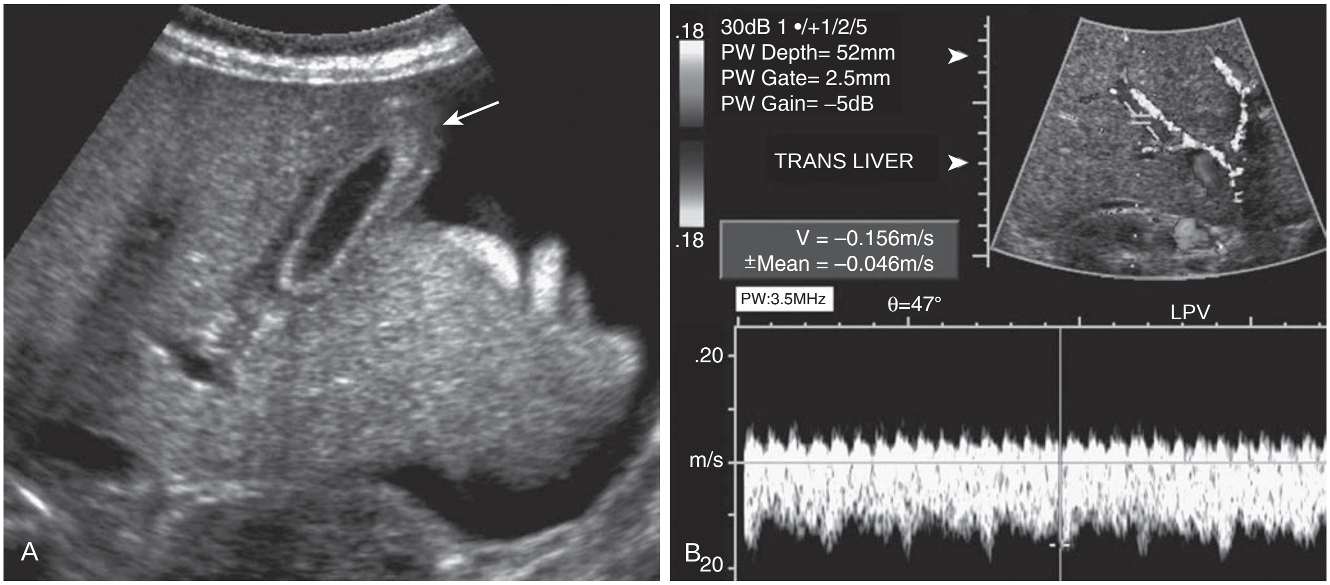

**Figure 92.12. Hepatic veno-occlusive disease.** (A) Longitudinal sonogram shows thickening of the gallbladder wall *(arrow)* and ascites. (B) Doppler image shows reversal of portal venous flow.

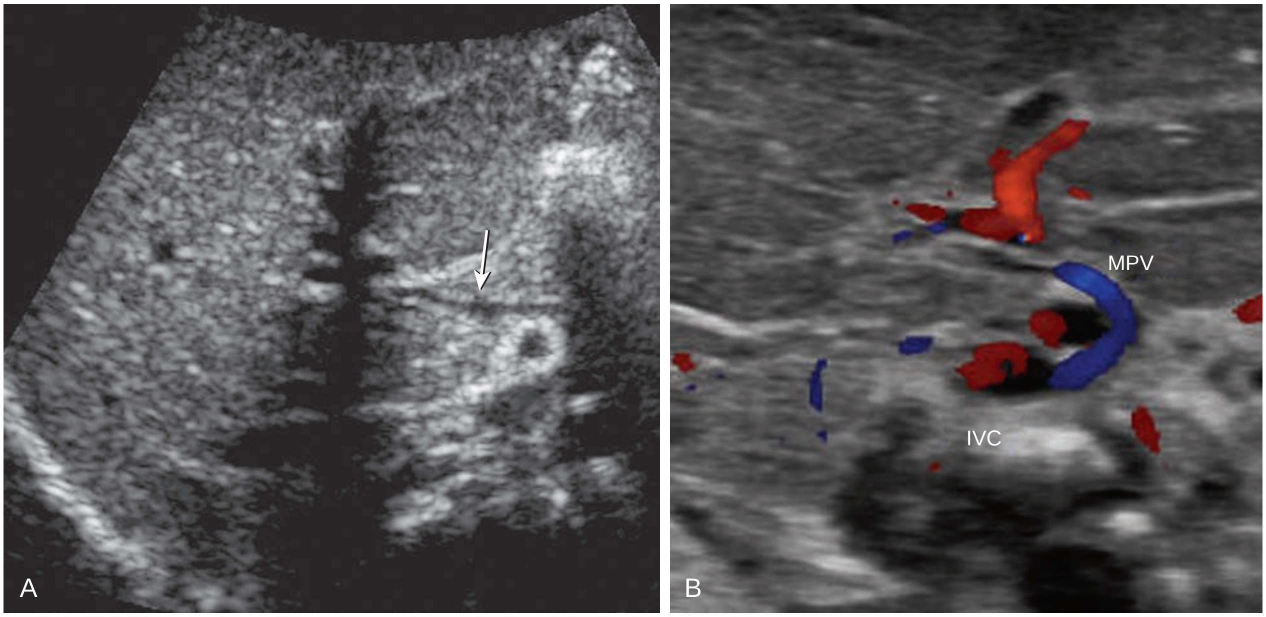

**Figure 92.14. Congenital extrahepatic portosystemic shunt.** (A) Transverse sonogram shows a diminutive MPV is present *(arrow).* (B) Transverse Doppler image in another infant shows the *MPV* draining into the *IVC.*

***Clinical Presentation.*** Extrahepatic portosystemic shunts are associated with other anomalies, such as polysplenia, biliary atresia, and cardiac and renal anomalies. They also are associated with the development of liver lesions, including focal nodular hyperplasia. Malignancies, including hepatoblastoma, hepatocellular carcinoma, and sarcoma, also have been reported in these patients. With the bypass of the hepatic circulation, systemic hyperammonemia also can be present, although hyperammonemic encephalopathy is more typically seen in older and adult patients, dependent in part on the volume of the shunt; increased circulation of galactose and bile acids also occurs.[49–52]

***Imaging.*** Absence of the portal vein may be noted prenatally, with congenital agenesis of the ductus venosus and umbilical vein drainage into the IVC or directly into the heart.[53]

When the portal vein is absent, the hepatic artery is larger than expected relative to the size of the liver and the patient's age.[52] When the portal vein is present, it is small (Fig. 92.14A). The shunt's vascular connection may be demonstrated by ultrasound imaging, particularly with the aid of color Doppler imaging (Fig. 92.14B), but CTA and MRA are more likely to demonstrate its complete course and anatomy (Fig. 92.15). Associated hepatic parenchymal nodules may be demonstrated by all cross-sectional imaging modalities.

***Treatment and Prognosis.*** Treatment, particularly in symptomatic patients, is aimed at surgical or endovascular occlusion of the abnormal connection if evidence exists that intrahepatic flow can be restored; otherwise, extrahepatic portal hypertension will ensue. Liver transplantation may be needed in persons with symptomatic extrahepatic shunts with agenesis of the portal vein and its branches.[51,52,54]

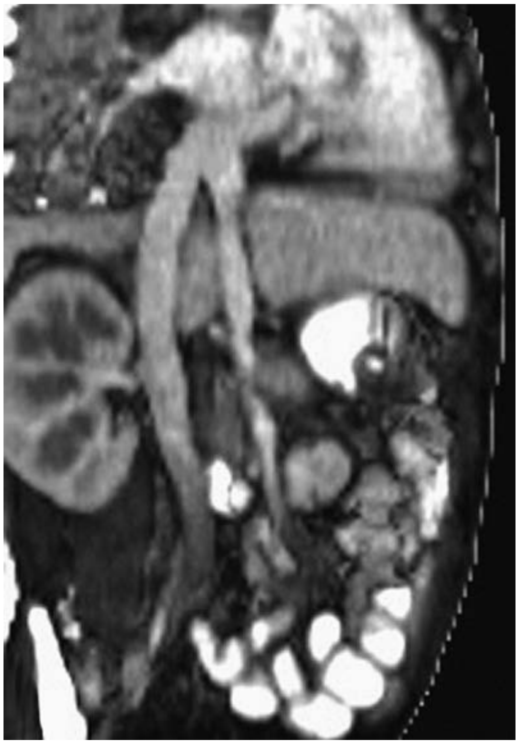

**Figure 92.15. Extrahepatic portosystemic shunt.** Coronal oblique reformatted CTA image shows the superior mesenteric vein connecting to the suprahepatic IVC, bypassing the liver.

## Intrahepatic Congenital Portosystemic Shunts

***Overview.*** Intrahepatic congenital portosystemic shunts are relatively rare anomalies, in which one or more intrahepatic portosystemic venous shunts may be present. They are classified into four types.[55] Type I, the most common, is a single large vein connecting the right portal and hepatic veins. Type II features peripheral single or multiple communications in one segment. Type III consists of an aneurysm connecting a peripheral portal vein and a hepatic vein branch. Type IV represents diffuse communications in multiple lobes.

***Etiology.*** Intrahepatic congenital portosystemic shunts represent persistent communications between the portal and hepatic venous derivatives of the embryologic vitelline veins, or between the vitelline and subcardinal veins (Fig. 92.16).[52,56] A patent ductus venous represents a form of portosystemic shunt from the left portal vein into the IVC.

***Clinical Presentation.*** These shunts may be asymptomatic and diagnosed incidentally. When encountered in neonates, some of

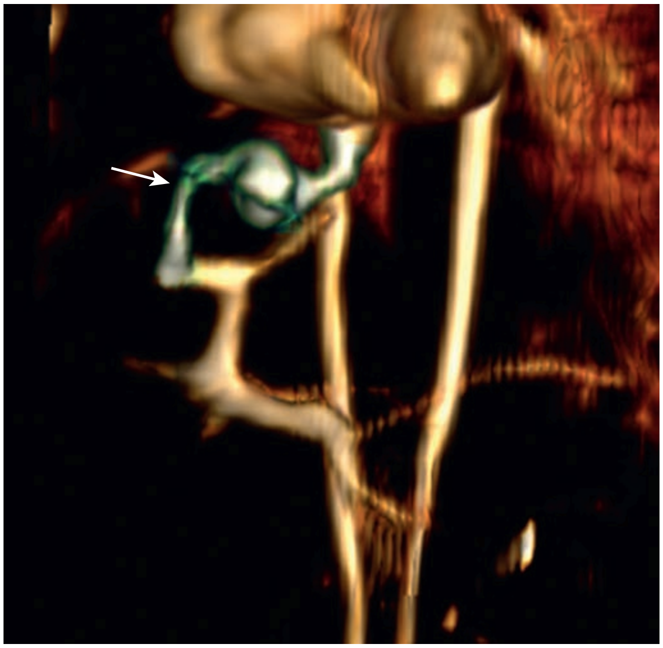

**Figure 92.16. Intrahepatic portosystemic shunt.** 3D reconstructed contrast-enhanced CT image shows a tortuous anomalous connection *(arrow)* between the left portal vein and intrahepatic IVC.

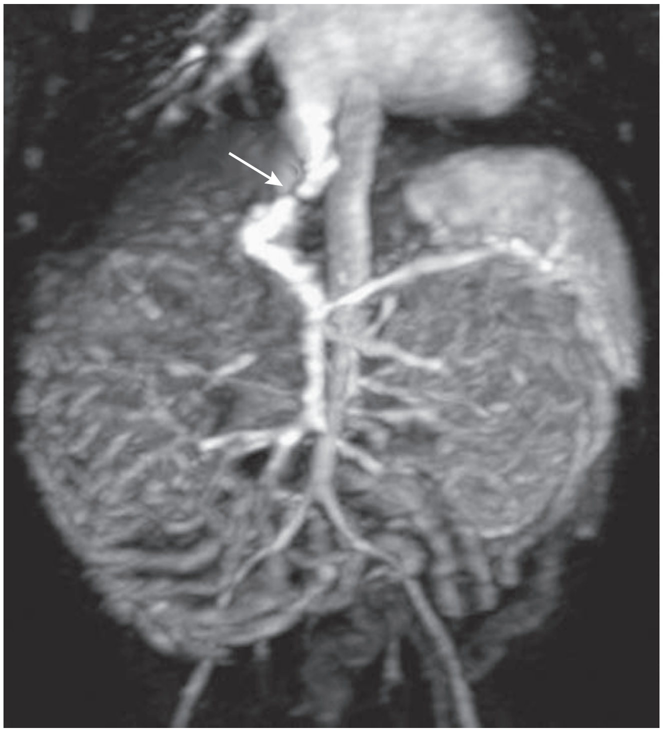

**Figure 92.17. Intrahepatic portosystemic shunt in an infant with hyperammonemia.** MR venographic image shows the anomalous connection *(arrow)* between the intrahepatic portal vein and the IVC. The portal vein was larger than normal on ultrasound.

these shunts may resolve spontaneously within the first 12 to 24 months of life; however, the proportion of patients in whom this occurs is not known.[52]

When these shunts are clinically apparent, presentation can include jaundice, hyperammonemia, hypergalactosemia, encephalopathy, and pulmonary hypertension.[51,52] Type IV shunts may be associated with massive shunting and heart failure. Cutaneous hemangiomas have been described in neonates with intrahepatic portosystemic shunts.

***Imaging.*** Intrahepatic congenital portosystemic shunts often are demonstrated by ultrasound imaging, sometimes when evaluating a child with a cutaneous hemangioma. The nonuniform size of the portal vein and hepatic vein branches may locate additional communications. The flow pattern in the portal veins, and at times also in the splenic vein, may demonstrate a biphasic or triphasic pattern, reflecting bypass of the hepatic parenchyma. Intrahepatic shunts are well demonstrated by CTA and MRA (Fig. 92.17).

***Treatment.*** Asymptomatic children with mild metabolic abnormalities can be treated conservatively by dietary means and Doppler imaging follow-up, because some of these shunts may close spontaneously.[51] Contemporary literature has described endovascular treatment with increasing frequency using a variety of surgical techniques and devices.[54,56]

## Subdiaphragmatic Anomalous Pulmonary Venous Connections

***Overview.*** Although anomalous pulmonary venous connections usually occur above the diaphragms, multiple subdiaphragmatic embryonal connections may persist, with subdiaphragmatic partial or total pulmonary venous drainage.

***Etiology.*** Pulmonary veins develop as a plexus that initially drains into both the cardinal veins and the umbilicovitelline venous system. As lung development proceeds, the common pulmonary vein is formed by the confluence of the four pulmonary veins and fuses with the posterior wall of the left atrium. If this normal fusion and drainage into the left atrium does not occur, embryonic connections to the splanchnic and umbilicovitelline systems persist.[44,57] Total anomalous pulmonary venous return below the diaphragm drains most frequently into the portal vein or ductus venosus.

***Clinical Presentation.*** Patients with infradiaphragmatic venous return are invariably obstructed and present with severe pulmonary edema. The obstruction may be at the level of the diaphragm, through intrinsic stenosis of the anomalous vessel, through closure of the ductus venosus, or through passage across the hepatic vascular bed in cases of drainage into the portal vein.[57,58]

***Imaging.*** On sonography, the anomalous common pulmonary vein is seen as a large vascular channel that enters the diaphragmatic hiatus anterior to the esophagus and inserts into the left portal vein or ductus venosus. CT and MRI show the same findings (Fig. 92.18).

***Treatment and Prognosis.*** Treatment of this anomaly is surgical (see Chapter 71).[59]

## HEPATIC ARTERIOVENOUS MALFORMATION AND FISTULA

***Overview.*** Arteriovenous malformations refer to a tangled collection of nonneoplastic vessels; they are much less common than infantile hemangiomas, although occasionally the two may be difficult to differentiate. Unlike hemangiomas, they do not regress and do not respond to medical therapy.[44,60]

Arterioportal fistulas refer to direct connections between the hepatic arterial and portal venous system, which can be intrahepatic or extrahepatic. They are classified according to their afferent supply[61]: Type 1 is supplied by either the right or left hepatic artery; type 2 is supplied by both right and left hepatic arteries or their braches; and type 3 refers to a complex lesion, with vascular supply including extrahepatic arteries. Fistulas between the arterial and the systemic hepatic venous system are exceedingly rare, and when congenital, they are seen most often in the setting of other anomalies, such as hemorrhagic telangiectasia, hepatic carcinoma, and hemangioma.[11]

***Etiology.*** Congenital arteriovenous fistulas may be single or multiple and may be isolated lesions or part of the spectrum of hereditary hemorrhagic telangiectasia and Ehlers–Danlos syndrome. Most lesions are not congenital but are acquired in patients with biliary cirrhosis or after blunt or penetrating trauma, such as a liver biopsy.[60,62]

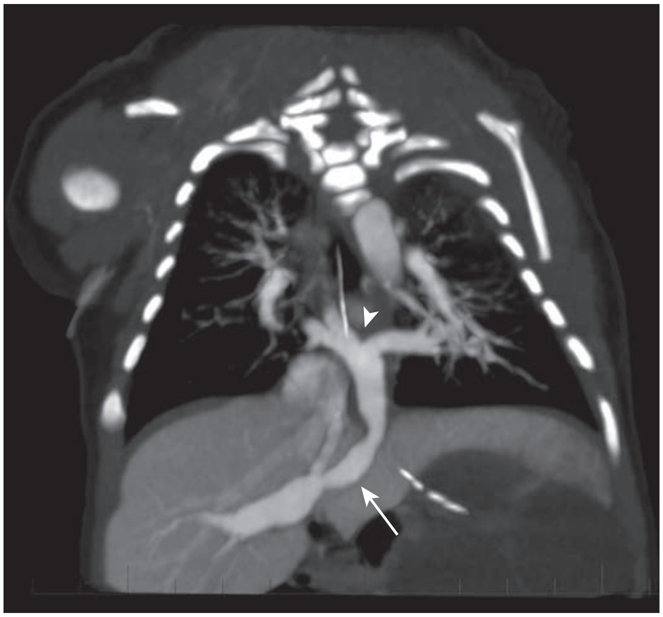

**Figure 92.18. Total anomalous pulmonary venous return.** Angled coronal MIP image from a CTA shows abnormal pulmonary venous return into the left portal vein *(arrow)*. The anomalous vein at the confluence of the inferior pulmonary veins *(arrowhead)* courses caudally through the diaphragm (where it is mildly constricted) to join the left portal vein.

***Clinical Presentation.*** Arteriovenous malformations may present with congestive heart failure, hepatic ischemia, or portal hypertension.[60] Clinical manifestations of arterioportal fistulas are presinusoidal portal hypertension, with consequent ascites, splenomegaly, and gastrointestinal bleeding, as well as malabsorption and failure to thrive.[60,61] A murmur and thrill may be detectable over the right upper quadrant in approximately 50% of cases.[61] High-output heart failure may be seen in infants, mainly when the ductus venosus is patent; acute closure of the ductus venosus can result in fatal gastrointestinal bleeding.[60] Acquired postbiopsy fistulas that are small, peripheral, and produce no symptoms are usually self-limited.

***Imaging.*** Hepatic congenital arteriovenous malformations and arteriovenous fistulas can be diagnosed with ultrasound, CT, and MRI. In congenital arteriovenous malformations, ultrasound demonstrates a tangle of vessels of variable size.[60] The size of the hepatic artery is proportional to the size of the shunt; the draining hepatic veins are distended, and the aorta may taper after the takeoff of the celiac axis (Fig. 92.19). The hepatic artery demonstrates very high systolic Doppler shifts and high diastolic flow, whereas the hepatic veins demonstrate pulsatile or arterialized high-velocity flow.

In patients with arteriovenous fistulas, ultrasound demonstrates enlargement of the hepatic artery as well as dilatation of the portal vein at the site of the fistulous connection.[44] Portal venous flow is reversed on Doppler sonography in the draining vein of an arterioportal fistula and may be reversed in the MPV as well as in the splenic and superior mesenteric veins, depending on shunt size.[1] The reversed portal venous flow usually is arterialized on spectral Doppler evaluation, with high flow velocity. The hepatic artery, or the branch that leads into the fistula, demonstrates high velocity and a decreased resistive index. Ascites and bowel wall thickening may be present. The fistula is intensely visible by color and power Doppler imaging, with vibration artifact in the hepatic vein. CT and CTA demonstrate intense enhancement and rapid washout in malformations and fistulas; rapid appearance of the portal vein occurs during the arterial phase, with enhancement

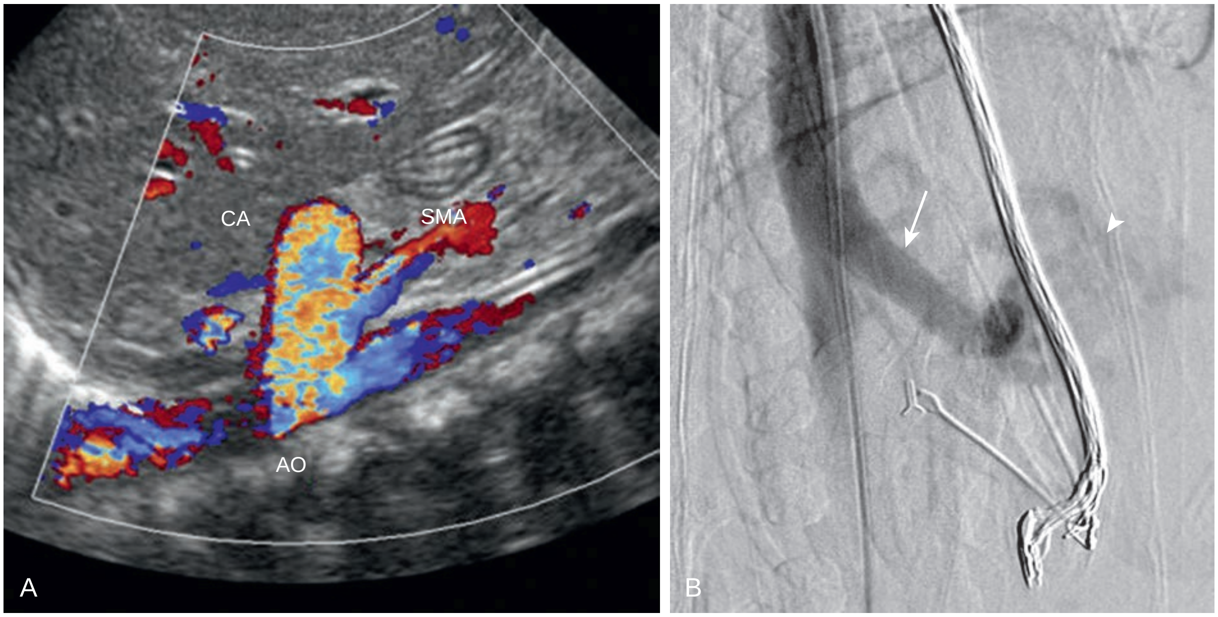

**Figure 92.19. Congenital hepatic arterioportal shunt.** (A) Color Doppler sonogram in a 4-month-girl with heart failure secondary to a congenital arterioportal shunt shows an enlarged celiac artery *(CA)* relative to the adjacent aorta *(AO)* and superior mesenteric artery *(SMA),* with color aliasing indicative of high flow velocity. (B) Lateral aortogram confirms an enlarged celiac trunk *(arrow)* and decreased caliber of the more distal aorta. Early filling of the shunt vessels *(arrowhead)* is seen over the liver.

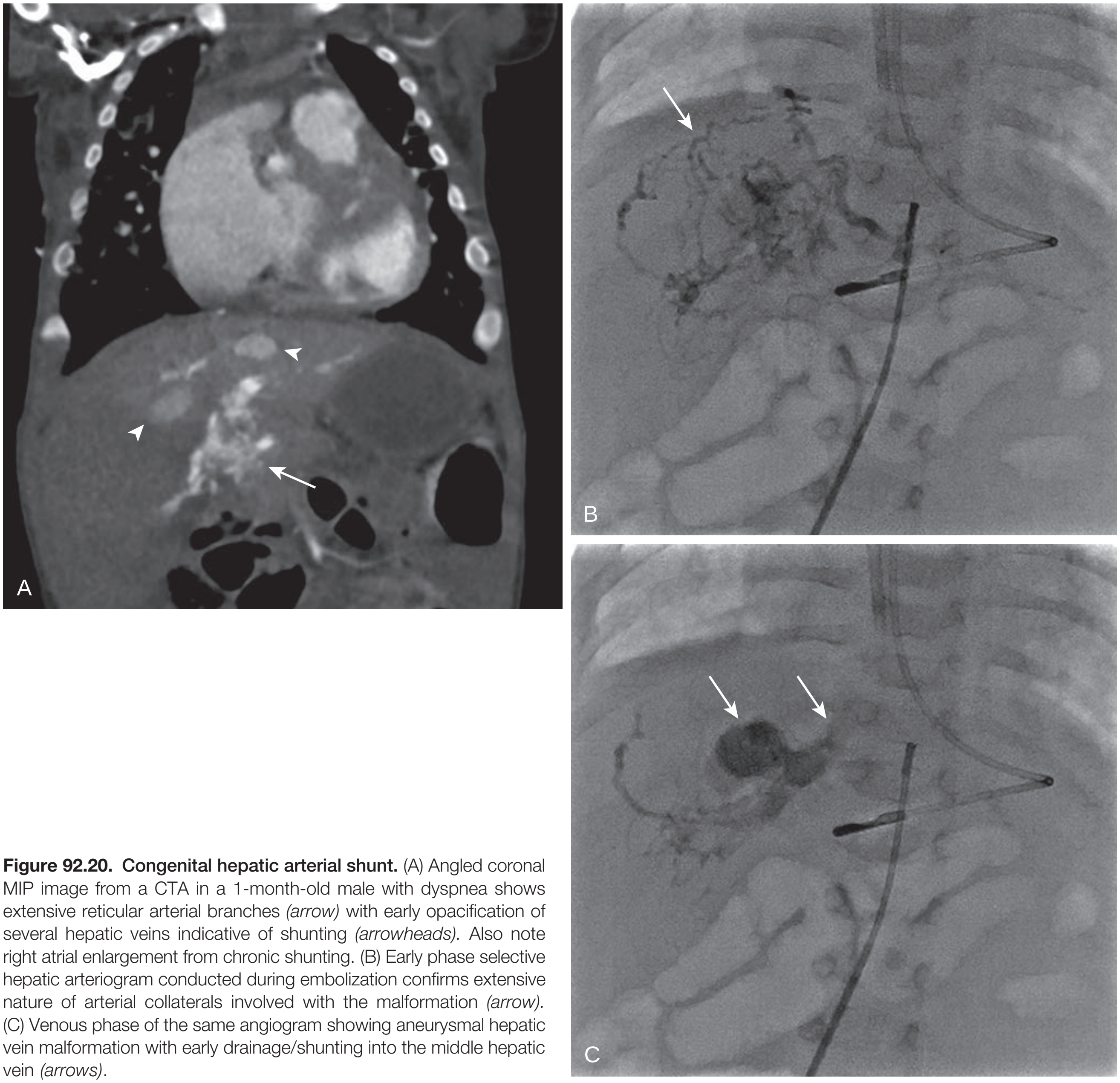

**Figure 92.20. Congenital hepatic arterial shunt.** (A) Angled coronal MIP image from a CTA in a 1-month-old male with dyspnea shows extensive reticular arterial branches *(arrow)* with early opacification of several hepatic veins indicative of shunting *(arrowheads).* Also note right atrial enlargement from chronic shunting. (B) Early phase selective hepatic arteriogram conducted during embolization confirms extensive nature of arterial collaterals involved with the malformation *(arrow).* (C) Venous phase of the same angiogram showing aneurysmal hepatic vein malformation with early drainage/shunting into the middle hepatic vein *(arrows)*.

intensity similar to that of the aorta.[44] The enlarged arterial supply and venous drainage are well demonstrated by CTA, with early appearance of the draining veins.[44] The excellent temporal resolution of fast-sequence MRA allows visualization of the vascular nidus and identification of fast clearance in arteriovenous malformations and fistulas. Angiography shows similar findings (Fig. 92.20) and is reserved for imaging before therapeutic embolization.[60]

***Treatment and Prognosis.*** Congenital hepatic arteriovenous malformations and fistulas do not respond to medical management. Treatment is aimed at obliteration of the abnormal arteriovenous connection and consists of embolization, surgical ligation, hepatic lobectomy, or liver transplantation.[1,44] As noted earlier, infants with biliary atresia and arterioportal shunt present a special problem; they are unlikely to tolerate interruption in hepatic arterial flow, and early liver transplantation may be the treatment of choice.[44,63,64] Prognosis depends on the severity of the underlying disease and the success of various treatments.

## KEY POINTS

- Portal hypertension is defined as a rise in pressure within the splanchnic venous system above 10 mm Hg.
- Cirrhosis is the most common cause of portal hypertension.
- HPS is associated with hepatic vascular abnormalities that alter the normal portosystemic circulation, leading to right to left intrapulmonary shunting.
- Budd–Chiari syndrome may be caused by a caval web, hepatic vein or IVC thrombosis, tumor extension into the IVC, external compression, or be idiopathic.
- Hepatic SOS develops most frequently in patients undergoing myeloablative therapy for hematopoietic stem cell transplantation and is primarily a clinical diagnosis.
- Abnormalities in development of the vitelline and subcardinal veins can result in a variety of vascular anomalies and intrahepatic shunts.

## SUGGESTED READINGS

Alonso-Gamarra E, Parron M, Perez A, et al. Clinical and radiologic manifestations of congenital extrahepatic portosystemic shunts: a comprehensive review. *Radiographics*. 2011;31:707–731.

Biyyam DR, Chapman T, Ferguson MR, et al. Congenital lung abnormalities: embryologic features, prenatal diagnosis, and postnatal radiologic-pathologic correlation. *Radiographics*. 2010;30(6):1721–1738.

Cheung KM, Lee CY, Wong CT, et al. Congenital absence of portal vein presenting as hepatopulmonary syndrome. *J Paediatr Child Health*. 2005;41:72–75.

Fink MA, Berry SR, Gow PJ, et al. Risk factors for liver transplantation waiting list mortality. *J Gastroenterol Hepatol*. 2007;22(1):119–124.

Kim MJ, Ko JS, Seo JK, et al. Clinical features of congenital portosystemic shunt in children. *Eur J Pediatr*. 2012;171:395–400.

Lee SH, Yoo KH, Sung KW, et al. Hepatic veno-occlusive disease in children after hematopoietic stem cell transplantation: incidence, risk factors, and outcome. *Bone Marrow Transplant*. 2010;45:1287–1293.

Lee W, Chang S, Duddalwar VA, et al. Imaging assessment of congenital and acquired abnormalities of the portal venous system. *Radiographics*. 2011;31:905–926.

Ryckman FC, Alonso MH. Causes and management of portal hypertension in the pediatric population. *Clin Liver Dis*. 2001;5:789–818.

## REFERENCES

Full references for this chapter can be found on www.expertconsult.com.

## REFERENCES

1. Tannuri AC, Tannuri U, Lima FR, et al. Congenital intrahepatic arterioportal fistula presenting as severe undernutrition and chronic watery diarrhea in a 2-year-old girl. *J Pediatr Surg*. 2009;44:e19–e22.
2. Ryckman FC, Alonso MH. Causes and management of portal hypertension in the pediatric population. *Clin Liver Dis*. 2001;5:789–818.
3. Weiss B, Shteyer E, Vivante A, et al. Etiology and long-term outcome of extrahepatic portal vein obstruction in children. *World J Gastroenterol*. 2010;16:4968–4972.
4. De Gaetano AM, Lafortune M, Patriquin H, et al. Cavernous transformation of the portal vein: patterns of intrahepatic and splanchnic collateral circulation detected with Doppler sonography. *AJR Am J Roentgenol*. 1995;165:1151–1155.
5. Morag I, Shah PS, Epelman M, et al. Childhood outcomes of neonates diagnosed with portal vein thrombosis. *J Paediatr Child Health*. 2011;47:356–360.
6. Schettino GC, Fagundes ED, Roquete ML, et al. Portal vein thrombosis in children and adolescents. *J Pediatr (Rio J)*. 2006;82:171–178.
7. Dehghani SM, Gholami S, Bahador A, et al. Comparison of Child-Turcotte-Pugh and pediatric end-stage liver disease scoring systems to predict morbidity and mortality of children awaiting liver transplantation. *Transplant Proc*. 2007;39:3175–3177.
8. Pugh RN, Murray-Lyon IM, Dawson JL, et al. Transection of the oesophagus for bleeding oesophageal varices. *Br J Surg*. 1973;60:646–649.
9. Kok T, van der Jagt EJ, Haagsma EB, et al. The value of Doppler ultrasound in cirrhosis and portal hypertension. *Scand J Gastroenterol Suppl*. 1999;230:82–88.
10. Yoon HM, Kim SY, Kim KM, et al. Liver stiffness measured by shear-wave elastography for evaluating intra-hepatic portal hypertension in children. *J Pediatr Gastroenterol Nutr*. 2017.
11. Gallego C, Velasco M, Marcuello P, et al. Congenital and acquired anomalies of the portal venous system. *Radiographics*. 2002;22:141–159.
12. Zargar SA, Javid G, Khan BA, et al. Endoscopic ligation compared with sclerotherapy for bleeding esophageal varices in children with extrahepatic portal venous obstruction. *Hepatology*. 2002;36:666–672.
13. Alonso J, Sierre S, Lipsich J, et al. Endovascular treatment of congenital portal vein fistulas with the Amplatzer occlusion device. *J Vasc Interv Radiol*. 2004;15:989–993.
14. Shigeta T, Kasahara M, Sakamoto S, et al. Balloon-occluded retrograde transvenous obliteration for a portosystemic shunt after pediatric living-donor liver transplantation. *J Pediatr Surg*. 2011;46:e19–e22.
15. Emre S, Dugan C, Frankenberg T, et al. Surgical portosystemic shunts and the Rex bypass in children: a single-centre experience. *HPB (Oxford)*. 2009;11:252–257.
16. Krebs-Schmitt D, Briem-Richter A, Grabhorn E, et al. Effectiveness of Rex shunt in children with portal hypertension following liver transplantation or with primary portal hypertension. *Pediatr Transplant*. 2009;13:540–544.
17. Chaves IJ, Rigsby CK, Schoeneman SE, et al. Pre- and postoperative imaging and interventions for the meso-Rex bypass in children and young adults. *Pediatr Radiol*. 2012;42:220–232.
18. Van Ha TG, Funaki BS, Ehrhardt J, et al. Transjugular intrahepatic portosystemic shunt placement in liver transplant recipients: experiences with pediatric and adult patients. *AJR Am J Roentgenol*. 2005;184:920–925.
19. Cheung KM, Lee CY, Wong CT, et al. Congenital absence of portal vein presenting as hepatopulmonary syndrome. *J Paediatr Child Health*. 2005;41:72–75.
20. Deep A, Jose B, Dhawan A. Hepatopulmonary syndrome in children—an update. *J Paediatr Child Health*. 2015;25(6):282–285.
21. Tang L, Luo B, Patel RP, et al. Modulation of pulmonary endothelial endothelin B receptor expression and signaling: implications for experimental hepatopulmonary syndrome. *Am J Physiol Lung Cell Mol Physiol*. 2007;292:L1467–L1472.
22. Chiu S-N, Ni Y-H, Wang J-K, et al. Resolution of secondary pulmonary arteriovenous malformations after embolization of a congenital superior-mesenteric-vein-to left-renal-vein shunt. *J Vasc Interv Radiol*. 2002;13:333–336.
23. Plessier A, Valla DC. Budd-Chiari syndrome. *Semin Liver Dis*. 2008;28:259–269.
24. Cura M, Haskal Z, Lopera J. Diagnostic and interventional radiology for Budd-Chiari syndrome. *Radiographics*. 2009;29:669–681.
25. Murad S, Plessier A, Hernandez-Guerra M, et al. Etiology, management, and outcome of the budd-chiari syndrome. *Ann Intern Med*. 2009;151:167.
26. Bittencourt PL, Couto CA, Ribeiro DD. Portal vein thrombosis and Budd-Chiari syndrome. *Clin Liver Dis*. 2009;13:127–144.
27. Pariente D, Franchi-Abella S. Paediatric chronic liver diseases: how to investigate and follow up? Role of imaging in the diagnosis of fibrosis. *Pediatr Radiol*. 2010;40:906–919.
28. Orloff MJ, Isenberg JI, Wheeler HO, et al. Budd-Chiari syndrome revisited: 38 years' experience with surgical portal decompression. *J Gastrointest Surg*. 2012;16:286–300, discussion 300.
29. Cesaro S, Pillon M, Talenti E, et al. A prospective survey on incidence, risk factors and therapy of hepatic veno-occlusive disease in children after hematopoietic stem cell transplantation. *Haematologica*. 2005;90:1396–1404.
30. Cheuk DK, Wang P, Lee TL, et al. Risk factors and mortality predictors of hepatic veno-occlusive disease after pediatric hematopoietic stem cell transplantation. *Bone Marrow Transplant*. 2007;40:935–944.
31. Corbacioglu S, Honig M, Lahr G, et al. Stem cell transplantation in children with infantile osteopetrosis is associated with a high incidence of VOD, which could be prevented with defibrotide. *Bone Marrow Transplant*. 2006;38:547–553.
32. Lee SH, Yoo KH, Sung KW, et al. Hepatic veno-occlusive disease in children after hematopoietic stem cell transplantation: incidence, risk factors, and outcome. *Bone Marrow Transplant*. 2010;45:1287–1293.
33. Jones RJ, Lee KS, Beschorner WE, et al. Venoocclusive disease of the liver following bone marrow transplantation. *Transplantation*. 1987;44:778–783.
34. McDonald GB, Hinds MS, Fisher LD, et al. Veno-occlusive disease of the liver and multiorgan failure after bone marrow transplantation: a cohort study of 355 patients. *Ann Intern Med*. 1993;118:255–267.
35. Lassau N, Auperin A, Leclere J, et al. Prognostic value of Doppler-ultrasonography in hepatic veno-occlusive disease. *Transplantation*. 2002;74:60–66.
36. McCarville MB, Hoffer FA, Howard SC, et al. Hepatic veno-occlusive disease in children undergoing bone-marrow transplantation: usefulness of sonographic findings. *Pediatr Radiol*. 2001;31:102–105.
37. Mortele KJ, Van Vlierberghe H, Wiesner W, et al. Hepatic veno-occlusive disease: MRI findings. *Abdom Imaging*. 2002;27:523–526.
38. Wadleigh M, Ho V, Momtaz P, et al. Hepatic veno-occlusive disease: pathogenesis, diagnosis and treatment. *Curr Opin Hematol*. 2003;10:451–462.
39. Chopra R, Eaton JD, Grassi A, et al. Defibrotide for the treatment of hepatic veno-occlusive disease: results of the European compassionate-use study. *Br J Haematol*. 2008;111:1122–1129.
40. DeLeve LD, Shulman HM, McDonald GB. Toxic injury to hepatic sinusoids: sinusoidal obstruction syndrome (veno-occlusive disease). *Semin Liver Dis*. 2002;22:27–42.
41. Mimatsu K, Oida T, Kano H, et al. Preduodenal portal vein, intestinal malrotation, polysplenia, and interruption of the inferior vena cava: a review of anatomical anomalies associated with gastric cancer. *Surg Radiol Anat*. 2012;34:179–186.
42. Singal AK, Ramu C, Paul S, et al. Preduodenal portal vein in association with midgut malrotation and duodenal web-triple anomaly? *J Pediatr Surg*. 2009;44:e5–e7.
43. Hernanz-Schulman M, Ambrosino MM, Genieser NB, et al. Pictorial essay. Current evaluation of the patient with abnormal visceroatrial situs. *AJR Am J Roentgenol*. 1990;154:797–802.
44. Gallego C, Miralles M, Marin C, et al. Congenital hepatic shunts. *Radiographics*. 2004;24:755–772.
45. Ohno K, Nakamura T, Azuma T, et al. Evaluation of the portal vein after duodenoduodenostomy for congenital duodenal stenosis associated with the preduodenal superior mesenteric vein, situs inversus, polysplenia, and malrotation. *J Pediatr Surg*. 2007;42:436–439.
46. Abernethy J, Banks J. Account of two instances of uncommon formation, in the viscera of the human body. By Mr. John Abernethy, Assistant Surgeon to St. Bartholomew's Hospital. Communicated by Sir Joseph Banks, Bart. P. R. S. *Philoso Trans Roy Soc Lond*. 1793;83:59–66.
47. Morgan G, Superina R. Congenital absence of the portal vein: two cases and a proposed classification system for portasystemic vascular anomalies. *J Pediatr Surg*. 1994;29:1239–1241.
48. Niwa T, Aida N, Tachibana K, et al. Congenital absence of the portal vein: clinical and radiologic findings. *J Comput Assist Tomogr*. 2002;26:681–686.
49. Murray CP, Yoo SJ, Babyn PS. Congenital extrahepatic portosystemic shunts. *Pediatr Radiol*. 2003;33:614–620.
50. Botha JF, Campos BD, Grant WJ, et al. Portosystemic shunts in children: a 15-year experience. *J Am Coll Surg*. 2004;199:179–185.

51. Kim MJ, Ko JS, Seo JK, et al. Clinical features of congenital portosystemic shunt in children. *Eur J Pediatr*. 2012;171:395–400.
52. Stringer MD. The clinical anatomy of congenital portosystemic venous shunts. *Clin Anat*. 2008;21:147–157.
53. Shen O, Valsky DV, Messing B, et al. Shunt diameter in agenesis of the ductus venosus with extrahepatic portosystemic shunt impacts on prognosis. *Ultrasound Obstet Gynecol*. 2011;37:184–190.
54. Stewart JK, Kuo WT, Hovsepian DM, et al. Portal venous remodeling after endovascular reduction of pediatric autogenous portosystemic shunts. *J Vasc Interv Radiol*. 2011;22:1199–1205.
55. Park JH, Cha SH, Han JK, et al. Intrahepatic portosystemic venous shunt. *AJR Am J Roentgenol*. 1990;155:527–528.
56. Tanoue S, Kiyosue H, Komatsu E, et al. Symptomatic intrahepatic portosystemic venous shunt: embolization with an alternative approach. *AJR Am J Roentgenol*. 2003;181:71–78.
57. Hines MH, Hammon JW. Anatomy of total anomalous pulmonary venous connection. *Oper Tech Thorac Cardiovasc Surg*. 2001;6:2–7.
58. Lucas RV Jr, Lock JE, Tandon R, et al. Gross and histologic anatomy of total anomalous pulmonary venous connections. *Am J Cardiol*. 1988;62:292–300.
59. Seale AN, Uemura H, Webber SA, et al. Total anomalous pulmonary venous connection: morphology and outcome from an international population-based study. *Circulation*. 2010;122:2718–2726.
60. Burrows PE, Dubois J, Kassarjian A. Pediatric hepatic vascular anomalies. *Pediatr Radiol*. 2001;31:533–545.
61. Norton SP, Jacobson K, Moroz SP, et al. The congenital intrahepatic arterioportal fistula syndrome: elucidation and proposed classification. *J Pediatr Gastroenterol Nutr*. 2006;43:248–255.
62. Khalid SK, Garcia-Tsao G. Hepatic vascular malformations in hereditary hemorrhagic telangiectasia. *Semin Liver Dis*. 2008;28:247–258.
63. Nishimori A, Okajima H, Okumura K, et al. Living donor liver transplantation as a means of rescuing post-embolization hepatic failure in a patient with idiopathic intrahepatic arteriovenous malformation in the liver. *J Hepatobiliary Pancreat Surg*. 2009;16:382–385.
64. Tercier S, Delarue A, Rouault F, et al. Congenital portocaval fistula associated with hepatopulmonary syndrome: ligation vs liver transplantation. *J Pediatr Surg*. 2006;41:e1–e3.

# 93 Liver Transplantation in Children

*Douglas C. Rivard and Geetika Khanna*

## OVERVIEW

The first liver transplantation was performed in 1963, with posttransplant survival reaching 1 year in 1968.[1] Subsequent use of immunosuppressants such as cyclosporine and tacrolimus, coupled with improved surgical techniques, has resulted in 1-year survival rates exceeding 90%.[2,3] The development of surgical techniques that allow surgeons to transplant portions of livers from adult donors has completely changed the fate of liver transplantation in pediatric patients.[4–6] Pediatric liver transplants account for approximately 7.8% of all liver transplants in the United States.[7]

The major indications for liver transplantation in children in North America include biliary atresia (32%), metabolic/genetic conditions (22%), acute liver failure (11%), cirrhosis (9%), liver tumor (9%), immune mediated liver and biliary injury (4%), and other miscellaneous conditions.[7] At least 80% of patients with biliary atresia receive transplants by 20 years of age, with the majority undergoing the procedure at younger than 4 years of age.[8] Technical variant grafts (i.e., split liver, living donor) are often used in smaller children, and the 10-year actuarial graft and patient survival for liver transplantation in biliary atresia is 73% and 86%, respectively.[9]

Other cholestatic causes of cirrhosis include bile duct hypoplasia syndromes (e.g., Alagille), cystic fibrosis, and primary sclerosing cholangitis.[10–12] Children with cholestasis related to total parenteral nutrition may have underlying short-bowel syndrome and may require combined liver and small bowel transplantation.

Diffuse nonbiliary liver diseases necessitating transplantation include metabolic liver disease, autoimmune hepatitis, neonatal hemochromatosis, graft-versus-host disease, and fulminant liver failure.[13–15] Liver transplantation is a well-established therapeutic option in children with metabolic disorders such as glycogen storage disease, tyrosinemia, and Wilson disease.[16–18] Congenital hepatic fibrosis is associated with autosomal recessive polycystic kidney disease; patients with these diseases may require combined liver and kidney transplantation.[19] Liver transplantation for hepatoblastoma and hepatocellular carcinoma has improved survival and is a viable option for children with unresectable or multifocal tumors without extrahepatic disease or vascular involvement. Patients with unresectable hepatoblastoma and pulmonary metastases can be considered for liver transplantation if the pulmonary metastases show complete response to chemotherapy or pulmonary metastatectomy is performed with tumor-free margins.

Liver transplants performed in older children usually involve the use of a whole cadaveric liver (Fig. 93.1), whereas most young children receive reduced transplants. Liver segments are defined according to the segmental and vascular anatomy.[20] Most living donor transplants use the donor's left lateral segments or left hemiliver, although the right lobe also may be used. A cadaveric liver may be split between two recipients with the left lateral segment used for a pediatric recipient and the rest of the liver used for an adult recipient; however, this results in challenging vascular and biliary connections because of limited pedicle lengths.[5]

Left hemiliver and left lateral segment hila and their cut surfaces face to the right; however, they can be differentiated by the presence of the falciform ligament separating lateral segments two and three from medial segment four in the left lobe transplant, which is absent in left lateral segment grafts. The small bowel, duodenum, colon, and right kidney often migrate into the vacated liver bed; a migrated cecum and right colon may imitate malrotation.

The portal vein usually is connected end-to-end to the recipient portal vein, with as much of the native portal vein preserved during hepatectomy as possible.[21] In case of short vascular pedicles, extension grafts may be used, which are also used in patients with unsuitable native portal veins (small caliber or thrombosed).

The donor hepatic artery usually is anastomosed to the recipient's hepatic artery as a fish mouth anastomosis or to the celiac axis. The hepatic artery may be connected to the infrarenal aorta if technically required (Fig. 93.2). In such cases, the native hepatic artery is ligated and should not be confused with arterial occlusion on imaging. Preoperative knowledge of variant hepatic artery anatomy (which can be present in up to 50% of the population) is essential for the donor and the recipient. The bile duct typically is attached to a Roux-en-Y jejunal loop (Fig. 93.3) in young children and children with biliary atresia, though direct duct-to-duct anastomosis can also be performed.

In split liver transplants, the donor hepatic vein is connected to the recipient's inferior vena cava. In full-size liver grafts, the donor liver is removed with the intrahepatic inferior vena cava (IVC), which is then interposed between the infraatrial and distal native IVC. The "piggyback" technique (with preservation of the recipient vena cava and cavocaval anastomosis) has gained wide acceptance and is the preferred technique for orthotopic liver transplantation at many institutions. In patients with polysplenia and biliary atresia, vascular connections may be modified as a result of the frequent absence of the hepatic segment of the IVC, azygous continuation, malrotation, a preduodenal portal vein, and other anomalies.[5,21,22]

Vascular, biliary, infectious, and immunosuppression-related complications may befall liver recipients postoperatively, including posttransplant lymphoproliferative disease (PTLD). The most common complication of liver transplant is infection, but vascular thrombosis and primary graft nonfunction account for most cases of graft loss leading to retransplantation. Death in most pediatric liver recipients is caused by infection, neurologic complications, or multisystem organ failure. Enteric complications include bowel perforation and obstruction, gastrointestinal hemorrhage, and infectious enteritis. Neurologic complications include cerebral hemorrhage and infarction, infection, and drug toxicity.[23–25] Immunosuppressive drug-induced nephrotoxicity is common, but imaging features generally are nonspecific.

Other complications include hepatic parenchymal defects, pleural effusions, and splenic infarcts, which may occur after splenic artery ligation.[26,27] Right adrenal hemorrhage and right phrenic nerve injury are potential complications seen after the standard transplant operation, but they rarely occur after a cava-sparing operation.

## IMAGING

Postoperative imaging is centered on evaluation of vascular, biliary, and enteric complications. Therefore an understanding of specific surgical practice is essential.

Intraoperative sonography may be performed when vascular anastomoses are difficult or revised and their patency is uncertain. Vascular patency is evaluated daily with Doppler ultrasound for the first few posttransplant days because the fate of the transplant

## Abstract:

Pediatric liver transplant is performed for a variety of indications. Knowledge of various surgical techniques and potential complications is relevant to the radiologist as medical imaging plays an integral role in evaluation of children receiving liver transplant.

## Keywords:

Pediatric liver transplant

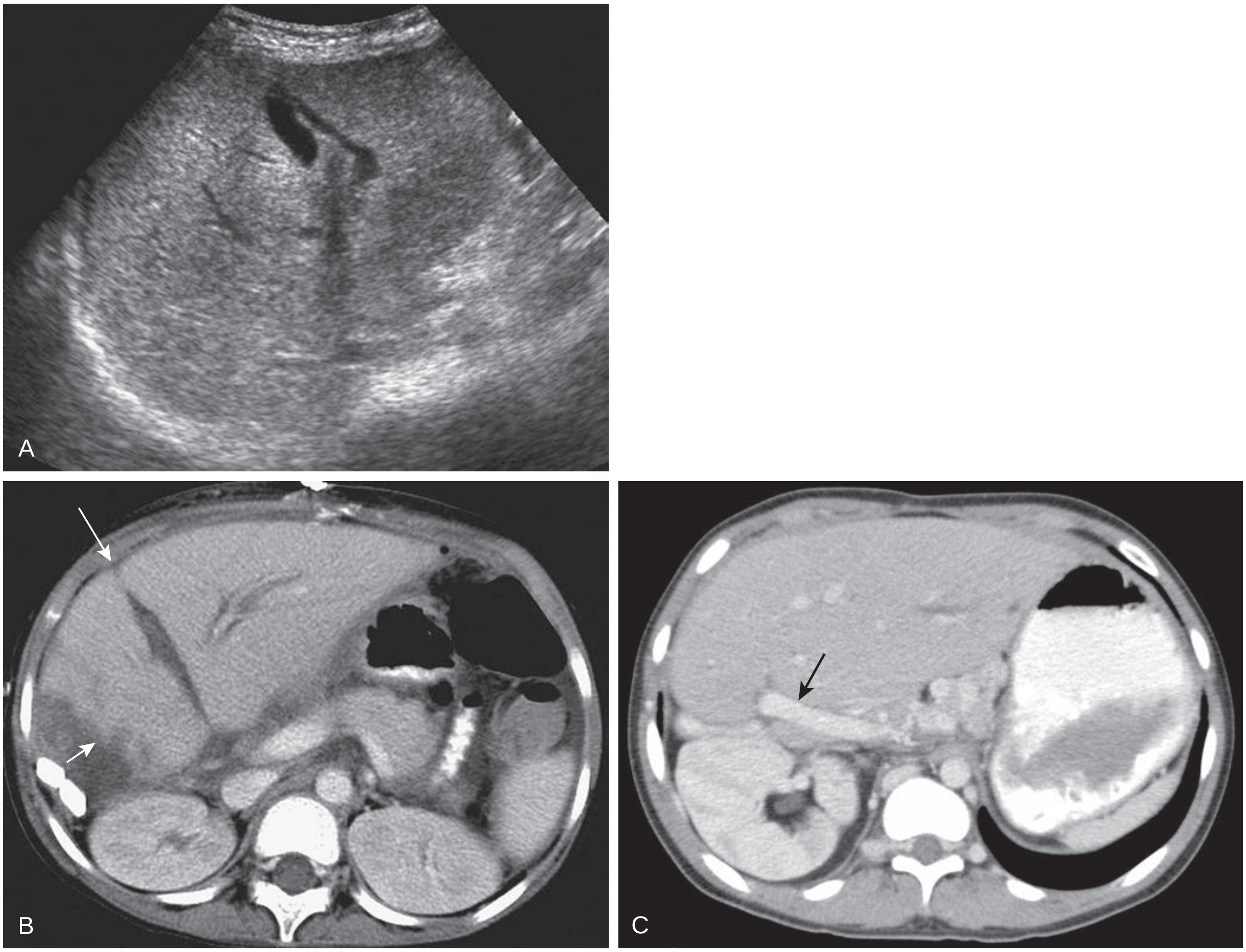

**Figure 93.1. Types of liver transplants.** (A) Transverse sonogram of a whole liver transplant. Fluid along the falciform ligament demarcates the left lateral and medial segments. A right lobe is also present. (B) Axial contrast-enhanced CT image of a left lobe liver graft shows an ill-defined, irregular cut edge with adjacent fluid *(short arrow)*. Fluid along the falciform ligament *(long arrow)* separates the left lateral segment (segments two and three) from the medial segment (segment four). (C) Axial contrast-enhanced CT image of a left lateral segment graft shows the portal vein entering from the right *(arrow)* and the absence of the falciform ligament. Also note the position of the right kidney in the upper abdomen.

is much improved if vascular occlusions are diagnosed and managed early. The frequency of required ultrasound examinations then decreases, based on individual needs and clinical concerns.[28,29]

Early postoperative ultrasound may be challenging because of poor acoustic windows caused by dressings, open incisions, free intraabdominal air, and body wall edema. The flow patterns in all vessels vary in the early postoperative period because of edema of the anastomosis and surrounding tissues, as well as hemodynamic changes in the graft's vascular bed. Vascular patency, flow direction, pulsatility pattern, and velocity can be evaluated using gray-scale, spectral, and color Doppler ultrasound techniques. The color velocity scale may have to be adjusted for each vessel separately to avoid aliasing in the faster flowing vessels, which can lead to ambiguity of flow direction. Efforts must be made to interrogate at the anastomoses, where stenosis, thrombosis, and occlusion are most likely.[28]

Early findings seen in otherwise normal liver grafts include increased periportal echogenicity (low attenuation on computed tomography [CT] and increased signal on water-sensitive magnetic resonance [MR] sequences) related to transient lymphatic engorgement (Fig. 93.4), which can last up to 1 year posttransplantation. Other postoperative findings include right pleural effusion, subhepatic fluid collections, and biliary air in recipients with choledochojejunostomies.[26,27]

Periodic long-term ultrasound screening of liver recipients is mandatory because vascular complications may be clinically silent. CT, CT angiography (CTA), magnetic resonance cholangiopancreatography (MRCP), and magnetic resonance angiography (MRA) are used to determine the need for biliary and vascular interventions in selected patients. The choice of CT versus magnetic resonance imaging (MRI) depends on the individual center's expertise. CT is preferred in the acutely sick patient and provides better spatial resolution for evaluation small vessels. Biliary complications such as strictures and bilomas can be well evaluated with MRCP with or without the use of hepatocyte-specific contrast agents.

## PRETRANSPLANT IMAGING

Preoperative imaging is tailored to the patient's underlying disease and coexistent conditions. The goals are to document vascular

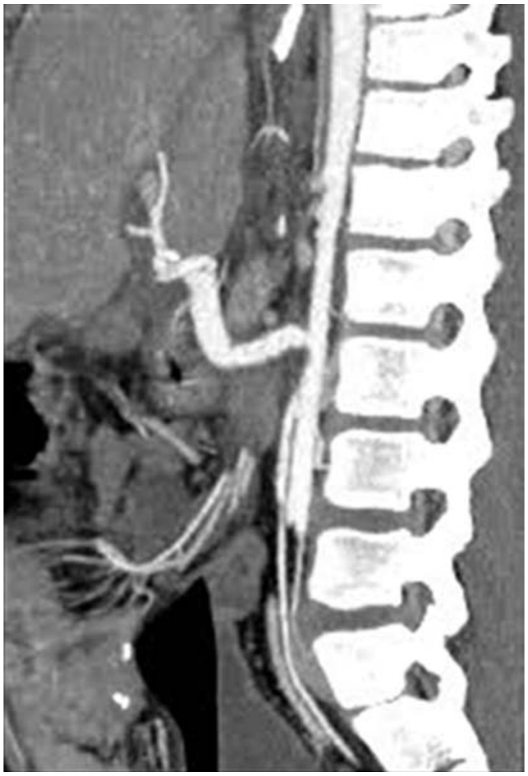

**Figure 93.2. Hepatic artery conduit.** Sagittal oblique reformatted contrast-enhanced CT maximum intensity projection (MIP) image shows an infrarenal conduit, arising just above the level of the inferior mesenteric artery, feeding the transplanted hepatic artery.

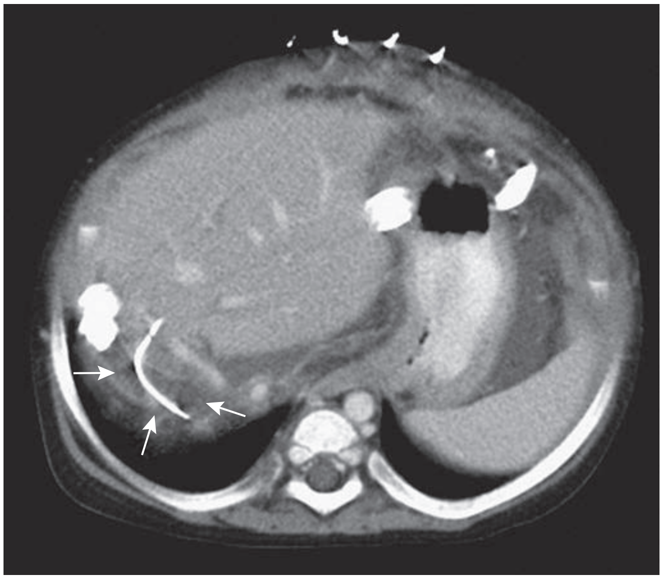

**Figure 93.3. Roux-en-Y biliary anastomosis.** Axial contrast-enhanced CT image early after transplantation show the biliary anastomosis and loop are marked by a small biliary stent *(arrows)*. Being an efferent loop from the liver, it frequently does not fill with intestinal contrast, making it difficult to differentiate from a pathologic fluid collection. Diffuse mesenteric edema and skin staples are noted.

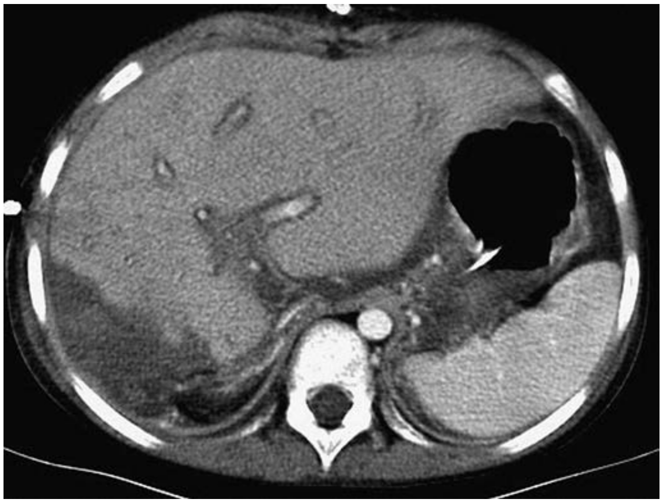

**Figure 93.4. Early CT findings in liver transplantation.** Axial contrast-enhanced CT image shows diffuse periportal hypoattenuation, irregularity of the liver cut surface edge with adjacent fluid. These are expected findings in the immediate post operative period.

patency, define visceral and vascular anatomy, exclude contraindications, evaluate the extent of liver disease and portal hypertension, and assess liver volumes.

Pertinent anatomic features for surgical planning include a small, absent, or occluded portal vein; IVC thrombosis; biliary atresia associated with polysplenia syndrome and absent intrahepatic IVC, with hepatic veins draining into the right atrium; systemic drainage of the splenic veins; congenital portosystemic shunts; and malrotation. Transplantation may be impossible when the portal and superior mesenteric veins are occluded or in cases of nonresponsive metastatic hepatoblastoma. Detection of hepatocellular carcinoma in a patient with cirrhosis changes the transplant urgency and requires tumor staging and decisions about pretransplant therapy, which affect the timing and feasibility of transplantation.[28]

Ultrasound is the first-line imaging modality in the preoperative evaluation of pediatric transplant candidates. Doppler ultrasound assesses vascular patency and hemodynamics. CT or MRI with intravenous contrast is excellent for showing vascular and visceral anatomy. Bone radiographs may detect rickets, osteopenia, and fractures, and chest radiographs may show cardiomegaly and vascular prominence in patients with hepatopulmonary disease (see Chapter 92).[30,31] Angiography is seldom needed but is reserved for patients for whom additional information may be required, such as if the patency of portal tract is questionable.

## VASCULAR COMPLICATIONS

### Hepatic Artery

***Overview.*** Hepatic arterial complications include thrombosis, occlusion, stenosis, peripheral arteriovenous fistula, and aneurysm. Hepatic artery thrombosis is the most common vascular complication as well as a major cause of graft loss and mortality in the early postoperative period. Early hepatic artery thrombosis is associated with a high incidence of transplant loss secondary to liver infarction.[32] If the problem is diagnosed within the first 2 to 3 days and the patient is still asymptomatic, most transplanted livers with hepatic artery thrombosis can be salvaged. However, if elevated liver function tests, bile leak, liver abscess, or sepsis have supervened, graft loss may reach 75%.[33] Late thrombosis typically presents with biliary complications.

***Imaging.*** The hepatic artery is much more difficult to visualize by gray-scale ultrasound than the portal vein because of its small

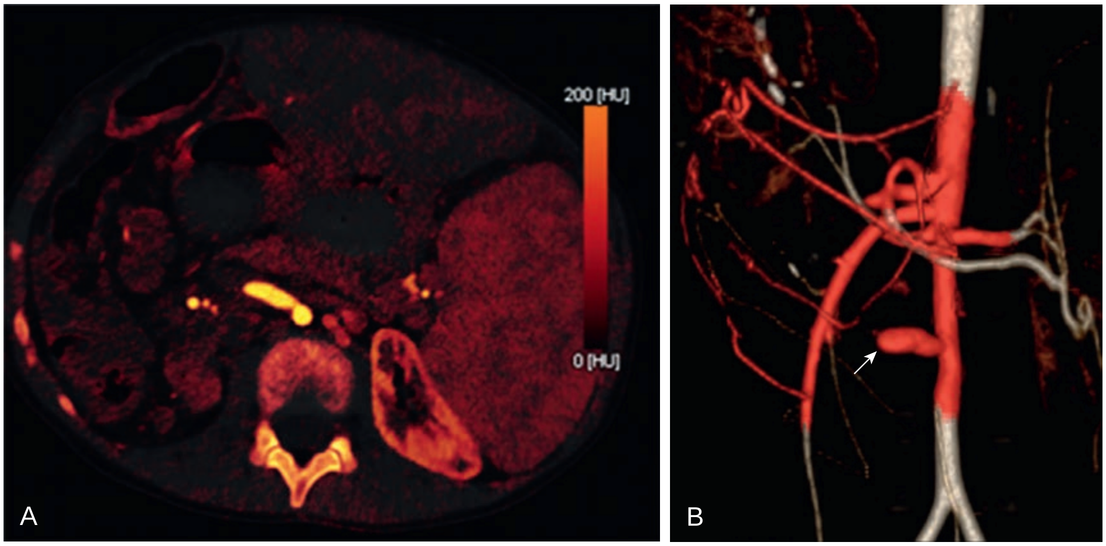

**Figure 93.5. Hepatic artery occlusion.** (A) Dual-energy CT iodine map shows abrupt termination of the infrarenal hepatic artery conduit with a nonperfused parenchyma of the transplanted liver. (B) 3D rendered reconstruction also demonstrates abrupt occlusion of the infrarenal arterial conduit *(arrow)*.

size. It is best evaluated by color and power Doppler ultrasound.[26] It is easier to follow the artery to its anastomosis when it is attached to the native hepatic artery or celiac axis rather than to the infrarenal aorta, where much of its course may be obscured by bowel gas. CTA and MRA are useful in showing hepatic artery anatomy, course, and complications, though CTA maybe preferred in the immediate postoperative period due to short examination time (Fig. 93.5).[27]

The hepatic artery flow pattern may vary considerably in the early postoperative days, demonstrating high and low resistive indices, without consistent prognostic implications.

The diagnosis of hepatic artery thrombosis is made by the inability to detect hepatic artery signal on color and spectral Doppler ultrasound.[26] Acute arterial thrombosis is treated by thrombectomy, revision, and occasionally retransplantation.[34] High-grade narrowing is manifested by turbulence and severely attenuated velocity distally with a parvus-tardus pattern in intrahepatic branches, with narrow systolic peaks and absent diastolic flow beyond the anastomosis.[32]

Later-onset hepatic artery occlusion may manifest with biliary leaks, strictures, and infection, including peribiliary abscess and sepsis because the biliary tree depends on hepatic arterial supply. In longstanding hepatic artery occlusion, hilar or transcapsular collaterals may result in a detectable arterial Doppler signal.[32]

Stenosis of the hepatic artery may be silent or may manifest with biliary complications and infection. High velocity and turbulence may be seen at the stenotic site. The flow pattern is abnormal, with a low-amplitude, parvus-tardus waveform representing a systolic acceleration time longer than 0.08 second and a resistive index lower than 0.5.[32] Very high-grade stenosis manifests with narrow and low-amplitude systolic peaks and absence of diastolic flow. The stenosis itself is usually extrahepatic and difficult to demonstrate directly by Doppler ultrasound (Fig. 93.6).[27,32] The hemodynamic changes of hepatic artery stenosis may be more dramatic than its appearance on CTA or MRA.

Hepatic artery pseudoaneurysm may occur at the anastomosis or within the liver at a biopsy site.[27,32] Liver biopsy also is a cause of intrahepatic arteriovenous fistulas.[34]

## Venous System

***Overview.*** Obstructive lesions of the portal vein, hepatic vein, and IVC may manifest with progressive ascites, deterioration of liver function, gastrointestinal bleeding, decreased platelet count, and increased spleen size. Pulmonary hypertension and intrapulmonary shunting may develop. Doppler signal in the intrahepatic portions of the portal vein do not exclude stenosis or obstruction, which may be present in the extrahepatic segment, with intrahepatic flow reconstituted by collateral vessels.[30] Portal vein, hepatic vein, and IVC stenosis result in flow acceleration at the stenosis and a jet of increased flow at the poststenotic segment, which appears as a contrasting color as a result of aliasing when the scale is adjusted to the velocity below the stenosis. The jet velocity is proportional to the pressure gradient across the stenosis.[26,27]

### Imaging

***Portal Vein.*** Ultrasound of the transplant portal vein requires visualization of its entire course. One must measure the diameter at any site of narrowing and interrogate the portal vein by spectral and color Doppler along its extrahepatic and hilar course, as well as its major intrahepatic branches. The curved course of the portal vein in left lobe and left lateral segment transplants and the size discrepancy between donor and recipient veins frequently cause dilation at the neohilum because of altered flow dynamics (Fig. 93.7) with a "yin-and-yang" swirling pattern on color Doppler. This pattern has not been proved clinically important. Anastomotic and periportal edema causing relative narrowing with jet formation is very common in the early postoperative period; these instances of edema are most often transient but may progress or persist and should be monitored. Complications include early thrombosis, stenosis, and late occlusion (Fig. 93.8).[26,27]

A hypoechoic thrombus may not be recognized by gray-scale ultrasound but shows absence of signal on color Doppler imaging. Reversal of superior mesenteric or splenic vein flow also is seen. Early thrombosis usually is treated by surgical thrombectomy and revision. Early posttransplant reversal of entire portal vein flow may reflect extensive hepatic necrosis and arterioportal shunting—an ominous sign associated with frequent organ loss.[27]

Later onset of portal vein thrombosis or occlusion may be clinically silent, manifesting with increasing plasma levels of hepatic enzymes, an enlarging spleen, and gastrointestinal bleeding. Intrahepatic portal venous flow frequently is reconstructed from collaterals recruited from superior mesenteric vein branches via varices in the Roux-en-Y loop and from transcapsular collaterals.

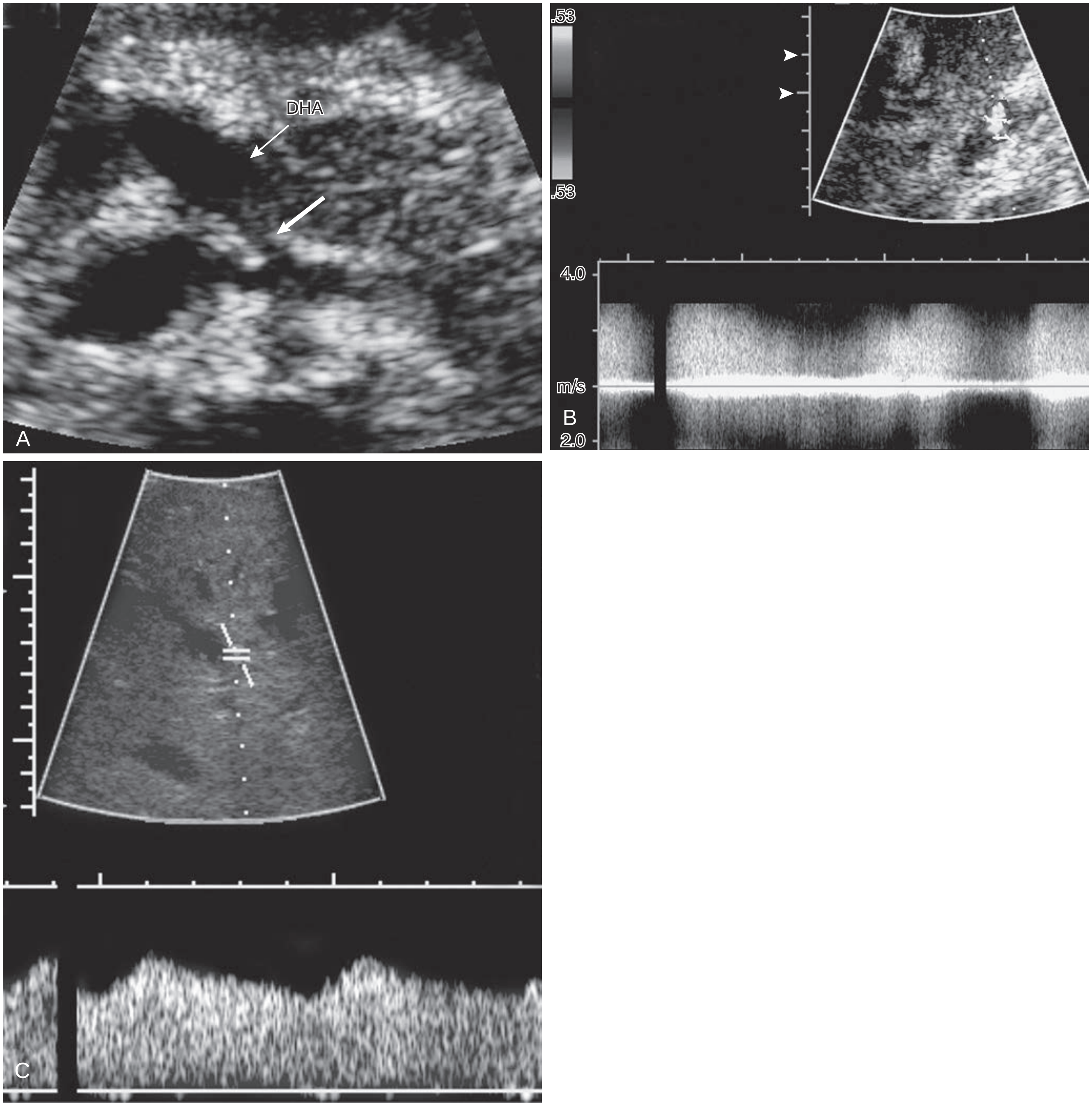

**Figure 93.6. Ultrasound and Doppler characteristics of hepatic artery stenosis.** (A) Transverse sonogram shows stenosis immediately distal to the celiac axis *(thick arrow)*. The donor hepatic artery *(DHA)* distal to the anastomotic stenosis is marked by a *thin arrow*. (B) Spectral and color Doppler at the stenosis show extreme turbulence and high velocity. The normal arterial signal is difficult to recognize because of aliasing. (C) Spectral and color Doppler in an intrahepatic hepatic artery branch show a slow systolic upstroke (parvus-tardus waveform), and relatively high diastolic flow producing an abnormally low resistive index.

In the latter event, flow in the receiving portal vein branches may be reversed with segment-to-segment shunting.

Stenosis usually occurs at anastomoses and in extension grafts (Fig. 93.9).[35] Because of the curved extrahepatic course of the portal vein, it may be difficult to demonstrate stenosis by ultrasound. The jet created at the stenotic site dissipates, such that flow velocity measured at the hilum is frequently normal despite a hemodynamically significant portal vein stenosis more proximally.[27] The jet also may exaggerate the dilation of the portal vein at the hilum. After successful angioplasty, the jet velocity decreases and the diameter at the stenotic site increases (Fig. 93.10). Less operator-dependent CT and MRI are highly useful and more consistent than ultrasound in the evaluation of portal vein occlusion and stenosis.[30,32,36]

***Hepatic Vein.*** Hepatic vein stenosis occurs mainly in reduced-size transplants at the anastomosis to the recipient IVC. In a posttransplant patient with the onset of portal hypertension, special efforts must be made to evaluate the hepatic veins and IVC if a

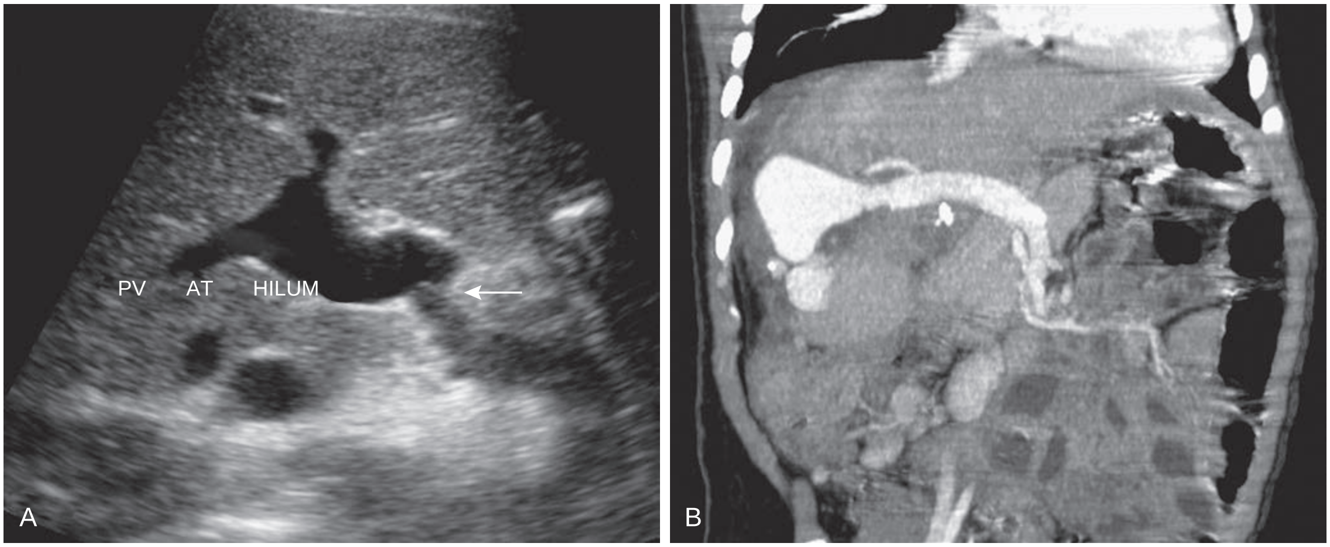

**Figure 93.7. Portal vein in segmental transplantation.** (A) Transverse sonogram shows a size discrepancy *(arrow)* between the native and donor portal veins *(PV AT HILUM)*. (B) Coronal CTA reconstruction demonstrates the extrahepatic portal vein coursing from the left to the right edge of the transplant, near the right abdominal wall. The portal vein is dilated at the neohilum. Note slight narrowing at the anastomosis in this early transplant, which can be a transient finding.

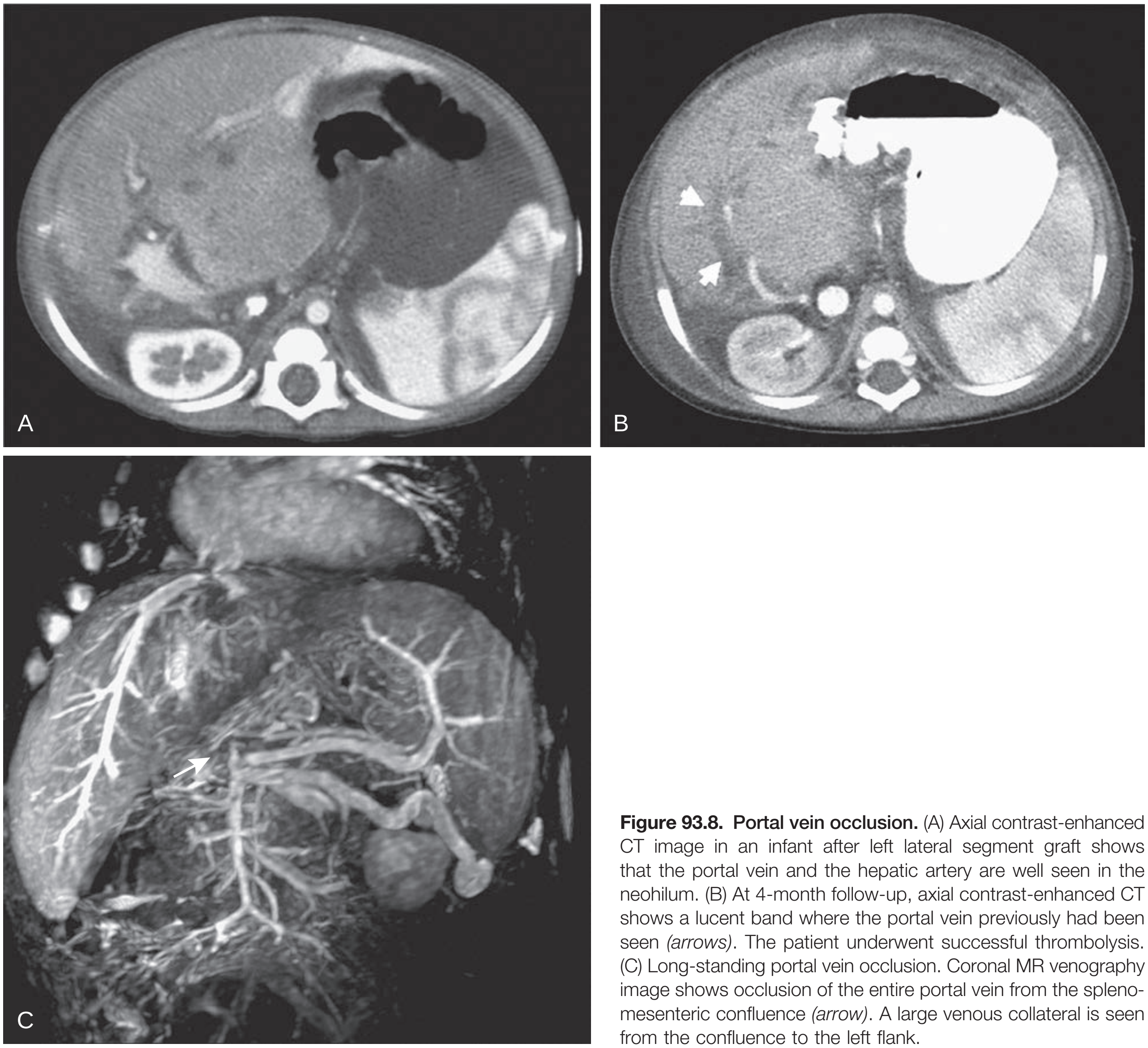

**Figure 93.8. Portal vein occlusion.** (A) Axial contrast-enhanced CT image in an infant after left lateral segment graft shows that the portal vein and the hepatic artery are well seen in the neohilum. (B) At 4-month follow-up, axial contrast-enhanced CT shows a lucent band where the portal vein previously had been seen *(arrows)*. The patient underwent successful thrombolysis. (C) Long-standing portal vein occlusion. Coronal MR venography image shows occlusion of the entire portal vein from the splenomesenteric confluence *(arrow)*. A large venous collateral is seen from the confluence to the left flank.

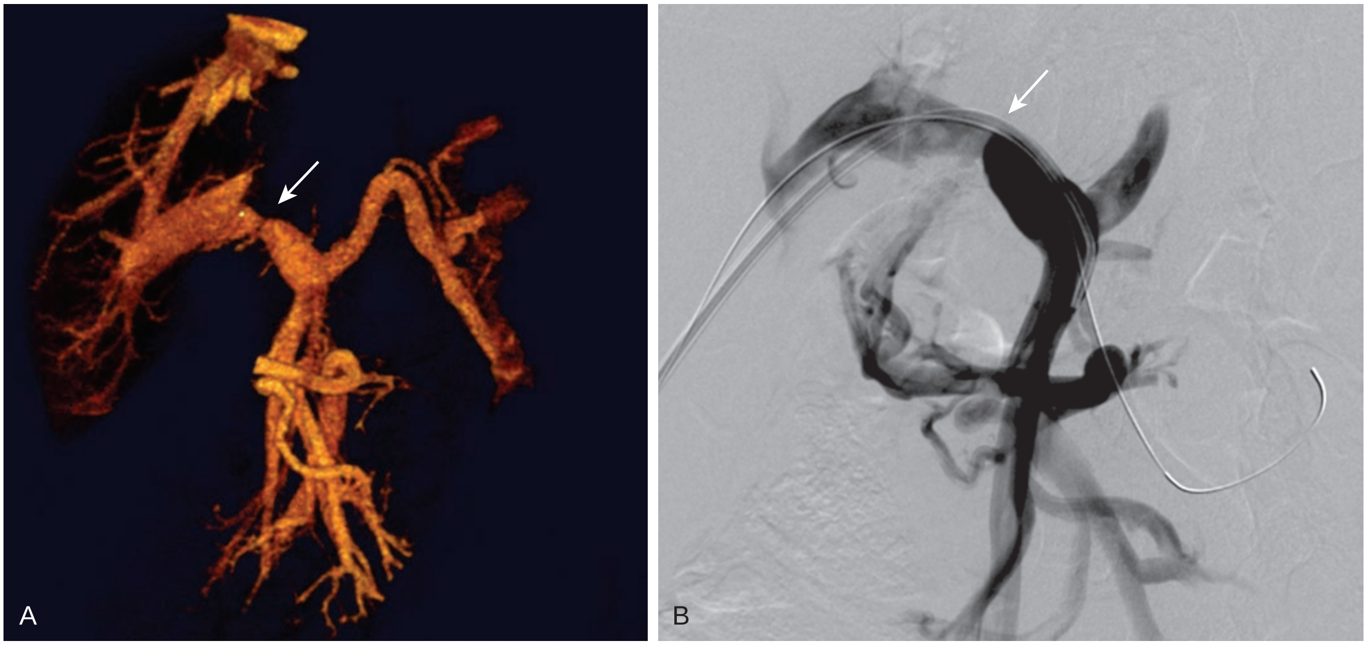

**Figure 93.9. Portal vein stenosis.** (A) Reconstructed images from contrast-enhanced CT shows anastomotic stenosis *(arrow)* in a patient with a whole liver transplant. (B) A portal venogram in the same patient confirms the portal vein stenosis *(arrow)*.

portal vein complication is not seen. Stenosis is near the diaphragm, making it difficult to demonstrate by ultrasound (Fig. 93.11). Doppler ultrasound demonstrates increased flow velocity and a jet with loss of triphasic flow.[32,37] A caveat is that triphasic flow may be absent without obstruction. CTA and MRA are excellent to demonstrate or confirm the diagnosis.[27]

***Inferior Vena Cava.*** IVC stenosis and obstruction may occur at the anastomosis. Anastomotic stenosis and obstruction may be short or long segment and may result from compression or graft torsion (Fig. 93.12). The clinical manifestations of IVC stenosis or obstruction depend on the location. If the problem is at or above the hepatic veins, it manifests with ascites and portal hypertension. If it is at a lower level, it may be clinically silent.[27]

IVC obstruction can be diagnosed by all cross-sectional modalities; however, several pitfalls may be encountered with Doppler ultrasound. Flow in the hepatic veins may be normal and triphasic if the IVC obstruction is distal to their insertion. On the other hand, when the obstruction is proximal to the hepatic vein insertion, hepatic venous blood may enter the IVC and flow retrograde to decompress into systemic collaterals. In patients with a surgical portosystemic shunt, IVC obstruction prevents adequate decompression, sometimes reversing flow in the shunt and increasing preexistent varices.[32,35]

## Biliary Complications

Biliary complications have been reported in up to 14.5% of children undergoing liver transplantation.[38] The small caliber of bile ducts and the presence of multiple ducts in segmental grafts increases the risk of these complications. Bile leaks and strictures occurring early after transplantation are related to technical surgical problems, such as anastomotic leak and narrowing or kinking. Biliary complications with a later onset commonly are associated with arterial ischemia.[32] Biliary strictures are more common in reduced-size liver transplants than in full-sized ones.[39] Inspissated bile and biliary compression by a mucocele or cystic duct remnant have been described.[30] Chronic rejection may be associated with loss of bile ducts and mild chronic dilation. Biliary strictures can be focal (at the site of the anastomosis) secondary to fibrotic proliferation or multifocal/intrahepatic secondary to arterial insufficiency. Hepatic arterial insufficiency can also result in biliary ischemia, bilomas, and biliary necrosis with sloughing of the duct epithelium into the biliary channels (Fig. 93.13).

Ultrasound identifies biliary dilation and is the primary screening modality. When bile duct dilation is found, further imaging is indicated.[26] MRCP increasingly is used to assess biliary obstruction and the need for intervention.[40–42] Direct transhepatic cholangiogram usually is performed as part of the therapeutic approach and patients can require multiple biliary interventions and indwelling draining catheters (Fig. 93.14).

## Fluid Collections

Early postoperative bleeding from leaking anastomoses or inadequate hemostasis leading to visible fluid collections occurs in as many as 15% of recipients. Up to half of these patients undergo operative exploration. Most fluid collections occur at the cut edge, contain serous fluid, blood, or bile, and are transient and clinically insignificant. Other collections may result from an anastomotic bile leak, abscess, or bowel perforation. The imaging appearance of perihepatic fluid collections is nonspecific; most contain some debris.[26] Specific diagnosis may require fluid aspiration or surgery.

When a fluid collection is suspected, it is important to realize that, although the blind end of the Roux-en-Y loop may dilate, the normal loop at the hilum of the transplanted liver may mimic a fluid collection on ultrasound and may not fill with oral contrast during CT scanning.[29,35]

Though the diagnosis for a bile leak can typically be established by the nature of the draining fluid, if clinically indicated, hepatobiliary iminodiacetic acid scan (HIDA) scan or delayed phase imaging with hepatocyte-specific contrast agents can be used to confirm the diagnosis of bile leak and identify the exact source of the leak (Fig. 93.15). Ascites is also common in the days after transplantation and usually is self-limited. If large in amount or prolonged in duration, an evaluation for the cause may be required.

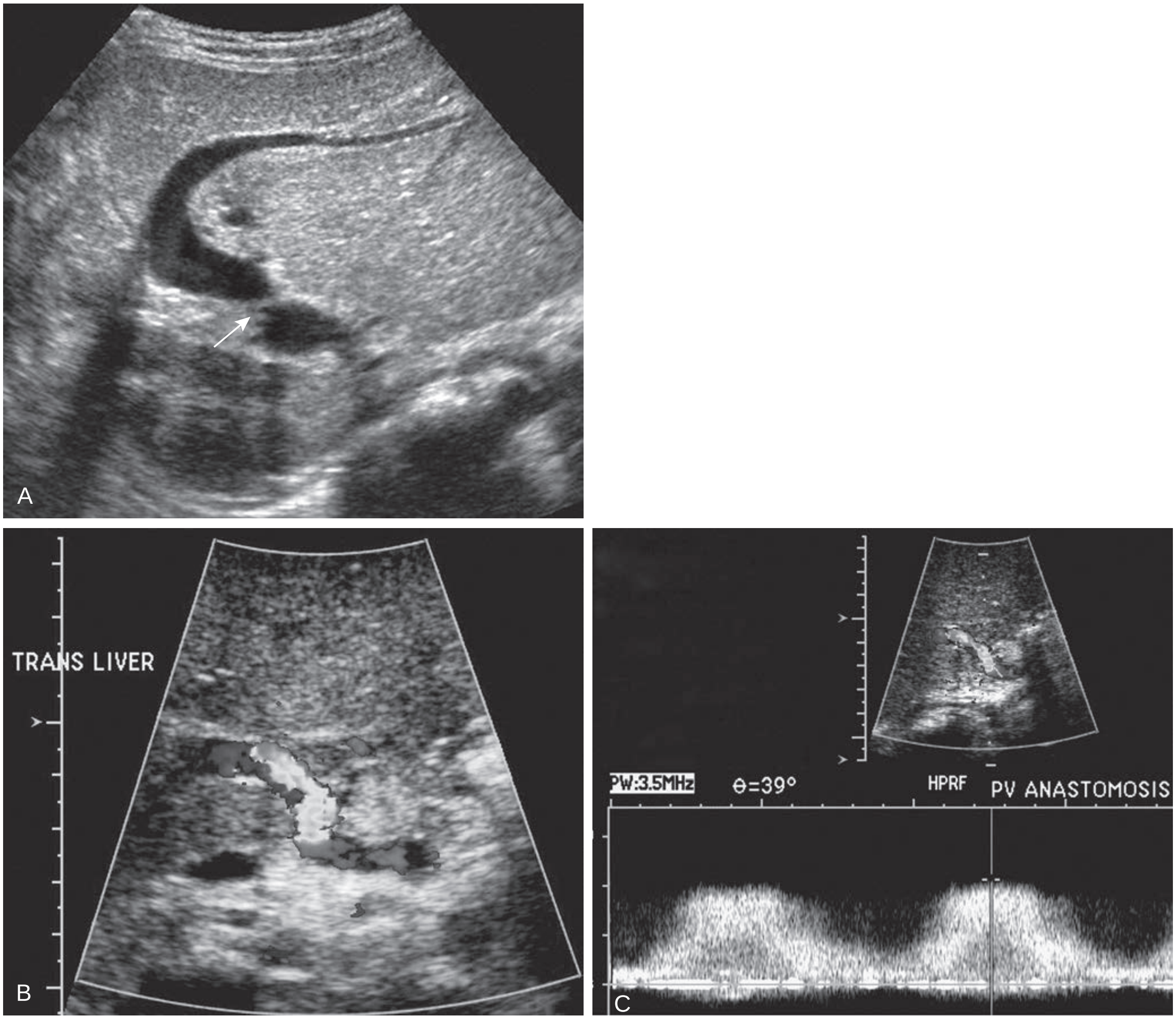

**Figure 93.10. Ultrasound and Doppler characteristics of portal vein stenosis.** (A) Transverse sonogram of a child with a left lateral segment graft shows a stenosis *(arrow)* outside the liver hilum, beyond the portal vein curvature. (B) On color Doppler, the velocity scale is adjusted such that aliasing demonstrates the higher velocity jet outlining the stenotic site. (C) On spectral and color Doppler with sampling at the jet, maximal flow velocity is obtained to assess the hemodynamic impact of the stenosis. The maximal jet velocity exceeds 2 m/sec.

## Infection

Postoperative infection develops in most liver recipients at some time, although consequent mortality is less than 10%. Bacterial and fungal infections are most common during the first postoperative month. Risk factors include hepatic artery occlusion, immunosuppression, central venous catheters, and nosocomial exposure. Viral and opportunistic infections usually occur between 30 and 180 days after transplantation.[43] Ultrasound and CT are the mainstay for assessing intraabdominal infections, particularly abscesses.[44] Cholangitis may prompt evaluation with MRI or percutaneous transhepatic cholangiography.[40]

## Rejection

Imaging plays a relatively minor role in the diagnosis of rejection, which is established mainly by liver biopsy. Rejection may be associated with mild degrees of nonobstructive bile duct dilation and an increase in hepatic arterial resistive indices. However, neither hepatic arterial waveforms nor flow pattern in the hepatic veins have proved to be predictive of rejection.[36]

## Posttransplantation Lymphoproliferative Disease

PTLD represents a spectrum of abnormalities of lymphoid proliferation linked with Epstein-Barr virus (in 98% of pediatric patients) and immune cell proliferation that ranges from polyclonal reversible B cell proliferation to aggressive monoclonal B cell lymphoma.[45] Risk factors for the development of PTLD are seronegativity for Epstein-Barr virus at transplantation, young age, intensity and type of immunosuppression (especially antilymphocyte antibody), cytomegalovirus infection, and type of transplant.[41] PTLD develops in children about three times as often as in adults, reported at 9.7% versus 2.9%, respectively.[46]

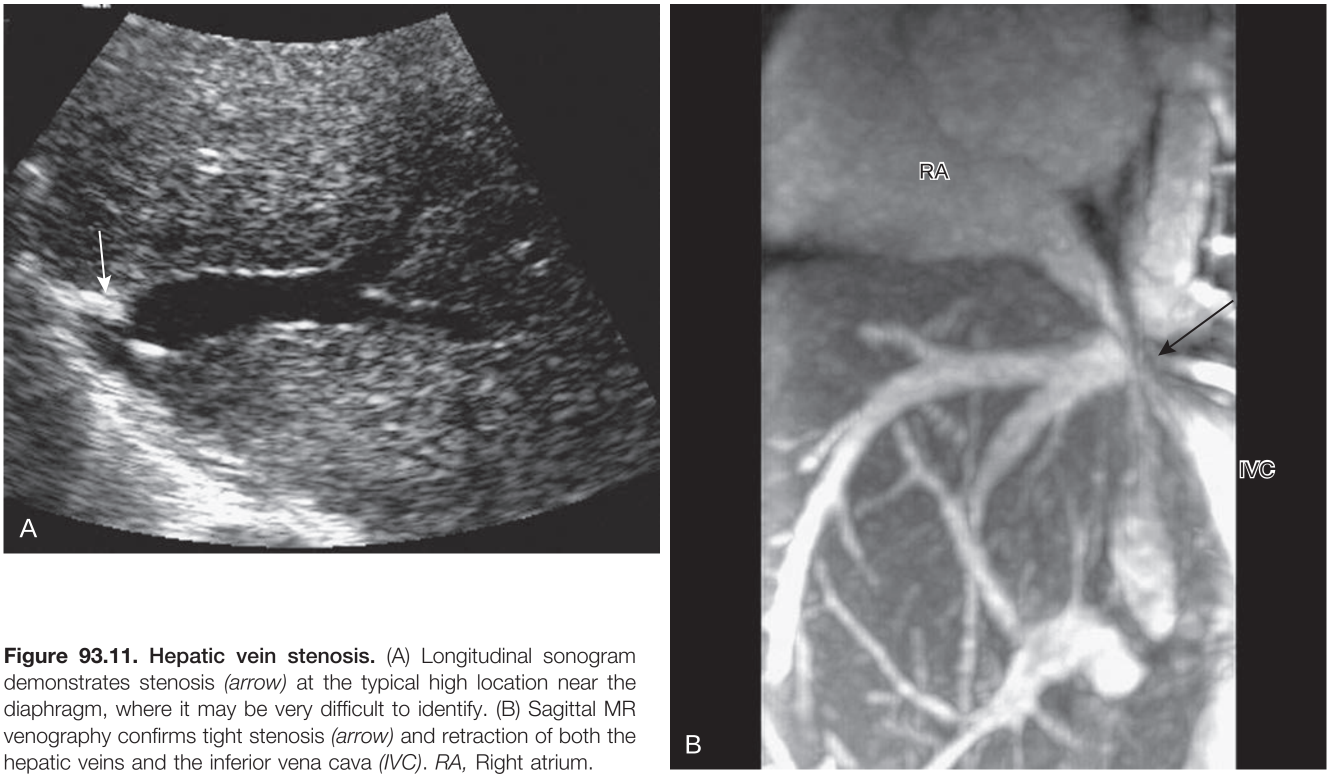

**Figure 93.11. Hepatic vein stenosis.** (A) Longitudinal sonogram demonstrates stenosis *(arrow)* at the typical high location near the diaphragm, where it may be very difficult to identify. (B) Sagittal MR venography confirms tight stenosis *(arrow)* and retraction of both the hepatic veins and the inferior vena cava *(IVC)*. *RA,* Right atrium.

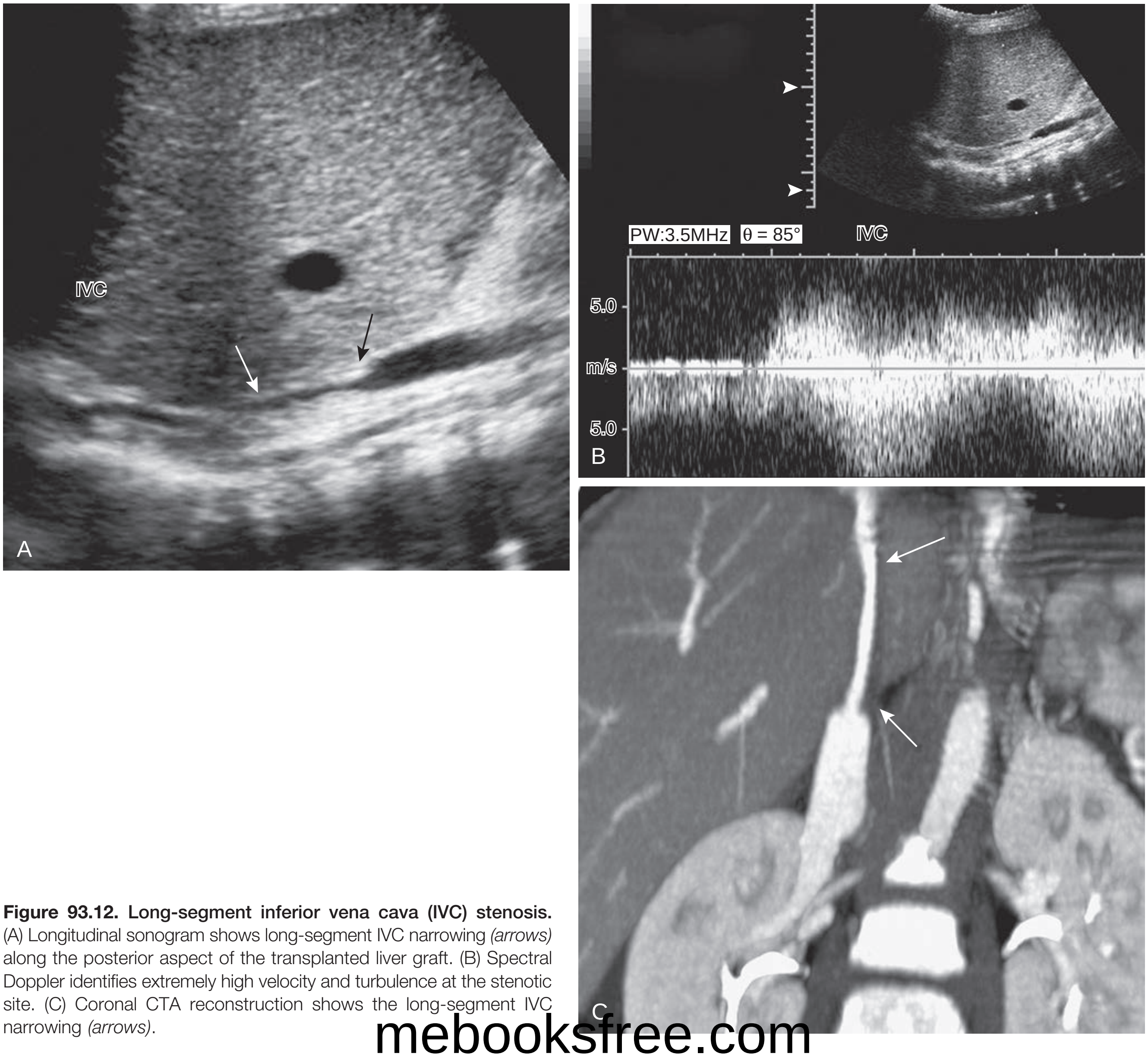

**Figure 93.12. Long-segment inferior vena cava (IVC) stenosis.** (A) Longitudinal sonogram shows long-segment IVC narrowing *(arrows)* along the posterior aspect of the transplanted liver graft. (B) Spectral Doppler identifies extremely high velocity and turbulence at the stenotic site. (C) Coronal CTA reconstruction shows the long-segment IVC narrowing *(arrows)*.

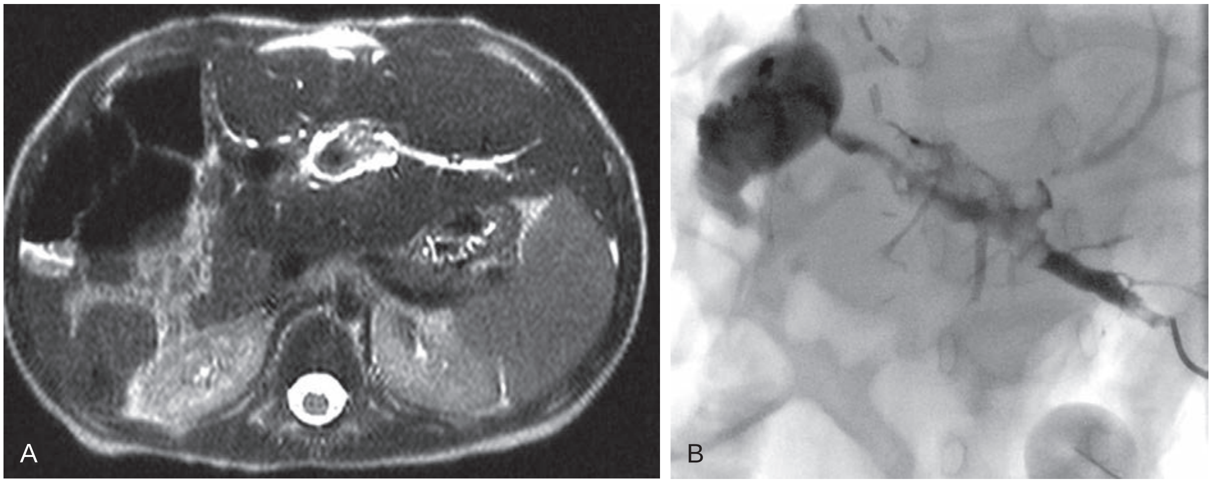

**Figure 93.13. Biliary necrosis secondary to late hepatic artery thrombosis.** (A) Axial T2-weighted MR image shows biliary duct dilation with hypointense filling defects in the bile duct. (B) Percutaneous cholangiogram shows irregular biliary channel with multiple filling defects secondary to sloughed biliary epithelium.

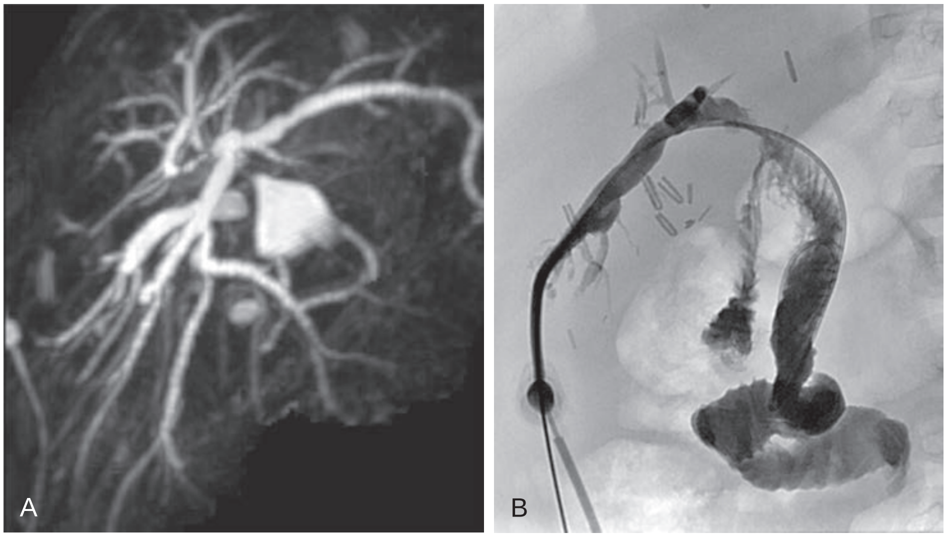

**Figure 93.14.** (A) 3D maximum intensity projection MRCP image shows marked intrahepatic biliary dilation with a tight stricture near the Roux-en-Y loop. (B) Percutaneous cholangiogram confirms the stricture and is used to deploy a biliary drainage catheter after stricturoplasty.

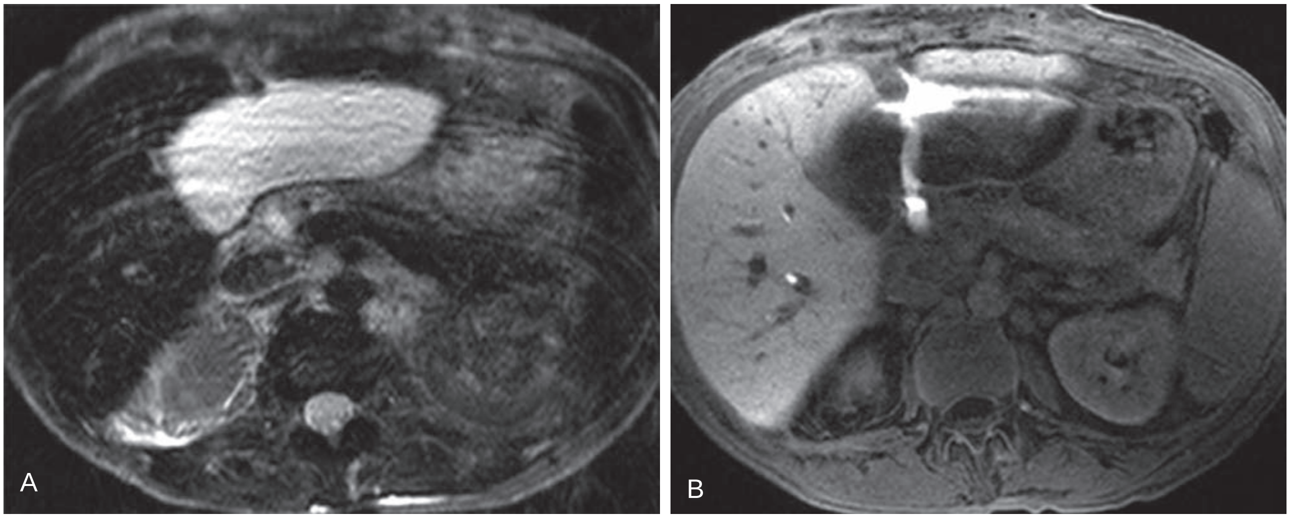

**Figure 93.15. Bile leak.** (A) Axial T2-weighted MR image shows a large fluid collection adjacent to the left lobe of the liver in a patient with a whole liver transplant. (B) 1-hour delayed T1-weighted image obtained after injection of hepatocyte-specific contrast agent confirms the bile leak and helps determine the exact site of the leak at the level of the duct anastomosis.

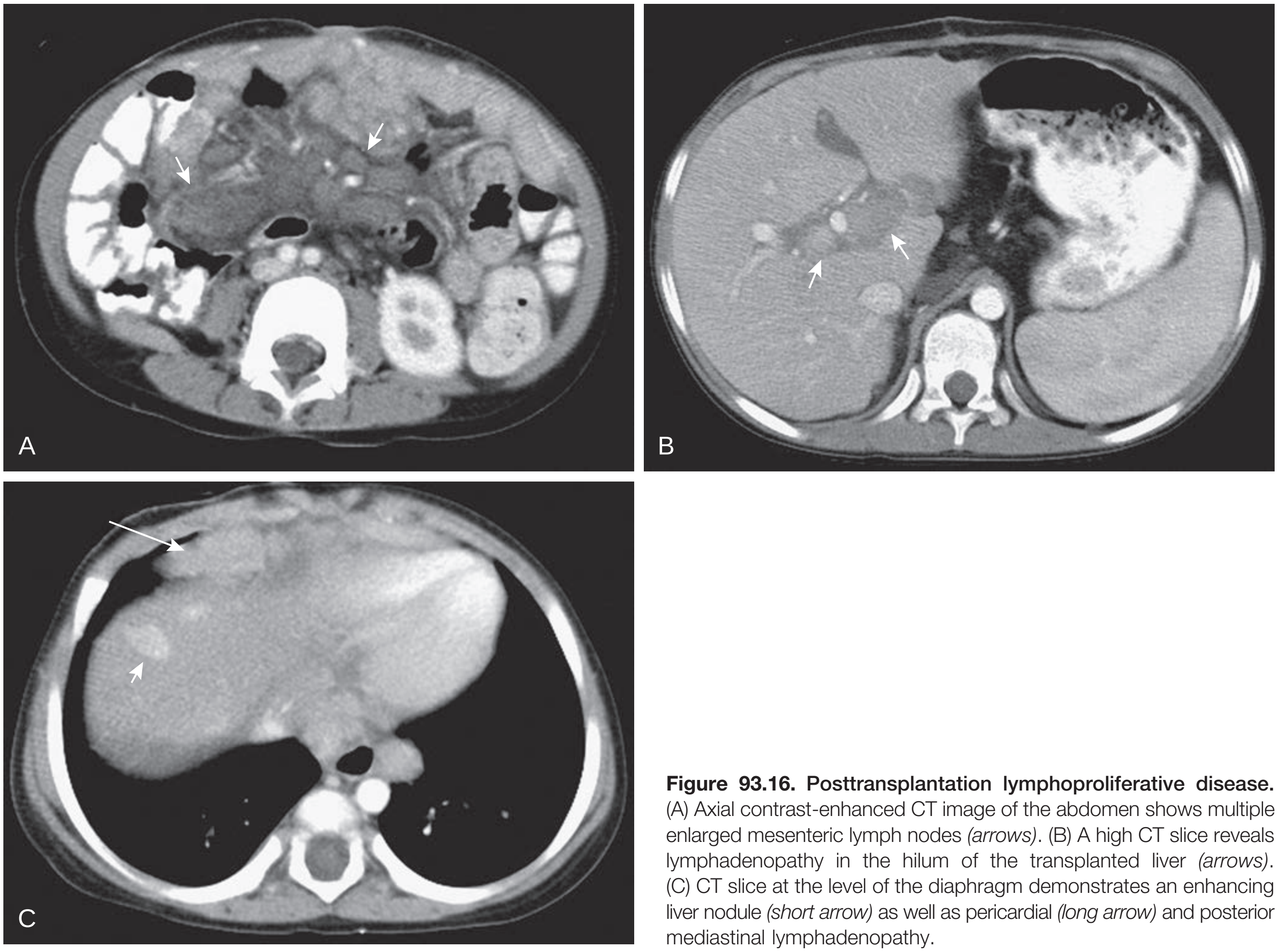

**Figure 93.16. Posttransplantation lymphoproliferative disease.** (A) Axial contrast-enhanced CT image of the abdomen shows multiple enlarged mesenteric lymph nodes *(arrows)*. (B) A high CT slice reveals lymphadenopathy in the hilum of the transplanted liver *(arrows)*. (C) CT slice at the level of the diaphragm demonstrates an enhancing liver nodule *(short arrow)* as well as pericardial *(long arrow)* and posterior mediastinal lymphadenopathy.

The time from transplantation to the development of PTLD averages about 8 months in children, although it may be shorter in patients treated with tacrolimus, occurring as early as within a few weeks.[47] Survival is better in patients with polyclonal PTLD and those with limited disease. In persons with polyclonal disease, PTLD may reverse completely with modifications of immune suppression.[48]

Sites of involvement in children include lymphoid tissue (particularly Waldeyer ring, pericardial, and mesenteric nodes), the gastrointestinal tract, the spleen, and the transplanted liver (Fig. 93.16). Newly enlarged tonsils and adenoids in a child with a transplanted liver should raise suspicion of PTLD. Unusually large mesenteric nodes are common in children with PTLD, although lack of normal standards makes it difficult to set a threshold size for diagnosis. Central nervous system involvement is uncommon.[42] The appearance of PTLD in the transplanted liver consists of multiple nonspecific focal lesions.[49]

## KEY POINTS

- Pretransplant imaging should include information on the patency and size of the portal vein, hepatic vascular variants, absence of hepatic neoplasm, and volumetric assessment of the liver.
- Early posttransplantation flow patterns may suggest vascular stenosis as a result of edema of the anastomosis and surrounding tissues. These findings are usually reversible but should be monitored.
- Doppler signal in the intrahepatic portions of the hepatic artery and portal vein may be present in spite of stenosis or obstruction in the extrahepatic segment as a result of collateral vessels. When transplant vessels are evaluated, screening ultrasound must be performed at the anastomosis, the narrowest portion, and at the site of maximal jet seen by color Doppler ultrasound.
- Reversal of portal venous flow in a lobar or segmental branch is a strong indication of main portal vein occlusion.

## SUGGESTED READINGS

Horvat N, Marcelino ASZ, Horvat JV, et al. Pediatric liver transplant: techniques and complications. *Radiographics*. 2017;37(6):1612–1631.
Spada G, Riva S, Maggiore G, et al. Pediatric liver transplantation. *World J Gastroenterol*. 2009;15(6):648–674.

## REFERENCES

Full references for this chapter can be found on www.expertconsult.com.

## REFERENCES

1. Otte JB. History of pediatric liver transplantation. Where are we coming from? Where do we stand? *Pediatr Transplant*. 2002;6(5):378–387.
2. Rook M, Rand E. Predictors of long-term outcome after liver transplant. *Curr Opin Organ Transplant*. 2011;16(5):499–504.
3. Ryckman FC, Bucuvalas JC, Nathan J, et al. Outcomes following liver transplantation. *Semin Pediatr Surg*. 2008;17(2):123–130.
4. Bourdeaux C, Darwish A, Jamart J, et al. Living-related versus deceased donor pediatric liver transplantation: a multivariate analysis of technical and immunological complications in 235 recipients. *Am J Transplant*. 2007;7(2):440–447.
5. Mehrabi A, Fonouni H, Müller SA, et al. Current concepts in transplant surgery: liver transplantation today. *Langenbecks Arch Surg*. 2008;393(3):245–260.
6. Hong JC, Yersiz H, Busuttil RW. Where are we today in split liver transplantation? *Curr Opin Organ Transplant*. 2011;16(3):269–273.
7. Squires RH, Ng V, Romero R, et al. Evaluation of the pediatric patient for liver transplantation: 2014 practice guideline by the American Association for the Study of Liver Diseases, American Society of Transplantation and the North American Society for Pediatric Gastroenterology, Hepatology and Nutrition. *Hepatology*. 2014;60:362–398.
8. Sokol RJ, Shepherd RW, Superina R, et al. Screening and outcomes in biliary atresia: summary of a National Institutes of Health workshop. *Hepatology*. 2007;46:566–581.
9. Barshes NR, Lee TC, Balkrishnan R, et al. Orthotopic liver transplantation for biliary atresia: the U.S. experience. *Liver transpl*. 2005;11:1193–1200.
10. Kamath BM, Schwarz KB, Hadzic N, et al. Alagille syndrome and liver transplantation. *J Pediatr Gastroenterol Nutr*. 2010;50(1):11–15.
11. Aydogdu S, Cakir M, Arikan C, et al. Liver transplantation for progressive familial intrahepatic cholestasis: clinical and histopathological findings, outcome and impact on growth. *Pediatr Transplant*. 2007;11(6):634–640.
12. Lu BR, Esquivel CO. A review of abdominal organ transplantation in cystic fibrosis. *Pediatr Transplant*. 2010;14(8):954–960.
13. Mieli-Vergani G, Vergani D. Autoimmune paediatric liver disease. *World J Gastroenterol*. 2008;14(21):3360–3367.
14. Heffron T, Pillen T, Welch D, et al. Medical and surgical treatment of neonatal hemochromatosis: single center experience. *Pediatr Transplant*. 2007;11(4):374–378.
15. Barshes NR, Myers GD, Lee D, et al. Liver transplantation for severe hepatic graft-versus-host disease: an analysis of aggregate survival data. *Liver Transpl*. 2005;11(5):525–531.
16. Arnon R, Annunziato R, Schilsky M, et al. Liver transplantation for children with Wilson disease: comparison of outcomes between children and adults. *Clin Transplant*. 2011;25(1):E52–E60.
17. Büyükpamukçu M, Varan A, Haberal M, et al. The efficacy of liver transplantation in malignant liver tumors associated with tyrosinemia: clinical and laboratory findings of five cases. *Pediatr Transplant*. 2006;10(4):517–520.
18. Stevenson T, Millan MT, Wayman K, et al. Long-term outcome following pediatric liver transplantation for metabolic disorders. *Pediatr Transplant*. 2010;14(2):268–275.
19. Chapal M, Debout A, Dufay A, et al. Kidney and liver transplantation in patients with autosomal recessive polycystic kidney disease: a multicentric study. *Nephrol Dial Transplant*. 2012;27(5):2083–2088.
20. Oliveira DA, Feitosa RQ, Correia MM. Segmentation of liver, its vessels and lesions from CT images for surgical planning. *Biomed Eng Online*. 2011;10:30.
21. Fung J, Kelly D, Kadry Z, et al. Immunosuppression in liver transplantation: beyond calcineurin inhibitors. *Liver Transpl*. 2005;11(3):267–280.
22. Hernanz-Schulman M, Ambrosino MM, Genieser NB, et al. Current evaluation of the patient with abnormal visceroatrial situs. *AJR Am J Roentgenol*. 1990;154(4):797–802.
23. Welling TH, Heidt DG, Englesbe MJ, et al. Biliary complications following liver transplantation in the model for end-stage liver disease era: effect of donor, recipient, and technical factors. *Liver Transpl*. 2008;14(1):73–80.
24. Berrocal T, Parrón M, Alvarez-Luque A, et al. Pediatric liver transplantation: a pictorial essay of early and late complications. *Radiographics*. 2006;26(4):1187–1209.
25. Diamond IR, Fecteau A, Millis JM, et al. Impact of graft type on outcome in pediatric liver transplantation: a report from Studies of Pediatric Liver Transplantation (SPLIT). *Ann Surg*. 2007;246(2):301–310.
26. O'Brien J, Buckley AR, Browne R. Comprehensive ultrasound assessment of complications post-liver transplantation. *Eur J Radiol*. 2010;74(1):206–213.
27. Zamboni GA, Pedrosa I, Kruskal JB, et al. Multimodality postoperative imaging of liver transplantation. *Eur Radiol*. 2008;18(5):882–891.
28. Huang TL. The role of color Doppler ultrasound in living donor liver transplantation. *J Med Ultrasound*. 2008;16:177–187.
29. Andronikou S, Millar AJ, Kader E, et al. Anatomical considerations in the imaging of 'reduced-size' liver transplantation in children. *Pediatr Radiol*. 2002;32(11):793–797.
30. Caruso S, Miraglia R, Maruzzelli L, et al. Imaging in liver transplantation. *World J Gastroenterol*. 2009;15(6):675–683.
31. Babyn PS. Imaging of the transplant liver. *Pediatr Radiol*. 2010;40(4):442–446.
32. Caiado AH, Blasbalg R, Marcelino AS, et al. Complications of liver transplantation: multimodality imaging approach. *Radiographics*. 2007;27(5):1401–4017.
33. Duffy JP, Hong JC, Farmer DG, et al. Vascular complications of orthotopic liver transplantation: experience in more than 4,200 patients. *J Am Coll Surg*. 2009;208(5):896–903, discussion 903-905.
34. Miraglia R, Maruzzelli L, Caruso S, et al. Interventional radiology procedures in pediatric patients with complications after liver transplantation. *Radiographics*. 2009;29(2):567–584.
35. Singh AK, Nachiappan AC, Verma HA, et al. Postoperative imaging in liver transplantation: what radiologists should know. *Radiographics*. 2010;30(2):339–351.
36. Cheng YF, Chen CL, Huang TL, et al. 3DCT angiography for detection of vascular complications in pediatric liver transplantation. *Liver Transpl*. 2004;10(2):248–252.
37. Suzuki L, de Oliveira IR, Widman A, et al. Real-time and Doppler US after pediatric segmental liver transplantation: II. Hepatic vein stenosis. *Pediatr Radiol*. 2008;38(4):409–414.
38. Feier FH, Chapchap P, Pugliese R, et al. Diagnosis and management of biliary complications in pediatric living donor liver transplant recipients. *Liver transpl*. 2014;20:882–892.
39. Anderson CD, Turmelle YP, Darcy M, et al. Biliary strictures in pediatric liver transplant recipients—early diagnosis and treatment results in excellent graft outcomes. *Pediatr Transplant*. 2010;14(3):358–363.
40. Rozel C, Garel L, Rypens F, et al. Imaging of biliary disorders in children. *Pediatr Radiol*. 2011;41(2):208–220.
41. Fernández MC, Bes D, De Dávila M, et al. Post-transplant lymphoproliferative disorder after pediatric liver transplantation: characteristics and outcome. *Pediatr Transplant*. 2009;13(3):307–310.
42. Sevmis S, Pehlivan S, Shabazov R, et al. Posttransplant lymphoproliferative disease in pediatric liver transplant recipients. *Transplant Proc*. 2009;41(7):2881–2883.
43. Shepherd RW, Turmelle Y, Nadler M, et al. Risk factors for rejection and infection in pediatric liver transplantation. *Am J Transplant*. 2008;8(2):396–403.
44. Almusa O, Federle MP. Abdominal imaging and intervention in liver transplantation. *Liver Transpl*. 2006;12(2):184–193.
45. Pasquale MA, Weppler D, Smith J, et al. Burkitt s lymphoma variant of post-transplant lymphoproliferative disease (PTLD). *Pathol Oncol Res*. 2002;8(2):105–108.
46. Jain A, Nalesnik M, Reyes J, et al. Posttransplant lymphoproliferative disorders in liver transplantation: a 20-year experience. *Ann Surg*. 2002;236(4):429–436, discussion 436-437.
47. George TI, Jeng M, Berquist W, et al. Epstein-Barr virus-associated peripheral T-cell lymphoma and hemophagocytic syndrome arising after liver transplantation: case report and review of the literature. *Pediatr Blood Cancer*. 2005;44(3):270–276.
48. Koh BY, Rosenthal P, Medeiros LJ, et al. Posttransplantation lymphoproliferative disorders in pediatric patients undergoing liver transplantation. *Arch Pathol Lab Med*. 2001;125(3):337–343.
49. Borhani AA, Hosseinzadeh K, Almusa O, et al. Imaging of posttransplantation lymphoproliferative disorder after solid organ transplantation. *Radiographics*. 2009;29(4):981–1000, discussion 1000-1002.

# 94

# The Spleen

*Josephine M. Ndolo, Stephanie E. Spottswood, and Marta Hernanz-Schulman*

## OVERVIEW

The spleen is an intraperitoneal organ supported by the gastrosplenic ligament and the splenorenal ligament (Fig. 94.1). Other ligaments that help support the spleen are the phrenicosplenic, splenocolic, pancreaticosplenic, phrenocolic, and pancreaticocolic.

The spleen is the largest of the body's lymphatic structures and the second largest organ of the reticuloendothelial system. A combination of red pulp (75%) and white pulp (25%) constitute the splenic parenchyma,[1] which is surrounded by a capsule. The red pulp is composed of the splenic cords and vascular sinuses, containing a large number of erythrocytes, while the white pulp is composed largely of lymphocytes and macrophages. The lymphoid cell organization within the white pulp is similar to that of the cortex of a lymph node.[2] The unique anatomy of the spleen is closely linked to its function and results in normal variants seen on computed tomography (CT) and magnetic resonance imaging (MRI), while the functional aspects can be evaluated scintigraphically. The primary function of the embryonic spleen is erythropoiesis, which decreases beyond the second trimester. The spleen is later responsible for filtering red blood cells that are aged or lack contractility, as well as antigen-coated cells, bacteria, and foreign particles. The spleen also acts as a platelet reservoir, releasing platelets in response to epinephrine release or consuming platelets in case of splenomegaly.[1]

## IMAGING

The spleen is seen in the left upper quadrant on abdominal radiographs (Fig. 94.2A) and may displace the left colon and/or stomach when enlarged.

The spleen has a homogeneous sonographic texture, slightly more echogenic than kidney, and iso- to slightly hyperechoic to the liver. The splenic hilar vessels are usually well seen (Fig. 94.2B), but intrasplenic branches typically require Doppler for identification.

On CT, the normal spleen has a higher attenuation than the liver, approximately 45 Hounsfield units (HU). A diffuse increase in splenic density can be observed in patients with hemosiderosis, sickle-cell disease, and lymphoma.[3] Transient heterogeneous splenic enhancement patterns are commonly encountered during rapid bolus contrast administration (Fig. 94.3). This normal phenomenon is thought to be secondary to variations in blood flow through the red and white pulp of the spleen; it is more pronounced with contrast injection rates of 1 mL/sec or greater and in children older than 1 year. Common patterns observed include archiform bands of alternating density, focal areas of low density, and diffuse mottled inhomogeneity.[4] More uniform enhancement is seen approximately 70 seconds after initiation of the contrast injection.

On MRI, the spleen signal intensity varies with age (Table 94.1 and Fig. 94.4). In the neonate, the spleen is T1 and T2 iso- to hypointense with respect to the liver. The T2 hypointensity is because of immaturity of the white pulp. After age 8 months, the spleen is T2 hyperintense relative to the liver due to white pulp maturation and maintains this appearance through adulthood.[5] The imaging sequences for the evaluation of the spleen can include T2-weighted, gradient-echo in and out of phase, pre- and post-contrast imaging, and the optional addition of T2* sequences to evaluate for the presence of hemosiderin.[6]

Scintigraphic splenic imaging with technetium-99m–labeled sulfur colloid, which is removed from the blood by the reticuloendothelial system, is useful for the identification of splenic ectopia, as well as several entities discussed later. It is not useful in cases of heterotaxy because splenic and hepatic tissue cannot be distinguished when neither location nor shape is an identifying criterion. Similarly, selective spleen scans can be misleading when the spleen is absent (e-Fig. 94.5).[7]

## ACCESSORY SPLEENS

***Overview.*** Accessory spleens are present in 20% to 35% of the normal population[8] and are usually found incidentally at autopsy or on imaging studies, most commonly located in the splenic hilum, in the gastrosplenic or splenorenal ligaments.[6] They can be found, however, virtually anywhere in the abdomen. They rarely exceed 2 cm in diameter and can be confused with splenic hilar or parapancreatic lymph nodes.

***Etiology.*** Accessory spleens are small splenic masses that fail to coalesce with the main mass of splenic tissue.

***Imaging.*** Accessory spleens can be identified on ultrasound (US), CT, or MRI; if questioned, definitive imaging study can be done with scintigraphy using technetium-99m sulfur colloid or denatured red blood cells.

***Treatment.*** Accessory spleens are considered a normal variant of development and, as such, require no treatment.

## SPLENOSIS

***Overview.*** These are acquired ectopic implants, which typically are seen in the peritoneum, but rarely can occur outside, such as in the pleural spaces.[6]

***Etiology.*** They are a result of seeding and implantation of splenic cells following trauma or splenectomy. The implants are usually multiple and of varying size.[6]

***Imaging.*** The ectopic splenic tissue demonstrates the same imaging characteristics as a normal spleen. It is important to differentiate these from adenopathy. Scintigraphy with Tc-99m sulfur colloid or denatured red cells is the most specific study for this purpose.[9]

***Treatment.*** No treatment is necessary.

## WANDERING SPLEEN

***Overview.*** This congenital anomaly results from maldevelopment of the splenic suspensory ligaments. Acquired cases may be a consequence of splenomegaly, traumatic injury, or ligamentous laxity.

***Etiology.*** Normally, during embryonic life, the residuum of the dorsal mesogastrium fuses with the posterior peritoneum, helping to support the spleen in its normal position. When this

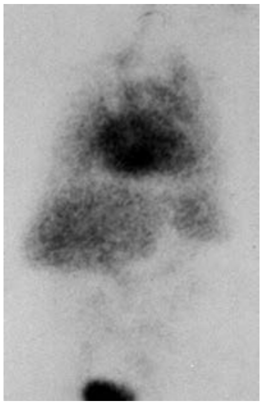

**e-Figure 94.5. Asplenia.** Damaged red blood cell (RBC) scan in an infant with asplenia shows midline liver, with extension into the left upper quadrant, which could be erroneously construed to represent the spleen.

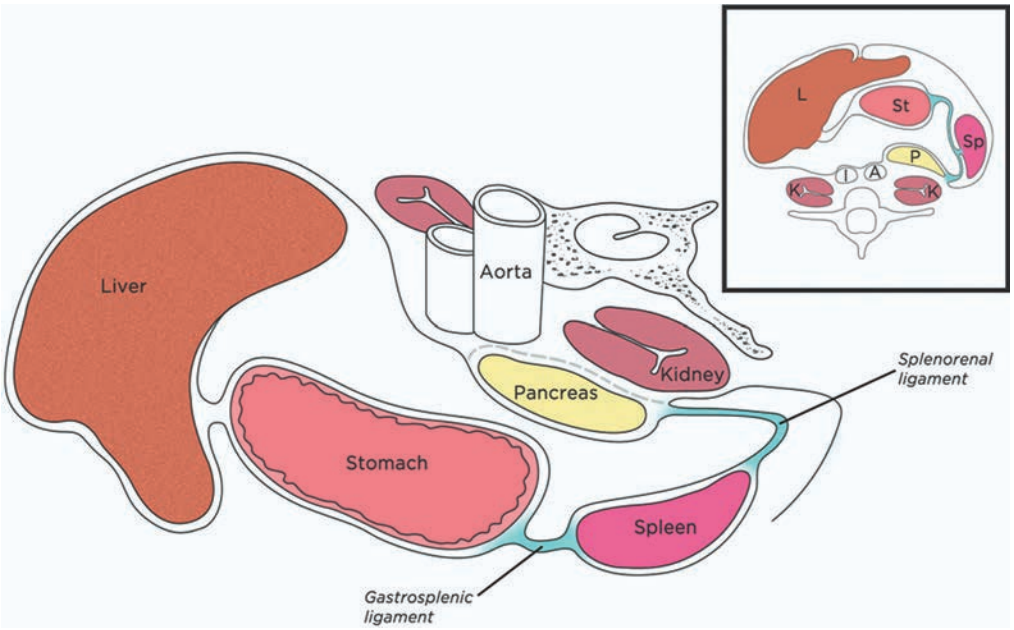

**Figure 94.1. Splenic attachments.** Oblique axial two-dimensional rendering of the fetal abdomen reveals the position of the gastrosplenic and splenorenal ligaments, which arise from the dorsal mesogastrium.

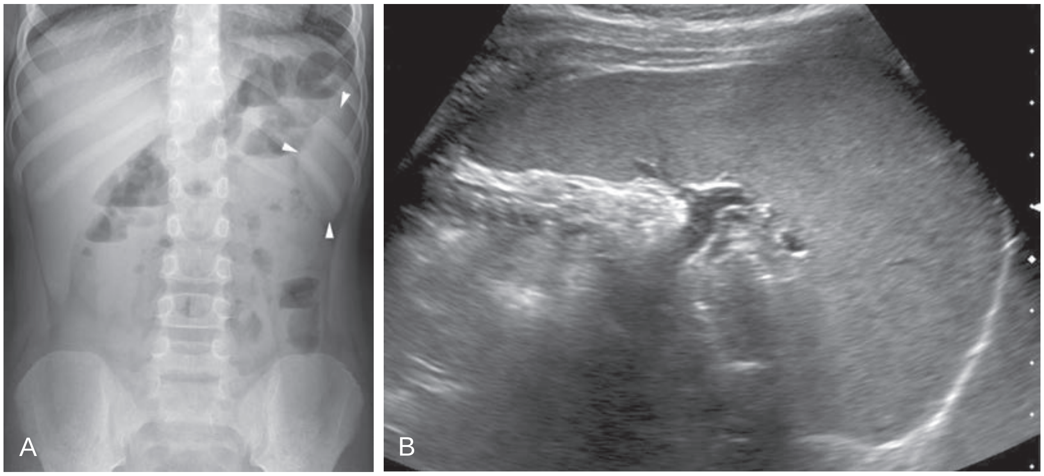

**Figure 94.2. Normal spleen.** (A) Frontal upright abdominal radiograph of a 6-year-old boy shows the normal spleen as circumscribed soft tissue fullness *(arrowheads)* in the left upper quadrant. (B) Transverse sonogram in a 15-year-old girl shows normal homogeneous parenchymal echotexture and hilar vessels.

**TABLE 94.1** MR Signal Intensity of Spleen Relative to Liver—By Age

| AGE | T1 | T2 |
|---|---|---|
| Neonate | Iso/Hypointense | Iso/Hypointense |
| Infant | Hypointense | Minimally hyperintense |
| >8 months | Hypointense | Hyperintense |

fusion does not take place, the dorsal mesogastrium may persist as a long mesentery, allowing the spleen to migrate, yielding the so-called *wandering spleen*. The most common location is the left lower quadrant.

***Clinical Presentation.*** The clinical presentation is variable; patients may be asymptomatic or present with a mobile mass on physical exam. More typically, the presentation is an acute abdomen, due to torsion of the vascular pedicle, with subsequent ischemia, impaired venous return, acute enlargement, and painful capsular tension.[10] Torsion is described in 64% of children[11] and may be a cause of recurrent abdominal pain due to intermittent torsion and detorsion.[12]

***Imaging.*** The abnormal position and orientation of the spleen can be identified by US, CT, MR, or radionuclide imaging, but this can be overlooked if close attention is not focused on these findings. If an ectopic spleen is found on ultrasound, scanning with the child in various positions can demonstrate splenic mobility.[13] When the spleen undergoes torsion, a "whorled" appearance of the splenic artery in the splenic pedicle has been described as a characteristic CT sign of torsion[14] (Fig. 94.6A). When ischemic secondary to torsion, the spleen has little or no uptake on radionuclide scintigraphy[15] and no contrast enhancement on CT (Fig. 94.6B). Color Doppler sonography similarly shows lack of flow in the splenic hilar vessels (Fig. 94.6C) and may also demonstrate the whorled appearance at the splenic hilum.

***Treatment.*** Treatment is operative, consisting of splenopexy if the spleen is viable or splenectomy if it is nonviable.[16] Because of the defective ligamentous support, gastric volvulus has been associated with wandering spleen[11] (Fig. 94.6D).

## SPLENOGONADAL SYNDROME

***Overview.*** The splenogonadal syndrome is a rare anomaly in which a portion of the spleen is conjoined with left gonadal tissue. Although this is an uncommon congenital anomaly, its identification is important because 30% to 50% of cases result in unnecessary orchiectomy for concern of extratesticular neoplasm.[17,18]

***Etiology.*** Splenogonadal fusion results when a portion of the splenic anlage fuses with primitive left gonadal tissue between the fifth and eighth weeks of gestation. Despite the fused splenic tissue, a normal spleen is present in the left upper quadrant. The splenogonadal fusion shows a splenic cord continuous with the ectopic, fused splenic tissue in approximately 55% of cases; it is discontinuous in approximately 45% of cases.[17] Splenogonadal fusion has been reported in association with transverse testicular ectopia.[19]

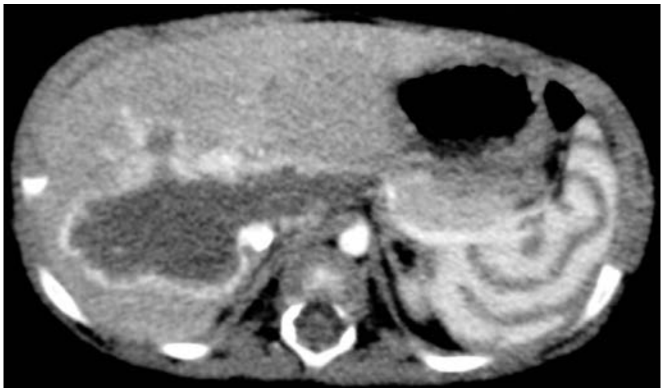

**Figure 94.3. Contrast bolus artifact on early arterial phase CT.** An arcuate or "archiform" contrast enhancement pattern is seen in the spleen, with ringlike or zebra-stripe bands of alternating density. CT with rapid bolus technique was performed to evaluate the hepatic hemangioma.

***Clinical Presentation.*** Splenogonadal fusion is much more common in males, with a male-female ratio of 16:1. The condition may be asymptomatic and discovered incidentally or at autopsy. It may be associated with left cryptorchidism, inguinal hernia, or testicular torsion, particularly when continuous. Multiple other anomalies may be present, particularly in the continuous type. In females, there is fusion of splenic tissue with the left ovary or mesovarium; this connection does not result in ovarian ectopia.

***Imaging.*** Sonography can reliably demonstrate the extratesticular location of a palpable scrotal mass in these cases, although at times it may resemble an intratesticular lesion.[20] The mass is typically oval or round and of similar echotexture to the adjacent normal testis but often is a slightly different size or configuration (e-Fig. 94.7A). Using a high frequency linear transducer, the ectopic splenic tissue has a nodular pattern caused by the lymphoid system and follicles of the white pulp in children between the age of 1 year to 5 years.[21] Color Doppler sonography shows abundant vascularity in the splenic tissue (e-Fig. 94.7B). Radionuclide imaging with technetium-99m sulfur colloid adds specificity to the diagnosis by revealing radiopharmaceutical uptake in the ectopic splenic tissue either in the left hemiscrotum or in the left inguinal canal when associated with cryptorchidism. A linear pattern extending from the left upper quadrant of the abdomen to the pelvis or scrotum may be detected in the continuous type (e-Fig. 94.7C).

MR or contrast-enhanced CT may reveal a rounded, enhancing, well-circumscribed soft tissue mass in the left hemiscrotum or left hemipelvis that may or may not continue cephalad toward the spleen.[22]

***Treatment.*** When the diagnosis is confirmed by means of imaging and the child is asymptomatic, no treatment is necessary. However, if surgical exploration is performed, the splenic tissue can be dissected safely off the tunica albuginea and the testis can be preserved.[17]

## SPLENORENAL FUSION

***Overview.*** Splenorenal fusion is a rare but well-recognized developmental anomaly in which there is congenital fusion of splenic and renal tissue. Fusion usually involves the left kidney and rarely the right.[23] Unlike posttraumatic splenosis, patients with congenital splenorenal fusion demonstrate an intact spleen with a separate blood supply. The importance of recognizing this anomaly is to prevent unnecessary nephrectomy for presumed malignancy.

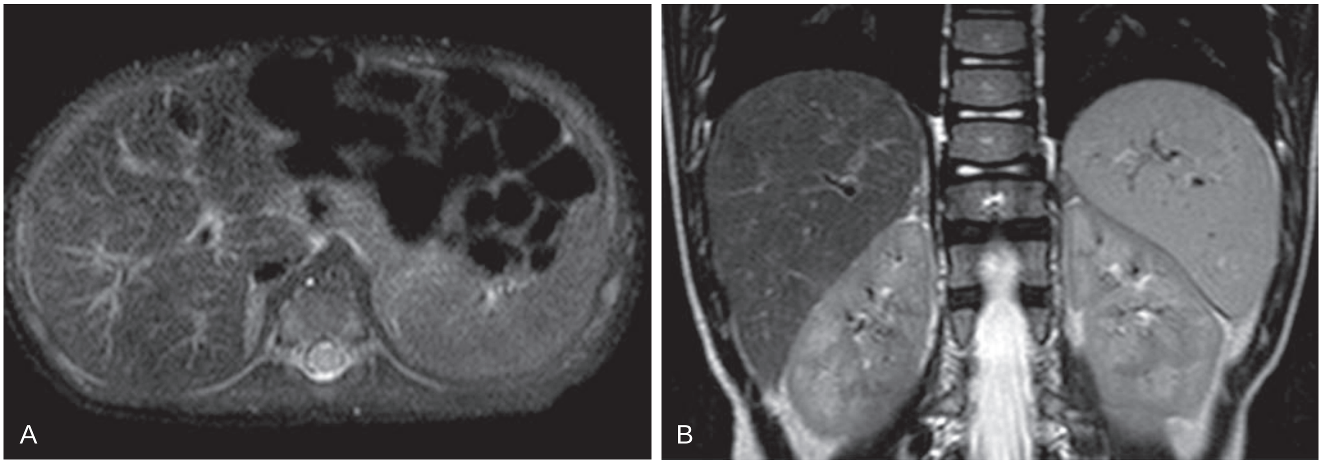

**Figure 94.4. Change in spleen T2 MR signal with age.** (A) Axial T2-weighted fat-suppressed MR image of the upper abdomen in a 2-month-old child shows that the spleen is nearly isointense to the liver. (B) Coronal T2-weighted fat-suppressed MR image of the upper abdomen in a 4-year-old child shows hyperintensity of the spleen compared with the liver.

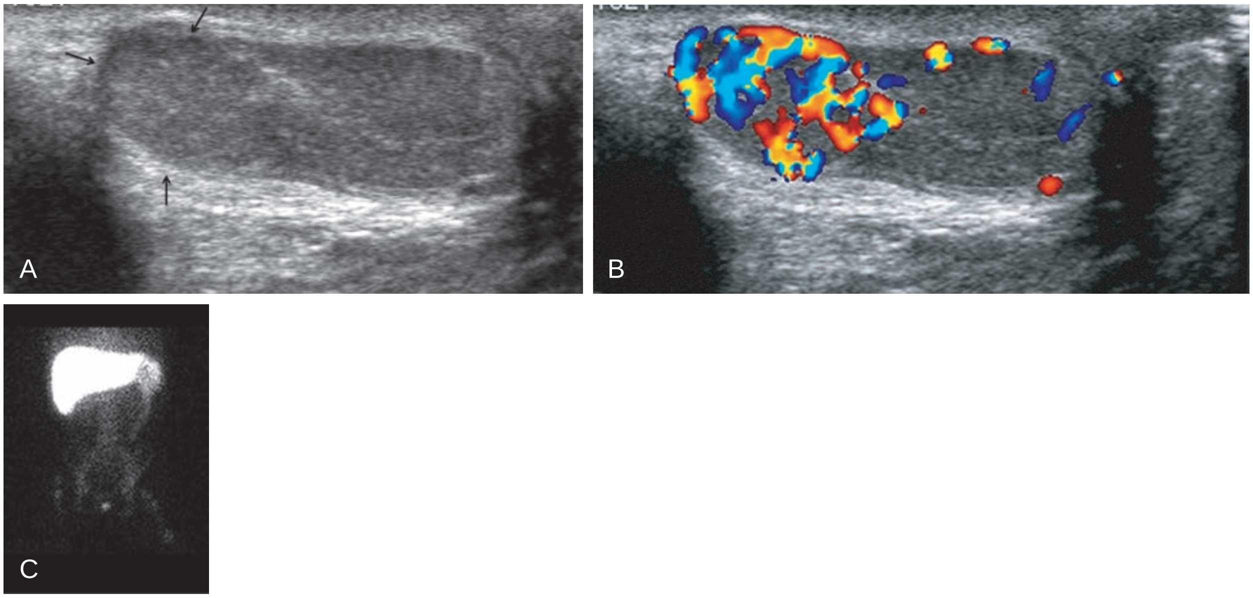

**e-Figure 94.7.** Splenogonadal fusion in a boy with a painless left scrotal mass. (A) Longitudinal sonogram of the left hemiscrotum reveals round-shaped splenic tissue cephalad to the testicle *(arrows)*, similar in echotexture and fused to the more oval-shaped testis below. (B) Color Doppler image shows increased vascularity of the splenic tissue compared with that of the testicle. (C) Technetium-99m sulfur colloid liver-spleen scan shows radiopharmaceutical uptake in the spleen in the left upper quadrant as well as in the left hemiscrotum; note continuous radiopharmaceutical uptake within the persistent cord of tissue connecting the spleen with the left testis. *(Courtesy of A. Schlesinger, MD, Houston, TX.)*

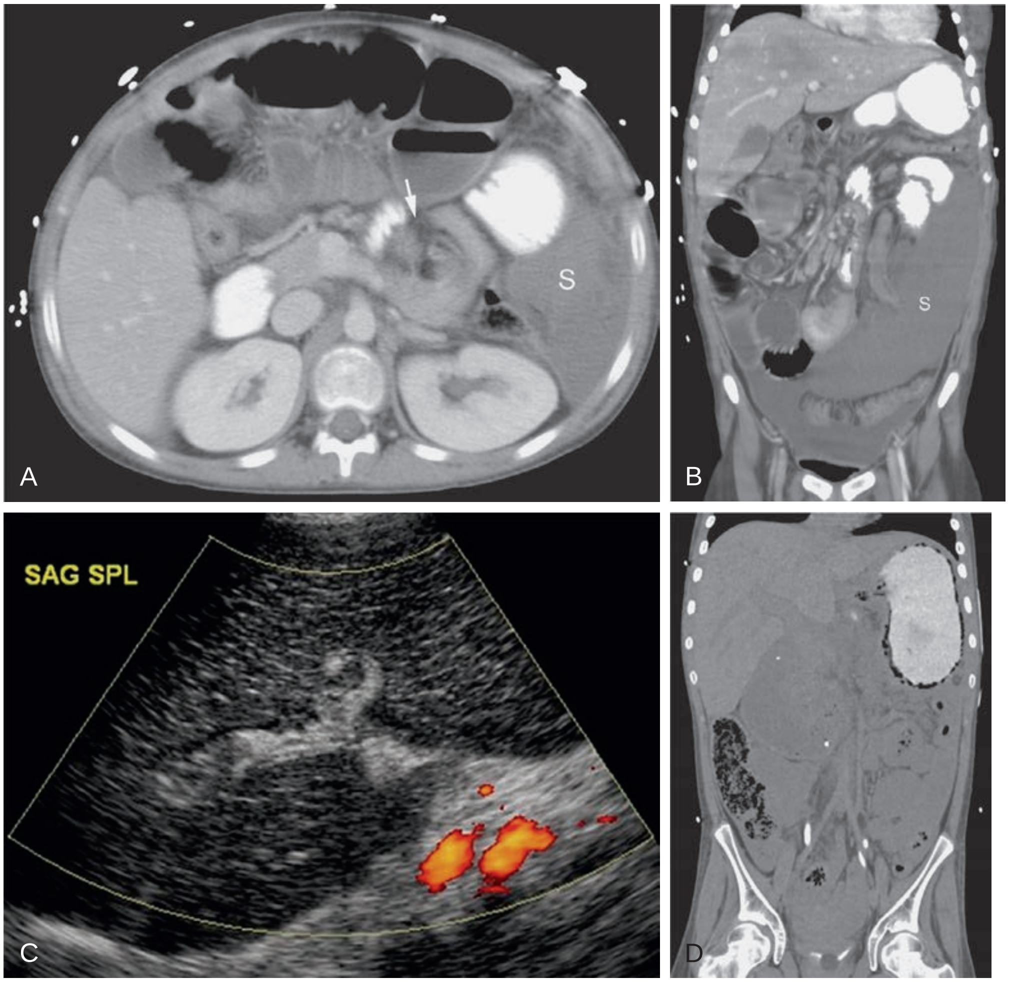

**Figure 94.6. Wandering spleen.** A 14-year-old girl with Niemann-Pick disease and acute abdominal pain. (A) Contrast-enhanced CT image of the abdomen show a “whorled” appearance of the splenic vessels and pancreatic tail *(arrow)* at the expected location of the splenic hilum. The spleen *(S)* shows low attenuation without contrast enhancement secondary to absent perfusion. (B) Coronal reformat underscores the displacement and abnormal orientation of the spleen *(S)* and again shows lack of contrast enhancement. (C) Color Doppler US image shows no vascular flow in the splenic hilum. Also note the abnormal echotexture of the spleen. (D) One year after splenectomy, the child presented with hypotension and abdominal distension. Coronal reconstruction of abdominal CT performed with oral contrast reveals reversal of the usual relationship of the gastric fundus and gastric outlet, consistent with gastric volvulus. Note the gastric pneumatosis. *(Courtesy of Jeanne G. Hill, MD, MUSC.)*

***Etiology.*** One theory to explain the origin of this anomaly is that fusion of the mesogastrium and left posterior peritoneum brings the splenic anlage and the left mesonephric ridge in close proximity during the eighth week of gestation, allowing the two organs to fuse.[24] Alternatively, it is postulated that splenic cells could migrate caudally to reach the metanephros and retroperitoneum, where there is no barrier to crossing the midline; this theory would explain reported right-sided fusion anomalies.[24,25] Splenorenal fusion may also be acquired from posttraumatic or postsplenectomy splenosis, where splenic tissue implants on the kidney and regrowth occurs.[24]

***Clinical Presentation.*** The condition may present incidentally on imaging or may cause symptoms due to mass effect or hypersplenism, manifesting as anemia and thrombocytopenia.

***Imaging.*** Conventional imaging with US, CT, or MR typically will not reliably distinguish this entity from a renal or retroperitoneal malignancy. When suspected, the diagnosis can be reliably made with technetium-99m sulfur colloid imaging, or, in the case of hypersplenism, with technetium-99m labeled, heat-damaged red blood cell imaging.

***Treatment.*** When the diagnosis is confirmed by means of imaging and the child is asymptomatic, no treatment is necessary.

## ABNORMAL VISCEROATRIAL SITUS

***Overview.*** Abnormal visceroatrial situs is an intriguing spectrum of abnormalities in which there is derangement of the normal viscerovascular asymmetry, with ambiguity of many asymmetric structures which may partially resemble their right- or left-sided counterparts, and typically involve abnormalities of the spleen. This is a relatively rare condition, cited to occur in approximately 1:10,000 patients,[26] although it is fairly common in pediatric centers that care for children with congenital heart disease. The normal visceroatrial anatomy is known as situs solitus, which translates from the Latin as “usual position.” Situs inversus refers to mirror-image visceroatrial anatomy *in toto*. Patients with situs inversus are frequently asymptomatic, although there is a slightly higher incidence of congenital heart disease than in patients with situs solitus. Situs ambiguous, or visceroatrial heterotaxia, refers to deranged visceroatrial asymmetry, which is neither situs solitus nor situs inversus. Patients with this abnormality are divided into two major groups: those with a tendency toward right-sided symmetry and those with a tendency toward left-sided symmetry; therefore each patient, within broad categories, has a unique constellation of anatomic findings that must be evaluated and described within the individual context.[7,27]

***Etiology.*** Although the exact mechanism by which normal viscerovascular asymmetry is established is not yet clear, it is clear that this occurs very early in the embryo. One theory relates to cellular chirality such as derived from cytoskeleton as early as the blastomere stage in some animal embryos.[28] A theory supported by considerable evidence in mammalian embryos suggests involvement of ciliated structures related to the midline embryo node, a pitlike transient structure in the anterior tip of the primitive streak.[29] Rotating cilia in cells in nodal cells generate a right-to-left flow leading to asymmetric expression of signaling molecules,[30] leading to asymmetric structures.[31] The exact mechanism by which this cascade is generated remains unclear.[32,33]

In humans, there is significant genetic heterogeneity in the heterotaxy population, with autosomal dominant, recessive, and X-linked inheritance patterns in some family units, but only a minority of patients demonstrate mutations in likely genetic pathways. Genetic copy number variants and genes with cilia-related functions have been implicated.[26,28]

***Clinical Presentation.*** Congenital heart disease occurs in approximately 96% of patients with heterotaxy,[26] although this is likely an overestimate, as those children who are asymptomatic are underdiagnosed. However, for any given congenital heart disease, patients with heterotaxy have greater comorbidities, complications, and poorer outcomes.[26]

Patients with right-sided atrial isomerism typically lack the spleen, a condition known as asplenia, which is associated with immune deficiency and overwhelming sepsis, particularly due to *S. pneumoniae*.[34] The ambiguous atrium resembles the right atrium, and severe congenital cardiac lesions are typically present, usually with cyanosis and diminished pulmonary blood flow. Patients will thus present with cyanosis and/or pulmonary edema.[7,27] Despite modern palliative procedures, mortality remains high.[35,36] Intestinal malrotation is typically present.

Patients with left-sided atrial isomerism characteristically have multiple splenules or polysplenia. Congenital heart disease is often present, although some patients with polysplenia are asymptomatic, and the diagnosis of heterotaxy may be made incidentally. Approximately 14% of patients in a large series of left atrial isomerism had a normal heart and presented with extracardiac abnormalities. This condition is associated with biliary atresia in as many as 10% of patients.[37] As in patients with asplenia, intestinal malrotation is the rule.

***Imaging.*** In patients with situs ambiguous plain radiographs may denote abnormal situs, with discordance of heart, stomach, and liver position. Patients with right-sided atrial isomerism may demonstrate bilateral right lungs with bilateral minor fissure and eparterial bronchi. Patients with left-sided isomerism on the other hand may demonstrate bilateral left-sided hila with hyparterial bronchi. However, in pediatric patients, hilar anatomy is often not clear due to overlying thymus, and plain films are at times normal.[7,38]

Ultrasound, CT, and MRI are very helpful in determining the viscerovascular anatomy. In patients with left-sided atrial isomerism, splenules will be invariably identified dorsal to the stomach, along its greater curvature, whether the stomach lies predominantly in the right or left upper quadrants,[7] because splenic tissue develops in the dorsal mesogastrium.[39] The appearance of the splenules is variable and ranges from a conglomerate of multiple splenules to a sometimes septated, largely single splenic mass (Fig. 94.8 and e-Fig. 94.9A). Interruption of the intrahepatic inferior vena cava (IVC) is seen in at least 50% of patients, with either right- or left-sided azygous continuation (e-Fig. 94.9B).[7] When the IVC is present, it may lie to the right or left of the aorta. A preduodenal portal vein may be seen (see Chapter 102). In patients presenting with biliary atresia, it is important to evaluate the continuity of the IVC and the course of the portal vein, because these vascular derangements are important in patients later referred for liver transplantation.[40–42]

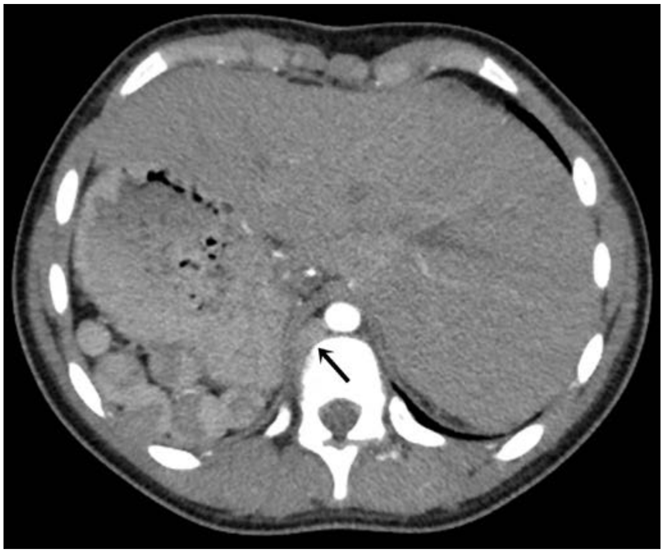

**Figure 94.8. Polysplenia.** Axial upper abdominal image from chest CTA on a 12-year-old girl with polysplenia and complex heart disease. There are multiple small splenules along the greater curvature of the right-sided stomach. An enlarged, not yet opacified retrocrural azygous vein *(arrow)* denotes azygous continuation of the suprarenal IVC.

In patients with right-sided atrial isomerism, imaging confirms absence of the spleen (e-Fig. 94.10A) and may identify other anomalies such as horseshoe adrenals fused in the midline (e-Fig. 94.10B).[43,44] Subdiaphragmatic total anomalous venous connections are easily identified, as the anomalous vessel courses anterior to the esophagus into the abdomen (e-Fig. 94.10C and D).[7] The IVC is nearly invariably present and may lie to the right or left of the aorta, crossing the midline anterior to the aorta to enter the atrium, if necessary.[7,38] A preduodenal portal vein may be present. On UGI, microgastria may be seen; malrotation is the norm. Scintigraphy can be misleading as hepatic activity can erroneously suggest the presence of splenic tissue (e-Fig. 94.5).[7]

***Treatment.*** Treatment is individualized based on the associated anomalies. Patients with asplenia are at risk for sepsis and need to be treated for immunodeficiency. Those with congenital heart disease or gastrointestinal anomalies, such as biliary atresia, typically require surgical intervention. Although some have advocated prophylactic Ladd procedure for malrotation, more recently others have shown that, in these patients with significant comorbidities, complications resulting from a prophylactic Ladd procedure are greater than those resulting from observation alone.[45–49]

## SPLENOMEGALY

***Overview.*** Splenomegaly refers to enlargement of the spleen, usually as a result of excessive destruction of abnormal blood cells, excessive antigenic stimulation, storage or infiltrative disorders, or portal venous congestion. Hypersplenism refers to the syndrome of sequestration of blood cell lines, particularly platelets by the enlarged spleen.

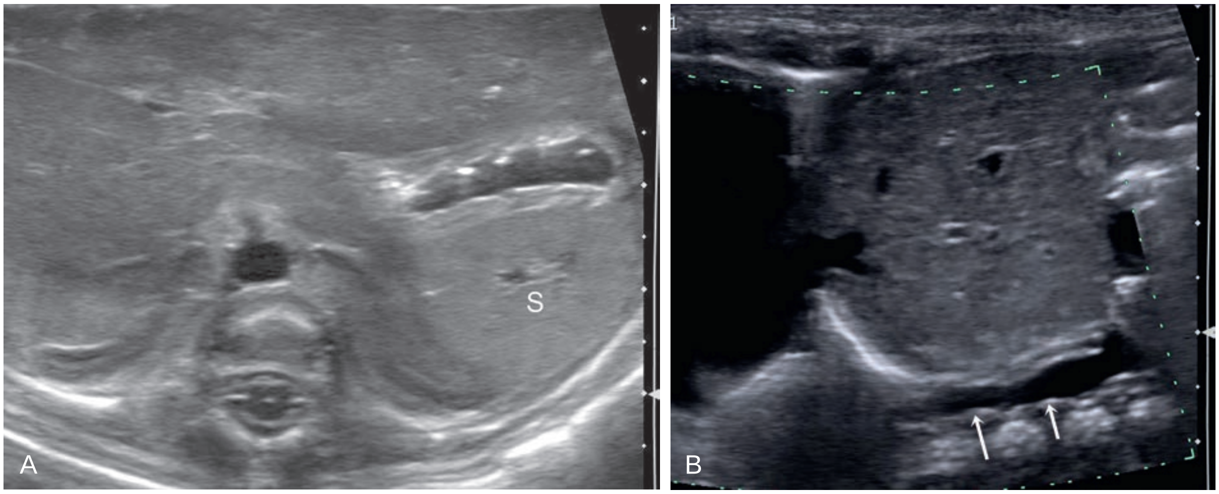

**e-Figure 94.9. Polysplenia.** (A) Axial sonogram on 1-day-old infant with polysplenia and complex congenital heart disease shows splenic tissue in a conformation that seems to be a single spleen *(S)* in the left upper quadrant, posterior to the greater curvature of the stomach. Prominent central vessel is due to an unusually oriented hilum. (B) Sagittal image on same patient shown in (A) shows azygous continuation, with the enlarged, retrocrural azygous vein *(arrows)* coursing immediately anterior to the spine. There was no intrahepatic IVC.

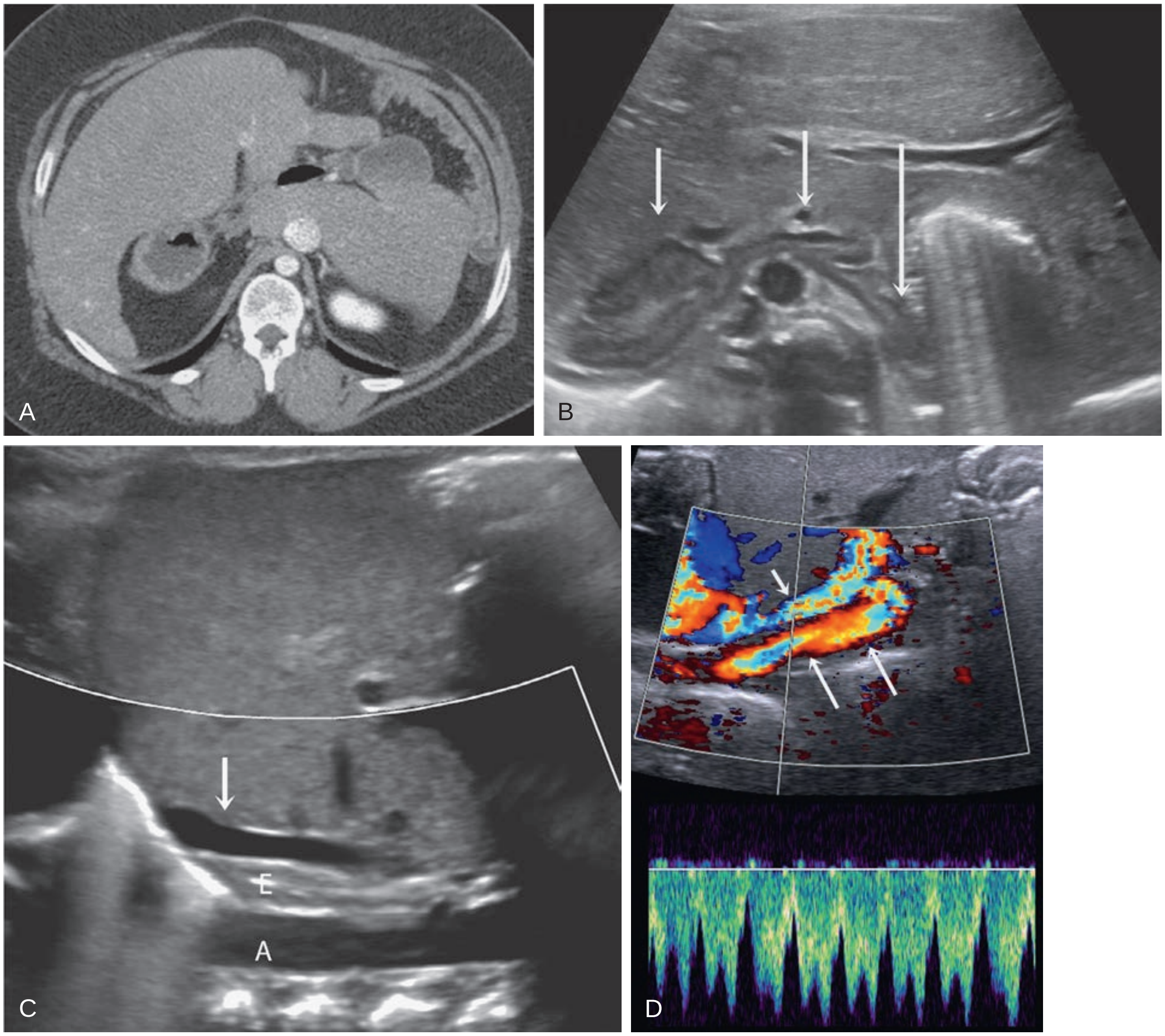

**e-Figure 94.10. Asplenia.** (A) Axial contrast-enhanced CT on a 12-year-old girl with complex congenital heart disease and asplenia. A portion of the liver extends behind the right-sided stomach, but there is no spleen. The IVC is seen anterior to the crus and anterior to the aorta. She also had a preduodenal portal vein *(not shown)*. (B) Horseshoe adrenal gland in a 1-day-old with asplenia. The adrenal gland *(arrows)* crosses the midline in continuity, anterior to the aorta. As in the patient in (A), a portion of the liver extends behind the stomach, but there is no spleen. (C) Total anomalous venous connection to left portal vein in a 1-day-old with asplenia. The anomalous vein *(white arrow)* extends into the abdomen anterior to the esophagus *(E)* and the aorta *(A)*. (D) Doppler image in same child as shown in (C) but in a different plane shows the anomalous vein *(long white arrows)* draining into the portal vein, with the flow returning to the right atrium via the ductus venosus *(short white arrow)*.

## BOX 94.1 Causes of Splenomegaly in Children

**INFECTION**

Bacterial, viral (e.g., Epstein-Barr), fungal, protozoan

**CONGESTIVE STATES RELATED TO PORTAL HYPERTENSION**

Cirrhosis
Portal or splenic vein thrombosis
Right heart failure

**LYMPHOHEMATOGENOUS DISORDERS**

Hodgkin lymphoma
Non-Hodgkin lymphoma
Lymphoproliferative disease
Hemolytic anemias (e.g., acute splenic sequestration in sickle cell anemia)
Thalassemia
Extramedullary hematopoiesis

**STORAGE DISEASES**

Gaucher, Niemann-Pick, Mucopolysaccharidoses

**IMMUNOLOGIC–INFLAMMATORY**

Idiopathic thrombocytopenic Purpura
Systemic lupus erythematosus
Juvenile Idiopathic arthritis

**CYSTS**

Congenital
Acquired

**BENIGN NEOPLASMS/MASSES**

Hemangioma
Lymphangioma
Hamartoma

**MISCELLANEOUS**

Sarcoidosis
Langerhans cell histiocytosis
Collagen vascular diseases

***Etiology.*** The spleen may become enlarged in several inherited conditions (Box 94.1). The hemolytic anemias frequently lead to splenomegaly, with hereditary spherocytosis, hereditary elliptocytosis, and thalassemia among the most common causes. Sickle cell anemia initially leads to splenomegaly; the pathophysiology is sequestration of impaired red blood cells by the spleen, leading to splenomegaly, anemia, and thrombocytopenia. This is followed by splenic atrophy in older children, secondary to multiple infarcts.

Patients with portal hypertension from a number of causes may have congestive splenomegaly.

Splenomegaly has been reported in a group of neonates who have undergone extracorporeal membrane oxygenation (ECMO) cannulation; the mechanism proposed was sequestration of cells damaged in the ECMO circuit.[50]

Splenomegaly can also occur in a variety of acquired disorders, including infection and neoplasm.

***Clinical Presentation.*** Patients with splenomegaly present with the signs and symptoms of the underlying condition. Acute splenic sequestration crisis is manifested clinically by sudden enlargement of the spleen and a rapid fall in hematocrit. This condition typically occurs in young children, with 76% of episodes occurring before 2 years of age. The episode can manifest emergently, with hypovolemic shock potentially progressing to death within a few hours.[51] The condition is rare beyond age 8, due to developing splenic fibrosis. Once a child has a sequestration crisis, there is a higher risk of recurrence.

**TABLE 94.2** Spleen Length in Children and Adolescents*

| Group | No. | 10th Centile | Median | 90th Centile | Upper Limit |
|---|---|---|---|---|---|
| 0–3 mo | 28 | 3.3 | 4.5 | 5.8 | 6.0 |
| 3–6 mo | 13 | 4.9 | 5.3 | 6.4 | 6.5 |
| 6–12 mo | 17 | 5.2 | 6.2 | 6.8 | 7.0 |
| 1–2 yr | 12 | 5.4 | 6.9 | 7.5 | 8.0 |
| 2–4 yr | 24 | 6.4 | 7.4 | 8.6 | 9.0 |
| 4–6 yr | 39 | 6.9 | 7.8 | 8.8 | 9.5 |
| 6–8 yr | 21 | 7.0 | 8.2 | 9.6 | 10.0 |
| 8–10 yr | 16 | 7.9 | 9.2 | 10.5 | 11.0 |
| 10–12 yr | 17 | 8.6 | 9.9 | 10.9 | 11.5 |
| 12–15 yr | 26 | 8.7 | 10.1 | 11.4 | 12.0 |
| 15–20 yr (male) | 5 | 9.0 | 10.0 | 11.7 | 12.0 |
| 15–20 yr (female) | 12 | 10.1 | 11.2 | 12.6 | 13.0 |

*All measurements are in centimeters. Upper limits are the next highest whole integer over the 90th percentile.

**TABLE 94.3** Length of Spleen in Children Versus Body Height and Age*

| Body Height (cm) | No. | Age Range (mo) | Mean ± SD | Range | Normal Limits |
|---|---|---|---|---|---|
| 48–64 | 52 | 1–3 | 53 ± 7.8 | 33–71 | 30–70 |
| 54–73 | 39 | 4–6 | 59 ± 6.3 | 45–71 | 40–75 |
| 65–78 | 18 | 7–8 | 63 ± 7.6 | 50–77 | 45–80 |
| 71–92 | 18 | 12–30 | 70 ± 9.6 | 54–86 | 54–85 |
| 85–109 | 27 | 36–59 | 75 ± 8.4 | 60–91 | 55–95 |
| 100–130 | 30 | 60–83 | 84 ± 9.0 | 61–100 | 60–105 |
| 110–131 | 36 | 84–107 | 85 ± 10.5 | 65–102 | 65–105 |
| 125–149 | 29 | 108–131 | 86 ± 10.7 | 64–114 | 65–110 |
| 137–153 | 17 | 132–155 | 97 ± 9.7 | 72–100 | 75–115 |
| 143–168 | 21 | 156–179 | 101 ± 11.7 | 84–120 | 80–120 |
| 152–175 | 12 | 180–200 | 101 ± 10.3 | 88–120 | 85–120 |

*All measurements are in centimeters.
*From Rosenberg HK, Markowitz RI, Kolberg H, et al: Normal splenic size in infants and children. sonographic measurements.* AJR Am J Roentgenol *1991;157:119–121.*

***Imaging.*** Plain radiographs of the abdomen may reveal an enlarged spleen in the left upper quadrant, displacing the stomach medially and the colon inferiorly.

Ultrasound readily detects splenomegaly, using the coronal imaging plane with the splenic hilum in view. Splenic length has been correlated with patient age[52] (Table 94.2) and with body height/length[53–56] (Table 94.3). When correlated against body mass index, the strongest correlate was with body weight according to the formula:

$$69.875 + \text{body weight [kg]} \times 0.371.$$ [57]

Reference ranges based on gestational age exist.[58] As a general rule, the tip of the spleen should not extend below the inferior pole of the left kidney (e-Fig. 94.11), and the spleen should not exceed 1.25 times renal length.[56]

CT and MRI also readily reveal an enlarged spleen and may allow for more standardized and reproducible measurement. Spleen volume can be readily measured with CT or MRI. Normal pediatric spleen volume, as measured on CT, correlates with body weight in a linear relationship.[59,60]

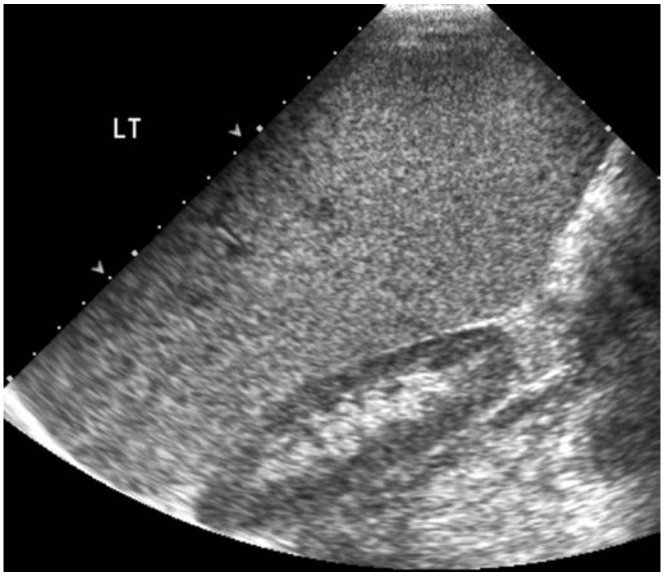

**e-Figure 94.11. Splenomegaly.** Splenomegaly in a 14-year-old boy with anemia. Coronal ultrasound image shows that the spleen extends below (caudad to) the lower pole of the left kidney.

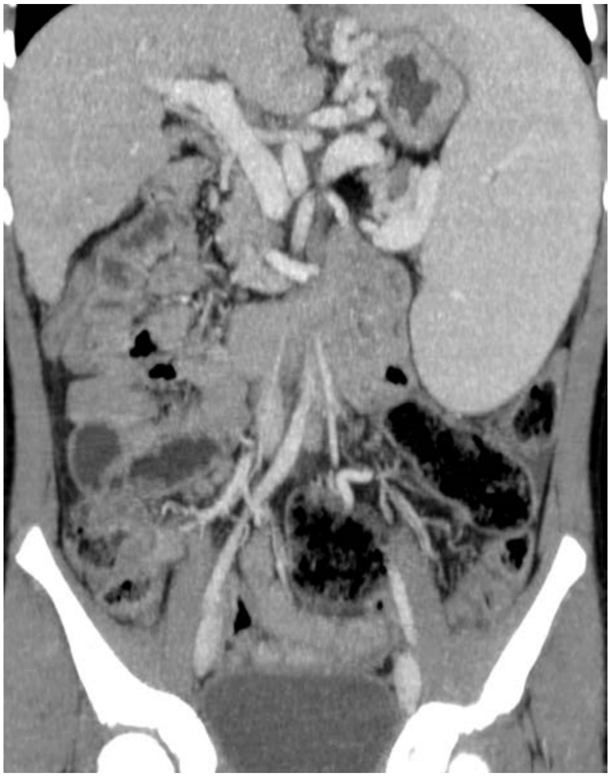

**Figure 94.12. Splenomegaly.** Splenomegaly secondary to portal hypertension in an 11-year-old girl with liver disease. Coronal reconstruction of contrast-enhanced CT of the abdomen shows splenic extension to the left mid abdomen. Multiple variceal collaterals are clearly depicted.

The imaging findings in splenomegaly are nonspecific as to cause, unless there is evidence of extramedullary hematopoiesis or infarcts, or ancillary findings are identified, such as varices in patients with congestive splenomegaly (Fig. 94.12). Extramedullary hematopoiesis may demonstrate focal areas of increased echogenicity on sonography, whereas infarcts may appear as hypoechoic areas. The storage diseases generally cause nonspecific splenomegaly,[61] but Gaucher disease may lead to focal hyper/hypoechoic or mixed echogenic foci, reflecting collections of Gaucher cells, or extramedullary hematopoiesis.[62] The focal collections may occasionally be hyperechoic secondary to fibrosis. They are isointense on T1-weighted MR imaging and hyperintense on T2-weighted imaging,[62,63] with low signal intensity on gradient recalled echo imaging due to the iron contained in Gaucher cells.[64]

In patients with sickle cell anemia experiencing acute sequestration crisis, the spleen appears larger than expected, and hypoechoic splenic lesions can be seen peripherally on US (Fig. 94.13) due to hemorrhage or infarction. Low attenuation peripheral lesions are demonstrated on contrast-enhanced CT[65] with patency of the splenic artery and vein.[66]

***Treatment.*** Treatment of splenomegaly is directed at the underlying cause. Splenectomy is used sparingly in children. Treatment of children with sickle cell disease is complex and includes supportive care, infection prophylaxis, and transfusion therapy in selected cases.[67]

The long-term management of sequestration syndrome consists of increased awareness of symptoms (primarily worsening anemia), signs (enlarging spleen), and, in some cases, short-term chronic transfusion.[51] In most sickle cell patients, splenic function is diminished because of splenic infarcts, and autosplenectomy is nearly 94% by age 5 to 6 years.[65] Although transfusion has been shown to reverse functional hyposplenism and preserve splenic function,[68–70] hyposplenism is not considered an indication for hypertransfusion.[67] Hematopoietic stem cell transplantation not only prevents further damage to the spleen but has demonstrated recovery of splenic function in children with sickle cell disease.[71]

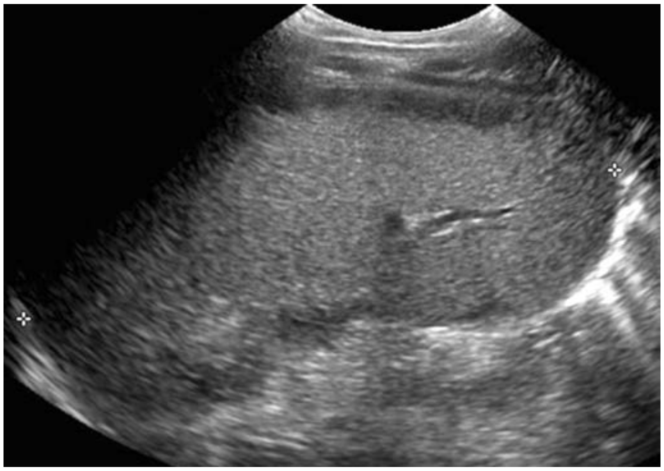

**Figure 94.13. Splenic sequestration crisis.** Longitudinal sonogram of the spleen of a young child with acute splenic sequestration crisis demonstrates numerous peripheral hypoechoic lesions. *(Courtesy of Sarah Fitch, MD, Richmond, VA.)*

## SPLENIC INFARCTION

***Overview.*** Splenic infarction is caused by a lack of perfusion to regions of the spleen or to the entire organ. The causes are numerous including embolic, hematologic, vascular disease, torsion, trauma, malignancy, and pancreatic disease.[72] The most common cause is partial or total occlusion of the splenic artery or its branches. Microinfarctions can be seen in patients with sickle cell anemia, lymphoma, or leukemia.[3]

***Clinical Presentation.*** Most patients will present with left upper quadrant pain, with or without fever and chills. Referred pain to the left shoulder is also a reported feature.[3,5]

***Imaging.*** At US, an acute, focal splenic infarct will typically appear as wedge-shaped, hypoechoic (Fig. 94.14A) and well demarcated lesion pointing toward the splenic hilum, with absent flow on Doppler interrogation.[5] On contrast-enhanced CT, typical splenic infarcts present as wedge-shaped, hypodense areas with the base facing the splenic capsule. Enhancement of the affected region may be observed in delayed phase images. When the entire spleen is infarcted, it results in diffuse splenic hypodensity with a rim of enhancing capsule. This is the so-called "rim sign" that results from persistent arterial supply to small capsular vessels. Splenic infarction as seen in sickle cell can also result in a small, calcified spleen (Fig. 94.14B). Complications include splenic rupture, hemorrhage, or abscess formation.[3]

Gamna-Gandy bodies are small hemorrhages in the spleen caused by hemolytic anemias (sickle cell disease, spherocytosis), portal hypertension, hemochromatosis, lymphoma, leukemia, portal hypertension, or splenic/portal venous thrombosis. They contain hemosiderin and a variable amount of fibrous tissue and calcium.[73] They are best imaged using MR and appear as multiple small foci of low signal intensity on all pulse sequences, due to iron deposition. On gradient-echo sequences or susceptibility weighted imaging, a blooming artifact is seen due to the paramagnetic effect of hemosiderin.[74,75]

***Treatment.*** Treatment consists of management of complications and infection prophylaxis as appropriate.

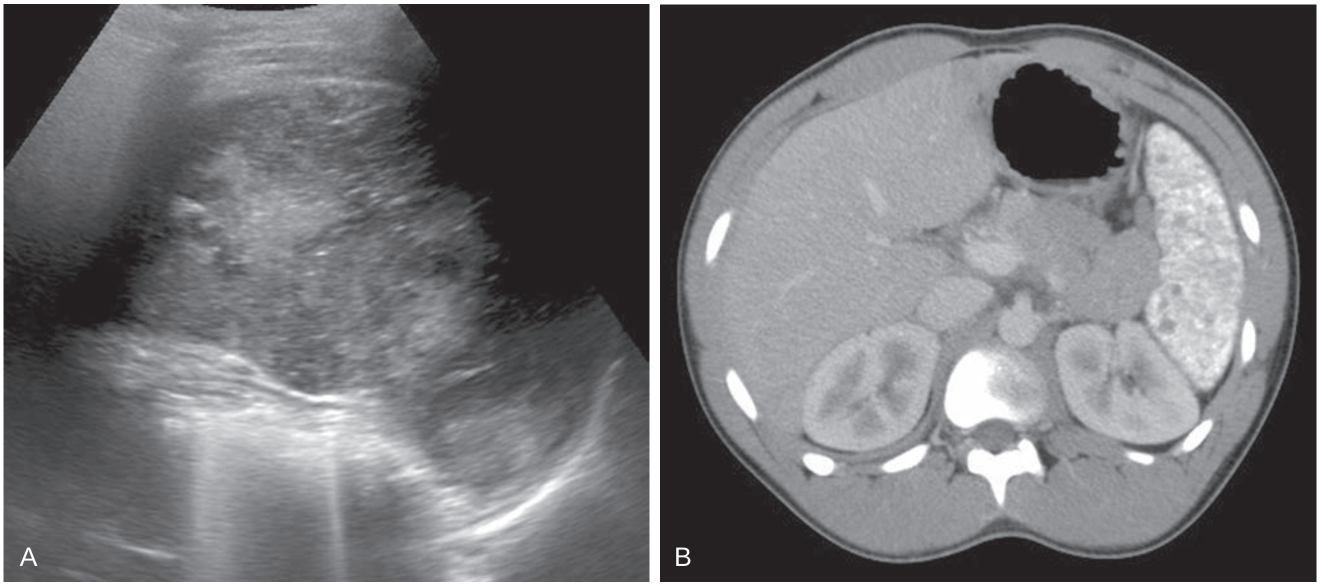

**Figure 94.14. Sickle cell disease complications.** (A) Transverse sonogram of the spleen in a15-year-old boy with sickle cell disease presenting with severe periumbilical pain reveals multiple hypoechoic areas, some peripheral and wedge-shaped, consistent with acute splenic infarcts. (B) Axial contrast-enhanced CT in an 18-year-old boy with sickle cell disease reveals a calcified spleen secondary to chronic infarction.

## INFECTIOUS DISEASES

***Overview.*** Involvement of the spleen in systemic infectious disease is most common in immunocompromised patients, with increasing incidence due to the increasing use of steroids and chemotherapeutic agents.[64] Bacterial, fungal, and granulomatous agents are frequently involved. Splenic involvement can also occur in immune-competent hosts with cat scratch fever, granulomatous diseases such as histoplasmosis, and viral infections. Viral infections, including infectious mononucleosis, are more likely to cause nonspecific splenomegaly due to reactive hyperplasia of the spleen's reticuloendothelial tissue. Splenic abscesses are uncommon lesions and are rare in the pediatric population.[76] Hydatid cysts may rarely involve the spleen.[77]

***Etiology.*** Bacterial splenic abscesses can develop via hematogenous spread, such as from bacterial endocarditis; spread from a contiguous infection, such as pancreatitis or perinephric abscess; and seeding in a spleen compromised by infarction or trauma. In cat scratch fever, the agent, *Bartonella henselae*, is transmitted from asymptomatic cats through biting and clawing. Hydatid disease is caused by echinococcal infection and may involve the spleen in up to 8% of cases (following liver and lung in frequency), typically arising through systemic dissemination or via intraperitoneal spread secondary to intraperitoneal rupture of hepatic disease.[78]

***Clinical Presentation.*** Symptoms of splenic involvement in an infectious process can be nonspecific and may be related to the systemic illness or to the secondary development of splenomegaly. Patients may present with fever, lethargy, and weight loss. Abdominal distension, tenderness, and leukocytosis are commonly found.[76] Cat scratch disease is a relatively common infection in children that typically presents with fever and tender lymphadenopathy.

***Imaging.*** Imaging has an important role in diagnosis, as signs and symptoms can be nonspecific. Early diagnosis and prompt treatment are critical to decrease mortality and morbidity. Splenic abscesses can be solitary, multiple, or multilocular, depending on the source of infection.

Large pyogenic abscesses appear as complex fluid collections with surrounding hyperemia on Doppler interrogation. On contrast-enhanced CT, pyogenic abscesses demonstrate rim-enhancement.[3]

Microabscesses are most commonly seen with fungal infection such as candidiasis. On US, these lesions exhibit a "bull's-eye" appearance due to a central hyperechoic inflammatory core surrounded by hypoechoic fibrous tissue.[79] High resolution imaging, including high frequency and linear transducers, may be necessary for detection of microabscesses. They appear as low-attenuation lesions on contrast-enhanced CT or MRI. It is important to note that small fungal abscesses lack contrast enhancement and may be difficult to detect or may be easily overlooked on CT images.[3] However, CT is generally superior to abdominal sonography in the detection of hepatosplenic fungal lesions.[80] *Candida* species are a frequent causative pathogen of microabscesses, although larger, solitary abscesses may also occur with candidiasis. They may be seen as hypoechoic areas on US, as low-attenuation areas on CT, and as T2-hyperintense lesions without peripheral enhancement.[81] In late stages, calcification may be seen on CT.[79]

MRI can be utilized for the evaluation of microabscesses, which appear as high signal intensity foci on water-sensitive, fat-suppressed sequences.[81]

In cat scratch disease, US may show hypoechoic lesions ranging from well-defined and homogeneous to indistinct and heterogeneous, while contrast-enhanced CT may show hypoattenuating lesions, isoattenuating lesions, or lesions with marginal enhancement (e-Fig. 94.15). On MRI, lesions demonstrate low signal intensity on T1-weighted sequences and high signal intensity on T2-weighted sequences.[3,82]

Hydatid cysts may demonstrate calcifications, which can be visible on plain films. The cysts are generally anechoic, although the presence of daughter cysts and membranes may produce septations and internal echoes. CT shows a focal lesion of lower attenuation than the surrounding splenic tissue, and it is the best modality to show rim calcification, when present.[78,83]

Tuberculosis, histoplasmosis, and coccidioidomycosis may produce multiple splenic granulomas, almost always associated with diffuse organ involvement secondary to hematogenous spread (e-Fig. 94.16). Splenic granulomas may be also be detected in patients with chronic granulomatous disease of childhood.

***Treatment.*** Treatment is geared to the underlying diagnosis. Cat scratch disease is usually self-limited and typically does not

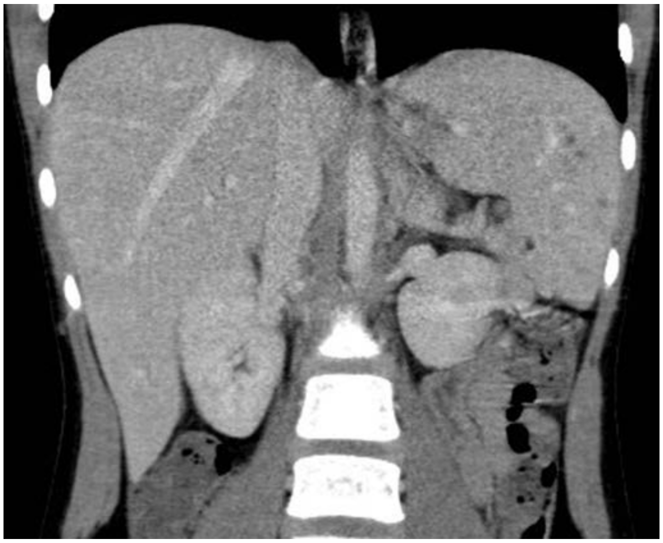

**e-Figure 94.15. Cat scratch disease.** Coronal reformatted contrast-enhanced CT image in a 10-year-old girl reveals a normal sized spleen with small round, hypodense lesions of slightly varying size.

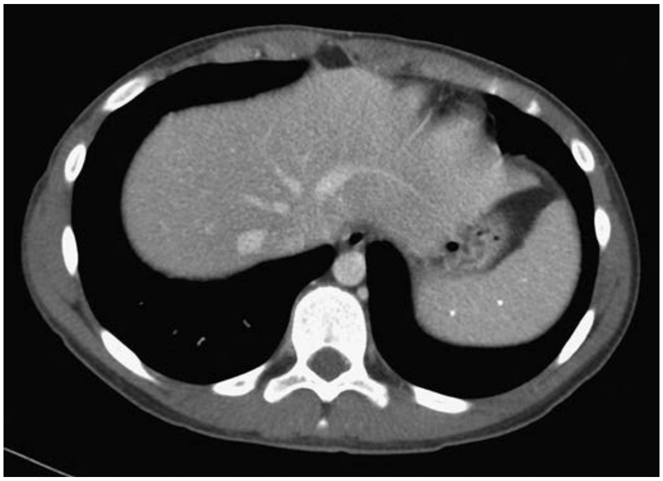

**e-Figure 94.16. Histoplasmosis.** Splenic granulomas in a 13-year-old girl with histoplasmosis. Two small foci of calcification representing calcified granulomas are seen within the spleen.

require antibiotic therapy. Hydatid cysts are first medically treated with antihelminthic drugs.[84] Splenectomy, with partial resection whenever possible, is considered a mainstay of treatment; a meticulous surgical approach is important in the treatment of splenic hydatidosis because of the risk of recurrence, spillage, and anaphylaxis.[77,85]

## BENIGN CYSTS AND NEOPLASMS

***Overview.*** Cysts are the most common benign lesions of the spleen. Splenic cysts can be primary or true cysts, which are defined by the presence of an epithelial lining and can be congenital. In most classification systems, secondary cysts or pseudocysts are typically related to antecedent trauma, infection, or infarction.[86,87] A more recent classification proposes that most nonparasitic splenic cysts are congenital in origin and have lost their epithelial lining over time.[88,89] Neoplasms of the spleen include benign lesions, such as hamartomas, and malignant lesions, which are most commonly part of a systemic ailment, such as splenic involvement with lymphoma, and rare primary splenic lesions, such as angiosarcoma.

### Epithelial Cysts

***Overview.*** Epithelial cysts are congenital representing approximately 10% of pediatric splenic lesions worldwide and are thus the most common nonparasitic cysts in the pediatric spleen.[90]

***Etiology.*** Epithelial cysts are believed to be derived from inclusions of the mesothelial lining of the spleen or from adjacent epithelial cells within the embryonic splenic anlage.[90] A few cases of familial occurrence have been reported, which lends support to the congenital origin of these lesions.[91]

***Clinical Presentation.*** Splenic cysts are frequently discovered incidentally on physical examination or imaging performed for other reasons. However, sufficiently large cysts can present as splenomegaly, renal compression with hypertension or varicocele, or radiating lumbar or left shoulder pain. They can also present with cyst rupture and peritonitis, particularly after trauma, which could be relatively minor.[88,92]

***Imaging.*** Primary epithelial/epidermoid cysts are usually solitary but can be multiple, with occasional calcification.[93] Epidermoid/epithelial cysts are frequently large enough to visibly enlarge the spleen on plain radiographs as a left upper quadrant mass displacing the stomach and colon (Fig. 94.17A and B). A rim of calcification may be seen. On US, the cysts are characteristically anechoic and sharply demarcated from the surrounding normal splenic tissue. However, hemorrhage, inflammatory debris, or internal fat droplets may cause the cyst to contain internal echoes, at times resembling a hypoechoic solid mass; movement of the internal echoes may be detectable and can be documented on video clips. Doppler interrogation reveals no internal flow. Liver-spleen scintigraphy demonstrates a focal photopenic defect. CT may be best at identifying calcifications. On CT and MRI, an uncomplicated epidermoid cyst appears as a rounded, sharply demarcated, nonenhancing mass with cystic imaging characteristics (Fig. 94.17C). If it is complicated by hemorrhage, the internal signal intensity of the lesion on MRI reflects the chemical state of the hemoglobin. Posttraumatic cysts may be difficult or impossible to distinguish radiologically from other cysts, but may have irregular walls and internal echoes from debris.

***Treatment.*** Cyst size is not the major impetus for intervention, and splenic cysts should be managed according to the patient's symptoms.[94] Surgical options for symptomatic cysts include: total splenectomy, hemisplenectomy,[95] or total cystectomy.[92]

### Hemangiomas

***Overview.*** Splenic hemangiomas are vascular proliferations made up of channels filled with slow-flowing blood. Hemangiomas are classified as capillary or cavernous, depending on the size of these vascular channels. They are the most common primary neoplasm of the spleen.

***Etiology.*** Splenic hemangiomas are likely congenital in origin, arising from the sinusoidal epithelium. Histologically, they contain a proliferation of vascular channels lined with a single layer of epithelium. They may be single, multiple, or may occur as part of a generalized angiomatosis, such as in Klippel-Trenaunay-Weber, Beckwith-Wiedemann, and Turner syndromes.[96]

***Clinical Presentation.*** Most patients are asymptomatic; when symptoms occur, they may not be manifest until adulthood. Symptoms are typically left upper quadrant fullness and pain. Symptomatic masses are usually a consequence of complications of such as hypersplenism, anemia, thrombocytopenia, and coagulopathy (Kasabach-Merritt syndrome).[90]

***Imaging.*** On US, the solid lesions are typically well-marginated and hyperechoic but may be hypoechoic; they demonstrate internal vascular flow, and calcifications may be seen.[2] On noncontrast CT, hemangiomas are well-defined, hypoattenuating, or isoattenuating masses. Capillary hemangiomas homogeneously enhance with contrast (Fig. 94.18), while cavernous hemangiomas may demonstrate a centripetal or a mottled attenuation on delayed contrast enhancement, due to the presence of fibrosis and microinfarctions.[3] On MRI, splenic hemangiomas are hypo- to isointense on T1-weighted images and hyperintense on T2-weighted images. As on CT, cavernous hemangiomas show peripheral enhancement extending toward the center, while capillary hemangiomas have a more homogenous enhancement.[6] Technetium-99m-labeled red blood cell scans may be helpful in characterizing atypical lesions by demonstrating increased activity on delayed images.[97]

***Treatment.*** Small or asymptomatic lesions are observed; larger lesions may require resection and may necessitate splenectomy.[90]

### Hamartomas

***Overview.*** Hamartomas, also known as splenomas or nodular hyperplasia of the spleen, are rare, nonneoplastic malformations composed of an anomalous mixture of normal splenic red pulp and lymphoid white pulp.[2]

***Etiology.*** It is proposed that splenic hamartomas result from splenic injury and reparative response.[98] Histologically, splenic hamartomas are composed of splenic sinusoidal tissue with no lymphoid follicles (red pulp) and variable chronic inflammation with macrophages, lymphocytes, plasma cells, extramedullary hematopoietic cells, fibrosis, hemosiderosis, and calcification.[98]

***Clinical Presentation.*** Most patients are asymptomatic, and the lesion is found incidentally; if it is large, there is the potential for rupture and hemoperitoneum. In some instances, they can be associated with tuberous sclerosis, Wiskott-Aldrich syndrome, or other hematologic conditions.[3,98]

***Imaging.*** Because hamartomas are composed of normal splenic tissue, they may not be detected with US or CT unless they alter the contour of the spleen, producing a focal bulge. Those that are identified by US are most commonly well-circumscribed, solid, and homogeneous, but some may be partly cystic and heterogeneous. They are variably described as hyperechoic,[2,99] hypoechoic,[100–102] or of mixed echogenicity. The variety of described morphologic patterns is likely derived from the preponderant growth of one or another of several histologic components. Hamartomas typically reveal increased blood flow on Doppler interrogation.[2] On contrast-enhanced CT, they demonstrate prolonged contrast enhancement due to stagnant blood flow within the sinuses of the red pulp. This assists in differentiating hamartomas from malignant tumors. Calcification, central areas of necrosis, and fat can be seen on CT.[3] The fibrous hamartomas are iso- or hyperintense on T1-weighted and hypointense on T2-weighted MRI. The nonfibrous hamartomas, which are more common, are isointense on T1-weighted and hyperintense on T2-weighted MRI.[103] They both demonstrate

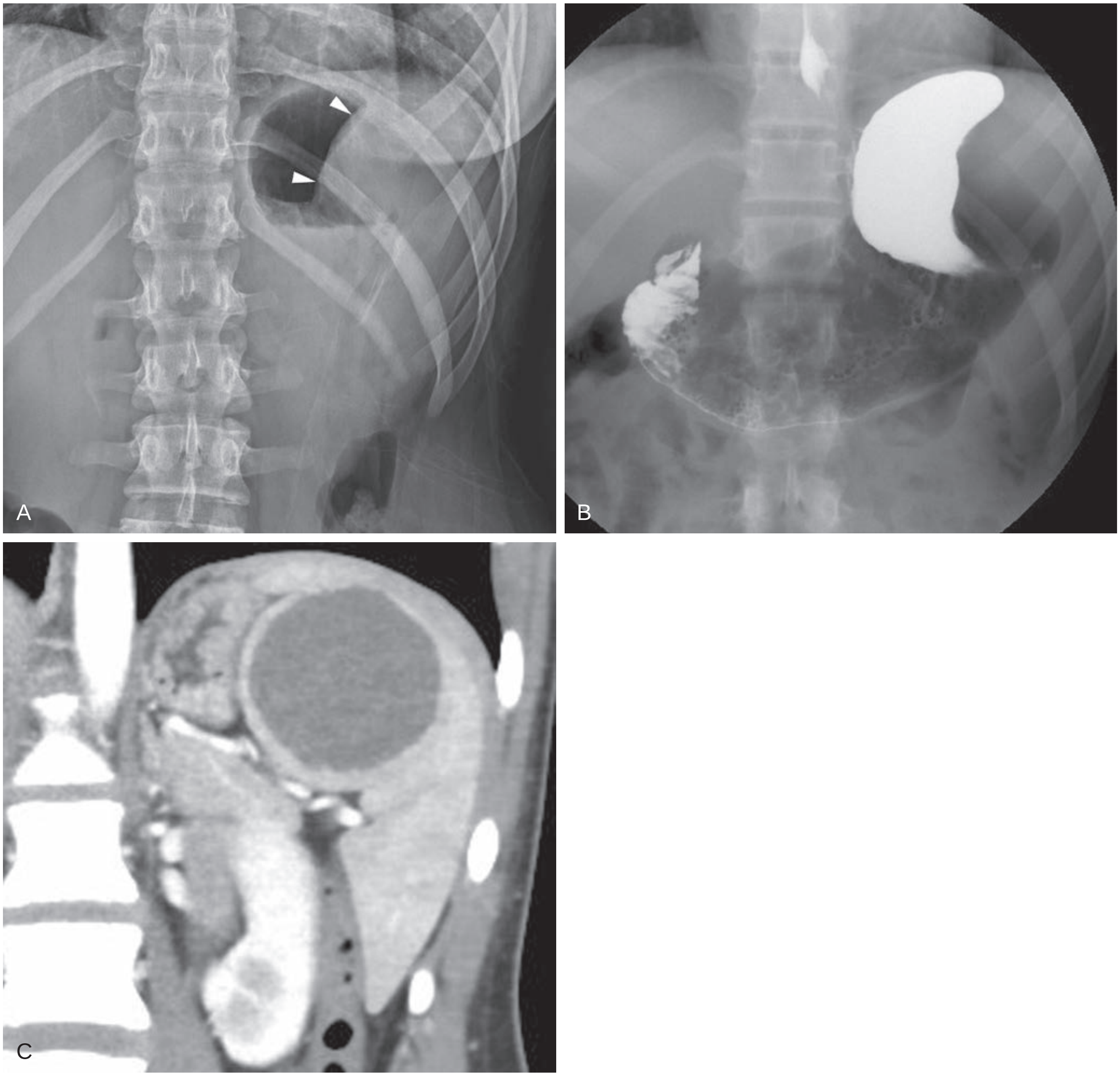

**Figure 94.17. Epithelial cyst.** (A) Frontal upright abdominal radiograph in a 14-year-old girl reveals a well-circumscribed curvilinear mass effect *(arrowheads)* on the lateral gastric air bubble. (B) Supine fluoroscopic image of the upper abdomen obtained during an upper GI examination confirms the mass effect on the fundus, arising from the spleen. (C) Coronal reformatted contrast-enhanced CT reveals a well-circumscribed, round, hypodense lesion in the upper portion of the spleen with mass effect on the decompressed stomach. The lesion measured 40 HU, consistent with a cyst.

diffuse heterogeneous contrast enhancement, with more uniform enhancement on delayed images.[64,96] On technetium-99m sulfur colloid scintigraphy, they may have radiopharmaceutical uptake greater than that in the surrounding normal spleen.[99]

***Treatment.*** If hypersplenism is associated, splenectomy can resolve the hematologic abnormalities.[98]

## Lymphatic Malformation

***Overview.*** Lymphatic malformations are rare, benign tumors, which may be single or multiple and may cause splenic enlargement. Splenic lymphangiomatosis is usually associated with lymphangiomas found elsewhere.

***Etiology.*** As in other sites, splenic lymphangioma is due to an abnormal congenital development of lymphatic channels.

***Clinical Presentation.*** Clinical manifestations range from an asymptomatic incidental finding to a large, symptomatic mass, which may cause symptoms from compression of adjacent structures.[2,104] The presence of splenic lymphangiomas should prompt a search for these lesions in other organs; multiorgan involvement describes lymphangiomatosis syndrome, where the liver, pericardium, mediastinum, lung, and bone may be involved.[2,104]

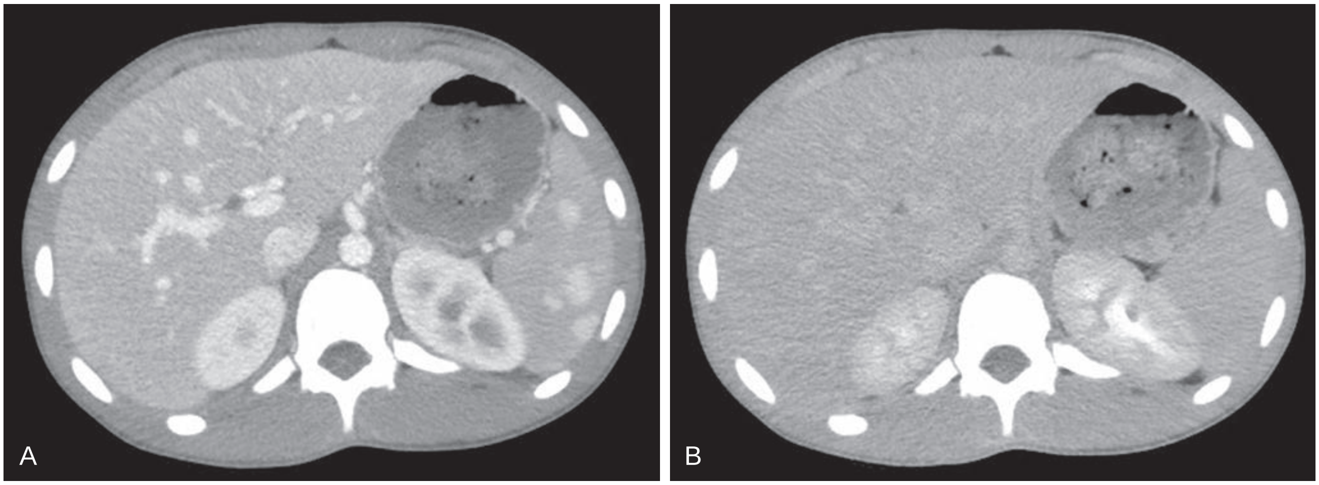

**Figure 94.18. Hemangioma.** (A) Axial contrast-enhanced CT in a 14-year-old boy shows multiple well-circumscribed oblong hyper-enhancing lesions. (B) Delayed image shows equilibration with the diffusely enhancing spleen.

***Imaging.*** On US, CT, and MRI, lymphatic malformations are most commonly sharply marginated, nonenhancing unilocular or multilocular cystic lesions, typically located close to the splenic capsule.[3] Though typically anechoic on US, they may contain internal floating echoes. On CT, they appear as single or multiple thin-walled, low-density, nonenhancing masses with sharp margins and occasional mural calcifications. The cysts generally have low signal intensity on T1-weighted and high signal intensity on T2-weighted MR images (e-Fig. 94.19); however, they may have high signal intensity on T1-weighted images secondary to internal hemorrhage or proteinaceous fluid.

***Treatment.*** Typically, with solitary small or asymptomatic lesions, no surgical intervention is required. Symptomatic lesions may be treated with partial or complete splenectomy, or sclerotherapy.[104]

## Peliosis

***Overview.*** Peliosis is an uncommon entity, consisting of blood-filled cavities, which lend the spleen a dark or purplish hue on gross examination. It is often seen in the setting of peliosis hepatis.

***Etiology.*** The etiology of the sinusoidal dilation leading to formation of multiple cystlike, blood-filled cavities within the splenic parenchyma is not certain.[105] It is associated with the use of anabolic steroids, blood dyscrasias such as aplastic anemia, infectious entities such as tuberculosis, and neoplasia.[90]

***Clinical Presentation.*** Many cases are asymptomatic and discovered incidentally; however, if it occurs along the periphery of the spleen, there is a potential for life-threatening rupture and hemoperitoneum.[106–108]

***Imaging.*** On US, splenic peliosis may reveal an echogenic mass with poorly defined foci of varying echogenicity.[2] The condition may also demonstrate multiple, well-defined, hypoechoic lesions of varying size, and occasionally fluid-fluid levels within the nodules. On CT, it appears as many small lesions of low attenuation without calcification.[109] Due to hemorrhage, peliosis can present as hyperdense lesions.[3] Centripetal enhancement, similar to hemangiomas, has been reported.[110] On MRI, fluid-fluid levels of varying intensity may be present due to blood in the cystic spaces.

***Treatment.*** Surgery is usually required for definitive diagnosis and treatment.[2]

## MALIGNANT NEOPLASMS

Malignant neoplasms of the spleen are usually related to multifocal neoplastic disorders, such as leukemia and lymphoma, and rarely metastases. Angiomatous tumors include littoral cell angioma, hemangiopericytoma, and angiosarcoma.

### Acute Leukemia

***Overview.*** Splenic involvement is often present in children with leukemia. Chronic myelogenous leukemia is rare in children but is frequently accompanied by massive splenomegaly.

***Etiology.*** Diffuse infiltration of the spleen by the leukemic cells leads to splenomegaly.

***Clinical Presentation.*** Splenomegaly is characteristic. Rarely, leukemic infiltration of the spleen can present with splenic infarction, characterized by severe abdominal pain.[111]

***Imaging.*** Imaging studies of the spleen are rarely performed in children with leukemia because the diagnosis is made by other means, and the results of splenic imaging have no impact on staging or prognosis. The spleen is often involved during the hematologically active stages of acute leukemia, and it frequently serves as a sanctuary site during hematologic remission. Cross-sectional imaging may reveal splenomegaly. Low attenuation splenic nodules can be difficult to differentiate from fungal microabscesses based on imaging alone; infarctions may also occur.[112]

***Treatment.*** Treatment is geared to the underlying malignancy and its complications.

### Lymphoma

***Overview.*** Lymphoma is the most common malignant tumor of the spleen, although primary splenic lymphoma accounts for less than 2% of all lymphomas.[113] The spleen is usually involved secondarily, and accurate imaging of splenic lesions is important because it can alter staging, treatment protocols, and overall prognosis. Nonmalignant conditions may mimic tumor involvement and lead to an erroneous diagnosis.

***Etiology.*** Pediatric lymphoma is a heterogeneous group of malignancies derived from the immune system, characterized by enlargement and proliferation of lymph nodes and secondary lymphoid tissues. Risk factors include immune system disorders, genetic factors, infections such as HIV, and iatrogenic conditions such as after transplantation.[112]

***Clinical Presentation.*** In non-Hodgkin lymphoma, the spleen is affected in 20% of patients, while in Hodgkin disease, the spleen is involved in 30% to 40% of cases at presentation.[114] Organ size alone should not be used to assess splenic

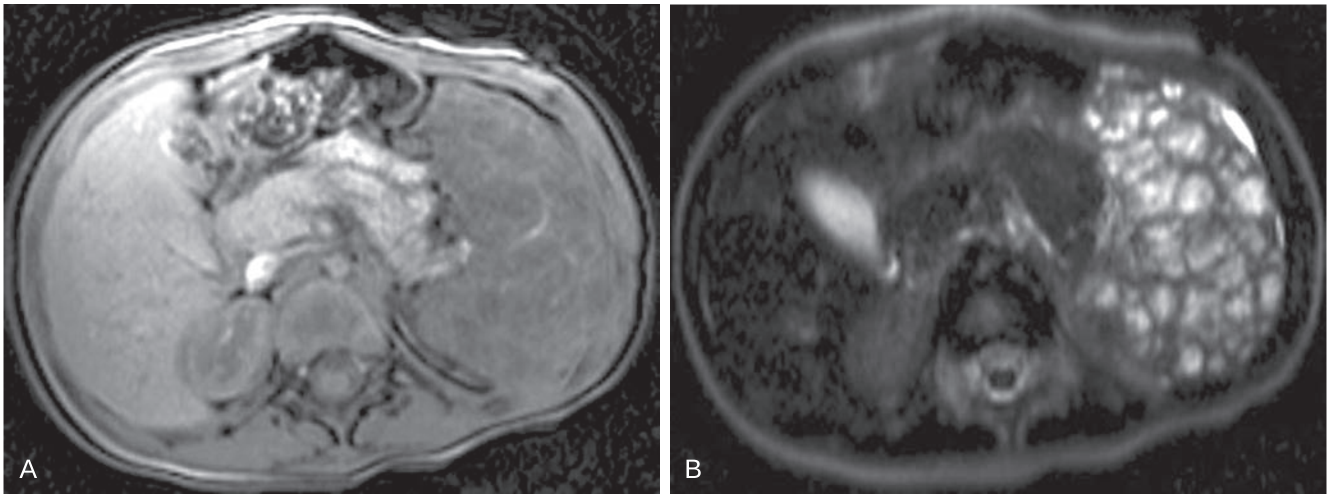

**e-Figure 94.19. Splenic lymphangiomas.** (A) T1-weighted MR image shows numerous lesions of low signal intensity diffusely involving the splenic parenchyma in an 18-month-old girl. (B) On a T2-weighted MR image, the lesions have high signal intensity. *(Courtesy of Jeanne G. Hill, MD, MUSC.)*

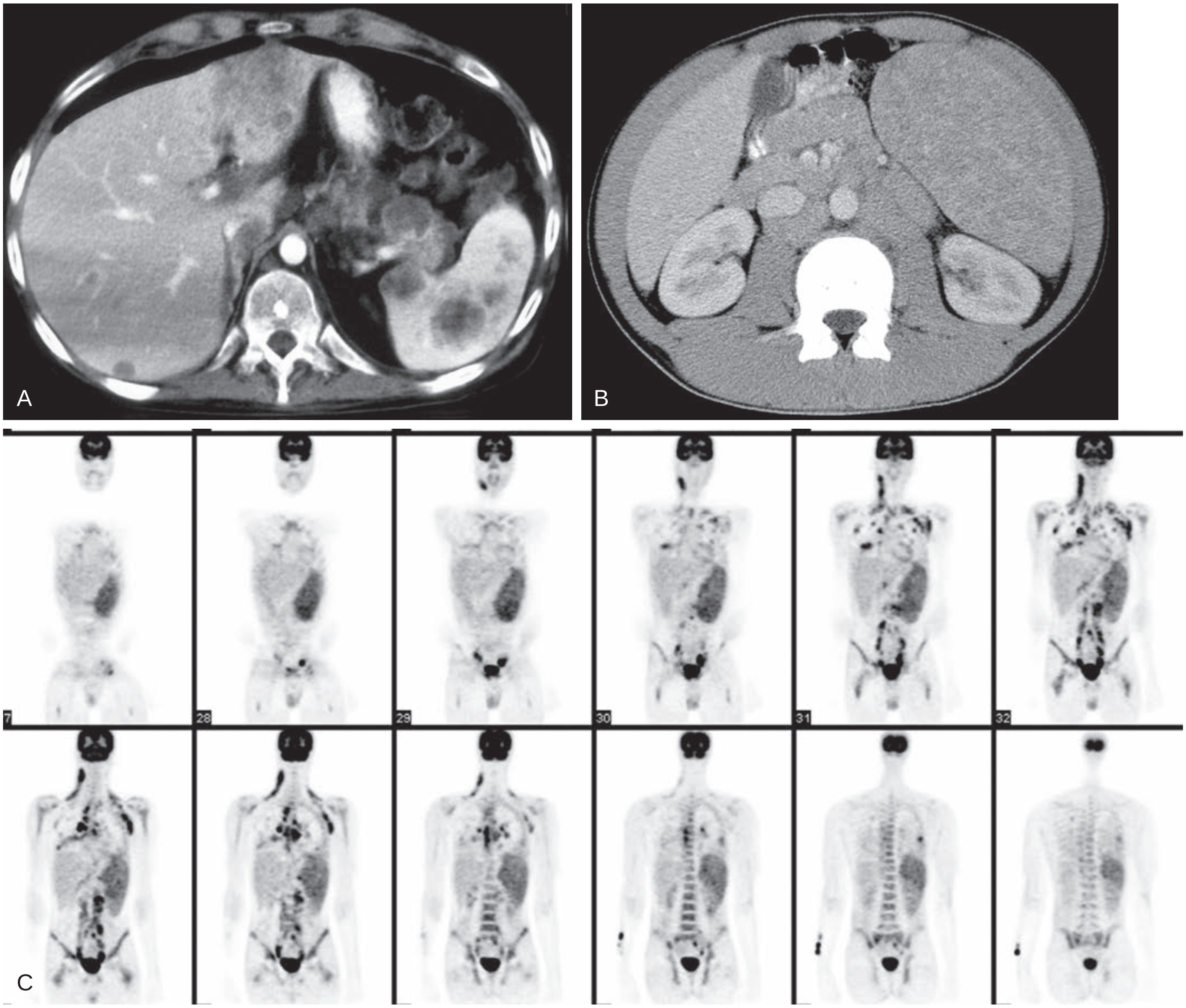

**Figure 94.20. Hodgkin lymphoma.** (A) Axial contrast-enhanced CT image in a 19-year-old with multiple episodes of relapsing disease and new left upper quadrant pain reveals multiple large, round, hypodense, nonenhancing masses in the spleen. Note additional foci of disease in the liver. (B) Axial contrast-enhanced CT image in a 14-year-old boy shows splenomegaly with numerous low-attenuation lesions throughout the spleen. (C) Coronal $^{18}$F FDG-PET images in a 15-year old reveal marked enlargement of the spleen with moderate-to-markedly increased FDG uptake. Note also nodal disease in the neck, supraclavicular regions, mediastinum, lungs, porta hepatis, retroperitoneum, iliac and inguinal regions, as well as the bone marrow.

involvement, because the spleen can be normal in size with tumor infiltration, and it may be enlarged without neoplastic involvement.

***Imaging.*** Non-Hodgkin lymphoma often may appear as splenic enlargement but may also have focal lesions large enough to be seen on US as ill-defined hypoechoic areas, especially in patients with high-grade malignancy. On CT, the low-attenuation lesions may not show appreciable enhancement compared with adjacent parenchyma after intravenous contrast administration. Lymphoma nodules can be challenging to differentiate from sarcoidosis or fungal abscesses, but the presence of splenic hilar lymphadenopathy is suggestive of lymphoma.[115] Hodgkin disease can also cause diffuse splenic infiltration that may or may not be detectable as focal splenic masses on CT (Fig. 94.20). If splenic involvement is the only subdiaphragmatic site, its detection is important for purposes of staging and prognosis. However, false-negative US, CT, and MRI examinations are common because these modalities depend on morphologic changes of enlargement or discrete nodules to diagnose lymphomatous involvement. Unfortunately, the imaging tissue characteristics of Hodgkin disease lesions are similar to those of normal spleen when the organ is diffusely infiltrated with disease that is only microscopically detectable.[112]

Metabolic imaging with 18F fluorodeoxyglucose (FDG) positron emission tomography (PET) is superior to US, CT, and MRI in identifying splenic involvement with lymphoma. F18-FDG PET/CT detects lymphomatous involvement of the spleen by identifying elevated glucose metabolism in tumor cells, regardless of whether there are gross morphologic changes. A meta-analysis reported sensitivity and specificity of F18-FDG

PET for the initial staging and restaging of non-Hodgkin lymphoma and Hodgkin disease as 90.3% and 91.1%, respectively.[116] In a small series, FDG PET correctly identified all patients with and without splenic disease with an accuracy of 100%; the accuracy of CT alone was only 57%.[117] In another study, F18-FDG PET/CT showed a comparable sensitivity of 96.2%, a specificity of 91.7%, and accuracy of 94% in the staging of primary splenic lymphoma.[118] F18-FDG PET/CT is superior to separate CT and F18-FDG PET in the staging and restaging of lymphoma and is the study of choice for staging and follow-up of Hodgkin disease and aggressive Non-Hodgkin lymphoma.[119,120] Treated splenic lymphomatous lesions may appear as necrotic and can eventually become calcific.[121]

***Treatment.*** Treatment options include chemotherapy, radiotherapy, radioimmunotherapy, and splenectomy.

## Littoral Cell Angioma

***Overview.*** Littoral cell angioma is an uncommon tumor that can occur at any age and may have some malignant potential with transformation to angiosarcoma.[122]

***Etiology.*** The lesion originates from the littoral cells of the red pulp with a network of connecting vascular channels.

***Clinical Presentation.*** Patients may be asymptomatic or present with splenomegaly, thrombocytopenia, and anemia. This entity presents as multiple lesions within an enlarged, heterogeneous spleen. The diagnosis should be considered in cases of multiple splenic lesions and hypersplenism. Associations with malignancies including colorectal carcinoma, hepatocellular carcinoma, lymphoma, and pancreatic adenocarcinoma have been reported.[123] It has been postulated that systemic immunosuppression related to the malignant state may be a factor in the development of littoral cell angioma.[124]

***Imaging.*** These lesions are heterogeneously hypoechoic on US and are initially of low attenuation on CT but typically become progressively isodense on delayed images after contrast enhancement[2,125] due to their histologic structure of multiple vascular channels.[126] On MRI, the lesions are well circumscribed and are predominantly T1 hypointense. On T2-weighted images, they may appear hyperintense or they may remain hypointense against the normal bright spleen parenchyma, presumably due to hemosiderin within the lesions.[2] The lesions show progressive contrast enhancement following gadolinium administration.

***Treatment.*** Treatment includes supportive therapy for the coagulopathy and endovascular embolization of the spleen to increase platelet count; when these fail, splenectomy may be indicated.[125]

## Hemangiopericytoma

***Overview.*** Hemangiopericytoma is a rare vascular tumor that most commonly occurs in the soft tissues of the extremities. It rarely originates as a primary tumor in the spleen.

***Etiology.*** Previously thought to originate from capillary pericytes, this tumor is now believed to represent a sarcoma of fibroblastic origin.[112] The tumor has variable biologic behavior and high potential for malignancy.[2,112]

***Clinical Presentation.*** When it occurs in the spleen, patients may be asymptomatic or they may present with splenomegaly, abdominal discomfort or left upper quadrant abdominal pain, hemorrhage, or infection.[112,127]

***Imaging.*** In the spleen, hemangiopericytomas may appear as a single large mass with smaller lesions within the parenchyma. Multiple hypoechoic lesions may be seen on ultrasound. Central Doppler flow has also been described.[128] Calcifications may be seen in the lesions on CT, as well as contrast enhancement of the solid portions and septations. The lesions demonstrate hypointensity on T1-weighted MR sequences and hyperintensity on T2-weighted sequences.

***Treatment.*** The treatment for splenic hemangiopericytoma is wide surgical excision[129] or splenectomy.[127] Careful long-term follow-up is required due to its aggressive behavior and a recurrence rate of 50%.[2]

## Angiosarcoma

***Overview.*** Angiosarcoma is a rare, highly malignant neoplasm that can occur at any age and is less common in children than in adults. It has no gender predilection, and it is considered the most common nonhematolymphoid malignant tumor of the spleen.[2,112]

***Etiology.*** Although the etiology of this lesion is unknown, it originates from endothelial cells in the splenic sinuses.[112] In older patients, angiosarcomas of the spleen are associated with previous chemotherapy for lymphoma and radiation therapy for breast cancer.[2]

***Clinical Presentation.*** The presentation may include left upper quadrant pain, fever, fatigue, weight loss, anemia, and thrombocytopenia. Splenomegaly is common[130] and can lead to splenic rupture at presentation in up to 30% of patients. Prognosis is poor, and metastases are common, typically to liver, lungs, and bone.[112,121]

***Imaging.*** US most commonly reveals a complex, heterogeneous mass, with hypoechoic cystic areas, likely reflecting foci of hemorrhage and necrosis. Solid hyperechoic regions display increased flow on color Doppler imaging. On CT, the lesions are ill-defined, with lower attenuation than the surrounding spleen, and demonstrate heterogeneous contrast enhancement and areas of necrosis.[2] MRI also reflects the heterogeneity of the mass with mixed signal on T1-weighted and T2-weighted images, and heterogeneous enhancement in the solid parts of the tumor. Intra- or perisplenic hemorrhage or hemoperitoneum can be seen on CT or MRI.[131]

***Treatment.*** If suspected, special care should be taken when performing a biopsy due to the high risk of hemorrhage.[121] Splenectomy is typically performed, followed by chemotherapy, but prognosis remains very poor.[112]

## Histiocytic Sarcoma

Histiocytic sarcoma is a rare hematopoietic neoplasm with malignant proliferation of cells presenting morphologic and immunophenotypic characteristics of mature tissue histiocytes.[132] It often localizes to the skin, lymph nodes, intestinal tract, or soft tissues, and primary splenic involvement is exceedingly rare. The patients present with general symptoms including fever, wasting, lymphadenopathy, hepatosplenomegaly, and progressive pancytopenia.[132] Imaging findings are variable and include splenomegaly, multiple, partially confluent, hypoattenuating masses (e-Fig. 94.21A) and possible hepatic infiltration. Splenectomy or splenic biopsy is useful for definitive diagnosis.[133] Splenic histiocytic sarcoma has a poor prognosis due to aggressive behavior with liver or bone marrow infiltration (e-Fig. 94.21B and C) and a poor response to therapy, though a splenectomy might induce temporary remission.[133]

## Splenic Metastases

Splenic metastases are uncommon and are thought to be due to lack of secondary afferent lymphatics.[134] Metastases from pediatric solid primary tumors are less common than with adult tumors. In general, tumors that most commonly metastasize to the spleen include melanoma and tumors of the lung, breast, and testicular germ cell tumors, particularly choriocarcinoma. Metastases may be single or multiple and frequently do not cause splenomegaly. Splenic metastases portend a poor prognosis.

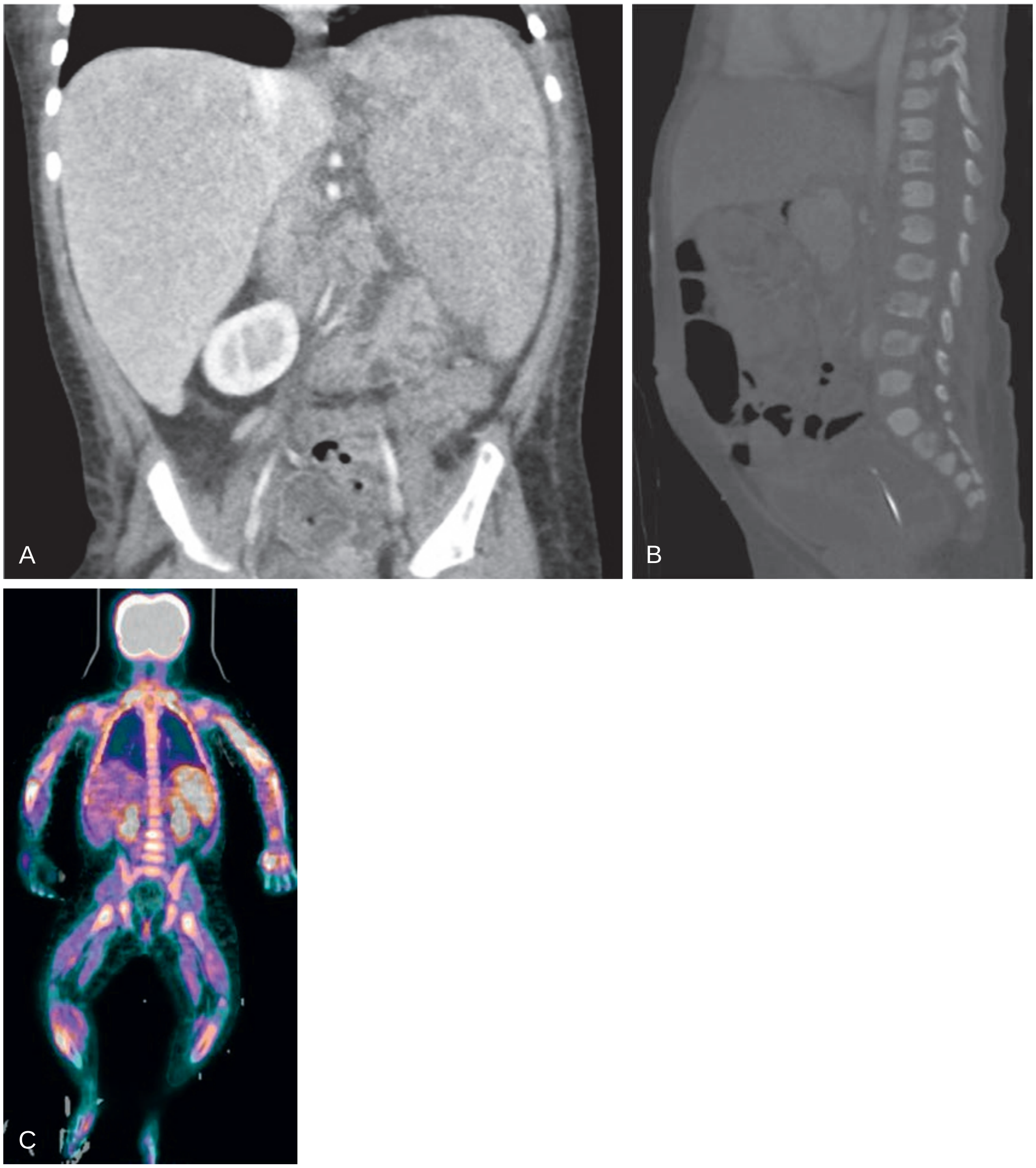

**e-Figure 94.21. Histiocytic sarcoma.** (A) Coronal reformatted contrast-enhanced CT image in an 8-month-old girl shows a markedly enlarged spleen with patchy areas of heterogeneity. (B) Sagittal reformatted image in bone window shows multilevel lytic lesions of the spine. (C) F18-FDG PET/CT whole body image demonstrates hypermetabolic uptake in the spleen and multiple bones.

## KEY POINTS

- Sonography is the primary imaging modality for evaluating splenic size, shape, location, and multiplicity.
- Radionuclide imaging with $^{99m}$Tc sulfur colloid helps in the assessment of ectopic splenic tissue, such as splenosis or splenogonadal fusion.
- In heterotaxy syndromes, splenic tissue, if present, will be located along the greater curvature of the stomach.
- Transient heterogeneous splenic enhancement patterns are commonly encountered during rapid bolus techniques on contrast-enhanced CT.
- Splenomegaly is usually a manifestation of an underlying systemic condition.
- Hypersplenism is a syndrome of sequestration of blood elements within an enlarged spleen.
- Hamartoma and hemangioma are the most common primary tumors of the spleen.
- Lymphoma is the most common malignancy of the spleen.

## SUGGESTED READINGS

Abbott RM, Levy AD, Aguilera NS, et al. From the archives of the AFIP: primary vascular neoplasms of the spleen: radiologic-pathologic correlation. *Radiographics*. 2004;24:1137.

Applegate KE, Goske MJ, Pierce G, et al. Situs revisited: imaging of the heterotaxy syndrome. *Radiographics*. 1999;19:837.

Elsayes KM, Vamsidhar RN, Mukundan G, et al. MR imaging of the spleen: spectrum of abnormalities. *Radiographics*. 2005;25:967–982.

Hilmes MA, Strouse PJ. The pediatric spleen. *Semin Ultrasound CT MR*. 2007;28:3–11.

Morgenstern L. Nonparasitic splenic cysts: pathogenesis, classification, and treatment. *J Am Coll Surg*. 2002;194:306–314.

Paterson A, Frush DP, Donnelly LF, et al. A pattern-oriented approach to splenic imaging in infants and children. *Radiographics*. 1999;19:1465.

Shabtaie SS, Hogan AR, Slidell MB. Splenic cysts. *Pediatr Ann*. 2016;45:e251–e256.

Vancauwenberghe T, Snoeckx A, Vanbeckevoort D, et al. Imaging of the spleen: what the clinician needs to know. *Singapore Med J*. 2015;56:133–144.

## REFERENCES

Full references for this chapter can be found on www.expertconsult.com.

## REFERENCES

1. Chadburn A. The spleen: anatomy and anatomical function. *Semin Hematol*. 2000;37(1 suppl 1):13–21.
2. Abbott RM, et al. From the archives of the AFIP: primary vascular neoplasms of the spleen: radiologic-pathologic correlation. *Radiographics*. 2004;24(4):1137–1163.
3. Karlo CA, et al. Computed tomography of the spleen: how to interpret the hypodense lesion. *Insights Imaging*. 2013;4(1):65–76.
4. Donnelly LF, et al. Heterogeneous splenic enhancement patterns on spiral CT images in children: minimizing misinterpretation. *Radiology*. 1999;210(2):493–497.
5. Hilmes MA, Strouse PJ. The pediatric spleen. *Semin Ultrasound CT MR*. 2007;28(1):3–11.
6. Vancauwenberghe T, et al. Imaging of the spleen: what the clinician needs to know. *Singapore Med J*. 2015;56(3):133–144.
7. Hernanz-Schulman M, et al. Current evaluation of the patient with abnormal visceroatrial situs. *AJR Am J Roentgenol*. 1990;154(4):797–802.
8. Kumar V, et al. *Robbins and Cotran Pathologic Basis of Disease*. 8th ed. Philadelphia: Saunders; 2010.
9. Hagan I, Hopkins R, Lyburn I. Superior demonstration of splenosis by heat-denatured Tc-99m red blood cell scintigraphy compared with Tc-99m sulfur colloid scintigraphy. *Clin Nucl Med*. 2006;31(8):463–466.
10. Lien CH, et al. Acute torsion of wandering spleen: report of one case. *Pediatr Neonatol*. 2009;50(4):177–180.
11. Liu HT, Lau KK. Wandering spleen: an unusual association with gastric volvulus. *AJR Am J Roentgenol*. 2007;188(4):W328–W330.
12. Lombardi R, et al. Wandering spleen in children: a report of 3 cases and a brief literature review underlining the importance of diagnostic imaging. *Pediatr Radiol*. 2014;44(3):279–288.
13. Taori K, et al. Pseudocyst formation: a rare complication of wandering spleen. *Br J Radiol*. 2005;78(935):1050–1052.
14. Ben Ely A, et al. The wandering spleen: CT findings and possible pitfalls in diagnosis. *Clin Radiol*. 2006;61(11):954–958.
15. Yilmaz O, et al. Torsion of wandering spleen as a rare reason for acute abdomen: a presentation of two cases. *Ulus Cerrahi Derg*. 2013;29(4):200–202.
16. Fiquet-Francois C, et al. Wandering spleen in children: multicenter retrospective study. *J Pediatr Surg*. 2010;45(7):1519–1524.
17. Karaman MI, Gonzales ET Jr. Splenogonadal fusion: report of 2 cases and review of the literature. *J Urol*. 1996;155(1):309–311.
18. Kocher NJ, et al. Splenogonadal fusion: a rare etiology of solid testicular mass. *Urology*. 2014;83(1):e1–e2.
19. Hasegawa Y, Kanemitsu I, Ueoka K. Transverse testicular ectopia with splenogonadal fusion: a case report. *Int J Urol*. 2011;18(6):466–468.
20. Uglialoro AD, et al. Splenogonadal fusion presenting as an asymptomatic testicular mass. *Urology*. 2016;97:1–4.
21. Ferron SA, Arce JD. Discontinuous splenogonadal fusion: new sonographic findings. *Pediatr Radiol*. 2013;43(12):1652–1655.
22. Varma DR, et al. Sonographic and CT features of splenogonadal fusion. *Pediatr Radiol*. 2007;37(9):916–919.
23. Khairat AB, Ismail AM. Splenogonadal fusion: case presentation and literature review. *J Pediatr Surg*. 2005;40(8):1357–1360.
24. Al Ahmad A, Jourabian M, Pipelzadeh M. Splenorenal fusion in a 26-month-old girl. *Pediatr Radiol*. 2009;39(7):735–738.
25. Rosenthal JT, et al. Right splenorenal fusion with associated hypersplenism. *J Urol*. 1981;126(6):812–814.
26. Cowan JR, et al. Copy number variation as a genetic basis for heterotaxy and heterotaxy-spectrum congenital heart defects. *Philos Trans R Soc Lond B Biol Sci*. 2016;371(1710).
27. Applegate KE, et al. Situs revisited: imaging of the heterotaxy syndrome. *Radiographics*. 1999;19(4):837–852, discussion 853-854.
28. Levin M, Klar AJ, Ramsdell AF. Introduction to provocative questions in left-right asymmetry. *Philos Trans R Soc Lond B Biol Sci*. 2016;371(1710).
29. Raya A, Izpisua Belmonte JC. Left-right asymmetry in the vertebrate embryo: from early information to higher-level integration. *Nat Rev Genet*. 2006;7(4):283–293.
30. Norris DP, Grimes DT. Developmental biology. Cilia discern left from right. *Science*. 2012;338(6104):206–207.
31. Blum M, et al. Symmetry breakage in the vertebrate embryo: when does it happen and how does it work? *Dev Biol*. 2014;393(1):109–123.
32. Grimes DT, et al. Genetic analysis reveals a hierarchy of interactions between polycystin-encoding genes and genes controlling cilia function during left-right determination. *PLoS Genet*. 2016;12(6):e1006070.
33. Norris DP, Jackson PK. Cell biology: calcium contradictions in cilia. *Nature*. 2016;531(7596):582–583.
34. Schutze GE, et al. Invasive pneumococcal infections in children with asplenia. *Pediatr Infect Dis J*. 2002;21(4):278–282.
35. Freedom RM, et al. Hearts with isomerism of the right atrial appendages—one of the worst forms of disease in 2005. *Cardiol Young*. 2005;15(6):554–567.
36. Lim JS, et al. Clinical features, management, and outcome of children with fetal and postnatal diagnoses of isomerism syndromes. *Circulation*. 2005;112(16):2454–2461.
37. Gilljam T, et al. Outcomes of left atrial isomerism over a 28-year period at a single institution. *J Am Coll Cardiol*. 2000;36(3):908–916.
38. Freedom RM, Fellows KE Jr. Radiographic visceral patterns in the asplenia syndrome. *Radiology*. 1973;107(2):387–391.
39. Paterson A, et al. A pattern-oriented approach to splenic imaging in infants and children. *Radiographics*. 1999;19(6):1465–1485.
40. Abramson SJ, et al. Biliary atresia and noncardiac polysplenic syndrome: US and surgical considerations. *Radiology*. 1987;163(2):377–379.
41. Davenport M, et al. The biliary atresia splenic malformation syndrome: a 28-year single-center retrospective study. *J Pediatr*. 2006;149(3):393–400.
42. Varela-Fascinetto G, et al. Biliary atresia-polysplenia syndrome: surgical and clinical relevance in liver transplantation. *Ann Surg*. 1998;227(4):583–589.
43. Rose V, Izukawa T, Moes CA. Syndromes of asplenia and polysplenia. A review of cardiac and non-cardiac malformations in 60 cases with special reference to diagnosis and prognosis. *Br Heart J*. 1975;37(8):840–852.
44. Strouse PJ, et al. Horseshoe adrenal gland in association with asplenia: presentation of six new cases and review of the literature. *Pediatr Radiol*. 2002;32(11):778–782.
45. Abbas PI, Dickerson HA, Wesson DE. Evaluating a management strategy for malrotation in heterotaxy patients. *J Pediatr Surg*. 2016;51(5):859–862.
46. Cullis PS, Siminas S, Losty PD. Is screening of intestinal foregut anatomy in heterotaxy patients really necessary?: a systematic review in search of the evidence. *Ann Surg*. 2016;264(6):1156–1161.
47. Salavitabar A, et al. Heterotaxy syndrome and intestinal rotational anomalies: impact of the Ladd procedure. *J Pediatr Surg*. 2015;50(10):1695–1700.
48. Sen S, et al. Heterotaxy syndrome infants are at risk for early shunt failure after Ladd procedure. *Ann Thorac Surg*. 2015;99(3):918–925.
49. Elder CT, et al. The role of screening and prophylactic surgery for malrotation in heterotaxy patients. *J Pediatr Surg*. 2014;49(12):1746–1748.
50. Klippenstein DL, et al. Splenic enlargement in neonates during ECMO. *Radiology*. 1994;190(2):411–412.
51. Rezende PV, et al. Acute splenic sequestration in a cohort of children with sickle cell anemia. *J Pediatr (Rio J)*. 2009;85(2):163–169.
52. Rosenberg HK, et al. Normal splenic size in infants and children: sonographic measurements. *AJR Am J Roentgenol*. 1991;157(1):119–121.
53. Dhingra B, et al. Normal values of liver and spleen size by ultrasonography in Indian children. *Indian Pediatr*. 2010;47(6):487–492.
54. Megremis SD, Vlachonikolis IG, Tsilimigaki AM. Spleen length in childhood with US: normal values based on age, sex, and somatometric parameters. *Radiology*. 2004;231(1):129–134.
55. Konus OL, et al. Normal liver, spleen, and kidney dimensions in neonates, infants, and children: evaluation with sonography. *AJR Am J Roentgenol*. 1998;171(6):1693–1698.
56. Loftus WK, Metreweli C. Ultrasound assessment of mild splenomegaly: spleen/kidney ratio. *Pediatr Radiol*. 1998;28(2):98–100.
57. Safak AA, Simsek E, Bahcebasi T. Sonographic assessment of the normal limits and percentile curves of liver, spleen, and kidney dimensions in healthy school-aged children. *J Ultrasound Med*. 2005;24(10):1359–1364.
58. Soyupak SK, et al. Sonographic measurements of the liver, spleen and kidney dimensions in the healthy term and preterm newborns. *Eur J Radiol*. 2002;43(1):73–78.
59. Schlesinger AE, Edgar KA, Boxer LA. Volume of the spleen in children as measured on CT scans: normal standards as a function of body weight. *AJR Am J Roentgenol*. 1993;160(5):1107–1109.
60. Watanabe Y, et al. Standard splenic volume in children and young adults measured from CT images. *Surg Today*. 1997;27(8):726–728.
61. Green BA, et al. Imaging findings in pediatric type 1 Gaucher disease: what the clinician needs to know. *J Pediatr Hematol Oncol*. 2011;33(4):301–305.

62. Simpson WL, Hermann G, Balwani M. Imaging of Gaucher disease. *World J Radiol*. 2014;6(9):657–668.
63. Hill SC, et al. Gaucher disease: abdominal MR imaging findings in 46 patients. *Radiology*. 1992;184(2):561–566.
64. Elsayes KM, et al. MR imaging of the spleen: spectrum of abnormalities. *Radiographics*. 2005;25(4):967–982.
65. Lonergan GJ, Cline DB, Abbondanzo SL. Sickle cell anemia. *Radiographics*. 2001;21(4):971–994.
66. Unal E, et al. Imaging findings of splenic emergencies: a pictorial review. *Insights Imaging*. 2016;7(2):215–222.
67. Brousse V, Buffet P, Rees D. The spleen and sickle cell disease: the sick(led) spleen. *Br J Haematol*. 2014;166(2):165–176.
68. Campbell PJ, et al. Splenic regrowth in sickle cell anaemia following hypertransfusion. *Br J Haematol*. 1997;96(1):77–79.
69. Barrios NJ, et al. Reversible splenic hypofunction in hypertransfused children with homozygous sickle cell disease. *J Natl Med Assoc*. 1993;85(9):677–680.
70. Buchanan GR, et al. Splenic phagocytic function in children with sickle cell anemia receiving long-term hypertransfusion therapy. *J Pediatr*. 1989;115(4):568–572.
71. Nickel RS, et al. Improved splenic function after hematopoietic stem cell transplant for sickle cell disease. *Pediatr Blood Cancer*. 2016;63(5):908–913.
72. Robertson F, Leander P, Ekberg O. Radiology of the spleen. *Eur Radiol*. 2001;11(1):80–95.
73. Piccin A, et al. Composition and significance of splenic Gamna-Gandy bodies in sickle cell anemia. *Hum Pathol*. 2012;43(7):1028–1036.
74. Zhang J, et al. Gamna-Gandy bodies of the spleen detected with susceptibility weighted imaging: maybe a new potential non-invasive marker of esophageal varices. *PLoS ONE*. 2013;8(1):e55626.
75. Dobritz M, et al. Gamna-Gandy bodies of the spleen detected with MR imaging: a case report. *Magn Reson Imaging*. 2001;19(9):1249–1251.
76. Rattan KN, et al. Splenic abscess in children: a report of three patients. *Afr J Paediatr Surg*. 2009;6(2):106–109.
77. Rasheed K, Zargar SA, Telwani AA. Hydatid cyst of spleen: a diagnostic challenge. *N Am J Med Sci*. 2013;5(1):10–20.
78. Pedrosa I, et al. Hydatid disease: radiologic and pathologic features and complications. *Radiographics*. 2000;20(3):795–817.
79. Cornely OA, Bangard C, Jaspers NI. Hepatosplenic Candidiasis. *Clin Liver Dis (Hoboken)*. 2015;6(2):47–50.
80. Yen TY, et al. Clinical characteristics of hepatosplenic fungal infection in pediatric patients. *J Microbiol Immunol Infect*. 2011;44(4):296–302.
81. Luna A, et al. MRI of focal splenic lesions without and with dynamic gadolinium enhancement. *AJR Am J Roentgenol*. 2006;186(6):1533–1547.
82. Weinspach S, et al. Cat scratch disease–heterogeneous in clinical presentation: five unusual cases of an infection caused by Bartonella henselae. *Klin Padiatr*. 2010;222(2):73–78.
83. Kalinova K, Stefanova P, Bosheva M. Surgery in children with hydatid disease of the spleen. *J Pediatr Surg*. 2006;41(7):1264–1266.
84. Hodge MG, et al. Splenic cysts in the pediatric population: a report of 21 cases with review of the literature. *Fetal Pediatr Pathol*. 2012;31(2):54–62.
85. Durgun V, et al. Primary splenic hydatidosis. *Dig Surg*. 2003;20(1):38–41.
86. Fowler RH. Nonparasitic benign cystic tumors of the spleen. *Int Abstr Surg*. 1953;96(3):209–227.
87. Martin JW. Congenital splenic cysts. *Am J Surg*. 1958;96(2):302–308.
88. Morgenstern L. Nonparasitic splenic cysts: pathogenesis, classification, and treatment. *J Am Coll Surg*. 2002;194(3):306–314.
89. Sinha CK, Agrawal M. Nonparasitic splenic cysts in children: current status. *Surgeon*. 2011;9(1):49–53.
90. Shabtaie SA, Hogan AR, Slidell MB. Splenic cysts. *Pediatr Ann*. 2016;45(7):e251–e256.
91. Kubo M, et al. Familial epidermoid cysts of the spleen: report of two cases. *Surg Today*. 2006;36(9):853–856.
92. Czauderna P, et al. Nonparasitic splenic cysts in children: a multicentric study. *Eur J Pediatr Surg*. 2006;16(6):415–419.
93. Ingle SB, Hinge Ingle CR, Patrike S. Epithelial cysts of the spleen: a minireview. *World J Gastroenterol*. 2014;20(38):13899–13903.
94. Kenney CD, et al. Management of non-parasitic splenic cysts: does size really matter? *J Gastrointest Surg*. 2014;18(9):1658–1663.
95. Kimber C, et al. Hemisplenectomy for giant splenic cysts in children. *Pediatr Surg Int*. 1998;14(1–2):116–118.
96. Ramani M, et al. Splenic hemangiomas and hamartomas: MR imaging characteristics of 28 lesions. *Radiology*. 1997;202(1):166–172.
97. Wijaya J, Kapoor R, Roach P. Tc-99m-labeled RBC scintigraphy and splenic hemangioma. *Clin Nucl Med*. 2001;26(12):1022–1023.
98. Abramowsky C, et al. "Hamartoma" of the spleen (splenoma) in children. *Pediatr Dev Pathol*. 2004;7(3):231–236.
99. Okada J, et al. Increased activity on radiocolloid scintigraphy in splenic hamartoma. *Clin Nucl Med*. 1990;15(2):112–115.
100. Brinkley AA, Lee JK. Cystic hamartoma of the spleen: CT and sonographic findings. *J Clin Ultrasound*. 1981;9(3):136–138.
101. Wang JH, et al. Multi-modality imaging findings of splenic hamartoma: a report of nine cases and review of the literature. *Abdom Imaging*. 2013;38(1):154–162.
102. Yamaguchi K, Maeda S, Kitamura K. Splenic hamartoma: report of a case and review of the literature. *Jpn J Surg*. 1989;19(3):381–386.
103. Yu RS, Zhang SZ, Hua JM. Imaging findings of splenic hamartoma. *World J Gastroenterol*. 2004;10(17):2613–2615.
104. Ioannidis I, Kahn AG. Splenic lymphangioma. *Arch Pathol Lab Med*. 2015;139(2):278–282.
105. Tsokos M, Erbersdobler A. Pathology of peliosis. *Forensic Sci Int*. 2005;149(1):25–33.
106. Kohr RM, Haendiges M, Taube RR. Peliosis of the spleen: a rare cause of spontaneous splenic rupture with surgical implications. *Am Surg*. 1993;59(3):197–199.
107. Lashbrook DJ, et al. Splenic peliosis with spontaneous splenic rupture: report of two cases. *BMC Surg*. 2006;6:9.
108. Shimono T, et al. Peliosis of the spleen: splenic rupture with intraperitoneal hemorrhage. *Abdom Imaging*. 1998;23(2):201–202.
109. Stojanovic V, et al. Splenic peliosis in the course of IgA nephropathy. *Pediatr Nephrol*. 2007;22(12):2137–2140.
110. Iannaccone R, et al. Peliosis hepatis: spectrum of imaging findings. *AJR Am J Roentgenol*. 2006;187(1):W43–W52.
111. Nath UK, et al. Acute abdomen due to splenic infarction as the initial presentation of pediatric acute lymphoblastic leukemia. *Int J Hematol*. 2013;97(3):433–434.
112. Ricci ZJ, et al. Improving diagnosis of atraumatic splenic lesions, Part III: malignant lesions. *Clin Imaging*. 2016;40(5):846–855.
113. Ahmed S, Horton KM, Fishman EK. Splenic incidentalomas. *Radiol Clin North Am*. 2011;49(2):323–347.
114. Paes FM, et al. FDG PET/CT of extranodal involvement in non-Hodgkin lymphoma and Hodgkin disease. *Radiographics*. 2010;30(1):269–291.
115. Leite NP, et al. Cross-sectional imaging of extranodal involvement in abdominopelvic lymphoproliferative malignancies. *Radiographics*. 2007;27(6):1613–1634.
116. Isasi CR, Lu P, Blaufox MD. A metaanalysis of 18F-2-deoxy-2-fluoro-D-glucose positron emission tomography in the staging and restaging of patients with lymphoma. *Cancer*. 2005;104(5):1066–1074.
117. Rini JN, et al. 18F-FDG PET versus CT for evaluating the spleen during initial staging of lymphoma. *J Nucl Med*. 2003;44(7):1072–1074.
118. Karunanithi S, et al. Use of 18F-FDG PET/CT imaging for evaluation of patients with primary splenic lymphoma. *Clin Nucl Med*. 2014;39(9):772–776.
119. Schaefer NG, et al. Non-Hodgkin lymphoma and Hodgkin disease: coregistered FDG PET and CT at staging and restaging–do we need contrast-enhanced CT? *Radiology*. 2004;232(3):823–829.
120. Saboo SS, et al. Spleen in haematological malignancies: spectrum of imaging findings. *Br J Radiol*. 2012;85(1009):81–92.
121. Kaza RK, et al. Primary and secondary neoplasms of the spleen. *Cancer Imaging*. 2010;10:173–182.
122. Ricci ZJ, et al. Improving diagnosis of atraumatic splenic lesions, part II: benign neoplasms/nonneoplastic mass-like lesions. *Clin Imaging*. 2016;40(4):691–704.
123. Bhavsar T, et al. Littoral cell angiomas of the spleen associated with solid pseudopapillary tumor of the pancreas. *World J Gastrointest Pathophysiol*. 2011;2(3):53–56.
124. Harmon RL, Cerruto CA, Scheckner A. Littoral cell angioma: a case report and review. *Curr Surg*. 2006;63(5):345–350.
125. Ertan G, et al. Pediatric littoral cell angioma of the spleen: multimodality imaging including diffusion-weighted imaging. *Pediatr Radiol*. 2009;39(10):1105–1109.
126. Levy AD, Abbott RM, Abbondanzo SL. Littoral cell angioma of the spleen: CT features with clinicopathologic comparison. *Radiology*. 2004;230(2):485–490.
127. Illuminati G, et al. Hemangiopericytoma of the spleen. *Int J Surg*. 2015;15:6–10.

128. Yang W, et al. Splenic hemangiopericytoma in a one-month-old infant. *J Pediatr Surg*. 2013;48(3):e21–e24.
129. Uygun I, et al. An infantile splenic hemangiopericytoma case treated with partial splenectomy. *Fetal Pediatr Pathol*. 2012;31(4): 248–253.
130. Hsu JT, et al. Primary angiosarcoma of the spleen. *J Surg Oncol*. 2005;92(4):312–316.
131. Thompson WM, et al. Angiosarcoma of the spleen: imaging characteristics in 12 patients. *Radiology*. 2005;235(1):106–115.
132. Yamada S, et al. Primary splenic histiocytic sarcoma complicated with prolonged idiopathic thrombocytopenia and secondary bone marrow involvement: a unique surgical case presenting with splenomegaly but non-nodular lesions. *Diagn Pathol*. 2012;7:143.
133. Kobayashi S, et al. Histiocytic sarcoma of the spleen: case report of asymptomatic onset of thrombocytopenia and complex imaging features. *Int J Hematol*. 2008;87(1):83–87.
134. Lam KY, Tang V. Metastatic tumors to the spleen: a 25-year clinicopathologic study. *Arch Pathol Lab Med*. 2000;124(4):526–530.

# 95

# The Pancreas

Anuradha S. Shenoy-Bhangle, Sudha A. Anupindi, and Michael S. Gee*

## EMBRYOLOGY, ANATOMY, AND PHYSIOLOGY

The pancreas (from the Greek words *pan*, meaning "all," and *kreas*, meaning "flesh") arises from two anlagen that develop from the endodermal lining of the duodenum. Before 28 days of gestation, the dorsal pancreatic bud develops as a diverticulum from the dorsal aspect of the duodenum caudal to the hepatic diverticulum. It grows upward and invaginates into the dorsal mesogastrium to form part of the head and the entire neck, body, and tail. The ventral pancreatic bud develops between 30 and 35 days of gestation as a diverticulum from the primitive bile duct that forms part of the head and uncinate process. The ventral pancreas rotates counterclockwise posterior to the duodenum at day 37 of gestation, and the two pancreatic buds fuse at about the sixth week of embryonic life. The ductal systems also fuse, and the duct from the dorsal bud becomes the accessory pancreatic duct (of Santorini) that drains into the minor duodenal papilla; the duct from the ventral bud enlarges to become the main pancreatic duct (of Wirsung) after fusion, with the distal two-thirds of the dorsal duct, which drains into the major duodenal papilla.

Developmental variants of the pancreatic ducts include: bifid pancreas, formed by the ducts of Wirsung and Santorini (60% of cases); a rudimentary duct of Santorini (30%); a dominant duct of Santorini (1%); and *ansa pancreatica*, in which the duct of Santorini curves as it courses to the duct of Wirsung. Ductal narrowing can be seen at the site of fusion of the dorsal and ventral ducts. The absence of proximal dilation allows differentiation of this normal variant from a true stricture. Duodenal obstruction, pancreatobiliary maljunction pancreatitis, and biliary cysts occur secondary to developmental variants. Pancreatobiliary maljunction is associated with congenital common bile duct webs.[1]

The pancreas grows substantially in the first year of life, and growth slows from years 1 through 18. The gland is relatively larger in children than in adults, and the overall ratio of gland size to patient body size decreases with age (Table 95.1). The pancreatic head is more prominent in children compared with the body and tail. The diameter of the pancreatic duct also varies with age (Table 95.2). Enlarged ducts (>1.5 mm at 1–6 years, >1.9 mm at 7–9 years, and >2.2 mm at 13–18 years) are associated with pancreatitis.[2]

The pancreas is a transversely oriented retroperitoneal organ that is divided into the head, neck, uncinate process, body, and tail (Fig. 95.1). The head is to the right of the midline, situated within the "C-loop" of the duodenum. At the junction of the inferior and left margins of the pancreatic head is an extension of the gland called the *uncinate process*. The anterior surface of the pancreatic head is in contact with the transverse colon, gastroduodenal artery, and loops of small intestine. The anterior surface of the uncinate process is in contact with the superior mesenteric artery and vein. The posterior surface of the head is adjacent to the inferior vena cava, common bile duct, renal veins, and the abdominal aorta.

The pancreatic body is in contact with the stomach anteriorly and superiorly. Its posterior portion abuts the abdominal aorta, splenic vein, left kidney, adrenal gland, and origin of the superior mesenteric artery. Loops of jejunum and ileum lie inferiorly. The tail may be more bulbous in children than the head or body and is narrower in adults. The pancreatic tail lies in the phrenicolienal ligament in contact with the gastric surface of the spleen and the splenic flexure of the colon.

The pancreas has both exocrine and endocrine functions. Exocrine function is directed toward digestion, with pancreatic enzymes secreted through the pancreatic duct into the small bowel to aid in breakdown of ingested fats (lipase), proteins (protease), and carbohydrates (amylase). The islets of Langerhans represent endocrine tissue that contains several types of hormone-producing cells (e.g., insulin, glucagon, somatostatin) that help regulate blood glucose levels and digestive function. The B cells produce insulin; A cells, glucagon; G cells, gastrin; D cells, somatostatin; and $D_1$ cells, vasoactive intestinal peptide (VIP) and secretin.

## IMAGING THE PANCREAS IN CHILDREN

The pancreas is not seen on plain radiographs, although calcifications in patients with chronic pancreatitis or cystic fibrosis (CF) may be identified (Fig. 95.2). In acute pancreatitis, dilated loops of bowel and fluid levels within the upper midabdomen indicate localized ileus. A pancreatic mass may be sufficiently large to lead to a paucity of bowel gas in the upper abdomen from displaced bowel loops.[3]

Ultrasonography (US) is the primary modality to evaluate the pediatric pancreas.[4] The pancreas is most easily seen if the stomach and duodenum are not distended with gas. Ingestion of water may improve pancreatic visualization by displacing air within the adjacent duodenum and stomach. The distal body and tail may also be imaged in the prone position using the left kidney or spleen as an acoustic window. Age-matched normal dimensions of the pancreas are given in Table 95.1.[4] Pancreatic size is best measured at its body, but individual variation is sufficient to warrant caution when determining pancreatic size. Enlargement of the pancreas should be mentioned when the anteroposterior dimension of the pancreatic body is greater than 1.5 cm.[5] The normal duct may be seen as a single- or double-track echogenic line anterior to the junction of the splenic and mesenteric veins (see Fig. 95.1). The pancreas has a spectrum of echogenicity relative to that of the liver, but in most children, the pancreas is hypoechoic or nearly isoechoic with the liver. In neonates, particularly premature infants, the pancreatic gland is more echogenic.[6]

Computed tomography (CT) of the pancreas is sparingly performed to avoid radiation. The pancreas is best visualized during bolus injection of intravenous (IV) contrast material during the mesenteric phase, which uniformly enhances the pancreatic parenchyma as well as the adjacent vasculature. The pancreas is hypodense compared with the liver, both on noncontrast and contrast-enhanced CT. The contour of the pancreas may be smooth or mildly lobulated due to the acinar lobar architecture. Contrast-enhanced CT is useful for evaluating pancreatic trauma, pancreatitis and its complications, and for further evaluation of abnormalities detected on US. Thin-collimation volumetric CT coupled with curved planar reformations produces quality imaging of pancreatic and peripancreatic tissues.[7]

Magnetic resonance imaging (MRI) of the pancreas[8,9] is increasingly used in children because it does not require ionizing radiation

---

*We acknowledge and thank Sue C. Kaste, Paritosh C Khanna, and Sumit Pruthi for contributions to the current chapter from prior editions.

## Abstract:

The pancreas is an important retroperitoneal organ with key exocrine and endocrine functions responsible for digestion and blood glucose regulation. The pediatric pancreas is subject to developmental variants; infections; inflammation and tumors. In our chapter, we explore the entire gamut of developmental and acquired conditions of the pancreas in the pediatric age group. We discuss congenital and hereditary pancreatic abnormalities; pancreatic tumors including solid-cystic papillary tumor; pancreatoblastoma; neuroendocrine tumors among others. We discuss the role of various imaging modalities with advantages and disadvantages in imaging pancreatic abnormalities in children with interesting illustrations demonstrating these abnormalities.

## Keywords:

congenital pancreatic abnormalities
pancreatoblastoma
hereditary pancreatitis
primary alveolar rhabdomyosarcoma of the pancreas
primary pancreatic neuroblastoma

**TABLE 95.1** Normal Sonographic and Computed Tomographic Dimensions of the Pancreas

| Age | Head | Body | Tail |
|---|---|---|---|
| **ULTRASOUND (MEAN ± SD, cm)** | | | |
| <1 month | 1.0 ± 0.4 | 0.6 ± 0.2 | 1.0 ± 0.4 |
| 1 month to 1 year | 1.5 ± 0.5 | 0.8 ± 0.3 | 1.2 ± 0.4 |
| 1-5 years | 1.7 ± 0.3 | 1.0 ± 0.2 | 1.8 ± 0.4 |
| 5-10 years | 1.6 ± 0.4 | 1.0 ± 0.3 | 1.8 ± 0.4 |
| 10-19 years | 2.0 ± 0.5 | 1.1 ± 0.3 | 2.0 ± 0.4 |
| **CT (MEAN ± SD, mm)** | | | |
| 20-30 years | 28.6 ± 3.8 | 19.1 ± 2.1 | 18.0 ± 1.6 |
| 21-40 years | 26.0 ± 3.4 | 18.2 ± 2.4 | 16.5 ± 1.8 |
| 41-50 years | 25.2 ± 3.6 | 17.8 ± 2.2 | 15.8 ± 1.7 |
| 51-60 years | 24.0 ± 3.6 | 16.0 ± 2.0 | 15.1 ± 1.9 |
| 61-70 years | 23.4 ± 3.5 | 15.8 ± 2.4 | 14.7 ± 1.8 |
| 71-80 years | 21.2 ± 4.3 | 14.4 ± 2.7 | 13.0 ± 2.1 |

*Modified from Heuck A, Maubach PA, Reiser M, et al. Age-related morphology of the normal pancreas on computed tomography.* Gastrointest Radiol. *1987;12:18–22; Siegel MJ, Martin KW, Worthington JL. Normal and abnormal pancreas in children: US studies.* Radiology. *1987;165:15–18.*

**TABLE 95.2** Normal Diameter of the Pancreatic Duct by Ultrasound and Computed Tomography

| Age (Years) | Diameter (Mean ± SD, mm [Range]) |
|---|---|
| **ULTRASOUND** | |
| 1-3 | 1.13 ± 0.15 (0.9-1.3) |
| 4-6 | 1.35 ± 0.15 (1.0-1.5) |
| 7-9 | 1.67 ± 0.17 (1.3-1.9) |
| 10-12 | 1.78 ± 0.17 (1.5-2.2) |
| 13-15 | 1.92 ± 0.18 (1.6-2.4) |
| 16-18 | 2.05 ± 0.15 (1.8-2.4) |
| **COMPUTED TOMOGRAPHY** | |
| 18-29 | 1.5 ± 0.5 |
| 30-39 | 1.6 ± 0.5 |
| 40-49 | 1.9 ± 0.3 |
| 50-59 | 2.0 ± 0.5 |
| 60-69 | 2.1 ± 0.4 |
| 70-81 | 2.0 ± 0.5 |

*Modified from Siegel MJ, Martin KW, Worthington JL. Normal and abnormal pancreas in children: US studies.* Radiology. *1987;165:15–18; Heuck A, Maubach PA, Reiser M, et al. Age-related morphology of the normal pancreas on computed tomography.* Gastrointest Radiol. *1987;12:18–22; Chao HC, Lin SJ, Kong MS, et al. Sonographic evaluation of the pancreatic duct in normal children and children with pancreatitis.* J Ultrasound Med. *2000;19:757–763; Glaser J, Hogemann B, Krummenerl T, et al. Sonographic imaging of the pancreatic duct. New diagnostic possibilities using secretin stimulation.* Dig Dis Sci. *1987;32:1075–1081.*

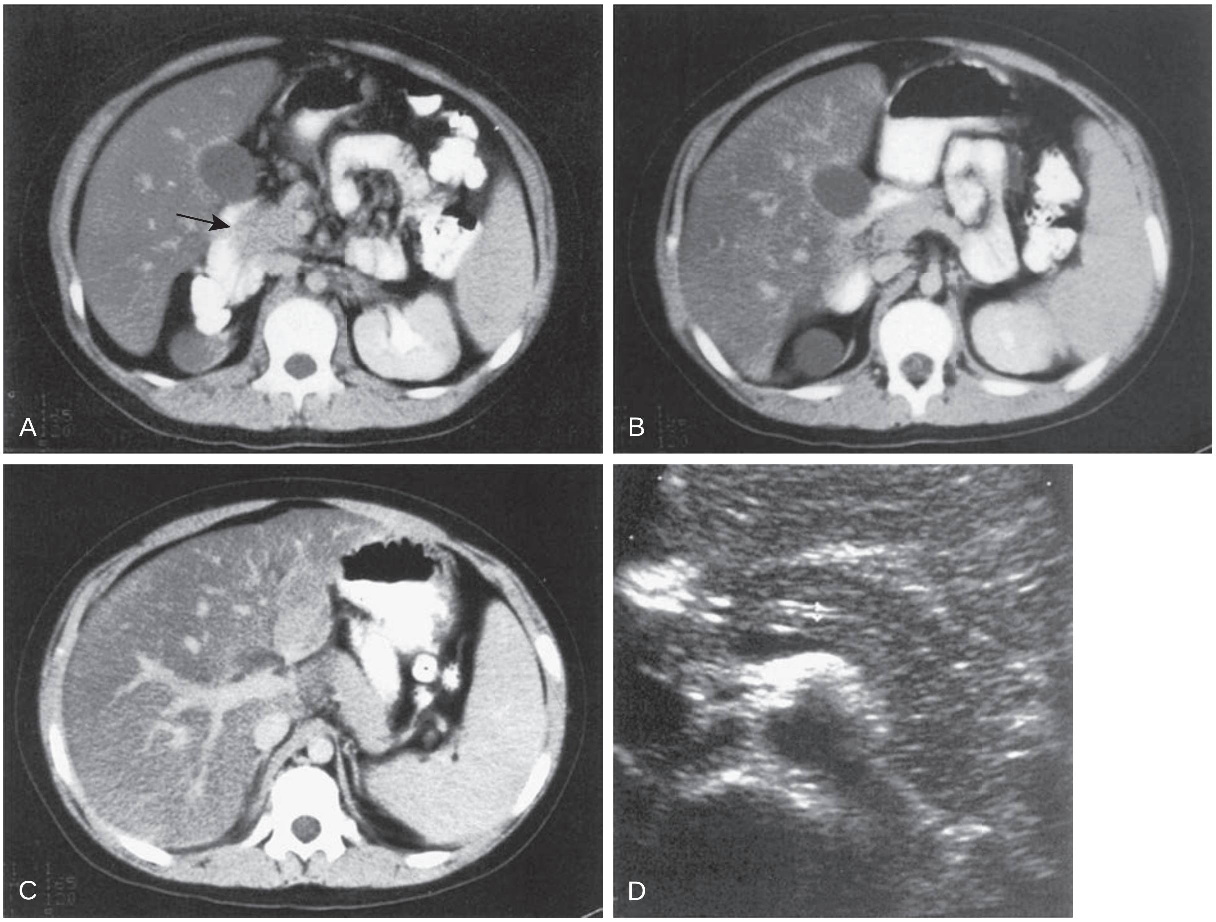

**Figure 95.1. Normal pancreas in an 11-year-old boy.** (A–C) Computed tomography (CT) sections of the pancreas. The head of the pancreas (*arrow* in A) is slightly bulbous and distinct from the contrast-filled duodenal sweep. The body of the pancreas (B) is narrower than the head or tail and is seen anterior to the aorta, from which the superior mesenteric artery arises. The tail of the pancreas (C) is thicker in children than in adults and extends to the spleen. (D) Transverse ultrasound shows the double track of a normal pancreatic duct.

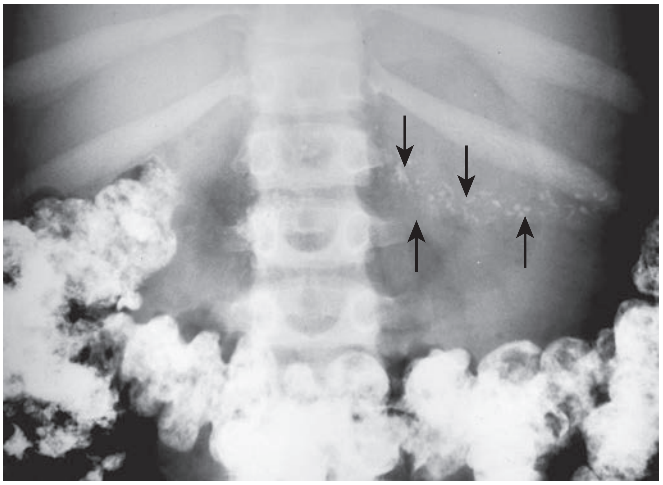

**Figure 95.2. Cystic fibrosis in a 9-year-old girl.** Multiple pancreatic calcifications *(arrows)* are seen on radiography.

and has high soft tissue contrast for characterizing the pancreatic parenchyma and ductal system.[8] Magnetic resonance (MR) images of the pancreas in children can be degraded by motion artifacts from respiration and patient movement, as well as susceptibility artifacts from air within bowel.[10] However, advances in rapid MR image acquisition, motion correction, and image reconstruction have greatly improved image quality in infants and young children.[11,12] On T1-weighted MRI, the pancreas demonstrates uniformly high signal intensity related to high protein content of the acinar cells.[13] The pancreas typically demonstrates similar signal intensity to the liver on T2-weighted images. Respiratory motion in older children is minimized by acquiring images during breath-holding, whereas in infants and young children, respiratory triggering or signal averaging techniques are typically required[11] (Fig. 95.3). T1-weighted imaging with fat suppression is very helpful for detection of focal pancreatic pathology, while T2-weighted imaging with fat suppression is helpful for detection of fluid collections and edema associated with pancreatitis or pancreatic masses.

Because of its noninvasive nature, magnetic resonance cholangiopancreatography (MRCP)[14] may be more useful than endoscopic

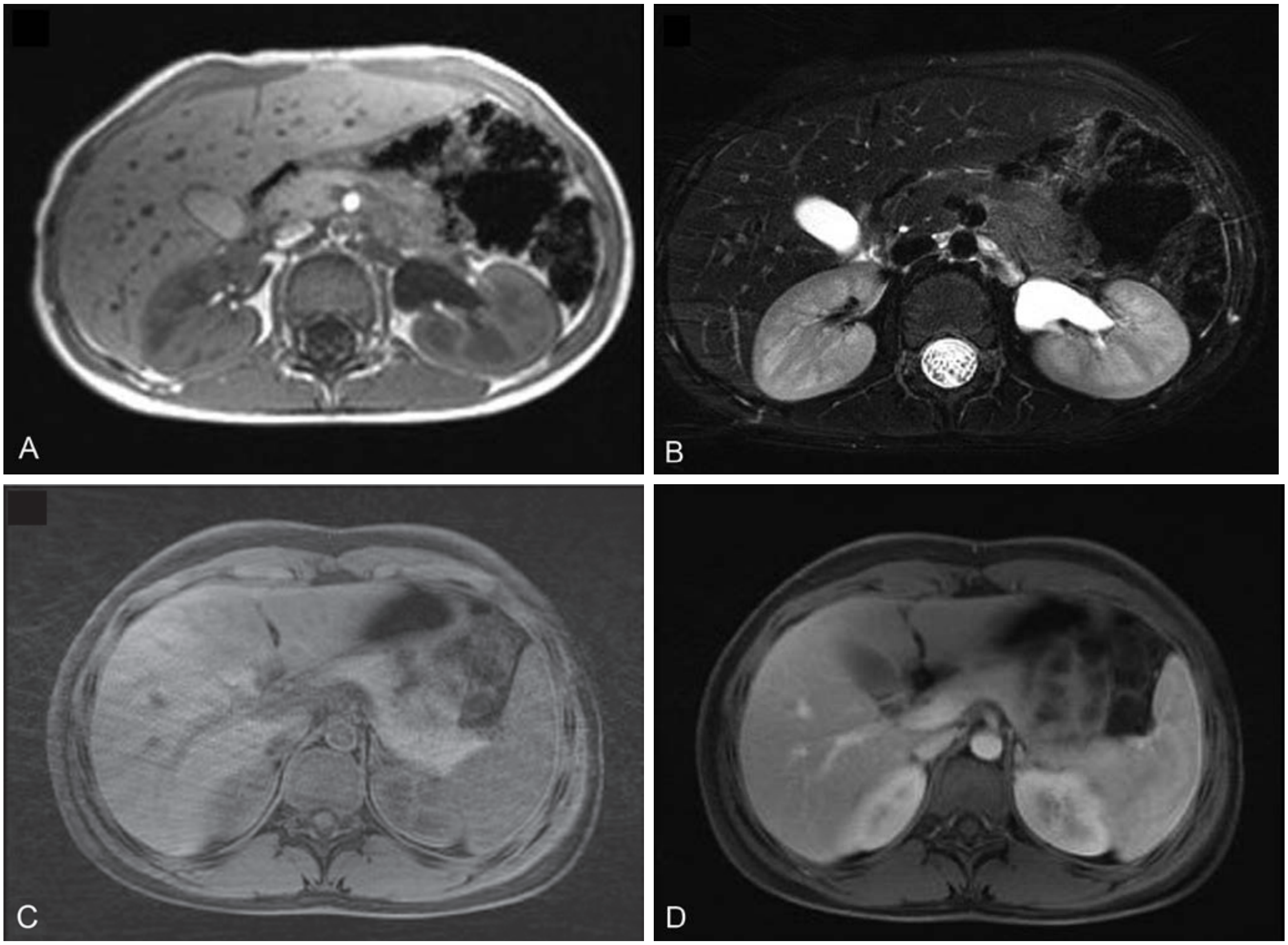

**Figure 95.3. MRI of normal pancreas in a 10-year-old girl.** (A) Axial T1-weighted, (B) T2-weighted fat-saturated, (C) T1-weighted fat-saturated precontrast, and (D) T1-weighted fat-saturated postcontrast images in a normal 10-year-old. Note that the normal pancreas is the brightest organ on T1-weighted images (with or without contrast) in the upper abdomen.

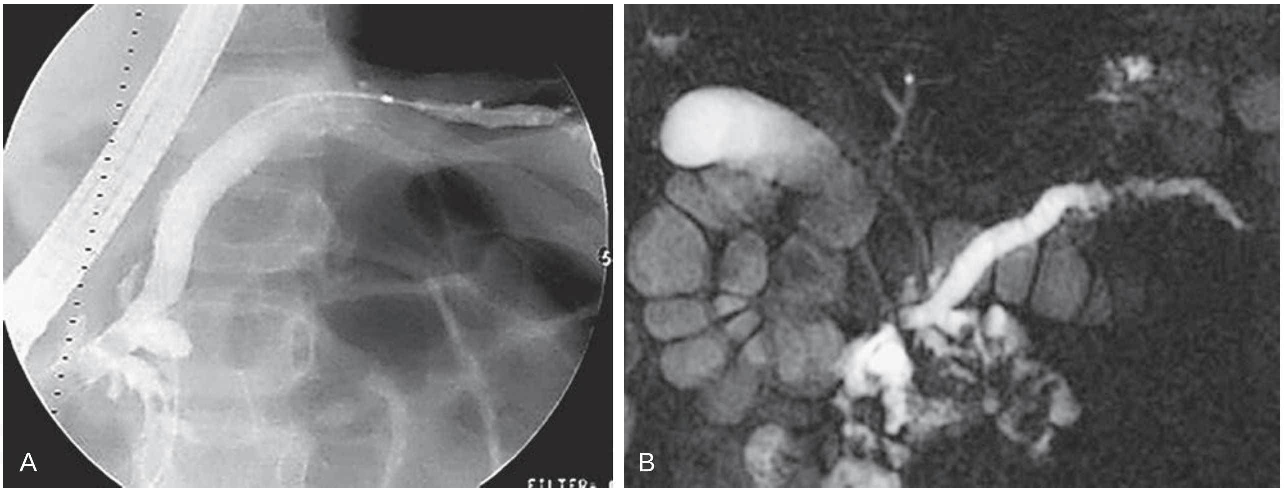

**Figure 95.4. Endoscopic retrograde cholangiopancreatography (ERCP) and magnetic resonance cholangiopancreatography (MRCP) in a 9-year-old with recurrent pancreatitis and stones.** (A) Anteroposterior image from ERCP shows abnormal dilation of the proximal pancreatic duct and narrowing, irregularity, beading, and an undulating caliber of the distal pancreatic duct. (B) Anterior MRCP image of the same patient exquisitely defines the abnormal caliber and irregularity of the pancreatic duct, consistent with recurrent pancreatitis. The common bile duct is normal. *(Courtesy Dr. Kimberly Applegate, Indianapolis, IN.)*

retrograde cholangiopancreatography (ERCP)[15] in children (Fig. 95.4). Reported sensitivity, specificity, and accuracy are 87%, 90%, and 89%, respectively, for stones; 100%, 98%, and 98% for cholangitis; 92%, 97%, and 96% for bile duct tumors; and 89%, 96%, and 95% for periampullary stenosis.[16] MRCP is useful in congenital abnormalities such as pancreas divisum, after pancreatic trauma to identify duct of Wirsung transections, in delineating postoperative anatomy after choledochal cyst repair, pancreatobiliary maljunction, common channel,[17] and pancreatic duct.[18] Similarly, MRCP accurately depicts the postoperative anatomy and complications after liver transplantation.[19] A normal MRCP may obviate the need for ERCP or percutaneous transhepatic cholangiography, and abnormalities visualized with MRCP can direct the modality and route for further intervention. An overview of MRCP pitfalls has been provided by Van Hoe and colleagues.[20]

Secretin stimulation with MRCP further enhances the imaging information obtained, because it gives additional valuable, functional, and anatomic information about the pancreatic duct and pancreatic excretory capacity. Secretin-enhanced MRCP has been described in detail in recent years[21–25] and may be useful for detection and diagnosis of a variety of congenital, inflammatory, and neoplastic pancreatic conditions.[26] Secretin stimulates pancreatic exocrine secretion, which in turn leads to transient pancreatic duct dilation and fluid excretion into the duodenum. Imaging the distended pancreatic duct during secretin stimulation can improve sensitivity for detecting anatomic abnormalities such as pancreas divisum. In addition, the volume and location of secretin-stimulated duodenal fluid production during MRCP has been shown to be an accurate surrogate marker of pancreatic exocrine function in patients with pancreatitis.[27] MRI can be used as a noninvasive tool to detect pancreatic iron overload and endocrine function due to magnetic susceptibility effects of iron.[28]

## CONGENITAL AND HEREDITARY PANCREATIC ABNORMALITIES

### Congenital Pancreatic Abnormalities[29,30]

#### Pancreas Divisum

***Overview.*** Pancreas divisum occurs in 4% to 14% of the population when the dorsal and ventral ducts fail to fuse, although the pancreas is otherwise anatomically normal. This fusion abnormality leads to the smaller minor papilla and duct of Santorini draining the major portion of the pancreas and is associated with an increased risk of pancreatitis.

***Clinical Presentation.*** Pancreas divisum is present in 12% to 50% of cases of acute pancreatitis in patients whose pancreatitis would otherwise be considered idiopathic.[31]

***Imaging.*** MRCP has been shown to be highly sensitive and specific for pancreas divisum (Fig. 95.5). The most commonly observed finding is a main pancreatic duct entering the duodenum at a location that is superior to the common bile duct and major papilla. Increased thickness of the pancreatic head has also been described.[32] Thin-section CT can demonstrate the unfused ducts and two distinct pancreatic moieties separated by a fat cleft in some patients.[33] Pancreas divisum may be associated with minor papilla adenoma beyond childhood. Secretin MRCP may be useful in better demonstration of pancreas divisum[34]

***Treatment.*** Minor papilla sphincterotomy to facilitate normal egress of pancreatic enzymes and duct stenting has been attempted.[35]

#### Congenital Short Pancreas

***Overview.*** Congenital short pancreas, also known as *agenesis of the dorsal pancreatic anlage*,[36] occurs when the portion of the pancreas derived from the dorsal embryonic bud is absent, and only the smaller portion, derived from the ventral anlage, is present. Thus the pancreatic neck, body, and tail are absent. This anomaly has been described in patients with polysplenia syndrome or as a sporadic finding.

***Clinical Presentation.*** Patients may have variable symptoms of abdominal pain and epigastric discomfort to diabetes.[37]

***Imaging.*** Only the globular pancreatic head can be identified on CT (Fig. 95.6). Size is variable, ranging from an enlarged or prominent pancreatic head, to a normal-sized or even mildly atrophic and small pancreatic head. The diagnosis of agenesis of the dorsal pancreas is inconclusive without demonstration of the absence of the dorsal pancreatic duct, either with MRCP or ERCP. Patients with this abnormality have an increased risk of developing diabetes mellitus[38] because of the paucity of islet cells, most of which are located in the distal pancreas. This condition may also be associated in later life with pancreatic tumors[39] such as intraductal papillary mucinous neoplasms.

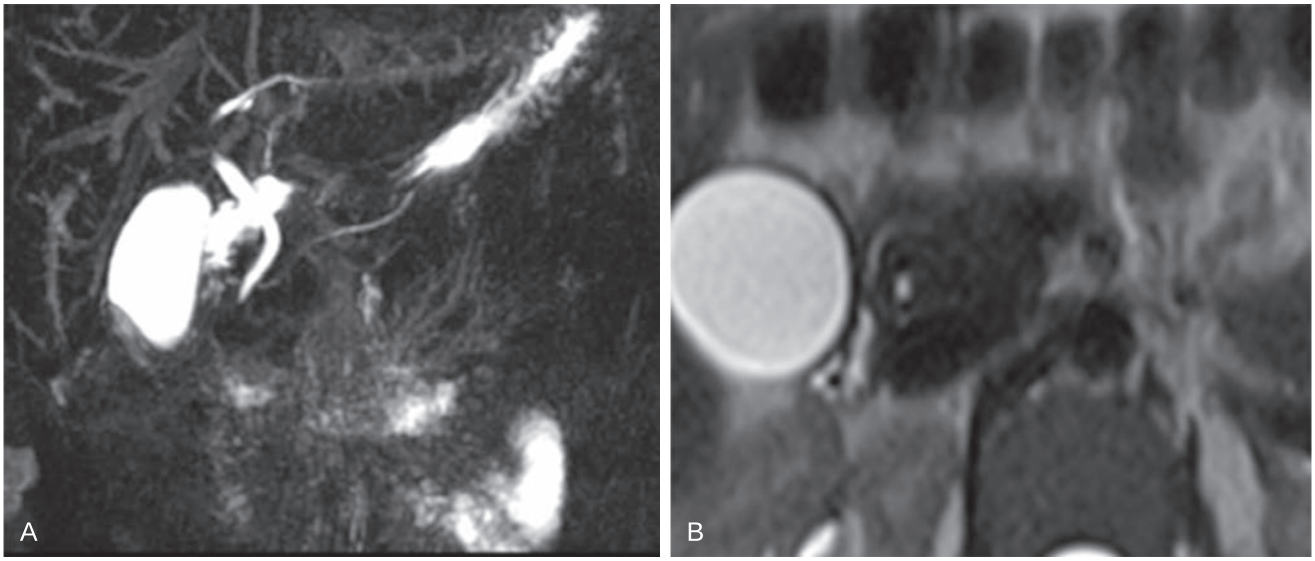

**Figure 95.5. Pancreas divisum.** (A) Coronal T2-weighted MR image shows the pancreatic body and tail draining through minor papilla. (B) Axial T2-weighted MR image shows separate ducts of Santorini (anterior duct) and Wirsung (posterior duct) in the pancreatic head.

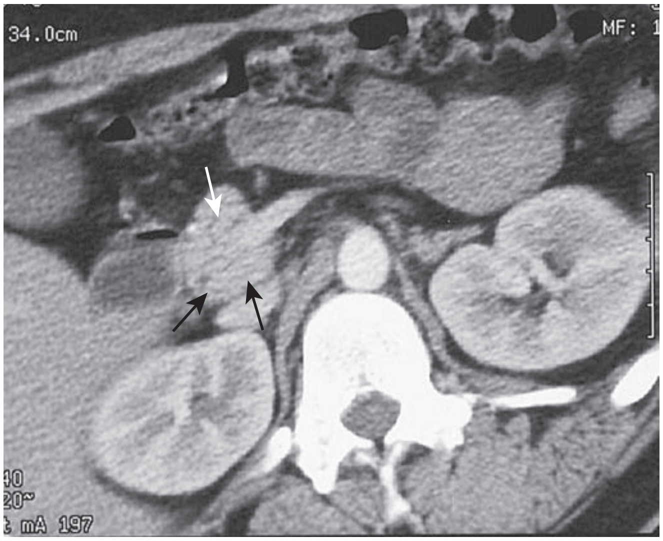

**Figure 95.6. Congenital short pancreas.** Axial contrast-enhanced abdominal CT image through the pancreatic bed shows a congenital short pancreas, with only a bulbous pancreatic head present *(arrows)*. *(Courtesy Dr. George Taylor, Boston, MA.)*

***Treatment.*** Treatment is supportive and is directed at the abdominal pain, pancreatitis, and diabetes.

## Ectopic Pancreas

***Overview.*** Ectopic pancreatic tissue[40] is an aberrant rest of normal pancreatic tissue remote from the pancreatic body that occurs in 1% to 13% of the population. The vast majority of pancreatic rests (about 70%) are located in the stomach, duodenum, and jejunum,[41] but they can occur elsewhere, such as omphaloenteric duct rests.[42] An association with Beckwith-Wiedemann syndrome (BWS)[43] and noncommunicating gastric duplication cyst containing ectopic pancreatic ducts and islet cells without acini has been described.[44]

***Clinical Presentation.*** Most pancreatic rests are incidental findings and are asymptomatic.

***Imaging.*** Detection of ectopic pancreatic tissue needs a high index of suspicion. Kim et al.[45] have described CT findings of ectopic pancreas and CT features to differentiate it from other common tumors found in these locations.

***Treatment.*** Laparoscopic gastric wedge resection is a safe and effective treatment for symptomatic pancreatic rests located in the stomach.

## Annular Pancreas

***Overview.*** Several theories of embryonic dysgenesis have been proposed for annular pancreas, but most suggest some form of rotational anomaly of the ventral bud. The pancreatic annulus, or the portion surrounding the duodenum, frequently has a separate duct entering the duodenum opposite the ampulla of Vater. Duodenal contents may reflux through this duct into the annulus. Affected patients present with duodenal stenosis or obstruction in infancy, but adults present with pancreatitis.[46] Other associated abnormalities (especially in patients with trisomy 21) include intestinal malrotation, tracheoesophageal fistula, anal atresia, and cardiac abnormalities and has been described in de Lange syndrome.

***Clinical Presentation.*** Infants frequently present because of associated duodenal obstruction. However, in approximately half the cases, the diagnosis is made beyond infancy. Annular pancreas has also been a cause of extrahepatic biliary obstruction.[47]

***Imaging.*** It is easier to detect and characterize the tissue surrounding the duodenum as pancreatic on MRI than CT. Diagnosis by US has also been described.[48] ERCP and MRCP are used to investigate ductal anatomy (Fig. 95.7).

***Treatment.*** Treatment requires bypass of the obstructed segment of duodenum usually by duodenoduodenostomy or gastrojejunostomy.[49]

## Congenital Pancreatic Cysts

***Overview.*** Congenital cysts of the pancreas are rare and are often confused with choledochal,[50] omental, or mesenteric cysts. Single congenital pancreatic cysts are very rare and occur predominantly in females.[51]

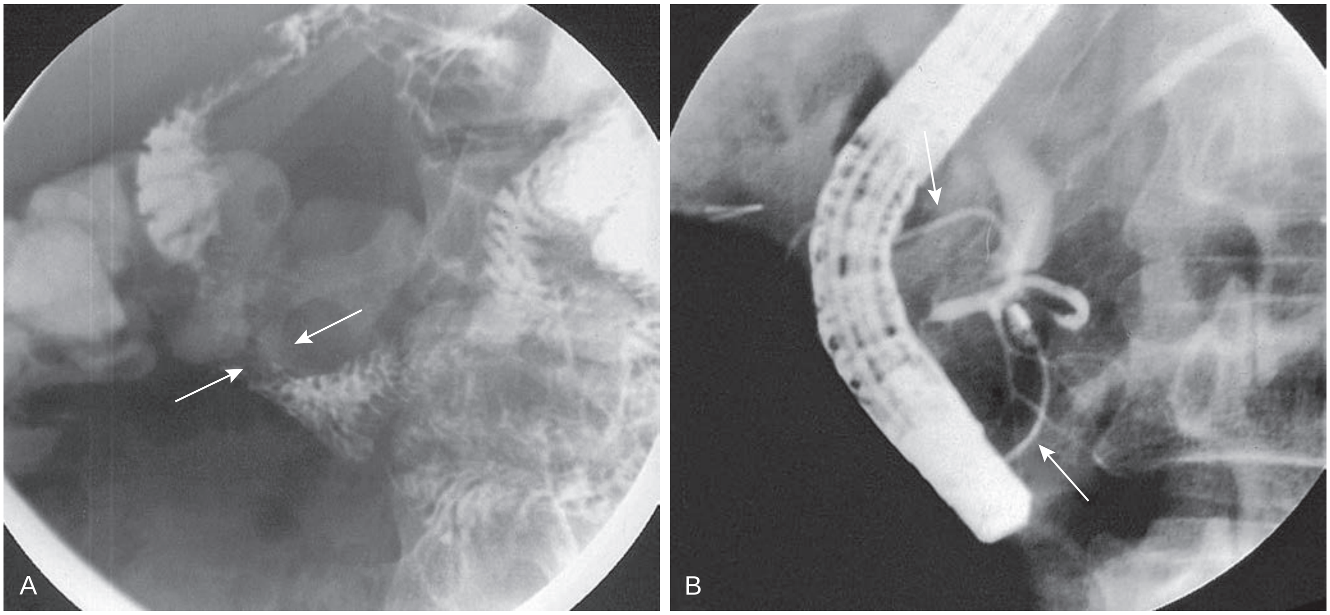

**Figure 95.7. Annular pancreas.** (A) Oblique view during an upper gastrointestinal series shows extrinsic narrowing of the duodenal C-loop *(arrows)*. (B) Endoscopic retrograde cholangiopancreatography confirms the presence of small ducts *(arrows)* encircling the duodenum, consistent with an annular pancreas.

***Clinical Presentation.*** Usually asymptomatic, but when symptoms do occur, they are related to mass effect and compression of adjacent structures.

***Imaging.*** Congenital cysts are anechoic on US. They are usually unilocular, located in the pancreatic tail, and range in size from microscopic to 5 cm.[52] Rarely, they may communicate with the ductal system. In contrast to single congenital pancreatic cysts, multiple congenital cysts may be associated with a polycystic disorder such as von Hippel-Lindau disease.[53] Juxtapancreatic gastrointestinal (GI) duplication cysts occur as abnormalities of the developing foregut and therefore usually have an alimentary tract epithelial lining. Most of these cysts arise from the stomach or duodenum but may rarely be sequestered within the pancreas.[54]

***Treatment.*** Surgical removal is usually only necessary for symptomatic cysts or those concerning for neoplasia.

## Hereditary Systemic Conditions With Pancreatic Involvement

### Cystic Fibrosis

***Overview.*** CF, an autosomal recessive genetic disease related to chloride channel dysfunction, leads to exocrine pancreatic insufficiency in 80% of affected patients. The etiology of pancreatic pathology in CF is multifactorial but is thought to include a combination of increased intra-acinar pressure from retained viscous pancreatic secretions, precipitation of proteins, and increased pancreatic enzyme concentration.[55]

***Clinical Presentation.*** Patients have pancreatic insufficiency, mainly exocrine, with failure to thrive, abdominal distension, steatorrhea, and occasional rectal prolapse. Patients with pancreatic cystosis (see the following text) are usually asymptomatic.

***Imaging.*** Four general imaging patterns of the pancreas have been observed, including normal, atrophic, lipomatous, and cystotic appearances.[56] In young patients with CF, US[57] shows a normal pancreas or pancreatic enlargement, but chronic obstruction ultimately results in atrophy of the gland with fatty infiltration and fibrosis, leading to increased echogenicity. CT shows reduced attenuation secondary to fatty infiltration (Fig. 95.8). Fibrosis without fatty infiltration is found infrequently. Unenhanced scans may show pancreatic calcifications, ductal dilation, and pancreatic cysts.[58] MRI findings are variable but can accurately depict the changes of fatty infiltration, fibrosis, and atrophy.[59,60]

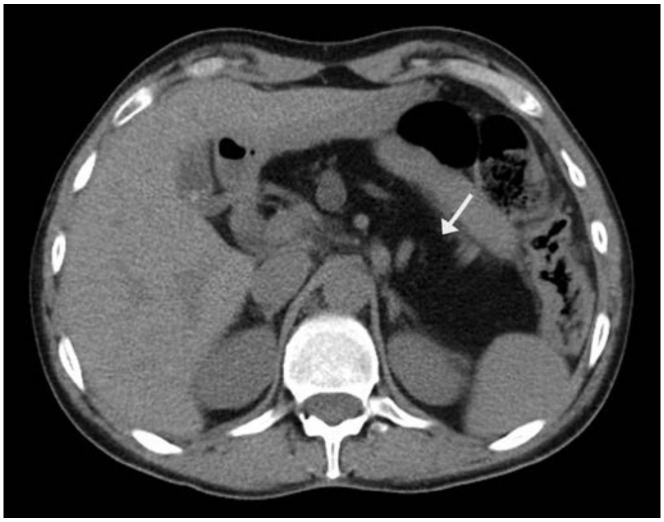

**Figure 95.8. Cystic fibrosis (CF) with diffuse fatty replacement of the pancreas.** Axial noncontrast CT of the abdomen in an 18-year-old girl with CF demonstrates diffuse fatty replacement *(arrow)*.

Cystic transformation of the pancreas, or *pancreatic cystosis*, in children and young adults may occur.[61] Here, the pancreas is replaced by macrocysts that are rarely more than 1 cm in diameter. These are true, epithelium-lined cysts that result from the accumulation of inspissated mucus, produced as a result of residual exocrine secretory function in the acinar cells, proximal to ducts obstructed from inflammation. This can be imaged with US, CT (Fig. 95.9), and MRI. Secretin-stimulated MRI with diffusion-weighted imaging is being investigated for assessment of exocrine pancreatic insufficiency in patients with CF.[62]

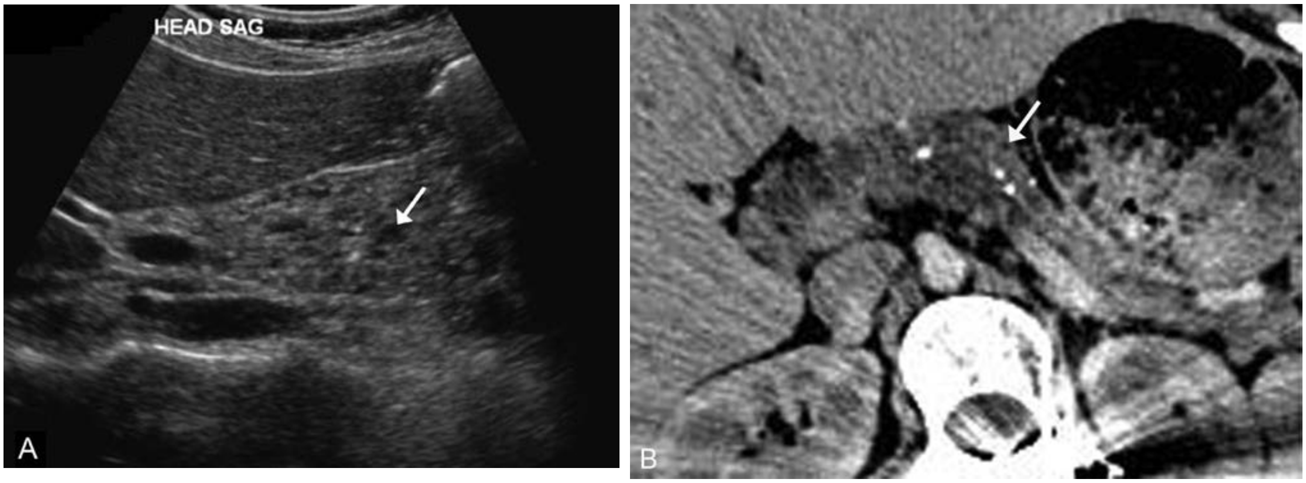

**Figure 95.9. Cystic fibrosis with pancreatic cystosis.** A 13-year-old girl with CF demonstrates pancreatic cystosis *(arrows)* on (A) US and (B) contrast-enhanced axial CT.

***Treatment.*** Exocrine pancreatic insufficiency is treated by supplementation with pancreatic enzyme products. Treatment otherwise is supportive and directed toward the underlying CF.

## Shwachman-Diamond Syndrome

***Overview and Clinical Presentation.*** Shwachman-Diamond syndrome is an autosomal-recessive disorder that results in short stature, exocrine pancreatic insufficiency, metaphyseal chondrodysplasia, and bone marrow dysfunction.

***Imaging.*** US and CT evaluations of the pancreas demonstrate fatty replacement (pancreatic lipomatosis)[63] as described earlier in patients with CF (e-Fig. 95.10). Other causes of pancreatic lipomatosis include chronic pancreatitis, prolonged steroid use, obesity, Cushing syndrome, hemochromatosis, obstruction of the duct of Wirsung, and Johanson-Blizzard syndrome.

***Treatment.*** Exocrine pancreatic insufficiency is treated by supplementation with pancreatic enzyme products. Other current treatment strategies include surgery for skeletal deformities, granulocyte colony-stimulating factor for neutropenia, and bone marrow transplantation for marrow failure.

## von Hippel-Lindau Disease

***Overview and Clinical Presentation.*** von Hippel–Lindau disease (VHL) is an autosomal-dominant disorder characterized by hemangioblastoma in multiple organs (especially the retina and central nervous system), skin lesions, and cysts of numerous organs, including the pancreas. Pancreatic involvement is seen in approximately 21% of patients.[64] Up to 75% of these multiple pancreatic lesions (e-Fig. 95.11) likely originate from progenitor cells, not mature endocrine cells as previously thought.[65]

***Imaging.*** VHL-associated cysts are typically anechoic on US and have reduced attenuation on CT compared with the surrounding pancreatic tissue. Multiple cysts—as well as serous and mucinous cystadenomas of the pancreas, carcinoma, adenocarcinoma, and islet cell tumors—are also associated with VHL.[64]

***Treatment.*** Although symptoms are rare, specific treatment of pancreatic lesions is required in selected patients, mainly those with large neuroendocrine tumors that require surgical resection.[66]

## Autosomal-Dominant Polycystic Kidney Disease

***Overview.*** Autosomal-dominant polycystic disease is a hereditary disorder with 100% penetrance but variable expressivity. The genetic mutations underlying the disease are in *PKD1* and *PKD2* that encode for components of a calcium channel receptor within primary cilia.[67] This ciliary defect leads to problems with mechanical stimulus sensing and membrane reception signal transmission, giving rise to tissue degeneration and cyst formation in a number of organs including the pancreas.[68]

***Clinical Presentation.*** Symptoms of large pancreatic cysts include abdominal pain, jaundice, and fever.

***Imaging.*** Renal cysts are the dominant feature, but cysts may also be found in the liver, spleen, adrenal glands, and pancreas. Pancreatic cysts are present in about 10% of patients, and the gland is typically less involved than the kidneys or liver.

***Treatment.*** Large, symptomatic pancreatic cysts may require surgical or percutaneous intervention.

## Hereditary Pancreatitis

Hereditary pancreatitis is an autosomal-dominant disease in which patients have recurrent episodes of pancreatitis. This condition is discussed later in the chapter.

## Beckwith-Wiedemann Syndrome

***Overview and Clinical Presentation.*** BWS is a relatively frequent overgrowth syndrome with an incidence estimated at 1 in 14,000 births. It is probably an autosomal-dominant disorder with variable transmission. The BWS gene has been identified on the short arm of chromosome 11 (11p15.5). The syndrome is characterized by visceromegaly, hemihypertrophy, and development of malignant tumors in 10% to 15% of affected patients; benign tumors are also found.

***Imaging.*** Imaging studies may show nonspecific pancreatic enlargement. Patients may develop pancreatoblastoma or focal adenomatosis, as discussed later under Pancreatic Neoplasms. Because of this risk, routine US screening is initiated at an early age.

***Treatment.*** Surgical intervention is required for pancreatic tumors.

## Hemochromatosis

***Overview.*** Hemochromatosis is an autosomal-recessive disorder that manifests as iron accumulation mainly in the liver, pancreas, and heart secondary to excessive iron reabsorption from the intestine, leading to organ dysfunction (see also Chapter 89).

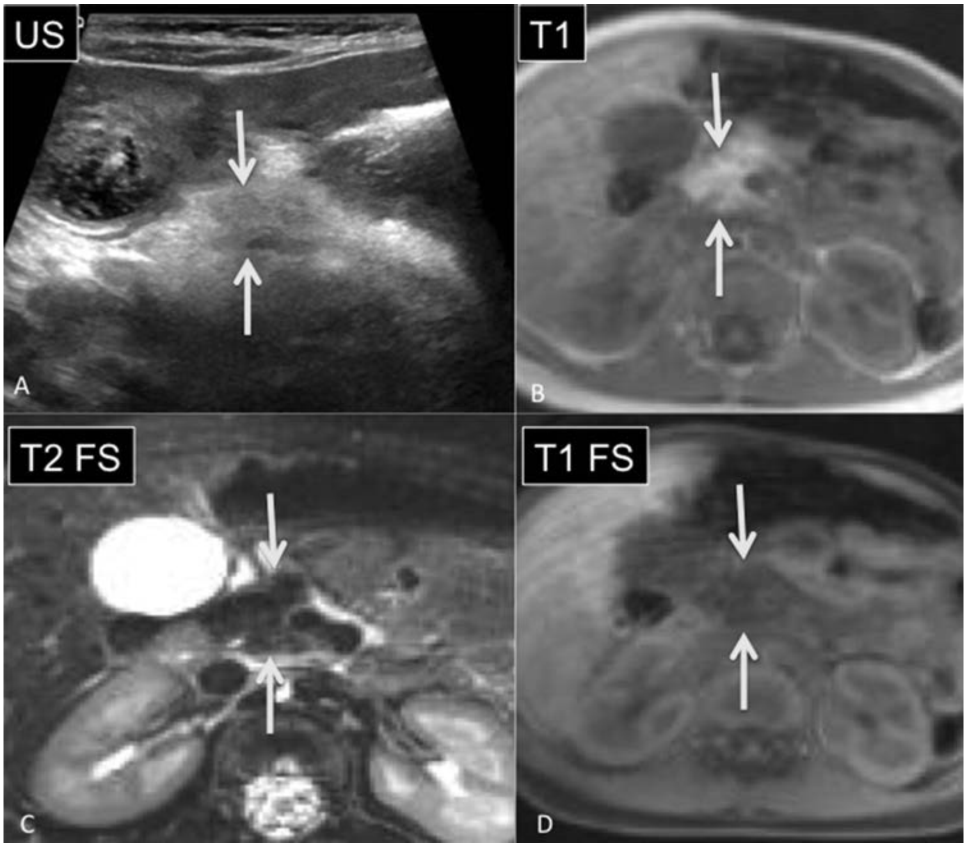

**e-Figure 95.10. Shwachman-Diamond syndrome.** (A) US demonstrates diffusely echogenic pancreas in a 9-year-old boy *(arrow)*. (B–D) Axial MR images demonstrate high signal pancreas on (B) T1-weighted images with (C) signal loss on T1-weighted and (D) T2-weighted fat-suppressed images *(arrows)*.

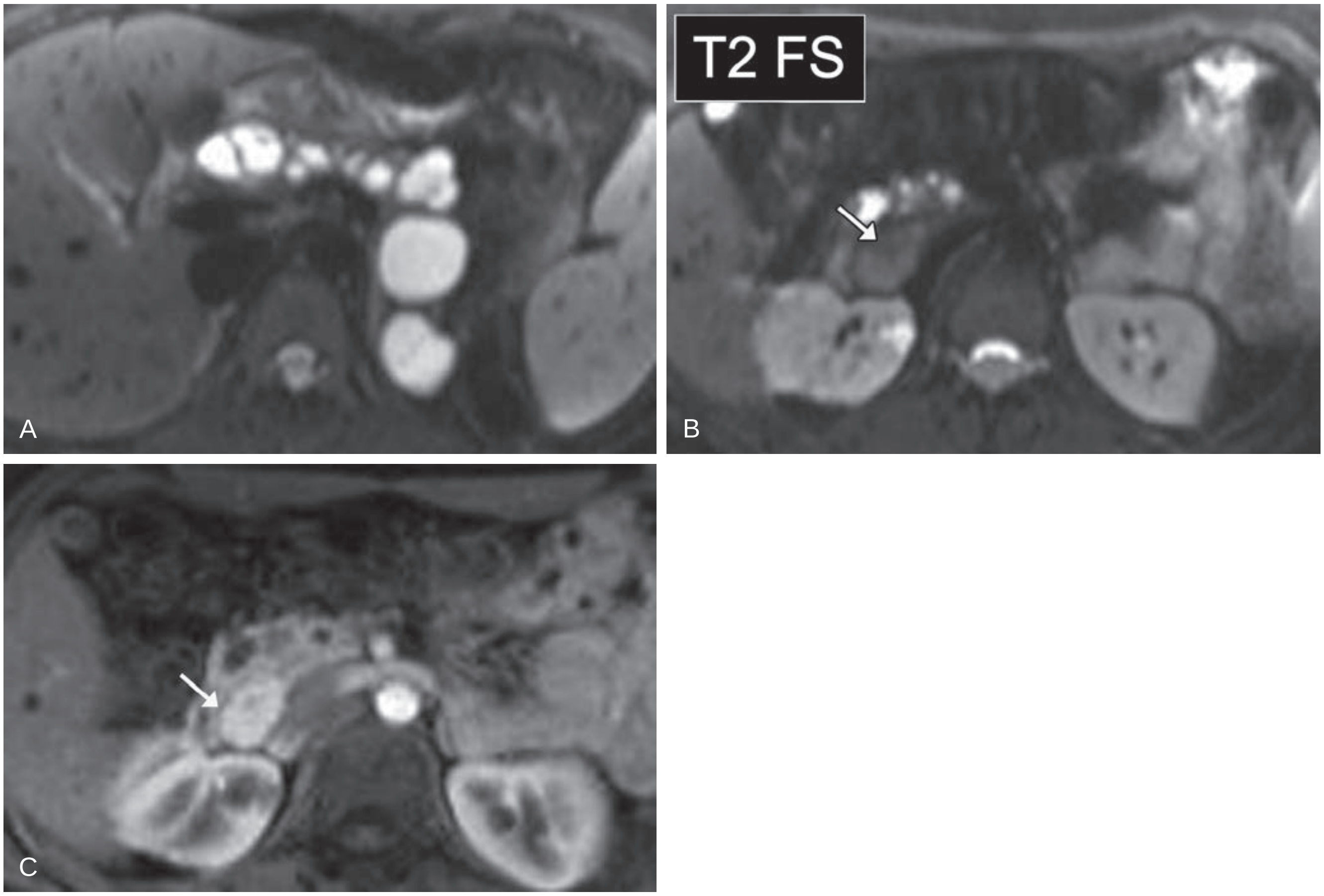

**e-Figure 95.11. von Hippel-Lindau (VHL) syndrome.** A 10-year-old girl with VHL demonstrates cysts on T2-weighted MR images (A and B). An arterial enhancing islet cell tumor is seen in the pancreatic head *(arrows)* on (B) T2-weighted fat-saturated and (C) T1-weighted fat-saturated images.

***Clinical Presentation.*** Symptoms referable to the pancreas may be absent or nonspecific, such as malaise and fatigue, or they may be those of insulin resistance due to pancreatic damage from iron deposition, culminating in diabetes.

***Imaging.*** The pancreatic changes from hemochromatosis are better appreciated with MRI, rather than CT, because of the magnetic susceptibility effects of iron. The liver and pancreas appear diffusely hypointense on T2*- and T2-weighted sequences. Distinction should be made from acquired transfusional iron overload (hemosiderosis), in which iron accumulates in the reticuloendothelial cells causing T2 hypointensity in the liver and spleen, but typically spares the pancreas.

***Treatment.*** Treatment is directed toward the resultant diabetes, and supportive treatment—such as phlebotomy, iron chelation therapy, and restriction of oral intake of iron-rich foods and beverages—is undertaken to prevent further damage from iron overload.

## PANCREATITIS

### Acute Pancreatitis

***Overview.*** Recent studies have reported an increasing incidence of acute pancreatitis in the pediatric age group.[69–71] This has been proposed to be secondary to both better detection as well as a rising incidence of obesity, which in turn is considered a risk factor for acute biliary pancreatitis.[72] Other demonstrated factors include multisystem disease, including sepsis, shock, hemolytic uremic syndrome, and viral infection, specifically mumps. Blunt trauma is the cause in 15% of patients (including bicycle handlebar injuries), congenital anatomic abnormalities in 10%, metabolic diseases in 10%, and drug toxicity in 3%. No cause may be identified in 25% of patients.[73]

Anatomic abnormalities associated with pancreatitis include pancreas divisum, congenital bile duct dilation, cysts with pancreatobiliary malunion/maljunction (40%–50%),[74] duodenal web, and congenital pancreatic cyst. An anomalous pancreatobiliary ductal junction may cause pancreatitis, by facilitating reflux of bile into the pancreas.[75–77] The frequency of acute pancreatitis in children with a choledochal cyst is reportedly as high as 68%. Associated metabolic disorders include hypercalcemia, hyperlipidemia, and CF; the drugs implicated most frequently are L-asparaginase (e-Fig. 95.12), steroids, and acetaminophen. A reported increased incidence of biliary sludge in adult patients with pancreatitis suggests that biliary sludge may be the probable cause in as many as 70% of patients with idiopathic pancreatitis.[78]

Autoimmune pancreatitis is a part of IgG4-related disease affecting the pancreas but is uncommon in the pediatric population.[79] Diffuse, focal, and multifocal involvement of the pancreas has been described; the diffuse type being the most common leading to “sausage”-shaped enlargement of the gland.[80]

***Clinical Presentation.*** Patients with nontraumatic acute pancreatitis typically present with epigastric pain, nausea, and vomiting. Elevation of serum concentrations of pancreatic enzymes—amylase, lipase, and trypsinogen—is common. Although abnormal laboratory values are typically considerably more sensitive than imaging in identifying acute pancreatitis, imaging studies are useful to confirm the diagnosis and to determine the extent of associated inflammatory changes and complications. Very rarely, pancreatitis may be the presenting symptom of a pancreatic malignancy in children and adolescents.

***Imaging.*** Abdominal radiographic findings are nonspecific. Reactive ileus or localized ileus from focal dilation of the duodenal loop (“sentinel loop”) and asymmetric left pleural effusion are suggestive findings.

US is the best initial imaging study for evaluation of acute pancreatitis and biliary abnormalities in children.[80] Pancreatic parenchymal echogenicity and size are unreliable indicators of acute pancreatitis. The edema that accompanies acute pancreatitis often results in a diffusely enlarged hypoechoic gland, although some will appear normal. A minority of affected patients have increased pancreatic echogenicity (see e-Fig. 95.12). The pancreatic duct may be dilated,[2] but this is an inconsistent finding. Masses may be identified in the pancreas that represent focal areas of fluid, hemorrhage, or phlegmon formation. US is sensitive in detecting peripancreatic fluid collections and assessing feasibility for image-guided interventions. The most commonly involved areas are the lesser sac, anterior pararenal space,[81] transverse mesocolon, and perirenal space. US can also detect vascular complications, including pseudoaneurysms and venous thromboses.

CT with IV contrast is more sensitive in detecting acute pancreatitis and its complications compared with US. CT features include focal or diffuse pancreatic enlargement, presence of hemorrhage, peripancreatic fluid collections, thickening of adjacent fascial planes, and ascites. Abscesses, necrosis, and vascular complications are particularly well delineated on CT.[82] Presence of gas locules without prior intervention is an indicator of underlying infection.

The CT severity index (CTSI), originally developed by Balthazar et al. for the adult population, has been shown to be a better indicator of acute severe pancreatitis than clinical scores in the pediatric population.[83] CT findings help triage early institution of antibiotics, ICU transfer in anticipation of renal or respiratory complications, or early administration of parenteral nutrition. However, serial follow-up with CT should be limited due to the risk of radiation exposure.

ERCP has no role in acute pancreatitis except when a therapeutic intervention is planned due to a known biliary etiology. ERCP is more useful to evaluate complicated or recurrent pancreatitis[84] and in cases of unusual pseudocyst formation. The findings range from mild irregularity of the duct to ductal narrowing with wall ectasia and acinar enlargement, which has been likened to a “string of beads.” Marked ductal ectasia is usually not seen in acute pancreatitis.

MRCP[85] is preferred to ERCP in the evaluation of childhood pancreatitis because it is noninvasive (see Fig. 95.4). MRCP is more sensitive in detection of choledocholithiasis compared with US, and pancreaticobiliary ductal anomalies are better evaluated. Secretin administration may help in visualizing the pancreatic duct and structural abnormalities.

MRI features of acute pancreatitis include low T1 signal intensity of the pancreatic parenchyma as well as heterogeneous or diminished parenchymal enhancement on the postcontrast imaging. T2-weighted and diffusion-weighted images are sensitive for detection of parenchymal edema and fluid collections as well as surrounding inflammation. Gas and calcification are better visualized on CT when compared with MRI.

Complications of acute pancreatitis can broadly be divided into vascular and nonvascular complications, the latter including collections and fistulizing disease. The latest revised version of the Atlanta classification[86] can be extrapolated to the pediatric population as the nature of collections is the same in adults and children. Acute edematous interstitial pancreatitis is associated with acute peripancreatic fluid collections that do not demonstrate a well-delineated wall and are seen up to 4 weeks from the start of inflammation, compared with pseudocysts that take 4 or more weeks to develop. Although most pseudocysts are in the region of the pancreas itself (see e-Fig. 95.12), they can appear nearly anywhere in the abdomen and in the mediastinum.[75,76] About 13% of pediatric patients with acute pancreatitis develop pseudocysts.[80] Although most pseudocysts resolve spontaneously within an average of 5 months,[87] some persist and require intervention.[88,89] Features associated with spontaneous resolution include a pseudocyst diameter less than 7.5 cm, absence of internal debris, and total pseudocyst volume less than 250 mL.

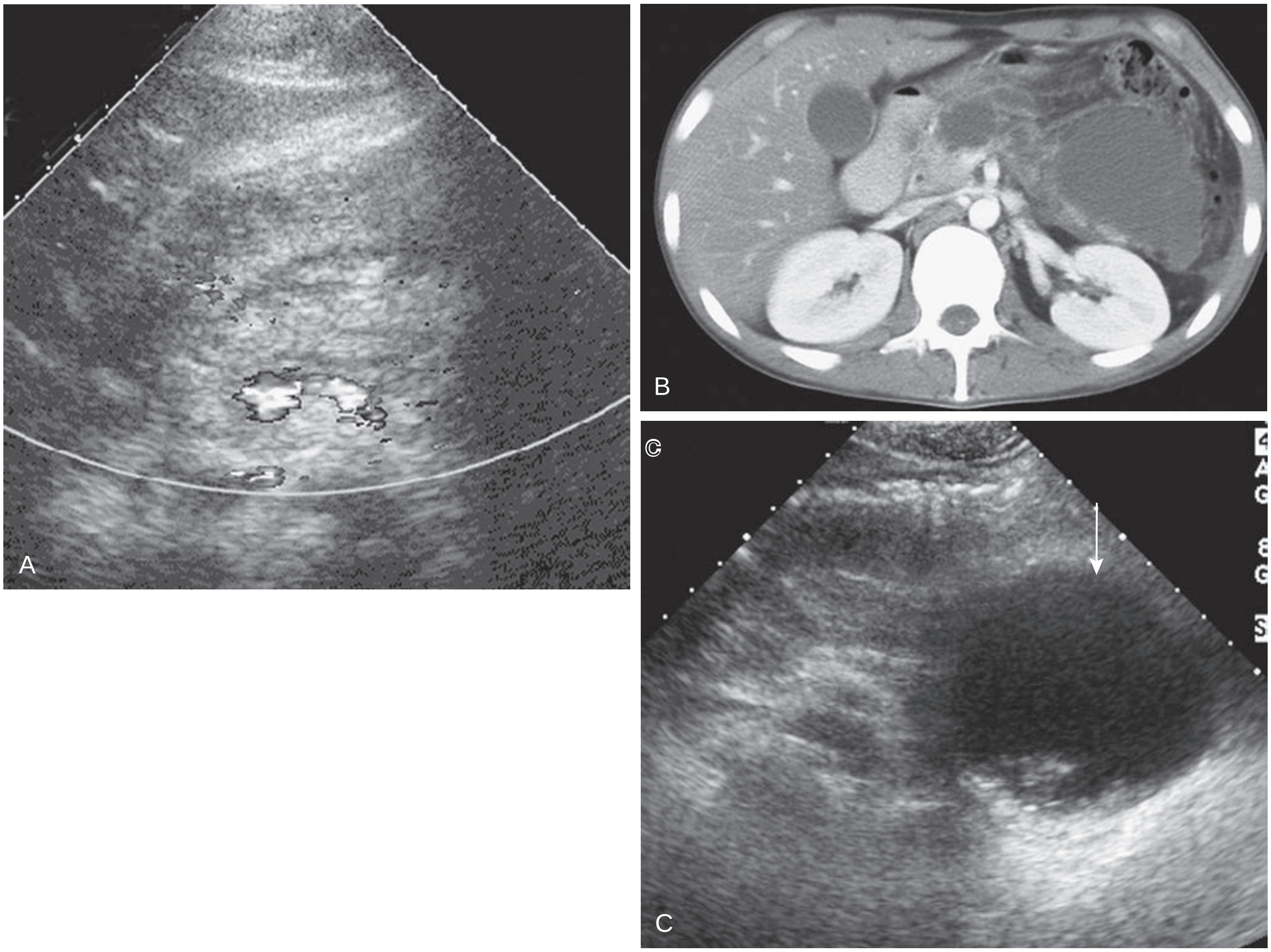

**e-Figure 95.12. Asparaginase-induced pancreatitis and pseudocyst formation.** (A) Transverse US in a 17-year-old boy undergoing treatment for acute lymphoblastic leukemia who developed acute pancreatitis. The body of the pancreas is enlarged and mildly hyperechoic, with indistinct margins. Doppler signal indicates the splenic vein dorsal to the pancreas. (B) Axial contrast-enhanced CT scan 2 days later shows peripancreatic edema and two pseudocysts in the body and tail. (C) Additional follow-up with US shows a large pseudocyst *(arrow)* involving the pancreatic tail and containing complex debris.

Collections associated with necrotizing pancreatitis are classified as acute necrotic collections in the first 4 weeks and walled off necrosis thereafter. Although contrast-enhanced CT is sensitive in diagnosing fluid collections, US or MRI is more sensitive in characterizing fluid composition. They frequently cause mass effect on adjacent structures, especially the stomach and duodenum, and this may be seen on radiographs or upper GI studies performed for unexplained abdominal pain. Pseudocysts are typically anechoic, although some may contain debris. ERCP usually shows the irregular ductal dilation of chronic inflammation (see Fig. 95.3A). Skeletal changes, particularly bone marrow infarcts, have long been recognized as a complication of pancreatitis, possibly related to increased levels of circulating lipase and to generalized enzymatic dysfunction of the pancreas.[90]

***Treatment.*** Primary treatment includes analgesia and bowel rest with parenteral nutrition.[91,92] Postpyloric enteral feeds may be begun before oral refeeding to prevent relapse and to provide nutritional support while preventing gut mucosal atrophy. Antibiotic use is recommended for necrotic pancreatitis. Surgery and interventional procedures are indicated for infected necrotic pancreatitis and complications such as pseudocyst and abscess formation, splenic artery and vein thrombosis, hemorrhage, and pseudoaneurysms.

## Chronic Pancreatitis

***Overview.*** Chronic pancreatitis in children is less common than acute pancreatitis. Although it occurs as a sequela of the acute disease, chronic pancreatitis can also be found in association with other entities, such as CF. Familial hereditary pancreatitis is an autosomal-dominant disease that usually presents during childhood or the teenage years.

***Clinical Presentation.*** Patients with chronic pancreatitis usually present with persistent abdominal pain; some have constant, debilitating pain, whereas others have pain related to food intake, especially fats and protein-rich meals. Steatorrhea as a result of fat malabsorption is common, and weight loss is attributed to malabsorption and a reduction in food intake secondary to pain and food aversion. Diabetes may result from chronic pancreatic damage, and chronic pancreatitis may result in obstructive jaundice secondary to biliary strictures.[93]

***Imaging.*** Ductal dilation with strictures and visibility of pancreatic duct side branches, pseudocysts, and calcifications are the most common imaging abnormalities in chronic hereditary pancreatitis,[94] and pancreatic atrophy may also occur. Chronic fibrosing pancreatitis is characterized by bands of collagen enclosing normal acini[95]; the resulting mass simulates a tumor.

***Treatment.*** Pancreatic enzyme supplementation is used for treatment of malabsorption and steatorrhea. Dietary fat restriction, analgesics and opiates for pain, and insulin for diabetes are other treatment strategies. Therapeutic endoscopy and surgery may also be used.[96]

## Trauma

***Overview.*** Traumatic pancreatic injury in children is typically caused by blunt abdominal injury. Bicycle handlebar injuries and motor vehicle trauma account for the majority of pancreatic trauma; however, pancreatic injury can also be seen with nonaccidental trauma, and this mechanism should always be excluded in children.[97] Please refer to Chapter 109 on abdominal trauma for further details.

# PANCREATIC NEOPLASMS

Primary pancreatic tumors, both benign and malignant, are very rare in childhood and adolescence (Table 95.3).[98] Pancreatic tumors that occur in pediatric patients include solid-cystic pseudopapillary tumor (Frantz tumor), pancreatoblastoma, and islet cell tumors with carcinomas being rare. Other tumors that typically occur elsewhere, but can arise within the pancreas, include lymphoma,[99] rhabdomyosarcoma, and rare cases of pancreatic neuroblastoma. Secondary involvement of the pancreas by adjacent tumor, especially neuroblastoma, may be difficult to distinguish from a primary pancreatic tumor.

**TABLE 95.3** Classification of Common Pancreatic Tumors of Childhood

| Location | Benign | Malignant |
|---|---|---|
| **EXOCRINE PANCREAS** | | |
| | Pancreatic cysts | Pancreatoblastoma |
| | Papillary-cystic tumor | Duct cell adenocarcinoma |
| | Duct adenoma | Acinar cell carcinoma |
| | Mucinous cystadenoma | |
| | Serous cystadenoma | |
| | Intraductal papilloma | |
| **CONNECTIVE TISSUE** | | |
| | Hemangioendothelioma | Sarcoma |
| | Lymphangioma | Lymphoma |
| | Teratoma | Leiomyosarcoma |
| **SECRETORY/ENDOCRINE** | | |
| | Islet cell hyperplasia | Insulinoma (10%) |
| | Insulinoma (90%) | Gastrinoma (60%) |
| | Gastrinoma (40%) | Gastrinoma (60%) |

*Modified from Enríquez G, Vázquez E, Aso C, et al. Pediatric pancreas: an overview.* Eur Radiol. *1998;8:1236–1244.*

## Solid-Cystic Papillary Tumor

***Overview.*** Solid-cystic papillary tumor is also known by many other terms: Frantz tumor, solid pseudopapillary tumor, papillary epithelial neoplasm (PEN), solid pseudopapillary epithelial neoplasm (SPEN), solid and cystic acinar cell tumor, papillary and solid neoplasm, papillary-cystic epithelial neoplasm, papillary-cystic carcinoma, solid and cystic tumor, solid and papillary neoplasm, papillary cystic tumor, and low-grade papillary neoplasm.[100] Recent studies have shown that this is the most common pancreatic neoplasm in children.[101,102] It accounts for about 0.2% to 2.7% of all nonendocrine pancreatic tumors. Solid-cystic papillary tumor is histologically low grade, with a reported 5-year survival of 97%.

***Clinical Presentation.*** This tumor has a predilection for women[103] and for persons of Asian origin; it is the most common pancreatic tumor in Asian children. Girls between the ages of 12 to 16 are commonly affected, although 10% do occur in males.[104] Children usually have a better prognosis than adults, owing to less frequent metastatic disease. Abdominal pain is the presenting symptom in about one-third of cases, with a palpable abdominal mass or as an incidental finding.

***Imaging.*** US shows a solid and cystic mass. CT findings include a large, well-defined, solid mass with varying degrees of cystic components that usually represent necrosis but are unrelated to tumor size (Fig. 95.13A and B).[105] Calcifications may also be present. On T1-weighted MR sequences, a low signal rim may represent either a fibrous capsule or compressed pancreatic parenchyma; central high-signal areas that represent debris or hemorrhagic necrosis have also been reported. Almost half of all lesions occur in the pancreatic head. Invasion of adjacent structures occurs and is often associated with liver and lymph node metastases.[106,107]

## Pancreatoblastoma

***Overview.*** Pancreatoblastoma, or pancreaticoblastoma,[108] arises from the pancreatic acinar cells, usually in the head or tail of the gland. The cells of these tumors represent persistence of the fetal anlage containing immature pancreatic acinar cells.

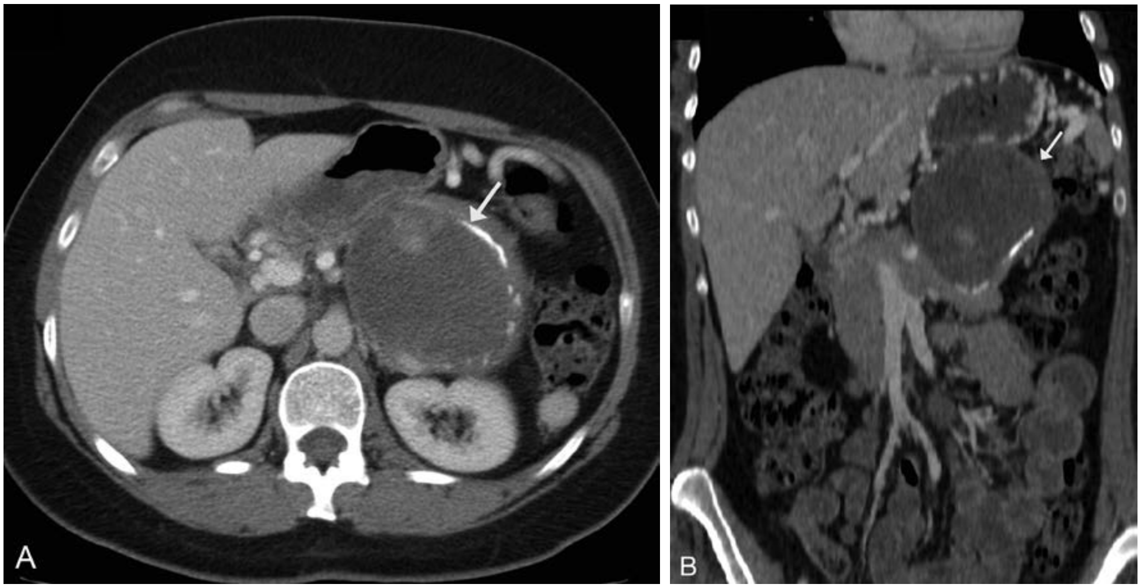

**Figure 95.13. Solid-cystic papillary tumor.** (A) Contrast-enhanced axial and (B) coronal reformatted CT in an 18-year-old girl presenting with an enlarging palpable abdominal mass demonstrates a hypoattenuating mass in the pancreatic tail with rim calcification and enhancing solid nodules.

Pancreatoblastoma is one of the most common exocrine tumors in pediatric patients and represents about 0.5% of all pancreatic epithelial tumors.

***Clinical Presentation.*** These tumors are found in boys twice as often as in girls. The incidence is higher in East Asia. Serum α-fetoprotein is elevated in 25% to 55% of cases, and an association with Beckwith-Wiedemann syndrome has been reported. A review of 153 patients with pancreatoblastoma found that the median age at presentation was 5 years, although this tumor has been diagnosed in patients as old as 68 years.[109] Seventeen percent of patients have metastatic disease, mostly involving the liver (88% of metastatic sites). Factors associated with a worse prognosis include metastatic or nonresectable disease and age older than 16 years at diagnosis. Pancreatoblastomas are often large at presentation, up to 12 cm, and may have central necrosis.

***Imaging.*** US and CT findings of pancreatoblastoma are often indistinguishable from those of pancreatic adenocarcinoma. Masses are typically hypoechoic and heterogeneous on US.[109] On CT, pancreatoblastoma is hypodense and appears to be multiloculated with enhancing septa (Fig. 95.14). Calcifications are not uncommon. When vascular encasement is present, it usually involves the inferior vena cava or mesenteric vessels. Despite the typically large size of pancreatoblastomas, obstruction of the biliary system is infrequent. Although variable, MRI characteristics include typically low signal intensity compared with the liver on T1-weighted images and isointensity to hyperintensity on T2-weighted images; enhancement varies.[110] Although findings are nonspecific as to tumor type, imaging suggests the malignant nature of the tumor and can clearly exclude the kidney and adrenal glands as organs of origin.

## Neuroendocrine Tumors

***Overview.*** Pancreatic neuroendocrine tumors arising from the pancreatic islet cells may be functioning (hormone-producing) or nonfunctioning.[97,104] In general, functioning neuroendocrine tumors tend to grow undiagnosed and present at a larger size at the time of diagnosis, while functioning tumors tend to be detected at a smaller size due to clinical symptoms related to hormone production (Fig. 95.15 and e-Fig. 95.16). Functioning neuroendocrine tumors produce increased amounts of polypeptide hormones such as insulin, gastrin, glucagon, VIP, and somatostatin.[104] Congenital hyperinsulinism (CHI, formerly called nesidioblastosis[111]) is due to beta-islet cell hyperplasia or adenomatosis and comes in two patterns: *diffuse adenomatosis*, where the gland is diffusely involved, and *focal adenomatous hyperplasia* due to a hyperfunctioning focal lesion.

***Clinical Presentation.*** Pancreatic neuroendocrine tumors present more commonly in adults but can present in older children. Pancreatic neuroendocrine tumors are observed in higher frequency in children with some genetic syndromes (e.g., multiple endocrine neoplasia type 1, Beckwith-Wiedemann, von Hippel-Lindau, tuberous sclerosis complex).[112] Nonfunctioning neuroendocrine tumors typically present with abdominal pain or distension, while patients with functioning tumors usually present with symptoms related to hormone production. Patients with insulinoma are seen initially with hypoglycemia, which typically manifests in children as erratic behavior and seizures. Tumors that secrete vasoactive intestinal peptide (VIP), so-called VIPomas, are associated with the syndrome of secretory diarrhea, hypokalemia, and achlorhydria. VIPomas are rare, with an estimated annual incidence of 0.2 to 0.5 per million population.

***Imaging.*** The most common site for pancreatic neuroendocrine tumors is in the pancreatic body and tail, where the majority of the islet cells reside.[113] These tumors are round or oval and are well circumscribed on US. They are hypoechoic but may have a hyperechoic rim; isoechoic and hyperechoic lesions have also been described in children and young adults. Endoscopic ultrasound (EUS) is more sensitive in detection of these tumors; however, it requires sedation/anesthesia and hence is less favored in children. On CT, these tumors demonstrate marked IV contrast enhancement particularly in the arterial phase (see Fig. 95.15, e-Fig. 95.16). Because these tumors are hypervascular, arteriography may be necessary in high-risk patients in whom US and CT are nondiagnostic, although magnetic resonance angiography (MRA) may replace this invasive technique. Intraoperative US has been used successfully to locate functioning islet cell tumors in children.[114] Selective venous sampling in children with hyperinsulinism can also help diagnose and localize tumors.[115] Indium-111-pentetreotide (Octreoscan) scintigraphy may also be useful in the diagnosis of primary or metastatic tumors.[116]

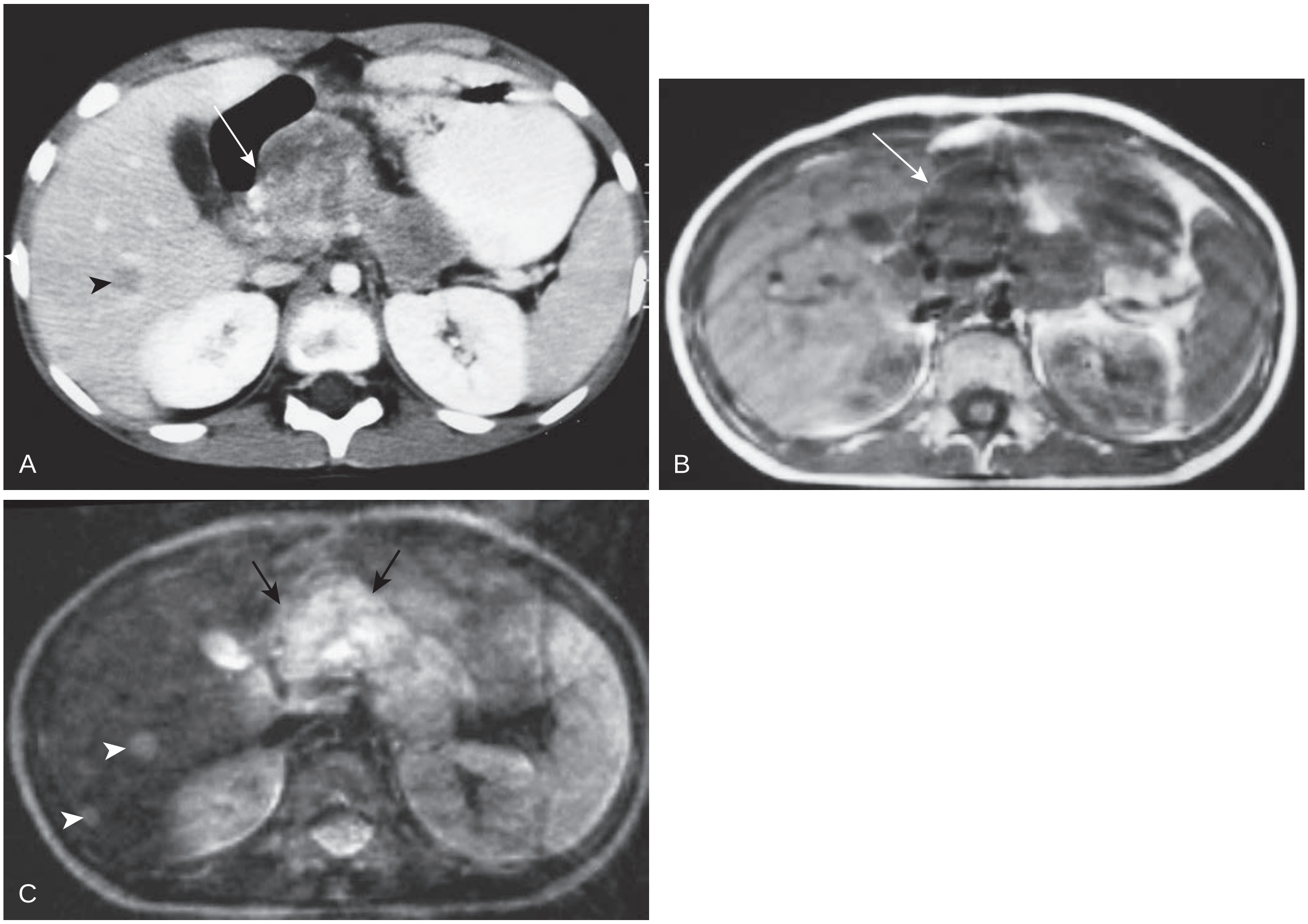

**e-Figure 95.16. Insulinoma.** (A) Axial contrast-enhanced CT through the pancreas of a 10-year-old girl with hypoglycemia. A large, heterogeneously enhancing mass involves the pancreatic head *(arrow)*. The remainder of the pancreas is also somewhat enlarged. Note the low-density hepatic metastasis *(arrowhead)*. (B) Axial T1-weighted MR image at the same level shows the intermediate-intensity pancreatic mass *(arrow)*. (C) T2-weighted sequence shows intensely increased signal *(arrows)*. Note also the conspicuity of the liver metastases on T2 weighting and a second, smaller metastatic focus located more peripherally *(arrowheads)*.

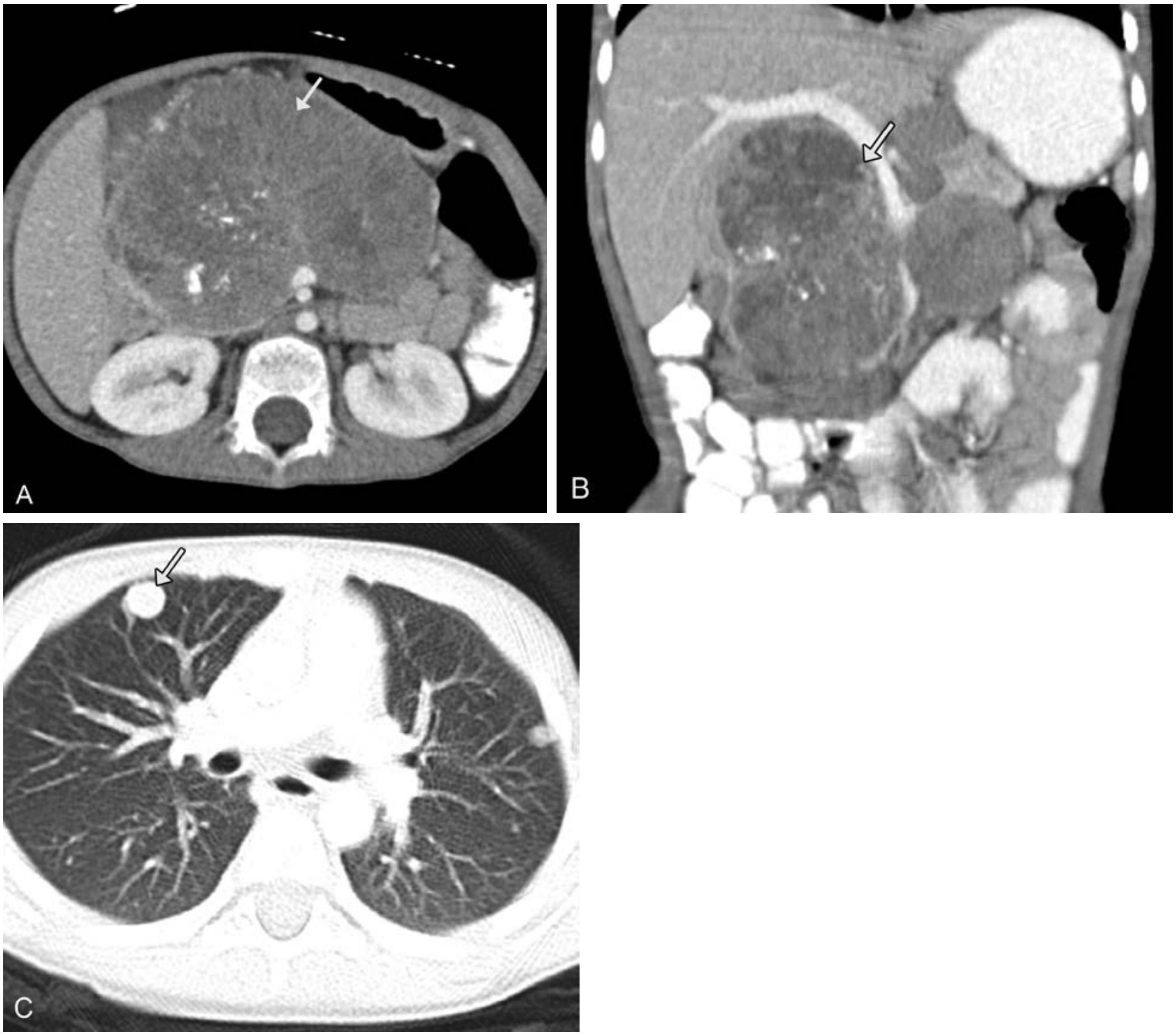

**Figure 95.14. Pancreatoblastoma.** (A) Axial contrast-enhanced and (B) coronal reformatted CT in a 3-year-old boy demonstrate a large, heterogeneously enhancing mass *(arrows)* arising from the pancreatic head and body. (C) Pulmonary metastases *(arrow)* are seen on the axial CT chest in lung windows.

Other islet cell tumors are rare in children, but they may be found in association with tumors in other organs as part of a genetic syndrome, in which case multiple synchronous neuroendocrine tumors can be observed.[104] Gastrinomas may be found in children with Zollinger-Ellison syndrome. In one series, 2 of 56 reported cases of VIP-producing tumors in children were islet cell tumors; neurogenic tumors generated the hormone in the other patients.[117] Pancreatic neuroendocrine tumors in the setting of tuberous sclerosis complex may be functioning or nonfunctioning but typically are diagnosed at a small size[118] incidentally on imaging performed to evaluate renal involvement of disease.

## Other Pancreatic Tumors

***Overview.*** The exocrine tissues of the pancreas give rise to benign and malignant tumors that are hormonally inactive, such as cystadenoma, adenocarcinoma, and adenosarcoma.

***Clinical Presentation.*** The most common presenting symptoms include abdominal pain in 55.8%, nausea or vomiting in 32.6%, fatigue in 25.6%, and an abdominal mass in 23.3%.[119] Cystadenomas and adenocarcinomas of the pancreas rarely occur in children and have been described in infants as well.[120] Pancreatic adenocarcinoma has been described in an adolescent boy with Peutz-Jeghers syndrome,[121] which carries a 100-fold increased risk.[122]

***Imaging.*** On US, solid tumors are typically hyperechoic, and cystic lesions are anechoic or hypoechoic. Adenocarcinomas may have cystic or hemorrhagic areas that result in mixed echogenicity. CT usually identifies a pancreatic mass of variable size, often causing biliary obstruction. In a recent study, pancreatic duct adenocarcinomas were identified in only 3 patients younger than 20 years among a total cohort of 439 cases.[123] Such tumors are often associated with a genetic predisposition. Because the diagnosis of pancreatic carcinoma is so rare in children (only about 50 cases have been reported), imaging evaluation is often delayed, and vascular invasion and metastases to lymph nodes and liver may be noted on imaging.[123]

Rhabdomyosarcoma may arise primarily in the pancreas (e-Fig. 95.17), as may lymphoma (Fig. 95.18). Neuroblastoma has been reported in the pancreas either as primary (e-Fig. 95.19) or secondary to direct extension. A single case of abdominal desmoid tumor presenting in the pancreas was reported in a 17-year-old boy with familial adenomatous polyposis syndrome.[124]

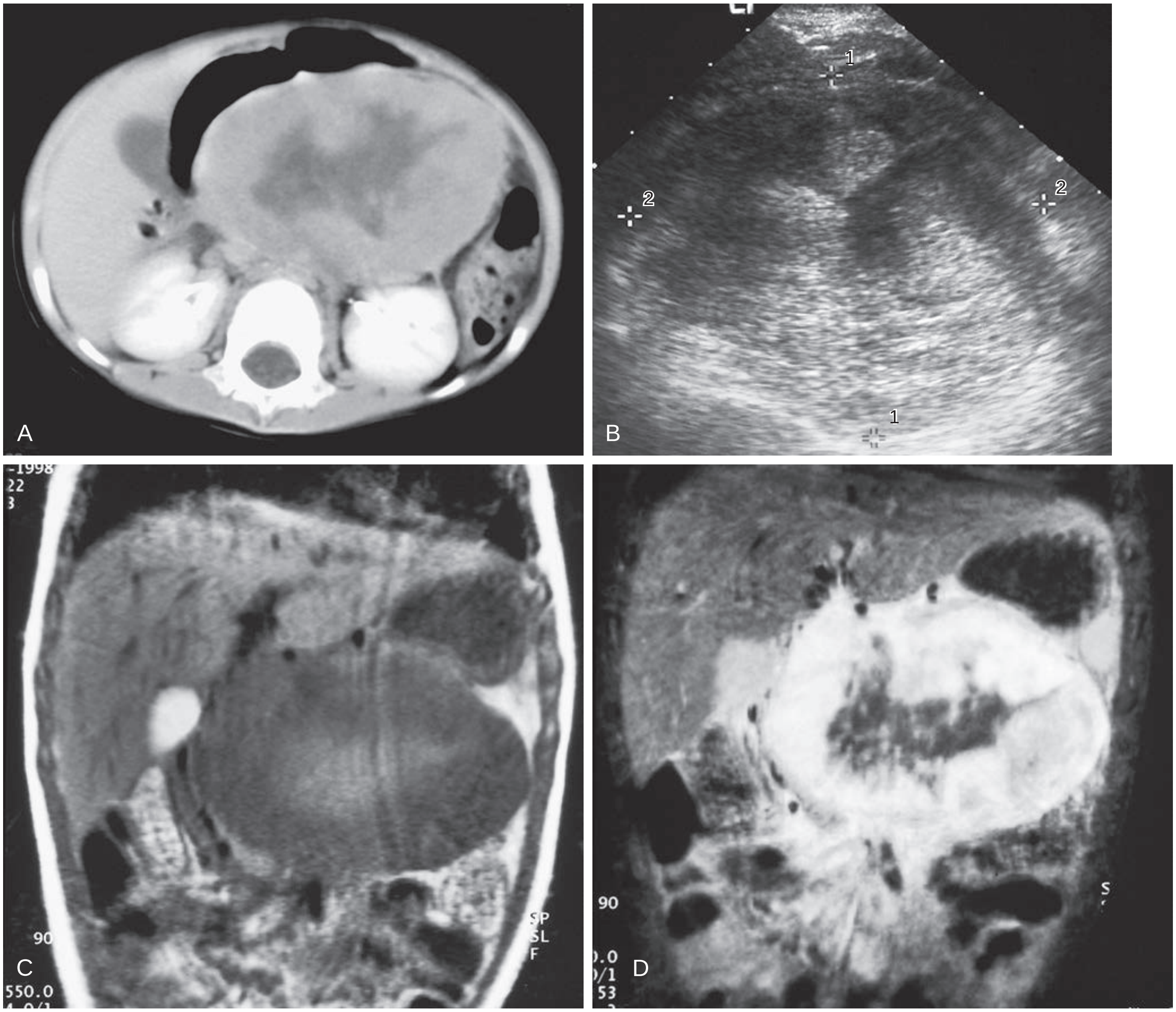

**e-Figure 95.17. Primary alveolar rhabdomyosarcoma of the pancreas in a 3-year-old boy.** (A) Axial, contrast-enhanced abdominal CT shows a large midabdominal mass that arises from the pancreatic body with a central hypodense area. (B) Axial US through the upper abdomen shows the mass *(between cursors)* to be of heterogeneous echogenicity. (C) Coronal, noncontrast, T1-weighted MR image shows irregular high signal centrally, surrounded by decreased signal in the bulk of the mass. (D) Coronal, contrast-enhanced, T1-weighted MR image with fat saturation shows diffuse, intense peripheral enhancement of the bulk of the mass around the central area in addition to surrounding edema.

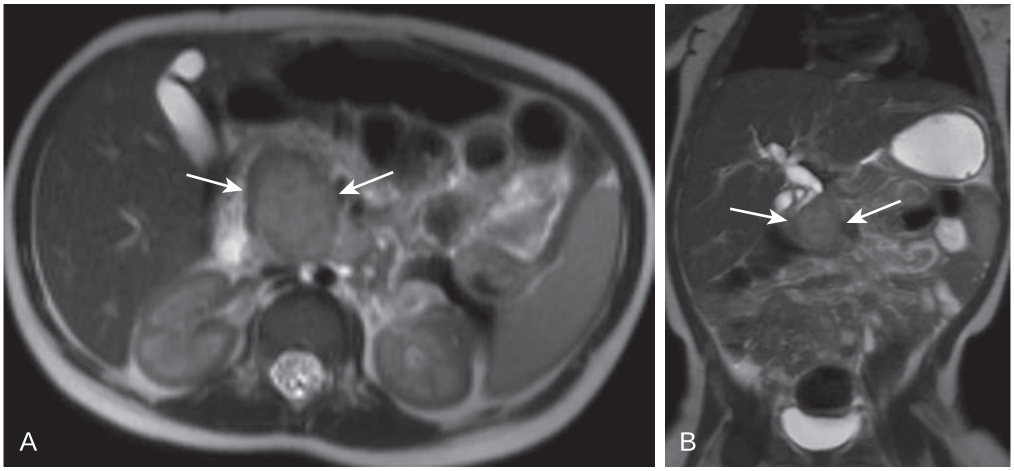

**e-Figure 95.19. Primary pancreatic neuroblastoma in a 15-month-old boy with intermittent jaundice.** Axial (A) and coronal (B) T2-weighted MR image of the abdomen demonstrates a gently lobulated, T2-hyperintense mass in the head of the pancreas *(arrows)*. Pathology after a pylorus-sparing Whipple pancreaticoduodenectomy revealed a poorly differentiated primary pancreatic neuroblastoma.

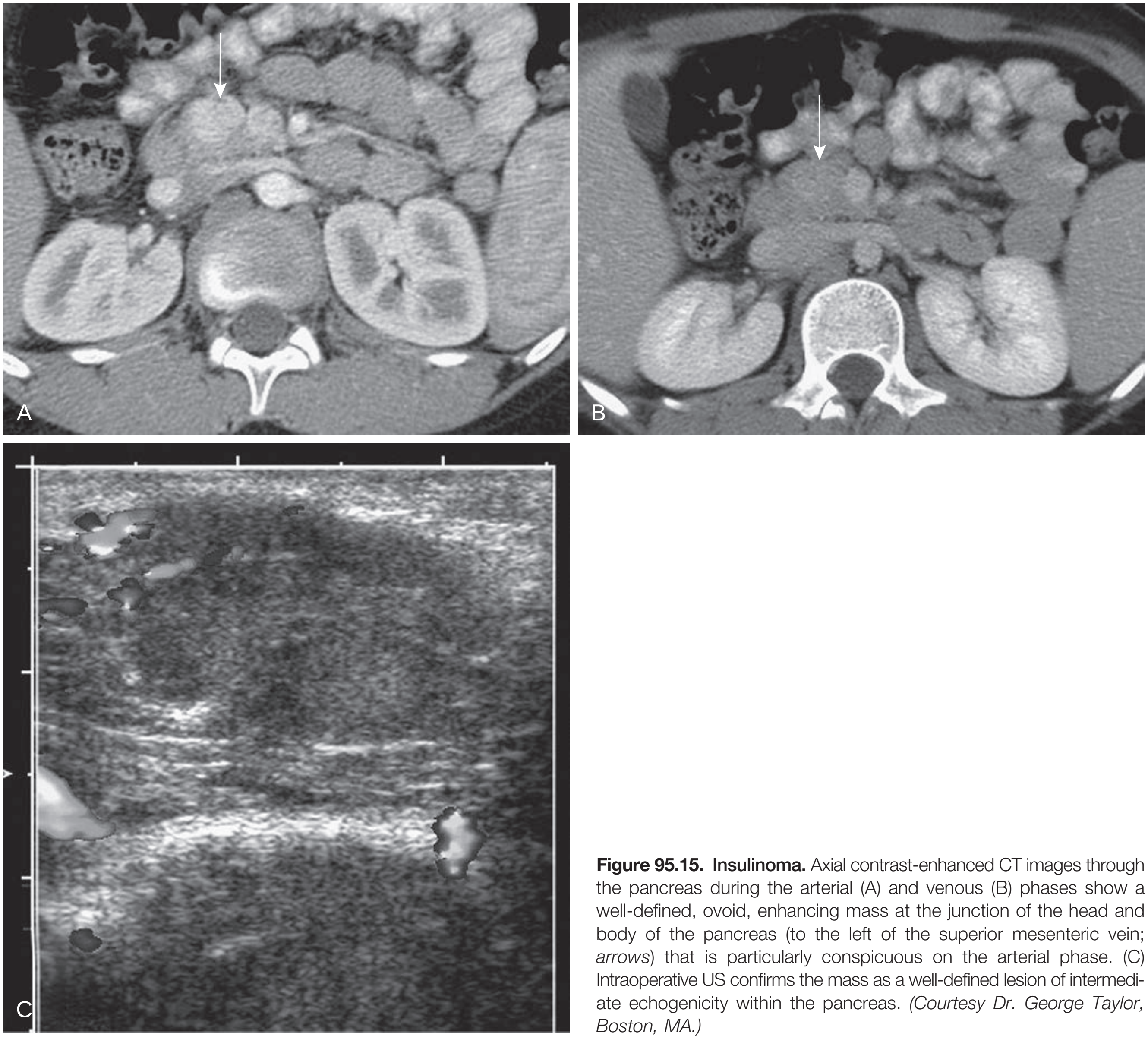

**Figure 95.15. Insulinoma.** Axial contrast-enhanced CT images through the pancreas during the arterial (A) and venous (B) phases show a well-defined, ovoid, enhancing mass at the junction of the head and body of the pancreas (to the left of the superior mesenteric vein; *arrows*) that is particularly conspicuous on the arterial phase. (C) Intraoperative US confirms the mass as a well-defined lesion of intermediate echogenicity within the pancreas. *(Courtesy Dr. George Taylor, Boston, MA.)*

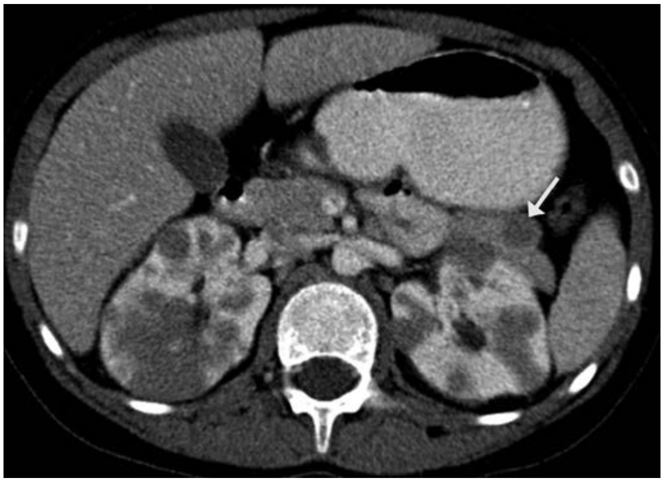

**Figure 95.18. Widely disseminated non-Hodgkin lymphoma involving the pancreas.** Axial contrast-enhanced CT image through the abdomen show, multiple rounded lymphomatous deposits in both kidneys and the pancreatic tail *(arrow)*.

Lymphatic malformations of the pancreas are extremely rare and account for less than 1% of cases.[125] They may occur in any portion of the pancreas at any age and are more frequent in females. On imaging, lymphatic malformations appear as septated, fluid-filled masses. Clinical presentation is nonspecific and includes nausea, vomiting, vague abdominal pain, and a palpable mass.

Exceptionally rare tumors of the pancreas include anaplastic large cell lymphoma,[99] infantile myofibromatosis,[126] and mature cystic teratoma.[127] Cystic teratoma of the pancreas has been reported in at least seven pediatric patients, who ranged in age from 2 to 16 years. These tumors arise from pluripotent cells of ectodermal cell lines and, like other extragonadal teratomas, likely originate from aberrant germ cells. Such tumors may be indistinguishable from other cystic abdominal masses.

Pancreatic involvement with metastatic disease is also rare but includes malignant melanoma, lymphoma (e-Fig. 95.20), rhabdomyosarcoma (Fig. 95.21), acute lymphoblastic leukemia, and osteosarcoma (e-Fig. 95.22).[128,129]

## Treatment of Pancreatic Neoplasms

Most pancreatic tumors are treated primarily with pancreatic resection and pancreatoduodenectomy. Resection is complete for

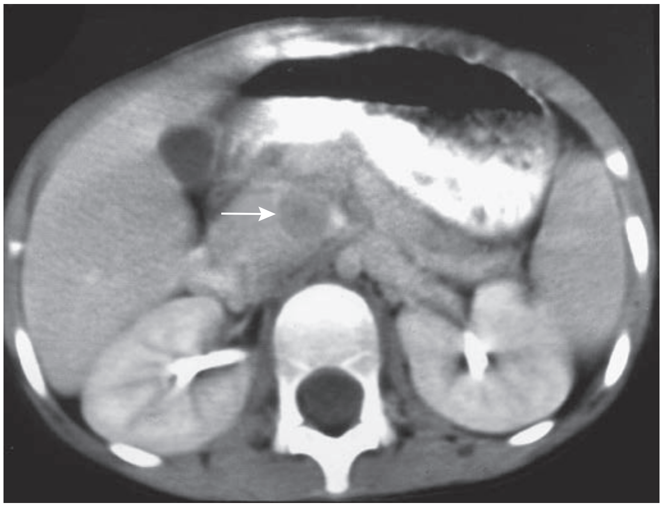

**e-Figure 95.20. Primary lymphoma of bone metastatic to the pancreas.** Axial computed tomographic image of the abdomen in an 8-year-old boy with known lymphoma of bone shows a focal, well-defined, hypoattenuating mass within the body of the pancreas *(arrow)*. This lesion showed mild gallium uptake on scintigraphy *(not shown)*.

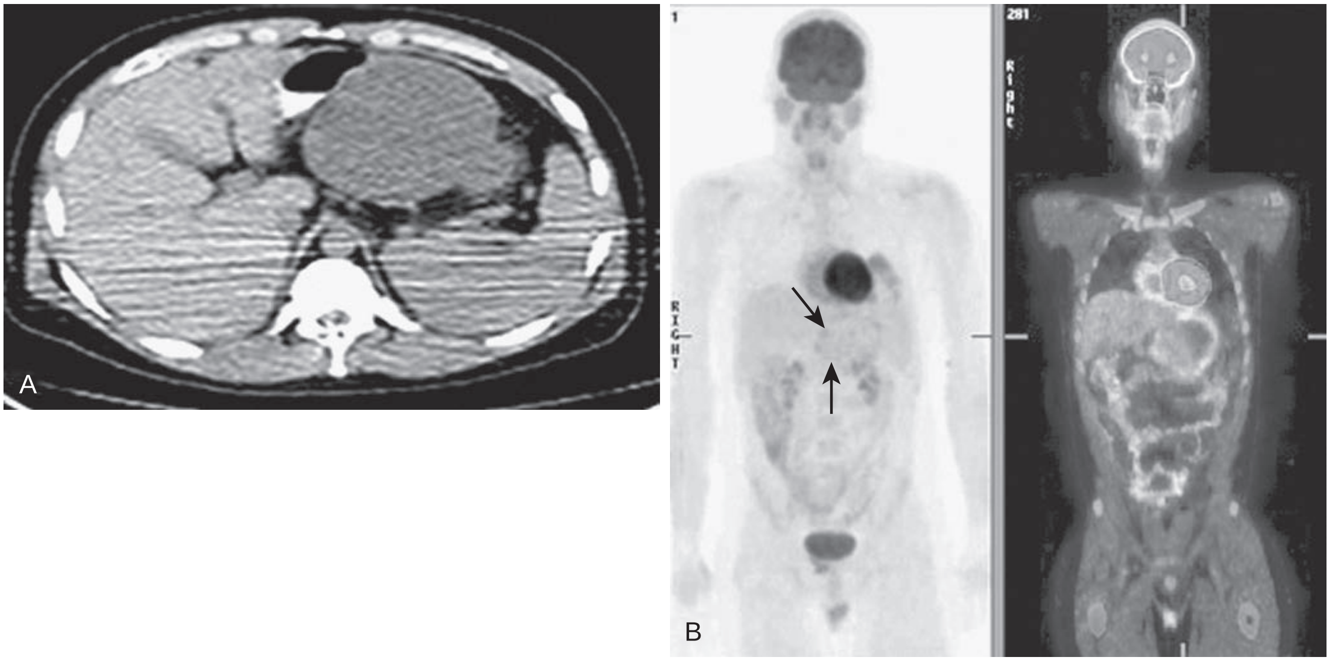

**e-Figure 95.22. Recurrent osteosarcoma metastatic to the pancreas in a 19-year-old man.** Five years earlier, the patient had been treated with multi-drug chemotherapy and limb-sparing surgery for nonmetastatic primary femoral osteosarcoma. He had been well until coming to medical attention with abdominal pain and fatigue. (A) Noncontrast axial CT through the upper abdomen as part of a fluorodeoxyglucose PET scan shows a large, low-density midabdominal mass arising from the midbody of the pancreas. (B) Anterior planar attenuation-corrected PET image *(left)* shows a subtle blush of uptake in the distribution of the mass *(arrows)*. Fused FDG-PET CT image *(right)* shows minimal peripheral uptake in the mass and central photopenia consistent with central necrosis; this was confirmed by aspiration and biopsy.

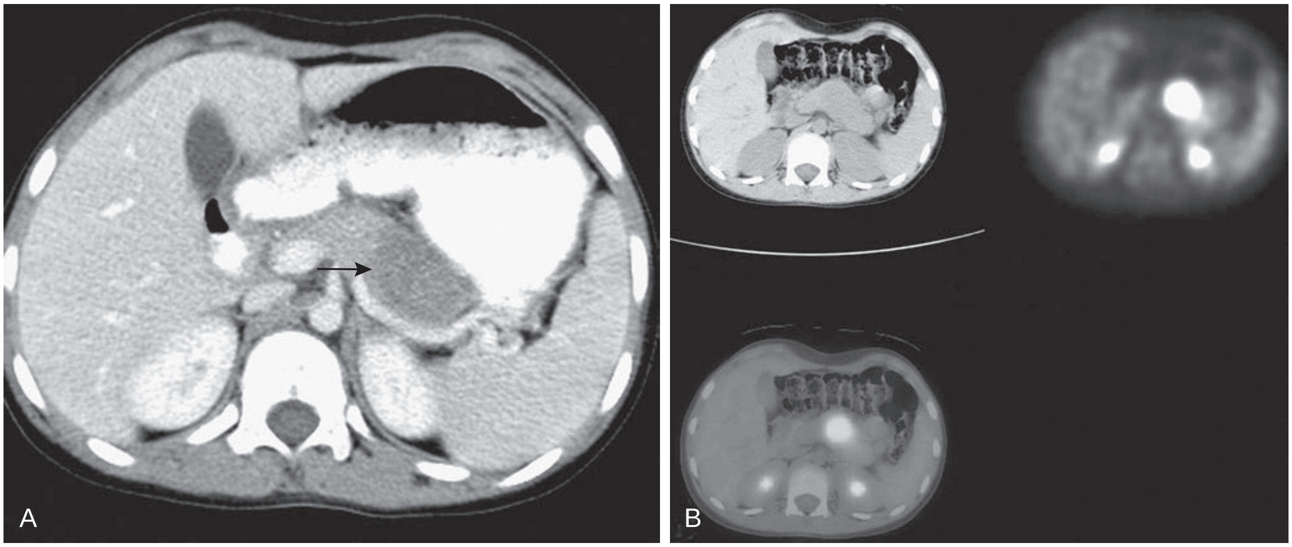

**Figure 95.21. Recurrent rhabdomyosarcoma metastatic to the pancreas.** Three years earlier, this 10-year-old girl had been treated for alveolar rhabdomyosarcoma of the calf. (A) Axial contrast-enhanced abdominal CT shows a well-defined low-density mass in the pancreas *(arrow)*. (B) Axial fluorodeoxyglucose PET CT image shows the lesion as a focal mass with intense uptake of radiopharmaceutical in the midbody of the pancreas.

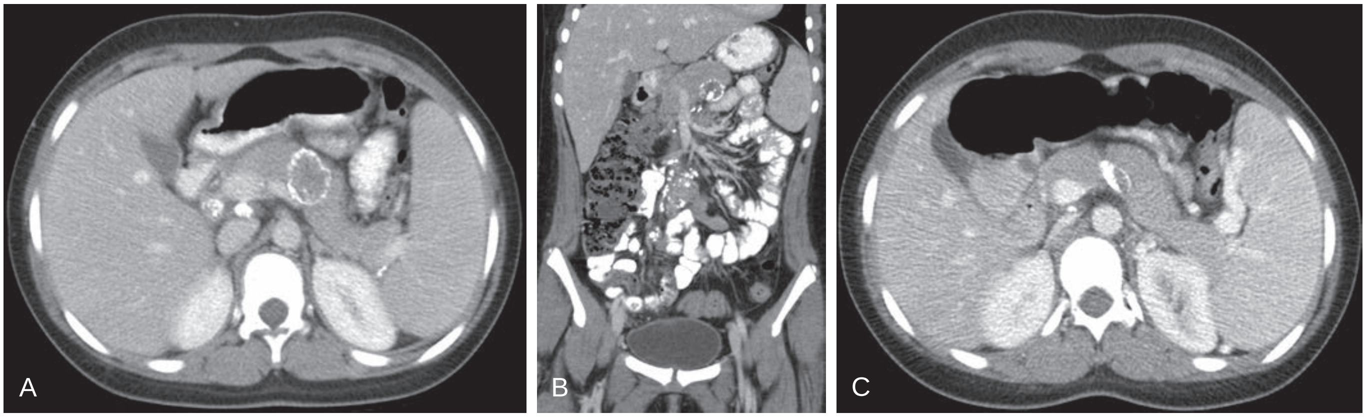

**Figure 95.23. Pancreatic tuberculosis in an HIV-positive teen.** (A) Axial contrast-enhanced CT through the upper abdomen shows a large, peripherally calcified, relatively hypodense lesion in the pancreatic body. (B) Coronal CT image through the abdomen demonstrates this lesion again; both axial and coronal images demonstrate calcified retroperitoneal lymph nodes. This patient was on multidrug therapy for abdominal tuberculosis. (C) Axial CT through the upper abdomen 2 years later demonstrates interval shrinkage of the peripherally calcified pancreatic body lesion; calcific foci appear more coarse and chunky as a result.

aggressive and advanced tumors; partial pancreatectomy[130] and enucleation may be indicated for less aggressive or small neoplasms. Radiotherapy or chemotherapy is less frequently indicated in the pediatric population.[104] Supportive medical therapy may be indicated, such as IV glucose for insulinoma or adenomatosis-induced hypoglycemia and for gastrinoma-induced Zollinger-Ellison syndrome.

## PANCREATIC INFECTIONS

### Hydatid Disease

***Overview.*** Pancreatic hydatid disease, or echinococcosis, is extremely rare and can result from parasitic infestation with *Echinococcus granulosus*, a parasite that affects humans and other mammals, most notably dogs and sheep.[131] The disease manifests as cysts in the affected organ.

***Clinical Presentation.*** Jaundice and abdominal pain may be the first symptoms of hydatid disease of the pancreas, and hydatid disease may also be a rare cause of recurrent pancreatitis.[132]

***Imaging.*** Abdominal CT demonstrates a complex, cystic pancreatic mass, most commonly in the pancreatic head.[131] Larger cysts may have smaller "daughter" cysts within them.

***Treatment.*** Conservative therapy with albendazole and surgical procedures such as subtotal cystectomy, distal pancreatectomy, cystoenteric anastomosis, Whipple resection, marsupialization, and external drainage have been used.

### Tuberculosis

***Overview and Clinical Presentation.*** Patients with abdominal tuberculosis are human immunodeficiency virus positive or otherwise immune compromised, or are from areas endemic for tuberculosis.

***Imaging.*** Abdominal tuberculosis (Fig. 95.23) can result in focal pancreatic parenchymal lesions or tuberculous abscesses, usually with one or more calcified components and imaging evidence of abdominal tuberculosis elsewhere (retroperitoneal adenopathy that is usually matted and may or may not be centrally necrotic or calcified; tuberculous ascites; matting of bowel loops or omentum, so-called omental cake; and intraperitoneal adhesions).[133]

***Treatment.*** Antituberculous multidrug therapy is recommended for up to 1 year; three to four drugs are given for the first 2 months, and then two drugs are given for up to 10 months. Surgical intervention is used for complicated cases.

## KEY POINTS

- Pancreas divisum is a normal variant due to failure of fusion of the dorsal and ventral anlage. The incidence of pancreatitis is slightly higher in individuals with pancreas divisum.
- Annular pancreas typically presents with duodenal obstruction in the neonatal period or pancreatitis/extrahepatic biliary obstruction in adults. There are often associated abnormalities.
- Imaging of patients with CF may reveal a spectrum of findings, from a normal to mildly enlarged pancreas in early stages of the disease to complete fatty replacement with calcification or “pancreatic cystosis” in advanced stages.
- Nonaccidental trauma should be considered as a potential etiology in children with unexplained pancreatic trauma or pancreatitis.
- Complications of acute pancreatitis evident by imaging include pseudocysts, splenic vein thrombosis, and splenic artery pseudoaneurysms.
- Direct evidence of pancreatic trauma at imaging includes contusion, transection, laceration, and comminution. Indirect findings include findings of acute pancreatitis and/or duodenal hematoma.
- Solid-cystic papillary tumor is the most common pancreatic tumor in children.
- Pancreatoblastoma and focal adenomatosis are pancreatic tumors associated with BWS.

## SUGGESTED READING

Anupindi SA, Chauvin NA, Khwaja A, et al. Magnetic resonance imaging of pancreaticobiliary diseases in children: from technique to practice. *Pediatr Radiol*. 2016;46(6):778–790.

Bollen TL, Singh VK, Maurer R, et al. A comparative evaluation of radiologic and clinical scoring systems in the early prediction of severity in acute pancreatitis. *Am J Gastroenterol*. 2011;107(4):612–619.

Chung EM, Travis MD, Conran RM. Pancreatic tumors in children: radiologic-pathologic correlation. *Radiographics*. 2006;26(4):1211–1238.

Foster BR, Jensen KK, Bakis G, et al. Revised Atlanta Classification for acute pancreatitis: a pictorial essay. *Radiographics*. 2016;36(3):675–687.

Shet NS, Cole BL, Iyer R. Imaging of pediatric pancreatic neoplasms with radiologic-histopathologic correlation. *AJR*. 2014;202(6):1337–1348.

## REFERENCES

Full references for this chapter can be found on www.expertconsult.com.

## REFERENCES

1. Shera A, Shah O. Congenital common bile duct web in association with hepatobiliary pancreatic ductal anomalies. *Eur J Pediatr Surg*. 2008;18(5):350–351. doi:10.1055/s-2008-1038444.
2. Chao HC, Lin SJ, Kong MS, et al. Sonographic evaluation of the pancreatic duct in normal children and children with pancreatitis. *J Ultrasound Med Off J Am Inst Ultrasound Med*. 2000;19(11):757–763.
3. Nijs E, Callahan MJ, Taylor GA. Disorders of the pediatric pancreas: imaging features. *Pediatr Radiol*. 2005;35(4):358–373. doi:10.1007/s00247-004-1326-1.
4. Siegel MJ, Martin KW, Worthington JL. Normal and abnormal pancreas in children: US studies. *Radiology*. 1987;165(1):15–18. doi:10.1148/radiology.165.1.3306783.
5. Teele RL, Share JC. *Ultrasonography of Infants and Children*. Philadelphia, Pa.: Saunders; 1991.
6. Walsh E, Cramer B, Pushpanathan C. Pancreatic echogenicity in premature and newborn infants. *Pediatr Radiol*. 1990;20(5):323–325.
7. Gong J-S, Xu J-M. Role of curved planar reformations using multidetector spiral CT in diagnosis of pancreatic and peripancreatic diseases. *World J Gastroenterol*. 2004;10(13):1943–1947.
8. Thai TC, Riherd DM, Rust KR. MRI Manifestations of pancreatic disease, especially pancreatitis, in the pediatric population. *Am J Roentgenol*. 2013;201(6):W877–W892. doi:10.2214/AJR.13.10834.
9. Keppke AL, Miller FH. Magnetic resonance imaging of the pancreas: the future is now. *Semin Ultrasound CT MR*. 2005;26(3):132–152.
10. Hakimé A, Giraud M, Vullierme M-P, et al. [MR imaging of the pancreas]. *J Radiol*. 2007;88(1 Pt 1):11–25.
11. Jaimes C, Gee MS. Strategies to minimize sedation in pediatric body magnetic resonance imaging. *Pediatr Radiol*. 2016;46(6):916–927. doi:10.1007/s00247-016-3613-z.
12. Chavhan GB, Babyn PS, Vasanawala SS. Abdominal MR imaging in children: motion compensation, sequence optimization, and protocol organization. *Radiographics*. 2013;33(3):703–719. doi:10.1148/rg.333125027.
13. Semelka RC, Ascher SM. MR imaging of the pancreas. *Radiology*. 1993;188(3):593–602. doi:10.1148/radiology.188.3.8351317.
14. Arcement CM, Meza MP, Arumanla S, et al. MRCP in the evaluation of pancreaticobiliary disease in children. *Pediatr Radiol*. 2001;31(2):92–97. doi:10.1007/s002470000326.
15. Kolodziejczyk E, Jurkiewicz E, Pertkiewicz J, et al. MRCP versus ERCP in the evaluation of chronic pancreatitis in children: which is the better choice? *Pancreas*. 2016;45(8):1115–1119. doi:10.1097/MPA.0000000000000644.
16. Bolog N, Constantinescu G, Oancea I, et al. Magnetic resonance imaging of bile and pancreatic ducts: a retrospective study. *Romanian J Gastroenterol*. 2004;13(2):91–97.
17. Suarez F, Bernard O, Gauthier F, et al. Bilio-pancreatic common channel in children: clinical, biological and radiological findings in 12 children. *Pediatr Radiol*. 1987;17(3):206–211. doi:10.1007/BF02388161.
18. Hamada Y, Tanano A, Takada K, et al. Magnetic resonance cholangiopancreatography on postoperative work-up in children with choledochal cysts. *Pediatr Surg Int*. 2004;20(1):43–46. doi:10.1007/s00383-003-1079-1.
19. Fulcher AS, Turner MA. Orthotopic liver transplantation: evaluation with MR cholangiography. *Radiology*. 1999;211(3):715–722. doi:10.1148/radiology.211.3.r99jn17715.
20. Van Hoe L, Mermuys K, Vanhoenacker P. MRCP pitfalls. *Abdom Imaging*. 2004;29(3):doi:10.1007/s00261-003-0119-6.
21. Akisik MF, Sandrasegaran K, Aisen AA, et al. Dynamic Secretin-enhanced MR Cholangiopancreatography. *Radiographics*. 2006;26(3):665–677. doi:10.1148/rg.263055077.
22. Calculli L, Pezzilli R, Fiscaletti M, et al. Exocrine pancreatic function assessed by secretin cholangio-Wirsung magnetic resonance imaging. *Hepatobiliary Pancreat Dis Int*. 2008;7(2):192–195.
23. Fukukura Y, Fujiyoshi F, Sasaki M, et al. Pancreatic duct: morphologic evaluation with MR cholangiopancreatography after secretin stimulation. *Radiology*. 2002;222(3):674–680. doi:10.1148/radiol.2223010684.
24. Tirkes T, Akisik F, Tann M, et al. Imaging of the pancreas with secretin enhancement. *Top Magn Reson Imaging*. 2009;20(1):19–24. doi:10.1097/RMR.0b013e3181b483f0.
25. Trout AT, Podberesky DJ, Serai SD, et al. Does secretin add value in pediatric magnetic resonance cholangiopancreatography? *Pediatr Radiol*. 2013;43(4):479–486.
26. Lopez Hänninen E, Amthauer H, Hosten N, et al. Prospective evaluation of pancreatic tumors: accuracy of MR imaging with MR cholangiopancreatography and MR angiography. *Radiology*. 2002;224(1):34–41. doi:10.1148/radiol.2241010798.
27. Cappeliez O, Delhaye M, Devière J, et al. Chronic pancreatitis: evaluation of pancreatic exocrine function with MR pancreatography after secretin stimulation. *Radiology*. 2000;215(2):358–364. doi:10.1148/radiology.215.2.r00ma10358.
28. Wood JC. Use of magnetic resonance imaging to monitor iron overload. *Hematol Oncol Clin North Am*. 2014;28(4):747–764. doi:10.1016/j.hoc.2014.04.002.
29. Nijs ELF, Callahan MJ. Congenital and developmental pancreatic anomalies: ultrasound, computed tomography, and magnetic resonance imaging features. *Semin Ultrasound CT MR*. 2007;28(5):395–401.
30. Benya EC. Pancreas and biliary system: imaging of developmental anomalies and diseases unique to children. *Radiol Clin North Am*. 2002;40(6):1355–1362.
31. Cotton PB. Congenital anomaly of pancreas divisum as cause of obstructive pain and pancreatitis. *Gut*. 1980;21(2):105–114.
32. Soulen MC, Zerhouni EA, Fishman EK, et al. Enlargement of the pancreatic head in patients with pancreas divisum. *Clin Imaging*. 1989;13(1):51–57.
33. Zeman RK, McVay LV, Silverman PM, et al. Pancreas divisum: thin-section CT. *Radiology*. 1988;169(2):395–398. doi:10.1148/radiology.169.2.3174986.
34. Manfredi R, Costamagna G, Brizi MG, et al. Pancreas divisum and "Santorinicele": diagnosis with dynamic MR cholangiopancreatography with secretin stimulation. *Radiology*. 2000;217(2):403–408. doi:10.1148/radiology.217.2.r00nv29403.
35. Kanamori A, Kumada T, Kiriyama S, et al. Endoscopic papillectomy of minor papillar adenoma associated with pancreas divisum. *World J Gastroenterol*. 2009;15(9):1138–1140.
36. Schnedl WJ, Piswanger-Soelkner C, Wallner SJ, et al. Agenesis of the dorsal pancreas. *World J Gastroenterol*. 2009;15(3):376–377.
37. Gilinsky NH, Del Favero G, Cotton PB, et al. Congenital short pancreas: a report of two cases. *Gut*. 1985;26(3):304–310.
38. Schnedl WJ, Piswanger-Soelkner C, Wallner SJ, et al. Agenesis of the dorsal pancreas and associated diseases. *Dig Dis Sci*. 2009;54(3):481–487. doi:10.1007/s10620-008-0370-3.
39. Sakpal SV, Sexcius L, Babel N, et al. Agenesis of the dorsal pancreas and its association with pancreatic tumors. *Pancreas*. 2009;38(4):367–373. doi:10.1097/MPA.0b013e318196c401.
40. Complete pancreatic ectopia in a gastric duplication cyst: a case report and review of the literature. *Eur J Pediatr Surg*. 2004;14(1):60–62. doi:10.1055/s-2004-815783.
41. Kilman WJ, Berk RN. The spectrum of radiographic features of aberrant pancreatic rests involving the stomach. *Radiology*. 1977;123(2):291–296. doi:10.1148/123.2.291.
42. Tillig B, Gerein V, Coerdt W, et al. Large supraumbilical pseudocystic tumour due to ectopic pancreatic tissue located in a rest of the omphaloenteric duct. *Eur J Pediatr Surg*. 2004;14(2):126–129. doi:10.1055/s-2004-815861.
43. Rahmah R, Yong JF, Sharifa NA, et al. Bilateral adrenal cysts and ectopic pancreatic tissue in Beckwith-Wiedemann syndrome: is a conservative approach acceptable? *J Pediatr Endocrinol Metab*. 2004;17(6):909–912.
44. Ueda D, Taketazu M, Itoh S, et al. A case of gastric duplication cyst with aberrant pancreas. *Pediatr Radiol*. 1991;21(5):379–380.
45. Kim JY, Lee JM, Kim KW, et al. Ectopic pancreas: CT findings with emphasis on differentiation from small gastrointestinal stromal tumor and leiomyoma. *Radiology*. 2009;252(1):92–100. doi:10.1148/radiol.2521081441.
46. Zyromski NJ, Sandoval JA, Pitt HA, et al. Annular pancreas: dramatic differences between children and adults. *J Am Coll Surg*. 2008;206(5):1019–1025. doi:10.1016/j.jamcollsurg.2007.12.009.
47. Baggott BB, Long WB. Annular pancreas as a cause of extrahepatic biliary obstruction. *Am J Gastroenterol*. 1991;86(2):224–226.
48. Vijayaraghavan SB. Sonography of pancreatic ductal anatomic characteristics in annular pancreas. *J Ultrasound Med Off J Am Inst Ultrasound Med*. 2002;21(11):1315–1318.
49. De Ugarte DA, Dutson EP, Hiyama DT. Annular pancreas in the adult: management with laparoscopic gastrojejunostomy. *Am Surg*. 2006;72(1):71–73.
50. To'o KJ, Raman SS, Yu NC, et al. Pancreatic and peripancreatic diseases mimicking primary pancreatic neoplasia. *Radiographics*. 2005;25(4):949–965. doi:10.1148/rg.254045167.

51. Handrich SJ, Hough DM, Fletcher JG, et al. The natural history of the incidentally discovered small simple pancreatic cyst: long-term follow-up and clinical implications. *Am J Roentgenol*. 2005;184(1):20–23. doi:10.2214/ajr.184.1.01840020.
52. Baker LL, Hartman GE, Northway WH. Sonographic detection of congenital pancreatic cysts in the newborn: report of a case and review of the literature. *Pediatr Radiol*. 1990;20(6):488–490.
53. Choyke PL, Filling-Katz MR, Shawker TH, et al. von Hippel-Lindau disease: radiologic screening for visceral manifestations. *Radiology*. 1990;174(3):815–820. doi:10.1148/radiology.174.3.2305064.
54. Claudon M, Verain AL, Bigard MA, et al. Cyst formation in gastric heterotopic pancreas: report of two cases. *Radiology*. 1988;169(3):659–660. doi:10.1148/radiology.169.3.3055030.
55. Feigelson J, Pécau Y, Poquet M, et al. Imaging changes in the pancreas in cystic fibrosis: a retrospective evaluation of 55 cases seen over a period of 9 years. *J Pediatr Gastroenterol Nutr*. 2000;30(2):145–151.
56. Ferrozzi F, Bova D, Campodonico F, et al. Cystic fibrosis: MR assessment of pancreatic damage. *Radiology*. 1996;198(3):875–879. doi:10.1148/radiology.198.3.8628886.
57. Daneman A, Gaskin K, Martin D, et al. Pancreatic changes in cystic fibrosis: CT and sonographic appearances. *Am J Roentgenol*. 1983;141(4):653–655. doi:10.2214/ajr.141.4.653.
58. Liu P, Daneman A, Stringer DA, et al. Pancreatic cysts and calcification in cystic fibrosis. *Can Assoc Radiol J*. 1986;37(4):279–282.
59. Tham RT, Heyerman HG, Falke TH, et al. Cystic fibrosis: MR imaging of the pancreas. *Radiology*. 1991;179(1):183–186. doi:10.1148/radiology.179.1.2006275.
60. Murayama S, Robinson AE, Mulvihill DM, et al. MR imaging of pancreas in cystic fibrosis. *Pediatr Radiol*. 1990;20(7):536–539.
61. Berrocal T, Pajares MP, Zubillaga AF. Pancreatic cystosis in children and young adults with cystic fibrosis: sonographic, CT, and MRI findings. *Am J Roentgenol*. 2005;184(4):1305–1309. doi:10.2214/ajr.184.4.01841305.
62. Madzak A, Engjom T, Wathle GK, et al. Secretin-stimulated MRI assessment of exocrine pancreatic function in patients with cystic fibrosis and healthy controls. *Abdom Radiol*. 2016;doi:10.1007/s00261-016-0972-8.
63. Sodhi KS, Thapa BR, Khandelwal S, et al. Pancreatic lipomatosis in an infant with cystic fibrosis. *Pediatr Radiol*. 2005;35(11):1157–1158. doi:10.1007/s00247-005-1520-9.
64. Eras M, Yenigun M, Acar C, et al. Pancreatic involvement in Von Hippel-Lindau disease. *Indian J Cancer*. 2004;41(4):159–161.
65. Shen H-CJ, Adem A, Ylaya K, et al. Deciphering von Hippel-Lindau (VHL/Vhl)-associated pancreatic manifestations by inactivating Vhl in specific pancreatic cell populations. Beier DR, ed. *PLoS ONE*. 2009;4(4):e4897. doi:10.1371/journal.pone.0004897.
66. Hammel PR, Vilgrain V, Terris B, et al. Pancreatic involvement in von Hippel-Lindau disease. The Groupe Francophone d'Etude de la Maladie de von Hippel-Lindau. *Gastroenterology*. 2000;119(4):1087–1095.
67. Sweeney WE, Avner ED. Diagnosis and management of childhood polycystic kidney disease. *Pediatr Nephrol*. 2011;26(5):675–692. doi:10.1007/s00467-010-1656-1.
68. Chung EM, Conran RM, Schroeder JW, et al. From the radiologic pathology archives: pediatric polycystic kidney disease and other ciliopathies: radiologic-pathologic correlation. *Radiographics*. 2014;34(1):155–178. doi:10.1148/rg.341135179.
69. Lopez MJ. The changing incidence of acute pancreatitis in children: a single-institution perspective. *J Pediatr*. 2002;140(5):622–624. doi:10.1067/mpd.2002.123880.
70. Nydegger A, Heine RG, Ranuh R, et al. Changing incidence of acute pancreatitis: 10-year experience at the Royal Children's Hospital, Melbourne. *J Gastroenterol Hepatol*. 2007;22(8):1313–1316. doi:10.1111/j.1440-1746.2007.04936.x.
71. Morinville VD, Barmada MM, Lowe ME. Increasing incidence of acute pancreatitis at an American pediatric tertiary care center: is greater awareness among physicians Responsible? *Pancreas*. 2010;39(1):5–8. doi:10.1097/MPA.0b013e3181baac47.
72. Ma MH, Bai HX, Park AJ, et al. Risk factors associated with biliary pancreatitis in children. *J Pediatr Gastroenterol Nutr*. 2012;54(5):651–656. doi:10.1097/MPG.0b013e31823a897d.
73. Weizman Z, Durie PR. Acute pancreatitis in childhood. *J Pediatr*. 1988;113(1 Pt 1):24–29.
74. Gananadha S, Smith R. Hepatobiliary and pancreatic: anomalous pancreatobiliary junction with choledochal cyst. *J Gastroenterol Hepatol*. 2006;21(4):776. doi:10.1111/j.1440-1746.2006.04439.x.
75. Roberts-Thomson I. Hepatobiliary and pancreatic: anomalous pancreatobiliary ductal junction. *J Gastroenterol Hepatol*. 2006;21(4):775. doi:10.1111/j.1440-1746.2006.04438.x.
76. Jeong JB, Whang JH, Ryu JK, et al. Risk factors for pancreatitis in patients with anomalous union of pancreatobiliary duct. *Hepatogastroenterology*. 2004;51(58):1187–1190.
77. Kamisawa T, Kurata M, Honda G, et al. Biliopancreatic reflux—pathophysiology and clinical implications. *J Hepatobiliary Pancreat Surg*. 2009;16(1):19–24. doi:10.1007/s00534-008-0010-5.
78. Lee SP, Nicholls JF, Park HZ. Biliary sludge as a cause of acute pancreatitis. *N Engl J Med*. 1992;326(9):589–593. doi:10.1056/NEJM199202273260902.
79. Hirabayashi K, Zamboni G. IgG4-related disease. *Pathologica*. 2012;104(2):43–55.
80. Restrepo R, Hagerott HE, Kulkarni S, et al. Acute pancreatitis in pediatric patients: demographics, etiology, and diagnostic imaging. *Am J Roentgenol*. 2016;206(3):632–644. doi:10.2214/AJR.14.14223.
81. Swischuk L, Hayden C. Pararenal space hyperechogenicity in childhood pancreatitis. *Am J Roentgenol*. 1985;145(5):1085–1086. doi:10.2214/ajr.145.5.1085.
82. Balthazar EJ, Robinson DL, Megibow AJ, et al. Acute pancreatitis: value of CT in establishing prognosis. *Radiology*. 1990;174(2):331–336. doi:10.1148/radiology.174.2.2296641.
83. Lautz TB, Turkel G, Radhakrishnan J, et al. Utility of the computed tomography severity index (Balthazar score) in children with acute pancreatitis. *J Pediatr Surg*. 2012;47(6):1185–1191. doi:10.1016/j.jpedsurg.2012.03.023.
84. Delhaye M, Matos C, Arvanitakis M, et al. Pancreatic ductal system obstruction and acute recurrent pancreatitis. *World J Gastroenterol*. 2008;14(7):1027–1033.
85. Shimizu T, Suzuki R, Yamashiro Y, et al. Magnetic resonance cholangiopancreatography in assessing the cause of acute pancreatitis in children. *Pancreas*. 2001;22(2):196–199.
86. Thoeni RF. The Revised Atlanta classification of acute pancreatitis: its importance for the radiologist and its effect on treatment. *Radiology*. 2012;262(3):751–764. doi:10.1148/radiol.11110947.
87. Mehta R, Suvarna D, Sadasivan S, et al. Natural course of asymptomatic pancreatic pseudocyst: a prospective study. *Indian J Gastroenterol*. 2004;23(4):140–142.
88. Garel L, Brunelle F, Lallemand D, et al. Pseudocysts of the pancreas in children: which cases require surgery? *Pediatr Radiol*. 1983;13(3):120–124.
89. Amundson GM, Towbin RB, Mueller DL, et al. Percutaneous transgastric drainage of the lesser sac in children. *Pediatr Radiol*. 1990;20(8):590–593.
90. Haller J, Greenway G, Resnick D, et al. Intraosseous fat necrosis associated with acute pancreatitis: MR imaging. *Radiology*. 1989;173(1):193–195. doi:10.1148/radiology.173.1.2781007.
91. Yin W-Y. The role of surgery in pancreatic pseudocyst. *Hepatogastroenterology*. 2005;52(64):1266–1273.
92. Bassi C, Larvin M, Villatoro E. Antibiotic therapy for prophylaxis against infection of pancreatic necrosis in acute pancreatitis. *Cochrane Database Syst Rev*. 2003;(4):CD002941, doi:10.1002/14651858.CD002941.
93. Wheatley MJ, Coran AG. Obstructive jaundice secondary to chronic pancreatitis in children: report of two cases and review of the literature. *Surgery*. 1988;104(5):863–869.
94. Spencer JA, Lindsell DR, Isaacs D. Hereditary pancreatitis: early ultrasound appearances. *Pediatr Radiol*. 1990;20(4):293–295.
95. Atkinson GO, Wyly JB, Gay BB, et al. Idiopathic fibrosing pancreatitis: a cause of obstructive jaundice in childhood. *Pediatr Radiol*. 1988;18(1):28–31.
96. Rollins MD, Meyers RL. Frey procedure for surgical management of chronic pancreatitis in children. *J Pediatr Surg*. 2004;39(6):817–820.
97. Anupindi SA, Chauvin NA, Khwaja A, et al. Magnetic resonance imaging of pancreaticobiliary diseases in children: from technique to practice. *Pediatr Radiol*. 2016;46(6):778–790. doi:10.1007/s00247-016-3608-9.
98. Ahmed TS, Chavhan GB, Navarro OM, et al. Imaging features of pancreatic tumors in children: 13-year experience at a pediatric tertiary hospital. *Pediatr Radiol*. 2013;43(11):1435–1443. doi:10.1007/s00247-013-2721-2.
99. Fraser CJ, Chan YF, Heath JA. Anaplastic large cell lymphoma of the pancreas: a pediatric case and literature review. *J Pediatr Hematol Oncol*. 2004;26(12):840–842.

100. Kosmahl M, Pauser U, Peters K, et al. Cystic neoplasms of the pancreas and tumor-like lesions with cystic features: a review of 418 cases and a classification proposal. *Virchows Arch*. 2004;445(2):doi:10.1007/s00428-004-1043-z.
101. Park M, Koh KN, Kim BE, et al. Pancreatic neoplasms in childhood and adolescence. *J Pediatr Hematol Oncol*. 2011;33(4):295–300. doi:10.1097/MPH.0b013e318206990a.
102. Dall'Igna P, Cecchetto G, Bisogno G, et al. Pancreatic tumors in children and adolescents: the Italian TREP project experience. *Pediatr Blood Cancer*. 2009:n/a-n/a. doi:10.1002/pbc.22385.
103. Tien Y, Ser K, Hu R, et al. Solid pseudopapillary neoplasms of the pancreas: Is there a pathologic basis for the observed gender differences in incidence? *Surgery*. 2005;137(6):591–596. doi:10.1016/j.surg.2005.01.015.
104. Chung EM, Travis MD, Conran RM. Pancreatic tumors in children: radiologic-pathologic correlation. *Radiographics*. 2006;26(4):1211–1238. doi:10.1148/rg.264065012.
105. Moholkar S, Sebire NJ, Roebuck DJ. Solid-pseudopapillary neoplasm of the pancreas: radiological-pathological correlation. *Pediatr Radiol*. 2005;35(8):819–822. doi:10.1007/s00247-005-1461-3.
106. Hassan I, Celik I, Nies C, et al. Successful treatment of solid-Pseudopapillary tumor of the pancreas with multiple liver metastases. *Pancreatology*. 2005;5(2–3):289–294. doi:10.1159/000085285.
107. Tang LH, Aydin H, Brennan MF, et al. Clinically aggressive solid pseudopapillary tumors of the pancreas: a report of two cases with components of undifferentiated carcinoma and a comparative clinicopathologic analysis of 34 conventional cases. *Am J Surg Pathol*. 2005;29(4):512–519.
108. Roebuck DJ, Yuen MK, Wong YC, et al. Imaging features of pancreatoblastoma. *Pediatr Radiol*. 2001;31(7):501–506. doi:10.1007/s002470100448.
109. Dhebri AR, Connor S, Campbell F, et al. Diagnosis, treatment and outcome of pancreatoblastoma. *Pancreatology*. 2004;4(5):441–453. doi:10.1159/000079823.
110. Stephenson CA, Kletzel M, Seibert JJ, et al. Pancreatoblastoma: MR appearance. *J Comput Assist Tomogr*. 1990;14(3):492–493.
111. Kaczirek K, Niederle B. Nesidioblastosis: an old term and a new understanding. *World J Surg*. 2004;28(12):1227–1230. doi:10.1007/s00268-004-7598-7.
112. Koc G, Sugimoto S, Kuperman R, et al. Pancreatic tumors in children and young adults with tuberous sclerosis complex. *Pediatr Radiol*. 2016;Sep 17.
113. Gouya H, Vignaux O, Augui J, et al. CT, Endoscopic sonography, and a combined protocol for preoperative evaluation of pancreatic insulinomas. *Am J Roentgenol*. 2003;181(4):987–992. doi:10.2214/ajr.181.4.1810987.
114. Galiber AK, Reading CC, Charboneau JW, et al. Localization of pancreatic insulinoma: comparison of pre- and intraoperative US with CT and angiography. *Radiology*. 1988;166(2):405–408. doi:10.1148/radiology.166.2.2827232.
115. Brunelle F, Negre V, Barth MO, et al. Pancreatic venous samplings in infants and children with primary hyperinsulinism. *Pediatr Radiol*. 1989;19(2):100–103.
116. Nikou GC, Toubanakis C, Nikolaou P, et al. VIPomas: an update in diagnosis and management in a series of 11 patients. *Hepatogastroenterology*. 2005;52(64):1259–1265.
117. Grosfeld JL, Vane DW, Rescorla FJ, et al. Pancreatic tumors in childhood: analysis of 13 cases. *J Pediatr Surg*. 1990;25(10):1057–1062.
118. Koc G, Sugimoto S, Kuperman R, et al. Pancreatic tumors in children and young adults with tuberous sclerosis complex. *Pediatr Radiol*. 2016 September;doi:10.1007/s00247-016-3701-0.
119. Liang H, Wang P, Wang X-N, et al. Management of nonfunctioning islet cell tumors. *World J Gastroenterol*. 2004;10(12):1806–1809.
120. Lau ST, Kim SS, Lee SL, et al. Mucinous cystadenoma of the pancreas in a one-year-old child. *J Pediatr Surg*. 2004;39(10):1574–1575.
121. Bowlby LS. Pancreatic adenocarcinoma in an adolescent male with Peutz-Jeghers syndrome. *Hum Pathol*. 1986;17(1):97–99.
122. Giardiello FM, Welsh SB, Hamilton SR, et al. Increased risk of cancer in the Peutz-Jeghers syndrome. *N Engl J Med*. 1987;316(24):1511–1514. doi:10.1056/NEJM198706113162404.
123. Lüttges J, Stigge C, Pacena M, et al. Rare ductal adenocarcinoma of the pancreas in patients younger than age 40 years: an analysis of its features and a literature review. *Cancer*. 2004;100(1):173–182. doi:10.1002/cncr.11860.
124. Pho LN, Coffin CM, Burt RW. Abdominal desmoid in familial adenomatous polyposis presenting as a pancreatic cystic lesion. *Fam Cancer*. 2005;4(2):135–138. doi:10.1007/s10689-004-1923-z.
125. Paal E, Thompson LD, Heffess CS. A clinicopathologic and immunohistochemical study of ten pancreatic lymphangiomas and a review of the literature. *Cancer*. 1998;82(11):2150–2158.
126. Rohrer K, Murphy R, Thresher C, et al. Infantile myofibromatosis: a most unusual cause of gastric outlet obstruction. *Pediatr Radiol*. 2005;35(8):808–811. doi:10.1007/s00247-005-1449-z.
127. Salimi J, Karbakhsh M, Dolatshahi S, et al. Cystic teratoma of the pancreas: a case report. *Ann Saudi Med*. 2004;24(3):206–209.
128. Kim SJ, Choi J-A, Lee SH, et al. Imaging findings of extrapulmonary metastases of osteosarcoma. *Clin Imaging*. 2004;28(4):291–300. doi:10.1016/S0899-7071(03)00206-7.
129. Jha P, Frölich AM, McCarville B, et al. Unusual association of alveolar rhabdomyosarcoma with pancreatic metastasis: emerging role of PET-CT in tumor staging. *Pediatr Radiol*. 2010;40(8):1380–1386.
130. Carricaburu E, Enezian G, Bonnard A, et al. Laparoscopic distal pancreatectomy for Frantz's tumor in a child. *Surg Endosc*. 2003;17(12):2028–2031. doi:10.1007/s00464-003-4222-0.
131. Krige JEJ, Mirza K, Bornman PC, et al. Primary hydatid cysts of the pancreas. *S Afr J Surg*. 2005;43(2):37–40.
132. Ozmen MM, Moran M, Karakahya M, et al. Recurrent acute pancreatitis due to a hydatid cyst of the pancreatic head: a case report and review of the literature. *JOP J Pancreas*. 2005;6(4):354–358.
133. Rao R, Pandey R, Rana M, et al. Pancreatic and peripancreatic tuberculosis presenting as hypoechoic mass and malignancy diagnosed by ultrasound-guided fine-needle aspiration cytology. *J Cytol*. 2013;30(2):130.

## PART 5 Esophagus

# 96 Congenital and Neonatal Abnormalities

Wendy Drew Ellis

## OVERVIEW

Severe congenital esophageal malformations, such as esophageal atresia, are usually diagnosed in the neonate; other congenital lesions, such as isolated tracheoesophageal fistulae (TEF), may remain undetected until later in life. Others, such as duplication cysts, may remain asymptomatic and identified incidentally later in life or even in adulthood.

## ESOPHAGEAL ATRESIA WITH AND WITHOUT TRACHEOESOPHAGEAL FISTULA

***Overview.*** Esophageal atresia with and without TEF is part of a heterogeneous spectrum of anomalies that ranges from isolated esophageal atresia to isolated fistula without atresia. Lesions are typically classified according to the association and location of the fistulous connection between the esophagus and the airway (Fig. 96.1). First described in 1670, esophageal atresia was a universally fatal anomaly until the fifth decade of the 20th century, when pediatric surgeons began successfully treating these children.[1,2] The incidence of esophageal atresia is approximately 1 in 3500 to 5000 births worldwide, with a tendency to occur more commonly in boys, although the gender difference varies with the type of lesion. Maternal risk factors include white race, first pregnancy, and advanced maternal age. There is also an increased risk in the siblings of affected patients.[1,3,4]

***Etiology.*** The development of esophageal atresia is poorly understood and still debated. Dominant theories in the past have been based on the model of a tracheoesophageal septum, a lateral ridge of tissue believed to separate the foregut into a dorsal component (the esophagus) from a ventral component (the trachea) in a caudocephalic direction. However, more recent investigations have suggested that this process does not occur in humans and instead suggest that the formation of the esophagus and trachea is the result of "a system of folds" in the cranial and caudal ends of the tracheoesophageal space that move toward each other, thus separating the space into the ventral trachea and dorsal esophagus. Following this theory, esophageal atresia with fistula results from an abnormally ventral position of the dorsal fold; isolated esophageal atresia is attributed to a vascular accident rather than abnormal separation of the alimentary and respiratory canals.[1,4–6] The association of the esophageal atresia complex with conotruncal anomalies and anomalies associated with DiGeorge syndrome suggests that abnormal development of pharyngeal arches may be related to this malformation.[1]

Further research with animal models concerns the investigation of genes that influence the temporal and spatial sequence of expression of molecular and genetic pathways, including retinoic acid receptors, and sonic hedgehog pathway effectors. Human teratogens that have been associated with this anomaly include abnormal maternal hormonal milieu (including estrogen, progesterone, and thyroid hormones), intrauterine exposure to thalidomide and diethylstilbestrol, and maternal diabetes.[1,7]

***Clinical Presentation.*** Patients with esophageal atresia with or without fistula typically come to medical attention prenatally or soon after birth. At prenatal evaluation patients with isolated esophageal atresia are most likely to be seen in the setting of maternal polyhydramnios with findings of a small or absent stomach bubble. Esophageal atresia and TEF may be suspected during pregnancy with similar findings. Neonates generally come to medical attention in the first few hours of life with excessive salivation and drooling, choking and regurgitation during feeds, and sometimes with cyanosis and/or respiratory distress.[1,3,4]

The incidence of associated congenital anomalies has been reported to be between 50% and 70%; it is most common in infants with isolated esophageal atresia and less common in children with isolated TEF.[3] The most common associated anomalies, in descending order of frequency, include cardiac, genitourinary, gastrointestinal, musculoskeletal, and neurologic anomalies. Approximately half of the children with esophageal atresia who have associated anomalies can eventually be classified as having a known syndrome, either chromosomal or named, such as VACTERL (*v*ertebral anomaly, *a*norectal atresia, *c*ardiac lesion, *t*racheo*e*sophageal fistula, *r*enal anomaly, *l*imb defect) (Fig. 96.2), CHARGE (*c*oloboma, *h*eart malformation, choanal *a*tresia, mental *r*etardation, *g*enitourinary and *e*ar malformations), Fanconi anemia, Opitz, and Goldenhar syndromes. VACTERL alone is present in approximately 20% of patients with esophageal atresia; patients with isolated esophageal atresia have an increased incidence of trisomy 21 (11%) and duodenal atresia (10%).[4,8,9]

***Imaging.*** Imaging is used in both the prenatal and neonatal diagnosis of esophageal atresia. Esophageal atresia is a cause of polyhydramnios. Fetuses with esophageal atresia may also have a small or absent stomach bubble.[4] These ultrasound findings alone lack specificity, with a reported 20% to 40% positive predictive value, and prenatal diagnosis may be made in as few as 10% of patients.[4,10] Diagnostic accuracy is improved when a blind-ending pouch is visualized in the fetal neck, and newer data suggest that fetal magnetic resonance imaging (MRI) may play an increasingly important role in prenatal diagnosis.[11,12] More commonly, the diagnosis is made in the immediate neonatal period. If the diagnosis of esophageal atresia is suspected in the first few hours of life, placement of a flexible feeding tube or enteric tube should be attempted (see Fig. 96.2). Introduction of contrast into the pouch is not typically necessary for confirmation of the diagnosis and can result in aspiration, although air may improve its identification and elucidate proximal pouch length.[4] Careful introduction of contrast into the pouch may reveal the rare patient who has a proximal fistula with or without atresia, but the danger of aspiration remains, and this diagnosis is typically made endoscopically.

On radiographs of the abdomen, absence of bowel gas indicates esophageal atresia without a distal TEF (e-Fig. 96.3), while the presence of gas in the abdomen indicates that there is a distal TEF (see Figs. 96.2 and 96.4). TEF from the proximal pouch cannot be excluded with chest radiographs and requires endoscopy for diagnosis. In patients who are on assisted ventilation, air may be forced into the stomach through the fistula, resulting in gastric overdistension and even perforation, particularly in infants who are intubated or have duodenal atresia. Approximately 2.5% of patients will have a right-sided aortic arch that should be identified on preoperative echo or ultrasound as esophageal repair is performed on the side opposite the arch.[1,4,13,14]

## Abstract:

Esophageal abnormalities of the newborn represent a diverse group of conditions, and include congenital anomalies ranging from various types of atresia, duplications and enteric fistulae, duplications as well as acquired conditions such as pharyngeal and esophageal perforation.

## Keywords:

esophageal atresia
tracheoesophageal fistula
foregut duplication
pharyngeoesophageal perforation
neurenteric cyst

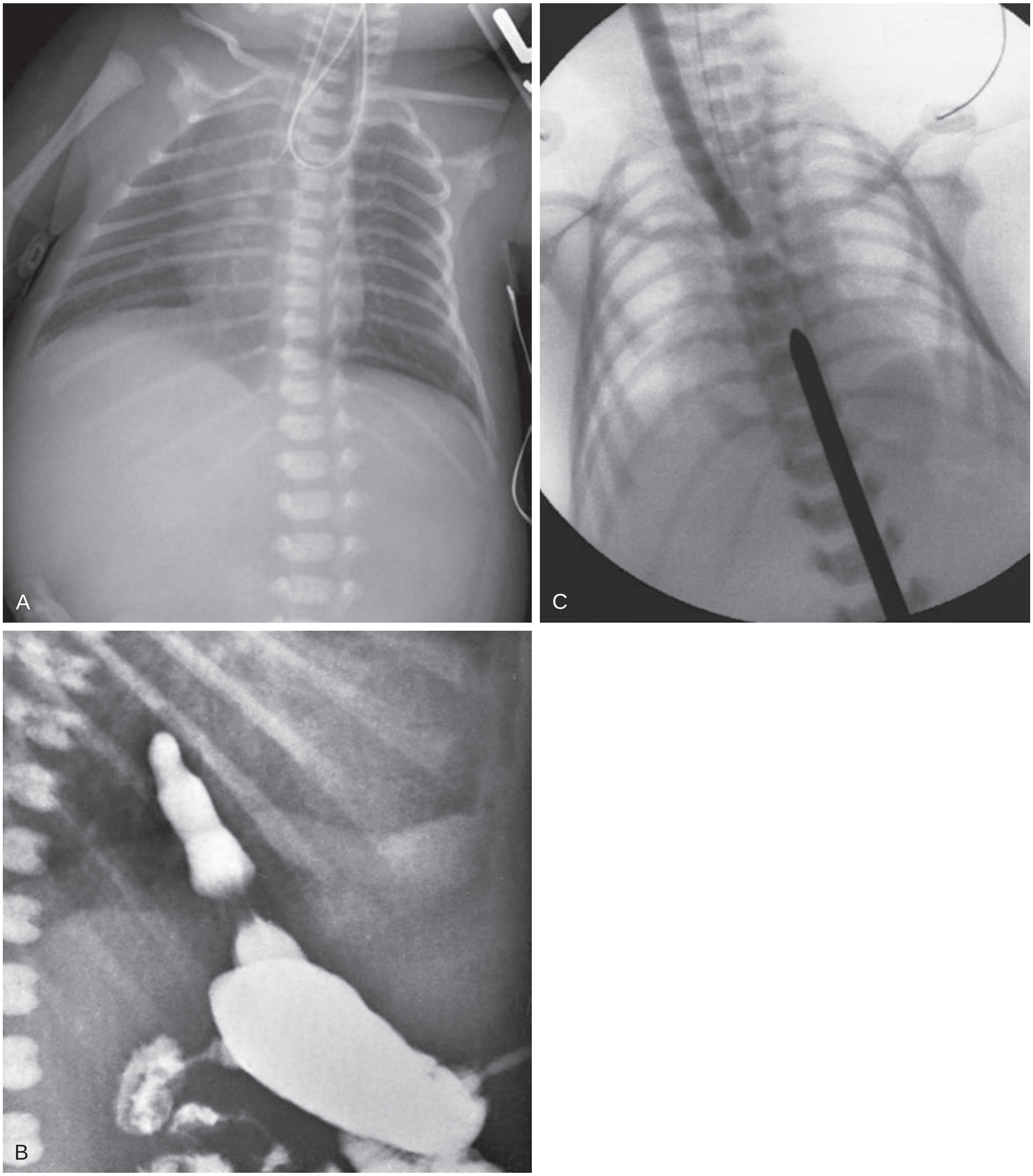

**e-Figure 96.3. Isolated esophageal atresia.** (A) Newborn boy born at 37 weeks' gestation with isolated esophageal atresia. The enteric tube turns cephalad in the blind-ending proximal esophageal pouch, and abdominal bowel gas is absent. (B) Gastrostomy injection with reflux into the short distal esophageal segment in a patient with esophageal atresia without a distal fistula. (C) Esophageal atresia with the gap between the segments confirmed at surgery. Frontal view reveals bougies in both the proximal and distal segments, showing a long gap between them.

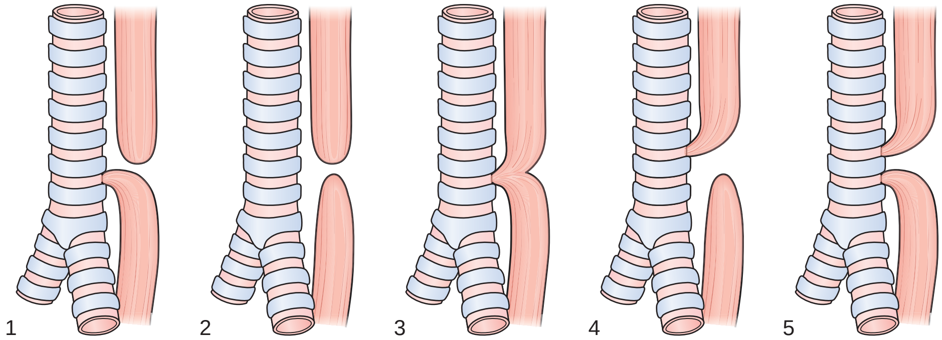

**Figure 96.1. Types of esophageal atresia, with and without tracheoesophageal fistula.** *Type 1* represents esophageal atresia with a distal fistula and is the most common form, occurring in approximately 84% of patients. *Type 2* illustrates esophageal atresia without a fistula, seen in about 6%. *Type 3* is an isolated H-type fistula (4%), and *type 4* describes esophageal atresia with the fistula arising from the proximal pouch (5%); *type 5,* with fistulae arising from both the proximal and distal pouch, is the least common (~1%).[1]

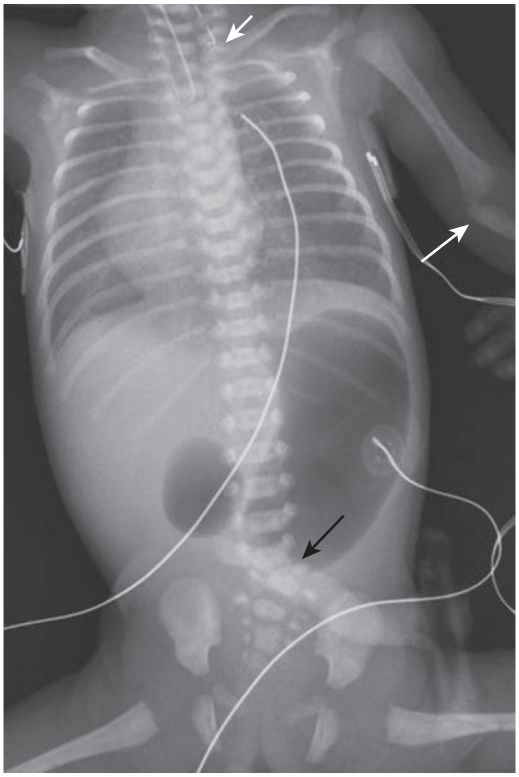

**Figure 96.2. VACTERL (*v*ertebral anomaly, *a*norectal atresia, *c*ardiac lesion, *t*racheoesophageal fistula, *r*enal anomaly, *l*imb defect) syndrome.** Newborn girl born at 32 weeks' gestation demonstrates the abnormalities seen with the VACTERL association. The patient is intubated because of the lung disease of prematurity. The enteric tube *(short white arrow)* ends just above thoracic inlet in the proximal esophageal pouch, and abdominal bowel gas indicates a distal tracheoesophageal fistula, whereas a "double bubble" sign and absence of distal bowel gas indicate duodenal atresia. There are 13 pairs of ribs, and a hemivertebra between L5 and S1 *(black arrow)*. Note the absent radius in the left arm (*white arrow* points to the ulna).

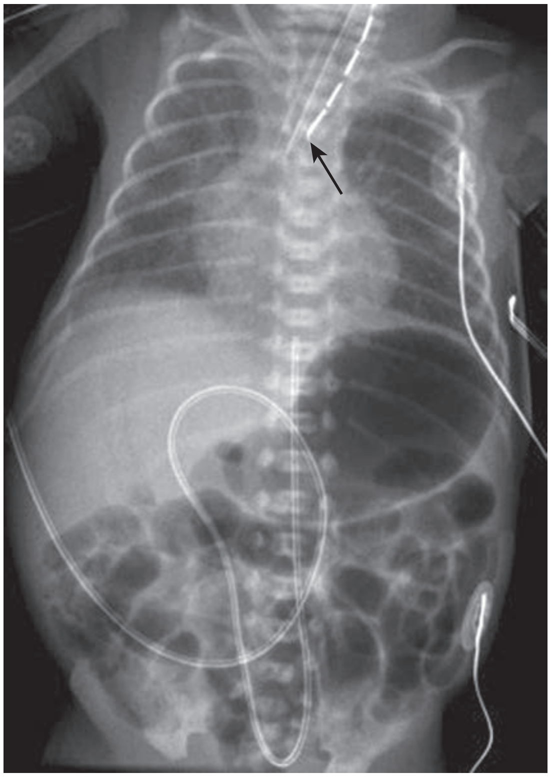

**Figure 96.4. Esophageal atresia with tracheoesophageal fistula.** Radiograph of a newborn preterm girl shows that the enteric tube *(arrow)* ends in the proximal esophageal pouch with abundant distal gas.

***Treatment/Follow-up.*** Surgical repair is typically undertaken within 1 to 2 days, after the clinical workup is complete, including treatment of more emergent medical issues. Open or thoracoscopic division/ligation of the fistula and primary esophageal anastomosis is the treatment of choice. Long-gap atresia, which accounts for approximately 25% of patients with esophageal atresia, is defined as a separation between the proximal and distal segments of greater than 2.5 cm. For these patients, a staged approach is employed, including early placement of a gastrostomy tube for nutritional support while mechanical traction is used to more closely appose the proximal and distal pouches before repair.[4] Isolated esophageal atresia is typically associated with a small proximal pouch and almost no thoracic esophagus (see e-Fig. 96.3), and patients are typically palliated with a gastrostomy in the first 24 to 48 hours of life, followed by delayed repair. Alternatively, if these procedures fail, a gastric pull-up or an esophageal substitute (usually jejunum or colon) can be interposed between the proximal and distal

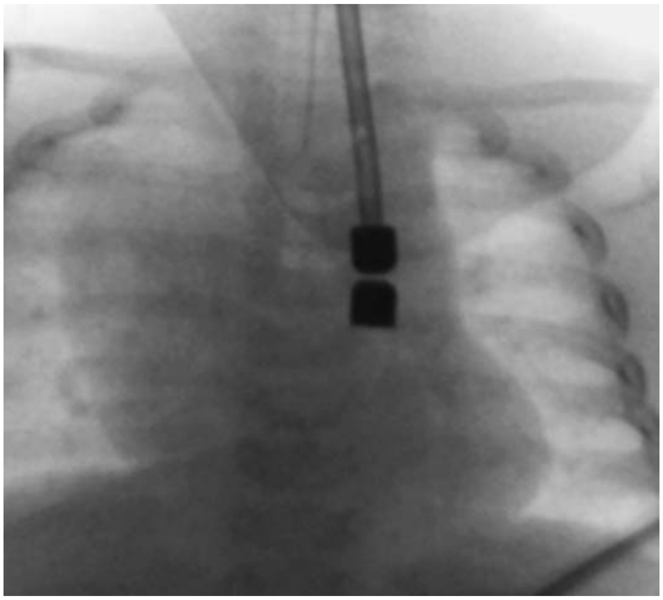

**Figure 96.5. Magnets in esophageal atresia.** Single fluoroscopic image demonstrates the magnetic probes placed in the proximal esophageal pouch and into the distal segment through the gastrostomy.

segments.[1,4] More recently, some centers, particularly in Europe, have used magnets to approximate and unite long gap segments shorter than 4.5 cm (Fig. 96.5).[15,16]

Imaging also plays an important role in the evaluation of early and late complications of esophageal atresia repair. Complications include anastomotic leak, anastomotic stricture, and recurrent TEF[17]; these are evaluated with esophagram (e-Fig. 96.6). Because standard esophageal contrast studies reportedly may miss as many as 50% of recurrent fistulae, bronchoscopy may also be required if a recurrent fistula is suspected.[1]

## ISOLATED TRACHEOESOPHAGEAL FISTULA

***Overview.*** Congenital, isolated TEF without atresia of the esophagus (type 3 in Fig. 96.1) is often termed an *H-type fistula*, and it differs significantly from the other types of tracheoesophageal malformations. Large fistulae usually present very early in life and are relatively easy to see on an esophagram (Fig. 96.7). More commonly, the fistulae are small, inconstantly patent, difficult to identify both clinically and radiographically, and may require repeated examinations and/or endoscopy for diagnosis.[4,18,19] A major reason for inconstant patency of a fistula is that normal esophageal mucosa can be redundant, which can transiently occlude the esophageal side.[20] Although rare, multiple fistulae can be present.[21]

Rarely, a bronchus originates directly from the esophagus, termed an *esophageal bronchus* (see also Chapter 52). If the connection is to the entire lung rather than a segment or lobe, it is termed *esophagotrachea* or *esophageal lung*.[22,23] This anomaly may be associated with esophageal atresia, TEF, or both.[22]

***Clinical Presentation.*** These patients typically present with recurrent episodes of coughing or choking and may progress to recurrent pneumonias, either in infancy or later in childhood; very rarely the presentation may be in early adulthood.[4,22,24,25] Patients with unexplained, intermittent respiratory distress and recurrent pneumonia should always be considered at risk for the presence of a TEF, and radiographic examination is warranted. Esophageal bronchus likewise presents with respiratory distress and pneumonia.

***Imaging.*** The term *H-type fistula* refers to its appearance on esophagram: the fistula courses cephalad from the esophagus posteriorly to the trachea anteriorly as it connects these two structures (see Fig. 96.7).

The examination should begin as a single-contrast esophagram using digital, pulsed fluoroscopy in the right lateral to slightly right anterior oblique position. The position should be optimized during the examination to allow the best view of the anterior wall of the esophagus and posterior wall of the trachea. A key element to the success of this examination is achieving full distension of the esophagus, to optimize filling and visualization of the fistula. If the esophagus does not distend optimally and no abnormality is detected while the patient is swallowing, an esophageal catheter may be placed for introduction of contrast under fluoroscopic guidance. This is considered especially in patients with normal prior examinations in whom a fistula remains suspect or in those in whom contrast is seen within the trachea from an unclear source (i.e., patients in whom aspiration versus fistulous connection cannot be differentiated).[26,27] The examiner slowly withdraws the catheter from the distal esophagus in the cephalic direction, while carefully injecting contrast material with enough velocity and volume to distend the esophagus maximally under constant fluoroscopic monitoring. The catheter should have an end hole, without more proximal side holes, for adequate control of the contrast infusion. Even if a fistula is noted, the injection should continue until the catheter is withdrawn into the hypopharynx, but care must be taken not to allow contrast material to spill over into the trachea. Although there is a danger of spilling contrast material into the airway with injection of the high cervical esophagus, it is important to examine this area because many fistulae occur at the level of the lower cervical or upper thoracic spine (see Fig. 96.7C).[28] Slow retraction of the catheter and careful fluoroscopic monitoring allow constant visualization and help to prevent overflow into the trachea.[28] Esophageal bronchus is well outlined on upper GI examination, and also with cross-sectional imaging, particularly computed tomography (CT) (Fig. 96.8A and e-Figs. 96.8B and 96.8C).[29]

***Treatment/Follow-up.*** Surgical correction of the connection between the esophagus and the airway is the treatment of choice. Endoscopic, thoracoscopic, and open thoracotomy surgical techniques can be used.[30,31]

Esophageal dysmotility, stenosis at the anastomotic site, and gastroesophageal reflux are common long-term issues in patients who require repeat imaging and often additional treatments.[4,31]

## LARYNGOTRACHEOESOPHAGEAL CLEFTS

***Overview.*** Laryngotracheoesophageal clefts occur in approximately 1 in 10,000 to 20,000 live births and consist of fistulous communications between the alimentary canal and the airway, either confined to the hypopharynx and larynx (Fig. 96.9) or extending inferiorly to include the esophagus.[32,33] Several related classifications have been proposed based on the extent of the communication between the respiratory and alimentary pathways.

The Benjamin-Inglis classification system, first published in 1989 and since modified to include therapeutic implications, describes four basic lesions (Table 96.1) that are classified on the length and location of the cleft.[32,33]

***Etiology.*** The larynx forms from the endoderm of the foregut caudally and from the mesenchyme of branchial arches four and six cranially.[32,34] Incomplete separation and/or incomplete midline fusion of these concurrent processes during early gestation is believed to result in the persistent midline defect with varying extent and severity.

***Clinical Presentation.*** The clinical presentation varies with the extent of the cleft; varying degrees of respiratory distress that begin early in infancy are aggravated during feeding with choking, stridor, aspiration, recurrent pneumonia, and cyanosis.[32,34] Patients with smaller defects, particularly type I, may present and come to diagnosis later; infants with type III and IV lesions typically present very soon after birth. In some patients, esophageal mucosa

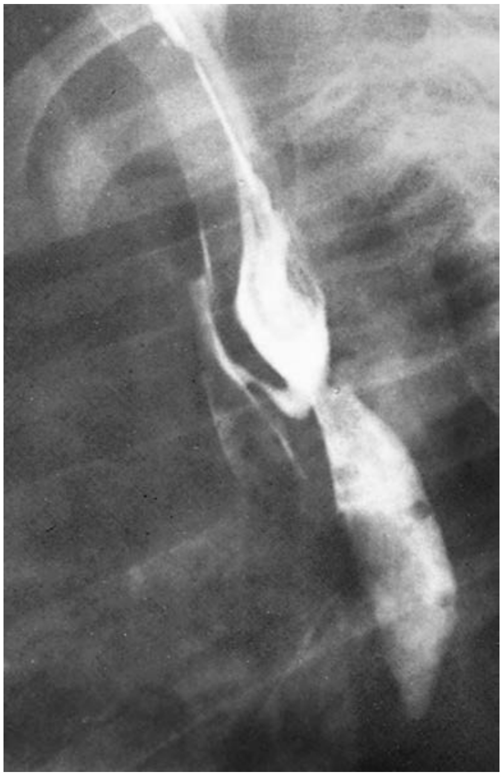

**e-Figure 96.6. Recurrent tracheoesophageal fistula.** Contrast esophagram demonstrates a fistulous connection with the airway at the site of the anastomosis, a finding typical of fistula developing as a postoperative complication.

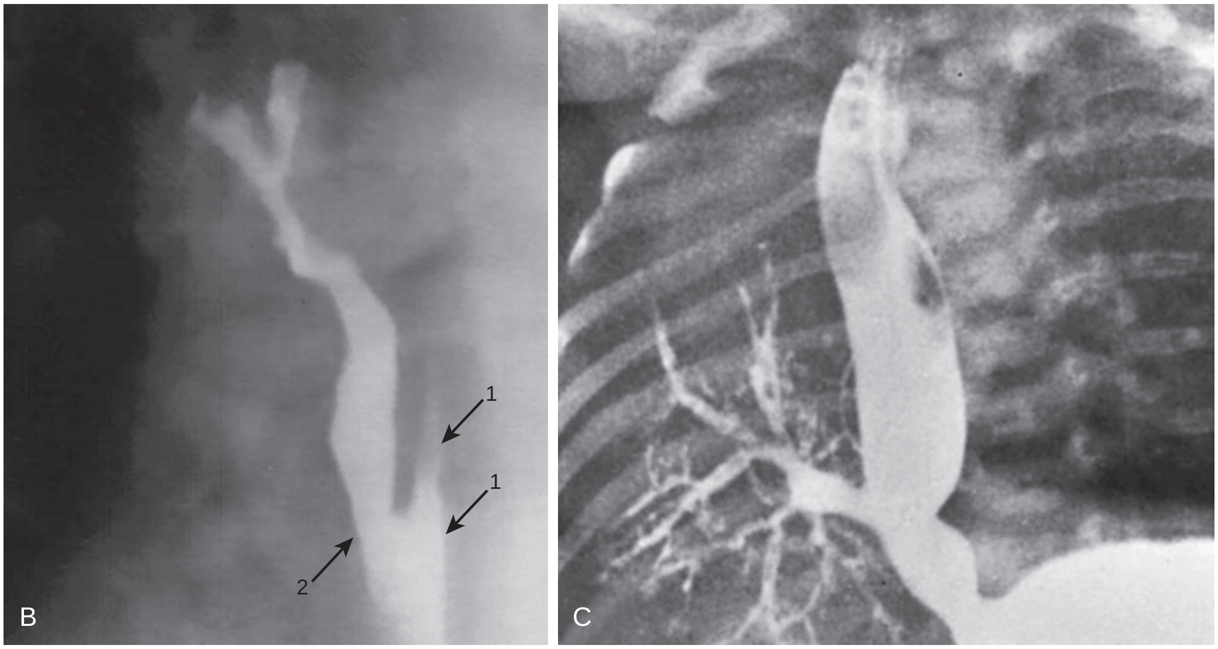

**e-Figure 96.8.** (B) Congenital esophagobronchial fistula. Oblique view shows esophagus (*arrows* with 1) and bronchus to right upper lobe (*arrow* with 2). (C) Esophageal bronchus. Frontal view from an esophagram demonstrates the origin of the right main bronchus from the distal esophagus.

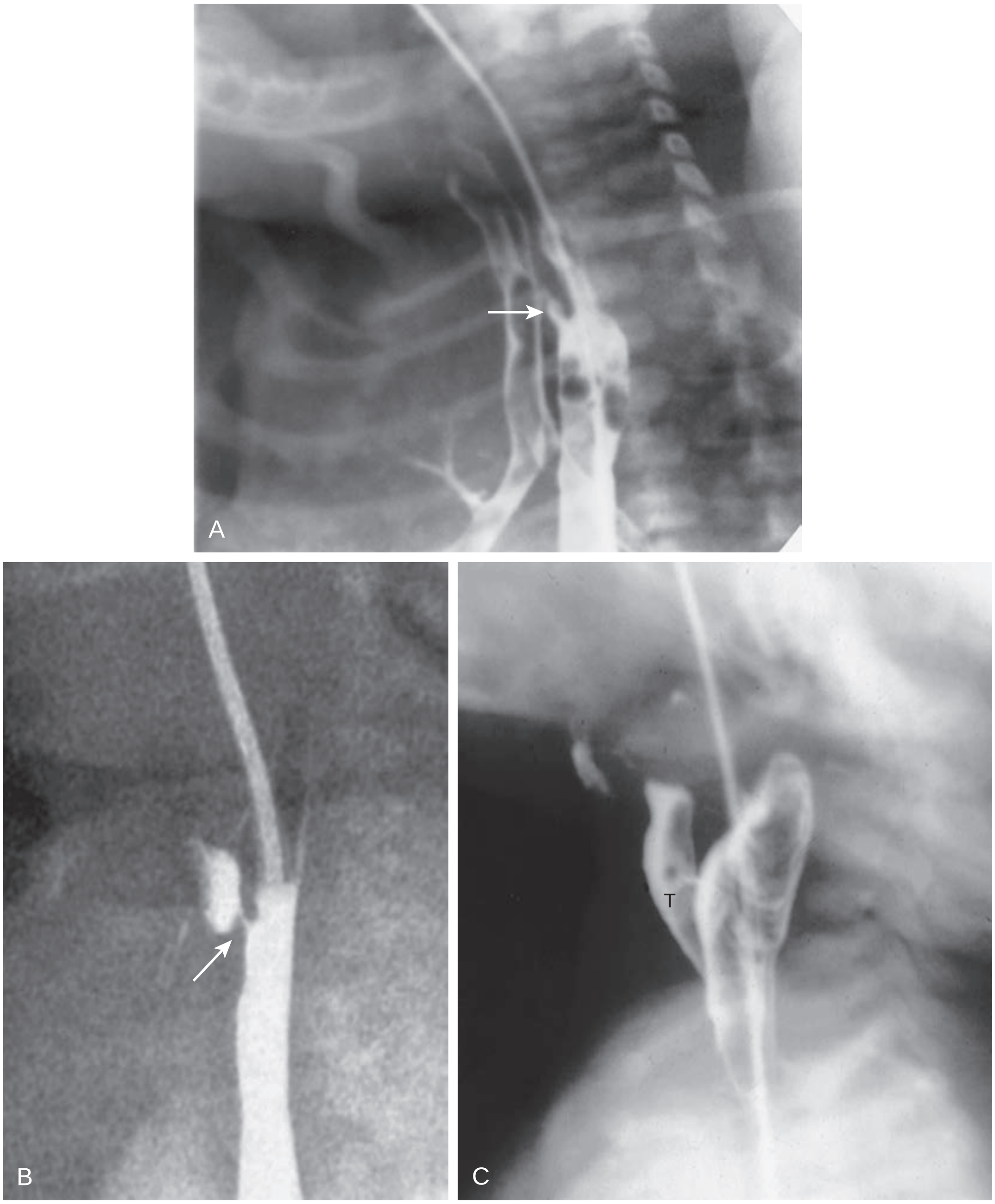

**Figure 96.7. H-type tracheoesophageal fistula.** (A) Tracheoesophageal fistula *(arrow)* in a 7-day-old boy with imperforate anus. (B) Demonstration of another H-type fistula *(arrow)* from the upper cervical esophagus to the trachea, using the technique of contrast injection through a feeding tube with very careful volume control. (C) Large H-type fistula from the upper cervical esophagus to the trachea *(T)*.

**TABLE 96.1** Benjamin-Inglis Classification of Laryngotracheoesophageal Clefts

| **Lesion Type** | **Type I** | **Type II** | **Type III** | **Type IV** |
|---|---|---|---|---|
| **Description** | Interarytenoid defect to the level of the vocal cords | Extension below vocal cords with incomplete extension through posterior cricoid | Complete extension through the posterior cricoid cartilage to the cervical trachea and esophagus | Extension to the intrathoracic trachea and esophagus |

herniates into the defect and offers some protection against aspiration, but symptoms of respiratory distress secondary to compromise of the airway typically worsen.[32] Associated anomalies such as esophageal atresia, VACTERL association, and other abnormalities such as anal atresia, bronchial or tracheal stenosis and pulmonary hypoplasia, hypospadias, and coarctation of the aorta may occur. Laryngotracheoesophageal clefts may also occur as part of syndromes such as CHARGE, Opitz G/BBB (laryngeal malformations, craniofacial anomalies, genitourinary anomalies, and ventral midline anomalies), and Pallister-Hall (laryngeal, gastrointestinal [GI], cardiopulmonary, limb, and neurologic malformations) syndromes.[32–34]

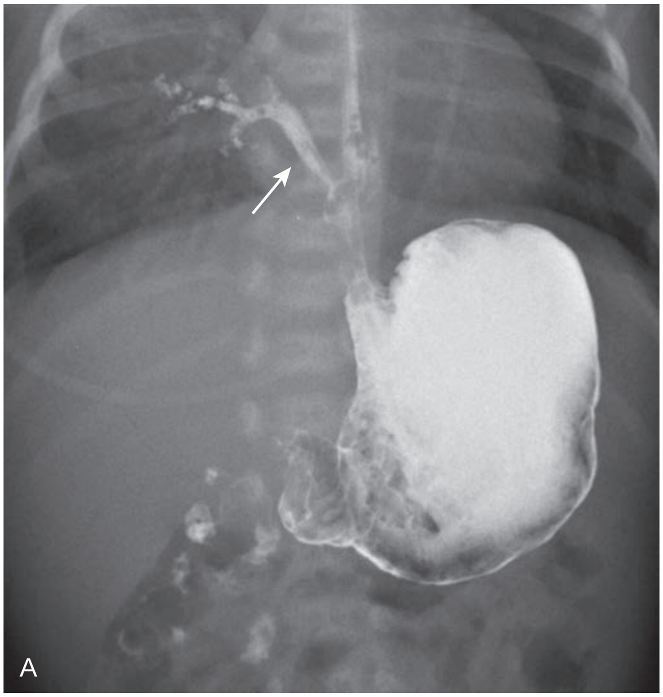

**Figure 96.8. Connections between esophagus and airway.** (A) Spot radiograph from an esophagram in a neonate with recurrent coughing/choking during feeds shows an esophageal bronchus *(arrow)* extending to the right lower lobe. *(Courtesy Alex Towbin, MD, Cincinnati, OH.)*

***Imaging.*** Diagnosis is usually made by direct laryngoscopy (see Fig. 96.9B). In some patients, such as those with type III and IV clefts, the diagnosis may be made during bronchoscopy undertaken to investigate symptoms of respiratory distress. On chest radiography, findings of chronic aspiration such as pneumonia, peribronchial wall thickening, and scarring can be seen.[34] On contrast esophagram (see Fig. 96.9A), contrast is seen within the airway, although this can be confused with aspiration or with TEF. If CT is performed, a common tracheoesophagus may be seen in extensive lesions, containing both the endotracheal and orogastric tubes, or expected tissue between trachea and esophagus may be absent.[32]

***Treatment Follow-up.*** The goal of treatment is to maintain the airway and ventilation while minimizing aspiration and allowing adequate nutrition. For minor clefts, medical therapy may be attempted initially.[33,34] Endoscopic surgical repair should be considered for types I, II, and some type III clefts. The remaining type III and IV are usually corrected with an open surgical approach,[34,35] and extensive clefts may require both cervical and thoracic approaches.[1,34] Postoperative survival rates range between 50% and 75%, depending on the extent of the cleft and severity of associated anomalies.[1,34] Late complications include anastomotic leaks, pharyngeal and esophageal dysfunction, and gastroesophageal reflux.[1,34]

## ACQUIRED PHARYNGOESOPHAGEAL PERFORATION

***Overview.*** Iatrogenic perforation of the pharynx and esophagus was first reported more than 40 years ago and, while reportedly rare, may occur more frequently than is recognized by the literature.

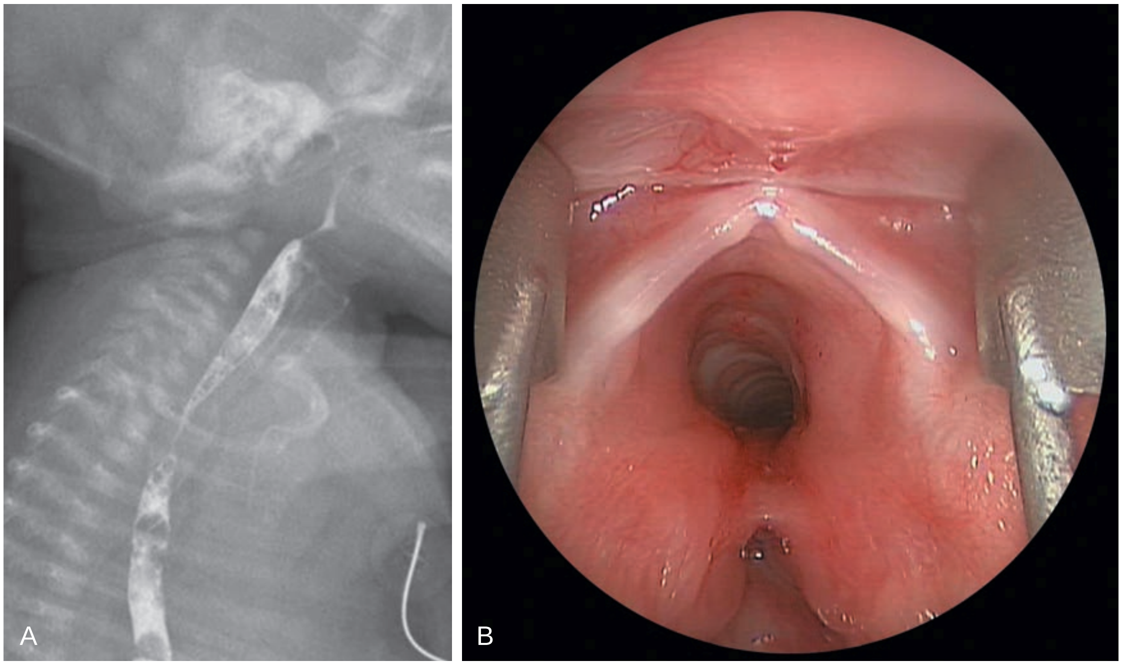

**Figure 96.9. Laryngotracheal cleft.** (A) Laryngotracheal cleft. Contrast swallow demonstrates large-volume aspiration from a posterior laryngeal wall defect. (B) Endoscopic photograph from the same patient shows a posterior laryngeal wall defect and type 2 or 3 laryngotracheal cleft.

It is typically secondary to manipulation, such as intubation and enteric tube placement. The imaging findings may overlap with those of esophageal atresia and can lead to misdiagnosis.[4,36,37]

***Etiology.*** This injury is more common among premature infants.[38] The mechanism of injury to the pharynx and upper esophagus is believed to relate to reflexive contraction of the cricopharyngeus muscle and narrowing of the esophageal introitus as it is compressed against the cervical vertebrae with hyperextension of the infant's neck. This leads to formation of a retroesophageal tract, which descends along the posterior mediastinum. The path of the catheter, or that of subsequently inserted catheters, may follow the perforation and enter the blind-ending tract in the prevertebral space; this may resemble the appearance of esophageal atresia on radiographs.[36,39] Alternatively, the catheter may pass into the right pleural space, presumably as the tube passes above the cricopharyngeal "roll bar" (the posterior and transverse hypopharyngeal portions of the cricopharyngeal muscle) and is deflected to the right by the brachiocephalic vessels. Saliva, formula, and gas collect in the pleural space.[40,41]

***Imaging.*** On chest radiographs, the findings of air or of a coiled enteric tube over the cervicothoracic junction may resemble the findings in esophageal atresia; distinguishing features include an unusually long blind pouch representing the false lumen, with irregular outline. Alternatively, an abnormal course of an enteric tube may be diagnostic (Fig. 96.10A–C). Esophagrams should be performed with water-soluble contrast at or near iso-osmolar concentration. Contrast extravasates into the newly created retroesophageal space (Fig. 96.10D). Introduced contrast material with time dissipates along adjacent tissue. Coexisting pneumomediastinum and pneumothorax or hydropneumothorax are helpful signs in detecting this complication and in differentiating it from esophageal atresia (see Fig. 96.10).[36–38]

***Clinical Findings.*** Although the initial clinical presentation may be relatively silent, patients typically manifest increased secretions with episodes of choking and cyanosis associated with feeding, and the development of crepitus and clinical deterioration follows. There is inability to easily pass a feeding catheter. Early diagnosis is critical as delay leads to increased morbidity and mortality.[4,38]

***Treatment/Follow-up.*** Once the injury has been recognized, the majority of these patients can be managed conservatively, with withdrawal of enteral feedings, broad spectrum antibiotics, and drainage of pleural effusion or pneumothorax if present. This management is successful in the vast majority of patients, and surgical treatment is reserved for complications, such as mediastinal abscess.[36–38]

## ESOPHAGEAL STENOSIS

***Overview.*** Congenital esophageal stenosis is a rare condition that occurs in 1 in 25,000 to 50,000 live births. The three histologic subtypes are fibromuscular stenosis, membranous web, or tracheobronchial remnants.[42]

Membranous stenosis is considered one of the rarest forms of this rare lesion and is usually located in the middle or distal third of the esophagus; it typically demonstrates an eccentric opening and is covered with squamous epithelium. Fibromuscular stenosis demonstrates subepithelial proliferation of smooth muscle and fibrosis. Stenosis associated with tracheobronchial remnants demonstrates cartilaginous tissue proliferation that partially or completely encircles the esophagus—usually in the lower third, within 3 cm of the gastroesophageal junction—and is often associated with esophageal atresia and TEF.[1,43,44]

***Etiology.*** The etiology of fibromuscular stenosis is uncertain, whereas that of membranous stenosis may be similar to that of membranous stenosis elsewhere in the GI tract. Stenosis as a result of tracheobronchial rests is thought to arise from incomplete separation of the tracheoesophageal septum during gestation with sequestration of the tracheal cartilage in the esophageal wall; this is carried distally by the growth of the esophagus.[1,44,45]

***Clinical Presentation.*** The typical presentation is that of dysphagia later in infancy, especially after introduction of solids.[1,46] Older patients may present with regurgitation, choking, vomiting, or failure to thrive.[42,44] Patients may also come to medical attention with retention of a foreign body outside of the cervicothoracic junction, the aortic arch, the left bronchial crossing, or the gastroesophageal junction, which are the typical locations in which foreign bodies lodge in the normal esophagus.[42]

***Imaging.*** Esophagram in patients with esophageal stenosis demonstrates an area of narrowing with partial obstruction. Stenoses secondary to web or to fibromuscular hypertrophy may be seen in the upper or mid portion of the esophagus. Stenoses secondary to tracheobronchial remnants appear as a discrete narrowing of the esophagus along its distal portion, typically within 3 cm of the gastroesophageal junction (Fig. 96.11A and e-Fig. 96.11B), particularly in a patient with esophageal atresia. The diagnosis may be confirmed by endoscopy and histopathology.[4,42,47]

Because of the rarity of congenital esophageal stenosis, the findings at esophagram may be misinterpreted as stricture, such as secondary to gastroesophageal reflux, or as achalasia, if located very close to the gastroesophageal junction.[45,47] In such cases, specific reflux studies and manometric studies to exclude the diagnosis of achalasia may be helpful.[47]

If the diagnosis is delayed, cross-sectional imaging may demonstrate marked thickening of the wall of the esophagus, resembling esophageal leiomyomatosis.[47]

***Treatment/Follow-up.*** It is essential that a stricture as a result of gastroesophageal reflux be excluded before the diagnosis of esophageal stenosis is made.[1] Endoscopic balloon dilatation can be used as a primary and therapeutic procedure and is most successful in those patients without a true cartilaginous component of the stenosis.[42,48,49] Membranous stenoses are amenable to endoscopic dilation and resection, although surgical resection of the stenotic segment is reserved for strictures that are not amenable to dilation or that recur.[42,50] A follow-up esophagram can be performed to assess for perforation, recurrent stenosis, or stricture after dilation or surgical resection.[42]

## ESOPHAGEAL DUPLICATION CYSTS

***Overview.*** Duplication cysts of the esophagus represent part of the spectrum of foregut duplication cysts, which in addition to esophageal duplication cysts, also include bronchogenic cysts and neurenteric cysts. Bronchogenic cysts typically include mural cartilage or respiratory glands and are discussed in Chapter 53. Neurenteric cysts communicate with the spinal canal through a vertebral defect and are additionally discussed in Chapters 43 and 58.

Esophageal duplication cysts represent approximately 10% of mediastinal masses in children and approximately 20% of alimentary tract duplications, being the most common site of duplications after the ileum.[51,52] They are found most commonly in the chest associated with the thoracic esophagus; however, they also may occur in the neck, associated with the cervical esophagus, or they may involve the thorax and the upper abdomen as in a thoracoabdominal duplication cyst. Approximately two-thirds occur in the right side of the mediastinum.[52–54]

Diagnostic criteria met by esophageal duplication cysts include attachment to the esophagus, two muscular layers enveloping the cyst, and lining by squamous, columnar, cuboidal, pseudostratified, or ciliated epithelium, or epithelium that "demonstrates some level of the gastrointestinal tract."[4,53] The vast majority of esophageal duplications are of the cystic, noncommunicating type; true tubular duplications of the esophagus are rare.[55–57] These cysts may extend below the diaphragm to involve the stomach, and they may communicate with the stomach or esophagus.[51]

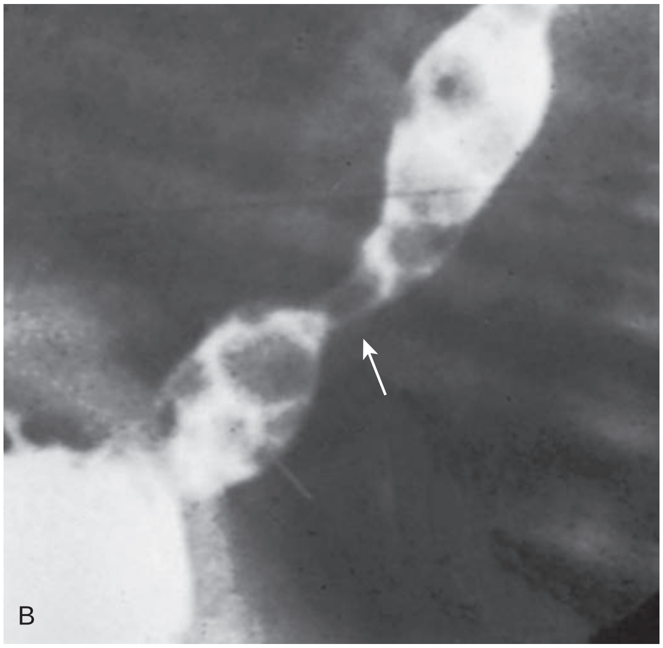

**e-Figure 96.11.** (B) Esophagram on another patient demonstrates stenosis in the distal portion of the esophagus (*arrow*) secondary to cartilaginous remnants. *(Courtesy Dr. E. Afshani, Buffalo NY.)*

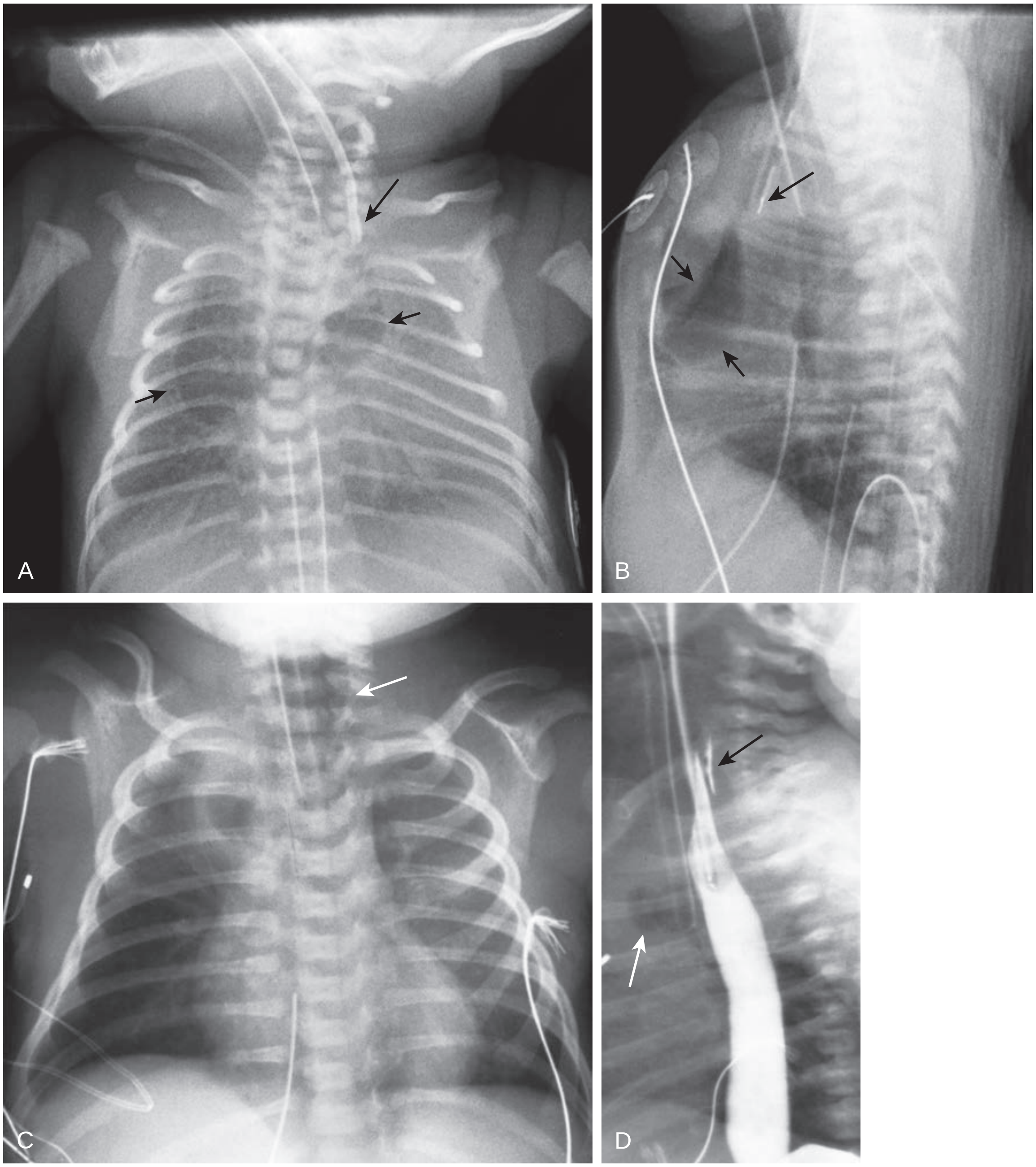

**Figure 96.10. Traumatic pharyngoesophageal perforation.** (A) Frontal chest in a 24-week premature infant reveals an unusual course of the enteric tube, terminating at a level that might suggest esophageal atresia *(long arrow)*. However, there is also an abnormal gas collection in the mediastinum *(short arrows)*. (B) Lateral view on same infant shown in A illustrates an abnormally anterior course of the enteric tube *(long arrow)* and anterior location of the loculated gas collection *(short arrows),* confirming traumatic pharyngeal perforation. This case is unusual in the anterior location of the collection, which clearly excludes esophageal atresia. The perforation healed spontaneously and the patient did well. (C) Frontal chest radiograph reveals an opacity in the right upper lobe with air in its center, consistent with hydropneumothorax. Note the hyperlucency in the lower neck, resembling the findings of an esophageal pouch in esophageal atresia *(arrow)*. (D) Esophagram shows air in the mediastinum *(white arrow)* and contrast extending behind the esophagus, a more typical location for perforation *(black arrow)*.

Neurenteric cysts are duplication cysts that communicate with the spinal canal. The typical example of this spectrum of anomalies is the dorsal enteric fistula, a patent communication between the gut and the dorsal midline skin surface, which traverses the vertebral body or the interspace, spinal canal and its contents, and the posterior vertebral elements (Fig. 96.12) (see also Chapter 58).

***Etiology.*** Esophageal duplication cysts are believed to be the result of a budding error of the dorsal portion of the foregut between the third and sixth weeks of gestation. These cysts arise from the posterior portion of the foregut and contain mucosa that, by histologic examination, is usually gastric or, more rarely, intestinal.[53] True tubular esophageal duplications likely develop

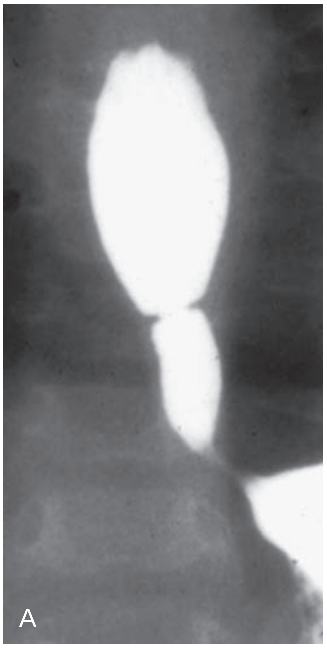

**Figure 96.11. Esophageal stenosis.** (A) Weblike narrowing of the distal esophagus with proximal dilatation secondary to esophageal cartilaginous rests. The diagnosis is suggested by the location of the narrowed segment.

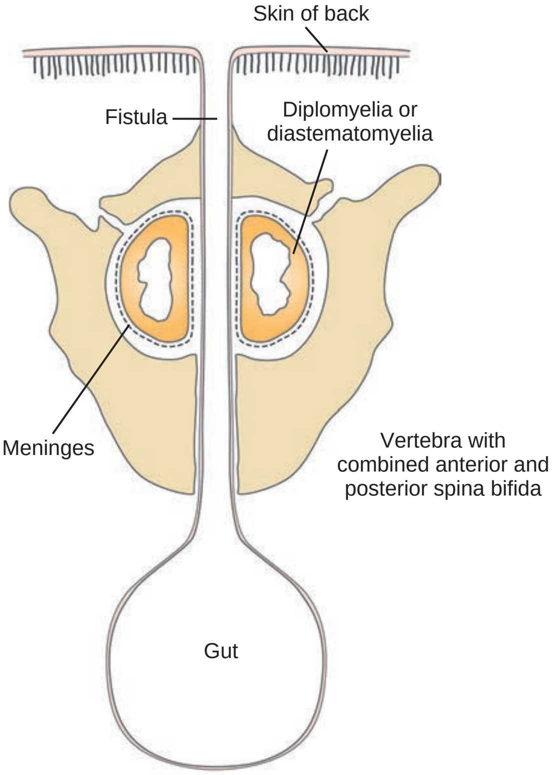
Skin of back
Fistula
Diplomyelia or diastematomyelia
Meninges
Vertebra with combined anterior and posterior spina bifida
Gut

**Figure 96.12. Diagrammatic representation of a typical dorsal enteric fistula.** *(From Naidich TP, McLone DG, Harwood-Nash DC. Spinal dysraphism. In: Newton TH, Potts DG, eds.* Computed Tomography of the Spine and Spinal Cord*. San Anselmo, CA: Clavadel Press; 1983:299–353.)*

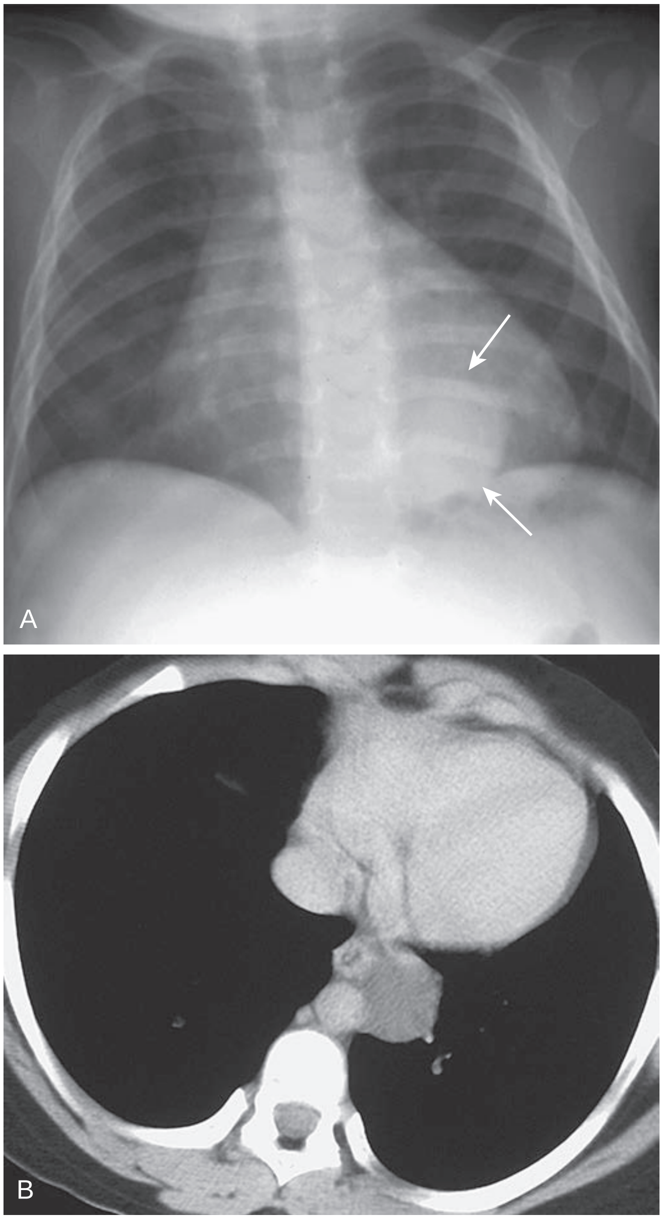

**Figure 96.14. Lower esophageal duplication cyst.** (A) Frontal chest radiograph reveals a paraspinal retrocardiac mass at the left base *(arrows)*. (B) Contrast-enhanced CT image demonstrates the persistently low attenuation of the duplication and its relationship to the esophagus.

from faulty recanalization of the esophageal lumen during the tenth week of gestation. They may or may not communicate with the esophageal lumen.[51,54–56,58]

***Clinical Presentation.*** Cervical duplication cysts are usually symptomatic very early in life, and patients come to medical attention with respiratory distress. Potential for respiratory compromise may be evident in fetal life, and an ex utero intrapartum treatment may be needed at delivery.[53] Thoracic duplication cysts that occur in the superior mediastinum may be found incidentally, but, if large, the patient may present with respiratory distress or dysphagia because of compression of adjacent structures (e-Fig. 96.13).[52] Duplication cysts that occur in the lower esophagus are often asymptomatic and may be discovered incidentally (Fig. 96.14), although they may become symptomatic as a result of inflammation,

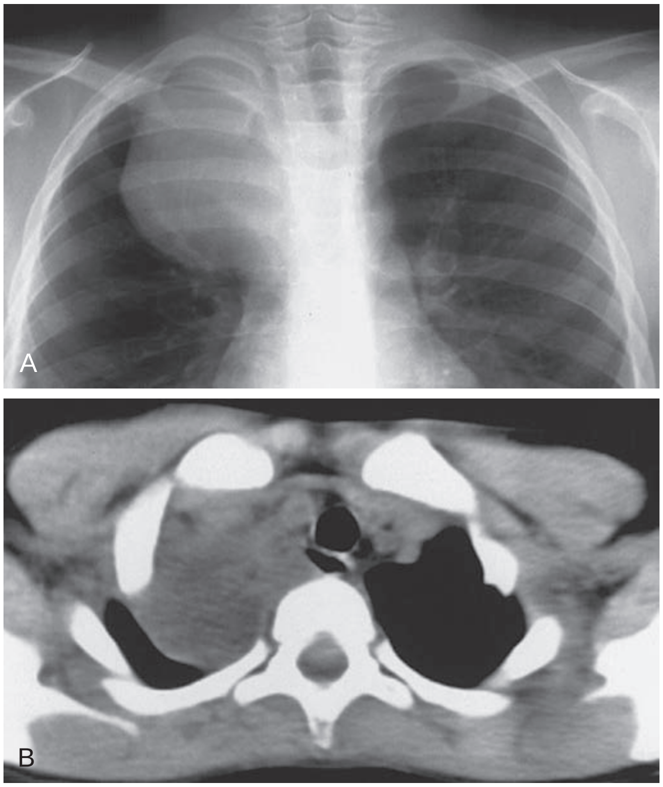

**e-Figure 96.13. Upper esophageal duplication cyst.** (A) Chest radiograph demonstrates a large mass projecting over the right thoracic apex, without evidence of effect upon the adjacent ribs. (B) CT demonstrates the low-attenuation cystic lesion and its relationship to the mediastinum and the adjacent, air-filled esophagus seen posterior to the airway.

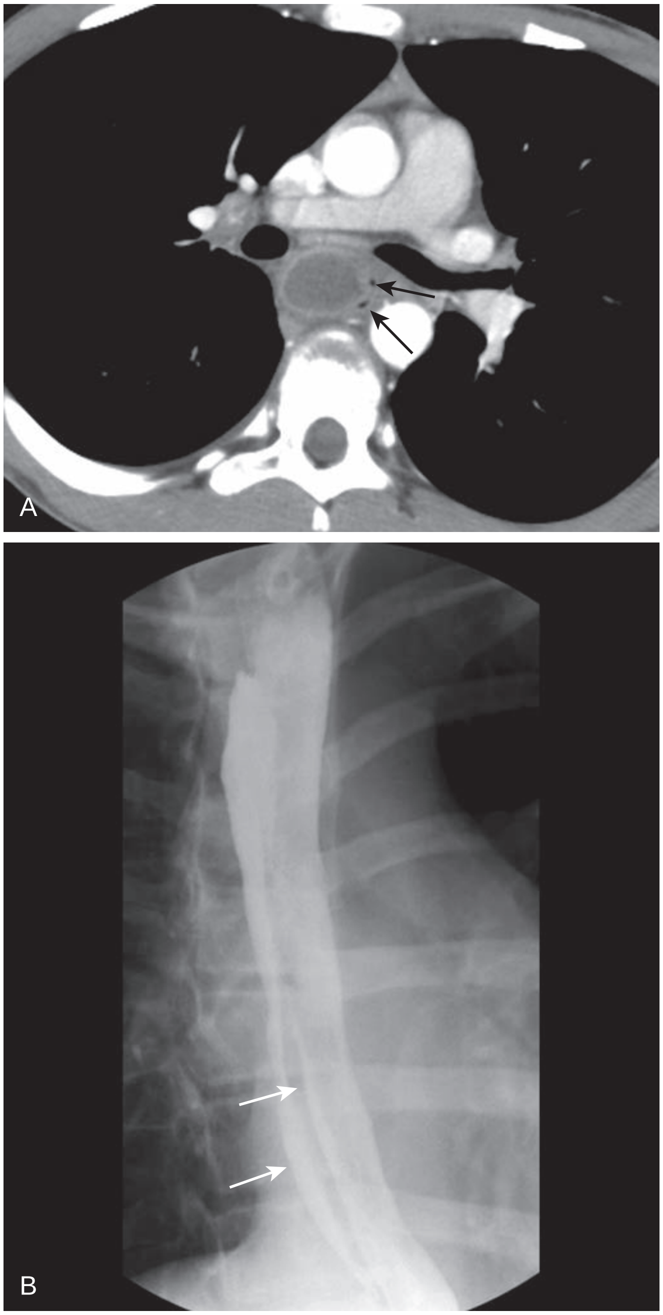

**Figure 96.15. Esophageal duplication cyst complication.** (A) CTA performed to evaluate for pulmonary embolus in a 17-year-old boy presenting with fever, vomiting, and chest pain shows a cystic structure with mildly enhancing walls to the right of the attenuated esophageal lumen *(arrows)*. (B) Subsequent water-soluble esophagram shows a filling defect *(upper arrow)* separating the lumen of the true esophagus from that of the duplication *(lower arrow)*. Duplication became superinfected, leading to symptoms at presentation and to erosion, allowing communication with the lumen of the esophagus.

if they contain gastric mucosa, or as a result of superinfection or hemorrhage (Fig. 96.15).[59]

Neurenteric cysts may present with back pain and progressive neurologic deficit if not diagnosed prenatally or in early infancy.[60] Infants may be brought to medical attention with meningitis. These defects are typically associated with midline vertebral lesions such as spina bifida, other dysraphic defects, or scoliosis (see Fig. 96.12 and e-Figs. 96.16 and 96.17).[60,61]

The combination of esophageal duplication with other anomalies, such as spinal defects, should prompt a search for additional duplications along the alimentary tract, which can be found in up to one-third of cases.[52]

***Imaging.*** Radiographs may demonstrate a sharply demarcated middle or posterior mediastinal mass and associated vertebral anomalies in cases of neurenteric cyst (see Fig. 96.14 and e-Fig. 96.16A).

Esophagrams (e-Fig. 96.16B) will suggest an intramural mass, but typically no connection between the two structures is seen.[58] Ultrasound can confirm the cystic nature of the mass in utero but is rarely utilized after birth.[62] CT and MRI are the modalities of choice to confirm the cystic nature of the mass and to best delineate the abnormality. The cyst fluid typically has the attenuation and signal characteristics of water, although this can be affected by hemorrhage or infection (see e-Fig. 96.13B and Figs. 96.14B and 96.15A).[58]

For neurenteric cysts, CT myelography (see e-Fig. 96.17) can demonstrate the extent of the lesion and any associated vertebral anomaly. MRI, however, is the current study of choice to evaluate the presence and extent of intraspinal abnormalities. These lesions are usually intradural and extramedullary.[63,64] Those enteric cysts that contain gastric mucosa with acid and pepsin secretion can be identified by nuclear imaging and are at risk for hemorrhage.[65]

***Treatment/Follow-up.*** Complete surgical resection of cystic duplications is the rule, although this treatment may be modified in case of complications such as infection and erosion into the true lumen of the esophagus.[60] Even if asymptomatic at discovery, esophageal duplication cysts are at risk for development of bleeding, infection, and cancer.[54] Some cysts are amenable to endoscopic treatment.[57]

## KEY POINTS

- Patients with esophageal atresia and distal fistula will have air in the abdomen, whereas patients without a distal fistula will not have abdominal bowel gas.
- Approximately 2.5% of patients with esophageal atresia have a right-sided aortic arch, which is important to identify preoperatively for surgical planning.
- The majority of patients with esophageal atresia complex have associated anomalies, although this decreases to approximately 25% among those with isolated or H-type fistulae.
- Distinguishing features between esophageal atresia and traumatic pharyngoesophageal perforation include an unusually long pouch, irregularity of its lumen, presence of pneumomediastinum, and contrast on esophagram that outlines both true and false lumens.
- Laryngotracheoesophageal clefts may be confused with TEFs or mistaken for aspiration during esophagram.
- The clinical and radiographic diagnosis of an isolated TEF can be elusive, and repeat examination can be considered in difficult cases.
- Congenital esophageal stenosis with tracheobronchial remnants is typically located in the distal esophagus, and when abutting the esophagogastric junction, can be mistaken for achalasia.
- Duplication cysts in the esophagus are second only to the ileum in frequency and are most commonly intrathoracic and cystic. Thoracic duplication cysts are often asymptomatic, but cervical duplication cysts become symptomatic very early in life.

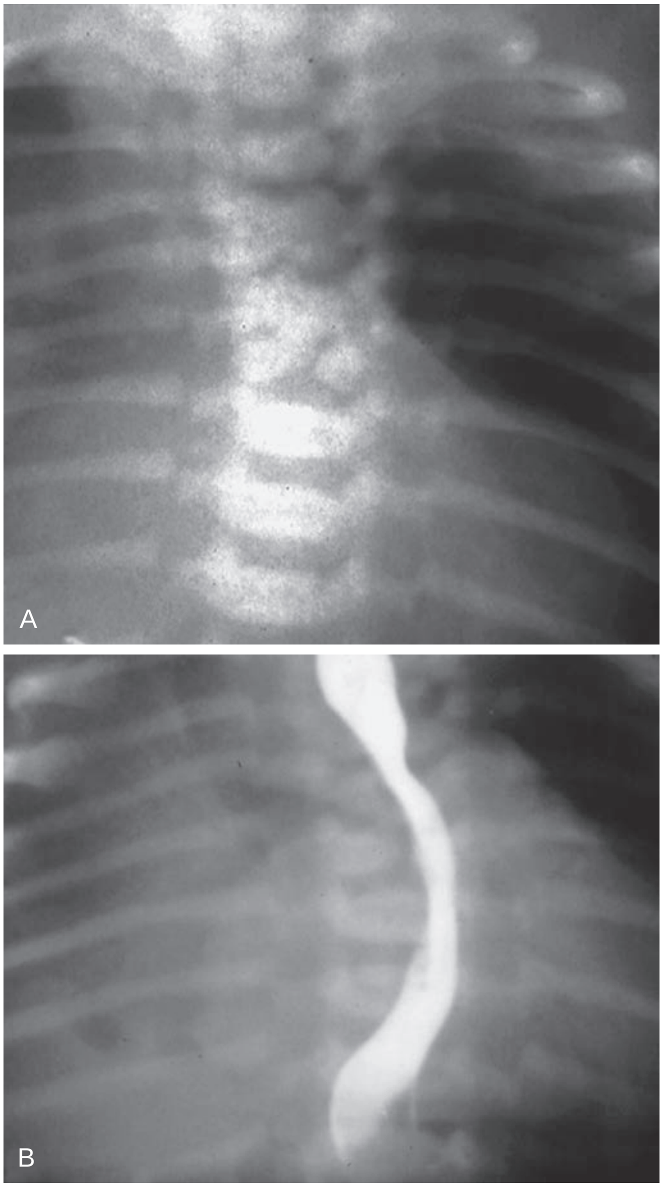

**e-Figure 96.16.** (A) Frontal chest radiograph demonstrates a right-sided mass lesion associated with a midthoracic vertebral segmentation anomaly. (B) Esophagram demonstrates the vertebral body malformations and paravertebral soft tissue mass and further outlines displacement of the esophagus. These findings in conjunction are suggestive of a neurenteric cyst.

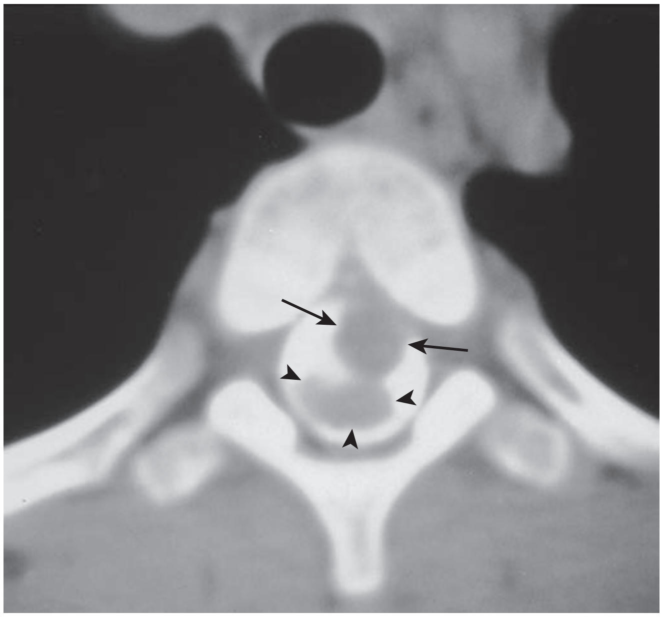

**e-Figure 96.17. Intraspinal neurenteric cyst.** Axial CT image with intrathecal contrast demonstrates an intraspinal mass *(arrows)* anterior to the compressed spinal cord *(arrowheads)* surgically proven to represent an intraspinal neurenteric cyst. Note the associated congenital cleft in the vertebral body.

## SUGGESTED READINGS

Berrocal T, Torres I, Gutiérrez J, et al. Congenital anomalies of the upper gastrointestinal tract. *Radiographics*. 1999;19(4):855–872.

Ioannides AS, Copp AJ. Embryology of oesophageal atresia. *Semin Pediatr Surg*. 2009;18(1):2–11.

Jones DW, Kunisaki SM, Teitelbaum DH, et al. Congenital esophageal stenosis: the differential diagnosis and management. *Pediatr Surg Int*. 2010;26(5):547–551.

Kluth D, et al. The embryology of foregut malformations. *J Pediatr Surg*. 1987;22:389–393.

Laffan EE, Daneman A, Ein SH, et al. Tracheoesophageal fistula without esophageal atresia: Are pull-back tube esophagograms needed for diagnosis? *Pediatr Radiol*. 2006;36(11):1141–1147.

Leboulanger N, Garabedian EN. Laryngo-tracheo-oesophageal clefts. *Orphanet J Rare Dis*. 2011;6:81.

## REFERENCES

Full references for this chapter can be found on www.expertconsult.com.

## REFERENCES

1. Harmon C, Coran A. Congenital anomalies of the esophagus. In: Coran A, et al, eds. *Coran: Pediatric Surgery*. Philadelphia: Elsevier; 2012.
2. Haight C, Towsley HA. Congenital atresia of the esophagus with tracheoesophageal fistula (extrapleural ligation of fistula and end-to-end anastomosis of esophageal segments). *Surg Gynecol Obstet*. 1943;76:672–688.
3. Sfeir R, et al. Esophageal atresia: data from a national Cohort. *J Pediatr Surg*. 2013;48:1664–1669.
4. Hryhorczuk A, Lee E, Eisenberg R. Esophageal abnormalities in pediatric patients. *AJR Am J Roentgenol*. 2013;201:W519–W532.
5. Oddsberg J, et al. Influence of maternal parity, age, and ethnicity on risk of esophageal atresia in the infant in a population-based study. *J Pediatr Surg*. 2008;43(9):1660–1665.
6. Kluth D, Fiegel H. The embryology of the foregut. *Semin Pediatr Surg*. 2003;12(1):3–9.
7. Billmyre KK, Hutson M, Klingensmith J. One shall become two: separation of the esophagus and trachea from the common foregut tube. *Dev Dyn*. 2015;244(3):277–288.
8. Stoll C, et al. Associated malformations in patients with esophageal atresia. *Eur J Med Genet*. 2009;52(5):287–290.
9. Burjonrappa S, et al. Type A esophageal atresia: a critical review of management strategies at a single center. *J Pediatr Surg*. 2010;45(5):865–871.
10. Sparey C, et al. Esophageal atresia in the Northern Region Congenital Anomaly Survey, 1985-1997: prenatal diagnosis and outcome. *Am J Obstet Gynecol*. 2000;182(2):427–431.
11. Shulman A, et al. Prenatal identification of esophageal atresia: the role of ultrasonography for evaluation of functional anatomy. *Prenat Diagn*. 2002;22(8):669–674.
12. Salomon LJ, et al. Real-time fetal magnetic resonance imaging for the dynamic visualization of the pouch in esophageal atresia. *Ultrasound Obstet Gynecol*. 2009;34(4):471–474.
13. Hernanz-Schulman M. Vascular rings: a practical approach to imaging diagnosis. *Pediatr Radiol*. 2005;35(10):961–979.
14. Lillehei CW, Colan S. Echocardiography in the preoperative evaluation of vascular rings. *J Pediatr Surg*. 1992;27(8):1118–1120.
15. Dorman RM, Vali K, Harmon CM, et al. Repair of esophageal atresia with proximal fistula using endoscopic magnetic compression anastomosis (magnamosis) after staged lengthening. *Pediatr Surg Int*. 2016;32(5):525–528. doi:10.1007/s00383-016-3889-y. [Epub 2016 Mar 24].
16. Lovvorn HN, Baron CM, Danko ME, et al. Staged repair of esophageal atresia: pouch approximation and catheter-based magnetic anastomosis. *J Pediatr Surg Case Rep*. 2014;2(4):170–175.
17. Smithers CJ, Hamilton TE, Manfredi MA, et al. Categorization and repair of recurrent and acquired tracheoesophageal fistulae occurring after esophageal atresia repair. *J Pediatr Surg*. 2017;52(3):424–430.
18. Al-Salem AH, Mohaidly MA, Al-Buainain HM, et al. Congenital H-type tracheoesophageal fistula: a national multicenter study. *Pediatr Surg Int*. 2016;32(5):487–491.
19. Sahnoun L, Aloui S, Nouri S, et al. [Isolated congenital tracheoesophageal fistula]. *Arch Pediatr*. 2013;20(2):186–191.
20. Guo W, et al. Tracheoesophageal fistula after primary repair of type C esophageal atresia in the neonatal period: recurrent or missed second congenital fistula. *J Pediatr Surg*. 2010;45(12):2351–2355.
21. Lallemand D, Quignodon JF, Courtel JV. The anomalous origin of bronchus from the esophagus: report of three cases. *Pediatr Radiol*. 1996;26(3):179–182.
22. Verma A, Mohan S, Kathuria M, et al. Esophageal bronchus: case report and review of the literature. *Acta Radiol*. 2008;49(2):138–141.
23. Sugandhi N, Sharma P, Agarwala S, et al. Esophageal lung: presentation, management, and review of literature. *J Pediatr Surg*. 2011;46(8):1634–1637. doi:10.1016/j.jpedsurg.2011.04.057.
24. Crabbe DC. Isolated tracheo-oesophageal fistula. *Paediatr Respir Rev*. 2003;4(1):74–78.
25. Biechlin A, Delattre A, Fayoux P. [Isolated congenital tracheoesophageal fistula. Retrospective analysis of 8 cases and review of the literature]. *Rev Laryngol Otol Rhinol (Bord)*. 2008;129(3):147–152.
26. Laffan EE, et al. Tracheoesophageal fistula without esophageal atresia: Are pull-back tube esophagograms needed for diagnosis? *Pediatr Radiol*. 2006;36(11):1141–1147.
27. Gopal M, Woodward M. Potential hazards of contrast study diagnosis of esophageal atresia. *J Pediatr Surg*. 2007;42(6):E9–E10.
28. Bax KN, Roskott AM, van der Zee DC. Esophageal atresia without distal tracheoesophageal fistula: high incidence of proximal fistula. *J Pediatr Surg*. 2008;43(3):522–525.
29. Colleran GC, Ryan CE, Lee EY, et al. Computed tomography and upper gastrointestinal series findings of esophageal bronchi in infants. *Pediatr Radiol*. 2017;47(2):154–160.
30. Richter GT, et al. Endoscopic management of recurrent tracheoesophageal fistula. *J Pediatr Surg*. 2008;43(1):238–245.
31. Rothenberg S. Thorascopic repair of esophageal atresia and tracheoesophageal fistula in neonates, First Decade's Experience. *Dis Esophagus*. 2012;26:359–364.
32. Leboulanger N, Garabedian EN. Laryngo-tracheo-oesophageal clefts. *Orphanet J Rare Dis*. 2011;6:81.
33. Strychowsky JE, Rahbar R. Laryngotracheoesophaeal clefts. *Semin Pediatr Surg*. 2016;25:128–131.
34. Johnston DR, Watters K, Ferrari LR, et al. Laryngeal cleft: evaluation and management. *Int J Pediatr Otorhinolaryngol*. 2014;78:905–911.
35. Sandu K, Monnier P. Endoscopic laryngotracheal cleft repair without tracheotomy or intubation. *Laryngoscope*. 2006;116(4):630–634.
36. Emil SGS. Pediatric surgical images, neonatal esophageal perforation. *J Pediatr Surg*. 2004;39(8):1296–1298.
37. Panieri E, Millar AJW, Rode H, et al. Iatrogenic esophageal perforation in children: patterns of injury, presentation, management, and outcome. *J Pediatr Surg*. 1996;31(7):890–895.
38. Onwuka EA, Saadai P, Boomer LA, et al. Nonoperative management of esophageal perforations in the newborn. *J Surg Res*. 2016;205:102–107.
39. Gander JW, Berdon WE, Cowles RA. Iatrogenic esophageal perforation in children. *Pediatr Surg Int*. 2009;25(5):395–401. doi:10.1007/s00383-009-2362-6. [Epub 2009 Apr 21].
40. Kassner EG, Baumstark A, Balsam D, et al. Passage of feeding catheters into the pleural space: a radiographic sign of trauma to the pharynx and esophagus in the newborn. *AJR Am J Roentgenol*. 1977;128(1):19–22.
41. Parelkar S, Mundada D, Joshi P, et al. Iatrogenic perforation of upper pouch in pure esophageal atresia: a rare complication and review of literature. *European J Pediatr Surg Rep*. 2013;1(1):21–23.
42. Michaud L, et al. Characteristics and management of congenital esophageal stenosis: findings from a multicenter study. *Orphanet J Rare Dis*. 2013;8:186.
43. Takamizawa S, et al. Congenital esophageal stenosis: therapeutic strategy based on etiology. *J Pediatr Surg*. 2002;37(2):197–201.
44. Nemolato S, et al. Oesophageal tracheobronchial remnants. *Gastroenterol Clin Biol*. 2008;32(8–9):779–781.
45. Neilson IR, et al. Distal congenital esophageal stenosis associated with esophageal atresia. *J Pediatr Surg*. 1991;26(4):478–481, discussion 481-482.
46. Pumberger W, Geissler W, Horcher E. [Congenital oesophageal stenosis due to tracheobronchial remnants]. *Chirurg*. 1999;70(9):1031–1035.
47. Jones DW, et al. Congenital esophageal stenosis: the differential diagnosis and management. *Pediatr Surg Int*. 2010;26(5):547–551.
48. Deiraniya AK. Congenital oesophageal stenosis due to tracheobronchial remnants. *Thorax*. 1974;29(6):720–725.
49. Ibrahim AH, et al. Congenital esophageal stenosis associated with esophageal atresia: new concepts. *Pediatr Surg Int*. 2007;23(6):533–537.
50. Elhalaby EE, et al. Congenital esophageal stenosis: to dilate or to resect. *Ann Pediatr Surg*. 2006;2(1):2–9.
51. Berrocal T, et al. Congenital anomalies of the upper gastrointestinal tract. *Radiographics*. 1999;19(4):855–872.
52. Lund D. Alimentary tract duplications. In: Coran A, et al, eds. *Coran: Pediatric Surgery*. Philadelphia: Elsevier; 2012.
53. Nayan S, et al. Cervical esophageal duplication cyst: case report and review of the literature. *J Pediatr Surg*. 2010;45(9):e1–e5.
54. Martin ND, et al. Intra-abdominal esophageal duplication cysts: a review. *J Gastrointest Surg*. 2007;11(6):773–777.
55. Kim JH, Kwon CI, Rho JY, et al. Communicating tubular esophageal duplication combined with bronchoesophageal fistula. *Clin Endosc*. 2016;49(1):81–85.
56. Rathod J, Disawal A, Taori K, et al. Communicating tubular duplication of upper esophagus-a rare occurrence. *J Clin Imaging Sci*. 2011;1:33.
57. Coumaros D, Schneider A, Tsesmeli N, et al. Endoscopic management of a tubular esophageal duplication diagnosed in adolescence (with videos). *Gastrointest Endosc*. 2010;71(4):827–830.
58. Fitch SJ, Tonkin IL, Tonkin AK. Imaging of foregut duplication cysts. *Radiographics*. 1986;6(2):189–201.
59. Al-Majali R, et al. Mediastinal foregut duplication cyst. *J Res Med Sci*. 2004;11(1):48–50.

60. Savage JJ, et al. Neurenteric cysts of the spine. *J Craniovertebr Junction Spine*. 2010;1(1):58–63.
61. Garg N, et al. Is total excision of spinal neurenteric cysts possible? *Br J Neurosurg*. 2008;22(2):241–251.
62. Sherer DM, et al. Prenatal sonographic findings of an isolated cervical esophageal duplication cyst. *J Ultrasound Med*. 2009;28(3):405–407.
63. Cai C, et al. Intraspinal neurenteric cysts in children. *Can J Neurol Sci*. 2008;35(5):609–615.
64. Menezes AH, Traynelis VC. Spinal neurenteric cysts in the magnetic resonance imaging era. *Neurosurgery*. 2006;58(1):97–105.
65. Kumar R, et al. Diagnosis of ectopic gastric mucosa using 99Tcm-pertechnetate: spectrum of scintigraphic findings. *Br J Radiol*. 2005;78(932):714–720.

# 97 Disorders of Swallowing

Steven Kraus, Jayne M. Seekins, and Henrique M. Lederman

## OVERVIEW

Swallowing, the coordinated movement of liquids, purees, and/or solids, is a complex sensorimotor process that depends on integrated information from multiple levels of the central and peripheral nervous system. It involves complex excitatory and inhibitory signals from multiple regions of the cortex and subcortex, and ascending sensory signals from the oropharyngeal area that trigger the central pattern generator in the bulbar reticular formation. This makes up a network of premotor neurons and interneurons that drive motor neurons of swallowing in cranial nerves V, VII, IX, X, and XII. The muscles of the lips, submental muscle group, tongue, palate, larynx, pharynx, and esophagus that are innervated by these cranial nerves are then excited and inhibited sequentially to form an oral bolus and swallow. There are three phases of swallowing, (1) the oral phase, which is under voluntary control (preparing the food or liquid in the oral cavity to form a bolus on the tongue-including sucking liquids, manipulating soft boluses, chewing solid food, and moving or propelling the bolus posteriorly through the oral cavity); (2) the pharyngeal phase, which is under involuntary control (initiating the swallow and moving it through the pharynx); and (3) the esophageal phase, which is also under involuntary control (moving the bolus into and through the cervical and thoracic esophagus and into the stomach via esophageal peristalsis).[1,2] When swallowing function is abnormal (dysphagic) due to developmental disability; neurologic disorders (e.g., cerebral palsy, meningitis, encephalopathy, traumatic brain injury, neuromuscular disease); factors affecting neuromuscular coordination (prematurity); complex medical conditions (e.g., heart disease, pulmonary disease, gastroesophageal reflux disease); structural abnormalities of the head and neck (e.g., cleft lip and/or palate, esophageal atresia, head and neck abnormalities); genetic syndromes (e.g., Pierre-Robin, Prader-Willi, Treacher-Collins); medication side effects; sensory issues as a primary cause or secondary to limited food availability in early development; behavioral factors; or social, emotional, and environmental issues; a radiologic study of swallowing function can assess and help therapists treat the dysphagia.[3] Most swallowing disorders in infants and children are secondary to developmental disorders, of which cerebral palsy is the most common.[4,5]

## GENERAL EXAMINATION PRINCIPLES

The Videofluoroscopic Swallow Study or VFSS is the radiographic study of deglutition performed in association with occupational therapists and/or speech pathologists, depending upon the institutional referral pattern. The primary purposes of the VFSS are (1) to assess the structure and function of swallowing and to assess the risk of aspiration; and (2) once a functional abnormality of swallowing is detected, to identify compensatory strategies and a management plan that enables the patient to feed functionally and safely. These strategies may include adjustments in bolus characteristics (e.g., volume or texture), method of presentation (cup, spoon, straw, suckle feeder, syringe), body posture or position, sensory input, or the use of active maneuvers to protect the airway (e.g., supraglottic swallow, Mendelssohn maneuver, coughing, and clearing the throat between swallows).[6]

As a prerequisite to performing the VFSS, the patient's history related to feeding and associated clinical conditions should be obtained and include data about the acuity of the clinical complaint, the child's feeding history, ability to suck, use of utensils, positioning and irritability during and after feeding, usual appetite, and signs of fatigue during feeding. Having this history can help streamline the evaluation and limit the duration of the examination to limit radiation exposure. The historical review should also include review of prior radiologic studies that may have already been performed including prior VFSS studies, upper gastrointestinal series (GIs), chest radiographs, high resolution computed tomography (HRCT) of the chest, etc., which may show radiologic evidence of dysphagia such as aspiration on a prior VFSS or upper GI, or secondary signs of aspiration on a chest radiograph or HRCT such as right upper lobe and bibasilar lung disease pattern.

The initial step in the evaluation of swallowing is to assess the anatomic structures of the naso- and oropharynx. Note the presence of a nasoenteric tube or tracheostomy tube and realize that the presence of a nasoenteric feeding tube has been shown to have no significant effect on the results of the VFSS.[7] For feeding, parents are asked to bring food and liquid that the child typically eats or drinks at home, as well as familiar utensils. The VFSS is then completed with this food or liquid mixed with contrast (usually barium). In some patients, flavoring can be added to the liquid to increase patient cooperation in swallowing although making sure not to modify the thickness of the standard thin and thickened liquids. The patient is placed in the true lateral position in a swallowing chair (or side-lying on the fluoroscopy table tilted at 15 degrees head up if neonate or small infant to simulate breast-feeding position) and is fed the liquid/contrast mixture of varying thickness by bottle with a nipple, sippy cup, cup with straw, or open cup depending on their level of development. Swallowing is evaluated in real time with video fluoroscopy (15–30 frames per second), examining mostly from the mouth through the cervical esophagus. At least one swallow should be followed to the gastroesophageal junction to detect any unexpected esophageal abnormality such as an unknown or recurrent H-type tracheoesophageal fistula or esophageal stricture that might occur in a patient with history of repaired esophageal atresia, a prominent vascular impression such as an aberrant subclavian artery (dysphagia lusoria) or esophageal achalasia in an older patient.[8–15] Imaging in the frontal projection may be done after lateral imaging, sometimes using a basal or Towne view.[12] This allows for evaluation of lateral wall movement, as well as correlation with the clinical evaluation of swallowing by fiberoptic endoscopic evaluation of swallowing, which is often performed as a complementary examination.[3,16,17]

If the infant will not take liquid/contrast from the nipple, it can be carefully introduced into the baby's mouth with a blunt-tipped syringe (between the cheek and the lateral aspect of the teeth or gums) or a feeding tube can be inserted through the nipple (e-Fig. 97.1) into the baby's mouth and controlled introduction of contrast under fluoroscopic guidance can be made to initiate swallowing. However, this type of "force-feeding" is artificial because it bypasses the oral phase of swallowing and so the results should be interpreted with caution. Force-feeding should be avoided and if a patient refuses to eat or drink; discontinuing the examination and performing when the infant or child is more cooperative is recommended for the best and most clinically relevant results. Contrast medium is mixed with increasingly thick food mixtures from puree to solid and swallowing of these are evaluated (if age-appropriate). Evaluation of the patient's ability to handle

## Abstract:

Swallowing is a complex sensorimotor process that depends on integrated information from multiple levels of the central and peripheral nervous system. It can be separated into the oral, pharyngeal, and esophageal phases. Swallowing can be evaluated radiologically by the Videofluoroscopic Swallow Study, VFSS, which is performed in conjunction with speech or occupational therapists. The purpose of the VFSS is not only to assess the structure and function of swallowing and the risk of aspiration; if an abnormality of swallow function including aspiration is detected, it is also important to attempt to identify compensatory strategies and a management plan that enables the patient to feed functionally and safely. Knowing the anatomy and physiology of swallowing and the patients clinical status can help predict which phase of swallowing will be abnormal. The most common causes of swallowing dysfunction in children include central neurologic dysfunction, congenital anomalies that cause mechanical interference in the swallowing apparatus, congenital and acquired retropharyngeal processes, and connective tissue disorders. In otherwise normal infants with dysphagia, gastroesophageal reflux (GER) is a common associated abnormality.

## Keywords:

Videofluoroscopic
dysphagia
tracheal aspiration
laryngeal penetration
cricopharyngeal achalasia
pharyngonasal backflow

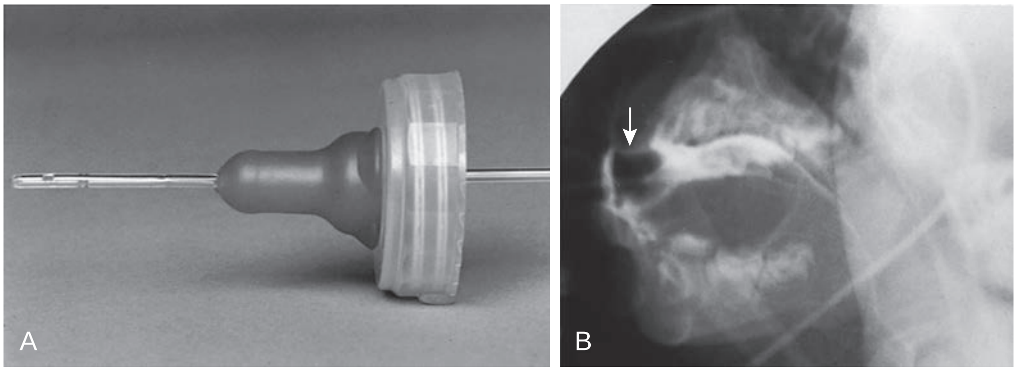

**e-Figure 97.1.** Modified feeding technique. (A) A number 8 silastic feeding tube is placed through a nipple so that a controlled introduction of contrast material can be made into the mouth, as the swallowing mechanism is observed. (B) Barium outlines the nipple *(arrow)* and the tube. *(Modified from Poznanski A. A simple device for administering barium to infants.* Radiology. *1969;93:1106.)*

differently textured foods aids in planning appropriate diet to meet nutritional needs and for future therapy. If the patient needs a special diet or only eats certain foods, those can be brought to the examination and used. If aspiration is seen during the VFSS, the study is not usually discontinued. Rather, the therapist will modify feeding strategies to help the patient swallow without aspirating; for example, (1) pacing the swallow, allowing only several swallows with intervening breaks; (2) utilizing nipples with a smaller opening resulting in a slower flow rate; and (3) thickening the fluid. One or all of these strategies are sometimes utilized to obtain safe swallowing.

## ABNORMAL FINDINGS ON VIDEOFLUOROSCOPIC SWALLOWING STUDIES

Typical abnormal findings in the oral phase of swallowing on a VFSS include (1) loss of food out of the mouth due to reduced lip closure, tongue thrust, and reduced tongue control; (2) piecemeal deglutition (requiring multiple swallows to clear the oral cavity of a single bolus) due to reduced tongue movements or strength; (3) prolonged oral transport (liquid >3 seconds) and (4) oral transport of puree with no bolus formation, both due to reduced tongue coordination; and (5) prolonged presence of material in valleculae or pyriform sinuses preinitiation due to prolonged delay in pharyngeal initiation of swallowing.[2]

Typical abnormal findings in the pharyngeal phase of swallowing include (1) pharyngonasal backflow due to reduced velopharyngeal closure or incoordination of pharyngeal contraction (Fig. 97.2 and e-Fig. 97.3); (2) laryngeal penetration due to reduced or delayed closure of airway entrance (laryngeal vestibule) (Fig. 97.4 and Video 97.1); (3) aspiration: (a) before swallow due to delayed swallow initiation, (b) during swallow due to incoordination of pharyngeal contraction and airway closure or vocal fold paresis or paralysis, (c) after swallow due to reduced pharyngeal pressure or contractions from residue; and/or (4) postswallow residue: (a) in valleculae due to reduced tongue base contraction, (b) in pyriform sinuses or posterior pharyngeal wall due to reduced submental muscle group and pharyngeal contraction.[2]

Typical abnormal findings in the esophageal phase of swallowing include (1) postswallow residue in the upper esophageal sphincter region due to reduced contraction of submental muscle group, tongue base, and reduced pharyngeal contractions and (2) prominence of or incomplete relaxation of the cricopharyngeus muscle (cricopharyngeal bar) due to reduced upper esophageal sphincter (UES) opening or premature UES closure.[2]

## CAUSES OF SWALLOWING DYSFUNCTION

The most common causes of swallowing dysfunction in pediatric patients include central neurologic dysfunction, congenital anomalies that cause anatomic abnormalities with mechanical interference in the swallowing apparatus, congenital and acquired retropharyngeal processes, and connective tissue disorders.

### Central Neurologic Dysfunction

***Overview.*** Cerebral palsy[1] is the most common cause of swallowing dysfunction in infants and children. Other neuromuscular disorders to be considered are brainstem dysfunction, cranial nerve abnormalities, intracranial neoplasms, meningomyelocele, muscular dystrophies, and myasthenia gravis. Familial dysautonomia (Riley-Day syndrome) leads to autonomic dysfunction with esophageal

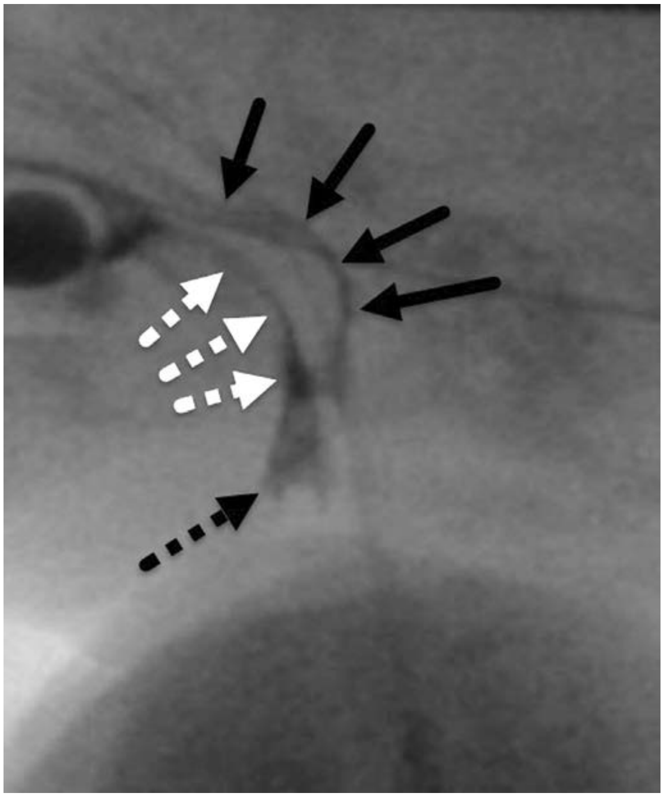

**Figure 97.2.** Pharyngonasal backflow. Lateral still image from a VFSS shows contrast from pharyngonasal backflow outlining the nasopharynx due to velopalatine insufficiency *(black arrows)*; contrast along the posterior tongue *(white dashed arrows)* and in the vallecula *(black dashed arrow)* is normal during swallowing.

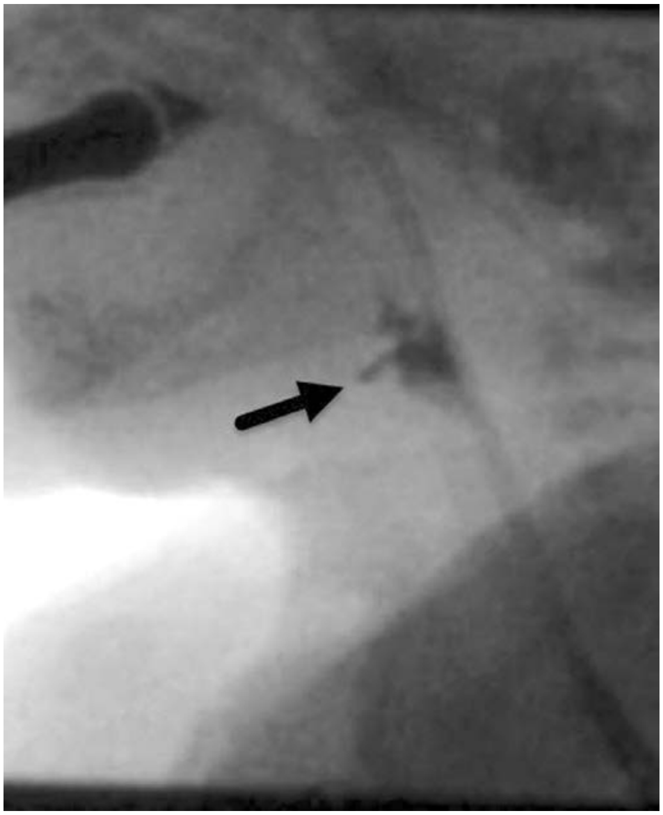

**Figure 97.4.** Shallow laryngeal penetration. Lateral still image from a VFSS shows contrast penetrating into the upper aspect of the laryngeal vestibule *(arrow)* but no contrast on the vocal cords or in the trachea.

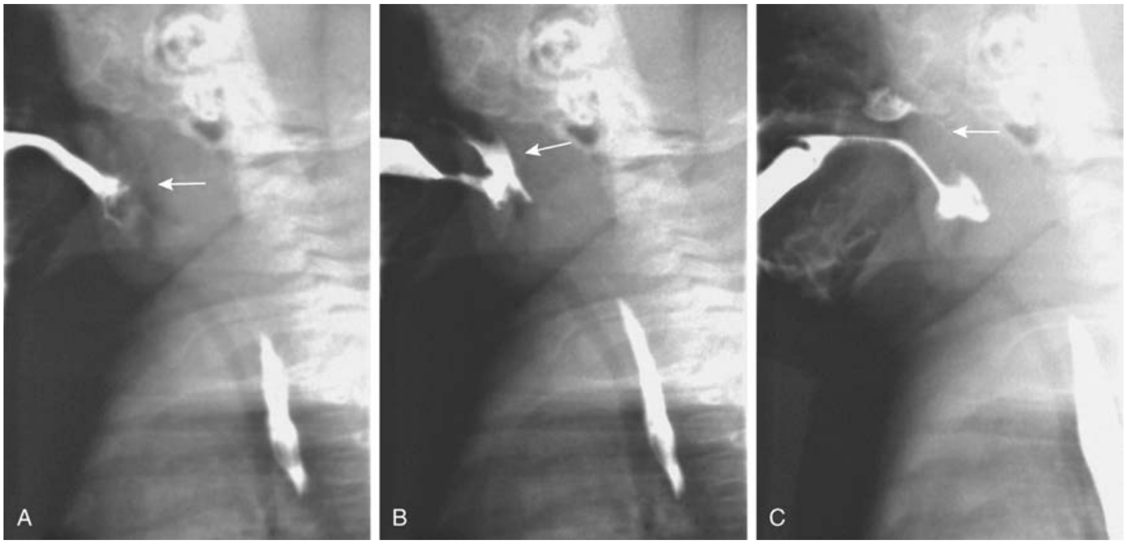

**e-Figure 97.3.** Pharyngonasal backflow. (A) As the nipple is inserted into the infant's mouth, the tongue and soft palate are relaxed and the nasopharynx opens *(arrow)*. (B) Normally, the tongue elevates, pushing the nipple to the roof of the mouth, and the soft palate elevates. In this example, the soft palate did not elevate and close off the nasopharynx, resulting in nasopharyngeal backflow *(arrow)*. (C) The infant finally did close the nasopharynx by elevation of the soft palate against the adenoid tissue *(arrow)*. Contrast material remains in the nose and in the hypopharynx.

dysmotility and frequent aspiration pneumonia. Abnormality of the neuromuscular mechanism elevating the soft palate (velopharyngeal closure) may lead to reflux of contrast material into the nasopharynx (pharyngonasal backflow or reflux), with subsequent pooling of contrast in the pharynx and potential aspiration into the airway. Abnormalities of other muscle groups lead to defective function of the epiglottis and upper esophageal sphincter, with aspiration into the airway being common.[18,19]

***Etiology.*** The etiology of swallowing dysfunction is related to dysfunction in one of the three phases of swallowing: oral phase with inability to deliver the food into the mouth (e.g., poor suck); pharyngeal phase with failure to move the food through the pharynx, elevation of the soft palate and closure of the epiglottis; or in the upper esophageal phase, with abnormal coordination of relaxation and contraction phase of the UES as previously detailed.[18] The coordination necessary to effect the swallowing process correctly is mediated through the cranial nerves responsible for both sensation and motor function, as well as osseous and muscular structures supplied by both the autonomic and voluntary nervous system. Thus depending on the level of the central nervous system (CNS) defect, one can predict which phase of swallowing will be most effected.

***Clinical Presentation.*** The severity of disordered swallowing and presence or absence of aspiration will depend on the level of neurologic deficit. Depending on the specific neurologic defect, any or all components of the swallowing mechanism may be affected. Symptoms may include pharyngonasal backflow, gagging, coughing and choking during feedings, recurrent pneumonia, malnutrition, and failure to thrive.[18,20] However, in some patients at risk for disordered swallowing and aspiration, the gagging and coughing reflex may itself be inherently absent or secondarily impaired, and these patients are at risk to aspirate without the protective cough reflex (silent aspiration). Due to the risk of silent aspiration in these patients, VFSS should be performed to aid nutritional management and to help reduce aspiration where possible.[21]

***Imaging.*** The abnormalities detected during VFSS will depend on the level of CNS defect. In upper cortical motor neuron dysfunction, oral phase dysfunction will dominate with loss of food from the mouth anteriorly, poor oral control of the bolus, fluid flowing off the tongue into the sulci of the mouth, and multiple small swallows required for a single bolus (piecemeal swallowing). In these patients, the pharyngeal phase is not as affected although if the oral phase of swallowing is markedly impaired, the pharyngeal phase will not be able to accommodate and contrast material may be seen within the nasopharynx or trachea (Fig. 97.5 and Video 97.2). Dysfunction in the pharyngeal phase may be related to brainstem dysfunction such as Chiari malformation, brainstem neoplasm, after resection of posterior fossa tumors, or demyelinating diseases involving brainstem structures. This may result in weak pharyngeal contraction or lack of adequate forward passage of pharyngeal contents resulting in pharyngeal residue or findings of a cricopharyngeal bar suggestive of cricopharyngeal achalasia.[18,22,23] It is also important to note if the patient can spontaneously clear the residue by repetitive dry swallows and if a cough reflex is present during episodes of aspiration.[21]

***Treatment and Follow-up.*** Treatment can begin at the time of the study as previously described by altering the liquid or food presentation or by altering the density of liquid by thickening agents to prevent aspiration, or treatment can extend to complete oral restriction with enteric tube feeding or total parenteral nutrition. VFSS can be repeated as the patient's clinical status improves or deteriorates further to assess the effect of any interval medical or surgical treatment.

## Congenital Anomalies

***Overview.*** Multiple congenital anomalies can lead to abnormal swallowing. Mechanical problems such as seen in the Pierre-Robin sequence with a small mandible can lead to significant feeding difficulties. Macroglossia as seen in patients with Beckwith-Wiedemann syndrome or trisomy 21 can present with similar problems. Disorders of the mouth and jaw such as cleft lip and cleft palate can lead to difficulties with oral and pharyngeal phases of swallowing.[16] These disorders are usually physically apparent or diagnosed prenatally. Disorders of the palate and tongue can be seen with both ultrasound and magnetic resonance imaging (MRI).[24–26]

***Etiology.*** The etiologies of the various congenital anomalies that can result in abnormal swallowing are obviously quite different. As an example, cleft palate is a result of partial or total lack of

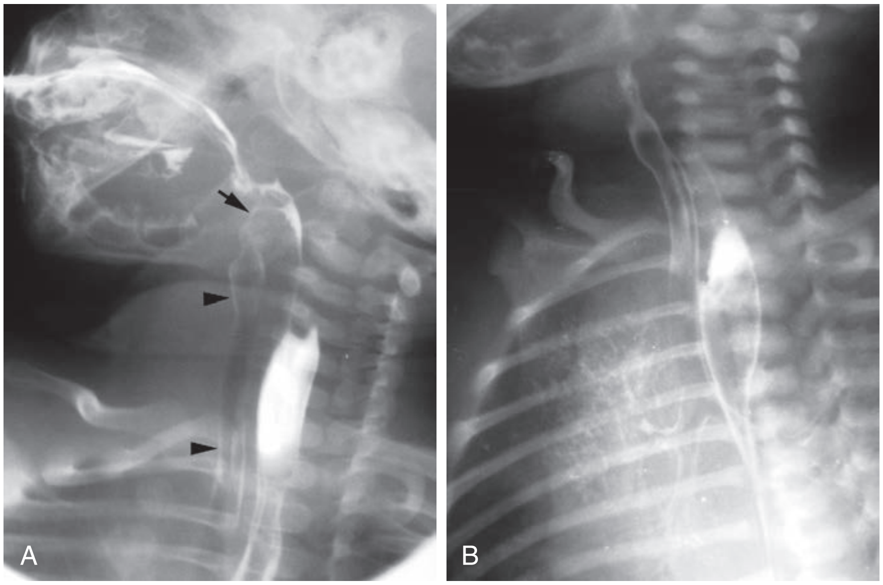

**Figure 97.5.** Aspiration. (A) Oblique image shows laryngeal penetration *(arrow)* and aspiration of contrast into the trachea *(arrowheads)*, secondary to lack of coordination during swallowing. (B) Oblique view reveals the extensive airway aspiration outlining bronchi and airspaces.

fusion of the palatal shelves between the 8th and 12th weeks of gestation.[24,27] Micrognathia may be seen alone or as part of a syndrome such as the Robin sequence[28] and is usually due to syndromic incomplete mandibular maturation or failure of normal mandibular development due to external causes.[29,30]

***Clinical Presentation.*** Symptoms correlate with the anatomic abnormality and therefore can vary widely, but all may present with choking, nasal regurgitation, pneumonia, or repeated pneumonitis. Cleft lip and cleft palate occur in varying degrees but usually are clinically apparent either externally or during the neonatal physical examination.

***Imaging.*** Conditions such as cleft lip/palate, micrognathia, and macroglossia are not routinely imaged postnatally beyond evaluation of the functional difficulties presented and may be identified prenatally with ultrasound or MRI.[24–26,28] On VFSS, one would note anterior loss in the oral phase in patients with cleft lip and pharyngonasal backflow potentially resulting in nasal regurgitation in the pharyngeal phase in patients with cleft palate. In the absence of other abnormalities, the pharyngeal phase of swallowing would be otherwise normal and aspiration is less likely. However, with more severe craniofacial anomalies, alteration in the muscles of deglutition increases the risk of significant swallowing dysfunction and aspiration.

***Treatment and Follow-up.*** Cleft lip and cleft palate are corrected surgically in infancy to allow for adequate feeding. Follow-up is usually endoscopic. Micrognathia treatment depends upon the severity. Mild micrognathia may be relieved with prone positioning and a nasopharyngeal airway until the patient grows. More severe mandibular hypoplasia may be treated by distraction osteotomy.[29] Macroglossia is treated clinically or surgically with partial anterior wedge lingual resection to allow for the return of normal swallow function.[31]

## Retropharyngeal Processes

***Overview.*** Retropharyngeal processes can be congenital or acquired. Cricopharyngeal spasm or achalasia is sometimes associated with an underlying neuromuscular disorder but often occurs as a primary abnormality.[22] Masses, both benign and malignant, are rare causes of dysphagia and range from congenital masses such as lymphatic malformation or cervical esophageal duplication, to acquired lesions such as foreign bodies, or traumatic or infectious abnormalities.

***Etiology.*** The swallowing abnormality in these patients is related to the mass effect of the lesion, which interferes with the coordinated peristaltic activity needed to effect proper swallowing. In patients with cricopharyngeal achalasia, the normal relaxation of the cricopharyngeus muscle in response to contraction of the middle and inferior pharyngeal constrictors does not occur, resulting in varying degree of obstruction to propulsion of the bolus into the esophagus.[22,23]

***Clinical Presentation.*** Symptoms of dysphagia will vary in presentation with the underlying abnormality. Cricopharyngeal achalasia presents with symptoms of aspiration, choking, and pharyngonasal regurgitation. Congenital masses may have been noted on prenatal imaging and in some cases may be visible externally on physical examination. Onset of dysphagia in conjunction with fever or other signs of infection suggest the presence of a retropharyngeal abscess or superinfection of a preexistent lesion. Prior trauma, such as insertion of orogastric tube or caustic or foreign body ingestion, represent other causes of dysphagia and disordered swallowing.

***Imaging.*** Radiographs of the neck are helpful in assessing whether there are pertinent abnormalities, such as narrowing or mass impression upon the airway, or evidence of foreign body. In patients with a retropharyngeal or prevertebral process, radiographs demonstrate increased density along the prevertebral space or posterior mediastinum, with mass effect bowing and/or narrowing the airway. Swallow study demonstrates similar findings upon the esophagus (Fig. 97.6).

Ultrasound, computed tomography, and MRI all have roles in the evaluation of neck masses. If present prenatally, imaging may guide any immediate intervention needed at birth.

In patients with cricopharyngeal spasm or achalasia, the VFSS study demonstrates a cricopharyngeal "bar", the posterior impression of the cricopharyngeus muscle that persists on multiple swallows and is associated with either partial or complete obstruction at the upper esophageal sphincter, often resulting in pharyngeal residue, aspiration, and pharyngonasal regurgitation (Fig. 97.7).

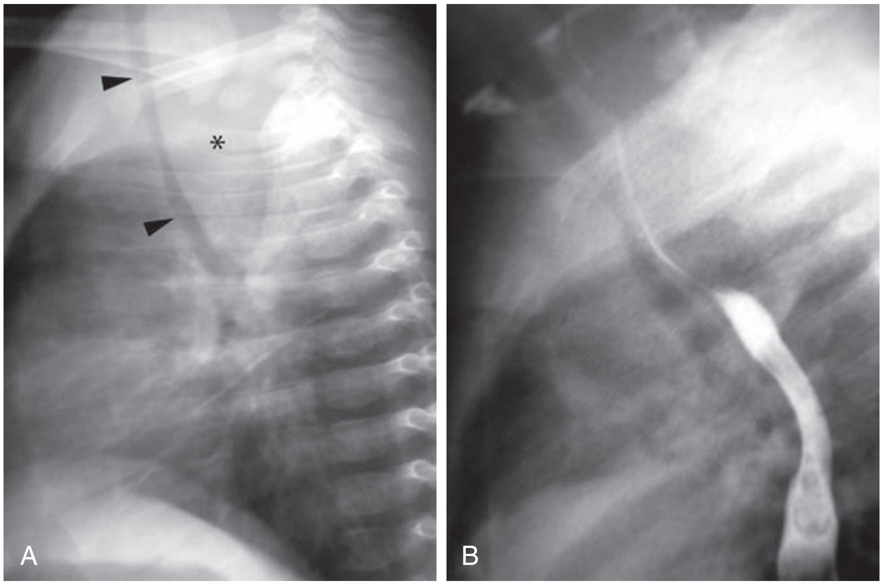

**Figure 97.6.** Prevertebral abscess. (A) Lateral chest radiograph shows a soft tissue density mass in the posterior mediastinum *(asterisk)* compressing and displacing the trachea anteriorly *(arrowheads)*. (B) Barium swallow demonstrates narrowing and anterior displacement of the esophagus and trachea.

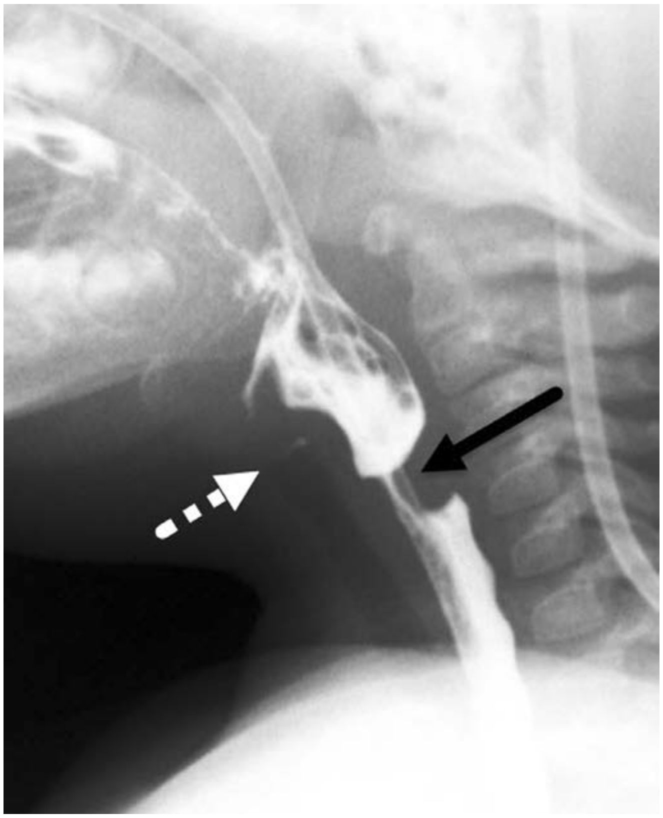

**Figure 97.7.** Cricopharyngeal achalasia and aspiration. Lateral image from a barium swallow shows a fixed filling defect in the posterior esophagus resulting from persistent contraction of the cricopharyngeus muscle *(black arrow)*. This has resulted in pharyngeal pooling of contrast, with resultant tracheal aspiration *(white dashed arrow)*.

***Treatment and Follow-up.*** The treatment depends upon the etiology of the lesion and ranges from medical, radiologic, oncologic, or surgical intervention. In patients with cricopharyngeal achalasia without significant obstruction, waiting may allow time for maturation, particularly when found in otherwise normal premature infants. In patients with primary cricopharyngeal achalasia, balloon dilatation has been advocated; surgical management remains controversial.[22,23]

## Connective Tissue Disorders

***Overview.*** Scleroderma and other connective tissue disorders are rare in childhood, most frequently occurring in adolescents and adults. While the esophagus is commonly involved, pharyngeal and upper esophageal function is usually normal. However, in adults with scleroderma, 26% may show swallowing dysfunction, and those with oropharyngeal abnormalities had more severe clinical disease and a higher incidence of pulmonary disease.[32,33] Gastroesophageal reflux (GER) that results in regurgitation or that reaches that pharynx and is swallowed has been associated with delay in swallowing initiation in children and can result in aspiration.[34] Anecdotally, GER is one of the most frequent associated abnormalities in otherwise normal infants with aspiration on VFSS performed for swallowing difficulties.

***Etiology.*** In patients with scleroderma, there is swelling of endothelial cells, with an adventitial periarterial fibrotic cuff.[35] Esophageal dysmotility typically begins at the level of the aortic arch. At this level, the esophageal muscle layer changes from striated to smooth muscle, which is affected more in patients with scleroderma.[33] Poor to absent primary peristalsis occurs in the distal two-thirds of the esophagus. Secondary gastroesophageal reflux, with or without esophagitis, may occur.

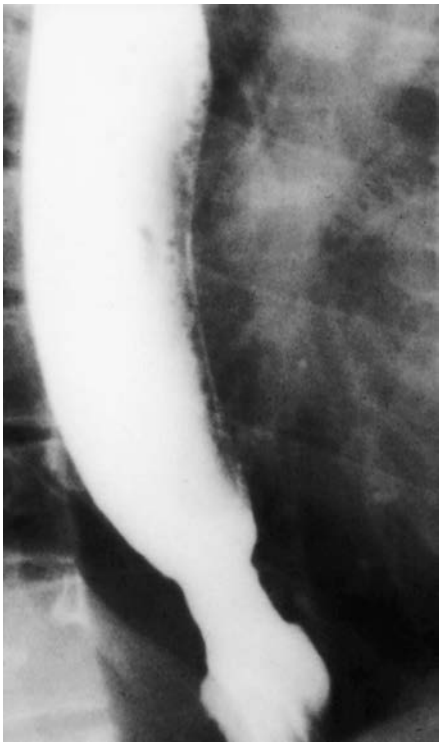

**Figure 97.8.** Scleroderma and distal esophageal stricture. Esophagram demonstrates narrowing of the distal esophagus with proximal dilatation. There was poor esophageal motility.

Dermatomyositis is an inflammatory myositis associated with a complement-mediated microangiopathy. In contrast to scleroderma, it primarily affects the striated muscle of the pharynx and upper esophagus. Dilation of these structures with disordered peristalsis frequently occurs, as does reflux of ingested material into the nasopharynx. The associated vasculitis may result in esophageal ulceration and perforation.[34]

***Clinical Manifestations.*** The esophagus is involved in nearly all patients with scleroderma, and approximately 50% to 90% have clinical symptoms of esophageal dysfunction, most commonly dysphagia and dyspepsia.[35] Those with moderate to severe esophageal manifestations have associated swallowing symptoms as well. Dermatomyositis involves the pharynx and upper esophageal sphincter, thus interfering with the appropriate direction of the bolus into the esophagus. In addition to dysphagia and inability to swallow without the aid of gravity if lying down, patients have hoarseness, nasal speech, and nasal regurgitation.

***Imaging.*** In older children and adolescents, a chest radiograph may aid with the initial workup. This may demonstrate a dilated esophagus with possibly an air-fluid level or interstitial lung disease.

VFSS in patients with mild scleroderma usually demonstrates a normal swallow mechanism but abnormal distal esophageal motility and dilation. Distal stricture formation is usually related to gastroesophageal reflux secondary to the incompetent lower esophageal sphincter (Fig. 97.8). In patients with moderate to severe disease, one may detect oral leakage, oropharyngeal residue, vestibular penetration, aspiration, and transient cricopharyngeal dysfunction.

Dermatomyositis can cause disordered swallowing of the pharynx and upper esophagus with similar findings, and pharyngeal-nasal reflux may also be detected.

***Treatment and Follow-up.*** Treatment of the underlying disease is the primary goal; findings and symptoms of reflux can be addressed medically.[35]

## KEY POINTS

- Swallowing is divided into oral, pharyngeal, and esophageal phases.
- Swallowing abnormalities can be due to a central neurologic disorder, anatomic disorders of the tongue, mouth, jaw, or esophagus, or an acquired condition.
- The primary purposes of the VFSS are to assess the structure and function of swallowing and the risk of aspiration, and to identify compensatory strategies and a management plan that enables the patient to feed functionally and safely.
- The assessment of swallow function in most departments is combined with speech therapy or occupational therapy.

## SUGGESTED READINGS

Barbiera F, Condello S, De Palo A, et al. Role of videofluorography swallow study in management of dysphagia in neurologically compromised patients. *Radiol Med*. 2006;111(6):818–827.

Derkay CS, Schechter GL. Anatomy and physiology of pediatric swallowing disorders. *Otolaryngol Clin North Am*. 1998;31(3):397–404.

Kim BR, Sung IY, Choi KH, et al. Long-term outcomes in children with swallowing dysfunction. *Dev Neurorehabil*. 2014;17(5):298–305.

Kramer SS. Radiologic examination of the swallowing impaired child. *Dysphagia*. 1989;3:117.

van den Engel-Hoek L, Erasmus CE, van Hulst KC, et al. Children with central and peripheral neurologic disorders have distinguishable patterns of dysphagia on videofluoroscopic swallow study. *J Child Neurol*. 2014;29(5):646–653.

## REFERENCES

Full references for this chapter can be found on www.expertconsult.com.

## REFERENCES

1. Erasmus CE, et al. Clinical practice: swallowing problems in cerebral palsy. *Eur J Pediatr*. 2012;171(3):409–414.
2. van den Engel-Hoek L, et al. Children with central and peripheral neurologic disorders have distinguishable patterns of dysphagia on videofluoroscopic swallow study. *J Child Neurol*. 2014;29(5):646–653.
3. American Speech Language Hearing Association. *Pediatric Dysphagia*; October 24, 2017. Available from: http://www.asha.org/Practice-Portal/Clinical-Topics/Pediatric-Dysphagia/.
4. Kakodkar K, Schroeder JW Jr. Pediatric dysphagia. *Pediatr Clin North Am*. 2013;60(4):969–977.
5. Durvasula VS, O'Neill AC, Richter GT. Oropharyngeal dysphagia in children: mechanism, source, and management. *Otolaryngol Clin North Am*. 2014;47(5):691–720.
6. Arvedson JC, Lefton-Greif MA. *Pediatric Videofluoroscopic Swallow Studies: A Professional Manual With Caregiver Guidelines;* 1998. San Antonio, Tex.: Communication Skill Builders/Psychological Corporation. x, 286 p.
7. Alnassar M, Oudjhane K, Davila J. Nasogastric tubes and videofluoroscopic swallowing studies in children. *Pediatr Radiol*. 2011;41(3):317–321.
8. Barone C, Carucci NS, Romano C. A rare case of esophageal dysphagia in children: aberrant right subclavian artery. *Case Rep Pediatr*. 2016;2016:2539374.
9. Cartabuke RH, Lopez R, Thota PN. Long-term esophageal and respiratory outcomes in children with esophageal atresia and tracheoesophageal fistula. *Gastroenterol Rep (Oxf)*. 2016;4(4):310–314.
10. Franklin AL, Petrosyan M, Kane TD. Childhood achalasia: a comprehensive review of disease, diagnosis and therapeutic management. *World J Gastrointest Endosc*. 2014;6(4):105–111.
11. Kramer SS. Radiologic examination of the swallowing impaired child. *Dysphagia*. 1989;3(3):117–125.
12. La Rossa D, et al. Video-radiography of the velopharyngeal portal using the towne's view. *J Maxillofac Surg*. 1980;8(3):203–205.
13. Martin GR, et al. Dysphagia lusorum in children. *Am J Dis Child*. 1986;140(8):815–816.
14. Perry JL. Anatomy and physiology of the velopharyngeal mechanism. *Semin Speech Lang*. 2011;32(2):83–92.
15. Skolnick ML, Cohn ER. *Videofluoroscopic Studies of Speech in Patients With Cleft Palate*. New York: Springer-Verlag; 1989.
16. Stringer DA, Witzel MA. Velopharyngeal insufficiency on videofluoroscopy: comparison of projections. *AJR Am J Roentgenol*. 1986;146(1):15–19.
17. Stringer DA, Witzel MA. Comparison of multi-view videofluoroscopy and nasopharyngoscopy in the assessment of velopharyngeal insufficiency. *Cleft Palate J*. 1989;26(2):88–92.
18. Fisher SE, Painter M, Milmoe G. Swallowing disorders in infancy. *Pediatr Clin North Am*. 1981;28(4):845–853.
19. van den Engel-Hoek L, et al. Feeding and swallowing disorders in pediatric neuromuscular diseases: an overview. *J Neuromuscul Dis*. 2015;2(4):357–369.
20. Kramer SS. Special swallowing problems in children. *Gastrointest Radiol*. 1985;10(3):241–250.
21. Weir KA, et al. Oropharyngeal aspiration and silent aspiration in children. *Chest*. 2011;140(3):589–597.
22. Erdeve O, et al. Primary cricopharyngeal achalasia in a newborn treated by balloon dilatation: a case report and review of the literature. *Int J Pediatr Otorhinolaryngol*. 2007;71(1):165–168.
23. Huoh KC, Messner AH. Cricopharyngeal achalasia in children: indications for treatment and management options. *Curr Opin Otolaryngol Head Neck Surg*. 2013;21(6):576–580.
24. Abramson ZR, et al. Radiology of cleft lip and palate: imaging for the prenatal period and throughout life. *Radiographics*. 2015;35(7):2053–2063.
25. Descamps MJ, et al. MRI for definitive in utero diagnosis of cleft palate: a useful adjunct to antenatal care? *Cleft Palate Craniofac J*. 2010;47(6):578–585.
26. Maarse W, et al. Prenatal ultrasound screening for orofacial clefts. *Ultrasound Obstet Gynecol*. 2011;38(4):434–439.
27. Tolarova MM. *Pediatric Cleft Lip and Palate*; 2009 March 23. Available from: http://emedicine.medscape.com/article/995535-overview.
28. Rogers-Vizena CR, et al. Prenatal features predictive of robin sequence identified by fetal magnetic resonance imaging. *Plast Reconstr Surg*. 2016;137(6):999e–1006e.
29. Mackay DR. Controversies in the diagnosis and management of the Robin sequence. *J Craniofac Surg*. 2011;22(2):415–420.
30. Morokuma S, et al. Abnormal fetal movements, micrognathia and pulmonary hypoplasia: a case report. Abnormal fetal movements. *BMC Pregnancy Childbirth*. 2010;10:46.
31. Heggie AA, et al. Tongue reduction for macroglossia in Beckwith Wiedemann syndrome: review and application of new technique. *Int J Oral Maxillofac Surg*. 2012.
32. Montesi A, et al. Oropharyngeal and esophageal function in scleroderma. *Dysphagia*. 1991;6(4):219–223.
33. Gaillard F, Yang N. *Gastrointestinal Manifestations of Scleroderma;* 2010 October 10, 2012. Available from: http://radiopaedia.org/articles/gastrointestinal-manifestations-of-scleroderma.
34. Ansell BM. Juvenile dermatomyositis. *J Rheumatol Suppl*. 1992;33:60–62.
35. Ntoumazios SK, et al. Esophageal involvement in scleroderma: gastroesophageal reflux, the common problem. *Semin Arthritis Rheum*. 2006;36(3):173–181.

# 98

# Acquired Esophageal Disorders

Alexander J. Towbin and Lincoln O. Diniz

## OVERVIEW

The esophagus is a muscular tube that transports food and oral secretions from the mouth to the stomach via coordinated peristalsis of striated and smooth muscle.[1] Acquired abnormalities of the esophagus can be separated into several broad categories: gastroesophageal reflux (GER), trauma including foreign bodies, inflammatory conditions, infections, motility disorders, postsurgical changes, neoplasms, and other conditions.

An esophagram or upper gastrointestinal (UGI) series is the most common method used to image the esophagus directly; the esophagram focuses on the esophagus, while the UGI is a more general examination of esophagus, stomach, and duodenum. See Chapter 84 for a description of the technique.

Computed tomography (CT) and magnatic resonance imaging (MRI) are rarely used as primary methods of imaging the esophagus; however, both CT and MRI have the advantage of allowing the radiologist to visualize the esophageal wall and lesions extrinsic to the esophagus.[2] There are several major limitations of cross-sectional imaging in evaluating the esophagus that prevent their use as a primary imaging modality: first, neither CT nor MRI provides functional information of esophageal motility; second, the esophagus is not able to be distended reliably to evaluate wall thickness accurately; third, neither study is able to provide mucosal detail; and finally, CT uses ionizing radiation.

## GASTROESOPHAGEAL REFLUX

***Overview and Etiology.*** Gastroesophageal reflux is defined as the retrograde passage of gastric contents into the esophagus.[3] When symptoms or lesions occur due to GER, it is referred to as gastroesophageal reflux disease (GERD).[4]

The primary mechanism of GER is transient relaxation of the lower esophageal sphincter. This relaxation can be triggered by a vasovagal reflex initiated by gastric distension or cardiopulmonary receptors, or a swallow that does not trigger esophageal peristalsis.[3] In children, severe GERD has several known underlying risk factors, including neurologic disorders such as spastic quadriplegia and cerebral palsy, esophageal atresia, chronic lung disease such as cystic fibrosis, and hiatal hernia.[5,6]

***Clinical Presentation.*** GER is ubiquitous in infants, occurring in 100% of 3-month-olds, 40% of 6-month-olds, and 5% to 20% of 1-year-olds.[4,6] In older children and adolescents, reported prevalence of weekly GERD symptoms increases with age, from 2% of 3- to 9-year-olds to 5% to 8.2% of children aged 10 to 17 years.[7]

The symptoms of GERD depend on age. In infants, symptoms include irritability, feeding difficulty, poor weight gain, and sleep disturbance. In older children, these include heartburn, abdominal pain, regurgitation or vomiting, and dysphagia.[3] Extraesophageal symptoms of GERD include chronic cough, asthma, apnea, bradycardia, sore throat, dental erosions, and recurrent otitis or sinusitis.[3] When compared with adults, children have fewer episodes of heartburn, dysphagia, and chest pain and more episodes of vomiting and regurgitation.[4]

GERD is often diagnosed based on symptoms and a trial of acid-reduction therapy. When symptoms are not specific or are atypical, confirmatory testing can be performed. Intraesophageal pH monitoring has traditionally been considered the gold standard due to its ability to measure the pH in the esophagus over a long period of time. The main limitation of this technique is that patients may have abnormal esophageal acid exposure without symptoms of GERD or retrograde bolus movement in the esophagus.[3,8] To evaluate for the retrograde passage of gastric contents as well as esophageal acidity, combined pH/impedance probes are used.[8]

***Imaging.*** According to the North American and European Pediatric Gastroesophageal Reflux Clinical Practice Guidelines, imaging studies are not required to make a diagnosis of GER.[9] UGI is often performed in the setting of GER to evaluate for an anatomic abnormality; however, it should not be used as the primary method of diagnosing GER or GERD. There are multiple limitations of UGI in diagnosing GER, including use of nonstandard techniques, lack of correlation with symptoms, and use of ionizing radiation. Methods used to provoke reflux such as Valsalva maneuver, positional changes, abdominal compression, or leg lifting may increase the sensitivity of detecting GER but lower the specificity.[3] Because there are more sensitive diagnostic tests and the radiologic findings do not correlate with symptoms, the collaborative practice parameter set forth by the American College of Radiology and the Society for Pediatric Radiology do not recommend provocative maneuvers or prolonged fluoroscopy for the detection of GER.[10]

Although UGI should not be prolonged to identify GER, it should be documented when present (Fig. 98.1). The percentage of patients who have GER on UGI decreases with age from 80% of infants less than 18 months to 30% of adolescents between 12 and 18 years old.[3] It should be noted that, although the height of reflux is often reported as a surrogate for its severity, there is no correlation with GERD symptoms.[3]

Technetium-99m (Tc-99m) sulphur colloid can also be used to diagnose GER. While scintigraphy is a sensitive method of detecting GER, it suffers many of the same limitations of UGI; mainly, the presence of GER does not correlate with symptoms of GERD and also requires ionizing radiation. A limitation of scintigraphy is its inability to diagnose some of the complications of GERD. Scintigraphy is thus reserved for cases where pH monitoring is not able to be performed or when evaluation of gastric motility is required.

Ultrasound benefits include its low cost, rapid performance, lack of ionizing radiation, and ability to perform a dynamic scan. While the North American and European Pediatric Gastroesophageal Reflux Clinical Practice Guidelines state that ultrasound is not recommended for routine evaluation of GER, some authors have described its use in evaluating the length of the abdominal esophagus, position of the lower esophageal sphincter relative to the diaphragm, and the presence of other potential causes of vomiting such as hiatal hernia.[9,11]

Esophageal complications of GERD include strictures and Barrett esophagitis. Esophageal strictures, also known as peptic strictures when caused by GERD, typically occur in the lower third of the esophagus and are a result of acidic injury. They are cited as being present in up to 15% of children with GERD and can occur at any age.[12] Many of the patients who develop strictures have an associated comorbidity, with 25% having a neurologic impairment.[12]

## Abstract:

The esophagus is a muscular tube that transports food and oral secretions from the mouth to the stomach via coordinated peristalsis of striated and smooth muscle. Acquired abnormalities of the esophagus can be separated into several broad categories: gastroesophageal reflux (GER), trauma including foreign bodies, inflammatory conditions, infections, motility disorders, postsurgical changes, neoplasms, and other conditions. This chapter will review the common abnormalities that affect the esophagus focusing on the unique imaging findings of each entity.

## Keywords:

gastroesophageal reflux (GER)
inflammatory conditions
motility disorders
postsurgical changes
neoplasms

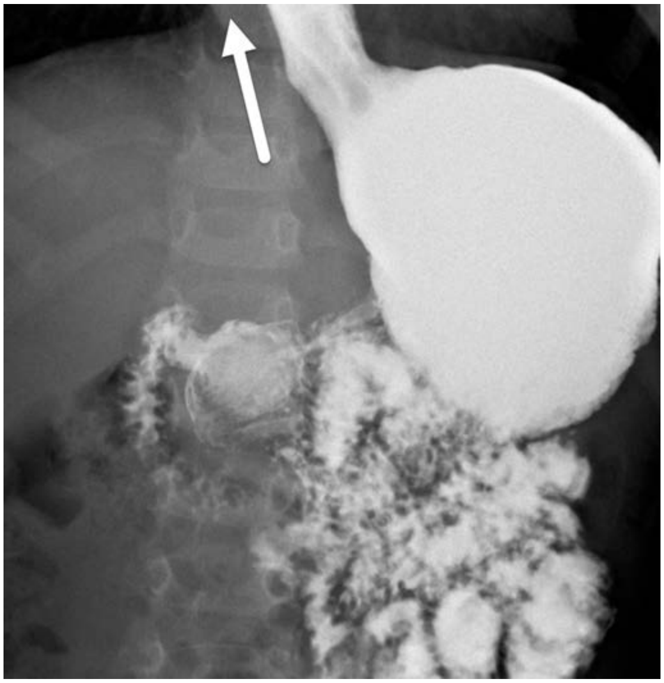

**Figure 98.1. Gastroesophageal reflux.** Image from an upper gastrointestinal examination shows retrograde flow of contrast from the stomach into the esophagus. The *arrow* shows the direction of contrast passage.

Barrett esophagus is defined as metaplasia of cells in the distal esophagus from squamous to columnar epithelium. Its prevalence in children with GERD ranges from 0.25% to 4.8%.[6,13] Risk factors for developing Barrett esophagus in children include severe chronic GERD, congenital abnormalities, neurologic impairment, hiatal hernia, and family history.[6] While it is associated with a 30-fold increase in esophageal adenocarcinoma in adults, the risk of developing adenocarcinoma is not defined in children.[6]

***Treatment.*** There are multiple options for treating GERD depending on the patient's age, comorbidities, and severity of symptoms. Generally, lifestyle changes and pharmacotherapy are first-line options. Lifestyle changes include avoidance of overfeeding, thickening feeds, upright positioning during sleep, and avoidance of second-hand smoke.[3] A goal of medical therapy is to decrease the acidity of the refluxed gastric contents. This is generally performed by using proton pump inhibitors and histamine receptor antagonists.[3] In patients with continued severe GERD after pharmacotherapy or who have other comorbidities such as neurologic impairment, antireflux surgery such as Nissen fundoplication is performed. Strictures are treated with esophageal dilation and fundoplication. In a small percentage of patients, severe and recurrent strictures will require extensive and repeated dilatations, and may come to surgical resection or esophageal replacement.[12]

## TRAUMA

Esophageal injury can occur through ingestion of foreign bodies or caustic substances, blunt injury, or forceful vomiting.

### Foreign Bodies

Ingested foreign bodies are common in children with the majority occurring in those younger than 3 years of age.[14] There were 86,261 pediatric foreign body ingestions in 2014 reported to the American Association of Poison Control Centers,[15] representing a fraction of the actual number of foreign bodies ingested.

#### Coins

***Overview and Etiology.*** In the United States and Europe, coins are the most commonly ingested foreign body.[16] It is estimated that there are more than 250,000 coin ingestions per decade.[16] While most coins spontaneously pass through the gastrointestinal tract, they can lodge in the esophagus. Coins typically lodge in one of three locations: the thoracic inlet (60%–70%), midesophagus at the level of the aortic arch (10%–20%), and just above the lower esophageal sphincter (20%).[14] When not witnessed, the patient may present beyond the acute stage.

***Clinical Presentation.*** Symptoms of chronic foreign body impaction include respiratory distress, asthma-like symptoms, cough, nausea, vomiting, and dysphagia. Respiratory symptoms are due to local inflammation surrounding the foreign body.[17] Patients with chronic foreign body impaction are at risk of esophageal perforation.

***Imaging.*** Radiographs are useful to identify the location of the coin and to look for signs of chronic impaction (e-Fig. 98.2). Coins are generally described as oriented in the coronal plane when located in the esophagus on the frontal radiograph, although there have been reports of sagitally oriented esophageal coins.[18] Inflammatory changes that develop in patients with chronic foreign body impaction cause thickening of the space between the esophagus and trachea on lateral chest radiographs, and often tracheal narrowing (e-Fig. 98.2B); lateral radiographs are therefore useful in patients in whom the episode was not witnessed and the time course is not known. Esophagram may be performed in patients with a chronic foreign body impaction after removal to evaluate for perforation or development of a tracheoesophageal fistula.

***Treatment.*** Coins, like other esophageal foreign bodies, can be removed via Foley catheter balloon extraction or endoscopy. Foley catheter extraction has been used as a safe and effective method of coin removal in children older than 1.5 years with acute ingestion, before the development of esophageal edema.[19] Despite its history of safe extractions and lower cost, Foley balloon extraction has fallen from favor due to concerns for patient safety related to airway compromise or esophageal injury.[20] Endoscopy is now the preferred method for extraction at most centers.

#### Batteries

***Overview and Etiology.*** Esophageal injury in children caused by button battery ingestion is increasing in frequency.[20,21] This increase in injury is thought to be due to an increase in size of the batteries coupled with the shift to a lithium cell.[16,22] Button batteries are often found in objects such as watches, calculators, toys, and hearing aids. Management of battery ingestion is different than that of coins because batteries lodged in the esophagus can cause severe damage in as little as 15 minutes.[16] Tissue damage is caused primarily by the generation of hydroxy ion radicals in the mucosa. This results in a caustic injury from high pH.[16]

***Clinical Presentation.*** If ingestion is witnessed, extraction should occur before the development of symptoms. If these develop, they include drooling, chest discomfort, choking, gagging, and airway obstruction. Damage can include esophageal perforation, or fistula to the trachea or to the aorta leading to exsanguination.[21] Children at greatest risk for developing aortoesophageal fistula are those younger than 5 years of age and those who have ingested batteries larger than 20 mm.[16]

***Imaging.*** Imaging is crucial in the diagnosis and management of button battery ingestion. Batteries can be distinguished on radiographs by their characteristic halo appearance with a circle of lucency just within the outer border (Fig. 98.3A and B).

Progression of injury, even days to weeks after the battery ingestion, is a hallmark of this disease entity. Therefore imaging

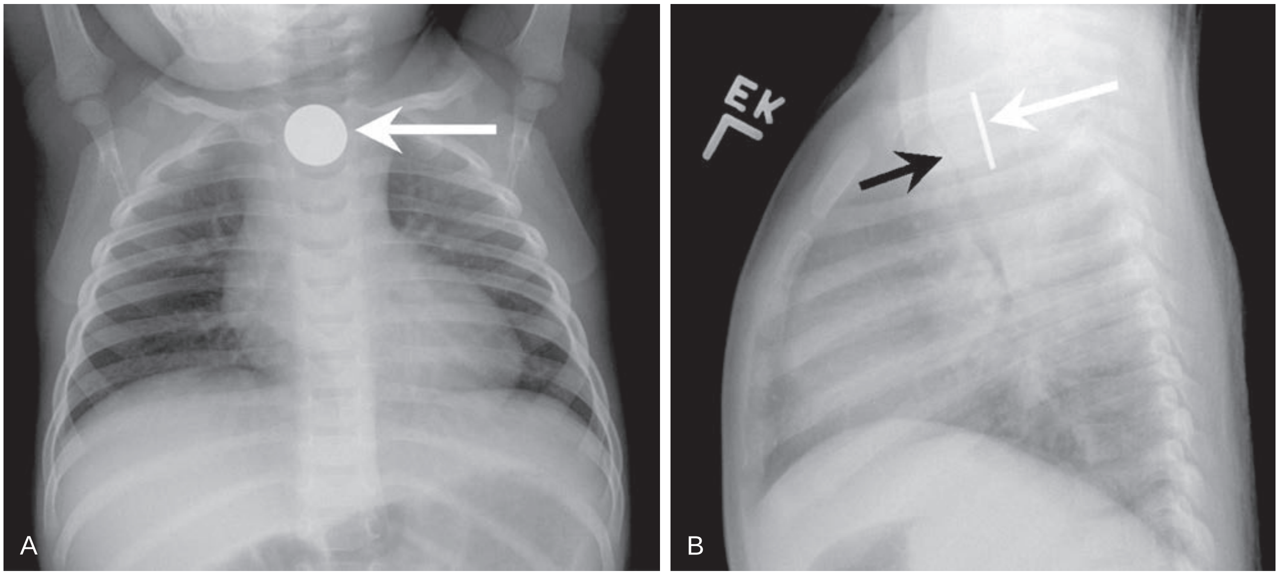

**e-Figure 98.2. Coin in esophagus.** (A) Frontal chest radiograph shows a coin lodged in the proximal esophagus *(arrow)* at the level of the thoracic inlet. (B) Lateral view of the chest shows the coin *(white arrow)* lodged in the proximal esophagus. The trachea *(black arrow)* is located anterior to the esophagus. The trachea is narrowed at the level of the foreign body. There is thickening of the space between the esophagus and trachea.

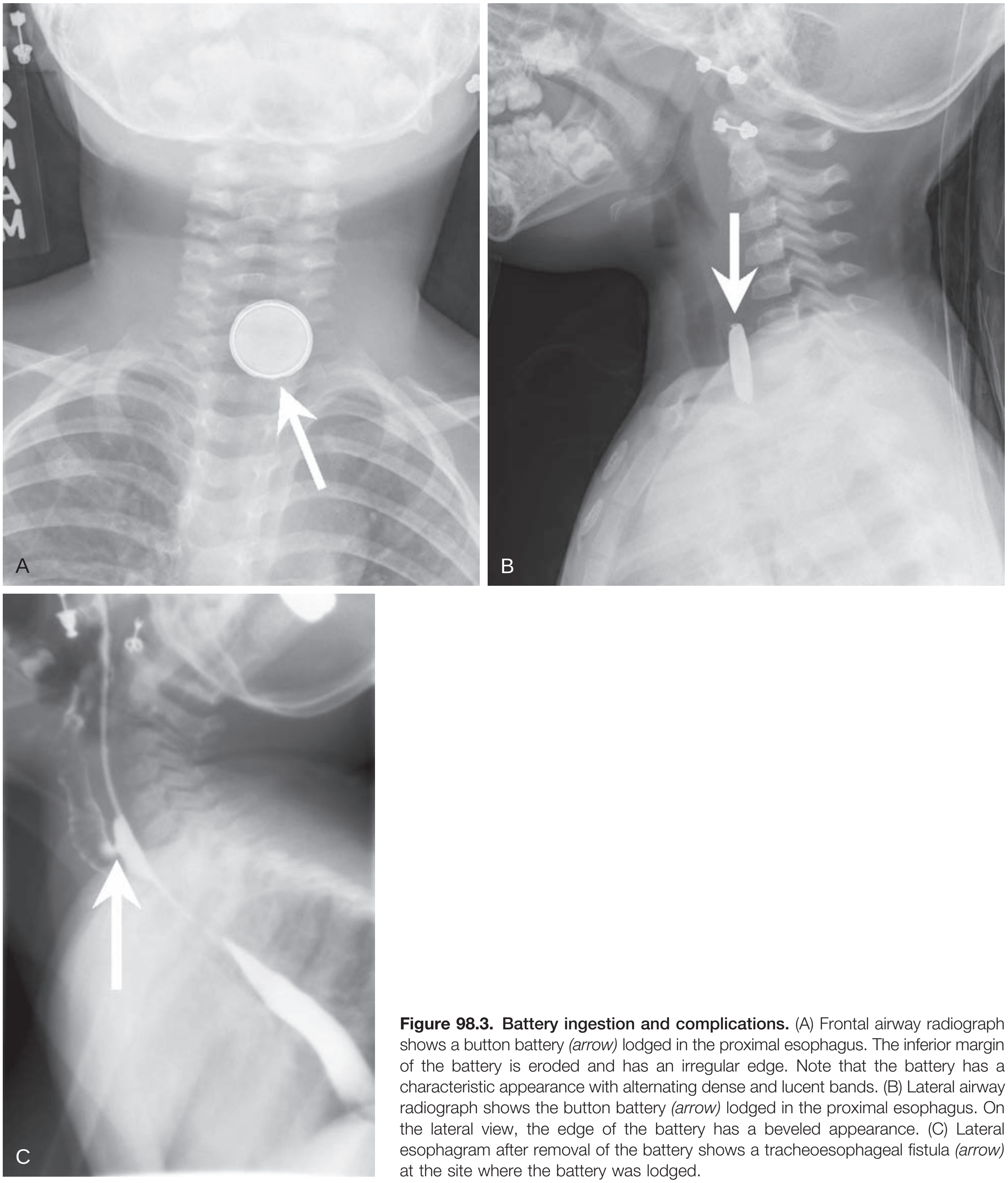

**Figure 98.3. Battery ingestion and complications.** (A) Frontal airway radiograph shows a button battery *(arrow)* lodged in the proximal esophagus. The inferior margin of the battery is eroded and has an irregular edge. Note that the battery has a characteristic appearance with alternating dense and lucent bands. (B) Lateral airway radiograph shows the button battery *(arrow)* lodged in the proximal esophagus. On the lateral view, the edge of the battery has a beveled appearance. (C) Lateral esophagram after removal of the battery shows a tracheoesophageal fistula *(arrow)* at the site where the battery was lodged.

plays a role in the continued management of these patients.[23] Esophagram with water-soluble iso-osmolal contrast can be performed after removal to evaluate for the presence of complications, such as esophageal perforation or tracheoesophageal fistula. (Fig. 98.3C and eD). Long-term complications, such as esophageal stricture, can also be diagnosed.[23]

Recently, the North American Society for Pediatric Gastroenterology, Hepatology, and Nutrition (NASPGHAN) has advocated for CT or MR angiography in the setting of a button battery ingestion when an esophageal injury is identified at the level of the aorta on endoscopy.[16] This recommendation was echoed by the Button Battery Task Force which further recommended using CT or MRI to evaluate for signs of mediastinitis and inflammation surrounding the aorta.[24]

***Treatment.*** If a battery is lodged in the esophagus, the requesting clinician should be contacted immediately to arrange emergent extraction. Follow-up imaging may be indicated, as previously discussed. There is no consensus recommendation for follow-up in the setting of esophageal inflammation, mediastinitis, or inflammation surrounding the aorta.

## Food Bolus Impaction

***Overview and Etiology.*** Impacted food boluses are relatively infrequent in children but may represent the initial presenting symptom of eosinophilic esophagitis, peptic stricture, achalasia, vascular rings, or an extrinsic mass.[25,26] Eosinophilic esophagitis is the major cause of food bolus impaction in children accounting for more than 50% of all cases. The second most common cause is an area of narrowing in a patient with prior esophageal atresia repair or Nissen fundoplication surgery.[27]

***Clinical Presentation.*** Acute impaction of food typically leads to symptoms of dysphagia and drooling; difficulty swallowing may lead to aspiration.

***Imaging.*** On esophagram, an impacted food bolus appears as a persistent filling defect in the esophagus (e-Fig. 98.4). The impacted food can completely obstruct the esophagus. This is seen on esophagram as a standing column of contrast that does not pass beyond the food bolus.

***Treatment.*** When identified, the food bolus is removed endoscopically. Esophagram can be performed after extraction or passage of the food bolus, to evaluate for the underlying cause, if not already known. Esophageal biopsy is recommended in patients diagnosed with food bolus impaction to assess for eosinophilic esophagitis, particularly in those who do not have a history of prior esophageal surgery.[27]

## Caustic Ingestion

***Overview and Etiology.*** Ingestion of caustic materials in childhood is relatively common and typically accidental. In 2014, there were 198,018 ingestions of household cleansers reported to the American Poison Control Centers, more than 65% of which occurred in children.[15] The age group at highest risk for caustic ingestion is children under 5 years of age,[15] with a peak around 2 years when children are learning to explore but not yet able to distinguish between harmless and harmful substances.[28]

The extent and severity of injury depends on several factors: the corrosiveness of the ingested substance, the quantity ingested, the physical state of the substance, the duration of the contact time of the substance with the esophagus, and subsequent secondary infection.[28,29]

A variety of substances can cause a caustic injury, including alkalis (pH up to 12), acids (pH as low as 2), and bleaches (pH near 7). In contrast to acidic substances that are sour, alkalis have a relatively innocuous taste, leading to a greater volume ingested.[28] Further, alkaline agents produce liquefaction necrosis and rapid penetration leading to more severe injury.[29]

***Clinical Presentation.*** After caustic ingestion, patients with severe injury typically present with pain, drooling, and airway symptoms; more visible signs of tissue damage include lip swelling, mouth ulcers, and erythema of the tongue.[28] Esophageal stricture is an important late complication with a reported frequency between 2% and 63% of patients.[29] A stricture can form in as little as 3 weeks after injury.[30]

***Imaging.*** Initial management of patients with caustic ingestion includes a radiograph of the chest and lateral neck to evaluate for pneumomediastinum. Esophagram is not indicated in the acute phase because it delays endoscopy and does not detail mucosal injuries.[28]

When strictures develop, they can be diagnosed based on symptoms, and confirmed with esophagram (Fig. 98.5). Caustic strictures can be focal or occupy a long segment of the esophagus depending on the substance ingested; acid ingestion typically causes a focal or short segment stricture while alkali substances cause a long segment stricture.[30] Strictures most commonly occur in the upper or midesophagus. Multiple strictures can also occur.

***Treatment.*** Acutely patients are treated with steroids, proton pump inhibitors, and antibiotics; endoscopic evaluation is performed to assess the extent of damage and to grade the injury. Strictures are first treated with balloon dilation under fluoroscopy. The advantage of balloon dilation over dilation using a bougie is that balloons dilate strictures in a radial direction rather than a longitudinal direction. This is thought to be less likely to cause an esophageal perforation.[28] After the balloon is inflated and the waist is seen to disappear, an esophagram is performed to evaluate for a leak that occurs in 4% to 30% of patients.[30] If balloon dilation fails, operative treatment with stricture resection is performed; esophageal replacement may be necessary.

Patients with a history of caustic ingestion are at risk of developing squamous cell carcinoma of the esophagus. These patients should undergo endoscopic surveillance as adults.[28]

## Pill Esophagitis

***Overview and Etiology.*** Pill esophagitis is an injury caused by medications; the drugs most frequently implicated are doxycycline and alendronate.[31] Other drugs reported to cause esophageal injury include nonsteroidal antiinflammatory drugs, potassium chloride, ferrous sulfate, phenytoin, and quinidine.[31] Characteristics of medications that are more likely to cause esophageal injury include the acidity of the medication and a capsule formulation that renders it more likely to stick in the esophagus.[32] Pill esophagitis is also more likely to occur in patients with delayed esophageal transit time including taking a pill with little or no water immediately before going to bed, decreased saliva production, and anatomic areas of narrowing.[32]

***Clinical Presesentation.*** Patients with pill esophagitis typically present with dysphagia, odynophagia, and chest pain. Pill esophagitis can often be diagnosed by history alone.

***Imaging.*** Esophagram is not commonly performed due to the classic history but can show a circular area of ulceration. If endoscopy is performed, a circular ulceration is identified with normal surrounding mucosa. The ulceration typically occurs at an anatomic area of narrowing such as at the level of the aortic arch, left mainstem bronchus, or gastroesophageal junction.[32]

***Treatment.*** Pill esophagitis is treated and prevented with changing pill-taking habits (taking pills with more water, taking pills long before going to bed), crushing pills, taking a liquid suspension, or switching medications.

## Iatrogenic Trauma

***Overview and Etiology.*** Iatrogenic trauma is the most common cause of esophageal perforation in children, representing 75% to 85% of all cases.[33] Esophageal perforation can be life-threatening

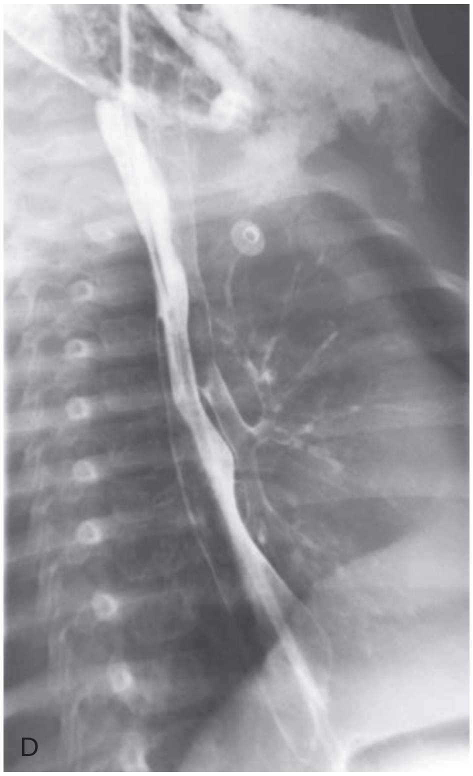

**e-Figure 98.3.** (D) Oblique view from an esophagram shows contrast in both the esophagus and the tracheobronchial tree due to the tracheoesophageal fistula.

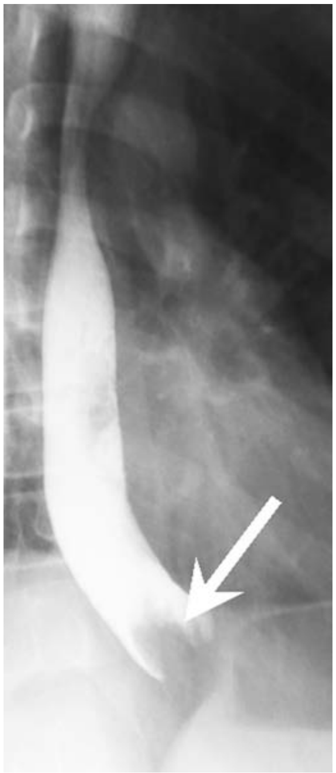

**e-Figure 98.4.** Esophagram shows a persistent filling defect *(arrow)* in the distal esophagus. The patient underwent endoscopy to remove the food bolus. The biopsy obtained during endoscopy confirmed a diagnosis of eosinophilic esophagitis.

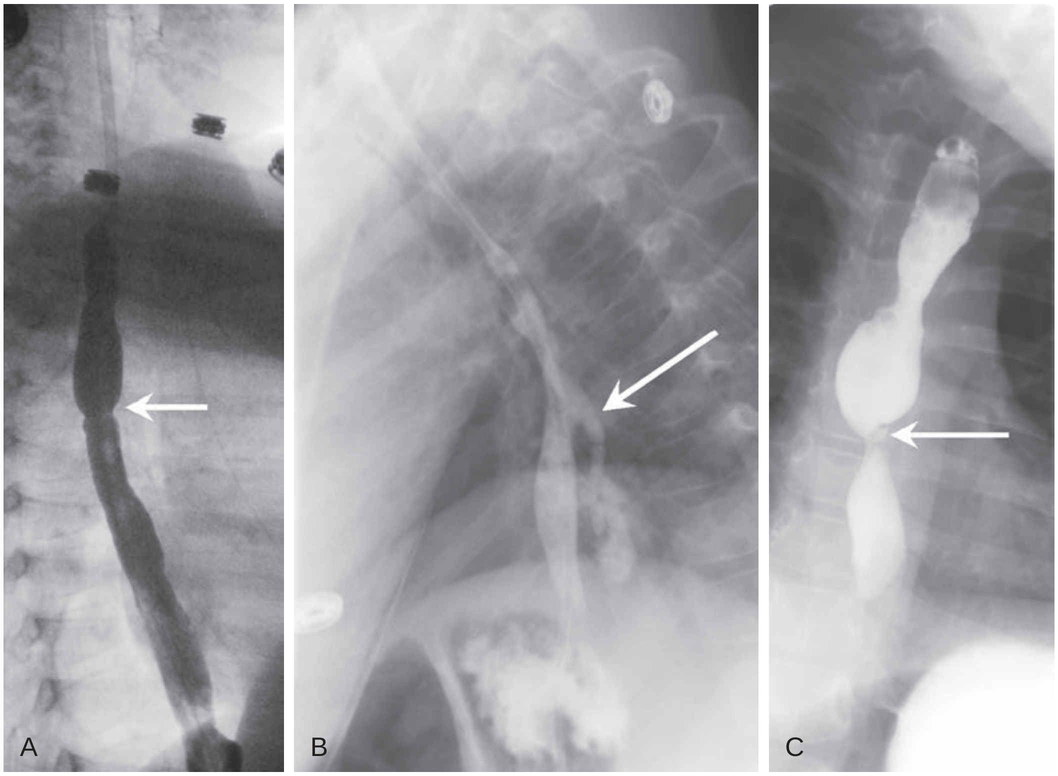

**Figure 98.5. Stricture and other complications of caustic ingestion.** (A) Esophagram in a patient with a recent history of lye ingestion shows an irregular contour of the esophagus and a focal area of narrowing *(arrow)*. (B) Esophagram in the same patient 3 months later and immediately after dilation of an esophageal stricture shows an esophageal perforation with a contrast leak *(arrow)*. (C) Esophagram in the same patient after the esophageal perforation had healed shows a stricture *(arrow)* in the midesophagus. The esophagus proximal to the stricture is dilated.

as the esophagus lacks a serosa, and the surrounding loose areolar connective tissue is unable to prevent the spread of infection; thus oral flora and digestive enzymes are able to spread to the mediastinum.[33]

The most common cause of iatrogenic perforation in children is from stricture dilation (see Fig. 98.5B). Other causes include complications of nasogastric tube placement, endotracheal intubation, endoscopy, pedicle screw placement, and sclerotherapy of esophageal varices.[34–36] The typical location of perforation depends on the age of the patient. In neonates, perforation typically occurs in the cervical esophagus at the pharyngeal/esophageal junction.[33] (See Chapter 96.)

***Clinical Presentation.*** Neonates often present after a difficult intubation with nonspecific symptoms, including drooling, choking, or coughing with feeds. In older children, perforation is more common in the thoracic esophagus. They typically present with respiratory distress, chest pain, or subcutaneous emphysema.[33]

***Imaging.*** The initial diagnostic examination is often frontal and lateral radiographs of the chest. Findings on the chest x-ray include pneumothorax, pneumomediastinum, pleural effusion, and, if the event was caused by nasogastric tube placement, an abnormal course of the tube may be seen (Fig. 98.6).[33] The location of the perforation can often be determined from the radiograph. Left-sided pneumothorax and effusion are more likely to occur in the setting of an upper thoracic perforation while right-sided findings are more likely to occur with perforations in the distal esophagus.[33]

Esophagram can be useful in diagnosing and locating a perforation. Water-soluble iso-osmolal contrast should be used first. If no contrast extravasation is noted, barium may then be used, as it is more sensitive in the detection of an esophageal leak.[33] Three patterns of perforation have been described on esophagram: a local cervical leak is identified if there is a retropharyngeal pocket of contrast; a submucosal leak appears as a linear tract posterior and lateral to the esophagus; finally, free perforation appears as contrast flowing into the pleural space.[33]

CT is not generally used to diagnose an esophageal perforation; however, in a complex, acutely ill patient, this may be the first study performed. Signs of esophageal perforation on CT include pneumomediastinum, mediastinal fluid, esophageal wall thickening, and a catheter extending beyond the esophagus.

***Treatment.*** Treatment usually consists of expectant medical management, with broad spectrum antibiotics, pleural drainage via chest tube and nutritional support with total parenteral nutrition or gastrostomy; a nasogastric (NG) tube may be placed beyond the perforation under direct visualization. Operative exploration is considered in patients in whom the above more conservative management fails.[33]

## Blunt Esophageal Trauma

***Overview and Etiology.*** The esophagus is rarely injured after chest trauma due to its flexibility and ability to decompress via the mouth and stomach.[37] Reported causes of esophageal injury include handlebar injury, crush injury, opening a bottle of carbonated drinks in the mouth, and child abuse.[38–41] Tracheoesophageal fistula is an even rarer complication of trauma.

***Clinical Presentation.*** Patients usually present with coughing induced by swallowing. Other findings include subcutaneous emphysema, pneumothorax, dysphagia, dyspnea, and hoarseness.

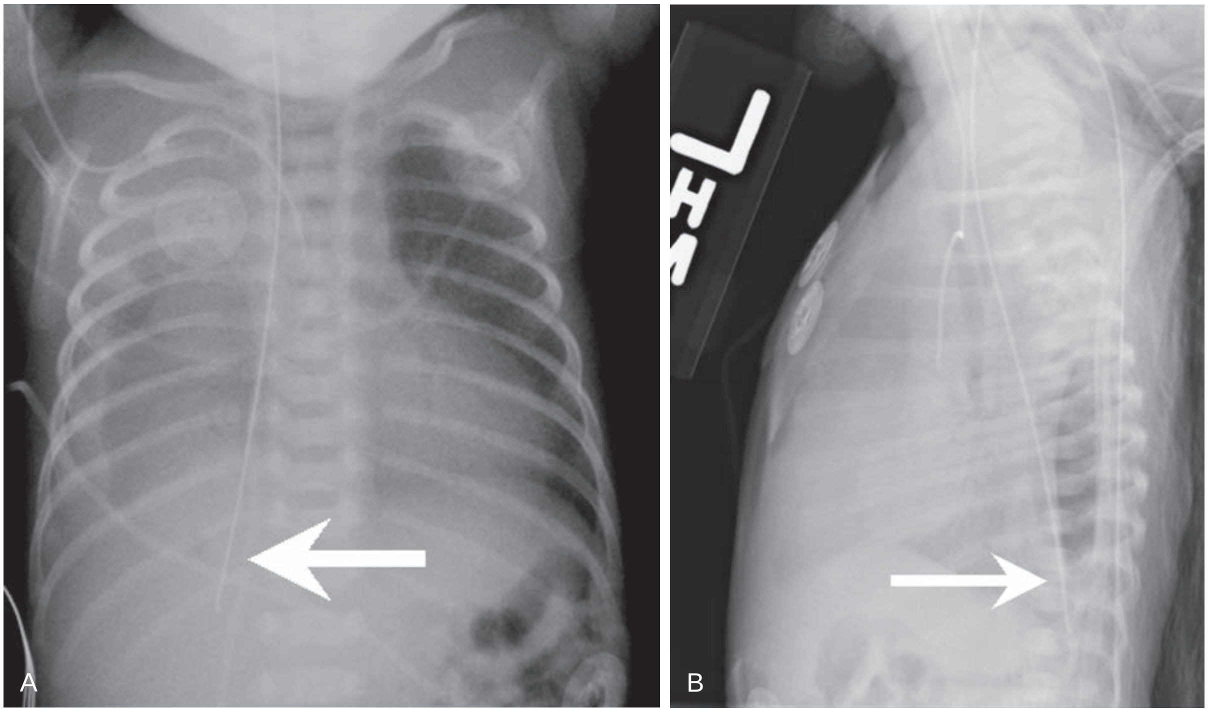

**Figure 98.6. Esophageal perforation.** (A) Frontal chest radiograph in a premature infant shows an abnormal course of the nasogastric tube *(arrow);* the tip of the tube overlies the right upper quadrant. There is a right pleural effusion. (B) Lateral chest radiograph also shows the abnormal course of the nasogastric tube *(arrow);* the tip of the tube projects in the pleural space over the posterior costophrenic sulcus.

***Imaging.*** Chest radiograph or CT may show pneumomediastinum and pleural effusion in a child presenting with blunt trauma. Esophagram can be performed for confirmation and to diagnose a tracheoesophageal fistula.[42] Water-soluble iso-osmolal contrast material should be used in these cases, as noted in previous section.

## Boerhaave Syndrome

***Overview and Etiology.*** Boerhaave syndrome is defined as spontaneous rupture of the esophagus, often related to vomiting. The rupture typically involves the distal portion of the thoracic esophagus. Boerhaave syndrome is rare in children, but nearly 50% of cases occur in neonates.[43]

***Clinical Presentation.*** Patients typically present with vomiting, lower thoracic pain, and subcutaneous emphysema.

***Imaging.*** In most children, the rupture occurs on the right side in contrast to adults in whom rupture is usually left-sided[43] and therefore chest radiograph will demonstrate right sided pneumothorax and pleural effusion. Diagnosis is confirmed with esophagram and/or endoscopy; however, insufflation may lead to life-threatening pneumothorax.

***Treatment.*** While children and neonates are more likely to have a better prognosis than adults, surgery remains the treatment of choice of Boerhaave syndrome. Conservative approach can be used in patients with small tears and is used in patients with presentation or diagnosis greater than 24 hours.[43]

# INFLAMMATORY CONDITIONS

## Eosinophilic Esophagitis

***Overview and Etiology.*** Eosinophilic esophagitis is a chronic inflammatory disease characterized by dense esophageal eosinophilia. Over the past decade, there has been an increase in awareness of the disease as well as an increase in the number of cases diagnosed. Currently it is thought that eosinophilic esophagitis occurs with an incidence of up to 1:10,000 children per year.[44] Eosinophilic esophagitis is three to four times more common in males and can occur at any age.[45] To be diagnosed with eosinophilic esophagitis, patients must have both the histologic and clinical features of the disease. Histologically, eosinophilic esophagitis is characterized by an esophageal mucosal biopsy with more than 15 eosinophils per high-power field.

***Clinical Presentation.*** Patients present with esophageal symptoms mimicking GERD. Older children tend to present with vomiting and abdominal pain, although in infants the presentation is more likely feeding difficulties; diagnosis at age less than 6 months is rare. Patients often have other signs of atopy, including dermatitis, food allergies, and asthma.[45]

***Imaging.*** Because the symptoms of eosinophilic esophagitis are protean and simulate those of GERD, diagnosis is often delayed. UGI is frequently performed as part of the diagnostic work of patients due to their esophageal symptoms. On UGI, the most common finding is a normal esophagus.[46] The most common positive findings are GER, irregular contractions, esophageal dysmotility, esophageal strictures, esophageal rings, small caliber esophagus, and food bolus impaction (Fig. 98.7).[46]

***Treatment.*** Eosinophilic esophagitis is thought to represent an allergic response to food and is usually treated with attempts to identify and eliminate the offending agent(s), or with an elemental diet. Steroids may also be used alone or in combination with diet therapy.[45]

## Epidermolysis Bullosa

***Overview and Etiology.*** Epidermolysis bullosa is a rare group of hereditary blistering disorders caused by mutations in genes

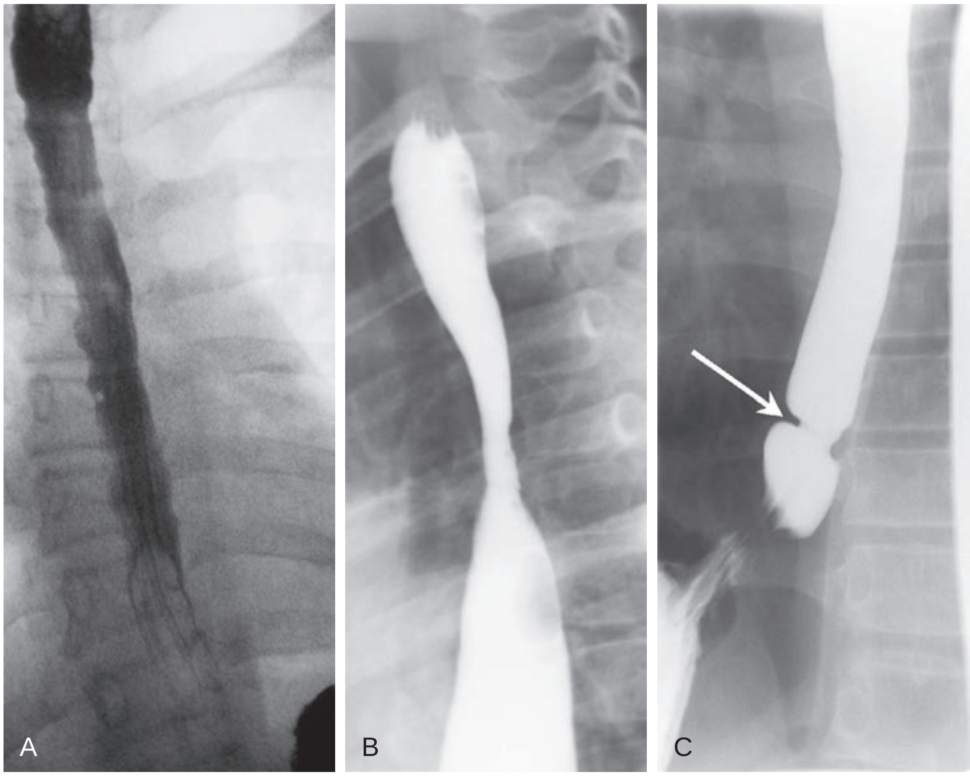

**Figure 98.7. Eosinophilic esophagitis.** (A) Esophagram shows diffuse irregular esophageal contractions. (B) Esophagram shows a stricture *(arrow)* of the mid esophagus. (C) Esophagram shows a Schatzki ring *(arrow)* of the distal esophagus.

expressed at the dermal-epidermal junction. More than 100 distinct genotypes and 20 phenotypes of disease of varying severity have been described.[47]

***Clinical Presentation.*** Patients often develop skin blistering and erosions with minor mechanical trauma. Repeated blistering leads to scar formation and causes symptoms such as contractures. Extracutaneous sites can also be affected and include the esophagus, bowel, rectum, anus, bladder, urethra, and trachea.[47]

***Imaging.*** In the esophagus and oropharynx, scar formation leads to dysphagia and esophageal strictures. Any segment of the esophagus may be involved, although approximately half of strictures occur in the cervical esophagus.[48]

***Treatment.*** The initial treatment of choice for esophageal strictures in children is balloon dilation under fluoroscopic or endoscopic visualization (Fig. 98.8).[47,48] Patients often require multiple dilations to treat recurrent or persistent strictures.[48]

## Crohn Disease

***Overview and Etiology.*** Crohn disease is a chronic inflammatory disease of the gastrointestinal tract characterized by waxing and waning symptoms, transmural inflammation of the bowel wall, and skip lesions. It can affect any portion of the gastrointestinal tract from the mouth to the anus, but it most commonly affects the small bowel and colon in children. Esophageal symptoms of Crohn disease are uncommon; however, endoscopic and histologic findings are more frequent and occur in 7.6% and 17.6%, respectively.[49]

***Clinical Presentation.*** Dysphagia is the most common symptom of esophageal Crohn disease followed by odynophagia, chest pain, nausea, and vomiting.[50]

***Imaging.*** While the esophagram is often normal, esophageal Crohn disease can manifest with mucosal irregularity, aphthous ulcers, or stricture.[49]

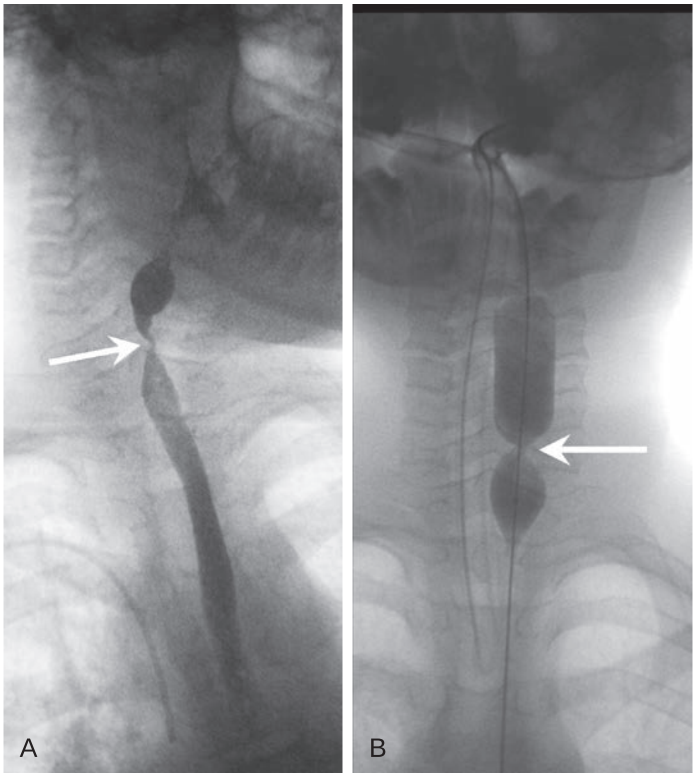

**Figure 98.8. Epidermolysis bullosa.** (A) Esophagram shows a tight stricture *(arrow)* in the cervical esophagus. (B) Image from esophageal dilation shows a balloon dilated in the cervical esophagus. There is a focal area of narrowing *(arrow)* at the site of stricture.

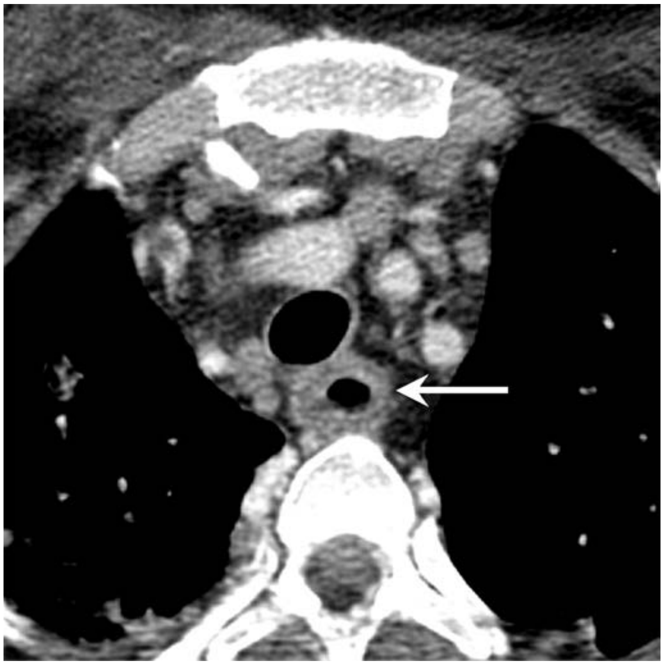

**Figure 98.9. Chronic granulomatous disease.** Axial contrast-enhanced CT in a patient with chronic granulomatous disease shows thickening of the wall of the proximal esophagus *(arrow)*.

## Chronic Granulomatous Disease

***Overview and Etiology.*** Chronic granulomatous disease is an uncommon primary immunodeficiency characterized by recurrent bacterial and fungal infections occurring at epithelial surfaces. Gastrointestinal manifestations are present in most patients with chronic granulomatous disease. Any portion of the gastroesophageal tract may be involved from the mouth to the anus. Esophageal involvement is uncommon.

***Clinical Manifestations.*** The symptoms overlap those of other entities affecting the esophagus, and include vomiting, dysphagia, heartburn, and odynophagia.[49]

***Imaging.*** In the esophagus, dysmotility and strictures have been seen on esophagram. CT of the chest can demonstrate esophageal wall thickening (Fig. 98.9).[51]

***Treatment.*** Treatment is with pharmacologic agents targeted at the infection and esophageal dilatation when necessary.[52]

## Behçet Syndrome

***Overview and Etiology.*** Behçet disease is an immune-mediated systemic vasculitis which affects multiple systems, likely representing an exaggerated inflammatory endothelial response. The entity is more prevalent in Mediterranean and Middle Eastern countries, Japan, and Southeast Asia.

***Clinical Manifestations.*** Behçet syndrome is characterized by pyoderma, gastrointestinal and genital mucous membrane ulceration, uveitis, and central nervous system vasculitis.[53] Oral ulcerations are often the first manifestation of disease. Because these ulcerations are nonspecific, diagnosis is often delayed until abnormalities of the genitals, gastrointestinal system, or central nervous system develop. Patients are also at risk of developing venous thrombosis and arterial aneurysms which can be life-threatening.

***Imaging.*** In the esophagus, dysmotility, ulceration, and stricture have been described on UGI.[53] These findings are often difficult to distinguish from Crohn disease. Diagnosis is made by the presence of mouth ulcers in association with two other major criteria, including skin lesions, recurrent genital ulcerations, or the presence of an excessive dermal inflammatory response termed pathergy.

***Treatment.*** Treatment is geared at reducing the overactive inflammatory response, and includes corticosteroids, azathioprine, and interferon.[10,54]

## INFECTIOUS ESOPHAGITIS

Infectious esophagitis is typically seen in children with congenital or acquired immunodeficiency such as chemotherapy or post-transplant immunosuppression. Endoscopy has replaced esophagram as the method of diagnosing infective esophagitis due to its ability to visualize the abnormality directly and to obtain a tissue sample for culture. If esophagram is performed for infectious esophagitis, the double-contrast technique is preferred, if possible, to better define mucosal detail.

### Candida Esophagitis

***Overview and Etiology.*** *Candida albicans* is the most common infective agent to cause esophagitis.[55] Oropharyngeal candidiasis is the strongest risk factor for the development of esophagitis in patients with neutropenia or human immunodeficiency virus (HIV) infection. On endoscopy, the appearance of esophageal Candidiasis varies from a few small, raised white plaques to confluent plaques with hyperemia and ulceration.[55]

***Clinical Manifestations.*** Patients typically present with odynophagia, dysphagia, and chest pain.

***Imaging.*** Esophagram is less sensitive than endoscopy in making the diagnosis.[55] On esophagram, severe infection is characterized by a shaggy appearance of the esophagus due to multiple ulcers and nodular plaques.

***Treatment.*** Treatment is with antifungal medications including fluconazole and nystatin; caspofungin and amphotericin are reserved for systemic cases and cases resistant to therapy. Prophylactic therapy is employed in immunocompromised patients.

### Cytomegalovirus Esophagitis

***Overview and Etiology.*** Cytomegalovirus (CMV) is common in the population at large and is one of the more common opportunistic infections in immunocompromised patients. When affecting the gastrointestinal tract, CMV most commonly involves the esophagus and the colon.

***Clinical Manifestations.*** Patients with CMV involving the gastrointestinal tract present with chronic diarrhea, abdominal pain, bleeding, perforation, odynophagia, peritonitis, and bowel obstruction.[56]

***Imaging.*** Esophagitis is the second most common gastrointestinal manifestation of CMV infection after colitis.[56] Endoscopy is the diagnostic method of choice; however, esophagram can demonstrate the large, shallow ulcers characteristic of CMV infection.

***Treatment.*** The most effective treatment for CMV infection in immunocompromised patients is restoration of immunocompetence, such as the use of antiretrovirals in patients with HIV.[56]

### Human Immunodeficiency Virus Esophagitis

***Overview and Etiology.*** Giant esophageal ulcers can occur in patients with HIV infection. There are several different causes of ulcers in immunocompromised patients including those with HIV infection, and these include CMV, *Candida albicans*, mycobacteria, and herpes simplex virus.[57] The ulcer is called an HIV-related or idiopathic giant ulcer when the cause of the ulcer cannot be attributed to other known pathogens, such as those previously described.

***Clinical Presentation.*** Patients present with esophageal symptoms of odynophagia, dysphagia, and retrosternal chest pain and may experience hematemesis. Complications include bleeding, strictures, and fistulas into the tracheobronchial tree.[58]

***Imaging.*** Idiopathic giant ulcers typically occur in the middle to distal third of the esophagus. Smaller satellite ulcers may also be present.[57] Idiopathic giant ulcers are difficult to distinguish from ulcers caused by CMV infection, although idiopathic giant ulcers are said to be larger and have overhanging edges.[57]

***Treatment.*** Treatment is geared to the infectious agent identified; if the ulcer is idiopathic, treatment is with steroids; thalidomide may also be added.[58]

## Tuberculosis

***Overview and Etiology.*** Involvement of the esophagus by tuberculosis is rare. There have been several reports of esophageal erosion with formation of a tracheoesophageal fistula in patients with tuberculosis.[59,60] Esophageal perforation is thought to occur by one of three methods: rupture of a mediastinal abscess into the esophagus, formation of a traction diverticulum due to tuberculous mediastinitis, or erosion due to pressure necrosis of adjacent lymph nodes.[59]

***Clinical Presentation.*** Symptoms depend on the complications; patients with esophagotracheal or esophagobronchial fistulas may experience extensive coughing after ingestion of fluids, and hematemesis.[61]

***Imaging.*** When perforation occurs, esophagram shows extraluminal extension into the mediastinum or into the fistula. On CT, there are large, low-density mediastinal lymph nodes in addition to pneumomediastinum.

***Treatment.*** Treatment is geared to addressing the complications in addition to antituberculous medications.Esophageal Motility Disorders

Primary esophageal motility disorders are uncommon in children. Esophageal dysmotility is most commonly seen in patients with esophageal atresia, due to an underlying inflammatory condition such as GERD, or rarely to a primary motor disorder such as achalasia.

## Esophageal Atresia

***Overview and Etiology.*** Esophageal atresia (see Chapter 96) is corrected via surgical repair in the early neonatal period. There are several potential complications of the repair: recurrent tracheoesophageal fistula, esophageal strictures at the site of anastomosis, and food bolus impaction (e-Fig. 98.10 and Fig. 98.11).

Esophageal dysmotility is near ubiquitous in patients with a history of esophageal atresia. There are two potential theories for the etiology of esophageal dysmotility: primary dysgenesis or postoperative sequela to the esophageal nerve supply.[62]

## Achalasia

***Overview and Etiology.*** Achalasia is a primary motor disorder characterized by failure of the lower esophageal sphincter to relax with swallowing.[63] Diagnosis can be made via manometry, upper endoscopy, or esophagram. Manometry is the gold standard for diagnosis and shows aperistalsis of the smooth muscle of the esophagus, and incomplete relaxation and elevated resting pressure in the lower esophageal sphincter.[64] Biopsy confirms the diagnosis of achalasia with hypertrophy of the muscularis and absent ganglion cells.

***Clinical Presentation.*** Patients present with progressive dysphagia, regurgitation, chest pain, nocturnal cough, and heartburn.[64]

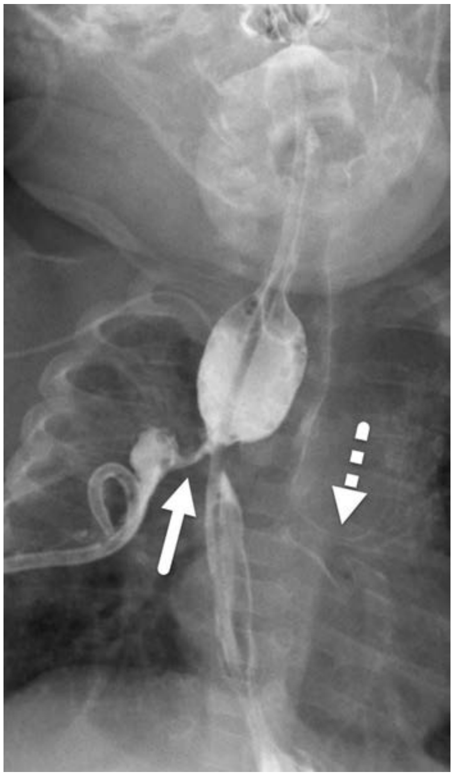

**Figure 98.11. Esophageal leak at anastomosis, and aspiration status postesophageal atresia repair.** Frontal image from an esophagram in a neonate with esophageal atresia status post repair shows a leak *(solid arrow)* at the esophageal anastomosis. Note that aspiration also occurred and contrast is visible in the left bronchial tree *(dashed arrow)*.

***Imaging.*** On chest x-ray, the esophagus can appear dilated and air-filled (Fig. 98.12). This appearance is often unusual and can mimic a medial pneumothorax. Esophagram shows dilation of the proximal esophagus, lack of peristalsis, and smooth tapering of the distal esophagus with a bird's beak appearance near the gastroesophageal junction.[64] This appearance of the distal esophagus can also be seen on sonography[64] and should be recognized if captured incidentally during abdominal ultrasound.

***Treatment.*** Achalasia can be treated with balloon dilation or Heller myotomy. Patients with untreated achalasia can develop aspiration pneumonia and esophageal perforation, and are at higher risk to develop esophageal cancer.[64,65]

# ESOPHAGEAL MASSES

## Leiomyomas

***Overview and Etiology.*** Although rare, leiomyomas are the most common esophageal tumor in children. In contrast to adults, the lesions in children are more likely to be multiple or diffuse.[66] Diffuse esophageal leiomyomatosis is a rare hamartomatous condition in which there is proliferation of the smooth muscle of the esophagus. Esophageal leiomyomatosis can be associated with leiomyomas at other sites or with Alport syndrome (nephropathy, astigmatism, and myopia).[67]

***Clinical Presentation.*** Isolated leiomyomas may be an incidental finding; leiomyomatosis presents with progressive symptoms of dysphagia, vomiting, regurgitation, weight loss, and retrosternal pain.[67]

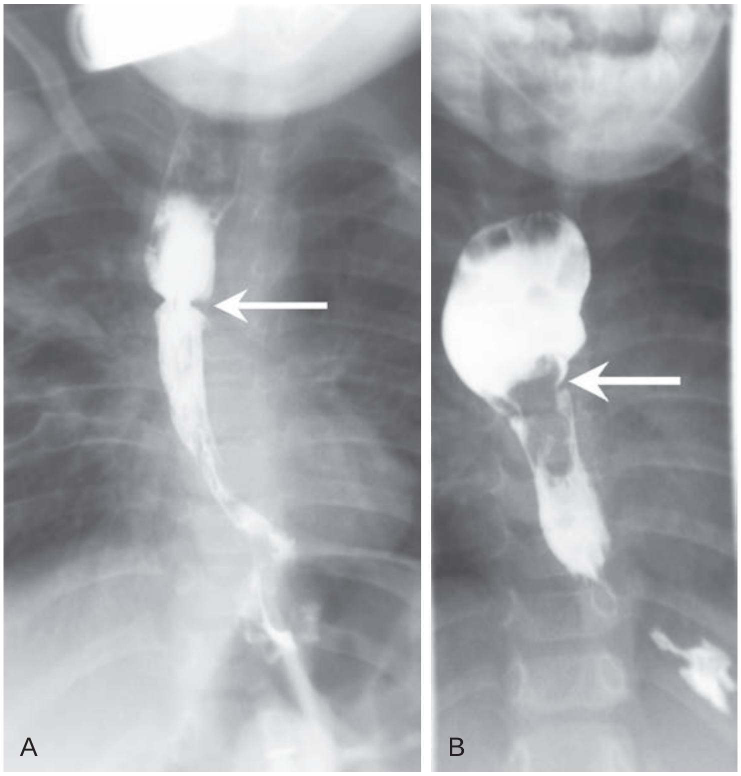

**e-Figure 98.10. Esophageal stricture after esophageal atresia repair.** (A) Esophagram in a patient with a history of previously repaired esophageal atresia and tracheoesophageal fistula shows a persistent filling defect at the site of the esophageal anastomosis *(arrow)*. Obstruction is denoted by dilatation of the proximal esophagus. (B) Esophagram in a different patient with a history of esophageal atresia repair shows a lobulated filling defect *(arrow)* at the site of anastomosis. The filling defect represented an impacted food bolus.

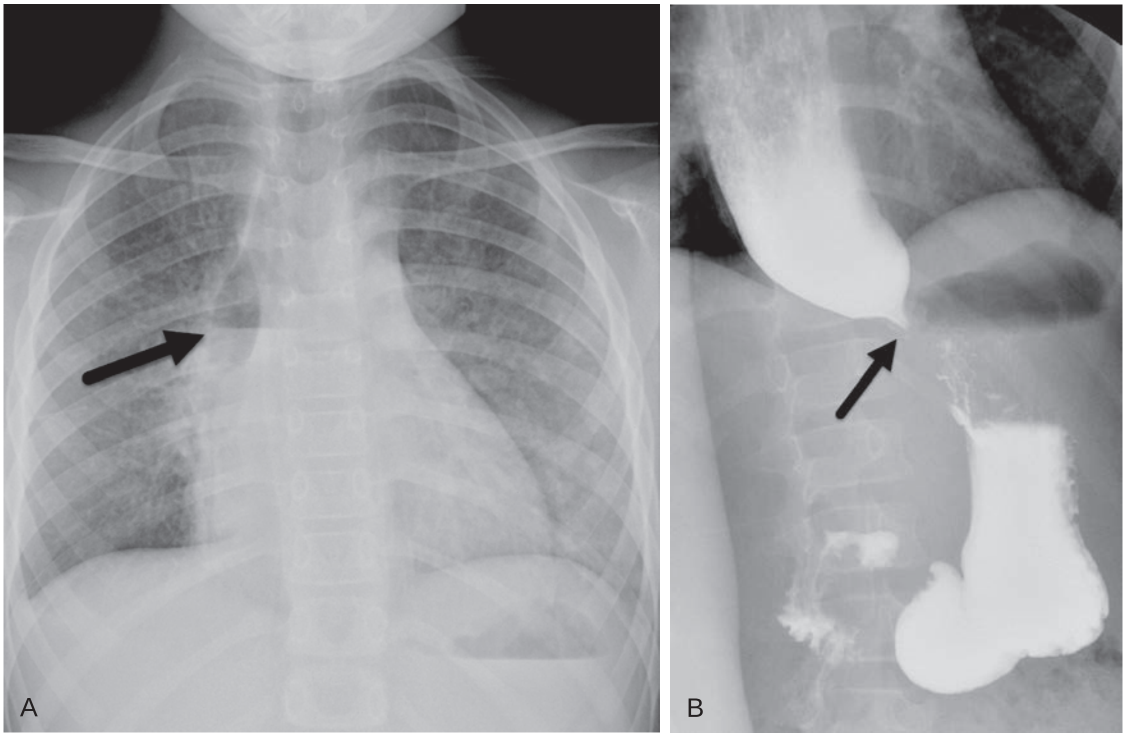

**Figure 98.12. Achalasia.** (A) Frontal chest radiograph in a patient with achalasia shows an oblong lucency of the dilated air-filled esophagus with an air-fluid level *(arrow)* in the right paraspinal region. (B) Spot image from esophagram shows the dilated distal esophagus coming to a point at the gastroesophageal junction. The distal narrowing gives the characteristic "bird's beak" appearance of achalasia *(arrow)*.

***Imaging.*** There are two potential findings on chest x-ray, including a tubular posterior mediastinal mass and rightward deviation of the azygoesophageal stripe.[66,67] Findings on esophagram can mimic achalasia and demonstrate a dilated tortuous esophagus with decreased peristalsis, tapered narrowing, and deviation from midline caused by the intramural masses.[67] If performed, cross-sectional imaging can show diffuse circumferential wall thickening of the esophagus; a discrete soft tissue mass protruding from the esophagus may also be present.[67]

***Treatment.*** Esophageal leiomyomatosis is generally treated with esophagectomy and gastric pull through.

### Malignancies

***Overview and Etiology.*** Esophageal malignancies are very rare in children. There are several conditions that place patients at a higher risk for malignancy including GERD with Barrett esophagitis, caustic ingestion, and achalasia. Esophageal carcinoma is more common in certain regions of the world due to nutrient deficiency of trace elements, consumption of pickled moldy foods, nitrosamines, and thermal injury. Areas with endemic human papilloma virus infection also have a higher incidence of esophageal carcinoma.[68]

### Extraesophgeal Tumors Affecting the Esophagus

***Overview and Etiology.*** The most common thoracic tumors to affect the esophagus are thoracic neuroblastomas and plexiform neurofibromas (Fig. 98.13),[69] with other tumors such as lipoblastoma being much less common (Fig. 98.14). These tumors can cause displacement or mass effect on the esophagus but rarely invade it. Depending on the degree of mass effect, the patient may present with dysphagia.

## OTHER ESOPHAGEL LESIONS

### Esophageal Varices

***Overview and Etiology.*** Esophageal varices are seen in the setting of portal hypertension. They occur primarily around the esophagus, stomach, spleen, and retroperitoneum. When portal hypertension is suspected, endoscopy is the best method to screen for varices.

***Clinical Presentation.*** The symptoms are those associated with portal hypertension; varices themselves are clinically silent until an episode of bleeding ensues. Variceal bleeding is the most serious complication of portal hypertension, and is associated with a mortality of up to 30%.[70]

***Imaging.*** Varices can be identified on contrast-enhanced CT as dilated serpiginous vessels and when very large can be seen on chest radiographs (Fig. 98.15). On esophagram, they appear as lobulated filling defects in the distal esophagus.

***Treatment.*** Varices are typically treated with sclerotherapy, banding, or placement of a portosystemic shunt.

### Esophageal Diverticula

***Overview and Etiology.*** Esophageal diverticula are uncommon in children. They can be associated with stricture, prior esophageal atresia repair, prior injury such as with a chronic foreign body, and connective tissue disorders such as Ehlers–Danlos syndrome.[71–73]

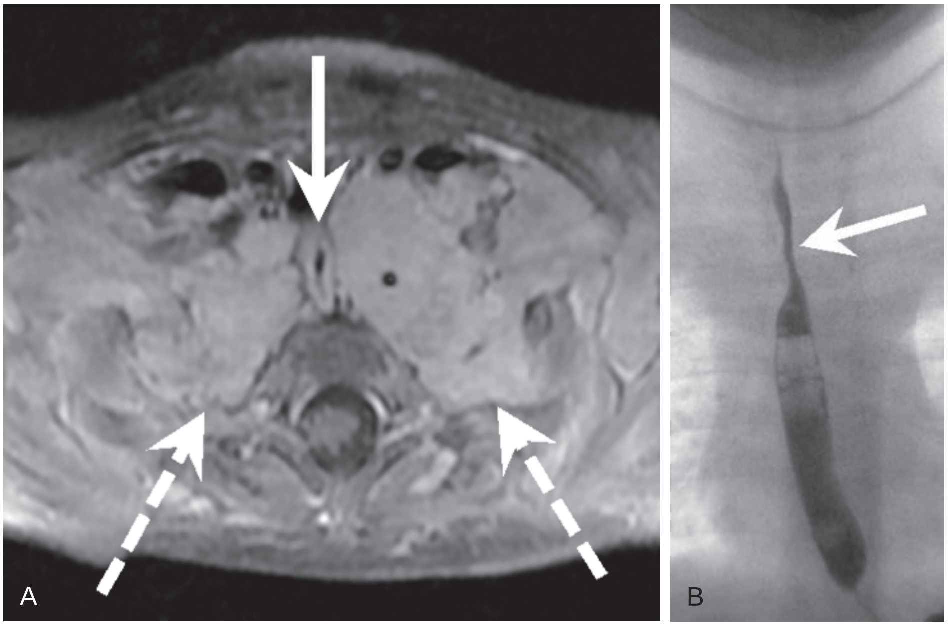

**Figure 98.13. Plexiform neurofibromas in neurofibromatosis type 1.** (A) Axial T1-weighted fat-saturated postcontrast image of the upper chest in a patient with neurofibromatosis, type 1 shows bilateral plexiform neurofibromas *(dashed arrows)* occupying the lung apices and extending to the axillae. The bilateral masses are compressing the esophagus *(arrow)*. (B) Esophagram in the same patient shows narrowing of the proximal esophagus *(arrow)* as it passes between the plexiform neurofibromas; the density from the masses can also be appreciated extending to the thoracic apices.

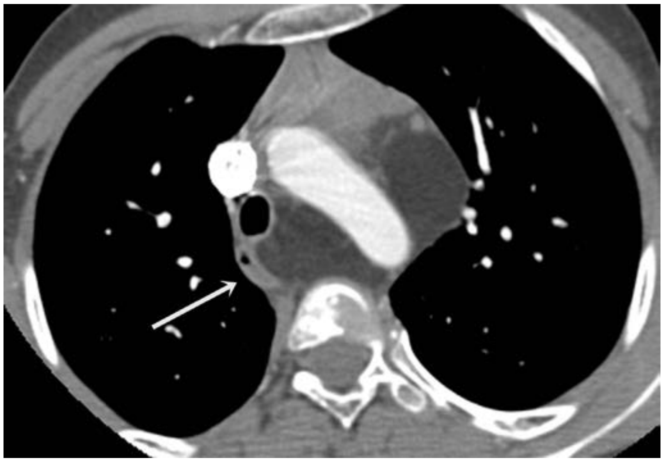

**Figure 98.14. Thoracic lipoblastoma.** Axial contrast-enhanced CT shows a large lipoblastoma displacing the trachea and the esophagus *(arrow)* leftward. *(Courtesy of Marta Hernanz-Schulman, Nashville, TN.)*

## KEY POINTS

- The symptoms of GERD depend on age.
- When compared with adults, children with GERD report fewer episodes of heartburn, dysphagia, and chest pain and more episodes of vomiting and regurgitation.
- Provocative maneuvers or prolonged fluoroscopy is not recommended for the detection of GER.
- Coins are the most common ingested foreign body.
- Button batteries lodged in the esophagus should be removed emergently.
- Food bolus impaction is commonly associated with eosinophilic esophagitis.
- Iatrogenic trauma is the most common cause of esophageal perforation in children.
- Infectious esophagitis is typically seen in immunocompromised children.

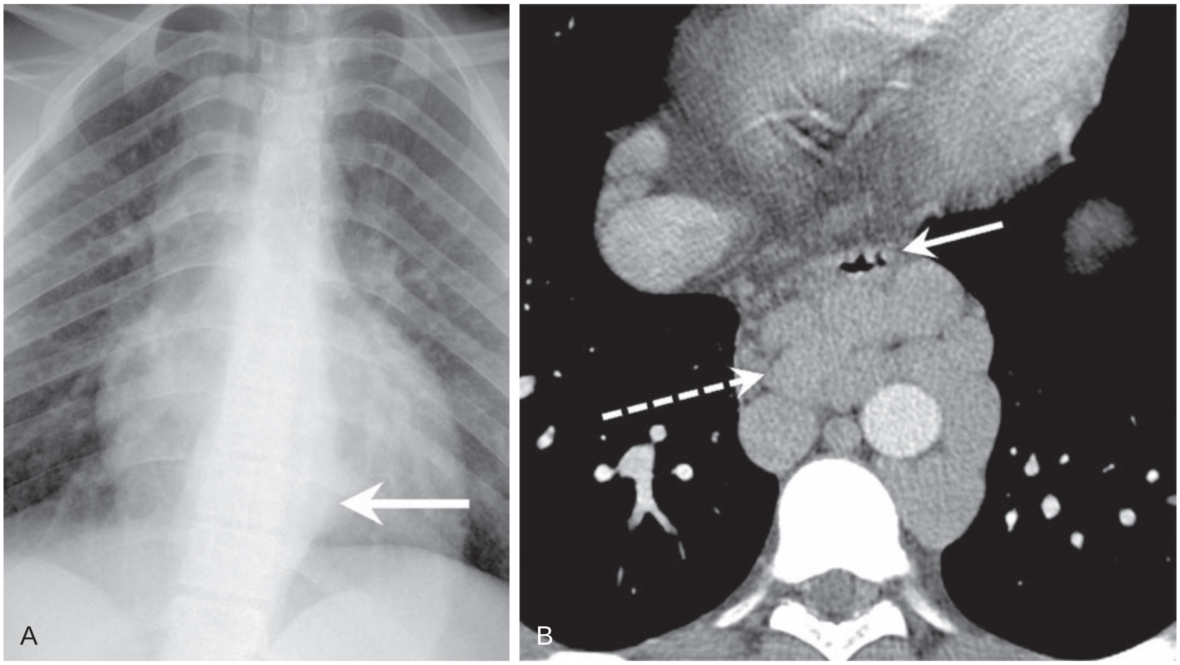

**Figure 98.15. Esophageal varices.** (A) Frontal chest radiograph in a patient with portal hypertension shows a soft tissue mass *(arrow)* in the left paraspinal region. (B) Axial contrast-enhanced CT in the same patient shows multiple dilated esophageal varices *(dashed arrow)* responsible for the paraspinal soft tissue mass on the chest radiograph, and displacing the esophagus *(arrow)* anteriorly, away from the aorta.

## SUGGESTED READINGS

Boyle JT. Gastroesophageal reflux disease in 2006. The imperfect diagnosis. *Pediatr Radiol*. 2006;36 Suppl 2:192–195.

Callahan MJ, Taylor GA. CT of the pediatric esophagus. *AJR Am J Roentgenol*. 2003;181:1391–1396.

Fordham LA. Imaging of the esophagus in children. *Radiol Clin North Am*. 2005;43:283–302.

Hryhorczuk AL, Lee EY, Eisenberg RL. Esophageal abnormalities in pediatric patients. *AJR Am J Roentgenol*. 2013;201:W519–W532.

## REFERENCES

Full references for this chapter can be found on www.expertconsult.com.

## REFERENCES

1. Fordham LA. Imaging of the esophagus in children. *Radiol Clin North Am*. 2005;43(2):283–302.
2. Callahan MJ, Taylor GA. CT of the pediatric esophagus. *AJR Am J Roentgenol*. 2003;181(5):1391–1396.
3. Boyle JT. Gastroesophageal reflux disease in 2006. The imperfect diagnosis. *Pediatr Radiol*. 2006;36 Suppl 2:192–195.
4. Hoffman I, et al. Esophageal motility in children with suspected gastroesophageal reflux disease. *J Pediatr Gastroenterol Nutr*. 2010;50(6):601–608.
5. Gilger MA, et al. Prevalence of endoscopic findings of erosive esophagitis in children: a population-based study. *J Pediatr Gastroenterol Nutr*. 2008;47(2):141–146.
6. Jeurnink SM, et al. Barrett's esophagus in children: does it need more attention? *Dig Liver Dis*. 2011;43(9):682–687.
7. Nelson SP, et al. Prevalence of symptoms of gastroesophageal reflux during childhood: a pediatric practice-based survey. Pediatric Practice Research Group. *Arch Pediatr Adolesc Med*. 2000;154(2):150–154.
8. Woodley FW, Mousa H. Acid gastroesophageal reflux reports in infants: a comparison of esophageal pH monitoring and multichannel intraluminal impedance measurements. *Dig Dis Sci*. 2006;51(11):1910–1916.
9. Vandenplas Y, et al. Pediatric gastroesophageal reflux clinical practice guidelines: joint recommendations of the North American Society for Pediatric Gastroenterology, Hepatology, and Nutrition (NASPGHAN) and the European Society for Pediatric Gastroenterology, Hepatology, and Nutrition (ESPGHAN). *J Pediatr Gastroenterol Nutr*. 2009;49(4):498–547.
10. Rokutanda R, Kishimoto M, Okada M. Update on the diagnosis and management of Behcet's disease. *Open Access Rheumatol*. 2015;7:1–8.
11. Savino A, et al. US in the diagnosis of gastroesophageal reflux in children. *Pediatr Radiol*. 2012;42(5):515–524.
12. Pearson EG, et al. Reflux esophageal stricture–a review of 30 years' experience in children. *J Pediatr Surg*. 2010;45(12):2356–2360.
13. El-Serag HB, et al. The prevalence of suspected Barrett's esophagus in children and adolescents: a multicenter endoscopic study. *Gastrointest Endosc*. 2006;64(5):671–675.
14. Kay M, Wyllie R. Pediatric foreign bodies and their management. *Curr Gastroenterol Rep*. 2005;7(3):212–218.
15. Mowry JB, et al. 2014 Annual Report of the American Association of Poison Control Centers' National Poison Data System (NPDS): 32nd Annual Report. *Clin Toxicol (Phila)*. 2015;53(10):962–1147.
16. Kramer RE, et al. Management of ingested foreign bodies in children: a clinical report of the NASPGHAN Endoscopy Committee. *J Pediatr Gastroenterol Nutr*. 2015;60(4):562–574.
17. Miller RS, et al. Chronic esophageal foreign bodies in pediatric patients: a retrospective review. *Int J Pediatr Otorhinolaryngol*. 2004;68(3): 265–272.
18. Schlesinger AE, Crowe JE. Sagittal orientation of ingested coins in the esophagus in children. *AJR Am J Roentgenol*. 2011;196(3): 670–672.
19. Towbin R, et al. Esophageal edema as a predictor of unsuccessful balloon extraction of esophageal foreign body. *Pediatr Radiol*. 1989;19(6–7):359–360.
20. Little DC, et al. Esophageal foreign bodies in the pediatric population: our first 500 cases. *J Pediatr Surg*. 2006;41(5):914–918.
21. Litovitz T, Whitaker N, Clark L. Preventing battery ingestions: an analysis of 8648 cases. *Pediatrics*. 2010;125(6):1178–1183.
22. Centers for Disease, C. and Prevention. Injuries from batteries among children aged <13 years–United States, 1995-2010. *MMWR Morb Mortal Wkly Rep*. 2012;61(34):661–666.
23. Pugmire BS, et al. Imaging button battery ingestions and insertions in children: a 15-year single-center review. *Pediatr Radiol*. 2017; 47(2):178–185.
24. Jatana KR, et al. Pediatric button battery injuries: 2013 task force update. *Int J Pediatr Otorhinolaryngol*. 2013;77(9):1392–1399.
25. Lao J, et al. Esophageal food impaction in children. *Pediatr Emerg Care*. 2003;19(6):402–407.
26. Underberg-Davis S, Levine MS. Giant thoracic osteophyte causing esophageal food impaction. *AJR Am J Roentgenol*. 1991;157(2):319–320.
27. Diniz LO, Towbin AJ. Causes of esophageal food bolus impaction in the pediatric population. *Dig Dis Sci*. 2012;57(3):690–693.
28. Riffat F, Cheng A. Pediatric caustic ingestion: 50 consecutive cases and a review of the literature. *Dis Esophagus*. 2009;22(1):89–94.
29. Dogan Y, et al. Caustic gastroesophageal lesions in childhood: an analysis of 473 cases. *Clin Pediatr (Phila)*. 2006;45(5):435–438.
30. Youn BJ, et al. Balloon dilatation for corrosive esophageal strictures in children: radiologic and clinical outcomes. *Korean J Radiol*. 2010; 11(2):203–210.
31. Glenn SM, Parakh K. Education and imaging. Gastrointestinal: pill esophagitis. *J Gastroenterol Hepatol*. 2008;23(2):339.
32. Grochenig HP, Tilg H, Vogetseder W. Clinical challenges and images in GI. Pill esophagitis. *Gastroenterology*. 2006;131(4):996–1365.
33. Gander JW, Berdon WE, Cowles RA. Iatrogenic esophageal perforation in children. *Pediatr Surg Int*. 2009;25(5):395–401.
34. Emil SG. Neonatal esophageal perforation. *J Pediatr Surg*. 2004;39(8):1296–1298.
35. Iqbal CW, et al. Pediatric endoscopic injuries: incidence, management, and outcomes. *J Pediatr Surg*. 2008;43(5):911–915.
36. O'Brien JR, et al. Esophageal injury from thoracic pedicle screw placement in a polytrauma patient: a case report and literature review. *J Orthop Trauma*. 2006;20(6):431–434.
37. Moore MA, Wallace EC, Westra SJ. The imaging of paediatric thoracic trauma. *Pediatr Radiol*. 2009;39(5):485–496.
38. Ablin DS, Reinhart MA. Esophageal perforation with mediastinal abscess in child abuse. *Pediatr Radiol*. 1990;20(7):524–525.
39. John V, et al. Tracheoesophageal fistula in a child after blunt chest trauma. *J Pediatr Surg*. 2006;41(10):E27–E29.
40. Meyerovitch J, et al. Pneumatic rupture of the esophagus caused by carbonated drinks. *Pediatr Radiol*. 1988;18(6):468–470.
41. Mukherjee K, Isbell JM, Yang E. Blunt posterior tracheal laceration and esophageal injury in a child. *J Pediatr Surg*. 2009;44(6):1292–1294.
42. Jacob R, et al. Traumatic tracheoesophageal fistula in a 5-year old. *Paediatr Anaesth*. 2006;16(10):1068–1072.
43. Antonis JH, Poeze M, Van Heurn LW. Boerhaave's syndrome in children: a case report and review of the literature. *J Pediatr Surg*. 2006;41(9):1620–1623.
44. Noel RJ, Putnam PE, Rothenberg ME. Eosinophilic esophagitis. *N Engl J Med*. 2004;351(9):940–941.
45. Putnam PE, Rothenberg ME. Eosinophilic esophagitis: concepts, controversies, and evidence. *Curr Gastroenterol Rep*. 2009;11(3):220–225.
46. Diniz LO, Putnam PE, Towbin AJ. Fluoroscopic findings in children and adolescents with Eosinophilic esophagitis. *Pediatr Radiol*. 2012;42(6):721–727.
47. Gottschalk A, et al. Anesthesia for balloon dilatation of esophageal strictures in children with epidermolysis bullosa dystrophica: from intubation to sedation. *Curr Opin Anaesthesiol*. 2010;23(4):518–522.
48. Fine JD, et al. Gastrointestinal complications of inherited epidermolysis bullosa: cumulative experience of the National Epidermolysis Bullosa Registry. *J Pediatr Gastroenterol Nutr*. 2008;46(2):147–158.
49. Ramaswamy K, et al. Esophageal Crohn disease in children: a clinical spectrum. *J Pediatr Gastroenterol Nutr*. 2003;36(4):454–458.
50. Rahhal RM, Banerjee S, Jensen CS. Pediatric Crohn disease presenting as an esophageal stricture. *J Pediatr Gastroenterol Nutr*. 2007;45(1):125–129.
51. Towbin AJ, Chaves I. Chronic granulomatous disease. *Pediatr Radiol*. 2010;40(5):657–668, quiz 792-793.
52. Huang A, Abbasakoor F, Vaizey CJ. Gastrointestinal manifestations of chronic granulomatous disease. *Colorectal Dis*. 2006;8(8):637–644.
53. Vlymen WJ, Moskowitz PS. Roentgenographic manifestations of esophageal and intestinal involvement in Behcet's disease in children. *Pediatr Radiol*. 1981;10(4):193–196.
54. Bang D. Treatment of Behcet's disease. *Yonsei Med J*. 1997;38(6):401–410.
55. Chiou CC, et al. Esophageal candidiasis in pediatric acquired immunodeficiency syndrome: clinical manifestations and risk factors. *Pediatr Infect Dis J*. 2000;19(8):729–734.
56. Ukarapol N, et al. Cytomegalovirus-associated manifestations involving the digestive tract in children with human immunodeficiency virus infection. *J Pediatr Gastroenterol Nutr*. 2002;35(5):669–673.
57. Blitman NM, Ali M. Idiopathic giant esophageal ulcer in an HIV-positive child. *Pediatr Radiol*. 2002;32(12):907–909.
58. Epstein DP, Locketz M. Oesophageal ulceration in HIV-infected patients. *S Afr Med J*. 2009;99(2):107–109.
59. Erlank A, et al. Oesophageal perforation as a complication of primary pulmonary tuberculous lymphadenopathy in children. *Pediatr Radiol*. 2007;37(7):636–639.
60. Goussard P, Andronikou S. Tuberculous broncho-oesophageal fistula: images demonstrating the pathogenesis. *Pediatr Radiol*. 2010;40 Suppl 1:S78.
61. Lucaya J, et al. Bronchial perforation and bronchoesophageal fistulas: tuberculous origin in children. *AJR Am J Roentgenol*. 1980;135(3): 525–528.

62. Lilja HE, Wester T. Outcome in neonates with esophageal atresia treated over the last 20 years. *Pediatr Surg Int*. 2008;24(5):531–536.
63. Lee CW, et al. Outcomes of treatment of childhood achalasia. *J Pediatr Surg*. 2010;45(6):1173–1177.
64. Iacob D, et al. Clinical and ultrasound approach to achalasia in a child. Case report. *Med Ultrason*. 2010;12(1):66–70.
65. Jung C, et al. Treatments for pediatric achalasia: Heller myotomy or pneumatic dilatation? *Gastroenterol Clin Biol*. 2010;34(3):202–208.
66. Guest AR, et al. Progressive esophageal leiomyomatosis with respiratory compromise. *Pediatr Radiol*. 2000;30(4):247–250.
67. Gupta V, et al. Leiomyomatosis of the esophagus: experience over a decade. *J Gastrointest Surg*. 2009;13(2):206–211.
68. Khurshed A, Ahmed R, Bhurgri Y. Primary gastrointestinal malignancies in childhood and adolescence–an Asian perspective. *Asian Pac J Cancer Prev*. 2007;8(4):613–617.
69. Retrosi G, et al. Plexiform schwannoma of the esophagus in a child with neurofibromatosis type 2. *J Pediatr Surg*. 2009;44(7):1458–1461.
70. Mileti E, Rosenthal P. Management of portal hypertension in children. *Curr Gastroenterol Rep*. 2011;13(1):10–16.
71. Heinen FL, Vallone P, Elmo G. Esophageal diverticulum in an infant with Down's syndrome and type III esophageal atresia. *J Pediatr Surg*. 2003;38(4):E9.
72. Herman TE, McAlister WH. Esophageal diverticula in childhood associated with strictures from unsuspected foreign bodies of the esophagus. *Pediatr Radiol*. 1991;21(6):410–412.
73. Toyohara T, et al. Giant epiphrenic diverticulum in a boy with Ehlers-Danlos syndrome. *Pediatr Radiol*. 1989;19(6–7):437.

# PART 6 Stomach

## 99

## Congenital and Neonatal Abnormalities of the Stomach

*Nancy R. Fefferman, Sudha P. Singh, and Marta Hernanz-Schulman*

Congenital abnormalities of the stomach, and those manifested in the neonatal period, are uncommon and include such entities as duplication cysts, diverticula, microgastria, and anomalies involving the antropyloric region.

### GASTRIC DUPLICATION CYST

***Overview.*** Duplication cysts may occur anywhere along the gastrointestinal tract, from the mouth to the rectum (see Chapters 96, 102, and 105). Gastric duplication cysts are rare and comprise approximately 4% to 7% of intestinal duplications.[1,2]

The cysts are most commonly located along the greater curvature of the stomach, share blood supply with the stomach, are invested in an outer smooth muscle layer, and typically contain gastric epithelial lining, although they may also contain pancreatic tissue or even small intestinal or colonic mucosa.[1,2] More than 80% of gastric duplications are spherical rather than tubular and do not communicate with the gastric lumen.[3] Complete duplications of the pylorus have also been described.[4] Rarely, communication with the pancreatic ductal system has been reported.[1,5]

***Etiology.*** The etiology remains controversial with several hypotheses postulated to explain the embryology of gastrointestinal tract duplications, as no single theory is sufficient to explain the characteristics of all types of duplication cysts; these theories include abortive twinning, split notochord, and persistence of an embryologic diverticulum (see Chapter 102).[6]

***Clinical Presentation.*** Gastric duplication cysts occur more frequently in females at a ratio of 2 : 1.[7] If not discovered prenatally,[8,9] postnatal clinical presentation of gastric duplication cysts usually occurs during the first year of life with symptoms including intestinal obstruction, abdominal pain, palpable mass, gastrointestinal bleeding, and hematemesis[10,11] or melena. Uncommon complications of gastric duplication cysts include pancreatitis[1,12] and gastric outlet obstruction simulating hypertrophic pyloric stenosis when abutting the distal antrum.[3,13] Malignancy has developed within the duplication cyst in some cases.[14,15]

***Imaging.*** Although gastric duplication cysts may be evident on plain radiography as a masslike density in the upper abdomen,[10] the low sensitivity and specificity limits the utility of plain radiography in the evaluation of gastric duplication cysts. Upper gastrointestinal (UGI) contrast examination may demonstrate mass effect by the cyst (Fig. 99.1A and B). Ultrasonography is an excellent imaging modality for characterization of these cystic masses, which often demonstrate the typical “gut signature” or “double-wall” sign representing the inner hyperechoic mucosal layer and peripheral hypoechoic muscle layers (Figs. 99.1C and 99.2); free fluid may be found in cases of perforation (e-Fig. 99.3). Cysts may be completely anechoic, or may contain septations and internal echoes representing proteinaceous material, blood products, or debris related to infection. Computed tomography (CT) demonstrates a well-circumscribed homogeneously low attenuating mass in the left upper quadrant. Peripheral enhancement, wall thickening, and heterogeneous attenuation of the cyst wall may be present if complicated by inflammation. On magnetic resonance imaging (MRI), the cysts exhibit fluid characteristics at T1 and T2 weighting, but the signal may increase on T1-weighted sequences in the presence of hemorrhage or other proteinaceous material.[3] Imaging with technetium 99m-pertechnate is helpful when there is gastric mucosa lining the cysts.[16,17] Meticulous technique is necessary to differentiate the duplication cyst from the adjacent stomach; multiple views may be required, and SPECT CT may be useful in defining the abnormality.[17]

***Treatment.*** Treatment of both symptomatic and asymptomatic gastric duplication cysts entails surgical resection with complete excision of the cyst.[18,19] If the cyst cannot be resected without violating the adjacent gastric lumen, a partial gastric resection with mucosal stripping may be necessary.[5] Laparoscopic resection of gastric duplication cysts has also been described.[19–23]

### GASTRIC DIVERTICULA

***Overview.*** Gastric diverticula are rare in the general population, with a reported prevalence of 0.02% in autopsy studies and 0.04% in contrast studies. They are most commonly diagnosed in the sixth and seventh decades but are even more uncommon in children, with only 4% of gastric diverticula occurring in patients less than 20 years of age.[24–27]

Approximately 70% of gastric diverticula are congenital, consist of all three layers of the gastric wall, with approximately 75% of them located in the posterior wall of the fundus 2 to 3 cm from the gastroesophageal junction. Acquired diverticula are more likely to be located near the antrum and represent false diverticula secondary to inflammatory comorbidity.[24–27]

***Etiology.*** The cause of congenital gastric diverticula is thought to be related to the division of the longitudinal fibers of the wall of the stomach resulting in a defect in the musculature of the gastric wall, impacted by arterial perforators and focal absence of peritoneal investment contributing to mural weakness.[24] Alternatively a diverticulum could result from faulty fusion of the dorsal mesentery of the stomach with the left posterior body wall.[26] Acquired diverticula as previously noted are usually related to peptic ulcer disease or pancreatitis.[24,28]

***Clinical Presentation.*** Although most gastric diverticula are clinically asymptomatic, symptomatic lesions in children tend to present in late childhood and adolescence. The symptoms can range from nonspecific complaints, such as recurrent abdominal pain, nausea, and vomiting, to massive hemorrhage and perforation; such symptoms may relate to the presence of ectopic pancreatic tissue within the diverticula causing erosions and ulceration.[24,28,29]

***Imaging.*** Imaging evaluation of suspected gastric diverticula includes UGI, which demonstrates an outpouching of the gastric wall that communicates with the gastric lumen. Right anterior oblique positioning optimizes the sensitivity of this imaging study due to the posterior wall location of most congenital gastric diverticula. Antral diverticula are similarly identified (Fig. 99.4). On CT and ultrasound, the diverticulum can be confused with other cystic lesions; positive oral contrast material is very helpful in establishing the correct diagnosis.[27,30,31]

## Abstract:

To detail the etiologies, clinical presentation, imaging appearances, and treatment plan of congenital and neonatal abnormalities of the stomach. Gastric duplication cyst, gastric diverticula, congenital microgastria are reviewed. Antropyloric obstructions including pyloric web, diaphragm and atresia are reviewed. Ectopic pancreas is also reviewed.

## Keywords:

Stomach, congenital anomalies
Gastric duplication cyst
Congenital gastric diverticula
Congenital microgastria and associations
Pyloric web
Pyloric atresia, multiple atresias (MIA), Epidermolysis bullosa
Ectopic pancreas

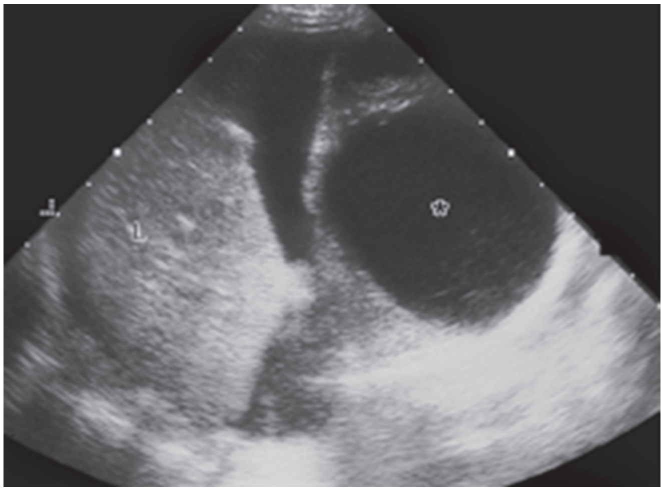

**e-Figure 99.3. Ruptured gastric duplication cyst.** Sagittal sonogram through the medial portion of the right lobe of the liver (L) demonstrates a thin-walled, approximately 4-cm cyst *(asterisk)*. Free fluid, complex in its dependent portion, was confirmed at surgery to represent hemorrhage secondary to perforation of the cyst. *(Courtesy of Dr. C. Mitchell, Peoria, IL.)*

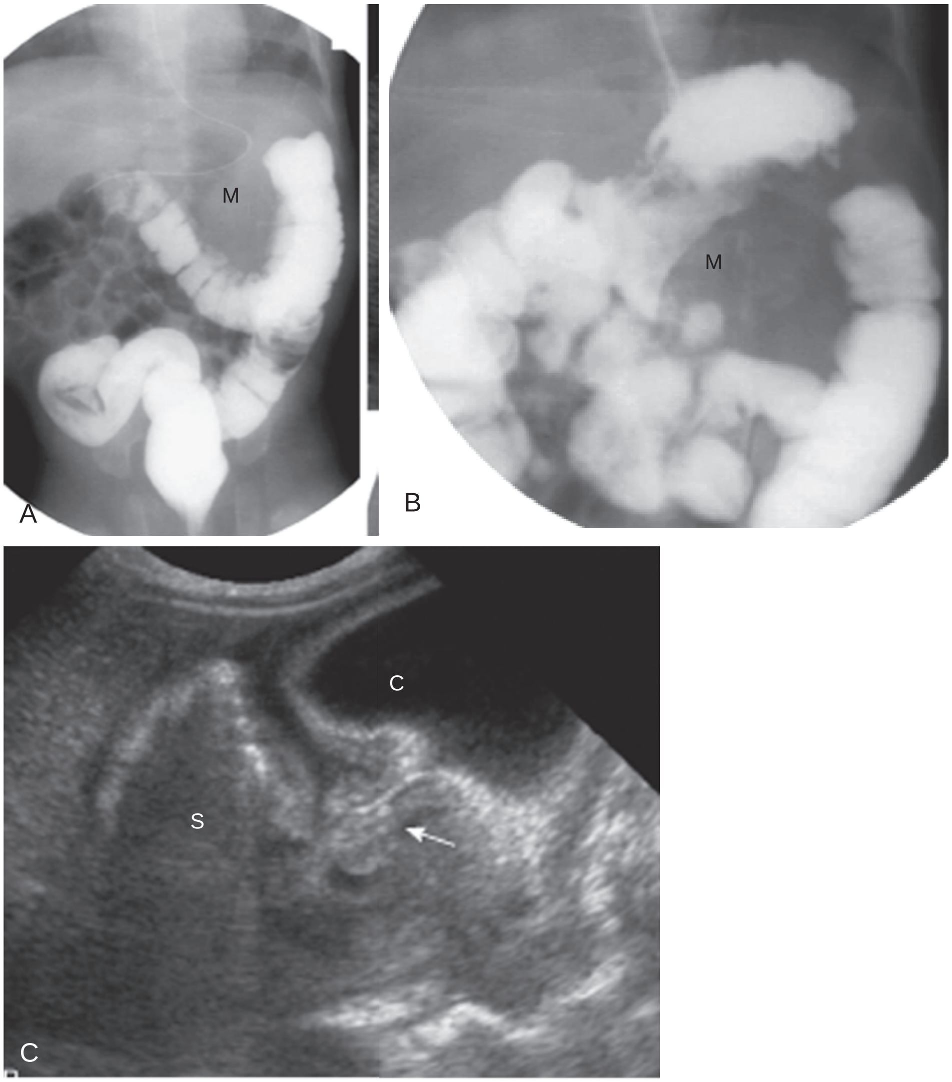

**Figure 99.1. Gastric duplication cyst.** (A) Contrast enema study in a 6-week-old infant demonstrates a mass (*M*) between the greater curvature of the stomach and the contrast-filled transverse colon. (B) UGI performed after the enema demonstrates mass effect (*M*) on the greater curvature of the stomach. (C) Ultrasound study demonstrates a fluid-filled cyst (C) with a hypo-hyperechoic bilayered outline typical of duplication cyst. The stomach (S) contains shadowing gas. The connection of the cyst with the gas-filled stomach is seen *(arrow)*. *(Courtesy of Dr. D. Barlev, New York, NY.)*

***Treatment.*** Symptomatic gastric diverticula may be treated pharmacologically with histamine-2 blockade. Surgical resection is reserved for patients whose symptoms are unresponsive to pharmacotherapy and can be performed with either laparotomy or laparoscopic excision.[29,32,33]

## CONGENITAL MICROGASTRIA

***Overview.*** Congenital microgastria is a rare anomaly characterized by a small, tubular stomach, located in the midline and typically associated with a distended esophagus. In persons with microgastria, the stomach is lined by normal gastric mucosa, but the total cell mass is significantly reduced.[34,35] Agastria, or complete absence of the stomach, is the most extreme form of microgastria.

Isolated congenital microgastria is extremely rare,[36] and this condition is nearly always accompanied by other congenital anomalies such as heterotaxy with splenic anomalies;[37,38] congenital diaphragmatic hernia;[39] trachea-esophageal clefts; hiatal hernia;[35] jaw and palate abnormalities;[40] DiGeorge syndrome; central nervous system abnormalities; and vertebral, cardiac, renal, and limb reduction anomalies (VACTERL association). The combination of microgastria in association with limb reduction defects and central nervous system anomalies may have an autosomal recessive mode of inheritance.[41,42]

***Etiology.*** Microgastria is thought to result from impaired foregut development (see also Chapter 83). The embryonic foregut elongates to form the primordial stomach during the fourth week of gestation. Dilatation of the region of the future stomach occurs in the fifth week. Lateral flattening of the stomach and a 90-degree rotation occur during the sixth week, and the lesser and greater curvatures become established during the sixth and seventh weeks. The growth of the fundus appears during the eighth or ninth week.[34] Early arrest of the process leads to microgastria; the size and the shape of the stomach therefore depend on when the arrest of development occurs.[35] During the fifth week of gestation, the spleen begins to form along the dorsal mesogastrium of the stomach; this association in development of the stomach and the spleen serves to explain the association of microgastria with splenic

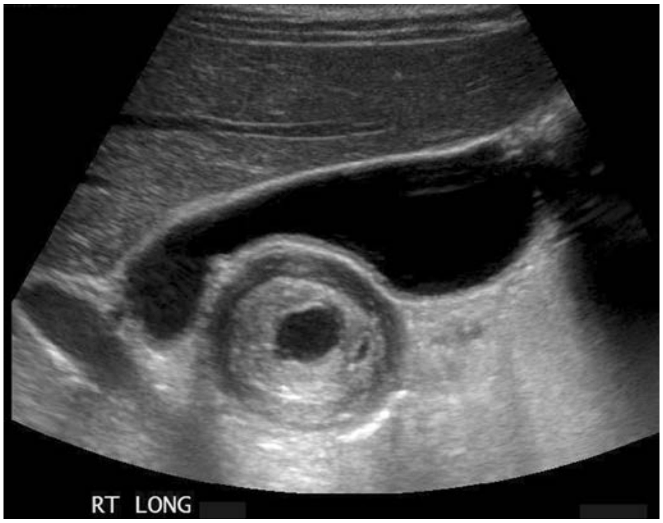

**Figure 99.2. Gastric duplication cyst.** Ultrasound image of the upper abdomen demonstrates a mass contiguous with the greater curvature of the stomach, with a bilayered hyper/hypoechoic wall suggesting the muscular and mucosal layers of gut signature. The wall and mucosa appear thickened suggesting inflammatory changes.

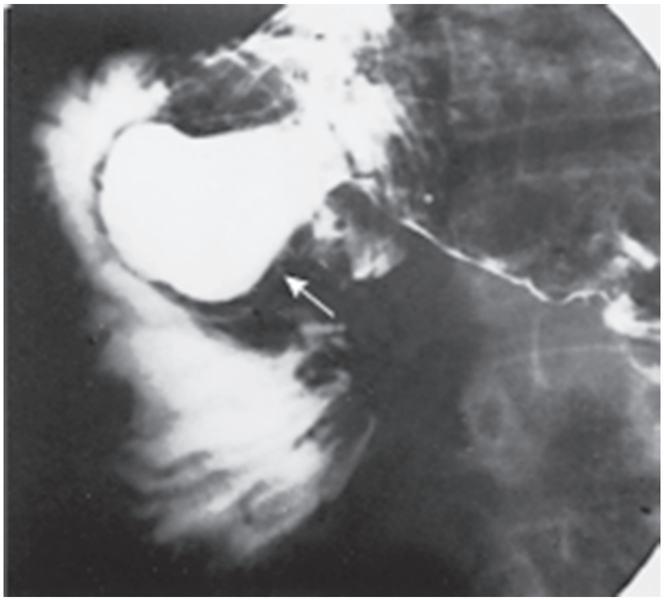

**Figure 99.4. Gastric diverticulum.** The barium-filled diverticulum is seen to be featureless with air-filled antrum *(arrow)* proximal and barium-filled duodenal sweep distal to it. The diverticulum originated at the gastroduodenal junction and was lined with gastric mucosa.

anomalies as in the heterotaxy syndromes. Association of microgastria with limb reduction anomalies is attributed to impairment of early mesodermal development.[42]

***Clinical Presentation.*** The infant may present with feeding intolerance, severe gastroesophageal reflux, and associated anomalies, which will modulate the clinical presentation and determine overall prognosis and mortality. Rare infants with isolated microgastria may present with failure to thrive, stridor or cyanosis during feeding,[43] feeding intolerance, recurrent aspiration pneumonia, and malnutrition as a result of severe gastroesophageal reflux.[36] Pernicious anemia may be present as a result of decreased intrinsic factor production because of the decreased gastric cell mass.[44]

***Imaging.*** Prenatally, failure of visualization of the fetal stomach with normal amniotic fluid volume raises concern for microgastria.[45] Chest and abdominal radiographs may show absence of the normal stomach bubble and, in some cases, the outline of a very dilated or megaesophagus might be visualized in the lower chest. UGI shows a small tubular stomach (less than 25% of the normal size) located in the midline, and associated with severe gastroesophageal reflux and a megaesophagus as a result of the overflow from the small capacity stomach (Fig. 99.5). Esophageal motility is ineffectual as a result of the gross dilatation, although after treatment the esophagus has been described as able to return to normal.[44] Additional imaging studies including spine radiographs, cardiac echo, ultrasound, CT, and MRI can be done as indicated to identify associated anomalies.

***Treatment.*** The treatment for microgastria is individualized, dependent on the severity of the microgastria and associated anomalies. Conservative or medical treatment may be tried initially but usually is not effective in severe cases because the stomach does not enlarge with time. Recent literature suggests that an early operation may be indicated for better growth and development and an improved quality of life overall. Most of the patients are treated with a Hunt–Lawrence pouch (a double lumen roux-en-Y jejunal pouch) for increasing the size of the gastric reservoir with improved growth patterns after surgery.[36,44]

## PYLORIC WEB, DIAPHRAGM, AND ATRESIA

***Overview.*** Pyloric atresia is a rare congenital anomaly which comprises less than 1% of intestinal atresias with a reported frequency of approximately 1 : 100,000 live births.[46] Although it can occur in isolation, in approximately 30% of cases, it has two major systemic associations: multiple intestinal atresias (MIA) and dermatologic abnormalities: epidermolysis bullosa (EB) and aplasia cutis congenita.[47,48] According to the Third International Consensus Meeting on Diagnosis and Classification of EB, pyloric atresia is associated with the simplex (EBS) and junctional (JEB) forms of EB.[49] Pyloric atresia is seen in three distinct anatomic types which somewhat mirror those of other intestinal atresias: (1) membranous, (2) atresia without a gap, and (3) atresia with an intervening gap. Membranous atresia is reported to be the most common, seen in approximately 60% of affected infants.[47,50]

Incomplete obstructions due to antral webs or diaphragms are reported to be the more commonly encountered form of this rare abnormality.[51] The webs are thin circumferential membranes measuring between 2 and 4 mm that span the lumen of the stomach, perpendicular to its long axis[52] typically located 1 to 2 cm from the pylorus, and composed of mucosal layers without a muscular component.[53,54]

***Etiology.*** The exact etiology remains controversial with a number of theories postulated including incomplete or abnormal canalization of the foregut during embryologic development or intrauterine mechanical or chemical injury.[46,55] When associated with EB, this has been thought to represent a specific clinical entity related to an abnormality in the cell surface signaling protein alpha 6 integrin or its ligands.[47]

***Clinical Presentation.*** Pyloric atresia presents in the neonate with nonbilious vomiting. Neonatal gastric perforation has been reported.[47] There is polyhydramnios in approximately 50% of cases, and the patients may be born prematurely.[48,56] When associated with EB, the skin changes are self-explanatory. In addition to multiple atresias, immunodeficiency has also been reported in some patients with pyloric atresia.[57]

Incomplete gastric outlet obstruction due to the presence of antropyloric webs or diaphragms has a variable clinical presentation depending on the size of the orifice, which can range from 2 to 30 mm. Clinical manifestations include vomiting, failure to thrive, and intermittent abdominal pain.[58]

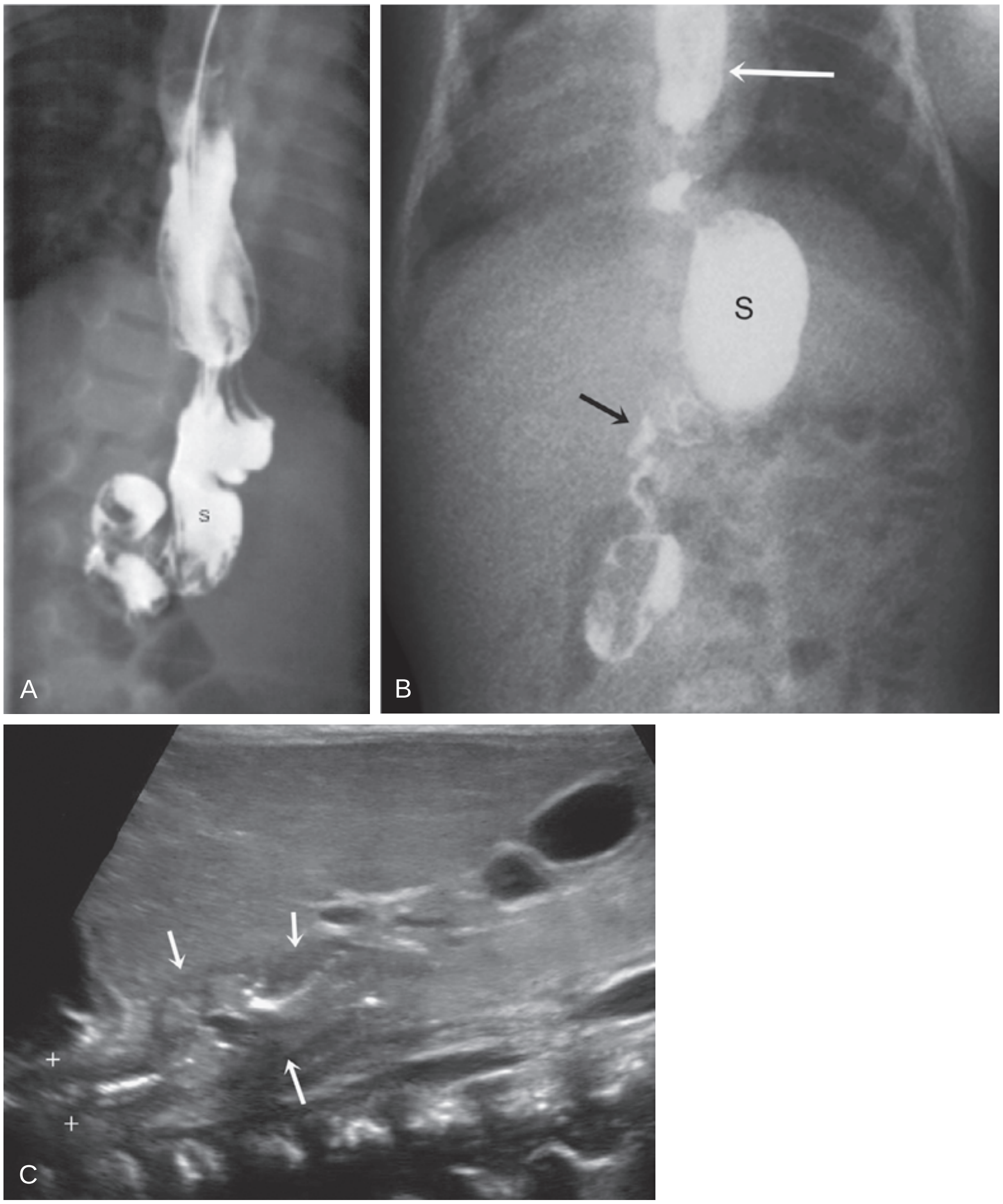

**Figure 99.5. Microgastria.** (A) Frontal image from an UGI performed with a nasogastric tube demonstrates a small midline stomach *(S)* with grossly patent gastroesophageal junction and megaesophagus. The patient also has malrotation of the bowel. (B) Frontal image from UGI in neonate with heterotaxy, asplenia and microgastria. Note the small, poorly differentiated midline stomach *(S),* large esophagus *(white arrow),* and malrotated duodenum *(black arrow)*. The heart is on the right, and the bulk of the liver mass is also on the right. (C) Midline sagittal sonogram in a neonate with heterotaxy and asplenia. The image shows a small midline stomach *(arrows)* and a large distal thoracic esophagus *(between calipers)*.

***Imaging.*** Prenatally, polyhydramnios, a dilated stomach and esophagus with collapsed distal bowel may be seen. “Snow flake” appearance of the amniotic fluid may be seen in cases associated with EB.[56] In patients with pyloric atresia, postnatal abdominal radiographs demonstrate a single bubble, representing the distended stomach, with absence of distal bowel gas.[59] Fluoroscopic contrast examination, if performed, will confirm gastric outlet obstruction. Ultrasound will reveal a blind-ending gastric antrum with no gas distally (Fig. 99.6).

In patients with antral web or diaphragm, fluoroscopic imaging evaluation of the stomach may demonstrate a double bulb appearance representing the distended antral segment interposed between the web and the true duodenal bulb, and/or linear filling defect in the distal stomach outlining the antral membrane (e-Fig. 99.7 and Fig. 99.8). Early filling images of the stomach are recommended as visualization of the filling defect may be obscured by dense contrast. Failure to achieve maximal distal antral distension may be associated with presence of a diaphragm or web that may not be visualized.[55] Sonographic demonstration of antropyloric webs has also been described in the literature.[60] Sonography needs meticulous technique and a fluid-filled stomach; sonographic findings include gastric distension, the presence of persistent linear echogenic structure projecting into the distal gastric lumen, and delayed gastric emptying. Recently, intramuscular fibrous bands

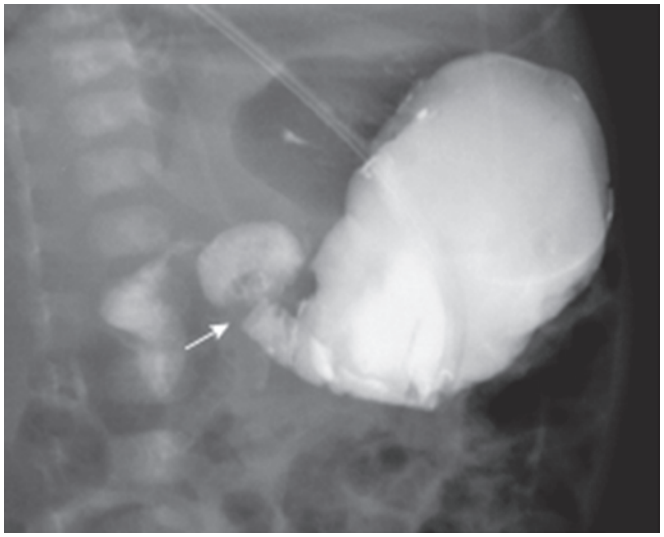

**e-Figure 99.7. Pyloric web in an infant with vomiting since birth.** Contrast demonstrates a circular band or indentation in the distal antrum *(arrow)*. Endoscopy demonstrated a pyloric web. *(Courtesy of Dr. Stuart C. Morrison, Cleveland, OH.)*

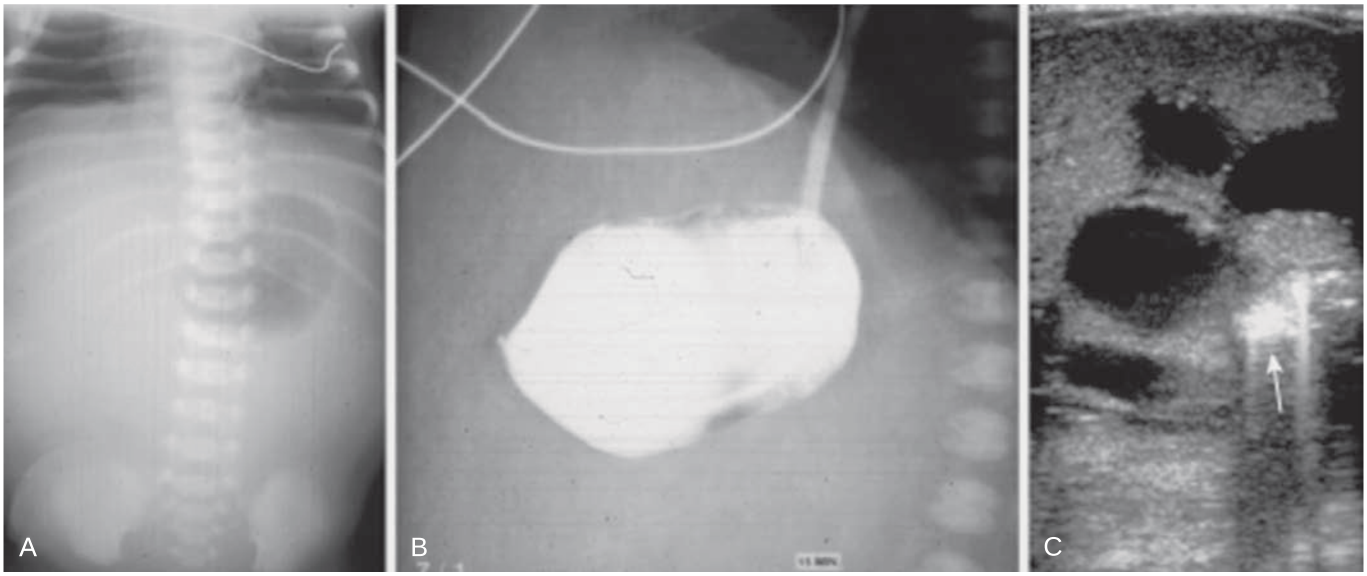

**Figure 99.6. Infant with pyloric atresia associated with multiple atresias.** (A) Abdominal radiograph shows some distension of the stomach with gas, and otherwise gasless abdomen. The distension of the flanks suggests that either the distal bowel loops are not collapsed, or that there is ascites. (B) UGI through orogastric tube shows blind-ending stomach, with no further passage of contrast. (C) Ultrasound examination shows gas within the blind-ending gastric antrum *(arrow)*. Other loops of bowel are distended with fluid due to the multiple atresias and retained gastrointestinal secretions, but there was no gas in any loop distal to the stomach.

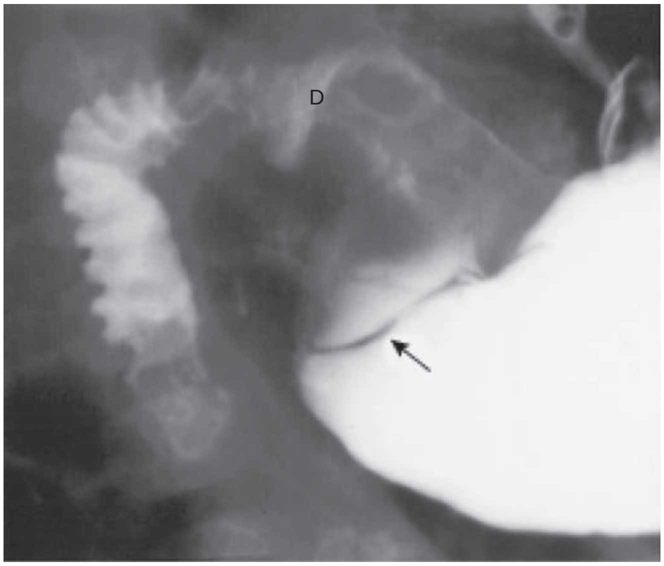

**Figure 99.8. Antropyloric web.** Spot image from UGI demonstrates barium in the antrum with a thin radiolucent band *(arrow)* representing a web in an older child who presented with long history of intermittent vomiting. *D*, Duodenal bulb.

resembling diaphragms on imaging have been reported.[54] Definitive diagnosis is made endoscopically.

***Treatment.*** Treatment of pyloric atresia is surgical, although mortality in cases associated with EB is high, as many of these children succumb to electrolyte imbalance, protein loss, and sepsis. The type of operation performed varies with the type of atresia that is present and ranges from membrane excision and pyloroplasty to gastroduodenostomy.[47,48,56] Antral membranes can be resected endoscopically.[60]

## ECTOPIC PANCREAS

***Overview.*** Ectopic pancreas is defined as the presence of pancreatic tissue outside of the pancreas without anatomic connection to the gland; it is most commonly found in the stomach, duodenum, and Meckel diverticulum, although it can be found in multiple locations, including the umbilicus, fallopian tube, liver, mediastinum, and lung.[61,62] Because most patients are asymptomatic, the reported incidence varies widely, between 0.5% and 14%.[62] Approximately 90% of gastric heterotopic pancreas lesions are located in the antrum and along the greater curvature.[61]

***Etiology.*** The etiology of ectopic pancreas remains unclear. One theory proposes that metaplasia of pluripotential endodermal cells, through errors in the Notch signaling pathway, give rise to pancreatic tissue in ectopic location; another theory suggests that embryonic pancreatic tissue is deposited in ectopic location through errors during the time of rotation of the foregut.[62–64]

***Clinical Presentation.*** Most patients are asymptomatic and therefore ectopic pancreas is usually an incidental finding.[65] If symptoms occur, it is typically in adulthood; children represented between 6% and 16% of symptomatic cases in series reporting both pediatric and adult patients.[66] In adults, symptoms occur more often in males, although in children girls represent a larger proportion of the total.[66] Typically the lesions are small and symptoms are secondary to inflammatory changes, such as pancreatitis and ulceration, resulting in abdominal pain or bleeding. When large enough, antral lesions can lead to gastric outlet obstruction.[61]

***Imaging.*** UGI demonstrates an intramural mound of tissue projecting into the gastric lumen in the prepyloric region along the greater curvature with a characteristic central umbilication (representing the attempt at duct formation). Diagnosis can be suggested only if the central umbilication is seen (Fig. 99.9). Endoscopic ultrasound demonstrates nonspecific findings such as a submucosal solid mass with intermediate echogenicity.[67] CT may show localized wall thickening or a small mass, which may demonstrate marked enhancement that can help to differentiate this

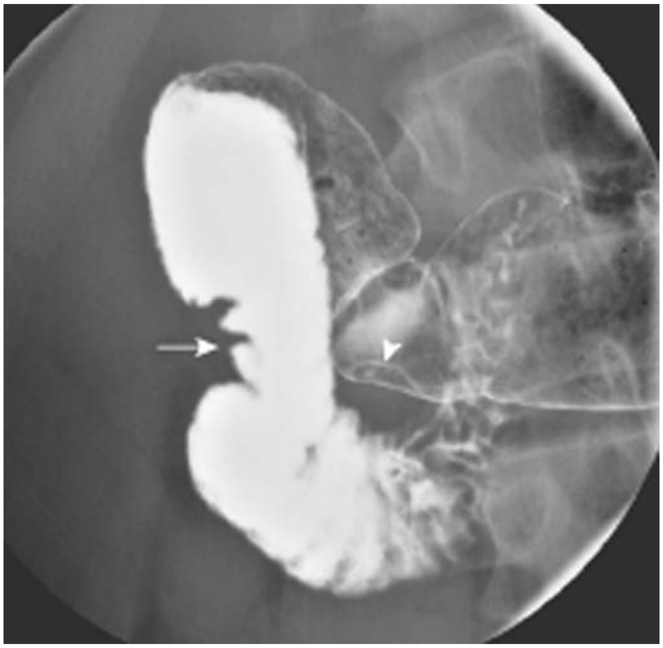

**Figure 99.9. Ectopic pancreas in a teenage girl with chronic vomiting.** Air contrast UGI demonstrates a small mass in the pylorus with central umbilication, proven at surgery to represent ectopic pancreas *(arrowhead)*. Annular pancreas/duodenal stenosis was also diagnosed, as demonstrated by narrowing along the second portion of the duodenum, also confirmed at surgery *(arrow)*.

lesion from gastrointestinal stromal tumor (GIST).[68] Distending the bowel lumen with negative oral contrast may be helpful.[69] MRI may help localize the ectopic pancreatic tissue by demonstrating an area with signal characteristics and enhancement similar to pancreatic tissue on all sequences; demonstration of ducts in the tissue or mass on MRI in a mesenteric lesion has been described.[67]

***Treatment.*** An ectopic pancreas diagnosed incidentally does not need treatment. Cases with symptoms are treated by surgical resection of the involved segment.[67]

## KEY POINTS

- Gastric duplication cysts are rare among the gastrointestinal duplications and are most commonly located along the greater curvature of the stomach.
- Microgastria is usually associated with other congenital anomalies such as the heterotaxy syndromes.
- The imaging hallmark of microgastria is a small midline stomach with significant reflux into a megaesophagus.
- Complete atresias involving the pylorus or antrum are extremely rare comprising less than 1% of all gastrointestinal atresias. Incomplete obstructions due to webs or diaphragms are the more commonly encountered form of this rare abnormality.

## SUGGESTED READING

Al-Salem A, Abdulla MR, Kothari MR, et al. Congenital pyloric atresia, presentation, management, and outcome: a report of 20 cases. *J Pediatr Surg*. 2014;49:1078–1082.

Erginel B, Soysal FG, Ozbey J, et al. Enteric duplication cysts in children: a single institution series with forty patients in twenty-six years. *World J Surg*. 2017;61:620–624.

Jones VS, Cohen RC. An eighteen-year follow-up after surgery for congenital microgastria- case report and review of literature. *J Pediatr Surg*. 2007;42:1957–1960.

Mortelé KJ, Rocha TC, Streeter JL. et.al. Multimodality imaging of pancreatic and biliary congenital anomalies. *Radiographics*. 2006;26:715–731.

Rodeberg DA, Zaheer S, Moir CR, et al. Gastric diverticulum: a series of four pediatric patients. *J Pediatr Gastroenterol Nutr*. 2002;34:564–567.

## REFERENCES

Full references for this chapter can be found on www.expertconsult.com.

## REFERENCES

1. Magnusson D, Scjwartz M. Stomach and duodenum. In: Oldham K, et al, eds. *Principles and Practice of Pediatric Surgery*. 2nd ed. Philadelphia: Lippincott Williams & Wilkins; 2005.
2. Liu R, Adler DG. Duplication cysts: diagnosis, management, and the role of endoscopic ultrasound. *Endosc Ultrasound*. 2014;3(3):152–160.
3. Singh JP, et al. Gastric duplication cyst: two case reports and review of the literature. *Case Rep Surg*. 2013;2013:605059.
4. Berrocal T, et al. Congenital anomalies of the upper gastrointestinal tract. *Radiographics*. 1999;19(4):855–872.
5. Holcomb GW 3rd, et al. Surgical management of alimentary tract duplications. *Ann Surg*. 1989;209(2):167–174.
6. Lund D. Alimentary tract duplications. In: *Pediatric Surgery*. Elsevier Health Sciences; 2012.
7. Agha FP, Gabriele OF, Abdulla FH. Complete gastric duplication. *AJR Am J Roentgenol*. 1981;137(2):406–407.
8. Nakazawa N, Okazaki T, Miyano T. Prenatal detection of isolated gastric duplication cyst. *Pediatr Surg Int*. 2005;21(10):831–834.
9. Granata C, et al. Gastric duplication cyst: appearance on prenatal US and MRI. *Pediatr Radiol*. 2003;33(2):148–149.
10. Barlev DM, Weinberg G. Acute gastrointestinal hemorrhage in infancy from gastric duplication: imaging findings. *Emerg Radiol*. 2004;10(4):204–206.
11. Prinsloo H, et al. Gastric duplication cysts as a rare cause of haematemesis: diagnostic challenges in two children. *Pediatr Surg Int*. 2011;27(10):1127–1130.
12. Steyaert H, et al. Uncommon complication of gastric duplication in a three-year-old child. *Eur J Pediatr Surg*. 1997;7(4):243–244.
13. Lopez-Fernandez S, et al. Pyloroduodenal duplication cysts: treatment of 11 cases. *Eur J Pediatr Surg*. 2013;23(4):312–316.
14. Zheng J, Jing H. Adenocarcinoma arising from a gastric duplication cyst. *Surg Oncol*. 2012;21(2):e97–e101.
15. Kaminski JP, Xu H, Hyser M. Symptomatic abdominal mass. Gastric duplication. *JAMA Surg*. 2015;150(6):593–594.
16. Kumar R, et al. Diagnosis of ectopic gastric mucosa using 99Tcm-pertechnetate: spectrum of scintigraphic findings. *Br J Radiol*. 2005; 78(932):714–720.
17. Hosseinnezhad T, et al. 99mTc-pertechnetate imaging for detection of ectopic gastric mucosa: a systematic review and meta-analysis of the pertinent literature. *Acta Gastroenterol Belg*. 2014;77(3):318–327.
18. Erginel B, et al. Enteric duplication cysts in children: a single-institution series with forty patients in twenty-six years. *World J Surg*. 2017;41(2):620–624.
19. Patino Mayer J, Bettolli M. Alimentary tract duplications in newborns and children: diagnostic aspects and the role of laparoscopic treatment. *World J Gastroenterol*. 2014;20(39):14263–14271.
20. Ford WD, et al. Laparoscopic excision of a gastric duplication cyst detected on antenatal ultrasound scan. *J Pediatr Surg*. 2004;39(10): e8–e10.
21. Machado MA, et al. Laparoscopic resection of gastric duplication: successful treatment of a rare entity. *Surg Laparosc Endosc Percutan Tech*. 2003;13(4):268–270.
22. Wakabayashi H, et al. Laparoscopically resected foregut duplication cyst (bronchogenic) of the stomach. *Dig Dis Sci*. 2007;52(8): 1767–1770.
23. Gorecki W, et al. Laparoscopic and laparoscopy-assisted resection of enteric duplication cysts in children. *J Laparoendosc Adv Surg Tech A*. 2015;25(10):838–840.
24. Rodeberg DA, et al. Gastric diverticulum: a series of four pediatric patients. *J Pediatr Gastroenterol Nutr*. 2002;34(5):564–567.
25. Kubiak R, Hamill J. Laparoscopic gastric diverticulectomy in a 13-year-old girl. *Surg Laparosc Endosc Percutan Tech*. 2006;16(1):29–31.
26. Rashid F, Aber A, Iftikhar SY. A review on gastric diverticulum. *World J Emerg Surg*. 2012;7(1):1.
27. Elliott S, et al. Surgical treatment of a gastric diverticulum in an adolescent. *J Pediatr Surg*. 2006;41(8):1467–1469.
28. Lhewa T, et al. Gastric antral diverticulum with heterotopic pancreas in a teenage patient. *J Pediatr Gastroenterol Nutr*. 2011;53(5):471.
29. Donkervoort SC, et al. Laparoscopic resection of a symptomatic gastric diverticulum: a minimally invasive solution. *JSLS*. 2006;10(4):525–527.
30. Schramm D, et al. Imaging findings of gastric diverticula. *ScientificWorldJournal*. 2014;2014:923098.
31. Feng Y, Zhang Z. Gastric diverticulum simulating a left adrenal mass: a case report and review of the literature. *Oncol Lett*. 2015;10:2477–2480.
32. Lopez ME, et al. Laparoscopic excision of a gastric diverticulum in a child. *J Laparoendosc Adv Surg Tech A*. 2007;17(2):246–248.
33. Zelisko A, et al. Laparoscopic resection of symptomatic gastric diverticula. *JSLS*. 2014;18(1):120–124.
34. Kroes EJ, Festen C. Congenital microgastria: a case report and review of literature. *Pediatr Surg Int*. 1998;13(5–6):416–418.
35. Kunisaki SM, et al. Gastric dissociation for the treatment of congenital microgastria with paraesophageal hiatal hernia. *J Pediatr Surg*. 2011;46(6):e1–e4.
36. Jones VS, Cohen RC. An eighteen year follow-up after surgery for congenital microgastria–case report and review of literature. *J Pediatr Surg*. 2007;42(11):1957–1960.
37. Hill LM. Congenital microgastria: absence of the fetal stomach and normal third trimester amniotic fluid volume. *J Ultrasound Med*. 1994;13(11):894–896.
38. Herman TE, Siegel MJ. Imaging casebook. Asplenia syndrome with congenital microgastria and malrotation. *J Perinatol*. 2004;24(1):50–52.
39. Sharma SC, Menon P. Congenital microgastria with esophageal stenosis and diaphragmatic hernia. *Pediatr Surg Int*. 2005;21(4):292–294.
40. Laurie DE, Wakeling EL. Congenital microgastria in association with Pierre-Robin sequence. *Clin Dysmorphol*. 2008;17(2):143–144.
41. al-Gazali LI, et al. Recurrence of the severe form of microgastria-limb reduction defect in a consanguineous family. *Clin Dysmorphol*. 1999;8(4):253–258.
42. Stewart C, Stewart M, Stewart F. Microgastria-limb reduction anomaly with total amelia. *Clin Dysmorphol*. 2002;11(3):187–190.
43. Waasdorp CE, Rooks V, Sullivan C. Congenital microgastria presenting as stridor. *Pediatr Radiol*. 2003;33(9):662–663.
44. Ala S, et al. Congenital microgastria in a two-month-old boy. *J Compr Ped*. 2014;5(3):221353.
45. Shepherd P, et al. Congenital microgastria: a rare cause of failure to visualise the fetal stomach. *Prenat Diagn*. 2011;31(10):1010–1012.
46. Andriessen MJ, Matthyssens LE, Heij HA. Pyloric atresia. *J Pediatr Surg*. 2010;45(12):2470–2472.
47. Al-Salem AH, et al. Congenital pyloric atresia, presentation, management, and outcome: a report of 20 cases. *J Pediatr Surg*. 2014;49(7):1078–1082.
48. Parelkar SV, et al. Pyloric atresia–three cases and review of literature. *Afr J Paediatr Surg*. 2014;11(4):362–365.
49. Chung HJ, Uitto J. Epidermolysis bullosa with pyloric atresia. *Dermatol Clin*. 2010;28(1):43–54.
50. Heinen FL. [Pyloric atresia: a report of 3 cases]. *Arch Argent Pediatr*. 2014;112(5):e227–e230.
51. Sharony R, et al. Prenatal ultrasound diagnosis of gastric outlet obstruction due to a pyloric web. *Prenat Diagn*. 1995;15(1):56–59.
52. Tiao MM, et al. Antral web associated with distal antral hypertrophy and prepyloric stenosis mimicking hypertrophic pyloric stenosis. *World J Gastroenterol*. 2005;11(4):609–611.
53. Nam SH, et al. Congenital antral web in premature baby. *Pediatr Gastroenterol Hepatol Nutr*. 2013;16(1):49–52.
54. Medsinge A, et al. Isolated intramuscular fibrous band masquerading antral web in a premature neonate. A case report. *J Pediatr Surg*. 2012;47(8):e17–e19.
55. Bell MJ, et al. Antral diaphragm–a cause of gastric outlet obstruction in infants and children. *J Pediatr*. 1977;90(2):196–202.
56. Yu DC, et al. In utero diagnosis of congenital pyloric atresia in a single twin using MRI and ultrasound. *J Pediatr Surg*. 2009;44(11): e21–e24.
57. Bass J. Pyloric atresia associated with multiple intestinal atresias and immune difficiency. *J Pediatr Surg*. 2002;37(6):941–942.
58. Lui KW, et al. Antral web–a rare cause of vomiting in children. *Pediatr Surg Int*. 2000;16(5–6):424–425.
59. Hermanowicz A, Debek W. IMAGES IN CLINICAL MEDICINE. Single Bubble–Pyloric Atresia. *N Engl J Med*. 2015;373(9):863.
60. Pratap A, et al. Antral mucosal valve: a rare cause of gastric outlet obstruction in newborn. *J Pediatr Surg*. 2006;41(4):856–858.
61. Trifan A, et al. Gastric heterotopic pancreas: an unusual case and review of the literature. *J Gastrointestin Liver Dis*. 2012;21(2):209–212.
62. Kim DU, et al. Heterotopic pancreatic rests: imaging features, complications, and unifying concepts. *Abdom Radiol (NY)*. 2017;42(1):216–225.
63. Kim DW, et al. Heterotopic pancreas of the jejunum: associations between CT and pathology features. *Abdom Imaging*. 2015;40(1):38–45.
64. Fukuda A, et al. Ectopic pancreas formation in Hes1-knockout mice reveals plasticity of endodermal progenitors of the gut, bile duct, and pancreas. *J Clin Invest*. 2006;116(6):1484–1493.

65. Nijs E, Callahan MJ, Taylor GA. Disorders of the pediatric pancreas: imaging features. *Pediatr Radiol*. 2005;35(4):358–373, quiz 457.
66. Ogata H, et al. Heterotopic pancreas in children: review of the literature and report of 12 cases. *Pediatr Surg Int*. 2008;24(3):271–275.
67. Shanbhogue AK, et al. A clinical and radiologic review of uncommon types and causes of pancreatitis. *Radiographics*. 2009;29(4):1003–1026.
68. Kim JY, et al. Ectopic pancreas: CT findings with emphasis on differentiation from small gastrointestinal stromal tumor and leiomyoma. *Radiology*. 2009;252(1):92–100.
69. Cho JS, et al. Heterotopic pancreas in the stomach: CT findings. *Radiology*. 2000;217(1):139–144.

# 100 Hypertrophic Pyloric Stenosis

*Marta Hernanz-Schulman*

## OVERVIEW

Hypertrophic pyloric stenosis (HPS) is the most common urgent surgical entity affecting infants during the first 6 months of life.[1] Incorrectly assumed to be congenital by Hirschsprung in his seminal postmortem description in two patients,[2] empirical data indicate that pyloric stenosis is not present at birth; although some exceptions may exist, the symptoms and characteristic anatomic changes of pyloric stenosis typically present in infants between 3 and 12 weeks of age.[3–6] There are occasional case reports of the diagnosis of pyloric stenosis made earlier in life,[7] but they remain exceedingly rare.

The epidemiology varies with racial and geographic extraction, with an incidence of approximately 2–5/1000 births among children of European descent; however, among children of African American or Asian extraction, this decreases to approximately 0.7/1000 births. There is a familial predisposition that suggests a polygenic inheritance with greater penetrance in males. Among children of affected fathers, the risk is approximately 5% for sons and 2.5% for daughters, while among children of affected mothers, the corresponding risk is 20% for boys and 7% for daughters. Proband concordance in monozygotic twins is cited to be between 0.25 and 0.44, whereas that in dizygotic twins is reduced to between 0.05 and 0.10, very similar to that of nontwin siblings.[8] The incidence of pyloric stenosis is inversely proportional to birth order, with odds ratio to birth order cited as: 1, 2, 3, 4+, roughly equivalent to increased risk levels of 1.9, 1.5, 1.3, and 1.0, respectively.[8]

## ANATOMY

### Normal

The stomach is divided by the incisura angularis into a fundus and body proximally, and the antrum distally; the latter is further subdivided by the sulcus intermedius into a proximal pyloric vestibule, and a distal pyloric antrum or pyloric canal, which is approximately 2.5 cm in length, and terminates in the pyloric sphincter and orifice, which lead into the duodenum (Fig. 100.1A and B).[9]

### Abnormal

In infants with pyloric stenosis, the muscle of the pyloric antrum hypertrophies, is unable to relax, and the pyloric antrum is no longer distensible; the mucosa is edematous and thickened (Fig. 100.2A and B). This complex of nonrelaxing musculature and thickened mucosa resembles an "elongated" canal on imaging and presents an obstruction to gastric emptying.[4,10–12]

## ETIOLOGY

Although the diagnosis and surgical treatment of HPS have undergone a remarkable evolution over the last century, no fundamental leap has been made in elucidating its cause, which remains unknown. The final common pathway seems to be one of work hypertrophy of the circular muscle of the pyloric antrum, which becomes unable to relax; the mucosa becomes edematous and hypertrophied, sometimes markedly, rarely simulating a polypoid mass.[12–14]

Due to lack of an obvious etiologic agent or process, in a *cum hoc ergo propter hoc* reasoning, associated findings have long been linked to etiology. In the 18th and early 20th centuries, etiology was linked to associated paucity of omentum (likely due to emaciation) and to "higher development of the nervous system" in children of "intellectual classes" due to its more common occurrence and identification in children of northern European extraction and professional families,[15] connections that seem blatantly absurd to us in the 21st century. More recent scientific inquiry has centered on the hypertrophied muscle, which has been found to be also abnormal at the microscopic and biochemical level. The thickened muscle is depleted of inhibitory peptides such as vasoactive polypeptide; of synaptic vesicles, presynaptic terminals, and neural cell adhesion molecules; of markers for enteric glia; of interstitial cell of Cajal; and of nitric oxide synthase activity at the messenger RNA level. There are increases in insulin-like and platelet-derived growth factors. Immunoreactivity studies evaluating desmin content suggest immaturity of the intermediate filaments in the hypertrophied pyloric muscle.[16–26] Pathologic material in pyloric stenosis is thankfully no longer typically available, but older pathology reports are revealing of the histology of the abnormal pylorus, demonstrating that "varying degrees of submucosal edema are always present" typically with "a mild to moderate lymphocytic infiltrate in the submucosa and muscularis" (see Fig. 100.2B).[12] Today, this is substantiated on preoperative ultrasound (US) imaging, where the mucosa is seen to be thickened and edematous, and both muscle and mucosa are hyperemic when evaluated with color and spectral Doppler.[4,13] Prostaglandin E1 and E2 have been reported to induce proliferation of gastric mucosa[27] and are related to muscle contraction in the human gastrointestinal tract[20]; prostaglandin therapy has preceded the development of pyloric stenosis requiring surgery.[28] Prostaglandin E2 generation in the gastric mucosa and increased concentration in the gastric secretions of patients with pyloric stenosis have been reported.[29]

Genetic susceptibility loci have been identified, with cases mapped to loci on chromosomes 3p25.1, 5q35.2, 16q-24, 16p12-p13, and 11q14-q22, the latter affecting ion channels with a potential role in smooth muscle control and hypertrophy.[30–33] In patients with pyloric stenosis, simple nucleotide polymorphisms (SNPs) have been mapped to 3p25.1, 3p25.2, and 5q35.2, located in proximity to genes that control muscle and gut development. Differential activity levels in the early postnatal period suggest a parallelism in the development of HPS.[34,35] SNPs have also been mapped to 11q23.3, and associations with cholesterol metabolism have also been proposed.[36,37]

A hypothesis that a genetically influenced increased parietal cell mass leads to a vicious cycle of increased acid secretion, increased gastric contraction, and secondary development of muscular hypertrophy and mucosal redundancy with delayed gastric emptying has also been advanced.[38,39] This concept is supported by the redundant mucosa that fills the pyloric channel,[13,28,40,41] induction of HPS with infusion of pentagastrin,[42] and the rarity of HPS before the inception of feedings. Despite the extensive anatomic and biochemical changes documented in this condition, as early as 4 months after surgical relief of the obstruction, the anatomic changes as well as assays for nerve growth factor, interstitial cells of Cajal, and nitric oxide synthase activity revert to normal.[24,43]

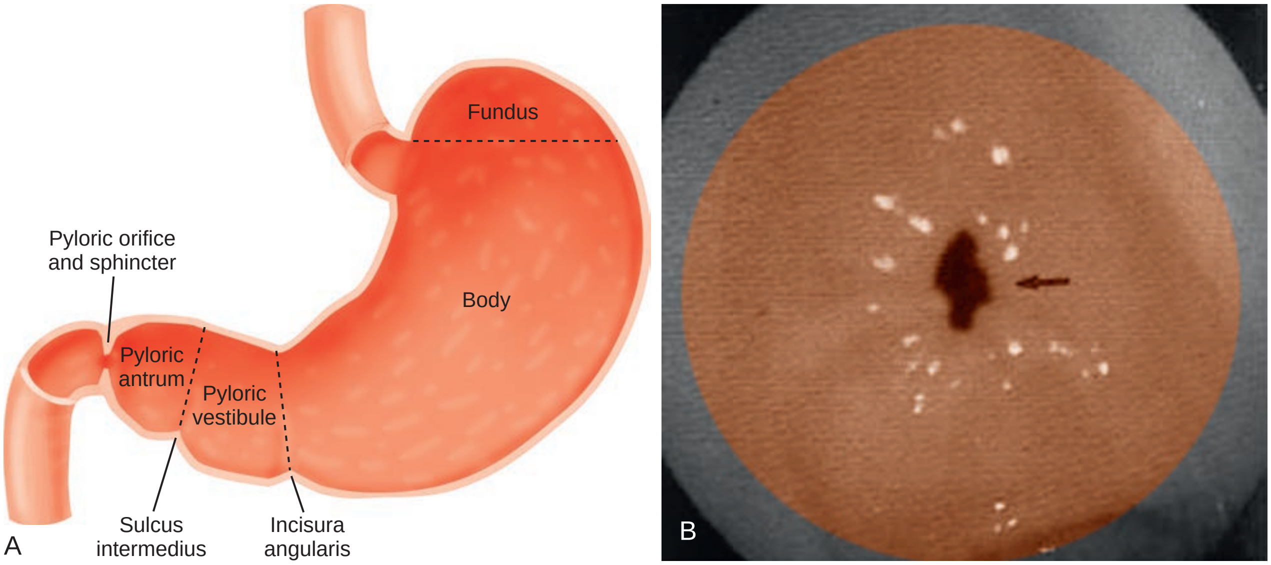

**Figure 100.1. Normal gastric and pyloric anatomy.** (A) Schematic illustration of gastric segmental anatomy. (B) Endoscopic appearance of the normal pyloric sphincteric orifice *(arrow)*.

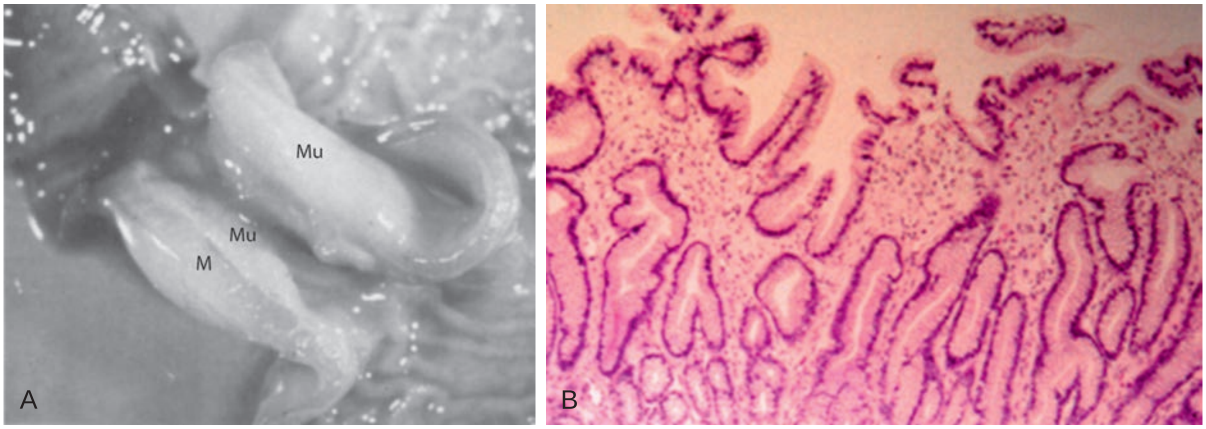

**Figure 100.2. Histopathologic anatomy in pyloric stenosis.** (A) Gross postmortem specimen of hypertrophied pylorus in an infant who succumbed to this condition. Note the thickened muscle *(M)* and the thickened mucosa *(Mu)* which would fill and obstruct the lumen of the unsectioned antropyloric canal. (B) Histologic specimen of antropyloric mucosa in infant with HPS with typical presentation, operative findings and postoperative recovery. The H&E (hematoxylin & eosin) stain shows mucosal hyperplasia with elongated, branched and mildly distorted pits, and abundant edematous lamina propria.

The macrolide antibiotic, erythromycin, is a prokinetic agent and has been associated with increased risk of developing HPS in some series, particularly when the infants are exposed very early in life, but further studies have determined that the link, if it exists, is weak and potential risk very small.[8]

As in the 19th century and despite our sophisticated tools, it remains difficult to extricate an initiating event from the multiplicity of associated abnormalities in this intriguing condition. The inciting event(s) of HPS remain obscure, and whether any or all of the multiple reversible abnormalities represent cause or effect of the initial condition remains a challenge for present and future investigators.

## CLINICAL PRESENTATION

Babies with HPS typically present with a history of forceful nonbilious vomiting, often described as "projectile." Although the color of the emesis may be yellow-tinged, if it is green, the differential shifts radically to malrotation and its emergent complication of midgut volvulus. In patients with HPS, vomiting may be relatively sudden in onset or be preceded by initially mild symptoms consistent with preexistent gastroesophageal reflux. Patients with long-standing HPS are voraciously hungry and may be sucking at their fists in a futile attempt to obtain nourishment. If the diagnosis is not made promptly, protracted vomiting and dehydration lead to a characteristic profile of electrolyte abnormalities, consisting of hypochloremic metabolic alkalosis secondary to the loss of hydrochloric acid from the stomach, with paradoxical aciduria, as renal mechanisms designed to maintain intravascular volume supervene to conserve sodium at the expense of hydrogen ion, which is excreted in the urine. Indirect hyperbilirubinemia may be found in a small minority of infants, secondary to decreased hepatic glucoronyl transferase activity induced by starvation. In patients who present after significant weight loss and are thin and dehydrated (thankfully few today), peristaltic waves may be seen on the wall of the scaphoid abdomen, progressing from the left upper quadrant across the epigastrium, flanked by a protuberant rib cage.[10] Fortunately, over the last several decades, the tendency has been for infants to present earlier, with less severe physical findings and laboratory abnormalities. Investigators have emphasized the changing pattern of presentation of infants with HPS, with a large majority of infants today diagnosed without evidence of metabolic abnormalities. The increased availability and diagnostic accuracy of US has been considered a factor in earlier diagnosis.[44–47]

## DIAGNOSIS AND IMAGING

### Physical Examination

Physical examination in experienced hands is often diagnostic by successfully palpating the *olive* or *pyloric tumor*, terms often used to designate the tactile detection of the olive-shaped thickened antropyloric muscle. This examination requires a calm infant and a committed and experienced examiner willing to dedicate 15 minutes or longer to the examination,[48] which may require decompression of the overdistended stomach via nasogastric tube.[49] If the muscle or "olive" is palpable, the examination is diagnostic. The sensitivity of abdominal palpation varies with the experience of the examiner, and ranges between 24% and 99%; specificity ranges between 92% and 99%.[49–53] False positives have been reported to be as high as 14% due to anatomic variants such as unusual extensions of the left lobe of the liver, and congenital abnormalities such as malrotation and duplication cysts; however, some of these reports do not specify the experience of the examiner.[54,55]

The diagnostic accuracy of US has generated a trend toward reliance on imaging rather than on physical examination and has led to a deterioration of the acumen of the clinical examination. In one retrospective study of two groups of patients separated by two decades, 212 evaluated between 1974 and 1977, and 187 patients between 1988 and 1991, investigators found that surgeons' success decreased from 99% to 79%; while that of nonsurgeons decreased from 47% to 33%.[52] In a series of 118 patients seen between 2006 and 2008, 100% of patients were evaluated with US, while the olive was palpated in only 13%.[45]

While the loss of clinical skills may be lamentable in some respects, and some have argued that imaging increases the financial cost of the workup of HPS, others have recognized that, despite "fading skills," the rapidity and accuracy of US diagnosis can result in "better patients," that is, better surgical candidates at the time of diagnosis.[44,45]

### Radiographic Studies

#### Plain Films

Plain films may strongly suggest the diagnosis, when revealing a markedly distended stomach, particularly if several peristaltic waves are seen, with little gas distally (Fig. 100.3),[56] although absence of these findings does not negate the diagnosis. In rare instances, HPS has been reported in association with isolated gastric pneumatosis that resolves after the stomach is decompressed (e-Fig. 100.4).[57]

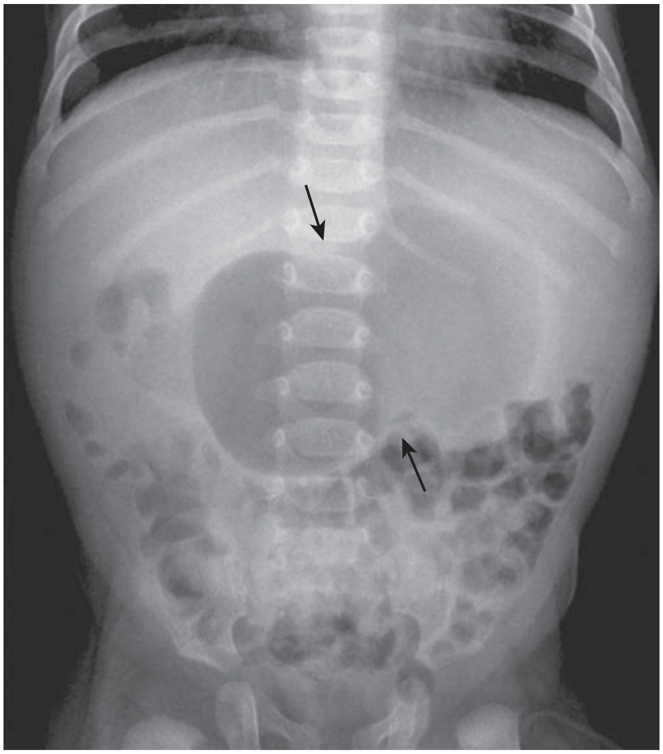

**Figure 100.3. Abdominal radiograph in infants with hypertrophic pyloric stenosis (HPS).** Abdominal radiograph demonstrates a distended stomach with a peristaltic wave *(arrow)*, with normal to mildly decreased distal gas. In the appropriate clinical setting, this is suggestive of pyloric stenosis.

#### Upper Gastrointestinal Series

The upper gastrointestinal (GI) as a diagnostic tool in patients with HPS was introduced in 1932 by Neuwissen and Sloof, with proponents such as Rigler in the United States.[58] In 1964, Currarino advocated double contrast examination with compression spots.[59] Before the advent of real-time US imaging, the upper GI series was the mainstay for imaging diagnosis and may still be utilized by radiologists with limited pediatric sonographic experience. If US shows a normal antropyloric canal, an upper GI may be performed to evaluate and document other potential causes of the patient's vomiting, such as reflux or more distal obstruction. Barium or a water-soluble agent may be used for oral contrast; if the latter, use a low-osmolality contrast medium approximating physiologic serum osmolality, as the child may vomit and aspiration may occur. To obtain a technically satisfactory contrast study, it may be necessary to decompress the stomach with an enteric tube, as a large amount of preexistent gastric contents will dilute the contrast medium and increase the chance of vomiting and aspiration during the examination. If the enteric tube is used, placing it distally and introducing the contrast with the patient in the prone right oblique position tends to require less contrast material to outline the gastric outlet. Because the diagnosis depends on passage of contrast through the abnormal, obstructed channel, fluoroscopic examination can be lengthy.

In addition to delay in the passage of contrast from the stomach, several other radiographic signs are present in infants with pyloric stenosis (Fig. 100.5). The antropyloric channel of the stomach is narrowed, and as contrast begins to enter the narrowed channel, it may appear as a "beak," which evolves into a "string" or a "double track" sign as contrast courses between the interstices of the thickened mucosa within the antropyloric lumen, compressed by the thickened, unrelaxing antropyloric muscle. The canal typically curves upward and posteriorly. The enlarged muscle mass encroaches upon the lumen of the antrum proximally, resulting in the "shoulder sign." When the duodenal base is also deformed by the thickened muscle, the appearance may resemble an "apple core" lesion. The "pyloric tit" can occasionally be seen along the lesser curve just proximal to the impression of the pyloric mass; it represents contrast trapped within the lumen of the stomach, compressed between a peristaltic wave and the impression of the pyloric muscle upon the adjacent more distal portion of the stomach. Antropyloric contraction during peristalsis or "pylorospasm" can transiently mimic the findings in HPS; therefore the study should document the persistence of the abnormal findings to establish the diagnosis.

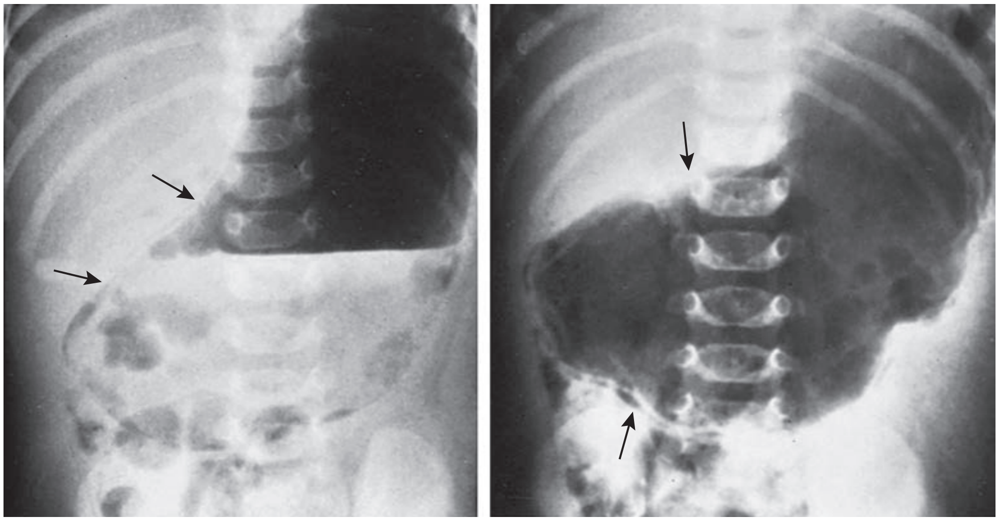

**e-Figure 100.4.** Gastric pneumatosis in an infant with hypertrophic pyloric stenosis (HPS). Supine abdominal radiograph in a 6-week-old girl with HPS shows a markedly dilated stomach with several peristaltic waves and decreased distal gas. There is intramural gas *(arrows)* which resolved within 24 hours after decompression with gastric intubation. *(Courtesy Dr. J. Leonidas, New Hyde Park, NY.)*

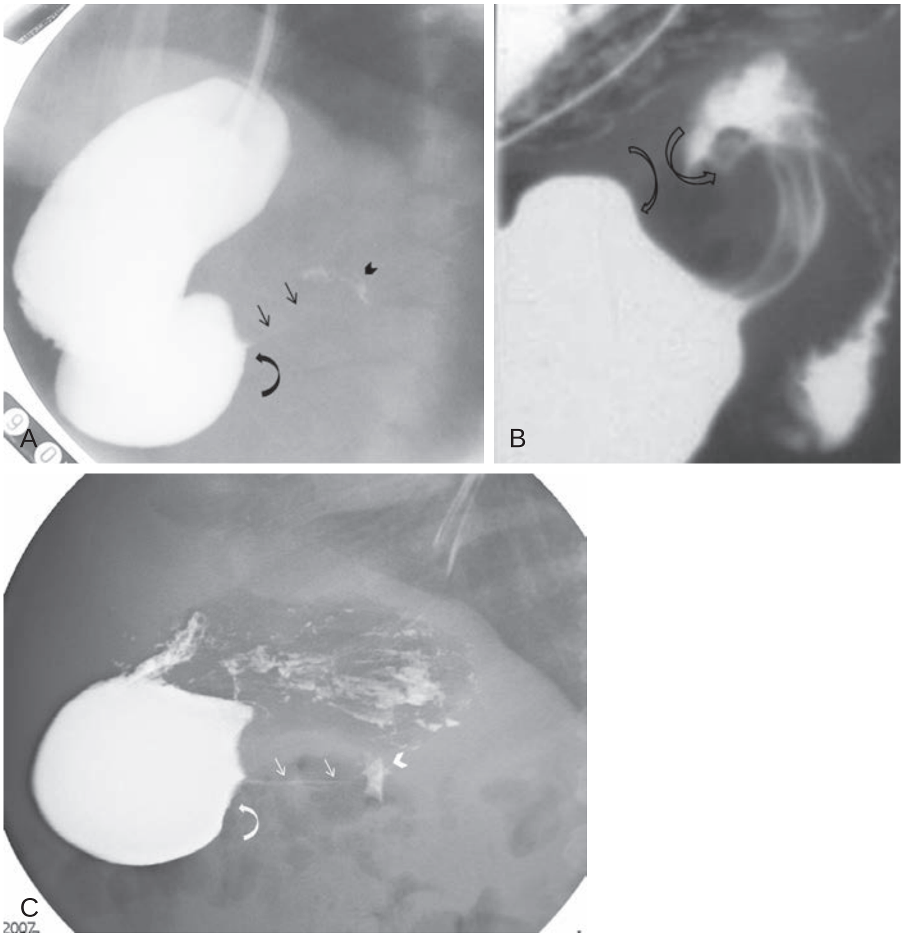

**Figure 100.5. Upper gastrointestinal imaging series in patients with hypertrophic pyloric stenosis (HPS).** (A) Orogastric tube was used to evacuate the stomach, and barium was instilled under fluoroscopic control. The image demonstrates a peristaltic wave and a small amount of contrast entering the narrowed canal, demonstrating both a beak *(curved arrow)* and string sign *(straight arrows)*. *Arrowhead* points to a small amount of contrast outlining the base of the duodenal bulb. (B) Oblique radiograph in another infant with HPS shows mass impression upon the proximal antrum and the distal duodenal base (*curved arrows* "shoulder signs"). The pyloric canal curves upwardly and posteriorly. Note the filling defect within the canal secondary to the hypertrophied mucosa, and the contrast tracks between the mucosal interstices, giving rise to what is termed the *double track sign;* there is a third linear track distally in the canal. (C) Oblique radiograph in another infant with HPS outlines deep shoulders on the gastric antrum *(curved arrow)* and a thin string sign *(arrows)*. The *arrowhead* points to the base of the duodenal bulb.

## Ultrasonography

The initial and seminal report of US as a diagnostic modality in infants with HPS was that of Teele and Smith, reported in the *New England Journal of Medicine* in 1977.[60] Since that time, US has become the modality of choice in the diagnosis of pyloric stenosis in most pediatric centers and is now considered the "gold standard" by many.[10,45,49] Similar to the clinical examination by manual palpation, the operator-dependent US examination requires a skilled and experienced examiner. Unlike the clinical examination, the US diagnosis can be performed quickly even on a crying infant, without the need to pass a gastric tube to empty the stomach or any other such relatively invasive and time-consuming maneuvers. Unlike the upper GI, the US examination does not require contrast to traverse the obstructed canal for diagnosis; again allowing for a rapid diagnosis, without the need of additional distension of the stomach, and without radiation exposure to the infant.

*Performance of the examination:* The examination is typically performed with linear transducers operating at a frequency of 7.5 MHz or higher. The time of the last feeding may be annotated on the image, and the degree of gastric distension related to the last feeding can give an initial clue as to the presence or absence of gastric outlet obstruction.

The examination is begun with the patient in the supine position. The transducer is placed in transverse position over the gastroesophageal junction, which is constant in location anterior to the aortic hiatus; the transducer is then swept along the length of the stomach, until the distal antrum and duodenal cap are identified; once the duodenal bulb is identified, the immediately proximal antropyloric canal can be evaluated for morphology and relaxation, thus identifying either pyloric stenosis or a normal antropyloric canal (Videos 100.1 and 100.2). The gallbladder and right kidney are typically, but not always, seen near the antropyloric canal, as the location of the antropyloric canal will vary with the degree of gastric distension.

*Criteria and dimensions:* Much emphasis has been placed on the measurements used to diagnose pyloric stenosis. Certainly, these are helpful and necessary but cannot be used in a vacuum without understanding of the underlying anatomy.

The report by Teele and Smith considered pyloric diameter as the major size criterion, likely due to the inability to resolve the internal anatomy of the abnormal pyloric complex by the poor detail depicted by the US equipment at the time. Muscle thickness became more important in subsequent reports with real-time capability; mucosal hypertrophy within the abnormal canal and increased flow on Doppler interrogation were also recognized in parallel with advances in equipment design and imaging detail.

Multiple studies have provided data to determine the normal and abnormal values. A 1986 prospective study of 200 infants[55] found a mean muscle thickness of 3.4 mm (range 3–5 mm), and a mean pyloric length of 22.3 mm (range 18–28 mm); despite the relative limitations of the US equipment of the day, the investigators were able to discriminate between normal and abnormal patients with 100% success rate. A study of 323 patients[61] found a mean muscle thickness was 4.8 mm (range 3.5–6 mm) and mean pyloric length 17.8 mm (range 11–25 mm); muscle thickness was found to be the most helpful discriminant, with an accuracy of 99.4%. In a 1991 series reporting on 145 consecutive patients,[5] a muscle thickness of 3 mm or greater was determined to be diagnostic of HPS, with muscle thickness <1.5 mm in 98% of normal patients. These results were validated in the series published by Hernanz-Schulman et al.[62] reporting on 152 infants with nonpalpable olives evaluated with sonography, in whom a maintained muscle thickness of 3 mm or greater was diagnostic of HPS, with no false positive examinations.

In younger and previously premature infants, there is a tendency for pyloric measurements to be smaller than in full-term, older infants at presentation.[62,63] In a more recent review of these patients, investigators found significant associations between pyloric dimensions and patient age and weight; however, these changes did not affect the existing diagnostic criteria for HPS, as a muscle thickness of ≥3 mm, and length ≥15 mm are diagnostic in all patient groups.[64]

The thicker the muscle and the longer the length of abnormal antropyloric muscle, the faster and more certain the diagnosis; however, literature and experience indicate that a *persistent* muscle thickness of 3 mm or greater along with a nonrelaxing antropyloric length of 11 to 14 mm or greater is diagnostic of pyloric stenosis. However, *persistence* is key, as a transient appearance of pyloric stenosis can occur in many normal patients (see the following text).

*Normal and abnormal pylorus:* The normal antropyloric channel has a sonographic appearance similar to that at upper GI, with relaxed, open lumen directly adjacent to the duodenal bulb via the pyloric orifice (Fig. 100.6).

The abnormal antropyloric canal, on the other hand, shows thickening of the muscle and mucosa to variable degrees. The mucosa can be markedly thickened in many patients, and may be mistaken for a polyp (Fig. 100.7). The length of the hypertrophied canal is variable, ranging from as little as 14 mm to greater than 20 mm. The lower limit of muscle thickness is 3 mm, a value that

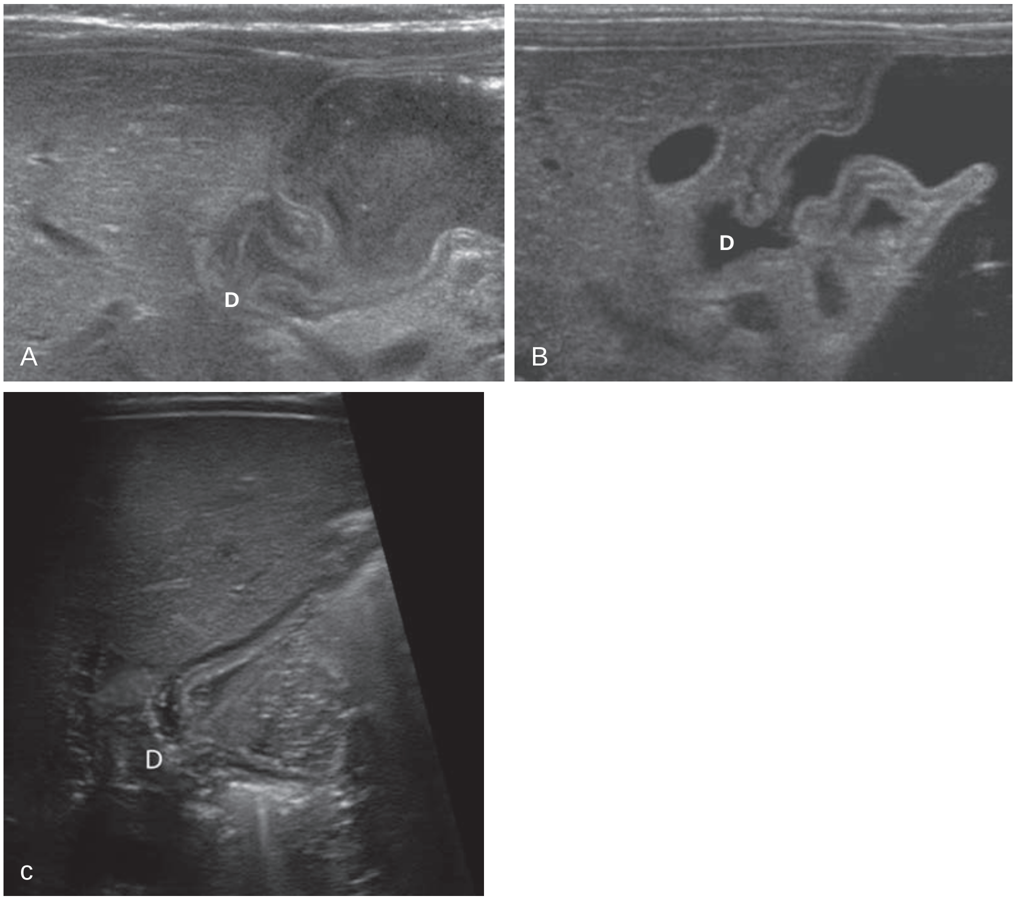

**Figure 100.6. Normal antropyloric canal in two infants.** (A) The stomach is filled with formula. Note that the antropyloric muscle is mildly thickened, but the mucosa is normal, and the antropyloric canal is distensible and filled with gastric contents. *D*, Duodenal bulb. (B) The stomach is filled with Pedialyte. Again, the antropyloric muscle is mildly thickened, but the lumen is distensible and filled with gastric contents. *D*, Duodenal bulb. (C) The antropyloric portion of the stomach is widely open, muscle layer is uniform and normal. *D*, Duodenal bulb.

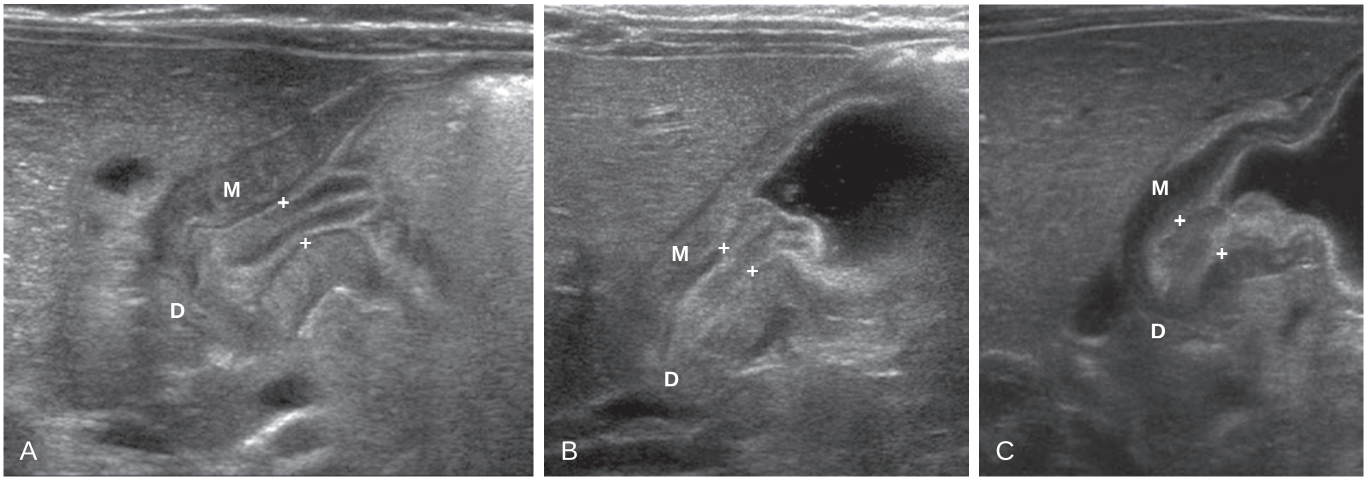

**Figure 100.7. Hypertrophic pyloric stenosis (HPS) in three infants.** (A) Abnormal pylorus in infant with HPS shows double layer of edematous mucosa (*between crosshairs*) sandwiched within the thickened muscle *(M)*, protruding into the gas and formula-filled antrum as the "nipple sign." *D*, Duodenal bulb. (B) Abnormal pylorus in another infant shows thickened muscle *(M)* and mucosa *(between crosshairs)* with protrusion into the proximal antrum. *D*, Duodenal bulb. Note the marked redundancy and prominence of the antropyloric mucosa, resembling a "polyp." (C) Another infant with progressive vomiting and poor weight gain. The muscle *(M)* is thickened to >3 mm, the mucosa *(between crosshairs)* measured 8 mm in thickness, protruding proximally into the fluid-filled antrum. *D,* Duodenal bulb. Again, notice the marked redundancy and prominence of the antropyloric mucosa, protruding into the antrum; it is easy to see how on endoscopy this could be mistaken for a "polyp."

is diagnostic if persistent without evidence of relaxation of the antropyloric canal throughout the examination.[10] Similar to Cohen et al.,[65] we emphasize that increased but transient contractions of the pylorus, or pylorospasm, may mimic pyloric stenosis in both appearance and measurement if the examination is performed quickly (Fig. 100.8A and B; e-Fig. 100.8C and D; Video 100.3). Evaluation of the antropyloric portion of the stomach over a period of time is important to confirm the diagnosis.

The muscle and mucosa typically show abundant flow as seen on color and spectral Doppler interrogation, although this is not a diagnostic criterion, but merely an associated finding in most patients (Fig. 100.9A; e-Fig. 100.9B and C). Although the patient might not have been fed for hours, the stomach is typically distended. It is important to realize that despite the lack of relaxation of the abnormal antropyloric canal, some gastric contents will pass through in many patients; HPS is not a complete obstruction, the fact on which diagnosis by upper GI is obviously based (e-Fig. 100.10; Video 100.4). In some patients, the muscle is very active, and visible contractions temporarily shorten and thicken, and lengthen and thin, the pyloric muscle; the appearance suggests that more proximal muscle, which has not lost its ability to relax and return to normal, is being actively recruited; this is an intriguing finding when considering the development and etiology of pyloric stenosis (Fig. 100.11; Video 100.5).

## Pitfalls

The normal pylorus might be difficult to visualize because of excessive amount of overlying bowel gas. In such cases, it is helpful to use the left lobe of the liver as an acoustic window, and angle inferiorly to identify the pylorus.

*False positives:* If the stomach is empty, or if the child lies supine such that the antrum is empty, or if there is active peristalsis, as noted earlier, the normal antropyloric canal may be mistaken for pyloric stenosis, particularly if the operator is inexperienced. First, if the stomach is empty, the child is unlikely to have HPS. However, exclusion of pyloric stenosis relies on demonstration of a normal antropyloric canal. If there is some fluid within the stomach, the child may be turned right side down, directing the fluid from the fundus into the antrum (Fig. 100.12A and B). If the stomach is empty, the child may be given a clear fluid, such as Pedialyte or glucose water; this will not only improve the ability to identify the pylorus and duodenal bulb, but will also allow definitive documentation of the normal anatomy (Fig. 100.12C and D).[10,62,66]

*False negatives:* In patients with HPS, the pylorus may be difficult to identify because a very distended stomach displaces it posterior to the antrum; this is also the cause of one of the false negative pitfalls in palpation (e-Fig. 100.13A). Some investigators have advocated emptying the stomach with a nasogastric catheter[67]; however, we prefer to turn the supine infant toward his/her left side, thus displacing the bulk of the fluid toward the fundus and away from the antrum, allowing the hypertrophied pylorus to rise anteriorly for optimal evaluation (e-Fig. 100.13B).

*Equivocal examinations:* Equivocal examinations are rare, but they occur when, after sufficient observation, the muscle measures between 2 and 3 mm in thickness. In such cases, the patient may be developing HPS, and follow-up examination is indicated if vomiting is unabated. It must be realized that neither the inciting event nor the time course for the development of HPS are known; the important point is to recognize that, although these patients do not have HPS, they are not entirely normal, and follow-up is needed if vomiting continues.[5,6,11]

## DIFFERENTIAL DIAGNOSIS

Other entities that can mimic HPS on sonographic examination are antropyloric gastritis, with or without ulcer disease, and chronic granulomatous disease of childhood; however, these conditions present at a later age, and do not typically present a clinical uncertainty.

The most common antropyloric abnormality mimicking HPS on upper GI series is pylorospasm. Although spasm may also cause the pyloric muscle to appear thicker on US, this is a transient phenomenon usually distinguishable from pyloric stenosis or which may necessitate a follow-up examination, as previously discussed under equivocal examinations. Focal foveolar hyperplasia, or

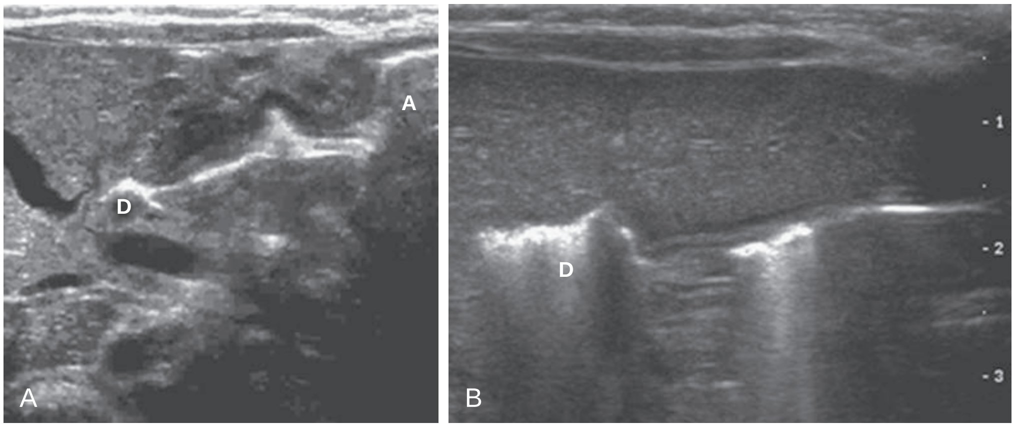

**e-Figure 100.10. Air passing through both abnormal and normal pyloric canal (see** Video 100.4**).** (A) A 3-week-old boy with pyloric stenosis. Hyperechoic air is seen along the anterior wall of the gastric antrum *(A)* and continues through the hypertrophied antropyloric canal into the duodenal cap. This was observed on real-time. *D*, Duodenal bulb. (B) A 4-week-old boy with normal pylorus also shows hyperechoic gas moving through the nearly empty but normal antropyloric canal, into the duodenal bulb. *D*, Duodenal bulb.

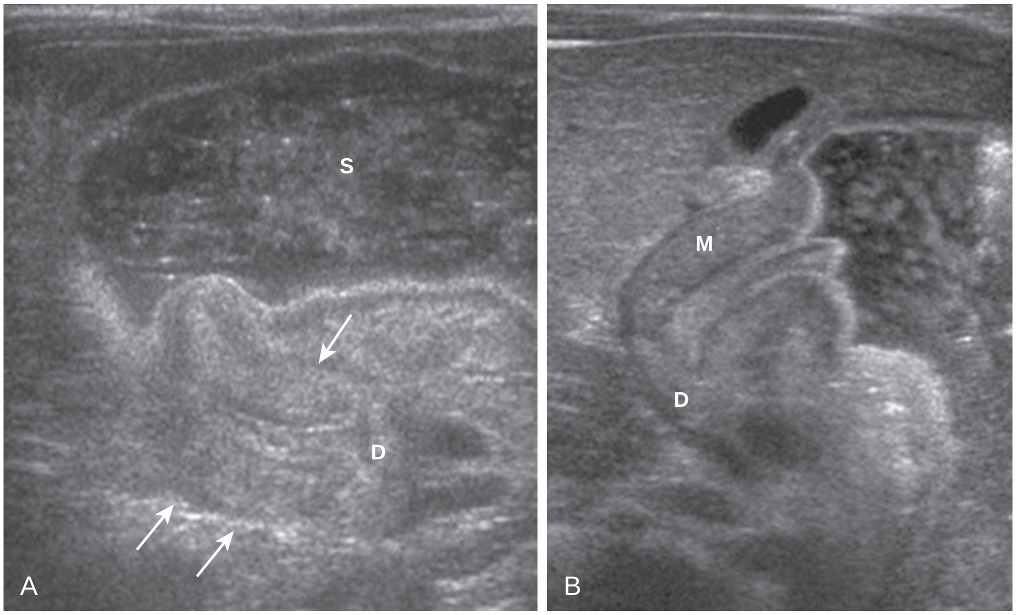

**e-Figure 100.13. Pitfall when scanning an overdistended stomach in infant with hypertrophic pyloric stenosis (HPS).** (A) Image of the overdistended distal stomach in an infant with HPS shows the hypertrophied pylorus *(arrows)* folded behind the stomach *(S)*. *D*, Duodenal bulb. (B) When the infant is turned towards a left posterior oblique position, the hypertrophied pylorus is allowed to rise anteriorly, and is much more easily detected and detailed. Note the nipple sign as the pyloric mucosa protrudes into the fluid-filled antrum. *M*, Muscle; *D*, duodenal bulb.

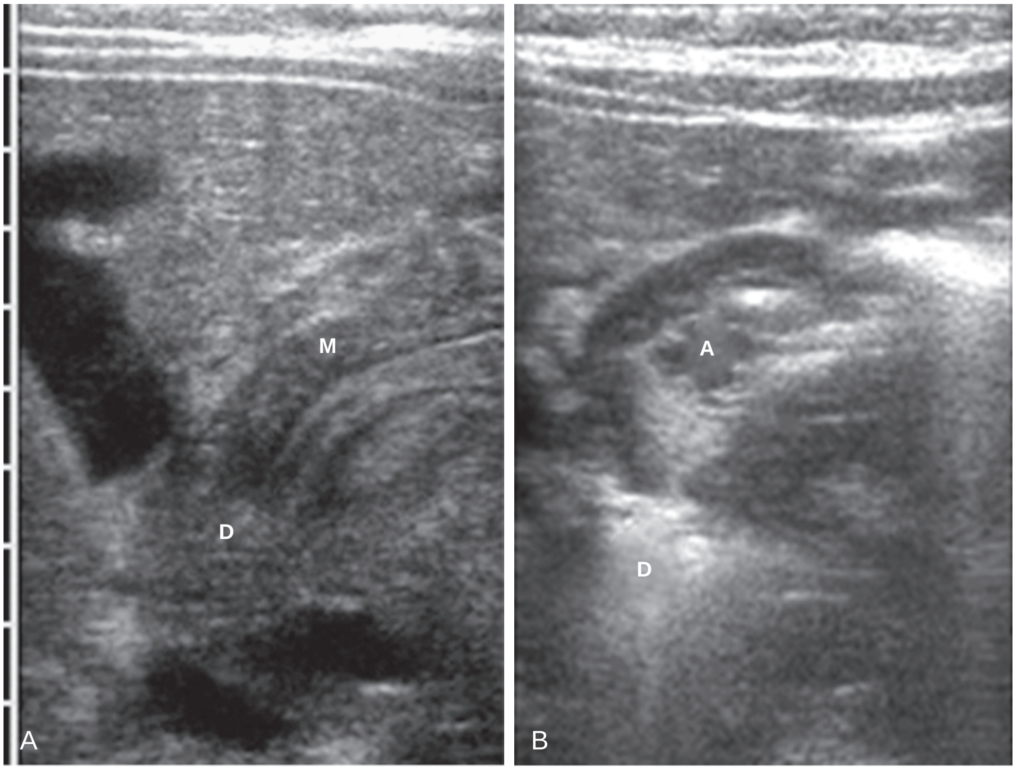

**Figure 100.8. Transient ultrasound findings (see** Video 100.3**).** (A) Antropyloric channel in infant with vomiting, shows narrowing with thickened muscle which measured up to 4 mm in thickness. *M*, Muscle; *D*, duodenal bulb. (B) Antropyloric channel in same infant as depicted in (A), 4 minutes later. The canal is open. *A*, Open antropyloric canal; *D*, duodenal bulb.

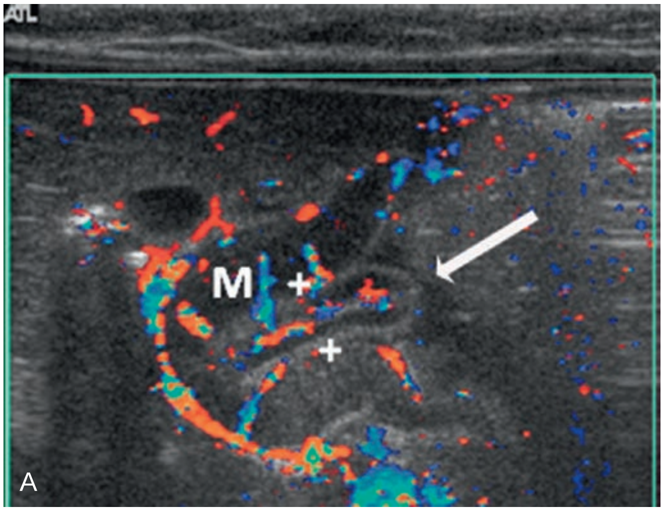

**Figure 100.9.** (A) Color Doppler image of antropyloric canal in infant with HPS. Note flow within the hypertrophied muscle *(M)* and mucosa (between crosshairs). Also note the antral nipple sign *(arrow)*.

polypoid mucosa in the antropyloric portion of the stomach, is usually associated with a history of congenital heart disease and prostaglandin therapy, and resembles the thickened mucosa that is seen in patients with HPS. The lobulated mucosal mass has been reported as causing gastric outlet obstruction and has developed into full-fledged HPS in some cases.[27,28,68]

## DIAGNOSTIC ALGORITHM

Palpation of the pyloric mass is the first diagnostic examination by the physician to whom the child presents. In further evaluation and referral, consideration can be given to the investment of time and relative invasiveness of inserting an orogastric tube to evacuate the stomach. The choice is to make a direct referral to the surgeon for additional palpation or to the radiologist for a diagnostic imaging examination. The cost and time delay of obtaining a surgical consultation/clinic visit versus the cost and time delay to obtain an imaging examination are obvious considerations, and these circumstances may differ across geographical venues and clinical practices. If the pyloric mass is palpated by the surgeon, no diagnostic imaging is necessary; if it cannot be palpated by the surgeon, again consideration falls upon a diagnostic imaging examination. Waiting and re-examining the patient with prolongation of inpatient care is likely not cost-effective in most settings and may lead to delay in diagnosis and treatment. We do not advocate, as has been suggested in the past, sedating an infant at high risk for vomiting to increase sensitivity in palpating the pyloric mass.[50] Trial feeds have been advocated as well, with reported negative exploratory rates ranging between 1% and 4%.[69]

Some investigators have advocated the upper GI series as the first examination in patients with symptoms of HPS for two reasons: although US in experienced hands is extremely accurate in the diagnosis of HPS, it will not always be diagnostic in infants with vomiting from other causes. An upper GI series is deemed by some to be more cost-effective as the first imaging examination compared with US, as a follow-up upper GI may be requested in patients with normal US, increasing the monetary cost of diagnosis.[53,70] However, US is more informative than upper GI, as it

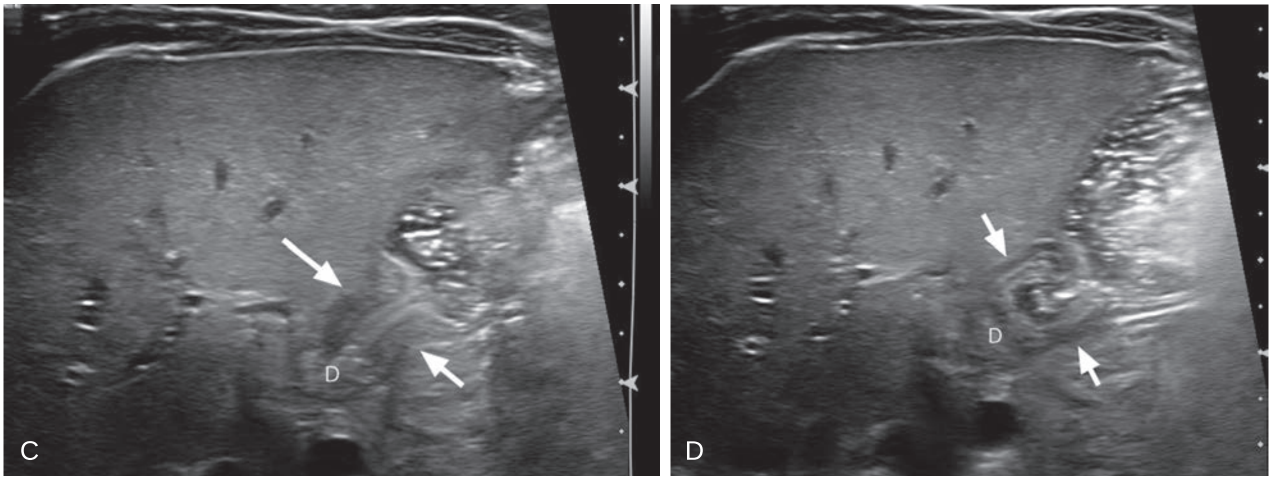

**e-Figure 100.8.** (C) Antropyloric channel in another infant with vomiting, shows narrowing with thickened muscle which measured up to 3.5 mm in thickness. *Arrows* point to the antropyloric muscle, *D*, Duodenal bulb. (D) Antropyloric channel in same infant as depicted in (C), 10 seconds apart. The canal is open *(arrows)*. *D*, Duodenal bulb.

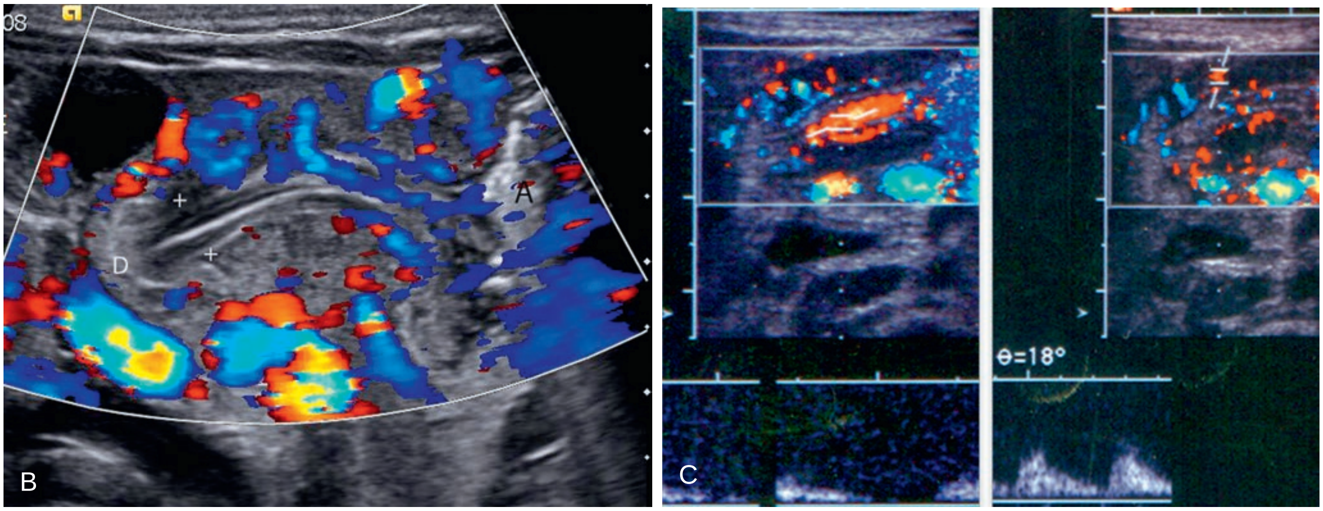

**e-Figure 100.9.** (B) Color Doppler image of antropyloric canal in another infant with hypertrophic pyloric stenosis (HPS). Note flow within muscle and mucosa. *A*, Antrum; *D*, duodenum, crosshairs outline the more distal mucosa. (C) Spectral evaluation of color flow in antropyloric canal of another infant demonstrates flow waveform spectra in mucosa *(left)* and muscle *(right)*.

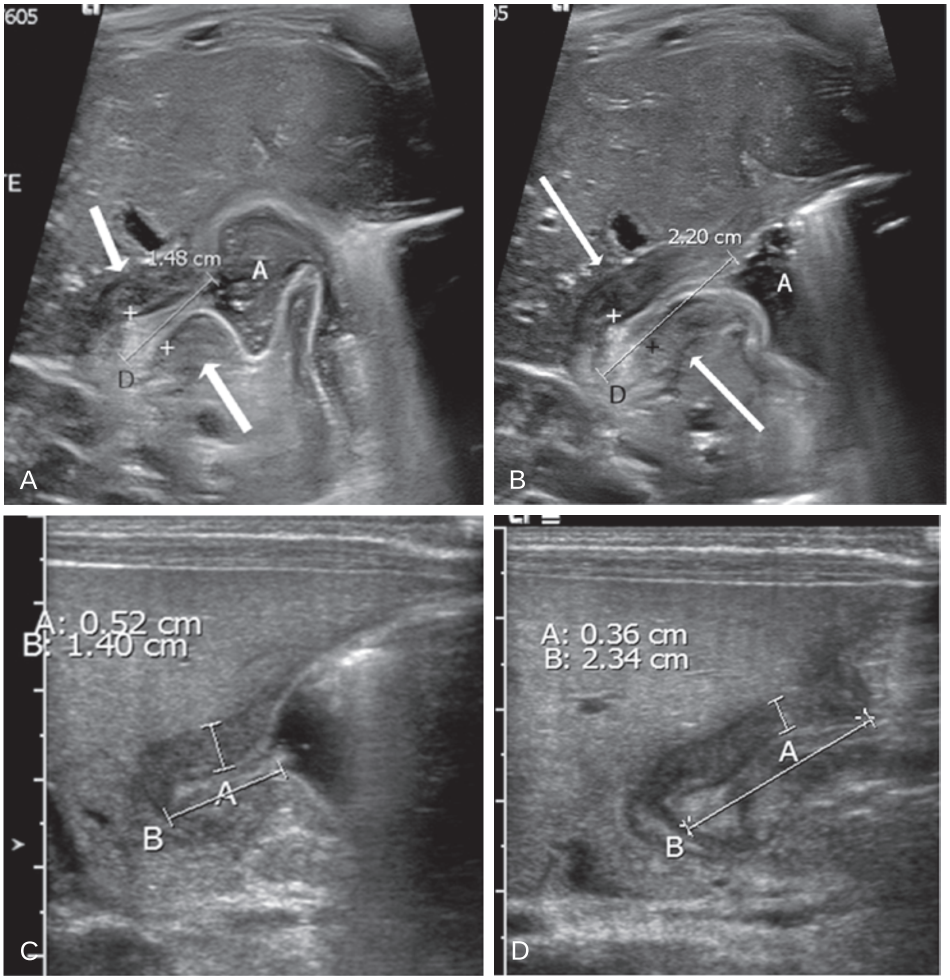

**Figure 100.11. Changing dimensions.** (A) Infant with HPS. Longitudinal image of antropyloric canal shows a thickened muscle, with relatively short abnormal canal, measuring 14.8 mm. *D*, duodenal bulb. Crosshairs define mucosa within canal, arrows point to the muscle complex. (B) Same patient 5 seconds later, shows lengthening of the abnormal canal now measuring 22 mm. *D*, duodenal bulb. Crosshairs define mucosa within canal, arrows point to the muscle complex. (C) A 4-week-old boy with HPS. Longitudinal image of antropyloric canal shows a thickened muscle *(between calipers, A)* measuring approximately 5.2 mm, and a relatively short canal *(between calipers, B)*, measuring 14 mm. *B* marking the longitudinal calipers overlies the duodenal bulb. (D) Same patient as in (C), 2 minutes later, shows a thinner muscle *(between calipers, A)* measuring approximately 3.6 mm, and a longer canal *(between calipers, B)*, measuring 23.4 mm. *B* marking the longitudinal calipers overlies the duodenal bulb.

is able to image beyond the lumen of the pylorus and assess the thickness of the muscle while posing no need to distend the stomach by addition of contrast media. More importantly, as we adopt the as low as reasonably achievable (ALARA) approach as outlined by The Image Gently Alliance, we believe that US should be the first examination in patients suspected of HPS in whom imaging is indicated, particularly pertinent in these young infants in whom fluoroscopy could be prolonged.[10,62,71] If the US shows that the pylorus is normal, vomiting is clearly nonbilious, and the duodenum is normal in caliber, the likelihood is high that the cause of vomiting is reflux, which could be initially treated empirically or documented with scintigraphy (e-Fig. 100.14).

## TREATMENT

Introduced by Ramstedt in 1912, surgical pyloromyotomy via a right upper quadrant or semicircumbilical incision is the traditional therapy for infants with HPS. In this procedure, the muscle is incised, and the mucosa is allowed to protrude through the incision without resuturing (Fig. 100.15).

*Medical therapy:* Several publications have redirected attention to medical therapy, which is based on the theory that muscle spasm is a contributing factor to the muscular hypertrophy and obstruction. In a prospective trial of infants treated with surgical or medical therapy, medical therapy was successful in 85% of cases, with 2/14 requiring pyloromyotomy; mean time to full feeds was 2.7 days in the surgical group, and 5.3 days in the medically treated group.[72] In a larger prospective trial including 52 medically treated infants, there was an 87% success rate; mean hospital stay was 5 days in the surgical group and 13 days in the successfully medically treated group.[73] A subsequently published trial reported a 75% success rate of medical therapy, although the prolonged resolution of symptoms resulted in some of the parents in the medical treatment group opting for surgery before completion of medical treatment.[74] A more recent 2013 investigation on 180 medically treated infants compared with 397 surgical patients reported a 79% success rate

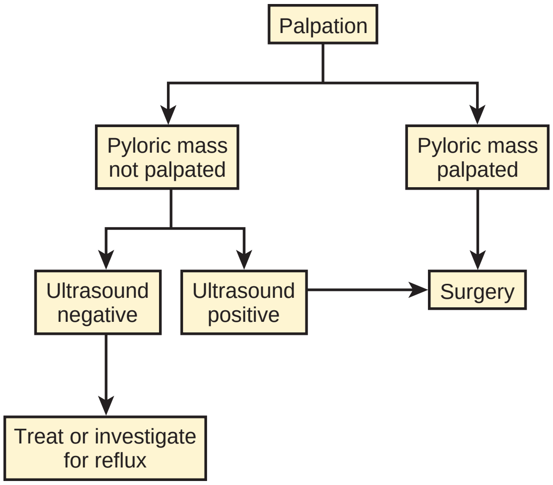

**e-Figure 100.14.** Diagnostic algorithm for infants suspected of having HPS.

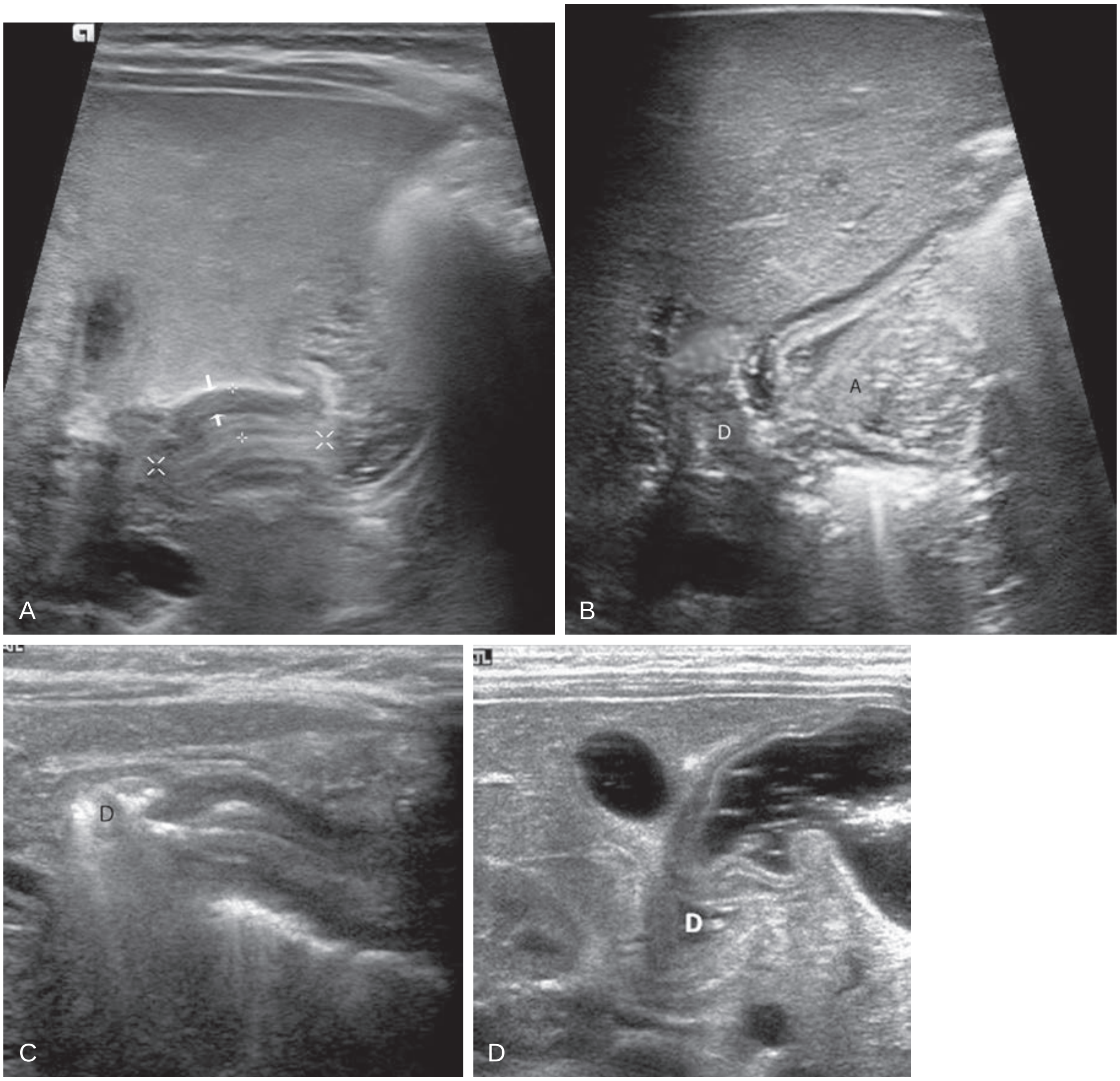

**Figure 100.12. Empty antrum mimicking HPS.** (A) A 2-month-old normal infant. With the child supine with a nondistended stomach, the empty antrum suggests HPS, with a muscle thickness measured at 4.9 mm and a length measured at 17 mm. However, please note that the muscle measurement is incorrectly placed, and includes the mucosa within the antral lumen; when the muscle alone was measured *(between white arrows)*, it measured 2 mm. (B) Same infant as in (A), a few minutes later. Turning the infant right side down, redirecting the gastric fluid into the antrum, shows normal distension of the antropyloric portion of the stomach and normal anatomy. *A,* Antrum; *D,* duodenum. (C) 8-week-old girl with vomiting. The stomach was initially empty, which is initial evidence against the presence of HPS in most infants. However, the collapsed distal antropyloric canal appears "elongated" thus mimicking some of the findings in pyloric stenosis. The muscle measured between 1.7 and 2.8 mm. *D*, Duodenum. (D) Same infant as in (C). After drinking Pedialyte ad lib, the antrum distends with a completely normal appearance. *D*, Duodenal bulb.

for the atropine group over a period of 8 days of therapy;[75] a second report found that continued projectile vomiting for greater than 3 days after medical therapy was predictive of failure and the need to convert to pyloromyotomy.[76]

*Laparoscopic pyloromyotomy:* Reported in 1991 by Alain et al.,[77] laparoscopic pyloromyotomy has been advocated recently by pediatric surgeons. Meta-analyses and prospective trials suggested that mucosal perforation might be more problematic with laparoscopy, but that wound infection appeared to be slightly less frequent. Data to date suggest that, once the learning curve for the laparoscopic approach is mastered, there is little difference in the overall outcome between these two procedures, with some prospective studies suggesting that the laparoscopic group shows less postoperative emesis and requires less postoperative analgesia, with improved cosmetic results as well.[78–84] A 2014 meta-analysis involving 1802 laparoscopic and 1028 open procedures found a very small although statistically significant higher incidence of incomplete pyloromyotomies in the laparoscopic group, although the adjusted difference was only 0.87%, raising the question of whether the difference is clinically relevant.[85]

Balloon dilatation has been attempted unsuccessfully in a limited number of patients; however, a potential role after failed pyloromyotomy or recurrent pyloric stenosis has been investigated with partial success in a very limited number of patients.[86–88]

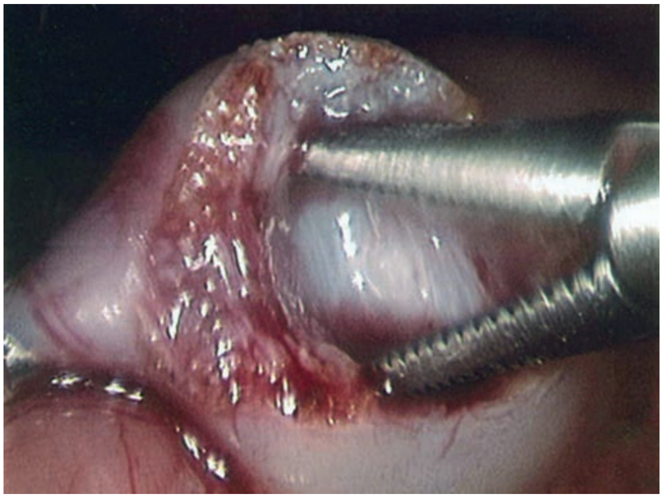

**Figure 100.15.** Intraoperative photograph of muscle-splitting Ramstedt pyloromyotomy. *(Courtesy of Dr. Robert Cywes.)*

## KEY POINTS

Radiographic findings on upper GI in HPS may include the following:

- Gastric distension and visible peristaltic waves on radiograph
- Narrowed, elongated, curved pyloric channel
- Beak sign
- String or double tract sign
- Shoulder sign
- "Pyloric tit" on lesser curve

Ultrasound findings in HPS include the following:

- Retained gastric contents
- Thickened, nonrelaxing antropyloric muscle measuring ≥3 mm
- Length of the abnormal channel typically ≥15 to 20 mm
- Redundant mucosa measuring similar or greater than muscle thickness
- Increased Doppler flow signal of mucosa and/or muscular layer

## SUGGESTED READINGS

Cohen HL, et al. Ultrasonography of pylorospasm: findings may simulate hypertrophic pyloric stenosis. *J Ultrasound Med*. 1998;17(11):705–711.

Dassinger M, Fuchs GJ. Infantile hypertrophic pyloric stenosis: closing in on the cause. *J Pediatr Gastroenterol Nutr*. 2014;58(5):545.

Hernanz-Schulman M. Infantile hypertrophic pyloric stenosis. *Radiology*. 2003;227(2):319–331.

## REFERENCES

Full references for this chapter can be found on www.expertconsult.com.

## REFERENCES

1. Oue T, Puri P. Smooth muscle cell hypertrophy versus hyperplasia in infantile hypertrophic pyloric stenosis. *Pediatr Res*. 1999;45(6):853–857.
2. Hirschsprung H. Falle von angeborener pylorusstenose, beobachtet bei Sauglingen. *Jahrb D. Kinderh*. 1888;27:61–68.
3. Rollins MD, et al. Pyloric stenosis: congenital or acquired? *Arch Dis Child*. 1989;64(1):138–139.
4. Hernanz-Schulman M, et al. Hypertrophic pyloric stenosis in infants: US evaluation of vascularity of the pyloric canal. *Radiology*. 2003;229(2):389–393.
5. O'Keeffe FN, et al. Antropyloric muscle thickness at US in infants: what is normal? *Radiology*. 1991;178(3):827–830.
6. Keckler SJ, et al. The progressive development of pyloric stenosis: a role for repeat ultrasound. *Eur J Pediatr Surg*. 2008;18(3):168–170.
7. Zenn MR, Redo SF. Hypertrophic pyloric stenosis in the newborn. *J Pediatr Surg*. 1993;28(12):1577–1578.
8. MacMahon B. The continuing enigma of pyloric stenosis of infancy: a review. *Epidemiology*. 2006;17(2):195–201.
9. Gray H. The digestive system. In: Goss C, ed. *Anatomy of the Human Body*. Philadelphia, PA: Lea & Febiger; 1973:1220.
10. Hernanz-Schulman M. Infantile hypertrophic pyloric stenosis. *Radiology*. 2003;227(2):319–331.
11. Hernanz-Schulman M, et al. Hypertrophied pyloric mucosa in patients with hypertrophic pyloric stenosis. *Pediatr Radiol*. 1998;28(11):901.
12. Kissane J. Stomach and Duodenum. In: *Pathology of Infancy and Childhood*. St. Louis: The C.V.Mosby Company; 1975:175–178.
13. Hernanz-Schulman M, et al. In vivo visualization of pyloric mucosal hypertrophy in infants with hypertrophic pyloric stenosis: is there an etiologic role? *AJR Am J Roentgenol*. 2001;177(4):843–848.
14. Markowitz RI, et al. Infantile hypertrophic pyloric stenosis–congenital or acquired? *J Clin Gastroenterol*. 1982;4(1):39–44.
15. Mack H. A history of hypertrophic pyloric stenosis and its treatment. *Bull Hist Med*. 1942;XII(3):465–689.
16. Kobayashi H, O'Briain DS, Puri P. Immunochemical characterization of neural cell adhesion molecule (NCAM), nitric oxide synthase, and neurofilament protein expression in pyloric muscle of patients with pyloric stenosis. *J Pediatr Gastroenterol Nutr*. 1995;20(3):319–325.
17. Kusafuka T, Puri P. Altered messenger RNA expression of the neuronal nitric oxide synthase gene in infantile hypertrophic pyloric stenosis. *Pediatr Surg Int*. 1997;12(8):576–579.
18. Langer JC, Berezin I, Daniel EE. Hypertrophic pyloric stenosis: ultrastructural abnormalities of enteric nerves and the interstitial cells of Cajal. *J Pediatr Surg*. 1995;30(11):1535–1543.
19. Malmfors G, Sundler F. Peptidergic innervation in infantile hypertrophic pyloric stenosis. *J Pediatr Surg*. 1986;21(4):303–306.
20. Ohshiro K, Puri P. Increased insulin-like growth factor and platelet-derived growth factor system in the pyloric muscle in infantile hypertrophic pyloric stenosis. *J Pediatr Surg*. 1998;33(2):378–381.
21. Ohshiro K, Puri P. Increased insulin-like growth factor-I mRNA expression in pyloric muscle in infantile hypertrophic pyloric stenosis. *Pediatr Surg Int*. 1998;13:253–255.
22. Okazaki T, et al. Abnormal distribution of nerve terminals in Infantile Hypertrophic Pyloric Stenosis. *J Ped Surg*. 1994;29:655–658.
23. Vanderwinden J, et al. Nitric Oxide Synthase activity in infantile hypertrophic pyloric stenosis. *NEJM*. 1992;327:511–515.
24. Vanderwinden JM, et al. Study of the interstitial cells of Cajal in infantile hypertrophic pyloric stenosis [published erratum appears in Gastroenterology 1996 Nov;111(5):1403]. *Gastroenterology*. 1996;111(2):279–288.
25. Wattchow D, et al. Abnormalities of peptide-cotaining nerve fibers in infantile hypertrophic pyloric stenosis. *Gastroenterology*. 1987;92:443–448.
26. Guarino N, Shima H, Puri P. Structural immaturity of the pylorus muscle in infantile hypertrophic pyloric stenosis. *Pediatr Surg Int*. 2000;16(4):282–284.
27. Peled N, et al. Gastric-outlet obstruction induced by prostaglandin therapy in neonates. *N Engl J Med*. 1992;327(8):505–510.
28. Callahan MJ, et al. The development of hypertrophic pyloric stenosis in a patient with prostaglandin-induced foveolar hyperplasia. *Pediatr Radiol*. 1999;29(10):748–751.
29. Shinohara K, et al. Correlation of prostaglandin E2 production and gastric acid secretion in infants with hypertrophic pyloric stenosis. *J Pediatr Surg*. 1998;33(10):1483–1485.
30. Capon F, et al. Linkage of monogenic infantile hypertrophic pyloric stenosis to chromosome 16p12-p13 and evidence for genetic heterogeneity. *Am J Hum Genet*. 2006;79(2):378–382.
31. Everett KV, et al. Linkage of monogenic infantile hypertrophic pyloric stenosis to chromosome 16q24. *Eur J Hum Genet*. 2008;16(9):1151–1154.
32. Everett KV, et al. Genome-wide high-density SNP-based linkage analysis of infantile hypertrophic pyloric stenosis identifies loci on chromosomes 11q14-q22 and Xq23. *Am J Hum Genet*. 2008;82(3):756–762.
33. Everett KV, Chung EM. Confirmation of two novel loci for infantile hypertrophic pyloric stenosis on chromosomes 3 and 5. *J Hum Genet*. 2013;58(4):236–237.
34. Feenstra B, et al. Plasma lipids, genetic variants near APOA1, and the risk of infantile hypertrophic pyloric stenosis. *JAMA*. 2013;310(7):714–721.
35. Feenstra B, et al. Common variants near MBNL1 and NKX2-5 are associated with infantile hypertrophic pyloric stenosis. *Nat Genet*. 2012;44(3):334–337.
36. Barnhart DC. Beyond the firstborn son: epidemiology to enlighten the pathogenesis of hypertrophic pyloric stenosis. *JAMA Pediatr*. 2013;167(12):1100–1101.
37. Dassinger M, Fuchs GJ. Infantile hypertrophic pyloric stenosis: closing in on the cause. *J Pediatr Gastroenterol Nutr*. 2014;58(5):545.
38. Rogers IM. The enigma of pyloric stenosis. Some thoughts on the aetiology. *Acta Paediatr*. 1997;86(1):6–9.
39. Rogers IM. The true cause of pyloric stenosis is hyperacidity. *Acta Paediatr*. 2006;95(2):132–136.
40. Hernanz-Schulman M, et al. The antral nipple sign of pyloric mucosal prolapse: endoscopic correlation of a new sonographic observation in patients with pyloric stenosis. *J Ultrasound Med*. 1995;14(4):283–287.
41. Holland AJ, et al. Idiopathic focal foveolar hyperplasia in infants. *Pediatr Surg Int*. 1997;12(7):497–500.
42. Dodge JA, Karim AA. Induction of pyloric hypertrophy by pentagastrin. An animal model for infantile hypertrophic pyloric stenosis. *Gut*. 1976;17(4):280–284.
43. Yoshizawa J, et al. Ultrasonographic features of normalization of the pylorus after pyloromyotomy for hypertrophic pyloric stenosis. *J Pediatr Surg*. 2001;36(4):582–586.
44. Chen E, et al. Pyloric stenosis in the age of ultrasonography: fading skills, better patients? *J Pediatr Surg*. 1996;31(6):829–830.
45. Glatstein M, et al. The changing clinical presentation of hypertrophic pyloric stenosis: the experience of a large, tertiary care pediatric hospital. *Clin Pediatr (Phila)*. 2011;50(3):192–195.
46. Papadakis K, et al. The changing presentation of pyloric stenosis. *Am J Emerg Med*. 1999;17(1):67–69.
47. Tutay GJ, et al. Electrolyte profile of pediatric patients with hypertrophic pyloric stenosis. *Pediatr Emerg Care*. 2013;29(4):465–468.
48. Grosfeld JL, O'Neill JA, Jr Coran AG, et al, eds. *Pediatric Surgery*. 6th ed. Philadelphia: Mosby Elsevier; 2006.
49. Schwartz MZ. Hypertrophic pyloric stenosis. In: Grosfeld J, et al, eds. *Grosfeld: Pediatric Surgery*. Philadelphia, PA: Mosby Elsevier; 2006.
50. Freund H, et al. Diagnosis of pyloric stenosis. *Lancet*. 1976;2(7983):473.
51. Godbole P, et al. Ultrasound compared with clinical examination in infantile hypertrophic pyloric stenosis. *Arch Dis Child*. 1996;75(4):335–337.
52. Macdessi J, Oates R. Clinical diagnosis of pyloric stenosis: a declining art. *BMJ*. 1993;306:553–555.
53. White MC, et al. Sensitivity and cost minimization analysis of radiology versus olive palpation for the diagnosis of hypertrophic pyloric stenosis. *J Pediatr Surg*. 1998;33(6):913–917.
54. Scharli A, Sieber WK, Kiesewetter WB. Hypertrophic pyloric stenosis at the Children's Hospital of Pittsburgh from 1912 to 1967. A critical review of current problems and complications. *J Pediatr Surg*. 1969;4(1):108–114.
55. Stunden RJ, LeQuesne GW, Little KE. The improved ultrasound diagnosis of hypertrophic pyloric stenosis. *Pediatr Radiol*. 1986;16(3):200–205.
56. Riggs W Jr, Long L. The value of the plain film roentgenogram in pyloric stenosis. *Am J Roentgenol Radium Ther Nucl Med*. 1971;112(1):77–82.
57. Lim R, et al. Massive gastric pneumatosis from pyloric stenosis. *CMAJ*. 2010;182(5):E227.
58. Hefke H. The roentgen diagnosis of hypertrophic pyloric stenosis in infants. *Radiology*. 1944;43:267–271.
59. Currarino G. The value of double-contrast examination of the stomach with pressure "spots" in the diagnosis of infantile hypertrophic pyloric stenosis. *Radiology*. 1964;83:873–878.
60. Teele RL, Smith EH. Ultrasound in the diagnosis of idiopathic hypertrophic pyloric stenosis. *N Engl J Med*. 1977;296(20):1149–1150.
61. Blumhagen JD, et al. Sonographic diagnosis of hypertrophic pyloric stenosis. *AJR Am J Roentgenol*. 1988;150(6):1367–1370.

62. Hernanz-Schulman M, et al. Hypertrophic pyloric stenosis in the infant without a palpable olive: accuracy of sonographic diagnosis. *Radiology*. 1994;193(3):771–776.
63. McKeown T, MacMahon B, Record R. Size of tumor in infantile pyloric stenosis related to age at operation. *Lancet*. 1951;1:556–558.
64. Iqbal C, et al. Evaluation of ultrasonographic parameters in the diagnosis of pyloric stenosis relative to patient age and size. *J Pediatr Surg*. 2012;47(8).
65. Cohen HL, et al. Ultrasonography of pylorospasm: findings may simulate hypertrophic pyloric stenosis. *J Ultrasound Med*. 1998;17(11): 705–711.
66. Blumhagen JD. The role of ultrasonography in the evaluation of vomiting in infants. *Pediatr Radiol*. 1986;16(4):267–270.
67. Mandell GA, et al. Cost-effective imaging approach to the nonbilious vomiting infant. *Pediatrics*. 1999;103(6 Pt 1):1198–1202.
68. Babyn P, et al. Radiologic features of gastric outlet obstruction in infants after long-term prostaglandin administration. *Pediatr Radiol*. 1995;25(1):41–43, discussion 44.
69. Mullassery D, et al. Negative exploration for pyloric stenosis–is it preventable? *BMC Pediatr*. 2008;8:37.
70. Olson AD, Hernandez R, Hirschl RB. The role of ultrasonography in the diagnosis of pyloric stenosis: a decision analysis. *J Pediatr Surg*. 1998;33(5):676–681.
71. Leonidas JC. Letter to the Editor. Commentary on Olson AD et al The role of ultrasonography in the diagnosis of pyloric stenosis: a decision analysis. *J Pediatr Surg*. 1999;34(10):1583–1584.
72. Yamataka A, et al. Pyloromyotomy versus atropine sulfate for infantile hypertrophic pyloric stenosis. *J Pediatr Surg*. 2000;35(2):338–341, discussion 342.
73. Kawahara H, et al. Medical treatment of infantile hypertrophic pyloric stenosis: should we always slice the "olive"? *J Pediatr Surg*. 2005;40(12):1848–1851.
74. Meissner PE, et al. Conservative treatment of infantile hypertrophic pyloric stenosis with intravenous atropine sulfate does not replace pyloromyotomy. *Pediatr Surg Int*. 2006;22(12):1021–1024.
75. Takeuchi M, et al. Pyloromyotomy versus i.v. atropine therapy for the treatment of infantile pyloric stenosis: nationwide hospital discharge database analysis. *Pediatr Int*. 2013;55(4):488–491.
76. Koike Y, et al. Predictive factors of negative outcome in initial atropine therapy for infantile hypertrophic pyloric stenosis. *Pediatr Int*. 2013;55(5):619–623.
77. Alain JL, Grousseau D, Terrier G. Extramucosal pyloromyotomy by laparoscopy. *Surg Endosc*. 1991;5(4):174–175.
78. Campbell BT, et al. Ghosts in the machine: a multi-institutional comparison of laparoscopic and open pyloromyotomy. *J Pediatr Surg*. 2007;42(12):2026–2029.
79. Fujimoto T, et al. Laparoscopic extramucosal pyloromyotomy versus open pyloromyotomy for infantile hypertrophic pyloric stenosis: which is better? *J Pediatr Surg*. 1999;34(2):370–372.
80. Hall NJ, et al. Recovery after open versus laparoscopic pyloromyotomy for pyloric stenosis: a double-blind multicentre randomised controlled trial. *Lancet*. 2009;373(9661):390–398.
81. Leclair MD, et al. Laparoscopic pyloromyotomy for hypertrophic pyloric stenosis: a prospective, randomized controlled trial. *J Pediatr Surg*. 2007;42(4):692–698.
82. St Peter SD, et al. Open versus laparoscopic pyloromyotomy for pyloric stenosis: a prospective, randomized trial. *Ann Surg*. 2006;244(3):363–370.
83. Siddiqui S, et al. Pyloromyotomy: randomized control trial of laparoscopic vs open technique. *J Pediatr Surg*. 2012;47(1):93–98.
84. Carrington EV, et al. Cost-effectiveness of laparoscopic versus open pyloromyotomy. *J Surg Res*. 2012;178(1):315–320.
85. Hall NJ, et al. Risk of incomplete pyloromyotomy and mucosal perforation in open and laparoscopic pyloromyotomy. *J Pediatr Surg*. 2014;49(7):1083–1086.
86. Hayashi AH, et al. Balloon catheter dilatation for hypertrophic pyloric stenosis. *J Pediatr Surg*. 1990;25(11):1119–1121.
87. Khoshoo V, et al. Endoscopic balloon dilatation of failed pyloromyotomy in young infants. *J Pediatr Gastroenterol Nutr*. 1996;23(4):447–451.
88. Nasr A, Ein SH, Connolly B. Recurrent pyloric stenosis: to dilate or operate? A preliminary report. *J Pediatr Surg*. 2008;43(2):e17–e20.

# 101 Acquired Disorders

Ellen Cecilia Benya

## OVERVIEW

Acquired disorders of the stomach in children are uncommon and may be the result of an underlying congenital predisposition, such as gastric volvulus; an inflammatory process, such as peptic ulcer disease (PUD); or a neoplastic or neoplastic-like condition. In addition to fluoroscopic contrast studies, ultrasonography (US), computed tomography (CT), and, less frequently, magnetic resonance imaging (MRI) and nuclear medicine may be used for evaluation.

## GASTRIC VOLVULUS

***Overview and Etiology.*** The stomach is normally fixed in the peritoneal cavity at the gastroesophageal (GE) junction and by the gastrohepatic, gastrosplenic, gastrocolic, and gastrophrenic ligaments (Fig. 101.1). Gastric volvulus is defined as an abnormal rotation of the stomach of more than 180 degrees around its long (organoaxial) or short (mesenteroaxial) axes (Figs. 101.2A and B). In the organoaxial type of gastric volvulus, there is an inversion of the position of the greater and lesser curves of the stomach, with the greater curvature positioned to the right and superior to the lesser curvature. In the mesenteroaxial type, the stomach rotates on its short axis, leading to a reversal of the relationship between the gastroesophageal junction and the antrum.[1]

***Clinical Presentation.*** Clinically, there are two primary scenarios. The first is the acute fulminant presentation, most often encountered in the mesenteroaxial type, with sudden and persistent vomiting and acute abdominal pain.[2] The chronic intermittent presentation is more often associated with the organoaxial type, with less specific symptoms including recurrent abdominal pain, vomiting, and gastric distension.[3] Predisposing factors for gastric volvulus include congenital or acquired absence of one or more of the fixating ligaments as isolated abnormalities, or occurring in association with a diaphragmatic defect, wandering spleen,[4] or heterotaxy syndrome.[5]

***Imaging.*** Abdominal radiographs in patients with gastric volvulus typically show marked gastric distension, often with a very unusual, "rounded" outline, or two air fluid levels on an upright view, with paucity of distal bowel gas indicating gastric outlet obstruction (Fig. 101.3A). Other findings include an unusual nasogastric tube course or diaphragmatic elevation. While plain radiographs are usually highly suggestive of the diagnosis, CT may be diagnostic in demonstrating the abnormal orientation and obstruction of the stomach and may detect the presence of heterotaxy or a wandering spleen (Fig. 101.3B).[4–6] Upper gastrointestinal (UGI) confirms the presence of gastric outlet obstruction and characterizes the type of gastric volvulus present (Fig. 101.3C). As noted earlier, in organoaxial volvulus, there is an inversion of the relationship of the greater and lesser curvatures, while in mesenteroaxial volvulus, the antrum and pylorus projects over the gastric fundus at the level of the GE junction; mixed types can also occur.[3]

***Treatment and Follow-up.*** Gastropexy is the treatment of choice and can be performed laparoscopically.[7–9]

## GASTRIC PERFORATION

***Overview and Etiology.*** Perforation of the stomach is an uncommon event, mainly seen in preterm and full-term neonates as a cause of massive pneumoperitoneum.[10] Potential etiologies include nasal ventilation, distal intestinal obstruction, ischemia, corticosteroid administration, or a combination of factors[11]; infants with esophageal atresia and distal fistula born prematurely are at particular risk if the diagnosis is not known before ventilatory support is instituted. Concomitant necrotizing enterocolitis has also been described.[12] Beyond the neonatal period, perforation is rare and usually secondary to trauma such as iatrogenic insertion of tubes and catheters, surgery such as fundoplication, caustic ingestion, or PUD.[2]

***Clinical Presentation.*** The most common presenting manifestations of perforation include sudden onset of abdominal distension, ileus, respiratory distress, and, less frequently, cyanosis, fever, vomiting, and bloody stool.[13]

***Imaging.*** Abdominal radiography is the imaging method of choice when perforation of the GI tract is suspected. As in other locations of GI perforation, abdominal radiographs will typically demonstrate free intraperitoneal air.

***Treatment and Follow-up.*** Gastric perforations require surgical repair. A higher mortality rate is seen in preterm and low birth weight infants who present with gastric perforation.[11]

## GASTRITIS AND GASTROPATHY

***Overview.*** Gastritis is a nonspecific term referring to conditions that result in inflammation of the gastric mucosa, such as PUD and/or *Helicobacter pylori* infection. In children, inflammatory changes in the stomach may also be the result of immunologic alterations (eosinophilic gastritis) or be related to other systemic entities such as Crohn disease or chronic granulomatous disease. Gastropathy is a disorder of the gastric mucosa that may demonstrate evidence of epithelial damage and regeneration but has little to no associated inflammatory change as seen in hypertrophic gastropathy (Menetrier disease).

### Peptic Ulcer Disease

***Overview and Etiology.*** PUD occurs less commonly in children than adults and, when seen, presents with duodenal ulceration more frequently than gastric ulceration (see Chapter 103).[14,15] The two main risk factors for PUD in children are *Helicobacter pylori* infection and nonsteroidal antiinflammatory medications.[15] *Helicobacter pylori*, a common human pathogen, is associated with both inflammatory conditions (chronic gastritis and PUD) and malignancy (gastric MALT "mucosa-associated lymphoid tissue" lymphoma).[16] Zollinger-Ellison syndrome results in PUD, with multiple, recurrent ulcerations seen in the distal duodenum and proximal jejunum due to the increased acid production generated by a gastrin-secreting tumor (Fig. 101.4).[17,18]

***Clinical Presentation.*** Symptoms of ulcer disease are varied and include abdominal pain, anorexia, early satiety, recurrent vomiting, and anemia.[19] In a few patients, PUD may result in severe gastrointestinal hemorrhage or acute abdominal pain due to perforation.[17]

***Imaging.*** Endoscopy has assumed the primary role in the diagnosis of ulcer disease.[19,20] Only rarely does UGI performed to evaluate the child with abdominal pain and vomiting demonstrate the presence of a gastric ulcer. Perforated ulcers may be identified

## Abstract:

Acquired disorders of the stomach in children are uncommon and may be the result of an underlying congenital predisposition, such as gastric volvulus; an inflammatory process, such as peptic ulcer disease (PUD); or a neoplastic or neoplastic-like condition. In addition to fluoroscopic contrast studies, ultrasonography (US), computed tomography (CT), and, less frequently, magnetic resonance imaging (MRI) and nuclear medicine may be used for evaluation.

## Keywords:

gastric volvulus
bezoar
gastritis
gastric tumors
ulcer

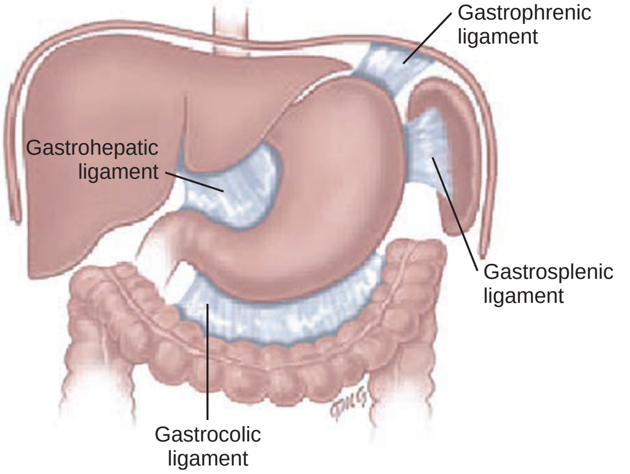

**Figure 101.1. Schematic drawing of stomach and its anchoring ligaments.** *(From Timpone VM, et al. Abdominal twists and turns: part I, gastrointestinal tract torsions with pathologic correlation.* AJR Am J Roentgenol*. 2011;197[1]:86–96.)*

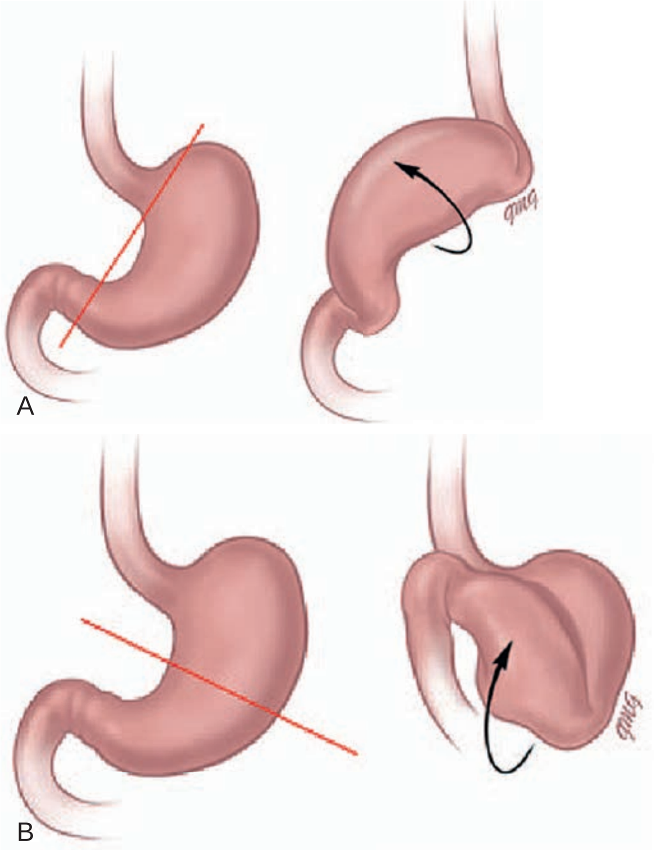

**Figure 101.2. Schematic drawing illustrating gastric volvulus.** (A) Organoaxial volvulus. Note rotation of the stomach along its long axis, such that the greater curvature is superior and to the right of the lesser curvature. The relationship of the gastroesophageal (GE) junction and the pylorus has not changed. (B) Mesenteroaxial volvulus. Note rotation of the stomach along its short axis, with reversal of the relationship of the GE junction and the pylorus. *(From Timpone VM, et al. Abdominal twists and turns: part I, gastrointestinal tract torsions with pathologic correlation.* AJR Am J Roentgenol*. 2011;197[1]:86–96.)*

on CT in the evaluation of a child with acute abdominal pain (e-Fig. 101.5).

***Treatment and Follow-up.*** Current therapy usually consists of a proton pump inhibitor to decrease acid production as well as antibiotics for *H. pylori*-associated ulcer disease.[19]

## Hypertrophic Gastropathy (Menetrier Disease)

***Overview and Etiology.*** Hypertrophy of the gastric rugal folds in association with protein-losing enteropathy in childhood is labeled Menetrier disease, or hypertrophic gastropathy of childhood.[20] The clinical, pathologic, and etiologic factors differ from the adult form. In adults, the disease is chronic and premalignant. In children, the disease is self-limited, with a peak age of 5 years at presentation. The etiology of the disease remains unknown; however, associated *H. pylori* and/or cytomegalovirus infection has been reported.[21,22]

***Clinical Presentation.*** Presentation typically includes acute vomiting, diarrhea, upper abdominal pain, and anorexia. Peripheral edema is usually present and may be associated with ascites and pleural effusions.[21] Rarely, there may be signs of gastrointestinal bleeding when there is ulceration of the gastric rugae.

***Imaging.*** This condition should be considered when diffuse and polypoid gastric fold thickening is seen involving the fundus and sparing the antrum on UGI, US, or CT studies (Fig. 101.6).[23,24] FDG-PET studies are not routinely performed but may show hypermetabolic activity in the regions of gastric wall thickening.[24] Differential diagnostic considerations include eosinophilic gastritis, *H. pylori*–related gastritis, gastric Crohn disease, Zollinger-Ellison syndrome, primary gastric lymphoma, and gastrointestinal stromal tumor (GIST).[24] Endoscopy with biopsy is needed for definitive diagnosis.

***Treatment and Follow-up.*** The entity in children is self-limited.[20] After correction of hypoproteinemia, complete recovery usually occurs within 2 to 4 weeks.[21]

## Chronic Granulomatous Disease

***Overview and Etiology.*** Chronic granulomatous disease (CGD) of childhood is a rare hereditary disorder of phagocyte function. It is most commonly inherited as an X-linked recessive gene mutation but also as an autosomal recessive defect, with three autosomal recessive mutations identified. The genetic mutation leads to a defect in activation of NADPH oxidase within the phagocytes that leaves them unable to kill and digest catalase-positive bacteria and fungi.[25,26] Histologically, there is granuloma formation within the thickened antral wall, which may develop due to chronic antigenic stimulation from organisms not killed by the defective phagocytes.[27]

***Clinical Presentation.*** Individuals with CGD develop recurrent infections, inflammation, and granulomas.[25] Involvement of the antrum resulting in gastric outlet obstruction occurs in the X-linked recessive form more commonly than in the autosomal recessive form and presents at a mean age of 44 months,[28] usually with severe vomiting.

***Imaging.*** Narrowing of the gastric antrum is a distinctive manifestation of CGD, occurring in 16% of cases.[29] Gastric outlet obstruction related to CGD is most commonly diagnosed by ultrasound or UGI series but may also be detected on abdominal CT studies done to evaluate other infectious complications such as hepatic abscesses. Ultrasound and CT studies demonstrate the circumferential antral wall thickening (Fig. 101.7). In addition to demonstrating antral narrowing, UGI series or nuclear medicine gastric emptying study can evaluate the degree of gastric obstruction. The differential diagnosis of gastric antral involvement includes PUD, Crohn disease, and eosinophilic gastritis.[30,31]

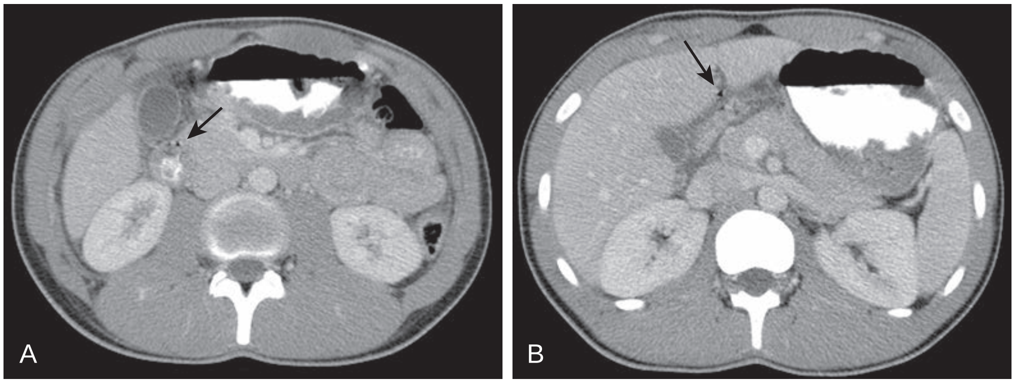

**e-Figure 101.5. Perforated duodenal ulcer in 16-year-old boy on nonsteroidal antiinflammatory regimen.** (A) Contrast-enhanced CT image shows marked thickening of the duodenal wall and small amount of free air *(arrow)*. (B) Image slightly more cephalad shows fluid about the duodenum, and additional free air extending toward the area of the falciform ligament *(arrow)*.

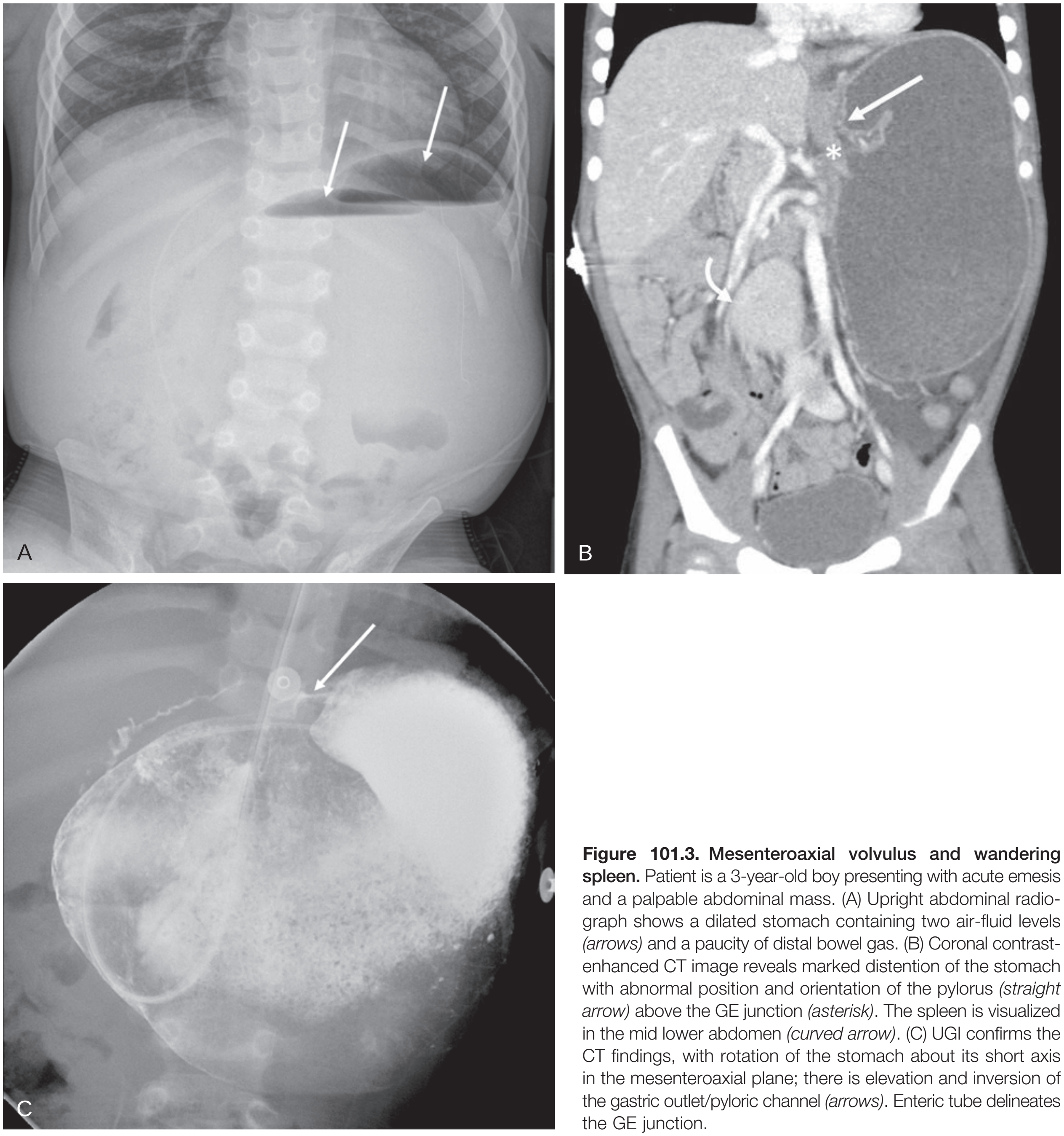

**Figure 101.3. Mesenteroaxial volvulus and wandering spleen.** Patient is a 3-year-old boy presenting with acute emesis and a palpable abdominal mass. (A) Upright abdominal radiograph shows a dilated stomach containing two air-fluid levels *(arrows)* and a paucity of distal bowel gas. (B) Coronal contrast-enhanced CT image reveals marked distention of the stomach with abnormal position and orientation of the pylorus *(straight arrow)* above the GE junction *(asterisk)*. The spleen is visualized in the mid lower abdomen *(curved arrow)*. (C) UGI confirms the CT findings, with rotation of the stomach about its short axis in the mesenteroaxial plane; there is elevation and inversion of the gastric outlet/pyloric channel *(arrows)*. Enteric tube delineates the GE junction.

***Treatment and Follow-up.*** Most patients respond in a few weeks to conservative medical management with nutritional support, steroids, and antibiotics.[28]

## Eosinophilic Gastritis

***Overview and Etiology.*** Eosinophilic gastroenteritis is a rare, poorly understood disorder, which may involve the esophagus, stomach, duodenum, small bowel, or colon. It can present any time between infancy and advanced age.[32] Eosinophilic gastritis differs from allergic gastritis, which histologically only involves the mucosal layer of the stomach and is caused by a specific antigen, most frequently cow's milk protein or soy milk protein.[33] Diagnostic criteria for eosinophilic gastritis include presence of gastrointestinal symptoms and biopsies demonstrating eosinophilic infiltration of the mucosal, muscular, and/or subserosal layer of the bowel without evidence of bacterial or parasitic infection or extraintestinal disease causing eosinophilia.[34,35]

***Clinical Presentation.*** Patients present with symptoms of abdominal pain, anorexia, failure to thrive, gastrointestinal bleeding, anemia, gastric obstruction, protein-losing enteropathy, and ascites.[32] Peripheral eosinophilia is usually but not always present.[36] Bowel obstruction and pancreatitis are more unusual manifestations of this condition.[32]

***Imaging.*** On UGI, findings of eosinophilic gastritis may include rigidity of the gastric antrum, thickened gastric folds, and mucosal nodules (Fig. 101.8).[37] On ultrasound, the predominantly antral abnormality can mimic findings seen in hypertrophic pyloric

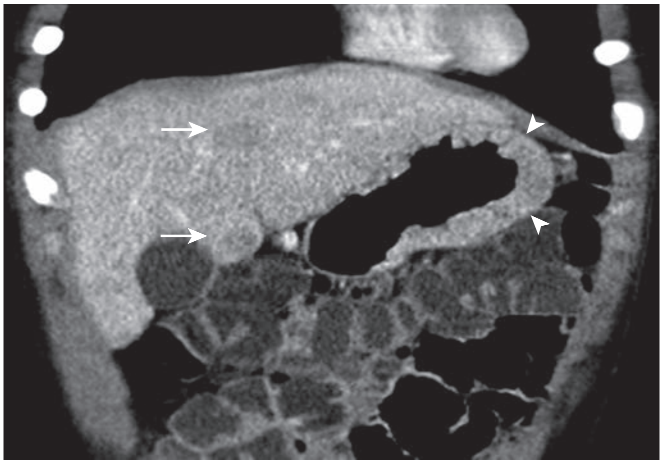

**Figure 101.4. Zollinger-Ellison syndrome secondary to a pancreatic gastrinoma in a 10-year-old boy.** Coronal contrast-enhanced CT image shows marked segmental thickening of the gastric fundus and body *(arrowheads)*. Two hypodense lesion in the liver are consistent with metastases *(arrows)*.

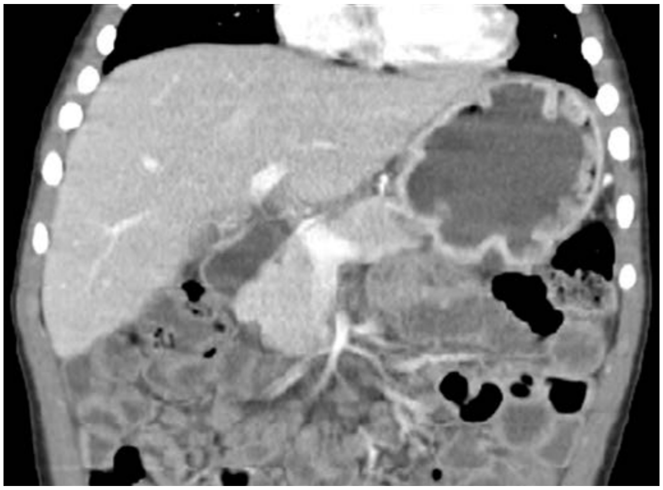

**Figure 101.6. Menetrier disease.** Coronal-reformatted contrast-enhanced CT image shows the typical thickening of the gastric folds in the fundus of the well-distended stomach in a 4-year-old boy presenting with 10 days of vomiting with streaks of blood, palpebral edema, and hypoalbuminemia. Menetrier disease was confirmed with endoscopy and gastric biopsy.

stenosis, and this condition should be suspected if such findings are seen in conjunction with eosinophilia.[38] However, in the majority of cases, radiologic imaging studies are normal.[32,39]

***Treatment.*** A variety of dietary and drug treatments have been employed for eosinophilic gastroenteritis with no consensus regarding the optimal regimen.[32] Oral corticosteroid treatment is currently the most frequently utilized therapy for eosinophilic gastroenteritis.[34,35]

## GASTRIC MASSES: FOREIGN BODIES, TUMORS, AND TUMOR-LIKE CONDITIONS

### Gastrointestinal Foreign Bodies

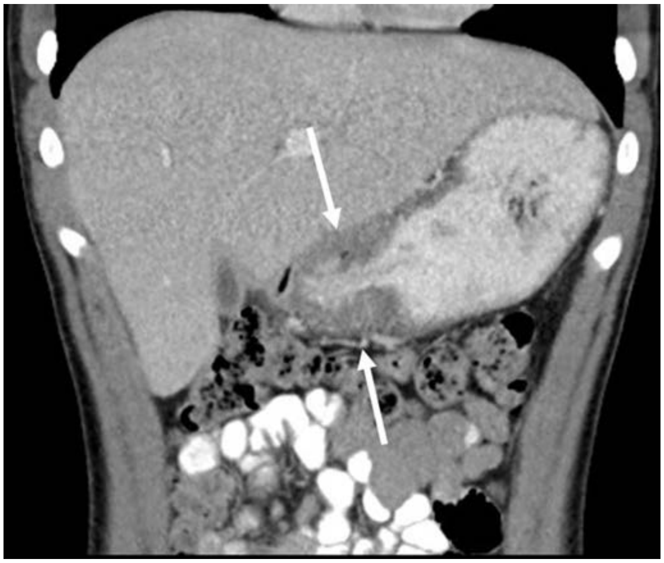

**Figure 101.7. Chronic granulomatous disease in a 15-year-old boy with intermittent epigastric pain, and occasional vomiting.** Coronal contrast-enhanced CT image shows marked circumferential thickening of the antral wall *(arrows)*.

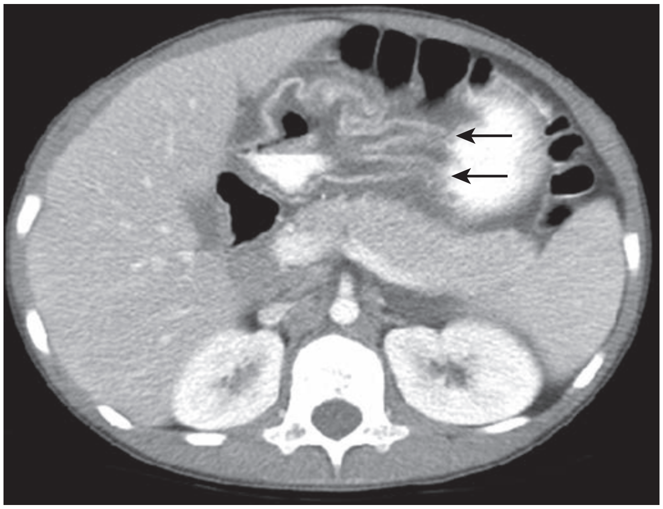

**Figure 101.8. Eosinophilic gastritis in a 14-year-old with chronic abdominal pain, failure to thrive, and nausea.** Axial contrast-enhanced CT image shows marked thickening of the gastric rugae predominantly in the antrum *(arrows)*. There is mural stratification indicating edema. Note the lack of subcutaneous fat in this child with failure to thrive.

***Overview and Etiology.*** The ingestion of foreign objects is relatively common in pediatric patients with peak age occurrence between 6 months and 3 years. Significant morbidity occurs in approximately 1% of children after foreign body ingestion[40] (see also Chapter 98).

Coins and smooth, blunt objects account for most ingested foreign bodies.[41] Complications, when they occur, are related to position (esophageal or gastric), size, shape, and sharpness of the foreign object, as well as its composition. Button batteries, especially those containing lithium and those larger than 20 mm in diameter, can lead to severe esophageal tissue injury from high pH resulting from the generation of hydroxide radicals. Finding the battery in the stomach does not exclude the possibility that esophageal injury might have occurred[42] (Fig. 101.9A). Multiple magnet ingestion (Fig. 101.9B) may result in tissue damage with formation of enteroenteric fistulae or bowel ischemia/necrosis and subsequent perforation due to attraction of magnets when present in adjacent bowel loops.[42]

***Imaging.*** Approximately 64% of foreign bodies are radiopaque and can be identified on plain films.[43] Nonradiopaque-ingested objects include those made of wood or plastic. Radiographs from nose to anus are indicated when foreign body ingestion is suspected. Fluoroscopy studies using water-soluble contrast may be useful to identify nonradiopaque foreign bodies.[41] US imaging of the stomach after water ingestion has been described to locate intraluminal foreign objects and to monitor progression through the gastrointestinal tract.[44]

***Treatment and Follow-up.*** Although 90% of foreign bodies that have cleared the esophagus will pass spontaneously, experts recommend removing sharp objects before they enter the duodenum.[41,45] Once the foreign body has passed the stomach, the stool should be checked to verify that the object has been expelled. If, after a week, the child has not excreted the object, a radiograph should be obtained to determine its location if present.[46] Button batteries and multiple magnets require special attention. All button batteries seen in the esophagus must be removed emergently due to their associated high morbidity and mortality rates. Guidelines for removal of button batteries from the stomach are evolving.[40,44,47,48]

## Bezoars

***Overview and Etiology.*** Bezoars are foreign bodies within the stomach or other portions of the gastrointestinal tract that form from the accretion of nondigestible materials and increase in size over time. The three most common types are: trichobezoars composed of ingested hair, phytobezoars composed of plant matter, and lactobezoars composed of undigested milk curds (Table 101.1). *Trichobezoars* usually result from swallowing of multiple small amounts of hair plucked from the head, or fibers from fur, rugs, or garments. The hairs or fibers become lodged in the gastric mucosal folds and over a period of time; an intraluminal mass or bezoar develops, forming a cast of the lumen of the stomach. Occasionally, a tail of material from the bezoar may extend into the duodenum and small bowel leading to the "Rapunzel syndrome" with potential complications, including small bowel intussusception, perforation, and bowel obstruction.[49,50] Patients with developmental delay and psychiatric illnesses are at increased risk for bezoars. Lactobezoars may occur in infants with a history of prematurity receiving a highly concentrated formula, with additional risk factors including poor neonatal gastric motility and dehydration.[49]

***Clinical Presentation.*** Patients with bezoars can be asymptomatic or present with relatively nonspecific symptoms, such as epigastric discomfort. Other complaints may include bloating, nausea and vomiting, early satiety, halitosis, dysphagia, and failure to thrive; rarely GI bleeding and acute abdominal pain can occur.[49]

**TABLE 101.1** Types of Bezoar According to the Ingested Material

| | |
|---|---|
| Phytobezoar | Nondigestible food particles found in fruits (dates, persimmons) and vegetables (cellulose, hemicellulose, lignin) |
| Trichobezoar | Hair bezoar. Associated with young females and/or patients with psychiatric illnesses who ingest hair, carpet, rope, string, etc. |
| Lactobezoar | Compact mass of undigested milk concretions traditionally described in preterm neonates on highly concentrated formula |
| Pharmacobezoar | Conglomeration of medications or medication vehicles |
| Others | Mixture hair, fruit, and fiber<br>Worms |

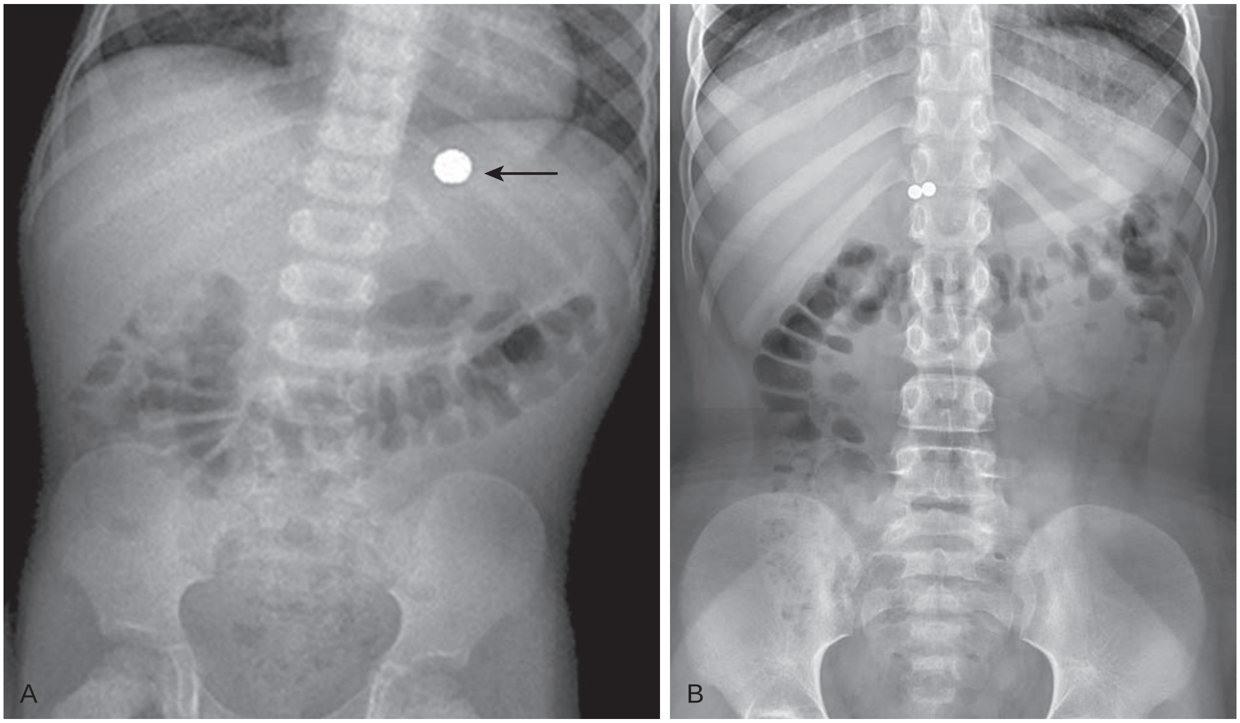

**Figure 101.9. Ingested gastric foreign bodies** (A) Ingested watch battery in a 2-year-old child. Supine radiograph shows the ingested battery with irregular outline indicating corrosion *(arrow)* in the gastric fundus. (B) A 6-year-old was playing with magnets, which were accidentally swallowed. Two opposed magnets are clearly seen in contact within the gastric antrum. *(Courtesy Marta Hernanz-Schulman, Nashville, TN.)*

***Imaging.*** Plain radiographs may demonstrate a mass within the stomach if outlined by gas, in addition to gastric distension without history of ingestion of a large meal. Fluoroscopic contrast studies will show the mass as contrast coats the bezoar and infiltrates within its interstices, producing the characteristic mottled appearance (Fig. 101.10A). CT can also identify a bezoar, typically without the need for ingestion of contrast and may also identify additional bezoars (Fig. 101.10B), as well as potential complications such as obstruction or perforation.[2,50]

***Treatment and Follow-up.*** Therapeutic options for treating amenable bezoars include fragmentation and dissolution with enzymatic therapy, or gastric lavage with saline in cases of lactobezoars, and subsequent dietary modification. In cases of motility disorders, the administration of prokinetic agents is important to prevent recurrence. Surgical or endoscopic extraction is reserved for trichobezoars or for those instances in which the previously described measures fail.[49,50]

## Gastric Tumors

***Overview and Etiology.*** Gastric tumors in children are rare but include gastric polyps, lymphoma, GIST, leiomyosarcoma, teratoma, and inflammatory pseudotumor.

Polyps, which may occur anywhere along the GI tract, are the most common gastric tumor in children. Isolated gastric polyps are usually benign, with a hyperplastic inflammatory histology most frequently identified.[51] Polyps can be part of a syndrome, such as hamartomatous polyps in Peutz-Jeghers syndrome, or fundic gland polyps in familial adenomatous polyposis.[51] Gastric polyps may be seen in up to 60% of patients with familial polyposis syndrome,[52] and lifelong endoscopic surveillance of these patients is warranted because of the potential for malignant transformation of adenomatous polyps.[53] An increased risk of malignancy is also seen in patients with Peutz-Jeghers syndrome.[54–56]

Primary gastric lymphoma can be divided into mucosa-associated lymphoid tissue (MALT) lymphoma and non-MALT lymphoma. MALT lesions typically arise in response to a stimulus such as *H. pylori* infection and are rare in children.[57,58] Non-MALT primary gastric lymphomas are also rare and are usually high-grade non-Hodgkin lymphomas of B-cell origin, usually of the Burkitt type.[59]

GIST are mesenchymal neoplasms derived from the muscle wall of hollow viscera in the GI tract, most of which are positive for mutations in the *KIT* and *PDGFRA* (platelet derived growth factor alpha receptor) tyrosine kinase genes. These tumors are very rare in pediatric patients, predominantly occurring in young girls and differing in pathogenesis from adult GIST typically with an epitheloid rather than spindle cell cytology.[60,61] These tumors are usually located in the gastric antrum, are frequently multifocal, and may be associated with a paraganglioma (Carney-Stratakis syndrome); pulmonary chondroma and extra-adrenal paraganglioma (Carney triad); and neurofibromatosis type-1.[60,61]

Leiomyoma and leiomyosarcoma are also mesenchymal neoplasms, but unlike GIST, these tumors demonstrate smooth muscle markers and are KIT and PDGFRA negative. They are much less prevalent in children, with peak age at presentation in the sixth decade. Although polypoid leiomyomas are the most common smooth muscle neoplasm arising in the GI tract, they are very

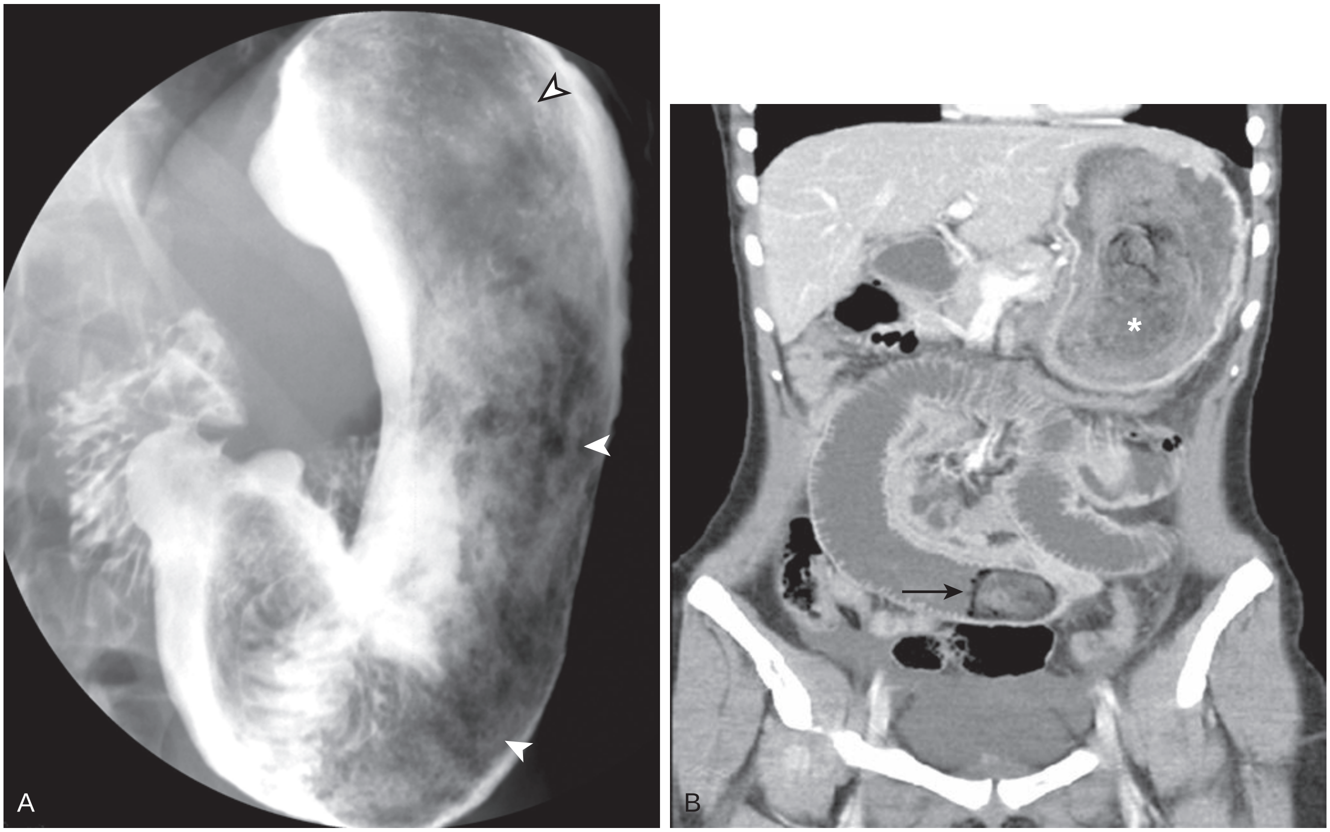

**Figure 101.10. Gastric bezoars A.** (A) Lactobezoar in a 6-month-old infant. Oblique view of an upper GI series shows a well-defined oval filling defect in the gastric lumen *(arrows)* subsequently confirmed to be a lactobezoar. (B) Trichobezoar in an adolescent girl with anorexia nervosa. Coronal contrast-enhanced CT image shows a trichobezoar *(asterisk)* of multiple densities forming a cast within the gastric lumen. An additional trichobezoar in the mid jejunum *(arrow)* is causing proximal small bowel obstruction.

rare outside of the esophagus and rectosigmoid; likewise, the malignant leiomyosarcoma is very rare in the stomach.[62]

Gastric teratomas make up less than 1% of teratomas in pediatric patients, and occur much more frequently in the sacrococcygeal region, the mediastinum, and gonads.[63] Gastric teratomas show a striking male predominance and present early in life in neonates and infants.[64,65]

Inflammatory pseudotumor, also known as plasma cell granuloma and inflammatory myofibroblastic tumor, is composed histologically of lymphocytes, plasma cells, myofibroblastic spindle cells, and collagen.[66] It is most common in the lung but can rarely occur in the stomach and is associated with microcytic anemia, hypergammaglobulinema, and elevated sedimentation rate.[67]

***Clinical Presentation.*** With the exception of gastric polyps, which may be discovered incidentally, the clinical presentation of all gastric tumors is similar and may include GI bleeding, anemia, abdominal pain, palpable mass, and, less frequently, gastric outlet obstruction. In cases of lymphoma, constitutional symptoms can be present.

***Imaging.*** Polyps can be seen on UGI series as pedunculated or sessile smooth mucosal lesions arising from the gastric wall. Adenomatous polyps are usually antral and multiple. The appearance is similar on CT, requiring appropriate gastric distension to secure the diagnosis. Oral positive or negative contrast material is usually helpful (e-Fig. 101.11).

In the rare primary and the more common secondary gastric lymphoma, CT reveals focal or diffuse mural masses that can protrude into the gastric lumen (Fig. 101.12) or cause mass effects upon adjacent structures. Multifocal intestinal involvement can be present, as well as hepatosplenomegaly, and regional or distant adenopathy. On UGI series, mucosal nodularity, rugal thickening, and masses with or without associated ulceration can be seen.[58] PET/CT is used in staging of lymphoma in children to assess disease activity and involvement of distant sites, particularly in lymph nodes that do not meet size criteria for pathologic involvement.[68,69]

Other mass lesions, such as GIST, are similarly seen on CT as masses with extension into the gastric lumen (Fig. 101.13) or mass effect upon adjacent structures. Inflammatory myofibroblastic tumor in the stomach tends to present as an infiltrative lesion which may demonstrate low attenuation areas as well as calcifications (Fig. 101.14).[70,71] Extension beyond the stomach is best appreciated on cross-sectional imaging, such as CT or MRI. PET/CT is useful in the assessment of distant metastases.[60]

***Treatment and Follow-up.*** Mass lesions identified on imaging studies require endoscopic evaluation for confirmation and biopsy. Treatment varies depending on the tumor histology.

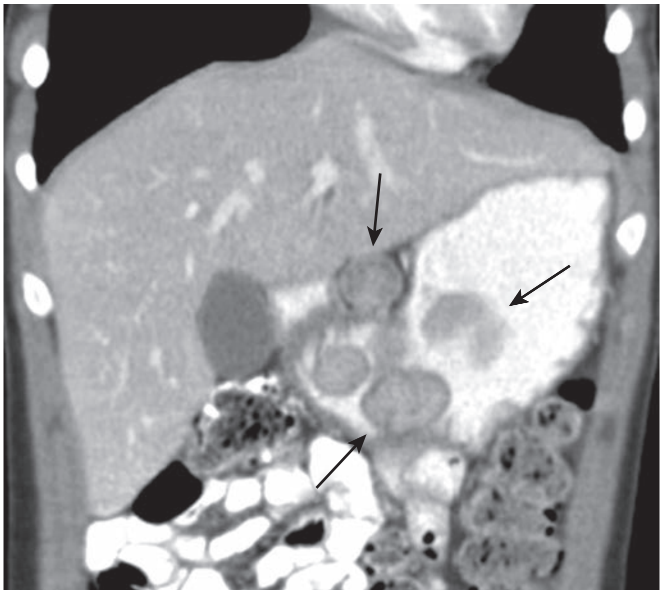

**Figure 101.13. Multifocal gastrointestinal stromal tumor in an adolescent girl presenting with chronic abdominal pain and anemia.** Coronal contrast-enhanced CT image shows multiple masses *(arrows)* arising from the wall of the gastric antrum.

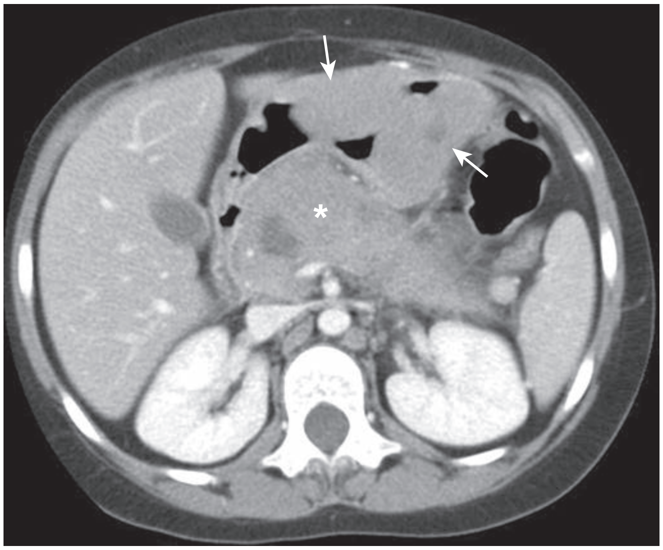

**Figure 101.12. Burkitt lymphoma in a 14-year-old African American girl presenting with vomiting and fever.** Axial contrast-enhanced CT image shows two large smooth and homogeneous masses *(arrows)* arising from the gastric wall protruding into the gastric lumen *(arrows)*. There is also a large more heterogeneous mass involving the pancreas *(asterisk)*.

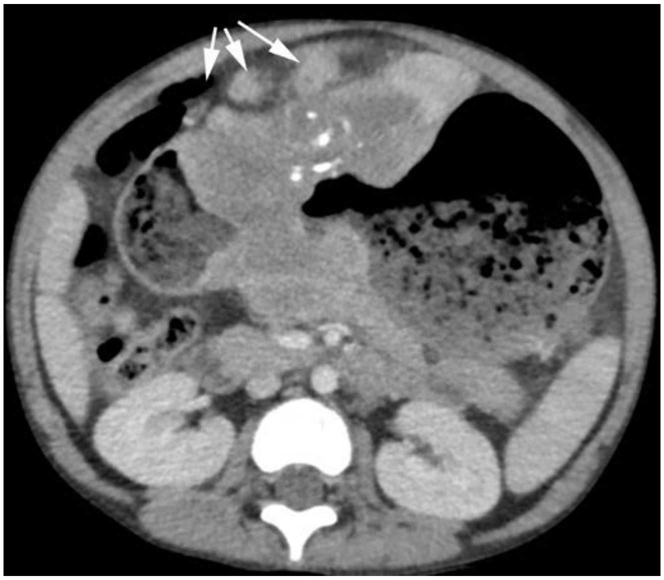

**Figure 101.14. Inflammatory myofibroblastic tumor of the stomach.** Axial contrast-enhanced CT image of 4-year-old girl presenting with abdominal pain demonstrates an infiltrative solid tumor with calcification. Two omental implants *(arrows)* are also visible. *(Courtesy Marta Hernanz-Schulman MD, Nashville, TN.)*

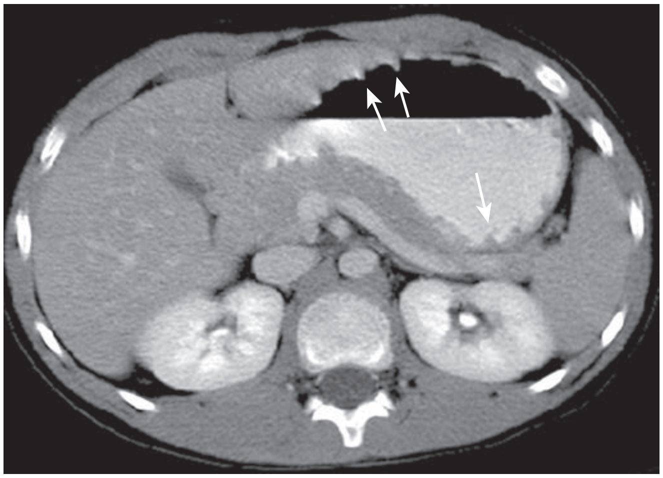

**e-Figure 101.11. Multiple gastric polyps in a patient with Gardner syndrome.** The patient is status post total colectomy. Axial contrast-enhanced CT image shows multiple tiny polyps arising diffusely from the gastric wall protruding into the lumen *(arrows)*, confirmed at endoscopy.

## KEY POINTS

- There are two types of gastric volvulus with different presentations. The organoaxial type usually presents with chronic abdominal pain, vomiting, and gastric distension. The mesenteroaxial type typically has a sudden presentation, with vomiting and acute abdominal pain.
- Ingested magnets and batteries, particularly lithium batteries, pose risk of esophageal or intestinal injury.
- Predisposing factors for bezoars are psychiatric problems, previous gastric surgery, gastroparesis, cystic fibrosis, and renal failure, among others.
- Gastric wall thickening in children can be due to several conditions. When it involves the antrum, eosinophilic gastritis and CGD are considerations. When it involves the fundus and body, Menetrier disease can be considered.

## SUGGESTED READINGS

Attard TM, Yardley JH, Cuffari C. Gastric polyps in pediatrics: an 18-year hospital-based analysis. *Am J Gastroenterol*. 2002;97(2):298–301.

Kramer RE, et al. Management of ingested foreign bodies in children: a clinical report of the NASPGHAN Endoscopy Committee. *J Pediatr Gastroenterol Nutr*. 2015;60(4):562–574.

Miettinen M, Lasota J. Gastrointestinal stromal tumors. *Gastroenterol Clin North Am*. 2013;42(2):399–415.

Oh SK, Han BK, Levin TL, et al. Gastric volvulus in children: the twists and turns of an unusual entity. *Pediatr Radiol*. 2008;38:297–304.

Zhang M, Li Y. Eosinophilic gastroenteritis: a state-of-the-art review. *J Gastroenterol Hepatol*. 2017;32(1):64–72.

## REFERENCES

Full references for this chapter can be found on www.expertconsult.com.

## REFERENCES

1. Timpone VM, et al. Abdominal twists and turns: part I, gastrointestinal tract torsions with pathologic correlation. *AJR Am J Roentgenol*. 2011;197(1):86–96.
2. Nijs E. Radiological imaging of the digestive tract in infants and children. *Med Radiol*. 2008;3:109–132.
3. Oh SK, et al. Gastric volvulus in children: the twists and turns of an unusual entity. *Pediatr Radiol*. 2008;38(3):297–304.
4. Uc A, et al. Gastric volvulus and wandering spleen. *Am J Gastroenterol*. 1998;93(7):1146–1148.
5. Nakada K, et al. Digestive tract disorders associated with asplenia/polysplenia syndrome. *J Pediatr Surg*. 1997;32(1):91–94.
6. Dodge JA, Karin AA. Induction of pyloric hypertrophy by pentagastrin: an animal model for infantile hypertrophic pyloric stenosis. *Gut*. 1976;17(4):280–284.
7. Elhalaby EA, Mashaly EM. Infants with radiologic diagnosis of gastric volvulus: are they over-treated? *Pediatr Surg Int*. 2001;17(8):596–600.
8. Al-Salem AH. Acute and chronic gastric volvulus in infants and children: who should be treated surgically? *Pediatr Surg Int*. 2007;23(11):1095–1099.
9. Al-Faraj D, et al. A case of acute mesentero-axial gastric volvulus in a patient with a diaphragmatic hernia: experience with a laparoscopic approach. *J Surg Case Rep*. 2015;2015(9).
10. Buonomo C, Taylor GA, Share JC. Idiopathic gastric preforation. In: *Practical Pediatric Imaging*. 3rd ed. Kirks; 1998:893.
11. Terui K, et al. Etiology of neonatal gastric perforation: a review of 20 years' experience. *Pediatr Surg Int*. 2012;28(1):9–14.
12. Yang CY, et al. Prognostic factors and concomitant anomalies in neonatal gastric perforation. *J Pediatr Surg*. 2015;50(8):1278–1282.
13. Lin CM, et al. Neonatal gastric perforation: report of 15 cases and review of the literature. *Pediatr Neonatol*. 2008;49(3):65–70.
14. Hernandez C, et al. Peptic ulcer disease in Helicobacter pylori-infected children: clinical findings and mucosal immune response. *J Pediatr Gastroenterol Nutr*. 2014;59(6):773–778.
15. Koca T, et al. Peptic ulcers and erosions in children at a pediatric unit in Turkey. *Indian Pediatr*. 2016;53(8):692–694.
16. Gold BD, Gilger MA, Czinn SJ. New diagnostic strategies for detection of Helicobacter pylori infection in pediatric patients. *Gastroenterol Hepatol (N Y)*. 2014;10(12 suppl 7):1–19.
17. Gryboski JD. Peptic ulcer disease in children. *Pediatr Rev*. 1990;12(1):15–21.
18. Wolfe MM, Soll AH. The physiology of gastric acid secretion. *N Engl J Med*. 1988;319(26):1707–1715.
19. Dohil R, Hassall E. Peptic ulcer disease in children. *Baillieres Best Pract Res Clin Gastroenterol*. 2000;14(1):53–73.
20. Jacobe S, Lam A, Elliott E. Transient hypertrophic gastropathy. *J Pediatr Gastroenterol Nutr*. 1998;26(2):211–215.
21. Hochman JA, Witte DP, Cohen MB. Diagnosis of cytomegalovirus infection in pediatric Menetrier's disease by in situ hybridization. *J Clin Microbiol*. 1996;34(10):2588–2589.
22. Occena RO, et al. Association of cytomegalovirus with Menetrier's disease in childhood: report of two new cases with a review of literature. *J Pediatr Gastroenterol Nutr*. 1993;17(2):217–224.
23. Takaya J, et al. Menetrier's disease evaluated serially by abdominal ultrasonography. *Pediatr Radiol*. 1997;27(2):178–180.
24. Trout AT, et al. Case 189: Pediatric Menetrier disease. *Radiology*. 2013;266(1):357–361.
25. Huang A, Abbasakoor F, Vaizey CJ. Gastrointestinal manifestations of chronic granulomatous disease. *Colorectal Dis*. 2006;8(8):637–644.
26. Khanna G, et al. Imaging of chronic granulomatous disease in children. *Radiographics*. 2005;25(5):1183–1195.
27. Rosh JR, et al. Treatment of intractable gastrointestinal manifestations of chronic granulomatous disease with cyclosporine. *J Pediatr*. 1995;126(1):143–145.
28. Dickerman JD, Colletti RB, Tampas JP. Gastric outlet obstruction in chronic granulomatous disease of childhood. *Am J Dis Child*. 1986;140(6):567–570.
29. Griscom NT, et al. Gastric antral narrowing in chronic granulomatous disease of childhood. *Pediatrics*. 1974;54(4):456–460.
30. Manson DE, et al. Primary immunodeficiencies: a pictorial immunology primer for radiologists. *Pediatr Radiol*. 2000;30(8):501–510.
31. Kenney PJ, Brinkso RE, Patel DV. Gastric involvement in CGD. *J Comput Assist Tomogr*. 1985;9(3):563–565.
32. Zhang M, Li Y. Eosinophilic gastroenteritis: a state-of-the-art review. *J Gastroenterol Hepatol*. 2017;32(1):64–72.
33. Dohil R, et al. Gastritis and gastropathy of childhood. *J Pediatr Gastroenterol Nutr*. 1999;29(4):378–394.
34. Katiyar R, et al. Primary eosinophilic gastritis in a child with gastric outlet obstruction. *J Gastrointest Surg*. 2016;20(6):1270–1271.
35. Talley NJ, et al. Eosinophilic gastroenteritis: a clinicopathological study of patients with disease of the mucosa, muscle layer, and subserosal tissues. *Gut*. 1990;31(1):54–58.
36. Garcia-Careaga M Jr, Kerner JA Jr. Gastrointestinal manifestations of food allergies in pediatric patients. *Nutr Clin Pract*. 2005;20(5):526–535.
37. Wehut WD, et al. Eosinophilic gastritis. Radiologic-pathologic correlation (RPC) from the Armed Forces Institute of Pathology (AFIP). *Radiology*. 1976;120(1):85–89.
38. Hummer-Ehret BH, et al. Eosinophilic gastroenteritis mimicking idiopathic hypertrophic pyloric stenosis. *Pediatr Radiol*. 1998;28(9):711–713.
39. Chang JY, et al. A shift in the clinical spectrum of eosinophilic gastroenteritis toward the mucosal disease type. *Clin Gastroenterol Hepatol*. 2010;8(8):669–675; quiz e88.
40. Arana A, et al. Management of ingested foreign bodies in childhood and review of the literature. *Eur J Pediatr*. 2001;160(8):468–472.
41. Chen MK, Beierle EA. Gastrointestinal foreign bodies. *Pediatr Ann*. 2001;30(12):736–742.
42. Kramer RE, et al. Management of ingested foreign bodies in children: a clinical report of the NASPGHAN Endoscopy Committee. *J Pediatr Gastroenterol Nutr*. 2015;60(4):562–574.
43. Uyeimura MC. Foreign body ingestion in children. *Am Fam Physician*. 2005;72:287–291.
44. Jeckovic M, et al. Is ultrasound useful in detection and follow-up of gastric foreign bodies in children? *Clin Imaging*. 2013;37(6):1043–1047.
45. Kay M, Wyllie R. Pediatric foreign bodies and their management. *Curr Gastroenterol Rep*. 2005;7(3):212–218.
46. Wunsch R, et al. [Foreign body ingestion]. *Radiologe*. 1999;39(6):472–477.
47. Burgos A, Rabago L, Triana P. Western view of the management of gastroesophageal foreign bodies. *World J Gastrointest Endosc*. 2016;8(9):378–384.
48. Pugmire BS, Lim R, Avery LL. Review of ingested and aspirated foreign bodies in children and their clinical significance for radiologists. *Radiographics*. 2015;35(5):1528–1538.
49. Sanders MK. Bezoars: from mystical charms to medical and nutritional management. *Pract Gastroenterol*. 2004;13:37–50.
50. Fallon SC, et al. The surgical management of Rapunzel syndrome: a case series and literature review. *J Pediatr Surg*. 2013;48(4):830–834.
51. Attard TM, Yardley JH, Cuffari C. Gastric polyps in pediatrics: an 18-year hospital-based analysis. *Am J Gastroenterol*. 2002;97(2):298–301.
52. Goedde TA, et al. Gastroduodenal polyps in familial adenomatous polyposis. *Surg Oncol*. 1992;1(5):357–361.
53. Gallagher MC, Phillips RK, Bulow S. Surveillance and management of upper gastrointestinal disease in familial adenomatous polyposis. *Fam Cancer*. 2006;5(3):263–273.
54. Goldstein SA, Hoffenberg EJ. Peutz-Jegher syndrome in childhood: need for updated recommendations? *J Pediatr Gastroenterol Nutr*. 2013;56(2):191–195.
55. Tomas C, et al. Update on imaging of Peutz-Jeghers syndrome. *World J Gastroenterol*. 2014;20(31):10864–10875.
56. Wang LC, et al. Gastrointestinal polyps in children. *Pediatr Neonatol*. 2009;50(5):196–201.
57. Claviez A, et al. MALT lymphoma in children: a report from the NHL-BFM Study Group. *Pediatr Blood Cancer*. 2006;47(2):210–214.
58. Kurugoglu S, et al. Radiological features in paediatric primary gastric MALT lymphoma and association with Helicobacter pylori. *Pediatr Radiol*. 2002;32(2):82–87.
59. Mitra S, et al. Primary gastric Burkitt's Lymphoma. *Rare Tumors*. 2014;6(4):5300.
60. Miettinen M, Lasota J. Gastrointestinal stromal tumors. *Gastroenterol Clin North Am*. 2013;42(2):399–415.
61. Prakash S, et al. Gastrointestinal stromal tumors in children and young adults: a clinicopathologic, molecular, and genomic study of 15 cases and review of the literature. *J Pediatr Hematol Oncol*. 2005;27(4):179–187.
62. Agaimy A, Wunsch PH. True smooth muscle neoplasms of the gastrointestinal tract: morphological spectrum and classification in a series of 85 cases from a single institute. *Langenbecks Arch Surg*. 2007;392(1):75–81.
63. Chandrasekharam VV, Gupta AK, Bhatnagar V. Infantile gastric teratoma. *Trop Gastroenterol*. 2000;21(4):192–193.

64. Sharma A, et al. Immature gastric teratoma in an infant: report of a case and review of the literature. *Indian J Pathol Microbiol*. 2010;53(4):868–870.
65. Gupta DK, et al. Gastric teratoma in children. *Pediatr Surg Int*. 2000;16(5–6):329–332.
66. Patnana M, et al. Inflammatory pseudotumor: the great mimicker. *AJR Am J Roentgenol*. 2012;198(3):W217–W227.
67. Taratuta E, et al. Pediatric inflammatory pseudotumor of the stomach: contrast-enhanced CT and MR imaging findings. *AJR Am J Roentgenol*. 1996;167(4):919–920.
68. Perry C, et al. Diagnostic accuracy of PET/CT in patients with extranodal marginal zone MALT lymphoma. *Eur J Haematol*. 2007;79(3):205–209.
69. Kaste SC, Shulkin BL. 18F-Fluorodeoxyglucose PET/CT in childhood lymphoma. *PET Clin N Am*. 2006;1:265–273.
70. Kim SJ, et al. Inflammatory myofibroblastic tumors of the abdomen as mimickers of malignancy: imaging features in nine children. *AJR Am J Roentgenol*. 2009;193(5):1419–1424.
71. Groenveld RL, et al. Abdominal inflammatory myofibroblastic tumor. *Case Rep Gastroenterol*. 2014;8(1):67–71.

# 102 Duodenum and Small Bowel: Congenital and Neonatal Abnormalities

*Marta Hernanz-Schulman*

## PART I: DUODENUM

Congenital anomalies of the duodenum often present with obstructive symptoms and consist of intrinsic obstructing lesions, such as duodenal atresia and stenosis, or extrinsic lesions that affect the duodenum, such as midgut volvulus or Ladd bands, annular pancreas, preduodenal portal vein, and duplications cysts; intrinsic and extrinsic lesions may coexist in the same patient.

### Intrinsic Lesions: Duodenal Atresia and Stenosis

***Overview.*** Duodenal atresia and stenosis represent a spectrum ranging from complete to partial obstruction, and corresponding presentation that ranges from prenatal life to late childhood or even adulthood. Duodenal atresia represents approximately one-half of all intestinal atresias, with a reported incidence of approximately 1 : 7,000 live births.[1,2] The classification of duodenal atresia by Gray and Skandalakis is most often cited[3,4] and is similar to that of more distal atresias: type I atresia (approximately 90% of cases) consists of a membrane that may obstruct completely or partially; in type II atresia, the segments are connected by a fibrous cord; in type III atresia, there is a gap separation with a mesenteric defect.

***Etiology.*** The lumen of the duodenum is obliterated during the 4th to 6th weeks of gestation due to rapid cell division, and it normally recanalizes by the 12th week; duodenal atresia is believed to result from failure of this recanalization process. This differs from atresia of the small and large bowel, which is believed to result from a vascular accident later in gestation.[5,6] The recanalization error theory was first suggested in 1900 but is very difficult to confirm.[7] Recent studies suggest that disruptions in fibroblast growth factor receptor 2 (FGFR2) function and retinoic acid signaling pathways may play a role in the development of duodenal and possibly other intestinal atresias.[7–10]

***Clinical Presentation.*** In approximately half of patients, duodenal atresia does not occur in isolation but rather as part of a syndrome or association, such as Down or esophageal atresia. Polyhydramnios, resulting from the proximal bowel obstruction, is seen in 30% to 50% of patients and leads to premature birth in half.[3,6,8] Thus the clinical presentation is often modified by associated anomalies and by prematurity.

Postnatally, infants with atresia typically present with vomiting within the first 24 hours of life; however, one-third of infants presenting in the neonatal period will have severe stenosis.[6] The infants who have not been diagnosed prenatally will present with bilious vomiting in greater than two-thirds of the cases, in which the obstruction is sited distal to the ampulla of Vater.[11] However, the obstruction occurs proximal to the ampulla of Vater in as many as 23% of patients,[12] and these will present with nonbilious vomiting. Thus the presentation of infants with duodenal stenosis can overlap that of infants with the much more common diagnosis of pyloric stenosis and may be initially encountered at ultrasound (Fig. 102.1). Because the duodenal obstruction is proximal, abdominal distension is not a typical finding, although epigastric fullness may be present secondary to the dilated stomach and duodenum.

Patients with less severe forms of duodenal stenosis may not come to medical attention until later in life, depending on the degree of obstruction. In such patients, presentation may be relatively nonspecific, such as failure to thrive, or rarely pancreatitis, secondary to reflux into the pancreatic duct, proximal to the site of obstruction.[13,14] Late presentation secondary to obstruction may be precipitated by ingestion of a foreign body that fails to pass and may exacerbate the degree of obstruction, leading to abdominal pain and/or vomiting (e-Fig. 102.2).[15,16] Annular pancreas and malrotation are seen in approximately one-third of cases.[6]

Associated anomalies are common in patients with duodenal atresia/stenosis. Approximately 25% to 40% of infants with duodenal atresia/stenosis have Down syndrome; conversely, approximately 4% of infants with Down syndrome have duodenal obstruction.[6,17] Hirschsprung disease has been reported in approximately 1% to 3% of patients with duodenal atresia and Down syndrome.[18,19] Approximately 5% of infants with esophageal atresia, with or without fistula, will also have duodenal atresia.[20] Heterotaxy with left isomerism/polysplenia has been reported in patients with duodenal diaphragm/intraluminal diverticulum.[13,21,22] Duodenal atresia can also be part of several familial syndromes with autosomal inheritance, such as Feingold syndrome (autosomal dominant) and Fryns syndrome (autosomal recessive).[23]

***Imaging.*** Abdominal radiographs are the starting point in the evaluation of a child with suspected gastrointestinal (GI) obstruction. In the neonate with duodenal atresia, the abdominal radiograph demonstrates the classic “double bubble” representing the dilated stomach and duodenum.[24,25] Because obstruction has been present in utero, the obstructed proximal duodenum is typically large, approximately one-half to one-third the size of the stomach (Fig. 102.3A); at times the pylorus is wide open, and the two bubbles are not distinctly separated (Fig. 102.3B) but should still be recognized. This appearance on the abdominal radiograph is diagnostic, and confirmatory contrast examinations are unnecessary. Rarely, air can be seen distally in a patient with complete atresia; this occurs when the atresia is flanked by the branches of an anomalous bifid common bile duct, with separate insertions into the duodenum above and below the point of atresia. Air or contrast may be seen refluxing into the anomalous ducts, which allow the contents of the obstructed proximal duodenum to course into the distal duodenum, bypassing the point of obstruction (Fig. 102.4).[12,26,27] In patients with duodenal atresia associated with esophageal atresia with a distal fistula, plain films will demonstrate the double bubble and are diagnostic (e-Fig. 102.5); perforation may occur if these infants need to be mechanically ventilated.

In patients with duodenal stenosis, distension of the stomach and proximal duodenum and decrease in distal gas is commensurate with the degree of obstruction present. However, if the stenosis is mild or the stomach is decompressed via enteric tube, the plain

## Abstract:

This chapter describes congenital anomalies of the duodenum and of the small bowel. Duodenal lesions described include intrinsic lesions, such as duodenal atresia and stenosis, extrinsic lesions including annual pancreas, preduodenal portal vein and duplications cysts, and malrotation and its complications, particularly midgut volvulus.

Small bowel lesions include small bowel atresias and stenoses, apple peel mesentery and other causes of obstruction or atresia including meconium ileus, both simple and complicated. Meckel diverticulum and its complications, small bowel duplication cysts, and other abnormalities such as omental and mesenteric cysts are also discussed.

## Keywords:

Congenital duodenum
duodenal atresia
duodenal stenosis
annual pancreas
preduodenal portal vein
duodenal duplication cysts
malrotation
midgut volvulus
jejunal atresia
ileal atresia
jejunal stenosis
meconium ileus
meconium peritonitis
meconium cyst
Meckel diverticulum
heterotopic gastric mucosa
mesenteric cysts
mesothelial cysts

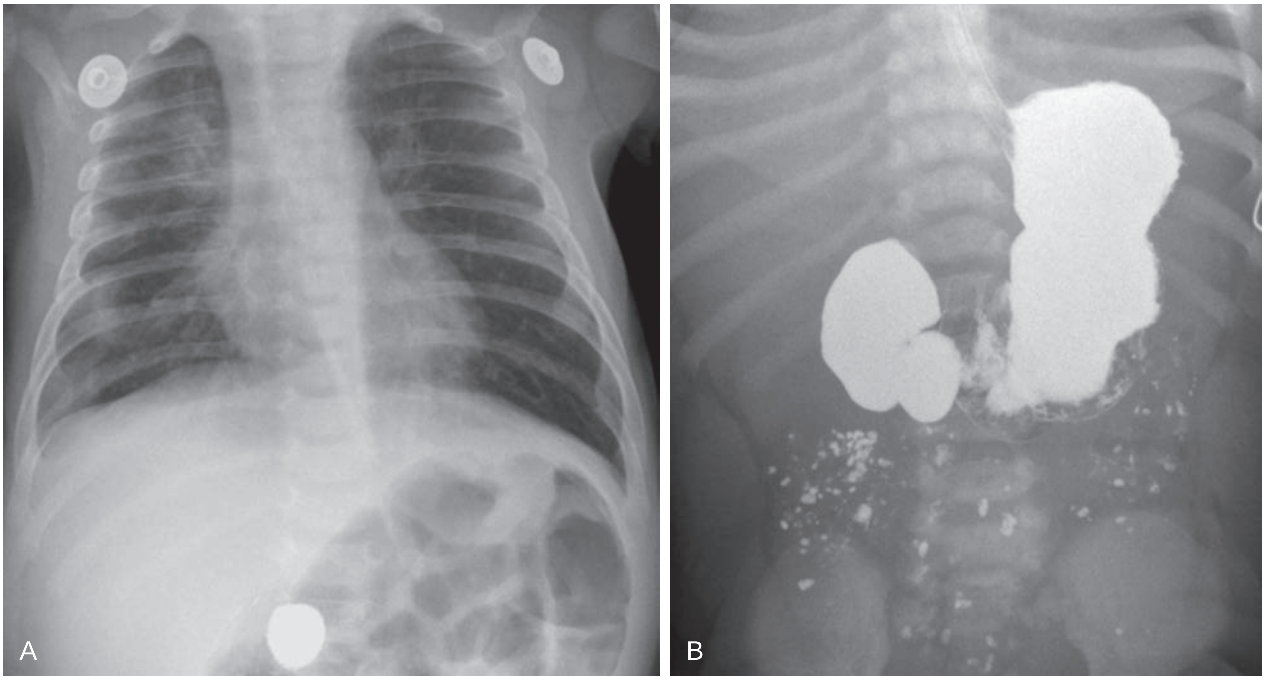

**e-Figure 102.2. Duodenal stenosis with foreign body.** (A) Chest radiograph of a 6-month-old shows a rock that had been ingested several weeks previously. (B) Subsequent UGI demonstrates a dilated duodenum proximal to a web, which was confirmed at surgery. The rock is obscured by the barium.

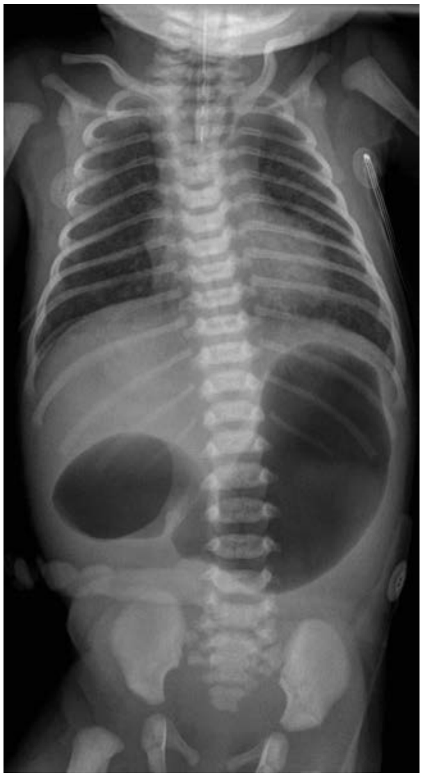

**e-Figure 102.5. Duodenal and esophageal atresia.** Radiograph of a 1-day-old infant shows the orogastric tube in the proximal esophageal pouch; abdominal double bubble indicates a distal fistula and duodenal atresia. This patient is at risk for perforation if there is a need for positive pressure ventilation.

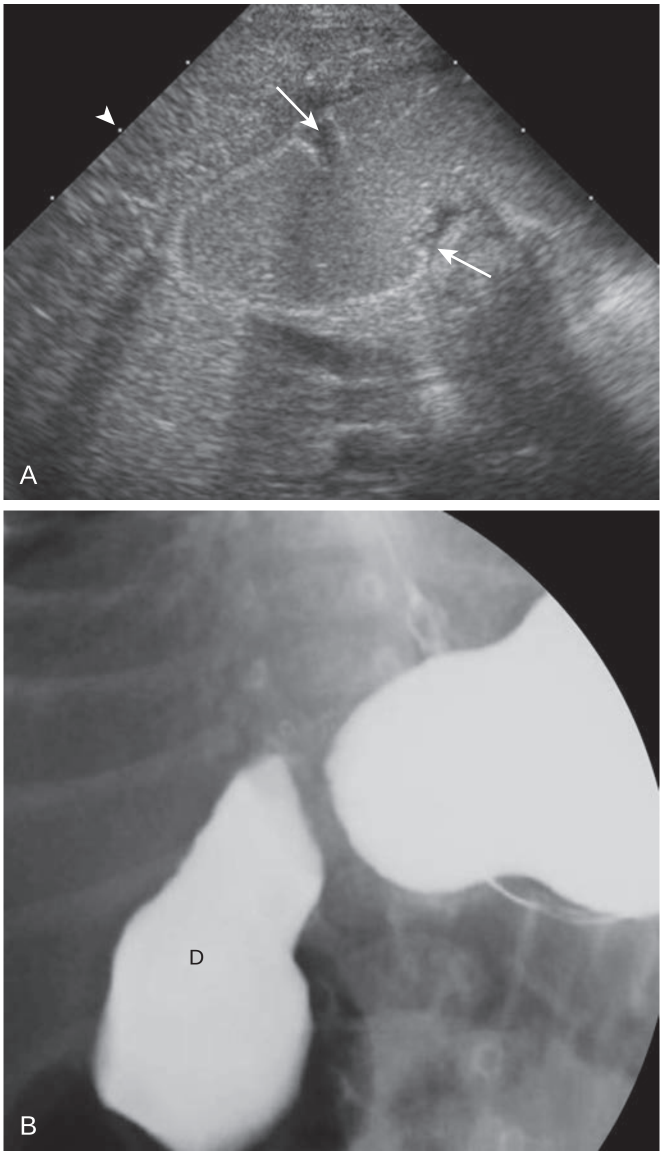

**Figure 102.1. Duodenal stenosis.** (A) Ultrasound image of 4-week-old girl with nonbilious vomiting and suspected pyloric stenosis shows a widely dilated pylorus *(arrows)* and duodenal bulb. The diagnosis of duodenal stenosis was confirmed at subsequent surgery. (B) Upper GI demonstrates a dilated duodenum *(D)*. Note that there is distal bowel gas.

abdominal radiographs may be nonrevealing or even misleading (e-Fig. 102.6).

An upper gastrointestinal (UGI) series may be needed to diagnose duodenal stenosis if potentially associated malrotation is a concern or if surgery is to be delayed (Fig. 102.7).[28] Contrast enema has been done in the past to assess the rotation of the bowel, but this examination is not helpful if it is normal or if the cecum is high-riding; cross-sectional imaging may be done in such cases for further evaluation,[29] discussed in greater detail later in this chapter.

On the UGI examination, patients with duodenal stenosis will demonstrate a partial obstruction (Fig. 102.8); when a web is present, the membrane may be seen as a thin linear filling defect (see Fig. 102.8B). In older patients, the elongated membrane may have the appearance of an intraluminal diverticulum or "windsock" (see Fig. 102.7). As noted earlier, some children with duodenal stenosis may present after ingestion of a foreign body too large to pass through the narrowed canal or orifice (see e-Fig. 102.2). In patients with duodenal atresia simulating duodenal stenosis secondary to bypass of the obstruction by anomalous ducts, contrast may be seen within the ducts, as discussed earlier (see Fig. 102.4B).

***Treatment.*** Treatment of duodenal atresia and stenosis is surgical. When Ladd described surgical correction of duodenal obstruction in 1932,[30] the reported mortality was approximately 40%. In 1990, Kimura et al. described the technique of diamond-shaped anastomosis, which has become standard procedure for open repair, with a mortality of 5% to 10% now largely due only to associated anomalies, particularly those involving cardiac lesions.[31,32] More recently, laparoscopic duodenoduodenostomy has been introduced, with increasingly good results, and reported improvement in return of bowel function, resulting in reduced length of hospital stay.[31,33–35]

## Extrinsic Lesions: Annular Pancreas, Malrotation, Preduodenal Portal Vein, and Duplication Cysts

### Annular Pancreas

***Overview.*** Annular pancreas refers to encirclement of the descending portion of the duodenum by pancreatic tissue. The prevalence of annular pancreas is not known, as asymptomatic cases are not always identified; among adults, autopsy series prevalence varies between 1–15 : 100,000 adults, while endoscopic retrograde cholangiopancreatography (ERCP) studies in symptomatic patients indicates a prevalence of 1–4 : 1000.[36,37] In children, the incidence is estimated at approximately 1–12 : 15,000 births,[38] with a 2 : 1 male:female ratio.[39] Annular pancreas may result in extrinsic duodenal obstruction; however, most cases of duodenal obstruction with annular pancreas are most likely the result of an associated intrinsic duodenal abnormality.[3]

***Etiology.*** The pancreas arises as a ventral and larger dorsal bud from the duodenum. Normally the ventral bud rotates and fuses with the dorsal bud. When the ventral bud becomes tethered to the duodenum before the onset of the rotation, or if the ventral bud fails to rotate completely before fusion, the result is the annular pancreas.[3,37,40] The pancreatic annulus, the portion surrounding the duodenum, frequently has a separate duct entering the duodenum, opposite the ampulla of Vater. Duodenal contents may reflux through this duct into the annulus. Studies in transgenic mice have shown that the annular tissue is derived from the ventral bud; molecular studies have implicated the hedgehog signaling pathway and the transmembrane 4 superfamily 3 gene *(TM4SF3)*.[41]

***Clinical Presentation.*** Children present with vomiting or feeding intolerance, with a median age of 1 day at diagnosis.[37] Presentation in older children who do not have duodenal obstruction is similar to that in adults, with pancreatitis and jaundice.[37,39,42,43] Associated anomalies are common, and these include malrotation, esophageal atresia, anal atresia, and cardiac defects, particularly in patients with trisomy 21 and Cornelia de Lange syndrome[17,37]; annular pancreas has also been reported in patients with heterotaxy.[44]

***Imaging.*** Plain films will show duodenal dilatation in those patients in whom there is intrinsic and/or extrinsic obstruction. UGI will show narrowing of the descending portion of the duodenum (Fig. 102.9A). On ultrasonography, a ring of pancreatic tissue may be seen about the descending portion of the duodenum, although the duodenum might be difficult to follow, and the appearance may resemble a mass at the level of the head of the pancreas (Fig. 102.9B). Computed tomography (CT) likewise can show the pancreatic tissue surrounding the duodenum (Fig. 102.9C and D), probably more clearly if aided by positive luminal contrast in the duodenum. Magnetic resonance imaging (MRI) also may show the ring of pancreatic tissue (Fig. 102.9E), but magnetic resonance cholangiopancreatography (MRCP) will show more definitive findings outlining the annular course of the pancreatic

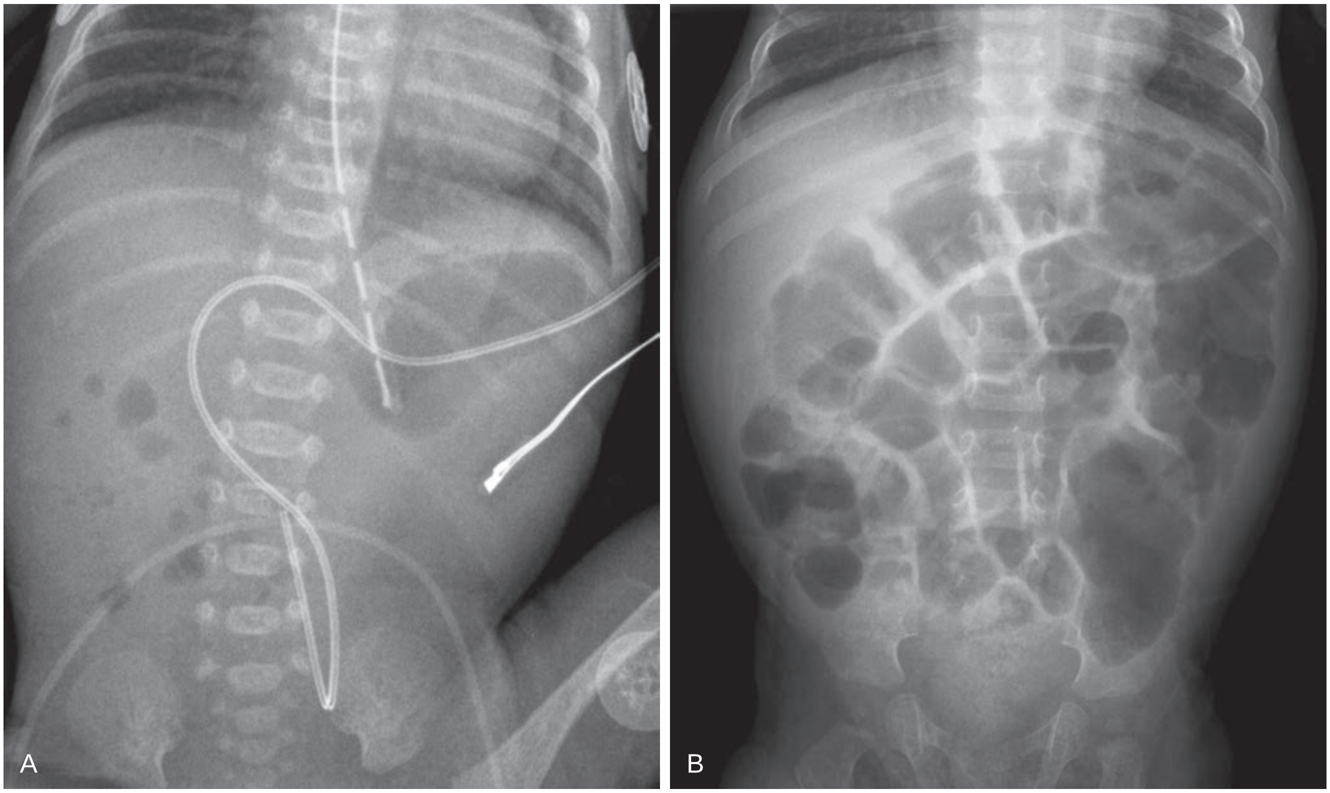

**e-Figure 102.6. Duodenal stenosis.** (A) Radiography of a 1-day-old premature twin infant with bilious aspirates shows minimal distal bowel gas. Duodenal stenosis was shown on subsequent UGI (see Fig. 102.8A) and confirmed at duodenoduodenostomy. (B) Radiograph of an 8-month-old with Down syndrome, admitted for investigation of failure to thrive. Despite the abundant distal bowel gas, duodenal stenosis with membrane was demonstrated on UGI (see Fig. 102.8B) and confirmed at subsequent surgery.

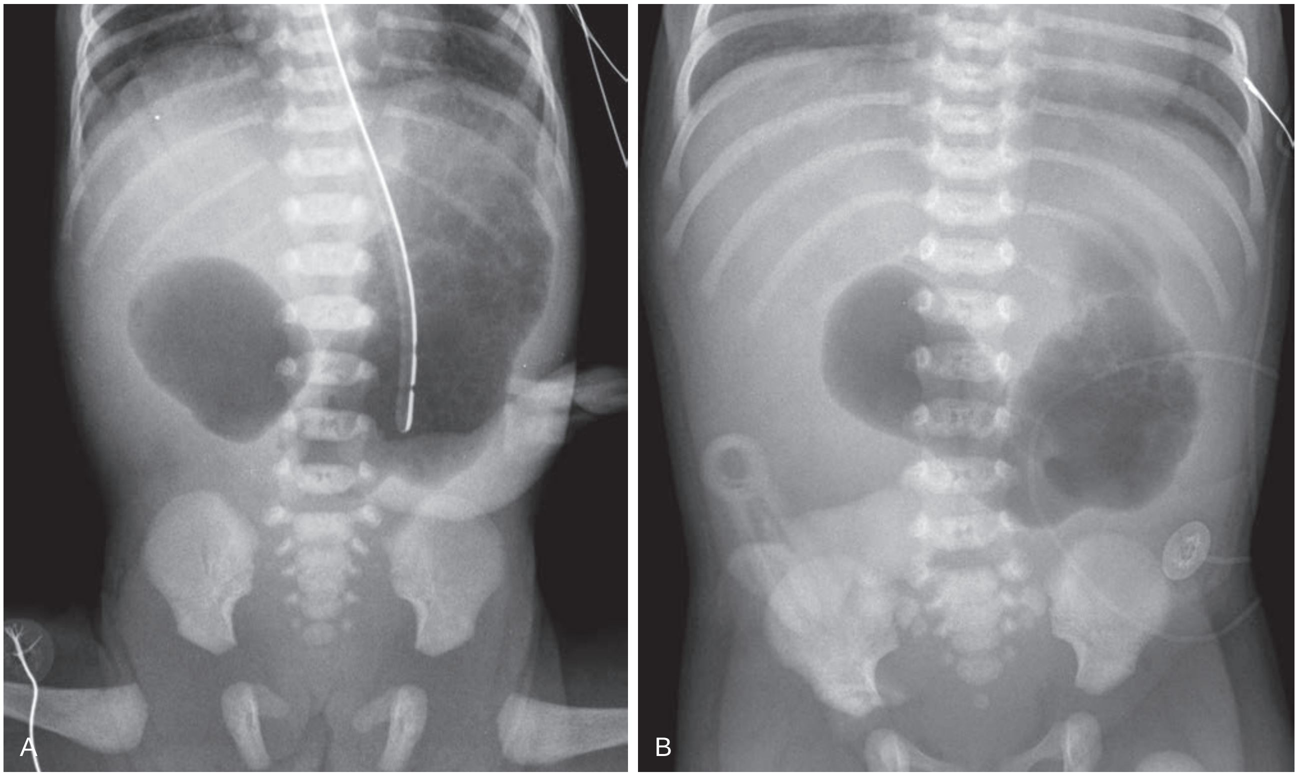

**Figure 102.3. Duodenal atresia.** (A) Radiograph of a 32-week gestation premature infant on day 1 of life, with prenatally diagnosed duodenal atresia shows the classic double bubble, with a distended stomach and duodenum, and no distal gas. (B) Full-term infant with prenatal diagnosis of duodenal atresia. The radiograph shows a gaping pylorus through which there is wide continuity between the dilated stomach and the dilated duodenum, with no distal gas.

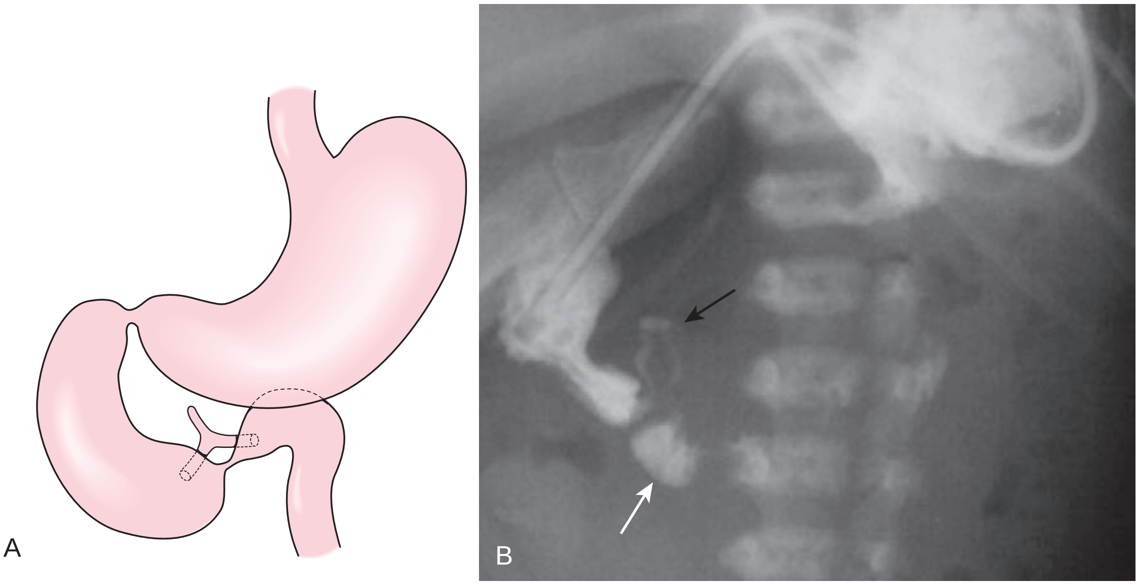

**Figure 102.4. Duodenal atresia with anomalous ducts.** (A) Schematic rendering of duodenal obstruction bypass by dual anomalous ducts. (B) UGI in a neonate with duodenal atresia, showing contrast in the ductal system *(black arrow)* bypassing the site of atresia into the distal segment *(white arrow)*. *(Reproduced with permission from Komuro H, et al. Bile duct duplication as a cause of distal bowel gas in neonatal duodenal obstruction.* J Pediatr Surg. *2011;46[12]:2301–2304.)*

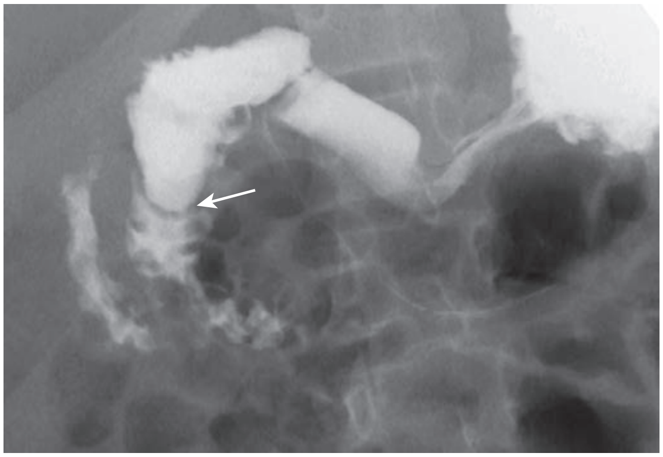

**Figure 102.7.** Duodenal web and malrotation UGI in adolescent with history of intermittent abdominal pain shows a duodenal web *(arrow)*. Note that duodenal contrast does not cross to the left of midline, indicating malrotation.

ducts (Fig. 102.9F), analogous to the findings seen at ERCP (e-Fig. 102.10).

***Treatment.*** As in the case of intrinsic duodenal obstruction, treatment is surgical bypass; interruption or division of the pancreatic tissue around the duodenum is not indicated, due to the likelihood of postoperative leakage or pancreatitis.[3] More recently, laparoscopic surgery has also been undertaken with good results in experienced hands.[33,45]

## Malrotation

**Overview.** The embryonic midgut, which is supplied by the superior mesenteric artery and extends from the distal descending duodenum to the distal transverse colon, undergoes 270 degrees of counterclockwise rotation (as viewed from the front) through a complex series of steps to achieve its final position, with the duodenojejunal junction in the left upper quadrant and the cecum in the right lower quadrant.

The term malrotation indicates that the normal rotation of the midgut was not completed, and therefore represents a misnomer, as the term "incomplete rotation" would more accurately characterize the resulting spectrum of abnormalities, which affect both the duodenojejunal and the cecal poles of the midgut, singly or in unison. The prevalence of malrotation is difficult to determine, inasmuch as asymptomatic cases may not be recognized; it has been most often quoted as 1 : 500 live births,[46–50] which seems excessive as that is similar to the incidence of pyloric stenosis (2–5 : 1000). More recent information suggests that malrotation is far less common, approximately 3.9 per 10,000.[51]

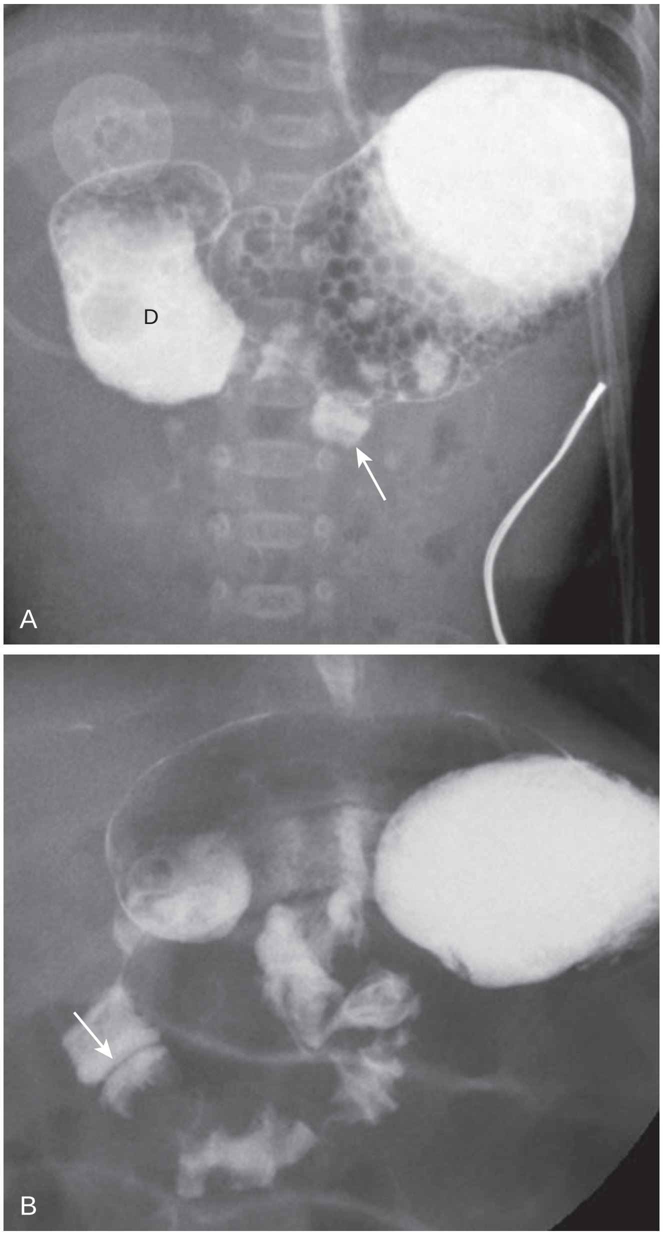

**Figure 102.8. Duodenal stenosis.** (A) UGI from same infant as shown in e-Fig. 102.6A shows the duodenal obstruction, with dilatation of the duodenum *(D)* and decreased duodenal caliber distally *(arrow)*. (B) UGI from same infant as shown in e-Fig. 102.6B shows a duodenal web *(arrow)*.

**Etiology.** To understand the etiology of malrotation, or incomplete rotation, the normal process of rotation must be understood. The gut begins as a straight tube, with the duodenojejunal junction and the cecum along a straight line. As the gut begins to grow, it forms a primary loop about the axis of the superior mesenteric artery, with the apex at the omphalomesenteric duct: the proximal portion is the prearterial (duodenojejunal) limb, and the distal portion is the postarterial (ileocecal or cecocolic) limb. Postnatally, the site of the Meckel diverticulum marks the junction of the pre- and postarterial limbs. Initially, the duodenum and cecum rotate 90 degrees counterclockwise, such that the duodenojejunal junction comes to lie in the right upper quadrant, and the cecum comes to lie in the left lower quadrant. At approximately 6 weeks of gestation, continued growth of the intestinal tube results in herniation of the bowel into the umbilical cord and a second counterclockwise turn of 90 degrees at the duodenojejunal junction. By the 10th week of gestation, the bowel begins its return into the abdominal cavity, beginning with the prearterial segment, and the duodenum undergoes its final 90 degrees of rotation and fixation at the ligament of Treitz in the left upper quadrant; the cecum similarly undergoes its final 180 degrees of rotation, to terminate in the right lower quadrant, and undergo fixation to the posterior peritoneum through shortening and resorption of its dorsal mesentery. The bowel is thus suspended from a mesentery, which is attached to the posterior abdominal wall, and which extends from the left upper to the right lower quadrants (Fig. 102.11). The configuration of the duodenal C-loop mirrors the 270 degrees of rotation that it has undergone.[46,48,52–54] The final steps in bowel

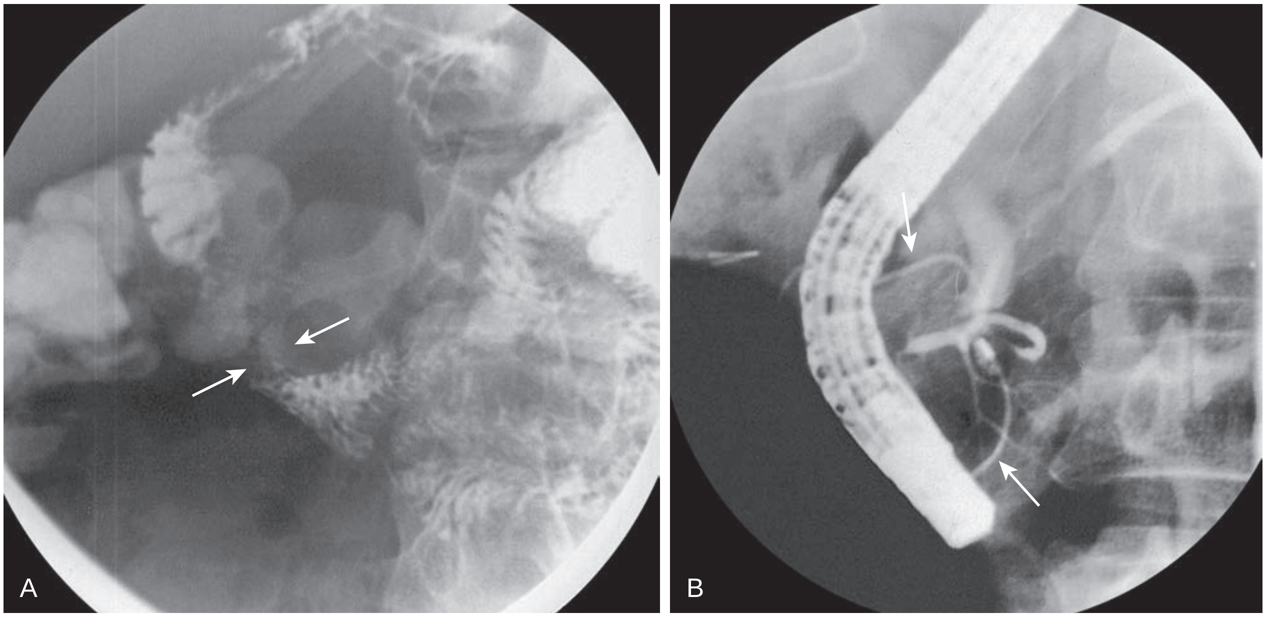

**e-Figure 102.10. Annular pancreas.** (A) Oblique view of the duodenal C-loop during an upper gastrointestinal series shows extrinsic narrowing *(arrows)*. (B) Image from subsequent ERCP confirms circumferential pancreatic ducts *(arrows)* and annular pancreas. *(Courtesy of Dr. George Taylor, Boston, MA.)*

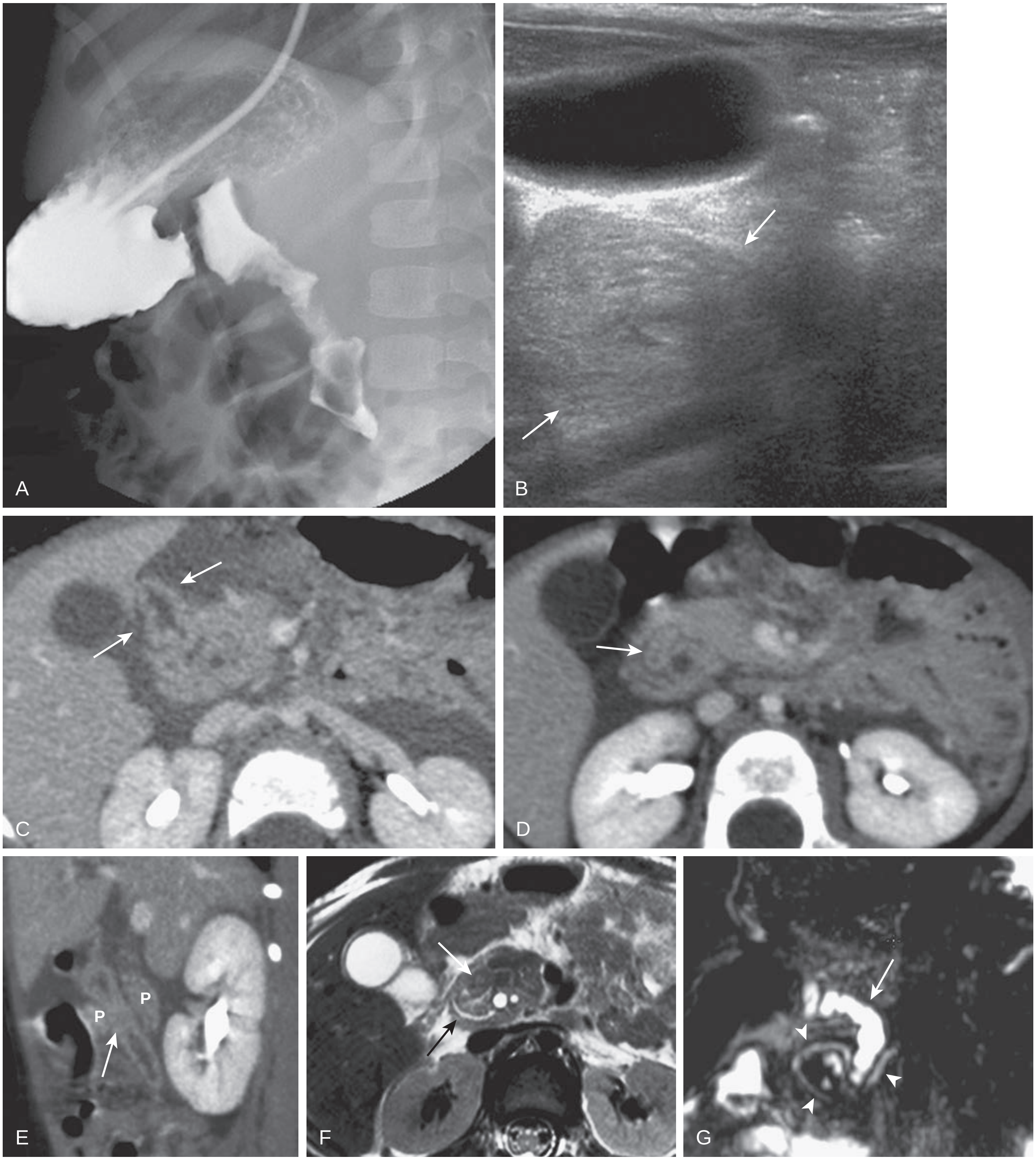

**Figure 102.9. Annular pancreas.** (A) UGI in 2-year-old girl with annular pancreas demonstrates a circumferential impression upon the descending duodenum. The patient had presented with pancreatitis; UGI was done after her symptoms had subsided to assess for an underlying element of duodenal obstruction. (B) Ultrasound at initial presentation shows a thickened head of the pancreas *(arrows)*. (C–E) Contrast-enhanced CT at initial presentation shows the duodenum *(arrows)* entering the head of the pancreas (C), within the head of the pancreas *(arrow)* (D), just lateral to the dilated common bile duct. Sagittal reformat (E) shows the duodenum *(arrow)* with pancreatic tissue *(P)* anterior and posterior to its descending portion. Free fluid is secondary to pancreatitis. (F) Axial T2-weighted magnetic resonance (MR) image shows the duodenum *(white arrow)* within the head of the pancreas, with circumferential pancreatic tissue, outlined by a portion of the encircling pancreatic duct *(black arrow)*. (G) MRCP delineates the pancreatic duct *(arrowheads)* and its circumferential course at the head of the pancreas. *Arrow* points to the dilated common bile duct. *(Courtesy of Melissa A. Hilmes, Nashville, TN.)*

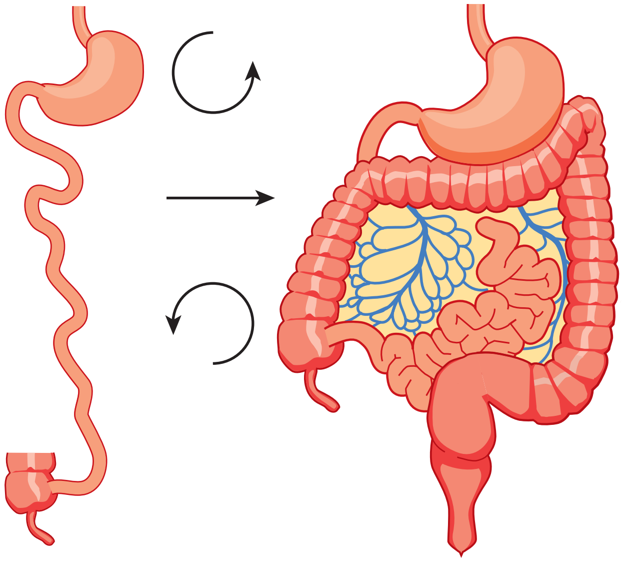

**Figure 102.11. Normal rotation of midgut.** The midgut starts as a straight tube; 270 degrees of counterclockwise rotation of the duodenojejunal junction places it in the left upper quadrant, while 270 degrees of counterclockwise rotation of the cecum places it in the right lower quadrant. After rotation is completed, normal fixation of the bowel results in the midgut being suspended from a broad-based mesentery, with retroperitoneal attachment at both ends.

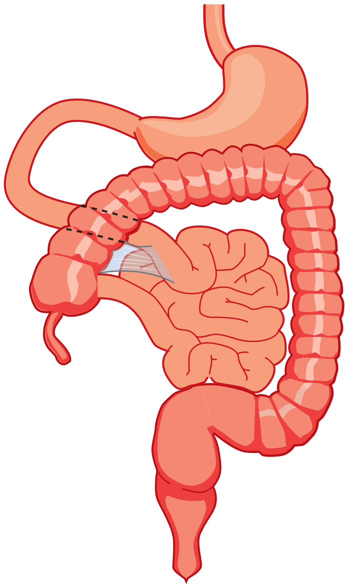

**Figure 102.12. Malrotation.** As the gut rotation proceeds beyond the initial 90 degrees ("nonrotation") and is arrested before the normal 270 degrees, the duodenojejunal junction and the cecum approximate, resulting in suspension of the midgut from a narrow mesenteric pedicle without normal attachments. This arrangement is at high risk for midgut volvulus.

rotation and fixation involve resorption of the dorsal mesenteries of the ascending and descending colon and elongation of the ascending colon with descent of the cecum, processes that are ongoing until several months of postnatal life.[49]

Malrotation arises when the process of normal rotation is arrested, and this can occur at any point along the 270-degree arc of rotation of the duodenojejunal or cecal segments. If it is arrested after the initial 90 degrees of counterclockwise rotation, the duodenojejunal junction and the small bowel will be located on the right side of the abdomen, and the cecum and the rest of the colon will be located in the left side of the abdomen, with the terminal ileum entering the cecum from right to left. Despite the fact that the initial 90 degrees of counterclockwise rotation have occurred in both the duodenojejunal junction and the cecum, this arrangement is nevertheless known as *nonrotation*, because of the parallel appearance of the small and large bowel and the absence of the duodenal C-loop; this type of malrotation is characterized by a relatively long mesenteric pedicle. Progression of the rotation process beyond the nonrotation stage brings the duodenojejunal junction and the cecum into closer proximity, and arrest along this spectrum typically results in a shorter mesenteric pedicle from which the bowel is suspended (Fig. 102.12), which increases the risk for midgut volvulus. Reversed rotation is a rare form of malrotation, in which the gut undergoes 90 degrees of clockwise rotation, instead of the normal 270 degrees of counterclockwise rotation. Starting from the initial straight tube, this rotation results in the location of the duodenojejunal junction in the left upper quadrant and of the cecum in the right lower quadrant. However, in these cases, the ceco-colic loop returns into the abdomen first, and this results in location of the transverse colon, not the duodenum, between the aorta and the superior mesenteric artery.[55,56]

There are also several disorders of fixation that commonly occur in patients with malrotation. Ladd bands are the result of abnormal mesenteric attachments that are formed in patients in whom the rotational process is incomplete. These bands, named after Dr. William E. Ladd, typically extend from the liver edge to the malrotated cecum, crossing over and causing obstruction and kinking of the duodenum (e-Fig. 102.13); however, they can rarely occur more distally, crossing over the jejunum, ileum, or colon.[52,57]

Internal hernias are the result of abnormal or incomplete fixation of the ascending or descending portions of the colon, resulting in a defect through which the bowel can herniate. Herniation into a defect in the ascending colon results in a right paraduodenal or mesocolic hernia, whereas herniation into a descending colonic defect results in a left paraduodenal or mesocolic hernia.[48,52] In persons with normal bowel rotation, failure of complete fixation of the ascending colon, cecum, or sigmoid colon can result in volvulus of these structures, typically not occurring until late adult life.

**Clinical Presentation.** The presentation of patients with malrotation depends on whether there is obstruction, whether the obstruction is acute or chronic, and on associated malformations. Presentation may occur in utero, and the neonate may demonstrate short bowel secondary to in utero bowel necrosis and resorption, or with apple-peel type of atresia.[58,59] In asymptomatic patients, malrotation may be discovered in the course of evaluation for other clinical concerns.

***Acute Midgut Volvulus.*** It is important to differentiate the midgut volvulus that occurs in patients with malrotation from the segmental volvulus that can occur in multiple other conditions, which involves only a small segment of small or large bowel, many of which will be discussed later. In midgut volvulus, the duodenum rotates clockwise about the axis of the superior mesenteric artery (Fig. 102.14) and is obstructed at its third portion, distal to the ampulla of Vater. Because approximately 60% to 80% of patients with midgut volvulus present in the first month of life,[47,49,52,60,61] the typical presentation is that of a previously well neonate who experiences the acute onset of bilious vomiting. The infant may experience crampy abdominal pain, which could be confused with colic. If the obstruction is significant, the abdomen may become initially scaphoid after distal intestinal contents are evacuated; this lack of distension, together with lack of abdominal tenderness during this early stage, may lead to underappreciation of the urgency

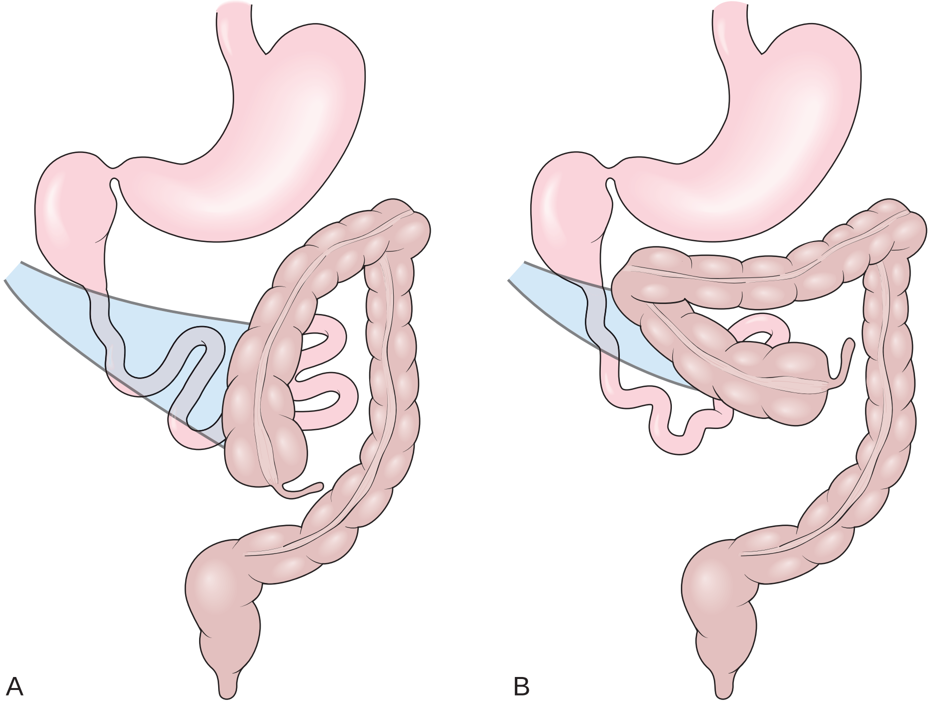

**e-Figure 102.13. Ladd bands.** Illustration of two instances (A and B) in the spectrum of malrotation, demonstrating dense peritoneal bands (Ladd bands) extending from the cecum to the right upper quadrant, crossing over and obstructing the duodenum. These bands can cause obstruction without volvulus, but if there is a volvulus, the bands must be divided after reduction of the volvulus to relieve the obstruction.

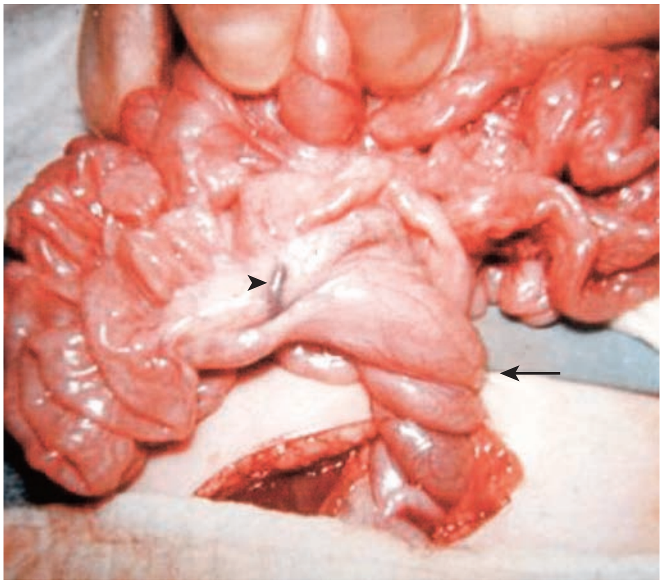

**Figure 102.14.** Acute midgut volvulus. At surgery, the duodenum is twisted clockwise *(arrow)* about the axis of the superior mesenteric artery *(arrowhead)*.

of the condition. Vascular compromise may lead to intraluminal bleeding and hematochezia, seen in 10% to 15% of patients with volvulus.[48] As ischemia of the midgut continues, the abdomen becomes distended and firm, with physical signs of peritonitis, and the patient will present in shock with cardiovascular collapse.[52]

Diagnosis of malrotation and midgut volvulus is even more challenging in premature infants. Preterm infants are less likely to present with bilious vomiting and instead display nonspecific signs and symptoms, including apnea and gastric retention, culminating in abdominal distension and shock with necrotic bowel at operation.[62,63]

***Chronic Midgut Volvulus.*** Partial or intermittent midgut volvulus tends to present more insidiously, with an average duration of symptoms of 28 months or more before the diagnosis.[52] There is usually a history of abdominal pain, which is often vague and intermittent but could be severe, often associated with intermittent vomiting and/or failure to thrive. Impairment of venous and lymphatic flow leads to signs and symptoms of malabsorption.[64,65] The correct diagnosis is frequently delayed, with interim diagnoses including central or psychogenic vomiting, milk or other food allergies, and various malabsorption syndromes, such as celiac disease.[28,52,66,67]

### Other Presentations

***Ladd Bands.*** Patients with duodenal obstruction secondary to Ladd bands may present acutely, with sudden onset of bilious vomiting, or may present with more chronic symptoms such as failure to thrive and intermittent abdominal pain.[52] Patients may also present with more distal obstruction.[57]

***Internal Hernias.*** Either right or left paraduodenal or mesocolic hernias produce symptoms by entrapment of bowel. Left hernias are more common and herniate through the fossa of Landzert; right hernias extend through the fossa of Waldeyer. These present with abdominal pain and vomiting secondary to obstruction, which can progress from partial to complete obstruction, and to ischemia and bowel necrosis.[68,69]

**Associated Conditions.** Malrotation occurs as part of a constellation of anomalies in as many as 30% to 60% of patients, depending on the reporting series.[52,60] Malrotation can occur in patients with duodenal stenosis and annular pancreas, which have been previously discussed but can also be found in patients with other intestinal atresias.[6,60] Malrotation can also be found as part of the spectrum of findings in patients with Hirschsprung disease and anorectal malformations, cloacal exstrophy, Eagle-Barrett (prune belly) syndrome, megacystis-microcolon-intestinal hypoperistalsis (Berdon syndrome), Cornelia de Lange, Marfan, and Meckel syndrome.[46,48,60,70] Malrotation is reported to be 25 times more common than in the general population in patients with trisomy 13, 18, and 21.[46,71] Malrotation is an intrinsic component of entities in which gut rotation cannot occur, such as gastroschisis, omphalocele, and Bochdalek diaphragmatic hernia; it is also extremely common if not invariable in patients with heterotaxy.[72–75]

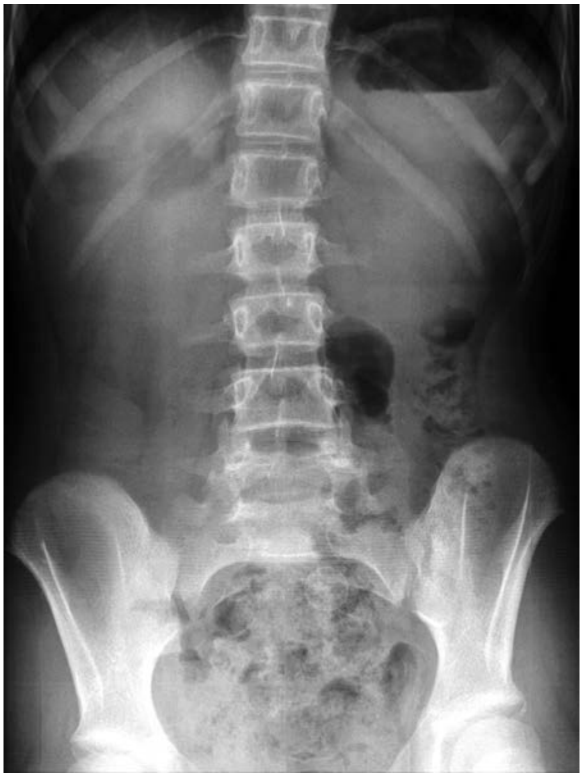

**Figure 102.15.** Nonrotation. Abdominal radiograph in an adolescent with nonrotation. Note that there is no evidence of colon in the right abdomen. The stool-filled colon is confined to the left side of the abdomen.

**Imaging.** Plain abdominal radiographic findings in patients with malrotation without obstruction or volvulus may show an abnormal distribution of stool, with absence of stool pattern in the right lower quadrant.[66] In patients with nonrotation, all colonic stool may be seen confined to the left half of the abdomen (Fig. 102.15). However, although it may occasionally be suspected, malrotation is not a plain film diagnosis.

In patients with volvulus, the radiographs may be completely normal at the onset of the bilious vomiting (Fig. 102.16A) and should not lead to a false sense of security. As unabated or increased duodenal obstruction occurs, distal bowel contents are evacuated; this lack of abdominal distension may again lead to a false sense of security or to the suspicion of pyloric stenosis if the stomach is distended and the significance of the bilious vomiting is overlooked (Fig. 102.16B). It is important to note that in acute volvulus the duodenum may be distended, but typically duodenal distension is subtle (Fig. 102.16C), different from the obvious double bubble of duodenal atresia, because the time span for the development of dilatation is typically much shorter.

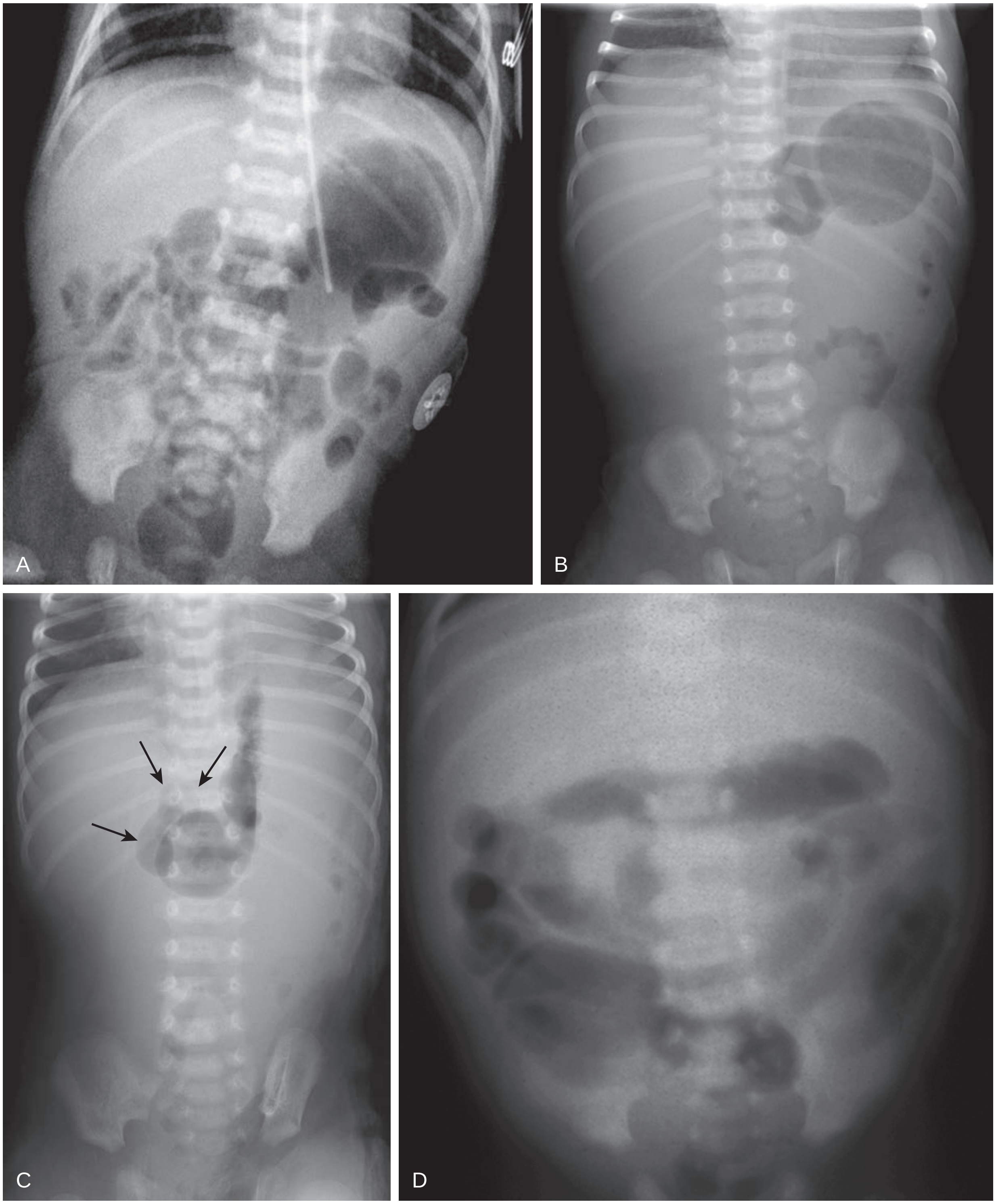

**Figure 102.16. Malrotation and midgut volvulus.** (A) Abdominal radiograph in 2-day-old infant with bilious vomiting and midgut volvulus. The bowel gas pattern is easily interpreted as within normal limits; a normal abdominal radiograph does not exclude the presence of volvulus. (B and C) Supine (B) and left decubitus (C) radiographs in 7-day-old infant with bilious vomiting and midgut volvulus. In (B), although the stomach is normal in size, there is discrepancy between the size of the stomach and the marked lack of gas distally. No distension of the duodenum is appreciated. In (C), the decubitus radiograph reveals gaseous distension of the duodenum, which was not appreciated on the supine image. This duodenal distension coupled with the history of new onset of bilious vomiting, and the paucity of distal gas, are extremely concerning for acute volvulus. (D) Radiograph of a 2-week-old infant with bilious vomiting for several days shows a severe ileus pattern, with fluid and gas distending loops of bowel throughout the abdomen. His bowel was necrotic at subsequent surgery, and the infant expired.

Ominous plain radiographic findings of supervening ischemia in patients with volvulus include abdominal distension, separation of the gas within bowel loops secondary to increased luminal fluid, tubular appearance of bowel loops, and fold thickening. Diffuse fluid and gaseous distension of the bowel suggests gangrenous bowel and a poor prognosis (Fig. 102.16D).

In premature infants, bilious vomiting may be absent, and the clinical picture may be nonspecific and suggestive of the more common entities of sepsis and necrotizing enterocolitis[62,63]; radiographs obtained at the time of systemic manifestations may show dilated bowel loops and suggest profound ileus and/or necrotizing enterocolitis (e-Fig. 102.17).

***Upper Gastrointestinal Tract.*** Although cross-sectional imaging is increasingly recognized as accurate in the evaluation of malrotation and volvulus, in most centers, UGI is considered the standard examination.

Documentation of normally rotated bowel can be challenging, and technique is very important. In pediatric patients, documentation of the normally rotated C-loop needs to be made on passage of the first bolus of contrast from the stomach; missing this opportunity can result in confusing and misleading findings. The course of the duodenum must be documented in both frontal and lateral projections, as the lateral view is essential to document the parallel orientation of the ascending and descending portions of the retroperitoneal duodenum.[48,76,77] On the frontal view, the duodenojejunal junction, recognized by the acute flexure as the duodenum returns to the peritoneal cavity, should be located just to the left of the left pedicle of the adjacent lumbar vertebra, at the same craniocaudal level as the bulb. The lateral view should show ascending and descending portions entirely superimposed anterior to the spine—anterior deviation of the ascending limb is abnormal. The technique is discussed and illustrated in Chapter 84.

The radiologist should be familiar with normal variants of the duodenum, such as duodenum inversum, in which the duodenum shows parallel ascending and descending course to the right of the spine, before crossing to the left and emerging into the peritoneal cavity at a normally positioned ligament of Treitz (Fig. 102.18, Video 102.1).[78,79] Conversely, it is imperative that the abnormal course of a malrotated duodenum in patients without volvulus be recognized, including abnormal location of the duodenojejunal junction on the frontal image (Fig. 102.19A) and abnormally anterior course of all or part of the duodenum on the lateral view.

In symptomatic patients with malrotation, the UGI examination may reveal the volvulus itself, showing a spiral twisting of the duodenum as it wraps around the axis of the superior mesenteric artery, classically described as a "corkscrew" (Fig. 102.19B). When there is complete obstruction, the contrast column may terminate in a beaklike configuration, as the contrast is propelled into the entrance of the spiral, but cannot proceed further (Fig. 102.19C).

In patients with obstruction secondary to Ladd bands, the duodenum may demonstrate a kinked configuration which at times resembles a Z-shape instead of the normal C-loop.[80] The Z-shape is the result of tacking down and kinking of the duodenum by the abnormal attempts at fixation and at times may be difficult to differentiate from volvulus (Fig. 102.19D).

***Contrast Enema.*** In the mid-20th century, barium enema was advocated in the investigation of patients suspected of malrotation and volvulus in the belief that cecal position would define the presence or absence of malrotation, while avoiding introduction of barium contrast proximal to the obstructed duodenum. However, with the understanding that up to 30% of patients with malrotation and its complications could have a normally rotated cecum, and with the realization that a high-riding cecum in a neonate may in fact be normally rotated,[28,81–83] the contrast enema is no longer favored as the appropriate first examination. In problem cases when the UGI is confusing, a follow-through small bowel to determine cecal position may be helpful. Although the caveats just noted regarding cecal position, and additional pitfalls in antegrade recognition of the cecum if the appendix or terminal ileum are not clearly visualized, a clearly abnormal cecal position, especially in children with an equivocal location of the duodenal-jejunal flexure, is diagnostic of malrotation. If there is continued concern, cross-sectional imaging, discussed later, can be considered.[84]

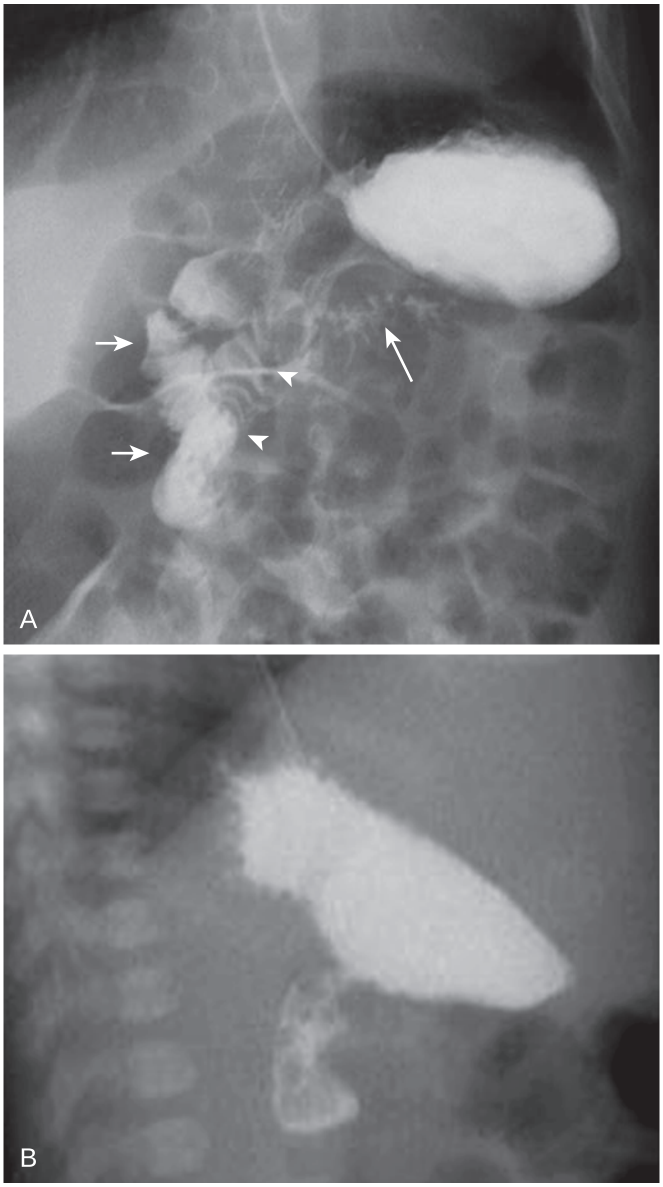

**Figure 102.18. Duodenum inversum.** (A) Frontal UGI image (A) of infant with duodenum inversum, a normal variant. Note that, after the vertical course of the duodenum on the right *(short arrows)* it ascends *(arrowheads)* to the right of the midline, before crossing to a normally positioned duodenojejunal junction at the ligament of Treitz *(large arrow)*. (B) Lateral view in a patient with duodenum inversum shows normal posterior position of the duodenal course, with superimposed ascending and descending limbs. (See Video 102.1.)

### Challenging Cases

***Overview and Pitfalls.*** A clearly abnormal course of the duodenum renders the diagnosis of malrotation straightforward. Unfortunately, false-positive and false-negative results may occur in as many as 15% and 6% of cases, respectively.[85–88] False positive interpretations usually result from failure to recognize normal

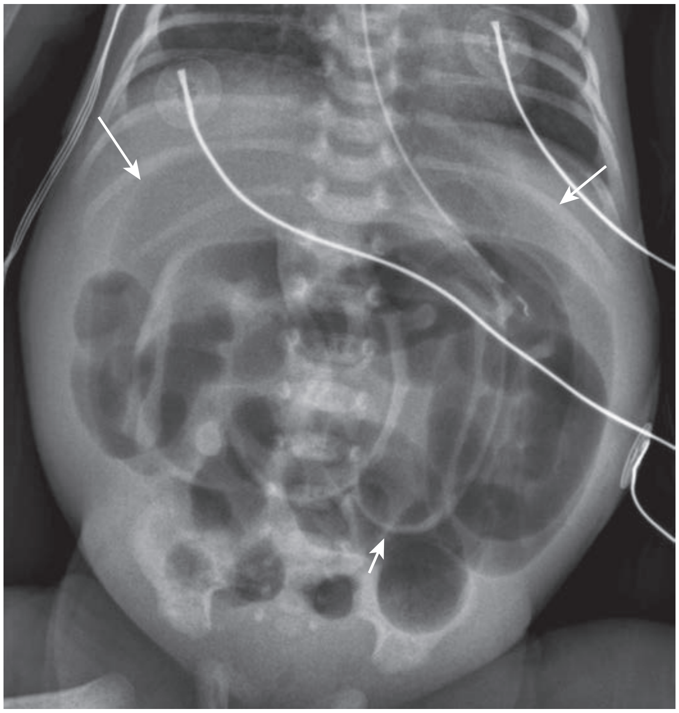

**e-Figure 102.17.** Midgut volvulus in a premature infant. The infant was tolerating increased feedings, when overnight he began having nonbilious residuals and had systemic symptoms consistent with sepsis. Radiograph shows generalized dilatation of bowel loops and free air *(arrows)*. At surgery, there was malrotation with midgut volvulus and bowel necrosis.

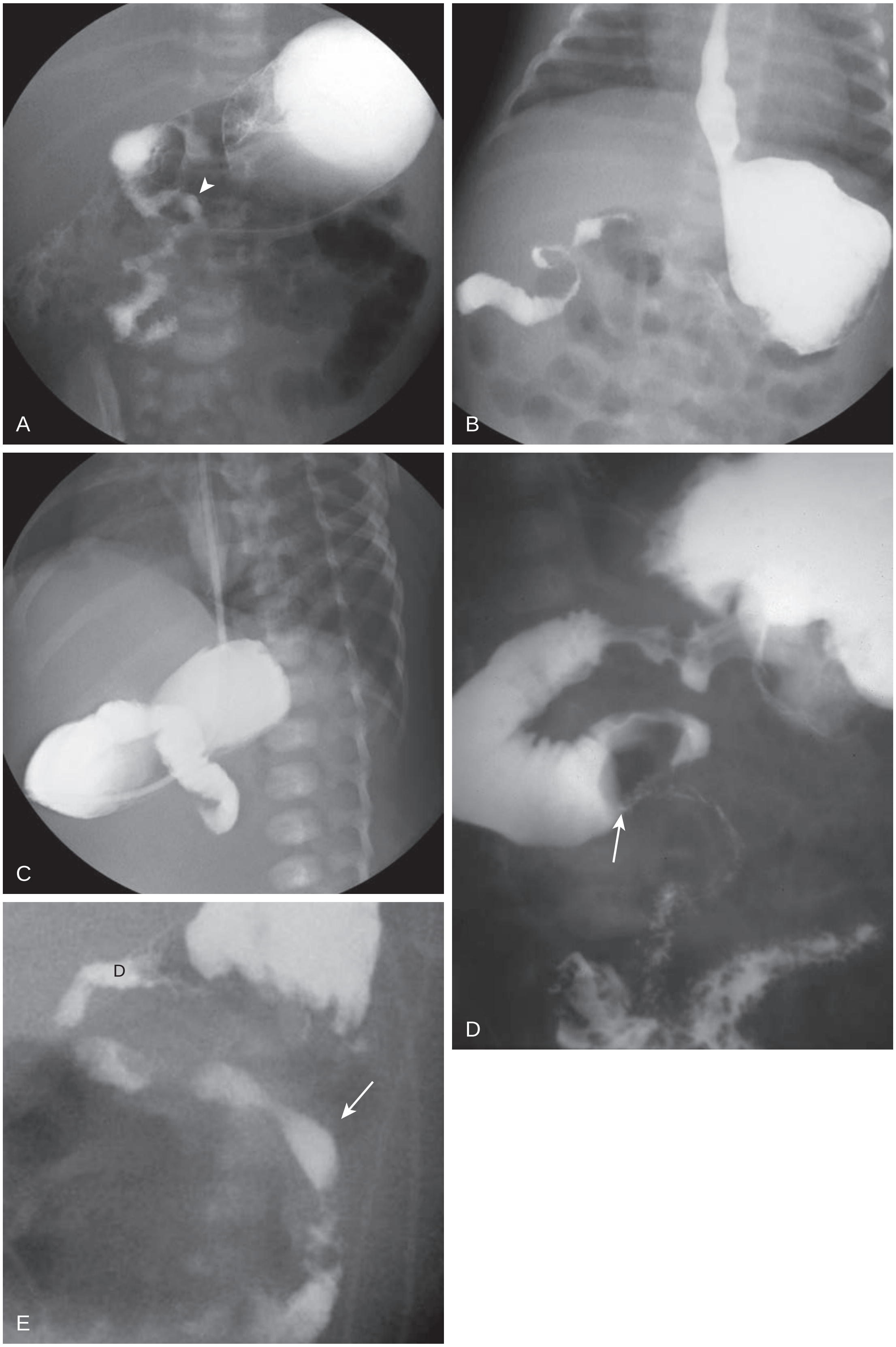

**Figure 102.19. Malrotation, volvulus, and Ladd bands on UGI.** (A) Malrotation in an infant without midgut volvulus. Frontal image demonstrates that the presumed duodenojejunal junction *(arrowhead)* is low and to the right of the midline. (B) Image obtained during UGI in infant with malrotation and midgut volvulus. Note the classic "corkscrew" configuration of the duodenum as it wraps around the mesenteric pedicle. There was significant reflux secondary to the obstruction. (C) Image from UGI on another infant with 1 day history of bilious vomiting, presenting to the ED with dehydration. There was complete obstruction of the duodenum, terminating in a configuration resembling a beak. (D) Ladd bands in 2-month-old girl with malrotation. Left posterior oblique spot image from an upper GI demonstrates the abnormal course of the duodenum, and dilatation of the proximal duodenum due to crossing bands at its third portion; note the kinking of the duodenum *(arrow)* and the resemblance to a corkscrew. This appearance does not exclude midgut volvulus. (E) Note the depression of the duodenojejunal junction *(arrow)* below the level of the duodenum (D) in this surgically confirmed normally rotated infant, secondary to the mass effect of dilated loops from a closed loop obstruction in the lower abdomen.

variants, such as the duodenum inversum previously discussed. Position of the proximal small bowel in the right upper quadrant, as an isolated finding, is not indicative of malrotation.[78,79,87] Displacement of a normal ligament of Treitz is another cause of false-positive results. We know that the neonatal duodenum is mobile[82] and can be displaced secondary to peritoneal masses; abnormal, dilated bowel loops[89] (Fig. 102.19E); or postoperatively.[90] A mobile or high position of the cecum, particularly in a neonate, can be a normal finding that overlaps with malrotation and renders evaluation for malrotation particularly challenging in individual patients.

Potential false-negative outcomes may result from suboptimal technique, such as failing to delineate the course of the duodenum on the first bolus of contrast from the stomach, or from failure to identify the subtle finding of malrotation, such as kinking of the duodenum along its course, or failing to appreciate an abnormally low location of the duodenojejunal junction, or one that is to the right of the left pedicle of the spine.[46,48,76,82,87] Limitations of the lateral view itself include the fact that the aorta and the superior mesenteric artery are not visualized, and therefore true retroperitoneal position of the duodenum cannot be ascertained unequivocally,[29] despite the parallel course of its ascending and descending portions anterior to the spine.

**Cross-Sectional Imaging.** Cross-sectional imaging is receiving further attention as a means of diagnosing malrotation and volvulus.[29,84,91–93] Even when cross-sectional imaging is not the first line examination, ultrasound may be the first examination performed in a child with vomiting in whom the presence or significance of bile in the vomitus has not been appreciated, or CT may be performed in an older child to assess atypical abdominal pain. Ultrasound can also be very helpful in patients with complete obstruction at the duodenum, in whom the rotation of the bowel or the presence of volvulus cannot be ascertained at UGI.

***Ultrasound.*** The normal retroperitoneal course of the duodenum is an indication of normal rotation of the bowel and has been underscored recently as an important finding on abdominal ultrasound.[29,84,91–94] That said, this is not an easy task, and as is true of the UGI, the ultrasound examination requires a knowledgeable and skilled operator, and utmost attention to detail. It is important to note that the peritoneal membrane is not visualized, and therefore the retroperitoneal location of the crossing duodenum is implied by the surrounding anatomy. It is easiest to find the duodenum as it courses beyond the pylorus and around the head of the pancreas, and follow its course between the aorta posteriorly and the superior mesenteric artery (SMA) and vein (SMV) anteriorly, noting the proximity of this crossing to the renal hila and to the origin of the SMA from the aorta (Fig. 102.20). Duodenal proximity to the origin of the SMA is important, as the duodenum crossing well below the renal hila does not document its retroperitoneal location.[93–96]

Alteration or inversion of the normal left-right relationship of the superior mesenteric artery and vein is often mentioned in the context of malrotation. Although the relationship can be abnormal in many patients with malrotation,[97] the finding is neither highly sensitive nor highly specific in the diagnosis of malrotation, with or without volvulus.[98]

The corkscrew findings of midgut volvulus have been termed the *whirlpool sign* at ultrasound,[99] where not just the duodenum, but also the SMV, can be seen turning clockwise about the axis of the SMA. As on UGI, the duodenum can be followed from the antrum and pylorus, around the head of the pancreas, and can be seen entering into the twist, indicating the presence of midgut volvulus (Fig. 102.21). As the transducer is moved craniocaudally, the clockwise twisting can be appreciated (Videos 102.2 and 102. 3). The relatively new advent of ultrasound in this emergent diagnosis begs the question of its sensitivity and specificity. Published data on smaller cohorts suggest that it is sensitive and specific for malrotation with volvulus,[100,101] with more recent presentations reporting sensitivity and specificity as high as 100%.[91] Despite these reports, experience with this modality is not widespread, and UGI remains the mainstay of diagnosis at most centers. On the other hand, if there is complete obstruction at UGI, consideration can be given to ultrasound to confirm the suspected diagnosis of volvulus. Ultrasound can further confirm flow within the SMA, within and distal to the volvulus (e-Fig. 102.22). In patients with bowel ischemia and gaseous distension of bowel, it is possible that the whirlpool sign may not be identified. Menten et al. propose that demonstration of a parallel orientation of the superior mesenteric artery and vein can exclude the presence of volvulus at the time of the examination.[102]

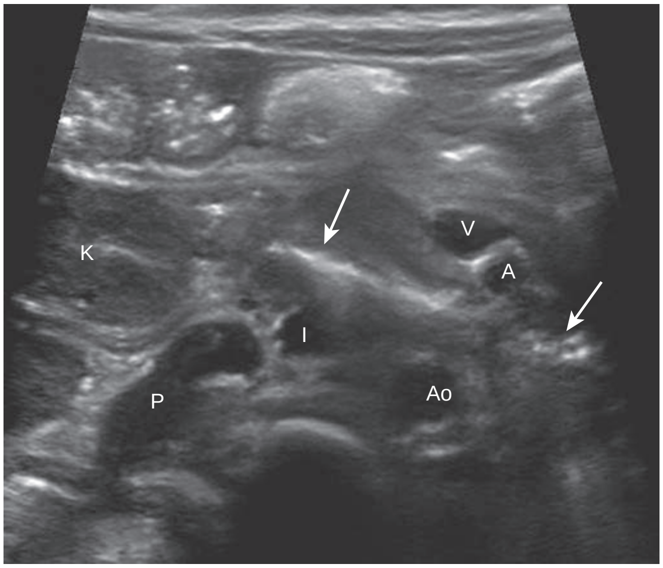

**Figure 102.20. Normal duodenum and rotation on ultrasound.** Normally rotated duodenum. Transverse ultrasound at the level of the renal hila, showing the gas-containing transverse duodenum (D3, *arrows*) crossing between the Aorta *(Ao)* and IVC *(I)* posteriorly, and the SMA *(A)* and SMV *(V)* anteriorly. *K*, Right kidney; *P*, right psoas.

In older patients presenting with chronic volvulus, the sonographic findings are similar, although the duodenum may be considerably larger, as it has had time to become dilated, in contradistinction to the acute presentation (Fig. 102.23, Video 102.4).

***Other Cross-Sectional Imaging.*** CT demonstrates the retroperitoneal course of the normally rotated duodenum, as well as the position of the cecum, unencumbered by overlying bowel gas, and therefore is an excellent modality to document bowel rotation. Identification of midgut volvulus, with incorporation of the duodenum and the superior mesenteric vessels in the twist, is also possible (Fig. 102.24). Although CT currently is not considered a primary modality in the assessment of malrotation, the findings should be recognized if encountered on examinations performed for other reasons. With low dose and ultrafast scanners that do not require sedation, the role of CT may need to be re-examined.

***Treatment.*** The surgical Ladd procedure for treatment for malrotation with volvulus consists of surgical detorsion, identification and lysis of Ladd bands, straightening of the duodenum along the right abdomen, and placement of the cecum in the left lower quadrant, broadening the base of the mesentery and creating a separation between the duodenojejunal junction and the cecum resembling nonrotation, with incidental appendectomy.[30,103] When accompanied by volvulus, the surgery is emergent, and correction of existing metabolic and electrolyte derangements must be undertaken. Laparoscopic surgery is an alternative approach in older children,[104] and there may be fewer short- and long-term complications hopefully without increased risk of recurrent volvulus.[105]

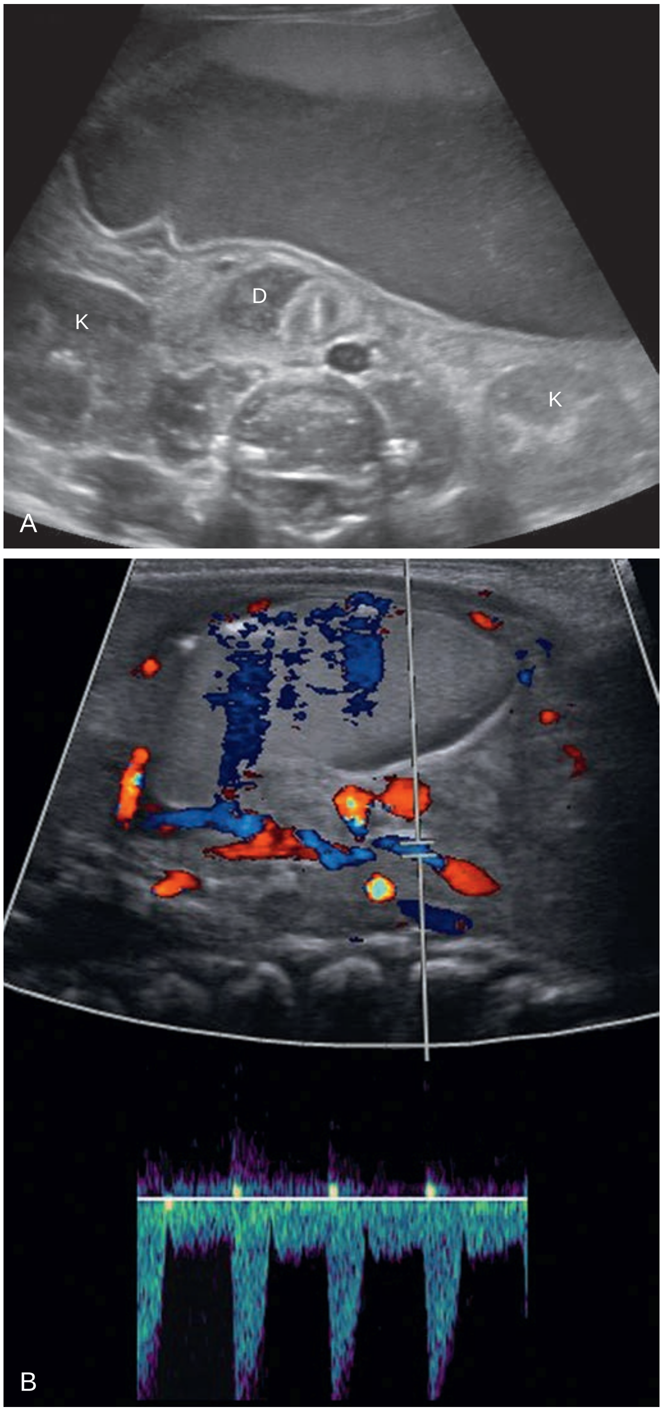

**e-Figure 102.22. Midgut volvulus.** (A) Ultrasound in a 4-day-old neonate with bilious vomiting shows a markedly dilated stomach, and the duodenum *(D)* entering into the volvulus with a beaklike configuration. *K*, Right and left kidneys. Video 102.3 shows the distended duodenum and the superior mesenteric vessels within the clockwise rotation of the midgut volvulus complex. (B) Sagittal image demonstrating flow in the SMA distal to the midgut volvulus. At surgery, the midgut volvulus without bowel compromise was confirmed.

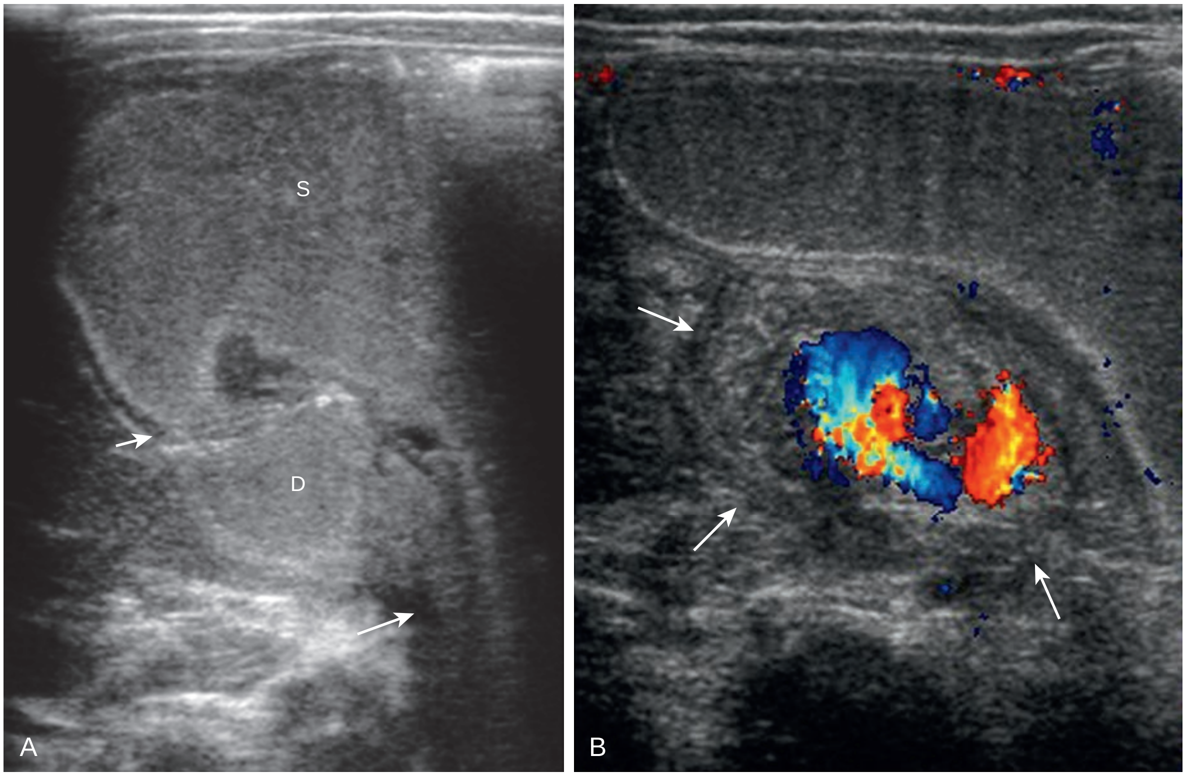

**Figure 102.21. Midgut volvulus on ultrasound.** (A) Ultrasound image of an 18-day-old boy with history of vomiting since birth, which had recently become "projectile" and was "occasionally yellow" shows a dilated stomach *(S)* and duodenum *(D)*, with the latter deviated medially as it enters into the midgut volvulus *(long arrow)*. The pylorus *(short arrow)* is widely open. (B) Color Doppler image shows the duodenum at the outer edge of the twist *(arrows)*, with the twisting superior mesenteric vein, and the centrally located superior mesenteric artery. Video 102.2 demonstrates the clockwise turning as the transducer moves in a cephalocaudal direction.

When malrotation in the absence of volvulus is found in the older child or adult, surgery is indicated if the patient is symptomatic. The role of surgery versus conservative management in the asymptomatic older patient with malrotation without volvulus, such as patients with heterotaxy,[106] remains controversial.[107] More recent literature suggests that observation, particularly in patients with heterotaxy, is preferable.[72,105,108–111]

### Preduodenal Portal Vein

***Overview.*** The portal vein forms at the junction of the superior mesenteric and splenic veins, and its normal course is retropancreatic and retroduodenal. The preduodenal portal vein courses anterior to the pancreas and duodenum; it is important because of its associated anomalies, but its major significance is surgical recognition.[112]

***Etiology.*** Preduodenal portal vein is the result of abnormal resorption of segments of the paired embryonic vitelline veins and their connections (e-Fig. 102.25). Normally there is persistence of the upper communicating branch between the left and right vitelline veins, resorption of the cephalad segment of the left vitelline vein, the caudal segment of the right, and of the lower communicating branch, resulting in the duodenum coursing ventral to the portal vein. The preduodenal portal vein results when the upper communicating branch is resorbed, with persistence of the lower communicating branch, which courses ventral to the duodenum; there is resorption of the left and persistence of the right vitelline veins.[113,114] It is often seen in disorders with failure of recognition of asymmetry, particularly heterotaxy, most often with left isomerism and polysplenia.[75,115]

***Clinical Presentation.*** The preduodenal portal vein is associated with conditions that cause duodenal obstruction, including duodenal web, annular pancreas, and malrotation. Therefore although often asymptomatic, the major presenting symptom is duodenal obstruction, believed to be secondary to the associated anomaly in most cases.[116,117] Preduodenal portal vein is highly associated with heterotaxy, particularly polysplenia.[75,118] The most important concern is inadvertent injury during surgery.[117,119,120] This anatomy should be identified before surgery whenever possible, particularly in presurgical candidates at risk for this anatomy.[73,75,121]

***Imaging.*** The preduodenal portal vein is well seen at cross-sectional anatomy. On sonography, the normal SMV is seen dorsal to the pancreas, where it is joined by the splenic vein to enter the liver. In the preduodenal arrangement, the SMV instead moves ventrally over the pancreas and hence, in a stepladder-like fashion, into the liver (e-Fig. 102.26).[75,122] On CT and MRI, the findings are similar (Fig. 102.27).[123]

***Treatment.*** There is no treatment necessary for asymptomatic preduodenal portal vein. When associated with obstruction, bypass of the obstruction or correction of malrotation or Ladd bands is indicated.[120,124]

# PART II: SMALL BOWEL

## Congenital/Neonatal Anomalies of the Small Bowel

### Small Bowel Atresia and Stenosis

***Overview.*** Atresia and stenosis affect the jejunum and ileum more commonly than any other portion of the abdominal GI

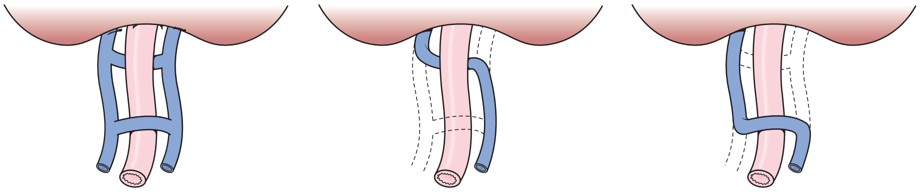

**e-Figure 102.25. Schematic illustration of formation of preduodenal portal vein.** Figure on *left* shows the paired vitelline veins with embryonic connections coursing dorsal (upper rung) and ventral (lower rung) to the duodenum. Normally (*middle* figure) there is persistence of the upper communicating branch, with resorption of the cephalad segment of the left vitelline vein, and the caudal segment of the right. The preduodenal portal vein (figure on the *right*) results from resorption of the upper communicating branch and persistence of the lower one, with resorption of the left vitelline vein and persistence of the right.

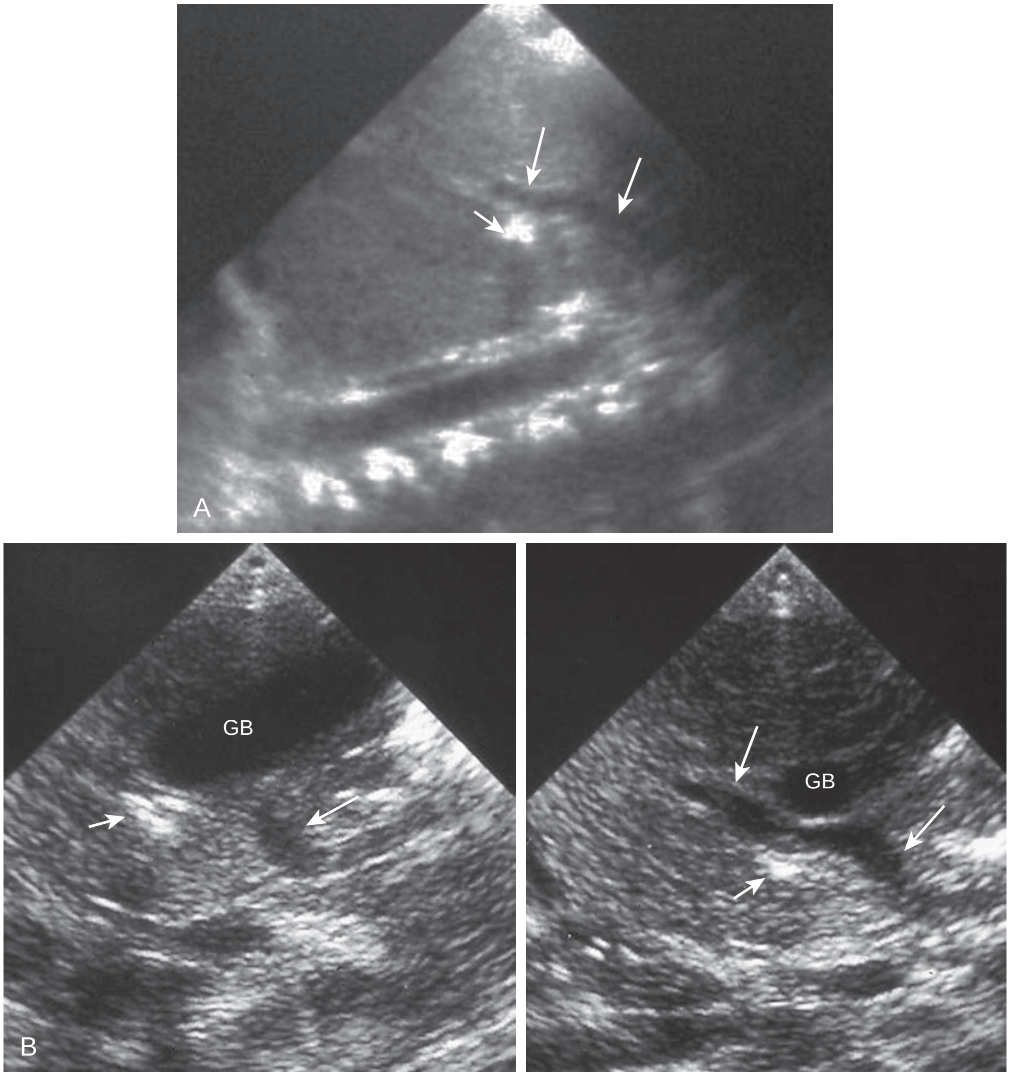

**e-Figure 102.26. Preduodenal portal vein.** (A) Sagittal sonogram in a child with asplenia shows the SMV/portal vein continuation into the liver *(long arrows)* passing anterior to the duodenum, outlined by a small amount of gas *(short arrow)*. (B) Sagittal sonogram in another child with polysplenia demonstrates the course of the SMV *(long arrows)* coursing over the pancreas and the duodenal bulb *(short arrows)* again outlined by a small amount of air. *GB* indicates a midline gallbladder.

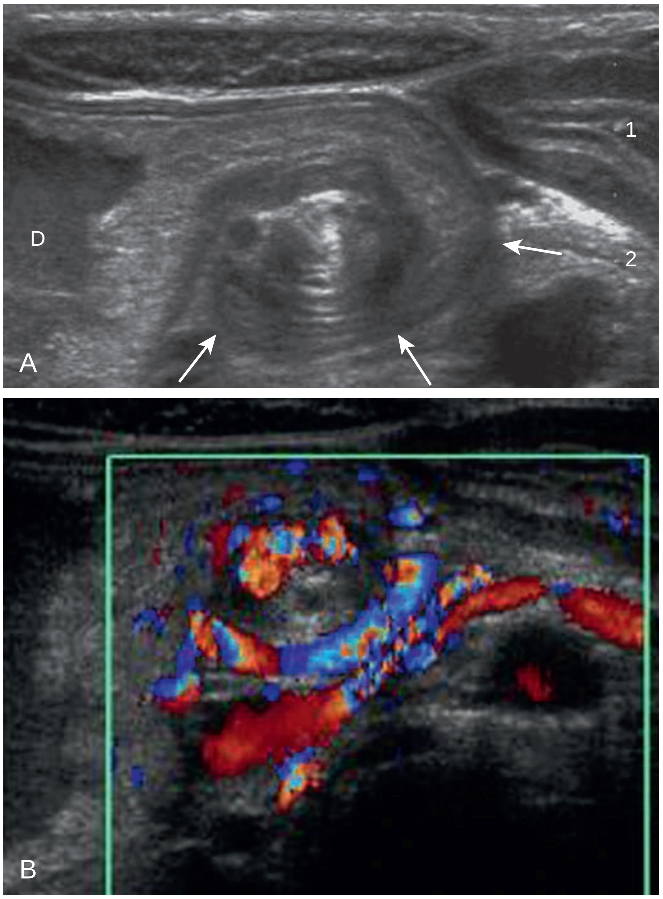

**Figure 102.23.** Video 102.4. **Chronic midgut volvulus.** A 5-year-old boy with a long history of vomiting, who weighed 15 kg at presentation to the ED, with a 14-pound weight loss over the previous 3 weeks, on a gluten-free diet for a recent diagnosis of gluten enteropathy. (See Video 102.4.) (A) Transverse sonogram of the upper abdomen shows a markedly dilated duodenum *(D)* narrowing as it enters into the midgut volvulus *(arrows)*. (B) Color Doppler at a similar level as (A) shows the mesenteric vein around the twist. Video 102.4 shows the clockwise twist, with distended distal mesenteric vasculature. Detorsion of a 720-degree twist and division of Ladd bands was accomplished at surgery.

tract: approximately 51% involve the jejunum and ileum, compared with the duodenum in 40% and the colon in approximately 9%.[125] Atresia is much more common than stenosis, which is seen in only 5% of cases. The incidence of jejunoileal atresia ranges between 1 and 3 cases per 10,000 live births, depending on geographic location, the incidence being greater in persons of European extraction and in African Americans, and lower in Latin Americans. Small bowel atresias affect the jejunum and ileum nearly equally; of those in the ileum, nearly two-thirds occur distally, while in the jejunum nearly two-thirds occur proximally.[126]

Jejunoileal atresias have been subdivided into five types and subtypes[125,127,128] (Fig. 102.28). Type I represents mucosal or membranous atresia, limited to luminal discontinuity. In type II, the blind ends of the bowel are connected by a fibrous cord, with continuity of the underlying mesentery. Type IIIa indicates discontinuity between the bowel ends, with an adjacent mesenteric defect, while IIIb is the specific long-segment atresia with wide mesenteric defect, typically described as “apple-peel,” “Christmas tree,” or “maypole” mesentery, due to the appearance of the residual distal small bowel, coiled around its tenuous vascular supply through retrograde flow via the ileocolic, right colic, or inferior mesenteric

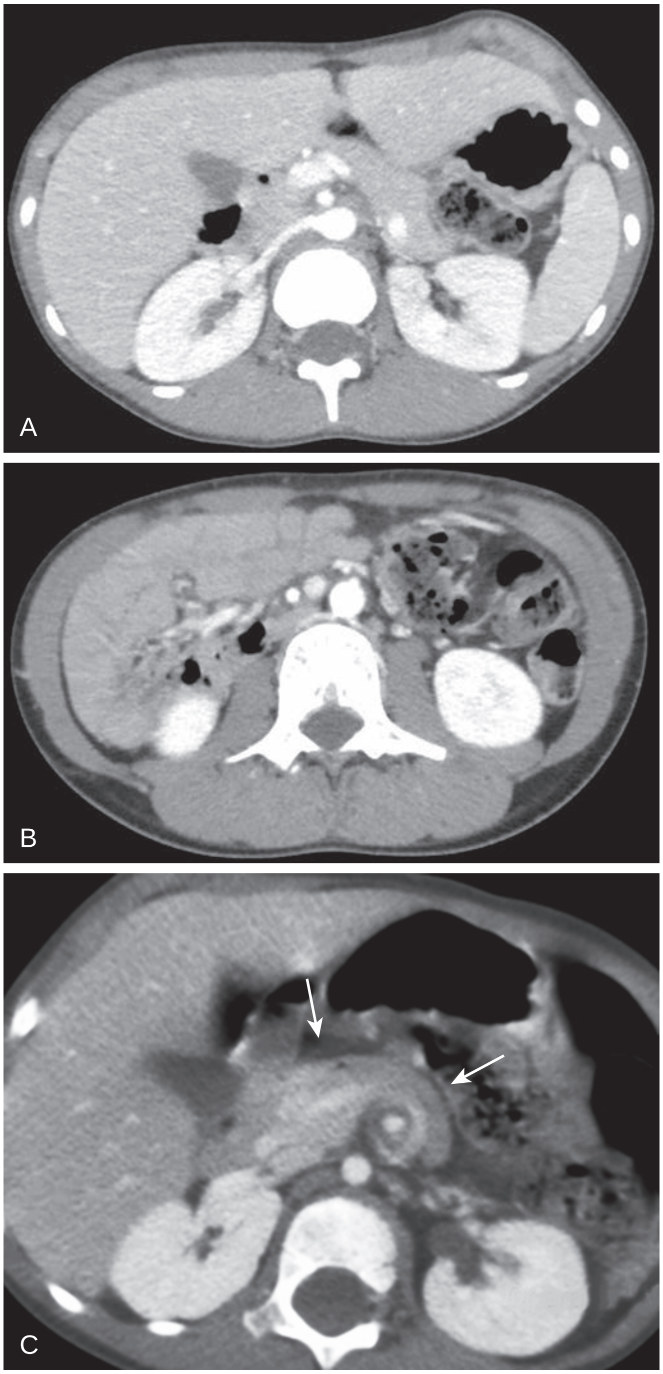

**Figure 102.24. Malrotation on CT.** (A and B) Two images from a contrast-enhanced CT scan in adolescent with abdominal pain (same patient as depicted in Fig. 102.15). (A) At the level of the renal hila, the duodenum does not cross the midline and remains intraperitoneal. (B) At the level of the inferior mesenteric artery, all the small bowel can be seen on the right side of the abdomen, and the colon on the left. (C) Contrast-enhanced CT scan in 2-year-old child with long history of intermittent abdominal pain and emesis. CT demonstrates a volvulus with duodenum *(arrows)*, which contains small bubbles of gas, entering into the twist.

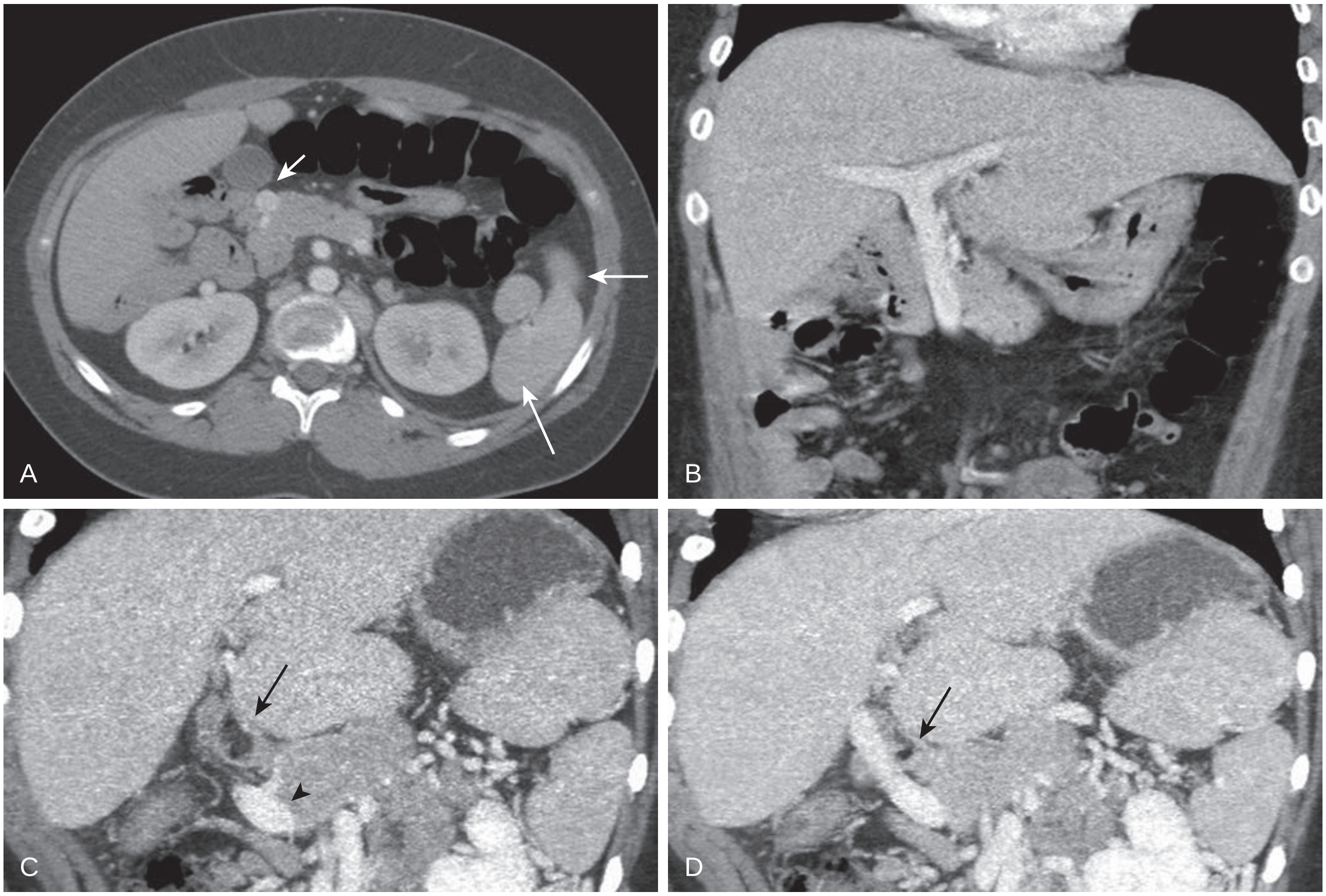

**Figure 102.27. Preduodenal portal vein.** (A) Axial contrast-enhanced CT image from a child with polysplenia *(long arrows)* shows a preduodenal portal vein *(short arrow)* ventral to the pancreas and duodenum. SMA is in normal position anterior to the aorta and dorsal to the pancreas. Note the congenitally short pancreas and the malrotation. (B) Coronal reformat shows the abnormal course of the portal vein as it extends into the liver. (C and D) Angled coronal reformats showing the anterior course of the portal vein. (C) The duodenum *(arrow)*, and the caudal portion of the portal vein, coursing anteriorly. (D) On the adjacent image, the portal vein is about to enter the liver directly ventral to the duodenum *(arrow)*. Note the similar anatomy displayed by ultrasound on another patient shown in Fig. 102.20.

arteries, further discussed later in this chapter.[129] Type IV refers to multiple atresias (Fig. 102.29).

***Etiology.*** Unlike the duodenum, in which the etiology of atresia and stenosis is believed to be failure of recanalization, the most accepted etiology in the jejunum, ileum, and colon is a vascular accident, the location and extent of which governs the location and severity of the resultant defect.[126,128,130,131]

Conditions that can result in prenatal gut ischemia include gastroschisis, intrauterine volvulus, intussusception, and internal hernias.[132] Atresias are found in patients who have undergone significant compression of bowel segments, such as incarceration in omphalocele or in tight gastroschisis defects. Moreover, signs of peritonitis have been found in up to 48% of atresia patients.[126] Extensive apple-peel small bowel atresia is postulated to occur secondary to occlusion of the superior mesenteric artery distal to the origin of the right colic and ileocolic arteries (e-Fig. 102.30). Genetic abnormalities disrupting apicobasal polarity of gut epithelial cells and cellular apoptosis have been implicated in patients with the rare hereditary multiple intestinal atresias (HMIA), which may be associated with combined immunodeficiency and is characterized by multiple atresias with a very poor prognosis.[133–136]

***Clinical Presentation.*** Patients with intestinal atresia may present prenatally with polyhydramnios. Because there is increased bowel surface to absorb the swallowed amniotic fluid in more distal atresias, the percentage of infants with polyhydramnios increases with more proximal atresias; it is approximately 38% in jejunal atresia. Similarly, the percentage of patients presenting with bilious emesis postnatally also increases with more proximal atresia, approximately 84% in patients with jejunal atresia. Jaundice can also occur due to changes in the enterohepatic circulation and is seen in approximately 32% of infants with jejunal and 20% of infants with ileal atresia. The more distal the atresia, the greater the degree of clinical abdominal distension; patients with more proximal atresias may show some distension of the upper abdomen.

Other anomalies outside of the GI system may be present in nearly one-third of patients, but this is more common in patients with jejunal than with ileal atresia.[137] Although duodenal atresia shows a high association with trisomy 21, this is not the case with jejunoileal atresia, which is seen in approximately 0.5% to 3% of patients with Down syndrome. Multiple atresias and the apple-peel variant of intestinal atresia can show a genetic pattern, and patients with the apple-peel variant have been reported with a constellation of other anomalies, including ocular abnormalities and microcephaly. More than two-thirds of these patients are born prematurely, and more than half have malrotation.[126]

***Imaging.*** Radiographs in patients with bowel obstruction will demonstrate proximal dilatation and collapse of bowel distal to the obstruction, or to the most proximal level of obstruction in

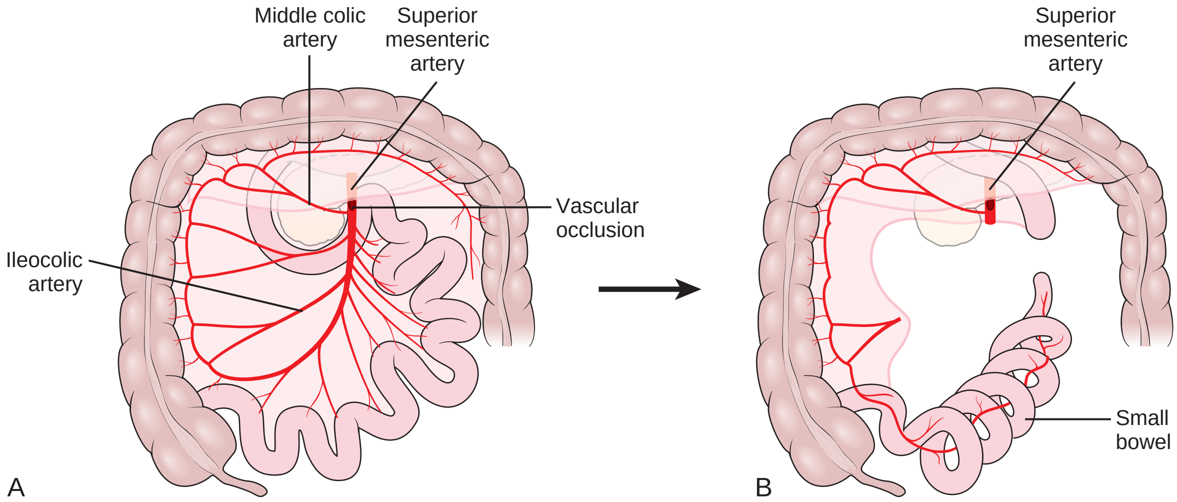

**e-Figure 102.30. Type IIIB atresia apple-peel variant of intestinal atresia.** (A) Schematic drawing of normal distribution of superior mesenteric artery and its branches. If there is prenatal occlusion at the point indicated, part of the jejunum and the accompanying dorsal mesentery will involute. (B) Sequelae of (A) with collateral supply of the residual distal small bowel via ileocolic branches of the distal superior mesenteric artery that are supplied by connections to the inferior mesenteric artery. The residual distal ileal loops wrap around their collateral supply, resembling an apple peel; an arrangement that is also descriptively known as a *Christmas tree* or *maypole.*

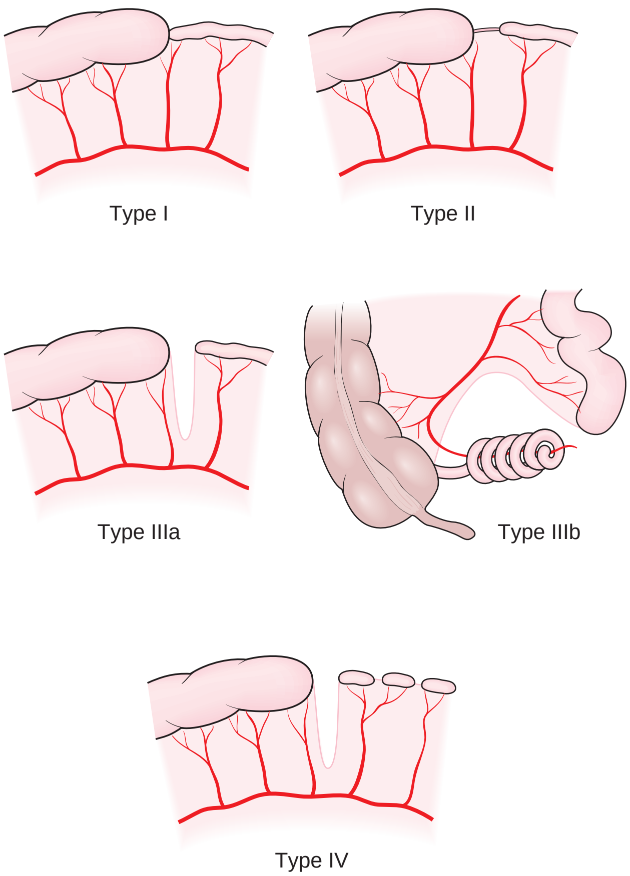

**Figure 102.28. Classification of jejunoileal atresias.** Type I is a mucosal or membranous atresia, in which only the lumen is atretic, with continuity of outer wall and mesentery. In type II atresia, the atretic segment is connected to the distal bowel by a fibrous cord, with an intact mesentery. Type IIIa indicates discontinuity between the atretic segment and the distal bowel, with an associated mesenteric defect, while in type IIIb, the mesenteric defect is large, with absence of a portion of the bowel; the remaining distal bowel is wrapped in "Christmas tree" or "apple-peel" fashion around a remnant arterial supply. Type IV refers to multiple atresias. *(Reproduced with permission of Grosfeld JL, Ballantine TV, and Shoemaker R. Operative mangement of intestinal atresia and stenosis based on pathologic findings.* J Pediatr Surg. *1979;14[3]:368–375.)*

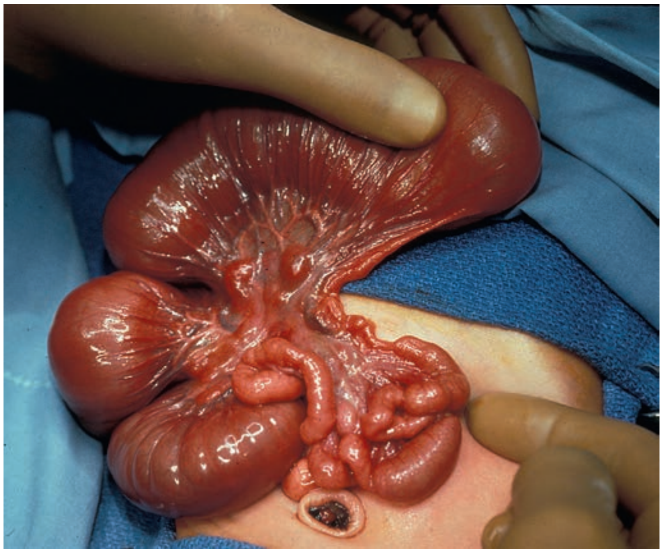

**Figure 102.29. Type IV atresia.** Intraoperative radiograph of an infant with multiple atresias. Note the dilatation of the bowel proximal to the first atresia, and the multiple, sausage-like distal atresias. *(Image courtesy of Dr. Wallace W. Neblett III, Nashville, TN.)*

patients with multiple atresias. Abdominal radiographs in patients with jejunal atresia will show dilatation of the stomach, duodenum and jejunum to the point of atresia, although the degree of dilatation may be much decreased if decompressed via enteric tube (Fig. 102.31A and B). In patients with proximal jejunal atresia, radiographs with the above findings are usually diagnostic. UGI will demonstrate the dilated stomach, duodenum, and small bowel to the point of first atresia (Fig. 102.31C).

In patients with ileal atresia, abdominal radiographs will reveal dilatation of gas-filled loops of bowel, often with protuberance of the flanks and elevation of the hemidiaphragms (Fig. 102.32A). In neonates, it is not possible to distinguish small from large bowel, despite the degree of dilatation or location.[138] However, in distal small bowel obstruction, there will not be gas in the rectum, a finding that can be optimized by obtaining a prone cross-table lateral radiograph (Fig. 102.32B). In patients with radiographic findings of distal obstruction, the differential includes distal small bowel obstruction and colonic abnormalities; therefore in such patients a contrast enema is indicated for diagnosis. Water-soluble contrast material diluted to a near iso-osmolal concentration is preferred (see Chapter 84). In patients with ileal atresia, the contrast enema will reveal a very small, unused colon, known as a *microcolon*, whose lumen has not been distended by swallowed material or succus entericus (Fig. 102.32C). The differential diagnosis of microcolon is that of distal small bowel obstruction: ileal atresia, meconium ileus, or long segment Hirschsprung disease.

In patients with apple-peel atresia, in whom the atresia is at the jejunum, with a long gap to the residual distal small bowel, radiographs will reveal findings suggestive of proximal atresia. In patients with jejunal stenosis, there will be distal gas and proximal dilatation dependent upon the degree of stenosis (e-Fig. 102.33). Ileal stenosis is much less common.

***Treatment.*** The treatment and management of jejunal and ileal atresia or stenosis is surgical. Although considerable morbidity still plagues the survivors of these abnormalities,[132] the prognosis of these infants has undergone a revolutionary improvement. Survival has improved from approximately 1% to 10% in the first half of the 20th century, to 84% in the 1970s, to 95% currently, related to improvement in surgical techniques and in pre-, peri-, and postoperative care and nutritional support.[6,132] Surgical challenges arise in the caliber discrepancy between dilated proximal and collapsed distal bowel. In patients with multiple atresias or apple-peel lesion, modified surgical procedures are used to improve the prognosis in infants with residual short bowel, such as the serial transverse enteroplasty (STEP) procedure.[139–141]

## Meconium Ileus

***Overview.*** Meconium ileus denotes an obstruction in the terminal ileum secondary to inspissated meconium within the distal ileum and is responsible for approximately 20% of neonatal intestinal obstruction.[142] Meconium ileus is the initial presentation in approximately 15% to 20% of patients with cystic fibrosis (CF). Although most patients who present with meconium ileus will be diagnosed with CF, up to 25% to 50% of infants with meconium ileus might have other diagnoses such as pancreatic insufficiency due to partial pancreatic aplasia or pancreatic duct stenosis or very long segment Hirschsprung disease encompassing the small bowel. Very low birth weight premature infants, infants of diabetic mothers, and those born via cesarean section may also present with meconium ileus.[143–148]

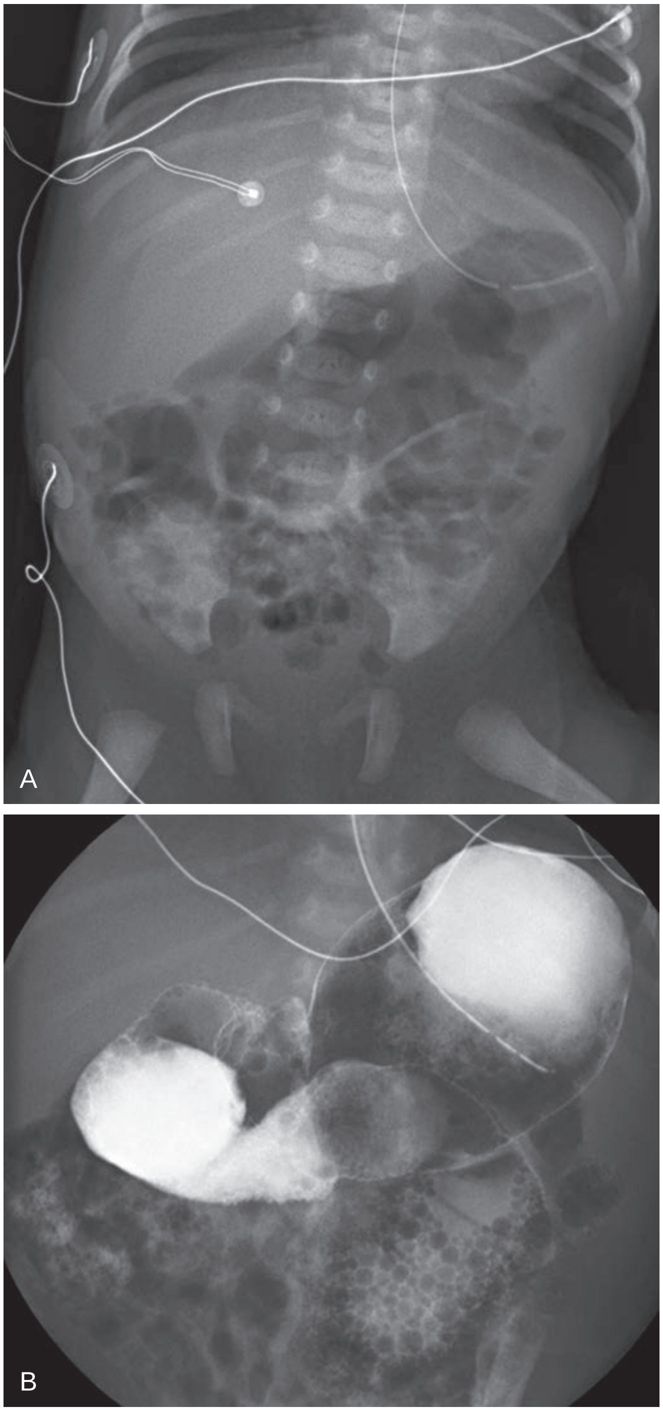

**e-Figure 102.33. Jejunal stenosis.** (A) Abdominal radiograph on day 2 of life in an infant shows several dilated upper abdominal loops with normal distal bowel gas pattern. (B) UGI confirms dilatation of the proximal jejunum, with some passage of contrast into distal loops beyond the point of stenosis.

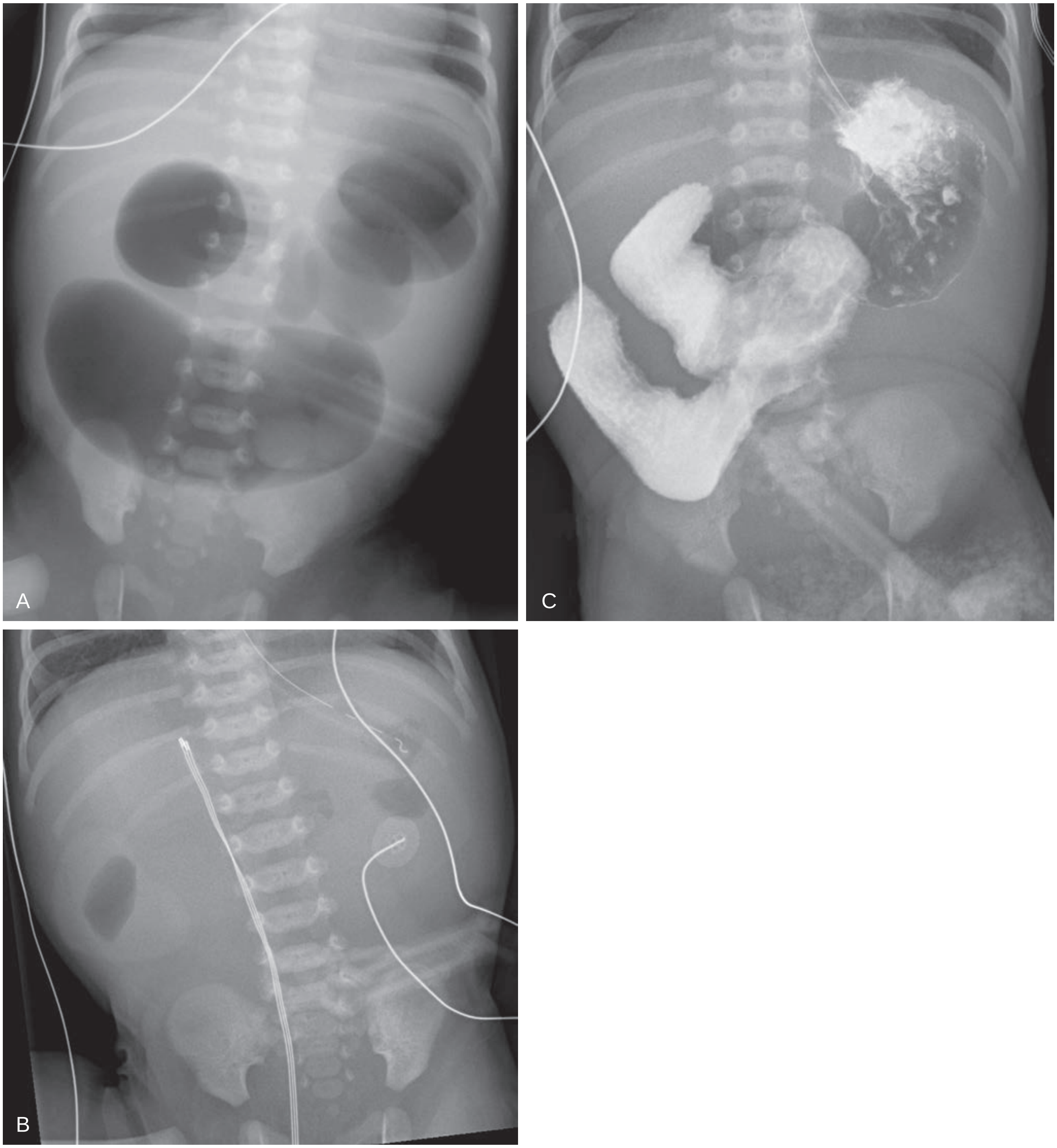

**Figure 102.31. Jejunal atresia.** (A) Abdominal radiograph on the first day of life in infant with jejunal atresia shows marked dilatation of proximal jejunal loops to the point of obstruction. Note that despite the very severe bowel dilatation, there is little distension of the flanks, and no elevation of the diaphragms, reflecting the fact that the more numerous distal bowel loops are collapsed. (B) After placement of orogastric tube, abdominal radiograph on the following day no longer demonstrates the dilated loops of bowel that were diagnostic on the initial radiograph. (C) UGI with iso-osmolal water-soluble contrast material shows close correlation with the gas-filled loops on the initial abdominal radiograph. This examination is not imperative to diagnosis but, if performed, will outline the dilated jejunal loops to the point of atresia.

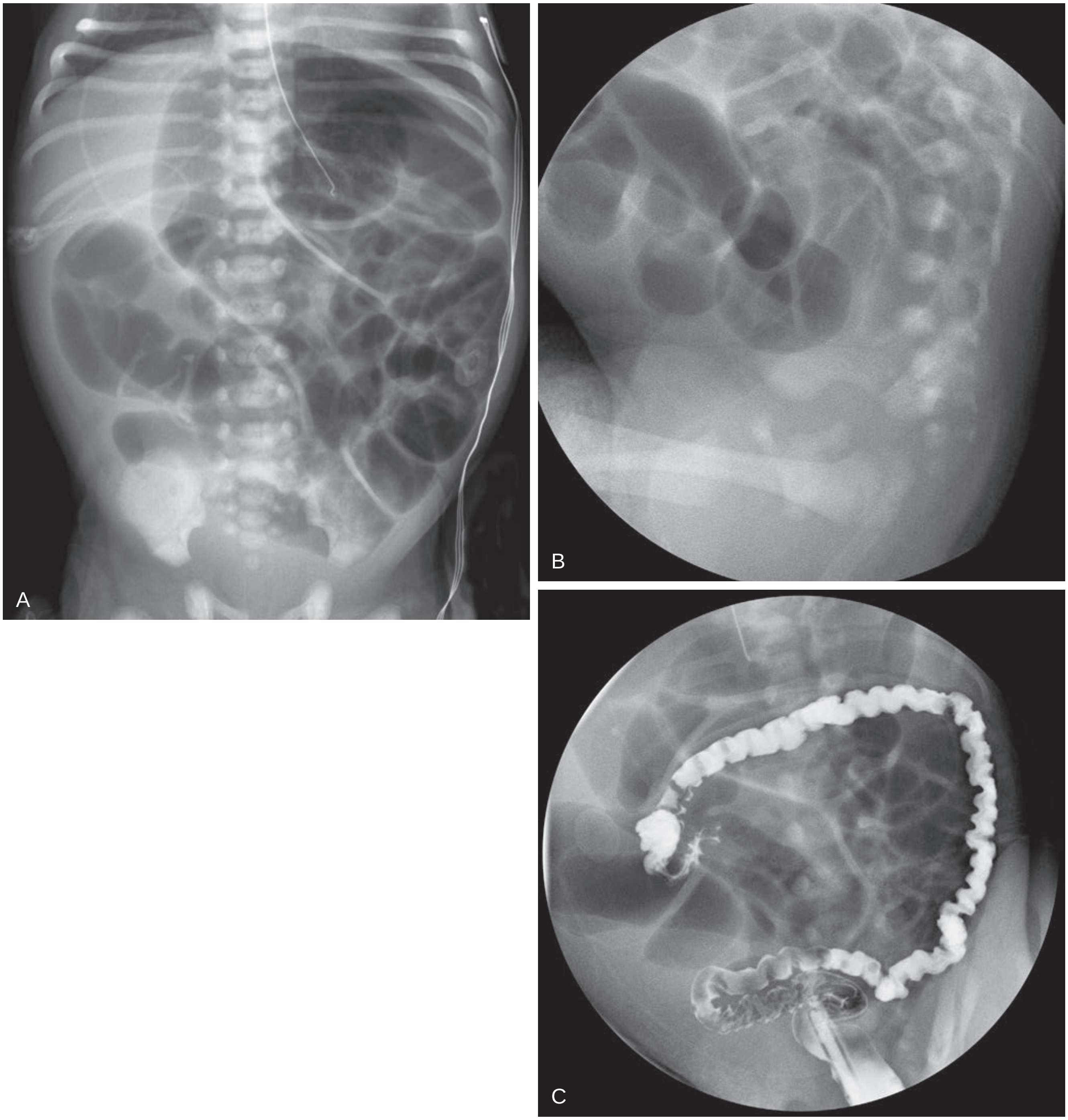

**Figure 102.32. Ileal atresia.** (A) Abdominal radiograph in infant boy demonstrates multiple dilated loops of bowel filling the abdomen. There is some distension of the flanks and elevation of the diaphragms, despite upper decompression via orogastric tube. Despite their large caliber, all of these loops represent small bowel. (B) Lateral radiograph before contrast enema demonstrates complete lack of distal gas, and none in the rectum. A catheter is present in the distal rectum. (C) Image from contrast enema demonstrates a microcolon. The colon is empty, without evidence of meconium pellets.

***Etiology.*** Patients with CF have a defect in the gene sited in locus q31.2 of chromosome 7, which encodes for the CF transmembrane conductance regulator (CFTR) protein and renders it ineffective in the regulation of chloride ion transport across the cell membranes in lungs, liver, pancreas, skin, digestive, and reproductive tracts. In the fetal gut, abnormal secretory products of the intestinal epithelial cells result in meconium with an abnormal electrolyte environment and increased concentration of protein (particularly albumin), which interact with other components of meconium, such as mucopolysaccharides. Degradation of this resultant material is impeded by abnormal concentration of pancreatic enzymes, also the result of the abnormal secretions produced by defective CFTR protein.[149,150] The meconium is markedly viscid and tenacious, and inspissates within the distal

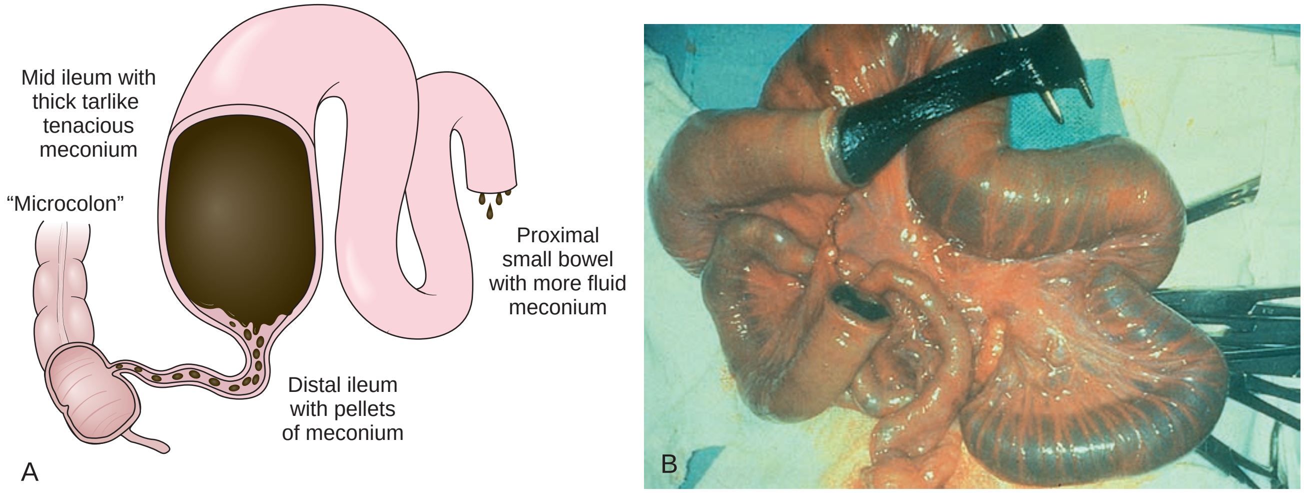
Mid ileum with thick tarlike tenacious meconium
"Microcolon"
Proximal small bowel with more fluid meconium
Distal ileum with pellets of meconium
A
B

**Figure 102.34. Meconium ileus.** (A) Schematic drawing of uncomplicated meconium ileus. Pellets of inspissated meconium fill the terminal ileum proximal to a microcolon. Several loops of more proximal ileum contain thick, tenacious meconium. (From Leonidas J.C., et al., Meconium ileus and its complications. A reappraisal of plain film roentgen diagnostic criteria. *Am J Roentgenol Radium Ther Nucl Med*. 1970;108[3]:598–609.) (B) Intraoperative radiograph shows an enterotomy of proximal bowel and the nature of the thick and tenacious meconium. Note the dilated proximal loops of bowel filled with meconium and the progressively small caliber of the distal bowel leading to the microcolon. *(Image courtesy of Dr. Wallace W. Neblett III, Nashville, TN.)*

small bowel lumen (Fig. 102.34), causing high-grade small bowel obstruction. More than 1,900 mutations of the CFTR gene have been reported with various genotype-phenotype correlations.[151]

***Clinical Presentation.*** The presentation of infants with meconium ileus is one of distal bowel obstruction, which may be complicated by in utero bowel perforation. Patients with uncomplicated or simple meconium ileus have been identified prenatally with abdominal distension, dilatation of bowel loops, and hyperechoic bowel.[152–154] Approximately 20% of the infants will have shown polyhydramnios in utero, more frequently in the subgroup with complicated meconium ileus discussed below. Postnatally the presentation will be similar to that of other infants with distal obstruction: abdominal distension, failure to pass meconium, and bilious vomiting.

Complicated meconium ileus occurs in approximately 40% to 50% of cases[143,155] and results from an in utero event secondary to the sheer volume and weight of the tenacious meconium; this can lead to a segmental volvulus, perforation with meconium peritonitis, and/or a small bowel atresia. Peritoneal meconium may be free in the peritoneal cavity or loculated into a persistent meconium cyst. Prenatal perforation might seal over in utero or may persist postnatally.

CF patients with the ΔF508 and G542X mutations have been reported to have a higher incidence of meconium ileus than patients with other mutations,[147] whereas complicated meconium ileus has been reported more frequently in patients homozygous for the ΔF508 mutation. Modifier genes located on chromosomes 4q35.1, 8p23.1, 11q25, and 19q13 have also been reported to affect the clinical presentation of infants with CF and the development of meconium ileus.[147,151] However, by the time the patients reach the age of 6 months, their prognosis is similar to those who did not present with meconium ileus.[155]

Meconium peritonitis is not specific to meconium ileus but occurs in patients in whom there has been intrauterine perforation for any reason. Occasionally a child is born with intraperitoneal calcifications in whom the perforation has sealed over and who is otherwise well, with no definable clinical sequelae (Fig. 102.35).

***Imaging.*** In infants without complicated meconium ileus, abdominal radiographs will show abdominal distension and multiple

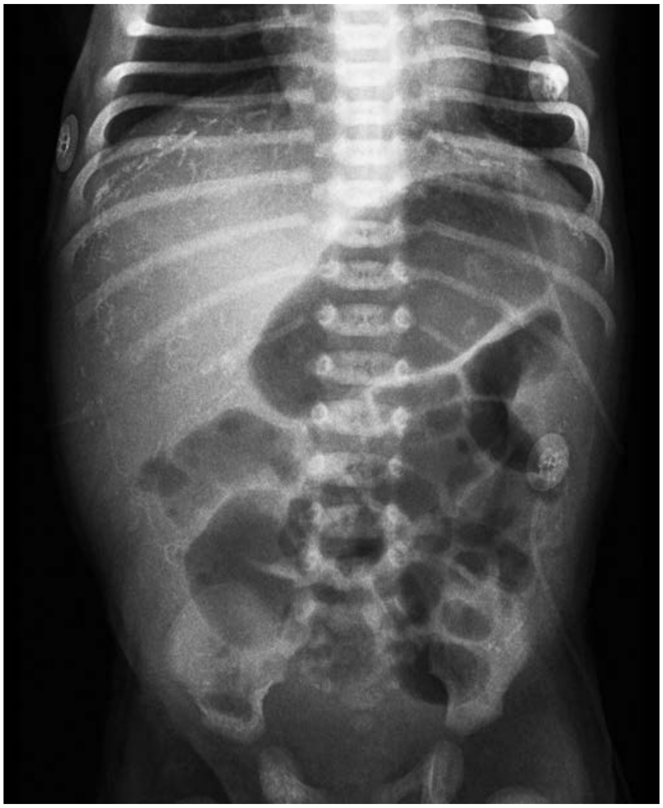

**Figure 102.35. Meconium peritonitis.** Abdominal radiograph of a 2-day-old infant with extensive intraperitoneal calcifications consistent with in utero perforation and meconium peritonitis. The child did well, without evidence of persistent perforation or obstruction, tolerated full feeds, and after appropriate observation, was discharged home.

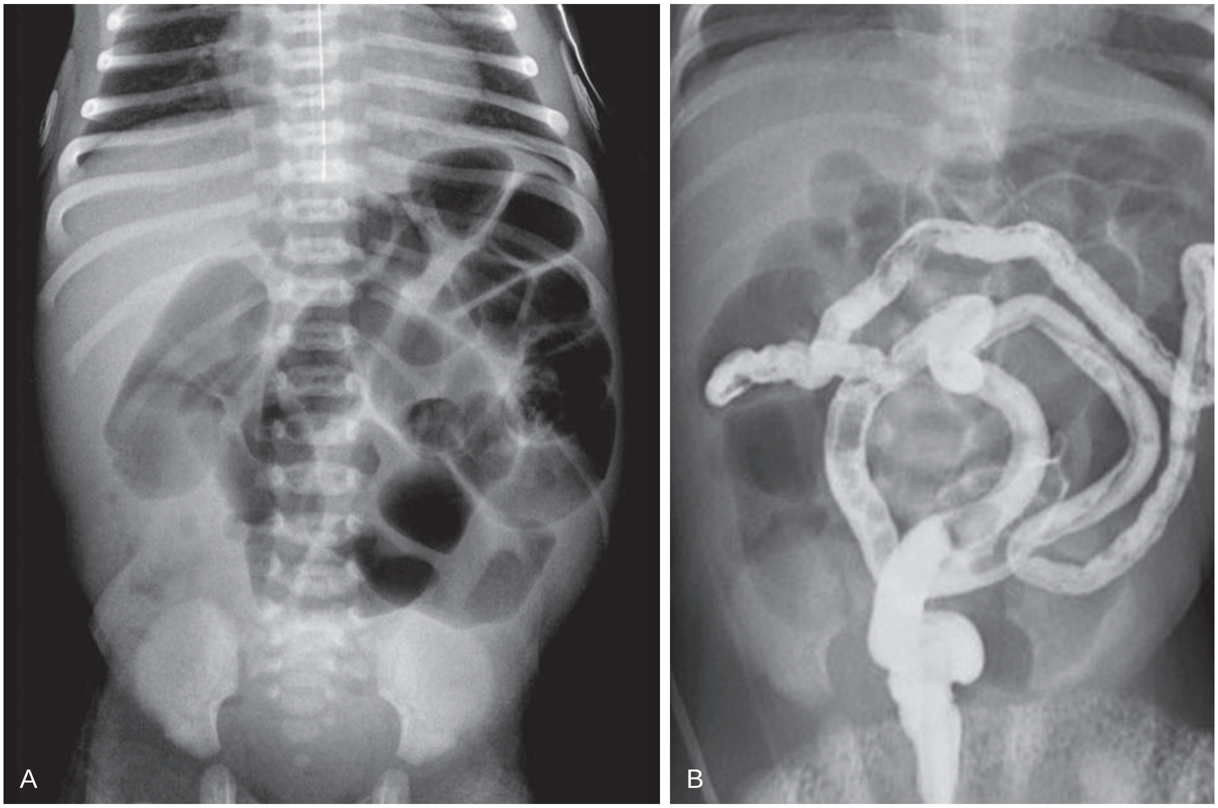

**Figure 102.36. Uncomplicated meconium ileus.** (A) Abdominal radiograph in 3-day-old infant with abdominal distension and bilious aspirates shows dilatation of multiple loops of bowel. No calcifications are seen on the radiograph to suggest complicated meconium ileus. There is an orogastric tube near the GE junction, which was subsequently advanced. (B) Contrast enema demonstrates a microcolon, with multiple meconium plugs, consistent with the diagnosis of meconium ileus. Compare with findings in Fig. 102.32C.

dilated loops of bowel, consistent with a distal obstruction (Fig. 102.36). In meconium ileus, the ileal loops are packed with meconium, which often renders a characteristic "soap bubble" appearance.[156] Air fluid levels are more typically described in patients with ileal atresia,[157] although their presence does not negate the diagnosis of meconium ileus, as loops proximal to the inspissated meconium may accumulate gas and fluid.

Radiographs of infants with complicated meconium ileus, in addition to signs of distal bowel obstruction, may show intraperitoneal calcifications consistent with meconium peritonitis and/or mass effect from a meconium cyst (Fig. 102.37A–E). Patients with such signs of complicated meconium ileus are operative candidates, not candidates for contrast fluoroscopic evaluation. Ultrasound is useful in some infants with complicated meconium ileus to document the location and size of a suspected meconium cyst (see Fig. 102.37B). Hyperechoic bowel loops, described in the fetus,[152–154] may also be seen postnatally (see Fig. 102.37C).

Similar to patients with ileal atresia, initial diagnostic imaging evaluation in the infant with simple meconium ileus is via contrast enema. As previously discussed, the diagnostic examination is with water-soluble contrast material diluted to a near iso-osmolal concentration. Barium is not recommended, as barium inspissated within the tarry meconium is unlikely to prove helpful, it is not necessary for diagnosis and can cause complications in case of perforation. Hyperosmolal material as the initial contrast medium may be harmful if the diagnosis proves to be a different abnormality, such as Hirschsprung disease. (See Chapter 84 for additional information on technique.) As is the case in patients with ileal atresia, the contrast enema in patients with meconium ileus will reveal an unused microcolon. However, in patients with meconium ileus in whom the distal ileum is impacted with tarry, tenacious meconium, small meconium pellets may be seen within the microcolon (see Fig. 102.36B). If contrast refluxes into the distal ileum, meconium pellets may be identified; if contrast reaches into the dilated loops of bowel, ileal atresia is excluded. However, contrast may not reflux readily into the dilated bowel loops in patients with meconium ileus due to inability to traverse the segments with inspissated meconium; in some cases, final diagnosis may rest on the surgical findings.

***Treatment.*** Patients with complicated meconium ileus are managed surgically; there is no role for an enema procedure in these patients.

Surgical removal of the obstructing meconium was the original treatment for simple meconium ileus,[158] but since Noblett's 1969 report, the Gastrograffin contrast enema is usually the initial treatment in patients with uncomplicated meconium ileus. Its success has been attributed to the hyperosmolarity of the contrast medium, as well as to the surfactant properties of polysorbate 80 (Tween 80).[159] Expected complications related to hyperosmolarity of the agent and subsequent fluid and electrolyte shifts can be managed with careful monitoring and replacement. Before the procedure, the patient should undergo adequate fluid and electrolyte replacement. Surgical consultation and stand-by are imperative.

Subsequent investigators have reported problems with bowel necrosis after administration of the Gastrografin enema[160] ascribed to the polysorbate component, which has been found to cause mucosal damage and necrosis in experimental animals.[161] For these reasons, many pediatric radiologists avoid Gastrografin during the therapeutic enema and utilize other moderately hyperosmolar media for relief of obstruction. A 1995 survey of pediatric radiologists in

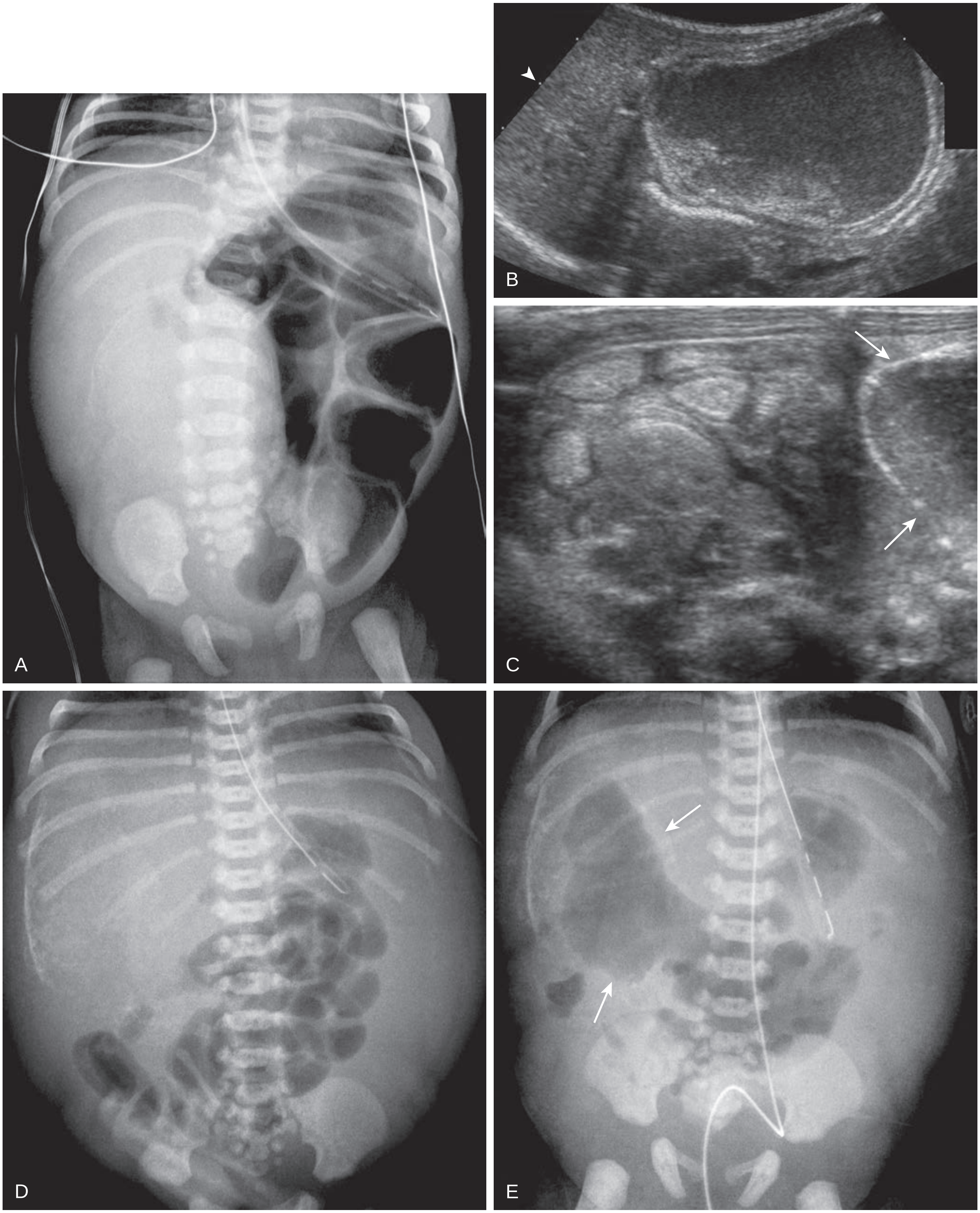

**Figure 102.37. Complicated meconium ileus.** (A) Abdominal radiograph in a 2-day-old girl with abdominal distension and bilious aspirates shows absence of bowel gas in the right abdomen with a partly calcified mass displacing gas-filled dilated loops of bowel to the left. (B) Ultrasound image demonstrates the subhepatic partly calcified mass with internal debris and fluid-fluid level. (C) Additional ultrasound image shows a portion of the cyst wall *(arrows)* and multiple, abnormal, hyperechoic loops of bowel. (D) Abdominal radiograph on a different 1-day-old infant shows a calcified mass in right upper quadrant, shown at sonography to represent a loculated complex meconium collection. (E) Radiograph a few hours later of the same infant shown in (D) shows a persistent perforation with gas entering into the right upper quadrant collection.

North America showed a higher success rate when an additive such as N-acetylcysteine (Mucomyst) was used but showed no correlation of success rate with contrast medium; reported perforation rate was 2.75%, with a higher risk of perforation in cases in which balloon occlusion of the rectum was used.[162]

Therapeutic enema may need to be repeated for definitive resolution of the obstruction; success may be at least partly dependent on perseverance of the operator, as the contrast material does not easily advance beyond the obstructing meconium into the dilated loops of bowel. The reported success rates vary but are most often quoted to be between 40% and 65%.[155,162,163] Close postprocedure monitoring of the infant is mandatory.

Surgery is indicated for patients in whom the therapeutic enema is unsuccessful.

## Meckel Diverticulum and Other Omphalomesenteric Duct Remnants

***Overview.*** Meckel diverticulum is found in approximately 1% to 4% of the population and is typically located within 100 cm from the ileocecal junction[164]; however, its location can be variable, being reported as up to 5 feet from the ileocecal valve.[165]

***Etiology.*** The Meckel diverticulum is a remnant of the vitelline or omphalomesenteric duct, the communication between the embryonic gut and the yolk sac that normally obliterates by the fifth to seventh week of gestation. Failure of obliteration of the duct leads to several results (e-Fig. 102.38). The ileal portion of the duct may remain as a Meckel diverticulum, located on the antimesenteric border, and containing all layers of the bowel wall. If the entire duct remains patent, the result is an umbilicoileal fistula. The lumen of the duct may obliterate, but the duct may remain as a fibrous cord, attaching the ileum or a Meckel to the anterior abdominal wall at the umbilicus. A focal, isolated part of the duct may remain open as a vitelline cyst.[165,166]

***Clinical Presentation.*** The vast majority of Meckel diverticula remain asymptomatic, with a complication rate estimated at 4% to 6%, decreasing with age.[166–168] Although the prevalence of diverticula is similar in both genders, symptoms are more likely to occur in males and in younger patients.[166–168] In a recent series encompassing more than four million admissions to children's hospitals, symptomatic Meckel were found to be more prevalent in whites and less frequent in African Americans.[167] The most common clinical presentation is that of painless rectal bleeding; Meckel diverticulum accounts for approximately 50% of lower GI bleeding in infants and toddlers, typically occurring as a complication of gastric mucosa within the diverticulum. The incidence of gastric mucosa within bleeding Meckel diverticula is estimated at approximately 23% to 80%.[165,166] Heterotopic pancreatic tissue, consisting of acini, ducts, and islets, is found in 5% to 16% of cases.[166] In addition to bleeding, gastric and pancreatic mucosa can lead to inflammation of the diverticulum, with abdominal pain mimicking appendicitis that can similarly evolve into perforation and/or obstruction.[165,169,170] Meckel diverticula can also torse,[171] particularly when very large (so called "giant diverticula").

Meckel diverticulum can present as distal small bowel obstruction through a variety of other mechanisms. The diverticulum may invert into the ileal lumen and serve as a lead point for intussusception. If there is a persistent attachment of the ileum or of the diverticulum to the umbilicus, this anchor can serve as a pivot point for a segmental volvulus, or the umbilical attachment can act as an adhesion to cause simple or closed loop obstruction. The Meckel diverticulum can become incarcerated in an inguinal hernia, known as a *Littre hernia*.[166] Patients with obstruction present with abdominal pain and vomiting, which can be complicated by bleeding in cases of intussusception.

Meckel can also present with neoplasia, typically in adult patients; the tumors are most commonly carcinoids, and complications include luminal obstruction and intussusception. Meckel diverticula may contain enteroliths and may also present with parasitic infections and lodged ingested foreign bodies.[165] Ulceration of the diverticulum can result in perforation, and this has been reported in preterm neonates[172]; ulceration is associated with gastric mucosa but not with *Helicobacter pylori* infection.[165,173]

***Imaging.*** Radiographs are not particularly helpful in the diagnosis of Meckel diverticula except as indicators of some of its complications. Fluoroscopic examination such as small bowel follow-through requires very careful technique and may be able to demonstrate the antimesenteric saccular outpouch from the distal ileum, particularly when enteroclysis is performed, or when the diverticula are larger, such as the "giant" diverticula that measure greater than 5 to 6 cm in diameter and up to 15 cm in length.[166] However, small diverticula may be inconspicuous and difficult to detect among multiple bowel loops.

The most well-known imaging examination for detection of Meckel diverticula is the technetium pertechnetate abdominal scintigram (see Chapter 84).[174] This examination is dependent upon the presence of gastric mucosa, with a reported sensitivity of 80% to 90%, specificity of 95%, and accuracy of 90% in pediatric patients[175]; accuracy may be lower in patients with bleeding who present with a hemoglobin less than 11g/dL.[174] Use of single photon emission computed tomography (SPECT) has been reported to improve detection over conventional planar imaging.[166,176] Duplication cysts with gastric mucosa are part of the differential diagnosis in a positive scan but often can be differentiated clinically or with other cross-sectional imaging modalities.

In patients with inflamed diverticula, sonography can detect the inflamed diverticulum, which appears as a blind-ending structure, surrounded by inflammation (Fig. 102.39A).[177,178] On cross-sectional imaging, the findings may be very difficult to distinguish from appendicitis (Fig. 102.39B); however, in other cases, a larger size and periumbilical location may indicate the correct diagnosis preoperatively (Fig. 102.39C). In patients in whom there is intussusception, the diagnosis can be made with cross-sectional imaging (e-Fig. 102.40).[166,179,180] Inverted diverticulum can also act as a lead point in ileo-ileo-colic intussusception (Fig. 102.41). On MRI, the inflamed Meckel may be visible, and differentiation from appendicitis may be aided by the identification of blood products within some diverticula.[181]

***Treatment.*** The treatment of complicated Meckel diverticula is surgical resection, including the adjacent base to ensure removal of all ectopic mucosa. However, the treatment of diverticula that are asymptomatic and incidentally discovered during surgery for another reason is less clear. The potential for the development of complications needs to be weighed against the potential for postsurgical complications, reported as 1% to 2% for patients with incidental resection, with a mortality rate of 0.001%.[165] Considerations include higher risk factors for complications existing at the time of incidental discovery, such as younger age and male gender,[182] and the increased risk of neoplasia in older age groups.[183] Laparoscopic or laparoscopically assisted removal is advocated,[184,185] and some investigators suggest that laparoscopy can replace the Meckel technetium scan in patients with a high clinical suspicion.[165,184]

## Duplication Cysts

***Overview.*** Duplication cysts of the GI tract are characterized by contiguity with and adherence to a segment of the alimentary tract by a smooth muscle coat, mucosal lining including one or more types of cells found within any portion of the alimentary canal, and a shared blood supply with native GI structures.[186] They can occur anywhere along the length of the GI tract from the mouth to the anus. In the abdomen, they are most common in the terminal ileum and ileocecal valve[187]; duodenal duplications account for approximately 6% of the total and are therefore

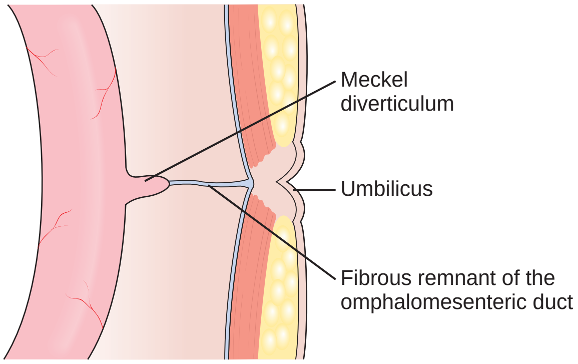

**e-Figure 102.38.** Diagrammatic representation of omphalomesenteric duct remnants. Meckel diverticulum is a true diverticulum containing all layers of the bowel wall, arising from the antimesenteric wall of the ileum. It may be free in the peritoneal cavity, or may remain attached to the abdominal wall at the umbilicus via a fibrous remnant of the omphalomesenteric duct, as depicted here. The omphalomesenteric duct can exist without a Meckel, either patent as an umbilicoileal fistula, as a fibrous cord, or a portion may be patent as a vitelline cyst.

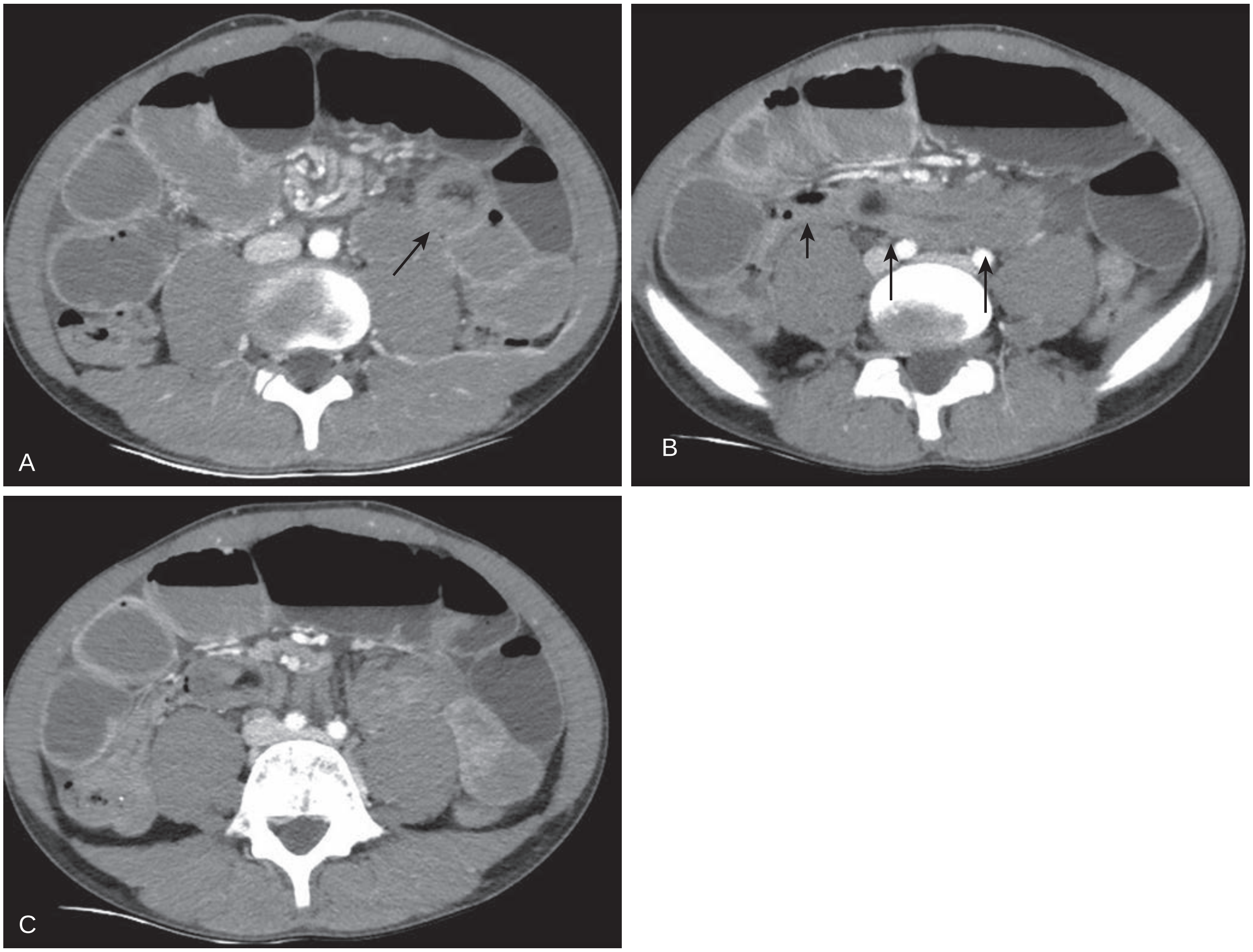

**e-Figure 102.40. Meckel diverticula with intussusception.** (A–C) Small bowel intussusception with Meckel diverticulum lead point. More proximal CT image (A) shows a small bowel obstruction, with multiple dilated small bowel loops and collapsed right and left colon. *Arrow* points to the beginning of a small bowel intussusception. More distal CT image (B) shows the small bowel intussusception with a fat density lead point *(arrows)*, which at surgery and pathology proved to be a lipoma at the base of a Meckel diverticulum. Additional image (C) below the level of the long intussuscepted loop shows the diverticulum to better advantage.

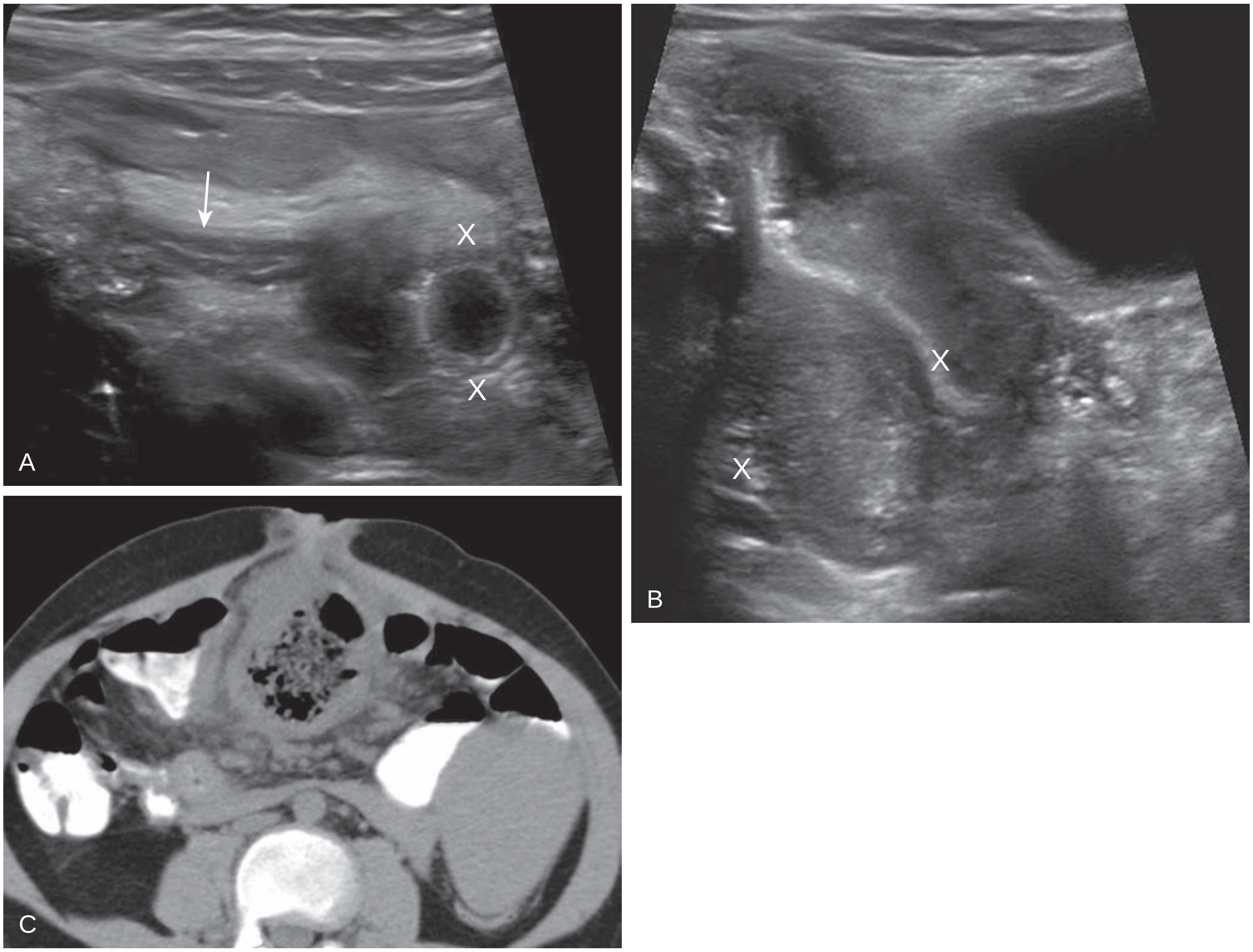

**Figure 102.39. Meckel diverticulum.** (A) Sonogram in a 4-year-old girl with abdominal pain and concern for appendicitis shows a normal appendix *(arrow)* with surrounding inflammation. There is a blind ending structure (between *X calipers*) measuring approximately 10 mm in diameter, which at surgery was a perforated Meckel diverticulum. (B) Sonogram in a 2-year-old girl with abdominal pain and concern for appendicitis. A normal appendix was seen on other images. There is a 12-mm thick-walled structure (between *X calipers*) that at surgery was an inflamed Meckel diverticulum with tip perforation. (C) CT image of an adolescent boy with abdominal pain demonstrates a large, inflamed loop of bowel with fecalized contents in close association with the umbilicus, representing an inflamed Meckel diverticulum.

uncommon.[188] Unlike the Meckel diverticulum, which is located on the antimesenteric border of the intestine, duplication cysts occur along the mesenteric border of the involved bowel loop and, in the duodenum, are found medial to the descending limb or along its third portion. Most of the cysts do not communicate with the intestinal lumen; a communication may be present in some of the tubular duplications.

***Etiology.*** The exact etiology of alimentary tract duplications remains unknown, although there are several theories that attempt to explain their origin. One theory is that duplication cysts result from incomplete attempts at twinning, a theory that also suggests an explanation for duplications of other organs, such as the bladder and urethra, which at times can accompany GI duplications. Duplications associated with anomalies of the spine (neurenteric cysts, found more commonly in the chest) may result from a split notochord with herniation of a foregut diverticulum. A third theory is that these anomalies are the result of diverticula that form during the recanalization stage of the bowel. A fourth hypothesis suggests that environmental factors, such as trauma or hypoxia, can induce events that can result in an enteric duplication.[188] No single theory explains all the instances of duplication anomalies, and it may be that more than one theory may be pertinent to the various types of anomalies.

***Clinical Presentation.*** The presentation of duplication cysts is usually related to their size, to their location, to the type of mucosal lining, to whether they are cystic or tubular, and to whether they are associated with other anomalies. Large cysts can present with mass effect or as a palpable mass. Duodenal duplication cysts can present as gastric outlet obstruction, failure to thrive, or pancreatitis possibly related to compression of the pancreatic duct,[189] and have also been reported to cause a fluid collection within the lesser sac.[190] Cysts containing gastric mucosa can ulcerate, bleed, and lead to inflammatory changes, presenting with abdominal pain and vomiting. Duplication cysts may act as a fulcrum for segmental volvulus[187]; those located in the terminal ileum and ileocecal valve may act as a lead point in intussusception and should be suspected when intussusception occurs in infants within the first 3 months of life (see chapter 107). Duplications may be multiple in as many

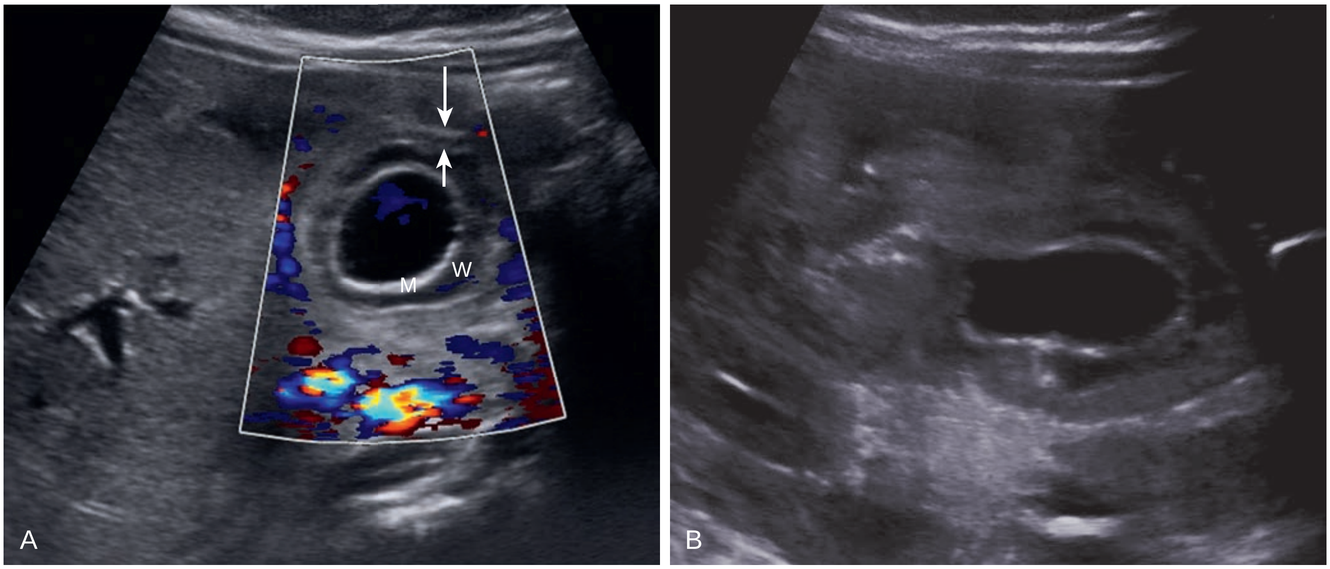

**Figure 102.41. Inverted Meckel diverticulum with ileo-ileo-colic intussusception in a 2-month-old infant.** (A) Transverse color Doppler sonogram of the distal tip of the intussusceptum complex shows a cystic lead point. *Arrows* outline the wall of the intussuscipiens; *W*, Diverticular wall; *M*, hyperechoic mucosal lining. (B) Longitudinal sonogram shows the diverticulum at the leading edge of the intussusception.

as 10% to 20% of patients, vertebral anomalies may be present, particularly in lesions that are supplied by vessels on both sides of the mesentery,[191] and there may be urinary tract anomalies.[192]

***Imaging.*** In duodenal duplication cysts, plain radiographs may demonstrate a soft-tissue mass or obstruction, with the mass effect seen along the distal aspect of the stomach or the duodenum.

Upper GI series could be the first study obtained in a child presenting with vomiting; in cases of duplication cysts of the duodenum, the examination reveals a filling defect along the mesenteric wall of the duodenum or extrinsic compression (Fig. 102.42A). Compression of the gastric outlet or of the first portion of the duodenum by the cyst has been described as a “beak” sign.[193] If there is focal communication between the cyst and the duodenum, contrast will enter the duplication. On CT and ultrasound (Fig. 102.42B–D), duodenal duplication cysts will be seen as cystic structures along the mesenteric border of the duodenum, with the characteristic hypo/hyperechoic wall typical of gut signature.

In large duplications of the small bowel, abdominal radiographs may demonstrate a mass (e-Fig. 102.43A and B). Cross-sectional imaging will demonstrate the cystic structure of the lesion, and the specific segment of bowel involved should be identified (e-Fig. 102.43C).

Small bowel duplication cysts may also present with obstruction, inflammation, intussusception, or a combination. As noted earlier, ultrasound typically reveals an anechoic cyst, but the fluid may contain debris if there has been infection or hemorrhage from associated ectopic gastric mucosa and ulceration (e-Fig. 102.43D). Typical “bowel wall signature” of an enteric duplication cyst is usually present.[194–196] The presence of bowel wall signature may help to differentiate a duplication cyst from a pancreatic pseudocyst in a patient presenting with pancreatitis, if the cyst is located within the pancreatic head. However, the gut signature is not fully sensitive or specific to duplication cysts; the gut signature may be obliterated by superimposed inflammatory changes and may be mimicked in other conditions, such as mesenteric cyst, cystic teratoma,[197] and ovarian cysts.

CT demonstrates a discrete fluid-filled cyst on the mesenteric border of the involved bowel segment often with bright enhancement of the cyst wall if there is inflammation (e-Fig. 102.43E). On MRI, as is the case with ultrasonography, hemorrhage or infection can alter the signal characteristics of the cyst contents. MRI is particularly helpful in cases of duodenal duplication cyst, when accompanied by MRCP, which can demonstrate the relationship of the cyst to the duodenal wall, as well as to the pancreatic head and the pancreatic and biliary ductal systems, which is important preoperative information.[188]

***Treatment.*** The most common treatment for duplication cysts is resection, although marsupialization with internal drainage may also be utilized in appropriate cases. Cysts with gastric mucosa should be excised or stripped of the mucosal lining; complex cases may require more extensive surgical excision.[188]

## Heterotopic Gastric Mucosa

***Overview.*** Although heterotopic gastric mucosa is most commonly associated with Meckel diverticula and with duplication cysts, it can also be found as an isolated anomaly anywhere along the intestinal tract.[198,199]

***Clinical Presentation.*** Patients can present with bleeding which can be life-threatening.

***Imaging.*** In the jejunum, heterotopic gastric mucosa often has an appearance of polypoid masses that extend into the bowel lumen. Because by definition these rests contain gastric mucosa, the diagnosis is best made with a technetium pertechnetate scan, although this rare lesion can be confused with the more common Meckel diverticulum. The diagnosis can also be made on contrast-enhanced CT with negative oral contrast material, in which the lesions may appear as hyperenhancing polypoid intraluminal lesions (Fig. 102.44).

***Treatment.*** As with Meckel diverticula and duplication cysts, the treatment is lesional excision.

## Lymphatic Malformations, Mesenteric and Omental Cysts

***Overview.*** Abdominal lymphatic malformations can be located in the mesentery or omentum as mesenteric or omental cysts. Lymphatic malformations have only an endothelial lining and contain lymphoid tissue within their walls, are usually multiloculated,

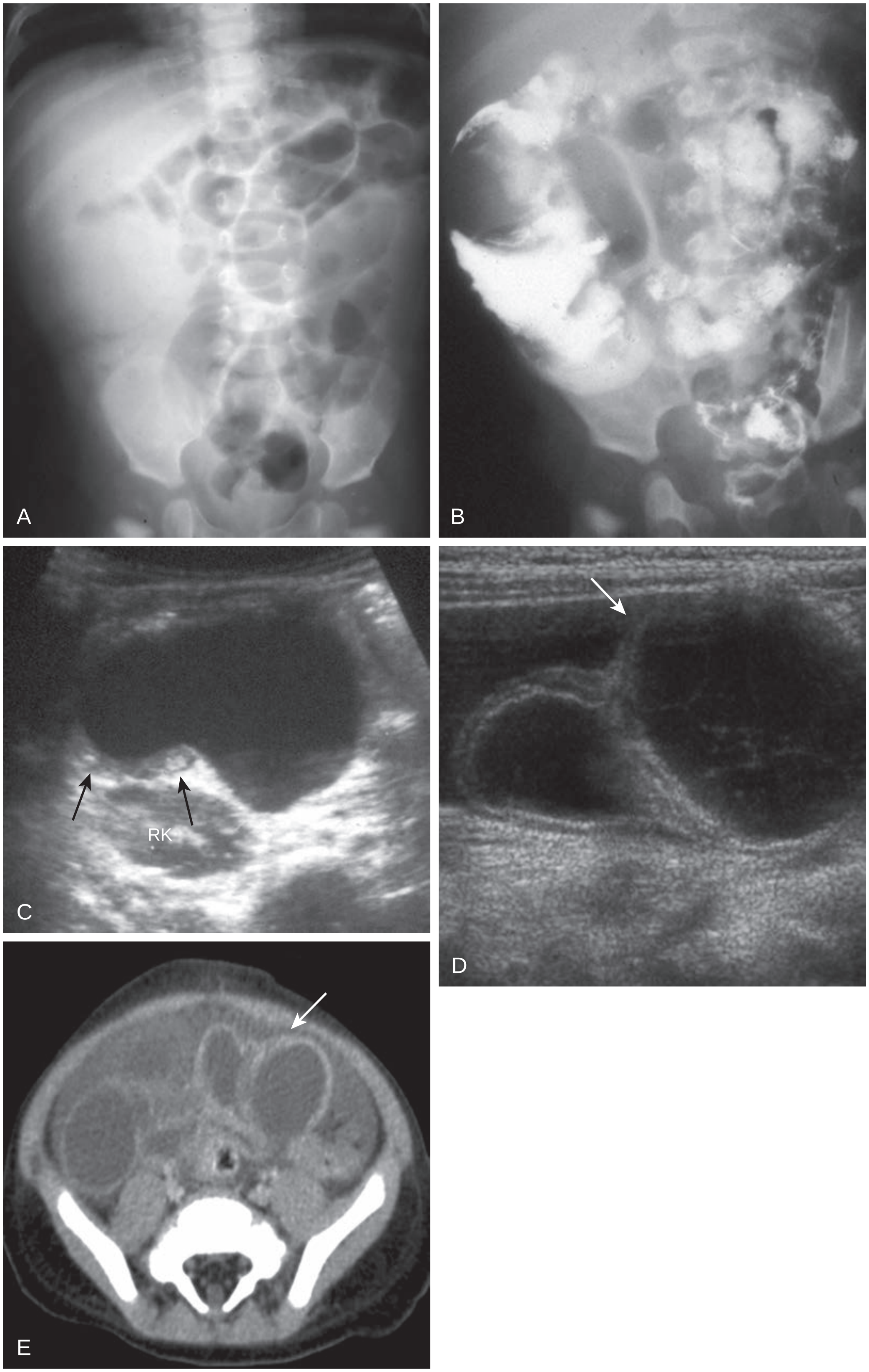

**e-Figure 102.43. Ileal duplication cysts.** (A) Plain abdominal radiograph on a 4-month-old infant presenting with vomiting at an outside institution demonstrates dilated loops of small bowel and mass effect along the right flank. (B) UGI was followed through to the ascending colon. The mass effect upon the ascending colon was mistaken for an intussusception, and the child was referred to a pediatric institution for further evaluation and reduction. (C) Axial sonogram demonstrates a large cystic mass in the right flank, with mass effect upon the adjacent, empty colon *(arrows)*. At surgery, a duplication cyst attached to the terminal ileum was identified and resected. *RK*, Right kidney. (D) Ultrasound of lower abdomen in a 3-year-old girl presenting with vomiting, abdominal pain, and abdominal distension reveals duplication cyst *(arrow)* containing echogenic debris, sharing a common wall with the distal ileum. Note that the distal ileum retains the gut signature, but this is partly absent within the duplication cyst. There is surrounding ascites. (E) Contrast-enhanced CT scan demonstrates enhancement of both the duplication cyst *(arrow)* and the adjacent ileal loop with which it shares a common wall. Ascites and findings of bowel obstruction with dilated loops of proximal bowel are seen. At surgery, an ileal duplication cyst was resected.

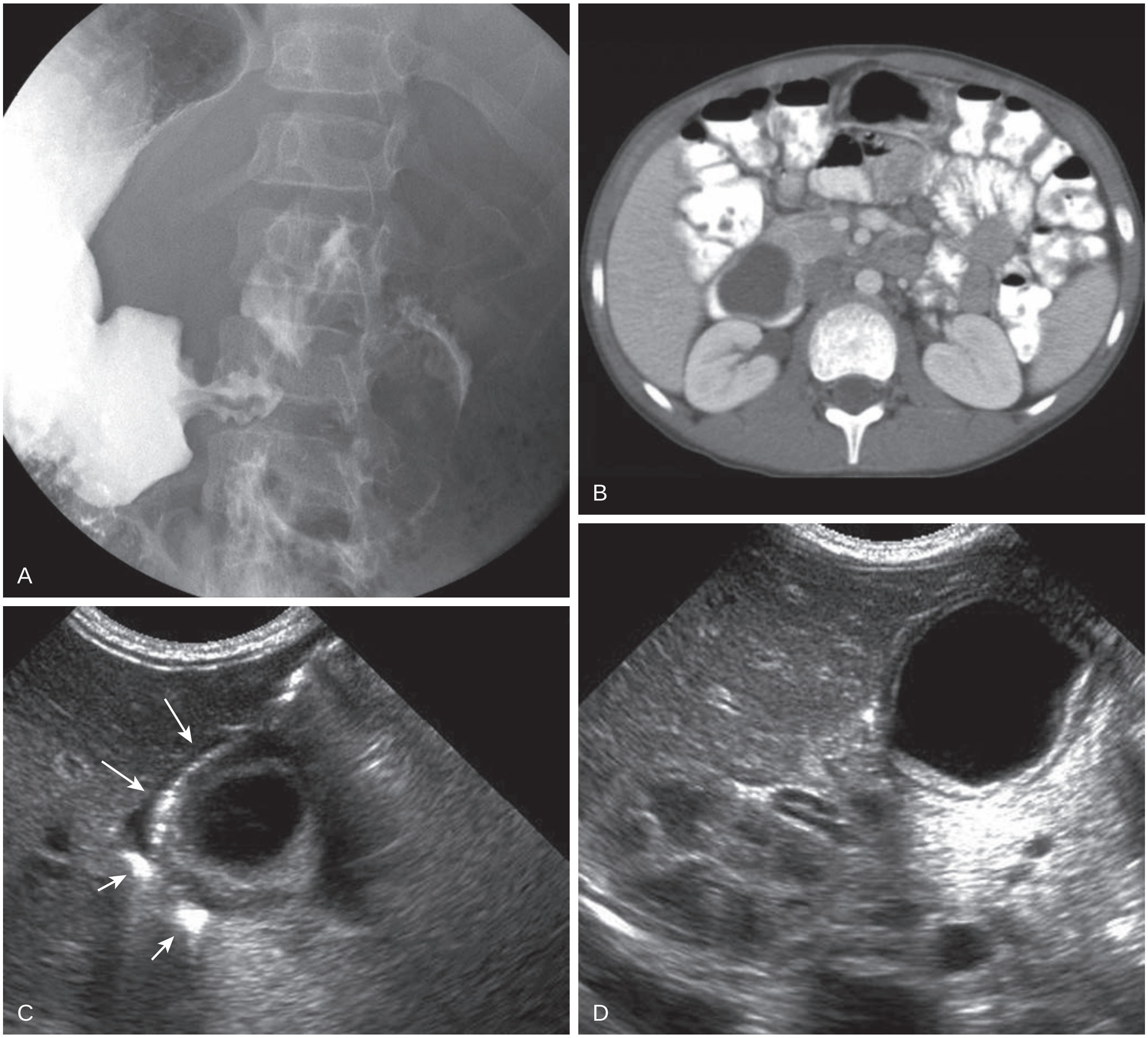

**Figure 102.42. Duodenal duplication cysts.** (A) UGI image in an 11-year-old boy demonstrates intramural mass effect upon the mesenteric border of the duodenum. (B) CT with oral and intravenous contrast on same patient in (A) again shows the location of the cystic mass along the mesenteric border of the duodenum encroaching upon its lumen. (C and D) 1-day-old infant with vomiting and prenatal diagnosis of abdominal cyst. (C) Sonogram shows the cyst to be intimately related to the distal antrum *(long arrows)* and the descending duodenum *(short arrows)*. (D) Additional image on same patient demonstrates the typical hypo/hyperechoic double layer of a duplication cyst, typical of gut signature.

and may contain chyle. The most common type of mesenteric or omental cyst is the lymphatic malformation, and most of these tend to occur in the mesentery rather than the omentum, because of its richer lymphatic content, most commonly in the ileal mesentery.[200,201]

Mesothelial cysts, on the other hand, occur in the small bowel, the mesentery, and the mesocolon, and are the result of accumulation of fluid between mesothelial layers. These cysts are therefore lined by mesothelium, without mural muscle fibers or lymphatic structures.[202] Nonpancreatic pseudocysts may also occur in the mesentery, or more often, in the omentum, and are believed to result from prior trauma or infection, with no inner cellular lining on histology.

***Etiology.*** The etiology of lymphatic mesenteric and omental cysts is not known; hypotheses include failure of embryonic lymphatic spaces to develop normal connections and drainage into the venous system, and benign proliferation of ectopic lymphatics sequestered from the venous system.[200] Mesothelial cysts and nonpancreatic pseudocysts are previously discussed.

***Clinical Presentation.*** Abdominal lymphatic malformations are rare, representing approximately 5% of lymphatic malformations occurring in all other areas, and with a prevalence of approximately 1 per 20,000 admissions, with a lower incidence in African Americans.[200,203] In the pediatric population, presentation is more common in males, although in adults the presentation is more common in females, through a putative estrogenic effect.[204] These

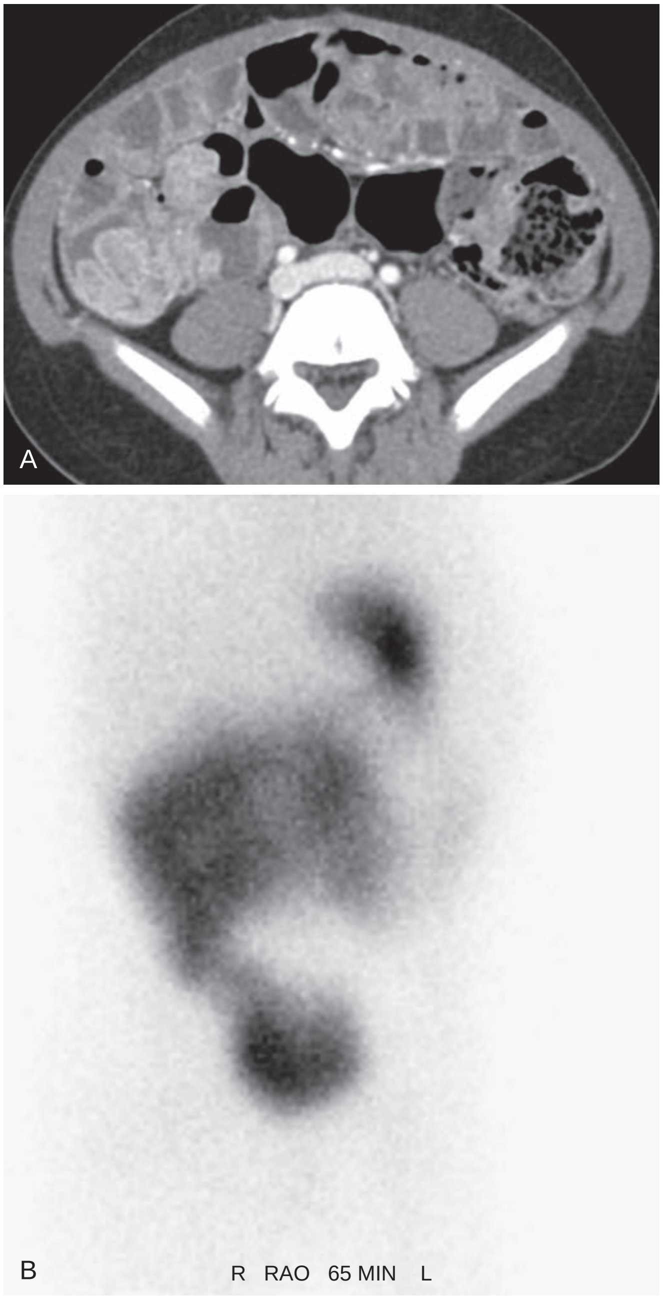

**Figure 102.44. Heterotopic gastric mucosa.** (A) Contrast-enhanced CT enterography in 12-year-old boy with heterotopic gastric mucosa shows multiple hyperenhancing nodular lesions encroaching upon the bowel lumen. (B) Technetium pertechnetate scan on the same patient several years earlier shows diffuse uptake throughout the bowel. *(Images courtesy of Andrew Trout, Cincinnati, OH.)*

lesions may be asymptomatic and discovered incidentally, or they may present as a result of size or complications of the lesion. Mass effect can result in partial obstruction developing over time or acutely due to acute enlargement of the cyst secondary to acute event such as hemorrhage.[205,206] Abdominal pain can occur through torsion of the cyst or one of its components (e-Fig. 102.45) or of adjacent bowel loops with the cyst acting as a fulcrum. The cysts can become infected, producing fever, abdominal pain, or sepsis.[200,201]

***Imaging.*** Radiographs show a large mass displacing intestinal loops. Dilated loops may be seen in patients with obstruction. GI contrast studies show displacement of bowel. Ultrasound demonstrates the multilocular nature of the mass with fine septations. The masses are usually anechoic, but some of the loculated spaces may be hypoechoic or even hyperechoic, depending on the chyle or blood content.[207] If the malformation is composed of microscopic cysts, it may simulate a solid lesion.[208] In case of omental cysts, it is important to recognize the blanket-like distribution of the fluid to differentiate it from ascites (Fig. 102.46). On CT, the attenuation values of the fluid range from near-fat to near-water, depending on its composition. On CT, septa and loculations are usually demonstrated, unless their attenuation value merges with that of the surrounding fluid. Fine calcifications may be present in some cases.[200] MRI studies of patients with lymphatic malformations show characteristics of the cyst ranging from fluid with low-intensity signal on T1-weighted images to fat with high-intensity signal.[209] Mesothelial cysts typically do not contain internal septations.[210]

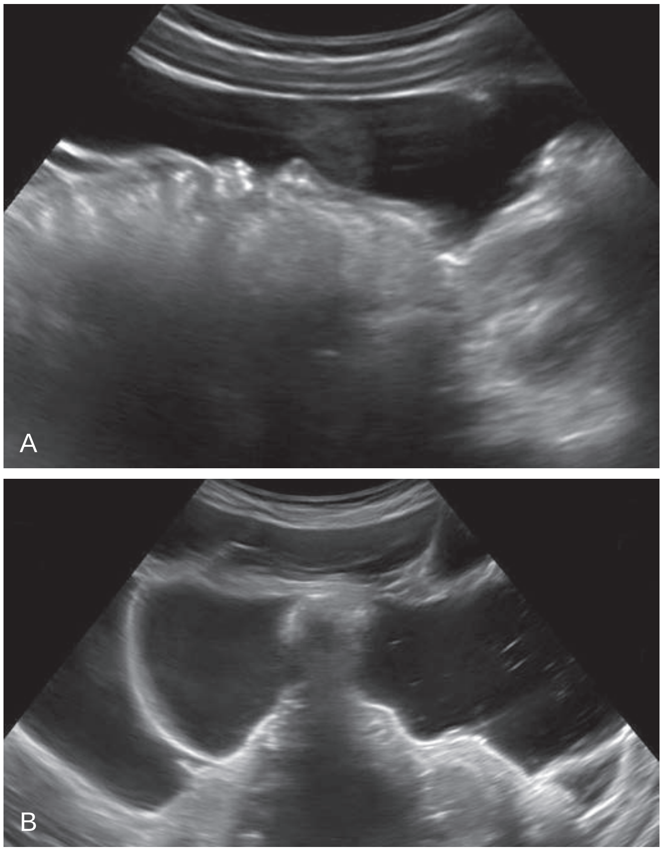

**Figure 102.46. Omental cyst.** (A) Transverse sonogram just below the liver in a 9-month-old infant thought to have ascites shows a cystic fluid-filled lesion, blanketed over the gas-containing bowel. (B) Transverse sonogram through the lower abdomen shows the large size of the lesion, containing septa, covering the bowel. At surgery, a large omental cyst was removed.

***Treatment.*** Traditional treatment is surgical resection with complete extirpation of the cyst. In children with mesenteric cysts, this is more likely to require segmental bowel resection than in adults (50%–60% vs. 33%).[200] If complete resection is not possible, marsupialization of the cyst with sclerosis of the lining can be performed. A surgical classification of mesenteric cysts, based on operative management, includes four types: type 1 is on a pedicle, and easily removed. Type 2 is sessile, restricted to the mesenteric boundaries, whereas type 3 has retroperitoneal extension and may involve the aorta, inferior vena cava, and other retroperitoneal

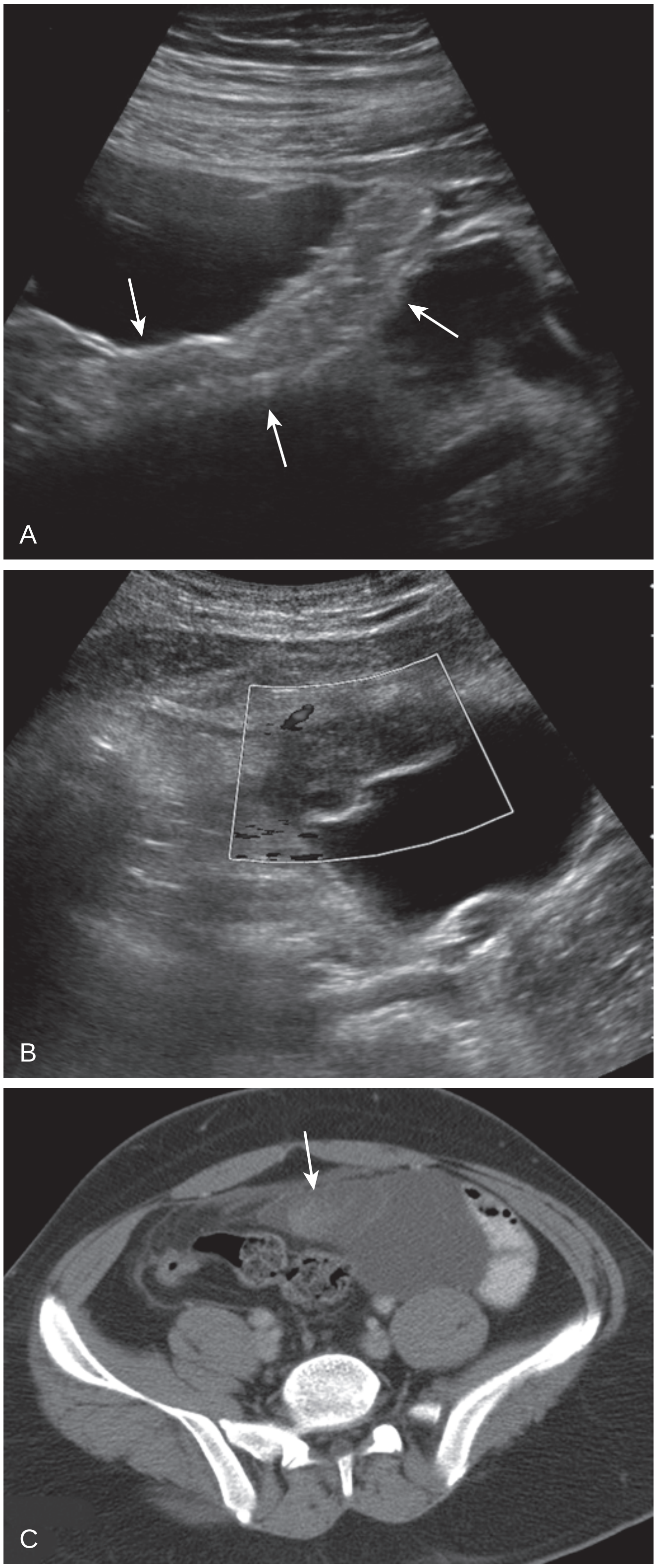

**e-Figure 102.45. Mesenteric cyst.** (A) A 14-year-old boy presented with abdominal pain and dysuria. Ultrasound of left midabdomen reveals multiseptated cystic mass, with intervening loop of small bowel *(arrows)*. (B) Color Doppler image obtained more inferiorly in the supravesical area shows an avascular solid-appearing component to the cystic lesions, with surrounding hyperechogenicity consistent with inflammation and edema. (C) Contrast-enhanced CT scan which had been done earlier at another institution shows the solid-appearing component *(arrow)* corresponding to the avascular structure noted on sonography in (B), and surrounding inflammation with fat stranding in the supravesical area. At surgery, a loculated mesenteric cyst was removed, with volvulus and infarction of a supravesical component, leading to the presenting symptoms and imaging findings.

structures, representing a severe surgical challenge. Type 4 refers to multicentric cysts.[203,211]

Laparoscopic resection is possible; however, this is best approached with caution if the diagnosis is not certain preoperatively or if the procedure will necessitate segmental bowel resection.[212–214]

Alternatively, lymphatic malformations may be treated via image-guided sclerotherapy with a variety of sclerosants. Multiple procedures may be required for complete resolution.

## KEY POINTS

- The finding of a double bubble on plain film is diagnostic of duodenal atresia/stenosis and does not need contrast studies for confirmation.
- Air can rarely be seen distal to the site of complete duodenal atresia in patients in whom an anomalous bifid biliary duct straddles and bypasses the point of obstruction.
- Polyhydramnios occurs in 30% to 50% of patients with duodenal atresia, and approximately half of these may be born prematurely.
- Associated anomalies in patients with duodenal atresia/stenosis include trisomy 21, Hirschsprung disease, esophageal atresia, and heterotaxy.
- In many patients with annular pancreas with obstruction, the obstruction is intrinsic and not secondary to the annular pancreas itself.
- Malrotation is the overarching term for incomplete rotation of the gut, before completion of the 270 degrees of counterclockwise rotation and normal fixation of duodenojejunal junction and cecum.
- Malrotation can lead to midgut volvulus due to the lack of normal fixation of the bowel and the short mesenteric pedicle that results from failure of completion of the normal rotation.
- Preduodenal portal vein is often found in patients with intrinsic duodenal obstruction, such as a duodenal membrane. The vein itself is not believed to be the primary cause of obstruction in most cases.
- Conditions that can result in prenatal gut ischemia and atresia include gastroschisis, intrauterine volvulus, intussusception, and internal hernias.
- Meconium ileus is the result of tarry, tenacious meconium impacted in the distal small bowel, causing distal small bowel obstruction.
- Calcifications in abdominal radiographs of infants with meconium ileus are a sign of meconium peritonitis and complicated meconium ileus. Such patients are operative candidates without further imaging or attempts at nonoperative treatment.
- Painless rectal bleeding is the most common presentation of Meckel diverticulum.
- Gut signature is a suggestive diagnostic finding of duplication cyst on sonography, but it is not completely specific.
- Duplication cysts are most common in the ileum, where they can act as lead points for intussusception.
- Lymphatic cysts are lined by endothelial cells and contain lymphoid tissue in their walls. Mesothelial cysts are the result of accumulation of fluid between mesothelial layers and are lined by mesothelium.

## SUGGESTED READINGS

Adams SD, Stanton MP. Malrotation and intestinal atresias. *Early Hum Dev*. 2014;90:921–925.

Cheng G, et al. Sonographic pitfalls in the diagnosis of enteric duplication cysts. *AJR Am J Roentgenol*. 2005;184(2):521–525.

Gorter RR, et al. Clinical and genetic characteristics of meconium ileus in newborns with and without cystic fibrosis. *J Pediatr Gastroenterol Nutr*. 2010;50(5):569–572.

Grant M, Kennedy A, Cochran W. Small bowel congenital anomalies: a review and update. *Curr Gastroenterol Rep*. 2016;18:16.

Lampl B, et al. Malrotation and midgut volvulus: a historical review and current controversies in diagnosis and management. *Pediatr Radiol*. 2009;39(4):359–366.

Levy AD, Hobbs CM. From the archives of the AFIP. Meckel diverticulum: radiologic features with pathologic correlation. *Radiographics*. 2004;24(2):565–587.

Sizemore AW, et al. Diagnostic performance of the upper gastrointestinal series in the evaluation of children with clinically suspected malrotation. *Pediatr Radiol*. 2008;38(5):518–528.

Strouse PJ. Disorders of intestinal rotation and fixation (“malrotation”). *Pediatr Radiol*. 2004;34(11):837–851.

Yousefzadeh DK. The position of the duodenojejunal junction: the wrong horse to bet on in diagnosing or excluding malrotation. *Pediatr Radiol*. 2009;39(suppl 2):S172–S177.

## REFERENCES

Full references for this chapter can be found on www.expertconsult.com.

## REFERENCES

1. Cragan JD, et al. Descriptive epidemiology of small intestinal atresia, Atlanta, Georgia. *Teratology*. 1993;48(5):441–450.
2. Magnuson D, Schwartz M, et al. Stomach and duodenum. In: Oldham K, ed. *Principles and Practice of Pediatric Surgery*. Philadelphia: Lippincott Williams & Wilkins; 2005.
3. Applebaum H, Sydorak R, et al. Duodenal atresia and stenosis - annular pancreas. In: Coran A, ed. *Coran: Pediatric Surgery*. Philadelphia: CV Mosby, an imprint of Elsevier; 2012.
4. Gray S, Skandalakis J. *Embryology for Surgeons: The Embryological Basis for the Treatment of Congenital Defects*. Philadelphia: Saunders; 1986.
5. Bailey PV, et al. Congenital duodenal obstruction: a 32-year review. *J Pediatr Surg*. 1993;28(1):92–95.
6. Dalla Vecchia LK, et al. Intestinal atresia and stenosis: a 25-year experience with 277 cases. *Arch Surg*. 1998;133(5):490–496, discussion 496–497.
7. Botham RA, et al. Formation of duodenal atresias in fibroblast growth factor receptor 2IIIb-/- mouse embryos occurs in the absence of an endodermal plug. *J Pediatr Surg*. 2012;47(7):1369–1379.
8. Celli J. Genetics of gastrointestinal atresias. *Eur J Med Genet*. 2014;57(8):424–439.
9. Nichol PF, Tyrrell JD, Saijoh Y. Retinaldehyde dehydrogenase 2 is down-regulated during duodenal atresia formation in Fgfr2IIIb-/- mice. *J Surg Res*. 2012;175(1):82–87.
10. Reeder AL, et al. Haploinsufficiency of retinaldehyde dehydrogenase 2 decreases the severity and incidence of duodenal atresia in the fibroblast growth factor receptor 2IIIb-/- mouse model. *Surgery*. 2012;152(4):768–775, discussion 775–776.
11. Brinkley MF, Tracy ET, Maxfield CM. Congenital duodenal obstruction: causes and imaging approach. *Pediatr Radiol*. 2016;46(8):1084–1095.
12. Tashjian DB, Moriarty KP. Duodenal atresia with an anomalous common bile duct masquerading as a midgut volvulus. *J Pediatr Surg*. 2001;36(6):956–957.
13. Lundstedt C, Lyttkens K, Andren S. Intraluminal duodenal diverticulum causing pancreatitis in a patient with a polysplenia syndrome. *Eur Radiol*. 1998;8(3):454–457.
14. Tasu JP, et al. Intraluminal duodenal diverticulum: radiological and endoscopic ultrasonography findings of an unusual cause of acute pancreatitis. *Eur Radiol*. 1999;9(9):1898–1900.
15. Fujiwara T, et al. Intraluminal duodenal diverticulum in a child: incidental onset possibly associated with the ingestion of a foreign body. *Eur J Pediatr*. 1999;158(2):108–110.
16. Kassner EG, et al. Retention of small foreign objects in the stomach and duodenum. A sign of partial obstruction caused by duodenal anomalies. *Radiology*. 1975;114(3):683–686.
17. Freeman SB, et al. Congenital gastrointestinal defects in Down syndrome: a report from the Atlanta and National Down Syndrome Projects. *Clin Genet*. 2009;75(2):180–184.
18. Kimble RM, Harding J, Kolbe A. Additional congenital anomalies in babies with gut atresia or stenosis: when to investigate, and which investigation. *Pediatr Surg Int*. 1997;12(8):565–570.
19. Sekmenli T, et al. Duodenal atresia and Hirschsprung disease in a patient with Down syndrome. *Eur J Gen Med*. 2011;8(2):157–159.
20. Ein SH, Palder SB, Filler RM. Babies with esophageal and duodenal atresia: a 30-year review of a multifaceted problem. *J Pediatr Surg*. 2006;41(3):530–532.
21. Kim JH, et al. Heterotaxia syndrome with intraluminal duodenal diverticulum. *J Korean Surg Soc*. 2010;79(1):75–78.
22. Shankar R, Rao SP, Shetty KB. Duodenal atresia in association with situs inversus abdominus. *J Indian Assoc Pediatr Surg*. 2012;17(2):71–72.
23. Holder-Espinasse M, et al. Familial syndromic duodenal atresia: Feingold syndrome. *Eur J Pediatr Surg*. 2004;14(2):112–116.
24. Rathaus V, et al. The bubble sign in the gasless abdomen of the newborn. *Pediatr Radiol*. 1992;22(2):106–109.
25. Traubici J. The double bubble sign. *Radiology*. 2001;220(2):463–464.
26. Knechtle SJ, Filston HC. Anomalous biliary ducts associated with duodenal atresia. *J Pediatr Surg*. 1990;25(12):1266–1269.
27. Komuro H, et al. Bile duct duplication as a cause of distal bowel gas in neonatal duodenal obstruction. *J Pediatr Surg*. 2011;46(12):2301–2304.
28. Berdon WE, et al. Midgut malrotation and volvulus. Which films are most helpful? *Radiology*. 1970;96(2):375–384.
29. Yousefzadeh DK. The position of the duodenojejunal junction: the wrong horse to bet on in diagnosing or excluding malrotation. *Pediatr Radiol*. 2009;39(suppl 2):S172–S177.
30. Ladd W. Congenital obstruction of the duodenum in children. *NEJM*. 1932;206(6):277–283.
31. Kay S, Yoder S, Rothenberg S. Laparoscopic duodenoduodenostomy in the neonate. *J Pediatr Surg*. 2009;44(5):906–908.
32. Kimura K, et al. Diamond-shaped anastomosis for duodenal atresia: an experience with 44 patients over 15 years. *J Pediatr Surg*. 1990;25(9):977–979.
33. Lacher M, et al. Minimal invasive surgery in the newborn: current status and evidence. *Semin Pediatr Surg*. 2014;23(5):249–256.
34. Spilde TL, et al. Open vs laparoscopic repair of congenital duodenal obstructions: a concurrent series. *J Pediatr Surg*. 2008;43(6):1002–1005.
35. van der Zee DC. Laparoscopic repair of duodenal atresia: revisited. *World J Surg*. 2011;35(8):1781–1784.
36. Sandrasegaran K, et al. Annular pancreas in adults. *AJR Am J Roentgenol*. 2009;193(2):455–460.
37. Zyromski NJ, et al. Annular pancreas: dramatic differences between children and adults. *J Am Coll Surg*. 2008;206(5):1019–1025, discussion 1025–1027.
38. Lainakis N, et al. Annular pancreas in two consecutive siblings: an extremely rare case. *Eur J Pediatr Surg*. 2005;15(5):364–368.
39. Saghir A, et al. Annular pancreas: radiologic features of a case with recurrent acute pancreatitis. *Radiol Case Rep*. 2011;6(3):1–4.
40. Kamisawa T, et al. A new embryologic hypothesis of annular pancreas. *Hepatogastroenterology*. 2001;48(37):277–278.
41. Etienne D, et al. Annular pancreas: a review of its molecular embryology, genetic basis and clinical considerations. *Ann Anat*. 2012;194(5):422–428.
42. Patra DP, et al. Annular pancreas: a rare cause of duodenal obstruction in adults. *Indian J Surg*. 2011;73(2):163–165.
43. Shan YS, Sy ED, Lin PW. Annular pancreas with obstructive jaundice: beware of underlying neoplasm. *Pancreas*. 2002;25(3):314–316.
44. Ruben GD, Templeton JM Jr, Ziegler MM. Situs inversus: the complex inducing neonatal intestinal obstruction. *J Pediatr Surg*. 1983;18(6):751–756.
45. Li B, et al. Laparoscopic diagnosis and treatment of neonates with duodenal obstruction associated with an annular pancreas: report of 11 cases. *Surg Today*. 2015;45(1):17–21.
46. Applegate KE, Anderson JM, Klatte EC. Intestinal malrotation in children: a problem-solving approach to the upper gastrointestinal series. *Radiographics*. 2006;26(5):1485–1500.
47. Stewart D, Colodny A. Malrotation of the bowel in infants and children: a 15 year review. *Surgery*. 1976;79(6):716–720.
48. Strouse PJ. Disorders of intestinal rotation and fixation (“malrotation”). *Pediatr Radiol*. 2004;34(11):837–851.
49. Torres AM, Ziegler MM. Malrotation of the intestine. *World J Surg*. 1993;17(3):326–331.
50. Kantor J. Anomalies of the colon: their roentgen diagnosis and clinical significance. *Radiology*. 1934;23(6):651–662.
51. Applegate KE. Imaging of clinically suspected malrotation in children. In: Medina L, Applegate KE, eds. *Evidence-Based Imaging in Pediatrics*. Philadelphia.: Springer; 2010:435–446.
52. Dassinger M, Smith S, et al. Disorders of intestinal rotation and fixation. In: Coran A, ed. *Coran: Pediatric Surgery*. Philadelphia: CV Mosby, an imprint of Elsevier; 2012.
53. Lampl B, et al. Malrotation and midgut volvulus: a historical review and current controversies in diagnosis and management. *Pediatr Radiol*. 2009;39(4):359–366.
54. Sadler T. Digestive system. In: *Langman's Medical Embryology*. Williams & Wilkins; 2010.
55. DePrima SJ, Hardy DC, Brant WE. Reversed intestinal rotation. *Radiology*. 1985;157(3):603–604.
56. Estrada RL, Gurd FN. Surgical correction of reversed rotation of the midgut loop. *Surg Gynecol Obstet*. 1962;114:707–717.
57. Raphaeli T, et al. Acute colonic obstruction from Ladd bands: a unique complication from intestinal malrotation. *J Pediatr Surg*. 2010;45(3):630–631.
58. Leonidas JC, et al. Duodenojejunal atresia with “apple-peel” small bowel. A distinct form of intestinal atresia. *Radiology*. 1976;118(3):661–665.
59. Seashore JH, et al. Familial apple peel jejunal atresia: surgical, genetic, and radiographic aspects. *Pediatrics*. 1987;80(4):540–544.
60. Filston HC, Kirks DR. Malrotation - the ubiquitous anomaly. *J Pediatr Surg*. 1981;16(4 suppl 1):614–620.
61. Potts SR, et al. The duodenal triangle: a plain film sign of midgut malrotation and volvulus in the neonate. *Clin Radiol*. 1985;36(1):47–49.

62. Horsch S, et al. Volvulus in term and preterm infants - clinical presentation and outcome. *Acta Paediatr*. 2016;105(6):623–627.
63. Kanellos-Becker I, et al. Early prediction of complex midgut volvulus in neonates and infants. *Pediatr Surg Int*. 2014;30(6):579–586.
64. Imamoglu M, et al. Rare clinical presentation mode of intestinal malrotation after neonatal period: malabsorption-like symptoms due to chronic midgut volvulus. *Pediatr Int*. 2004;46(2):167–170.
65. Zellos A, et al. Malrotation of the intestine and chronic volvulus as a cause of protein-losing enteropathy in infancy. *Pediatrics*. 2012;129(2):e515–e518.
66. Berdon WE. The diagnosis of malrotation and volvulus in the older child and adult: a trap for radiologists. *Pediatr Radiol*. 1995; 25(2):101–103.
67. Spigland N, Brandt ML, Yazbeck S. Malrotation presenting beyond the neonatal period. *J Pediatr Surg*. 1990;25(11):1139–1142.
68. Salar O, et al. Internal hernias: a brief review. *Hernia*. 2013;17(3): 373–377.
69. Zizzo M, et al. Laparoscopic treatment of acute small bowel obstruction due to left paraduodenal hernia: a case report and literature review. *Int J Surg Case Rep*. 2016;20:87–91.
70. Berdon WE, et al. Megacystis-microcolon-intestinal hypoperistalsis syndrome: a new cause of intestinal obstruction in the newborn. Report of radiologic findings in five newborn girls. *AJR Am J Roentgenol*. 1976;126(5):957–964.
71. Torfs CP, Christianson RE. Anomalies in Down syndrome individuals in a large population-based registry. *Am J Med Genet*. 1998;77(5):431–438.
72. Abbas PI, Dickerson HA, Wesson DE. Evaluating a management strategy for malrotation in heterotaxy patients. *J Pediatr Surg*. 2016;51(5):859–862.
73. Applegate KE, et al. Situs revisited: imaging of the heterotaxy syndrome. *Radiographics*. 1999;19(4):837–852, discussion 853–854.
74. Chang J, Brueckner M, Touloukian RJ. Intestinal rotation and fixation abnormalities in heterotaxia: early detection and management. *J Pediatr Surg*. 1993;28(10):1281–1284, discussion 1285.
75. Hernanz-Schulman M, et al. Current evaluation of the patient with abnormal visceroatrial situs. *AJR Am J Roentgenol*. 1990;154(4):797–802.
76. Koplewitz BZ, Daneman A. The lateral view: a useful adjunct in the diagnosis of malrotation. *Pediatr Radiol*. 1999;29(2):144–145.
77. Tang V, et al. Disorders of midgut rotation: making the correct diagnosis on UGI series in difficult cases. *Pediatr Radiol*. 2013;43(9):1093–1102.
78. Long FR, et al. Radiographic patterns of intestinal malrotation in children. *Radiographics*. 1996;16(3):547–556, discussion 556–560.
79. Long FR, et al. Intestinal malrotation in children: tutorial on radiographic diagnosis in difficult cases. *Radiology*. 1996;198(3):775–780.
80. Ablow RC, et al. Z-shaped duodenojejunal loop: sign of mesenteric fixation anomaly and congenital bands. *AJR Am J Roentgenol*. 1983;141(3):461–464.
81. Kiesewetter W, Smith J. Malrotation of the midgut in infancy and childhood. *AMA Arch Surg*. 1958;77:483–491.
82. Katz ME, et al. The position and mobility of the duodenum in children. *AJR Am J Roentgenol*. 1987;148(5):947–951.
83. Slovis TL, Klein MD, Watts FB. Incomplete rotation of the intestine with a normal cecal position. *Surgery*. 1987;87:325–330.
84. Daneman A. Malrotation: the balance of evidence. *Pediatr Radiol*. 2009;39(suppl 2):S164–S166.
85. Applegate KE. Evidence-based diagnosis of malrotation and volvulus. *Pediatr Radiol*. 2009;39(suppl 2):S161–S163.
86. Dilley AV, et al. The radiologist says malrotation: does the surgeon operate? *Pediatr Surg Int*. 2000;16(1–2):45–49.
87. Sizemore AW, et al. Diagnostic performance of the upper gastrointestinal series in the evaluation of children with clinically suspected malrotation. *Pediatr Radiol*. 2008;38(5):518–528.
88. Stephens LR, Donoghue V, Gillick J. Radiological versus clinical evidence of malrotation, a tortuous tale–10-year review. *Eur J Pediatr Surg*. 2012;22(3):238–242.
89. Taylor GA, Teele RL. Chronic intestinal obstruction mimicking malrotation in children. *Pediatr Radiol*. 1985;15(6):392–394.
90. Benya EC, et al. Duodenum and duodenal-jejunal junction in children: position and appearance after liver transplantation. *Radiology*. 1998;207(1):233–236.
91. Dao T. Ultrasound as a definitive imaging predictor of midgut volvulus. *Pediatr Radiol*. 2015;45(1 suppl):p. Paper #006, S71.
92. Menten R, et al. Sonographic assessment of the retroperitoneal position of the third portion of the duodenum: an indicator of normal intestinal rotation. *Pediatr Radiol*. 2012;42(8):941–945.
93. Yousefzadeh DK, et al. US as a primary tool in the work-up of malrotation: reply to Anuradha. *Pediatr Radiol*. 2010;40:1846–1847.
94. Yousefzadeh DK, Kang L, Tessicini L. Assessment of retromesenteric position of the third portion of the duodenum: an US feasibility study in 33 newborns. *Pediatr Radiol*. 2010;40(9):1476–1484.
95. Taylor GA. CT appearance of the duodenum and mesenteric vessels in children with normal and abnormal bowel rotation. *Pediatr Radiol*. 2011;41(11):1378–1383.
96. Yousefzadeh DK. Regarding online publication of CT appearance of the duodenum and mesenteric vessels in children with normal and abnormal bowel rotation. *Pediatr Radiol*. 2011;41(11):1481–1482.
97. Weinberger E, et al. Sonographic diagnosis of intestinal malrotation in infants: importance of the relative positions of the superior mesenteric vein and artery. *AJR Am J Roentgenol*. 1992;159(4):825–828.
98. Zerin JM, DiPietro MA. Superior mesenteric vascular anatomy at US in patients with surgically proved malrotation of the midgut. *Radiology*. 1992;183(3):693–694.
99. Pracros JP, et al. Ultrasound diagnosis of midgut volvulus: the “whirlpool” sign. *Pediatr Radiol*. 1992;22(1):18–20.
100. Chao HC, et al. Sonographic features related to volvulus in neonatal intestinal malrotation. *J Ultrasound Med*. 2000;19(6):371–376.
101. Patino MO, Munden MM. Utility of the sonographic whirlpool sign in diagnosing midgut volvulus in patients with atypical clinical presentations. *J Ultrasound Med*. 2004;23(3):397–401.
102. Menten R, et al. Reply to Dr. B. Karmazyn regarding duodenum between the aorta and the SMA does not exclude malrotation. *Pediatr Radiol*. 2013;43(1):123.
103. Ladd W. Surgical diseases of the alimentary tract. *NEJM*. 1936; 216(16):705–708.
104. Hsiao M, Langer JC. Surgery for suspected rotation abnormality: selection of open vs laparoscopic surgery using a rational approach. *J Pediatr Surg*. 2012;47(5):904–910.
105. Ooms N, et al. Laparoscopic treatment of intestinal malrotation in children. *Eur J Pediatr Surg*. 2016;26(4):376–381.
106. Chang R, Andreoli S, Ziegler MM. Malrotation. In: Johnson L, ed. *Encyclopedia of Gastroenterology*. Academic Press; 2004.
107. McVay MR, et al. Jack Barney Award. The changing spectrum of intestinal malrotation: diagnosis and management. *Am J Surg*. 2007;194(6):712–717, discussion 718–719.
108. Covey SE, et al. Prophylactic versus symptomatic Ladd procedures for pediatric malrotation. *J Surg Res*. 2016;205(2):327–330.
109. Elder CT, et al. The role of screening and prophylactic surgery for malrotation in heterotaxy patients. *J Pediatr Surg*. 2014;49(12):1746–1748.
110. Graziano K, et al. Asymptomatic malrotation: diagnosis and surgical management: an American Pediatric Surgical Association outcomes and evidence based practice committee systematic review. *J Pediatr Surg*. 2015;50(10):1783–1790.
111. Papillon S, et al. Congenital heart disease and heterotaxy: upper gastrointestinal fluoroscopy can be misleading and surgery in an asymptomatic patient is not beneficial. *J Pediatr Surg*. 2013;48(1): 164–169.
112. Knight HO. An anomalous portal vein with its surgical dangers. *Ann Surg*. 1921;74(6):697–699.
113. Bower RJ, Ternberg JL. Preduodenal portal vein. *J Pediatr Surg*. 1972;7(5):579–584.
114. De Wailly P, et al. Pre-duodenal portal vein in polysplenia syndrome: clinical effects and surgical application. *Surg Radiol Anat*. 2011;33(5):451–454.
115. Kim SH, Cho YH, Kim HY. Preduodenal portal vein: a 3-case series demonstrating varied presentations in infants. *J Korean Surg Soc*. 2013;85(4):195–197.
116. Esscher T. Preduodenal portal vein–a cause of intestinal obstruction? *J Pediatr Surg*. 1980;15(5):609–612.
117. Mordehai J, et al. Preduodenal portal vein causing duodenal obstruction associated with situs inversus, intestinal malrotation, and polysplenia: a case report. *J Pediatr Surg*. 2002;37(4):E5.
118. Ohno K, et al. Evaluation of the portal vein after duodenoduodenostomy for congenital duodenal stenosis associated with the preduodenal superior mesenteric vein, situs inversus, polysplenia, and malrotation. *J Pediatr Surg*. 2007;42(2):436–439.
119. Bhorat N, Thomson SR, Anderson F. Preduodenal portal vein: a potential laparoscopic cholecystectomy nightmare. *S Afr J Surg*. 2009;47(1):17–18.
120. Weber WF, Draus JM Jr. Preduodenal portal vein: a rare cause of neonatal bowel obstruction. *Am Surg*. 2016;82(9):775–776.

121. Abramson SJ, et al. Biliary atresia and noncardiac polysplenic syndrome: US and surgical considerations. *Radiology*. 1987;163(2):377–379.
122. McCarten K, Littlewood Teele R. Preduodenal portal vein: venography, ultrasonography and review of the literature. *Ann Radiol (Paris)*. 1978;21:155–160.
123. Tsuda Y, et al. Preduodenal portal vein and anomalous continuation of inferior vena cava: CT findings. *J Comput Assist Tomogr*. 1991;15(4):585–588.
124. Fernandes ET, et al. Preduodenal portal vein: surgery and radiographic appearance. *J Pediatr Surg*. 1990;25(12):1270–1272.
125. Grosfeld JL, Ballantine TV, Shoemaker R. Operative mangement of intestinal atresia and stenosis based on pathologic findings. *J Pediatr Surg*. 1979;14(3):368–375.
126. Frischer J, Azizkhan R. Jejunoileal atresia and stenosis. In: Coran A, et al, eds. *Coran: Pediatric Surgery*. Philadelphia: CV Mosby, an imprint of Elsevie; 2012.
127. Martin L, Zerella J. Jejuno-ileal atresia: a proposed classification. *J Pediatr Surg*. 1976;11:399–403.
128. Louw J, Barnard C. Congenital intestinal atresia observations on its origin. *Lancet*. 1955;266(6899):1065–1067.
129. Dickson JA. Apple peel small bowel: an uncommon variant of duodenal and jejunal atresia. *J Pediatr Surg*. 1970;5(6):595–600.
130. Davis D, Poynter CW. Congenital occlusions of intestine with report of a case of multiple atresias of jejunum. *Surg Gynecol Obstet*. 1922;34:35.
131. Santulli TV, Blanc WA. Congenital atresia of the intestine: pathogenesis and treatment. *Ann Surg*. 1961;154:939–948.
132. Stollman TH, et al. Decreased mortality but increased morbidity in neonates with jejunoileal atresia; a study of 114 cases over a 34-year period. *J Pediatr Surg*. 2009;44(1):217–221.
133. Bigorgne AE, et al. TTC7A mutations disrupt intestinal epithelial apicobasal polarity. *J Clin Invest*. 2014;124(1):328–337.
134. Bilodeau A, et al. Hereditary multiple intestinal atresia: thirty years later. *J Pediatr Surg*. 2004;39(5):726–730.
135. Chen R, et al. Whole-exome sequencing identifies tetratricopeptide repeat domain 7A (TTC7A) mutations for combined immunodeficiency with intestinal atresias. *J Allergy Clin Immunol*. 2013;132(3):656–664, e17.
136. Notarangelo LD. Multiple intestinal atresia with combined immune deficiency. *Curr Opin Pediatr*. 2014;26(6):690–696.
137. Harris J, Kallen B, Robert E. Descriptive epidemiology of alimentary tract atresia. *Teratology*. 1995;52(1):15–29.
138. Leonidas JC, et al. Meconium ileus and its complications. A reappraisal of plain film roentgen diagnostic criteria. *Am J Roentgenol Radium Ther Nucl Med*. 1970;108(3):598–609.
139. Garnett GM, et al. First STEPs: serial transverse enteroplasty as a primary procedure in neonates with congenital short bowel. *J Pediatr Surg*. 2014;49(1):104–107, discussion 108.
140. Ismail A, et al. Serial transverse enteroplasty in intestinal atresia management. *J Pediatr Surg*. 2005;40(2):E5–E6.
141. Onofre LS, et al. Apple-peel intestinal atresia: enteroplasty for intestinal lengthening and primary anastomosis. *J Pediatr Surg*. 2013;48(6):E5–E7.
142. DeLorimier AA, Fonkalsrud EW, Hays DM. Congenital atresia and stenosis of the jejunum and ileum. *Surgery*. 1969;65(5):819–827.
143. Fakhoury K, et al. Meconium ileus in the absence of cystic fibrosis. *Arch Dis Child*. 1992;67(10 Spec No):1204–1206.
144. Shigemoto H, et al. Neonatal meconium obstruction in the ileum without mucoviscidosis. *J Pediatr Surg*. 1978;13(6):475–479.
145. Stringer MD, et al. Meconium ileus due to extensive intestinal aganglionosis. *J Pediatr Surg*. 1994;29(4):501–503.
146. Tal A, et al. Familial meconium ileus with normal sweat electrolytes. *Clin Pediatr (Phila)*. 1985;24(8):460–462.
147. Gorter RR, et al. Clinical and genetic characteristics of meconium ileus in newborns with and without cystic fibrosis. *J Pediatr Gastroenterol Nutr*. 2010;50(5):569–572.
148. Paradiso VF, et al. Meconium obstruction in absence of cystic fibrosis in low birth weight infants: an emerging challenge from increasing survival. *Ital J Pediatr*. 2011;37:55.
149. Hernanz-Schulman M. CT as an outcome surrogate in patients with cystic fibrosis: does the effort justify the risks? *Radiology*. 2012;262(3):746–749.
150. Ziegler MM. Meconium ileus. In: Coran A, et al, eds. *Coran: Pediatric Surgery*. Philadelphia: Mosby; 2012.
151. Ferec C, Cutting GR. Assessing the disease—liability of mutations in CFTR. *Cold Spring Harb Perspect Med*. 2012;2(12):a009480.
152. Benacerraf BR, Chaudhury AK. Echogenic fetal bowel in the third trimester associated with meconium ileus secondary to cystic fibrosis. A case report. *J Reprod Med*. 1989;34(4):299–300.
153. Yaron Y, et al. Evaluation of fetal echogenic bowel in the second trimester. *Fetal Diagn Ther*. 1999;14(3):176–180.
154. De Oronzo MA. Hyperechogenic fetal bowel: an ultrasonographic marker for adverse fetal and neonatal outcome? *J Prenat Med*. 2011;5(1):9–13.
155. Murshed R, et al. Meconium ileus: a ten-year review of thirty-six patients. *Eur J Pediatr Surg*. 1997;7(5):275–277.
156. Neuhauser EB. Roentgen changes associated with pancreatic insufficiency in early life. *Radiology*. 1946;46:319–328.
157. White H. Meconium ileus: a new roentgen sign. *Radiology*. 1956; 66(4):567–571.
158. Donnison AB, Shwachman H, Gross RE. A review of 164 children with meconium ileus seen at the Children's Hospital Medical Center, Boston. *Pediatrics*. 1966;37(5):833–850.
159. Noblett HR. Treatment of uncomplicated meconium ileus by Gastrografin enema: a preliminary report. *J Pediatr Surg*. 1969;4(2):190–197.
160. Leonidas JC, et al. Possible adverse effect of methylglucamine diatrizoate compounds on the bowel of newborn infants with meconium ileus. *Radiology*. 1976;121(3 Pt 1):693–696.
161. Lutzger LG, Factor SM. Effects of some water-soluble contrast media on the colonic mucosa. *Radiology*. 1976;118(3):545–548.
162. Kao SC, Franken EA Jr. Nonoperative treatment of simple meconium ileus: a survey of the Society for Pediatric Radiology. *Pediatr Radiol*. 1995;25(2):97–100.
163. Karimi A, et al. Issues in the management of simple and complex meconium ileus. *Pediatr Surg Int*. 2011;27(9):963–968.
164. Matsagas MI, et al. Incidence, complications, and management of Meckel's diverticulum. *Arch Surg*. 1995;130(2):143–146.
165. Snyder C. Meckel diverticulum. In: Coran A, et al, eds. *Coran: Pediatric Surgery*. Philadelphia: CV Mosby, an imprint of Elsevier; 2012.
166. Levy AD, Hobbs CM. From the archives of the AFIP. Meckel diverticulum: radiologic features with pathologic correlation. *Radiographics*. 2004;24(2):565–587.
167. Alemayehu H, et al. Demographic disparities of children presenting with symptomatic Meckel's diverticulum in children's hospitals. *Pediatr Surg Int*. 2014;30(6):649–653.
168. Bani-Hani KE, Shatnawi NJ. Meckel's diverticulum: comparison of incidental and symptomatic cases. *World J Surg*. 2004;28(9):917–920.
169. Baldisserotto M, Maffazzoni DR, Dora MD. Sonographic findings of Meckel's diverticulitis in children. *AJR Am J Roentgenol*. 2003;180(2):425–428.
170. Sung T, Callahan MJ, Taylor GA. Clinical and imaging mimickers of acute appendicitis in the pediatric population. *AJR Am J Roentgenol*. 2006;186(1):67–74.
171. Rosenbaum DG, Pollock AN. Torsed meckel diverticulum mimicking a cystic teratoma. *Pediatr Emerg Care*. 2016;32(7):493–495.
172. Alvares BR, Yumioka AS, Dos Santos GG. Uncommon presentation of perforated Meckel's diverticulum in preterm newborn. *Radiol Bras*. 2015;48(4):265–266.
173. Karagin PH, et al. Helicobacter species and gut bacterial DNA in Meckel's diverticulum and the appendix. *World J Gastroenterol*. 2011;17(36):4104–4108.
174. Swaniker F, Soldes O, Hirschl RB. The utility of technetium 99m pertechnetate scintigraphy in the evaluation of patients with Meckel's diverticulum. *J Pediatr Surg*. 1999;34(5):760–764, discussion 765.
175. Sagar J, Kumar V, Shah DK. Meckel's diverticulum: a systematic review. *J R Soc Med*. 2006;99(10):501–505.
176. Xie Q, et al. Incremental value of SPECT/CT in detection of Meckel's diverticulum in a 10-year-old child. *Springerplus*. 2016;5(1):1270.
177. Kawamoto S, et al. CT Detection of symptomatic and asymptomatic meckel diverticulum. *AJR Am J Roentgenol*. 2015;205(2):281–291.
178. Kotha VK, et al. Radiologist's perspective for the Meckel's diverticulum and its complications. *Br J Radiol*. 2014;87(1037):20130743.
179. Bennett GL, Birnbaum BA, Balthazar EJ. CT of Meckel's diverticulitis in 11 patients. *AJR Am J Roentgenol*. 2004;182(3):625–629.
180. Daneman A, et al. Sonographic appearances of inverted Meckel diverticulum with intussusception. *Pediatr Radiol*. 1997;27(4):295–298.
181. Epifanio M, et al. Magnetic resonance findings of a meckel's diverticulum at 3 tesla. *J Pediatr Gastroenterol Nutr*. 2015.
182. Sai Prasad TR, et al. Meckel's diverticular complications in children: is laparoscopy the order of the day? *Pediatr Surg Int*. 2007;23(2): 141–147.

183. Jadlowiec CC, Bayron J, Marshall WT 3rd. Is an incidental meckel's diverticulum truly benign? *Case Rep Surg*. 2015;2015:679097.
184. Chan KW, et al. Laparoscopic excision of Meckel's diverticulum in children: what is the current evidence? *World J Gastroenterol*. 2014;20(41):15158–15162.
185. Duan X, et al. Laparoscopic vs. laparoscopically assisted management of Meckel's diverticulum in children. *Int J Clin Exp Med*. 2015;8(1):94–100.
186. Ladd W. Duplications of the alimentary tract. *Southern Med J*. 1937;30(4):363–371.
187. Puligandla PS, et al. Gastrointestinal duplications. *J Pediatr Surg*. 2003;38(5):740–744.
188. Lund D. Alimentary tract duplications. In: Coran A, et al, eds. *Coran: Pediatric Surgery*. Philadelphia: CV Mosby, an imprint of Elsevier; 2012.
189. Keller MS, et al. Duodenal duplication cysts: a rare cause of acute pancreatitis in children. *Surgery*. 2001;130(1):112–115.
190. Cauchi JA, Buick RG. Duodenal duplication cyst: beware of the lesser sac collection. *Pediatr Surg Int*. 2006;22(5):456–458.
191. Li L, Zhang JZ, Wang YX. Vascular classification for small intestinal duplications: experience with 80 cases. *J Pediatr Surg*. 1998;33(8):1243–1245.
192. Ildstad ST, et al. Duplications of the alimentary tract. Clinical characteristics, preferred treatment, and associated malformations. *Ann Surg*. 1988;208(2):184–189.
193. Blake NS. Beak sign in duodenal duplication cyst. *Pediatr Radiol*. 1984;14(4):232–233.
194. Barr LL, et al. Enteric duplication cysts in children: are their ultrasonographic wall characteristics diagnostic? *Pediatr Radiol*. 1990;20(5):326–328.
195. Narlawar RS, et al. Sonographic findings in a duodenal duplication cyst. *J Clin Ultrasound*. 2002;30(9):566–568.
196. Segal SR, et al. Ultrasonographic features of gastrointestinal duplications. *J Ultrasound Med*. 1994;13(11):863–870.
197. Cheng G, et al. Sonographic pitfalls in the diagnosis of enteric duplication cysts. *AJR Am J Roentgenol*. 2005;184(2):521–525.
198. Davis JS, et al. Heterotopic gastric mucosa mimicking a Meckel's diverticulum in a young girl. *J Pediatr Surg*. 2015;50(5):879–881.
199. Jimenez JC, et al. Recurrent gastrointestinal tract bleeding secondary to jejunal gastric heterotopia. *J Pediatr Surg*. 2005;40(10):1654–1657.
200. Ricketts R. Mesenteric and omental cysts. In: Coran A, et al, eds. *Coran: Pediatric Surgery*. Philadelphia: CV Mosby, an imprint of Elsevier; 2012.
201. Tan JJ, Tan KK, Chew SP. Mesenteric cysts: an institution experience over 14 years and review of literature. *World J Surg*. 2009;33(9):1961–1965.
202. de Perrot M, et al. Mesenteric cysts. Toward less confusion? *Dig Surg*. 2000;17(4):323–328.
203. Losanoff JE, et al. Mesenteric cystic lymphangioma. *J Am Coll Surg*. 2003;196(4):598–603.
204. Goh BK, et al. Intra-abdominal and retroperitoneal lymphangiomas in pediatric and adult patients. *World J Surg*. 2005;29(7):837–840.
205. Kokhanovsky N, et al. Giant omental hemorrhagic cyst presenting as acute hemorrhagic anemia in a 21-month-old infant. *Pediatr Emerg Care*. 2014;30(3):188–190.
206. Tomizawa Y, Garner K, Sohnen A. Lymphangioma of the small bowel mesentery: a rare intra-abdominal tumor causing anemia. *Clin Gastroenterol Hepatol*. 2013;11(8):e57.
207. Khong PL, et al. Ultrasonography of intra-abdominal cystic lesions in the newborn. *Clin Radiol*. 2003;58(6):449–454.
208. Chung EM, et al. Solid tumors of the peritoneum, omentum, and mesentery in children: radiologic-pathologic correlation: from the radiologic pathology archives. *Radiographics*. 2015;35(2):521–546.
209. Levy AD, Cantisani V, Miettinen M. Abdominal lymphangiomas: imaging features with pathologic correlation. *AJR Am J Roentgenol*. 2004;182(6):1485–1491.
210. Arraiza M, et al. Primary cystic peritoneal masses and mimickers: spectrum of diseases with pathologic correlation. *Abdom Imaging*. 2015;40(4):875–906.
211. Kim SH, et al. Clinical features of mesenteric lymphatic malformation in children. *J Pediatr Surg*. 2016;51(4):582–587.
212. Conzo G, et al. Laparoscopic treatment of an omental cyst: a case report and review of the literature. *Surg Laparosc Endosc Percutan Tech*. 2005;15(1):33–35.
213. Jain V, et al. A case of laparoscopic mesenteric cyst excision. *Case Rep Surg*. 2012;2012:594095.
214. Trompetas V, Varsamidakis N. Laparoscopic management of mesenteric cysts. *Surg Endosc*. 2003;17(12):2036.

# 103 Acquired Abnormalities

Marta Hernanz-Schulman

Acquired duodenal abnormalities can be generalized into conditions that cause obstruction, inflammation, and neoplasia.

## ABNORMALITIES THAT RESULT IN DUODENAL OBSTRUCTION

### Superior Mesenteric Artery Syndrome

***Overview.*** First described at autopsy by von Rokitansky in 1861,[1] the term *superior mesenteric artery* or *SMA syndrome* refers to obstruction to the third portion of the duodenum at its crossing between the aorta and the superior mesenteric artery. It is also known by other terms, including cast syndrome and Wilkie syndrome.[2] The overall prevalence is cited to be between 0.013% and 0.3% of patients undergoing upper gastrointestinal (UGI) examinations;[3–5] a 20-year series confined to pediatric patients reports approximately one child per year diagnosed with this condition in the authors' pediatric hospital.[6]

***Etiology.*** The normal angle between the aorta and the SMA is between 25 and 60 degrees, and the normal aorto-SMA distance is 10 to 28 mm,[3] parameters that have been found to be significantly correlated to adult body mass index (BMI), particularly in females.[7] The etiology of SMA syndrome has been ascribed to an abnormally low angle between the aorta and the superior mesenteric artery, bringing them in close apposition at the crossing of the third portion of the duodenum. The low angle and decreased distance between the aorta and the SMA is thought to occur due to an abnormally low origin of the SMA, or an abnormally high position of the duodenojejunal junction at the ligament of Treitz, or "hypertrophy" of the ligament of Treitz.[1,7–9]

Although asthenic individuals, particularly after acute weight loss, are most susceptible to the development of SMA syndrome, Biank et al. found that this was not true in approximately 50% of their pediatric patients, who had a mean BMI at the 39th percentile. Premorbid conditions include Nissen fundoplication, cerebral palsy, traumatic brain injury, and posterior spinal fusion.[6] Other predisposed individuals include burn victims, and patients with lumbar hyperlordosis or in spinal traction/cast.[10] SMA syndrome may occur in families, raising the question of genetic predisposition.[11]

***Clinical Presentation.*** The clinical syndrome occurs more commonly in females between the ages of 10 and 39 years,[12] although it has been reported rarely in neonates and questionably prenatally.[12–14] The most common clinical presentation includes abdominal pain, vomiting, nausea, early satiety and anorexia;[6,15] acute presentation may follow one of the premorbid conditions previously described.[16]

***Imaging.*** Plain radiographs may show gastric dilatation, but the stomach may be decompressed by vomiting or via enteric tube. Contrast UGI study shows dilatation and partial obstruction of the third portion of the duodenum, terminating in a straight line at the expected location of the crossing of the SMA, with active but poorly effective peristalsis across the point of obstruction.

Ultrasound has been used to measure both the angle and the distance between the aorta and the SMA but may have difficulty outlining their relationship to the duodenum unless the latter is fluid-filled. As in the UGI, magnetic resonance imaging (MRI) and computed tomography (CT) (Fig. 103.1) are able to assess the dilatation of the duodenum and additionally can determine its relationship to the SMA, as well as the aorto-mesenteric angle and the aorto-mesenteric distance; angles less than 25 degrees and distances less than 8 mm are correlated with the clinical syndrome.[16]

***Treatment.*** Nonoperative medical treatment consists of measures for weight gain with high calorie enteral nutrition either by mouth, with transpyloric tube feedings beyond the point of obstruction, or with hyperalimentation. In one pediatric series, this was successful in 86% of patients, with a mean length of treatment of 65 days.[6] Medical treatment is most likely to be successful when the syndrome is of acute onset.[17]

Operative treatment is reserved for those who fail medical management and typically consists of duodenojejunostomy, with laparoscopic procedures resulting in a decreased length of hospital stay.[18,19]

### Duodenal Hematoma

***Overview.*** Duodenal hematoma is an infrequent injury in pediatric patients, occurring in less than 2% to 3% of children with abdominal injuries, usually associated with blunt abdominal trauma, both accidental and nonaccidental. The hematoma may extend beyond the ligament of Treitz into the proximal jejunum as a duodenojejunal hematoma.[20] Duodenal hematomas are graded as I or II, depending on whether a single portion or more than one portion of the duodenum is involved, according to The American Association for the Surgery of Trauma (AAST).[21]

***Etiology.*** The retroperitoneal duodenum contains a vascular submucosal and subserosal plexus and lies relatively fixed against the rigid spine, thus facilitating injury after blunt abdominal trauma. Bleeding is contained within the submucosa and subserosa and, as it increases in volume, it encroaches into the duodenal lumen. In children, this injury typically occurs after blunt trauma such as a direct punch or kick to the epigastrium, or handlebar injuries. Motor vehicle injuries involving sudden deceleration forces can also produce a shearing injury and result in intramural hematoma.[20] In a series of 33 children with blunt duodenal injury, nonaccidental trauma was the most common cause of duodenal injury (24%), followed by motor vehicle crashes, handlebar injuries, sports injuries, and other forms of direct trauma.[23] Duodenal hematoma has also been reported after endoscopic duodenal biopsy,[22,24–27] in patients with coagulation abnormalities after relatively minor trauma, or patients with pancreatitis, the latter postulated to be secondary to disruption of intramural vasculature by pancreatic enzymes.[28,29]

***Clinical Presentation.*** The clinical presentation includes abdominal pain and vomiting, typically bilious. When occurring after blunt trauma, there may be an associated pancreatic injury. Luminal obstruction sufficient to produce symptoms may not occur immediately after injury, and children may not present until several days after the traumatic event. When occurring after significant trauma such as a motor vehicle accident, the injury may be identified at CT evaluation. In the appropriate clinical setting, this injury should raise the concern for nonaccidental, inflicted trauma.[20,24,30] Rarely, the hematoma can act as a lead point of an intussusception into the adjacent jejunum.[31]

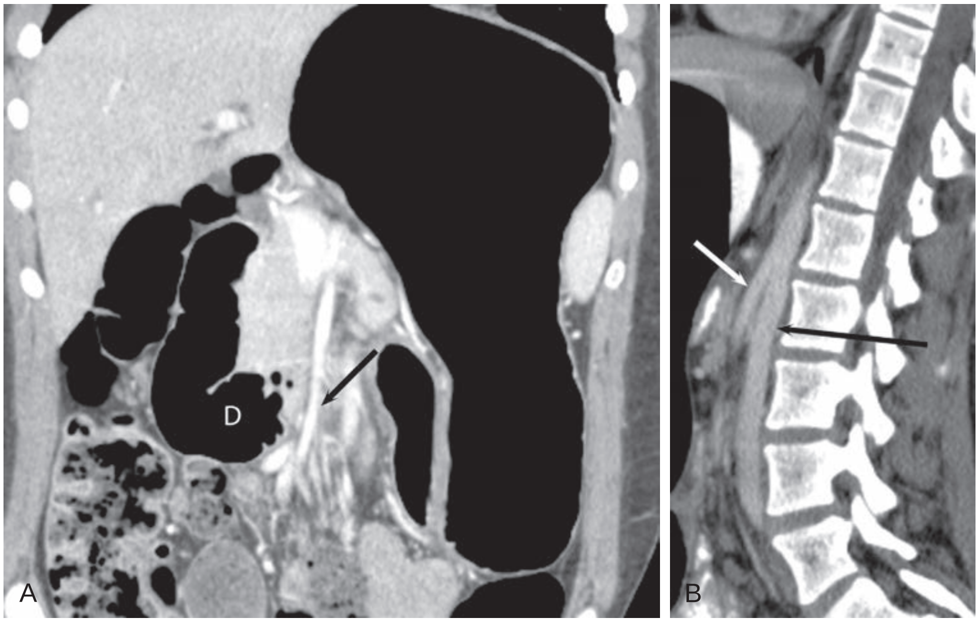

**Figure 103.1. Superior mesenteric artery syndrome.** Adolescent boy with cerebral palsy and vomiting. (A) Coronal reformatted contrast-enhanced CT image shows a dilated duodenum *(D)* to the crossing of the SMA *(black arrow)*. (B) Sagittal image on the same patient shows the narrow angle between the aorta *(black arrow)* and the SMA *(white arrow)*, which measured less than 12 degrees.

***Imaging.*** Plain films may be the initial modality in a child presenting with epigastric abdominal pain, tenderness, and vomiting. Depending upon the degree of obstruction and the severity of vomiting, the radiographs may show distension of the stomach and duodenum, with paucity of distal bowel contents; rarely, the outline of the hematoma may be visible against the gas in an adjacent viscus (Fig. 103.2A).

The findings on UGI depend on the ability of some of the contrast to traverse the obstructed portion of the duodenum. If very little contrast passes, the luminal border of the distended duodenum may show a lobulated contour. As contrast passes through the obstruction, it will outline the contour of the hematoma as a lobulated filling defect (Fig. 103.2B). Smaller hematomas may demonstrate more subtle findings, such as duodenal fold thickening.[20]

Ultrasound typically shows a distended proximal duodenum, with a mass of variable echogenicity encroaching upon and obliterating the more distal lumen (Fig. 103.2C).[32,33] The echogenicity of the mass is variable, depending on the status of the clot; the clue to the diagnosis is that the mass follows the course of the duodenum. On Doppler interrogation, there is no internal flow.

CT demonstrates similar findings, with dilatation of the more proximal duodenum, and a nonenhancing mass that follows the course of the duodenum obliterating its more distal lumen (Fig. 103.2D and E). (See also Fig. 109.11.)

MR is not often performed in children with duodenal hematomas. If performed, it will again show a mass following the course of the duodenum, obliterating its lumen, with signal characteristics consistent with evolving hematoma.

***Treatment.*** Patients with duodenal perforation need emergent surgery, but the treatment for duodenal hematoma generally consists of decompression of the stomach and duodenum via nasogastric tube, and maintenance of hydration and parenteral nutrition until resolution of the hematoma. In one series, the mean time to resolution of symptoms ranged between 12 and 16 days.[23,34] More severe grade II injuries are associated with longer intervals to resolution and discharge but typically also respond to expectant and supportive management.[35] If there is complete obstruction without improvement, it may be necessary to evacuate the hematoma surgically or via percutaneous drainage.[23,35]

## Duodenal Intussusception

***Overview.*** Duodenal intussusception may be seen in both antegrade and retrograde direction, typically around a gastrojejunostomy (GJ) tube.

***Etiology.*** Antegrade duodenojejunal intussusception is a relatively common complication of postpyloric GJ tubes, as the tube acts as a lead point for the intussusception. In large series, the rate of intussusception ranges from 16% to nearly 50%.[36,37] Intussusceptions are more likely in boys, in younger patients, with larger bore tubes and tubes with a distal pigtail that may act as a lead point, and administration of prokinetic agents.[37,38] Intussusception can also occur around a weighted nasojejunal tube.[39] Retrograde intussusception, on the other hand, is much less common and is believed to occur as a tube with an inflated terminal balloon, which has migrated distally due to peristalsis, is pulled back toward the stomach.[40,41]

***Clinical Presentation.*** The presentation is typically the onset of vomiting, bilious in approximately half the cases,[36] which may be accompanied by abdominal pain/irritability. However, these intussusceptions may be discovered incidentally at the time of routine tube check,[42] and therefore may be asymptomatic and transient in some cases. Uncommonly, intussusceptions lead to bowel necrosis requiring resection.[38] Hematemesis or bloody gastric aspirates are described in patients with retrograde intussusceptions.[40,41] Retrograde intussusception also occurs after gastric surgery, such as gastrojejunostomy, although in those cases the duodenum is bypassed. The intussuscepted jejunum may be gangrenous; obstruction and hematemesis are typical in acute presentation.[43]

***Imaging.*** Abdominal radiographs and ultrasound are helpful in diagnosis. Radiographs may reveal gastric outlet obstruction, and in retrograde intussusception, gas within the stomach will demonstrate the distal mass protruding into the gastric antrum

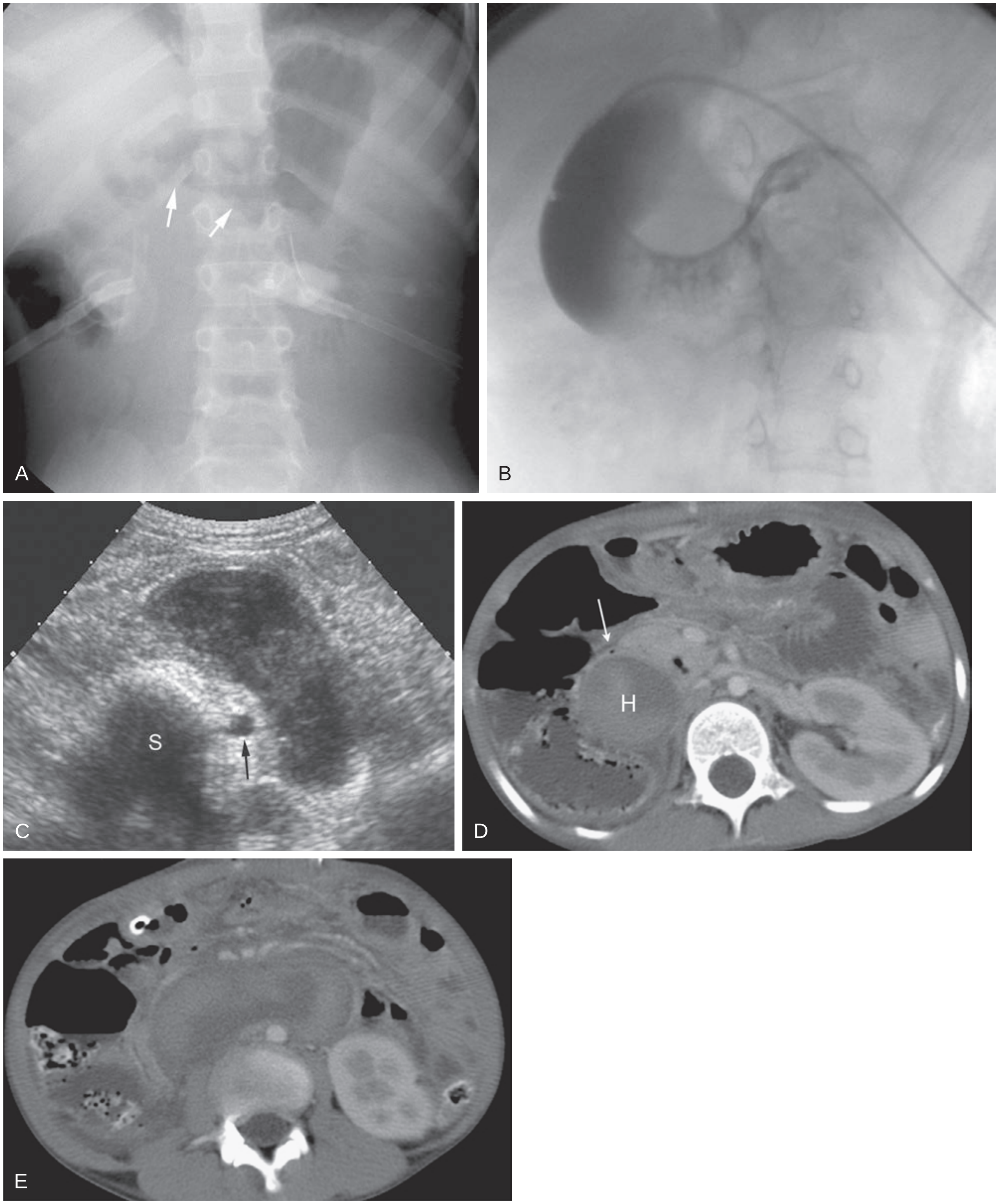

**Figure 103.2. Duodenal hematomas.** (A) An 8-year-old who had undergone an upper endoscopy with duodenal biopsy, and developed persistent bilious vomiting. Radiograph shows a polypoid density *(arrows)* encroaching upon the gas along the inferior border of the antrum. There is gaseous distension of the more proximal duodenum, with very little gas distally. (B) Fluoroscopic UGI image of a 10-year-old boy with cerebral palsy and mental retardation who presented to the ED with dehydration and inability to tolerate feedings. Introduction of contrast during unsuccessful GJ tube placement shows an obstructing duodenal hematoma as a filling defect upon the third and distal second portions of the duodenum. (C) Transverse sonogram on same patient as shown in (A), demonstrates the heterogeneous duodenal hematoma, following the course of the third portion of the duodenum. *S*, Spine. *Arrow* points to the aorta. (D) Contrast-enhanced CT at the level of the junction of the second and third portions of the duodenum, same patient as illustrated in (A) and (C), shows the large heterogeneous hematoma *(H)* obliterating the duodenal lumen. *Arrow* points to the duodenal wall and gas bubble in residual obliterated lumen. (E) More distal CT section through the third portion of the duodenum shows the heterogeneous hematoma, obliterating the lumen of the third portion of the duodenum.

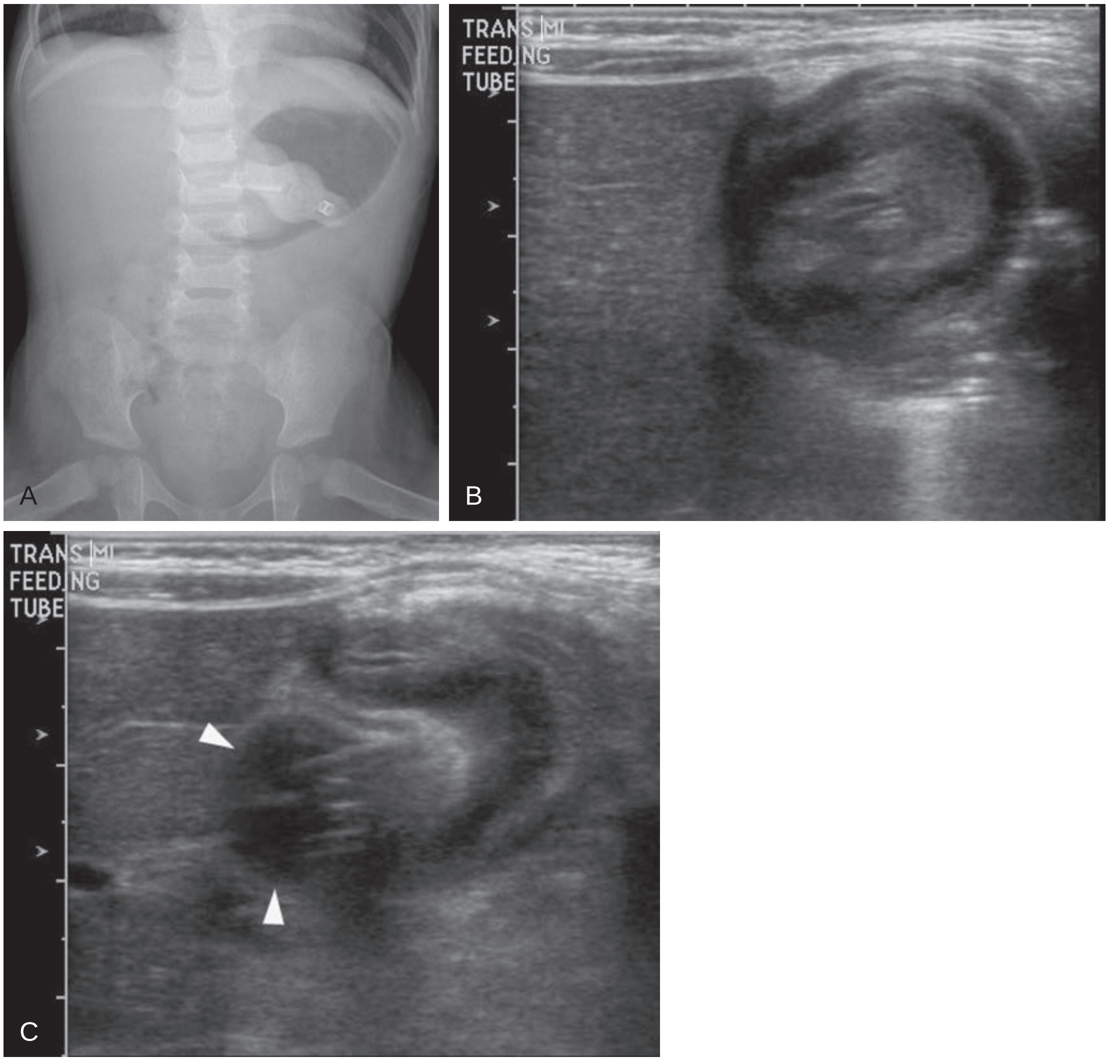

**Figure 103.3. Retrograde duodeno-gastric intussusception.** (A) Radiograph of a 3-year-old boy with a gastrostomy tube, who presented with vomiting demonstrates a gastrostomy tube, a dilated air-filled stomach with a mass-like lesion at the antrum, and a paucity of distal bowel gas consistent with gastric outlet obstruction. (B) Right upper quadrant sonogram demonstrates an intussusception. (C) US image immediately adjacent to (B) confirms that the gastrostomy tube balloon *(arrowheads)* is related to the intussusception.

(Fig. 103.3A). Ultrasound demonstrates the classic appearance of bowel within bowel at the gastric outlet[36,40,44] and may show a balloon as a lead point, particularly in retrograde intussusception (Fig. 103.3B and C). UGI will demonstrate a coiled spring appearance as the contrast passes into the intussusception; the amount of contrast may be small and the findings relatively subtle, therefore a high index of suspicion is helpful in arriving at the correct diagnosis.[44] On CT, the intussusceptum will be seen extending along the course of the duodenum, particularly well when outlined by air or contrast medium.[45]

***Treatment.*** Introduction of air or saline through the tube has been successful in reduction of intussusception,[36] although antegrade intussusceptions can be treated by replacement of the GJ tube over a wire.[38] This complication can be prevented by changing to a smaller bore GJ tube, removing the pigtail, or shortening the length of GJ tube.[46] If the intussusception occurs around a nasojejunal tube, the tube should be removed.[42] Retrograde intussusception is usually managed by deflation of the balloon,[40] although, in some cases of supervening ischemia, surgical resection has become necessary.[47]

## INFLAMMATORY CONDITIONS

### Duodenal Ulcer Disease

***Overview.*** Ulcer disease can involve the stomach and/or the duodenum and, as in the stomach, it is often associated with *Helicobacter pylori* infection, a pathogen that is estimated to colonize/infect approximately half the world's population.[48] Gastritis and gastric ulcers are discussed in Chapter 101.

***Etiology.*** The etiology of duodenal ulcerations is a result of overwhelming the inherent defense mechanisms, which include epithelial cell renewal and regeneration, duodenal bicarbonate production, preservation of mucosal blood flow, and production of prostaglandins.[49] The understanding of peptic and duodenal ulcer disease in both adults and children has changed dramatically since the elucidation of the role of *H. pylori* infection by Warren and Marshall in 1984[50,51] for which they were awarded the Nobel Prize in 2005. Because *H. pylori* is trophic for gastric epithelium, duodenal ulcers related to *H. pylori* are believed to occur over sites of gastric metaplasia[52]; they are thus related to increased acid secretion and decreased bicarbonate output by the duodenum, thus lowering luminal pH and precipitating bile acids, which would otherwise exert an inhibitory effect on *H. pylori* growth. Acid hypersecretion additionally promotes the activation of pepsinogen to pepsin facilitating mucosal ulceration.[52]

A higher rate of *H. pylori* infection has been reported in children with duodenal ulcers (62%) than in those with peptic ulcers (20%), although other sources do not confirm this relationship.[53] Transmission of *H. pylori* is mainly by the oral-oral or fecal-oral route, and requires contact with intestinal secretions.[54,55] Colonization with this pathogen has greater prevalence in locations with suboptimal sanitary infrastructure and crowded living conditions.[55] Childhood is the primary period of colonization by *H. pylori*, with cases often clustering within families secondary to intrafamilial transmission.[55] In Western nations, there is a decreasing prevalence of *H. pylori* colonization, being reported as low as 27% in children from Western European centers, although this may be underreported secondary to culture of specimens from the stomach rather than the duodenum.[56]

With reduction of *H. pylori*, the proportion of duodenal ulcers unrelated to *H. pylori* increases. Other causes of duodenal ulcer disease include therapy with nonsteroidal anti-inflammatory medications (NSAIDs). These agents promote ulceration by inhibition of cyclooxygenase 1 and 2 enzymes, which have a role in maintaining the integrity of the gastric epithelium and its mucous barrier, as well as in the response to inflammatory processes. NSAIDs may also increase the production of inflammatory mediators such as leukotrienes.[49]

***Clinical Presentation.*** Most children with duodenal ulcer disease present with symptoms that include epigastric tenderness, pain that wakes the child from sleep at night, hematemesis, melena, anorexia, poor weight gain, and vomiting.[53,56,57] Extragastric or extraduodenal manifestations include failure to thrive with growth disturbance in addition to poor weight gain, iron deficiency anemia, and idiopathic thrombocytopenic purpura.[55]

***Imaging.*** UGI has been largely supplanted in the diagnosis of duodenal ulcer disease by endoscopy, which has become the diagnostic gold standard and also allows the biopsy and culture of detected abnormalities. When UGI is performed, double contrast technique is more sensitive in the detection of ulcer disease, although this is much more difficult to perform in younger patients and impossible to perform in infants.

Despite the shift to endoscopy, ulcers should be detected during UGI if present. Duodenitis, which could be secondary to multiple etiologies beyond ulcer disease, is manifested by thickening of the duodenal folds, with a historically cited sensitivity of 45% in detecting duodenal inflammation.[57] The imaging appearance of duodenal ulcers in children is similar to that in adults, with the most common finding in an acute ulcer being contrast within an ulcer crater (Fig. 103.4). Radiating folds representing surrounding mucosal edema may also be seen. When the ulcer is on the nondependent wall of the duodenum, air will fill the ulcer outlined by barium. Chronic duodenal ulcers may lead to a scarred and deformed duodenum, but these are uncommon in children. So-called "giant duodenal ulcers" are rare, occur more commonly in association with NSAIDs, and have been found in patients with end stage renal disease and with Crohn disease.[52]

Ultrasound is not typically performed in patients with known duodenal ulcer disease; however, thickening of the bowel wall has been described, as well as surrounding fluid and gas in cases of perforation.[58]

On CT, thickening of the duodenal wall may be detected, as well as contrast within an ulcer crater.[59] In cases of perforation, periduodenal fluid and retroperitoneal and intraperitoneal free air may be identified, along with contrast extravasation if oral contrast was used (Fig. 103.5).[28]

***Treatment.*** *H. pylori* is considered a group I carcinogen, and the goal of therapy is eradication.[60] Although in the initial reports the pyloric organisms were sensitive to multiple antibiotics,[61] not all current strains demonstrate similarly wide susceptibility. Eradication of the organisms in symptomatic patients requires triple or quadruple therapy, with testing of resistance profiles recommended.[60,62,63]

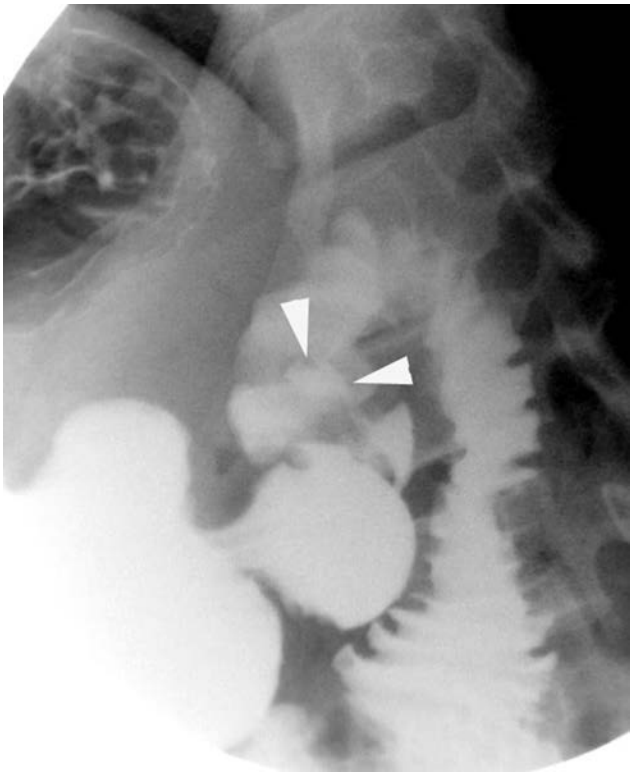

**Figure 103.4. Duodenal ulcer.** UGI spot image of the duodenal bulb in a boy with 1-week history of abdominal pain reveals a collection of contrast in the ulcer crater *(arrowheads)*. *(Case courtesy of Dr. Tamar Ben-Ami, Chicago, IL.)*

## Zollinger-Ellison Syndrome

***Overview.*** The Zollinger-Ellison syndrome refers to autonomous oversecretion of the hormone gastrin by a gastrinoma of the duodenum or pancreas, resulting in unusually severe and refractory ulcer disease, typically accompanied by diarrhea. The condition is rare, with an incidence quoted as 1 to 3 new cases per million population.[64] Gastrinomas and the Zollinger-Ellison syndrome can occur sporadically or, in approximately 15% to 38% of cases, as part of the multiple endocrine neoplasia Type 1 (MEN-1) syndrome;[64–66] conversely, the Zollinger-Ellison syndrome occurs in approximately 21% to 70% of patients with MEN-1.

The Zollinger-Ellison syndrome is typically diagnosed in the fifth decade, with approximately 90% presenting between the ages of 20 and 60 years of age.[66] The syndrome tends to present at a younger age when part of the MEN-1 syndrome. Approximately 8.6% occur in children, about 4 times more commonly in boys, typically no earlier than the second decade, although the diagnosis has been reported in a 5-year-old girl.[65,67,68]

Most tumors are located in the wall of the duodenum or in the head of the pancreas but can also be located in more distant regions, including the heart, ovary, kidneys, and mesentery. Tumors can be both small and multiple, presenting a challenge to diagnosis.[69–71] However, the majority of gastrinomas occur in the so-called gastrinoma triangle, which is located to the right of the superior mesenteric artery, and bounded superiorly by the confluence of the cystic and common bile ducts, inferiorly by the junction of

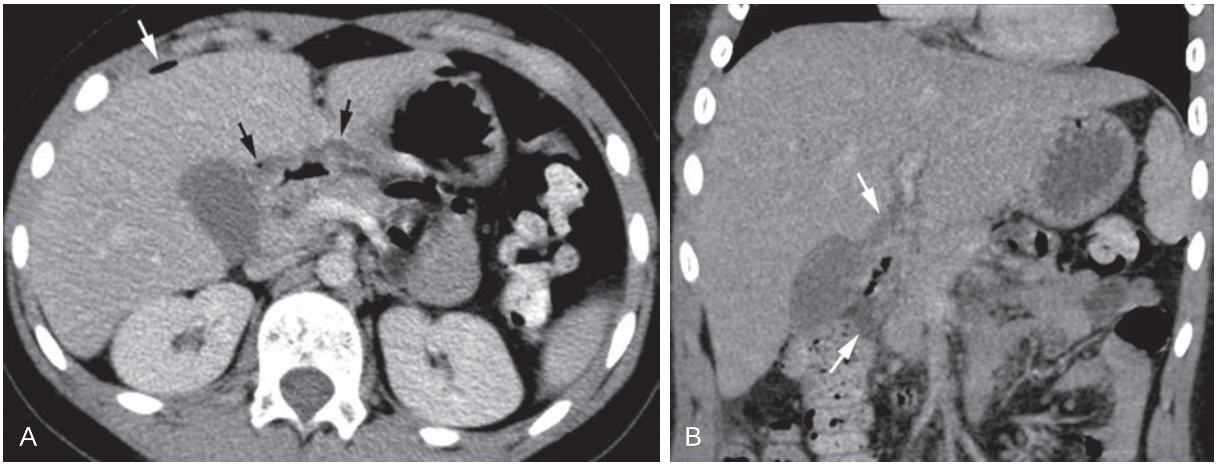

**Figure 103.5. Perforated duodenal ulcer.** (A) Contrast-enhanced CT image in a 9-year-old boy with 2-day history of abdominal pain, fever, and decreased activity shows thickening of the duodenum, with a small amount of periduodenal fluid and free air *(black arrows)* as well as intraperitoneal free air *(white arrow)*. (B) Coronal reformatted CT image shows thickening of the duodenum, and periduodenal fluid *(arrows)*.

the second and third portions of the duodenum, and medially by the junction of the head and body of the pancreas.[69,72]

***Etiology.*** Autonomous neoplastic overproduction of gastrin results in acid hypersecretion and extensive ulcer disease. The cause of sporadic gastric tumors is not known; however, MEN-1 is the result of an autosomal dominant mutation in the tumor suppressor gene MEN-1, encoding the protein MENIN. Parathyroid hyperplasia, pancreatic endocrine tumors (of which gastrinoma is the most common), pituitary adenomas, and adrenal adenomas occur in this syndrome. Patients are also prone to develop carcinoid tumors; gastric, thymic, and bronchial lesions; lipomas; and skin lesions including melanomas.[66]

***Clinical Presentation.*** The triad of abdominal pain, weight loss, and diarrhea in conjunction with ulcer disease (typically negative for *H. pylori*) is highly suggestive of Zollinger-Ellison syndrome. Patients may also present with hematemesis, tarry stools, and anemia. The diagnosis of gastrinoma and Zollinger-Ellison syndrome should prompt investigation for MEN-1, particularly in children.[66,67] Some patients with MEN-1 may present initially with evidence of hyperparathyroidism, such as urolithiasis; manifestation of gastrinoma may follow, sometimes as much as 25 years later.[73] Approximately 60% of gastrinomas are malignant, and 50% have metastasized at diagnosis.[69,74]

The primary ulcer site is the duodenum, and ulcers can occur in the distal duodenum as well as the jejunum, sites that should raise concern for gastrinoma. In a pediatric series of patients with Zollinger-Ellison syndrome, the primary ulcer site was duodenum in 72% and the jejunum in 28%.[67]

Successful treatment with proton pump inhibitors may delay the diagnosis by assuaging symptoms.[64,66] The diagnosis is made by demonstrating gastrin hypersecretion by measurement of fasting gastrin levels and acid secretion. However, in patients who are on proton pump inhibitors, fasting serum gastrin levels may be sufficiently elevated to overlap with those seen in patients with Zollinger-Ellison syndrome[66]; in such cases, proton pump inhibitors should be withdrawn for approximately 1 week before repeating the test.[64] In addition to fasting gastrin levels, provocative tests are also employed, utilizing secretin, calcium, and meal stimulation.[66]

***Imaging.*** The classic finding on UGI examination is the presence of ulcers in the duodenum, particularly distal duodenum, or in the jejunum, as well as thickening of duodenal and gastric folds.[66] Ulcer disease is now more often evaluated endoscopically, which shows thickened gastric folds in up to 94% of patients with Zollinger-Ellison syndrome.[64]

Ultrasonography has not been found to be sensitive in detecting gastrinomas either inside or outside the liver and pancreas. However, endoscopic ultrasound (EUS) is much more sensitive, with detection rates as high as 93% in some patients; however, it is much less helpful in distal lesions located close to or in the tail of the pancreas.[75] On CT, identification of hypervascular pancreatic gastrinomas is optimized with rapid bolus technique, with thin collimation and reformats, possibly requiring dual phase arterial and portal venous imaging.[76] A recent review found a nearly 100% sensitivity of EUS and CT in detection of pancreatic neuroendocrine tumors.[77] Contrast-enhanced MRI was thought to be sensitive and complementary to EUS in a recent report.[75] Somatostatin receptor scintigraphy using [$^{111}$In-DTPA-DPhe$^{1}$]octreotide was found to be 70% sensitive in the detection of the tumors.[66] More recently, PET-CT with $^{68}$Ga-labelled somatostatin analogues has shown great sensitivity in detection of neuroendocrine tumors.[78] PET-CT with these agents showed superior sensitivity when compared with MRI, CT, and 18F-FDG PET (approaching or reaching 100%), and identified extrapancreatic and duodenal lesions.[77–80] Direct venous sampling after selective arterial injection of secretin or calcium to elicit gastrin release (selective arterial secretagogue injection [SASI] test) can detect more than 90% of gastrinomas smaller than 5 mm that may otherwise elude imaging diagnosis.[71,81]

***Treatment.*** Control of hyperacidity is one of the key elements in survival.[66,82] Historically, this was achieved with gastrectomy, but today suppression of excess acid production is achieved medically with proton pump inhibitors. The management of patients is geared toward treatment of other manifestations of the MEN-1 syndrome if present, as well as the gastrinoma itself. Although most gastrinomas demonstrate slow growth, 25% show more rapid growth, and approximately 60% to 90% demonstrate malignant behavior.[70] In a study of 151 patients, more than half of those with sporadic gastrinomas were free of disease after surgery, and most of these were able to achieve long-term cure; this approach is preferred in patients with sporadic gastrinoma.[70] In patients with MEN-1 and gastrinoma, some authors advocate a pancreas-preserving total duodenectomy to achieve cure in some of the patients, as well as laparoscopic intervention.[71,83,84]

## Inflammatory Bowel Disease

***Overview.*** Although involvement of the duodenum with Crohn disease is nearly universally accompanied by ileal or ileocolic disease,[85,86] there is a wide difference in the reported percentage with duodenal involvement.[87] This is likely related to the fact that patients with duodenal disease do not have symptoms distinct from those with more distal involvement.[86,88,89] In one endoscopic study of Crohn patients, 31.9% had involvement of the duodenal bulb and 18.1% of the second portion of the duodenum.[90] Another review found that 53.3% of children with Crohn disease had upper GI involvement, and of these 63% had duodenal involvement alone or in combination with esophageal and gastric lesions.[91]

***Etiology.*** The etiology of Crohn disease remains unknown, although a genetic predisposition is underscored by familial occurrence and concordance of the disease in monozygotic twins (44%–58%).[92] Please see Chapters 104 and 106 for additional discussion.

***Clinical Presentation.*** Patients with duodenal involvement tend to present at a younger age than patients with distal involvement,[93] typically with abdominal pain, general malaise, and weight loss.[94] These patients tend to have more severe clinical manifestations and course.[91]

Complications related to duodenal involvement include involvement of the ampullary region of the duodenum, leading to biliary and pancreatic duct obstruction,[95] as well as pancreatitis, although the latter could be related to other causes such as medications used to treat the primary disease.[96] Fistula formation also occurs, although it is believed that fistulas between the duodenum and small bowel or colon usually originate in the latter, rather than in the duodenum.[86]

***Imaging.*** Just as the diagnosis of Crohn disease has shifted from radiography to endoscopy, the imaging modalities have shifted from radiography to cross-sectional imaging, including ultrasound with color or power Doppler, CT, and MRI, with MR enterography (MRE) largely being used to follow patients in many centers.[97] However, if a UGI is requested in a patient with abdominal pain and weight loss, the diagnostic findings should be appreciated.

The findings on UGI are similar to those found in distal bowel. Double contrast studies are more sensitive than single contrast examinations in identifying the aphthous lesions that characterize the early stages of the disease. These will most typically be found in the antrum, pylorus, and duodenum. Duodenal fold thickening, luminal narrowing, wall thickening, and fistula and sinus tract formation may also be seen (Fig. 103.6).

Ultrasound is able to detect bowel wall thickening, and Doppler is able to detect the hyperemia characteristic of active Crohn disease, findings that are well documented in terminal ileal disease.[98–101]

CT is helpful in patients with bowel obstruction and other patients who are unable to tolerate MRI because of procedure length and other requirements such as sedation. Duodenal findings include fold thickening, increased enhancement, and stricture formation.[28,59,102]

MRE is becoming the ideal modality in the routine imaging evaluation of patients with Crohn disease. The findings in the duodenum are similar to those in other bowel segments.[103,104]

***Treatment.*** Therapy for duodenal Crohn disease typically includes exclusion of *H. pylori*, and its treatment if found. Treatment then consists of proton pump inhibition to inhibit gastric secretion and promote ulcer healing, as well as corticosteroids. Biologics such as anti-TNFα (tumor necrosis factor) and immunomodulators continue to be evaluated for efficacy in achieving mucosal healing.[105] Strictures are amenable to endoscopic balloon dilatation. Patients who do not respond to medical management or who develop gastrointestinal hemorrhage may need surgical intervention.[86]

## Cystic Fibrosis

***Overview.*** There are multiple manifestations of cystic fibrosis (CF) in the gastrointestinal tract; duodenal involvement includes duodenal fold thickening, ulceration, and strictures.[106] Duodenal and gastric ulceration has been reported in as many as 10% of autopsy reports of pediatric patients with CF.[107]

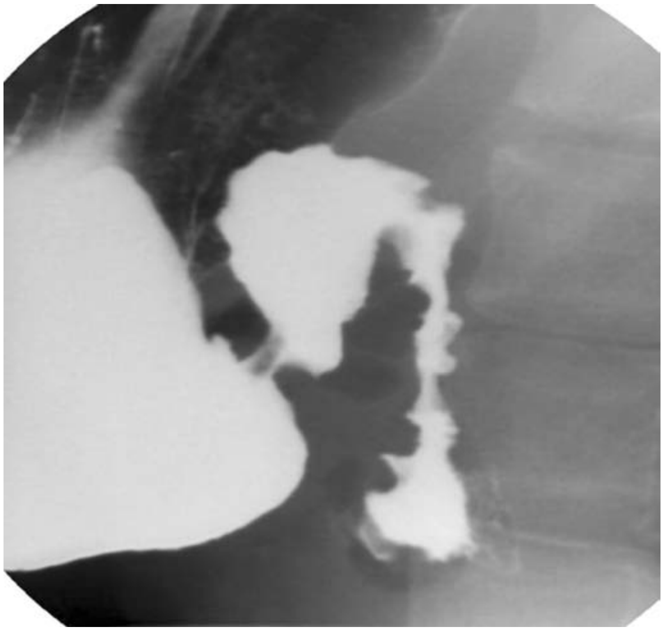

**Figure 103.6. Crohn disease.** UGI spot image demonstrates mucosal fold thickening in the duodenum. There was extensive disease elsewhere in the bowel. *(Case courtesy of Lakshmana Das Narla, Richmond, VA.)*

***Etiology.*** Impaired secretion of bicarbonate by the duodenum and pancreas curtails the ability to buffer gastric acid.[108] Thickening of duodenal folds is believed to be related both to hyperacidity in the environment, abnormal mucus production, and hypertrophy of Brunner glands.[107] Hyperacid duodenal environment also leads to precipitation of bile salts and decreased fat absorption.

Inflammatory changes in the gut of CF patients have been found through identification of products of T-cell activation[109] and output of inflammatory proteins.[110] The etiology of inflammatory changes in the duodenal mucosa may include factors such as increased antigenic load secondary to pancreatic insufficiency and defective digestion of luminal contents,[109] and altered intestinal flora.[111]

***Clinical Presentation.*** Patients usually present with abdominal pain; hematemesis may occur if there is ulcer disease.[107] Patients may also manifest symptoms of severe gastroesophageal reflux, thought partly related to gastrointestinal dysmotility and the need for frequent postural drainage.[112]

***Imaging.*** UGI typically demonstrates thick and coarse duodenal folds, particularly along its first and second portions, with some distortion and kinking of the duodenal contours, at times simulating a mass lesion,[113] ulceration,[107] or frank stricture formation (e-Fig. 103.7).[106,108]

***Treatment.*** Patients are treated with proton pump inhibitors or histamine-2 ($H_2$) receptor antagonists to decrease the acidity of the duodenal environment, which helps prevent ulceration as well as increase the ability to absorb fats and fat-soluble vitamins.[114,115]

## NEOPLASMS

***Overview.*** Duodenal neoplasms are uncommon lesions. Neoplasms that are characteristic to the duodenum include lesions related to Brunner glands, adenomas associated with polyposis syndromes, and neuroendocrine tumors. Gastrointestinal stromal tumors (GIST), clear cell sarcomas, and clear cell myomelanocytic tumor (PEComa) have also been reported, although these are highly unusual.[116,117] Brunner gland hyperplasia has been described as three types: diffuse through the duodenum, circumscribed and confined

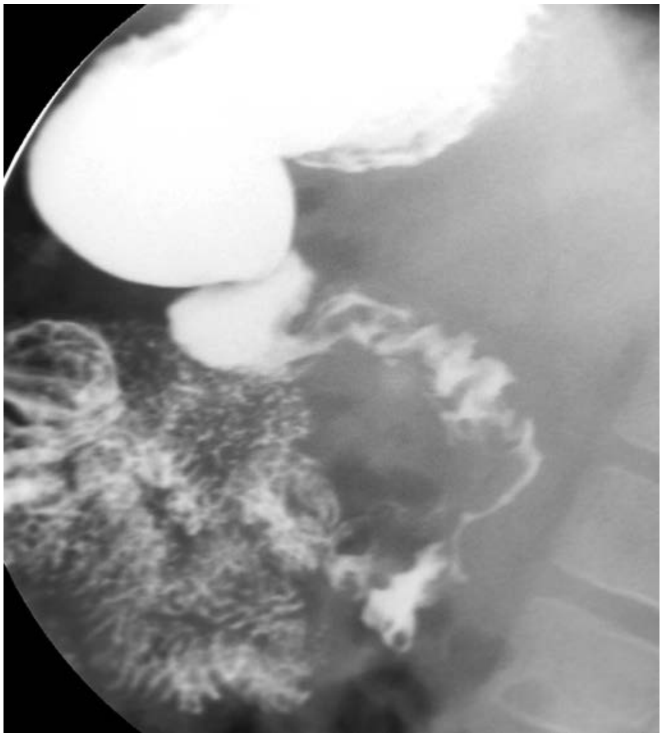

**e-Figure 103.7. Cystic fibrosis.** UGI spot image in a patient with cystic fibrosis demonstrates duodenal fold thickening. *(Case courtesy of Dr. Steven Kraus, Cincinnati, OH.)*

to its first portion, and Brunner gland hamartoma, which refers to lesions larger than one centimeter.[118] These hamartomatous lesions are rare, more often occurring in adults during or after middle age, but can occur in children and have been reported in early infancy, more commonly in the more proximal duodenum.[119,120]

Most duodenal polypoid lesions in pediatric patients are associated with polyposis syndromes. Familial adenomatous polyposis (FAP) is the most common systemic abnormality in patients with duodenal adenomatous polyps; conversely, adenomatous duodenal polyps occur in approximately 90% of FAP patients. Periampullary duodenal carcinoma is the most common extracolonic tumor in adult patients with FAP.[121,122] In an endoscopic study of 24 pediatric patients with FAP, periampullary adenomas were present in 41%.[123] Children with Peutz-Jeghers syndrome develop hamartomatous polyps in the duodenum,[121] although 3% to 6% of hamartomas develop adenomatous changes.[122] Brunner gland hypertrophy develops in patients with juvenile polyposis,[121] but cancers of the duodenum have also been reported in this population.[122]

Duodenal neuroendocrine tumors may be sporadic, or associated with MEN-1 or neurofibromatosis type 1. Approximately two-thirds of duodenal neuroendocrine tumors are G cell gastrin tumors, of which nearly one-third are associated with the Zollinger-Ellison syndrome. Somatostatin-producing D cell tumors represent approximately one-fifth of duodenal lesions, nearly exclusively located in the periampullary region.[124,125]

***Etiology.*** The hyperplasia of Brunner glands that occurs in uremic patients is thought to be related to the elevated gastrin levels and hyperacidity that occurs in patients with end-stage renal insufficiency.[118,126,127] Brunner gland hamartomas are associated with chronic renal failure, chronic pancreatitis, peptic ulcer disease. and infection with *H. pylori*.[128]

Mutations that render the product of tumor suppressor genes ineffective are of paramount importance in the development of malignancy. FAP patients have a mutation within the adenomatous polyposis coli *(APC)* gene located at chromosome 5q21. Peutz-Jeghers has been mapped to the *STK* (serine threonine kinase 11) gene on chromosome 19p13.3. Genetic loci in separate kindred with juvenile polyposis have been reported in the *SMAD4* gene located on chromosome 18q21.1 and the *PTEN* gene on chromosome 10q23.[121,122]

***Clinical Manifestations.*** Patients with Brunner gland hyperplasia are typically asymptomatic. When symptoms occur, patients tend to present with bleeding, obstruction, pain, vomiting, and diarrhea.[118] Large lesions such as Brunner gland hamartoma can present with gastric outlet obstruction, and biliary obstruction and pancreatitis when affecting the periampullary region.[128]

Duodenal carcinoids may manifest as Zollinger-Ellison syndrome. D cell somatostatin-producing tumors arising in the duodenum are usually too small to produce clinically apparent symptoms related to hormone overproduction.[129]

***Imaging.*** A large lesion, such as a giant Brunner gland hamartoma may demonstrate evidence of gastric outlet obstruction on abdominal radiographs.[128] On UGI, a filling defect within the duodenal bulb may be demonstrated (Fig. 103.8). Single or multiple polyps, seen with FAP or Peutz-Jeghers syndromes, appear as a multitude of filling defects, at times complicated by intussusception (e-Fig. 103.9). Duodenal carcinoids have been described as intraluminal or mural filling defects, sometimes with ulcerations, and occasionally producing obstruction by intussusception.[124] CT detection is optimized by the use of negative luminal contrast, with marked arterial enhancement decreasing on the portal venous phase.[76,125] On MR, they have been described as low signal on T1-weighted images, heterogeneously high signal on water-sensitive sequences, and have early arterial hyperenhancement.[124,129]

***Treatment.*** Brunner gland hyperplasia does not require specific treatment if asymptomatic. Conservative treatment consists of control of gastric acidity with proton pump antagonists and $H_2$ blockers. Brunner gland hamartomas may be amenable to endoscopic removal, although larger or more diffuse lesions may need more extensive surgical polypectomy, or segmental or more extensive duodenal resection.[128] Children with FAP undergo periodic endoscopic screening, as most duodenal adenomas are not symptomatic. Management of periampullary adenocarcinoma includes pancreaticoduodenectomy. Endoscopic ampullectomy may be helpful in some patients with early lesions.[123]

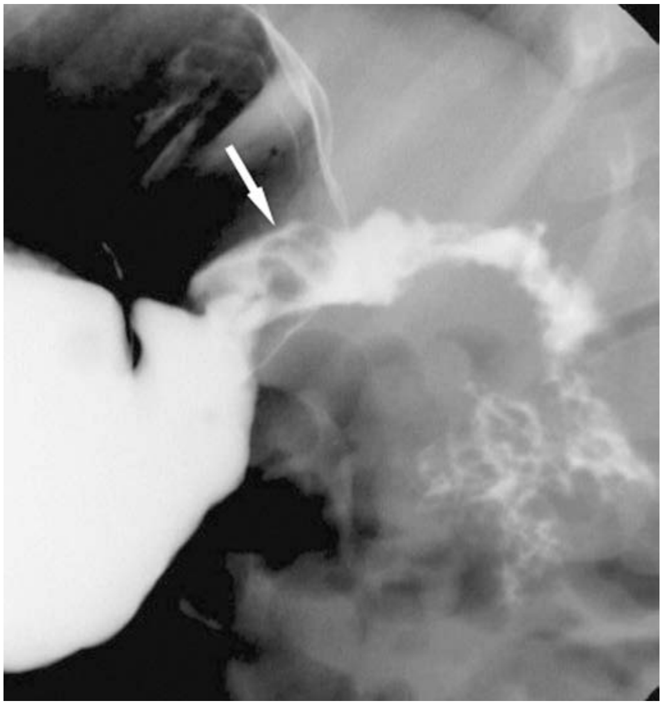

**Figure 103.8. Brunner gland hyperplasia.** UGI spot image shows a less than 1 cm filling defect *(arrow)* in the duodenal bulb consistent with Brunner gland hyperplasia. *(Case courtesy of Kimberly Applegate; Lexington, KY.)*

KEY POINTS

- The normal angle between the aorta and the SMA is 25 to 60 degrees, and the distance between the aorta and the SMA is 10 to 28 mm.
- SMA syndrome-predisposing conditions include Nissen fundoplication, cerebral palsy, traumatic brain injury, posterior spinal fusion, burn, lumbar hyperlordosis, and spinal traction/cast.
- Causes of duodenal hematoma include nonaccidental trauma and other blunt injuries to the epigastrium, such as handlebar injuries, motor vehicle crashes, and sports injuries.
- Duodenal intussusception is a complication of post-pyloric GJ tubes, which act as a lead point.
- Duodenal ulcer disease is associated with infection by *Helicobacter pylori*, which is estimated to colonize/infect approximately half the world's population.
- Zollinger-Ellison syndrome refers to autonomous oversecretion of the hormone gastrin by a gastrinoma, resulting in unusually severe and refractory ulcer disease, accompanied by diarrhea. Approximately 15% to 38% of cases occur as part of MEN-1.
- Duodenal involvement in patients with Crohn disease is identified more frequently with endoscopic evaluation.

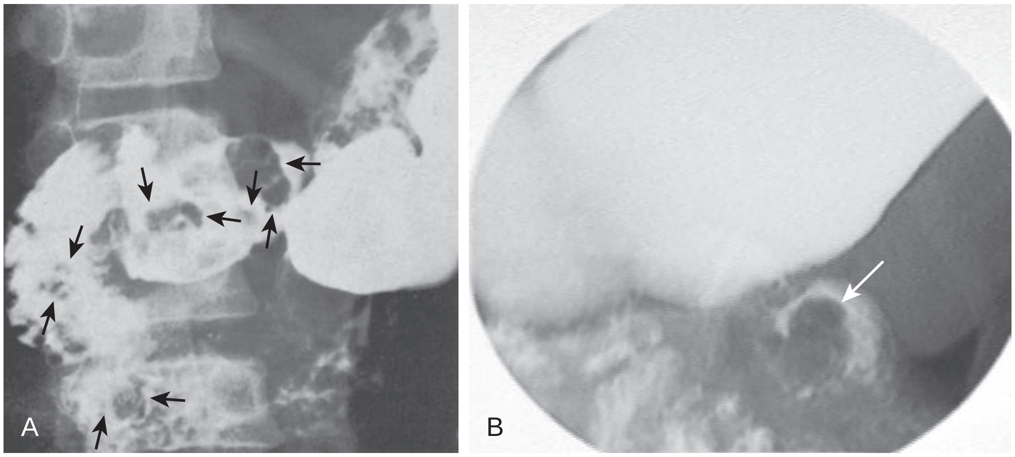

**e-Figure 103.9. Peutz-Jeghers syndrome.** (A) UGI shows multiple polyps in the duodenum *(arrows)* in a 12-year-old boy with Peutz-Jeghers syndrome. He also had polyps in the stomach, the colon, and the remainder of the small intestine. (B) A 9-year-old boy with Peutz-Jeghers syndrome presenting with symptoms of intermittent obstruction. UGI spot image of the proximal jejunum demonstrates a filling defect *(arrow)* due to duodenojejunal intussusception. A hamartomatous duodenal polyp was found to be the lead point at endoscopy. *(Case courtesy of R. Paul Guillerman, Houston, TX.)*

- Duodenal ulceration in patients with CF is related to impaired secretion of bicarbonate and increased acid production, producing an acidic duodenal environment.
- Most pediatric duodenal polyps that are not associated with Brunner gland hyperplasia are associated with polyposis syndromes. Duodenal adenomatous polyps occur in approximately 90% of patients with familial adenomatous polyps.

## SUGGESTED READINGS

Agrons GA, et al. Gastrointestinal manifestations of cystic fibrosis: radiologic-pathologic correlation. *Radiographics*. 1996;16(4):871–893.

Anupindi SA, Podberesky DJ, Towbin AJ, et al. Pediatric inflammatory bowel disease: imaging issues with targeted solutions. *Abdom Imaging*. 2015;40(5):975–992. doi:10.1007/s00261-015-0423-y.

Biank V, Werlin S. Superior mesenteric artery syndrome in children: a 20-year experience. *J Pediatr Gastroenterol Nutr*. 2006;42(5):522–525.

Dillman JR, Trout AT, Smith EA. MR enterography: how to deliver added value. *Pediatr Radiol*. 2016;46(6):829–837. doi:10.1007/s00247-016-3555-5.

Gaines BA, et al. Duodenal injuries in children: beware of child abuse. *J Pediatr Surg*. 2004;39(4):600–602.

Hughes UM, et al. Further report of small-bowel intussusceptions related to gastrojejunostomy tubes. *Pediatr Radiol*. 2000;30(9):614–617.

Kalach N, et al. Frequency and risk factors of gastric and duodenal ulcers or erosions in children: a prospective 1-month European multicenter study. *Eur J Gastroenterol Hepatol*. 2010;22(10):1174–1181.

Khanna G, et al. Gastroenteropancreatic neuroendocrine tumors in children and young adults. *Pediatr Radiol*. 2008;38(3):251–259.

Sakuraba A, et al. Endoscopic and pathologic changes of the upper gastrointestinal tract in Crohn's disease. *Biomed Res Int*. 2014;2014:610767.

## REFERENCES

Full references for this chapter can be found on www.expertconsult.com.

## REFERENCES

1. Raissi B, Taylor BM, Taves DH. Recurrent superior mesenteric artery (Wilkie's) syndrome: a case report. *Can J Surg*. 1996;39(5):410–416.
2. Wilkie D. Chronic duodenal ileus. *Am J Med Sci*. 1927;173(5):643.
3. Neri S, et al. Ultrasound imaging in diagnosis of superior mesenteric artery syndrome. *J Intern Med*. 2005;257(4):346–351.
4. Anderson JR, Earnshaw PM, Fraser GM. Extrinsic compression of the third part of the duodenum. *Clin Radiol*. 1982;33(1):75–81.
5. Goin LS, Wilk SP. Intermittent arteriomesenteric occlusion of the duodenum. *Radiology*. 1956;67(5):729–737.
6. Biank V, Werlin S. Superior mesenteric artery syndrome in children: a 20-year experience. *J Pediatr Gastroenterol Nutr*. 2006;42(5):522–525.
7. Ozkurt H, et al. Measurement of the distance and angle between the aorta and superior mesenteric artery: normal values in different BMI categories. *Surg Radiol Anat*. 2007;29(7):595–599.
8. Strong E. Mechanics of arteriomesenteric duodenal obstruction and direct surgical attack upon etiology. *Ann Surg*. 1958;148(5):725–730.
9. Suhani, et al. Short and hypertrophic ligament of treitz: a rare cause of superior mesentric artery syndrome. *J Clin Diagn Res*. 2014;8(10):ND3–ND4.
10. Jain R. Superior mesenteric artery syndrome. *Curr Treat Options Gastroenterol*. 2007;10(1):24–27.
11. Ortiz C, et al. Familial superior mesenteric artery syndrome. *Pediatr Radiol*. 1990;20(8):588–589.
12. Mosalli R, et al. Superior mesenteric artery syndrome: a rare cause of complete intestinal obstruction in neonates. *J Pediatr Surg*. 2011;46(12):e29–e31.
13. Okugawa Y, et al. Superior mesenteric artery syndrome in an infant: case report and literature review. *J Pediatr Surg*. 2007;42(10):E5–E8.
14. Caspi B, et al. Prenatal manifestation of superior mesenteric artery syndrome. *Prenat Diagn*. 2003;23(11):932–934.
15. Marchant EA, Alvear DT, Fagelman KM. True clinical entity of vascular compression of the duodenum in adolescence. *Surg Gynecol Obstet*. 1989;168(5):381–386.
16. Lee TH, et al. Superior mesenteric artery syndrome: where do we stand today? *J Gastrointest Surg*. 2012;16(12):2203–2211.
17. Makam R, et al. Laparoscopic management of superior mesentric artery syndrome: a case report and review of literature. *J Minim Access Surg*. 2008;4(3):80–82.
18. Bohanon FJ, et al. A case series of laparoscopic duodenojejunostomy for the treatment of pediatric superior mesenteric artery syndrome. *Int J Surg Res*. 2016;2016(suppl 1):1–5.
19. Sun Z, et al. Minimally invasive duodenojejunostomy for superior mesenteric artery syndrome: a case series and review of the literature. *Surg Endosc*. 2015;29(5):1137–1144.
20. Kleinman PK, Brill PW, Winchester P. Resolving duodenal-jejunal hematoma in abused children. *Radiology*. 1986;160(3):747–750.
21. Trauma T.A.A.f.t.S.o. *AAST Injury Scoring Scale*. 2017. p. Table 13, Duodenum Injury Scale.
22. Deambrosis K, et al. Delayed duodenal hematoma and pancreatitis from a seatbelt injury. *West J Emerg Med*. 2011;12(1):128–130.
23. Clendenon JN, et al. Management of duodenal injuries in children. *J Pediatr Surg*. 2004;39(6):964–968.
24. Gaines BA, et al. Duodenal injuries in children: beware of child abuse. *J Pediatr Surg*. 2004;39(4):600–602.
25. Dunkin D, Benkov KJ, Rosenberg HK. Duodenal and rectal hematomas complicating endoscopic biopsy: use of sonography in pediatrics. *J Ultrasound Med*. 2009;28(11):1575–1580.
26. Iuchtman M, et al. Post-traumatic intramural duodenal hematoma in children. *Isr Med Assoc J*. 2006;8(2):95–97.
27. Szajewska H, et al. Intramural duodenal hematoma: an unusual complication of duodenal biopsy sampling. *J Pediatr Gastroenterol Nutr*. 1993;16(3):331–333.
28. Jayaraman MV, et al. CT of the duodenum: an overlooked segment gets its due. *Radiographics*. 2001;21(Spec No):S147–S160.
29. Ma JK, et al. Pancreatic-induced intramural duodenal haematoma. *Asian J Surg*. 2008;31(2):83–86.
30. Hilmes MA, et al. CT identification of abdominal injuries in abused pre-school-age children. *Pediatr Radiol*. 2011;41(5):643–651.
31. Lu SJ, Goh PS. Traumatic intussusception with intramural haematoma. *Pediatr Radiol*. 2009;39(4):403–405.
32. Hernanz-Schulman M, Genieser NB, Ambrosino M. Sonographic diagnosis of intramural duodenal hematoma. *J Ultrasound Med*. 1989;8(5):273–276.
33. Megremis S, et al. Sonographic diagnosis and monitoring of an obstructing duodenal hematoma after blunt trauma: correlation with computed tomographic and surgical findings. *J Ultrasound Med*. 2004;23(12):1679–1683.
34. Shilyansky J, et al. Diagnosis and management of duodenal injuries in children. *J Pediatr Surg*. 1997;32(6):880–886.
35. Peterson ML, et al. Management of traumatic duodenal hematomas in children. *J Surg Res*. 2015;199(1):126–129.
36. Hughes UM, et al. Further report of small-bowel intussusceptions related to gastrojejunostomy tubes. *Pediatr Radiol*. 2000;30(9):614–617.
37. Friedman JN, et al. Complications associated with image-guided gastrostomy and gastrojejunostomy tubes in children. *Pediatrics*. 2004;114(2):458–461.
38. Connolly BL. Gastrointestinal interventions–emphasis on children. *Tech Vasc Interv Radiol*. 2003;6(4):182–191.
39. Hughes U, Connolly B. Small-bowel intussusceptions occurring around nasojejunal enteral tubes–three cases occurring in children. *Pediatr Radiol*. 2001;31(6):456–457.
40. Fisher D, Hadas-Halpern I. Jejunoduodenogastric intussusception–a rare complication of gastrostomy tube migration. *Pediatr Radiol*. 2001;31(6):455.
41. Gasparri MG, et al. Retrograde jejunogastric intussusception. *South Med J*. 2000;93(5):499–500.
42. Navarro O, Daneman A. Intussusception. Part 3: Diagnosis and management of those with an identifiable or predisposing cause and those that reduce spontaneously. *Pediatr Radiol*. 2004;34(4):305–312; quiz 369.
43. Prasad S, Ramachandra L, Deepak S. Gangrenous jejunogastric intussusception. *Internet J Surg*. 2009;19(1).
44. Connolly BL, et al. Recognition of intussusception around gastrojejunostomy tubes in children. *AJR Am J Roentgenol*. 1998;170(2):467–470.
45. Weber A, Nadel S. CT appearance of retrograde jejunoduodenogastric intussusception: a rare complication of gastrostomy tubes. *AJR Am J Roentgenol*. 1991;156(5):957–959.
46. Soscia J, Friedman JN. A guide to the management of common gastrostomy and gastrojejunostomy tube problems. *Paediatr Child Health*. 2011;16(5):281–287.
47. Osuntokun B, et al. Duodenogastric intussusception: a rare cause of gastric outlet obstruction. *J Pediatr Gastroenterol Nutr*. 2004;39(3):299–301.
48. Pacheco AR, et al. Involvement of the Helicobacter pylori plasticity region and cag pathogenicity island genes in the development of gastroduodenal diseases. *Eur J Clin Microbiol Infect Dis*. 2008;27(11):1053–1059.
49. Vakil N. Peptic ulcer disease. In: Feldman M, Friedman L, Brandt L, eds. *Sleisenger and Fordtran's Gastrointestinal and Liver Disease*. Philadelphia: Saunders, an imprint of Elsevier; 2010.
50. Marshall BJ, et al. Attempt to fulfil Koch's postulates for pyloric Campylobacter. *Med J Aust*. 1985;142(8):436–439.
51. Marshall BJ, Warren JR. Unidentified curved bacilli in the stomach of patients with gastritis and peptic ulceration. *Lancet*. 1984;1(8390):1311–1315.
52. Soll A, Graham D. Peptic ulcer disease. In: Yamada T, ed. *Textbook of Gastroenterology*. Hoboken, NJ: Wiley-Blackwell; 2009.
53. Kalach N, et al. Frequency and risk factors of gastric and duodenal ulcers or erosions in children: a prospective 1-month European multicenter study. *Eur J Gastroenterol Hepatol*. 2010;22(10):1174–1181.
54. Boyanova L, et al. Helicobacter pylori and Helicobacter heilmannii in untreated Bulgarian children over a period of 10 years. *J Med Microbiol*. 2007;56(Pt 8):1081–1085.
55. Gold B. Helicobacter pylori infection. In: Liacouras CA, Piccoli D, eds. *Liacouras & Piccoli; Pediatric Gastroenterology: Requisites*. 1st ed. Philadelphia: Mosby, an Imprint of Elsevier; 2008.
56. Morrison S, Ngo P, Chiu B. Perforated pepetic ulcer in the pediatric population: a case report and literature review. *J Ped Surg Case Reports*. 2013;1:416–419.
57. Long FR, et al. Duodenitis in children: correlation of radiologic findings with endoscopic and pathologic findings. *Radiology*. 1998;206(1):103–108.
58. Minardos I, et al. Peptic ulcer perforation: sonographic imaging of active fluid leakage. *J Clin Ultrasound*. 2006;34(1):38–41.
59. Zissin R, et al. Pictorial review. CT of duodenal pathology. *Br J Radiol*. 2002;75(889):78–84.
60. Thung I, et al. Review article: the global emergence of Helicobacter pylori antibiotic resistance. *Aliment Pharmacol Ther*. 2016;43(4):514–533.

61. Marshall BJ, et al. Pyloric Campylobacter infection and gastroduodenal disease. *Med J Aust*. 1985;142(8):439–444.
62. Park JY, et al. Helicobacter pylori clarithromycin resistance and treatment failure are common in the USA. *Dig Dis Sci*. 2016; 61(8):2373–2380.
63. Rogers BB, Gold BD. Helicobacter pylori gastritis: susceptible to further testing? *Dig Dis Sci*. 2016;61(8):2156–2159.
64. Gibril F, Jensen RT. Zollinger-Ellison syndrome revisited: diagnosis, biologic markers, associated inherited disorders, and acid hypersecretion. *Curr Gastroenterol Rep*. 2004;6(6):454–463.
65. Grosfeld JL, et al. Pancreatic tumors in childhood: analysis of 13 cases. *J Pediatr Surg*. 1990;25(10):1057–1062.
66. Ellison EC, Johnson JA. The Zollinger-Ellison syndrome: a comprehensive review of historical, scientific, and clinical considerations. *Curr Probl Surg*. 2009;46(1):13–106.
67. Rosenlund ML. The Zollinger-Ellison syndrome in children: a review. *Am J Med Sci*. 1967;254(6):884–892.
68. Abe K, Niikawa N, Sasaki H. Zollinger-Ellison syndrome with Marden-Walker syndrome. Association of two rare diseases in a 5-year-old girl. *Am J Dis Child*. 1979;133(7):735–738.
69. Eire PF, et al. Uncommon case of gastrinoma in a child. *Eur J Pediatr Surg*. 1996;6(3):173–174.
70. Norton JA, et al. Surgery to cure the Zollinger-Ellison syndrome. *N Engl J Med*. 1999;341(9):635–644.
71. Imamura M, Komoto I, Ota S. Changing treatment strategy for gastrinoma in patients with Zollinger-Ellison syndrome. *World J Surg*. 2006;30(1):1–11.
72. Passaro E Jr, et al. The origin of sporadic gastrinomas within the gastrinoma triangle: a theory. *Arch Surg*. 1998;133(1):13–16; discussion 17.
73. Gibril F, et al. Multiple endocrine neoplasia type 1 and Zollinger-Ellison syndrome: a prospective study of 107 cases and comparison with 1009 cases from the literature. *Medicine (Baltimore)*. 2004;83(1):43–83.
74. Gibril F, et al. Somatostatin receptor scintigraphy: its sensitivity compared with that of other imaging methods in detecting primary and metastatic gastrinomas. A prospective study. *Ann Intern Med*. 1996;125(1):26–34.
75. Barbe C, et al. Magnetic resonance imaging versus endoscopic ultrasonography for the detection of pancreatic tumours in multiple endocrine neoplasia type 1. *Dig Liver Dis*. 2012;44(3):228–234.
76. Khanna G, et al. Gastroenteropancreatic neuroendocrine tumors in children and young adults. *Pediatr Radiol*. 2008;38(3):251–259, quiz 358-359.
77. Lastoria S, et al. Role of (68)Ga-DOTATATE PET/CT in patients with multiple endocrine neoplasia type 1 (MEN1). *Endocrine*. 2016;52(3):488–494.
78. Sharma P, et al. PET/CT imaging of neuroendocrine tumors with (68)Gallium-labeled somatostatin analogues: an overview and single institutional experience from India. *Indian J Nucl Med*. 2014;29(1): 2–12.
79. Mojtahedi A, et al. The value of (68)Ga-DOTATATE PET/CT in diagnosis and management of neuroendocrine tumors compared to current FDA approved imaging modalities: a review of literature. *Am J Nucl Med Mol Imaging*. 2014;4(5):426–434.
80. Sadowski SM, et al. Results of (68)Gallium-DOTATATE PET/CT scanning in patients with multiple endocrine neoplasia type 1. *J Am Coll Surg*. 2015;221(2):509–517.
81. Imamura M, et al. Usefulness of selective arterial secretin injection test for localization of gastrinoma in the Zollinger-Ellison syndrome. *Ann Surg*. 1987;205(3):230–239.
82. Wilson SD. Zollinger-Ellison syndrome in children: a 25-year follow-up. *Surgery*. 1991;110(4):696–702; discussion 702-703.
83. Ito T, Igarashi H, Jensen RT. Zollinger-Ellison syndrome: recent advances and controversies. *Curr Opin Gastroenterol*. 2013; 29(6):650–661.
84. Massaro SA, Emre SH. Metastatic gastrinoma in a pediatric patient with Zollinger-Ellison syndrome. *J Pediatr Hematol Oncol*. 2014;36(1):e13–e15.
85. Wagtmans MJ, et al. Crohn's disease of the upper gastrointestinal tract. *Neth J Med*. 1997;50(2):S2–S7.
86. Kefalas CH. Gastroduodenal Crohn's disease. *Proc (Bayl Univ Med Cent)*. 2003;16(2):147–151.
87. van Hogezand RA, et al. Proximal Crohn's disease: review of the clinicopathologic features and therapy. *Inflamm Bowel Dis*. 2001;7(4):328–337.
88. Lenaerts C, et al. High incidence of upper gastrointestinal tract involvement in children with Crohn disease. *Pediatrics*. 1989;83(5): 777–781.
89. Mashako MN, et al. Crohn's disease lesions in the upper gastrointestinal tract: correlation between clinical, radiological, endoscopic, and histological features in adolescents and children. *J Pediatr Gastroenterol Nutr*. 1989;8(4):442–446.
90. Sakuraba A, et al. Endoscopic and pathologic changes of the upper gastrointestinal tract in Crohn's disease. *Biomed Res Int*. 2014;2014:610767.
91. Crocco S, et al. Upper gastrointestinal involvement in paediatric onset Crohn's disease: prevalence and clinical implications. *J Crohns Colitis*. 2012;6(1):51–55.
92. Beattie RM, et al. Inflammatory bowel disease. *Arch Dis Child*. 2006;91(5):426–432.
93. Wagtmans MJ, et al. Clinical aspects of Crohn's disease of the upper gastrointestinal tract: a comparison with distal Crohn's disease. *Am J Gastroenterol*. 1997;92(9):1467–1471.
94. Lukovich P, et al. [Crohn's disease of the duodenum. Clinical signs, diagnosis, conservative and surgical treatment]. *Orv Hetil*. 2008;149(11):505–508.
95. Yung K, et al. Ampullary stenosis with biliary obstruction in duodenal Crohn's disease: a case report and review of the literature. *Dig Dis Sci*. 2005;50(6):1118–1121.
96. Pitchumoni CS, Rubin A, Das K. Pancreatitis in inflammatory bowel diseases. *J Clin Gastroenterol*. 2010;44(4):246–253.
97. Griffin N, et al. Small bowel MR enterography: problem solving in Crohn's disease. *Insights Imaging*. 2012;3(3):251–263.
98. Parente F, et al. Bowel ultrasound in assessment of Crohn's disease and detection of related small bowel strictures: a prospective comparative study versus x ray and intraoperative findings. *Gut*. 2002;50(4): 490–495.
99. Thomson M, et al. Graded compression and power Doppler ultrasonography versus endoscopy to assess paediatric Crohn disease activity pre- and posttreatment. *J Pediatr Gastroenterol Nutr*. 2012;54(3):404–408.
100. Alison M, et al. Ultrasonography of Crohn disease in children. *Pediatr Radiol*. 2007;37(11):1071–1082.
101. Spalinger J, et al. Doppler US in patients with Crohn disease: vessel density in the diseased bowel reflects disease activity. *Radiology*. 2000;217(3):787–791.
102. Dillman JR, et al. CT enterography of pediatric Crohn disease. *Pediatr Radiol*. 2010;40(1):97–105.
103. Tolan DJ, et al. MR enterographic manifestations of small bowel Crohn disease. *Radiographics*. 2010;30(2):367–384.
104. Toma P, et al. CT and MRI of paediatric Crohn disease. *Pediatr Radiol*. 2007;37(11):1083–1092.
105. Nuti F, et al. Prospective evaluation of the achievement of mucosal healing with anti-TNF-alpha therapy in a paediatric Crohn's disease cohort. *J Crohns Colitis*. 2016;10(1):5–12.
106. Phelan MS, et al. Radiographic abnormalities of the duodenum in cystic fibrosis. *Clin Radiol*. 1983;34(5):573–577.
107. Agrons GA, et al. Gastrointestinal manifestations of cystic fibrosis: radiologic-pathologic correlation. *Radiographics*. 1996;16(4):871–893.
108. Robertson MB, Choe KA, Joseph PM. Review of the abdominal manifestations of cystic fibrosis in the adult patient. *Radiographics*. 2006;26(3):679–690.
109. Raia V, et al. Evidence of chronic inflammation in morphologically normal small intestine of cystic fibrosis patients. *Pediatr Res*. 2000;47(3):344–350.
110. Smyth RL, et al. Intestinal inflammation in cystic fibrosis. *Arch Dis Child*. 2000;82(5):394–399.
111. Bruzzese E, et al. Intestinal inflammation is a frequent feature of cystic fibrosis and is reduced by probiotic administration. *Aliment Pharmacol Ther*. 2004;20(7):813–819.
112. Levine J. Gastrointestinal manifestations of systemic diseases. In: Yamada T, ed. *Textbook of Gastroenterology*. Wiley Online Library; 2009.
113. Taussig LM, Saldino RM, Di Sant'Agnese PA. Radiographic abnormalities of the duodenum and small bowel in cystic fibrosis of the pancreas (mucoviscidosis). *Radiology*. 1973;106(2):369–376.
114. van der Doef HP, et al. Gastric acid inhibition for fat malabsorption or gastroesophageal reflux disease in cystic fibrosis: longitudinal effect on bacterial colonization and pulmonary function. *J Pediatr*. 2009;155(5):629–633.

115. De Matos V, Mascarenhas M. Cystic fibrosis. In: Liacouras C, Piccoli D, eds. *Liacouras & Piccoli: Pediatric Gastroenterology: Requisites*. 1st ed. Philadelphia: Mosby, and Imprint of Elsevier; 2007.
116. Chiarugi M, et al. Gastrointestinal stromal tumour of the duodenum in childhood: a rare case report. *BMC Cancer*. 2007;7:79.
117. Mhanna T, et al. Clear cell myomelanocytic tumor (PEComa) of the duodenum in a child with a history of neuroblastoma. *Arch Pathol Lab Med*. 2005;129(11):1484–1486.
118. Paimela H, et al. Multiple duodenal polyps in uraemia: a little known clinical entity. *Gut*. 1984;25(3):259–263.
119. Abbass R, Al-Kawas FH. Brunner gland hamartoma. *Gastroenterol Hepatol (N Y)*. 2008;4(7):473–475.
120. Sedano J, et al. Brunner's gland hamartoma of the duodenum. *Ann R Coll Surg Engl*. 2015;97(5):e70–e72.
121. Attard TM, Abraham SC, Cuffari C. The clinical spectrum of duodenal polyps in pediatrics. *J Pediatr Gastroenterol Nutr*. 2003;36(1):116–119.
122. Bresalier R, Anadasabapathy S. Tumors of the small intestine. In: Yamada T, ed. *Textbook of Gastroenterology*. Wiley Online Library; 2009.
123. Attard TM, et al. Multicenter experience with upper gastrointestinal polyps in pediatric patients with familial adenomatous polyposis. *Am J Gastroenterol*. 2004;99(4):681–686.
124. Levy AD, et al. Duodenal carcinoids: imaging features with clinical-pathologic comparison. *Radiology*. 2005;237(3):967–972.
125. Tsai SD, et al. Duodenal neuroendocrine tumors: retrospective evaluation of CT imaging features and pattern of metastatic disease on dual-phase MDCT with pathologic correlation. *Abdom Imaging*. 2015;40(5):1121–1130.
126. Dekker W. Clinical relevance of gastric and duodenal polyps. *Scand J Gastroenterol Suppl*. 1990;178:7–12.
127. Tori A, Gupta SK. Clinical quiz. Uremia. *J Pediatr Gastroenterol Nutr*. 2005;40(5):609–610.
128. Gupta V, Gupta P, Jain A. Giant Brunner's gland adenoma of the duodenal bulb presenting with ampullary and duodenal obstruction mimicking pancreatic malignancy. *JOP*. 2011;12(4):413–419.
129. Glockner J, Lee C. MRI of uncommon and unusual lesions of the duodenum, small bowel, and mesentery. *Int J Diag Imag*. 2015;2(2).

# 104 Acquired Lesions of the Small Intestines

Mary-Louise C. Greer

The pediatric duodenum, jejunum, and ileum are subject to a range of acquired pathologies. In this chapter, the etiology, pathophysiology, and clinical manifestations of small bowel obstruction (SBO), infectious and noninfectious inflammatory bowel disease (IBD), and intestinal infiltrative and neoplastic disorders will be discussed.

## SMALL BOWEL OBSTRUCTION

***Overview.*** Acquired SBO may be partial or complete, acute or chronic, and intermittent. It is relatively uncommon in children, particularly in infants under 1 year of age, in whom congenital causes of obstruction are more common (see Chapter 102). Congenital anomalies can, however, result in acquired SBO, with an inguinal hernia containing herniated bowel causing obstruction if incarcerated, or adhesions after neonatal gastroschisis repair. Acquired neonatal insults such as necrotizing enterocolitis (NEC) can cause ischemic strictures.

Abnormalities that mimic obstruction include chronic intestinal pseudoobstruction, manifest by variable distension of the gastrointestinal (GI) tract, defined as being “repetitive episodes or continuous symptoms and signs of bowel obstruction, including radiographic documentation of dilated bowel with air-fluid levels, in the absence of a fixed, lumen-occluding lesion.”[1,2]

***Etiology.*** As in adults, the majority of acquired SBO in children is secondary to adhesions or hernias.[3,4] Less common causes include tumors, inflammatory or fibrotic strictures in IBD, volvulus associated with malrotation or Meckel diverticulum, foreign body (FB) ingestion, and small bowel intussusception (see Chapter 107).[3–6]

### Adhesions

Adhesions are a common cause of obstruction in patients who have undergone prior abdominal surgery, reportedly affecting 1% to 6% postoperatively, 80% occurring within 3 months.[3,7] In neonates, adhesions are seen particularly after surgery for repair of abdominal wall defects such as gastroschisis. In older children, adhesive obstruction occurs most often after ileostomy formation and closure (25%) and Ladd’s procedure for malrotation (24%), with lower rates for general laparotomy (6.5%). Rates are less than 1% after appendectomy, although higher if perforated.[3,7]

### Incarcerated Hernia

Hernias are responsible for approximately 10% of bowel obstructions.[3] Inguinal hernias are a relatively common condition in children, with an overall incidence between 0.8% and 4.4%.[8] The vast majority are indirect hernias related to a patent processus vaginalis.[9] The incidence of inguinal hernia is 10 times higher in boys than girls.[10] Inguinal hernias have both a higher incidence (~30%) and a higher risk of incarceration (31%) in premature infants.[11] Internal hernias can be paraduodenal (see Chapter 102), occurring around an incompletely fixated falciform ligament or a Meckel diverticulum.[5,12]

### Tumors

Tumors may cause bowel obstruction from extrinsic compression or as intrinsic lesions triggering intussusception secondary to polyps or to lymphoma, typically Burkitt lymphoma. Tumors are further discussed later in this chapter.

### Omphalomesenteric Duct Remnants

Omphalomesenteric remnants or Meckel diverticula are the residua of the embryologic yolk stalk. Present in 2% to 4% of the population, 4.8% of people will develop a spectrum of GI complications that make diagnosis challenging.[12] When failing to regress, the obliterated lumen can form a fibrous cord, sometimes with cystic remnants, attaching the mid–small intestine to the anterior abdominal wall. Distal SBO in Meckel diverticulum can result from a mechanism similar to adhesions, bowel herniation, or from intussusception.[5,12] Other manifestations include GI bleeding from ectopic gastric or rarely pancreatic tissue. Gastric ectopia is usually seen without SBO, but ectopic pancreatic tissue is strongly associated with intussusceptions (see Chapter 102).[5]

### Adynamic Ileus

Adynamic ileus can cause bowel distension and may mimic mechanical obstruction. Adynamic ileus occurs after major abdominal operations, and if prolonged it may be difficult to differentiate from an early postoperative or recurrent obstruction.[3] Adynamic ileus may also occur in the setting of burns, trauma, and certain medications. The pathophysiology of postoperative ileus remains incompletely understood, but the disruption of normal autonomic GI motility is multifactorial and related to pharmacologic, inflammatory, hormonal, metabolic, and neuropsychologic influences.[13]

### Foreign Body Ingestion

Ingestion of FBs by infants and children, most frequently between 6 months and 6 years, can potentially cause SBO if held up at the terminal ileum.[3,14] The increasing incidence of multiple magnet ingestion poses unique risks; if self-apposing across different parts of the intestine, they may cause obstruction and/or mucosal erosion and perforation.[15]

***Clinical Presentation.*** SBO in children presents most frequently with crampy abdominal pain, vomiting (variably bilious), anorexia and obstipation, with constant pain, lethargy, and abdominal distention if prolonged.[7] Nausea and bilious vomiting predominate in proximal obstruction, with less distension.[4] Infants and young children may display only irritability and food refusal. Peritonitis, tachycardia, and fever can be indicative of bowel ischemia, with accompanying leukocytosis or lactic acidosis.

***Imaging.*** Patients with long-standing complete obstruction will demonstrate dilated loops of bowel with differential air-fluid levels on horizontal-beam images and absence of stool and gas in the colon (Fig. 104.1A and B). In partial obstruction, gas and stool may be present in the colon; however, a caliber difference between

## Abstract:

Acquired lesions of the small intestines range from commonly encountered small bowel obstruction (SBO), infectious and non-infectious inflammatory disorders, to infiltrative diseases, and more rarely, intestinal neoplasms. This review considers these and other acquired small bowel diseases in neonates, children and adolescents. Their etiologies, pathophysiology, clinical manifestations, imaging and treatment are discussed.

Adhesions are the commonest cause of pediatric SBO, less frequently incarcerated hernias, Meckel diverticulae, intussusceptions and tumors. Ingested foreign bodies (FB) have the added risk of possible perforation if a battery or more than one magnet is swallowed. Early recognition is important as surgical intervention may be warranted e.g. FB removal. Radiographs show dilated bowel with air-fluid levels. Although hyperperistalsis seen on ultrasound can help differentiate SBO from adynamic ileus, computed tomography (CT) remains a key tool in diagnosis.

Whilst infectious enteritis is a major cause of childhood morbidity and mortality, the role of imaging is limited. In comparison, imaging is central to the diagnosis of pediatric inflammatory bowel disease (IBD), helping distinguish Crohn disease from ulcerative colitis and IBD-unclassified, document extent, complications and treatment response. Magnetic resonance enterography, ultrasound and CT have largely replaced fluoroscopy.

This diagnostic imaging pathway change is similar in the evaluation of functional and infiltrative disorders such as cystic fibrosis, protein-losing enteropathies, graft-versus-host disease and IgA vasculitis, considered here in more detail. So too is the diagnosis and staging of benign and malignant small bowel neoplasms, nuclear medicine having a greater role in lymphoma, neuroendocrine and gastrointestinal stromal tumors.

## Keywords:

small bowel obstruction
gastrointestinal foreign bodies
infectious diarrhea
pediatric inflammatory bowel disease
protein-losing enteropathy
small intestinal tumors

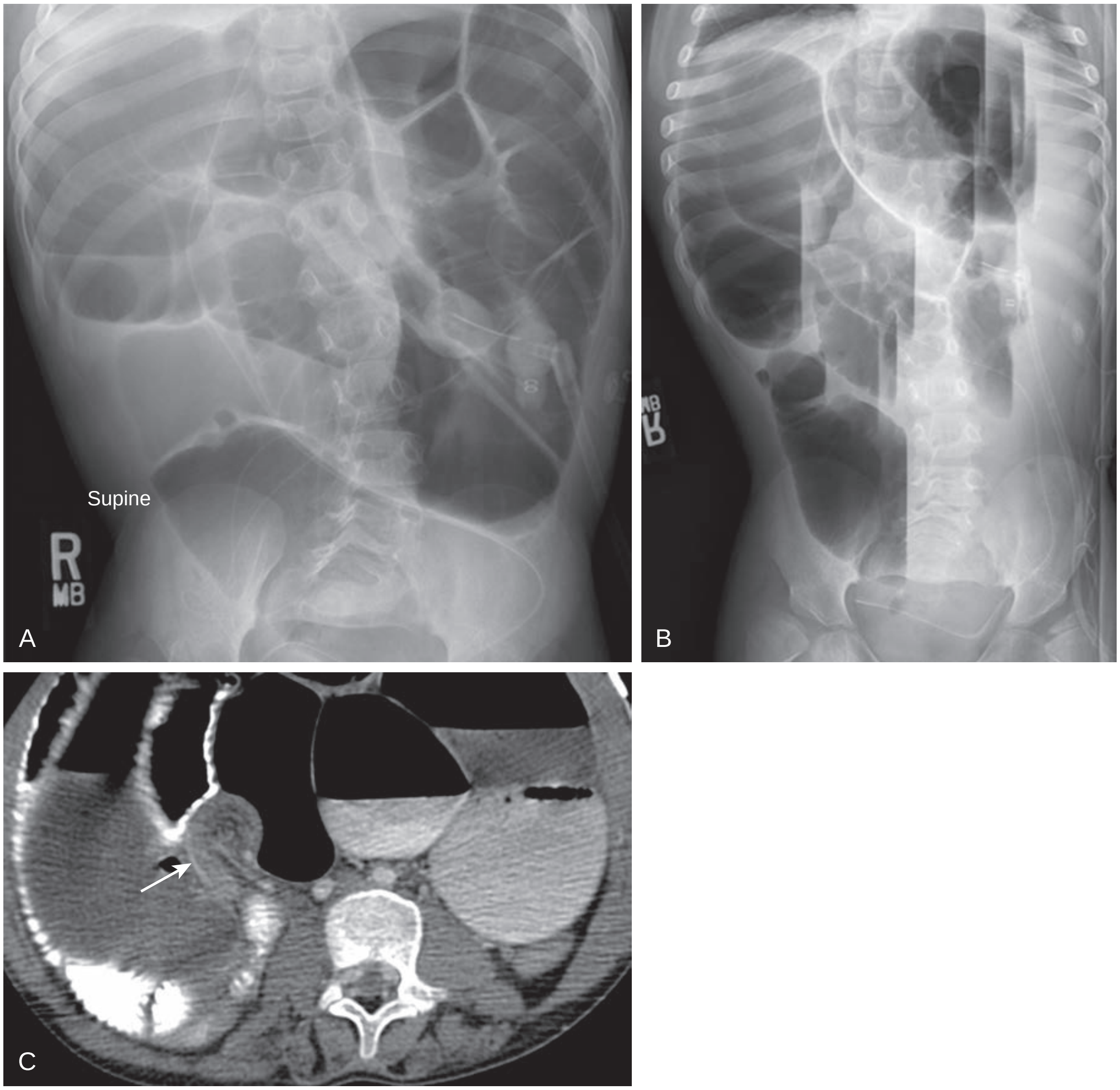

**Figure 104.1. Small bowel obstruction caused by adhesions.** (A) Supine radiograph of the abdomen in an 8-year-old boy with a history of multiple abdominal operations and increasing abdominal distension shows dilated, gas-filled loops of bowel. (B) Horizontal-beam left lateral decubitus image demonstrates multiple differential air-fluid levels. (C) Axial contrast-enhanced CT image shows a transition zone *(arrow)* between dilated proximal bowel loops and collapsed distal bowel loops. As oral contrast is seen in dilated proximal and nondilated distal bowel loops, the obstruction is incomplete. Adhesions resulting in a small bowel obstruction were lysed at surgery.

proximal loops of dilated bowel and bowel distal to the obstruction should remain evident.

Conventional radiographs may reveal the level of obstruction but in many cases poorly differentiate incomplete obstruction from adynamic ileus. Radioopaque FBs such as magnets or batteries may be evident on x-ray, with serial imaging advocated depending on FB location.[3,14] The level and, at times, the cause of obstruction may be more readily demonstrated on computed tomography (CT) or ultrasound (US), including FBs that may be radiolucent on radiographs (Fig. 104.2). Small bowel follow-through (SBFT) is rarely done, usually reserved now for young infants.

Adynamic ileus can simulate mechanical obstruction on plain radiographs. Supine radiographs of the abdomen show dilated loops of bowel in both conditions; however, mechanical obstruction usually causes proximal dilation with reduced caliber of the distal bowel, whereas adynamic ileus typically causes uniform dilatation of the entire small and large bowel.

In neonates, it is often not possible to differentiate small and large bowel; a prone cross-table lateral view of the rectum can be helpful to assess caliber of distal bowel when obstruction is suspected. In older children, on upright views, mechanical obstruction can show a step-laddered arrangement to bowel, often with pronounced fluid distension accompanying the air-fluid levels. Conversely with adynamic ileus the air-fluid levels are frequently more scattered and with more gaseous distension, both better seen with decubitus views. Decubitus views are also important in evaluating for free intraperitoneal air.

There is a renewed interest in US in diagnosing SBO. Point-of-care US for pediatric SBO is evolving although is not yet

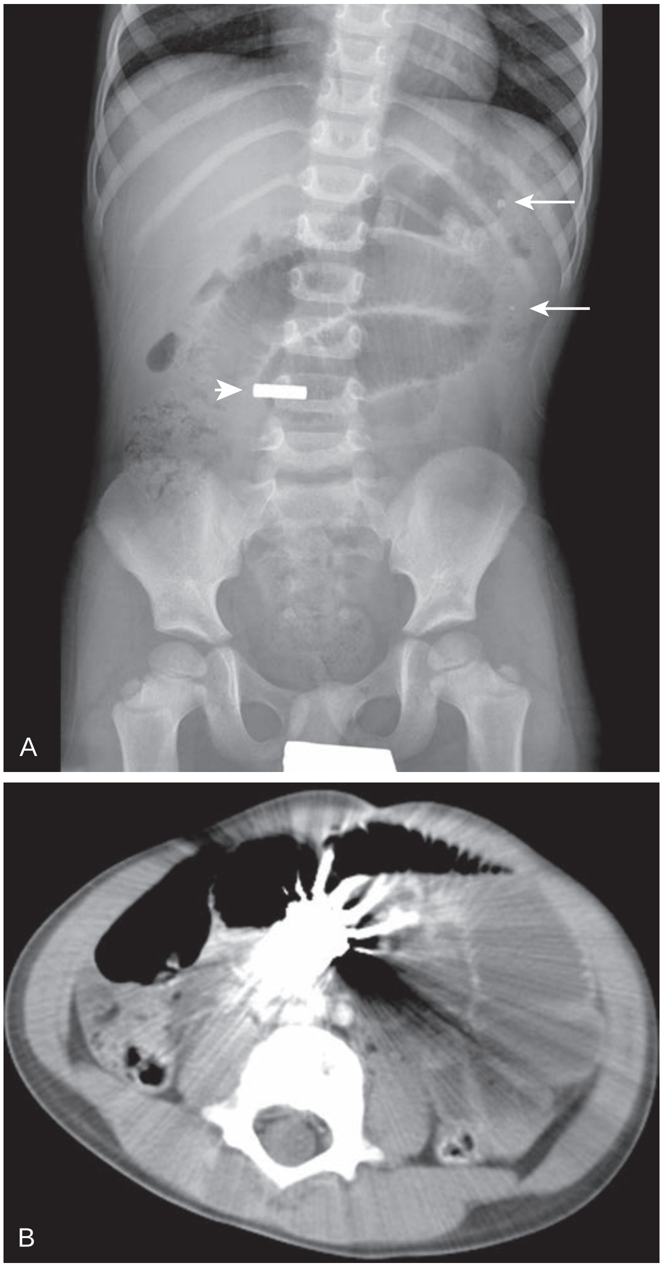

**Figure 104.2. Foreign body ingestion from a magnet causing small bowel obstruction.** A 5-year-old boy presented with a 24-hour history of abdominal pain and bilious vomiting after ingestion of a radioopaque FB, presumed to be a battery *(broad arrow),* seen on supine abdominal radiograph (A) in the midabdomen. There is marked gaseous distension of proximal small bowel loops with a paucity of bowel gas distally indicating SBO. Note numerous folds in dilated segment in keeping with jejunum. Smaller radioopaque foci seen remote from the large FB *(small arrows)* were later confirmed to be in colon. (B) Abdominal CT without oral contrast demonstrated the obstructing FB at level of transition point in the umbilical region, with grossly dilated fluid-filled proximal small bowel loops and collapsed bowel distally. At surgery, localized perforation was found with a protruding FB—a magnet—with one large and several smaller parts at level of the SBO.

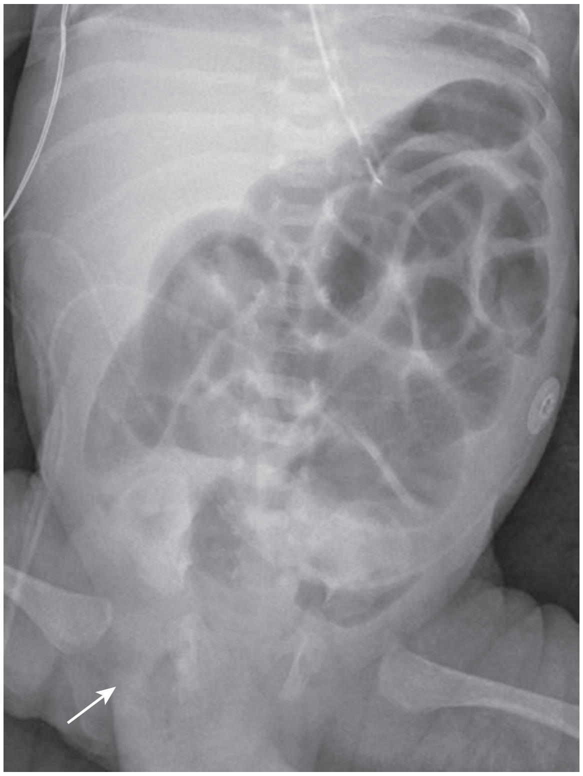

**Figure 104.3. Small bowel obstruction caused by inguinal hernia.** Supine radiograph of the abdomen in a 1-month-old, former 26-week preterm boy, who presented with a distended abdomen and a right inguinal hernia, demonstrates dilated, gas-filled loops of bowel. Bowel gas is seen within the right inguinal hernia *(arrow)*. Obstructive symptoms improved after manual reduction of the hernia.

validated.[16,17] In mechanical obstruction, US can show distended fluid-filled proximal loops (>2.5 cm) and collapsed distal loops, hyperperistalsis, and "to-and-fro" motion upstream from the obstruction. In contrast, peristalsis may be diminished in adynamic ileus, with uniformly distended fluid-filled bowel loops. On occasion, intrinsic lesions can be seen, such as strictures in IBD (Video 104.1) or intussusceptions (without or with pathologic lead point such as Meckel diverticulum or lymphoma), or extrinsic causes such as a tumor. Infrequently, bowel tethering with or without volvulus or angulation from an adhesion or peritoneal band is evident.

CT can be helpful in revealing the level and occasionally the cause of the obstruction. Administration of oral contrast is not always necessary (see Fig. 104.1C), and only water-soluble agents should be administered if bowel perforation is suspected. CT is particularly helpful in diagnosing closed-loop obstruction and obstruction related to adhesions, with dilated bowel loops seen proximally and collapsed bowel distal to a transition point of obstruction, sometimes with swirling vessels. The diagnosis of an incarcerated hernia is typically established by history and physical exam, although radiographs (Fig. 104.3) or US may occasionally be used to confirm the diagnosis.

***Treatment.*** Although a majority of children are managed conservatively, more require surgical intervention than adults to minimize gut ischemia and necrosis, which remains a high risk.[4,7] This requires careful triage and monitoring for clinical change. Those with symptoms of partial obstruction usually respond well to bowel decompression. Prompt surgical intervention is warranted if fever, leukocytosis, or unremitting pain are present or develop, or conservative treatment does not resolve symptoms of partial SBO within 48 hours.[7]

In the absence of peritoneal signs, the treatment of choice for an incarcerated inguinal hernia is manual reduction, which has a success rate of 80%, followed by repair 24 to 48 hours after reduction.[10,11] For umbilical hernias persisting beyond 4 years of age, surgery is advocated because of the increasing risk of incarceration with age.[18]

Early postoperative SBO has traditionally consisted of prolonged bowel rest and decompression via nasogastric tube. However small bowel intussusception should be excluded, as this may require laparotomy.[7] In FB ingestion, particularly multiple magnet ingestion in a symptomatic patient, early surgical review is required to consider endoscopic or laparoscopic removal.[15] Some advocate magnet removal even when asymptomatic due to the risk for severe GI injury and death (see Fig. 104.2).[14] In chronic intestinal pseudoobstruction, treatment depends on the underlying cause and may include prokinetics; surgery in the form of gastrostomy, jejunostomy, and/or loop enterostomy; and total parenteral nutrition (TPN).[2]

## INFLAMMATORY CONDITIONS OF THE SMALL BOWEL

### Infectious Diseases

***Overview.*** Infectious diarrhea is a major source of childhood morbidity and mortality under 5 years of age, with 1.7 billion episodes reported in 2010, and an estimated 700,000 deaths attributable to it in 2011, 72% under 2 years. Undernutrition is a major risk factor. Viruses, bacteria, and parasites are causative agents of acute gastroenteritis in children, with the leading causes rotavirus and cholera preventable by vaccination.[19–21]

***Etiology.*** *Viral Infection.* Viruses are one of the most common causes of acute infectious diarrhea, defined as at least "three loose stools per day for less than 14 days."[21] Globally, the most common and severe viral gastroenteritis is due to rotavirus, highest in number in Africa but with peak severity and mortality in the Western Pacific (32.6%), and lowest in the Americas (23.4%). Less common severe viral infections are astrovirus, adenovirus, and norovirus *(Caliciviridae)*.[19–21]

*Bacterial Infection.* Bacterial pathogens are estimated to cause between 2% and 10% of infectious diarrhea cases in developed countries[20]; *Vibrio cholerae* accounts for 1% globally, with severe diarrhea and mortality rates of up to up to 4.5%.[19] *Shigella*, *Salmonella*, *Escherichia coli*, and *Campylobacter* are the most common in the United States.[20]

*Clostridium difficile* can be isolated from the intestine of up to 50% of normal neonates, decreasing to less than 5% by 2 years of age. Illness-associated *C. difficile* infection is seen with a decrease in other intestinal flora secondary to exposure to broad-spectrum antibiotics, resulting in antimicrobial-associated diarrhea or pseudomembranous colitis.[20]

Rarely, *Mycobacterium tuberculosis* (TB) can involve the intestine in children.[22–24]

*Parasitic Infection. Giardia lamblia*, *Entamoeba histolytica*, and *Cryptosporidium* are parasitic causes of infectious diarrhea, all seen globally, and mostly not severe, although occasionally *Cryptosporidium* can be.[19,20] The helminthes including nematodes or roundworms, and the platyhelminthes or flatworms, are estimated to infect one-third of those in developing countries, with children and adolescents harboring the largest loads.[25]

*Human Immunodeficiency Virus.* Approximately 3.2 million children under 15 years of age are infected with human immunodeficiency virus (HIV) worldwide, often in conjunction with other endemic conditions, such as TB, malaria, cytomegalovirus (CMV), and helminthic infections.[25–27] Although antiretroviral therapy (ART) has decreased the prevalence of vertical mother-to-child transmission (MTCT) and perinatal HIV in developing countries, approximately 240,000 children are newly infected annually, primarily through postnatal MTCT.[27]

***Clinical Presentation.*** *Viral Infection.* Viral gastroenteritis commonly manifests with vomiting followed by severe watery diarrhea, nausea, abdominal pain, headaches, and low-grade fever, often accompanied by upper respiratory tract symptoms.[28] Others like norovirus are often milder and self-limiting.

*Bacterial Infection.* Considerable overlap occurs in clinical symptoms of viral and bacterial enteritis. High fever, shaking chills, and blood and mucus in stools is infrequent in viral gastroenteritis.[20] Diagnosis may be established by stool leukocytes and positive stool culture. Intestinal TB can present with fever, anorexia, abdominal pain, distension and diarrhea, and weight loss that may mimic Crohn disease (CD).[24]

*Parasitic Infection.* Symptoms of *Giardia* infection vary from asymptomatic to foul-smelling diarrhea with flatulence, abdominal distension, and anorexia. Diagnosis is from stool microscopic smear examination or immunofluorescence antibody testing.[20]

*Cryptosporidium* infection is usually self-limited in the immune competent child, may be asymptomatic, or can be confused with viral gastroenteritis.[29] In immunocompromised patients, including those with HIV, the course can be protracted with severe, chronic diarrhea and subsequent malnutrition and dehydration, which may result in death.[20,29]

*Helminthic* infestations can present with low-grade fever and nonbloody watery diarrhea or gut obstruction as in intestinal *Ascaris lumbricoides*. Chronic infection can lead to physical and cognitive impairment in children.[3,25,30]

*Human Immunodeficiency Virus.* Persistent diarrhea is a manifestation of the clinical syndrome of AIDS.[19] HIV can directly affect the gut or coexist with other pathogens, leading to or compounding severe malnutrition and subsequent growth retardation.[27] The child with HIV may also be more susceptible to opportunistic infections (e.g., CMV, *Mycobacterium avium-intracellulare*, and fungi, especially *Candida albicans*).[19,26]

***Imaging.*** Imaging is not generally indicated in the evaluation of infectious diarrhea. Abdominal radiographs may demonstrate a nonobstructive pattern of dilated fluid-filled loops (see previous section). Absence of stool throughout the colon is common, with air-fluid levels in the rectum. Pneumatosis intestinalis is rarely seen, more so in immune-compromised patients.[31]

US may show fluid-filled small bowel loops, with or without wall thickening, free fluid, and lymphadenopathy in viral gastroenteritis (e-Fig. 104.4).[32] In intestinal TB, enlarged nodes may be centrally hypoechoic and the ascites finely septated; distortion of the ileocecal region/ascending colon rarely may be seen on barium enema.[22] US may reveal transient small bowel intussusception during periods of hyperperistalsis.

In *Ascaris* intestinal infestation, the roundworm may be seen at US as four echogenic lines in parallel, best seen with a high-frequency transducer, and US can exclude related complications such as intussusception or biliary ascariasis.[3,30] Features relating to helminthic infections can also be seen on SBFT, including barium dilution, mild mucosal fold thickening, rapid or delayed transit times, and, on occasion, delineation of the parasitic gut.

The terminal ileum and cecum are often involved in bacterial enteritis, such as with *Yersinia*, termed infectious ileocecitis. Unlike intestinal TB, infectious ileocecitis may be seen on US, CT, and SBFT and barium enema, as mural thickening with variable involvement of the more distal large bowel (Fig. 104.5). US or CT may also reveal regional lymphadenopathy.[28,33]

HIV enteropathy may be seen on SBFT as increased nodularity or mucosal effacement, more usually secondary to opportunistic infection with CMV or *Cryptosporidium* infection.[19,34]

***Treatment.*** Treatment is dependent upon the underlying causative agent. Viral gastroenteritis is typically a self-limited condition but may warrant supportive measures such as rehydration.

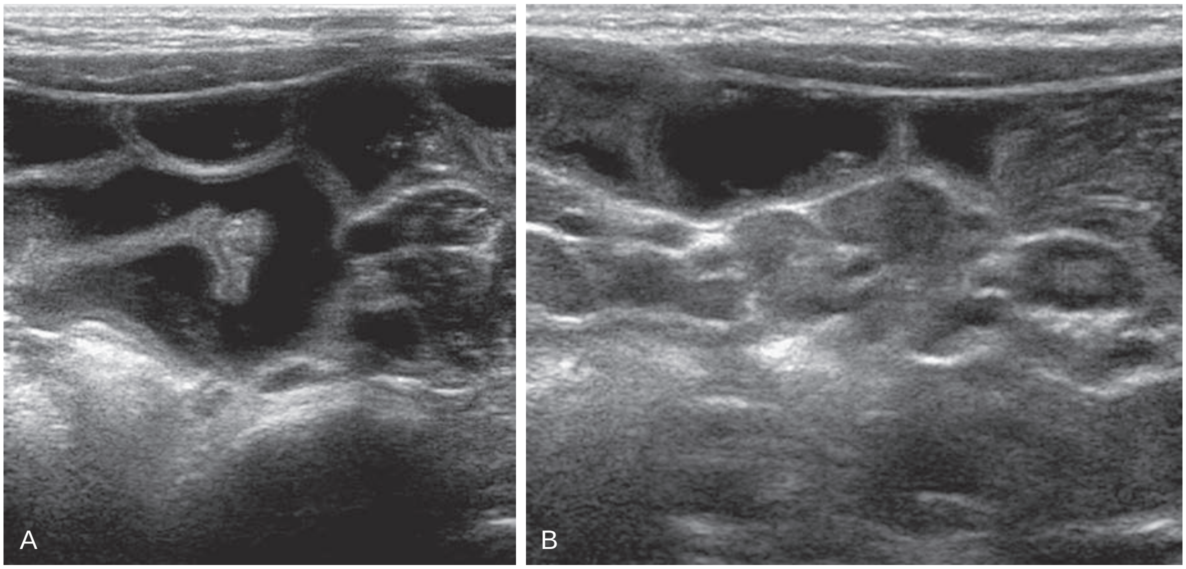

**e-Figure 104.4. Gastroenteritis.** A 21-month-old boy was seen with vomiting and irritability. (A) Ultrasonography requested for clinical concern of intussusception reveals distended, fluid-filled loops of bowel that are otherwise normal. (B) Additional image in the right lower quadrant reveals multiple enlarged mesenteric nodes, which were hyperemic on color Doppler interrogation (not shown). *(Courtesy Marta Hernanz-Schulman MD, Nashville, TN.)*

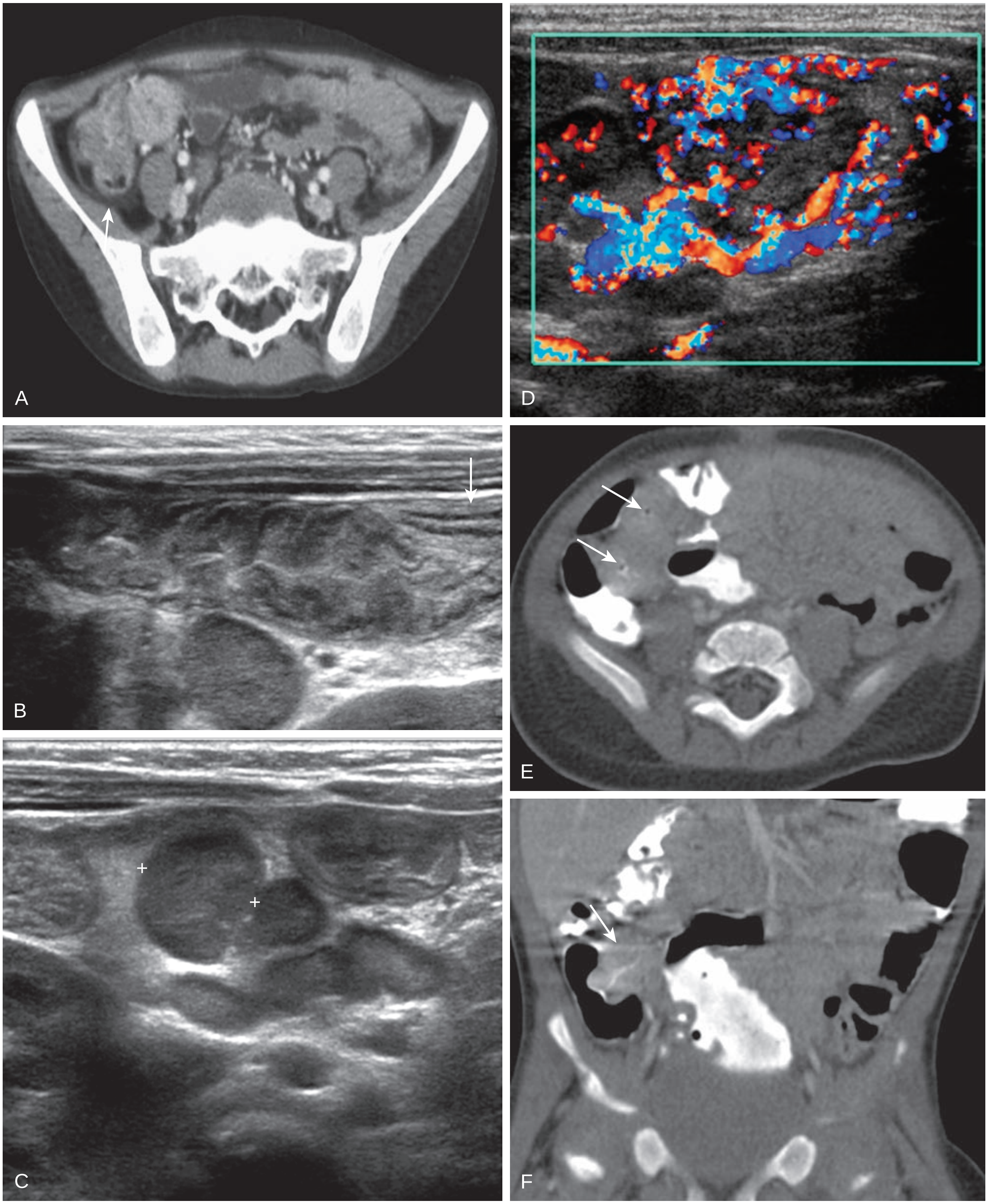

**Figure 104.5. Bacterial enterocolitis.** (A) *Shigella enteritis.* Axial contrast-enhanced CT reveals concentric thickening and enhancement of the terminal ileum and cecum, along with a small amount of pericecal fluid *(arrow)*. *Shigella sonnei* was cultured from the stool. (B) Transverse sonogram of the right lower quadrant in a 5-month-old with mucous diarrhea and abdominal pain and suspected intussusception shows a markedly thickened terminal ileum, along with a visible transition to normal bowel *(arrow)* more proximally. A large lymph node is seen deep to the terminal ileum. (C) Transverse sonogram in same infant as shown in (B), obtained slightly more cephalad, reveals a large nodal aggregate medial to the ascending colon and anterior to the lower pole of the right kidney (*calipers* outline one of the nodes). (D) Color Doppler image in the same infant shows marked hyperemia in the thick-walled terminal ileum and in the surrounding mesentery and lymph nodes. (E) *Yersinia* enteritis. Axial contrast-enhanced CT in a 9-month-old boy who had a 10-day history of fever, emesis, and voluminous diarrhea demonstrates pronounced thickening and luminal narrowing of the terminal ileum *(arrows)*. (F) Coronal reformat image of same patient as shown in (E) demonstrates similar findings. Stool cultures were positive for *Yersinia enterocolitica*.

Bacterial enterocolitis also includes supportive therapy, with antimicrobial therapy not always necessary depending on the severity of illness and immunocompetency of the patient. Agents such as metronidazole and nitazoxanide are active against *Giardia* and *Cryptosporidium*, respectively. Treatment of helminthic infections is relatively limited, particularly when considering the global ubiquity of these infections, and it includes diethylcarbamazine and newer agents such as albendazole and praziquantel.[20,25] Measures to increase vaccination for rotavirus and cholera, improve delivery of ART, and prevent MTCT of HIV will significantly reduce pediatric morbidity and mortality from infectious enterocolitis.[19,27]

## Inflammatory Bowel Disease

***Overview.*** IBD includes CD, ulcerative colitis (UC), and IBD-unclassified (IBD-U). CD, characterized by transmural granulomatous inflammation of the GI tract, can affect anywhere from the mouth to anus, whereas in UC, continuous nongranulomatous mucosal inflammation is limited to large bowel.[35] Inflammation can progress to penetrating and/or fibrostenotic disease. These are chronic, relapsing, and remitting conditions.[36,37] CD is almost three times more frequent than UC in children, with IBD-U comprising less than 10% of cases. The incidence of IBD is increasing worldwide with wide geographic variability; the highest annual incidence of CD is reported as 20.2 per 100,000 person-years in North America and UC 24.3 per 100,000 person-years in Europe.[38,39] Pediatric onset occurs in up to 25% of patients, often of greater severity than adult-onset IBD.[40,41] Increasingly recognized is a small cohort of very young children presenting with IBD less than 6 years, known as *very early onset IBD* (VEO-IBD).[38,41,42]

***Etiology and Pathophysiology.*** According to consensus guidelines on imaging in IBD, current understanding of causation suggests IBD "results from an inappropriate inflammatory response (immune dysregulation) to intestinal microbes in a genetically susceptible host," with both genetic and environmental contributors.[43–45] There are genotypes common to the major phenotypes of CD and UC, some overlapping and some unique, likely accounting for different phenotypic subtypes. This variability is accompanied by different rates of disease progression and severity, more pronounced in children and adolescence, particularly in VEO-IBD. This suggests a phenotype-genotype association, although inconstant, with evidence of genotypic susceptibility linked to single nucleotide polymorphism, with *NOD2* having the strongest link to CD.[46–49] To better understand this phenotype-genotype association, a classification system more accurately capturing pediatric IBD location and extent has been adapted from the adult Montreal Classification, known as the *Paris Classification*.[48] This incorporates age-based pediatric-specific disease elements such as greater extent/pancolitis in UC, increased upper GI tract disease and coexistent penetrating and stricturing disease in CD, and growth delay.[48] A 5-year review of phenotype in IBD patients from the EUROKIDS Registry with CD identified 16% with ileal/ileocecal disease (L1), 27% with isolated colonic disease (L2), 53% with ileocolonic disease (L3), and isolated upper GI tract disease in 4% (L4 a+b) (Fig. 104.6).[47]

On review of UC patients from this registry, atypical UC features were macroscopic rectal sparing (5%), cecal patches (2%), backwash or reflux ileitis (10%) with pancolitis, and mild upper GI erosions or ulcers (4%).[50] Perianal disease is almost exclusively seen in CD and IBD-U, and phenotypic variability is now being recognized, with increase in rectal and jejunal involvement in perianal CD.[51]

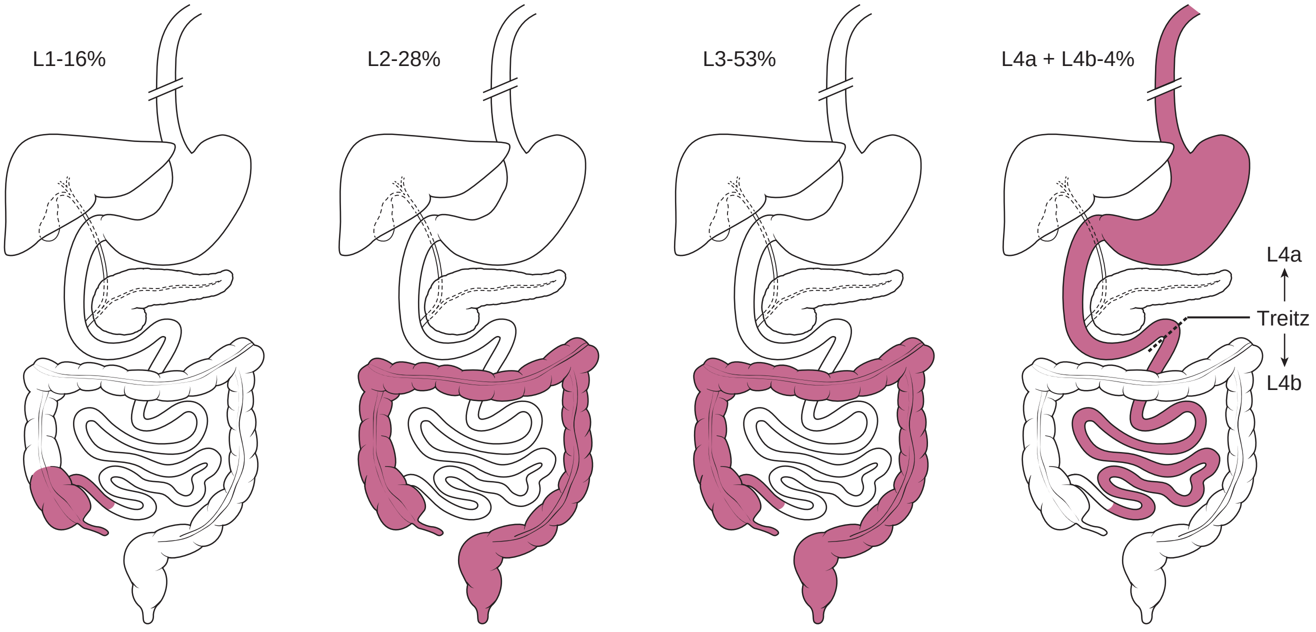

| | | | | | | | |
|---|---|---|---|---|---|---|---|
| L1 | N = 46 (7.9%) | L2 | N = 106 (18.2%) | L3 | N = 161 (27.7%) | | |
| L1 + L4a | N = 21 (3.0%) | L2 + L4a | N = 24 (4.1%) | L3 + L4a | N = 83 (14.3%) | L4a | N = 1 (0.2%) |
| L1 + L4b | N = 20 (3.4%) | L2 + L4b | N = 22 (3.8%) | L3 + L4b | N = 38 (6.5%) | L4b | N = 17 (2.9%) |
| L1 + L4ab | N = 8 (1.4%) | L2 + L4ab | N = 7 (1.2%) | L3 + L4ab | N = 25 (4.3%) | L4ab | N = 3 (0.5%) |

**Figure 104.6. Disease location according to the Paris classification in 582 newly diagnosed pediatric CD patients who underwent a complete diagnostic workup according to the Porto criteria.** L1: terminal ileal disease (± limited cecal disease); L2: colonic disease; L3: ileocolonic disease; L4: isolated upper gastrointestinal tract disease. L4A: esophagogastroduodenal disease; L4B: jejunal/proximal ileal disease. *(Redrawn from de Bie CI, Paerregaard A, Kolacek S, et al. Disease phenotype at diagnosis in pediatric Crohn's disease: 5-year analyses of the EUROKIDS Registry.* Inflamm Bowel Dis. *Feb 2013;19[2]:378–385.)*

***Clinical Presentation.*** As in adults, children and adolescents with IBD can present with diarrhea, often having mucus and/or bloodstained stool, vague abdominal pain, weight loss, and unexplained anemia.[35] Perianal disease can include fissures, ulcers, abscesses, fistulae, and skin tags, seen in approximately 10% of pediatric CD patients at diagnosis.[52] Distinct from adults is linear growth retardation, as reflected in the Paris Classification, delayed onset of puberty, reduced bone mineral density, and malnutrition.[41,48] VEO-IBD is more severe with isolated colonic disease, profound impact on growth and development, and can be fatal.[38,41,42] Patients may have ongoing subclinical inflammation and be asymptomatic.[53] Approximately 30% of affected individuals have a positive family history, and there is a 50% concordance between monozygotic twins.[54]

Extraintestinal manifestations of IBD include hepatobiliary disease (e.g. primary sclerosing cholangitis in UC) and musculoskeletal disorders such as sacroiliitis, with related symptoms sometimes triggering screening for IBD. They should be kept in mind when imaging for small and large bowel disease.[55]

Distinguishing CD and UC can be challenging, with diagnosis dependent upon a complete, standardized diagnostic workup including esophagogastroduodenoscopy (EGD) and ileocolonoscopy, and small bowel imaging with capsule endoscopy or magnetic resonance enterography (MRE) as defined by the revised Porto criteria. This is recommended in all except those with definitive UC, for accuracy and to minimize those designated as IBD-U (Fig. 104.7).[35,49]

A range of established pediatric clinical activity scores (e.g. PCDAI and PUCAI [Pediatric CD and UC Activity Indices, respectively]) incorporate history, examination, and laboratory data, quantifying baseline and ongoing disease activity; a score less than 10 being remission in PCDAI. As mucosal healing rather than symptom remission is increasingly the goal of treatment, poor correlation of these indices with endoscopic evidence of mucosal inflammation has prompted development of alternate noninvasive image-based scoring systems, MRE in particular, to define activity and guide treatment.[45,48,56] Multivariate logistical regression of itemized features of CD activity has been undertaken—bowel wall thickness, edema, ulceration, and relative contrast enhancement for inflammation in the MaRIA Score (validated with endoscopy/biopsy), adding diffusion-weighted imaging in the Clermont score; adding strictures for the Lémann damage score; and for an MRE global score (MEGS) length of disease (validated against fecal calprotectin), with varying sensitivities and specificities.[57–59] Although validation is ongoing and use is not yet standard in clinical practice, MRE is proving robust in assessing mucosal healing in adults as well in limited studies to date in children, with pediatric-specific MRE-based indices under development.[60–62]

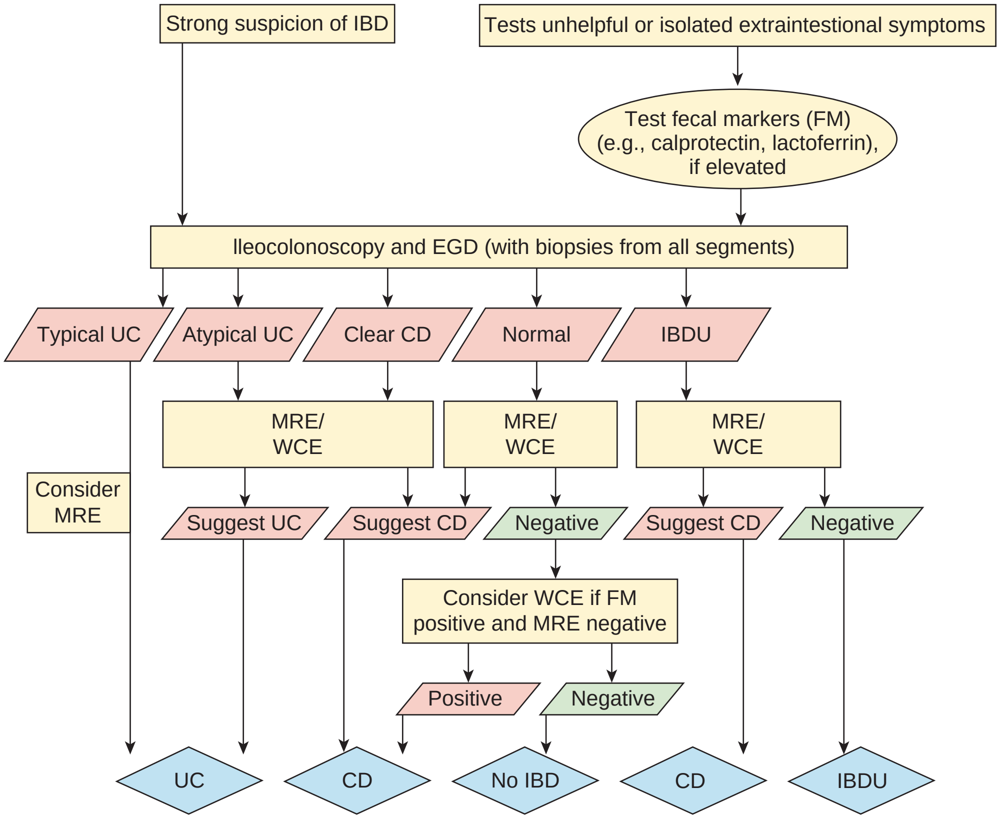
Strong suspicion of IBD
Tests unhelpful or isolated extraintestional symptoms
Test fecal markers (FM) (e.g., calprotectin, lactoferrin), if elevated
Ileocolonoscopy and EGD (with biopsies from all segments)
Typical UC
Atypical UC
Clear CD
Normal
IBDU
MRE/ WCE
MRE/ WCE
MRE/ WCE
Consider MRE
Suggest UC
Suggest CD
Negative
Suggest CD
Negative
Consider WCE if FM positive and MRE negative
Positive
Negative
UC
CD
No IBD
CD
IBDU

**Figure 104.7. Evaluation of child/adolescent with intestinal or extraintestinal symptoms suggestive of IBD.** Atypical UC is a new IBD category consisting of five phenotypes and reflects a phenotype that should be treated as UC. IBD-U may be entertained as a tentative diagnosis after endoscopy and can be used as a final diagnosis after imaging and a full endoscopic workup. UC is divided into typical UC and atypical UC. *CD*, Crohn disease; *EGD*, esophagogastroduodenoscopy; *FM*, fecal marker; *IBD*, inflammatory bowel disease; *MRE*, magnetic resonance enterography; *UC*, ulcerative colitis; *WCE*, wireless capsule endoscopy. *(Redrawn from Levine A, Koletzko S, Turner D, et al. ESPGHAN revised Porto criteria for the diagnosis of inflammatory bowel disease in children and adolescents.* J Pediatr Gastroenterol Nutr. *Jun 2014;58[6]:795–806.)*

**TABLE 104.1** Imaging Findings by Modality in Small Bowel Inflammatory Bowel Disease

| | **US**<br>**Sens/Spec** | **CTE**<br>**Sens/Spec** | **MRE**<br>**Sens/Spec** |
|---|---|---|---|
| **Active inflammation** | 75%-94%/67%-100%$^{\wedge>\circ}$ | 67%-100%/62%-100%$^{\circ*}$ | 55%-88%/79%-89%$^{*>+}$ |
| **Fibrosis** | N/A | 42%/68%$^{*}$ | 73%/82%$^{*}$ |
| **Fistula** | 31%-87%/95%-96%$^{\circ\wedge}$ | 70%-78%/87%-97%$^{\circ}$ | 76%-88%/93%-96%$^{\circ}$ |
| **Abscess** | 83%-91%/93%$^{\circ\wedge}$ | 85%-86%/88%-95%$^{\circ}$ | 86%-100%/93%-100%$^{\circ}$ |
| **Stenosis** | 58%-85%/92%$^{\wedge\circ}$ | 85%-92%/100%$^{\circ}$ | 86%-92%/90%-94%$^{\circ}$ |

^Anupindi et al.[63]/Alison et al.[64]—pediatrics; *Quencer et al.[65]—pediatrics; $^{>}$Aloi et al.[66]; $^{+}$Shenoy-Bhangle et al.[67]—pediatrics; $^{\circ}$Panes et al.[43]—not pediatric specific; *CTE/MRE*, Computed tomography/magnetic resonance enterography; *DWI*, diffusion weighted imaging; *N/A*, not available; *Sens*, sensitivity; *Spec*, specificity; *US*, abdominopelvic ultrasound.

***Imaging* (*Table 104.1*).** Imaging algorithms have substantially altered in recent years, in line with changing treatment targets and outcome measures.[49,68] Detection of IBD and distinction between CD and UC are key at presentation, as well as exclusion of other diseases such as infectious ileitis or appendicitis. At diagnosis and on follow-up, imaging objectives include defining disease location and extent (specifying involved segment length, activity and severity, and where possible characterizing as inflammation or damage), all with treatment implications. In the acute setting, assessment for acute flare, abscess, or obstruction from stricture should ideally occur within 24 hours.[43] Surgical planning is increasingly done with MRE rather than fluoroscopy.[69]

## Abdominal Radiography

With acute abdominal pain in IBD, radiography can demonstrate perforation or obstruction, with images likely to include an erect chest or upright abdominal image. Although no longer routinely used in IBD assessment, familiarity with the more reliable radiographic signs is still important. These include mucosal irregularity in the colon and small bowel and an abnormal stool pattern with stool absent or limited to a single loop.[43,70] Extraintestinal manifestations of IBD such as renal or biliary calculi or sacroiliitis may be seen.

## Ultrasound

Interrogation of bowel is now often used in imaging pediatric IBD because it lacks ionizing radiation, has wide availability and low cost, and is usually well tolerated, even with use of oral contrast.[66] However, its role in initial screening is limited as it has variable accuracy in disease detection (particularly MRE).[43,63,71] While used for monitoring disease activity, treatment response, assessment of acute flares, and disease complications, reproducibility has been questioned.[72] The use of nonabsorbable oral contrast and intravenous contrast-enhanced US has been shown to improve sensitivity, specificity, and accuracy for disease detection in CD including strictures.[43,63] Compared with MRE and capsule endoscopy, conventional or contrast-enhanced US have shown similar sensitivities, but variable specificities. In the small bowel, US is best for terminal and distal ileum but poor for proximal to midsmall bowel.[66,71–73] US shear wave elastography is one of a number of promising noninvasive techniques to assess bowel fibrosis.[74]

Mural features in IBD include (1) bowel wall thickening greater than 3 mm (normal 1.5–3 mm in the terminal ileum and 2–3 mm in the colon); (2) "stiffness" where thick or distended loop remains noncompressible/unchanging; (3) increased echogenicity/loss of stratification; (4) Doppler hypervascularity (Fig. 104.8); (5) serosal irregularity/speculation; and (6) reduced peristalsis.[63,64,66] Vessel density of density greater than 2 vessels/cm$^2$ and wall thickness greater than 5 mm have shown high specificity (88%) for active disease.[75] Stenoses can be seen as persistent luminal narrowing (≤2 mm), reduced or absent peristalsis, with upstream dilatation and hyperperistalsis. Extramural features include (1) a halo of echogenic, hyperemic mesentery (>4 mm) relating to fibrofatty proliferation, (2) regional lymphadenopathy (short axis ≥8 mm), (3) abscess (sensitivity 83%–91%), and (4) fistula–hypoechoic tracts, occasionally containing echogenic foci if gas, extending to adjacent bowel, genitourinary structures, or skin; they can be associated with tethered or sharply angulated juxtaposed bowel loops (sensitivity 31%–87%).[64,71] Backwash or reflux ileitis is seen in conjunction with pancolitis in UC with less mural thickening or extramural abnormality. Lymphoid hyperplasia can mimic both entities, again

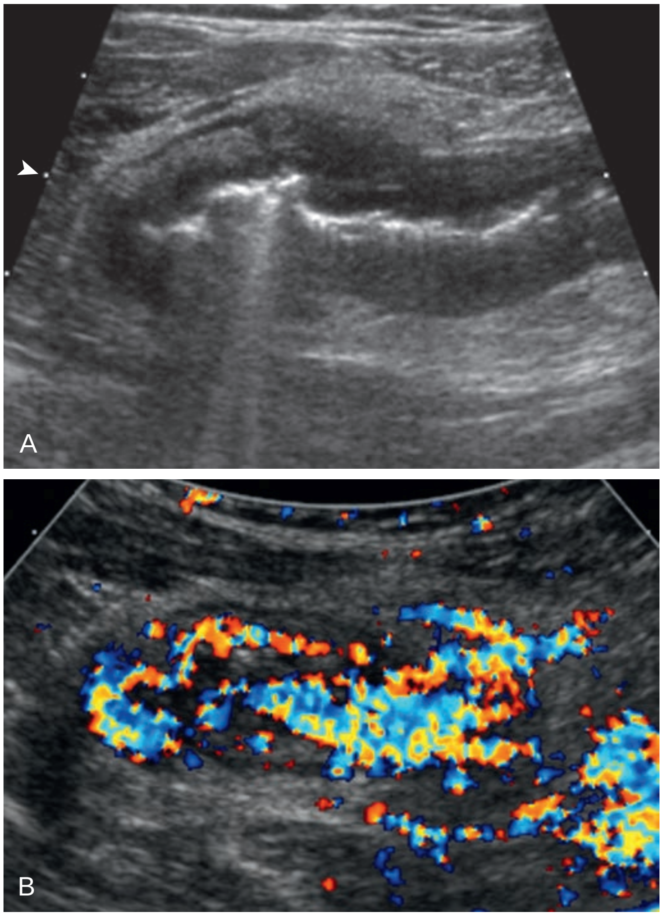

**Figure 104.8. Crohn disease.** Transverse gray-scale (A) and color Doppler (B) sonograms of the right lower quadrant of an adolescent boy with Crohn disease show a markedly thickened and hyperemic terminal ileum. *Arrowhead* in (A) is the focal zone centered on the bowel.

with less diffuse mural thickening, often with rounded hypoechoic lymphoid follicles and normal peristalsis.

## Fluoroscopy

SBFT and small bowel enteroclysis have largely been replaced by other modalities, in particular MRE and computed tomographic enterography (CTE) to a lesser extent.[49,68] Although more sensitive in demonstrating mucosal lesions such as erosions and superficial ulcers, these other modalities better demonstrate mural and transmural features of IBD, with the added advantage of no ionizing radiation with MRE and US.[76] Fluoroscopic studies are now reserved for patients in whom MRE or CTE is contraindicated. Typical features in terminal ileal CD include shallow poorly defined ulcers with surrounding edema; linear, serpiginous ulcers; and a swollen disorganized fold pattern, with loss of pliability on compression. In comparison, lymphoid hyperplasia has small nodular filling defected.[77] Loop separation from wall thickening and/or fibrofatty proliferation, strictures and fistulae can be demonstrated.

## Computed Tomography

CTE is performed after ingestion of sufficient low-density oral contrast to achieve bowel distension and intravenous iodinated contrast, imaging at either 45 seconds (enteric phase) or 70 seconds (portal venous phase).[78] With sensitivities ranging from 60% to 90% and specificities 90% to 100% for detection of CD, it is used in some pediatric centers as baseline imaging to document the presence and extent of IBD (although some prefer MRE to avoid ionizing radiation).[35,43,49] However, short acquisition times, less operator dependence than US, wide accessibility, high spatial resolution, and reduced need for sedation or anesthesia make it a viable alternative (see https://acsearch.acr.org/docs/69470/Narrative/).[43,78]

Bowel wall thickening (>3 mm) and hyperenhancement are hallmarks of CD on CTE.[79,80] Disease activity, with active inflammation evidenced by wall thickening, avid enhancement, submucosal edema, and mesenteric inflammation, correlate well with histologic evidence of inflammation. However, CTE is less predictive of fibrosis than MRE.[65] As with US, stenoses can be evidenced by luminal narrowing and prestenotic dilatation. Additionally, upstream fecalization or the “small bowel feces” sign can be indicative of SBO (Video 104.1; Fig. 104.9 and e-Fig. 104.10). The peri-intestinal features of comb sign, fibrofatty proliferation, phlegmon, and abscesses are well depicted. Fistulae are variably seen, with abscesses and fistulae often arising just proximal to stenosed bowel.[78,80] In the acute setting, when larger volumes of contrast may not be tolerated, conventional abdominal CT with no or limited oral contrast may be sufficient for a diagnosis of bowel obstruction, perforation, or abscess (see Video 104.1). IBD-related pathologies such as renal and biliary calculi, and some musculoskeletal changes can also be depicted on CT.

## Magnetic Resonance Imaging

In addition to detecting diseased segments in small bowel CD, MRE helps define extent, activity, and complications. MRE requires ingestion of weight-based doses of hyperosmolar biphasic oral contrast agents, typically up to 1400 mL, intravenous gadolinium-based contrast agents, and antispasmodic agents to optimize small bowel visualization. Conventional rapid and fluid-sensitive sequences provide anatomic and functional information, using dynamic (cine) and static pre- and postcontrast sequences to delineate the bowel wall and mesentery.[81–83] Advanced imaging techniques include delayed contrast enhancement (DCE) imaging with subtraction, diffusion-weighted imaging (DWI), and magnetization transfer pulses generating ratios (MTR), increasingly used to better define activity and differentiate active inflammation from fibrosis.[84–89] While validation sufficient to guide therapy is ongoing, enhancement gain greater than 24% between 70 seconds and 7 minutes, with or without ulcers, shows promise in distinguishing minimal and marked fibrosis and inflammation in CD.[85,90] The diagnostic capabilities plus the lack of ionizing radiation and excellent soft tissue contrast resolution have led to widespread use of MRE in pediatric IBD, particularly for serial imaging, and can be performed satisfactorily at 1.5 and 3 Tesla field strengths.[49,68,91]

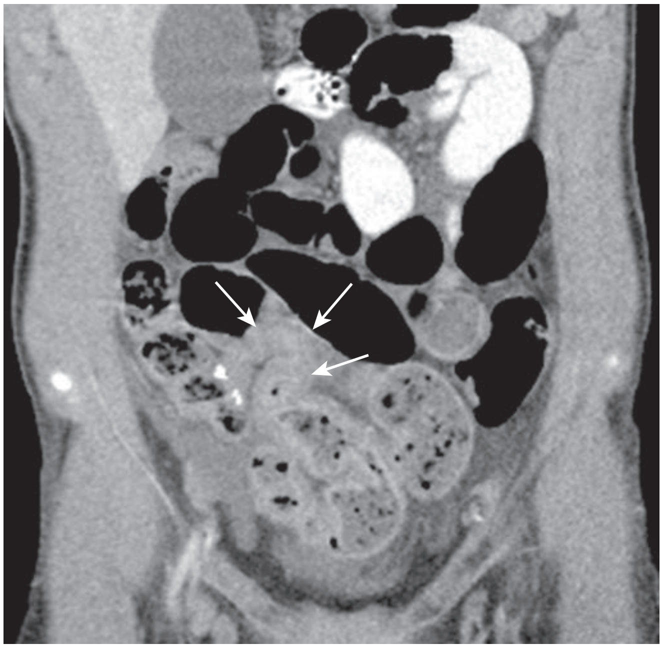

**Figure 104.9. Crohn disease stricture.** Coronal reformatted contrast-enhanced CT image through the pelvis of a 15-year-old boy with Crohn disease presenting with worsening abdominal pain and vomiting 2 years post ileal resection. An anastomotic stricture is demonstrated measuring 4.8 cm *(arrows)* with collapsed lumen, bowel wall thickening, and fecalization of upstream ileum, with staples to the right of the *arrows*.

The majority of CD small bowel findings on CTE apply equally to MRE. Mural features include skip or continuous lesions with bowel wall thickening greater than 3 mm (which can be eccentric), hyperenhancement, mucosal ulceration, pseudosacculation, and strictures with luminal narrowing and prestenotic dilatation (>3 cm).[59,92,93] MRE additionally can show mural edema with T2 hyperintensity and mucosal or stratified enhancement in active disease, reduced T2 signal relative to skeletal muscle, and variably transmural enhancement in chronic or fibrotic disease, with diseased segments having abnormally increased or decreased peristalsis on cine imaging (Video 104.2).[94,95] Restricted diffusion is seen in active inflammation with increased mural signal on trace images and reduced signal on the apparent diffusion coefficient (ADC) map (Fig. 104.11). While less reliable on its own, DWI accuracy improves when used in conjunction with conventional MRE sequences, particularly if DWI is viewed first.[96,97] Extramural features include penetrating lesions: sinuses, fistulae, and abscesses (Fig. 104.12). Abscesses, rim-enhancing fluid collections, can be difficult to distinguish from fluid-filled bowel, and central restriction on DWI improves conspicuity.[98] Sinuses and fistulae have variable signal depending on contents (gas, fluid, feces) and are better demonstrated when DWI supplements T2-weighted or postcontrast T1-weighted sequences. Fistulae occur in 8.2% of pediatric CD within 12 months of diagnosis and 24.5% by 10 years, and additional features include tethering of adjacent bowel loops, and simple or stellate tracts to bowel, skin, or genitourinary structures, often

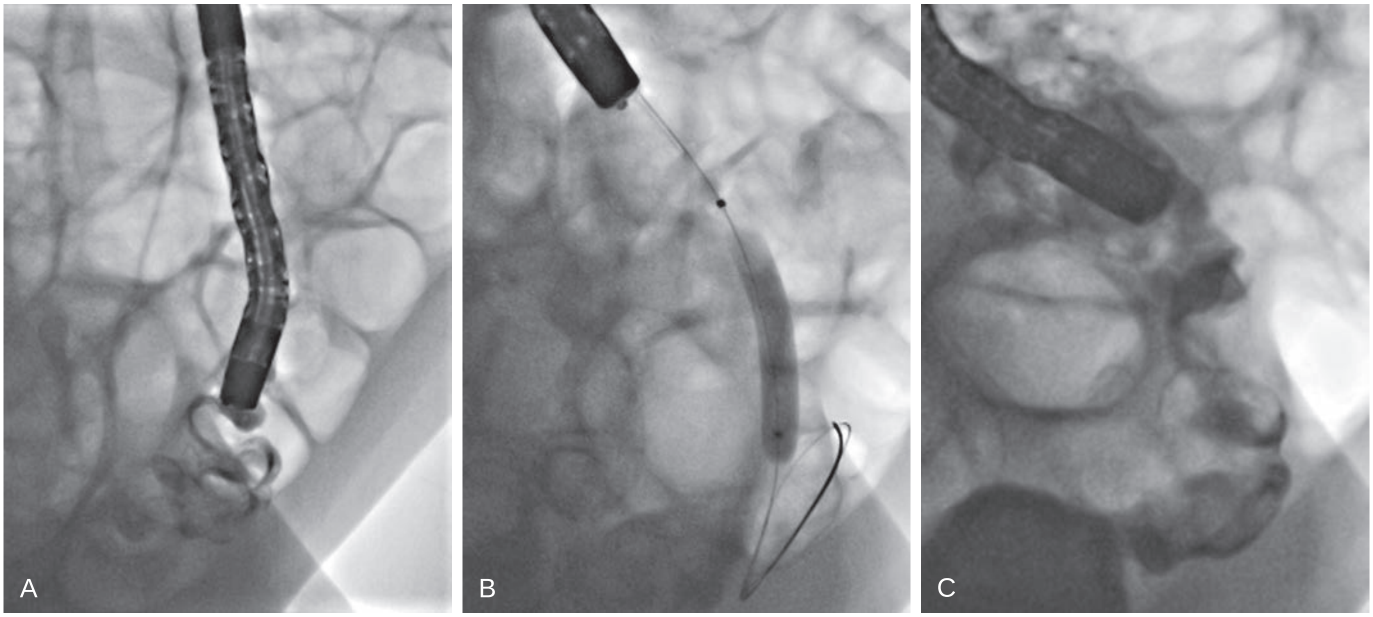

**e-Figure 104.10. Crohn disease stricture.** (A–C) Colonoscopy and pre-, mid-, and postballoon dilatation images show persistent narrowing that required resection.

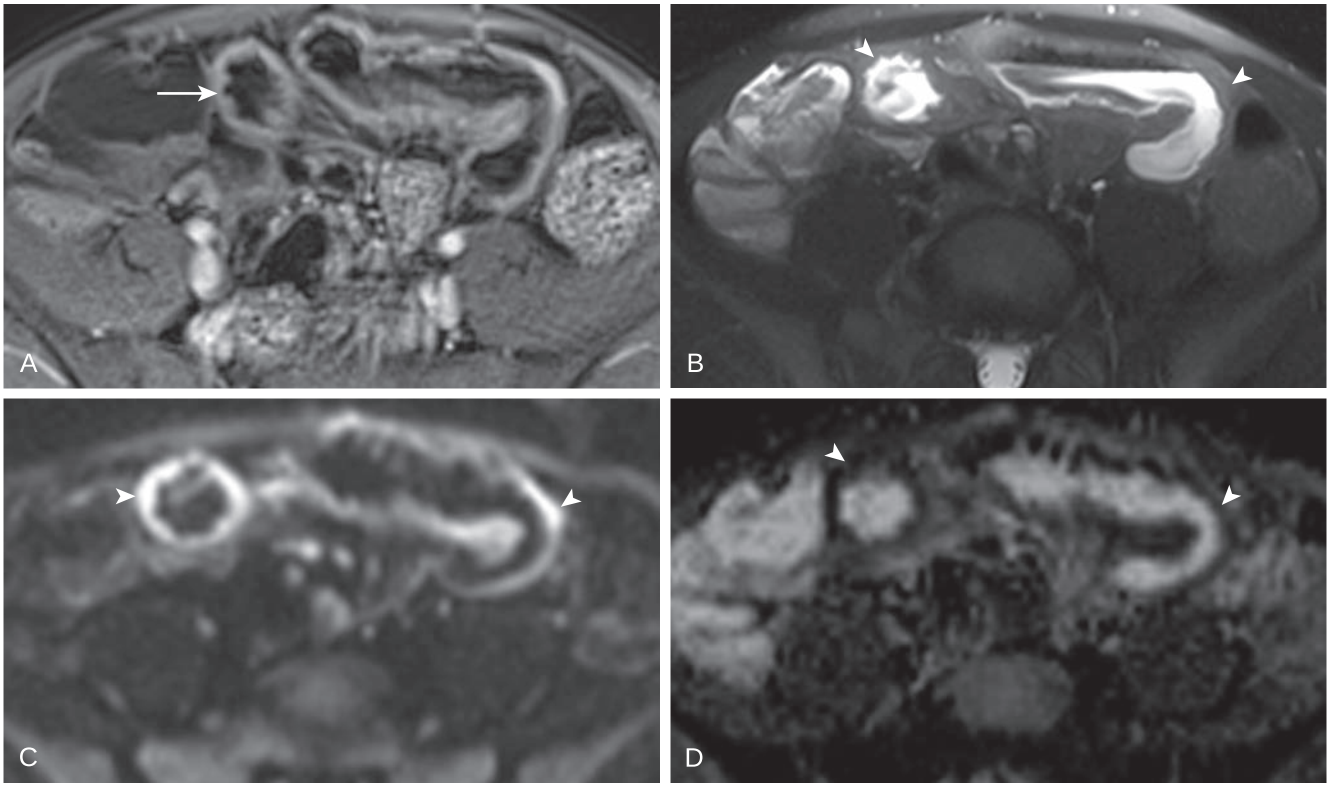

**Figure 104.11. Crohn disease with active inflammation in distal ileum in an 11-year-old boy.** (A) Axial fat-suppressed contrast-enhanced T1-weighted 3D gradient echo MR image, (B) axial single-shot T2-weighted image, and (C and D) diffusion-weighted imaging (DWI) with (C) trace image at $b = 800\ s/mm^2$ and (D) ADC map. Moderate transmural hyperenhancement is evident in an inflamed bowel loop in the midpelvis on (A) with deep ulceration *(arrow)*. There is T2 bowel wall hyperintensity on (B) and corresponding areas of restriction on DWI seen on trace image (C) as increased signal and on ADC map as decreased signal (D) *(arrowheads)*. Mild fibrofatty proliferation and comb sign are seen in the adjacent mesentery.

arising just proximal to or at the level of a stricture.[93,95] Other extraintestinal features are fibrofatty proliferation, vasa recta engorgement (comb sign), regional lymphadenopathy, perimural mesenteric edema and enhancement, intraperitoneal fluid, and phlegmons.[82] Increasingly, qualitative and quantitative MRE analyses are being used as biomarkers of treatment response.[83,99]

Identified IBD-related extraintestinal findings can include sclerosing cholangitis and biliary calculi, with magnetic resonance cholangiopancreatography (MRCP) usually performed separately (see Chapter 88), and enthesitis-related arthropathy and sacroiliitis, with bone marrow edema well seen on DWI.[55,100,101]

## Nuclear Medicine

Radiolabeled white blood cell scintigraphy and $^{18}$F-fluorodeoxyglucose (FDG) positron emission tomography (PET)/CT or PET/MRI can demonstrate active inflammation in small and large bowel in IBD, documenting extent and assessing treatment response. Decreased $^{18}$F-FDG uptake in areas of fibrosis can aid distinction of fibrotic and inflammatory structures. Radiation burden limits routine use in pediatric imaging.[43,74,102]

## Special Considerations

VEO-IBD rates special mention because of its more serious prognosis and the extra challenges in performing CTE and MRE in children under 6 years of age. While US may be used for initial imaging (with particular focus on colon), increasing utilization of MRE under general anesthesia has had good success, requiring only minor modification in technique.[103]

Fortunately, the risk of IBD-related malignancy is extremely low in children and adolescents, occurring more in CD. Leukemia and lymphoma are most common and usually treatment related. Long-term implications of therapy must thus be balanced against severe IBD outcomes.[41,104,105] Disease-related malignancies are less frequent and include small and large bowel adenocarcinoma and cholangiocarcinoma. Diagnostic imaging is neoplasm specific rather than surveillance focused.

***Treatment.*** In parallel with advances in GI tract imaging has been a paradigm shift in the treatment of pediatric CD and UC away from clinical endpoints and toward mucosal healing (and potentially transmural healing) with the primary goal of induction and maintenance of remission aided by biologic agents targeting molecular pathways.[45,53,83] Reversing inflammation and limiting progression has lead to improved quality of life, fewer complications, and less surgical intervention.[41,53] Medical therapies are implemented based on clinical and endoscopic disease activity indices, and increasingly imaging biomarkers, to promote to mucosal and transmural healing.[53,59] Treatment options include exclusive enteral nutrition, corticosteroids, immunomodulators, antibiotics, and biologic agents.[41] When refractory to medical therapy or with severe fistulizing or fibrostenotic disease, surgical intervention is indicated encompassing abscess drainage, balloon dilatation, strictureplasty, or surgical resection (see e-Fig. 104.10).[106]

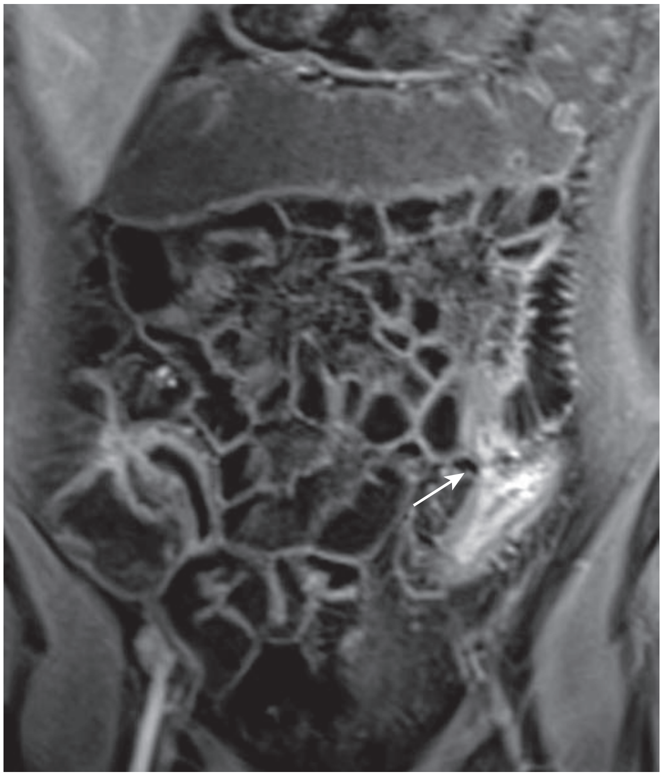

**Figure 104.12. Crohn disease enterocolic fistula and terminal ileitis.** Coronal fat-suppressed contrast-enhanced T1-weighted 3D gradient echo MR image demonstrates tethered loops of inflamed bowel with thick walls and transmural hyperenhancement in the left lower quadrant with fistula between the jejunum and distal descending/sigmoid colon *(arrow)*. Stratified hyperenhancement of thick-walled terminal ileum is more in keeping with active inflammation.

## Behçet Disease

***Overview.*** Behçet disease is an uncommon, immune-mediated vasculitis. This chronic, relapsing condition involves multiple organ systems, including the GI tract in 0.7% to 50%, neurologic, and cardiovascular systems.[107,108] Mean age of onset is 25 to 30 years, although rare presentations from 10 to 15 years of age occur.[109] Disease prevalence in Asia is approximately 30 per 100,000 population with more common GI involvement, with prevalence in North America of approximately 7 per 100,000.[107,108,110]

***Etiology.*** Behçet disease is an autoinflammatory disease of complex genetic trait, associated with mutations in the gene for familial Mediterranean fever, manifest as vascular endothelial dysfunction and an excessive inflammatory response, termed pathergy.[110]

***Clinical Presentation.*** Diagnosis is made by established clinical criteria from the International Study Group for Behçet disease with recurrent mouth ulcers plus at least two other major criteria: ocular involvement (e.g., uveitis), skin lesions (e.g., erythema nodosum), recurrent genital ulcerations, and a positive pathergy test.111 Most frequent GI symptoms include abdominal pain, diarrhea, and bleeding.[108]

***Imaging.*** Ulceration is most common in the ileocecal region. Double contrast barium enema (or enteroclysis), better than single contrast studies, demonstrate deep, localized, relatively large, "collar-button" ulcers, and long segment thickening of adjacent mucosal folds from lympangiectasia.107,108 Complications can include aneurysmal dilatation of the terminal ileum, perforation, fistulae, and cecal masses. The entire GI tract can be affected, mimicking CD.[107]

***Treatment.*** Medical therapies include corticosteroids and other immunosuppressants during disease exacerbations and increasingly biologic therapy for refractory lesions.[107,108,110] Surgical resection of severely involved segments can result in recurrence, between 40% and 80% within 2 years of surgery, often located near the initial anastomosis.[107]

# FUNCTIONAL AND INFILTRATIVE DISEASES

## Cystic Fibrosis

***Overview.*** Cystic fibrosis (CF) is an autosomal recessive condition caused by a lack or dysfunction of CF transmembrane conductance regulator *(CFTR)* protein resulting from a variety of mutations mapped to locus q31.2 of chromosome 7. This protein is involved in the regulation of chloride ion transport across cell membranes in the lungs, digestive system, reproductive tract, and skin. It is the most common genetic defect in Caucasians; 3.3% of white Americans are carriers of a *CFTR* mutation versus 1.1% of Asian Americans, with an homozygous prevalence approximating 1 in 3500 in white Americans.[112,113]

***Clinical Presentation.*** GI symptoms occur in 85% to 90% of CF patients, arising from constipation, obstruction, mucus accumulation, disturbed motility, dysbiosis with bacterial overgrowth, and chronic intestinal inflammation.[113] Meconium ileus occurs in the newborn period (see Chapter 102). In older children and adolescents, the most common intestinal abnormality is distal intestinal obstruction syndrome (DIOS), formerly known as *meconium ileus equivalent*, occurring in approximately 15% of patients.[114] Children present with colicky abdominal pain and a palpable right lower quadrant mass from impacted fecal material in the ileocolic region. Because mild to severe constipation is a common concomitant condition, the DIOS diagnosis is reserved for patients with signs and symptoms of SBO.

Intussusception, usually ileocolic, is seen in 1% to 17% of CF patients.[113,114] Presenting around 10 years of age, intermittent abdominal pain is often milder than in idiopathic intussusception, and some patients are asymptomatic.[115]

***Imaging.*** In DIOS, radiographs show small bowel dilatation with air-fluid levels; bubbly fecal material may also be present, particularly in the right lower quadrant.[115] If CT is performed; dilated small bowel loops can be followed to the site of impaction in the distal ileum (Fig. 104.13).

The appendix in patients with CF is typically distended by mucoid contents, and although its contents may be expressible with compression, appendiceal diameter alone is not a reliable criterion for diagnosis of appendicitis in these patients; periappendiceal findings therefore become particularly important.[116,117]

US is the modality of choice for diagnosing intussusception, sometimes demonstrating a pathologic lead-point (e.g., inspissated secretions, enlarged lymphoid follicles, or a distended appendix). In CF patients with malabsorption and less-specific GI symptoms, US may show bowel loop dilatation greater than 2 cm, short segments of moderate wall thickening and hypervascularization, and altered motility, especially in the ileocecal region.[113]

***Treatment.*** Although most patients with DIOS respond to enemas that include mucolytic agents, water-soluble contrast enemas given under fluoroscopic control also may be effective, refluxing into the terminal ileum and repeating over a 24- to 48-hour period as required to completely relieve the impaction.[115] Surgical management may be needed in patients who do not respond to nonsurgical techniques.

Some intussusceptions spontaneously resolve but if ileocolic, and there is no perforation or peritonitis, a fluoroscopically guided air or sonographically guided saline enema reduction is performed.[114,118]

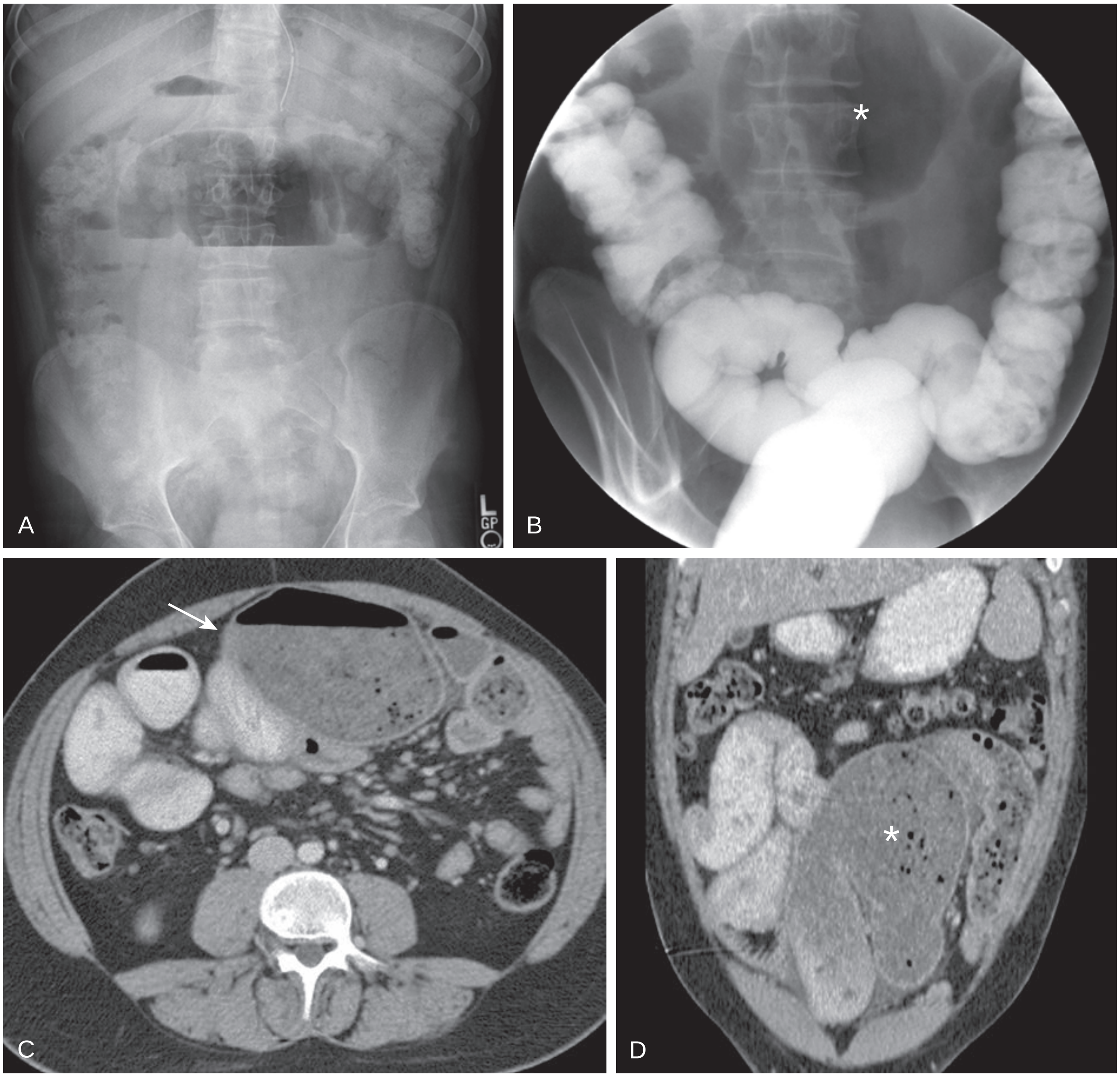

**Figure 104.13. Distal intestinal obstructive syndrome.** (A) Upright abdominal radiograph in a 7-month-old boy with cystic fibrosis and increasing abdominal distension, pain, and emesis shows a dilated, gas-filled bowel loop in the central abdomen with an increased air-fluid level. (B) Contrast enema image shows no substantial reflux into the terminal ileum and persistence of the abnormally dilated bowel loop in the midabdomen *(asterisk)*. (C) Axial contrast-enhanced CT image shows flocculent material in a dilated midabdominal bowel loop *(arrow)*. (D) Coronal reformat confirms the axial findings. Flocculent material dilating the small bowel is again seen *(asterisk)*. Distal ileal obstruction was confirmed at laparotomy.

## Protein-Losing Enteropathies

***Overview.*** Protein loss through the GI tract may be related to a range of underlying abnormalities, including immune-mediated dysfunction, such as celiac disease, or to lymphatic obstruction, such as in intestinal lymphangiectasia.

***Etiology.*** *Celiac Disease.* Celiac disease is the most common cause of intestinal malabsorption in childhood. Also known as *nontropical sprue* or *gluten enteropathy*, it is an autoimmune disease caused by gluten intolerance, a protein present in wheat and related species, including barley and rye. The disease is more prevalent in Western Europe and North America, affecting as many as 1 of every 80 to 300 persons.[119] The hypersensitivity to gluten is related to the tissue transglutaminase (TTG) enzyme, which acts as the autoantigen. Diagnostic tests include measurement of IgA antibody to human recombinant TTG, as well as quantitative serum IgA evaluation. Diagnosis is made when small bowel biopsy documents villous atrophy. The disorder is associated with type 1 diabetes mellitus; Down, Turner, and William syndromes; and IgA deficiency.[119]

*Whipple Disease.* Whipple disease is a chronic systemic bacterial infection caused by *Tropheryma whipplei* that is most common in middle-aged men but has been associated with acute illnesses such as diarrhea in young children.[120,121] While *T. whipplei* infection is common (incidence of 2%–11% in Europe), Whipple disease is rare but increasing.[122] It is characterized by the presence of macrophages that persist even after eradication of the initiating organism. Macrophages from affected patients have normal phagocytosis but appear to be unable to effectively handle the bacterial antigens.[120]

*Intestinal Lymphangiectasia.* Intestinal lymphangiectasia is characterized by dilation of intestinal lymphatics that results in protein loss as lymph leaks into the lumen of the intestine. Primary intestinal lymphangiectasia is associated with developmental abnormalities of the intestinal lymphatics and may be associated with abnormal lymphatics elsewhere in the body. Secondary intestinal lymphangiectasia occurs in patients with diseases such as sarcoid or lymphoma that cause obstruction of the intestinal lymphatics.[123] Secondary disease may also be seen when there is an increase in intralymphatic pressure because of an increase in venous pressure (e.g., constrictive pericarditis) or increased right atrial pressures (e.g., Fontan physiology after single ventricle repair or congestive heart failure).[119,124]

*Miscellaneous Protein-Losing Enteropathies.* Patients with immunodeficiency syndromes may have a clinical and radiographic picture similar to celiac disease. Other causes of protein-losing enteropathy include allergic gastroenteropathy, IBD, infectious mononucleosis, and polyarteritis nodosa.

***Clinical Presentation.*** *Celiac Disease.* Most children affected with celiac disease come to medical attention between 4 and 24 months of age with failure to thrive, abdominal distension, and diarrhea. Diarrhea is considered one of the hallmarks of the disease, although it is absent in 10% of patients; in fact, some children may present with constipation. Children may experience anemia with iron and folate deficiency, hypertransaminemia, arthritis, and behavioral disturbances. Adolescents have delayed puberty, anorexia, and clinical findings related to the hypocalcemia and hypoproteinemia of malabsorption.[119]

*Whipple Disease.* Patients with classic Whipple disease present with systemic manifestations, most commonly migratory arthralgias involving larger joints, chronic diarrhea and weight loss, and chronic localized infections (e.g., endocarditis, uveitis, encephalitis, and hyperpigmentation resembling Addison disease). Acute infections include gastroenteritis, pneumonia, and/or bacteremia, although some carriers are asymptomatic.[120,122]

*Intestinal Lymphangiectasia.* Several syndromes are associated with intestinal lymphangiectasia, such as neurofibromatosis type 1 (NF1), Turner, Noonan, Klippel-Trénaunay, and Hennekam. Patients with either primary or secondary intestinal lymphangiectasia typically have diarrhea and edema related to hypoproteinemia, failure to thrive, and other symptoms related to malabsorption.[123]

***Imaging.*** The first step in the evaluation of the patient with protein-losing enteropathy is to exclude common etiologies such as malnutrition and liver and renal disease. Diagnosis is made by documentation of enteral protein loss by determining the clearance of alpha$_1$-antitrypsin (A1AT) from plasma.[125]

$^{99m}$Technetium or $^{111}$In-labeled human serum albumin ($^{99m}$Tc/$^{111}$In-HSA) scintigraphy has also been used to document enteral protein leakage. $^{99m}$Tc has higher sensitivity but lower specificity than $^{111}$In-labeled tracers, with pooled sensitivities and specificities of 87% (81%–92%) and 62% (51%–72%).[126] Because of the intermittent nature of the protein loss and the need for serial scanning for up to 24 hours, many centers now utilize A1AT testing. However, scintigraphy has a distinct advantage of localizing the site of protein loss (i.e., large and/or small bowel or stomach).[127]

Abdominal radiographs in patients with celiac disease may show nonspecific small bowel distension, whereas Whipple disease lacks distension.

US findings in celiac disease include bowel dilatation (>2.5 cm), bowel wall thickening (≥3 mm), fold reversal (effaced mucosa in the jejunum and thickened in the ileum), increased or decreased peristalsis, and extraintestinal features including mesenteric lymphadenopathy and ascites. Small bowel intussusceptions are also seen.[128] These findings resolve when a gluten-free diet is instituted. Any significant mesenteric adenopathy in celiac disease should raise a suspicion for lymphoma.[129] Intestinal lymphangiectasia may have features related to edema with gallbladder and bowel wall thickening, mesenteric edema and ascites, and occasionally lymphatic malformations.

Classic SBFT imaging findings described in celiac disease consist of luminal distension, thickened mucosal folds, and contrast flocculation and segmentation; the latter two are uncommonly seen with modern-day barium preparations. As in US, mucosal folds may show reversal. The duodenum may exhibit mucosal erosions or thickened nodular folds. Similar thickening of small bowel folds is seen without dilatation in Whipple disease (e-Fig. 104.14). Barium studies in patients with intestinal lymphangiectasia may show mild bowel dilatation and thickened folds (Fig. 104.15), although a substantial number of affected children have a normal SBFT.

Patients with immunodeficiency syndromes may have a clinical and radiographic picture similar to celiac disease. Some affected patients have radiographic findings of lymphoid hyperplasia, particularly in the distal ileum.[130]

Abdominal CT is not routinely used in investigation of protein-losing enteropathy. Low-density lymphadenopathy, hepatosplenomegaly, and ascites may be seen in Whipple disease, and similar features to that seen on US in intestinal lymphangiectasia. Bowel can also have a “halo” reflecting intramural edema (inner low density and outer high density), also seen in IBD and ischemic enteritis, with the lack of lymphadenopathy aiding distinction from celiac and Whipple disease.[131] MRE is an emerging tool in the investigation of protein-losing enteropathy.[95,132] Recent development of dynamic magnetic resonance (MR) lymphangiography, delineating the central conducting lymphatics, shows promise in investigation of unexplained protein-losing enteropathy.[133]

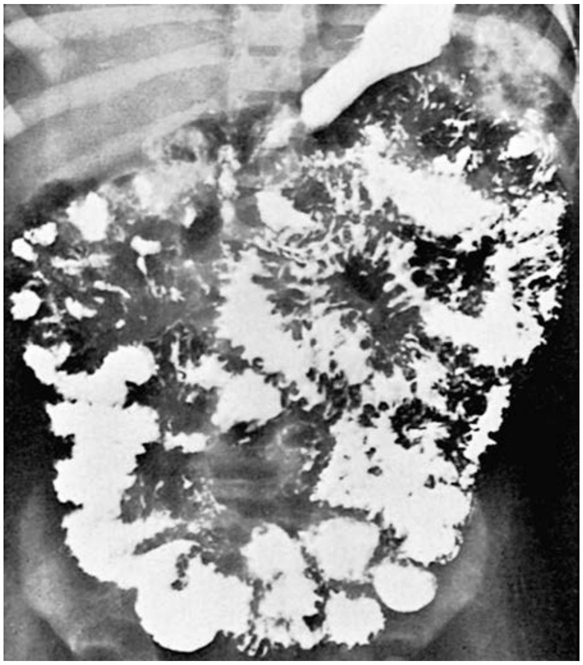

**Figure 104.15. Intestinal lymphangiectasia.** Small bowel series in a 3-year-old girl with intestinal lymphangiectasia shows marked coarsening and thickening of the mucosal folds.

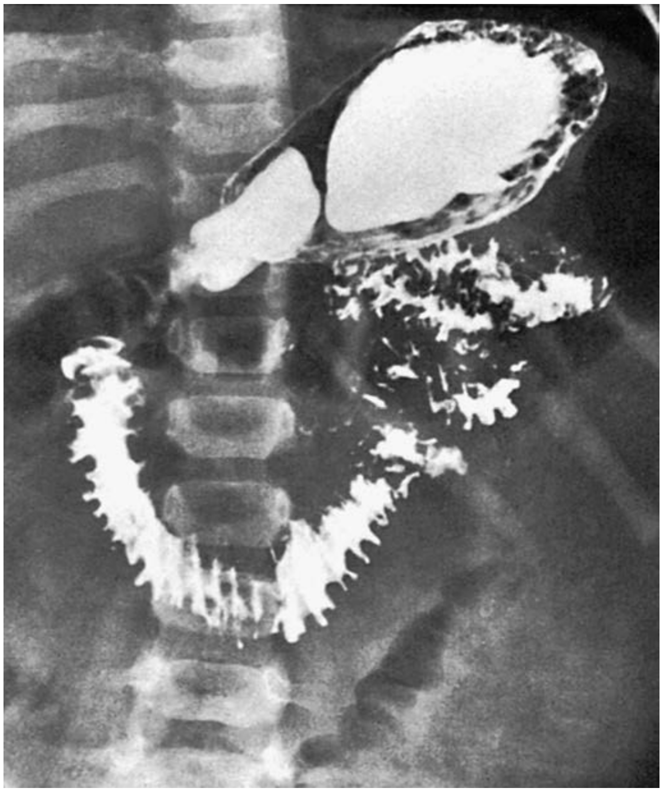

**e-Figure 104.14. Whipple disease.** Upper gastrointestinal series in a 2-year-old boy with Whipple disease reveals marked thickening of the duodenal and jejunal folds.

***Treatment.*** Therapeutic approaches for protein-losing enteropathy vary depending on the underlying etiology; the goal of the treatment is to correct the underlying abnormality and nutritional supplementation.

The treatment for celiac disease is a lifelong gluten-free diet. Prolonged antibiotic treatment is required for Whipple disease, with the combination of doxycycline and hydroxychloroquine now advocated. Even with this new regimen, lifelong monitoring is needed because of the risks of recurrence and reconstitution inflammatory syndrome.[122]

In patients with lymphangiectasia, treatment includes a low-fat diet primarily consisting of medium chain triglycerides and high protein. In secondary lymphangiectasia, attention is paid to the primary problem.

## Graft-versus-Host Disease

***Overview.*** Graft-versus-host disease (GVHD) can result from hematopoietic stem cell transplantation. GVHD occurs when the donor lymphocytes react with the tissues of the host, with an inflammatory cascade that often begins in the GI tract.[134,135] Three conditions are generally required for the development of GVHD: (1) the graft must contain immunologically competent cells; (2) the host must possess important transplant alloantigens that are lacking in the donor graft so that the host appears foreign to the graft; and (3) the host must be incapable of mounting an effective immunologic reaction against the graft.[136,137]

***Etiology.*** GVHD results from donor T-cell epithelial damage in the host target organs.[137] Pathophysiology of GVHD includes pretransplant host tissue injury secondary to preparative ablative radiation and chemotherapy, activation of donor T-lymphocytes, and cytotoxicity against target host cells through the effected inflammatory cascade mediated through histocompatibility antigens.[134,135] The most important elements in the development of GVHD relate to the degree of human leukocyte antigen mismatch.[135] GI symptoms are the sequelae of destruction of the intestinal crypts leading to patchy or diffuse mucosal ulceration.[137]

***Clinical Presentation.*** Acute GVHD occurs within the first 100 days, and commonly within 30 to 40 days, after transplantation.[137] Patients usually have a combination of dermal, hepatic, and GI abnormalities. Dermatitis is manifested as a pruritic, maculopapular rash that may proceed to desquamation. Hepatitis results from involvement of the biliary epithelium and may progress to coagulopathy, encephalopathy, and liver failure. GI manifestations include anorexia, nausea, vomiting, severe diarrhea (often bloody), hematochezia, crampy abdominal pain, and ileus. Other organs, including the esophagus and conjunctiva, may also be involved. The diagnosis of intestinal involvement in acute GVHD can be confounded by a concurrent infectious gastroenteritis.[137,138]

Chronic GVHD can develop as early as 40 to 50 days posttransplant, de novo, or as a variable progression of acute GVHD; clinical, histologic, and immunologic findings are most important in defining disease. The majority of patients have skin abnormalities that include desquamation and vitiligo, which may progress to scleroderma-like changes. Severe mucositis of the mouth and esophagus may occur, and, while infrequent, GI involvement can result in localized inflammation or strictures in the esophagus and rarely the small bowel. Chronic cholestatic liver disease may also occur. Involvement of the hematopoietic system may lead to thrombocytopenia, and this (along with progressive onset, elevated bilirubin, and lichen planus) points to a poor prognosis.[137]

In summary, intestinal damage is a feature of acute GVHD, while the esophagus is the major GI region affected in chronic GVHD.[138] Incidence of GVHD is slightly higher in intestinal transplant patients at 5%, especially isolated transplants, affecting the native GI tract along with usual sites of disease.[139]

***Imaging.*** Patients receiving bone marrow transplantation are at risk of GVHD and other complications related to direct toxicity from pretransplant ablative chemotherapy and radiation, and infections. Clinical presentations may overlap, and imaging may be required to narrow the differential diagnosis.

Abdominal radiographs show a pattern of adynamic ileus with separation of bowel loops, thickening of the bowel wall, and air-fluid levels. Less commonly seen are pneumatosis intestinalis and ascites. On occasion, the abdomen may be completely gasless (e-Fig. 104.16A).

Contrast studies are rarely performed in these patients but may show characteristic (though not pathognomonic) diffuse luminal narrowing with featureless bowel creating a “ribbon” or “toothpaste” appearance.[138,140]

US is usually the primary mode of intestinal evaluation in acute GVHD. This reveals loss of stratification of the bowel wall, with variable small bowel and colonic mural thickening, with two or more intestinal sites aiding distinction from other causes. Ileal and colonic dilatation is infrequent.[141,142] Doppler demonstrates a markedly hyperemic bowel wall with elevated velocities in the superior mesenteric artery (SMA). Supervening ischemic changes may be identified in patients with undetectable mural flow and decreased SMA velocities, which is associated with a poor prognosis.[143] Extraenteric features include ascites, periportal edema, pericholecystic fluid, and gallbladder wall thickening and hyperemia.

Less commonly performed, CT findings in GVHD can be striking (see e-Fig. 104.16B and C). Bowel loops are variably distended with fluid, with marked contrast enhancement of the mucosa.[144] Oral contrast can obscure the mucosal enhancement and is poorly tolerated by these children, so it is avoided.[144] Engorgement of the vasa recta is the most common extraintestinal finding seen on CT and is indicative of hyperdynamic circulation. The target-like appearance to bowel and extraenteric features as seen at US and CT are similar on MRI.[145]

***Treatment.*** Treatment is aimed primarily at prophylaxis to prevent GVHD by using immunosuppressive agents (initially corticosteroids). Posttransplant immunosuppressive therapeutic management after onset of GVHD is generally less effective.[137,140]

## Immunoglobulin A Vasculitis (Henoch-Schönlein Purpura)

***Overview.*** Immunoglobulin A vasculitis (IgAV), formerly known as *Henoch-Schönlein purpura*, is the most common vasculitis of childhood and affects the small vessels in the skin, joints, GI tract, and kidneys. The incidence of IgAV is approximately 10 to 20 per 100,000 population and is most common in children between 2 and 6 years of age, although 30% of cases are in patients over age 20 years.[146,147]

***Etiology.*** A vasculitis of small vessels, nongranulomatous and ANCA-negative, it is characterized by IgA-dominant immune complex deposits in capillaries, venules, and arterioles.[148] Pathogenesis remains unknown with suspected genetic predispositions and implication of a range of coexistent organisms including group A beta-hemolytic *Streptococcus* and *Mycoplasma*.[146]

***Clinical Features.*** Consensus criteria define IgAV as having a palpable purpura (mandatory) plus one of the following: diffuse abdominal pain, biopsy showing predominant IgA deposition, arthritis or arthralgia, or renal involvement (proteinuria or hematuria).[147] ANCA-negative laboratory findings can be a consideration.[148] Classically presenting after an upper respiratory tract infection with lower extremity palpable purpura, lesions above the waist, and clinically evident edema are associated with GI involvement.[149] Although 20% to 50% have renal involvement, only 1% to 3% progress to end-stage renal failure.[149] Arthralgias and GI symptoms may precede the characteristic rash in 30% to 43% of patients. GI symptoms are seen in

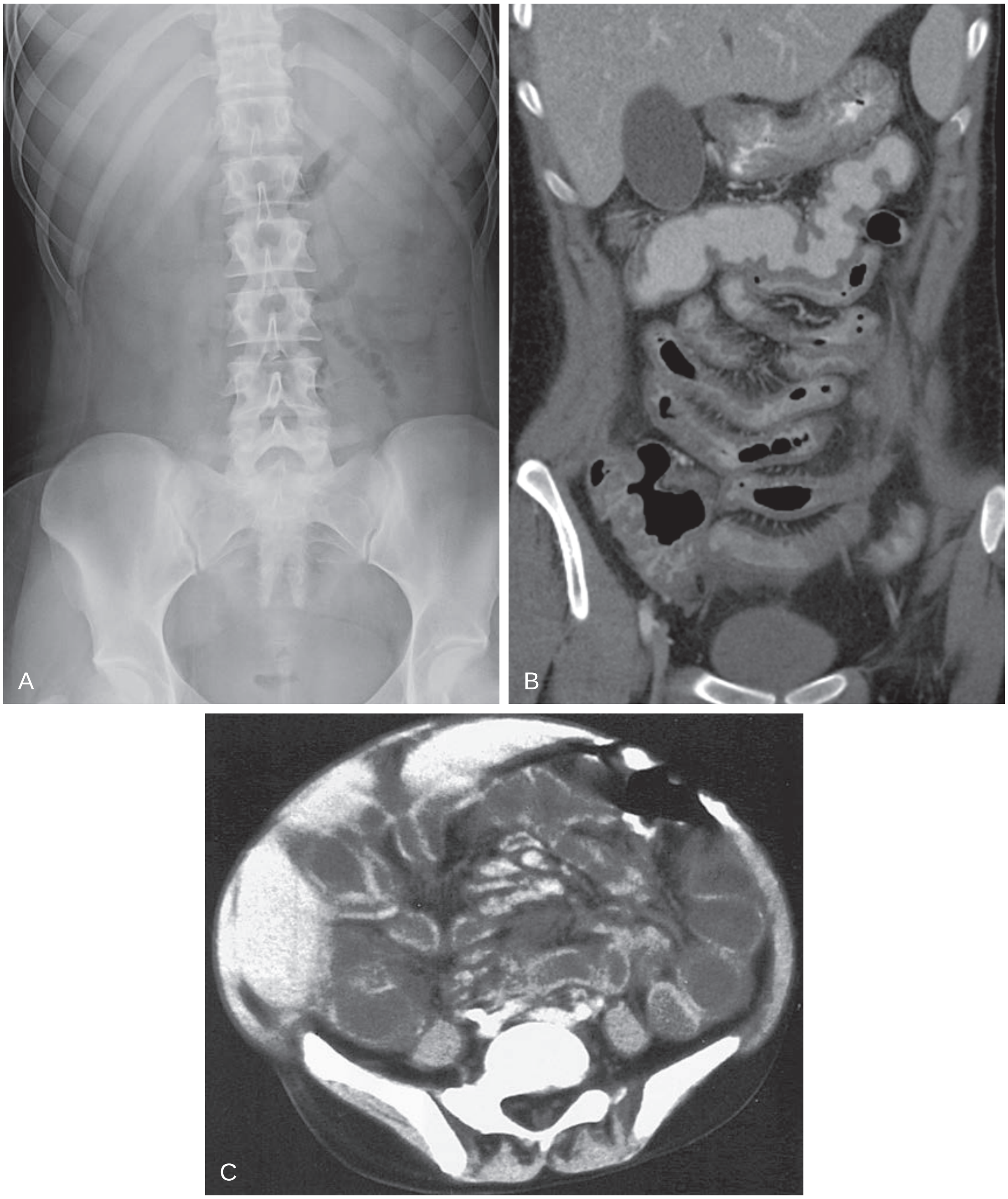

**e-Figure 104.16. Graft-versus-host disease (GVHD).** (A) Supine abdominal radiograph in an 18-year-old girl with voluminous watery diarrhea 95 days after unrelated-donor bone marrow transplant, shows a nonspecific paucity of bowel gas. (B) Coronal contrast-enhanced CT image demonstrates diffuse bowel wall thickening. Severe gastrointestinal GVHD was confirmed by additional clinical data. (C) Axial contrast-enhanced CT in another child with GVHD shows marked edema of the bowel wall with deep mucosal enhancement.

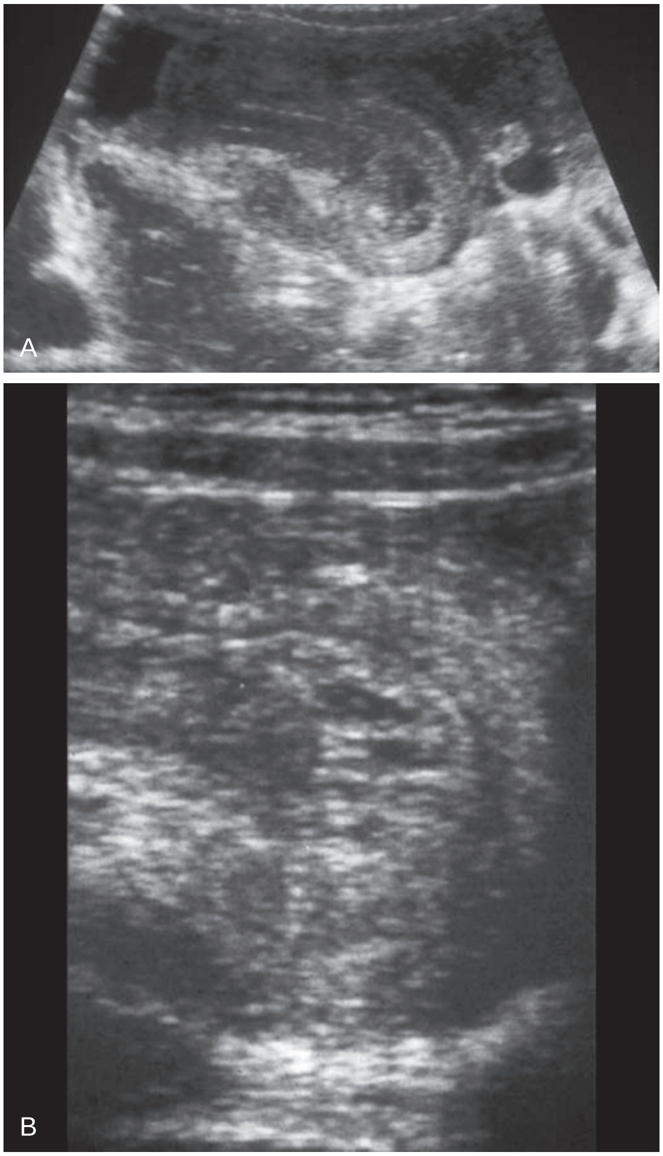

**Figure 104.17. IgA Vasculitis (Henoch-Schönlein purpura) with intussusceptions.** (A) Transverse sonogram of the left lower quadrant in a 6-year-old girl with acute abdominal pain reveals a thick-walled small bowel loop with intussusception. (B) Linear transducer image of the tip of the intussusception shows thick-walled bowel layers and sonolucent spaces in the intussuscepted mesentery consistent with edema. At surgery several hours later, an irreducible ileoileal intussusception was identified, which needed segmental bowel resection; the typical petechial rash appeared the following day. *(Courtesy Marta Hernanz-Schulman MD, Nashville, TN.)*

approximately 50% to 75% of patients and include nausea, vomiting, colicky abdominal pain, and hematochezia.[146] Bleeding into the bowel wall can rarely lead to intussusception, approximately 70% ileoileal. Complications include ischemia and perforation (Fig. 104.17).[148]

***Imaging.*** US may reveal bowel wall thickening with skip areas of abnormality (Fig. 104.17 and e-Fig. 104.18), reduced peristalsis, bowel dilation, mesenteric lymphadenopathy and edema, and intraperitoneal-free fluid, which are nonspecific.[146,148] Small bowel intussusception may be seen (see following section). Radiographs should be obtained if there is suspected bowel perforation.[146] Fluoroscopic contrast studies, CT, and MRI are not usually indicated. Intravenous radiographic contrast media (iodinated or gadolinium-based) should be avoided in the presence of renal impairment. Strictures may occur as a late sequela of the disease, likely from vasculitis with secondary focal areas of ischemia.

***Treatment.*** GI manifestations of IgAV generally require no treatment, although administration of corticosteroids has been reported to improve symptoms and shorten the symptomatic period.[146] While most intussusceptions reduce spontaneously, this is not always the case, and serial US may be needed to ensure resolution.[148]

## Small Bowel Intussusception

***Overview.*** Intussusceptions in young children are typically ileocolic or ileoileocolic (see Chapter 107). Small bowel intussusceptions are more frequently identified as an incidental finding with the widespread use of cross-sectional imaging.[150]

***Etiology.*** Small bowel intussusceptions are typically short segment, transient, and asymptomatic.[151,152] Exceptions include those caused by a focal lead point such as Meckel diverticulum, duplication cysts, polyps, small bowel hemangiomas, and lymphoma. Small bowel intussusceptions may also be seen with bowel thickening in gastroenteritis, IgAV, CF, or celiac disease (e-Fig. 104.18). In addition, small bowel intussusceptions may occur in association with gastrojejunostomy (GJ) tubes, typically in the jejunum, or during the postoperative period.[153]

***Clinical Presentation.*** Compared with ileocolic intussusception, symptoms in small bowel intussusception are less severe or absent, with only vomiting seen with any frequency.[154] Patients with a small bowel intussusception secondary to a lead point that does not reduce spontaneously present with abdominal pain and bowel obstruction.[151]

***Imaging.*** US is the first-line modality in intussusception evaluation; they appear as a laminated "pseudomass" longitudinally and "target" sign transversely. Findings that indicate a transient intussusception include short length (<3 cm), thin diameter (<2.5 cm), preserved wall motion, and absence of a lead point.[151] Additional features favoring small bowel versus ileocolic intussusception are absence of either a fat core or lymph nodes inside the lesion.[154] The findings are similar on US and CT (see Chapters 103 and 107).[150,151] Interrogation of the intussusception and adjacent bowel may demonstrate a focal or diffuse pathologic lead point as earlier discussed, mesenteric lymph nodes within the complex, and evidence of bowel obstruction. GJ tubes can be seen as a central shadowing, with or without a hyperechoic focus.[153]

***Treatment.*** Small bowel intussusception in the absence of a lead point or bowel obstruction should be treated symptomatically, with serial US usually demonstrating spontaneous resolution, often during a single examination. Pathologic SBOs are not amenable to image-guided enema reduction and require surgical management.

## TUMORS

### Benign Tumors

#### Polyps

Polyps can be occur throughout the GI tract, most commonly in the colon, and are histologically classified as neoplastic polyps (e.g. adenomas) and nonneoplastic polyps (e.g., hyperplastic, inflammatory, and hamartomatous polyps [HP]). Although rare compared with other polyps, HP are the most common in children, over 90% being solitary juvenile polyps in the rectosigmoid. Multiple HP occur in hamartomatous polyposis syndromes (such as Peutz-Jeghers syndrome [PJS]), which are associated with a high risk of malignancy (Chapter 108).[155]

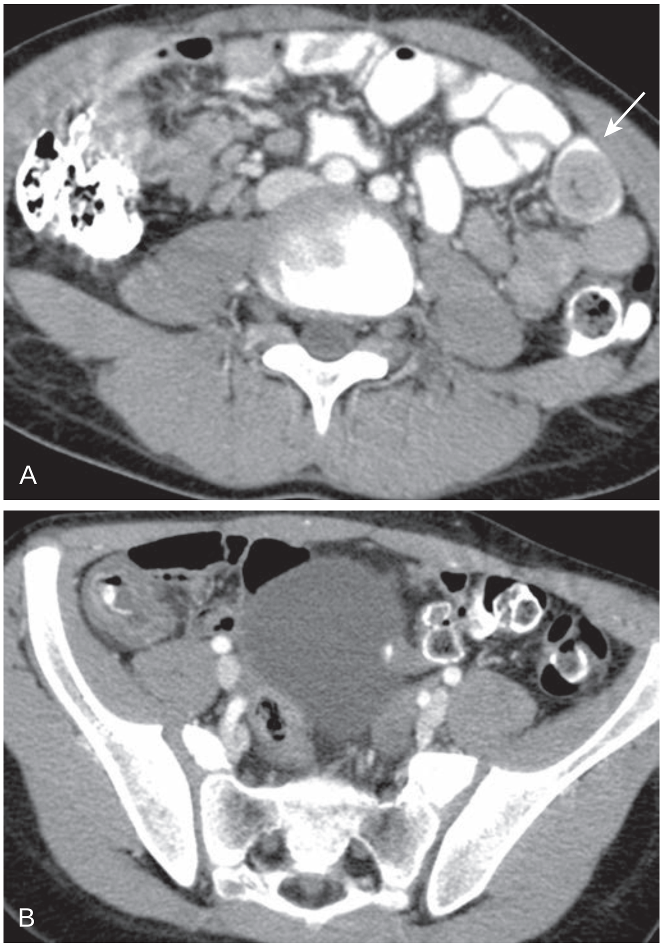

**e-Figure 104.18. IgA vasculitis (Henoch-Schönlein purpura).** (A) Axial contrast-enhanced CT images in a 9-year-old girl with abdominal pain, fever, and bloody stools demonstrate a transient small bowel (ileoileal) intussusception *(arrow)* and (B) pronounced thickening of the terminal ileum.

## Peutz-Jeghers Syndrome

***Overview.*** PJS is an autosomal-dominant syndrome with incomplete penetrance characterized by mucocutaneous pigmentation and hamartomatous polyps of the GI tract. The estimated prevalence is approximately 1 per 100,000–195,000 individuals.[155,156]

***Etiology.*** PJS has been attributed to mutations in the *STK11* gene (serine/threonine kinase 11, alias *LKB1*) on chromosome 19p13.3.[156]

***Clinical Presentation.*** The characteristic mucocutaneous pigmentation from pigment-laden macrophages usually precedes polyp formation and is seen in approximately 95% of patients as brown or black pigmentation of the vermillion border, buccal mucosa, face, palms, and soles. Typically present during early childhood, they often fade at adolescence.[156] Polyps occur most commonly in the small bowel, followed by the colon and stomach, sparing the esophagus. The most common clinical presentation is with symptoms of SBO with abdominal pain due to an intussusception (69% of patients having at least one episode by 16 years of age), followed by rectal bleeding and anemia. The first GI symptoms can occur in early childhood, with 50% to 75% of patients presenting before 20 years of age.[155,157] Patients with PJS have 1% to 2% risk of malignancy by 20 years increasing to 31% by 50 years, with GI tract malignancies the most common.[158] Associated extraintestinal malignancies may involve the testes, breasts, pancreas, reproductive organs, and less frequently the thyroid, gallbladder, and biliary tree.[158]

***Imaging.*** Diagnosis is usually made based on the combination of mucocutaneous rash and on biopsy of the polyp, most commonly in the small bowel, with decreasing frequency in the colon and stomach.

US is the main modality for diagnosis of small bowel intussusceptions as previously described. Although polyps are not well seen sonographically, they are variably described as hypo- or hyperechoic polypoidal masses (e-Fig. 104.19).[153]

For surveillance, SBFT, enteroclysis, and CT are now discouraged because of ionizing radiation risks.[159] MRE is as effective as SBFT in detecting polyps, and for polyps greater than or equal to 15 mm is equivalent to videocapsule endoscopy and has better localization.[159,160] It is likely MRE will be incorporated into surveillance protocols as these findings are further validated. For now, comprehensive surveillance for polyps involves upper GI endoscopy, videocapsule endoscopy, and ileocolonoscopy starting at 8 years of age, with additional organ screening from puberty onward.[160,161]

***Treatment.*** Intussusceptions require surgical resection unless they resolve spontaneously, which can be monitored with serial US. Polypectomy can be performed endoscopically, usually for polyps 10 to 15 mm, if symptomatic or rapidly growing. Experimental agents for chemoprevention, such as rapamycin, are being developed and tested.[156] Cancer surveillance is part of the patients' lifelong care.

## Benign Neoplasms

***Overview.*** Primary neoplasms in the GI tract represent less than 5% of all neoplasms in children, and are even rarer in the upper GI tract.[162] Benign neoplasms in the small intestine include hemangiomas, vascular malformations, neurofibromas, fibromas, leiomyomas, lipomas, and lipoblastomas. Most benign small bowel tumors manifest with GI bleeding or intussusception.

***Etiology.*** Hemangiomas can be solitary or multiple and may occur as an isolated finding or in association with a syndrome. Patients with Klippel-Trénaunay syndrome are seen with visceral and cutaneous hemangiomas. Telangiectasias (dilated superficial blood vessels) may occur in the small intestine in Osler-Weber-Rendu syndrome. Vascular malformations that involve the small intestine have also been reported in association with other soft tissue vascular malformations.[163]

Neurofibromas may occur in isolation or as a manifestation of NF1, where they are the most frequent bowel neoplasm, seen in approximately 10% to 25% of patients.[164]

Fat-containing small intestinal neoplasms include lipomas and lipoblastomas. These appear primarily within the intestinal wall or in the adjacent omentum or retroperitoneum. Lipoblastomas are rare tumors related to embryonal fat, occurring almost exclusively in children; 90% come to medical attention within the first 3 years of life.[165,166]

***Clinical Features.*** Hemangiomas may manifest with GI bleeding, obstruction as a lead point for intussusception, or perforation.[163] Neurofibromas that involve the small bowel are often asymptomatic, however, they may be seen initially with GI bleeding or with obstruction secondary to intussusception or segmental volvulus.[164] Lipomas may ulcerate when larger than 2 cm and may lead to intestinal bleeding or intussusception,[167] and lipoblastomas, although benign, may recur locally in as many as 25% of cases.[165]

***Imaging.*** Rarely, abdominal radiographs may reveal a soft tissue density with localized mass effect. More usually patients present with abdominal pain and signs of SBO, with dilated bowel loops and fluid air levels secondary to intussusception. Fluoroscopic contrast studies are rarely indicated but may reveal a luminal filling defect or a mural mass. US is the preferred modality for intussusception diagnosis, as well as looking for a focal pathologic lead point, although these are rarely discerned.[153] Lipomas and lipoblastomas demonstrate characteristic low density on CT and fat intensity on MRI.[165,167]

***Treatment.*** Neurofibromas that are symptomatic typically undergo surgical excision.[168] Lipoblastomas are treated by complete resection, and mesenteric lipoblastomas may require resection of adjacent intestinal loops.[165,166]

# Malignant Tumors

***Overview.*** With the exception of lymphoma, malignant tumors of the small intestine in children are exceedingly rare.[162] GI stromal cell tumors (GIST) are considered potentially malignant[169] and as such will be discussed here, along with lymphoma and neuroendocrine (carcinoid) tumors. Patients with PJS, considered previously, may also develop GI malignancies. Other polyposis syndromes that primarily affect colon are further discussed in Chapter 108.

## Gastrointestinal Stromal Tumors

***Etiology.*** The most common mesenchymal tumor of the stomach and intestine, GIST are very rare in children and adolescents, representing 1% to 2% of all GIST with an incidence of 0.02 per million under 14 years (median age 13 years) and up to 70% occurring in girls.[170,171] Arising from the interstitial cells of Cajal in smooth muscle, pediatric GIST are similar to adult GIST demonstrating positive stains for CD117/c-KIT and CD34 but different in that only 15% have mutations in somatic receptor tyrosine kinase gene KIT and platelet-derived growth factor receptor alpha (PDGFRA), referred to as wild type (WT) GIST.[172] GIST can be sporadic, familial (Carney-Stratakis syndrome, both paragangliomas, and GIST), part of the nonhereditary syndrome Carney triad (gastric GIST, extra-adrenal paraganglioma, pulmonary chondroma), or associated with other syndromes (e.g., NF1).[171]

***Clinical.*** GIST most frequently manifest with GI bleeding and secondary anemia. Other symptoms can include vomiting, abdominal pain, early satiety, a palpable mass, weight loss, and obstruction.[172,173] They are often multifocal, particularly gastric GIST in Carney triad but can present as a single, often exophytic mass that can ulcerate. Sixty percent are gastric, 20% to 30% in small intestine; in children, 20% to 29% have metastases at diagnosis, usually to regional lymph nodes, liver, and peritoneum (<2% in adults).[170–172,174]

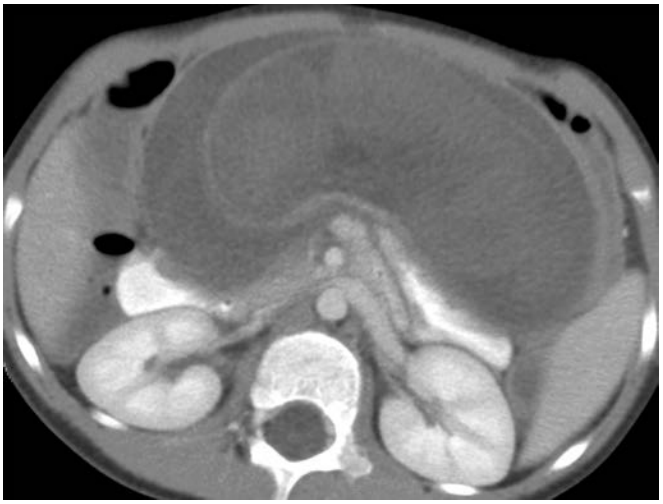

**e-Figure 104.19. Hamartomatous polyps causing intussusception.** Axial contrast-enhanced CT image in a 4-year-old boy with severe episodic abdominal pain shows a small bowel (jejunojejunal) intussusception with a high-grade obstruction. Infarcted hamartomatous polyps were present on the pathologic specimen of the resected intussuscepted bowel.

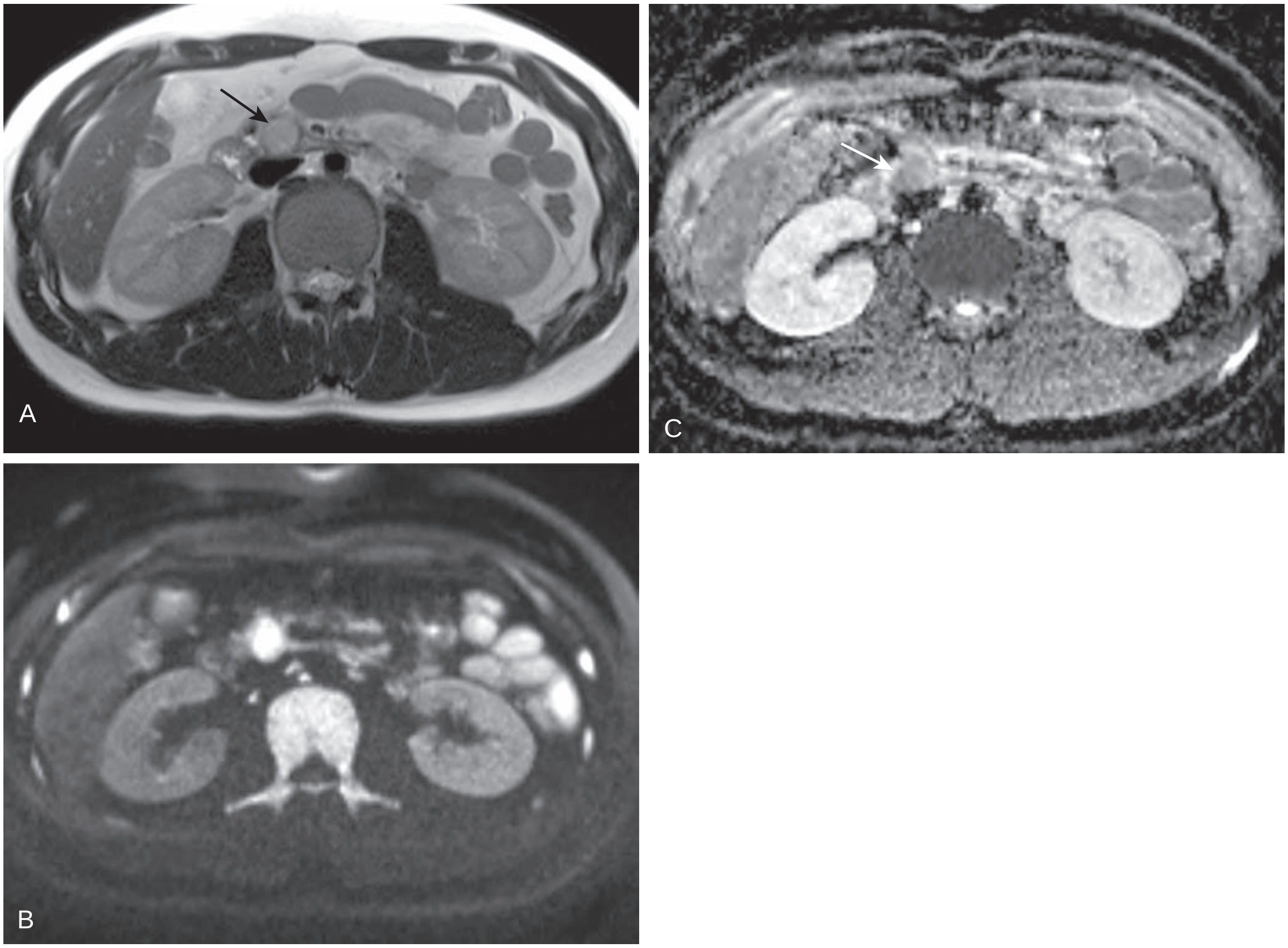

**Figure 104.20. Gastrointestinal stromal tumor (GIST).** A 14-year-old boy with melena. Axial single-shot fast spin echo (SSFSE) sequence (A), DWI b = 800 s/mm$^2$ (B), and ADC map (C) MR images show a T2 hyperintense, diffusion-restricting mass *(arrow)* arising from the third portion of the duodenum.

***Imaging.*** Abdominal radiographs may show a soft tissue mass with local mass effect, or SBO or gastric obstruction. With ionizing radiation concerns and reported sensitivity of 35%, fluoroscopic contrast studies are rarely performed but may demonstrate a circumscribed, rounded gastric or intestinal filling defect or obstruction. US is often the first study to detect a mass, which appears lobular and hypoechoic with central cysts or necrosis and intermediate peripheral vascularity; size varies between a few millimeters to 25 cm. US can localize GIST origin as well as screen for metastases.[175] CT and MRI postintravenous contrast are used in diagnosis and staging showing lobular, single or multifocal soft tissue density/intensity masses with peripheral enhancement, and central necrosis, cysts, or hemorrhage.[176] $^{18}$F-FDG PET/CT and PET/MRI are particularly sensitive for GIST and have a role in defining occult metastases, as well as monitoring treatment response or recurrence (Fig. 104.20).[170]

***Treatment.*** Pediatric GIST tend to be indolent in spite of metastatic disease, especially small tumors (<2 cm) that may be monitored with endoscopic US.[170] Local surgical resection is the primary treatment due to resistance to standard chemotherapy; however, recurrence is high (40%–90% in adults).[172] If KITc or PDGFRA mutation is positive, adjuvant therapy with ongoing surveillance imaging is an option, although this is yet to be standardized.

## Gastrointestinal Tract Lymphoma

***Overview.*** Burkitt lymphoma is the most frequent subtype of non-Hodgkin lymphoma (NHL) that occurs in children. More than one-third of the cases occur in children between 5 and 9 years of age (median age at presentation being 8 years), with a male predominance. The GI tract is involved in 22.5% to 57.5%.[177,178] The second-most common NHL in children is diffuse large B-cell lymphoma (DLBCL), accounting for 20% of pediatric NHL, more common in adolescents. While widely disseminated in 75%, the GI tract is the most common extranodal site. Anaplastic large cell and T-cell lymphoblastic NHL rarely involve the GI tract, and Hodgkin lymphoma is nodal.[179] Lastly, posttransplant lymphoproliferative disease (PTLD) commonly involves the GI tract after liver, kidney, pancreas, lung, or heart transplant. The incidence is from 5% to 33%, with a median onset 5 years posttransplant, and is highest after pancreas transplantation.[180] The distal small bowel is the most common site. Imaging features are similar to other NHL.

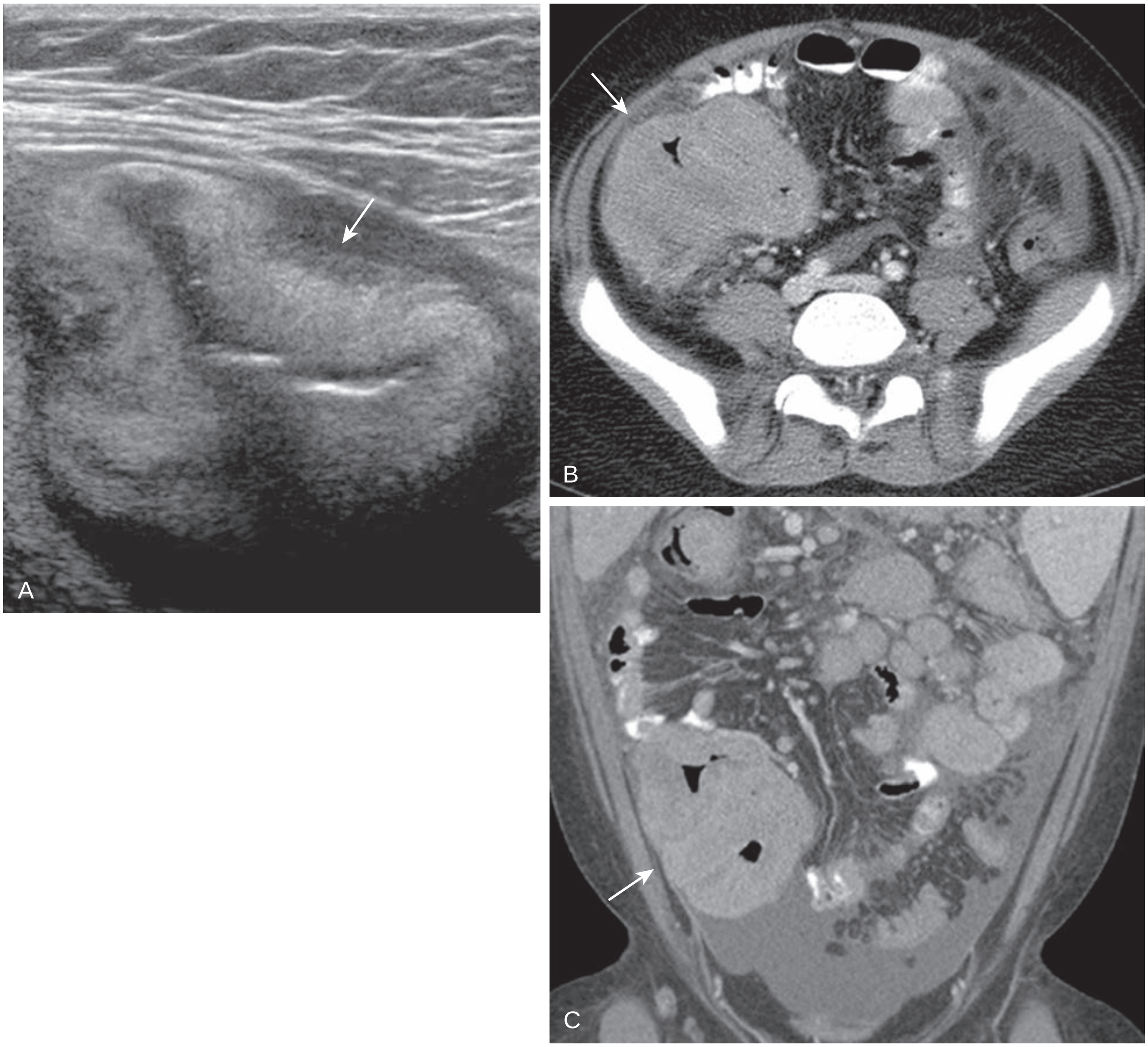

**Figure 104.21. Burkitt lymphoma.** (A) Transverse abdominal sonographic image in a 12-year-old boy who presented with abdominal pain, nausea, and diarrhea shows pronounced bowel wall thickening *(arrow)*. (B) Correlative axial contrast-enhanced CT image confirms thickening of bowel in the right lower quadrant *(arrow)* and moderate ascites. (C) Coronal reformat again shows the involvement of the bowel with tumor *(arrow)* and additionally demonstrates ascites.

## Burkitt Lymphoma

***Etiology.*** Burkitt lymphoma is a monoclonal B-cell lymphoma that occurs in three principal forms: endemic, sporadic, and immunodeficient. The endemic form, originally identified in Uganda in 1958, occurs in equatorial Africa and Papua New Guinea, with a 95% association with the Epstein-Barr virus (EBV). The sporadic form is seen in North America, Northern and Eastern Europe, and the Far East, and its association with EBV is 15%. The immunodeficient form is associated with immune-compromised states, particularly with HIV infection, congenital deficiencies, and iatrogenic immunodeficiencies such in allograft recipients.[177,179]

***Clinical Presentation.*** Primary pediatric GI tract lymphomas preferentially involve small and large bowel, rather than the stomach in adults.[181] Terminal ileum, cecum, and appendix are common sites of involvement by Burkitt lymphoma, the terminal ileum most commonly involved due to a high concentration of lymphatic nodal tissue.[177] Common presenting symptoms range from a painless, palpable abdominal mass to abdominal pain with intestinal obstruction or perforation, followed by neck swelling.[178] Obstruction may be related to an intussusception with a pathologic lead point (see Fig. 108.7). Burkitt lymphoma is one of the most rapidly growing tumors, with a doubling time of approximately 24 hours, making prompt diagnosis important.[177]

***Imaging.*** Abdominal radiographs may show evidence of mass effect or obstruction related to an intussusception, or appear normal. US can demonstrate an intussusception with lymphoma seen as a lobulated, hypoechoic mass in the intussusceptum acting as a pathologic lead point. Prominent reactive lymphoid hyperplasia can be a mimicker.[153] In the absence of intussusception, a mass of low or heterogeneous echogenicity with a hyperechoic center may be seen when the lymphoma infiltrates the bowel wall (Fig. 104.21A). CT and MRI may show circumferential or asymmetric bowel wall thickening or focal masses (Fig. 104.21B and C) with dilatation of the bowel lumen from obstruction, luminal narrowing, or intussusception.[177,182] Ascites may also be present (see Fig. 104.21C). Careful evaluation of retroperitoneal organs, liver, and spleen is mandatory for disseminated disease. Burkitt lymphoma demonstrates high avidity on $^{18}$F-FDG PET/CT and PET/MRI in active disease at nodal and extranodal sites, useful in tumor staging and assessing treatment response.[182,183]

***Treatment.*** Although it grows rapidly, Burkitt lymphoma is also rapidly responsive to chemotherapy, with no need for radiation or surgery (unless complicated by intussusception or perforation).[181,184] Image-guided enemas can be attempted in this setting but should be done with caution and in consultation with the referring surgeon.[153]

## Neuroendocrine Tumor (Carcinoid Tumor)

***Overview.*** Neuroendocrine tumors (NETs) were previously known as *carcinoid tumors*. A 2011 consensus guideline redefined them as follows[185]: “neuroendocrine neoplasms” (NEN) for all low-, intermediate-, and high-grade tumors; “tumor” (NET) reserved for low- to intermediate-grade neoplasms (previously “carcinoid” or “atypical carcinoid”); and “carcinoma” (NEC) for high-grade neoplasms (previously “poorly differentiated carcinoma”). Additionally, mid and hindgut NETs are further classified by location: gastroduodenal, jejuno-ileal (SI-NEN), appendiceal, cecal, colonic, or rectal.[186]

NETs are rare neoplasms defined by the expression of neuroendocrine markers.[185] Second only to lymphoma in incidence of pediatric GI tract neoplasms, they occur in the digestive tract in up to 95% of cases.[187] Most commonly found in young adults, NETs are rare in children, with a reported prevalence of 0.08%.[188]

***Etiology.*** NETs arise from neuroendocrine enterochromaffin or Kulchitsky cells. Although most lesions arise de novo, NETs are associated with multiple endocrine neoplasia types 1 and 2 as well as NF1.[189]

***Clinical Presentation.*** Unlike the rapidly growing Burkitt lymphoma, NETs have a slow growth rate and indolent course, with a relatively long asymptomatic period.[186] Presentation may mimic acute appendicitis; patients otherwise come to medical attention with intermittent abdominal pain, vomiting, bleeding, and bowel obstruction. In adults, metastases are seen at diagnosis in approximately one-fourth of patients.[190] Metastases and the carcinoid syndrome are uncommon in children.[188]

***Imaging.*** NETs are not typically detectable on radiographs unless complicated by a secondary process such as intussusception with obstruction. Rarely, a calcified appendiceal NET may mimic a fecalith.[189] On cross-sectional imaging, associated mesenteric desmoplastic reaction, nodal, or hepatic metastases may be more readily identifiable than the primary tumor. CT and MR enterography/enteroclysis may aid in primary tumor detection.[186] On MRI, carcinoids may be seen as a subtle, asymmetric mural thickening that is isointense on T1- and mildly hyperintense on T2-weighted sequences.[189] Isotope imaging with $^{68}$gallium-DOTATOC PET/CT is preferred for detection and staging of NEN; $^{18}$F-FDG PET/CT or PET/MRI is not useful in lower-grade tumors.[186]

***Treatment.*** Locoregional surgical resection is the first line of treatment for NET (with tumor debulking if symptomatic); antiproliferative agents (e.g., somatostatin analogs and interferon-$\alpha$) and rarely peptide receptor radionuclide therapy are options in more advanced disease.[189] Tumors less than 2 cm in diameter at diagnosis have a favorable prognosis especially for incidentally detected appendiceal NET, where right hemicolectomy is no longer advocated.[187,188,191,192]

### KEY POINTS

- The most common causes of small bowel obstruction in older children are adhesions, hernias and omphalomesenteric duct remnants.
- Infectious gastroenteritis is most commonly caused by viruses, and imaging generally plays little or no role in the evaluation of the disease.
- ALARA (as low as reasonably achievable) principles, minimizing ionizing radiation exposure, should be followed with respect to imaging children with CD.
- US, CT, and MRI have largely replaced the fluoroscopic examination of the bowel in the assessment of IBD, and CT and MRI have comparable sensitivities and specificities.
- MRI is the imaging modality of choice for assessing perianal disease and fistulae in patients with CD.
- Burkitt lymphoma often involves the GI tract in children and is a common lead point for intussusception for older children.

### SUGGESTED READINGS

Anupindi SA, Podberesky DJ, Towbin AJ, et al. Pediatric inflammatory bowel disease: imaging issues with targeted solutions. *Abdom Imaging*. 2015;40(5):975–992.

Guelfguat M, Kaplinskiy V, Reddy SH, et al. Clinical guidelines for imaging and reporting ingested foreign bodies. *AJR Am J Roentgenol*. 2014;203(1):37–53.

Hryhorczuk AL, Lee EY. Imaging evaluation of bowel obstruction in children: updates in imaging techniques and review of imaging findings. *Semin Roentgenol*. 2012;47(2):159–170.
Lewis RB, Mehrotra AK, Rodríguez P, et al. From the radiologic pathology archives: gastrointestinal lymphoma: radiologic and pathologic findings. *Radiographics*. 2014;34(7):1934–1953.
Masselli G, Mastroiacovo I, De Marco E, et al. Current techniques and new perspectives research of magnetic resonance enterography in pediatric Crohn's disease. *World J Radiol*. 2016;8(7):668–682.
Nay J, Menias CO, Mellnick VM, et al. Gastrointestinal manifestations of systemic disease: a multimodality review. *Abdom Imaging*. 2015;40(6):1926–1943.

## REFERENCES

Full references for this chapter can be found on www.expertconsult.com.

## REFERENCES

1. Rudolph CD, Hyman PE, Altschuler SM, et al. Diagnosis and treatment of chronic intestinal pseudo-obstruction in children: report of consensus workshop. *J Pediatr Gastroenterol Nutr*. 1997;24(1):102–112.
2. Di Lorenzo C, Youssef NN. Diagnosis and management of intestinal motility disorders. *Semin Pediatr Surg*. 2010;19(1):50–58.
3. Stehr W, Gingalewski C. Other causes of intestinal obstruction. In: Coran A, Adzick N, Krummel T, et al, eds. *Coran: Pediatric Surger*. 7th ed. Philadelphia: Mosby, an Imprint of Elsevier; 2012.
4. Hucl T. Acute GI obstruction. *Best Pract Res Clin Gastroenterol*. 2013;27(5):691–707.
5. Huang CC, Lai MW, Hwang FM, et al. Diverse presentations in pediatric Meckel's diverticulum: a review of 100 cases. *Pediatr Neonatol*. 2014;55(5):369–375.
6. Wright CC, Closson FT. Updates in pediatric gastrointestinal foreign bodies. *Pediatr Clin North Am*. 2013;60(5):1221–1239.
7. Lautz TB, Barsness KA. Adhesive small bowel obstruction–acute management and treatment in children. *Semin Pediatr Surg*. 2014;23(6):349–352.
8. Welch KJ, ed. *Pediatric Surgery*. 4th ed. Chicago: Year Book Medical Publishers; 1986.
9. Katz DA. Evaluation and management of inguinal and umbilical hernias. *Pediatr Ann*. 2001;30(12):729–735.
10. Brandt ML. Pediatric hernias. *Surg Clin North Am*. 2008;88(1):27–43, vii-viii.
11. Lau ST, Lee YH, Caty MG. Current management of hernias and hydroceles. *Semin Pediatr Surg*. 2007;16(1):50–57.
12. Stanescu GL, Plesea IE, Diaconu R, et al. Meckel's diverticulum in children, clinical and pathological aspects. *Rom J Morphol Embryol*. 2014;55(suppl 3):1167–1170.
13. Mattei P, Rombeau JL. Review of the pathophysiology and management of postoperative ileus. *World J Surg*. 2006;30(8):1382–1391.
14. ASGE. Standards of Practice Committee, Ikenberry SO, Jue TL, et al. Management of ingested foreign bodies and food impactions. *Gastrointest Endosc*. 2011;73(6):1085–1091.
15. Alfonzo MJ, Baum CR. Magnetic foreign body ingestions. *Pediatr Emerg Care*. 2016;32(10):698–702.
16. Jang TB, Schindler D, Kaji AH. Bedside ultrasonography for the detection of small bowel obstruction in the emergency department. *Emerg Med J*. 2011;28(8):676–678.
17. James V, Alsani FS, Fregonas C, et al. Point-of-care ultrasound in pediatric small bowel obstruction: an ED case series. *Am J Emerg Med*. 2016.
18. Graf JL, Caty MG, Martin DJ, et al. Pediatric hernias. *Semin Ultrasound CT MR*. 2002;23(2):197–200.
19. Walker CL, Rudan I, Liu L, et al. Global burden of childhood pneumonia and diarrhoea. *Lancet*. 2013;381(9875):1405–1416.
20. Dennehy PH. Acute diarrheal disease in children: epidemiology, prevention, and treatment. *Infect Dis Clin North Am*. 2005;19(3):585–602.
21. Goodgame R. Norovirus gastroenteritis. *Curr Infect Dis Rep*. 2007;9(2):102–109.
22. Tinsa F, Essaddam L, Fitouri Z, et al. Abdominal tuberculosis in children. *J Pediatr Gastroenterol Nutr*. 2010;50(6):634–638.
23. Dones P, Di Gangi M, Failla MC, et al. Intestinal tuberculosis in a child living in a country with a low incidence of tuberculosis: a case report. *BMC Res Notes*. 2014;7:762.
24. Larsson G, Shenoy T, Ramasubramanian R, et al. Routine diagnosis of intestinal tuberculosis and Crohn's disease in Southern India. *World J Gastroenterol*. 2014;20(17):5017–5024.
25. Hotez PJ, Brindley PJ, Bethony JM, et al. Helminth infections: the great neglected tropical diseases. *J Clin Invest*. 2008;118(4):1311–1321.
26. Miller TL, Agostoni C, Duggan C, et al. Gastrointestinal and nutritional complications of human immunodeficiency virus infection. *J Pediatr Gastroenterol Nutr*. 2008;47(2):247–253.
27. Jesson J, Leroy V. Challenges of malnutrition care among HIV-infected children on antiretroviral treatment in Africa. *Med Mal Infect*. 2015;45(5):149–156.
28. Blakelock RT, Beasley SW. Infection and the gut. *Semin Pediatr Surg*. 2003;12(4):265–274.
29. Huang DB, Chappell C, Okhuysen PC. Cryptosporidiosis in children. *Semin Pediatr Infect Dis*. 2004;15(4):253–259.
30. Kessler DO, Gurwitz A, Tsung JW. Point-of-care sonographic detection of intestinal ascaris lumbricoides in the pediatric emergency department. *Pediatr Emerg Care*. 2010;26(8):586–587.
31. Capitanio MA, Greenberg SB. Pneumatosis intestinalis in two infants with rotavirus gastroenteritis. *Pediatr Radiol*. 1991;21(5):361–362.
32. Belard S, Tamarozzi F, Bustinduy AL, et al. Point-of-care ultrasound assessment of tropical infectious diseases–a review of applications and perspectives. *Am J Trop Med Hyg*. 2016;94(1):8–21.
33. Matsumoto T, Iida M, Sakai T, et al. Yersinia terminal ileitis: sonographic findings in eight patients. *AJR Am J Roentgenol*. 1991;156(5):965–967.
34. Haller JO, Cohen HL. Pediatric HIV infection: an imaging update. *Pediatr Radiol*. 1994;24(3):224–230.
35. Levine A, Koletzko S, Turner D, et al. ESPGHAN revised porto criteria for the diagnosis of inflammatory bowel disease in children and adolescents. *J Pediatr Gastroenterol Nutr*. 2014;58(6):795–806.
36. Sauer CG, Kugathasan S. Pediatric inflammatory bowel disease: highlighting pediatric differences in IBD. *Gastroenterol Clin North Am*. 2009;38(4):611–628.
37. Winter DA, Karolewska-Bochenek K, Lazowska-Przeorek I, et al. Pediatric IBD-unclassified is less common than previously reported; results of an 8-year audit of the EUROKIDS Registry. *Inflamm Bowel Dis*. 2015;21(9):2145–2153.
38. Gasparetto M, Guariso G. Highlights in IBD epidemiology and its natural history in the paediatric age. *Gastroenterol Res Pract*. 2013;2013:829040.
39. Molodecky NA, Soon IS, Rabi DM, et al. Increasing incidence and prevalence of the inflammatory bowel diseases with time, based on systematic review. *Gastroenterology*. 2012;142(1):46–54 e42, quiz e30.
40. Benchimol EI, Fortinsky KJ, Gozdyra P, et al. Epidemiology of pediatric inflammatory bowel disease: a systematic review of international trends. *Inflamm Bowel Dis*. 2011;17(1):423–439.
41. Corica D, Romano C. Biological therapy in pediatric inflammatory bowel disease: a systematic review. *J Clin Gastroenterol*. 2016.
42. Mamula P, Telega GW, Markowitz JE, et al. Inflammatory bowel disease in children 5 years of age and younger. *Am J Gastroenterol*. 2002;97(8):2005–2010.
43. Panes J, Bouhnik Y, Reinisch W, et al. Imaging techniques for assessment of inflammatory bowel disease: joint ECCO and ESGAR evidence-based consensus guidelines. *J Crohns Colitis*. 2013;7(7):556–585.
44. Doecke JD, Simms LA, Zhao ZZ, et al. Genetic susceptibility in IBD: overlap between ulcerative colitis and Crohn's disease. *Inflamm Bowel Dis*. 2013;19(2):240–245.
45. Osterman MT. Mucosal healing in inflammatory bowel disease. *J Clin Gastroenterol*. 2013;47(3):212–221.
46. Hafen GM, Ranganathan SC, Robertson CF, et al. Clinical scoring systems in cystic fibrosis. *Pediatr Pulmonol*. 2006;41(7):602–617.
47. de Bie CI, Paerregaard A, Kolacek S, et al. Disease phenotype at diagnosis in pediatric Crohn's disease: 5-year analyses of the EUROKIDS Registry. *Inflamm Bowel Dis*. 2013;19(2):378–385.
48. Levine A, Griffiths A, Markowitz J, et al. Pediatric modification of the Montreal classification for inflammatory bowel disease: the Paris classification. *Inflamm Bowel Dis*. 2011;17(6):1314–1321.
49. de Bie CI, Buderus S, Sandhu BK, et al. Diagnostic workup of paediatric patients with inflammatory bowel disease in Europe: results of a 5-year audit of the EUROKIDS registry. *J Pediatr Gastroenterol Nutr*. 2012;54(3):374–380.
50. Levine A, de Bie CI, Turner D, et al. Atypical disease phenotypes in pediatric ulcerative colitis: 5-year analyses of the EUROKIDS Registry. *Inflamm Bowel Dis*. 2013;19(2):370–377.
51. Assa A, Amitai M, Greer ML, et al. Perianal pediatric Crohn disease is associated with a distinct phenotype and greater inflammatory burden. *J Pediatr Gastroenterol Nutr*. 2017;65(3):293–298.
52. Keljo DJ, Markowitz J, Langton C, et al. Course and treatment of perianal disease in children newly diagnosed with Crohn's disease. *Inflamm Bowel Dis*. 2009;15(3):383–387.
53. Civitelli F, Nuti F, Oliva S, et al. Looking beyond mucosal healing: effect of biologic therapy on transmural healing in pediatric Crohn's disease. *Inflamm Bowel Dis*. 2016;22(10):2418–2424.
54. Ruemmele FM. Pediatric inflammatory bowel diseases: coming of age. *Curr Opin Gastroenterol*. 2010;26(4):332–336.
55. Sheybani EF, Sheikh N, Chavhan GB, et al. Extra-intestinal findings on magnetic resonance enterography in children with inflammatory bowel disease. *Clin Radiol*. 2016;71(9):828–836.
56. Turner D, Levine A, Walters TD, et al. Which PCDAI version best reflects intestinal inflammation in pediatric Crohn's disease? *J Pediatr Gastroenterol Nutr*. 2016.

57. Rimola J, Ordas I, Rodriguez S, et al. Magnetic resonance imaging for evaluation of Crohn's disease: validation of parameters of severity and quantitative index of activity. *Inflamm Bowel Dis*. 2011;17(8):1759–1768.
58. Pariente B, Cosnes J, Danese S, et al. Development of the Crohn's disease digestive damage score, the Lemann score. *Inflamm Bowel Dis*. 2011;17(6):1415–1422.
59. Moy MP, Sauk J, Gee MS. The role of MR enterography in assessing Crohn's disease activity and treatment response. *Gastroenterol Res Pract*. 2016;2016:8168695.
60. Church PC, Turner D, Feldman BM, et al. Systematic review with meta-analysis: magnetic resonance enterography signs for the detection of inflammation and intestinal damage in Crohn's disease. *Aliment Pharmacol Ther*. 2015;41(2):153–166.
61. Moy MP, Kaplan JL, Moran CJ, et al. MR enterographic findings as biomarkers of mucosal healing in young patients with Crohn disease. *AJR Am J Roentgenol*. 2016;1–7.
62. Church PC, Greer MC, Cytter-Kuint R, et al. Magnetic resonance enterography has good inter-rater agreement and diagnostic accuracy for detecting inflammation in pediatric Crohn disease. *Pediatr Radiol*. 2017;47(5):565–575.
63. Anupindi SA, Halverson M, Khwaja A, et al. Common and uncommon applications of bowel ultrasound with pathologic correlation in children. *AJR Am J Roentgenol*. 2014;202(5):946–959.
64. Alison M, Kheniche A, Azoulay R, et al. Ultrasonography of Crohn disease in children. *Pediatr Radiol*. 2007;37(11):1071–1082.
65. Quencer KB, Nimkin K, Mino-Kenudson M, et al. Detecting active inflammation and fibrosis in pediatric Crohn's disease: prospective evaluation of MR-E and CT-E. *Abdom Imaging*. 2013;38(4):705–713.
66. Aloi M, Di Nardo G, Romano G, et al. Magnetic resonance enterography, small-intestine contrast US, and capsule endoscopy to evaluate the small bowel in pediatric Crohn's disease: a prospective, blinded, comparison study. *Gastrointest Endosc*. 2015;81(2):420–427.
67. Shenoy-Bhangle A, Nimkin K, Goldner D, et al. MRI predictors of treatment response for perianal fistulizing Crohn disease in children and young adults. *Pediatr Radiol*. 2014;44(1):23–29.
68. Domina JG, Dillman JR, Adler J, et al. Imaging trends and radiation exposure in pediatric inflammatory bowel disease at an academic children's hospital. *AJR Am J Roentgenol*. 2013;201(1):W133–W140.
69. Seemann NM, Radhakrishnan S, Gazendam A, et al. The role of imaging in the preoperative assessment of children with inflammatory colitis. *J Pediatr Surg*. 2017;52(6):970–974.
70. Taylor GA, Nancarrow PA, Hernanz-Schulman M, et al. Plain abdominal radiographs in children with inflammatory bowel disease. *Pediatr Radiol*. 1986;16(3):206–209.
71. Ahmad TM, Greer ML, Walters TD, et al. Bowel Sonography and MR Enterography in Children. *AJR Am J Roentgenol*. 2016;206(1): 173–181.
72. Dillman JR, Smith EA, Sanchez R, et al. Prospective cohort study of ultrasound-ultrasound and ultrasound-MR enterography agreement in the evaluation of pediatric small bowel Crohn disease. *Pediatr Radiol*. 2016;46(4):490–497.
73. Horsthuis K, Bipat S, Bennink RJ, et al. Inflammatory bowel disease diagnosed with US, MR, scintigraphy, and CT: meta-analysis of prospective studies. *Radiology*. 2008;247(1):64–79.
74. Stidham RW, Higgins PD. Imaging of intestinal fibrosis: current challenges and future methods. *United European Gastroenterol J*. 2016;4(4):515–522.
75. Spalinger J, Patriquin H, Miron MC, et al. Doppler US in patients with Crohn disease: vessel density in the diseased bowel reflects disease activity. *Radiology*. 2000;217(3):787–791.
76. Masselli G, Casciani E, Polettini E, et al. Comparison of MR enteroclysis with MR enterography and conventional enteroclysis in patients with Crohn's disease. *Eur Radiol*. 2008;18(3):438–447.
77. Lipson A, Bartram CI, Williams CB, et al. Barium studies and ileoscopy compared in children with suspected Crohn's disease. *Clin Radiol*. 1990;41(1):5–8.
78. Dillman JR, Adler J, Zimmermann EM, et al. CT enterography of pediatric Crohn disease. *Pediatr Radiol*. 2010;40(1):97–105.
79. Siddiki HA, Fidler JL, Fletcher JG, et al. Prospective comparison of state-of-the-art MR enterography and CT enterography in small-bowel Crohn's disease. *AJR Am J Roentgenol*. 2009;193(1):113–121.
80. Toma P, Granata C, Magnano G, et al. CT and MRI of paediatric Crohn disease. *Pediatr Radiol*. 2007;37(11):1083–1092.
81. Greer ML. How we do it: MR enterography. *Pediatr Radiol*. 2016; 46(6):818–828.
82. Grand DJ, Guglielmo FF, Al-Hawary MM. MR enterography in Crohn's disease: current consensus on optimal imaging technique and future advances from the SAR Crohn's disease-focused panel. *Abdom Imaging*. 2015;40(5):953–964.
83. Gee MS, Harisinghani MG. MRI in patients with inflammatory bowel disease. *J Magn Reson Imaging*. 2011;33(3):527–534.
84. Seo N, Park SH, Kim KJ, et al. MR enterography for the evaluation of small-bowel inflammation in Crohn disease by using diffusion-weighted imaging without intravenous contrast material: a prospective noninferiority study. *Radiology*. 2016;278(3):762–772.
85. Rimola J, Planell N, Rodriguez S, et al. Characterization of inflammation and fibrosis in Crohn's disease lesions by magnetic resonance imaging. *Am J Gastroenterol*. 2015;110(3):432–440.
86. Dillman JR, Swanson SD, Johnson LA, et al. Comparison of noncontrast MRI magnetization transfer and T2 -Weighted signal intensity ratios for detection of bowel wall fibrosis in a Crohn's disease animal model. *J Magn Reson Imaging*. 2015;42(3):801–810.
87. Pazahr S, Blume I, Frei P, et al. Magnetization transfer for the assessment of bowel fibrosis in patients with Crohn's disease: initial experience. *MAGMA*. 2013;26(3):291–301.
88. Tielbeek JA, Ziech ML, Li Z, et al. Evaluation of conventional, dynamic contrast enhanced and diffusion weighted MRI for quantitative Crohn's disease assessment with histopathology of surgical specimens. *Eur Radiol*. 2014;24(3):619–629.
89. Dillman JR, Smith EA, Sanchez R, et al. DWI in pediatric small-bowel Crohn disease: are apparent diffusion coefficients surrogates for disease activity in patients receiving infliximab therapy? *AJR Am J Roentgenol*. 2016;207(5):1002–1008.
90. Rimola J, Planell N, Rodriguez S, et al. Corrigendum: Characterization of inflammation and fibrosis in Crohn's disease lesions by magnetic resonance imaging. *Am J Gastroenterol*. 2015;110(3):480.
91. Patak MA, von Weymarn C, Froehlich JM. Small bowel MR imaging: 1.5T versus 3T. *Magn Reson Imaging Clin N Am*. 2007;15(3):383–393, vii.
92. Sinha R, Rajiah P, Murphy P, et al. Utility of high-resolution MR imaging in demonstrating transmural pathologic changes in Crohn disease. *Radiographics*. 2009;29(6):1847–1867.
93. Barkmeier DT, Dillman JR, Al-Hawary M, et al. MR enterography-histology comparison in resected pediatric small bowel Crohn disease strictures: can imaging predict fibrosis? *Pediatr Radiol*. 2016;46(4):498–507.
94. Sinha R, Murphy P, Sanders S, et al. Diagnostic accuracy of high-resolution MR enterography in Crohn's disease: comparison with surgical and pathological specimen. *Clin Radiol*. 2013;68(9): 917–927.
95. Mollard BJ, Smith EA, Dillman JR. Pediatric MR enterography: technique and approach to interpretation-how we do it. *Radiology*. 2015;274(1):29–43.
96. Shenoy-Bhangle AS, Nimkin K, Aranson T, et al. Value of diffusion-weighted imaging when added to magnetic resonance enterographic evaluation of Crohn disease in children. *Pediatr Radiol*. 2016;46(1):34–42.
97. AlSabban Z, Church P, Moineddin R, et al. Accuracy and interobserver agreement of diffusion-weighted imaging in pediatric inflammatory bowel disease. *Clin Imaging*. 2016;41:14–22.
98. Morani AC, Smith EA, Ganeshan D, et al. Diffusion-weighted MRI in pediatric inflammatory bowel disease. *AJR Am J Roentgenol*. 2015;204(6):1269–1277.
99. Dillman JR, Trout AT, Smith EA. MR enterography: how to deliver added value. *Pediatr Radiol*. 2016;46(6):829–837.
100. Vendhan K, Bray TJ, Atkinson D, et al. A diffusion-based quantification technique for assessment of sacroiliitis in adolescents with enthesitis-related arthritis. *Br J Radiol*. 2016;89(1059):20150775.
101. Gotler J, Amitai MM, Lidar M, et al. Utilizing MR enterography for detection of sacroiliitis in patients with inflammatory bowel disease. *J Magn Reson Imaging*. 2015;42(1):121–127.
102. Catalano OA, Gee MS, Nicolai E, et al. Evaluation of quantitative PET/MR enterography biomarkers for discrimination of inflammatory strictures from fibrotic strictures in Crohn disease. *Radiology*. 2016;278(3):792–800.
103. Mollard BJ, Smith EA, Lai ME, et al. MR enterography under the age of 10 years: a single institutional experience. *Pediatr Radiol*. 2016;46(1):43–49.
104. Dulai PS, Thompson KD, Blunt HB, et al. Risks of serious infection or lymphoma with anti-tumor necrosis factor therapy for pediatric

inflammatory bowel disease: a systematic review. *Clin Gastroenterol Hepatol*. 2014;12(9):1443–1451, quiz e1488-1449.

105. de Ridder L, Turner D, Wilson DC, et al. Malignancy and mortality in pediatric patients with inflammatory bowel disease: a multinational study from the porto pediatric IBD group. *Inflamm Bowel Dis*. 2014;20(2):291–300.
106. Romeo E, Jasonni V, Caldaro T, et al. Strictureplasty and intestinal resection: different options in complicated pediatric-onset Crohn disease. *J Pediatr Surg*. 2012;47(5):944–948.
107. Chae EJ, Do KH, Seo JB, et al. Radiologic and clinical findings of Behcet disease: comprehensive review of multisystemic involvement. *Radiographics*. 2008;28(5):e31.
108. Ideguchi H, Suda A, Takeno M, et al. Behcet disease: evolution of clinical manifestations. *Medicine (Baltimore)*. 2011;90(2):125–132.
109. Kitaichi N, Ohno S. Behcet disease in children. *Int Ophthalmol Clin*. 2008;48(3):87–91.
110. Ozen S. Pediatric onset Behcet disease. *Curr Opin Rheumatol*. 2010;22(5):585–589.
111. Matthews JG, Parks TG. Ischaemic colitis in the experimental animal. I. Comparison of the effects of acute and subacute vascular occlusion. *Gut*. 1976;17(9):671–676.
112. Hernanz-Schulman M. CT as an outcome surrogate in patients with cystic fibrosis: does the effort justify the risks? *Radiology*. 2012;262(3):746–749.
113. Fraquelli M, Baccarin A, Corti F, et al. Bowel ultrasound imaging in patients with cystic fibrosis: Relationship with clinical symptoms and CFTR genotype. *Dig Liver Dis*. 2016;48(3):271–276.
114. Chaudry G, Navarro OM, Levine DS. Oudjhane K. Abdominal manifestations of cystic fibrosis in children. *Pediatr Radiol*. 2006;36(3):233–240.
115. Agrons GA, Corse WR, Markowitz RI, et al. Gastrointestinal manifestations of cystic fibrosis: radiologic-pathologic correlation. *Radiographics*. 1996;16(4):871–893.
116. Lardenoye SW, Puylaert JB, Smit MJ, et al. Appendix in children with cystic fibrosis: US features. *Radiology*. 2004;232(1):187–189.
117. Fields TM, Michel SJ, Butler CL, et al. Abdominal manifestations of cystic fibrosis in older children and adults. *AJR Am J Roentgenol*. 2006;187(5):1199–1203.
118. Flaum V, Schneider A, Gomes Ferreira C, et al. Twenty years' experience for reduction of ileocolic intussusceptions by saline enema under sonography control. *J Pediatr Surg*. 2016;51(1):179–182.
119. Ammoury RF, Croffie JM. Malabsorptive disorders of childhood. *Pediatr Rev*. 2010;31(10):407–415, quiz 415-406.
120. Fenollar F, Puechal X, Raoult D. Whipple's disease. *N Engl J Med*. 2007;356(1):55–66.
121. Fenollar F, Minodier P, Boutin A, et al. Tropheryma whipplei associated with diarrhoea in young children. *Clin Microbiol Infect*. 2016;22(10):869–874.
122. Fenollar F, Lagier JC, Raoult D. Tropheryma whipplei and Whipple's disease. *J Infect*. 2014;69(2):103–112.
123. Braamskamp MJ, Dolman KM, Tabbers MM. Clinical practice. Protein-losing enteropathy in children. *Eur J Pediatr*. 2010;169(10):1179–1185.
124. Khanna G, Bhalla S, Krishnamurthy R, et al. Extracardiac complications of the Fontan circuit. *Pediatr Radiol*. 2012;42(2):233–241.
125. Umar SB, DiBaise JK. Protein-losing enteropathy: case illustrations and clinical review. *Am J Gastroenterol*. 2010;105(1):43–49, quiz 50.
126. Khalesi M, Nakhaei AA, Seyed AJ, et al. Diagnostic accuracy of nuclear medicine imaging in protein losing enteropathy : systematic review and meta-analysis of the literature. *Acta Gastroenterol Belg*. 2013;76(4):413–422.
127. Chiu NT, Lee BF, Hwang SJ, et al. Protein-losing enteropathy: diagnosis with (99m)Tc-labeled human serum albumin scintigraphy. *Radiology*. 2001;219(1):86–90.
128. Gale HI, Gee MS, Westra SJ. Nimkin K. Abdominal ultrasonography of the pediatric gastrointestinal tract. *World J Radiol*. 2016;8(7):656–667.
129. Shannahan S, Leffler DA. Diagnosis and updates in celiac disease. *Gastrointest Endosc Clin N Am*. 2017;27(1):79–92.
130. Bastlein C, Burlefinger R, Holzberg E, et al. Ottenjann R. Common variable immunodeficiency syndrome and nodular lymphoid hyperplasia in the small intestine. *Endoscopy*. 1988;20(5):272–275.
131. Stevens RL, Jones B, Fishman EK. The CT halo sign: a new finding in intestinal lymphangiectasia. *J Comput Assist Tomogr*. 1997;21(6):1005–1007.
132. Kavaliauskiene G, Ziech ML, Nio CY, et al. Small bowel MRI in adult patients: not just Crohn's disease—a tutorial. *Insights Imaging*. 2011;2(5):501–513.
133. Krishnamurthy R, Hernandez A, Kavuk S, et al. Imaging the central conducting lymphatics: initial experience with dynamic MR lymphangiography. *Radiology*. 2015;274(3):871–878.
134. Hill GR, Ferrara JL. The primacy of the gastrointestinal tract as a target organ of acute graft-versus-host disease: rationale for the use of cytokine shields in allogeneic bone marrow transplantation. *Blood*. 2000;95(9):2754–2759.
135. Jacobsohn DA. Acute graft-versus-host disease in children. *Bone Marrow Transplant*. 2008;41(2):215–221.
136. Billingham RE. The biology of graft-versus-host reactions. *Harvey Lect*. 1966;62:21–78.
137. Ferrara JL, Deeg HJ. Graft-versus-host disease. *N Engl J Med*. 1991;324(10):667–674.
138. Jones B, Wall SD. Gastrointestinal disease in the immunocompromised host. *Radiol Clin North Am*. 1992;30(3):555–577.
139. Boluda ER. Pediatric small bowel transplantation. *Curr Opin Organ Transplant*. 2015;20(5):550–556.
140. Servaes S. Intestinal graft-versus-host disease. *Pediatr Radiol*. 2010;40(suppl 1):S101.
141. Gorg C, Wollenberg B, Beyer J, et al. High-resolution ultrasonography in gastrointestinal graft-versus-host disease. *Ann Hematol*. 2005;84(1):33–39.
142. Calabrese E, Zorzi F, Visconti E, et al. Bowel ultrasonography as an aid for diagnosis of intestinal acute graft-versus-host-disease after allogeneic haematopoietic stem cell transplantation. *Dig Liver Dis*. 2013;45(11):899–904.
143. Klein SA, Martin H, Schreiber-Dietrich D, et al. A new approach to evaluating intestinal acute graft-versus-host disease by transabdominal sonography and colour Doppler imaging. *Br J Haematol*. 2001;115(4):929–934.
144. Donnelly LF, Morris CL. Acute graft-versus-host disease in children: abdominal CT findings. *Radiology*. 1996;199(1):265–268.
145. Kalantari BN, Mortele KJ, Cantisani V, et al. CT features with pathologic correlation of acute gastrointestinal graft-versus-host disease after bone marrow transplantation in adults. *AJR Am J Roentgenol*. 2003;181(6):1621–1625.
146. McCarthy HJ, Tizard EJ. Clinical practice: Diagnosis and management of Henoch-Schonlein purpura. *Eur J Pediatr*. 2010;169(6):643–650.
147. Waller R, Ahmed A, Patel I, et al. Update on the classification of vasculitis. *Best Pract Res Clin Rheumatol*. 2013;27(1):3–17.
148. Soliman M, Laxer R, Manson D, et al. Imaging of systemic vasculitis in childhood. *Pediatr Radiol*. 2015;45(8):1110–1125.
149. Johnson EF, Lehman JS, Wetter DA, et al. Henoch-Schonlein purpura and systemic disease in children: retrospective study of clinical findings, histopathology and direct immunofluorescence in 34 paediatric patients. *Br J Dermatol*. 2015;172(5):1358–1363.
150. Strouse PJ, DiPietro MA, Saez F. Transient small-bowel intussusception in children on CT. *Pediatr Radiol*. 2003;33(5):316–320.
151. Kim JH. US features of transient small bowel intussusception in pediatric patients. *Korean J Radiol*. 2004;5(3):178–184.
152. Kornecki A, Daneman A, Navarro O, et al. Spontaneous reduction of intussusception: clinical spectrum, management and outcome. *Pediatr Radiol*. 2000;30(1):58–63.
153. Navarro O, Daneman A. Intussusception. Part 3: Diagnosis and management of those with an identifiable or predisposing cause and those that reduce spontaneously. *Pediatr Radiol*. 2004;34(4):305–312, quiz 369.
154. Lioubashevsky N, Hiller N, Rozovsky K, et al. Ileocolic versus small-bowel intussusception in children: can US enable reliable differentiation? *Radiology*. 2013;269(1):266–271.
155. Jelsig AM. Hamartomatous polyps - a clinical and molecular genetic study. *Dan Med J*. 2016;63(8).
156. Kopacova M, Tacheci I, Rejchrt S, et al. Peutz-Jeghers syndrome: diagnostic and therapeutic approach. *World J Gastroenterol*. 2009;15(43):5397–5408.
157. van Lier MG, Mathus-Vliegen EM, Wagner A, et al. High cumulative risk of intussusception in patients with Peutz-Jeghers syndrome: time to update surveillance guidelines? *Am J Gastroenterol*. 2011;106(5):940–945.
158. Hearle N, Schumacher V, Menko FH, et al. Frequency and spectrum of cancers in the Peutz-Jeghers syndrome. *Clin Cancer Res*. 2006;12(10):3209–3215.

159. Tomas C, Soyer P, Dohan A, et al. Update on imaging of Peutz-Jeghers syndrome. *World J Gastroenterol*. 2014;20(31):10864–10875.
160. Beggs AD, Latchford AR, Vasen HF, et al. Peutz-Jeghers syndrome: a systematic review and recommendations for management. *Gut*. 2010;59(7):975–986.
161. Goldstein SA, Hoffenberg EJ. Peutz-Jegher syndrome in childhood: need for updated recommendations? *J Pediatr Gastroenterol Nutr*. 2013;56(2):191–195.
162. Zhuge Y, Cheung MC, Yang R, et al. Pediatric intestinal foregut and small bowel solid tumors: a review of 105 cases. *J Surg Res*. 2009;156(1):95–102.
163. Levy AD, Abbott RM, Rohrmann CA Jr, et al. Gastrointestinal hemangiomas: imaging findings with pathologic correlation in pediatric and adult patients. *AJR Am J Roentgenol*. 2001;177(5):1073–1081.
164. Levy AD, Patel N, Dow N, et al. From the archives of the AFIP: abdominal neoplasms in patients with neurofibromatosis type 1: radiologic-pathologic correlation. *Radiographics*. 2005;25(2):455–480.
165. Kok KY. Telisinghe PU. Lipoblastoma: clinical features, treatment, and outcome. *World J Surg*. 2010;34(7):1517–1522.
166. Kucera A, Snajdauf J, Vyhnanek M, et al. Lipoblastoma in children: an analysis of 5 cases. *Acta Chir Belg*. 2008;108(5):580–582.
167. Thompson WM. Imaging and findings of lipomas of the gastrointestinal tract. *AJR Am J Roentgenol*. 2005;184(4):1163–1171.
168. Rastogi R. Intra-abdominal manifestations of von Recklinghausen's neurofibromatosis. *Saudi J Gastroenterol*. 2008;14(2):80–82.
169. Nishida T, Goto O, Raut CP, et al. Diagnostic and treatment strategy for small gastrointestinal stromal tumors. *Cancer*. 2016;122(20):3110–3118.
170. Benesch M, Wardelmann E, Ferrari A, et al. Gastrointestinal stromal tumors (GIST) in children and adolescents: a comprehensive review of the current literature. *Pediatr Blood Cancer*. 2009;53(7):1171–1179.
171. Otto C, Agaimy A, Braun A, et al. Multifocal gastric gastrointestinal stromal tumors (GISTs) with lymph node metastases in children and young adults: a comparative clinical and histomorphological study of three cases including a new case of Carney triad. *Diagn Pathol*. 2011;6:52.
172. Janeway KA, Weldon CB. Pediatric gastrointestinal stromal tumor. *Semin Pediatr Surg*. 2012;21(1):31–43.
173. Nishida T, Blay JY, Hirota S, et al. The standard diagnosis, treatment, and follow-up of gastrointestinal stromal tumors based on guidelines. *Gastric Cancer*. 2016;19(1):3–14.
174. Nishida T, Tsujimoto M, Takahashi T, et al. Gastrointestinal stromal tumors in Japanese patients with neurofibromatosis type I. *J Gastroenterol*. 2016;51(6):571–578.
175. Falcone M. Pediatric Gastrointestinal Tumors. *J Diagn Med Sonogr*. 2012;28(3):4.
176. Levy AD, Remotti HE, Thompson WM, et al. Gastrointestinal stromal tumors: radiologic features with pathologic correlation. *Radiographics*. 2003;23(2):283–304, 456; quiz 532.
177. Biko DM, Anupindi SA, Hernandez A, et al. Childhood Burkitt lymphoma: abdominal and pelvic imaging findings. *AJR Am J Roentgenol*. 2009;192(5):1304–1315.
178. Kamona AA, El-Khatib MA, Swaidan MY, et al. Pediatric Burkitt's lymphoma: CT findings. *Abdom Imaging*. 2007;32(3):381–386.
179. Abramson SJ, Price AP. Imaging of pediatric lymphomas. *Radiol Clin North Am*. 2008;46(2):313–338, ix.
180. Borhani AA, Hosseinzadeh K, Almusa O, et al. Imaging of post-transplantation lymphoproliferative disorder after solid organ transplantation. *Radiographics*. 2009;29(4):981–1000, discussion 1000-1002.
181. Kassira N, Pedroso FE, Cheung MC, et al. Primary gastrointestinal tract lymphoma in the pediatric patient: review of 265 patients from the SEER registry. *J Pediatr Surg*. 2011;46(10):1956–1964.
182. Grajo JR, Kayton ML, Steffensen TS, et al. Presentation of ileal Burkitt lymphoma in children. *J Radiol Case Rep*. 2012;6(8): 27–38.
183. Karantanis D, Durski JM, Lowe VJ, et al. 18F-FDG PET and PET/CT in Burkitt's lymphoma. *Eur J Radiol*. 2010;75(1):e68–e73.
184. Yustein JT, Dang CV. Biology and treatment of Burkitt's lymphoma. *Curr Opin Hematol*. 2007;14(4):375–381.
185. Salazar R, Wiedenmann B, Rindi G, et al. ENETS 2011 Consensus Guidelines for the Management of Patients with Digestive Neuroendocrine Tumors: an update. *Neuroendocrinology*. 2012;95(2): 71–73.
186. Niederle B, Pape UF, Costa F, et al. ENETS Consensus Guidelines Update for Neuroendocrine Neoplasms of the Jejunum and Ileum. *Neuroendocrinology*. 2016;103(2):125–138.
187. Henderson L, Fehily C, Folaranmi S, et al. Management and outcome of neuroendocrine tumours of the appendix-a two centre UK experience. *J Pediatr Surg*. 2014;49(10):1513–1517.
188. Spunt SL, Pratt CB, Rao BN, et al. Childhood carcinoid tumors: the St Jude Children's Research Hospital experience. *J Pediatr Surg*. 2000;35(9):1282–1286.
189. Scarsbrook AF, Ganeshan A, Statham J, et al. Anatomic and functional imaging of metastatic carcinoid tumors. *Radiographics*. 2007;27(2):455–477.
190. Pavel M, O'Toole D, Costa F, et al. ENETS Consensus Guidelines Update for the Management of Distant Metastatic Disease of Intestinal, Pancreatic, Bronchial Neuroendocrine Neoplasms (NEN) and NEN of Unknown Primary Site. *Neuroendocrinology*. 2016;103(2): 172–185.
191. Virgone C, Cecchetto G, Alaggio R, et al. Appendiceal neuroendocrine tumours in childhood: Italian TREP project. *J Pediatr Gastroenterol Nutr*. 2014;58(3):333–338.
192. Amr B, Froghi F, Edmond M, et al. Management and outcomes of appendicular neuroendocrine tumours: retrospective review with 5-year follow-up. *Eur J Surg Oncol*. 2015;41(9):1243–1246.

# 105

# Congenital and Neonatal Disorders

Marta Hernanz-Schulman

## OVERVIEW

Congenital and neonatal abnormalities of the colon can be divided into those that present in the neonatal period, such as colonic atresia and stenosis, imperforate anus, and functional colonic abnormalities, such as small left colon syndrome and meconium plug. Entities such as Hirschsprung disease, anorectal stenosis, duplication cysts, and chronic intestinal pseudoobstruction (CIPO) are congenital abnormalities that can or even typically present later in life, while acquired entities, such as necrotizing enterocolitis, routinely affect the newborn, particularly the premature.

## COLONIC ATRESIA AND STENOSIS

***Overview.*** The colon is the least involved segment in intestinal atresias, with colonic atresia comprising between 1.8% and 15% of intestinal atresias, with an overall incidence of 1 in 1498 to 1 in 66,000 births.[1] The anatomic descriptive classification of intestinal atresias (as described in Chapter 102, Fig. 102.28) is applied to colonic atresias: type I membranous; type II blind ends separated by fibrous cord; type III mesenteric defect; and type IV multiple atresias.[2,3] Atresia involves the right colon in approximately half the cases, particularly type III lesions.[1]

Colonic atresia is associated with other colonic abnormalities, as well as extracolonic and extraintestinal comorbidities in as many as 47% of cases.[1] Approximately 22% of patients may have Hirschsprung disease or hypoganglionosis[4–6]; other associations include malrotation, abdominal wall defect, and other atresias.[1] Extraintestinal anomalies include the musculoskeletal system, heart, abdominal wall, eyes, and central nervous system (CNS).[6,7]

Congenital colonic stenosis is very rare, with less than 20 cases reported in the literature, typically consisting of stricture-like stenosis, although membranous stenosis has also been reported. Most cases of colonic stenosis in infants are acquired, particularly as sequela of conditions such as necrotizing enterocolitis.[8,9]

***Etiology.*** Similar to small bowel atresias, colonic atresias are thought to result from an ischemic event in utero leading to resorption of the involved bowel and discontinuity of the proximal and distal segments.[10] More recently, mutations in fibroblast growth factor 10 (FGF10) or its receptor have resulted in intestinal atresia in mice, even in the absence of vascular insult, suggesting that this genetic determinant may also play a role in the intrauterine development of intestinal atresias.[11,12] Most isolated cases are sporadic, but syndromic cases share a genetic basis. Hereditary multiple intestinal atresias, which include immune deficiencies and carries a very high mortality, is believed to be an autosomal recessive lesion, with mutations in the *TTC7A* gene.[13]

***Clinical Presentation.*** Polyhydramnios is uncommon, because the atresia is sufficiently distal to allow resorption of swallowed amniotic fluid. Infants with colonic atresia present with abdominal distension, vomiting, and failure to pass meconium. Because the obstruction is distal, the onset of vomiting may be delayed in comparison to more proximal atresias.[7,14]

***Imaging.*** Abdominal radiographs in patients with colonic atresia often show that the proximal colon is dilated far more than the other loops of bowel (Figs. 105.1A and B), and air-fluid levels and absence of gas in the rectum will be seen on prone cross-table lateral views (Fig. 105.1C). The disproportionate dilatation of the proximal colon is due to competence of the ileocecal valve, which allows intestinal contents forward into the atretic proximal colonic segment but does not allow decompression proximally. This finding is characteristic and highly suggestive of the diagnosis on plain films, although not always present. Contrast enema demonstrates a blind-ending microcolon, devoid of the filling defects that characterize meconium ileus (Fig. 105.1D).

***Treatment.*** Surgery is required. Because 15% to 20% of patients with colonic atresia will also have proximal intestinal atresia, the proximal bowel should be evaluated. Hirschsprung disease should be excluded before reestablishing intestinal continuity, and existing extraintestinal anomalies should be identified.[6,7] The size discrepancy between the markedly dilated proximal segment and the distal microcolon may necessitate resection of the dilated proximal segment.[15]

## ANORECTAL MALFORMATIONS

***Overview.*** Anorectal malformations (ARM) encompass the spectrum of anal atresia and stenosis, with an incidence estimated at approximately 1:5000 live births worldwide. Approximately one-third of patients have isolated lesions, whereas two-thirds are affected by other abnormalities in multiple organ systems as well as other portions of the gastrointestinal (GI) tract.[16] Approximately 95% of the patients have a fistula to the urethra (males), vagina (females), or the perineum; however, among patients with Down syndrome and ARM, approximately 95% have no fistula.[17]

ARM lesions were classified in 1953 by Gross as high and low, with respect to position of the atresia above or below the levator mechanism.[18,19] Two decades later, the concept of intermediate or translevator lesions was introduced to denote the more continuous spectrum of these lesions (Fig. 105.2). More recently Levitt and Peña have introduced a gender-inclusive classification that has prognostic implications as well as implications regarding optimal surgical management and outcome.[20] Under this framework, females with high lesions (high rectovaginal fistula) who later present with a persistent/unrepaired urogenital sinus abnormality represent girls with persistent cloaca, initially confused with high anal atresia; these are classified by the length of the persistent cloacal canal (Table 105.1).[20]

Rectal atresia and stenosis are discussed among the ARM lesions, although such patients have a normal anal canal and external physical findings. These lesions constitute approximately 1% of ARM lesions. In patients with rectal atresia, the rectum is atretic 1 to 2 cm above the anus.[20–22]

***Etiology.*** Anorectal atresia with rectourethral or rectovaginal fistulas may be the result of failure of the urorectal septum to descend to the cloacal membrane and the eventual site of the perineal body; if the cloaca is too small, the hindgut may then terminate anteriorly, entering either the urethra in the male or the vagina in the female. Rectoanal atresias are thought to be related to vascular accidents similar to those that occur in atresias of the small bowel and colon; imperforate anus is due to failure of breakdown of the anal membrane.[23]

## Abstract:

This chapter discusses congenital anomalies of the colon, and acquired abnormalities characteristic of the neonatal period.

Colonic atresia and stenosis are reviewed, including associations such as the Currarino syndrome. Anorectal malformations are discussed with respect to the level of termination, characteristics in males and females, and associated anomalies. Hirschsprung disease, its differential presentation in neonates and older patients, and diagnostic criteria, as well as complications such as Hirschsprung colitis are discussed.

Obstructive colonic lesions involving colonic dysmaturity and their relationship to Hirschsprung are also addressed, in conjunction with rarer entities such as the Berdon syndrome. The various types of colonic and rectal duplication cysts are discussed. Necrotizing enterocolitis, diagnosis, severity and Bell Criteria are also reviewed.

## Keywords:

Colon atresia
colon stenosis
congenital anomalies of colon
Currarino syndrome
Hirschsprung disease
Hirschsprung enterocolitis
Berdon syndrome
megacystis-microcolon-intestinal hypoperistalsis syndrome
chronic intestinal pseudoobstruction (CIPO)
colonic duplications
necrotizing enterocolitis (NEC)

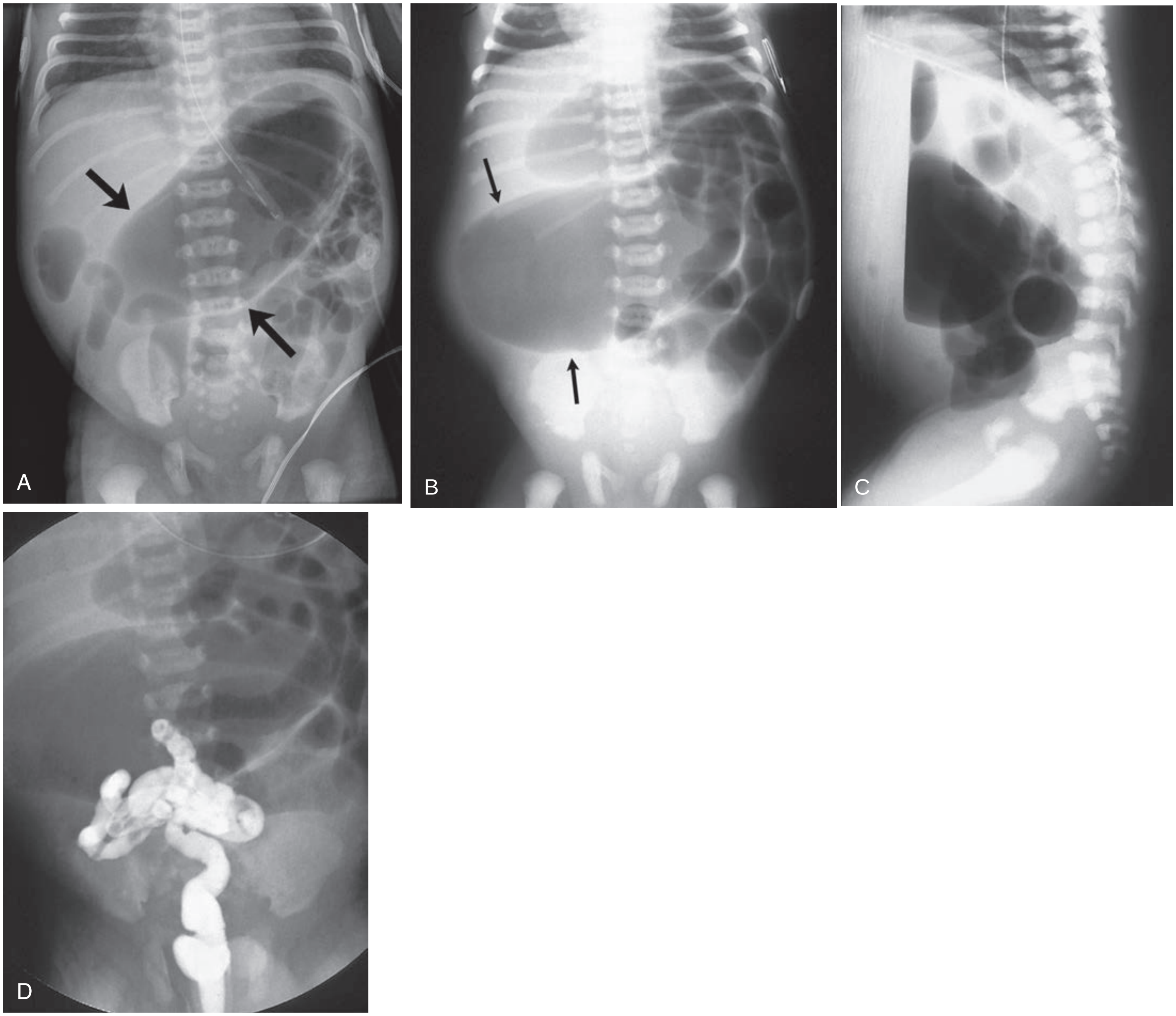

**Figure 105.1. Colonic atresia.** (A) Supine abdominal radiograph of neonate shows a markedly dilated proximal colonic segment *(arrows)* that could be mistaken for the stomach and also shows the relatively mild distension of the distal small bowel loops, despite the complete obstruction. Atresia of the ascending colon was found at surgery. (B) Supine abdominal radiograph of another infant with abdominal distension and bilious vomiting demonstrates protuberance of the flanks and elevation of the diaphragm. There are gas-filled dilated loops of bowel, but one loop is dilated far more than other loops; this represents the atretic proximal colonic segment *(arrows)*. Orogastric tube decompresses the stomach. (C) Prone cross-table lateral radiograph in same patient as shown in B. The large air-fluid level is located within the atretic proximal colonic segment. There is no gas in the rectum. (D) Contrast enema in same infant as shown in B and C shows a microcolon terminating blindly at the atretic segment.

No single genetic abnormality has been identified in association with ARM, but a genetic susceptibility is considered likely in many cases due to the increased risk in affected families, knock-out mice models, and the association of ARM with conditions that are part of chromosomal anomalies[24]; the most common chromosomal abnormalities are trisomy 21 and a microdeletion at chromosome 22q11.2, although abnormalities have been identified in multiple chromosomes.[16] Approximately 15% of patients with rectovestibular or rectoperineal fistulas indicative of low lesions have a positive family history for ARM. Genetic studies in both animals and humans have implicated defects in the sonic hedgehog, *Wnt5a*, and *Skt* genes. These studies suggest that the pathogenetic mechanisms of high and low fistulas differ and that it may be a genetic mutation, rather than obstruction, that leads to fistula formation in some cases.[16,24]

***Clinical Manifestations.*** Patients with ARM are clinically apparent by physical examination at birth, with the exception of patients with rectal atresia or stenosis, who are externally normal. The physical examination may reveal a perineal or vestibular fistula, although in both genders this is best evaluated after 24 hours, as

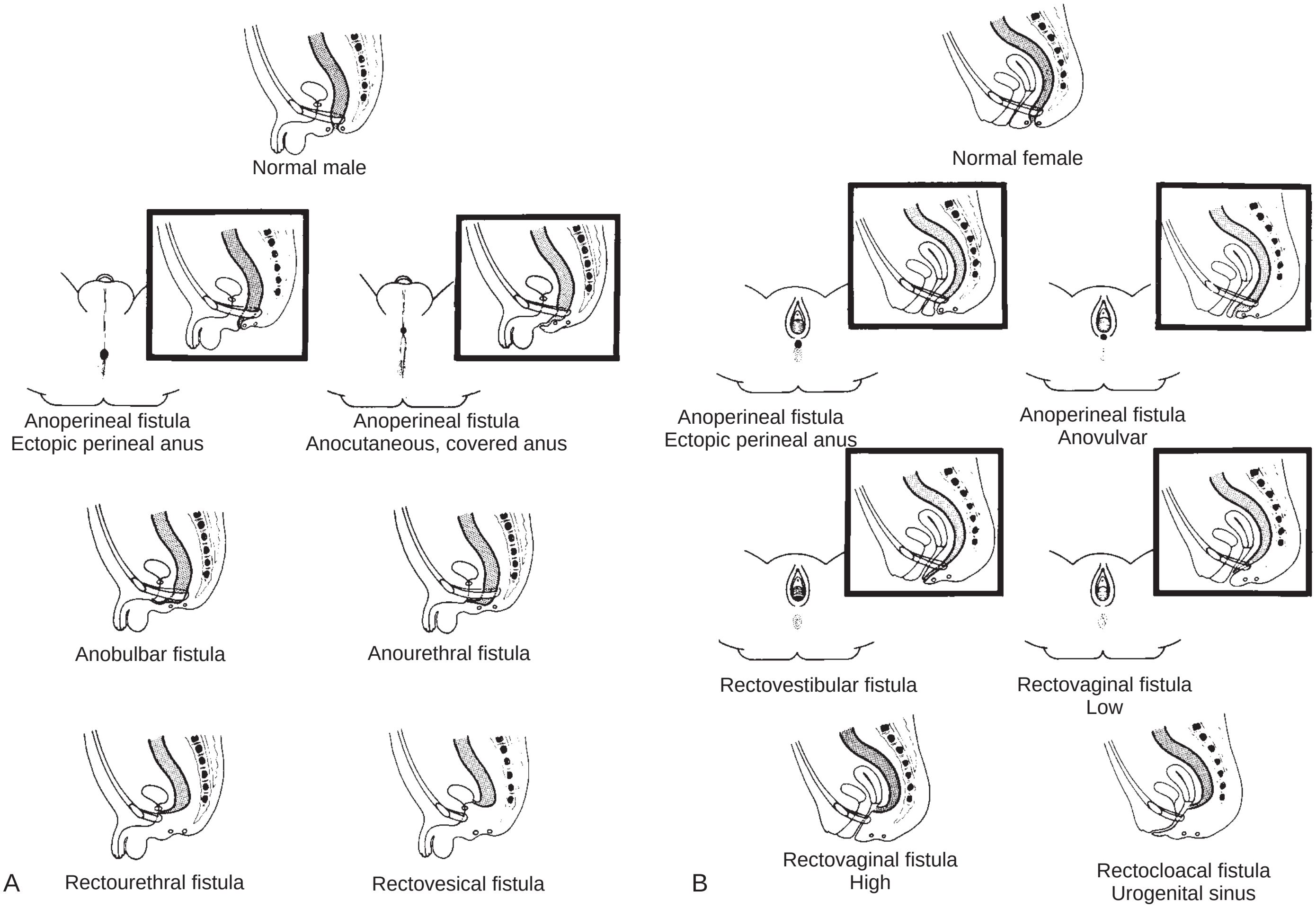

**Figure 105.2. Physical examination findings in boys and girls with anorectal malformations.** (A) Schematic diagram of normal and ectopic termination of the hindgut in the male. (B) Schematic diagram of normal termination and common sites of ectopic termination of the hindgut in the female. *(From Santulli TV. In: Mustard WT, et al, eds.* Pediatric Surgery. *2nd ed. St. Louis: Mosby–Year Book; 1969, with permission.)*

**TABLE 105.1** Classification of Anorectal Malformations

| Males | Females |
|---|---|
| Perineal fistula | Perineal fistula |
| Rectourethral fistula | Vestibular fistula |
| Bulbar | Persistent cloaca |
| Prostatic | ≤3 cm common channel |
| Rectobladder neck fistula | >3 cm common channel |
| Imperforate anus without fistula | Imperforate anus without fistula |
| Rectal atresia | Rectal atresia |
| Complex defects | Complex defects |

*From Levitt M, Peña A. Anorectal malformations. In: Coran A, et al, eds.* Pediatric Surgery, *Philadelphia: CV Mosby, an Imprint of Elsevier; 2012.*

meconium may not appear in the perineum before this time.[20] The presence of a rectourethral fistula may be revealed by identification of fecal material in the urine. Patients who demonstrate a “flat bottom” (i.e., the buttock crease is not visible) have poor development of pelvic musculature, which typically implies a more guarded prognosis.[17] Girls with a single perineal orifice have a cloacal malformation.[20]

Other congenital anomalies are seen in greater than 50% of patients with ARM.[24] The best known group of anomalies associated with ARM is the VACTERL association, which includes *v*ertebral anomalies, *a*nal atresia, *c*ardiac abnormalities, esophageal atresia with or without *te* fistula, *r*enal and *l*imb abnormalities. Esophageal atresia complex is seen in approximately 10% of patients, and abnormalities affecting the duodenum, such as atresia or malrotation, are seen in 1% to 2%. Vertebral anomalies occur in approximately one-third of patients (Figs. 105.3A and B), and their severity may be correlated with the complexity of the anorectal lesion. Coronal clefts in particular are often seen in patients with imperforate anus and have been reported as being nine times more common in boys than in girls.[25] Genetic syndromes include trisomy 21, trisomy 8, and fragile X syndrome.[16] Cardiovascular abnormalities are seen in about one-third of patients and most commonly consist of atrial septal defect and persistent ductus arteriosus, followed by tetralogy of Fallot and ventricular septal defect.[17] Hirschsprung disease is rare, being seen in only 3 out of 2100 patients.[26] Genitourinary anomalies are common, presenting in one-third to one-half of cases, again correlated with increasing complexity of the defect. These range from reflux to renal dysplasia or agenesis, with cryptorchidism and hypospadias seen in male patients. Females may demonstrate Müllerian abnormalities, including duplications and obstructions, particularly in the setting of cloacal abnormalities.[17,20]

***Imaging.*** Patients with ARM undergo imaging to elucidate associated anomalies and to determine the fistulous anatomy. The

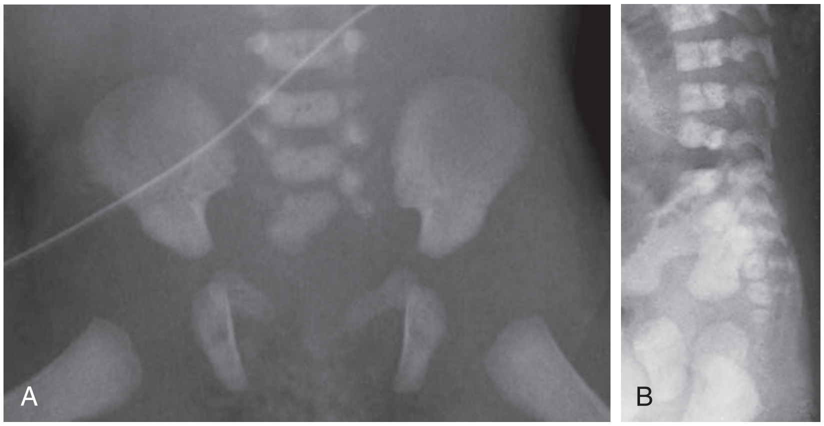

**Figure 105.3. Bony abnormalities in patients with anorectal malformations.** (A) Pelvic radiograph in a neonate shows an abnormal sacrum. (B) Lateral spine radiograph on another patient shows numerous lumbar coronal clefts.

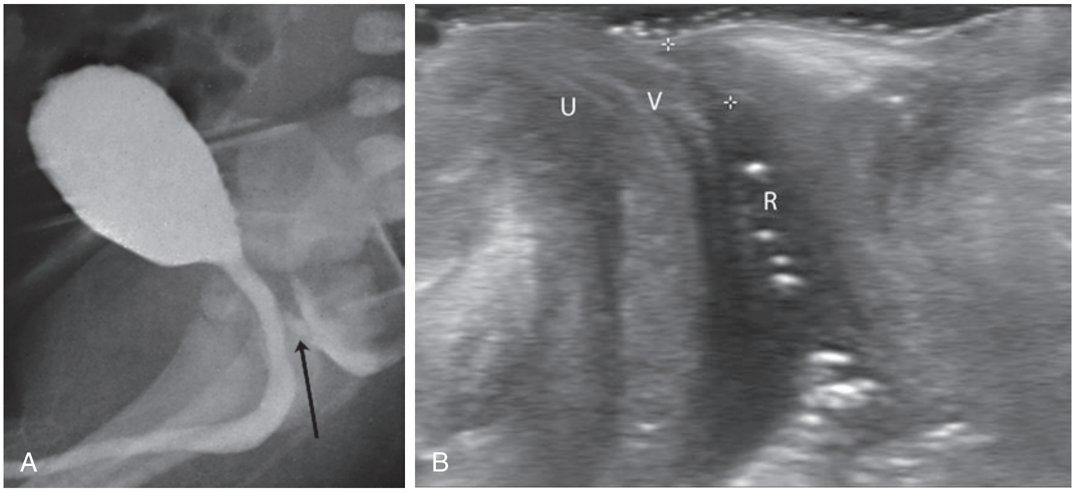

**Figure 105.4. Anorectal malformation: preoperative imaging.** (A) Voiding cystourethrogram in a male demonstrates a fistulous connection to the posterior urethra *(arrow)*. Note that the rectum bulges inferiorly below the level of the fistula. This could cause a spuriously short distance that might be seen on abdominal radiographs and transperineal sonography. (B) Sagittal transperineal ultrasound in a female infant shows the urethra *(U)*, vagina *(V)*, and rectum *(R)*; the latter contains multiple tiny gas bubbles. Calipers delineate the distance to the perineum. No fistulas were identified at imaging or subsequent repair.

sacral ratio[17] quantifies the degree of sacral hypoplasia by measuring the distance between the iliac crests and the inferior border of the sacroiliac joints (A–B) and the distance between the inferior border of the sacroiliac joints and the tip of the sacrum (B–C); the BC/CD ratio should be greater than 0.4. Increase in the ratio to approach 1.0 indicates better sacral development and better potential prognosis.

Imaging of these infants usually includes cardiac evaluation, radiographs of the spine, ultrasound of the kidneys and of the spinal canal, as well as ultrasound of the pelvis in girls, particularly those with cloacal anomaly, as uterine anomalies often exist. Perineal scanning is an important supplement to the imaging of these patients.[27]

In patients who do not have a perineal fistula, several imaging methods have been used for evaluation of the distal anatomy. One of the earliest methods, still in use by some,[17] is the lateral invertogram, or more recently the prone cross-table lateral view of the rectum, which relies on visualizing the gas-filled rectum and relating its termination to pelvic bony landmarks, particularly extension below the coccyx, which would classify it as part of a low lesion. However, problems such as meconium distal to gas, and movement of the rectum with infant straining and crying (Fig. 105.4A), render this examination often inexact and problematic, and it has been abandoned by many. Some investigators advocate performing a voiding cystourethrogram (VCUG) during initial evaluation, as it may reveal the fistulous connection (see Fig. 105.4A).[28] This procedure is not always successful because voiding pressure at the urethra may be insufficient to overcome blockage of meconium in the fistula.

Ultrasound is also used to evaluate the distal position of the rectum (Fig. 105.4B). The meconium in the pouch allows easy visualization of the distal rectum; however, changes in apparent position with straining make it somewhat challenging; measurements of 10±4 mm correlate with a low lesion, whereas measurements of 24±6 mm correlate with intermediate and high lesions. Other authors use 15 mm as the differentiator of low verus intermediate and high lesions.[27,29,30] Transverse rather than sagittal transperineal scanning can identify the puborectalis musculature; the presence of this musculature correlated with low-type lesions, whereas its absence correlated with high-type lesions.[31]

In patients without a perineal fistula who are initially managed with colostomy, evaluation after colostomy can be done through a colostogram, considered by many to be one of the most important anatomic imaging studies, outlining the presence and location of the fistula, the bowel that will be used in the pull-through procedure, and the bony pelvic anatomy (e-Figs. 105.5A and B).[32] The examination is performed under fluoroscopic control, and once the distal rectal vault has reached a rounded appearance, the examination should be considered complete.[33]

Magnetic resonance imaging (MRI) has also been used to identify the internal anatomy. High field strengths, small field of view, and sequences without fat suppression increase the conspicuity of the muscles of the pelvic floor and help visualize the position of the distal rectal pouch with respect to the levator mechanism.[34] Instillation of gadolinium can facilitate delineation of the anatomy. Magnetic resonance (MR) can also delineate Müllerian anomalies associated with cloacal malformation in girls with ARM. Three-dimensional (3D) reformats offer additional global information for the surgeon (e-Figs. 105.5C and D). MR is superior to colostogram in its ability to delineate the musculature of the pelvic floor, the levator group including the pubococcygeus, puborectalis, and iliococcygeus muscles, as well as the external anal sphincter (EAS).[29,35] This modality can also be used to evaluate the rectum and levator sling after definitive surgical repair (Figs. 105.6A and B).

Patients with rectal atresia who have normal-appearing external anal apparatus are imaged in the same manner as patients presenting with distal obstruction, by performing a contrast enema. The enema is diagnostic in that it demonstrates a very short distal rectum that terminates blindly (e-Fig. 105.7).

***Treatment.*** The treatment is surgical but varies with the level and complexity of the lesions. Most boys can be repaired with a posterior sagittal approach alone, although some with a high lesion will require an additional abdominal surgical component to mobilize a very high rectum. In girls, operative repair of the cloacal anomaly can be extremely challenging when there is a long channel.[32] Babies with rectal atresia typically undergo initial colostomy, with subsequent anastomotic repair of the atretic rectum with the anal canal.[20]

## CURRARINO ASSOCIATION

***Overview.*** This entity was initially described in 1981 as a triad of anorectal stenosis or other type of low anorectal malformation: anterior sacral defect such as scimitar, crescent or sickle deformity, and a presacral mass such as meningocele, teratoma, or enteric cyst.[36] Since that time, our understanding of this abnormality has undergone an evolution, with recognition of a much wider spectrum of phenotypic abnormalities and of an underlying genetic defect.

***Etiology.*** Currarino syndrome is an autosomal dominant disorder with variable penetrance; approximately 50% of the cases are sporadic. A mutation located at 7q36 encoding for the *HLXB9* (*MNX1*) gene that encodes for nuclear transcription factor HB9, which plays a role in the dorsoventral separation of the caudal embryo. Other genes related to the same differentiation pathway may be involved in cases that are negative for *HLXB9* mutations.[37–39] A phenotype has been described that includes abnormal facies and development, associated with a normal *MNX1* gene and a larger distal 7q deletion.[40]

***Clinical Presentation.*** Age at presentation is a spectrum that spans the fetal and adult age groups. A fetus may present with a presacral mass, a neonate with anal atresia, and an older child and adult with constipation, meningitis, or presacral malignancy. The spectrum of presacral masses includes teratoma, rectal duplication cyst, anterior meningocele, leiomyosarcoma, and ectopic nephroblastoma.[38,39,41–43]

Other features of the full spectrum of the syndrome include Hirschsprung disease, dysganglionosis, bladder motility abnormalities, vesicoureteral reflux, rib anomalies, urinary and gynecologic abnormalities, cord tethering, and intraspinal lipomas.[42,44]

***Imaging.*** Radiographs of the sacrum may reveal the typical scimitar-shaped sacral abnormality (Fig. 105.8A); however, other sacral defects, typically deletion abnormalities, may be present. In a minority of patients, the sacrum is normal.[39]

Patients with anorectal stenosis may have a rectoperineal fistula or an anteriorly placed anus, and present with constipation, sometimes in early adulthood. Contrast enema shows marked narrowing of distal rectum, with excessive stool proximally (Fig. 105.8B). If of sufficient size, the presacral mass will exert a visible mass effect upon the posterior wall of the distal rectum.

MRI demonstrates the presacral mass and images the spinal canal well (Fig. 105.8C). In young infants, the presacral mass is often visible sonographically (Fig. 105.8D).

***Treatment.*** Surgical treatment depends on the specific phenotypic manifestations, and each is treated accordingly, involving general surgeons, neurosurgeons, and oncologists.

## HIRSCHSPRUNG DISEASE

***Overview.*** This condition that bears his name was first recognized as a distinct entity by Hirschsprung, who in 1887 carefully described and published a detailed description of two infants who had died before 1 year of age.[46,47] Once uniformly

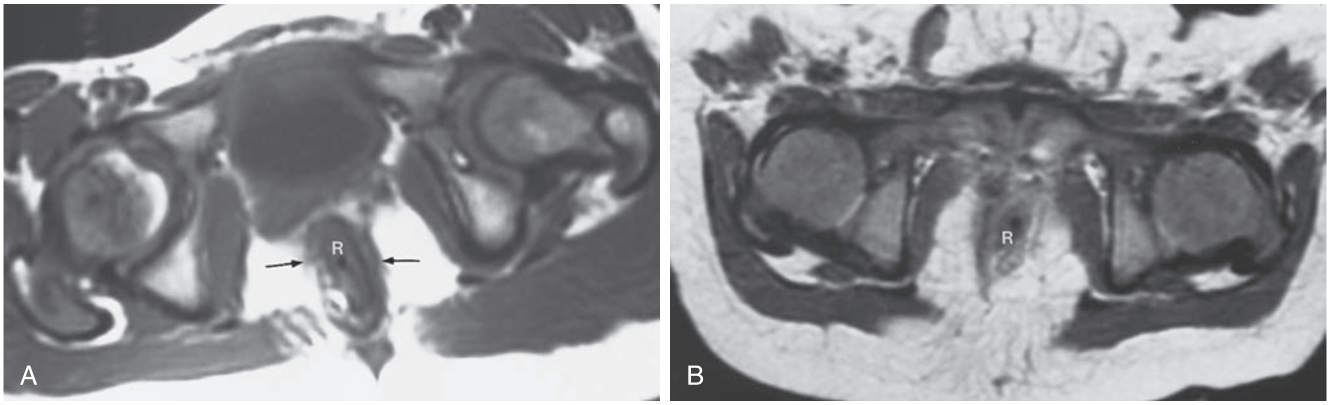

**Figure 105.6. Anorectal malformation after definitive repair.** (A) Axial T1-weighted MR image at the level of the pubic bone shows the rectum *(R)* contained within the puborectalis muscle *(arrows)*. (B) Axial T1-weighted MR image through the region of the pubic bone on another postoperative child shows that the rectum *(R)* is not enclosed by muscle on the left side. There is little puborectalis muscle on the left.

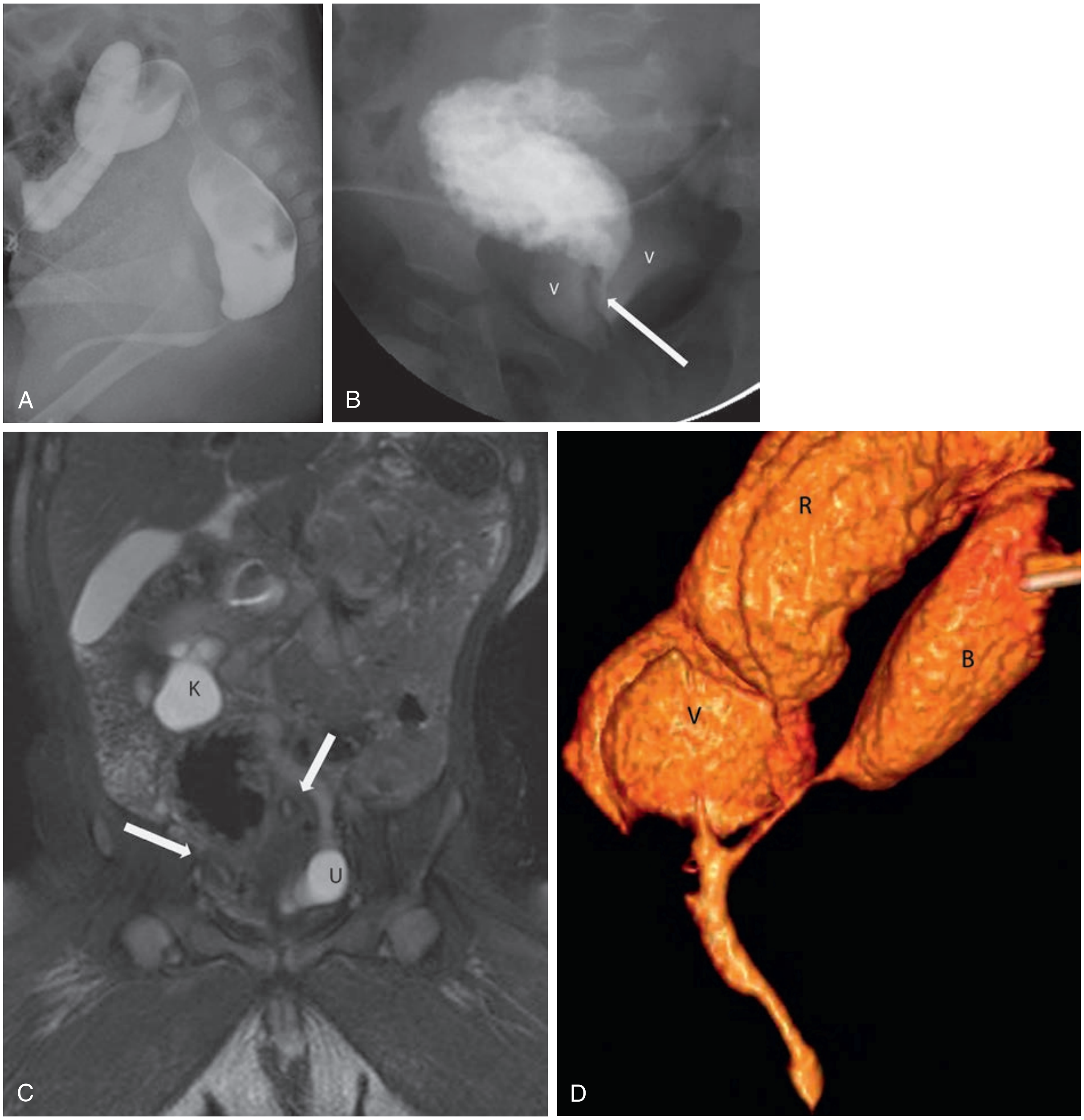

**e-Figure 105.5. Anorectal malformation (ARM).** (A) Colostogram in a male infant demonstrates a fistula from the atretic rectal segment to the posterior urethra. (B) Colostogram in a female infant with ARM, cloaca, and uterovaginal duplication. Contrast outlines the fistulous connection *(arrow)* between the atretic colonic segment and the left-sided vagina (*V*, Right and left vaginal canals). (C) Coronal T2-weighted MR image on same infant as shown in (B) shows the two uterine horns *(arrows)*. *K*, Partly visualized renal pelvis of a pancake kidney with dilated left ureter *(U)*. (D) Sagittal 3D reformat of ARM and cloacal anatomy in same patient as shown in (B) and (C). Vaginal canal and urethra unite into a common channel that terminates in a single orifice at the perineum. *B*, Bladder; *R*, atretic rectum; *V*, one of two superimposed vaginal canals, shown to communicate with vagina on other images and in (B).

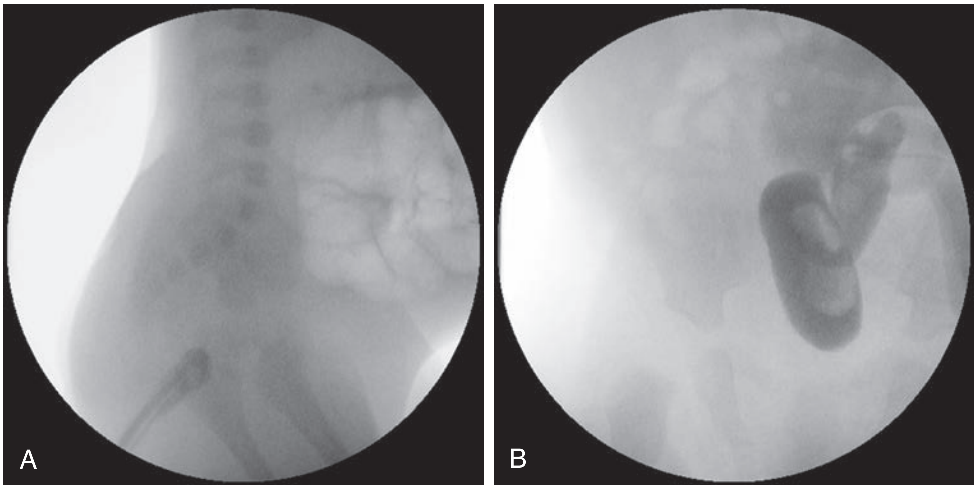

**e-Figure 105.7. Rectal atresia.** (A) Initial lateral image of attempted contrast enema in neonate with distal obstruction. Note the dilated loops of bowel and the lack of air in the rectum. The catheter and the contrast could not advance further than 2 cm. (B) Colostogram before definite repair shows the termination of the colon proximal to the atresia. Compare with the location of the catheter outlining the distal segment in (A).

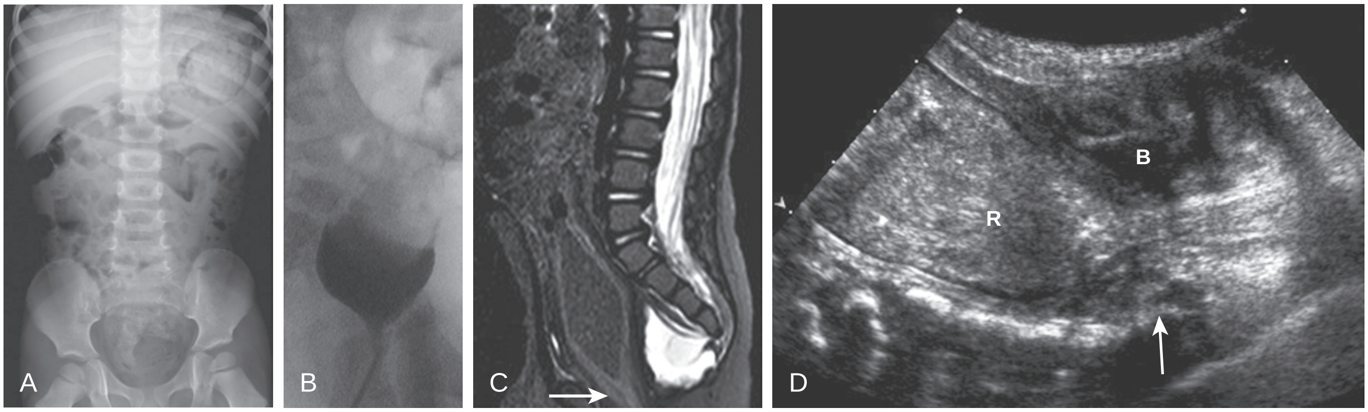

**Figure 105.8. Currarino syndrome.** (A) Supine abdominal radiograph in 23-month-old boy with history of constipation demonstrates increased amount of stool in the colon, and a bony deletion anomaly, resembling a scimitar, along the left side of the sacrum. (B) Contrast enema demonstrates narrowing of the distal rectum. (C) Sagittal T2-weighted MR image demonstrates a cystic presacral mass that proved to represent an anterior meningocele. Note the narrowing of the distal rectum *(arrow)*. (D) Anterior sagittal pelvic sonogram of a different male neonate shows a dilated proximal rectum *(R)* with distal narrowing, and a retrorectal hypoechoic mass *(arrow)*, which proved to represent a mature teratoma. *B*, Bladder.

lethal, Hirschsprung disease remains a serious condition with potential mortality and morbidity. It is a familiar condition to most pediatricians, occurring in approximately 1 per 5000 live births.[45] Hirschsprung disease is responsible for approximately 15% to 20% of cases of neonatal bowel obstruction, presenting in the newborn period in approximately 80% of cases. The transition point between normal and abnormal bowel can occur at any point and can extend through a variable length of the small bowel, to rarely include the entire bowel as total intestinal aganglionosis.[45] When the transition point is located at the rectosigmoid, it is termed *short-segment aganglionosis* and occurs in approximately 80% to 90% of cases. Males predominate in short-segment aganglionosis (4:1 boy:girl ratio); however, male preponderance diminishes in longer segment involvement.

Hirschsprung disease is the result of failure of propagation of normal innervation of the bowel, due to arrest of the proximal to distal migration of vagal neural crest cells, and is therefore considered a neurocristopathy. As a result of abnormal arrest of migration, a variable length of distal bowel lacks parasympathetic Auerbach (intermuscular) and Meissner (submucosal) plexuses, and is unable to participate in normal peristaltic propulsion of the colonic contents, resulting in failure of relaxation and functional obstruction. In addition to absence of ganglion cells, histologic evaluation of the abnormal bowel also shows abnormal acetylcholinesterase staining and hypertrophied nerve fibers (e-Fig. 105.9).

***Etiology.*** The etiology of the absence of ganglion cells from the involved segments in Hirschsprung disease is not known, but the migration is controlled by a hierarchical gene regulatory network.[51] One of the theories is that the migrating ganglion cells do not reach the distal segment because they are fewer in number, or mature prematurely; on the other hand, it is also possible that the ganglion cells reach the distal segment but perish or are unable to proliferate because of a deficient microenvironment.[52] A variety of gene mutations have been found, suggesting that this may be a multifactorial disease. The most commonly identified abnormality is in the *RET* proto-oncogene located at 10q11, found in approximately 15% to 35% of sporadic cases and 50% of familial cases. *EDNRB* located at 13q22 is identified in approximately 5% of cases.[53–55] A positive family history is encountered in a minority of patients (<10%), but this increases to nearly 25% in patients with total aganglionosis, with the degree of risk proportional to the length of the affected segment and degree of consanguinity.[56,57]

***Clinical Presentation.*** The clinical presentation of Hirschsprung disease in the neonate is one of distal obstruction, including abdominal distension and bilious vomiting, as well as failure to pass meconium beyond the first 24 hours, seen in up to 90% of patients.[52] Rarely perforation of the cecum or appendix can occur in neonates, typically those with long-segment disease.[58,59] In patients with total colonic aganglionosis, ganglion cells tend to be absent from the appendix as well.[60] In older children, Hirschsprung disease presents with constipation, with abdominal distension, vomiting, and failure to thrive in more severe cases. In late presentation, the zone of transition is typically low-segment, as longer segment disease usually presents early.[52] Among infants diagnosed with Hirschsprung disease, 6% to 19% have been premature; in these patients the presentation can be confusing due to comorbidities and overlap with findings of immature enteric nervous system.[61,62]

Hirschsprung disease is associated with multiple other conditions in up to 30% of cases.[63] It is most commonly associated with Down syndrome, which is present in approximately 2% to 10% of patients with Hirschsprung disease, in a 5:1 boy:girl ratio.[45] Other associated syndromes include Waardenburg syndrome (pigmentary anomalies and sensorineural hearing loss), Goldberg-Shprintzen syndrome (mental retardation, cleft palate, and Hirschsprung disease), McKusick-Kaufman syndrome (hydrometrocolpos, polydactyly, congenital heart disease), Bardet-Biedl syndrome (pigmentary retinopathy, obesity, hypogonadism), the Currarino association, and central hypoventilation syndrome (Ondine curse).[45,64,65] Patients with longer segment aganglionosis are more likely to demonstrate central hypoventilation syndrome than those with short-segment disease.[66] Other isolated abnormalities include malrotation, limb, skin, CNS, kidney, cardiac, and other malformations.[52,64,67,68]

Enterocolitis, also known as *Hirschsprung-associated enterocolitis*, is a major cause of morbidity and mortality in Hirschsprung disease, affecting approximately 10% to 50% of patients.[52,69] Clinically, it can present insidiously or abruptly, with diarrhea, fever, abdominal distension, colicky abdominal pain, and hematochezia, and may occur before or after surgery. If the child is not known to have Hirschsprung disease at the time of enterocolitis onset, the clinical situation can be confusing, as the expected clinical finding in patients with Hirschsprung is constipation rather than diarrhea. A Hirschsprung-associated enterocolitis score, which incorporates clinical, laboratory, and radiologic findings, may prove helpful in

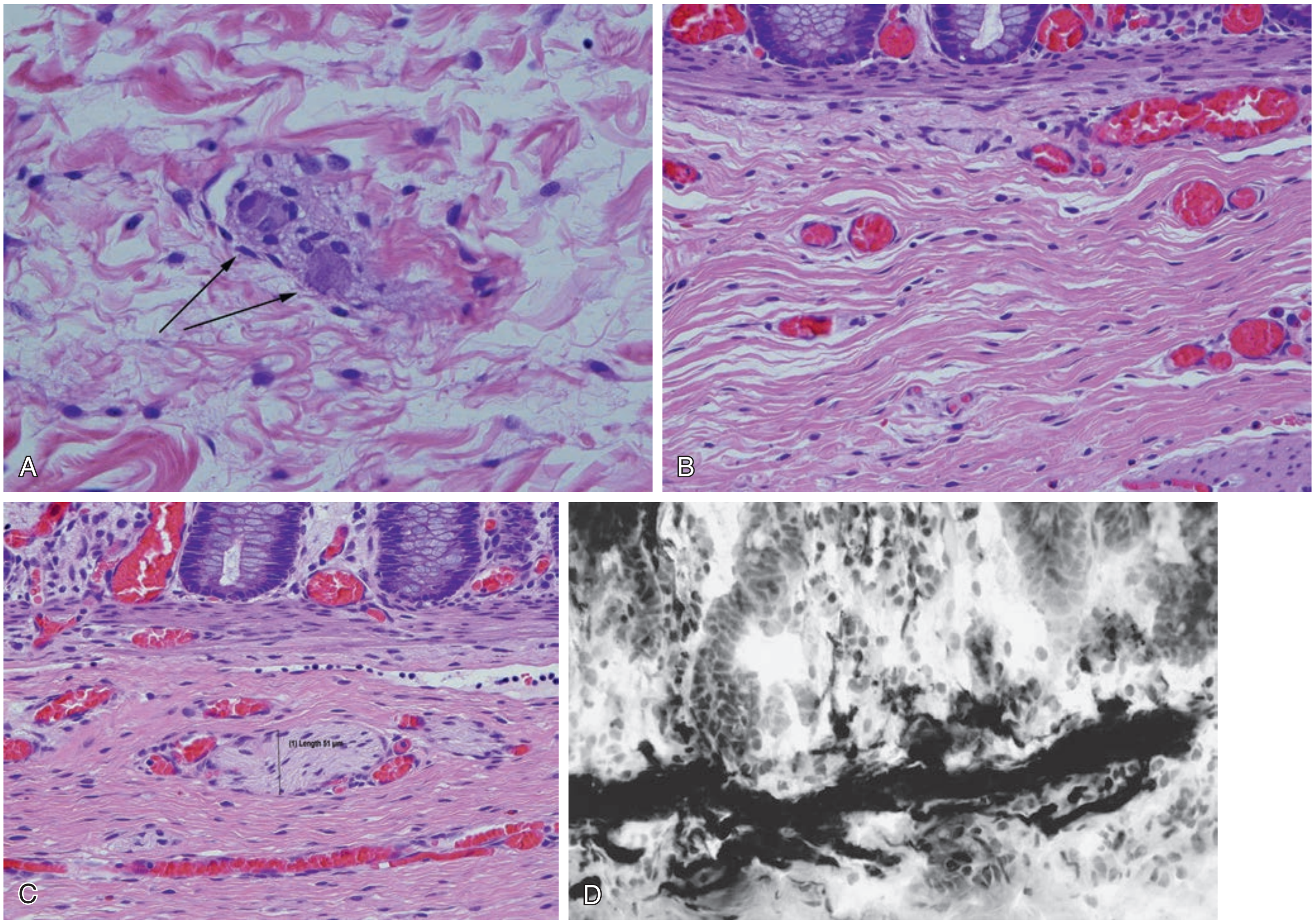

**e-Figure 105.9. Pathologic findings in Hirschsprung disease.** (A) Normal newborn hematoxylin and eosin staining reveals submucosal ganglion cells *(arrows)*. (B and C) Newborn with Hirschsprung disease. Biopsy shows no ganglion cells (B) and hypertrophic nerve (C) outlined by linear caliper measurement. (Courtesy Dr. Hernan Correa, Vanderbilt Children's Hospital of Nashville, TN.) (D) Newborn with Hirschsprung disease. Acetylcholinesterase stain of biopsy reveals abnormal stain of twiglike nerve processes in the lamina propria.

establishing the diagnosis and determining the severity of this condition.[70] Pathogenesis is unknown, but implicated mechanisms include abnormal epithelial lining, abnormal mucin production, abnormal local immune mechanisms, and viral and bacterial pathogens, notably *Clostridium difficile*, promoted by intestinal stasis. Studies in mice have implicated abnormal goblet cell differentiation and splenic lymphopenia.[71,72] Incidence of enterocolitis increases with delayed diagnosis, long-segment disease, and comorbid conditions, such as found in patients with Down syndrome.[69] Implicated postoperative risk factors include development of postoperative intestinal obstruction secondary to anastomotic stricture or adhesions, or development of anastomotic leak.[69]

***Imaging.*** In neonates, the abdominal radiographs demonstrate evidence of distal bowel obstruction (Fig. 105.10A). On prone cross-table lateral radiographs, there is usually gas in the rectum, unlike with small bowel or colonic atresias; however, the caliber of the air-filled rectum is clearly smaller than that of more proximal bowel, and a zone of transition may be identifiable if located at the rectosigmoid junction. In older patients, a retained rectal foreign body may provide an initial clue to the diagnosis (Fig. 105.10B).

Radiologic diagnosis is made with contrast enema, which is geared toward identification of the zone of transition (Figs. 105.10C–E). Routine enemas before the diagnostic procedure should be avoided. The study is done with a small catheter, which should be placed as close to the sphincter as possible in neonates. In neonates, water-soluble iso-osmolal agents are preferred, as hyperosmolal media will lead to increased bowel distension. Barium is not optimal if there is another cause of obstruction, such as meconium ileus, and undesirable in case of perforation. In older patients being evaluated for constipation, barium is the usual contrast agent. Initial images must be obtained in the lateral projection, as soon as the contrast begins to enter the colon, before any potential obliteration of the zone of transition has occurred. Multiple fluorostore images are used to document the flow of contrast and the caliber of the colon, as they offer a temporal documentation of the findings without additional radiation exposure. The enema is terminated when the zone of transition is identified.

The distal, aganglionic colon is typically normal in caliber, with a variably abrupt transition to dilated proximal colon. The aganglionic segment may exhibit a changing, serrated appearance, due to aperistaltic contractions of the abnormally innervated bowel. A rectosigmoid diameter ratio less than 0.9 will typically be present in patients with low-segment Hirschsprung disease. However, the rectosigmoid ratio is rarely needed to identify the zone of transition, and it can be misleading in cases of more extensive aganglionosis; it is only helpful when the zone of transition is located at the rectosigmoid junction and can be misleading if the zone of transition is located elsewhere. This is the opposite of patients with functional constipation, where there will be greater distension of the rectum, or of the rectum and sigmoid, in comparison with the more proximal colon. Postevacuation and delayed films are helpful in the neonate, particularly in patients with total colonic aganglionosis in whom the colon may have normal or nonspecific appearance.[73]

In older patients, retained stool may distend the aganglionic segment. However, a caliber difference may be maintained, and coupled with an appropriate index of suspicion, can lead to recognition of the diagnosis (Figs. 105.10F–H).

In patients with total colonic aganglionosis, the findings are variable and the diagnosis can be problematic; as with the older patient, an appropriately high index of suspicion is needed. The colon in these infants may present a normal or near-normal appearance with normal and uniform caliber. Although often relatively featureless, there can be a pseudotransition zone, sometimes at the splenic flexure, or the patient may demonstrate a microcolon,

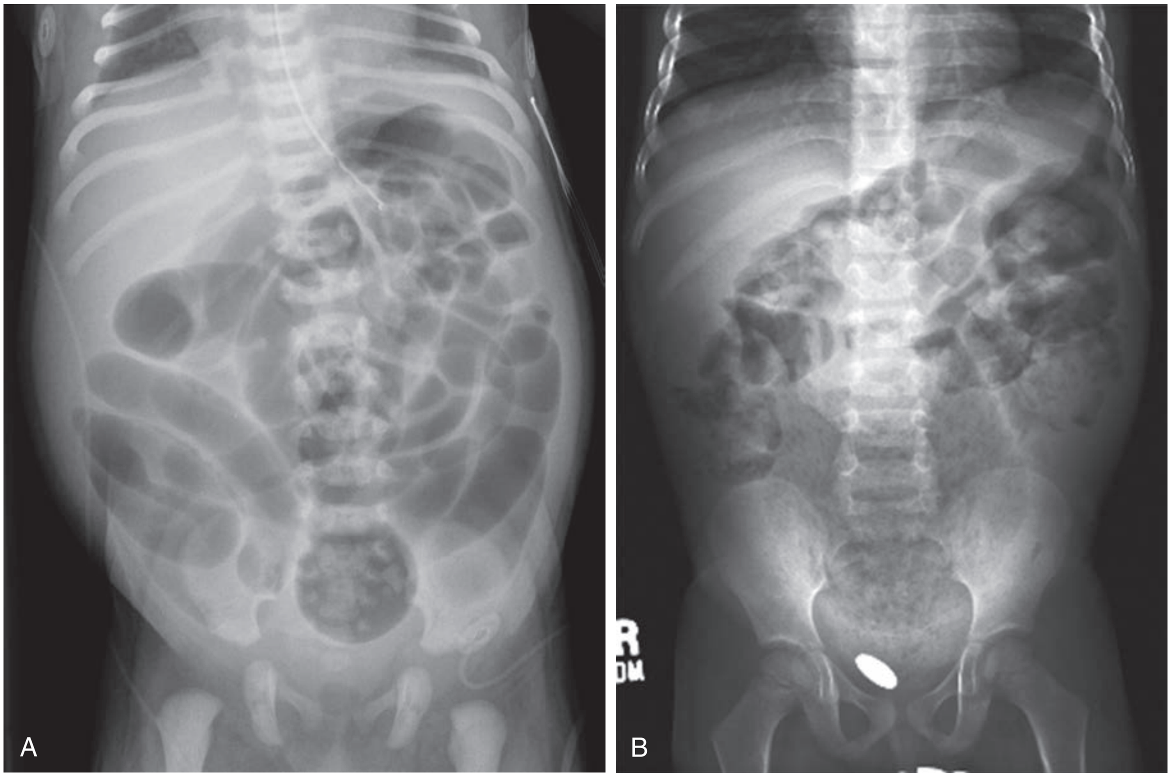

**Figure 105.10. Hirschsprung disease: early and late diagnosis.** (A) Supine abdominal radiograph on 3-day-old baby with abdominal distension reveals multiple dilated loops of bowel, indicating a distal obstruction. (B) Abdominal radiograph in a 4-year-old status-post repair of interrupted aortic arch, who presented with constipation and retained coin within the rectum for several months. There is marked fecal dilatation of the sigmoid, which does not extend into the rectum; the rectum contains a retained coin.

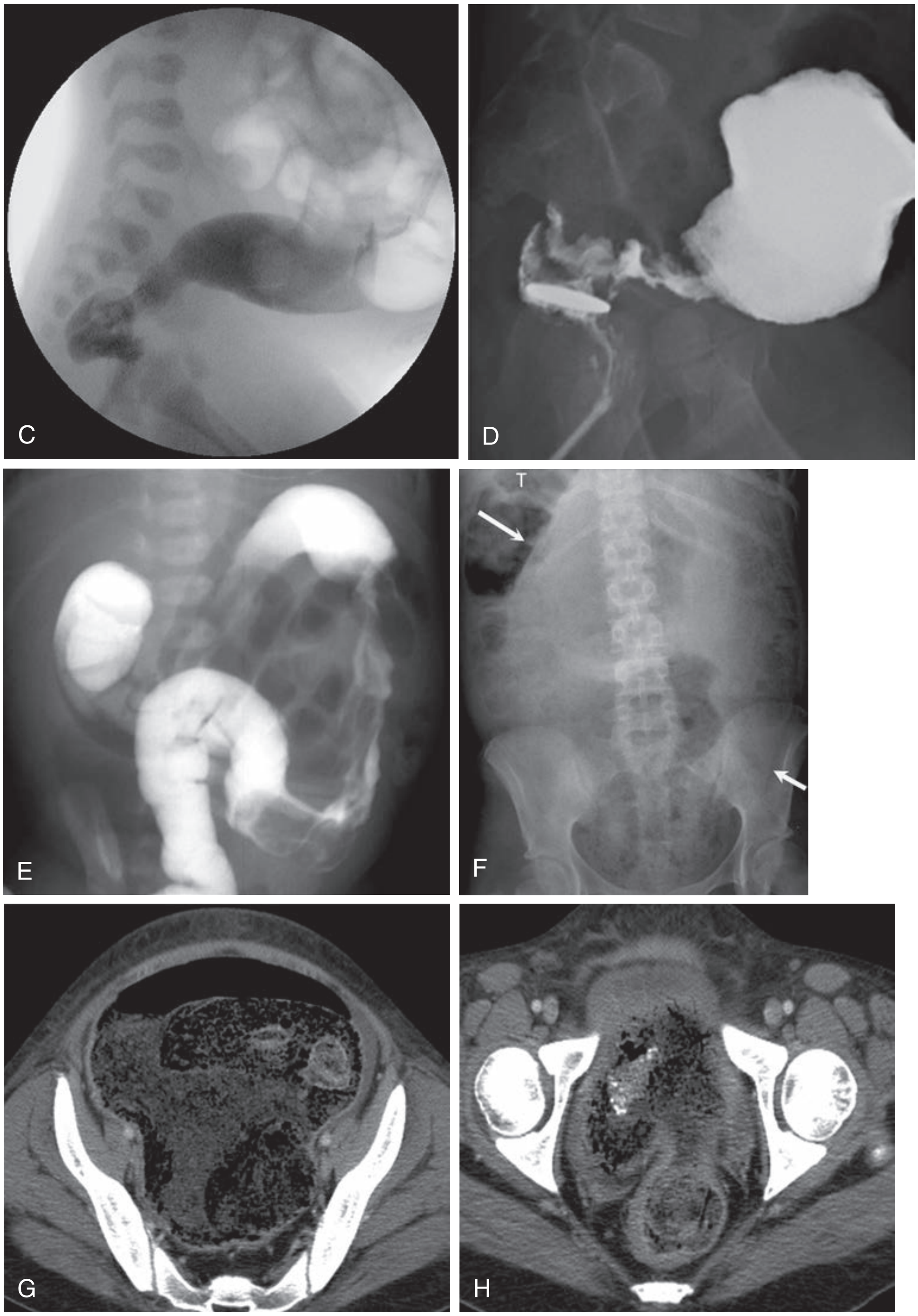

**Figure 105.10, cont'd.** (C) Contrast enema in a lateral projection on same patient as shown in (A) shows a caliber change at the rectosigmoid junction consistent with a rectosigmoid transition zone. (D) Lateral view of contrast enema in same patient as shown in (C) clearly shows the zone of transition, and the retained coin. (E) Abdominal image during contrast enema in a 2-day-old girl with positive family history of Hirschsprung disease and signs of distal bowel obstruction. Note the multiple dilated loops of bowel. The examination shows an abnormal distal descending colon, with irregular wall resulting from disordered contraction, and an apparent transition at the splenic flexure. At surgery, Hirschsprung was confirmed, with transition at the splenic flexure. (F) Abdominal radiograph of 15-year-old girl with diabetes and history of intermittent diarrhea, who presented acutely to the emergency department with diarrhea and abdominal distension. The abdominal radiograph shows marked stool burden and colonic dilatation. The sigmoid colon *(arrows)* extends into the abdomen, and displaces transverse colon *(T)* cephalad. (G) CT on same patient as shown in (F) was requested for clinical concern of appendicitis. CT at upper pelvis shows dilated sigmoid entering the pelvis. (H) CT lower in pelvis shows the zone of transition.

at times with the development of a meconium ileus pattern (e-Figs. 105.11A–F).

Newborns with Hirschsprung disease can initially present as meconium plug (e-Figs. 105.11E) or small left colon syndrome; such patients should be carefully monitored, and if normal bowel function does not return, further evaluation such as suction biopsy should be considered.

Definitive diagnosis is made by characteristic biopsy findings, showing absence of ganglion cells and abnormal acetylcholinesterase staining and hypertrophied nerve fibers. Manometric studies, with failure of relaxation of the internal sphincter with rectal distension, are helpful after the immediate neonatal period, and therefore helpful in older children.

Abdominal radiographs of patients with Hirschsprung-associated enterocolitis may show dilatation of bowel loops, with irregular outline consistent with spasm and mucosal disruption and ulceration (Fig. 105.12A). Contrast enemas are not indicated but if performed will show ulceration and spasm (Fig. 105.12B).

***Treatment.*** Surgical repair of Hirschsprung disease involves resecting the denervated bowel and bringing normally innervated bowel distally through the sphincteric mechanism. Swenson devised and performed the first successful surgical repair; his procedure consists of resection of the aganglionic segment and anastomosis of normal, ganglion-containing bowel to the sphincteric mechanism. The Duhamel procedure involves leaving the anterior portion of the aganglionic rectum in place and anastomosis of ganglion-containing bowel to its posterior wall. The Soave or endorectal pull-through involves resection of the mucosa and submucosa of the aganglionic bowel, and pulling the normal ganglion-containing bowel through the muscular rectal sleeve.[20] The Duhamel and Soave procedures are modifications of the Swenson, designed to minimize risk of injury to the sphincteric mechanism. Complications include postoperative leaks, strictures, and delayed bowel control. Residual obstruction predisposes to stasis and the consequent risk of enterocolitis. Postoperatively, some narrowing may be seen at the distal muscular sleeve, or the barium enema may appear normal, except for the double-density from the retained rectal pouch in patients treated with the Duhamel procedure (e-Figs. 105.13A and B). Strictures and the appearance of a zone of transition are not normal postoperative findings.

More recently there has been work investigating the possibility of introducing stem cells to populate the aganglionic bowel; although promising, these investigations are in the early stages of animal testing.[74–76]

## COLONIC DYSMOTILITY: MECONIUM PLUG, SMALL LEFT COLON, AND DYSMOTILITY OF PREMATURITY

***Overview.*** Meconium plug and small left colon syndromes refer to conditions of colonic dysmotility, which present as distal bowel obstruction in neonates, and which overlap with each other as well as with Hirschsprung disease. In meconium plug syndrome, a plug of meconium is identified within the colon, which, when evacuated, has a characteristic "white head" (Fig. 105.14A). The colon in patients with the small left colon syndrome may also contain meconium plugs but, in addition, a variable portion of the left colon, typically encompassing the descending colon and sigmoid, have a characteristically small caliber resembling a microcolon. In these patients, the rectum is typically of normal caliber. These conditions also overlap with the failure to pass meconium and, at times, obstructive symptoms that may be seen in very low or extremely low birth weight infants (<1500 and <1000 grams birth weight, respectively).

***Etiology.*** The etiology of these conditions is believed to be a delayed maturation of effective peristalsis in these patients and/or abnormally increased water absorption by the colon leading to a more tenacious meconium. Approximately 40% to 50% of small left colon syndrome cases occur in conjunction with maternal diabetes; conversely, small left colon syndrome has been cited to occur in approximately 4.7% of infants with history of maternal diabetes.[77] An increased viscosity of exocrine secretions and an immature intestinal nervous system are thought to be responsible for the obstructive symptoms seen in some low birth weight infants.[78,79]

***Clinical Presentation.*** Patients present with abdominal distension and bilious vomiting, typically in a term infant. Meconium

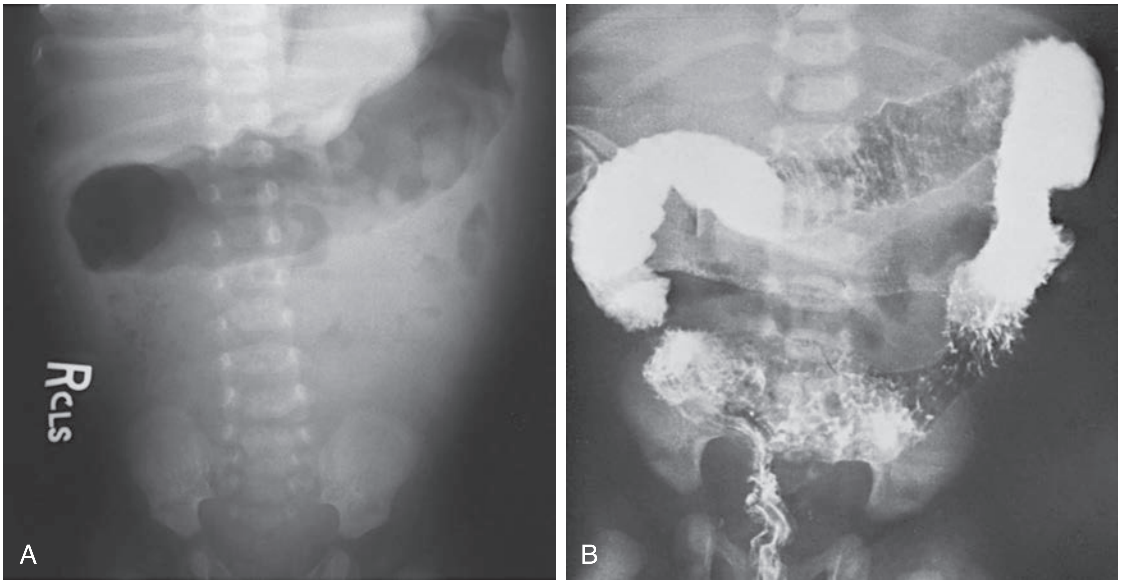

**Figure 105.12. Hirschsprung enterocolitis.** (A) Abdominal radiograph of a child who developed Hirschsprung-associated enterocolitis shows the irregular wall and thumb printing in the gas-filled transverse colon. (B) Lethal enterocolitis in a 12-day-old boy who presented with fever, foul diarrhea, and shock. Contrast enema shows extensive edema, ulceration, and spasm. The patient expired on arrival at the referral institution.

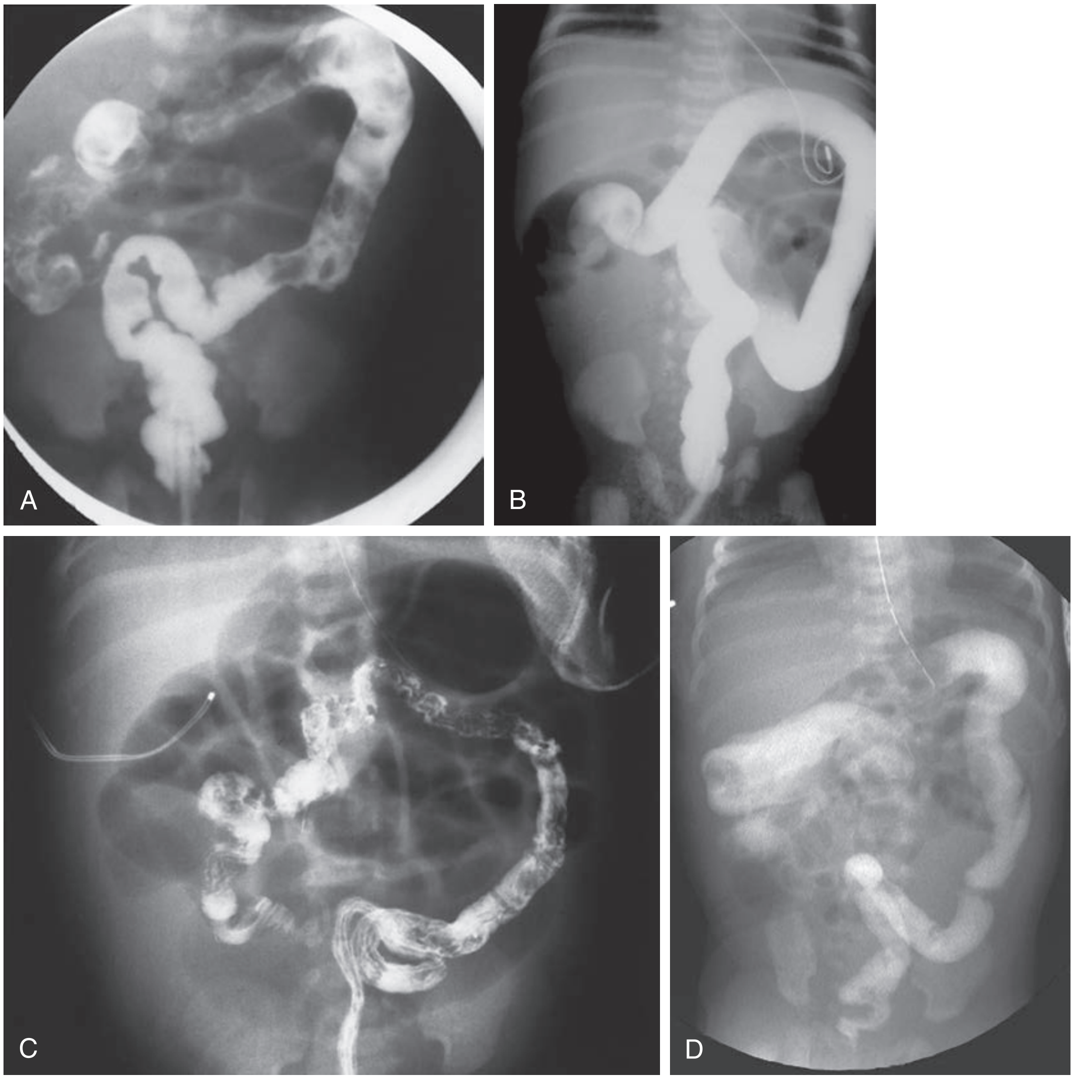

**e-Figure 105.11. Hirschsprung disease: contrast enema in total colon and small bowel aganglionosis.** (A) Anteroposterior image of contrast enema of neonate with distal bowel obstruction; the colon shows a normal and uniform caliber, without evidence of zone of transition, although it is somewhat featureless and contains multiple filling defects; note the dilated loops of small bowel in the background. Total colonic aganglionosis was documented at surgery. (B) Anteroposterior image of contrast enema of a neonate with Down syndrome. The examination shows a colon of uniform caliber, although less redundant than typical. Total colonic aganglionosis was found at surgery. (C) Image from contrast enema in another neonate with total colonic aganglionosis, demonstrating the appearance of a microcolon. (D) Image from contrast enema in a 6-day-old girl with distal obstruction. The examination shows a gradual caliber change, with a questionable transition point at the distal transverse colon. Total colonic aganglionosis was documented at surgery.

*Continued*

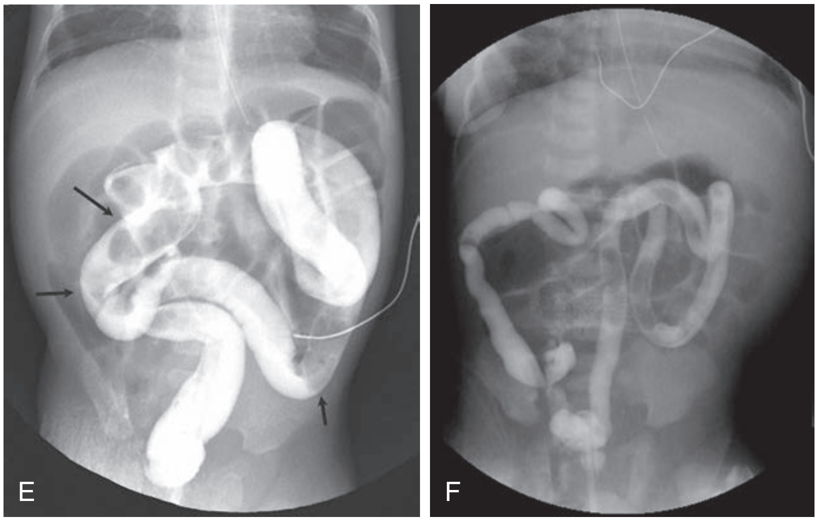

**e-Figure 105.11, cont'd.** (E) Image from contrast enema in neonate with distal bowel obstruction demonstrates a uniform caliber colon with multiple filling defects *(arrows)* suggesting meconium plugs. At surgery, Hirschsprung was identified involving the entire colon and the distal 20 cm of ileum. (F) Image from contrast enema in a 1-day-old infant with distal obstruction. The examination shows a colon only slightly larger than a typical microcolon. At surgery, there was aganglionosis of the entire colon, and of the small bowel to the jejunum, 51 cm from the ligament of Treitz. Because of the short length of his normal bowel, the child became TPN-dependent.

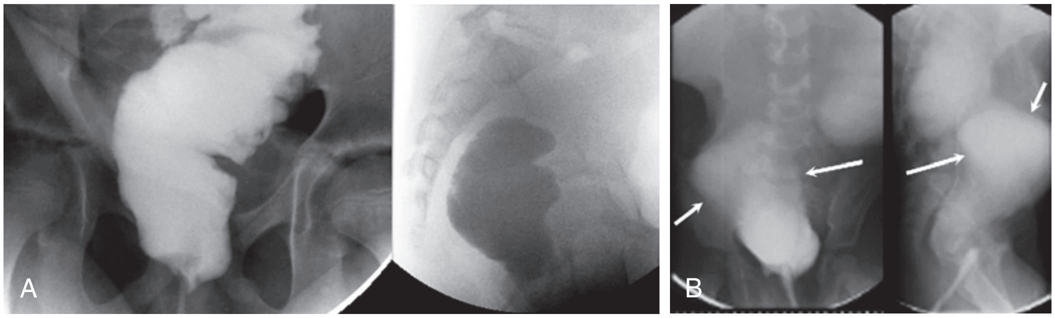

**e-Figure 105.13. Hirschprung disease after pull-through surgery.** (A) Frontal and lateral radiographs of contrast enema in child after Soave procedure. Note the smooth appearance of the colon through the pull-through sleeve. (B) Frontal and lateral radiographs of contrast enema in child after Duhamel procedure. Note the double density appearance of contrast within the wider Duhamel pouch *(arrows)*.

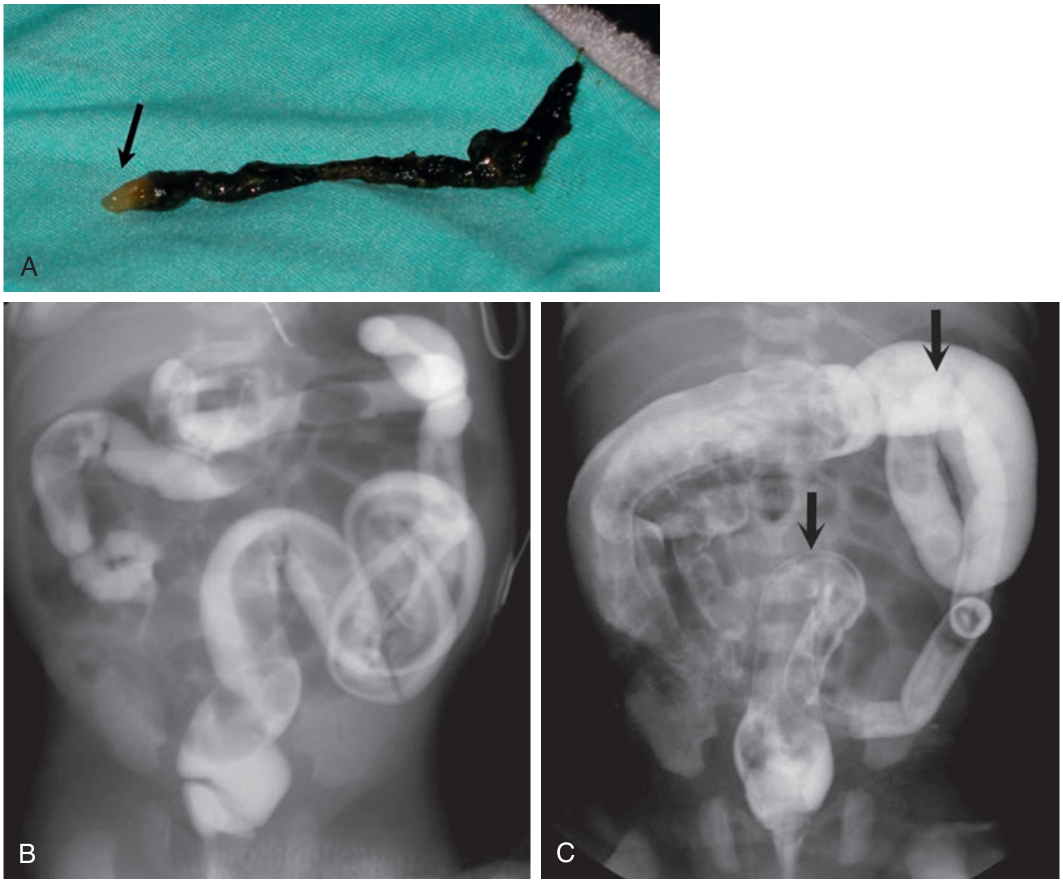

**Figure 105.14. Colonic dysmotility.** (A) Photograph of a meconium plug evacuated after diagnostic contrast enema, demonstrating the distinctive white tip *(arrow)*. (B) Water-soluble enema in infant with meconium plug. Note the long plug outlined as a filling defect within the contrast column in the distal colon. After this examination, the patient did well, relieved of the obstruction. (C) Water-soluble enema in infant with small left colon. Note the normal caliber rectum, and the small diameter of the colon, beginning in the sigmoid, and continuing along the left colon (outlined by distal and proximal *arrows*). Meconium plugs are also evident. This infant also did well after this examination, relieved of the obstruction.

plug and small left colon syndromes could be the presenting findings in patients with Hirschsprung disease. It is important to monitor these patients closely after initial relief of obstruction; if symptoms recur or do not abate, biopsy is necessary to evaluate for Hirschsprung disease.[80]

The very low and extremely low birth weight patients typically present around 10 to 14 days of age, with increasing abdominal distension and failure to pass meconium.[78] Abdominal examination is usually benign, but complications such as bowel perforation can occur.

***Imaging.*** Radiographs show typical findings of distal obstruction with multiple dilated loops of bowel, although the degree of dilatation tends to be less than that seen in other causes of distal obstruction, such as distal atresias or meconium ileus.[81] As with other cases of distal bowel obstruction, a diagnostic contrast enema with water-soluble contrast material with a near-iso-osmolal concentration should be performed. In cases of meconium plug, the enema demonstrates a colon of normal caliber, with a typically long filling defect caused by the meconium plug (Fig. 105.14B), which the patient may evacuate at the conclusion of the radiographic examination. Patients with small left colon syndrome will show a small caliber colon involving a variable length of sigmoid and descending colon, with a typically normal caliber rectum (Fig. 105.14C). Low birth weight infants typically do not come to diagnostic contrast enema; if the infants have obstruction secondary to other causes as outlined in this chapter, findings may be diagnostic.[78]

***Treatment.*** Patients with meconium plug and small left colon syndrome typically do well after the enema examinations. In patients with a protracted recovery or in whom there is recurrence of symptoms, biopsy for Hirschsprung disease should be performed. Premature infants with obstruction may be treated with enemas,[78] although it carries more risk in these much more labile, very small infants; guidance with ultrasound has also been reported.[82]

## CHRONIC INTESTINAL PSEUDOOBSTRUCTION

***Overview.*** CIPO refers to a characteristic, chronically recurring, and at times massive dilatation of the intestinal tract without identifiable mechanical cause. The term encompasses a heterogeneous group of disorders that affect the enteric nervous system and intestinal smooth muscle, resulting in failure of normal intestinal motility. The condition can be primary or secondary. Secondary disease is associated with multiple conditions, including scleroderma, dermatomyositis, and muscular dystrophies; infiltrative diseases such as amyloidosis; nervous system diseases such as myotonic dystrophy and familial dysautonomia; postviral syndromes such as Epstein-Barr, cytomegalovirus (CMV), herpes zoster and rotavirus; fetal alcohol syndrome; and mitochondrial disorders.[83]

In the pediatric population, primary disease predominates and is subdivided into neuropathic or myopathic forms; patients with the myopathic form of primary disease tend to have involvement of other systems, particularly the urinary system.

Approximately 40% of patients become symptomatic within the first month and 65% within the first year of life. Chronicity is defined as either congenital disease persisting during the first 2 months of life or as persistence for greater than 6 months. Histopathology may demonstrate diverse findings, such as hypoganglionosis, degenerative changes in smooth muscle fibers, additional muscle layer, collagen deposition, degeneration of neurons and axons, and proliferation of neurons, nerve fibers, or glial cells.

Neuronal intestinal dysplasia (NID) constitutes a form of primary disease with two subtypes and is a disorder of intestinal innervation that can be diffuse or localized.[84] Type A consists of aplasia or hypoplasia of sympathetic innervation of the intestine and constitutes less than 5% of cases. Type B accounts for approximately 95% of cases and affects the parasympathetic system with hyperplasia of the submucosal and myenteric plexus with dysplastic and ectopic ganglion cells and increased acetylcholinesterase staining.[51] Type B NID has been found in the proximal intestine of patients with Hirschsprung disease.[85–87]

***Etiology.*** The enteric nervous system generates rhythmic enteric activity and includes the interstitial cells of Cajal, neurons, and glial cells. The network of interstitial cells of Cajal has been found to be abnormal in some patients with CIPO, and delayed maturation of these cells has been reported in neonates with transient CIPO. Ganglion cells containing nitric oxide synthase, which mediates sphincteric relaxation, have been found to be increased in some patients with CIPO.[83] Animal models targeting the *Hox11L1* gene and the endothelin B receptor develop phenotypic and histologic findings similar to NID type B, with hyperplasia of myenteric ganglia. However, genetic investigation in humans with NID has been unproductive.[51,85] Most cases of this disease are sporadic, and although a genetic locus in humans has not been isolated, familial clusters with autosomal dominant inheritance have been reported.[44] More recently, mutations in *RAD21* disrupting regulation of apolipoprotein B have been found in patients with CIPO, with animal experiments suggesting a role in transit and development of intestinal neurons.[88]

***Clinical Findings.*** Children present with periodic vomiting, diarrhea, abdominal distension, constipation, pain, and weight loss. Patients with NID type A present in the neonatal period with acute episodes of intestinal spasticity, diarrhea, and hematochezia. Patients with NID type B present with chronic constipation and/or pseudoobstruction, typically in the first 3 years of life.[44] Patients who develop small bowel bacterial overgrowth secondary to intestinal stasis may develop diarrhea, weight loss, and macrocytic anemia.[83]

Multiple anomalies have been documented in patients with primary disease, in addition to Hirschsprung disease, which occurs in as many as 10% of cases.[44] Related associations include multiple endocrine neoplasia type IIb and neurofibromatosis.[89] Other associations include malrotation, ARM, congenital short small bowel, and intestinal atresia, as well as extraintestinal problems such as vesical dysfunction, Down syndrome, and histiocytosis.[44]

***Imaging.*** Imaging demonstrates dilated loops of bowel, particularly the colon, with air-fluid levels suggestive of obstruction but which really represent severe adynamic ileus. Megacolon is typically found with contrast enema, without the diagnostic transition zone findings of Hirschsprung disease. Contrast small bowel and enema studies show poor motor activity in affected parts of the bowel, but otherwise are nonspecific. Gut dilatation is common in the colon, the stomach, and the small bowel, and can assume massive proportions (e-Fig. 105.15).

***Treatment.*** Gastrostomy may be used for feeding (although is often not tolerated) and for venting. Enteral feedings through a jejunostomy are sometimes tolerated. Medical management includes prokinetic agents and antiemetics. Management of patients who develop small bowel bacterial overgrowth includes vitamins, antibiotics, and possibly probiotics.[83] Some patients may need intestinal transplantation, or combined hepatic and intestinal transplantation if liver disease secondary to total parenteral nutrition supervenes.[83] Stem cell transplantation may have a future role in treatment of these conditions.

## MEGACYSTIS-MICROCOLON-INTESTINAL HYPOPERISTALSIS SYNDROME

***Overview.*** The megacystis-microcolon-intestinal hypoperistalsis syndrome (MMIHS or Berdon syndrome) was first described by Berdon and colleagues in 1976[90] and is a well-recognized clinical entity[51,85] with an approximately 2:1 female predominance.[91] Malrotation is present in many patients.[90,91] This syndrome is considered one of the most severe forms of functional intestinal obstruction in the newborn and is often fatal[91]; without treatment, most patients succumb within the first 6 months of life.[92]

***Etiology.*** Approximately 20% of reported cases are familial, with a pattern suggesting autosomal recessive inheritance.[93] *nAchR* genes on chromosome 15 affecting the nicotinic acetylcholine unit have been implicated.[51,93] Histologic evaluation shows normal ganglion cells in most patients, but these are decreased in some patients and increased in others, who show hyperganglionosis as well as giant ganglia.[91] Interstitial cells of Cajal are responsible for generating coordinated peristaltic activity, and abnormalities in the interstitial cells of Cajal in the urinary bladder[94] and in the intestinal myenteric plexus[95] have been found in patients with MMIHS. In addition, abnormalities of the smooth muscle cells have been found, with evidence of thinning, vacuolar degeneration, and increased connective tissue in both the bowel and bladder.[95–97]

***Clinical Presentation.*** These infants present with abdominal distension and bilious vomiting secondary to obstruction; abdominal distension is exacerbated by urinary bladder dilatation. Bowel sounds are decreased or absent.

***Imaging.*** Radiographs show marked abdominal distension, a largely gasless abdomen with the markedly distended urinary bladder displacing bowel loops. Ultrasound demonstrates the markedly distended urinary bladder, typically in association with hydroureteronephrosis. Upper GI demonstrates hypo- or aperistalsis of stomach, duodenum, and small bowel. Contrast enema demonstrates a microcolon. Malrotation is seen in more than one-half of cases (Fig. 105.16).[85]

***Treatment.*** This condition carries a poor prognosis, with one series reporting only 7 of 44 patients surviving.[93] Medical treatment with prokinetics and GI hormones is most often unsuccessful, and total parenteral nutrition becomes necessary to maintain the infants.[85] Patients who develop hepatic disease become candidates for multivisceral transplantation.[92]

## COLONIC DUPLICATIONS

***Overview.*** GI duplications are also discussed in Chapters 96, 99, and 102, with the specific associated gut segments; this chapter will address findings characteristic of colonic duplications. Approximately 17% of GI duplications are colonic,[98] and 5% are rectal. Colonic duplications can be cystic or tubular. Cystic duplications consist of a short duplicated segment typically not communicating with the adjacent lumen. Tubular duplications typically connect with the GI tract and often drain into a single or duplicated anal orifice or into the perineum via a fistula. The colon proper is that portion ending in a perineal anus; the duplicated colon is that portion ending at a perineal fistula, at a communication with the colon proper, or blindly. In some cases, both colons end in a duplicated perineal anus or in perineal fistulae.[99] The duplications are of variable length and can be classified as extending above or below the peritoneal reflection. If the duplication does extend

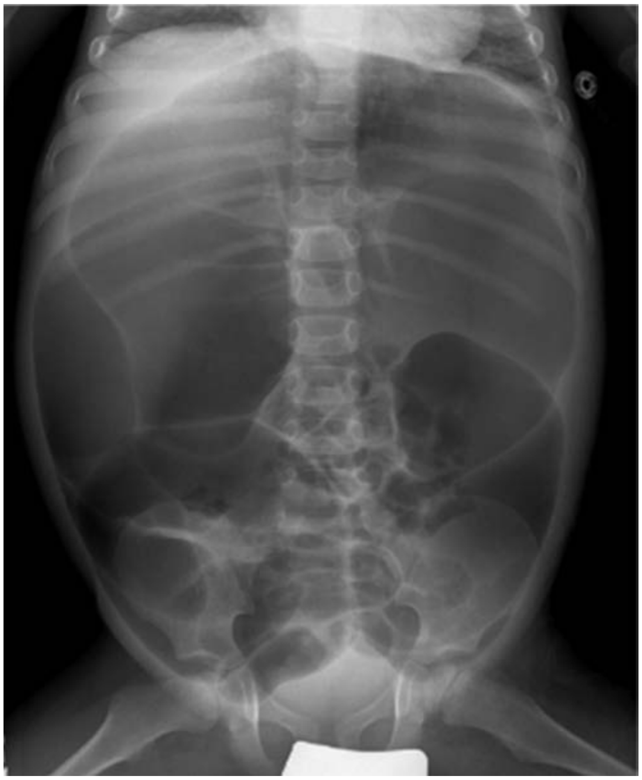

**e-Figure 105.15. Chronic intestinal pseudoobstruction.** Abdominal radiograph of a 5-year-old boy with myopathic type pseudoobstruction, largely dependent on total parenteral nutrition due to prolonged episodes of feeding intolerance. During this acute presentation, the radiograph demonstrates massive dilatation of the colon.

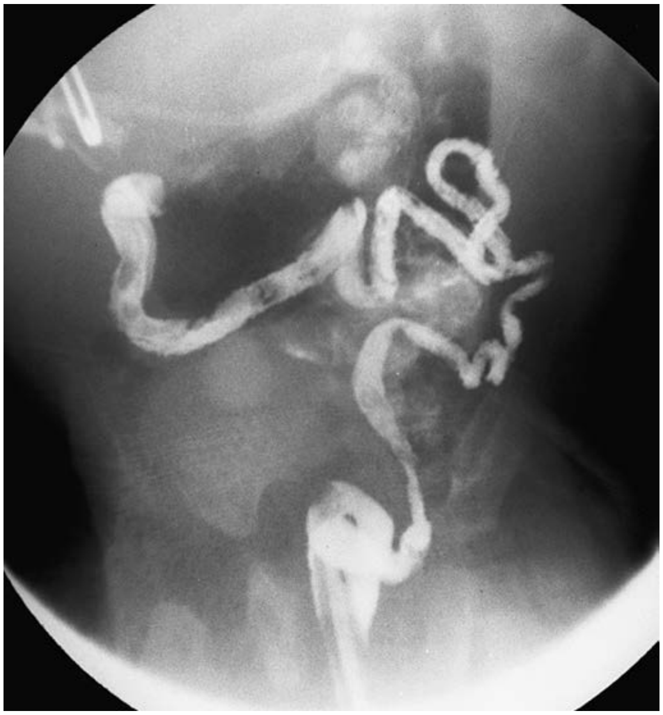

**Figure 105.16. Megacystis-microcolon-intestinal hypoperistalsis syndrome.** Single frontal view of newborn female reveals the microcolon characteristic of this entity. Note the malposition of the cecum, consistent with the malrotation that is common in these patients. Soft tissue density in the pelvis is consistent with a distended urinary bladder.

below the peritoneal reflection, and therefore does not have a perineal opening, communication with the lumen can be at one or both ends. They can extend proximally to involve the cecum, appendix, and terminal ileum.

Approximately 75% of tubular colonic duplications are associated with multiple other anomalies, including renal anomalies. When associated with duplication of the genitourinary tract (uterus, bladder, urethra, penis), and vertebral and cord abnormalities, it is termed *caudal duplication anomaly* (e-Fig. 105.17).[100,101] Although anterior rectal duplications have been reported,[98] cystic rectal duplications are typically located in the presacral space (e-Fig. 105.18).

***Etiology.*** The partial or abortive twinning theory invokes a split in the primitive streak during the embryonic period, with a relatively late split resulting in duplications of the colon. In cases of caudal duplication anomaly, a mechanical cause may interfere by dividing developing precursor structures leading to duplication.[102]

***Clinical Findings.*** The presentation of colonic duplication varies with the type and location. The incidence of gastric mucosa within colonic duplications is reportedly less than in other types, and they can therefore remain asymptomatic and discovered incidentally in late childhood or adulthood. Cystic duplications may be complicated by bowel obstruction due to volvulus, intussusception with the duplication cyst as a leading point, or as an acutely enlarging mass. Duplications may also become symptomatic secondary to inflammation and ulceration; nausea, vomiting, abdominal pain, and identification of a mass on physical examination or imaging are common presentations. Rectal duplications, when large or enlarging, can present with constipation as well as urinary obstruction; because they are located behind the rectum, they may also mimic presacral meningoceles or cystic teratomas.[98,99] Colon and rectal duplications may present as a second opening in the perineum. In girls in whom the duplication terminates in a perineal/vaginal opening, the duplication may simulate a rectovaginal fistula.[104]

***Imaging.*** Initial suspicion on physical examination or on plain films can be followed up with sonography, fluoroscopy, computed tomography (CT), or MRI. Tubular duplications with a perineal fistula are best diagnosed with contrast enema via both perineal orifices, outlining both lumina; antegrade contrast studies may also be diagnostic. CT and MRI will likely be diagnostic, but at the present time their exact role in the workup of these lesions remains undefined. Rectal duplications can be identified in plain films and contrast enemas via a mass effect upon the rectum, and upon the adjacent genitourinary structures if sufficiently large. Sonography and MRI are likely the best modalities to evaluate noncommunicating cysts (see e-Fig. 105.18). A search for other system anomalies should also be undertaken, with the appropriate imaging modality.

***Treatment.*** Symptomatic simple cystic duplications can be resected. If a presacral rectal duplication presents as an abscess, drainage is advocated as initial treatment.[98] Long colonic duplications can be treated by extensive fenestration between the two lumina, with resection of the perineal fistula.

## NECROTIZING ENTEROCOLITIS

***Overview.*** The term necrotizing enterocolitis (NEC) was coined in 1952[105] to describe an inflammatory condition affecting the GI tract of neonates, most commonly premature infants surviving the first few days of life who were receiving enteral nutrition. Today, necrotizing enterocolitis is considered the most common newborn surgical emergency, with greater morbidity and mortality than all other surgical GI conditions in this age group combined.[106] Approximately 90% of cases of NEC occur in premature infants; the incidence of NEC is inversely proportional to gestational age, with the majority of cases occurring in infants weighing between 500 and 750 grams, and only approximately 7% to 13% of cases occurring in full-term infants.[106] NEC affects up to 11.5% of infants weighing less than 750 grams and 4% of infants weighing between 1250 and 1500 grams.[107,108] Risk factors for NEC in term infants include congenital heart disease and other conditions that affect splanchnic blood flow, such as maternal cocaine use and decreased prenatal umbilical blood flow.

The Bell classification of enterocolitis severity, introduced in 1978,[109] is still used with modifications today (Table 105.2).[110,111] Stage I is sensitive but nonspecific, as it includes infants in whom NEC is suspected, but not definitely diagnosed; stage IIA is mild but definite NEC; stage IIB is NEC of moderate severity, while stage IIIA refers to advanced NEC, and stage IIIB refers to NEC that has advanced to perforation. Some investigators suggest excluding stage I, which is relatively nonspecific and may include patients without true NEC and suggest grouping NEC by suspected etiologies.[113]

***Etiology.*** Ischemia leading to intestinal mucosal injury, prior feedings, and a substrate of intestinal flora have been recognized for decades as central to the pathophysiology and development of NEC.[106,112] A complex process involving cytokines and growth factors initiates an inflammatory cascade leading to intestinal injury, cellular apoptosis, breach of the mucosal barrier, and bacterial translocation in susceptible infants.

The most important risk factors for the development of NEC are prematurity and enteral feedings, which have been instituted in 90% of infants who develop NEC. The premature neonate has poorly developed intestinal motility leading to stasis, altered ability to maintain homeostasis between proinflammatory and antiinflammatory compounds, to regulate splanchnic vasoconstriction and blood flow, and to maintain mucosal integrity. Proinflammatory compounds are upregulated in NEC, including platelet activating factor, tumor necrosis factor, and certain types of interleukins, leukotrienes, and oxygen free radicals. Toll-like receptor 4 (TLR4)

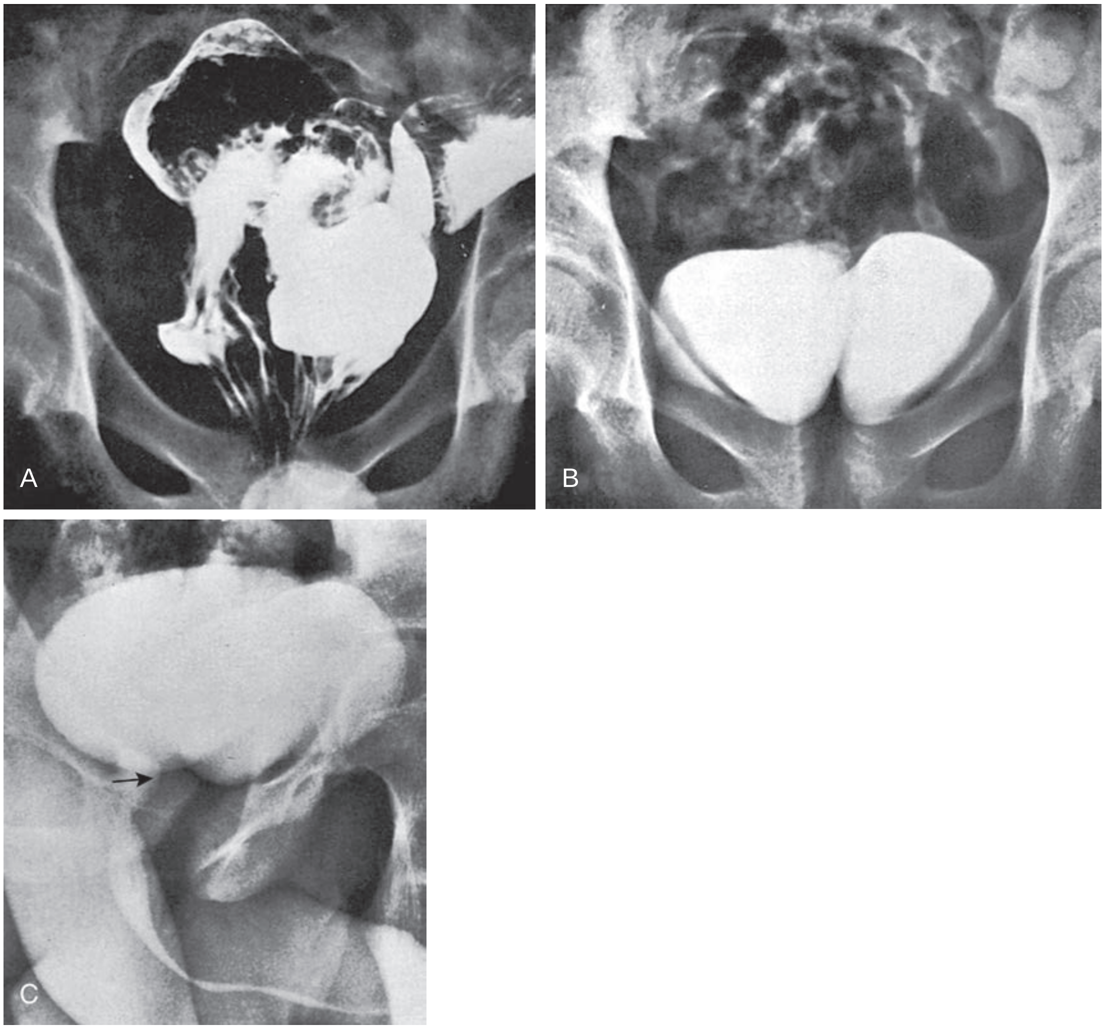

**e-Figure 105.17. Duplication of the entire colon and bladder.** (A) Contrast enema of the pelvis after excretory urography in a 15-year-old boy who had been treated in the newborn period for anal atresia, demonstrates two rectums. Surgical exploration revealed duplication of the entire colon, from appendix to rectum. (B) Frontal radiograph of the pelvis after excretory urography shows two bladders. Each upper urinary tract emptied into the bladder on its respective side. (C) Voiding urethrogram demonstrates a single urethra *(arrow)* originating from the right side.

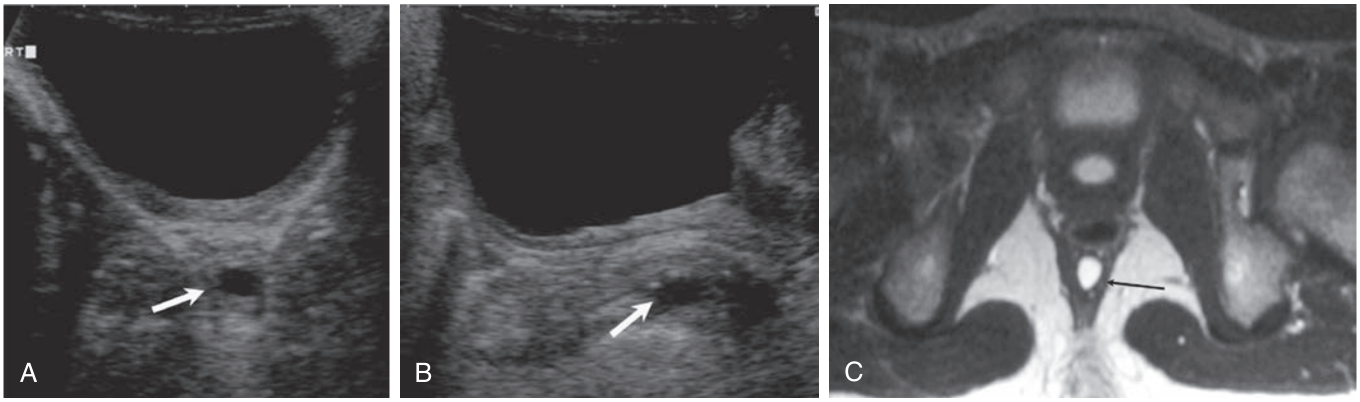

**e-Figure 105.18. Rectal duplication.** (A) Transverse sonogram in a 6-year-old girl who presented with abdominal pain shows an incidental finding of a small cyst *(arrow)* inseparable from the rectal wall. (B) Sagittal sonogram demonstrates the retrorectal location of the cyst *(arrow)*. (C) Axial T2-weighted MR image confirms the small cystic lesion *(arrow)* and better demonstrates its retrorectal location.

**TABLE 105.2** Modified Bell Staging Criteria

| Stage | Systemic Findings | Abdominal Findings | X-rays |
|---|---|---|---|
| IA, B – Suspected | Apnea, bradycardia, temperature instability | Distension, blood in stools | Mild ileus |
| IIA – Definite, mild severity | Apnea, bradycardia, temperature instability | Absent bowel sounds +/– abdominal tenderness | Ileus, pneumatosis |
| IIB – Definite, moderate severity | Metabolic acidosis, thrombocytopenia | Abdominal tenderness +/– cellulitis, RLQ mass | Ileus, pneumatosis, ascites |
| IIIA – Definite, severe | Apnea, hypotension, bradycardia, metabolic and respiratory acidosis, neutropenia, DIC | Abdominal distension, abdominal tenderness, signs of peritonitis | Ileus, pneumatosis, ascites |
| IIIB – Definite, severe, bowel perforation | Apnea, hypotension, bradycardia, metabolic and respiratory acidosis, neutropenia, DIC | Abdominal distension, abdominal tenderness, signs of peritonitis | Pneumoperitoneum |

*Adapted from Sylvester K, Liu G, Albanese CT. Necrotizing enterocolitis. In: Coran A, et al, eds.* Pediatric Surgery, *Philadelphia: CV Mosby, an Imprint of Elsevier; 2012.*

senses lipopolysaccharide, and its expression is associated with increased severity of NEC; its concentration falls precipitously at birth, but its expression is attenuated by breast milk.[113] Accelerated apoptosis resulting from overproduction of inflammatory compounds has been shown to result in a break at the villus tip of the intestinal mucosal barrier, facilitating bacterial translocation and the inflammatory cascade.[106,107,114]

***Clinical Findings.*** The clinical findings reflect the severity and evolution of the disease. In Bell stage I disease, the infant exhibits relatively nonspecific symptoms, including systemic signs such as apnea, bradycardia, and temperature instability, and abdominal signs consisting of abdominal distension, hemoccult positive stools, and increased gastric residuals. These signs could also be present in other conditions, such as sepsis, and therefore are sensitive, but relatively nonspecific. By stage IIA, the diagnosis of NEC can be made, and clinical findings include abdominal tenderness and grossly bloody stools; by stage IIB, the child has progressed to thrombocytopenia and mild acidosis, as well as abdominal wall edema and tenderness. Infants in stage IIIA have severe disease with metabolic and respiratory acidosis requiring intubation, signs of disseminated intravascular coagulation, with worsening abdominal wall erythema, edema, and induration. Patients with stage IIIB disease show clinical evidence of shock and gut perforation.

Complications of NEC in survivors relate to whether the patients have developed short bowel syndrome, with dependence on total parenteral nutrition and its attendant complications. Strictures occur in 9% to 36% of survivors of NEC, most often in the colon (70%–80%), and 21% of these occur at the splenic flexure. Strictures develop most often in patients who have been managed medically and present with failure to gain weight, rectal bleeding, or signs and symptoms of obstruction.[7,106]

***Imaging.*** Abdominal radiographs have been the mainstay of imaging evaluation of infants with NEC, and the Bell criteria therefore have corresponding radiographic findings.

The radiographs of infants with Bell stage I disease, similar to the physical findings, are nonspecific, demonstrating a bowel gas pattern that is within normal limits or shows a mild ileus. Stage IIA disease is specific, because in addition to an ileus pattern, focal pneumatosis can be seen. As NEC progresses to stage IIB, radiographs show extensive pneumatosis ± portal venous gas and early ascites (Figs. 105.19A and B). Stage IIIA demonstrates more prominent ascites and persistent bowel loops; pneumoperitoneum is the hallmark of stage IIIB disease (Fig. 105.19C). Periodic imaging is important and is employed more frequently in patients who have more advanced disease.

Ultrasound is a useful and often complementary modality to abdominal radiographs.[115,116] In stage IIA disease, intramural gas has a characteristic appearance as it wraps around the subserosa of the involved bowel loops (Fig. 105.20A); absent peristalsis correlates with the clinical absence of bowel sounds. In stage IIB disease, ultrasound identifies ascites more easily than radiographs, while the pneumatosis and portal venous gas are also seen (Fig. 105.20B). In stage IIIA disease, thinning of the bowel wall can be evident. The hallmark of stage IIIB disease, pneumoperitoneum, is seen on ultrasound, most easily as gas anterior to the liver. However, pneumoperitoneum may not be present in as many as 37% of infants with perforation[106]; when there is perforation, ultrasound can demonstrate complex ascites, which has been correlated with bowel perforation and need for surgery.[117] Several sonographic findings are associated with an adverse outcome, particularly focal fluid collections, and three or more of these additional findings: abnormal bowel wall echogenicity, bowel wall thickening or thinning, free fluid with internal echoes, absent bowel wall perfusion, and intramural gas.[118]

Patients who develop strictures may be evaluated with fluoroscopic examinations, typically contrast enema, as 80% of strictures develop in the colon, and 15% in the terminal ileum (Fig. 105.21).[106]

***Treatment.*** Initial medical treatment consists of fluid resuscitation, antibiotics, and total parenteral nutrition. Surgical intervention is required to remove bowel that has become gangrenous, while preserving intestinal length. Optimal surgical timing, when the bowel is gangrenous but before perforation, is difficult to define clinically or by imaging.[106] Pneumoperitoneum in infants with surgically proven perforation is present in only approximately 63% of cases.[106] Criteria that suggest gangrene before perforation include abdominal wall erythema, fixed appearance of intestinal loop(s) on radiography or ultrasound, and clinical deterioration while receiving medical therapy.[106,119] Patients with perforation who are deemed very poor surgical candidates may undergo initial peritoneal drainage.[106,119]

## KEY POINTS

- Colonic atresia is uncommon, representing between 1.8% and 15% of all intestinal atresias.
- Approximately 95% of patients with ARM have a fistula to the urethra, vagina, or perineum; however, fistulae are much less common in patients with Down syndrome and ARM.
- The Currarino association was initially described as a triad of ARM, presacral mass, and sacral anomaly, but current understanding recognizes a much wider spectrum of phenotypic abnormalities and an underlying genetic defect.
- Hirschsprung disease histopathology includes absent ganglion cells, hypertrophied nerve fibers, and increased acetylcholinesterase staining.
- Diagnostic findings at contrast enema in patients with Hirschsprung disease include a zone of transition between normal caliber aganglionic bowel distally and dilated bowel proximally; irregular outline of the aganglionic segment may be present due to nonperistaltic contractions.

*Continued*

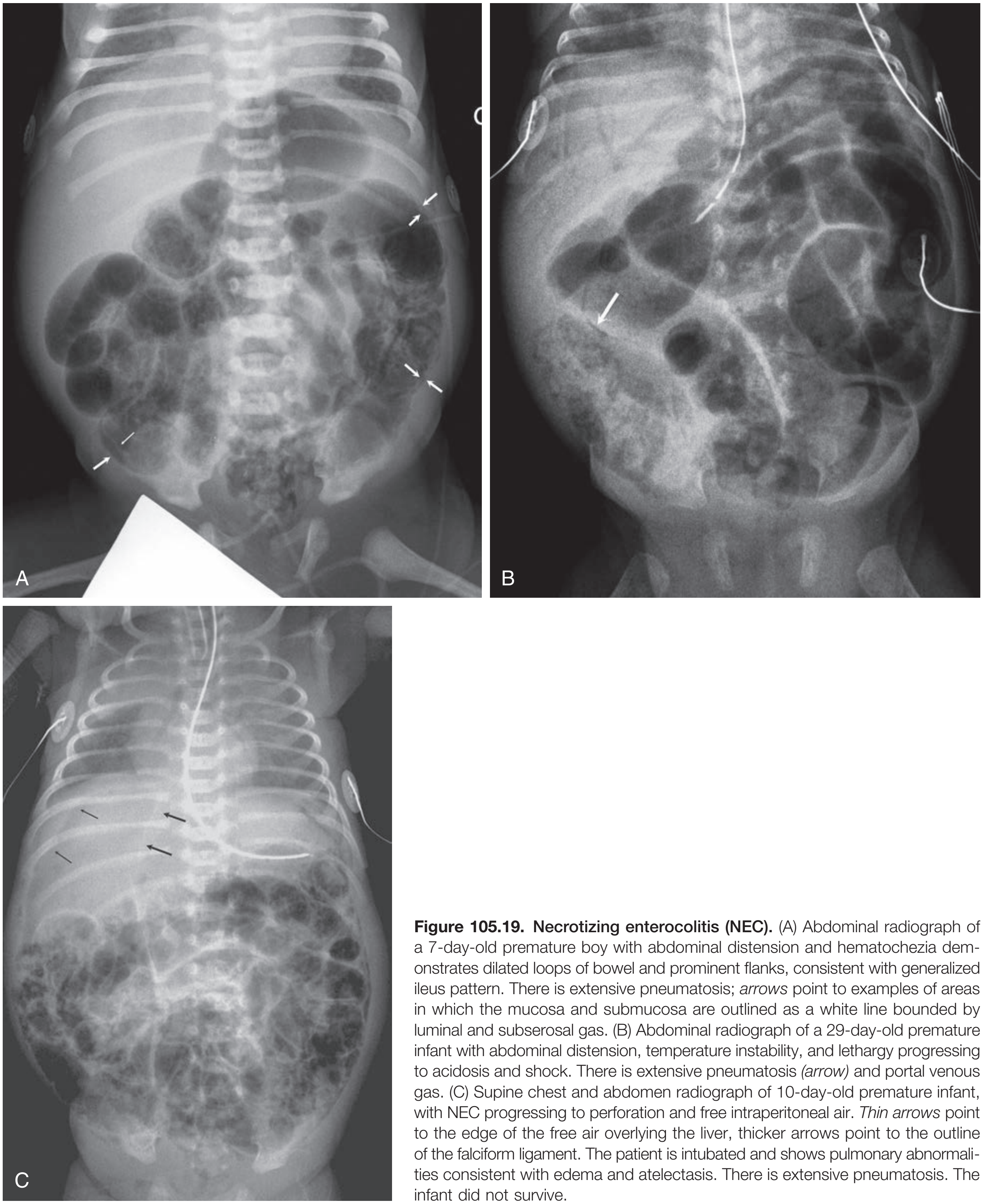

**Figure 105.19. Necrotizing enterocolitis (NEC).** (A) Abdominal radiograph of a 7-day-old premature boy with abdominal distension and hematochezia demonstrates dilated loops of bowel and prominent flanks, consistent with generalized ileus pattern. There is extensive pneumatosis; *arrows* point to examples of areas in which the mucosa and submucosa are outlined as a white line bounded by luminal and subserosal gas. (B) Abdominal radiograph of a 29-day-old premature infant with abdominal distension, temperature instability, and lethargy progressing to acidosis and shock. There is extensive pneumatosis *(arrow)* and portal venous gas. (C) Supine chest and abdomen radiograph of 10-day-old premature infant, with NEC progressing to perforation and free intraperitoneal air. *Thin arrows* point to the edge of the free air overlying the liver, thicker arrows point to the outline of the falciform ligament. The patient is intubated and shows pulmonary abnormalities consistent with edema and atelectasis. There is extensive pneumatosis. The infant did not survive.

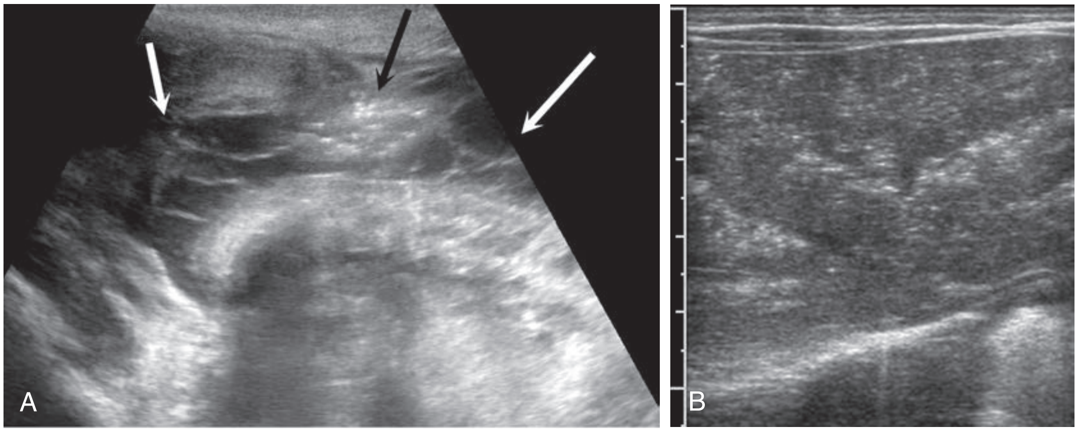

**Figure 105.20. Necrotizing enterocolitis (NEC).** (A) Ultrasound of an infant with severe NEC and perforation. *Black arrow* outlines bowel loop with circumferential punctate echoes consistent with pneumatosis. *White arrows* point to complex fluid collection. (B) Transverse sonogram of the liver in infant with portal venous gas demonstrates the multiple intrahepatic echoes along the vascular distribution.

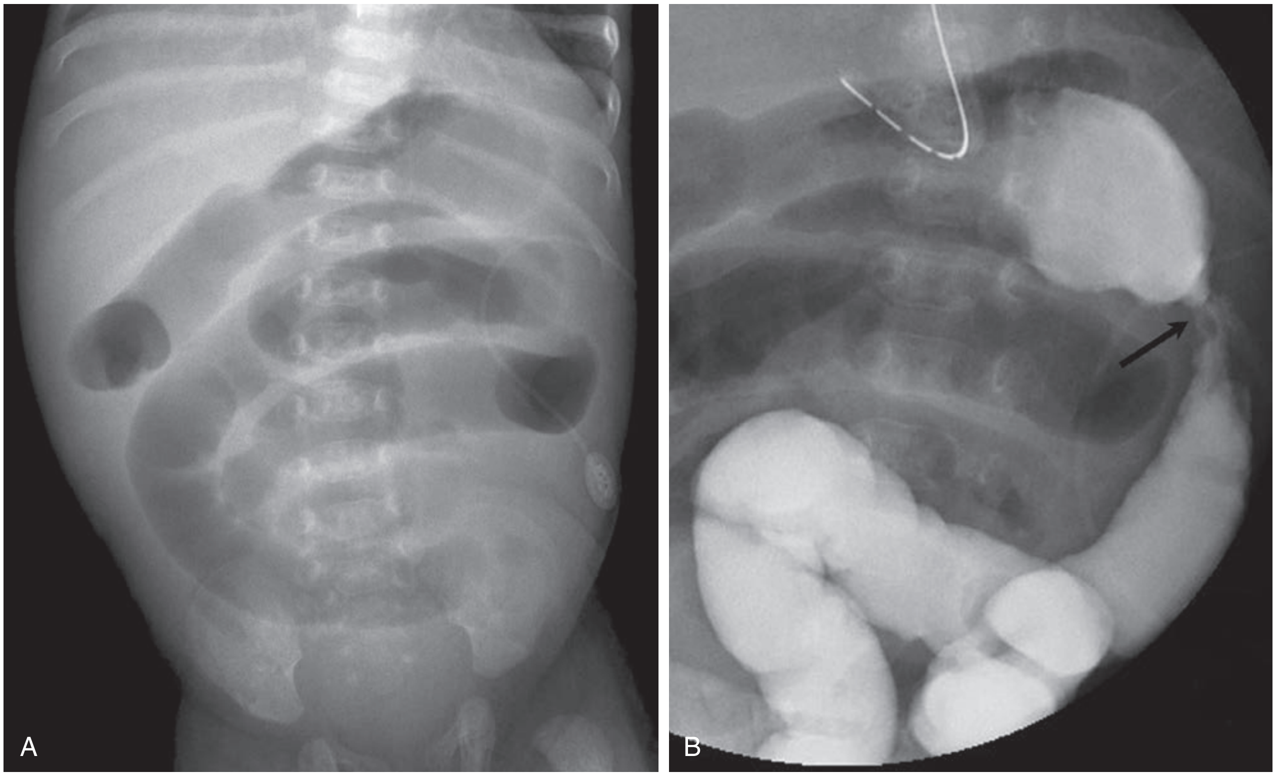

**Figure 105.21. Necrotizing enterocolitis (NEC): development of strictures.** (A) A 7-week-old premature infant with past history of NEC presents with increasing residuals, vomiting, and abdominal distension. Abdominal radiograph shows dilated loops of bowel consistent with a distal, partial obstruction. (B) Spot image from contrast enema demonstrates an area of narrowing in the proximal descending colon, consistent with a stricture *(arrow)*.

- Meconium plug and small left colon syndrome are considered functional obstructions and are usually transient; failure to resolve requires exclusion of Hirschsprung disease.
- Chronic intestinal pseudoobstruction may be primary or secondary. The primary form is most common in children and is, in turn, subdivided into neuropathic and myopathic forms.
- Megacystis-microcolon-intestinal hypoperistalsis syndrome presents within the first 6 months of life, is associated with malrotation, and has a poor prognosis.
- Tubular colonic duplications of the colon often drain to the perineum; typically, although not invariably, they connect to the gastrointestinal tract.
- NEC is most commonly seen in premature infants, with a triad of intestinal ischemia, oral feedings, and luminal bacteria. Bell criteria differentiate the level of severity of the condition, which correlates with clinical and imaging findings.

## SUGGESTED READINGS

Bischoff A, Levitt MA, Pena A. Update on the management of anorectal malformations. *Pediatr Surg Int*. 2013;29(9):899–904.

Cox SG, et al. Colonic atresia: spectrum of presentation and pitfalls in management. A review of 14 cases. *Pediatr Surg Int*. 2005;21(10):813–818.

Cuturilo G, et al. Phenotype analysis impacts testing strategy in patients with Currarino syndrome. *Clin Genet*. 2016;89(1):109–114.

Emil S, et al. Meconium obstruction in extremely low-birth-weight neonates: guidelines for diagnosis and management. *J Pediatr Surg*. 2004;39(5):731–737.

Epelman M, et al. Necrotizing enterocolitis: review of state-of-the-art imaging findings with pathologic correlation. *Radiographics*. 2007;27(2):285–305.

Panza E, et al. Genetics of human enteric neuropathies. *Prog Neurobiol*. 2012;96(2):176–189.

Puri P, Shinkai M. Megacystis microcolon intestinal hypoperistalsis syndrome. *Semin Pediatr Surg*. 2005;14(1):58–63.

## REFERENCES

Full references for this chapter can be found on www.expertconsult.com.

## REFERENCES

1. Etensel B, et al. Atresia of the colon. *J Pediatr Surg*. 2005;40(8):1258–1268.
2. Grosfeld JL, Ballantine TV, Shoemaker R. Operative mangement of intestinal atresia and stenosis based on pathologic findings. *J Pediatr Surg*. 1979;14(3):368–375.
3. Martin L, Zerella J. Jejuno-ileal atresia: a proposed classification. *J Pediatr Surg*. 1976;11:399–403.
4. Cox SG, et al. Colonic atresia: spectrum of presentation and pitfalls in management. A review of 14 cases. *Pediatr Surg Int*. 2005;21(10):813–818.
5. Fishman SJ, et al. Nonfixation of an atretic colon predicts Hirschsprung's disease. *J Pediatr Surg*. 2001;36(1):202–204.
6. El-Asmar KM, et al. Colonic atresia: association with other anomalies. *J Neonatal Surg*. 2016;5(4):47.
7. Arca M, Oldham K. Atresia, stenosis and other obstructions of the colon. In: Coran A, et al, eds. *Coran: Pediatric Surgery*. Philadelphia: CV Mosby, an Imprint of Elsevier; 2012.
8. Elisa Z, et al. Multiple congenital colonic stenosis: a rare gastrointestinal malformation. *Case Rep Pediatr*. 2016;2016:6329793.
9. Mizuno M, et al. Congenital membranous colonic stenosis–case report of an extremely rare anomaly. *J Pediatr Surg*. 2003;38(8):E13–E15.
10. Louw J, Barnard C. Congenital intestinal atresia observations on its origin. *Lancet*. 1955;266(6899):1065–1067.
11. Celli J. Genetics of gastrointestinal atresias. *Eur J Med Genet*. 2014;57(8):424–439.
12. Fairbanks TJ, et al. A genetic mechanism for cecal atresia: the role of the Fgf10 signaling pathway. *J Surg Res*. 2004;120(2):201–209.
13. Githu T, et al. Fetal MRI of hereditary multiple intestinal atresia with postnatal correlation. *Pediatr Radiol*. 2014;44(3):349–354.
14. Dalla Vecchia LK, et al. Intestinal atresia and stenosis: a 25-year experience with 277 cases. *Arch Surg*. 1998;133(5):490–496, discussion 496–7.
15. England RJ, Scammell S, Murthi GV. Proximal colonic atresia: is right hemicolectomy inevitable? *Pediatr Surg Int*. 2011;27(10):1059–1062.
16. Herman RS, Teitelbaum DH. Anorectal malformations. *Clin Perinatol*. 2012;39(2):403–422.
17. Levitt M, Peña A. Anorectal malformations. In: Coran A, et al, eds. *Coran: Pediatric Surgery*. Philadelphia: CV Mosby, an Imprint of Elsevier; 2012.
18. Gross RE. Malformations of the anus and rectum. In: Gross RE, ed. *The Surgery of Infancy and Childhood*. Philadelphia: WB Saunders; 1953.
19. Bhatnagar S. Anorectal malformations (part 1). *J Neonatal Surg*. 2015;4(1):7.
20. Levitt MA, Pena A. Anorectal malformations. *Orphanet J Rare Dis*. 2007;2:33.
21. M B, et al. Primary transanal management of rectal atresia in a neonate. *J Neonatal Surg*. 2016;5(2):20.
22. Hamrick M, et al. Rectal atresia and stenosis: unique anorectal malformations. *J Pediatr Surg*. 2012;47(6):1280–1284.
23. Sadler T. Digestive System. In: *Langman's Medical Embryology*. Philadelphia: Lippincott Williams & Wilkins; 2010.
24. Wang C, Li L, Cheng W. Anorectal malformation: the etiological factors. *Pediatr Surg Int*. 2015;31(9):795–804.
25. Berdon WE, et al. The radiologic evaluation of imperforate anus. An approach correlated with current surgical concepts. *Radiology*. 1968;90(3):466–471.
26. Levitt MA, Kant A, Pena A. The morbidity of constipation in patients with anorectal malformations. *J Pediatr Surg*. 2010;45(6):1228–1233.
27. Son JK, Taylor GA. Transperineal ultrasonography. *Pediatr Radiol*. 2014;44(2):193–201.
28. Karsten K, Rothe K, Marzheuser S. Voiding Cystourethrography in the diagnosis of anorectal malformations. *Eur J Pediatr Surg*. 2016;26(6):494–499.
29. Alamo L, et al. Anorectal malformations: finding the pathway out of the labyrinth. *Radiographics*. 2013;33(2):491–512.
30. Haber HP, et al. Transperineal sonography for determination of the type of imperforate anus. *AJR Am J Roentgenol*. 2007;189(6):1525–1529.
31. Han TI I., Kim O, Kim WS. Imperforate anus: US determination of the type with infracoccygeal approach. *Radiology*. 2003;228(1):226–229.
32. Bischoff A, Levitt MA, Pena A. Update on the management of anorectal malformations. *Pediatr Surg Int*. 2013;29(9):899–904.
33. Lee JK, Towbin AJ. Currarino syndrome and the effect of a large anterior sacral meningocele on distal colostogram in an anorectal malformation. *J Radiol Case Rep*. 2016;10(6):16–21.
34. Nievelstein RA, et al. Magnetic resonance imaging in children with anorectal malformations: embryologic implications. *J Pediatr Surg*. 2002;37(8):1138–1145.
35. Kavalcova L, et al. The diagnostic value of MRI fistulogram and MRI distal colostogram in patients with anorectal malformations. *J Pediatr Surg*. 2013;48(8):1806–1809.
36. Currarino G, Coln D, Votteler T. Triad of anorectal, sacral, and presacral anomalies. *AJR Am J Roentgenol*. 1981;137(2):395–398.
37. Ross AJ, et al. A homeobox gene, HLXB9, is the major locus for dominantly inherited sacral agenesis. *Nat Genet*. 1998;20(4):358–361.
38. Fleury J, et al. Currarino syndrome as an etiology of a neonatal Escherichia coli meningitis. *J Perinatol*. 2007;27(9):589–591.
39. Cretolle C, et al. Spectrum of HLXB9 gene mutations in Currarino syndrome and genotype-phenotype correlation. *Hum Mutat*. 2008;29(7):903–910.
40. Cuturilo G, et al. Phenotype analysis impacts testing strategy in patients with Currarino syndrome. *Clin Genet*. 2016;89(1):109–114.
41. Caro-Dominguez P, Bass J, Hurteau-Miller J. Currarino syndrome in a fetus, infant, child, and adolescent: spectrum of clinical presentations and imaging findings. *Can Assoc Radiol J*. 2016.
42. Martucciello G, et al. Currarino syndrome: proposal of a diagnostic and therapeutic protocol. *J Pediatr Surg*. 2004;39(9):1305–1311.
43. Sen G, et al. Familial Currarino syndrome presenting with peripheral primitive neuroectodermal tumour arising with a sacral teratoma. *Pediatr Blood Cancer*. 2008;50(1):172–175.
44. Martucciello G, et al. Associated anomalies in intestinal neuronal dysplasia. *J Pediatr Surg*. 2002;37(2):219–223.
45. Parisi MA. Hirschsprung Disease Overview. In: Pagon RA, Adam MP, Ardinger HH, et al, eds. *GeneReviews®[Internet]*. Seattle (WA): University of Washington, Seattle; 2002 Jul 12 [updated 2015 Oct 1]:1993–2017.
46. Hirschsprung H. Stuhlträgheit Neugeborenenr in Folge von Dilatation und Hypertrophie des Colons. *Jahrb F Kinderh*. 1887;27:1.
47. Tiffin M, Chandler L, Faber H. Localized absence of the ganglion cells of the myenteric plexus in congenital megacolon. *Arch Pediatr Adolesc Med*. 1940;59(5):1071–1082.
48. [deleted in review]
49. [deleted in review]
50. [deleted in review]
51. Panza E, et al. Genetics of human enteric neuropathies. *Prog Neurobiol*. 2012;96(2):176–189.
52. Langer JC. Hirschsprung Disease. In: Coran A, et al, eds. *Coran: Pediatric Surgery*. Philadelphia: CV Mosby, an Imprint of Elsevier; 2012.
53. Carrasquillo MM, et al. Genome-wide association study and mouse model identify interaction between RET and EDNRB pathways in Hirschsprung disease. *Nat Genet*. 2002;32(2):237–244.
54. Heanue TA, Pachnis V. Prospective identification and isolation of enteric nervous system progenitors using Sox2. *Stem Cells*. 2011;29(1):128–140.
55. Widowati T, et al. RET and EDNRB mutation screening in patients with Hirschsprung disease: functional studies and its implications for genetic counseling. *Eur J Hum Genet*. 2016;24(6):823–829.
56. Rudolph C, Benaroch L. Hirschsprung disease. *Pediatr Rev*. 1995;16(1):5–11.
57. Badner JA, et al. A genetic study of Hirschsprung disease. *Am J Hum Genet*. 1990;46(3):568–580.
58. Newman B, Nussbaum A, Kirkpatrick JA Jr. Bowel perforation in Hirschsprung's disease. *AJR Am J Roentgenol*. 1987;148(6):1195–1197.
59. Newman B, et al. Appendiceal perforation, pneumoperitoneum, and Hirschsprung's disease. *J Pediatr Surg*. 1988;23(9):854–856.
60. O'Hare T, et al. A retrospective cohort study of total colonic aganglionosis: is the appendix a reliable diagnostic tool? *J Neonatal Surg*. 2016;5(4):44.
61. Baxter KJ, Bhatia AM. Hirschsprung's disease in the preterm infant: implications for diagnosis and outcome. *Am Surg*. 2013;79(7):734–738.
62. Duess JW, Hofmann AD, Puri P. Prevalence of Hirschsprung's disease in premature infants: a systematic review. *Pediatr Surg Int*. 2014;30(8):791–795.
63. Moore SW. The contribution of associated congenital anomalies in understanding Hirschsprung's disease. *Pediatr Surg Int*. 2006;22(4):305–315.

64. Amiel J, Lyonnet S. Hirschsprung disease, associated syndromes, and genetics: a review. *J Med Genet*. 2001;38(11):729–739.
65. Haddad GG, et al. Congenital failure of automatic control of ventilation, gastrointestinal motility and heart rate. *Medicine (Baltimore)*. 1978;57(6):517–526.
66. Bajaj R, et al. Congenital central hypoventilation syndrome and Hirschsprung's disease in an extremely preterm infant. *Pediatrics*. 2005;115(6):e737–e738.
67. Stratulat-Chiriac I, McLaughlin D, Antao B. Rare association of extended total colonic aganglionosis and intestinal malrotation. *J Neonatal Surg*. 2016;5(4):61.
68. Hofmann AD, Duess JW, Puri P. Congenital anomalies of the kidney and urinary tract (CAKUT) associated with Hirschsprung's disease: a systematic review. *Pediatr Surg Int*. 2014;30(8):757–761.
69. Hackam DJ, Filler RM, Pearl RH. Enterocolitis after the surgical treatment of Hirschsprung's disease: risk factors and financial impact. *J Pediatr Surg*. 1998;33(6):830–833.
70. Pastor AC, et al. Development of a standardized definition for Hirschsprung's-associated enterocolitis: a Delphi analysis. *J Pediatr Surg*. 2009;44(1):251–256.
71. Frykman PK, et al. Enterocolitis causes profound lymphoid depletion in endothelin receptor B- and endothelin 3-null mouse models of Hirschsprung-associated enterocolitis. *Eur J Immunol*. 2015;45(3):807–817.
72. Thiagarajah JR, et al. Altered goblet cell differentiation and surface mucus properties in Hirschsprung disease. *PLoS ONE*. 2014;9(6):e99944.
73. Wong CW, et al. The value of the 24-h delayed abdominal radiograph of barium enema in the diagnosis of Hirschsprung's disease. *Pediatr Surg Int*. 2015;31(1):11–15.
74. Heuckeroth RO. Regeneration: stem cells make the bowel nervous. *Nature*. 2016;531(7592):44–45.
75. Stamp LA, Young HM. Recent advances in regenerative medicine to treat enteric neuropathies: use of human cells. *Neurogastroenterol Motil*. 2017;29(1).
76. Fattahi F, et al. Deriving human ENS lineages for cell therapy and drug discovery in Hirschsprung disease. *Nature*. 2016;531(7592):105–109.
77. Ellis H, Kumar R, Kostyrka B. Neonatal small left colon syndrome in the offspring of diabetic mothers—an analysis of 105 children. *J Pediatr Surg*. 2009;44(12):2343–2346.
78. Siddiqui MM, Drewett M, Burge DM. Meconium obstruction of prematurity. *Arch Dis Child Fetal Neonatal Ed*. 2012;97(2):F147–F150.
79. Arnoldi R, et al. Delayed meconium passage in very low birth weight infants. *Eur J Pediatr Surg*. 2011;21(6):395–398.
80. Keckler SJ, et al. Current significance of meconium plug syndrome. *J Pediatr Surg*. 2008;43(5):896–898.
81. Berrocal T, et al. Congenital anomalies of the small intestine, colon, and rectum. *Radiographics*. 1999;19(5):1219–1236.
82. Cho HH, et al. Ultrasound-guided contrast enema for meconium obstruction in very low birth weight infants: factors that affect treatment success. *Eur J Radiol*. 2015;84(10):2024–2031.
83. Rodriguez L, Flores A. Chronic intestinal pseudo-obstruction. In: Liacouras C, Piccoli D, Bell L, eds. *Liacouras & Piccoli: Pediatric Gastroenterology: Requisite*. Philadelphia: Mosby: an Imprint of Elsevier; 2008.
84. Fadda B, et al. [Neuronal intestinal dysplasia. Critical 10-years' analysis of clinical and biopsy diagnosis]. *Z Kinderchir*. 1983;38(5):305–311.
85. Puri P. Intestinal dysganglionosis and other disorders of intestinal motility. In: Coran A, et al, eds. *Coran: Pediatric Surgery*. Philadelphia: CV Mosby, an Imprint of Elsevie; 2012.
86. Puri P, et al. Neuronal colonic dysplasia: an unusual association of Hirschsprung's disease. *J Pediatr Surg*. 1977;12(5):681–685.
87. Berger S, et al. Congenital malformations and perinatal morbidity associated with intestinal neuronal dysplasia. *Pediatr Surg Int*. 1998;13(7):474–479.
88. Bonora E, et al. Mutations in RAD21 disrupt regulation of APOB in patients with chronic intestinal pseudo-obstruction. *Gastroenterology*. 2015;148(4):771–782 e11.
89. Case records of the Massachusetts General Hospital. Weekly clinicopathological exercises. Case 52-1991. An eight-year-old girl with recurrent abdominal distention after surgical correction of Hirschsprung's disease. *N Engl J Med*. 1991;325(26):1865–1874.
90. Berdon WE, et al. Megacystis-microcolon-intestinal hypoperistalsis syndrome: a new cause of intestinal obstruction in the newborn. Report of radiologic findings in five newborn girls. *AJR Am J Roentgenol*. 1976;126(5):957–964.
91. Puri P, Shinkai M. Megacystis microcolon intestinal hypoperistalsis syndrome. *Semin Pediatr Surg*. 2005;14(1):58–63.
92. Raofi V, et al. Combined living-related segmental liver and bowel transplantation for megacystis-microcolon-intestinal hypoperistalsis syndrome. *J Pediatr Surg*. 2008;43(2):e9–e11.
93. McLaughlin D, Puri P. Familial megacystis microcolon intestinal hypoperistalsis syndrome: a systematic review. *Pediatr Surg Int*. 2013;29(9):947–951.
94. Piaseczna Piotrowska A, et al. Interstitial cells of Cajal in the human normal urinary bladder and in the bladder of patients with megacystis-microcolon intestinal hypoperistalsis syndrome. *BJU Int*. 2004;94(1):143–146.
95. Piotrowska AP, et al. Alterations in smooth muscle contractile and cytoskeleton proteins and interstitial cells of Cajal in megacystis microcolon intestinal hypoperistalsis syndrome. *J Pediatr Surg*. 2003;38(5):749–755.
96. Rolle U, et al. Megacystis-microcolon-intestinal hypoperistalsis syndrome: evidence of intestinal myopathy. *Pediatr Surg Int*. 2002; 18(1):2–5.
97. Rolle U, Puri P. Structural basis of voiding dysfunction in megacystis microcolon intestinal hypoperistalsis syndrome. *J Pediatr Urol*. 2006;2(4):277–284.
98. Lund D. Alimentary Tract Duplications. In: Coran A, et al, eds. *Coran: Pediatric Surgery*. Philadelphia: CV Mosby, an Imprint of Elsevier; 2012.
99. Yousefzadeh DK, et al. Tubular colonic duplication–review of 1876-1981 literature. *Pediatr Radiol*. 1983;13(2):65–71.
100. Pampal A, et al. Rectal duplications accompanying rectovestibular fistula: report of two cases. *Pediatr Int*. 2013;55(4):e86–e89.
101. Piolat C, et al. Perforated tubular duplication of the transverse colon: a rare cause of meconium peritonitis with prenatal diagnosis. *Pediatr Surg Int*. 2005;21(2):110–112.
102. Kroes HY, et al. Two cases of the caudal duplication anomaly including a discordant monozygotic twin. *Am J Med Genet*. 2002;112(4): 390–393.
103. [deleted in review]
104. Kwak JM, Boo YJ, Kim J. Tubular colorectal duplication presenting as rectovaginal fistula. *ANZ J Surg*. 2014;84(4):289–290.
105. Schmid KO. [A specially severe form of enteritis in newborn, enterocolitis ulcerosa necroticans. I. Pathological anatomy]. *Osterr Z Kinderheilkd Kinderfuersorge*. 1952;8(2):114–135.
106. Sylvester K, Liu G, Albanese CT. Necrotizing enterocolitis. In: Coran A, et al, eds. *Coran: Pediatric Surgery*. Philadelphia: CV Mosby an Imprint of Elsevier; 2012.
107. Wu SF, Caplan M, Lin HC. Necrotizing enterocolitis: old problem with new hope. *Pediatr Neonatol*. 2012;53(3):158–163.
108. Caplan MS, Fanaroff A. Necrotizing: a historical perspective. *Semin Perinatol*. 2016.
109. Bell MJ, et al. Neonatal necrotizing enterocolitis. Therapeutic decisions based upon clinical staging. *Ann Surg*. 1978;187(1):1–7.
110. Walsh MC, Kliegman RM. Necrotizing enterocolitis: treatment based on staging criteria. *Pediatr Clin North Am*. 1986;33(1):179–201.
111. Kliegman RM, Walsh MC. Neonatal necrotizing enterocolitis: pathogenesis, classification, and spectrum of illness. *Curr Probl Pediatr*. 1987;17(4):213–288.
112. Santulli TV, et al. Acute necrotizing enterocolitis in infancy: a review of 64 cases. *Pediatrics*. 1975;55(3):376–387.
113. Gordon P, et al. Mapping the new world of necrotizing enterocolitis (NEC): review and opinion. *EJ Neonatol Res*. 2012;2(4):145–172.
114. Posencheg M, Pereira G. Necrotizing enterocolitis. In: Liacouras C, Piccoli D, Bell L, eds. *Liacouras & Piccoli: Pediatric Gastroenterology: Requisites*. Philadelphia: Mosby: an Imprint of Elsevier; 2008.
115. Garbi-Goutel A, et al. Prognostic value of abdominal sonography in necrotizing enterocolitis of premature infants born before 33 weeks gestational age. *J Pediatr Surg*. 2014;49(4):508–513.
116. Silva CT, et al. A prospective comparison of intestinal sonography and abdominal radiographs in a neonatal intensive care unit. *Pediatr Radiol*. 2013;43(11):1453–1463.
117. Palleri E, et al. Complex fluid collection on abdominal ultrasound indicates need for surgery in neonates with necrotizing enterocolitis. *Eur J Pediatr Surg*. 2016.
118. Silva CT, et al. Correlation of sonographic findings and outcome in necrotizing enterocolitis. *Pediatr Radiol*. 2007;37(3):274–282.
119. Epelman M, et al. Necrotizing enterocolitis: review of state-of-the-art imaging findings with pathologic correlation. *Radiographics*. 2007;27(2):285–305.

# 106 Inflammatory and Infectious Diseases

*Mary-Louise C. Greer and Tahani M. Ahmad*

Colitis encompasses a spectrum of infectious and noninfectious inflammatory conditions. Infectious colitides, with etiologies often overlapping with enteritis (see Chapter 104), are typically acute in onset and may be localized as in acute appendicitis. The causative agent may not be known in inflammatory colitis. Some patients with hemolytic uremic syndrome (HUS) or inflammatory bowel disease (IBD) are recognized as having altered immune regulation,[1,2] and more often this form of colitis is chronic. Etiologies, clinical manifestations, imaging, and treatment options of these colitides, and others including treatment-related colitis (e.g., pseudomembranous and radiation-induced colitis), will be discussed. For some, such as IBD, this will be expanding on the discussion from Chapter 104.

## INFLAMMATORY BOWEL DISEASE

IBD includes Crohn disease (CD), ulcerative colitis (UC), and unclassified IBD. For the incidence, etiology, pathophysiology, and clinical presentation of IBD in the pediatric population, including very early onset IBD, please refer to Chapter 104. In this chapter, we will be addressing imaging of CD and UC, including perianal disease, and treatment where it differs from IBD of the upper gastrointestinal (GI) tract.

### Imaging

A summary of the diagnostic performance of various modalities in diagnosing features of IBD is listed in Table 106.1.

### Radiography

Radiography has an emergent role in IBD and, while not routinely used, familiarity with more reliable features of IBD remains important including "thumbprinting."[3] Of importance in UC and ileocolonic CD is toxic megacolon, with colonic dilatation seen on abdominal radiographs.[4] Dilatation of the transverse colon exceeding 56 mm in patients greater than 11 years (normal rarely >40 mm in younger patients) is a strong indicator of toxic megacolon, particularly if seen in conjunction with three of four criteria: fever, tachycardia, leukocytosis, or anemia (Fig. 106.1).[5]

### Ultrasound

As discussed in Chapter 104, abdominal and pelvic ultrasound (US) now plays an important role in pediatric IBD, for monitoring disease, diagnosis if magnetic resonance imaging (MRI) is not an option, and problem solving in acute situations by demonstrating abscesses, stenoses, fistulae or an acute flare, with advantages and limitations as previously considered.[6] US after ingestion of nonabsorbable oral contrast can assist if colonic strictures render ileocolonoscopy nondiagnostic.[4] Good specificity but lower sensitivity of conventional US is primarily due to differences in detection of colonic inflammation by location, limiting its usefulness as a screening tool. US accuracy is high in a majority of the large bowel but lower in the transverse colon and rectum.[4,7]

Mural and extramural features in colonic CD emulate small bowel findings (see Chapter 104). Crohn colitis can have skip lesions or be right side only (e-Fig. 106.2). In comparison, UC is characterized by continuous involvement of the colon from the rectum progressing retrograde with intermediate wall thickening, slightly hypoechoic and nonhomogenous mucosa, and submucosal edema (acute phase) with preserved mural stratification. Chronic UC can have submucosal fibrosis ± fat deposits, loss of haustrations, and stiffness. Even so, distinction from Crohn colitis is poor (Fig. 106.3).[8] Pancolitis can be associated with backwash ileitis (6%–20%).[9] Transmural involvement is rare in UC, as are extramural findings. Regional variations with macroscopic rectal sparing and cecal patches are not usually evident on cross-sectional imaging.

Perianal and perineal US have a small role in the acute setting to rapidly identify a perianal abscess that may require urgent drainage. A percutaneous approach can demonstrate fistulae, although with variable accuracy, and classification largely depends on use of endoanal probes that are seldom utilized in children and adolescents.[4]

### Fluoroscopy

Single or double contrast enemas are now rarely used in IBD imaging due to the ionizing radiation and inability to evaluate transmural and extramural features. Infants and young children may still benefit from this technique for diagnosis and documenting extent of very early onset IBD (e-Fig. 106.4). Water-soluble contrast agents are now often used in preference to barium. Mucosal ulceration, pseudopolyps, loss of haustrations, stenoses, and fistulae have all been documented in CD. Enteroenteric fistulae may be demonstrated to lesser extent with fluoroscopy than with other techniques.[10] UC typically has shallower ulcers, with less wall deformity and stricturing.

### Computed Tomography and Magnetic Resonance Imaging

#### Computed Tomography/Magnetic Resonance Enterography and Colonography

The colon is evaluated when included in computed tomographic enterography (CT) and magnetic resonance enterography (MRE) assessment of small bowel, without any special colonic preparation. CD features are similar to that seen in small bowel (see Chapter 104) with deep ulcers, pseudopolyps, mural thickening and hyperenhancement, engorged vasa recta, and on MRE, T2 hyperintensity and restricted diffusion. In UC, mural thickening can be subtler with preservation of the smooth outer contour of the bowel wall (Fig. 106.5). As with US, MRI can occasionally demonstrate mural fat in chronic UC, although infrequently seen in children (e-Fig. 106.6). In both, loss of colonic haustrations can be seen ("lead pipe" configuration).[11] In Crohn colitis in particular, extramural changes can include fibrofatty proliferation, mesenteric enhancement, or edema, abscesses, and fistulae.[4,12] Although strictures can be difficult to appreciate in collapsed large bowel, this was not an impediment to detection of colonic inflammation, with a recent small study comparing MRE with endoscopic biopsies showing a sensitivity of 90% and specificity of 60% for active inflammation (Fig. 106.7).[13] Unsuspected perianal disease is increasingly recognized on MRE, and this region warrants careful review (see later in this chapter).[14]

CT colonography (virtual colonoscopy) uses colonic air insufflation, and MR colonography uses rectal instillation of warm water or saline to distend the colon, although colonic IBD can be seen

## Abstract:

A diverse range of acquired colonic disorders resulting from inflammatory and infectious etiologies is discussed in this chapter. Their pathophysiology, clinical manifestations, imaging features and treatment options will be reviewed.

Inflammatory bowel disease (IBD) manifests in the large bowel as ulcerative or Crohn colitis, with or without perianal disease, and hemolytic uremic syndrome can result in hemorrhagic colitis. They may arise from immunologic defects and/or infections. Colitides with more defined etiologies include antibiotic-associated pseudomembranous colitis from *Clostridium difficile*, radiation and neutropenic colitis.

Where diagnostic imaging is indicated, abdominal radiographs or ultrasound are usually sufficient, largely replacing contrast enemas. Magnetic resonance imaging (MRI) and to lesser extent computed tomography (CT), are utilized selectively as in evaluation of IBD. Although imaging of infectious colitis is seldom required, in rare instances imaging can aid distinction from other diseases, such as the invasive fungal infection gastrointestinal basidiobolomycosis that can mimic lymphoma. CT and MRI are of limited value in diseases such as Graft-Versus-Host colitis as imaging findings are usually non-specific.

Appendicitis warrants special attention. A common condition in childhood and adolescence, inflammation of the appendix can be challenging to diagnose, symptoms non-specific in up to a third of cases, particularly in younger patients. Complications from delayed or missed diagnoses can be significant. Changing diagnostic pathways have greater reliance on imaging, ultrasound usually first line. In equivocal cases, CT and more recently MRI have a useful role. These modifications have contributed to improved patient outcomes with a decline in negative appendectomy rates.

## Keywords:

Ulcerative colitis
Crohn colitis
pseudomembranous colitis
infectious colitides
appendicitis

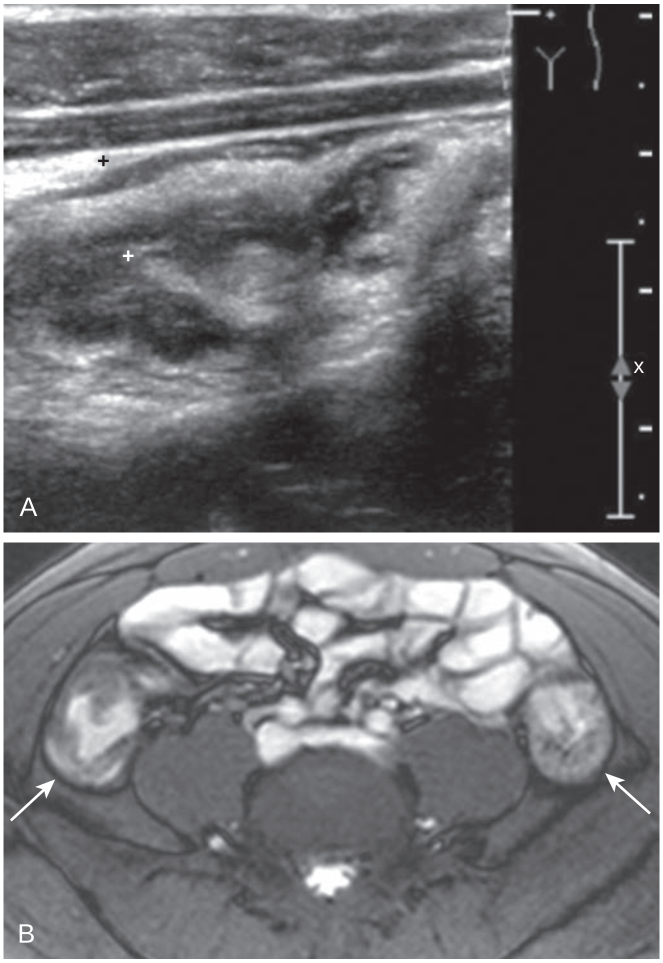

**e-Figure 106.2. Crohn disease flare in a 15-year-old boy.** Ultrasound (US) and corresponding magnetic resonance enterography (MRE) images show circumferential wall thickening of the cecum that is hyperechoic on US (A) and hyperintense on axial T2-weighted steady-state free precession fat-saturated MRE (B), with similar finding in the descending colon *(arrows)*.

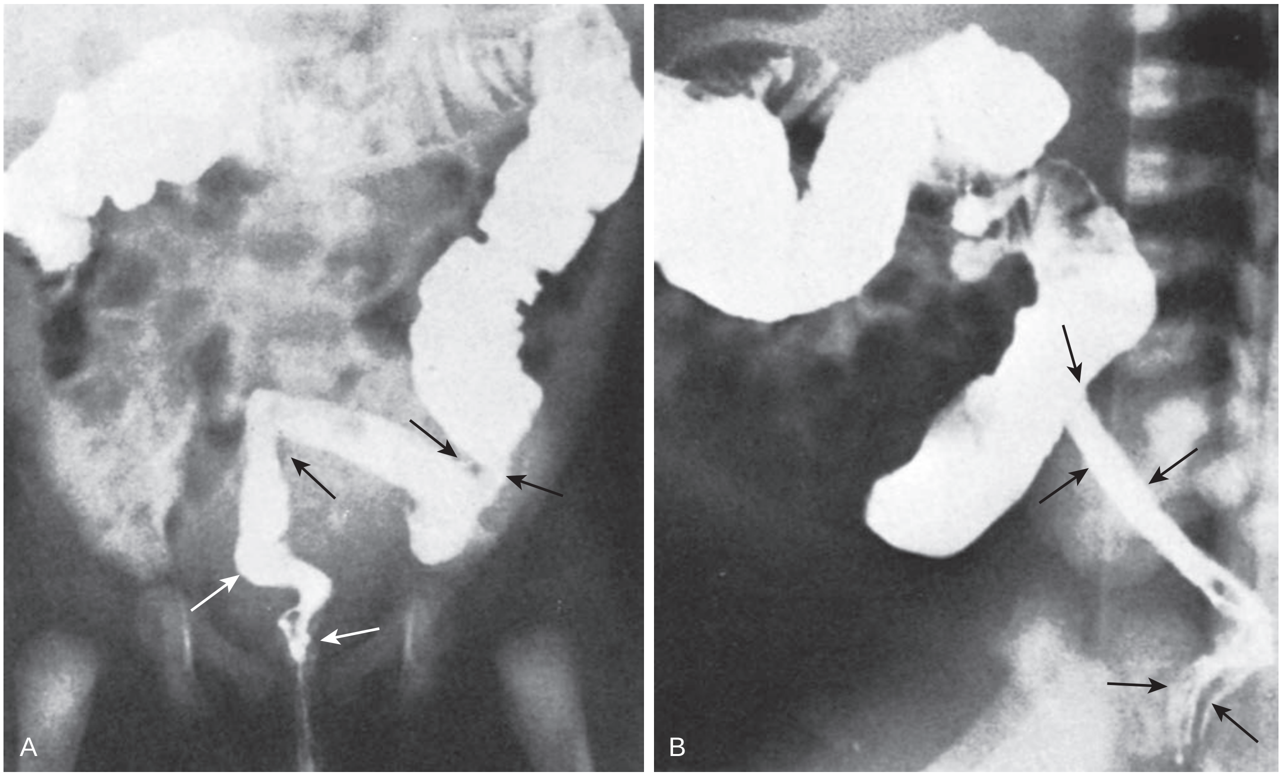

**e-Figure 106.4. Infantile ulcerative colitis in a 3-week-old girl with rectal bleeding.** Frontal (A) and lateral (B) projections during barium enema show tubular narrowing of the rectum and sigmoid colon *(arrows)* with an abrupt transition zone. The findings were suggestive of aganglionosis, but biopsy revealed ulcerative colitis.

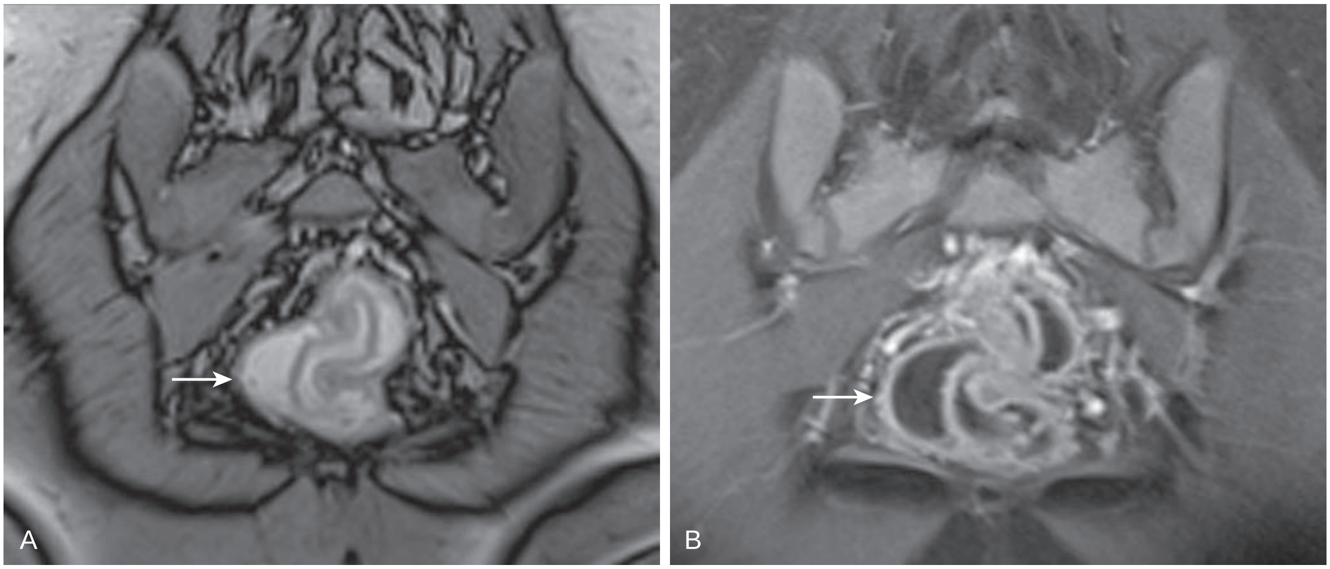

**e-Figure 106.6. Chronic ulcerative colitis on MR enterography.** Intramural fat in the rectosigmoid in a 16-year-old boy is demonstrated by increased signal on (A) coronal non–fat-suppressed T2-weighted steady-state free precession image and deceased signal on (B) coronal contrast-enhanced T1-weighted 3D gradient echo sequence *(arrows)*.

even without good distension (e-Fig. 106.8).[12,15] MR colonography, lacking ionizing radiation, may have value if ileocolonoscopy is incomplete due to strictures or patient contraindications. This provides mucosal, mural, as well extramural information, which in undifferentiated IBD can aid in distinguishing CD from UC.[4,12] In pediatric IBD, patient tolerance precludes MR colonoscopy from being employed routinely in conjunction with MRE, although it is done in some centers. There are variable rates of detection reported for CD on MR colonography (which performs better for UC), such that ileocolonoscopy remains the mainstay of evaluation in pediatric IBD.[4,15]

**TABLE 106.1** Imaging Findings by Modality in Colonic Inflammatory Bowel Disease*

| | US<br>Sens./Spec. | CT^<br>Sens./Spec. | MRI^<br>Sens./Spec. |
|---|---|---|---|
| **Crohn colitis** | 63%-100% / 77%-100% | 60%-90% / 90%-100% | 78%-100% / 46%-100%<br>#(60% / 90%) |
| **Ulcerative colitis** | 48%-100% / 82%-90% | 74% / N/A | 59%-68% / 32%-40% |
| **Fistula** | 71%-87% / 90%-100% | 68% / 91% | 71%-100% / 92%-100% |
| **Abscess** | 81%-100% / 92%-94% | 86%-100% / 95%-100% | 75%-86% / 91%-93% |
| **Stenosis** | 100% / 90% | N/A | 75%-100% / 91%-100% |

*Summary of "Imaging techniques for assessment of inflammatory bowel disease: Joint ECCO and ESGAR evidence-based consensus guidelines"[4]—not specific to pediatrics

#"Detecting inflammation in the unprepared pediatric colon – how reliable is magnetic resonance enterography?"—pediatric[13]

^technique, e.g., enterography, colonography, not always specified

*CT*, computed tomography; *MRI*, magnetic resonance imaging; *N/A*, not available; *Sens*, sensitivity; *Spec*, specificity; *US*, ultrasound.

### Pelvic MRI

For perianal disease, occurring in up to 21% of pediatric CD patients, pelvic MRI is the imaging reference standard (Fig. 106.9).[12,16–18] Fistulae and abscesses are well depicted, and MRI is superior to US and examination under anesthesia, although accuracy is increased when these are combined.[4] Skin tags can also be seen. Described according to Parks' or St. James University Hospital classifications, one review has suggested the Parks' classification is more suited to children due to shorter anal canal length, typically performed without an endoanal coil.[19–22] Contrast-enhanced and diffusion-weighted imaging can help define disease activity as well as distinguishing fistulae from abscesses. Activity measures (e.g., Van Assche and predictors of treatment response) are increasingly used to guide therapy, with better responses seen with maximum fistula length less than 2.5 cm and abscess volume less than 1 mL.[23,24] Contraindications for MRI and risks relating to iodinated and gadolinium-based contrast agents will be discussed elsewhere. There is seldom a role for CT in perianal disease in children.

## Nuclear Medicine

A negative scintigraphy study in CD (e.g., radiolabeled leucocytes or positron emission tomography (PET)/CT or PET/MR) can exclude active disease with high accuracy.[4] While monitoring

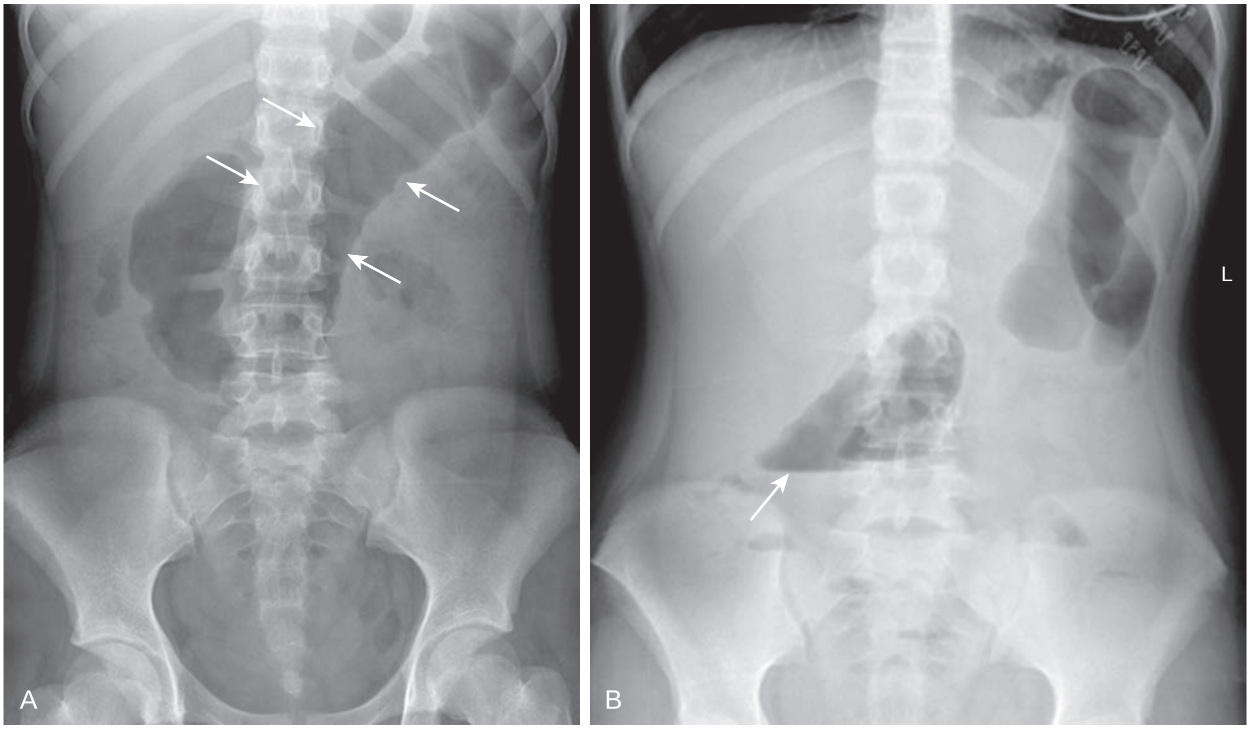

**Figure 106.1. Toxic megacolon in a 13-year-old girl with ulcerative colitis.** (A) Supine abdominal radiograph shows dilated transverse colon (5.9 cm) with loss of haustrations and mild wall thickening *(arrows)*. The remainder of the abdomen and pelvis is relatively gasless with a paucity of stool. (B) Upright radiograph shows multiple air-fluid levels *(arrow)*.

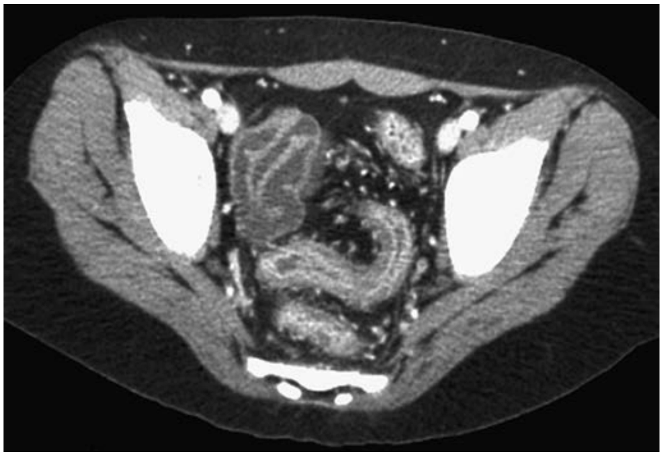

**e-Figure 106.8. Ulcerative colitis in a 12-year-old.** Contrast-enhanced CT image shows a smooth outer wall with marked mucosal enhancement of the rectosigmoid colon and engorgement of pelvic vessels. *(Courtesy Dr. Marta Hernanz-Schulman, Nashville, TN.)*

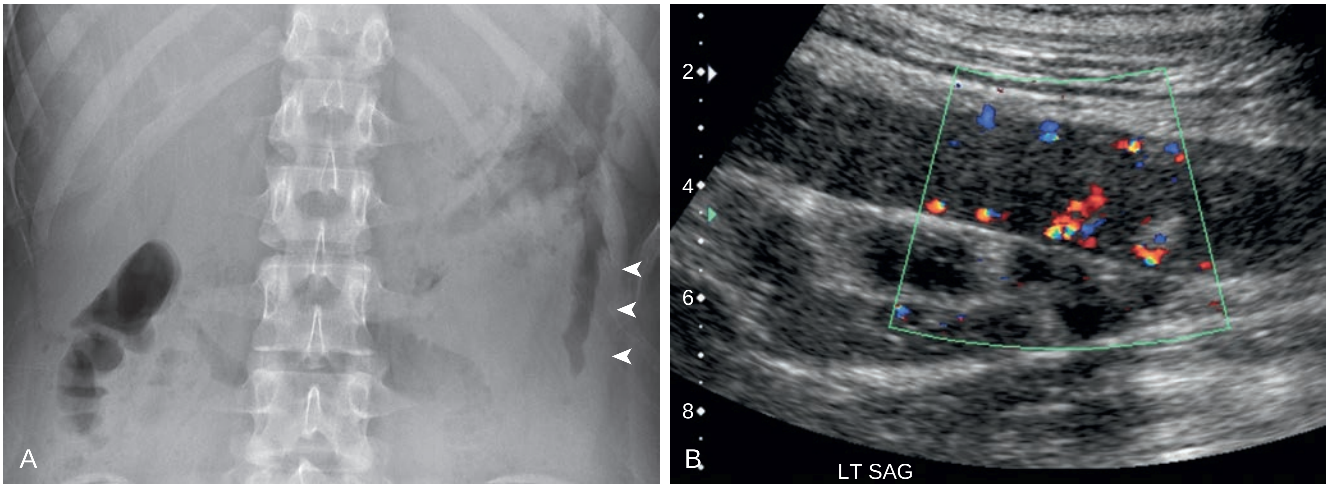

**Figure 106.3. Ulcerative colitis in a 15-year-old with acute-on-chronic changes.** (A) Abdominal radiograph shows diffuse thickening of featureless descending colon with "lead pipe" configuration and no stool contents *(arrowheads)*. (B) Color Doppler sonogram reveals diffuse mural thickening, hyperemia, and luminal narrowing. Note the absence of extracolonic soft tissue changes.

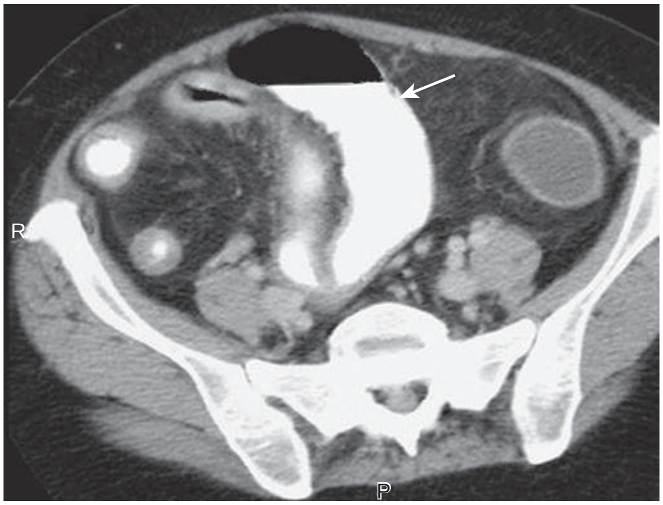

**Figure 106.5. Active Crohn disease in a 19-year-old.** Contrast-enhanced CT shows the distended ileum *(arrow)* proximal to the thick-walled ileal loops and mesenteric stranding and vascular engorgement, resulting from active inflammation. Mural thickening and vascular engorgement of colonic segments is apparent. Positive oral contrast in the lumen interferes with evaluation of mucosal enhancement.

treatment response and distinction of inflammatory and fibrotic strictures is promising, as with small bowel (see Chapter 104), there is limited application for pediatric IBD due to the ionizing radiation and poor evaluation of perianal disease.[4,25,26]

***Treatment.*** *Toxic megacolon* requires aggressive therapy combining medical and surgical approaches due to a high risk of perforation. Managing the underlying cause and supportive therapy with bowel rest, then enteral feeds, low-dose heparin for deep venous thrombosis prophylaxis, high-dose steroids, and antibiotics should not exceed 48 hours. Nasogastric suction is not beneficial. Subtotal colectomy and end ileostomy with a Hartmann's closure of the rectum, required in 47%, has a lower mortality rates than total colectomy, although emergent total colectomy is sometimes needed.[5,27]

Medical treatment and surgical intervention in Crohn colitis is discussed in Chapter 104.[28,29] In UC, corticosteroids and 5-aminosalicylates are initially used to achieve and maintain mucosal healing. Antitumor necrosis α (anti-TNFα) therapies such as infliximab are reserved for persistently active UC in up to 20% of steroid-dependent patients.[28] Colectomy rates vary geographically, approximating 15% at 5 years and 20% 10 years after presentation and, while curative, is not without morbidity.[30,31]

Perianal fistulae and abscesses involve both medical and surgical options such as antibiotics, topical or systemic biologic agents, fistulotomy, fecal diversion, and primary incision and drainage. The choice depends on severity, activity, and prognostic features of fistula length and abscess volume.[23] Anti-TNFα agents should be avoided with abscesses but in combination with seton drainage achieves a 90% response, although relapse rates are high.[32]

## PSEUDOMEMBRANOUS COLITIS

Pseudomembranous colitis refers to severe colonic disease that occurs in approximately 15% to 25% of patients with antibiotic-associated diarrhea.[33]

***Etiology.*** The toxins produced by the bacterium *Clostridium difficile* are the most important cause of antibiotic-associated pseudomembranous colitis, producing whitish, raised, plaquelike lesions restricted to the colon, as distinct from nonantibiotic-associated pseudomembranous colitis, which can also involve small bowel.[33–35] Other less common toxins include those produced by *C. perfringens* and *Staphylococcus aureus*. The diagnosis is a combined clinical and laboratory one (enzyme immunoassay detection of toxin A and B in stool and higher sensitivity polymerase chain reaction toxin gene detection). Infants exposed to *C. difficile* do not become unwell due to inability of the toxin to bind to immature colonic mucosa, thus pseudomembranous colitis is more common in adults than in children and rare in infants.[34] Recently, studies have shown an association of recurrent *C. difficile* colitis in older patients who had undergone remote appendectomy, suggesting a role of immune protection by the normal appendix.[36,37]

***Clinical Presentation.*** Pseudomembranous colitis is characterized by fever, bloody diarrhea, cramping, and colonic mucositis and can be life-threatening. The condition most commonly follows

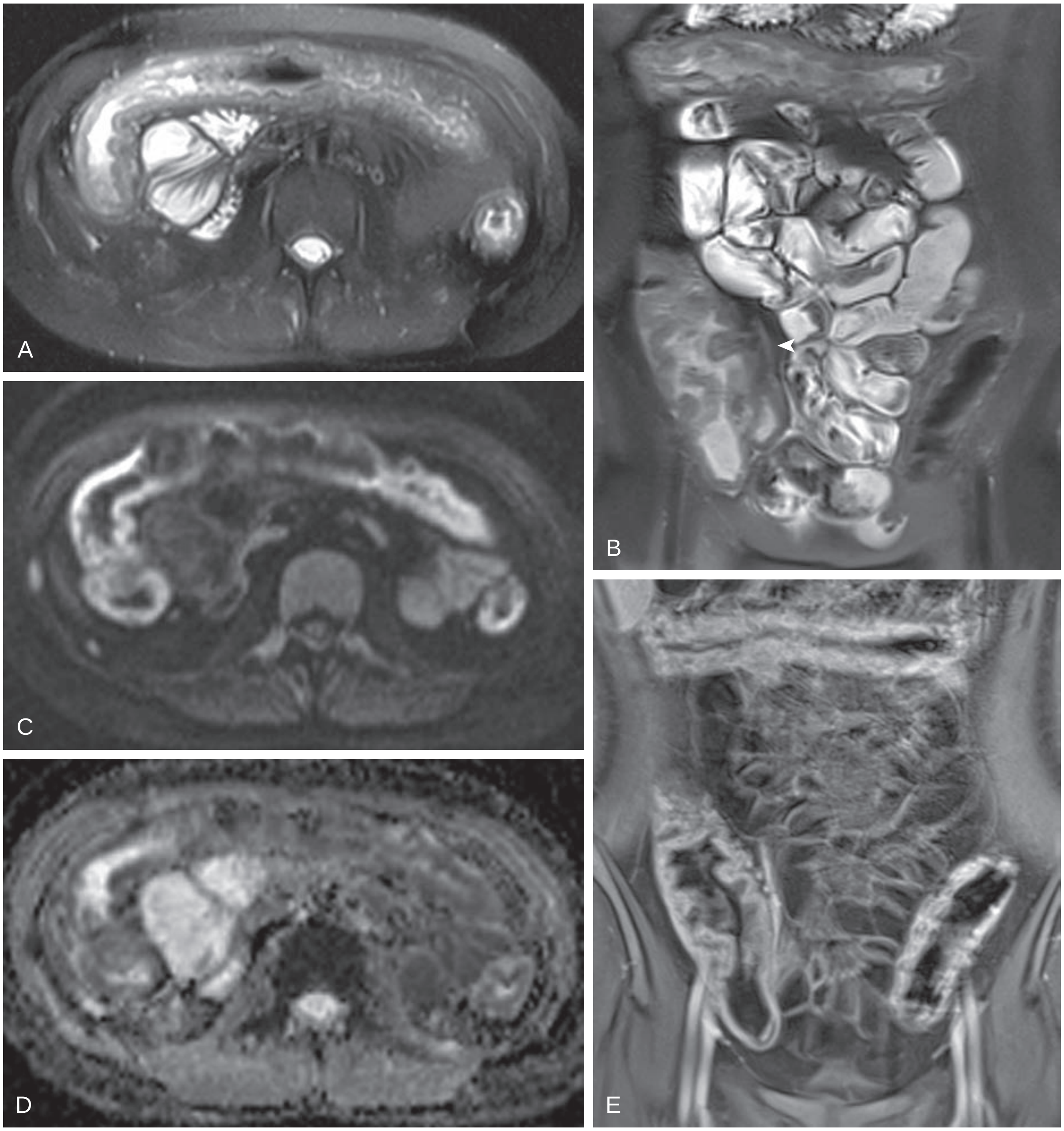

**Figure 106.7. Ulcerative colitis with pancolitis on MR enterography.** The same 16-year-old boy in e-Fig. 106.6 with precolectomy MR enterography. There is continuous transmural involvement of the colon with severe acute-on-chronic inflammation showing deep ulceration, increased mural signal on (A) axial and (B) coronal T2-weighted single-shot images; restricted diffusion on axial diffusion weighted imaging (DWI) with increased mucosal signal on b = 800 s/mm$^2$ (C) and corresponding decreased signal on apparent diffusion coefficient (ADC) map (D); and transmural hyperenhancement on (E) coronal contrast-enhanced fat-suppressed T1-weighted 3D gradient echo images. Note sparing of the terminal ileum, partially seen on (B) *(arrowhead)* and remainder of the small bowel, and smooth serosal surface of the colon with no significant pericolonic inflammation that help distinguish this from Crohn colitis.

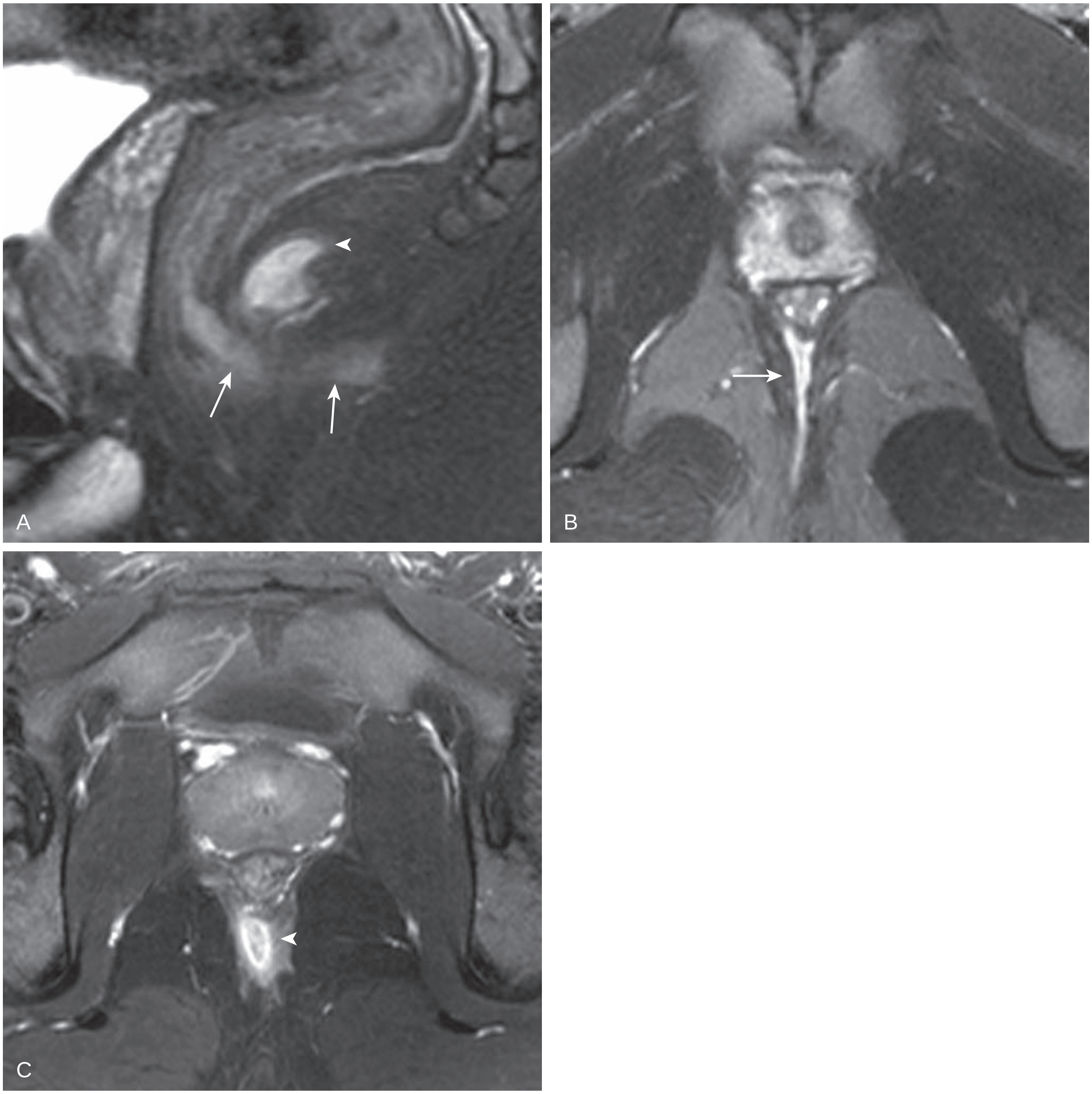

**Figure 106.9. Perianal Crohn disease in a 17-year-old male.** Pelvic MRI reveals a perianal abscess at 6 o'clock superiorly *(arrowheads* in A and C*)*, rim enhancing with fluid signal centrally, and trans-sphincteric fistula (TSF) *(arrows)* more inferiorly at 6 o'clock, with a high signal enhancing tract in (A) sagittal fat-suppressed T2-weighted and (B and C) axial fat-suppressed, contrast-enhanced, T1-weighted sequences.

broad-spectrum antibiotic therapy occurring in hospitalized patients who are often debilitated, immunocompromised, or recovering from surgery.[34,38] However, it may occur without preceding antibiotic therapy in patients in whom the gut flora has been altered, such as after weaning or surgery. The onset of diarrhea may occur within weeks after cessation of antibiotic therapy.

***Imaging.*** Imaging is less specific than clinical and laboratory findings.[39] On abdominal radiographs, findings of pseudomembranous colitis are similar to other colitides unless it is severe, with small bowel dilatation, "thumbprinting" in segments of variable length, haustral thickening and colon dilatation, and rarely gross cecal distension.[35,40] Enemas should be avoided. US, MR, or CT findings of pancolitis, with or without ascites, can be seen. Bowel wall thickening on US is predominantly hypoechoic, and on CT and MR, occasionally nodular haustral thickening can be seen (the "accordion" pattern).[39,40]

***Treatment.*** Preceding antibiotic therapy associated with the colitis should be stopped. The first line of antibiotic treatment is oral metronidazole and supportive measures including rehydration. Other oral or intravenous (IV) antibiotics may be needed initially and with recurrence; colectomy is now rarely indicated.

## HEMOLYTIC UREMIC SYNDROME

Hemolytic uremic syndrome (HUS) is a thrombotic, nonimmune, microangiopathic condition characterized by renal failure, hemolytic anemia, and thrombocytopenia.[2,41] In children, it can be related to foods such as undercooked meat in 90% of cases, causing infection often with diarrhea. The syndrome has a peak incidence of approximately 6.1 per 100,000 in children aged less than 5 years.[41]

***Etiology.*** Most cases of HUS are caused by a Shiga-like toxin produced by *Escherichia coli* serotype 0157:H7 (STEC-HUS). This is found in raw or incompletely cooked beef and unpasteurized dairy products. Rarely HUS can arise from severe disseminated *Streptococcus pneumoniae* (pneumococcal-HUS). When these infections are excluded, HUS is designated atypical (aHUS), usually without diarrhea, and dysregulation of the complement system is recognized as the pathogenic effector mechanism.[2,41] Hemorrhagic colitis is common. Renal and central nervous system complications can markedly affect the course and prognosis of this disease; outcomes typically are more severe in aHUS.[41–43]

***Clinical Presentation.*** STEC-HUS is most common during the summer months in children younger than 5 years of age. It has a spectrum of clinical manifestations from asymptomatic carrier, to a short GI prodrome averaging 3 days from ingestion with nonbloody diarrhea, to clinical evidence of acute renal failure, fever, anemia, and thrombocytopenia.[2,42–44] A positive stool culture for the specific Shiga toxin–producing *E. coli* pathogen is definitive when positive. Pneumococcal-HUS may have respiratory and neurologic features in addition to the more severe HUS triad.[2] aHUS occurs as a single event, more frequently progressing to a chronic condition.[41]

***Imaging.*** In hemorrhagic colitis, US reveals concentric wall thickening, echogenic pericolonic fat, and narrowing of the bowel lumen, primarily affecting the cecum and ascending colon, although the small bowel may be affected.[45] These features are nonspecific and may be seen in other infiltrative and inflammatory colitides. Radiographs may show colon "thumbprinting."[46] This is better seen on CT and MRI (which are rarely indicated), with contiguous bowel wall thickening, free fluid, and fat stranding.[47] Radiographic IV contrast media should be avoided due to renal impairment. There is no role for fluoroscopy. Toxic megacolon and colonic perforation have been reported, and colonic strictures can occur as a late complication.[48]

***Treatment.*** Initial treatment for HUS is supportive and may include IV fluids, transfusion of blood products, and management of hypertension. Supportive renal dialysis, if needed, is usually for 10 days in 40% to 50% with STEC-HUS, with recovery of renal function in 55% to 70% of cases.[41] Patients with aHUS may need longer renal replacement support and have worse outcomes. Use of a monoclonal antibody eculizimab, blocking the C5 cascade, is showing promising results in limiting duration of HUS in the acute phase and improving outcomes after transplantation, reducing HUS recurrence.[2]

## RADIATION COLITIS

Secondary toxicity to the GI tract is a known complication of radiation therapy. The incidence of radiotherapy-related bowel toxicity is variable depending on the radiation port, radiation dose, dosing schedule, underlying bowel condition, and comorbidities. The presentation can be acute or chronic, and different mechanisms are responsible for each. The changes can occur months to years after exposure and may involve the small bowel, colon, or rectum.[49]

***Etiology.*** Radiation injury leads to activation of mucosal cytokines and increased levels of inflammatory mediators such as interleukin (IL)-2, IL-6, and IL-8.[50] The acute changes are attributed to inhibition of epithelial cell mitotic activity and thus denudation of the mucosal surface. The chronic changes are sequelae of progressive obliterative endarteritis and fibrosis that result in variable degrees of ischemia, necrosis, and eventually stricture and fistulae formations.[51] Radiation enteritis tends to develop in patients who have received in the order of 45 Gy but can occur with doses as low as 5 to 12 Gy.[49,52]

***Clinical Presentation.*** Diarrhea, cramping, and sometimes lower intestinal bleeding occur in the acute phase, which is usually self-limiting. Urgency and tenesmus can also be seen with radiation proctitis. Eventually, fibrosis may occur, which leads to stiffness and loss of mobility and distensibility of the affected portions of the colon. Additional complications include partial obstruction, chronic adhesions, and fragility of the bowel, which may culminate in perforation.[50] Perianal fistula, hematochezia, and incontinence have been reported in patients receiving pelvic radiation.[50,51]

***Imaging.*** Patients with radiation colitis do not usually undergo imaging examinations during the acute phase. Fluoroscopic imaging with contrast enema may delineate the chronic, fibrotic change to the affected colon (e-Fig. 106.10). The imaging findings range from normal (seen in 15%) to ulceration and contour abnormalities, intestinal fixation, decreased distensibility, and stenosis.[51] The "omega sign," caused by bilateral retraction at the base of a narrowed sigmoid loop, was seen in nearly 60% of patients with radiation colitis.[51] CT and MR show relatively nonspecific findings of bowel wall thickening with an occasional target sign in acute stages and stenosis later on. The main diagnostic clue is the distribution of these changes within the radiation port.[49]

***Treatment.*** Treatment is geared toward symptom relief and includes dietary changes in addition to medications for nausea and diarrhea. Initial medical treatment usually includes antiinflammatory medications such as oral- or enema-delivered steroid or 5-aminosalicylic acid preparations.[51] Treatment options also include sucralfate, short-chain fatty acids, misoprostol, hyperbaric oxygen, and antioxidant vitamins.[51] Management of patients with chronic disease can be challenging; as many as 30% of patients may require surgery for fistulae, perforation, or bowel obstruction that does not respond to nonsurgical management.[52]

## NEUTROPENIC COLITIS

Neutropenic colitis, also known as *typhlitis*, is a necrotizing colitis primarily seen in children with low neutrophil counts from hematopoietic malignancies, although it is also seen in children with solid tumors who undergo high-dosage chemotherapy.[53] There are no definitive diagnostic criteria, although diagnosis is typically made when clinical and imaging findings are suggestive.

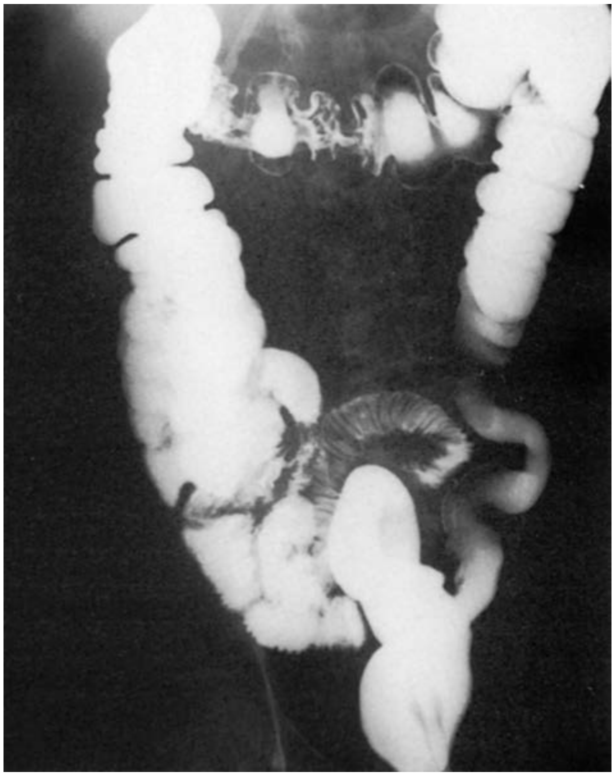

**e-Figure 106.10. Radiation colitis in an 8-year-old boy who had received radiation therapy for pelvic tumor 3 years earlier.** Barium enema shows narrowing, rigidity, and loss of haustration in the distal descending and sigmoid portions of the colon.

***Etiology.*** Development of the condition is associated with chemotherapy-related low neutrophil counts (usually less than $1.5 \times 10^9$/L) at which point the host immune system is impaired. It usually occurs between weeks 1 and 2 postchemotherapy corresponding to the neutrophil count nadir.[54] Acute lymphocytic and myelogenous leukemia are the most common underlying malignancies in pediatric patients.

The disease most often affects the cecum, hence the term typhlitis. This preferential vulnerability of the cecum is thought to be attributed to its relative low vascularity and blood supply.[54] The appendix may be involved and may produce clinical findings that mimic acute appendicitis.[55] Edema and inflammation of the colon (mainly the ascending colon) and the terminal ileum may occur, although other bowel segments can be involved.[54,56] Pneumatosis, perforation, or abscess may supervene. Bowel wall thickening, transmural edema with mucosal ulceration, ecchymoses, fibrin exudates, and partial- to full-thickness hemorrhagic necrosis are often discovered only at autopsy.[54]

***Clinical Presentation.*** This condition occurs in less than 5% of children with neutropenia. Abdominal pain, diarrhea, fever, and distended abdomen are the common presenting symptoms.

***Imaging.*** Radiographs are typically nonspecific and may show a focal ileus in the right lower quadrant. Often, a sentinel loop of dilated terminal ileum may be seen.[57] Enema studies are contraindicated in the acute phase and while there is neutropenia. Because the clinical presentation may mimic acute appendicitis, cross-sectional imaging is a critical diagnostic differentiating tool. US shows a markedly thickened cecal wall that may be either hyperechoic or hypoechoic.[58] Intraluminal fluid and ascites may also be identified. CT shows marked thickening of the affected portions of the colon, which is usually more marked in the cecum, surrounding inflammatory change and free fluid (Fig. 106.11).[56] Extension of this process may involve the terminal ileum and the appendix.

***Treatment.*** Management most often is conservative and includes antibiotics, but rarely bowel resection is necessary. Recovery is more related to the presence and severity of comorbidities than to the neutropenic colitis.[59]

## GRAFT-VERSUS-HOST DISEASE COLITIS

Graft-versus-host disease (GVHD) colitis can be seen in the immunocompromised patient postallogenic bone marrow transplantation. It occurs when the donor lymphocytes in the graft mount an immune reaction against the host. GVHD usually affect the skin, liver, and GI tract (predominantly the ileum and colon).[60]

***Clinical Presentation.*** GVHD is classified as acute when it occurs during the first 100 days and chronic when it happens after 100 days, although there can be overlap.[61] Patients can present with maculopapular rash, increased conjugated bilirubin and alkaline phosphatase, watery or bloody diarrhea and abdominal pain, anemia or thrombocytopenia, and possible nephrotic syndrome.

***Imaging.*** CT imaging findings are not very specific and include wall thickening with a halo of decreased attenuation within the wall. With severe mucosal disease, there may be prolonged coating of both the small and large bowel with oral contrast material with incorporation of contrast into the bowel wall with healing.[60] The main diagnostic clue is the clinical history of bone marrow transplantation.

## INFECTIOUS COLITIS

The same agents that affect the small bowel, discussed in Chapter 104, usually cause the infectious colitides. Imaging is rarely needed, and when performed shows nonspecific colitis. However, there are potential emerging infections to consider.

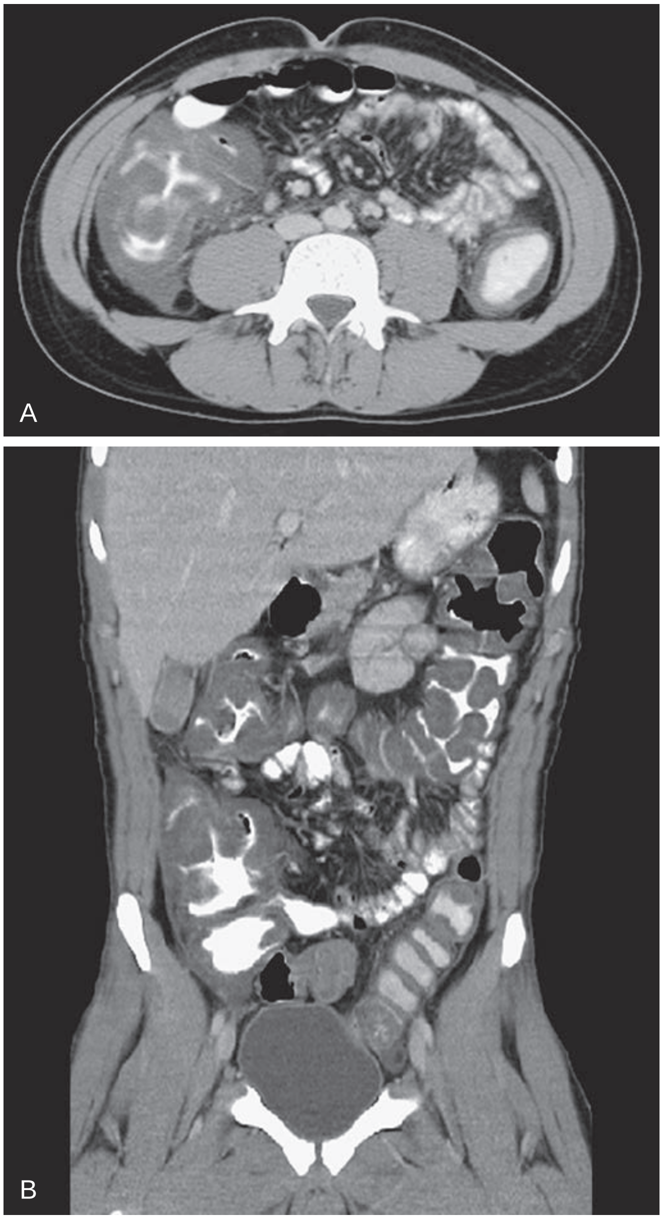

**Figure 106.11. Neutropenic colitis.** Contrast-enhanced CT in an 18-year-old man with acute myelogenous leukemia, fever, and neutropenia. (A) Axial image shows the marked thickening of the cecum and a small amount of free fluid. (B) Coronal reformat image shows pancolitis, affecting the right colon to a greater extent.

### Gastrointestinal Basidiobolomycosis

***Etiology.*** Previously known as a *chronic skin fungal infection*, gastrointestinal basidiobolomycosis infection (GIB) is a very rare invasive fungal infection caused by *Basiodobolus ranarum* with a predilection for large bowel. It is a mimicker of lymphoma and CD, the differential also including intestinal tuberculosis, sarcoidosis, schistosomiasis, and amebiasis. Left untreated, there is a high risk of perforation and a mortality rate of 18%.[62–64]

*B. ranarum* is found in soil and vegetation worldwide and is likely of low virulence given the small number of cases reported. However, GI infection is increasingly recognized in immunocompromised and, more recently, immune competent patients.

Males are affected more than females, with a slight increase in number of cases in the late first decade.[63]

***Clinical Presentation.*** Patients typically present with fever and vomiting, abdominal pain, constipation, weight loss, and a palpable abdominal mass.[63,64] Marked eosinophilia and raised erythrocyte sedimentation rate (ESR) and C-reactive protein (CRP) are also present.[65] Blood, urine, and fecal samples are usually negative for fungi.[63] Biopsy shows transmural granulomatous inflammation and a prominent eosinophilic component, and the diagnosis is confirmed by tissue biopsy with polymerase chain reaction (PCR), with fungal hyphae and zygospores on staining.[63]

***Imaging.*** US is the first imaging modality and may show a large soft tissue mass involving the cecum and extending beyond the wall, typically sparing the appendix, with multiple regional mesenteric lymph nodes. CT has a similar appearance with bowel wall thickening, large lobulated soft tissue mass(es) centered in the cecum and ascending colon, with luminal narrowing with or without obstruction (e-Fig. 106.12). Perforation or abscess can be seen.[63,64] One study showed the large bowel was involved in 82% and small bowel in 36%, with liver and gallbladder disease in 30%.[64]

***Treatment.*** Early recognition to avoid perforation is critical. Surgical resection of the infected tissue followed by a prolonged course of itraconazole is the preferred treatment, with good results.[62–64]

## FIBROSING COLONOPATHY

Fibrosing colonopathy was first described in 1994 in patients with cystic fibrosis (CF) who received lipase replacement therapy.[66]

***Etiology.*** The majority of CF patients depend on pancreatic-enzyme supplements to treat exocrine pancreatic insufficiency. With the introduction of oral, enteric-coated, high-dose pancreatic enzyme medication, clinicians increased the amount of enzyme supplements to many of these patients. Some who received particularly high doses later came to medical attention with what has been termed *fibrosing colonopathy*.[67] Children were at higher risk than adults, until strict dosage guidelines were implemented. This entity is now rare because of compliance with appropriate dosage recommendations.[68]

***Clinical Presentation.*** The clinical presentation includes abdominal pain, distension, nausea, vomiting, constipation, and occasionally colonic obstruction. Although nonspecific, these signs and symptoms do not respond to medical therapy.

***Imaging.*** The most common contrast enema findings are colonic strictures, loss of haustra, and colonic shortening.[69] The bowel wall may be thickened, and ascites may be evident on cross-sectional imaging.

***Treatment.*** Some of these patients require surgery to relieve the obstruction, and they may also require resection of the fibrotic segment of colon.[68]

## APPENDICITIS

The vermiform appendix is a thin, tubular, intestinal diverticulum attached to the base of the cecum that is often referred to as a *vestigial organ*. Although conventional wisdom asserts that the appendix has no function, there is increasing evidence suggesting that it plays a role in immune function and as a reservoir for normal gut flora.[36,37] Inflammation of the appendix remains the most common indication for surgery in both children and adults. There are approximately 70,000 to 90,000 pediatric cases annually in the United States with an estimated incidence of 75 to 233 per 100,000 children. The incidence increases with age and peaks in adolescence. The lifetime risk to develop appendicitis is 8.6% for males and 6.7% for females.[70] Although rare, appendicitis does occur in young children and infants. Boys are affected more frequently than girls by a ratio of 1.4 to 1.0. Classically, appendicitis has been considered a clinical diagnosis with reported negative appendectomy rates between 12% and 20%.[70,71] This rate is no longer considered acceptable given operative complication rates and improvements in imaging diagnoses.[72] Preoperative imaging results in noticeable decrease of the negative appendectomy rate without increasing the rate of perforations.[73] Negative appendectomy rates have declined to 5% in many centers with the increased use of preoperative US and CT.[74]

***Etiology.*** Appendicitis commonly occurs in the setting of luminal obstruction. Subsequent distension of the appendix and ischemic mucosal damage leads to bacterial overgrowth and invasion of the wall that, in turn, results in transmural inflammation and ultimately in perforation. Luminal obstruction may be secondary to the presence of fecaliths, hyperplasia of lymphoid follicles, and foreign bodies that include parasites and neuroendocrine (carcinoid) tumors.[75] The pathophysiology of appendicitis is believed to be a dynamic process that occurs over 24 to 36 hours. Although infrequent, subacute appendicitis and spontaneous resolution of acute appendicitis have been described. Spontaneous resolution of luminal obstruction is the proposed pathophysiology in these cases and has been mostly associated with CF and appendiceal lymphoid hyperplasia.[76,77]

***Clinical Presentation.*** Appendicitis can be a challenging diagnosis in children; the clinical presentation is nonspecific in approximately one-third of patients.[78] The classic clinical presentation—early periumbilical pain, followed by migration of localized pain to the right lower quadrant, with associated fever and vomiting—occurs in less than 50% of pediatric patients.[79] More often, the constellation of findings is nonspecific. Younger children may be unable to communicate symptoms effectively, resulting in delayed diagnosis and higher perforation rates. Initial relief of pain and/or more generalized abdominal pain with fever occurs after perforation, which usually results in a local phlegmon or walled off abscess adjacent to the appendix. Perforation is usually contained by the omentum, but generalized peritonitis can also occur. Reported perforation rates in children range from 23% to 88%.[78]

***Imaging.*** Imaging plays a vital role in diagnosing suspected appendicitis. The effectiveness of imaging for suspected appendicitis in children has been debated in the medical literature, which has specifically looked at the impact of imaging on the negative appendectomy and perforation rates. Several studies suggest a stable perforation rate with preoperative imaging,[80–82] whereas others demonstrate a significant decrease in perforation rate, from 35% to 15.5%, with preoperative imaging.[83] A decrease in the negative appendectomy rate has been demonstrated in numerous studies.[83–85] CT generally outperforms US in depicting the inflamed appendix, but increased awareness and concerns about radiation dose and long-term adverse effects has restricted CT use in children with suspected appendicitis.[86,87] Most pediatric centers use US as a first imaging modality, reserving CT (and increasingly MRI) for unclear/equivocal or problematic cases.

When the appendix is normal, alternative diagnoses, particularly in young children, must be considered. The differential diagnoses, in decreasing order of prevalence, are mesenteric adenitis, ovarian cyst, pyelonephritis, infectious or inflammatory colitis, omental infarction (e-Fig. 106.13), urinary system stones, and inflamed Meckel's diverticulum.[88,89] A summary of imaging findings is listed in Box 106.1.

### Radiographs

Before the advent of current cross-sectional imaging modalities, imaging of appendicitis relied on abdominal radiographic findings, which are often normal or nonspecific in approximately 77% of

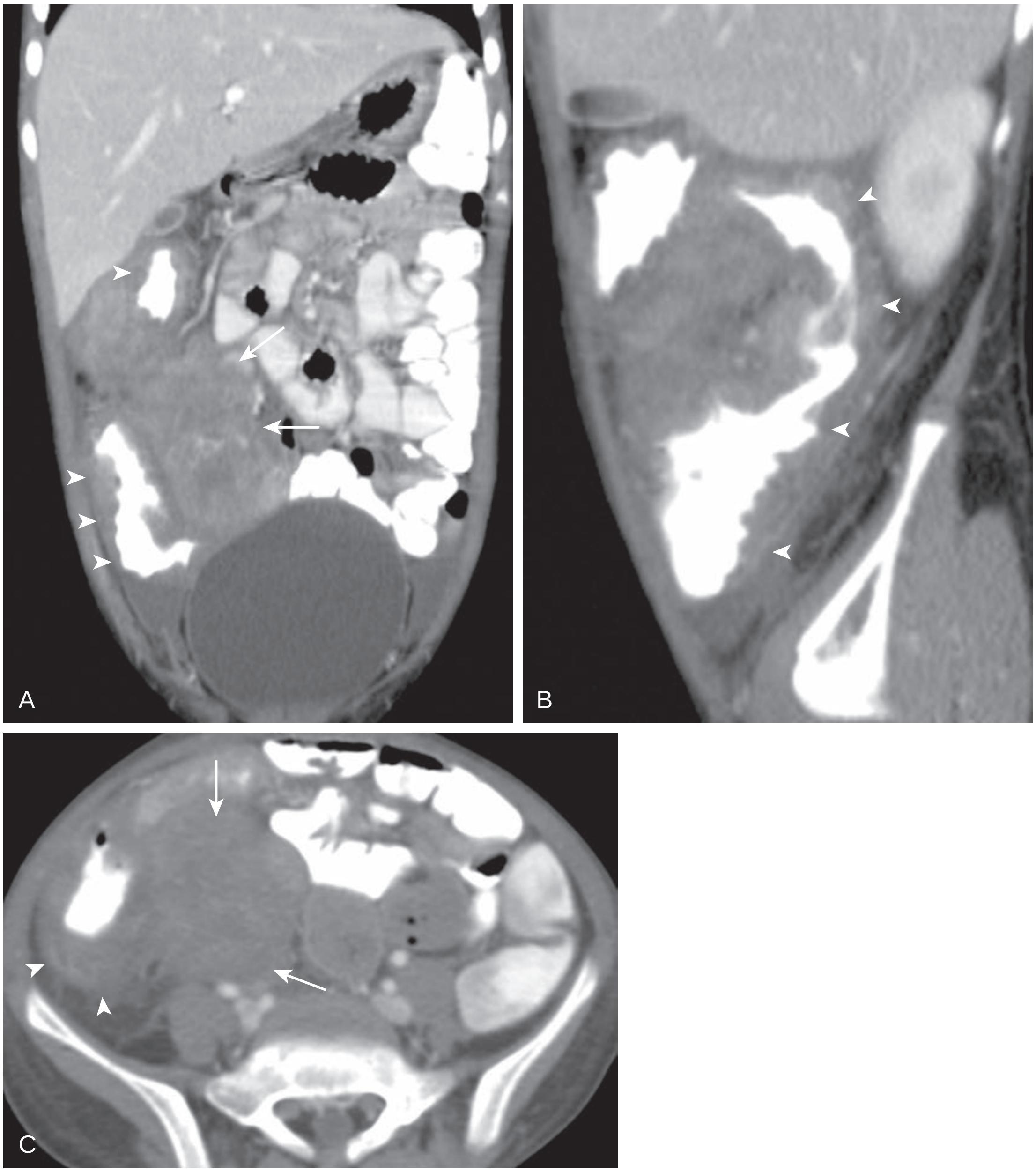

**e-Figure 106.12. Gastrointestinal basidiobolomycosis (GIB).** Abdominal CT with oral and intravenous contrast in a 6-year-old boy who presented with fever, abdominal pain, and diarrhea for 2 weeks. (A) Coronal, (B) sagittal and (C) axial images demonstrate diffuse mural thickening of large bowel *(arrowheads)* secondary to this invasive fungal infection, preferentially involving cecum, ascending colon and hepatic flexure. Medially, in the right lower quadrant, there are large, rounded soft tissue density masses extending beyond bowel into the retroperitoneum *(arrows in A and C)* with intermingled nodal enlargement. The differential includes Burkitt lymphoma. *(Courtesy Dr. Abeer Almehdar, King Abdulaziz Medical City, Jeddah, Saudi Arabia.)*

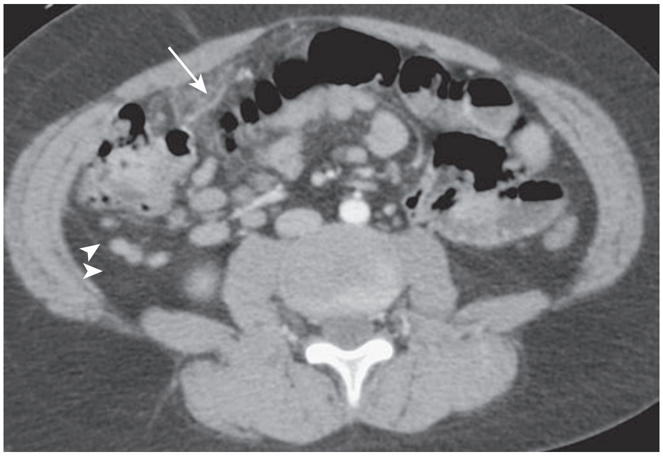

**e-Figure 106.13. Omental infarction.** Contrast-enhanced CT through the lower abdomen in a young boy who underwent CT for clinically suspected appendicitis. Note typical location of edematous omentum anterior to the cecum with a prominent central vein *(arrow)*, a classic finding in omental torsion. Portions of the normal retrocecal appendix *(arrowheads)* are seen, as are several incidental mesenteric nodes medial to the cecum. The patient was managed expectantly, with resolution of the symptoms. *(Courtesy Dr. Marta Hernanz-Schulman, Nashville, TN.)*

children with appendicitis.[79] The presence of a radiographically visible appendicolith, considered to be the most specific radiographic sign of appendicitis, is only present in 5% to 15% of patients with appendicitis.[79,90] Appendicoliths are seen in 43% to 50% of cases on CT and are multiple in 30% (e-Fig. 106.14).[91,92] Additional nonspecific radiographic findings include a paucity of bowel gas or a soft tissue mass in the right lower quadrant, ileus that may be either focal or diffuse, and less often, small bowel obstruction.[93] Mild levoconvex curvature of the spine may be present as a result of splinting in response to abdominal pain.

## Ultrasound

US using a graded compression technique for evaluation of appendicitis was first described in 1986.[93] Numerous studies have addressed the efficacy of US and to evaluate additional sonographic findings.[94–98] The limitations of US include operator experience, larger patient body habitus, and limited field of view. Optimized technique for US evaluation of suspected appendicitis is essential. The examination is performed with a high-frequency linear transducer that ranges from 9 to 15 MHz, depending on the size of the patient. A linear transducer is necessary not just to obtain the appropriate resolution but also to effect adequate graded compression. Graded compression is essential, because it displaces overlying bowel gas and helps decrease the distance between the transducer and the appendix. Additionally, compression helps differentiate normal bowel from an inflamed appendix. The compression is "graded" in that it is exerted slowly, without sudden release, to optimize patient tolerance and prevent rebound tenderness. Transverse and longitudinal scans are performed over the point of maximal tenderness. A recommended approach is to start by locating the cecum, ileocecal valve, and the terminal ileum, then to gently angle the probe caudally. The appendix is most commonly seen in the midpelvic region over the right common iliac vessels. If the appendix is not identified at this point, additional sonographic interrogation is necessary given the variability in location of the appendiceal tip. The appendix can be found in the retrocecal region, deep pelvic region, and abdomen above the iliac crests.[99] Visualization of the tip of the appendix, the base, and the full length of the blind-ending tubular structure should be clearly described in the report.

US demonstration of the normal appendix is useful in excluding the diagnosis of appendicitis, characterized as a compressible, blind-ending tubular structure originating from the base of the cecum without peristalsis; diameter less than 6 mm; absence of wall thickening (<3 mm); and presence of a central echogenic line that represents acoustic reflection from the collapsed luminal interface (Fig. 106.15).[98,100,101] The terminal ileum can mimic the appendix but is distinguished by its hypoechoic folds and peristalsis.

The US signs of an inflamed appendix include a noncompressible, blind-ending tubular structure with a transverse diameter measuring greater than 6 mm. Additional features include appendiceal wall thickness greater than 3 mm, wall hyperemia on color Doppler, periappendiceal hypoechoic halo that reflects appendiceal wall edema, periappendiceal hyperechogenicity that reflects periappendiceal edema, and the presence of an appendicolith, variably accompanied by bright periportal echoes in the liver (Fig. 106.16).[97,102]

These secondary sonographic findings vary depending on the progression of the inflammatory process. In a multivariate analysis by Trout et al.,[103] the inflammation of the periappendiceal fat (Fig. 106.17) was the only finding statistically significant in predicting acute appendicitis (odds ratio (OR) = 68.93, $P < 0.0001$), other criteria, though not independently predictive of appendicitis, remain important markers pointing toward the diagnosis of appendicitis. Kessler et al.[104] found that the most accurate appendiceal finding for appendicitis was a diameter of 6 mm or larger, with a sensitivity, specificity, negative predictive value and positive predictive value of 98%. These and other studies support that a constellation of findings is the most accurate in making the diagnosis of appendicitis.

Early uncomplicated appendicitis will demonstrate a target-like appearance with hypoechogenicity centrally as a result of luminal distension with pus or fluid, increased echogenicity of the inflamed submucosa, hypoechoic edematous serosa, and increased periappendiceal echogenicity (see Fig. 106.17). As the inflammatory process advances and suppurative appendicitis ensues, the periappendiceal tissues demonstrate a heterogeneous pattern of increased

### BOX 106.1 Imaging Features in Acute Appendicitis

**PLAIN RADIOGRAPHS**

- Ileus, often localized to right lower quadrant
- Antalgic scoliosis from splinting
- Appendicolith
- Small bowel obstruction, most commonly in younger children
- Abscess with mass effect and/or atypical air collection

**ULTRASOUND**

- Appendiceal diameter >6 mm
- Noncompressible appendix
- Increased flow in wall with color Doppler
- Appendicolith with acoustic shadowing
- Periappendiceal fluid or abscess
- Periappendiceal echogenic fat
- Perforation that may decompress the appendix
- Abscess

**COMPUTED TOMOGRAPHY AND MAGNETIC RESONANCE**

- Dilated appendix >7 mm
- Wall enhancement and thickening with surrounding fat stranding
- Appendicolith or luminal pus
- Abscess or phlegmon

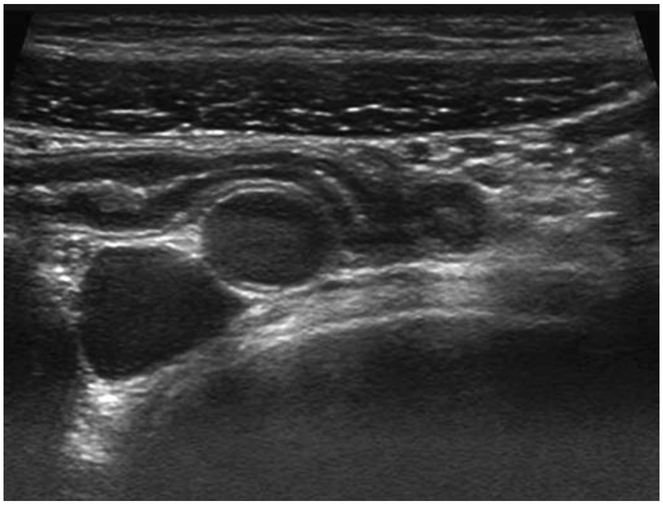

**Figure 106.15. Normal appendix.** Ultrasound image of the normal appendix shows typical location of a nondilated, blind-ending tubular structure posterior to the terminal ileum and anterior to the iliac vessels with a central echogenic line within the nondistended appendix.

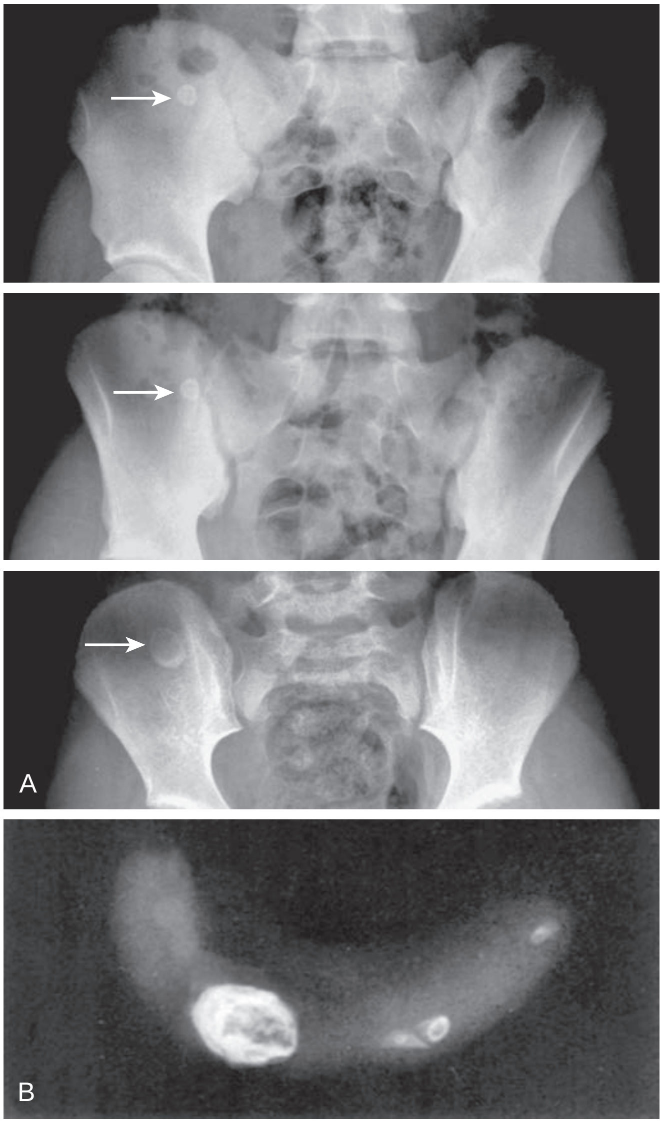

**e-Figure 106.14. Acute appendicitis.** (A) Radiographs showing appendicoliths *(arrow)* in three different patients. (B) Resected appendiceal specimen in another patient shows a large appendicolith obstructing the appendiceal lumen.

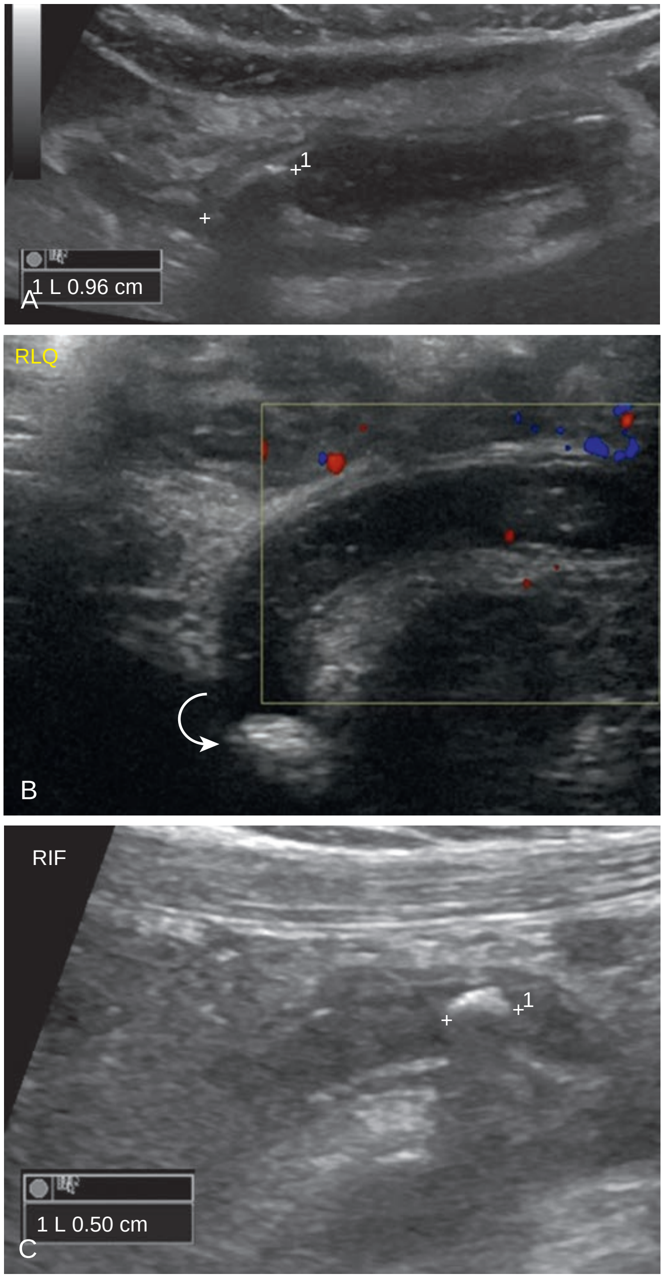

**Figure 106.16. Appendicoliths.** (A) Gray-scale and (B) color Doppler sonograms in two patients with appendicoliths at the base of dilated fluid-filled inflamed appendices (indicated by *calipers* in A, *curved arrow* in B). (C) Companion sonogram of an appendicolith (indicated by *calipers*) with no other sonographic signs of acute inflammation.

echogenicity with hyperemia on color Doppler (Fig. 106.18). Increasing appendiceal dilatation, interruption or loss of the echogenic submucosal layer, and absence of vascularity with color Doppler are signs of supervening gangrenous change and portends pending microperforations (Fig. 106.19). Although the abnormal appendix may not be visualized with perforated appendicitis, sonographic findings suggestive of perforation include phlegmon with poorly defined bowel loops in the right lower quadrant demonstrating increased echogenicity, a mass of mixed echogenicity, focal bowel wall thickening, intraperitoneal fluid, loculated fluid collections, or frank abscess. On occasion, the perforated appendix may appear decompressed with a diameter less than 6 mm.

Absence of visualization of an abnormal appendix in the setting of acute appendicitis may be due to a retrocecal location, obscuration by superimposed bowel gas, or limited US penetration. Additionally, appendiceal inflammatory changes may be confined to the tip of the appendix which is commonly referred to as *tip appendicitis*.[105] If the entire appendix has not been visualized on US, and clinical symptoms suggest appendicitis or other intraperitoneal pathology, further imaging may be warranted, particularly if there are secondary signs of right lower quadrant inflammation.

## Computed Tomography

CT is highly sensitive and specific for the diagnosis or exclusion of appendicitis in children. It is often utilized in the setting of a negative or equivocal US or perforated appendicitis. Scanning parameters should be adjusted appropriately for the size of the child to optimize dose. CT protocols vary with respect to the administration of oral, IV, and rectal contrast in addition to targeted imaging versus imaging the entire abdomen and pelvis.[74] A systematic review concluded that IV contrast alone performs as well as or better than CT with IV and positive enteral contrast for the diagnosis or exclusion of appendicitis.[106]

Although the average diameter of the normal appendix typically approximates 6 mm, actual size may vary on CT, from 2 to 11 mm, because the examination is not done with compression, and the appendiceal lumen may distend with gas or feces. The absence of associated CT signs of appendicitis is helpful to confirm a normal appendix. In a recent study, there were significant differences in intra- and interreviewer appendiceal diameter measurements, indicating that measurement alone is not a definitive appendicitis indicator and should not be interpreted in isolation of the other pertinent signs.[107]

As is the case with US, the appearance of the abnormal appendix varies with the histopathologic stage and severity of the disease process. The inflamed appendix on CT is a dilated, thick-walled tubular structure with centrally decreased attenuation that demonstrates wall contrast enhancement (e-Fig. 106.20 and Fig. 106.21). An obstructing appendicolith may be present in up to 50% of cases (Fig. 106.22).[91,92] Adjacent inflammation produces periappendiceal stranding and fluid. Additional nonspecific findings include intraperitoneal free fluid, cecal wall thickening and thickening of adjacent terminal ileum and sigmoid colon, small bowel obstruction, and mesenteric lymphadenopathy.[108]

With perforation, the appendix may decompress or may even fail to be visualized. Perforation may result in diffuse intraperitoneal inflammation or, more commonly, in localized phlegmon and abscess formation (e-Fig. 106.23). Diffuse peritonitis is more common in infants younger than age 2 than in older children. Hepatic abscesses and mesenteric or portal pyelophlebitis can also occur. CT is extremely helpful in identifying and characterizing smaller abscesses and extruded fecaliths that may act as a potential source of recurrent infection.

## Computed Tomography and Ultrasound

CT and US are reported to have a nearly equivalent specificity, 95% and 94%, respectively.[109] Although CT has a greater sensitivity than US (94% and 88%, respectively, bearing in mind that US is much more variable and operator dependent),[109] concerns regarding the potential risks of ionizing radiation exposure associated with CT have prompted increasing use of US in the imaging evaluation of suspected appendicitis.[110,111] US is considered the most appropriate initial imaging modality to evaluate children with suspected appendicitis by the American College of Radiology appropriateness criteria. Various imaging algorithms have been described in the literature that includes the staged utilization of initial evaluation

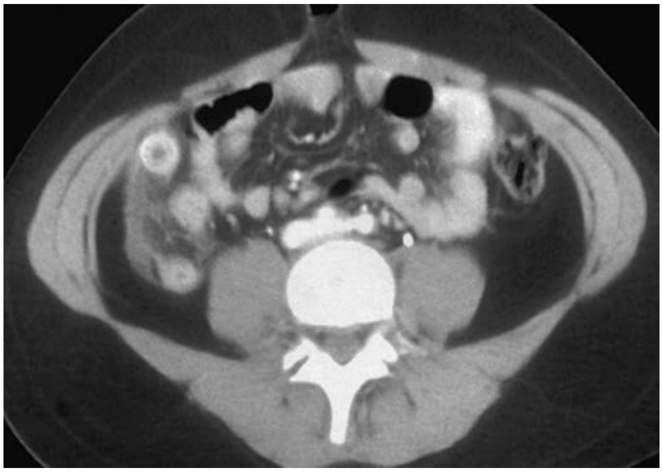

**e-Figure 106.20. Acute appendicitis.** Contrast-enhanced CT image shows a dilated, enhancing appendix with marked periappendiceal inflammation.

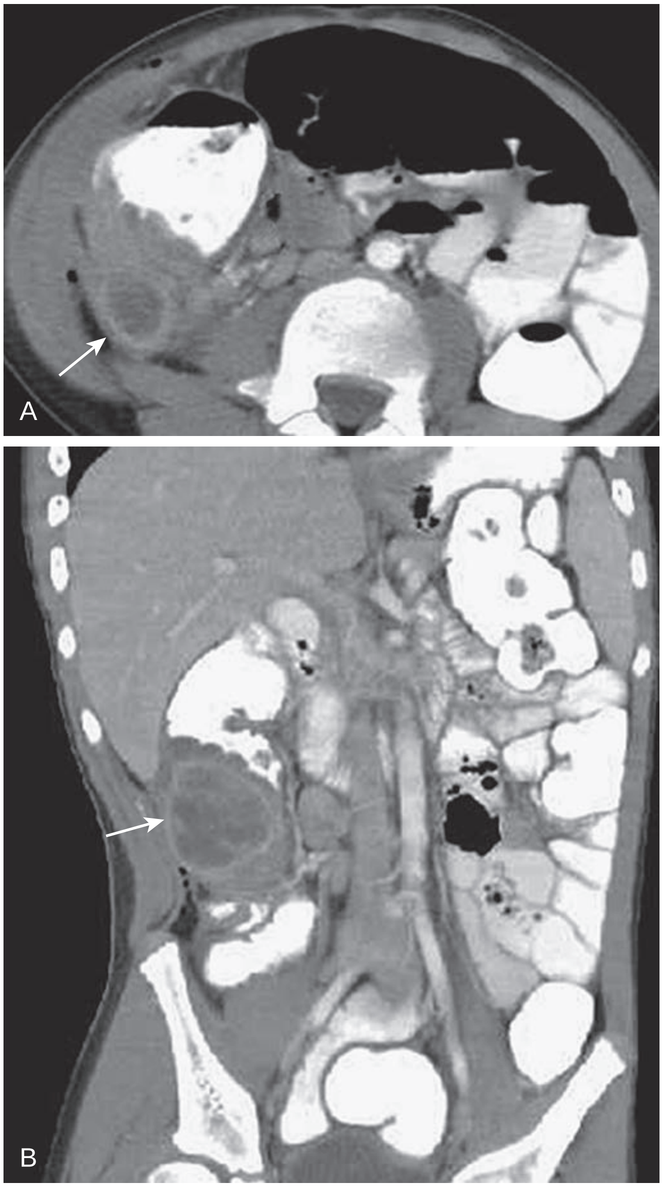

**e-Figure 106.23. Perforated appendix.** (A) Contrast-enhanced CT image with enteric contrast shows a well-defined retrocecal abscess *(arrow)* with adjacent cecal wall thickening and mesenteric adenopathy medial to the cecum. (B) Coronal CT reformat shows the full craniocaudal extent of the abscess *(arrow)*.

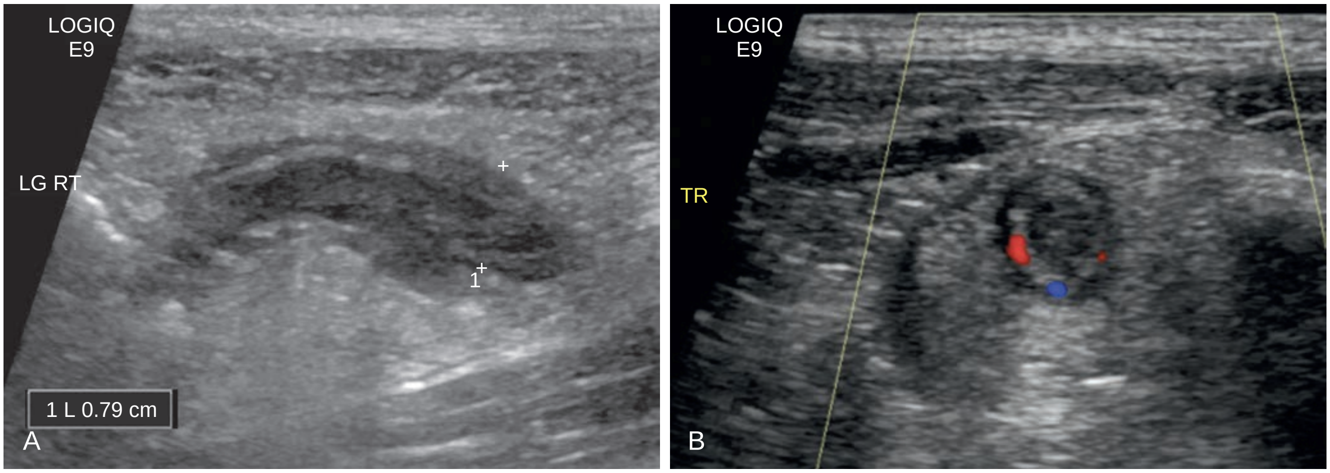

**Figure 106.17. Acute appendicitis.** (A) Longitudinal and (B) transverse color Doppler sonograms from a 13-year-old boy with acute right lower quadrant pain demonstrate a distended hypoechoic lumen, thick-walled, hyperemic appendix *(target sign)*. Circumferential zone of increased echogenic tissue around appendix in keeping with regional inflammation, possibly walled off by omentum.

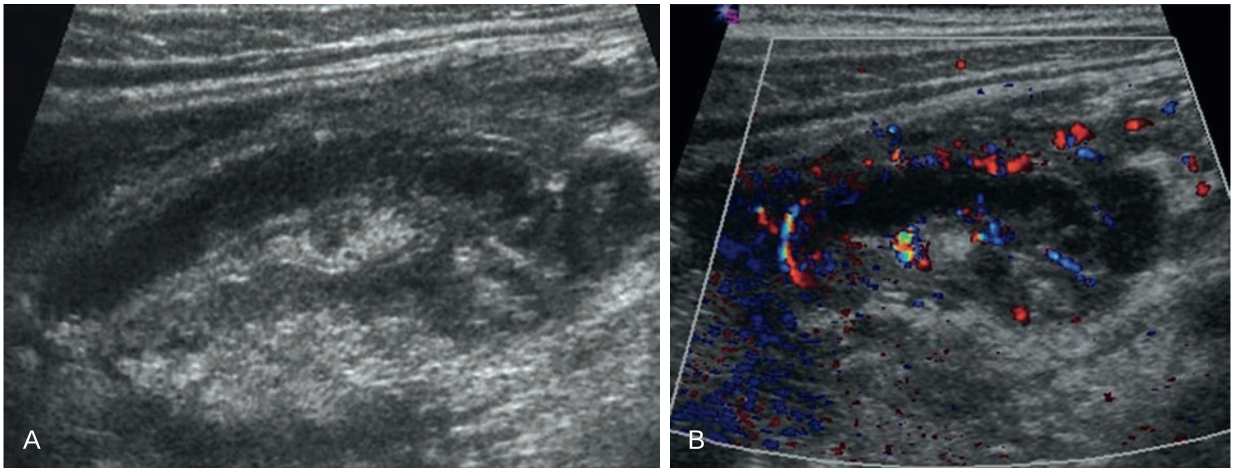

**Figure 106.18. Advanced acute appendicitis.** (A) Sonogram shows an abnormal appendix with increased mixed echogenicity of the adjacent tissues and a small amount of periappendiceal fluid. (B) Color Doppler sonogram demonstrates hyperemia in the wall of the appendix and in the adjacent soft tissues.

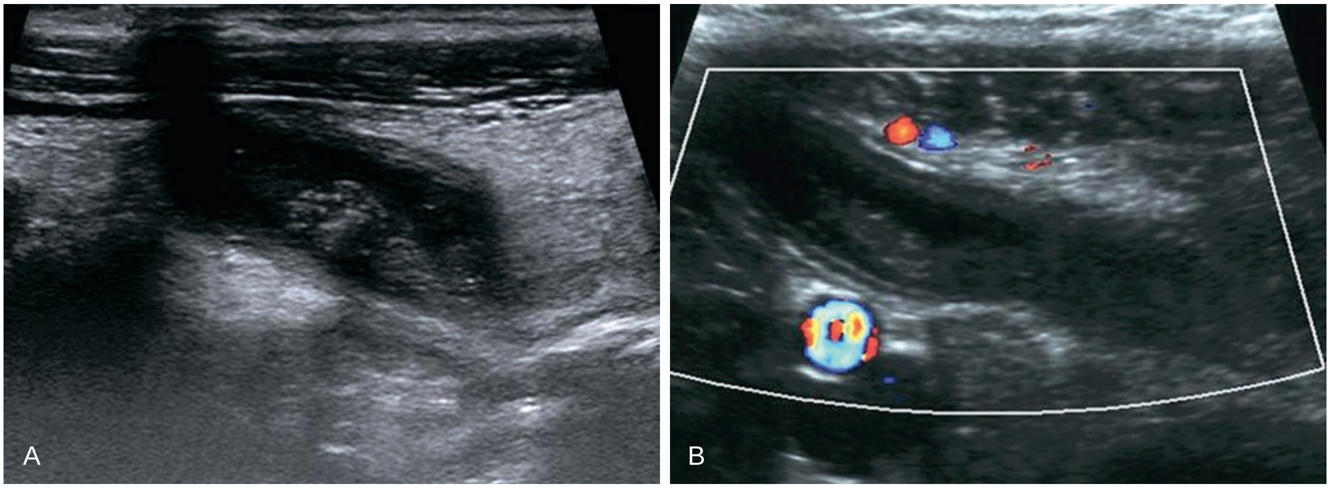

**Figure 106.19. Gangrenous appendicitis.** Longitudinal gray-scale (A) and color Doppler (B) sonograms show a dilated appendix with loss of the echogenic submucosal layer and absence of vascularity with color Doppler evaluation. There is increased echogenicity of the periappendiceal fat.

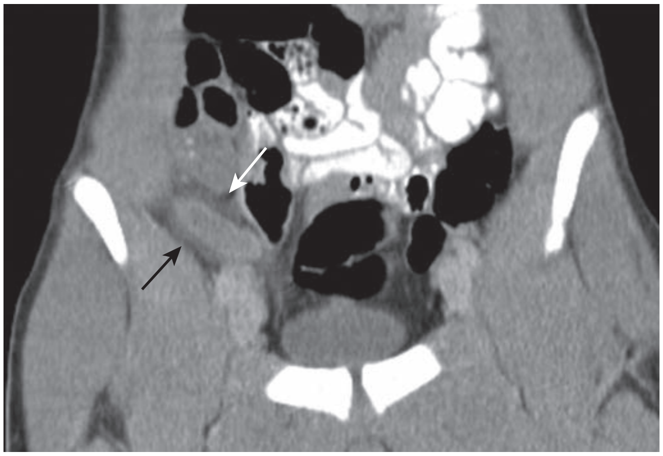

**Figure 106.21. Acute appendicitis.** Coronal reformatted contrast-enhanced CT image of the pelvis demonstrates a dilated appendix with wall enhancement and periappendiceal inflammation *(arrows)*.

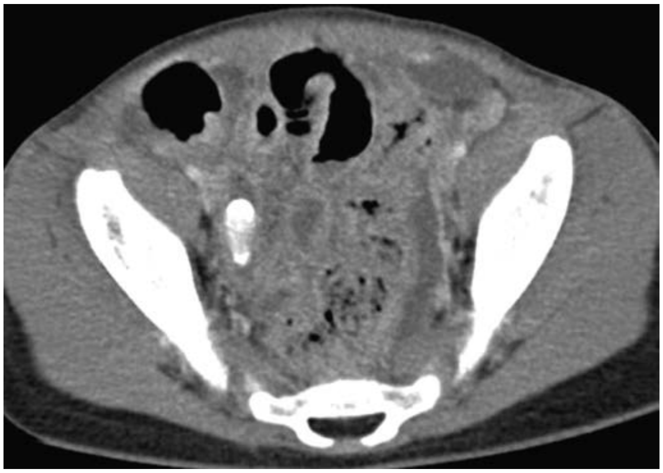

**Figure 106.22. Perforated appendicitis.** Axial contrast-enhanced CT image shows an appendicolith in the right lower quadrant in the remnant of the appendix. Extensive peritoneal inflammation is present with several abscesses.

**TABLE 106.2** Diagnostic Performance (%) of MRI Versus US and CT in Children With Suspected Appendicitis

| | MRI^ | US^ | MRI ** | CT** |
|---|---|---|---|---|
| Sensitivity | 93.3 | 90.0 | 94.4 | 100 |
| Specificity | 98 | 86.3 | 100 | 97.9 |
| PPV | 96.5 | 79.4 | 100 | 97.8 |
| NPV | 96.2 | 93.6 | 98.8 | 100 |

^Orth R, et al. Prospective Comparison of MR Imaging and US for the Diagnosis of Pediatric Appendicitis. *Radiology*. 2014;272(1):233-239.

**Dillman J, et al. Equivocal Pediatric Appendicitis: Unenhanced MR Imaging Protocol for Nonsedated Children—A Clinical Effectiveness Study. *Radiology*. 2016;279(1):216-225.

*CT,* Computed tomography; *MRI,* magnetic resonance imaging; *NPV,* negative predictive value; *PPV,* positive predictive value; *US,* ultrasound.

with US followed by CT for equivocal or nondiagnostic US studies.[74,112,113] The reported ratio of US to CT in one of the largest prospective studies that follow this algorithm was about 6:1 overall and 24:1 in children.[113]

## Magnetic Resonance Imaging

MRI has been reported to yield excellent results in the evaluation of suspected appendicitis with high sensitivity and specificity (Table 106.2).[114,115] Imaging protocols vary between institutions, but typically use unenhanced sequences with average examination times of 14 to 25 minutes.[116,117] The abnormal appendix demonstrates thickening of the appendiceal wall with high-signal intensity on T2-weighted images, a dilated lumen with high T2-signal intensity contents with restricted diffusion (indicating pus), and increased signal intensity of the periappendiceal tissues (Fig. 106.24).[118]

Although MRI has the appealing advantage of no ionizing radiation, current limitations precluding routine use of MRI for suspected appendicitis include a relatively long examination time and limited availability compared with CT. Sedation may be needed for very young children, although faster sequences and imaging protocols have been described and performed without sedation in children as young as 3 years.[114,118]

Fig. 106.25 is a suggested imaging algorithm for suspected appendicitis in children and adolescents. This proposal draws

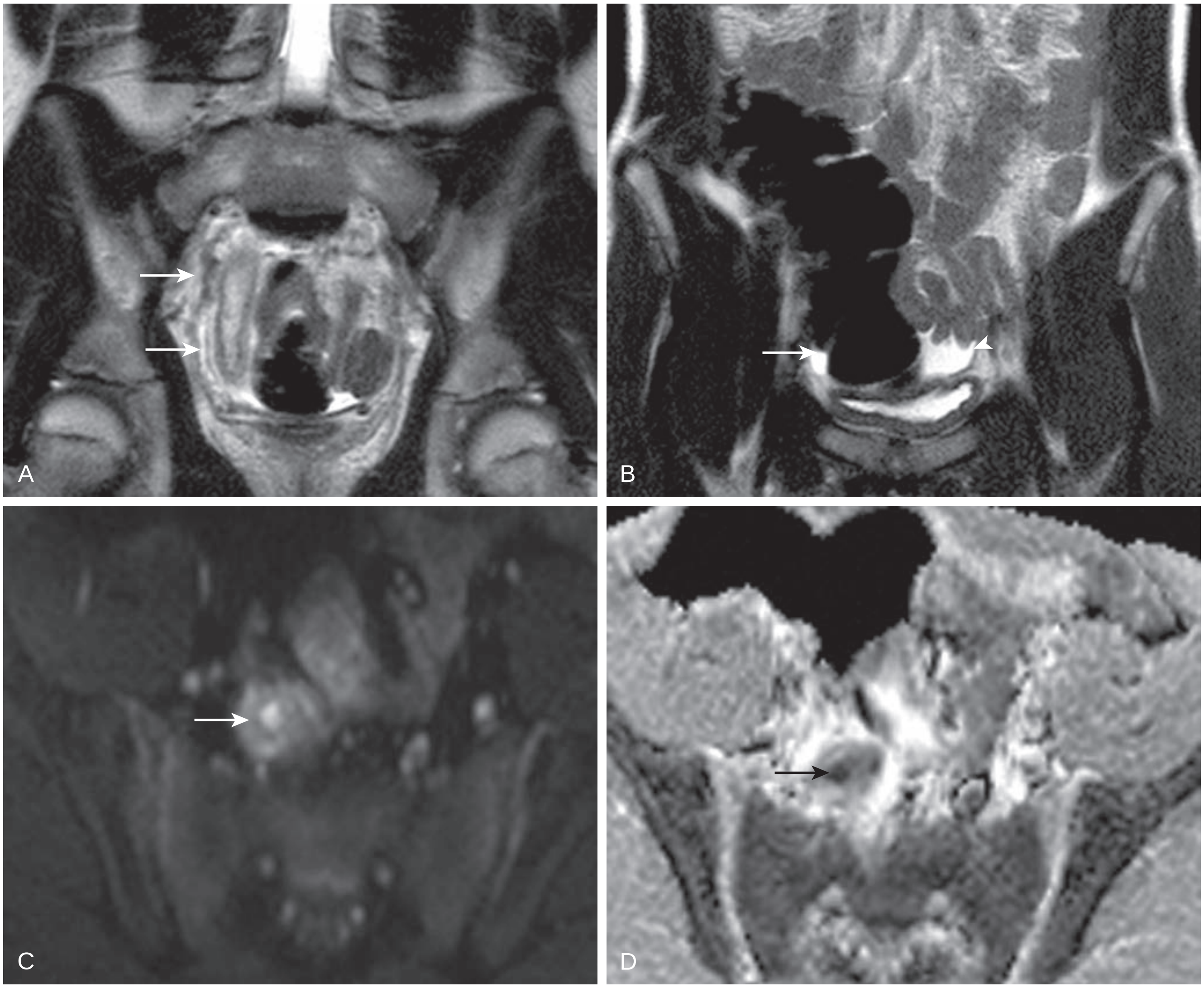

**Figure 106.24. Magnetic resonance imaging (MRI) of acute appendicitis.** A 13-year-old boy with vomiting and right lower quadrant (RLQ) pain. Ultrasound done initially was not diagnostic due to gassy RLQ. Coronal single-shot T2-weighted sequence with (A) distended blind-ending tubular appendix in RLQ *(arrows)* with wall and periappendiceal edema, and immediately anterior to this is (B) a gas-filled low lying cecum *(arrow)* and pelvic free fluid *(arrowhead)*. Axial diffusion weighted imaging through the appendix with bright luminal contents on (C) trace image ($b = 600\ s/mm^2$), dark on (D) apparent diffusion coefficient map, showing restricted fluid in appendix in keeping with pus.

on available literature and the experience of various pediatric institutions.

***Treatment.*** Although appendectomy is the mainstay in the treatment of acute appendicitis, the literature is variable on the management of appendicitis and depends on the institution and the individual surgeon with respect to surgical procedure, timing of the surgical procedure, antibiotic therapy, and the clinical presentation of the patient.[119–121] Laparoscopic appendectomy has become a preferred surgical approach.[122,123] Several studies suggest that emergent appendectomy may not be necessary, and that IV antibiotics with appendectomies delayed for 12 to 24 hours after presentation do not significantly increase the rate of perforations, operative time, or length of hospital stay.[124,125] Timely imaging, however, remains essential for proper diagnosis and treatment planning. Patients with perforated appendicitis generally undergo antibiotic therapy followed by interval appendectomy several weeks later. If an abscess is present, the child will typically undergo image-guided drainage.[126]

## MISCELLANEOUS DISORDERS

### Colonic Volvulus

Colonic volvulus refers to a twisting or torsion of a portion of the colon, such as the cecum or the sigmoid. It is less common in children than in adults. When it occurs in children, the cecum is the most common area to twist; in adults, the sigmoid colon is the most common location.

***Etiology.*** A mobile cecum is a normal variant, seen in as many as 15% of individuals. Cecal volvulus is very rare in the pediatric population and results from dilatation of a mobile cecum, typically in patients with relative immobility, such as that resulting from neurologic impairment; cecal volvulus leads to obstruction and bowel distension.[127–129]

Iatrogenic causes of cecal volvulus include the presence of a ventriculoperitoneal shunt and the Malone antegrade continence enema (MACE) procedure.[130] This procedure provides a

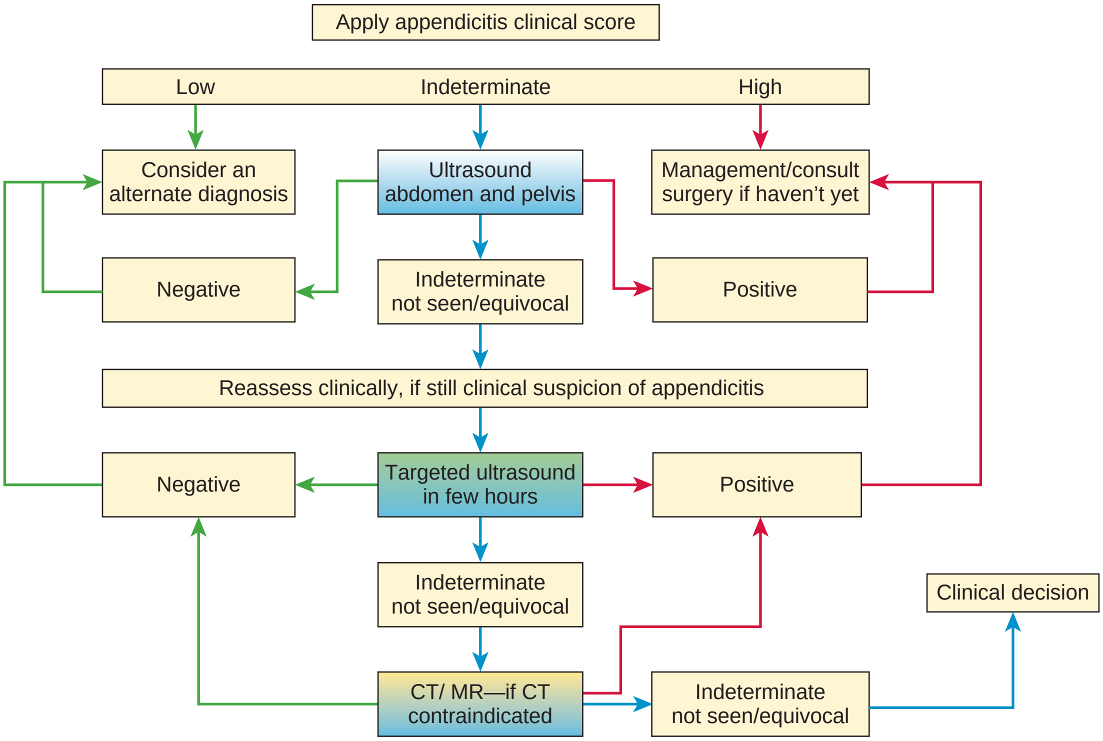
Apply appendicitis clinical score
Low
Indeterminate
High
Consider an alternate diagnosis
Ultrasound abdomen and pelvis
Management/consult surgery if haven't yet
Negative
Indeterminate not seen/equivocal
Positive
Reassess clinically, if still clinical suspicion of appendicitis
Negative
Targeted ultrasound in few hours
Positive
Indeterminate not seen/equivocal
Clinical decision
CT/ MR—if CT contraindicated
Indeterminate not seen/equivocal

**Figure 106.25.** Suggested imaging algorithm for suspected appendicitis in pediatric patients.

catheterizable stoma for colonic enema in patients with chronic constipation, and it may provide a focal point for the bowel to twist around.

Sigmoid volvulus[131,132] and volvulus of the transverse colon can also rarely occur in children.[129,133] Predisposing factors are abnormal mesenteric attachments or neurologic impairment, and these lead to hypomobility and severe obstipation.[128]

***Clinical Presentation.*** Colonic volvulus presents with signs of obstruction—nausea, vomiting, abdominal pain, and distension—although the findings may be relatively nonspecific and confused with other causes of obstruction or even gastroenteritis.[128]

***Imaging.*** Radiographs demonstrate bowel obstruction with marked dilatation of the colonic segment, which may be present in the right lower quadrant or over the midabdomen, if the volvulus involves the right colon (Fig. 106.26). The typical appearance on contrast enema of the site of volvulus obstruction is the "bird beak" sign. On CT, enlargement of the twisted portion of the colon is apparent, as is a "whirl sign" at the site of the twist.[129] The markedly enlarged colonic segment may have an enhancing thickened wall (e-Fig. 106.27). If the bowel becomes ischemic, the wall may not enhance, and pneumatosis may be present.[129]

***Treatment.*** Most children undergo surgical exploration and reduction of the volvulus as an emergency procedure, with resection of necrotic bowel when necessary. There are reports of enema reduction of both cecal and more distal volvulus in children, although now using water-soluble contrast agents rather than barium.[134]

## Pneumatosis Coli

***Overview.*** Pneumatosis intestinalis and pneumatosis coli, are terms that refer to the radiographic, US, or CT finding of air in the wall of the intestine or colon respectively, and it may be due to both benign and serious clinical conditions.

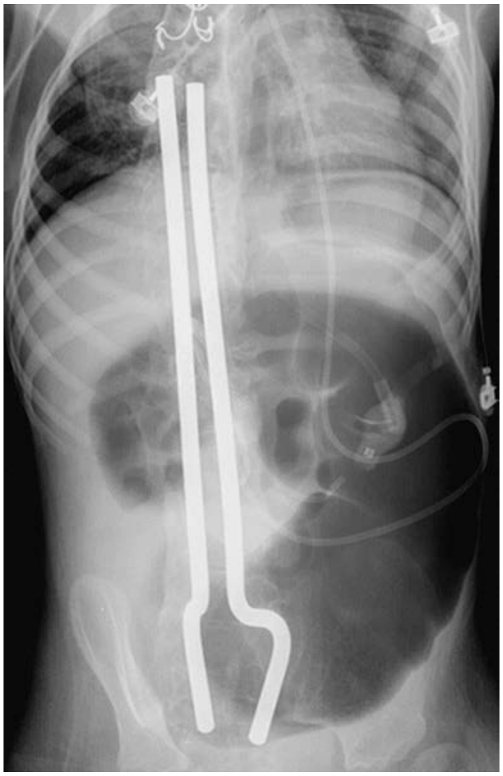

**Figure 106.26. Acute cecal volvulus around ventriculoperitoneal shunt tubing.** Frontal abdominal radiograph of a teenage boy with developmental delay and chronic constipation, who presented with acute onset of vomiting and abdominal pain. The radiograph shows marked distension of a colonic loop in the left abdomen, which was found at surgery to represent an acutely twisted right colon.

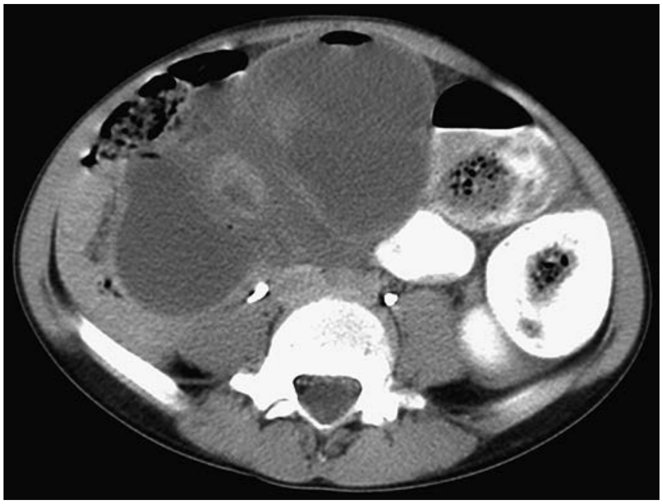

**e-Figure 106.27. Acute cecal volvulus around a Malone antegrade continence enema (MACE) procedure.** This 12-year-old boy came to medical attention with acute abdominal pain and vomiting without fever. He underwent rectal and intravenous contrast-enhanced CT, which showed a markedly dilated cecum. At surgery, the cecum had twisted around the MACE and was resected.

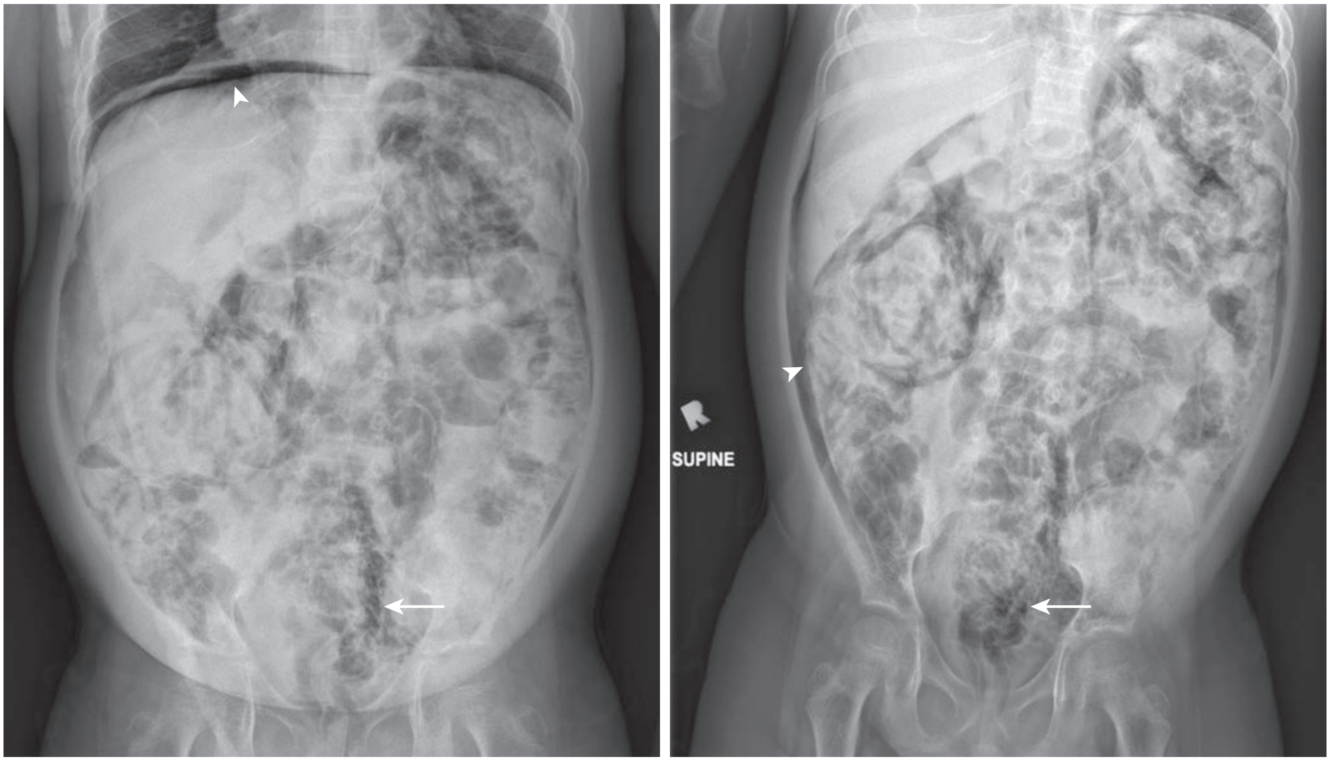

**Figure 106.28. Pneumatosis.** Erect (left) and supine (right) abdominal radiographs showing extensive pneumatosis intestinalis and pneumatosis coli *(arrows)* with pneumoperitoneum *(arrowheads)* in an adolescent on long-term steroid therapy for chronic bowel graft-versus-host disease.

***Etiology.*** Pneumatosis is well known to occur in patients with underlying ischemic bowel disease, such as necrotizing enterocolitis (NEC), and in some cases of bowel obstruction. However, it is also described in a wide variety of more benign or chronic conditions, such as CD, UC, AIDS, in transplant patients, and with viral infections, particularly cytomegalovirus.[135–140] Children are more likely to have pneumatosis than are adults, and depending on the etiology, the condition may generate few symptoms or may be asymptomatic. In most, the mechanism is not evident, however bacterial overgrowth and mechanical factors have been postulated.[135,139] It is also described as an epiphenomenon probably caused by gas dissection in CF,[138,141] and in some cases it is related to steroid therapy.

***Imaging.*** When NEC is a clinical concern, abdominal radiography is used for the detection of associated findings that include pneumatosis, ileus, perforation, or portal venous air (see Chapter 105). When perforation is a concern, cross-table lateral projections in unstable neonates and upright views in otherwise well patients are performed (Fig. 106.28). In some, pneumatosis may be an unexpected finding on radiographs. For the many associated benign conditions, and in those children who are asymptomatic, there is no evidence that serial radiographs are useful.

There is considerable variability in interpretation of the objective radiographic signs in detecting NEC.[142,143] Sonography may detect pneumatosis of the small or large bowel and may predict outcome in patients with NEC.[144,145] Standardization in approach and complementary use of US can assist in accurate detection.

***Treatment.*** Treatment is directed to the underlying condition.

## KEY POINTS

- Transmural disease is characteristic of Crohn disease but not of ulcerative colitis.
- Magnetic resonance enterography is increasingly used for evaluation and monitoring of disease activity in inflammatory bowel disease.
- The toxins produced by the bacterium *C. difficile* are the most important cause of antibiotic-associated pseudomembranous colitis.
- Most cases of HUS are caused by a Shiga-like toxin–producing *E. coli*, serotype 0157:H7, found in raw or incompletely cooked meats and in unpasteurized dairy products.
- Radiation colitis can occur months to years after exposure. Endarteritis with end-vessel and microvascular circulation compromise is the hallmark of supervening chronic ischemia.
- Neutropenic colitis (typhlitis) is a necrotizing colitis primarily seen in children with hematopoietic malignancies.
- Sonography is the initial cross-sectional imaging test recommended for appendicitis evaluation, followed by CT or alternately MRI if available, as necessary.
- CT imaging should be justified and optimized for the clinical indication and size of the child (see www.imagegently.org).
- Segmental colonic volvulus occurs in the setting of inanition associated with marked obstipation and distension and deficient supporting ligaments.
- Pneumatosis intestinalis occurs in a variety of benign and serious conditions in children.

## SUGGESTED READINGS

Athans BS, Depinet HE, Towbin AJ, et al. Use of clinical data to predict appendicitis in patients with equivocal US findings. *Radiology*. 2016;280(2):557–567.

Borali E, De Giacomo C. Clostridium difficile infection in children: a review. *J Pediatr Gastroenterol Nutr*. 2016;63(6):e130–e140.

Garel C, Blouet M, Belloy F, et al. Diagnosis of pediatric gastric, small-bowel and colonic volvulus. *Pediatr Radiol*. 2016;46(1):130–138.

Kirkpatrick ID, Greenberg HM. Gastrointestinal complications in the neutropenic patient: characterization and differentiation with abdominal CT. *Radiology*. 2003;226(3):668–674.

McCarville MB, Adelman CS, Li C, et al. Typhlitis in childhood cancer. *Cancer*. 2005;104(2):380–387. PubMed PMID: 15952190.

McCarville MB, Thompson J, Li C, et al. Significance of appendiceal thickening in association with typhlitis in pediatric oncology patients. *Pediatr Radiol*. 2004;34(3):245–249. PubMed PMID: 14722695.

Shenoy-Bhangle A, Gee MS. Magnetic resonance imaging of perianal Crohn disease in children. *Pediatr Radiol*. 2016;46(6):838–846.

## REFERENCES

Full references for this chapter can be found on www.expertconsult.com.

## REFERENCES

1. Doecke JD, Simms LA, Zhao ZZ, et al. Genetic susceptibility in IBD: overlap between ulcerative colitis and Crohn's disease. *Inflamm Bowel Dis*. 2013;19(2):240–245.
2. Talarico V, Aloe M, Monzani A, et al. Hemolytic uremic syndrome in children. *Minerva Pediatr*. 2016;68(6):441–455.
3. Taylor GA, Nancarrow PA, Hernanz-Schulman M, et al. Plain abdominal radiographs in children with inflammatory bowel disease. *Pediatr Radiol*. 1986;16(3):206–209.
4. Panes J, Bouhnik Y, Reinisch W, et al. Imaging techniques for assessment of inflammatory bowel disease: joint ECCO and ESGAR evidence-based consensus guidelines. *J Crohns Colitis*. 2013;7(7):556–585.
5. Autenrieth DM, Baumgart DC. Toxic megacolon. *Inflamm Bowel Dis*. 2012;18(3):584–591.
6. Anupindi SA, Halverson M, Khwaja A, et al. Common and uncommon applications of bowel ultrasound with pathologic correlation in children. *AJR Am J Roentgenol*. 2014;202(5):946–959.
7. Ahmad TM, Greer ML, Walters TD, et al. Bowel sonography and MR enterography in children. *AJR Am J Roentgenol*. 2016;206(1):173–181.
8. Alison M, Kheniche A, Azoulay R, et al. Ultrasonography of Crohn disease in children. *Pediatr Radiol*. 2007;37(11):1071–1082.
9. Levine A, de Bie CI, Turner D, et al. Atypical disease phenotypes in pediatric ulcerative colitis: 5-year analyses of the EUROKIDS Registry. *Inflamm Bowel Dis*. 2013;19(2):370–377.
10. Maconi G, Sampietro GM, Parente F, et al. Contrast radiology, computed tomography and ultrasonography in detecting internal fistulas and intra-abdominal abscesses in Crohn's disease: a prospective comparative study. *Am J Gastroenterol*. 2003;98(7):1545–1555.
11. Mollard BJ, Smith EA, Dillman JR. Pediatric MR enterography: technique and approach to interpretation-how we do it. *Radiology*. 2015;274(1):29–43.
12. Gee MS, Harisinghani MG. MRI in patients with inflammatory bowel disease. *J Magn Reson Imaging*. 2011;33(3):527–534.
13. Barber JL, Lozinsky AC, Kiparissi F, et al. Detecting inflammation in the unprepared pediatric colon - how reliable is magnetic resonance enterography? *Pediatr Radiol*. 2016;46(5):646–652.
14. Dillman JR, Trout AT, Smith EA. MR enterography: how to deliver added value. *Pediatr Radiol*. 2016;46(6):829–837.
15. Thornton E, Morrin MM, Yee J. Current status of MR colonography. *Radiographics*. 2010;30(1):201–218.
16. Tutein Nolthenius CJ, Bipat S, Mearadji B, et al. MRI characteristics of proctitis in Crohn's disease on perianal MRI. *Abdom Radiol (NY)*. 2016;41(10):1918–1930.
17. Szurowska E, Wypych J, Izycka-Swieszewska E. Perianal fistulas in Crohn's disease: MRI diagnosis and surgical planning: MRI in fistulazing perianal Crohn's disease. *Abdom Imaging*. 2007;32(6):705–718.
18. Adler J, Dong S, Eder SJ, et al. ImproveCareNow Pediatric IBDLHS. Perianal Crohn's disease in a large multicenter pediatric collaborative. *J Pediatr Gastroenterol Nutr*. 2016.
19. Compton GL, Bartlett M. Perianal disease in pediatric Crohn disease: a review of MRI findings. *Pediatr Radiol*. 2014;44(10):1198–1208, quiz 1195–1197.
20. Parks AG. Pathogenesis and treatment of fistuila-in-ano. *Br Med J*. 1961;1(5224):463–469.
21. Parks AG, Gordon PH. Fistula-in-ano: perineal fistula of intra-abdominal or intrapelvic origin simulating fistula-in-ano–report of seven cases. *Dis Colon Rectum*. 1976;19(6):500–506.
22. Morris J, Spencer JA, Ambrose NS. MR imaging classification of perianal fistulas and its implications for patient management. *Radiographics*. 2000;20(3):623–635, discussion 635–627.
23. Shenoy-Bhangle A, Nimkin K, Goldner D, et al. MRI predictors of treatment response for perianal fistulizing Crohn disease in children and young adults. *Pediatr Radiol*. 2014;44(1):23–29.
24. Kulkarni S, Gomara R, Reeves-Garcia J, et al. MRI-based score helps in assessing the severity and in follow-up of pediatric patients with perianal Crohn disease. *J Pediatr Gastroenterol Nutr*. 2014;58(2):252–257.
25. Catalano OA, Gee MS, Nicolai E, et al. Evaluation of quantitative PET/MR enterography biomarkers for discrimination of inflammatory strictures from fibrotic strictures in Crohn disease. *Radiology*. 2016;278(3):792–800.
26. Stidham RW, Higgins PD. Imaging of intestinal fibrosis: current challenges and future methods. *United European Gastroenterol J*. 2016;4(4):515–522.
27. Miniello S, Marzaioli R, Balzanelli MG, et al. Toxic megacolon in ulcerative rectocolitis. Current trends in clinical evaluation, diagnosis and treatment. *Ann Ital Chir*. 2014;85(1):45–49.
28. Corica D, Romano C. Biological therapy in pediatric inflammatory bowel disease: a systematic review. *J Clin Gastroenterol*. 2016;Sep 15.
29. Romeo E, Jasonni V, Caldaro T, et al. Strictureplasty and intestinal resection: different options in complicated pediatric-onset Crohn disease. *J Pediatr Surg*. 2012;47(5):944–948.
30. Fumery M, Duricova D, Gower-Rousseau C, et al. Review article: the natural history of paediatric-onset ulcerative colitis in population-based studies. *Aliment Pharmacol Ther*. 2016;43(3):346–355.
31. de Ridder L, Turner D, Wilson DC, et al. Malignancy and mortality in pediatric patients with inflammatory bowel disease: a multinational study from the porto pediatric IBD group. *Inflamm Bowel Dis*. 2014;20(2):291–300.
32. Hukkinen M, Pakarinen MP, Piekkala M, et al. Treatment of complex perianal fistulas with seton and infliximab in adolescents with Crohn's disease. *J Crohns Colitis*. 2014;8(8):756–762.
33. Bartlett JG. Antimicrobial agents implicated in Clostridium difficile toxin-associated diarrhea of colitis. *Johns Hopkins Med J*. 1981;149(1):6–9.
34. Faris B, Blackmore A, Haboubi N. Review of medical and surgical management of Clostridium difficile infection. *Tech Coloproctol*. 2010;14(2):97–105.
35. Loughran CF, Tappin JA, Whitehouse GH. The plain abdominal radiograph in pseudomembranous colitis due to Clostridium difficile. *Clin Radiol*. 1982;33(3):277–281.
36. Im GY, Modayil RJ, Lin CT, et al. The appendix may protect against Clostridium difficile recurrence. *Clin Gastroenterol Hepatol*. 2011;9(12):1072–1077.
37. Bollinger RR, Barbas AS, Bush EL, et al. Biofilms in the normal human large bowel: fact rather than fiction. *Gut*. 2007;56(10):1481–1482.
38. Peterson LR, Manson RU, Paule SM, et al. Detection of toxigenic Clostridium difficile in stool samples by real-time polymerase chain reaction for the diagnosis of C. difficile-associated diarrhea. *Clin Infect Dis*. 2007;45(9):1152–1160.
39. Blickman JG, Boland GW, Cleveland RH, et al. Pseudomembranous colitis: CT findings in children. *Pediatr Radiol*. 1995;25(suppl 1):S157–S159.
40. Bolondi L, Ferrentino M, Trevisani F, et al. Sonographic appearance of pseudomembranous colitis. *J Ultrasound Med*. 1985;4(9):489–492.
41. Mele C, Remuzzi G, Noris M. Hemolytic uremic syndrome. *Semin Immunopathol*. 2014;36(4):399–420.
42. Griffin PM, Ostroff SM, Tauxe RV, et al. Illnesses associated with Escherichia coli O157:H7 infections. A broad clinical spectrum. *Ann Intern Med*. 1988;109(9):705–712.
43. Griffin PM, Tauxe RV. The epidemiology of infections caused by Escherichia coli O157:H7, other enterohemorrhagic E. coli, and the associated hemolytic uremic syndrome. *Epidemiol Rev*. 1991;13:60–98.
44. Tochen ML, Campbell JR. Colitis in children with the hemolytic-uremic syndrome. *J Pediatr Surg*. 1977;12(2):213–219.
45. Nay J, Menias CO, Mellnick VM, et al. Gastrointestinal manifestations of systemic disease: a multimodality review. *Abdom Imaging*. 2015;40(6):1926–1943.
46. Kirks DR. The radiology of enteritis due to hemolytic-uremic syndrome. *Pediatr Radiol*. 1982;12(4):179–183.
47. Miller FH, Ma JJ, Scholz FJ. Imaging features of enterohemorrhagic Escherichia coli colitis. *AJR Am J Roentgenol*. 2001;177(3):619–623.
48. Sebbag H, Lemelle JL, Moller C, et al. Colonic stenosis after hemolytic-uremic syndrome. *Eur J Pediatr Surg*. 1999;9(2):119–120.
49. Rha SE, Ha HK, Lee SH, et al. CT and MR imaging findings of bowel ischemia from various primary causes. *Radiographics*. 2000;20(1):29–42.
50. Kountouras J, Zavos C. Recent advances in the management of radiation colitis. *World J Gastroenterol*. 2008;14(48):7289–7301.
51. Kennedy GD, Heise CP. Radiation colitis and proctitis. *Clin Colon Rectal Surg*. 2007;20(1):64–72.
52. Theis VS, Sripadam R, Ramani V, et al. Chronic radiation enteritis. *Clin Oncol (R Coll Radiol)*. 2010;22(1):70–83.
53. Abramson SJ, Berdon WE, Baker DH. Childhood typhlitis: its increasing association with acute myelogenous leukemia. Report of five cases. *Radiology*. 1983;146(1):61–64.
54. Mehdi I, Al Bahrani B. Chemotherapy-induced neutropenic necrotizing enterocolitis: a review. *J Pak Med Assoc*. 2012;62(7):718–723.

55. Hobson MJ, Carney DE, Molik KA, et al. Appendicitis in childhood hematologic malignancies: analysis and comparison with typhlitis. *J Pediatr Surg*. 2005;40(1):214–219, discussion 219–220.
56. Kirkpatrick ID, Greenberg HM. Gastrointestinal complications in the neutropenic patient: characterization and differentiation with abdominal CT. *Radiology*. 2003;226(3):668–674.
57. McNamara MJ, Chalmers AG, Morgan M, et al. Typhlitis in acute childhood leukaemia: radiological features. *Clin Radiol*. 1986;37(1):83–86.
58. Lee JH, Lim GY, Im SA, et al. Gastrointestinal complications following hematopoietic stem cell transplantation in children. *Korean J Radiol*. 2008;9(5):449–457.
59. Fike FB, Mortellaro V, Juang D, et al. Neutropenic colitis in children. *J Surg Res*. 2011;170(1):73–76.
60. Horton KM, Corl FM, Fishman EK. CT evaluation of the colon: inflammatory disease. *Radiographics*. 2000;20(2):399–418.
61. Dignan FL, Clark A, Amrolia P, et al. Diagnosis and management of acute graft-versus-host disease. *Br J Haematol*. 2012;158(1):30–45.
62. El-Shabrawi MH, Kamal NM, Jouini R, et al. Gastrointestinal basidiobolomycosis: an emerging fungal infection causing bowel perforation in a child. *J Med Microbiol*. 2011;60(Pt 9):1395–1402.
63. El-Shabrawi MH, Kamal NM. Gastrointestinal basidiobolomycosis in children: an overlooked emerging infection? *J Med Microbiol*. 2011;60(Pt 7):871–880.
64. Vikram HR, Smilack JD, Leighton JA, et al. Emergence of gastrointestinal basidiobolomycosis in the United States, with a review of worldwide cases. *Clin Infect Dis*. 2012;54(12):1685–1691.
65. Turner D, Hyams J, Markowitz J, et al. Appraisal of the pediatric ulcerative colitis activity index (PUCAI). *Inflamm Bowel Dis*. 2009;15(8):1218–1223.
66. Smyth RL. Fibrosing colonopathy in cystic fibrosis. *Arch Dis Child*. 1996;74(5):464–468.
67. FitzSimmons SC, Burkhart GA, Borowitz D, et al. High-dose pancreatic-enzyme supplements and fibrosing colonopathy in children with cystic fibrosis. *N Engl J Med*. 1997;336(18):1283–1289.
68. Lloyd-Still JD, Beno DW, Kimura RM. Cystic fibrosis colonopathy. *Curr Gastroenterol Rep*. 1999;1(3):231–237.
69. Zerin JM, Kuhn-Fulton J, White SJ, et al. Colonic strictures in children with cystic fibrosis. *Radiology*. 1995;194(1):223–226.
70. Puig S, Staudenherz A, Felder-Puig R, et al. Imaging of appendicitis in children and adolescents: useful or useless? A comparison of imaging techniques and a critical review of the current literature. *Semin Roentgenol*. 2008;43(1):22–28.
71. Addiss DG, Shaffer N, Fowler BS, et al. The epidemiology of appendicitis and appendectomy in the United States. *Am J Epidemiol*. 1990;132(5):910–925.
72. Holscher HC, Heij HA. Imaging of acute appendicitis in children: EU versus U.S. … or US versus CT? A European perspective. *Pediatr Radiol*. 2009;39(5):497–499.
73. Kosloske AM, Love CL, Rohrer JE, et al. The diagnosis of appendicitis in children: outcomes of a strategy based on pediatric surgical evaluation. *Pediatrics*. 2004;113(1 Pt 1):29–34.
74. Hernanz-Schulman M. CT and US in the diagnosis of appendicitis: an argument for CT. *Radiology*. 2010;255(1):3–7.
75. Lamps LW. Appendicitis and infections of the appendix. *Semin Diagn Pathol*. 2004;21(2):86–97.
76. Migraine S, Atri M, Bret PM, et al. Spontaneously resolving acute appendicitis: clinical and sonographic documentation. *Radiology*. 1997;205(1):55–58.
77. Heller MB, Skolnick ML. Ultrasound documentation of spontaneously resolving appendicitis. *Am J Emerg Med*. 1993;11(1):51–53.
78. Sivit CJ, Applegate KE. Imaging of acute appendicitis in children. *Semin Ultrasound CT MR*. 2003;24(2):74–82.
79. Rothrock SG. Pagane J. Acute appendicitis in children: emergency department diagnosis and management. *Ann Emerg Med*. 2000;36(1):39–51.
80. Applegate KE, Sivit CJ, Salvator AE, et al. Effect of cross-sectional imaging on negative appendectomy and perforation rates in children. *Radiology*. 2001;220(1):103–107.
81. Partrick DA, Janik JE, Janik JS, et al. Increased CT scan utilization does not improve the diagnostic accuracy of appendicitis in children. *J Pediatr Surg*. 2003;38(5):659–662.
82. York D, Smith A, Phillips JD, et al. The influence of advanced radiographic imaging on the treatment of pediatric appendicitis. *J Pediatr Surg*. 2005;40(12):1908–1911.
83. Pena BM, Taylor GA, Fishman SJ, et al. Effect of an imaging protocol on clinical outcomes among pediatric patients with appendicitis. *Pediatrics*. 2002;110(6):1088–1093.
84. Smink DS, Finkelstein JA, Garcia Pena BM, et al. Diagnosis of acute appendicitis in children using a clinical practice guideline. *J Pediatr Surg*. 2004;39(3):458–463, discussion 458–463.
85. Rao PM, Rhea JT, Rattner DW, et al. Introduction of appendiceal CT: impact on negative appendectomy and appendiceal perforation rates. *Ann Surg*. 1999;229(3):344–349.
86. Larson DB, Johnson LW, Schnell BM, et al. National trends in CT use in the emergency department: 1995-2007. *Radiology*. 2011;258(1):164–173.
87. Broder J, Fordham LA, Warshauer DM. Increasing utilization of computed tomography in the pediatric emergency department, 2000-2006. *Emerg Radiol*. 2007;14(4):227–232.
88. Siegel MJ, Carel C, Surratt S. Ultrasonography of acute abdominal pain in children. *JAMA*. 1991;266(14):1987–1989.
89. Sivit CJ, Applegate KE, Berlin SC, et al. Evaluation of suspected appendicitis in children and young adults: helical CT. *Radiology*. 2000;216(2):430–433.
90. Brennan GD. Pediatric appendicitis: pathophysiology and appropriate use of diagnostic imaging. *CJEM*. 2006;8(6):425–432.
91. Lowe LH, Penney MW, Scheker LE, et al. Appendicolith revealed on CT in children with suspected appendicitis: how specific is it in the diagnosis of appendicitis? *AJR Am J Roentgenol*. 2000;175(4):981–984.
92. Friedland JA, Siegel MJ. CT appearance of acute appendicitis in childhood. *AJR Am J Roentgenol*. 1997;168(2):439–442.
93. Puylaert JB. Acute appendicitis: US evaluation using graded compression. *Radiology*. 1986;158(2):355–360.
94. Jeffrey RB Jr, Laing FC, Townsend RR. Acute appendicitis: sonographic criteria based on 250 cases. *Radiology*. 1988;167(2):327–329.
95. Kao SC, Smith WL, Abu-Yousef MM, et al. Acute appendicitis in children: sonographic findings. *AJR Am J Roentgenol*. 1989;153(2):375–379.
96. Wiersma F, Toorenvliet BR, Bloem JL, et al. US examination of the appendix in children with suspected appendicitis: the additional value of secondary signs. *Eur Radiol*. 2009;19(2):455–461.
97. Goldin AB, Khanna P, Thapa M, et al. Revised ultrasound criteria for appendicitis in children improve diagnostic accuracy. *Pediatr Radiol*. 2011;41(8):993–999.
98. Chan L, Shin LK, Pai RK, et al. Pathologic continuum of acute appendicitis: sonographic findings and clinical management implications. *Ultrasound Q*. 2011;27(2):71–79.
99. Peletti AB, Baldisserotto M. Optimizing US examination to detect the normal and abnormal appendix in children. *Pediatr Radiol*. 2006;36(11):1171–1176.
100. Wiersma F, Sramek A, Holscher HC. US features of the normal appendix and surrounding area in children. *Radiology*. 2005;235(3):1018–1022.
101. Balthazar EJ, Birnbaum BA, Yee J, et al. Acute appendicitis: CT and US correlation in 100 patients. *Radiology*. 1994;190(1):31–35.
102. Patriquin HB, Garcier JM, Lafortune M, et al. Appendicitis in children and young adults: Doppler sonographic-pathologic correlation. *AJR Am J Roentgenol*. 1996;166(3):629–633.
103. Trout AT, Sanchez R, Ladino-Torres MF. Reevaluating the sonographic criteria for acute appendicitis in children: a review of the literature and a retrospective analysis of 246 cases. *Acad Radiol*. 2012;19(11):1382–1394.
104. Kessler N, Cyteval C, Gallix B, et al. Appendicitis: evaluation of sensitivity, specificity, and predictive values of US, Doppler US, and laboratory findings. *Radiology*. 2004;230(2):472–478.
105. Lim HK, Lee WJ, Lee SJ, et al. Focal appendicitis confined to the tip: diagnosis at US. *Radiology*. 1996;200(3):799–801.
106. Anderson BA, Salem L, Flum DR. A systematic review of whether oral contrast is necessary for the computed tomography diagnosis of appendicitis in adults. *Am J Surg*. 2005;190(3):474–478.
107. Trout AT, Zhang B, Towbin AJ. Measurement error in CT assessment of appendix diameter. *Pediatr Radiol*. 2016;46(13):1831–1836.
108. Applegate KE, Sivit CJ, Myers MT. Pschesang B. Using helical CT to diagnosis acute appendicitis in children: spectrum of findings. *AJR Am J Roentgenol*. 2001;176(2):501–505.
109. Doria AS, Moineddin R, Kellenberger CJ, et al. US or CT for diagnosis of appendicitis in children and adults? A meta-analysis. *Radiology*. 2006;241(1):83–94.
110. Pearce MS, Salotti JA, Little MP, et al. Radiation exposure from CT scans in childhood and subsequent risk of leukaemia and brain tumours: a retrospective cohort study. *Lancet*. 2012;380(9840):499–505.

111. Mathews JD, Forsythe AV, Brady Z, et al. Cancer risk in 680,000 people exposed to computed tomography scans in childhood or adolescence: data linkage study of 11 million Australians. *BMJ*. 2013;346: f2360.
112. Strouse PJ. Pediatric appendicitis: an argument for US. *Radiology*. 2010;255(1):8–13.
113. Toorenvliet BR, Wiersma F, Bakker RF, et al. Routine ultrasound and limited computed tomography for the diagnosis of acute appendicitis. *World J Surg*. 2010;34(10):2278–2285.
114. Moore MM, Gustas CN, Choudhary AK, et al. MRI for clinically suspected pediatric appendicitis: an implemented program. *Pediatr Radiol*. 2012;42(9):1056–1063.
115. Cobben L, Groot I, Kingma L, et al. A simple MRI protocol in patients with clinically suspected appendicitis: results in 138 patients and effect on outcome of appendectomy. *Eur Radiol*. 2009;19(5):1175–1183.
116. Dillman JR, Gadepalli S, Sroufe NS, et al. Equivocal pediatric appendicitis: unenhanced MR imaging protocol for nonsedated children-a clinical effectiveness study. *Radiology*. 2016;279(1):216–225.
117. Petkovska I, Martin DR, Covington MF, et al. Accuracy of unenhanced MR imaging in the detection of acute appendicitis: single-institution clinical performance review. *Radiology*. 2016;279(2):451–460.
118. Nitta N, Takahashi M, Furukawa A, et al. MR imaging of the normal appendix and acute appendicitis. *J Magn Reson Imaging*. 2005;21(2):156–165.
119. Muehlstedt SG, Pham TQ, Schmeling DJ. The management of pediatric appendicitis: a survey of North American Pediatric Surgeons. *J Pediatr Surg*. 2004;39(6):875–879, discussion 875–879.
120. Newman K, Ponsky T, Kittle K, et al. Appendicitis 2000: variability in practice, outcomes, and resource utilization at thirty pediatric hospitals. *J Pediatr Surg*. 2003;38(3):372–379, discussion 372–379.
121. Chen C, Botelho C, Cooper A, et al. Current practice patterns in the treatment of perforated appendicitis in children. *J Am Coll Surg*. 2003;196(2):212–221.
122. Lee SL, Yaghoubian A, Kaji A. Laparoscopic vs open appendectomy in children: outcomes comparison based on age, sex, and perforation status. *Arch Surg*. 2011;146(10):1118–1121.
123. Rentea RM, Peter SD, Snyder CL. Pediatric appendicitis: state of the art review. *Pediatr Surg Int*. 2016;Oct 14.
124. Abou-Nukta F, Bakhos C, Arroyo K, et al. Effects of delaying appendectomy for acute appendicitis for 12 to 24 hours. *Arch Surg*. 2006;141(5):504–506, discussioin 506–507.
125. Yardeni D, Hirschl RB, Drongowski RA, et al. Delayed versus immediate surgery in acute appendicitis: do we need to operate during the night? *J Pediatr Surg*. 2004;39(3):464–469, discussion 464–469.
126. St Peter SD, Snyder CL. Operative management of appendicitis. *Semin Pediatr Surg*. 2016;25(4):208–211.
127. Berger RB, Hillemeier AC, Stahl RS, et al. Volvulus of the ascending colon: an unusual complication of non-rotation of the midgut. *Pediatr Radiol*. 1982;12(6):298–300.
128. Andersen JF, Eklof O, Thomasson B. Large bowel volvulus in children. Review of a case material and the literature. *Pediatr Radiol*. 1981;11(3):129–138.
129. Peterson CM, Anderson JS, Hara AK, et al. Volvulus of the gastrointestinal tract: appearances at multimodality imaging. *Radiographics*. 2009;29(5):1281–1293.
130. Kokoska ER, Herndon CD, Carney DE, et al. Cecal volvulus: a report of two cases occurring after the antegrade colonic enema procedure. *J Pediatr Surg*. 2004;39(6):916–919, discussion 916–919.
131. Ton MN, Ruzal-Shapiro C, Stolar C. Kazlow PG. Recurrent sigmoid volvulus in a sixteen-year-old boy: case report and review of the literature. *J Pediatr Surg*. 2004;39(9):1434–1436.
132. Campbell JR, Blank E. Sigmoid volvulus in children. *Pediatrics*. 1974;53(5):702–705.
133. Reinarz S, Smith WL, Franken EA Jr, et al. Splenic flexure volvulus: a complication of pseudoobstruction in infancy. *AJR Am J Roentgenol*. 1985;145(6):1303–1304.
134. Mellor MF, Drake DG. Colonic volvulus in children: value of barium enema for diagnosis and treatment in 14 children. *AJR Am J Roentgenol*. 1994;162(5):1157–1159.
135. Dubinsky MC, Deslandres C, Patriquin H, et al. Pneumatosis intestinalis and colocolic intussusception complicating Crohn's disease. *J Pediatr Gastroenterol Nutr*. 2000;30(1):96–98.
136. Kurbegov AC, Sondheimer JM. Pneumatosis intestinalis in non-neonatal pediatric patients. *Pediatrics*. 2001;108(2):402–406.
137. Yeager AM, Kanof ME, Kramer SS, et al. Pneumatosis intestinalis in children after allogeneic bone marrow transplantation. *Pediatr Radiol*. 1987;17(1):18–22.
138. Hernanz-Schulman M, Kirkpatrick J Jr, Shwachman H, et al. Pneumatosis intestinalis in cystic fibrosis. *Radiology*. 1986;160(2):497–499.
139. Chelimsky G, Blanchard S, Sivit C, et al. Pneumatosis intestinalis and diarrhea in a child following renal transplantation. *Pediatr Transplant*. 2003;7(3):236–239.
140. Sivit CJ, Josephs SH, Taylor GA, et al. Pneumatosis intestinalis in children with AIDS. *AJR Am J Roentgenol*. 1990;155(1):133–134.
141. Spalinger J, Patriquin H, Miron MC, et al. Doppler US in patients with crohn disease: vessel density in the diseased bowel reflects disease activity. *Radiology*. 2000;217(3):787–791.
142. El-Kady S, Petel D, Baird R. Inter-rater agreement in the evaluation of abdominal radiographs for necrotizing enterocolitis. *J Pediatr Surg*. 2014;49(5):733–735.
143. Markiet K, Szymanska-Dubowik A, Janczewska I, et al. Agreement and reproducibility of radiological signs in NEC using The Duke Abdominal Assessment Scale (DAAS). *Pediatr Surg Int*. 2016.
144. Silva CT, Daneman A, Navarro OM, et al. Correlation of sonographic findings and outcome in necrotizing enterocolitis. *Pediatr Radiol*. 2007;37(3):274–282.
145. Goske MJ, Goldblum JR, Applegate KE, et al. The "circle sign": a new sonographic sign of pneumatosis intestinalis - clinical, pathologic and experimental findings. *Pediatr Radiol*. 1999;29(7):530–535.

# 107 Intussusception

Kimberly E. Applegate and Marta Hernanz-Schulman

## OVERVIEW

Intussusception is an acquired invagination of the bowel into itself (Fig. 107.1). The more proximal bowel that invaginates into more distal bowel is termed the *intussusceptum*, whereas the recipient bowel that contains the intussusceptum is termed the *intussuscipiens*. Invagination of the bowel, if sustained, leads to edema, and ischemic changes eventually supervene. Intussusception is thus an urgent condition, and delay in diagnosis results in increased risk for bowel necrosis and perforation.

Intussusception can occur in any part of the bowel at any age. In infants and young children, idiopathic ileocolic intussusception is by far the most common, comprising approximately 95% of all cases, and is the most common cause of small bowel obstruction in patients aged 3 months to 5 years.[1] The documented incidence of intussusception varies with geographic location, averaging approximately 74 cases in infants younger than 1 year of age per 100,000 infant-years worldwide, ranging in the United States between 33 and 52 per 100,00 infant-years with a male:female ratio of approximately 2 : 1.[2,3]

## ETIOLOGY

### Idiopathic

Approximately 90% to 95% of cases of intussusception in children are ileocolic and idiopathic.[4,5] The majority occur in the first year of life, with a peak age of 5 to 9 months. Circumferential lymphoid hypertrophy about the terminal ileum is thought to play an etiologic role in the onset of idiopathic intussusception.[4,6,7] Antecedent infection with adenovirus has been implicated in cases of idiopathic intussusception,[8] likely as a cofactor in the development of lymphoid hyperplasia. Other infectious agents, particularly enterovirus, also have been implicated.[9–11] Although typically associated with seasonal peaks in the May, June, and July,[4] recent reports have identified no specific seasonality, suggesting no, or more than one, antecedent gastrointestinal pathogen.[12]

### Rotavirus Vaccine

Shortly after the first rotavirus vaccine was introduced in the United States in 1998 for routine vaccination of infants at ages 2, 4, and 6 months, several reports to the Centers for Disease Control and Prevention (CDC) suggested an association between the vaccine and intussusception, prompting vaccine removal from the market. A subsequent case-controlled study of this tetravalent vaccine found “a strong, temporal, and specific” relationship, sufficient to provide “evidence of a causal association” between the vaccine and intussusception.[13] Since then, a monovalent and a pentavalent vaccine have been developed, and both have undergone extensive evaluation worldwide.[14] They have been found to have a lower but not nonexistent risk of intussusception, particularly within a week of receiving the first dose. However, institution of these vaccines has significantly lowered the mortality and morbidity associated with rotavirus disease, for a positive risk-benefit ratio.[3,15–19]

### Lead Points

There may be a definable, pathologic, lead point, such as a focal mass, or a more diffuse bowel wall abnormality accompanying the intussusception, particularly when intussusception occurs outside of the typical idiopathic age range, or when nontransient intussusception is confined to the small bowel or to the colon. Lead points may be found in approximately 5% of children presenting with intussusception in the first year of life but are present in 60% of intussusceptions in 5- to 14-year-old patients and are also more frequently found in infants less than 3 months of age; 44% of lead points present by 5 years of age. Although the absolute number of lead points is approximately equal in infants and in older children,[20] the percentage of lead points in children outside the typical age bracket for idiopathic intussusception is much higher because the denominator is so much smaller. The most common focal lead points in infants are Meckel diverticulum and duplication cyst, whereas in older children polyps and lymphoma are more common. Parasitic infestations can act as or produce lead points for intussusception in the large or small bowel, particularly ascariasis, although others such as schistosomiasis have also been reported.[21–24] Diffuse bowel thickening, such as is seen with Henoch-Schönlein purpura, typically leads to small bowel intussusception. Polyps can act as lead points in the small bowel or in the colon and can present with colocolic intussusceptions. Although patients with detected lead points will eventually have surgery, nonoperative reduction may be attempted in ileocolic intussusceptions to allow for nonurgent surgery.

Lead points are more likely in patients with recurrent intussusception but only represent approximately 14% to 19% of recurrent intussusception cases[4,20]; the majority of patients with recurrent intussusceptions do not have lead points.

Intussusception can also occur around gastrostomy and gastrojejunostomy tubes (see Chapter 103).

## CLINICAL PRESENTATION

Idiopathic intussusception occurs most commonly in infants aged between 3 months and 3 years, with a peak age of 5 to 9 months; large series report 57% to 85% of cases presenting before the age of 1 year (an average of 67% occur by age 1 year).[7,25]

The classic clinical presentation of the child with intussusception is the triad of colicky abdominal pain, vomiting, and bloody stools.[7] Individually, each of these symptoms is present in a large number of patients, although all three are found less frequently. Colicky abdominal pain is found in 58% to 100% of cases, vomiting in up to 85% of cases, and bloody stools in up to 75% of cases, but the triad is seen in 25% to 65% of patients, depending on the series and age group.[5,26–28] In patients presenting in the first year of life, irritability, bile-stained vomit, and lethargy are more likely to be present.[5] In other patients, clinical signs and symptoms of intussusception may be nonspecific and overlap with those of more common conditions, such as gastroenteritis, and some authors have found no reliable clinical prediction models that identify all children with intussusception.[27,29,30] One retrospective analysis of patients found that only 50% of children were correctly diagnosed clinically at initial presentation.[31] Vomiting or diarrhea may lead to dehydration, which exaggerates lethargy. Venous hypertension leads to hematochezia, with a typical mixture of stool, blood, and blood clots that has been described as “currant jelly stools,” a clinical finding highly suggestive of intussusception.

## DIAGNOSIS AND IMAGING

Box 107.1 summarizes the evidence regarding imaging management of intussusception.

## Abstract:

To describe the various types of bowel intussusception that occur in pediatric patients. Ileocolic intussusception with and without lead points is discussed. Additional discussion includes ileoileal intussusceptions, and key points in differentiation from ileocolic intussusception, as well as differentiation between transient clinically insignificant small bowel intussusceptions, as well as those which are significant and may produce ischemic bowel. The various methods of nonsurgical reduction are described and discussed, including complications and success rate.

## Keywords:

Intussusception
ileoileal
ilelileocolic
ileocolic
colocolic
lead points
plain film diagnosis
ultrasound diagnosis
nonsurgical reduction
air enema
liquid enema
complications
recurrence

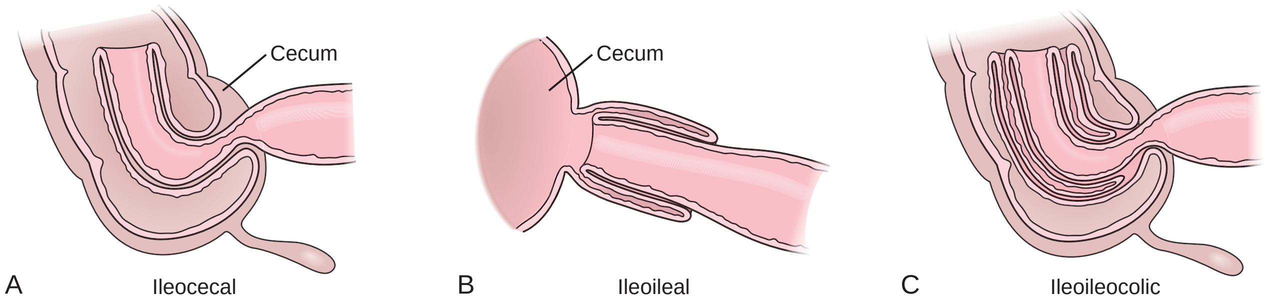

**Figure 107.1. Types of pediatric intussusception, in longitudinal section.** (A) Ileocecal. (B) Ileoileal. (C) Ileoileocolic.

**BOX 107.1** Diagnosis and Management of Intussusception

Plain radiographs are useful for:
- Differential diagnosis; screen for other conditions
- Detect bowel obstruction
- Free air

Ultrasound is highly sensitive and specific in detecting intussusception
- Ultrasound can also detect lead points
- Findings suggesting decreased chance of nonoperative reduction
  - Trapped fluid at the leading edge of the intussusceptum
  - Absence of flow on Doppler evaluation

Enema is indicated for reduction in the absence of:
- Free air
- Peritoneal signs

## Abdominal Radiographs

Overall, abdominal radiographs are considered to have a low sensitivity and specificity for intussusception; sensitivities of 45% to 62% and specificities of up to 87% have been reported,[32,33] with reports of higher sensitivity although with lower specificity when employing a three-view examination.[34] Abdominal radiographs typically include a frontal view and a horizontal ray view; left side down decubitus is most helpful, because in addition to assessing air-fluid levels and free air, gas is gravitationally directed into the ascending colon, which can help in diagnosis or exclusion of intussusception. In one series, the addition of the decubitus radiograph improved diagnostic performance, with 67% of studies considered determinate for diagnosis, and a sensitivity and specificity of 74% and 58%, respectively.[35] The visualization of the intussusceptum as an intracolonic mass outlined by gas, termed the *crescent sign*, is nearly pathognomonic of intussusception but is seen in only approximately one-third of cases (Fig. 107.2).[35] The absence of stool and bowel gas in the ascending colon is one of the more suggestive radiographic signs of intussusception, while the clear presence of stool or an air-fluid level within the cecum is the most specific sign to exclude it. However, small bowel or sigmoid gas located in the right abdomen on radiographs may mimic ascending colon or cecal gas, and fluid filling the right colon in a patient with gastroenteritis may also show a similar appearance.

In this era of widely available ultrasound, perhaps the more important role of abdominal radiographs is to screen for other conditions, ranging from constipation to free air to foreign body, and to assess for the presence of bowel obstruction, which helps guide the ultrasound and is also an important prognostic factor for reduction.

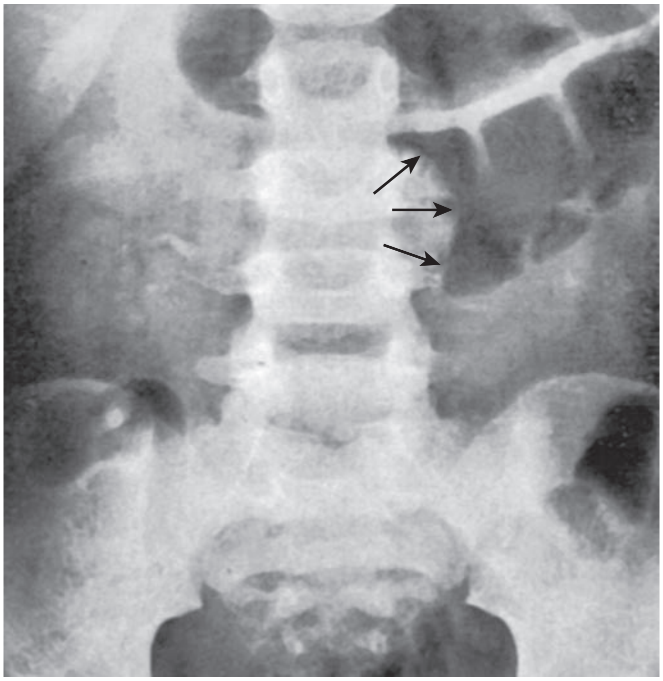

**Figure 107.2. Ileocolic intussusception in a 4-year-old child.** The leading edge of the intussusception *(arrows)* is outlined by gas within the transverse colon. No gas or other colonic contents can be seen in the cecum or in the ascending colon, which are occupied by the intussusceptum.

## Ultrasonography

Ultrasound is highly sensitive in the detection of intussusception, with sensitivity and specificity at or close to 100%, even when performed by relatively inexperienced operators.[36,37] Ultrasound is the primary imaging modality used by more than 90% of European pediatric radiologists[38] and is highly accurate when used as the primary imaging modality for the diagnosis and exclusion of this condition.[33] Initial evaluation by ultrasound circumvents the more invasive enema in patients who do not have intussusception and allows diagnosis of other conditions in which performance of an enema would be noncontributory or contraindicated mesenteric adenitis or colitis.[27,39,40] Ultrasound evaluation has been found to be part of the most cost-effective strategy in the diagnosis and treatment of children with intussusception.[41]

Intussusception is diagnosed by identifying the bowel-within-bowel appearance of the intussusceptum within the intussuscipiens, which are clearly visible with high-resolution equipment. Initial reports described pseudokidney, donut, and target signs, resulting from the central hyperechoic mesentery resembling a renal hilus, and the surrounding loops of bowel resembling the kidney when imaged longitudinally, and a donut or target on transverse images.[42] Today, much greater detail allows the bowel-within-bowel appearance to be easily demonstrated; the leading edge shows the inversion of the inner and outer sleeves of the intussusceptum, with or without trapped fluid or lead point. Typically, flow can be identified with color Doppler (Fig. 107.3).

Ileocolic intussusception is most often encountered in the right upper quadrant, but all four quadrants are evaluated and documented; review of abdominal radiographs that can localize bowel gas and determine the presence of dilated small bowel loops can be helpful in performing and interpreting the ultrasound. Overview with a curved transducer may be done, but the diagnostic examination is typically performed with a linear transducer focused to encompass the entire abdominal thickness. Once the intussusception is encountered, it should be followed to its leading edge to determine the presence of anechoic trapped fluid and/or a potential lead point.

Ultrasound findings have prognostic correlations with the nonoperative reducibility of an intussusception. Anechoic fluid trapped between the intussusceptum and the intussuscipiens (Fig. 107.4) has been associated with lack of reducibility.[39] Lack of color Doppler signal in the wall of the intussuscepted bowel suggests bowel ischemia.[39,43] Because ischemia and perforation can be focal, identification of flow does not exclude underlying ischemic changes or potential for perforation. There are conflicting reports as to whether free peritoneal fluid is associated with fewer successful reductions,[44,45] but it is present in approximately one-half of patients.[42] Although these findings are associated with fewer successful reductions, none represents a contraindication to enema reduction. The only absolute contraindications to enema reduction are signs of peritonitis and free intraperitoneal air.

The detection of lead points by imaging is best accomplished by ultrasound at presentation by paying careful attention to the leading edge of the intussusception (Fig. 107.5). In a recent review, focal lead points were detected in 74% of infants at presentation.[20] Before the incorporation of ultrasound into the routine diagnosis

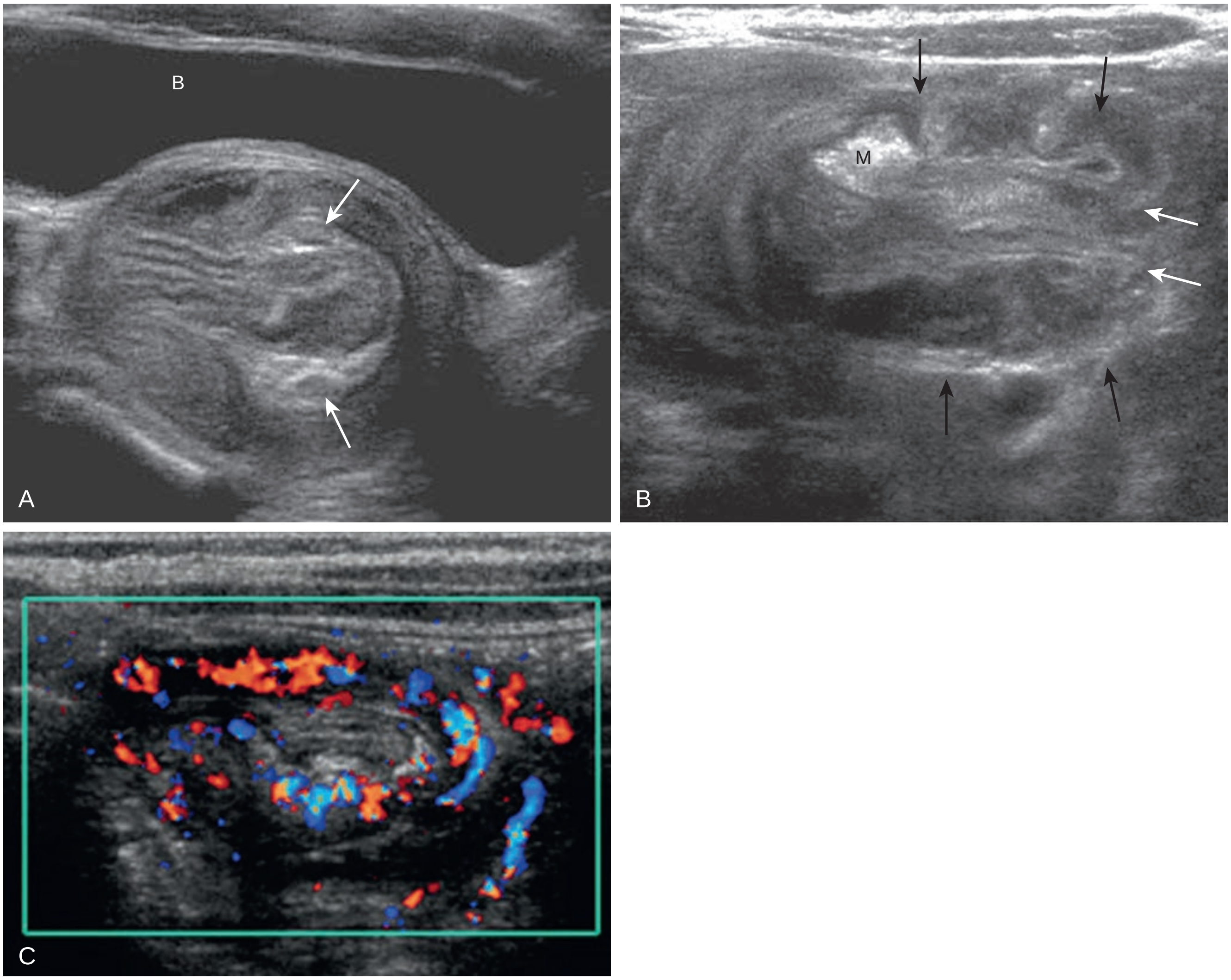

**Figure 107.3. Intussusception.** (A) Transverse sonogram in a 5-year-old boy through the intussusceptum complex shows mesentery and lymph nodes *(arrows)* in the space between the inner and outer sleeves of the intussusceptum. The intussusception was in the rectum. *B*, Bladder. (B) Longitudinal sonogram in a 3-month-old child shows mesentery *(M)* between the inner and outer sleeves of the intussusceptum *(white arrows)*, which represent the entering limb and the everted, returning limb. *Black arrows* outline the outer edge of the intussuscipiens. Note that there is no evidence of a lead point. (C) Transverse color Doppler sonogram of an intussusception demonstrating typical concentric rings of flow.

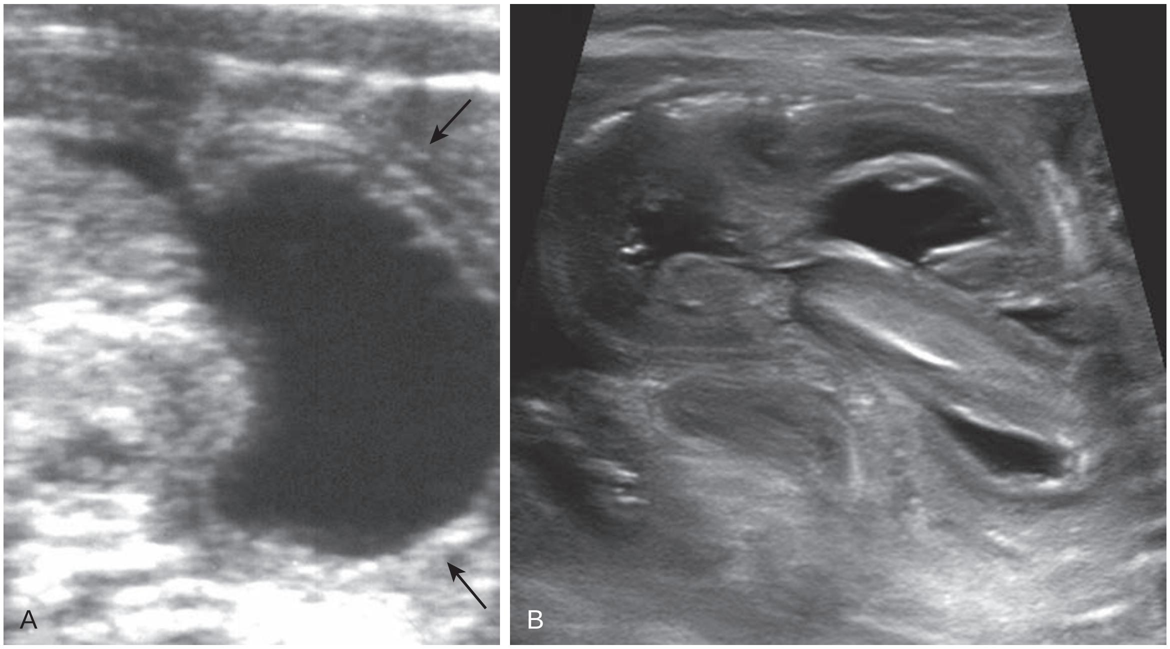

**Figure 107.4. Intussusception.** (A) Sonogram shows fluid at the leading edge of the intussusceptum complex, outlining the eversion of the inner and outer sleeves of the intussusceptum. *Arrows* point to the outer edge of the intussuscipiens. (B) Longitudinal sonogram of intussusception in a 3-month-old boy with high-grade small bowel obstruction. Note the large amount of fluid trapped within the intussusceptum complex. The intussusception was only partially reducible, and a partial colectomy was necessary for nonviable bowel.

of intussusception, approximately 40% of lead points were identified by liquid enema, while detection by air enema is approximately 11%.[20] Patients in whom a lead point has not been identified but is suspected may need further evaluation, with consideration of follow-up ultrasound, computed tomography, contrast studies, or endoscopy based on the etiology of concern.[20]

## Small Bowel and Colocolic Intussusceptions

Small bowel intussusceptions are more often encountered in the mid, lower, or left side of the abdomen. There are two types of small bowel intussusceptions: transient, asymptomatic intussusceptions and significant intussusceptions, often associated with lead point, which may have undergone ischemia and require bowel resection.

Transient, typically asymptomatic small bowel intussusceptions are characterized by a smaller diameter and a length less than 3.5 cm, often visible peristalsis (e-Fig. 107.6, Video 107.1). They are often compressible, there is no evidence of abnormal flow on color Doppler interrogation, and there is no central mesenteric echogenicity and lymph nodes so characteristic of the ileocolic intussusceptions.[46–48]

Nontransient, symptomatic small bowel and colocolic intussusceptions are typically large and may be associated with ascites and small bowel obstruction (Fig. 107.7).[49] Lead points are often evident, identified by computed tomography or ultrasound (Fig. 107.5 and e-Fig. 107.8). Significant small bowel intussusceptions typically require surgery; enema is not considered appropriate or effective in reduction, because of the presence of the ileocecal valve, and the possibility of ischemic changes.[50–53]

## Nonoperative Treatment

### Techniques and Reduction Rates

Enema reduction should be undertaken in children with intussusception after surgical consultation. The only absolute contraindications to enema reduction are signs of peritonitis on clinical examination or free air on imaging (Box 107.2). The most important factor that predicts an unsuccessful enema reduction is longer duration of symptoms: 48–72 hours is considered a significant delay.[7,25] Other factors associated with lower rates of successful reduction include age less than 3 months, dehydration, small bowel obstruction, and intussusception encountered in the rectum (25% reduction rate).[7,25,32,54]

**BOX 107.2** Image-Guided Reduction of Intussusception

**ABSOLUTE CONTRAINDICATIONS**

- Peritonitis
- Free intraperitoneal air

**PNEUMATIC REDUCTION TECHNIQUE**

- Patient should be well hydrated
- Use available measurement devices to control pressure; may use a pop-off valve
- May begin at 80 mm Hg; do not exceed 120 mm Hg mean pressure
- Compare small bowel gas pre- and postreduction into cecum (Most helpful in patients with small bowel obstruction)

**HYDROSTATIC REDUCTION TECHNIQUE**

- Patient should be well hydrated
- Maintain pressure head no greater than 1 meter $H_2O$
- Make three attempts of 3 minutes each
- Be sure buttocks are well sealed
- Reduction is incomplete until distal small bowel loops are easily filled

Air and liquid contrast enemas are used for intussusception reduction. The air enema is considered by most to be superior to positive-contrast liquid enema for several reasons. If perforation occurs, there is considerably less spillage of fecal material in the peritoneal cavity with air than with liquid agents, and the contrast material in the peritoneum may cause additional complications

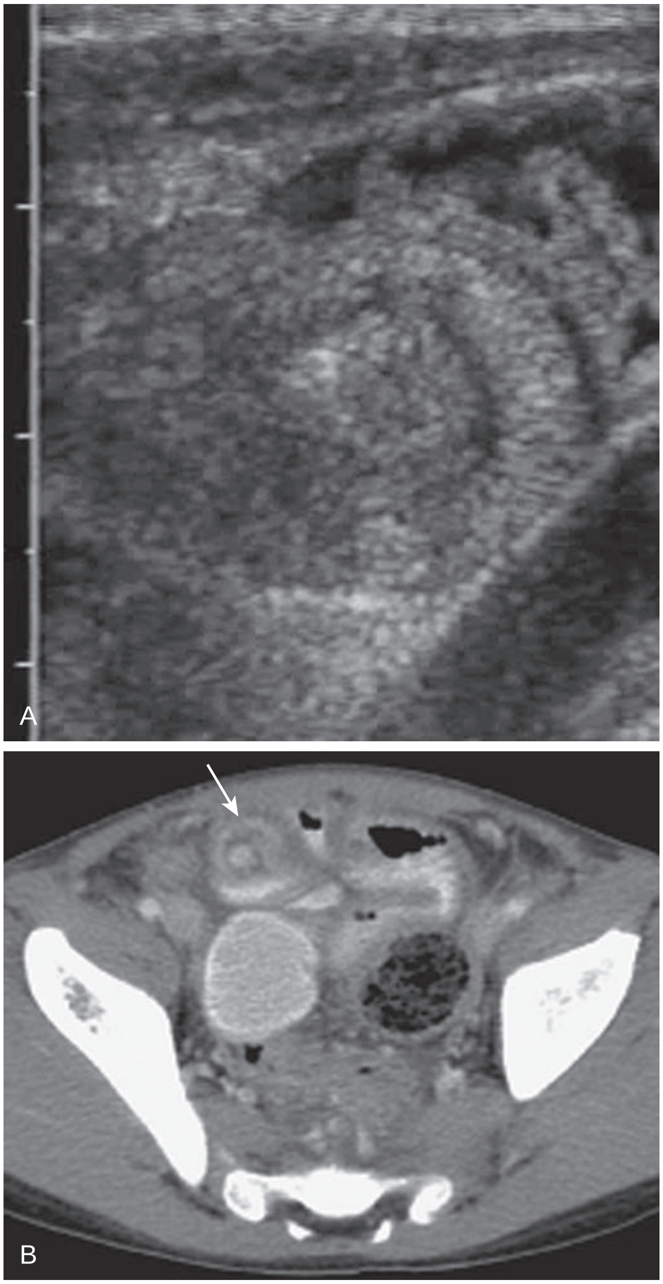

**e-Figure 107.6. Transient asymptomatic intussusception of the small bowel (also see Video 107.1).** (A) Transverse sonogram of an ileoileal intussusception incidentally identified in an infant with gastroenteritis; on longitudinal image, it measured less than 3 cm and could not be identified on rescanning of the area. (B) Contrast-enhanced CT of young child undergoing routine follow-up imaging of a testicular tumor. There is an asymptomatic, short-segment small bowel intussusception *(arrow)* that resolved spontaneously.

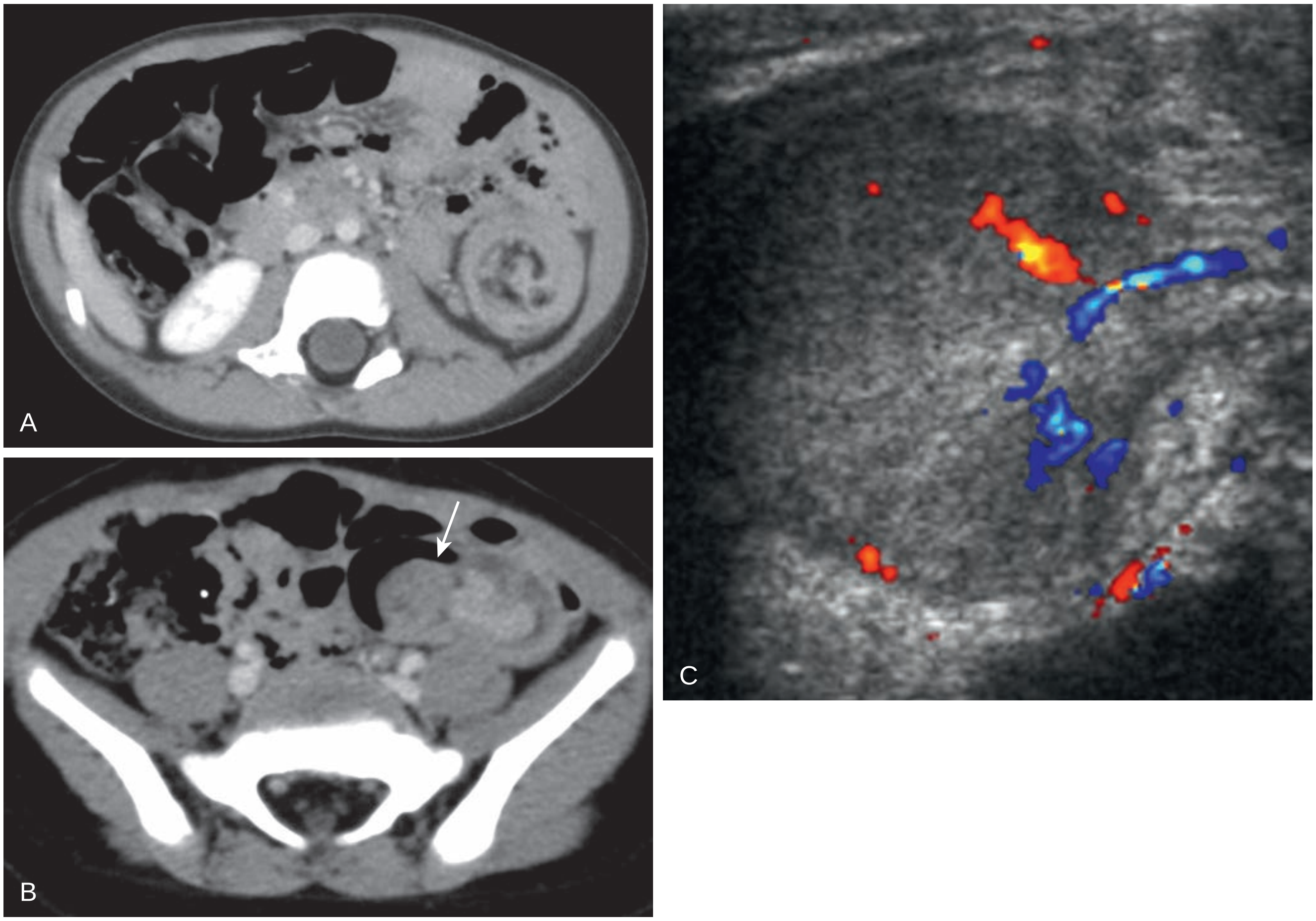

**e-Figure 107.8. Colocolic intussusception secondary to a polyp.** (A) Contrast-enhanced CT shows the intussusception in the descending colon. (B) The *arrow* points to the polyp. (C) Color Doppler image shows flow within the polyp.

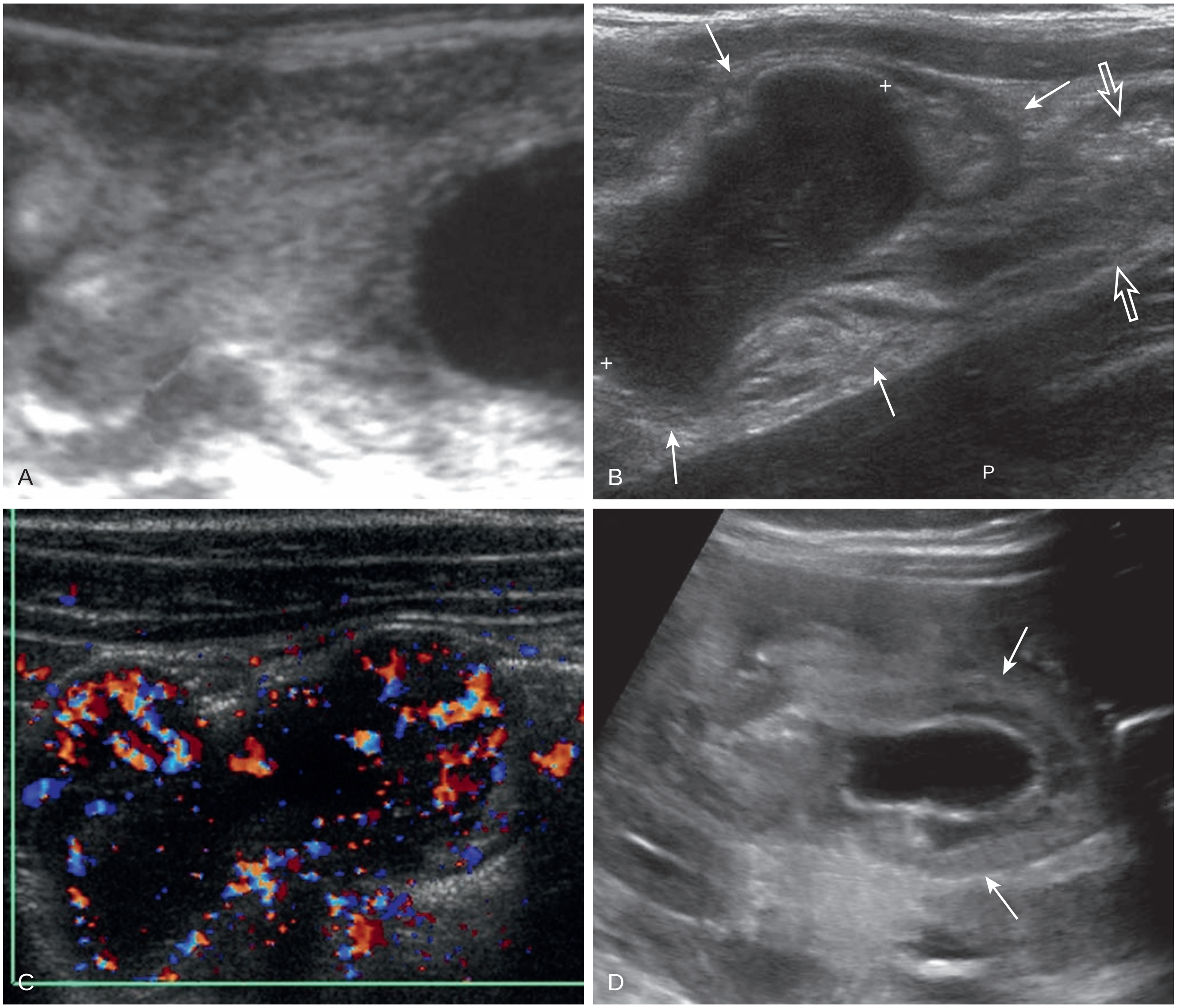

**Figure 107.5. Lead points.** (A) A 3-month-old infant with intussusception secondary to an ileal duplication cyst acting as a lead point. Note the difference in appearance from that of trapped fluid in a child without a lead point (Fig. 107.4A). (B and C) An 8-year-old boy presenting with severe, intermittent abdominal pain. Examination of the right lower quadrant shows an anechoic, solid mass with abundant flow on color Doppler interrogation (C), intussuscepted into the cecum *(arrows)*. Open arrows indicate the terminal ileum. *P*, Psoas muscle. Pathologic diagnosis was Burkitt lymphoma. (D) A 2-month-old infant with intussusception. A thick-walled hollow viscus *(white arrows)* was the leading edge, which was proved at surgery and pathology to represent a Meckel diverticulum. Air reduction was only partly successful; at surgery, a small segment of ischemic bowel was resected.

after perforation. There is no liquid or stool spillage on the patient or on the field of view, and the air-filled sigmoid and distal colon do not block the field of view as happens with radiodense contrast material. The rates of recurrence of intussusception after air or after liquid enema reductions do not differ (both are approximately 10%). Importantly, the radiation exposure is 2.3-fold lower when air is used.[28,55–60]

More than 70 published studies of enema reduction report an average reduction rate of 76% (Table 107.1).[25,61] More recent reports suggest a higher success rate for air enema over liquid (80% vs. 70%).[62] A recent meta-analysis that included 16,187 children undergoing air enema reduction and 13,081 children undergoing liquid enema reduction reported a success rate of 82.7% for air and 69.6% for liquid; perforation rates were 0.39% and 0.43%, respectively.[63]

Relative disadvantage of the air enema is a lower rate of detection of lead points, although these are best detected at preceding sonography.[20] Positive-contrast liquid enema also tends to outline the small bowel loops to determine reduction more easily, and ileoileal components may be more conspicuously identified. In 2004, 65% of pediatric radiologists in the United States reported using air enema, 33% liquid enema, and 3% liquid enema with sonographic guidance[64]; the proportion currently using air enemas is likely much higher.

All children should have surgical consultation before enema: (1) to assess for peritoneal signs precluding enema, (2) to alert the surgeons about a potential surgical candidate, (3) for urgent surgery in case of perforation, and (4) for management after reduction. Before enema reduction, dehydration should be treated with intravenous fluid resuscitation. Children with evidence of

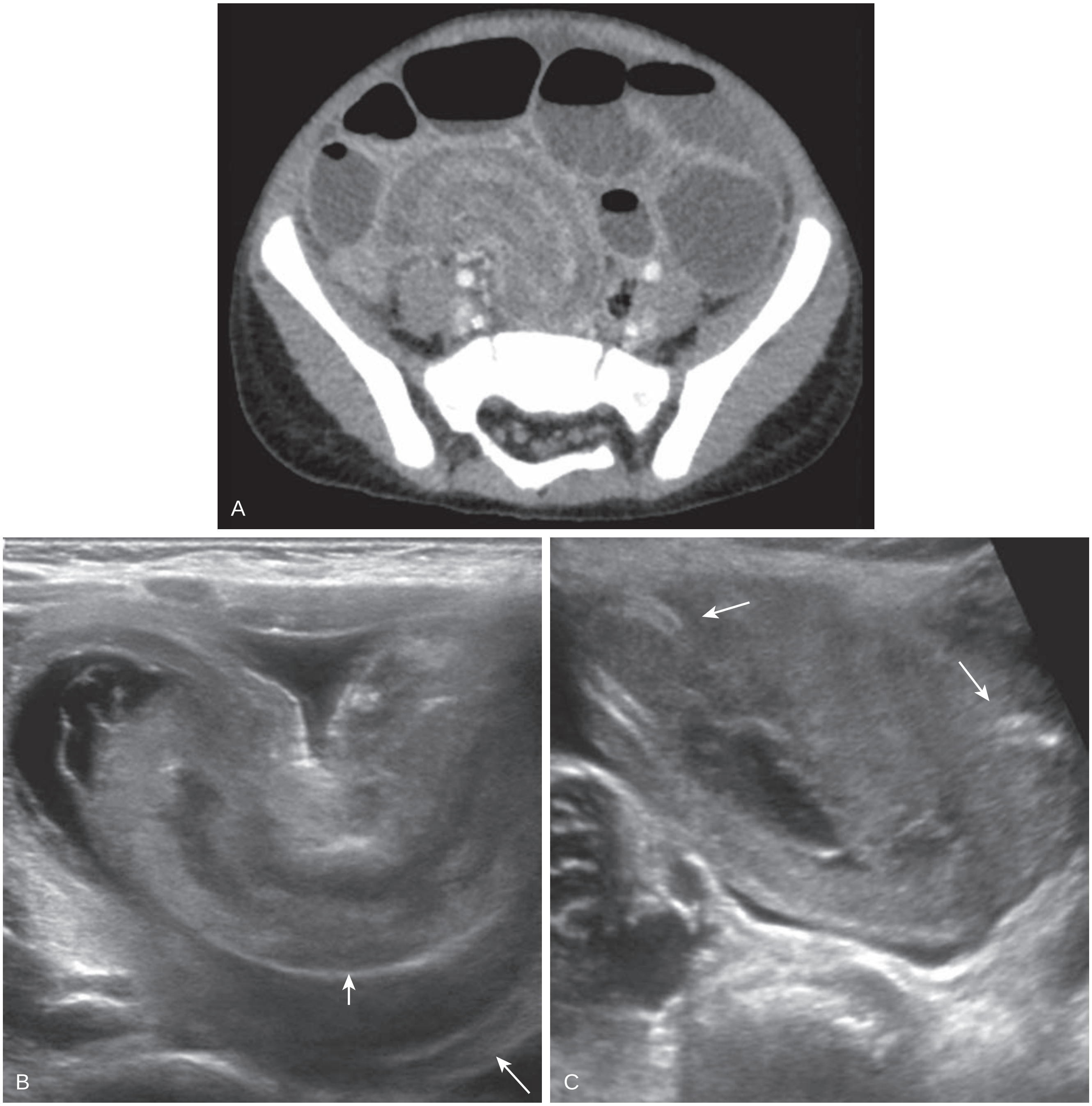

**Figure 107.7. Symptomatic small bowel intussusceptions.** (A) Contrast-enhanced CT shows a small bowel intussusception in a 3-year-old child presenting with bowel obstruction. No discrete lead point is identified. At surgery ischemic bowel segment had to be resected, and the child proved to have Henoch-Schönlein purpura. (B and C) Small bowel intussusception in a 5-year-old boy presenting with high-grade small bowel obstruction. The intussusception located in the mid abdomen shows an unusual linear echo *(short arrow)* between the inner sleeve of the intussusception and the trapped fluid; the *long arrow* points to the outer edge of the large intussusception complex. (C) Sonogram shows two portions of an Ascaris worm embedded within the intussusception *(arrows)*. The live worm was found at surgery, where ischemic bowel had to be resected.

peritonitis, shock, sepsis, or free air on abdominal radiographs are not candidates for enema.

## Air Enema Technique

In the air enema technique, the enema tip should be placed in the child's rectum and securely taped in place. The tape can be shaped into a funnel along the tube, to help form a seal. The buttocks are taped tightly together, and an assistant should also aid by holding the buttocks closed, whether the child is in a supine or a prone position. This technique is important because air leaking around the tube diminishes the pressure head. Air is rapidly insufflated into the colon under fluoroscopic observation, up to a constant, mean pressure of 120 mm Hg, thus maximizing reduction and

**TABLE 107.1**

**Main Outcomes: Effectiveness and Safety of Air Versus Liquid Enema Reduction of Intussusception (Excluding Direct Comparison Studies)**

| | Air | | | | | Liquid | | | | | |
|---|---|---|---|---|---|---|---|---|---|---|---|
| | | | | Heterogeneity | | | | | Heterogeneity | | |
| **Outcome Measure** | **No. of Studies** | **No. of Patients** | **Rate (%)** | **$I^2$ (%)** | ***P*** | **No. of Studies** | **No. of Patients** | **Rate (%)** | **$I^2$ (%)** | ***P*** | ***P*** |
| Success (reduction) rate | 44 | 16,187 | 82.7 (79.9-85.6) | 97 | <0.001 | 52 | 13,081 | 69.6 (65.0-74.1) | 98 | <0.001 | <0.001 |
| Perforation rate | 38 | 15,752 | 0.39 (0.23-0.55) | 40 | 0.04 | 30 | 9429 | 0.43 (0.24-0.62) | 9 | 0.87 | 0.73 |
| Rate of first recurrence after enema reduction | 26 | 10,494 | 6.0 (4.5-7.5) | 89 | <0.001 | 24 | 4004 | 7.3 (5.8-8.8) | 71 | <0.001 | 0.01 |
| Rate of recurrence within 48 h after enema reduction | 9 | 1586 | 3.1 (1.1-5.1) | 89 | <0.001 | 11 | 1178 | 3.2 (1.9-4.51) | 44 | 0.03 | 0.93 |

**Subgroup Analysis of Success Rates of Air Versus Liquid Enema Reduction (Excluding Direct Comparison Studies)**

| | Air | | | Liquid | | | |
|---|---|---|---|---|---|---|---|
| **Factor Analyzed** | **No. of Studies** | **No. of Patients** | **Rate (%)** | **No. of Studies** | **No. of Patients** | **Rate (%)** | ***P*** |
| Rate of presence of a lead point[a] | 27 | 4791 | 2.0 (1.3-2.7) | 33 | 4665 | 6.3 (4.2-8.3) | <0.001 |
| Enema reduction guidance | | | | | | | |
| Fluoroscopy | 23 | 6038 | 84 (82-86) | 26 | 3534 | 68 (62-74) | <0.001 |
| Ultrasound | 4 | 454 | 89 (79-99) | 7 | 994 | 86 (81-91) | 0.10 |
| Publication period | | | | | | | |
| 1970s | 0 | 0 | NA | 3 | 584 | 73.3 (57.3-89.3) | NA |
| 1980s | 6 | 9386 | 82.9 (74.4-91.0) | 20 | 2897 | 61.1 (52.7-69.6) | <0.001 |
| 1990s | 17 | 2961 | 76.4 (65.5-87.2) | 15 | 1822 | 73.7 (67.8-79.5) | <0.001 |
| 2000s | 14 | 2309 | 86.6 (83.6-89.6) | 12 | 7052 | 77.9 (70.2-85.5) | <0.001 |
| 2010s | 8 | 2181 | 77.2 (67.8-86.7) | 2 | 726 | 65.9 (31.7-1.00) | <0.001 |
| Country of publication | | | | | | | |
| United States | 4 | 476 | 74.3 (56.7-92.0) | 10 | 1092 | 61.3 (54.7-68.0) | <0.001 |
| Outside United States | 40 | 15,711 | 83.5 (80.7-86.3) | 42 | 11,989 | 71.5 (66.2-76.7) | <0.001 |
| Type of hospital | | | | | | | |
| Children's | 26 | 12,666 | 83.1 (79.4-86.7) | 19 | 2191 | 69.1 (63.5-74.6) | <0.001 |
| Other than children's | 18 | 3521 | 82.3 (77.7-87) | 33 | 10,890 | 69.8 (63.3-76.2) | <0.001 |
| Recruitment | | | | | | | |
| Consecutive | 13 | 1774 | 80.7 (74.3-87.1) | 9 | 1393 | 75.6 (66.8-84.3) | <0.001 |
| Nonconsecutive | 30 | 14,132 | 83.4 (80.1-86.7) | 42 | 11,601 | 67.8 (62.6-73) | <0.001 |
| Prospective | 16 | 4674 | 83.6 (79.4-87.9) | 8 | 809 | 79.9 (70.5-89.3) | 0.01 |
| Retrospective | 28 | 11,513 | 82.1 (78.2-86) | 44 | 12,272 | 67.7 (62.8-72.6) | <0.001 |

Note: Values in parentheses are 95% CI. $I^2$, Inconsistency index; *NA,* not applicable.

[a] Not limited to the patients who had unsuccessful enema reduction. Rate is for all the patients evaluated in each study; some underwent primary surgery and not enema reduction.

*From Sadigh G, et al. Meta-analysis of air versus liquid enema for intussusception reduction in children.* AJR Am J Roentgenol. *2015;205(5):W542–W549.*

minimizing the risk for perforation. One device to perform the air enema has been described by Shiels et al.[65] A less laborious modification that uses the hospital air supply system has been recently described.[66]

Once the intussusception is encountered, its reduction is followed fluoroscopically until it is complete (Fig. 107.9). The use of pulsed fluoroscopy at a low setting, if available, is very important for reducing the radiation dosage, particularly when the reduction is lengthy. Fluoro "last image hold" images can document the progress of the reduction without additional exposures (Video 107.2). Air should flow freely from the cecum into the distal small bowel loops to signify complete reduction. Obtaining an image when the intussusceptum has reached the cecum is usually very helpful in documenting complete reduction, particularly in patients who already have abundant small bowel gas secondary to a bowel obstruction, by comparing the number of filled loops.

The examination is tailored to the patient and performed in collaboration with the surgeon. In general, we continue with the enema so long as there is progress and the procedure is tolerated, and stop when there is no movement of the intussusceptum. The attempts are tempered by information regarding the likelihood of reducibility gathered earlier from history, clinical examination, and prior imaging, again in consultation with the surgeons.

The radiologist should be vigilant for the appearance of free intraperitoneal air, which can be inconspicuous at first. In case of perforation, it is very important to open the buttocks and the rectal tube to allow colonic air to escape outside the patient; in addition, it is essential to have a large-gauge needle available to decompress the peritoneal cavity, as colonic perforation can result in tension pneumoperitoneum that impedes adequate breathing and may cause impaired venous return.

## Liquid Enema Technique

A general guideline to the liquid enema technique, often taught to radiology residents, is the "rule of threes": three attempts of 3 minutes' duration, with the liquid enema bag at 3 feet above the fluoroscopy table. Although there is little empirical evidence to support this rule, particularly regarding the height of the enema bag,[25,67] it serves well as a general guideline, although it has been

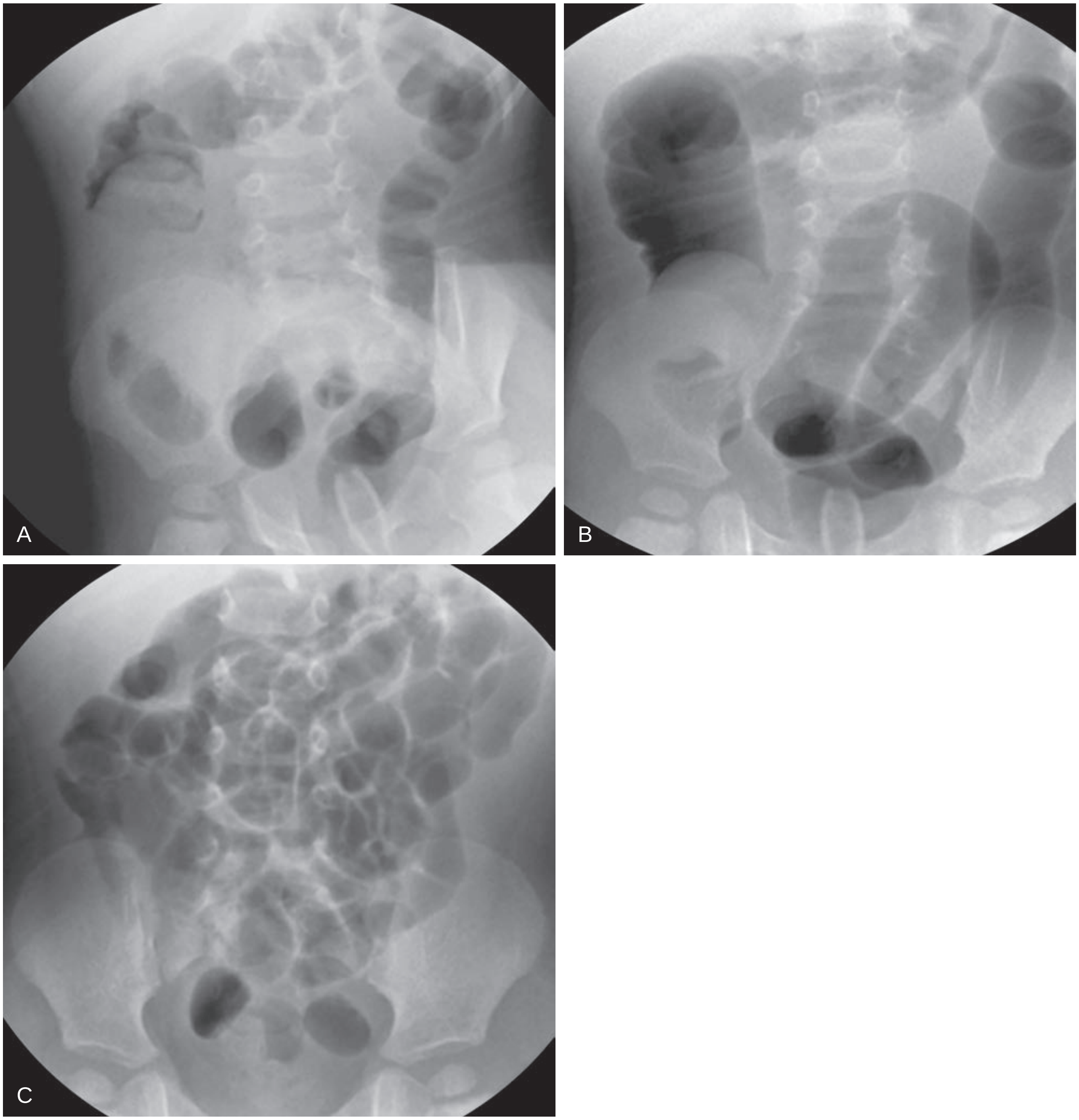

**Figure 107.9. Pneumatic reduction of intussusception (see Video 107.2).** (A) Initial fluoroscopic image shows the tube tip in the rectum, and the leading edge of the intussusception at the hepatic flexure. (B) With continued insufflation and further distension of the colon, the leading edge has moved into the right lower quadrant. (C) After successful reduction, there is gas filling multiple loops of small bowel.

documented that columns of various liquid media differ in the height at which a pressure of 120 mm Hg is generated.[68] As with the air enema, the buttocks are tightly taped and held together to prevent escape of the liquid and loss of the pressure head (e-Fig. 107.10).

## Radiation Dosage

The radiation dosage a child receives depends on a number of factors, particularly the capabilities of the fluoroscopy equipment, the use of pulsed fluoroscopy, the use of fluorosaves versus exposures for documentation, the ease of reduction (that affects the fluoroscopy time), and the contrast medium used. Experienced pediatric radiologists using air enema averaged 95 seconds of fluoroscopy time to reduce an intussusception.[56] Air enema radiation dosages have been estimated to be one-third to one-half less than the dosage for liquid enema[69] and more recently were documented to be 2.3 times lower with air reduction due to interaction of the contrast medium with the automatic exposure control system.[60]

## Complications and Perforation

The most concerning potential complication of enema reduction is the perforation of weakened, ischemic bowel, or the uncovering

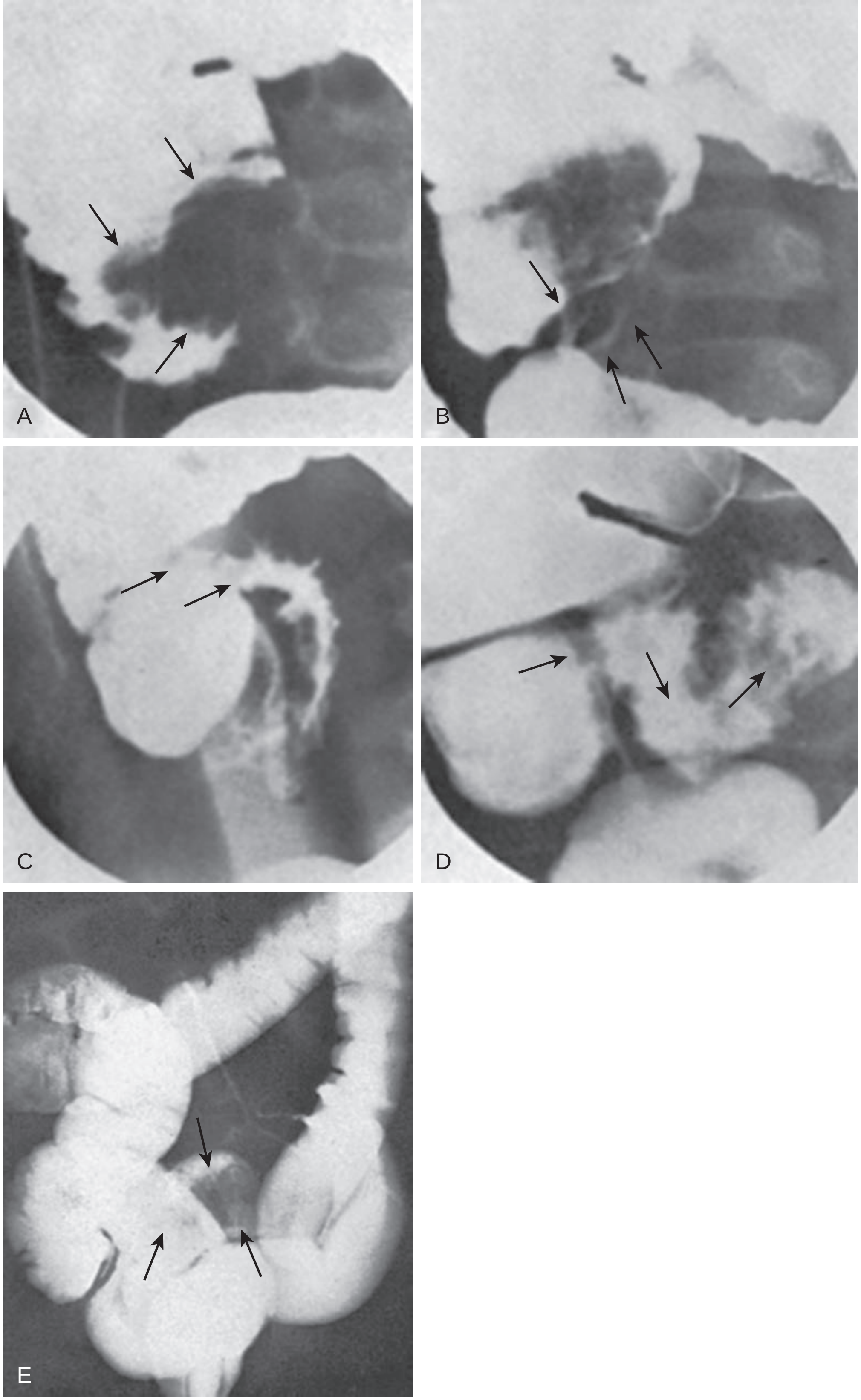

**e-Figure 107.10. Hydrostatic reduction of intussusception.** Serial radiographic changes at the ileocecal valve during hydrostatic reduction of intussusception in an 18-month-old infant. (A) The intussusception has already moved proximally from the transverse colon into the cecum, where it causes a filling defect *(arrows)*. (B) The appendix is beginning to fill *(arrows)*, and the cecal filling defect is smaller. (C) The terminal ileum is beginning to fill *(arrows)*, and the cecal filling defect has disappeared. (D) The terminal ileum is normally distended *(arrows)*, with visible mucosal relief. (E) In another child, residual ileoileal intussusception *(arrows)* in the terminal ileum after hydrostatic reduction of the colic component of an ileoileocolic intussusception. The leading edge was initially encountered at splenic flexure.

of a preexistent perforation during reduction. The risk for perforation depends on the patient population, but multiple series describe it as less than 1%.[70] A recent meta-analysis reported perforation rates of 0.39% for air and 0.43% for liquid enema.[63] The published difference in perforation rate between air and liquid enema is either nonexistent or not statistically significant (see Table 107.1). Although determination of clinical predictors of perforation is complicated by a lack of randomized prospective studies, a key factor is symptom length greater than 48 hours. Several reports in both porcine models and children suggest that there may be preexisting focal perforation in the necrotic intussuscipiens, or less commonly the intussusceptum, that are inapparent before reduction but are uncovered during the reduction process. The most common site of perforation is at or just proximal to the intussusception in the transverse colon.[25,28,71–74]

Barium should not be used for intussusception reduction because of the risks for barium peritonitis, infection, and adhesions if perforation occurs. Although among positive contrast media iodinated contrast is now preferred and is considered a safer agent than barium, it nevertheless may produce fluid and electrolyte shifts if perforation occurs.[28,59,69,74]

One complication unique to air enema is the tension pneumoperitoneum. In an early report, two deaths occurred from this complication, leading the proponents of air enema to advise having an 18-gauge needle readily available in the fluoroscopy room for emergent decompression. As previously discussed, it is important upon noting a perforation to immediately open the valve of the enema tube and also open the buttocks so that the colonic air may escape to the outside. Although it is theoretically possible, there have been no reports of air embolism.

## Alternative Enema Approaches

A number of different approaches have been described to try to improve intussusception reduction via enema. These include sedation, anesthesia, use of glucagon, manual palpation, and delayed repeat enema. Except for the delayed repeat enema, none of these approaches has been proven to increase the rate of successful reduction.

## Fluoroscopy Versus Sonography

In North America, fluoroscopy is most often used during enema reduction. Initial reports from Asia on the use of sonography with fluid show rates of successful reduction as high or higher than with fluoroscopic techniques.[75] More recent reports show sustained successful performance of this procedure, with reduction rates reported at approximately 83%.[76,77] Recognition of perforation with spillage of fluid into the peritoneal cavity might be difficult, particularly in those patients who already present with ascites, and with less experienced operators.[78] Fecal contamination upon perforation is likely to resemble that seen with liquid positive contrast media in fluoroscopy-guided reduction.

## Delayed Repeat Enema

In children in whom the initial enema reduction attempt is only partially successful, a delayed repeat enema may avoid the need for surgical reduction. The use of this additional delayed attempt, between 30 minutes and several hours after the initial procedure, has shown promise in increasing the success of nonoperative reductions by allowing some of the edema to subside after the initial, partial reduction. Published reports have achieved further reduction in 50% to 82% of cases that do not reduce at the initial enema.[79–83] The largest series to date reports fewer bowel resections after delayed enema than after immediate surgery after a single enema procedure, 26.4% versus 11.8%[84]; however, this is most likely due to the fact that the patients who went directly to surgery are those at greater risk of ischemia, either through risk factors as enumerated earlier, or by lack of progress on the initial reduction attempt. Further research to understand optimal timing and technique for delayed repeat enemas is needed. The child must remain clinically stable and be appropriately monitored during this time interval. Delayed enema should not be attempted if the initial enema does not move the intussusception at all.

## Management of Recurrent Cases

Intussusception recurrence rates average up to 10% (range, 5%–15%), regardless of whether the technique involved air or liquid enema. The recurrence rates are less than or equal to 5% when surgical reduction is performed, presumably because of the development of adhesions.[85] Approximately 50% of children who develop recurrent intussusception present within 48 hours, but recurrences have been reported up to 18 months later. Although the only known risk factors for recurrent intussusceptions are lead points, a pathologic lead point is only present in approximately 15% to 19% of children with recurrent intussusceptions, more likely when there is more than one recurrence.[4,20] On the hypothesis that hypertrophied Peyer patches are implicated in both initial and recurrent cases of intussusception, a randomized double-blind trial showed no recurrences among children receiving dexamethasone compared with 5% in the placebo group, but the actual utility of this treatment remains unclear.[86]

## Surgical Management and Financial Costs

Approximately 20% to 40% of children who undergo surgical reduction of their intussusception will require bowel resection.[87] The long-term risk for small bowel obstruction from adhesions is approximately 3% to 5% for children older than 1 month.[88] The costs of surgical care are considerably higher than those of nonsurgical reduction. Earlier reports indicate a four- to fivefold increase in the cost of surgical management.[89,90] A more recent report that included the performance of repeat delayed enemas shows a mean hospital cost of $9205 for the group receiving delayed enema and $14,422 for those receiving immediate surgery after first enema. For those patients who are successfully managed as outpatients and discharged from the emergency department, there are additional cost savings and reduced length of stay.[91]

### KEY POINTS

- Intussusception is the most common cause of small bowel obstruction in children aged 3 months to 5 years.
- Ninety to ninety-five percent of intussusceptions in children are ileocolic and idiopathic. Lead point mass lesions are found in approximately 5% in the first year of life.
- The most common lead points are Meckel diverticulum, duplication cyst, polyp, and lymphoma, the latter typically in the older children.
- The classic clinical symptom triad is vomiting, abdominal pain, and bloody stools; each of these is found in 58% to 100% of cases, but the full triad is documented in approximately 25% to 65%.
- Ultrasound is the primary imaging modality for diagnosing intussusception.
- Air enema overall has a reported higher success rate than liquid enema.
- Perforation rate is less than 1% for both air and liquid enema reduction.
- The most consistent factor that predicts unsuccessful enema reduction is duration of the symptoms.
- Recurrence rates range between 5% and 15%, regardless of reduction method, typically within the first 48 hours.

## SUGGESTED READINGS

Beres AL, Baird R. An institutional analysis and systematic review with meta-analysis of pneumatic versus hydrostatic reduction for pediatric intussusception. *Surgery*. 2013;154(2):328–334.

Daneman A, Navarro O. Intussusception. Part 1: a review of diagnostic approaches. *Pediatr Radiol*. 2003;33(2):79–85.

del-Pozo G, et al. Intussusception: trapped peritoneal fluid detected with US–relationship to reducibility and ischemia. *Radiology*. 1996; 201(2):379–383.

Lautz TB, Thurm CW, Rothstein DH. Delayed repeat enemas are safe and cost-effective in the management of pediatric intussusception. *J Pediatr Surg*. 2015;50(3):423–427.

Lioubashevsky N, et al. Ileocolic versus small bowel intussusception in children: can US enable reliable differentiation? *Radiology*. 2013;269(1):266–271.

Navarro O, Daneman A. Intussusception. Part 3: Diagnosis and management of those with an identifiable or predisposing cause and those that reduce spontaneously. *Pediatr Radiol*. 2004;34(4):305–312, quiz 369.

Sadigh G, et al. Meta-analysis of air versus liquid enema for intussusception reduction in children. *AJR Am J Roentgenol*. 2015;205(5):W542–W549.

Shiels WE 2nd, et al. Air enema for diagnosis and reduction of intussusception: clinical experience and pressure correlates. *Radiology*. 1991;181(1):169–172.

## REFERENCES

Full references for this chapter can be found on www.expertconsult.com.

## REFERENCES

1. Parashar UD, et al. Trends in intussusception-associated hospitalizations and deaths among US infants. *Pediatrics*. 2000;106(6):1413–1421.
2. Eng PM, et al. Incidence of intussusception among infants in a large commercially insured population in the United States. *Pediatr Infect Dis J*. 2012;31(3):287–291.
3. Jiang J, et al. Childhood intussusception: a literature review. *PLoS ONE*. 2013;8(7):e68482.
4. Columbani PM, Scholz S. Intussusception. In: Coran AG, et al, eds. *Pediatric Surgery*. Philadelphia: Elsevier; 2012.
5. Mandeville K, et al. Intussusception: clinical presentations and imaging characteristics. *Pediatr Emerg Care*. 2012;28(9):842–844.
6. Bisset GS 3rd, Kirks DR. Intussusception in infants and children: diagnosis and therapy. *Radiology*. 1988;168(1):141–145.
7. Daneman A, Navarro O. Intussusception. Part 1: a review of diagnostic approaches. *Pediatr Radiol*. 2003;33(2):79–85.
8. Bines JE, et al. Risk factors for intussusception in infants in Vietnam and Australia: adenovirus implicated, but not rotavirus. *J Pediatr*. 2006;149(4):452–460.
9. Minney-Smith CA, et al. Intussusception is associated with the detection of adenovirus C, enterovirus B and rotavirus in a rotavirus vaccinated population. *J Clin Virol*. 2014;61(4):579–584.
10. Khalifa AB, et al. [Infectious etiology of acute idiopathic intussusception in children]. *Ann Biol Clin (Paris)*. 2013;71(4):389–393.
11. Mansour AM, et al. Enteric viral infections as potential risk factors for intussusception. *J Infect Dev Ctries*. 2013;7(1):28–35.
12. Serayssol C, et al. [Seasonal pattern of intussusceptions in infants and children: is fall/winter predominance still worth consideration? A 10-year retrospective epidemiological study]. *Arch Pediatr*. 2014;21(5):476–482.
13. Murphy TV, et al. Intussusception among infants given an oral rotavirus vaccine. *N Engl J Med*. 2001;344(8):564–572.
14. Soares-Weiser K, et al. Vaccines for preventing rotavirus diarrhoea: vaccines in use. *Cochrane Database Syst Rev*. 2012;(11):CD008521.
15. Oberle D, et al. Rotavirus vaccination: a risk factor for intussusception? *Bundesgesundheitsblatt Gesundheitsforschung Gesundheitsschutz*. 2014;57(2):234–241.
16. Yen C, et al. Rotavirus vaccination and intussusception - Science, surveillance, and safety: A review of evidence and recommendations for future research priorities in low and middle income countries. *Hum Vaccin Immunother*. 2016;12(10):2580–2589.
17. Tate JE, et al. Intussusception rates before and after the introduction of rotavirus vaccine. *Pediatrics*. 2016;138(3).
18. Rha B, et al. Intussusception following rotavirus vaccination: an updated review of the available evidence. *Expert Rev Vaccines*. 2014;13(11):1339–1348.
19. Stowe J, et al. The risk of intussusception following monovalent rotavirus vaccination in England: A self-controlled case-series evaluation. *Vaccine*. 2016;34(32):3684–3689.
20. Navarro O, Daneman A. Intussusception. Part 3: Diagnosis and management of those with an identifiable or predisposing cause and those that reduce spontaneously. *Pediatr Radiol*. 2004;34(4):305–312, quiz 369.
21. Nikolic H, et al. Chronic intussusception in children caused by Ascaris lumbricoides. *Wien Klin Wochenschr*. 2011;123(9–10):294–296.
22. Ramareddy RS, et al. Surgical complications of Ascaris lumbricoides in children. *J Indian Assoc Pediatr Surg*. 2012;17(3):116–119.
23. Mazigo HD, et al. Intestinal schistosomiasis associated with intussusception: a case report. *Tanzan J Health Res*. 2011;13(2):139–141.
24. Khuroo MS. Ascariasis. *Gastroenterol Clin North Am*. 1996;25(3):553–577.
25. Daneman A, Navarro O. Intussusception. Part 2: An update on the evolution of management. *Pediatr Radiol*. 2004;34(2):97–108, quiz 187.
26. Losek JD, Fiete RL. Intussusception and the diagnostic value of testing stool for occult blood. *Am J Emerg Med*. 1991;9(1):1–3.
27. Harrington L, et al. Ultrasonographic and clinical predictors of intussusception. *J Pediatr*. 1998;132(5):836–839.
28. Shiels WE 2nd, et al. John Caffey Award. Colonic perforation by air and liquid enemas: comparison study in young pigs. *AJR Am J Roentgenol*. 1993;160(5):931–935.
29. Klein EJ, Kapoor D, Shugerman RP. The diagnosis of intussusception. *Clin Pediatr (Phila)*. 2004;43(4):343–347.
30. Kuppermann N, et al. Predictors of intussusception in young children. *Arch Pediatr Adolesc Med*. 2000;154(3):250–255.
31. Beasley SW, Auldist AW, Stokes KB. The diagnostically difficult intussusception: its characteristics and consequences. *Pediatr Surg Int*. 1988;3:135–138.
32. Sargent MA, Babyn P, Alton DJ. Plain abdominal radiography in suspected intussusception: a reassessment. *Pediatr Radiol*. 1994;24(1):17–20.
33. Henderson AA, et al. Comparison of 2-view abdominal radiographs with ultrasound in children with suspected intussusception. *Pediatr Emerg Care*. 2013;29(2):145–150.
34. Roskind CG, et al. Test characteristics of the 3-view abdominal radiograph series in the diagnosis of intussusception. *Pediatr Emerg Care*. 2007;23(11):785–789.
35. Hooker RL, et al. Radiographic evaluation of intussusception: utility of left-side-down decubitus view. *Radiology*. 2008;248(3):987–994.
36. Pracros JP, et al. Acute intestinal intussusception in children. Contribution of ultrasonography (145 cases). *Ann Radiol (Paris)*. 1987;30(7):525–530.
37. Verschelden P, et al. Intussusception in children: reliability of US in diagnosis–a prospective study. *Radiology*. 1992;184(3):741–744.
38. Schmit P, Rohrschneider WK, Christmann D. Intestinal intussusception survey about diagnostic and nonsurgical therapeutic procedures. *Pediatr Radiol*. 1999;29(10):752–761.
39. del-Pozo G, et al. Intussusception: trapped peritoneal fluid detected with US–relationship to reducibility and ischemia. *Radiology*. 1996;201(2):379–383.
40. Henrikson S, et al. The effect of screening sonography on the positive rate of enemas for intussusception. *Pediatr Radiol*. 2003;33(3):190–193.
41. Bucher BT, et al. Intussusception in children: cost-effectiveness of ultrasound vs diagnostic contrast enema. *J Pediatr Surg*. 2011;46(6):1099–1105.
42. Swischuk LE, Hayden CK, Boulden T. Intussusception: indications for ultrasonography and an explanation of the doughnut and pseudokidney signs. *Pediatr Radiol*. 1985;15(6):388–391.
43. Lim HK, et al. Assessment of reducibility of ileocolic intussusception in children: usefulness of color Doppler sonography. *Radiology*. 1994;191(3):781–785.
44. del Pozo G, et al. Intussusception in children: current concepts in diagnosis and enema reduction. *Radiographics*. 1999;19(2):299–319.
45. Littlewood Teele R, Vogel SA. Intussusception: the paediatric radiologist's perspective. *Pediatr Surg Int*. 1998;14(3):158–162.
46. Lioubashevsky N, et al. Ileocolic versus small bowel intussusception in children: can US enable reliable differentiation? *Radiology*. 2013;269(1):266–271.
47. Mateen MA, et al. Transient small bowel intussusceptions: ultrasound findings and clinical significance. *Abdom Imaging*. 2006;31(4):410–416.
48. Strouse PJ, DiPietro MA, Saez F. Transient small bowel intussusception in children on CT. *Pediatr Radiol*. 2003;33(5):316–320.
49. Munden MM, et al. Sonography of pediatric small bowel intussusception: differentiating surgical from nonsurgical cases. *AJR Am J Roentgenol*. 2007;188(1):275–279.
50. Ko SF, et al. Pediatric small bowel intussusception disease: feasibility of screening for surgery with early computed tomographic evaluation. *Surgery*. 2010;147(4):521–528.
51. Chua JH, Chui CH, Jacobsen AS. Role of surgery in the era of highly successful air enema reduction of intussusception. *Asian J Surg*. 2006;29(4):267–273.
52. Koh EP, et al. A report of 6 children with small bowel intussusception that required surgical intervention. *J Pediatr Surg*. 2006;41(4):817–820.
53. Rajagopal R, et al. Transient versus surgically managed small bowel intussusception in children: role of ultrasound. *Afr J Paediatr Surg*. 2015;12(2):140–142.
54. West KW, et al. Intussusception: current management in infants and children. *Surgery*. 1987;102(4):704–710.
55. Shiels WE 2nd, et al. Air enema for diagnosis and reduction of intussusception: clinical experience and pressure correlates. *Radiology*. 1991;181(1):169–172.
56. Gu L, et al. John Caffey Award. Intussusception reduction in children by rectal insufflation of air. *AJR Am J Roentgenol*. 1988;150(6):1345–1348.
57. Guo JZ X., Ma Y, Zhou QH. Results of air pressure enema reduction of intussusception: 6,396 cases in 13 years. *J Pediatr Surg*. 1986;21(12):1201–1203.
58. Hernanz-Schulman M, et al. Effect of radiographic contrast agents on leukocyte metabolic response. *Pediatr Radiol*. 2000;30(6):361–368.
59. Hernanz-Schulman M, et al. Experimental study of mortality and morbidity of contrast media and standardized fecal dose in the peritoneal cavity. *Pediatr Radiol*. 2000;30(6):369–378.
60. Kaplan SL, et al. Intussusception reduction: effect of air vs. liquid enema on radiation dose. *Pediatr Radiol*. 2017.

61. Applegate KE. Intussusception in children: diagnostic imaging and treatment. In: Medina LS, Applegate KE, Blackmore CC, eds. *Evidence-Based Imaging in Pediatrics*. New York: Springer; 2010.
62. Beres AL, Baird R. An institutional analysis and systematic review with meta-analysis of pneumatic versus hydrostatic reduction for pediatric intussusception. *Surgery*. 2013;154(2):328–334.
63. Sadigh G, et al. Meta-analysis of air versus liquid enema for intussusception reduction in children. *AJR Am J Roentgenol*. 2015; 205(5):W542–W549.
64. Daneman A. *Unpublished Survey*. SPR Annual Meeting. Savannah, GA: 2004.
65. Shiels WE 2nd, Bisset GS 3rd, Kirks DR. Simple device for air reduction of intussusception. *Pediatr Radiol*. 1990;20(6):472–474.
66. Jindal G, et al. Assessment of a modified technique for air delivery during fluoroscopic-monitored pneumatic intussusception reduction. *Pediatr Radiol*. 2017.
67. McAlister WH. Intussusception: even Hippocrates did not standardize his technique of enema reduction. *Radiology*. 1998;206(3):595–598.
68. Kuta AJ, Benator RM. Intussusception: hydrostatic pressure equivalents for barium and meglumine sodium diatrizoate. *Radiology*. 1990;175(1):125–126.
69. Kirks DR. Diagnosis and treatment of pediatric intussusception: how far should we push our radiologic techniques? *Radiology*. 1994; 191(3):622–623.
70. Campbell JB. Contrast media in intussusception. *Pediatr Radiol*. 1989; 19(5):293–296.
71. Beasley S. Intussusception. *Pediatr Radiol*. 2004;34(4):302–304.
72. Armstrong EA, et al. Intussusception complicated by distal perforation of the colon. *Radiology*. 1980;136(1):77–81.
73. Mercer S, Carpenter B. Mechanism of perforation occurring in the intussuscipiens during hydrostatic reduction of intussusception. *Can J Surg*. 1982;25(5):481–483.
74. Daneman A, et al. Patterns of recurrence of intussusception in children: a 17-year review. *Pediatr Radiol*. 1998;28(12):913–919.
75. Wang GD, Liu SJ. Enema reduction of intussusception by hydrostatic pressure under ultrasound guidance: a report of 377 cases. *J Pediatr Surg*. 1988;23(9):814–818.
76. Karadag CA, et al. Ultrasound-guided hydrostatic reduction of intussusception with saline: safe and effective. *J Pediatr Surg*. 2015; 50(9):1563–1565.
77. Flaum V, et al. Twenty years' experience for reduction of ileocolic intussusceptions by saline enema under sonography control. *J Pediatr Surg*. 2016;51(1):179–182.
78. Sanchez TR, et al. Sonographically guided enema for intussusception reduction: a safer alternative to fluoroscopy. *J Ultrasound Med*. 2012;31(10):1505–1508.
79. Gorenstein A, et al. Intussusception in children: reduction with repeated, delayed air enema. *Radiology*. 1998;206(3):721–724.
80. Saxton V, et al. Intussusception: a repeat delayed gas enema increases the nonoperative reduction rate. *J Pediatr Surg*. 1994;29(5):588–589.
81. Sandler AD, et al. Unsuccessful air-enema reduction of intussusception: is a second attempt worthwhile? *Pediatr Surg Int*. 1999;15(3–4): 214–216.
82. Dahab M, et al. The second trial pneumatic reduction for idiopathic intussusception: therapeutic effect and hazards. *Ann Pediatr Surg*. 2012;8:77–79.
83. Pazo A, Hill J, Losek JD. Delayed repeat enema in the management of intussusception. *Pediatr Emerg Care*. 2010;26(9):640–645.
84. Lautz TB, Thurm CW, Rothstein DH. Delayed repeat enemas are safe and cost-effective in the management of pediatric intussusception. *J Pediatr Surg*. 2015;50(3):423–427.
85. Niramis R, et al. Management of recurrent intussusception: non-operative or operative reduction? *J Pediatr Surg*. 2010;45(11):2175–2180.
86. Lin SL, Kong MS, Houng DS. Decreasing early recurrence rate of acute intussusception by the use of dexamethasone. *Eur J Pediatr*. 2000;159(7):551–552.
87. Kaiser AD, Applegate KE, Ladd AP. Current success in the treatment of intussusception in children. *Surgery*. 2007;142(4):469–475, discussion 475-7.
88. Janik JS, et al. An assessment of the surgical treatment of adhesive small bowel obstruction in infants and children. *J Pediatr Surg*. 1981;16(3):225–235.
89. Bratton SL, et al. Intussusception: hospital size and risk of surgery. *Pediatrics*. 2001;107(2):299–303.
90. Stein JE, Beasley SW, Phelan E. The cost benefit of changing protocols in the management of intussusception. *Aust N Z J Surg*. 1997;67(6):330–331.
91. Beres AL, et al. Comparative outcome analysis of the management of pediatric intussusception with or without surgical admission. *J Pediatr Surg*. 2014;49(5):750–752.
92. Chen SC, et al. Epidemiology of childhood intussusception and determinants of recurrence and operation: analysis of national health insurance data between 1998 and 2007 in Taiwan. *Pediatr Neonatol*. 2010;51(5):285–291.

# 108 Tumors and Tumor-like Conditions

M. Beth McCarville*

Tumors and tumor-like conditions affecting the colon in children can be divided into several categories. For the purpose of this chapter, we will discuss benign lymphoid hyperplasia, vascular lesions of the colon, and neoplasms. Several neoplasms arise in patients with genetic disorders, and in those cases,[1] we provide a brief description of the disorder. Although these colonic lesions, particularly neoplasms, tend to be rare in children, it is incumbent on the radiologist to be familiar with them to provide a thoughtful, thorough consultation regarding imaging findings.

## NONNEOPLASTIC LESIONS

### Benign Lymphoid Hyperplasia

***Overview.*** Benign lymphoid hyperplasia is a benign condition of the bowel most frequently found in the distal ileum and the colon. These lesions represent patches of lymphoid tissue and can be seen in both adults and children. The precise prevalence in children is unknown, but the entity has been found in up to 30% of symptomatic patients undergoing colonoscopy.[1]

***Etiology, Pathophysiology, and Clinical Presentation.*** The observation of benign lymphoid hyperplasia in families suggests that genetic or environmental factors could be pertinent.[2] A high prevalence of lymphoid hyperplasia in adults has also been found, possibly related to an enhanced immune response.[3] In children, a number of theories have been proposed, including a local response to infection, immunodeficiency states, and local hypersensitivity reaction. Controversy also exists regarding the association of benign lymphoid hyperplasia with autism spectrum disorder.[4]

Benign lymphoid hyperplasia is usually discovered incidentally either on imaging or at endoscopy. As such, it is almost certainly underrecognized, and its true prevalence is unknown. Visual inspection at colonoscopy will demonstrate multiple raised, closely spaced areas along the bowel wall.

***Imaging.*** The appearance on imaging studies is that of innumerable small filling defects, mostly uniform in size, at times centrally umbilicated, and most commonly seen on double-contrast imaging of the colon (Fig. 108.1). The lesions typically range in size from 2 to 3 mm and are often too small to be detected on a single-contrast examination. One of the earliest imaging descriptions stressed the need to distinguish lymphoid hyperplasia from true polyps,[5] citing instances in which colectomies were performed because the benign nature of these lesions was not recognized. The characteristic pattern of innumerable small, uniform lesions also should be distinguished from benign lymphoid polyps, which are more common in adults and can become large and pedunculated.[6]

***Treatment.*** Lymphoid hyperplasia itself requires no specific treatment. If it is associated with another condition, then that condition would be treated accordingly.

### Vascular Lesions

***Overview.*** A number of vascular lesions and vascular tumors can arise within the colon. Although rare in children, they usually have specific clinical and imaging findings that can allow for a specific diagnosis. Some vascular lesions will be found incidentally while others present as lower gastrointestinal (GI) tract bleeding.

***Etiology, Pathophysiology, and Clinical Presentation.*** Vascular lesions of the colon represent a wide array of conditions. Colonic varices (particularly in the rectal region) appear as mural lesions and typically are associated with portal hypertension, providing a collateral pathway between the portomesenteric and the systemic venous systems. This collateral pathway has been reported to occur in nearly one-third of children with portal hypertension, in whom rectal bleeding is seen in 7%.[7]

Other colonic vascular lesions that cause lower GI bleeding include venous malformations, arteriovenous malformations, angiodysplasia, telangiectasias, and hemangiomas.[8] Most vascular malformations of the pediatric GI tract are vascular malformations of the cavernous type. These can be components of syndromes of anomalous vascular development such as Klippel–Trenaunay syndrome and blue rubber bleb nevus syndrome.

Because vascular lesions of the colon tend to come to light when they are symptomatic, the true incidence is unknown, but they are believed to be rare in children. The presentation can be that of lower GI bleeding or iron deficiency anemia. It should be noted that hemangiomas, though discussed here, fall under the category of vascular tumors of the GI tract and are associated with cutaneous hemangiomas in up to 50% of cases.

***Imaging.*** The lesions are difficult to resolve with most imaging modalities, but imaging with CT in the early arterial phase after contrast injection can demonstrate these lesions. Involved bowel will show intense enhancement (Fig. 108.2), and occasionally abnormal supplying arteries or draining veins are visible. In a minority of cases with bleeding, active extravasation can be seen.[9]

***Treatment.*** Much like vascular lesions elsewhere in the GI tract and indeed elsewhere in the body, the treatment depends on the specific lesion, its location, the degree and extent of involvement, and the clinical status of the patient. These lesions can be treated medically or surgically, embolized angiographically, or sclerosed endoscopically.

## NEOPLASTIC LESIONS

Neoplasms of the colon are rare in children. Most are benign juvenile polyps. Polyps associated with the hereditary polyposis syndromes are quite rare, and there is often a known family history. Primary malignancies arising from the colon and metastatic disease to the colon are rarer still. These three groups will constitute the remainder of this chapter.

Double-contrast barium enema has been essentially replaced by ultrasound, computed tomography (CT), and magnetic resonance imaging (MRI) for evaluation of colonic masses. These modalities are used in conjunction with endoscopy, snare resection, and/or surgical intervention for diagnosis and staging.

### Juvenile Polyps

***Overview.*** Juvenile or hamartomatous polyps are the most common intestinal tumors in childhood, with a prevalence of 1% to 3%. They may be single or multiple, and most are found in the sigmoid colon and rectum, but they can arise anywhere along the GI tract.

---

*The author acknowledges the contributions to this chapter of Jeffrey Traubici and Alan Daneman from the previous edition.

***Etiology, Pathophysiology, and Clinical Presentation.*** Histologically these lesions appear as mucus-filled glands, and they might be related to blocked, hyperplastic mucus glands. A dense infiltrate of inflammatory cells suggests an inflammatory inciting event, and thus the synonymous term "inflammatory polyp." However, the underlying etiology of these isolated polyps remains to be determined.

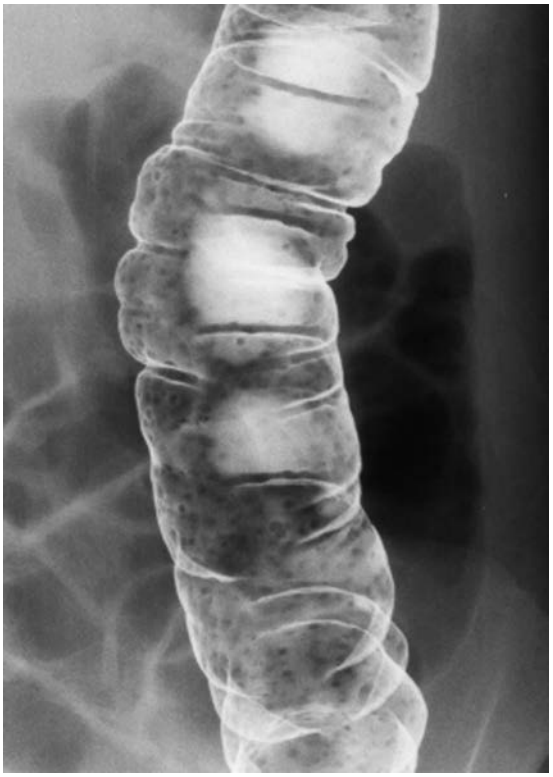

**Figure 108.1. Benign lymphoid hyperplasia.** An 11-year-old girl had a double-contrast barium enema as part of the workup for rectal bleeding. A spot image of the descending colon demonstrates numerous filling defects that are uniform in size. The findings are consistent with benign lymphoid hyperplasia. Similar findings were seen throughout the colon.

Most patients present in the first decade, typically between 2 and 5 years of age. The most common presenting symptom is painless, bright-red rectal bleeding. Pain is associated with the rare complication of colocolic intussusception. Some children present with iron deficiency anemia and others with a prolapsing mass, which can be mistaken for rectal prolapse.[12]

***Imaging.*** In the past, investigation for colonic neoplasms such as the juvenile polyp in a child with rectal bleeding often included a double-contrast enema. On such an examination, the lesions are typically smooth, can be sessile or pedunculated, and measure 3 cm or less. Currently the diagnosis is frequently made endoscopically or on cross-sectional imaging, with the lesions appearing as nonspecific intraluminal masses (Fig. 108.3).

***Treatment.*** Because these solitary lesions carry no increased risk of malignancy, the treatment is polypectomy alone. Most commonly, a polypectomy is performed with snare resection during a colonoscopy. Anemia is treated with iron supplementation or transfusion if necessary. With resection of the polyp, the blood loss should cease. If multiple polyps are present or a family history of juvenile polyps is uncovered, then the patient should be evaluated for the juvenile polyposis syndrome (JPS), discussed later.

## POLYPOSIS SYNDROMES

Although the inherited polyposis syndromes are rare, they have the potential to cause serious morbidity and mortality within affected families. A proper understanding of the various conditions is important for the primary clinician and consultant. Genetic screening and initiation of a surveillance plan is mandatory. Surveillance should include the GI tract as well as extraintestinal sites of potential disease.[13]

### Syndromes Associated With Juvenile or Hamartomatous Polyps

#### Juvenile Polyposis Syndrome

***Overview.*** First described in the literature in 1964,[14] JPS is an autosomal-dominant condition characterized by a multiplicity of

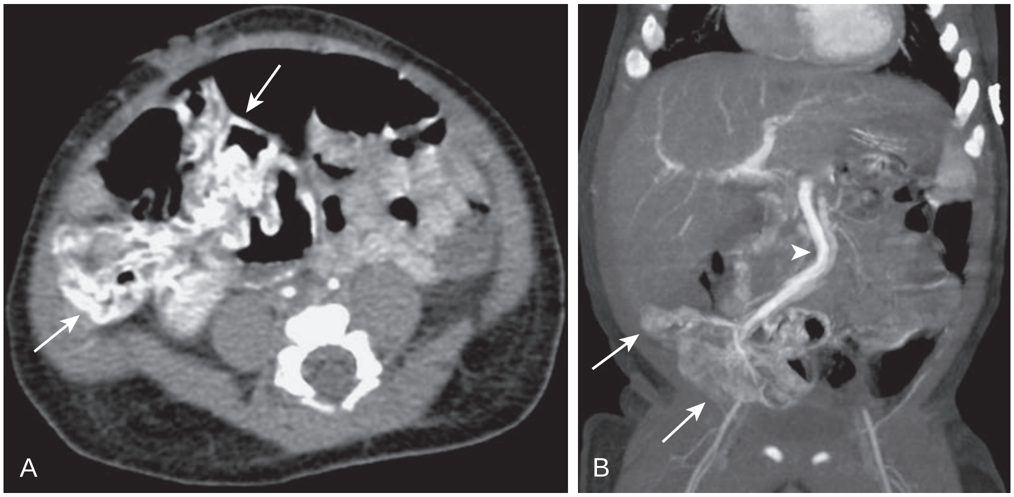

**Figure 108.2. Colonic infantile hemangioma.** An infant presented at 4 weeks of age with gastrointestinal bleeding requiring multiple transfusions. An enhanced computed tomography scan of the abdomen and pelvis was done in the arterial phase. Axial (A) and coronal reconstruction (B) demonstrates intense enhancement of the wall of the distal ileum and cecum *(arrows)*. Venous drainage is through a markedly dilated mesenteric vein (*arrowhead* in B). The affected segment was resected, and pathology confirmed that it was an infantile hemangioma.

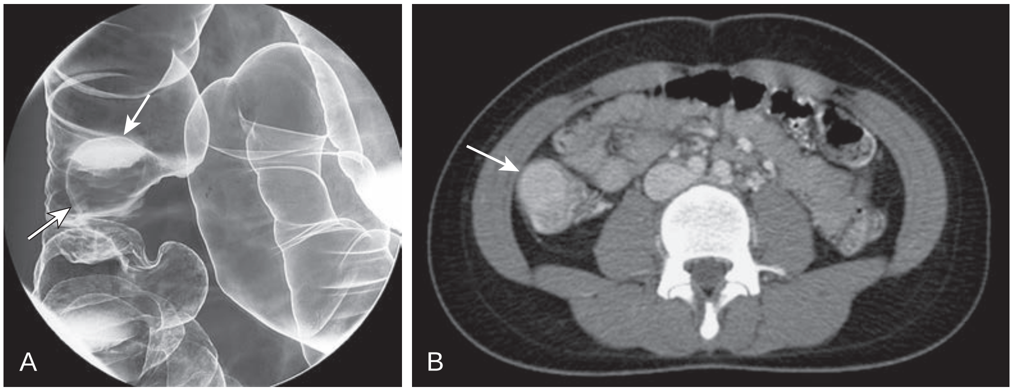

**Figure 108.3. Juvenile polyp.** A 15-year-old girl presented with a 2-month history of abdominal pain. (A) A double-contrast enema demonstrates a sessile mass consistent with a polyp arising from the wall of the ascending colon *(arrows)*. (B) A computed tomography scan in the same patient demonstrated an enhancing mass *(arrow)* within the lumen of the ascending colon.

GI hamartomatous polyps. It is the most common of the hamartomatous syndromes.

***Etiology, Pathophysiology, and Clinical Presentation.*** In approximately 75% of cases, a family history of the disease will be present. Mutations have been identified in the *SMAD4* gene on chromosome 18 and the *BMPR1A* gene on chromosome 10.[15]

From a clinical standpoint, the disease should be considered in any patient with five or more juvenile polyps in the colon, extracolonic juvenile polyps, or with any number of polyps when associated with a positive family history.[16] The clinical presentation can be more variable than in the patient with nonsyndromic juvenile polyps. In addition to rectal bleeding, anemia, and intussusception, patients with JPS in whom there is involvement of a large segment of the GI tract can present with failure to thrive, malabsorption, or hypoalbuminemia. Associated congenital anomalies include hydrocephalus and hypertelorism. Small series have described JPS in association with other conditions, including hereditary hemorrhagic telangiectasia.[17]

***Imaging.*** The imaging appearance of polyps in JPS differs in the number of polyps identified, but otherwise it is similar to that of isolated lesions.

***Treatment.*** Patients with JPS have an increased risk of colonic malignancy reported to be as high as 50%.[18] Screening of these children can be done with a combination of endoscopy, various imaging modalities, and capsule endoscopy. Polyps typically are removed via snare polypectomy.

## Cowden Syndrome

***Overview.*** Cowden syndrome is a rare autosomal-dominant syndrome with an estimated prevalence of 1 : 200,000 individuals.[19] Features include hamartomatous polyps of the GI tract; hamartomatous lesions of the skin; hamartomas of other solid organs; and neoplasms of the breast, thyroid, and endometrium.[19] GI tract polyps arising in these patients include inflammatory, hyperplastic, lipomatous, and even adenomatous lesions.

***Etiology, Pathophysiology, and Clinical Presentation.*** Cowden syndrome is one of several disorders that fall under the category of the protein tyrosine phosphatase and tensin (PTEN) hamartoma tumor syndromes. Mutations in the tumor suppressor gene *PTEN* are present in up to 80% of patients with Cowden syndrome.[19,20]

The presentation of patients with Cowden syndrome can be similar to the other conditions in which colonic polyps occur. Patients with Cowden syndrome also have an increased risk of neoplasms of the thyroid, endometrium, and breast. The lifetime risk of breast cancer in women with Cowden syndrome is between 25% and 50%. In these women, the onset of breast cancer is earlier than in sporadic cases. At present, the risk of GI malignancy in these patients is unknown.[19]

***Imaging.*** The imaging appearance of polyps in Cowden syndrome is similar to that of polyps described earlier in the chapter.

***Treatment.*** Polyps in patients with Cowden syndrome are treated with snare polypectomy; screening can include endoscopy, fluoroscopic and cross-sectional imaging modalities, and capsule endoscopy. Anemia is treated with iron supplementation and transfusion if necessary. Appropriate screening for the associated neoplasms also must be initiated. This screening consists of early breast self-examination and perhaps early initiation of mammography. Thyroid and uterine surveillance with screening ultrasound also is recommended.

## Peutz–Jeghers Syndrome

***Overview.*** Peutz–Jeghers syndrome is an autosomal-dominant syndrome with an incidence of approximately 1 : 120,000 people.[21] It was described separately, in 1921 and 1949, by the authors after whom the syndrome was named. In this condition, hamartomatous polyps develop in the GI tract, in association with skin and mucosal hyperpigmented lesions.

***Etiology, Pathophysiology, and Clinical Presentation.*** In familial Peutz–Jeghers syndrome, evidence indicates that the syndrome relates to mutations in the *STK11* (serine threonine kinase) gene. In up to 50% of cases, no family history of the disease is present, which suggests a fairly high rate of new mutation.[22]

The condition is characterized by pigmented lesions of the lips and buccal mucosa and hamartomatous polyps of the GI tract. The polyps can occur anywhere in the GI tract, but are most commonly found in the small bowel, particularly the jejunum. Polyps in the large and small bowel tend to be pedunculated, while those in the stomach tend to be sessile (Fig. 108.4A). Polyps also can arise in the gallbladder, bronchi, urinary bladder, and ureter.

The most common GI-related clinical presentation is abdominal pain as a result of intussusception, with a polyp as a pathologic lead point. Patients also can present with clinical findings related to GI hemorrhage.

***Imaging.*** The appearance of the polyps in Peutz–Jeghers syndrome does not differ significantly from that seen in other hamartomatous polyposes. It is not unusual for patients to present with intussusception and the typical associated imaging findings (see Chapter 107), with the polyp acting as a pathologic lead point (Fig. 108.4B and C).

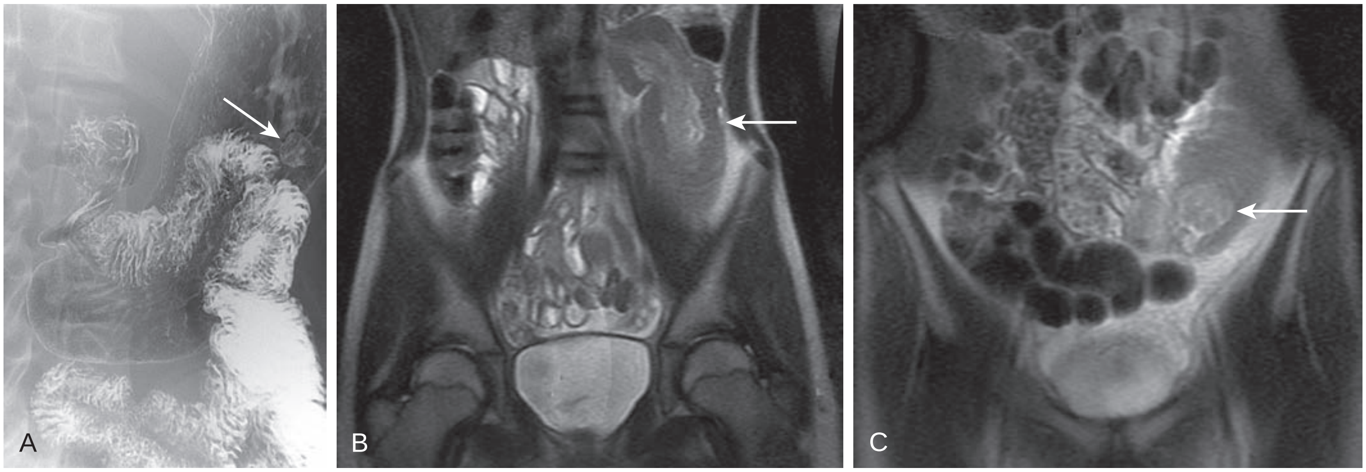

**Figure 108.4. Peutz–Jeghers syndrome in a 14-year-old girl.** (A) A double-contrast upper gastrointestinal series demonstrates a small polyp *(arrow)* arising in the proximal body of the stomach. (B) and (C) Several years later, the patient presented with abdominal pain and was found to have a small bowel intussusception *(arrow)*. (B) A coronal magnetic resonance imaging single shot fast spin echo sequence demonstrates the intussusception along the left flank *(arrow)*. (C) What was believed to be a polyp functioning as a lead point *(arrow)* was seen lower in the pelvis on a more anterior image of the same sequence.

***Treatment.*** The treatment of the polyps is removal, either surgically or endoscopically, when necessary. Anemia is treated with iron supplementation and transfusion if necessary. Although it is not clear whether the polyps themselves have malignant potential, it is now accepted that there is an overall increased risk of neoplasms in patients with Peutz–Jeghers syndrome, typically in adulthood. Colorectal, breast, and ovarian tumors predominate.[21]

## Polyposis Syndromes Associated With Adenomatous Polyps

Several conditions fall under the category of polyposis syndromes associated with adenomatous polyps. These conditions include familial adenomatous polyposis (FAP), attenuated FAP, Gardner syndrome, and Turcot syndrome. In all these conditions, a germline mutation occurs in the adenomatous polyposis coli *(APC)* gene, located on the long arm of chromosome 5.

### Familial Adenomatous Polyposis and Variants

***Overview.*** The prevalence of FAP is between 1:5000 and 1:17,000.[23] Although the condition is defined by the presence of more than five adenomatous polyps, affected persons often will have hundreds, if not thousands, of polyps.

Extraintestinal lesions also are well described. In nearly one in five patients, a desmoid tumor will develop (e-Fig. 108.5), which will be discussed further later in this chapter. About 60% to 90% of patients have congenital hypertrophy of the retinal pigment epithelial cells, which is present at birth and is assessed by fundoscopy. Lesions that can develop later in life include osteomas (often in the skull and mandible), lipomas, fibromas, and epidermoid cysts. An increased risk exists of developing hepatoblastoma (e-Fig. 108.6), thyroid and pancreatic cancers, cholangiocarcinoma, and central nervous system (CNS) tumors, particularly medulloblastoma.[24] It is believed that, with better management of the intestinal manifestations of FAP and subsequent longer life spans of affected patients, the incidence of these extraintestinal processes will likely increase.

In patients with attenuated FAP, fewer polyps are present and the inevitable development of malignancy occurs nearly a decade later than in the classic form. Patients with attenuated FAP manifest similar extraintestinal lesions and also exhibit a propensity for extracolonic polyps.

Gardner syndrome is believed to represent a variant of FAP, rather than a separate syndrome; some clinicians include these patients within the FAP group and agree that the term Gardner syndrome is now obsolete. Others continue to use the term Gardner syndrome in cases where the extraintestinal disease is particularly prominent. In Gardner syndrome, one sees the typical GI manifestations of FAP, including the plethora of polyps and the associated malignancies. Desmoid tumors often are cited as a classic extracolonic lesion in persons with Gardner syndrome; these tumors are a locally aggressive form of fibromatosis and arise from the fascial tissue associated with muscle or from the mesentery. The tumors typically appear in the abdomen or in the abdominal wall.[25] They may develop after trauma, such as after a prophylactic colectomy, and are a major cause of morbidity and mortality in these patients.[25]

In addition to desmoid tumors, patients with Gardner syndrome develop osteomas (particularly of the mandible), periampullary duodenal polyps, lipomas, fibromas, nasopharyngeal angiofibromas, and epidermoid cysts.

***Etiology, Pathophysiology, and Clinical Presentation.*** FAP is an autosomal-dominant condition in which a mutation is present in the *APC* gene; approximately 30% of cases result from spontaneous mutations.[26] This mutation results in a failure of apoptosis and in uncontrolled cell growth, with the ultimate development of polyps—in this case, adenomatous ones.

Polyps tend to develop late in the first decade and in the second decade of life, with symptoms arising in the third decade. Therefore, unless screened, patients may not be diagnosed until adulthood. The most common presentation in childhood is rectal bleeding.[23]

***Imaging.*** In classic FAP, the colon is carpeted with lesions. The polyps tend to vary in size and lack the central umbilication often seen in benign lymphoid hyperplasia.

A desmoid tumor is most often hypoechoic and at times nearly anechoic on ultrasound. On CT, the lesion often will be low attenuation, exhibit little enhancement in the portal venous phase, and may show increased enhancement in a delayed phase. Signal characteristics vary on MR although the lesion is usually of low signal intensity on T1-weighted sequences and of high signal on T2-weighted sequences (see e-Fig. 108.5).

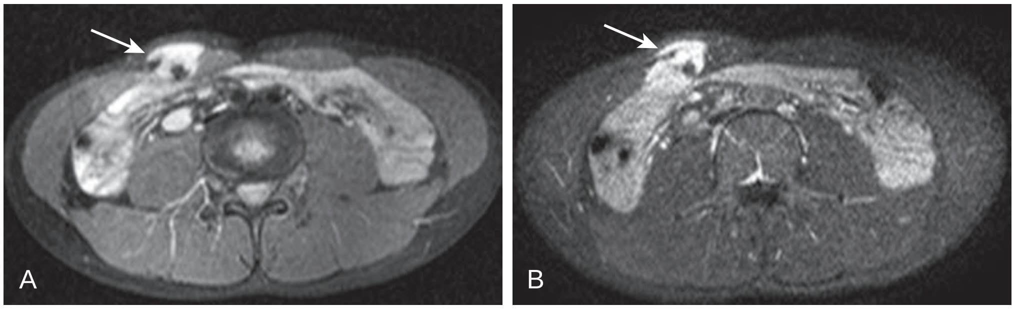

**e-Figure 108.5. Desmoid tumor in a patient with familial adenomatous polyposis.** A 16-year-old boy with a history of familial adenomatous polyposis presented with a palpable mass of the abdominal wall. (A) An axial T2-weighted spectral presaturation with inversion recovery MR image demonstrates a lesion with high signal *(arrow)* that has arisen in or infiltrated the right rectus abdominis muscle. (B) A gadolinium-enhanced axial T1-weighted fat-saturated MR image demonstrates mostly avid enhancement. Some areas within the lesion on both sequences are low in signal and may represent areas of fibrosis.

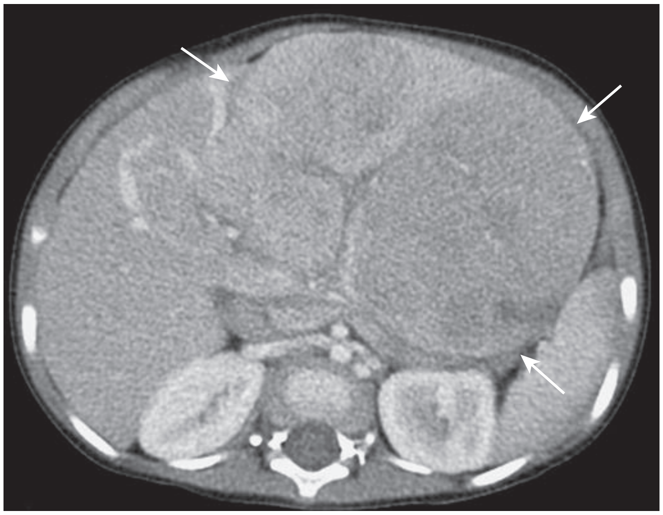

**e-Figure 108.6. Hepatoblastoma in a patient with familial adenomatous polyposis (FAP).** A 22-month-old boy presented with an abdominal mass. The family history included FAP. An axial contrast-enhanced computed tomography image though the upper abdomen demonstrates a large mass *(arrows)* that arises from the left lobe of the liver. A biopsy was performed, and the findings were consistent with hepatoblastoma.

***Treatment.*** Colorectal carcinoma will develop in nearly all patients with FAP if it is left untreated. The accepted standard of care, therefore, is prophylactic colectomy. Polyps also can develop in other parts of the GI tract, and periampullary polyps of the duodenum are well described. Although the development of duodenal carcinoma is rare, particularly in children,[27] surveillance of the upper GI tract is recommended after prophylactic colectomy. Any polyps found are removed endoscopically.

### Turcot Syndrome

***Overview.*** Turcot syndrome originally was described in 1959 in siblings found to have adenomatous polyps of the colon and malignancies of the CNS.[28] It is now understood that the condition is one of adenomatous polyposis, with an increased risk of colorectal carcinoma and of CNS tumors. Within the past decade, the syndrome has been reclassified to include two separate conditions with distinct genetic and molecular abnormalities and phenotypes: brain tumor-polyposis syndrome-1 and -2.

***Etiology, Pathophysiology, and Clinical Presentation.*** Brain tumor-polyposis syndrome-1 is inherited as an autosomal-recessive condition and is the result of a defect in mismatch repair *(MMR)* genes, which correct deoxyribonucleic acid replication errors. This genetic abnormality is unusual in that, when heterozygous, the gene expresses a different phenotype, termed Lynch syndrome, also known as hereditary nonpolyposis colorectal cancer syndrome. Brain tumor-polyposis syndrome-2 is inherited as an autosomal-dominant condition, with mutations in the *APC* gene.[29,30]

The clinical presentation is similar to that seen in FAP. Patients also can exhibit café au lait–type lesions and multiple lipomas. Patients with brain tumor-polyposis syndrome-1 are characterized by development of primarily astrocytomas and glioblastomas, as well as hematologic malignancies. Colorectal carcinomas arise at a mean age of 16 years; colon adenomas and carcinomas of the small bowel also develop in persons with this syndrome. Myriad colonic polyps occur in patients with brain tumor-polyposis syndrome-2, with carcinoma typically developing by 40 years of age; medulloblastoma is the more common CNS tumor that develops in these patients.[29]

***Imaging.*** The imaging of colonic polyps has been described earlier. The appearance of the polyps in patients with Turcot syndrome does not differ from that seen in other polyposes. The CNS malignancies typically are investigated with MRI.

***Treatment.*** The treatment in patients with Turcot syndrome depends on the individual clinical presentation and concerns. Polyps can be removed by snare polypectomy; however, given the risk of colorectal carcinoma, the patient may undergo a prophylactic colectomy. The CNS malignancies or other tumors are treated accordingly.

## OTHER COLONIC NEOPLASMS

### Benign Neoplasms

Rarely, other benign neoplasms can arise in the pediatric colon; they are largely sporadic and are not associated with other conditions. Lipomas (e-Fig. 108.7), leiomyomas, and neurofibromas have all been described. Hemangiomas and vascular malformations were discussed earlier in this chapter.

### Malignant Neoplasms

Isolated malignant colorectal neoplasms are quite rare in pediatric patients, and large series are limited and tend to represent years and decades of collected cases, during which time diagnostic methods and treatment protocols changed. In addition, such reports tend to represent the experience of referral centers where more complicated patients with more advanced disease might be treated.

### Adenocarcinoma

***Overview.*** Adenocarcinoma of the colon is exceedingly rare in children, with a prevalence of 1 in 1,000,000 persons younger than 19 years of age.[31] Mucinous carcinoma is the most common subtype described in sporadic cases of pediatric colon cancer. The tumor is more often associated with underlying predisposing conditions, such as FAP and its variants, hereditary nonpolyposis colorectal cancer syndrome, Peutz–Jeghers syndrome, and JPS, as well as Crohn disease and ulcerative colitis (Fig. 108.8).[31]

***Etiology, Pathophysiology, and Clinical Presentation.*** The etiology of colorectal adenocarcinoma is not completely understood although there are a number of risk factors that relate to age, ethnicity, diet, other medical conditions, smoking, and alcohol consumption.

Presenting symptoms include abdominal pain, an abdominal mass, "constipation," weight loss, and GI bleeding. Whereas these symptoms might lead to immediate consideration of a GI malignancy in adults, the clinical suspicion of colon cancer in children is low and may result in delayed diagnosis.[32]

***Imaging.*** Radiographs may be normal or suggest a bowel obstruction. Rarely one might see a mass or mass effect. Calcifications can be seen in the mucinous forms, both in the primary tumor and in the metastatic lesions. Contrast enema may show irregularity of the bowel wall, a mural lesion, or circumferential narrowing (Fig. 108.9). CT and MRI are the modalities used to evaluate for local and distant spread. The most common sites of metastases are lymph nodes, liver, lung, and adrenal glands.

***Treatment.*** The treatment is primarily surgical, followed by chemotherapy and, at times, radiation therapy. In some cases of metastatic disease, particularly to the liver, locally directed therapy is used.

### Neuroendocrine Tumors

***Overview.*** Well differentiated neuroendocrine tumors, previously referred to as "carcinoid tumors," are neoplasms of epithelial origin, which, when they arise in the colon, are most commonly periappendiceal (Fig. 108.10). Attempts have been made to establish a staging system that would help predict prognosis.[33] The most important prognostic criteria appear to be patient age, tumor size, histology, and the presence or absence of lymph node involvement or distant metastases. In larger series, approximately 40% of lesions are well differentiated. The remainder are almost equally split between moderately and poorly differentiated lesions.[33]

***Etiology, Pathophysiology, and Clinical Presentation.*** The inciting event for the development of carcinoid tumor is not yet clear. These tumors may be seen in patients who have other malignant neoplasms. Appendiceal neuroendocrine tumors are the most common pediatric GI neuroendocrine tumors.[34]

Patients can present with abdominal pain. Commonly the lesion is discovered incidentally at appendectomy in a patient thought to have acute appendicitis. In some cases the lesion may act as a lead point for an intussusception. Patients with liver metastases can manifest the carcinoid syndrome (flushing, tachycardia, diarrhea), although it is extremely rare in the pediatric age group.

***Imaging.*** The imaging findings depend on the size of the mass, its location, and the extent of disease. If it is sufficiently small, the lesion can occlude the appendiceal lumen, resulting in a distended/obstructed appendix (see Fig. 108.10) mimicking acute appendicitis. Otherwise a nonspecific mass is seen with or without metastatic spread. As with adenocarcinoma, CT and MRI can be used to assess for extent of disease. The tumor can metastasize to the liver, lungs, and bone.

***Treatment.*** If the lesion is small (less than 2 cm) and localized, treatment is surgery alone. Chemotherapy is administered for metastatic disease.

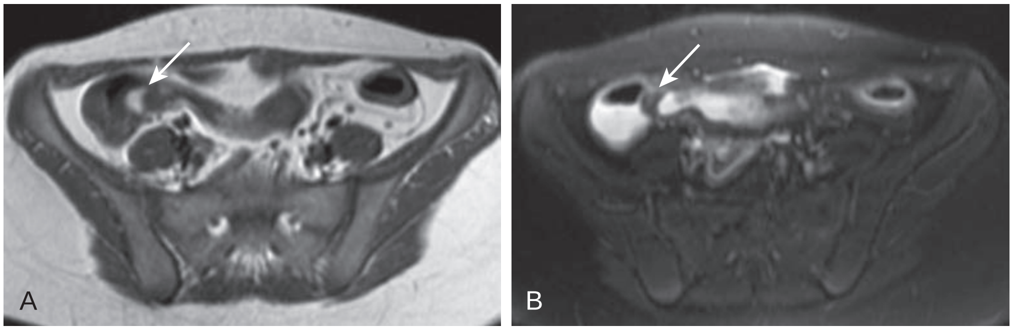

**e-Figure 108.7. Lipoma at the ileocecal valve.** A 14-year-old girl presented with abdominal pain. T1-weighted (A) and fat-saturated T2-weighted (B) magnetic resonance images through the pelvis demonstrate a small mass at the level of the ileocecal valve *(arrows)*. The lesion is high in signal on the T1-weighted sequence and low in signal on the fat-saturated T2-weighted sequence.

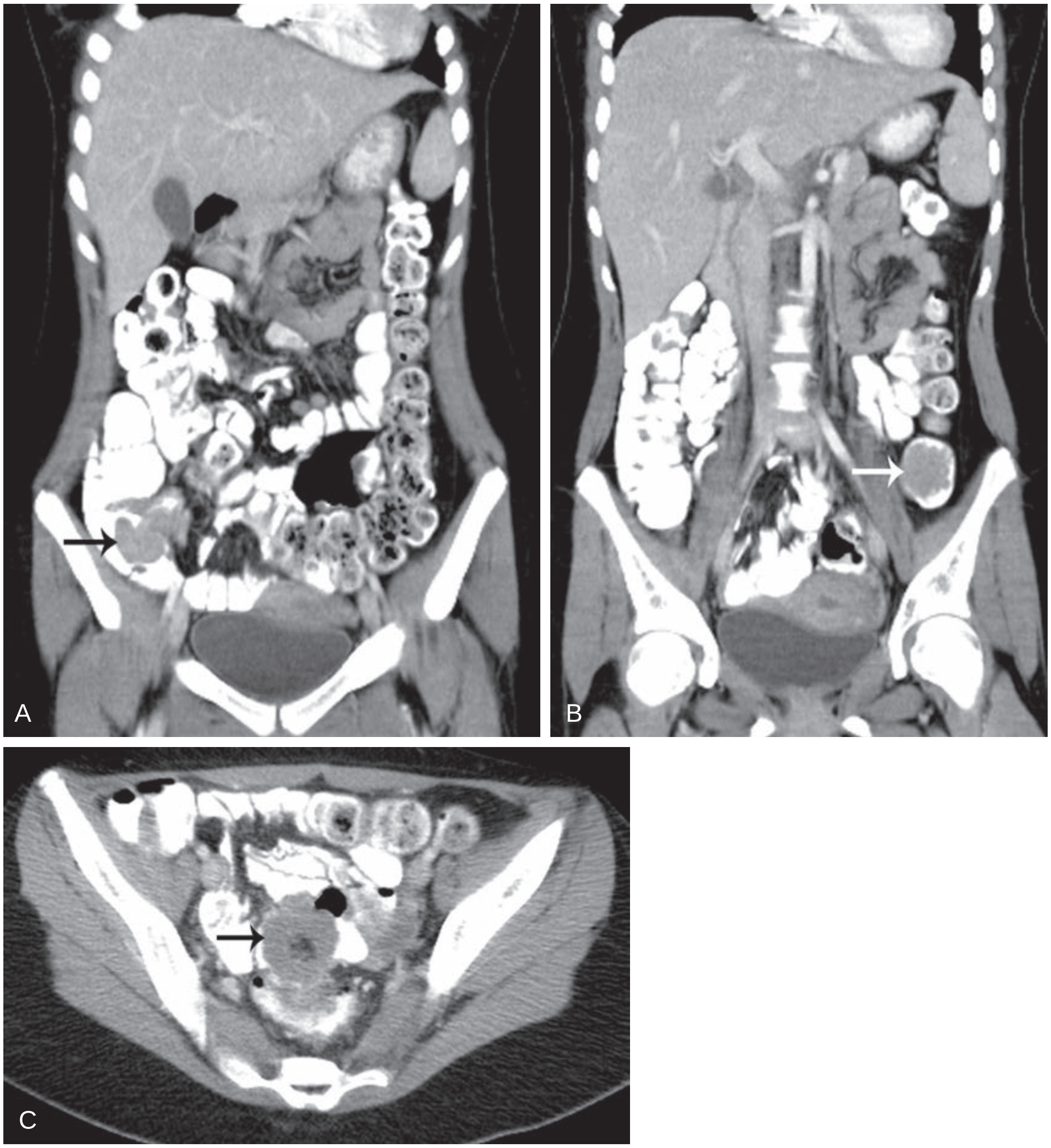

**Figure 108.8. Adenomatous polyps and rectal mucinous adenocarcinoma.** Screening colonoscopy in a 13-year-old girl with constitutional mismatch repair deficiency syndrome and anaplastic astrocytoma revealed several adenomatous polyps and rectal adenocarcinoma. Coronal reconstructed contrast-enhanced CT images demonstrate large, solid filling defects (A) at the ileocecal junction *(arrow)* and (B) in the descending colon *(arrow)*. Biopsy showed these to be adenomatous polyps. (C) Axial image from same CT examination shows an adenomatous polyp in the rectum that had undergone transformation to mucinous adenocarcinoma *(arrow)*.

## Lymphoma

***Overview.*** The colon can be a site of involvement in patients with lymphoma, although the small bowel is more commonly involved. Primary colorectal lymphoma accounts for less than 1% of all colorectal malignancies and occurs most often in the cecum.[35] Disorders predisposing to bowel lymphoma include ataxia-telangiectasia, Wiskott–Aldrich syndrome, agammaglobulinemia, severe combined immunodeficiency, and solid organ or bone marrow transplantation. There also appears to be an association between inflammatory bowel disease (IBD) and lymphoma. IBD may result in chronic antigenic stimulation.[35] Recent data shows that, when these patients are treated with immunosuppressive and biologic agents, they are at greater risk of developing lymphoma.[36] The risk of developing a neoplasm must be weighed against the risks associated with not adequately treating the primary disease.

***Etiology, Pathophysiology, and Clinical Presentation.*** As noted above, lymphoma arising in the colon may result from conditions such as immunosuppression after transplantation. Some investigators postulate a genetic component because a family history can sometimes be elicited. Others suggest a role for infectious agents, particularly the Epstein–Barr virus in patients with underlying IBD.[37]

The presenting symptoms in patients with GI lymphoma are often nonspecific and include abdominal pain and weight

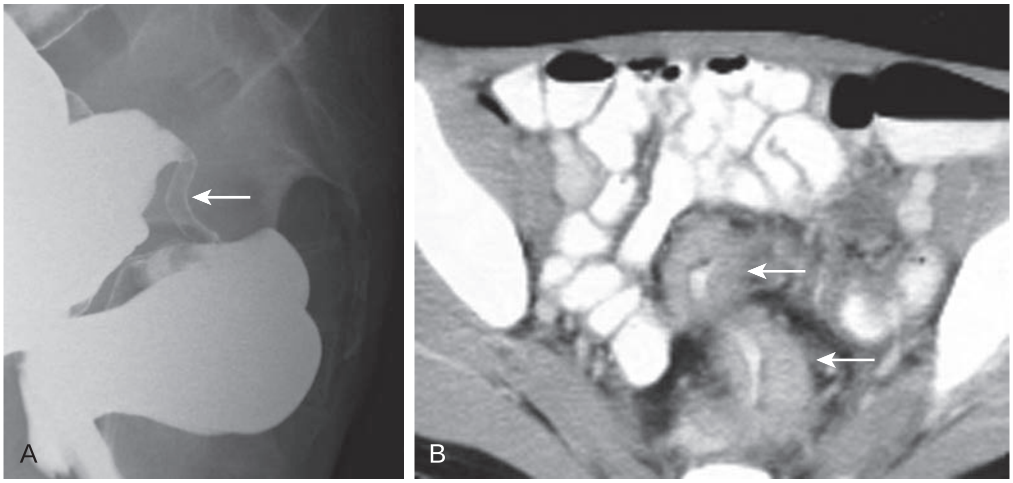

**Figure 108.9. Rectosigmoid adenocarcinoma.** A 14-year-old boy presented with rectal bleeding. (A) Lateral projection from a double-contrast barium enema demonstrates an area of circumferential narrowing *(arrow)* near the junction of the sigmoid colon and rectum. (B) A contrast-enhanced computed tomography scan also demonstrates circumferential soft tissue narrowing the lumen *(arrows)*. The lesion was resected and found to be an adenocarcinoma.

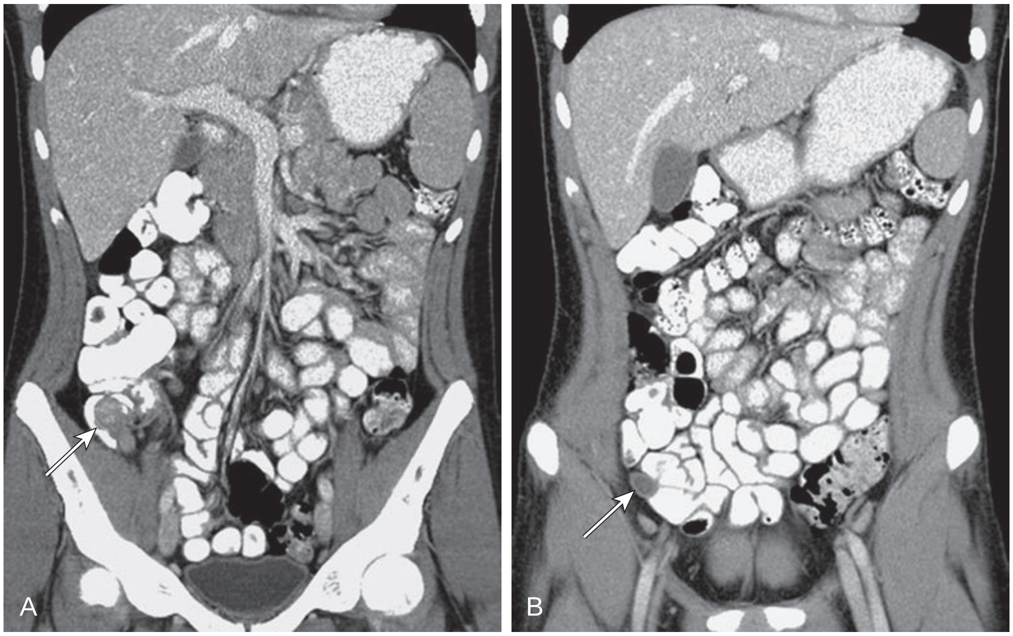

**Figure 108.10. Appendiceal neuroendocrine tumor.** A 16-year-old boy presented with intermittent right lower quadrant pain. (A) Contrast-enhanced coronal reformat CT demonstrates a mass at the base of the appendix invaginating into the cecum *(arrow)*. (B) The obstructed appendix is distended to its tip with fluid *(arrow)*.

loss. Bleeding and a change in bowel habits occur less frequently. If the lesion is large enough, it can present as a palpable mass. In some cases, the presentation is one of a colocolic intussusception.[38]

***Imaging.*** If contrast enema is performed, the appearance can be one of irregularity of the bowel wall, a smooth or lobulated mural mass, or circumferential narrowing. A long segment of the bowel can be affected. On ultrasound, the lesion is typically, although not always, hypoechoic, but is proved to be a solid mass by demonstration of flow on Doppler imaging. On CT or MRI an enhancing soft tissue mass is seen, which can be associated with adenopathy and/or solid visceral involvement (Fig. 108.11).

***Treatment.*** Treatment consists of chemotherapy and radiation therapy. In cases of relapse, high-dose chemotherapy followed by stem cell transplantation has been used.

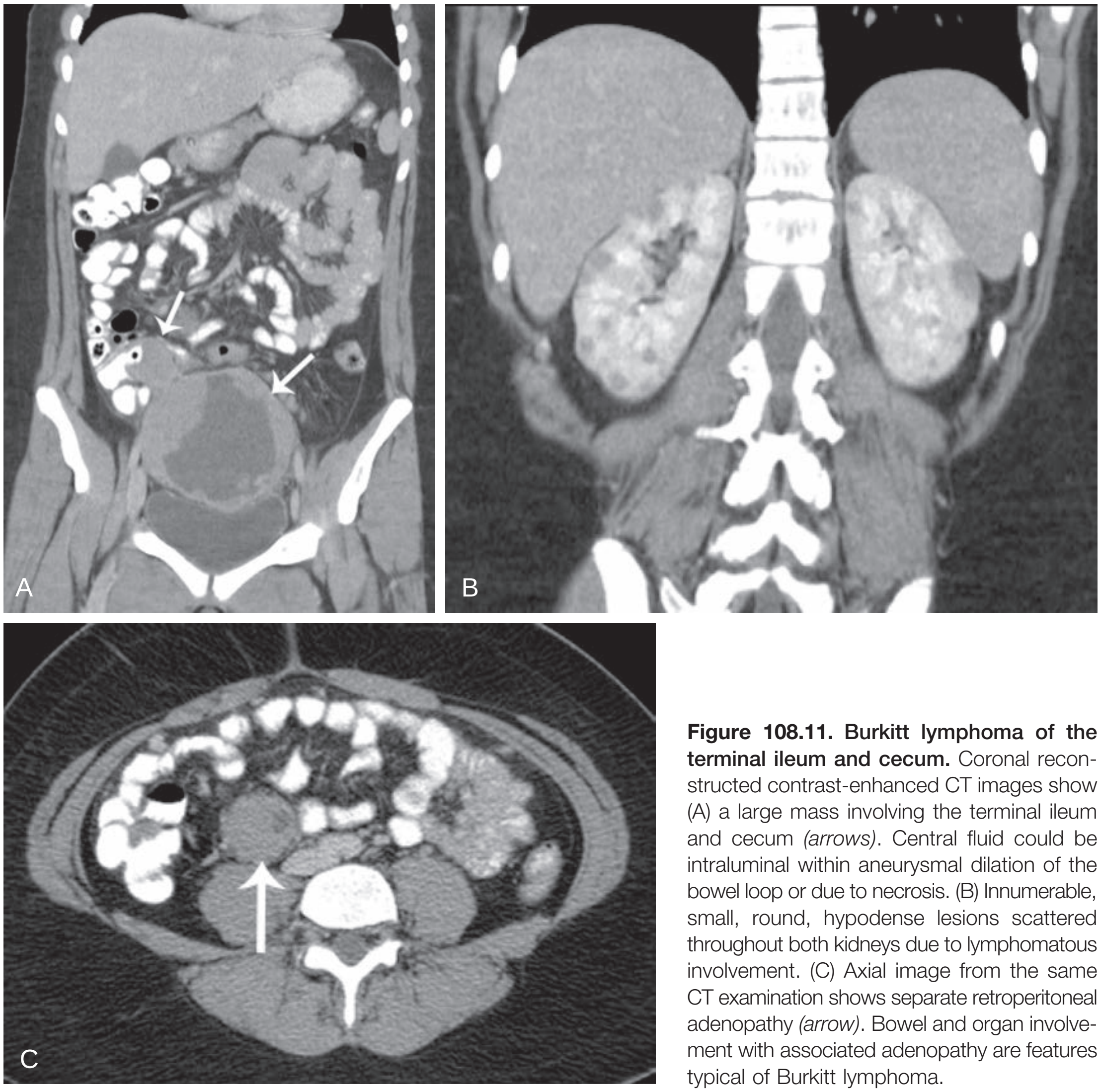

**Figure 108.11. Burkitt lymphoma of the terminal ileum and cecum.** Coronal reconstructed contrast-enhanced CT images show (A) a large mass involving the terminal ileum and cecum *(arrows)*. Central fluid could be intraluminal within aneurysmal dilation of the bowel loop or due to necrosis. (B) Innumerable, small, round, hypodense lesions scattered throughout both kidneys due to lymphomatous involvement. (C) Axial image from the same CT examination shows separate retroperitoneal adenopathy *(arrow)*. Bowel and organ involvement with associated adenopathy are features typical of Burkitt lymphoma.

## KEY POINTS

- Benign lymphoid hyperplasia most frequently involves the terminal ileum and colon. On double-contrast enema, the lesions are uniform in size (usually 2–3 mm) and can be umbilicated.
- Vascular lesions of the colon are rare but can present as lower GI bleeding. They can be difficult to demonstrate with imaging, although cross-sectional imaging may be useful, particularly arterial phase CT.
- The isolated juvenile polyp is the most common intestinal tumor in childhood. It has no known malignant potential and is treated with polypectomy alone.
- The hamartomatous syndromes include JPS, Peutz–Jeghers syndrome, and Cowden syndrome.
- The adenomatous syndromes include classic FAP, attenuated FAP, Gardner syndrome, and Turcot syndrome. Most persons believe that the term Gardner syndrome is obsolete and include the condition in FAP.
- Benign tumors of the colon tend to be sporadic and include lipomas, leiomyomas, and neurofibromas.
- Malignancies are rare but include lymphoma, adenocarcinoma, and well differentiated neuroendocrine tumors.

## SUGGESTED READINGS

Alkhouri N, Franciosi JP, Mamula P. Familial adenomatous polyposis in children and adolescents. *J Pediatr Gastroenterol Nutr*. 2010;51:727–732.

Barnard J. Screening and surveillance recommendations for pediatric gastrointestinal polyposis syndromes. *J Pediatr Gastroenterol Nutr*. 2009;48(suppl 2):S75–S78.

Hill DA, Furman WL, Billups CA, et al. Colorectal carcinoma in childhood and adolescence: a clinicopathologic review. *J Clin Oncol*. 2007;25:5808–5814.

Krauss E, Konturek P, Maiss J, et al. Clinical significance of lymphoid hyperplasia of the lower gastrointestinal tract. *Endoscopy*. 2010;42:334–337.

Landry CS, Woodall C, Scoggins CR, et al. Analysis of 900 appendiceal carcinoid tumors for a proposed predictive staging system. *Arch Surg*. 2008;143:664–670.

Pickhardt PJ, Kim DH, Menias CO, et al. Evaluation of submucosal lesions of the large intestine: part 2. Nonneoplastic causes. *Radiographics*. 2007;27:1693–1703.

Shih SL, Liu YP, Tsai YS, et al. Evaluation of arterial phase MDCT for the characterization of lower gastrointestinal bleeding in infants and children: preliminary results. *AJR Am J Roentgenol*. 2010;194:496–499.

Wong MT, Eu KW. Primary colorectal lymphomas. *Colorectal Dis*. 2006;8:586–591.

## REFERENCES

Full references for this chapter can be found on www.expertconsult.com.

## REFERENCES

1. Iacono G, et al. Colonic lymphoid nodular hyperplasia in children: relationship to food hypersensitivity. *Clin Gastroenterol Hepatol*. 2007;5(3):361–366.
2. Kleinman R. Nodular lymphoid hyperplasia. In: Kleinman R, ed. *Atlas of Pediatric Gastrointestinal Disease*. Hamilton, Canada: B.C. Becker; 1998:205–207.
3. Krauss E, et al. Clinical significance of lymphoid hyperplasia of the lower gastrointestinal tract. *Endoscopy*. 2010;42(4):334–337.
4. Galiatsatos P, Gologan A, Lamoureux E. Autistic enterocolitis: fact or fiction? *Can J Gastroenterol*. 2009;23(2):95–98.
5. Capitanio MA, Kirkpatrick JA. Lymphoid hyperplasia of the colon in children. Roentgen observations. *Radiology*. 1970;94(2):323–327.
6. Pickhardt PJ, et al. Evaluation of submucosal lesions of the large intestine: part 2. Nonneoplastic causes. *Radiographics*. 2007;27(6):1693–1703.
7. Heaton ND, Davenport M, Howard ER. Incidence of haemorrhoids and anorectal varices in children with portal hypertension. *Br J Surg*. 1993;80(5):616–618.
8. Turck D, Michaud L. Lower gastrointestinal bleeding. In: Kleinman R, ed. *Walker's Pediatric Gastrointestinal Disease*. Hamilton, Canada: B.C. Decker; 2008:1309–1319.
9. Shih SL, et al. Evaluation of arterial phase MDCT for the characterization of lower gastrointestinal bleeding in infants and children: preliminary results. *AJR Am J Roentgenol*. 2010;194(2):496–499.
10. Fishman SJ, Mulliken JB. Hemangiomas and vascular malformations of infancy and childhood. *Pediatr Clin North Am*. 1993;40(6):1177–1200.
11. Defreyne L, et al. Colonic arteriovenous malformation in a child misinterpreted as an idiopathic colonic varicosis on angiography: remarks on current classification of childhood intestinal vascular malformations. *Eur Radiol*. 2003;13(suppl 4):L138–L141.
12. Durno CA. Colonic polyps in children and adolescents. *Can J Gastroenterol*. 2007;21(4):233–239.
13. Barnard J. Screening and surveillance recommendations for pediatric gastrointestinal polyposis syndromes. *J Pediatr Gastroenterol Nutr*. 2009;48(suppl 2):S75–S78.
14. McColl I, et al. Juvenile polyposis coli. *Proc R Soc Med*. 1964;57:896–897.
15. Schreibman IR, et al. The hamartomatous polyposis syndromes: a clinical and molecular review. *Am J Gastroenterol*. 2005;100(2):476–490.
16. Chow E, Macrae F. A review of juvenile polyposis syndrome. *J Gastroenterol Hepatol*. 2005;20(11):1634–1640.
17. Schwenter F, et al. Juvenile polyposis syndrome, SMAD4 mutations, and hereditary hemorrhagic telangiectasia. *J Pediatr Gastroenterol Nutr*. 2012;54(1):120–122.
18. Howe JR, Mitros FA, Summers RW. The risk of gastrointestinal carcinoma in familial juvenile polyposis. *Ann Surg Oncol*. 1998;5(8):751–756.
19. Gustafson S, et al. Cowden syndrome. *Semin Oncol*. 2007;34(5):428–434.
20. Eng C. PTEN: one gene, many syndromes. *Hum Mutat*. 2003;22(3):183–198.
21. McGarrity TJ, Kulin HE, Zaino RJ. Peutz-Jeghers syndrome. *Am J Gastroenterol*. 2000;95(3):596–604.
22. Beggs AD, et al. Peutz-Jeghers syndrome: a systematic review and recommendations for management. *Gut*. 2010;59(7):975–986.
23. Alkhouri N, Franciosi JP, Mamula P. Familial adenomatous polyposis in children and adolescents. *J Pediatr Gastroenterol Nutr*. 2010;51(6):727–732.
24. Groen EJ, et al. Extra-intestinal manifestations of familial adenomatous polyposis. *Ann Surg Oncol*. 2008;15(9):2439–2450.
25. Sturt NJ, et al. Evidence for genetic predisposition to desmoid tumours in familial adenomatous polyposis independent of the germline APC mutation. *Gut*. 2004;53(12):1832–1836.
26. Erdman SH, Barnard JA. Gastrointestinal polyps and polyposis syndromes in children. *Curr Opin Pediatr*. 2002;14(5):576–582.
27. Groves CJ, et al. Duodenal cancer in patients with familial adenomatous polyposis (FAP): results of a 10 year prospective study. *Gut*. 2002;50(5):636–641.
28. Turcot J, Despres JP, St Pierre F. Malignant tumors of the central nervous system associated with familial polyposis of the colon: report of two cases. *Dis Colon Rectum*. 1959;2:465–468.
29. Villani A, Malkin D, Tabori U. Syndromes predisposing to pediatric central nervous system tumors: lessons learned and new promises. *Curr Neurol Neurosci Rep*. 2012;12(2):153–164.
30. Hamilton SR, et al. The molecular basis of Turcot's syndrome. *N Engl J Med*. 1995;332(13):839–847.
31. Donoghue L, Klein M. Tumors of the digestive tract. In: Kliegman R, ed. *Nelson Textbook of Pediatrics*. Philadelphia: Saunders; 2007:1641–1644.
32. Hill DA, et al. Colorectal carcinoma in childhood and adolescence: a clinicopathologic review. *J Clin Oncol*. 2007;25(36):5808–5814.
33. Landry CS, et al. Analysis of 900 appendiceal carcinoid tumors for a proposed predictive staging system. *Arch Surg*. 2008;143(7):664–670.
34. Khanna G, O'Dorisio SM, Menda Y, et al. Gastroenteropancreatic neuroendocrine tumors in children and young adults. *Pediatr Radiol*. 2008;38(3):251–259.
35. Wong MT, Eu KW. Primary colorectal lymphomas. *Colorectal Dis*. 2006;8(7):586–591.
36. Jones JL, Loftus EV Jr. Lymphoma risk in inflammatory bowel disease: is it the disease or its treatment? *Inflamm Bowel Dis*. 2007;13(10):1299–1307.
37. Wong NA, et al. Epstein-Barr virus infection in colorectal neoplasms associated with inflammatory bowel disease: detection of the virus in lymphomas but not in adenocarcinomas. *J Pathol*. 2003;201(2):312–318.
38. Gollub MJ. Colonic intussusception: clinical and radiographic features. *AJR Am J Roentgenol*. 2011;196(5):W580–W585.

# 109 Abdominal Trauma

*George A. Taylor and Carlos J. Sivit*

## OVERVIEW

Trauma in children accounts for more than 500,000 hospital admissions and 20,000 deaths per year. After cranial trauma, the abdomen is the second most common site of injury, and approximately 80% of abdominal injuries are due to blunt force trauma. The most common reported mechanism is motor vehicle crashes, followed by automobile–pedestrian injuries. Other common causes of injury include bicycle trauma and falls from a height. In young children, injuries also may result from intentional or nonaccidental trauma.[1]

## CLINICAL PRESENTATION

Clinical variables that have been associated with a high risk of injury include gross hematuria, abdominal tenderness, seat belt ecchymoses, and a high trauma score. Seat belt ecchymoses across the lower abdomen or flank represent an important high-risk marker for injury.[2,3] Such ecchymoses are associated with an injury complex to the lumbar spine, bowel, and bladder that accounts for most injuries to belted motor vehicle passengers.

Several points to be noted regarding hematuria and abdominal injury include the following: (1) most children with hematuria do not have a urinary tract injury; (2) a nonurinary tract injury is observed more frequently than a urinary tract injury in children with hematuria; (3) a negative urinalysis is associated with a very low risk of genitourinary (GU) injury; and (4) asymptomatic hematuria is a low-risk indicator for abdominal injury.

## IMAGING

Computed tomography (CT) is the imaging method of choice in the evaluation of abdominal and pelvic injury after blunt trauma in hemodynamically stable children. Evaluation with CT allows accurate detection and characterization of injury to solid and hollow viscera. CT also identifies and quantifies intraperitoneal and extraperitoneal fluid and blood, and can detect active bleeding. Additionally, CT reveals associated bony injury to the ribs, spine, and pelvis. The role of CT in the assessment of injured children includes establishing the presence or absence of visceral and bony injury, identifying injury that requires close monitoring and operative or endovascular intervention, and estimating associated blood loss. Normal CT findings also serve an important function in management of the injured child and in exclusion of an intraabdominal or pelvic source of blood loss.

The rapid and accurate evaluation of injured children with CT has resulted in improved triage, has contributed to reduced morbidity and mortality, and, along with improvements in supportive care, has played a critical role in the success of nonoperative management of solid organ injuries. While CT is the preferred imaging test in the setting of blunt abdominal trauma, intraabdominal injuries are only present in 5% to 15.5% of children sustaining blunt trauma. Yet, CT findings have been shown to change the initial management plan in nearly half of children assessed after blunt abdominal trauma.[4–6]

### Computed Tomography Technique

Children should be hemodynamically stable before undergoing a CT scan. An unstable patient must be stabilized or should proceed directly to surgery for evaluation and treatment.

A precise size-based protocol is important in minimizing the length of the examination and radiation dose exposure and in maximizing the information obtained. Sedation is rarely required before performing a CT scan in an injured child. However, because excessive patient motion results in image degradation, in select instances, a short-acting sedative may be necessary if diagnostic images are to be obtained.

The use of intravenous (IV) contrast material by rapid bolus injection is essential for maximizing the opacification of solid viscera and ensuring adequate injury detection (commonly 2 mL/kg to a maximum amount of 120 mL). Without appropriate IV administration of contrast material, solid organ laceration or hematoma may be relatively inconspicuous or missed. Additionally, the use of IV contrast material permits the detection of active hemorrhage. Multiphase and "total body" imaging are not necessary for the detection of abdominal injury and add an unnecessary radiation burden.

The use of oral contrast material in CT scanning after blunt abdominal trauma has not been found to improve the detection of intraabdominal injuries in children.[7] In our experience, the potential advantages of enhanced detection of small intramural or mesenteric hematomas and the detection of oral contrast extravasation as a sign of bowel rupture are small and outweighed by its potential disadvantages, including delay in performance of the examination and possibility of aspiration. If oral contrast material is used, diluted (2%) water-soluble contrast material should be administered at least 30 minutes before the scan is performed.

### Sonography in the Assessment of Abdominal Trauma

Sonography remains widely used in the screening of injured children and adults, and has been shown to have high sensitivity and specificity in the detection of hemoperitoneum; however, its utility is limited in comparison with CT. Solely identifying fluid does not necessarily reveal the cause or the site of injury, and the presence of hemoperitoneum in a hemodynamically stable child typically does not affect clinical management decisions. Furthermore, sonography provides no diagnostic information regarding injury to the bony pelvis or lumbar spine, it cannot be used in the diagnosis of hollow viscus injury, and it has been shown to miss approximately one-fourth to one-third of solid organ injuries.[8] Thus if one relies on identification of peritoneal fluid as a marker for hepatic and splenic injury, one will miss a significant number of injuries. Nevertheless, sonography has a potential role in diagnosing hemodynamically unstable patients because it can be performed rapidly at the bedside before the patient is taken to the operating room. In this role, it serves as a fast, noninvasive replacement for diagnostic peritoneal lavage. Recent studies suggest that contrast-enhanced sonography may have improved accuracy in delineating solid organ injuries.[9]

## Abstract:

Background: Blunt abdominal trauma is a common occurrence in children, and imaging plays an important role in initial medical management.

Findings: The most common mechanisms of injury are due to motor vehicle crashes and automobile-pedestrian injuries.

Contrast-enhanced CT is the imaging method of choice for identifying both solid and hollow visceral injuries. Contrast-enhanced sonography has also shown promise in evaluation of solid organ lacerations. The grade of injury has poor correlation with the need for surgical intervention.

Conclusions: CT information is currently most frequently used in deciding on admission to hospital, as well as the intensity and duration of hospitalization, and activity restriction.

## Keywords:

abdominal trauma
computed tomography
liver injury
spleen injury
kidney injury
bowel injury

## COMPUTED TOMOGRAPHY FINDINGS

### Splenic Injury

The spleen is the most commonly injured organ after blunt trauma, and frequently is associated with other organ injuries (Fig. 109.1). Because the spleen is much smaller than the liver, complex injury results in shattering or fragmentation of the organ (Fig. 109.2). Associated intraparenchymal or subcapsular hematoma may be present. As with hepatic injury, associated intraperitoneal hemorrhage is not always present, especially when the splenic capsule remains intact. Absence of hemoperitoneum is observed in approximately 25% of splenic injuries. After injury involving the splenic hilum, blood also can track along the splenorenal ligament into the anterior pararenal space surrounding the pancreas.

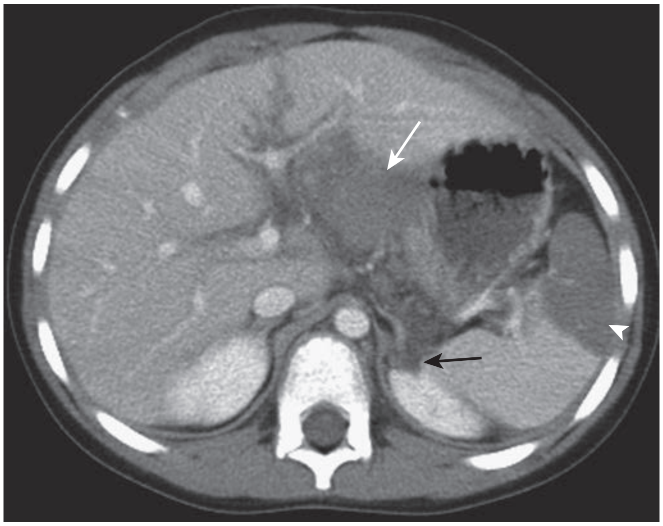

**Figure 109.1. Hepatic, splenic, and renal injury.** Contrast-enhanced axial CT image through the upper abdomen reveals a laceration to segment III of the left hepatic lobe *(white arrow)*, a splenic hematoma *(arrowhead)*, and a small laceration to the left kidney *(black arrow)*.

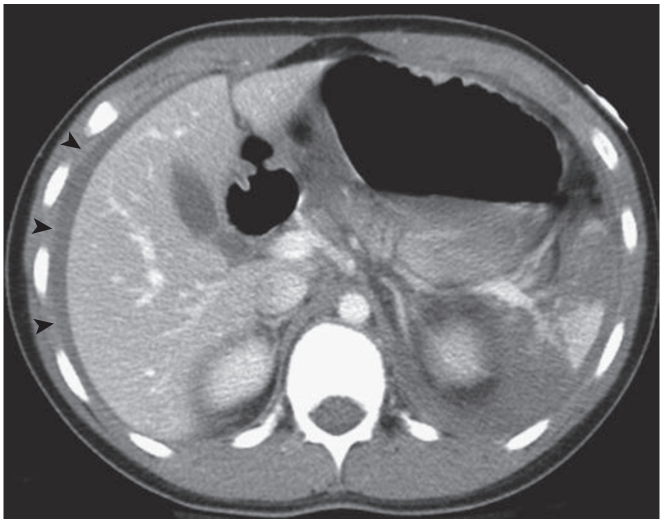

**Figure 109.2. Shattered spleen.** Contrast-enhanced axial CT image through the upper abdomen shows a shattered spleen with only a small amount of central contrast enhancement. Note right perihepatic hemoperitoneum *(arrowheads)*.

Pitfalls that may result in false-positive diagnosis of splenic injury include heterogeneous early splenic enhancement and splenic lobulations or clefts that mimic a laceration. The heterogeneous splenic enhancement is due to differences in enhancement between red and white pulp in the spleen. This artifact can be avoided by instituting a delay of at least 70 seconds after IV contrast material administration before scanning. Splenic clefts and lobulations typically have smooth contours and thus can be differentiated from lacerations, which typically have irregular contours.

***Treatment.*** Various injury grading scales have been described to objectively quantify injury to the spleen. As is true for hepatic injury, these scales are not predictive of surgical treatment in children because bleeding typically stops spontaneously, and nonoperative management is successful in most splenic injuries. Grade of injury often is used for nonoperative clinical decision making, similar to the use of grading in hepatic injury.[10,11]

### Hepatic Injury

Hepatic injury also is common after blunt trauma in children, in whom this organ is poorly protected from injury by overlying ribs because the immature chest wall is easily deformed by external forces. A hepatic laceration appears as a nonenhancing region of varying configuration (Figs. 109.1 and 109.3) that may be linear or branching. Lacerations may be associated with a parenchymal or a subcapsular hematoma.

The liver is surrounded by a thin capsule that, in turn, is covered by a peritoneal reflection of thin connective tissue. The presence of hemoperitoneum associated with hepatic injury principally relates to violation of the liver capsule at the site of injury. In several large series, hepatic injury was associated with hemoperitoneum in approximately two-thirds of cases. Associated hemoperitoneum may be seen throughout the greater peritoneal cavity. Often, the largest fluid pockets are located in the pelvis. Hepatic injury may not be associated with intraperitoneal hemorrhage if the injury does not extend to the surface of the liver, if the hepatic capsule is not disrupted, or if the injury extends to the liver surface in the bare area of the liver, which is devoid of peritoneal reflection (Fig. 109.4). Injury that extends to the bare area may lead to associated retroperitoneal hemorrhage, with blood often surrounding the right adrenal gland or extending into the anterior pararenal space.

Circumferential zones of periportal low attenuation may be seen in the liver after trauma. The presence of these low attenuation zones does not indicate hepatic injury. They most likely represent distended periportal lymphatics as a result of intravascular third-space fluid losses that occur after fluid resuscitation.[12,13]

***Treatment.*** A number of grading scales have been proposed to quantify the severity of hepatic injury. These scales emphasize the anatomic extent of the injury, including capsular integrity, extent of subcapsular collection, extent of parenchymal disruption, and involvement of the vascular pedicle. The most widely used grading scale was developed by the American Association for the Surgery of Trauma. It was devised initially to reflect surgical findings but often is used to report severity of organ injury upon CT scanning. In children, these scales are not predictive of the need for operative management because, in the vast majority of hepatic injuries, bleeding typically stops spontaneously and the injuries can be managed successfully without surgery regardless of the severity.[10] This response likely is a result of the relatively smaller size of blood vessels and the enhanced vasoconstrictive response in children relative to adults. Between 1% and 3% of children with hepatic injury require surgical or endovascular hemostasis. However, injury grading scales often are used in the decision algorithm of patient management regarding intensity and length of hospitalization and activity restriction.

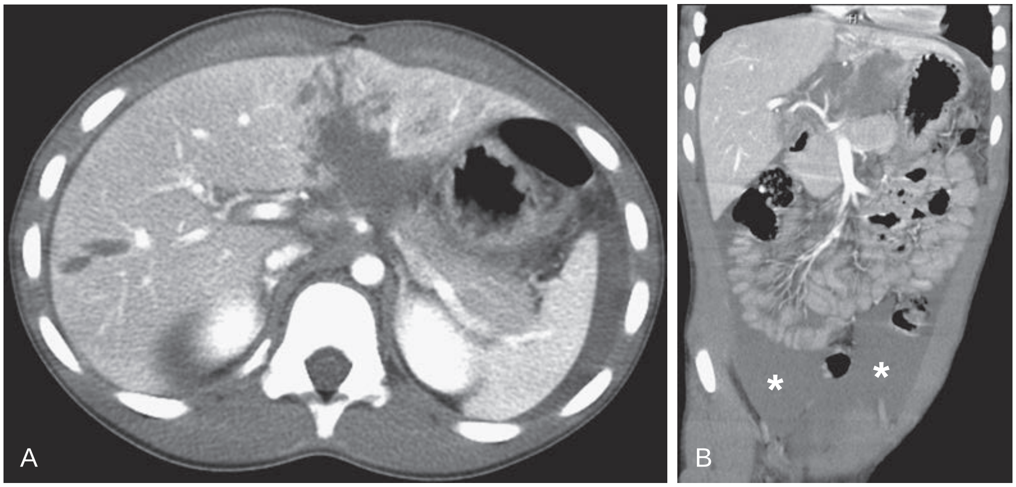

**Figure 109.3. Hepatic laceration and hemoperitoneum.** Contrast-enhanced axial CT image through the upper abdomen (A) reveals a complex hepatic laceration involving segment IV and a simple laceration of segment V. A coronal reformat image (B) shows a large associated hemoperitoneum in the pelvis *(asterisks)*.

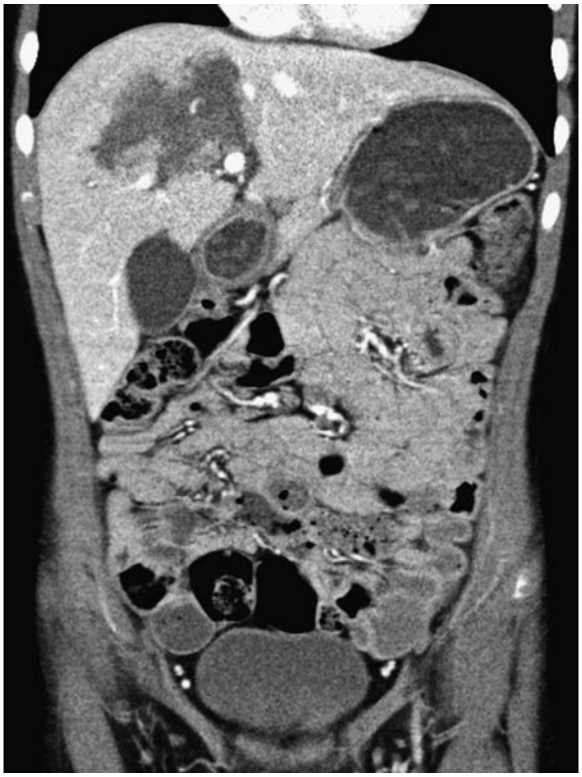

**Figure 109.4. Hepatic laceration without hemoperitoneum.** Coronal reformat of a contrast-enhanced CT scan reveals a laceration of segment VIII. No associated hemoperitoneum is present.

## Pancreatic Injury

Pancreatic injury is relatively uncommon in children. Injury to the body of the pancreas typically results from direct compression of the gland against the vertebral column, whereas injury to the head or tail of the pancreas results from a blow to the flank. Impact by bicycle handlebars is a common mechanism of injury to the pancreas. Direct signs of injury may be difficult to identify because of the small size of the gland, the paucity of surrounding fat, and the minimal separation of fracture fragments.

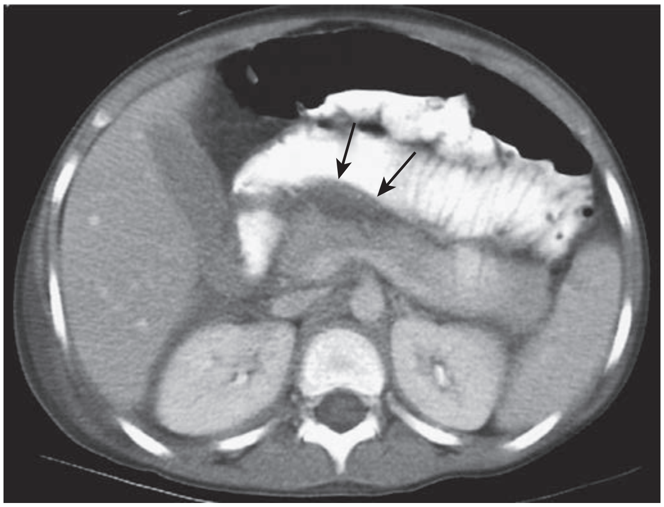

**Figure 109.5. Pancreatic injury with associated peripancreatic fluid.** Contrast-enhanced axial CT image through the upper abdomen shows fluid in the anterior pararenal space surrounding the pancreas *(arrows)*.

The best indicator of pancreatic injury at CT is unexplained peripancreatic fluid (i.e., fluid in the anterior pararenal space or lesser sac) (Fig. 109.5). This finding may be seen more often than the actual laceration. When fluid collects in the anterior pararenal space, it also may dissect between the pancreas and the splenic vein. However, pancreatic injury is only one cause of fluid in the anterior pararenal space.[1] Other causes include third-space intravascular fluid loss, blood that extends from injury to the spleen or to the bare area of the liver, blood or bowel contents from a duodenal injury, and blood or urine that exudes from a renal injury after disruption of the renal fascia.

Additional CT signs of posttraumatic pancreatitis include focal or diffuse gland enlargement, stranding of peripancreatic and/or mesenteric fat, thickening of the anterior renal fascia, and free peritoneal fluid.

A false-positive diagnosis of pancreatic injury may result from the partial volume effect caused by the gland's small size and undulating nature. This pitfall may be avoided by obtaining thin-section axial reconstructions and by creating coronal reformatted images.

Pancreatic injury may be complicated by peripancreatic fluid collections, which may evolve into pancreatic pseudocysts. Approximately half of focal fluid collections that develop after pancreatic injury spontaneously resolve, and half evolve into pseudocysts that may require percutaneous or surgical drainage. The most common location for pseudocyst formation is the intrapancreatic or peripancreatic anterior pararenal space, or lesser sac (Fig. 109.6). However, pseudocysts may develop anywhere in the abdomen or pelvis.

MR can be very useful in subsequent imaging evaluation of pancreatic injury, (Fig. 109.7); the addition of cholangiopancreatography may be of additional value in transection of the pancreatic duct.

***Treatment.*** Currently, there are divergent opinions regarding the management of pancreatic injury. Some practitioners have shown that nonoperative management of most pancreatic injury is successful, even when the pancreatic duct is involved. Others believe that distal pancreatectomy for transections occurring to the left of the spine is the treatment of choice because it is definitive and accompanied by an acceptable level of morbidity.[14–16]

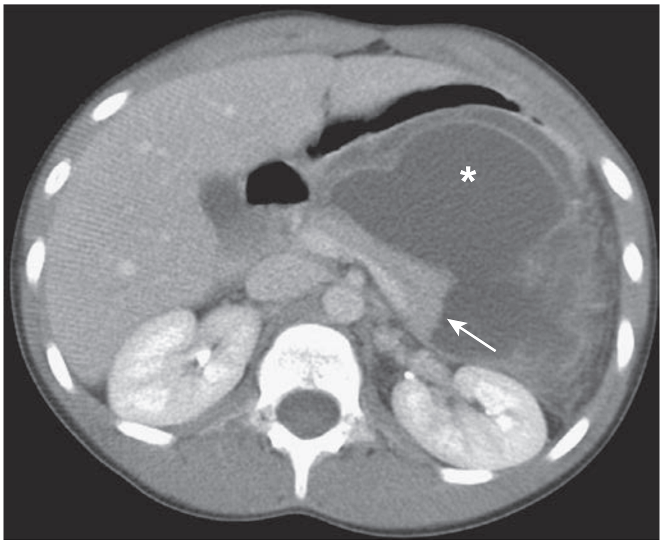

**Figure 109.6. Pancreatic pseudocyst.** Contrast-enhanced axial CT image through the upper abdomen shows a laceration of the pancreatic tail *(arrow)* with a large, thick-walled focal fluid collection *(asterisk)* representing a pancreatic pseudocyst in the anterior pararenal space.

## Peritoneal Fluid and Hemorrhage

Attenuation values of blood in the peritoneal cavity vary widely, depending on whether it is unclotted blood (hemoperitoneum), clotted blood, or active hemorrhage. Furthermore, several factors affect measured attenuation values for peritoneal fluid on CT, including measurement technique, fluid location within the field, artifacts, and delayed fluid enhancement after IV administration of contrast material. Unclotted hemoperitoneum has attenuation values that range from 20 to 60 Hounsfield units (HU). Approximately one-third of fluid pockets exhibit attenuation values lower than 30 HU. Low attenuation fluid (<60 HU) in an acutely injured child also may represent bile, urine, bowel contents, third-space fluid losses, or preexisting ascites.

Clotted blood has higher attenuation values (60–90 HU) than does free-flowing blood because of its greater density and hemoglobin content. Because clotted blood typically is seen adjacent to the site of injury, the presence of focal, higher attenuation clotted blood has been described as the "sentinel clot" sign; it is a marker for the principal site of hemorrhage and occasionally may be useful in localizing the site of injury.

Occasionally, CT may reveal active hemorrhage in children who appear hemodynamically stable. The amount of hemoperitoneum noted on CT is not a measure of ongoing hemorrhage; rather, it reflects the cumulative amount of bleeding that occurred between the time of injury and the time the CT scan was obtained. The only sign of active hemorrhage on CT is the presence of focal or high attenuation areas (>90 HU) (Fig. 109.8), referred to in the literature as a contrast blush.[17] The rate of active bleeding required for detection on CT is unclear. CT is useful in identifying active bleeding but may have difficulty in localizing the site of the hemorrhage. The torn blood vessel may be difficult to see because of diminished contrast enhancement caused by vasoconstriction and loss of blood containing contrast material. Occasionally, this finding may be observed only on delayed scanning.

The absence of peritoneal fluid or blood does not exclude the presence of hepatic or splenic injury. More than one-third of hepatic injuries and one-fourth of splenic injuries in children have no associated peritoneal fluid. The relatively high prevalence of hepatic and splenic injury without associated peritoneal fluid has significant implications for imaging strategies in the assessment of injured children.

***Treatment.*** Most children with active hemorrhage detected on CT do not require operative intervention. It has been reported that 20% or fewer children with hepatic or splenic injury and active hemorrhage have required operative hemostasis.[17–19]

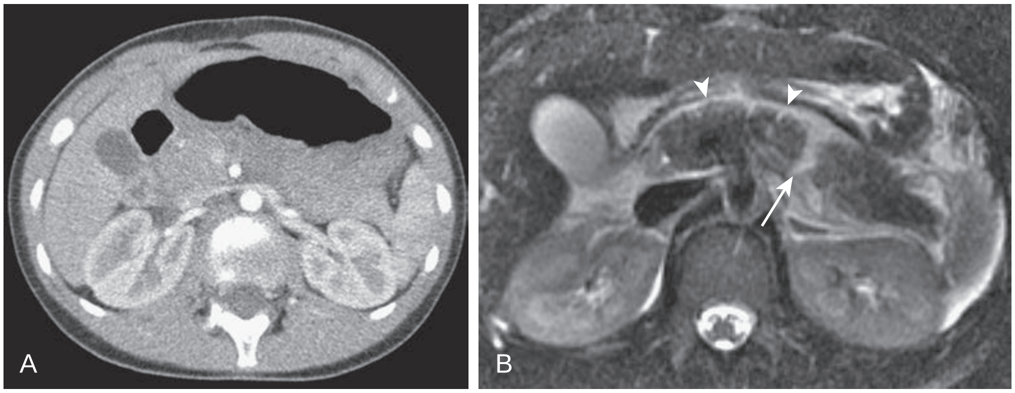

**Figure 109.7. Pancreatic injury missed on an initial CT scan.** A contrast-enhanced CT image through the upper abdomen (A) shows a heterogeneous ill-defined pancreas but no focal laceration. Axial T2-weighted fast spin echo MR image with fat saturation obtained the same day (B) shows peripancreatic fluid *(arrowheads)* and a laceration of the pancreatic body *(arrow)*.

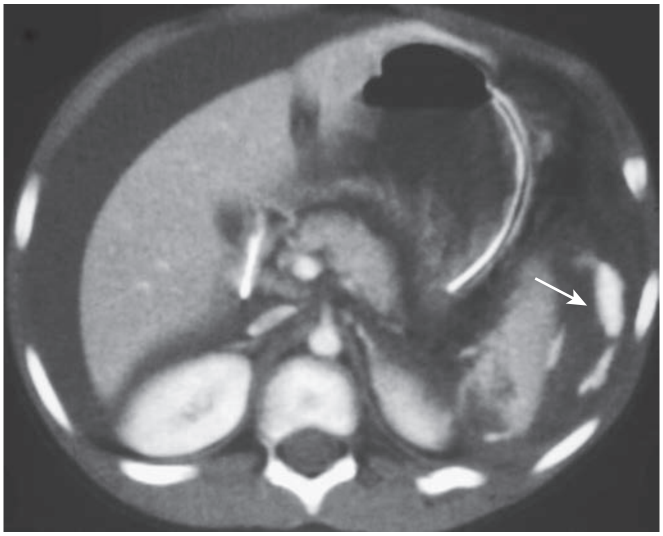

**Figure 109.8. Active hemorrhage.** Contrast-enhanced axial CT image through the upper abdomen shows a focal high attenuation collection representing intravenous contrast extravasation from a splenic arterial tear *(arrow)*.

## Bowel and Mesenteric Injury

Bowel and mesenteric injuries are uncommon after blunt trauma, occurring in 6% to 16% of injured children. The most common mechanisms of injury associated with bowel and mesenteric injury are motor vehicle crashes, handlebar injuries, nonaccidental trauma, and falls. Intestinal injury is the result of direct force on the gastrointestinal tract and mesentery leading to a crush injury, rapid deceleration producing a shearing force between fixed and mobile portions of bowel or mesenteric attachments, and a sharp increase in intraluminal pressure resulting in rupture of the gut.[20] Bowel rupture most commonly occurs in the mid to distal small intestine. The presence of seat belt ecchymosis and an acute hyperflexion (Chance) fracture of the lumbar spine are the only physical findings found to have a strong and significant association with bowel and mesenteric injury.[3] Nonaccidental injury always must be considered in a child with a history of minor blunt trauma who has a bowel perforation.[20,21]

Clinical signs and symptoms may be absent, minimal, or delayed, and CT plays an important role in early and accurate diagnosis. Delayed diagnosis can result in bowel ischemia, peritonitis, and, in rare cases, death as a result of sepsis. The main challenge for the radiologist is to distinguish between injuries that do and do not require surgical intervention. CT findings specific to bowel injury include the presence of extraluminal gas, extravasation of oral contrast material, and bowel discontinuity (Fig. 109.9).[22–24] The latter two findings are very uncommon in pediatric practice. Extraluminal gas, however, is present in 20% to 30% of children with bowel injury and is a highly specific finding, albeit with low sensitivity. In a supine patient, extraluminal gas tends to accumulate at the convexity of the abdominal wall and in the porta hepatis (Fig. 109.10). Blunt abdominal injury also can lead to intravasation of gas into the mesenteric and portal venous system, presumably through mucosal disruption, or because of ischemic changes resulting from mesenteric tears.[25] Injury to the retroperitoneal duodenum often results in localized bubbles of gas immediately adjacent to a thickened and distorted duodenum and pancreas. Review of the examination at a wide window setting is helpful in the detection of small amounts of extraluminal gas. Several other CT findings are common in injured patients but are less specific for significant bowel injury; these findings include focal bowel wall thickening and mesenteric fluid or stranding.

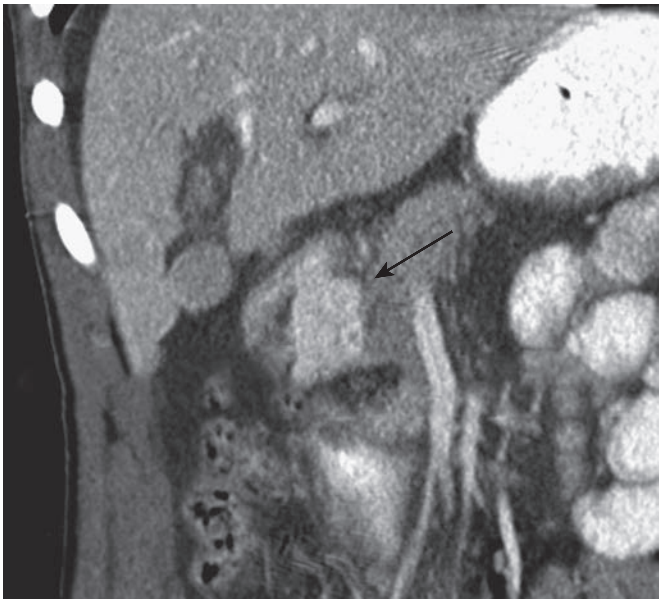

**Figure 109.9. Duodenal perforation with extravasation of oral contrast material.** Coronal reformat of a contrast-enhanced CT scan shows extravasation of oral contrast in the retroperitoneum *(arrow)* medial to the duodenal sweep.

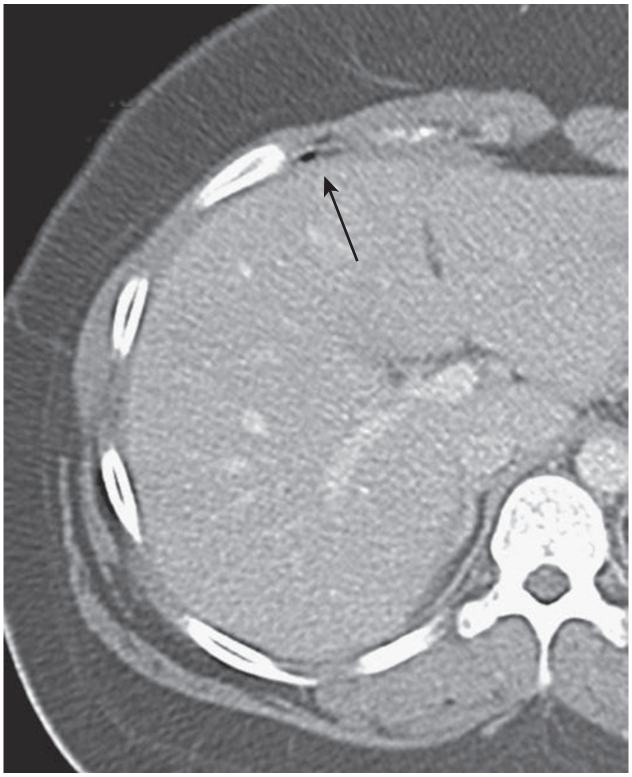

**Figure 109.10. Ileal perforation and extraluminal gas.** Contrast-enhanced CT image through the liver shows a small collection of extraluminal gas anterior to the right hepatic lobe *(arrow)*.

Intramural hematoma results from hemorrhage into the bowel wall after a partial-thickness tear has occurred; these injuries usually can be managed nonoperatively. The most common location is the duodenum. The CT appearance is that of focal bowel wall thickening that often is eccentric (Fig. 109.11). Large duodenal hematomas may appear dumbbell-shaped. Because the injury is

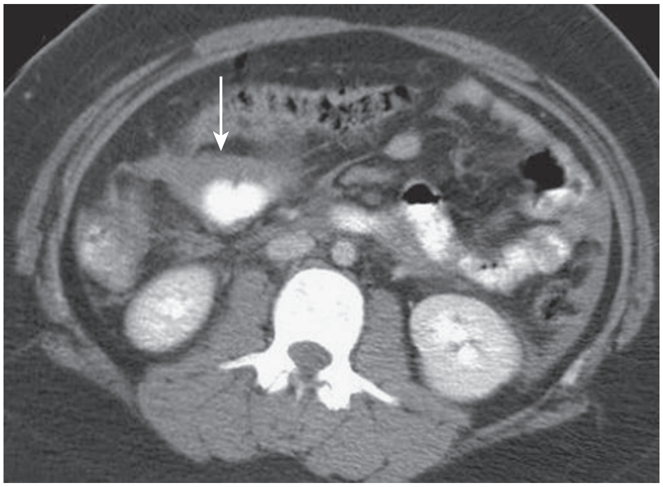

**Figure 109.11. Mesenteric tear and ischemic bowel.** Contrast-enhanced axial CT image through the mid abdomen shows a focal area of eccentric bowel wall thickening *(arrow)* due to a mesenteric tear. Ischemic bowel was confirmed at surgery.

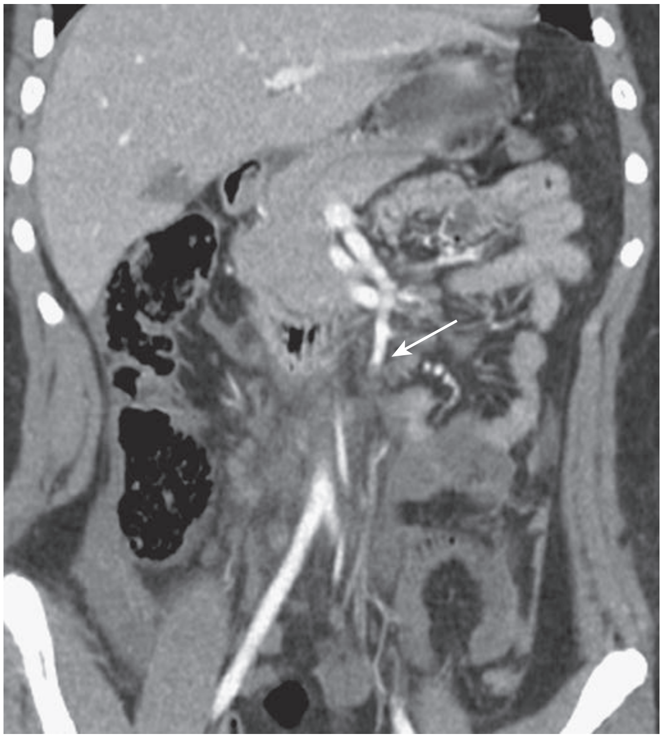

**Figure 109.12. Superior mesenteric artery occlusion.** Coronal reformat of a contrast-enhanced CT scan shows abrupt termination of the superior mesenteric artery *(arrow)*. The patient had subsequent mesenteric ischemia and bowel perforation.

intramural, no extraluminal air or extravasated contrast material should be present. Large hematomas can result in obstruction of the bowel proximal to the injury.

CT signs that are highly specific for significant mesenteric injury are related to vascular injury and include mesenteric vascular beading, abrupt termination of mesenteric vessels, and mesenteric vascular extravasation (Fig. 109.12 and Box 109.1).[24] These findings are rare in children, and their sensitivity and specificity are not known. Abnormalities that are less specific for the need for surgical intervention in mesenteric injury are mesenteric stranding and hematoma; these findings may represent a range of injuries from minor mesenteric bruising to underlying vascular disruption.

The most frequent CT finding associated with bowel rupture and mesenteric injury is "unexplained" peritoneal fluid (i.e., moderate to large amounts of fluid in the absence of solid viscus injury or bony pelvic fracture) (Fig. 109.13). Although nonspecific, unexplained peritoneal fluid is an important marker of potentially serious bowel or mesenteric injury. Approximately half the children with a moderate to large quantity of peritoneal fluid as the only finding on CT after blunt trauma have intestinal injury.[25] Follow-up CT imaging in patients with initially equivocal findings and persistent abdominal symptoms has been reported to improve the detectability of intestinal injuries.[23]

Multidetector scanners have improved the accuracy of CT for the diagnosis of bowel and mesenteric injuries. However, the reported sensitivity values (80%–95%) and specificity values (48%–84%) vary widely among studies.[24,26]

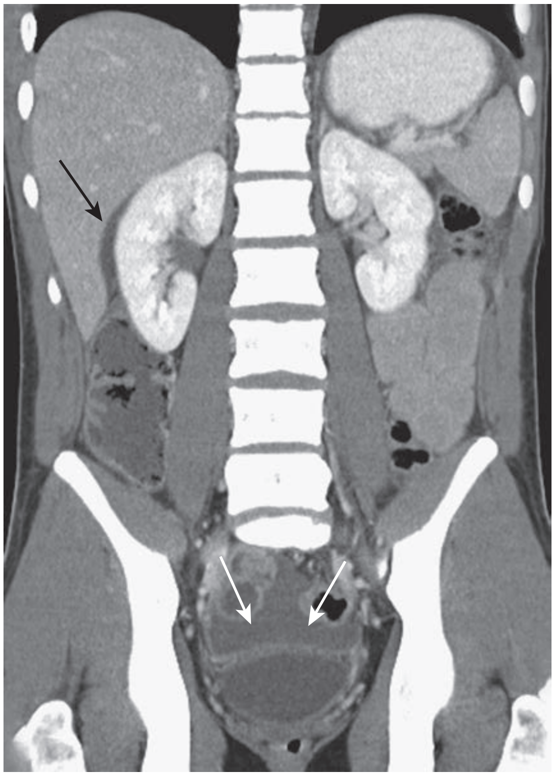

**Figure 109.13. Bowel rupture with a moderate amount of "unexplained" peritoneal fluid.** Coronal reformat of a contrast-enhanced CT scan shows a moderate amount of peritoneal fluid in the cul-de-sac *(white arrows)*, and in the subhepatic space *(black arrow)*. No other abnormalities were noted on CT. A jejunal rupture was identified at surgery.

**BOX 109.1** High-Specificity Computed Tomography Findings in Bowel and Mesenteric Injury

Extraluminal gas
Extraluminal oral contrast material
Bowel discontinuity
Mesenteric vascular beading
Abrupt termination of mesenteric vessels
Mesenteric vascular extravasation

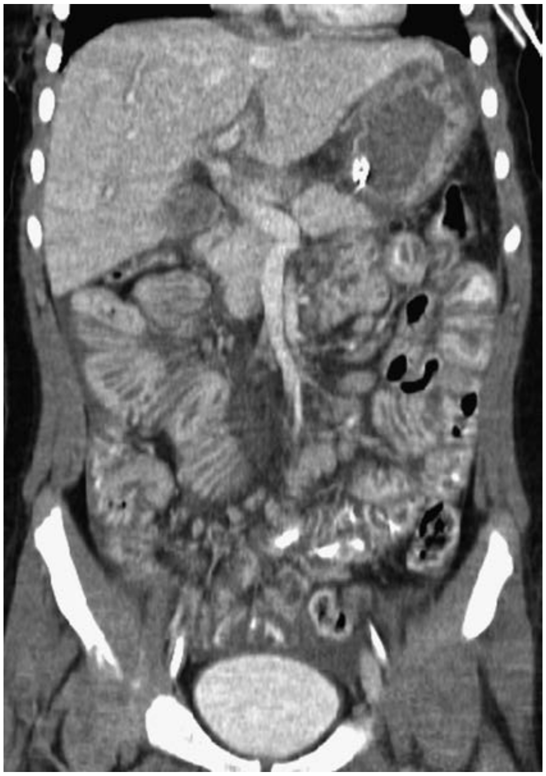

**Figure 109.14. Hypoperfusion complex.** Coronal reformat of a contrast-enhanced CT scan shows diffuse intestinal thickening, dilation with fluid, intense contrast enhancement of the bowel wall, low periportal attenuation, and ascites indicative of partially compensated shock.

## Hypoperfusion Complex

A characteristic complex of CT findings associated with partially compensated hypovolemic shock in severely injured children has been characterized as the "hypoperfusion complex." Most of these children have required extensive resuscitation for arterial hypotension on admission.[27]

CT findings in all children with the hypoperfusion complex include diffuse intestinal dilation with fluid. Abnormally intense contrast enhancement of bowel wall, mesentery, kidneys, aorta, and inferior vena cava is present, as well as diminished caliber of the aorta and inferior vena cava (Fig. 109.14). Variable findings include periportal low attenuation zones; intense adrenal, pancreatic, and mesenteric enhancement; decreased pancreatic and splenic enhancement; peritoneal and retroperitoneal fluid; and bowel wall thickening.[27,28]

The hypoperfusion complex is a marker for a tenuous hemodynamic state and a predictor of a poor outcome. The mortality rate in children with this constellation of findings on CT approaches 80%.[27]

### KEY POINTS

- Clinical variables associated with a high risk of injury include gross hematuria, abdominal tenderness, and seat belt ecchymoses.
- Multiphase CT scanning is not necessary in children who have sustained blunt trauma.
- Hepatic injury extending to the bare area of the liver may be associated with retroperitoneal hemorrhage.
- Heterogeneous early splenic enhancement, splenic lobulations, or clefts may mimic a splenic laceration.
- Most hepatic and splenic injuries in children can be treated safely without operative intervention.
- Pancreatic injury may be difficult to identify in children because of a paucity of surrounding fat and the minimal separation of fracture fragments. The best indicator of pancreatic injury at CT is unexplained peripancreatic fluid.
- The size of hemoperitoneum on CT reflects the cumulative amount of bleeding; it is not a measure of ongoing hemorrhage.
- The absence of peritoneal fluid or blood does not exclude the presence of hepatic or splenic injury.
- A sentinel clot can indicate the site of injury.
- The most frequent CT finding associated with bowel rupture and mesenteric injury is "unexplained" peritoneal fluid.

### SUGGESTED READINGS

Borgialli DA, Ellison AM, Erlich P, et al. Association between the seat belt sign and intra-abdominal injuries in children with blunt torso trauma in motor vehicle collisions. *Acad Emerg Med*. 2014;21:1240–1248.

Brofman N, Atri M, Epid D, et al. Evaluation of bowel and mesenteric trauma with multi-detector CT. *Radiographics*. 2006;26:1119–1131.

Lynn KN, Werder GM, Callaghan RM, et al. Pediatric blunt splenic trauma: a comprehensive review. *Pediatr Radiol*. 2009;39:904–916.

Mattix KD, Tataria M, Holes J, et al. Pediatric pancreatic trauma: predictors of nonoperative management failure and associated outcomes. *J Pediatr Surg*. 2007;42:340–344.

Van der Vlies CH, Saltzherr TP, Wilde JCH, et al. The failure rate of nonoperative management in children with splenic or liver injury with contrast blush on computed tomography: a systematic review. *J Pediatr Surg*. 2010;45:1044–1051.

### REFERENCES

Full references for this chapter can be found on www.expertconsult.com.

## REFERENCES

1. Bixby SD, Callahan MJ, Taylor GA. Imaging in pediatric blunt abdominal trauma. *Semin Roentgenol*. 2008;43(1):72–82.
2. Sharma OP, Oswanski MF, Kaminsky BP, et al. Clinical implications of the seat belt sign in blunt trauma. *Am Surg*. 2009;75(9):822–827.
3. Borgialli DA, Ellison AM, Erlich P, et al. Association between the seat belt sign and intra-abdominal injuries in children with blunt torso trauma in motor vehicle collisions. *Acad Emerg Med*. 2014;21:1240–1248.
4. Bond SJ, Eichelberger MR, Gotschall CS, et al. Nonoperative management of blunt hepatic and splenic injury in children. *Ann Surg*. 1996;223(3):286–289.
5. Ruess L, Sivit CJ, Eichelberger MR, et al. Blunt abdominal trauma in children: impact of CT on operative and nonoperative management. *AJR Am J Roentgenol*. 1997;169(4):1011–1014.
6. Neish AS, Taylor GA, Lund DP, et al. Effect of CT information on the diagnosis and management of acute abdominal injury in children. *Radiology*. 1998;206(2):327–331.
7. Ellison A, Quayle KS, Bonsu B, et al. Use of oral contrast for abdominal computed tomography in children with blunt torso trauma. *Ann Emerg Med*. 2015;66:107–114.
8. Ben-Ishay O, Daoud M, Peled Z, et al. Focused abdominal sonography for trauma in the clinical evaluation of children with blunt abdominal trauma. *World J Emerg Surg*. 2015;10:27. doi:10.1186/s13017-015-0021-x.
9. McGahan JP, Horton S, Gersovich EO, et al. Appearance of solid organ injury with contrast-enhanced sonography in blunt abdominal trauma: preliminary experience. *AJR Am J Roentgenol*. 2006;187(3):658–666.
10. Ruess L, Sivit CJ, Eichelberger MR, et al. Blunt hepatic and splenic trauma in children: correlation of a CT injury severity scale with clinical outcome. *Pediatr Radiol*. 1995;25(5):321–325.
11. Lynn KN, Werder GM, Callaghan RM, et al. Pediatric blunt splenic trauma: a comprehensive review. *Pediatr Radiol*. 2009;39(9):904–916, quiz 1029-1030.
12. Patrick LE, Ball TI, Atkinson GO, et al. Pediatric blunt abdominal trauma: periportal tracking at CT. *Radiology*. 1992;183(3):689–691.
13. Sivit CJ, Taylor GA, Eichelberger MR, et al. Significance of periportal low-attenuation zones following blunt trauma in children. *Pediatr Radiol*. 1993;23(5):388–390.
14. Canty TG Sr, Weinman D. Management of major pancreatic duct injuries in children. *J Trauma*. 2001;50(6):1001–1007.
15. Mattix KD, Tataria M, Holmes J, et al. Pediatric pancreatic trauma: predictors of nonoperative management failure and associated outcomes. *J Pediatr Surg*. 2007;42(2):340–344.
16. Shilyansky J, Sena LM, Kreller M, et al. Nonoperative management of pancreatic injuries in children. *J Pediatr Surg*. 1998;33(2):343–349.
17. Lutz N, Mahboubi S, Nance ML, et al. The significance of contrast blush on computed tomography in children with splenic injuries. *J Pediatr Surg*. 2004;39(3):491–494.
18. Cloutier DR, Baird TB, Gormley P, et al. Pediatric splenic injuries with a contrast blush: successful nonoperative management without angiography and embolization. *J Pediatr Surg*. 2004;39(6):969–971.
19. Nwomeh BC, Nadler EP, Meza MP, et al. Contrast extravasation predicts the need for operative intervention in children with blunt splenic trauma. *J Trauma*. 2004;56(3):537–541.
20. Sivit CJ, Taylor GA, Eichelberger MR. Visceral injury in battered children: a changing perspective. *Radiology*. 1989;173(3):659–661.
21. Hilmes MA, Hernanz-Schulman M, Greeley CS, et al. CT identification of abdominal injuries in abused pre-school-age children. *Pediatr Radiol*. 2011;41:643–651.
22. Abbas SM, Upadhyay V. Hollow viscus injury in children: Starship Hospital experience. *World J Emerg Surg*. 2007;2:14.
23. Atri M, Hanson JM, Grinblat L, et al. Surgically important bowel and/or mesenteric injury in blunt trauma: accuracy of multidetector CT for evaluation. *Radiology*. 2008;249(2):524–533.
24. Brofman N, Atri M, Hanson JM, et al. Evaluation of bowel and mesenteric blunt trauma with multidetector CT. *Radiographics*. 2006;26(4):1119–1131.
25. Christiano JG, Tummers M, Kennedy A. Clinical significance of isolated intraperitoneal fluid on computed tomography in pediatric blunt abdominal trauma. *J Pediatr Surg*. 2009;44(6):1242–1248.
26. Gurland B, Dolgin SE, Shlasko E, et al. Pneumatosis intestinalis and portal vein gas after blunt abdominal trauma. *J Pediatr Surg*. 1998;33(8):1309–1311.
27. Sivit CJ, Taylor GA, Bulas DI, et al. Posttraumatic shock in children: CT findings associated with hemodynamic instability. *Radiology*. 1992;182(3):723–726.
28. Sivit CJ, Eichelberger MR, Taylor GA. CT in children with rupture of the bowel caused by blunt trauma: diagnostic efficacy and comparison with hypoperfusion complex. *AJR Am J Roentgenol*. 1994;163(5):1195–1198.

## PART 1 Overview

# 110 Embryology, Anatomy, and Variants of the Kidneys and Genitourinary Tract

*Sally J. Smith, Brooke S. Lampl, and Jonathan R. Dillman*

The urinary system and the genital system are closely associated embryologically and begin to develop during the fourth week of gestation.[1,2] Both develop from the intermediate mesoderm along the posterior wall of the abdominal cavity. A longitudinal elevation of the mesoderm, the urogenital ridge, forms on both sides of the abdominal aorta. Part of the urogenital ridge gives rise to the nephrogenic cord, which will form the urinary system, and another part gives rise to the gonadal ridge, which will form the genital system.[1]

The nephrogenic cord gives rise to the mesonephros, which consists of glomeruli and mesonephric tubules. The mesonephric tubules open into the mesonephric duct, which soon opens into the cloaca.[1,3] The mesonephros degenerates toward the end of the first trimester, although their tubules persist in males and participate in the formation of the genital system.[2] During the fifth week of gestation, the metanephros begins to develop. The definitive kidneys develop from the ureteric bud (metanephric diverticulum), an outgrowth of the mesonephric duct, and the metanephric blastema, which is derived from the nephrogenic cord.

The ureteric bud is responsible for the development of the collecting system (ureter, renal pelvis, and calyces).[1,2,4] The stalk of the ureteric bud forms the ureter. The ureteric bud grows into the metanephric blastema, where branching leads to the formation of the renal pelvis, major and minor calyces, and the collecting tubules (Figs. 110.1 and 110.2). Nephrons form in the metanephric blastema as the result of induction by the collecting tubules. The embryonic kidneys initially lie in the pelvis. As the abdomen grows, the kidneys “ascend” and rotate 90 degrees. By the ninth week of gestation, the kidneys come in contact with the adrenal glands as they attain their final position. The fetal kidney has a lobulated external contour that will disappear as the nephrons continue to grow. The full complement of glomeruli is present by 36 weeks’ gestation.

Congenital anomalies of the kidney and urinary tract are common.[1,4] Early degeneration of a ureteric bud or involution of the metanephros leads to regression of the metanephric blastema and renal agenesis. Bifurcation of the ureteric bud results in urinary tract duplication. When the location of the origin of the ureteric bud is abnormal or if the origin itself is maldeveloped, the potential for vesicoureteral reflux (VUR) or ureteral ectopia exists (Fig. 110.3).

The bladder arises from the most superior portion of the urogenital sinus.[1,2,5] It is initially continuous with the allantois. With constriction of the allantois, the lumen is obliterated, and a fibrous cord, the urachus, remains. The urachus connects the apex of the bladder with the umbilicus. Persistence of the allantoic lumen may result in urachal fistulas, sinuses, or cysts. The ureterovesical junction (UVJ) develops as the distal parts of the mesonephric duct are incorporated into the enlarging bladder. As the mesonephric ducts are absorbed, the ureters come to open separately into the urinary bladder with the orifice moving superolaterally and the distal ureteral segments entering obliquely through the base of the bladder. The middle portion of the urogenital sinus develops into the prostatic urethra in males and the entire urethra in females. The distal portion of the male urethra is derived from a cord of ectoderm that grows from the tip of the glans penis to meet the spongy portion of the urethra derived from the caudal (phallic) portion of the urogenital sinus. Development of the ureters and bladder is complete by the fourth gestational month.

The fetus begins to make urine by the ninth week of gestation, and the urine contributes the largest component of the amniotic fluid.[6] Oligohydramnios is often a marker of renal or urinary tract abnormalities, and severe oligohydramnios may lead to pulmonary hypoplasia.

During the first few days after birth, the neonate has a low glomerular filtration rate (GFR) and low urine output.[7] This is especially true of premature infants. The newborn kidney also has a limited ability to concentrate urine and decreased tubular reabsorption of sodium. GFR and urine output increase significantly over the first week of life. This immaturity of renal function is an important factor to keep in mind in the ordering and interpretation of renal imaging studies in the setting of antenatal hydronephrosis.

## NORMAL ANATOMY

### Kidney

Multiple renal lobules fuse to form the kidney. Each lobule is composed of two distinct regions: (1) the outer cortex and (2) the inner medulla (Fig. 110.4). The medulla is composed of 8 to 13 pyramids, which terminate in the renal papillae at the level of the calyces. Two or more pyramids may drain into the same papilla (confluent papilla), and two or more papillae may drain into a single calyx (compound calyx). Occasionally, when lobules fuse, the renal cortex remains and extends centrally between the pyramids, representing a column of Bertin (e-Fig. 110.5). A column of Bertin often occurs at the interpolar region or between the two moieties of a duplex kidney.[8,9] Additionally, the junction of these lobules may persist and be seen as a scalloping or lobation of the cortical border (Fig. 110.6). The junctional parenchymal defect is similarly derived from a variation in the fusion of the fetal lobules. It appears as a thick, triangular, echogenic notch in the anterosuperior or posteroinferior aspect of the kidney (more often on the right) and mimics a cortical scar. The junctional parenchymal defect may be connected to the renal hilum by an echogenic line called the *interrenuncular septum* (Fig. 110.7). The left kidney is apt to be more triangular, with a distinct bulge along its lateral aspect, the *dromedary hump* (Fig. 110.8).[10–13]

## Abstract:

The kidneys, upper urinary tract, and genital tract are closely associated embryologically. These structures begin to develop in the embryo very early in gestation from the intermediate mesoderm along the posterior wall of the abdominal cavity. The urinary bladder develops separately, arising from the most superior portion of the urogenital sinus. While these structures most often develop normally, a variety of congenital anomalies can occur, with varying frequencies and degrees of clinical importance. In this chapter we will present in detail the normal embryology of the kidneys and urinary tract as well as review normal anatomy and a variety of developmental variants (congenital anomalies).

## Keywords:

Genitourinary tract
Kidney
Ureter
Embryology
Anatomy
Congenital Anomaly
Children

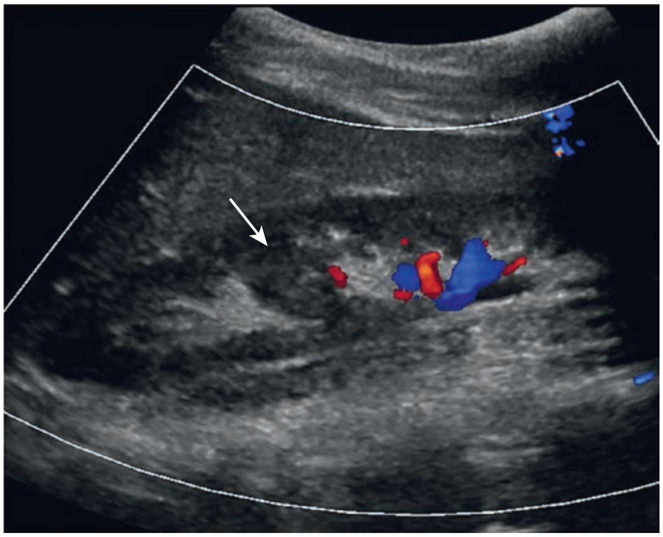

**e-Figure 110.5. Column of Bertin.** Longitudinal sonogram shows a central column of cortical tissue *(arrow)* extending into the central sinus echoes.

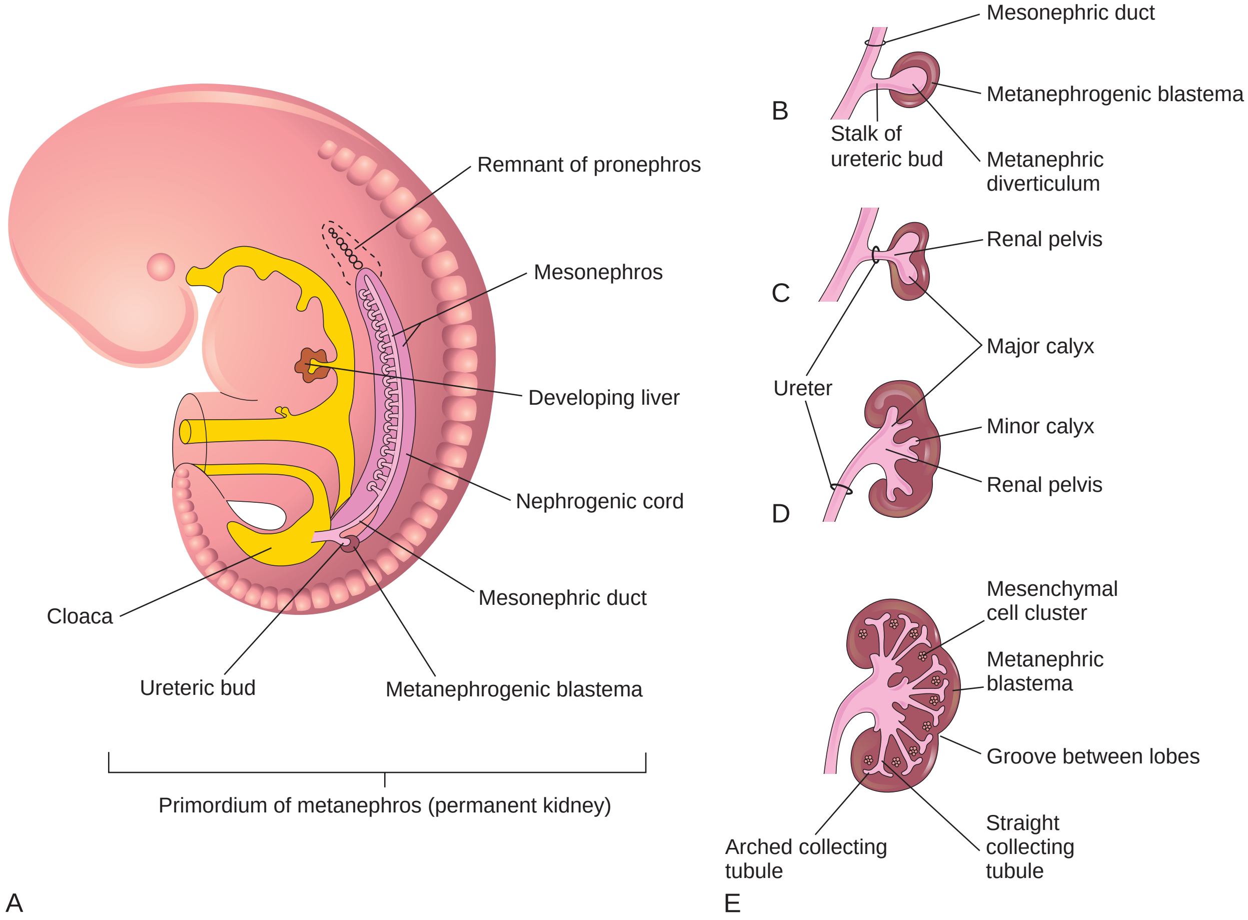

**Figure 110.1. Development of the metanephros, the primordium of the permanent kidney.** (A) Lateral view of a 5-week embryo, showing the primordium of the metanephros. (B–E) Successive stages in the development of the metanephric diverticulum or ureteric bud (fifth to eighth weeks). Observe the development of the ureter, renal pelvis, calyces, and collecting tubules. *(From Moore KL, Persaud TVN. The urogenital system. In:* Before We Are Born: Essentials of Embryology and Birth Defects*. 7th ed. Philadelphia: Saunders Elsevier; 2003.)*

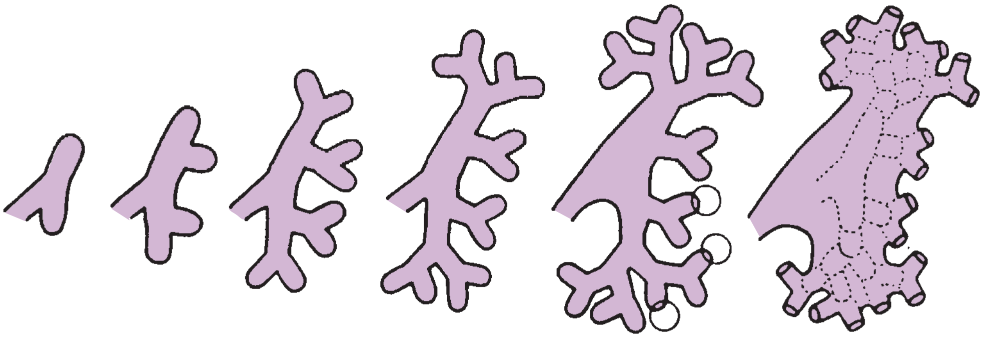

**Figure 110.2. Ureteric bud with multiple divisions leading to development of the pelvicalyceal system.** *(Adapted from Parrott TS, Skandalakis JE, Gray SW. The kidney and ureter. In: Skandalakis JE, Gray SW, eds.* Embryology for Surgeons: The Embryological Basis for the Treatment of Congenital Anomalies*. 2nd ed. Baltimore: Williams & Wilkins; 1994.)*

In newborns and infants, the kidneys have a larger medullary and smaller cortical volume than in later life. On ultrasonography, the neonatal renal cortex is moderately hyperechoic, close to the echogenicity of adjacent liver and spleen and can be greater than that of the liver in newborns and premature infants (see Fig. 110.8). The pyramids are relatively hypoechoic, maintaining corticomedullary differentiation. Between ages 6 months and 2 years, the echogenicity of the medulla and cortex resembles that of adult kidneys.[14–17]

The kidney is usually supplied by a single artery arising from the abdominal aorta. After the renal artery enters the renal hilum, posterior and slightly superior to the renal vein, it divides into

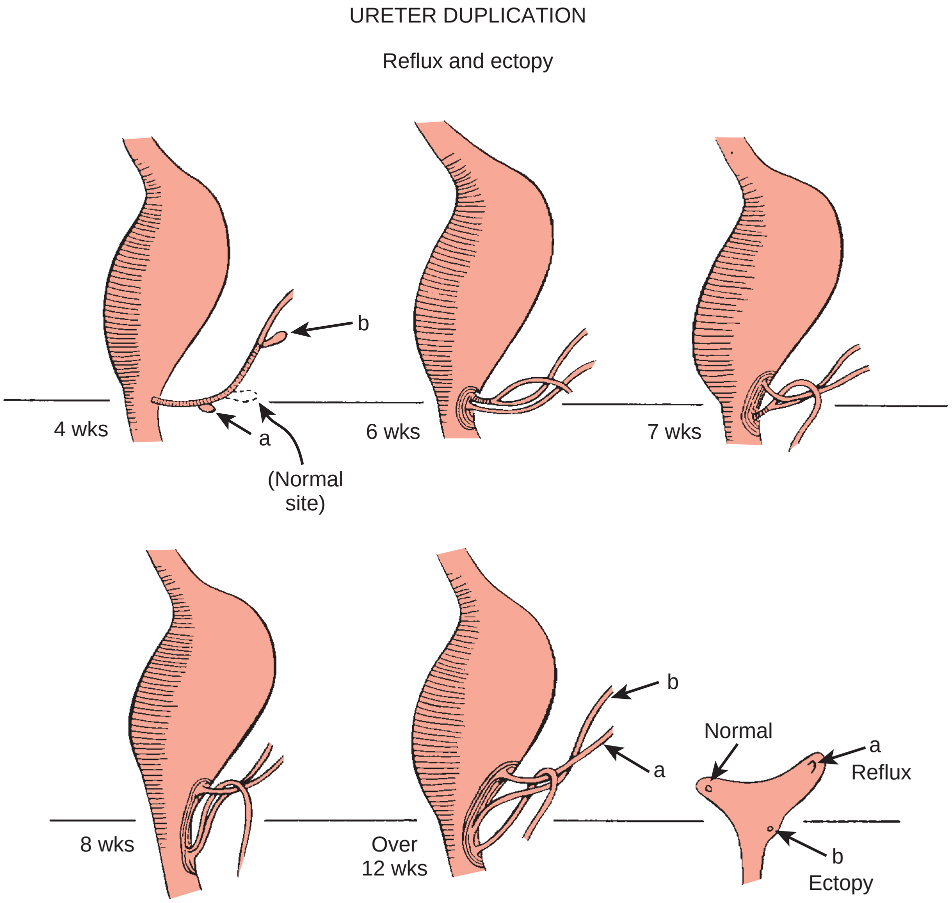

**Figure 110.3. The ureteric bud and its relationship to the bladder.** The drawing shows how ectopia and vesicoureteral reflux may occur.

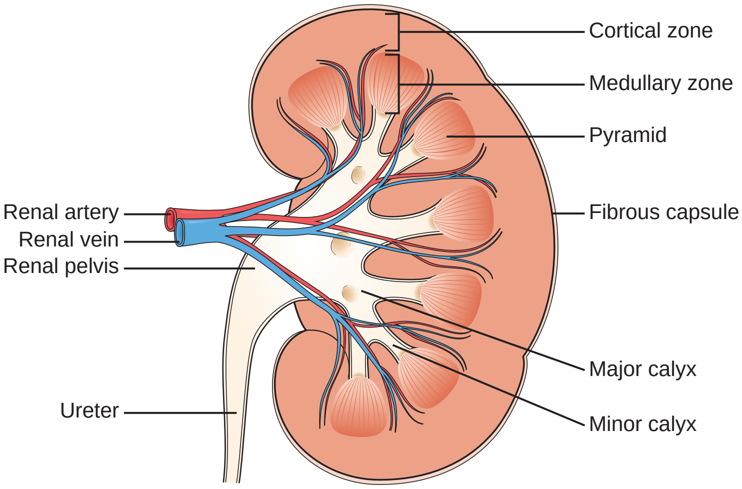

**Figure 110.4. Macroscopic anatomy of the kidney in longitudinal section.** The left kidney as viewed anteriorly. *(Redrawn from Kelly HA, Burnam CF.* Diseases of the Kidneys, Ureters and Bladder. *2nd ed. New York: Appleton; 1922.)*

anterior and posterior branches, which, in turn, generally divide into superior and inferior branches (e-Fig. 110.9). About 20% to 30% of kidneys have a second or accessory renal artery arising from the aorta. The left renal vein is longer than the right, courses anterior to the aorta, and receives the ipsilateral suprarenal and gonadal veins before entering the inferior vena cava.[8,18] Variations exist at all levels.

Renal length is the most commonly measured morphologic parameter and has been correlated to age, body height, and body weight. Standards for renal length have been developed for ultrasonography (e-Fig. 110.10). The left kidney may be slightly longer than the right. Kidneys with complete or partial collecting system duplication are often longer than normal kidneys. The width of the kidney is approximately 50% of its length and is relatively thicker in neonates than older children. Cortical thickness of the upper renal pole is normally slightly thicker than the lower pole. Extra cortical tissue may be noted about the renal hilum and may impinge on the renal pelvis (suprahilar/infrahilar bulge, or hilar lips).[17,19–25]

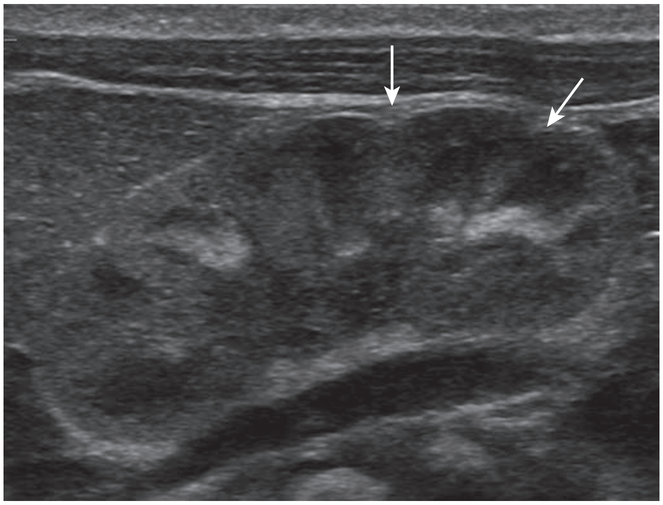

**Figure 110.6. Fetal lobulations.** Residual fetal lobations are responsible for the scalloped border of the kidney *(arrows)* on this sagittal sonogram.

## Pelvocalyceal System

The renal pelvis varies in size and shape and may lie entirely within (intrarenal) or partly beyond (extrarenal) the renal sinus. In most kidneys, the pelvis branches into two major infundibula (or major calyces). The inferior infundibulum is commonly broad and short and is connected with a larger number of minor calyces compared with the upper infundibulum. Each kidney has about 8 to 13 minor calyces. These have a cup-shaped appearance that results from the protrusion of the renal papilla into the calyx. Most calyces are directed laterally and either slightly anteriorly or posteriorly within the kidney.[4,6,18,24,26]

## Ureter

The ureter is a tubular structure that courses through the retroperitoneum from the kidney to the bladder and has three major components: (1) the ureteropelvic junction (UPJ) and proximal ureter, (2) the midureter, and (3) the distal ureter and UVJ (including the transmural ureter and the ureteral orifice). The proximal ureter starts at the UPJ with a smooth tapering from the renal pelvis. The ureter lies adjacent to the psoas muscle and is crossed by the gonadal vessels before passing over the iliac vessels. The lower ureter lies along the lateral pelvic wall, coursing behind the bladder. The ureter enters the bladder wall at an oblique angle and opens into the bladder. Its course through the bladder wall may be seen (called the *plica ureterica* at cystoscopy) and constitutes the lateral border of the bladder trigone. Three muscular layers constitute the ureteral wall, with a thick outer adventitial layer containing vessels and lymphatics.[4,6,27–29]

The vascular supply of the ureter is primarily from the inferior vesical artery inferiorly, and the gonadal artery (e.g., testicular artery) and renal artery superiorly. Nerves supplying the ureter follow the arteries. Rhythmic peristaltic ureteral contractions transport urine from the renal pelvis into the urinary bladder two to seven times per minute.[4,6]

The anatomic relationship of the distal ureter to the bladder wall at the UVJ is important in preventing VUR. Normally, the distal ureter courses through the bladder musculature at an oblique angle and then continues inferomedially and submucosally to its ostia in the lateral corner of the trigone (Fig. 110.11). The UVJ acts as a passive flap valve. Continence is ensured by apposition of the roof and floor of the submucosal tunnel when intravesical

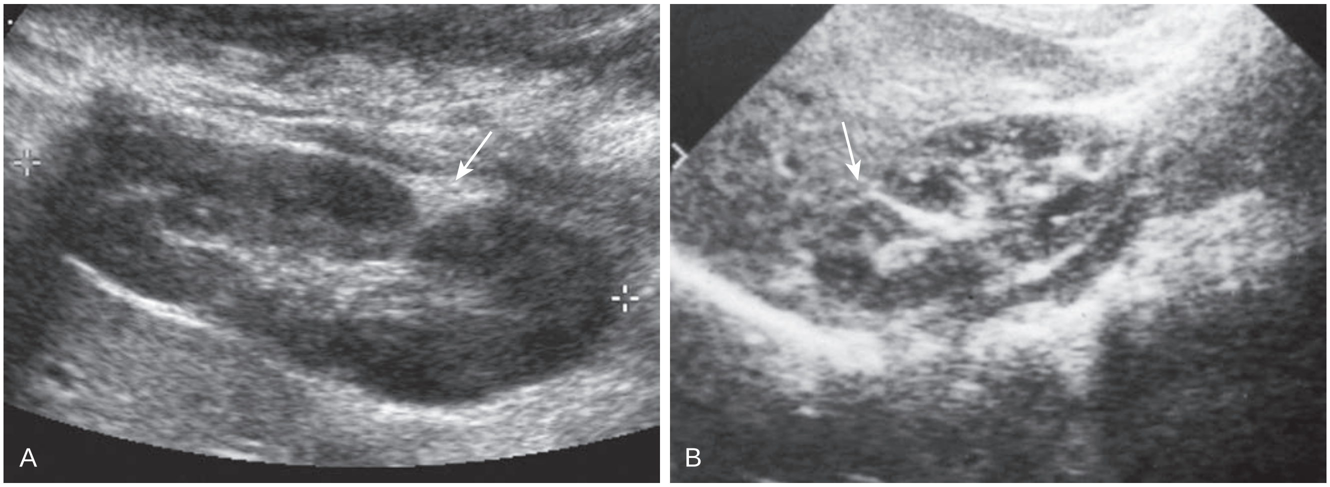

**Figure 110.7. Junctional parenchymal defects.** (A) Longitudinal prone sonogram shows a fat-filled cleft *(arrow)* in the posterior kidney. (B) Longitudinal supine sonogram in another patient shows a renicular septum *(arrow)*. Both are normal findings, probably related to a demarcation of embryonic reniculi.

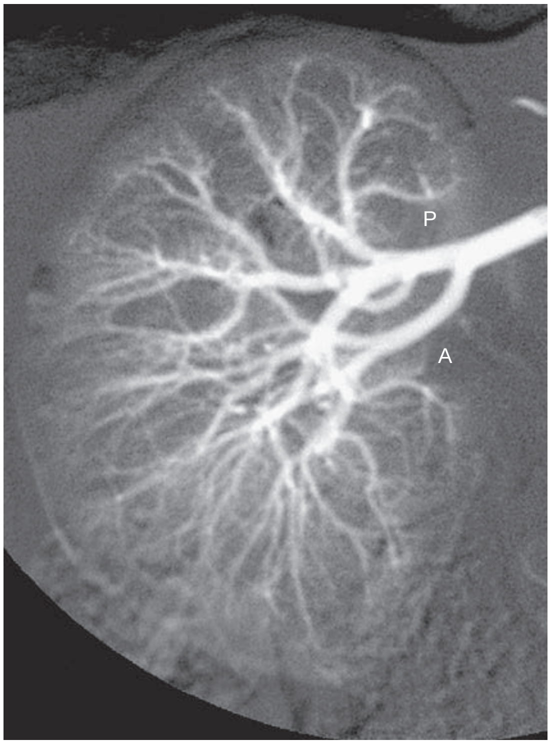

**e-Figure 110.9. Normal renal arterial anatomy.** Digital subtraction arteriogram of the right kidney in a 6-month-old shows a single main renal artery dividing into anterior *(A)* and posterior *(P)* branches. Normal opacification and distribution of vessels to the level of the arcuate arteries are seen.

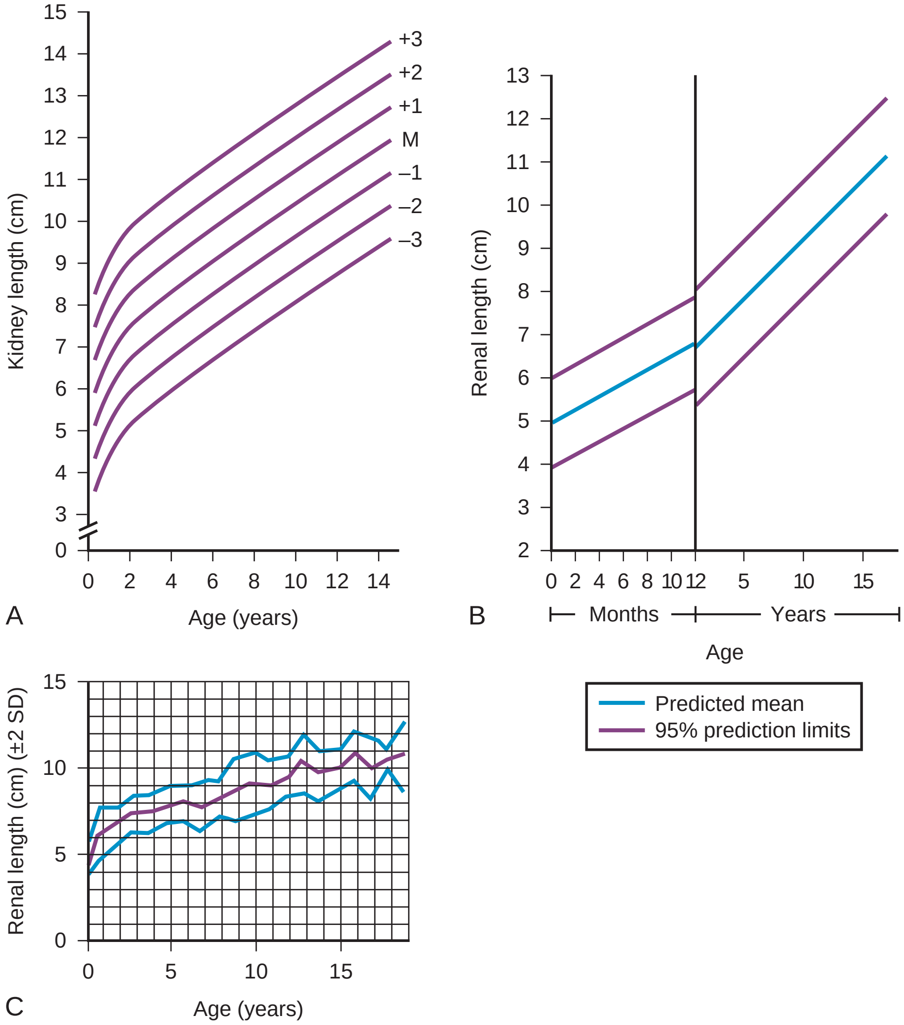

**e-Figure 110.10. Kidney length in centimeters.** (A) Measurements obtained from supine urographic films and correlated with age, including values for three standard deviations (SD) above and below the mean *(M)*. The SD is 0.75 cm. (B) Ultrasonographic measurements correlated with age; the values are slightly lower than those obtained from urographic films. (C) Ultrasonographic measurements correlated with age, including ± 2 SD. *(A, Modified from Currarino G, Williams B, Dana K. Kidney length correlated with age: normal values in children.* Radiology*. 1984;150:703; B, From Han BK, Babcock DS. Sonographic measurements and appearance of normal kidneys in children.* Am J Roentgenol*. 1985;145:611; C, From Rosenbaum DM, Korngold E, Teele RL. Sonographic assessment of renal length in normal children.* Am J Roentgenol*. 1984;142:467.)*

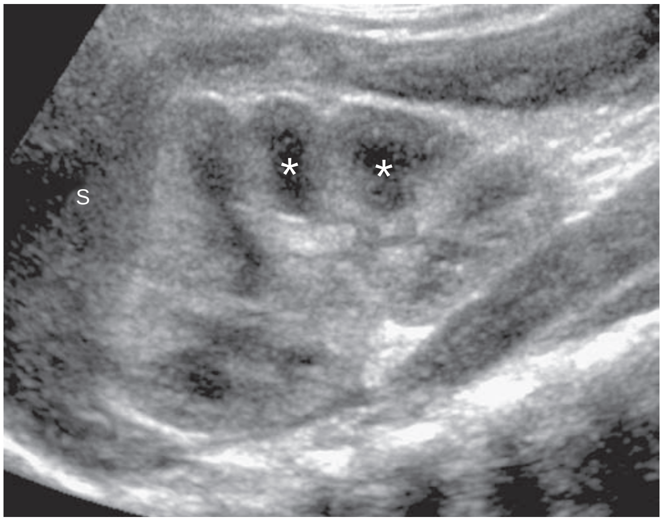

**Figure 110.8. Normal neonatal kidney.** Supine longitudinal sonogram of the left kidney shows the sharp corticomedullary differentiation common in infancy and early childhood. The hypoechoic triangular renal pyramids *(asterisks)* are surrounded by cortex that is more echogenic than the adjacent spleen *(S)*. The spleen has flattened the upper renal contour and produces the appearance of a dromedary kidney.

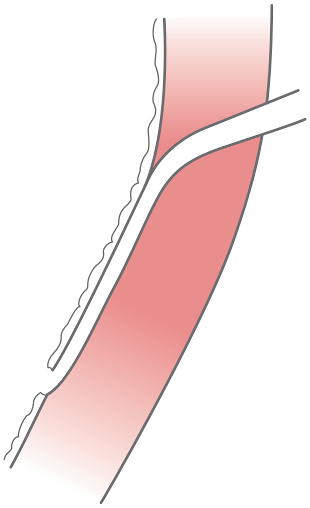

**Figure 110.11. Course of the distal segment of ureter within the bladder wall.** The ureter at first traverses the bladder musculature almost perpendicularly and then descends submucosally for a much longer segment (submucosal tunnel).

pressure increases and is enhanced by contraction of the intrinsic local musculature.

## Bladder

In the neonate and young child, the dome and body of the bladder are located primarily in the abdomen while the base is intrapelvic. Bowel impressions are common and may impress on the intra-abdominal bladder when it is distended. This normal appearance should not be confused with a pelvic mass. A urachal remnant may be seen at the bladder dome, best seen on ultrasound and computed tomography (CT). Normal bladder capacity can be predicted on the basis of weight in infancy and by age for the older child. For infants under 1 year of age, bladder capacity in milliliters is predicted by multiplying the weight in kilograms by 7. The predicted bladder capacity in milliliters of children more than 1 year old is the age in years plus 2 multiplied by 30. Ultrasonography best demonstrates normal bladder wall thickness, which should be no more than 3 mm when distended and 6 mm when collapsed.[5,30–38]

## Urethra

The female urethra is equivalent to the posterior urethra of the male. Anatomic features of the female urethra include the internal sphincter at the bladder neck, intermuscular incisura, membranous urethra at the level of the urogenital diaphragm or external urethral sphincter, and the fossa navicularis, although only the impressions of the sphincters are usually seen at imaging (e-Fig. 110.12).[5,39,40]

The components of the normal male urethra include the prostatic, membranous, bulbous, and penile urethra. Normal anatomic features of the male prostatic urethra include the internal sphincter, the intermuscular incisura, and the verumontanum. The verumontanum is a focal elevation in the posterior wall of the prostatic urethra, where the paired ejaculatory ducts enter, seen as a small ovoid filling defect in the posterior portion of the prostatic urethra. The plicae colliculae are normal folds that extend from the distal verumontanum and may produce circumferential impressions on urethral images.[5,39,41–45]

The membranous urethra runs through the urogenital diaphragm or the external urethral sphincter and becomes the anterior urethra, consisting of the bulbous and penile segments, and the fossa navicularis (e-Fig. 110.13). The muscles related to bladder continence and micturition are the detrusor muscle of the bladder, the musculature of the bladder neck and proximal urethra at the internal urethral sphincter, and the external urethral sphincter. The external sphincter is composed of striated voluntary muscles of the pelvic floor.

## CONGENITAL ANATOMIC VARIANTS AND ANOMALIES

## Kidney

### Renal Agenesis (Unilateral and Bilateral)

True renal agenesis is thought to be caused by failure of the ureteric bud to contact the ipsilateral metanephric blastema. Unilateral renal agenesis is present in about 1 : 1000 live births. Children with true unilateral renal agenesis lack the ipsilateral ureter and hemitrigone of the urinary bladder. Those children with an absent kidney but a normally developed bladder and a distal ureter of varying length probably represent the involution of a multicystic dysplastic kidney.[31] Associated anomalies include VACTERL (vertebral defects, anorectal malformation, cardiac defects, tracheo-esophageal fistula, renal anomalies, and limb abnormalities) association (e-Fig. 110.14), unicornuate uterus (e-Fig. 110.14), uterus didelphys (obstructed hemivagina with ipsilateral renal agenesis, or OHVIRA), and Mayer-Rokitansky-Küster-Hauser syndrome in girls, and seminal vesicle cysts, absence of the vas deferens, and cystic dysplasia of the rete testis in boys (Box 110.1).[31,46–53]

Bilateral renal agenesis is almost always lethal with an incidence of 1 : 10,000 to 3 : 10,000 live births. Boys are affected more commonly compared with girls. Pulmonary hypoplasia is generally the cause of death and may be associated with neonatal pneumothorax and pneumomediastinum. The Potter sequence is manifest at birth: small chest, abnormal facial features (micrognathia, beaked nose, epicanthic folds, low-set ears), and limb deformities (tightly apposed fingers, dislocated hips, clubfeet).[31]

***Imaging.*** Ultrasonography demonstrates the absence of the kidney (and excludes renal ectopia) and the presence of an abnormally configured (elongated or elliptical) adrenal gland,

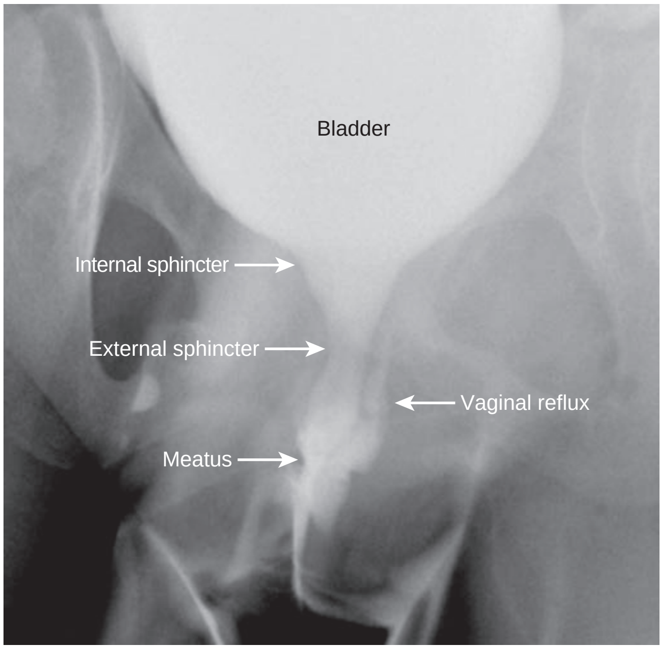

**e-Figure 110.12. Normal female urethra.** Voiding cystourethrogram in a young girl shows a normal urethra.

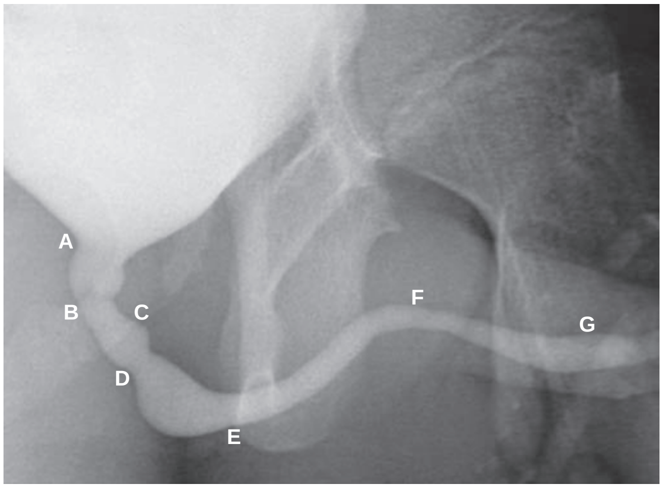

**e-Figure 110.13. Normal male urethra.** Voiding cystourethrogram in a 15-year-old boy shows a normal urethra. *A,* Internal urethral sphincter. *B,* Site of the verumontanum. *C,* Prostatic urethra. *D,* Membranous urethra. *E,* Bulbous urethra. *F,* Penile urethra. *G,* Fossa navicularis. *(From the* Radiographic atlas of the pediatric urethra*. Available at: www.nationwidechildrens.org/gd/applications/radiology/atlas/Urethra%20Atlas/Welcome.html.)*

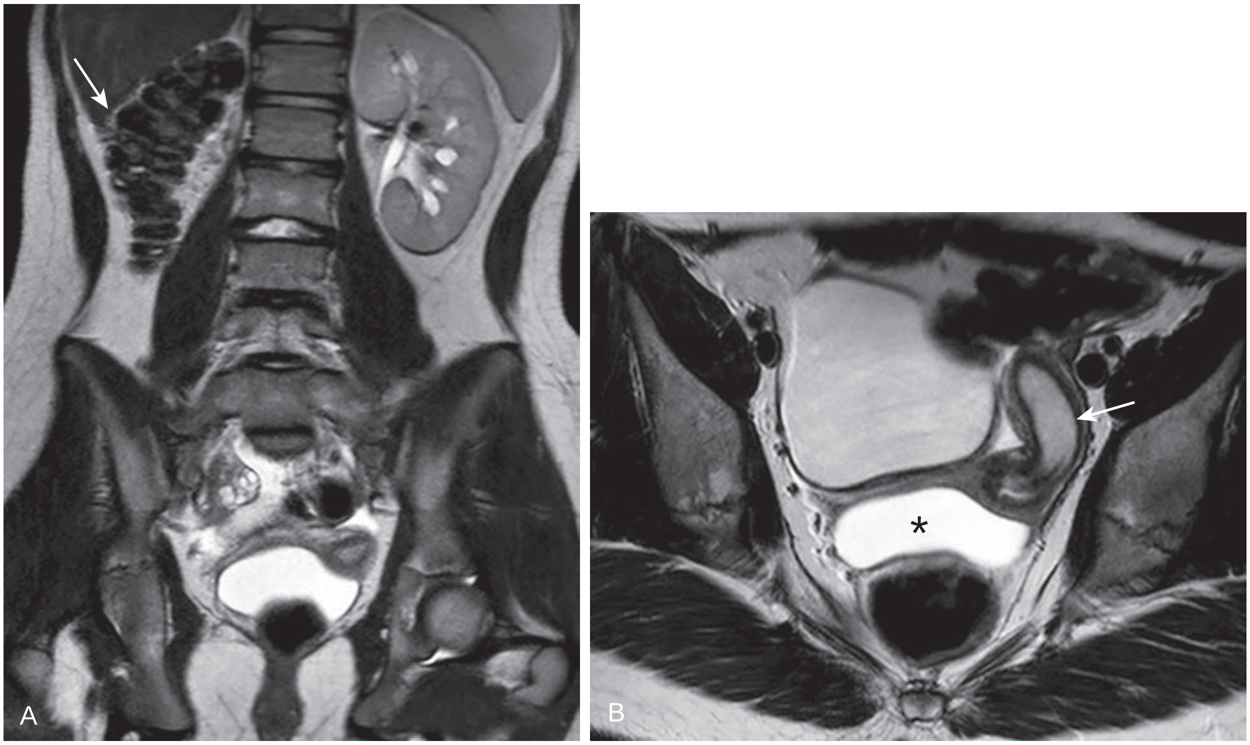

**e-Figure 110.14. Renal agenesis in teenage girl.** (A) Coronal T2-weighted MR image shows absence of the right kidney. Bowel is present in the right renal fossa *(arrow)*; the left kidney is normal. (B) Axial T2-weighted MR image shows a left unicornuate uterus *(arrow)*. The vagina is obstructed and contains fluid *(asterisk)*.

rather than its normal triangular or inverted Y-configuration (Fig. 110.15).[31,54–56] Because the embryology of the adrenal gland is independent of that of the kidney, it is usually located in its expected position, even when the kidney does not reach the renal fossa. Ultrasonography and magnetic resonance imaging (MRI) are most commonly used to evaluate associated uterine and vaginal anomalies in girls and seminal vesicle cysts in boys (Fig. 110.16).[45–49]

### BOX 110.1 Genital Anomalies Associated With Unilateral Renal Agenesis

**FEMALE**

- Absence or hypoplasia of vagina
- Absence of uterus
- Failure of fusion of midline structures (Müllerian derivatives)
  - Bicornuate uterus, uterus didelphys
  - Obstructed hemivagina +/– hemiuterus, fallopian tube
- Gartner duct cyst
- Ipsilateral absence of uterine horn and fallopian tube (unicornuate uterus)

**MALE**

- Ipsilateral anomalies
  - Absence of epididymis
  - Absence of seminal vesicle
  - Absence of vas deferens
  - Absence or hypoplasia of testis
  - Seminal vesicle cysts
  - Cystic dysplasia of rete testis

Because of the increased incidence of VUR into the remaining solitary kidney and the need to protect its parenchyma, a study to exclude vesicoureteral reflux is recommended early in life.

## Renal Ectopia

Renal ectopia is diagnosed when a kidney fails to migrate to its appropriate renal fossa, occurring with an incidence of 1 : 800 to 1 : 1000.[57] The pelvic kidney is the most common type of renal ectopia (accounting for ~60% of cases). Pelvic kidneys are prone to VUR and in about 10% of children may be the only kidney. In some children, both kidneys are in the pelvis and may be fused into a single unit, the so-called *cake kidney* or *lump kidney*. Ectopic intrathoracic kidney is the least common form of renal ectopia, representing less than 5% of cases.[58,59] This condition may occur as an isolated lesion with an intact diaphragm but is more often part of a larger intrathoracic herniation through the foramen of Bochdalek.[58] Anomalies of rotation and blood supply are to be expected with renal ectopia.[31]

***Imaging.*** On ultrasonography, the pelvicalyceal system of the pelvic kidney may be predominantly extrarenal, resulting in images in which the kidney lacks the usual central renal echo complex.[57] Corticomedullary differentiation may be indistinct (Fig. 110.17). UPJ obstruction is common in pelvic kidneys because the abnormal orientation of the ureter relative to the renal pelvis impedes drainage. Renal scintigraphy is often used to both locate and define the morphology of ectopic kidneys, but CT, MRI, and excretory urography are also effective (e-Fig. 110.18).[60] The thoracic kidney is located in the posterior mediastinum and on chest radiographs may be mistaken for neurogenic tumors that develop in this region (e-Fig. 110.19).

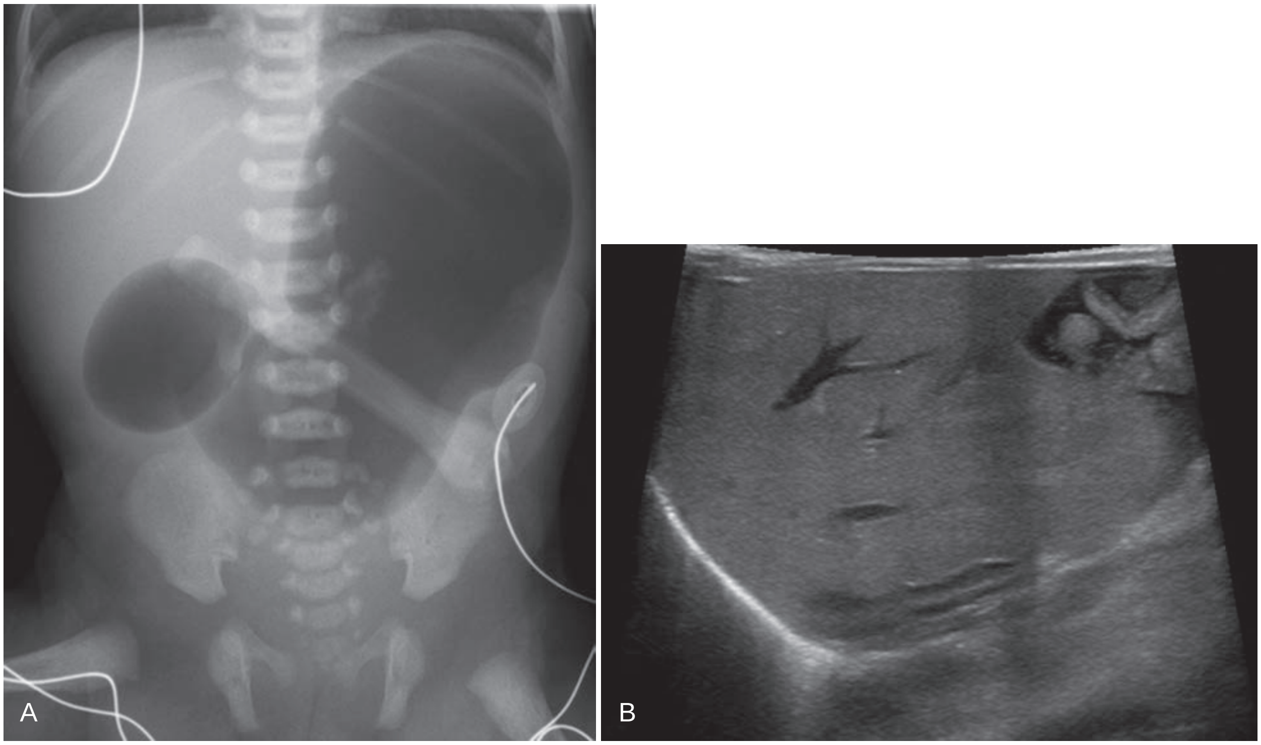

**Figure 110.15. Newborn with unilateral renal agenesis and VACTERL association.** (A) Supine abdominal radiograph shows marked gastric and proximal duodenal gaseous distention, the so-called "double bubble sign." No identifiable distal bowel gas exists. Both esophageal atresia (with distal fistula) and duodenal atresia were confirmed at surgery. (B) Longitudinal sonogram through the right renal fossa confirms congenital absence of the right kidney. The right adrenal gland is abnormally elongated.

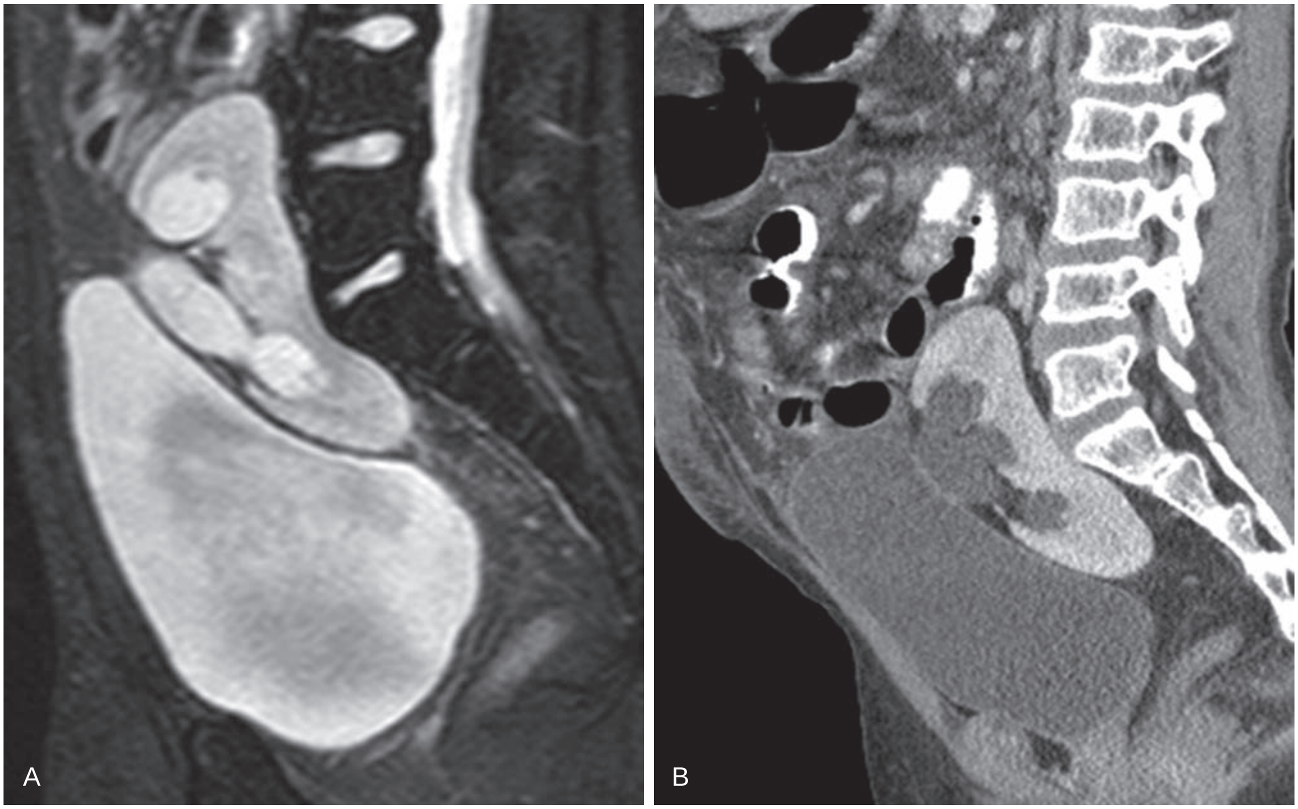

**e-Figure 110.18. A 7-year-old boy with pelvic kidney.** (A) Sagittal T2-weighted magnetic resonance and (B) sagittal contrast-enhanced computed tomography images from the same child in Fig. 110.17 reveal a pelvic kidney located posterior to the urinary bladder. There is mild pelvicaliectasis without actual obstruction, and the pelvic kidney is nonrotated with its pelvis oriented anteriorly.

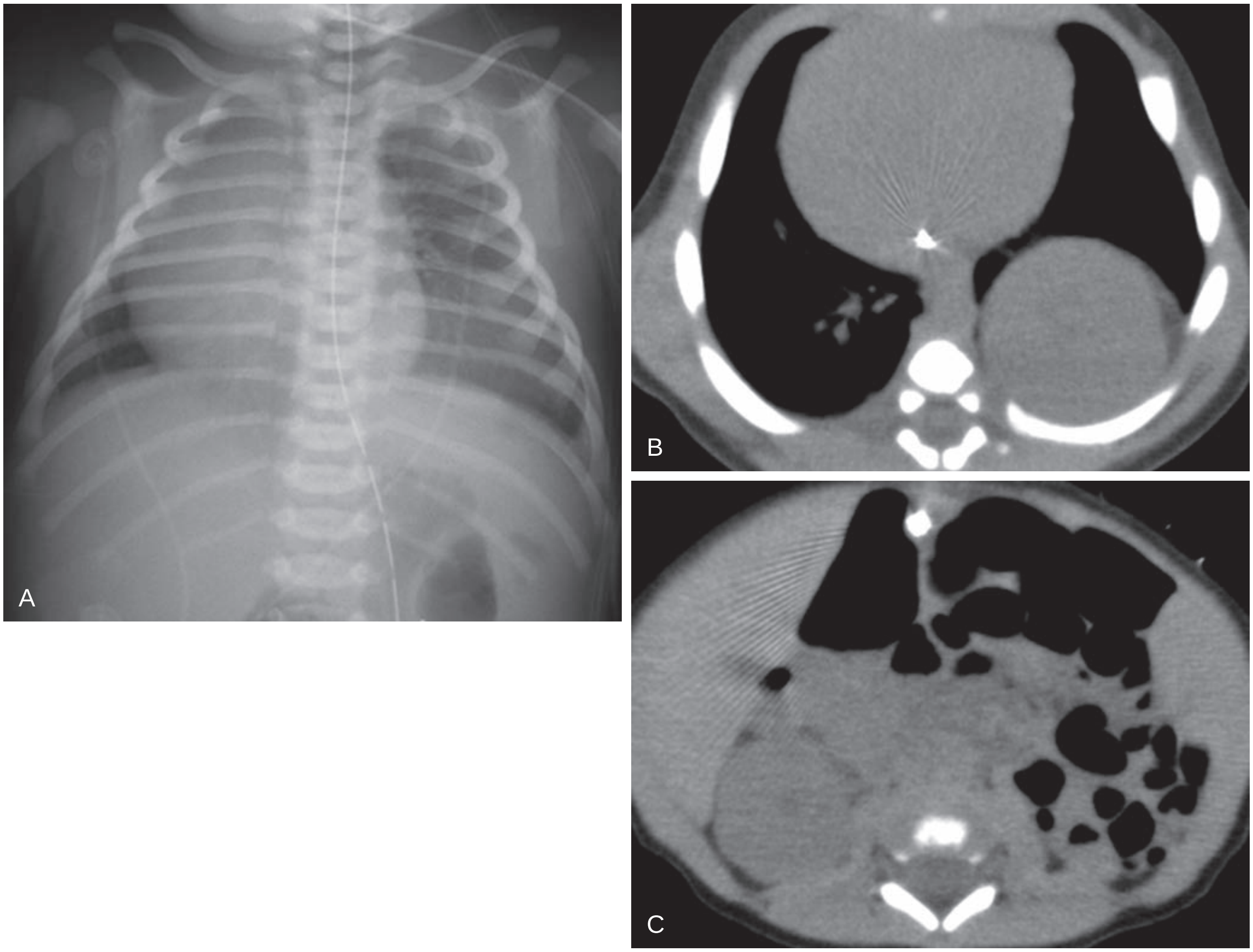

**e-Figure 110.19. A newborn boy with superior renal ectopia caused by left congenital diaphragmatic hernia.** (A) Anteroposterior chest radiograph shows increased opacity at the left lung base and rightward shift of mediastinal structures. (B and C) Axial computed tomography images without intravenous contrast material show a posteriorly located intrathoracic left kidney. Small bowel loops are located in the left renal fossa. The right kidney resides in its normal location. This neonate was proved to have a left Bochdalek-type congenital diaphragmatic hernia at surgery.

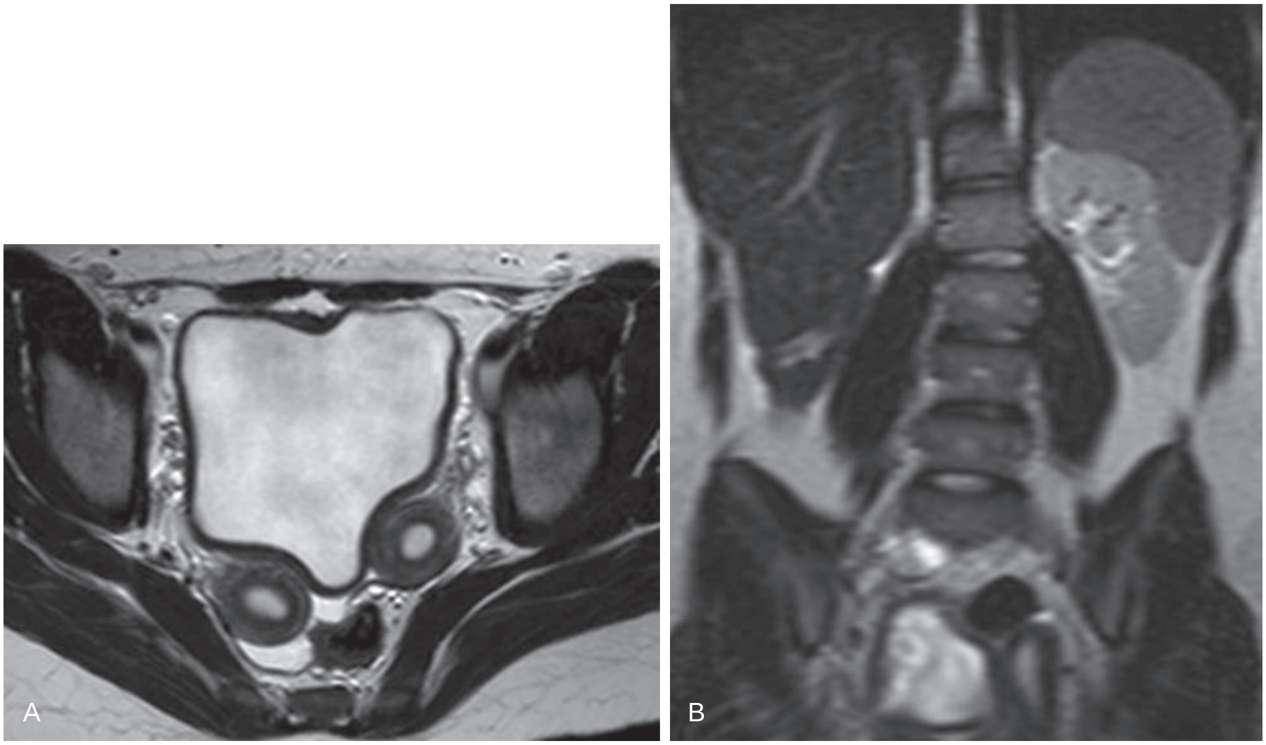

**Figure 110.16. Unilateral renal agenesis and Mullerian anomaly in a 14-year-old girl.** (A) Axial T2-weighted MR image through the pelvis shows two separate uterine horns, proven to be uterus didelphys. (B) A coronal single-shot fast spin-echo image through the retroperitoneum confirms congenital absence of the right kidney.

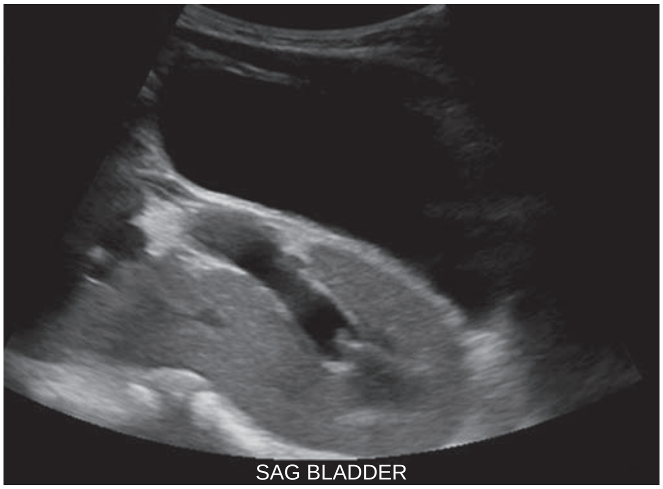

**Figure 110.17. Pelvic kidney.** Longitudinal sonogram through the pelvis of a 5-year-old boy reveals an ectopic kidney located posterior to the urinary bladder. The kidney is nonrotated with its hilum and extrarenal pelvis oriented anteriorly. Corticomedullary differentiation is diminished.

## Anomalies of Fusion: Horseshoe Kidney and Crossed Renal Ectopia

### Horseshoe Kidney

Horseshoe kidney is the most common renal fusion anomaly, noted in 1 : 400 to 1 : 1000 autopsies.[31,61–63] It derives its name from the U-shape configuration of the kidneys, produced by the fusion of the lower pole moieties, which are more medially located than the upper poles (Fig. 110.20).[61–63] The bridging tissue, known as the *isthmus*, is more commonly composed of functioning renal parenchyma than fibrous tissue.[31,61,64] The isthmus is located just below the origin of the inferior mesenteric artery.[31,63] This condition is caused by in utero fusion of the metanephric blastemas in the pelvis during the sixth or seventh week of gestation.[62] The vascular supply of horseshoe kidneys is quite variable, arising from the abdominal aorta, iliac arteries, and inferior mesenteric artery.[61,63,64]

***Clinical Presentation.*** Horseshoe kidneys may be asymptomatic; however, an increased incidence of UPJ obstruction, VUR, and ureteral duplication predispose affected individuals to both urolithiasis and infection.[31,63–65] Because horseshoe kidneys overlie the spine and lack protective surrounding ribs, they are prone to injury from direct trauma.[63] A slight increased risk of Wilms tumor in horseshoe kidneys compared with normal kidneys has been reported.[31,62,63,66,67]

***Imaging.*** Ultrasonography demonstrates the upper portion of each kidney in a low paraspinal location. The isthmus may be identified in many cases anterior to the lumbar spine, especially when mild compression is used to displace interposed bowel loops. The renal long axis is abnormal and may be curved (Fig. 110.21).[68] Anterior orientation of the renal pelvis from nonrotation/malrotation is common as are extrarenal pelves.[64,68] CT and magnetic resonance (MR) angiography may be used to establish renal artery anatomy. CT also excellently depicts renal parenchymal and collecting system injuries in the setting of abdominal trauma (e-Fig. 110.22). MR urography or renal scintigraphy may be performed to assess for suspected UPJ obstruction (e-Fig. 110.23).[63] Voiding cystourethrogram (VCUG) may help assess for VUR.

### Crossed Renal Ectopia

***Clinical Presentation.*** Crossed renal ectopia occurs when both kidneys are located on one side of the spine; a portion of the lower kidney, usually the one that has moved from its normal

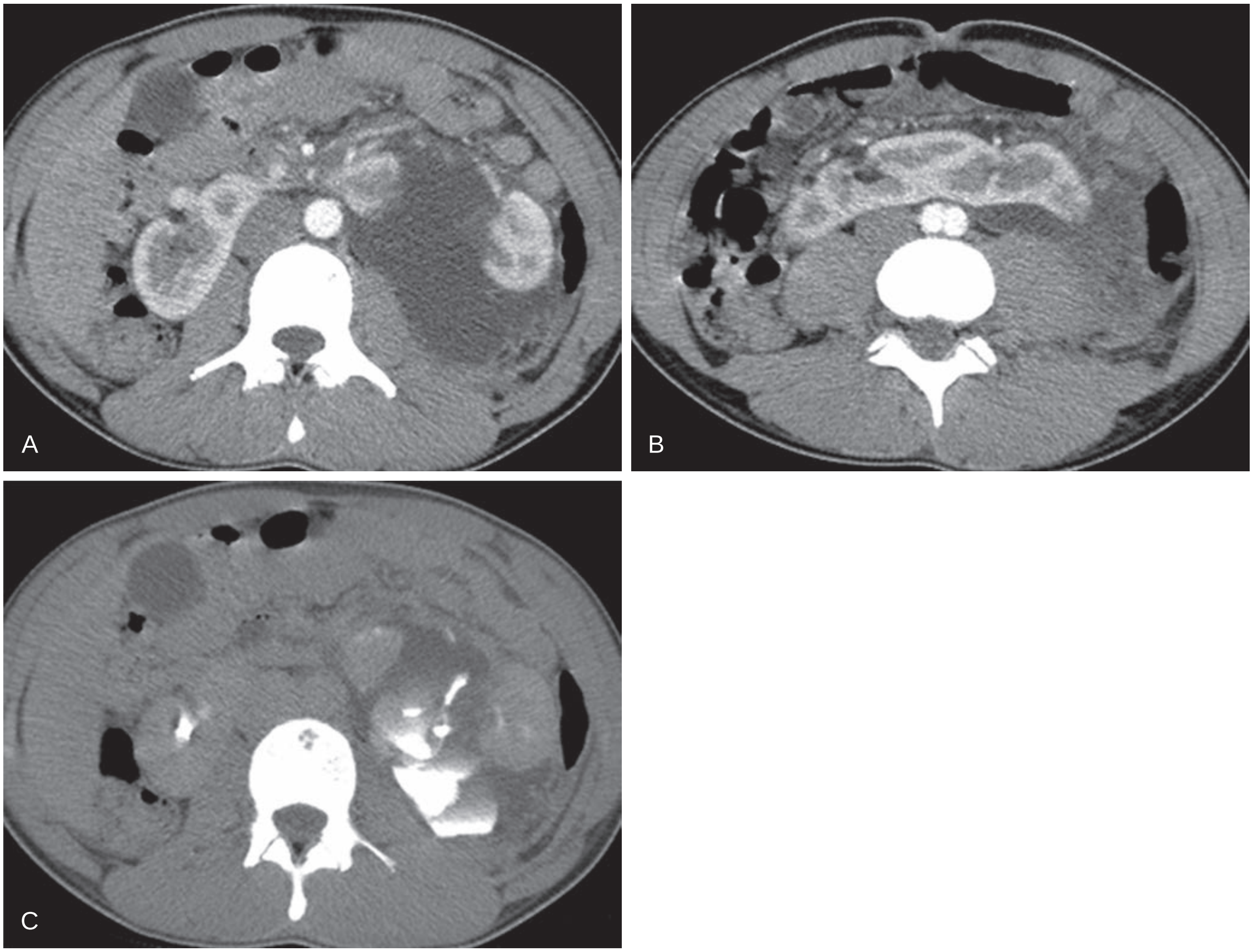

**e-Figure 110.22. Horseshoe kidney, traumatic injury.** (A and B) Axial contrast-enhanced computed tomography (CT) images through the abdomen confirm the presence of a horseshoe kidney with a thick parenchymal isthmus. A large amount of fluid is present within the left perinephric space, and there is a large laceration involving the left renal moiety. (C) An axial excretory phase CT image acquired 10 minutes later shows multiple fluid-contrast material levels in the left retroperitoneum caused by renal collecting system injury.

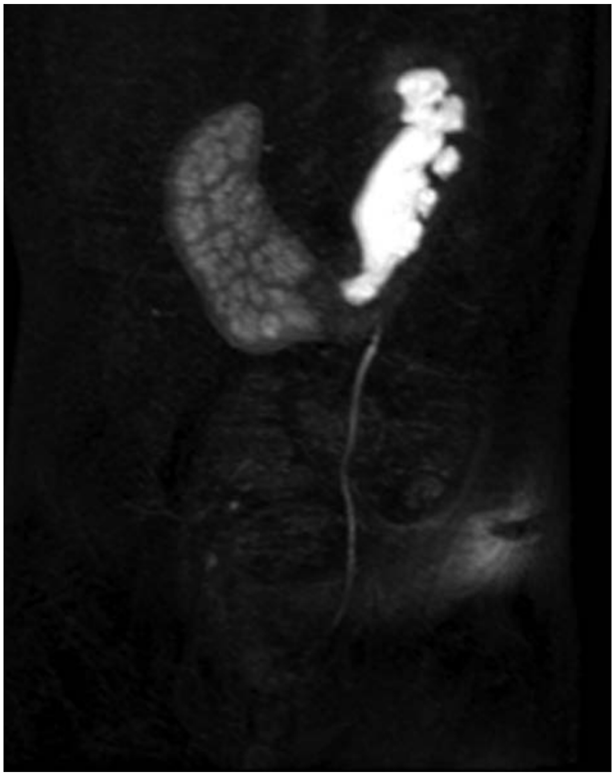

**e-Figure 110.23. Horseshoe kidney and magnetic resonance imaging.** A coronal T1-weighted postcontrast magnetic resonance urogram maximum intensity projection image shows abnormal long-axis of the kidneys and fusion of the lower renal poles. A delayed nephrogram is seen on the right, consistent with upper urinary tract obstruction. Normal excretion of contrast material is present by the left moiety. *(Courtesy Damien Grattan-Smith, MD, Atlanta, GA: Scottish Rite Children's Medical Center.)*

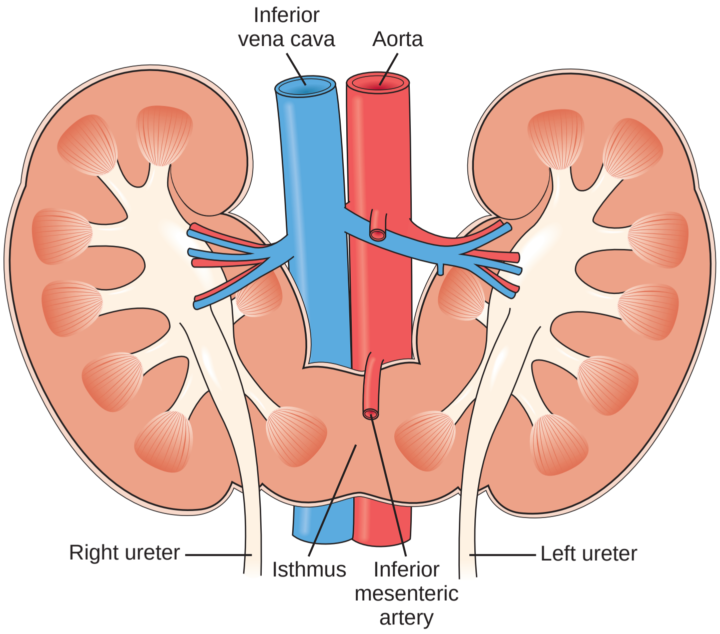

**Figure 110.20. Horseshoe kidney with fusion of the inferior poles, separation of the superior poles, and failure of rotation.** The renal pelves enter the kidneys on their anterior aspect. *(Redrawn from Kelly HA, Burnam CF.* Diseases of the Kidneys, Ureters and Bladder. *2nd ed. New York: Appleton; 1922.)*

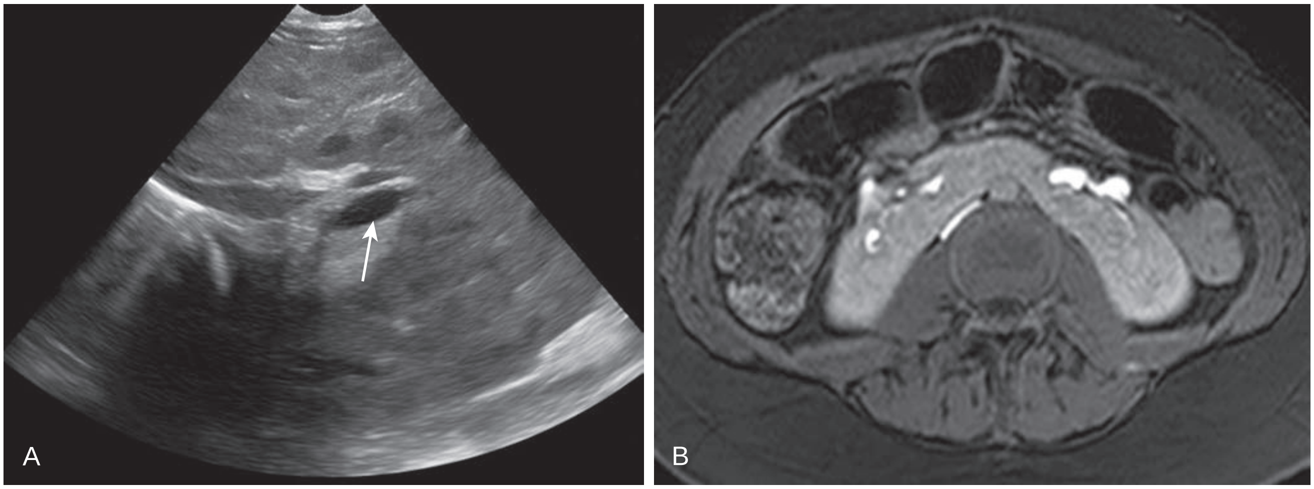

**Figure 110.21. Horseshoe kidney.** (A) Coronal oblique sonogram through the retroperitoneum shows a horseshoe kidney with a parenchymal isthmus overlying the abdominal aorta *(arrow)*. Abnormal longitudinal axis of the kidneys is seen. (B) An axial T1-weighted postcontrast magnetic resonance image with fat saturation shows fusion of the kidneys in the midline just below the level of the inferior mesenteric artery *(arrow)*. The kidneys are malrotated with the collecting systems oriented anteriorly.

position (most commonly the left kidney), may extend over the spine.[31,69] This anomaly is seen in 1:7500 children, affects boys more often than girls, and is the second most common renal fusion anomaly after horseshoe kidney.[31,61,69,70] The ureter from the lower kidney crosses the midline to insert into the bladder in its normal position.[69] Although most are oriented in a relatively vertical axis, the lower kidney may be obliquely or horizontally related to the superior kidney (Fig. 110.24). The position of the upper (uncrossed) kidney may also be ectopically low. Approximately 85% of crossed kidneys are fused and encompassed by a common renal fascia—hence the term *crossed fused renal ectopia*.[31] As expected in any type of ectopia, the arterial vascularity and venous drainage may be anomalous, and the renal pelvis, especially of the lower kidney, may be malrotated.[59,69,71]

***Imaging.*** Imaging demonstrates an empty renal fossa on one side and both kidneys located on the opposite side of the spine (Fig. 110.25).[72] MRI and CT show two separate ureters, each entering its appropriate trigone.[31] Doppler ultrasonography may be used to demonstrate jets of urine emanating from the normally positioned UVJs. Ultrasonography, MRI, and CT may allow visualization of a small indentation at the site of renal parenchymal fusion (e-Fig. 110.26).[72,73]

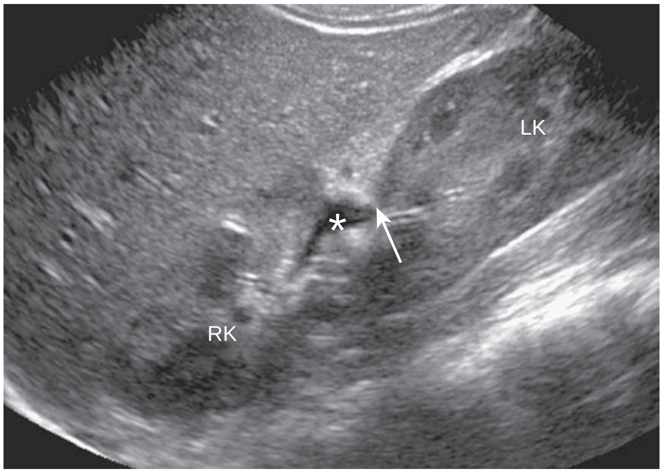

**e-Figure 110.26. Crossed fused renal ectopia.** Longitudinal ultrasonographic image of the right upper quadrant shows a well-defined indentation or notch *(arrow)* at the junction between the right kidney *(RK)* and the crossed, fused left kidney *(LK)*. The right renal pelvis has a small amount of visible urine within it *(asterisk)*.

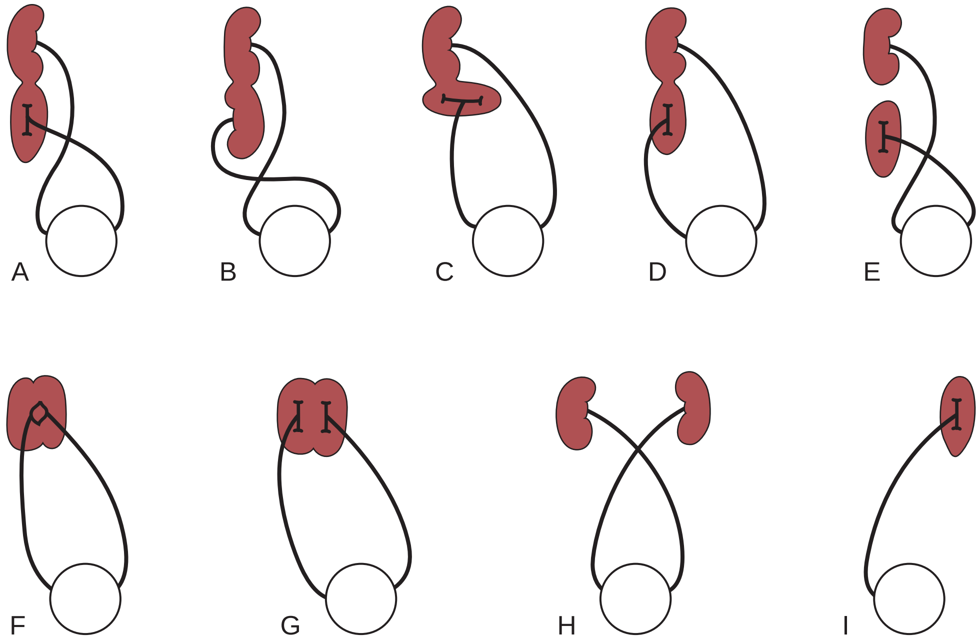

**Figure 110.24. Various types of crossed renal ectopia.** (A) Unilateral fused kidney (inferior renal ectopia), the most common form. (B) Sigmoid or S-shaped kidney. (C) L-shaped kidney. (D) Unilateral fused kidney (superior renal ectopia). (E) Crossed ectopia without fusion. (F) Unilateral disk kidney. (G) Unilateral lump kidney. (H) Bilateral crossed ectopia. (I) Crossed ectopia of a solitary kidney (solitary crossed renal ectopia).

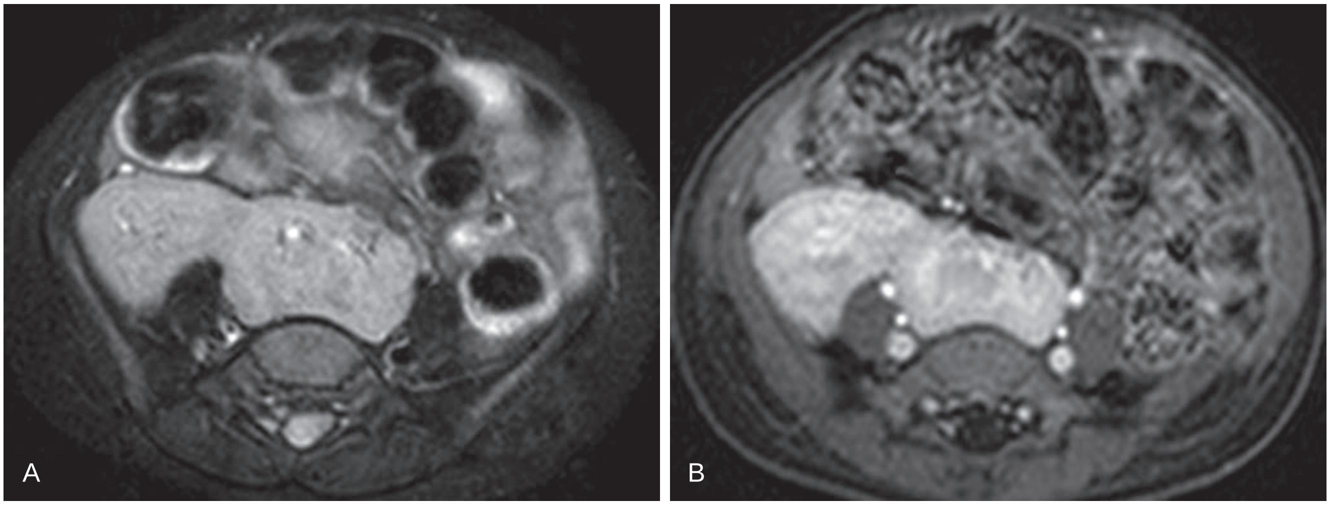

**Figure 110.25. Crossed fused renal ectopia in a 2-year-old girl.** (A) Axial T2-weighted and (B) postcontrast T1-weighted MR images with fat saturation show renal fusion, with both kidneys located to the right of the midline. The left (lower) moiety partly overlies the spine.

# URETER

## Ureteropelvic Junction and Proximal Ureter

The transition between the renal pelvis and the ureter, or the UPJ, may be sharply or poorly defined. Both extrinsic filling defects and local narrowing are commonly observed at the UPJ without resultant hydronephrosis. An inferior polar artery may produce a small extrinsic defect or notch in the ureter near the UPJ (e-Fig. 110.27). A sharp kink without obstruction is occasionally seen in the proximal portion of the ureter as a transient or constant finding. Retained fetal folds in the upper ureter (e-Fig. 110.28), mild elongation and tortuosity of the ureter, and mild widening of the midureter may all be seen normally in the urogram in the infant. They are believed to represent a persistence of fetal characteristics and disappear in early childhood.[74–78]

## Duplication

Ureteral duplication (duplication of the renal pelvis ± ureter) is one of the most common anomalies of the urinary tract (Fig. 110.29). Incomplete duplication ranges from a bifid renal pelvis

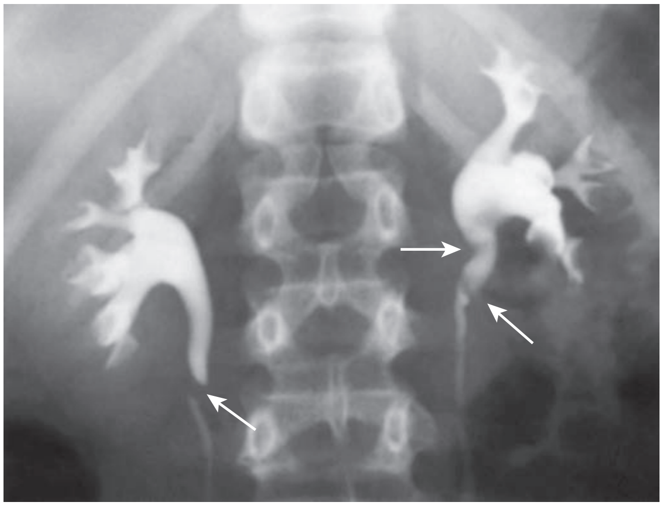

**e-Figure 110.27. Renal arterial impressions.** Intravenous urography in a 14-year-old girl shows several defects at the ureteropelvic junction and proximal ureter *(arrows)*, presumably caused by nonobstructing crossing arteries.

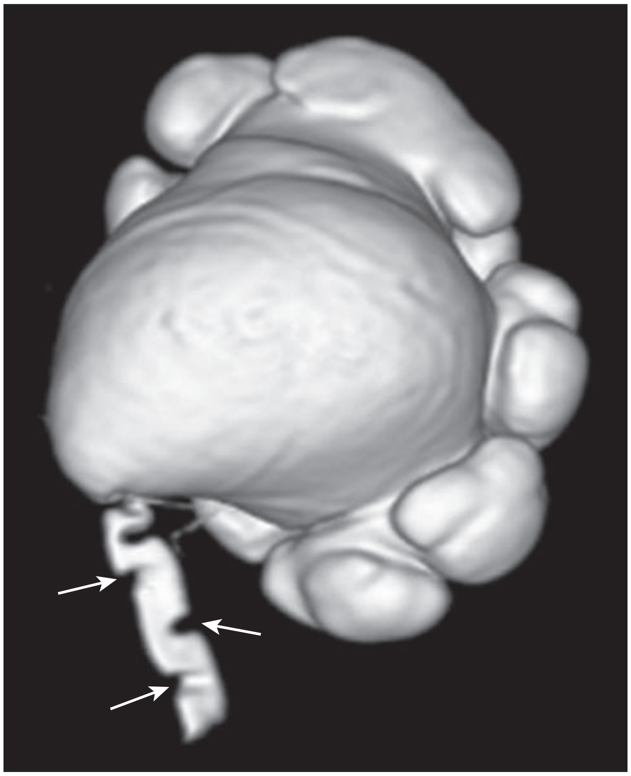

**e-Figure 110.28. Retained fetal folds.** 3D rendering from an MR urogram in a child with UPJ obstruction shows multiple nonobstructive filling defects *(arrows)* in the proximal portion of the ureter. In most children, these disappear over time.

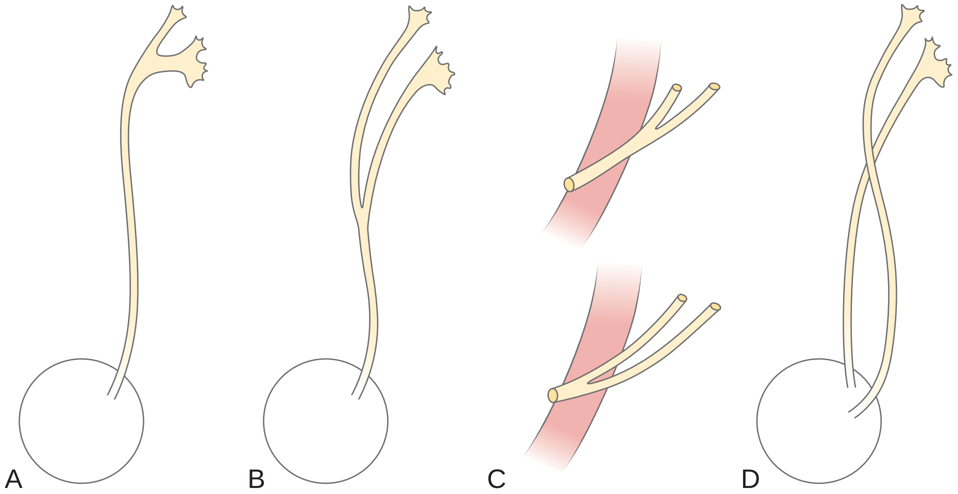

**Figure 110.29. Various forms of ureteral duplication.** (A) Bifid pelvis. (B) Partial ureteral duplication (Y-ureter). (C) Incomplete ureteral duplication with the ureters joining near the bladder or within the bladder wall (V-ureter). (D) Complete ureteral duplication with separate ureteral orifices. The upper pole ureter inserts distally and medially to the lower pole ureter (Weigert-Meyer rule).

to two ureters joining anywhere along their course and continuing inferiorly as a single structure. In completely duplicated systems, the two ureters are separate throughout their entire course. The ureter draining the upper pole of the kidney normally inserts into the bladder more caudad and more medially than the lower pole ureter (Weigert-Meyer rule) and has a longer submucosal tunnel than the lower pole ureter. Ureteral duplication is more commonly unilateral, although it may be bilateral. Ureteral duplication is of no clinical importance unless complicated by another congenital lesion or an acquired process. These conditions, such as ureteral ectopia, ureterocele, VUR, urinary tract infection, and UPJ obstruction, are addressed in later chapters.[79–86]

Other variants probably related to ureteral duplication include the accessory ureter or a ureteral stump. The accessory ureter is a tubular structure originating from a distal normal ureter at the bladder and extending cephalad along the normal ureter to end blindly proximally, without connection to a pelvocalyceal system or renal parenchyma. The ureteral stump varies in length from a few centimeters to a narrow but patent cord that extends almost to the kidney (e-Fig. 110.30).[87–91]

Ureteral triplication (e-Fig. 110.31) is another rare anomaly in which three ureters arise from the kidney; one from the upper pole, the second from the midzone of the kidney, and the third from the lower pole. The three ureters may drain separately into the bladder, or one may end ectopically; the parenchyma drained by the ectopic ureter is usually small and poorly functioning. In a second type, two of the three ureters may join in the lumbar area to form a single Y-shaped ureter that drains usually into the bladder, together with a normal third ureter. In a third type, the three ureters join in the lumbar area to form a common distal ureter that drains into the bladder. More than half the cases of ureteral triplication defy the Weigert-Meyer rule. Four ureters emanating from a single kidney have been described.[92–95]

## BLADDER

Bladder ears are normal lateral protrusions of the urinary bladder (e-Fig. 110.32). They are most frequently seen in infants less than 6 months of age as transient protrusions that are most apparent when the bladder is partially full. Bladder ears represent extraperitoneal herniations of the bladder through the internal inguinal ring into the inguinal canal. An association of bladder ears with inguinal hernia may reflect the presence of a patent processus vaginalis. Rarely, lateral protrusions of the rectum occur in this same location, producing a normal anatomic variant termed *rectal ears*.[96–98]

## URETHRA

Several normal findings exist and should not be confused with pathologic processes, including normal anatomic folds of the posterior urethra of the male, and urinal and foreskin artifact. Normal anatomic folds are frequently visualized in the posterior urethra of the male and should not be confused with congenital obstructing membranes. Unlike congenital obstructing membranes, these folds do not produce dilatation of the proximal posterior urethra or decrease the urinary stream.[99–103]

Urinal artifact may be produced in the male during voiding. The urethral stream is compressed at the level of the penoscrotal junction by the plastic urinal and should not be confused with a stricture of the penile urethra. A film during voiding without urethral compression by the urinal confirms normal urethral caliber.[104]

Foreskin artifact is caused by retraction of a tight foreskin and consequent narrowing of the distal urethra. This appearance may also mimic a urethral stricture. Reduction of the foreskin while voiding makes the appearance normal.

### KEY POINTS

- The kidney, urinary tract, and genital tract are closely associated embryologically.
- The neonatal kidney has immature function during the first days after birth with decreased GFR and urine output, and limited concentrating ability.
- Variants in imaging of the childhood kidney include the column of Bertin, junctional parenchymal defect, scalloping of the cortical border, interrenuncular septum, dromedary hump, hilar lips, and hypoechoic pyramids.

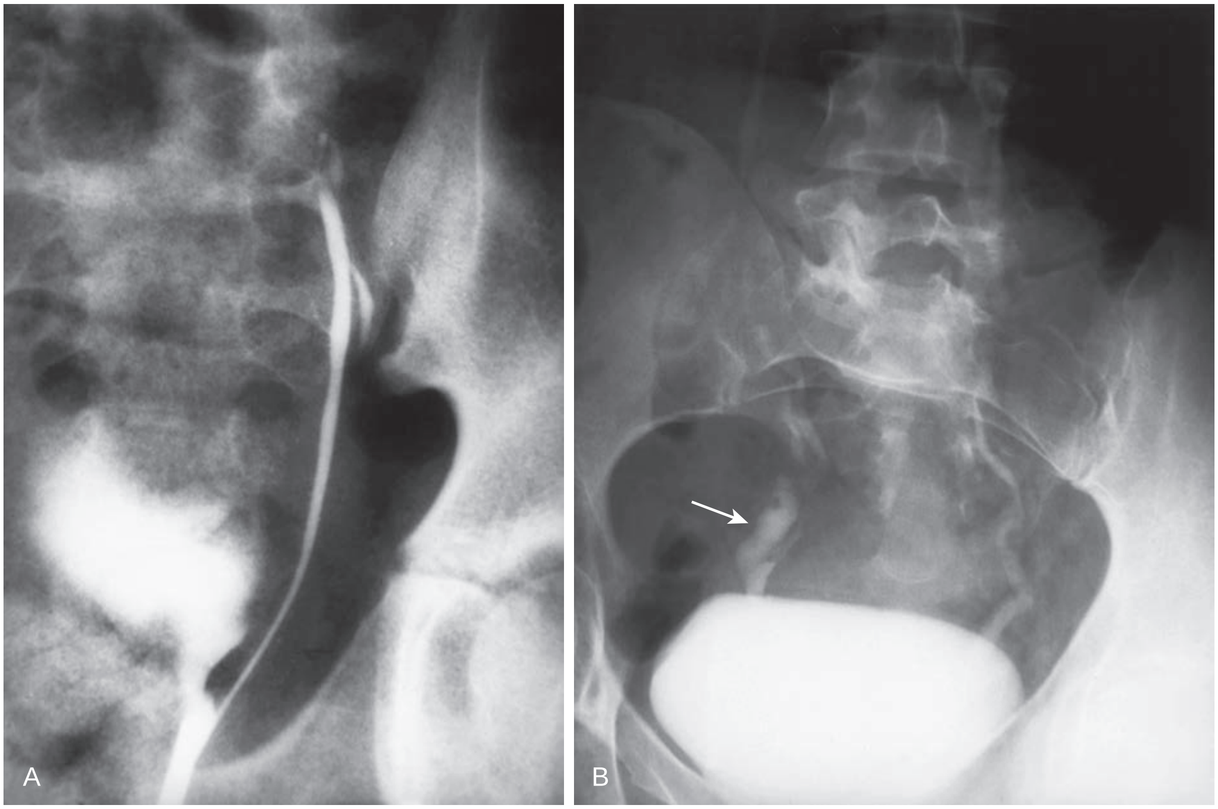

**e-Figure 110.30. Rare forms of ureteral duplication.** (A) A retrograde ureterogram demonstrates a blind-ending accessory ureter. (B) A voiding cystourethrogram demonstrates vesicoureteral reflux into normal right and left ureters and a blind-ending right ureteral stump *(arrow)*.

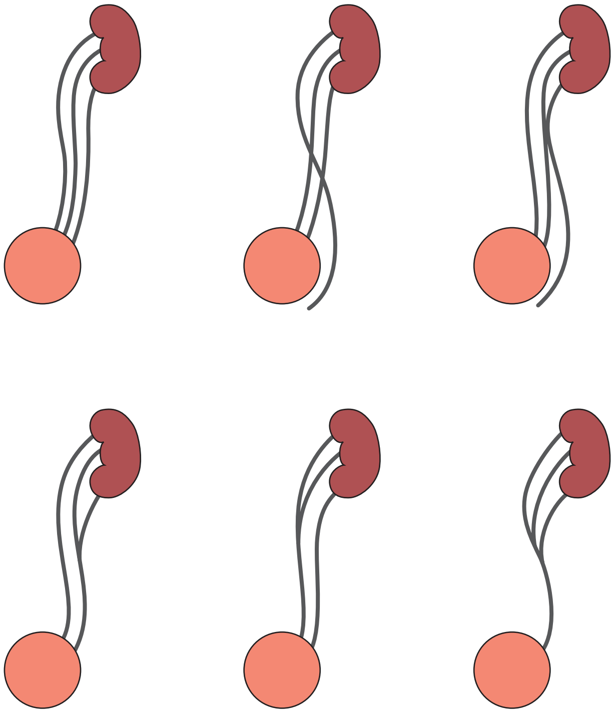

**e-Figure 110.31. Types of ureteral triplication.** *Top*, Complete triplication: all three ureters enter the bladder separately, or one may insert ectopically. *Bottom*, Incomplete triplication: varying degrees of communication with one or two separate ureteral orifices into the bladder.

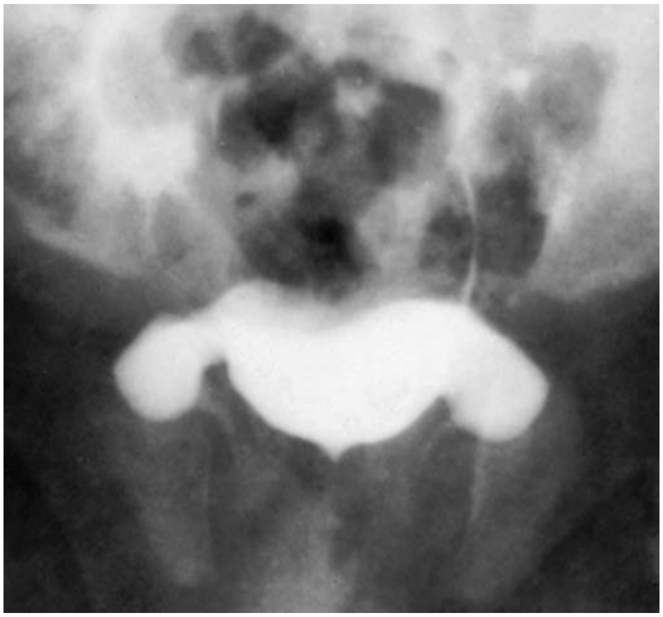

**e-Figure 110.32. Bladder ears.** A voiding cystourethrogram shows transient lateral herniation of the bladder ("bladder ears") in a normal infant. *(Courtesy Sandra K. Fernbach, MD, and Kate A. Feinstein, MD.)*

- Renal length is correlated to age, height, and weight.
- Horseshoe kidneys have an increased incidence of UPJ obstruction, VUR, ureteral duplication, and injury from direct trauma. A slight increased risk of Wilms tumor has been reported.
- The ureter from the lower kidney of crossed, fused kidneys crosses midline to insert into the bladder in its normal position.
- Ureteral duplication may be partial or complete. Incomplete duplication ranges from a bifid renal pelvis to two ureters joining anywhere along their course and continuing inferiorly as a single structure. In completely duplicated systems, the two ureters are separate throughout their entire course.

## SUGGESTED READINGS

Fernbach SK, Feinstein KA, Schmidt MB. Pediatric voiding cystourethrography: a pictorial guide. *Radiographics*. 2000;20(1):155–168.

Glodny B, Petersen J, Hofmann KJ, et al. Kidney fusion anomalies revisited: clinical and radiological analysis of 209 cases of crossed fused ectopia and horseshoe kidney. *BJU Int*. 2009;103:224–235.

Moore KL, Persaud TVN. The urogenital system. In: *Before We are Born: Essentials of Embryology and Birth Defects*. 7th ed. Philadelphia, PA: WB Saunders; 2003.

Patel U. *Congenital Anomalies of the Bladder Imaging and Urodynamics of the Lower Urinary Tract*. London, U.K.: Springer; 2010:23–27.

Shapiro E. Clinical implications of genitourinary embryology. *Curr Opin Urol*. 2009;19(4):427–433.

## REFERENCES

Full references for this chapter can be found on www.expertconsult.com.

## REFERENCES

1. Moore KL, Persaud TVN. The urogenital system. In: *Before We Are Born: Essentials of Embryology and Birth Defects*. 7th ed. Philadelphia, PA: WB Saunders; 2003:162–189.
2. Sadler TW. Urogenital system. In: *Langman's Medical Embryology*. 8th ed. Baltimore, MD: Lippincott Williams & Wilkins; 2000:304–344.
3. O'Rahilly RO, Müller F. The urinary system. In: *Human Embryology & Teratology*. 2nd ed. New York: Wiley-Liss; 1996:273–290.
4. Parrott TS, Skandalakis JE, Gray SW. The kidney and ureter. In: Skandalakis JE, Gray SW, eds. *Embryology for Surgeons: The Embryological Basis for the Treatment of Congenital Anomalies*. 2nd ed. Baltimore, MD: Williams & Wilkins; 1994:594–670.
5. Parrott TS, Skandalakis JE, Gray SW. The bladder and urethra. In: Skandalakis JE, Gray SW, eds. *Embryology for Surgeons: The Embryological Basis for the Treatment of Congenital Anomalies*. 2nd ed. Baltimore, MD: Williams & Wilkins; 1994:671–717.
6. Vogt BA, MacRae Dell K, Davis ID. The kidney and urinary tract. In: Martin RJ, Fanaroff AA, Walsh MC, eds. *Neonatal-perinatal Medicine*. 8th ed. Philadelphia, PA: Mosby; 2006:1659–1683.
7. Brophy PD, Robillard JE. Functional development of the kidney in utero. In: Polin RA, Fox WW, Abman SH, eds. *Fetal and Neonatal Physiology*. 3rd ed. Philadelphia, PA: Saunders; 2004:1229–1241.
8. Dodds WJ, Darweesh RM, Lawson TL, et al. The retroperitoneal spaces revisited. *AJR Am J Roentgenol*. 1986;147:1155.
9. Lafortune M, Constantin A, Breton G, et al. Sonography of hypertrophied column of Bertin. *AJR Am J Roentgenol*. 1986;146:53.
10. Auh YH, Rubinstein WA, Markisz JA, et al. Extraperitoneal paravesical spaces: CT delineation with US correlation. *Radiology*. 1986;159:319–328.
11. Auh YH, Rubinstein WA, Markisz JA, et al. Intraperitoneal paravesical spaces: CT delineation with US correlation. *Radiology*. 1986;159:311–317.
12. Hoffer FA, Hanabergh AM, Teele RL. The interrenicular junction: a mimic of renal scarring on normal pediatric sonograms. *AJR Am J Roentgenol*. 1985;145:1075.
13. Kenney IJ, Wild SR. Renal parenchymal junctional line in children: ultrasonic frequency and appearance. *Br J Radiol*. 1987;60:865.
14. Erwin BC, Carroll BA, Muller H. A sonographic assessment of neonatal renal parameters. *J Ultrasound Med*. 1985;4:217.
15. Haller JO, Berdon WE, Friedman AP. Increased renal cortical echogenicity: a normal finding in neonates and infants. *Radiology*. 1982;142:173.
16. Gordon I, Riccabona M. Investigating the newborn kidney—update on imaging techniques. *Semin Neonatol*. 2003;8:269–278.
17. Han BK, Babcock DS. Sonographic measurements and appearance of normal kidneys in children. *AJR Am J Roentgenol*. 1985;145:611.
18. McClennan BL, Lee JKT, Peterson RR. Anatomy of the perirenal area. *Radiology*. 1986;158:555.
19. Currarino G, Williams B, Dana K. Kidney length correlated with age: normal values in children. *Radiology*. 1984;150:703.
20. Jequier S, Paltiel H, Lafortune M. Ureterovesical jets in infants and children: duplex and color Doppler US studies. *Radiology*. 1990;175:349.
21. Rosenbaum DM, Korngold E, Teele R. Sonographic assessment of renal length in normal children. *AJR Am J Roentgenol*. 1984; 142:467.
22. Schlesinger AE, Hedlund GL, Pierson WP, et al. Normal standards for kidney length in premature infants: determination with US. Work in progress. *Radiology*. 1987;164:127.
23. Schlesinger AE, Hernandez RJ, Zerin JM, et al. Interobserver and intraobserver variations in sonographic renal length measurements in children. *AJR Am J Roentgenol*. 1991;156:1029.
24. Vade A, Lau P, Smick J, et al. Sonographic renal parameters as related to age. *Pediatr Radiol*. 1987;17:212.
25. Zerin JM, Meyer RD. Sonographic assessment of renal length in the first year of life: the problem of "spurious nephromegaly." *Pediatr Radiol*. 2000;30:52.
26. Kaufman RA, Dunbar JS, Gole DE. Normal dilatation of the proximal ureters in children. *AJR Am J Roentgenol*. 1981;137:945.
27. Herman TE, McAlister OH. Radiographic manifestations of congenital anomalies of the lower urinary tract. *Radiol Clin North Am*. 1991;29:365.
28. Shapiro E. Clinical implications of genitourinary embryology. *Curr Opin Urol*. 2009;19(4):427–433.
29. Uetani N, Bouchard M. Plumbing in the embryo: developmental defects of the urinary tracts. *Clin Genet*. 2009;75(4):307–317.
30. Berrocal T, Lopez-Pereira P, Arjonilla A, et al. Anomalies of the distal ureter, bladder, and urethra in children: embryologic, radiologic, and pathologic features. *Radiographics*. 2002;22:1139–1164.
31. Cohen HL, Kravets F, Zucconi W, et al. Congenital abnormalities of the genitourinary system. *Semin Roentgenol*. 2004;39:282–303.
32. Koff SA. Evaluation and management of voiding disorders in children. *Urol Clin North Am*. 1988;15:769.
33. Fernbach SK, Feinstein KA. Abnormalities of the bladder in children: imaging findings. *AJR Am J Roentgenol*. 1994;162:1143.
34. Fernbach SK, Feinstein KA, Schmidt MB. Pediatric voiding cystourethrography: a pictorial guide. *Radiographics*. 2000;20:155.
35. Riccabona M, Lindbichler F, Sinzig M. Conventional imaging in paediatric uroradiology. *Eur J Radiol*. 2002;43:100.
36. Herman TE, McAllister WH. Radiographic manifestations of the lower urinary tract. *Radiol Clin North Am*. 1991;29:365.
37. Berger RM, Maizels M, Moran GC, et al. Bladder capacity (ounces) equals age (years) plus 2 predicts normal bladder capacity and aids in the diagnosis of abnormal voiding patterns. *J Urol*. 1983;129: 347–349.
38. Zerin JM, Chen E, Ritchey ML, et al. Bladder capacity as measured at voiding cystourethrography in children: relationship to toilet training and frequency of micturition. *Radiology*. 1993;187:803–806.
39. Ludwikowski B, Oesch Hayward I, Brenner E, et al. The development of the external urethral sphincter in humans. *BJU Int*. 2001;87:565–568.
40. Sebe P, Fritsch H, Oswald J, et al. Fetal development of the female external urinary sphincter complex: an anatomical and histological study. *J Urol*. 2005;173:1738–1742.
41. Kawashima A, Sandler CM, Wasserman NF, et al. Imaging of urethral disease: a pictorial review. *Radiographics*. 2004;24(suppl 1):S195–S216.
42. Lo WC, Wang CR, Lim KE. Diagnosis of the congenital urethral anomalies of male child by voiding cystourethrography. *Acta Paediatr Taiwan*. 1999;40:152–156.
43. Pavlica P, Barozzi L, Menchi I. Imaging of the male urethra. *Eur Radiol*. 2003;13:1583–1596.
44. Klimberg I. The development of voiding control. *Am Urol Assoc Update Series*. 1988;7:161.
45. Volmar KE, Fritsch MK, Perlman EJ, et al. Patterns of congenital lower urinary tract obstructive uropathy: relation to abnormal prostate and bladder development and the prune belly syndrome. *Pediatr Dev Pathol*. 2001;4:467.
46. Fedele L, Bianchi S, Agnoli B, et al. Urinary tract anomalies associated with unicornuate uterus. *J Urol*. 1996;155:847–848.
47. Oppelt P, Renner SP, Kellermann A, et al. Clinical aspects of Mayer-Rokitansky-Kuester-Hauser syndrome: recommendations for clinical diagnosis and staging. *Hum Reprod*. 2006;21:792–797.
48. Tanaka YO, Kurosaki Y, Kobayashi T, et al. Uterus didelphys associated with obstructed hemivagina and ipsilateral renal agenesis: MR findings in seven cases. *Abdom Imaging*. 1998;23:437–441.
49. Tarry WF, Duckett JW, Stephens FD. The Mayer-Rokitansky syndrome: pathogenesis, classification and management. *J Urol*. 1986;136:648–652.
50. Schlegel PN, Shin D, Goldstein M. Urogenital anomalies in men with congenital absence of the vas deferens. *J Urol*. 1996;155:1644–1648.
51. van den Ouden D, Blom JH, Bangma C, et al. Diagnosis and management of seminal vesicle cysts associated with ipsilateral renal agenesis: a pooled analysis of 52 cases. *Eur Urol*. 1998;33:433–440.
52. Kim B, Kawashima A, Ryu JA, et al. Imaging of the seminal vesicle and vas deferens. *Radiographics*. 2009;29:1105–1121.
53. Wojcik LJ, Hansen K, Diamond DA, et al. Cystic dysplasia of the rete testis: benign congenital lesion associated with ipsilateral urological anomalies. *J Urol*. 1997;158:600–604.
54. McGahan JP, Myracle MR. Adrenal hypertrophy: possible pitfall in the sonographic diagnosis of renal agenesis. *J Ultrasound Med*. 1986;5:265–268.
55. Hoffman CK, Filly RA, Callen PW. The "lying down" adrenal sign: a sonographic indicator of renal agenesis or ectopia in fetuses and neonates. *J Ultrasound Med*. 1992;11:533–536.
56. Kenney PJ, Robbins GL, Ellis DA, et al. Adrenal glands in patients with congenital renal anomalies: CT appearance. *Radiology*. 1985;155: 181–182.
57. Barnewolt CE, Lebowitz RL. Absence of a renal sinus echo complex in the ectopic kidney of a child: a normal finding. *Pediatr Radiol*. 1996;26:318–323.
58. Rouanne M, Le Mandat A, Dorgeret S, et al. A rare case of ectopic intrathoracic kidney in a 1-year-old child. *Urology*. 2010;76:57–59.

59. Liddell RM, Rosenbaum DM, Blumhagen JD. Delayed radiologic appearance of bilateral thoracic ectopic kidneys. *AJR Am J Roentgenol*. 1989;152:120–122.
60. Sharma R, Savita N, Chakravarty KL, et al. Pancake kidney detected on renal scintigraphy. *Clin Nucl Med*. 2006;31:729–730.
61. Glodny B, Petersen J, Hofmann KJ, et al. Kidney fusion anomalies revisited: clinical and radiological analysis of 209 cases of crossed fused ectopia and horseshoe kidney. *BJU Int*. 2009;103: 224–235.
62. Huang EY, Mascarenhas L, Mahour GH. Wilms' tumor and horseshoe kidneys: a case report and review of the literature. *J Pediatr Surg*. 2004;39:207–212.
63. O'Brien J, Buckley O, Doody O, et al. Imaging of horseshoe kidneys and their complications. *J Med Imaging Radiat Oncol*. 2008;52: 216–226.
64. Kaakaji Y, Pfister RC. Case 1: Horseshoe kidney with severe congenital hydronephrosis (ureteropelvic junction obstruction). *AJR Am J Roentgenol*. 1998;171(826):829–830.
65. Cascio S, Sweeney B, Granata C, et al. Vesicoureteral reflux and ureteropelvic junction obstruction in children with horseshoe kidney: treatment and outcome. *J Urol*. 2002;167:2566–2568.
66. Neville H, Ritchey ML, Shamberger RC, et al. The occurrence of Wilms tumor in horseshoe kidneys: a report from the National Wilms Tumor Study Group (NWTSG). *J Pediatr Surg*. 2002;37:1134–1137.
67. Mesrobian HG, Kelalis PP, Hrabovsky E, et al. Wilms tumor in horseshoe kidneys: a report from the National Wilms Tumor Study. *J Urol*. 1985;133:1002–1003.
68. Strauss S, Dushnitsky T, Peer A, et al. Sonographic features of horseshoe kidney: review of 34 patients. *J Ultrasound Med*. 2000;19:27–31.
69. Patel TV, Singh AK. Crossed fused ectopia of the kidneys. *Kidney Int*. 2008;73:662.
70. Watanabe T. Reflux nephropathy in a patient with crossed renal ectopia with fusion. *Pediatr Nephrol*. 2002;17:617–619.
71. Hertz M, Rubinstein ZJ, Shahin N, et al. Crossed renal ectopia: clinical and radiological findings in 22 cases. *Clin Radiol*. 1977;28:339–344.
72. Goodman JD, Norton KI, Carr L, et al. Crossed fused renal ectopia: sonographic diagnosis. *Urol Radiol*. 1986;8:13–16.
73. McCarthy S, Rosenfield AT. Ultrasonography in crossed renal ectopia. *J Ultrasound Med*. 1984;3:107–112.
74. Rigas A, Karamanolakis D, Bogdanos I, et al. Pelvi-ureteric junction obstruction by crossing renal vessels: clinical and imaging features. *BJU Int*. 2003;92(1):101–103.
75. Riccabona M. The ureter and vesicoureteral reflux. In: Slovis T, ed. *Caffey's Pediatric Diagnostic Imaging*. 11th ed. Philadelphia, PA: Mosby; 2008:2315–2355.
76. Rabinowitz R, Kingston TE, Wesselhoeft C, et al. Ureteral valves in children. *Urology*. 1998;51(suppl 5A):7–11.
77. Stringer MD, Yassaie S. Is the pelviureteric junction an anatomical entity? *J Pediatr Urol*. 2011; [Epub ahead of print].
78. Patel U. *Congenital Anomalies of the Bladder. Imaging and Urodynamics of the Lower Urinary Tract*. London, U.K.: Springer; 2010:23–27.
79. Caldamone AA. Duplication anomalies of the upper tract in infants and children. *Urol Clin North Am*. 1991;12:75.
80. Berdon WE. Contemporary imaging approach to pediatric urologic problems. *Radiol Clin North Am*. 1991;29:605.
81. Churchill BM, Abara EO, McLorie GA. Ureteral duplication, ectopy and ureteroceles. *Pediatr Clin North Am*. 1987;34:1273.
82. Bisset GS, Strife JL. The duplex collecting system in girls with urinary tract infection: prevalence and significance. *AJR Am J Roentgenol*. 1987;148:497.
83. Kaefer M, Barnewolt C, Retik AB, et al. The ultrasound diagnosis of infravesical obstruction in children: evaluation of bladder wall thickness indexed to bladder filling. *J Urol*. 1997;157:989.
84. Nussbaum AR, Dorst JP, Jeffs RD, et al. Ectopic ureter and ureterocele: their varied radiographic manifestations. *Radiology*. 1986;159:227.
85. Sorantin E, Fotter R, Aigner R, et al. The sonographically thickened wall of the upper urinary tract: correlation with other imaging methods. *Pediatr Radiol*. 1997;27:667.
86. Gylys-Morin VM, Minevich E, Tackett LD, et al. Magnetic resonance imaging of the dysplastic renal moiety and ectopic ureter. *J Urol*. 2000;164:2034.
87. Gupta PK. Letter to the editor: Blind-ending branch of bifid ureter: multidetector CT imaging findings. *Br J Radiol*. 2011;84(1004):769.
88. Chang E, Santillan C, O'Boyle MK. Blind-ending branch of a bifid ureter: multidetector CT imaging findings. *Br J Radiol*. 2011;84(998):e38–e40.
89. Blair D, Rigsby C, Rosenfield AT. The nubbin sign on computed tomography and sonography. *Urol Radiol*. 1987;9:149.
90. Hawas N, Noah M, Pattel PJ. Blind-ending ureter: clinical significance? An analysis of 13 cases with review of the literature. *Eur Urol*. 1987;13:39.
91. Tilley EA, Dow CJ. Cranial blind-ending branch of a bifid ureter: report of 3 cases. *Br J Urol*. 1988;62:127.
92. Kokabi N, Price N, Smith GH, et al. Ureteral triplication: a rare anomaly with a variety of presentations. *J Pediatr Urol*. 2011;7(4):484–487.
93. Xu Z, Li Z, Wang D, et al. Ureteral triplication combined with right renal ectopia and ureteral cyst. *Urol Int*. 2009;83(4):476–478.
94. Bloom RA, Crooks EK, Wise HA. Complete ureteral triplication with ectopia. *Urology*. 1984;25:176.
95. Gosalbez R Jr, Gosalbez R, Piro C, et al. Ureteral triplication and ureterocele: report of 3 cases and review of the literature. *J Urol*. 1991;145:105.
96. Lakshminarayana G, Mathew A, Rajesh R, et al. A rare congenital anomaly of urinary bladder—Bladder ears. *Indian J Nephrol*. 2010; 20(4):220–221.
97. Aygen M, Akduman IE, Osman MM. Bladder ear: a potential source of false interpretation on F-18 FDG PET. *Clin Nucl Med*. 2008;33(10):721–722.
98. Kassner EG, Schussheim A, Gordon DH. Rectal ears. *J Can Assoc Radiol*. 1975;26(2):125–127.
99. Fernbach SK, Feinstein KA, Schmidt MB. Pediatric voiding cystourethrography: a pictorial guide. *Radiographics*. 2000;20(1):155–168.
100. Kawashima A, Sandler CM, Wasserman NF, et al. Imaging of urethral disease: a pictorial review. *Radiographics*. 2004;24:S195–S216.
101. Schöllnast H, Lindbichler F, Riccabona M. Ultrasound (US) of the urethra in infants: comparison US versus VCUG. *J Ultrasound Med*. 2004;23:769.
102. Teele RL, Share JC. Transperineal sonography in children. *AJR Am J Roentgenol*. 1997;168:1263.
103. Giordano M, Marzolla R, Puteo F, et al. Voiding urosonography as first step in diagnosis of vesicoureteral reflux in children: a clinical experience. *Pediatr Radiol*. 2007;37:674–677.
104. Ramos AJ, Watts FB Jr, Timmons JW. The urinal artifact. *Radiology*. 1978;128(3):807–808.

# 111 Imaging Techniques

Amy B. Kolbe, Larry A. Binkovitz, M. Beth McCarville, and J. Damien Grattan-Smith

## RADIOGRAPHIC PROCEDURES

### Intravenous Urography

Intravenous urography (IVU) was historically the imaging method of choice for the kidneys and upper urinary tracts but has been supplanted by magnetic resonance imaging (MRI) and computed tomography (CT). It is rarely the preferred imaging method in current pediatric practice. IVU uses the physiologic excretion of injected iodinated contrast media for anatomic visualization of the renal cortex, medulla, collecting system, and ureter and provides general information about renal function.

Imaging begins with a frontal radiograph of the abdomen to identify any calcifications or masses. Subsequently, low osmolar contrast media with a high iodine content is administered intravenously at a dose of 2 mL/kg (maximum, 150 mL) to obtain adequate iodine concentration in the renal tubules and collecting system. The filming sequence is tailored to the individual examination. An initial frontal radiograph within 1 to 2 minutes of injection images the nephrographic phase. Assessment of this radiograph determines subsequent filming. For routine examination, a radiograph at approximately 5 to 10 minutes allows visualization of the kidneys and their collecting systems, the ureters, and bladder (e-Fig. 111.1). In the prone position, the higher specific gravity of the contrast material allows better visualization of the anteriorly positioned renal pelves and proximal ureters.

The nephrographic phase provides a gross estimate of renal function, as well as information on renal size and parenchymal contour. A poorly visible nephrogram may indicate a technical problem in achieving optimal plasma concentration of contrast material or some degree of renal failure or diminished renal function. A dense and prolonged nephrogram indicates obstruction of the renal collecting system or renal tubules, hypotension, hypovolemia, or acute tubular necrosis.

### Retrograde Urethrography

Retrograde urethrograms are obtained infrequently in children but sometimes are performed in boys to evaluate possible urethral injury or rupture after a straddle injury or pelvic trauma. A small catheter is introduced into the anterior urethra to or slightly past the fossa navicularis, and the meatus is occluded. With the patient in a steep oblique position, a small amount of contrast material is injected through a syringe to allow evaluation of the urethra to the level of the external sphincter. Spasm of the external sphincter sometimes prevents filling of the most proximal portion of the posterior urethra. Although urethrograms are rarely performed in girls, the tip of a small Foley catheter with the balloon distended can be placed into the urethra and then taped to the perineum to allow retrograde evaluation of the urethra.

### Voiding Cystourethrography

Antegrade voiding cystourethrography (VCUG) is the traditional examination of choice for detailed anatomic evaluation of the bladder, study of the anatomy of the male urethra, and identification of vesicoureteral reflux (VUR). The bladder is filled by gravity pressure, using dilute sterile contrast media with an iodine concentration of 80 to 100 mg/mL. The predicted bladder capacity (in milliliters) for children younger than 1 year is the child's weight in kilograms multiplied by 7. In children older than 1 year, the predicted capacity is the child's age in years plus 2, multiplied by 30.[1,2]

An early bladder filling image is obtained to evaluate for ureteroceles or masses. Images with a full urinary bladder are obtained in the lateral oblique projections to look for VUR. Voiding films are useful to evaluate the bladder and urethra (particularly the male urethra) and for the diagnosis of VUR, which may occur only during voiding. After voiding, an image of the bladder documents any postvoid residual, and an image of the kidneys documents any reflux that occurred during the examination. Neonates should undergo at least two filling and voiding cycles to increase the chance of detecting VUR.[3–6] Pulsed fluoroscopy, last image hold recording, and videotaping are important imaging strategies for reducing radiation exposure.[7–10]

## ULTRASOUND

### Contrast-Enhanced Voiding Urosonography

The intravesical instillation of ultrasound contrast agents in the urinary bladder allows the sonographic evaluation of VUR without the use of ionizing radiation.[11–14] These microbubble contrast agents are composed of an outer shell of lipid, protein, or polymer that encases a gas, commonly perfluorocarbon or sulfur hexafluoride.[15] The gas is highly reflective on ultrasound imaging (Fig. 111.2) and can be detected even when administered in very small volumes. The ultrasound transducer is positioned intermittently over the bladder, ureters, and kidneys while the bladder is filled. On gray-scale imaging, the microbubbles appear echogenic. Refluxed contrast material is easily detected in the ureters and kidneys (Fig. 111.3). Although this technique does not avoid catheterization, it does eliminate radiation exposure. Results indicate that the sensitivity for VUR detection is comparable with that of standard techniques. A reflux grading system for contrast-enhanced voiding ultrasonography has been developed and is similar to the international grading system for VCUG.[12] Urethral visualization is possible with contrast-enhanced voiding ultrasonography but remains challenging (Fig. 111.4).

### Renal Ultrasonography

Ultrasonography is an ideal method for examining the kidneys and bladder in infants and children because of their small physical habitus and lack of abdominal fat and because ultrasonography does not utilize ionizing radiation. Variable transducer frequencies and transducer design (e.g., sector, phased, curvilinear, and linear array) allow for individualized approaches. Doppler ultrasound is valuable for the detection of blood flow, to confirm arterial perfusion, or to exclude venous thrombosis. Measurable blood flow parameters from spectral Doppler analysis include peak systolic velocity, end-diastolic velocity, and acceleration time. The normal renal artery has a prompt systolic upstroke with an acceleration time of 70 msec or less and a visible early systolic peak. The normal resistive index depends on the patient's age; it may be as high as 0.9 in a preterm infant and falls to around the adult value

## Abstract:

This chapter describes the radiologic and nuclear medicine imaging techniques available for evaluating the kidneys and urinary system and their disorders in children. Renal ultrasonography is the most widely used and appropriate initial screening exam. Advanced techniques include contrast-enhanced ultrasonography, fluoroscopic voiding cystourethrography, nuclear cystography, diuretic renography, nuclear scintigraphy, and magnetic resonance urography, each having varying ability to assess anatomy and function of the urinary system. Common urinary disorders including hydronephrosis, obstructive uropathy, vesicourethral reflux, and renal cortical scarring are discussed in context of the different imaging modalities and their findings.

## Keywords:

voiding cystourethrography
MR urography
vesicoureteral reflux
renal scintigraphy
DMSA
MAG-3
nuclear cystography

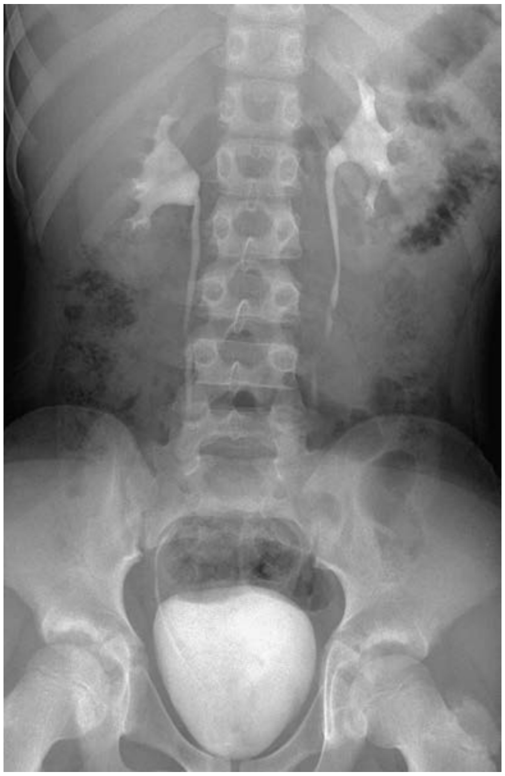

**e-Figure 111.1. Normal intravenous urography image.** A 5-minute image shows opacification of the collecting systems with normal thin, delicate calyces, normal nondilated ureters, and filling of the bladder.

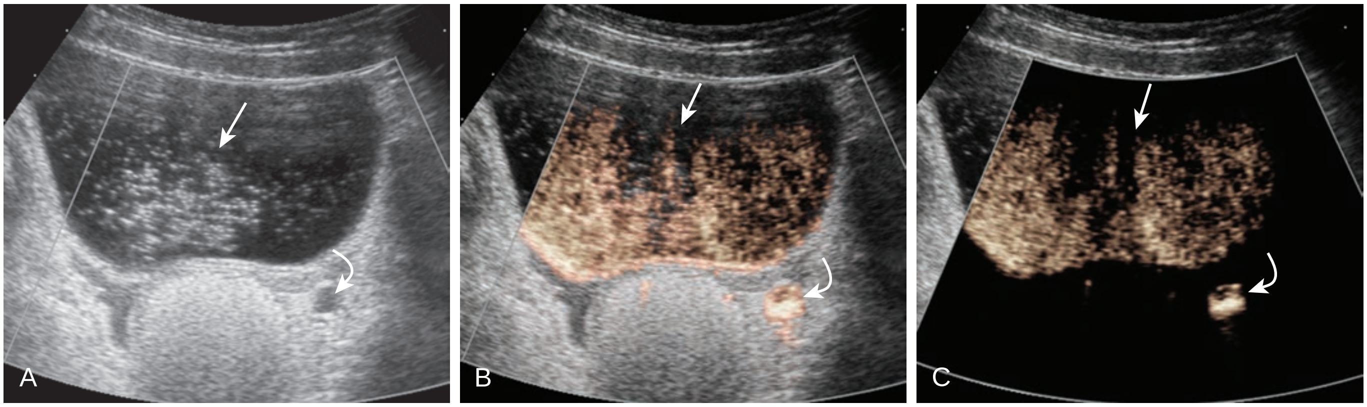

**Figure 111.2. Contrast-enhanced cystosonography.** Transverse ultrasound images after instillation of an ultrasound microbubble contrast agent into the urinary bladder. (A) On gray-scale imaging, the contrast agent appears as hyperechoic material in the bladder *(straight arrow)* surrounded by anechoic urine. Reflux into the distal left ureter *(curved arrow)* is present but somewhat difficult to appreciate. (B) Color overlay technology shows the contrast agent to better advantage as bright orange material in the bladder *(straight arrow)* and distal ureter *(curved arrow)*. (C) Subtraction technology further accentuates the presence of contrast material by eliminating non–contrast-enhanced background tissue. Contrast material in the bladder *(straight arrow)* and ureter *(curved arrow)* are readily apparent. *(Images courtesy Dr. Kassa Darge, Children's Hospital of Philadelphia.)*

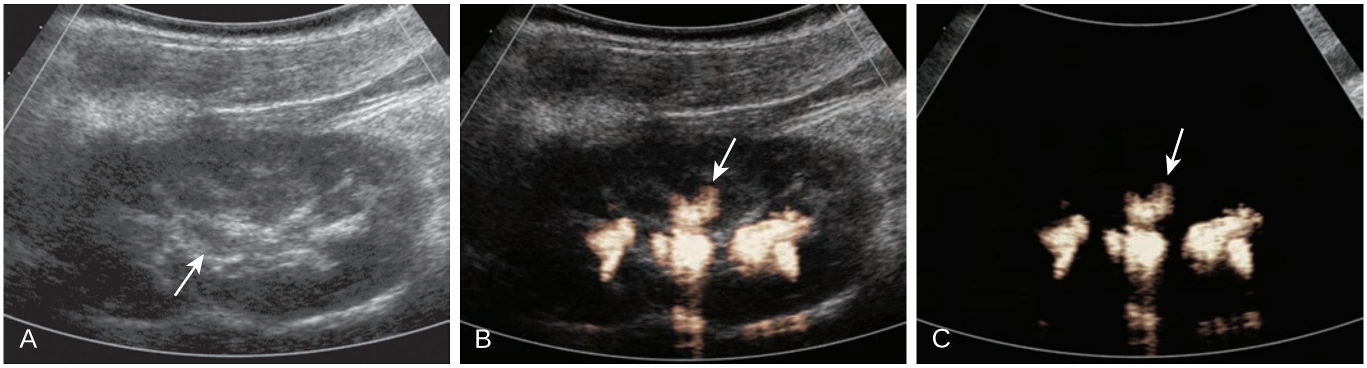

**Figure 111.3. Contrast-enhanced cystosonography.** Longitudinal ultrasound images of the kidney, obtained during contrast-enhanced voiding urosonography, demonstrate reflux into the renal collecting system *(arrows)* on gray-scale (A), color-overlay (B), and subtraction (C) images. *(Images courtesy Dr. Kassa Darge, Children's Hospital of Philadelphia.)*

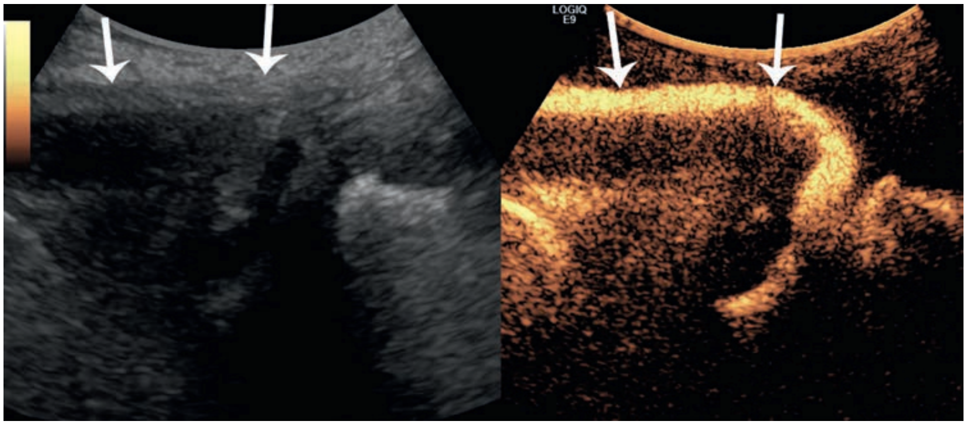

**Figure 111.4. Contrast-enhanced urethral ultrasound.** Longitudinal contrast-enhanced ultrasound gray-scale (left) and color (right) images demonstrate a normal male urethra *(arrows)*. *(Images courtesy Dr. Harriet Paltiel, Boston Children's Hospital.)*

of 0.7 in the first few months of life.[16–19] Color Doppler twinkling artifact can also be used to detect urinary tract calculi.[20]

In young children, it is advisable to initiate the urogenital ultrasound examination with an examination of the bladder. The full bladder of an infant commonly empties when the transducer is placed in the suprapubic region. Kidneys are imaged in the longitudinal and transverse planes. The kidneys are ovoid solid organs with fine, medium-level echoes arising from the cortex, a well-delineated corticomedullary junction with brightly echoic arcuate arteries, and pyramid-shaped, relatively large medullary rays that are hypoechoic. Cortical echogenicity in neonates and young infants is higher and the medullary pyramids are more hypoechoic than in older children (Fig. 111.5). The cortical echogenicity is increased compared with the liver and spleen in preterm infants, isoechoic in neonates and young infants, and diminishes progressively in older children. The transition from the infant renal echo pattern to that of the child typically occurs between 6 and 9 months (Fig. 111.6). Normal pediatric sonographic measurements of right and left kidney length, based on height and age, are provided in Table 111.1.[21–26]

## NUCLEAR MEDICINE

### Nuclear Cystography

Nuclear cystography is performed for the assessment of VUR and is an alternative to fluoroscopic VCUG. The examination is performed by direct instillation of radiotracer (technetium-99m–mertiatide [MAG-3] or technetium-99m-diethylenetriaminepentaacetic acid [DTPA]) and sterile saline solution into the bladder after sterile catheterization[27] or indirectly after nuclear renography with planar images obtained during voiding.[28] Dynamic imaging of the bladder and kidney regions is acquired with use of a posterior gamma camera throughout the filling and voiding cycle. The data can be grouped (in 10- or 60-second intervals) and viewed dynamically. VUR is documented when tracer is shown to ascend into a tubular structure corresponding to the ureter or when the renal collecting system is visualized. The dose of tracer is dependent on bladder volume: 300 mCi for bladder volumes up to 300 mL and 600 mCi for larger bladder volumes. A cyclic cystogram is recommended for children younger than 2 years, for children

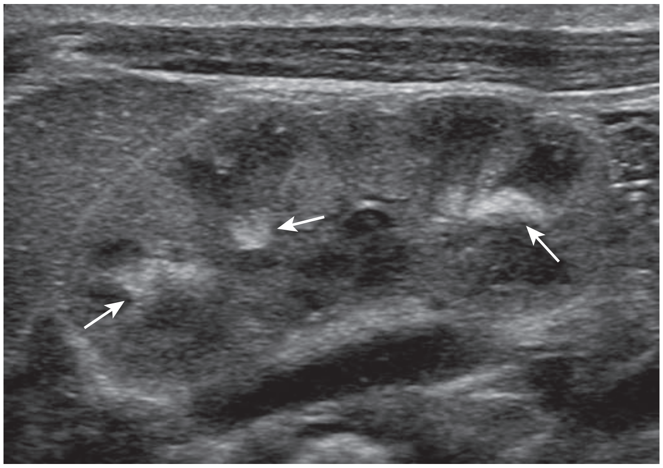

**Figure 111.5. Normal newborn kidney.** A longitudinal sonogram shows that the right renal cortex is isoechoic to the adjacent liver. The hypoechoic medullary pyramids are quite distinct. Areas of medullary pyramid increased echogenicity *(arrows)* are likely due to Tamm-Horsfall protein, a normal finding in a neonate.

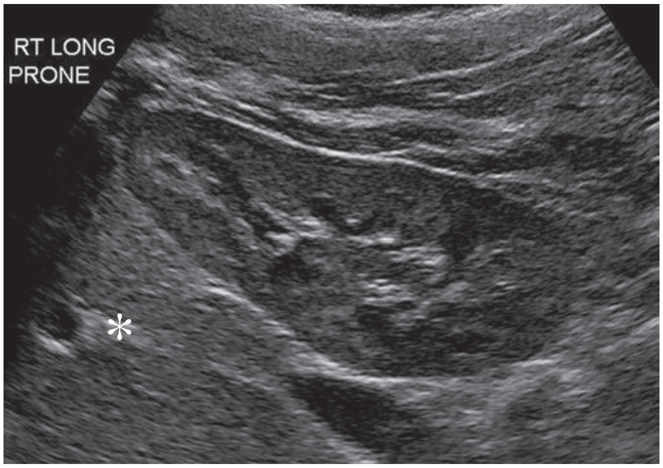

**Figure 111.6. Normal pediatric kidney.** A prone longitudinal sonogram in an 8-year-old child shows that the renal cortex is hypoechoic relative to the adjacent liver *(asterisk)*. The medullary pyramids are still distinct. Note the minimal echogenicity of the renal sinus as a result of a paucity of renal sinus fat.

**TABLE 111.1** Normal Sonographic Renal Lengths in Children Based on Height and Age

| Subjects | | | Left Kidney Length (mm) | | | | | Right Kidney Length (mm) | | | | |
|---|---|---|---|---|---|---|---|---|---|---|---|---|
| | | | | Percentile | | Suggested Limits of Normal | | | Percentile | | Suggested Limits of Normal | |
| Body Height (cm) | No. | Age Range | Mean (SD) | 5th | 95th | Lower | Upper | Mean (SD) | 5th | 95th | Lower | Upper |
| 48-64 | 50 | 1-3 mo | 50 (5.5) | 42 | 59 | 35 | 65 | 50 (5.8) | 40 | 58 | 35 | 65 |
| 54-73 | 39 | 4-6 mo | 56 (5.5) | 47 | 64 | 40 | 70 | 53 (5.3) | 50 | 64 | 40 | 70 |
| 65-78 | 17 | 7-9 mo | 61 (4.6) | 54 | 68 | 45 | 75 | 59 (5.2) | 52 | 66 | 45 | 70 |
| 71-92 | 18 | 1-2.5 y | 66 (5.3) | 57 | 72 | 50 | 80 | 61 (3.4) | 55 | 65 | 50 | 75 |
| 85-109 | 22 | 3-4.9 y | 71 (4.5) | 61 | 76 | 55 | 85 | 67 (5.1) | 59 | 75 | 55 | 80 |
| 100-130 | 26 | 5-6.9 y | 79 (5.9) | 70 | 87 | 60 | 95 | 74 (5.5) | 65 | 83 | 60 | 85 |
| 110-131 | 32 | 7-8.9 y | 84 (6.6) | 73 | 93 | 65 | 100 | 80 (6.6) | 70 | 91 | 65 | 95 |
| 124-149 | 27 | 9-10.9 y | 84 (7.4) | 75 | 97 | 65 | 105 | 80 (7.0) | 69 | 89 | 65 | 100 |
| 137-153 | 15 | 11-12.9 y | 91 (8.4) | 77 | 102 | 70 | 110 | 89 (6.2) | 82 | 100 | 70 | 105 |
| 143-168 | 22 | 13-14.9 y | 96 (8.9) | 84 | 110 | 75 | 115 | 94 (5.9) | 85 | 102 | 75 | 110 |
| 152-175 | 11 | 15-16.7 y | 99 (7.5) | 90 | 110 | 80 | 120 | 92 (7.0) | 83 | 102 | 75 | 110 |

*From Konus OL, Ozdemir A, Akkaya A, et al. Normal liver, spleen, and kidney dimensions in neonates, infants, and children: evaluation with sonography.* AJR. *1998;171:1693–1698.*

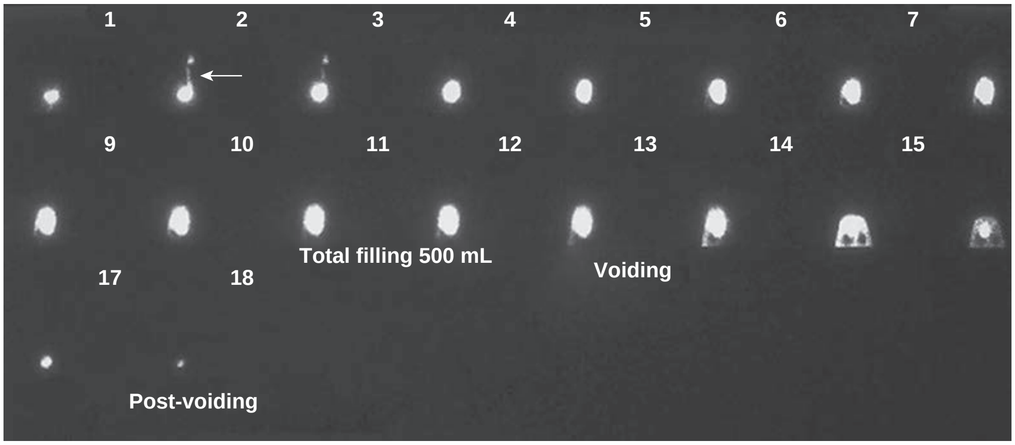

**Figure 111.8. Vesicoureteral reflux.** Early in the study, this nuclear cystogram shows intermediate-grade right vesicoureteral reflux *(arrow)* that later fully drains and does not recur through voiding. Continuous acquisition of the nuclear cystogram allowed the demonstration of this transient reflux, which likely would have been missed with fluoroscopic voiding cystourethrography.

with previously documented VUR or a high suspicion for VUR, and for children who void well before the expected bladder capacity is reached. The procedure is identical to the standard cystogram; however, the catheter is left in the bladder after the first voiding cycle and is used to refill the bladder for a repeat void. As with VCUG, cyclic studies increase the diagnostic yield (e-Fig. 111.7), identifying an additional 10% to 15% of children with VUR compared with noncyclic voiding studies.[29]

Nuclear cystography offers three main advantages over fluoroscopic VCUG: increased detection of VUR (up to an additional 20%) (Fig. 111.8), frequent detection of a higher grade of VUR,[30,31] and reduced radiation dose (approximately 10–25-fold).[32] Disadvantages of nuclear cystography include a lack of detailed anatomic visualization of the urethra and collecting systems and limited identification of bladder abnormalities (such as periureteric diverticula); in addition, the classification of VUR with nuclear cystography is less refined than that with VCUG. The nuclear cystography VUR grades of low, intermediate, and high roughly correspond to the fluoroscopic grades of 1 (low), 2 or 3 (intermediate), and 4 or 5 (high).[27]

## Diuretic Renography

Diuretic renography is used to distinguish obstructive from nonobstructive hydronephrosis.[33] It attempts to quantify urinary obstruction based on the relative function of the hydronephrotic kidney compared with the normal kidney and the rate of urinary excretion of radiotracer (MAG-3 or DTPA) from the renal pelvis (and, in the presence of hydroureter, from the ureter) after a diuretic challenge (typically 1 mg/kg IV furosemide). The graphic presentation of renal excretion using a time versus intensity curve is termed a *renogram* (e-Fig. 111.9); normal, equivocal, and obstructed patterns of excretion after a diuretic challenge, termed *washout*, have been described[33] (Fig. 111.10). Additionally, the time required for half the tracer in the collecting system to pass across the ureteropelvic junction after the administration of furosemide, termed *diuretic* $T_{1/2}$, is stratified to indicate a normal (0–10 minutes), equivocal (10–20 minutes), or obstructed (>20 minutes) pattern.[34,35] These values are useful in distinguishing obstructive from nonobstructive hydronephrosis in older children and adults. However, application of these guidelines can lead to the misdiagnosis of obstruction in a large number of young infants with hydronephrosis demonstrated on routine prenatal sonography (e-Fig. 111.11).[36] The high capacitance of the dilated renal pelvis and relatively low renal urine output in young infants limit the accuracy of this test in the setting of hydronephrosis in children younger than 2 years.[35] Increasing hydronephrosis, decreasing split renal function of the hydronephrotic kidney, and a worsening washout curve all suggest the possibility of significant obstruction (Fig. 111.12).

## Cortical Scintigraphy

A renal cortical scan is performed for the assessment of acute pyelonephritis or its sequela, atrophic pyelonephritic scarring, or for the identification and characterization of functioning renal tissue. A cortical scan also can be used to identify renal anomalies of fusion or location, although sonography is the examination of choice because of its lack of ionizing radiation, increased availability, better anatomic detail, and lower cost.

The renal cortical scan typically is performed with technetium-99m–labeled dimercaptosuccinic acid (DMSA) or glucoheptonate. These agents are extracted by and then bind to cells of the proximal convoluted tubule. It does not accumulate in the medulla or collecting system, thus accounting for the scan appearance of cortical uptake with relative central photopenia of the medulla and renal sinus (Fig. 111.13). Imaging typically occurs 2 to 3 hours after injection and should be performed with pinhole collimation or single photon emission CT acquisition with a dual-headed camera.[37,38] The accuracy in demonstrating acute pyelonephritis exceeds 95%.[39] A defect that appears as a vague area of photopenia not associated with volume loss is more consistent with acute pyelonephritis, whereas a triangular, well-demarcated photopenic focus with volume loss typically is considered an atrophic scar (Fig. 111.14), although it also may be related to focal renal dysplasia. Most areas of infection resolve without residual scarring, especially in older children, but resolution may not occur until 6 months or longer after the acute event. Therefore a definitive diagnosis of a scar requires a follow-up study at least 6 months after the acute infection.[40] Rounded defects identified with cortical scintigraphy should be further characterized with ultrasound to assess for a cyst or mass (e-Fig. 111.15).

## Miscellaneous Renal Nuclear Studies

Quantitation of renal function is possible with nuclear imaging techniques.[41] The relative function of each kidney can be assessed during renography before tracer exits the renal pelvis or with cortical scintigraphy. Regions of interest for each kidney are drawn

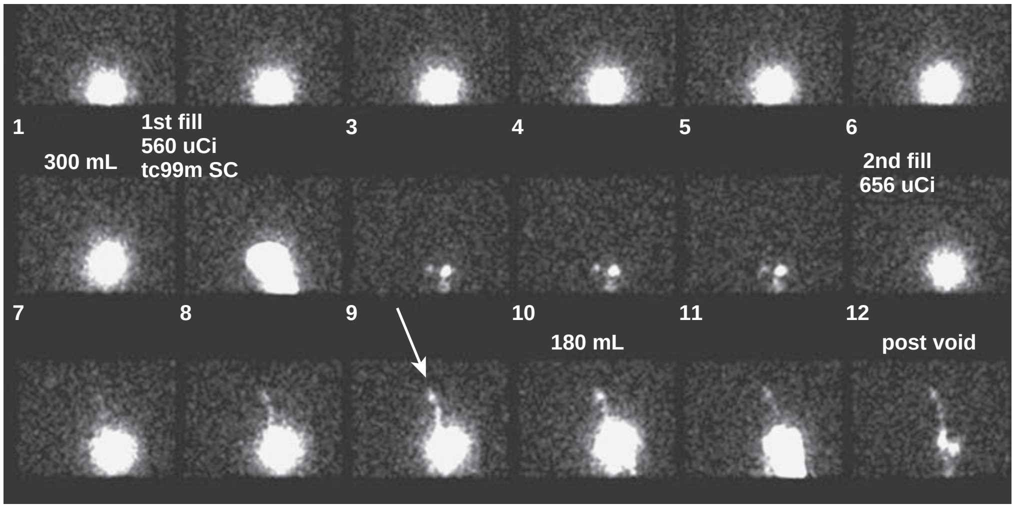

**e-Figure 111.7. Vesicoureteral reflux.** A cyclic nuclear cystogram demonstrates a normal first cycle, with intermediate-grade left reflux present on the second cycle only *(arrow)*.

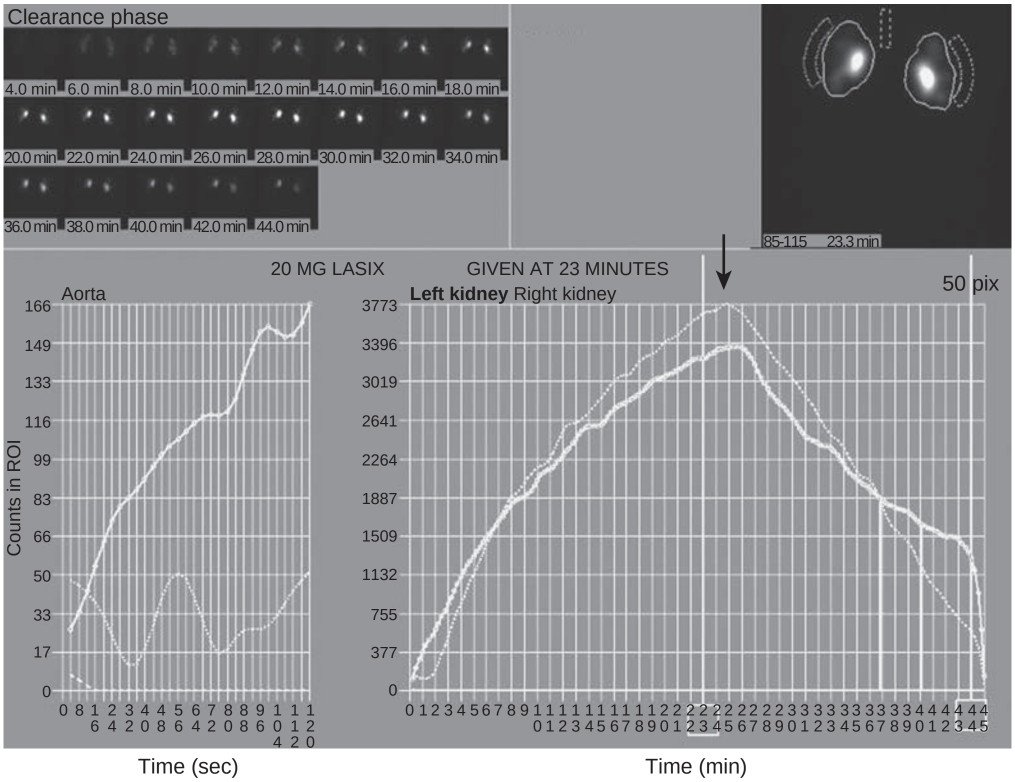

**e-Figure 111.9.** Time versus activity graph shows a steady accumulation of tracer in the renal region of interest until washout occurs, starting 3 minutes after injection of a diuretic agent *(arrow)*. Note the superolateral background region of interest adjacent to both kidneys. Also note mild urinary stasis and hydronephrosis, with no spontaneous excretion until after administration of a diuretic agent. The diuretic $T_{1/2}$ is approximately 10 minutes, which is considered normal in the presence of mild hydronephrosis.

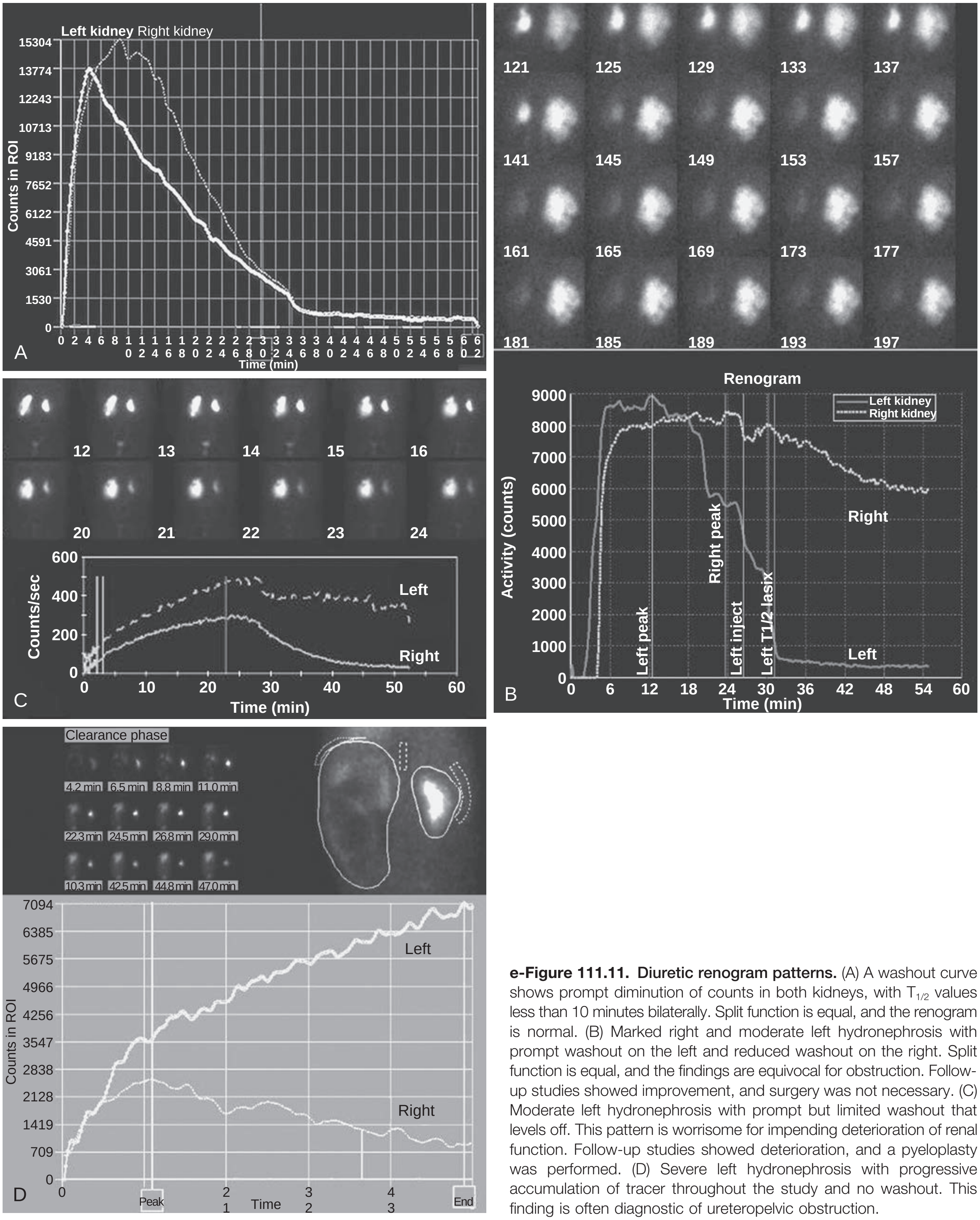

**e-Figure 111.11. Diuretic renogram patterns.** (A) A washout curve shows prompt diminution of counts in both kidneys, with $T_{1/2}$ values less than 10 minutes bilaterally. Split function is equal, and the renogram is normal. (B) Marked right and moderate left hydronephrosis with prompt washout on the left and reduced washout on the right. Split function is equal, and the findings are equivocal for obstruction. Follow-up studies showed improvement, and surgery was not necessary. (C) Moderate left hydronephrosis with prompt but limited washout that levels off. This pattern is worrisome for impending deterioration of renal function. Follow-up studies showed deterioration, and a pyeloplasty was performed. (D) Severe left hydronephrosis with progressive accumulation of tracer throughout the study and no washout. This finding is often diagnostic of ureteropelvic obstruction.

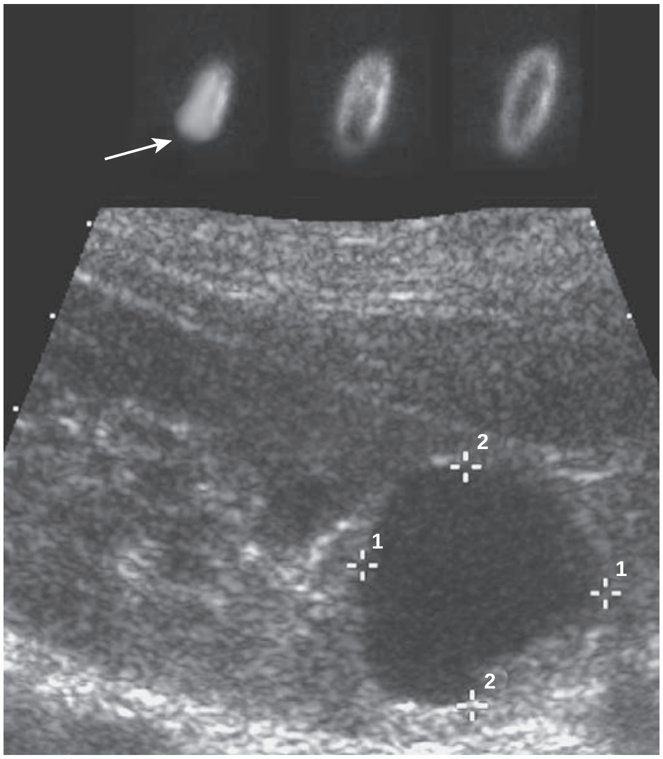

**e-Figure 111.15. Renal cyst.** Sagittal single photon emission computed tomography dimercaptosuccinic acid images show a rounded, photopenic defect in the lower pole *(arrow)*, which was shown to be a cyst on follow-up ultrasound.

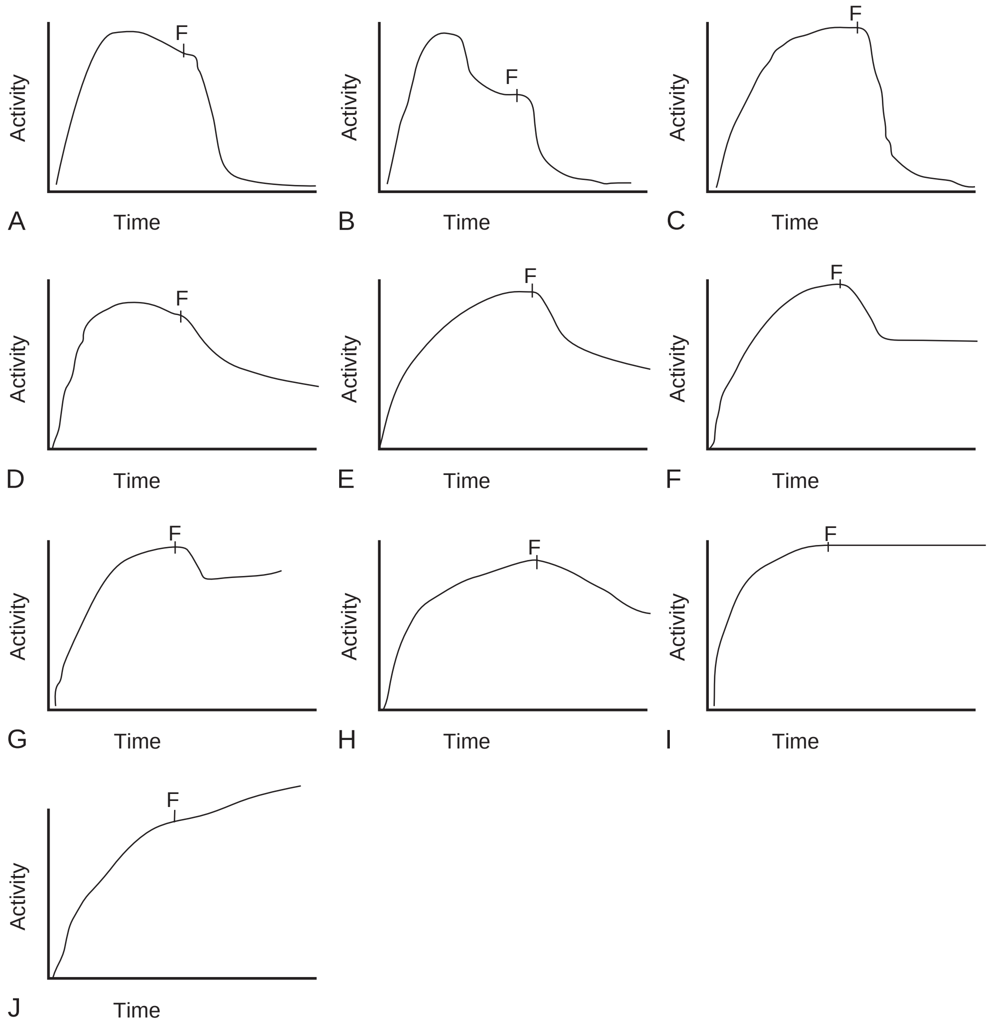

**Figure 111.10. Diuretic renogram patterns.** Patterns (A–C) are typically indicative of nonobstructed systems. Patterns (D and E) are equivocal in older children but usually indicate no obstruction in neonates and young infants with hydronephrosis. Patterns (F and G) often indicate flow-related obstruction. Patterns (H–J) typically indicate obstruction in older children but are seen frequently in neonates and infants with nonobstructive hydronephrosis. *F,* Furosemide injection.

from a posterior image, and relative function is given in terms of a percentage of total renal counts. The normal value is 50% ± 5%. Absolute renal function quantitation in terms of glomerular filtration rate or effective renal plasma flow can be performed with technetium-labeled DTPA and MAG-3, respectively, but these techniques require one to four blood samples.[41] Renal function increases rapidly in the first 2 years of life and reaches adult values, when normalized to body surface area, by age 2 years (normal values range from 80 to 140 mL/min/1.73 $m^2$).[41]

## COMPUTED TOMOGRAPHY

CT is one of our most powerful imaging tools. High-quality CT can be performed in patients of all ages and sizes and is not limited by bone or bowel gas. Relative immobility is required, and in children, reassurance, explanation of the procedure, the presence of a parent, sedation, and immobilization all contribute to a successful diagnostic study. Multidetector scanners that operate quickly obviate the need for sedation in many patients. Multiplanar reformatting, especially in the coronal plane, can aid in the depiction of the urinary tract.[42–44]

Noncontrast imaging is performed for calcifications or nephrolithiasis, but most CT imaging of the genitourinary system is performed with IV contrast material. Contrast enhancement is required for the evaluation of renal lesions and the vessels of the abdomen. Delayed imaging is useful for assessing the integrity of the collecting system (such as after trauma), assessing the course of the ureter, and evaluating certain renal masses and cystic lesions. CT radiation doses should be optimized based on patient size and the purpose of the study. Scanning begins based on the speed of the particular CT scanner and the information being sought. By showing the progression of contrast enhancement of the cortex, medulla, and collecting system of the kidneys, CT provides some assessment of renal function and anatomy.[45–50]

## MAGNETIC RESONANCE IMAGING

MRI has excellent tissue characterization, multiplanar capabilities, and the ability to gather functional and anatomic information. Meticulous attention to patient preparation and scanning technique is essential to reliably obtain high-quality images. Urine in the collecting system and ureter has low signal intensity on T1-weighted images and high signal intensity on T2-weighted scans. The kidney is easily visualized with intermediate signal on T1-weighted sequences and typically high signal on T2-weighted sequences. The renal cortex and medulla may demonstrate slightly different signal intensities on MRI (thus allowing visualization of corticomedullary differentiation), depending on the echo and repetition times chosen (Fig. 111.16).[51–58] A common indication for renal MRI in the pediatric population is the characterization of renal masses and cystic lesions.

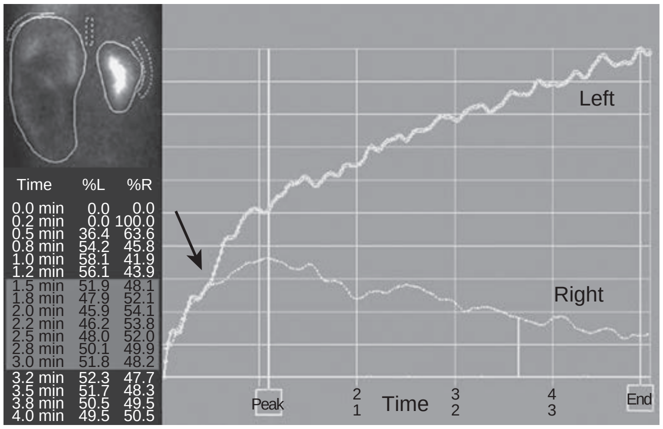

| Time | %L | %R |
|---|---|---|
| 0.0 min | 0.0 | 0.0 |
| 0.2 min | 0.0 | 100.0 |
| 0.5 min | 36.4 | 63.6 |
| 0.8 min | 54.2 | 45.8 |
| 1.0 min | 58.1 | 41.9 |
| 1.2 min | 56.1 | 43.9 |
| 1.5 min | 51.9 | 48.1 |
| 1.8 min | 47.9 | 52.1 |
| 2.0 min | 45.9 | 54.1 |
| 2.2 min | 46.2 | 53.8 |
| 2.5 min | 48.0 | 52.0 |
| 2.8 min | 50.1 | 49.9 |
| 3.0 min | 51.8 | 48.2 |
| 3.2 min | 52.3 | 47.7 |
| 3.5 min | 51.7 | 48.3 |
| 3.8 min | 50.5 | 49.5 |
| 4.0 min | 49.5 | 50.5 |

**Figure 111.12. Hydronephrosis.** A markedly enlarged left kidney with central photopenic regions consistent with marked hydronephrosis. The renogram shows tracer accumulation and retention throughout, with no discernible washout after administration of a diuretic. Note that the renogram tracings of the two kidneys are superimposed during the first few minutes after injection of the tracer *(arrow)*, which indicates nearly equal split renal function, as shown on the function table between 1.5 and 3 minutes.

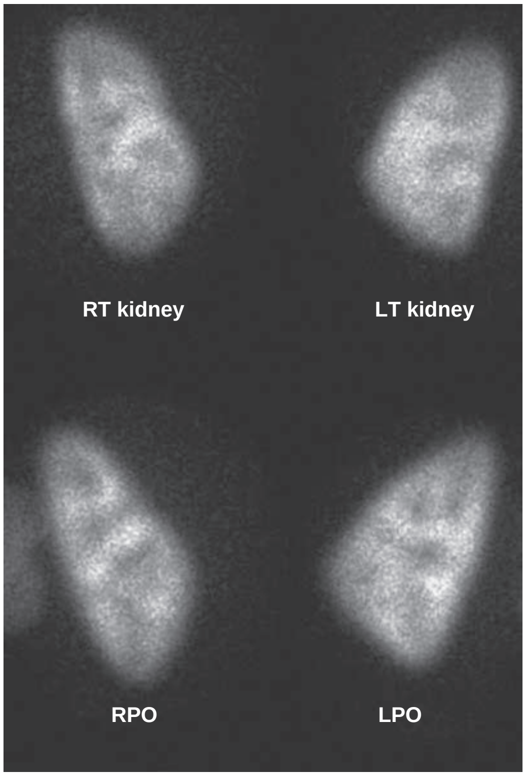

**Figure 111.13. Normal dimercaptosuccinic acid cortical scan.** Note the relative photopenia of the medulla due to a lack of uptake by the deeper portions of the loop of Henle. Also note the decreased intensity of the polar regions as a result of the relatively thinner polar cortex when compared with the midpolar region. *LPO,* Left posterior oblique; *LT,* left; *RPO,* right posterior oblique; *RT,* right.

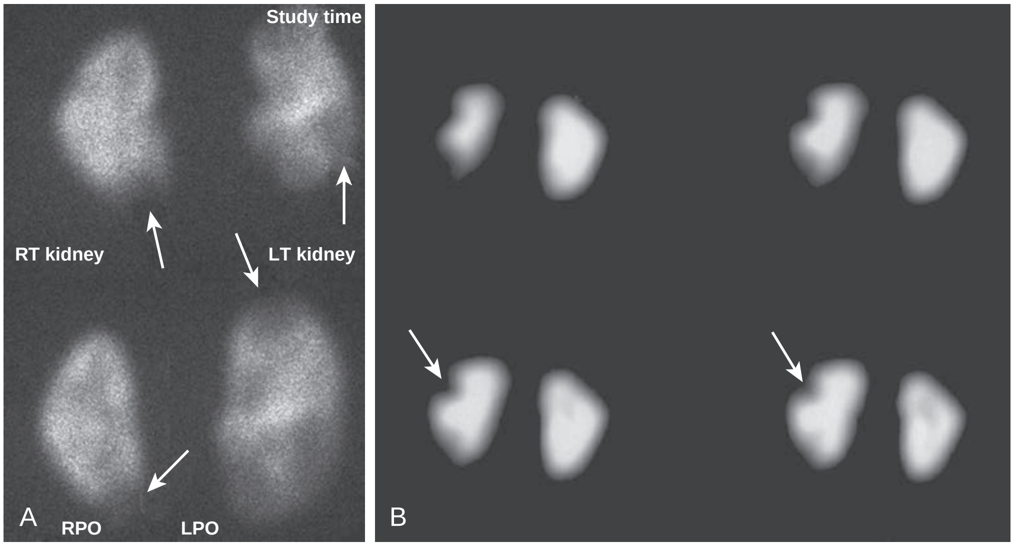

**Figure 111.14. Pyelonephritis versus scarring.** (A) Pinhole dimercaptosuccinic acid (DMSA) images obtained for split uptake assessment show bilateral photopenic defects that are rather poorly defined and not associated with renal parenchymal volume loss *(arrows)* indicating pyelonephritis. (B) Coronal single photon emission computed tomography glucoheptonate images show sharply defined wedge-shaped defects *(arrows)* indicative of renal scars. Glucoheptonate has been largely replaced by DMSA for cortical scintigraphy because of better binding characteristics. *LPO,* Left posterior oblique; *LT,* left; *RPO,* right posterior oblique; *RT,* right.

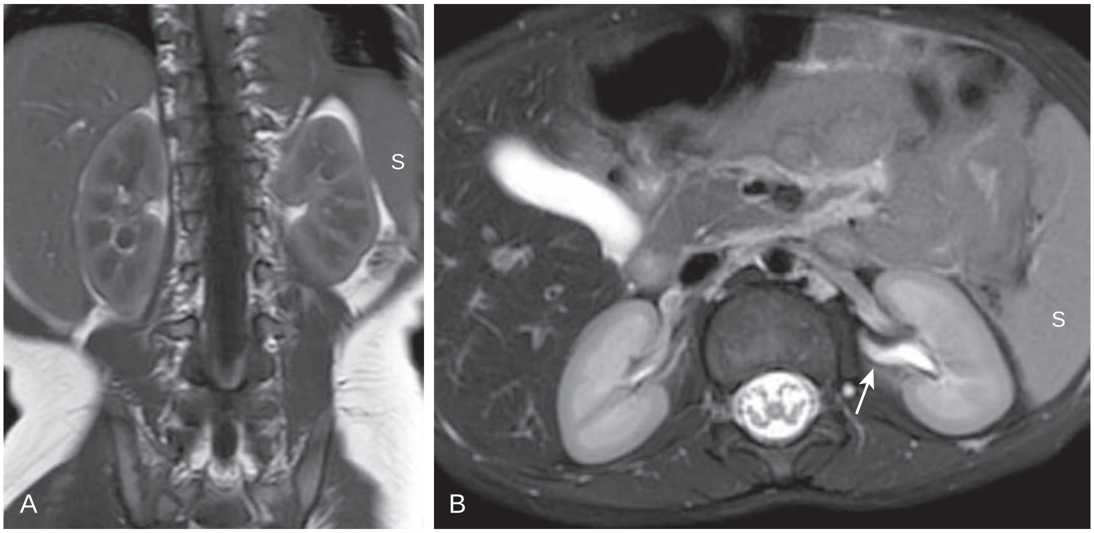

**Figure 111.16. Normal renal magnetic resonance image in a 1-year-old.** (A) A coronal T1-weighted fast spin-echo image shows that the renal cortex is near-isointense to the adjacent spleen *(S)* and the medulla is hypointense relative to the cortex. (B) An axial T2-weighted fast spin-echo fat-saturated image shows renal parenchyma is slightly hyperintense relative to the spleen *(S)*, with the medulla appearing brighter than cortex and the urine in the central pelvis appearing quite hyperintense *(arrow)*.

## Magnetic Resonance Urography

Magnetic resonance urography (MRU) represents the next stage in the evolution of uroradiology, fusing superb anatomic and functional imaging into a single test that does not use ionizing radiation (Fig. 111.17).[59–65] In addition to conventional T1- and T2-weighted images, dynamic imaging is performed in conjunction with the injection of a gadolinium-based contrast agent to assess the concentrating and excretory functions of the kidney (e-Fig. 111.18). The evaluation of the contrast dynamics is similar to renal scintigraphy but with the important distinction that the signals originating from the renal parenchyma can be separated from those originating from the collecting system. The primary indication for MRU is in the evaluation of hydronephrosis (e-Fig. 111.19). Other evolving indications for MRU include evaluation of renal scarring and dysplasia, identification of ectopic ureters in children with urinary incontinence, and characterization of complex urinary tract anatomy.

### Hydronephrosis and Obstructive Uropathy

Hydronephrosis is the most common indication for MRU in infants and children.[66] Ureteropelvic junction obstruction is the most common cause of neonatal hydronephrosis. Obstructive uropathy occurs in a subset of children with hydronephrosis and refers to obstruction that results in an injury to the kidney.[67] The kidney damage is not simply a result of mechanical impairment of urine flow but rather occurs as a result of a complex syndrome caused by the interaction of a variety of vasoactive factors and cytokines, leading to alterations of both glomerular hemodynamics and tubular function.[68] It is necessary to try to determine if the degree of obstruction present will lead to either a loss of renal function in the future or, in the case of children, will limit the future development of the kidney.

In children, obstruction is usually both chronic and partial. The partial obstruction results in equilibrium between urine production, impaired urine outflow, and pelvic reservoir capacity.[69] A steady state is reached between the amount of urine produced and the volume of the renal pelvis so that the pressure in the renal pelvis is in the normal range. This dynamic balance may be upset during diuresis or when the obstruction is exacerbated. The loss of balance results in a transient increase in pelvic pressure. It is unclear whether it is the frequency, duration, or severity of these transitory elevations in renal pelvic pressure that are responsible for renal damage and progressive loss of renal function.

One of the key strengths of MRU (also known as *functional MRU*, or fMRU) is its ability to dynamically assess signal intensity changes occurring within the renal parenchyma after administration of contrast material and in response to a fluid and diuretic challenge. Changes in renal physiology can be evaluated rapidly by examining how the perfusion, filtration, and concentration affect the handling of the contrast agent by the kidney.

With MRU, the hydronephrotic kidney is subjected to both a fluid challenge (IV hydration) and a diuretic challenge (IV furosemide administered ~15 minutes before the administration of contrast material). The response of the kidney to this challenge determines the appearance of the MR nephrogram. If symmetric changes in the signal intensity of the nephrogram occur, the hydronephrosis is classified as a compensated hydronephrotic system—that is, the fluid challenge has been accommodated without increasing the pressure in the pelvicalyceal system. However, when the signal intensity changes are asymmetric, they most often indicate acute or chronic obstruction—that is, the fluid challenge has exceeded the capacity for renal drainage, and the pressure in the collecting system rises. This hydronephrosis is classified as a decompensated hydronephrotic system. Signs associated with decompensation include parenchymal edema on the T2-weighted images, delayed calyceal transit time, and a delayed and increasingly dense (intense) nephrogram (Fig. 111.20). These two patterns have different prognostic implications; little improvement in renal function can be expected after pyeloplasty in compensated kidneys, but significant improvement is seen in decompensated systems.[70]

The quality of the renal parenchyma is assessed both on the high-resolution T2-weighted images and during the parenchymal phase of the nephrogram. Signs that suggest underlying uropathy and permanent damage include architectural disorganization with loss of the corticomedullary differentiation, small cysts,

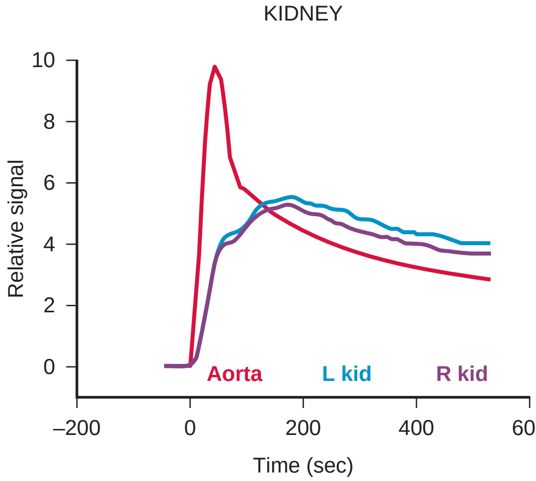

**e-Figure 111.18. Time intensity curves for the patient shown in Fig. 111.17.** These curves allow assessment and comparison of renal perfusion, concentration, and excretion similar to the time activity curves generated with diuretic renal scintigraphy.

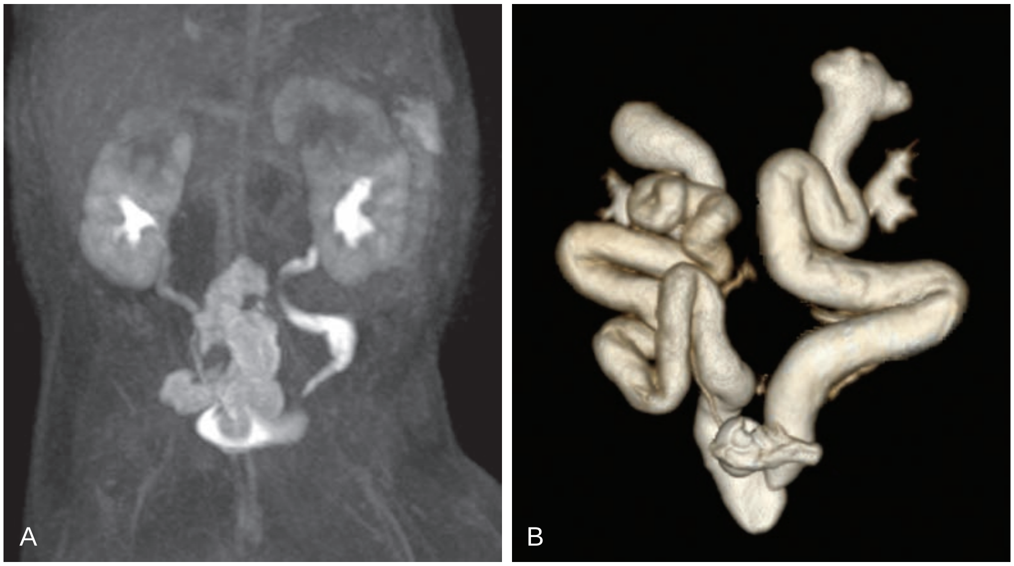

**e-Figure 111.19. Hydronephrosis and poor renal function.** Postcontrast T1-weighted maximum intensity projection (A) and 3D T2-weighted volume-rendered (B) MRU images show the anatomy and morphology of hydronephrotic and poorly functioning systems. Both kidneys are duplex with poorly functioning upper poles and associated megaureters. The lower pole ureters are seen on both the contrast-enhanced and the T2-weighted images. The ureters of the upper poles are only seen on the T2-weighted volume-rendered image, whereas the T1-weighted MIP only shows poorly enhancing parenchyma of the upper pole. The anatomy and insertion of the megaureters can be assessed on the T2-weighted urogram.

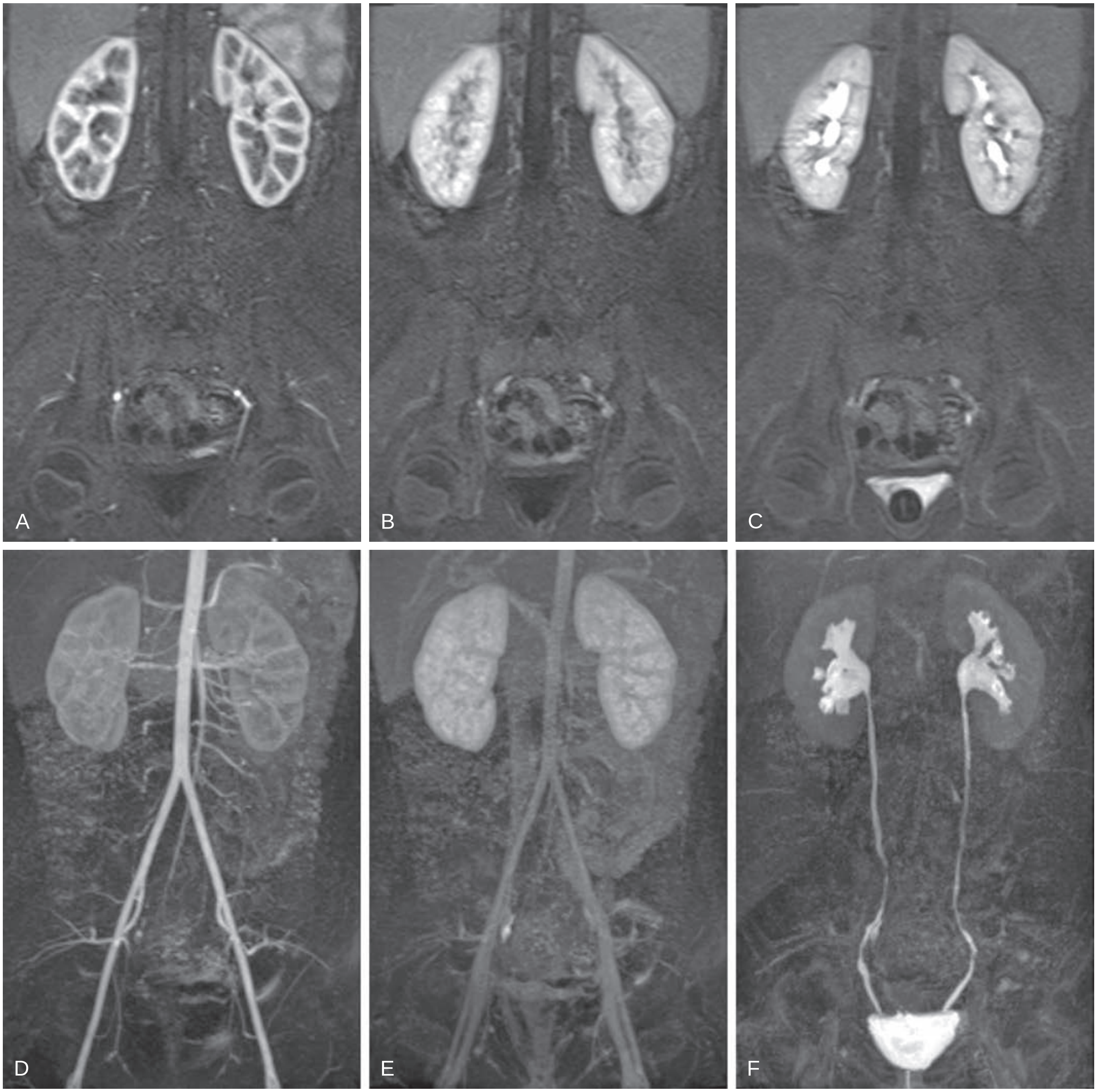

**Figure 111.17. Normal magnetic resonance urogram in an 8-year-old girl.** Images (A–C) show the same slice from three volume acquisitions acquired at time points corresponding to the cortical (arterial), parenchymal (nephrographic), and excretory phases of renal function, respectively. Images (D–F) are maximum intensity projections derived from the total volume for the three same time points.

and low cortical T2-weighted signal intensity (e-Fig. 111.21). The nephrogram in these cases usually shows dim and patchy contrast enhancement reflecting damage to the microvasculature, as well as to the glomeruli and tubules. These imaging findings probably reflect the histologic changes of renal damage based on reduced glomerular number, glomerular hyalinization, cortical cysts, and interstitial inflammation and fibrosis.[71] In contrast to uropathic kidneys, edematous kidneys typically show increased signal intensity on the T2-weighted images, as well as a delayed hyperintense nephrogram. The edematous pattern typically is seen either with decompensated hydronephrosis or acute pyelonephritis.

Anatomic information includes grading the hydronephrosis, identification of transition in the caliber of the ureter, and evaluation of underlying causes such as kinks, strictures, or crossing vessels.[72,73] Both the T2-weighted and delayed postcontrast images are used to define the pelvicalyceal and ureteric anatomy. The T2-weighted images (magnetic resonance [MR] hydrography) are particularly helpful in children with severe hydronephrosis and/or poorly functioning systems. Volumetric T2-weighted and

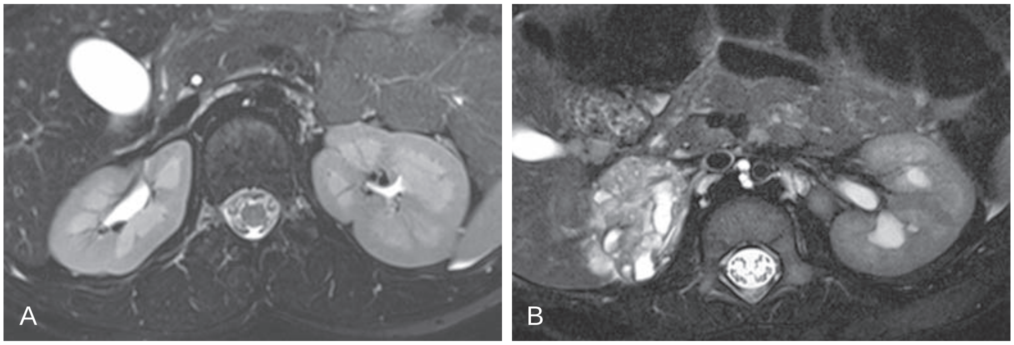

**e-Figure 111.21. Renal dysplasia.** High-resolution T2-weighted MR images show a patient with normal renal anatomy (A), whereas part (B) shows a patient with right renal dysplasia. MRU allows assessment of both the renal cortex and medulla and detection of cysts, scarring, edema, and architectural disorganization.

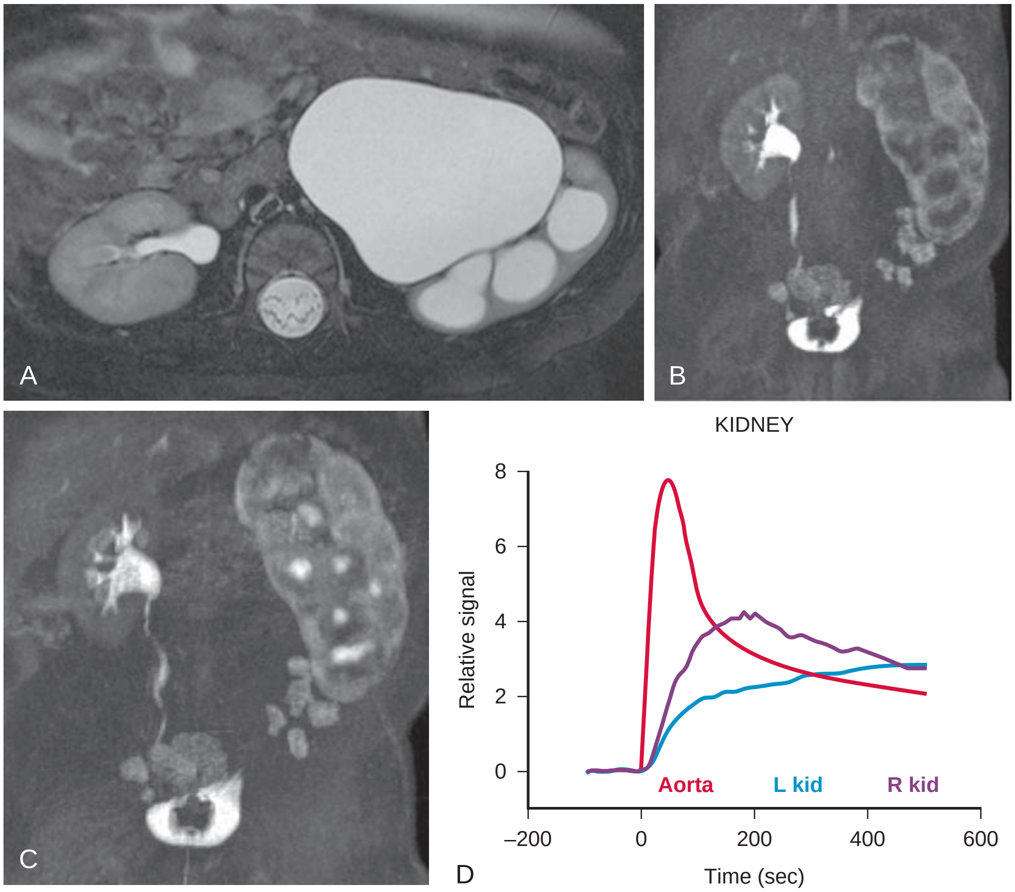

**Figure 111.20. Decompensated ureteropelvic junction obstruction in a 3-month-old girl.** (A) The axial T2-weighted MR image demonstrates marked hydronephrosis of the left kidney with ballooning of the calyces and thinning of the renal parenchyma. After administration of contrast material, calyceal excretion of contrast material is delayed on the left side (B), and an increasingly dense (intense) nephrogram is seen (C). The signal intensity versus time curve (D) shows delayed peak enhancement with gradual accumulation of signal within the parenchyma of the left kidney. *L,* Left; *R,* right.

postcontrast images can be used to generate exquisite volume-rendered and maximum intensity projection images of the pelvicalyceal systems and ureters.

## Congenital Malformations, Renal Scarring, and Dysplasia

Anomalies of renal fusion, position, and rotation are clearly demonstrated with MRU. Horseshoe and ectopic kidneys easily can be separated from the background and overlying tissues. Pelvic kidneys in particular are clearly demonstrated with MRU. Hypoplastic kidneys associated with ureteric ectopia and supernumerary kidneys usually can be demonstrated even if minimal renal function exists. MRU is the method of choice in the evaluation of incontinence associated with ectopic insertion of the ureter (Fig. 111.22).[74]

MRU enables identification of the acquired segmental scars most often associated with pyelonephritis and differentiation of areas of acute pyelonephritis from developed scars on the basis of mass effect and inflammatory changes. Acute pyelonephritis is associated with edema, mass effect, and swelling of the kidney. Mature scars are characterized by volume loss and contour defects of the kidney on T2-weighted images and perfusion defects on the dynamic contrast-enhanced images, and they exhibit dilatation of the adjacent calyx, indicating transmural parenchymal loss. Affected regions demonstrate no appreciable contrast enhancement, reflecting fibrosis and microvascular damage (Fig. 111.23).

The typical imaging features associated with dysplastic kidneys include small size, disorganized architecture with loss of normal corticomedullary differentiation, small cysts, decrease in signal intensity on T2-weighted images, poor perfusion, a dim and patchy nephrogram, and dysmorphic calyces.

### KEY POINTS

- Ultrasound is generally the first-line test for evaluating the kidneys and urinary tract in children.
- Antegrade VCUG is the examination of choice for detailed anatomic evaluation of the bladder, study of the anatomy of the male urethra, and identification of VUR.
- Nuclear cystography is performed as an alternative to VCUG for the assessment of VUR. Advantages include continuous imaging, which increases detection of VUR, reduced radiation dose, and detection of higher-grade VUR. Disadvantages include lack of detailed anatomic information and decreased information about the grade of VUR.
- Contrast-enhanced voiding urosonography sensitivity for VUR detection is comparable with that of standard techniques.

*Continued*

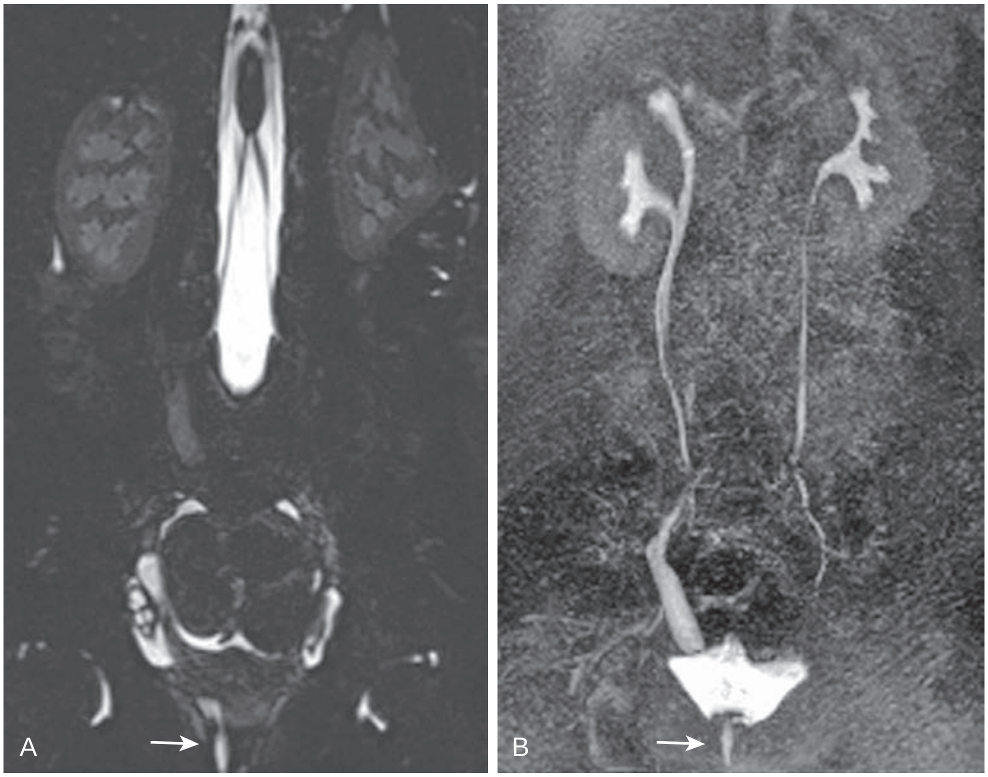

**Figure 111.22. Ectopic ureteric insertion in a 9-year-old girl with incontinence.** The T2-weighted MR image (A) shows a small cystic and dysplastic right upper pole moiety with a dilated ureter seen extending below the bladder base. On the delayed postcontrast maximum intensity projection image (B), the dilated ectopic ureter is seen inserting distally into the vagina *(arrows)*.

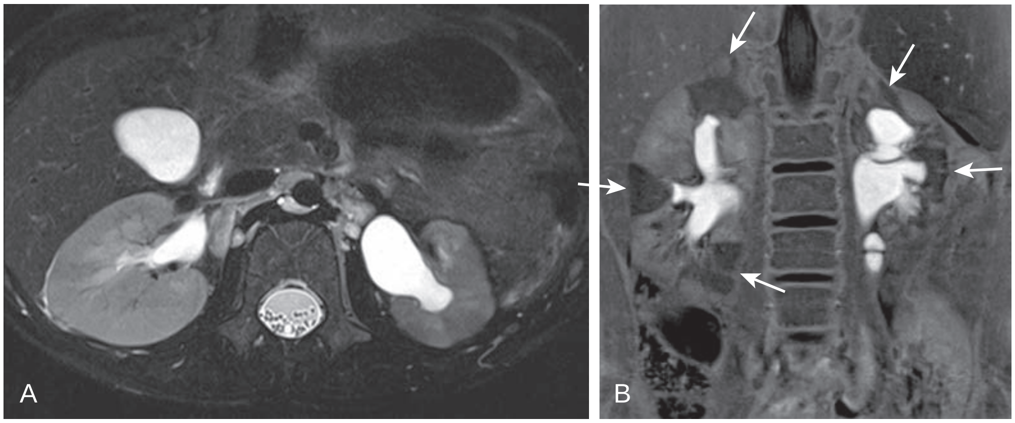

**Figure 111.23. Renal scarring in a 5-year-old girl with a history of a recurrent urinary tract infection.** An axial T2-weighted image (A) shows a smaller left kidney with disorganization of the renal parenchyma and focal areas of low signal intensity. Minimal abnormality is seen on the right. The inversion recovery image after administration of contrast material (B) shows triangular areas of decreased intensity with associated deformity of the renal contour bilaterally *(arrows)*. The scars are seen adjacent to the calyces.

- Cyclic voiding studies increase the detection of VUR in infants.
- Diuretic nuclear renography distinguishes obstructive from nonobstructive hydronephrosis based on the characteristics of the renogram generated, including differential renal function, renal extraction of radiotracer, and washout of radiotracer from the urinary collecting system. The examination is less accurate in young infants because of a high capacitance renal pelvis and relatively low urine output.
- The ability of MRU to provide a more complete characterization of renal anatomy and physiology has provided insights into the pathophysiology of hydronephrosis and the complex interaction of renal development, dysplasia, and scarring. MRU has the potential to revolutionize the imaging approach to renal disease in children.
- MRU is the method of choice in the evaluation of incontinence associated with ectopic insertion of the ureter.

## SUGGESTED READINGS

Darge K. Voiding urosonography with ultrasound contrast agents for the diagnosis of vesicoureteric reflux in children. I. Procedure. *Pediatr Radiol*. 2008;38(1):40–53.

Darge K, Grattan-Smith JD, Riccabona M. Pediatric uroradiology: state of the art. *Pediatr Radiol*. 2011;41(1):82–91.

Dickerson EC, Dillman JR, Smith EA, et al. Pediatric MR Urography: indications, techniques, and approach to review. *Radiographics*. 2015;35(4):1208–1230.

Jones RA, Grattan-Smith JD, Little S. Pediatric magnetic resonance urography. *J Magn Reson Imaging*. 2011;33:510–526.

Jones RA, Votaw JR, Salman K, et al. Magnetic resonance imaging evaluation of renal structure and function related to disease: technical review of image acquisition, postprocessing, and mathematical modeling steps. *J Magn Reson Imaging*. 2011;33:1270–1283.

Riccabona M, Lindbichler F, Sinzig M. Conventional imaging in pediatric uroradiology. *Eur J Radiol*. 2002;43:100–109.

## REFERENCES

Full references for this chapter can be found on www.expertconsult.com.

## REFERENCES

1. Darge K, Riedmiller H. Current status of vesicoureteral reflux diagnosis. *World J Urol*. 2004;22:88–95.
2. Riccabona M, Lindbichler F, Sinzig M. Conventional imaging in pediatric uroradiology. *Eur J Radiol*. 2002;43:100–109.
3. McEwing RL, Anderson NG, Hellewell S. Comparison of echo-enhanced ultrasound with fluoroscopic MCU for the detection of vesicoureteral reflux in neonates. *Pediatr Radiol*. 2002;32:853–858.
4. Medina LS, Aguirre E, Altman NR. Vesicoureteral reflux imaging in children: comparative cost analysis. *Acad Radiol*. 2003;10:139–144.
5. Papdopoulou F, Efremidis SC, Oiconomou A, et al. Cyclic voiding cystourethrography: is vesicoureteral reflux missed with standard voiding cystourethrography. *Eur Radiol*. 2002;12:666–670.
6. Piaggio G, Degl' Innocenti ML, Toma P. Cystosonography and voiding cystourethrography in the diagnosis of vesicoureteral reflux. *Pediatr Nephrol*. 2003;18:18–22.
7. Persinakis K, Raissaki M, Damilakis J, et al. Fluoroscopy-controlled voiding cystourethrography in infants and children: are the radiation risks trivial? *Eur Radiol*. 2006;16:846–851.
8. Persliden J, Helmrot E, Hjort P, et al. Dose and image quality in the comparison of analogue and digital techniques in paediatric urology examinations. *Eur Radiol*. 2004;14:638–644.
9. Lederman HM, Khademian ZP, Felice M. Dose reduction fluoroscopy in pediatrics. *Pediatr Radiol*. 2002;32:844–848.
10. Ward VL, Barnewolt CE, Strauss KY, et al. Radiation exposure reduction during voiding cystourethrography in a pediatric porcine model of vesicoureteral reflux. *Radiology*. 2006;238:96–106.
11. Kis E, Nyitrai A, Várkonyi I, et al. Voiding urosonography with second-generation contrast agent versus voiding cystourethrography. *Pediatr Nephrol*. 2010;25(11):2289–2293.
12. Darge K. Voiding urosonography with ultrasound contrast agents for the diagnosis of vesicoureteric reflux in children. I. Procedure. *Pediatr Radiol*. 2008;38(1):40–53.
13. Riccabona M. Urinary tract imaging in infancy. *Pediatr Radiol*. 2009;39(suppl 3):436–445.
14. Darge K. Voiding urosonography with US contrast agent for the diagnosis of vesicoureteric reflux in children: an update. *Pediatr Radiol*. 2010;40(6):956–962.
15. Kiessling I, Bzyl J, Kiessling F. Molecular ultrasound imaging and its potential for paediatric radiology. *Pediatr Radiol*. 2011;41(2):176–184.
16. Avni EF, Brion LE. Ultrasound of the neonate urinary tract. *Urol Radiol*. 1983;5:177–183.
17. Hricak H, Slovis TL, Callen CW, et al. Neonatal kidneys: sonographic-anatomic correlation. *Radiology*. 1983;147:699–702.
18. Keller MS. Renal Doppler sonography in infants and children. *Radiology*. 1989;172:603–604.
19. Coley BD. Pediatric applications of abdominal vascular Doppler: part II. *Pediatr Radiol*. 2004;34:772–786.
20. Masch WR, Cohan RH, Ellis JH, et al. Clinical effectiveness of prospectively reported sonographic twinkling artifact for the diagnosis of renal calculus in patients without known urolithiasis. *AJR Am J Roentgenol*. 2016;206(2):326–331.
21. Haller JO, Berdon WE, Friedman AP. Increased renal cortical echogenicity: a normal finding in neonates and infants. *Radiology*. 1982;142:173–174.
22. Jequier S, Paltiel H, Lafortune M. Ureterovesical jets in infants and children: duplex and color Doppler US studies. *Radiology*. 1990;175:349–353.
23. Kraus RA, Gaisie G, Young LW. Increased renal parenchymal echogenicity: causes in pediatric patients. *Radiographics*. 1990;10:1009–1018.
24. Riccabona M. Modern pediatric ultrasound: potential applications and clinical significance: a review. *Clin Imaging*. 2006;30:77–86.
25. Scoutt LM, Zawin ML, Taylor KWJ, et al. Clinical applications. *Radiology*. 1990;174:309–319.
26. Wiener JS, O'Hara SM. Optimal timing of initial postnatal ultrasonography in newborns with prenatal hydronephrosis. *J Urol*. 2002;168:1826–1829.
27. Mandell GA, Eggli DF, Gilday DL, et al *Society of Nuclear Medicine procedure guideline for radionuclide cystography in children* (pdf): http://interactive.snm.org/docs/pg_ch32_0703.pdf. Accessed January 3, 2013.
28. Bower G, Lovegrove FT, Geijsel H, et al. Comparison of "direct" and "indirect" radionuclide cystography. *J Nucl Med*. 1985;26(5):465–468.
29. Gelfand MJ, Koch BL, Elgazzar AH, et al. Cyclic cystography: diagnostic yield in selected pediatric populations. *Radiology*. 1999;213:118–120.
30. Dikshit MP, Acharya VN, Shikare S, et al. Comparison of direct radionuclide cystography with micturating cystourethrography for the diagnosis of vesicoureteric reflux, and its correlation with cystoscopic appearances of the ureteric orifices. *Nephrol Dial Transplant*. 1993;8(7):600–602.
31. Merrick MV, Notghi A, Chalmers N, et al. Long-term follow up to determine the prognostic value of imaging after urinary tract infections. Part 1: Reflux. *Arch Dis Child*. 1995;72(5):388–392.
32. Ward VL, Strauss KJ, Barnewolt CE, et al. Pediatric radiation exposure and effective dose reduction during voiding cystourethrography. *Radiology*. 2008;249(Iss 3).
33. Conway JJ, Maizels M. The "well tempered" diuretic renogram: a standard method to examine the asymptomatic neonate with hydronephrosis or hydroureteronephrosis. A report from combined meetings of the Society for Fetal Urology and members of the Pediatric Nuclear Medicine Council–Society of Nuclear Medicine. *J Nucl Med*. 1992;33:2047–2051.
34. Mandell GA, Cooper JA, Leonard JC, et al *Society of Nuclear Medicine procedure guideline for diuretic renography in children* (pdf): http://interactive.snm.org/docs/pg_ch29_0403.pdf. Accessed January 3, 2013.
35. Koff SA, Binkovitz L, Coley B, et al. Renal pelvis volume during diuresis in children with hydronephrosis: implications for diagnosing obstruction with diuretic renography. *J Urol*. 2005;174:303–307.
36. Gordon I. Diuretic renography in infants with prenatal unilateral hydronephrosis: an explanation for the controversy about poor drainage. *BJU Int*. 2001;87:551–555.
37. Mandell GA, Eggli DF, Gilday DL, et al *Society of Nuclear Medicine procedure guideline for renal cortical scintigraphy in children* (pdf): http://interactive.snm.org/docs/pg_ch32_0403.pdf. Accessed January 3, 2013.
38. Piepsz A, Colarinha P, Gordon I, et al *Guidelines on* $^{99m}$*Tc-DMSA scintigraphy in children* (pdf): http://www.eanm.org/publications/guidelines/gl_paed_dmsa_scin.pdf. Accessed January 3, 2013.
39. Ruston HG, Majd M, Chandra R, et al. Evaluation of 99m technetium-dimercapto-succinic acid renal scans in experimental acute pyelonephritis in piglet. *J Urol*. 1988;140:1169–1174.
40. Stokland E, Hellstrom M, Jacobsson B, et al. Renal damage one year after first urinary tract infection: role of dimercaptosuccinic acid scintigraphy. *J Pediatr*. 1996;129(6):815–820.
41. Piepsz A, Colarinha P, Gordon I, et al *Guidelines for glomerular filtration rate determination in children* (pdf): http://www.eanm.org/publications/guidelines/gl_paed_gfrd.pdf. Accessed January 3, 2012.
42. Donnelly LF, Frush DP. Pediatric multidetector body CT. *Radiol Clin North Am*. 2003;41:637–655.
43. Huang J, Kim YH, Shankar S, et al. Multidetector CT urography: comparison of two different scanning protocols for improved visualization of the urinary tract. *J Comput Assist Tomogr*. 2006;30:33–36.
44. Siegel MJ. Protocols for helical CT in pediatrics. In: Silverman PM, ed. *Helical (Spiral) Computed Tomography: A Practical Approach to Clinical Protocols*. New York: Lippincott-Raven; 1998.
45. Strouse PJ, Bates DG, Bloom DA, et al. Non-contrast thin-section helical CT of urinary tract calculi in children. *Pediatr Radiol*. 2002;32:326–332.
46. Kawamoto S, Horton KM, Fishman EK. Opacification of the collecting system and ureters on excretory-phase CT using oral water as contrast medium. *AJR Am J Roentgenol*. 2006;186:136–140.
47. Frush DP. Pediatric CT: practical approach to diminish the radiation dose. *Pediatr Radiol*. 2002;32:714–717.
48. Frush DP. Review of radiation issues for computed tomography. *Semen Ultrasound CT MR*. 2004;25:17–24.
49. Kokako E, Bratt S, Dora VS. Renal multidetector row CT. *Radiol Clin North Am*. 2005;43:1021–1047.
50. Nakayama Y, Awai K, Fenamate Y, et al. Abdominal CT with low tube voltage: preliminary observations about radiation dose, contrast enhancement, image quality, and noise. *Radiology*. 2005;237:945–951.
51. Borthen A, Pierre-Jerome C, Gestalt KI. Pediatric excretory MR urography: comparative study of enhanced and non-enhanced techniques. *Eur Radiol*. 2003;13:1423–1427.
52. Grant PE, Matsuda KM. Applications of new MR techniques in pediatric patients. *Magn Reson Imaging Clin N Am*. 2003;11:493–522.
53. Riccabona M. Pediatric MRU—its potential and its role in the diagnostic work-up of upper urinary tract dilatation in infants and children. *World J Urol*. 2004;22:79–87.
54. Riccabona M, Ruppert-Kohlmayr A, Ring E, et al. Potential impact of pediatric MR urography on the imaging algorithm in patients with a functional single kidney. *AJR Am J Roentgenol*. 2004;183:795–800.

55. Rohrschneider WK, Haufe S, Clorius JH. MR to assess renal function in children. *Eur Radiol*. 2003;13:1033–1045.
56. Staatz G, Nolte-Ernsting CC, Adam GB, et al. Feasibility and utility of respiratory-gated, gadolinium-enhanced T1-weighted magnetic resonance urography in children. *Invest Radiol*. 2000;35:504–512.
57. Verswijvel GA, Oyen RH, Van Poppel HP, et al. Magnetic resonance imaging in the assessment of urologic disease: an all-in-one approach. *Eur Radiol*. 2000;10:1614–1619.
58. Bennett HF, Debiao L. MR imaging of renal function. *Magn Reson Imaging Clin N Am*. 1997;5:107–126.
59. Jones RA, Grattan-Smith JD, Little S. Pediatric magnetic resonance urography. *J Magn Reson Imaging*. 2011;33:510–526.
60. Grattan-Smith JD, Jones RA. Magnetic resonance urography in children. *Magn Reson Imaging Clin N Am*. 2008;16:515–531.
61. Grattan-Smith JD, Jones RA. MR urography: technique and results for the evaluation of urinary obstruction in the pediatric population. *Magn Reson Imaging Clin N Am*. 2008;16:643–660.
62. Rohrschneider WK, Becker K, Hoffend J, et al. Combined static-dynamic MR urography for the simultaneous evaluation of morphology and function in urinary tract obstruction. II. Findings in experimentally induced ureteric stenosis. *Pediatr Radiol*. 2000;30:523–532.
63. Rohrschneider WK, Haufe S, Wiesel M, et al. Functional and morphologic evaluation of congenital urinary tract dilatation by using combined static-dynamic MR urography: findings in kidneys with a single collecting system. *Radiology*. 2002;224:683–694.
64. Vivier PH, Dolores M, Taylor M, et al. MR urography in children. Part 1: how we do the F0 technique. *Pediatr Radiol*. 2010;40:732–738.
65. Vivier PH, Dolores M, Taylor M, et al. MR urography in children. Part 2: how to use ImageJ MR urography processing software. *Pediatr Radiol*. 2010;40:739–746.
66. Lebowitz RL, Griscom NT. Neonatal hydronephrosis: 146 cases. *Radiol Clin North Am*. 1977;15:49–59.
67. O'Reilly PH. Obstructive uropathy. *Q J Nucl Med*. 2002;46:295–303.
68. Chevalier RL, Thornhill BA, Forbes MS, et al. Mechanisms of renal injury and progression of renal disease in congenital obstructive nephropathy. *Pediatr Nephrol*. 2010;25:687–697.
69. Koff SA. Pathophysiology of ureteropelvic junction obstruction. Clinical and experimental observations. *Urol Clin North Am*. 1990;17:263–272.
70. Little SB, Jones RA, Grattan-Smith JD. Evaluation of UPJ obstruction before and after pyeloplasty using MR urography. *Pediatr Radiol*. 2008;38(suppl 1):S106–S124.
71. Elder JS, Stansbrey R, Dahms BB, et al. Renal histological changes secondary to ureteropelvic junction obstruction. *J Urol*. 1995;154:719–722.
72. Weiss DA, Kadakia S, Kurzweil R, et al. Detection of crossing vessels in pediatric ureteropelvic junction obstruction: clinical patterns and imaging findings. *J Pediatr Urol*. 2015;11(4):173.e1–173.e5. doi:10.1016/j.jpurol.2015.04.017. [Epub 2015 May 27].
73. Parikh KR, Hammer MR, Kraft KH, et al. Pediatric ureteropelvic junction obstruction: can magnetic resonance urography identify crossing vessels? *Pediatr Radiol*. 2015;45(12):1788–1795. doi:10.1007/s00247-015-3412-y. PMID: 26216155.
74. Avni FE, Nicaise N, Hall M, et al. The role of MR imaging for the assessment of complicated duplex kidneys in children: preliminary report. *Pediatr Radiol*. 2001;31:215–223.

# 112 Prenatal Imaging and Intervention

*Teresa Chapman and Judy A. Estroff*

## OVERVIEW

Fetal genitourinary system abnormalities encompass a wide spectrum of disorders varying in degrees of severity and include developmental anomalies, obstructive lesions in the urinary tract, and renal parenchymal diseases. The prenatal evaluation of the genitourinary system includes assessment of the amniotic fluid, the kidneys, the bladder, and associated anomalies. Amniotic fluid is important for normal fetal development, particularly the fetal lungs. In the first trimester, amniotic fluid forms as a dialysate of maternal serum. Fetal urine production begins by 12 weeks of gestation and becomes the major source of amniotic fluid by 16 weeks. Fetal urine production is typically 120 mL/day at 20 weeks and increases gradually to 1200 mL/day by term. The fetus voids every 30 to 60 minutes. The bladder should be visualized at least once during a prenatal imaging examination.[1,2]

Identification of the fetal urinary bladder is attempted in the first trimester ultrasound, and more detailed evaluation of the kidneys and bladder is a fundamental part of the second trimester fetal anatomic assessment. Complex cases, such as bladder exstrophy, confusing duplex collecting systems, and obstructive masses, may be further evaluated by fetal magnetic resonance imaging (MRI).[3–5] Sonographic fetal anatomic assessment may be limited in the setting of oligohydramnios, and MRI may be particularly useful. Prenatal findings may influence the further pursuit of genetic and laboratory testing or surgical intervention and may guide the delivery plan.

## NORMAL FETAL GENITOURINARY TRACT

***Overview and Imaging.*** Fetal kidneys can be identified at 13 weeks of gestation. Normal renal sizes through gestation (mean kidney length in millimeters is slightly longer than weeks of gestation) are shown in Table 112.1.[6,7] Corticomedullary differentiation is apparent by 20 weeks of gestation (Fig. 112.1). Renal calyces and ureters typically are not seen on ultrasound unless they are pathologically dilated,[8] and the renal pelvis is only readily visualized once the anterior-posterior diameter exceeds 2 mm.[9] The fetal bladder can be visualized at 10 weeks of gestation. The bladder wall should not measure more than 3 mm. Bladder wall thickening may be a sign of outlet obstruction.[10,11]

Amniotic fluid volume can be a reflection of renal health. Oligohydramnios (defined by an amniotic fluid index less than 8 cm)[12] may be seen in the setting of placental insufficiency, intrauterine growth retardation, chromosomal abnormality, premature rupture of membranes, post-dates gestation, or urologic pathology (Box 112.1).[13]

## RENAL PARENCHYMAL DISORDERS

***Overview.*** Fetal renal echogenicity may be abnormally increased as a normal variant but more often reflects an underlying abnormality. The fetal kidney is considered echogenic if it is brighter than the fetal liver. Echogenic kidneys are observed in approximately 1 to 2 per 1000 fetal ultrasounds, and approximately 10% of cases of renal malformations include echogenic kidneys.[14,15] Etiologic considerations for the echogenic kidney are summarized in Box 112.2.[16–24] If echogenic kidneys are identified and the amniotic fluid volume is normal, the findings suggest nonlethal renal disease. Echogenic kidneys with oligohydramnios are highly concerning for a poor outcome.[25]

## CYSTIC RENAL DISEASE

***Overview.*** Congenital cystic renal diseases occur in about 2 to 4 in 1000 live births and include autosomal dominant and autosomal recessive polycystic kidney disease (Fig. 112.2 and Video 112.1), multicystic dysplastic kidney (Fig. 112.3), cystic glomerulopathies, and other cystic renal dysplasias. The complex pathogenesis of these disorders involves an abnormal orchestration of transcription and growth factor expression (Table 112.2), as well as ciliopathies affecting the renal tubule primary cilium (Table 112.3).[26–29] Structural and functional abnormalities in primary cilia contribute to various cystic phenotypes that involve the kidney and liver.[27]

***Imaging.*** These types of renal cystic abnormalities may be demonstrated in the fetus either by ultrasound or MRI.[27,30–36] Fetal sonographic evaluation of the kidneys should include renal length,

**TABLE 112.1** Normal Fetal Renal Lengths

| Gestational Age (wk) | Mean Kidney Length (cm) | 95% Confidence Interval (cm) |
|---|---|---|
| 18 | 2.2 | 1.6-2.8 |
| 19 | 2.3 | 1.5-3.1 |
| 20 | 2.6 | 1.8-3.4 |
| 21 | 2.7 | 2.1-3.2 |
| 22 | 2.7 | 2-3.4 |
| 23 | 3 | 2.2-3.7 |
| 24 | 3.1 | 1.9-4.4 |
| 25 | 3.3 | 2.5-4.2 |
| 26 | 3.4 | 2.4-4.4 |
| 27 | 3.5 | 2.7-4.4 |
| 28 | 3.4 | 2.6-4.2 |
| 29 | 3.6 | 2.3-4.8 |
| 30 | 3.8 | 3.9-4.6 |
| 31 | 3.7 | 2.8-4.6 |
| 32 | 4.1 | 3.1-5.1 |
| 33 | 4 | 3.3-4.7 |
| 34 | 4.2 | 3.3-5 |
| 35 | 4.2 | 3.2-5.2 |
| 36 | 4.2 | 3.3-5 |
| 37 | 4.2 | 3.3-5.1 |
| 38 | 4.4 | 3.2-5.6 |
| 39 | 4.2 | 3.5-4.8 |
| 40 | 4.3 | 3.2-5.3 |
| 41 | 4.5 | 3.9-5.1 |

*Modified from Cohen HL, Cooper J, Eisenberg P, et al. Normal length of fetal kidneys.* Am J Roentgenol. *1991;157:545–548.*

**BOX 112.1** Renal Etiologies for Oligohydramnios

- Bilateral renal agenesis
- Bilateral multicystic dysplastic kidney
- Bilateral severe ureteropelvic junction obstruction
- Bilateral renal disease with one kidney each involved with items 1, 2, or 3 above
- Severe prune-belly syndrome
- Severe autosomal recessive polycystic kidney disease
- Severe renal dysplasia as a result of posterior urethral valves or urethral atresia

## Abstract:

Fetal genitourinary system abnormalities including congenital malformations, obstructive lesions in the urinary tract, and renal parenchymal diseases may be identified by prenatal ultrasound. The prenatal evaluation of the genitourinary system includes assessment of the amniotic fluid, the kidneys, the bladder, and associated anomalies. Fetal magnetic resonance imaging (MRI) adds to the sonographic evaluation in the setting of oligohydramnios or in complex or confusing cases. Prenatal findings may influence the further pursuit of genetic and laboratory testing or surgical intervention, and may guide the delivery plan. In this chapter, the normal sonographic and MRI appearance of the genitourinary system is reviewed. Abnormalities of renal parenchyma, including renal masses, as well as urinary tract dilatation and its appropriate management are discussed. Lower urinary tract outlet obstruction and potential prenatal surgical interventions are reviewed as well.

## Keywords:

Fetal MRI
urinary tract dilatation
megacystitis
renal cystic disease
renal tumor
lower urinary tract obstruction

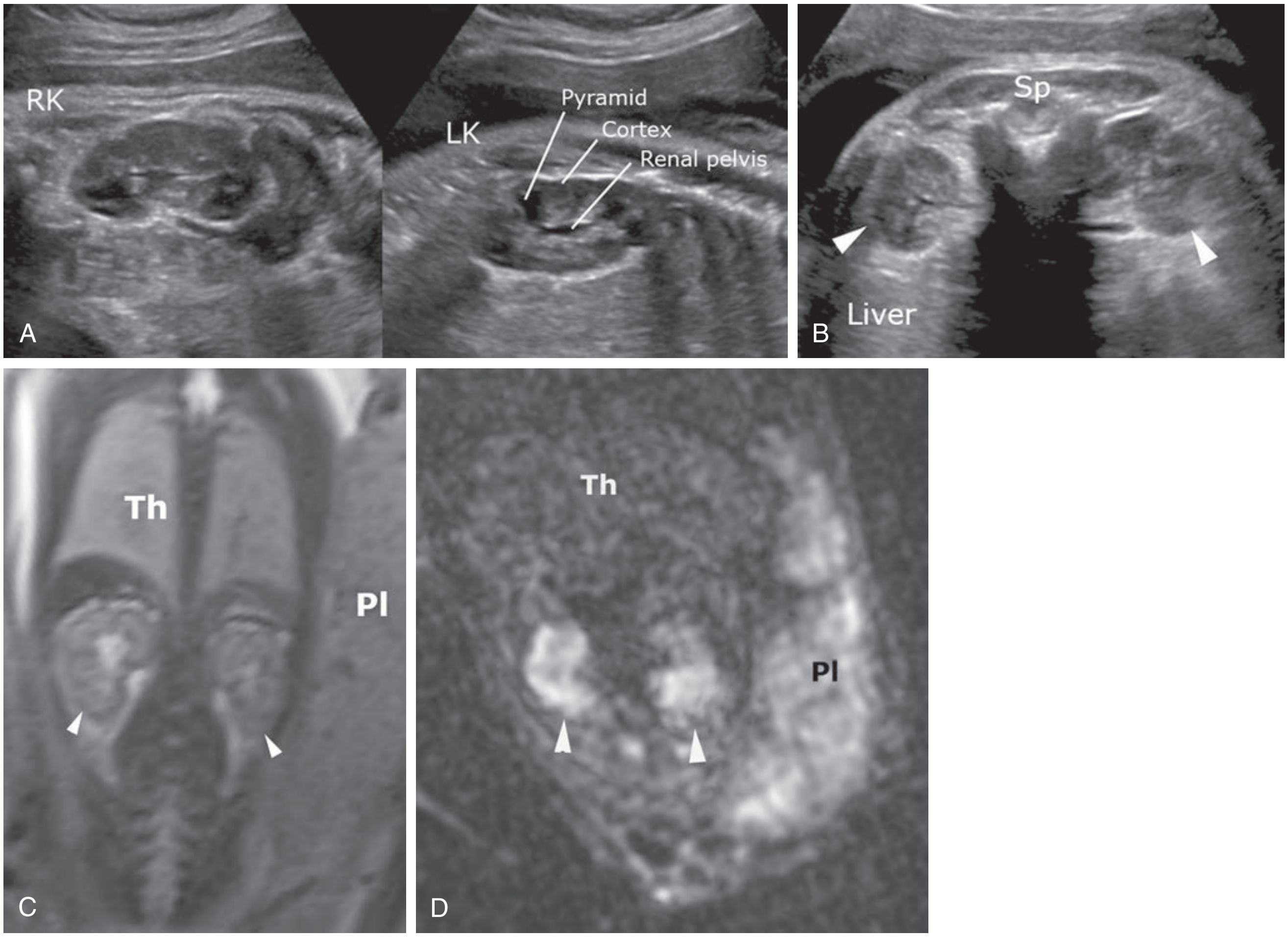

**Figure 112.1. Normal fetal kidneys.** (A) Longitudinal sonogram of the fetal kidneys at 32 weeks' gestational age shows a thin layer of perinephric fat with normal corticomedullary differentiation. A small amount of fluid is present in the central renal pelvis. (B) Transverse sonogram of the fetal kidneys shows the renal parenchyma *(arrowheads)* is hypoechoic to liver. (C) Coronal T2-weighted single-shot fast-spin echo magnetic resonance (MR) image through the fetal abdomen at 27 weeks' gestational age shows normal corticomedullary differentiation of the kidneys *(arrowheads)*. The renal cortex is isointense to muscle. The renal medulla is mildly hyperintense. (D) Large field-of-view diffusion-weighted MR image in coronal plane through the same fetus shows normal hyperintense kidneys *(arrowheads)*. *LK*, Left kidney; *Pl*, placenta; *RK*, right kidney; *Sp*, spine; *Th*, Thorax.

**BOX 112.2** Causes of Fetal Echogenic Kidney

- Idiopathic
- Cystic renal disease
- Infection
- Chromosomal abnormalities
- Toxic and ischemic insults

overall echogenicity, preservation of corticomedullary differentiation, and presence of macroscopic cysts. Renal size may be considered abnormally increased if it is greater than or equal to 2 standard deviations (moderately enlarged) or greater than or equal to 4 standard deviations (markedly enlarged) greater than expected for gestational age.[6] Renal echogenicity greater than that of the liver or spleen is abnormal (Fig. 112.4), and corticomedullary differentiation may be lost or reversed if renal parenchymal disease is present.[27] MRI also readily shows abnormalities in renal size and detects renal cysts. Dysplastic parenchyma typically increases the T2-weighted signal intensity (e-Fig. 112.5).

***Approach to Diagnosis.*** A differential diagnostic approach to fetal echogenic renal cystic diseases is summarized in Table 112.4. If macroscopic cysts are observed without abnormal renal echogenicity, possible etiologies will depend on the number of cysts observed. Visualization of a single renal cyst should prompt consideration of a cystic tumor, a duplex collecting system with cystic dysplasia of the upper pole, urinoma, asymmetric presentation of autosomal dominant polycystic kidney disease (ADPKD), or an isolated cyst in an otherwise normal kidney. Multiple cysts may be seen with multicystic dysplastic kidney, ADPKD, tuberous sclerosis complex, and *TCF2* gene mutation–associated nephropathy.

## RENAL TUMORS

***Overview and Imaging.*** A solid, round echogenic mass in the fetal kidney (Fig. 112.6) is most likely to be a congenital mesoblastic nephroma (CMN), also known as a *leiomyomatous hamartoma* or a *fetal renal hamartoma*, although a Wilms tumor may present in the fetus as well.[37] Both tumor types can replace the kidney or be localized. Tumors may be vascular with cystic areas as a result of hemorrhage and cystic degeneration. Polyhydramnios may occur (seen in 40% of renal tumor cases) and may lead to premature

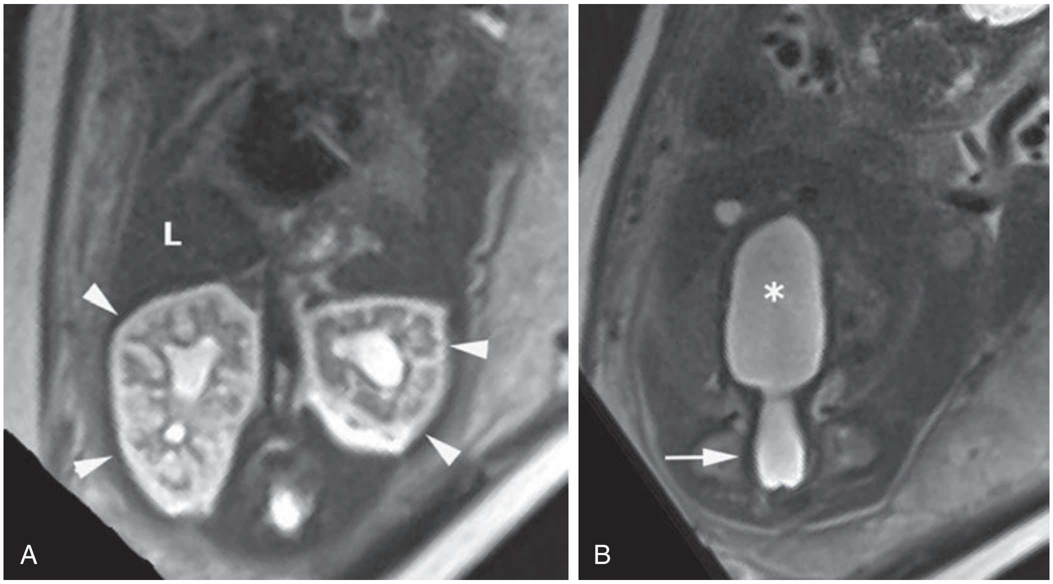

**e-Figure 112.5. Abnormal intensity of renal parenchyma on fetal MRI.** (A) Coronal T2-weighted single-shot fast spin-echo MR image through the abdomen of a fetus at 27 weeks' gestational age shows markedly hyperintense renal cortices *(arrowheads)* bilaterally. Urinary tract dilatation is evident bilaterally. (B) Coronal image through the fetal pelvis shows an abnormally dilated urinary bladder *(asterisk)* and dilated posterior urethra *(small arrow)*, with urinary bladder wall thickening, consistent with urinary bladder outlet obstruction by posterior urethral valves. Note the absence of amniotic fluid.

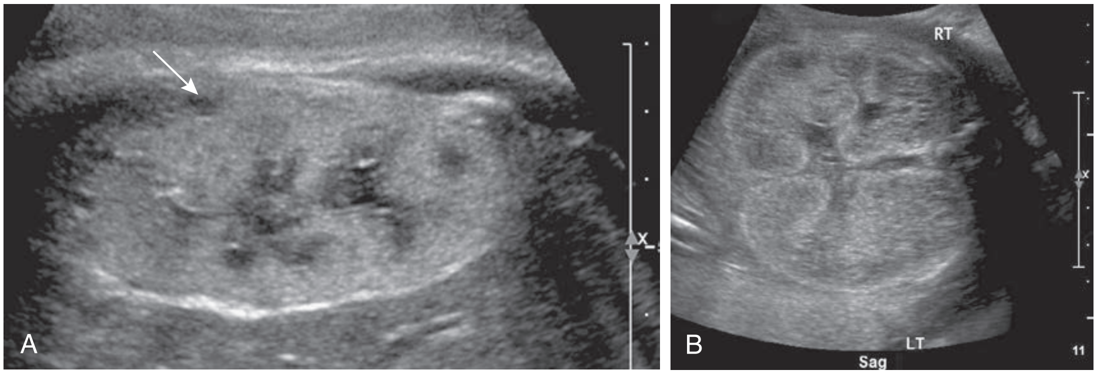

**Figure 112.2. Autosomal dominant polycystic kidney disease (ADPKD) and autosomal recessive polycystic kidney disease (ARPKD).** (A) Longitudinal sonogram of a fetus at 36 weeks' gestational age shows an enlarged echogenic kidney measuring more than 6 cm in length with small peripheral cysts *(arrow)*. The contralateral kidney also was large and echogenic. Amniotic fluid remained normal throughout the pregnancy. The father also had ADPKD. (B) Coronal sonogram of both kidneys of a different fetus at 23 weeks' gestational age shows marked nephromegaly and diffusely increased echogenicity with poor corticomedullary differentiation. This appearance is created by the innumerable acoustic reflections by dilated tubules. *LT*, Left kidney; *RT*, right kidney.

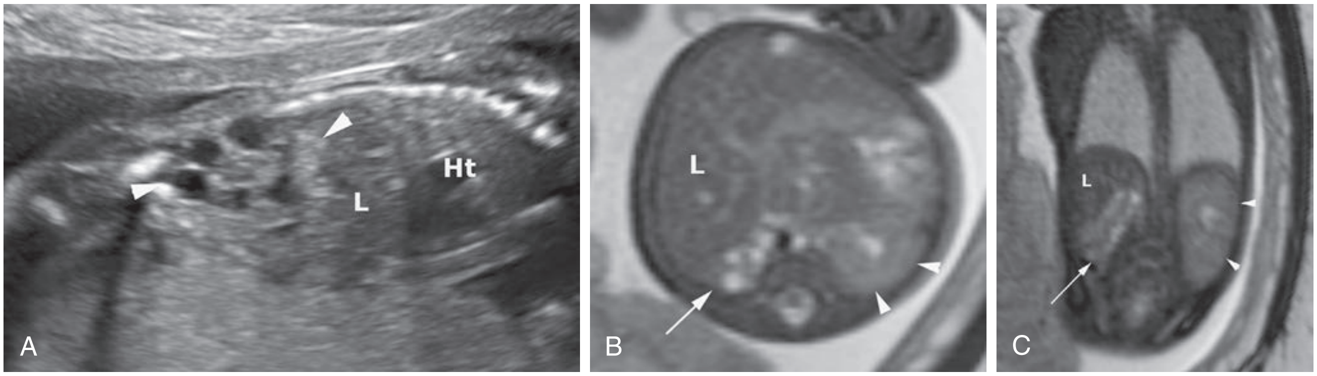

**Figure 112.3. Multicystic dysplastic kidney.** (A) Longitudinal sonogram of the right kidney in a fetus at 20 weeks' gestational age shows an enlarged kidney (outlined by *arrowheads* at superior and inferior poles) with macroscopic cysts not communicating with the collecting system. There is minimally discernible renal parenchyma that is echogenic and disorganized. (B) Axial and (C) coronal steady-state free precession MR image of the same fetus at 31 weeks' gestational age shows decreased size of the multicystic mass *(arrow)* in the right renal fossa with no normal renal tissue. Left kidney *(arrowheads)* is normal. *Ht*, Heart; *L*, liver.

**TABLE 112.2** Selected Examples of Gene Mutations Resulting in Congenital Urinary Tract Abnormalities

| Renal Abnormality | PAX2 (paired box 2 gene, 10q24.31) | HNF1B (HNF1B Homeobox B, 17q12) | EYA1 (EYA transcriptional coactivator and phosphatase 1 gene, 8q13.3) | SIX1 (SIX Homeobox 1, 14q23.1) | SALL1 (Spalt like transcription factor 1, 16q12.1) | GATA3 (GATA binding protein 3 gene, 10p14) |
|---|---|---|---|---|---|---|
| Dysplasia | √ | √ | √ | √ | √ | √ |
| Renal agenesis | | | √ | √ | | √ |
| Renal hypoplasia | √ | √ | | | √ | |
| Ureteropelvic junction obstruction | √ | √ | | | √ | |
| Vesicoureteral reflux | | | | | √ | √ |
| Glomerulocystic kidney disease | | √ | | | | |
| Syndrome | Renal-coloboma | MODY5 | BOR | BOR | Townes-Brock | HDR |

*BOR,* Brachio-oto-renal; *HDR,* hypoparathyroidism, deafness, and renal dysplasia; *MODY5,* maturity-onset diabetes, type 5.

*Modified from Bonsib SM. The classification of renal cystic diseases and other congenital malformations of the kidney and urinary tract.* Arch Pathol Lab Med. *2010;134(4):554–568.*

**TABLE 112.3** Ciliopathies: Molecular, Genetic, and Pathologic Features

| Ciliopathy | Protein | Inheritance | Lesions |
|---|---|---|---|
| Autosomal dominant PKD | Polycystin 1, Polycystin 2 | AD | Cysts within the entire nephron |
| Autosomal recessive PKD | Fibrocystin | AR | Collecting duct cysts |
| Meckel-Gruber syndrome | MKS proteins 1, 3 | AR | Cystic dysplasia |
| Oral-facial-digital syndrome | OFD protein | X-linked | Glomerular kidney disease |
| Bardet-Beidl syndrome | BBS proteins 1-8 | Digenic | Tubulointerstitial nephritis |
| Von Hippel-Lindau | VHL protein | AR | Renal cysts (premalignant) and renal cell carcinoma |

*AD,* Autosomal dominant; *AR,* autosomal recessive; *PKD,* polycystic kidney disease.
*Modified from Bonsib SM. The classification of renal cystic diseases and other congenital malformations of the kidney and urinary tract.* Arch Pathol Lab Med. *2010;134(4):554–568.*

**TABLE 112.4** Differential Diagnosis: Fetal Renal Cystic Disease With Echogenic Kidneys by Ultrasound[33]

| Diagnosis | Gestational Age at Diagnosis | Degree of Renal Enlargement | Additional Findings |
|---|---|---|---|
| Meckel-Gruber Syndrome | Late first trimester, early second trimester | Markedly enlarged | Hypoechoic renal medulla; polydactyly; cerebral anomalies |
| ARPKD | Mid to late second trimester, third trimester | Moderately to markedly enlarged | Reversal of corticomedullary differentiation; possible oligohydramnios; few visible cysts are rare but possible |
| Bardet-Biedl syndrome | Second trimester, third trimester | Markedly enlarged | Postaxial polydactyly; cysts may be observed |
| ADPKD | Second trimester, third trimester | Moderately enlarged | |
| TCF2 gene mutation–associated nephropathy | Second trimester, third trimester | Moderately enlarged | Family history of diabetes is frequent; spectrum of expression includes glomerulocystic change, renal dysplasia, and renal agenesis; cysts may be observed |

*ADPKD,* Autosomal dominant polycystic kidney disease; *ARPKD,* autosomal recessive polycystic kidney disease.
*From Avni FE, Hall M. Renal cystic diseases in children: new concepts.* Pediatr Radiol. *2010;40:9399–9946; Cassart M, Eruin D, Didier F, et al. Antenatal renal sonographic anomalies and postnatal follow-up of renal involvement in Bardet-Biedl syndrome.* Ultrasound Obstet Gynecol. *2004;24:51–54.*

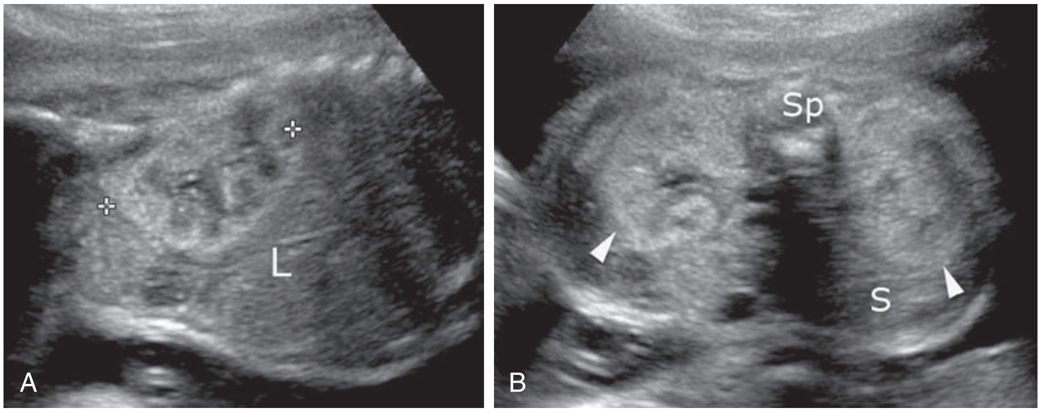

**Figure 112.4. Echogenic kidneys in a fetus at 29 weeks' gestational age by ultrasound.** (A) Longitudinal sonogram through the right kidney, which measures 37 mm. (B) Transverse sonogram through both kidneys *(arrowheads)*. The renal cortices are brighter than the liver *(L)* and spleen *(S)*. Renal length is normal for this gestational age, and the amniotic fluid volume is normal. *Sp*, Spine.

labor, and fetal renal tumor patients have increased perinatal complications.[38] Although CMN is generally benign, resection is recommended as a small percentage exhibit aggressive or malignant behavior.

## ANTENATAL HYDRONEPHROSIS

***Overview.*** Pyelectasis (dilatation of the fetal renal collecting system) is seen in 1% to 5% of screened fetuses.[39–45] Numerous factors influence renal pelvis dilation, including maternal hydration, fetal bladder filling, or the presence of an extrarenal pelvis (e-Fig. 112.7). Fetuses with trisomy 21 have an increased incidence of mild pyelectasis (>4 mm in the second trimester).[46] If mild pyelectasis is observed, other anomalies or risk factors should be present before pursuing cell-free fetal DNA testing, because the specificity of aneuploidy with isolated pyelectasis is low.[47–49] Most fetuses with mild pyelectasis are normal (approximately 90% or more).[42,45,50,51] Apart from the risk for chromosomal aneuploidy,

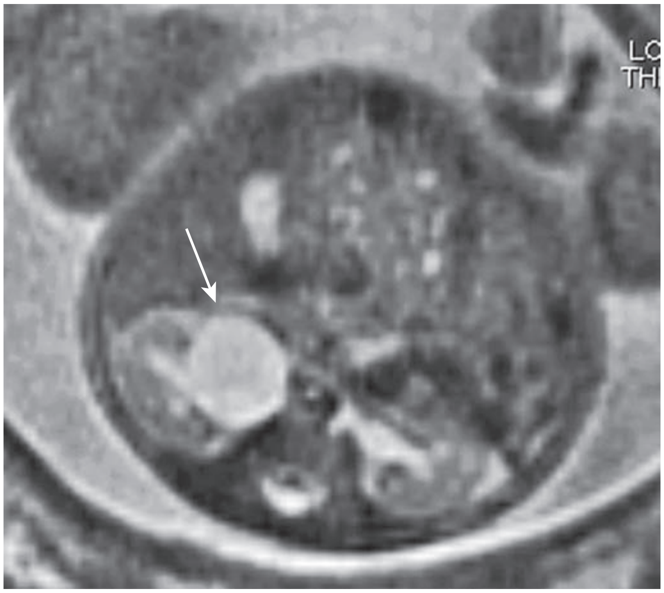

**e-Figure 112.7. Extrarenal pelvis versus ureteropelvic junction obstruction.** Axial single-shot fast spin-echo T2-weighted MR image of both fetal kidneys shows a large extrarenal pelvis on the right *(arrow)*. The renal cortex remains thick. Postnatal imaging (not shown here) confirmed a mildly dilated extrarenal pelvis without obstruction.

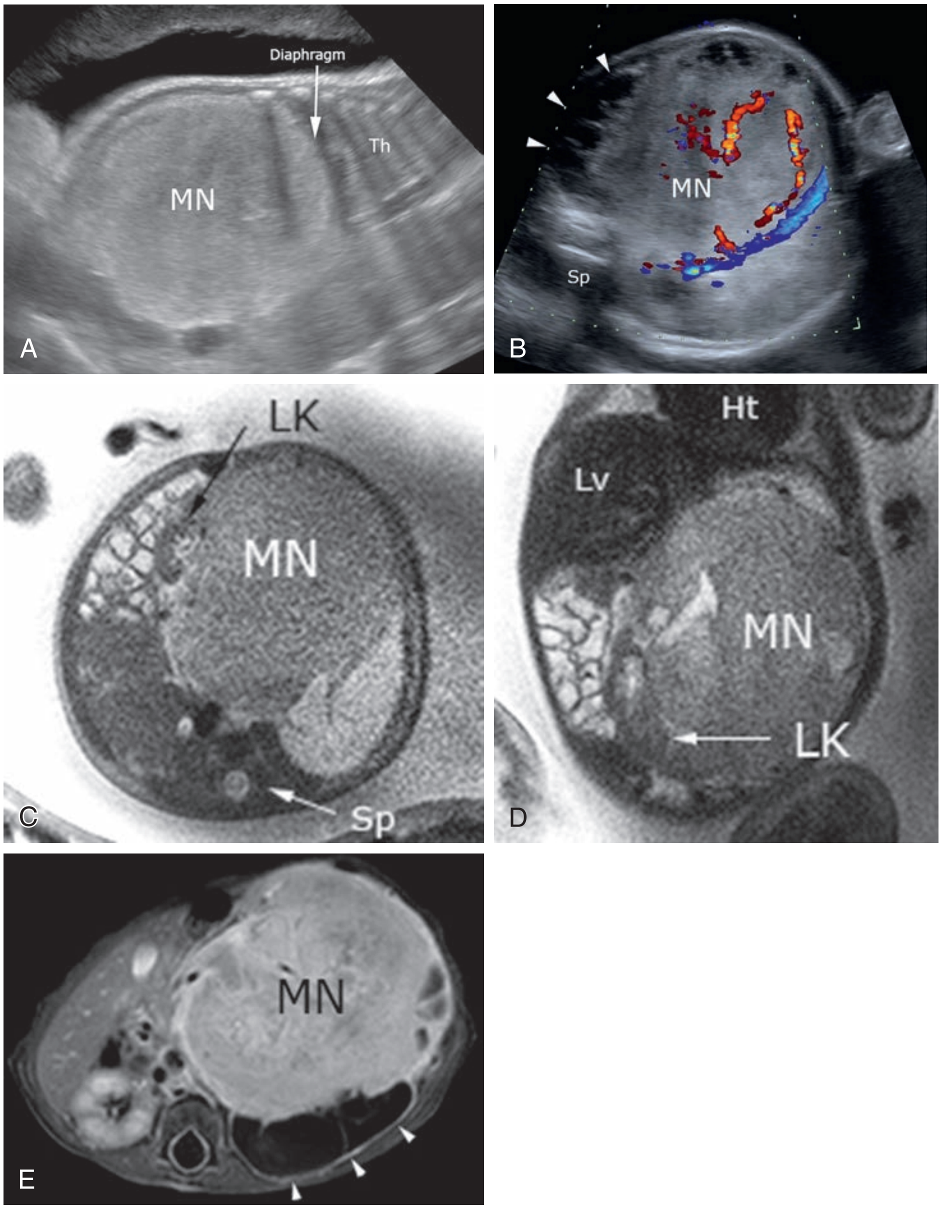

**Figure 112.6. Fetal mesoblastic nephroma.** (A) Longitudinal gray-scale and (B) transverse color Doppler prenatal ultrasound images at 36 weeks' gestational age show a large left retroperitoneal echogenic vascular mass with marginal anechoic spaces *(white arrowheads)* consistent with cystic components. Subsequent single-shot fast spin-echo fetal 3T MR images in (C) axial and (D) coronal planes show mass displacing the left renal parenchyma *(LK)* anteriorly. (E) Postnatal contrast-enhanced MR image in axial plane shows enhancing solid tissue with rim-enhancing marginal cystic components *(arrowheads)*. Pathology was confirmed after nephrectomy. *Ht*, Heart; *Lv*, liver; *MN*, mesoblastic nephroma; *Sp*, spine; *Th*, thorax. *(Images courtesy Dr. Pinar Karakas-Rothey, Benioff Children's Hospital Oakland, Oakland, California.)*

pyelectasis in the fetus may signify either obstruction or vesicoureteral reflux, so follow-up later in gestation and postnatally must be considered. Causes of bilateral hydronephrosis are presented in Box 112.3.

***Imaging.*** In 2014 a consensus classification system for urinary tract dilatation (UTD) was established by eight relevant societies.[45] The UTD Classification System applies to both prenatal and postnatal diagnosis. The severity of the urinary tract dilation is based on six categories: (1) anterior-posterior renal pelvic diameter (APRPD); (2) calyceal dilation; (3) renal parenchymal thickness; (4) renal parenchymal appearance; (5) bladder abnormalities; and (6) ureteral abnormalities. The classification system is stratified based on gestational age (16–27 weeks vs. 28 weeks or greater). Antenatal urinary tract dilation is declared as either low risk (UTD A1) or increased risk (UTD A2-3). If the APRPD is 4 to less than 7 mm at 16 to 27 weeks gestational age (GA) or 7 to less than 10 mm at 28 weeks or greater, and if no other abnormality of the urinary tract is present (Fig. 112.8), then the UTD is classified as A1 (low risk). However, if the APRPD is greater than or equal to 7 mm at 16 to 27 weeks or greater than or equal to 10 mm at 28 weeks or greater, or if any additional abnormality is present (unexplained oligohydramnios, peripheral caliectasis,

### BOX 112.3 Bilateral Hydronephrosis: Etiologies in a Fetus

**URETERAL LESIONS**

- Ureteropelvic junction obstruction
- Ureterovesicular junction obstruction/congenital primary megaureter
- Mid ureteral stricture/valve

**BLADDER OUTLET LESIONS**

- Ureterocele with obstruction
- Posterior urethral valves
- Urethral atresia
- Vesicoureteral reflux
- Prune-belly syndrome
- Megacystis-microcolon-hypoperistalsis syndrome

### BOX 112.4 Urinary Tract Dilatation (UTD) Classification System

| | |
|---|---|
| UTD A1 | Minimal dilation of renal pelvis only:<br>4 to <7 mm (16–27 wks GA)<br>7 to <10 mm (28 wks GA or older) |
| UTD A2-3 | Moderate to severe dilation of renal pelvis and possibly peripheral calices:<br>>7 mm (16–27 wks GA)<br>>10 mm (28 wks GA or older)<br>Parenchyma abnormal: thinning, cysts, or echogenic<br>Unexplained oligohydramnios; abnormal ureter; abnormal urinary bladder |

*From Nguyen HT, Benson CB, Bromley B, et al. Multidisciplinary consensus on the classification of prenatal and postnatal urinary tract dilation (UTD classification system).* J Pediatr Urol. *2014;10:982–998.*
*GA,* Gestational age.

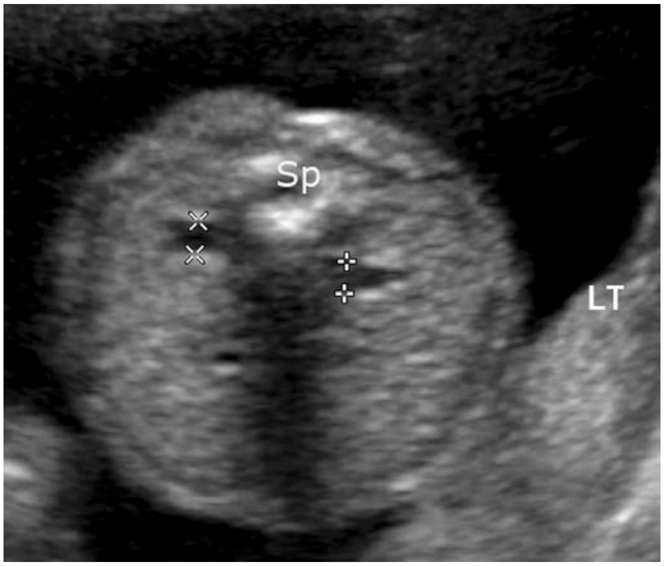

**Figure 112.8. Fetal urinary tract dilatation, low risk (UTD A1).** A transverse ultrasound image of a fetus at 20 weeks' gestational age shows calipers marking the anterior-posterior diameter of both renal pelves, measuring between 4 to 7 mm. The renal parenchyma is normal, and ureters and urinary bladder were normal *(not shown)*. This mild degree of UTD is classified as low risk. *LT,* Left; *Sp,* spine.

renal parenchymal abnormality, ureterectasis, or urinary bladder abnormality), then the UTD is classified as increased risk (A2-3) (Box 112.4 and Fig. 112.9).

Management recommendations based on the UTD classification are also proposed.[45] The main goals of follow-up imaging are to identify fetal kidneys at risk for renal failure or infection, and to identify fetuses that may benefit from fetal surgical intervention (discussed later in this chapter). For UTD A1 diagnosed before 32 weeks, a follow-up prenatal ultrasound is recommended at greater than or equal to 32 weeks. If the repeat ultrasound at greater than or equal to 32 weeks shows resolution of the UTD and no abnormality of the renal parenchyma, bladder, and ureters, then no further prenatal or postnatal follow-up is necessary. However, if there is persistent UTD A1 or UTD A2-3, evaluation after birth is recommended.

Postnatal evaluation should include two ultrasound evaluations. The first ultrasound usually is performed at least 2 days after birth to avoid underestimating collecting system dilatation as a result of physiologic oliguria in the first 48 hours of life and within 1 month after birth; the second ultrasound study is then performed 1 to 6 months later.[45,52,53] Follow-up should be performed sooner for suspected obstructive uropathies, such as posterior urethral valves (as suggested by a thick-walled bladder with persistent urinary tract dilation and/or posterior urethral dilation on prenatal ultrasound) or for bilateral conditions.[45]

Counseling patients about the significance of antenatally detected pyelectasis is based on a large number of studies reviewing outcomes of otherwise normal fetuses found to have varying degrees of UTD.[40–45,54] A meta-analysis[44] combining the findings 1678 cases of antenatal hydronephrosis gathered from 17 independent studies found that even mild degrees of prenatally diagnosed hydronephrosis may indicate pathology requiring postnatal management (11.9%). Prenatal consultation with a pediatric urologist and/or pediatric nephrologist is recommended in situations where there is substantial risk for surgery or renal dysfunction.[45]

## MEGACYSTIS

***Overview and Imaging.*** An abnormally large bladder, or megacystis, manifests in the first trimester in approximately 1 : 330 to 1 : 1800 pregnancies.[55–59] A longitudinal bladder diameter greater than 7 mm during the second or third trimester is considered abnormal.[55–58] Early diagnoses of megacystis may resolve later in pregnancy.[11,55–59] An enlarged fetal bladder observed by ultrasound or MRI may simply reflect normal variation in bladder filling, although if bilateral hydroureteronephrosis is observed, then pathologies such as obstruction or functional emptying abnormalities must be considered. If an abnormal longitudinal bladder diameter persists after 23 weeks gestational age, the prognosis is more likely to be poor.[59] Potentially severe abnormalities include posterior urethral valves (Fig. 112.10), prune-belly syndrome (Eagle-Barrett syndrome) (e-Fig. 112.11), and megacystis-microcolon-intestinal hypoperistalsis syndrome. An enlarged fetal bladder also merits close evaluation of the spine, given that caudal regression and neural tube defects may present with a neurogenic bladder.[60]

## FETAL BLADDER OUTLET OBSTRUCTION: SURGICAL INTERVENTIONS

***Overview.*** At a minimum, management of urinary tract outlet obstruction in the fetus involves serial ultrasounds through the second and third trimester and may merit delivery of the fetus at a tertiary care center. The role for procedural intervention in the fetus with bladder outlet obstruction has been well investigated during the past few decades, especially in identifying the appropriate fetal population that would benefit from intervention. Although the

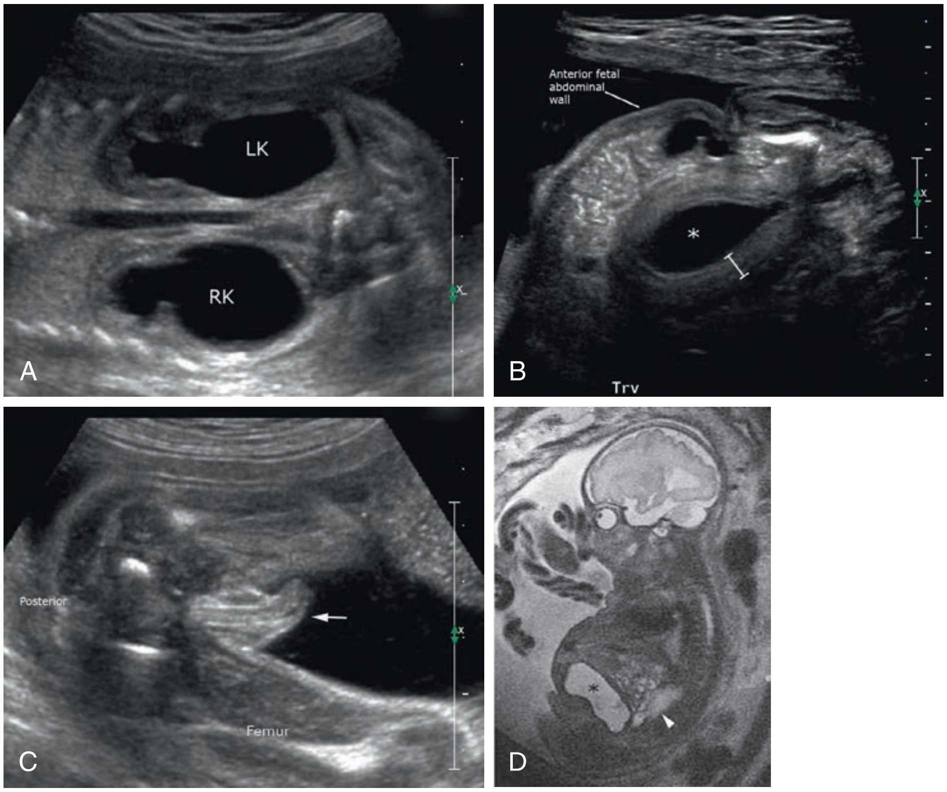

**e-Figure 112.11. Fetal prune-belly (Eagle-Barrett syndrome).** (A) Coronal sonogram through the kidneys in a fetus at 24 weeks' gestational age shows bilateral marked urinary tract dilatation. (B) Transverse sonogram through the fetal urinary bladder *(asterisk)* shows marked thickening of the urinary bladder wall (denoted by *caliper*). Abnormal contour of the anterior abdominal wall is also appreciable. (C) Normal male phallus is observed *(arrow)*. Amniotic fluid index is normal. (D) Sagittal T2-weighted single-shot fast spin-echo MR image performed later at 30 weeks' gestational age shows abnormal urinary bladder *(asterisk)* enlargement and abnormal abdominal wall contour. Volume-averaging of partially viewed dilated renal collecting system is noted by *arrowhead*. *LK*, Left kidney; *RK*, right kidney.

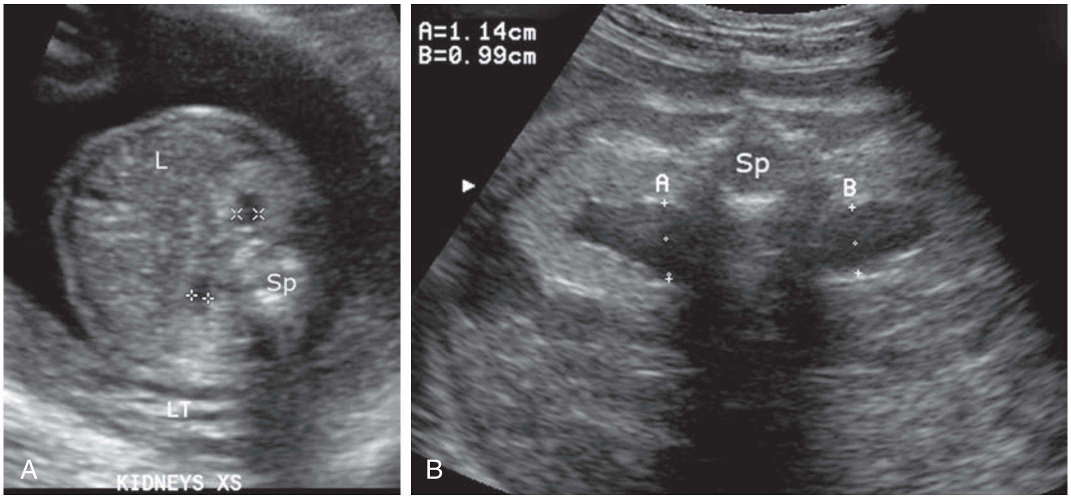

**Figure 112.9. Fetal urinary tract dilatation, high risk (UTD A2-3).** (A) Transverse sonogram of a fetus at 23 weeks' gestational age shows a mildly dilated right renal pelvis, measuring 4.4 mm. Because of increased renal echogenicity, the UTD classification is A2-3 (high risk). (B) Transverse sonogram of a different fetus at 35 weeks' gestational age shows abnormal dilatation of the bilateral kidneys, with anterior-posterior renal pelvis diameters measuring 10 mm and 11 mm. Renal echogenicity is mildly echogenic as well. Urinary bladder was normal *(not shown)*. In the third trimester, this degree of urinary tract dilatation is classified as A2-3. *L*, Liver; *Sp*, spine.

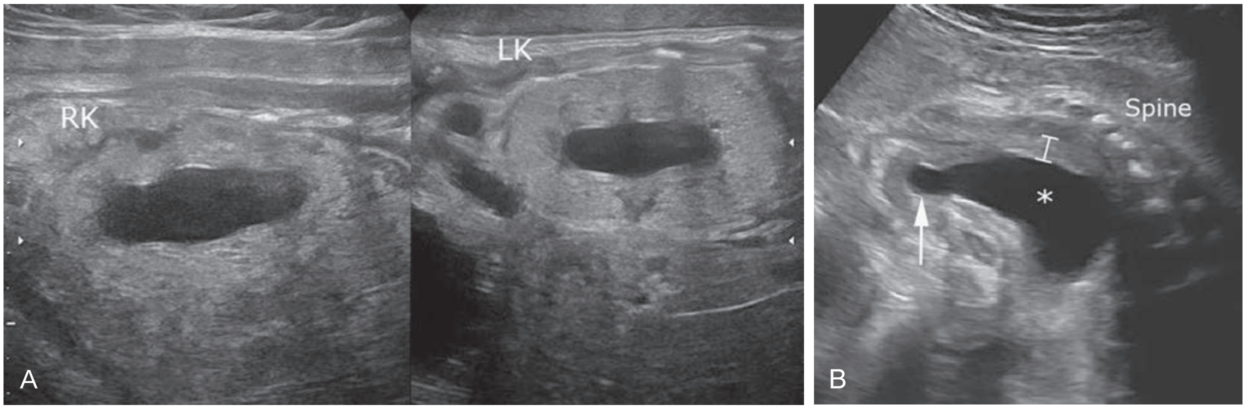

**Figure 112.10. Posterior urethral valves and oligohydramnios.** (A) Longitudinal sonogram at 32 weeks' gestational age shows echogenic kidneys. The renal pelves measured 13 mm on left and 7 mm on right (not shown). With the increased renal echogenicity, the UTD classification is A2-3 (high risk). (B) The fetal bladder *(asterisk)* is abnormally large with distension of the posterior urethra *(arrow)* in a configuration called the *keyhole* sign. Bladder wall thickening is noted by caliper. *LK*, Left kidney; *RK*, right kidney.

fetus with a high-grade bladder outlet obstruction may progress during pregnancy and be accompanied by development of renal dysplasia, second trimester cases have been reported that spontaneously improve and later manifest only a low-grade obstruction with normal amniotic fluid volume.[61,62] Further, animal studies have shown that the severity of renal damage from obstruction depends on numerous factors, including the timing, duration, and severity of the obstruction.[62–64] The primary challenge is to identify the fetuses for intervention that have severe enough obstruction that renal function and pulmonary development would be compromised by progression of disease but that maintain the potential for improved renal development after the obstruction is relieved.

Monitoring the function of fetal kidneys primarily requires assessing amniotic fluid volume and the sonographic appearance of the kidneys; more eloquent measurements include sampling various fetal urine electrolytes and proteins after 20 weeks' gestational age. Many investigators have evaluated the potential of fetal urine electrolyte concentrations in identifying renal functional prognosis.[65–67] Fetuses with obstructive uropathy and a subsequent poor outcome are "salt wasters," and fetuses with a decent outcome have hypotonic urine.[68] Nicolini et al.[67] found that elevated fetal urinary calcium levels was the most sensitive (100%) predictor of renal dysplasia (specificity 60%), and elevated urinary sodium levels were the most specific (80%) predictor of renal dysplasia. Urinary phosphate, creatinine, and urea were not useful in predicting the likelihood of renal dysplasia. Elevated levels of the protein β2-microglobulin within fetal urine also has been shown to be useful in the prediction of postnatal renal function,[68] particularly in identifying fetuses at risk for renal damage by obstruction even when amniotic fluid volume remains normal.

***Treatment and Complications.*** Surgical intervention for bladder outlet obstruction and decreasing amniotic fluid volume or oligohydramnios is considered in the fetus with a good prognostic electrolyte panel (i.e., Na <100 mEq per liter, Cl <90 mEq per liter, and osmolarity <210 mEq per liter) and no evidence of renal dysplasia by ultrasound.[69,70] Surgical interventions to treat bladder outlet obstruction include vesicoamniotic shunt, fetoscopic valve ablation, fetoscopic urethral stent placement, and open fetal surgery for vesicostomy.

The vesicoamniotic shunt is placed percutaneously under ultrasound guidance to allow for emptying of the obstructed bladder directly into the amniotic cavity. Seven nonrandomized, controlled clinical series in the literature[66,71–76] offer the combined experience of 195 treated fetuses. A meta-analysis[77] incorporating studies of both controlled series and additional case studies pooled the odds ratios to summarize measures of effect of this procedure. This analysis found that bladder drainage markedly improved perinatal survival, specifically in the subgroup of fetuses with a poor predicted prognosis (based on urine electrolytes and amniotic fluid volume). The procedure, when successful, restores amniotic fluid volume and allows for improved development of the fetal lungs. Although the vesicoamniotic shunt has the potential to improve pulmonary development, the shunt does not necessarily benefit the kidneys. Further, shunt placement does not address the severe bladder dysfunction seen with outlet obstruction, and animal studies have shown that decompressing a normal fetal bladder by shunting leads to a fibrotic and noncompliant bladder wall.[78] The bladder dysfunction is a potential obstacle to renal transplantation. Complication rates from vesicoamniotic shunt placement are as high as 60%[79,80] and include inadequate shunt drainage, shunt migration, premature labor, urinary fetal ascites, chorioamnionitis, and iatrogenic gastroschisis.

Only one randomized control trial (RCT) has been performed to evaluate the effective outcomes of this procedure.[81] The percutaneous shunting in lower urinary tract obstruction (PLUTO) RCT included 31 patients and sought to determine the effectiveness of vesicoamniotic shunting (VAS) as a treatment for lower urinary tract obstruction.[81] Survival seemed to be higher in the fetuses receiving vesicoamniotic shunting, but because of poor recruitment, the study was closed early and the benefit could not be definitively proven. The authors concluded that the chance of newborn infants surviving with normal renal function is very low irrespective of whether vesicoamniotic shunting is done,[81] as suggested in previous studies.[82] A follow-up study reported on the remaining patients in the PLUTO registry who did not wish to be randomly assigned to a treatment group and who instead chose their own management plan (either conservative management or VAS).[83] There was a higher number of voluntary terminations of pregnancy than the authors had expected. Of 144 total patients in the registry, 68 patients pursued termination, 31 patients were enrolled in the RCT, and the remaining 45 patients were compared with the RCT. The authors observed no difference in live-birth rates for those who received either VAS or conservative management, highlighting the poor prognosis when lower urinary tract obstruction (LUTO) is associated with pulmonary hypoplasia. The chance of the infant surviving with normal renal function was also higher in the group that registered for conservative management than in those who were randomized. Those in the registry who elected to pursue conservative management were less likely to have presented at an earlier age and were less likely to have low amniotic fluid volume; given the prediction for a poor outcome when either early GA or low amniotic fluid volume are present, it is likely that the apparent difference in findings could be explained by these confounding patient cohort factors. More recently published retrospective single center studies, however, demonstrate that VAS may still be a valid treatment option in adequately selected cases.[54,84]

As an alternative to VAS, fetal cystoscopy may allow for diagnosis of the obstructive lesion and for intervention, such as by ablation of posterior urethral valves, fenestration of ureterocele, or placement of a stent across a stenotic urethra.[84–95] This method also avoids the need for amnioinfusion and some of the potential risks associated with vesicoamniotic shunt migration.[86] Recent experience shows that laser fulguration and hydroablation are the best option for disruption of posterior urethral valves, with neonatal survival rates of approximately 70% to 75%.[89,90] There is a lack of evidence for the effectiveness of fetal cystoscopy over VAS for LUTO. Sananes et al suggest the main advantage of the fetal cystoscopy over VAS is that it provides the correct diagnosis of the etiology of LUTO and consequently to allow a better selection of candidates for fetal therapy that contribute to better long-term outcome related to renal function.[92]

Open fetal surgery for vesicostomy (bladder marsupialization) is the only approach that completely decompresses the entire urinary tract and eliminates the transmission of pressure to the kidney. Candidates for this procedure are male fetuses with posterior urethral valves less than 24 weeks' gestational age presenting with oligohydramnios, normal fetal urine electrolytes, and no evidence of renal cystic dysplasia or abnormally increased renal echogenicity, and who have normal karyotypes. Only a small amount of clinical experience exists in this advanced arena of fetal surgical intervention, and vesicostomy currently carries a 50% neonatal mortality.[96–98]

## KEY POINTS

- The prenatal evaluation of the genitourinary system includes assessment of the amniotic fluid, the kidneys, the bladder, and associated anomalies.
- Fetal urine production begins by 12 weeks of gestation.
- The fetal kidney is considered echogenic if it is brighter than the fetal liver. Echogenic kidneys with oligohydramnios portend a poor prognosis.
- Visualization of a single renal cyst should prompt consideration of a cystic tumor, duplex collecting system with cystic dysplasia of the upper pole, urinoma, asymmetric presentation of ADPKD, or an isolated cyst in an otherwise normal kidney. Multiple cysts may be seen with multicystic dysplastic kidney, ADPKD, tuberous sclerosis complex, and TCF2 gene mutation–associated nephropathy.
- A solid, rounded echogenic mass in the fetal kidney is most likely to be a CMN.
- If at 32 weeks, the anterior-posterior renal pelvic diameter of the renal pelvis remains less than 7.0 mm, then parents can be counseled regarding the association with a good postnatal outcome.
- If an enlarged fetal bladder is associated with bilateral hydroureteronephrosis, a serious obstruction or functional emptying abnormality must be considered. These abnormalities include posterior urethral valves, prune-belly syndrome (Eagle-Barrett syndrome) and megacystis-microcolon-intestinal hypoperistalsis syndrome.
- Complex cases such as bladder exstrophy, confusing duplex collecting systems, and obstructive masses may be evaluated further by fetal MRI.
- Surgical intervention for bladder outlet obstruction and decreasing amniotic fluid volume or oligohydramnios is considered in the fetus with a good prognostic electrolyte panel (Na <100 mEq per liter, Cl <90 mEq per liter, and osmolarity <210 mEq per liter) and no evidence of renal dysplasia by ultrasound.
- Fetal surgical interventions to treat bladder outlet obstruction include a vesicoamniotic shunt, fetoscopic valve ablation, fetoscopic urethral stent placement, and open fetal surgery for vesicostomy.

## SUGGESTED READINGS

Aksu N, Yavascan O, Kangin M, et al. Postnatal management of infants with antenatally detected hydronephrosis. *Pediatr Nephrol*. 2005;20:1253–1259.

Bonsib SM. The classification of renal cystic diseases and other congenital malformations of the kidney and urinary tract. *Arch Pathol Lab Med*. 2010;134:554–568.

Fievet L, Faure A, Coze S, et al. Fetal megacystis: etiologies, management, and outcome according to the trimester. *Urology*. 2014;84(1):185–190.

Hormann M, Brugger PC, Balassy C, et al. Fetal MRI of the urinary system. *Eur J Radiol*. 2006;57:303–311.

Leclair MD, El-Ghoneimi A, Audry G, et al; French Pediatric Urology Study Group. The outcome of prenatally diagnosed renal tumors. *J Urol*. 2005;173:186–189.

Morris RK, Malin GL, Quinlan-Jones E, et al. Percutaneous vesicoamniotic shunting versus conservative management for fetal lower urinary tract obstruction (PLUTO): a randomized trial. *Lancet*. 2013;382:1496–1506.

Nguyen HT, Benson CB, Bromley B, et al. Multidisciplinary consensus on the classification of prenatal and postnatal urinary tract dilation (UTD classification system). *J Pediatr Urol*. 2014;10:982–998.

Ruano R, Sananes N, Wilson C, et al. Fetal lower urinary tract obstruction: proposal for standardized multidisciplinary prenatal management based on disease severity. *Ultrasound Obstet Gynecol*. 2016;48(4):476–482.

## REFERENCES

Full references for this chapter can be found on www.expertconsult.com.

## REFERENCES

1. Rabinowitz R, Peters MT, Vyas S, et al. Measurement of fetal urine production in normal pregnancy by real-time ultrasonography. *Am J Obstet Gynecol*. 1989;161:1264–1266.
2. Fagerquist M, Fagrquist U, Oden A, et al. Fetal urine production and accuracy when estimating fetal urinary bladder volume. *Ultrasound Obstet Gynecol*. 2001;17:132–139.
3. Cassart M, Massez A, Metens T, et al. Complementary role of MRI after sonography in assessing bilateral urinary tract anomalies in the fetus. *AJR Am J Roentgenol*. 2004;182:689–695.
4. Hormann M, Brugger PC, Balassy C, et al. Fetal MRI of the urinary system. *Eur J Radiol*. 2006;57:303–311.
5. Poutamo J, Vanninen R, Partanen K, et al. Diagnosing fetal urinary tract anomalies: benefits of MRI compared to US. *Acta Obstet Gynecol Scand*. 2000;79:65–71.
6. Cohen HL, Cooper J, Eisenberg P, et al. Normal length of fetal kidneys. *AJR Am J Roentgenol*. 1991;157:545–548.
7. Witzani L, Brugger PC, Hormann M, et al. Normal renal development investigated with fetal MRI. *Eur J Radiol*. 2006;57:294–302.
8. Grignon A, Filion R, Filiatrault D, et al. Urinary tract dilatation in utero: classification and clinical applications. *Radiology*. 1986;160:645–647.
9. Mure PY, Pierre Mouriquand P. Upper urinary tract dilatation: prenatal diagnosis, management and outcome. *Semin Fetal Neonatal Med*. 2008;13:152–163.
10. Rosati P, Guariglia L. Transvaginal sonographic assessment of the fetal urinary tract in early pregnancy. *Ultrasound Obstet Gynecol*. 1996;7:95–100.
11. Bronshtein M, Kushnir O, Ben RZ, et al. Transvaginal sonographic measurement of fetal kidneys in the first trimester of pregnancy. *J Clin Ultrasound*. 1990;18:299–301.
12. Hoskins IA, McGovern PG, Ordorica SA, et al. Amniotic fluid index: correlation with amniotic fluid volume. *Am J Perinatol*. 1992;9:315–318.
13. Kemper MJ, Mueller-Wiefel DE. Prognosis of antenatally diagnosed oligohydramnios of renal origin. *Eur J Pediatr*. 2007;166:393–398.
14. Han CCC, Woo BH, Tan JVK, et al. A single center review of antenatally diagnosed fetal echogenic kidney. *Ultrasound Obstet Gynecol*. 2003;22(suppl 1):16.
15. De La Vega A, Torres E. Prenatal diagnosis of renal disease. *P R Health Sci J*. 2005;24:141–144.
16. Lilford RJ, Irving HC, Allibone EB. A tale of two prior probabilities—avoiding the false positive antenatal diagnosis of autosomal recessive polycystic kidney disease. *Br J Obstet Gynaecol*. 1992;99:216–219.
17. Choong KKL, Gruenwald SM, Hodson EM. Echogenic fetal kidneys in cytomegalovirus infection. *J Clin Ultrasound*. 1993;21:128–132.
18. Silver DA, Ashworth MT, Andrews HS. Prenatal ultrasound diagnosis of fetal candida infection: a complication of a retained intrauterine contraceptive device. *Ultrasound Obstet Gynecol*. 1994;4:154–157.
19. Carr MC, Benacerraf BR, Estroff JA, et al. Prenatally diagnosed bilateral hyperechoic kidneys with normal amniotic fluid: postnatal outcome. *J Urol*. 1995;153:442–444.
20. MacDermot KD, Saggar-Malik AK, Economides DL, et al. Prenatal diagnosis of autosomal dominant polycystic kidney disease (PKD1) presenting in utero and prognosis for very early onset disease. *J Med Genet*. 1998;35:13–16.
21. Verdin SM, Economides DL. The role of ultrasonographic markers for trisomy 21 in women with positive serum biochemistry. *Br J Obstet Gynaecol*. 1998;105:63–67.
22. Sandoval R, Sepulveda W, Gutierrez J, et al. Prenatal diagnosis of nonmosaic trisomy 9 in a fetus with severe renal disease. *Gynecol Obstet Invest*. 1999;48:69–72.
23. Schilke K, Schaefer F, Waldherr R, et al. A case of Perlman syndrome: fetal gigantism, renal dysplasia, and severe neurological deficits. *Am J Med Genet*. 2000;91:29–33.
24. Tsatsaris V, Gagnadoux MF, Aubry MC, et al. Prenatal diagnosis of bilateral isolated fetal hyperechogenic kidneys. Is it possible to predict long term outcome? *BJOG*. 2002;109:1388–1393.
25. Estroff JA, Mandell J, Benacerraf BR. Increased renal parenchymal echogenicity in the fetus: importance and clinical outcome. *Radiology*. 1991;181:135–139.
26. Bonsib SM. The classification of renal cystic diseases and other congenital malformations of the kidney and urinary tract. *Arch Pathol Lab Med*. 2010;134:554–568.
27. Avni FE, Hall M. Renal cystic diseases in children: new concepts. *Pediatr Radiol*. 2010;40:939–946.
28. Rodriguez MM. Developmental renal pathology: its past, present, and future. *Fetal Pediatr Pathol*. 2004;23:211–229.
29. Rosenblum ND. Developmental biology of the human kidney. *Semin Fetal Neonatal Med*. 2008;13:125–132.
30. Breysem L, Bosmans H, Dymarkowski S, et al. The value of fast MR imaging as an adjunct to ultrasound in prenatal diagnosis. *Eur Radiol*. 2003;13:1538–1548.
31. Koplay M, Onbas O, Alper F, et al. Prenatal MRI findings of polycystic kidney disease associated with holoprosencephaly. *Korean J Radiol*. 2009;10:307–309.
32. Liu YP, Cheng SJ, Shih SL, et al. Autosomal recessive polycystic kidney disease: appearance on fetal MRI. *Pediatr Radiol*. 2006;36:169.
33. Avni FE, Garel L, Cassart M, et al. Perinatal assessment of hereditary cystic renal diseases: the contribution of sonography. *Pediatr Radiol*. 2006;35:405–414.
34. Rzk D, Chapman AB. Cystic and inherited kidney diseases. *Am J Kidney Dis*. 2003;42:1305–1317.
35. Deshpande C, Hennekam RCM. Genetic syndromes and prenatally detected renal anomalies. *Semin Fetal Neonatal Med*. 2008;13:171–180.
36. Winyard P, Chitty LS. Dysplastic kidneys. *Semin Fetal Neonatal Med*. 2008;13:142–151.
37. Walter J, McGahan J. Mesoblastic nephroma: prenatal sonographic detection. *J Clin Ultrasound*. 1985;13:686–689.
38. Leclair MD, El-Ghoneimi A, Audry G, et al; French Pediatric Urology Study Group. The outcome of prenatally diagnosed renal tumors. *J Urol*. 2005;173:186–189.
39. Herndon CDA, McKenna PH, Kolon TF, et al. A multicenter outcomes analysis of patients with neonatal reflux presenting with prenatal hydronephrosis. *J Urol*. 1999;162:1203–1208.
40. Kent A, Cox D, Downey P, et al. A study of mild fetal pyelectasis: outcome and proposed strategy of management. *Prenat Diagn*. 2000;20:206–209.
41. Sairam S, Al-Habib A, Sasson S, et al. Natural history of fetal hydronephrosis diagnosed on mid-trimester ultrasound. *Ultrasound Obstet Gynecol*. 2001;17:191–196.
42. Ismaili K, Hall M, Donner C, et al. Results of systematic screening for minor degrees of fetal renal pelvis dilatation in an unselected population. *Am J Obstet Gynecol*. 2003;188:242–246.
43. Odibo AO, Raab E, Elovitz M, et al. Prenatal mild pyelectasis evaluating the thresholds of renal pelvic diameter associated with normal postnatal renal function. *J Ultrasound Med*. 2004;23:513–517.
44. Lee RS, Cendron M, Kinnamon DD, et al. Antenatal hydronephrosis as a predictor of postnatal outcome: a meta-analysis. *Pediatrics*. 2006;118:586–593.
45. Nguyen HT, Benson CB, Bromley B, et al. Multidisciplinary consensus on the classification of prenatal and postnatal urinary tract dilation (UTD classification system). *J Pediatr Urol*. 2014;10:982–998.
46. Benacerraf BR, Mandell J, Estroff J. Fetal pyelectasis: a possible association with Down syndrome. *Obstet Gynecol*. 1990;76:58–60.
47. Nyberg DA, Resta RG, Luthy DA, et al. Isolated sonographic markers for detection of fetal Down syndrome in the second trimester of pregnancy. *J Ultrasound Med*. 2001;20:1053–1063.
48. Bromley B, Lieberman E, Shipp TD, et al. The genetic sonogram: a method of risk assessment for Down syndrome in the second trimester. *J Ultrasound Med*. 2002;21:1087–1096.
49. American College of Obstetricians and Gynecologists. *Screening for fetal chromosomal abnormalities (ACOG practice bulletin; no. 77)*. Washington, DC: American College of Obstetricians and Gynecologists; 2007.
50. Aksu N, Yavascan O, Kangin M, et al. Postnatal management of infants with antenatally detected hydronephrosis. *Pediatr Nephrol*. 2005;20:1253–1259.
51. Mallik M, Watson AR. Antenatally detected urinary tract abnormalities: more detection but less action. *Pediatr Nephrol*. 2008;23:897–904.
52. Dejter SW, Gibbons MD. The fate of infant kidneys with fetal hydronephrosis but initially normal postnatal sonography. *J Urol*. 1989;142:661–662.
53. Laing FC, Burke VD, Wing VW, et al. Postpartum evaluation of fetal hydronephrosis: optimal timing for follow-up sonography. *Radiology*. 1984;152:423–424.
54. Anderson N, Clautice-Engle T, Allan R, et al. Detection of obstructive uropathy in the fetus: predictive value of sonographic measurements of renal pelvic diameter at various gestational ages. *AJR Am J Roentgenol*. 1995;164:719–723.

55. Müller Brochut AC, Thomann D, Kluwe W, et al. Fetal megacystis: experience of a single tertiary center in Switzerland over 20 years. *Fetal Diagn Ther*. 2014;36(3):215–222.
56. Dias T, Sairam S, Kumarasiri S. Ultrasound diagnosis of fetal renal abnormalities. *Best Pract Res Clin Obstet Gynaecol*. 2014;28(3):403–415.
57. Fievet L, Faure A, Coze S, et al. Fetal megacystis: etiologies, management, and outcome according to the trimester. *Urology*. 2014;84(1):185–190.
58. Taghavi K, Sharpe C, Stringer MD. Fetal megacystis: a systematic review. *J Pediatr Urol*. 2016 Oct 8. pii: S1477-5131(16)30285-6; doi:10.1016/j.jpurol.2016.09.003. [Epub ahead of print].
59. Fontanella F, Duin L, Adama van Scheltema PN, et al. Fetal megacystis: prediction of spontaneous resolution and outcome. *Ultrasound Obstet Gynecol*. 2017 Jan 30; doi:10.1002/uog.17422. [Epub ahead of print]; PubMed PMID: 28133847.
60. Calvo-Garcia MA. Imaging evaluation of fetal megacystis: how can magnetic resonance imaging help? *Semin Ultrasound CT MR*. 2015;36(6):537–549.
61. Bianchi DW, Crombleholme TM, D'Alton ME, et al. Renal agenesis. In: *Fetology: Diagnosis and Management of the Fetal Patient*. 2nd ed. New York: McGraw Hill; 2010.
62. Harrison MR, Ross N, Noall R, et al. Correction of congenital hydronephrosis in utero. I. The model: fetal urethral obstruction produces hydronephrosis and pulmonary hypoplasia in fetal lambs. *J Pediatr Surg*. 1983;18:247–256.
63. Glick PL, Harrison MR, Noall RA, et al. Correction of congenital hydronephrosis in utero III. Early mid-trimester ureteral obstruction produces renal dysplasia. *J Pediatr Surg*. 1983;18:681–687.
64. Glick PL, Harrison MR, Adzick NS, et al. Correction of congenital hydronephrosis in utero IV: in utero decompression prevents renal dysplasia. *J Pediatr Surg*. 1984;19:649–657.
65. Wilkins IA, Chitkara U, Lynch L, et al. The nonpredictive value of fetal urinary electrolytes: preliminary report of outcomes and correlations with pathologic diagnosis. *Am J Obstet Gynecol*. 1987;157:694–698.
66. Crombleholme TM, Harrison MR, Golbus MS, et al. Fetal intervention in obstructive uropathy: prognostic indicators and efficacy of intervention. *Am J Obstet Gynecol*. 1990;162:1239–1244.
67. Nicolini U, Fisk NM, Rodeck CH, et al. Fetal urine biochemistry: an index of renal maturation and dysfunction. *Br J Obstet Gynaecol*. 1992;99:46–50.
68. Muller F, Dommergues M, Mandelbrot L, et al. Fetal urinary biochemistry predicts postnatal renal function in children with bilateral obstructive uropathies. *Obstet Gynecol*. 1993;82:813–820.
69. Glick PL, Harrison MR, Golbus MS, et al. Management of the fetus with congenital hydronephrosis II: Prognostic criteria and selection for treatment. *J Pediatr Surg*. 1985;20:376–387.
70. Cendron M, D'Alton ME, Crombleholme TM. Prenatal diagnosis and management of the fetus with hydronephrosis. *Semin Perinatol*. 1994;18:163–181.
71. Evans MI, Sacks AJ, Johnson MP, et al. Sequential invasive assessment of fetal renal function and the intrauterine treatment of fetal obstructive uropathies. *Obstet Gynecol*. 1991;77:545–550.
72. Nicolini U, Tannirandorn Y, Vaughan J, et al. Further predictors of renal dysplasia in fetal obstructive uropathy: bladder pressure and biochemistry of "fresh" urine. *Prenat Diagn*. 1991;11:159–166.
73. Lipitz S, Robson SC, Ryan G, et al. Management and outcome of obstructive uropathy in twin pregnancies. *Br J Obstet Gynaecol*. 1993;100:879–880.
74. Johnson MP, Bukowski TP, Reitleman C, et al. In utero surgical treatment of fetal obstructive uropathy: a new comprehensive approach to identify appropriate candidates for vesicoamniotic shunt therapy. *Am J Obstet Gynecol*. 1994;170:1770–1776.
75. Quintero RA, Johnson MP, Romero R, et al. In-utero percutaneous cystoscopy in the management of fetal lower obstructive uropathy. *Lancet*. 1995;346:537–540.
76. Freedman AL, Bukowski TP, Smith CA, et al. Fetal therapy for obstructive uropathy: diagnosis specific outcomes. *J Urol*. 1996;156:720–723.
77. Clark TJ, Martin WL, Divakaran TG, et al. Prenatal bladder drainage in the management of fetal lower urinary tract obstruction: a systematic review and meta-analysis. *Obstet Gynecol*. 2003;102:367–382.
78. Kitagawa H, Pringle KC, Koike J, et al. Is a vesicoamniotic shunt intrinsically bad? Shunting a normal fetal bladder. *J Pediatr Surg*. 2007;42:2002–2006.
79. Elder JS, Duckett JW Jr, Snyder HM. Intervention for fetal obstructive uropathy: has it been effective? *Lancet*. 1987;2:1007–1010.
80. Wilson RD, Johnson MP. Prenatal ultrasound guided percutaneous shunts for obstructive uropathy and thoracic disease. *Semin Pediatr Surg*. 2003;12:182–189.
81. Morris RK, Malin GL, Quinlan-Jones E, et al. Percutaneous vesicoamniotic shunting versus conservative management for fetal lower urinary tract obstruction (PLUTO): a randomized trial. *Lancet*. 2013;382:1496–1506.
82. Morris RK, Ruano R, Kilby MD. Effectiveness of fetal cystoscopy as a diagnostic and therapeutic intervention for lower urinary tract obstruction: a systematic review. *Ultrasound Obstet Gynecol*. 2011;37(6):629–637.
83. Morris RK, Middleton LJ, Malin GL, et al; PLUTO Collaborative Group. Outcome in fetal lower urinary tract obstruction: a prospective registry study. *Ultrasound Obstet Gynecol*. 2015;46(4):424–431.
84. Ruano R, Sananes N, Wilson C, et al. Fetal lower urinary tract obstruction: proposal for standardized multidisciplinary prenatal management based on disease severity. *Ultrasound Obstet Gynecol*. 2016;48(4):476–482.
85. Kohl T. Minimally invasive fetoscopic interventions: an overview in 2010. *Surg Endosc*. 2010;24:2056–2067.
86. Quintero RA, Johnson MP, Romero R, et al. In-utero percutaneous cystoscopy in the management of fetal lower obstructive uropathy. *Lancet*. 1995;346:537–540.
87. Quintero RA, Morales WJ, Allen MH, et al. Fetal hydrolaparoscopy and endoscopic cystotomy in complicated cases of lower urinary tract obstruction. *Am J Obstet Gynecol*. 2000;183:324–330.
88. Quintero RA. Fetal obstructive uropathy. *Clin Obstet Gynecol*. 2005;48:923–941.
89. Clifton MS, Harrison MR, Ball R, et al. Fetoscopic transuterine release of posterior urethral valves: a new technique. *Fetal Diagn Ther*. 2008;23:89–94.
90. Ruano R, Duarte S, Bunduki V, et al. Fetal cystoscopy for severe lower urinary tract obstruction—initial experience of a single center. *Prenat Diagn*. 2010;30:30–39.
91. Ruano R. Fetal surgery for severe lower urinary tract obstruction. *Prenat Diagn*. 2011;31(7):667–674.
92. Sananes N, Cruz-Martinez R, Favre R, et al. Two-year outcomes after diagnostic and therapeutic fetal cystoscopy for lower urinary tract obstruction. *Prenat Diagn*. 2016;36(4):297–303.
93. Ruano R, Sananes N, Sangi-Haghpeykar H, et al. Fetal intervention for severe lower urinary tract obstruction: a multicenter case-control study comparing fetal cystoscopy with vesicoamniotic shunting. *Ultrasound Obstet Gynecol*. 2015;45(4):452–458.
94. Persico N, Berettini A, Fabietti I, et al. A new minimally invasive technique for cystoscopic laser treatment of fetal ureterocele. *Ultrasound Obstet Gynecol*. 2016 Sep 8; doi:10.1002/uog.17296. [Epub ahead of print]; PubMed PMID: 27607564.
95. Torres Montebruno X, Martinez JM, Eixarch E, et al. Fetoscopic laser surgery to decompress distal urethral obstruction caused by prolapsed ureterocele. *Ultrasound Obstet Gynecol*. 2015;46(5):623–626.
96. Harrison MR, Nakayama DK, Noall R, et al. Correction of congenital hydronephrosis in utero II. Decompression reverses the effects of obstruction on the fetal lung and urinary tract. *J Pediatr Surg*. 1982;17:965–974.
97. Crombleholme TM, Harrison MR, Langer JC, et al. Early experience with open fetal surgery for congenital hydronephrosis. *J Pediatr Surg*. 1988;23:1114–1121.
98. Holmes N, Harrison MR, Baskin LS. Fetal surgery for posterior urethral valves: long-term postnatal outcomes. *Pediatrics*. 2001;108:E7.

# 113 Congenital and Neonatal Abnormalities

Jonathan R. Dillman and Kassa Darge

## KIDNEY AND URETER

### Multicystic Dysplastic Kidney

***Overview, Etiology, and Clinical Presentation.*** A multicystic dysplastic kidney (MCDK) is the most common form of cystic renal dysplasia. With high-grade obstruction or atresia of the upper urinary tract (renal pelvis and/or ureter) during early renogenesis, disordered parenchymal development results in an MCDK.[1] Two types of MCDK exist: the pelvoinfundibular type (common) and the hydronephrotic type (uncommon).[2,3] MCDK can occur in half of a duplex kidney (usually the upper moiety) or in renal fusion anomalies, such as a horseshoe kidney and crossed fused renal ectopia. MCDK is sporadic in most cases, although familial cases have been described.[1,4] Vesicoureteral reflux (VUR) (both ipsilateral [into an atretic ureter] and contralateral) and contralateral ureteropelvic junction (UPJ) obstruction are associated with this anomaly, and Müllerian anomalies may coexist in girls.[1,5,6] Long-term sequelae (e.g., infection and hypertension) are rare, because most affected kidneys either partially or completely involute on their own over time.[7–11]

***Imaging.*** On ultrasound, computed tomography (CT), and magnetic resonance imaging (MRI), a classic MCDK is characterized by multiple cysts of various sizes (ranging from 1 mm to several cm) that do not communicate, with no identifiable normal renal parenchyma (Fig. 113.1). The size of the affected kidney may be small, normal, or enlarged.[1] Compensatory hypertrophy of the contralateral kidney often is present.[12] The hydronephrotic form has cysts that communicate, mimicking pelvicaliectasis, but no normal functioning renal tissue.[2] The diagnosis of both pelvoinfundibular and hydronephrotic MCDK can be confirmed by diuretic renal scintigraphy (e-Fig. 113.2) or magnetic resonance urography (MRU) (e-Fig. 113.3). A voiding cystourethrogram (VCUG) may reveal VUR into a blind-ending ureter on the side of the MCDK.[13,14]

***Treatment.*** Follow-up ultrasound typically demonstrates involution of the cysts over time, eventually resulting in remnant dysplastic renal tissue that may be difficult to visualize (e-Fig. 113.4).[15,16] Resection of an MCDK is rarely indicated[17] and is usually reserved for cases in which there is increasing kidney size rather than involution. In the past, routine nephrectomies were performed due to a fear of malignant degeneration. Current evidence discounts this possibility, and, if no other complication exists, surgery is not indicated and limited radiologic follow-up may be appropriate.[11]

### Autosomal Dominant Polycystic Kidney Disease

***Overview and Etiology.*** Autosomal dominant polycystic kidney disease (ADPKD), the most common form of inherited renal cystic disease, is now recognized to be a ciliopathy (disorder of the primary cilia) and is seen in about 1 in 800 live births.[18–20] Two types of ADPKD exist, each with clearly defined chromosomal mutations. The more severe form (PKD1) accounts for about 85% to 90% of cases, whereas the milder phenotype (PKD2) presents later in life, results in less morbidity, and is less common.[18,21] Cysts arise from both the renal cortex and the medulla.[18,22]

***Clinical Presentation.*** Systemic hypertension, hematuria, and slowly progressive chronic kidney disease are the typical clinical manifestations.[1,23] ADPKD is very rarely detected prenatally because fewer than 5% of nephrons are cystic before birth.[1] Diagnosis of ADPKD early in life portends a poor prognosis; 43% of affected persons die in the first year of life, hypertension develops in 67%, and some affected children progress rapidly to end-stage renal disease.[23] Because in some instances it can be difficult to delineate between autosomal recessive and autosomal dominant forms of polycystic kidney disease, screening of siblings and parents may be helpful. ADPKD can coexist with tuberous sclerosis as a "contiguous gene syndrome," and the recognition of this specific syndromic form has implications for management.[24]

***Imaging.*** The diagnosis of ADPKD usually is made on the basis of ultrasound (Fig. 113.5), although CT or MRI also can suggest it. While the kidneys may be normal during the first decade of life, they also may contain one or more simple cysts (Fig. 113.6).[18,25] The kidneys may be abnormally enlarged and echogenic, mimicking autosomal recessive polycystic kidney disease (ARPKD) in early life[18,26] Although it is typically a bilateral process, imaging findings may be asymmetric, and in young children they can manifest as a unilateral abnormality.[18,25,27] Microscopic cysts, as well as larger cysts that can be detected by cross-sectional imaging techniques, can involve the liver and less frequently other organs.[22,28] Nephrolithiasis may be seen at ultrasound or CT.[29] The remainder of the urinary tract is usually normal.

***Treatment.*** Although renal function is generally maintained during childhood, ADPKD is responsible for the need for chronic dialysis in 10% to 12% of adult dialysis patients.[1] Hypertension should be managed medically to prevent long-term complications. While 12% to 15% of patients with ADPKD have an intracranial aneurysm,[22,27,30,31] screening magnetic resonance (MR) angiography usually is not performed in childhood because aneurysm rupture is rare in this period.

### Autosomal Recessive Polycystic Kidney Disease

***Overview and Etiology.*** ARPKD is a rare disorder that is seen in about 1 : 20,000 live births and that is also recognized to be a ciliopathy.[32,33] Genetic studies have localized the inheritance of ARPKD to chromosome 6p.[33,34] The *PKHD1* gene is expressed in fetal and adult kidneys and livers, the two major sites affected by the disease.[34] Approximately 1 in 70 persons is a carrier for this condition.[32,33] Histologically, the kidneys have a spongelike appearance, replaced by myriad mostly minute 1- to 2-mm cysts of relatively uniform size, representing dilated and elongated collecting ducts.[1,33] These cysts radiate from the hilum toward the surface of the kidney without a clear demarcation between the medulla and cortex; fibrosis is present in the renal interstitium.

***Clinical Presentation.*** ARPKD has been subdivided into categories based on clinical presentation. The perinatal and neonatal forms, which have the poorest prognosis, are associated with severe renal dysfunction, and affected patients may die of the disease early in life.[33,35] While the degrees of renal and hepatic abnormalities

## Abstract:

There are numerous congenital anomalies and developmental conditions that can affect the kidneys, ureters, and urinary bladder. These abnormalities are frequently detected *in utero* or during the neonatal period. Some of these conditions are quite common (e.g., multicystic dysplastic kidney, ureteropelvic junction obstruction, upper urinary tract duplication), while other conditions are quite rare (e.g., congenital megacalyces, megacystis-microcolon-intestinal hypoperistalsis-malrotation syndrome, cloacal exstrophy). In this chapter, we will review the etiology, clinical presentation, and imaging features of several common and less common genitourinary congenital and neonatal abnormalities.

## Keywords:

Congenital
Neonate
Kidney
Ureter
Urinary Bladder

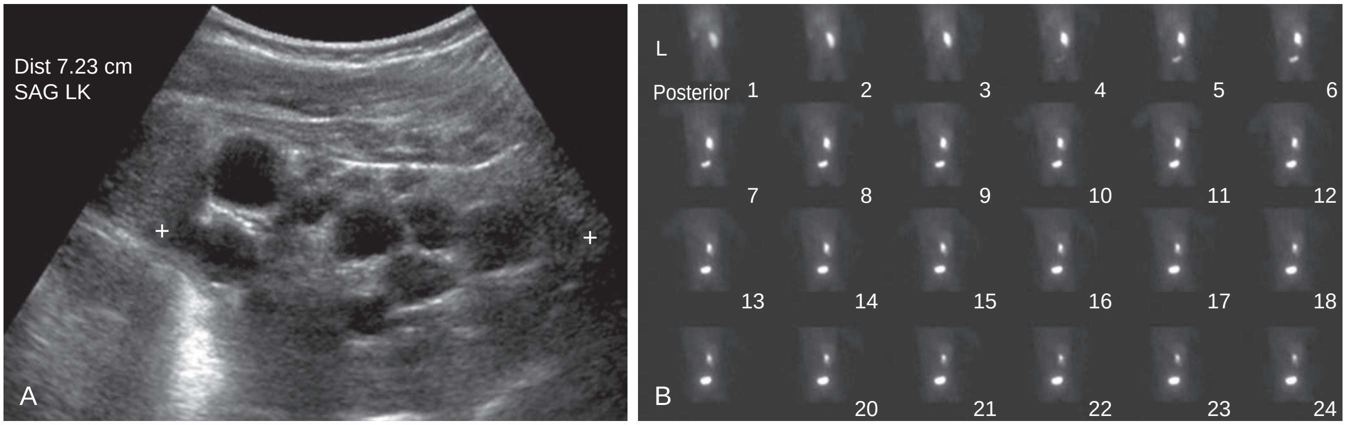

**e-Figure 113.2. A multicystic dysplastic kidney in a 6-month-old boy.** (A) Longitudinal ultrasound image of the left kidney shows multiple noncommunicating cysts of variable size. Visualized renal parenchyma is abnormally echogenic. (B) Posterior diuretic renal scintigraphy images show no appreciable left kidney function with no uptake or excretion of radiotracer. Right kidney function is normal.

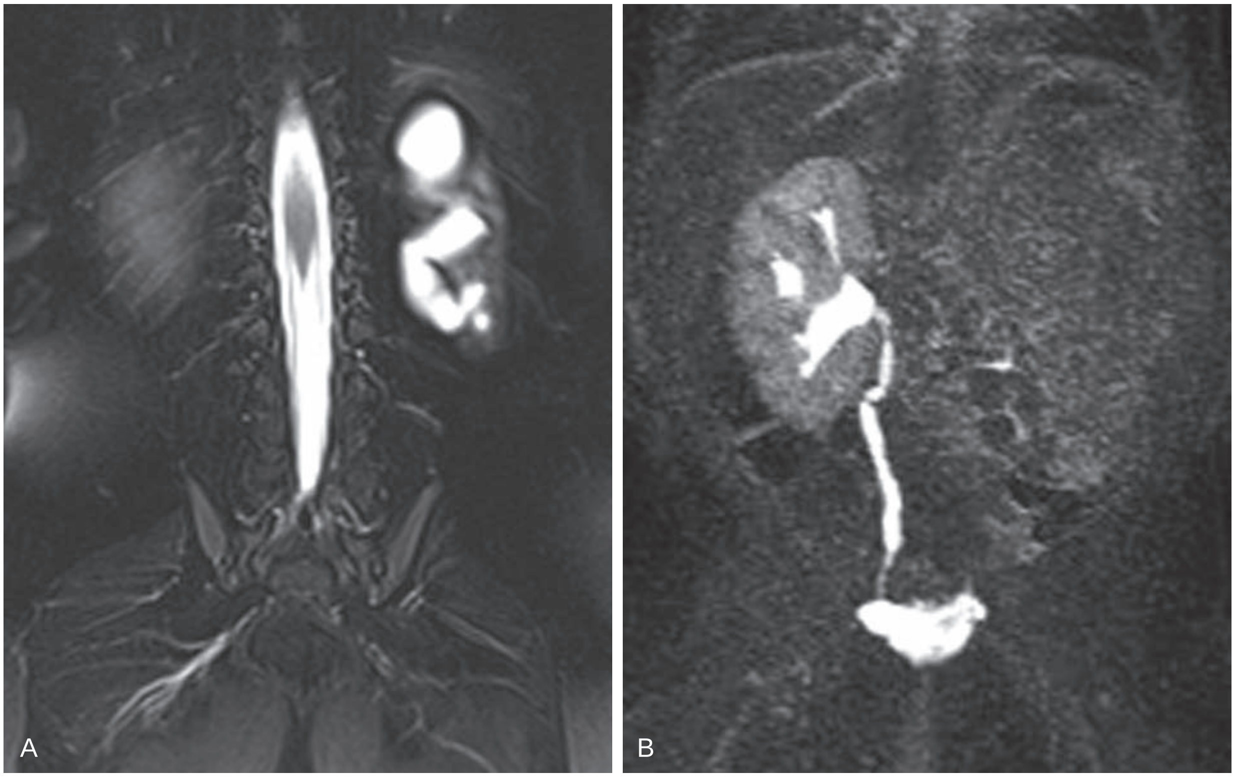

**e-Figure 113.3. Multicystic dysplastic kidney and MRI, hydronephrotic form.** (A) A coronal T2-weighted MR image with fat saturation shows a fluid signal within the left kidney that has a configuration similar to that of the renal collecting system. Only a small amount of left kidney parenchyma is present. (B) A coronal T1-weighted maximum intensity projection (MIP) MR image obtained 15 minutes after contrast material injection confirms the absence of the left kidney function. The right kidney is normal.

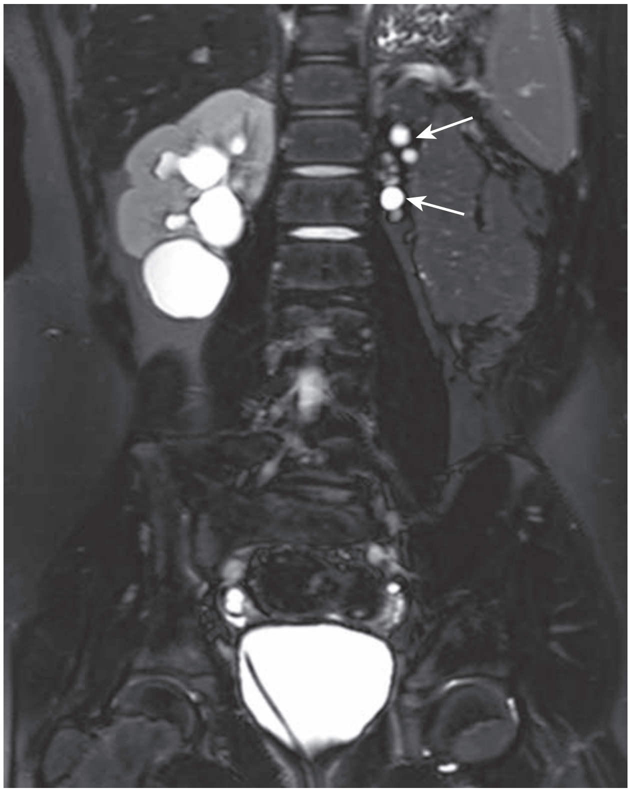

**e-Figure 113.4. Involuting multicystic dysplastic kidney.** A coronal T2-weighted MR image with fat saturation from a 14-year-old girl shows multiple small hyperintense cysts in the left renal fossa *(arrows)*, consistent with an involuting multicystic dysplastic kidney. This kidney was no longer visible by ultrasound. The right kidney is duplex in structure, with severe lower moiety parenchymal thinning due to ureteropelvic junction obstruction as well as multiple areas of upper moiety scarring.

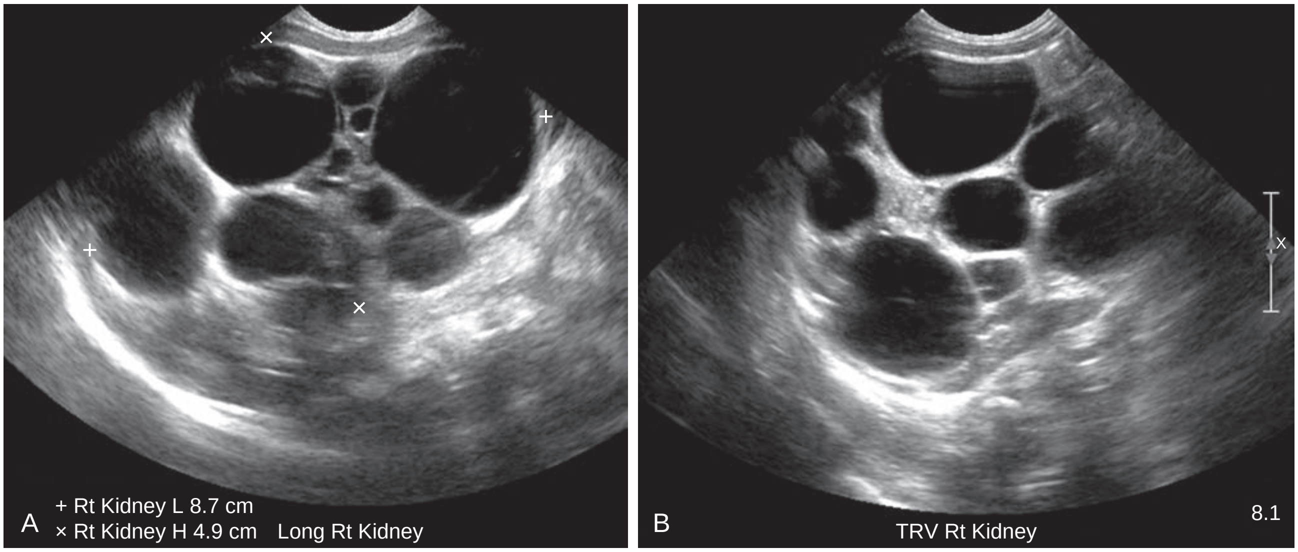

**Figure 113.1. Multicystic dysplastic kidney in a 1-day-old boy.** (A) Longitudinal ultrasound image of an enlarged left kidney shows multiple noncommunicating simple cysts of variable size, mimicking hydronephrosis. The very small amount of remaining renal parenchyma is abnormally echogenic. (B) A transverse ultrasound image shows similar findings.

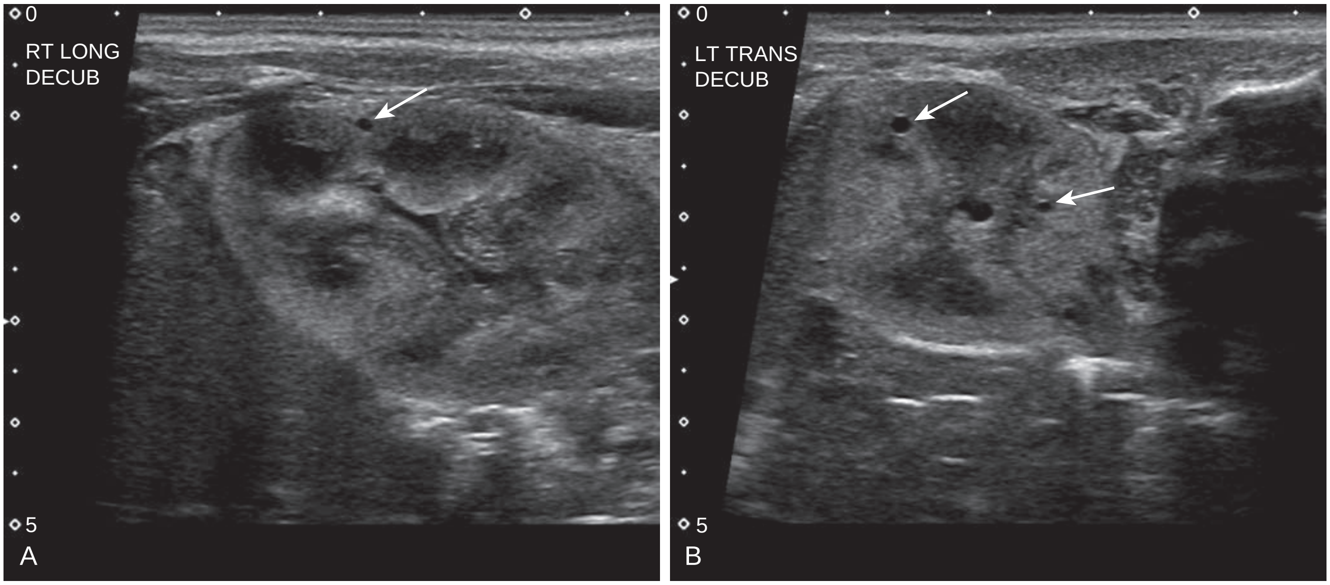

**Figure 113.5. Autosomal dominant polycystic kidney disease in a newborn.** (A) Longitudinal right kidney and (B) transverse left kidney ultrasound images show small bilateral simple renal cysts *(arrows)*. The renal cortex appears echogenic as well. There was a documented history of maternal and maternal grandfather autosomal dominant polycystic kidney disease.

historically have been considered to be inversely proportional,[19,33] a recent study suggests that the severity of renal and liver involvement are independent.[36] Liver involvement may be the cause of clinical presentation in a minority of affected children due to ductal plate malformations (e.g., congenital hepatic fibrosis and intrahepatic bile duct ectasia, or Caroli syndrome) and associated complications, such as portal hypertension and cholangitis.[33,36]

***Imaging.*** Abdominal radiography in the neonatal period commonly reveals bilateral abdominal or flank masses with centralized gas-filled bowel loops. The lungs may appear small because of a combination of pulmonary hypoplasia and mass effect from marked nephromegaly (e-Fig. 113.7).[33] On ultrasound, affected neonatal kidneys tend to be smoothly enlarged (frequently more than four standard deviations above the mean expected length for age), are hyperechoic as a result of the multiple acoustic interfaces at the walls of the dilated ducts, and have poor corticomedullary differentiation (Fig. 113.8).[1,33,35,37] On occasion, discrete cysts (solitary or multiple) of variable size (most commonly <1 cm) may be seen (Fig. 113.9).[32,37] A sonolucent rim may be seen at the periphery of the kidney as a result of cortical compression and relative sparing.[32,33] Contrast-enhanced CT (Fig. 113.10), while rarely performed, can show delayed opacification of the renal parenchyma with a prolonged and striated nephrogram. When studied with MRI, the dilated tubules in affected kidneys can appear linear and

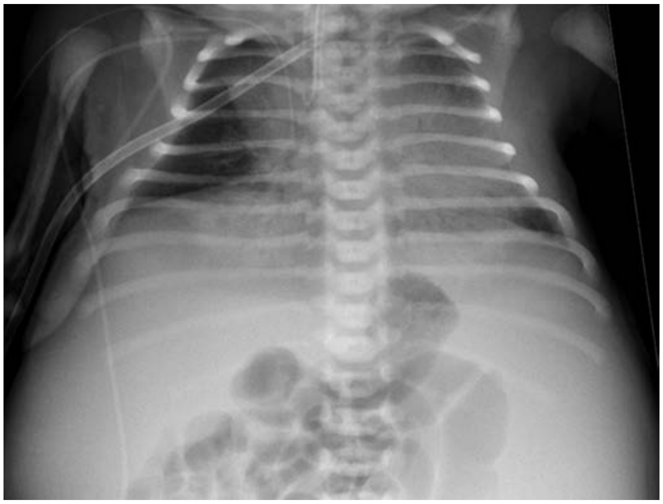

**e-Figure 113.7. Autosomal recessive polycystic kidney disease in a newborn boy.** Anteroposterior chest radiograph shows small lungs due to pulmonary hypoplasia. Bulging of the flanks and centralization of bowel gas is due to bilateral nephromegaly.

hyperintense on T2-weighted imaging, radiating from the medulla toward the cortex giving rise to a "spoke wheel" appearance (Fig. 113.11).[38] Ultrasound and MRI are most often used to evaluate for liver involvement, typically showing altered liver echogenicity and signal intensity due to congenital hepatic fibrosis, dilated intrahepatic bile ducts (sometimes appearing cystic and showing the central dot sign), and splenomegaly (e-Fig. 113.12).

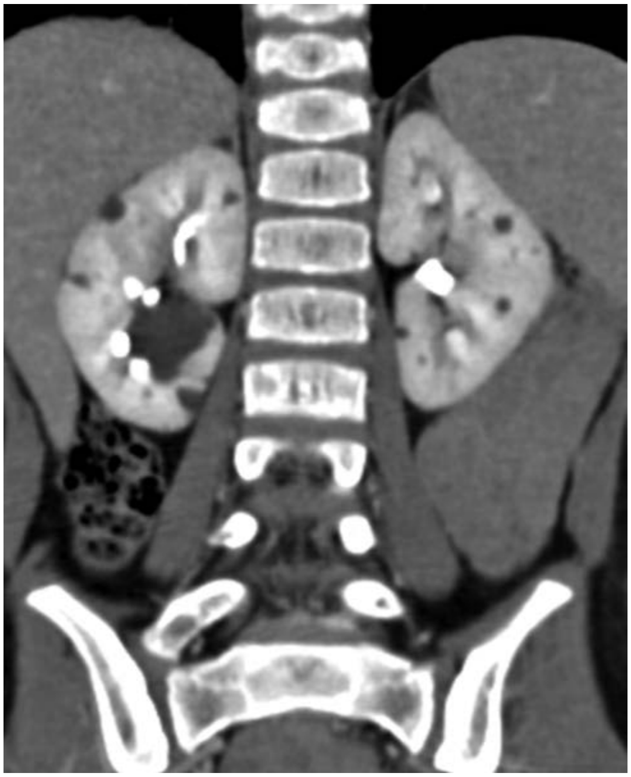

**Figure 113.6. Autosomal dominant polycystic kidney disease in an 8-year-old girl.** Coronal reformatted contrast-enhanced CT image shows multiple low attenuation lesions in both kidneys due to the presence of cysts.

***Treatment.*** Eighty-six percent of patients who survive beyond 1 month of age are alive at 1 year, and 67% are alive at 15 years.[39] Bilateral nephrectomy and renal replacement therapy may be required in neonates or infants when renal enlargement is massive and causes symptomatic mass effect or pulmonary compromise.[40] In infants who have initially adequate (although not normal) renal function, the disease may not be detected until later in the first decade. Systemic renovascular hypertension may occur and require medical management.[19,33] Many patients with ARPKD eventually will require renal replacement therapy, either dialysis or renal transplantation; combined liver-kidney transplantation may be performed in some children.[41]

## Other Renal Cystic Diseases in Children

Other uncommon genetic disorders (syndromes) are associated with renal cysts (Box 113.1). Recent studies suggest that several of these conditions are also due to genetic mutations that affect primary cilia or centromere function (sometimes referred to as *nephronopthisis*), with a variety of genes implicated.[20,28] Depending

**BOX 113.1** Other Causes of Renal Cystic Disease

- Tuberous sclerosis
- von Hippel-Lindau disease
- Trisomies 13 and 18
- Medullary cystic kidney disease
- Other ciliary disorders/nephronophthisis
  Asphyxiating thoracic dystrophy (Jeune syndrome)
  Bardet-Biedl syndrome
  Meckel-Gruber syndrome
  Joubert syndrome
  Oral-facial-digital syndrome type 1
  Short rib polydactyly
  Zellweger syndrome (cerebrohepatorenal syndrome)

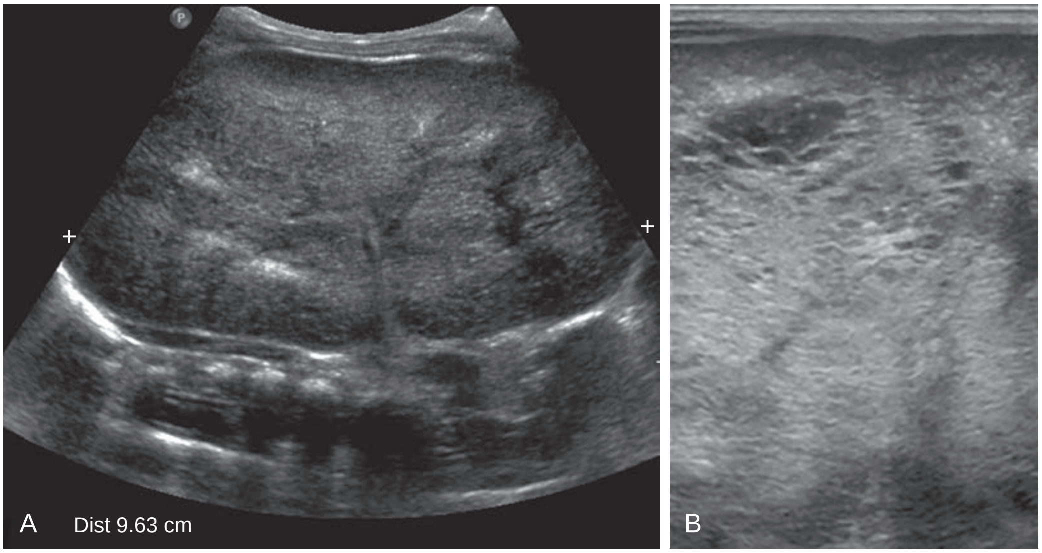

**Figure 113.8. Autosomal recessive polycystic kidney disease in a newborn girl.** (A) Longitudinal ultrasound image of the left kidney confirms the presence of a nephromegaly with loss of corticomedullary differentiation. The kidney is centrally echogenic and peripherally hypoechoic. (B) Linear high-frequency transducer ultrasound evaluation from a different newborn with autosomal recessive polycystic kidney disease reveals numerous tiny cystic structures within the kidney due to dilated ducts and tubules. The peripheral cortex is relatively hypoechoic.

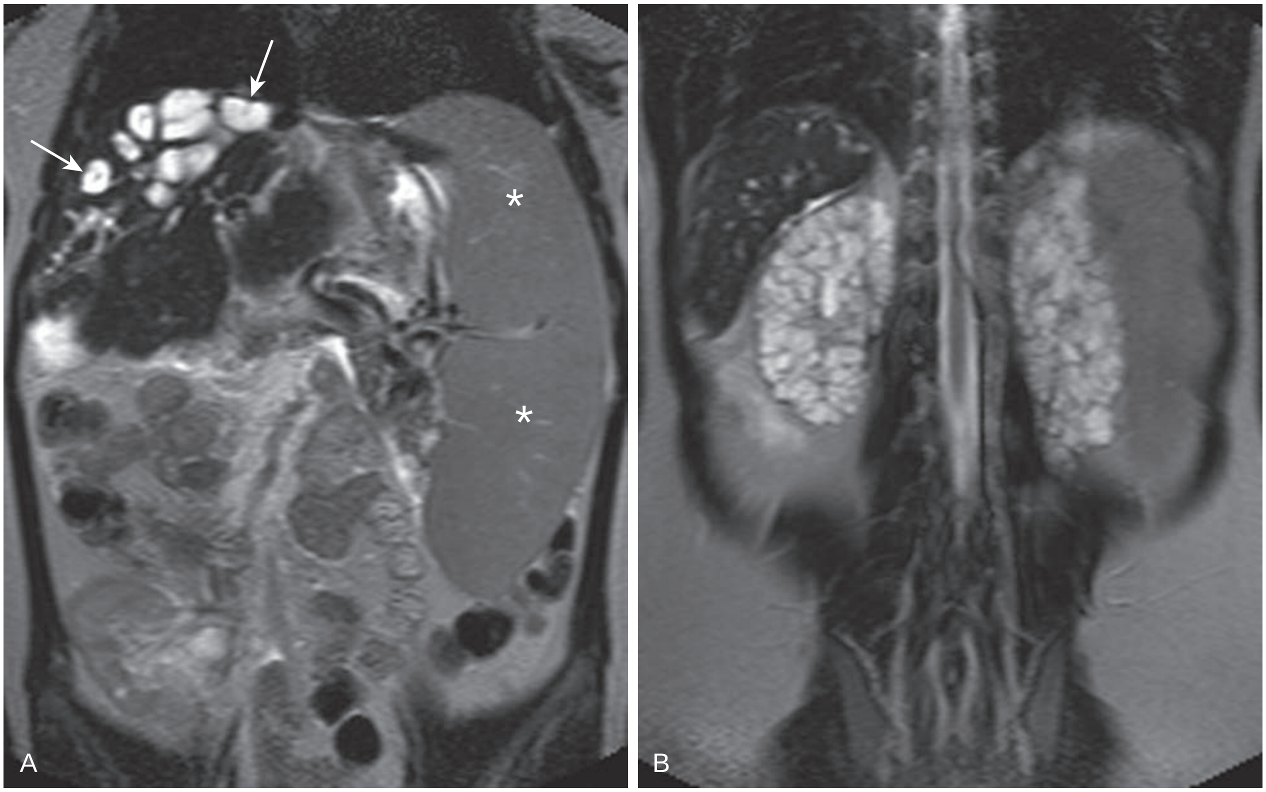

**e-Figure 113.12. Autosomal recessive polycystic kidney disease with severe liver involvement.** A coronal T2-weighted magnetic resonance (MR) image from a 14-year-old boy shows (A) shrunken appearance of the liver, multiple dilated intrahepatic bile ducts *(arrows)*, and splenomegaly *(asterisks)*. Findings suggest congenital hepatic fibrosis, Caroli syndrome, and portal hypertension. (B) More posterior image shows complete replacement of both kidneys by many small cysts.

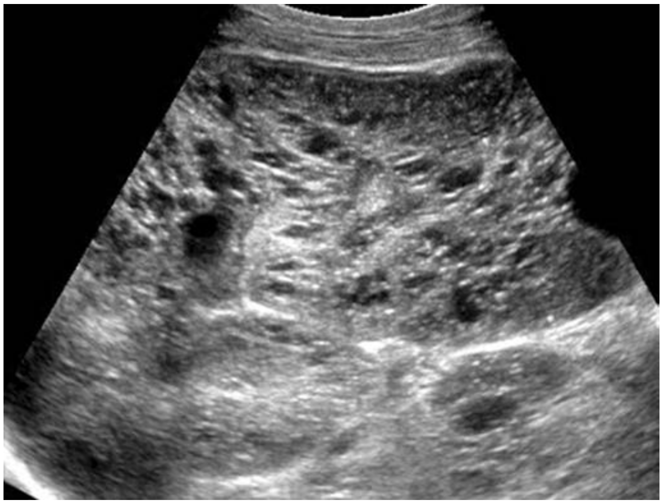

**Figure 113.9. Autosomal recessive polycystic kidney disease in a 6-month-old boy presenting with acute renal failure and bilateral flank masses.** Longitudinal ultrasound image of the right kidney shows nephromegaly, loss of normal corticomedullary differentiation, and many tiny cystic structures replacing the renal parenchyma.

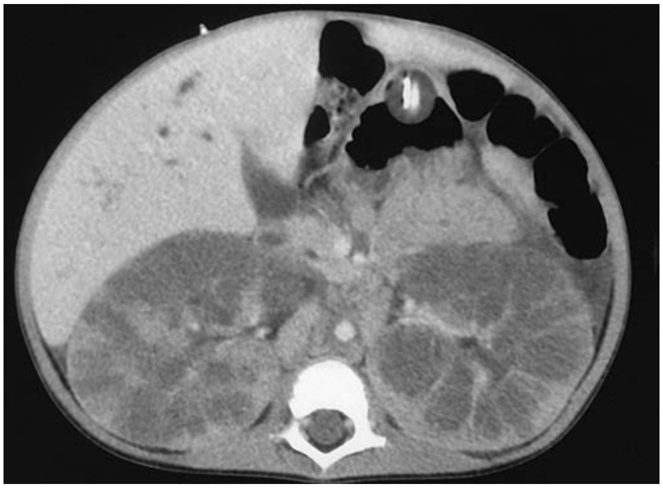

**Figure 113.10. Autosomal recessive polycystic kidney disease and CT.** A CT image shows that the pathologic process is primarily medullary. The dilated tubules have produced a linear pattern that can be seen clearly in a few regions. Areas of cortex appear spared.

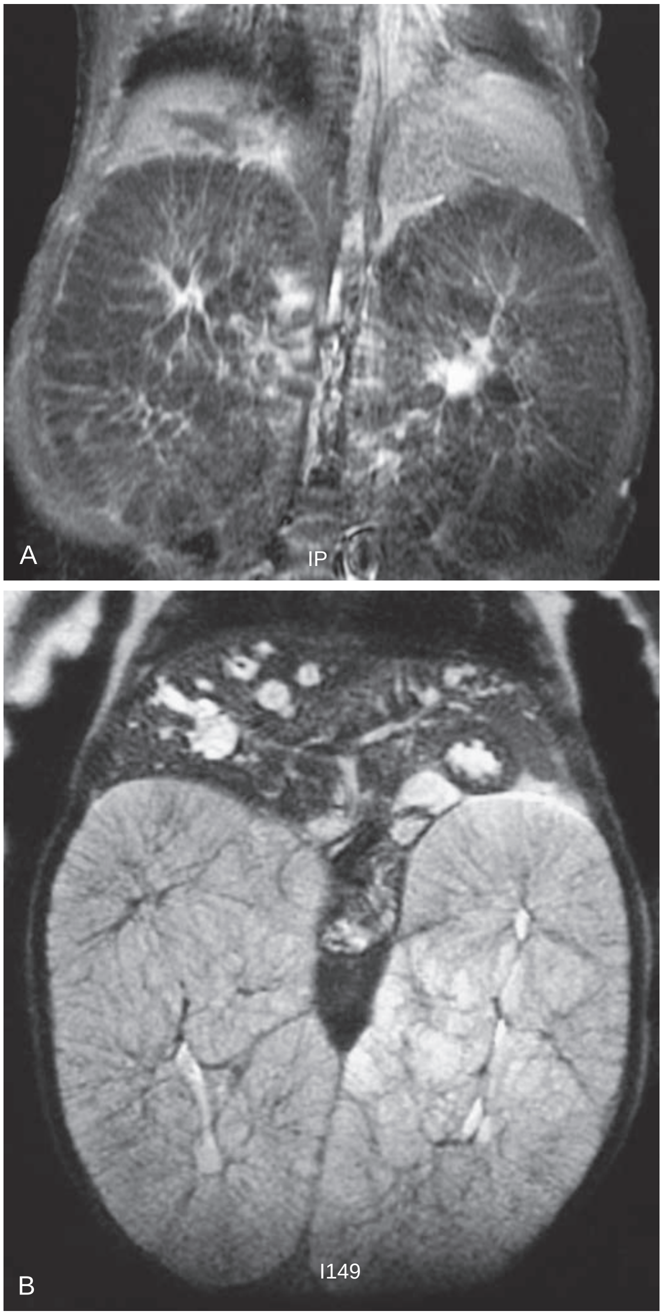

**Figure 113.11. Autosomal recessive polycystic kidney disease and MRI.** (A) T1-weighted and (B) T2-weighted MR images from an infant show that the kidneys are enormously enlarged and have a "spoke wheel" appearance. The patient also has intrahepatic biliary ectasia (Caroli syndrome), appearing as liver cysts on the T2-weighted image.

on the specific mutation, clinical presentation, associated anomalies, and age of presentation with regard to renal disease may vary.

## Calyceal Diverticulum

***Overview, Etiology, and Clinical Presentation.*** A calyceal diverticulum represents a focal outpouching of the renal collecting system that is located within the renal parenchyma and that contains urine.[42] This condition has an incidence of 3.3 to 4.5 : 1000 in children, based on excretory urography.[43–45] Calyceal diverticula are likely developmental in origin; they are lined with urothelium and surrounded by muscularis mucosa.[42,44] Although these structures most commonly are an incidental finding, they can be associated with pain as well as infection and calculus formation as a result of urinary stasis.[42,44,46,47]

***Imaging.*** Abdominal radiographs may be normal or may demonstrate one or more calculi (or milk of calcium) within a calyceal diverticulum.[44] On ultrasound, such diverticula may mimic a solitary renal cyst, appearing round, thin-walled, and anechoic.[43] They can vary in size ranging from a few millimeters to several centimeters (with a mean size around 11 mm),[44,46] and they most commonly occur within the upper pole of the kidney.[42] Calyceal diverticula can rarely be bilateral and/or multiple.[48] Upon excretory phase imaging (including MRI and CT), calyceal diverticula may fill with contrast material (Fig. 113.13). A thin connection, or neck, to an adjacent calyceal fornix may or may not be identified.[44]

***Treatment.*** A symptomatic calyceal diverticulum may require endoscopic or laparoscopic ablation.[47] Although both lithotripsy

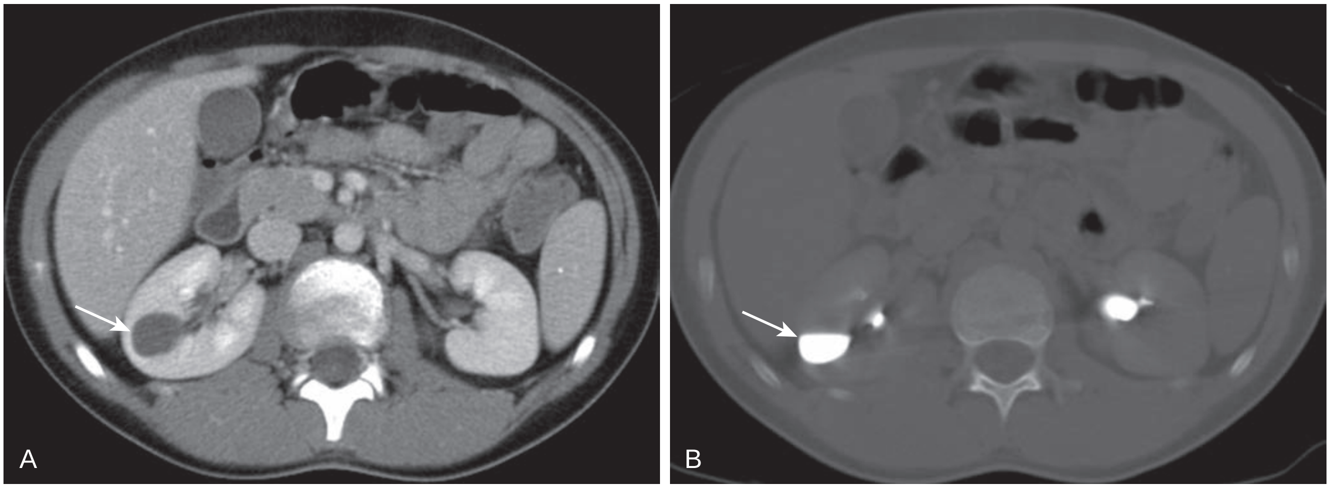

**Figure 113.13. Calyceal diverticulum in a 10-year-old girl.** (A) Axial contrast-enhanced CT image shows a low-attenuation cystic structure in the right kidney *(arrow)*. (B) An axial postcontrast excretory phase CT image shows excreted contrast material layering with this abnormality.

of calculi within the diverticulum and percutaneous ablation of the cavity have been described in adults,[46,49] such techniques have not been applied widely to children.

## Congenital Infundibulopelvic Stenosis

***Overview, Etiology, and Clinical Presentation.*** Congenital infundibulopelvic stenosis is a very rare congenital anomaly of the renal collecting system that presents as unilateral or bilateral caliectasis.[50] Although the exact etiology of this condition is uncertain, Lucaya et al[51] hypothesized that this abnormality is a milder manifestation of the process that results in MCDK. Affected children may be predisposed to urinary tract infections, and this condition may be associated with other renal and urinary tract anomalies.[50,51] Renal function may be normal to severely impaired.[50,51]

***Imaging.*** Upon contrast-enhanced excretory phase imaging studies (including excretory urography, MRU, and CT), this condition has a specific appearance: the renal collecting system infundibula are abnormally narrowed but not entirely obliterated, and the calyces appear abnormally rounded and dilated (Fig. 113.14). The renal pelvis also typically appears narrowed as a result of stenosis or hypoplasia. This condition may be unilateral or bilateral. Despite the cystlike appearance of the calyces on contrast-enhanced studies, the ultrasound appearance of the kidneys can be normal.

***Treatment.*** Most affected individuals demonstrate normal or stable impaired renal function and do not require treatment. Surgical approaches to manage this condition have been described, including multiple infundibuloplasties, ureterocalicostomy, and renal transplantation.[51] MRU with three-dimensional volumetric rendering can provide detailed anatomic depiction of the pelvocalyceal system and aid surgical planning.[50]

## Congenital Megacalyces (Megacalycosis)

***Overview, Etiology, and Clinical Presentation.*** Congenital megacalyces is a very rare anomaly of the renal collecting system that may be confused for obstructive hydronephrosis.[52] Calyceal involvement may be unilateral or bilateral. This abnormal calyceal dilatation is likely a result of underdevelopment/hypoplasia of the renal medullary pyramids.[53,54] Boys are more commonly affected than girls. Associated urinary stasis may predispose affected children to urinary tract infection and urolithiasis.[53]

***Imaging.*** Congenital megacalyces may appear similar to obstructive caliectasis by ultrasound. With excretory urography and MRU, however, this condition may be more readily identifiable because of the presence of abnormally dilated calyces that lack normal papillary impressions, have a polygonal or faceted shape, and appear to be increased in number (20 or more) (Fig. 113.15).[54] The renal parenchyma overlying affected calyces may appear thin. The renal pelvis can be normal in caliber or mildly dilated,[53] and classically, no related urinary tract obstruction should be present.

***Treatment.*** Congenital megacalyces usually is an incidental finding that requires no specific treatment.

## Ureteropelvic Junction Obstruction

***Overview.*** UPJ obstruction is the most common type of congenital urinary tract obstruction, occurring in about 3 per 1000 live births. Boys are more frequently affected than are girls, and the left kidney is more commonly involved than the right kidney. About 30% of cases are bilateral, although severity of obstruction and pelvicaliectasis may be asymmetric.[1]

***Pathophysiology.*** In the majority of cases, an intrinsic narrowing (e.g., smooth muscle deficiency, fibrosis/stricture, valve, kinking, or altered peristalsis) occurs at the level of the UPJ, leading to dilatation of the pelvicalyceal system.[1,55] Secondary intrinsic obstruction of the UPJ also can be caused by fibroepithelial polyps. On occasion, extrinsic narrowing can be seen from a crossing renal vessel, particularly in older children and adults.[56,57] UPJ obstruction can be found in association with other urinary tract anomalies, such as contralateral MCDK, upper urinary tract duplication,[58,59] VUR,[60] and ureterovesical junction obstruction.[61]

***Clinical Presentation.*** When UPJ obstruction is not detected prenatally, affected children can present with a palpable abdominal mass in the neonatal period. Older children may present with intermittent hydronephrosis and flank pain, often associated with crossing vessels. UPJ obstruction can be complicated by calculi, infection, forniceal rupture and urinoma, and posttraumatic hematuria, especially when diagnosis is delayed.[35]

***Imaging.*** On ultrasound, abnormal dilatation of the pelvicalyceal system of varying degrees is seen, whereas the ureter is generally normal in caliber.[1,35] Ultrasound findings suggestive of renal dysplasia may be present in cases of severe obstruction. Debris within the collecting system can represent infection or hemorrhage (Fig. 113.16). Careful interrogation of the UPJ region with Doppler

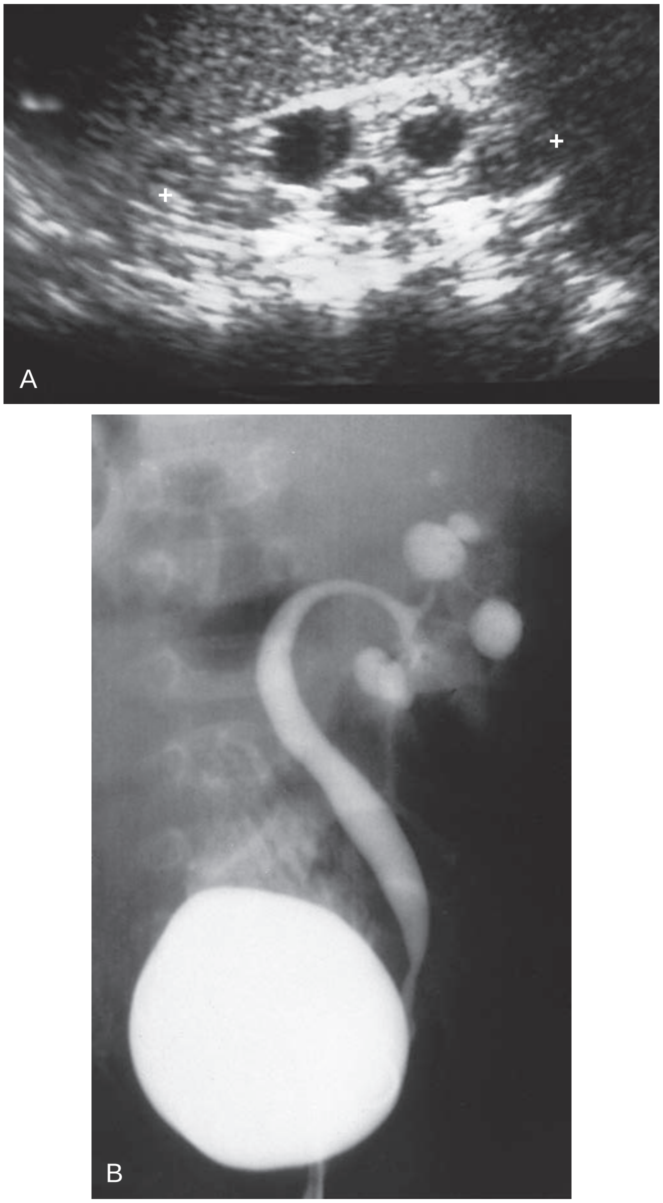

**Figure 113.14. Infundibulopelvic stenosis simulating cystic kidney disease.** (A) Longitudinal ultrasound image shows multiple “cysts” scattered throughout the kidney in this child with VACTERL association. (B) A voiding cystourethrogram shows vesicoureteral reflux into the abnormal pelvocalyceal system. The ureter has a greater caliber than the renal pelvis, infundibula, and calyces. The most peripheral portion of each calyx is rounded, producing the cystic spaces seen with ultrasound.

ultrasound may identify a crossing vessel, when present.[62] Frequently, separating dilated nonobstructed from dilated obstructed renal collecting systems is difficult by ultrasound alone.

Abdominal radiographs may show soft tissue fullness, bulging of the flank, and displacement of bowel loops from the affected side (e-Fig. 113.17). While not typically performed for pediatric UPJ obstructions, contrast-enhanced excretory phase CT commonly demonstrates delayed enhancement and excretion of contrast material.[55] CT angiography with multiplanar reformatted and three-dimensional images as well as MRU may be used to depict suspected crossing vessels as a cause of UPJ obstruction in older children and adults (Fig. 113.18).[57,63,64]

Diuretic renal scintigraphy is most often used to evaluate renal function (including perfusion and differential function) and drainage in the setting of suspected or known UPJ obstruction (e-Fig. 113.19).[65,66] Functional MRU is an increasingly important tool in the evaluation of untreated and treated UPJ obstructions.[67] This imaging technique currently allows for the detailed assessment of urinary tract anatomy, while also providing information regarding differential renal function and the presence or absence of obstructive uropathy (Fig. 113.20).[67–69] Both retrograde and antegrade pyelography may be performed to establish the level of upper urinary tract obstruction, if clinically necessary.

***Treatment.*** Recent literature has emphasized the conservative management of neonates with pelvocalyceal dilatation and suspected UPJ obstruction, especially with preserved renal function shown by biochemical parameters and imaging.[1,70–72] A substantial number of cases that are identified prenatally with pelvocalyceal dilation resolve spontaneously without requiring surgery.[70–72] Indications for surgery include reduced renal function, considerably delayed excretion of contrast material or radiotracer, sustained increase in pelvicalyceal dilation, breakthrough infections, a solitary kidney, and severe bilateral hydronephrosis.[72,73] Treatment, when necessary, usually is accomplished with a dismembered pyeloplasty (open, laparoscopic, or robotic).[1]

## Upper Urinary Tract Duplication

***Overview and Etiology.*** A duplex kidney consists of a single renal unit that is drained by two collecting systems. If two ureteric buds are present or the ureteric bud bifurcates before meeting the metanephric blastema, duplication of the renal collecting system and/or ureter occur.[74] Possibilities include a simple bifid renal pelvis, a bifid ureter (i.e., incomplete ureteral duplication), complete ureteral duplication, an ectopic ureter, and an ectopic ureterocele. Incomplete duplication of the upper urinary tract is more common than is complete duplication. Even when two ureters are present distally, they frequently enter the bladder via a common sheath.

In cases of complete ureteral duplication, one ureter takes up a near-normal position within the urinary bladder, and the other moves inferiorly with the mesonephric (wolffian) duct into an abnormal location (e.g., the bladder neck, urethra, vagina, or perineum in girls or the ejaculatory system in boys).[74] The Weigert-Meyer rule, which is applied only to complete duplications, states that the ureter that drains the upper moiety inserts inferior and medial to the lower moiety ureter (Fig. 113.21). In addition, the ectopic ureter is more likely to be obstructed, whereas the lower moiety ureter is more likely to reflux. Extravesical ureter insertion is far more common in girls than in boys. Extravesical ureter insertions in boys are above the sphincter mechanism; they can be below the sphincter mechanism in girls and present with urinary incontinence. On occasion, ectopic ureteroceles may be detected in the setting of a diminutive pelvicalyceal system, the so-called “ureterocele disproportion.”[74,75]

***Clinical Presentation.*** Clinically, incomplete duplication of the upper urinary tract may be asymptomatic or may present with urinary tract infections as a result of ureteroureteral reflux and stasis (so-called “yo-yo” reflux).[74] Children with complete duplication may present in a variety of manners, including hydronephrosis, urinary tract infection, and bladder outlet obstruction due to a large ureterocele.[74,76] Complete duplications in girls also may present with enuresis (both daytime and nocturnal wetness) as a result of insertion of the ectopic ureter into the urethra below the level of the sphincter mechanism or vagina.[74] In boys, complete duplications may complicated by infection (e.g., urinary tract or epididymitis) or pelvic pain.

***Imaging.*** Ultrasound may identify a prominent renal parenchymal column that appears to completely separate the sinus fat, providing indirect evidence of collecting system duplication (Fig. 113.22). More commonly, complete duplications present with

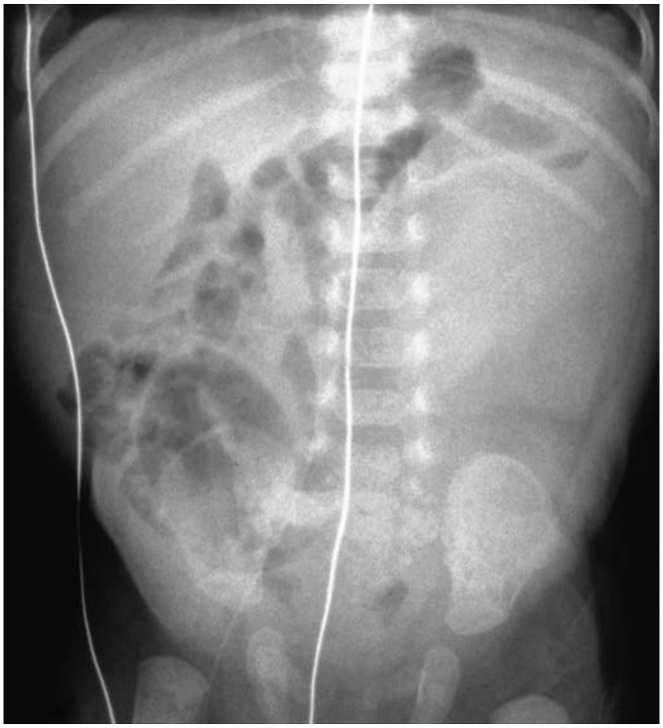

**e-Figure 113.17. Ureteropelvic junction obstruction.** Abdominal radiograph reveals mass effect in the central and left abdomen, displacing bowel to the right.

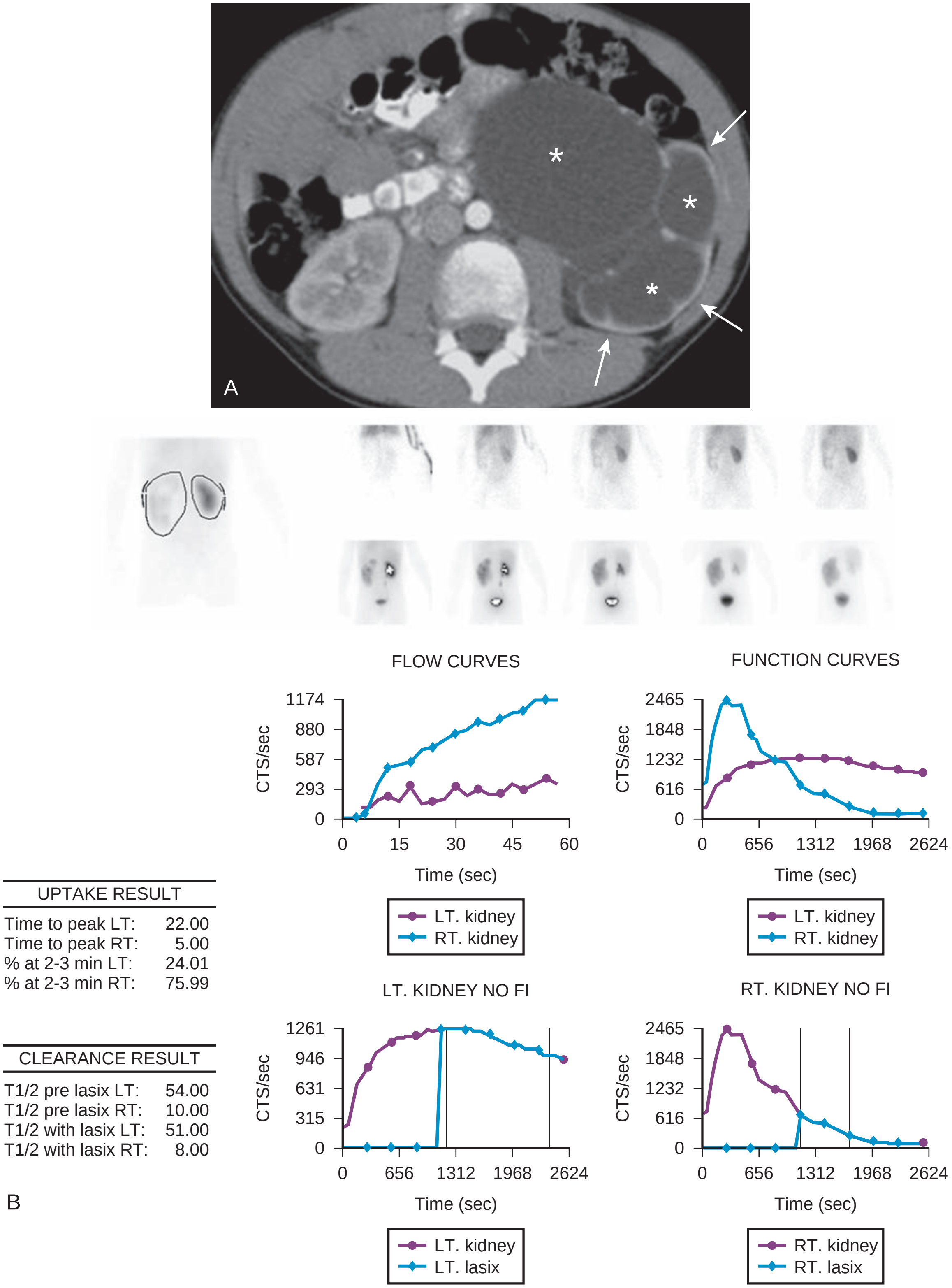

| UPTAKE RESULT | |
|---|---|
| Time to peak LT: | 22.00 |
| Time to peak RT: | 5.00 |
| % at 2-3 min LT: | 24.01 |
| % at 2-3 min RT: | 75.99 |

| CLEARANCE RESULT | |
|---|---|
| T1/2 pre lasix LT: | 54.00 |
| T1/2 pre lasix RT: | 10.00 |
| T1/2 with lasix LT: | 51.00 |
| T1/2 with lasix RT: | 8.00 |

**e-Figure 113.19. Ureteropelvic junction obstruction in a 7-year-old with gross hematuria after a fall.** (A) Axial contrast-enhanced CT image demonstrates marked left pelvicaliectasis *(asterisks)* and renal parenchymal thinning *(arrows)*. The left ureter was normal in caliber. (B) Diuretic renal scintigraphy demonstrates decreased perfusion of the left kidney. The left kidney shows substantially delayed uptake and excretion of radiotracer despite intravenous furosemide administration, a pattern consistent with obstruction. *CTS,* Counts; *LT,* left; *RT,* right.

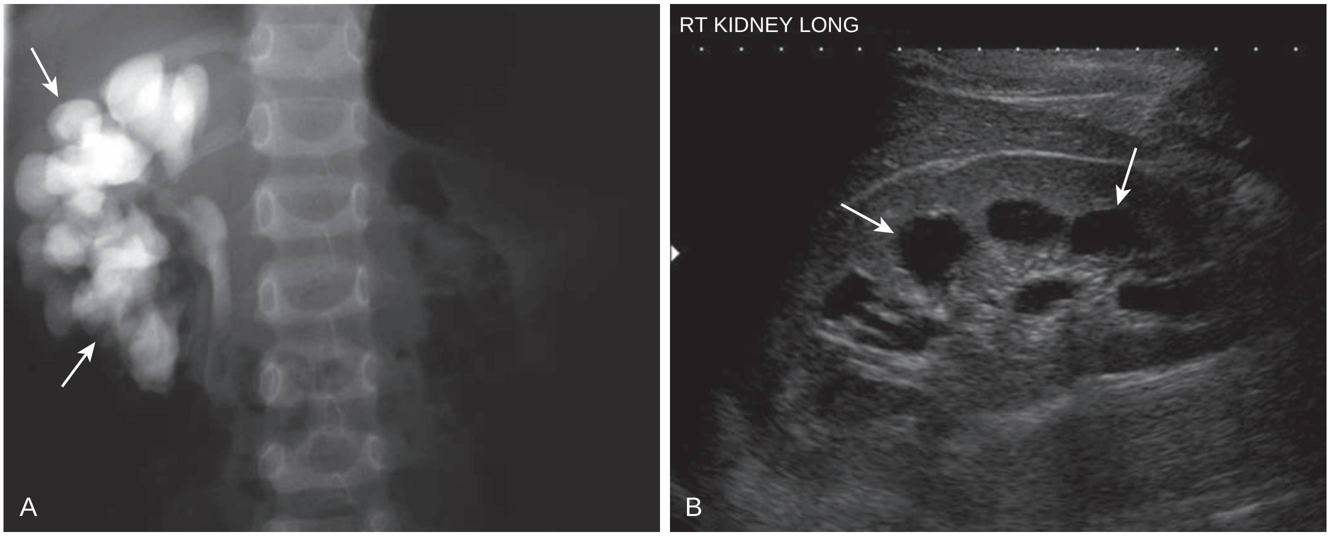

**Figure 113.15. Congenital megacalyces in a 5-year-old boy.** (A) An excretory urography image demonstrates contrast material filling an increased number of right kidney polygon-shaped calyces *(arrows)*, confirming the diagnosis of congenital megacalyces. The right renal pelvis is normal in diameter. (B) A longitudinal ultrasound image of the right kidney shows multiple dilated calyces that appear as cysts *(arrows)* with overlying parenchymal thinning.

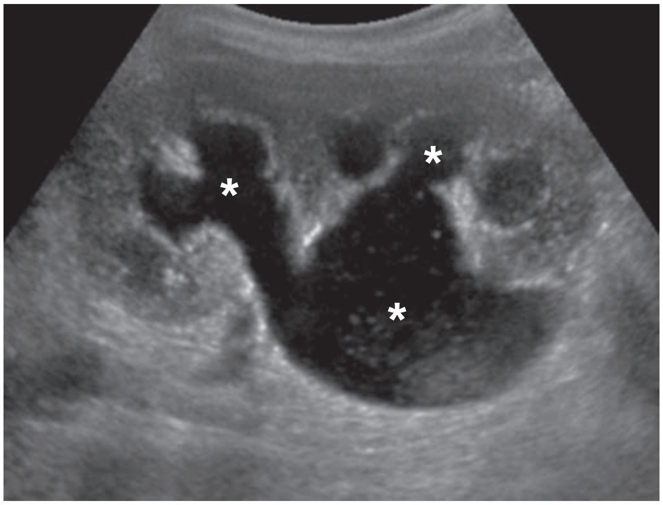

**Figure 113.16. Ureteropelvic junction obstruction in a newborn boy with a typical ultrasound appearance.** Longitudinal image of the left kidney shows moderate to severe dilatation of the pelvicalyceal system *(asterisks)*, with the renal pelvis being more dilated that the calyces. The proximal ureter could not be seen. Debris is present in the renal pelvis.

upper moiety hydronephrosis. Dilatation of the lower moiety can be due to VUR or, less often, concomitant UPJ obstruction (e-Fig. 113.23).[58,74] Ultrasound of the urinary bladder may show a thin-walled intraluminal cystic structure, consistent with a ureterocele (Fig. 113.24).[1] Ureteroceles vary in size and may appear septated or multiloculated, and when they are located in the midline, it may be difficult to establish the exact side from which they arise.[76]

In the early bladder filling phase of a VCUG examination, a smooth, round filling defect is consistent with a ureterocele (Fig. 113.25). Ureteroceles become more difficult to visualize as the urinary bladder distends with contrast material because of obscuration, flattening, or even eversion.[74,76] VUR into the lower moiety collecting system of a duplex kidney commonly reveals too few calyces and has a “drooping lily” appearance as a result of abnormal long-axis orientation (Fig. 113.26).[74] The normal long axis of the renal collecting system should parallel that of the ipsilateral psoas muscle. On occasion, VUR may be noted involving the upper moiety of a duplicated system (in about 11% of children), sometimes only after ureterocele incision.[74,77] VUR also can be used to separate incomplete from complete ureteral duplications (Fig. 113.27).

MRU provides a precise assessment of duplicated upper urinary tract anatomy (Figs. 113.28 and 113.29).[78] A variety of T2-weighted imaging techniques can be used to image urine-filled structures without exogenous contrast material. MRU also can evaluate renal function, detect evidence of obstructive uropathy and dysplasia, and confidently identify ectopic ureteric insertions (Fig. 113.29).[74,79]

***Treatment.*** Incomplete duplications of the upper urinary tract are frequently asymptomatic and require no specific treatment. Treatments for upper moiety obstruction include endoscopic puncture or excision of an obstructing ureterocele, ureteroureterostomy, and upper moiety heminephrectomy in the setting of poor or absent function.[74,80,81] Lower moiety dilatation due to VUR may require ureteral reimplantation, whereas dilatation due to UPJ obstruction may require pyeloplasty. Multicystic dysplastic upper moieties may involute over time without need for intervention.[82]

## URINARY BLADDER

### Prune-Belly Syndrome (Eagle-Barrett Syndrome)

***Overview, Etiology, and Clinical Presentation.*** Prune-belly syndrome, also known as *Eagle-Barrett* or *triad syndrome*, includes the constellation of bilateral cryptorchidism, anterior abdominal wall muscular deficiency, and a variety of urinary tract anomalies, including megacystis and hydroureteronephrosis.[83,84] The appearance of the abdominal wall on physical examination and radiographs has a characteristic appearance. Although the pathogenesis of prune-belly syndrome is controversial, two main theories have been suggested: (1) bladder outlet obstruction early in utero and (2) a primary mesodermal defect.[83–85] This condition is usually nonhereditary (although familial cases have been reported), usually affects boys (3%–5% of cases occur in girls), and is present in

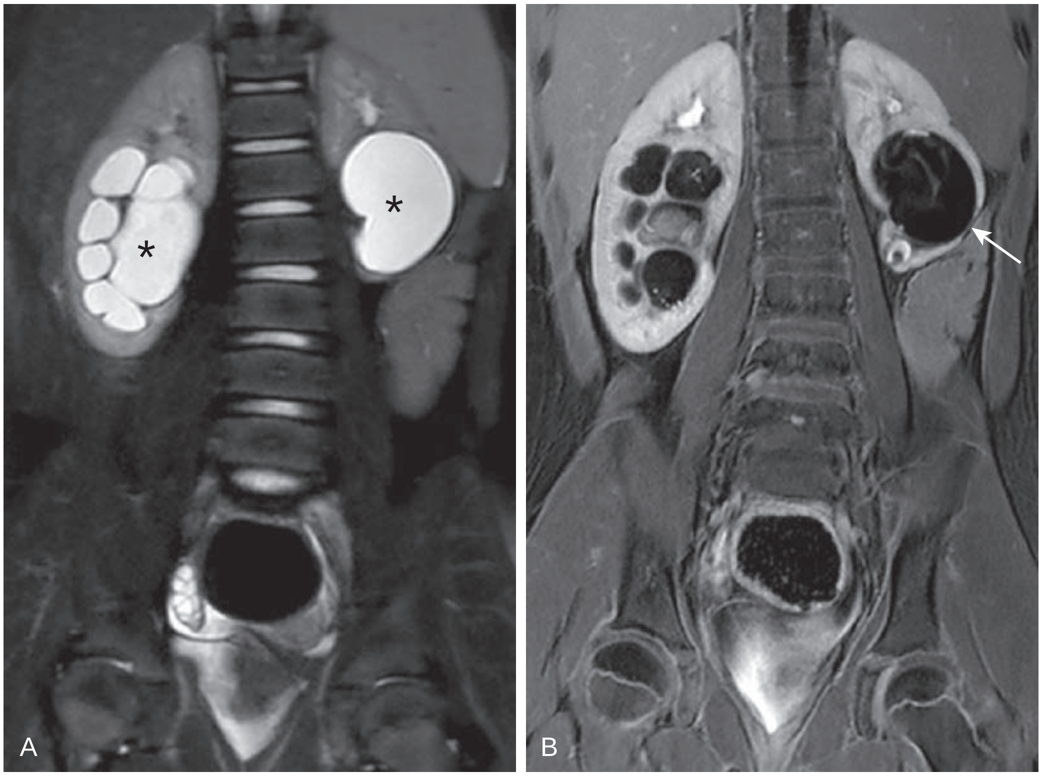

**e-Figure 113.23. Bilateral upper urinary tract duplication with bilateral lower moiety ureteropelvic junction obstructions in an 8-year-old girl.** (A) Coronal T2-weighted fat-saturated MR image shows bilateral duplex kidneys with bilateral lower moiety pelvicaliectasis *(asterisks)*. (B) A coronal postcontrast excretory phase T1-weighted MR image shows delayed passage of contrast material into the bilateral lower moiety collecting systems due to ureteropelvic junction obstructions. There is severe left lower moiety parenchymal thinning *(arrow)*. There was timely excretion of contrast material into the bilateral upper moiety collecting systems.

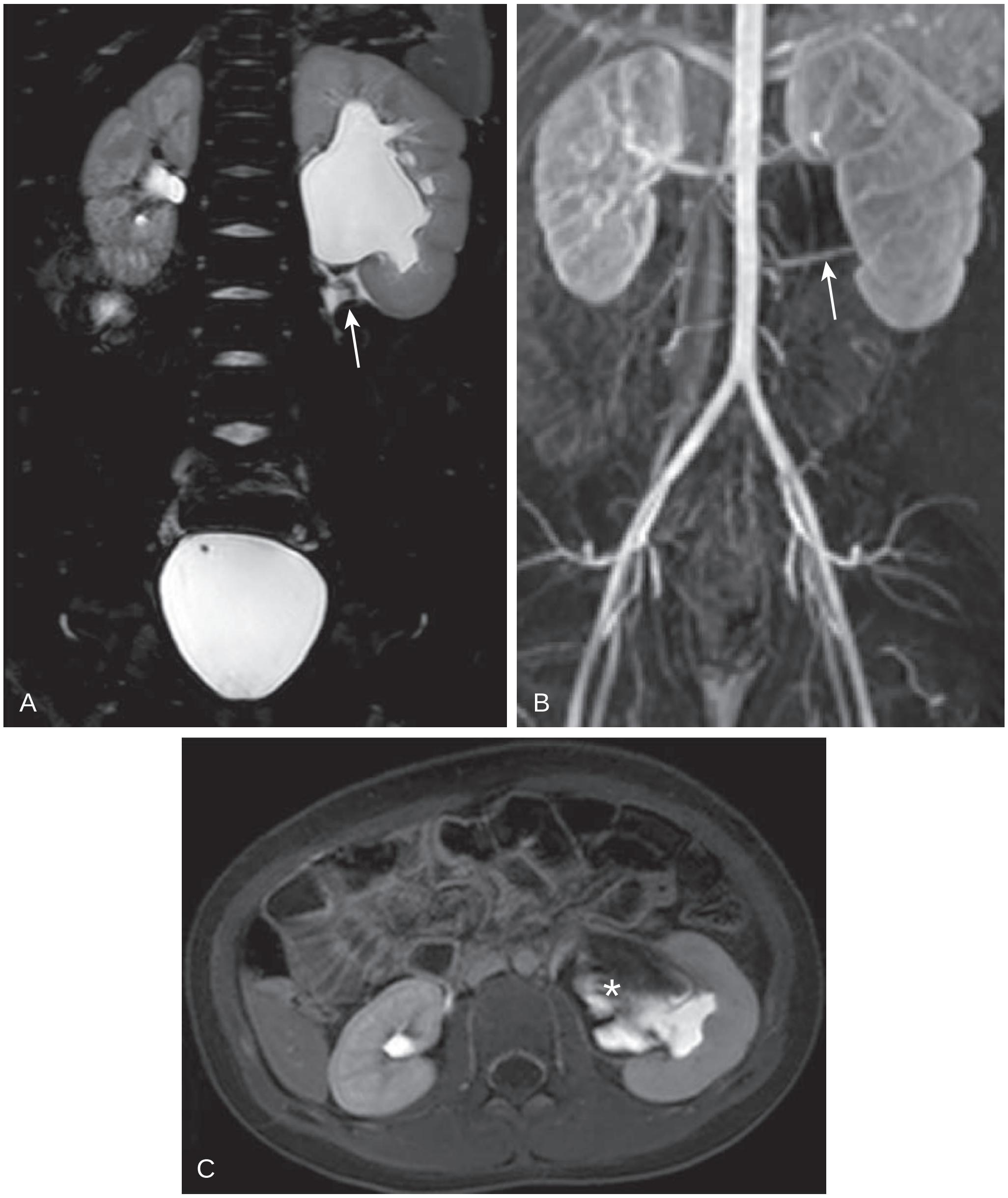

**Figure 113.18. Ureteropelvic junction obstruction due to surgically confirmed crossing vessel.** (A) Coronal T2-weighted fat-saturated magnetic resonance (MR) image shows left pelvicaliectasis; fluid *(arrow)* adjacent to the left renal collecting system is likely due to diuretic challenge and related forniceal rupture or transudation of urine. (B) Coronal postcontrast arterial phase T1-weighted maximum intensity projection (MIP) MR image shows slight hypoenhancement of the left kidney as well as an accessory left renal artery *(arrow)* crossing the left ureteropelvic junction region. (C) Axial postcontrast T1-weighted MR image shows delayed excretion of contrast material into the left renal collecting system *(asterisk)*.

1:29,000 to 1:50,000 live births.[83,84] Associated anomalies of the cardiovascular, musculoskeletal, and gastrointestinal systems also may be present.[86]

***Imaging.*** On physical examination and radiographs, the abdominal wall of affected neonates has a characteristic wrinkled appearance with bulging of the flanks resulting from muscular deficiency (e-Fig. 113.30). VCUG allows depiction of the urinary bladder and urethral anatomy, identifies VUR, and determines whether a urachal anomaly is present. Markedly dilated, tortuous ureters are common because of a combination of muscular deficiency and VUR, which is present in approximately 75% of patients with prune-belly syndrome (Fig. 113.31).[84] Upper urinary tract obstruction typically is not present. The urinary bladder usually has a smooth wall and an increased capacity (megacystis) and may contain multiple diverticula. Urethral findings include dilatation and elongation of the prostatic urethra (e-Fig. 113.32), an enlarged utricle, megalourethra (see e-Fig. 113.32), and rarely urethral atresia.[83] A minority of patients with prune-belly syndrome have urethral obstruction due to an obstructing membrane or valve.[83] The primary role of ultrasound in the neonatal period is to establish the status of the kidneys. The kidneys commonly show findings compatible with renal dysplasia, including small size, abnormally

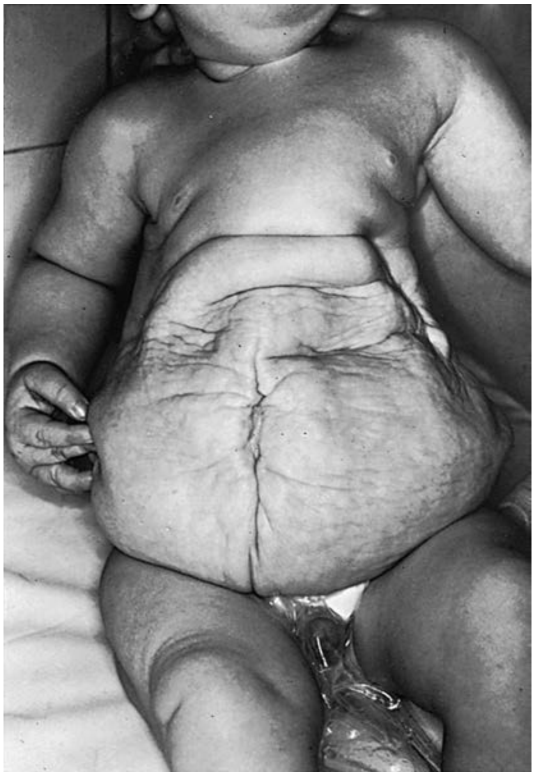

**e-Figure 113.30. Prune-belly syndrome in a newborn boy.** There is marked abdominal wall laxity. The testes were undescended, and flank masses representing huge ureters were easily palpated.

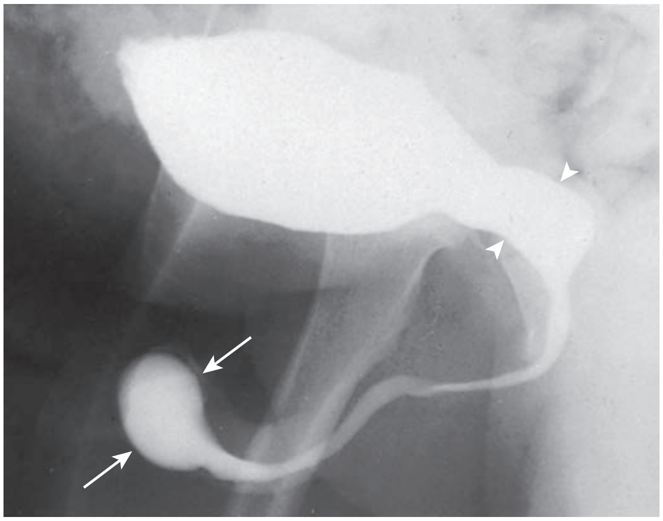

**e-Figure 113.32. Neonatal boy with prune-belly syndrome.** A voiding cystourethrogram image shows an elongated and dilated nonobstructed posterior urethra *(arrowheads)* as well as localized dilatation of the distal segment of the urethra *(arrows)*, consistent with a localized form of fusiform megalourethra.

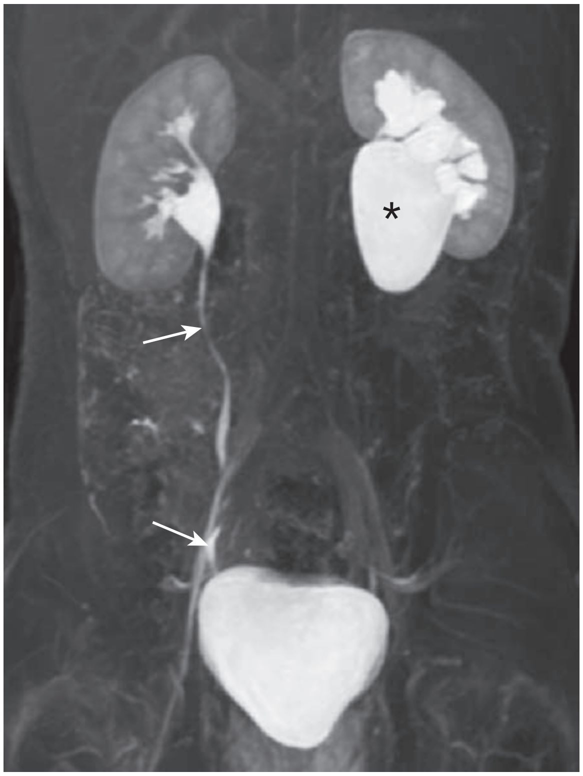

**Figure 113.20. Ureteropelvic junction obstruction in an 8-year-old girl.** Coronal postcontrast excretory phase T1-weighted maximum intensity projection (MIP) MR image shows dilated left renal collecting system *(asterisk)* and delayed passage of contrast material into the left ureter. The right upper urinary tract is normal in caliber, with contrast filling the right ureter *(arrows)*.

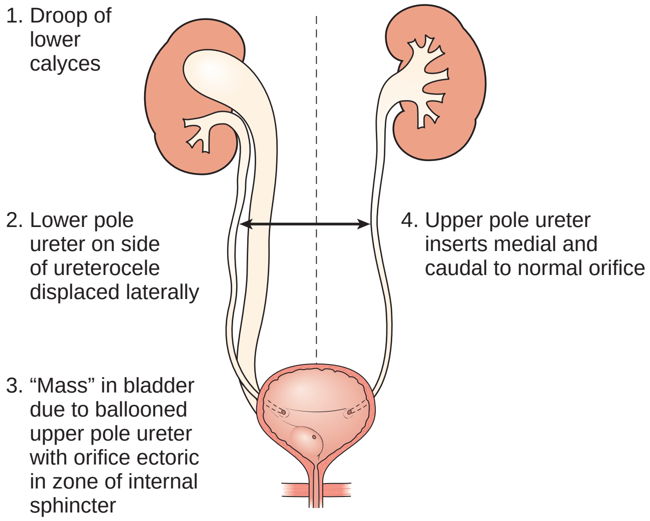
1. Droop of lower calyces
2. Lower pole ureter on side of ureterocele displaced laterally
3. "Mass" in bladder due to ballooned upper pole ureter with orifice ectoric in zone of internal sphincter
4. Upper pole ureter inserts medial and caudal to normal orifice

**Figure 113.21.** Diagram of the Weigert-Meyer rule. *(Redrawn from Berdon WE, Baker DH, Becker JA, et al. Ectopic ureterocele.* Radiol Clin North Am*. 1968;6:205–214.)*

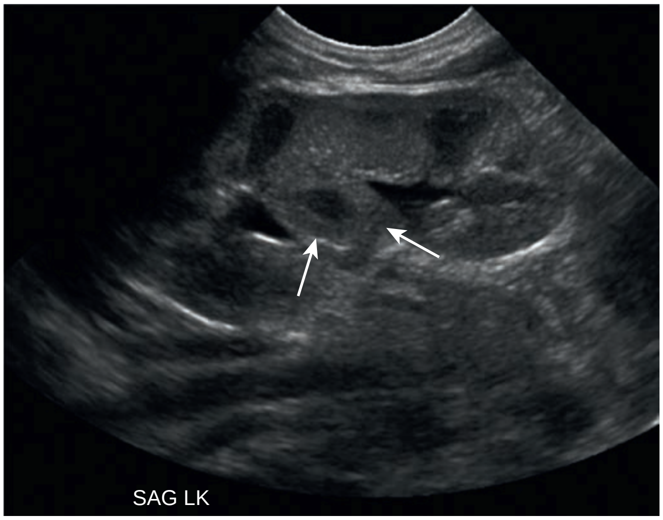

**Figure 113.22. Upper urinary tract duplication in a 1-month-old girl.** A longitudinal ultrasound image through the left kidney shows a prominent column *(arrows)* separating upper and lower moiety collecting systems.

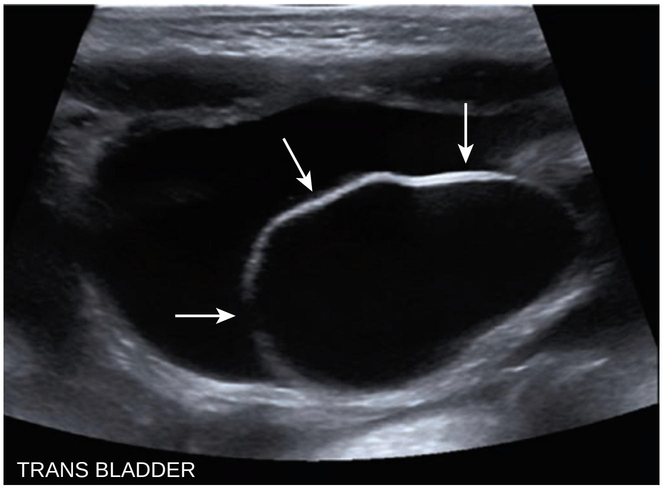

**Figure 113.24. Upper urinary tract duplication in a 6-week-old girl.** Transverse ultrasound image through the bladder confirms the presence of a large left ureterocele *(arrows)*.

increased parenchymal echogenicity, loss of corticomedullary differentiation, and cortical cysts.

***Treatment.*** Children with prune-belly syndrome may require multiple surgical procedures. The testes should be relocated from the abdomen to the scrotum (orchiopexy) to minimize the risk of future testicular torsion and neoplasm.[83] Any urethral obstruction should be surgically addressed. VUR and poor upper urinary tract drainage may be managed with chronic antibiotic prophylaxis or surgical reimplantation of the ureters to attempt to preserve renal function. Megacystis and poor urinary bladder emptying may be treated with reduction cystoplasty or vesicostomy.[87] In more severe cases, anterior abdominal wall surgical reconstruction (abdominoplasty) is performed and may improve urinary bladder emptying.[83,87] Because of renal dysplasia and chronic kidney disease, affected children eventually may require renal transplantation or dialysis therapy.[86]

## Megacystis-Microcolon-Intestinal Hypoperistalsis Syndrome

***Overview, Etiology, and Clinical Presentation.*** The name "megacystis-microcolon-intestinal hypoperistalsis syndrome" describes the pertinent clinical and radiologic findings.[88] Originally termed *Berdon syndrome*, features of this syndrome may overlap

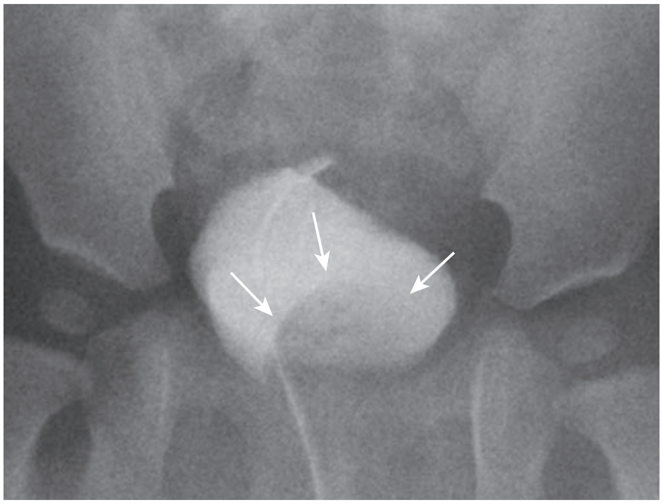

**Figure 113.25. Left upper urinary tract duplication in a 1-year-old girl.** Voiding cystourethrogram image demonstrates a large urinary bladder filling defect *(arrows)*, indicating a ureterocele. No vesicoureteral reflux was visualized.

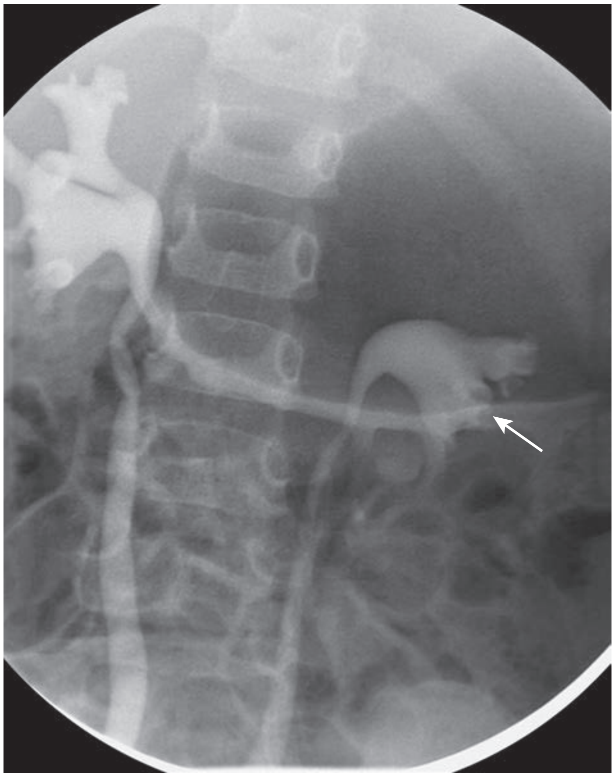

**Figure 113.26. Left upper urinary tract duplication in a 2-year-old girl.** Voiding cystourethrogram image shows bilateral vesicoureteral reflux. The left renal collecting system has too few calyces and its axis is abnormally oriented, giving rise to the "drooping lily" appearance *(arrow)*.

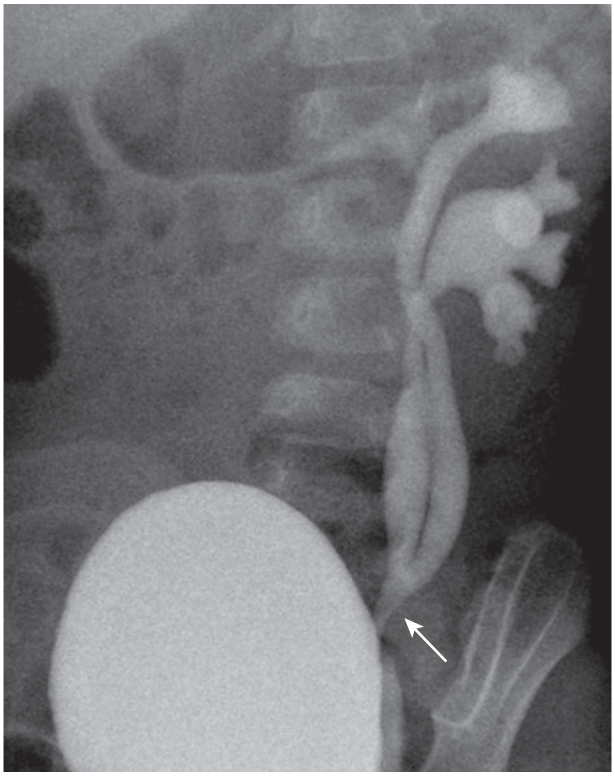

**Figure 113.27. Incomplete duplication of the left upper urinary tract in a 1-year-old girl.** A voiding cystourethrogram image shows reflux of contrast material into two separate left renal collecting systems and proximal/mid ureters. The ureters join distally *(arrow)*, above the left ureterovesical junction.

with prune-belly syndrome. This syndrome is an autosomal recessive disorder seen mostly in girls.[89] It presents clinically with severe abdominal distention during the neonatal period because of functional bowel obstruction and severe urinary bladder distention; prenatal detection also has been described.[90,91]

***Imaging.*** Abdominal radiography may demonstrate a large, round mass emanating from the pelvis because of megacystis; ultrasound and VCUG can confirm marked urinary bladder distention (Fig. 113.33) and, in most cases, hydroureteronephrosis.[91] Urinary bladder emptying is abnormal, although no anatomic obstruction is found. Contrast enema examination reveals a severe microcolon and diminished or absent colonic peristalsis (Fig. 113.34).[90,91] Upper gastrointestinal (GI) series and small bowel follow-through can be used to document malrotation and hypoperistaltic small bowel.[88,92]

***Treatment.*** This syndrome is often fatal in the first year of life because of malnutrition or sepsis, unless the patient receives parenteral nutrition and aggressive supportive care.[90,91,93,94] Bowel transplantation has been attempted as a treatment option.[95] A cutaneous vesicostomy or suprapubic cystostomy may assist urinary bladder drainage.[91]

## Bladder Exstrophy

***Overview, Etiology, and Clinical Presentation.*** Deficiency of the anterior abdominal wall with an open, everted, incompletely formed urinary bladder is called *bladder exstrophy*. The anterior wall of the urinary bladder and overlying skin are absent, and the rectus abdominis muscles are separated inferiorly.[1,96] The remaining posterior urinary bladder wall is continuous with the skin.[96] Failure of migration of mesenchymal cells between ectoderm and cloaca during the fourth week of fetal life leads to incomplete closure of the midline lower anterior abdominal wall in utero.[1,96,97] This rare, unpredictable, congenital defect occurs in 1:10,000 to 1:40,000 live births and is more common in boys.[1] Epispadias in boys and bifid clitoris in girls often are noted as well.[96] Other skeletal, spinal, scrotal, and anorectal anomalies also may be present,[1,96] whereas renal anomalies are relatively uncommon.[98]

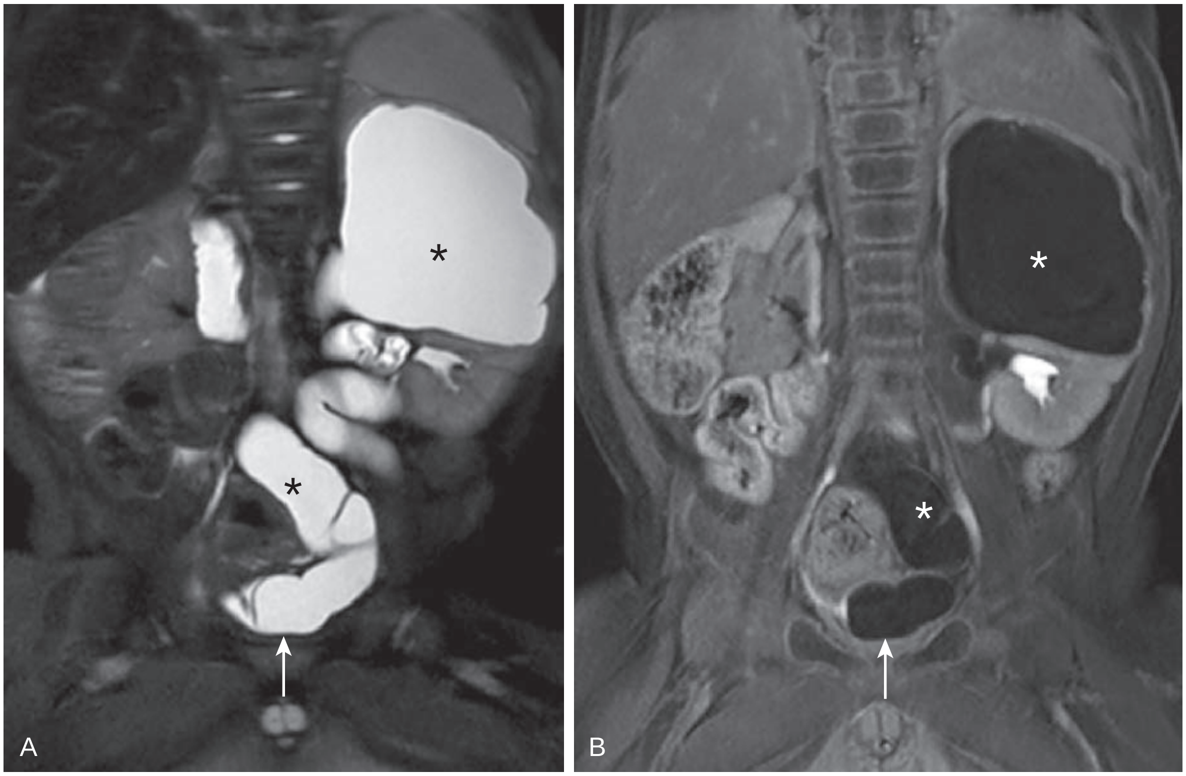

**Figure 113.28. Complete duplication of the left upper urinary tract in a 6-month-old boy.** Coronal (A) T2-weighted fat-saturated and (B) postcontrast excretory phase T1-weighted MR images show severely dilated left upper moiety collecting system and ureter *(asterisks)* due to an obstructing ureterocele *(arrows)*. There is severe left upper moiety parenchymal thinning. The left lower moiety collecting system has a "drooping lily" appearance, and the left lower moiety urinary tract is nonobstructed and normal in caliber.

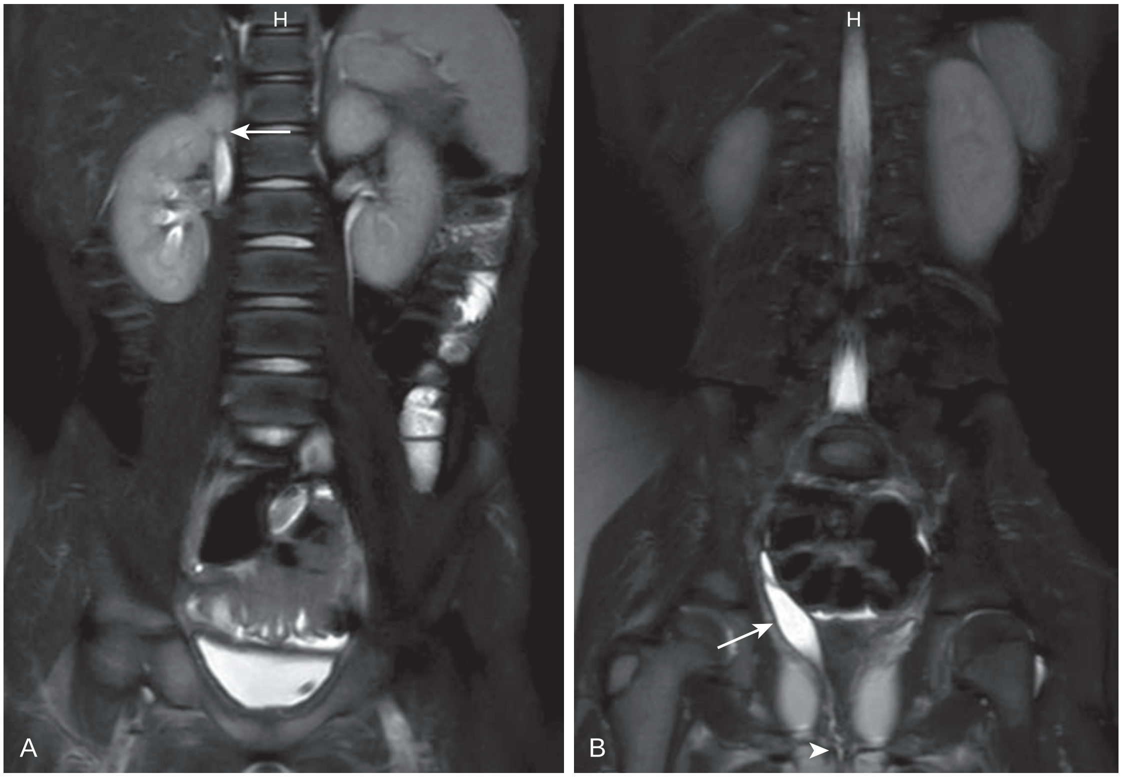

**Figure 113.29. Upper urinary tract duplication and an ectopic ureter in a 6-year-old girl with enuresis.** (A) A coronal T2-weighted fat saturated MR image shows duplication of the right upper urinary tract, which was not appreciated at ultrasound. A single upper moiety calyx was identified *(arrow)*. (B) A more posterior image shows that the right upper moiety ureter is dilated distally *(arrow)*, before narrowing as it passes through the pelvic floor and opening onto the vaginal introitus *(arrowhead)*.

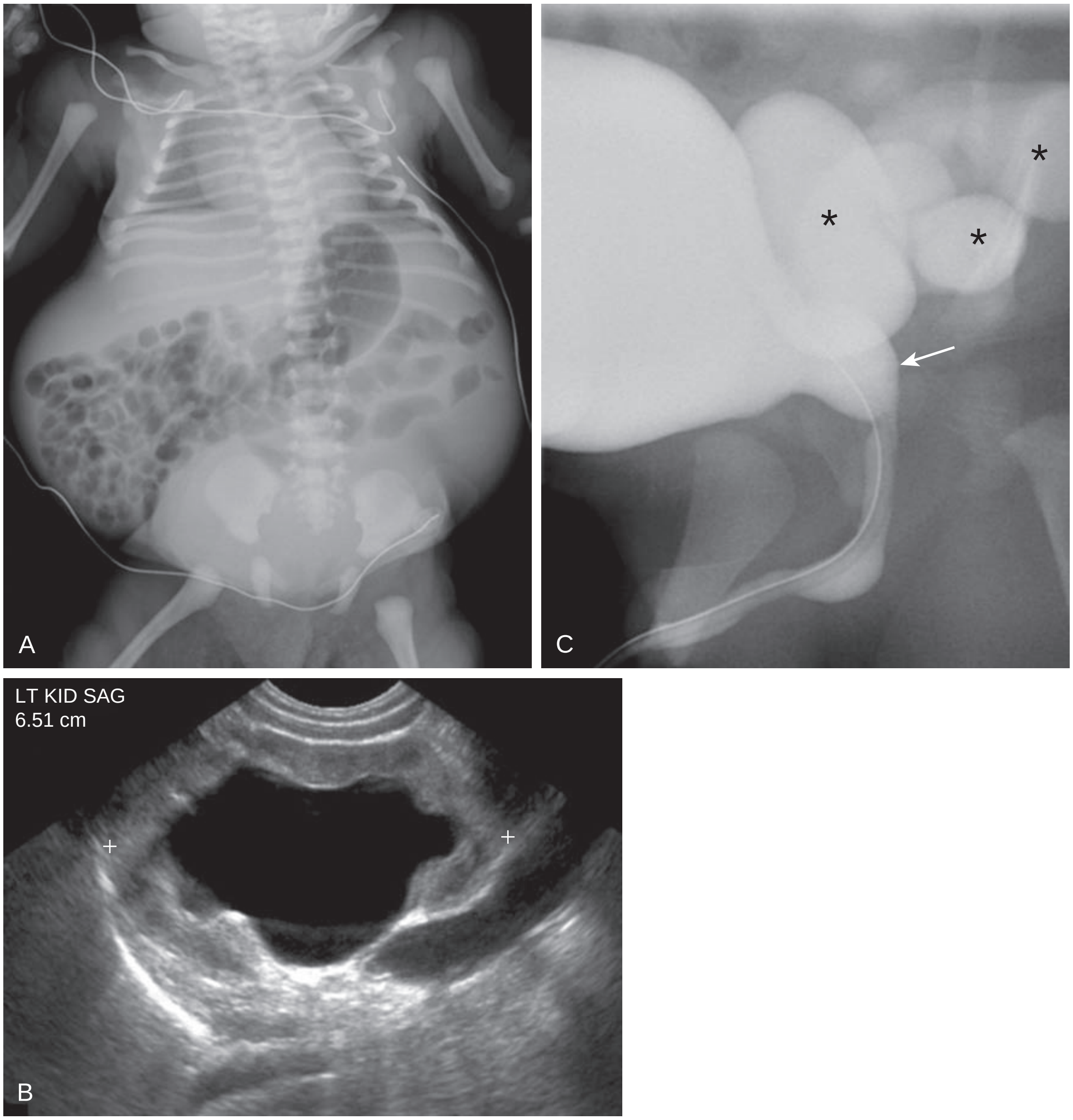

**Figure 113.31. A neonatal boy with prune-belly syndrome.** (A) Abdominal radiograph shows laxity of the anterior abdominal wall and bulging flanks. (B) Longitudinal ultrasound image of the left kidney shows dilatation of the collecting system and proximal ureter. The kidney demonstrates abnormally increased parenchymal echogenicity and contains a few subcortical cysts (not shown), suggestive of renal dysplasia. (C) Voiding cystourethrogram demonstrates dilatation of the posterior urethra *(arrow)* and high-grade vesicoureteric reflux *(asterisks)*.

***Imaging.*** Radiographs show abnormal pubic symphyseal widening (Fig. 113.35).[96,99] The hips may be dislocated. Renal imaging is most commonly normal at birth.[96] Recently, MRI has been used to assess pelvic floor anatomy after bladder exstrophy repair.[100]

***Treatment.*** The prognosis for bladder exstrophy is generally good. Although certain patients may be amenable to complete primary closure,[101] others may require multiple surgeries involving the genitourinary and skeletal systems early in life. An increased incidence of adenocarcinoma of the bladder later in life is found compared with age-matched control subjects.[1,102]

## CLOACAL EXSTROPHY

***Overview, Etiology, and Clinical Presentation.*** Cloacal exstrophy is a nonhereditary constellation of congenital anomalies that involves the anterior abdominal wall and multiple organ systems, and it is a result of maldevelopment of the cloacal membrane during organogenesis. The infraumbilical cloacal membrane persists, which interferes with normal infraumbilical anterior abdominal wall closure and leads to failure of urogenital septum separation from the rectum. Two hemibladders are separated by ileocecal bowel mucosa.[103] The terminal ileum prolapses through the exposed cecum (“elephant trunk” deformity).[103] Associated anomalies include omphalocele, abnormal genitalia, two-vessel umbilical cord, closed spinal defects, renal abnormalities, and Müllerian anomalies in girls.[104]

***Imaging.*** Radiographs may demonstrate a variety of abnormalities, including abnormal widening of the pubic symphysis, lumbosacral spine anomalies, dislocated hips, and clubfoot. Imaging of the kidneys may reveal agenesis or ectopia, and various Müllerian anomalies may be detected in girls (Fig. 113.36). Ultrasound and

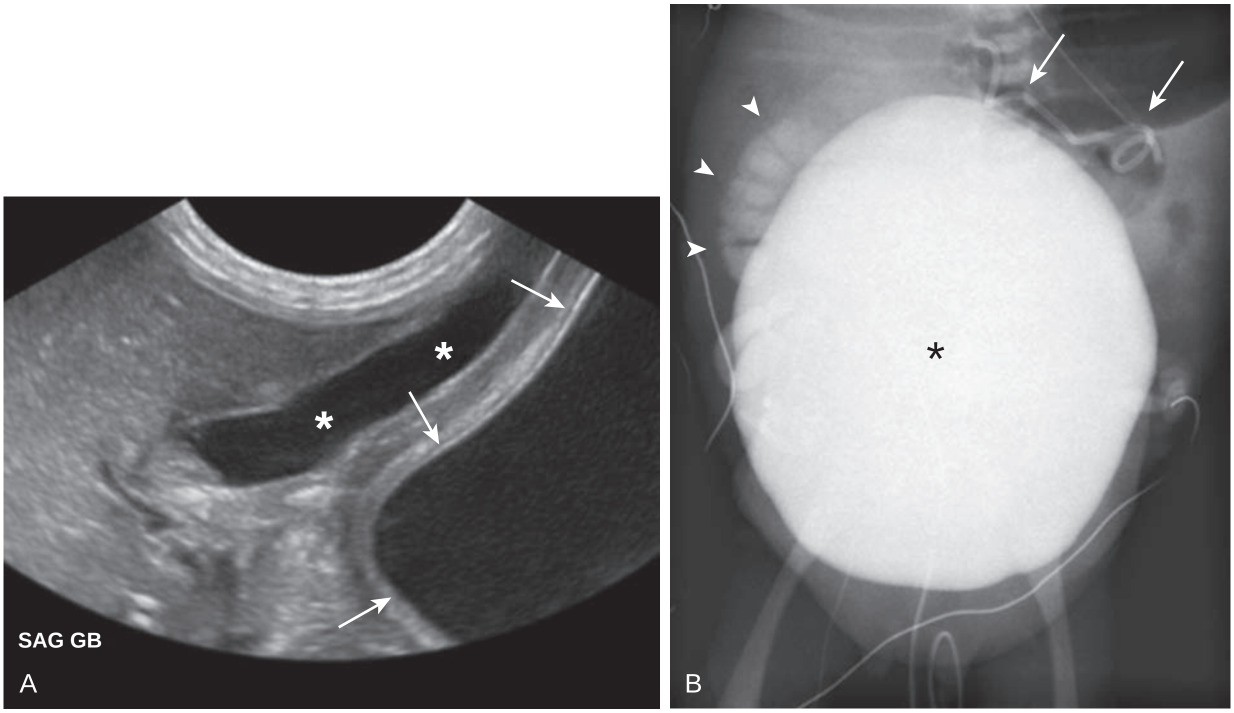

**Figure 113.33. Newborn boy with megacystis-microcolon-intestinal hypoperistalsis syndrome (Berdon syndrome).** (A) Longitudinal ultrasound image demonstrates a markedly dilated urinary bladder *(arrows)*, which extends into the upper abdomen and abuts the gallbladder *(asterisks)*. (B) Voiding cystourethrogram image shows the urinary bladder *(asterisk)* occupying most of the abdomen and pelvis. High-grade right vesicoureteral reflux is present *(arrowheads)*, and a retained vesicoamniotic shunt *(arrows)* projects over the left upper quadrant of the abdomen.

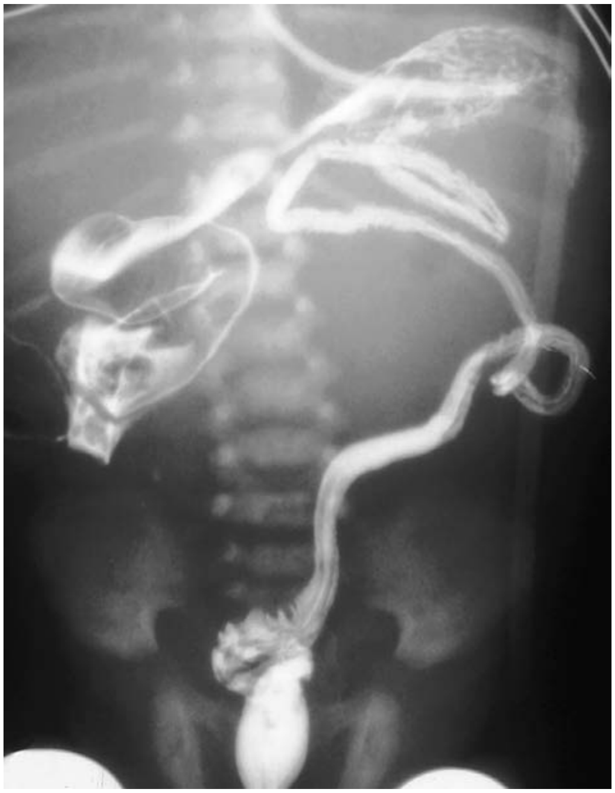

**Figure 113.34. Megacystis-microcolon-intestinal hypoperistalsis syndrome (Berdon syndrome).** The anterior view from a contrast enema reveals a severe microcolon. Contrast material in the upper GI tract shows abnormal duodenal course, consistent with malrotation.

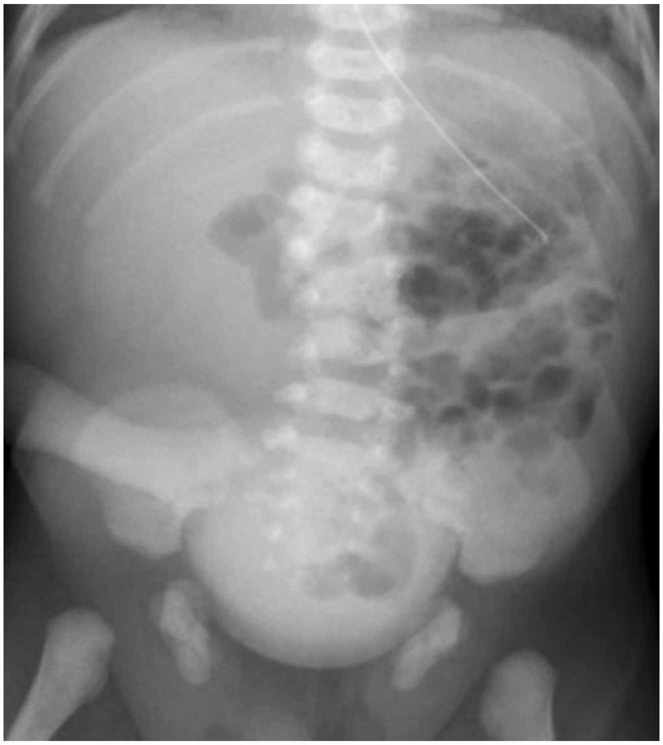

**Figure 113.35. Neonate with bladder exstrophy and a bifid scrotum.** Abdominal radiograph shows diastasis of the pubic symphysis, consistent with bladder exstrophy. A round, masslike opacity projecting over the pelvis is due to a large umbilical hernia. Incidental note is made of multiple lumbar vertebral anomalies.

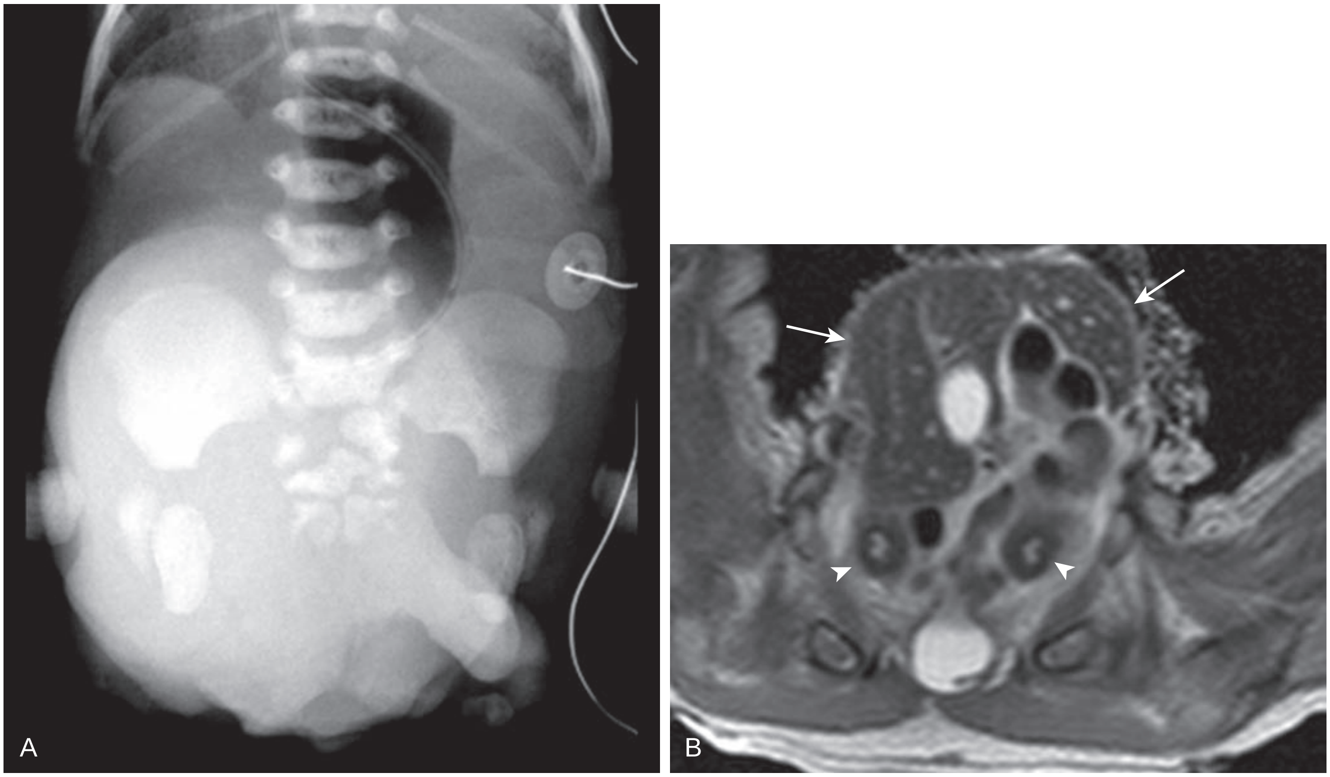

**Figure 113.36. A neonate with cloacal exstrophy.** (A) Abdominal radiograph shows multiple sacral anomalies and abnormal widening of the pubic symphysis. A masslike opacity projecting over the lower abdomen and pelvis was due to a large omphalocele. (B) Axial T2-weighted MR image shows a large liver-containing omphalocele at the level of the pelvis *(arrows)*. Two separate uterine horns *(arrowheads)* can be seen, consistent with uterus didelphys.

MRI imaging of the spine commonly reveal spinal dysraphism and spinal cord tethering (e-Fig. 113.37). Upper GI series evaluation should be performed because midgut malrotation may be present in up to 30% of affected children.[103]

***Treatment.*** This condition commonly requires a multistage approach to surgical reconstruction, with closure of spinal detects and management of gastrointestinal tract anomalies taking preference to urinary bladder and genital recontruction.[105] Advances in surgical technique and supportive care have improved survival and functional outcomes.

## CLOACAL MALFORMATION

***Overview, Etiology, and Clinical Presentation.*** Cloacal malformation is diagnosed when the urinary, genital, and gastrointestinal tracts all come together to form a single outflow channel of variable length.[76,106] On physical examination, the perineum has a single opening that eliminates urine, feces, and genital tract secretions.[106] Unlike with cloacal exstrophy, the anterior abdominal wall is intact.[76] Although the etiology of this congenital anomaly is not entirely understood, it is thought to be due to failure of urorectal septum to join the cloacal membrane in utero.[76] This condition only affects 1:40,000 to 1:50,000 phenotypic newborn girls.[106]

***Imaging.*** Contrast injection through a catheter placed within the single perineal orifice under fluoroscopic observation can be used to confirm the diagnosis and definitely characterize perineal anatomy.[76,106] Jaramillo et al[106] divided these malformations into urethral and vaginal subtypes based on the appearance of the common channel. Numerous genitourinary tract abnormalities may be seen in the setting of cloacal malformation, including VUR, ureteral ectopia, urinary bladder duplication, urethral duplication, urachal anomalies, and a variety of uterine and vaginal anomalies.[106] Renal abnormalities may include agenesis, horseshoe kidney, and obstruction, whereas osseous abnormalities may include widening of the pubic symphysis and partial sacral agenesis. Abnormalities of the spinal cord may be present and are best characterized by ultrasound or MRI. Contrast material injection through the distal limb of a diverting colostomy also can further assess perineal anatomy (Fig. 113.38).[76,106,107] Authors have described a combined fluoroscopic-MRI approach for anatomic assessment of infants with cloacal malformations allowing evaluation of the urinary, genital, and gastrointestinal tracts as well as the spine, kidneys, and Müllerian structures.[108,109]

***Treatment.*** The goals of surgery are to achieve urinary and fecal continence and to preserve future sexual function. A diverting colostomy is often performed soon after birth as a temporizing measure. Hematocolpos/hydrocolpos due to vaginal obstruction should be drained. Posterior sagittal anorectovaginourethroplasty is commonly performed to definitely repair the entire malformation with good results, although laparotomy also may be required.[110,111]

### Acknowledgment

The editors acknowledge the contributions of D. Gregory Bates to this chapter from the previous edition.

KEY POINTS

- MCDK usually involutes over time, eventually resulting in remnant dysplastic renal tissue that may be difficult to visualize by ultrasound.
- Two types of ADPKD (a ciliopathy) exist, each with clearly defined chromosomal mutations and prognoses.

*Continued*

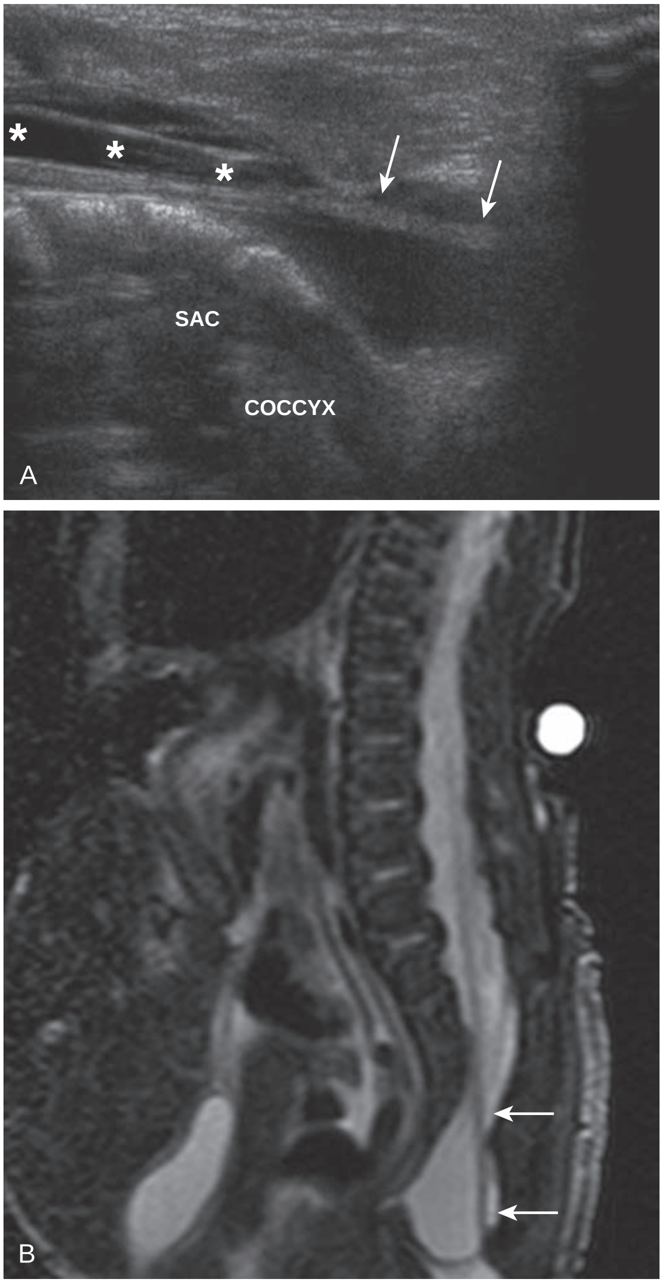

**e-Figure 113.37. Neonate with cloacal exstrophy and a tethered spinal cord.** (A) Longitudinal ultrasound image of the lumbosacral spinal canal demonstrates a low-lying, elongated conus medullaris *(asterisks)* with thickening of the filum terminale *(arrows)*. The sacral portion of the thecal sac is abnormally dilated. (B) Sagittal T2-weighted MR image of the lumbosacral spine reveals a thickened, tethered filum terminale *(arrows)*. *SAC,* sacrum.

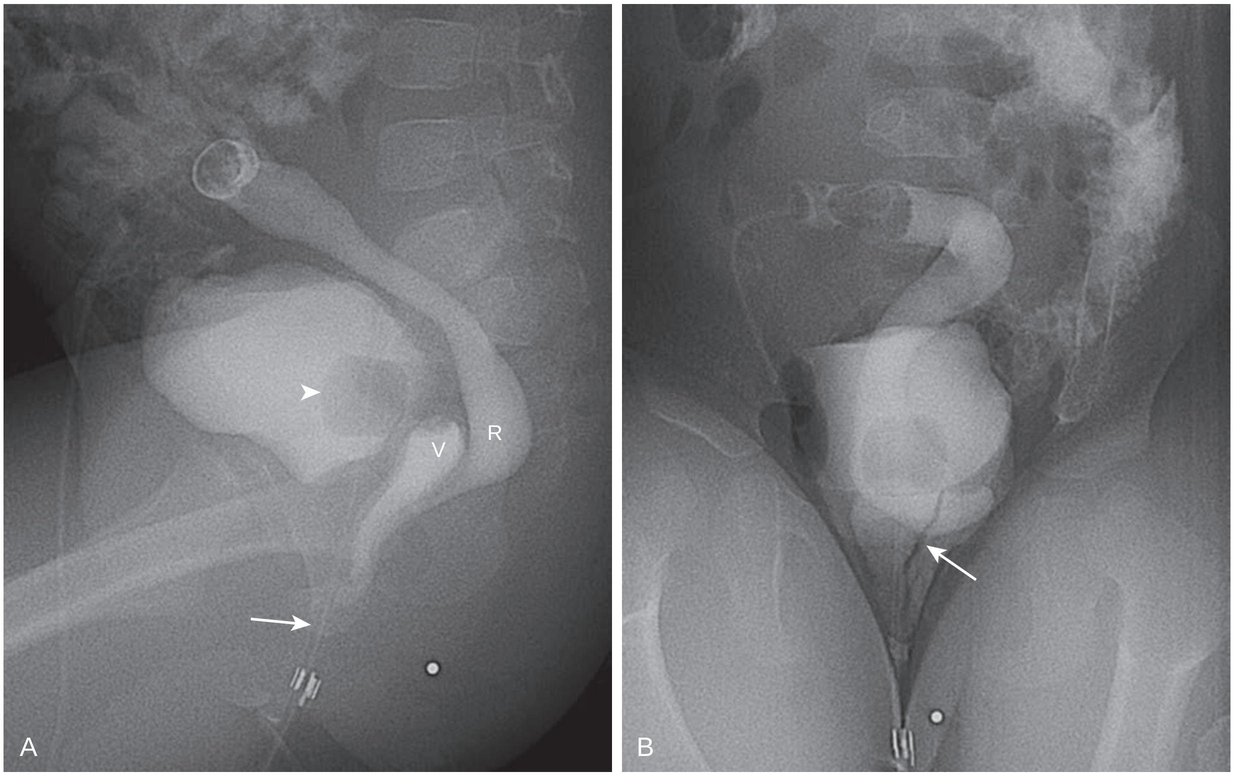

**Figure 113.38. Cloacal malformation in a 16-month-old girl.** (A) Sagittal fluoroscopic image obtained after injection of the contrast material into the child's mucous fistula and urinary bladder shows findings consistent with cloacal malformation. A catheter is present in the common channel *(arrow)*, and a metallic BB marker is on the skin surface at the expected location of the anus. *arrowhead*, Foley catheter balloon; *R*, rectum; *V*, vagina. (B) Frontal image shows two hemivaginas, separated by a thin septum *(arrow)*.

- ARPKD presenting early in life commonly requires renal replacement therapy; recent studies suggest that the severity renal and hepatic abnormalities are independent and not necessarily inversely proportional.
- About 30% of UPJ cases are bilateral, although the severity of obstruction and pelvicaliectasis may be asymmetric.
- The Weigert-Meyer rule, which applies only to complete duplications, states that the ureter that drains the upper moiety inserts inferior and medial to the lower moiety ureter. The upper moiety ectopic ureter is more likely to be obstructed (ectopic ureterocele or stenotic ectopic orifice), whereas the lower moiety ureter is more likely to reflux.
- Calyceal diverticula most commonly occur within the upper pole.
- Congenital megacalyces is a very rare nonobstructive anomaly of the renal collecting system that may be confused easily with obstructive hydronephrosis.
- Prune-belly syndrome, also known as *Eagle-Barrett* or *triad syndrome*, includes the constellation of bilateral cryptorchidism, anterior abdominal wall muscular deficiency, and a variety of urinary tract anomalies, including megacystis and hydroureteronephrosis.
- Megacystis-microcolon-intestinal hypoperistalsis-malrotation syndrome presents clinically with severe abdominal distention during the neonatal period as a result of functional bowel obstruction and severe urinary bladder distention.
- Cloacal malformation has a single perineal opening that eliminates urine, feces, and genital tract secretions. Unlike with cloacal exstrophy, the anterior abdominal wall is intact.

## SUGGESTED READINGS

Adeb M, Darge K, Dillman JR, Carr M, Epelman M. Magnetic resonance urography in evaluation of duplicated renal collecting systems. *Magn Reson Imaging Clin N Am*. 2013;21:717–730.

Berrocal T, Lopez-Pereira P, Arjonilla A, et al. Anomalies of the distal ureter, bladder, and urethra in children: embryologic, radiologic, and pathologic features. *Radiographics*. 2002;22:1139–1164.

Chung EM, Conran RM, Schroeder JW, Rohena-Quinquilla IR, Rooks VJ. From the radiologic pathology archives: pediatric polycystic kidney disease and other ciliopathies: radiologic-pathologic correlation. *Radiographics*. 2014;34:155–178.

Eickmeyer AB, Casanova NF, He C, et al. The natural history of the multicystic dysplastic kidney–is limited follow-up warranted? *J Pediatr Urol*. 2014;10:655–661.

Jaramillo D, Lebowitz RL, Hendren WH. The cloacal malformation: radiologic findings and imaging recommendations. *Radiology*. 1990;177:441–448.

McDaniel BB, Jones RA, Scherz H, et al. Dynamic contrast-enhanced MR urography in the evaluation of pediatric hydronephrosis: part 2, anatomic and functional assessment of ureteropelvic junction obstruction. *AJR Am J Roentgenol*. 2005;185:1608–1614.

Rabelo EA, Oliveira EA, Diniz JS, et al. Natural history of multicystic kidney conservatively managed: a prospective study. *Pediatr Nephrol*. 2004;19:1102–1107.

Traubici J, Daneman A. High-resolution renal sonography in children with autosomal recessive polycystic kidney disease. *AJR Am J Roentgenol*. 2005;184(5):1630–1633.

## REFERENCES

Full references for this chapter can be found on www.expertconsult.com.

## REFERENCES

1. Cohen HL, Kravets F, Zucconi W, et al. Congenital abnormalities of the genitourinary system. *Semin Roentgenol*. 2004;39:282–303.
2. Felson B, Cussen LJ. The hydronephrotic type of unilateral congenital multicystic disease of the kidney. *Semin Roentgenol*. 1975;10:113–123.
3. Griscom NT, Vawter GF, Fellers FX. Pelvoinfundibular atresia: the usual form of multicystic kidney: 44 unilateral and two bilateral cases. *Semin Roentgenol*. 1975;10:125–131.
4. Belk RA, Thomas DF, Mueller RF, et al. A family study and the natural history of prenatally detected unilateral multicystic dysplastic kidney. *J Urol*. 2002;167:666–669.
5. Aslam M, Watson AR. Unilateral multicystic dysplastic kidney: long term outcomes. *Arch Dis Child*. 2006;91:820–823.
6. Kiechl-Kohlendorfer U, Geley T, Maurer K, Gassner I. Uterus didelphys with unilateral vaginal atresia: multicystic dysplastic kidney is the precursor of "renal agenesis" and the key to early diagnosis of this genital anomaly. *Pediatr Radiol*. 2011;41(9):1112–1116.
7. Snodgrass WT. Hypertension associated with multicystic dysplastic kidney in children. *J Urol*. 2000;164:472–473, discussion 473-474.
8. Rabelo EA, Oliveira EA, Diniz JS, et al. Natural history of multicystic kidney conservatively managed: a prospective study. *Pediatr Nephrol*. 2004;19:1102–1107.
9. Rickwood AM, Anderson PA, Williams MP. Multicystic renal dysplasia detected by prenatal ultrasonography. Natural history and results of conservative management. *Br J Urol*. 1992;69:538–540.
10. Vinocur L, Slovis TL, Perlmutter AD, et al. Follow-up studies of multicystic dysplastic kidneys. *Radiology*. 1988;167:311–315.
11. Eickmeyer AB, Casanova NF, He C, et al. The natural history of the multicystic dysplastic kidney–is limited follow-up warranted? *J Pediatr Urol*. 2014;10(4):655–661.
12. Rottenberg GT, De Bruyn R, Gordon I. Sonographic standards for a single functioning kidney in children. *AJR Am J Roentgenol*. 1996;167:1255–1259.
13. Flack CE, Bellinger MF. The multicystic dysplastic kidney and contralateral vesicoureteral reflux: protection of the solitary kidney. *J Urol*. 1993;150:1873–1874.
14. Karmazyn B, Zerin JM. Lower urinary tract abnormalities in children with multicystic dysplastic kidney. *Radiology*. 1997;203:223–226.
15. Strife JL, Souza AS, Kirks DR, et al. Multicystic dysplastic kidney in children: US follow-up. *Radiology*. 1993;186(3):785–788.
16. Avni EF, Thoua Y, Lalmand B, et al. Multicystic dysplastic kidney: natural history from in utero diagnosis and postnatal followup. *J Urol*. 1987;138:1420–1424.
17. Gordon AC, Thomas DF, Arthur RJ, et al. Multicystic dysplastic kidney: is nephrectomy still appropriate? *J Urol*. 1988;140:1231–1234.
18. Avni FE, Garel L, Cassart M, et al. Perinatal assessment of hereditary cystic renal diseases: the contribution of sonography. *Pediatr Radiol*. 2006;36:405–414.
19. Wood BP. Renal cystic disease in infants and children. *Urol Radiol*. 1992;14(4):284–295.
20. Hildebrandt F, Benzing T, Katsanis N. Ciliopathies. *N Engl J Med*. 2011;364(16):1533–1543.
21. Hateboer N, v Dijk MA, Bogdanova N, et al. Comparison of phenotypes of polycystic kidney disease types 1 and 2. European PKD1-PKD2 Study Group. *Lancet*. 1999;353:103–107.
22. Hartman DS. Renal cystic disease in multisystem conditions. *Urol Radiol*. 1992;14:13–17.
23. MacDermot KD, Saggar-Malik AK, Economides DL, et al. Prenatal diagnosis of autosomal dominant polycystic kidney disease (PKD1) presenting in utero and prognosis for very early onset disease. *J Med Genet*. 1998;35:13–16.
24. Back SJ, Andronikou S, Kilborn T, Kaplan BS, Darge K. Imaging features of tuberous sclerosis complex with autosomal-dominant polycystic kidney disease: a contiguous gene syndrome. *Pediatr Radiol*. 2015;45(3):386–395.
25. Hayden CK Jr, Swischuk LE. Renal cystic disease. *Semin Ultrasound CT MR*. 1991;12:361–373.
26. Pretorius DH, Lee ME, Manco-Johnson ML, et al. Diagnosis of autosomal dominant polycystic kidney disease in utero and in the young infant. *J Ultrasound Med*. 1987;6:249–255.
27. Wood BP. Renal cystic disease in infants and children. *Urol Radiol*. 1992;14(4):284–295.
28. Chung EM, Conran RM, Schroeder JW, Rohena-Quinquilla IR, Rooks VJ From the radiologic pathology archives: pediatric polycystic kidney disease and other ciliopathies: radiologic-pathologic correlation. *Radiographics*. 2014;34(1):155-178. doi:10.1148/rg.341135179. Review. Erratum in: Radiographics. 2014 Jan-Feb;34(1):15a.
29. Mufti UB, Nalagatla SK. Nephrolithiasis in autosomal dominant polycystic kidney disease. *J Endourol*. 2010;24(10):1557–1561.
30. Xu HW, Yu SQ, Mei CL, et al. Screening for intracranial aneurysm in 355 patients with autosomal-dominant polycystic kidney disease. *Stroke*. 2011;42:204–206.
31. Butler WE, Barker FG 2nd, Crowell RM. Patients with polycystic kidney disease would benefit from routine magnetic resonance angiographic screening for intracerebral aneurysms: a decision analysis. *Neurosurgery*. 1996;38:506–515, discussion 515-516.
32. Traubici J, Daneman A. High-resolution renal sonography in children with autosomal recessive polycystic kidney disease. *AJR Am J Roentgenol*. 2005;184(5):1630–1633.
33. Lonergan GJ, Rice RR, Suarez ES. Autosomal recessive polycystic kidney disease: radiologic-pathologic correlation. *Radiographics*. 2000;20:837–855.
34. Ward CJ, Hogan MC, Rossetti S, et al. The gene mutated in autosomal recessive polycystic kidney disease encodes a large, receptor-like protein. *Nat Genet*. 2002;30:259–269.
35. Mercado-Deane MG, Beeson JE, John SD. US of renal insufficiency in neonates. *Radiographics*. 2002;22:1429–1438.
36. Gunay-Aygun M, Font-Montgomery E, Lukose L, et al. Characteristics of congenital hepatic fibrosis in a large cohort of patients with autosomal recessive polycystic kidney disease. *Gastroenterology*. 2013;144(1):112–121, e2.
37. Avni FE, Guissard G, Hall M, et al. Hereditary polycystic kidney diseases in children: changing sonographic patterns through childhood. *Pediatr Radiol*. 2002;32:169–174.
38. Kern S, Zimmerhackl LB, Hildebrandt F, et al. Rare-MR-urography—a new diagnostic method in autosomal recessive polycystic kidney disease. *Acta Radiol*. 1999;40:543–544.
39. Roy S, Dillon MJ, Trompeter RS, et al. Autosomal recessive polycystic kidney disease: long-term outcome of neonatal survivors. *Pediatr Nephrol*. 1997;11:302–306.
40. Beaunoyer M1, Snehal M, Li L, et al. Optimizing outcomes for neonatal ARPKD. *Pediatr Transplant*. 2007;11(3):267–271.
41. Brinkert F1, Lehnhardt A, Montoya C, et al. Combined liver-kidney transplantation for children with autosomal recessive polycystic kidney disease (ARPKD): indication and outcome. *Transpl Int*. 2013;26(6):640–650.
42. Stunell H, McNeill G, Browne RF, et al. The imaging appearances of calyceal diverticula complicated by urolithiasis. *Br J Radiol*. 2010;83:888–894.
43. Kavukcu S, Cakmakci H, Babayigit A. Diagnosis of caliceal diverticulum in two pediatric patients: a comparison of sonography, CT, and urography. *J Clin Ultrasound*. 2003;31:218–221.
44. Siegel MJ, McAlister WH. Calyceal diverticula in children: unusual features and complications. *Radiology*. 1979;131:79–82.
45. Timmons JW Jr, Malek RS, Hattery RR, et al. Caliceal diverticulum. *J Urol*. 1975;114:6–9.
46. Monga M, Smith R, Ferral H, et al. Percutaneous ablation of caliceal diverticulum: long-term followup. *J Urol*. 2000;163:28–32.
47. Long CJ, Weiss DA, Kolon TF, Srinivasan AK, Shukla AR. Pediatric calyceal diverticulum treatment: an experience with endoscopic and laparoscopic approaches. *J Pediatr Urol*. 2015;11(4):172.e1–172.e6.
48. Karmazyn B, et al. Caliceal diverticulum in pediatric patients: the spectrum of imaging findings. *Pediatr Radiol*. 2011;41(11):1369–1373.
49. Gross AJ, Herrmann TR. Management of stones in calyceal diverticulum. *Curr Opin Urol*. 2007;17:136–140.
50. Bayne CE, Peters CA. Congenital infundibulopelvic stenosis: indications for intervention, surgical technique, and review of literature. *J Pediatr Urol*. 2016. pii: S1477-5131(16)30133-4.
51. Lucaya J, Enriquez G, Delgado R, et al. Infundibulopelvic stenosis in children. *AJR Am J Roentgenol*. 1984;142:471–474.
52. Gittes RF, Talner LB. Congenital megacalices versus obstructive hydronephrosis. *J Urol*. 1972;108:833–836.
53. Pieretti-Vanmarcke R, Pieretti A, Pieretti RV. Megacalycosis: a rare condition. *Pediatr Nephrol*. 2009;24:1077–1079.
54. Vargas B, Lebowitz RL. The coexistence of congenital megacalyces and primary megaureter. *AJR Am J Roentgenol*. 1986;147:313–316.
55. Shopfner CE. Ureteropelvic junction obstruction. *Am J Roentgenol Radium Ther Nucl Med*. 1966;98:148–159.

56. Ross JH, Kay R, Knipper NS, et al. The absence of crossing vessels in association with ureteropelvic junction obstruction detected by prenatal ultrasonography. *J Urol*. 1998;160:973–975, discussion 994.
57. Weiss DA, Kadakia S, Kurzweil R, et al. Detection of crossing vessels in pediatric ureteropelvic junction obstruction: clinical patterns and imaging findings. *J Pediatr Urol*. 2015;11(4):173.e1–173.e5.
58. Fernbach SK, Zawin JK, Lebowitz RL. Complete duplication of the ureter with ureteropelvic junction obstruction of the lower pole of the kidney: imaging findings. *AJR Am J Roentgenol*. 1995;164:701–704.
59. Joseph DB, Bauer SB, Colodny AH, et al. Lower pole ureteropelvic junction obstruction and incomplete renal duplication. *J Urol*. 1989;141:896–899.
60. Lebowitz RL, Blickman JG. The coexistence of ureteropelvic junction obstruction and reflux. *AJR Am J Roentgenol*. 1983;140:231–238.
61. McGrath MA, Estroff J, Lebowitz RL. The coexistence of obstruction at the ureteropelvic and ureterovesical junctions. *AJR Am J Roentgenol*. 1987;149:403–406.
62. Frauscher F. Value of contrast-enhanced color Doppler imaging for detection of crossing vessels in patients with ureteropelvic junction obstruction. *Radiology*. 2000;217:916–917.
63. Mitsumori A, Yasui K, Akaki S, et al. Evaluation of crossing vessels in patients with ureteropelvic junction obstruction by means of helical CT. *Radiographics*. 2000;20:1383–1393, discussion 1393-1395.
64. Parikh KR, Hammer MR, Kraft KH, et al. Pediatric ureteropelvic junction obstruction: can magnetic resonance urography identify crossing vessels? *Pediatr Radiol*. 2015;45(12):1788–1795.
65. Conway JJ, Maizels M. The “well tempered” diuretic renogram: a standard method to examine the asymptomatic neonate with hydronephrosis or hydroureteronephrosis. A report from combined meetings of The Society for Fetal Urology and members of The Pediatric Nuclear Medicine Council—The Society of Nuclear Medicine. *J Nucl Med*. 1992;33:2047–2051.
66. Rossleigh MA. Renal cortical scintigraphy and diuresis renography in infants and children. *J Nucl Med*. 2001;42:91–95.
67. Little SB, Jones RA, Grattan-Smith JD. Evaluation of UPJ obstruction before and after pyeloplasty using MR urography. *Pediatr Radiol*. 2008;38(suppl 1):S106–S124.
68. McDaniel BB, Jones RA, Scherz H, et al. Dynamic contrast-enhanced MR urography in the evaluation of pediatric hydronephrosis: part 2, anatomic and functional assessment of ureteropelvic junction obstruction. *AJR Am J Roentgenol*. 2005;185:1608–1614.
69. Perez-Brayfield MR, Kirsch AJ, Jones RA, et al. A prospective study comparing ultrasound, nuclear scintigraphy and dynamic contrast enhanced magnetic resonance imaging in the evaluation of hydronephrosis. *J Urol*. 2003;170:1330–1334.
70. Takla NV, Hamilton BD, Cartwright PC, et al. Apparent unilateral ureteropelvic junction obstruction in the newborn: expectations for resolution. *J Urol*. 1998;160:2175–2178.
71. Ylinen E, Ala-Houhala M, Wikstrom S. Outcome of patients with antenatally detected pelviureteric junction obstruction. *Pediatr Nephrol*. 2004;19:880–887.
72. Chertin B, Pollack A, Koulikov D, et al. Conservative treatment of ureteropelvic junction obstruction in children with antenatal diagnosis of hydronephrosis: lessons learned after 16 years of follow-up. *Eur Urol*. 2006;49:734–738.
73. Gonzalez R, Schimke CM. Ureteropelvic junction obstruction in infants and children. *Pediatr Clin North Am*. 2001;48:1505–1518.
74. Fernbach SK, Feinstein KA, Spencer K, et al. Ureteral duplication and its complications. *Radiographics*. 1997;17:109–127.
75. Share JC, Lebowitz RL. Ectopic ureterocele without ureteral and calyceal dilatation (ureterocele disproportion): findings on urography and sonography. *AJR Am J Roentgenol*. 1989;152:567–571.
76. Berrocal T, Lopez-Pereira P, Arjonilla A, et al. Anomalies of the distal ureter, bladder, and urethra in children: embryologic, radiologic, and pathologic features. *Radiographics*. 2002;22:1139–1164.
77. Lee PH, Diamond DA, Duffy PG, et al. Duplex reflux: a study of 105 children. *J Urol*. 1991;146:657–659.
78. Adeb M, Darge K, Dillman JR, Carr M, Epelman M. Magnetic resonance urography in evaluation of duplicated renal collecting systems. *Magn Reson Imaging Clin N Am*. 2013;21(4):717–730.
79. Avni FE, Nicaise N, Hall M, et al. The role of MR imaging for the assessment of complicated duplex kidneys in children: preliminary report. *Pediatr Radiol*. 2001;31:215–223.
80. Dorisio O, Elia A, Landi L, et al. Effectiveness of primary endoscopic incision in treatment of ectopic ureterocele associated with duplex system. *Urology*. 2011;77:191–194.
81. Garcia-Aparicio L, Krauel L, Tarrado X, et al. Heminephroureterectomy for duplex kidney: laparoscopy versus open surgery. *J Pediatr Urol*. 2009;6(2):157–160.
82. Lin CC, Tsai JD, Sheu JC, et al. Segmental multicystic dysplastic kidney in children: clinical presentation, imaging finding, management, and outcome. *J Pediatr Surg*. 2010;45:1856–1862.
83. Das Narla L, Doherty RD, Hingsbergen EA, et al. Pediatric case of the day. Prune-belly syndrome (Eagle-Barrett syndrome, triad syndrome). *Radiographics*. 1998;18:1318–1322.
84. Herman TE, Siegel MJ. Prune belly syndrome. *J Perinatol*. 2009;29:69–71.
85. Volmar KE, Fritsch MK, Perlman EJ, et al. Patterns of congenital lower urinary tract obstructive uropathy: relation to abnormal prostate and bladder development and the prune belly syndrome. *Pediatr Dev Pathol*. 2001;4:467–472.
86. Seidel NE, Arlen AM, Smith EA, Kirsch AJ. Clinical manifestations and management of prune-belly syndrome in a large contemporary pediatric population. *Urology*. 2015;85(1):211–215.
87. Strand WR. Initial management of complex pediatric disorders: prune belly syndrome, posterior urethral valves. *Urol Clin North Am*. 2004;31:399–415, vii.
88. Berdon WE, Baker DH, Blanc WA, et al. Megacystis-microcolon-intestinal hypoperistalsis syndrome: a new cause of intestinal obstruction in the newborn. Report of radiologic findings in five newborn girls. *AJR Am J Roentgenol*. 1976;126(5):957–964.
89. Adeb M1, Anupindi S, Carr M, Darge K. An unusual urinary tract presentation in a case of megacystis microcolon intestinal hypoperistalsis syndrome. *J Radiol Case Rep*. 2012;6(11):1–7.
90. Levin TL, Soghier L, Blitman NM, et al. Megacystis-microcolon-intestinal hypoperistalsis and prune belly: overlapping syndromes. *Pediatr Radiol*. 2004;34:995–998.
91. Berdon WE, Baker DH, Blanc WA, et al. Megacystis-microcolon-intestinal hypoperistalsis syndrome: a new cause of intestinal obstruction in the newborn. Report of radiologic findings in five newborn girls. *AJR Am J Roentgenol*. 1976;126:957–964.
92. Ballisty MM, Braithwaite KA, Shehata BM, Dickson PN. Imaging findings in megacystis-microcolon-intestinal hypoperistalsis syndrome. *Pediatr Radiol*. 2013;43(4):454–459.
93. Munch EM, Cisek LJ Jr, Roth DR. Magnetic resonance imaging for prenatal diagnosis of multisystem disease: megacystis microcolon intestinal hypoperistalsis syndrome. *Urology*. 2009;74:592–594.
94. Magana Pintiado MI, Al-Kassam Martinez M, Bousono Garcia C, et al. The megacystis-microcolon-intestinal hypoperistalsis syndrome: apropos of a case with prolonged survival. *Nutr Hosp*. 2008;23:513–515.
95. Masetti M, Rodriguez MM, Thompson JF, et al. Multivisceral transplantation for megacystis microcolon intestinal hypoperistalsis syndrome. *Transplantation*. 1999;68:228–232.
96. White P, Lebowitz RL. Exstrophy of the bladder. *Radiol Clin North Am*. 1977;15:93–107.
97. Mildenberger H, Kluth D, Dziuba M. Embryology of bladder exstrophy. *J Pediatr Surg*. 1988;23:166–170.
98. Stec AA, Baradaran N, Gearhart JP. Congenital renal anomalies in patients with classic bladder exstrophy. *Urology*. 2012;79(1):207–209.
99. Muecke EC, Currarino G. Congenital widening of the pubic symphysis: associated clinical disorders and roentgen anatomy of affected bony pelves. *Am J Roentgenol Radium Ther Nucl Med*. 1968;103:179–185.
100. Halachmi S, Farhat W, Konen O, et al. Pelvic floor magnetic resonance imaging after neonatal single stage reconstruction in male patients with classic bladder exstrophy. *J Urol*. 2003;170:1505–1509.
101. Grady RW, Carr MC, Mitchell ME. Complete primary closure of bladder exstrophy. Epispadias and bladder exstrophy repair. *Urol Clin North Am*. 1999;26:95–109, viii.
102. Paulhac P, Maisonnette F, Bourg S, et al. Adenocarcinoma in the exstrophic bladder. *Urology*. 1999;54:744.
103. Meglin AJ, Balotin RJ, Jelinek JS, et al. Cloacal exstrophy: radiologic findings in 13 patients. *AJR Am J Roentgenol*. 1990;155:1267–1272.
104. Suson KD, Inouye B, Carl A, Gearhart JP. Congenital renal anomalies in cloacal exstrophy: is there a difference? *J Pediatr Urol*. 2016. pii: S1477-5131(16)30032-8.
105. Thomas JC, DeMarco RT, Pope JC 4th, et al. First stage approximation of the exstrophic bladder in patients with cloacal exstrophy—should

this be the initial surgical approach in all patients? *J Urol*. 2007;178:1632–1635, discussion 1635-1636.

106. Jaramillo D, Lebowitz RL, Hendren WH. The cloacal malformation: radiologic findings and imaging recommendations. *Radiology*. 1990;177:441–448.
107. Patel MN, Racadio JM, Levitt MA, et al. Complex cloacal malformations: use of rotational fluoroscopy and 3-D reconstruction in diagnosis and surgical planning. *Pediatr Radiol*. 2012;42(3):355–363.
108. Jarboe MD, Teitelbaum DH, Dillman JR. Combined 3D rotational fluoroscopic-MRI cloacagram procedure defines luminal and extraluminal pelvic anatomy prior to surgical reconstruction of cloacal and other complex pelvic malformations. *Pediatr Surg Int*. 2012;28(8):757–763.
109. Patel MN. Use of rotational fluoroscopy and 3-D reconstruction for pre-operative imaging of complex cloacal malformations. *Semin Pediatr Surg*. 2016;25(2):96–101.
110. Pena A, Levitt MA, Hong A, et al. Surgical management of cloacal malformations: a review of 339 patients. *J Pediatr Surg*. 2004;39:470–479.
111. Levitt MA, Peña A. Cloacal malformations: lessons learned from 490 cases. *Semin Pediatr Surg*. 2010;19(2):128–138.

# 114 Acquired Abnormalities

Robert G. Wells

## RENAL INFECTION

### Acute Bacterial Pyelonephritis

***Overview.*** The term *pyelonephritis* encompasses infections of the renal parenchyma and pelvocaliceal system. Renal infections can be acute or chronic; unilateral or bilateral; and focal, multifocal, or diffuse. Potential complications include renal or perinephric abscess.[1]

***Pathophysiology and Clinical Presentation.*** The most common cause of acute bacterial pyelonephritis is ascending infection from the lower urinary tract. Parenchymal renal infection may also occur as a result of hematogenous inoculation; this mechanism is most common in infants. Risk factors for pyelonephritis include high-grade vesicoureteral reflux, urinary tract congenital anomalies, voiding dysfunction, intermittent catheterization, and urinary diversion. Potential clinical manifestations include flank pain, abdominal pain, fever, pyuria, nausea, and vomiting. Young infants with pyelonephritis often have nonspecific findings such as irritability, vomiting, and poor feeding; fever is sometimes lacking.[2–4]

***Imaging.*** Renal cortical scintigraphy with technetium-99m dimercaptosuccinic acid (DMSA) is highly sensitive (at least 90%) for the detection of acute bacterial pyelonephritis. Infected regions of the kidneys have diminished or absent radiotracer uptake, often with a spherical or flarelike pattern (Fig. 114.1). The scintigraphic defect of a renal abscess is usually indistinguishable from that of uncomplicated parenchymal infection.[5–7]

Contrast-enhanced computed tomography (CT) provides sensitivity similar to renal cortical scintigraphy for the diagnosis of acute bacterial pyelonephritis. CT findings include diminished nephrogram intensity; radially oriented linear streaks of diminished attenuation; round, masslike, or irregular hypoattenuating foci; wedge-shaped defects; and heterogeneous diminished enhancement throughout an enlarged kidney (Fig. 114.2). Delayed CT images of the infected kidney show retention of contrast material in obstructed tubules. A parenchymal or perinephric abscess appears as a hypoattenuating focus, sometimes with a prominently enhancing rim.[8]

Renal parenchymal edema resulting from infection leads to diminished signal intensity on T1-weighted magnetic resonance imaging (MRI) and increased signal intensity on T2-weighted images. Alternatively, the kidneys may show one or more focal areas of decreased T2-weighted signal intensity (Fig. 114.3). MRI findings can include nephromegaly, localized parenchymal expansion, diminished corticomedullary differentiation, parenchymal striation, perinephric edema/fluid, urothelial thickening, and decreased contrast enhancement of infected parenchyma.[9–11]

Reported sensitivities of sonography for the detection of acute bacterial pyelonephritis range from 25% to 50%. Potential findings include nephromegaly, abnormal parenchymal echogenicity, deficient corticomedullary differentiation, renal sinus hyperechogenicity, and urothelial thickening. Color Doppler or power Doppler imaging demonstrates diminished perfusion of the infected regions of parenchyma, sometimes with a wedge shape (Fig. 114.4). A parenchymal abscess usually appears as a spherical avascular hypoechoic focus with acoustic enhancement. Occasionally, pus within the cavity results in an isoechoic or hyperechoic appearance. A perinephric abscess appears as a hypoechoic, sometimes complex fluid collection immediately peripheral to the renal capsule.[7,12–14]

***Treatment and Follow-up.*** The treatment of bacterial pyelonephritis is antibiotic therapy. Follow-up sonography or scintigraphy serves to detect progression to scarring. Defects on renal cortical scintigraphy can persist for a few months after clinical resolution of the infection; therefore scintigraphy for scar detection should be delayed for at least 3 to 6 months.[15,16]

### Pyonephrosis

***Overview.*** Pyonephrosis is a bacterial infection of the kidney in which purulent material fills a dilated collecting system. Most often, a preexisting chronic urinary tract obstruction is present, such as ureteropelvic junction obstruction. Acute obstruction because of a calculus is an occasional cause in children. The clinical presentation of pyonephrosis is similar to that of other bacterial urinary tract infections. Fever, flank pain, pyuria, and hematuria are common.[17]

***Imaging.*** Sonography shows echogenic material within a dilated pelvocaliceal system (e-Fig. 114.5). The purulent material often layers in the dependent portions of the collecting system and may shift with changes in patient position. Thickening of the wall of the dilated renal pelvis is usually present. Echogenic foci in the urinary tract due to gas-forming organisms is an uncommon finding.[18,19]

CT, MRI, or scintigraphy shows diminished function of the involved kidney. Contrast enhancement of the renal parenchyma is heterogeneous and delayed on CT. Excreted contrast material may outline filling defects in the dilated collecting system on delayed images. Debris usually is visible in the dilated renal collecting system on MRI. The renal parenchyma has abnormal heterogeneous signal intensity. The pus-filled collecting system is markedly hyperintense on diffusion-weighted images.[20,21]

***Treatment and Follow-up.*** The treatment of pyonephrosis includes prompt initiation of aggressive antimicrobial therapy. Drainage of the obstructed collecting system often is required, usually by percutaneous nephrostomy. Surgical correction of an underlying obstruction is delayed until resolution of the acute infection.

### Xanthogranulomatous Pyelonephritis

***Overview.*** Xanthogranulomatous pyelonephritis (XGP) is an uncommon form of severe chronic renal parenchymal infection that can sometimes mimic a renal tumor. The pathogenesis typically involves chronic infection of an obstructed kidney, often due to a large calculus. Diffuse involvement of the kidney is most common; segmental or focal forms also can occur, sometimes in association with obstruction of a duplicated collecting system or infundibulum. Clinical findings may be nonspecific and can include fever, flank pain, malaise, pyuria, weight loss, and anemia.[22–25]

***Imaging.*** In the early stages of XGP, the involved portion of the kidney typically has an irregular hyperechoic character on sonography. With the diffuse form, the kidney may be massively enlarged but usually maintains a reniform shape. Echogenic foci with shadowing indicate calcifications. With progression, necrotic

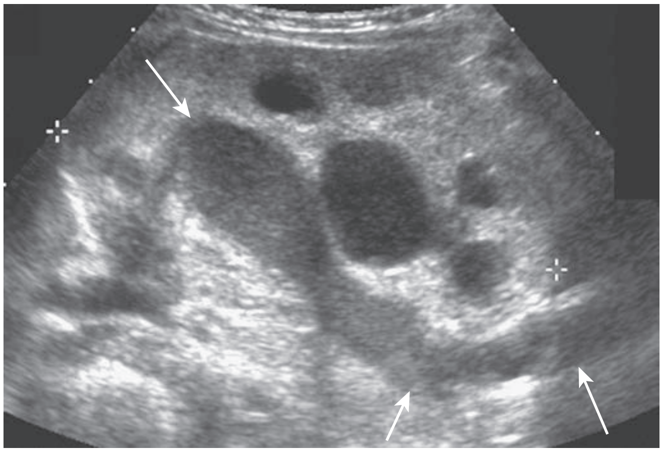

**e-Figure 114.5. Pyonephrosis.** Longitudinal sonogram shows a hydronephrotic duplex collecting system. There is echogenic debris within the upper pole collecting system and ureter *(arrows)*. Lesser debris is present within the lower pole collecting system.

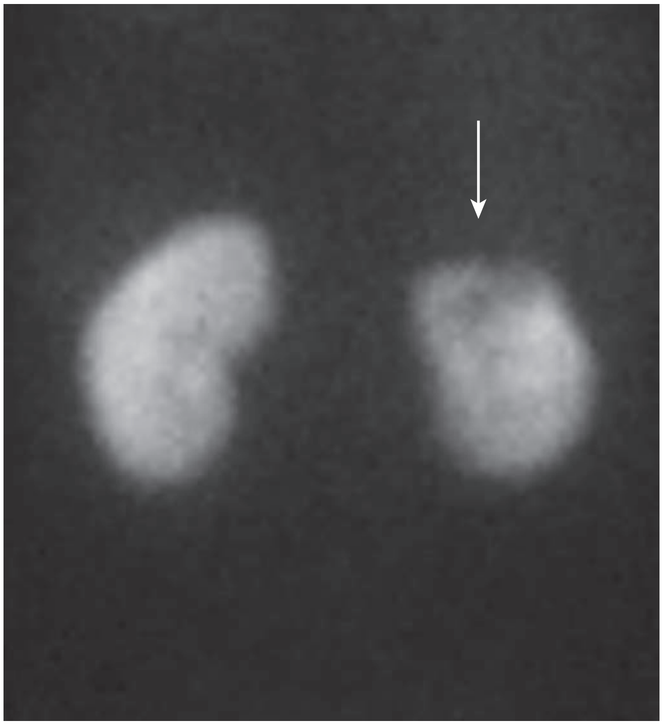

**Figure 114.1. Acute bacterial pyelonephritis.** Posterior technetium-99m DMSA image of a febrile 16-year-old shows absent uptake in the upper pole of the right kidney *(arrow)*.

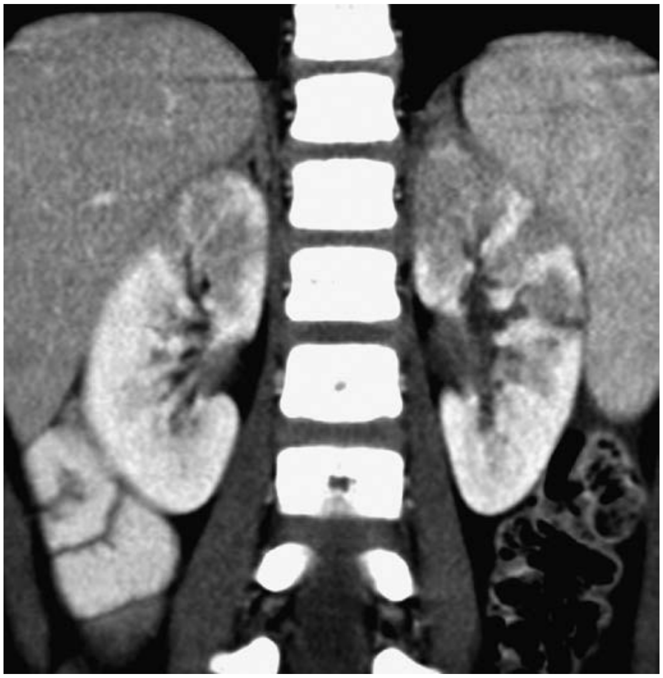

**Figure 114.2. Multifocal bacterial pyelonephritis.** Multiple areas of decreased contrast enhancement of the kidneys are present on this coronal CT image of a 6-year-old girl.

tissue and fluid are usually hypoechoic. Echogenic debris is sometimes visible within abscesses or the dilated collecting system.[26]

CT of diffuse XGP typically demonstrates an enlarged nonfunctioning kidney that has multiple low-attenuation parenchymal foci (Fig. 114.6). Most patients have a staghorn calculus in a contracted renal pelvis. Perinephric fat stranding is common. Perinephric abscesses are moderately hypoattenuating with peripheral enhancement. The pus-filled collecting system is hypoattenuating. Little or no contrast excretion occurs on delayed imaging. Regional retroperitoneal lymphadenopathy is common. With the focal form of XGP, CT typically demonstrates an expansile renal "mass". Peripheral granulation tissue or compressed renal parenchyma may result in an enhancing peripheral rim. The involved renal parenchyma typically has low or intermediate signal intensity on T1-weighted MRI and high intensity on T2-weighted images.[27]

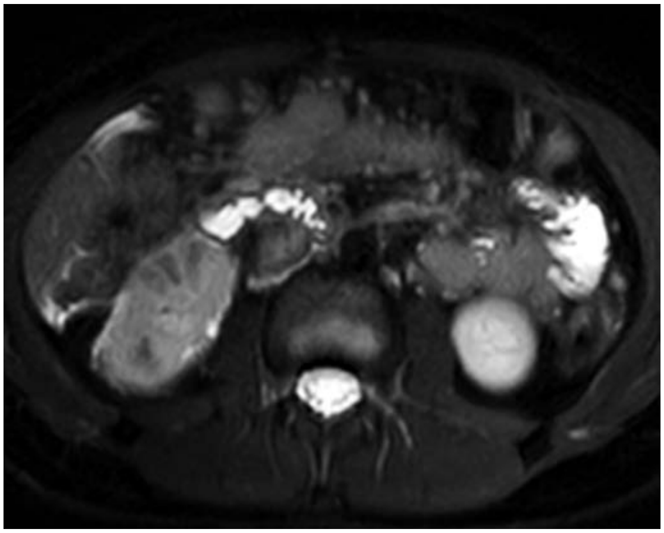

**Figure 114.3. Acute bacterial pyelonephritis.** Axial T2-weighted fat-saturated magnetic resonance (MR) image shows multiple areas of right kidney focal signal hypointensity and perinephric fluid in a 10-year-old girl with clinically suspected acute appendicitis and history of multiple urinary tract infections.

***Treatment and Follow-up.*** The usual treatment for XGP is antibiotic therapy followed by nephrectomy or heminephrectomy. A percutaneous biopsy occasionally is useful to allow differentiation from a neoplasm and to provide material for culture. With acute disease, percutaneous abscess drainage can serve as a temporizing measure.

## Candidiasis

***Overview.*** Candidiasis, typically due to *Candida albicans*, accounts for about 80% of renal fungal infections. Premature neonates are particularly susceptible. The clinical presentation in neonates usually is nonspecific: hypertension, oliguria, or anuria. Older children with renal candidiasis usually have immunocompromise. The clinical findings typically are indistinguishable from those of a bacterial infection: fever, chills, dysuria, and flank pain.[28]

***Imaging.*** Potential sonographic findings of renal candidiasis include parenchymal hyperechogenicity, nephromegaly, one or more small abscesses, and debris within the collecting system. A fungus ball (mycetoma) in the pelvocalyceal system appears as an echogenic object, with or without acoustic shadowing (Fig. 114.7). Dilation of the collecting system proximal to a fungus ball is common.

Findings on contrast-enhanced CT include nephromegaly, diffuse or multifocal edema, renal abscess, and hydronephrosis. Infected parenchyma lacks normal contrast enhancement. Disseminated candidiasis sometimes results in numerous tiny bilateral hypoattenuating renal lesions, often associated with splenic and hepatic disease. CT may demonstrate organ enlargement and a heterogeneous (salt and pepper) pattern of contrast enhancement.[29,30]

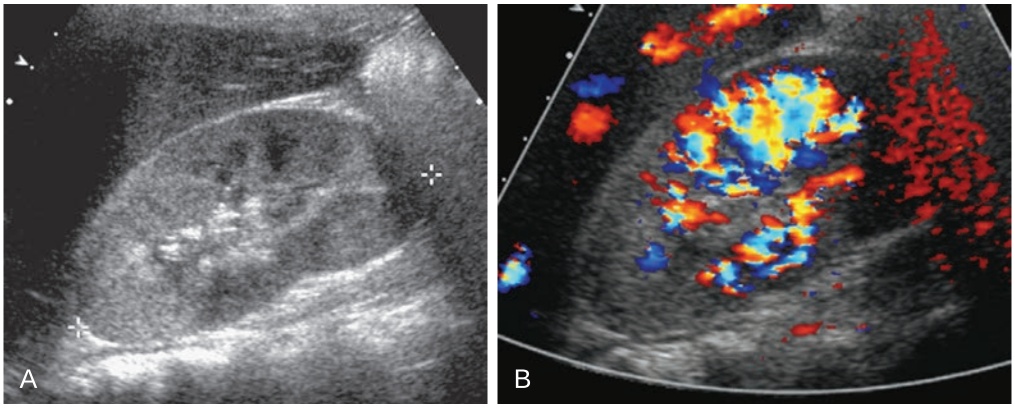

**Figure 114.4. Acute bacterial pyelonephritis.** (A) Gray-scale sonogram shows increased echogenicity and deficient corticomedullary differentiation in the upper pole. (B) There is diminished perfusion in the edematous infected upper pole upon color Doppler assessment.

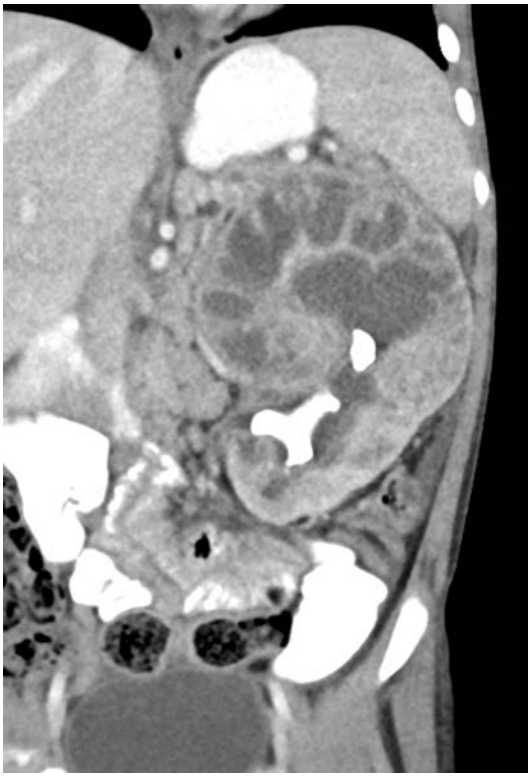

**Figure 114.6. Xanthogranulomatous pyelonephritis.** Coronal contrast-enhanced CT shows an enlarged left kidney that contains large calculi. There is no excretion of contrast into the dilated collecting system. There are multiple peripheral low attenuation areas in the upper pole due to parenchymal necrosis. *(Courtesy of Dr. Michael Mullin, DO, Milwaukee, WI.)*

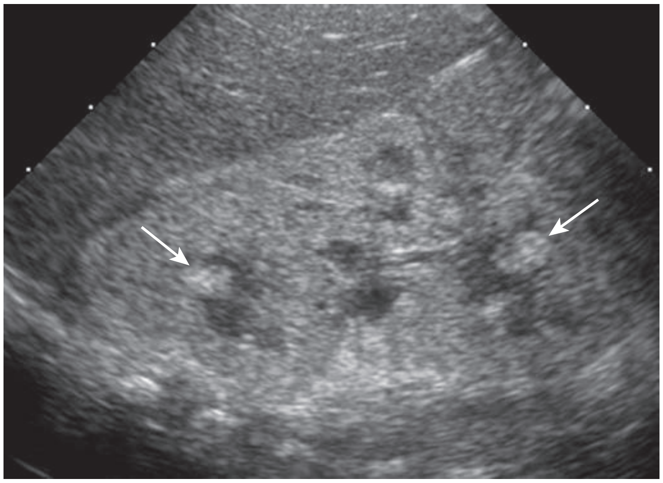

**Figure 114.7. Candidiasis.** Longitudinal renal sonogram of a premature infant with urinary candidiasis shows an echogenic right kidney with poor corticomedullary differentiation and echogenic fungus balls in the collecting system *(arrows)*.

***Treatment and Follow-up.*** The typical treatment is systemic antifungal medication. Percutaneous nephrostomy is an option for children with an obstructing fungus ball. This treatment allows decompression of the collecting system and provides a pathway for installation of antifungal or fibrinolytic medication.[31]

## Tuberculosis

***Overview.*** The urinary system is the most common site of extrapulmonary tuberculosis. Initial infection of the kidney consists of small caseous foci in the renal parenchyma that release the organism into the collecting tubules. Eventually, a larger mass may develop in the renal cortex, resulting in additional discharge of mycobacteria. Antegrade seeding frequently allows spread of infection to the ureters, prostate, or epididymis. Involvement of the collecting system can progress to fibrosis and calcification, sometimes leading to obstruction. Potential symptoms of urinary tuberculosis include dysuria, flank pain, and gross hematuria.[32]

***Imaging.*** In the acute phase of tuberculous infection, imaging of the renal parenchyma may be normal or show manifestations of edema and vasoconstriction. Involved areas lack normal contrast enhancement on CT and MRI, and sometimes have altered echogenicity on sonography. Inflamed urothelium may appear thickened and show prominent contrast enhancement. Parenchymal edema and large tubercles may cause distortion of the calyceal system. Excreted contrast sometimes pools within parenchymal cavitations. Multiple small filling defects may be present in the collecting system or ureter. Fibrotic strictures of the collecting system that are common late in the course of the disease result in focal dilation or hydronephrosis. Dystrophic calcifications can develop in necrotic parenchyma.[33–35]

***Treatment and Follow-up.*** The mainstay treatment is systemic antituberculous medication. Imaging studies serve to monitor treatment effectiveness and to detect complications. Apparent obstructive strictures of the ureter sometimes are due to edema that can regress during treatment. A persistent stricture may require surgical intervention.

**BOX 114.1** Causes of Medullary Nephrocalcinosis

**HYPERCALCIURIA**

Endocrine
- Hyperparathyroidism
- Cushing syndrome
- Diabetes insipidus
- Hyperthyroidism

Renal
- Type 1 renal tubular acidosis

Alimentary
- Milk alkali syndrome
- Hypervitaminosis D

Skeletal
- Immobilization
- Metastatic disease

Drugs
- Furosemide
- Steroids

Miscellaneous
- Idiopathic hypercalciuria
- Idiopathic hypercalcemia
- Nephropathic cystinosis

**URINARY STASIS**

Obstructive uropathy
Medullary sponge kidney

**HYPEROXALURIA**

Primary

**HYPERURICOSURIA**

Secondary

## STONE DISEASE

### Overview

Urinary system calcifications can occur within the kidneys, ureters, bladder, or urethra. *Urolithiasis* refers to intraluminal stones. The term *nephrolithiasis* indicates calculi within the pelvicalyceal system. *Nephrocalcinosis* refers to intraparenchymal renal calcifications, either medullary or cortical. *Dystrophic* calcification of abnormal tissue, such as the wall of a renal cyst, inflammatory tissue, or a neoplasm, is a potential source of calcifications throughout the urinary system.

### Nephrocalcinosis

#### Medullary Nephrocalcinosis

***Overview.*** In more than 90% of children with nephrocalcinosis, the calcification predominantly is in the medullary region. The most common causes of pediatric medullary renal calcification are metabolic conditions that produce hypercalcemia and hypercalciuria (Box 114.1).[36–38]

***Etiologies, Pathophysiology, and Clinical Presentation.*** Type 1 (distal) renal tubular acidosis (RTA) is the most common metabolic condition associated with nephrocalcinosis in children. Nephrocalcinosis occurs in about three-quarters of patients with type 1 RTA. Progression to urolithiasis can occur.

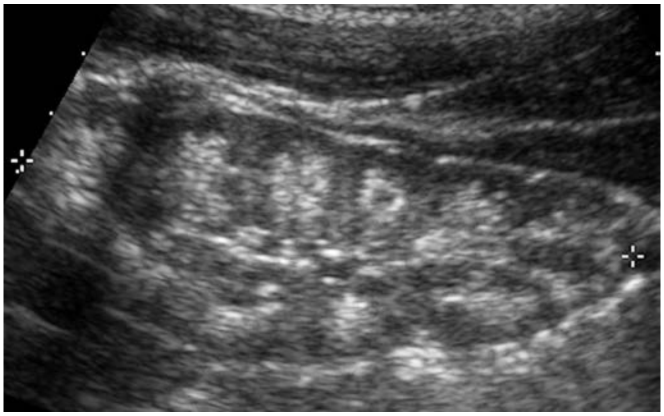

**Figure 114.8. Medullary nephrocalcinosis.** Longitudinal sonogram shows multiple punctate echogenicities involving the renal pyramids.

The administration of loop diuretics, such as furosemide, is an important cause of nephrocalcinosis in neonates. The typical time course to the earliest manifestations of stone formation is approximately 30 days after the start of diuretic therapy. Spontaneous resolution occurs in most, but not all, of these infants within several months.

In patients with primary hyperoxaluria, deposition of insoluble calcium oxalate monohydrate crystals in renal tubules leads to medullary nephrocalcinosis, interstitial fibrosis, and progressive renal functional impairment. Renal cortical calcification and urolithiasis can also occur.[39] Medullary sponge kidney is another cause of medullary nephrocalcinosis.

***Imaging.*** The major sonographic feature of medullary nephrocalcinosis is hyperechogenicity of one or more renal pyramids (Fig. 114.8). With macroscopic calcification, acoustic shadowing and color Doppler twinkling artifact may be present. The earliest sonographic sign of medullary nephrocalcinosis is loss of normal papillary hypoechogenicity. In some instances, hyperechogenicity occurs only at the tips or periphery of the pyramids.[40,41]

With extensive nephrocalcinosis, medullary calcifications are visible on standard radiographs. Most common are diffuse or uniform calcifications within the medullary pyramids, resulting in a triangular pattern. Renal calcification in patients with type 1 RTA typically is quite dense and involves all the medullary pyramids in a uniform fashion. Calcifications associated with medullary sponge kidney tend to be asymmetric.[42,43]

CT allows definitive localization of calcifications to the medullary or cortical regions (Fig. 114.9). With medullary sponge kidney, medullary calculi typically occur in clusters within the renal pyramids. Stagnation of contrast material is evident within the dilated collecting tubules on enhanced CT. With mild disease, stagnation of contrast material appears as linear papillary opacities; small cystic components may be visible with more advanced disease. The excreted contrast surrounds any calculi that are within the collecting tubules.[44,45]

The Anderson-Carr-Randall progression theory of urolithiasis suggests that microscopic calcifications within a renal pyramid can coalesce to form a plaque that migrates toward the calyx and thereby form a stone nidus. High-resolution ultrasonography of young children may reveal papillary hyperechogenicity caused by these microscopic calcifications, despite normal findings on other imaging studies. Hyperechoic pyramids are present in about 50% of children with diseases that predispose to nephrocalcinosis. Subepithelial calcium phosphate plaques sometimes are visible on radiographs or CT as slivers of calcification adjacent to the papillary tip.[46]

***Treatment and Follow-up.*** Adequate hydration is an important preventive measure in patients with known nephrocalcinosis or a

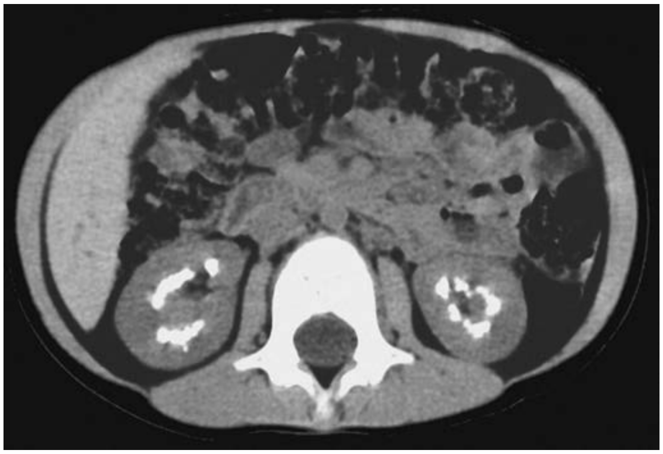

**Figure 114.9. Medullary nephrocalcinosis.** Unenhanced CT image shows dense renal pyramid calcifications in a child with type 1 renal tubular acidosis.

**BOX 114.2** Causes of Cortical Nephrocalcinosis

- Renal cortical necrosis
- Chronic glomerulonephritis
- Renal transplant rejection
- Alport syndrome
- Ethylene glycol poisoning
- Hyperoxaluria
- Acquired immunodeficiency syndrome–associated infections

**TABLE 114.1** Causes of Urolithiasis and the Most Commonly Associated Types of Stones

| Underlying Condition | Associated Stones |
|---|---|
| Idiopathic | Calcium |
| Urinary stasis | Calcium |
| Congenital obstruction | |
| Neurogenic bladder | |
| Pyelocalyceal diverticulum | |
| Surgical urinary diversions | |
| Urinary tract infection | Struvite, triple phosphate |
| Hypercalciuria | Calcium |
| Idiopathic hypercalciuria | |
| Idiopathic infantile hypercalcemia | |
| Hyperparathyroidism | |
| Sarcoidosis | |
| Type 1 renal tubular acidosis | |
| Immobilization | |
| Long-term diuretic use | |
| Hypervitaminosis D | |
| Hyperthyroidism | |
| Bone metastasis | |
| Prolonged corticosteroid therapy | |
| Fanconi syndrome | |
| Hyperoxaluria | Calcium oxalate |
| Primary oxaluria | |
| Small bowel disease | |
| Hyperuricosuria | Uric acid |
| Lymphoproliferative and myeloproliferative disorders | |
| Tumor lysis | |
| Lesch-Nyhan syndrome | |
| Cystinuria | Cystine |
| Hereditary cystinuria | |
| Xanthinuria | Xanthine |
| Hereditary xanthinuria | |
| Allopurinol therapy | |

metabolic condition that can cause nephrocalcinosis. Various medical therapies serve to reduce renal calcium excretion and increase the solubility of urinary calcium. These techniques occasionally lessen the severity of nephrocalcinosis over time. However, nephrocalcinosis is irreversible for most patients. Imaging studies provide early detection of renal calcifications, monitor response to therapy, and detect complications such as obstructive urolithiasis.

### Cortical Nephrocalcinosis

***Overview and Imaging.*** Cortical nephrocalcinosis involves the periphery of the kidney and the central septa of Bertin. In the pure forms of cortical nephrocalcinosis, the medullary pyramids are spared. The most common causes of cortical nephrocalcinosis are chronic glomerulonephritis, acute cortical necrosis, and oxalosis (Box 114.2).

Standard abdominal radiographs may show thin linear peripheral calcifications, diffuse homogeneous renal calcification, or diffuse punctate calcifications. On sonography, the involved cortex is echogenic, but acoustic shadowing does not occur unless conglomerate calcifications are present. CT accurately demonstrates the cortical location of calcification.[37,47,48]

Cortical hyperechogenicity in patients with acute renal cortical necrosis may be visible on sonography within a few weeks of the injury. Calcifications become more obvious sonographically and radiographically over time. Progressive renal atrophy also occurs. Various patterns of nephrocalcinosis can occur: (1) punctate;[49] (2) bandlike peripheral calcification with perpendicular extensions into the columns of Bertin; or (3) thin, parallel curvilinear calcifications at the interface between the necrotic cortex and the viable subcapsular cortex (i.e., the "tram-track" pattern).

## Urolithiasis

***Overview.*** The prevalence of urolithiasis varies according to geographic area, age, gender, and race. In the United States, urolithiasis affects approximately 1 in 1,000 children. Urolithiasis is slightly more common in Europe than in North America and is considerably more common in Asia. In American children, the prevalence of urolithiasis is greatest in southern California and the southeastern states. Urolithiasis is more common in white persons than in African Americans.[38,50–52]

***Pathophysiology.*** About 70% of patients with urolithiasis have a known predisposing condition, such as hypercalciuria, urinary stasis, or chronic infection (Table 114.1). A genitourinary anomaly is present in at least one-third of children with nephrocalcinosis and in nearly all patients with renal calculi related to infection. Urolithiasis is common in patients with urinary tract infections caused by a urea-splitting gram-negative enteric organism. These "infection stones" usually are a mixture of magnesium ammonium phosphate (struvite) and calcium phosphate (apatite), that is, a "triple phosphate stone." Struvite is the predominant composition of most staghorn calculi. Nonstruvite stones that occur in association with urinary tract infections are termed "infection-associated stones." Patients with neurogenic bladder, congenital urinary tract obstruction, surgical urinary diversion, or other types of urinary stasis have a propensity for calcium stones and infection stones.[53–55]

Hypercalciuria and hyperoxaluria are common causes of calcium stones. Uric acid stones due to hyperuricosuria account for only 5% of stones in North American children, but they are common in some areas of the world. Cystinuria and xanthinuria are rare causes of urolithiasis. Matrix stones are rare stones that consist of nonradiopaque inspissated mucoproteins, usually in conjunction

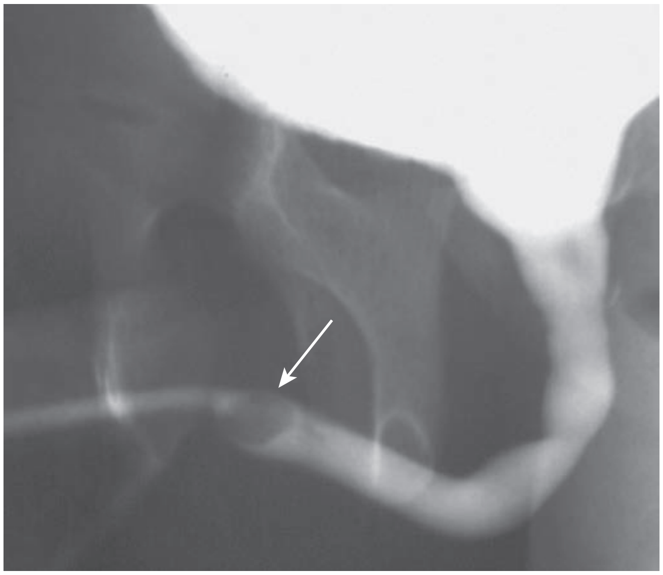

**Figure 114.11. Urethral calculus.** Urethrogram shows a partially obstructing urethral calculus as a filling defect *(arrow)* in the contrast column.

**TABLE 114.2** Radiopacity of Urinary Stones and Relative Frequency in North American Children

| Stone | Opacity | % of Stones |
|---|---|---|
| Calcium stones | +++ | 75–80 |
| Struvite | – | 10–15 |
| Triple phosphate | ++ | 5–15 |
| Cystine | + | Rare |
| Uric acid | – | 5 |
| Xanthine | – | Rare |
| Matrix | – | Rare |

with laminated or scattered calcific components. About 30% of pediatric urolithiasis is idiopathic. The typical composition of idiopathic stones is calcium phosphate or calcium oxalate. Idiopathic calcium stones sometimes have a nucleus of urate.[56]

Bladder stones can either originate from the upper urinary tract or develop within the bladder (e-Fig. 114.10). Bladder stones often are laminated and sometimes reach a very large size. Bladder stones also can form in a bladder diverticulum, surgical pouch/reservoir, or urachal remnant.

Urethral calculi are rare and only occur in males (Fig. 114.11). They can originate from a more proximal portion of the urinary tract or arise locally. Primary urethral calculi sometimes develop in association with prolonged obstruction or within a urethral diverticulum or prostatic utricle.

***Clinical Presentation.*** Pain is present in 50% to 75% of children with urolithiasis at the time of diagnosis. Pain can localize to the abdomen or flank, and may or may not radiate. Additional potential clinical manifestations include hematuria (common), urgency, dysuria, frequency, fever, pyuria, and bacteriuria. Urinary retention can occur in patients with stones of the bladder or urethra.

***Imaging.*** From 60% to 90% of urinary tract calculi are sufficiently radiopaque for visualization on standard radiographs (Table 114.2). Classification of a stone as radiopaque versus nonopaque is based on its appearance on standard radiographs (e-Fig. 114.12). In general, calcium stones are radiopaque. Stones composed of pure uric acid, xanthine, or struvite usually are nonopaque. Cystine stones are moderately radiopaque.[57,58]

The European Society of Pediatric Radiology recommends ultrasound as the initial cross-sectional imaging study for children with suspected nephrolithiasis, with reservation of CT for instances of complicated or equivocal urolithiasis.[59–61] Both radiopaque and nonopaque urinary tract stones appear echogenic on sonography and produce acoustic shadowing (Fig. 114.13). Twinkling artifact refers to a discrete focus of alternating colors that can occur at or deep to the site of a calculus on color Doppler images.[62] This is sometimes accompanied by a color comet-tail artifact distal to the stone (Fig. 114.14).[62] Secondary signs of an obstructing ureteral calculus include ureteropelvocalyectasis, nephromegaly, parenchymal hyperechogenicity, and elevated renal arterial resistive index. The sonographic appearance of acoustic shadowing aids in the differentiation of a bladder calculus from blood clot, debris, or tumor.

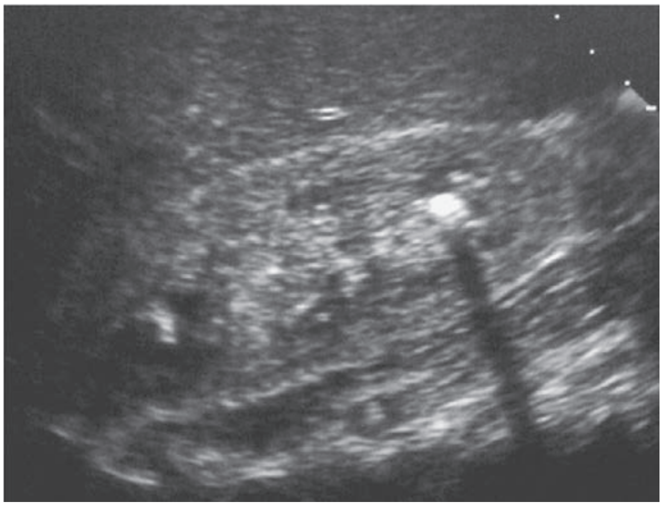

**Figure 114.13. Nephrolithiasis.** Longitudinal sonographic image of an infant with hypercalcemia and Williams syndrome reveals an echogenic, shadowing calculus in a right lower pole calyx.

CT is the most sensitive imaging technique for the detection of urolithiasis (Fig. 114.15). Regardless of composition, most urinary tract stones are hyperattenuating on CT. Calcium oxalate stones generally have attenuation values between 800 and 1,000 Hounsfield unit (HU) range, infection stones between 300 to 900 HU, and uric acid stones between 150 and 500 HU. Secondary CT signs of an obstructing urinary tract stone include hydronephrosis, hydroureter, nephromegaly, delayed nephrogram, periureteral edema, and perinephric stranding or fluid. Usually, the portion of the ureteral wall that surrounds a calculus thickens (the "rim sign"); this sign typically is lacking with a phlebolith or other mimicking calcification. A linear soft tissue density (the involved pelvic vein) often extends from a phlebolith; this feature is the "comet tail sign."[58,63,64]

## KEY POINTS

- Renal cortical scintigraphy, contrast-enhanced CT, and MRI are highly sensitive for the detection of parenchymal renal infections.
- Pyelonephritis in children can occur without pyuria or vesicoureteral reflux.
- Pediatric renal candidiasis usually is associated with prematurity or immunocompromise.
- Most children with nephrocalcinosis have hypercalcemia and/or hypercalciuria.
- Most children with urolithiasis have a known predisposing condition such as hypercalciuria, urinary stasis, or chronic infection.

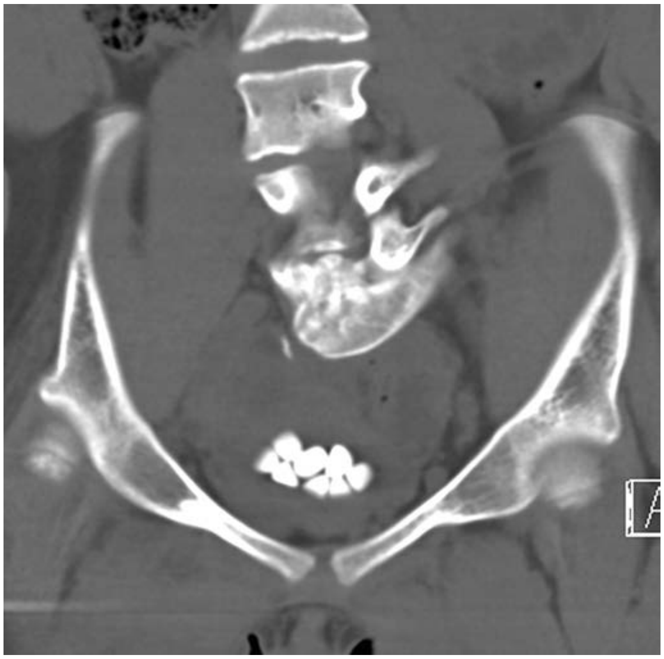

**e-Figure 114.10. Bladder calculi.** Coronal unenhanced CT image shows multiple stones in the urinary bladder of this child with spina bifida.

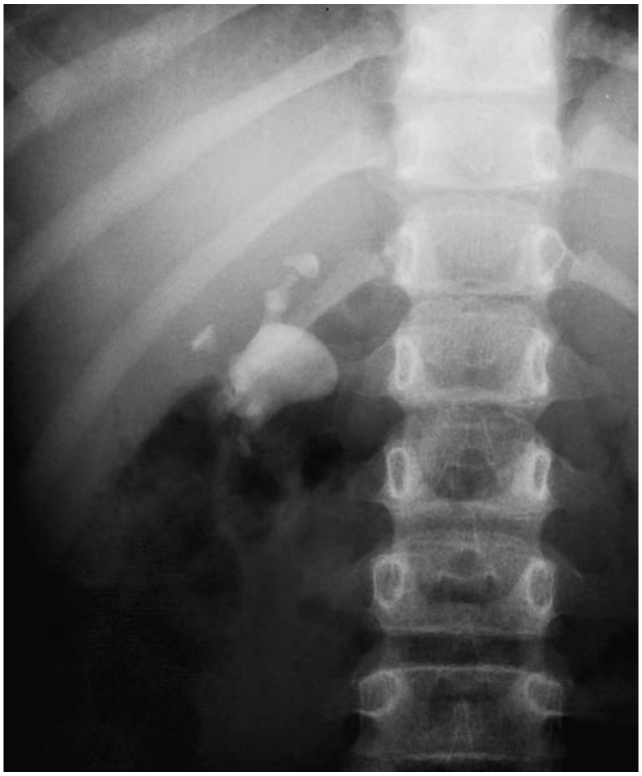

**e-Figure 114.12. Staghorn calculus.** Large opaque triple phosphate infection stone occupies the renal pelvis and extends into the calyces.

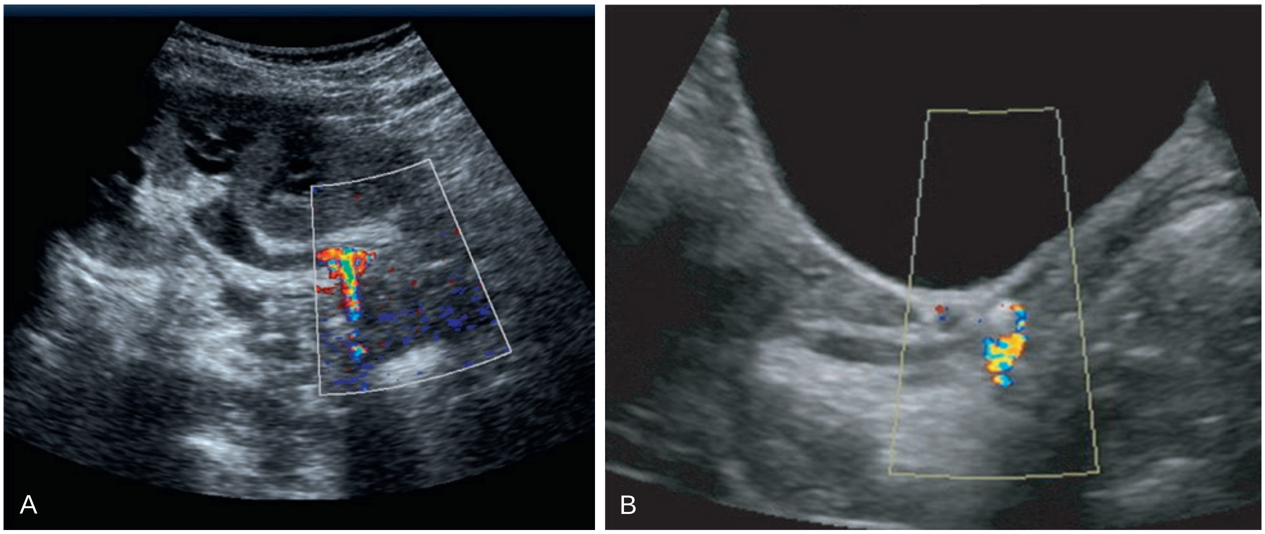

**Figure 114.14. Ureteral calculi showing twinkling artifact.** (A) Longitudinal color Doppler image shows twinkling and associated comet tail artifacts due to a calculus in the proximal aspect of the ureter. (B) Longitudinal color Doppler image shows twinkling and associated comet tail artifacts due to an echogenic calculus in the distal aspect of the ureter.

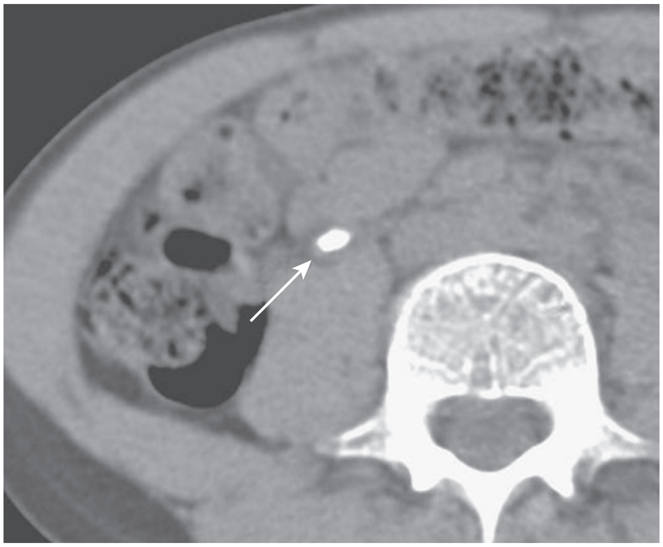

**Figure 114.15. Ureteral calculus.** Unenhanced CT image shows a right ureteral calculus with a surrounding thickened ureteral wall *(arrow)*.

## SUGGESTED READINGS

Colleran GC, Callahan MJ, Paltiel HJ, et al. Imaging in the diagnosis of pediatric urolithiasis. *Pediatr Radiol*. 2017;47(1):5–16.
Craig WD, Wagner BJ, Travis MD. Pyelonephritis: radiologic-pathologic review. *Radiographics*. 2008;28(1):255–277, quiz 327-328.
Hoppe B, Kemper MJ. Diagnostic examination of the child with urolithiasis or nephrocalcinosis. *Pediatr Nephrol*. 2010;25(3):403–413.
Kraus SJ, Lebowitz RL, Royal SA. Renal calculi in children: imaging features that lead to diagnoses: a pictorial essay. *Pediatr Radiol*. 1999;29(8):624–630.
Lavocat MP, Granjon D, Allard D, et al. Imaging of pyelonephritis. *Pediatr Radiol*. 1997;27:159–165.

## REFERENCES

Full references for this chapter can be found on www.expertconsult.com.

## REFERENCES

1. Raszka WV Jr, Khan O. Pyelonephritis. *Pediatr Rev*. 2005;26(10):364–370.
2. Smith EA. Pyelonephritis, renal scarring, and reflux nephropathy: a pediatric urologist's perspective. *Pediatr Radiol*. 2008;38(suppl 1):S76–S82.
3. Rollino C, Boero R, Ferro M, et al. Acute pyelonephritis: analysis of 52 cases. *Ren Fail*. 2002;24(5):601–608.
4. Chang SL, Shortliffe LD. Pediatric urinary tract infections. *Pediatr Clin North Am*. 2006;53(3):379–400, vi.
5. Majd M, Nussbaum Blask AR, Markle BM, et al. Acute pyelonephritis: comparison of diagnosis with 99mTc-DMSA, SPECT, spiral CT, MR imaging, and power Doppler US in an experimental pig model. *Radiology*. 2001;218(1):101–108.
6. Lavocat MP, Granjon D, Allard D, et al. Imaging of pyelonephritis. *Pediatr Radiol*. 1997;27(2):159–165.
7. Jaksic E, Bogdanovic R, Artiko V, et al. Diagnostic role of initial renal cortical scintigraphy in children with the first episode of acute pyelonephritis. *Ann Nucl Med*. 2011;25(1):37–43.
8. Dacher JN, Boillot B, Eurin D, et al. Rational use of CT in acute pyelonephritis: findings and relationships with reflux. *Pediatr Radiol*. 1993;23(4):281–285.
9. Poustchi-Amin M, Leonidas JC, Palestro C, et al. Magnetic resonance imaging in acute pyelonephritis. *Pediatr Nephrol*. 1998;12(7):579–580.
10. Lonergan GJ, Pennington DJ, Morrison JC, et al. Childhood pyelonephritis: comparison of gadolinium-enhanced MR imaging and renal cortical scintigraphy for diagnosis. *Radiology*. 1998;207(2):377–384.
11. Dickerson EC, Dillman JR, Smith EA, et al. Pediatric MR urography: indications, techniques, and approach to review. *Radiographics*. 2015;35(4):1208–1230.
12. Dacher JN, Pfister C, Monroc M, et al. Power Doppler sonographic pattern of acute pyelonephritis in children: comparison with CT. *AJR Am J Roentgenol*. 1996;166(6):1451–1455.
13. Eggli KD, Eggli D. Color Doppler sonography in pyelonephritis. *Pediatr Radiol*. 1992;22(6):422–425.
14. Sorantin E, Fotter R, Aigner R, et al. The sonographically thickened wall of the upper urinary tract system: correlation with other imaging methods. *Pediatr Radiol*. 1997;27(8):667–671.
15. Roberts JA. Management of pyelonephritis and upper urinary tract infections. *Urol Clin North Am*. 1999;26(4):753–763.
16. Pecile P, Miorin E, Romanello C, et al. Age-related renal parenchymal lesions in children with first febrile urinary tract infections. *Pediatrics*. 2009;124(1):23–29.
17. Yoder IC, Lindfors KK, Pfister RC. Diagnosis and treatment of pyonephrosis. *Radiol Clin North Am*. 1984;22(2):407–414.
18. Jeffrey RB, Laing FC, Wing VW, et al. Sensitivity of sonography in pyonephrosis: a reevaluation. *AJR Am J Roentgenol*. 1985;144(1):71–73.
19. Schneider K, Helmig FJ, Eife R, et al. Pyonephrosis in childhood–is ultrasound sufficient for diagnosis? *Pediatr Radiol*. 1989;19(5):302–307.
20. Chan JH, Tsui EY, Luk SH, et al. MR diffusion-weighted imaging of kidney: differentiation between hydronephrosis and pyonephrosis. *Clin Imaging*. 2001;25(2):110–113.
21. Subramanyam BR, Raghavendra BN, Bosniak MA, et al. Sonography of pyonephrosis: a prospective study. *AJR Am J Roentgenol*. 1983;140(5):991–993.
22. Korkes F, Favoretto RL, Broglio M, et al. Xanthogranulomatous pyelonephritis: clinical experience with 41 cases. *Urology*. 2008;71(2):178–180.
23. Smith EA, Styn N, Wan J, et al. Xanthogranulomatous pyelonephritis: an uncommon pediatric renal mass. *Pediatr Radiol*. 2010;40(8): 1421–1425.
24. Zugor V, Schott GE, Labanaris AP. Xanthogranulomatous pyelonephritis in childhood: a critical analysis of 10 cases and of the literature. *Urology*. 2007;70(1):157–160.
25. Bingol-Kologlu M, Ciftci AO, Senocak ME, et al. Xanthogranulomatous pyelonephritis in children: diagnostic and therapeutic aspects. *Eur J Pediatr Surg*. 2002;12(1):42–48.
26. Kim J. Ultrasonographic features of focal xanthogranulomatous pyelonephritis. *J Ultrasound Med*. 2004;23(3):409–416.
27. Kim JC. US and CT findings of xanthogranulomatous pyelonephritis. *Clin Imaging*. 2001;25(2):118–121.
28. Bryant K, Maxfield C, Rabalais G. Renal candidiasis in neonates with candiduria. *Pediatr Infect Dis J*. 1999;18(11):959–963.
29. Erden A, Fitoz S, Karagulle T, et al. Radiological findings in the diagnosis of genitourinary candidiasis. *Pediatr Radiol*. 2000;30(12):875–877.
30. Kale H, Narlawar RS, Rathod K. Renal fungal ball: an unusual sonographic finding. *Journal of Clinical Ultrasound : JCU*. 2002;30(3):178–180.
31. Bisht V, Voort JV. Clinical practice: obstructive renal candidiasis in infancy. *Eur J Pediatr*. 2011;170(10):1227–1235.
32. Eastwood JB, Corbishley CM, Grange JM. Tuberculosis and the kidney. *Journal of the American Society of Nephrology : JASN*. 2001;12(6):1307–1314.
33. Mapukata A, Andronikou S, Fasulakis S, et al. Modern imaging of renal tuberculosis in children. *Australas Radiol*. 2007;51(6):538–542.
34. Rui X, Li XD, Cai S, et al. Ultrasonographic diagnosis and typing of renal tuberculosis. *International Journal of Urology : Official Journal of the Japanese Urological Association*. 2008;15(2):135–139.
35. Wong A, Dhingra S, Surabhi VR. AIRP best cases in radiologic-pathologic correlation: genitourinary tuberculosis. *Radiographics*. 2012;32(3):839–844.
36. Ammenti A, Pelizzoni A, Cecconi M, et al. Nephrocalcinosis in children: a retrospective multi-centre study. *Acta Paediatr*. 2009;98(10):1628–1631.
37. Cremin B, Wiggelinkhuizen J, Bonnici F. Nephrocalcinosis in children. *Br J Radiol*. 1982;55(654):413–418.
38. Hoppe B, Kemper MJ. Diagnostic examination of the child with urolithiasis or nephrocalcinosis. *Pediatr Nephrol*. 2010;25(3):403–413.
39. Strauss SB, Waltuch T, Bivin W, et al. Primary hyperoxaluria: spectrum of clinical and imaging findings. *Pediatr Radiol*. 2016.
40. Glazer GM, Callen PW, Filly RA. Medullary nephrocalcinosis: sonographic evaluation. *AJR Am J Roentgenol*. 1982;138(1):55–57.
41. Weber G, Cazzuffi MA, Frisone F, et al. Nephrocalcinosis in children and adolescents: sonographic evaluation during long-term treatment with 1,25-dihydroxycholecalciferol. *Child Nephrol Urol*. 1988;9(5):273–276.
42. Manz F, Jaschke W, van Kaick G, et al. Nephrocalcinosis in radiographs, computed tomography, sonography and histology. *Pediatr Radiol*. 1980;9(1):19–26.
43. Dyer RB, Chen MY, Zagoria RJ. Abnormal calcifications in the urinary tract. *Radiographics*. 1998;18(6):1405–1424.
44. Afschrift M, Nachtegaele P, Van Rattinghe R, et al. Nephrocalcinosis demonstrated by ultrasound and CT. *Pediatr Radiol*. 1983;13(1):42–43.
45. Kawamoto S, Duggan P, Sheth S, et al. Renal papillary and calyceal lesions at CT urography: genitourinary imaging. *Radiographics*. 2017;37(1):358–359.
46. Patriquin H, Robitaille P. Renal calcium deposition in children: sonographic demonstration of the Anderson-Carr progression. *AJR Am J Roentgenol*. 1986;146(6):1253–1256.
47. Alon US. Nephrocalcinosis. *Curr Opin Pediatr*. 1997;9(2):160–165.
48. Sefczek RJ, Beckman I, Lupetin AR, et al. Sonography of acute renal cortical necrosis. *AJR Am J Roentgenol*. 1984;142(3):553–554.
49. Papanicolaou N, Pfister RC, Young HH 2nd, et al. Percutaneous ultrasonic lithotripsy of symptomatic renal calculi in children. *Pediatr Radiol*. 1986;16(1):13–16.
50. Knoll T, Schubert AB, Fahlenkamp D, et al. Urolithiasis through the ages: data on more than 200,000 urinary stone analyses. *J Urol*. 2011;185(4):1304–1311.
51. Mandeville JA, Nelson CP. Pediatric urolithiasis. *Curr Opin Urol*. 2009;19(4):419–423.
52. Routh JC, Graham DA, Nelson CP. Trends in imaging and surgical management of pediatric urolithiasis at American pediatric hospitals. *J Urol*. 2010;184(4 suppl):1816–1822.
53. Abrahams HM, Stoller ML. Infection and urinary stones. *Curr Opin Urol*. 2003;13(1):63–67.
54. Cameron MA, Sakhaee K, Moe OW. Nephrolithiasis in children. *Pediatr Nephrol*. 2005;20(11):1587–1592.
55. Gillespie RS, Stapleton FB. Nephrolithiasis in children. *Pediatr Rev*. 2004;25(4):131–139.
56. DeFoor WR, Jackson E, Minevich E, et al. The risk of recurrent urolithiasis in children is dependent on urinary calcium and citrate. *Urology*. 2010;76(1):242–245.
57. Kraus SJ, Lebowitz RL, Royal SA. Renal calculi in children: imaging features that lead to diagnoses: a pictorial essay. *Pediatr Radiol*. 1999;29(8):624–630.
58. Palmer JS, Donaher ER, O'Riordan MA, et al. Diagnosis of pediatric urolithiasis: role of ultrasound and computerized tomography. *J Urol*. 2005;174(4 Pt 1):1413–1416.
59. Riccabona M, Avni FE, Blickman JG, et al. Imaging recommendations in paediatric uroradiology: minutes of the ESPR workgroup session on urinary tract infection, fetal hydronephrosis, urinary tract ultrasonography and voiding cystourethrography, Barcelona, Spain, June 2007. *Pediatr Radiol*. 2008;38(2):138–145.
60. Riccabona M, Avni FE, Dacher JN, et al. ESPR uroradiology task force and ESUR paediatric working group: imaging and procedural

recommendations in paediatric uroradiology, part III. Minutes of the ESPR uroradiology task force minisymposium on intravenous urography, uro-CT and MR-urography in childhood. *Pediatr Radiol*. 2010;40(7):1315–1320.

61. Riccabona M, Avni FE, Blickman JG, et al. Imaging recommendations in paediatric uroradiology. Minutes of the ESPR uroradiology task force session on childhood obstructive uropathy, high-grade fetal hydronephrosis, childhood haematuria, and urolithiasis in childhood. ESPR Annual Congress, Edinburgh, UK, June 2008. *Pediatr Radiol*. 2009;39(8):891–898.
62. Dillman JR, Kappil M, Weadock WJ, et al. Sonographic twinkling artifact for renal calculus detection: correlation with CT. *Radiology*. 2011;259(3):911–916.
63. Bellin MF, Renard-Penna R, Conort P, et al. Helical CT evaluation of the chemical composition of urinary tract calculi with a discriminant analysis of CT-attenuation values and density. *Eur Radiol*. 2004;14(11):2134–2140.
64. Strouse PJ, Bates DG, Bloom DA, et al. Non-contrast thin-section helical CT of urinary tract calculi in children. *Pediatr Radiol*. 2002;32(5):326–332.

# 115 Renal Neoplasms

Ethan A. Smith and D. Gregory Bates

## NEPHROGENIC RESTS AND NEPHROBLASTOMATOSIS

***Overview and Pathophysiology.*** Embryologic development of the kidneys is completed by the 36th gestational week. Residual embryonic fetal tissue (metanephric blastema) that persists beyond 36 weeks' gestation is called a *nephrogenic rest*. Multifocal or diffuse nephrogenic rests are termed *nephroblastomatosis*. Nephrogenic rests are identified in about 1% of neonatal autopsies. The vast majority of nephrogenic rests resolve spontaneously by 4 months of age. However, approximately 1% of nephrogenic rests will undergo malignant transformation into Wilms tumor (previously known as *nephroblastoma*).[1–3]

Nephrogenic rests can occur anywhere in the kidney and are usually found either within a renal lobule (intralobar) or peripherally within the cortex (perilobar). Intralobar nephrogenic rests develop earlier in nephrogenesis and are more likely to undergo malignant transformation into Wilms tumor. Nephrogenic rests also are classified according to histologic features of development; hyperplastic and neoplastic rests are thought to be active and to have higher malignant potential, whereas dormant or sclerosing nephrogenic rests are considered inactive.[1–4]

Intralobar nephrogenic rests are less common than perilobar nephrogenic rests. Intralobar nephrogenic rests tend to be few and are located randomly in the renal lobe. Intralobar rests are associated with sporadic aniridia, Drash syndrome (male pseudohermaphrodism and nephritis), and WAGR syndrome (Wilms tumor, aniridia, genital anomalies, and mental retardation). Patients with sporadic aniridia have a 30% to 40% risk of Wilms tumor, which represents the greatest likelihood of all of the genetic and syndromic abnormalities associated with nephroblastomatosis.[1–4]

Perilobar nephrogenic rests are often multiple and are located at the corticomedullary junction or in the cortex. Diffuse perilobar nephrogenic rests or diffuse perilobar nephroblastomatosis describes the presence of multiple perilobar rests involving the periphery of the renal cortex. Perilobar nephrogenic rests are associated with hemihypertrophy syndromes, Beckwith-Wiedemann syndrome (macroglossia, macrosomia, and omphalocele), Perlman syndrome (fetal gigantism and multiple congenital anomalies), and trisomy 18. Patients with hemihypertrophy and Beckwith-Wiedemann syndrome have about a 5% risk of developing a Wilms tumor.[1,3–5]

***Imaging.*** Some nephrogenic rests are microscopic and cannot be identified by imaging. Larger nephrogenic rests can be evaluated with ultrasonography (US), computed tomography (CT), and magnetic resonance imaging (MRI). In diffuse perilobar nephrogenic rests, the affected kidney may be enlarged. On sonography, corticomedullary differentiation is absent. Nephrogenic rests and areas of diffuse nephroblastomatosis may be hypoechoic or isoechoic with respect to normal renal cortex. Multifocal nephroblastomatosis is more difficult to identify on sonography due to the diffuse nature of the disease.[2,3,6]

CT is more sensitive than ultrasound for the evaluation of nephrogenic rests and nephroblastomatosis. On contrast-enhanced CT, nephrogenic rests appear as low attenuation lesions that enhance less than normal renal cortex (Figs. 115.1 and 115.2). Bulky masses may distort the pelvicalyceal system. Bilateral involvement may be symmetric or asymmetric. Lenticular or plaquelike lesions may be more difficult to identify on CT than round masses.[2,3,6] In diffuse perilobar nephrogenic rests, a thick rind of low attenuation tissue encases normally enhancing but architecturally distorted parenchyma (e-Fig. 115.3).

On MRI, nephrogenic rests are isointense to normal renal parenchyma on T1-weighted sequences and isointense to hyperintense on T2-weighted sequences. Similar to CT, nephrogenic rests enhance less than normal renal parenchyma after intravenous gadolinium chelate administration and hence appear as hypointense to enhancing renal parenchyma on T1-weighted postcontrast images. In general, the signal intensity and enhancement of nephroblastomatosis is homogeneous, whereas foci of Wilms tumor tend to be more heterogeneous.[2,3,6–8]

***Treatment and Follow-up.*** Presently, no specific treatment is advocated for nephrogenic rests/nephroblastomatosis unless Wilms tumor develops. Close radiologic follow-up is recommended for children with genetic abnormalities or syndromes associated with nephroblastomatosis. Children with hemihypertrophy or Beckwith-Wiedemann syndrome are at risk for the development of other embryonal tumors, such as hepatoblastoma. No large studies have been performed to establish the optimal screening interval for Wilms tumor surveillance. A baseline CT of patients with nephroblastomatosis-related genetic abnormalities or syndromes at 6 months of age (or at diagnosis if the patient is older than 6 months), followed by surveillance ultrasound examinations every 3 to 4 months until the child is at least 8 years of age, is recommended on the basis of results from the National Wilms Tumor Studies.[2,3,9–13]

## WILMS TUMOR

***Overview, Pathophysiology, and Staging.*** Wilms tumor is one of the most common abdominal malignancies of childhood, and it accounts for approximately 90% of pediatric renal masses. Its peak incidence is at 3 to 4 years of age (80% occur in children <5 years old), but it has been described in the fetus, neonate, teenager, and adult. Clinical presentation includes a palpable mass, abdominal pain, hematuria, and occasionally hypertension (from tumor renin production). As discussed, certain syndromes and genetic abnormalities predispose to development of a Wilms tumor (e-Fig. 115.4). Two loci on chromosome 11 have been implicated in the genesis of Wilms tumors: 11p13 (*WT1* gene —WAGR or Drash syndrome) and 11p15 (*WT2* gene — Beckwith-Wiedemann syndrome or hemihypertrophy). Approximately 5% of children have bilateral Wilms tumor, and up to 7% have multicentric disease. Most Wilms tumors arise from the renal parenchyma; however, extrarenal Wilms tumors rarely may develop in the abdomen or at distant sites.[1,14–18]

In the United States, tumor stage (Box 115.1) is determined by a combination of preoperative imaging, intraoperative findings, and pathology, while the grade is established on histopathologic examination. Metastatic disease is present in 15% to 20% of patients at presentation and is most commonly seen in the lungs, followed by the liver.[17] The classic triphasic Wilms tumor arises from mesodermal precursors of the renal parenchyma (metanephros) and contains blastemal, stromal, and epithelial elements. The prognosis for tumors with a favorable histology is excellent, even for those at higher stages. Approximately 7% of tumors contain anaplastic elements and have a worse prognosis.[18] In Europe, the staging system is based completely on radiologic findings. Tumors

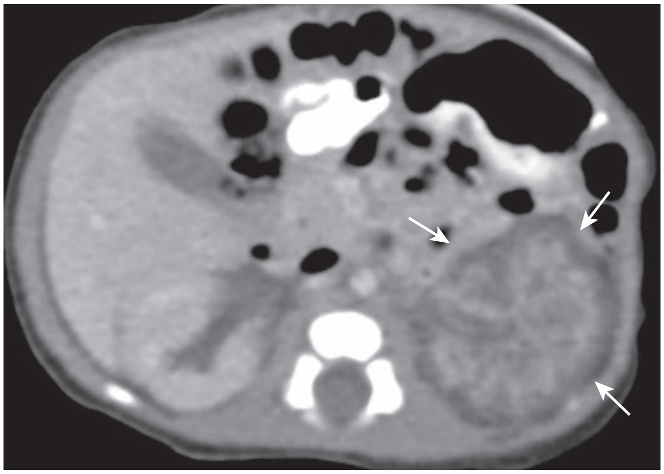

**e-Figure 115.3. Asymmetric diffuse perilobar nephroblastomatosis.** Axial contrast-enhanced CT image in a neonate shows a rind of hypoenhancing tissue involving the periphery of the left kidney *(arrows)*. The right kidney is normal.

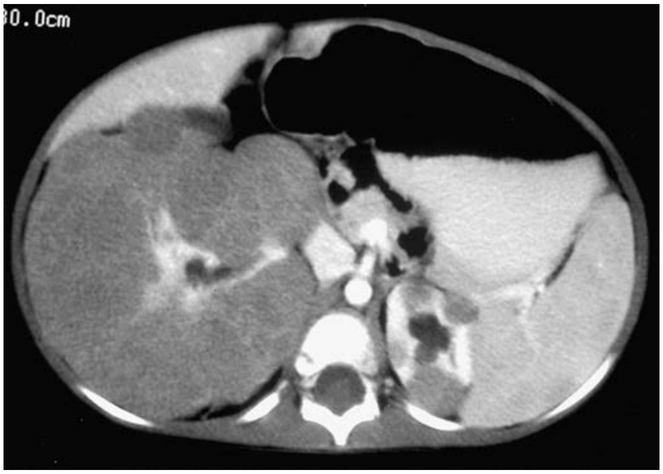

**e-Figure 115.4. Diffuse perilobar nephroblastomatosis and right Wilms tumor.** Axial contrast-enhanced CT image demonstrates round, peripheral masses that enhance to a lesser extent than normal renal parenchyma in the upper pole of the left kidney. The right kidney has a thick rind of lobulated, hypoattenuating tissue without a discrete mass. A biopsy showed Wilms tumor on the right, and a nephrectomy was performed.

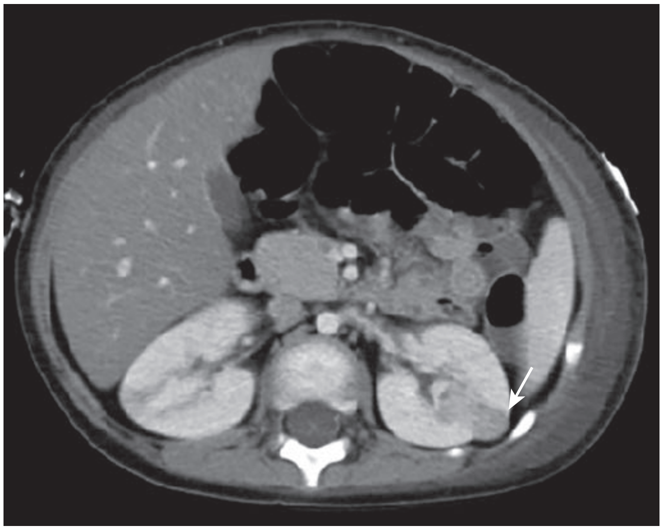

**Figure 115.1. Solitary nephrogenic rest.** Axial contrast-enhanced CT image shows a small, well-circumscribed hypoenhancing mass *(arrow)* in the left kidney.

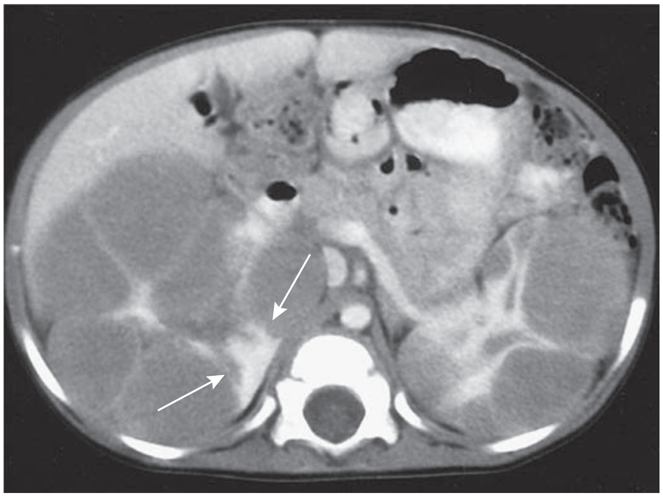

**Figure 115.2. Diffuse perilobar nephroblastomatosis with symmetric involvement.** Axial contrast-enhanced CT image shows enlarged kidneys with multiple, round, peripheral low attenuation masses. Only small areas of normally enhancing kidney tissue *(arrows)* are present.

**BOX 115.1** Children's Oncology Group (COG) Staging of Wilms Tumor

**STAGE I**

- A completely resected tumor limited to the kidney with an intact capsule
- No biopsy or rupture of tumor before removal
- No involvement of vessels or renal sinuses
- No tumor at or beyond the margins of resection
- Regional lymph nodes are negative for tumor

**STAGE II**

- A completely resected tumor
- No tumor at or beyond the margins of resection
- Regional lymph nodes are negative for tumor
- One or more of the following findings:
  - Penetration of the renal capsule
  - Invasion of vasculature extending beyond the renal parenchyma

**STAGE III**

- Residual tumor is present after surgery, confined to the abdomen, with one or more of the following attributes present:
  - One or more regional lymph nodes are positive for tumor
  - The tumor is implanted on or penetrating through the peritoneum
  - The presence of gross unresected tumor or tumor at the margin of resection
  - Any tumor spillage occurring before or during surgery, including biopsy
  - The tumor was removed in more than one piece

**STAGE IV**

- The presence of hematogenous metastasis (e.g., lung, liver, bone, or brain)
- The presence of lymph node metastasis outside the abdomen and pelvis

**STAGE V**

- Wilms tumor in both kidneys

*From Gratias EJ, Dome JS. Current and emerging chemotherapy treatment strategies for Wilms tumor in North America.* Paediatr Drugs. *2008;10(2):115–124.*

are classified on the basis of their imaging appearance, and chemotherapy is usually given before definitive surgery is performed. In the United States, neoadjuvant chemotherapy is reserved for tumors that are considered unresectable at presentation due to vascular invasion or other features.[1,2,18]

***Imaging.*** Radiologic evaluation of Wilms tumor is focused on identifying the site(s) of involvement, defining local extent of disease to assist in surgical planning, and evaluating for metastases. Preoperative imaging may include conventional radiography, abdominal sonography, and thoracic, abdominal, and pelvic CT, and/or MRI. The role of $F^{18}$-fluorodeoxyglucose positron emission tomography (FDG-PET) fused with CT (PET-CT) at diagnosis is less clear. PET-CT is often reserved for evaluating for residual disease or recurrence after therapy.[1,2,19,20]

On sonography, Wilms tumor typically appears as a large, heterogeneous intrarenal mass. Some Wilms tumors may contain cystic components, portions of obstructed and entrapped pelvicalyceal systems, or hemorrhagic and necrotic tumor. Identification of vascular invasion with extension into the renal vein, inferior vena cava, or right atrium is important for surgical planning and can be assessed with ultrasound (e-Fig. 115.5), CT (Fig. 115.6), or MRI. The tumor may invade the renal capsule, seed the peritoneal space, or grow directly into the mesentery and omentum. Hepatic metastases, if present, appear as rounded, hypoechoic liver lesions. The contralateral kidney should be carefully evaluated for synchronous Wilms tumor, nephrogenic rests, or nephroblastomatosis.[1,2,6]

On CT, Wilms tumor typically appears as a large, heterogeneous mass arising from the kidney (Fig. 115.7). The tumor enhances to a lesser extent than does normal renal parenchyma. There is characteristically a rim of enhancing renal tissue surrounding at least a portion of the mass (the so-called "claw sign"), confirming the mass to be of renal origin. Calcifications are uncommon, being present in only about 9% of Wilms tumors (e-Fig. 115.8). CT of the chest is used to identify pulmonary metastases.[1,2,6,21,22]

On MRI, a Wilms tumor is isointense with respect to normal renal parenchyma on T1-weighted sequences and heterogeneously hyperintense with respect to normal renal parenchyma on T2-weighted sequences. After administration of intravenous contrast material, a Wilms tumor is typically hypoenhancing relative

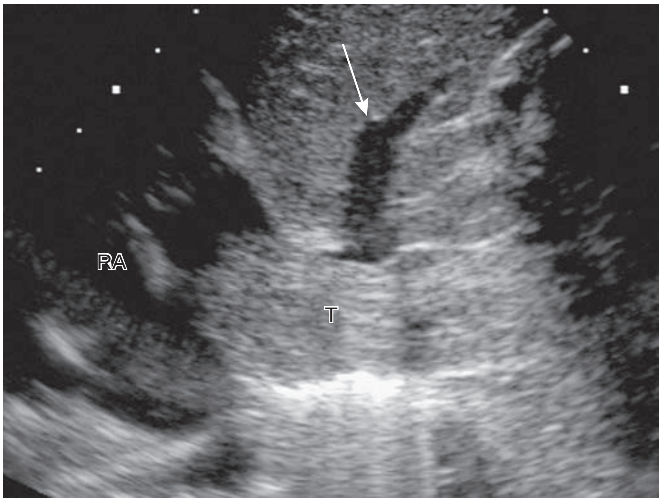

**e-Figure 115.5. Wilms tumor extending into the inferior vena cava and the right atrium *(RA)*.** Longitudinal gray-scale ultrasound image demonstrates tumor thrombus *(T)* expanding the inferior vena cava and extending into the right atrium. The tumor partially occludes drainage from one of the hepatic veins *(arrow)*.

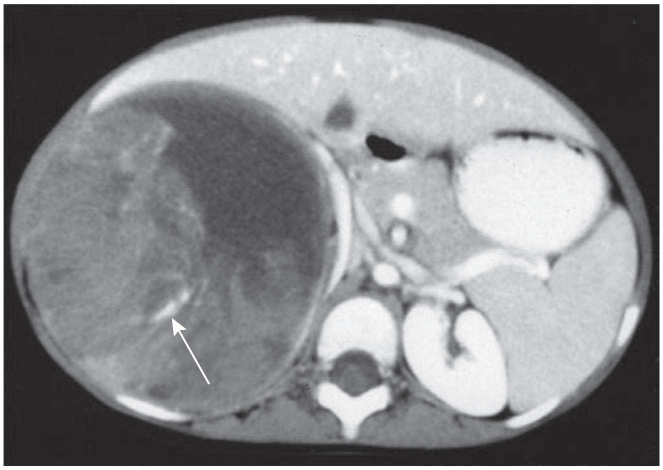

**e-Figure 115.8. Wilms tumor containing calcification.** Coronal contrast-enhanced CT image shows a large, heterogeneous renal mass with linear calcification present posteriorly *(arrow)*. Calcification may be dystrophic or indicate teratoid differentiation.

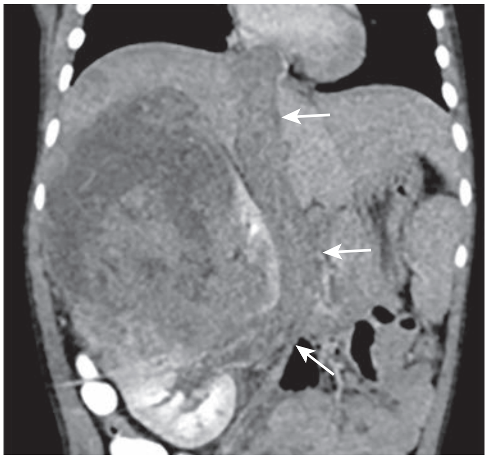

**Figure 115.6. Wilms tumor extending into the inferior vena cava and right atrium.** Coronal contrast-enhanced CT image demonstrates a large right Wilms tumor with heterogeneous soft tissue *(arrows)* filling the right renal vein and IVC, extending to the lower right atrium, consistent with extensive tumor thrombus.

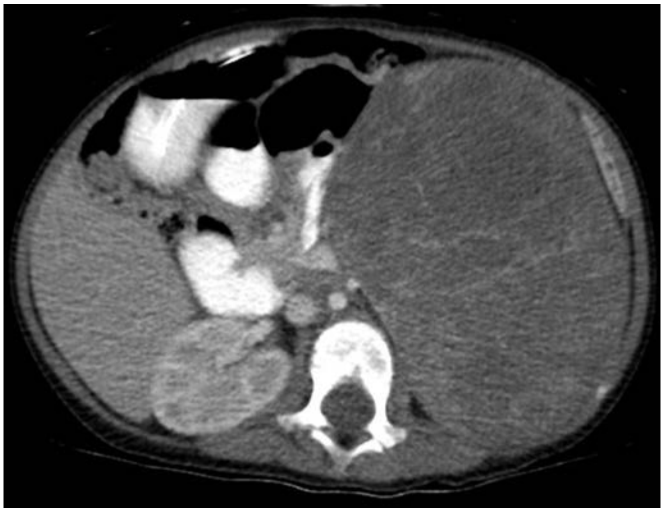

**Figure 115.7. Wilms tumor.** Axial contrast-enhanced CT in a 2-year-old girl shows a large, heterogeneous predominantly low attenuation left renal mass, consistent with Wilms tumor.

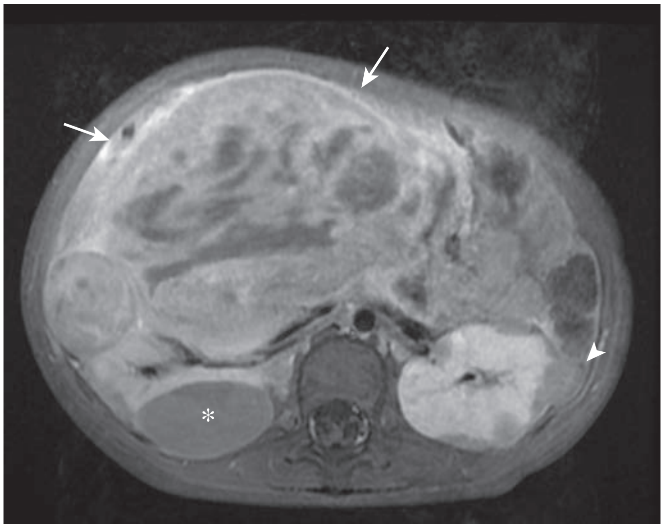

**Figure 115.9. Bilateral Wilms tumor.** Axial T1-weighted postcontrast magnetic resonance (MR) image in a 2-year-old boy shows a large, heterogeneous mass arising from the right kidney *(arrows)*. There is an additional mass in the right kidney *(asterisk)* as well as multiple smaller left renal masses *(arrowhead)*, proven to be multifocal bilateral Wilms tumors.

to normal renal parenchyma (Fig. 115.9). On diffusion-weighted imaging, the tumor typically has heterogeneous signal with areas of impeded diffusion reflecting the high cellularity of the viable tumor. T2-weighted sequences and diffusion-weighted imaging also readily depict liver metastases and enlarged retroperitoneal lymph nodes. Vascular invasion can be assessed on T2-weighted spin-echo images, seen as filling defects instead of the expected vascular flow voids, or as filling defects on T1-weighted postcontrast images.[1,2,7,8,23]

Wilms tumors are typically FDG-avid, but the role of FDG-PET in Wilms evaluation is as yet unclear. FDG-PET can help with a targeted biopsy of a viable Wilms tumor and biologically aggressive elements (e.g., anaplastic Wilms). Currently, FDG-PET is primarily used for evaluating for residual tumor after treatment or confirming local/regional recurrence.[2,19]

***Treatment.*** In the United States, therapy for Wilms tumor depends on the stage and primary resectability of the tumor. Up front *en bloc* resection of the mass and the entire affected kidney is performed if possible, followed by adjuvant chemotherapy. If needed based on disease stage (stage III or IV disease), radiation therapy to the flank, entire abdomen, and/or lungs is considered. If the primary tumor is not initially resectable, or if there is bilateral disease, neoadjuvant chemotherapy is given before resection. In bilateral disease, resection often involves partial nephrectomy as opposed to total nephrectomy to spare as much renal tissue as possible. In Europe, up-front chemotherapy is given before surgery based on data showing possible reduced rates of tumor rupture (stage III disease) when neoadjuvant chemotherapy is given. Ongoing clinical trials are focused on limiting surgical morbidity and therapy-related toxicity, especially with regard to limiting abdominal and pulmonary radiation therapy to only certain subsets of patients. Advancements in therapy over recent decades has resulted in a greater than 90% long-term survival for localized disease and greater than 70% survival for metastatic disease.[1,2,17,18,24–30]

## CLEAR CELL SARCOMA OF THE KIDNEY

***Overview.*** Clear cell sarcoma of the kidney accounts for approximately 5% of primary renal tumors in childhood. Clear cell sarcoma occurs in an age group similar to that affected by Wilms tumor (1–4 years of age) and has a male predominance. No familial or syndromic association has been identified. Immunohistochemical staining has shown no characteristic marker pattern, but negativity to the *WT1* gene is important.

***Imaging.*** Imaging features of the primary tumor are similar to those of Wilms tumor, typically a large, heterogeneous renal mass (Fig. 115.10). Distinct from Wilms tumor, clear cell sarcoma has a predilection for bone metastases (even being formerly known as "the bone-metastasizing renal tumor of childhood"). A pathologic diagnosis of clear cell sarcoma necessitates an evaluation of the skeletal system. Bone scintigraphy or a conventional radiographic skeletal survey may be used. However, metastases to lymph nodes, lung, and liver still are seen more frequently than bone metastases.

***Treatment.*** Due to the aggressive behavior of clear cell sarcoma, it is associated with a higher rate or relapse and mortality than Wilms tumor, with a reported long-term survival of 60% to 70%. Treatment consists of nephrectomy and aggressive chemotherapy.[1,31–38]

## RHABDOID TUMOR OF THE KIDNEY

***Overview.*** Rhabdoid tumor of the kidney accounts for 2% of pediatric renal malignancies. The name is derived from its monomorphous histologic appearance resembling that of skeletal muscle, although a myogenic origin has not been proved. Rhabdoid tumors occur in a younger age group than do Wilms tumors (80% occur in children younger than 2 years of age). The most common clinical presentation is hematuria secondary to invasion of the renal pelvis.

***Imaging.*** Rhabdoid tumors of the kidney also have imaging characteristics similar to those of Wilms tumors. Imaging features that may suggest the diagnosis include subcapsular fluid collections, medial location within the kidney, and tumor lobules separated by low-density hemorrhage or necrosis with peripheral calcifications. These tumors are highly aggressive, metastasize early, and often present with advanced disease. A distinct association with synchronous or metachronous primary or metastatic central nervous system lesions is seen, often in the posterior fossa. Primitive neuroectodermal tumors, medulloblastomas, ependymomas, and cerebellar and brainstem astrocytomas all have been reported. After tissue diagnosis of rhabdoid tumor of the kidney, MRI of the brain is often recommended.

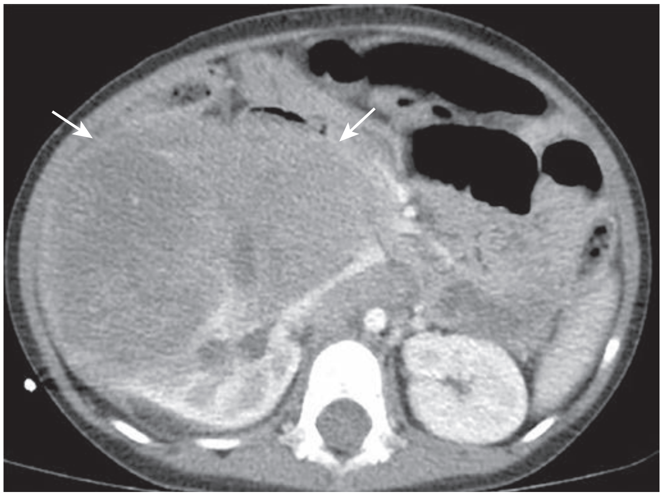

**Figure 115.10. Clear cell sarcoma of the kidney.** Axial contrast-enhanced CT image in an 18-month-old girl shows a large heterogeneous mass in the right kidney *(arrows)* found to be clear cell sarcoma of the kidney at pathology. This mass is indistinguishable from Wilms tumor.

***Treatment.*** Rhabdoid tumors have a poor prognosis, with an 18-month survival of only 20%. Treatment includes nephrectomy, radiation therapy to the tumor bed, and aggressive chemotherapy.[1,39–46]

## CONGENITAL MESOBLASTIC NEPHROMA

***Overview.*** Congenital mesoblastic nephroma (CMN) is the most common solid renal tumor in infants under 6 months of age and is typically identified within the first 3 months of life. Originally thought to represent a congenital Wilms tumor, it is now recognized as a distinct neoplasm. Clinical presentation is that of a palpable abdominal mass and, less frequently, hematuria. Histologically, the tumor is composed of monomorphic infiltrating spindle-shaped mesenchymal cells and embryonal metaplasia of entrapped renal tissue. CMN is subtyped into classic, cellular, and mixed forms.

***Imaging.*** CMN tends to be a large heterogeneous mass, often with poorly defined margins and lacking a capsule. At ultrasound, CMN is a predominantly solid intrarenal mass but may contain cystic components. The mass may distort and displace the pelvicalyceal system. On CT, CMN may show homogeneous or heterogeneous enhancement, is unilateral and unifocal, displaces adjacent vasculature without invasion, and typically does not have calcifications (Fig. 115.11). Low attenuation foci representing necrosis, fluid-filled cysts, or hemorrhage may be seen. On MRI, the tumor typically has a low signal on T1-weighted images (although foci of hemorrhage may be hyperintense) and has a variable signal on T2-weighted sequences. After intravenous contrast administration, the mass is typically heterogeneously enhancing but may also demonstrate homogeneous enhancement.

***Treatment.*** Complete surgical excision is the treatment of choice. CMN is associated with a favorable outcome after complete surgical resection. However, the cellular variant (resembling congenital infantile fibrosarcoma and often sharing a common chromosomal translocation) is associated with local recurrences (10%) and metastases. Adjuvant chemotherapy is not recommended

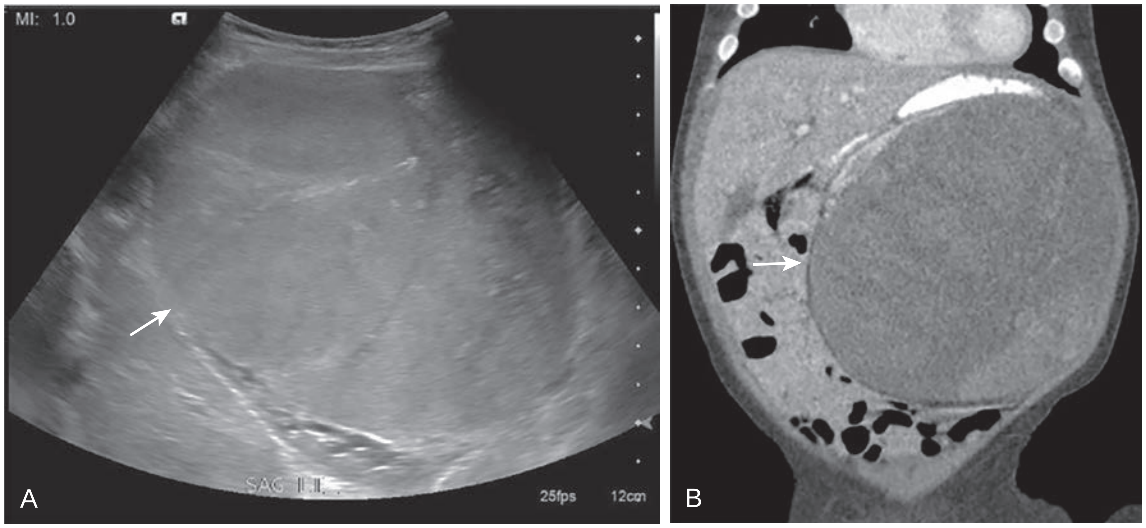

**Figure 115.11. Congenital mesoblastic nephroma.** (A) Longitudinal gray-scale ultrasound image shows a large, solid mass *(arrow)* arising from the left kidney in a 3-month-old boy. (B) Coronal contrast-enhanced CT image in the same child shows the mass *(arrow)* to be heterogeneously hypoenhancing. The “claw sign” is present.

if complete resection is feasible in either classic or cellular variants of CMN.[1,47–53]

## MULTILOCULAR CYSTIC RENAL TUMOR

***Overview and Pathophysiology.*** Multilocular cystic renal tumor occurs predominantly in boys during infancy and early childhood (3 months to 4 years) and in women during their seventh and eighth decades.[54] Multilocular cystic tumors with fibrous septa that contain mature tubules are called *cystic nephroma*. When the cystic mass has blastemal elements within its septa, it is called a *cystic partially differentiated nephroblastoma*. While multilocular cystic tumors can be sporadic, an association with the *DICER1* mutations is becoming more frequently recognized. *DICER1* mutations are also associated with pleuropulmonary blastoma, multinodular goiter and thyroid cancer, and sex cord-stromal tumors of the gonads.[55]

***Imaging.*** Partially differentiated cystic nephroblastomas and cystic nephromas cannot be distinguished from one another on the basis of imaging features. The multilocular cystic renal tumor may involve the entire kidney or only a small portion of it. Ultrasound is more sensitive than CT for identification of septa (Fig. 115.12). The lesions are typically well-circumscribed masses of multiple anechoic cysts varying in size from a few millimeters to several centimeters. Unilocular tumors are less common but do occur. One characteristic imaging feature is extension of the mass toward the renal pelvis. In a recent series of 44 cystic nephromas, all lesions abutted the renal pelvis and 42% had visible herniation into the renal pelvis on imaging.[55] On contrast-enhanced CT and MRI, the septa enhance but the locules do not enhance, and contrast material does not accumulate within individual locules (Figs. 115.12 and 115.13). Small curvilinear calcifications may rarely be present.[55]

***Treatment.*** Surgical excision generally is curative, and the prognosis is excellent. Local recurrence may occur if the tumor is incompletely excised. Metastases have not been reported. In the setting of *DICER1* mutation, additional imaging to investigate for other phenotypical features, such as pleuropulmonary blastoma, should be considered.[1,54–66]

## RENAL CELL CARCINOMA

***Overview.*** Renal cell carcinoma (RCC) is rare in the first two decades of life and accounts for approximately 5% of all pediatric renal tumors. Increasing evidence indicates that RCC in children differs from adult RCC in biology and behavior. Translocation RCC accounts for most instances of childhood RCC and generally involves the *TFE3* gene on chromosome Xp11.2 and less commonly the *TEFB* gene on chromosome 6p21. Prior chemotherapy currently is the only known risk factor for the development of Xp11 translocation RCC. Children with tuberous sclerosis complex,

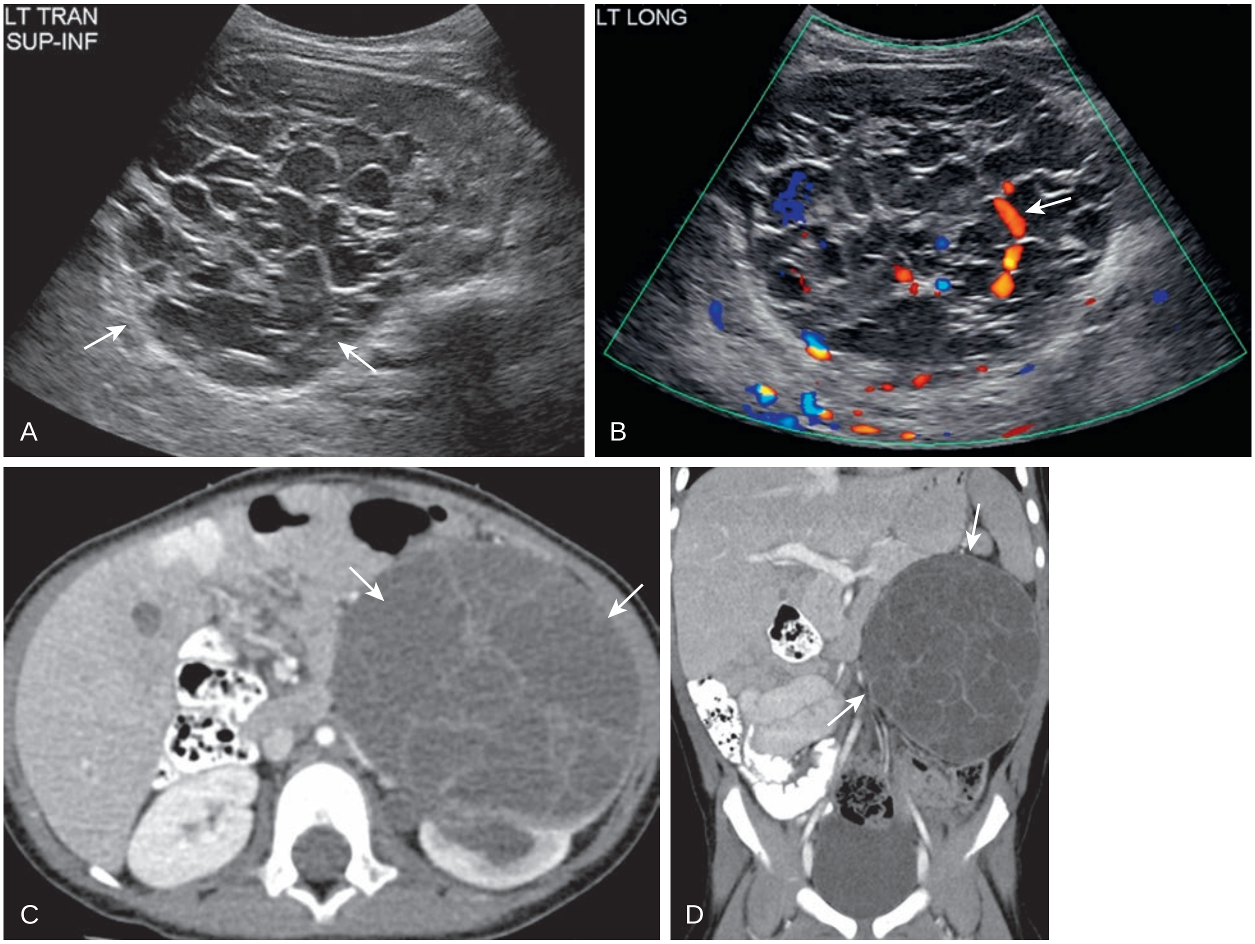

**Figure 115.12. Cystic nephroma.** (A) Transverse gray-scale ultrasound image of the left kidney shows a cystic mass *(arrows)* that contains many septa and locules of varying sizes. (B) Longitudinal color Doppler ultrasound image shows blood flow within the septations *(arrow)*. (C) Axial and (D) coronal contrast-enhanced CT images demonstrate a large hypoattenuating mass *(arrows)* arising from the left kidney with multiple thin septa. There is mild left pelvicaliectasis due to mass effect.

von Hippel-Lindau syndrome, and neuroblastoma appear to be at increased risk for the development of RCC. Wilms tumors outnumber RCCs in the first decade of life by a ratio of 30:1. During the second decade of life, a solid renal mass is equally likely to be an RCC or a Wilms tumor. Clinical presentation includes gross hematuria, flank pain, and a palpable abdominal mass. Fever, hypercalcemia, polycythemia, and hypertension are uncommon.

***Imaging.*** Although an RCC tends to be smaller than a Wilms tumor, its morphology can be similar, and the two can be indistinguishable preoperatively. Ultrasound, CT, and MRI will all show a solid, heterogeneous mass with variable necrosis, hemorrhage, calcification, and cystic degeneration (Fig. 115.14).[67] The tumor invades locally and spreads to retroperitoneal nodes. Vascular invasion into the renal vein and inferior vena cava (IVC) is also possible. Metastases to the lungs, bones, liver, or brain are found in 20% of patients at diagnosis.

***Treatment.*** Staging of RCC uses the Tumor, Node, Metastasis (TNM) system. The standard therapy for RCC in children and adolescents remains radical nephrectomy. RCC is often relatively resistant to systemic chemotherapy or radiotherapy. Nephron-sparing surgery currently is recommended only in adults, although it may be considered in children with predisposing conditions, such as von Hippel-Lindau syndrome. Retroperitoneal lymph node dissection remains controversial in children. Overall survival rates are approximately 50% to 60%, with the best prognosis for localized disease confined to the kidney. Xp11 translocation RCC has the potential to metastasize late, as many as 20 or 30 years after diagnosis.[1,68–79]

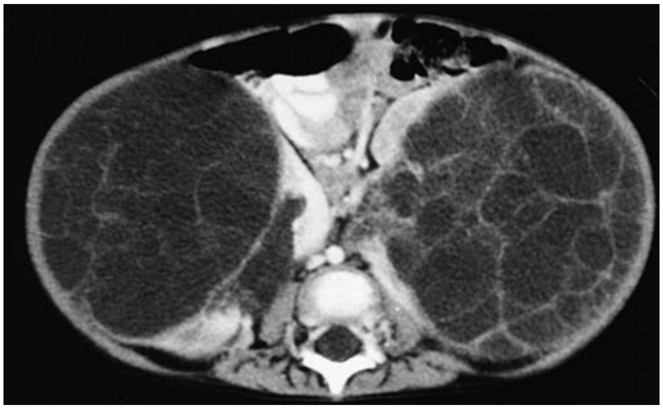

**Figure 115.13. Bilateral, partially differentiated cystic nephroblastoma.** Axial contrast-enhanced CT image shows multiple thin septa coursing through the bilateral renal low-attenuation masses. Both masses bulge into the renal hilar region.

## MEDULLARY CARCINOMA OF THE KIDNEY

***Overview.*** Medullary carcinoma of the kidney was described as a distinct entity in 1995. It is a highly aggressive malignant tumor of epithelial origin that appears almost exclusively in patients with the sickle cell trait or hemoglobin SC disease. The tissue of origin appears to be within the calyceal epithelium, a common region of papillary necrosis in the hemoglobin SC population. The mean age at presentation is 20 years (range, 10–39 years). A male-to-female ratio of 3:1 is seen in patients younger than 25 years. Presenting symptoms include gross hematuria, abdominal or flank pain, a palpable mass, and weight loss. Medullary carcinoma spreads aggressively with metastatic disease to regional lymph nodes and the lungs.

***Imaging.*** Medullary carcinomas develop in the renal medulla, infiltrate the cortex, encase the renal pelvis, invade the lymphatics and vasculature, and have a predilection for the right kidney. Ultrasound, CT, and MRI will all show a centrally located, infiltrative lesion with peripheral caliectasis, reniform enlargement, and peripheral satellite nodules (Fig. 115.15). The tumor has a heterogeneous echotexture on ultrasound and shows heterogeneous enhancement on CT and MRI secondary to intratumoral hemorrhage and extensive necrosis. CT and MRI also excellently depict collecting system involvement and metastatic disease to the regional lymph nodes.

***Treatment.*** Treatment includes a combination of surgery, aggressive chemotherapy, and radiation. The tumor generally responds poorly to therapy, with a mean survival of 15 weeks from diagnosis.[1,80–83]

## RENAL ANGIOMYOLIPOMA

***Overview.*** Angiomyolipomas are lesions consisting of a disordered arrangement of vascular, smooth muscle, and fatty elements. Histologic composition suggests a hamartoma, but currently angiomyolipomas are thought to represent a true neoplasm. In children, angiomyolipomas are rare in the absence of tuberous sclerosis. Angiomyolipomas also are associated with neurofibromatosis and von Hippel-Lindau syndrome. These lesions are usually asymptomatic; however, larger lesions (over 4 cm) are susceptible to spontaneous hemorrhage, resulting in flank or abdominal pain, hematuria, and severe retroperitoneal hemorrhage.

***Imaging.*** The imaging appearance of angiomyolipomas is variable depending on the histologic contents. CT and MRI are diagnostic when macroscopic fat is identified within the lesion,

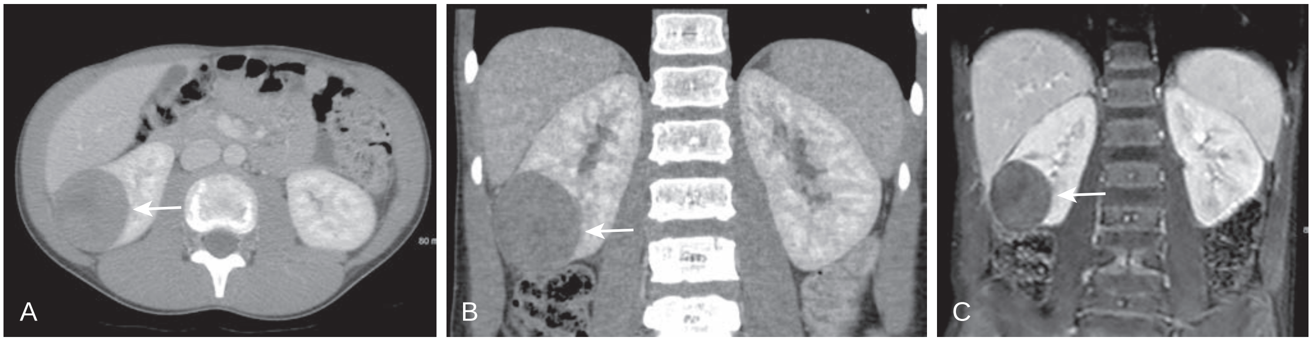

**Figure 115.14. Renal cell carcinoma.** (A) Axial and (B) coronal contrast-enhanced CT images in a 12-year-old boy show a well-circumscribed, mildly heterogeneous mass arising from the lower pole of the right kidney *(arrow)* found to be renal cell carcinoma at histopathology. (C) Coronal T1-weighted postcontrast MR image in the same patient shows the mass *(arrow)* to be hypoenhancing compared with normal renal tissue.

remembering that fat may very rarely be seen in Wilms tumors and RCCs. In addition to traditional T1-weighted MRI and fat suppression techniques, Dixon techniques can be used to definitely show the presence of fat. Fat can also be identified as areas of hyperechogenicity at US. Sporadic lesions are rare and are usually unilateral, while bilateral lesions often are seen in persons with tuberous sclerosis (Fig. 115.16). Angiomyolipomas without visible fat are commonly hypointense on T2-weighted MRI sequences and may be indistinguishable from other solid renal masses at CT and MRI. On angiography, angiomyolipomas demonstrate characteristic tortuous, dilated vessels with aneurysm formation.

***Treatment.*** Lesions larger than 4 cm may be selectively embolized or surgically removed to prevent a life-threatening hemorrhage. Serial imaging to monitor angiomyolipoma size is recommended every 2 to 3 years before puberty and then annually after puberty.[1,84–93]

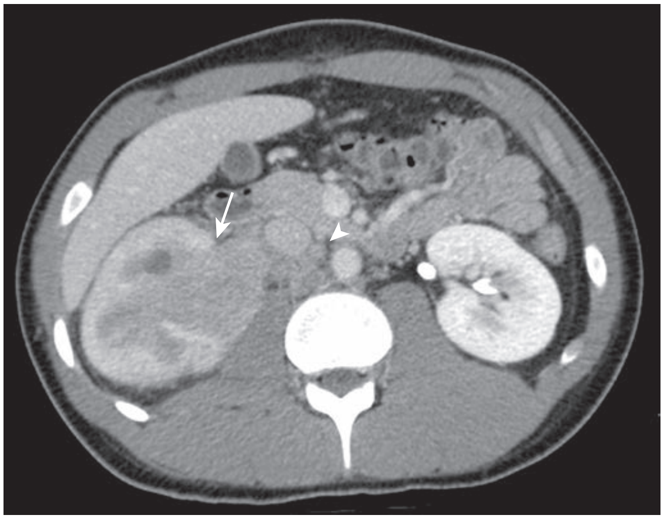

**Figure 115.15. Medullary carcinoma of the kidney.** Axial contrast-enhanced CT image in an 18-year-old young man with sickle cell trait demonstrates an infiltrative, enhancing mass involving the right renal hilum and central portion of the kidney *(arrow)*. There were multiple prominent and mildly enlarged retroperitoneal lymph nodes *(arrowhead)*, and tumor extended into the proximal right ureter.

## RENAL LYMPHOMA

***Overview.*** Lymphomatous involvement of the kidney is due to hematogenous spread or direct extension from retroperitoneal sites. The kidney normally does not contain lymphoid tissue, and for this reason, primary renal lymphoma is rare. In children, non-Hodgkin lymphoma (especially Burkitt lymphoma) is most common. Lymphomatous involvement of the kidney typically does not produce symptoms until late in its course. Flank pain, abdominal pain, hematuria, anemia, weight loss, and a palpable mass are most common.

***Imaging.*** The most common imaging pattern is multiple parenchymal masses distorting the collecting system; less common findings are a solitary renal mass, diffuse infiltration, and isolated perinephric disease. Both CT and MRI are better than sonography for locating renal lesions and identifying extension into adjacent structures. On CT and MRI, multiple round homogeneous and hypoenhancing masses are seen (Fig. 115.17). The findings of perinephric disease include thickening of Gerota fascia, soft tissue nodules, or soft tissue plaques that are typically hypoenhancing relative to normal enhancing renal parenchyma. On sonography, the lesions are typically hypoechoic, with frequent through transmission. Hypoechoic, isoechoic, and hyperechoic subcortical masses all have been described (e-Fig. 115.18). Lymphomatous lesions, however, may be occult or may present as diffuse nephromegaly because of tumor infiltration as the only finding.[1,94–100]

## OSSIFYING RENAL TUMOR OF INFANCY

***Overview.*** Ossifying renal tumor of infancy is an exceedingly rare benign renal mass. The age at presentation ranges from 6 days to 14 months. Hematuria is the presenting symptom. Histologically, the lesion consists of an osteoid core, osteoblasts, and spindle cells.

***Imaging.*** At imaging, ossifying renal tumor of infancy is a small renal mass (usually 2–3 cm) arising from the papillary region of the renal pyramid and extending into the collecting system, with or without evidence of obstruction. Calcifications are typically present, with hyperechogenicity and posterior acoustic shadowing on US, high attenuation on CT, and signal loss on MRI.

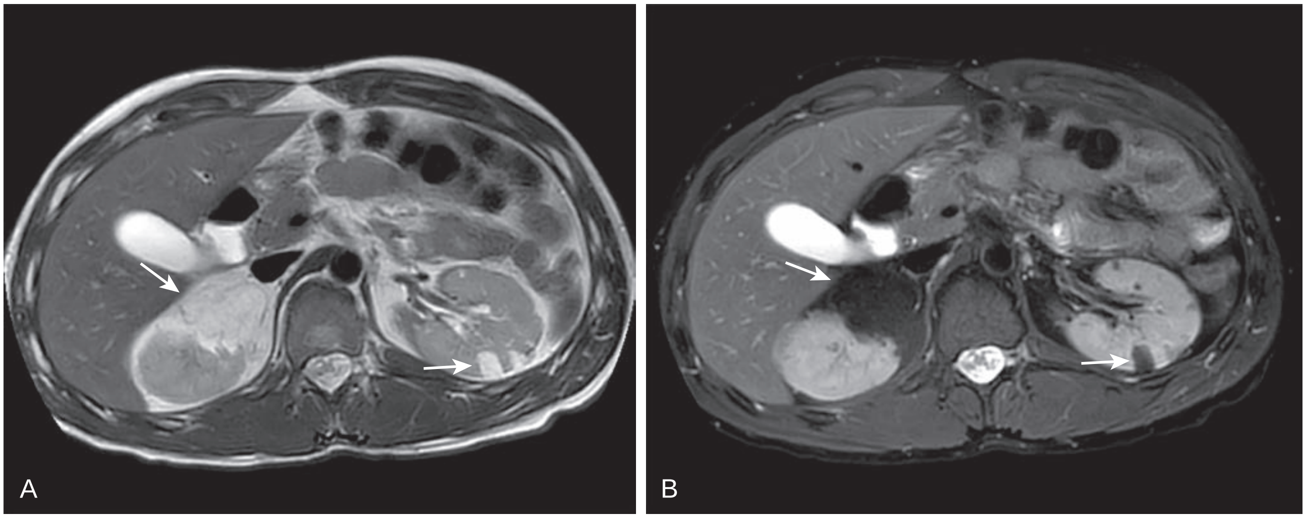

**Figure 115.16. Angiomyolipomas of the kidneys.** (A) Axial T2-weighted MR image without fat saturation in a teenage boy with tuberous sclerosis demonstrates multiple hyperintense masses *(arrows)* in both kidneys. (B) The same lesions all lose signal on a T2-weighted fat-saturated MR image at the same level, confirming the presence of macroscopic fat *(arrows)*.

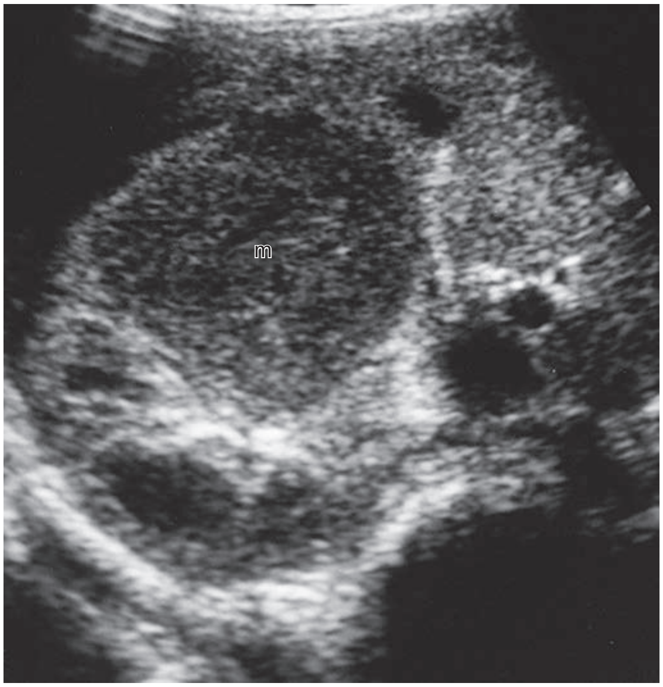

**e-Figure 115.18. Non-Hodgkin lymphoma of the kidney.** Transverse gray-scale ultrasound image of the right kidney demonstrates a hypoechoic mass *(m)* that is replacing the anteromedial portion of the kidney.

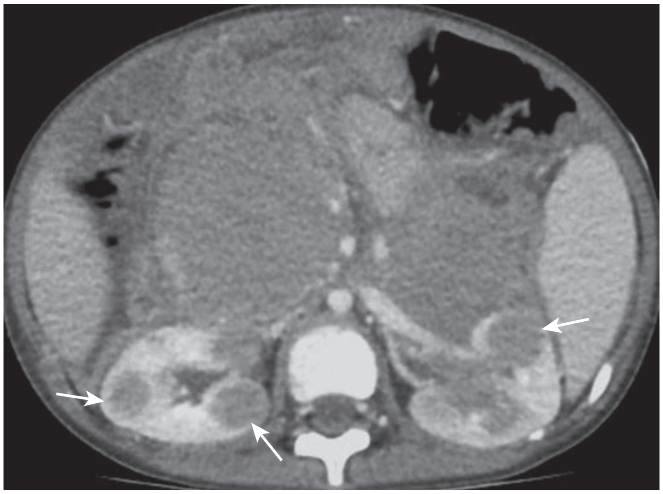

**Figure 115.17. Non-Hodgkin (Burkett) lymphoma of the kidneys.** Axial contrast-enhanced CT image in a 5-year-old boy with abdominal pain shows multiple, bilateral round hypoattenuating renal masses *(arrows)*. There is extensive lymphomatous involvement of the mesentery and omentum as well.

***Treatment.*** The treatment is resection; either complete or partial nephrectomy was performed in the reported cases. The biologic behavior appears to be benign, with no case of malignant spread or postsurgical disease at follow-up.[1,101–103]

## KEY POINTS

- Nephroblastomatosis commonly regresses and resolves spontaneously; however, it may degenerate into a Wilms tumor.
- Children with genetic and syndromic abnormalities associated with nephroblastomatosis should be screened for Wilms tumor by ultrasound.
- The imaging features of clear cell sarcoma of the kidney are similar to those of Wilms tumor, and it has a predilection for bone metastases.
- Rhabdoid tumor of the kidney has the worst prognosis of all of the childhood renal tumors and is associated with primary or metastatic central nervous system lesions.
- CMN is the most common primary renal mass in infants under 6 months of age.
- Multilocular cystic renal tumors occur in two distinct age and gender groups: young boys and adult women.
- RCC in children differs from adult RCC in biology and behavior.
- Life-threatening retroperitoneal hemorrhage is a complication of angiomyolipomas; the risk of hemorrhage increases in lesions that are larger than 4 cm.
- Medullary carcinoma of the kidney is a highly aggressive malignant tumor of epithelial origin that occurs almost exclusively in patients who have sickle cell trait or hemoglobin SC disease.

## SUGGESTED READINGS

Chung EM, Graeber AR, Conran RM. Renal tumors of childhood: radiologic-pathologic correlation part 1. The first decade. *Radiographics*. 2016;36:499–522.

Geller E, Kochan PS. Renal neoplasms of childhood. *Radiol Clin North Am*. 2011;49(4):689–709, vi.

Kaste SC, Dome JS, Babyn PS, et al. Wilms tumor: prognostic factors, staging, therapy and late effects. *Pediatr Radiol*. 2008;38:2–17.

Lowe LH, Isuani BH, Heller RM, et al. Pediatric renal masses: Wilms tumor and beyond. *Radiographics*. 2000;20(6):1585–1603.

Northrup BE, Jokerst CE, Grubb RL, et al. Hereditary renal tumor syndromes: imaging findings and management strategies. *AJR Am J Roentgenol*. 2012;199:1294–1304.

Powis M. Neonatal renal tumours. *Early Hum Dev*. 2010;86(10):607–612.

Sebire NJ, Vujanic GM. Paediatric renal tumours: recent developments, new entities and pathological features. *Histopathology*. 2009;54(5):516–528.

## REFERENCES

Full references for this chapter can be found on www.expertconsult.com.

## REFERENCES

1. Lowe LH, Isuani BH, Heller RM, et al. Pediatric renal masses: Wilms tumor and beyond. *Radiographics*. 2000;20(6):1585–1603.
2. Owens CM, Brisse HJ, Olsen ØE, et al. Bilateral disease and new trends in Wilms tumour. *Pediatr Radiol*. 2008;38(1):30–39.
3. Lonergan GJ, Martínez-León MI, Agrons GA, et al. Nephrogenic rests, nephroblastomatosis, and associated lesions of the kidney. *Radiographics*. 1998;18(4):947–968.
4. Hennigar RA, O'Shea PA, Grattan-Smith JD. Clinicopathologic features of nephrogenic rests and nephroblastomatosis. *Adv Anat Pathol*. 2001;8(5):276–289.
5. Hoyme HE, Seaver LH, Jones KL, et al. Isolated hemihyperplasia (hemihypertrophy): report of a prospective multicenter study of the incidence of neoplasia and review. *Am J Med Genet*. 1998;79:274.
6. Rohrschneider WK, Weirich A, Rieden K, et al. US, CT, and MR imaging characteristics of nephroblastomatosis. *Pediatr Radiol*. 1998;28:435.
7. Hoffer FA. Magnetic resonance imaging of abdominal masses in the pediatric patient. *Semin Ultrasound CT MR*. 2005;26(4):212–223.
8. Gylys-Morin V, Hoffer FA, Kozakewich H, et al. Wilms' tumor and nephroblastomatosis: imaging characteristics at gadolinium-enhanced MR imaging. *Radiology*. 1993;188:517.
9. Cozzi DA, Zani A. Nephron-sparing surgery in children with primary renal tumor: indications and results. *Semin Pediatr Surg*. 2006;15(1):3–9.
10. Beckwith JB. Questions and answers: Wilms' tumor screening. *AJR Am J Roentgenol*. 1995;164:1294.
11. Choyke PL, Siegel MJ, Craft AW, et al. Screening for Wilms' tumor in children with Beckwith-Wiedemann syndrome or idiopathic hemihypertrophy. *Med Pediatr Oncol*. 1999;32:196.
12. Borer JG, Kaefer M, Barnewolt CE, et al. Renal findings on radiological follow-up of patients with Beckwith-Wiedemann syndrome. *J Urol*. 1999;161:235.
13. Perlman EJ, Faria P, Soares A, et al. Hyperplastic perilobar nephroblastomatosis: long-term survival of 52 patients. *Pediatr Blood Cancer*. 2006;46:203.
14. Applegate KE, Ghei M, Perez-Atayde AR. Prenatal detection of a Wilms' tumor. *Pediatr Radiol*. 1999;29:64.
15. Md Zin R, Murch A, Charles A. Pathology, genetics and cytogenetics of Wilms' tumour. *Pathology*. 2011;43(4):302–312.
16. Suzuki K, Miyake H, Tashiro M, et al. Extrarenal Wilms' tumor. *Pediatr Radiol*. 1993;23:149.
17. Smets AM, de Kraker J. Malignant tumors of the kidney: imaging strategy. *Pediatr Radiol*. 2010;40:1010–1018.
18. Kaste SC, Dome JS, Babyn PS, et al. Wilms tumor: prognostic factors, staging, therapy and late effects. *Pediatr Radiol*. 2008;38:2–17.
19. Jadvar H, Connolly LP, Fahey FH, et al. PET and PET/CT in pediatric oncology. *Semin Nucl Med*. 2007;37:316–331.
20. Goske MJ, Mitchell C, Reslan WA. Imaging of patients with Wilms' tumor. *Semin Urol Oncol*. 1999;17:11.
21. Slasky BS, Bar-Ziv J, Freeman AI, et al. CT appearance of involvement of the peritoneum, mesentery and omentum in Wilms' tumor. *Pediatr Radiol*. 1997;27:14.
22. Wootton-Gorges SL, Albano EA, Riggs JM, et al. Chest radiography versus chest CT in the evaluation for pulmonary metastases in patients with Wilms' tumor: a retrospective review. *Pediatr Radiol*. 2000;30:533.
23. Linam LE, Yu X, Calvo-Garcia MA, et al. Contribution of magnetic resonance imaging to prenatal differential diagnosis of renal tumors: report of two cases and review of the literature. *Fetal Diagn Ther*. 2010;28(2):100–108.
24. Gratias EJ, Dome JS. Current and emerging chemotherapy treatment strategies for Wilms tumor in North America. *Paediatr Drugs*. 2008;10(2):115–124.
25. Grundy P, Perlman E, Rosen NS, et al. Current issues in Wilms tumor management. *Curr Probl Cancer*. 2005;29(5):221–260.
26. Ko EY, Ritchey ML. Current management of Wilms' tumor in children. *J Pediatr Urol*. 2009;5(1):56–65.
27. Ehrlich PF, Hamilton TE, Grundy P, et al. The value of surgery in directing therapy for patients with Wilms' tumor with pulmonary disease: a report from the National Wilms' Tumor Study Group (National Wilms' Tumor Study 5). *J Pediatr Surg*. 2006;41:162.
28. Olsen OE, Jeanes AC, Sebire NJ, et al. Changes in computed tomography features following preoperative chemotherapy for nephroblastoma: relation to histopathological classification. *Eur Radiol*. 2004;14:990.
29. Meisel JA, Guthrie KA, Breslow NE, et al. Significance and management of computed tomography detected pulmonary nodules: a report from the National Wilms' Tumor Study Group. *Int J Radiat Oncol Biol Phys*. 1999;44:579.
30. Porteus MH, Narkool P, Neuberg D, et al. Characteristics and outcome of children with Beckwith-Wiedemann syndrome and Wilms' tumor: a report from the National Wilms' Tumor Study Group. *J Clin Oncol*. 2000;18:2026.
31. Hadley GP, Sheik-Gafoor MH. Clear cell sarcoma of the kidney in children: experience in a developing country. *Pediatr Surg Int*. 2010;26(4):345–348.
32. Boo YJ, Fisher JC, Haley MJ, et al. Vascular characterization of clear cell sarcoma of the kidney in a child: a case report and review. *J Pediatr Surg*. 2009;44(10):2031–2036.
33. Hung NA. Congenital "clear cell sarcoma of the kidney." *Virchows Arch*. 2005;446(5):566–568.
34. Ahmed HU, Arya M, Levitt G, et al. Part I: primary malignant non-Wilms' renal tumours in children. *Lancet Oncol*. 2007;8(8):730–737.
35. Ahmed HU, Arya M, Levitt G, et al. Part II: treatment of primary malignant non-Wilms' renal tumours in children. *Lancet Oncol*. 2007;8(9):842–848.
36. Portugal R, Barroca H. Clear cell sarcoma, cellular mesoblastic nephroma and metanephric adenoma: cytological features and differential diagnosis with Wilms tumour. *Cytopathology*. 2008;19(2):80–85.
37. Argani P, Perlman EJ, Breslow NE, et al. Clear cell sarcoma of the kidney: a review of 351 cases from the National Wilms' Tumor Study Group Pathology Center. *Am J Surg Pathol*. 2000;24:4.
38. Glass RBJ, Davidson AJ, Fernbach SK. Clear cell sarcoma of the kidney: CT, sonographic, and pathological correlation. *Radiology*. 1991;180:715.
39. Chang CJ, Yeh ML, Chen CC. Rhabdoid tumor of the kidney with spontaneous rupture: case report and review of literature. *Pediatr Surg Int*. 2008;24(4):451–453.
40. Winger DI, Buyuk A, Bohrer S, et al. Radiology-Pathology Conference: rhabdoid tumor of the kidney. *Clin Imaging*. 2006;30(2):132–136.
41. Luo CC, Lin JN, Jaing TH, et al. Malignant rhabdoid tumour of the kidney occurring simultaneously with a brain tumour: a report of two cases and review of the literature. *Eur J Pediatr*. 2002;161(6):340–342.
42. Amar AM, Tomlinson G, Green DM, et al. Clinical presentation of rhabdoid tumors of the kidney. *J Pediatr Hematol Oncol*. 2001;23(2):105–108.
43. Isaacs H Jr. Fetal and neonatal rhabdoid tumor. *J Pediatr Surg*. 2010;45(3):619–626.
44. Agrons GA, Kingsman KD, Wagner BJ, et al. Rhabdoid tumor of the kidney in children: a comparative study of 21 cases. *AJR Am J Roentgenol*. 1997;168:447.
45. Chung CJ, Lorenzo R, Rayder S, et al. Rhabdoid tumors of the kidney in children: CT findings. *AJR Am J Roentgenol*. 1995;164:697.
46. Tomlinson GE, Breslow NE, Dome J, et al. Rhabdoid tumor of the kidney in The National Wilms' tumor study: age at diagnosis as a prognostic factor. *J Clin Oncol*. 2005;23:7641.
47. Bayindir P, Guillerman RP, Hicks MJ, et al. Cellular mesoblastic nephroma (infantile renal fibrosarcoma): institutional review of the clinical, diagnostic imaging, and pathologic features of a distinctive neoplasm of infancy. *Pediatr Radiol*. 2009;39(10):1066–1074.
48. England RJ, Haider N, Vujanic GM, et al. Mesoblastic nephroma: a report of the United Kingdom Children's Cancer and Leukaemia Group (CCLG). *Pediatr Blood Cancer*. 2011;56(5):744–748.
49. Chaudry G, Perez-Atayde AR, Ngan BY, et al. Imaging of congenital mesoblastic nephroma with pathological correlation. *Pediatr Radiol*. 2009;39(10):1080–1086.
50. Goldberg J, Liu P, Smith C. Congenital mesoblastic nephroma presenting with hemoperitoneum and shock. *Pediatr Radiol*. 1994;24:54.
51. Hartman DS, Lim Lesar MS, Madewell JE, et al. Mesoblastic nephroma: radiologic-pathologic correlation of 20 cases. *AJR Am J Roentgenol*. 1981;136:69.
52. Schlesinger AE, Rosenfield NS, Castle VP, et al. Congenital mesoblastic nephroma metastatic to the brain: a report of two cases. *Pediatr Radiol*. 1995;25:S73.
53. Willert JR, Feuser J, Beckwith JB. Congenital mesoblastic nephroma: a rare cause of perinatal anemia. *J Pediatr*. 1999;134:248.
54. Agrons GA, Wagner BJ, Davidson AJ, et al. Multilocular cystic renal tumor in children: radiologic-pathologic correlation. *Radiographics*. 1995;15:653.
55. Cajaiba MM, Khanna G, Smith EA, et al. Pediatric cystic nephromas: distinctive imaging features and frequent DICER1 mutations. *Hum Pathol*. 2016;48:81–87.

56. Bouhafs A, Cherradi N, Lamaalmi N, et al. An unusual case of multilocular cystic nephroma with prominent renal pelvis involvement. *Int J Urol*. 2006;13(4):436–438.
57. Sodhi KS, Suri S, Samujh R, et al. Case report: bilateral multilocular cystic nephromas: a rare occurrence. *Br J Radiol*. 2005;78(929):450–452.
58. Broecker B. Non-Wilms' renal tumors in children. *Urol Clin North Am*. 2000;27(3):463–469, ix.
59. MacLennan GT, Ross J, Cheng L. Cystic partially differentiated nephroblastoma. *J Urol*. 2010;183(4):1585–1586.
60. van den Hoek J, de Krijger R, van de Ven K, et al. Cystic nephroma, cystic partially differentiated nephroblastoma and cystic Wilms' tumor in children: a spectrum with therapeutic dilemmas. *Urol Int*. 2009;82(1):65–70.
61. Baker JM, Viero S, Kim PC, et al. Stage III cystic partially differentiated nephroblastoma recurring after nephrectomy and chemotherapy. *Pediatr Blood Cancer*. 2008;50(1):129–131.
62. Puvaneswary M, Macintosh J, Cassey J. Cystic partially differentiated nephroblastoma. *Australas Radiol*. 2006;50(3):255–257.
63. Blakely ML, Shamberger RC, Norkool P, et al. Outcome of children with cystic partially differentiated nephroblastoma treated with or without chemotherapy. *J Pediatr Surg*. 2003;38(6):897–900.
64. Rajangam K, Narasimhan KL, Trehan A, et al. Partial nephrectomy in cystic partially differentiated nephroblastoma. *J Pediatr Surg*. 2000;35(3):510–512.
65. Hartman DS, Davis CJ, Sanders RC, et al. The multiloculated renal mass: considerations and differential features. *Radiographics*. 1987;7:29.
66. Madewell JE, Goldman SM, Davis CJ, et al. Multilocular cystic nephroma: a radiographic-pathologic correlation of 58 patients. *Radiology*. 1983;146:309.
67. Downey RT, Dillman JR, Ladino-Torres MF, et al. CT and MRI appearances and radiologic staging of pediatric renal cell carcinoma. *Pediatr Radiol*. 2012;42(4):410–417, quiz 513-4.
68. Spreafico F, Collini P, Terenziani M, et al. Renal cell carcinoma in children and adolescents. *Expert Rev Anticancer Ther*. 2010;10(12):1967–1978.
69. Ross H, Argani P. Xp11 translocation renal cell carcinoma. *Pathology*. 2010;42(4):369–373.
70. Armah HB, Parwani AV. Xp11.2 translocation renal cell carcinoma. *Arch Pathol Lab Med*. 2010;134(1):124–129.
71. Sausville JE, Hernandez DJ, Argani P, et al. Pediatric renal cell carcinoma. *J Pediatr Urol*. 2009;5(4):308–314.
72. Selle B, Furtwängler R, Graf N, et al. Population-based study of renal cell carcinoma in children in Germany, 1980-2005: more frequently localized tumors and underlying disorders compared with adult counterparts. *Cancer*. 2006;107(12):2906–2914.
73. Silberstein J, Grabowski J, Saltzstein SL, et al. Renal cell carcinoma in the pediatric population: results from the California Cancer Registry. *Pediatr Blood Cancer*. 2009;52(2):237–241.
74. Schultz TD, Sergi C, Grundy P, et al. Papillary renal cell carcinoma: report of a rare entity in childhood with review of the clinical management. *J Pediatr Surg*. 2011;46(6):e31–e34.
75. Allison JW, James CA, Figarola MS. Pediatric case of the day: renal cell carcinoma in a child with tuberous sclerosis. *Radiographics*. 1999;19:1388.
76. Donnelly LF, Rencken IO, Shardell K, et al. Renal cell carcinoma after therapy for neuroblastoma. *AJR Am J Roentgenol*. 1996;167:915.
77. Fenton DS, Taub JW, Amundson GM, et al. Renal cell carcinoma occurring in a child 2 years after chemotherapy for neuroblastoma. *AJR Am J Roentgenol*. 1993;161:165.
78. Kabala JE, Shield J, Duncan A. Renal cell carcinoma in childhood. *Pediatr Radiol*. 1992;22:203.
79. Cook A, Lorenzo AJ, Salle JL, et al. Pediatric renal cell carcinoma: single institution 25-year case series and initial experience with partial nephrectomy. *J Urol*. 2006;175(4):1456–1460, discussion 1460.
80. Davidson AJ, Choyke PL, Hartman DS, et al. Renal medullary carcinoma associated with sickle cell trait: radiologic findings. *Radiology*. 1995;195:83.
81. Davis CJ, Mostofi FK, Sesterhenn IA. Renal medullary carcinoma: the seventh sickle cell nephropathy. *Am J Surg Pathol*. 1995;19:1.
82. Kalyanpur A, Schwartz DS, Fields JM, et al. Renal medulla carcinoma in a white adolescent. *AJR Am J Roentgenol*. 1997;169:1037.
83. Pickhardt PJ. Renal medullary carcinoma: an aggressive neoplasm in patients with sickle cell trait. *Abdom Imaging*. 1998;23:531.
84. Kim JY, Kim JK, Kim N, et al. CT histogram analysis: differentiation of angiomyolipoma without visible fat from renal cell carcinoma at CT imaging. *Radiology*. 2008;246(2):472–479.
85. Silverman SG, Mortele KJ, Tuncali K, et al. Hyperattenuating renal masses: etiologies, pathogenesis, and imaging evaluation. *Radiographics*. 2007;27(4):1131–1143.
86. Kim JK, Kim SH, Jang YJ, et al. Renal angiomyolipoma with minimal fat: differentiation from other neoplasms at double-echo chemical shift FLASH MR imaging. *Radiology*. 2006;239(1):174–180.
87. Winterkorn EB, Daouk GH, Anupindi S, et al. Tuberous sclerosis complex and renal angiomyolipoma: case report and review of the literature. *Pediatr Nephrol*. 2006;21(8):1189–1193.
88. Casper KA, Donnelly LF, Chen B, et al. Tuberous sclerosis complex: renal imaging findings. *Radiology*. 2002;225(2):451–456.
89. Carter TC, Angtuaco TL, Shah HR. Ultrasound case of the day: large, bilateral angiomyolipomas of the kidneys with tuberous sclerosis. *Radiographics*. 1999;19:555.
90. Ewalt DH, Sheffield E, Sparagana SP, et al. Renal lesion growth in children with tuberous sclerosis complex. *J Urol*. 1998;160:141.
91. Henske EP. Tuberous sclerosis and the kidney: from mesenchyme to epithelium, and beyond. *Pediatr Nephrol*. 2005;20:854.
92. Kim JK, Park SY, Shon JH, et al. Angiomyolipoma with minimal fat: differentiation from renal cell carcinoma at biphasic helical CT. *Radiology*. 2004;230:677.
93. Tchaprassian Z, Mognato G, Paradias G, et al. Renal angiomyolipoma in children: diagnostic difficulty in 3 patients. *J Urol*. 1998;159:1654.
94. Pedrosa I, Sun MR, Spencer M, et al. MR imaging of renal masses: correlation with findings at surgery and pathologic analysis. *Radiographics*. 2008;28(4):985–1003.
95. Zhang J, Pedrosa I, Rofsky NM. MR techniques for renal imaging. *Radiol Clin North Am*. 2003;41(5):877–907.
96. Weinberger E, Rosenbaum DM, Pendergrass TW. Renal involvement in children with lymphoma: comparison of CT with sonography. *AJR Am J Roentgenol*. 1990;155:347.
97. Sheth S, Ali S, Fishman E. Imaging of renal lymphoma: patterns of disease with pathologic correlation. *Radiographics*. 2006;26(4):1151–1168.
98. Urban BA, Fishman EK. Renal lymphoma: CT patterns with emphasis on helical CT. *Radiographics*. 2000;20(1):197–212.
99. Fernbach SK, Glass RBJ. Uroradiographic manifestations of Burkitt's lymphoma in children. *J Urol*. 1986;135:986.
100. Hartman DS, Davis CJ, Goldman SM, et al. Renal lymphoma: radiologic-pathologic correlation of 21 cases. *Radiology*. 1982;144:759.
101. Höglund HH, Kellner MW, Körber F, et al. Ossifying renal tumor of infancy (ORTI)—a rare diagnosis. *Klin Padiatr*. 2011;223(3):178–179.
102. Vazquez JL, Barnewolt CE, Shamberger RC, et al. Ossifying renal tumor of infancy presenting as a palpable abdominal mass. *Pediatr Radiol*. 1998;28(6):454–457.
103. Chatten J, Cromie WJ, Duckett JW. Ossifying tumor of infantile kidney: report of two cases. *Cancer*. 1980;45(3):609–612.

# 116 Vascular Conditions

Robert G. Wells

## RENOVASCULAR HYPERTENSION

***Overview.*** Approximately 5% to 10% of children and adolescents with severe hypertension have an underlying renal vascular lesion. In children younger than 5 years, up to 80% of clinically significant hypertension is due to renovascular disease. There are myriad developmental and acquired causes of renovascular hypertension (Box 116.1). A complication related to umbilical artery catheterization is the most common cause of renovascular hypertension in neonates. In older children, renal arterial dysplasia is the most common cause.[1–5]

***Imaging.*** Renal size asymmetry on sonography is an important sign of possible renovascular hypertension, as the affected kidney often is small. The examination should include assessment of the renal vessels and aorta with gray-scale and color Doppler images, as well as spectral Doppler of the renal arteries and suprarenal aorta. In children, the most specific diagnostic sonographic findings for renovascular hypertension are visualization of a stenosis on color Doppler images (with turbulent flow and aliasing) and a tardus-parvus spectral Doppler pattern distal to the stenosis (slow systolic acceleration and diminished peak systolic velocity, often associated with a decreased resistive index) (Fig. 116.1). Objective criteria for poststenotic blood flow alterations include acceleration index <300 cm/sec[2] and acceleration time >70 msec; there is commonly flattening of the systolic peak. Measurements at the stenotic segment show a renal artery-to-aorta peak systolic velocity ratio >3.5 and a peak systolic velocity of >200 cm/s.[6–11]

The most useful scintigraphic technique for detection of renovascular hypertension involves the evaluation of renal function without and with the use of an angiotensin-converting enzyme inhibitor, usually captopril or enalaprilat. Tc-99m mercaptoacetyltriglycine (MAG3) is the optimal imaging agent for this study. In the presence of renovascular disease, imaging in conjunction with angiotensin-converting enzyme inhibitor therapy typically shows diminished perfusion, diminished initial uptake, and poor parenchyma clearance of the affected kidney. Comparative imaging in the absence of the medication shows improved function (Fig. 116.2).[12] However, children often have segmental arterial or smaller disease, making perfusion changes difficult to detect, and thus scintigraphy has a limited role in children.

Computed tomographic angiography (CTA) and magnetic resonance angiography (MRA) are noninvasive techniques for visualization of renal vascular anatomy. Upon administration of contrast material, global and regional alterations in kidney perfusion and function also can be assessed. Both of these modalities have limited sensitivity for detecting intrarenal stenoses.

Transcatheter angiography remains the gold standard technique for detection and characterization of renal arterial stenosis and should be considered when noninvasive tests are nondiagnostic, or when there is a clinical suspicion of small vessel disease. In general, >50% narrowing of the renal arterial diameter is hemodynamically significant. The presence of enlarged collateral pathways is an additional indicator of significant renal artery stenosis. Transcatheter renal vein renin sampling is useful in selected cases of suspected renal hypertension (e-Fig. 116.3).[13–15]

## RENAL ARTERY DYSPLASIA

***Overview.*** Renal artery dysplasia (commonly referred to as *fibromuscular dysplasia*, or FMD) is the most common cause of renal artery stenosis in children (Fig. 116.4). Hypertension is the typical presenting feature; other potential clinical findings include headaches and an abdominal bruit. Subcategorization of FMD is based on the layer of the arterial wall that is involved.[16–22]

### Primary Intimal Fibroplasia

Primary intimal fibroplasia is characterized by circumferential accumulation of collagen subintimally and within the internal elastic membrane. This form is the most common cause of renal artery stenosis in children. Imaging shows a smooth, bandlike, tubular, or funnel-shaped stenosis that usually involves the distal two-thirds of the renal artery or a branch vessel.

### Perimedial or Subadventitial Fibrodysplasia

Perimedial or subadventitial fibrodysplasia involves collagen deposition in the outer border of the media over a variable length of the renal artery. Angiography typically shows severe long-segment beaded narrowing of the renal artery. This disease occurs almost exclusively in girls older than 10 years of age. About 15% of patients have bilateral involvement.

### Fibromuscular Hyperplasia

Fibromuscular hyperplasia is an extremely rare vasculopathy. Concentric thickening of the renal arterial wall is due to proliferating smooth muscle and fibrous tissue. Angiographically, this lesion appears as a smooth stenosis of the renal artery or its branches. The appearance often is indistinguishable from that of intimal fibroplasia.

### Medial Fibroplasia

Medial fibroplasia is rare in children. Alternating areas of focal thinning of the internal elastic membrane and focal collagenous thickening of the medial muscular layer are present. Angiographically, there is a “string-of-beads” appearance, typically involving the distal two-thirds of the main renal artery and its branches. Areas of dilation between stenoses are usually greater in caliber than the normal renal artery.

## NEUROFIBROMATOSIS TYPE 1

The most common vascular pathology in patients with neurofibromatosis type 1 is stenosis of the aorta or a large branch vessel. Occasionally, an aneurysm occurs. In the kidney, a small-vessel mesodermal dysplasia also can occur. Arterial stenosis in these patients is often long and tapered.[22–24]

## TAKAYASU ARTERITIS

Takayasu arteritis is a rare idiopathic chronic inflammatory vasculitis. Hypertension due to stenosis of a renal artery or the suprarenal aorta is common. Computed tomography (CT) and magnetic resonance imaging (MRI) features of Takayasu arteritis include luminal narrowing, mural thickening, adherent thrombus, and mural calcification of the aorta, pulmonary arteries, and major aortic branch vessels. With active disease, the thickened vascular wall has prominent contrast enhancement at CT and MRI, and

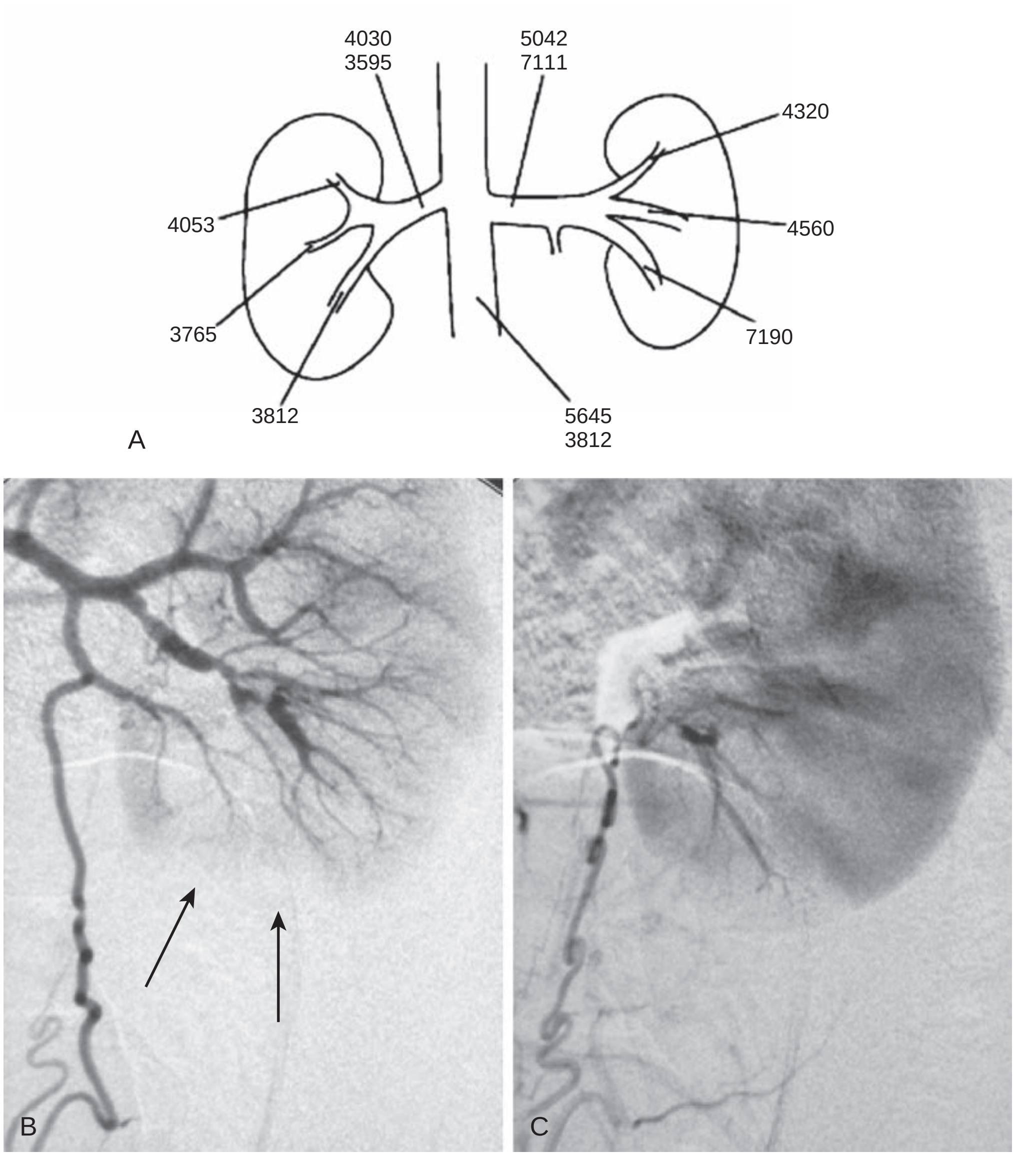

**e-Figure 116.3. Hypertension in an 11-year-old girl.** (A) Map of renal vein renin activity shows that the hypertension is driven by a focus in the left lower pole. (B) Arterial phase angiography shows complex segmental stenoses, an area of delayed perfusion owing to a "missing vessel" *(arrows)*, and a prominent collateral ureteric artery. (C) Capillary phase angiography shows that the ureteric artery collateral reconstitutes the "missing vessel," completing the nephrogram. *(From Roebuck DJ. Paediatric interventional radiology.* Imaging*. 2001;13:302–320.)*

### BOX 116.1 Causes of Renovascular Hypertension in Children

**Renal Artery (Fibromuscular) Dysplasia**

**Inflammatory Disease**

- Vasculitis (e.g., Takayasu arteritis)
- Moyamoya disease
- Irradiation

**Genetic Disorders**

- Williams syndrome
- Neurofibromatosis type 1
- Feuerstein-Mims syndrome (Schimmelpenning syndrome)
- Degos disease
- Marfan syndrome

**Atherosclerosis**

- Hyperlipidemias

**Vascular Anomaly**

- Renal arteriovenous malformation
- Renal artery aneurysm
- Renal artery hypoplasia

**Thromboembolism**

- Umbilical artery catheterization
- Neonate of diabetic mother
- Sepsis/dehydration

**Renal Transplantation**

- Rejection
- Arterial narrowing

**Other**

- Congenital rubella
- Compression by mass
- Congenital fibrous band
- Posttraumatic cause
- Retroperitoneal fibrosis

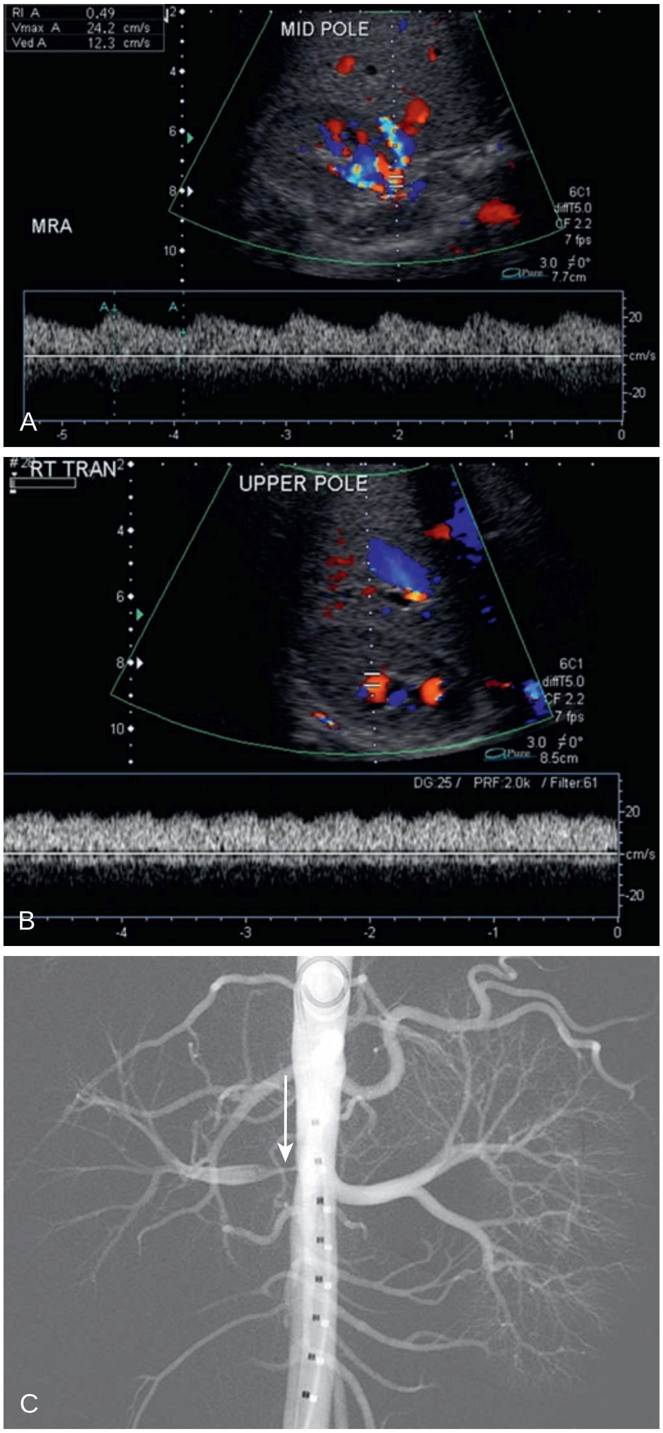

**Figure 116.1. Renal artery stenosis.** (A and B) Spectral Doppler evaluation of intrarenal arteries distal to a severe right main renal artery stenosis in a child with renal arterial dysplasia shows tardus parvus and nearly monophasic waveforms. (C) Catheter angiography confirms severe stenosis of the main renal artery *(arrow)*.

may appear T2 hyperintense; periarterial inflammation may also be seen (Fig. 116.5).[25–27]

## MIDDLE AORTIC SYNDROME

Middle aortic (or midaortic) syndrome is an often progressive vascular disorder that involves the midthoracic through abdominal segments of the aorta. Most affected individuals also have narrowing of major visceral branches, including the renal arteries. Imaging shows diffuse narrowing or even absence of the thoracoabdominal segment of the aorta and the major branch vessels (e-Fig. 116.6 and Fig. 116.7). If renal artery narrowing is severe, collateral flow to the kidneys usually occurs via ureteral, adrenal, and gonadal arteries that fill from lower intercostal vessels.[28,29] Middle aortic syndrome appearance may be caused by a congenital malformation, developmental arterial dysplasia, neurofibromatosis type 1, vasculitis (including radiation-induced), and rarely Williams syndrome.

## RENOVASCULAR TRAUMA

***Overview.*** Potential renal arterial injuries include intimal disruption, main renal artery avulsion, branch vessel transection, false aneurysm, and arteriovenous fistula. Most renal injuries in children result from blunt trauma; penetrating injuries are uncommon. The intimal layer is most susceptible to a stretching injury because it is less elastic than the media and adventitia. An intimal tear can precipitate dissection, luminal occlusion, or thrombosis. Stretching injury also can cause spasm of the renal artery without a tear. With severe, rapid motion of the kidney, vascular avulsion can occur. Penetrating injuries and iatrogenic mechanisms such as a needle biopsy can lead to an intrarenal arteriovenous fistula or pseudoaneurysm.[30]

***Imaging.*** Globally deficient parenchymal contrast enhancement is an important CT indicator of possible disruption, thrombosis, or spasm of the main renal artery. Contrast enhancement in the

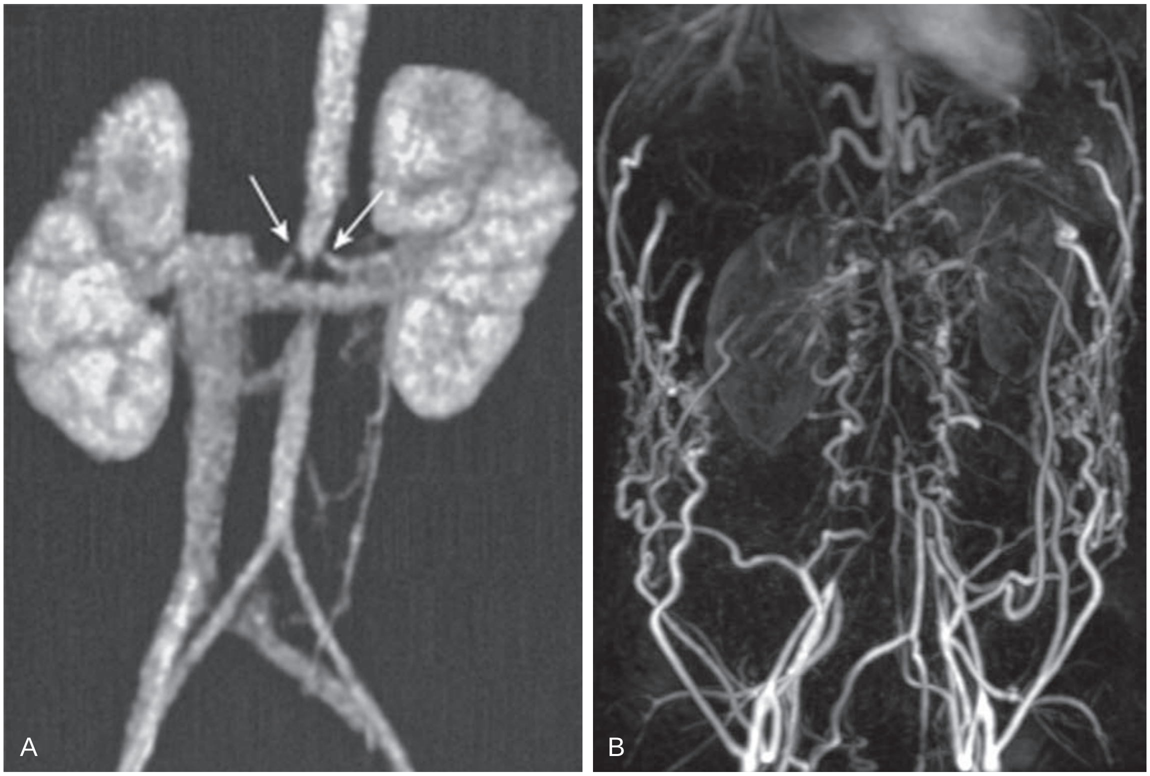

**e-Figure 116.6. Middle aortic syndrome and hypertension.** (A) Volume-rendered CTA image of a child with middle aortic syndrome reveals severe narrowing of the renal artery origins *(arrows)* and infrarenal portion of the abdominal aorta. (B) Maximum intensity projection MRA image from another child demonstrates nonvisualization of the entire abdominal aorta with reconstitution of lower extremity blood flow from extensive paraspinous and body wall collateral vessels.

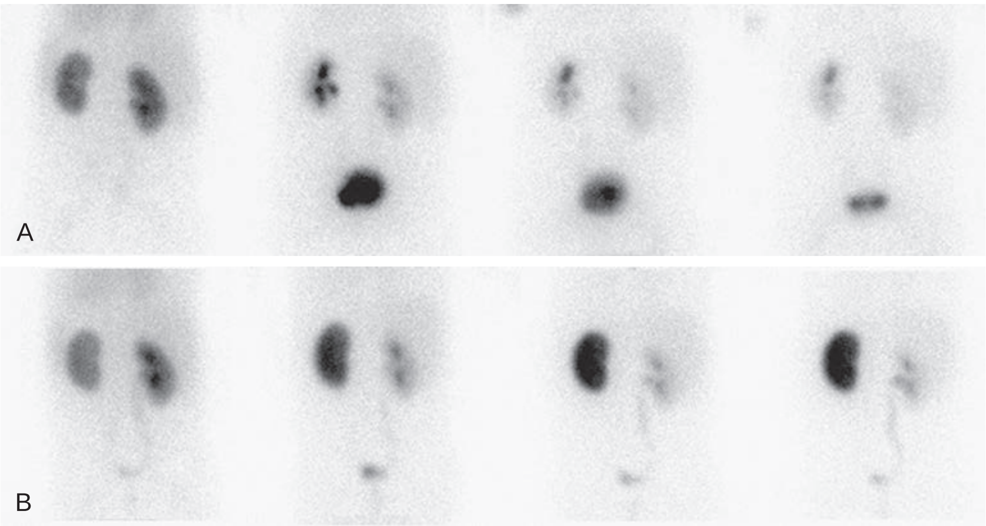

**Figure 116.2. Renovascular hypertension and angiotensin-converting enzyme (ACE) inhibition scintigraphy.** (A) Renogram shows normal uptake and excretion from both kidneys. (B) Renogram after administration of an ACE inhibitor shows marked radiopharmaceutical retention in the left kidney, indicating renal artery stenosis. *(Courtesy Douglas F. Eggli, MD, Hershey, PA.)*

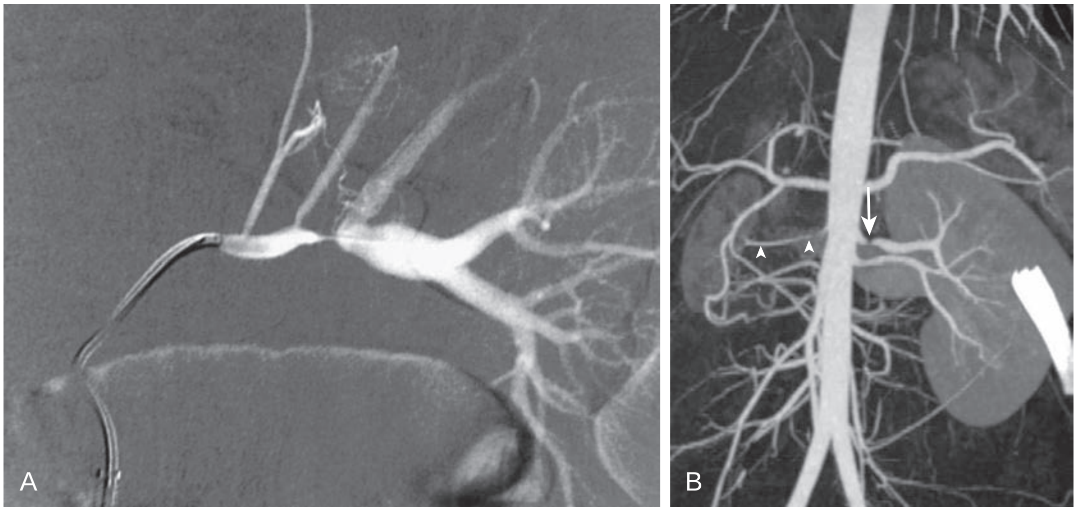

**Figure 116.4. Renal artery stenosis.** (A) Selective renal arteriogram of a 12-year-old girl with hypertension due to primary intimal fibroplasia shows severe stenosis and poststenotic dilatation of the left main renal artery. (B) Contrast-enhanced CT coronal maximum intensity projection image shows two left renal arteries; the superior artery has a severe focal stenosis proximally *(arrow)*. The right main renal artery is diffusely narrowed *(arrowheads)*, and the right kidney is atrophic.

periphery of an ischemic kidney (the "cortical rim sign") is an indicator of acute renal arterial occlusion, although this does not occur until at least several hours after the event. A localized renal infarction due to traumatic occlusion of an intrarenal vessel or embolic phenomenon results in a wedge-shaped or rounded area of absent enhancement, often with sharp margins. With partial main renal artery occlusion, the nephrogram intensity is diminished. Arterial phase CT is useful to detect occlusion, pseudoaneurysm, or active extravasation of the renal artery.[31–33]

## ANEURYSM

***Overview.*** Renal artery aneurysms are rare in childhood. Classifying features include location (extraparenchymal vs. intraparenchymal) and morphology (saccular, fusiform, dissecting, or false). Some pediatric renal artery aneurysms are idiopathic; others are due to infection (e.g., mycotic aneurysms), renal artery stenosis (often related to neurofibromatosis type 1 or FMD), or autoimmune vasculitis (e.g., polyarteritis nodosa). Aneurysms of the renal artery also can occur in patients with Kawasaki disease and Ehlers-Danlos syndrome. The most common clinical manifestations of a renal artery aneurysm are hematuria and flank pain.[34,35]

***Imaging.*** Renal artery aneurysms can be single or multiple. Most are saccular. Thrombus or calcification occasionally is present within the aneurysm (Fig. 116.8). Most are detectable with sonography, CTA, or MRA. Conventional angiography sometimes is required for the detection and characterization of small lesions, such as in patients with polyarteritis nodosa.[11,36]

## ARTERIOVENOUS MALFORMATION AND FISTULA

About three-quarters of renal arteriovenous fistulas are iatrogenic or related to trauma. Congenital arteriovenous malformations of the kidney are rare. Hematuria and a bruit are common clinical

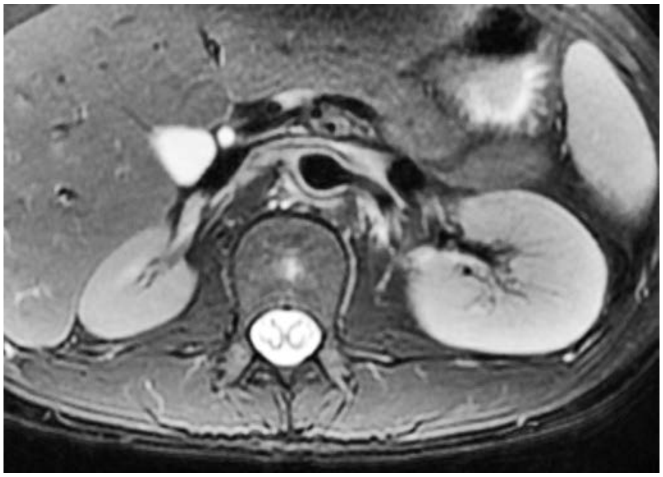

**Figure 116.5. Takayasu arteritis.** Axial T2-weighted fat-saturated magnetic resonance (MR) image of a child with hypertension shows abnormally increased signal in the walls of the abdominal aorta and renal arteries due to active inflammation. The right renal artery is narrowed, and the right kidney is atrophic. Periarterial signal hyperintensity is also due to inflammation.

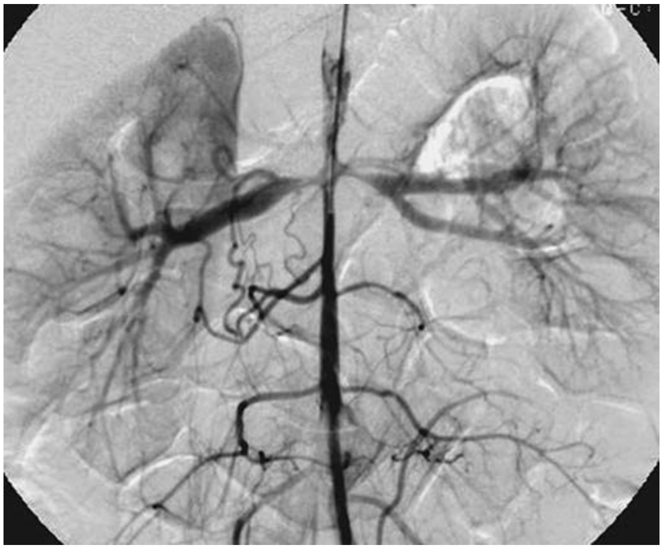

**Figure 116.7. Middle aortic syndrome.** Aortogram of a 3-month-old boy with severe hypertension reveals a hypoplastic abdominal aorta and bilateral proximal renal artery stenoses.

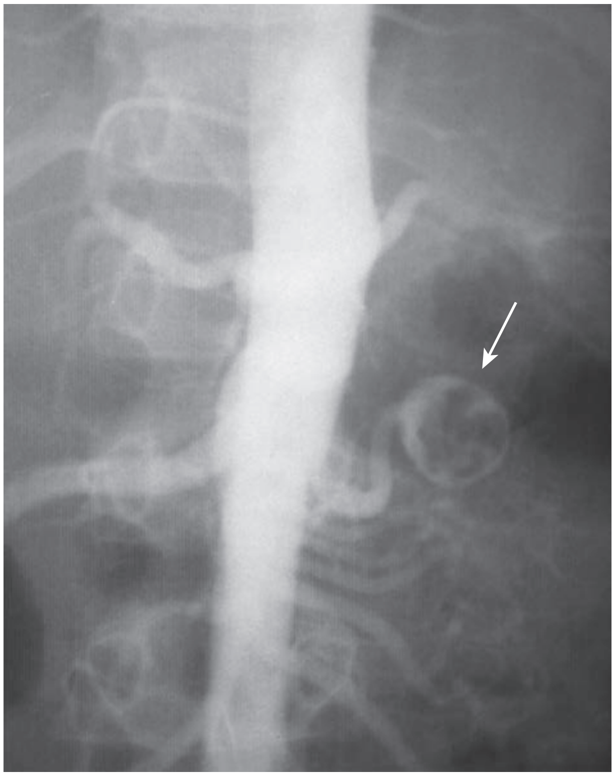

**Figure 116.8. Renal artery aneurysm.** Abdominal aortogram shows a partially thrombosed saccular aneurysm *(arrow)* of the left renal artery.

findings with both of these lesions. A large shunt can cause high-output heart failure. Imaging studies show a focal abnormal direct communication between an artery and a vein, whereas shunting in an arteriovenous malformation occurs through a nidus of abnormal vessels. Supplying and draining vessels are enlarged. Doppler analysis shows turbulent flow and arterial velocity in the draining veins. Angiography shows rapid flow through the lesion.[37–41]

## THROMBOSIS, EMBOLISM, AND INFARCTION

***Overview.*** Thromboembolic disease of the renal arteries is uncommon in children. Predisposing conditions include sepsis (endocarditis), prolonged hypotension, severe dehydration, congenital heart disease, trauma, and hypercoagulable disorders. In neonates, the most common cause is an umbilical arterial catheter. Infants of diabetic mothers are at increased risk for renal arterial thrombosis. In older children, acute occlusion of a major renal artery causes flank pain, nausea, vomiting, fever, and hematuria. Small emboli or minor thrombosis may be asymptomatic, although hypertension is a common complication.[42]

***Imaging.*** In the acute phase of renal artery thromboembolism, sonography is normal or shows nonspecific renal enlargement and cortical hyperechogenicity. Color or power Doppler evaluation sometimes reveals global, focal, or multifocal perfusion deficits. Blood flow within the capsule may be increased. Careful evaluation of the main renal artery sometimes demonstrates a clot, as well as abnormal arterial waveforms. If the main renal artery remains patent, the resistive index often is elevated.

CTA and MRA of patients with renal arterial thromboembolic disease may reveal filling defects or narrowing of the renal artery. With global renal infarction, renal parenchymal enhancement and contrast material excretion are mostly absent. One or more wedge-shaped enhancement defects may occur in the presence of segmental renal infarction. In about 50% of patients with renal infarction, a thin prominently enhancing rim is visible at the peripheral margin (e-Fig. 116.9).[11,33,40,43]

## DISEASES OF THE INTRARENAL ARTERIES

### Renal Vasculitis

The kidney is a relatively common site of involvement in various forms of vasculitis. The most widely used classification of vasculitis is based on the size of the predominantly involved vessels. Takayasu arteritis is an example of large vessel vasculitis. Polyarteritis nodosa and Kawasaki disease predominantly involve medium-sized vessels. The presence or absence of antineutrophil cytoplasmic antibodies (ANCAs) allows subcategorization of the small vessel vasculitides. Henoch-Schönlein purpura (HSP) is ANCA negative; ANCA-positive vasculitides that can affect the kidney include granulomatosis with polyangiitis (Wegener granulomatosis) and microscopic polyarteritis. Small-vessel vasculitis also can occur in

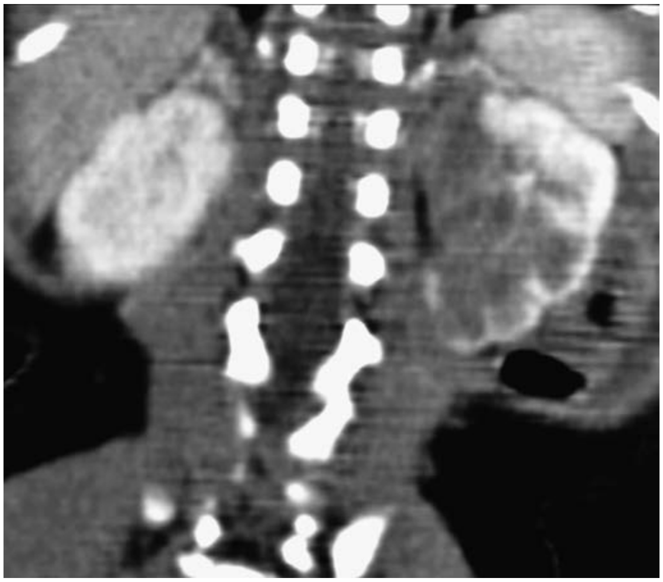

**e-Figure 116.9. Acute renal artery thrombosis in a neonate.** Coronal reformatted contrast-enhanced CT shows deficient enhancement in most of the left kidney. Note preserved enhancement of a thin peripheral rim of cortex.

association with various infectious diseases, such as Rocky Mountain spotted fever, human immunodeficiency virus, hepatitis B, and tuberculosis.[44–48]

## Polyarteritis Nodosa

Polyarteritis nodosa is a rare idiopathic focal segmental necrotizing vasculitis. Renal involvement occurs in about half of affected children. Clinical manifestations of kidney involvement include hematuria, proteinuria, and hypertension. Imaging studies of the kidneys may show manifestations of focal or multifocal renal ischemia. Intraparenchymal or perirenal hemorrhage can occur due to aneurysm rupture. Catheter arteriography reveals small (2–3 mm) aneurysms, typically located at the bifurcations of interlobular or arcuate arteries. Small intrarenal vessels are irregular and tortuous because of vascular and perivascular inflammation (Fig. 116.10).[49–51]

## Granulomatosis with Polyangiitis (Wegener Granulomatosis) and Microscopic Polyarteritis

Granulomatosis with polyangiitis (Wegener granulomatosis) is a rare necrotizing vasculitis that predominantly affects the respiratory tract. Up to 80% of patients have manifestations of renal involvement, such as hematuria, proteinuria, and diminished glomerular filtration rate. Similar clinical findings occur in patients with microscopic polyarteritis, although respiratory system involvement is lacking. Diagnostic imaging findings of kidney involvement with these two vasculitides are similar to those of polyarteritis nodosa. Foci of parenchymal scarring may occur as the result of ischemia. Rupture of a small-vessel aneurysm can lead to intrarenal or perirenal hemorrhage.[52–54]

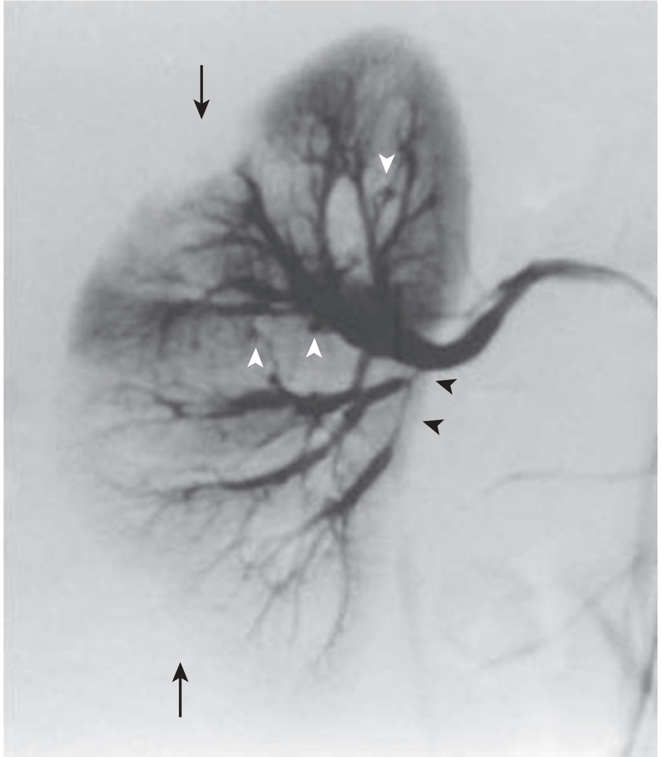

**Figure 116.10. Polyarteritis nodosa.** This patient had an established diagnosis of polyarteritis nodosa for 1 year and new-onset hypertension. Selective right renal angiogram shows segmental narrowing of the intrarenal branch to the lower pole *(black arrowheads)*, small saccular aneurysms at vessel branch points *(white arrowheads)*, and patchy perfusion deficits in the upper and lower poles *(arrows)*.

## Systemic Lupus Erythematosus

Up to 75% of children with systemic lupus erythematosus have clinical manifestations of renal involvement. The major pathologic manifestation is thickening of the basement membrane as a result of focal glomerulonephritis; inflammatory narrowing of interlobular arteries can also occur. In the absence of renal failure, the kidneys often appear normal on imaging studies. Mild nephromegaly is common. Diffuse or multifocal hyperechogenicity of the renal parenchyma may be present on sonography. Elevation of the resistive index on spectral Doppler evaluation may be predictive of worsening renal function.[55,56]

## Hemolytic-Uremic Syndrome

***Overview.*** Hemolytic-uremic syndrome is the most common cause of acute renal failure in early childhood. The pathogenesis involves bacterial infection (commonly *Escherichia coli*) and endothelial cell damage within glomeruli and renal arterioles. In most cases of hemolytic-uremic syndrome, anemia, fever, vomiting, bloody diarrhea, and abdominal discomfort develop in an otherwise healthy infant. Affected children beyond infancy are usually around 3 years of age. The child may become critically ill, with signs and symptoms that include pallor, irritability, seizures, heart failure, hypertension, gastrointestinal bleeding, and oliguria. Acute renal failure usually lasts for 1 to 4 weeks, with subsequent slow improvement[57]; a minority of patients develop end-stage renal disease.

***Imaging.*** Early in the disease, sonography is normal or shows minimal nephromegaly. Subsequent abnormally increased parenchymal echogenicity usually is most prominent in the glomerular and subcortical regions. The degree of cortical echogenicity correlates with the severity of the illness. Spectral Doppler shows diminished blood flow. In most patients, the kidney returns to a normal size as the disease resolves, but more severe injury can lead to atrophy and/or nephrocalcinosis.[58–60]

## Henoch-Schönlein Purpura

***Overview.*** HSP is a hypersensitivity vasculitis that affects small vessels and is an important cause of nephritis in children. The clinical tetrad includes a purpuric rash, arthralgias, abdominal pain, and glomerulonephritis. Between 20% to 30% of patients with HSP have hematuria, and 30% to 70% have proteinuria. Clinical signs of renal involvement may follow or coincide with the appearance of purpura, but they rarely antedate the skin findings.[61–64]

***Imaging.*** Sonography may show normal or bilaterally enlarged kidneys. Hyperechogenicity of the renal cortex is usually diffuse, and the medullary pyramids remain hypoechoic. Renal cortical hyperechogenicity diminishes as the acute disease regresses. Occasionally, cross-sectional imaging studies show an intramural hematoma of the bladder wall or ureter. Ureteral fibrosis is a rare complication. Imaging of the bowel may reveal mural thickening and small bowel intussusceptions.

## Sickle Cell Disease

***Overview.*** Stasis of red blood cells within the renal medulla is common in patients with sickle cell disease. Recurrent episodes of medullary ischemia lead to alterations in papillary morphology, sometimes with progression to papillary necrosis. Cortical hypertrophy can occur.[65,66]

***Imaging.*** Intravenous urography and CT may show calyceal blunting and prominent papillae with broad, deep calyces. The collecting system often is distorted (e-Fig. 116.11). In some patients, papillary necrosis is evident. Nephromegaly, usually bilateral, is common. Recurrent infarction and subsequent fibrosis eventually may lead to renal scarring and atrophy.[67,68]

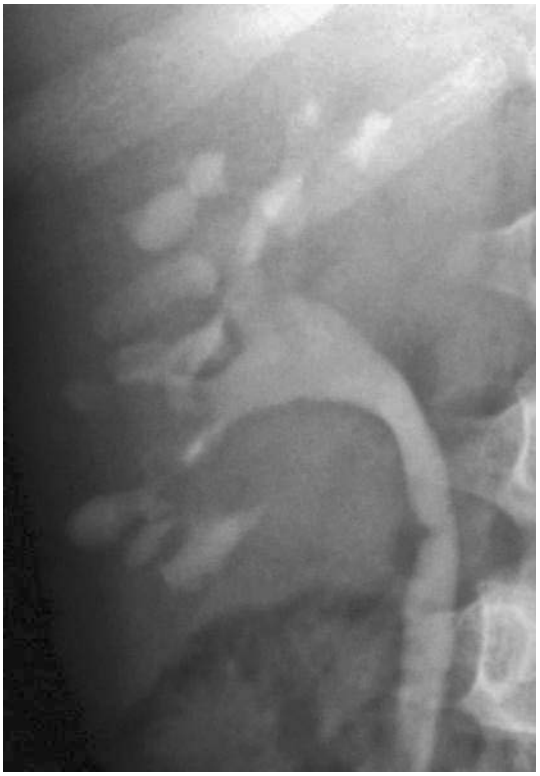

**e-Figure 116.11. Sickle cell disease.** Intravenous urogram of a 13-year-old child with sickle cell disease shows calyceal dilation and collecting system distortion.

Renal sonography typically shows mild diffuse enlargement, hyperechogenicity, and loss of corticomedullary differentiation (Fig. 116.12). A perirenal hematoma can occur as a complication of renal infarction. Doppler sonography may detect renovascular disease. MRI shows decreased cortical signal intensity relative to the medulla on T1-weighted and T2-weighted images due to iron deposition in the renal cortex (Fig. 116.13).[69,70]

## RENAL VEIN THROMBOSIS

***Overview.*** Renal vein thrombosis (RVT) is the most common renal vascular abnormality of neonates. Most affected infants have a predisposing systemic abnormality, such as dehydration, sepsis, polycythemia, or maternal diabetes mellitus. Small intrarenal vessels are the initial or only site of thrombosis in many children with RVT. Propagation of a central venous catheter–related inferior vena cava clot is an additional potential mechanism. RVT in older patients can occur as a complication of nephrotic syndrome, glomerulonephritis, a hypercoagulable state, trauma, retroperitoneal tumor, or renal transplantation. Typical clinical manifestations of RVT include nephromegaly, signs of renal insufficiency, hematuria, and hypertension.[71]

***Imaging.*** The typical sonographic features of RVT are abnormal parenchymal echogenicity and loss of corticomedullary differentiation (Fig. 116.14). In some patients, interlobular echogenic streaks are present. Interstitial hemorrhage occasionally leads to parenchymal hyperechogenicity. Elevation of the arterial resistive index occurs as a result of venous outflow obstruction (Fig. 116.15). Narrowing of the systolic peak also is common. Careful sonographic evaluation of the renal veins sometimes reveals an echogenic clot; however, the absence of a clot within the major renal veins does

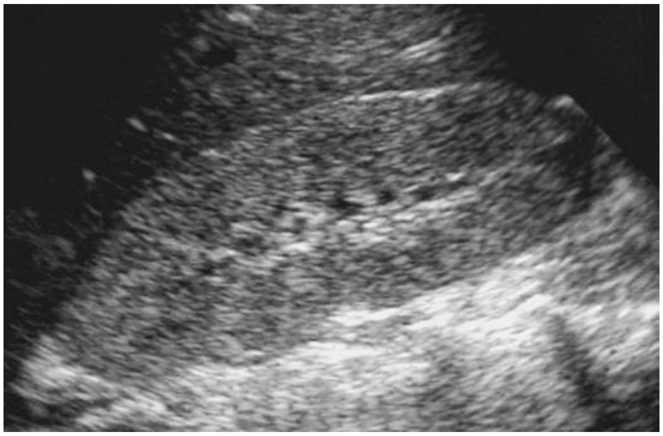

**Figure 116.12. Sickle cell disease.** Longitudinal sonogram of a 15-year-old boy with sickle cell disease shows hyperechogenicity of the kidney and absent corticomedullary differentiation.

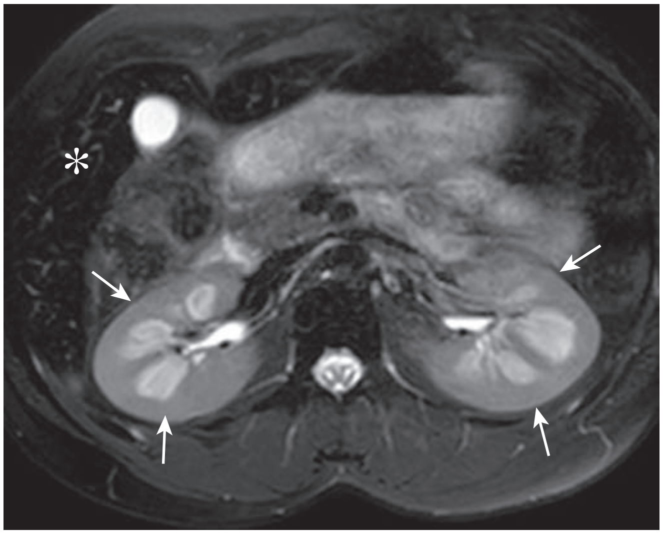

**Figure 116.13. Sickle cell disease.** Axial T2-weighted fat-saturated MR image shows abnormal signal hypointensity of the renal cortices *(arrows)* due to hemolysis and iron deposition. The liver is also markedly hypointense due to the presence of iron *(asterisk)*.

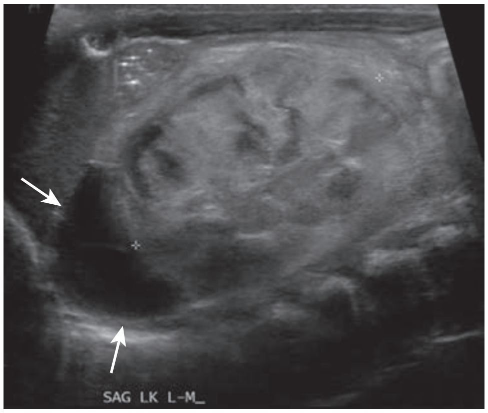

**Figure 116.14. Renal vein thrombosis.** Longitudinal sonogram from a neonate with renal vein thrombosis shows an enlarged, echogenic, heterogeneous left kidney with loss of corticomedullary differentiation. A hypoechoic collection superior to the kidney is due to concomitant adrenal hemorrhage *(arrows)*.

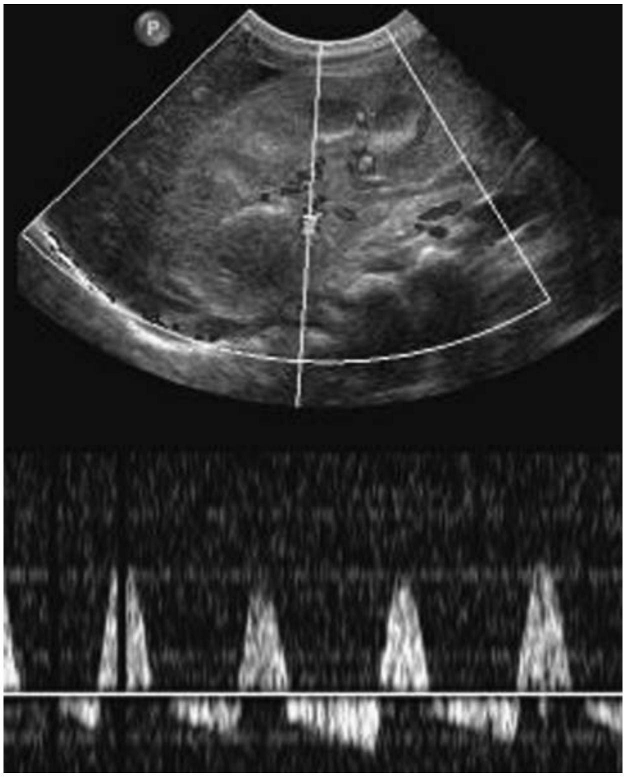

**Figure 116.15. Renal vein thrombosis.** Longitudinal sonogram of this 2-day-old infant shows an enlarged and echogenic kidney. A highly resistive pattern of intrarenal arterial flow is present with reversal of diastolic blood flow.

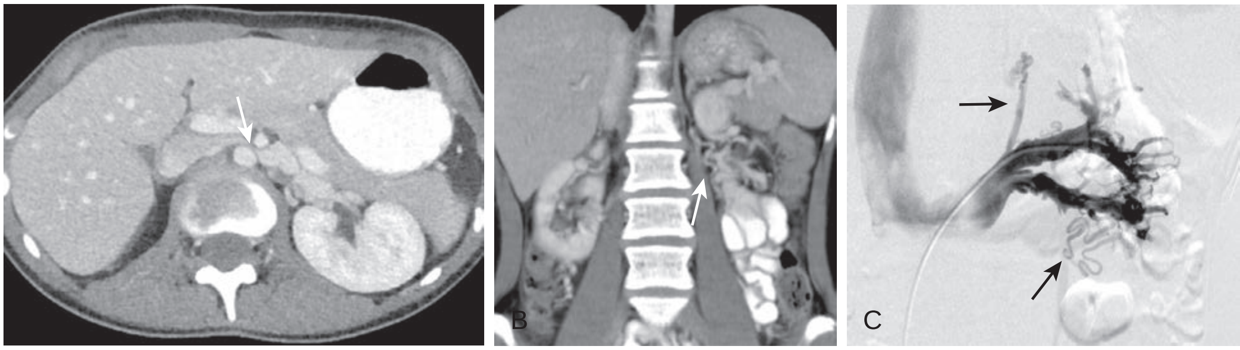

**Figure 116.17. Nutcracker syndrome.** (A) Axial contrast-enhanced CT image from a 17-year-old girl with hematuria and left flank pain shows narrowing of the left renal vein as it passes between the abdominal aorta and superior mesenteric artery *(arrow)*. (B) Coronal CT image shows multiple collateral veins in the left renal hilar region *(arrow)*. (C) Catheter venography shows enlargement of the left renal vein and multiple venous collateral vessels *(arrows)*.

not exclude the diagnosis of small-vessel RVT. Doppler evaluation of the main renal vein shows absent or monophasic flow.[72–74]

***Treatment and Follow-up.*** Therapy of RVT is supportive and directed toward treatment of the underlying cause. Renal scintigraphy during the acute phase provides prognostic information; mild compromise of uptake and excretion indicates a good prognosis (e-Fig. 116.16). Within a few weeks of onset of RVT, the affected kidney decreases in size. In some patients, progression to global atrophy occurs. Follow-up radiography or CT occasionally demonstrates a reticular pattern of calcification within the intrarenal veins; this finding is essentially pathognomonic of previous RVT.

## NUTCRACKER SYNDROME

***Overview.*** The nutcracker syndrome is clinically symptomatic venous hypertension of the left kidney due to compression of the left renal vein between the aorta and superior mesenteric artery (or narrowing of a retroaortic left renal vein). The most common clinical findings are hematuria and flank pain. Renal vein-to-gonadal vein reflux can lead to pelvic congestion syndrome in females and varicocele in males.

***Imaging.*** CT and MRI show abrupt narrowing of the aortomesenteric portion of the left renal vein and acute angulation of the superior mesenteric artery relative to the aorta (<35 degrees); prominent collateral veins may also be present (Fig. 116.17). Doppler shows elevated velocity of the narrowed segment (suggested criteria: peak systolic velocity >5 times that at the renal hilum). Clinically significant narrowing is suggested by sonographic demonstration of reduction of the AP diameter of the renal vein by ≥3 times that of the vein diameter at the renal hilum in the supine position or by >5 times after standing for ≥15 minutes.[11,75]

### KEY POINTS

- Sonography, including Doppler evaluation, is the most appropriate initial imaging technique for most children with suspected renovascular pathology.
- Renal arterial dysplasia is the most common cause of renal arterial stenosis in children. Renal artery thromboembolism in infants often is related to an umbilical artery catheter.
- Hemolytic-uremic syndrome is the most common cause of acute renal failure in childhood.
- RVT is the most common neonatal renovascular abnormality.

## SUGGESTED READINGS

Al-Katib S, Shetty M, Jafri SM, et al. Radiologic assessment of native renal vasculature: a multimodality review. *Radiographics*. 2017;37(1):136–156.
Cakar N, Ozcakar ZB, Soy D, et al. Renal involvement in childhood vasculitis. *Nephron Clin Pract*. 2008;108(3):c202–c206.
Castelli PK, Dillman JR, Smith EA, et al. Imaging of renin-mediated hypertension in children. *AJR Am J Roentgenol*. 2013;200(6):W661–W672.
Lau KK, Stoffman JM, Williams S, et al. Neonatal renal vein thrombosis: review of the English-language literature between 1992 and 2006. *Pediatrics*. 2007;120(5):e1278–e1284.
Olin JW, Sealove BA. Diagnosis, management, and future developments of fibromuscular dysplasia. *J Vasc Surg*. 2011;53(3):826–836, e821.
Tullus K, Brennan E, Hamilton G, et al. Renovascular hypertension in children. *Lancet*. 2008;371(9622):1453–1463.

## REFERENCES

Full references for this chapter can be found on www.expertconsult.com.

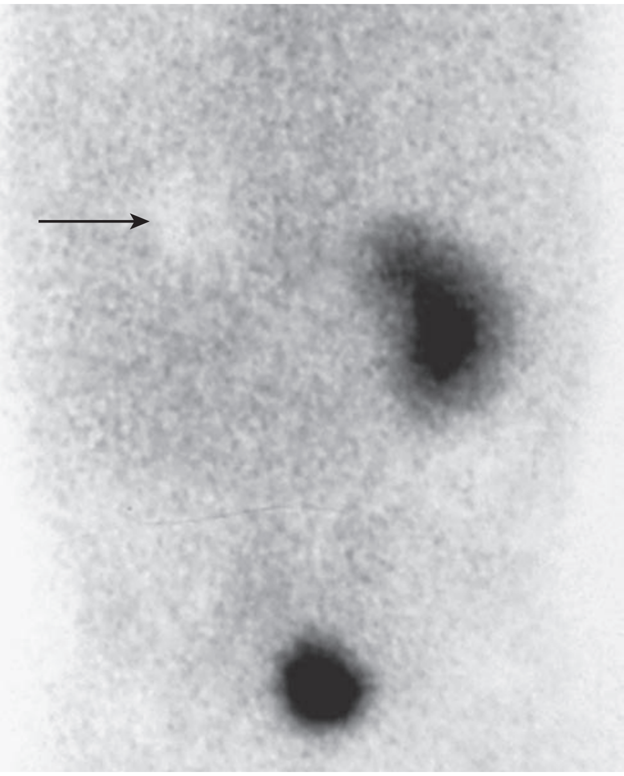

**e-Figure 116.16. Renal vein thrombosis.** A posterior technetium-99m diethylenetriaminepentaacetic acid (DTPA) scintigraphic image of an infant with left renal vein thrombosis shows absent left renal function. An oval suprarenal photopenic focus *(arrow)* is a result of concomitant adrenal hemorrhage.

## REFERENCES

1. Estepa R, Gallego N, Orte L, et al. Renovascular hypertension in children. *Scand J Urol Nephrol*. 2001;35(5):388–392.
2. Hiner LB, Falkner B. Renovascular hypertension in children. *Pediatr Clin North Am*. 1993;40(1):123–140.
3. Mentser M. Diagnosis and treatment of hypertension in children. *Pediatr Clin North Am*. 1982;29(4):933–945.
4. Tullus K, Brennan E, Hamilton G, et al. Renovascular hypertension in children. *Lancet*. 2008;371(9622):1453–1463.
5. Roth CG, Spottswood SE, Chan JC, et al. Evaluation of the hypertensive infant: a rational approach to diagnosis. *Radiol Clin North Am*. 2003;41(5):931–944.
6. Radermacher J, Chavan A, Schaffer J, et al. Detection of significant renal artery stenosis with color Doppler sonography: combining extrarenal and intrarenal approaches to minimize technical failure. *Clin Nephrol*. 2000;53(5):333–343.
7. Voiculescu A, Heusch A, Duppers P, et al. Duplex ultrasound findings before and after surgery in children and adolescents with renovascular hypertension. *Ultrasound Med Biol*. 2014;40(12):2786–2793.
8. Brun P, Kchouk H, Mouchet B, et al. Value of Doppler ultrasound for the diagnosis of renal artery stenosis in children. *Pediatr Nephrol*. 1997;11(1):27–30.
9. Riccabona M, Lobo ML, Papadopoulou F, et al. ESPR uroradiology task force and ESUR paediatric working group: imaging recommendations in paediatric uroradiology, part IV: Minutes of the ESPR uroradiology task force mini-symposium on imaging in childhood renal hypertension and imaging of renal trauma in children. *Pediatr Radiol*. 2011;41(7): 939–944.
10. Lee HY, Grant EG. Sonography in renovascular hypertension. *J Ultrasound Med*. 2002;21(4):431–441.
11. Al-Katib S, Shetty M, Jafri SM, et al. Radiologic assessment of native renal vasculature: a multimodality review. *Radiographics*. 2017; 37(1):136–156.
12. Abdulsamea S, Anderson P, Biassoni L, et al. Pre- and postcaptopril renal scintigraphy as a screening test for renovascular hypertension in children. *Pediatr Nephrol*. 2010;25(2):317–322.
13. Visrutaratna P, Srisuwan T, Sirivanichai C. Pediatric renovascular hypertension in Thailand: CT angiographic findings. *Pediatr Radiol*. 2009;39(12):1321–1326.
14. Vo NJ, Hammelman BD, Racadio JM, et al. Anatomic distribution of renal artery stenosis in children: implications for imaging. *Pediatr Radiol*. 2006;36(10):1032–1036.
15. Falesch LA, Foley WD. Computed tomograpy angiography of the renal circulation. *Radiol Clin North Am*. 2016;54(1):71–86.
16. Olin JW, Sealove BA. Diagnosis, management, and future developments of fibromuscular dysplasia. *J Vasc Surg*. 2011;53(3):826–836 e821.
17. Sabharwal R, Vladica P, Coleman P. Multidetector spiral CT renal angiography in the diagnosis of renal artery fibromuscular dysplasia. *Eur J Radiol*. 2007;61(3):520–527.
18. Willoteaux S, Faivre-Pierret M, Moranne O, et al. Fibromuscular dysplasia of the main renal arteries: comparison of contrast-enhanced MR angiography with digital subtraction angiography. *Radiology*. 2006;241(3):922–929.
19. Lewis S, Kadian-Dodov D, Bansal A, et al. Multimodality imaging of fibromuscular dysplasia. *Abdom Radiol (NY)*. 2016;41(10):2048–2060.
20. Green R, Gu X, Kline-Rogers E, et al. Differences between the pediatric and adult presentation of fibromuscular dysplasia: results from the US Registry. *Pediatr Nephrol*. 2016;31(4):641–650.
21. Bolen MA, Brinza E, Renapurkar RD, et al. Screening CT angiography of the aorta, visceral branch vessels, and pelvic arteries in fibromuscular dysplasia. *JACC Cardiovasc Imaging*. Sep 16 2016.
22. Srinivasan A, Krishnamurthy G, Fontalvo-Herazo L, et al. Spectrum of renal findings in pediatric fibromuscular dysplasia and neurofibromatosis type 1. *Pediatr Radiol*. 2011;41(3):308–316.
23. Booth C, Preston R, Clark G, et al. Management of renal vascular disease in neurofibromatosis type 1 and the role of percutaneous transluminal angioplasty. *Nephrol Dial Transplant*. 2002;17(7):1235–1240.
24. Oderich GS, Sullivan TM, Bower TC, et al. Vascular abnormalities in patients with neurofibromatosis syndrome type I: clinical spectrum, management, and results. *J Vasc Surg*. 2007;46(3):475–484.
25. Cakar N, Yalcinkaya F, Duzova A, et al. Takayasu arteritis in children. *J Rheumatol*. 2008;35(5):913–919.
26. McCulloch M, Andronikou S, Goddard E, et al. Angiographic features of 26 children with Takayasu's arteritis. *Pediatr Radiol*. 2003;33(4):230–235.
27. Nastri MV, Baptista LP, Baroni RH, et al. Gadolinium-enhanced three-dimensional MR angiography of Takayasu arteritis. *Radiographics*. 2004;24(3):773–786.
28. Sethna CB, Kaplan BS, Cahill AM, et al. Idiopathic mid-aortic syndrome in children. *Pediatr Nephrol*. 2008;23(7):1135–1142.
29. Adams WM, John PR. US demonstration and diagnosis of the midaortic syndrome. *Pediatr Radiol*. 1998;28(6):461–463.
30. Knudson MM, Harrison PB, Hoyt DB, et al. Outcome after major renovascular injuries: a Western trauma association multicenter report. *J Trauma*. 2000;49(6):1116–1122.
31. Vu M, Anderson SW, Shah N, et al. CT of blunt abdominal and pelvic vascular injury. *Emerg Radiol*. 2010;17(1):21–29.
32. Dayal M, Gamanagatti S, Kumar A. Imaging in renal trauma. *World J Radiol*. 2013;5(8):275–284.
33. Ambesh P, Lal H. Renal cortical rim sign. *Abdom Imaging*. 2015; 40(7):2914–2915.
34. Callicutt CS, Rush B, Eubanks T, et al. Idiopathic renal artery and infrarenal aortic aneurysms in a 6-year-old child: case report and literature review. *J Vasc Surg*. 2005;41(5):893–896.
35. Davis FM, Eliason JL, Ganesh SK, et al. Pediatric nonaortic arterial aneurysms. *J Vasc Surg*. 2016;63(2):466–476 e461.
36. Sarkar R, Coran AG, Cilley RE, et al. Arterial aneurysms in children: clinicopathologic classification. *J Vasc Surg*. 1991;13(1):47–56, discussion 56-47.
37. Renowden SA, Blethyn J, Cochlin DL. Duplex and colour flow sonography in the diagnosis of post-biopsy arteriovenous fistulae in the transplant kidney. *Clin Radiol*. 1992;45(4):233–237.
38. Riccabona M, Schwinger W, Ring E. Arteriovenous fistula after renal biopsy in children. *J Ultrasound Med*. 1998;17(8):505–508.
39. Cho KJ, Stanley JC. Non-neoplastic congenital and acquired renal arteriovenous malformations and fistulas. *Radiology*. 1978;129(2):333–343.
40. Sidhu R, Lockhart ME. Imaging of renovascular disease. *Semin Ultrasound CT MR*. 2009;30(4):271–288.
41. Kawashima A, Sandler CM, Ernst RD, et al. CT evaluation of renovascular disease. *Radiographics*. 2000;20(5):1321–1340.
42. Kavaler E, Hensle TW. Renal artery thrombosis in the newborn infant. *Urology*. 1997;50(2):282–284.
43. Johnson PT, Fishman EK. Computed tomography angiography of the renal and mesenteric vasculature: concepts and applications. *Semin Roentgenol*. 2011;46(2):115–124.
44. Cakar N, Ozcakar ZB, Soy D, et al. Renal involvement in childhood vasculitis. *Nephron Clin Pract*. 2008;108(3):c202–c206.
45. Maritati F, Iannuzzella F, Pavia MP, et al. Kidney involvement in medium- and large-vessel vasculitis. *J Nephrol*. 2016;29(4):495–505.
46. Barut K, Sahin S, Kasapcopur O. Pediatric vasculitis. *Curr Opin Rheumatol*. 2016;28(1):29–38.
47. Ozen S, Ruperto N, Dillon MJ, et al. EULAR/PReS endorsed consensus criteria for the classification of childhood vasculitides. *Ann Rheum Dis*. 2006;65(7):936–941.
48. Schmidt WA. Use of imaging studies in the diagnosis of vasculitis. *Curr Rheumatol Rep*. 2004;6(3):203–211.
49. Brogan PA, Davies R, Gordon I, et al. Renal angiography in children with polyarteritis nodosa. *Pediatr Nephrol*. 2002;17(4):277–283.
50. Ozaki K, Miyayama S, Ushiogi Y, et al. Renal involvement of polyarteritis nodosa: CT and MR findings. *Abdom Imaging*. 2009;34(2):265–270.
51. Singhal M, Gupta P, Sharma A, et al. Role of multidetector abdominal CT in the evaluation of abnormalities in polyarteritis nodosa. *Clin Radiol*. 2016;71(3):222–227.
52. Bansal PJ, Tobin MC. Neonatal microscopic polyangiitis secondary to transfer of maternal myeloperoxidase-antineutrophil cytoplasmic antibody resulting in neonatal pulmonary hemorrhage and renal involvement. *Ann Allergy Asthma Immunol* 2004;93(4):398–401.
53. Aasarod K, Iversen BM, Hammerstrom J, et al. Wegener's granulomatosis: clinical course in 108 patients with renal involvement. *Nephrol Dial Transplant*. 2000;15(5):611–618.
54. Belostotsky VM, Shah V, Dillon MJ. Clinical features in 17 paediatric patients with Wegener granulomatosis. *Pediatr Nephrol*. 2002;17(9):754–761.
55. Stanley JH, Cornella R, Loevinger E, et al. Sonography of systemic lupus nephritis. *AJR Am J Roentgenol*. 1984;142(6):1165–1168.
56. Kirby JM, Jhaveri KS, Maizlin ZV, et al. Abdominal manifestations of systemic lupus erythematosus: spectrum of imaging findings. *Can Assoc Radiol J*. 2009;60(3):121–132.
57. Siegler R, Oakes R. Hemolytic uremic syndrome; pathogenesis, treatment, and outcome. *Curr Opin Pediatr*. 2005;17(2):200–204.

58. Kraus RA, Gaisie G, Young LW. Increased renal parenchymal echogenicity: causes in pediatric patients. *Radiographics*. 1990;10(6):1009–1018.
59. Choyke PL, Grant EG, Hoffer FA, et al. Cortical echogenicity in the hemolytic uremic syndrome: clinical correlation. *J Ultrasound Med*. 1988;7(8):439–442.
60. Patriquin HB, O'Regan S, Robitaille P, et al. Hemolytic-uremic syndrome: intrarenal arterial Doppler patterns as a useful guide to therapy. *Radiology*. 1989;172(3):625–628.
61. Davin JC. Henoch-Schonlein purpura nephritis: pathophysiology, treatment, and future strategy. *Clin J Am Soc Nephrol*. 2011;6(3):679–689.
62. Trapani S, Micheli A, Grisolia F, et al. Henoch Schonlein purpura in childhood: epidemiological and clinical analysis of 150 cases over a 5-year period and review of literature. *Semin Arthritis Rheum*. 2005;35(3):143–153.
63. Komatsu H, Fujimoto S, Yoshikawa N, et al. Clinical manifestations of Henoch-Schonlein purpura nephritis and IgA nephropathy: comparative analysis of data from the Japan Renal Biopsy Registry (J-RBR). *Clin Exp Nephrol*. 2016;20(4):552–560.
64. Gedalia A. Henoch-Schonlein purpura. *Curr Rheumatol Rep*. 2004;6(3):195–202.
65. Scheinman JI. Sickle cell disease and the kidney. *Nat Clin Pract Nephrol*. 2009;5(2):78–88.
66. Stallworth JR, Tripathi A, Jerrell JM. Prevalence, treatment, and outcomes of renal conditions in pediatric sickle cell disease. *South Med J*. 2011;104(11):752–756.
67. Dyer RB, Chen MY, Zagoria RJ. Intravenous urography: technique and interpretation. *Radiographics*. 2001;21(4):799–821, discussion 822-794.
68. Kawamoto S, Duggan P, Sheth S, et al. Renal papillary and calyceal lesions at CT urography: genitourinary imaging. *Radiographics*. 2017;37(1):358–359.
69. Lande IM, Glazer GM, Sarnaik S, et al. Sickle-cell nephropathy: MR imaging. *Radiology*. 1986;158(2):379–383.
70. Taori KB, Chaudhary RS, Attarde V, et al. Renal Doppler indices in sickle cell disease: early radiologic predictors of renovascular changes. *AJR Am J Roentgenol*. 2008;191(1):239–242.
71. Lau KK, Stoffman JM, Williams S, et al. Neonatal renal vein thrombosis: review of the English-language literature between 1992 and 2006. *Pediatrics*. 2007;120(5):e1278–e1284.
72. Alexander AA, Merton DA, Mitchell DG, et al. Rapid diagnosis of neonatal renal vein thrombosis using color Doppler imaging. *J Clin Ultrasound*. 1993;21(7):468–471.
73. Elsaify WM. Neonatal renal vein thrombosis: grey-scale and Doppler ultrasonic features. *Abdom Imaging*. 2009;34(3):413–418.
74. Hibbert J, Howlett DC, Greenwood KL, et al. The ultrasound appearances of neonatal renal vein thrombosis. *Br J Radiol*. 1997;70(839):1191–1194.
75. Zhang H, Li M, Jin W, et al. The left renal entrapment syndrome: diagnosis and treatment. *Ann Vasc Surg*. 2007;21(2):198–203.

# 117 Renal Failure and Transplantation

Harriet J. Paltiel

## ACUTE RENAL INJURY

***Overview.*** Acute renal failure is defined as a sudden loss of renal function that may be due to inadequate renal perfusion, renal cell injury, or obstruction to urine flow. The term *acute kidney injury* (AKI) has been proposed to replace the term *acute renal failure* and is gaining wide acceptance.[1,2] AKI usually develops in hospitalized children as a result of systemic illness or its treatment and not from primary renal disease. The most common causes of AKI in children are renal ischemia, nephrotoxic drugs, and sepsis.[3,4] Other important causes are listed in Box 117.1. AKI from any cause can lead to chronic kidney disease.[5–9] Recovery of renal function, at least in part, depends on the underlying events leading to injury.

***Imaging.*** In general, sonography should be the first diagnostic imaging study in the workup of persons with AKI, and in most cases it is the only imaging required. The role of sonography is to determine renal size and to exclude anatomic abnormalities as the cause of AKI. The renal cortex, medulla, and collecting system have different acoustic properties, and pathologic changes are readily detected and correlate well with histologic findings. Doppler techniques provide information about renal perfusion and vascular abnormalities. Sonography also is used to localize the kidneys for percutaneous biopsy. More precise functional information may be obtained with nuclear medicine studies that can aid in differentiating between prerenal, intrinsic renal, and postrenal causes of AKI.

***Prerenal Injury.*** In persons with prerenal injury, the kidney is intrinsically normal, and renal function is diminished as a result of decreased renal perfusion (e.g., hypovolemia). Sonographic examination of the kidneys is normal. Restoration of renal perfusion results in a prompt return of renal function.

***Intrinsic Renal Disease.*** Renal ischemia due to a prolonged prerenal injury or a severe hypoxic/ischemic insult can lead to acute tubular necrosis. Imaging findings depend on the severity of parenchymal injury. A generalized increase in renal cortical echogenicity indicates intrinsic renal disease (Fig. 117.1). In mild cases, the kidneys may appear normal or may demonstrate slightly increased renal cortical echogenicity. Decreased corticomedullary differentiation may be noted. Doppler flow may be normal in mild disease, whereas poor peripheral perfusion and diminished arterial diastolic flow due to increased intrarenal vascular resistance occur in more severe cases.

Nephrotoxic drugs commonly associated with AKI include antibiotics, chemotherapeutic agents, nonsteroidal antiinflammatory medications, and iodinated contrast material.[10] Some agents such as aminoglycoside antibiotics cause tubular injury. Methicillin and other penicillin analogs, cimetidine, sulfonamides, rifampin, and nonsteroidal antiinflammatory drugs may cause acute interstitial nephritis, which is thought to be related to a hypersensitivity reaction with development of antitubular basement membrane antibodies in some cases. While iodinated contrast material has historically been considered a common cause of AKI in children and adults, recent adult studies suggest that the risk may be lower than previously thought.[11–13]

Children with acute lymphocytic leukemia and B-cell lymphoma are at risk for the development of uric acid nephropathy and tumor lysis syndrome. One mechanism of injury believed to be of importance in uric acid nephropathy is precipitation of uric acid crystals in the renal microvasculature leading to obstruction of renal blood flow, or precipitation in the renal tubules leading to obstruction of urine flow. Tumor lysis syndrome is a constellation of metabolic abnormalities resulting from spontaneous or treatment-related tumor necrosis. As tumor cells are lysed, rapid increases in serum potassium, uric acid, and phosphorus occur, with a decrease in serum calcium. Patients who are treated with allopurinol, a purine analog used to diminish the excretion of uric acid, instead excrete large quantities of the uric acid precursors xanthine and hypoxanthine. Precipitation of these compounds is thought to play a role in the development of AKI.

In patients who are in septic shock, AKI can develop from hypotension, leading to renal ischemia and acute tubular necrosis, or AKI can develop as a result of the use of nephrotoxic medications.

***Obstructive Uropathy and Lower Tract Lesions.*** Urinary tract obstruction can cause AKI if the obstruction affects a solitary kidney, both ureters, or the urethra. Congenital causes include ureteropelvic junction obstruction, ureterovesical junction obstruction, and posterior urethral valves. Acquired urinary tract obstruction can be caused by urinary tract stones or, rarely, tumors. Bladder rupture is another rare cause of AKI associated with ascites. Bladder rupture in children usually is due to trauma or as a complication of bladder augmentation. It can also occur rarely in patients with chronically unused bladders or conditions with outflow obstruction combined with a diseased bladder wall, such as posterior urethral valves or congenital bladder diverticula.[14–17]

## CHRONIC KIDNEY DISEASE

***Overview.*** The terms *chronic renal failure* and *chronic renal insufficiency* have been used historically to describe varying degrees of chronic renal dysfunction. Currently, the term *chronic kidney disease* (CKD) is used by both adult and pediatric nephrology communities throughout the world.[17] The classification of CKD published by the National Kidney Foundation's Kidney Disease Outcomes Quality Initiative is based on the estimated glomerular filtration rate and is applicable to children older than 2 years and to adults.[18] The classification categorizes CKD into five different stages and is widely used in clinical practice (Table 117.1).

It has been recognized that most patients with CKD (estimated to be one in eight adults) never reach end-stage renal disease and the need for renal replacement therapy because they are at risk for accelerated cardiovascular disease and are more likely to die prematurely from cerebrovascular or cardiovascular disease.[19] Therefore clinical management requires measures to diminish cardiovascular risk factors in both adult and pediatric patients.

According to the North American Pediatric Renal Trials and Collaborative Studies 2008 report,[20] the most common causes of pediatric CKD in North America are congenital disorders, such as obstructive uropathy (20.7%); renal aplasia, hypoplasia, and dysplasia (17.3%); and reflux nephropathy (8.4%) (Fig. 117.2; Table 117.2). In contrast, in Japan, 34% of pediatric CKD is due to glomerulonephritis, primary focal segmental glomerulosclerosis, and immunoglobulin A nephropathy.[21] In Jordan[22] and Iran,[23] where consanguinity is more common, heritable disorders such as cystic kidney diseases, primary hyperoxaluria, cystinosis, Alport syndrome, and congenital nephrotic syndrome represent a greater proportion of cases of CKD. In the developing world, acquired causes of CKD predominate, particularly infection-related glomerulopathies.[24,25]

## Abstract:

Sonography is the initial imaging study performed when assessing patients with acute and chronic renal failure and may be the only imaging that is necessary. The role of sonography is to determine renal size and to exclude anatomical abnormalities as the cause of renal failure, and to monitor the effects of treatment. When functional information is required, nuclear medicine studies are done to help differentiate prerenal, renal and postrenal causes of acute and chronic renal failure. Sonography is the imaging study of choice in the evaluation of renal transplants and detection of complications. Imaging is focused on an assessment of graft perfusion and vascular anastomoses. Late complications include chronic rejection and PTLD. Chronic rejection will be manifest as a gradual reduction in graft size, increased parenchymal echogenicity and decreased perfusion. PTLD is the most common neoplastic disorder in pediatric transplant recipients and sonography is used to search for enlarged lymph nodes and solid masses in the abdomen and pelvis. Sonographic monitoring of the native kidneys in transplant recipients is required because of an increased risk of malignancy in this population.

## Keywords:

Sonography
renal failure
renal transplantation
chronic rejection
PTLD

### BOX 117.1 Common Causes of Acute Kidney Injury

**PRERENAL FAILURE**

- Decreased true intravascular volume
- Decreased effective intravascular volume

**INTRINSIC RENAL DISEASE**

- Acute tubular necrosis
- Hypoxic/ischemic insults
- Drug-induced
- Toxin-mediated
  Endogenous toxins—hemoglobin, myoglobin
  Exogenous toxins—ethylene glycol, methanol

**URIC ACID NEPHROPATHY AND TUMOR LYSIS SYNDROME**

**Interstitial Nephritis**

- Drug-induced
- Idiopathic

**Glomerulonephritis**

**Vascular Lesions**

- Renal artery thrombosis
- Renal vein thrombosis
- Cortical necrosis
- Hemolytic uremic syndrome

**Hypoplasia/Dysplasia with or Without Obstructive Uropathy**

- Idiopathic
- Exposure to nephrotoxic drugs in utero

**Hereditary Renal Disease**

- Autosomal-dominant polycystic kidney disease
- Autosomal-recessive polycystic kidney disease
- Alport syndrome
- Sickle cell nephropathy
- Juvenile nephronophthisis

**Obstructive Uropathy/Lower Tract Lesions**

- Obstruction in a solitary kidney
- Bilateral ureteral obstruction
- Urethral obstruction
- Bladder rupture

*From Andreoli SP. Clinical evaluation of acute kidney injury in children. In: Avner ED, ed.* Pediatric nephrology. *6th ed. Berlin: Springer-Verlag; 2009.*

The worldwide incidence and prevalence of CKD is greater for boys than for girls because of the higher incidence of congenital causes of CKD in boys.[20–27]

***Imaging.*** Imaging plays an essential role in diagnosis, assessment of function, and monitoring of the effects of treatment at all stages of CKD, from the antenatal period to pretransplantation evaluation. Many urinary tract abnormalities are discovered by prenatal sonography or magnetic resonance imaging (MRI). Postnatal imaging usually focuses on growth, function, and assessment of complications. A multimodality approach often is required, including radiography, sonography, fluoroscopy, nuclear medicine, and MRI.

As with AKI, sonography is the primary imaging modality used to investigate CKD and guide performance of a percutaneous biopsy. Assessment of renal and bladder morphology permits detection of congenital anomalies, such as ureteropelvic junction obstruction, posterior urethral valves, duplex collecting systems and ureters, and ectopic ureteral insertion. Determination of kidney size is critical for long-term follow-up. Enlarged kidneys may occur in the setting of obstruction, certain cystic diseases, and glomerulonephritis. Hypoplastic/dysplastic and scarred kidneys usually are small. A gradual reduction in kidney size usually occurs in persons with CKD. With progressive CKD, a concomitant loss of corticomedullary differentiation usually occurs, and most patients will have echogenic renal parenchyma.[28]

Dysplastic kidneys have disordered development that generally is manifested as a combination of echogenic parenchyma and cysts (Fig. 117.3). Dysplasia may be focal or diffuse and generally appears sonographically as echogenic tissue without recognizable

**TABLE 117.1** Kidney Disease Outcomes Quality Initiative Stages of Chronic Kidney Disease

| Stage | Description | GFR (mL/min/1.73 m$^2$) |
|---|---|---|
| 1 | Kidney damage with normal or increased GFR | ≥90 |
| 2 | Kidney damage with mild decrease in GFR | 60–89 |
| 3 | Moderate decrease in GFR | 30–59 |
| 4 | Severe decrease in GFR | 15–29 |
| 5 | Kidney failure | <15 (or dialysis) |

*GFR,* Glomerular filtration rate.

*From VanDeVoorde RG, Warady BA. Management of chronic kidney disease. In: Avner ED, ed.* Pediatric nephrology. *6th ed. Berlin: Springer-Verlag; 2009.*

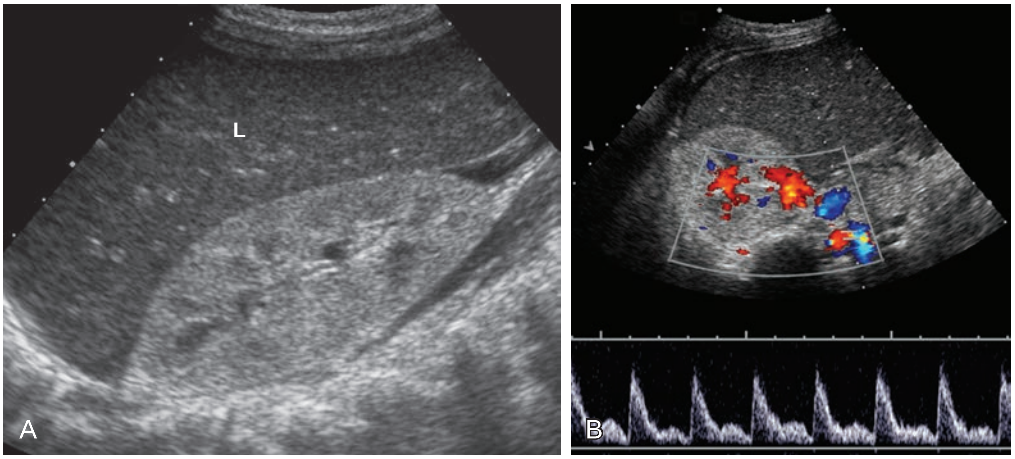

**Figure 117.1. Hemolytic-uremic syndrome.** (A) Longitudinal sonogram of an 18-month-old boy with acute kidney injury shows an enlarged right kidney with parenchymal echogenicity greater than that of the adjacent liver *(L)* and decreased corticomedullary differentiation. (B) Spectral Doppler waveform from the main renal artery shows diminished diastolic flow and an elevated resistive index.

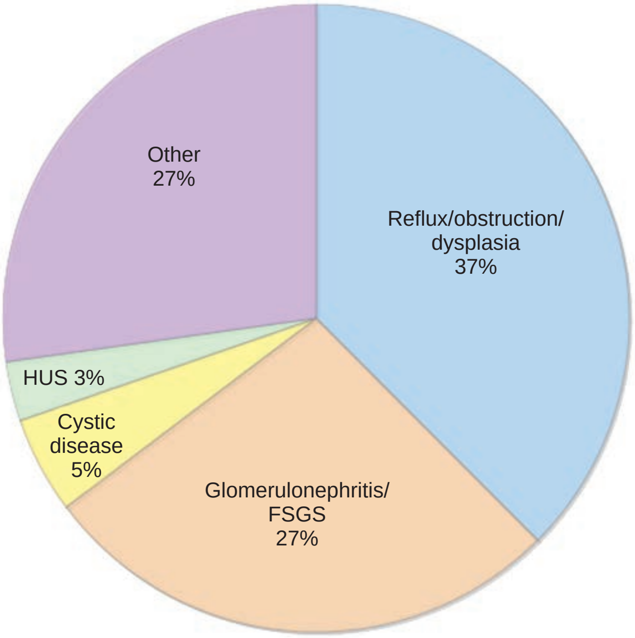

**Figure 117.2.** Primary causes of end-stage renal disease in pediatric patients. *HUS,* Hemolytic uremic syndrome; *FSGS,* focal segmental glomerulosclerosis. *(Modified from Eddy A. Pathophysiology of progressive renal disease. In Avner ED, ed.* Pediatric nephrology. *6th ed. Berlin: Springer-Verlag; 2009.)*

**TABLE 117.2** 2007 North American Pediatric Renal Trials and Collaborative Studies Report, Primary Diagnosis of Chronic Renal Insufficiency

| **Primary Diagnosis** | **No. of Patients (N = 6794)** | **%** |
|---|---|---|
| Obstructive uropathy | 1436 | 21.1 |
| Aplastic/hypoplastic/dysplastic kidney | 1187 | 17.5 |
| Focal segmental glomerulosclerosis | 589 | 8.7 |
| Reflux nephropathy | 568 | 8.4 |
| Polycystic disease | 271 | 4.0 |
| Prune belly | 192 | 2.8 |
| Renal infarct | 157 | 2.3 |
| Hemolytic uremic syndrome | 138 | 2.0 |
| Systemic lupus erythematosus nephritis | 108 | 1.6 |
| Familial nephritis | 108 | 1.6 |
| Membranoproliferative glomerulonephritis, types I and II | 102 | 1.5 |
| Cystinosis | 100 | 1.5 |
| Pyelonephritis/interstitial nephritis | 95 | 1.4 |
| Medullary cystic disease | 86 | 1.3 |
| Chronic glomerulonephritis | 81 | 1.2 |
| Congenital nephritic syndrome | 74 | 1.1 |
| Immunoglobulin A (Berger) nephropathy | 66 | 1.0 |
| Idiopathic crescentic glomerulonephritis | 46 | 0.7 |
| Henoch-Schönlein nephritis | 42 | 0.6 |
| Membranous nephropathy | 35 | 0.5 |
| Wilms tumor | 31 | 0.5 |
| Other systemic immunologic disorders | 25 | 0.4 |
| Wegener granulomatosis | 21 | 0.3 |
| Sickle cell nephropathy | 14 | 0.2 |
| Diabetic glomerulopathy | 11 | 0.2 |
| Oxalosis | 7 | 0.1 |
| Drash syndrome | 6 | 0.1 |
| Other | 1020 | 15.0 |

*From VanDeVoorde RG, Warady BA. Management of chronic kidney disease. In Avner ED, ed.* Pediatric nephrology. *6th ed. Berlin: Springer-Verlag; 2009.*

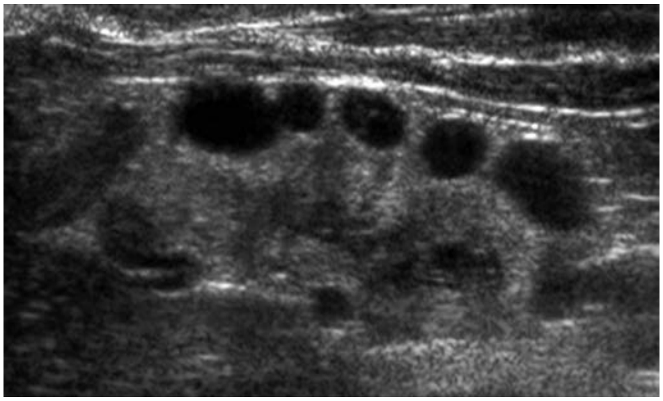

**Figure 117.3. Renal dysplasia.** Sagittal sonogram of the right kidney in a 7-week-old boy with renal failure shows a small kidney with echogenic parenchyma and multiple peripheral cysts. The left kidney had a similar appearance (not shown).

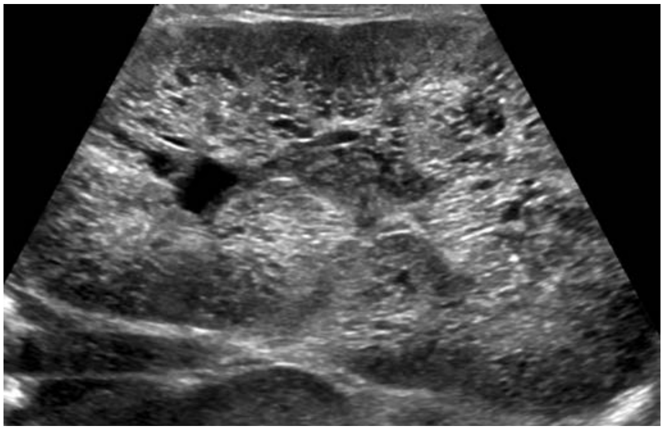

**Figure 117.4. Autosomal-recessive polycystic kidney disease.** Sagittal sonogram of the left kidney in a 3-day-old girl demonstrates nephromegaly, loss of normal corticomedullary differentiation, hypoechoic subcapsular cortex, and multiple cysts of varying size in the medullary region. The right kidney had a similar appearance (not shown).

corticomedullary differentiation. Severe bilateral renal dysplasia (i.e., bilateral multicystic dysplastic kidneys) is incompatible with life. Multicystic dysplastic kidney is the most common form of unilateral dysplasia and consists of multiple large, generally noncommunicating cysts of varying size and minimal intervening echogenic parenchyma. About half of these kidneys eventually will involute by ultrasound.[29] Monitoring of the contralateral functioning kidney is critical in these patients, because associated abnormalities are common.[30] Renal scarring may occur as a sequela of infection or vesicoureteral reflux. Sonography is relatively insensitive in the detection of scarring, and nuclear scintigraphy with dimercaptosuccinic acid or MRI may be required for more precise assessment of renal parenchymal integrity.[31,32]

Children with autosomal recessive polycystic kidney disease have large, echogenic kidneys with poor corticomedullary differentiation due to the presence of innumerable tiny (often microscopic) cysts. Visible cysts less than 1 cm in diameter are detected in about 50% of children (Fig. 117.4). Evaluation of the liver is necessary because of the high association of ductal plate malformations. Autosomal dominant polycystic kidney disease may manifest in childhood, although associated CKD is rare. The kidneys usually appear normal initially, with cystic changes developing later in life. Occasionally, cysts may be present at birth.[33–36]

Renal vascularity reflects functional status and will decrease in persons with CKD. Several recent publications suggest that the renal arterial resistive index may correlate with creatinine levels and may be an independent risk factor for the progression of CKD.[37,38]

## TRANSPLANTATION

***Overview.*** Renal transplantation is the treatment of choice in children with end-stage renal disease, with improved patient survival and quality of life compared with dialysis. However, renal transplantation in children is associated with a number of specific problems, including a higher incidence of graft failure and post-transplant malignancy than in adults, as well as growth retardation. Furthermore, it may be challenging technically to transplant a relatively large adult kidney into a small pediatric abdomen. Transplantation of kidneys from donors younger than 5 years usually is avoided because the risk of early graft failure is increased, mainly as a result of graft thrombosis.[39] Adult kidneys almost always are used. An allograft may be from a living, related donor; from a living, unrelated donor; or it may be cadaveric in origin. In the United States, more than 50% of transplanted kidneys in children are from living, adult donors.[40]

***Imaging.*** Assessment of the transplant kidney is similar to that of a native kidney, with an emphasis on graft perfusion and vascular anastomoses; sonography is the primary imaging technique. Familiarity with the surgical anatomy is essential to a complete evaluation of the vasculature. In small children, the kidney is often placed intraperitoneally with anastomosis of the donor renal artery and vein to the recipient distal aorta and inferior vena cava, respectively. In older children, the graft is placed in a retroperitoneal location within an iliac fossa. The donor renal artery is anastomosed either to the recipient external (more commonly) or internal iliac artery, and the donor vein is anastomosed to the recipient external iliac vein. The donor ureter is anastomosed to the recipient urinary bladder (ureteroneocystostomy).[41]

A normal kidney transplant allograft has a sonographic appearance similar to that of a normal native kidney. The close proximity of the graft to the body surface accentuates the distinction between the renal cortex, medullary pyramids, and central sinus. Doppler evaluation reveals continuous antegrade flow within the main renal artery throughout the cardiac cycle, with low-impedance arterial waveforms in the intrarenal vessels. The intrarenal arterial resistive indices range from 0.5 to 0.8.[42] Flow within the main renal vein and intrarenal veins is opposite in direction to that in the arteries and usually is mildly pulsatile, reflecting normal cardiac and respiratory motion.

In the immediate postoperative period, the most common complications are acute tubular necrosis, vascular narrowing or thrombosis, and rejection. These entities may be difficult to distinguish with imaging techniques. In all three entities, the graft will appear swollen, with loss of normal corticomedullary differentiation and abnormal (usually elevated) arterial resistive indices. Renal vein thrombosis usually occurs in the first postoperative week and manifests as decreased or absent flow within the main renal vein associated with elevated arterial resistive indices (including possible reversal of diastolic blood flow) (Fig. 117.5). Additional acute complications include urine leaks, other fluid collections (e.g., hematoma or abscess), urinary obstruction, and vesicoureteral reflux, all of which are readily demonstrated by imaging.[43–45] Lymphoceles are the most common fluid collections and are caused by lymphatic disruption. They usually develop weeks to months after transplantation (Fig. 117.6).[46]

Renal artery stenosis usually occurs within the first 3 years after transplantation.[47,48] Doppler sonography may demonstrate an elevated velocity within the main renal artery of greater than 200 cm/sec (Fig. 117.7), as well as a *pulsus parvus et tardus* waveform in the arteries distal to the stenotic site (including an abnormally low resistive index). Although Doppler sonography is the screening modality of choice, significant stenotic lesions can be missed. Computed tomographic angiography, magnetic resonance angiography, and catheter angiography are useful problem-solving techniques when sonography is inconclusive. Catheter angiography remains the definitive imaging technique for renal artery imaging.[48–50]

Important late complications include chronic rejection and posttransplant lymphoproliferative disorder (PTLD). Chronic rejection is manifested sonographically by a gradual reduction in graft size, increased parenchymal echogenicity, and decreased perfusion.[42,45] In the pediatric renal transplant population, two large series have reported an incidence of PTLD of 1.2%[51] and

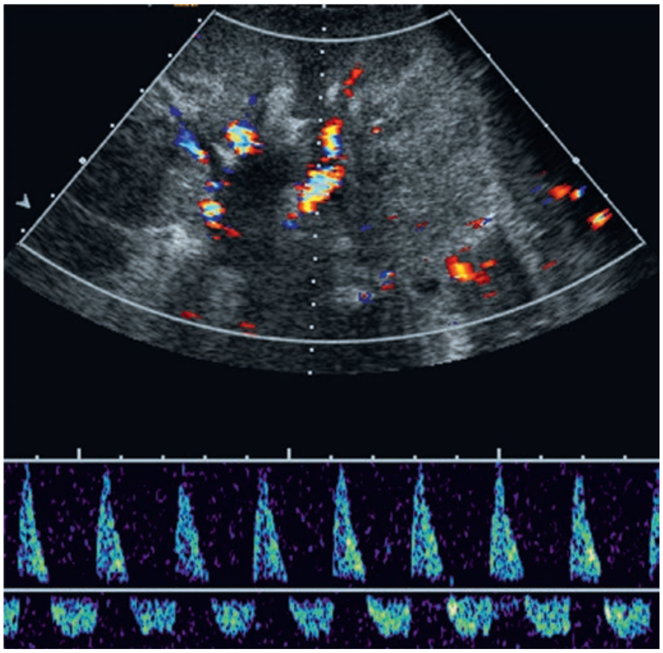

**Figure 117.5. Transplant renal vein thrombosis.** Longitudinal sonogram of a 20-month-old boy 1 day after living–related donor transplantation shows a swollen, echogenic kidney with diminished corticomedullary differentiation. Marked pulsatility of the main renal arterial waveform is noted with reversed diastolic flow, reflecting increased peripheral resistance.

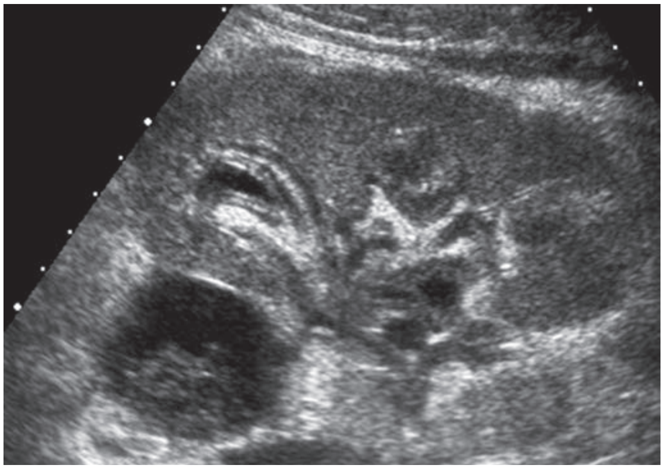

**Figure 117.6. Lymphocele.** Sagittal sonogram of a 16-year-old girl obtained 6 months after deceased donor renal transplantation depicts a small fluid collection with internal echogenic debris indenting the upper pole of the right-sided kidney.

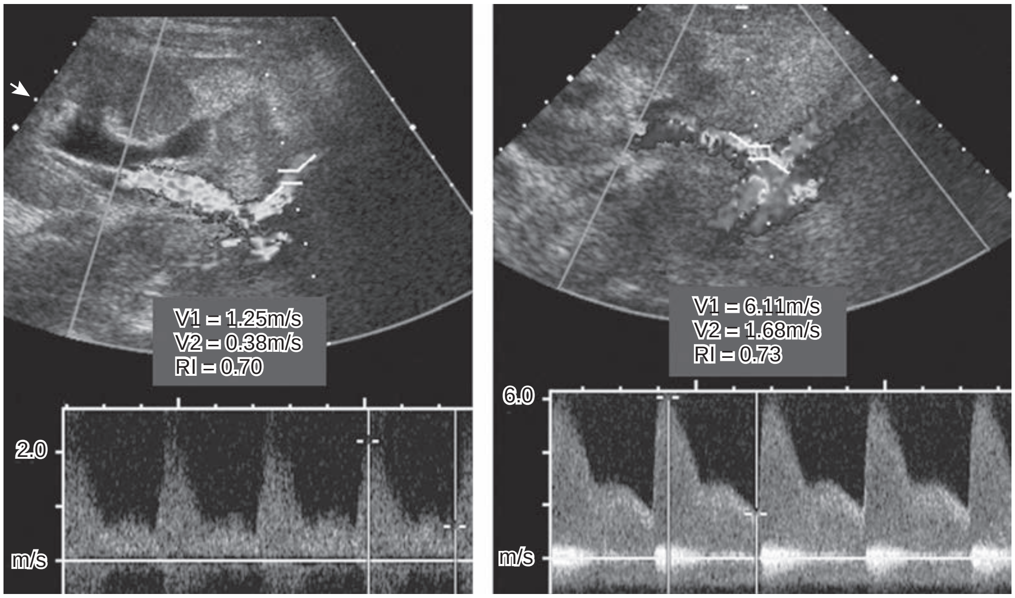

**Figure 117.7. Transplant renal arterial stenosis.** Spectral Doppler sonograms of a child with a rising serum creatinine level shows a nearly fivefold increase in renal arterial peak systolic velocity *(right image)* compared with the supplying external iliac artery *(left image)*, indicating hemodynamically significant stenosis.

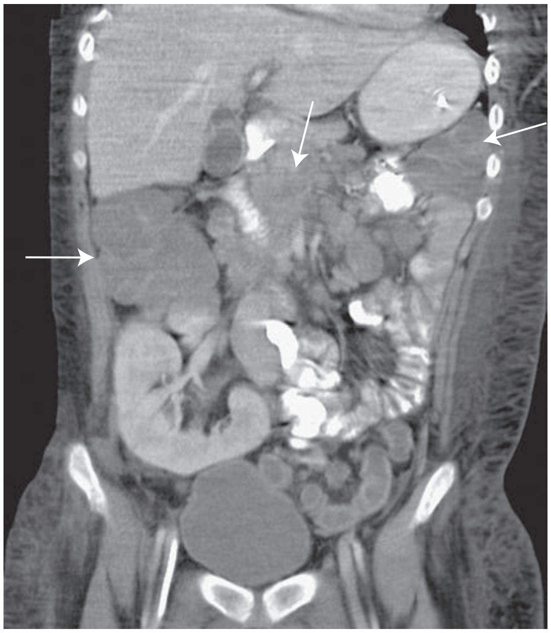

**Figure 117.8. Posttransplant lymphoproliferative disorder.** Coronal reformatted image from a contrast-enhanced CT in a 17-year-old boy shows a right lower quadrant renal transplant. Multiple low-density conglomerate masses within the abdomen represent lymphoproliferative tissue *(arrows)*.

4.5%, respectively.[52] PTLD is the most common neoplastic disorder in pediatric transplant recipients, accounting for 52% of all malignancies in this patient population[53] and is associated with Epstein-Barr virus (EBV) infection. In immune-suppressed persons with impaired T-cell immune surveillance, EBV infection can cause abnormal B-cell proliferation, especially in persons who were seronegative at the time of transplantation.[53,54] Patients at risk will have elevated EBV titers, and sonographic follow-up must include a search for lymph node enlargement and solid masses of the abdominal and pelvic viscera (Fig. 117.8).

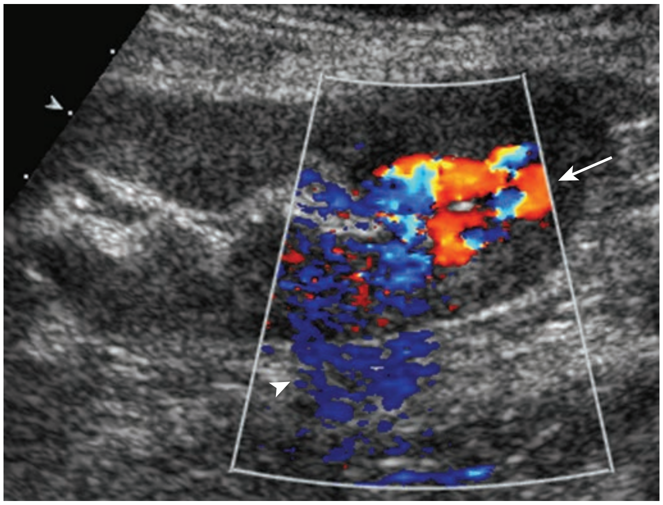

**Figure 117.9. Postbiopsy arteriovenous fistula.** Color Doppler sonogram shows enlarged vessels in the lower pole of a renal transplant *(arrow)* associated with soft tissue vibration artifact *(arrowhead)*.

Percutaneous renal biopsy may be indicated at any stage after transplantation and often is performed under sonographic guidance. Iatrogenic complications of biopsy include hemorrhage and arteriovenous fistula formation (Fig. 117.9). Sonographic monitoring of the native kidneys always should be performed because of an increased risk of malignancy.[55,56]

## KEY POINTS

- Sonography is the first imaging study performed for evaluation for AKI and CKD and often is the only imaging required.
- Nuclear medicine studies provide functional information that helps distinguish prerenal, renal, and postrenal causes of AKI and CKD.

*Continued*

- Sonography is the technique of choice for detecting complications of renal transplantation.
- PTLD is the most common neoplastic disorder in pediatric transplant recipients.
- Sonographic monitoring of native kidneys in transplant recipients is necessary because of an increased risk of malignancy.

## SUGGESTED READINGS

Camacho JC, Moreno CC, Harri PA, et al. Posttransplantation lymphoproliferative disease: proposed imaging classification. *Radiographics*. 2014;34(7):2025–2038.

Khati NJ, Hill MC, Kimmel PL. The role of ultrasound in renal insufficiency: the essentials. *Ultrasound Q*. 2005;21:227–244.

Stanescu AL, Hryhorczuk AL, Chang PT, et al. Pediatric abdominal organ transplantation: current indications, techniques, and imaging findings. *Radiol Clin North Am*. 2016;54(2):281–302.

## REFERENCES

Full references for this chapter can be found on www.expertconsult.com.

## REFERENCES

1. Bellomo R, Ronco C, Kellum JA, et al. Acute Dialysis Quality Initiative workgroup. Acute renal failure - definition, outcome measures, animal models, fluid therapy and information technology needs: the Second International Consensus Conference of the Acute Dialysis Quality Initiative (ADQI) Group. *Crit Care*. 2004;8(4):R204–R212.
2. Srisawat N, Kellum JA. Acute kidney injury: definition, epidemiology, and outcome. *Curr Opin Crit Care*. 2011;17(6):548–555.
3. Goldstein SL, Devarajan P. Acute kidney injury in childhood: should we be worried about progression to CKD? *Pediatr Nephrol*. 2011;26:509–522.
4. Rewa O, Bagshaw SM. Acute kidney injury-epidemiology, outcomes and economics. *Rev Nephrol*. 2014;10(4):193–207.
5. Nash K, Hafeez A, Hou S. Hospital-acquired renal insufficiency. *Am J Kidney Dis*. 2002;39:930–936.
6. Uchino S, Kellum JA, Bellomo R, et al. Acute renal failure in critically ill patients: a multinational, multicenter study. *JAMA*. 2005;294:813–818.
7. Chertow GM, Soroko SH, Paganini EP, et al. Mortality after acute renal failure: models for prognostic stratification and risk adjustment. *Kidney Int*. 2006;70:1120–1126.
8. Basile DP. The endothelial cell in ischemic acute kidney injury: implications for acute and chronic function. *Kidney Int*. 2007;72:151–156.
9. Hsu CY, McCulloch CE, Fan D, et al. Community-based incidence of acute renal failure. *Kidney Int*. 2007;72:208–212.
10. Hui-Stickle S, Brewer ED, Goldstein SL. Pediatric ARF epidemiology at a tertiary care center from 1999 to 2001. *Am J Kidney Dis*. 2005;45:96–101.
11. Davenport MS, Khalatbari S, Cohan RH, et al. Contrast material-induced nephrotoxicity and intravenous low-osmolality iodinated contrast material: risk stratification by using estimated glomerular filtration rate. *Radiology*. 2013;268(3):719–728.
12. Moore A, Dickerson E, Dillman JR, et al. Incidence of nonconfounded post-computed tomography acute kidney injury in hospitalized patients with stable renal function receiving intravenous iodinated contrast material. *Curr Probl Diagn Radiol*. 2014;43(5):237–241.
13. McDonald RJ, McDonald JS, Carter RE, et al. Intravenous contrast material exposure is not an independent risk factor for dialysis or mortality. *Radiology*. 2014;273(3):714–725.
14. Chan DP, Abujudeh HH, Cushing GL Jr, et al. CT cystography with multiplanar reformation for suspected bladder rupture: experience in 234 cases. *AJR Am J Roentgenol*. 2006;187(5):1296–1302.
15. Breen M, Phelps A, Estrada C, et al. The role of imaging in pediatric bladder augmentation. *Pediatr Radiol*. 2015;45(10):1440–1447.
16. Oktar T, Sanli O, Atar A, et al. Iatrogenic bladder rupture in a child following voiding cystourethrography and its laparoscopic management. *Eur J Pediatr Surg*. 2011;21(4):275–277.
17. VanDeVoorde RG, Warady BA. Management of chronic kidney disease. In Avner ED, ed. *Pediatric nephrology*. 6th ed, Berlin: Springer-Verlag; 2009.
18. Definition and classification of stages of chronic kidney disease. *Am J Kidney Dis*. 2002;39:S46–S75.
19. Coresh J, Selvin E, Stevens LA, et al. Prevalence of chronic kidney disease in the United States. *JAMA*. 2007;298:2038–2047.
20. North. American Pediatric Renal Trials and Collaborative Studies (NAPRTCS) *2008 annual report*. NAPRTCS, Boston, MA.
21. Hattori S, Yosioka K, Honda M, et al. The 1998 report of the Japanese National Registry data on pediatric end-stage renal disease patients. *Pediatr Nephrol*. 2002;17:456–461.
22. Hamed RM. The spectrum of chronic renal failure among Jordanian children. *J Nephrol*. 2002;15:130–135.
23. Madani K, Otoukesh H, Rastegar A, et al. Chronic renal failure in Iranian children. *Pediatr Nephrol*. 2001;16:140–144.
24. Anochie I, Eke F. Chronic renal failure in children: a report from Port Harcourt, Nigeria (1985-2000). *Pediatr Nephrol*. 2003;18:692–695.
25. Sirin A, Emre S, Alpay H, et al. Etiology of chronic renal failure in Turkish children. *Pediatr Nephrol*. 1995;9:549–552.
26. Ardissino G, Daccò V, Testa S, et al. Epidemiology of chronic renal failure in children: data from the ItalKid project. *Pediatrics*. 2003;111:e382–e387.
27. Ali. el TM, Abdelraheem MB, Mohamed RM, et al. Chronic renal failure in Sudanese children: aetiology and outcomes. *Pediatr Nephrol*. 2009;24(2):349–353.
28. Yaprak M, Çakır Ö, Turan MN, et al. Role of ultrasonographic chronic kidney disease score in the assessment of chronic kidney disease. *Int Urol Nephrol*. 2016;[Epub ahead of print].
29. Eickmeyer AB, Casanova NF, He C, et al. The natural history of the multicystic dysplastic kidney–is limited follow-up warranted? *J Pediatr Urol*. 2014;10(4):655–661.
30. Schreuder MF, Westland R, van Wijk JA. Unilateral multicystic dysplastic kidney: a meta-analysis of observational studies on the incidence, associated urinary tract malformations and the contralateral kidney. *Nephrol Dial Transplant*. 2009;24:1810–1818.
31. Moorthy I, Wheat D, Gordon I. Ultrasonography in the evaluation of renal scarring using DMSA scan as the gold standard. *Pediatr Nephrol*. 2004;19:153–156.
32. Cerwinka WH, Grattan-Smith JD, Jones RA, et al. Comparison of magnetic resonance urography to dimercaptosuccinic acid scan for the identification of renal parenchyma defects in children with vesicoureteral reflux. *J Pediatr Urol*. 2014;10(2):344–351.
33. Hartung EA, Guay-Woodford LM. Autosomal recessive polycystic kidney disease: a hepatorenal fibrocystic disorder with pleiotropic effects. *Pediatrics*. 2014;134(3):e833–E845.
34. Barua M, Pei Y. Diagnosis of autosomal-dominant polycystic kidney disease: an integrated approach. *Semin Nephrol*. 2010;30:356–365.
35. Rosetti S, Harris PC. Genotype-phenotype correlations in autosomal dominant and autosomal recessive polycystic kidney disease. *J Am Soc Nephrol*. 2007;18:1374–1380.
36. Gunay-Aygun M. Liver and kidney disease in ciliopathies. *Am J Med Genet C Semin Med Genet*. 2009;151C:296–306.
37. Sugiura T, Wada A. Resistive index predicts renal prognosis in chronic kidney disease. *Nephrol Dial Transplant*. 2009;24:2780–2785.
38. Parolini C, Noce A, Staffolani E, et al. Renal resistive index and long-term outcome in chronic nephropathies. *Radiology*. 2009;252:888–896.
39. Singh A, Stablein D, Tejani A. Risk factors for vascular thrombosis in pediatric renal transplantation: a special report of the North American Pediatric Renal Transplant Cooperative Study. *Transplantation*. 1997;63:1263–1267.
40. Shapiro R, Sarwal MM. Pediatric kidney transplantation. *Pediatr Clin North Am*. 2010;57(2):393–400.
41. McGuire MT, Phelps A, Paltiel HJ. Pediatric visceral transplantation. *Ultrasound Clin*. 2013;8:375–401.
42. Nixon JN, Biyyam DR, Stanescu L, et al. Imaging of pediatric renal transplants and their complications: a pictorial review. *Radiographics*. 2013;33(5):1227–1251.
43. Salvatierra O Jr, Millan M, Concepcion W. Pediatric renal transplantation with considerations for successful outcomes. *Semin Pediatr Surg*. 2006;15:208–217.
44. Kayler L, Kang D, Howard R. Kidney transplant ureteroneocystostomy techniques and complications: review of the literature. *Transplant Proc*. 2010;42:1413–1420.
45. Carmichael J, Easty M. Imaging chronic renal disease and renal transplant in children. *Pediatr Radiol*. 2010;40:963–974.
46. Kobayashi K, Censullo ML, Rossman LL, et al. Interventional radiologic management of renal transplant dysfunction: indications, limitations, and technical considerations. *Radiographics*. 2007;27:1109–1130.
47. Dodd GD III, Tublin ME, Shah A, et al. Imaging of vascular complications associated with renal transplants. *AJR Am J Roentgenol*. 1991;157:449–459.
48. Singh AK, Sahani DV. Imaging of the renal donor and transplant recipient. *Radiol Clin North Am*. 2008;46:79–93.
49. Browne RF, Tuite DJ. Imaging of the renal transplant: comparison of MRI with duplex sonography. *Abdom Imaging*. 2006;31:461–482.
50. Glockner JF, Vrtiska TJ. Renal MR and CT angiography: current concepts. *Abdom Imaging*. 2007;32:407–420.
51. Dharnidharka VR, Sullivan EK, Stablein DM, et al. *Risk factors for post transplant lymphoproliferative disorder (PTLD) in pediatric kidney transplantation: a report of the North American Pediatric Renal Transplant Cooperative Study (NAPRTCS)*.
52. Funch DP, Brady J, Ko HH, et al. Methods and objectives of a large US multicenter case-control study of post-transplant lymphoproliferative disorder in renal transplant patients. *Recent Results Cancer Res*. 2002;159:81–88.
53. Penn I. De novo malignancies in pediatric organ transplant recipients. *Pediatr Transplant*. 1998;2:56–63.
54. Pinkerton CR, Hann I, Weston CL, et al. Immunodeficiency-related lymphoproliferative disorders: prospective data from the United Kingdom Children's Cancer Study Group Registry. *Br J Haematol*. 2002;118:456–461.
55. Tsaur I, Obermüller N, Jonas D, et al. De novo renal cell carcinoma of native and graft kidneys in renal transplant recipients. *BJU Int*. 2011;108:229–234.
56. Tsaur I, Karalis A, Blaheta R, et al. Transitional cell carcinoma of the native urinary tract after kidney transplantation: recommendations following a long-term retrospective analysis. *Am J Med Sci*. 2011;341:478–483.

# 118 The Ureter

*Andrew H. Schapiro and Jonathan R. Dillman*

## EMBRYOLOGY

During the fifth week of gestation, the urinary collecting system begins development as an outpouching from the mesonephric duct known as the ureteral bud. Contact between the bulbous portion of the ureteral bud and the metanephric blastema induces this portion of the bud to branch and develop into the renal pelvis, calyces, and collecting tubules. Meanwhile, the stalk of the ureteral bud develops into the ureter. The segment of distal mesonephric duct located between the ureteral bud and developing bladder, known as the common nephric duct, undergoes apoptosis, bringing the distal ureter into contact with the developing bladder. The ureteral orifice then migrates cranially and laterally as the bladder tissue surrounding the ureteral insertion expands and differentiates.[1–3]

## IMAGING

Ultrasound is the first-line imaging technique in pediatric uroradiology. Unfortunately, the ureter can generally only be visualized when it is sufficiently filled with urine, and even then only the proximal and distal aspects are typically seen. Using the kidney as an acoustic window from a posterior or lateral approach, the ureteropelvic junction (UPJ) can usually be identified in well-hydrated patients with a tapering of the pelvis toward the proximal ureter. To visualize the ureterovesical junction (UVJ) and distal ureter, sufficient fluid distension of the urinary bladder is mandatory so that it can serve as a window to the retrovesical space. Once the bladder is sufficiently filled, the normal ureter can be followed superiorly for several centimeters. Further visualization up to the iliac vessels or higher is only possible in cases with a significantly dilated ureter and sufficient sonographic access.

Sonographic evaluation of the urine inflow jet from the ureteral orifice into the urinary bladder can provide useful information about the patency and peristaltic activity of the ureter, as well as the position and function of the UVJ. This ureteral jet can sometimes be seen on gray-scale ultrasound as a rush of echoes from the ureteral ostium into the bladder lumen, but it is more easily seen with color Doppler sonography. Sonographic visualization of this jet can be limited with patient dehydration or when the specific gravity of ureteral urine and bladder urine are similar after recent voiding.[4–8]

Modern multidetector computed tomography (CT) can rapidly acquire high spatial resolution images of the entire ureter and surrounding structures. In pediatric uroradiology, CT can be useful for evaluation of severe trauma, urolithiasis and its complications, inflammatory disease, suspected obstructing crossing vessels, and tumors.[8–11] For evaluation of urolithiasis, noncontrast enhanced CT is typically performed, but for other indications, opacification of the ureteral lumen with contrast is often beneficial. This can be achieved either with delayed, excretory phase imaging after a single contrast material injection or with a split-bolus CT urography technique in which the renal parenchyma and ureter are opacified with contrast material simultaneously.[12] CT angiography can be used to assess vascular anatomy. Although a useful technique, CT does impart ionizing radiation and often requires iodinated contrast, which carries its own inherent risks. Thus CT should be used only when necessary, and protocols should be tailored to minimize radiation exposure.[8]

Diuretic renography is a well-established nuclear medicine technique for assessment of renal function and urinary tract drainage, where serial image acquisitions are obtained after intravenous injection of 99m-technetium-mercaptoacetyltriglycine ($^{99m}$Tc-MAG3) or $^{99m}$Tc-diethylene triamine pentaacetic acid ($^{99m}$Tc-DTPA) both before and after diuretic stimulation.[13,14] With this technique, ureteral drainage can be visualized and quantified in a standardized fashion providing excellent functional information. Limitations and drawbacks include patient exposure to ionizing radiation, limited assessment of urinary tract drainage in the setting of poor renal function, and poor anatomic resolution.[13,15]

Magnetic resonance urography (MRU) can provide excellent spatial resolution and functional information in a single study without the use of ionizing radiation or iodinated contrast material. In children, MRU can be particularly useful in the investigation of congenital genitourinary anomalies and hydronephrosis.[16–18] With MRU, anatomic assessment of the entire ureter can be obtained without the need for intravascular contrast material by using a variety of T2-weighted pulse sequences. Postdiuretic contrast-enhanced MRU (so-called functional MRU) allows for functional assessment by using fast T1-weighted gradient recalled echo pulse sequences to image at multiple time points after contrast material administration, allowing assessment of the arterial, corticomedullary, nephrographic, and excretory phases.[19–20] Downsides of this technique at present include availability, cost, inability to image patients with certain implantable devices, need for sedation or anesthesia for many pediatric patients, and risk of nephrogenic systemic fibrosis if a linear gadolinium contrast agent is administered to patients with severe kidney disease.[17,18] There is also growing concern about detectable deposition of gadolinium in body tissues, but at present long-term effects remain uncertain.[21]

## URETERAL OBSTRUCTION

There is a spectrum of ureteral obstruction ranging from partial obstruction without any clinical consequence to severe obstruction that can threaten renal function. Most ureteral obstructions occur at the UPJ or UVJ. However, obstructive lesions between these two points can occur as a result of congenital and acquired causes.

### Congenital Obstruction

***Ureteral Valve.*** Congenital ureteral valves are transverse folds of mucosa and variable smooth muscle that are typically cusp-shaped or diaphragm-like in configuration.[22–25] They are by definition associated with upstream obstructive uropathy and a normal downstream urinary tract, without evidence of other cause for obstruction.[23] They are often associated with other urinary tract anomalies (Fig. 118.1).[24,26] Neonates and infants may have physiologic ureteral folds that can mimic ureteral valves, but the former are not associated with obstruction and typically disappear during the first years of life (Fig. 118.2).[27] Imaging will demonstrate dilation of the upstream ureter and renal collecting system with abrupt transition at the level of obstruction. The fold may be visible

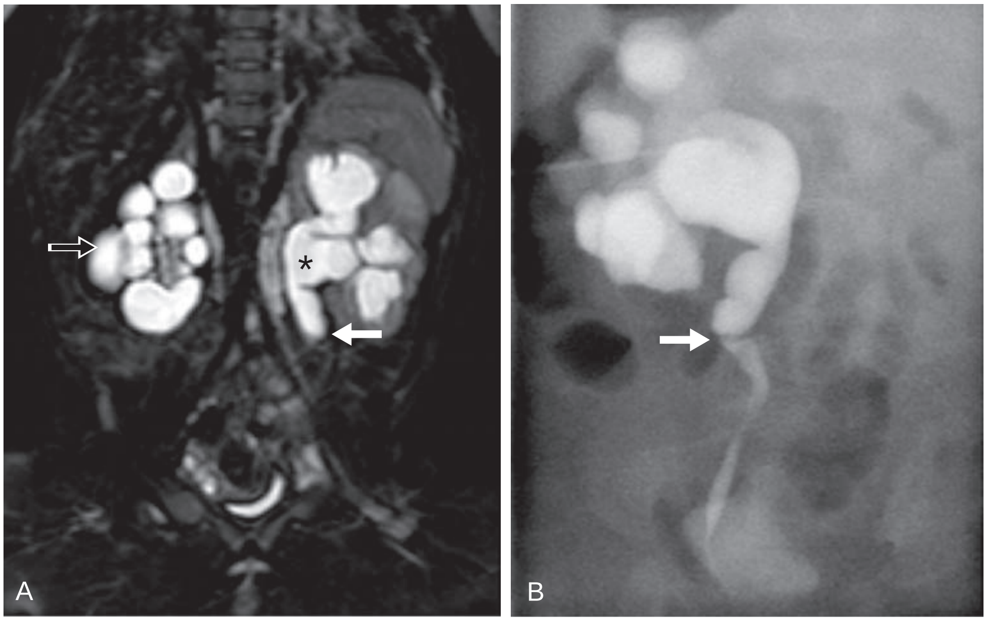

**Figure 118.1. Left ureteral valve in a 2-month-old girl.** (A) Coronal T2-weighted fat-saturated MRU image demonstrates dilation of the left pelvocalyceal system *(asterisk)* and proximal ureter with high-grade transition to a decompressed more distal ureter *(white arrow).* The right kidney consists of multiple cysts of variable size and a small amount of dysplastic parenchyma *(black arrow)*, compatible with multicystic dysplastic kidney (MCDK). (B) Percutaneous antegrade pyelogram of the same patient in the prone position demonstrates focal shelflike narrowing of the left ureter *(arrow)* at the level of transition seen on MRU.

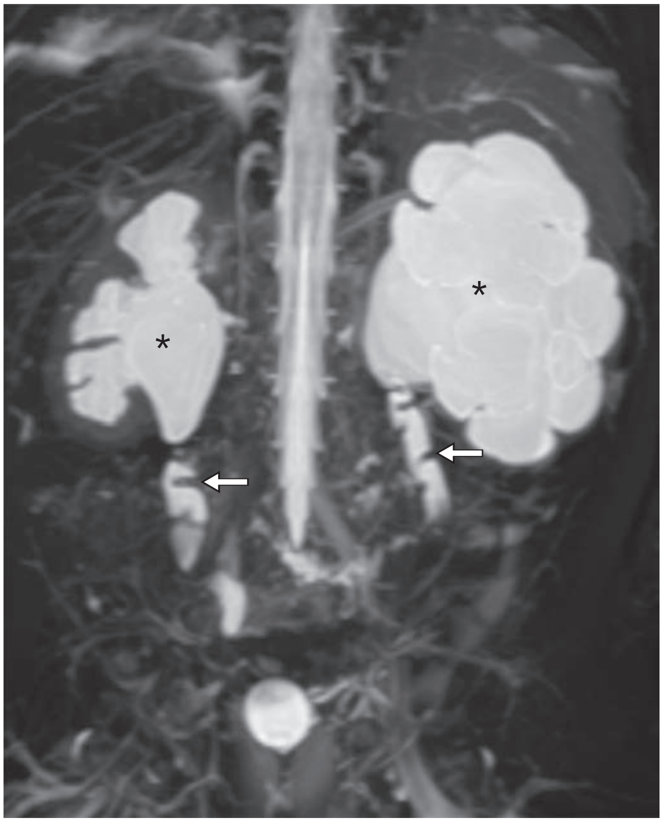

**Figure 118.2. Bilateral ureteral folds as well as bilateral UPJ obstructions in a neonate.** Coronal T2-weighted maximum intensity projection MRU image shows linear filling defects in both proximal ureters without associated ureteral caliber change at the level of the filling defects *(arrows)*, compatible with ureteral folds. Marked bilateral pelvocaliectasis *(asterisks)*, worse on the left, is due to superimposed bilateral UPJ obstructions.

as a membrane-like filling defect when the entire ureter is opacified with contrast material or on heavily T2-weighted noncontrast MRU sequences. Renal scintigraphy will demonstrate impaired collecting system drainage suggesting obstruction.[26] Treatment consists of resection of the valve-containing ureteral segment and ureteral end-to-end anastomosis.[26]

***Congenital Ureteral Stricture.*** A congenital ureteral stricture is a discrete segment of congenital narrowing along the length of the ureter that does not involve the UPJ and UVJ. It is most commonly seen in the middle third of the ureter, typically where the ureter crosses the common iliac vessels, and is therefore often referred to as a “midureteral stricture” (Fig. 118.3). However, it can also occur in the proximal or distal ureter.[28] Unlike with ureteral valves, there are no mucosal folds present, and at pathology, a smooth funnel-shaped narrowing of the lumen is seen. The etiology is uncertain, with possibilities including focal abnormalities of ureteral wall musculature or relative focal ischemia during development. Association with multicystic dysplastic kidney (MCDK), either ipsilateral or contralateral to the involved ureter, is not uncommon.[28-31] Detection on prenatal imaging has been reported, but differentiating a midureteral stricture from the more common UPJ or UVJ obstruction is challenging. On postnatal imaging, findings will often be similar to those of ureteral valves, with distinction between the two entities generally made at pathology (e-Fig. 118.4).[29,32,33] Most congenital ureteral strictures require surgical management, but patients with preserved function and no symptoms may be managed conservatively.[28]

***Vascular Compression.*** A retrocaval or circumcaval ureter is an uncommon anomaly more often seen in males in which the right ureter passes posterior to the inferior vena cava (IVC), emerges between the cava and the aorta, and then curves around and in front of the cava to return to its normal position in the pelvis (e-Fig. 118.5). This anomaly results from anomalous development of the infrarenal IVC from the more laterally located right posterior cardinal vein rather than the more typical right supracardinal vein.[34,35] At least some degree of ureteral obstruction is common. However, patients are often asymptomatic, and the abnormality

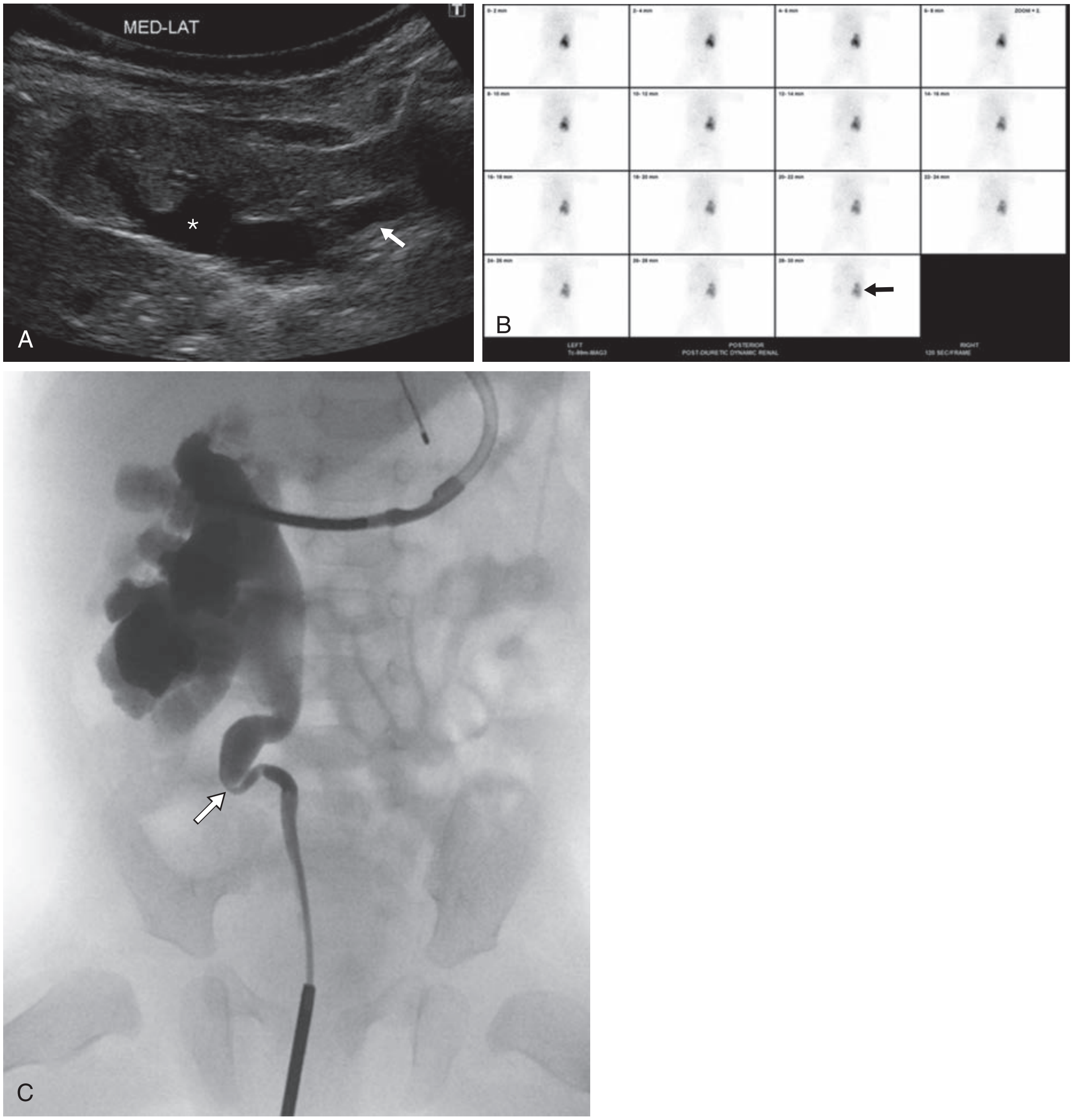

**e-Figure 118.4. Right congenital ureteral stricture and solitary right kidney in a 1-month-old girl.** (A) Ultrasound of the solitary right kidney shows pelvocaliectasis *(asterisk)* as well as dilation of the imaged proximal ureter *(arrow).* (B) Posterior post-diuretic images from diuretic renography show poor drainage of the dilated proximal right collecting system *(arrow).* (C) Retrograde pyelogram demonstrates focal narrowing of the middle third of the ureter, with ureteral caliber change at the level of narrowing *(arrow).* Excision of the narrowed segment and ureteroureterostomy were subsequently performed, with pathology confirming a congenital ureteral stricture.

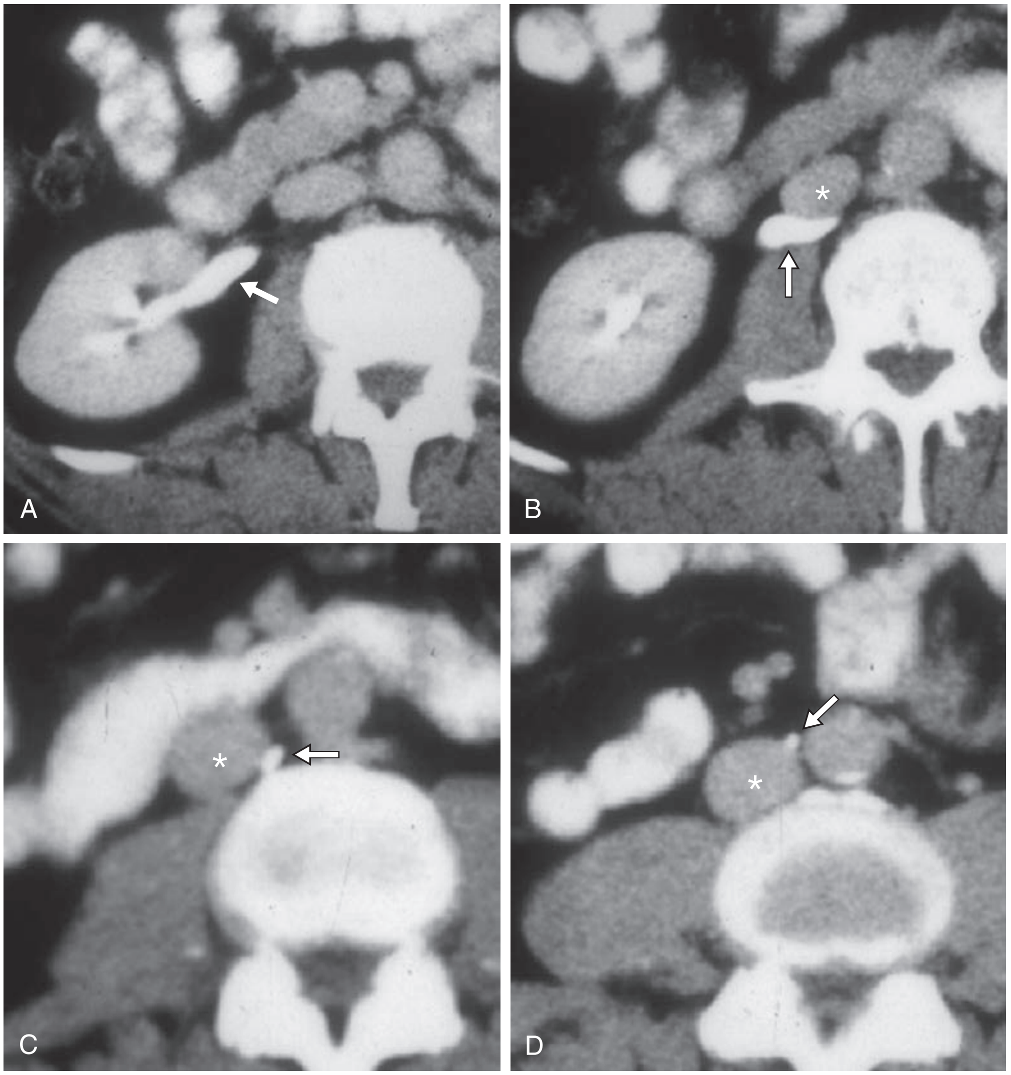

**e-Figure 118.5. Sequential cranial to caudal axial images of a retrocaval ureter on excretory phase contrast-enhanced CT.** (A) Contrast opacified right renal pelvis and proximal ureter *(arrow)*. (B) The right ureter *(arrow)* courses toward the posterior aspect of the IVC *(asterisk)*. (C) The right ureter *(arrow)* has passed posterior to the IVC *(asterisk)* and is seen along the posteromedial aspect of the IVC. (D) The ureter *(arrow)* has coursed between the aorta and IVC *(asterisk)*, and is seen along the anteromedial IVC in the aortocaval groove.

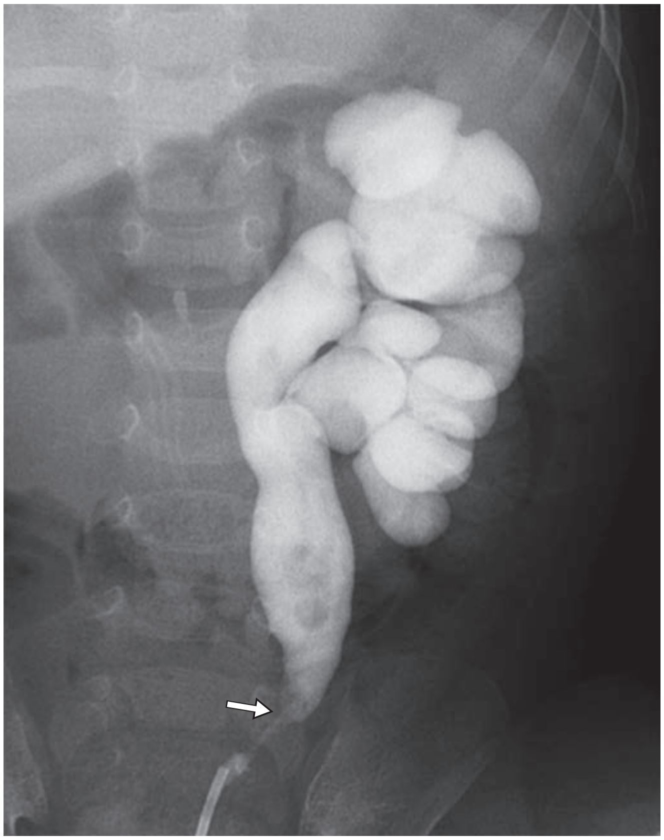

**Figure 118.3. Left congenital ureteral stricture in a 5-month-old girl.** Retrograde pyelogram demonstrates dilation of the left proximal ureter and pelvocalyceal system upstream to focal narrowing in the middle third of the ureter in the region where it crosses the iliac vessels *(arrow).* The left renal collecting system is duplicated, having a bifid appearance.

may be discovered on imaging for other reasons.[36,37] The anomaly may be demonstrated with contrast-enhanced CT, but MRU can establish the diagnosis and assess the degree of functional obstruction.[34,38,39] Surgery is performed when the patient is symptomatic or when there is decreased function of the affected kidney, and consists of division of the retrocaval ureter and ureteroureteric or ureteropelvic anastomosis anterior to the IVC.[36]

Crossing renal arteries and veins have been associated with urinary tract obstruction, particularly intermittent obstruction manifesting as recurrent renal colic and hydronephrosis.[40,41] These vessels typically cross anterior to the UPJ or proximal ureter and may be branches of the renal artery or vein, or accessory vessels (Fig. 118.6).[41,42] The crossing vessel may be demonstrated with either contrast-enhanced CT or MR angiography.[42,43] Normal vascular impressions can be seen on imaging but are not associated with secondary findings of obstruction. When a crossing vessel is identified in a patient with clinical and imaging findings suggesting intermittent obstruction and there is no intrinsic UPJ obstruction identified at surgery, a vessel transposition can be performed. When a crossing vessel is felt to be potentially aggravating an underlying intrinsic UPJ obstruction, a dismembered pyeloplasty is performed.[43]

## Acquired Obstruction

***Acquired Strictures.*** Acquired strictures of the ureter are uncommon in children. Potential causes are numerous and include: iatrogenesis (e.g., surgery, instrumentation, radiation therapy), chronic infection (e.g., tuberculosis, schistosomiasis, chronic granulomatous disease), inflammation from a passed stone, autoimmune etiologies (e.g., Henoch–Schönlein purpura and polyarteritis nodosa), and trauma (e-Fig. 118.7).[12,44–46] Strictures can be of variable length, can involve any segment of the ureter, and can be multiple. Fixed narrowing and associated upstream ureteral dilation can help differentiate strictures from physiologic narrowing, which is particularly common at the UPJ, pelvic brim, and UVJ.[12]

***Obstructing Filling Defects.*** Multiple different obstructing luminal filling defects can occur in the pediatric ureter, including crystalline debris, blood clots, calculi, and fungus balls.[12,47–51] Ultrasound may directly demonstrate an echogenic filling defect if it is contained within the visible ureter and may show posterior acoustic shadowing and twinkling artifact in the setting of urolithiasis. Ureteral dilation upstream of the filling defect suggests associated obstruction, but the degree of dilation may be very mild in the acute setting despite the patient having severe pain (Fig. 118.8). In this scenario, alterations in the bladder ureteral inflow jet on color Doppler sonography may be a helpful indirect sign of obstruction (Fig. 118.9).[52,53] All calculi except indinavir calculi are typically visible at noncontrast CT, with other types of filling defects visible at CT urography.[12] Although not typically used in the acute setting, contrast-enhanced MRU can confirm the presence of an obstructing filling defect and determine the level of the obstruction with high sensitivity.[18]

***Extrinsic Causes of Obstruction.*** Secondary ureteral inflammation and narrowing can result from adjacent infection, inflammatory bowel disease, or rarely retroperitoneal fibrosis (Fig. 118.10).[12,54] Mass-effect or encasement by adjacent tumor can also be associated with ureteral narrowing and obstruction (Fig. 118.11).[12] Imaging findings will be those of ureteral obstruction previously described with additional extraureteral findings dependent upon the extrinsic cause of obstruction.

## DISORDERS OF URETERAL MOTILITY

Impaired ureteral motility in the form of hypoperistalsis or dyskinesia may be transient or permanent, and can be seen in association with acute or chronic obstruction, abnormal ureteral implantation, vesicoureteral reflux, instrumentation or surgery, urinary tract infection, and certain medications.[55,56] There may be associated functional obstruction and upstream ureteral dilation, with urine drainage relying on gravity. Overall drainage of the collecting system can be assessed with renal scintigraphy or MRU, and direct assessment of ureteral peristalsis may be achieved with ultrasound, renal scintigraphy, or MRU.[55–58]

## PRIMARY MEGAURETER

Megaureter is a generic term used to describe an abnormally dilated ureter and can be primary or secondary. The term primary megaureter is reserved for ureteral dilation due to intrinsic abnormality of the ureter or UVJ rather than downstream abnormality in the bladder or urethra, or other extrinsic cause.[59,60] Megaureters are categorized as obstructed, refluxing, nonobstructed and nonrefluxing, and, occasionally, obstructed and refluxing.[59]

***Primary Obstructed Megaureter.*** Primary obstructed megaureter is caused by a congenital adynamic distal ureteral segment, usually 0.5 to 4 cm in length, which prevents normal caudal propagation of ureteral peristalsis and results in functional obstruction. The exact cause for the aperistaltic segment is uncertain, but ureteral wall muscular derangement and increased collagen infiltration have been described at histology and electron microscopy. At endoscopy, the distal ureter and ureteral orifice are typically normal in caliber and appearance.[61] Primary obstructed megaureter may manifest as recurrent urinary tract infection (UTI), renal scarring, abdominal or flank pain, hematuria, palpable mass, or, rarely, renal failure. However, a primary megaureter may also be discovered incidentally in asymptomatic patients.[62–64]

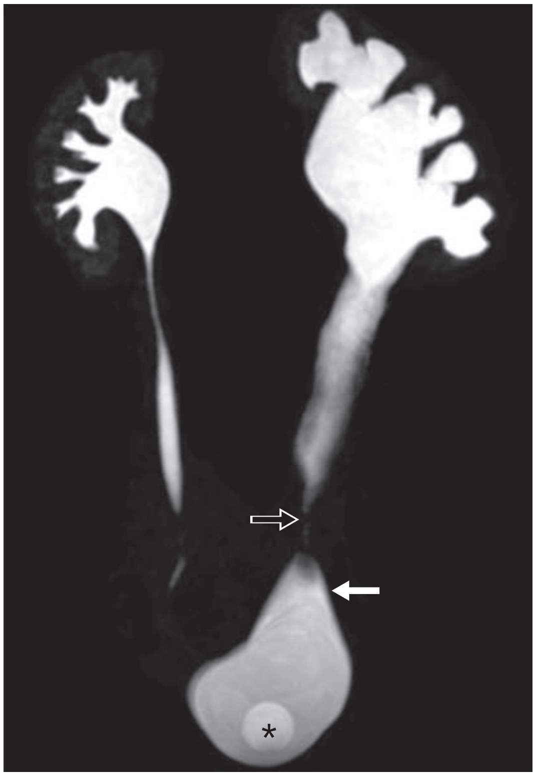

**e-Figure 118.7. Postsurgical ischemic stricture in a teenage boy with history of left ureteroneocystostomy and psoas hitch procedure.** Coronal T2-weighted maximum intensity projection MRU image demonstrates a tethered, conical appearance of the left superolateral bladder *(white arrow)*, compatible with history of prior psoas hitch procedure. There is segmental distal left ureteral narrowing at the site of stricture *(black arrow)* with upstream ureteral dilatation. A Foley balloon is seen in the bladder *(asterisk).*

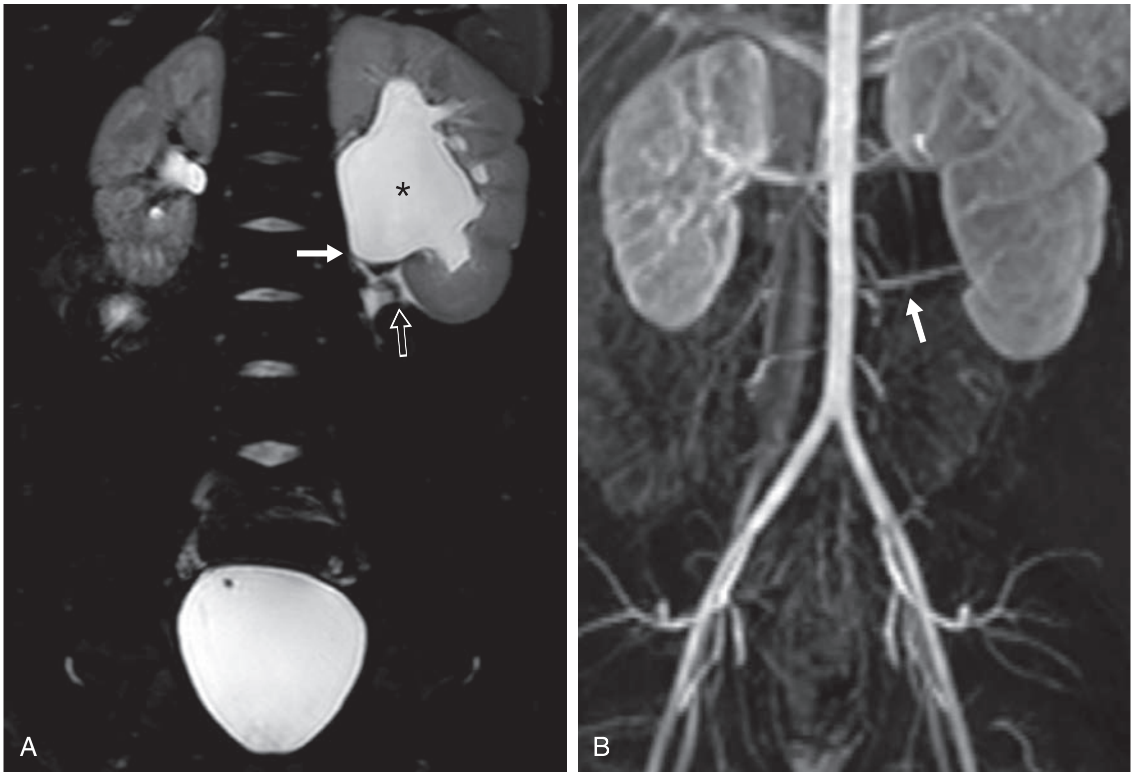

**Figure 118.6. UPJ obstruction due to a crossing vessel.** (A) Coronal T2-weighted MRU image demonstrates a dilated left renal pelvis and calyces *(asterisk)* with cutoff at the UPJ *(white arrow).* Inferior perirenal fluid *(black arrow)* may reflect forniceal rupture or urine transudation. (B) Coronal postcontrast maximum intensity projection MRU image shows a lower pole accessory artery *(arrow)* crossing the left collecting system at the level of the UPJ. UPJ obstruction due to a crossing vessel was confirmed at subsequent surgery.

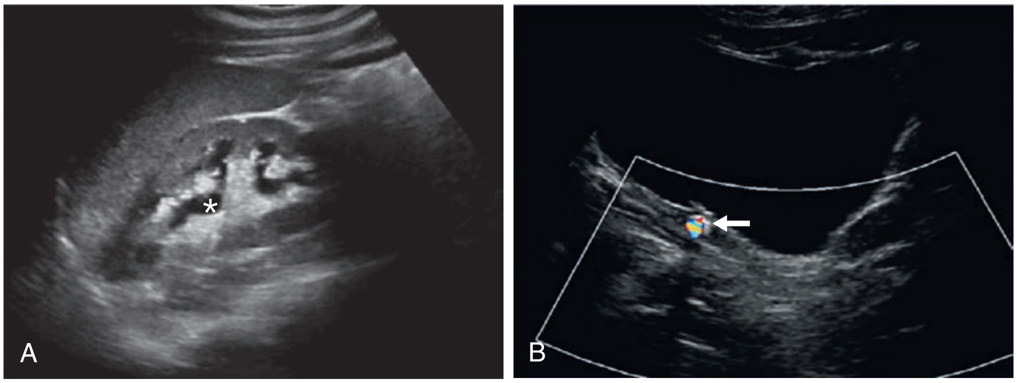

**Figure 118.8. Obstructing ureteral calculus in a 16-year-old girl with left flank.** (A) Gray-scale sonogram of the left kidney demonstrates mild pelvocaliectasis *(asterisk).* (B) An echogenic filling defect with posterior acoustic shadowing and twinkling artifact is present in the distal left ureter *(arrow).*

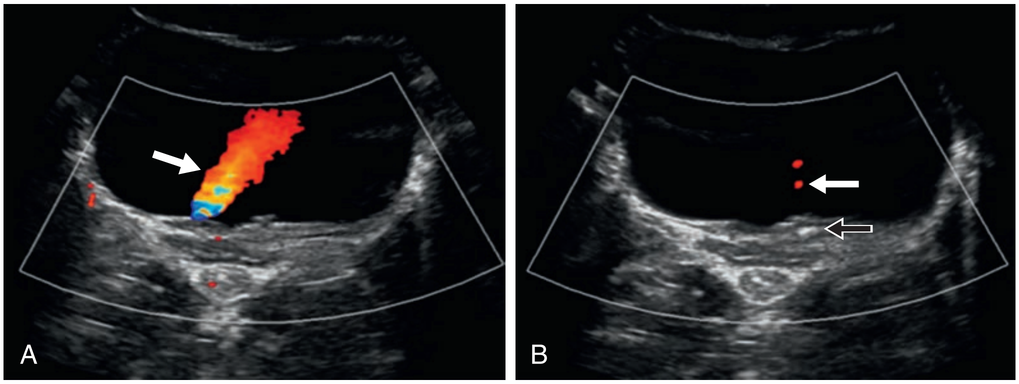

**Figure 118.9. Asymmetric ureteral jets in a teenage girl with left flank pain.** (A) Normal right ureteral jet *(arrow).* (B) Nearly absent left ureteral jet *(white arrow)* with echogenic filling defect *(black arrow)* seen in the distal left ureter at the UVJ, suggesting a partially obstructive left ureteral calculus.

On imaging, the affected ureter is variably dilated, typically affecting the lower ureter greater than the upper ureter and renal pelvis, with abrupt tapering to a relatively narrowed short distal segment (Fig. 118.12 and e-Fig. 118.13).[60] Absent peristalsis of the persistently relatively narrowed distal ureteral segment and/or abnormal to-and-fro peristalsis in the dilated upstream ureter may be seen at ultrasound.[65] Diuretic renal scintigraphy or MRU can be used to assess urinary tract drainage and obstruction. Vesicoureteral reflux (VUR) may occasionally be present in patients with obstructed primary megaureter. Patients with preserved renal function and no symptoms can be managed conservatively. However, resection of the aperistaltic segment and ureteral reimplantation

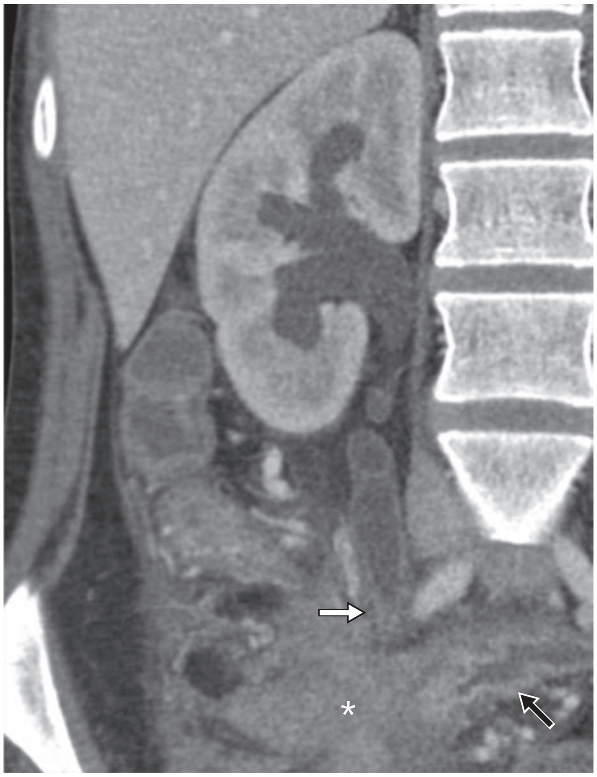

**Figure 118.10. Right ureteral obstruction from extensive bowel and mesenteric inflammation in a 16-year-old girl with Crohn disease.** Coronal postcontrast CT image shows narrowing of the midright ureter *(white arrow)* at the level of an inflammatory mass/phlegmon *(asterisk)*; inflamed bowel is present *(black arrow).* There is associated reactive ureteral wall thickening and upstream pyeloureteral dilation.

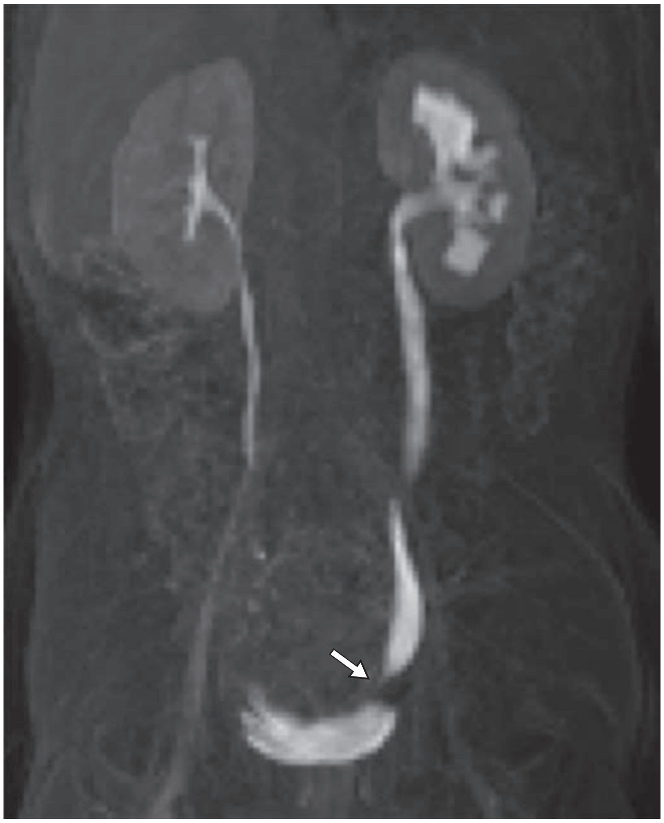

**Figure 118.12. Obstructed primary megaureter in a 12-year-old girl.** Coronal postcontrast T1-weighted excretory phase maximum intensity projection MRU image shows left collecting system and ureteral dilation that is most pronounced distally; there is abrupt narrowing of the very distal left ureter *(arrow).* There was substantially delayed passage of contrast material through the left collecting system and ureter compared with the contralateral side.

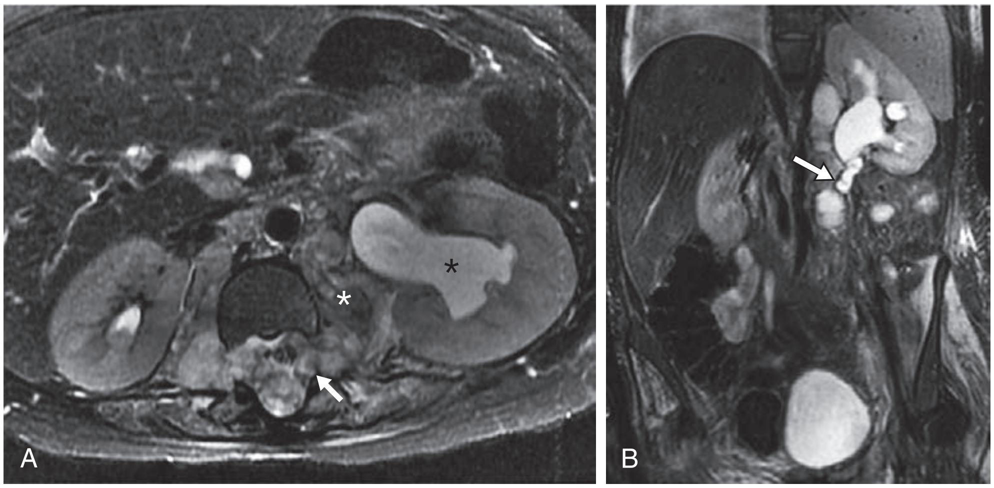

**Figure 118.11. Left ureteral obstruction due to compression by a malignant peripheral nerve sheath tumor in an 18-year-old girl.** (A) Axial T2-weighted MR image shows left pelvocaliectasis *(black asterisk)*. There is an immediately adjacent large predominantly retroperitoneal mass *(white asterisk)* with spinal canal invasion *(arrow)*. (B) Coronal T2-weighted MR image demonstrates abrupt cutoff of the ureter at the level of a portion of the mass *(arrow).*

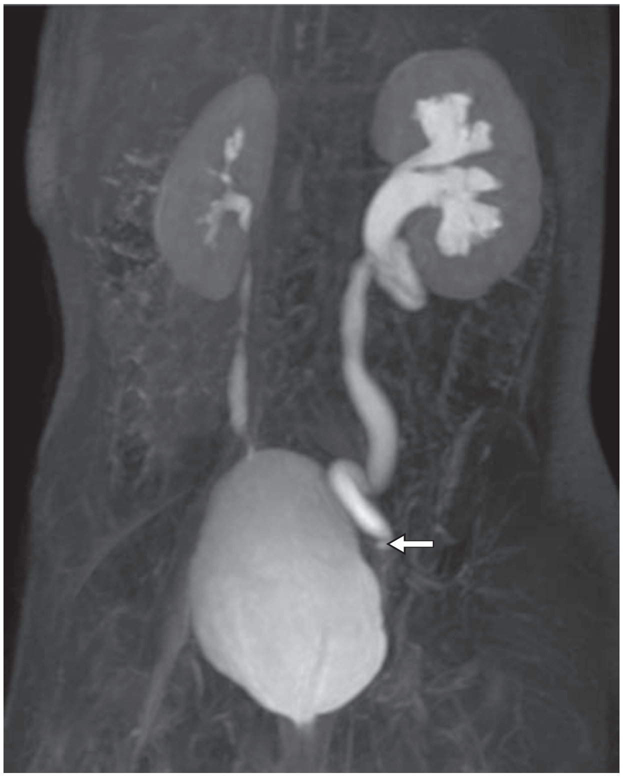

**e-Figure 118.13. Obstructed primary megaureter in a 6-year-old boy.** Coronal postcontrast T1-weighted excretory phase maximum intensity projection MRU image shows a dilated, tortuous left ureter with cutoff or high-grade transition of the distal ureter contrast column *(arrow)*. The narrowed distal ureteral segment is greater than 5 cm in length.

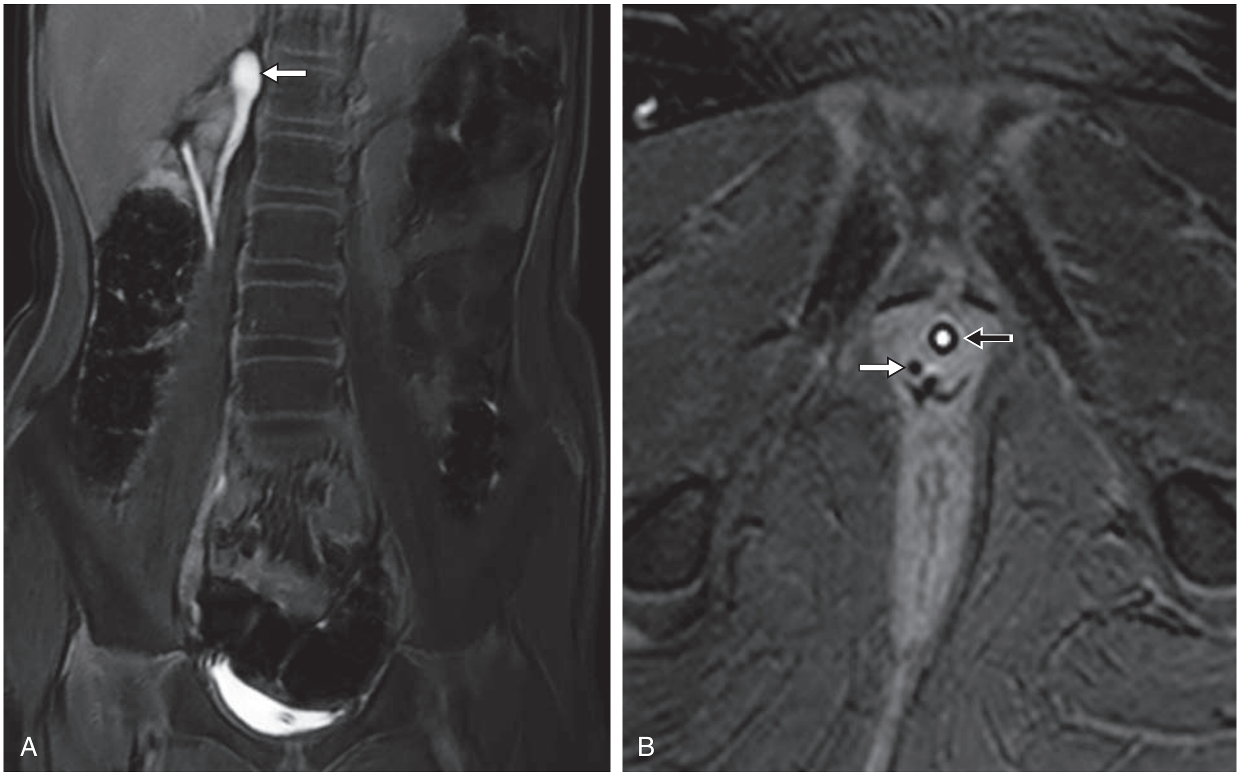

**Figure 118.14. Ectopic ureter in a 7-year-old girl with daytime and nighttime wetness.** (A) Coronal postcontrast T1-weighted excretory phase MRU image demonstrates a right duplex kidney with the upper pole ureter draining a single calyx *(arrow).* (B) Axial postcontrast T1-weighted fat-saturated MRU image through the lower pelvis shows the ectopic upper pole ureter *(white arrow)* coursing through the right anterolateral vaginal wall, appearing as a round hypointense focus. No contrast material is seen within the lumen due to obstruction. A bladder catheter with luminal contrast material demarcates the more anteriorly located urethra *(black arrow).*

may be performed for those with reduced renal function, recurrent pain, hematuria, multiple urinary tract infections, and urolithiasis. A temporizing procedure such as cutaneous ureterostomy or ureteral stent placement may be performed in neonates or infants before definitive surgery.[61]

***Primary Refluxing Megaureter.*** Refluxing megaureter may be the result of a short or absent intravesical ureter, or other abnormality of the UVJ, and is more fully discussed in the chapter on vesicoureteral reflux (see Chapter 119).[64] On imaging, a dilated ureter will be demonstrated in association with VUR. There should be no evidence of ureteral obstruction.

***Primary Nonobstructed, Nonrefluxing Megaureter.*** Nonobstructed, nonrefluxing megaureter is the most common form of megaureter detected in neonates. The cause is uncertain, but this form of megaureter may be the result of higher prenatal urine production seen in third trimester fetuses relative to postnatal urine production or impaired peristalsis as a result of delayed ureteral maturation. Regardless, nonobstructed, nonrefluxing megaureter typically resolves in the first 2 years of life.[61] As in any case of megaureter, voiding cystourethrography (VCUG) or radionuclide cystography should be performed to exclude VUR. Diuretic renal scintigraphy or MRU should be performed to exclude obstruction that may require surgery. This benign form of megaureter is generally managed conservatively.[60]

## URETERAL ECTOPIA

An ectopic ureter is one that drains to an abnormal site, either within the bladder outside the normal posterolateral angle of the trigone, or extravesically.[66] Ureteral ectopia is more common in girls than in boys. Although ectopic ureters can drain a single collecting system, they drain a duplicated collecting system in up to 80% of cases.[67–69]

In girls, the ectopic ureter may insert into the low bladder or urethra upstream of the external sphincter, preserving continence. However, commonly the ureter bypasses the sphincter complex and inserts into the vagina, vestibule, cervix, uterus, or into a Gartner duct cyst (Figs. 118.14 and 118.15).[60,70–72] As a result, female patients with an ectopic ureter commonly present with continuous dribbling of urine despite an otherwise normal voiding pattern.[60,70,73] While wetness often occurs during the day and at night, it may only occur during the day due to a capacious ectopic ureter or the vagina acting as a reservoir when the patient is recumbent at night.[70]

In boys, the ectopic ureter may insert into the low bladder, prostatic urethra, seminal vesicle, vas deferens, or ejaculatory duct.[60,70,74] Unlike in girls, the ectopic ureter inserts upstream of the sphincter. Therefore males do not present with incontinence but rather with pain, urinary tract infection, orchitis and/or epididymitis, or renal failure.[70,73] Ureteral ectopia to the genital ducts can manifest as a dilated, cystic mass behind the trigone of the bladder. In both sexes, the renal parenchyma drained by the ectopic ureter is commonly dysplastic, with some correlation between the degree of ectopia and the degree of renal dysfunction.[60,69,70,73]

Ultrasound is the initial imaging method of choice and can be diagnostic, particularly when the anomalous ureter is dilated and can be followed distally to its insertion. However, the renal parenchyma draining into an ectopic ureter often has poor excretion, limiting visibility of a nonobstructed ureter. In addition, the dysplastic renal parenchyma associated with an ectopic ureter may be small and subtle, often resulting in the dysplastic moiety or even an entire dysplastic kidney being missed.[60,68,75] CT acquired during the

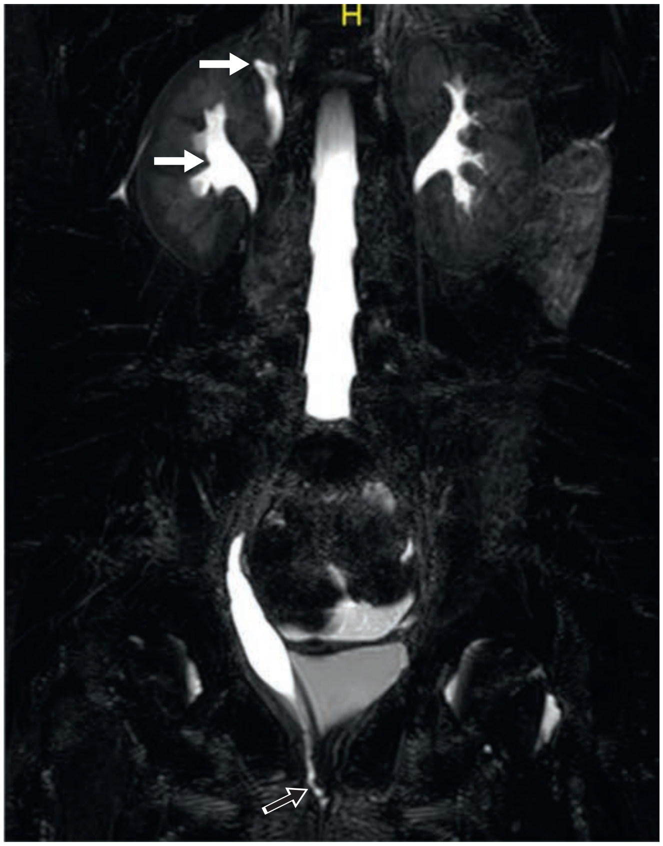

**Figure 118.15. Ectopic ureter in a 6-year-old girl with daytime and nighttime wetness.** Coronal T2-weighted MRU image shows a right duplex kidney *(white arrows).* An ectopic upper pole ureter courses past the bladder to the perineum *(black arrow).*

excretory phase of contrast enhancement may be more sensitive, with common findings being vaginal pooling of contrast material and a ureter coursing posterior to, and not inserting into, the bladder.[69] MRU has been shown to be highly accurate in depicting ectopic ureters, and in ruling out ureteral ectopia by demonstrating normal ureteral insertions. It can simultaneously assess renal function, which may play an important role in management decisions.[73]

Treatment depends on the functional status of the renal parenchyma drained by the ectopic ureter. If there is poor function, a partial or complete nephroureterectomy is performed in the setting of a duplicated system and single system, respectively. When renal function needs to be preserved, ureteroureterostomy or ureteral reimplantation can be performed.[68,69]

## URETEROCELE

A ureterocele is a cystlike submucosal expansion of the terminal segment of the ureter within the bladder or urethra. There are two subtypes: (1) intravesical ureterocele, located entirely within the bladder; and (2) ectopic ureterocele, in which some portion is situated permanently at the bladder neck or in the urethra.[66] In children, ureteroceles are most often associated with a duplicated system and have an ectopic insertion. In adults, they are commonly associated with a single system and insert orthotopically. In the setting of a duplicated system, ureteroceles are almost always associated with the upper pole moiety, but rare cases of lower pole moiety ureteroceles have been reported.[76,77] Ureteroceles are four to seven times more common in girls and are bilateral in 10% of cases.[78]

Ureteroceles may be associated with renal dysplasia or obstructive nephropathy (Fig. 118.16).[79] There is VUR into the ipsilateral lower pole moiety ureter or the contralateral ureter in 50% and 25% of children, respectively.[80] Large ureteroceles can obstruct the ipsilateral lower pole moiety ureter or the contralateral ureter. Bladder outlet obstruction by a ureterocele that has prolapsed into the urethra is rare, as most ureteroceles decompress during voiding but can occur and may necessitate emergent treatment (e-Fig. 118.17).[79]

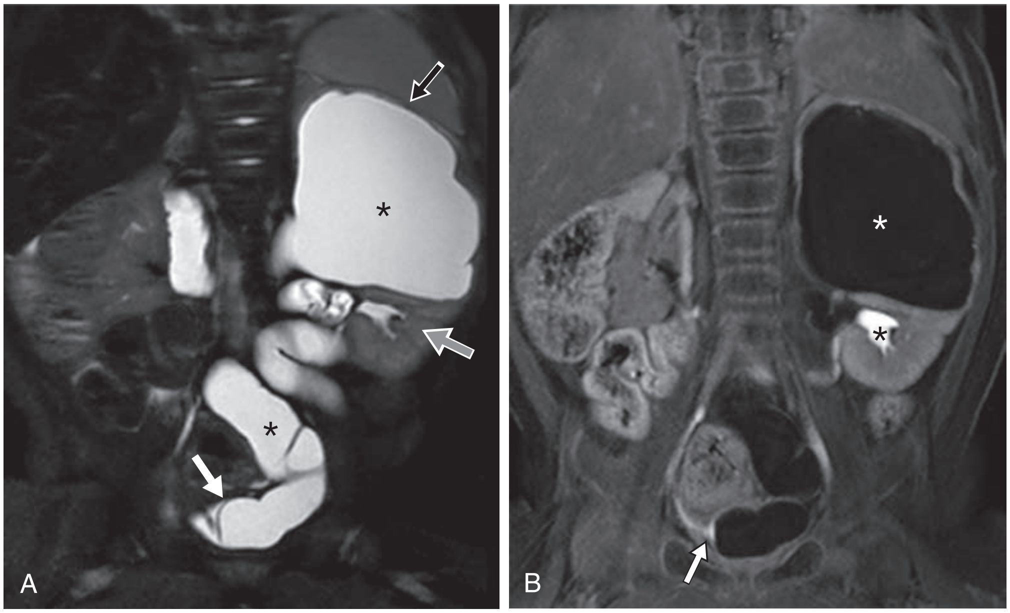

**Figure 118.16. Ureterocele-related obstructive nephropathy in a 6-month-old girl.** (A) Coronal T2-weighted fat-saturated MRU image demonstrates a left duplex system with severe upper moiety pyeloureteral dilation *(asterisk)* upstream of an intravesical ureterocele *(white arrow).* The ureterocele is surrounded by a small amount of urine in the bladder. The upper pole moiety parenchyma is markedly thinned *(black arrow).* The lower moiety collecting system is nondilated, and the parenchyma is normal *(gray arrow).* (B) Coronal postcontrast T1-weighted excretory phase MRU image shows contrast in the lower moiety collecting system *(black asterisk)* but no contrast within the upper moiety collecting system *(white asterisk)* due to obstruction and poorly functioning upper pole moiety parenchyma. A small amount of contrast is present within the bladder *(arrow).*

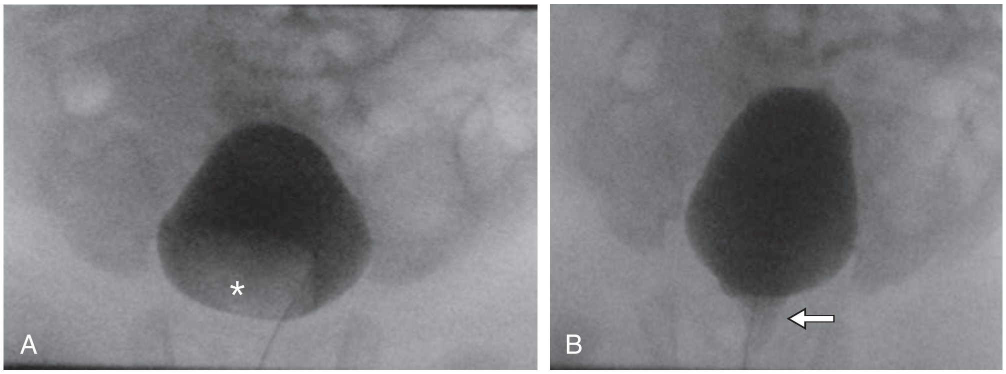

**e-Figure 118.17. Ureterocele decompression during voiding.** (A) Voiding cystourethrogram (VCUG) image acquired before voiding demonstrates a large, round filling defect *(asterisk)* in the right lower bladder, compatible with a ureterocele. (B) On a later image acquired during voiding, as demonstrated by contrast within the urethra *(arrow)*, the ureterocele has decompressed and is no longer visible.

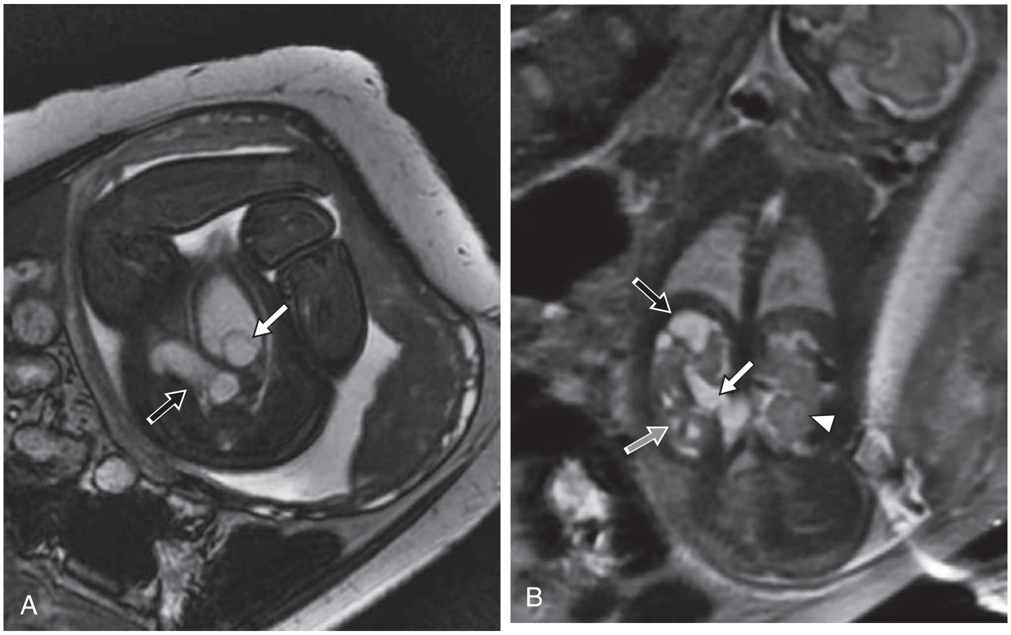

**Figure 118.18.** Ureterocele detected on fetal imaging. (A) Balanced steady-state free precession MR image in the axial plane of the fetus demonstrates a ureterocele *(white arrow)* with associated upstream ureteral dilation *(black arrow).* (B) Single-shot fast spin echo MR image in the coronal plane of the fetus shows the dilated ureter draining the upper moiety of a right duplex system *(white arrow).* There is cystic dysplasia of the upper moiety parenchyma *(black arrow).* There is also dilation of the lower moiety collecting system *(gray arrow)* that may be due to VUR or obstruction of the ureteral orifice by the large upper pole ureterocele. The left kidney is normal *(arrowhead).*

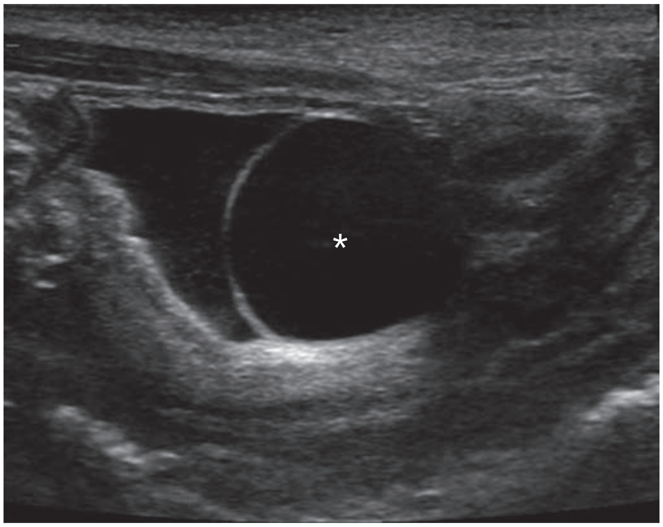

**Figure 118.19. Ureterocele in a 3-day-old girl.** Longitudinal sonogram of the bladder demonstrates a large ureterocele *(asterisk)* in the inferior bladder, giving a "cyst within a cyst" appearance.

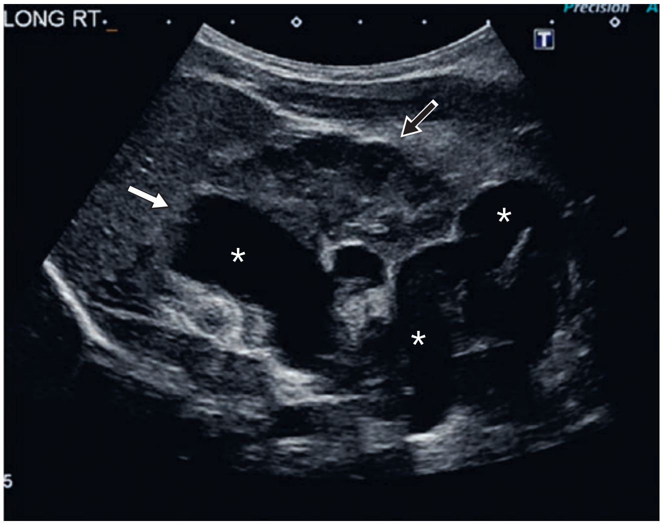

**Figure 118.21. Same 3-day-old girl with large ureterocele from Fig. 118.19.** Longitudinal sonogram shows dilation of the upper pole pelvocalyceal system and proximal ureter *(asterisks).* There is associated severe upper pole moiety parenchymal attenuation *(white arrow).* The lower pole moiety parenchyma is preserved *(black arrow).*

More than 90% of ureteroceles are discovered in children younger than 3 years of age and many are diagnosed prenatally (Fig. 118.18).[81] They commonly present clinically with UTI but can present as failure to thrive, abdominal or pelvic pain, hematuria, or acute bladder outlet obstruction. They may also be asymptomatic and incidentally detected.[78]

Ultrasound imaging of an intravesical ureterocele shows a cystic lesion of variable size attached to the posterolateral wall of the bladder and protruding into the lumen, giving a "cyst within cyst" appearance (Fig. 118.19).[60,78,79] An ectopic ureterocele will be seen as a cystic structure located more inferiorly than expected for an intravesical ureterocele.[60] Sometimes ureteroceles have a more complicated bilobed or septated appearance, and may contain debris or calculi (e-Fig. 118.20). On real-time sonography, partial or complete ureterocele collapse may be seen as a result of ureteral peristalsis.[60] There is often associated dilation of the upstream ureter as a result of obstruction (Fig. 118.21). However, even a large ureterocele can be associated with a diminutive ureter and calyces and minimal renal parenchyma, an entity known as "ureterocele disproportion."[82] Dilation of the contralateral ureter or of the ipsilateral lower moiety ureter in the case of duplication

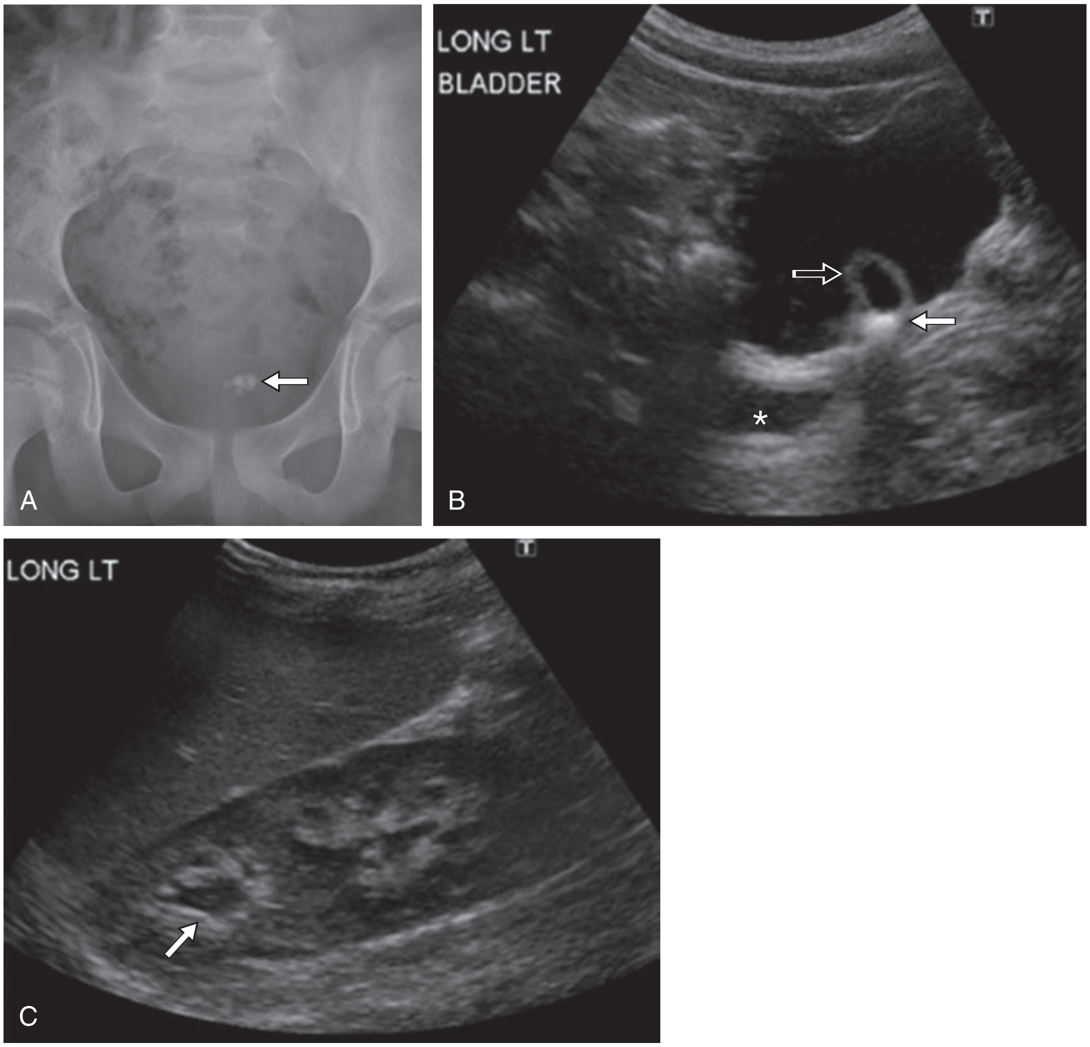

**e-Figure 118.20. 6-year-old boy with left upper quadrant pain.** (A) Abdominal radiograph shows small calcifications in the left lower pelvis *(arrow).* (B) Longitudinal sonogram of the bladder demonstrates echogenic calculi with posterior acoustic shadowing *(white arrow)* seen in association with a left ureterocele *(black arrow).* There is upstream left ureteral dilation *(asterisk).* (C) Longitudinal renal sonogram shows a duplex left kidney with mild upper moiety caliectasis *(arrow).*

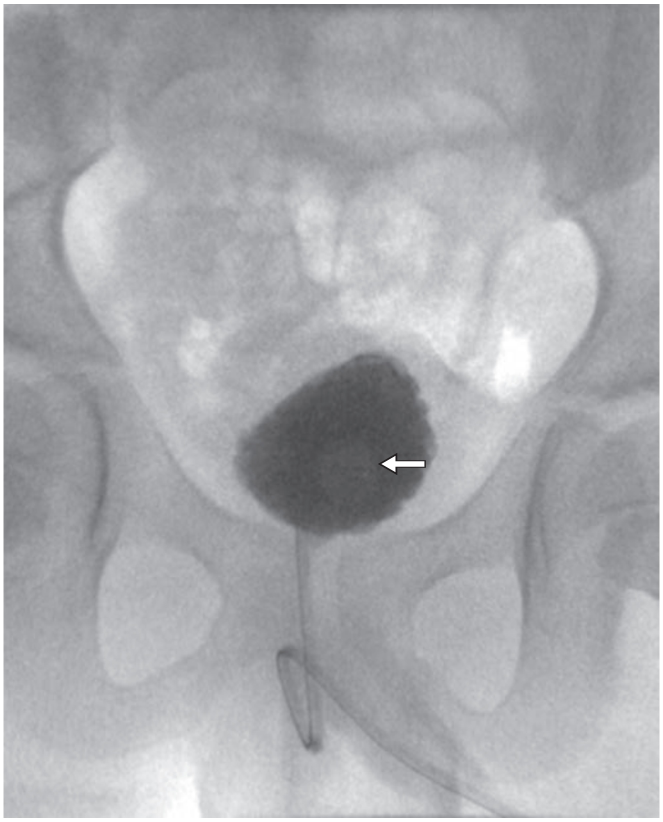

**Figure 118.22. Ureterocele on VCUG.** Frontal VCUG image acquired during early bladder filling demonstrates a round filling defect to the left of the midline.

may also be seen.[60,79] Ultrasound can also be useful for assessing the renal unit for findings of dysplasia or obstructive nephropathy, with the affected renal unit sometimes appearing as a cystic structure in cases of severe obstruction.

On VCUG, a ureterocele appears as a round or oval radiolucent filling defect within the bladder and is best imaged during early bladder filling (Fig. 118.22). As bladder luminal pressure rises with increased bladder filling, the ureterocele is compressed and flattened against the bladder wall, making it difficult to identify. With still higher bladder pressures, ureteroceles may even evert, simulating a paraureteral diverticulum. During voiding, a ureterocele may prolapse into the urethra. VUR into an untreated ureterocele is rare but common after endoscopic incision. Renal scintigraphy may reveal renal parenchymal functional impairment, particularly of an involved upper pole moiety. MRU can be useful for preoperative imaging because it provides functional information along with anatomic detail and can reveal any associated genitourinary abnormalities.[18]

Treatment depends on the type of ureterocele, the amount of renal function, and whether there is VUR into the ipsilateral lower pole moiety ureter and/or contralateral ureter. Endoscopic ureterocele incision alone can be successful for an intravesical ureterocele, but a second surgical procedure is generally required for an ectopic ureterocele. For an ectopic ureterocele with reasonably preserved renal function and no VUR of the lower pole moiety ureter, a ureteroureterostomy or ureteropyelostomy can be performed, connecting the upper and lower pole collecting systems. When there is poor renal function and no VUR, an upper pole partial nephrectomy is generally successful. In the setting of an ectopic ureterocele associated with poorly functioning upper pole moiety parenchyma and VUR of the lower pole moiety or contralateral ureter, an upper pole partial nephrectomy and likely second stage surgery consisting of ureterocele removal and double ureteral reimplantation is generally required.[79]

## URETERAL NEOPLASMS

Primary neoplasms of the upper urinary tract (renal pelvis and ureters), such as rhabdomyosarcoma or urothelial neoplasm, are extremely rare in children. The ureter is more often secondarily involved by tumors such as Wilms tumor, neuroblastoma, rhabdomyosarcoma, and malignant teratoma. Instances of benign and often pedunculated fibroepithelial polyps in the upper one-third of the ureter have been reported (e-Fig. 118.23) and can cause hematuria or rarely UPJ or ureteral obstruction. Ultrasound is only useful to detect large tumors with a significant extraureteral component or to visualize indirect signs of obstruction. Otherwise, imaging relies on CT or MRU.[83–89]

## POSTOPERATIVE IMAGING OF THE URETER

Postoperative imaging is heavily based on ultrasound. However, ultrasound is poor at assessing urinary drainage, and because a chronically dilated collecting system may remain dilated even after relief of obstruction, a functional scintigraphic or MRU study may prove helpful for distinguishing obstruction from chronic nonobstructive dilation. In the setting of postoperative ureteral obstruction (e.g., due to antireflux procedures, blood clots, or stricture), imaging may not only help in detection but also may assist interventions, such as ureteral balloon dilatation, ureteral stent placement, and percutaneous nephrostomy.

### KEY POINTS

- The ureter is more difficult to image than other parts of the urinary system.
- MRU is a powerful tool for imaging the upper urinary tract and can assess both anatomy and function without the use of ionizing radiation.
- Most ureteral obstructions occur at the UPJ or UVJ but can occur between these locations as a result of congenital or acquired causes.
- Megaureter may be obstructed, refluxing, nonobstructed and nonrefluxing, or obstructed and refluxing.
- A history of constant urine leakage in a girl with otherwise normal voiding should suggest extravesical ureteral ectopia.
- In children, ureteroceles are most often associated with the upper pole moiety of a duplicated system and have an ectopic insertion.
- Primary ureteral neoplasms are extremely rare in children, with secondary involvement of the ureter by extraureteral tumors more common.

### SUGGESTED READING

Arlen AM, et al. Magnetic resonance urography for diagnosis of pediatric ureteral stricture. *J Pediatr Urol.* 2014;10(5):792–798.

Berrocal T, et al. Anomalies of the distal ureter, bladder, and urethra in children: embryologic, radiologic, and pathologic features. *Radiographics.* 2002;22(5):1139–1164.

Cerwinka WH, Grattan-Smith JD, Kirsch AJ. Magnetic resonance urography in pediatric urology. *J Pediatr Urol.* 2008;4(1):74–82, quiz 82–83.

Darge K, Grattan-Smith JD, Riccabona M. Pediatric uroradiology: state of the art. *Pediatr Radiol.* 2011;41(1):82–91.

Figueroa VH, et al. Utility of MR urography in children suspected of having ectopic ureter. *Pediatr Radiol.* 2014;44(8):956–962.

Glassberg KI, et al. Suggested terminology for duplex systems, ectopic ureters and ureteroceles. *J Urol.* 1984;132(6):1153–1154.

Potenta SE, et al. CT urography for evaluation of the ureter. *Radiographics.* 2015;35(3):709–726.

Riccabona M. Urinary tract imaging in infancy. *Pediatr Radiol.* 2009;39(suppl 3):436–445.

### REFERENCES

Full references for this chapter can be found on www.expertconsult.com.

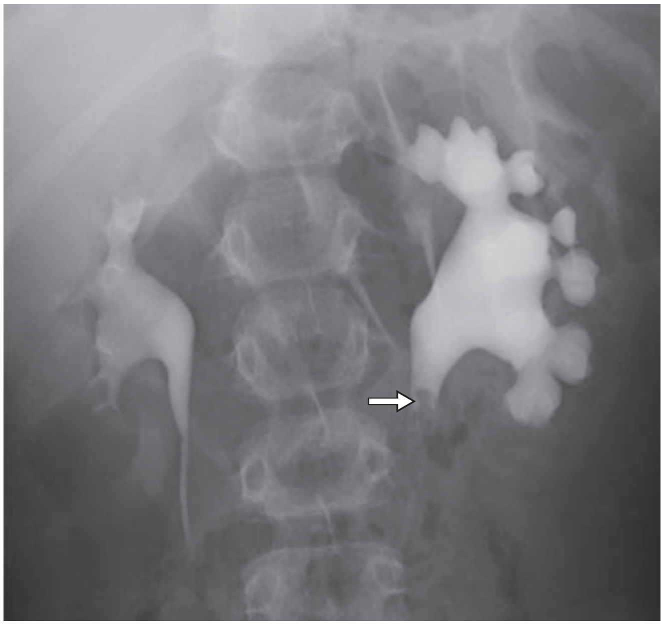

**e-Figure 118.23. Fibroepithelial polyp in a 10-year-old boy with intermittent left flank pain.** Intravenous pyelogram image shows a filling defect *(arrow)* in the proximal left ureter just distal to the UPJ. There is associated upstream left pelvocaliectasis and a small amount of distal ureteral contrast, compatible with partial obstruction. Pathology of the resected ureteral segment demonstrated a fibroepithelial polyp.

## REFERENCES

1. Moore KL, Persaud TVN, Torchia MG. Urogenital system. In: *Before We Are Born: Essentials of Embryology and Birth Defects*. Saunders; 2016:161–188.
2. Shapiro E. Clinical implications of genitourinary embryology. *Curr Opin Urol*. 2009;19(4):427–433.
3. Batourina E, et al. Apoptosis induced by vitamin A signaling is crucial for connecting the ureters to the bladder. *Nat Genet*. 2005;37(10):1082–1089.
4. Baker SM, Middleton WD. Color Doppler sonography of ureteral jets in normal volunteers: importance of the relative specific gravity of urine in the ureter and bladder. *AJR Am J Roentgenol*. 1992;159(4): 773–775.
5. Riccabona M. Potential of modern sonographic techniques in paediatric uroradiology. *Eur J Radiol*. 2002;43(2):110–121.
6. de Bessa J Jr, et al. Diagnostic accuracy of color Doppler sonographic study of the ureteric jets in evaluation of hydronephrosis. *J Pediatr Urol*. 2008;4(2):113–117.
7. Strehlau J, Winkler P, de la Roche J. The uretero-vesical jet as a functional diagnostic tool in childhood hydronephrosis. *Pediatr Nephrol*. 1997;11(4):460–467.
8. Darge K, Grattan-Smith JD, Riccabona M. Pediatric uroradiology: state of the art. *Pediatr Radiol*. 2011;41(1):82–91.
9. Mitsumori A, et al. Evaluation of crossing vessels in patients with ureteropelvic junction obstruction by means of helical CT. *Radiographics*. 2000;20(5):1383–1393, discussion 1393-1395.
10. Quillin SP, et al. Helical (spiral) CT angiography for identification of crossing vessels at the ureteropelvic junction. *AJR Am J Roentgenol*. 1996;166(5):1125–1130.
11. [deleted in review].
12. Potenta SE, et al. CT urography for evaluation of the ureter. *Radiographics*. 2015;35(3):709–726.
13. Piepsz A, Ham HR. Pediatric applications of renal nuclear medicine. *Semin Nucl Med*. 2006;36(1):16–35.
14. Shulkin BL, et al. Procedure guideline for diuretic renography in children 3.0. *J Nucl Med Technol*. 2008;36(3):162–168.
15. Riccabona M. Urinary tract imaging in infancy. *Pediatr Radiol*. 2009;39(suppl 3):436–445.
16. Perez-Brayfield MR, et al. A prospective study comparing ultrasound, nuclear scintigraphy and dynamic contrast enhanced magnetic resonance imaging in the evaluation of hydronephrosis. *J Urol*. 2003;170(4 Pt 1):1330–1334.
17. Cerwinka WH, Grattan-Smith JD, Kirsch AJ. Magnetic resonance urography in pediatric urology. *J Pediatr Urol*. 2008;4(1):74–82, quiz 82-83.
18. Cerwinka WH, Kirsch AJ. Magnetic resonance urography in pediatric urology. *Curr Opin Urol*. 2010;20(4):323–329.
19. Vivier PH, et al. MR urography in children. Part 1: How we do the F0 technique. *Pediatr Radiol*. 2010;40(5):732–738.
20. [deleted in review].
21. Murata N, et al. Gadolinium tissue deposition in brain and bone. *Magn Reson Imaging*. 2016;34(10):1359–1365.
22. Gosálbez R, et al. Congenital ureteral valves in children. *Urology*. 1983;21(3):237–241.
23. Wall B, Wachter E. Congenital ureteral valve: its role as a primary obstructive lesion: classification of the literature and report of an authentic case. *J Urol*. 1952;68(4):684–690.
24. Rabinowitz R, et al. Ureteral valves in children. *Urology*. 1998;51(5A suppl):7–11.
25. Reinberg Y, et al. Congenital ureteral valves in children: case report and review of the literature. *J Pediatr Surg*. 1987;22(4):379–381.
26. Rossi E, et al. Congenital ureteral valves: two new cases and a review of the literature. *J Pediatr Urol*. 2007;3(5):344–349.
27. Kirks DR, Currarino G, Weinberg AG. Transverse folds in the proximal ureter: a normal variant in infants. *AJR Am J Roentgenol*. 1978;130(3):463–464.
28. Arlen AM, et al. Magnetic resonance urography for diagnosis of pediatric ureteral stricture. *J Pediatr Urol*. 2014;10(5):792–798.
29. Hwang AH, et al. Congenital mid ureteral strictures. *J Urol*. 2005;174(5):1999–2002.
30. Docimo SG, et al. Congenital midureteral obstruction. *Urol Radiol*. 1989;11(3):156–160.
31. Smith BG, et al. Congenital midureteral stricture in children diagnosed with antenatal hydronephrosis. *Urology*. 2004;64(5):1014–1019.
32. Brugnara M, et al. Prenatal diagnosis of a rare form of congenital mid-ureteral stricture: a case report and literature revisited. *BMC Urol*. 2007;7:8.
33. Gitlin J, Kaefer M. Congenital mid ureteral stricture presenting as prenatal hydronephrosis. *J Urol*. 2002;168(3):1154–1155.
34. Lautin EM, et al. CT diagnosis of circumcaval ureter. *AJR Am J Roentgenol*. 1988;150(3):591–594.
35. Bass JE, et al. Spectrum of congenital anomalies of the inferior vena cava: cross-sectional imaging findings. *Radiographics*. 2000;20(3):639–652.
36. Acharya SK, et al. Retrocaval ureter: a rare cause of hydronephrosis in children. *J Pediatr Surg*. 2009;44(4):846–848.
37. Carrion H, et al. Retrocaval ureter: report of 8 cases and the surgical management. *J Urol*. 1979;121(4):514–517.
38. Leyendecker JR, Barnes CE, Zagoria RJ. MR urography: techniques and clinical applications. *Radiographics*. 2008;28(1):23–46, discussion 46-47.
39. Blandino A, et al. MR urography of the ureter. *AJR Am J Roentgenol*. 2002;179(5):1307–1314.
40. Rigas A, et al. Pelvi-ureteric junction obstruction by crossing renal vessels: clinical and imaging features. *BJU Int*. 2003;92(1):101–103.
41. Hoffer FA, Lebowitz RL. Intermittent hydronephrosis: a unique feature of ureteropelvic junction obstruction caused by a crossing renal vessel. *Radiology*. 1985;156(3):655–658.
42. Lamba R, et al. Multidetector CT of vascular compression syndromes in the abdomen and pelvis. *Radiographics*. 2014;34(1):93–115.
43. Calder AD, et al. Contrast-enhanced magnetic resonance angiography for the detection of crossing renal vessels in children with symptomatic ureteropelvic junction obstruction: comparison with operative findings. *Pediatr Radiol*. 2007;37(4):356–361.
44. Dalpiaz A, et al. Urological manifestations of henoch-schonlein purpura: a review. *Curr Urol*. 2015;8(2):66–73.
45. Walther MM, et al. The urological manifestations of chronic granulomatous disease. *J Urol*. 1992;147(5):1314–1318.
46. Gargollo PC, Barnewolt C, Diamond DA. Calcified ureteral stricture in a child with polyarteritis nodosa. *J Urol*. 2004;171(3):1254–1255.
47. [deleted in review].
48. Colleran GC, et al. Imaging in the diagnosis of pediatric urolithiasis. *Pediatr Radiol*. 2016.
49. Sobel JD, Vazquez JA. Fungal infections of the urinary tract. *World J Urol*. 1999;17(6):410–414.
50. Kale H, Narlawar RS, Rathod K. Renal fungal ball: an unusual sonographic finding. *J Clin Ultrasound*. 2002;30(3):178–180.
51. Dembner AG, Pfister RC. Fungal infection of the urinary tract: demonstration by antegrade pyelography and drainage by percutaneous nephrostomy. *AJR Am J Roentgenol*. 1977;129(3):415–418.
52. Jandaghi AB, et al. Assessment of ureterovesical jet dynamics in obstructed ureter by urinary stone with color Doppler and duplex Doppler examinations. *Urolithiasis*. 2013;41(2):159–163.
53. Burge HJ, et al. Ureteral jets in healthy subjects and in patients with unilateral ureteral calculi: comparison with color Doppler US. *Radiology*. 1991;180(2):437–442.
54. Miller OF, et al. Presentation of idiopathic retroperitoneal fibrosis in the pediatric population. *J Pediatr Surg*. 2003;38(11):1685–1688.
55. Müller-Suur R, Mesko L. Analysis of ureteral peristalsis in routine renography using a time-space approach. *Contrib Nephrol*. 1987;56:232–237.
56. Kim S, et al. Time-resolved dynamic contrast-enhanced MR urography for the evaluation of ureteral peristalsis: initial experience. *J Magn Reson Imaging*. 2008;28(5):1293–1298.
57. Keller MS, Weiss RM, Rosenfield NS. Sonographic evaluation of ureterectasis in children: the significance of peristalsis. *J Urol*. 1993;149(3):553–555.
58. Ropolo R, et al. Scintigraphic study of ureteral peristalsis using fast Fourier transforms. *J Nucl Biol Med*. 1993;37(4):223–227.
59. King LR. Megaloureter: definition, diagnosis and management. *J Urol*. 1980;123(2):222–223.
60. Berrocal T, et al. Anomalies of the distal ureter, bladder, and urethra in children: embryologic, radiologic, and pathologic features. *Radiographics*. 2002;22(5):1139–1164.
61. Merlini E, Spina P. Primary non-refluxing megaureters. *J Pediatr Urol*. 2005;1(6):409–417.
62. Meyer JS, Lebowitz RL. Primary megaureter in infants and children: a review. *Urol Radiol*. 1992;14(4):296–305.
63. Pfister RC, Hendren WH. Primary megaureter in children and adults. Clinical and pathophysiologic features of 150 ureters. *Urology*. 1978;12(2):160–176.
64. Shokeir AA, Nijman RJ. Primary megaureter: current trends in diagnosis and treatment. *BJU Int*. 2000;86(7):861–868.
65. Wood BP, et al. Ureterovesical obstruction and megaloureter: diagnosis by real-time US. *Radiology*. 1985;156(1):79–81.

66. Glassberg KI, et al. Suggested terminology for duplex systems, ectopic ureters and ureteroceles. *J Urol*. 1984;132(6):1153–1154.
67. Ahmed S, Morris LL, Byard RW. Ectopic ureter with complete ureteric duplication in the female child. *J Pediatr Surg*. 1992;27(11):1455–1460.
68. Chowdhary SK, et al. Single-system ectopic ureter: a 15-year review. *Pediatr Surg Int*. 2001;17(8):638–641.
69. Hanson GR, et al. Diagnosis of ectopic ureter as a cause of urinary incontinence. *J Pediatr Urol*. 2007;3(1):53–57.
70. Fernbach SK, et al. Ureteral duplication and its complications. *Radiographics*. 1997;17(1):109–127.
71. Ellerker AG. The extravesical ectopic ureter. *Br J Surg*. 1958;45(192):344–353.
72. Ghosh B, et al. Ectopic ureter draining into the uterus. *Urol Ann*. 2016;8(1):105–107.
73. Figueroa VH, et al. Utility of MR urography in children suspected of having ectopic ureter. *Pediatr Radiol*. 2014;44(8):956–962.
74. El-Ghar MA, El-Diasty T. Ectopic insertion of the ureter into the seminal vesicle. *World J Radiol*. 2013;5(9):349–351.
75. Lipson JA, et al. Subtle renal duplication as an unrecognized cause of childhood incontinence: diagnosis by magnetic resonance urography. *J Pediatr Urol*. 2008;4(5):398–400.
76. Arap S, et al. Ureterocele of the lower pole ureter and an ectopic upper pole ureter in a duplex system. *J Urol*. 1983;129(6):1227–1228.
77. Harb JF, et al. Ureterocele arising from a lower-pole moiety. *Urol Int*. 1999;63(4):245–246.
78. Coplen DE, Duckett JW. The modern approach to ureteroceles. *J Urol*. 1995;153(1):166–171.
79. Merlini E, Lelli Chiesa P. Obstructive ureterocele-an ongoing challenge. *World J Urol*. 2004;22(2):107–114.
80. Caldamone AA, Snyder HM, Duckett JW. Ureteroceles in children: followup of management with upper tract approach. *J Urol*. 1984;131(6):1130–1132.
81. Blyth B, et al. Endoscopic incision of ureteroceles: intravesical versus ectopic. *J Urol*. 1993;149(3):556–559, discussion 560.
82. Share JC, Lebowitz RL. Ectopic ureterocele without ureteral and calyceal dilatation (ureterocele disproportion): findings on urography and sonography. *AJR Am J Roentgenol*. 1989;152(3):567–571.
83. Rutigliano DN, et al. Ureteral reconstruction for retroperitoneal tumors in children. *J Pediatr Surg*. 2007;42(2):355–358.
84. Ritchey M, et al. Ureteral extension in Wilms' tumor: a report from the National Wilms' Tumor Study Group (NWTSG). *J Pediatr Surg*. 2008;43(9):1625–1629.
85. Droc CL, et al. Embryonal rhabdomyosarcoma arising in the ureter. *Fetal Pediatr Pathol*. 2008;27(1):1–11.
86. Townsend MF 3rd, et al. Ureteral rhabdomyosarcoma. *Urology*. 1999;54(3):561.
87. Kojima Y, et al. Multiple metachronous fibroepithelial polyps in children. *J Urol*. 2011;185(3):1053–1057.
88. Adey GS, et al. Fibroepithelial polyps causing ureteropelvic junction obstruction in children. *J Urol*. 2003;169(5):1834–1836.
89. Niu ZB, et al. Ureteral polyps: an etiological factor of hydronephrosis in children that should not be ignored. *Pediatr Surg Int*. 2007;23(4):323–326.

# 119 Vesicoureteral Reflux

*Boaz Karmazyn and Brandon P. Brown*

## DEFINITION AND IMAGING OBJECTIVES

***Overview.*** Vesicoureteral reflux (VUR) refers to the retrograde passage of urine from the urinary bladder into the ureter and often to the renal collecting system.[1,2] VUR mainly affects infants and young children with a prevalence of 25% to 40% (Box 119.1).[1] VUR is a risk factor for the development of pyelonephritis, with consequent renal scarring.[3–6]

Current evidence suggests that the long-term risks associated with pyelonephritis and renal scarring are low and that preventive antibiotics and surgery may be useful in only a subset of patients.[7–12] Therefore most children with an uncomplicated initial urinary tract infection (UTI) will not benefit from imaging, and the focus in the evaluation of VUR should be patients who have complicated or recurrent UTIs, as some of them may benefit from prophylactic antibiotics or surgery.[8,11,13] Another common indication in the evaluation of VUR is prenatal hydronephrosis. VUR may also be associated with anomalies that require prompt surgical treatment to prevent renal damage.[13,14]

## ETIOLOGY

***Overview.*** The etiology of VUR is not entirely understood. It is possible that VUR in some infants is physiologic and will spontaneously resolve.[1,2] VUR may be caused by abnormal ureteric budding or interaction with the metanephric mesenchyme, resulting in a lateralized ureteral orifice, with a subsequent shortened submucosal ureter that is deficient in longitudinal muscle fibers.[1,2] Primary VUR has a familial association with genetic heterogeneity.[15–17]

Secondary VUR is seen in patients with other urinary tract anomalies (Box 119.2).[18–20] In addition, increased bladder pressure from bladder outlet obstruction (e.g., posterior urethral valves), as well as increased detrusor muscle tone or uncoordinated bladder contraction (e.g., neurogenic bladder) can cause VUR.[21–26]

**BOX 119.1** Common Features in Patients With Vesicoureteral Reflux (VUR)

- VUR is common in infants and young children.
- African Americans have lower incidence of VUR.
- VUR has a familial association (parent-child or sibling-sibling) with genetic heterogeneity.
- Most VUR will resolve spontaneously within the first decade of life.
- In utero VUR is associated with renal dysplasia.
- The main indications to evaluate for VUR are UTI and antenatal hydronephrosis.
- Children with VUR have increased incidence of pyelonephritis and renal scarring.
- Initial management in most children with VUR is to await spontaneous resolution.
- Children with VUR should be evaluated for bowel and bladder dysfunction.
- Treatment of bowel and bladder dysfunction increases resolution of VUR and improves surgical outcomes.
- Prophylactic antibiotic therapy decreases the risk of recurrent UTIs in children with VUR but not the risk of renal scarring.
- Surgery for VUR is reserved for children with breakthrough infections and progressive scarring.

## IMAGING TECHNIQUES

***Overview.*** The diagnostic imaging modalities preferred for the evaluation of VUR include voiding cystourethrogram (VCUG), radionuclide cystography (RNC), and ultrasound (US) (Box 119.3). The optimal imaging modality in the assessment of VUR depends on the indication, radiologist preference and experience, and availability. VCUG is the gold standard for depicting VUR and is especially useful as the initial imaging examination for boys, while contrast-enhanced voiding urosonography (ce-VUS) involves no ionizing radiation and may be used as the first study in girls and in follow-up studies. In the past, RNC was considered

**BOX 119.2** Causes of Vesicoureteral Reflux (VUR)

**PRIMARY**

- Developmental, idiopathic, or immature urinary tract
- Anomalous development at the ureterovesical junction

**SECONDARY**

- Bladder outlet obstruction, particularly posterior urethral valves
- Neurogenic bladder
- Bladder dyssynergia and dysfunctional voiding
- Bladder diverticula
- Prune-belly syndrome
- Postoperative bladder, including ureterocele incision

**BOX 119.3** Imaging of Vesicoureteral Reflux (VUR)

**VOIDING CYSTOURETHROGRAM (VCUG)**

- Gold standard study for grading of VUR
- Defines anatomy (bladder, urethra, and refluxing ureters and ureterovesical junctions)

**RADIONUCLIDE CYSTOGRAPHY**

- Allows continuous imaging
- Similar accuracy in grading VUR as compared with VCUG
- Limited anatomic details (decreased ability to see the urethra in boys)
- Can be used as the initial study in girls, or as a follow-up study for boys or girls

**CONTRAST-ENHANCED UROSONOGRAPHY**

- No radiation
- Similar accuracy in grading VUR as compared with VCUG
- Smaller field-of-view as compared with VCUG
- Provides anatomic information regarding kidneys and urinary tract

## Abstract:

Vesicoureteral reflux (VUR) is common in infants and young children. VUR can be evaluated with voiding cystourethrogram (VCUG), radionuclear cystography or contrast-enhanced voiding urosonography. VCUG has the advantage of demonstrating detailed anatomy and is therefore the imaging of choice for initial evaluation in boys.

In children with urinary tract infection (UTI), VUR is a risk factor for the development of pyelonephritis, with consequent renal scarring. The long-term risks associated with pyelonephritis and renal scarring including hypertension and decreased renal function are low, and preventive antibiotics and surgery may be useful in only a subset of patients. Therefore, most children with an uncomplicated initial UTI will not benefit from imaging. The focus in the evaluation of VUR should be in patients who have complicated or recurrent UTIs who may benefit from preventive antibiotics or surgical intervention.

Another common indication in the evaluation of VUR is prenatal hydronephrosis. VUR may be associated with anomalies that require prompt surgical treatment to prevent renal damage.

## Keywords:

Vesicoureteral reflux
Urinary tract infection
Hydronephrosis
Voiding cystourethrogram
Radionuclear cystography
Contrast-enhanced voiding urosonography

to have lower levels of ionizing radiation compared with VCUG; however, with the use of modern fluoroscopy techniques, VCUG has been found to result in significantly lower radiation dose.[27]

For studying the renal parenchyma, US is useful in the evaluation of underlying congenital abnormalities; however, US has limited sensitivity for the detection of pyelonephritis and renal scarring.[28–30] Dimercaptosuccinic acid (DMSA) scintigraphy, contrast-enhanced computed tomography (CT), and magnetic resonance imaging (MRI) have higher accuracy for the detection of pyelonephritis and renal scarring.[31–33] Either CT or MRI can be used for evaluation of pyelonephritis complicated with an abscess.

## GRADING

The international criteria for grading VUR is based on the VCUG (Fig. 119.1).[34] Similar grading scales exist for nuclear cystography and ce-VUS.[35,36] In recent years, a simplified classification of nondilated (grades I and II; Fig. 119.2) versus dilated (grades III, IV, and V; Fig. 119.3) VUR has been used for evaluation of the effect of treatment on children with UTI.[37–39]

In patients with VUR to the level of the calyces, intrarenal reflux of material may be visualized (Fig. 119.4). Intrarenal reflux occurs through the presence of compound (concave) papillae that are a

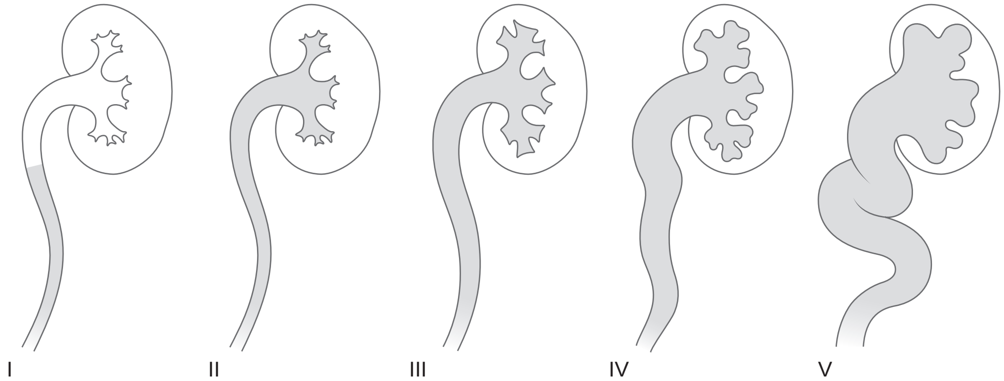

**Figure 119.1. Vesicoureteral reflux grading.** A schematic drawing demonstrating the vesicoureteral reflux grading system on a voiding cystourethrogram. *(From Lebowitz RL, Olbing H, Parkkulainen KV, et al. International reflux study in children: international system of radiographic grading of vesicoureteral reflux: International Reflux Study in Children.* Pediatr Radiol*. 1985;15:105.)*

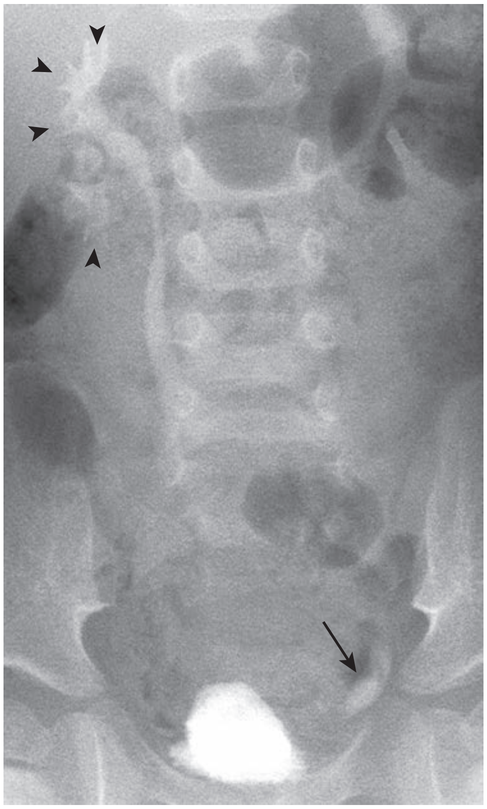

**Figure 119.2. Vesicoureteral reflux.** Voiding cystourethrogram image in a 2-year-old girl shows right grade II vesicoureteral reflux with thin and delicate calyces *(arrowheads)* and left grade I reflux in the distal ureter *(arrow)*.

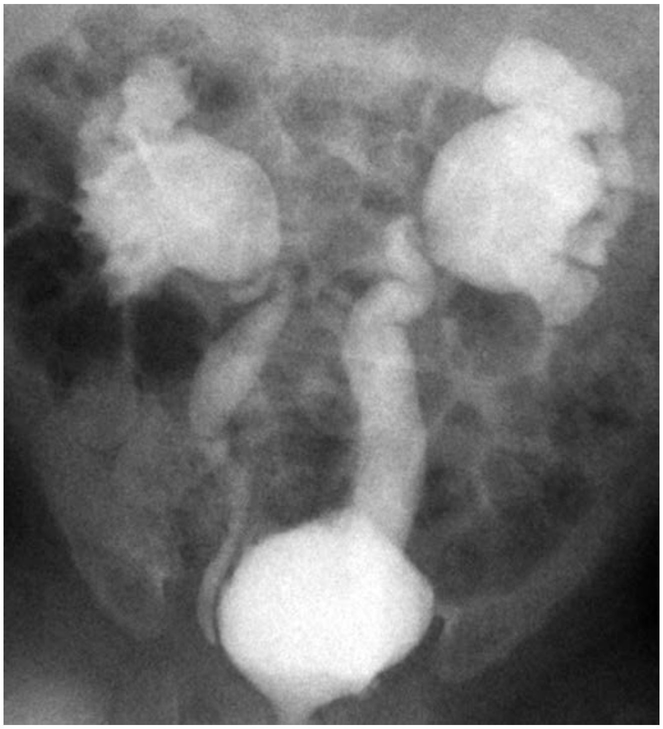

**Figure 119.3. Vesicoureteral reflux.** Voiding cystourethrogram image in a 2-month-old girl shows bilateral dilated vesicoureteral reflux. There is right grade IV vesicoureteral reflux with moderate dilatation and tortuosity of the ureter with extensive dilation of the renal pelvis, but the papillary impressions remain visible in the majority of calyces. There is left grade V vesicoureteral reflux with gross dilatation of a tortuous ureter, renal pelvis, and calyces; no papillary impressions are visible in the majority of calyces.

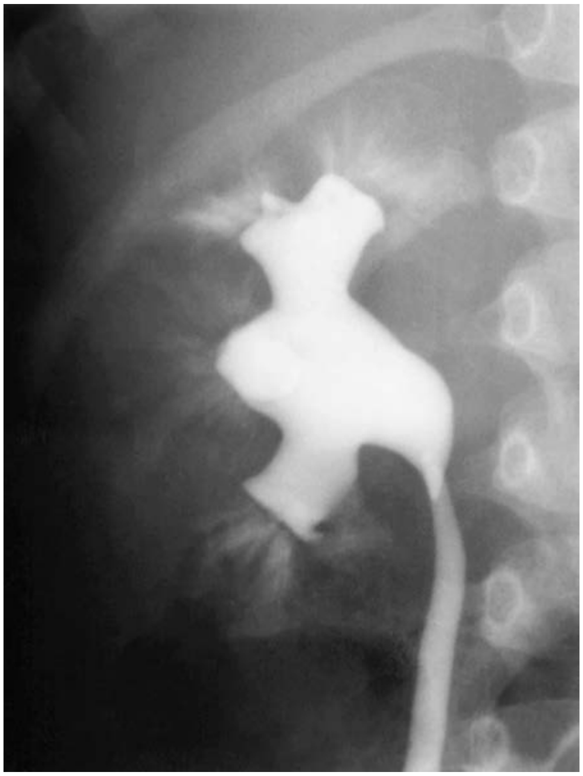

**Figure 119.4. Intrarenal reflux.** Vesicoureteral reflux in a 2-year-old girl shows right high-grade vesicoureteral reflux and diffuse intrarenal reflux, most pronounced at the poles.

result of fusion of two or more simple papillae. At the concave center of the compound papillae, the ductal orifices are open compared with the typical simple (convex) papillae that have oblique orifices that close with increased intrarenal pressure.[40,41] The compound papillae are more frequently seen at the upper and lower poles.[40,41] Intrarenal reflux is associated with increased risk of renal scarring. However, there is no consensus regarding whether the presence of this finding should change management.[42,43] Intrarenal reflux is not included in the international grading system,[34] and its presence should therefore be specifically mentioned in addition to grading of the VUR.

Consistency of the grading system based on VCUG is high when compared between radiologists who work in the same institution.[44] Nevertheless, a significant interobserver variability in grading VUR was found between radiology reports from different institutions.[45]

Reflux in ce-VUS is ranked in grades I to V similar to that for VCUG.[46] The RNC classification of reflux differs from the VCUG classification and is less exact. In RNC grade 1, activity is limited to the ureter, while in RNC grade 2, activity reaches the collecting system with no or minimal activity in ureter. RNC grade 3 is diagnosed when the collecting system and ureter are dilated.[47]

VUR grading does not take into consideration other important factors such as the age and sex of the patient, urinary tract obstruction, renal function and scarring, high- or low-pressure VUR, early or late VUR, slow or quick clearance from the upper collecting system, cystoscopic findings, and the presence or absence of associated disorders (e.g., ureteral duplication, ureteral ectopia, ureterocele, bladder diverticula, prune-belly syndrome, urethral obstruction, megacystis-megaureter association, or neurogenic bladder). This additional information can be essential for making decisions regarding therapy.

## VESICOURETERAL REFLUX IMAGING

### Voiding Cystourethrogram

VCUG may cause anxiety for both parents and children. The anxiety increases early during catheterization and later with discomfort from full distension of the bladder.[48] Sedation and nonsedation methods have been described for decreasing anxiety and pain during VCUG, although the degree of sedation use varies.[49–54] Sedation may especially help in the case of the child who has had previous traumatic experience with catheterization, a history of sexual abuse, or with older children who are known to be unable to cooperate. In older males, a retrograde transurethral infusion of 2% lidocaine can be used to decrease sensation.[55,56] Bladder catheterization is performed in a sterile fashion, and a 5 French catheter is often used in young infants, with an 8 French catheter used in older children.[55,56]

VCUG is performed following “as low as reasonably achievable” principles with the use of pulsed fluoroscopy collimated to the area of interest, with the tower as close as possible to the patient while the examination is performed, and commonly with image acquisition via the last image hold function.[27,57,58] Fluoroscopic observation of the early filling phase has the advantage of increased detection of small ureteroceles.[55,56] Near the end of the filling phase, and especially when VUR has been detected, oblique projections are obtained to evaluate the ureterovesical junctions. The maximal degree of urinary tract dilation should be documented, and then imaging should be continued intermittently during voiding, as about 20% of VUR occurs only during voiding. The urethra is evaluated in the anteroposterior projection in girls and oblique projection in boys. The catheter should not be removed before having an optimal documentation of the anatomy of the urethra when voiding around the catheter. Cyclic infusion of contrast, in which the examination is performed during a series of filling and voiding cycles, has been shown to increase the detection of VUR and severity of the VUR.[59–62]

In about 5% of the patients, VUR may be associated with ureteropelvic junction (UPJ) obstruction. Most commonly it is a coincidental association of these two most common urinary anomalies.[63,64] In some cases UPJ obstruction can be secondary to local scarring from infection or anatomic kinks in the ureter (Fig. 119.5). It is important to recognize this association as antireflux treatment can exacerbate UPJ obstruction.[63,64] The imaging signs suggesting coexistent VUR and UPJ obstruction are a disproportionally dilated renal collecting system compared with the ureter, dilution of the contrast within the renal collecting system, and delayed emptying. It is important to recognize pseudo-UPJ obstruction when pelvic dilatation is visualized on the VCUG, but drainage films or antegrade studies document good drainage (e-Fig. 119.6).[64]

### Radionuclear Cystography

RNC is performed after bladder catheterization, with normal saline mixed with Tc-99m pertechnetate (or other radiopharmaceutical) and administrated via gravity through the bladder catheter. The examination table is covered with plastic-lined absorbent paper to contain spilled radiopharmaceutical and reduce contamination of the table. Images are obtained at a rate of 3 to 5 seconds per frame.[47,65,66]

RNC has similar or higher sensitivity for detection of VUR compared with VCUG.[65–69] However, it has limited spatial resolution and anatomic details are inferior to those seen on a VCUG (Fig. 119.7). Therefore RNC should not be the first imaging evaluation in boys when there is a need for detailed anatomy of the urethra.

### Ultrasound

US without the use of intravesical contrast material has low sensitivity for detection of VUR and does not correlate with severity of

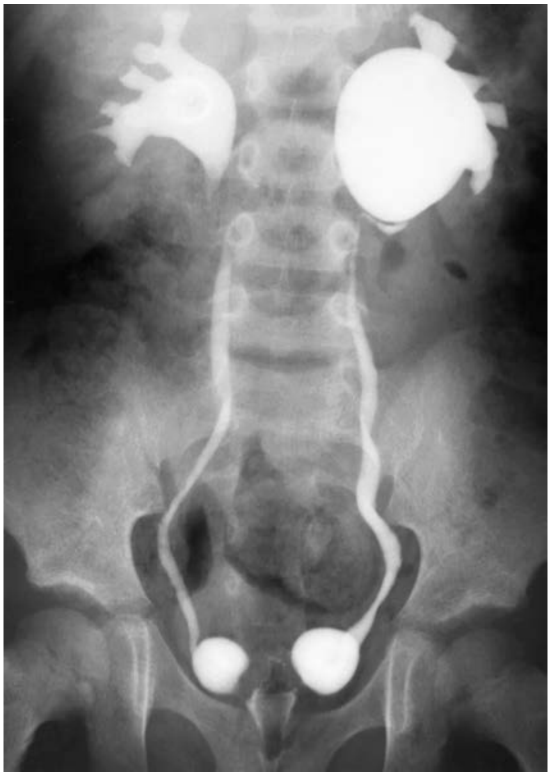

**e-Figure 119.6. Vesicoureteral reflux and left pseudoureteropelvic junction obstruction.** VCUG image after voiding shows right grade IV and left grade V vesicoureteral reflux with ballooning of the left renal pelvis. Intrarenal reflux is present as well. The intravenous urogram image (not shown) was entirely normal. Bilateral paraureteral (Hutch) diverticula also are present.

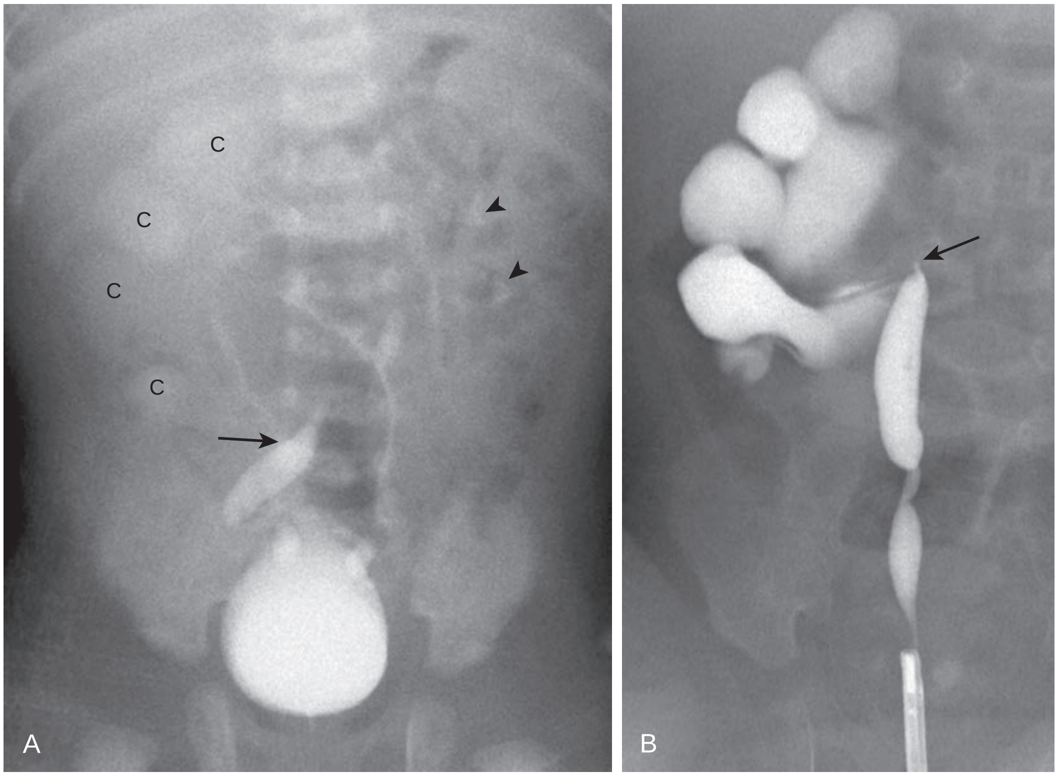

**Figure 119.5. Vesicoureteral reflux and right ureteropelvic junction obstruction.** (A) Voiding cystourethrogram image in a 12-day-old boy shows right prominent ureter *(arrow)* with disproportionally marked distended collecting system (C-calyces) with dilution of contrast. In the presence of ureteropelvic junction obstruction, it is not possible to grade the VUR. There is left VUR as well *(arrowheads)*. (B) Intraoperative retrograde study shows the narrowed ureteropelvic junction *(arrow)*.

VUR.[70,71] The ureters and pelvicalyceal system of patients with VUR often appear normal on sonography even if they appear dilated on VCUG (e-Fig. 119.8). Indirect sonographic signs for VUR are hydronephrosis, hydroureter, urothelial thickening, and changing diameter of the pelvocalyceal system and ureter during the examination.[72,73]

ce-VUS uses US microbubble contrast material instilled into the urinary bladder via transurethral catheterization.[36,46,74–79] The kidneys, bladder, and lower ureters are scanned alternately, and the urethra is scanned during voiding (Fig. 119.9 and e-Fig. 119.10). This method enables depiction of VUR as well as renal, upper urinary tract, and lower urinary tract anatomy.[36,46,74] The sensitivity and specificity of ce-VUS is similar to VCUG.[36,46,74–79]

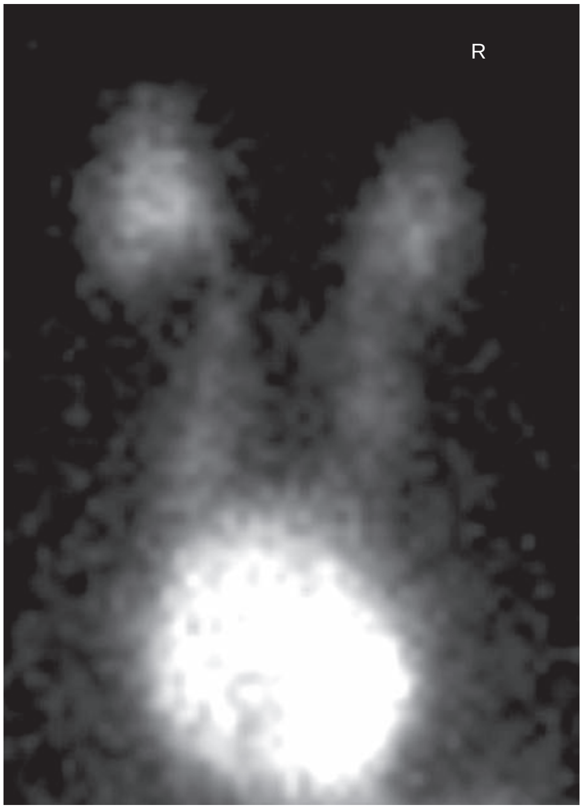

**Figure 119.7. Vesicoureteral reflux and radionuclide cystography.** Posterior view image of Tc-99m pertechnetate cystogram demonstrates radionuclide classification left grade 3 and right grade 2 vesicoureteral reflux.

## NATURAL HISTORY

***Overview.*** Most VUR resolves spontaneously during the first decade of life.[80] This tendency is attributed to a maturation process of the UVJ with age, with an increase in the length of the intramural ureter and strengthening of its musculature. In general, as the grade of the VUR increases, spontaneous resolution is seen with less frequency and often takes a longer time.[80–83] Complete resolution is achieved in 83% of nondilated (grades I–II) VUR and in 73% of dilated (grades III–V) VUR within 10 years.[80] The median time for resolution is 2.5 years for nondilated and 4.5 years for dilated VUR.[80] Dilated VUR is also associated with a higher risk of renal scarring.[84–86] There are multiple factors that affect the rate of VUR resolution. Higher rates are associated with presentation in children younger than 1 year, prenatal hydronephrosis, and reflux when bladder volume is greater than 50% of predicted capacity.[82,87] UTI, bilateral VUR, and voiding dysfunction are associated with lower rates of resolution.[82] Dysfunctional elimination syndromes (Fig. 119.11) are associated with delayed VUR

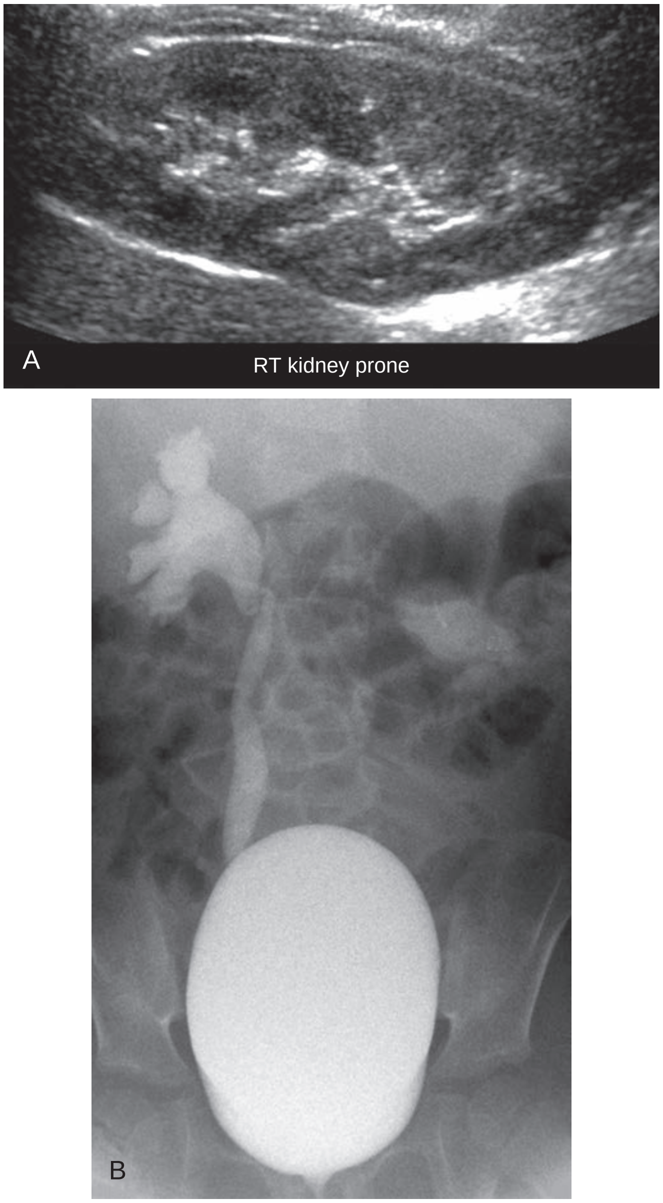

**e-Figure 119.8. Normal renal ultrasound with high-grade vesicoureteral reflux.** (A) A 3-year-old girl with normal longitudinal gray-scale sonogram of the right kidney. (B) Voiding cystourethrogram image shows right high-grade vesicoureteral reflux.

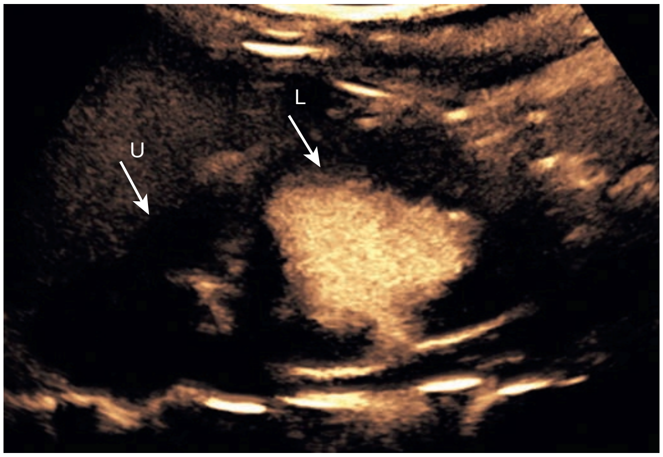

**e-Figure 119.10. Vesicoureteral reflux to the lower pole of a duplex kidney demonstrated by contrast-enhanced voiding urosonography.** Longitudinal sonogram using contrast-specific software in 2-year-old girl demonstrates high-grade vesicoureteral reflux to a dilated lower moiety collecting system (*arrow* L, lower moiety; *arrow* U, upper moiety). *(Image courtesy Dr. Kassa Darge, Children's Hospital of Philadelphia.)*

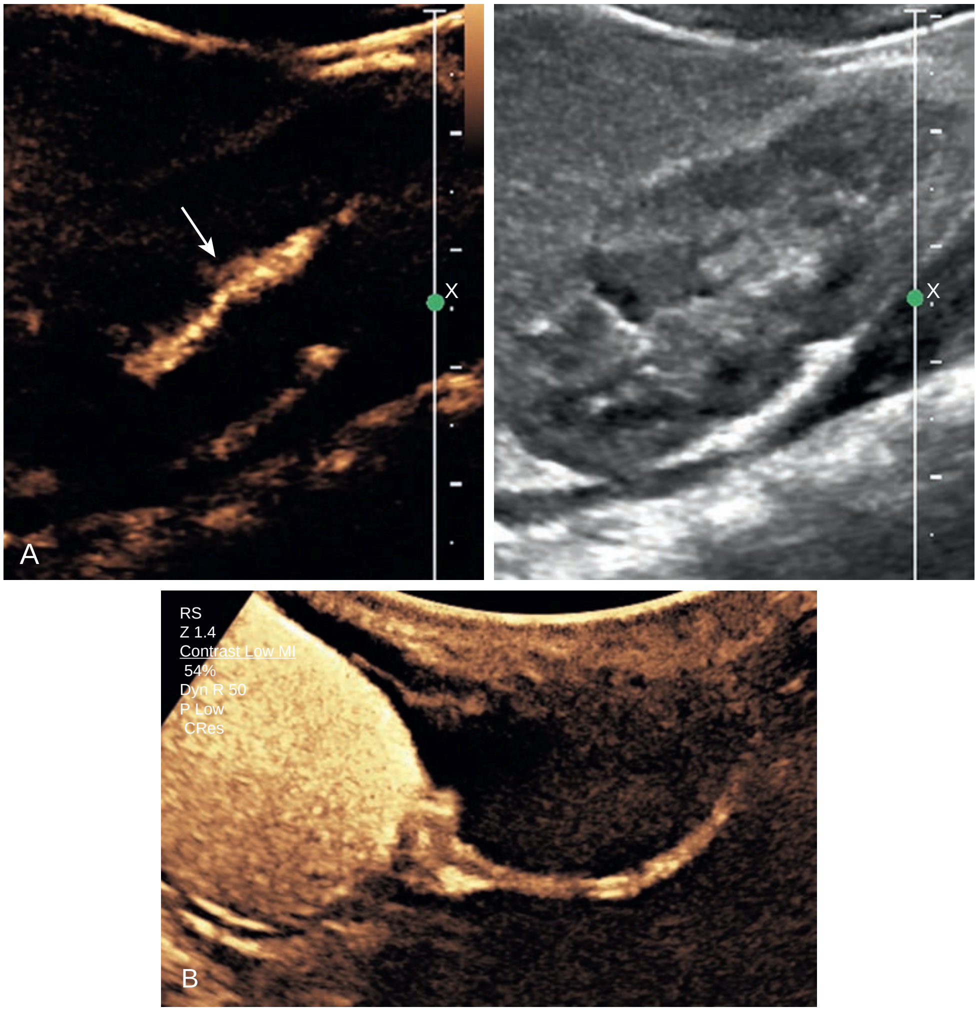

**Figure 119.9. Vesicoureteral reflux demonstrated by contrast-enhanced voiding urosonography.** (A) Longitudinal sonogram in an 11-month-old boy demonstrates right grade II vesicoureteral reflux in dual image mode. The left image was obtained using contrast-specific software that subtracts the background signal and increases the conspicuity of refluxed contrast agent in nondistended renal pelvis (*arrow*, orange material) compared with a gray-scale image. (B) Longitudinal sonogram during voiding shows a normal male urethra. *(Images courtesy Dr. Kassa Darge, Children's Hospital of Philadelphia.)*

resolution and an increased rate of breakthrough UTI.[88] Rates of spontaneous resolution of reflux to the lower moiety of a duplicated system (Fig. 119.12), and in the presence of paraureteral (Hutch) diverticula, were found to be similar to rates among patients with single, typical ureteral systems.[19,89,90]

## RENAL SCARRING AND VUR

***Overview and Pathophysiology.*** In children with normal kidneys, the likelihood of developing chronic kidney disease or hypertension from renal scarring derived from pyelonephritis is very low.[1,91–94]

From prenatal US screening, it was found that in most children with VUR, decreased renal function, and parenchymal abnormalities, the underlying mechanism is not renal scarring secondary to pyelonephritis but rather preexistent congenital hypoplastic/dysplastic kidneys (e-Fig. 119.13).[3,95] VUR is associated with hypoplastic and dysplastic kidneys, mainly in boys.[3,95] Many different types of gene signaling are involved during the interaction of the mesonephric duct with the metanephric mesenchyme during development of the embryonic kidney.[96] Failure of any of the molecular interactions can lead to unique congenital anomalies.[95,96] Another possibility is that intrauterine high-pressure VUR to the immature kidneys causes damage to the immature renal parenchyma.[3]

A meta-analysis of 33 studies found that among children with a first episode of UTI, 57% (95% confidence interval [CI]: 50%–64%) develop pyelonephritis and 18% (95% CI: 14%–23%) developed renal scarring.[84] The risk of renal scarring increases with recurrent pyelonephritis.[97] The prevalence of VUR also increases in children with recurrent UTIs.[97] In children with VUR, there is increased risk of pyelonephritis (relative risk [RR] = 1.5) and renal scarring (RR = 2.6).[83] Children with dilated VUR have about twice the risk to develop renal scarring compared with children with nondilated VUR,[83,97] yet many children with pyelonephritis and renal scarring will not have VUR.[96,98]

Accurate estimations of the long-term clinical consequences of febrile UTIs are difficult to ascertain, as available studies have wide population heterogeneity, limited follow-up, and there is a lack of prospective studies with a control group.[91] From a review of eight prospective studies (1029 children), it was found that only 0.4% of children with initially normal renal function presented with decreased renal function during later follow-up.[92] The risk of end-stage renal disease from acquired scarring is extremely

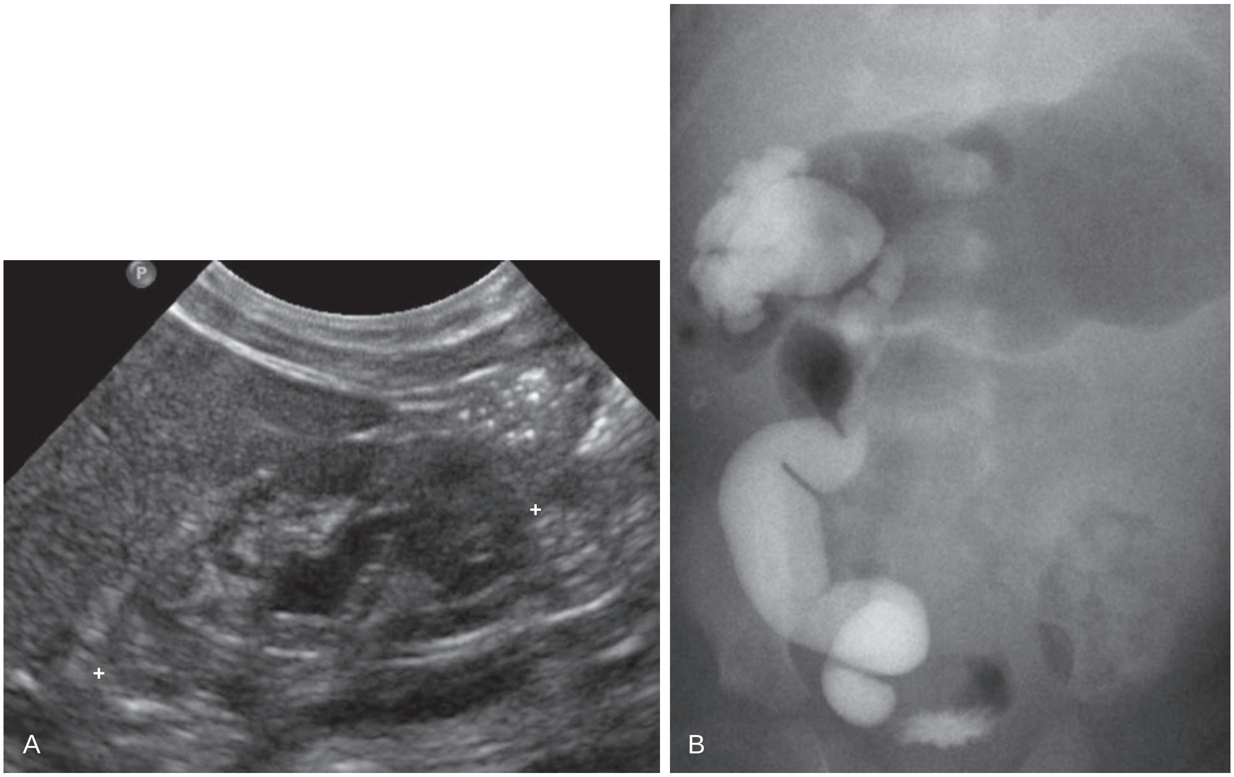

**e-Figure 119.13. Congenital hypoplastic dysplastic kidney with vesicoureteral reflux.** (A) Longitudinal gray-scale sonogram of the right kidney in a 1-month-old boy demonstrates a small kidney (length = 3.3 cm) with echogenic parenchyma with poor corticomedullary differentiation, urothelial thickening, and mild hydronephrosis. (B) Voiding cystourethrogram image shows right grade V vesicoureteral reflux.

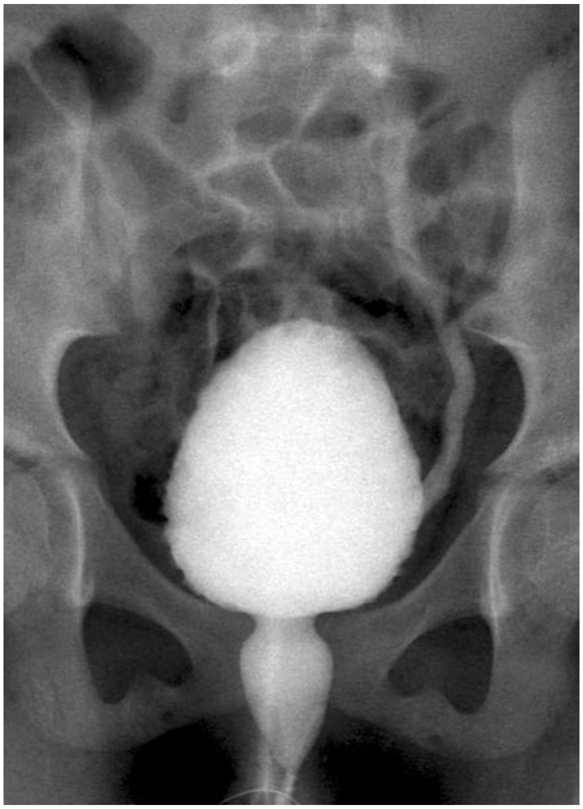

**Figure 119.11. Vesicoureteral reflux and detrusor sphincter dyssynergia.** Voiding cystourethrogram image in a 10-year-old girl with recurrent urinary tract infections and dysfunctional elimination syndrome shows trabeculation of the bladder, ballooning of the urethra ("spinning top" urethra) and left vesicoureteral reflux. Urodynamic study demonstrated abnormally high bladder pressure and dyssynergia with urination.

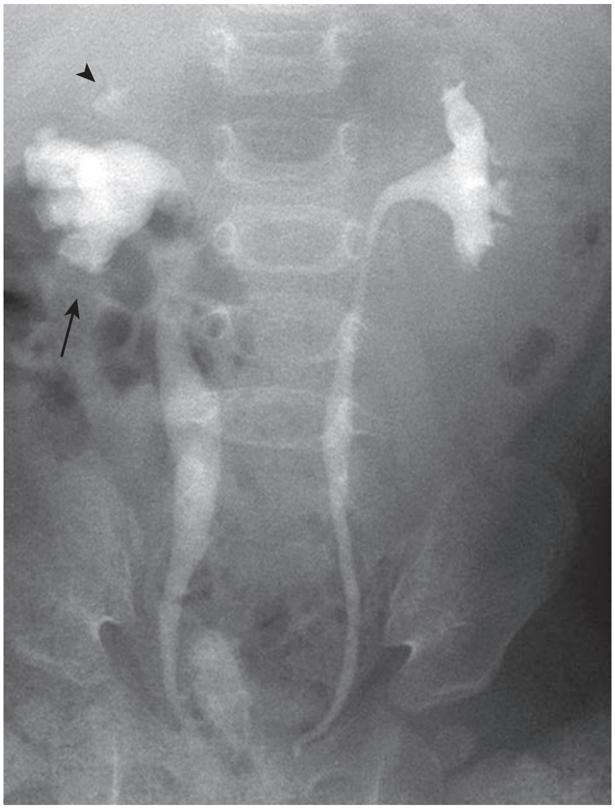

**Figure 119.12. Vesicoureteral reflux (VUR) affecting a duplex kidney.** Voiding cystourethrogram image in a 9-month-old girl demonstrates high-grade VUR into the lower moiety of the right duplex kidney. The collecting system is inferiorly displaced ("drooping lily" sign, *arrow*). There is also reflux into the right upper moiety *(arrowhead)* and left grade II reflux.

low. The overall incidence of end-stage renal disease (ESRD) in children ranges from about 7 (5–9 age group) to 31 (18–21 age group) per million.[99] Registries of children with end-stage renal disease or renal transplantation have reported that reflux nephropathy accounts for 2.6% to 5.1% of ESRD.[99,100]

The prevalence of hypertension secondary to renal scarring in most studies varies between 2% to 6%.[92] In a 10-year international prospective study, hypertension was reported in 1.6% (4/252) of children with VUR.[101]

***Imaging.*** Gray-scale renal US is the primary imaging modality for evaluation of the renal parenchyma in children with febrile UTI. However, gray-scale US has low sensitivity for detection of acute pyelonephritis and parenchymal scarring.[28,102,103] A few studies have suggested moderate to high (74%–89%) sensitivity and varied specificity (53%–81%) of power Doppler in the diagnosis of pyelonephritis.[30,31,104] The sensitivity of power Doppler in detection of renal scarring is low.[104] The parenchymal changes of pyelonephritis are increased or decreased echogenicity, loss of corticomedullary differentiation, and focal or diffuse renal enlargement.[102] Color Doppler imaging shows decreased vascularity.[30,104] Renal scarring may be depicted by US as focal or diffuse parenchymal thinning and areas of depression in the outline of the kidney with or without dilated and distorted adjacent calyces (Fig. 119.14).[28,104] Nuclear scintigraphy, using a cortical agent such as DMSA, contrast-enhanced MRI, and contrast-enhanced CT have all demonstrated high accuracy for detection of pyelonephritis.[31,105] DMSA is considered the gold standard for evaluation of renal scarring.[31,85,106,107] Focal areas of decreased or absent renal cortical uptake on DMSA that persist for months as well as distortion or indentation of the renal parenchyma can both indicate renal scarring (e-Fig. 119.15).[31,105] Recent studies suggest that MRI has high accuracy and can replace DMSA for evaluation of renal scarring (Fig. 119.16).[108,109]

## TREATMENT OF VUR

***Overview.*** The goal of VUR treatment is to prevent recurring febrile UTIs, avoid renal injury, and minimize morbidity.[13] The preferred initial management in most children with VUR is conservative, awaiting spontaneous resolution.[13] Preventive antibiotics in children with VUR have been shown to decrease the risk of recurrent UTIs but not renal scarring.[8]

Abnormal bowel and bladder dysfunction and VUR are associated with each other and with UTI. Children should be evaluated for symptoms of bowel and bladder dysfunction, such as urinary frequency and urgency, prolonged voiding intervals, daytime wetting, constipation, and encopresis. Treatment of bowel and bladder dysfunction increases the resolution rate of VUR, lowers the recurrence rate of febrile UTIs, and improves the outcome of endoscopic treatment for VUR.[13,24,110]

There is a trend toward increasingly minimal intervention for primary VUR in pediatric hospitals, as children with VUR but without pyelonephritis are observed to do well under conservative management.[111] Antireflux procedures are considered for patients with recurrent breakthrough UTIs despite preventive antibiotic treatment or after complicated UTIs.[13] The success rate of ureteral surgical reimplantation is high (98%).[13] Postoperatively, US can

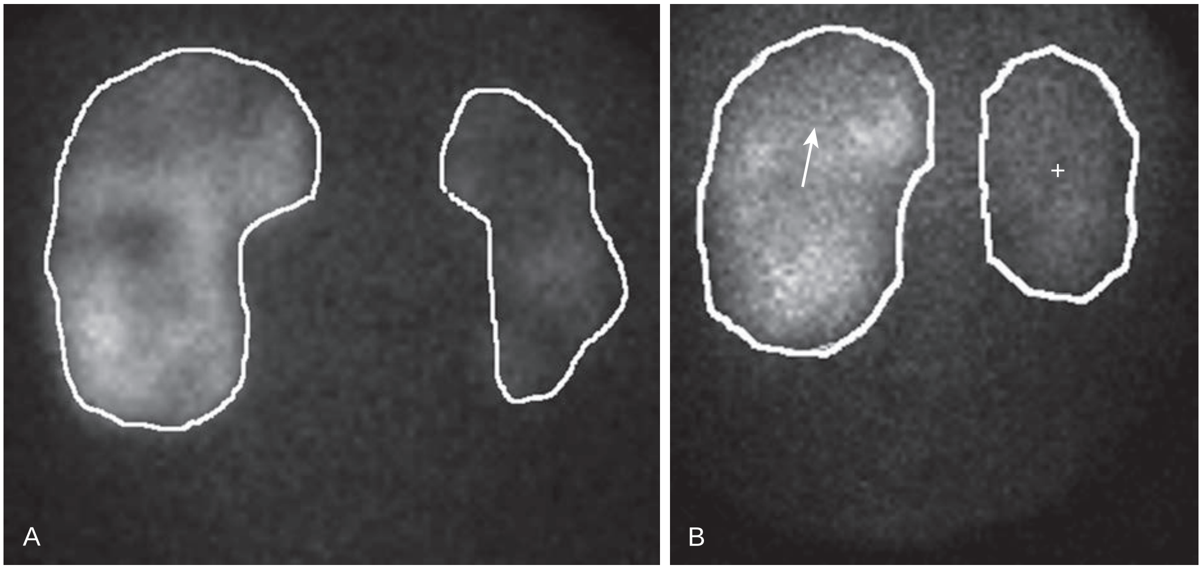

**e-Figure 119.15. Pyelonephritis and renal scarring on Tc-99m dimercaptosuccinic acid (DMSA) scan.** (A) Posterior view Tc-99m DMSA image of the kidneys in a 5-year-old boy with pyelonephritis demonstrates diffusely scarred right kidney and multiple photopenic areas in the left kidney. (B) Four months later, follow-up posterior view Tc-99m DMSA image shows decreased but persistent left upper pole photopenic area *(arrow)* consistent with renal scarring.

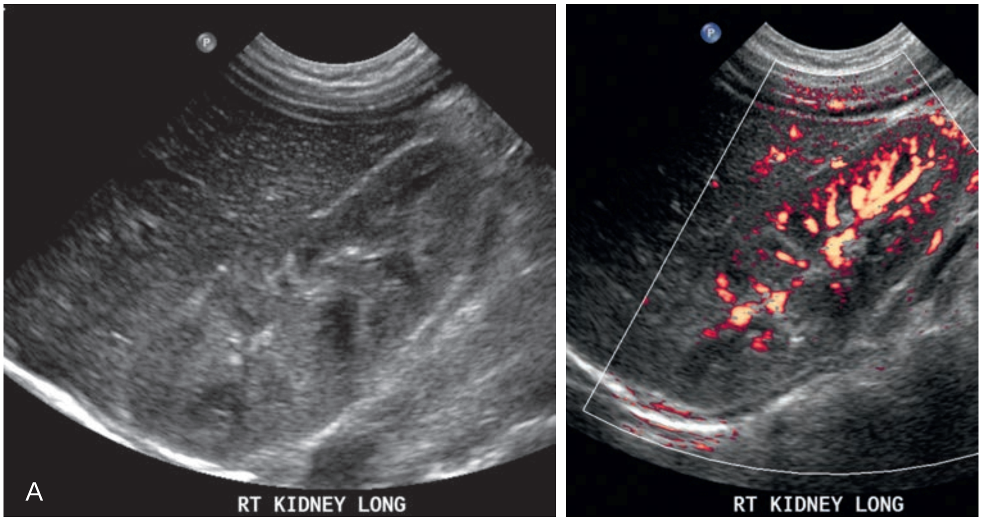

**Figure 119.14. Acute pyelonephritis in an 8-month-old girl with febrile urinary tract infection.** (A) Longitudinal gray-scale sonogram shows swelling and increased echogenicity of the upper pole. (B) Longitudinal power Doppler sonogram shows decreased vascularity in the upper pole.

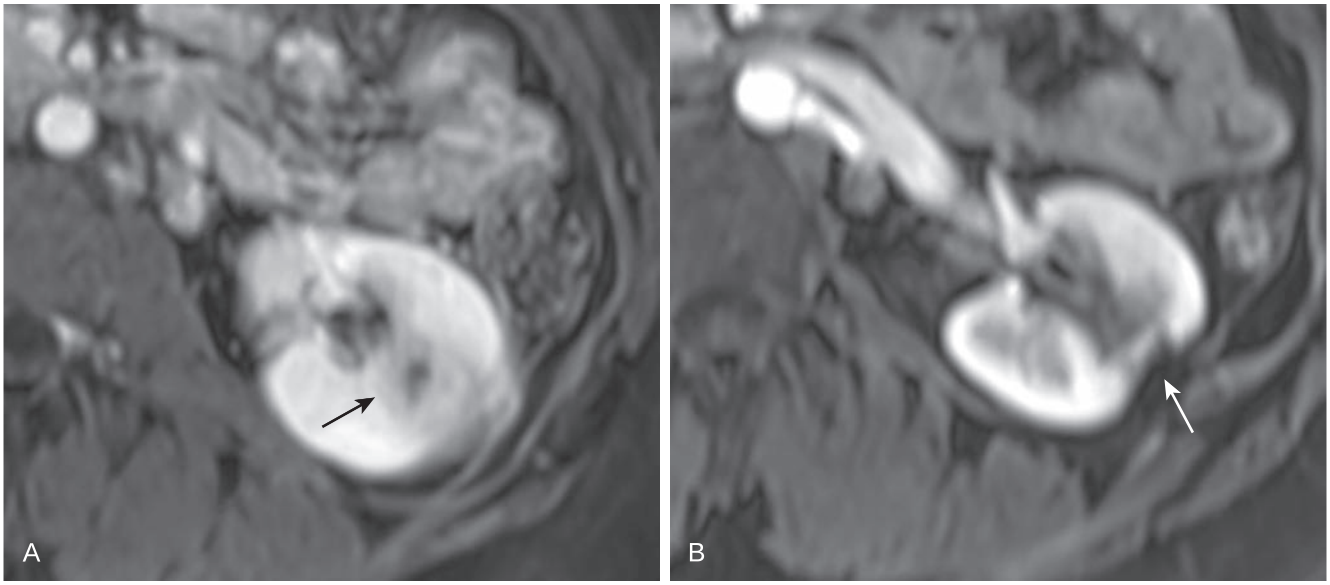

**Figure 119.16. Complicated pyelonephritis with an intrarenal abscess and renal scarring.** (A) Axial postcontrast T1-weighted magnetic resonance (MR) image in a 16-year-old girl with acute pyelonephritis demonstrates a left intrarenal abscess *(arrow)* with perirenal inflammatory standing. (B) Four months later, follow-up MR image demonstrates cortical scarring *(arrow)*.

demonstrate focal thickening of the posterior bladder wall and pseudodiverticular sacculations (e-Fig. 119.17).[112] Alternative therapies, such as endoscopic intravesical injection of a small amount of material (e.g., Silicon, Teflon paste, or dextranomer/hyaluronic acid [Deflux]) into the bladder wall behind the submucosal ureteral tunnel, are also available (Fig. 119.18).[113] The injected material elevates and narrows the ureteral tunnel and causes a localized protrusion of the bladder wall at the lateral angle of the trigone containing the ureteral orifice.[113] The injected material is well visualized by US as a round, echogenic focus that can calcify (Fig. 119.19).[114] The main limitation of this treatment is the lower success rate, which ranges from 50% to 92%.[13,115–118]

## IMAGING ALGORITHMS FOR EVALUATION OF VUR

***Overview.*** The most common indications for evaluation of VUR are prenatal hydronephrosis and UTI. Prenatal hydronephrosis is diagnosed in approximately 1% to 2% of all pregnancies. The grading of hydronephrosis and the clinical practice for evaluation of these children varies widely.[119] The purpose of postnatal imaging in patients with prenatally diagnosed hydronephrosis is to identify underlying urologic abnormalities and those that may benefit from treatment to prevent renal damage and morbidity.

The imaging of VUR in children with febrile UTI is controversial.[120] Overall, as there is no clear benefit of treatment for

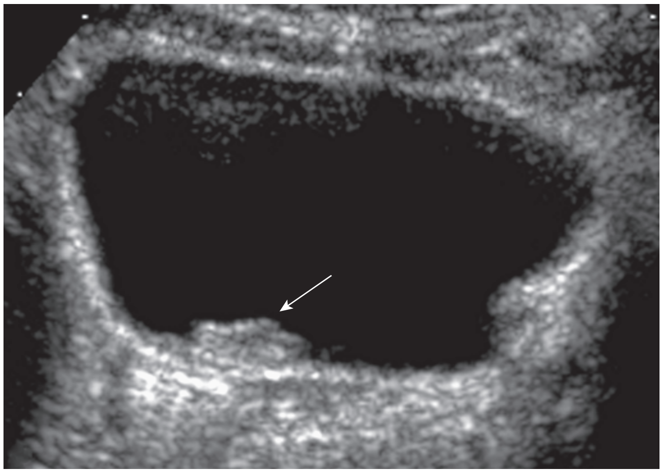

**e-Figure 119.17. Postoperative appearance of ureteral reimplantation.** Gray-scale sonogram of the bladder shows nodularity at the site of ureteral reimplantation *(arrow)*.

children with a first episode of uncomplicated febrile UTI, the tendency is to evaluate for VUR selectively in children with a higher risk of underlying urologic abnormalities or renal scarring. The main controversy is whether renal scintigraphy can be used as the first study (the "top down" approach), thus saving some children from the discomfort associated with the VCUG study. The main limitation of such an approach is that renal scintigraphy is associated with higher radiation dose and that it cannot reliably select all patients with VUR who may benefit from treatment. A meta-analysis study on use of DMSA in cases of acute UTI yielded sensitivity and specificity of 79% and 53%, respectively, for dilated VUR; however, there was marked statistical heterogeneity between the studies. The authors concluded that acute-phase DMSA renal scanning cannot be recommended as replacement for VCUG in the evaluation of young children with a first febrile UTI.[121]

***Imaging Algorithm.*** Evaluation for VUR is indicated in children with antenatal or postnatal moderate or severe hydronephrosis and hydronephrosis associated with oligohydramnios, abnormal renal parenchyma, presence of hydroureter, and bladder wall thickening.[14,122] There is no consensus regarding the need for all children with postnatal mild hydronephrosis to be evaluated for VUR (Fig. 119.20).[119,122,123]

In children older than 2 months with a first episode of uncomplicated febrile UTI, routine imaging of VUR is no longer recommended.[97] Imaging for VUR should still be considered for children with recurrent UTI, as they have been shown to have increased risk of VUR and renal scarring, and also in children with complicated febrile UTI to evaluate for underlying congenital urologic abnormalities.[97] For neonates, the presence of a UTI is associated with a higher percentage of underlying congenital urinary tract anomalies, and urinary infection is more commonly complicated with sepsis. Therefore evaluation with VUR should be considered

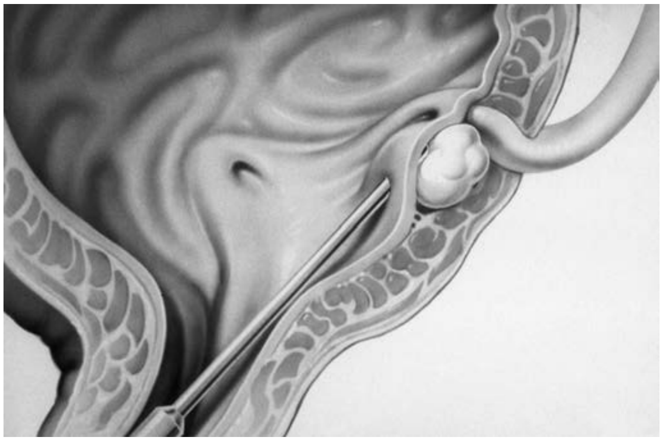

**Figure 119.18. Subureteric injection.** Diagram shows injection of material under the entrance of the ureter into the bladder to eliminate vesicoureteral reflux.

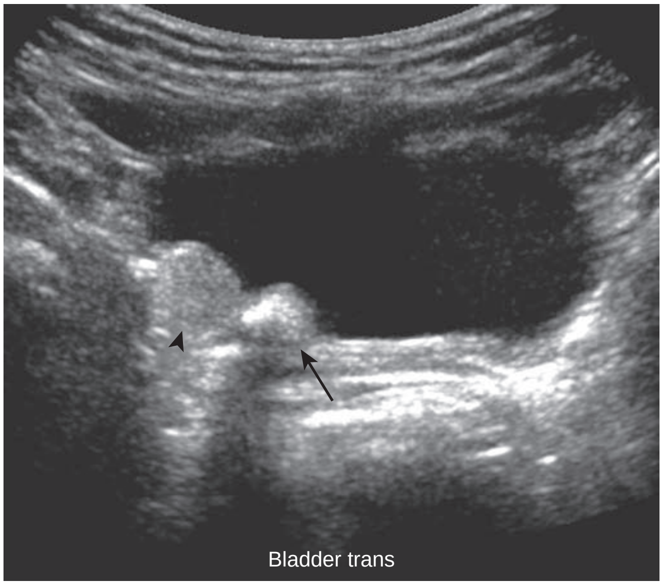

**Figure 119.19. Deflux injection.** Transverse gray-scale sonogram of the bladder in a 3-year-old boy 2 years after endoscopic Deflux injection demonstrates an echogenic mound in the right posterior bladder wall *(arrowhead)* with a focal area of posterior acoustic shadowing due to calcification *(arrow)*, mimicking a bladder stone.

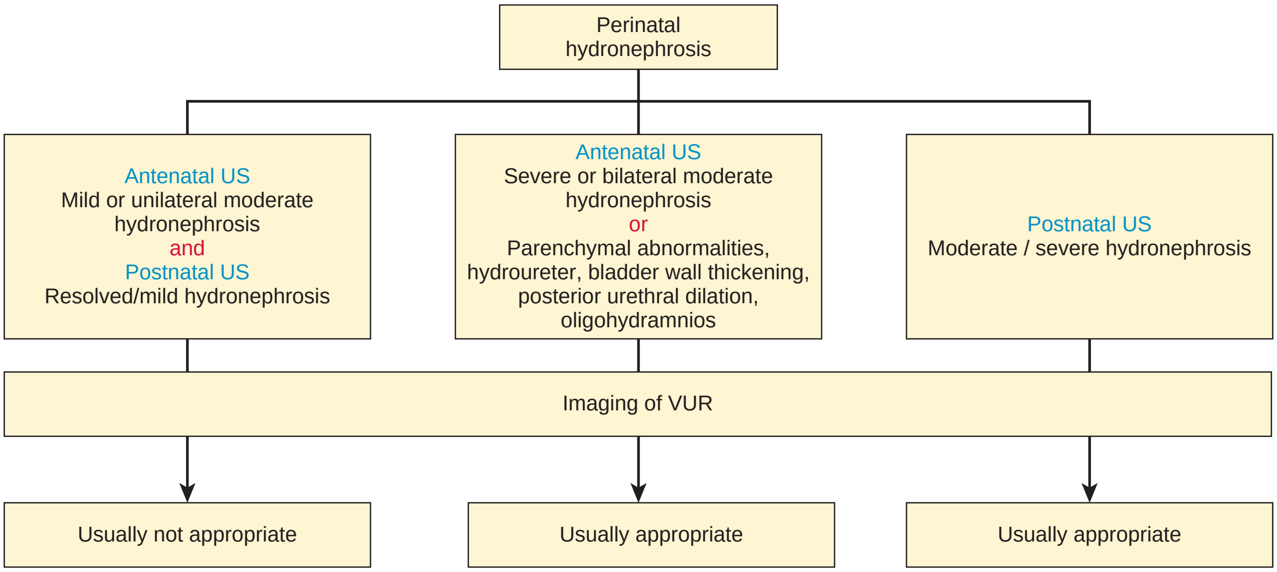
Perinatal hydronephrosis
Antenatal US
Mild or unilateral moderate hydronephrosis
and
Postnatal US
Resolved/mild hydronephrosis
Antenatal US
Severe or bilateral moderate hydronephrosis
or
Parenchymal abnormalities, hydroureter, bladder wall thickening, posterior urethral dilation, oligohydramnios
Postnatal US
Moderate / severe hydronephrosis
Imaging of VUR
Usually not appropriate
Usually appropriate
Usually appropriate

**Figure 119.20. Imaging algorithm for evaluation of vesicoureteral reflux (VUR) in children with perinatal hydronephrosis.**

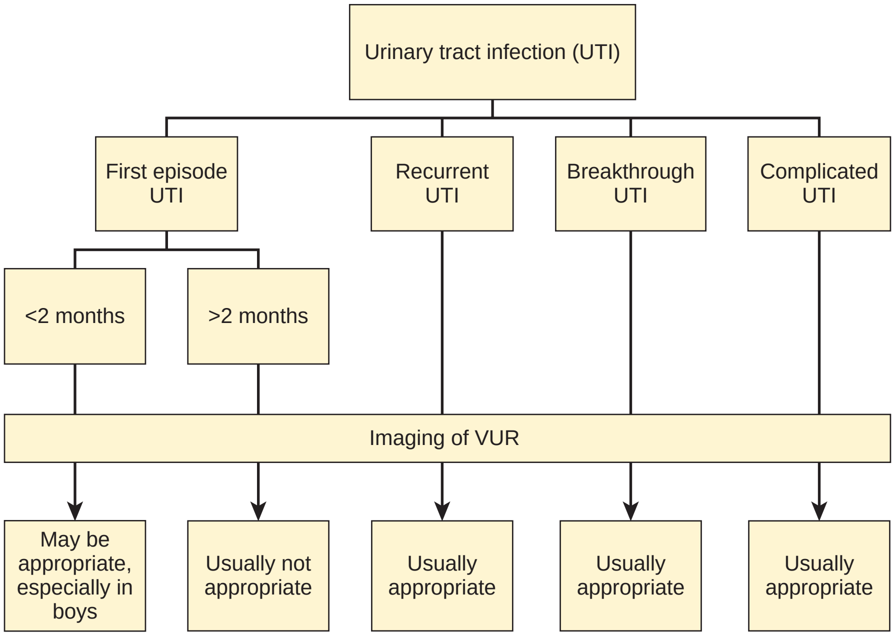

**Figure 119.21.** Imaging algorithm for evaluation of vesicoureteral reflux (VUR) in children with urinary tract infection.

in newborn boys, as it is important to identify the presence of posterior urethral valves.[124]

In boys, VCUG is the preferred first study as it is best for evaluation of the urethral anatomy. In girls and with all follow-up studies, ce-VUS or RNC can be used for evaluation of VUR (Fig. 119.21).[125] The additional use of DMSA or MRI can be beneficial for select pediatric patients with recurrent UTI to more accurately identify renal scarring. The identification of renal scarring may change medical management with antibiotics or surgical antireflux procedures.[125] Follow-up studies for VUR to document resolution depends on the VUR grading. The follow-up interval should increase with increased VUR grading, as the resolution rate in these more severe cases is slower.[80,81]

## KEY POINTS

- VUR does not cause UTI.
- VUR can be either primary or secondary to other urologic abnormalities.
- VUR is a risk factor for the development of pyelonephritis, with consequent renal scarring and potential long-term sequelae.
- Most VUR resolves spontaneously.
- The rate and time for resolution of VUR depends on the grade of VUR, with higher grades resolving more slowly.
- In children older than 2 months with uncomplicated first febrile UTI, imaging for VUR is usually not necessary.

## SUGGESTED READINGS

American College of Radiology Appropriateness Criteria. *Urinary tract infection–child*, 2016. https://acsearch.acr.org/docs/69444/Narrative/.
Hoberman A, Greenfield SP, Mattoo TK, et al. Antimicrobial prophylaxis for children with vesicoureteral reflux. *N Engl J Med*. 2014;370(25):2367–2376.
Nguyen HT, Herndon CD, Cooper C, et al. The Society for Fetal Urology consensus statement on the evaluation and management of antenatal hydronephrosis. *J Pediatr Urol*. 2010;6(3):212–231.
Peters CA, Skoog SJ, Arant BS Jr, et al. Summary of the AUA Guideline on Management of Primary Vesicoureteral Reflux in Children. *J Urol*. 2010;184(3):1134–1144.
Roberts KB. Urinary tract infection: clinical practice guideline for the diagnosis and management of the initial UTI in febrile infants and children 2 to 24 months. *Pediatrics*. 2011;128(3):595–610.
Tullus K. Vesicoureteric reflux in children. *Lancet*. 2015;385(9965):371–379.

## REFERENCES

Full references for this chapter can be found on www.expertconsult.com.

## REFERENCES

1. Tullus K. Vesicoureteric reflux in children. *Lancet*. 2015;385(9965):371–379.
2. Williams G, Fletcher JT, Alexander SI, et al. Vesicoureteral reflux. *Journal of the American Society of Nephrology : JASN*. 2008;19(5):847–862.
3. Peters C, Rushton HG. Vesicoureteral reflux associated renal damage: congenital reflux nephropathy and acquired renal scarring. *J Urol*. 2010;184(1):265–273.
4. Oh MM, Jin MH, Bae JH, et al. The role of vesicoureteral reflux in acute renal cortical scintigraphic lesion and ultimate scar formation. *J Urol*. 2008;180(5):2167–2170.
5. Mingin G. Vesicoureteral reflux, urinary tract infection and renal scarring: sorting it all out. *J Urol*. 2008;180(5):1884–1885.
6. Mohanan N, Colhoun E, Puri P. Renal parenchymal damage in intermediate and high grade infantile vesicoureteral reflux. *J Urol*. 2008;180(4 suppl):1635–1638. discussion 1638.
7. Pennesi M, Travan L, Peratoner L, et al. Is antibiotic prophylaxis in children with vesicoureteral reflux effective in preventing pyelonephritis and renal scars? A randomized, controlled trial. *Pediatrics*. 2008;121(6):e1489–e1494.
8. Hoberman A, Greenfield SP, Mattoo TK, et al. Antimicrobial prophylaxis for children with vesicoureteral reflux. *N Engl J Med*. 2014;370(25):2367–2376.
9. Montini G, Rigon L, Zucchetta P, et al. Prophylaxis after first febrile urinary tract infection in children? A multicenter, randomized, controlled, noninferiority trial. *Pediatrics*. 2008;122(5):1064–1071.
10. de Bessa J Jr, de Carvalho Mrad FC, Mendes EF, et al. Antibiotic prophylaxis for prevention of febrile urinary tract infections in children with vesicoureteral reflux: a meta-analysis of randomized, controlled trials comparing dilated to nondilated vesicoureteral reflux. *J Urol*. 2015;193(5 suppl):1772–1777.
11. Brandstrom P, Neveus T, Sixt R, et al. The Swedish reflux trial in children: IV. Renal damage. *J Urol*. 2010;184(1):292–297.
12. Hodson EM, Wheeler DM, Vimalchandra D, et al. Interventions for primary vesicoureteric reflux. *Cochrane Database Syst Rev*. 2007;(3):CD001532.
13. Peters CA, Skoog SJ, Arant BS Jr, et al. Summary of the AUA Guideline on Management of Primary Vesicoureteral Reflux in Children. *J Urol*. 2010;184(3):1134–1144.
14. St Aubin M, Willihnganz-Lawson K, Varda BK, et al. Society for fetal urology recommendations for postnatal evaluation of prenatal hydronephrosis–will fewer voiding cystourethrograms lead to more urinary tract infections? *J Urol*. 2013;190(4 suppl):1456–1461.
15. Skoog SJ, Peters CA, Arant BS Jr, et al. Pediatric Vesicoureteral Reflux Guidelines Panel summary report: clinical practice guidelines for screening siblings of children with vesicoureteral reflux and neonates/infants with prenatal hydronephrosis. *J Urol*. 2010;184(3):1145–1151.
16. Lambert HJ, Stewart A, Gullett AM, et al. Primary, nonsyndromic vesicoureteric reflux and nephropathy in sibling pairs: a United Kingdom cohort for a DNA bank. *Clin J Am Soc Nephrol*. 2011;6(4):760–766.
17. Carvas F, Silva A, Nguyen HT. The genetics of primary, nonsyndromic vesicoureteral reflux. *Curr Opin Urol*. 2010;20(4):336–342.
18. Shankar KR, Vishwanath N, Rickwood AM. Outcome of patients with prenatally detected duplex system ureterocele; natural history of those managed expectantly. *J Urol*. 2001;165(4):1226–1228.
19. Lee PH, Diamond DA, Duffy PG, et al. Duplex reflux: a study of 105 children. *J Urol*. 1991;146(2 Pt 2):657–659.
20. Je BK, Kim HK, Horn PS. Incidence and spectrum of renal complications and extrarenal diseases and syndromes in 380 children and young adults with horseshoe kidney. *AJR Am J Roentgenol*. 2015;205(6):1306–1314.
21. Heikkila J, Rintala R, Taskinen S. Vesicoureteral reflux in conjunction with posterior urethral valves. *J Urol*. 2009;182(4):1555–1560.
22. Hong YK, Altobelli E, Borer JG, et al. Urodynamic abnormalities in toilet trained children with primary vesicoureteral reflux. *J Urol*. 2011;185(5):1863–1868.
23. Ural Z, Ulman I, Avanoglu A. Bladder dynamics and vesicoureteral reflux: factors associated with idiopathic lower urinary tract dysfunction in children. *J Urol*. 2008;179(4):1564–1567.
24. Sillen U, Brandstrom P, Jodal U, et al. The Swedish reflux trial in children: v. Bladder dysfunction. *J Urol*. 2010;184(1):298–304.
25. Mazzola BL, von Vigier RO, Marchand S, et al. Behavioral and functional abnormalities linked with recurrent urinary tract infections in girls. *J Nephrol*. 2003;16(1):133–138.
26. Kajbafzadeh AM, Baradaran N, Sadeghi Z, et al. Vesicoureteral reflux and primary bladder neck dysfunction in children: urodynamic evaluation and randomized, double-blind, clinical trial on effect of alpha-blocker therapy. *J Urol*. 2010;184(5):2128–2133.
27. Haid B, Becker T, Koen M, et al. Lower radiation burden in state of the art fluoroscopic cystography compared to direct isotope cystography in children. *J Pediatr Urol*. 2015;11(1):35, e31–36.
28. Sinha MD, Gibson P, Kane T, et al. Accuracy of ultrasonic detection of renal scarring in different centres using DMSA as the gold standard. *Nephrol Dial Transplant*. 2007;22(8):2213–2216.
29. Bush NC, Keays M, Adams C, et al. Renal damage detected by DMSA, despite normal renal ultrasound, in children with febrile UTI. *J Pediatr Urol*. 2015;11(3):126, e121–127.
30. Basiratnia M, Noohi AH, Lotfi M, et al. Power Doppler sonographic evaluation of acute childhood pyelonephritis. *Pediatric nephrology*. 2006;21(12):1854–1857.
31. Majd M, Nussbaum Blask AR, Markle BM, et al. Acute pyelonephritis: comparison of diagnosis with 99mTc-DMSA, SPECT, spiral CT, MR imaging, and power Doppler US in an experimental pig model. *Radiology*. 2001;218(1):101–108.
32. Weiser AC, Amukele SA, Leonidas JC, et al. The role of gadolinium enhanced magnetic resonance imaging for children with suspected acute pyelonephritis. *J Urol*. 2003;169(6):2308–2311.
33. Cerwinka WH, Grattan-Smith JD, Jones RA, et al. Comparison of magnetic resonance urography to dimercaptosuccinic acid scan for the identification of renal parenchyma defects in children with vesicoureteral reflux. *J Pediatr Urol*. 2014;10(2):344–351.
34. Lebowitz RL, Olbing H, Parkkulainen KV, et al. International system of radiographic grading of vesicoureteric reflux. International Reflux Study in Children. *Pediatr Radiol*. 1985;15(2):105–109.
35. Fretzayas A, Karpathios T, Dimitriou P, et al. Grading of vesicoureteral reflux by radionuclide cystography. *Pediatr Radiol*. 1984;14(3):148–150.
36. Berrocal T, Gaya F, Arjonilla A, et al. Vesicoureteral reflux: diagnosis and grading with echo-enhanced cystosonography versus voiding cystourethrography. *Radiology*. 2001;221(2):359–365.
37. de Bessa J Jr, de Carvalho Mrad FC, Mendes EF, et al. Antibiotic prophylaxis for prevention of febrile urinary tract infections in children with vesicoureteral reflux: a meta-analysis of randomized, controlled trials comparing dilated to nondilated vesicoureteral reflux. *J Urol*. 2015;193(5 suppl):1772–1777.
38. Brandstrom P, Jodal U, Sillen U, et al. The Swedish reflux trial: review of a randomized, controlled trial in children with dilating vesicoureteral reflux. *J Pediatr Urol*. 2011;7(6):594–600.
39. Martin AD, Iqbal MW, Sprague BM, et al. Most infants with dilating vesicoureteral reflux can be treated nonoperatively. *J Urol*. 2014;191(5 suppl):1620–1626.
40. Ransley PG, Risdon RA. Renal papillary morphology in infants and young children. *Urol Res*. 1975;3(3):111–113.
41. Ransley PG, Risdon RA. Renal papillary morphology and intrarenal reflux in the young pig. *Urol Res*. 1975;3(3):105–109.
42. Kim SW, Im YJ, Hong CH, et al. The clinical significance of intrarenal reflux in voiding cystourethrography (VCUG). *Korean J Urol*. 2010;51(1):60–63.
43. Boubnova J, Sergent-Alaoui A, Deschenes G, et al. Evolution and prognosis value of intrarenal reflux. *J Pediatr Urol*. 2011;7(6):638–643.
44. O'Neil BB, Cartwright PC, Maves C, et al. Reliability of voiding cystourethrogram for the grading of vesicoureteral reflux. *J Pediatr Urol*. 2014;10(1):107–111.
45. Schaeffer AJ, Greenfield SP, Ivanova A, et al. Reliability of grading of vesicoureteral reflux and other findings on voiding cystourethrography. *J Pediatr Urol*. 2016.
46. Darge K. Voiding urosonography with US contrast agent for the diagnosis of vesicoureteric reflux in children: an update. *Pediatr Radiol*. 2010;40(6):956–962.
47. *Society of Nuclear Medicine Procedure Guideline for Radionuclide Cystography in Children hisodpcp*.
48. Thacker PG, Collins HR, Hill J. Distress experienced during pediatric VCUGs - a granular, prospective assessment using the brief behavioral distress scale. *Pediatr Radiol*. 2016;46(5):660–665.
49. Rao J, Kennedy SE, Cohen S, et al. A systematic review of interventions for reducing pain and distress in children undergoing voiding cystourethrography. *Acta Paediatr*. 2012;101(3):224–229.
50. Elder JS, Longenecker R. Premedication with oral midazolam for voiding cystourethrography in children: safety and efficacy. *AJR Am J Roentgenol*. 1995;164(5):1229–1232.

51. Ferguson GG, Chen C, Yan Y, et al. The efficacy of oral midazolam for decreasing anxiety in children undergoing voiding cystourethrogram: a randomized, double-blind, placebo controlled study. *J Urol*. 2011;185(6 suppl):2542–2546.
52. Phillips DA, Watson AR, MacKinlay D. Distress and the micturating cystourethrogram: does preparation help? *Acta Paediatr*. 1998;87(2):175–179.
53. Srivastava T, Betts G, Rosenberg AR, et al. Perception of fear, distress and pain by parents of children undergoing a micturating cystourethrogram: a prospective study. *J Paediatr Child Health*. 2001;37(3):271–273.
54. Zier JL, Kvam KA, Kurachek SC, et al. Sedation with nitrous oxide compared with no sedation during catheterization for urologic imaging in children. *Pediatr Radiol*. 2007;37(7):678–684.
55. Agrawalla S, Pearce R, Goodman TR. How to perform the perfect voiding cystourethrogram. *Pediatr Radiol*. 2004;34(2):114–119.
56. Fernbach SK, Feinstein KA, Schmidt MB. Pediatric voiding cystourethrography: a pictorial guide. *Radiographics*. 2000;20(1):155–168, discussion 168–171.
57. Jaju A, Shaw HL, Don S, et al. ALARA: Impact of practice quality improvement initiative on dose reduction in pediatric voiding cystourethrogram. *AJR Am J Roentgenol*. 2015;205(4):886–893.
58. Bazopoulos EV, Prassopoulos PK, Damilakis JE, et al. A comparison between digital fluoroscopic hard copies and 105-mm spot films in evaluating vesicoureteric reflux in children. *Pediatr Radiol*. 1998;28(3):162–166.
59. Gelfand MJ, Koch BL, Elgazzar AH, et al. Cyclic cystography: diagnostic yield in selected pediatric populations. *Radiology*. 1999;213(1):118–120.
60. Paltiel HJ, Rupich RC, Kiruluta HG. Enhanced detection of vesicoureteral reflux in infants and children with use of cyclic voiding cystourethrography. *Radiology*. 1992;184(3):753–755.
61. Papadopoulou F, Efremidis SC, Oiconomou A, et al. Cyclic voiding cystourethrography: is vesicoureteral reflux missed with standard voiding cystourethrography? *Eur Radiol*. 2002;12(3):666–670.
62. Polito C, Moggio G, La Manna A, et al. Cyclic voiding cystourethrography in the diagnosis of occult vesicoureteric reflux. *Pediatric nephrology*. 2000;14(1):39–41.
63. Lebowitz RL, Blickman JG. The coexistence of ureteropelvic junction obstruction and reflux. *AJR Am J Roentgenol*. 1983;140(2): 231–238.
64. Hollowell JG, Altman HG, Snyder HM 3rd, et al. Coexisting ureteropelvic junction obstruction and vesicoureteral reflux: diagnostic and therapeutic implications. *J Urol*. 1989;142(2 Pt 2):490–493. discussion 501.
65. Polito C, Rambaldi PF, La Manna A, et al. Enhanced detection of vesicoureteric reflux with isotopic cystography. *Pediatric nephrology*. 2000;14(8–9):827–830.
66. Unver T, Alpay H, Biyikli NK, et al. Comparison of direct radionuclide cystography and voiding cystourethrography in detecting vesicoureteral reflux. *Pediatr Int*. 2006;48(3):287–291.
67. Lee RS, Diamond DA, Chow JS. Applying the ALARA concept to the evaluation of vesicoureteric reflux. *Pediatr Radiol*. 2006;36(suppl 2):185–191.
68. Mandell GA, Eggli DF, Gilday DL, et al. Procedure guideline for radionuclide cystography in children. Society of Nuclear Medicine. *J Nucl Med*. 1997;38(10):1650–1654.
69. Poli-Merol ML, Francois S, Pfliger F, et al. Interest of direct radionuclide cystography in repeated urinary tract infection exploration in childhood. *Eur J Pediatr Surg*. 1998;8(6):339–342.
70. Mahant S, Friedman J, MacArthur C. Renal ultrasound findings and vesicoureteral reflux in children hospitalised with urinary tract infection. *Arch Dis Child*. 2002;86(6):419–420.
71. Nelson CP, Johnson EK, Logvinenko T, et al. Ultrasound as a screening test for genitourinary anomalies in children with UTI. *Pediatrics*. 2014;133(3):e394–e403.
72. Gordon ZN, McLeod DJ, Becknell B, et al. Uroepithelial thickening on sonography improves detection of vesicoureteral reflux in children with first febrile urinary tract infection. *J Urol*. 2015;194(4):1074–1079.
73. Leroy S, Vantalon S, Larakeb A, et al. Vesicoureteral reflux in children with urinary tract infection: comparison of diagnostic accuracy of renal US criteria. *Radiology*. 2010;255(3):890–898.
74. Duran C, del Riego J, Riera L, et al. Voiding urosonography including urethrosonography: high-quality examinations with an optimised procedure using a second-generation US contrast agent. *Pediatr Radiol*. 2012;42(6):660–667.
75. Kis E, Nyitrai A, Varkonyi I, et al. Voiding urosonography with second-generation contrast agent versus voiding cystourethrography. *Pediatric nephrology*. 2010;25(11):2289–2293.
76. Kljucevsek D, Battelino N, Tomazic M, et al. A comparison of echo-enhanced voiding urosonography with X-ray voiding cystourethrography in the first year of life. *Acta Paediatr*. 2012;101(5):e235–e239.
77. McCarville MB. Contrast-enhanced sonography in pediatrics. *Pediatr Radiol*. 2011;41(suppl 1):S238–S242.
78. Papadopoulou F, Ntoulia A, Siomou E, et al. Contrast-enhanced voiding urosonography with intravesical administration of a second-generation ultrasound contrast agent for diagnosis of vesicoureteral reflux: prospective evaluation of contrast safety in 1,010 children. *Pediatr Radiol*. 2014;44(6):719–728.
79. Wong LS, Tse KS, Fan TW, et al. Voiding urosonography with second-generation ultrasound contrast versus micturating cystourethrography in the diagnosis of vesicoureteric reflux. *Eur J Pediatr*. 2014;173(8):1095–1101.
80. Wennerstrom M, Hansson S, Jodal U, et al. Disappearance of vesicoureteral reflux in children. *Arch Pediatr Adolesc Med*. 1998;152(9):879–883.
81. Schwab CW Jr, Wu HY, Selman H, et al. Spontaneous resolution of vesicoureteral reflux: a 15-year perspective. *J Urol*. 2002;168(6):2594–2599.
82. Estrada CR Jr, Passerotti CC, Graham DA, et al. Nomograms for predicting annual resolution rate of primary vesicoureteral reflux: results from 2,462 children. *J Urol*. 2009;182(4):1535–1541.
83. Upadhyay J, McLorie GA, Bolduc S, et al. Natural history of neonatal reflux associated with prenatal hydronephrosis: long-term results of a prospective study. *J Urol*. 2003;169(5):1837–1841. discussion 1841; author reply 1841.
84. Shaikh N, Ewing AL, Bhatnagar S, et al. Risk of renal scarring in children with a first urinary tract infection: a systematic review. *Pediatrics*. 2010;126(6):1084–1091.
85. Peters C, Rushton HG. Vesicoureteral reflux associated renal damage: congenital reflux nephropathy and acquired renal scarring. *J Urol*. 2010;184(1):265–273.
86. Soylu A, Demir BK, Turkmen M, et al. Predictors of renal scar in children with urinary infection and vesicoureteral reflux. *Pediatric nephrology*. 2008;23(12):2227–2232.
87. Alexander SE, Arlen AM, Storm DW, et al. Bladder volume at onset of vesicoureteral reflux is an independent risk factor for breakthrough febrile urinary tract infection. *J Urol*. 2015;193(4):1342–1346.
88. Koff SA, Wagner TT, Jayanthi VR. The relationship among dysfunctional elimination syndromes, primary vesicoureteral reflux and urinary tract infections in children. *J Urol*. 1998;160(3 Pt 2):1019–1022.
89. Ben-Ami T, Gayer G, Hertz M, et al. The natural history of reflux in the lower pole of duplicated collecting systems: a controlled study. *Pediatr Radiol*. 1989;19(5):308–310.
90. Afshar K, Malek R, Bakhshi M, et al. Should the presence of congenital para-ureteral diverticulum affect the management of vesicoureteral reflux? *J Urol*. 2005;174(4 Pt 2):1590–1593.
91. Montini G, Tullus K, Hewitt I. Febrile urinary tract infections in children. *NEJM*. 2011;365(3):239–250.
92. Toffolo A, Ammenti A, Montini G. Long-term clinical consequences of urinary tract infections during childhood: a review. *Acta Paediatr*. 2012;101(10):1018–1031.
93. Salo J, Ikaheimo R, Tapiainen T, et al. Childhood urinary tract infections as a cause of chronic kidney disease. *Pediatrics*. 2011;128(5):840–847.
94. Novak TE, Mathews R, Martz K, et al. Progression of chronic kidney disease in children with vesicoureteral reflux: the North American Pediatric Renal Trials Collaborative Studies Database. *J Urol*. 2009;182(4 suppl):1678–1681.
95. Toka HR, Toka O, Hariri A, et al. Congenital anomalies of kidney and urinary tract. *Semin Nephrol*. 2010;30(4):374–386.
96. McMahon AP, Aronow BJ, Davidson DR, et al. GUDMAP: the genitourinary developmental molecular anatomy project. *Journal of the American Society of Nephrology : JASN*. 2008;19(4):667–671.
97. Roberts KB. Urinary tract infection: clinical practice guideline for the diagnosis and management of the initial UTI in febrile infants and children 2 to 24 months. *Pediatrics*. 2011;128(3):595–610.
98. Ditchfield MR, De Campo JF, Cook DJ, et al. Vesicoureteral reflux: an accurate predictor of acute pyelonephritis in childhood urinary tract infection? *Radiology*. 1994;190(2):413–415.
99. United States renal data system 2016 *Eac, adolescents, and young adults*. https://www.usrds.org/2016/view/v2_08.aspx.

100. North American Pediatric Renal Trials and Collaborative Studies, 2014 *Annual transplant report*. https://web.emmes.com/study/ped/annlrept/annualrept2014.pdf.
101. Jodal U, Smellie JM, Lax H, et al. Ten-year results of randomized treatment of children with severe vesicoureteral reflux. Final report of the International Reflux Study in Children. *Pediatric nephrology*. 2006;21(6):785–792.
102. Bjorgvinsson E, Majd M, Eggli KD. Diagnosis of acute pyelonephritis in children: comparison of sonography and 99mTc-DMSA scintigraphy. *AJR Am J Roentgenol*. 1991;157(3):539–543.
103. Moorthy I, Wheat D, Gordon I. Ultrasonography in the evaluation of renal scarring using DMSA scan as the gold standard. *Pediatric nephrology*. 2004;19(2):153–156.
104. Hitzel A, Liard A, Vera P, et al. Color and power Doppler sonography versus DMSA scintigraphy in acute pyelonephritis and in prediction of renal scarring. *J Nucl Med*. 2002;43(1):27–32.
105. Lonergan GJ, Pennington DJ, Morrison JC, et al. Childhood pyelonephritis: comparison of gadolinium-enhanced MR imaging and renal cortical scintigraphy for diagnosis. *Radiology*. 1998;207(2):377–384.
106. Rossleigh MA, Farnsworth RH, Leighton DM, et al. Technetium-99m dimercaptosuccinic acid scintigraphy studies of renal cortical scarring and renal length. *J Nucl Med*. 1998;39(7):1280–1285.
107. Rushton HG, Majd M. Dimercaptosuccinic acid renal scintigraphy for the evaluation of pyelonephritis and scarring: a review of experimental and clinical studies. *J Urol*. 1992;148(5 Pt 2):1726–1732.
108. Cerwinka WH, Grattan-Smith JD, Jones RA, et al. Comparison of magnetic resonance urography to dimercaptosuccinic acid scan for the identification of renal parenchyma defects in children with vesicoureteral reflux. *J Pediatr Urol*. 2014;10(2):344–351.
109. Kavanagh EC, Ryan S, Awan A, et al. Can MRI replace DMSA in the detection of renal parenchymal defects in children with urinary tract infections? *Pediatr Radiol*. 2005;35(3):275–281.
110. Mendez R, Somoza I, Tellado MG, et al. Predictive value of clinical factors for successful endoscopic correction of primary vesicoureteral reflux grades III-IV. *J Pediatr Urol*. 2006;2(6):545–550.
111. Herbst KW, Corbett ST, Lendvay TS, et al. Recent trends in the surgical management of primary vesicoureteral reflux in the era of dextranomer/hyaluronic acid. *J Urol*. 2014;191(5 suppl):1628–1633.
112. Rypens F, Avni EF, Bank WO, et al. The ureterovesical junction in children: sonographic findings after surgical or endoscopic treatment. *AJR Am J Roentgenol*. 1992;158(4):837–842.
113. Dawrant MJ, Mohanan N, Puri P. Endoscopic treatment for high grade vesicoureteral reflux in infants. *J Urol*. 2006;176(4 Pt 2):1847–1850.
114. Cerwinka WH, Kaye JD, Scherz HC, et al. Radiologic features of implants after endoscopic treatment of vesicoureteral reflux in children. *AJR Am J Roentgenol*. 2010;195(1):234–240.
115. Saperston K, Smith J, Putman S, et al. Endoscopic subureteral injection is not less expensive than outpatient open reimplantation for unilateral vesicoureteral reflux. *J Urol*. 2008;180(4 suppl):1626–1629. discussion 1629-1630.
116. Gupta A, Snodgrass W. Intra-orifice versus hydrodistention implantation technique in dextranomer/hyaluronic acid injection for vesicoureteral reflux. *J Urol*. 2008;180(4 suppl):1589–1592. discussion 1592-1583.
117. Kirsch AJ. Outpatient surgery for vesicoureteral reflux: endoscopic injection vs extravesical ureteral reimplantation. *J Urol*. 2011;186(5):1764–1765.
118. Routh JC, Inman BA, Reinberg Y. Dextranomer/hyaluronic acid for pediatric vesicoureteral reflux: systematic review. *Pediatrics*. 2010;125(5):1010–1019.
119. Nguyen HT, Benson CB, Bromley B, et al. Multidisciplinary consensus on the classification of prenatal and postnatal urinary tract dilation (UTD classification system). *J Pediatr Urol*. 2014;10(6):982–998.
120. Koyle MA, Elder JS, Skoog SJ, et al. Febrile urinary tract infection, vesicoureteral reflux, and renal scarring: current controversies in approach to evaluation. *Pediatr Surg Int*. 2011;27(4):337–346.
121. Mantadakis E, Vouloumanou EK, Georgantzi GG, et al. Acute Tc-99m DMSA scan for identifying dilating vesicoureteral reflux in children: a meta-analysis. *Pediatrics*. 2011;128(1):e169–e179.
122. Nguyen HT, Herndon CD, Cooper C, et al. The Society for Fetal Urology consensus statement on the evaluation and management of antenatal hydronephrosis. *J Pediatr Urol*. 2010;6(3):212–231.
123. Estrada CR, Peters CA, Retik AB, et al. Vesicoureteral reflux and urinary tract infection in children with a history of prenatal hydronephrosis–should voiding cystourethrography be performed in cases of postnatally persistent grade II hydronephrosis? *J Urol*. 2009;181(2):801–806, discussion 806–807.
124. Goldman M, Lahat E, Strauss S, et al. Imaging after urinary tract infection in male neonates. *Pediatrics*. 2000;105(6):1232–1235.
125. *American College of Radiology Appropriateness Criteria. Urinary tract infection–child*, 2016. https://acsearch.acr.org/docs/69444/Narrative/.

# 120 Bladder and Urethra

Hollie C. West and Christopher G. Anton

## URACHAL ANOMALIES

***Overview.*** The urachus is the fetal channel connecting the bladder and the allantosis. Fibrotic regression of the urachus typically extends from the umbilicus toward the bladder and results in the median umbilical ligament. Usually, this process is completed by 4 to 5 months of gestational age.[1,2] Failure of urachal regression may result in: (1) patent urachus, (2) urachal sinus, (3) urachal diverticulum, and (4) urachal cyst (Fig. 120.1). While many urachal anomalies are asymptomatic, symptoms can include umbilical discharge, localized or urinary tract infection (UTI), and lower abdominal pain.[3]

***Imaging.*** Ultrasound (US), voiding cystourethrography (VCUG), and fistulography are the primary imaging tools for initial evaluation of suspected urachal anomalies. A patent urachus results in a vesicoumbilical fistula and is the most common urachal anomaly (Fig. 120.2). US demonstrates a midline tubular connection between the bladder dome and umbilicus, which may be confirmed with bladder catheterization via the umbilicus (e-Fig. 120.3) or by VCUG. Echogenic debris within the urachal channel and surrounding inflammation suggest infection; abscesses may occur in some children. Clinically, a patent urachus typically presents with urine leakage from the umbilicus and is detected in the neonatal period.

A urachal sinus is defined as a blind-ending pouch extending from the umbilicus without continuity with the bladder, typically depicted by US and confirmed by umbilical catheterization or fistulography (sinography). This sinus may periodically produce discharge. A urachal diverticulum is usually asymptomatic and results from the failure of obliteration at the vesicular end only, resulting in an outpouching from the dome of the bladder. This is commonly demonstrated on both US and VCUG (Fig. 120.4). A urachal cyst forms when the urachus is obliterated at both the vesicular and umbilical ends but remains patent at some point along its length, usually the lower one-third of the urachus. Imaging with US, computed tomography (CT), or magnetic resonance imaging (MRI) will typically demonstrate a fluid-filled cyst with or without signs of superinfection (e-Fig. 120.5).[3,4]

***Treatment.*** Urachal remnants in children younger than 6 months have been reported to resolve with nonoperative management and initially may be managed conservatively. If resolution does not occur, resection is performed to minimize infection risk and the potential for neoplasia later in life.[1,2]

## BLADDER DIVERTICULA

***Overview.*** Bladder diverticula may be primary (congenital), secondary, or iatrogenic (postoperative). Congenital diverticula are the most common type and may be idiopathic or related to various syndromes including Ehlers-Danlos, Menkes, and Williams. They are more common in boys, and typically occur near the ureterovesicular junction (UVJ). While many children are asymptomatic, depending on the location and proximity to the ureteral orifice, these may contribute to vesicoureteral reflux, prenatal hydronephrosis, or result in bladder outlet obstruction. Secondary bladder diverticula are the result of prolonged bladder outlet obstruction (usually in the setting of posterior urethral valves or neurogenic dysfunction). Iatrogenic diverticula are seen most often in the anterior wall of the bladder at the site of a previous vesicostomy or suprapubic drainage catheter, and at the UVJ after ureteral reimplantation.[5] Patients with diverticula may present with recurrent UTI, urinary retention, incontinence, stone formation, vesicoureteral reflux (VUR), and ureteral and bladder outlet obstruction.

***Imaging.*** VCUG is the most sensitive method for detecting bladder diverticula. Diverticular outpouchings may enlarge or become visible during voiding when bladder contraction forces urine into the diverticulum (Fig. 120.6). A paraureteral diverticulum located lateral and cephalad to the ureteral orifice in an otherwise normal patient with a smooth-walled bladder is commonly referred to as a *Hutch diverticulum* (e-Fig. 120.7). Altered voiding dynamics may result in retained urine and VUR. If the diverticulum is large, it may engulf the ureteral orifice and the ureter may empty into the diverticulum (e-Fig. 120.8).[6,7] Multiple diverticula are commonly observed in the settings of bladder outlet obstruction and neurogenic bladder.

***Treatment.*** Though symptomatic patients with associated VUR have traditionally been managed with diverticulectomy and ureteral reimplantation, recent evidence has demonstrated comparable VUR resolution rates among patients with and without associated diverticula.[8] However, a diverticulum is more likely to be associated with high-grade VUR and recurrent UTI, and ureteral reimplantation is necessary for those cases in which the ureteral orifice is incorporated into the diverticulum.[9] Primary bladder diverticula not in a paraureteral location and not associated with VUR or obstruction are more likely to contribute to infection and voiding dysfunction when over 3 cm, and are often excised.[10]

## NEOPLASMS OF THE BLADDER

### Rhabdomyosarcoma

***Overview.*** Genitourinary rhabdomyosarcoma (RMS) accounts for about 20% of all RMS and includes those tumors arising from the bladder or prostate gland (often infiltrating both structures), testes and paratesticular structures, penis, perineum, vagina, cervix, and uterus. RMS is the most frequent bladder neoplasm in children in the first 2 decades of life, presenting typically in the ages between 2 to 6 years with a second peak at 15 to 19 years.[11] Histologically, RMS is divided into three main subtypes in children, which are distinguished cytogenetically: (1) embryonal, (2) alveolar, and (3) pleomorphic (mainly seen in adult patients and rarely in children). Embryonal RMS accounts for approximately 90% of all genitourinary RMS and has a more favorable prognosis. The embryonal botryoid variant has the most favorable prognosis, accounts for one-quarter of cases, and has a lobulated, polypoid appearance that resembles a bunch of grapes (hence the name sarcoma botryoides).[12,13]

Genitourinary RMS spreads by local extension to regional and retroperitoneal lymph nodes and adjacent soft tissues. Distant tumor spread (usually to lungs or bone) is present at the time of diagnosis in 10% to 20% of patients.[14] Presenting symptoms depend upon site of origin but may include bladder outlet obstruction and hydroureteronephrosis, hematuria, abdominal mass, painless scrotal enlargement, or a mass prolapsing into the vaginal introitus.[12]

***Imaging.*** US is the first study for a child with suspected bladder RMS. The tumor within the bladder may appear hyperechoic or

## Abstract:

In this chapter, we reviewing the radiologic evaluation of the pediatric urinary bladder and urethra. Common as well as less common congenital anomalies and neoplasms (benign and malignant) are discussed. The clinical presentation, imaging, and management of bladder outlet obstruction in the male child is also presented.

## Keywords:

Urinary bladder
urethra
children
congenital anomalies
neoplasms

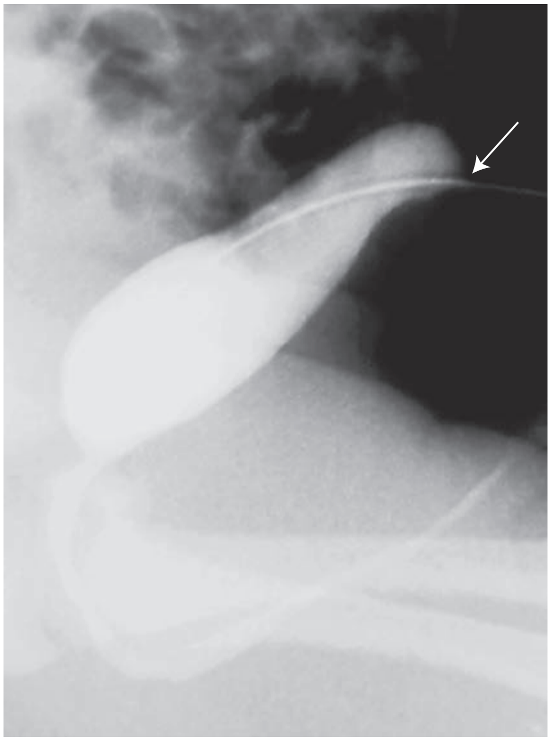

**e-Figure 120.3. Patent urachus.** Lateral view during voiding cystourethrography performed after catheterization of the bladder through the umbilicus *(arrow)*.

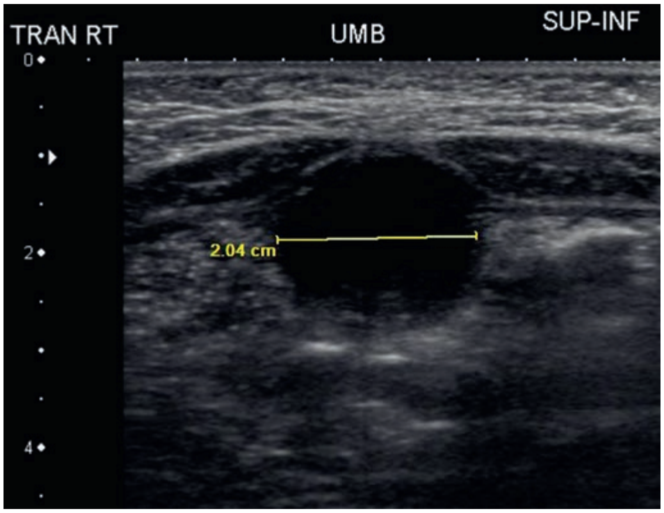

**e-Figure 120.5. Urachal cyst.** Transverse gray-scale sonogram shows an anechoic cyst in the infraumbilical region arising from the expected location of the median umbilical ligament.

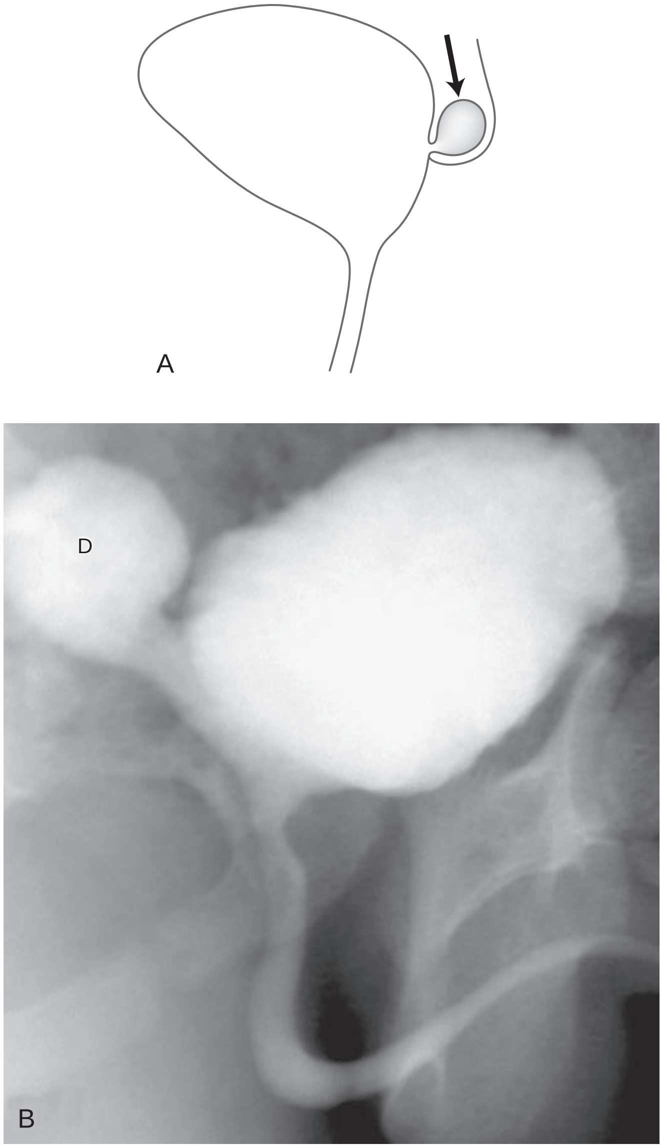

**e-Figure 120.7. Hutch diverticulum.** (A) Diagram of a paraureteral bladder diverticulum (Hutch diverticulum) *(arrow)* located immediately above the ureterovesical junction. (B) Left lateral oblique view during voiding cystourethrography shows a right-sided diverticulum *(D)* originating at the trigone.

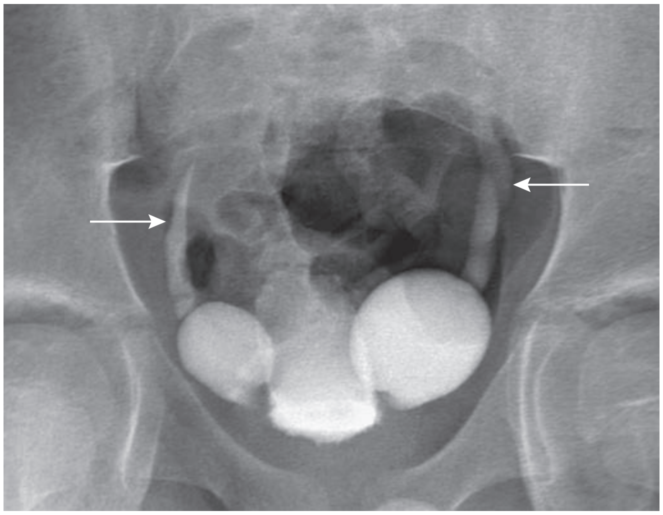

**e-Figure 120.8. Bilateral Hutch diverticula.** Anterior image during a voiding cystourethrography shows bilateral diverticula incorporating the ureteral orifices and associated with bilateral vesicoureteral reflux *(arrows)*.

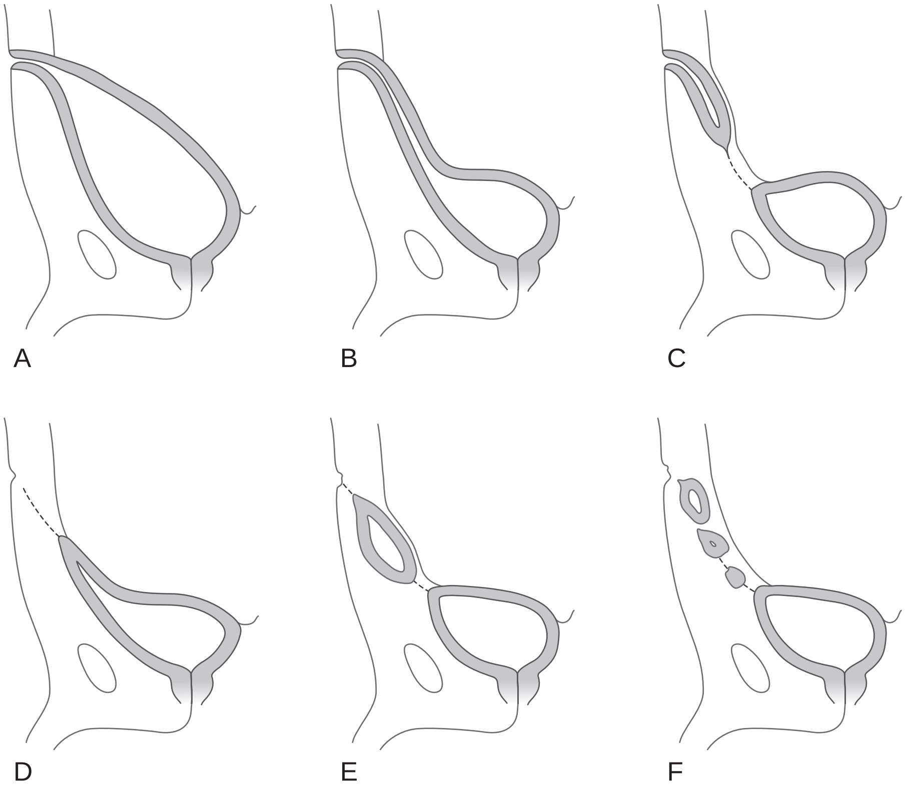

**Figure 120.1. Development of the urachus and types of urachal anomalies.** (A) Appearance of the bladder in early fetal life, before development of the urachus. (B) Patent urachus (vesicoumbilical fistula). (C) Urachal sinus. (D) Urachal (vesicourachal) diverticulum. (E and F) Urachal cyst(s).

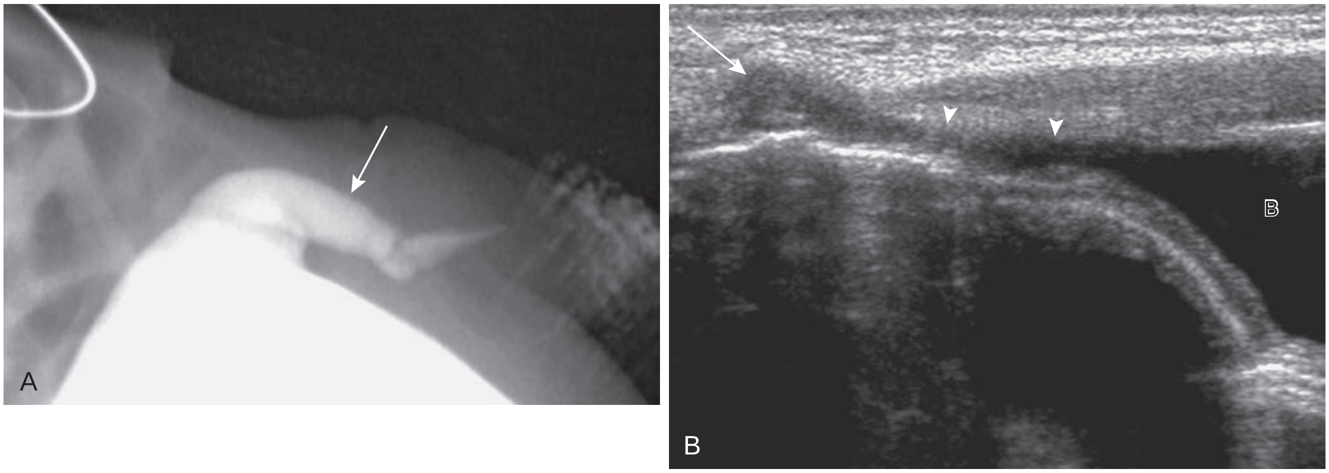

**Figure 120.2. Patent urachus.** (A) Lateral voiding cystourethrogram image shows a fistulous tract *(arrow)* leading from the dome of the bladder to the umbilicus. (B) Longitudinal sonogram shows a urine-filled patent urachus *(arrowheads)* extending from the dome of bladder *(B)* to the umbilicus *(arrow)*.

hypoechoic and may have focal anechoic regions representing necrosis, hemorrhage, or cystic areas. Color and spectral Doppler evaluation show hyperemia and increased diastolic flow. VCUG is less often used for screening but when obtained most often shows a filling defect in the posteroinferior aspect of the bladder (Fig. 120.9). When originating in the prostate gland (Fig. 120.10 and e-Fig. 120.11), the cystogram, CT, or MRI will show an upward displacement of the bladder floor or a smooth, lobulated mass at the base of the bladder. Contrast-enhanced CT often identifies RMS as a bulky bladder mass of heterogeneous attenuation that may invade periurethral and perivesical tissues or may extend into the ischiorectal fossa. Calcification is rare. Vaginal tumors arising high in the anterior vaginal vault may be indistinguishable from a primary bladder tumor. On MRI, RMS demonstrates low-signal intensity on T1-weighted sequences and high-signal intensity on T2-weighted sequences. After the administration of gadolinium-based contrast material, RMS typically enhances heterogeneously. Metastatic workup includes CT of the chest, bone scan, and

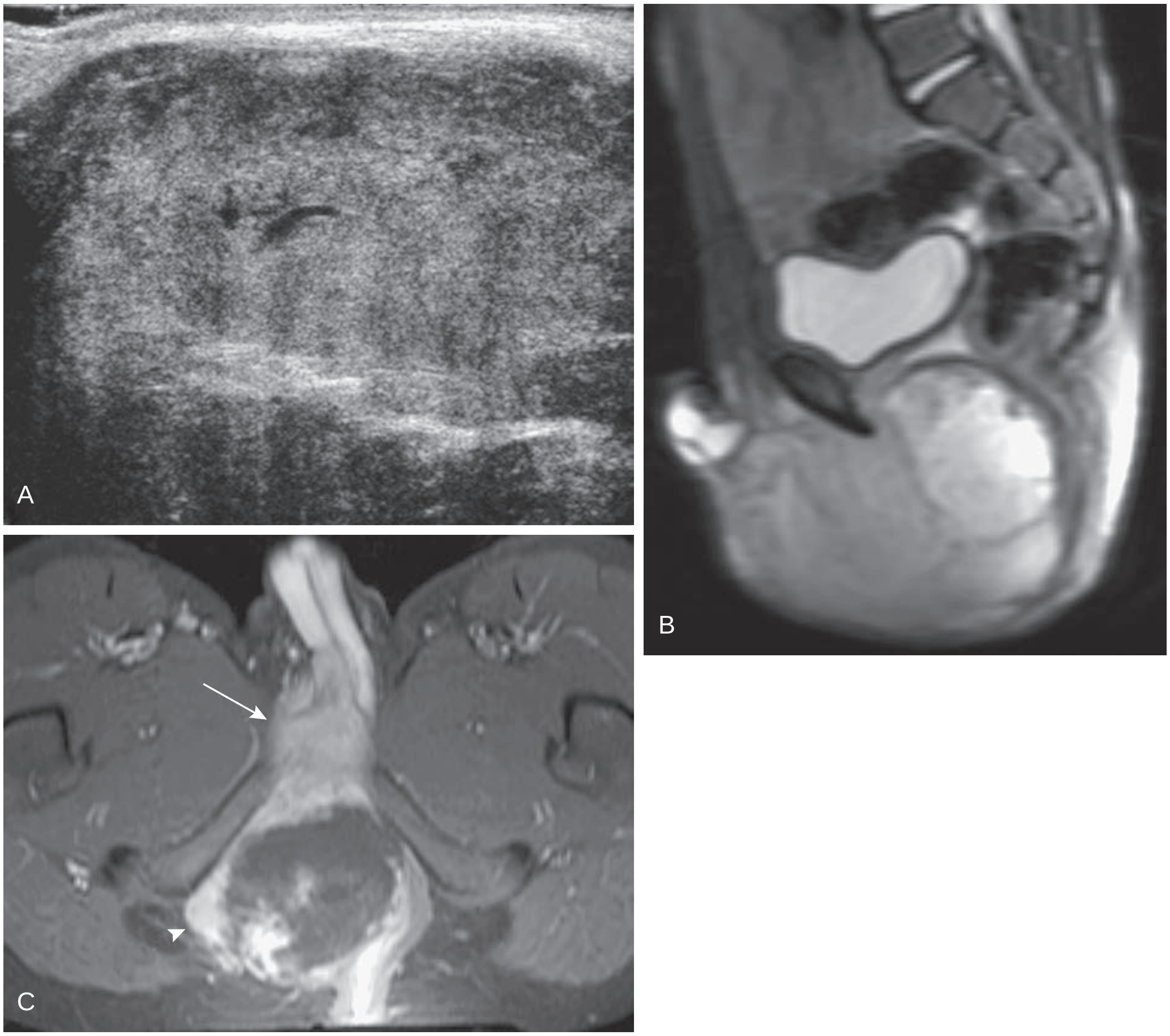

**e-Figure 120.11. Prostatic rhabdomyosarcoma.** (A) Longitudinal transperineal sonogram demonstrates a large, heterogeneous mass. (B) Sagittal T2-weighted MR image shows a large, lobulated, heterogeneously hyperintense mass extending from the bladder base to the perineum. The bladder base is elevated. (C) Axial postcontrast T1-weighted fat-saturated MR image shows a heterogeneously enhancing mass extending into the right ischiorectal fossa *(arrowhead)*, and there is direct invasion of the base of the penis *(arrow)*.

bone marrow biopsy.[11,12,14] F-18-fleurodeoxyglucose (FDG) positron emission tomography (PET)/computed tomography (CT) may also be used to evaluate for sites of metastatic disease.

***Treatment.*** The Children's Oncology Group and Intergroup Rhabdomyosarcoma Study staging system for genitourinary RMS is presented in Box 120.1.[11] Treatment combines surgical removal of as much of the tumor as possible, chemotherapy, and radiation therapy. Tumors of the urinary bladder and prostate gland may require pelvic exenteration and urinary reconstruction, and have an overall 5-year survival rate of approximately 70%. Genitourinary RMS originating from nonbladder/prostate gland sites and botryoid histology have more favorable prognoses and a better overall 5-year survival rate.[15]

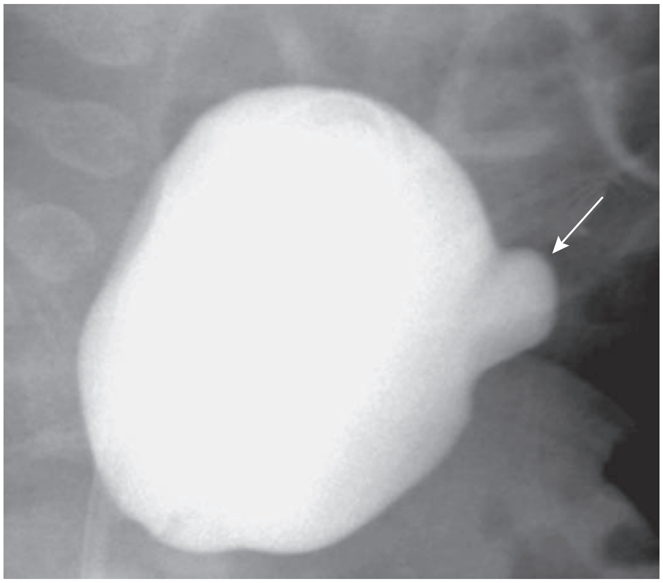

**Figure 120.4. Urachal diverticulum.** Lateral voiding cystourethrogram image shows a urachal diverticulum *(arrow)* extending from the bladder dome.

## BENIGN NEOPLASMS

***Overview and Imaging.*** Hemangioma or venous malformation of the bladder is probably the most common benign bladder "mass." Hemangioma typically presents as a discrete solitary mass of variable size (<1 cm to more than 10 cm) projecting from the posterior or lateral walls of the bladder. Hematuria is the most common clinical presentation. US will demonstrate bladder wall thickening, intramural anechoic spaces, and occasional calcification. CT and MRI may be required to fully define the extent of the lesion and for preoperative planning as cystoscopy may only reveal a small portion of the mass.[16]

Nephrogenic adenoma is a rare benign papillary lesion of the bladder and is considered a chronic metaplastic response to urothelial injury. In most cases, a history of UTI, inflammation, trauma or recent surgery (ureteral reimplantation), calculi, or catheterization is present. The bladder is the most common site in children. While the incidence is highest in adult males, pediatric patients are more commonly female. Dysuria and hematuria are the most common presenting symptoms and generally resolve after transurethral resection and fulguration. However, the recurrence rate is up to 80% in pediatric population and peaks at around

### BOX 120.1 Intergroup Rhabdomyosarcoma Study Staging System for Neoplasms of the Bladder

**Stage I:** Localized tumor, completely resected
**Stage IIA:** Localized tumor, grossly resected with microscopic residual
**Stage IIB:** Tumor with regional disease or lymph node involvement, completely resected
**Stage IIC:** Tumor with regional disease or involved lymph nodes, grossly resected with microscopic residual
**Stage IIIA:** Gross residual tumor after biopsy only
**Stage IIIB:** Distant metastases present at diagnosis

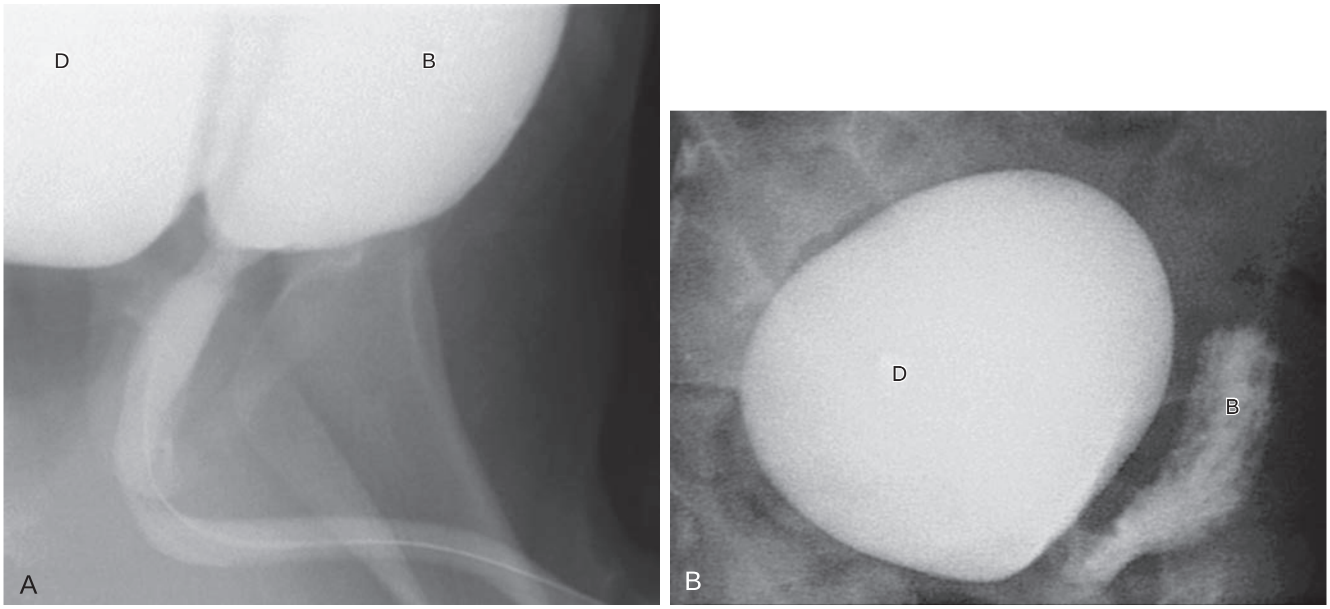

**Figure 120.6. Expanding diverticulum.** (A) Oblique voiding cystourethrogram image showing an expanding right bladder diverticulum *(D)* during voiding. *B*, Bladder. (B) At the end of voiding, a large contrast-filled diverticulum *(D)* remains with an empty bladder *(B)*.

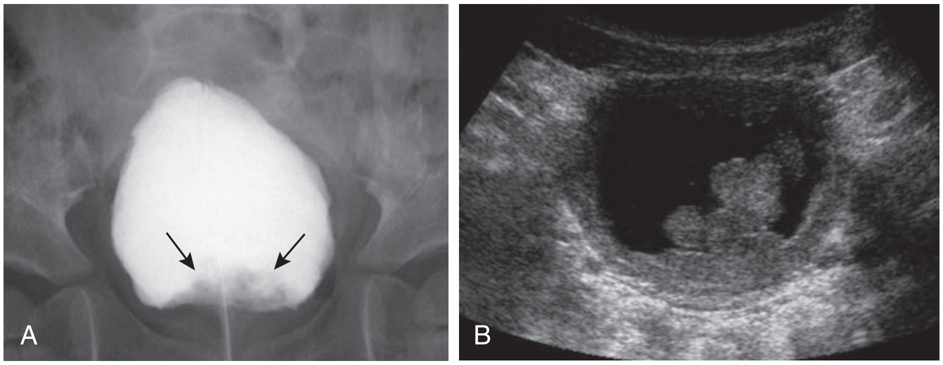

**Figure 120.9. Rhabdomyosarcoma.** (A) Cystogram from a 1-year-old girl with hematuria shows a lobular mass involving the bladder base *(arrows)*. (B) Traverse gray-scale sonogram shows a lobulated soft tissue mass arising from the posterior bladder base. The bladder wall is thickened due to outlet obstruction.

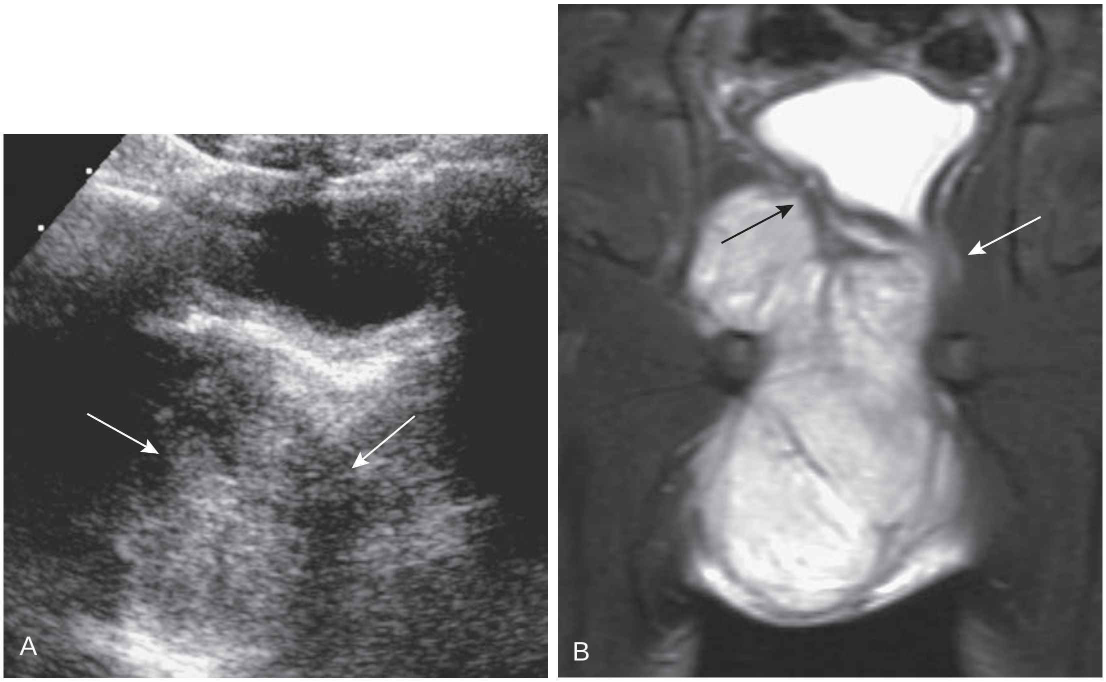

**Figure 120.10. Prostatic rhabdomyosarcoma.** (A) Transverse gray-scale sonogram of the pelvis in a 5-year-old boy shows a large predominantly hypoechoic mass below the bladder base *(arrows)*. (B) Coronal T2-weighted fat-saturated MR image shows the bladder base displaced to the left *(black arrow)* and the rectum displaced to the left and partially encased *(white arrow)*. See e-Fig. 120.11.

4 years posttreatment. Though considered a precursor to malignancy in adults, this is not the case in children.[17]

Inflammatory myofibroblastic tumor (IMT), or inflammatory pseudotumor, is a rare entity that may occur at multiple sites throughout the body. While rare, the bladder is the most common site of genitourinary involvement, with the tumor usually arising from the bladder dome in children (versus the lateral walls in adults). While the malignant potential of these lesions has been debated, the World Health Organization classifies these lesions as intermediate soft tissue tumors composed of spindle cells and an inflammatory infiltrate, including plasma cells. Many of these tumors demonstrate anaplastic lymphoma tyrosine kinase (ALK) gene rearrangements. IMT usually presents with gross hematuria, irritative or obstructive dysuria, and abdominal pain but may occasionally present with a palpable mass or fever and weight loss (postulated to be cytokine induced). Average size of the lesions is approximately 5.5 cm, but they may become quite large. These lesions can be indistinguishable on imaging from bladder RMS, and biopsy is required for diagnosis (Fig. 120.12). While metastatic disease and local recurrence may occur, this has not been reported with pediatric bladder IMT, and treatment with surgical resection and imaging surveillance are generally considered sufficient.[18]

## BLADDER OUTLET OBSTRUCTION AND POSTERIOR URETHRAL VALVES

***Overview.*** Lower urinary tract obstruction occurs in 1 per 5000 births with up to 90% of patients being boys. Approximately 70% to 80% of cases are due to the presence of posterior urethral valves (PUV) or membranes.[19,20] Additional less common anomalies of the male urethra resulting in lower urinary tract obstruction include anterior urethral valves, anterior urethral diverticulum, and megalourethra. These entities are generally considered together because of common features and transitional forms suggesting a

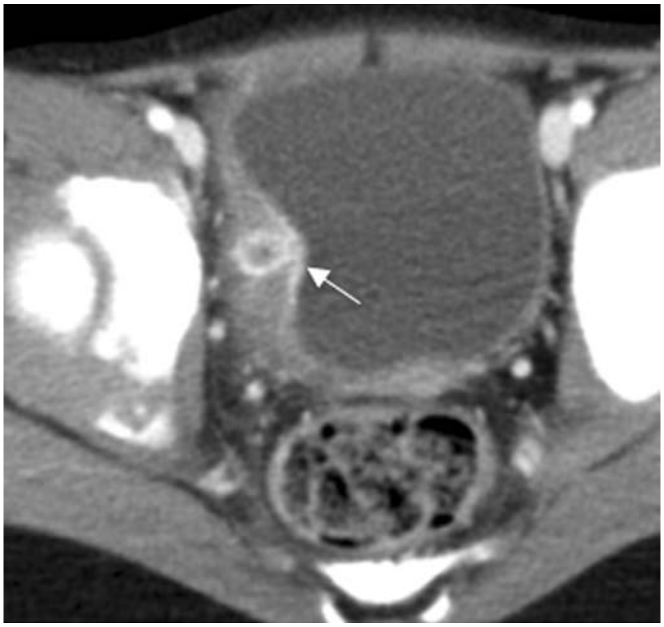

**Figure 120.12. Inflammatory myofibroblastic tumor.** Axial contrast-enhanced CT image demonstrates right bladder wall thickening and hyperenhancement *(arrow)*. Biopsy confirmed inflammatory myofibroblastic tumor, or inflammatory pseudotumor.

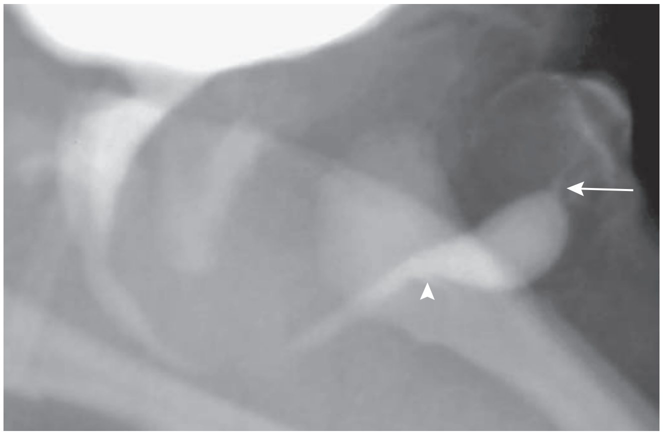

**Figure 120.13. Anterior urethral valve.** Oblique voiding cystourethrogram image shows a focal saccular dilation of the distal anterior urethra. Distally, an acute angle is formed at the junction with the narrowed urethra *(arrow)*. Proximally, an obtuse angle is present *(arrowhead)*. *(From Bates DG, Coley BD. Ultrasound diagnosis of the anterior urethral valve.* Pediatr Radiol. *2001;31:634–636.) See also* e-Fig. 120.14.

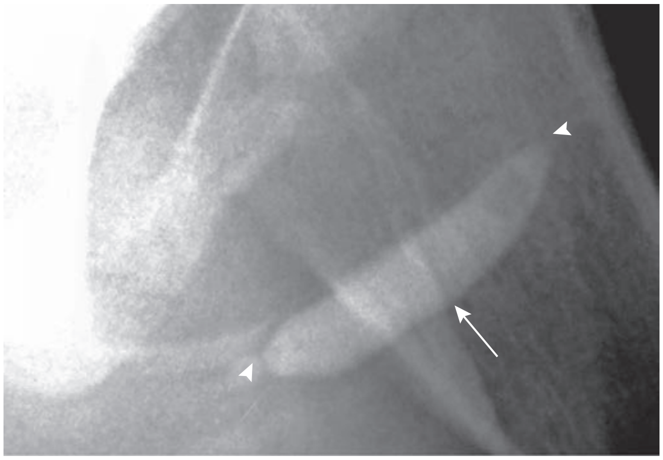

**Figure 120.15. Urethral diverticulum.** Oblique image during voiding cystourethrogram shows saccular outpouching *(arrow)* along the ventral urethra. Acute angles are formed at the junction of the anterior and posterior lips with the urethra *(arrowheads)*.

spectrum of related deformities, differing primarily in their relationship to the corpus spongiosum. VCUG is the initial diagnostic study of choice for all causes of bladder outlet obstruction.

Anterior urethral valves (AUV) are congenital mucosal folds located distal to the membranous urethra that obstruct the flow of urine (Fig. 120.13 and e-Fig. 120.14).[21] AUV may cause more proximal dilatation of the urethra mimicking a diverticulum; however, these “pseudodiverticula” form an obtuse angle with the ventral floor of the urethra (unlike true anterior urethral diverticula).

An anterior urethral diverticulum is an often quite large saccular outpouching of the ventral aspect of the anterior urethra into the corpus spongiosum, often near the penoscrotal junction, with intact corpora cavernosa (Fig. 120.15).[22–24] The more proximal urethra is commonly dilated, the proximal margin of the diverticulum forms an acute angle with the floor of the ventral urethra, and these lesions are commonly occult at retrograde urethrography (RUG). Clinical presentations include urinary dribbling, weak urinary stream, and UTI. The urethral diverticulum may be anatomically linked to the megalourethra, in which the corpus spongiosum (scaphoid megalourethra), corpora cavernosa (fusiform megalourethra), or both are deficient (e-Figs. 120.16 and 120.17).[25] Scaphoid megalourethra is more common, generally less severe, and saccular (as opposed to fusiform) in appearance.

## POSTERIOR URETHRAL VALVES

***Overview.*** Originally classified by Young into three types, all PUV are now considered to be the same type (Young’s type 1) and are formed by a membrane of Wolffian duct origin. The membrane originates in the region of the verumontanum and courses obliquely to the distal prostatic urethra.[20,26] The rigidity of the membrane along the line of fusion results in variable degrees of obstruction. When detected prenatally, obstruction is usually severe with renal dysplasia resulting from pressure damage to the developing renal pelvis, collecting ducts, and parenchyma as well as pulmonary hypoplasia secondary to oligohydramnios. If the fetus survives, up to 45% will develop renal insufficiency or end-stage renal disease requiring renal dialysis or transplantation before 5 years of age.[27–29] Those children who escape antenatal detection may present in the first months or years of life with UTIs, sepsis, voiding disorders, hematuria, vomiting, failure to thrive, urinary retention, hydronephrosis, ascites, and congestive heart failure. Patients with milder forms of the disease may escape detection until late as adolescence. These children may present with functional voiding disorders or UTIs.[30]

***Imaging.*** Antenatal and postnatal MRI and US show varying degrees of hydroureteronephrosis and bladder wall thickening (e-Fig. 120.18). Dysplastic kidneys with increased echogenicity, decreased corticomedullary differentiation, and cortical cyst formation may be seen. Perinephric fluid collections (urinomas) are usually related to forniceal rupture (Fig. 120.19 and e-Fig. 120.20). When unexplained ascites is discovered in a male fetus or newborn, the diagnosis of urinary tract obstruction caused by PUV should be strongly considered (Fig. 120.21). Associated hydroureteronephrosis may not be present because the forniceal rupture and communication to the peritoneal cavity act as a “pop off” mechanism, allowing one or both kidneys to decompress and therefore

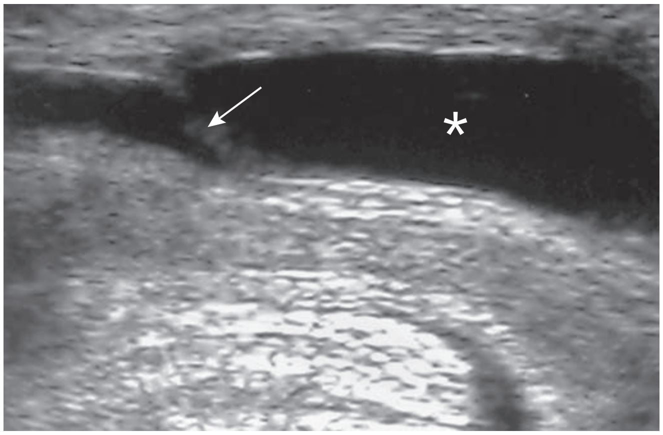

**e-Figure 120.14. Anterior urethral valve.** Longitudinal ultrasound image of the urethra during voiding shows thin echogenic valve traversing the urethra *(arrow)*. Proximal to the valve, urethral dilation is seen *(asterisk)*. *(From Bates DG, Coley BD. Ultrasound diagnosis of the anterior urethral valve.* Pediatr Radiol*. 2001;31:634–636.)*

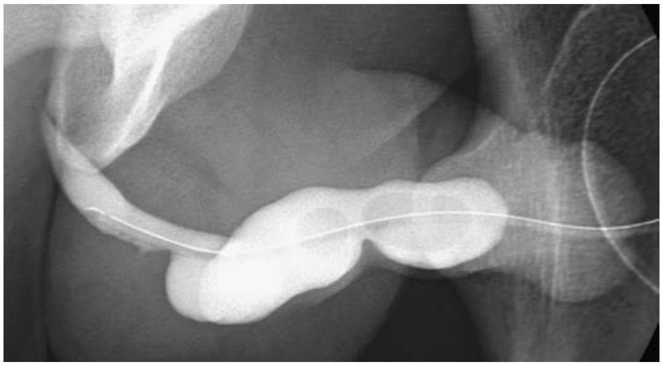

**e-Figure 120.16. Megalourethra.** An oblique image from a retrograde urethrogram shows fusiform dilation of the penile urethra.

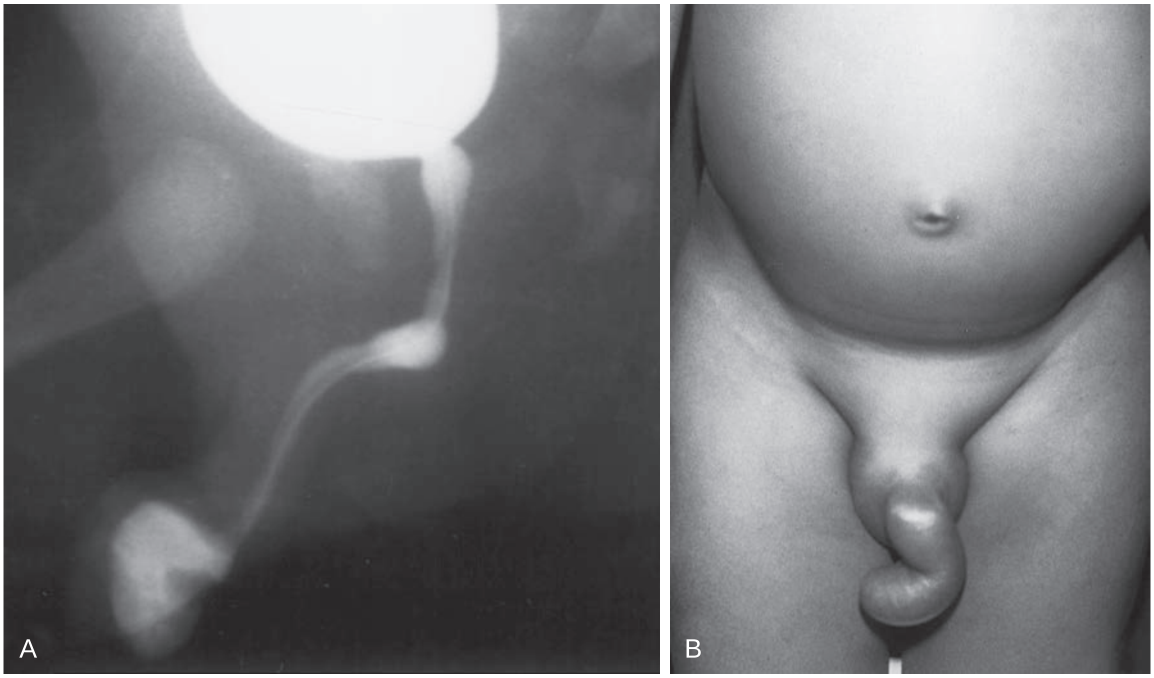

**e-Figure 120.17. Megalourethra.** (A) Voiding cystourethrogram shows dilation of the anterior penile urethra. (B) Postvoid photograph of the same child.

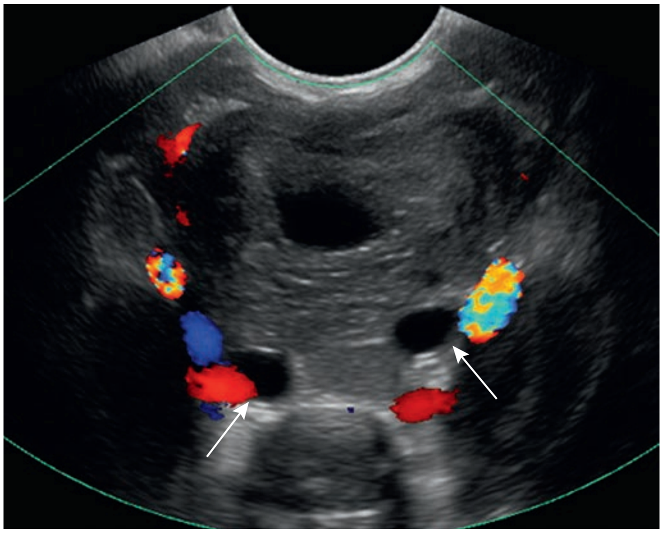

**e-Figure 120.18. Posterior urethral valves.** Transverse color Doppler sonogram shows marked bladder wall thickening and trabeculation due to outlet obstruction. The distal ureters *(arrows)* are dilated.

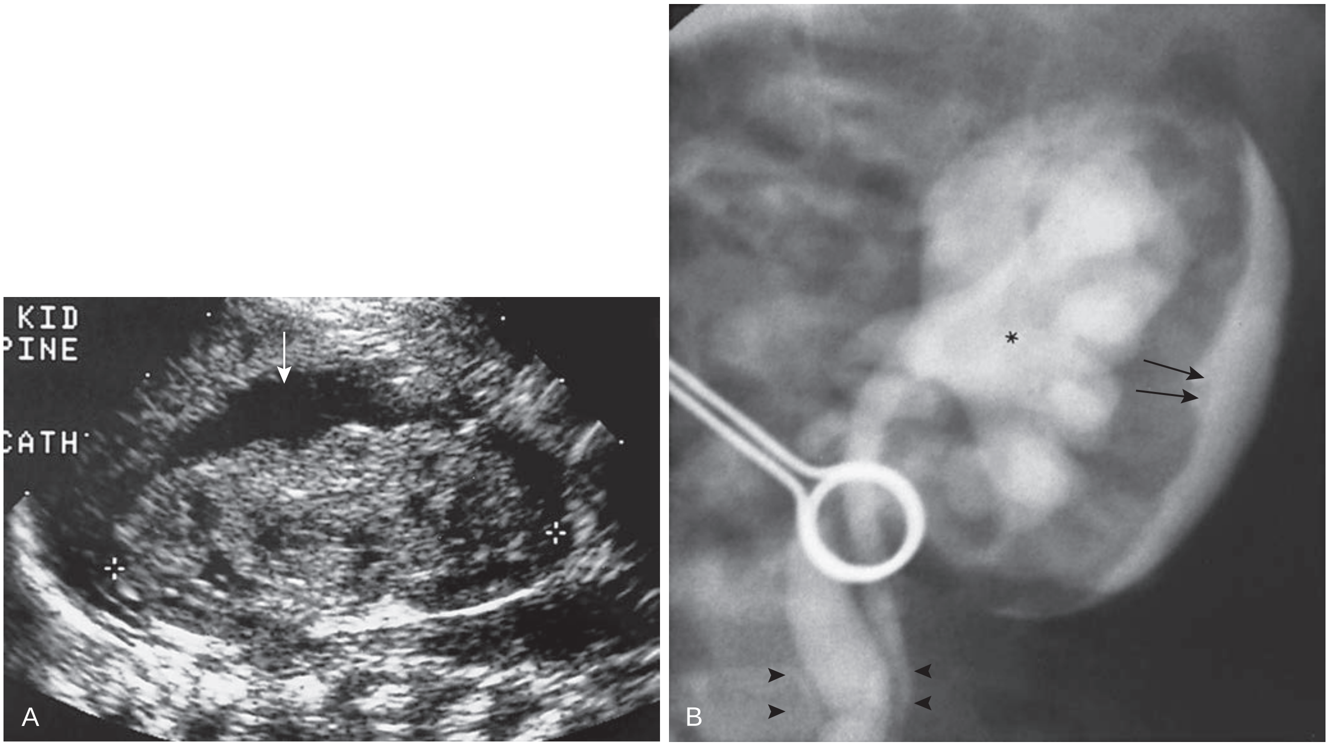

**e-Figure 120.20. Posterior urethral valves and perinephric fluid collection.** (A) Longitudinal gray-scale sonogram in a neonate shows a perinephric fluid collection *(arrow)*, likely a urinoma. No dilation of the intrarenal collecting system is present because it has decompressed into the subcapsular space. (B) Voiding cystourethrogram in a neonate with posterior urethral valves shows grade IV/V vesicoureteric reflux *(asterisk)*, intrarenal reflux, and either transparenchymal flow of contrast material into the subcapsular space or forniceal rupture with contrast material in the same location as the arrow on image (A) *(arrows)*. Contrast material also tracks down along the ureter *(arrowheads)*.

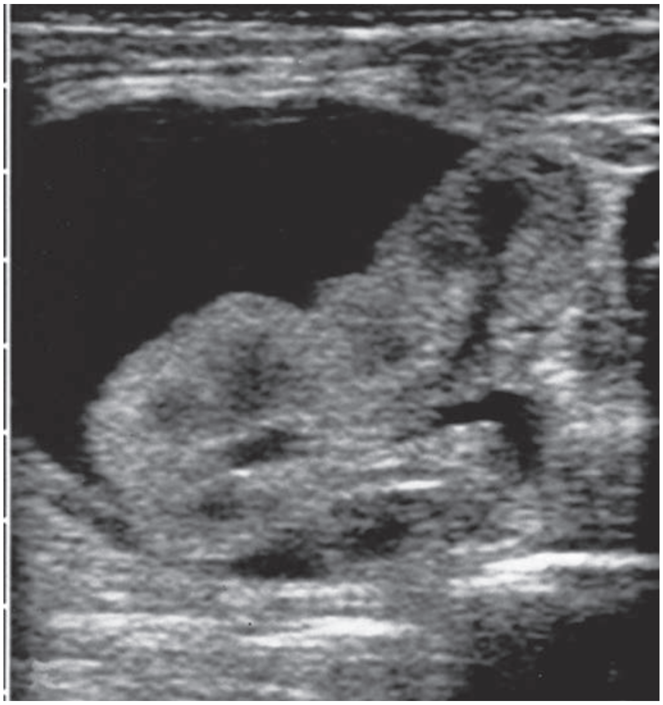

**Figure 120.19. Posterior urethral valve and perinephric fluid collection.** Transverse prone gray-scale sonogram shows a urinoma with mass effect on the left kidney.

attenuating the degree of renal damage. US can show the dilated posterior urethra, especially if the child is voiding at the time of the examination (e-Fig. 120.22).[31–36]

VCUG is the diagnostic study of choice for PUV (e-Fig. 120.23). VCUG directly shows the PUV and its effect on the urinary bladder: wall thickening, trabeculation with cellulae and sacculi, diverticula, and hypertrophy of the interureteric ridge (e-Fig. 120.24). The membrane itself may be visualized as a thin linear defect in the contrast-filled posterior urethra in some children (Fig. 120.25). VUR occurs in about one-half to two-thirds of boys with PUV, of whom approximately two-thirds have unilateral reflux (e-Fig. 120.26 and Box 120.2).[20,26,37,38]

***Treatment.*** When identified antenatally, severe obstruction can be treated with vesicoamniotic shunting; more recently developed fetoscopic laser ablation techniques are still considered experimental.[39] After birth, transurethral valvulotomy under direct visualization remains the treatment of choice. Residual valve tissue with obstruction is not uncommon, and stricture formation at the site of previous urethral valves or in the membranous urethra may occur.[40–43]

## POSTERIOR URETHRAL POLYPS

***Overview.*** Urethral polyps are benign growths usually of fibroepithelial histology that occur most commonly in boys 8 to 10 years of age. They typically arise from the posterior urethra in the region of the verumontanum as an elongated mobile mass.[44] The classic clinical triad includes intermittent urinary retention, intermittent hematuria, and intermittent lower urinary tract symptoms caused

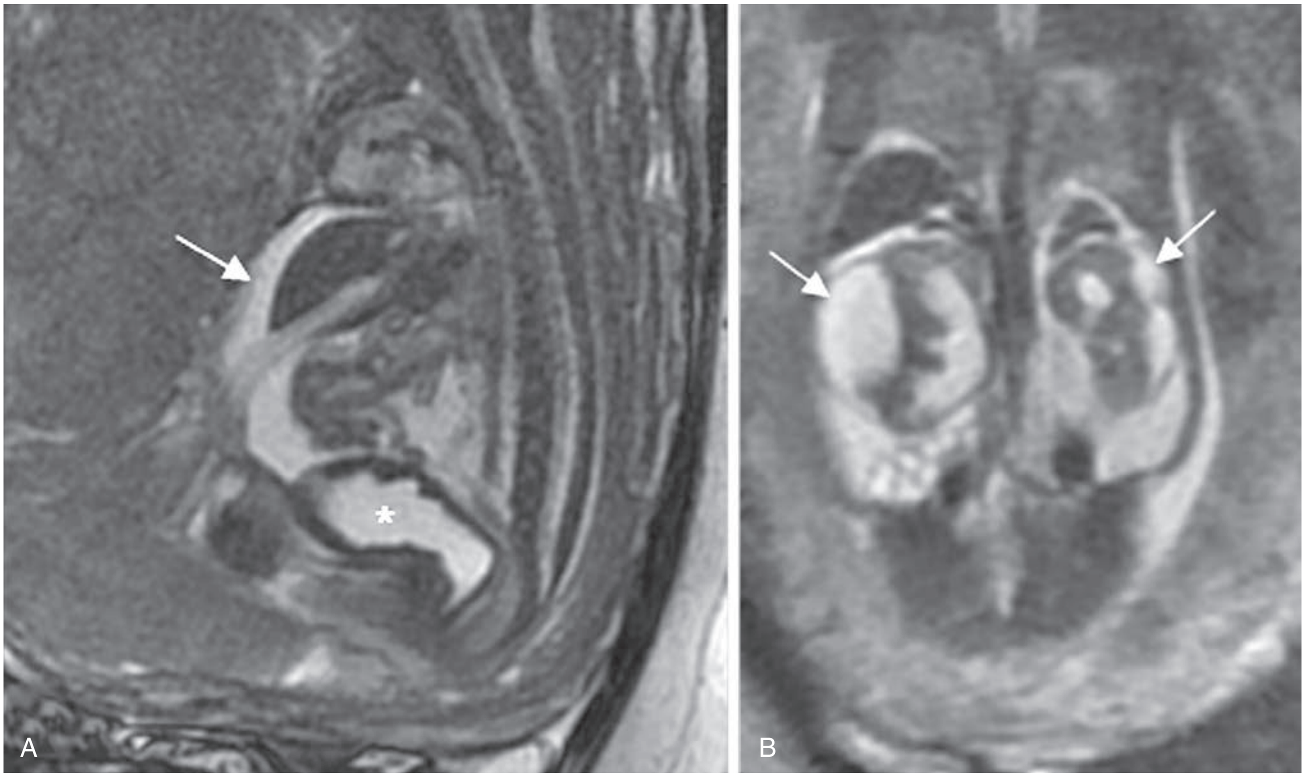

**Figure 120.21. Posterior urethral valves in a fetus.** (A) Sagittal T2-weighted MR image shows a dilated, thick-walled bladder *(asterisk)* and dilated posterior urethra. Ascites is also present *(arrow)*. (B) Coronal T2-weighted MR image through the kidneys shows bilateral pelvicaliectasis and subcapsular fluid collections *(arrows)*.

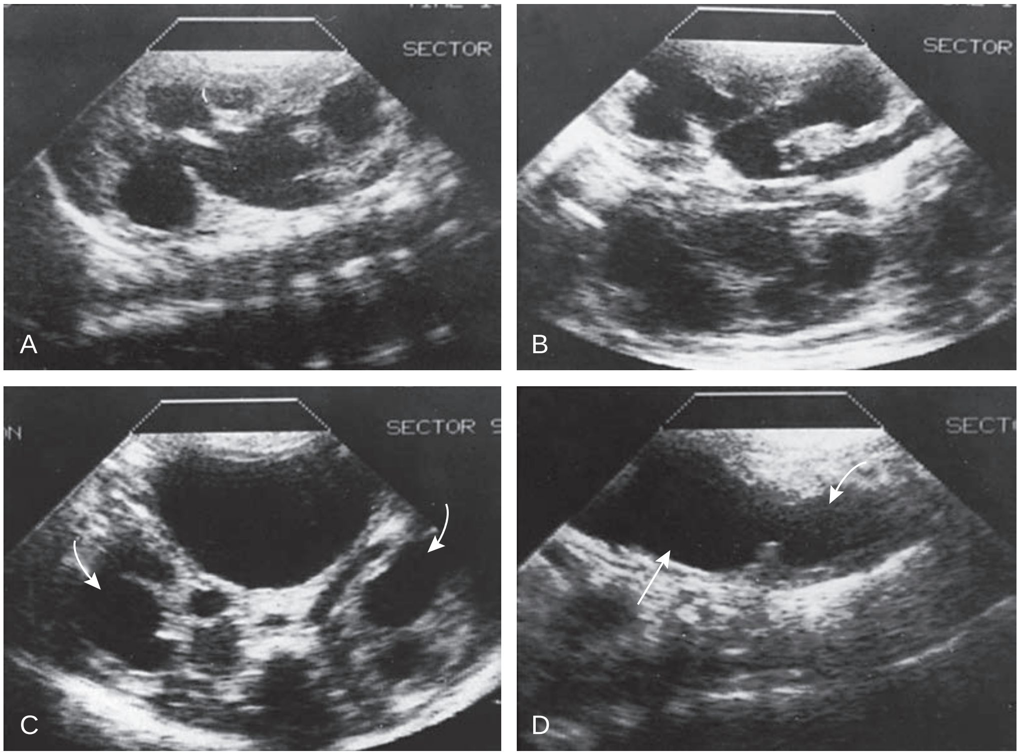

**e-Figure 120.22. Posterior urethral valves in a 7-day-old male infant strongly suspected on the basis of a fetal ultrasound examination.** (A and B) Longitudinal gray-scale sonogram of the right kidney (A) and left kidney (B) show bilateral dilation of the pelvicalyceal systems. (C) Bilateral ureterectasis also is present extending caudally to the bladder *(arrows)*. The bladder was markedly distended. (D) Midline longitudinal sonogram of the bladder with the transducer directly caudally shows dilation of the posterior urethra *(curved arrow)*. *Straight arrow* points to the bladder.

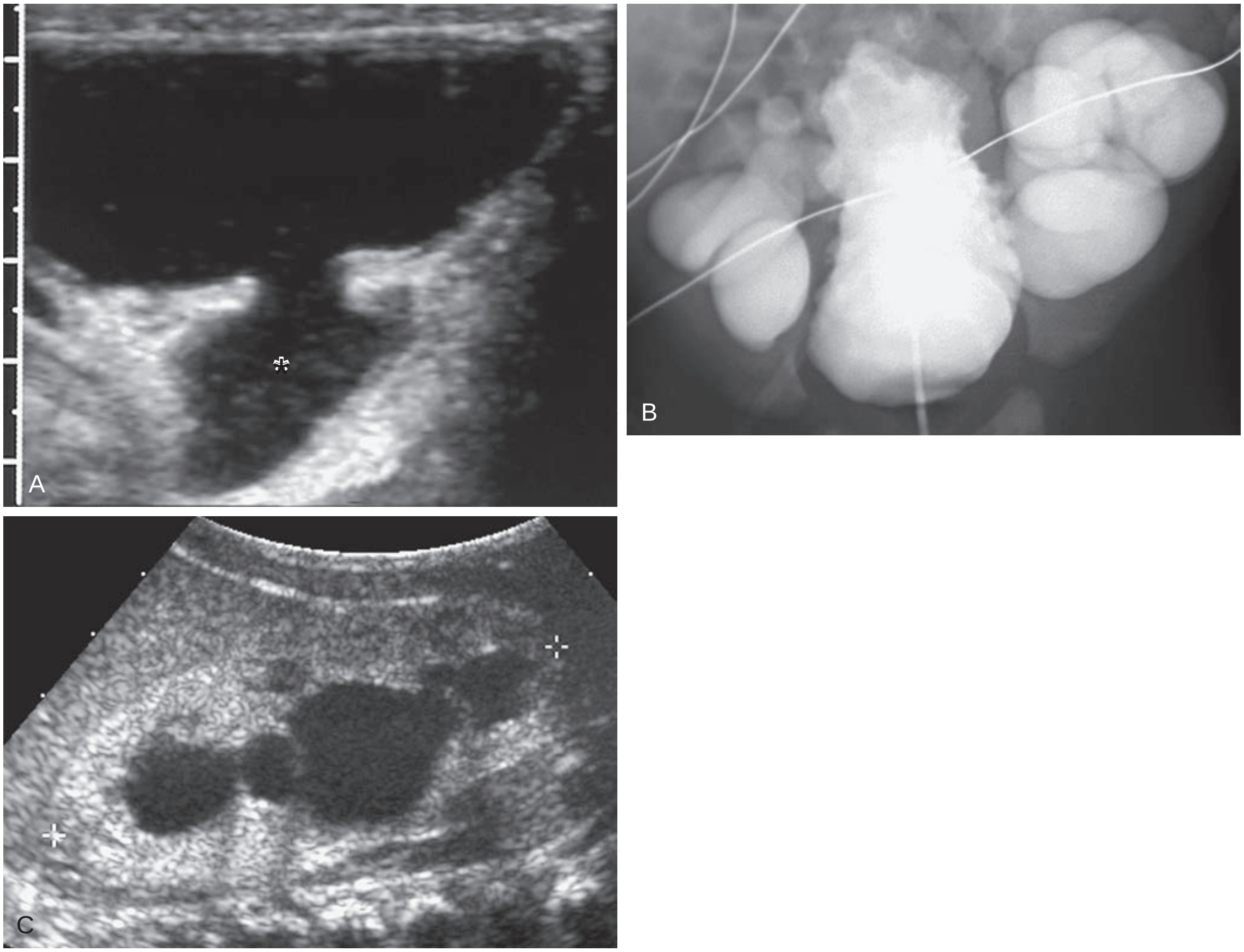

**e-Figure 120.23. Posterior urethral valves.** (A) Transverse gray-scale sonogram of the bladder shows a dilated posterior urethra *(asterisk)*, representing the "keyhole" sign. (B) Anterior image from a voiding cystourethrogram of the same patient demonstrates a trabeculated bladder with severe bilateral vesicoureteral reflux. (C) Longitudinal gray-scale sonogram of the same patient demonstrates an echogenic right kidney with absent corticomedullary differentiation and hydronephrosis indicating renal dysplasia.

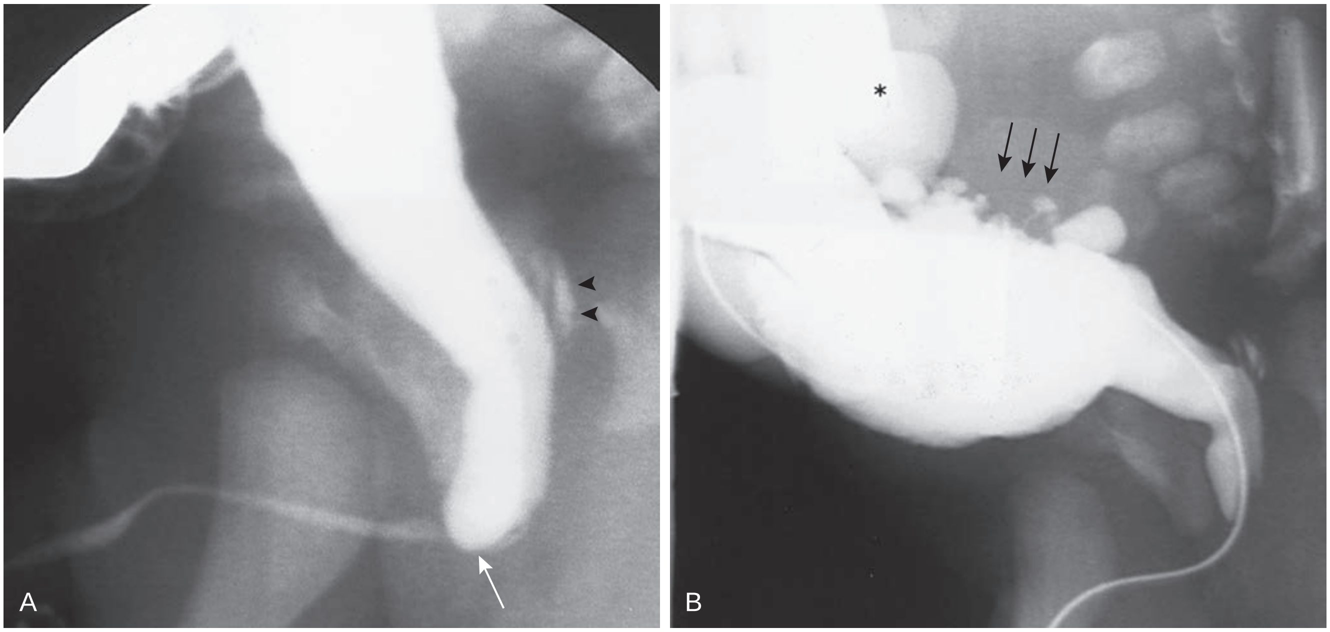

**e-Figure 120.24. Posterior urethral valve on voiding cystourethrogram.** (A) Steep oblique view from a voiding cystourethrogram shows posterior urethral valves *(arrow)*. The valves are clearly seen at the bottom of the verumontanum, with the distal urethral lumen eccentric and posterior in position. The posterior urethra related to the obstruction is dilated, and reflux into the ejaculatory ducts is seen *(arrowheads)*. (B) VCUG of the same neonate shows a trabeculated bladder with cellulae and sacculi *(arrows)*. Left-sided vesicoureteric reflux *(asterisk)* is seen.

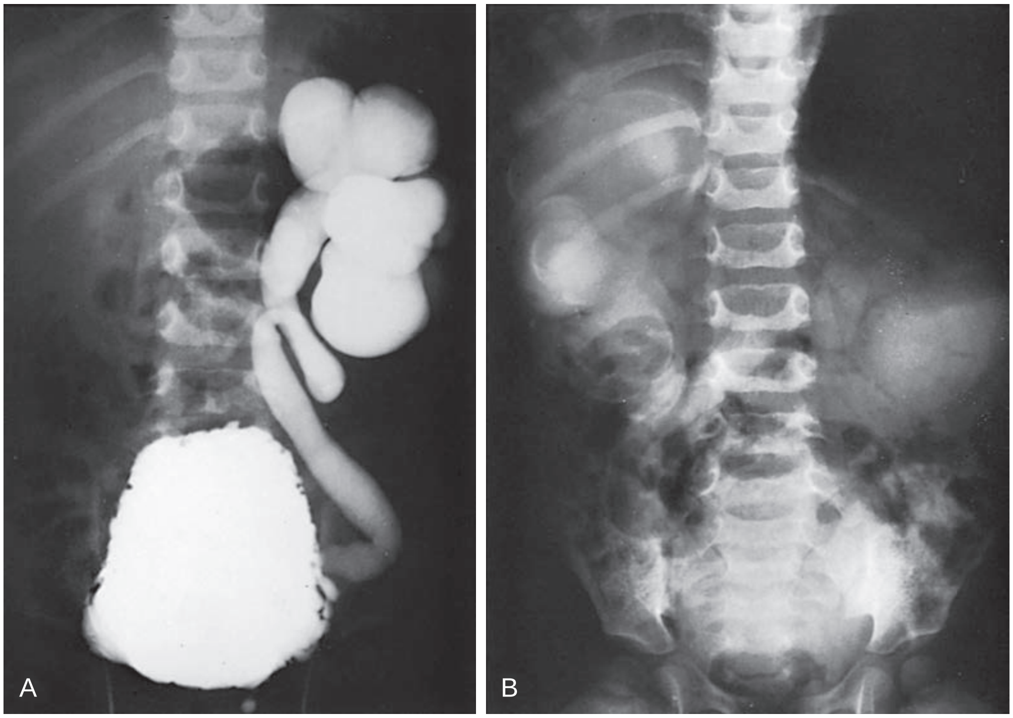

**e-Figure 120.26. Infant with posterior urethral valves.** (A) Voiding cystourethrogram shows severe left-sided reflux and bladder wall thickening. (B) Excretory urogram shows poor renal function and severe upper tract dilation bilaterally. Rim sign on the right represents a dense collection of contrast material in tubules around the dilated calyces.

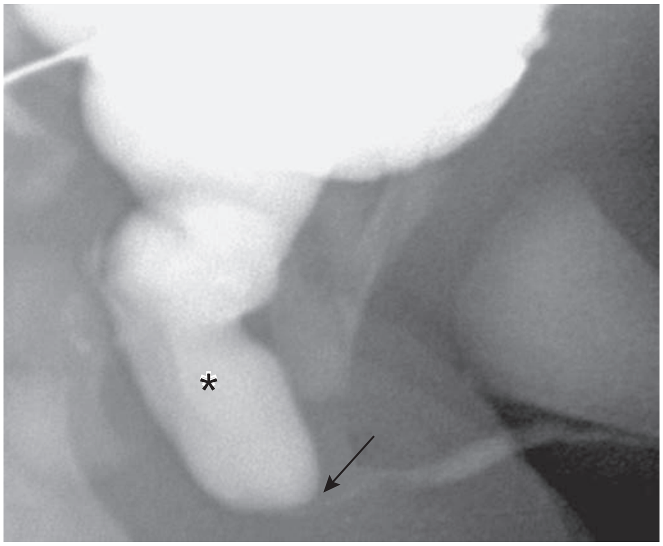

**Figure 120.25. Posterior urethral valves.** Oblique voiding cystourethrogram image shows a dilated posterior urethra *(asterisk)* with abrupt transition at level of valves *(arrow)* to a narrow anterior urethra. Incidental reflux into the ejaculatory ducts is seen.

**BOX 120.2** Imaging Findings in Patients With Posterior Urethral Valves

**ULTRASONOGRAPHY**

Renal cysts (dysplasia)
Bilateral (unilateral) hydronephrosis
Thick-walled bladder
Dilated posterior urethra
Membrane in posterior urethra

**VOIDING CYSTOURETHROGRAPHY**

Dilated posterior urethra
Membrane in posterior urethra
Reflux into prostatic ducts, ejaculatory ducts, or both
Thick bladder neck
Trabeculated bladder
Vesicoureteral reflux

by obstruction of the urethral lumen during voiding. Not uncommonly, patients may carry a diagnosis of psychosomatic voiding dysfunction due to the intermittent nature of the symptoms.[45] When females are affected, the most common presentation is an interlabial mass and external bloody discharge secondary to irritation of the polyp. Important differential considerations include prolapsed ectopic ureterocele, paraurethral cyst, hydrometrocolpos, and botryoid RMS.[46]

***Imaging.*** VCUG remains the imaging test of choice. Before voiding, the tip of the polyp is frequently located at the level of the bladder neck, causing a small rounded filling defect. In the voiding phase, the polyp moves downward into the distal posterior urethra and occasionally into the bulbar urethra (Fig. 120.27). At the end of voiding, the polyp is displaced retrograde to the level of the bladder outlet by the contraction of the external urethral sphincter. US may demonstrate a mobile pedunculated mass at the bladder base and indirect signs of bladder outlet obstruction (hydronephrosis and a large bladder with or without bladder wall hypertrophy).[47,48]

***Treatment.*** Treatment is transurethral resection with fulguration of the base of the polyp, and the risk of recurrence is nearly zero. Open surgery is reserved for when transurethral or endoscopic suprapubic resection is not feasible.[45]

## PROSTATIC UTRICLE

***Overview.*** The prostatic utricle is an epithelium-lined diverticulum of the prostatic urethra and is thought to be the remnant of the fused caudal ends of the Müllerian ducts. It is located at the level of the verumontanum between the openings of the two ejaculatory ducts. Normally, the urogenital sinus does not respond to Müllerian inhibiting factor but instead masculinizes in response to testosterone secretion in males. Abnormal hormonal input or sensitivity leads to development of the prostatic utricle and commonly varying degrees of hypospadias.[49] The increasing severity of the hypospadias correlates with increasing size of the utricle. While there is some debate, these are distinguished from Müllerian duct cysts in their earlier presentation, increased association with hypospadias and intersex disorders, and tubular shape. Though many are asymptomatic, poor emptying may lead to urine retention and stasis. Clinically, this presents as lower urinary tract voiding symptoms, urinary retention, UTI, epididymitis, stone formation, or postvoid dribbling caused by delayed utricle drainage.[50]

***Imaging.*** VCUG and RUG define the utricle size and its origin from the prostatic urethra and any associated hypospadias. Direct catheterization of the bladder during VCUG may be difficult secondary to preferential passage into the utricle (e-Fig. 120.28).

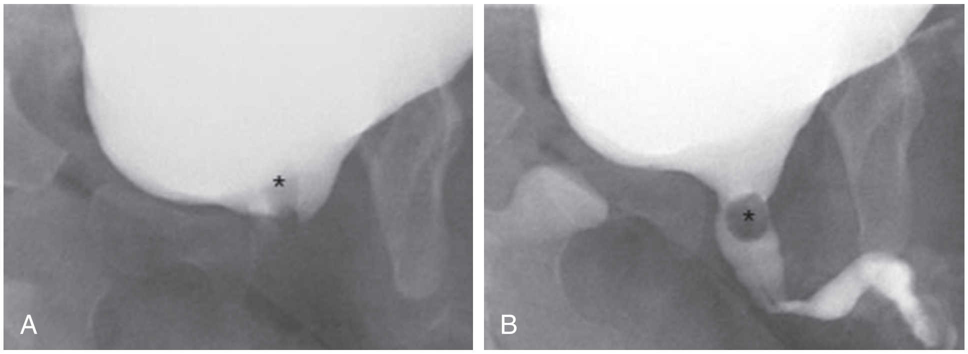

**Figure 120.27. Urethral polyp.** (A) Oblique image during voiding cystourethrography shows a lobular filling defect in the base of the bladder during initial filling phase *(asterisk)*. (B) The defect prolapses into the posterior urethra during voiding phase representing a polyp on a stalk *(asterisk)*.

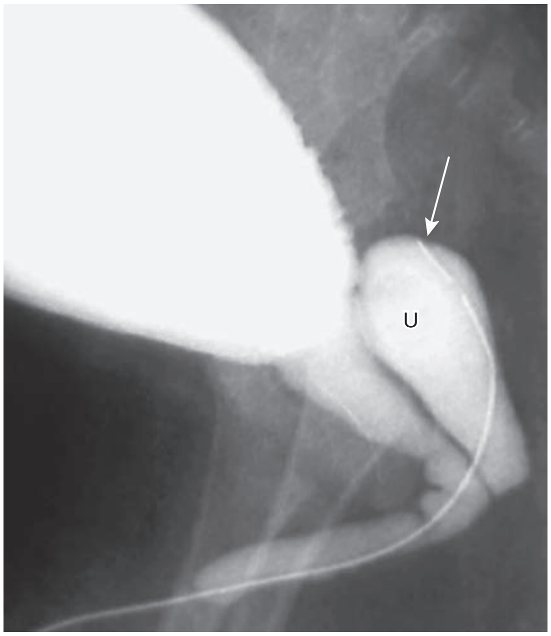

**e-Figure 120.28. Utricle.** Oblique voiding cystourethrogram image shows the catheter *(arrow)* positioned in the utricle *(U)*. Bladder filling and voiding were achieved without repositioning of the catheter.

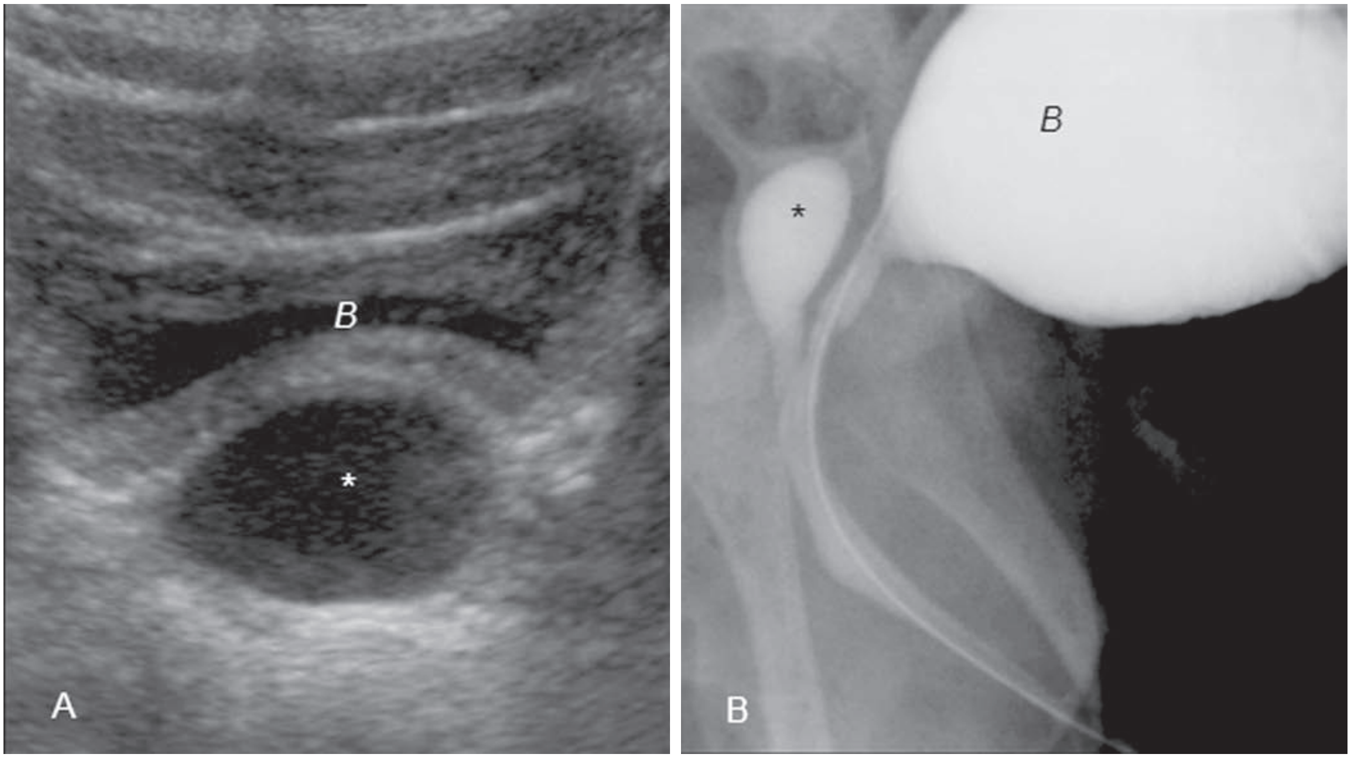

**Figure 120.29. Prostatic utricle.** (A) Transverse gray-scale sonogram through the level of the bladder demonstrates a fluid-filled cystic structure *(asterisk)* posteriorly. (B) Oblique voiding cystourethrogram demonstrates filling of a tubular structure arising from the verumontanum, consistent with a prostatic utricle.

Rarely the utricle may not be visible on RUG or VCUG, in which case US may be useful. Transabdominal US may demonstrate a retrovesical cystic mass, with or without internal debris, tapering to the expected location of the posterior urethra. CT and MRI will demonstrate a thin-walled cystic lesion originating from the prostatic urethral region, with or without associated mass effect on the bladder and ureters (Fig. 120.29).[51,52]

***Treatment.*** Surgical excision is the definitive treatment of symptomatic Müllerian duct remnants. Surgical management remains challenging because of the intimate association of these lesions to the ejaculatory ducts, vas deferens, ureters, pelvic nerves, and rectum.[53] More recently, laparoscopic excision has been reported with good success.[54]

## ABNORMALITIES OF COWPER'S GLANDS

***Overview.*** Bulbourethral (Cowper's) glands arise from the urethra in response to dihydrotestosterone and secrete a clear substance that serves as a lubricant. There are two pairs of glands, with the main pair within the urogenital diaphragm and an accessory pair within the bulbospongiosal tissue. The ducts measure 2 to 3 cm in length and course anteriorly to empty along the ventral surface of the bulbar urethra.[55,56]

***Imaging.*** The clinical significance of Cowper's glands in children usually lies in their recognition as a normal entity when visualized as a contrast-filled tubular structure paralleling the undersurface of the bulbar urethra during VCUG (e-Fig. 120.30). Rarely, a dilated gland and duct (syringocele) may be present (either congenital or acquired) and result in variable clinical presentation depending on whether or not the orifice is open (postvoid dribbling, uretheral discharge, UTI, and hematuria) or closed (obstructive symptoms, dysuria, urinary retention, and perineal pain).

These have been previously classified into four groups by Maizels et al according to morphology and symptoms: simple, perforate, imperforate, and ruptured.[57] When the orifice of the syringocele is open, contrast can be seen refluxing into the dilated duct, while when closed there will be smooth extrinsic mass effect along the ventral surface of the bulbar urethra (Fig. 120.31). On transperineal US, syringocele will appear as a generally anechoic cystic lesion within the characteristic location posterior to the bulbourethra. MRI may be useful for visualization of otherwise radiographically

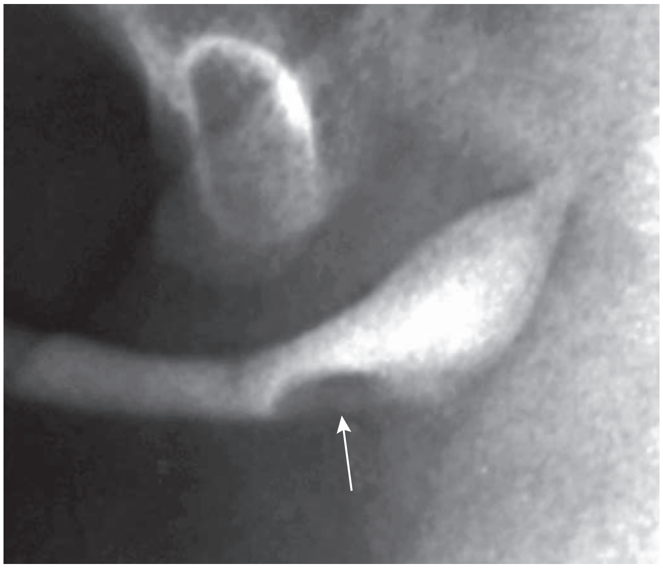

**Figure 120.31. Cowper's duct cyst (syringocele).** Oblique retrograde urethrogram image shows a lobular filling defect *(arrow)* along the ventral surface of the bulbar urethra.

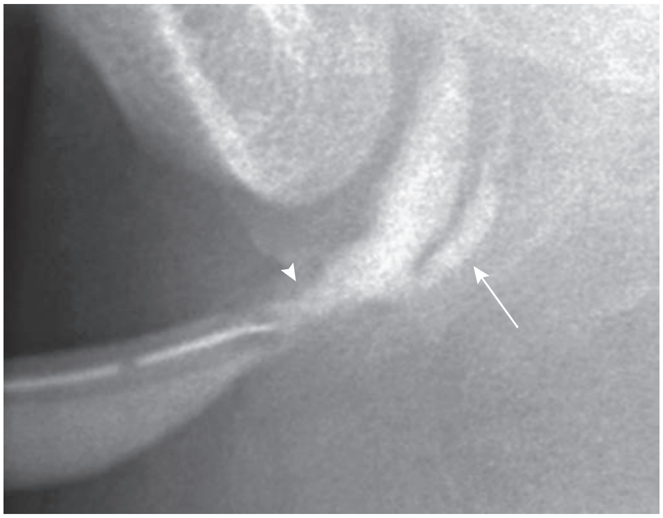

**e-Figure 120.30. Cowper's duct.** Oblique image from a retrograde urethrogram in a patient with a bulbar urethral stricture *(arrowhead)* shows retrograde filling of a ventral tubular structure *(arrow)* paralleling the urethra.

occult closed syringoceles which do not opacify with VCUG. Occasionally, asymptomatic retention cysts may be visualized as filling defects along the floor of the urethra during VCUG performed for other unrelated symptoms. When symptomatic, retention cysts will usually enlarge posteriorly and result in perineal masses or abscesses in the absence of voiding symptoms.[55,56,58,59]

Treatment when symptomatic is usually endoscopic incision. An important component of management is identification of secondary or coincidental pathology, which has been reported in up to 83% of patients, including minor urethral valves, VUR, ureteropelvic junction obstruction, and megaureter.[60]

## URETHRAL DUPLICATION

***Overview.*** These developmental anomalies are characterized by the presence of a complete or partial accessory urethral channel, which may arise anywhere from the bladder neck to the distal urethra and may occur in the sagittal plane (most common, with a ventral and dorsal urethra) or coronal plane (usually occurring in the setting of bladder duplication). It is important to remember that in almost all cases of sagittal duplication, the ventral urethra is the functioning channel and contains the sphincter mechanism and verumontanum.

A single unifying theory does not explain all the various forms of duplication, and more than one classification scheme exists in the literature, the most commonly referenced being the classification described by Effman et al.[61] In females, they are almost exclusively complete duplications with associated bladder duplication. In males, however, they most commonly occur as incomplete duplications that end blindly in the periurethral tissue or as a second meatus anywhere along the dorsal (epispadic variant, most common) or ventral (hypospadic variant) aspect of the penis.[62–66]

In the epispadic type, an incomplete accessory channel has a dorsal opening in the penis and ends blindly. The complete or partial forms originate from the bladder neck or proximal urethra and course through the dorsal aspect of the penis to end in an epispadic position anywhere between the glans and the root of the penis. Rarely, they originate from a minute cavity (nonfunctional sagittal plane duplicated bladder) located behind the pubic symphysis and in front of the normal bladder. The ventral urethra is normally positioned and ends in the glandular meatus (but may rarely be hypospadic).[65,66]

In the hypospadic type, an incomplete accessory channel has a ventral opening in the penis or originates from the normal proximal urethra and ends blindly in the periurethral tissue, similar in appearance to a urethral diverticulum or Cowper's duct. Complete or partial duplications arise from the bladder or proximal urethra and course through the ventral aspect of the penis to end in a hypospadic position along the shaft.[63,65,67] An important form of urethral duplication of the hypospadic type is referred to as *Y-type duplication*. The ventral urethra originates from the midprostatic urethra and terminates in the anal canal or on the perineum. Urine flows preferentially through this ventral channel and is considered the more functional urethra as it traverses the sphincter mechanism. A normally positioned dorsal urethra is usually stenotic or partially atretic.[68–71]

The congenital urethroperineal fistula has a similar location to the Y-type duplication, but is a distinctly different developmental anomaly (Fig. 120.32 and e-Fig. 120.33). The normally positioned dorsal channel is the functioning urethra in this case, and micturition is normal. Clinically, only a few drops of urine are present at the perineal opening.[72,73]

Accessory urethras may be asymptomatic or may cause a double urinary stream, urinary incontinence, UTIs, and urinary retention.

***Imaging.*** Appropriate evaluation of urethral duplication includes anatomic evaluation of all channels (rarely more than two channels may be seen), recognition of the functional urethra, and identification of associated anomalies.[64,65] VCUG is adequate if all urethral channels can be clearly identified (Fig. 120.34 and e-Fig. 120.35). RUG may be necessary for hypoplastic channels not visualized on VCUG. Cystoscopy may be performed to confirm the radiographic findings and to precisely identify which urethra contains the sphincteric mechanism and normal verumontanum.[63,67]

***Treatment.*** Preservation and surgical reconstruction of the functional urethral channel is the primary goal of treatment and must be individualized to the patient's unique anatomy. Ventral channel excision in congenital urethroperineal fistula is curative.[63,65,67,70,74]

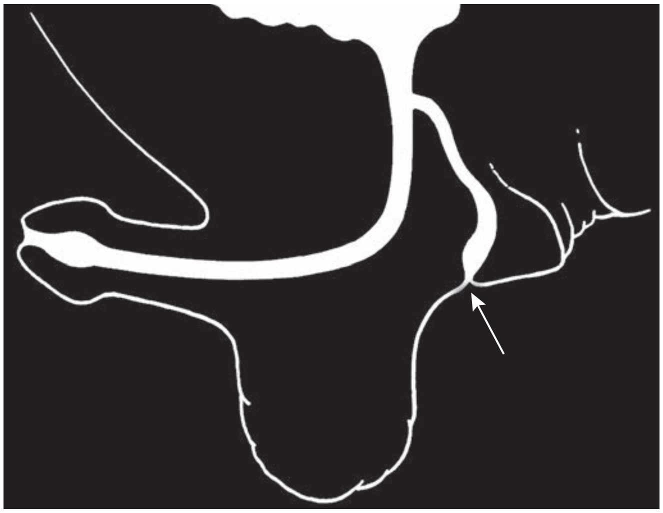

**Figure 120.32. Urethroperineal fistula.** Schematic diagram showing the perineal fistula *(arrow)* originating from the normal dorsal urethra. This is the exception to the rule that the ventral urethra is the normal urethra in duplications. *(From Bates DG, Lebowitz RL. Congenital urethroperineal fistula.* Radiology. *1995;194:501–504.) See* e-Fig. 120.33.

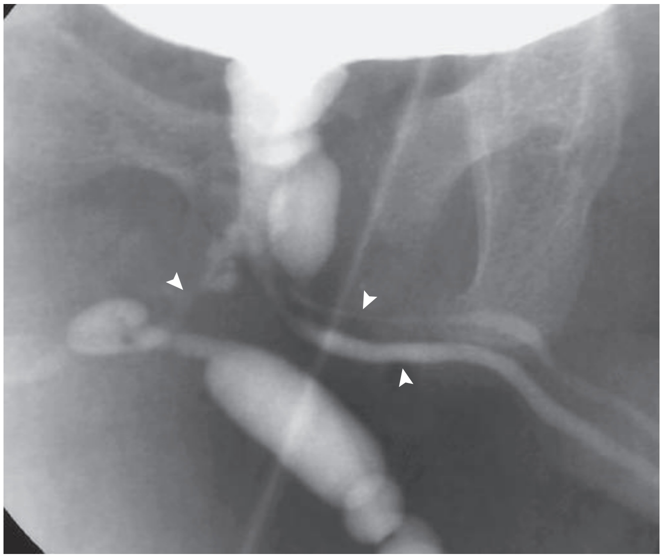

**Figure 120.34. Urethral duplications.** A voiding cystourethrogram oblique image shows triplication of the urethra *(arrowheads)* originating from the prostatic urethra.

## URETHRAL STRICTURES

***Overview.*** While sometimes congenital, most pediatric urethral strictures are secondary to trauma. Iatrogenic strictures account for about two-thirds of urethral strictures in children, located

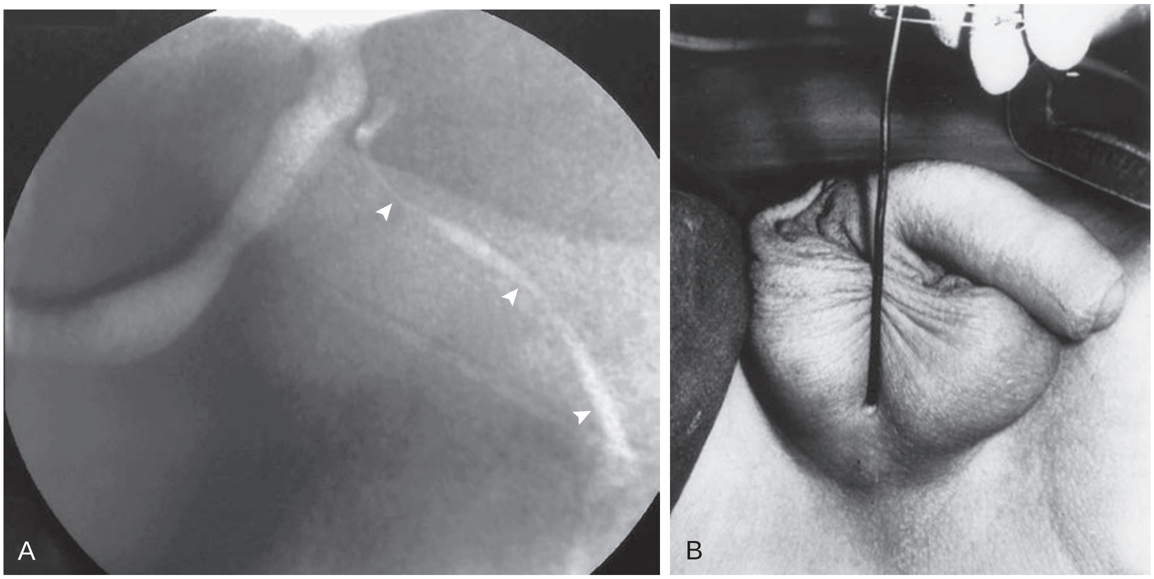

**e-Figure 120.33. Urethroperineal fistula.** (A) Oblique VCUG image shows a congenital perineal fistula *(arrowheads)* originating from the prostatic urethra. (B) A photograph of another patient, showing a probe within the perineal urethra. *(From Bates DG, Lebowitz RL. Congenital urethroperineal fistula.* Radiology. *1995;194:501–504.)*

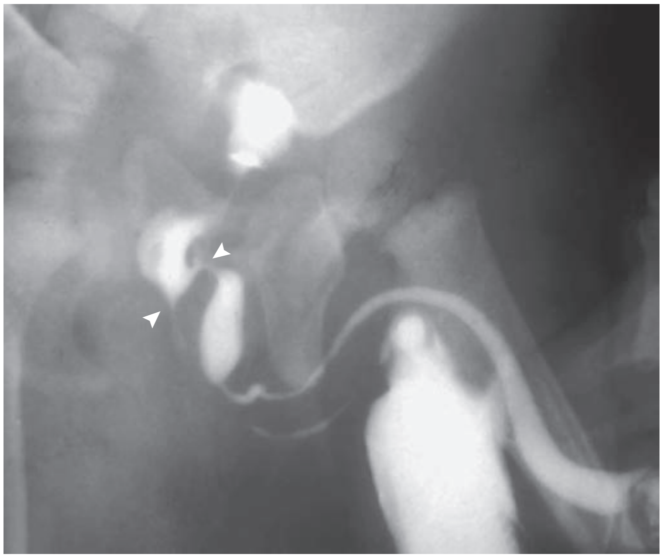

**e-Figure 120.35. Urethral duplications.** An oblique image from a retrograde urethrogram after simultaneous injection of both the glandular and ventral penile openings shows partial duplication of the urethra originating at the prostatic urethra *(arrowheads)*.

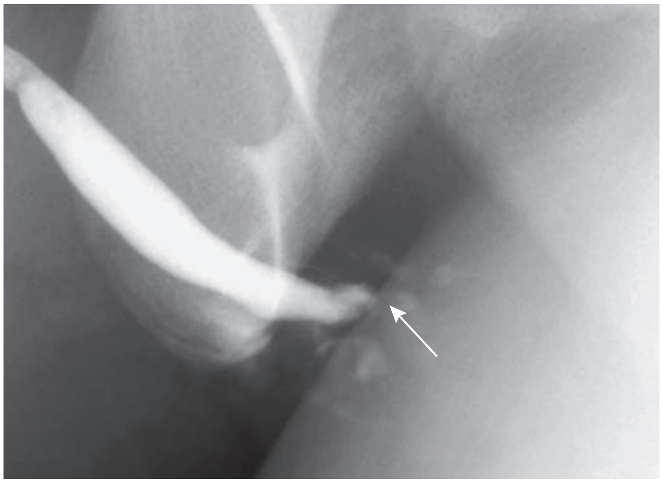

**Figure 120.36. Straddle injury.** A retrograde urethrogram shows bulbar urethral disruption *(arrow)* and contrast extravasation.

predominantly near the penoscrotal junction, an area that is particularly vulnerable to internal trauma. External trauma resulting in stricture disease may result from pelvic fractures, penetrating injuries, direct blows to the perineum, and straddle injuries. Urethral infections are uncommon causes of urethral strictures in children as opposed to young adults, in whom they are often due to *Neisseria gonorrhoeae* infection.[75–78] Urethral strictures of unknown cause in symptomatic boys are not rare and may be the result of unrecognized external trauma or urethritis, Cowper's duct infection, or rupture of a Cowper's duct cyst. They may also be secondary to incomplete dissolution of the urogenital membrane at the junction of the cloaca and genital groove (Cobb's collar) within the anterior urethra.[79] The clinical manifestations of urethral strictures include blood at the meatus after known trauma, poor urinary stream, straining to void, urinary retention, painful urination, hematuria, UTI, and recurrent epididymitis.

***Imaging.*** The diagnosis of urethral stricture is readily established by VCUG when the bladder can be catheterized. Compression of the distal penis during voiding or RUG results in distention of the normal urethra and better delineation of the true extent of the stricture. Strictures from straddle injuries are usually located in the bulbar urethra (Fig. 120.36 and e-Fig. 120.37). Congenital strictures also are located most often in the bulbar urethra and are usually very short and diaphragm-like. In the interpretation of the urethrogram, it is important to keep in mind those normal areas of narrowing at the level of the urogenital diaphragm or narrowing caused by spasm of the bulbocavernosus or external sphincter muscles that may simulate a stricture.[77,80–82] Complementary or alternative techniques to fluoroscopic evaluation that have emerged relatively recently include transperineal sonography and magnetic resonance (MR) urethrography, with the latter possessing the added ability to provide information about bladder and periurethral tissues in additional to accurately defining urethral anatomy.[80,82]

***Treatment.*** Three major forms of treatment exist for urethral stricture: (1) *urethral dilation*, which is the oldest and simplest treatment; (2) *open reconstruction with urethroplasty*, which is regarded as the gold standard; and (3) *internal urethrotomy*, by incising or ablating the stricture transurethrally.[83,84]

## KEY POINTS

- Failure of the urachus to normally regress can result in several anomalies: patent urachus (most common), urachal sinus, urachal diverticulum, and urachal cyst.
- Bladder diverticula may be primary (congenital), secondary, or iatrogenic (postoperative).
- Rhabdomysarcoma is the most common neoplasm of the lower genitourinary tract. The embryonal form is most common, accounting for approximately 90% of cases.
- Late renal insufficiency or failure may develop in 25% to 40% of patients with PUV throughout adolescence and into adulthood.
- Large prostatic utricles are commonly associated with male hypospadias.
- In Y-type urethral duplication, the ventral channel is considered the normal urethra. In congenital urethroperineal fistula, the normally positioned dorsal channel is the functioning urethra.
- Iatrogenesis accounts for about two-thirds of urethral strictures in children.

## SUGGESTED READINGS

Agrons GA, Wagner BJ, Lonergan GJ, et al. From the archives of the AFIP. Genitourinary rhabdomyosarcoma in children: radiologic-pathologic correlation. *Radiographics*. 1997;17(4):919–937.

Berrocal T, Lopez-Pereira P, Arjonilla A, et al. Anomalies of the distal ureter, bladder, and urethra in children: embryologic, radiologic, and pathologic features. *Radiographics*. 2002;22:1139–1164.

Kawashima A, Sandler CM, Wasserman NF, et al. Imaging of urethral disease: a pictorial review. *Radiographics*. 2004;24(suppl 1):S195–S216.

Krishnan A, deSouza A, Konijeti R, et al. The anatomy and embryology of posterior urethral valves. *J Urol*. 2006;175:1214–1220.

Levin TL, Han B, Little BP. Congenital anomalies of the male urethra. *Pediatr Radiol*. 2007;37(9):851–862, quiz 945.

Yapo BR, Gerges B, Holland AJ. Investigation and management of suspected urachal anomalies in children. *Pediatr Surg Int*. 2008;24(5):589–592.

## REFERENCES

Full references for this chapter can be found on www.expertconsult.com.

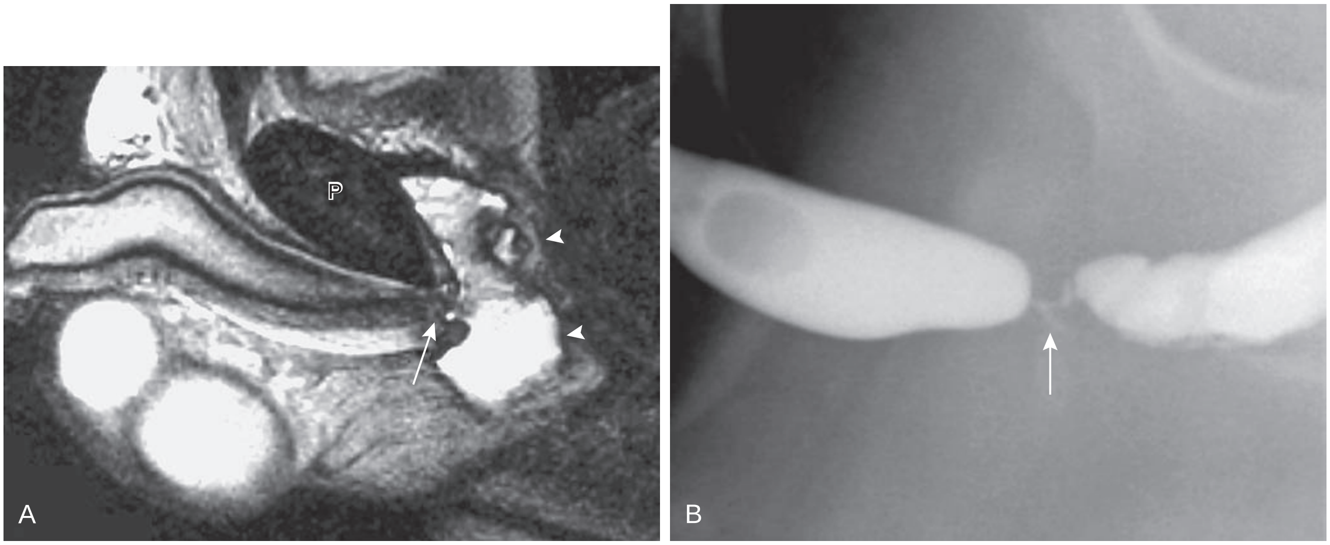

**e-Figure 120.37. Straddle injury.** (A) Sagittal T2-weighted MR image shows urethral disruption *(arrow)* directly beneath the pubis *(P)*. The urethral fragments are separated by an intervening hematoma *(arrowheads)*. (B) A follow-up retrograde urethrogram after repair shows high-grade urethral stricture *(arrow)*.

## REFERENCES

1. Galati V, Donovan B, Ramji F, et al. Management of urachal remnants in early childhood. *J Urol*. 2008;180(suppl 4):1824–1826. discussion 1827.
2. Yapo BR, Gerges B, Holland AJ. Investigation and management of suspected urachal anomalies in children. *Pediatr Surg Int*. 2008;24(5):589–592.
3. Yu JS, Kim KW, Lee HJ, et al. Urachal remnant diseases: spectrum of CT and US findings. *Radiographics*. 2001;21(2):451–461.
4. Ozbek SS, Pourbagher MA, Pourbagher A. Urachal remnants in asymptomatic children: gray-scale and color Doppler sonographic findings. *J Clin Ultrasound*. 2001;29(4):218–222.
5. Boechat MI, Lebowitz RL. Diverticula of the bladder in children. *Pediatr Radiol*. 1978;7(1):22–28.
6. Hernanz-Schulman M, Lebowitz RL. The elusiveness and importance of bladder diverticula in children. *Pediatr Radiol*. 1985;15(6):399–402.
7. Hutch JA. Saccule formation at the ureterovesical junction in smooth walled bladders. *J Urol*. 1961;86:390–399.
8. Afshar K, Malek R, Bakhshi M, et al. Should the presence of congenital para-ureteral diverticulum affect the management of vesicoureteral reflux? *J Urol*. 2005;174(4 Pt 2):1590–1593.
9. Im YJ, Lee YS, Kim SW, et al. Implications of paraureteral diverticulum for the management of vesicoureteral reflux. *Int J Urol*. 2015;22(9):850–853.
10. Celebi S, Sander S, Kuzdan O, et al. Current diagnosis and management of primary isolated bladder diverticula in children. *J Pediatr Urol*. 2015;11(2):61.e1–61.e65.
11. Wu HY, Snyder HM 3rd, Womer RB. Genitourinary rhabdomyosarcoma: which treatment, how much, and when? *J Pediatr Urol*. 2009;5(6):501–506.
12. Agrons GA, Wagner BJ, Lonergan GJ, et al. From the archives of the AFIP. Genitourinary rhabdomyosarcoma in children: radiologic-pathologic correlation. *Radiographics*. 1997;17(4):919–937.
13. Wu HY, Snyder HM 3rd. Pediatric urologic oncology: bladder, prostate, testis. *Urol Clin North Am*. 2004;31(3):619–627, xi.
14. Poggiani C, Teani M, Auriemma A, et al. Sonographic detection of rhabdomyosarcoma of the urinary bladder. *Eur J Ultrasound*. 2001;13(1):35–39.
15. Rodeberg DA, Anderson JR, Arndt CA, et al. Comparison of outcomes based on treatment algorithms for rhabdomyosarcoma of the bladder/prostate: combined results from the Children's Oncology Group, German Cooperative Soft Tissue Sarcoma Study, Italian Cooperative Group, and International Society of Pediatric Oncology Malignant Mesenchymal Tumors Committee. *Int J Cancer*. 2011;128(5):1232–1239.
16. Ashley RA, Figueroa TE. Gross hematuria in a 3-year-old girl caused by a large isolated bladder hemangioma. *Urology*. 2010;76(4):952–954.
17. Vemulakonda VM, Kopp RP, Sorensen MD, et al. Recurrent nephrogenic adenoma in a 10-year-old boy with prune belly syndrome: a case presentation. *Pediatr Surg Int*. 2008;24(5):605–607.
18. Collin M, Charles A, Barker A, et al. Inflammatory myofibroblastic tumour of the bladder in children: a review. *J Pediatr Urol*. 2015;11(5):239–245.
19. Imaji R, Dewan PA. Congenital posterior urethral obstruction: re-do fulguration. *Pediatr Surg Int*. 2002;18(5–6):444–446.
20. Young HH, Frontz WA, Baldwin JC. Congenital obstruction of the posterior urethra. J Urol, 3: 289-365, 1919. *J Urol*. 2002;167(1):265–267, discussion 268.
21. Bates DG, Coley BD. Ultrasound diagnosis of the anterior urethral valve. *Pediatr Radiol*. 2001;31(9):634–636.
22. Gupta DK, Srinivas M. Congenital anterior urethral diverticulum in children. *Pediatr Surg Int*. 2000;16(8):565–568.
23. Kajbafzadeh A. Congenital urethral anomalies in boys. Part II. *Urol J*. 2005;2(3):125–131.
24. McLellan DL, Gaston MV, Diamond DA, et al. Anterior urethral valves and diverticula in children: a result of ruptured Cowper's duct cyst? *BJU Int*. 2004;94(3):375–378.
25. Paulhac P, Fourcade L, Lesaux N, et al. Anterior urethral valves and diverticula. *BJU Int*. 2003;92(5):506–509.
26. Berrocal T, Lopez-Pereira P, Arjonilla A, et al. Anomalies of the distal ureter, bladder, and urethra in children: embryologic, radiologic, and pathologic features. *Radiographics*. 2002;22(5):1139–1164.
27. El-Ghoneimi A, Desgrippes A, Luton D, et al. Outcome of posterior urethral valves: to what extent is it improved by prenatal diagnosis? *J Urol*. 1999;162(3 Pt 1):849–853.
28. Reinberg Y, de Castano I, Gonzalez R. Prognosis for patients with prenatally diagnosed posterior urethral valves. *J Urol*. 1992;148(1):125–126.
29. Ylinen E, Ala-Houhala M, Wikstrom S. Prognostic factors of posterior urethral valves and the role of antenatal detection. *Pediatr Nephrol*. 2004;19(8):874–879.
30. Schober JM, Dulabon LM, Woodhouse CR. Outcome of valve ablation in late-presenting posterior urethral valves. *BJU Int*. 2004;94(4):616–619.
31. Chen C, Shih SL, Liu FF, et al. In utero urinary bladder perforation, urinary ascites, and bilateral contained urinomas secondary to posterior urethral valves: clinical and imaging findings. *Pediatr Radiol*. 1997;27(1):3–5.
32. Cohen HL, Susman M, Haller JO, et al. Posterior urethral valve: transperineal US for imaging and diagnosis in male infants. *Radiology*. 1994;192(1):261–264.
33. Cohen HL, Zinn HL, Patel A, et al. Prenatal sonographic diagnosis of posterior urethral valves: identification of valves and thickening of the posterior urethral wall. *J Clin Ultrasound*. 1998;26(7):366–370.
34. Feinstein KA, Fernbach SK. Septated urinomas in the neonate. *AJR Am J Roentgenol*. 1987;149(5):997–1000.
35. Kaefer M, Keating MA, Adams MC, et al. Posterior urethral valves, pressure pop-offs and bladder function. *J Urol*. 1995;154(2 Pt 2):708–711.
36. Mercado-Deane MG, Beeson JE, John SD. US of renal insufficiency in neonates. *Radiographics*. 2002;22(6):1429–1438.
37. Ditchfield MR, Grattan-Smith JD, de Campo JF, et al. Voiding cystourethrography in boys: does the presence of the catheter obscure the diagnosis of posterior urethral valves? *AJR Am J Roentgenol*. 1995;164(5):1233–1235.
38. Imaji R, Dewan PA. The clinical and radiological findings in boys with endoscopically severe congenital posterior urethral obstruction. *BJU Int*. 2001;88(3):263–267.
39. Martinez JM, Masoller N, Devlieger R, et al. Laser ablation of posterior urethral valves by fetal cystoscopy. *Fetal Diagn Ther*. 2015;37(4):267–273.
40. Barber T, Al-Omar O, McLorie GA. Cold knife valvulotomy for posterior urethral valves using novel optical urethrotome. *Urology*. 2009;73(5):1012–1015.
41. Lopez Pereira P, Martinez Urrutia MJ, Jaureguizar E. Initial and long-term management of posterior urethral valves. *World J Urol*. 2004;22(6):418–424.
42. Nijman RJ, Scholtmeijer RJ. Complications of transurethral electro-incision of posterior urethral valves. *Br J Urol*. 1991;67(3):324–326.
43. Youssif M, Dawood W, Shabaan S, et al. Early valve ablation can decrease the incidence of bladder dysfunction in boys with posterior urethral valves. *J Urol*. 2009;182(suppl 4):1765–1768.
44. Demircan M, Ceran C, Karaman A, et al. Urethral polyps in children: a review of the literature and report of two cases. *Int J Urol*. 2006;13(6):841–843.
45. Akbarzadeh A, Khorramirouz R, Kajbafzadeh AM. Congenital urethral polyps in children: report of 18 patients and review of literature. *J Pediatr Surg*. 2014;49(5):835–839.
46. Akbarzadeh A, Khorramirouz R, Saadat S, et al. Congenital urethral polyps in girls: as a differential diagnosis of interlabial masses. *J Pediatr Adolesc Gynecol*. 2014;27(6):330–334.
47. Beluffi G, Berton F, Gola G, et al. Urethral polyp in a 1-month-old child. *Pediatr Radiol*. 2005;35(7):691–693.
48. Ben-Meir D, Yin M, Chow CW, et al. Urethral polyps in prepubertal girls. *J Urol*. 2005;174(4 Pt 1):1443–1444.
49. Yeung CK, Sihoe JD, Tam YH, et al. Laparoscopic excision of prostatic utricles in children. *BJU Int*. 2001;87(6):505–508.
50. Krstic ZD, Smoljanic Z, Micovic Z, et al. Surgical treatment of the Müllerian duct remnants. *J Pediatr Surg*. 2001;36(6):870–876.
51. Kojima Y, Hayashi Y, Maruyama T, et al. Comparison between ultrasonography and retrograde urethrography for detection of prostatic utricle associated with hypospadias. *Urology*. 2001;57(6):1151–1155.
52. Li CC, Ko SF, Ng SH, et al. Symptomatic giant Müllerian duct cyst in an infant: radiographic and CT findings. *Abdom Imaging*. 2004;29(4):525–527.
53. Desautel MG, Stock J, Hanna MK. Müllerian duct remnants: surgical management and fertility issues. *J Urol*. 1999;162(3 Pt 2):1008–1013. discussion 1014.
54. Jia W, Liu GC, Zhang LY, et al. Comparison of laparoscopic excision versus open transvesical excision for symptomatic prostatic utricle in children. *J Pediatr Surg*. 2016;51(10):1597–1601.
55. Chughtai B, Sawas A, O'Malley RL, et al. A neglected gland: a review of Cowper's gland. *Int J Androl*. 2005;28(2):74–77.

56. Colodny AH, Lebowitz RL. Lesions of Cowper's ducts and glands in infants and children. *Urology*. 1978;11(4):321–325.
57. Maizels M, Stephens FD, King LR, et al. Cowper's syringocele: a classification of dilatations of Cowper's gland duct based upon clinical characteristics of 8 boys. *J Urol*. 1983;129(1):111–114.
58. Beluffi G, Fiori P, Pietrobono L, et al. Cowper's glands and ducts: radiological findings in children. *Radiol Med (Torino)*. 2006;111(6):855–862.
59. Kickuth R, Laufer U, Pannek J, et al. Cowper's syringocele: diagnosis based on MRI findings. *Pediatr Radiol*. 2002;32(1):56–58.
60. Blasl F, Rosch WH, Koen M, et al. Cowper's syringocele: a rare differential diagnosis of infravesical obstruction in boys and young adults. *J Pediatr Urol*. 2016.
61. Effmann EL, Lebowitz RL, Colodny AH. Duplication of the urethra. *Radiology*. 1976;119(1):179–185.
62. Coker AM, Allshouse MJ, Koyle MA. Complete duplication of bladder and urethra in a sagittal plane in a male infant: case report and literature review. *J Pediatr Urol*. 2008;4(4):255–259.
63. Mane SB, Obaidah A, Dhende NP, et al. Urethral duplication in children: our experience of eight cases. *J Pediatr Urol*. 2009;5(5):363–367.
64. Prasad N, Vivekanandhan KG, Ilangovan G, et al. Duplication of the urethra. *Pediatr Surg Int*. 1999;15(5–6):419–421.
65. Salle JL, Sibai H, Rosenstein D, et al. Urethral duplication in the male: review of 16 cases. *J Urol*. 2000;163(6):1936–1940.
66. Usami M, Hayashi Y, Kojima Y, et al. Congenital prepubic sinus: a variant of dorsal urethral duplication (Stephens type 3). *Int J Urol*. 2005;12(2):231–233.
67. Arena S, Arena C, Scuderi MG, et al. Urethral duplication in males: our experience in ten cases. *Pediatr Surg Int*. 2007;23(8):789–794.
68. Arda IS, Hicsonmez A. An unusual presentation of Y-type urethral duplication with perianal abscess: case report. *J Pediatr Surg*. 2002;37(8):1213–1215.
69. Haleblian G, Kraklau D, Wilcox D, et al. Y-type urethral duplication in the male. *BJU Int*. 2006;97(3):597–602.
70. Kumaravel S, Senthilnathan R, Sankkarabarathi C, et al. Y-type urethral duplication: an unusual variant of a rare anomaly. *Pediatr Surg Int*. 2004;20(11–12):866–868.
71. Sanchez MM, Vellibre RM, Castelo JL, et al. A new case of male Y-type urethral duplication and review of literature. *J Pediatr Surg*. 2006;41(1):e69–e71.
72. Sharma AK, Kothari SK, Menon P, et al. Congenital H-type recto-urethral fistula. *Pediatr Surg Int*. 2002;18(2–3):193–194.
73. Wagner JR, Carr MC, Bauer SB, et al. Congenital posterior urethral perineal fistulae: a unique form of urethral duplication. *Urology*. 1996;48(2):277–280.
74. Podesta ML, Medel R, Castera R, et al. Urethral duplication in children: surgical treatment and results. *J Urol*. 1998;160(5):1830–1833.
75. D'Cruz R, Soundappan SS, Cass DT, et al. Catheter balloon-related urethral trauma in children. *J Paediatr Child Health*. 2009;45(10): 564–566.
76. Holland AJ, Cohen RC, McKertich KM, et al. Urethral trauma in children. *Pediatr Surg Int*. 2001;17(1):58–61.
77. Kim B, Kawashima A, LeRoy AJ. Imaging of the male urethra. *Semin Ultrasound CT MR*. 2007;28(4):258–273.
78. Lendvay TS, Smith EA, Kirsch AJ, et al. Congenital urethral stricture. *J Urol*. 2002;168(3):1156–1157.
79. Sugimoto M, Kakehi Y, Yamashita M, et al. Ten cases of congenital urethral stricture in childhood with enuresis. *Int J Urol*. 2005;12(6): 558–562.
80. El-Ghar MA, Osman Y, Elbaz E, et al. MR urethrogram versus combined retrograde urethrogram and sonourethrography in diagnosis of urethral stricture. *Eur J Radiol*. 2010;74(3):e193–e198.
81. Morey AF, McAninch JW. Ultrasound evaluation of the male urethra for assessment of urethral stricture. *J Clin Ultrasound*. 1996;24(8):473–479.
82. Osman Y, El-Ghar MA, Mansour O, et al. Magnetic resonance urethrography in comparison to retrograde urethrography in diagnosis of male urethral strictures: is it clinically relevant? *Eur Urol*. 2006;50(3):587–593, discussion 594.
83. Koraitim MM. On the art of anastomotic posterior urethroplasty: a 27-year experience. *J Urol*. 2005;173(1):135–139.
84. Mazdak H, Izadpanahi MH, Ghalamkari A, et al. Internal urethrotomy and intraurethral submucosal injection of triamcinolone in short bulbar urethral strictures. *Int Urol Nephrol*. 2010;42(3):565–568.

# 121

# Congenital and Neonatal Conditions

Oscar M. Navarro and Alan Daneman

## NORMAL ADRENAL

The adrenal glands in the neonate are easily visualized on ultrasonography; they are relatively large because of the presence of the fetal adrenal cortex, which accounts for about 80% of the gland (Fig. 121.1).[1]

On ultrasonography, the normal adrenal gland has a central hyperechoic stripe surrounded by a hypoechoic rim. The peripheral hypoechoic rim represents fetal as well as definitive cortex (see Fig. 121.1). The central hyperechoic stripe includes the medulla, the central veins of the adrenal, connective tissue, and the inner part of the fetal cortex.[2] Morphologically, the normal adrenal gland has an inverted Y-shape. The surface of the adrenal gland is smooth or only slightly undulating. The easiest and most useful measurement of the adrenal gland is the limb width, which should normally be less than 4 mm.[3]

Computed tomography (CT) and magnetic resonance imaging (MRI) are rarely required to visualize the adrenals in a neonate unless a mass is present.

## STRAIGHT OR DISCOID ADRENAL

***Overview and Imaging.*** A straight or discoid shape of the adrenal gland is seen on ultrasonography in association with certain congenital anomalies of the ipsilateral kidney, in which the kidney either is absent from its normal position in the renal fossa or is extremely small as a result of antenatal damage and dysplasia.[4] The adrenal gland otherwise develops normally but assumes a flattened, discoid shape (Fig. 121.2). The adrenal retains its normal pattern of echogenicity. Straight adrenal glands are longer than otherwise normal glands, and they tend to be slightly thicker.

## HORSESHOE ADRENAL

***Overview and Imaging.*** Horseshoe adrenal gland is a rare congenital anomaly in which the right and left adrenal glands are fused. It is often associated with anomalies of the kidneys and the central nervous system, asplenia with visceral heterotaxy, and other anomalies.[5]

A horseshoe adrenal gland appears on ultrasonography as a band of normal adrenal tissue crossing the midline in the upper abdomen above the kidneys (e-Fig. 121.3). The adrenal gland maintains normal echogenicity. The isthmus of the horseshoe adrenal gland usually passes behind the aorta, but in asplenia it usually passes in front of the aorta.[5]

## ADRENAL CONGESTION

***Overview and Imaging.*** Adrenal congestion may occur in perinatal asphyxia or stress. On ultrasonography, the glands are enlarged but maintain their general overall shape and smooth surface (Fig. 121.4). This usually occurs bilaterally but may be seen unilaterally or focally within one gland.[2] Loss of the normal central echogenic stripe occurs, and the fetal cortex may become a broad band of slightly increased echogenicity. A very thin peripheral anechoic rim that represents the definitive cortex may be present. Follow-up ultrasonography may show development of focal hypoechoic areas that represent hemorrhage or infarction.[2] The changes may be reversible and the sonographic pattern may return to that of normal adrenal glands in patients who survive.

## CONGENITAL ADRENAL HYPERPLASIA

***Overview.*** Congenital adrenal hyperplasia (CAH) refers to a group of autosomal recessive disorders in which an enzymatic defect occurs in the pathway for cortisol biosynthesis in the adrenal cortex. The most common defect is a deficiency of the enzyme 21-hydroxylase, which affects females much more than males.[3] This leads to ambiguous sexual development in newborn girls or salt-losing crisis in newborns of either sex.

The diagnosis of CAH is confirmed by the presence of elevated serum 17-hydroxyprogesterone (17-OHP). In addition, in female neonates with genital ambiguity, normal internal genitalia are seen on pelvic ultrasonography, and there is a normal (46, XX) karyotype. The 17-OHP level is diagnostic only when measured after the third day of life because a relatively high level is present in the immediate neonatal period in normal newborns. Furthermore, 17-OHP assays may not be easily available. These delays, although relatively short, may contribute to the diagnostic uncertainty and heighten parental anxiety. Therefore ultrasonography in the immediate neonatal period may play a role as some specific signs of CAH are seen on ultrasonography.[3]

***Imaging.*** Ultrasonography has shown to have a diagnostic sensitivity of 92% and a specificity of 100% for the diagnosis of CAH in the presence at least two of these three characteristics: adrenal gland size (limb width > 4 mm), surface characteristics (cerebriform or crenated appearance), and internal echo pattern (diffusely stippled pattern of echogenicity or less commonly diffuse thickened band of increased echogenicity) (Fig. 121.5).[3] These changes may be present focally within the adrenal glands or may be asymmetric between both adrenal glands.[3] Rarely, the adrenal glands may appear normal, emphasizing the fact that the absence of the signs does not exclude the diagnosis of CAH.

The sonographic changes in the adrenal glands with CAH are reversible with the introduction of therapy. Administration of corticosteroids to the mother of the affected fetus results in a normal sonographic appearance of the adrenal glands at birth.

## WOLMAN DISEASE

***Overview.*** Wolman disease is a rare disorder of lipid metabolism (familial xanthomatosis). This inherited deficiency of lysosomal acid lipase leads to an accumulation of cholesterol esters and triglycerides in many organs, particularly the adrenal glands.[6] The disorder manifests in the early weeks of life, and hepatosplenomegaly, jaundice, vomiting, steatorrhea, abdominal distension, and growth failure may exist. The disease is rapidly progressive, and death occurs within the first year.

***Imaging.*** Marked enlargement of both adrenal glands, which retain their overall shape, is seen on imaging. This is associated with marked, diffuse, punctate calcification (e-Fig. 121.6).[6] This can be recognized on plain radiographs of the abdomen and cross-sectional imaging. On ultrasonography, the calcification in Wolman disease appears as dense punctate or granular hyperechogenicities with

## Abstract:

Normal adrenal glands in neonates are easily visualized on ultrasonography because of the presence of the fetal adrenal cortex. They have an inverted Y-shape with a hyperechoic central stripe, a hypoechoic rim, smooth contours, and a limb thickness < 4 mm. Computed tomography or magnetic resonance imaging are rarely required unless a mass is present.

A straight or discoid shape of the adrenal gland is an indicator of an ipsilateral renal anomaly. Congenital adrenal hyperplasia (CAH), usually due to 21-hydroxilase deficiency, presents with either ambiguous genitalia in girls or salt-losing crisis. Ultrasonography can help in diagnosis before final biochemical confirmation. In CAH, the adrenal is thicker, has a cerebriform shape, and shows increased echogenicity with loss of central echogenic stripe. In Wolman disease, a rare lipid metabolism disorder, the adrenal glands are enlarged and diffusely calcified.

Neonatal suprarenal masses include adrenal hemorrhage, usually associated with perinatal stress. On ultrasonography, it shows variable echogenicity with absence of Doppler blood flow and can be difficult to differentiate from neuroblastoma. Follow-up ultrasonography is useful in diagnosis of hemorrhage by showing decrease in size and changes in echogenicity. Neuroblastoma is the most common neonatal adrenal tumor with variable size, echogenicity and blood flow, and may present with metastases to the liver, skin and bone marrow.

Pulmonary sequestration may present as a neonatal suprarenal mass, more often left-sided and diagnosed earlier than neuroblastoma, in the second trimester. On ultrasonography, it is an echogenic mass many times with cystic spaces because of a congenital pulmonary airway malformation component.

## Keywords:

Adrenal gland
Adrenal hemorrhage
Congenital adrenal hyperplasia
Neuroblastoma
Pulmonary sequestration
Wolman disease

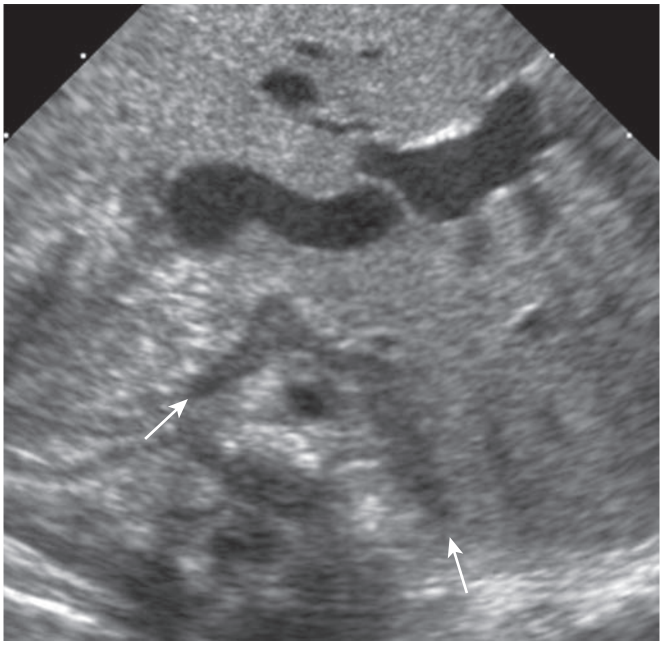

**e-Figure 121.3. Horseshoe adrenal gland *(arrows)* in a patient with heterotaxy syndrome (asplenia).** Transverse sonogram of the upper abdomen shows that the adrenal glands are fused across the midline, giving a horseshoe shape. The central echogenic stripe and surrounding hypoechoic zone and smooth surface are maintained. The gland lies anterior to the aorta, which is to the right of the midline, and behind the inferior vena cava, which is to the left. *(Courtesy Dr. Ulrich Willi, Kinderspital, Zürich, Switzerland.)*

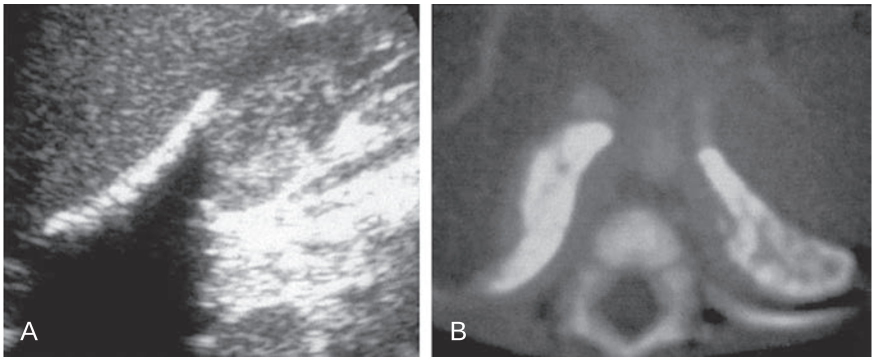

**e-Figure 121.6. Wolman disease.** Marked calcification and enlargement of both adrenal glands are seen. (A) A longitudinal sonogram of the right adrenal shows linear echogenicity in the anterior part of the gland with a strong acoustic shadow posteriorly. (B) On the computed tomography scan, the calcification appears to be more peripheral within the cortex of both adrenal glands.

posterior acoustic shadowing, the latter seldom seen with adrenal hemorrhage. On CT, the large size of both adrenal glands and the diffuse pattern of calcification differentiate this condition from resolving adrenal hemorrhage, in which the adrenal glands are smaller with more globular calcification.

## SUPRARENAL MASSES

***Overview.*** Adrenal masses in the neonate can be caused by hemorrhage or neoplasm, particularly neuroblastoma. Extraadrenal masses are rare with the most common being extralobar pulmonary sequestration. An accurate diagnosis is important for appropriate management. However, diagnoses may be difficult because of overlapping imaging features and thus may not be established on the initial imaging findings alone, often requiring follow-up imaging, correlation with clinical history, and measurement of urine catecholamines. Because of the relatively good prognosis of perinatal neuroblastoma, initial conservative management is often warranted. CT and MRI have a lesser role in the diagnosis of these lesions and are mainly indicated to assess extent and for staging of a suspected neuroblastoma.

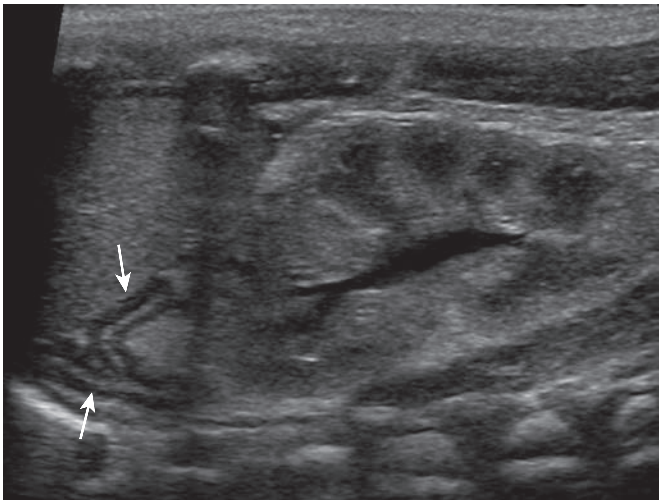

**Figure 121.1. Normal left adrenal in a 1-day-old newborn.** Longitudinal sonogram of the left adrenal gland *(arrows)* shows a central hyperechoic stripe representing the central veins, connective tissue, medullary tissue, and congested sinusoids of the inner part of the fetal cortex. The surrounding hypoechoic zone represents the less congested outer part of the fetal cortex and the thin peripheral definitive cortex. The surface of the gland is smooth.

## Adrenal Hemorrhage

***Overview.*** Adrenal hemorrhage is the most common adrenal gland masslike abnormality in neonates. It often occurs within the first few days of life but can occur prenatally and be seen on antenatal ultrasonography. It is more commonly right sided (70%) and may be bilateral (10%).[7] It usually occurs in situations of perinatal stress, including difficult or traumatic delivery, hypoxia, and sepsis. It may also occur in bleeding diatheses. Large infants and infants of mothers with diabetes are particularly susceptible. Adrenal hemorrhages in neonates may be an incidental finding.

***Imaging.*** Ultrasonography is the modality of choice for documentation of the presence of an adrenal hemorrhage and for follow-up. Ultrasonography shows a suprarenal mass of variable echogenicity (Fig. 121.7) without internal blood flow on color

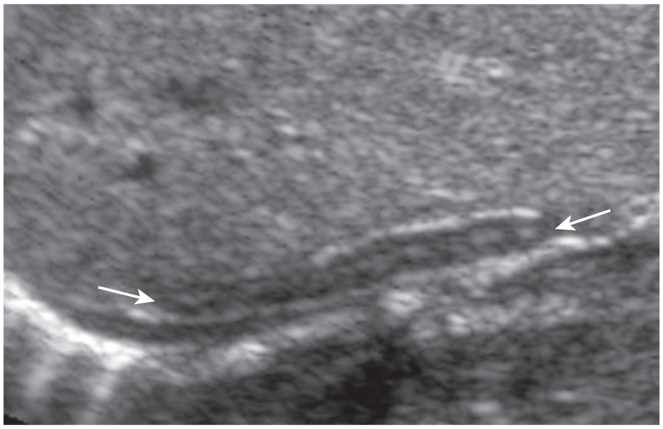

**Figure 121.2. Discoid adrenal gland in a patient with right renal agenesis.** Longitudinal sonogram of the right adrenal gland shows a straight adrenal *(arrows)* that lacks the morphology illustrated in Fig. 121.1. The central hyperechoic stripe, surrounding hypoechoic zone, and smooth surface are preserved.

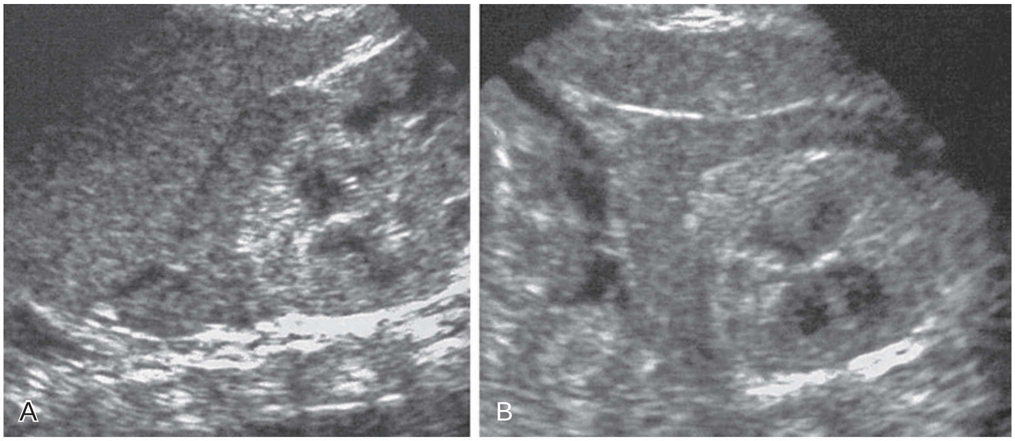

**Figure 121.4. Adrenal congestion in an 8-day-old full-term boy with necrotizing enterocolitis, cardiovascular collapse, and multiorgan failure.** Longitudinal (A) and transverse (B) sonograms reveal marked enlargement of the left adrenal gland. Although it has retained its normal shape and smooth surface, there is loss of the normal central echogenic stripe. The gland has a more homogeneous low-level echogenicity, and in parts, a peripheral anechoic thin rim is seen. A postmortem histologic examination revealed congestion of the fetal cortex. The peripheral thin rim represents the peripheral definitive cortex.

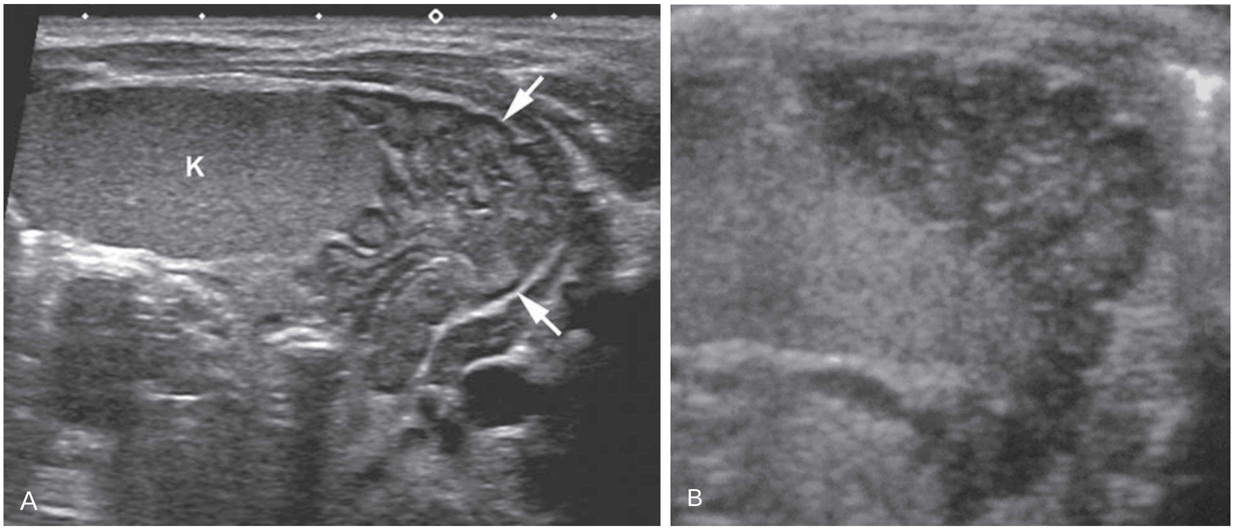

**Figure 121.5. Congenital adrenal hyperplasia.** (A) Transverse sonogram of the left adrenal gland in a newborn shows an enlarged thickened gland *(arrows)* with a cerebriform appearance; *K*, Kidney. (B) Transverse sonogram of the left adrenal gland in another patient shows marked enlargement of the gland, and the central echogenic stripe has been replaced by diffuse stippled echogenicity.

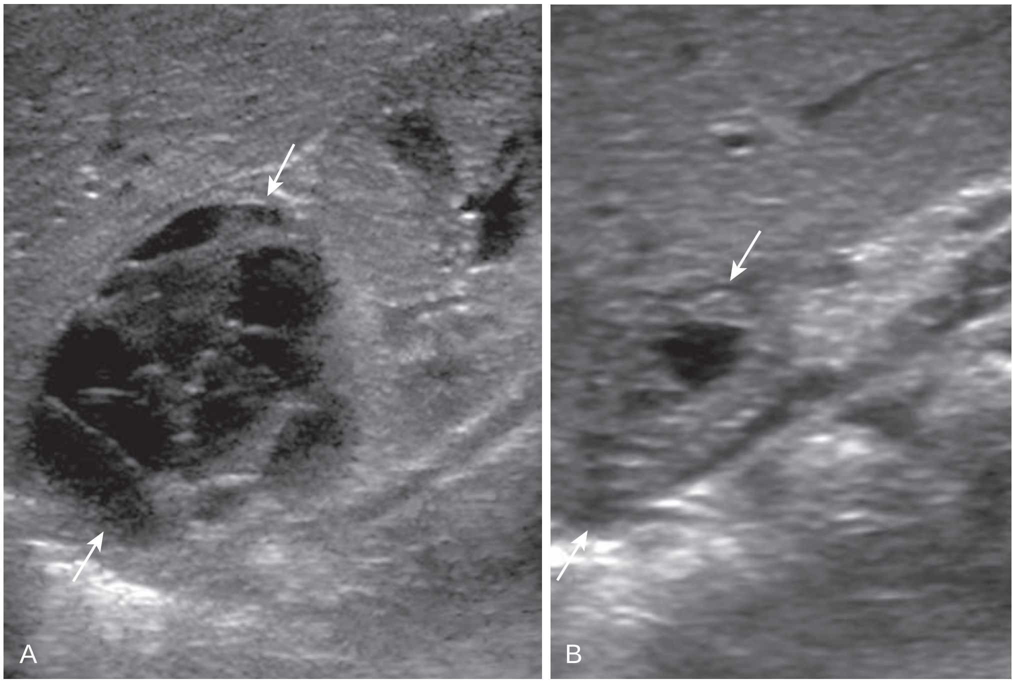

**Figure 121.7. Adrenal gland hemorrhage detected in the third trimester of pregnancy in a neonate.** (A) Longitudinal sonogram of the right upper quadrant at 17 days of age shows a multiseptated predominantly cystic mass *(arrows)* superior to the right kidney. No blood flow in the septa was evident on color Doppler interrogation (not shown). (B) The follow-up sonogram at 38 days of age shows significant decrease in size of the mass *(arrows)* as well as a change in its echogenicity. The pattern of evolution of this lesion is compatible with an adrenal hemorrhage. In addition, urine catecholamines and metaiodobenzylguanidine scan were negative in this patient.

Doppler ultrasonography. These findings may overlap with those of neuroblastoma, and therefore, further confirmation of the diagnosis may be obtained from follow-up ultrasonography.[7] The adrenal hemorrhage decreases in size and changes echogenicity within the first week (see Fig. 121.7), followed by development of peripheral increased echogenicity due to calcification. The calcification becomes more compacted as the mass becomes smaller, and the adrenal gland eventually resumes a more normal shape and size. Rarely, MRI may be used to discriminate adrenal hemorrhage from neuroblastoma, based on the detection of blood products and lack of postcontrast enhancement.

## Neuroblastoma

***Overview and Imaging.*** Neuroblastoma is the most common adrenal gland neoplasm found in the fetus and neonates.[8] When detected antenatally, it is generally diagnosed in the third trimester. It is frequently right-sided, may vary significantly in size (Fig. 121.8), and often has a more cystic appearance than in older infants and children (Fig. 121.9).[8,9] At sonography, the echogenicity varies; some may be homogeneously echogenic (Fig. 121.10), whereas others are highly heterogeneous. Blood flow is often detected on color Doppler ultrasonography aiding in the differentiation from hemorrhage (see Fig. 121.10). However, the absence of flow does not exclude the diagnosis of neuroblastoma.

Perinatal neuroblastoma also may present with metastatic disease, typically in the liver, skin, and bone marrow, corresponding to stage MS (equivalent to stage 4S of the formerly used International Neuroblastoma Staging System) (see Chapter 122). Diffuse infiltration of the liver may result in massive hepatomegaly (e-Fig. 121.11).

In contrast to neuroblastoma in older children, in perinatal neuroblastoma urinary catecholamine metabolites are elevated in only 40% of cases, and metaiodobenzylguanidine (MIBG) avidity exists in only 70% of cases.[8]

## Intraabdominal Pulmonary Sequestration

***Overview and Imaging.*** Intraabdominal extralobar pulmonary sequestration is a mass of pulmonary tissue separate from the lung with systemic arterial supply that can be found in the suprarenal region, usually on the left side. In contrast to adrenal neuroblastoma and hemorrhage, these are commonly diagnosed in the second trimester of pregnancy.[10] In fact, a suprarenal mass diagnosed in the third trimester of pregnancy but with a normal second trimester sonogram goes against a diagnosis of sequestration. On ultrasonography, sequestrations appear homogeneously hyperechoic, although in more than half the cases, small (<5 mm), well-defined intralesional cysts exist because of the presence of associated congenital pulmonary airway malformation (Fig. 121.12).[10,11] The normal adrenal gland is often identified, displaced anteriorly by the sequestration. These sequestrations may decrease in size and even disappear on follow-up ultrasonography.[11]

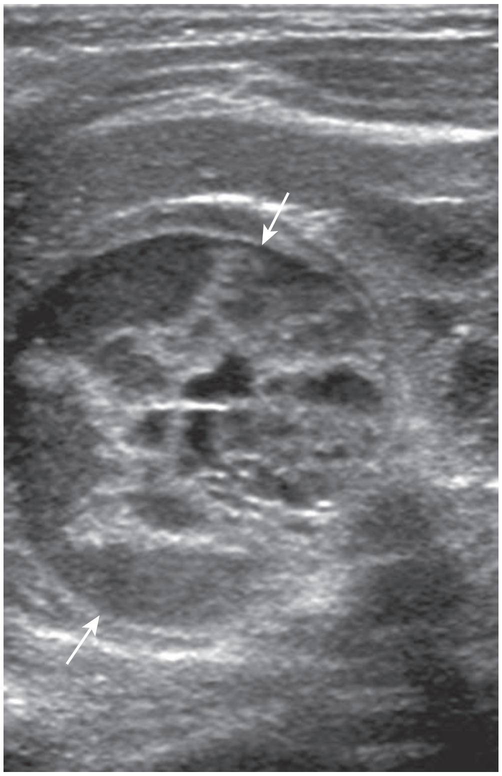

**Figure 121.9. Right adrenal neuroblastoma detected in the third trimester of pregnancy in an 8-day-old girl.** A longitudinal sonogram shows a complex, multiseptated, partly cystic mass *(arrows)* involving the right adrenal. No blood flow in the septa was evident on color Doppler interrogation (not shown). The mass has similar features to the adrenal hemorrhage illustrated in Fig. 121.7, although in this case, urine catecholamines were elevated and the mass was metaiodobenzylguanidine avid.

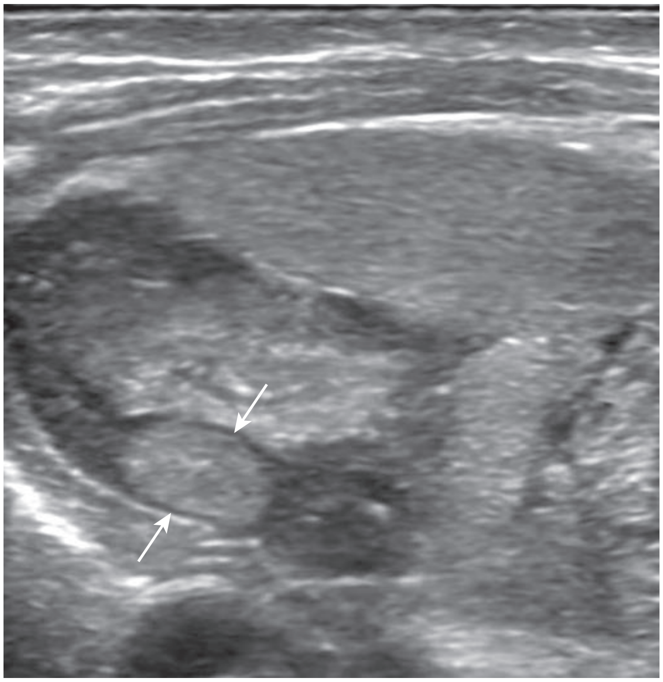

**Figure 121.8. Left adrenal neuroblastoma found incidentally in a 13-day-old boy.** Longitudinal sonogram of the left upper quadrant shows a very small hyperechoic mass *(arrows)* within one of the limbs of the left adrenal gland.

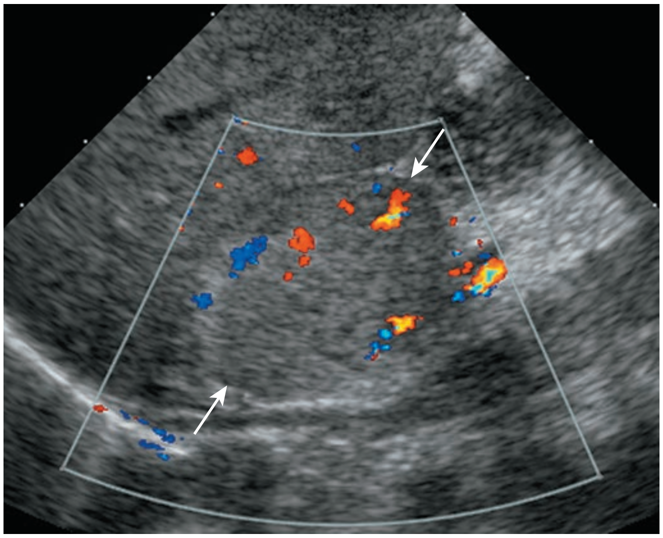

**Figure 121.10. Right adrenal neuroblastoma detected in the third trimester of pregnancy in a 10-day-old boy.** A longitudinal sonogram shows a relatively homogenous hyperechoic mass *(arrows)* arising in a somewhat exophytic fashion from the inferior and anterior aspect of the right adrenal gland. Intralesional blood flow is shown on color Doppler interrogation.

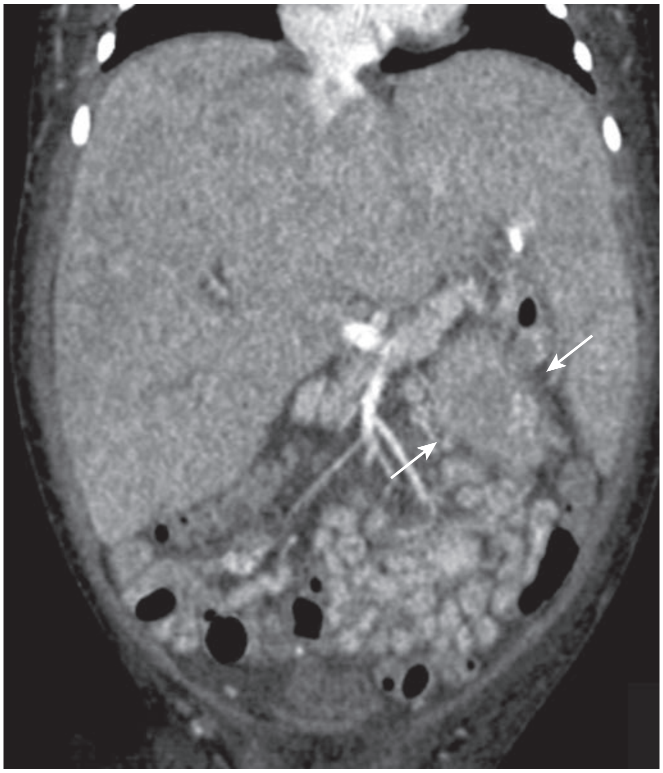

**e-Figure 121.11. Bilateral adrenal neuroblastoma with liver metastatic disease.** Coronal reformatted contrast-enhanced CT image shows marked hepatomegaly with heterogeneous attenuation of the parenchyma due to metastatic infiltration by neuroblastoma. Part of the left adrenal mass is evident *(arrows)*.

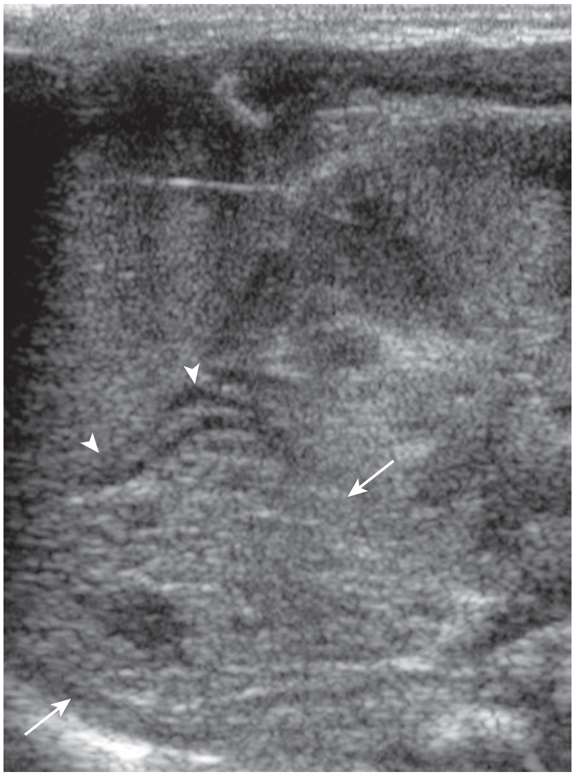

**Figure 121.12. Left-sided intraabdominal pulmonary sequestration detected in the second trimester of pregnancy in a 2-day-old girl.** A relatively echogenic left suprarenal mass *(arrows)* displaces the normal left adrenal anteriorly *(arrowheads)*, characteristic of sequestration. Within the mass, rounded hypoechoic areas represent cysts secondary to a component of congenital pulmonary airway malformation.

## KEY POINTS

- A straight or discoid adrenal gland is a marker for an ipsilateral renal anomaly.
- A horseshoe adrenal gland is associated with nongenitourinary anomalies, including asplenia.
- Ultrasonography can be helpful in the expedient diagnosis of CAH.
- Follow-up ultrasonography is helpful in the differentiation of adrenal gland neuroblastoma from hemorrhage.
- Time of antenatal diagnosis is extremely helpful in the differentiation of adrenal gland neuroblastoma from intraabdominal pulmonary sequestration.

## SUGGESTED READINGS

Balassy C, Navarro OM, Daneman A. Adrenal masses in children. *Radiol Clin North Am*. 2011;49:711–727.

Paterson A. Adrenal pathology in childhood: a spectrum of disease. *Eur Radiol*. 2002;12:2491–2508.

Rosado-de-Christenson ML, Frazier AA, Stocker JT, et al. Extralobar sequestration: radiologic-pathologic correlation. *Radiographics*. 1993;13:425–441.

## REFERENCES

Full references for this chapter can be found on www.expertconsult.com.

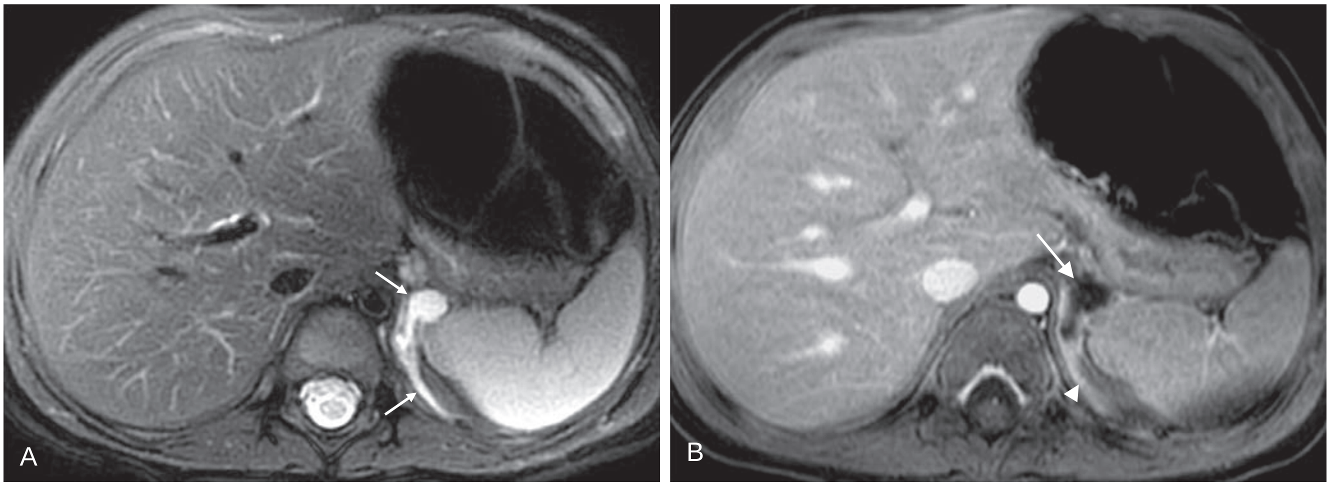

**e-Figure 121.13. 1 year-old boy with suprarenal extralobar pulmonary sequestration.** A left "adrenal" mass was detected *in utero* that decreased in size over time. (A) Axial T2-weighted fat-suppressed MR image shows a left suprarenal hyperintense curvilinear mass *(arrows)* located just below the left hemidiaphragm. (B) Postcontrast T1-weighted fat-suppressed image shows that the anterior portion of the lesion *(arrow)* is nonehancing due to a cystic component, while the posterior portion is solid and enhances *(arrowhead)*.

## REFERENCES

1. Rosenberg ER, Bowie JD, Andreotti RF, et al. Sonographic evaluation of fetal adrenal glands. *AJR Am J Roentgenol*. 1982;139:1145–1147.
2. Koplewitz BZ, Daneman A, Cutz E, et al. Neonatal adrenal congestion: a sonographic-pathologic correlation. *Pediatr Radiol*. 1998;28:958–962.
3. Al-Alwan I, Navarro O, Daneman D, et al. Clinical utility of adrenal ultrasonography in the diagnosis of congenital adrenal hyperplasia. *J Pediatr*. 1999;135:71–75.
4. Hoffman CK, Filly RA, Callen PW. The "lying down" adrenal sign: a sonographic indicator of renal agenesis or ectopia in fetuses and neonates. *J Ultrasound Med*. 1992;11:533–536.
5. Strouse PJ, Haller JO, Berdon WE, et al. Horseshoe adrenal gland in association with asplenia: presentation of six new cases and review of the literature. *Pediatr Radiol*. 2002;32:778–782.
6. Özmen MN, Aygün N, Kiliç I, et al. Wolman's disease: ultrasonographic and computed tomographic findings. *Pediatr Radiol*. 1992;22:541–542.
7. Deeg KH, Bettendorf U, Hofmann V. Differential diagnosis of neonatal adrenal haemorrhage and congenital neuroblastoma by colour coded Doppler sonography and power Doppler sonography. *Eur J Pediatr*. 1998;157:294–297.
8. Nuchtern JG. Perinatal neuroblastoma. *Semin Pediatr Surg*. 2006; 15:10–16.
9. Hwang SM, Yoo SM, Kim JH, et al. Congenital adrenal neuroblastoma with and without cystic change: differentiating features with an emphasis on the value on ultrasound. *AJR Am J Roentgenol*. 2016;207:1105–1111.
10. Curtis MR, Mooney DP, Vaccaro TJ, et al. Prenatal ultrasound characterization of the suprarenal mass: the distinction between neuroblastoma and subdiaphragmatic extralobar pulmonary sequestration. *J Ultrasound Med*. 1997;16:75–83.
11. Daneman A, Baunin C, Lobo E, et al. Disappearing suprarenal masses in fetuses and infants. *Pediatr Radiol*. 1997;27:675–681.

# 122 Acquired Conditions

*Oscar M. Navarro and Alan Daneman*

## NEUROBLASTOMA

***Overview.*** Neuroblastoma is the most common extracranial solid neoplasm in children and accounts for almost 10% of all childhood neoplasms.[1] Neuroblastoma arises in the abdomen in two-thirds of cases; of these, about two-thirds of lesions occur in the adrenal gland, whereas the remainder may arise anywhere along the sympathetic nerve chains.[1]

Neuroblastoma, ganglioneuroblastoma, and ganglioneuroma belong to a group of related neurogenic neoplasms arising from neural crest tissue that are distinguished by their degree of cellular maturation and differentiation. Neuroblastoma accounts for the vast majority and has the most primitive and malignant cells.[2] Ganglioneuroma represents the most differentiated end of the spectrum and is benign. Ganglioneuroblastomas represent an intermediate group with mixed histology and behavior.

Most children with neuroblastoma present between 1 and 5 years of age, with a median age of almost 2 years, although tumors may be uncommonly congenital and present at birth.[2] Neuroblastoma is more common in patients with neurofibromatosis type 1, Beckwith-Wiedemann syndrome, Hirschsprung disease, central hypoventilation syndrome, and DiGeorge syndrome.[2]

Neuroblastomas typically present as palpable masses or with symptoms and signs related to local tumor invasion, metastatic disease, and the effects of hormone production (e.g., catecholamines) or autoimmune response (opsoclonus-myoclonus syndrome). Metastatic disease is seen in up to 70% of patients at presentation.[3] The most common sites include local and distant lymph nodes, bone, bone marrow, liver, and skin.

The diagnosis of neuroblastoma can be made by tissue biopsy, but a combination of positive bone marrow aspirate and increased urinary catecholamine metabolites (vanillylmandelic acid and homovanillic acid) is sufficient to confirm the diagnosis. The urinary level of catecholamine metabolites is increased in almost 90% of cases of neuroblastoma.[4] The International Neuroblastoma Staging System has been the most commonly used worldwide for staging neuroblastoma.[1,2,4] However, its application has encountered many difficulties, as it relies on the extent of tumor resected at surgery. For this reason, the International Neuroblastoma Risk Group Staging System was developed in 2009 and relies on preoperative imaging findings and detection of metastatic disease. Specific involvement of vital structures represent image-defined risk factors (IDRFs) and upstage tumors from L1 to L2 (Box 122.1).[5] In general, IDRFs represent encasement of vessels and nerves, contiguous organ invasion or significant intraspinal extension, airway compression, and tumor in more than one body compartment (Box 122.2).[6]

The prognosis of neuroblastoma depends on stage at presentation, patient's age (children younger than 12 to 18 months have better prognosis), histologic category, grade of tumor differentiation, status of the *MYCN* oncogene, chromosome 11q status, and deoxyribonucleic acid ploidy.[7]

***Imaging.*** Adrenal neuroblastomas and those arising from the adjacent retroperitoneum are usually easily identified with ultrasound (US), computed tomography (CT), or magnetic resonance imaging (MRI) because the mass is generally quite large by the time of presentation (Fig. 122.1). Very small masses are uncommon, and in those cases seen beyond the neonatal age, CT and MRI play a more important role than ultrasonography (Fig. 122.2 and e-Fig. 122.3). The masses have a variety of appearances by US with the most characteristic being that of a solid, heterogeneous, hyperechoic mass, often with small hyperechoic calcifications with or without posterior acoustic shadowing (Fig. 122.4 and e-Fig. 122.5).[1,2,4] Anechoic areas resulting from cystic, hemorrhagic, or necrotic changes may be present (e-Fig. 122.6).

The new International Neuroblastoma Risk Group Staging System requires the use of CT, MRI, or both for staging.[5] On CT, neuroblastomas usually show heterogeneous enhancement, depicting solid areas along with areas of necrosis, hemorrhage, and cystic change (see Fig. 122.1). Calcification is present in more than 90% of cases (see Fig. 122.1 and e-Fig. 122.6).[4] On MRI, the lesions are usually heterogeneous, with predominantly low signal on T1-weighted images and high signal on T2-weighted images, and with variable degrees of enhancement (Fig. 122.7).[2,4]

A characteristic imaging feature of neuroblastoma is the displacement of adjacent organs and the displacement or encasement of adjacent major vessels (see Figs. 122.1 and 122.7).[4] Local spread may be to lymph nodes. Less frequently, direct invasion into the kidneys (Fig. 122.8) or liver may occur, and the tumor may extend into the spinal canal.

Neuroblastoma liver metastases may be single or multiple nodules, or may present with an infiltrative pattern, particularly in neonates (Fig. 122.9) (see Chapter 121). Metastases to bone are best identified with metaiodobenzylguanidine (MIBG) scintigraphy.

If the lesion responds to chemotherapy, the mass regresses and shrinks to a very small amount of soft tissue that often becomes calcified. Certain neuroblastomas in very young children, including individuals with metastatic disease, may undergo spontaneous regression.[8]

## GANGLIONEUROMA

***Overview.*** Ganglioneuroma represents the mature, benign form of neural crest neoplasm. This is far less frequent compared with neuroblastoma; it may develop from the maturation of a known malignant neuroblastoma, or it may be found de novo.[2]

Ganglioneuromas most frequently occur in the posterior mediastinum followed by the extra-adrenal retroperitoneum (e-Fig. 122.10) and the adrenal gland.[2] These tumors usually occur in older children, are frequently asymptomatic, and are often found incidentally on imaging. Occasionally, symptoms may result from tumor growth into the intervertebral foramina, causing spinal cord compression. Urinary catecholamine levels are usually normal.

***Imaging.*** The imaging appearance of ganglioneuroma has been traditionally considered to be indistinguishable from that of neuroblastoma (Figs. 122.11 and 122.12).[2] Therefore definitive diagnosis has usually relied on the histologic examination of tumor tissue. However, more recent studies using diffusion-weighted MRI have shown significantly lower apparent diffusion coefficient (ADC) values in neuroblastoma compared with ganglioneuroma/ganglioneuroblastoma, which may be helpful in tumor differentiation.[9] Ganglioneuromas are also less often calcified as well as generally smaller and more circumscribed than neuroblastoma.

## Abstract:

Acquired conditions of the adrenal glands and retroperitoneum are most commonly neurogenic neoplasms. Neuroblastoma, a malignant tumor, is the most frequent, often presenting in young children. Most arise from the adrenal gland. They usually present as a large, heterogeneous mass with calcifications that can be diagnosed with ultrasound although computed tomography (CT) or magnetic resonance imaging (MRI) are required for staging using the International Risk Group Staging System, which relies on identification of image-defined risk factors. Neuroblastomas often encase major abdominal vessels and may extend into the spinal canal. They can metastasize to the liver and bone. Ganglioneuroma, the benign counterpart, presents more often in older children and occurs most frequently in the retroperitoneum. On imaging ganglioneuroma is indistinguishable from neuroblastoma except for higher apparent diffusion coefficient values on diffusion-weighted MRI in the former. Pheochromocytoma (adrenal) and paraganglioma (extraadrenal) are uncommon, arise from chromaffin cells, are frequently benign and present with symptoms related to catecholamine secretion. CT and MRI are better than ultrasound for diagnosis although imaging features are not specific. Functional imaging with MIBG is more specific for diagnosis. Adrenocortical neoplasms (adenomas and carcinomas) are more commonly seen in girls, in patients with predisposing cancer conditions, particularly Li-Fraumeni syndrome, and are generally hormonally functioning. In children they are often large, heterogeneous masses on all imaging modalities. Other pediatric retroperitoneal masses include lymphadenopathy, vascular malformations, Kaposiform hemangioendothelioma, other neurogenic tumors, adipocytic tumors, germ cell neoplasms (including teratoma), rhabdomyosarcoma, fibromatosis, idiopathic fibrosis, hematoma and abscess.

## Keywords:

Adrenal gland
Adrenocortical neoplasms
Ganglioneuroma
Neuroblastoma
Pheochromocytoma
Retroperitoneum
Teratoma

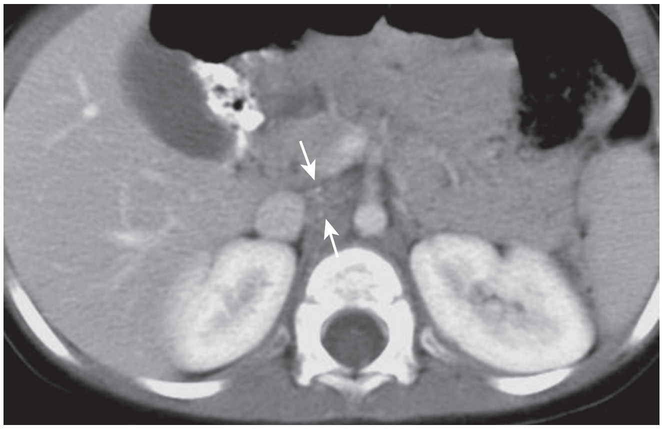

**eFigure 122.3. Retroperitoneal neuroblastoma in a 19-month-old boy presenting with ataxia and nystagmus.** Axial contrast-enhanced CT image shows a small hypodense mass with punctate calcifications in the aortocaval region *(arrows)*. Because of its location and small size, this mass was difficult to appreciate on US.

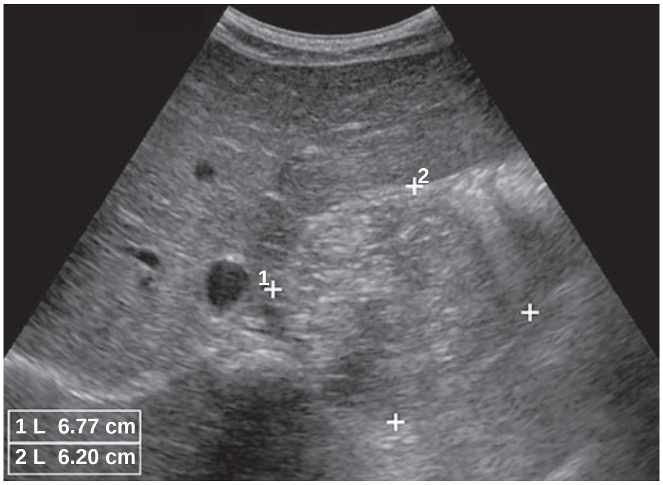

**e-Figure 122.5. Left adrenal neuroblastoma in a 7-year-old girl.** Transverse sonogram shows a round, solid mass (between cursors) posterior to the left lobe of the liver with multiple confluent hyperechoic foci.

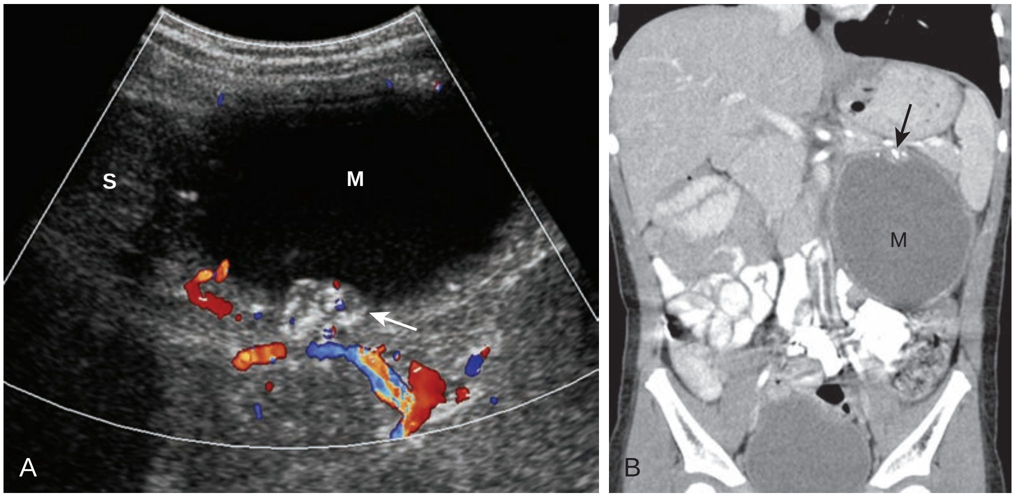

**e-Figure 122.6. Left adrenal neuroblastoma in a 3-year-old girl.** (A) Oblique sonogram shows a cystic mass *(M)* anterior and medial to the spleen *(S)* with foci of mural calcification *(arrow)*. (B) Coronal contrast-enhanced computed tomography image shows the left upper quadrant cystic mass *(M)* with mural calcifications *(arrow)*, which on histology proved to be neuroblastoma.

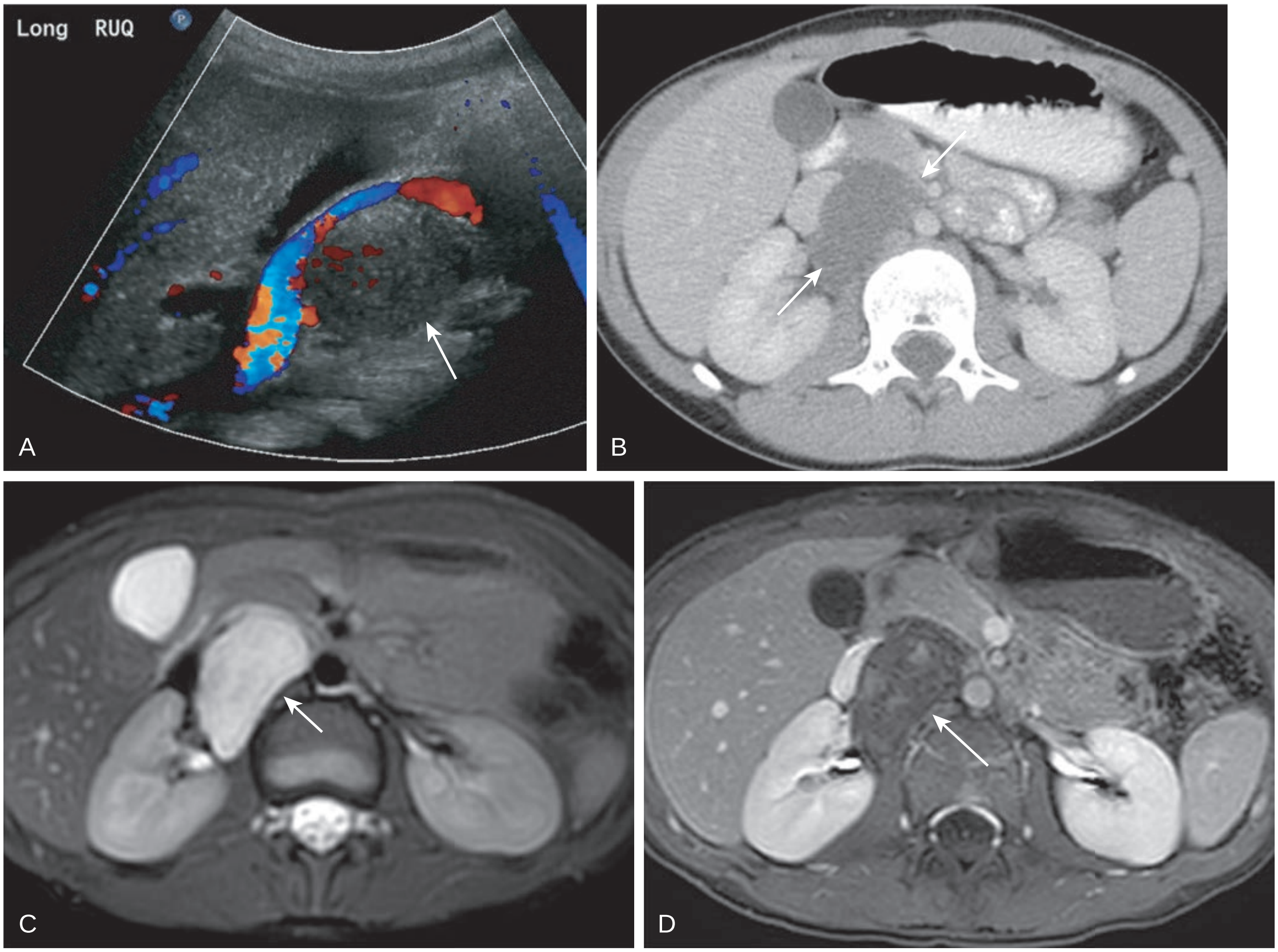

**e-Figure 122.10. Incidentally-detected retroperitoneal ganglioneuroma in a 10-year-old boy.** (A) Longitudinal color Doppler image shows a round, solid retrocaval mass *(arrow)*. (B) Axial contrast-enhanced CT image shows a homogeneous, low attenuation mass *(arrows)* posterior to the inferior vena cava. (C) Axial T2-weighted fat-saturated MR image shows that the mass *(arrow)* is homogeneously hyperintense. (D) Postcontrast T1-weighted fat-suppressed MR image shows only minimal patchy enhancement within the mass *(arrow)*. Surgical pathology confirmed the diagnosis of retroperitoneal ganglioneuroma.

## PHEOCHROMOCYTOMA

***Overview.*** Pheochromocytoma is an uncommon neural crest tumor of the adrenal gland arising from chromaffin cells. If the tumor is extra-adrenal, it is known as a paraganglioma, with most common abdominal locations being in the vicinity of the renal vessels and at the organ of Zuckerkandl near the origin of the inferior mesenteric artery. In children, 70% of pheochromocytomas occur in the adrenal gland, and 19% to 38% have bilateral adrenal gland involvement.[10] Malignancy is present in 12% of lesions in children.[11] The diagnosis of malignancy is often made on the basis of metastases rather than histology.[11]

Pheochromocytoma usually presents in older children (mean age = 11 years). In approximately 40% of cases, it may be part of cancer predisposition syndromes, mainly von Hippel-Lindau disease, multiple endocrine neoplasias (MEN) 2A and 2B, and familial paraganglioma-pheochromocytoma syndromes.[10,11]

The clinical presentation is usually related to the secretion of catecholamines. Patients may present with hypertension, headache, tachycardia, diaphoresis, nervousness, and weight loss.[10]

***Imaging.*** CT and MRI are better imaging modalities than ultrasonography for accurate localization of these tumors. Functional imaging with MIBG is more specific and has been reported to be more sensitive in detecting multifocal disease.[10,11]

Pheochromocytoma may have a solid homogeneous or heterogeneous appearance on US (e-Fig. 122.13 and Fig. 122.14A). Heterogeneity is more commonly seen with larger lesions because of hemorrhage, necrosis, and, less commonly, calcification (see Fig. 122.14).[12] On CT, the lesions show avid enhancement except for areas of necrosis or hemorrhage.[1] The use of nonionic low-osmolar intravenous contrast material for CT is safe in patients with pheochromocytoma.[13] On MRI, pheochromocytoma is hypointense to isointense compared with the liver on T1-weighted images and hyperintense on T2-weighted images (see Figs. 122.14 and 122.15), with a pattern of intense enhancement after the

### BOX 122.1 International Neuroblastoma Risk Group Staging System

**Stage L1:** Localized tumor confined to one body compartment without involvement of vital structures (no image-defined risk factor [IDRF])

**Stage L2:** Locoregional tumor with at least one IDRF

**Stage M:** Distant metastasis (excluding stage MS)

**Stage MS:** Child <18 months of age with metastasis confined to skin, liver, and/or bone marrow

*Modified from Monclair T, Brodeur GM, Ambros PF, et al. The international neuroblastoma risk group (INRG) staging system: an INRG task force report.* J Clin Oncol. *2009;27:298–303.*

### BOX 122.2 Image-Defined Risk Factors in Neuroblastoma

- Ipsilateral tumor extension into another body compartment
  - Neck-chest, chest-abdomen, abdomen-pelvis
- Neck
  - Major artery or vein encasement
  - Skull base extension
  - Tracheal compression
- Thorax
  - Brachial plexus or major vessel encasement
  - Tracheal or principal bronchial compression
  - Costovertebral junction invasion between T9 and T12
- Abdomen and Pelvis
  - Porta hepatis or hepatodeuodenal ligament invasion
  - Superior mesenteric artery origin or proximal branch encasement
  - Aorta, inferior vena cava, celiac axis, or iliac vessel encasement
  - Pelvic tumor crossing sciatic notch
- Intraspinal extension with >⅓ of spinal canal invaded, or perimedullary leptomeningeal spaces effaced, or abnormal spinal cord signal
- Adjacent organ infiltration
  - Including liver, kidney, pancreas, duodenum, diaphragm, mesentery, pericardium

Note: vessel encasement is defined as ≥50% circumference contact or complete compression of venous lumen.

*Modified from Dumba M et al. Neuroblastoma and nephroblastoma: a radiological review.* Cancer Imaging. *2015;15:5.*

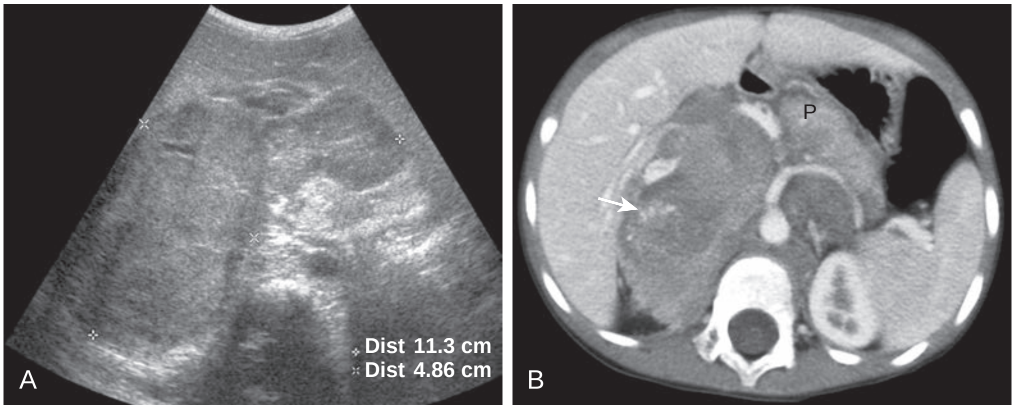

**Figure 122.1. Retroperitoneal neuroblastoma in a 4-year-old boy.** (A) Transverse sonogram and (B) axial contrast-enhanced CT image of the abdomen show a large lobulated, solid mass centered in the right upper quadrant but with a significant component crossing the midline and extending into the left hemiabdomen. At CT, the mass is heterogeneous with hypodense and hyperdense areas as well as foci of calcification *(arrow)*. Note the characteristic encasement of the major vessels by the mass, in this case the aorta, the celiac axis, and its major branches, which are image-defined risk factors. The pancreas *(P)* is displaced anteriorly and to the left by the mass.

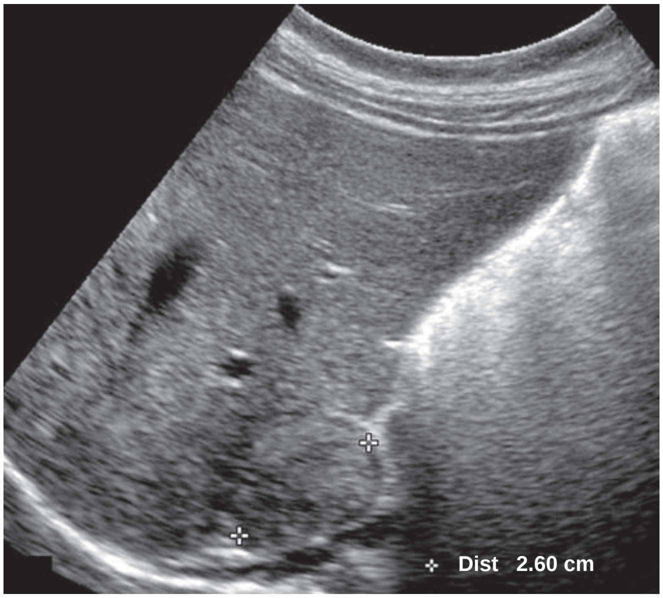

**e-Figure 122.13. Bilateral pheochromocytomas in an 11-year-old boy with von Hippel-Lindau disease and systemic arterial hypertension (same patient as shown in Fig. 122.15).** Longitudinal sonogram of the right upper quadrant shows a well-defined round, solid mass (between cursors) of slightly heterogeneous echogenicity.

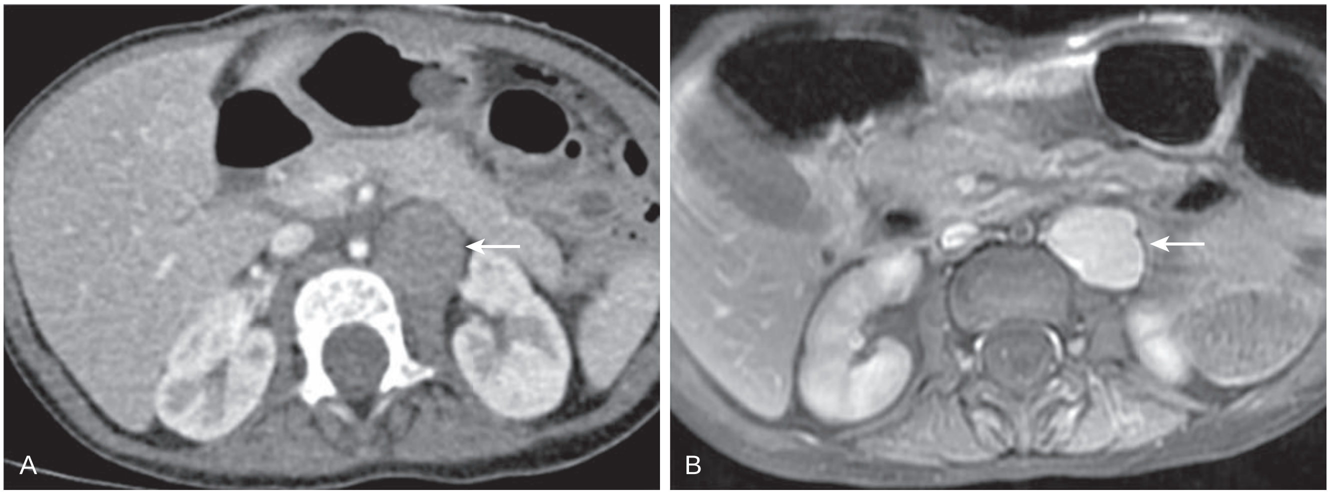

**Figure 122.2. Incidentally detected small neuroblastoma in a 2-year-old boy.** (A) Axial contrast-enhanced CT image shows a small round, enhancing retroperitoneal mass *(arrow)* located between the abdominal aorta and left kidney. (B) Axial postcontrast T1-weighted fat-suppressed MR image confirms the presence of a solid enhancing retroperitoneal mass, proven to be neuroblastoma.

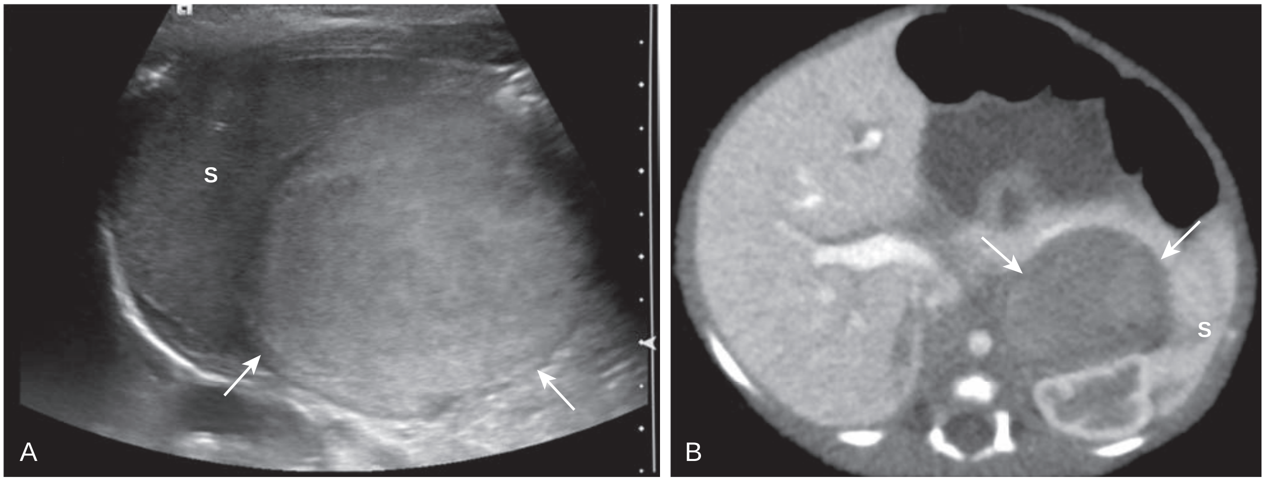

**Figure 122.4. Congenital neuroblastoma in an 8-day-old boy.** (A) Longitudinal sonogram shows a large round, circumscribed, echogenic left upper quadrant solid mass *(arrows)*, with mass-effect upon the spleen *(S)*. (B) Axial contrast-enhanced CT image confirms a mildly heterogenous, enhancing left upper quadrant mass, proven to be a congenital neuroblastoma arising from the left adrenal gland. The mass exerts mass-effect upon the spleen *(S)*, pancreas, and left kidney. Abnormal soft tissue also surrounds the abdominal aorta.

administration of gadolinium chelate.[1] Paragangliomas generally have a similar MRI appearance to adrenal pheochromocytomas (e-Fig. 122.16). Whole body MRI screening has also been shown effective for detecting pheochromocytomas and paragangliomas in patients with syndromes.[14]

***Treatment.*** Surgical removal of all known lesions is usually curative. However, clinical follow-up is essential, along with urinary catecholamine measurement to detect recurrence or the development of new lesions.

## ADRENOCORTICAL NEOPLASMS

***Overview.*** Adrenocortical neoplasms primarily comprise two types of tumor: adenomas and carcinomas. Both are uncommon in children. A higher incidence is seen in children under the age of 4 years.[15] Girls are affected more commonly compared with boys, and carcinomas are more common than adenomas.[16] The majority of these tumors are hormonally functioning, and the most common endocrine abnormality is overproduction of androgens. Girls present with virilization, and boys present with pseudoprecocious puberty. Often, mixed endocrine dysfunction is caused by the overproduction of both glucocorticoids and mineralocorticoids. Two cancer predisposition syndromes, Li-Fraumeni syndrome and Beckwith-Wiedemann syndrome, are associated with adrenocortical neoplasms.[16]

***Imaging.*** At presentation, adrenocortical neoplasms in children are usually larger than 5 cm.[12] Most lesions can be documented with US, but CT and MRI are particularly important for assessing large lesions, and local invasion and spread. On all three modalities, smaller lesions tend to have a fairly homogeneous appearance and may be either an adenoma or carcinoma (Fig. 122.17). Areas of heterogeneity reflecting hemorrhage, necrosis, and calcification are seen more commonly in larger lesions, usually carcinomas (Fig. 122.18).[12] In larger lesions, the characteristic appearance of

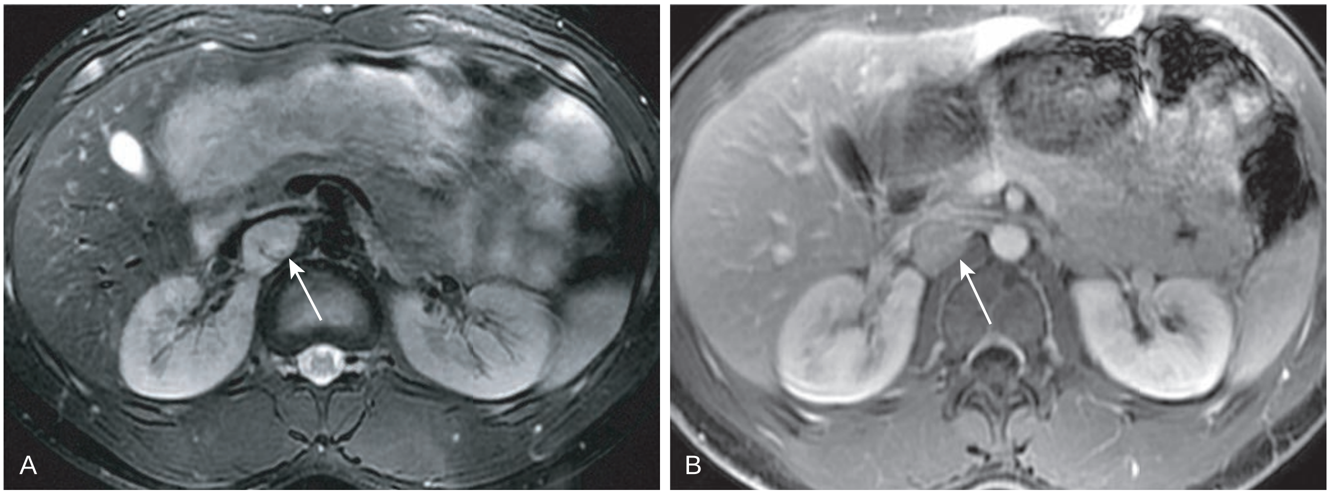

**e-Figure 122.16. Retroperitoneal paraganglioma in a 15-year-old boy with a family history of hereditary paraganglioma-pheochromocytoma syndrome.** (A) Axial T2-weighted fat-suppressed MR image shows a predominantly hyperintense, mildly heterogeneous retrocaval mass *(arrow)*. (B) Axial postcontrast, T1-weighted, fat-suppressed MR image shows that the mass mildly homogeneously enhances. Surgical pathology confirmed the diagnosis of paraganglioma.

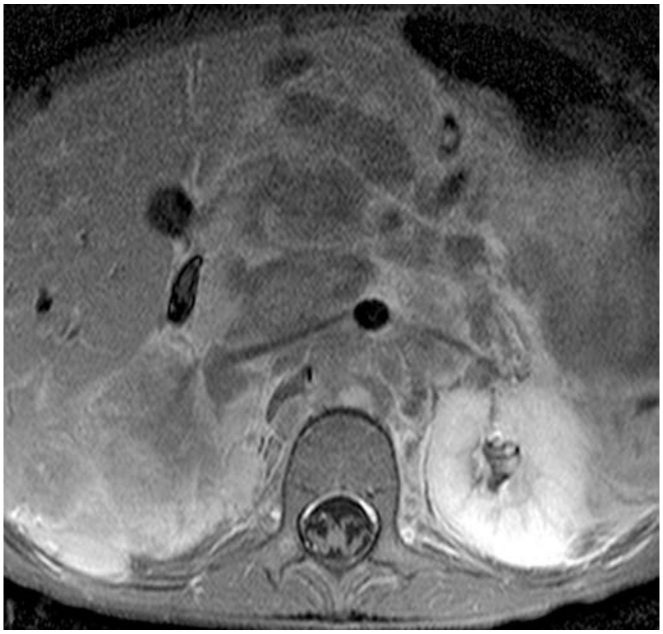

**Figure 122.7. Retroperitoneal neuroblastoma in a 4-year-old girl.** Axial postcontrast, T1-weighted, fat-suppressed MR image shows a large retroperitoneal mass encasing the aorta and renal arteries and displacing the inferior vena cava to the right. The mass shows heterogeneous enhancement.

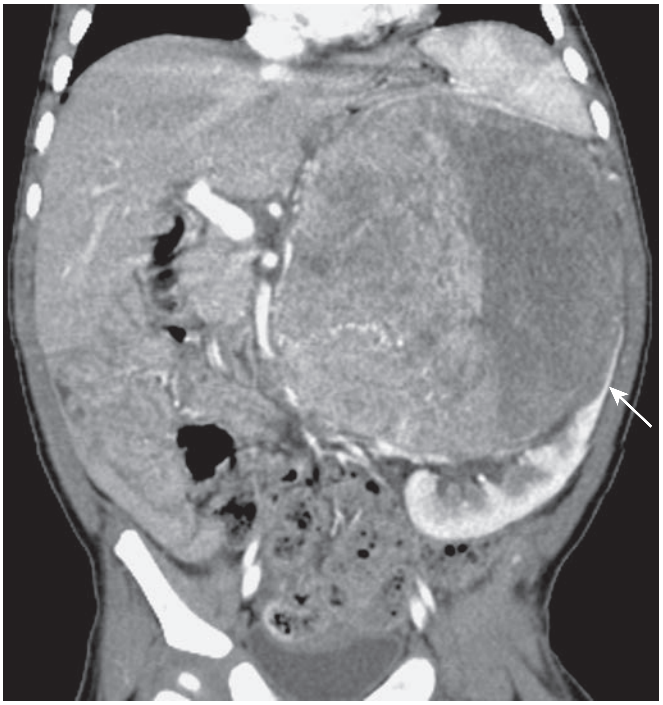

**Figure 122.8. Left adrenal neuroblastoma in a 9-month-old girl.** Coronal contrast-enhanced CT image shows a large heterogeneous retroperitoneal mass invading the left kidney. The left kidney is displaced caudally and laterally with suggestion of a partial “claw sign” *(arrow)*, which may lead to the erroneous interpretation that the mass is arising from the left kidney.

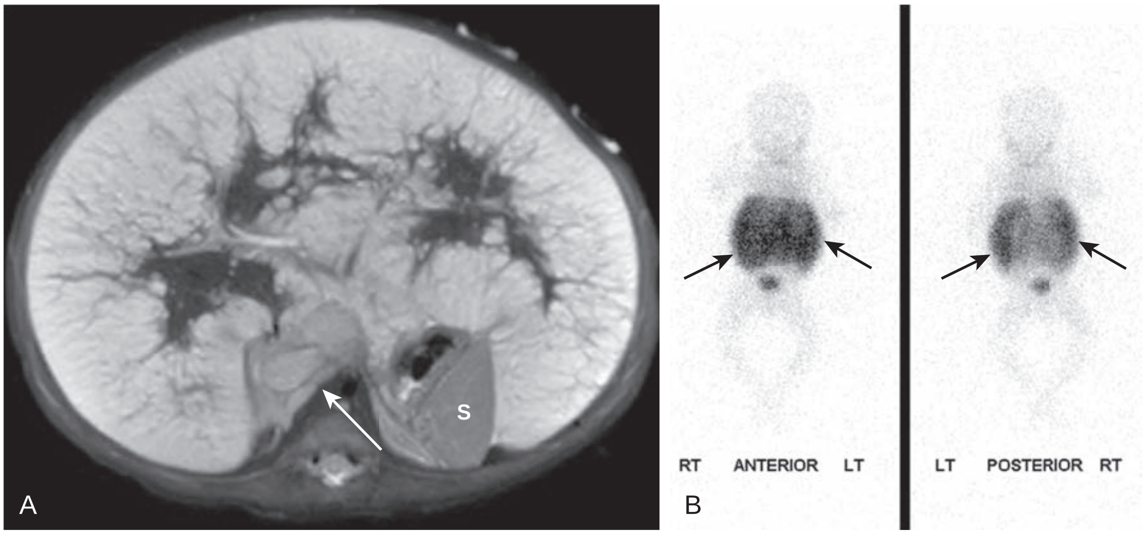

**Figure 122.9. Metastatic liver disease in neuroblastoma in an 8-day-old girl (stage MS [formerly 4S]).** (A) Axial T2-weighted fat-suppressed MR image shows extensive abnormal signal hyperintensity involving the periphery of the liver, proven by biopsy to be infiltrative metastatic neuroblastoma. The primary tumor is partially seen in the right suprarenal fossa *(arrow)*. *S*, Spleen. (B) Anterior and posterior planar MIBG scan images show marked hepatic radiotracer uptake *(arrows)*, indicating metastatic disease.

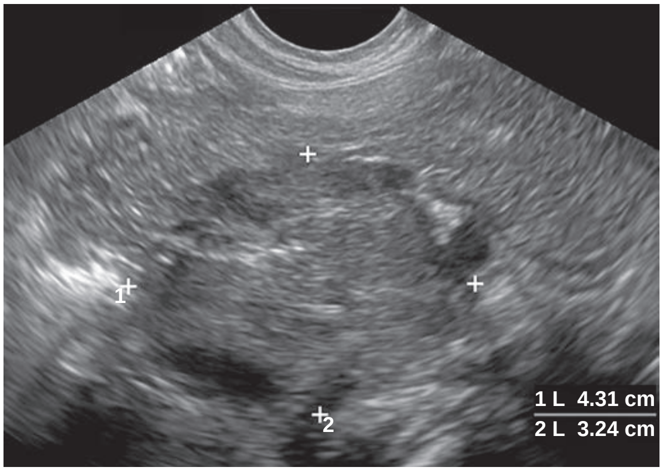

**Figure 122.11. Retroperitoneal ganglioneuroma in a 7-year-old girl.** Transverse sonogram shows a large round, solid mass (between cursors) of intermediate echogenicity with scattered punctate calcifications in the midline retroperitoneum. The sonographic appearance of ganglioneuroma is indistinguishable from neuroblastoma.

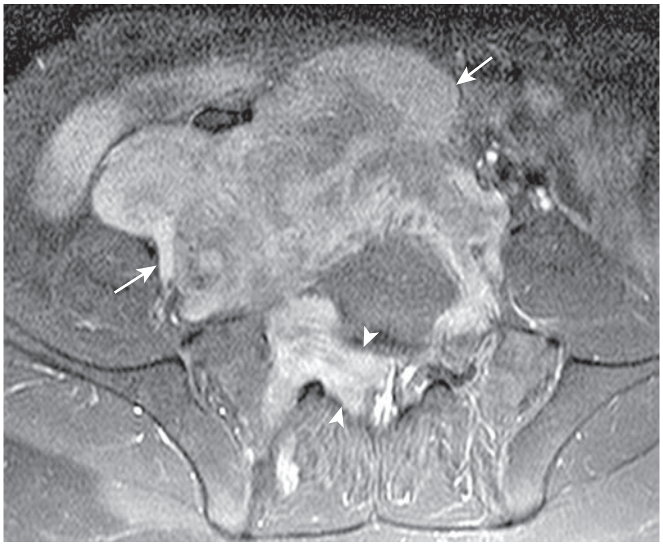

**Figure 122.12. Retroperitoneal ganglioneuroma in a 10-year-old girl.** Axial fat-suppressed, postcontrast, T1-weighted MR image shows a large, heterogeneous, retroperitoneal mass *(arrows)*, which extends into sacral foramina and into the distal spinal canal *(arrowheads)*. The imaging features are similar to those seen in neuroblastoma.

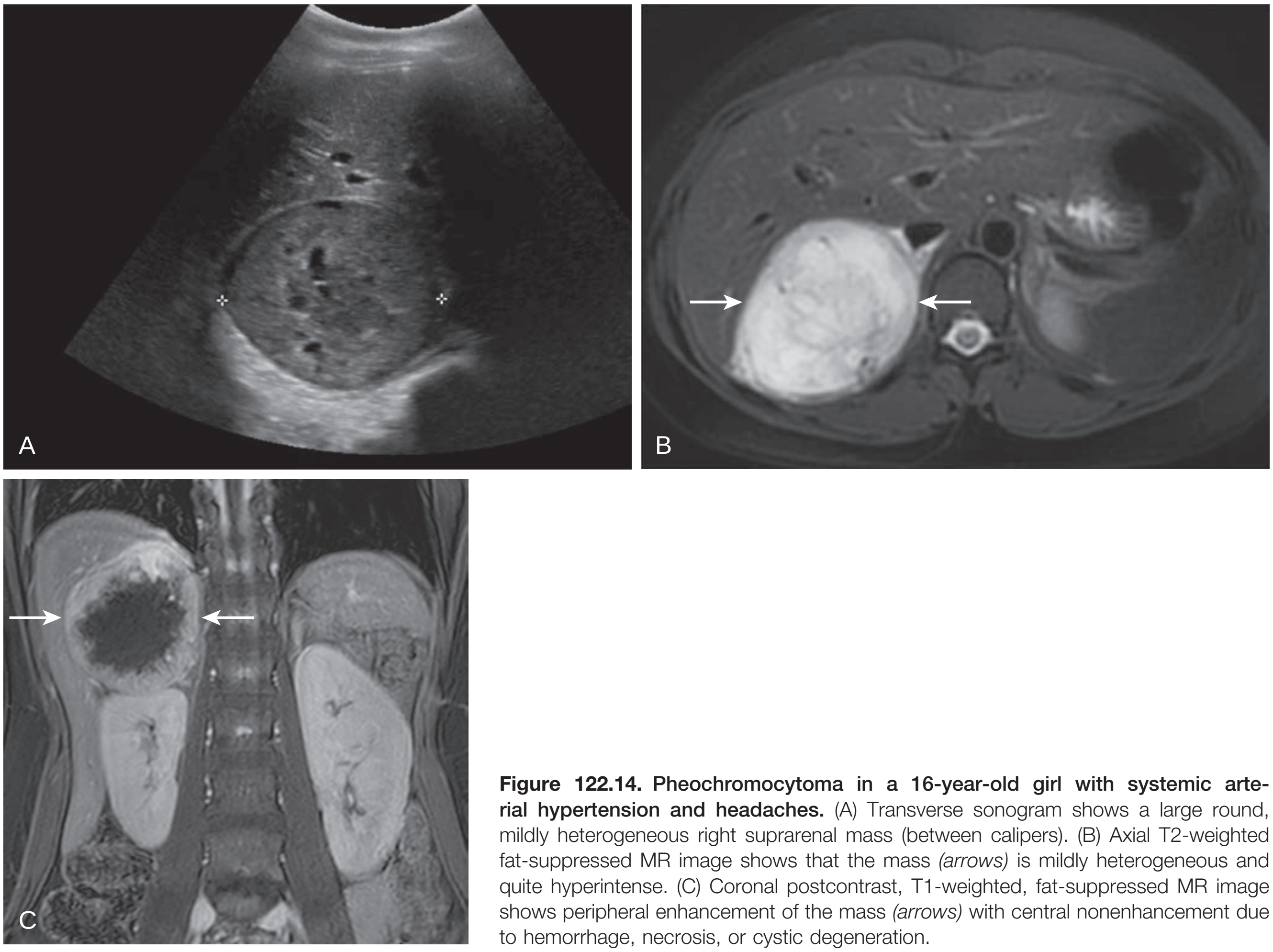

**Figure 122.14. Pheochromocytoma in a 16-year-old girl with systemic arterial hypertension and headaches.** (A) Transverse sonogram shows a large round, mildly heterogeneous right suprarenal mass (between calipers). (B) Axial T2-weighted fat-suppressed MR image shows that the mass *(arrows)* is mildly heterogeneous and quite hyperintense. (C) Coronal postcontrast, T1-weighted, fat-suppressed MR image shows peripheral enhancement of the mass *(arrows)* with central nonenhancement due to hemorrhage, necrosis, or cystic degeneration.

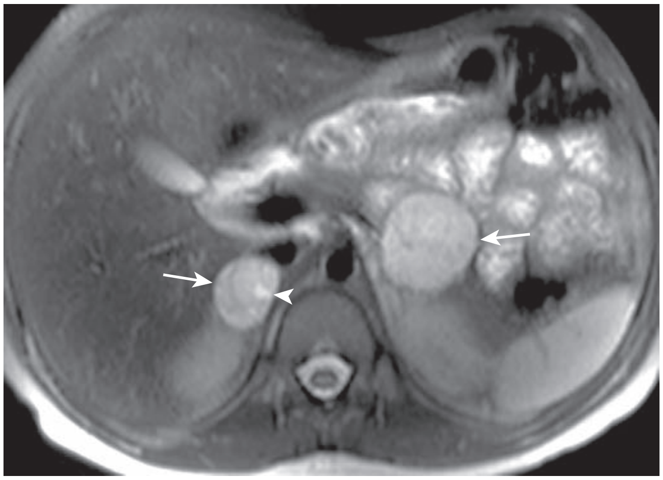

**Figure 122.15. Bilateral pheochromocytomas in an 11-year-old boy with von Hippel-Lindau disease and systemic arterial hypertension.** Axial fat-suppressed T2-weighted magnetic resonance image shows bilateral adrenal masses *(arrows)*, larger on the left. The masses are hyperintense with small cystic change on the right medially *(arrowhead)*. (See e-Fig. 122.13 for US of same patient.)

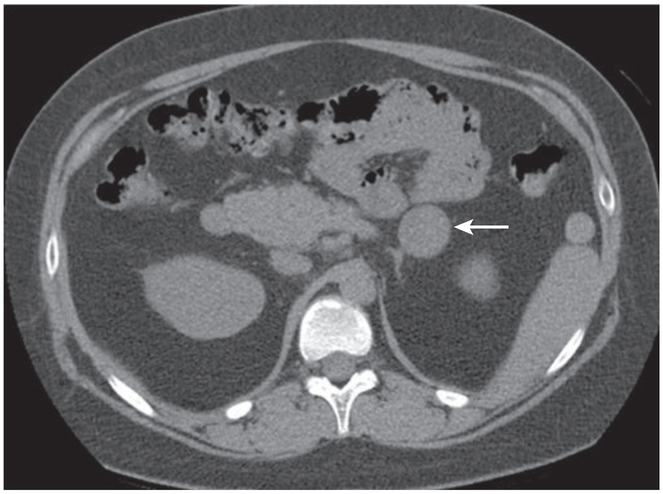

**Figure 122.17. Adrenocortical adenoma in a 2-year-old girl with Cushingoid features.** Axial noncontrast CT image shows a round mass *(arrow)* arising from the left adrenal gland, proven to be a functioning adrenocortical adenoma. There is a large amount of intraabdominal fat for the child's age.

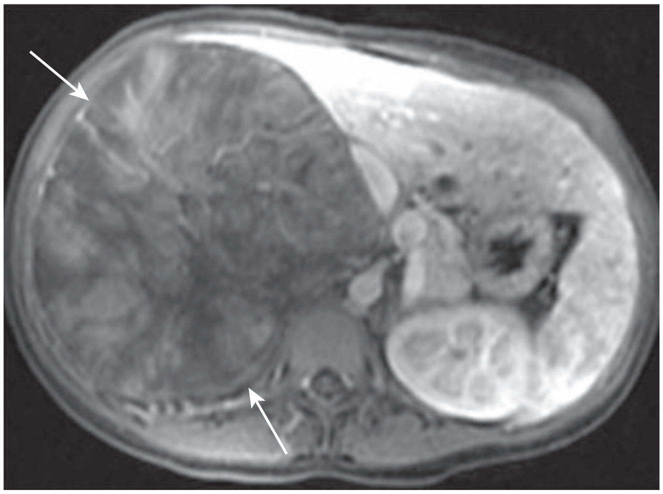

**Figure 122.18. Adrenocortical carcinoma in a 16-year-old girl with abdominal pain and weight loss.** Axial postcontrast, T1-weighted, fat-suppressed MR image shows a very large right suprarenal mass that exerts considerable mass-effect. The mass heterogeneously enhances with areas of alternating relatively increased and decreased signal intensity.

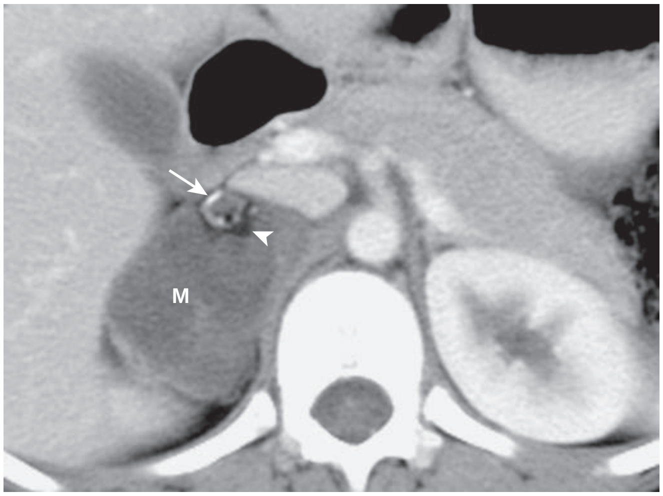

**Figure 122.19. Retroperitoneal teratoma in an 11-year-old girl.** Contrast-enhanced axial CT image shows a well-defined right suprarenal mass *(M)*, with mainly fluid attenuation and some soft tissue septa. Calcification *(arrow)* and fat attenuation *(arrowhead)* are seen anteriorly within the mass.

a central scar, with radiating linear bands that represent areas of necrosis and calcification, may be seen.[1] It is not always possible to predict accurately which adrenocortical lesions are malignant by imaging, unless local spread and invasion have occurred or metastatic disease is present. Metastatic disease most commonly occurs to the lungs, liver, and bone.[16]

***Treatment.*** Complete resection of the primary tumor is essential for survival in the setting of malignancy.[16] Adenomas clearly have a good prognosis, but clinical and imaging follow-up are essential because the histologic distinction between adenoma and carcinoma is not possible in all cases.

## OTHER RETROPERITONEAL CONDITIONS

***Overview.*** Apart from pathology arising from the urinary tract and adrenal gland and sympathetic chains, other less common retroperitoneal conditions include lymphadenopathy (mainly lymphoma or metastatic lymphadenopathy), vascular malformations, Kaposiform hemangioendotheliomas, other neurogenic tumors (schwannoma, neurofibroma, malignant peripheral nerve sheath tumor), adipocytic tumors, germ cell neoplasms (including teratomas) (Fig. 122.19 and e-Fig. 122.20), rhabdomyosarcoma, fibromatosis, idiopathic fibrosis, hematoma, and abscess.

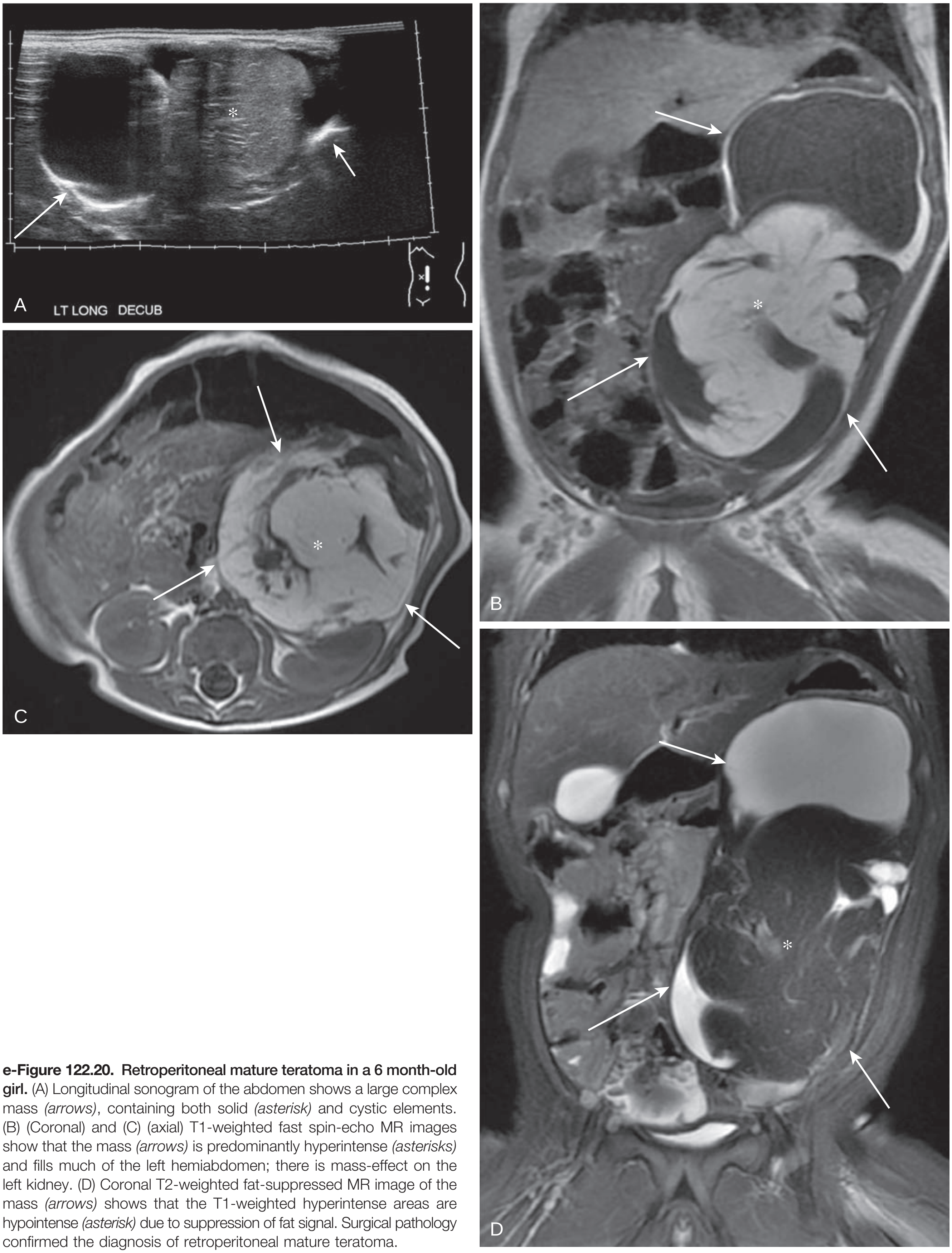

**e-Figure 122.20. Retroperitoneal mature teratoma in a 6 month-old girl.** (A) Longitudinal sonogram of the abdomen shows a large complex mass *(arrows)*, containing both solid *(asterisk)* and cystic elements. (B) (Coronal) and (C) (axial) T1-weighted fast spin-echo MR images show that the mass *(arrows)* is predominantly hyperintense *(asterisks)* and fills much of the left hemiabdomen; there is mass-effect on the left kidney. (D) Coronal T2-weighted fat-suppressed MR image of the mass *(arrows)* shows that the T1-weighted hyperintense areas are hypointense *(asterisk)* due to suppression of fat signal. Surgical pathology confirmed the diagnosis of retroperitoneal mature teratoma.

## KEY POINTS

- Neuroblastoma is the most common extracranial solid neoplasm in children and accounts for almost 10% of all childhood neoplasms.
- Metastatic disease in neuroblastoma is present in up to 70% of patients at presentation.
- A characteristic imaging feature of neuroblastoma is the displacement of adjacent organs and the displacement or encasement of adjacent major vessels.
- Ganglioneuroma may be unable to be differentiated from neuroblastoma/ganglioneuroblastoma solely on the basis of conventional imaging appearances.
- Li-Fraumeni and Beckwith-Wiedemann syndromes are associated with adrenocortical neoplasms.
- Adrenocortical tumors most often present with evidence of hormonal overproduction (e.g., precocious puberty, virilization, Cushing syndrome).

## SUGGESTED READINGS

Balassy C, Navarro OM, Daneman A. Adrenal masses in children. *Radiol Clin North Am*. 2011;49:711–727.
Havekes B, Romijn JA, Eisenhofer G, et al. Update on pediatric pheochromocytoma. *Pediatr Nephrol*. 2009;24:943–950.
Lonergan GJ, Schwab CM, Suarez ES, et al. Neuroblastoma, ganglioneuroblastoma and ganglioneuroma: radiologic-pathologic correlation. *Radiographics*. 2002;22:911–934.
McCarville MB. Imaging neuroblastoma: what the radiologist needs to know. *Cancer Imaging*. 2011;11:S44–S47.
Paterson A. Adrenal pathology in childhood spectrum of disease. *Eur Radiol*. 2002;12:2491–2508.

## REFERENCES

Full references for this chapter can be found on www.expertconsult.com.

## REFERENCES

1. Paterson A. Adrenal pathology in childhood, a spectrum of disease. *Eur Radiol*. 2002;12:2491–2508.
2. Lonergan GJ, Schwab CM, Suarez ES, et al. Neuroblastoma, ganglioneuroblastoma and ganglioneuroma: radiologic-pathologic correlation. *Radiographics*. 2002;22:911–934.
3. McHugh K, Pritchard J. Problems in the imaging of three common paediatric solid tumours. *Eur J Radiol*. 2001;37:72–78.
4. Hiorns MP, Owens CM. Radiology of neuroblastoma in children. *Eur Radiol*. 2001;11:2071–2081.
5. Monclair T, Brodeur GM, Ambros PF, et al. The international neuroblastoma risk group (INRG) staging system: an INRG task force report. *J Clin Oncol*. 2009;27:298–303.
6. McCarville MB. Imaging neuroblastoma: what the radiologist needs to know. *Cancer Imaging*. 2011;11(Spec No A):S44–S47.
7. Cohn SL, Pearson ADJ, London WB, et al. The international neuroblastoma risk group (INRG) staging system: an INRG task force report. *J Clin Oncol*. 2009;27:289–297.
8. Bénard J, Raguénez G, Kauffmann A, et al. MYCN-non-amplified metastatic neuroblastoma with good prognosis and spontaneous regression: a molecular portrait of stage 4S. *Mol Oncol*. 2008;2(3):261–271.
9. Gahr N, Darge K, Hahn G, et al. Diffusion-weighted MRI for differentiation of neuroblastoma and ganglioneuroblastoma/ganglioneuroma. *Eur J Radiol*. 2011;79:443–446.
10. Havekes B, Romijn JA, Eisenhofer G, et al. Update on pediatric pheochromocytoma. *Pediatr Nephrol*. 2009;24:943–950.
11. Waguespack SG, Rich T, Grubbs E, et al. A current review of the etiology, diagnosis, and treatment of pediatric pheochromocytoma and paraganglioma. *J Clin Endocrinol Metab*. 2010;95:2023–2037.
12. Siegel MJ, Chung EM. Adrenal glands, pancreas, and other retroperitoneal structures. In: Siegel MJ, ed. *Pediatric Sonography*. 4th ed. Philadelphia, PA: Lippincott Williams & Wilkins; 2011:461–508.
13. Baid SK, Lai EW, Wesley RA, et al. Brief communication: radiographic contrast infusion and catecholamine release in patients with pheochromocytoma. *Ann Intern Med*. 2009;150(1):27–32. Erratum in: Ann Intern Med. 2009 Feb 17;150(4):292.
14. Jasperson KW, Kohlmann W, Gammon A, et al. Role of rapid sequence whole-body MRI screening in SDH-associated hereditary paraganglioma families. *Fam Cancer*. 2014;13(2):257–265.
15. Ribeiro RC, Figueiredo B. Childhood adrenocortical tumors. *Eur J Cancer*. 2004;40:1117–1126.
16. Flynt KA, Dillman JR, Davenport MS, et al. Pediatric adrenocortical neoplasms: can imaging reliably discriminate adenomas from carcinomas? *Pediatr Radiol*. 2015;45(8):1160–1168.

# 123 Genitourinary Trauma

George A. Taylor

## RENAL INJURY

***Overview.*** The kidney is the third most frequently injured abdominal viscus in children and accounts for 1.3% to 15% of injuries in children who suffer blunt abdominal trauma. Children are more susceptible to renal injury during blunt trauma compared with adults because of the relatively increased mobility of the pediatric kidney, less perinephric fat, and reduced protection by a more compliant chest wall. Preexisting renal abnormalities such as a horseshoe kidney (Fig. 123.1 and e-Fig. 123.2) or pelvic kidney, hydronephrosis, cystic renal disease, and tumors may increase the size or alter the location of the kidney leading to an increased susceptibility to injury.[1]

Most children with clinically significant renal injury present with hematuria; the risk of underlying renal injury is markedly higher in patients with gross hematuria (22%) compared with those with lesser amounts of urinary blood (8%). However, the presence of asymptomatic microscopic hematuria is a low-yield sign for the presence of underlying renal injury, and the absence of hematuria correlates with a low risk for urinary injury (0.2%).[2,3] Isolated renal injury in children is relatively uncommon, with associated injuries typically present in the lungs (45%), spleen (33%), and liver (29%).

***Imaging.*** Computed tomography (CT) is the preferred modality for initial assessment of hemodynamically stable children with suspected renal injury because of its wide availability, rapid image acquisition, and accuracy. The use of intravenous contrast material is essential for the evaluation of the kidney, and scanning during the portal venous phase of opacification is recommended. A delayed scan may be helpful for the detection of urinary extravasation. Noncontrast scans are not generally helpful, and they unnecessarily increase radiation dose to the patient. Unstable patients who require immediate evaluation may be examined with ultrasonography at the bedside before complete resuscitation or surgery. Routine follow-up imaging can be performed with gray-scale and color Doppler ultrasonography in most patients, and CT can be reserved for selected patients with other associated injury or ambiguous findings on serial ultrasonography.[4]

The most common type of renal injury is parenchymal contusion, which manifests on CT as a focal or diffuse region of absent or delayed contrast enhancement (Fig. 123.3). The contusion is characterized by microscopic areas of hemorrhage and surrounding edema. The involved kidney may also appear larger on CT as a result of the associated edema.

Renal injury may be complicated by perirenal hematoma, which may be subcapsular or perinephric. These two types of hematoma can be differentiated on the basis of CT features. A subcapsular hematoma is limited in its extension by the renal capsule and therefore exerts greater mass effect on the renal parenchyma, whereas a perinephric hematoma is distributed throughout the perirenal space and typically exhibits less mass effect on the renal parenchyma.

Renal collecting system injury results in urinary extravasation of intravenous contrast material (see e-Fig. 123.2, Fig. 123.4, and e-Fig. 123.5). Urine leakage that remains encapsulated in the perirenal space is termed a urinoma. Occasionally, hemorrhage or urinary extravasation may extend into the pelvis owing to direct communication between the perirenal space in the abdomen and the prevesical extraperitoneal space in the pelvis.[1] Grade IV renal injuries with medial contrast material extravasation from the collecting system on CT have been shown to be a high-risk sign for surgical intervention.[3]

The American Association for the Surgery of Trauma has developed an injury scale to categorize the increasing severity of renal injury (Table 123.1). Grade I to grade III injuries are considered low-grade, and account for between 69% to 99% of all renal injuries. Grade IV and V injuries are less common and include the shattered kidney, ureteropelvic junction avulsion, and renal artery transection or thrombosis (Fig. 123.6).

***Treatment.*** The great majority of renal injuries (69%–99%) are treated nonsurgically with great success. Even in high-grade injuries, no surgical intervention is necessary in 60% to 70%. Early ureteral stent placement may be considered in patients with high-grade injuries who do not demonstrate contrast material in the ipsilateral ureter.[5]

## BLADDER INJURY

***Overview.*** Blunt injuries to the bladder typically result from a blow to the lower abdomen when the bladder is distended or when the pelvis is fractured. Fortunately, the incidence of lower urinary tract injury in children is quite low, estimated at 0.2% of pediatric trauma admissions. Although approximately 50% of children with bladder tears have a pelvic fracture, only 0.5% to 3.7% of children with pelvic fractures have associated bladder injuries.[6] High-yield indications for CT cystography include gross hematuria, pelvic fracture, and high-risk mechanisms of injury such as motor vehicle crashes and the presence of a seatbelt ecchymosis. Bladder injuries may be classified as intraperitoneal rupture, extraperitoneal rupture, and combined lesions.

***Imaging.*** Standard abdominal trauma CT scanning protocols may miss important bladder injuries because of incomplete bladder distension. CT cystography is the preferred technique for the detection of bladder tears with a reported sensitivity and specificity of 95% and 100% respectively.[7] The bladder is filled by gravity drip infusion of dilute water-soluble iodinated contrast material using age-based estimates of bladder capacity (e.g., 4.5 × age [0.40] = capacity in ounces).[8]

Extraperitoneal rupture accounts for approximately 83% of all bladder perforations in pediatric patients. They are often associated with pelvic fractures that distort and shear the bladder at its attachments near the trigone, below the peritoneal reflection. On CT cystography, extravasation is usually confined to the perivesical soft tissues (Fig. 123.7, and e-Figs. 123.8 and 123.9) but may extend into the scrotum, superiorly along the anterior abdominal wall, or up through retroperitoneal spaces to the level of the kidney.[1,9]

Intraperitoneal rupture occurs when the bladder is acutely compressed resulting in a sudden increase in pressure and a tear of the dome of the bladder. This results in extravasation of contrast-containing urine into the peritoneal cavity where it fills the cul-de-sac, surrounds the bowel, often extending into the paracolic

## Abstract:

The kidney is the third most frequently injured abdominal viscus in children who suffer blunt abdominal trauma. Children are more susceptible to renal injury during blunt trauma compared with adults because of the relatively increased mobility of the pediatric kidney, less perinephric fat, and reduced protection by a more compliant chest wall. Preexisting renal abnormalities such as a horseshoe kidney or pelvic kidney, hydronephrosis, cystic renal disease, and tumors may increase the size or alter the location of the kidney leading to an increased susceptibility to injury. Most children with clinically significant renal injury present with hematuria. Injuries to the bladder typically result from a blow to the lower abdomen when the bladder is distended or when the pelvis is fractured. Although approximately 50% of children with bladder tears have a pelvic fracture, only 0.5% to 3.7% of children with pelvic fractures have associated bladder injuries. Bladder injuries may be classified as intraperitoneal rupture, extraperitoneal rupture, and combined lesions. The majority of injuries to the scrotum occur in older boys and are the result of a direct blow to the groin during sport activities (50%), motor vehicle crashes (9%–17%), falls, or straddle injuries. Typical indications for imaging include an acute, painful, or ecchymotic scrotum, and a nonpalpable testis. Although common, scrotal injuries rarely need surgical intervention. In this chapter, we will review the various forms of genitourinary tract injury that occur in children as well as discuss strategies for imaging these injuries.

## Keywords:

Children
Trauma
Genitourinary
Kidney
Bladder
Testis

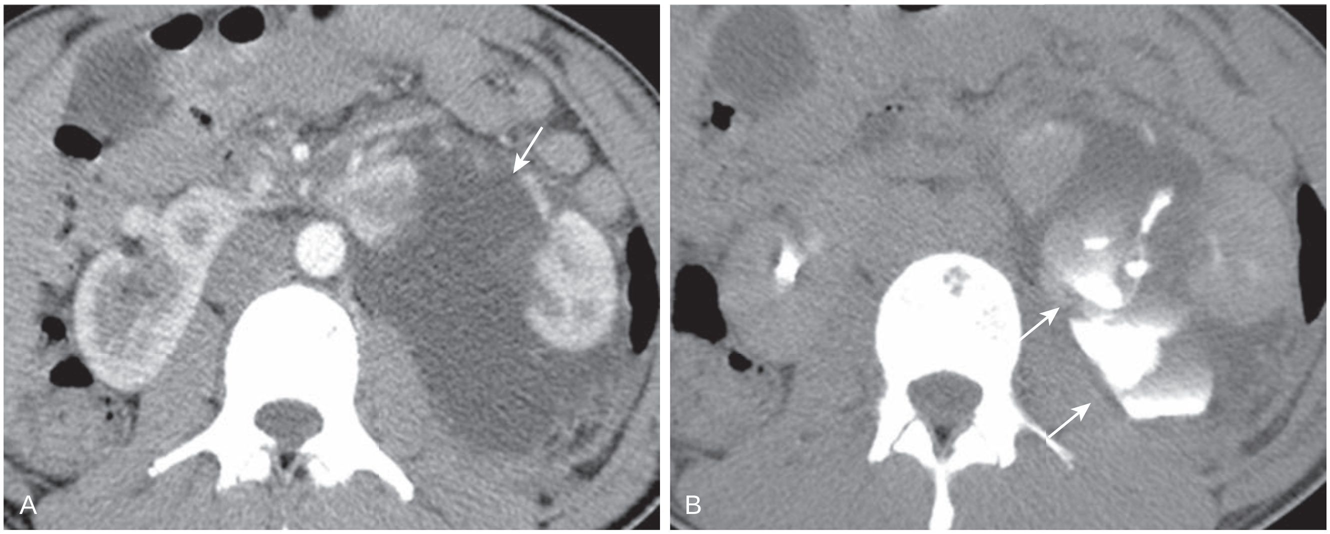

**e-Figure 123.2. Laceration in horseshoe kidney.** (A) Axial contrast-enhanced CT image from an 8-year-old in a motor vehicle accident shows a large laceration involving the left moiety of a horseshoe kidney. (B) Delayed excretory phase image shows urine mixed with contrast material outside of the renal collecting system *(arrows)*, consistent with grade IV injury.

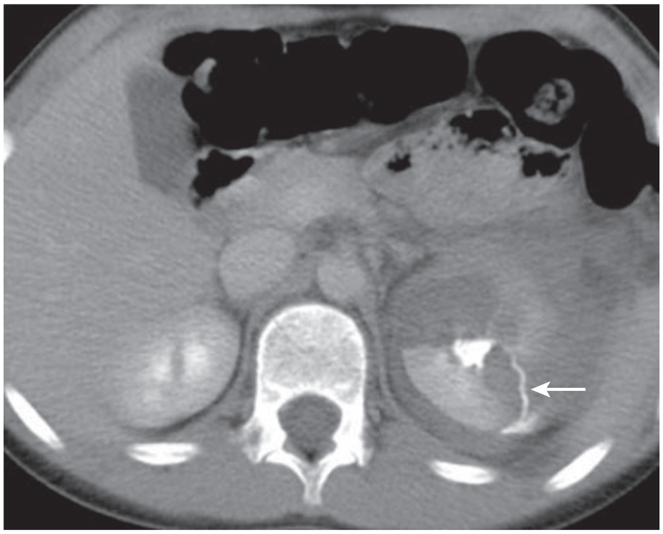

**e-Figure 123.5. Grade IV renal injury.** Axial excretory phase contrast-enhanced CT image from a 10-year-old boy that slipped on a pool deck shows multiple areas of posttraumatic left kidney parenchymal low attenuation. There is contrast material spilling from the left renal collecting system into the left perinephric space *(arrow)*.

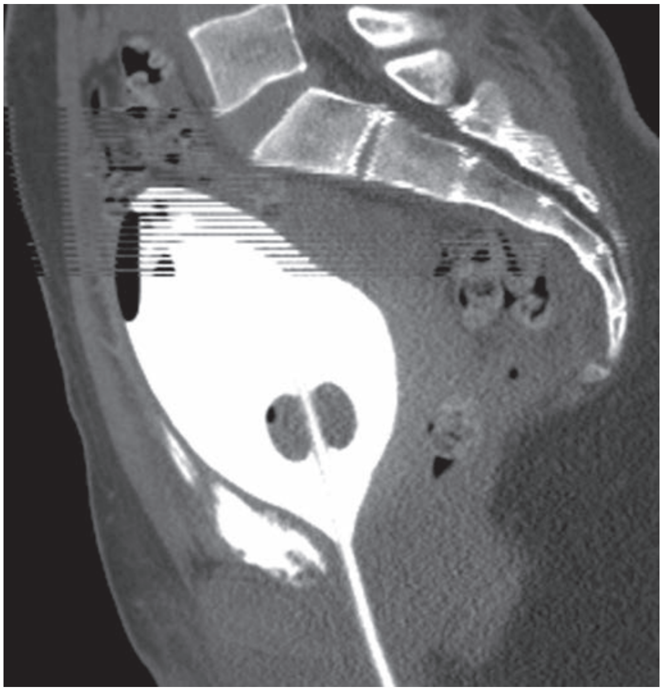

**e-Figure 123.8. Extraperitoneal bladder rupture.** A sagittal CT cystogram image shows contained extravasation of contrast-containing urine into the perivesical spaces.

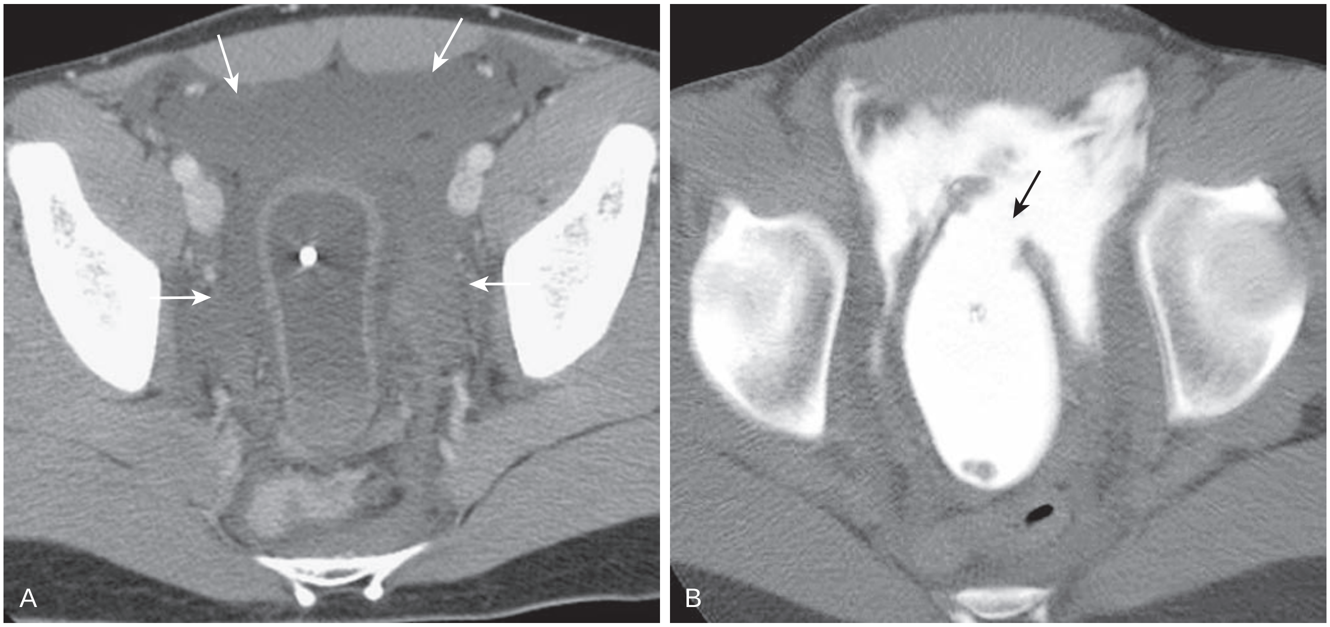

**e-Figure 123.9. Extraperitoneal bladder rupture.** (A) Axial contrast-enhanced CT image from a teenage boy in a motor vehicle accident shows a large amount of extraperitoneal fluid *(arrows)* demonstrating mass-effect upon the urinary bladder. (B) CT cystogram image shows a large defect *(arrow)* involving the anterior inferior wall of the bladder with leakage of contrast material into the prevesical space. Dependent filling defect in the bladder is likely a blood clot.

gutters and subhepatic space (Fig. 123.10 and e-Fig. 123.11). In children, intraperitoneal rupture accounts for up to 17% of all bladder tears.

***Treatment.*** Intraperitoneal ruptures require immediate surgical repair, whereas extraperitoneal ruptures are usually treated by catheter drainage alone. Combined intraperitoneal and extraperitoneal injuries are uncommon in children and are often identified during surgical exploration (Fig. 123.12). Bladder tears generally have a highly favorable outcome, unless the injury extends longitudinally through the bladder base into the proximal urethra. These injuries frequently lead to incontinence and the need for multiple additional surgeries (Fig. 123.13 and e-Fig. 123.14).[10,11]

## URETHRAL INJURY

***Overview.*** Urethral injuries can be divided into posterior and anterior urethral injuries. Most posterior urethral injuries are caused by direct blows to the perineum, falls, or motor vehicle accidents, and occur frequently in the setting of pelvic fractures. These injuries usually involve the membranous urethra and are caused by shearing and rupture of the puboprostatic ligaments. Anterior urethral injuries are usually straddle-type injuries that are rarely associated with pelvic fractures. Although any grade of hematuria may be associated with urethral injury, the strongest clinical sign is the presence of blood at the meatus. No urethral

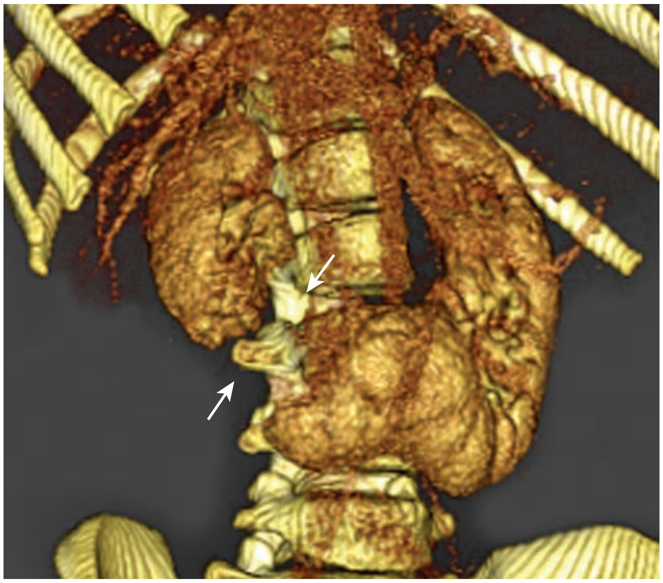

**Figure 123.1. Laceration in horseshoe kidney.** Oblique three-dimensional volume-rendered image from contrast-enhanced CT shows complete transection *(arrows)* of a horseshoe kidney.

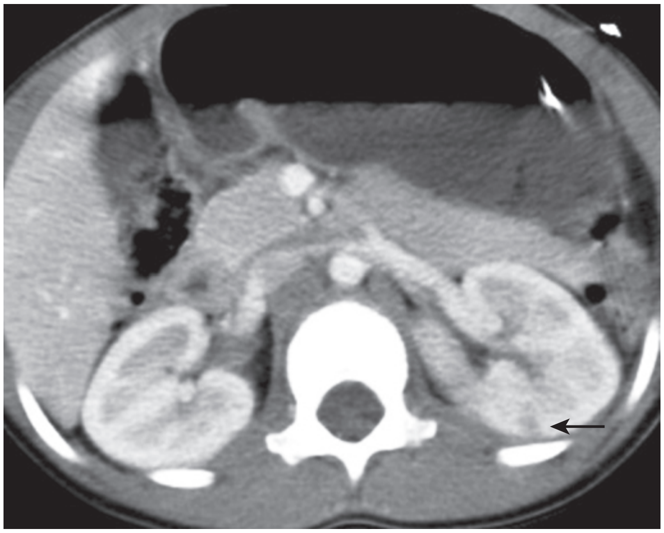

**Figure 123.3. Renal contusion.** A 6-year-old pedestrian hit by a car with multiple liver and splenic lacerations. Axial contrast-enhanced CT image shows a focal area of low attenuation in the left kidney posteriorly *(arrow)*, consistent with contusion (grade 1 injury).

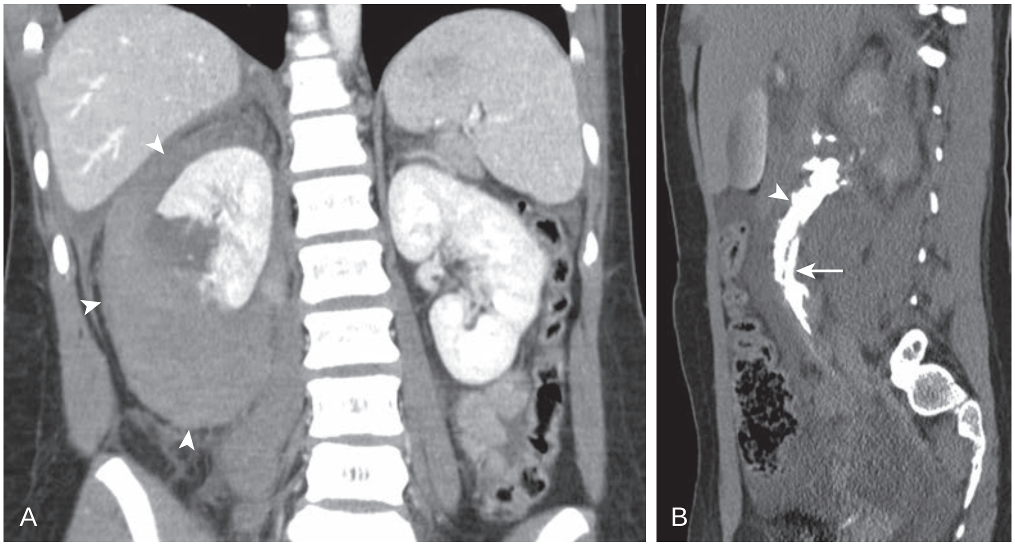

**Figure 123.4. Grade IV renal injury.** (A) Coronal contrast-enhanced CT image shows complete transection of right kidney and large perinephric hematoma *(arrowheads)*. (B) A delayed excretory phase CT image shows extravasation of contrast-containing urine *(arrowhead)* along the right ureter *(arrow)*.

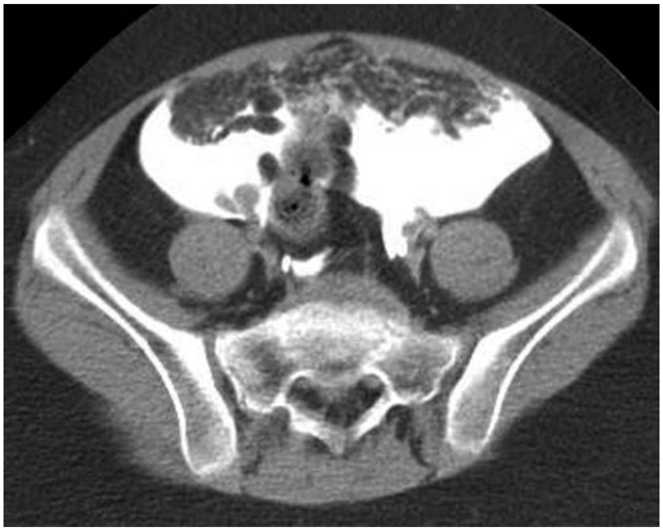

**e-Figure 123.11. Intraperitoneal bladder rupture.** Axial CT cystogram image through the sacral promontory shows extravasated contrast surrounding bowel and mesentery.

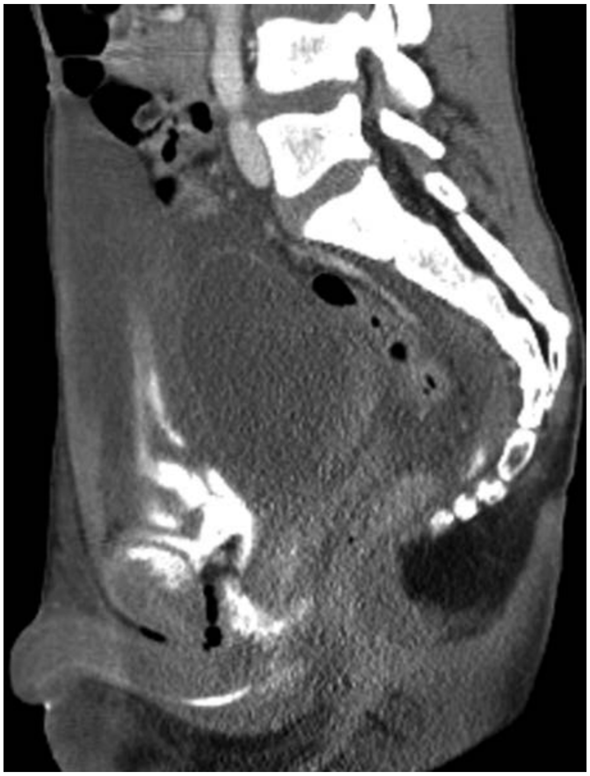

**e-Figure 123.14. Bladder neck and urethral tear.** A sagittal contrast-enhanced CT image of the pelvis shows elevated bladder base, perivesical "sentinel" hematoma, and extravasated contrast material.

**TABLE 123.1** American Association for the Surgery of Trauma (AAST) Renal Injury Scale

| Injury Grade | Renal Injury |
|---|---|
| I | Renal contusion, small nonexpanding subcapsular hematoma |
| II | Superficial renal laceration (<1 cm) not involving collecting system or deep medulla, nonexpanding perinephric hematoma |
| III | Deep renal laceration (>1 cm) without involvement of renal collecting system |
| IV | Laceration of renal collecting system, vascular injury with contained hemorrhage, segmental infarction without laceration, expanding subcapsular hematoma compressing the kidney |
| V | Shattered kidney, avulsion of renal hilum, ureteropelvic junction avulsion, complete laceration or thrombosis of main renal artery or vein |

*From http://www.aast.org/Library/TraumaTools/InjuryScoringScales.aspx#kidney.*

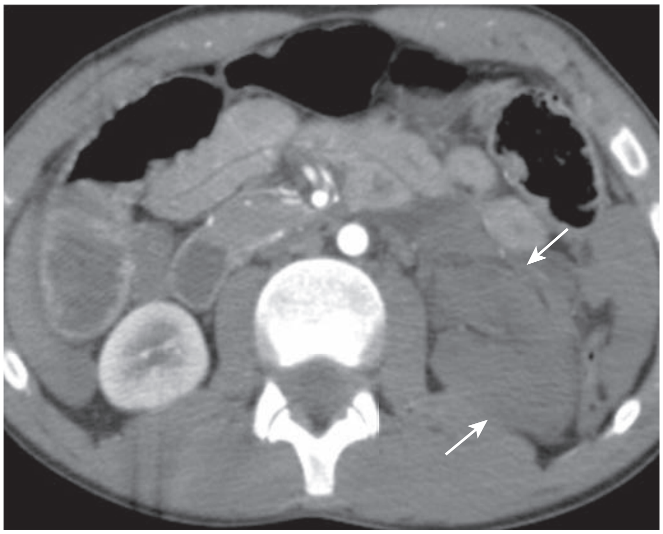

**Figure 123.6. Grade V renal injury.** Teenage boy hit by a truck while driving a snowmobile. Axial contrast-enhanced CT image shows nonenhancement of the left kidney *(arrows)* due to renal artery injury, likely dissection or thrombosis.

instrumentations should be performed in patients with suspected urethral injury until a retrograde urethrogram is performed to evaluate the integrity of the entire urethra. Attempts to catheterize the bladder may convert a partial urethral tear into a complete transection.[12]

***Imaging.*** Retrograde urethrography is performed by inserting the tip of a Foley catheter into the distal urethra. The balloon is slowly inflated in the fossa navicularis, and water-soluble iodinated contrast material is gently hand-injected via a syringe, with the patient positioned in the steep oblique or lateral position. Urethral injuries are manifested by irregular narrowing of the affected urethra and extravasation of contrast material into the surrounding tissues; intraluminal filling defects due to hematoma may be seen (Fig. 123.15 and e-Fig. 123.16).

Although retrograde urethrography is the preferred method of evaluating the urethra, placement of a urinary catheter is common in patients with multiple trauma, and retrograde urethrography may be initially considered only after a CT scan has already been performed. Therefore familiarity with CT findings associated with urethral injuries is important. These include obliteration of the fat plane around the urogenital diaphragm, obscured contours of the prostate, elevation of the bladder base, and blood along the obturator internus muscle (see Fig. 123.13 and e-Fig. 123.14).[13]

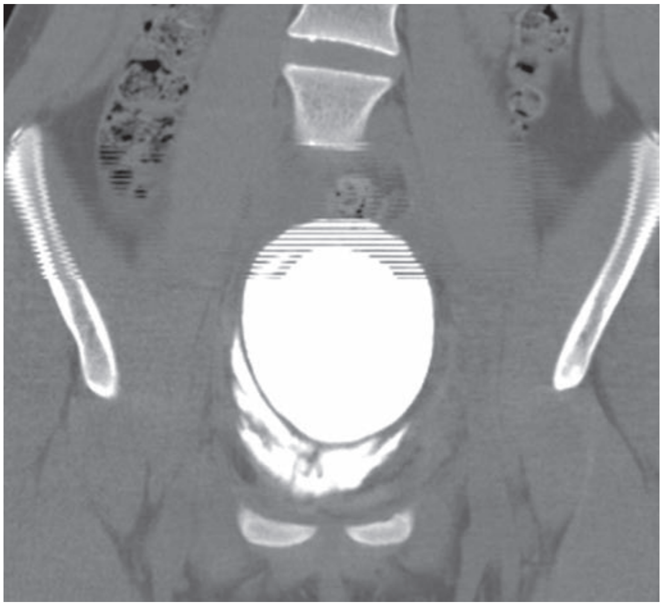

**Figure 123.7. Extraperitoneal bladder rupture.** A coronal reformatted CT cystogram image shows contained extravasation of contrast-containing urine into the perivesical space. A sagittal reformatted image is provided in e-Fig. 123.8.

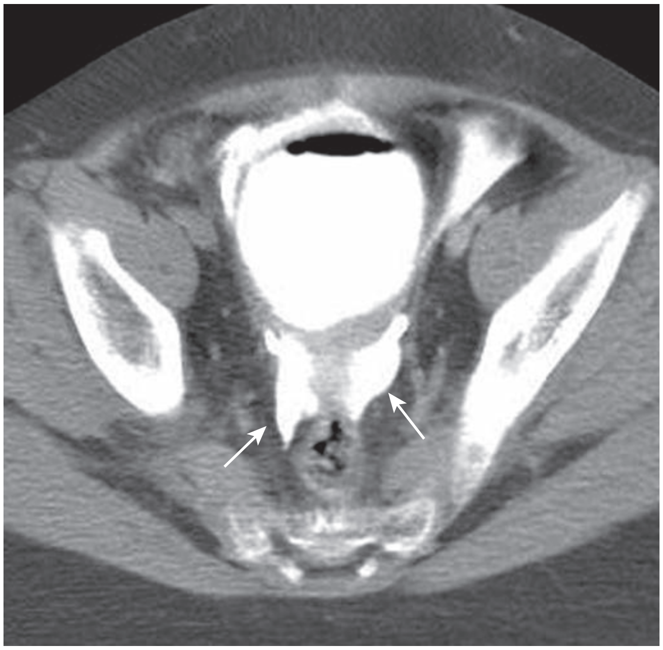

**Figure 123.10. Intraperitoneal bladder rupture.** An axial CT cystogram image through the pelvis shows extravasation of contrast-containing urine into the cul de sac *(arrows)*. A higher axial image showed contrast material surrounding bowel and mesentery (see e-Fig. 123.11).

## SCROTAL INJURY

***Overview.*** The majority of blunt injuries to the scrotum occur in older boys and are the result of a direct blow to the groin

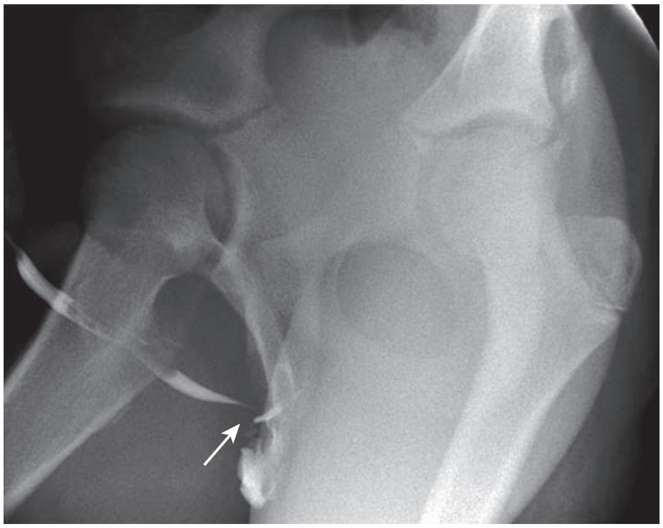

**e-Figure 123.16. Straddle injury, bulbous urethra.** Teenage boy with bulbous urethra injury that occurred when attempting to hurdle a chair. Retrograde urethrogram image shows a laceration *(arrow)* of the urethra with extravasation of contrast material into the scrotum.

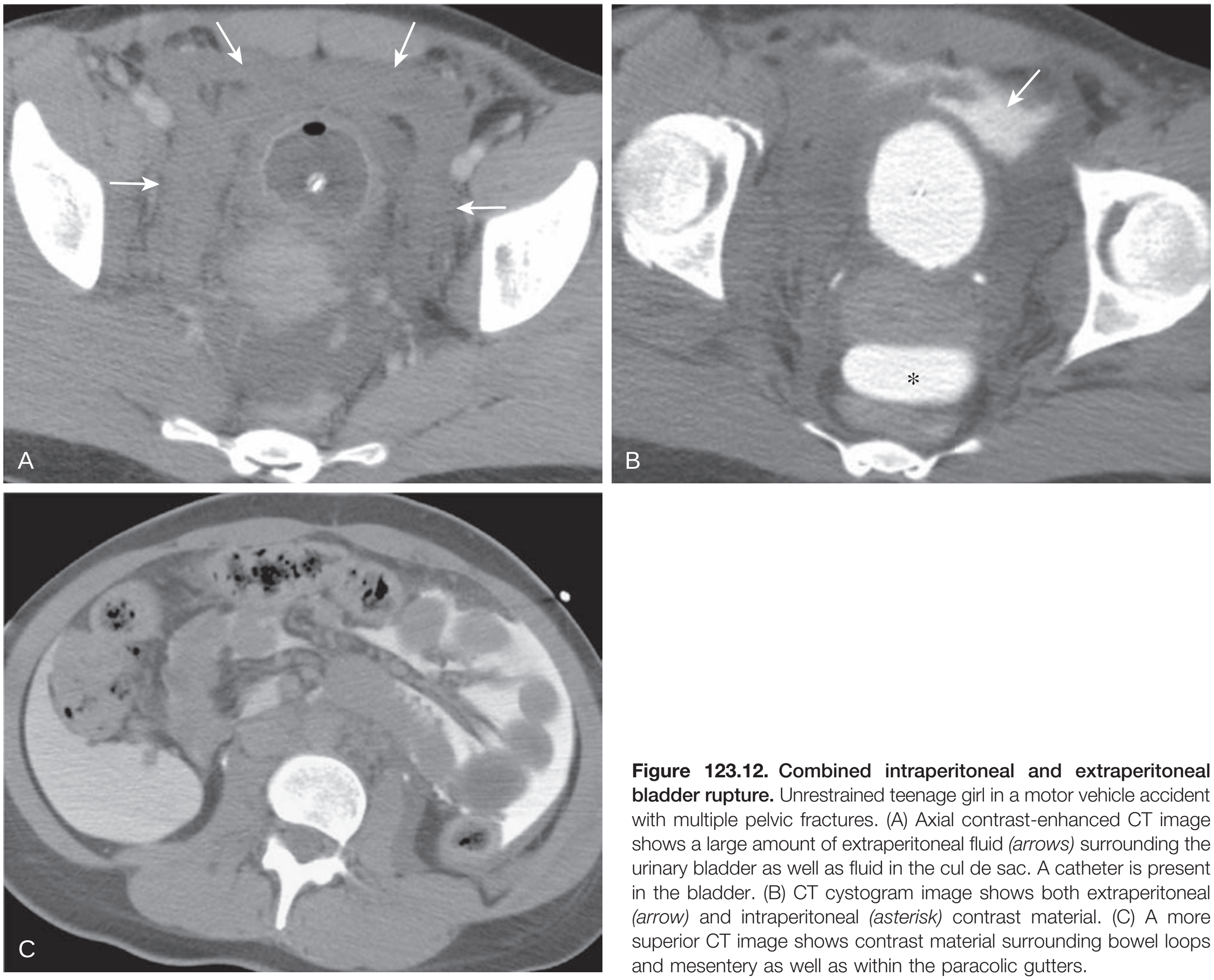

**Figure 123.12. Combined intraperitoneal and extraperitoneal bladder rupture.** Unrestrained teenage girl in a motor vehicle accident with multiple pelvic fractures. (A) Axial contrast-enhanced CT image shows a large amount of extraperitoneal fluid *(arrows)* surrounding the urinary bladder as well as fluid in the cul de sac. A catheter is present in the bladder. (B) CT cystogram image shows both extraperitoneal *(arrow)* and intraperitoneal *(asterisk)* contrast material. (C) A more superior CT image shows contrast material surrounding bowel loops and mesentery as well as within the paracolic gutters.

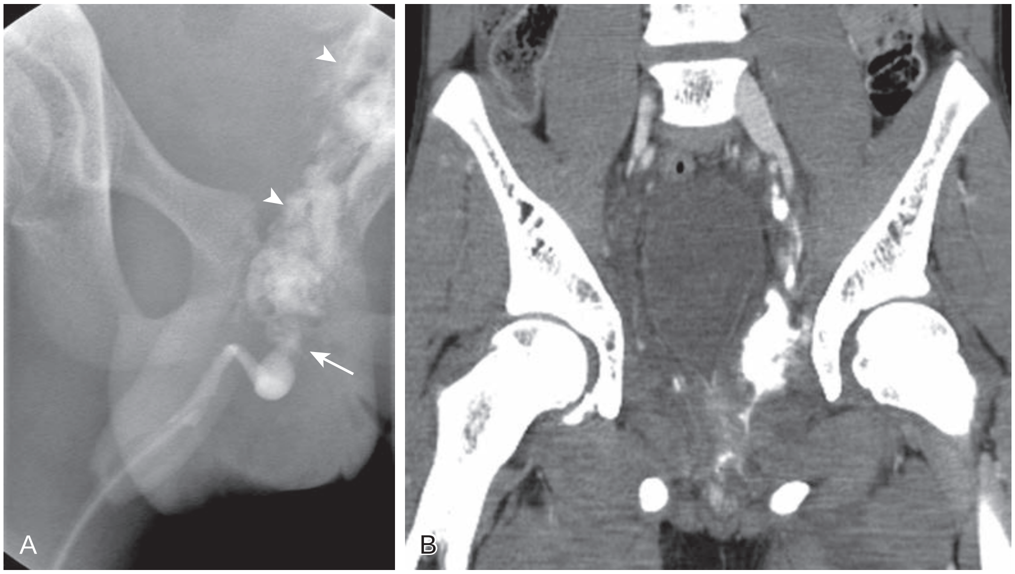

**Figure 123.13. Bladder neck and urethral tear.** (A) An oblique retrograde urethrogram image shows complete transection *(arrow)* of posterior urethra and bladder neck with extraperitoneal extravasation of contrast material *(arrowheads)*. (B) A coronal reformatted contrast-enhanced CT image of the pelvis shows elevated bladder base, perivesical “sentinel” hematoma, and extravasated contrast material. A sagittal reformatted image is provided in e-Fig. 123.14.

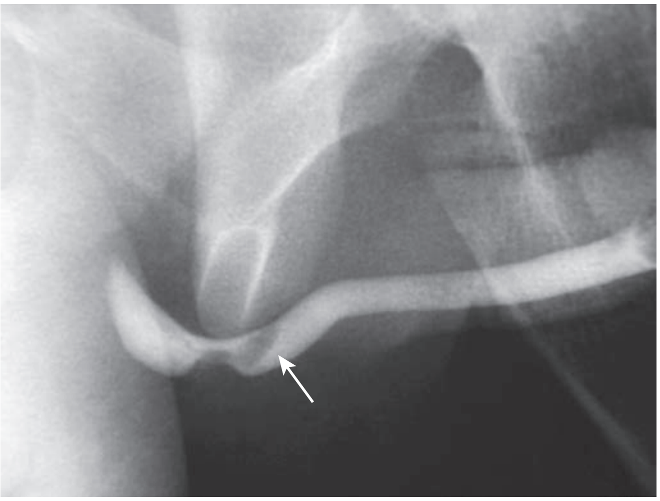

**Figure 123.15. Straddle injury, bulbous urethra.** An oblique retrograde urethrogram shows focal urethral narrowing and intraluminal hematoma *(arrow)*.

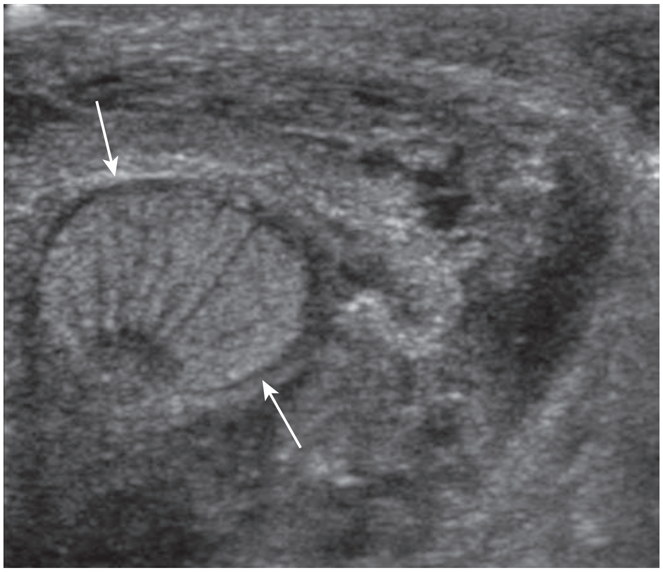

**Figure 123.17. Scrotal hematoma.** Transverse ultrasonogram of the right scrotum shows an intact testis *(arrows)* surrounded by heterogeneous peritesticular hematoma (hematocele). See e-Fig. 123.18 for the longitudinal view.

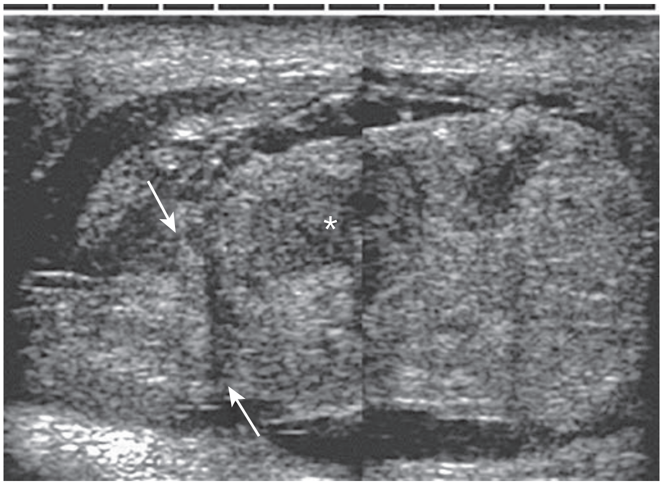

**Figure 123.19. Testicular rupture.** A longitudinal composite scrotal ultrasound image shows a heterogeneous testis with intratesticular hematoma *(asterisk)* and extrusion of testicular contents through a tear in the tunica albuginea *(arrows)*. See e-Fig. 123.20 for power Doppler image of the same testicle.

during sport activities (50%), motor vehicle crashes (9%–17%), falls, or straddle injuries. Typical indications for imaging include an acute, painful, or ecchymotic scrotum, and a nonpalpable testis. Although common, scrotal injuries rarely need surgical intervention. Fortunately, more than 80% of ruptured testes can be successfully salvaged if surgical repair is performed within 72 hours of injury.[12]

***Imaging.*** Sonography is the most effective method of assessing the injured scrotum. High-frequency (7–20 megahertz) linear array transducers should be used to evaluate both testes with gray-scale and color or power Doppler to determine the location and extent of injury. Ultrasonography plays a key role in the identification of testicular rupture allowing for immediate surgical exploration and repair.

Hematomas and hematoceles are the most common findings after scrotal injury. They may be single or multiple and may have a wide range of echogenicities, depending on the time interval between injury and imaging (Fig. 123.17 and e-Fig. 123.18). With time, the contained hemorrhage becomes less echogenic, and the fluid may become more typical of hydrocele.

Testicular fractures occur when a break occurs in the testicular parenchyma alone or is associated with a tear in the tunica albuginea (testicular rupture). Sonography demonstrates heterogeneous echogenicity of the testicular parenchyma, caused by infarction and hemorrhage. Irregularity of the normally smooth testicular border and, occasionally, nonvisualization of any normal testicular parenchyma are also encountered. Ultra-sonographic findings of an abnormal testicular contour and heterogeneous echotexture caused by hemorrhage and extrusion of seminiferous tubules have a high sensitivity and specificity for the diagnosis of testicular rupture (Fig. 123.19 and e-Fig. 123.20).[12–14]

One must be wary of the possibility that bizarre heterogeneous echogenicity in a traumatized scrotum may actually be a hematoma that has superiorly displaced a normal testis into the inguinal canal. Other extratesticular findings include reactive hydroceles, posttraumatic epididymitis, and testicular torsion.

## KEY POINTS

- Asymptomatic microscopic hematuria is a low-risk indicator of renal injury.
- Delayed CT imaging through an injured kidney should be considered to identify urinary extravasation.
- High-risk indicators of bladder injury include the combination of gross hematuria, pelvic fracture, and high-risk mechanism of injury.
- Fifty percent of children with bladder injury have a fracture of the bony pelvis.
- A retrograde urethrogram is essential in boys with suspected urethral injury.
- Ultrasonographic findings are both sensitive and specific for testicular rupture.
- Most genitourinary injuries can be treated nonsurgically. Exceptions include intraperitoneal bladder rupture, urethral transection, and testicular rupture.

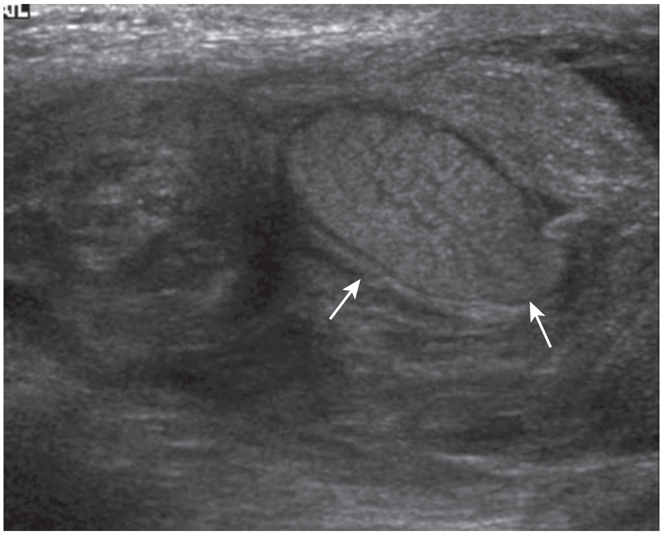

**e-Figure 123.18. Scrotal hematoma.** A longitudinal ultrasound image of the right scrotum shows an intact testis *(arrows)* surrounded by heterogeneous peritesticular hematoma (hematocele).

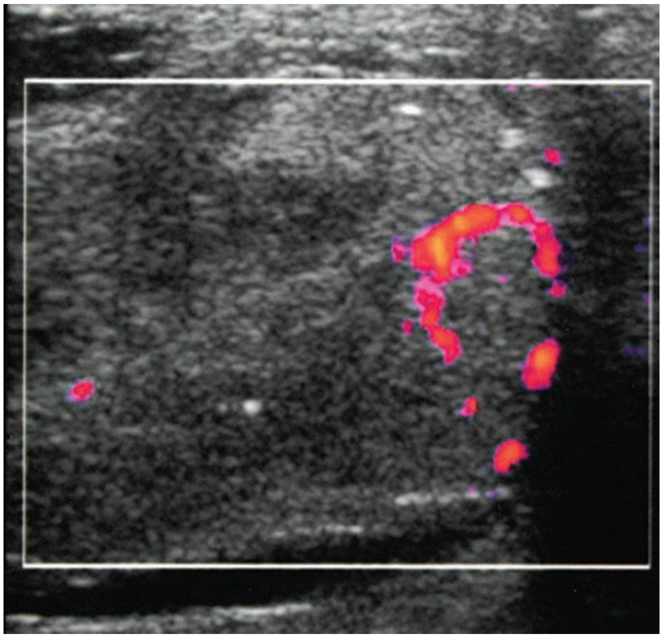

**e-Figure 123.20. Testicular rupture.** A power Doppler ultrasound image of the same patient shown in Fig. 123.19 shows only minimal flow in the remaining viable testis.

## SUGGESTED READINGS

Adu-Frimpong J. Genitourinary trauma in boys. *Clin Ped Emerg Med*. 2009;10:45.

Bixby SD, Callahan MJ, Taylor GA. Imaging in pediatric blunt abdominal trauma. *Semin Roentgenol*. 2008;43:72.

Dahlstrom K, Dunoski B, Zerin JM. Blunt renal trauma in children with pre-existing renal abnormalities. *Pediatr Radiol*. 2015;45(1):118–123.

Fenton LZ, Karakas SP, Baskin L, et al. Sonography of pediatric blunt scrotal trauma: what the pediatric urologist wants to know. *Pediatr Radiol*. 2016;46(7):1049–1058.

Gomez RG, Ceballos L, Coburn M, et al. Consensus statement on bladder injuries. *BJU Int*. 2004;94:27.

Harris AC, Zwirewich CV, Torreggiani WC, et al. CT findings in blunt renal trauma. *Radiographics*. 2001;21:S201–S214.

Ramchandani P, Buckler PM. Imaging of genitourinary trauma. *AJR Am J Roentgenol*. 2009;192:1514.

## REFERENCES

Full references for this chapter can be found on www.expertconsult.com.

## REFERENCES

1. Bixby SD, Callahan MJ, Taylor GA. Imaging in pediatric blunt abdominal trauma. *Semin Roentgenol*. 2008;43:72.
2. Taylor GA, Eichelberger MR, Potter BM. Hematuria: a marker of abdominal injury in children after blunt trauma. *Ann Surg*. 1988; 208:688.
3. Jones TS, Stovall RT, Jones EL, et al. A negative urinalysis is associated with a low likelihood of intra-abdominal injury after blunt abdominal trauma. *Am J Surg*. 2017;213(1):69-72.
4. Eeg KR, Khoury AE, Halachmi S, et al. Single center experience with application of the ALARA concept to serial imaging studies after blunt renal trauma in children—is ultrasound enough? *J Urol*. 2009; 181:1834.
5. Henderson CG, Sedberry-Ross S, Pickard R, et al. Management of high grade renal trauma: 20-year experience at a pediatric level I trauma center. *J Urol*. 2007;178:246.
6. Gomez RG, Ceballos L, Coburn M, et al. Consensus statement on bladder injuries. *BJU Int*. 2004;94:27.
7. Quagliano PV, Delair SM, Malhotra AK. Diagnosis of blunt bladder injury: a prospective comparative study of computed tomography cystography and conventional retrograde cystography. *J Trauma*. 2006;61:410.
8. Kaefer M, Zurakowski D, Bauer SB, et al. Estimating normal bladder capacity in children. *J Urol*. 1997;158:2261.
9. Sivit CJ, Cutting JP, Eichelberger MR. CT diagnosis and localization of rupture of the bladder in children with blunt abdominal trauma: significance of contrast material in the pelvis. *AJR Am J Roentgenol*. 1995;164:1243.
10. Routh JC, Husmann DA. Long-term continence outcomes after immediate repair of pediatric bladder neck lacerations extending into the urethra. *J Urol*. 2007;178:1816.
11. Deibert CM, Glassberg KI, Spencer BA. Repair of pediatric bladder rupture improves survival: results from the National Trauma Data Bank. *J Pediatr Surg*. 2012;47(9):1677–1681.
12. Adu-Frimpong J. Genitourinary trauma in boys. *Clin Ped Emerg Med*. 2009;10:45.
13. Ramchandani P, Buckler PM. Imaging of genitourinary trauma. *AJR Am J Roentgenol*. 2009;192:1514.
14. Nicola R, Carson N, Dogra VS. Imaging of traumatic injuries to the scrotum and penis. *AJR Am J Roentgenol*. 2014;202:W512–W520.

# 124

# Disorders of Sex Development

Harris L. Cohen and Stephen F. Miller

## EMBRYOLOGY, SEX DIFFERENTIATION, AND GONAD DIFFERENTIATION

***Overview.*** The three important precursor components needed for genital system development are the genital ridge and the two sets of internal sex ducts, the Müllerian-paramesonephric and the Wolffian-mesonephric. Around 7 weeks' gestation, the embryologic genital ridge becomes either an ovary or a testis. The development of the male genital system is an "active" process requiring testes and Müllerian inhibiting substance (MIS). The sex-determining region (*SRY* gene) on the short arm of the Y chromosome encodes a testis-determining factor. Under this factor's influence (and in the presence of H-Y antigens found in the cell membranes of normal XY males), there is normal testis development with germ cells in the genital ridge differentiating into Sertoli cells and Leydig cells. Sertoli cells secrete MIS, which causes complete Müllerian duct system involution. Leydig cells produce testosterone. The enzyme 5a-reductase converts testosterone intracellularly within the target tissues into the powerful androgen dihydrotestosterone (DHT). DHT allows the Wolffian duct system to develop into the epididymis, vas deferens, ejaculatory duct, and seminal vesicles.

If no Y chromosome exists or if abnormal encoding of testes-determining factor is present, the gonad will passively differentiate into an ovary between 11 weeks' to 17 weeks' gestation (typically in the presence of two X chromosomes). Absence of two X chromosomes may lead to abnormal or "streak" ovaries. The ovaries and their hormones, however, are thought to have no apparent role in sex differentiation of the female genital tract. The absence of MIS leads to persistence of Müllerian structures, which develop into the fallopian tubes, uterus, cervix, and upper two-thirds of the vagina. The Wolffian ducts involute in the absence of testosterone.

The undifferentiated external genitalia include the urogenital tubercle, urogenital swelling, and urogenital folds. DHT stimulation in males causes these structures to develop into the glans penis, scrotum, and penile shaft, respectively. In females, they develop into the clitoris, labia majora, and labia minora, respectively. The prostate gland develops from the urogenital sinus.[1–6] Disorders of Sexual Development (DSD) are diagnosed when there is discordance between chromosomal (genetic), gonadal, and anatomical sex.

## DISORDERS OF SEX DEVELOPMENT WITHOUT AMBIGUITY OF EXTERNAL GENITALIA (Box 124.1)

### Phenotypic Females

### Turner Syndrome (XO Gonadal Dysgenesis)

***Overview.*** Classic Turner syndrome (isochromatous 45,XO karyotype pattern) is the most common gonadal dysgenesis associated with an abnormal karyotype in girls and is nonfamilial. A single X chromosome is the probable cause for the presence of streak ovaries (streaks or ridges of connective tissue in the mesosalpinges parallel to the fallopian tubes), rather than normal ovaries. Some functional ovarian elements are present in a few cases. Fallopian tubes, a uterus, and a vagina are present, and no Wolffian duct derivatives are found.[1,5,6]

Patients with classic Turner syndrome have several somatic findings. Affected patients are short in stature with a distinctive facies that includes low-set ears, a low hairline, and a high-arched palate. They have a short, broad, and webbed neck; widely spaced nipples; and a shield chest. Classically, there is shortening of the fourth and/or fifth metacarpal bones. Cervical lymphatic malformations can be noted in fetal life, and the webbed neck is thought to be a residuum. Other variably seen findings include a bicuspid aortic valve, enlarged aortic root, coarctation of the aorta, renal anomalies (e.g., horseshoe kidney), and Hashimoto thyroiditis. Patients with Turner syndrome have delayed onset of puberty, no breast development or vaginal mucosal estrogenization (but presence of pubic and axillary hair), infantile internal and external genitalia, and primary amenorrhea.[1,7,8]

***Imaging.*** The prepubertal uterus (Fig. 124.1) and vagina are normally formed and will respond to exogenous hormone stimulation. The dysgenetic or streak gonads are difficult to image. When the adnexa are measurable, they are typically less than 1 mL in volume.

### Mosaic Turner Syndrome

Approximately 25% of patients with 45,XO Turner syndrome have a so-called chromatin-positive pattern. Their mosaic karyotype is most often of a mixture of 45,XO and 46,XX chromosomes. Less often, other mosaic patterns (e.g., XO/XXX or XO/XX/XXX) or 46,XX with an abnormal X chromosome are present. In such cases, the gonads may consist of a streak ovary on one side and a hypoplastic or normal ovary on the other side, bilateral hypoplastic ovaries, or essentially normal ovaries. External and internal genitalia are entirely female, without Wolffian duct remnants. These patients usually do not have the somatic abnormalities typically attributed to classic Turner syndrome, but many are short.[1] Patients with mosaic Turner syndrome may develop secondary sex characteristics at puberty (found to occur in about 50%), and some may menstruate regularly.[1,9]

### Amenorrhea Caused by Hypergonadotropic Hypogonadism

Primary amenorrhea (defined as a lack of menses by age 16 years), with high levels of circulating follicle-stimulating hormone and luteinizing hormone by serum assays, occurs because of ovarian failure; gonadal tissues fail to respond to endogenous gonadotropins. Patients included in this category may have classic Turner syndrome, gonadal dysgenesis (including 46,XY and familial 46,XX), secondary ovarian failure as a result of radiation or chemotherapy, or on an autoimmune basis (autoimmune oophoritis).[1,5,6,8]

### 46,XY Gonadal Dysgenesis

Patients with 46,XY gonadal dysgenesis (X-linked recessive or sex-limited autosomal dominant) are phenotypically female, with streak gonads and infantile internal and external female genitalia. Patients are usually first diagnosed as having an abnormality in adolescence. As with other forms of gonadal dysgenesis, in such patients, the sex chromosome may not be absent but is abnormal. A deletion of the small arm of the Y chromosome (responsible

## Abstract:

This chapter reviews disorders of sexual development (DSD) by noting normal embryology, sex differentiation and gonadal differentiation of the genital system and then reviewing disorders of these processes. Discussed disorders include: DSDs without external genital ambiguity such as Turner syndrome XO (gonadal dysgenesis) with its classic streak ovaries but present fallopian tubes, uterus and vagina as well as 46XY gonadal dysgenesis and familial 46XX gonadal dysgenesis. DSDs in phenotypic males including Klinefelter's syndrome and persistent Mullerian duct syndrome are discussed. DSDs with ambiguous external genitalia including patients with pseudohermaphroditism i.e. female intersex (46,XX DSD) and male intersex (46,XY DSD) patients and those with androgen insensitivity syndrome are reviewed. Various forms of complete and partial gonadal dysgenesis are discussed along with the association of gonadal dysgenesis and gonadoblastomas. The diagnostic imaging evaluation of the ambiguous genitalia patient is reviewed.

## Keywords:

DSD (disorders of sex development)
Turner syndrome
Gonadal dysgenesis
Male intersex
Female intersex
Gonadoblastoma
Hermaphroditism

**BOX 124.1** Disorders of Sex Differentiation Without Ambiguous External Genitalia

- Turner syndrome
- Mosaic Turner syndrome
- Gonadal dysgenesis, various forms
- Klinefelter syndrome
- Persistent Müllerian duct syndrome

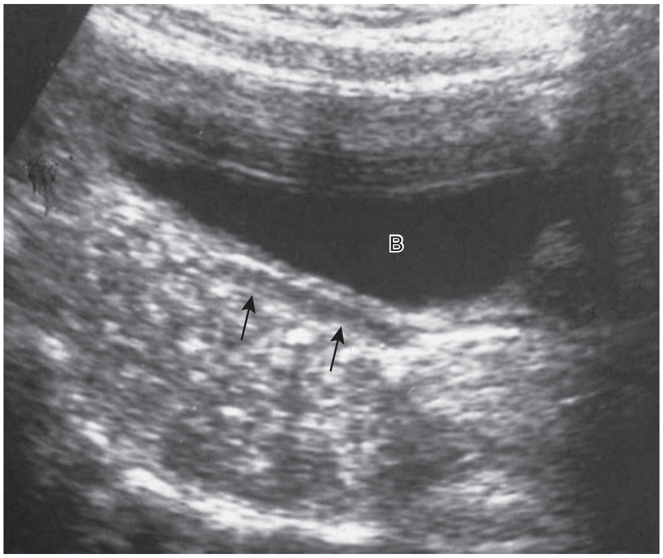

**Figure 124.1. Turner syndrome.** A longitudinal sonogram of the pelvis shows a small tubular uterus *(arrows)* in this 16-year-old with primary amenorrhea and 45,XO Turner syndrome. Her ovaries could not be identified. *B,* Bladder.

for production of testis-determining factor or MIS) may be present. Mosaicism may lead to the development of ovaries rather than streak gonads. If a Y chromosome is a component of the karyotype of a patient with gonadal dysgenesis and ovaries, the patient has an increased risk of developing a gonadoblastoma within a dysgenetic ovary. Seminomas also may occur in these patients.[1,2]

### Familial 46,XX Gonadal Dysgenesis

Patients with familial 46,XX gonadal (sporadic or autosomal recessive) dysgenesis have gonads that consist of bilateral streaks in some cases or hypoplastic ovaries in others. A hypoplastic ovary may present on one side with a streak gonad on the other. The internal and external genitalia are entirely female, without Wolffian duct derivatives. Incomplete puberty may be observed in patients with residual ovarian tissue. Sexual infantilism and primary amenorrhea are typical findings in those patients with bilateral streak gonads.[1,2]

## Phenotypic Males

### Klinefelter Syndrome (47,XXY Seminiferous Tubular Dysgenesis)

Seminiferous tubular dysgenesis (Klinefelter syndrome) is the most common aberration of the human sex chromosome. The typical 47,XXY karyotype is found in phenotypic males with primary hypogonadism. It is nonfamilial, occurring in 1 in every 750 to 1,000 males. Variants have been described with less common chromosomal abnormalities, including XX/XXY or XY/XXY mosaicism, as well as XXXY, XXXXY, XXYY, or XXXYY sex chromosomal karyotypes. The external genitalia, especially the testes, are small. The testes are usually less than 3 cm in length and are firm. Cryptorchidism and hypospadias are common, with most patients developing azoospermia and sterility. The diagnosis is usually not made until after puberty. Gynecomastia develops in almost half of the older patients, and affected patients (particularly those with the classic 47,XXY karyotype) are at an increased risk for breast cancer. Rare cases of testicular and extragonadal germ cell neoplasms have been reported.[1,5,6]

**BOX 124.2** Disorders of Sex Differentiation With Ambiguous External Genitalia

- 46,XX DSD, preferred term for female intersex (pseudohermaphroditism)
- 46,XY DSD, preferred term for male intersex (pseudohermaphroditism)
- Gonadal dysgenesis, various forms
- 46,XX/46,XY ovotesticular DSD (preferred term for true hermaphroditism)
- 46,XX testicular DSD

*DSD*, Disorders of sexual differentiation.

### Persistent Müllerian Duct Syndrome (46,XY PMDS)

Persistent Müllerian duct syndrome is a rare type of sexual differentiation abnormality in males caused by a deficiency of Müllerian inhibiting factor (MIF). These patients usually have a normal 46,XY karyotype and are phenotypically male, but they have a small uterus and fallopian tubes and a small vagina connected to the posterior urethra at the level of the verumontanum. Unilateral or bilateral cryptorchidism is common, as are unilateral or bilateral inguinal hernias. A uterus (uteri hernia syndrome), fallopian tubes, or sometimes a testis may be found in the hernia. The disorder, typically sporadic, has been reported in siblings.[1,2,10,11]

## DISORDERS OF SEX DEVELOPMENT WITH AMBIGUOUS EXTERNAL GENITALIA (Box 124.2)

## Pseudohermaphroditism (Intersex)

Disorders of sex differentiation formerly referred to as intersex, pseudohermaphroditism, or hermaphroditism are abnormalities in which nonaccord of chromosomal, gonadal, and genital sex is present. Unlike true hermaphroditism, in which two types of gonadal tissue are present, pseudohermaphroditism shows nonaccord but with only one gender's gonads present. By definition, male intersex patients have testes and female intersex patients have ovaries or ovarian tissue.[1]

## Female Intersex (46,XX DSD)

***Overview.*** 46,XX DSD or female intersex is usually diagnosed in neonatal life in chromosomally normal females with masculinized external genitalia. The cause is usually increased fetal adrenal androgen production, most commonly from congenital adrenal hyperplasia or adrenogenital syndrome. Congenital adrenal hyperplasia (Fig. 124.2) is the most common cause of abnormal sex differentiation in females, causes adrenal gland enlargement ("cerebriform" appearance), and occurs in 1 in 15,000 live births worldwide. It is caused by an inherited deficiency of enzymes involved in adrenocortical hormone biosynthesis. Affected patients have normal ovaries, a uterus, and fallopian tubes, and no testicular tissue or internal Wolffian duct derivatives. In most cases, the external genitalia are ambiguous (Fig. 124.3), with a prominent phallus/clitoris or partially fused labioscrotal folds.

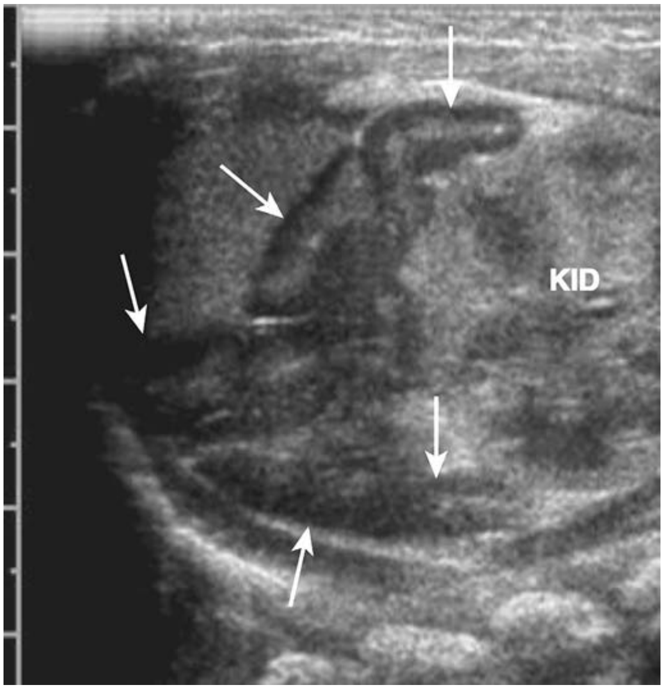

**Figure 124.2. Congenital adrenal hyperplasia.** A longitudinal gray-scale sonogram of the left adrenal gland and superior left kidney shows an enlarged, redundant adrenal gland *(arrows)*. The patient was a newborn with ambiguous genitalia and had three times the normal level of 17-hydroxyprogesterone. Her karyotype proved to be 46,XX. She was diagnosed with salt-wasting 21-hydroxylase deficiency as the cause of her congenital adrenal hyperplasia.

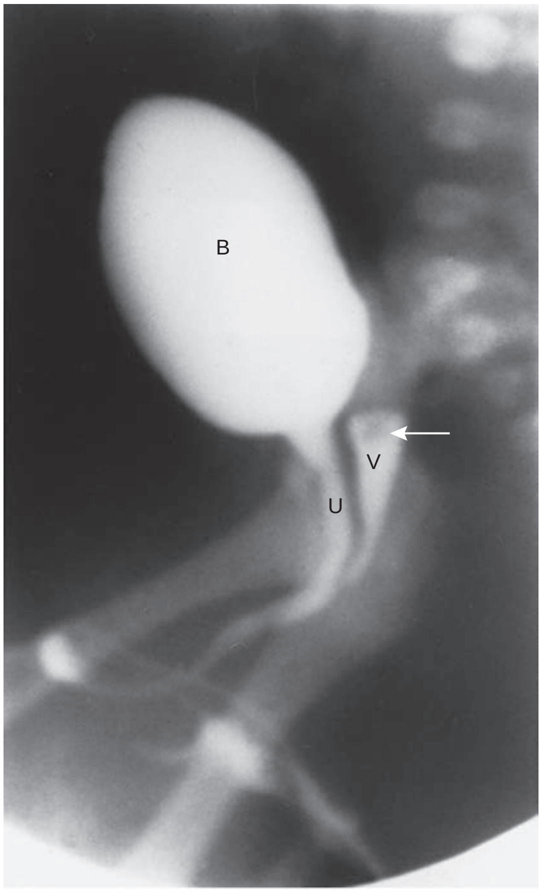

**Figure 124.4. Congenital adrenal hyperplasia.** Lateral voiding cystourethrogram shows a bladder *(B)* with an elongated male-type urethra *(U)*. Posterior to it is a vagina *(V)* with a subtle impression *(arrow)* of a cervix superiorly. The patient was a 46,XX neonate from an area in Puerto Rico, where congenital adrenal hyperplasia is common. *(From Cohen HL, Haller J. Pediatric and adolescent genital abnormalities.* Clin Diagn Ultrasound*. 1988;24:187–216. With permission. Copyright Elsevier Science USA.)*

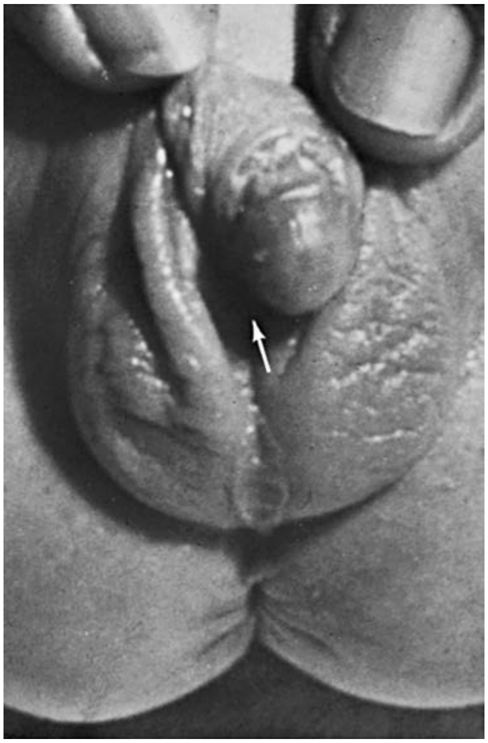

**Figure 124.3. Ambiguous external genitalia in a 1-month-old infant.** A penis and scrotum are present, but no gonads are palpable. A single perineal opening was found at the base of the penis *(arrow)*.

***Imaging.*** A variably-sized vagina is connected with the posterior urethra, forming a urogenital sinus, which commonly empties at the base of the penis. No gonads can be palpated in the labioscrotal folds or in the inguinal canal because they are located within the pelvis. Voiding cystourethrography (VCUG) often shows a male-type elongated urethra (Fig. 124.4). These patients are potentially fertile with external genital reconstruction and correct sex assignment.[1,2]

## Male Intersex (46,XY DSD)

46,XY DSD or male intersex patients are true males with a normal 46,XY male karyotype, present H-Y antigens, normal or mildly defective (and usually undescended) testes, but incomplete masculinization or frank ambiguity of their external genitalia. Decreased testosterone production and a lack of MIF production results in a karyotypically normal male with a female phenotype (except for partial masculinization of the external genitalia), and incomplete inhibition of the development of Müllerian-derived structures, such as the uterus, vagina, and fallopian tubes (Fig. 124.5 and e-Fig. 124.6). Such patients usually have no secondary sexual development at puberty and may have an infantile uterus

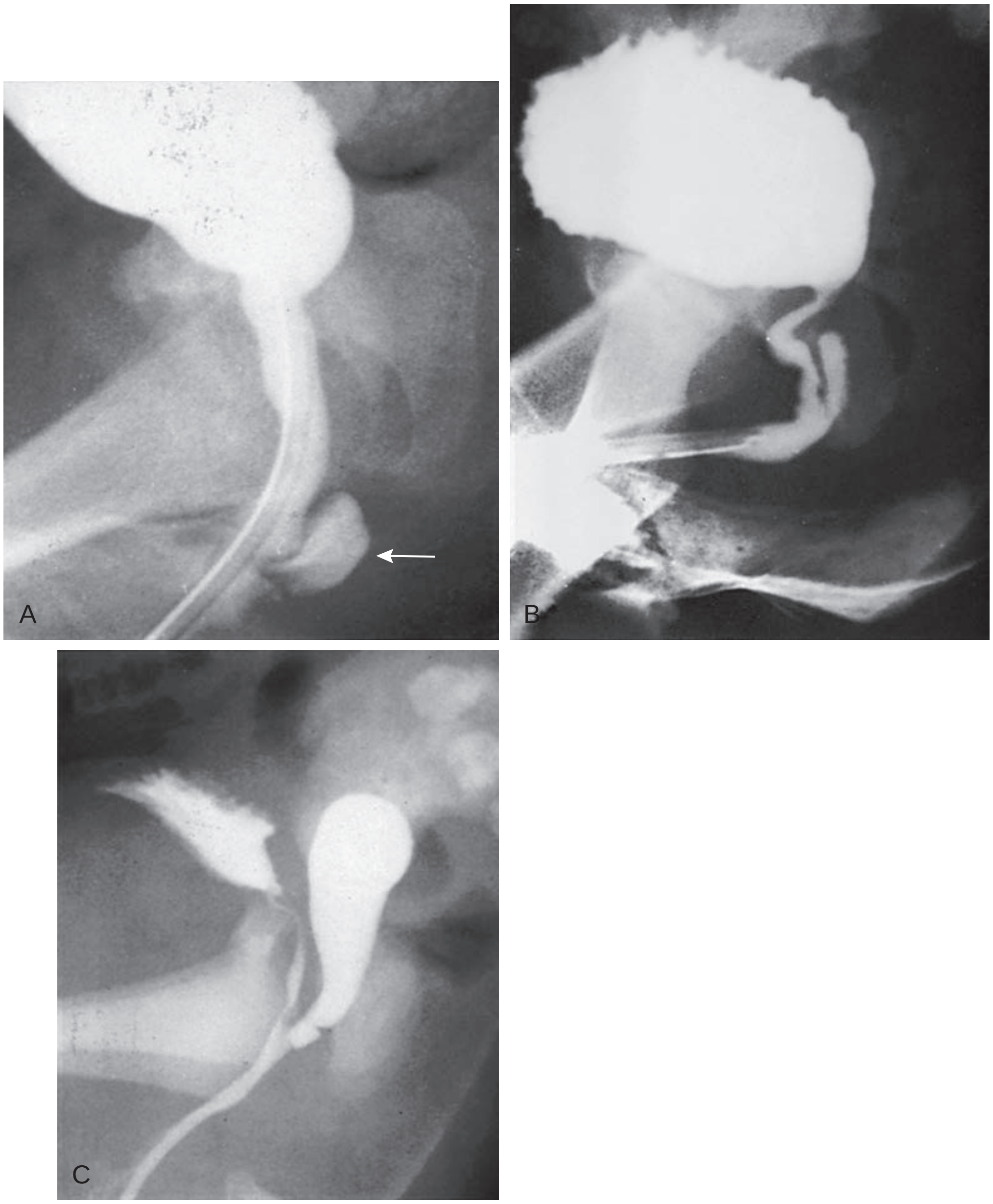

**e-Figure 124.6. 46,XY DSD (male pseudohermaphroditism).** (A) Incomplete testicular feminization syndrome in a patient with a predominantly female phenotype. Voiding cystourethrography shows a mildly elongated urethra and retrograde opacification of a short, blind-ending vaginal pouch *(arrow)* in the perineum behind the urethra. Seminal ducts may end in a vaginal pouch such as this. A similar configuration can be seen in patients with complete testicular feminization syndrome and in patients with 5-alpha-reductase deficiency. (B) Three-year-old child with ambiguous external genitalia and 5-alpha-reductase deficiency. A retrograde urethrogram shows a urogenital sinus and a small vagina without a cervical imprint. A more common pattern in 5-alpha-reductase deficiency is that shown in A. (C) Infant with severe hypospadias. A retrograde urethrogram shows a somewhat longer utricle connected with the distal end of the posterior urethra. The male urethra is somewhat short.

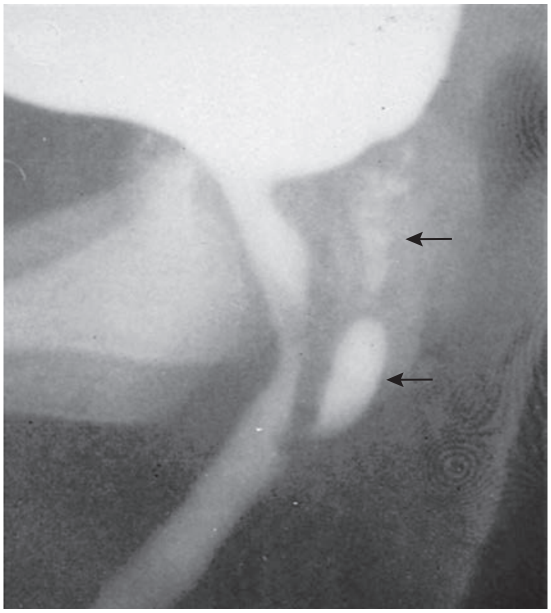

**Figure 124.5. A male infant with severe hypospadias (perineal and scrotoperineal), bilateral cryptorchidism, small penis, and unfused scrotal folds.** The image shows a utricle or blind vaginal pouch *(lower arrow)* that is very short and extending off the distal aspect of the posterior urethra. *Upper arrow* shows seminal ducts emptying into the utricle. The male urethra is somewhat short. See e-Fig. 124.6.

on ultrasonography. If the production of MIF by the testes is not affected, no internal Müllerian system structures (uterus and fallopian tubes) will develop. The biochemical defect may be decreased androgen synthesis, decreased DHT production as a result of 5-alpha-reductase deficiency, or a defect in androgen receptors. In many cases, the exact etiology remains unknown.[1,2,5,6,12,13]

### Androgen Insensitivity Syndrome

Androgen insensitivity syndrome (AIS; X-linked recessive), formerly known as testicular feminization syndrome, is a form of intersex in which patients with 46,XY karyotype have well-formed testes (usually undescended within the abdomen or inguinal region) that produce androgens and MIF. However, lack of end-organ response to androgens is caused by a defect in a specific cytoplasmic receptor protein that normally binds DHT to the plasma membrane and transports it to the nuclear chromatin. Müllerian system development is inhibited, and patients do not develop a uterus, fallopian tubes, or the upper two-thirds of the vagina. They do develop secondary female sexual characteristics via circulating estrogens (produced from the breakdown of testosterone and adrenal steroids as well as from direct production by the testes).

Patients with the complete form of the abnormality appear as phenotypically normal females, although they may have inguinal or labial masses resulting from the undescended testes (Fig. 124.7). They have normal breast development and may or may not have a short, blind-ending vagina behind the urethral opening. They usually present with amenorrhea and may respond to substitutional estrogen therapy. In the incomplete form (10%–20% of cases), patients present earlier in life because of ambiguous genitalia, not usually noted with the complete form of the disorder. Affected patients may have a predominantly female phenotype (incomplete testicular feminization) or a predominantly male phenotype (Reifenstein syndrome).[1,2]

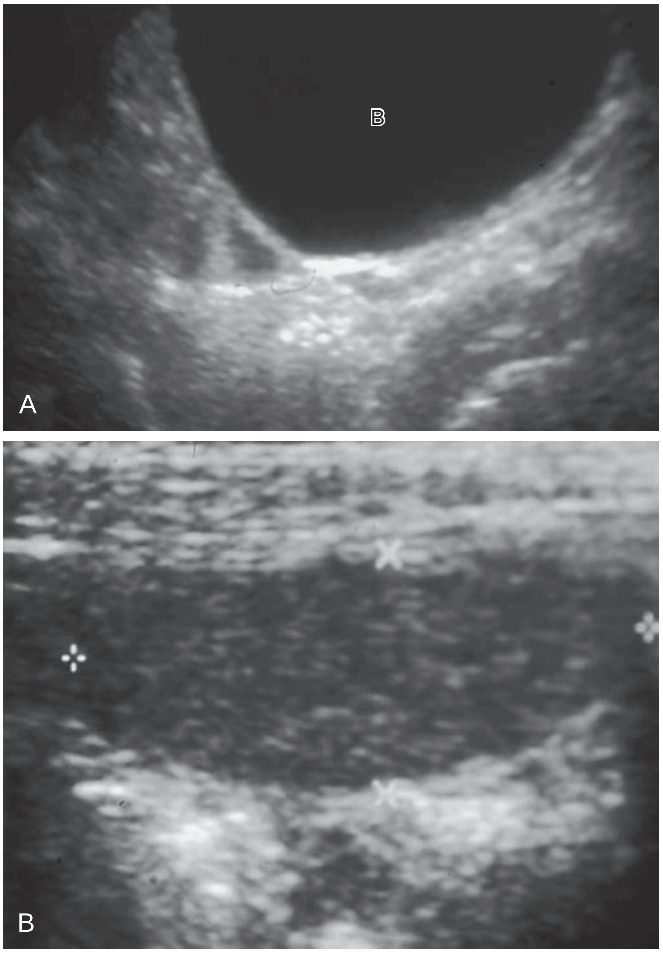

**Figure 124.7. Androgen insensitivity syndrome.** (A) Phenotypically normal 16-year-old girl, who presented with primary amenorrhea. Longitudinal midline gray-scale sonogram showed no uterus posterior to the bladder *(B)*. Ovaries were not seen. Karyotyping showed 46,XY, and the patient was proven to have androgen insensitivity syndrome. (B) This patient was noted to have bilateral inguinal masses. An oval structure *(cursors)* without cysts was found in the patient's left inguinal region on ultrasonography and proved to be an undescended testis. *(Courtesy of Joseph Yee, MD.)*

## Gonadal Dysgenesis

### Mixed Gonadal Dysgenesis (45,XO/46,XY MGD)

Mixed or asymmetric gonadal dysgenesis (also known as XO/XY gonadal dysgenesis) is a relatively common form of abnormal sexual differentiation, usually occurring sporadically. Affected patient karyotypes are most often a mosaic of 45,XO and 46,XY. At times, XO/XYY or other mosaicisms are seen. These patients often have a streak gonad similar to that seen in Turner syndrome on one side and a usually dysgenetic (but occasionally normal) testis on the other. A fallopian tube is often present on the side of the streak gonad, and a vas deferens may be present on the side of the testis. The testis is usually intraabdominal, but can be partially or completely descended. The external genitalia cover a wide spectrum of appearances from that of an almost normal female to that of an essentially normal male with hypospadias. Most patients have ambiguous external genitalia (as seen in other intersex situations), with a penis or clitoris of variable size, unfused labioscrotal folds, and a variably sized vagina connected with the

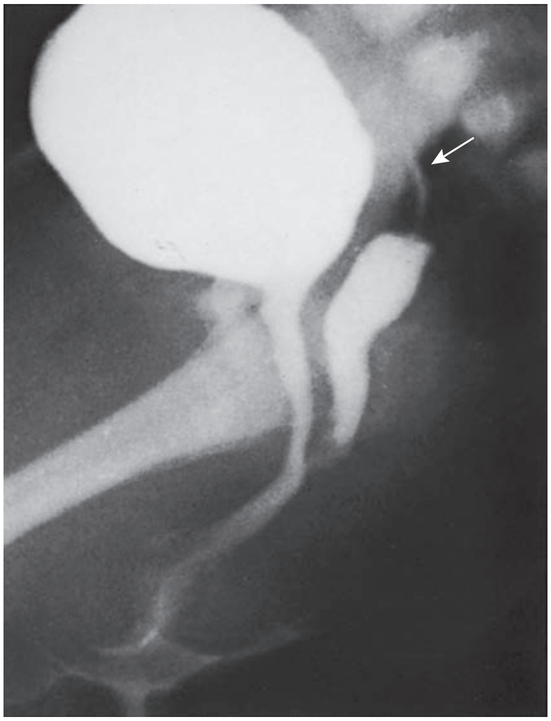

**Figure 124.8. Mixed gonadal dysgenesis.** Lateral voiding cystourethrography image shows a urogenital sinus with a well-developed vagina in an 11-day-old with ambiguous external genitalia. A cervical imprint is seen, and contrast material opacifies the uterine canal *(arrow)*.

urethra (urogenital sinus) that commonly empties at the base of the penis (Fig. 124.8). A uterus, said to be present in all cases, is usually small or rudimentary. Most patients are raised as females, but at puberty, some virilization may take place (usually without gynecomastia).[1,2]

## Familial Gonadal Dysgenesis

### 46,XY Complete Gonadal Dysgenesis

Familial 46,XY gonadal dysgenesis is typically an X-linked dominant abnormality (but can have Y-linked, autosomal dominant, or recessive inheritance patterns) that may be nonsyndromic or associated with several syndromes. The gonads are variable, and there may be bilateral streaks, bilateral dysgenetic testes, or a streak on one side and a dysgenetic testis on the other (mixed gonadal dysgenesis). Patients with bilateral streak gonads have a female phenotype with normal fallopian tubes, uterus, and vagina, usually clitoromegaly, and absence of Wolffian duct derivatives. Sexual infantilism and amenorrhea are expected at puberty. Patients with bilateral dysgenetic testes or with a mixed form of gonadal dysgenesis typically have ambiguous or incompletely masculinized external genitalia. Müllerian and Wolffian duct derivatives are present but may be hypoplastic or rudimentary. Swyer syndrome is a constitutional syndrome associated with CGD. [1,5,6]

### 46,XY Partial Gonadal Dysgenesis

There are several syndromes associated with Partial Gonadal Dysgenesis (PGD). Denys-Drash syndrome is an uncommon form of PGD and male intersex. Patients most often have a 46,XY karyotype, bilateral gonadal dysgenesis with a variable histologic pattern, ambiguous external genitalia, and intraabdominal testes. They have chronic glomerulonephritis with histologic features similar to those of congenital nephrosis, and they develop end-stage renal disease in early life. More than half of these patients develop a Wilms tumor at a young age, with the tumor purportedly occurring only in those patients with a female phenotype. Between 20% and 30% of Denys-Drash patients develop gonadal neoplasia. Camptomelic dysplasia as well as WAGR syndrome (*W*ilms tumor, *A*niridia, *G*enitourinary anomalies, and mental *R*etardation) are two other PGD syndromes.[1,5,6,14,15]

### 46,XY Gonadal Agenesis (Vanishing Testes Syndrome)

Patients with this condition are males with a 46,XY karyotype. No gonads are present, and male sex differentiation is absent or incomplete as a result of idiopathic testicular resorption of unknown cause in early fetal life (approximately 13–14 weeks' gestation). The external genitalia are ambiguous, and usually both Müllerian and Wolffian duct derivatives are completely absent. Vanishing testes syndrome is differentiated from cases of bilateral anorchia (congenital absence of the testes), which are presumably caused by resorption of the testes beyond 13 to 14 weeks' gestational age. Patients with bilateral anorchia have normal male sex development and no residual Müllerian structures.[1,16]

## 46, XX Testicular DSD

46,XX DSD (de la Chapelle syndrome), formerly known as XX maleness, is a very unusual cause of ambiguous genitalia occurring in 4 to 5 cases per 100,000 individuals. Because of errors in meiosis, an unequal interchange of sex chromosomes occurs, such that individuals may have one or two X chromosomes containing the male *SRY* gene. Patients are sterile but usually have two small testes, usually descended. Gynecomastia may be present, but more often the individuals are phenotypically male and have no intraabdominal Müllerian tissue despite being genetically female.[1,17]

## 46,XX/46,XY Ovotesticular DSD

46,XX/46,XY ovotesticular DSD, formerly known as true hermaphroditism, is a rare sporadic disorder in which the affected patient has both testicular and ovarian tissues in the same or contralateral gonads. More than half such patients have the 46,XX karyotype. Mosaic karyotype patterns with at least one line with a Y chromosome do exist, including XO/XY, XX/XXY, or XX/XY chimerism. Fifteen percent of patients have the 46,XY karyotype. All true hermaphrodites are H-Y antigen positive regardless of karyotype. In patients with the 45,XX karyotype, undetected Y chromosomal material is probably present and transferred to another chromosome. The testes or ovotestes may be intraabdominal, in the inguinal region, in the scrotal area, or in the labia majora. The ovaries are almost always intraabdominal. Internal gonadal ducts are usually consistent with the ipsilateral gonad (i.e., a vas on the side of a testis and a fallopian tube on the side of an ovary). In the case of ovotestes, the associated internal gonadal duct is usually a fallopian tube. A uterus is found in almost all cases but is most often hypoplastic.[1]

A wide spectrum of external genitalia exists ranging from normal male to ambiguous to female. Cryptorchidism and inguinal hernias are common. Hernias can contain a gonad with its internal gonadal duct or even a uterus. About 75% of affected patients are raised as males. At puberty, some virilization as well as gynecomastia usually occurs.[1,2]

## GONADAL NEOPLASIA OF PATIENTS WITH DISORDERS OF SEXUAL DEVELOPMENT

The gonads in several disorders of sexual development (with or without ambiguous genitalia) are at an increased risk for developing neoplasms. Patients with the highest risk of developing gonadal neoplasia are those with XO/XY mixed gonadal dysgenesis and those with 46,XY gonadal dysgenesis. The incidence of a gonadal tumor in these conditions increases from 3% to 4% in the first decade, from 10% to 20% by age 20, and from 15% to 40% or more in older patients. Neoplasms are almost always germ cell in type, including seminoma or dysgerminoma and gonadoblastoma. Less commonly, patients may develop a gonadal teratoma, teratocarcinoma, yolk sac tumor, embryonal carcinoma of the adult type, or choriocarcinoma. These neoplasms are rare in patients who do not have a Y chromosome as part of their karyotype. The risk is apparently related to the H-Y antigen.[1,2]

## DIAGNOSTIC EVALUATION OF PATIENTS WITH AMBIGUOUS GENITALIA

***Overview.*** The discovery of anomalous or ambiguous genitalia in a newborn has been described as an emergency from a social perspective. Optimal care should be provided by an experienced multidisciplinary team. The identification of the uterus, vagina, or urogenital sinus using ultrasonography and contrast genitogram aids in the decision on how to rear the child. These findings can then be correlated and sexual identification aided by karyotyping, including fluorescent studies for Y chromosomes, specific analysis of the Y chromosome for the testis-determining gene, culture of genital skin fibroblasts for androgen receptor binding, and tests for androgen responsiveness. The appearance of the external genitalia is seldom diagnostic of a specific disorder, but palpable gonads in the inguinal canal, labioscrotal folds, or scrotum can exclude female 46,XX DSD in most cases. Sometimes, the definitive anatomic diagnosis is made only at laparoscopy or laparotomy and on the basis of gonadal biopsy. The main role of ultrasonography is identification of the uterus, a relatively easy task in the newborn female.[1,2,18]

***Imaging.*** A detailed radiographic study of the lower genitourinary tract (genitography or vaginography) is important for diagnosis and as a guide in surgical reconstructive procedures. Patients commonly have a urogenital sinus, a common terminal channel for the anterior urethra and posterior vaginal pouch. This sinus usually empties at the base of the phallus. VCUG, particularly on lateral view, may outline the entire anatomy needed for evaluation. If the urethral catheter can be advanced only into the vagina, an injection with the catheter in that position may opacify the vagina, the urogenital sinus, and often the proximal urethra. If confusion about the anatomy persists during the VCUG examination, a retrograde injection of contrast material may be attempted through a catheter with the tip placed just inside the "urethral" meatus. At times, a coude catheter (with a curved tip) manipulated under fluoroscopic control into the urethra and bladder or into the vagina may improve contrast study of the area. An effort should be made on the VCUG or vaginogram to determine if a uterine cervix is present (see Fig. 124.4). A cervical impression at vaginography, however, may not be apparent if the vagina is not sufficiently distended or if the uterus is hypoplastic. A uterine cervix is present in all female intersex patients and is a common finding among many patients with mixed gonadal dysgenesis or ovotesticular DSD (true hermaphroditism) as well. All members of these groups may have a hypoplastic or rudimentary uterus that may not be noted radiographically. Cervical imprints are not seen in 46,XY DSD (male pseudohermaphrodites) or males with hypospadias.[1,2]

In some patients evaluated by VCUG or genitography, the urogenital sinus is quite short and joined by the vagina very close to the perineal surface (Fig. 124.9). In other patients, it is a much longer channel, joined by the vagina at a much higher level, occasionally near the bladder neck. A very high insertion of the vagina in the urogenital sinus may pose a problem at the time of vaginal reconstruction because of the danger of injuring the external urethral sphincter. In patients evaluated for disorders of sex development or ambiguous genitalia, the vagina may vary in size from a small cavity to an organ of normal size for the patient's age. Occasionally, its distal end is stenosed or is completely obliterated, resulting in hydrocolpos at birth or hematocolpos at puberty (Fig. 124.10).[1]

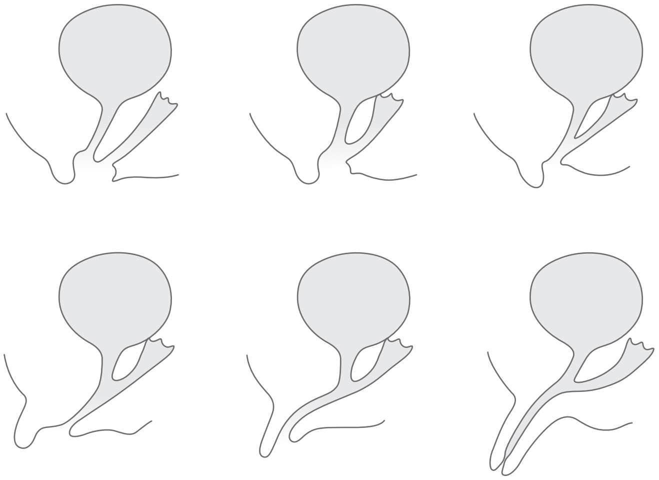

**Figure 124.9. Different types of urogenital sinus are arranged in order of increasing masculinization, from an almost normal female pattern to a penile urethra.** The urogenital sinus is of variable length, and the vagina may enter the urogenital sinus at various levels.

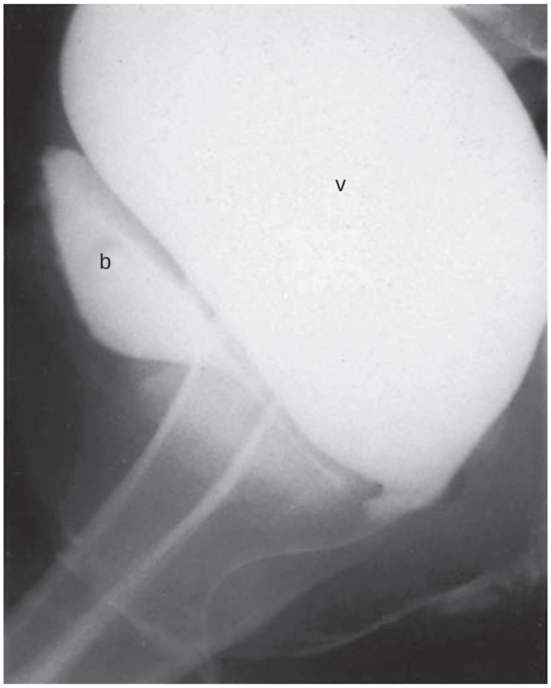

**Figure 124.10. Hydrocolpos in congenital adrenal hyperplasia syndrome.** Lateral view from a vaginogram of a 14-year-old girl with a urogenital sinus shows a catheter within a large obstructed vagina. She had presented with abdominal pain and a pelvic mass. *v*, Vagina; *b*, bladder.

Pelvic ultrasonography is valuable in evaluating infants and children with ambiguous genitalia. Ultrasonography is an excellent imaging tool for identification of uterine tissue (Fig. 124.11), although it may be difficult with hypoplastic uteri. The proximal vagina may also be demonstrated, particularly if it contains urine, but the urethra and urogenital sinus cannot be studied by this method. Ultrasonography does not replace genitography, but it is of particular value when genitography is unsuccessful. Ovaries are often seen, but fallopian tubes, unless obstructed, are more difficult to image. Ultrasonography is an excellent tool for the assessment of the adrenal gland in the newborn. Pelvic magnetic resonance imaging is of value in evaluating Müllerian duct system structures when ultrasonography and genitography do not provide sufficient information (Fig. 124.12).[1,19–21]

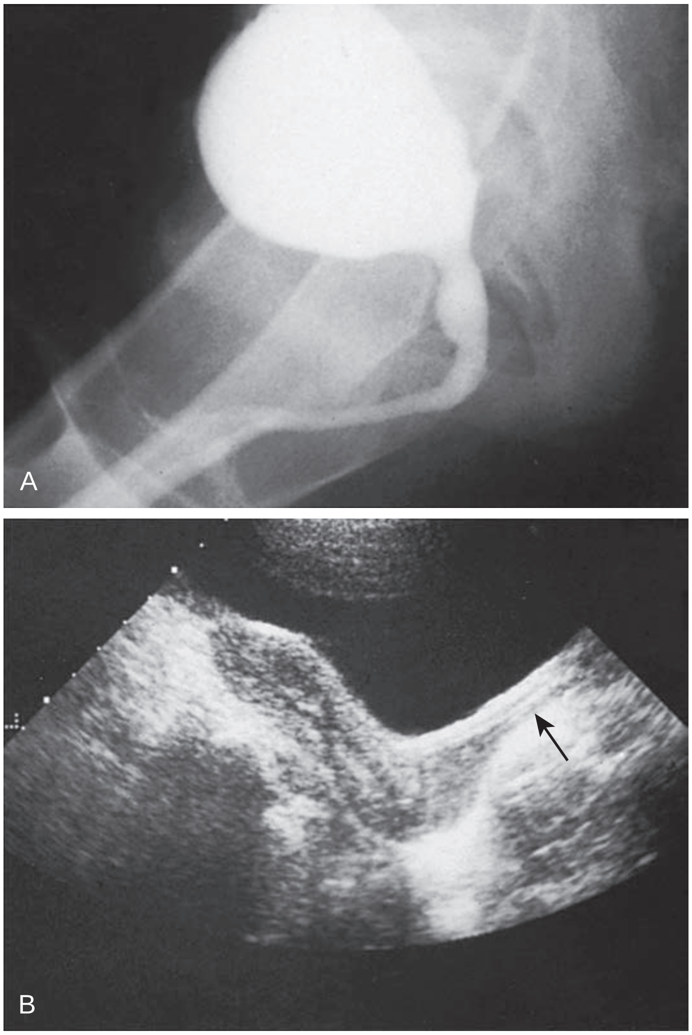

**Figure 124.11. Anatomic evaluation of a 13-year-old with known congenital adrenal hyperplasia being evaluated before surgical vaginoplasty.** (A) Voiding cystourethrography shows a phallic urethra. (B) Sagittal gray-scale sonogram shows a normal adult uterus. The proximal two-thirds of the vagina *(arrow)* are noted and appear normal.

## KEY POINTS

- DSD are abnormalities that have nonaccord of chromosomal, gonadal, and genital sex. 46,XY DSD (male intersex) patients have testes, and 46,XX DSD (female intersex) patients have ovarian tissue.
- DSD may be caused by abnormalities of hormone production, end-organ response, chromosomes, or gonads.
- The development of a male genital system requires the presence of testes and their production of MIS.
- Turner syndrome is the most common gonadal dysgenesis associated with an abnormal karyotype in girls.
- Primary amenorrhea is defined as a lack of menses by age 16 years. Many of the causes may also be linked to causes of delayed sexual development.
- 46,XX/46,XY ovotesticular DSD, once known a true hermaphroditism, is a rare sporadic disorder in which the affected patient has both testicular and ovarian tissues in the same or contralateral gonads.
- Patients with several of the DSD disorders are at an increased risk for developing gonadal neoplasms.
- The length of the urogenital sinus and the level of insertion of the vagina are indicators of the degree of virilization, but are nonspecific regarding the type of underlying disorder. Noting the presence or absence of a cervical imprint on the vaginogram is more important. A uterine cervix is present in all 46,XX DSD (female intersex) patients. Ultrasound, particularly in the young infant, can readily denote the presence of a normal uterus.

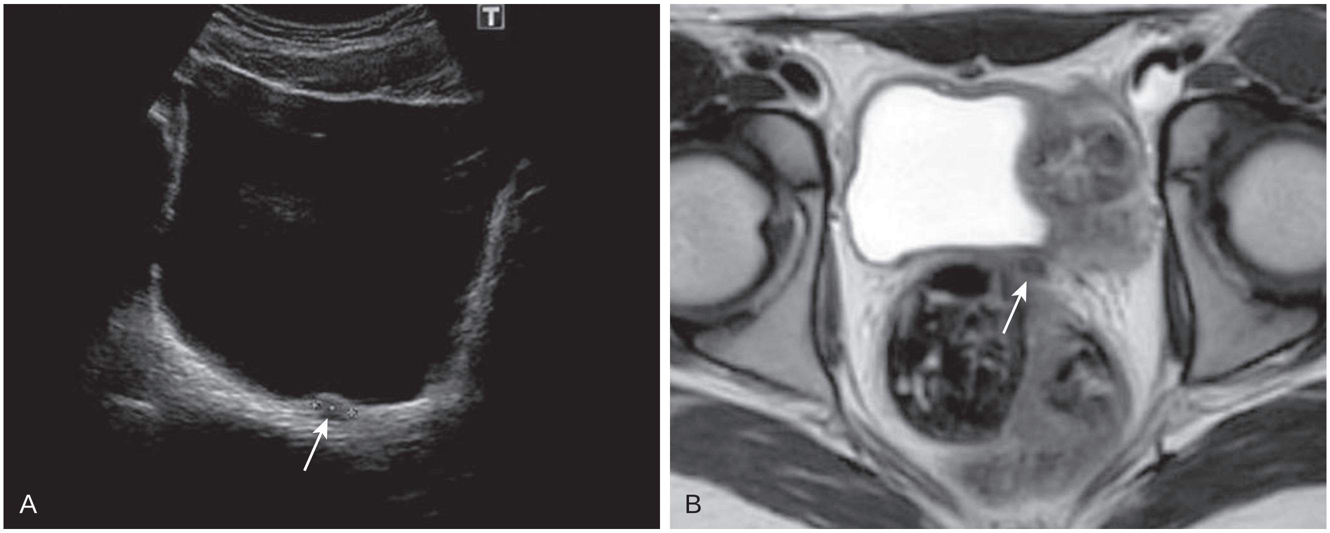

**Figure 124.12. Anatomic evaluation of a 12-year-old with known mixed gonadal dysgenesis.** (A) Transverse gray-scale sonogram through the pelvis shows a small, round, hypoechoic structure *(arrow)* posterior to the urinary bladder, thought to possibly represent a prepubertal uterus. (B) Axial T2-weighted MR image confirmed the presence of a tiny uterus *(arrow)*. The gonads had been previously removed.

## SUGGESTED READINGS

Ahmed SF, Rodie M. Investigation and initial management of ambiguous genitalia. *Best Pract Res Clin Endocrinol Metab*. 2010;24(2):197–218.

Ardinger HH, et al, eds. *GeneReviews [Internet]*. Seattle (WA): University of Washington, Seattle; 1993-2016. Available from: https://www.ncbi.nlm.nih.gov/books/NBK1547/.

Barthold JS. Disorders of sex differentiation: a pediatric urologist's perspective of new terminology and recommendations. *J Urol*. 2011; 185(2):393–400.

Chavhan GB, Parra DA, Oudjhane K, et al. Imaging of ambiguous genitalia: classification and diagnostic approach. *Radiographics*. 2008; 28(7):1891–1904.

Cohen-Kettenis PT. Psychosocial and psychosexual aspects of disorders of sex development. *Best Pract Res Clin Endocrinol Metab*. 2010;24(2):325–334.

Gillam LH, Hewitt JK, Warne GL. Ethical principles for the management of infants with disorders of sex development. *Horm Res Paediatr*. 2010;74(6):412–418.

Lambert SM, Vilain EJ, Kolon TF. A practical approach to ambiguous genitalia in the newborn period. *Urol Clin North Am*. 2010;37(2):195–205.

Lee PA, Houk CP, Ahmed SF, et al. Consensus statement on management of intersex disorders. *Pediatrics*. 2006;118(2):e488–e500.

## REFERENCES

Full references for this chapter can be found on www.expertconsult.com.

## REFERENCES

1. Cohen HL. Anomalies of sex differentiation. In: Slovis T, ed. *Caffey's Pediatric Diagnostic Imaging*. 11th ed. Philadelphia, PA: Mosby (Elsevier); 2008:2394–2405.
2. Currarino G, Wood B, Majd M. Abnormalities of the genital tract. In: Silverman F, Kuhn J, eds. *Caffey's Pediatric X-Ray Diagnosis*. 9th ed. St. Louis: Mosby–Year Book; 1993:1375–1401.
3. Rey RA, Grinspon RP. Normal male sexual differentiation and aetiology of disorders of sex development. *Best Pract Res Clin Endocrinol Metab*. 2011;25:221–238.
4. Kucinskas L, Just W. Human male sex determination and sexual differentiation: pathways, molecular interaction and genetic disorders. *Medicina (Kaunas)*. 2005;41:633–640.
5. Purcell K, Lingappa V, Taylor R. Disorders of the female reproductive tract. In: McPhee S, Ganong W, eds. *Pathophysiology of Disease. An Introduction to Clinical Medicine*. 5th ed. New York: McGraw-Hill; 2006:624–651.
6. McPhee S. Disorders of the male reproductive tract. In: McPhee S, Ganong W, eds. *Pathophysiology of Disease. An Introduction to Clinical Medicine*. 5th ed. New York: McGraw-Hill; 2006:652–675.
7. Boechat MI, Westra SJ, Lippe B. Normal US appearance of ovaries and uterus in four patients with Turner's syndrome and 45,X karyotype. *Pediatr Radiol*. 1996;26:37–39.
8. Nidecker A, Cohen HL, Zinn HL. Amenorrhea in the adolescent or young adult. In: Bluth E, Benson C, Ralls P, et al, eds. *Ultrasound. A Practical Approach to Clinical Problems*. 2nd ed. New York: Thieme; 2008:513–527.
9. Hall JG, Gilchrist DM. Turner syndrome and its variants. *Pediatr Clin North Am*. 1990;37:1421–1440.
10. Fernandes E, Fernandes E, Hollabaugh S, et al. Persistent Müllerian duct syndrome. *Urology*. 1990;36:516–518.
11. Halbertsma F, Otten B, Wijnen R, et al. A baby boy with cryptorchism, inguinal hernia and internal female genitalia: the persistent Müllerian duct syndrome. *Ned Tijdschr Geneeskd*. 2004;148:484–487.
12. Sivit CJ, Hung W, Taylor G, et al. Sonography in neonatal congenital adrenal hyperplasia. *AJR Am J Roentgenol*. 1991;156:141–143.
13. Speiser P. Prenatal treatment of congenital adrenal hyperplasia. *J Urol*. 1999;162:534–536.
14. Koziell A, Grundy R. Frasier and Denys-Drash syndromes: different disorders or part of a spectrum? *Arch Dis Child*. 1999;81(4):365–369.
15. Coppes MJ, Huff V, Pelletier J. Denys-Drash syndrome: relating a clinical disorder to genetic alterations in the tumor suppressor gene WT1. *J Pediatr*. 1993;123(5):673–678.
16. Marcantonio SM, Fechner PY, Migeon CJ, et al. Embryonic testicular regression sequence: a part of the clinical spectrum of 46,XY gonadal dysgenesis. *Am J Med Genet*. 1994;49:1–5.
17. de la Chapelle A. The etiology of maleness in XX men. *Hum Genet*. 1981;58:105–116.
18. Lee PA, Houk CP, Ahmed SF, et al. Consensus statement on management of intersex disorders. *Pediatrics*. 2006;118(2):e488–e500.
19. Cohen HL, Bober S, Bow S. Imaging the pediatric pelvis: the normal and abnormal genital tract and simulators of its diseases. *Urol Radiol*. 1992;14:273–283.
20. Ratani R, Cohen HL, Fiore E. Pediatric gynecologic ultrasound. *Ultrasound Q*. 2004;20:127–139.
21. Cohen HL, Lemond T. Gynecologic imaging of the pediatric patient. In: Fielding J, Brown D, Thurmond A, eds. *Gynecologic Imaging*. Philadelphia: Elsevier Saunders; 2011:547–564.

# 125 Abnormalities of the Male Genital Tract

Harris L. Cohen and Stephen F. Miller

## OVERVIEW

Ultrasound (US), including Doppler imaging in all its forms, is the main diagnostic imaging tool for evaluating the scrotum. Computed tomography (CT) is used predominantly to evaluate metastatic spread of testicular or other intrascrotal tumors. Magnetic resonance imaging (MRI) has been used in the search for undescended testes that remain in an intraabdominal position. MRI, like CT, also can be used to analyze metastatic spread of testicular tumor. Its uses in evaluating the male genital tract are evolving.

### Ultrasound Technique

Scrotal US is performed using a high-frequency transducer. The superficial position of testes in the normally thin-walled scrotum allows excellent imaging with a transducer of 7.5 MHz or higher. Longitudinal and transverse views are taken of each hemiscrotum. Transverse views, sometimes using a convex array transducer (e-Fig. 125.1), allow the best side-by-side comparison of both testes and their adnexa, especially when checking for differences in size, echogenicity, and vascularity.[1–5] Spectral Doppler ultrasound can be used to further characterize testicular blood flow and demonstrate both arterial and venous waveforms (e-Fig. 125.2).

### Normal Findings

The testes should be ovoid, nearly symmetric, and homogeneously echogenic. There is some discrepancy with regard to normal testicular volumes (Box 125.1). A highly echogenic linear focus (seen posteriorly and superiorly) represents the mediastinum testis (Fig. 125.3), which is the inward extension of the tightly adherent covering of the testis, the tunica albuginea. Fibrous septa extending from the mediastinum testes divide the testes into more than 250 lobules, each drained by one or more seminiferous tubules that merge into the rete testes. The rete testes, draining veins, lymphatics, nerves, and testicular artery course within the mediastinum testis.[5–8]

The head of the epididymis (e-Fig. 125.4) sits atop the superior pole of each testis. The head is continuous with the epididymal body and tail, which travel inferiorly along the posterolateral margin of the testis. The echotexture of the epididymis is normally homogeneous. It may be of equal or of slightly greater or lesser echogenicity than that of the testes.[5–8]

The scrotal wall should be between 3 and 6 mm thick. Beneath the scrotal wall are the two layers of the tunica vaginalis (Fig. 125.5), the outer (parietal) and the inner (visceral) layers, which are the residua of the processus vaginalis (i.e., peritoneum that descended with the testis from the abdomen). The visceral layer covers the testis on its anterior border and is attached to the tunica albuginea. Between the tunica's two layers is a potential space that normally may contain 1 to 2 mL of fluid. It is here that the fluid of a hydrocele may accumulate.[5–8]

**BOX 125.1** Normal Scrotal Volumes

0–9 months: 0.27–0.44 mL
1 year: 0.31 mL
6–12 years: 2–5 mL
13–15 years: 5–10 mL
16.5–18 years: 6–22 mL

Several small, persistent, vestigial remnants of the mesonephric (wolffian) and Müllerian duct systems may be found within the scrotum. Of these, usually only three may be seen on US examination, usually only if fluid (e.g., from a hydrocele) surrounds one of them. These remnants are the appendix testis (e-Fig. 125.6) (a remnant of the Müllerian duct), which is attached to the upper pole of the testis (and the most common appendix to potentially undergo torsion); the appendix epididymis (a remnant of the

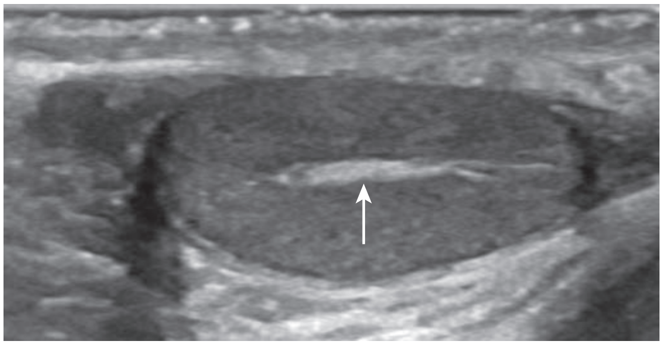

**Figure 125.3. Mediastinum testis.** A transverse sonogram shows a linear echogenic structure *(arrow)* within a normal testis, which is the mediastinum testis.

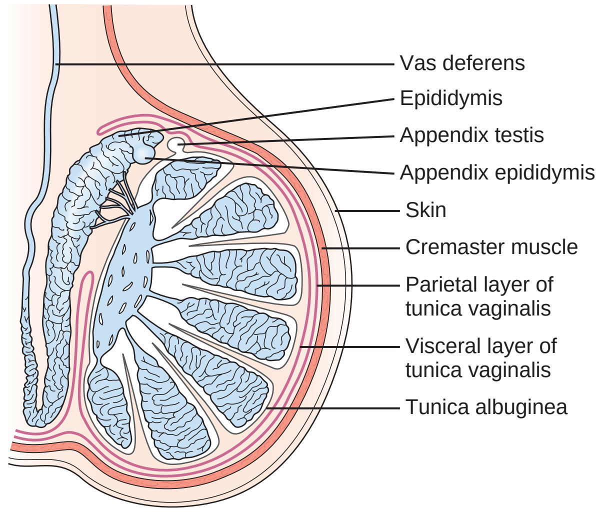

**Figure 125.5. A schematic drawing of the scrotum and its contents as seen in the longitudinal plane through a single testis.** Note the tunica albuginea surrounding the lobules of the testes. The tunica albuginea, in turn, is surrounded by the visceral layer of the tunica vaginalis and the more superficial parietal layer of the tunica vaginalis. *(From Cohen HL, Sivit C, eds.* Fetal and pediatric ultrasound: a casebook approach. *New York: McGraw-Hill; 2001. Reproduced with permission of McGraw-Hill Companies.)*

## Abstract:

This chapter discusses imaging of the normal and abnormal male genital tract. Ultrasound techniques and normal imaging findings of scrotal contents are presented. Current evaluation of cryptorchidism, causes of testicular and scrotal enlargement and/or pain (e.g., hydrocele, varicocele, trauma, testicular torsion, torsion of testicular and epididymal appendages, epididymitis or epididymo-orchitis, and neoplasm), and testicular microlithaisis are discussed.

## Keywords:

Children
Testicle
Neoplasm
Hydrocele
Testicular torsion
Epididymitis
Varicocele

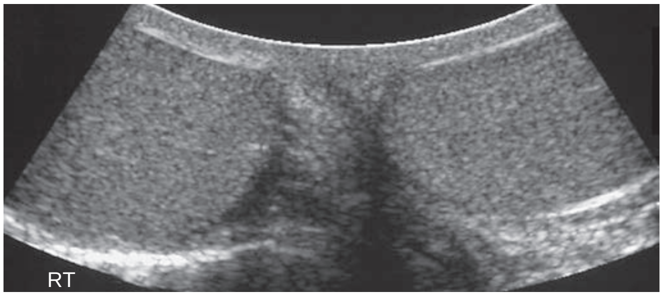

**e-Figure 125.1. Normal testes.** The testes of a teenager appear homogeneously echogenic on ultrasound in the transverse plane. This image was obtained using a convex linear array transducer that allowed imaging of most of both testes. These transducers can show both testes in their entirety in most cases and therefore are an improvement over linear array transducers (which are limited by the size of their footprint) for side-by-side comparisons of testes.

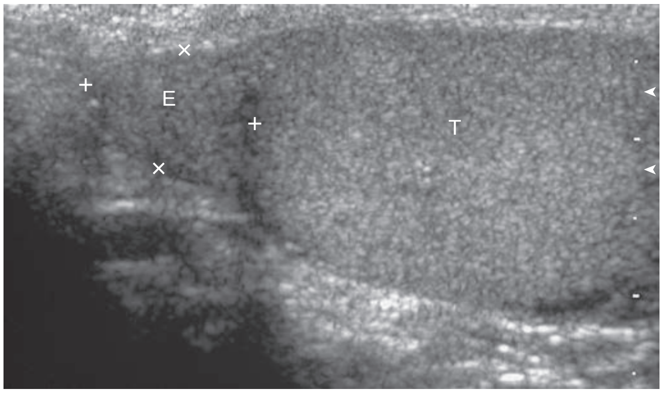

**e-Figure 125.4. Normal epididymis.** In this longitudinal sonogram, cursors mark off the head of the epididymis *(E)*, which sits atop the superior testis *(T)*. The normal epididymal body and tail, which travel along the side of the testis, are more difficult to separate from normal testis.

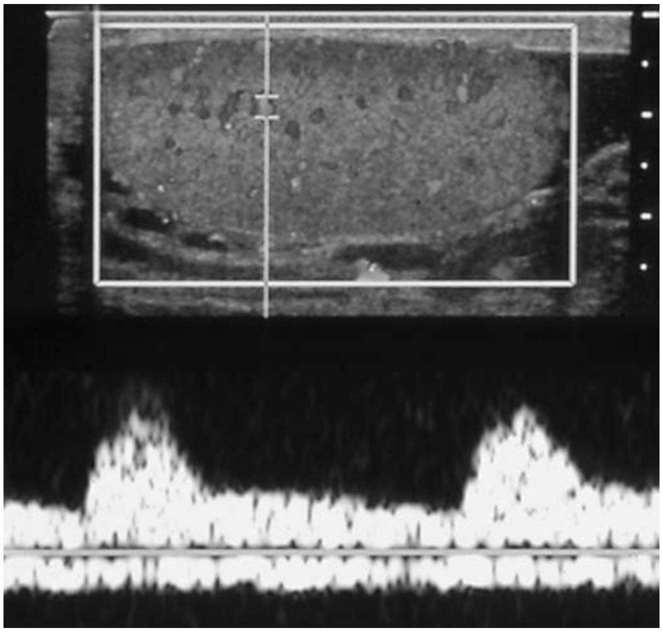

**e-Figure 125.2. Normal Doppler flow in a testis.** The upper half of the image shows the normal testis, with color signal filling vessels with moving blood. Insonation of a point in the upper third of the testis provides a spectral pattern that shows a classic arterial signal with its systolic and diastolic components above the baseline and a relatively unchanging and continuous venous signal below it.

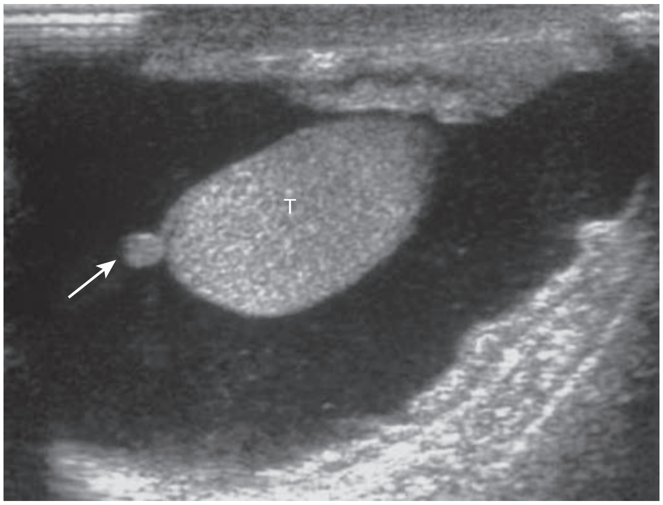

**e-Figure 125.6. Appendix testis.** Longitudinal sonogram shows a small circular structure *(arrow)* extending off the testis *(T)* that is a normal appendix testis. It was readily seen on this image because of the presence of a large hydrocele.

mesonephron), which is attached to the head of the epididymis; and the vas aberrans (a remnant of the mesonephron), which is attached to the epididymis at the junction of its body and tail.[5–8]

## CRYPTORCHIDISM

***Overview.*** By 32 weeks' gestational age, the testes have descended into the scrotum via the inguinal canal in 93% of all male fetuses. By 6 weeks of age, only 4% of term infants have a nonpalpable testis. Of these infants, 20% have true cryptorchidism (undescended testis). Cryptorchidism is more common on the right (70%) and is bilateral in 10% to 33% of cases. Beyond the age of 1 year, the prevalence of true cryptorchidism is approximately 1%. The etiology of cryptorchidism is not clear; it may be hormonal or mechanical (e.g., lack of proper fixation of the testis or an abnormal gubernaculum), or a combination of the two.

***Imaging.*** US is the initial procedure for localization of a testis that is not palpable within the scrotum (e-Fig. 125.7). The undescended testis may be smaller and hypoplastic, although usually is of equal echogenicity to the contralateral normal testis. T2-weighted MRI with fat-suppression generally is more effective than CT for finding an intraabdominal testes. Normal testes have a homogeneous high signal on T2-weighted images.[5,9] Alternatively, exploratory laparoscopy can be performed to identify a suspected intraabdominal testis that cannot be palpated by a pediatric urologist.

***Treatment.*** Surgical treatment for undescended testes is orchiopexy, fixation of the testes within the scrotum. It is performed, especially in cases of intraabdominal testes, because of the increased risk for the development of testicular neoplasia (a 10–40 times greater risk, with seminoma being the most common neoplasm).[10] Spontaneous descent during the first year of life may occur from an endogenous surge of luteinizing hormone, and thus surgical correction typically is delayed until 18 to 24 months.[5,11] After orchiopexy, 53% of the originally undescended testes are reported to be abnormal by either position, volume, structure, or perfusion.[12–15]

## HYDROCELE

***Overview.*** Hydrocele, the most common scrotal mass in a child (Fig. 125.8), results from fluid accumulated between the layers of the tunica vaginalis. Several types of hydroceles are identified (Fig. 125.9). The processus vaginalis is closed in 50% to 75% of children at birth and in most of the remainder by the end of the first year of life. Residual fluid from testicular descent is responsible for the noncommunicating hydroceles reported in at least 15% of male fetuses beyond 28 weeks of life. If the processus vaginalis fails to close, a communicating hydrocele can develop.

In a hydrocele of the spermatic cord (a funicular hydrocele), the processus vaginalis is obliterated in its proximal and distal end, and the hydrocele is contained in the patent space between these two points. In an inguinoscrotal hydrocele, the processus vaginalis is obliterated only at the internal inguinal ring, and the hydrocele extends cephalad from the scrotum into the inguinal canal. In an abdominoscrotal hydrocele (e-Fig. 125.10), the funicular process at the internal inguinal ring remains patent, allowing a dumbbell-shaped cystic mass to protrude into the extraperitoneal space above the inguinal area.[16]

In most cases, the etiology of a hydrocele found in the child or adolescent is idiopathic. Acquired (commonly reactive) hydroceles can develop after scrotal trauma or as a complication of epididymitis-orchitis, testicular torsion, or in the presence of an intrascrotal neoplasm. A hydrocele that increases in size without an intrascrotal cause suggests the presence of a patent processus vaginalis and the possibility of an associated inguinal hernia.

***Imaging.*** Scrotal US shows the cystic (fluid) nature of the hydrocele as it appears to surround the normal homogeneously echogenic testis. Septations and debris may be present, particularly if the hydrocele is infected (i.e., a pyocele) or hemorrhagic (i.e., a hematocele) (e-Fig. 125.11). Echogenic debris (e.g., cholesterol crystals) may be seen in the fluid of chronic hydroceles (e-Fig. 125.12), along with occasional calcifications.

***Treatment.*** After the age of 2 years, a hydrocele is unlikely to resolve, and surgery is required. This consists of a high ligation of the patent processus vaginalis and emptying of the distal fluid collection.[17,18]

## TESTICULAR TORSION

***Overview.*** Torsion may occur at any age but is seen most often in adolescent boys between 11 and 18 years of age, perhaps because of the increase in testicular growth and weight during this time.

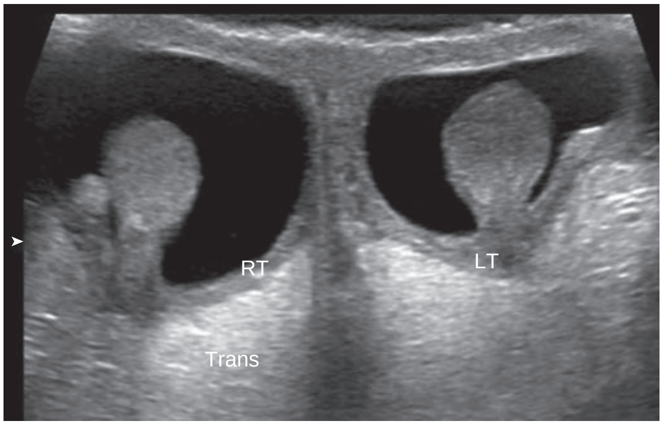

**Figure 125.8. Hydroceles.** Transverse gray-scale sonogram shows two normal testes appearing as echogenic structures within an enlarged fluid-filled scrotum of a young child due to large hydroceles. Note that the testes are normally affixed to the posterior scrotal wall.

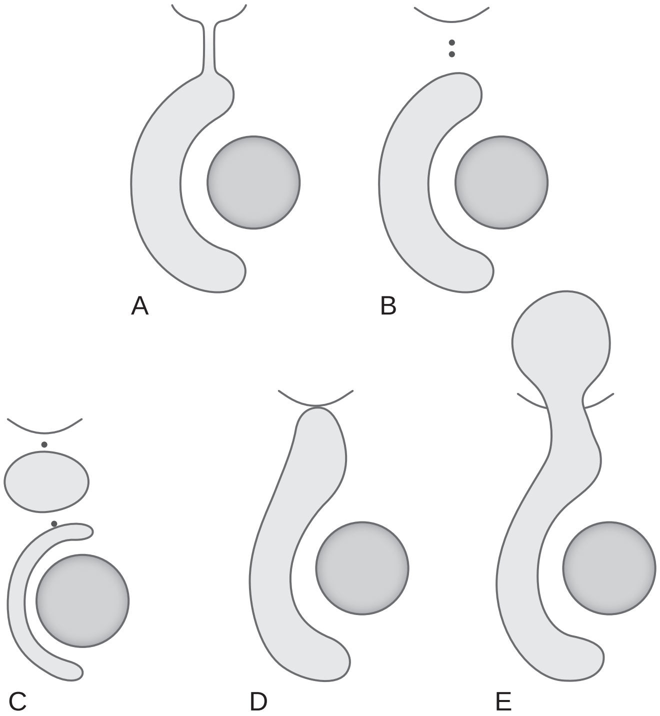

**Figure 125.9. Hydrocele types.** (A) Congenital or intermittent hydrocele. (B) Scrotal hydrocele. (C) Hydrocele of the cord. (D) Inguinoscrotal hydrocele. (E) Abdominoscrotal hydrocele.

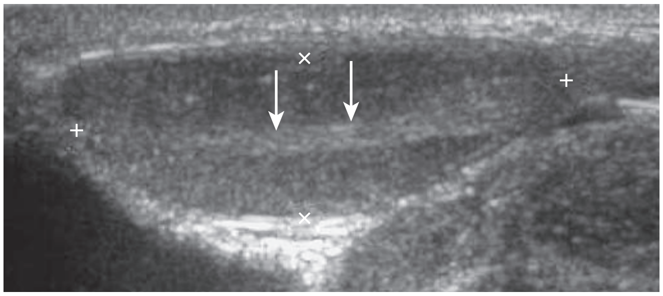

**e-Figure 125.7. Analysis of the inguinal region for undescended testis.** Longitudinal sonogram shows cursors *(graticules and x's)* marking off the borders of a normal undescended testis found in the right groin of a child. *Arrows* point to the mediastinum of the testis.

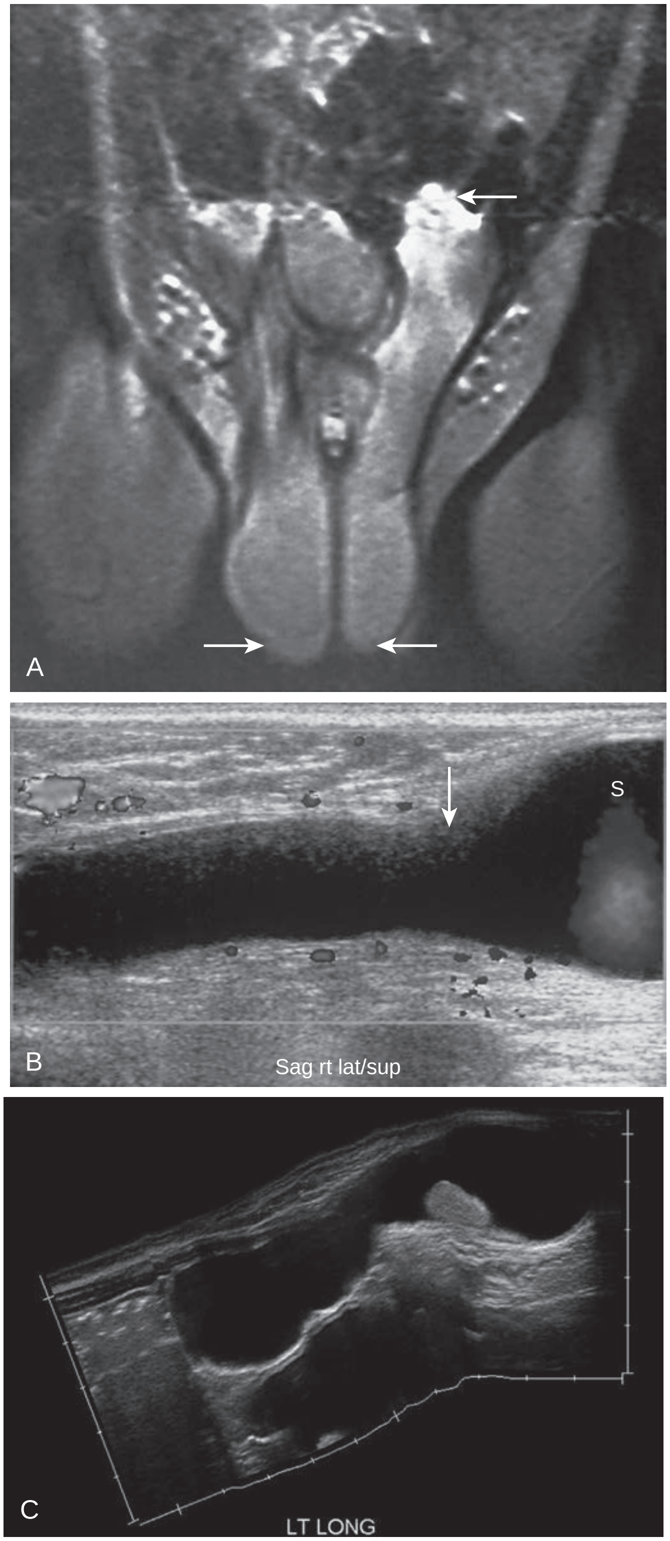

**e-Figure 125.10. Abdominoscrotal hydrocele.** (A) Tubular structures *(arrows)* are seen extending from each side of the scrotum superiorly into the abdominal cavity on a coronal T1-weighted magnetic resonance (MR) image. This child had bilateral abdominoscrotal hydroceles; the superior extent on the right is not well visualized on this image. He presented with an enlarged scrotum and palpable inguinal masses, the sizes of which changed with scrotal compression. (B) Longitudinal sonogram in another patient shows a right-sided tubular, fluid-filled structure extended from the scrotum *(S)* to above the inguinal area *(arrow)*. (C), Abdominoscrotal hydrocele in 6-month-old boy with scrotal swelling. *(A, from Cohen HL, Sivit C, eds.* Fetal and pediatric ultrasound: a casebook approach. *New York: McGraw-Hill; 2001. Reproduced with*

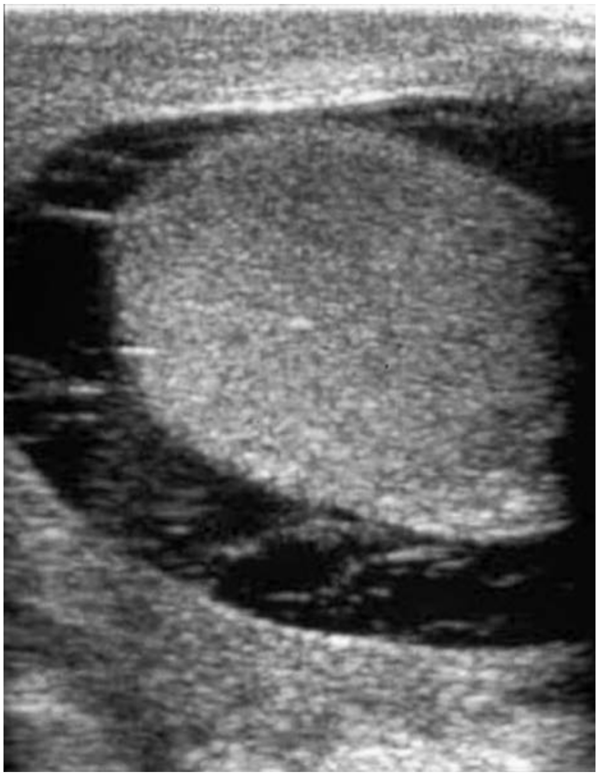

**e-Figure 125.11. Hematocele.** Longitudinal sonogram shows fluid containing echogenic material that surrounds the normal testis of a 14-year-old who was kicked in the scrotum several days before imaging.

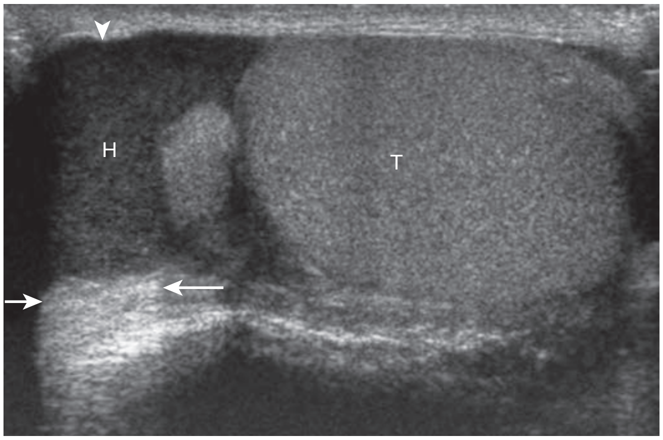

**e-Figure 125.12. Chronic hydrocele.** Longitudinal sonogram shows echogenic debris-filled fluid due to a chronic hydrocele *(H)* in the scrotum of a teenager. Excellent through transmission of sound *(arrows)* helps indicate that the echogenic material is complicated fluid rather than solid material. *T,* Testicle.

The normal testis is strongly attached to the epididymis, which in turn is applied to the posterior scrotal wall. If these attachments fail to develop properly (the "clapper-in-a-bell" phenomenon), the testis, suspended within the tunica vaginalis, may rotate and the spermatic cord undergoes torsion. A male with acute testicular torsion experiences sudden acute scrotal pain, often accompanied by nausea and vomiting. An important finding on physical examination is a change in testicular axis from the normal vertical positioning of the testis in the scrotum to a more horizontal positioning (Fig. 125.13). Within hours of torsion, a reddened scrotum develops, with or without enlargement.

***Imaging.*** Ultrasonography is the only diagnostic tool necessary to make the diagnosis of torsion and suggest surgical exploration. The testis is normal sized to enlarged, with normal to decreased echogenicity (see Fig. 125.13). Enlargement and hypoechogenicity are thought to be due to venous congestion. The echotexture pattern is usually homogeneous early with heterogeneity increasing over time. Epididymal enlargement may be an early finding in some cases of torsion. At least 10% of cases of torsion have associated reactive hydroceles. US performed more than 24 to 48 hours after symptomatology may show a heterogeneous or hyperechoic testis from hemorrhage or hemorrhagic necrosis (Fig. 125.14).

State-of-the-art color or power Doppler imaging methods have made US the reference standard for the imaging and preoperative diagnosis of testicular torsion. Venous flow is lost before arterial flow ceases. Color flow comparison to the contralateral testis is helpful and necessary, particularly when torsion is incomplete. Such a partial torsion is suggested not by absence of arterial flow but by blood flow asymmetry. The spermatic cord should always be imaged and, when seen, should be straight. When torsion is present, a spiral twist (whirlpool sign or knot) can be seen. Flow may be normal or increased in a torsed testis that spontaneously detorses.[19–22]

***Treatment.*** Torsion must be corrected in a timely manner to preserve testicular viability. Surgery within 24 hours leads to 60% to 70% testicular salvage, but after 24 hours salvage is only 20%. Because abnormal testicular fixation to the scrotum is usually bilateral, preventive orchiopexy often is performed on the contralateral testis.[15]

## Testicular Torsion in the Fetus and Newborn

***Overview.*** Testicular torsion that occurs in the newborn period usually presents as a painless, firm scrotal mass often associated with bluish-red scrotal discoloration. The affected testis is generally nonviable. If the torsion occurred in intrauterine life, one is imaging the neonatal equivalent of delayed torsion. This form of torsion is considered extravaginal and is not associated with the "clapper-in-a-bell" deformity. Such torsions may be bilateral.

***Imaging.*** Antenatal torsion may be diagnosed on fetal US examination. Antenatal torsion must be considered if the fetal testis or testes are heterogeneous in echogenicity or of asymmetric size (Fig. 125.15). Diagnosis in the newborn is made by similar imaging findings.[23–26] Infarcted testes due to intrauterine torsion may be small and may be located in the inguinal canal. They may have an echogenic rim due to calcification or infarction of the more central testicular parenchyma (see Fig. 125.15).

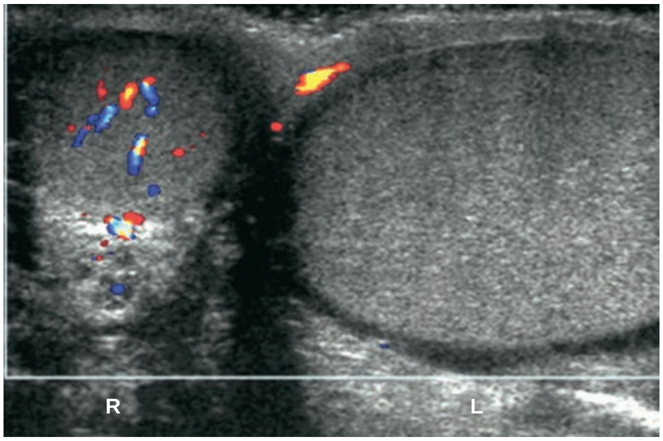

**Figure 125.13. Testicular torsion and axis change.** Color Doppler sonogram in the transverse plane shows flow in the right testicle. The right testicle is oval to circular, because it has been evaluated in the transverse plane. The left testicle is elongated as if it is in longitudinal plane, indicating an abnormal lie within the scrotum worrisome for torsion. Lack of color Doppler flow confirms left testicular torsion.

## Torsion of Testicular and Epididymal Appendages

***Overview.*** Testicular and epididymal appendage torsion occurs most often in the 6- to 12-year-old age group. Patients present with localized pain, a pea-sized mass in the area of the upper pole of the testis, and at times, a pinpoint discoloration (the "blue dot" sign) seen through the overlying scrotal skin. The clinical picture may be indistinguishable from that of testicular torsion, albeit in a somewhat younger age group.

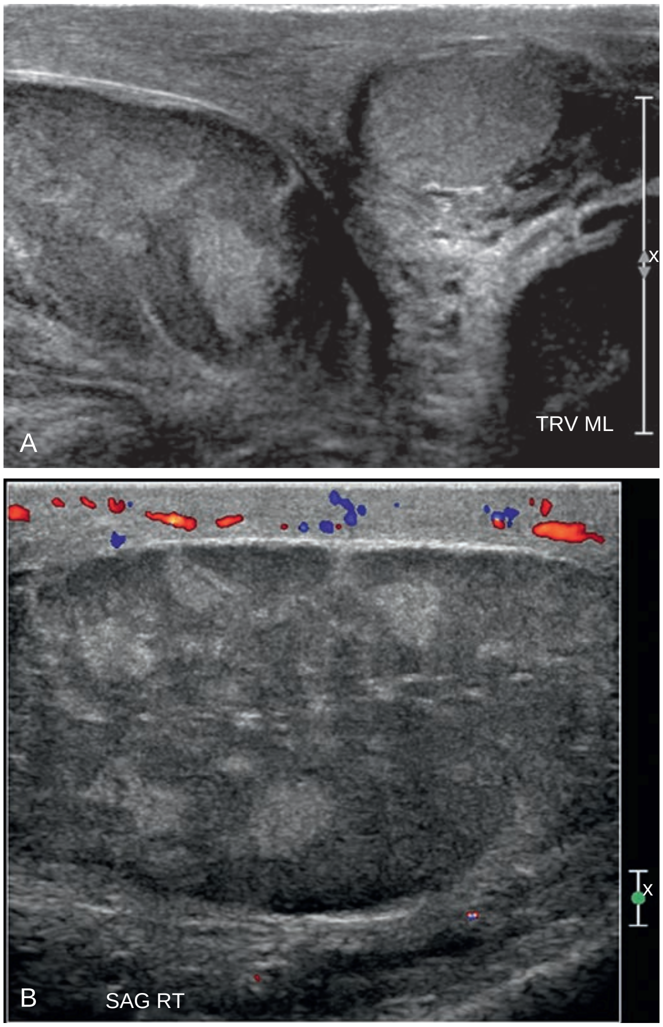

**Figure 125.14. Delayed diagnosis of testicular torsion in a boy with scrotal pain greater than 24 hours.** (A) Transverse sonogram shows an enlarged, heterogeneous right testis when compared with the left testis. (B) Longitudinal color Doppler image shows no blood flow within the right testis.

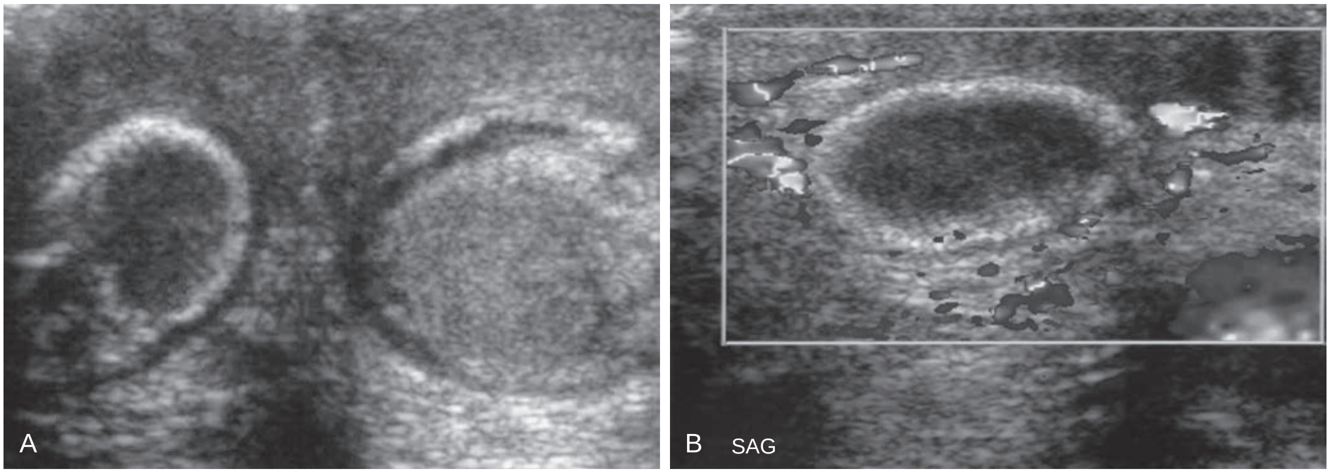

**Figure 125.15. Bilateral antenatal testicular torsion.** (A) Transverse sonogram shows two testes with torsion of different ages in a newborn with scrotal swelling. The testes are seen deep to a more superficial thickened scrotal wall. The right testis is hypoechoic with an echogenic rim, suggesting remote torsion. The more echogenic left testis does not appear particularly abnormal on this image, although its periphery is more echogenic than the remainder of its parenchyma. Color Doppler imaging showed no flow in either testis. Upon surgery, both testes proved to have undergone torsion. The torsion of the left testis probably occurred later in fetal life. Tiny hydroceles are present bilaterally. (B) Longitudinal color Doppler sonogram of the torsed right testis shows no color Doppler flow within the hypoechoic parenchyma.

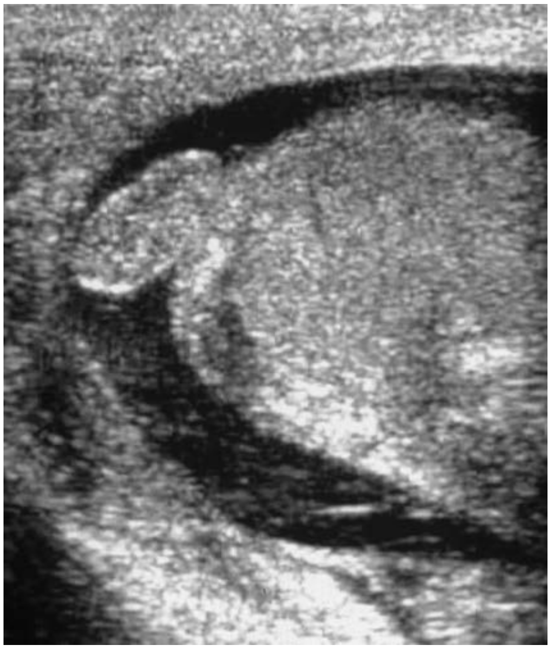

**Figure 125.16. Torsed appendix testis.** Longitudinal sonogram of the superior portion of the scrotum shows a prominent oval structure superior to the testis of a child who presented with sudden testicular pain. Some debris is present in a small surrounding hydrocele. Color Doppler imaging of the testis was normal, proving that no testicular torsion was present.

***Imaging.*** The US appearance of a torsed appendage shows it not to have its typical small comma-like shape but rather a larger circular or ovoid shape (Fig. 125.16). The torsed appendage can vary in echogenicity and is associated with the testis or epididymis on the affected side. Reactive epididymal swelling and hyperemia often are present. Usually the testicular echogenicity and vascular flow are normal.[23,27] Infarcted appendages may eventually calcify, appearing echogenic with posterior acoustic shadowing.

***Treatment.*** Appendage torsion generally is a self-limited disorder that responds to nonsteroidal antiinflammatory medications and comfort measures, such as limited activity and a warm compress. As the appendage infarcts and undergoes necrosis, the pain resolves. Surgical intervention is indicated when the symptoms are prolonged and spontaneous resolution does not occur.[28]

## EPIDIDYMITIS

***Overview.*** Epididymitis is the most common cause of an acute painful scrotum in the postpubescent male. The cause is usually bacterial, although in pediatric and some adolescent patients, epididymitis may be viral (e.g., as a result of the mumps virus). Patients with epididymitis often are febrile, and at least half report dysuria. Pyuria is common, and nausea, vomiting, and leukocytosis may be present. An enlarged epididymis may be palpated, and scrotal edema and tenderness often are present.

The infection usually reaches the epididymis through the spermatic ducts. Causative factors include urinary tract infections, urethral instrumentation and indwelling catheters, distal urethral obstruction, and reflux of urine from the urethra into the seminal ducts as a result of a congenitally patulous orifice, an ectopic ureter draining into the vas deferens, and an ectopic vas deferens draining into the bladder or ureter.

Complications of epididymitis include direct spread of the infection to the testis (i.e., epididymo-orchitis), which can be seen in as many as 20% of cases. Although it is an uncommon complication, an abscess may develop and require drainage. In unusual cases, acute epididymitis may impede testicular blood flow, resulting in focal or diffuse infarction of the testis or epididymis even in the absence of torsion.

***Imaging.*** US shows enlargement of the epididymis (e-Fig. 125.17) and commonly a reactive hydrocele or pyocele. Overlying scrotal wall thickening may be present. The echogenicity of the enlarged epididymis may be normal, slightly decreased, or slightly increased. The affected area of epididymis, although enlarged, usually maintains its normal shape. The diagnosis is supported by color Doppler imaging showing increased flow (Fig. 125.18). With epididymo-orchitis, a hypoechoic area of involvement is

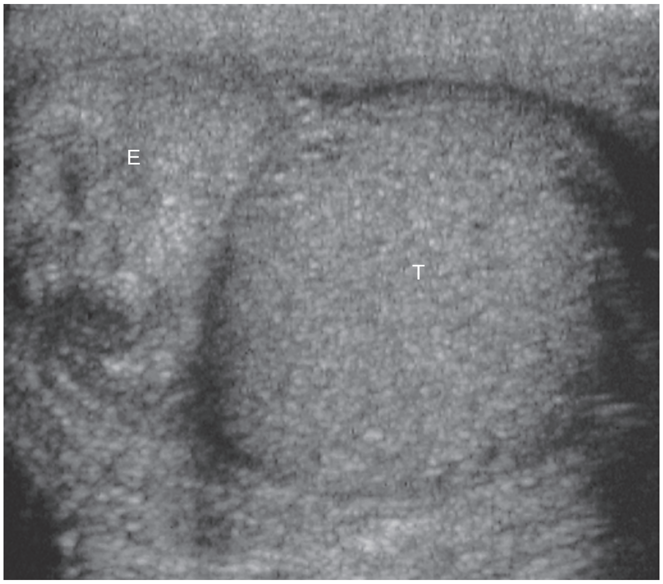

**e-Figure 125.17. Epididymitis.** A longitudinal gray-scale sonogram shows that the left epididymis *(E)* of this teenager is very large and heterogeneous compared with the normal testis *(T)*.

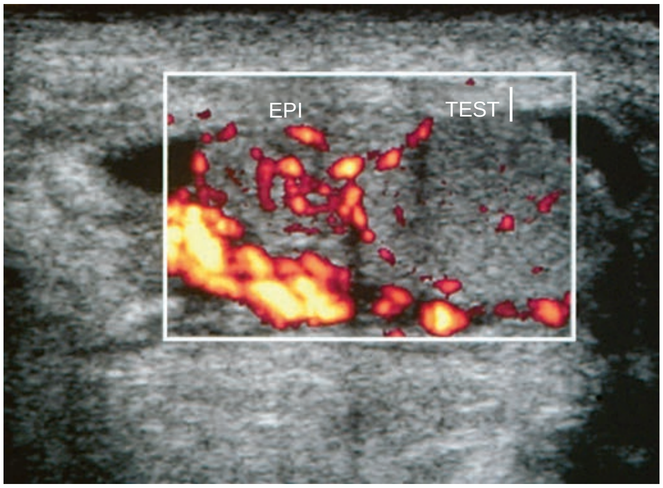

**Figure 125.18. Epididymitis in a child.** Longitudinal power Doppler sonogram shows that flow to the prominent right epididymis *(EPI)* of this 10-year-old child is greater than that to the testis *(TEST)*.

seen within the testis directly adjacent to the area of involved epididymis (e-Fig. 125.19). Color Doppler imaging usually shows increased flow to the involved portion of adjacent testis and the epididymis. In the prepubescent male, when epididymitis is the result of a congenital anomaly, a voiding cystourethrogram may be performed to detect abnormalities such as reflux of contrast agent into a vas deferens.[29–31]

***Treatment.*** Urine cultures should be obtained for all pediatric patients with epididymitis. Antibiotic therapy is reserved for young infants and those with pyuria and positive urine cultures.[32]

## HENOCH-SCHÖNLEIN PURPURA

***Overview and Imaging.*** Henoch-Schönlein purpura is a generalized vasculitis of unknown cause characterized clinically by a purpuric rash, abdominal pain, joint manifestations, and often hematuria secondary to glomerulonephritis. Involvement of the epididymis and less commonly the testis may result in scrotal swelling and tenderness. More often, however, the scrotum alone is involved by severe purpura and swelling. Imaging may be indicated to exclude testicular torsion. Imaging normal testes with normal flow despite marked edema of the scrotal wall helps suggest the diagnosis and can prevent the need to explore the scrotum surgically.[33,34]

## TESTICULAR AND PARATESTICULAR NEOPLASMS

### Primary Testicular Neoplasms

***Overview.*** Testicular neoplasms are uncommon in infants and children, representing only 1% to 1.5% of all childhood malignancies. When present, they tend to occur in very young children, with a peak incidence at 2 years of age and with 60% of the cases occurring in children younger than 2 years. Such tumors usually present as a painless, nontender, and firm scrotal mass often of weeks' to months' duration. Scrotal pain and tenderness may occur if associated torsion occurs. Testicular tumors occasionally are bilateral. Primary testicular tumors are classified according to their tissue of origin.

***Imaging.*** The predominant imaging tool used to search for and evaluate tumors of the scrotum and its contents is US. Most testicular neoplasms tend to be hypoechoic (e-Fig. 125.20). Contained anechoic areas within tumors represent either cystic components or more often are evidence of focal necrosis as the tumor outstrips its blood supply. Acute hemorrhage appears echogenic, and echogenic foci with posterior shadowing may be seen with intratumoral calcifications. Reactive hydroceles are associated in at least 15% to 20% of cases. Color Doppler and power Doppler US demonstrate increased vascularity in the majority of malignant tumors and may help define the mass itself. CT or MRI can be used to evaluate for retroperitoneal lymph node enlargement and search for solid organ metastases. Chest radiographs and CT are used to search for pulmonary metastases and thoracic lymph node enlargement.[5]

### Germ Cell Tumors

***Overview and Imaging.*** Most childhood testicular tumors (65%–75%) are germ cell in origin. Yolk sac tumor is by far the most common malignant germ cell tumor (80%–90%) in children. Three-fourths of yolk sac tumors are diagnosed by 24 months of age. Hemorrhage, particularly after clot dissolution, frequently causes echo-free areas within this typically hypoechoic, somewhat well-circumscribed mass. An elevated serum alpha-fetoprotein level is a tumor marker in approximately 90% of affected patients.[5]

Testicular teratomas represent 10% to 15% of childhood germ cell tumors, with 65% of cases diagnosed before 2 years of age. They are composed of elements derived from all three germ cell layers and may contain may contain cartilage, bone, fat, and epidermal elements, such as keratin. Teratomas appear on US as complex masses with cystic and solid components (Fig. 125.21). Bony and dental elements are echogenic with posterior shadowing on US, whereas the adipose component appears echogenic but without shadowing. Prepubertal teratomas are said to almost always follow a benign course even if they contain islands of malignant germ cells (15%). Postpubertal teratomas, in contrast, are potentially malignant because of their propensity to develop components of other germ cell tumors, resulting in teratocarcinomas. Serum human chorionic gonadotropin level in these cases usually is elevated.[5,35]

### Gonadal Stromal Tumors

***Overview and Imaging.*** Non–germ cell testicular tumor types represent only 25% to 30% of pediatric testicular tumors. Leydig cell and Sertoli cell tumors represent the most common gonadal stromal tumors of childhood. They are almost always benign. Almost half (45%) of Leydig cell tumors are diagnosed between the ages of 2 and 9 years, with a peak incidence at 4 years of age. Leydig cell tumors typically are painless but may be associated with premature virilization (Fig. 125.22) if androgen is produced or with gynecomastia if estrogen is produced. Sertoli cell tumors represent 20% of the non–germ cell tumors. Half are diagnosed in the first year of life. Gynecomastia may be caused by estrogen production. Tumors containing a mixture of non–germ cell histologic patterns may occur.[5,36,37]

### Epidermoid Cyst

***Overview and Imaging.*** The epidermoid cyst, also known as a keratocyst, is a benign tumor of germ cell origin representing less than 1% of all testis tumors. It consists of a simple squamous cell–lined echopenic area located within the testicular parenchyma, usually just below the tunica albuginea. The wall is made up of fibrous tissue, and its lumen contains "cheesy" keratinized material or amorphous debris. Patients usually present with a painless 0.5- to 4-cm nodule that often is found incidentally on a routine physical examination. Four basic US appearances are seen, including a halo with central increased echogenicity, a sharply defined mass with peripheral calcification, and a solid mass with an echogenic rim. However, the classic appearance is a mass with an onion-skin

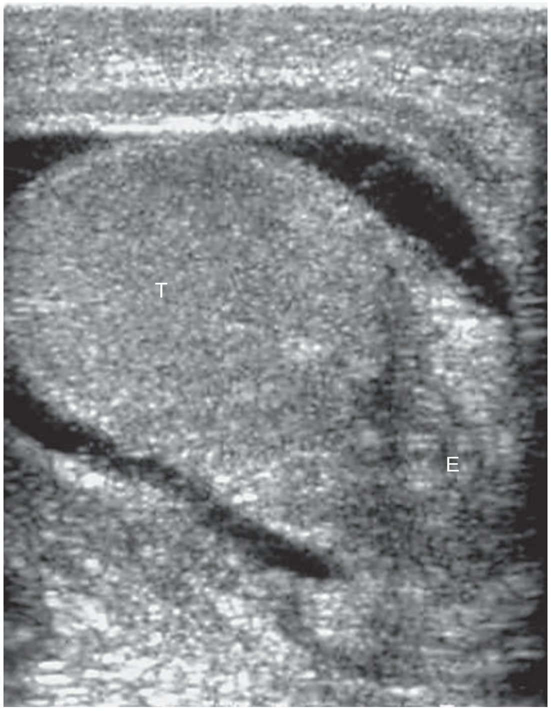

**e-Figure 125.19. Epididymo-orchitis.** A longitudinal gray-scale sonogram of the left testis shows that the scrotum is somewhat thickened, and a hydrocele is present. The echopenic portion of the epididymis *(E)* is seen inferiorly and is difficult to separate from the testis *(T)*. The testis is hypoechoic where it is in contact with the inflamed epididymis. The findings are consistent with extension of the infection into the testis.

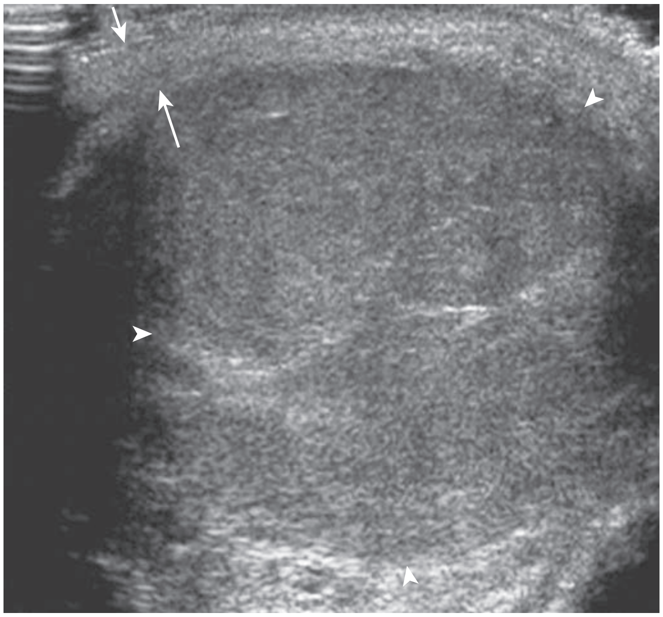

**e-Figure 125.20. Testicular seminoma.** Longitudinal gray-scale sonogram in a 17-year-old with an enlarging scrotum shows a large mass *(arrowheads)* surrounded by a periphery of normal testicular parenchyma *(arrows)*. It is hypoechoic compared with the normal testicle, as is typical of most testicular neoplasms.

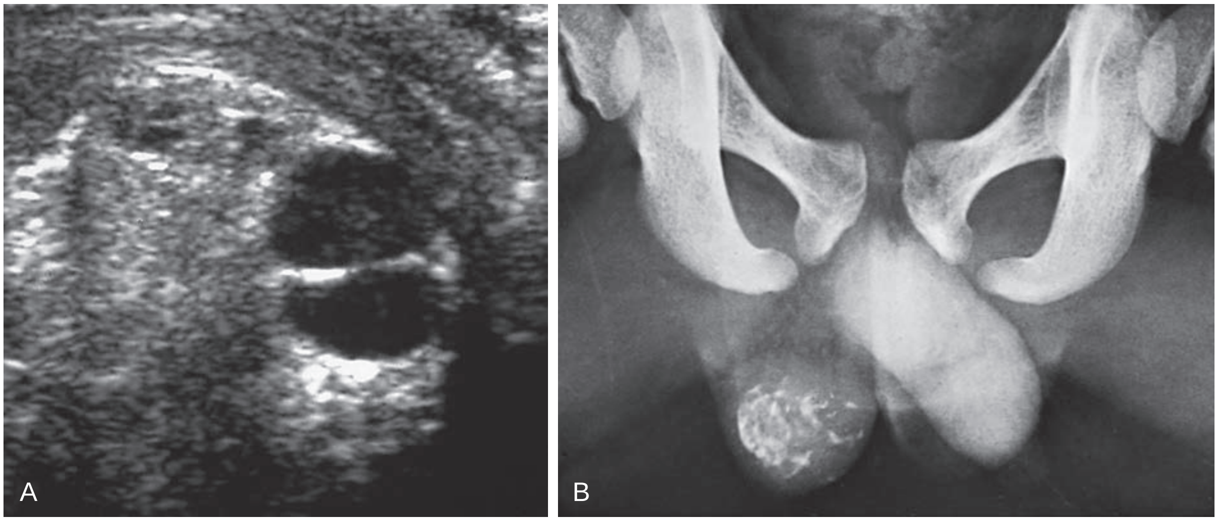

**Figure 125.21. Testicular teratoma.** (A) Transverse gray-scale sonogram of the right testicle shows a complex testicular mass with debris-filled cystic foci and surrounding hyperechogenicity. (B) A coned radiograph of the lower pelvis identifies a calcified right testicular lesion. *(Courtesy Dr. Leslie E. Grissom.)*

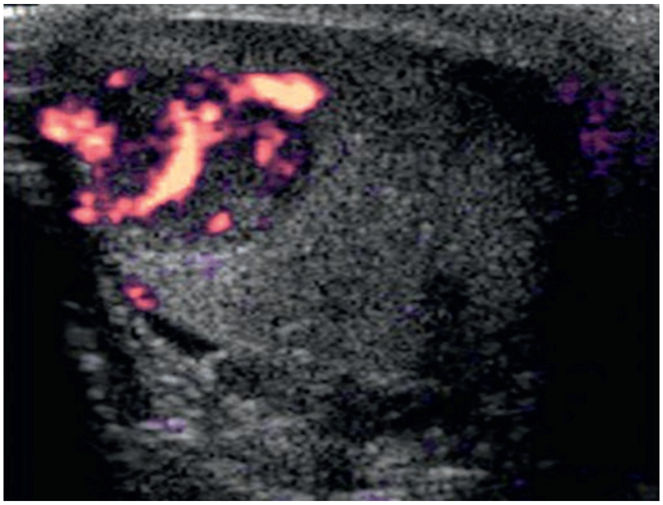

**Figure 125.22. Leydig cell tumor.** Transverse power Doppler image of the right testis in an 8-year-old boy with precocious puberty (early virilization) shows a round hypoechoic mass with associated increased blood flow.

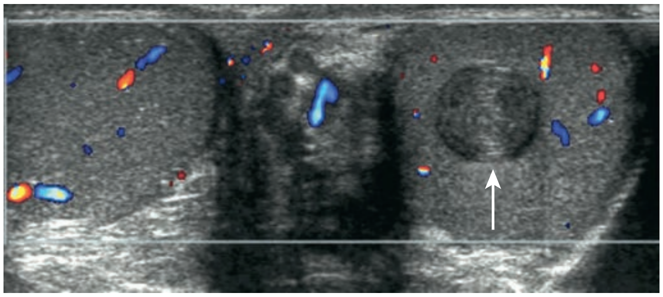

**Figure 125.23. Testicular epidermoid.** Transverse color Doppler sonogram in a teenager shows a normal right testicle. The left testicle contains an avascular mass *(arrow)* with onion skin layering, typical for a testicular epidermoid.

pattern of alternating hyperechoic and hypoechoic rings that is typically avascular (Fig. 125.23).[5,38–40]

## Secondary Testicular Neoplasms

***Overview and Imaging.*** Testicular metastases are rare in children, representing far less than 1% of testicular tumors. Leukemia and lymphoma are the most common causes. Enlarged testes caused by leukemic or lymphomatous infiltration may be the primary manifestation of these diseases or the first sign of relapse after bone marrow remission. The lesions often are bilateral. At least 8% of patients with acute lymphocytic leukemia have testicular involvement at some point during the course of their disease. These enlarged testes have focal or diffuse areas of decreased echogenicity (Fig. 125.24). Areas of hemorrhage appear echogenic, and lymphatic obstruction may lead to a hydrocele. Color Doppler imaging often shows significant increases in flow, often in an

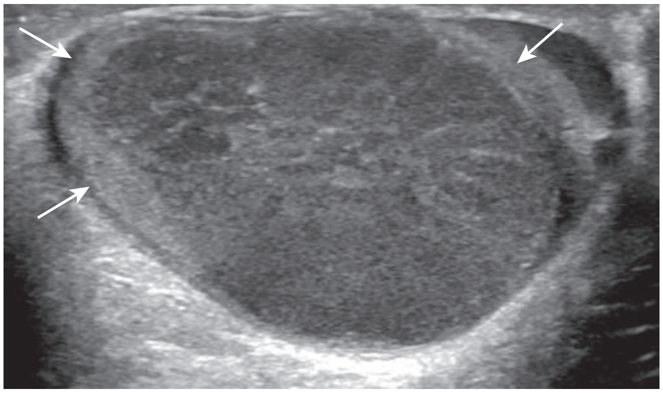

**Figure 125.24. Leukemia recurrence.** Longitudinal gray-scale scrotal sonogram in a 5-year-old boy with leukemia who was thought to be in remission. Patient presented with an enlarged scrotum. A large hypoechoic left testicular mass is seen with a small peripheral rim of normal testicular tissue *(arrows)*. The echopenic area proved to be due to leukemic involvement of the testis.

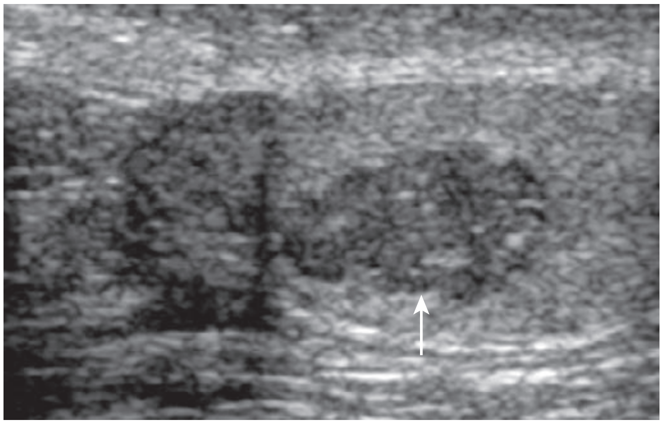

**Figure 125.25. Adrenal rests.** Longitudinal sonogram in a boy with congenital adrenal hyperplasia shows a hypoechoic mass *(arrow)* in the left testis.

asymmetric pattern related to the position of the infiltrating masses within the testis.

### Adrenal Rests

***Overview and Imaging.*** Adrenal rests are simulators of intratesticular tumors. At times, aberrant cells from the adrenal cortex may travel with gonadal tissue and be incorporated into the testis during fetal life. With high levels of adrenocorticotropic hormone and associated cortical cell stimulation (as in persons with congenital adrenal hyperplasia and Cushing syndrome), these rests may enlarge. Patients present with a testicular mass or enlargement. On US, one or more hypoechogenic or hyperechogenic masses generally are seen, typically along the mediastinum testis, usually bilaterally (Fig. 125.25). A typical color Doppler US pattern has been described in which multiple peripheral vessels radiate in a spokelike fashion from the centers of individual rests.[41,42]

### Testicular Microlithiasis

***Overview and Imaging.*** Testicular microlithiasis is characterized by calcifications within the lumina of seminiferous tubules. It is denoted on US by individual, tiny (1–3 mm), hyperechoic foci without shadowing (Fig. 125.26) within the testicular parenchyma. Some clinicians reserve the diagnosis for cases in which more than five microliths are noted on a single US image (classic or diffuse testicular microlithiasis). Testicular microlithiasis is reported in 2.4% of asymptomatic 0- to 19-year-old boys and also has been associated with cryptorchidism, infertility, male intersex, Klinefelter syndrome, and pulmonary alveolar microlithiasis. It usually is an incidental finding; however, there is a likely association between the presence of diffuse testicular microlithiasis and the presence or development of testicular neoplasm (reportedly 13–21.6 times greater than normal risk), particularly germ cell neoplasia (e.g., seminoma). Because of the association of microlithiasis and tumors, patients with testicular microlithiasis are sometimes followed up clinically and by US for possible tumor development.[43–47,47a]

## INTRASCROTAL EXTRATESTICULAR MASSES

### Paratesticular Rhabdomyosarcoma

***Overview and Imaging.*** Rhabdomyosarcoma is the most common malignant paratesticular mass in children, representing 10% of all intrascrotal tumors of childhood. It originates from the supporting stroma of the spermatic cord, testicular appendages, and paratesticular tunics and often is located superior to the testis. Two incidence peaks are seen for intrascrotal rhabdomyosarcoma, one at 2 to 4 years of age and the other between 15 and 17 years. Rhabdomyosarcomas present as a painless mass, grow rapidly, and frequently are large at presentation. They spread early to regional and retroperitoneal lymph nodes. Venous invasion and distant metastases, especially to the lungs, are not uncommon. On US examination, the mass is often heterogeneous, sometimes containing focal anechoic areas caused by necrosis (Fig. 125.27). As with all

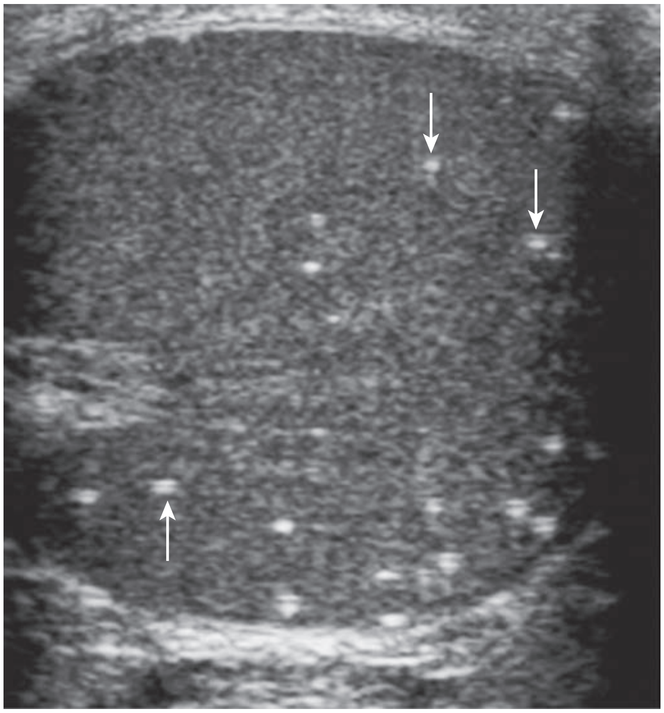

**Figure 125.26. Testicular microlithiasis.** Transverse gray-scale sonogram shows several small, nonshadowing, hyperechoic foci *(arrows)* in this right testicle of an older teenager. This finding was present bilaterally.

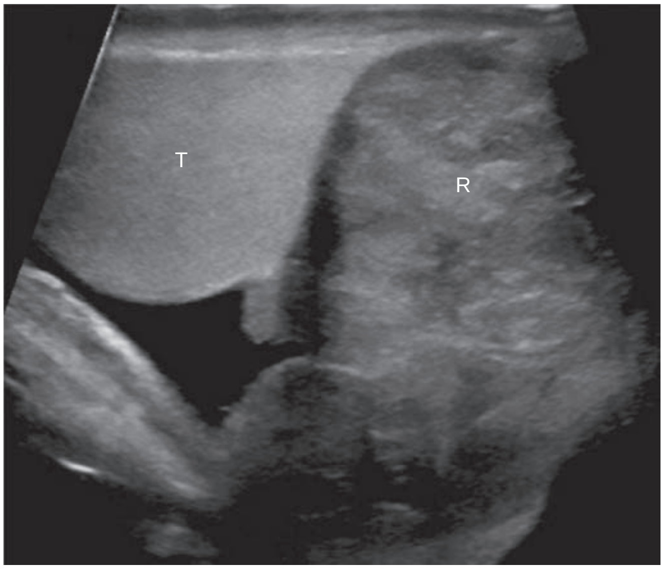

**Figure 125.27. Paratesticular rhabdomyosarcoma.** Longitudinal sonogram shows a large, heterogeneous mass *(R)* adjacent to a normal testis *(T)*. A small associated hydrocele is present.

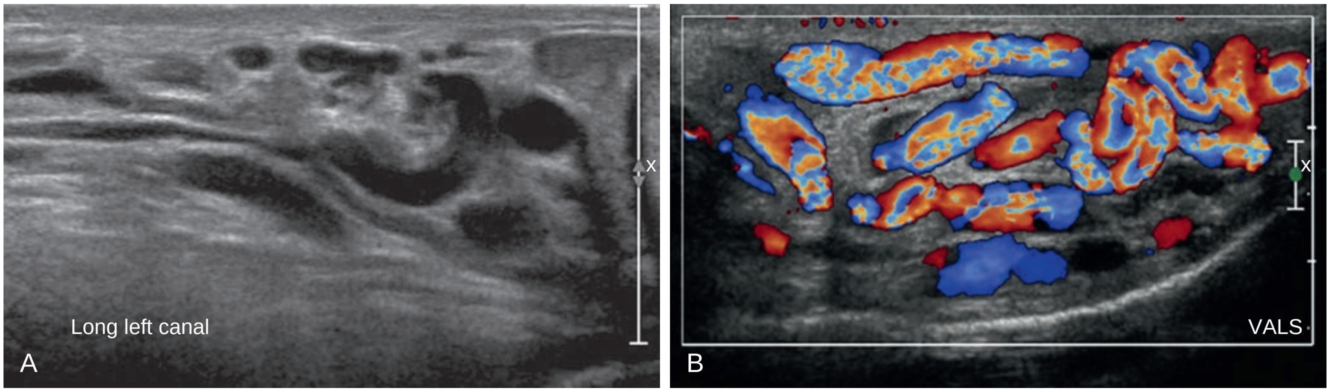

**Figure 125.28. Varicocele.** (A) Longitudinal gray-scale sonogram in a 12-year-old boy shows tubular anechoic structures in the left inguinal canal measuring up to 2 to 3 mm. (B) Longitudinal color Doppler image obtained during Valsalva shows color signal filling the tubular structures due to augmented retrograde blood flow.

### BOX 125.2 Grading of Varicoceles

**Grade I** (65%): Small varicoceles, appearing as only mild thickening of the spermatic cord
**Grade II** (25%): Moderate in size and consisting of a mass of veins up to 2 mm in diameter
**Grade III** (10%): Varicocele made up of individual veins greater than 2 mm in diameter

extratesticular masses, if the testes are invaded, differentiating the lesion from a mass of testicular origin may be difficult.

## Varicoceles

***Overview.*** Varicocele is a common pediatric scrotal mass, which is composed of dilated veins of the pampiniform plexus. Varicoceles are graded according to their size (Box 125.2). When they are unilateral, 99% of varicoceles are left-sided, perhaps because the left spermatic vein enters the left renal vein at a right angle. This anatomic situation is linked to a far greater incidence of venous incompetence compared with the right side, where the right spermatic vein enters the inferior vena cava directly at an oblique angle. The occurrence of bilateral varicoceles is common. However, finding a solitary right-sided varicocele is extremely uncommon, and, if found, the examiner must rule out an intraabdominal neoplasm or another mass as a cause.[5]

***Imaging.*** On US examination, varicoceles are tortuous, tubular, echo-free structures that typically are situated superior, lateral, and/or posterior to the testis (Fig. 125.28A). The diagnosis is confirmed by having the patient perform a Valsalva maneuver, supine or standing, and noting on color Doppler imaging that the tubular vessels, which may not show flow before the maneuver, will fill with color signal (Fig. 125.28B). Such increased flow may also be demonstrated by a change in the spectral Doppler waveform (e-Fig. 125.29).

***Treatment.*** Surgical or interventional varicocele ligation is recommended in cases in which ipsilateral testicular volume loss of 2 mL or greater occurs. Histologic analysis of such testes has shown various degrees of tubal hypoplasia, decreased spermatogenesis, focal fibrosis, or arrest of germ cell maturation.[5,48–53]

### KEY POINTS

- An undescended abdominal testis has a 10 to 40 times greater risk for a future malignancy.
- A hydrocele is the most common scrotal mass in a child.
- Testicular (and epididymal) appendages most typically torse in the 6- to 12-year-old age group.
- Epididymitis is the most common cause of an acute painful scrotum in the postpubescent male.
- Testicular torsion diagnosed in the newborn period can present as painless, firm scrotal mass(es) that appears heterogeneous when acute; in utero torsion may give rise to a small inguinal testis with peripheral calcification.
- Viable torsed testes undergo orchiopexy; nonviable testes are removed. Preventive orchiopexy is performed on the contralateral normal testis.
- Yolk sac tumor is the most common germ cell tumor in prepubertal children.
- Rhabdomyosarcoma is the most common malignant paratesticular mass in children.
- Unilateral right-sided varicoceles raise concern for an intraabdominal or retroperitoneal mass.

### SUGGESTED READINGS

Ahmed HU, Arya M, Muneer A, et al. Testicular and paratesticular tumours in the prepubertal population. *Lancet Oncol*. 2010;11(5):476–483.
Akbar SA, Sayyed TA, Jafri SZ, et al. Multimodality imaging of paratesticular neoplasms and their rare mimics. *Radiographics*. 2003;23(6):1461–1476.
Coley BD. Sonography of pediatric scrotal swelling. *Semin Ultrasound CT MR*. 2007;28(4):297–306.
Hörmann M, Balassy C, Philipp MO, et al. Imaging of the scrotum in children. *Eur Radiol*. 2004;14(6):974–983.
Karmazyn B, Steinberg R, Livne P, et al. Duplex sonographic findings in children with torsion of the testicular appendages: overlap with epididymitis and epididymoorchitis. *J Pediatr Surg*. 2006;41(3):500–504.
Marulaiah M, Gilhotra A, Moore L, et al. Testicular and paratesticular pathology in children: a 12-year histopathological review. *World J Surg*. 2010;34(5):969–974.
Munden MM, Trautwein LM. Scrotal pathology in pediatrics with sonographic imaging. *Curr Probl Diagn Radiol*. 2000;29(6):185–205.

### REFERENCES

Full references for this chapter can be found on www.expertconsult.com.

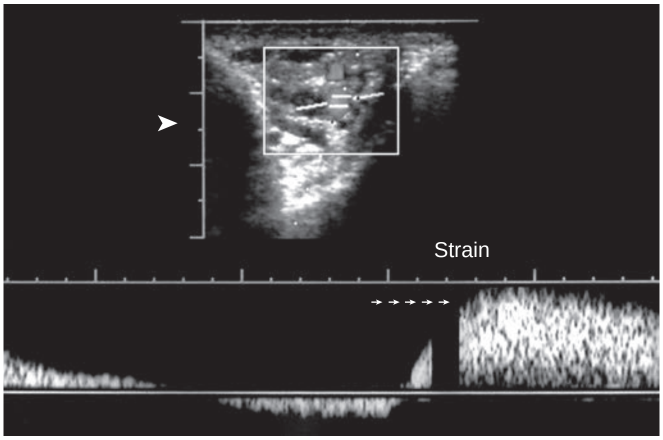

**e-Figure 125.29. Varicocele.** Doppler sonogram shows tubular structures in the scrotum. The lower half of the image shows the venous spectral pattern over time. *Arrows* point out when the patient strained, resulting in significant increased venous flow.

## REFERENCES

1. Prader A. Testicular size: assessment and clinical importance. *Triangle*. 1966;7:240–243.
2. Kuijper E, Van Kooten J, Verbeke J, et al. Ultrasonographically measured testicular volumes in 0- to 6-year-old boys. *Hum Reprod*. 2008;23:792–796.
3. Cassorla FG, Golden SM, Johnsonbaugh RD, et al. Testicular volume during early infancy. *J Pediatrics*. 1981;99:742–743.
4. Daniel WA Jr, Feinstein RA, Howard-Peebles P, et al. Testicular volumes of adolescents. *J Pediatrics*. 1982;101:1010–1012.
5. Cohen HL, Haller J. Scrotal ultrasound in the pediatric and adolescent patient. *Radiol Rep*. 1990;2:276–290.
6. Dogra VS, Gottlieb RH, Oka M, et al. Sonography of the scrotum. *Radiology*. 2003;227:18–36.
7. Cohen HL. Hematocle. In: Cohen HL, Sivit C, eds. *Fetal and Pediatric Ultrasound: A Casebook Approach*. New York: McGraw-Hill; 2001.
8. Akin EA, Khati NJ, Hill MC. Ultrasound of the scrotum. *Ultrasound Q*. 2004;20:181–200.
9. Troughton AH, Waring J, Longstaff A, et al. Role of magnetic resonance imaging in the investigation of undescended testes. *Clin Radiol*. 1990;41:178–181.
10. Woodward P. Case 70: seminoma in an undescended testis. *Radiology*. 2004;231:388–392.
11. Tekgül S, Riedmiller H, Gerharz E, et al. Cryptorchidism. In: *Guidelines on Paediatric Urology*. Arnhem, The Netherlands: European Association of Urology, European Society for Paediatric Urology; 2009.
12. Giwercman A, Grindsted J, Hansen B, et al. Testicular cancer risk in boys with maldescended testis: a cohort study. *J Urol*. 1987;138:1214–1216.
13. Riebel T, Herrmann C, Wit J, et al. Ultrasonographic late results after surgically treated cryptorchidism. *Pediatr Radiol*. 2000;30:151–155.
14. Pettersson A, Richiardi L, Nordenskjold A, et al. Age at surgery for undescended testis and risk of testicular cancer. *N Engl J Med*. 2007;356(18):1835–1841.
15. Hadziselimovic F. Treatment of cryptorchidism with GnRH. *Urol Clin North Am*. 1982;9:413–420.
16. Singh A, Kao S, D'Alessandro M, et al. Case 164; funicular type of spermatic hydrocele. *Radiology*. 2010;257:890–892.
17. Lau ST, Lee YH, Caty M. Current management of hernias and hydroceles. *Semin Pediatr Surg*. 2007;16(1):50–57.
18. Cimador M, Castagnetti M, De Grazia E. Management of hydrocele in adolescent patients. *Nat Rev Urol*. 2010;7(7):379–385.
19. Paltiel H. Acute left testicular torsion in an adolescent. In: Cohen HL, Sivit C, eds. *Fetal and Pediatric Ultrasound: A Casebook Approach*. New York: McGraw-Hill; 2001.
20. Jensen MC, Lee K, Halls J, et al. Color Doppler sonography in testicular torsion. *J Clin Ultrasound*. 1990;18:446–448.
21. Karmazyn B, Steinberg R, Kornreich L, et al. Clinical and sonographic criteria of acute scrotum in children: a retrospective study of 172 boys. *Pediatr Radiol*. 2005;35:302–310.
22. Baud C, Veyrac C, Couture A, et al. Spiral twist of spermatic cord: a reliable sign of testicular torsion. *Pediatr Radiol*. 1998;28:950–954.
23. Vijayaraghavan SB. Sonographic differential diagnosis of acute scrotum. *J Ultrasound Med*. 2006;25:563–574.
24. Zinn H, Cohen HL. Fetal and neonatal testicular torsion. In: Cohen HL, Sivit CJ, eds. *Fetal and Pediatric Ultrasound: A Casebook Approach*. New York: McGraw-Hill; 2001.
25. Zerin JM, DiPietro MA. Testicular infarction in a newborn: ultrasound findings. *Pediatr Radiol*. 1990;20:329–330.
26. Brown SM, Casillas V, Montalvo B, et al. Intrauterine spermatic cord torsion in the newborn with sonographic and pathologic correlation. *Radiology*. 1990;177:755.
27. Cohen HL, Shapiro M, Haller J, et al. Torsion of the testicular appendage. *J Ultrasound Med*. 1992;11:81–84.
28. Gatti JM, Patrick Murphy J. Current management of the acute scrotum. *Semin Pediatr Surg*. 2007;16(1):58–63.
29. Ralls PW. Acute epididymo-orchitis. In: Herzberg BS, Hill MC, Cohen HL, eds. *Ultrasound*. (third series). Reston, VA: American College of Radiology; 2005.
30. Trambert MA, Mattrey R, Levine D, et al. Subacute scrotal pain: evaluation of torsion versus epididymitis with MR imaging. *Radiology*. 1990;175:53–56.
31. Middleton WD, Siegel BA, Melson GL, et al. Acute scrotal disorders: prospective comparison of color Doppler US and testicular scintigraphy. *Radiology*. 1990;177:177–181.
32. Santillanes G, Gausche-Hill M, Lewis RJ. Are antibiotics necessary for pediatric epididymitis? *Pediatr Emerg Care*. 2011;27(3):174–178.
33. Laor T, Atala A, Teele RL. Scrotal ultrasonography in Henoch-Schönlein purpura. *Pediatr Radiol*. 1992;22(7):505–506.
34. Hara Y, Tajiri T, Matsuura K, et al. Acute scrotum caused by Henoch-Schönlein purpura. *Int J Urol*. 2004;11(7):578–580.
35. Connor S, Guest P. Conversion of multiple solid testicular teratoma metastases to fatty and cystic liver masses following chemotherapy: CT evidence of "maturation. *Br J Radiol*. 1999;72:1114–1116.
36. Kirsch A, Bastian W, Cohen HL, et al. Precocious puberty in a child with unilateral Leydig cell tumor of the testis following orchiopexy. *J Urol*. 1993;150:1483–1485.
37. Cohen HL, Torrisi J. Leydig cell tumor of the testicle. In: Cohen HL, Sivit C, eds. *Fetal and Pediatric Ultrasound: A Casebook Approach*. New York: McGraw-Hill; 2001.
38. Ulbright T, Srigley J. Dermoid cyst of the testis: a study of five postpubertal cases, including a pilomatrixoma-like variant, with evidence supporting its separate classification from mature testicular teratoma. *Am J Surg Pathol*. 2001;25:788–793.
39. Arellano CM, Kozakewich HP, Diamond D, et al. Testicular epidermoid cysts in children: sonographic characteristics with pathological correlation. *Pediatr Radiol*. 2011;41(6):683–689, quiz 796-797.
40. Neumann DP, Abrams GS, Hight DW. Testicular epidermoid cysts in prepubertal children: case report and review of the world literature. *J Pediatr Surg*. 1997;32(12):1786–1789.
41. Avila N, Premkumar A, Shawker T, et al. Testicular adrenal rest tissue in congenital adrenal hyperplasia: findings at gray-scale and color Doppler US. *Radiology*. 1996;198:99–104.
42. Vanzulli A, DelMaschio A, Paesano P, et al. Testicular masses in association with adrenogenital syndrome: US findings. *Radiology*. 1992;183:425–429.
43. Cast J, Nelson W, Early A, et al. Testicular microlithiasis: prevalence and tumor risk in a population referred for scrotal sonography. *AJR Am J Roentgenol*. 2000;175:1703–1706.
44. Skyrme R, Fenn N, Jones A, et al. Testicular microlithiasis in a UK population: its incidence, association and follow-up. *BJU Int*. 2000;86:482–485.
45. Bach A, Hann L, Shi W, et al. Is there an increased incidence of contralateral testicular cancer in patients with intratesticular microlithiasis? *AJR Am J Roentgenol*. 2003;180:497–500.
46. Hamper UM. Testicular microlithiasis with germ cell tumor. In: Herzberg BS, Hill MC, Cohen HL, eds. *Ultrasound*. (third series). Reston, AV: American College of Radiology; 2005.
47. Goede J, Hack W, Vander Voort-Doedens LM, et al. Prevalance of testicular microlithiasis in asymptomatic males 0 to 19 years old. *J Urol*. 2009;182(4):1516–1520.

47a. Trout AT, Chow J, McNamara ER, et al. Association between testicular microlithiasis and testicular neoplasia: large multicenter study in a pediatric population. *Radiology*. 2017;285(2):576–583.

48. Kass E, Chandra R, Belman A. Testicular histology in the adolescent with a varicocele. *Pediatrics*. 1987;79:996–998.
49. Kessler A, Meirsdorf S, Graif M, et al. Intratesticular varicocele: gray scale and color Doppler sonographic appearance. *J Ultrasound Med*. 2005;24:1711–1716.
50. Ozcan H, Aytac S, Yagci C, et al. Color Doppler ultrasonographic findings in intratesticular varicocele. *J Clin Ultrasound*. 1997;25:325–327.
51. Cohen HL, Zinn DL. Varicocele. In: Cohen HL, Sivit C, eds. *Fetal and Pediatric Ultrasound: A Casebook Approach*. New York: McGraw-Hill; 2001.
52. Castagnetti M, Cimador M, Catalano P, et al. Evolving management of adolescent varicocele. *J Pediatr Urol*. 2008;4(2):107–112.
53. Preston MA, Carnat T, Flood T, et al. Conservative management of adolescent varicoceles: a retrospective review. *Urology*. 2008;72(1):77–80.

# 126

# Abnormalities of the Female Genital Tract

*Harris L. Cohen and Anand Dorai Raju*

## IMAGING TECHNIQUES

Ultrasound is the primary imaging modality to assess the pediatric gynecologic tract, its diseases, and the simulators of those diseases. Ultrasound provides quick evaluation of the uterus, ovaries, and cul-de-sac. Computed tomography (CT) and magnetic resonance imaging (MRI) provide a more global view of the pelvis and abdomen than does ultrasound, and they are preferred for the evaluation of tumor extent and metastases. The drawbacks of radiation exposure for CT and potential need for sedation/anesthesia for MRI are of particular relevance in pediatric patients.[1,2]

## OVARIAN AND UTERINE DEVELOPMENT

### Normal Ovary

***Overview and Imaging.*** The two ovaries are ovoid structures generally located posterior or lateral to the uterus within the mesovarium of the broad ligament (Fig. 126.1). Ovaries may be located anywhere along their embryologic course from the inferior border of the kidney to the broad ligament. Ovaries may be involved in indirect inguinal hernias, 15% of which occur in females. Herniated ovaries can extend as low as the labia (Fig. 126.2), the female equivalent of the scrotum.[1–4]

Ovarian volume can be estimated using the formula for a modified prolate ellipse: $0.52 \times L \times W \times D$. Length (L) and depth (D) usually are measured on a longitudinal (parasagittal) image, and width (W) is measured on a transverse view. In the first three months of life, when maternal hormonal stimulation is greatest, ovarian volumes average 1.06 $cm^3$ but have a range of normal as high as 3.6 $cm^3$. The high end of the range of normal is 2.7 $cm^3$ for 4- to 12-month-olds and 1.7 $cm^3$ for 13- to 24-month-olds. The mean ovarian volume reported for children older than 2 years who have not undergone puberty is 1 $cm^3$. For menstruating females, the mean ovarian volume typically is 6 to 9.8 $cm^3$.[5–9]

Ultrasound routinely identifies follicles or cysts in most girls of all ages. Cystic structures were noted in 80% of the imaged ovaries of a group of healthy children who were newborn to 2 years old, 72% of a 2- to 6-year-old group, and 68% of a 7- to 10-year-old group (Fig. 126.3). Macrocysts occasionally are seen in all age groups. The ovary is not a quiescent organ in childhood but rather is a dynamic organ undergoing constant internal change.[10]

### Normal Uterus

***Overview and Imaging.*** The uterus of the newborn has a mean length of 3.5 cm, which decreases to 2.6 to 3 cm by the

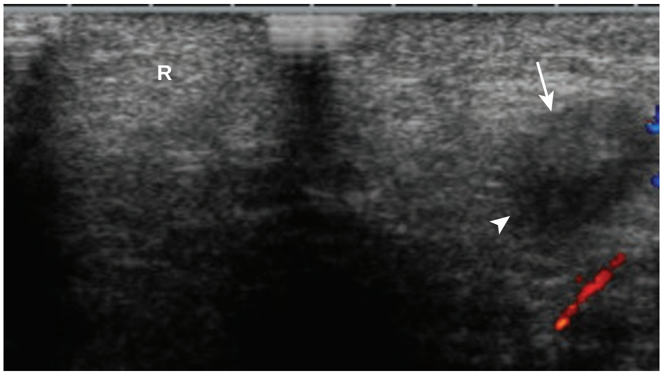

**Figure 126.2. Herniated left ovary.** Transverse color Doppler sonogram shows an unremarkable right labia *(R)*. The left labia contains a hypoechoic structure *(arrow)* with a likely cystic area *(arrowhead)*, proven to be a herniated ovary at surgery.

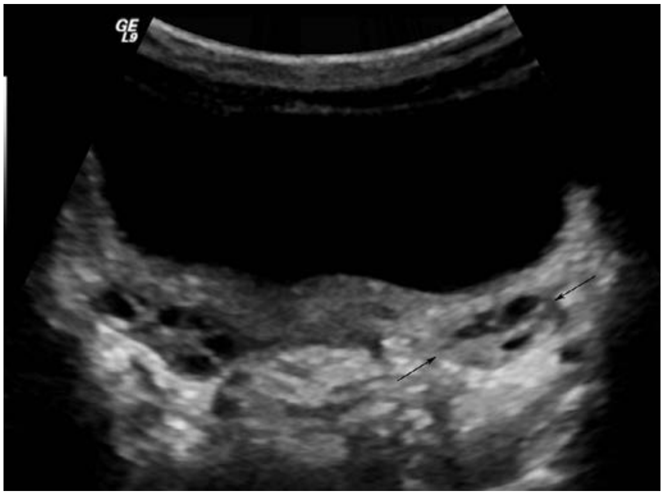

**Figure 126.1. Normal prepubertal ovaries in an 8-year-old girl.** Transverse gray-scale sonogram shows both ovaries located posterior to the bladder, containing a few small hypoechoic follicles. The left ovary is between the arrows.

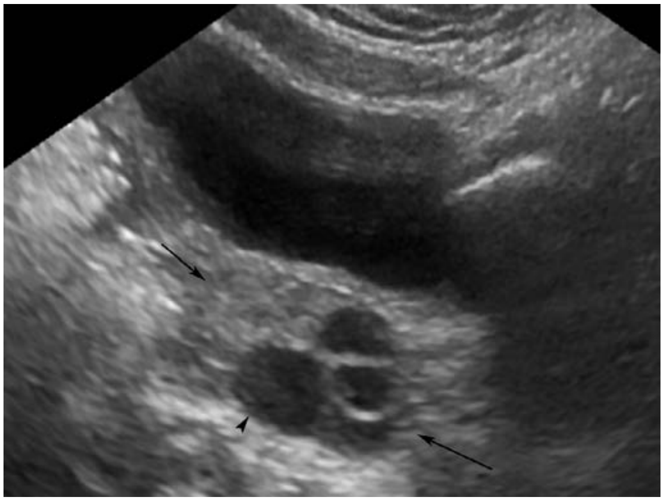

**Figure 126.3. Normal ovarian follicles in an infant.** Longitudinal gray-scale sonogram shows a normal ovary *(arrows)* in a 2-month-old. An *arrowhead* points to one of several prominent follicles seen in the ovary.

## Abstract:

This chapter reviews abnormalities of the female genital tract. It discusses imaging techniques and the imaging of normal ovary and uterus as well as non-neoplastic disorders of the pediatric and adolescent pelvis including Mullerian duct anomalies, causes of hydro and hematocolpos and hematometrocolpos, interlabial masses, pelvic inflammatory disease, ovarian cysts, hemorrhagic cysts and ovarian torsion. It discusses neoplasms of the pediatric and adolescent gynecological tract including vaginal, uterine and predominantly ovarian neoplasms including teratomas, dysgerminomas, cystadenoma and cystadenocarcinomas, granulosa cell tumor and sertoli leydig and leydig cell tumors.

## Keywords:

Pediatric ovary
Pediatric uterus
Mullerian duct system anomaly
Ovarian torsion
Hematometrocolpos

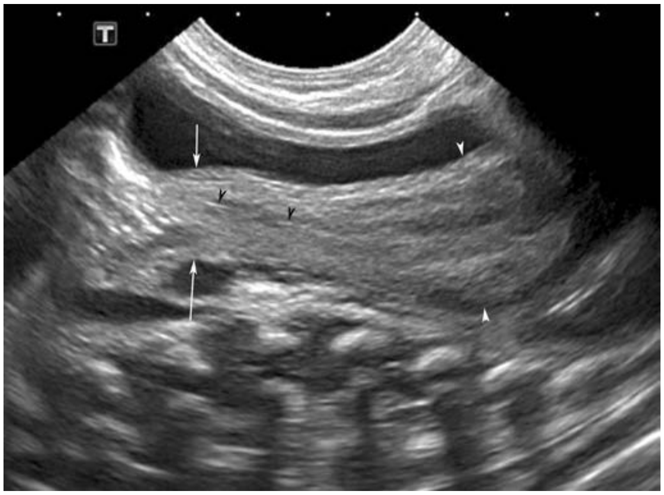

**Figure 126.4. Normal neonatal uterus.** A longitudinal sonogram shows a spade-shaped uterus posterior to the bladder. *White arrows* show a relatively narrow uterine fundus compared with the far wider cervix *(white arrowhead)*. Note the subtle central echogenic line *(black arrowheads)*, which is the coapted endometrial lining.

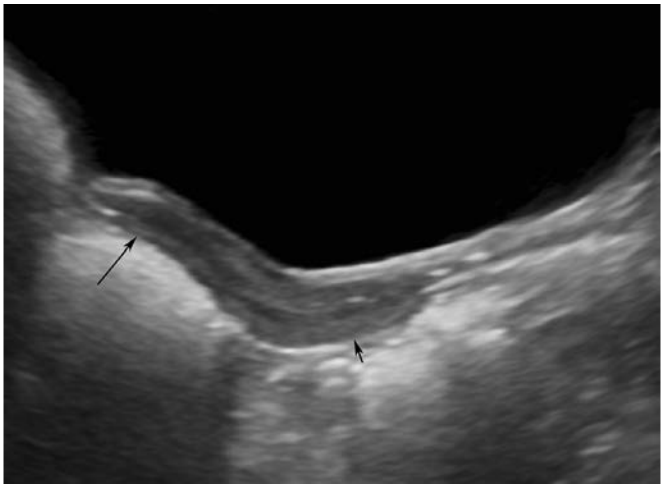

**Figure 126.5. Normal prepubertal uterus.** A longitudinal gray-scale sonogram from a 6-year-old girl shows a small, tubular-shaped uterus *(arrows)*. The cervix *(short arrow)* appears slightly larger than the uterine body and fundus *(long arrow)*. The uterus is smaller than the neonatal uterus shown in Fig. 126.4.

fourth month of life as maternal hormonal stimulation decreases. On ultrasound examination of a newborn's uterus, it is not uncommon to find either a hypoechoic halo around an echogenic endometrial cavity stripe or endometrial cavity fluid.[2,11] The typical newborn's uterus is shaped like a spade, with the anteroposterior diameter of the cervix as much as twice that of its fundus (Fig. 126.4). The newborn's cervix is also longer than the fundus. After the first year of life, the typical uterus is tube-shaped and remains that way for several years (Fig. 126.5).[2,12]

Uterine length increases gradually between 3 and 8 years of age. The mean perimenarchal measurement is 4.3 cm. After puberty and fundal development, the typical pear-shaped uterus measures 5 to 8 cm in length (Fig. 126.6). It is said to descend deeper in the pelvis and no longer maintains the typical neutral position of premenarchal life but instead may be anteverted or retroverted.[13]

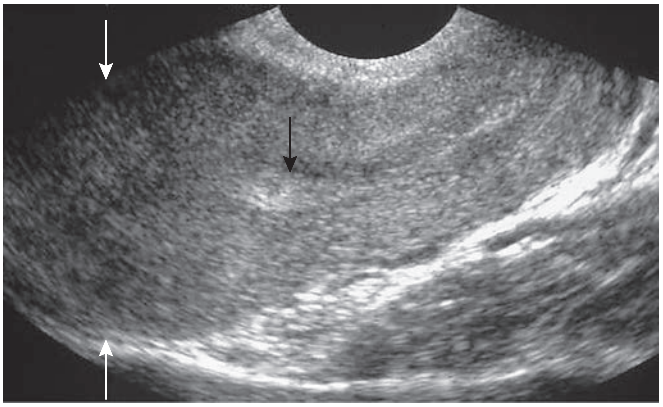

**Figure 126.6. Normal postmenarchal uterus.** Transvaginal longitudinal gray-scale sonogram from a teenager shows that the fundus is the widest part of the uterus (between the *white arrows*). The cervix, to the right, is far less wide. A *black arrow* points to the normally echogenic endometrial cavity.

## NONNEOPLASTIC DISORDERS OF THE FEMALE PELVIS

### Müllerian Duct Anomalies

***Overview.*** In females, the Müllerian duct system (MDS) normally develops into the fallopian tubes, uterus, and upper vagina, while the wolffian system involutes. External genital development proceeds along female lines except in the presence of androgens. By 11 weeks, a Y-shaped uterovaginal primordium has developed into the two fallopian tubes and fusion of a large portion of the bilateral MDS into a single uterus and upper vagina. Incomplete septal resorption of the fused bilateral MDS can lead to a septate uterus (which may extend into the cervix and vagina) or an arcuate uterus (generally considered a normal variant). Nonfusion or variably incomplete fusion of the MDS can lead to a wide spectrum of anomalies, including partial or complete absence of the uterus, fallopian tubes, and upper vagina (Mayer-Rokitansky-Küster-Hauser syndrome), uterus didelphys, and bicornuate uterus (Fig. 126.7). The association of uterine and renal anomalies is well established, including "obstructed hemivagina with ipsilateral renal agenesis (OHVIRA)," and when a gynecologic anomaly is present, one should evaluate the kidneys and urinary tract (e-Fig. 126.8) and vice versa.[14] While ultrasound may suggest anomalies of the MDS, postpubertal pelvic MRI is the imaging test of choice for characterization.

### Transverse Vaginal Septum and Imperforate Hymen

***Overview.*** In a girl with a transverse vaginal septum, the vagina is obliterated by fibrous connective tissue with vascular and muscular elements lined by squamous epithelium. The area of obliteration may be a thin membrane, but more commonly it involves a segment of the vagina (segmental vaginal atresia). The imperforate hymen is a thin membrane that forms at the junction of the caudal end of the MDS and the cranial end of the urogenital sinus. Both a transverse vaginal septum and imperforate hymen may present with an obstructed uterus and vagina.[11,15–18]

A distended vagina (colpos) or uterus (metros) is filled with secretions (muco), watery fluid (hydro), or blood (hemato). For example, hematometrocolpos is defined as hemorrhagic material filling a distended vagina and uterus. It is suggested on physical examination by either seeing an interlabial mass or palpating a pelvic mass. Clinical presentation in the teenage years includes amenorrhea

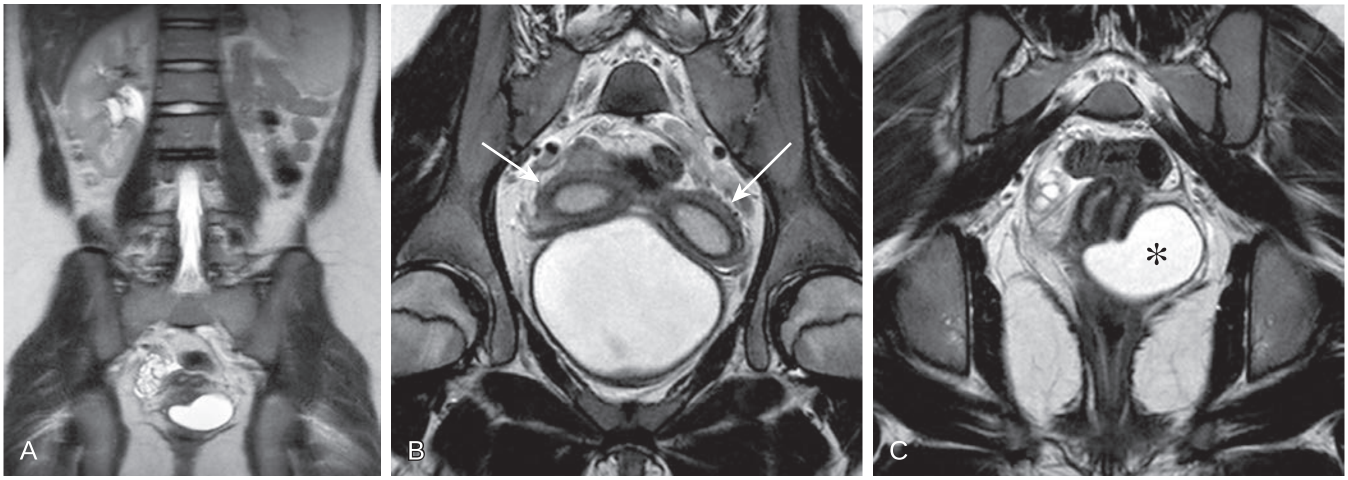

**e-Figure 126.8. Obstructed hemivagina with ipsilateral renal agenesis (OHVIRA).** (A) Coronal T2-weighted magnetic resonance (MR) image in a 13-year-old girl shows a normal right kidney; the left kidney is absent and bowel is present in the left renal fossa. (B) Coronal T2-weighted MR images shows two separate uteri *(arrows)*. (C) Coronal T2-weighted image shows two cervices. Imaging confirmed uterus didelphys. Fluid signal *(asterisk)* surrounds the left cervix and distends the left hemivagina due to an obstructing vaginal septum.

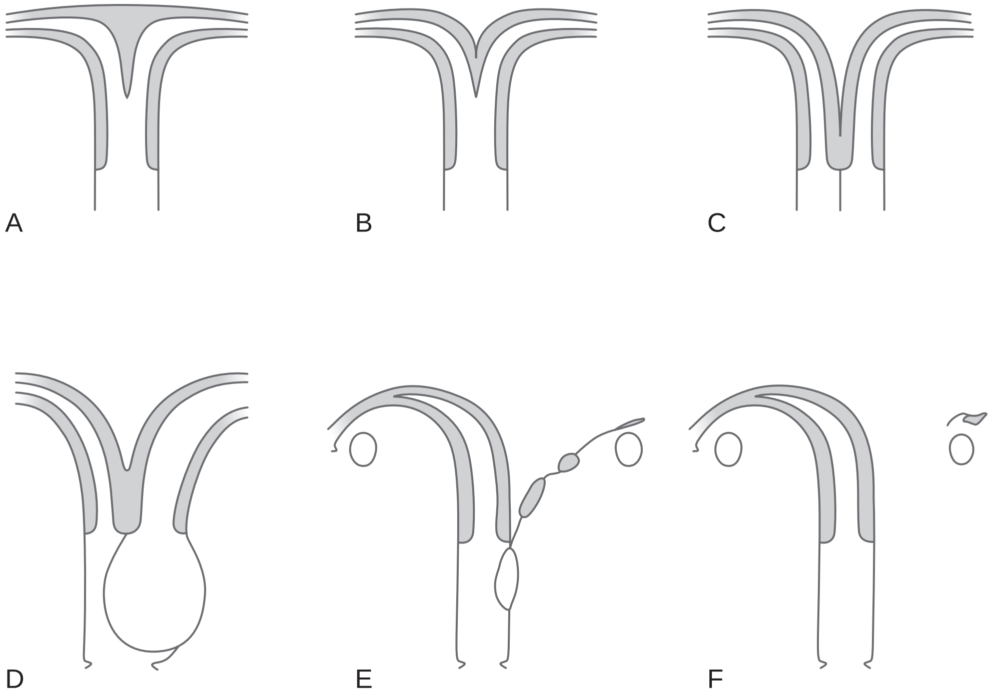

**Figure 126.7. Müllerian ductal system anomalies.** (A) Septate uterus. (B) Bicornuate uterus with single cervix. (C) Uterus didelphys with a septate vagina. (D) Uterus didelphys with congenitally obstructed hemivagina. (E) Unicornuate uterus with rudimentary hemiuterus (the rudimentary hemiuterus is nondilated, suggesting no functional endometrial tissue). (F) Unicornuate uterus with no rudimentary hemiuterus.

(despite normal development of secondary sex characteristics) and cyclic crampy abdominopelvic pains, or a pelvic mass resulting from accumulation of menstrual blood in the proximal vagina (and uterus and tubes). Complete or partial obstructions may occur in association with various MDS anomalies.[14,19–21]

***Imaging.*** Ultrasound images are similar in appearance whether seen in a neonate or a menarchal teenager. The distended vagina appears as a round or tubular cystic mass that usually is midline, often containing internal echoes from accumulated cervical mucus secretions or hemorrhage from sloughing of a hormonally stimulated endometrial lining. The uterus can be identified separately from the vagina by the thick muscular uterine wall, whereas the vaginal wall is thin. Pelvic MRI also can show the obstructed vagina and confirm the presence of blood products (Fig. 126.9).[14,15,22,23]

***Treatment.*** Vaginal obstruction detected in the neonate or infant is typically immediately corrected. In patients presenting with hematometrocolpos at puberty, the obstruction should be corrected as promptly as possible to avoid endometriosis from reverse spillage of menstrual blood into the peritoneal cavity through the fallopian tubes. Hysterectomy is indicated in patients with vaginal agenesis with a rudimentary uterus and a functional endometrium and in patients with cervical atresia occurring as an isolated lesion or in association with vaginal agenesis (forms of Mayer-Rokitansky-Küster-Hauser syndrome).[2,21–24]

## Interlabial Masses in Young Girls

***Overview and Imaging.*** The differential diagnosis of interlabial masses is usually made on visual inspection based on the location and external appearance of the mass. Masses associated with the urethral orifice include prolapse of an ectopic ureterocele (identified as a small, reddened, doughnut-like mass with its central opening being the ureteral meatus itself) and cystic dilatation of an obstructed paraurethral (Skene) gland (presenting as a mass located on either side of a displaced urethral meatus). Masses associated with the vaginal introitus include prolapse of a vaginal cyst (a remnant of the wolffian or Müllerian duct systems or epithelial inclusions originating from elements of the urogenital sinus), an imperforate hymen (e-Fig. 126.10), cystic dilatation of an obstructed Bartholin gland, and prolapse of a sarcoma botryoides (embryonal rhabdomyosarcoma) of the vagina.[2,6]

A cystogram or vaginogram as well as ultrasound of the bladder and vagina may be necessary to further define the lesion. CT or MRI may help if continued anatomic questions remain. At times, only examination under anesthesia and surgical exploration are conclusive.[6,21]

## Pelvic Inflammatory Disease

***Overview.*** Pelvic inflammatory disease (PID) is the most serious complication of sexually transmitted diseases. PID includes a spectrum of ascending infection that ranges from isolated endometritis to extension of infection into the Fallopian tubes (salpingitis) and ovaries (oophoritis), potentially resulting in a tuboovarian abscess (TOA), and even extension into the peritoneal cavity with resultant peritonitis. *Neisseria gonorrhoeae* and *Chlamydia trachomatis* are the most common etiologic agents.[25,26] Clinical presentation includes lower abdominal/pelvic pain, purulent vaginal discharge, fever, leukocytosis, and an elevated erythrocyte sedimentation rate. Adnexal tenderness, generally bilateral, and cervical motion tenderness are hallmarks for the clinical diagnosis on physical examination.[25,26]

***Imaging and Treatment.*** Early in the course of PID or salpingitis, no abnormal ultrasound findings may be present, and the diagnosis will be based solely on clinical and laboratory evaluation. A helpful ultrasound finding in cases of salpingo-oophoritis is prominent ovaries that may be adherent to the uterus. More advanced cases of acute or, more often, chronic PID may demonstrate evidence of hydrosalpinx, pyosalpinx, or TOA (Figs. 126.11, 126.12, and e-Fig. 126.13). The affected fallopian

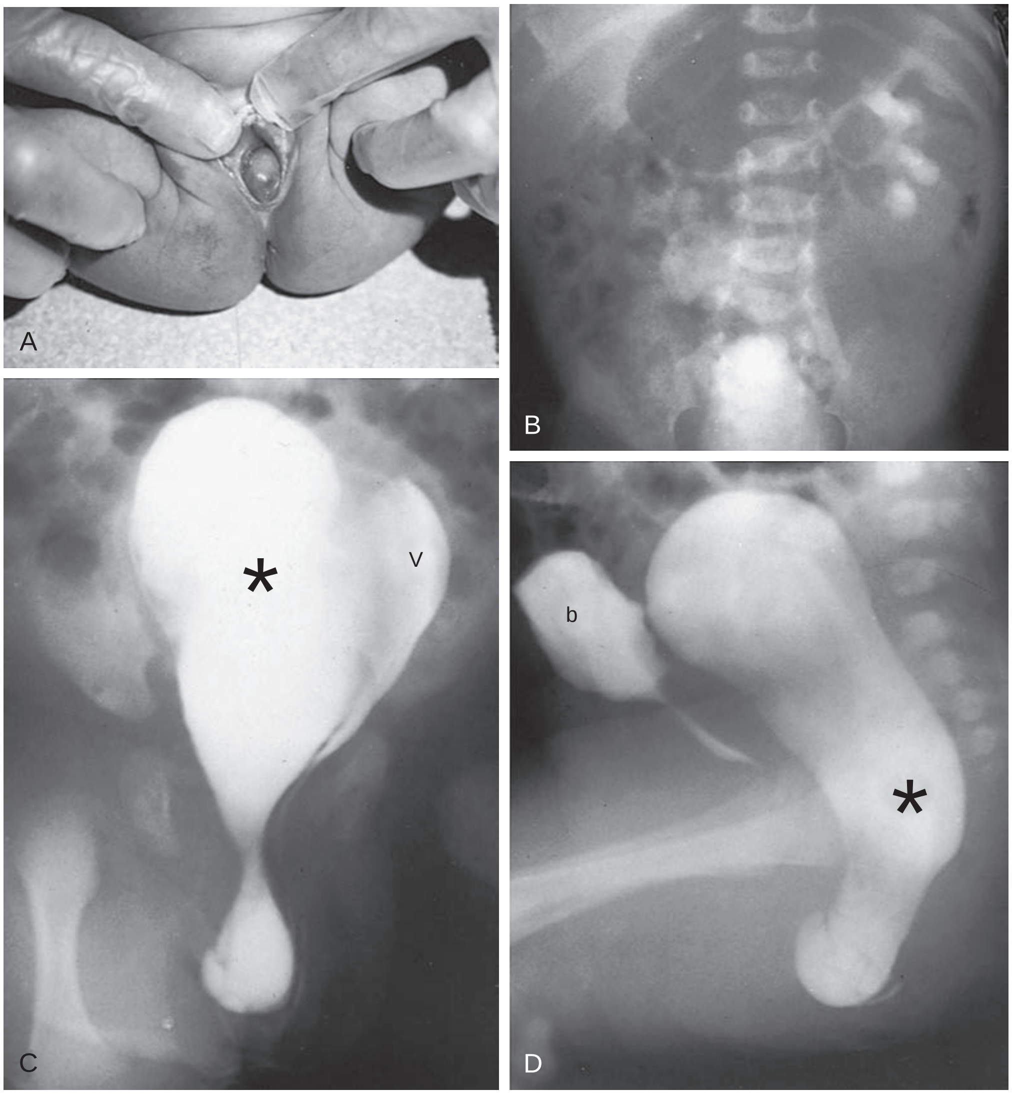

**e-Figure 126.10. Obstructed right hemivagina.** (A) A 2-day-old girl presented with a gray cystic mass at the vaginal introitus. (B) Intravenous urography shows no right renal function (probably because of an absent kidney). On frontal (C) and lateral (D) vaginograms, contrast material introduced through a needle inserted in the cystic mass at the introitus opacifies a markedly distended right hemivagina and uterus (unilateral hydrometrocolpos) *(asterisks)*. Contrast material from previous studies is still present in the patent left hemivagina *(V)* and bladder *(b)*.

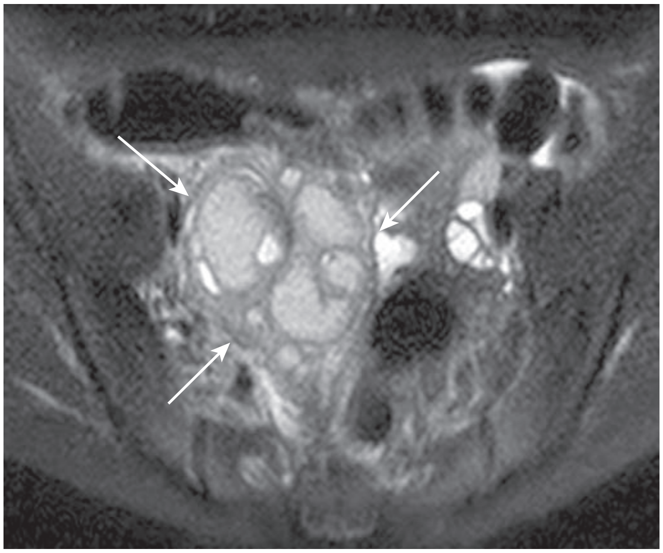

**e-Figure 126.13. Pyosalpinx and tubo-ovarian abscess.** Axial T2-weighted fat-saturated MR image from a 14-year-old sexually active girl shows a mass *(arrows)* consisting of multiple round and ovoid intermediate signal structures in the right hemipelvis surrounded by inflammation. A normal right ovary was not identified. The left adnexa is normal.

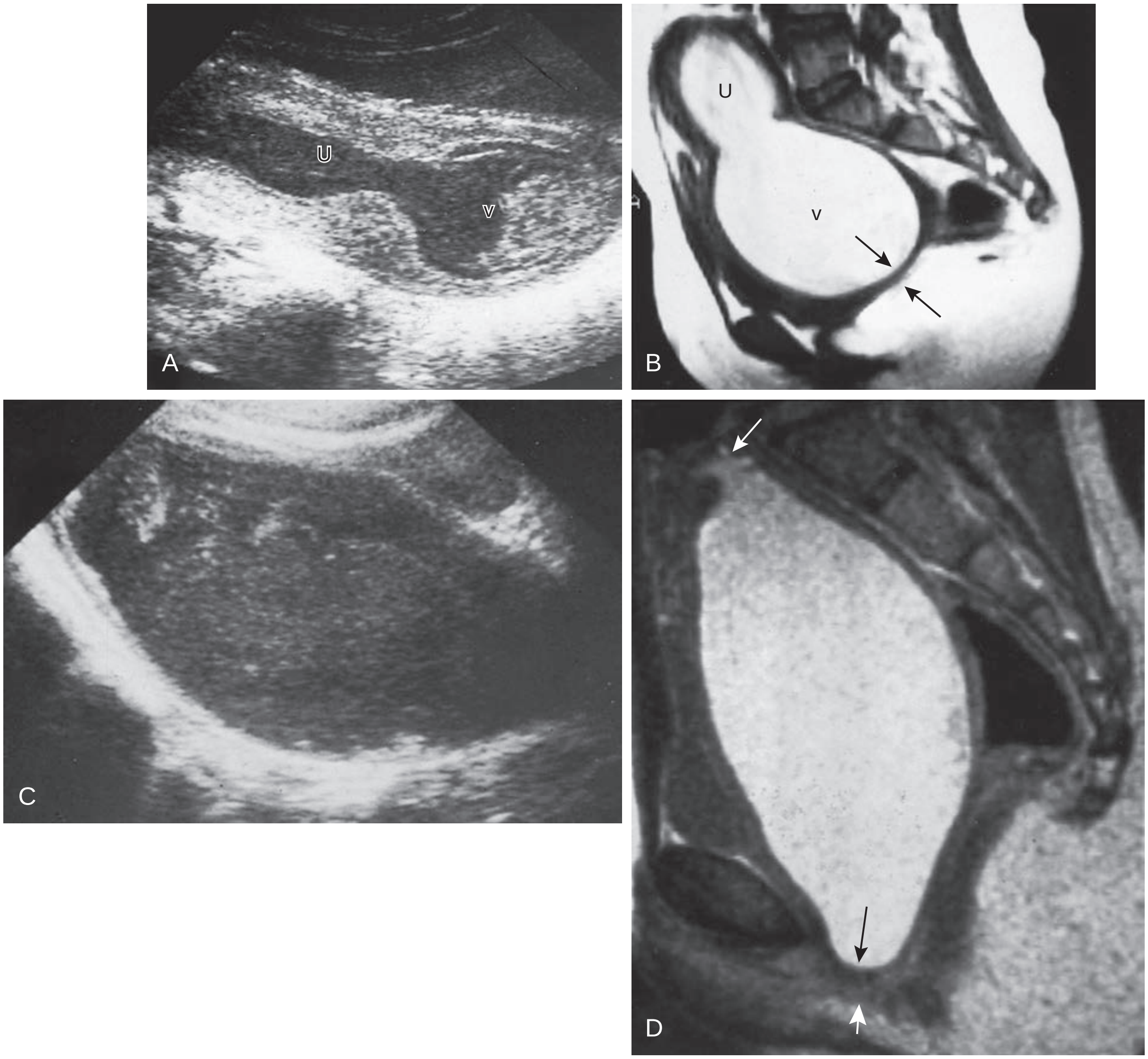

**Figure 126.9. Hematometrocolpos in two different girls.** (A) Longitudinal gray-scale sonogram shows a large midline cystic structure consistent with a distended vagina *(v)* and uterus *(U)*. The lower part of the vagina contains echogenic material. The external genitalia appeared normal on inspection. (B) Midline sagittal T1-weighted magnetic resonance (MR) image obtained for presurgical planning shows the enlarged vagina *(v)* and uterus *(U)* filled with material proven to be blood. The obstruction is at the level of the lower vagina and measures 0.5 cm in thickness *(arrows)*. At surgery, this was either a very low transverse vaginal septum or thick imperforate hymen. (C) Longitudinal gray-scale sonogram shows a large midline cystic structure containing debris, consistent with hematocolpos. (D) Midline T1-weighted MR image shows a markedly distended vagina filled with blood. The uterus *(long white arrow)* is not enlarged. The obstruction is at the level of the lower vagina and measures more than 0.5 cm in thickness *(between short white and black arrows)*. At surgery, the obstruction was found to be a thick transverse vaginal septum or short zone of vaginal atresia.

tube walls may be thickened with intraluminal linear echoes. The echogenicity of the fluid within the fallopian tube is not a reliable indicator of the presence or absence of infection. TOA appears on ultrasound as partial or complete replacement of the normal ovarian tissue by a heterogeneous mass or an echopenic region with contained debris. The contents of a suspected TOA often can be better evaluated by transvaginal ultrasound examination. CT and MRI can also be used to evaluate the extent of inflammation. TOA usually is treated aggressively with intravenous antibiotic regimens and, if necessary, percutaneous drainage or surgery.[26,27]

## Ovarian Torsion

***Overview.*** Ovarian torsion is caused by partial or complete rotation of the ovary on its pedicle, compromising first lymphatic flow, then venous drainage, and finally arterial inflow, leading to hemorrhagic infarction. Torsion of the ovary is most often seen in peripubertal or older girls. Ovarian torsion is often associated ovarian or paraovarian cysts or masses.[28,29] Classic ovarian torsion pain is sudden and acute. Associated complaints of nausea, vomiting, or constipation may occur and mislead the clinician; fever is rare. Leukocytosis with a left shift may be present. At least half of patients with ovarian torsion claim prior bouts of such pain, suggesting previous torsion and detorsion.[28,29]

***Imaging.*** Ovaries involved in torsion have a variable ultrasound appearance related to the degree of internal hemorrhage, stromal edema, and infarction that has occurred by the time they are imaged. The ovaries may appear cystic, cystic with septations, cystic with a debris layer, complex with mixed solid and cystic components, or solid. One relatively specific ultrasound image is a unilaterally enlarged solid ovary with multiple peripheral (cortical zone) follicles (Fig. 126.14).[30]

An ovary that has sustained acute torsion is generally much larger than a normal ovary. Reported volumes range from only 3.2 to 24 times normal, to ovarian volumes of 150 cm$^3$ or larger in postmenarchal patients. Comparison with the volume and morphology of the contralateral ovary may help make the diagnosis under the appropriate clinical circumstances.[29,30]

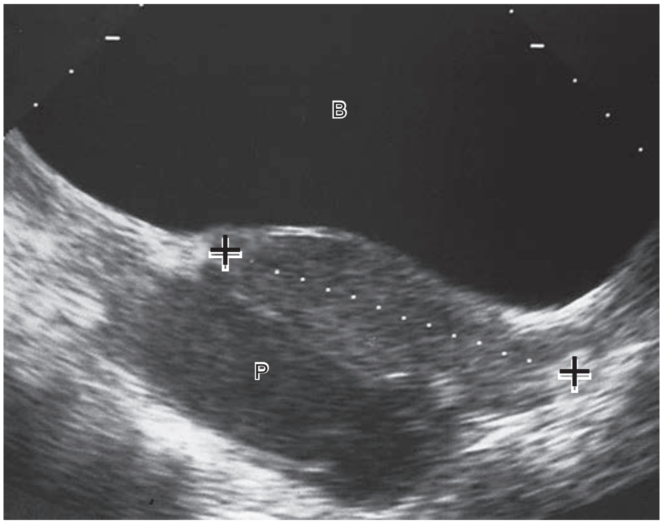

**Figure 126.11. Pyosalpinx.** Midline longitudinal gray-scale sonogram shows a fluid-filled tubular structure *(P)* containing debris, allowing through-transmission of sound, located posterior to the uterus *(cursors)*. *B,* Bladder.

Color Doppler imaging in the evaluation of cases of suspected ovarian torsion can sometimes be confusing. Well-documented cases exist of surgically proven torsed ovaries for which color Doppler imaging showed peripheral and even central arterial flow. Other investigators have reported that an assurance of viability can only be made by imaging central venous flow in an ovary that has undergone torsion. An 87% diagnostic accuracy for determining viability is reported by verifying blood flow changes at the twisted vascular pedicle itself. Patients with no blood flow at the twisted pedicle may have necrotic ovaries.[31–33]

A fallopian tube may rarely torse without torsion of the associated ovary (Fig. 126.15). When this occurs, patients may have sudden pain or nonspecific complaints. A cystic, sometimes tubular or C-shaped structure may be seen at ultrasound, CT, or MRI, and may be mistaken for acute appendicitis.

***Treatment.*** It is hoped that detorsion and, if necessary, removal of a mass causing torsion will save the gonad and preserve its function. The time from clinical complaint to diagnosis and treatment plays a large role in preserving ovarian function. Doppler imaging may have a role in assessing the recovery of an ovary that has undergone torsion in follow-up studies after surgical detorsion.[1,35,36] The role of oopheropexy remains controversial.

## Nonneoplastic Ovarian Cysts

***Overview and Imaging.*** Nonneoplastic cysts of follicular origin (i.e., functional ovarian cysts) are the most common cause of ovarian enlargement. Beyond puberty, the adolescent ovary is similar to that of the adult, developing several follicles early in the menstrual cycle until a dominant follicle develops and ruptures at midcycle, while the others atrophy and resorb. Occasionally, one or more of these follicles fails to resorb and instead enlarges as a functional or retention cyst. These cysts can reach a large size but usually are no larger than 3 cm. The classic cyst on ultrasound examination is echoless with a sharp back wall and excellent acoustic through-transmission. Most functional ovarian cysts are treated conservatively and resolve spontaneously. If there is concern for a neoplastic etiology, a 6-week follow-up ultrasound evaluation allows analysis of cyst in the other half of a different menstrual cycle, thus

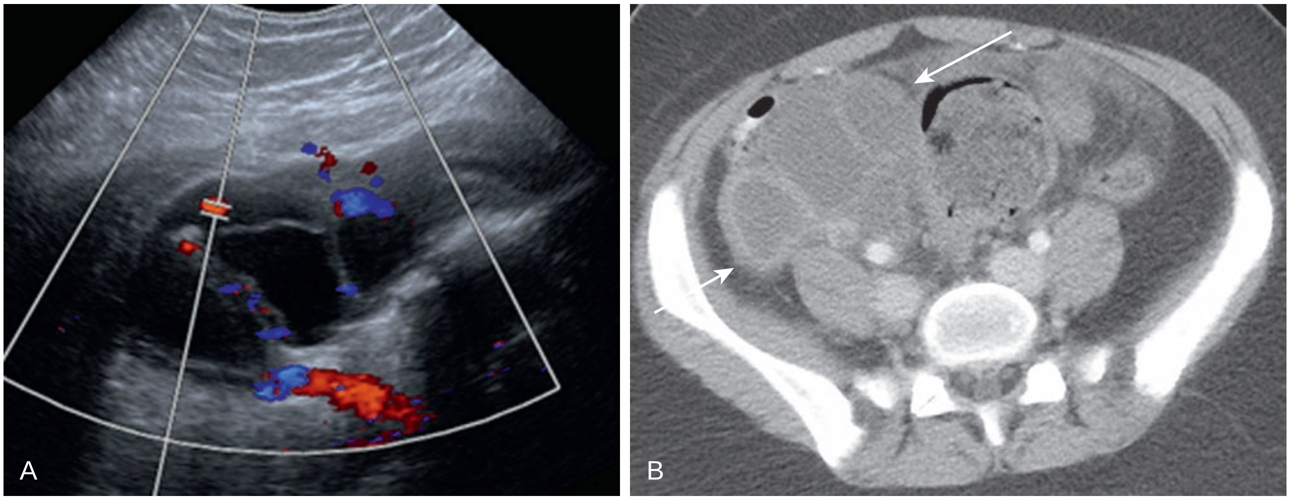

**Figure 126.12. Tubo-ovarian abscess from pelvic inflammatory disease.** (A) Color Doppler image through the right adnexa in a 16-year-old girl shows multiple fluid-filled structures with a discrete wall. (B) Axial contrast-enhanced CT image shows multiple peripherally enhancing fluid-filled structures *(arrows)* in the right lower quadrant, proven to be a tubo-ovarian abscess. Percutaneous image-guided needle aspiration yielded streptococcal species.

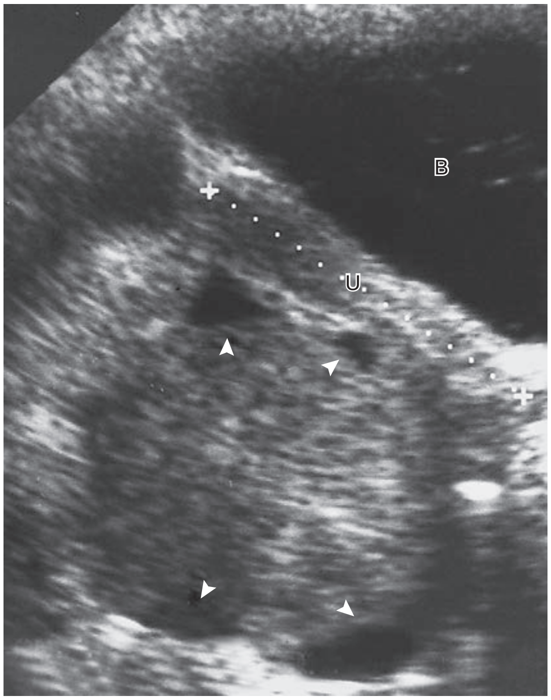

**Figure 126.14. Ovarian torsion.** Longitudinal sonogram shows a tubular uterus *(U*; *cursors)* that is posterior to the bladder *(B)* and anterior to a large solid mass with a few peripheral cysts *(arrowheads)*. This is a classic image of acute ovarian torsion. Infarction or acute hemorrhage would make the internal contents of the ovary more heterogeneous. *(From Cohen HL, Safriel YI. Ovarian torsion. In: Cohen HL, Sivit C, eds.* Fetal and Pediatric Ultrasound: A Casebook Approach*. New York: McGraw-Hill; 2001:516.)*

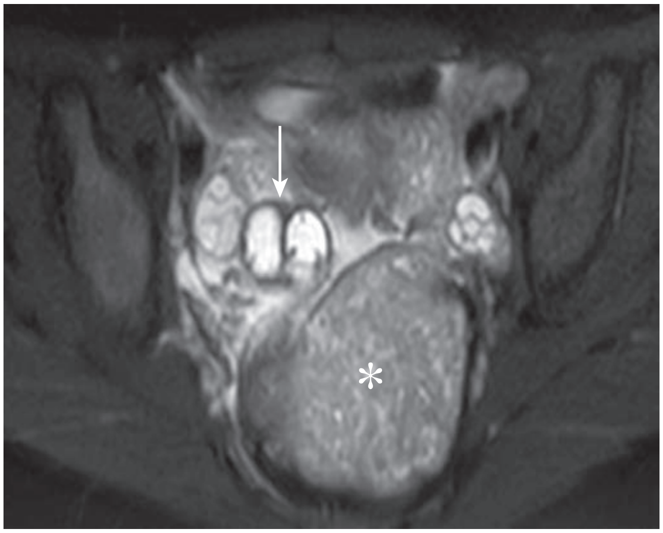

**Figure 126.15. Isolated fallopian tube torsion.** Axial T2-weighted fat-saturated MR image in an 11-year-old girl with suspected acute appendicitis shows two round fluid-filled structures *(arrows)* in the right adnexa adjacent to the normal right ovary. There is extensive inflammation in the right hemipelvis. A large amount of stool is present in the rectum *(asterisk)*. Surgical exploration confirmed isolated fallopian tube torsion.

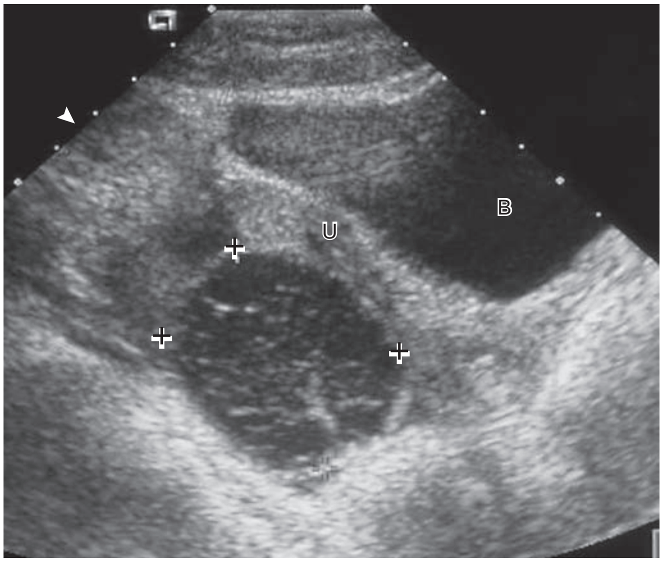

**Figure 126.16. Hemorrhagic ovarian cyst.** Longitudinal gray-scale sonogram shows a hypoechoic mass *(cursors)* containing mesh-like linear echogenicities in the adnexal area of a 12-year-old girl with acute abdominal pain. A tubo-ovarian abscess and endometrioma may look similar but present with different clinical scenarios. *B,* Bladder; *U,* uterus.

documenting resolution or diminution, and, thereby, helping to prove that it is a physiologic cyst and helping to disprove cystic neoplasm.[36–39]

### Hemorrhagic Ovarian Cysts

***Overview.*** Functional cysts may develop internal hemorrhage, which occurs when theca interna vessels rupture into the cyst cavity. Such hemorrhagic ovarian cysts can arise from ovarian follicles at any stage in their maturation, even as they involute. The typical clinical presentation of a hemorrhagic ovarian cyst is commonly sudden, severe, transient lower abdominal or pelvic pain of 1 to 3 hours' duration. The pain is thought to result from sudden distention of the ovarian cyst by the hemorrhage.[40]

***Imaging.*** Most hemorrhagic ovarian cysts are heterogeneous in echogenicity. There may be hypoechoic or hyperechoic areas separated by thin or thick linear echoes of various orientations (Fig. 126.16), echoless with a contained focal echogenicity of variable size clot, contain fluid-debris levels, or appear as a solid mass when clot fills the cyst. A changing ultrasound appearance over time can help confirm the diagnosis as the clot lyses and cyst resolves.[37,40]

## Polycystic Ovary Syndrome

***Overview.*** Polycystic ovary syndrome (PCOS; also known as *Stein-Leventhal syndrome*) is a hyperandrogenic state with resultant peripheral conversion of larger than normal amounts of estrogen. The chronic hyperestrogenic, hyperandrogenic stimulation leads to chronic anovulation and is responsible for the classic bilaterally enlarged ovaries, which may be asymmetric but usually contain numerous small follicles/cysts. PCOS is the most common secondary cause of amenorrhea in adolescents and young adults. Patients sometimes, but far from always, experience the classic triad of obesity (31%), hirsutism (62%), and menstrual abnormalities (80%), including amenorrhea, irregular menses, and prolonged uterine bleeding. Laboratory diagnosis is made by noting an increased luteinizing hormone: follicle-stimulating hormone ratio and elevated androstenedione level.[41]

***Imaging.*** A helpful indicator of PCOS is increased ovarian echogenicity, which is thought to be due to ovarian stromal hypertrophy and considered to be evidence of hyperandrogenism. Persons with PCOS have high numbers of subcapsular follicles in their ovaries (Fig. 126.17). Typically, numerous cysts of 5 to 8 mm in diameter are noted on transabdominal ultrasound evaluation of each ovary; a greater number of cysts may be appreciated on transvaginal examination. Follicles of classic cases should not be larger than 10 mm in diameter. Larger follicles or the presence of a single large (dominant) cyst makes the diagnosis of PCOS unlikely. Ovarian volumes may or may not be greater than the mean for their control group.[42–45]

## NEOPLASMS OF THE GYNECOLOGIC TRACT

### Vagina and Uterus

***Overview and Imaging.*** Embryonal rhabdomyosarcoma is the most common genital neoplasm in children of both sexes. It generally is seen before the age of 3 years, is rarely noted at birth, and is uncommon but can occur in older female patients. Urogenital sinus remnants are thought to be the origin of some rhabdomyosarcomas, usually originating from the anterior vagina near the cervix. Occasionally, they may arise from the cervix. The mass may protrude from the vaginal introitus, often with a polypoid or cluster-of-grapes appearance (sarcoma botryoides). These rhabdomyosarcomas are aggressive tumors that spread rapidly by direct invasion of the vaginal wall and pelvic structures. The tumor may extend to the uterus, bladder, ureters, or rectum. Metastases to regional lymph nodes, the lungs, and other organs may occur. Local recurrence is common.[46–48]

Endodermal sinus tumor of the vagina, also known as yolk sac carcinoma or adenocarcinoma of the infant vagina, usually is seen in infants between 8 and 15 months and rarely after the second year. It often originates in the posterior wall of the vagina (e-Fig. 126.18) and may have a polypoid appearance very similar to that of sarcoma botryoides. The tumor spreads to pelvic soft tissues, pelvic and retroperitoneal nodes, liver, and lungs.[46,48]

Clear cell (or mesonephric) adenocarcinoma usually originates from the vagina and uncommonly from the cervix. It usually is seen after menarche. In the past few decades, about two-thirds of patients with this tumor had a history of maternal exposure to diethylstilbestrol or related substances during the first 3 months of pregnancy. These tumors can become quite large, filling the entire vagina by the time of diagnosis. Tumor spread is via the lymphatics to pelvic nodes. Local recurrence is common, and pulmonary metastases can occur.[46,48]

### Ovary

***Overview.*** Ovarian neoplasms commonly are divided into groups based on the apparent origin of their cellular components: germ cell tumors, sex cord/stromal tumors, and surface epithelial tumors. Sixty percent of all pediatric ovarian neoplasms are of germ cell origin. Of the germ cell tumors, 70% are teratomas, 25% are dysgerminomas, and 5% are endodermal sinus or yolk sac tumors. About one-fifth of pediatric ovarian tumors are epithelial cell in origin, including cystadenoma (80%) and cystadenocarcinoma (10%). The remaining pediatric ovarian tumors are sex cord tumors or tumors of stromal/mesenchymal origin. Fifteen percent of those are arrhenoblastomas (also called Seroli-Leydig cell tumors), and 75% are granulosa/theca cell tumors.[46,47]

Overall, about one-third of ovarian neoplasms are malignant. This percentage decreases with increasing age. About 50% of hormonally active tumors are malignant. Of the malignant lesions, 85% are germ cell tumors (dysgerminomas, immature teratomas, endodermal sinus tumors, embryonal cell carcinomas, and choriocarcinomas), 10% are stromal (Sertoli–Leydig cell, granulosa/theca cell, and undifferentiated neoplasms), and 5% are epithelial cell tumors (serous and mucinous cystadenocarcinomas). Malignant neoplasms can break through the ovarian capsule and spread to adjacent organs. Metastases are most often to the peritoneal cavity, opposite ovary, pelvic and retroperitoneal lymph nodes, omentum, liver, and abdominal organs (Fig. 126.19). Involvement of peritoneal and pleural linings may lead to ascites or pleural effusions. Staging of malignant ovarian tumors is presented in Box 126.1.[46,49]

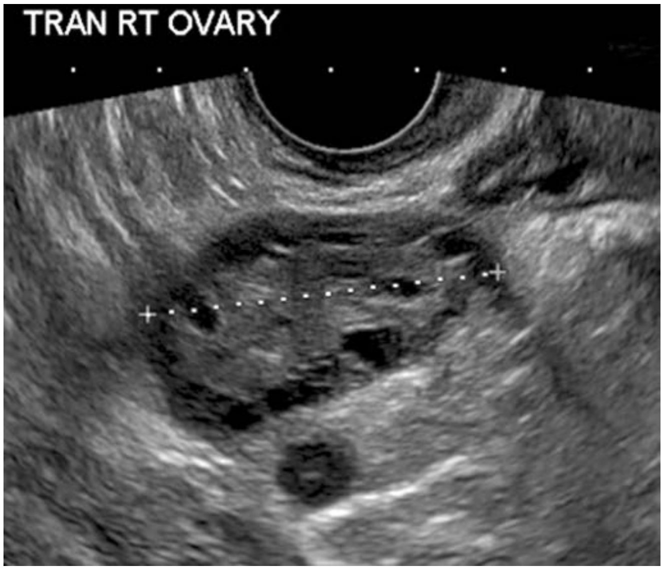

**Figure 126.17. Polycystic ovary disease.** Transverse gray-scale sonogram in an 18-year-old young woman with dysfunctional uterine bleeding shows increased echogenicity of the ovarian stroma and many peripheral follicles of similar size.

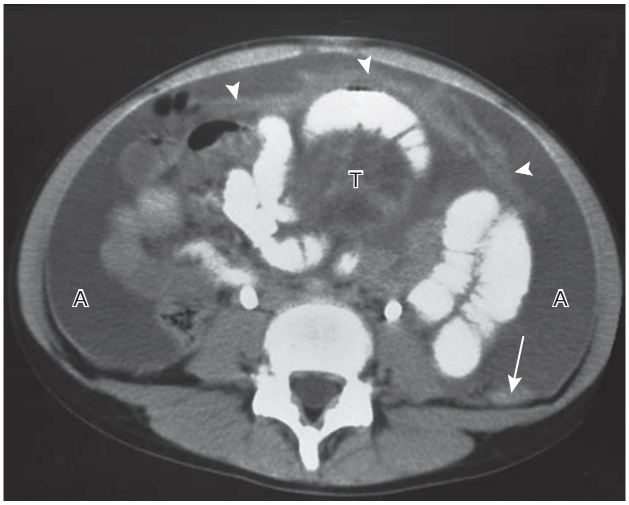

**Figure 126.19. Endodermal sinus tumor.** Axial contrast-enhanced CT image shows malignant omental spread with omental “caking” *(arrowheads)* and peritoneal implants in this 13-year-old girl with endodermal sinus tumor of the ovary. Moderate ascites *(A)* is present. An arrow points to a posterior left-sided peritoneal metastasis. *T,* The most superior portion of the ovarian tumor. *(From Cohen HL, Bober S, Bow S. Imaging the pediatric pelvis: the normal and abnormal genital tract and simulators of its diseases.* Urol Radiol. *1992;14:273-283.)*

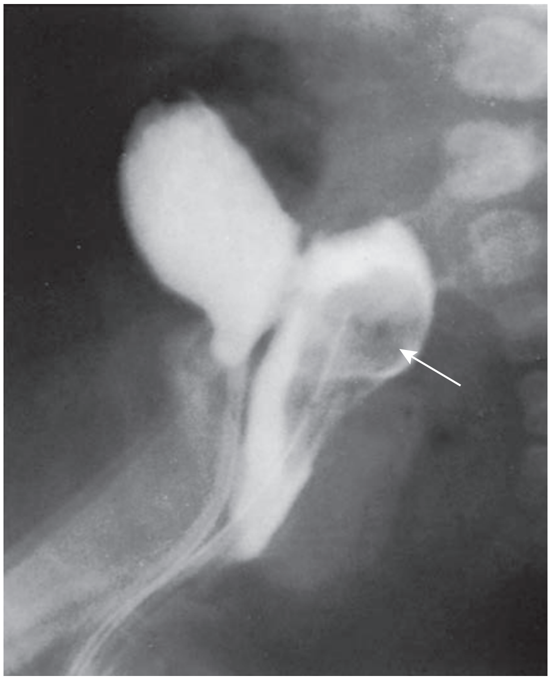

**e-Figure 126.18. Endodermal sinus tumor of the vagina.** A lateral vaginogram shows a mass *(arrow)* within the contrast-filled vagina of a 6-month-old girl, originating from the vagina's posterior wall. The contrast-filled bladder seen anterior to the vagina was filled by a separate injection.

**BOX 126.1** Staging for Ovarian Neoplasms

Stage I: Tumor limited to the ovaries
Stage IA: Tumor limited to one ovary, no malignant ascites
Stage IB: Tumor limited to both ovaries, no malignant ascites
Stage IC: Stage IA or IB with malignant ascites
Stage II: Tumor involves one or both ovaries with pelvic extension
Stage IIA: Extension or implants on the uterus or fallopian tubes, no malignant ascites
Stage IIB: Extension to other pelvic tissues, no malignant ascites
Stage IIC: Stage IIA or IIB with malignant ascites
Stage III: Tumor involves one or both ovaries with peritoneal implants outside the pelvis or retroperitoneal lymph node metastasis
Stage IIIA: Microscopic peritoneal metastasis beyond the pelvis
Stage IIIB: Macroscopic peritoneal metastasis beyond the pelvis 2 cm or less
Stage IIIC: Peritoneal metastasis beyond the pelvis more than 2 cm or regional lymph node metastasis
Stage IV: Distant metastasis, including liver parenchyma

*Based on the American Joint Committee on Cancer and the International Federation of Gynecology and Obstetrics staging of carcinoma of the ovary. Modified from Emans S, Laufer M, Goldstein D, eds.* Pediatric and Adolescent Gynecology, *5th ed. Philadelphia: Lippincott Williams & Wilkins; 2005.*

## Ovarian Teratomas

***Overview.*** Mature ovarian teratomas (or dermoid cysts) are the most common ovarian neoplasm in pediatric patients and usually are found in adolescents. The tumors may vary in size from those contained solely within the ovary itself to those that extend 5 to 10 cm beyond the ovary. Almost all teratomas are benign, with malignancy found in 2% to 10% of cases or less. Teratomas usually are discovered by chance during pelvic ultrasound examinations performed on adolescents for other reasons; about one-fourth are bilateral. Occasionally, they may be diagnosed by the incidental discovery of calcification or ossification (including teeth or bone) in the adnexal area on radiograph examinations (Fig. 126.20).[49,50]

***Imaging.*** Most teratomas appear sonographically as complex cysts with anechoic, hypoechoic, and echogenic components. A minority of cases are either anechoic (perhaps because the solid component is at the mass's periphery and not imaged) or entirely echogenic. The classic ultrasound appearance shows a prominent cystic component and at least one associated nodule (a dermoid plug or Rokitansky nodule) (Fig. 126.21) that often is echogenic, with posterior shadowing as a result of contained fat, hair, sebum, and/or calcium. The shadowing may obscure deeper portions of the mass, a phenomenon called the "tip of the iceberg" sign. The anechoic component of teratomas is made up of serous fluid or sebum, which is in a fluid state when at body temperature. Fat–fluid levels and hair–fluid levels may be seen as part of the cystic component.

Similar findings are seen on CT (e-Fig. 126.22) or MRI. CT may show calcifications that are not seen by other methods. MRI is particularly valuable in demonstrating the fatty components of the mass. Signal characteristics on MRI reflect the composition of a teratoma. Calcification, bone, and hair have low-signal intensity on both T1- and T2-weighted images. Fat has a high signal on T1-weighted studies and may show India ink artifact on T1-weighted gradient echo opposed-phase imaging. Fluid has a high signal on T2-weighted studies. Immature, partially differentiated malignant teratomas are uncommon and generally are solid and almost universally unilateral.[47,49–52]

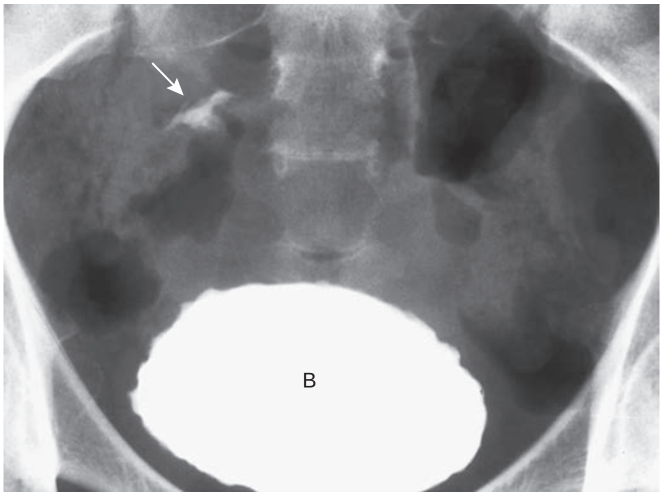

**Figure 126.20. Ovarian teratoma.** Plain radiograph of the pelvis shows a triangular calcification *(arrow)* in the right side of the pelvis. It was proven to be within a right ovarian teratoma. *B,* Bladder.

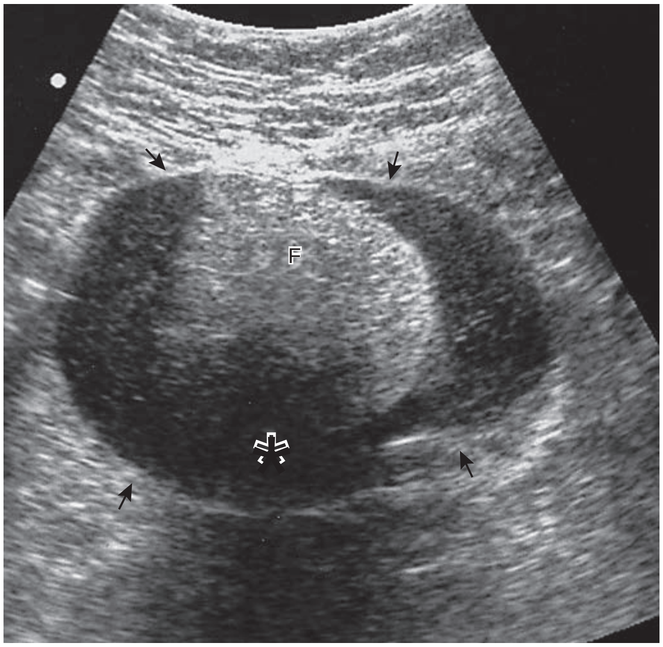

**Figure 126.21. Ovarian teratoma.** Transverse gray-scale sonogram shows a left adnexal mass *(arrows)* with a central highly echogenic component. Posterior shadowing is present *(asterisk)*, suggesting a dermoid plug. The periphery of the mass is composed of complex fluid. *(From Ruggierro M, Awobuluyi M, Cohen H, et al. Imaging the pediatric pelvis: role of ultrasound.* Radiologist. *1997;4:155-170.)*

## Ovarian Dysgerminoma

***Overview and Imaging.*** Dysgerminoma is the second-most common ovarian neoplasm in children and adolescents after mature teratoma. It is the most common malignant ovarian tumor of the pediatric period. It is said to be the histologic counterpart to the testicular seminoma of boys. Imaging or visual inspection shows it to be solid, smooth, and typically well encapsulated. These tumors often are large when first diagnosed (Fig. 126.23). About one-fifth of cases have bilateral involvement. Dysgerminomas may arise in dysgenetic gonads, but this presentation is much less common than

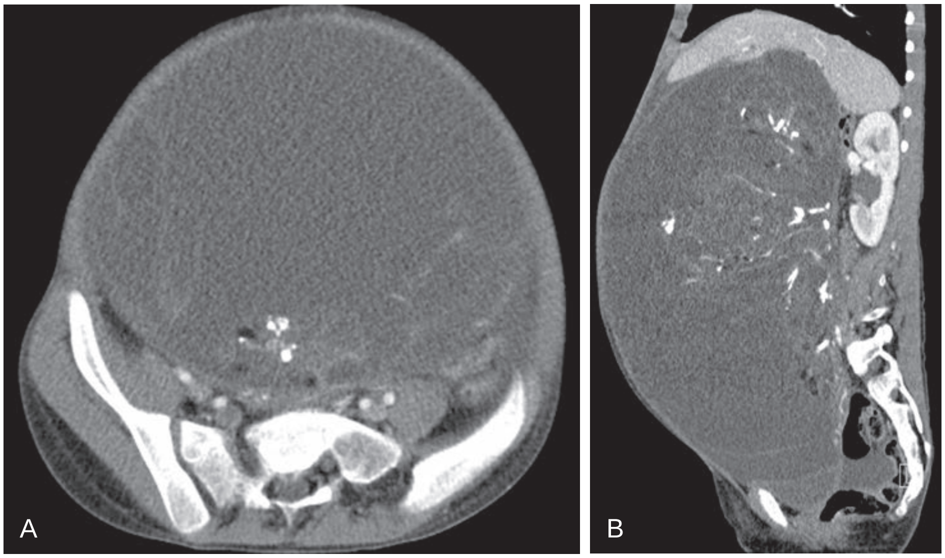

**e-Figure 126.22. Ovarian teratoma.** (A) Axial and (B) sagittal contrast-enhanced CT images in an 11-year-old girl with enlarging abdomen show a very large mass arising from the pelvis. The mass is predominantly fluid attenuation and contains high attenuation foci consistent with calcification/ossification and low attenuation foci consistent with fat.

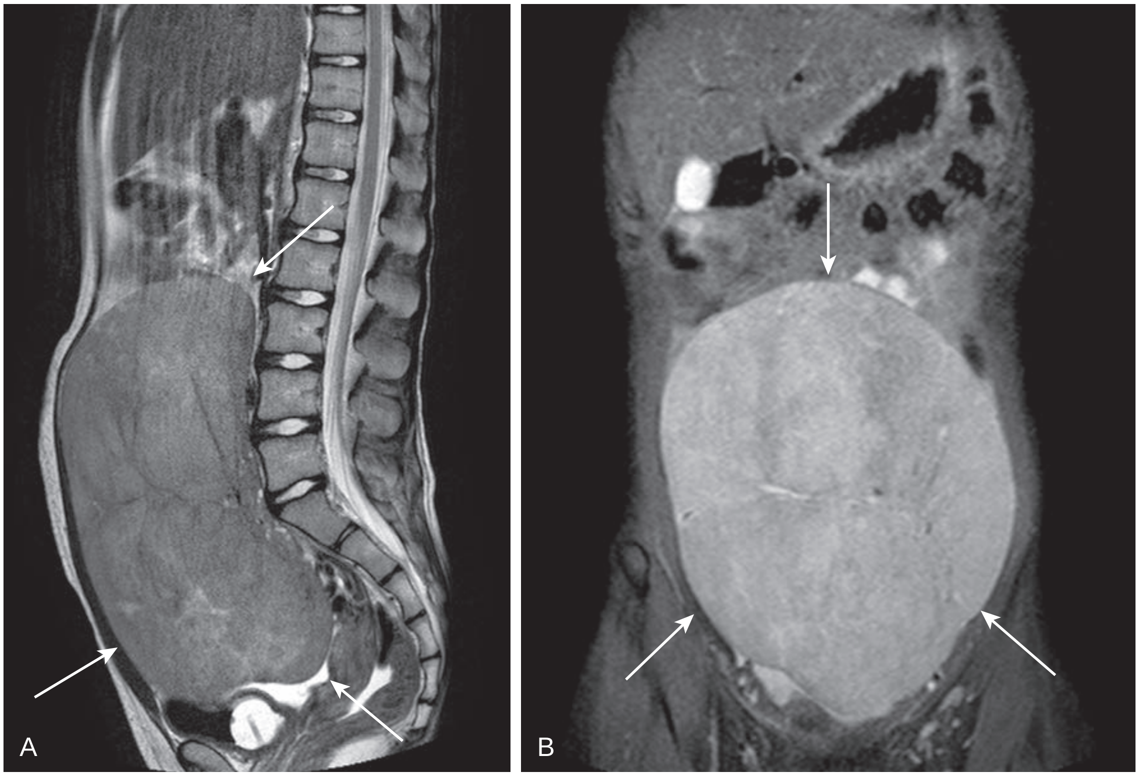

**Figure 126.23. Dysgerminoma.** (A) Sagittal T2-weighted and (B) coronal T2-weighted fat-saturated MR images in a 15-year-old girl with an enlarging abdomen show a large, heterogeneous, predominantly hyperintense mass *(arrows)* arising from the pelvis. The mass was proven to arise from the left ovary at surgery.

with gonadoblastomas. Pure dysgerminomas are nonfunctioning tumors, but hormonal function may be observed in dysgerminomas that contain islands of other germ cell tumors (mixed germ cell tumors). These tumors can spread locally and to retroperitoneal nodes. They are very radiosensitive, and prognosis with treatment is generally good, with an overall survival of more than 90%.[49,50]

## Endodermal Sinus Tumor

***Overview and Imaging.*** An endodermal sinus tumor (yolk sac tumor or carcinoma) is an uncommon malignant neoplasm that can occur at any age. It often is bulky at the time of diagnosis and is predominantly solid on ultrasound but may contain cystic spaces. In most cases, serum alpha-fetoprotein levels are increased. Some endodermal sinus tumors secrete human chorionic gonadotropin, causing incomplete precocious puberty by stimulating ovarian estrogen production. This phenomenon can cause menstrual irregularities in postpubertal girls. The tumor is radiosensitive. Although the incidence of recurrence is high, the survival rate is high among treated patients.[53]

## Cystadenomas and Cystadenocarcinomas

***Overview and Imaging.*** Surface epithelial tumors in children are similar to those in adults and consist predominantly of cystadenomas and cystadenocarcinomas. Cystadenomas are very uncommon before puberty and usually are unilateral, although they may be bilateral in some girls (Fig. 126.24). They vary in size from 3 to 30 cm. Of the two types of cystadenomas, serous cystadenomas contain clear, watery fluid, and the less common mucinous cystadenomas contain mucin, a jelly-like material. Most of these tumors are multiseptated cystic masses (Fig. 126.25) when imaged by ultrasound, CT, and MRI. Cystadenomas are benign neoplasms, but a serous papillary form is reported to be prone to rupture, with spillage of tumor material into the peritoneal cavity, causing a serous papillomatosis. Cystadenocarcinomas are much less common than their benign counterparts. They may appear similar to cystadenomas, but the presence of irregular margins, thick septations, and papillary projections suggests malignancy. Ascites, omental or peritoneal implants, lymphadenopathy, and hepatic metastases indicate malignant spread.[46,49]

## Juvenile Granulosa Cell Tumors

***Overview and Imaging.*** Juvenile granulosa cell tumors are predominantly solid, but mixed solid and cystic or predominantly cystic masses are seen. These lesions may be large at diagnosis and can appear complex at MRI. About three-fourths of juvenile granulosa cell tumors produce estrogen, which causes isosexual precocious puberty; uterine and endometrial stripe enlargement may be observed. Nonfunctioning tumors may be discovered incidentally as a mass on physical examination or ultrasound. The vast majority of juvenile granulosa cell tumors are successfully managed with surgical resection, with recurrences and metastases a rarity.[46,49]

## Sertoli-Leydig/Leydig Cell Tumors

***Overview and Imaging.*** Formerly called arrhenoblastomas, these tumors are usually large and unilateral. They may be solid or cystic. They usually are well differentiated and benign, but a poorly differentiated form also occurs. Most produce androgenic substances, causing virilization in prepubertal girls and signs of virilization, hirsutism, and oligomenorrhea or amenorrhea after puberty.[54] These tumors have recently been associated with *DICER1* germline mutations.[55]

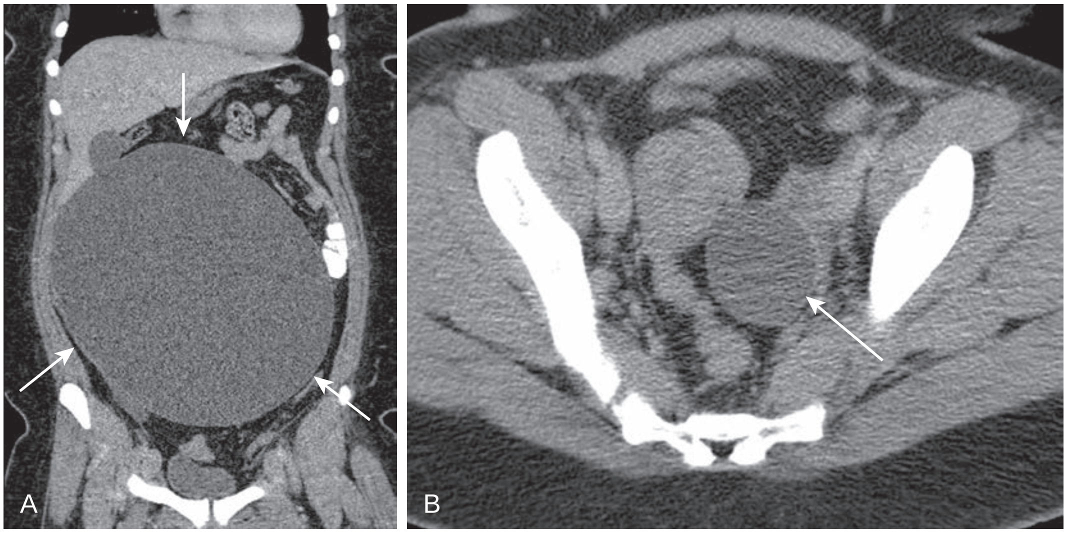

**Figure 126.24. Bilateral ovarian serous cystadenomas.** (A) Coronal contrast-enhanced CT image in a 17-year-old girl shows a very large cystic mass *(arrows)* filling most of the abdomen and pelvis, proven to be a serous cystadenoma arising from the right ovary. (B) Axial CT image through the pelvis shows a second cyst *(arrow)* arising from the left ovary, also proven to be a serous cystadenoma.

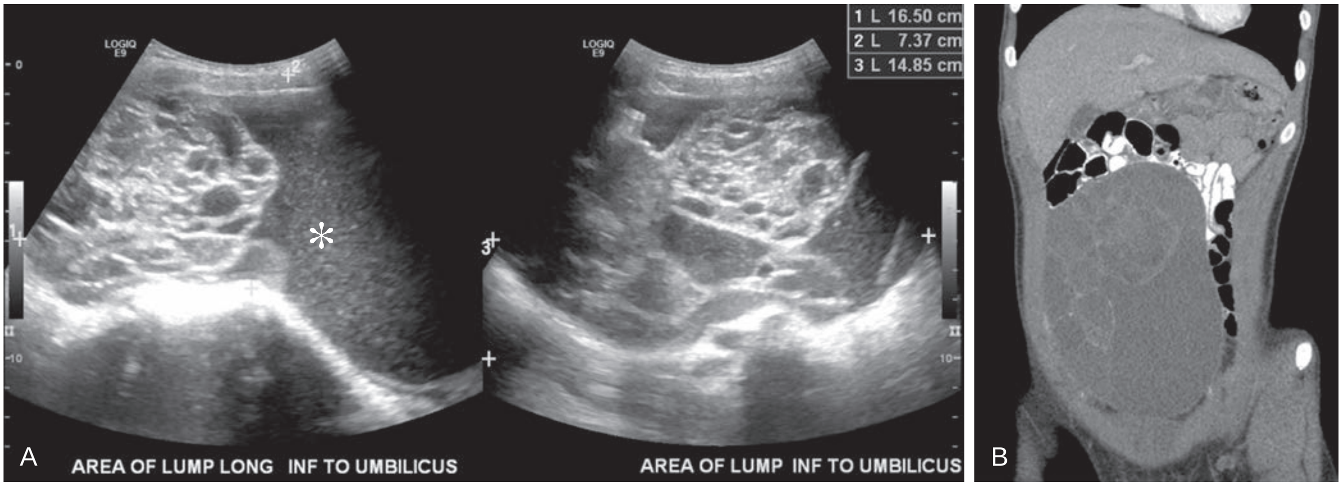
LOGIQ E9
LOGIQ E9
1 L 16.50 cm
2 L 7.37 cm
3 L 14.85 cm
*
A
AREA OF LUMP LONG INF TO UMBILICUS
AREA OF LUMP INF TO UMBILICUS
B

**Figure 126.25. Ovarian mucinous cystadenoma.** (A) Side-by-side longitudinal and transverse gray-scale ultrasound images in a 14-year-old girl show a large abdominopelvic complex cystic mass containing many septations and echogenic fluid *(asterisk)*. (B) Coronal contrast-enhanced CT image shows similar findings, including considerable mass-effect upon adjacent structures. Surgical pathology confirmed a mucinous cystadenoma arising from the right ovary.

## KEY POINTS

- Ultrasound is the primary imaging modality used to assess the pediatric gynecologic tract.
- Follicles/cysts exist in the ovaries of most girls of all ages.
- A changing ultrasound appearance over time can help confirm the diagnosis of a hemorrhagic ovarian cyst.
- The predominant pelvic mass found in neonates and infants is a distended, obstructed vagina or uterus filled with secretions, fluid, or blood.
- Patient history, physical examination, and laboratory findings may be necessary to differentiate among TOA, hemorrhagic cyst, and endometrioma, which may look alike on ultrasound.
- Ovaries in persons with PCOS show increased ovarian echogenicity and typically contain numerous 5 to 8 mm peripheral follicles on transabdominal ultrasound.
- An acutely torsed ovary is much larger than a normal ovary.
- Mature ovarian teratomas are the most common pediatric ovarian neoplasm.
- Embryonal rhabdomyosarcoma is the most common genital tract neoplasm in children of both sexes.
- About one-third of all ovarian neoplasms are malignant. As many as 50% of hormonally active tumors are malignant.

## SUGGESTED READINGS

Chiou SY, Lev-Toaff AS, Masuda E, et al. Adnexal torsion: new clinical and imaging observations by sonography, computed tomography, and magnetic resonance imaging. *J Ultrasound Med*. 2007;26(10):1289–1301.
de Vries L, Phillip M. Role of pelvic ultrasound in girls with precocious puberty. *Horm Res Paediatr*. 2011;75(2):148–152.
Garel L, Dubois J, Grignon A, et al. US of the pediatric female pelvis: a clinical perspective. *Radiographics*. 2001;21(6):1393–1407.

Li Y, Phelps A, Zapala MA, et al. Magnetic resonance imaging of Müllerian duct anomalies in children. *Pediatr Radiol*. 2016;46(6):796–805.

Schlomer B, Rodriguez E, Baskin L. Obstructed hemivagina and ipsilateral renal agenesis (OHVIRA) syndrome should be redefined as ipsilateral renal anomalies: cases of symptomatic atrophic and dysplastic kidney with ectopic ureter to obstructed hemivagina. *J Pediatr Urol*. 2015;11(2):77.e1–77.e6. doi:10.1016/j.jpurol.2014.12.004.

Schultz KA, Ness KK, Nagarajan R, et al. Adnexal masses in infancy and childhood. *Clin Obstet Gynecol*. 2006;49(3):464–479.

Servaes S, Victoria T, Lovrenski J, et al. Contemporary pediatric gynecologic imaging. *Semin Ultrasound CT MR*. 2010;31(2):116–140.

Shah RU, Lawrence C, Fickenscher KA, et al. Imaging of pediatric pelvic neoplasms. *Radiol Clin North Am*. 2011;49(4):729–748, vi.

Sintim-Damoa A, Majmudar AS, Cohen HL, et al. Pediatric ovarian torsion: spectrum of imaging findings. *Radiographics*. 2017;37:1892–1908.

Stranzinger E, Strouse PJ. Ultrasound of the pediatric female pelvis. *Semin Ultrasound CT MR*. 2008;29(2):98–113.

## REFERENCES

Full references for this chapter can be found on www.expertconsult.com.

## REFERENCES

1. Cohen HL, Lemond T. Gynecologic imaging of the pediatric patient. In: Fielding J, Brown D, Thurmond A, eds. *Gynecologic Imaging*. Philadelphia: Saunders (Elsevier); 2011.
2. Cohen HL, Bober S, Bow S. Imaging the pediatric pelvis: the normal and abnormal genital tract and simulators of its diseases. *Urol Radiol*. 1992;14:273.
3. Ruggierro M, Awobuluyi M, Cohen H, et al. Imaging the pediatric pelvis: role of ultrasound. *Radiologist*. 1997;4:155.
4. Ratani R, Cohen HL, Fiore E. Pediatric gynecologic ultrasound. *Ultrasound Q*. 2004;20:127.
5. Cohen HL, Shapiro MA, Mandel FS, et al. Normal ovaries in neonates and infants: a sonographic study of 77 patients 1 day to 24 months old. *AJR Am J Roentgenol*. 1993;160:583.
6. Currarino G, Wood B, Majd M. Abnormalities of the genital tract. In: Silverman F, Kuhn J, eds. *Caffey's Pediatric X-ray Diagnosis*. 9th ed. St Louis: Mosby–Year Book; 1993.
7. Herter L, Golendziner E, Flores J, et al. Ovarian and uterine sonography in healthy girls between 1 and 13 years old: correlation of findings with age and pubertal status. *AJR Am J Roentgenol*. 2002;178:1531.
8. Eisenberg P, Cohen H, Mandel F, et al. US analysis of premenarchal gynecological structures. *J Ultrasound Med*. 1991;10:S30.
9. Salardi S, Orsini L, Cacciari E, et al. Pelvic ultrasonography in premenarchal girls: relation to puberty and sex hormone concentrations. *Arch Dis Child*. 1985;60:120.
10. Cohen HL, Tice H, Mandel F. Ovarian volumes measured by US: bigger than we think. *Radiology*. 1990;177:189.
11. Nussbaum Blask AR, Sanders RC, Gearhart JP. Obstructed uterovaginal anomalies: demonstration with sonography: I. Neonates and infants. *Radiology*. 1991;179:79.
12. Cohen HL, Sivit CJ, eds. *Fetal and Pediatric Ultrasound: A Casebook Approach*. New York: McGraw-Hill; 2001.
13. Orsini L, Salardi S, Pilu G, et al. Pelvic organs in premenarchal girls: real-time ultrasonography. *Radiology*. 1984;153:113.
14. Woodward P, Sohaey R, Wagner B. Congenital uterine malformations. *Curr Probl Diagn Radiol*. 1995;24:177.
15. Emans S, Laufer M, Goldstein D, eds. The physiology of puberty. In: *Pediatric & Adolescent Gynecology*. 5th ed. Philadelphia: Lippincott Williams and Wilkins; 2005.
16. Caloia D, Morris H, Rahmani M. Congenital transverse vaginal septum: vaginal hydrosonographic diagnosis. *J Ultrasound Med*. 1998;17:261.
17. Scanlan KA, Pozniak M, Fagerholm M, et al. Value of transperineal sonography in the assessment of vaginal atresia. *AJR Am J Roentgenol*. 1990;154:545.
18. Reid R. Amenorrhea. In: Copeland L, ed. *Textbook of Gynecology*. Philadelphia: WB Saunders; 1993.
19. Reed M, Griscom N. Hydrometrocolpos in infancy. *Am J Roentgenol Radium Ther Nucl Med*. 1973;118:1.
20. Carrington B, Hricak H, Nuruddin R, et al. Mullerian duct anomalies: MR imaging evaluation. *Radiology*. 1990;176:715.
21. Hugosson C, Jorulf H, Bakri Y. MRI in distal vaginal atresia. *Pediatr Radiol*. 1991;21:281.
22. Rosenblatt M, Rosenblatt R, Kutcher R, et al. Utero-vaginal hypoplasia: sonographic, embryologic and clinical considerations. *Pediatr Radiol*. 1991;21:536.
23. Reinhold C, Hricak H, Forstner R, et al. Primary amenorrhea: evaluation with MR imaging. *Radiology*. 1997;203:383.
24. Fedele L, Dorta M, Brioschi D, et al. Magnetic resonance imaging in Mayer-Rokitansky-Küster-Hauser syndrome. *Obstet Gynecol*. 1990;76:593.
25. Westrom L. Incidence, prevalence and trends of acute pelvic inflammatory disease and its consequences in industrialized countries. *Am J Obstet Gynecol*. 1980;138:880.
26. Cohen HL, Smith W, Kushner D, et al. Imaging evaluation of acute right lower quadrant and pelvic pain in adolescent girls (ACR Appropriateness Criteria). *Radiology*. 2000;215S:833–840.
27. Bulas D, Ahlstrom P, Sivit C, et al. Pelvic inflammatory disease in the adolescent: comparison of transabdominal and transvaginal sonographic evaluation. *Radiology*. 1992;183:435.
28. Linam LE, Darolia R, Naffaa LN, et al. US findings of adnexal torsion in the pediatric and adolescent population: size really does matter. *Pediatr Radiol*. 2007;37(10):1013–1019.
29. Servaes S, Zurakowski D, Laufer MR, et al. Sonographic findings of ovarian torsion in children. *Pediatr Radiol*. 2007;37:446–451.
30. Graif M, Itzchak Y. Sonographic evaluation of ovarian torsion in childhood and adolescence. *AJR Am J Roentgenol*. 1988;150:647.
31. Cil A, Akgul M, Tulunay G, et al. Recovery of ovarian function after detorsion: Doppler findings. *Acta Radiol*. 2006;47:618.
32. Davis AJ, Fein NR. Subsequent asynchronous torsion of normal adnexa in children. *J Pediatr Surg*. 1990;25:687.
33. Fleischer AC, Brader KR. Sonographic depiction of ovarian vascularity and flow: current improvements and future applications. *J Ultrasound Med*. 2001;20:241.
34. Lee E, Kwon H, Joo H, et al. Diagnosis of ovarian torsion with color Doppler sonography: depiction of twisted vascular pedicle. *J Ultrasound Med*. 1998;17:83.
35. Quillin S, Siegel M. Color Doppler ultrasound of children with acute lower abdominal pain. *Radiographics*. 1993;13:293.
36. Cohen HL. Physiologic ovarian cysts in a newborn. In: Hertzberg B, Hill M, Cohen HL, eds. *Ultrasound (Third Series): Test and Syllabus*. Baltimore: ACR Publications; 2005.
37. Garel L, Filiatrault D, Brandt M, et al. Antenatal diagnosis of ovarian cysts: natural history and therapeutic implications. *Pediatr Radiol*. 1991;21:182.
38. Cohen HL, Eisenberg P, Mandel F, et al. Ovarian cysts are common in premenarchal girls: a sonographic study of 101 children 2 to 12 years of age. *AJR Am J Roentgenol*. 1992;159:89.
39. Galli-Tsinopoulou A, Moudiou T, Mamopoulos A, et al. Multifollicular ovaries in female adolescents with cystic fibrosis. *Fertil Steril*. 2006;85:1484.
40. Baltarowich OH, Kurtz A, Pasto M, et al. The spectrum of sonographic findings in hemorrhagic ovarian cysts. *AJR Am J Roentgenol*. 1987;148:901.
41. Herter L, Magalnaes J, Spritzer P. Association of ovarian volume and serum LH levels in adolescent patients with menstrual disorders and/or hirsutism. *Braz J Med Biol Res*. 1993;26:1041.
42. Atiomo W, Pearson S, Shaw S, et al. Ultrasound criteria in the diagnosis of polycystic ovary syndrome (PCOS). *Ultrasound Med Biol*. 2000;26:977.
43. Takahashi K, Okada M, Ozaki T, et al. Transvaginal ultrasonographic morphology in polycystic ovarian syndrome. *Gynecol Obstet Invest*. 1995;39:201.
44. Battaglia C, Artini P, Genazzani A, et al. Color Doppler analysis in oligo- and amenorrheic women with polycystic ovary syndrome. *Gynecol Endocrinol*. 1997;11:105.
45. Pinkas H, Mashiach R, Rabinerson D, et al. Doppler parameters of uterine and ovarian stromal blood flow in women with polycystic ovary syndrome and normally ovulating women undergoing controlled ovarian stimulation. *Ultrasound Obstet Gynecol*. 1998;12:197.
46. Wu A, Siegel MJ. Sonography of pelvic masses in children: diagnostic predictability. *AJR Am J Roentgenol*. 1987;148:1199.
47. Boechat M. Magnetic resonance imaging of abdominal and pelvic masses in children. *Top Magn Reson Imaging*. 1990;3:25.
48. McNall R, Nowicki P, Miller B, et al. Adenocarcinoma of the cervix and vagina in pediatric patients. *Pediatr Blood Cancer*. 2004;43:289–294.
49. Surratt J, Siegel M. Imaging of pediatric ovarian masses. *Radiographics*. 1991;11:533.
50. Sisler CL, Siegel MJ. Ovarian teratomas: a comparison of the sonographic appearance in prepubertal and postpubertal girls. *AJR Am J Roentgenol*. 1990;154:139.
51. Ulbright T, Srigley J. Dermoid cyst of the testis: a study of five postpubertal cases, including a pilomatrixoma-like variant, with evidence supporting its separate classification from mature testicular teratoma. *Am J Surg Pathol*. 2001;25:788.
52. Ekici E, Soysal M, Kara S, et al. The efficiency of ultrasonography in the diagnosis of dermoid cysts. *Zentralbl Gynakol*. 1996;118:136.
53. Levitin A, Haller K, Cohen HL, et al. Endodermal sinus tumor of the ovary: imaging evaluation. *AJR Am J Roentgenol*. 1996;167:791.
54. Larsen W, Felmar E, Wallace M, et al. Sertoli-Leydig cell tumor of the ovary: a rare cause of amenorrhea. *Obstet Gynecol*. 1992;79:831.
55. Schultz KA, Harris A, Messinger Y, et al. Ovarian tumors related to intronic mutations in DICER1: a report from the international ovarian and testicular stromal tumor registry. *Fam Cancer*. 2016;15(1):105–110.

# 127 Amenorrhea and Abnormalities of Puberty

Harris L. Cohen and Anand Dorai Raju

Indications for evaluation of the adolescent pelvis usually are based on complaints of abdominal pain, pelvic pain, or a mass. Other clinical symptoms resulting in imaging evaluation in female patients relate to abnormalities of development of secondary sexual characteristics of puberty. These changes may be seen earlier than normal (i.e., precocious puberty), may be delayed (i.e., delayed puberty), or may fail to develop (e.g., hypogonadism and sexual infantilism) in adolescents. The other key reason for adolescent gynecologic evaluation is amenorrhea (lack of menses), whether primary or secondary. Conditions causing pubertal delay may also cause primary or secondary amenorrhea.[1,2]

## PUBERTY

Puberty among girls is the stage of development between childhood and adulthood when activation of the hypothalamic-pituitary-ovarian-uterine axis produces maturation of the gonads, resulting in an increased production of sex hormones, development of secondary sex characteristics, a growth spurt, and development of reproductive capability. The earliest signs of puberty among girls are breast development (usually occurring between ages 8–13 years) and pubic hair growth (usually between ages 8–14 years). These signs are followed by a growth spurt (usually between ages 9.5–14.5 years), axillary hair development, and menarche (usually between ages 10–16 years). Puberty is typically completed within about 4 years.[1,3–5]

Puberty among boys usually begins between 9 and 14 years of age and is completed in 3.5 to 4 years. It begins with testicular enlargement (usually occurring between ages 9–13.5 years), followed by the appearance of pubic hair (usually between ages 10–15 years), enlargement of the penis (usually between ages 11–12.5 years), and development of axillary and facial hair as well as a growth spurt (usually between ages 10.5–16 years).[1,3]

### Physiologic Changes at Puberty and the Normal Ovulatory Menstrual Cycle

Ordinarily, until the age of at least 8 years, an unknown “central restraining mechanism” prevents the pulsatile release of gonadotropin-releasing hormone (GnRH) from the arcuate nucleus of the hypothalamus. Pulsatile release of GnRH appears necessary for ovulation and development of the corpus luteum. In early puberty, the pulsatile GnRH release is maximal only at night, but with time the typical adult pattern of continuous pulsatile GnRH secretion develops.[1,5,6]

With the earliest activation of GnRH, most girls undergo ovarian folliculogenesis without ovulation. Unopposed estrogen production leads to progressive uterine growth and endometrial proliferation. Breast budding, physiologic leukorrhea, and accelerated linear growth occur. As the hypothalamic-pituitary-ovarian-uterine axis matures over approximately a 2-year span, cycles with subnormal progesterone production and shortened intermenstrual intervals are replaced by fertile cycles and normal corpus luteum function.[1,5,6]

The typical ovulatory cycle has a 24- to 35-day intermenstrual interval and usually a premenstrual molimina (mild group of symptoms, including breast tenderness, food craving, fatigue, headaches, sleep problems, and/or fluid retention). Longer intervals often are associated with anovulation. Improved nutrition and living conditions are thought to be at least in part responsible for the gradual decrease in mean menarchal age during the past century. In North America, the mean menarchal age currently is 12.4 years, with a range of 9 to 17 years. Menarche usually occurs 2 to 5 years after breast bud development.[1,6]

### Premature Thelarche and Adrenarche

***Overview and Clinical Presentation.*** Premature thelarche and adrenarche are relatively common, self-limited variants of normal pubertal development in girls. Premature thelarche refers to premature breast development without other signs of precocious sexual maturation in girls younger than 8 years of age. It usually is seen between 1 and 4 years of age; one-third of the cases resolve spontaneously. Premature adrenarche refers to the appearance of pubic and axillary hair without other signs of precocious sexual maturity. In both premature thelarche and premature adrenarche, bone age and patient height are normal to only slightly advanced/increased. The cause of premature thelarche or adrenarche is not certain. The levels of circulating sex hormones usually are normal. Increased end-organ sensitivity to normal levels of estrogen or androgen is a possible cause.[1,7,8]

In boys, premature appearance of pubic and axillary hair without other signs or only minor signs of precocious puberty is a relatively common variant of normal development that may be due to an increase in circulating androgens from premature maturation of the adrenal glands of unknown cause. No penile enlargement is present, presumably because the levels of circulating androgens are not sufficiently elevated. The bone age and growth rate are slightly increased. The remainder of pubertal development occurs at a normal age.[1,8]

## PRECOCIOUS PUBERTY

Precocious puberty refers traditionally to the appearance of secondary sex characteristics before 8 years of age in girls and before 9 years of age in boys. A Pediatric Endocrine Society task force suggested that the definition ages be modified to secondary sexual characteristics noted in white girls under age 7 and African American girls under age 6. Precocious puberty is divided into two main types: (1) complete, central, gonadotropin-dependent, or true precocious puberty and (2) incomplete, peripheral, gonadotropin-independent, pseudoprecocious puberty, or precocious pseudopuberty. Whereas the complete form is characteristically isosexual, with development of secondary sex characteristics that are appropriate for the patient’s gender, the incomplete form may be either isosexual or heterosexual. Incomplete heterosexual precocious puberty is manifested by signs of virilization in girls and by gynecomastia or other signs of feminization in boys.[1,4,7,8]

### Complete or Central Isosexual Precocious Puberty

***Overview and Pathophysiology.*** Complete or central isosexual precocious puberty results from premature activation of the hypothalamic-pituitary-gonadal complex with increased production of gonadotropic and sex hormones and an early onset of ovulation or spermatogenesis. Complete precocious puberty may be idiopathic or secondary to organic central nervous system (CNS) lesions.[1,9,10]

## Abstract:

This chapter reviews amenorrhea and abnormalities related to puberty. The concepts of puberty, expected age-related physiologic changes, and the menstrual cycle are discussed. Definitions allowing the diagnosis of premature thelarche, premature adrenarche, and precocious puberty (PP) are presented. There are various forms including complete or central isosexual PP, incomplete PP, and virilizing disorders or heterosexual PP. The clinical, laboratory, and imaging evaluation of PP and delayed puberty are reviewed. Finally, amenorrhea, including both primary and secondary causes, is discussed.

## Keywords:

Amenorrhea
Congenital adrenal hyperplasia
Precocious puberty
Virilization
Feminization

***Etiology and Imaging.*** The cause of precocious puberty in girls is idiopathic in at least 80% of cases. About 20% of affected girls have a hypothalamic or pituitary lesion. Fewer than 10% of cases of true precocious puberty in boys have an idiopathic cause. A familial tendency to idiopathic early pubertal development is observed in some cases (i.e., constitutional or genetic precocious puberty).[1,9,10]

Possible causes of precocious puberty in either sex include intracranial tumors or cysts, hydrocephalus, sequelae of intracranial inflammatory processes or trauma, and other intracranial lesions that may activate the hypothalamus by pressure or invasion. Of the CNS tumors/neoplasms that may cause true precocious puberty, hamartoma of the hypothalamic tuber cinereum (Fig. 127.1) is the most common. This usually small CNS tumor secretes GnRH, is more common in boys than in girls, is generally benign and nonprogressive, and usually cannot be surgically corrected. It may be pedunculated or appear as an excrescence of the tuber cinereum, below the mammillary body. The onset of puberty in patients with this lesion is usually at a younger age (~2 years) than in patients with idiopathic precocious puberty. Other CNS neoplasms that may cause true precocious puberty in either sex usually are located in or near the hypothalamus and include hypothalamic or optic gliomas, astrocytoma, ependymoma, dysgerminoma, and prolactinoma. Suprasellar dysgerminoma in boys also may cause incomplete precocious puberty through tumor secretion of human chorionic gonadotropin (hCG).[1,10,11]

True precocious puberty may be observed in some children with long-standing untreated hypothyroidism. The increased production of gonadotropic hormones and prolactin seen in these patients may be due to a hormonal overlap in the pituitary response to thyroid deficiency. Affected patients show little, if any, development of secondary sexual characteristics, especially pubic hair. These changes regress with treatment of the hypothyroidism.[1,8]

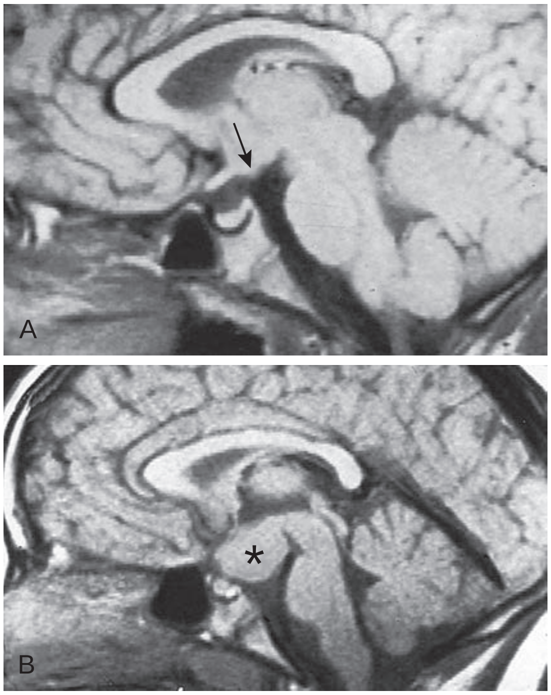

**Figure 127.1. Hamartoma of the tuber cinereum causing precocious puberty.** On midline sagittal T1-weighted magnetic resonance (MR) images of the brain from two different patients, an *arrow* points to a small hamartoma in an 8-year-old (A) and an *asterisk* indicates an unusually large hamartoma in a 7-year-old (B). Both patients had a history of precocious puberty.

## Incomplete (Pseudosexual) Precocious Puberty in Girls

***Overview.*** Pseudosexual (or incomplete) precocious puberty in girls usually presents before 5 years of age. Excess circulating estrogens or related substances develop independently of the hypothalamus and pituitary gland. These estrogens usually are produced by the ovaries or adrenal glands or may be from an exogenous source, such as food, parenteral or oral medications, or other substances.[1,7,12]

***Etiology and Imaging.*** Gonadotropin levels are low, and the gonads remain immature. The most common ovarian source is an autonomous estrogen-secreting follicular (granulosa-thecal) cyst (Fig. 127.2). Other causes are estrogen-producing ovarian neoplasms, particularly granulosa cell (or granulosa-theca cell) tumors (Fig. 127.3) and rare estrogen-secreting adrenal neoplasms (adenomas or carcinomas).[1,7,12]

McCune-Albright syndrome consists of polyostotic fibrous dysplasia, cutaneous café au lait spots, and precocious puberty. The syndrome is found predominantly in females. Autonomously functioning ovarian cysts are seen in some cases. In others, no anatomic cause is noted. McCune-Albright syndrome occasionally presents as complete or true precocious puberty. It has been suggested that the initially partial or incomplete precocious puberty in these patients becomes complete (gonadotropin dependent) as the result of an early maturation of the hypothalamic-pituitary-gonadal complex, which is caused by a long-standing exposure to estrogen.[1,7]

## Virilizing Disorders (Heterosexual Precocious Puberty)

***Overview and Clinical Presentation.*** Testosterone is produced in normal females by the adrenal gland (25%), by the ovary (25%), and by peripheral conversion of D4-androstenedione (50%), with only 1% typically free and biologically active. A form of pseudosexual precocity may occur in girls when androgen levels are excessive or end organs become excessively sensitive to normal amounts of circulating androgens. Either case may lead to heterosexual pseudoprecocious puberty as the girls undergo virilization and masculine secondary sexual characteristics develop. Clinical findings include increases in body and facial hair (hirsutism), acne, deepening of the voice, clitoromegaly, increased muscle mass, and temporal balding. Menstrual abnormalities are common among affected adolescents.[1,12]

### Congenital Adrenal Hyperplasia

***Overview and Imaging.*** Congenital adrenal hyperplasia (CAH) is the most common form of hyperandrogenism. The increased production of androgenic substance is due in most cases to a deficiency of 21-hydroxylase and far less commonly to deficiencies in 11β-hydroxylase, 3β-hydroxysteroid dehydrogenase, or other enzymes involved in cortisol and/or aldosterone synthesis. Imaging of the adrenal gland will show enlargement (Fig. 127.4) that is usually bilateral and diffuse. The normal adrenal gland shape is maintained.[1,13]

### Other Causes of Virilization in Girls

***Overview, Etiology, and Pathophysiology.*** Adrenal adenomas (Fig. 127.5) or adrenal carcinomas (Fig. 127.6) may produce increased levels of androgens and virilization. Signs of Cushing syndrome may be seen as a result of associated tumor secretion of glucocorticoid hormones.[1,13]

Ovarian neoplasms may secrete androgens and cause virilization. These neoplasms include Sertoli-Leydig cell tumors, thecomas (luteoma—a virilizing dysgerminoma that contains theca cells), or

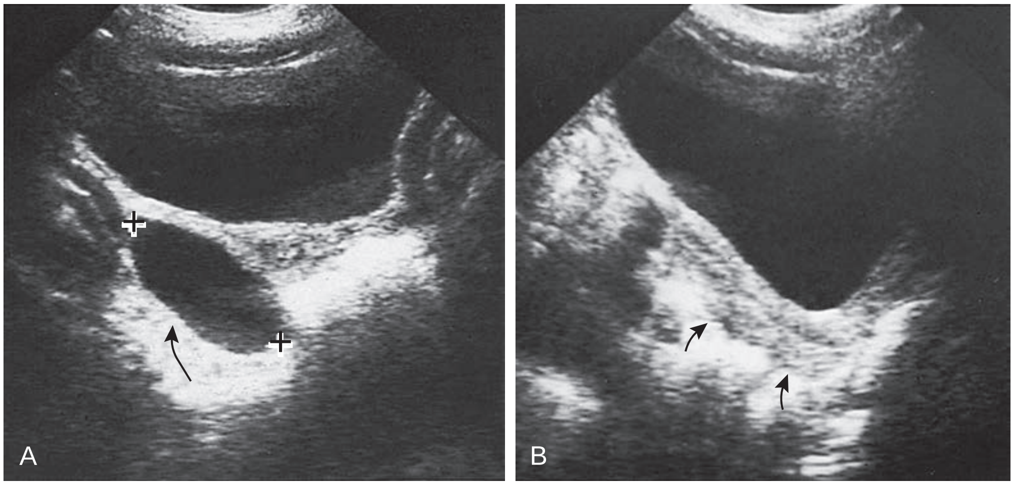

**Figure 127.2. Autonomous estrogen-secreting ovarian cyst causing precocious puberty.** (A) Longitudinal sonogram of the right adnexa *(arrow)* of a 3-year-old girl with precocious puberty shows a large cyst *(cursors)*. This cyst was proved to autonomously secrete estrogen. The left adnexa was normal. (B) Midline longitudinal sonogram shows that the child's uterus *(arrows)* is longer than normal for her age. It is not the tubular shape typical of childhood but appears almost pear-shaped, with an echogenic central endometrial cavity indicating estrogenization.

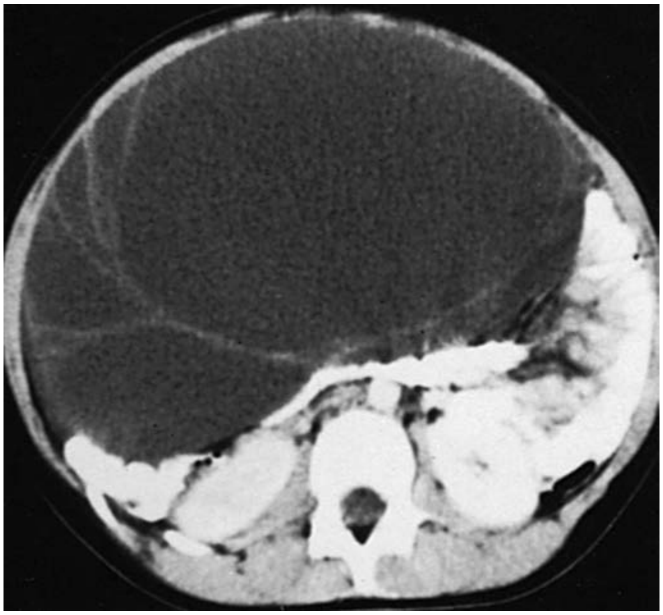

**Figure 127.3. Granulosa cell tumor of the ovary causing precocious puberty.** Axial contrast-enhanced CT image shows a large, cystic, multiseptated mass occupying most of the abdomen in a 10-year-old girl. The mass proved to be an ovarian estrogen-producing juvenile granulosa cell tumor.

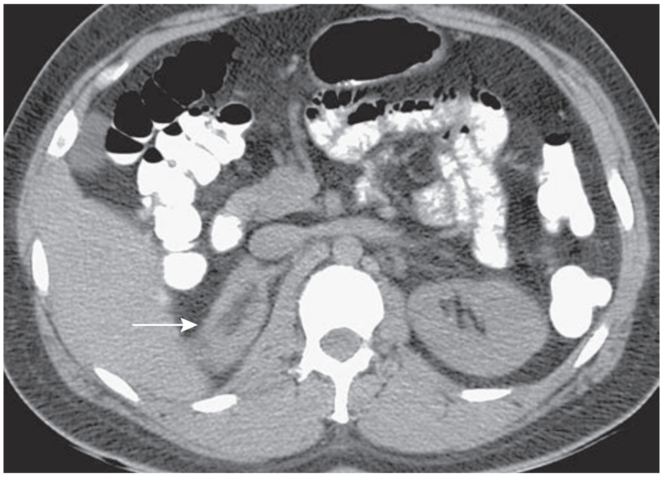

**Figure 127.4. Congenital adrenal hyperplasia.** Axial CT image shows that the right adrenal gland *(arrow)* is thicker than normal in this 24-year-old with simple virilizing congenital adrenal hyperplasia. As is typical with this disorder, the adrenal gland maintains its normal shape.

gonadoblastomas. Exogenous exposure to androgens or androgen-like substances may cause virilization at all ages. Again, virilization at puberty may develop in some girls with rare anomalies of sex differentiation, such as 46,XY gonadal dysgenesis, even though they are phenotypically normal females at birth.[1,14]

Idiopathic hirsutism and polycystic ovarian syndrome also are considered to be among the virilizing disorders of females. Idiopathic hirsutism consists of an increase in body and facial hair that occurs as the sole or predominant abnormality and is a relatively common problem in otherwise normal pubertal and postpubertal girls. Idiopathic hirsutism may be precipitated by any of the causes of virilization. It may be seen in families or as a result of polycystic ovary syndrome and the increased androgen production by the many small follicular cysts (see Chapter 126). The cause is usually idiopathic and believed to be a result of an altered response of the end organ (hair follicle) to normal levels of circulating androgens.[1,15–17]

## Incomplete Isosexual (Pseudoprecocious) Puberty in Boys

***Overview, Etiology, and Pathophysiology.*** Isosexual pseudoprecocity of sexual development in boys is due to an increase in circulating androgen or androgen-like substances either from production by adrenal glands or testes or from an exogenous source. CAH is the most common cause for excessive androgen production by the adrenal gland of either sex. Affected males are born with normal external genitalia, but if CAH is untreated, signs of sexual precocity soon develop. Isosexual pseudoprecocious puberty in males, sometimes associated with signs of glucocorticoid excess, also can occur because of androgen-secreting neoplasms of the adrenal cortex (e.g., adenocarcinoma or adenoma). A rare cause of isosexual precocity in boys is an androgen-secreting Leydig cell tumor of the testis (see Chapter 125). Several extrapituitary hCG-secreting tumors also can result in an incomplete form of isosexual precocious puberty by stimulating testosterone production by testicular Leydig cells. These tumors include some hepatocellular carcinomas, hepatoblastomas, teratomas or chorioepitheliomas of the mediastinum and retroperitoneum, and suprasellar germinomas. A familial form of gonadotropin-independent precocious puberty in boys is caused by premature maturation and sometimes hyperplasia of the Leydig cells of the testis, with production of testosterone. Exposure to exogenous androgens or the administration of hCG for undescended testes may be further causes of incomplete virilization in males.[1,8,13]

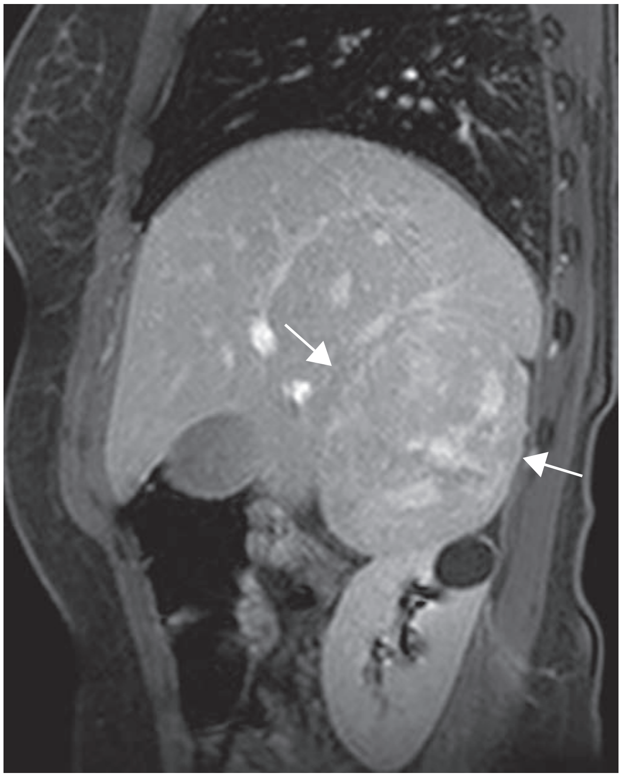

**Figure 127.5. Adrenocortical adenoma causing virilization in a 17-year-old girl presenting with secondary amenorrhea and hirsutism.** Sagittal postcontrast T1-weighted MR image shows a large heterogeneous mass arising from the right adrenal gland *(arrows)* proven to be a hormonally active adrenocortical adenoma. An incidental cyst is present in the right kidney.

## Adolescent Gynecomastia and Feminizing Disorders in Boys

***Overview and Etiology.*** Mild breast development may occur transiently in adolescent boys between 13 and 15 years of age. It is usually bilateral, idiopathic, and may be familial. Typically no hormonal abnormality is found. The gynecomastia generally regresses in 2 or 3 years, but in a few cases it may persist into adult life. Pathologic causes of gynecomastia in boys may be exposure to exogenous estrogens, an estrogen-secreting neoplasm of the testis or adrenal cortex, a prolactin-secreting neoplasm of the pituitary gland, Klinefelter syndrome, congenital bilateral anorchia, acquired testicular failure, and other conditions with some biochemical defect in testosterone production or androgen end-organ receptor.[1,18]

## Clinical and Laboratory Evaluation of Precocious Puberty

***Overview and Clinical Presentation.*** Physical examination can help determine the correct diagnosis. Physical examination should denote the type and degree of pubertal development as well as the size, shape, and firmness of the testes. In complete precocious puberty, both testes are enlarged; in partial sexual precocity, they often are of normal size. Unilateral testicular enlargement suggests a testicular neoplasm. The abdomen should be evaluated for a flank or pelvic mass. The presence of café au lait spots should suggest the diagnosis of fibrous dysplasia or neurofibromatosis. Laboratory studies may include luteinizing hormone, follicle-stimulating hormone, and estradiol levels; gonadotropin response to GnRH; thyroid studies; and a vaginal smear in girls, as well as plasma and urinary testosterone levels.[1,8]

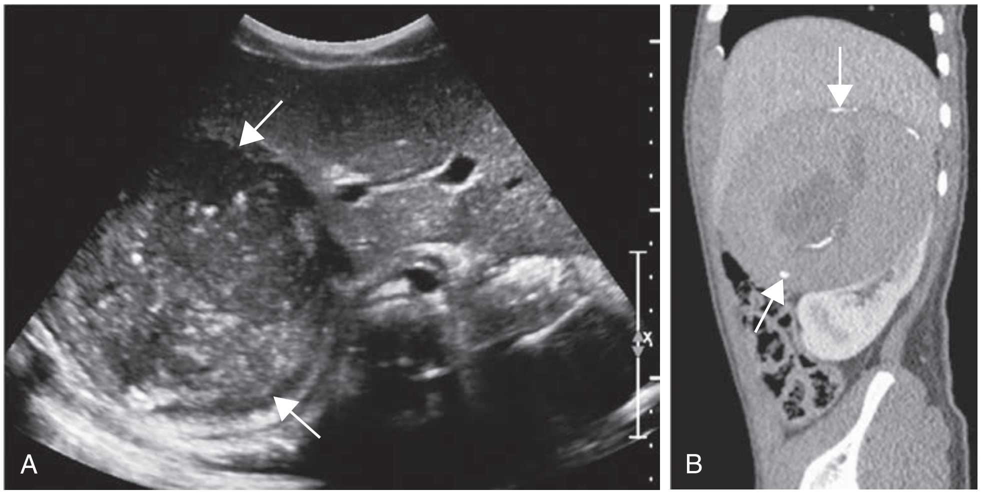

**Figure 127.6. Adrenocortical carcinoma causing virilization in a 3-year-old girl.** (A) Transverse sonogram through the upper abdomen shows a large heterogeneous mass *(arrows)* posterior to the right lobe of the liver. (B) Sagittal contrast-enhanced CT image shows that the mass arises from the right suprarenal fossa, exerts substantial mass effect upon the right kidney, and contains calcifications *(arrows)*.

### Imaging Evaluation of Precocious Puberty

***Imaging.*** An anteroposterior film of the left hand, including carpal bones and the distal forearm, is commonly used for bone age determination. Bone age often is advanced in patients with true precocious puberty and in patients with androgenic stimulation. The skeletal length often is increased early in patients with advanced bone age. However, if the precocious puberty is not treated, premature fusion of the epiphyses may develop and result in a limitation to the patient's potential height.[1,8]

Ultrasound, with emphasis on the adrenal glands and the ovaries, is the primary initial radiologic study of patients with precocious puberty. In girls with true precocious puberty, a pelvic ultrasound may show some bilateral enlargement of the ovaries and prominence of the uterus, and in rare cases a large estrogen-secreting ovarian cyst that has resulted from stimulation of the hypothalamic-pituitary complex. Small and multiple ovarian cysts/follicles may be seen in girls with true precocious puberty because of high gonadotropin levels. Pseudoprecocity caused by the autonomous estrogen secretion of an ovarian cyst or tumor will be denoted by ovarian asymmetry, with the autonomous lesion being found in the larger ovary (see Fig. 127.2). The finding in prepubertal girls of an increased uterine size and a well-defined central endometrial echo indicates an increase in circulating estrogen from any cause. A skeletal survey is indicated when fibrous dysplasia is suspected.[1,8,19]

Patients with isosexual precocious puberty that is suspected to be of the complete or central type should have magnetic resonance imaging (MRI) of the brain with special attention to the tuber cinereum. Skull radiographs are of limited diagnostic value but may show intracranial calcifications, enlargement of the sella turcica, signs of increased intracranial pressure, or skull changes of fibrous dysplasia.[1,8]

## DELAYED OR ABSENT PUBERTAL DEVELOPMENT

Puberty is considered to be delayed and should be investigated in girls when secondary sex characteristics fail to appear by 13 years of age, which is considered two standard deviations beyond the norm. Evaluation for pubertal delays in boys is suggested when pubic and axillary hair or other external secondary characteristics, particularly enlargement of the testes and penis, fail to appear by age 14 years. Delayed puberty or failure of puberty to develop may be idiopathic (constitutional) or due to chronic systemic disorders, disorders of the hypothalamic-pituitary complex causing decreased gonadotropin secretion (i.e., secondary or hypogonadotropic hypogonadism), or primary disorders of the gonads with a secondary elevation of gonadotropic hormone secretion (i.e., primary or hypergonadotropic hypogonadism).[1,20,21]

### Idiopathic (Constitutional) Pubertal Delay

***Overview and Clinical Presentation.*** In some otherwise normal children, the onset of puberty is delayed for up to several years. When puberty eventually starts, it usually continues to completely normal secondary sexual development. These occurrences underline the fact that there may be constitutional or genetic causes for delay in the maturation of the hypothalamic-pituitary complex. Often, such children may experience a delay in bone age and height development. The ability to differentiate between constitutional pubertal delays in otherwise normal children and true disorders of the hypothalamic-pituitary axis may not be simple.[1,21]

### Delayed Puberty in Chronic Systemic Disorders

***Overview and Etiology.*** Delayed puberty may occur on a physiologic basis in patients with chronic diseases. Patients with other long-term debilitating processes, as well as anorexia nervosa, may have delays in pubertal development. Such delays also may be noted in children or adolescents who undergo prolonged and vigorous physical exertion, such as long-distance running, gymnastics, or dance. Puberty may develop or proceed normally in some of these patients after improvement or removal of the precipitating cause. However, any halt in the pubertal development of a patient is a cause for concern and an immediate endocrinologic workup.[1,22,23]

### Hypogonadism Caused by Hypothalamic-Pituitary Disorders (Hypogonadotropic Hypogonadism)

***Overview and Clinical Presentation.*** Several disorders of the hypothalamic-pituitary complex result in decreased gonadotropin production, and secondarily a decrease in gonadal sex steroids. Impaired or absent gonadal function causes an absence of pubertal development. In girls, the uterus remains infantile, menses does not occur, and breast budding and other secondary sexual characteristics do not develop. In boys, the penis and scrotum are infantile, and the testes remain immature and smaller than expected for age. Pubic and axillary hair is scanty or absent, the voice remains high pitched, and increased fat deposition often occurs, particularly at the hips, pelvis, abdomen, and breast. Delayed closure of the epiphyses with elongation of the limbs is observed unless an associated growth hormone deficiency is present.[1,21,22]

***Etiology and Pathophysiology.*** Causative abnormalities include intracranial tumors such as craniopharyngioma, hypothalamic and optic gliomas, dysgerminoma, and other tumors of the pituitary gland and hypothalamus or adjacent areas. Other manifestations of pituitary insufficiency, such as diabetes insipidus and short stature, may be present. Primary or secondary hypogonadotropic hypogonadism also may be seen in patients with Langerhans cell histiocytosis and in patients with certain congenital midline defects of the face, the base of the skull, and the CNS (e.g., septo-optic dysplasia or holoprosencephaly), which may be associated with developmental anomalies of the hypothalamus and pituitary gland, resulting in hypogonadism.[1,21]

Functional causes of hypogonadism include idiopathic hypopituitarism, characterized by short stature resulting from growth hormone deficiency, and sometimes other findings associated with deficiencies of other pituitary hormones. Cases of isolated gonadotropic deficiency, sporadic or familial, may occur in association with anosmia or hyposmia and other abnormalities that characterize Kallmann syndrome. Isolated luteinizing hormone deficiency in males, which sometimes is familial, results in failure of pubertal development; it usually is associated with gynecomastia but with the preservation of spermatogenesis (i.e., fertile eunuch syndrome). Hypogonadism, which probably also is related to abnormalities of hypothalamic function, can be observed in Prader-Willi and Laurence-Moon-Biedl syndromes.[1,21]

### Hypogonadism Caused by Gonadal Lesions (Hypergonadotropic Hypogonadism)

***Overview, Etiology, and Pathophysiology.*** Certain congenital or acquired lesions of the gonads may result in hypogonadism and failure of pubertal development. Gonadal sex steroids are decreased, and as a result, an increase in pituitary secretion of gonadotropins occurs. Just as in hypogonadotropic hypogonadism, pubertal development is absent in girls or boys. The key gonadal lesions in girls include Turner syndrome (45,XO), XX gonadal dysgenesis, XY gonadal dysgenesis, and a gonadal dysgenesis with galactosemia and immune oophoritis (often associated with Hashimoto thyroiditis, hypoparathyroidism, adrenal insufficiency, pernicious anemia, chronic active hepatitis, and candidiasis). Hypergonadotropic hypogonadism also can occur among patients with normal karyotypes who experience secondary ovarian failure either by infarction, as with cases of bilateral ovarian torsion, surgical removal of both ovaries, radiation therapy to the pelvis (usually of 800 cGy or greater), chemotherapy, or autoimmune oophoritis.[1,21,24]

Gonadal lesions in boys leading to hypogonadism include congenital bilateral anorchia with otherwise normal external genitalia, which is caused by resorption of the testes after the 13th week of gestation (e.g., vanishing testes syndrome) and acquired testicular atrophy resulting from bilateral testicular torsion, surgical injury during bilateral orchiopexy, radiation, or other causes. Absence of puberty also is observed in some genetic males born with an entirely female phenotype, including those with XY gonadal dysgenesis and some forms of male intersex states with impaired biosynthesis of active sex steroids as a result of an inherited enzymatic deficiency.[1,25,26]

## Diagnostic and Historical Considerations

***Overview, Clinical Presentation, and Imaging.*** Important information may be obtained from the patient's family history, medical history, associated medical disorders, and physical examination. At the physical examination, special emphasis should be placed on pubertal staging (Tanner classification), assessment of general growth and maturation, detection of signs and symptoms of CNS disease, and systemic diseases or syndromes. Visual fields testing, gynecologic evaluation, and chromosomal analysis should be carried out if indicated. The hormonal studies include measurements of serum testosterone, estradiol, and gonadotropins; gonadotropic response to GnRH stimulation; and testosterone response to hCG stimulation. Measurements of circulating prolactin and growth hormone, as well as thyroid function tests, may be undertaken. Radiologic procedures include bone age determination, brain MRI, pelvic ultrasound to evaluate the size of the ovaries and uterus, and other studies as indicated.[1,21]

## Evaluation of Patients With Amenorrhea

***Overview and Etiology.*** Causes of pubertal delay in girls may be similar to causes of primary or secondary amenorrhea. Primary amenorrhea is defined as a lack of menses by age 16 years. Secondary amenorrhea is defined as a cessation of menses at any point in time after menarche and before menopause.[1,27,28]

Primary amenorrhea has many causes and involves several organ systems (Box 127.1). It may be seen in adolescents with normal pubertal development, as well as those with delayed sexual development, delayed menarche with some pubertal development, and delayed menarche plus virilization. Many of its causes have already been reviewed, including hypogonadotropic hypogonadism, hypergonadotropic hypogonadism, intersex states, female adolescents with virilization (see Fig. 127.6), polycystic ovarian syndrome (PCOS), genital obstruction (e.g., hematometra/hematometrocolpos), and uterine aplasia or hypoplasia. Secondary amenorrhea often is due physiologically to pregnancy and pathologically to PCOS.[1,27,28]

### KEY POINTS

- Unopposed estrogen production leads to progressive uterine growth and endometrial proliferation. Axillary and pubic hair development result from ovarian and adrenal gland androgen production.
- Precocious puberty classically refers to the appearance of external signs of adolescence before 8 years of age in girls and before 9 years of age in boys.
- The cause of precocious puberty is idiopathic in at least 80% of girls but in less than 10% of boys.
- Hypothalamic hamartoma is the most common CNS mass to cause true precocious puberty.
- Pseudosexual precocious puberty in girls usually presents before 5 years of age. Excess circulating estrogens or related substances develop independent of central stimulation.

*Continued*

### **BOX 127.1** Etiology of Primary Amenorrhea

**HYPOTHALAMUS**

- Systemic illness
- Chronic disease
- Familial
- Stress
- Competitive athletics
- Eating disorders
- Obesity
- Tumor
- Irradiation, surgery
- Drugs

**PITUITARY**

- Idiopathic hypopituitarism
- Tumor
- Hemochromatosis
- Infarction
- Irradiation, surgery

**THYROID GLAND**

- Hypothyroidism
- Hyperthyroidism

**ADRENAL GLANDS**

- Congenital adrenocortical hyperplasia
- Cushing disease (hypercortisolism)
- Addison disease (hypocortilsolism)
- Tumor

**OVARIES**

- Gonadal dysgenesis
- Ovarian failure
- Polycystic ovary syndrome
- Ovarian tumor
- Bilateral oophorectomy

**CERVIX**

- Agenesis

**VAGINA**

- Agenesis
- Transverse septum
- Imperforate hymen

*Modified from Emans SJ. Amenorrhea in the adolescent. In: Emans S, Goldstein D, eds.* Pediatric and adolescent gynecology. *5th ed, Philadelphia: Lippincott Williams and Wilkins; 2005.*

- The most common source is an autonomous estrogen-secreting ovarian follicular cyst.
- CAH is the most common form of hyperandrogenism; in most cases it is due to 21-hydroxylase deficiency.
- Puberty is considered to be delayed when secondary sex characteristics fail to appear by 13 years of age in girls and 14 years of age in boys.
- Delayed puberty may occur on a physiologic basis in patients with chronic or debilitating disease, extreme or prolonged exercise, and anorexia nervosa.
- Primary amenorrhea is defined as a lack of menses by age 16 years. Secondary amenorrhea is defined as a cessation of menses at any time after menarche and before menopause.

## SUGGESTED READINGS

Argyropoulos M, Kiortsis D. MRI of the hypothalamic-pituitary axis in children. *Pediatr Radiol*. 2005;35:1045.

Cohen HL, Bober S, Bow S. Imaging the pediatric pelvis: the normal and abnormal genital system and simulators of its diseases. *Urol Radiol*. 1992;14:273.

Garel L, Dubois J, Grignon A, et al. US of the pediatric female pelvis: a clinical perspective. *Radiographics*. 2001;21(6):1393–1407.

Stranzinger E, Strouse PJ. Ultrasound of the pediatric female pelvis. *Semin Ultrasound CT MR*. 2008;29(2):98–113.

Warren MP, Goodman LR. Exercise-induced endocrine pathologies. *J Endocrinol Invest*. 2003;26(9):873–878.

## REFERENCES

Full references for this chapter can be found on www.expertconsult.com.

## REFERENCES

1. Cohen HL. Abnormalities of puberty and amenorrhea. In: Slovis T, ed. *Caffey's Pediatric Diagnostic Imaging*. 11th ed. Philadelphia: Elsevier; 2008.
2. Cohen HL, Bober S, Bow S. Imaging the pediatric pelvis: the normal and abnormal genital system and simulators of its diseases. *Urol Radiol*. 1992;14:273.
3. Gordon CM, Laufer MR. The physiology of puberty. In: Emans SJ, Laufer MR, Goldstein DP, eds. *Pediatric and Adolescent Gynecology*. 5th ed. Philadelphia: Lippincott Williams & Wilkins; 2005.
4. Mansfield J. Precocious puberty. In: Emans SJ, Laufer MR, Goldstein DP, eds. *Pediatric and Adolescent Gynecology*. 5th ed. Philadelphia: Lippincott Williams & Wilkins; 2005.
5. Lee PA. Neuroendocrinology of puberty. *Semin Reprod Endocrinol*. 1988;6:13.
6. Lee PA. Physiology of puberty. In: Becker K, Bilezkian J, Brenner W, et al, eds. *Principles and Practice of Endocrinology and Metabolism*. Philadelphia: JB Lippincott; 1990.
7. Schwartz ID, Root AW. Puberty in girls: early, incomplete or precocious? *Contemp Pediatr*. 1990;7:147.
8. Wheeler MD, Styne DM. Diagnosis and management of precocious puberty. *Pediatr Clin North Am*. 1990;37:1255.
9. Bajpai A, Sharma J, Kabra M, et al. Precocious puberty: clinical and endocrine profile and factors indicating neurogenic precocity in Indian children. *J Pediatr Endocrinol Metab*. 2002;15:1173.
10. Argyropoulos M, Kiortsis D. MRI of the hypothalamic-pituitary axis in children. *Pediatr Radiol*. 2005;35:1045.
11. Starceski PJ. Hypothalamic hamartomas and sexual precocity. *Am J Dis Child*. 1990;144:225.
12. Rosenfield RL. Hyperandrogenism in peripubertal girls. *Pediatr Clin North Am*. 1990;37:1333.
13. Kawashima A, Sandler C, Fishman E, et al. Spectrum of CT findings in nonmalignant disease of the adrenal gland. *Radiographics*. 1998;18:393.
14. Larsen W, Felmar E, Wallace M, et al. Sertoli-Leydig cell tumor of the ovary: a rare cause of amenorrhea. *Obstet Gynecol*. 1992;79:831.
15. Herter L, Magalnaes J, Spritzer P. Association of ovarian volume and serum LH levels in adolescent patients with menstrual disorders and/or hirsutism. *Braz J Med Biol Res*. 1993;26:1041.
16. Battaglia C, Artini P, D'Ambrogio G, et al. The role of color Doppler imaging in the diagnosis of polycystic ovary syndrome. *Am J Obstet Gynecol*. 1995;172:108.
17. Takahashi K, Okada M, Ozaki T, et al. Transvaginal ultrasonographic morphology in polycystic ovarian syndrome. *Gynecol Obstet Invest*. 1995;39:201.
18. Mahoney CP. Adolescent gynecomastia: differential diagnosis and management. *Pediatr Clin North Am*. 1990;37:1389.
19. Cohen HL, Eisenberg P, Mandel F, et al. Ovarian cysts are common in premenarchal girls: a sonographic study of 101 children 2–12 years old. *AJR Am J Roentgenol*. 1992;159:89.
20. Currarino G, Wood B, Majd M. Abnormalities of the genital tract. In: Silverman F, Kuhn J, eds. *Caffey's Pediatric X-Ray Diagnosis*. 9th ed. St Louis: Mosby–Year Book; 1993.
21. Rosenfeld RL. Clinical review 6: diagnosis and management of delayed puberty. *J Clin Endocrinol Metab*. 1990;70:559.
22. Emans S. Amenorrhea in the adolescent. In: Emans S, Laufer J, Goldstein D, eds. *Pediatric and Adolescent Gynecology*. 5th ed. Philadelphia: Lippincott Williams and Wilkins; 2005.
23. Falsetti L, Pasinetti E, Mazzani M, et al. Weight loss and menstrual cycle: clinical and endocrinological evaluation. *Gynecol Endocrinol*. 1992;6:49.
24. Tarani L, Lampariello S, Raguso G, et al. Pregnancy in patients with Turner's syndrome: six new cases and review of literature. *Gynecol Endocrinol*. 1998;12:83.
25. Shah R, Woolley M, Costin G. Testicular feminization syndrome: the androgen insensitivity syndrome. *J Pediatr Surg*. 1992;27:757.
26. Lee PA, O'Dea L. Primary and secondary testicular insufficiency. *Pediatr Clin North Am*. 1990;37:1359.
27. Reid R. Amenorrhea. In: Copeland L, ed. *Textbook of Gynecology*. Philadelphia: WB Saunders; 1993.
28. Nidecker A, Cohen HL, Zinn HL. Amenorrhea in the adolescent or young adult. In: Bluth E, Benson C, Ralls P, et al, eds. *Ultrasound: A Practical Approach to Clinical Problems*. 2nd ed. New York: Thieme; 2008.

SECTION 8

# Musculoskeletal System

## PART 1 Overview

# 128 Embryology, Anatomy, and Normal Findings

J. Herman Kan and Peter J. Strouse

## EMBRYOLOGY

Both striated muscle and bone are derived from the mesodermal germ layer. The limb buds form at the end of the fourth week of fetal life. Near the end of the second month of fetal life, the embryonic cartilaginous skeleton is already subdivided into its principal segments, which are the forerunners of bones of the limbs. Primary ossification centers are formed by deposition of calcium in the cartilaginous matrix after hypertrophy and vacuolization of local cartilage cells.[1] In tubular bones, this process occurs at approximately the midpoint of the shaft and is followed by central resorption, which gives rise to the primary marrow cavity. Calcified disks proximal and distal to the primary cavity become preparatory zones of calcification after the development of the advancing, proliferating shaft during growth. Cartilage proximal and distal to the zones of calcification becomes the epiphyses. A layer of cells within the epiphyses near the shaft produces new cells interposed between the resting cartilage of the epiphysis and the older cells and calcified cartilage adjacent to the shaft. The matrix around the old cells calcifies and is invaded by capillaries and bone cells from the marrow. Bone is formed on the calcified cartilage, and new bone and cartilage undergo remodeling by osteoclasts and osteoblasts, so the length of the bone is increased (Fig. 128.1). The girth of the bone and the thickness of the cortex are increased by subperiosteal accretion via activity of subperiosteal osteoblasts. Peripheral resorption of bone at the advancing ends of the shaft maintains the gentle flaring that characterizes normal tubular bone and is the mechanism responsible for what is termed *modeling*. Disproportionate osteoclastic activity within the shaft of the bone reams out a marrow cavity. Continued, balanced activity of all these processes permits a small tubular bone to become a large tubular bone while functional shape and relations with adjacent structures are maintained.

Secondary ossification centers appear in the cartilaginous epiphyses and apophyses and enlarge by similar but much slower processes than those that enlarge the shaft. Irregularities in density and discontinuities in the structure of secondary ossification centers are frequent during normal mineralization and may simulate disease. The known ages at first appearance and upon fusion of these ossification centers can serve as indicators of physical maturation (Figs. 128.2 and 128.3; Table 128.1).

The cartilaginous epiphyses are terminal remnants of the original cartilaginous models of bone. Longitudinal growth takes place at the junction of the physis and the metaphysis by proliferation of cartilage cells in the physis, calcification of the surrounding matrix, and transformation to bone through the activity of metaphyseal vessels and accompanying osteoblasts and osteoclasts. Ossification centers develop within the epiphyses; growth ceases when these secondary centers fuse, through the physis, with the metaphysis. Apophyses are outgrowths of a bone that develop where muscle tendons originate or insert. Similar to the epiphyses, the apophyses develop ossification centers that eventually fuse with the main body of the underlying bone. Apophyses are different from epiphyses in that they do not contribute to longitudinal growth. Epiphyseal and apophyseal ossification and growth occur related to matrix deposition by the spherical growth plate, which has physiology similar to the physis. When epiphyseal ossification is complete, the spherical growth plate and epiphyseal cartilage are no longer appreciable, and only articular cartilage overlies the epiphyseal bone. This process occurs simultaneously with closure of the physis at skeletal maturity.

## PHYSIOLOGY

The bones provide rigid support for the body and sites of insertion for muscles, to which the bones respond as levers. The bones are active physiologically in infants and children, changing size and shape with growth and hormone activity (related to levels of vitamin D, parathyroid hormone, calcitonin, or serum calcium and phosphate levels) and in response to mechanical stresses.[2]

During growth, in addition to its constant increase in length and breadth, the shaft is continuously molded or reshaped to its final form in a process called *modeling* or *tubulation*. One of the most conspicuous features of modeling is progressive concentric contraction of the shaft behind the wider, advancing terminal segment (e-Fig. 128.4); this process results in the flared ends of tubular bones.

Significant disturbances in configuration of the shafts occur in many chronic diseases that affect the growing skeleton. With overtubulation, a diaphysis is abnormally narrow in caliber with accentuation of metaphyseal flaring. This usually is seen in children with cerebral palsy or other neuromuscular diseases in which normal muscular stresses are not present. With undertubulation, the diaphysis is abnormally broad in caliber with loss of the normal metaphyseal flaring; causes may include Gaucher disease, Pyle dysplasia, and osteochondromatosis.

Acute changes related to systemic disease are most commonly seen at the juxtaphyseal metaphysis, which is the most metabolically active component of the growing bone unit, and the location of primary bone deposition (e.g., metaphyseal fraying seen in persons with rickets or juxtaphyseal sclerosis with intervening areas of bony rarefaction in persons with leukemia).

## ANATOMY

Three types of bones are found in the limbs: (1) long and short tubular bones, (2) round bones in the wrists and ankles, and (3) sesamoids, which are small bones in the tendons and articular capsules. Functionally, a growing tubular bone is made up of the following segments: diaphysis, metaphysis, physis, and epiphysis (Fig. 128.5). "Long bones" have epiphyses at both ends. Short tubular bones ("short bones") have epiphyses at one end. In the

## Abstract:

To describe the embryology, anatomy, and normal variants of the growing skeleton and to differentiate from pathologic conditions. Normal developmental variants of the growing skeleton may superficially mimic traumatic and neoplastic entities. By understanding the embryologic and development of these normal variations, radiologists can improve identification of pathologic processes that may affect the growing skeleton.

## Keywords:

radiography
MRI
embryology
normal variants
accessory ossification centers

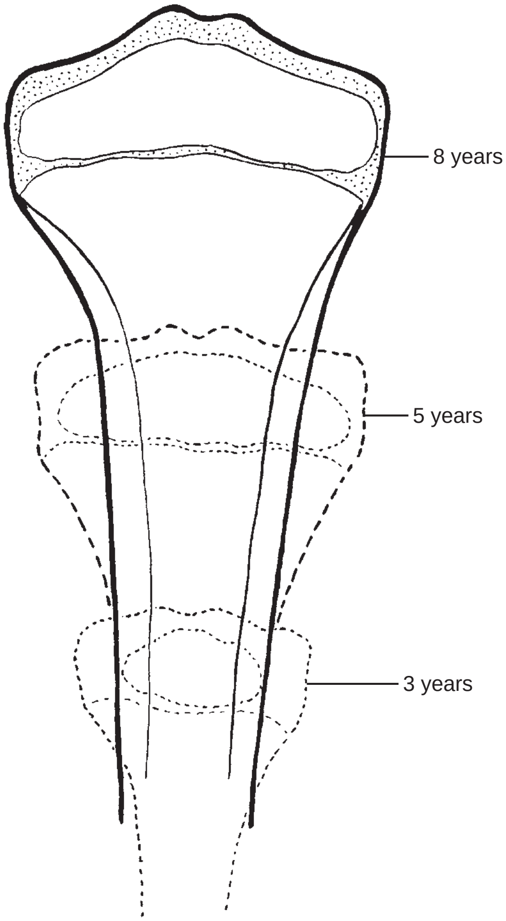

**e-Figure 128.4. Growth and configuration of the tibia with advancing age.** The progressive concentric constriction of the shaft away from the wider epiphyseal plate is shown schematically on superimposed tracings of radiographs.

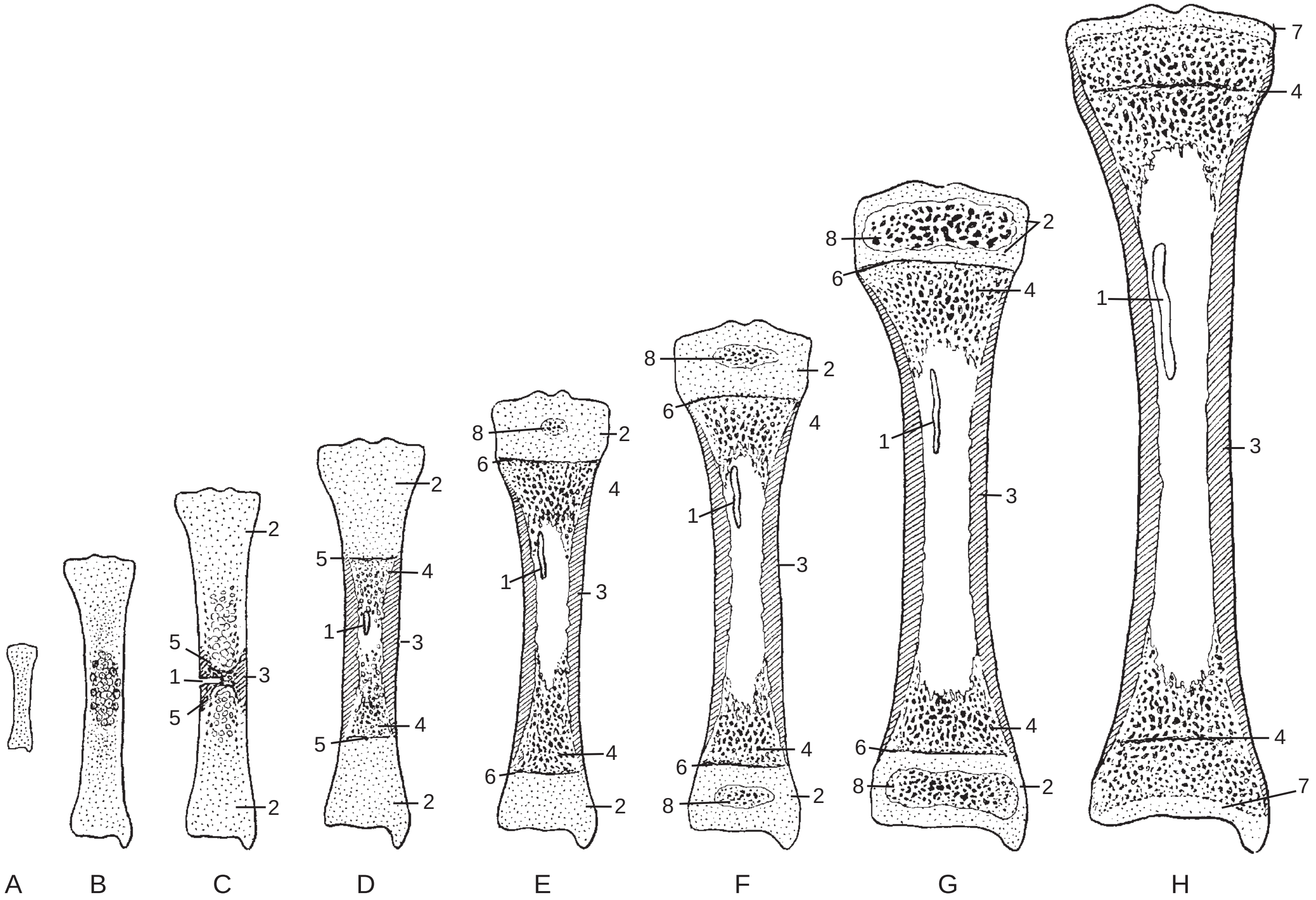

**Figure 128.1. Schema of progressive stages in the growth and maturation of the tibia.** (A) The mass of embryonal cartilage that is the anlage of the tibia. (B) Initial enlargement and multiplication of the central cartilage cells and an increase in cartilaginous matrix—the chondrification center that is the forerunner of the primary ossification center. (C) The early primary ossification center shows the formation of a central belt of subperiosteal bone (early cortex) and penetration of the cartilaginous matrix by the periosteal elements; the channel of this penetration persists as the nutrient canal. (D) Extension of ossification toward both ends of the shaft, with central resorption forming the medullary cavity. (E) The tibia at birth, with a secondary ossification center in the proximal epiphyseal cartilage. (F) At approximately the fourth postnatal month, ossification centers are seen in both of the epiphyseal cartilages. (G) The juvenile tibia shows the growth of all components and enlargement of the epiphyseal secondary ossification centers. (H) The adult tibia, with complete fusion of the shaft and both epiphyses. The narrow plates of articular cartilage that cap each end of the bone persist throughout life. *1,* nutrient canal; *2,* epiphyseal cartilage; *3,* corticalis; *4,* spongiosa; *5 and 6,* provisional zones of calcification or epiphyseal plates; *7,* articular cartilages; *8,* secondary epiphyseal ossification centers. *(Modified from an original drawing by W. M. Rogers, MD.)*

hands and feet, secondary ossification centers appear in the bases of the phalanges and in the distal ends of the second through fifth metacarpals and metatarsals. Epiphyses for the first metacarpal and first metatarsal are found in the proximal ends of the bones. The location of the secondary centers appears to be related to the sites of maximal joint motion of individual short tubular bones. Apparent epiphyseal ossification centers observed at the ends of short bones, where their occurrence is not expected, are termed *pseudoepiphyses*.

**TABLE 128.1** Epiphyseal Ossification in the Fetus and Neonate: Fifth and Ninety-Fifth Percentiles

| Ossification Center | Fifth Percentile | Ninety-Fifth Percentile |
|---|---|---|
| Humeral head | 37th week | 16 postnatal weeks |
| Distal femur | 31st week | 39th week (female)<br>40th week (male) |
| Proximal tibia | 34th week | 2 postnatal weeks (female)<br>5 postnatal weeks (male) |
| Calcaneus | 22nd week | 25th week |
| Talus | 25th week | 31st week |
| Cuboid | 37th week | 8 postnatal weeks (female)<br>16 postnatal weeks (male) |

*Data from Kuhns LR, Finnstrom O. New standards of ossification of the newborn.* Radiology. *1976;119:655–660.*

## NORMAL FINDINGS

### Determining Skeletal Age

The gestational age of a newborn can be estimated radiographically through several methods. The proximal humeral ossification center

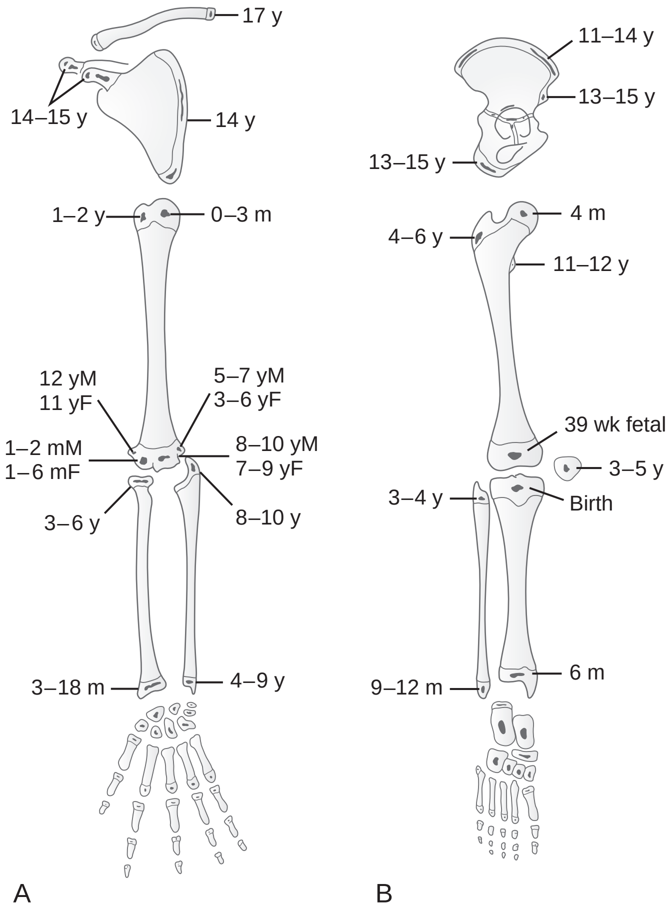

**Figure 128.2.** Ages of onset of secondary (epiphyseal and apophyseal) ossification of the major bones of the upper (A) and lower (B) extremity. *F,* Female; *M,* male; *m,* month; *wk,* week; *y,* year. *(Reproduced from Ogden JA.* Skeletal Injury in the Child. *3rd ed. New York: Springer; 2000.)*

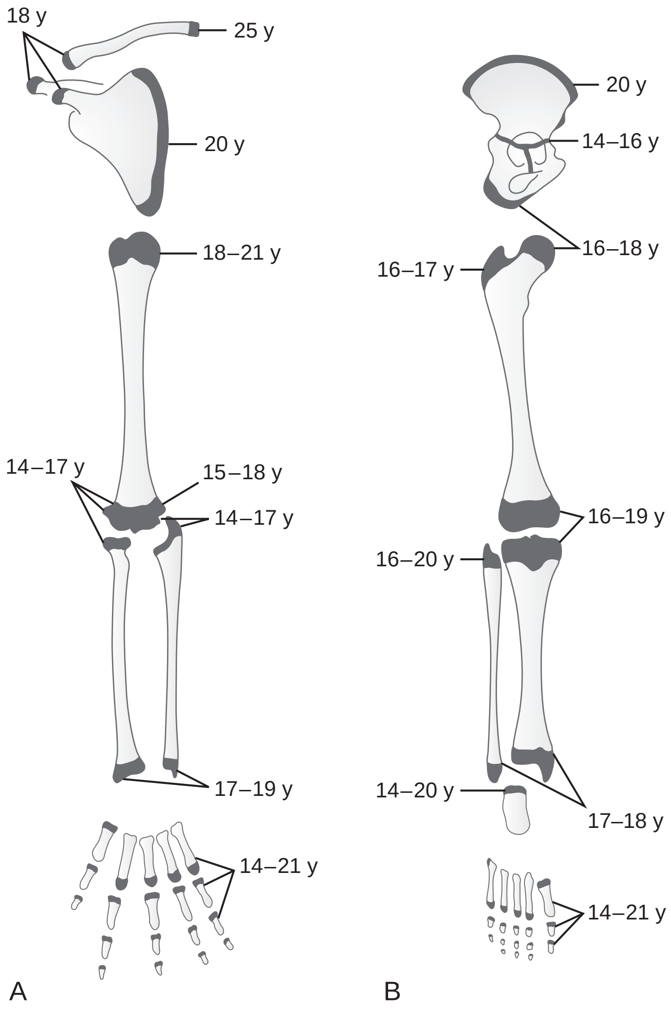

**Figure 128.3.** Ages of physeal closure of the major bones of the upper (A) and lower (B) extremities. *y,* Year. *(Reproduced from Ogden JA.* Skeletal Injury in the Child. *3rd ed. New York: Springer; 2000.)*

appears shortly after birth, with a 95% confidence interval between 37 weeks' gestation and 16 weeks' postnatal life.[3] Ossification before 37 weeks is unusual; therefore the presence of the proximal humeral ossification center is an indication that a newborn is at term or near term. Teeth appear at a characteristic time; the first deciduous molars form at 33 weeks, and the second deciduous molars form at 36 weeks. The range of values is great for the radiographic appearance of various appendicular bone epiphyseal ossification centers, even in premature infants (Table 128.1).

Evaluation of bone age is used to estimate biologic maturation relative to chronologic age. Differences in familial, racial, and socioeconomic factors limit the applicability of the standards of Greulich and Pyle (which were developed in the 1940s) to today's children.[4,5] It is well accepted that maturation varies between races. For instance, African American children mature faster than do white children.[6] The hand, with its numerous secondary centers in phalanges and metacarpals, and to a lesser degree the wrist, are used as an index of total skeletal maturation. Standard deviations, which are based on chronologic age, are somewhat broad. A bone age within the 5% to 95% confidence interval (or ±2 standard deviations) is considered normal.

In children younger than 2 years, use of the standards of Greulich and Pyle is limited because relatively little change is noted in the ossification centers of the hand and wrist during this period. More rapid changes may be observed in the knee or foot, however. Radiographs of the left knee or left foot—anteroposterior

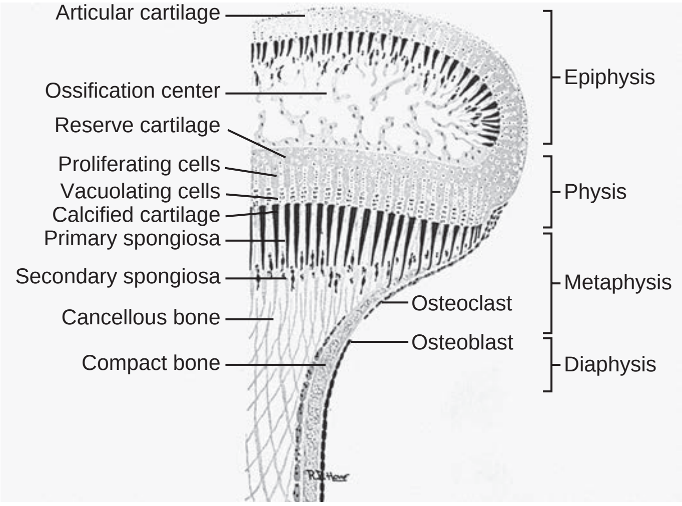

**Figure 128.5.** Functional components of the growing end of a tubular bone and their anatomic substrate.

and lateral—can be obtained in children younger than 2 years of age and compared with published standards.[7,8]

The Risser classification can be used to assess skeletal maturation through evaluation of the appearance and state of fusion of the iliac crest.[9] Ossification of the iliac crest begins laterally and proceeds medially: stage 0—no ossification; stage I—up to 25% ossified; stage II—25% to 50% ossified; stage III—50% to 75% ossified; stage IV—75% to 100% ossified; and stage V—fully ossified and fused (e-Fig. 128.6 and Fig. 134.2).

Assessment of skeletal age by radiography is useful in many clinical scenarios. Boxes 128.1 and 128.2 list causes of advanced and delayed skeletal maturation, respectively. Menarche typically occurs after fusion of the physes of the distal phalanges. Bone age can be used with long bone measurements to predict adult height. Assessment of bone age is also valuable in the planning of orthopedic treatments, including epiphysiodesis, leg-lengthening procedures, and scoliosis management.

**BOX 128.1** Causes of Advanced Skeletal Maturation

- Acrodysostosis
- Adrenogenital syndrome (adrenocortical tumor or hyperplasia)
- Cerebral gigantism
- Gonadal tumors (androgen or estrogen secreting)
- Growth hormone excess (gigantism)
- Hyperthyroidism (maternal or acquired)
- Hypothalamic tumors
- Idiopathic familial advanced bone age
- Idiopathic isosexual precocious puberty
- Lipodystrophy
- Liver tumors (choriocarcinoma, hepatoma)
- McCune-Albright syndrome (polyostotic fibrous dysplasia)
- Medication with sex hormones
- Pinealoma
- Premature adrenarche
- Premature thelarche
- Pseudohypoparathyroidism
- Various syndromes

**BOX 128.2** Causes of Delayed Skeletal Maturation

- Addison disease
- Chromosomal disorders (e.g., trisomy 21 and trisomy 18)
- Chronic illness
- Chronic renal disease
- Chronic severe anemia (e.g., sickle cell anemia and thalassemia)
- Congenital heart disease (especially cyanotic)
- Congenital malformation syndromes
- Constitutional delay
- Cushing syndrome
- Growth hormone deficiency
- Hypogonadism (e.g., Turner syndrome)
- Hypothyroidism
- Idiopathic causes
- Inflammatory bowel disease
- Intrauterine growth retardation
- Juvenile diabetes mellitus
- Malabsorption syndromes (e.g., celiac disease)
- Malnutrition
- Neurologic disorders
- Panhypopituitarism
- Rickets
- Skeletal dysplasias (most)
- Steroid therapy

## Anatomic Variants

Experience and knowledge often are the best resources for successfully identifying normal variants. Compendiums of normal variants (e.g., *An Atlas of Normal Roentgen Variants That May Simulate Disease* by Keats and Anderson[10] and *Borderlands of Normal and Early Pathological Findings in Skeletal Radiography* by Freyschmidt et al.[11]) are invaluable resources.

Many epiphyseal and apophyseal ossification centers are irregular and fragmented in their early development (Fig. 128.7). When evaluating the significance of irregular ossification in a single area, it is important to remember that normal irregularities of ossification usually are symmetric and accompanied by similar changes in other areas of the skeleton. Normal epiphyseal and apophyseal fragmentary ossification tends to have a smooth, round, and sclerotic appearance. Sometimes epiphyseal fragmentary ossification centers may have a jigsaw configuration. Normal epiphyseal fragmentary ossification should be differentiated from acute fractures that tend to have a linear contour with nonsclerotic margins with accompanying soft tissue swelling and joint effusions.

Physiologic osteosclerosis of the newborn is a common finding. The long tubular bones of fetuses, premature infants, and term newborn infants often appear sclerotic compared with the bones of older children because of proportionately thicker cortical bone and more abundant spongiosa during fetal and neonatal life (e-Fig. 128.8). The sclerotic features disappear gradually during the first weeks of life and resolve by 2 to 3 months of age.

Physiologic periosteal reaction in the newborn also is a common finding seen in infants from 1 to 4 months of age and in both premature and term infants. Physiologic periosteal new bone is diaphyseal, smooth, regular, and 2 mm or less in thickness (Fig. 128.9).[12] Physiologic periosteal new bone is most common in the tibia, femur, and humeral diaphysis and occasionally is seen in the radius and ulna. In most infants, physiologic periosteal new bone is symmetric; however, it may be asymmetric in one-third to one-half of patients. Traumatic periosteal new bone tends to be asymmetric, metaphyseal, thicker, and irregular compared with physiologic periosteal new bone.

A variety of normal variants in the metaphyses of infants may simulate injury. It is important to distinguish these findings from the classic metaphyseal lesions of child abuse (see Chapter 143). The most common variant is the subperiosteal bone collar of the juxtaphyseal metaphysis, which has a normal step-off that may mimic a metaphyseal lesion of child abuse (Fig. 128.10).[13]

Gas (nitrogen) is commonly seen in joints of young children as a result of traction needed to appropriately position the child. Some authors hold that the presence of this vacuum phenomenon within the joint on radiography excludes a joint effusion.

The following selected, important variants should not be confused with pathology.

### Hands and Feet

**Ivory Epiphyses.** Sclerotic epiphyseal ossification centers of the phalanges are called *ivory epiphyses* (e-Fig. 128.11).[14] They occur in approximately 1 in every 300 patients. Ivory epiphyses usually are found in the distal phalanges and in the middle phalanx of the fifth digit. Maturation may be retarded. Ivory epiphyses are usually sporadic and occur in developmentally normal children but may occur in association with cone-shaped epiphyses in dysplastic syndromes such as Cockayne's syndrome, trichorhinophalangeal syndrome, and multiple epiphyseal dysplasia.[14] Ivory epiphyses are more frequently found in the toes compared with the fingers.

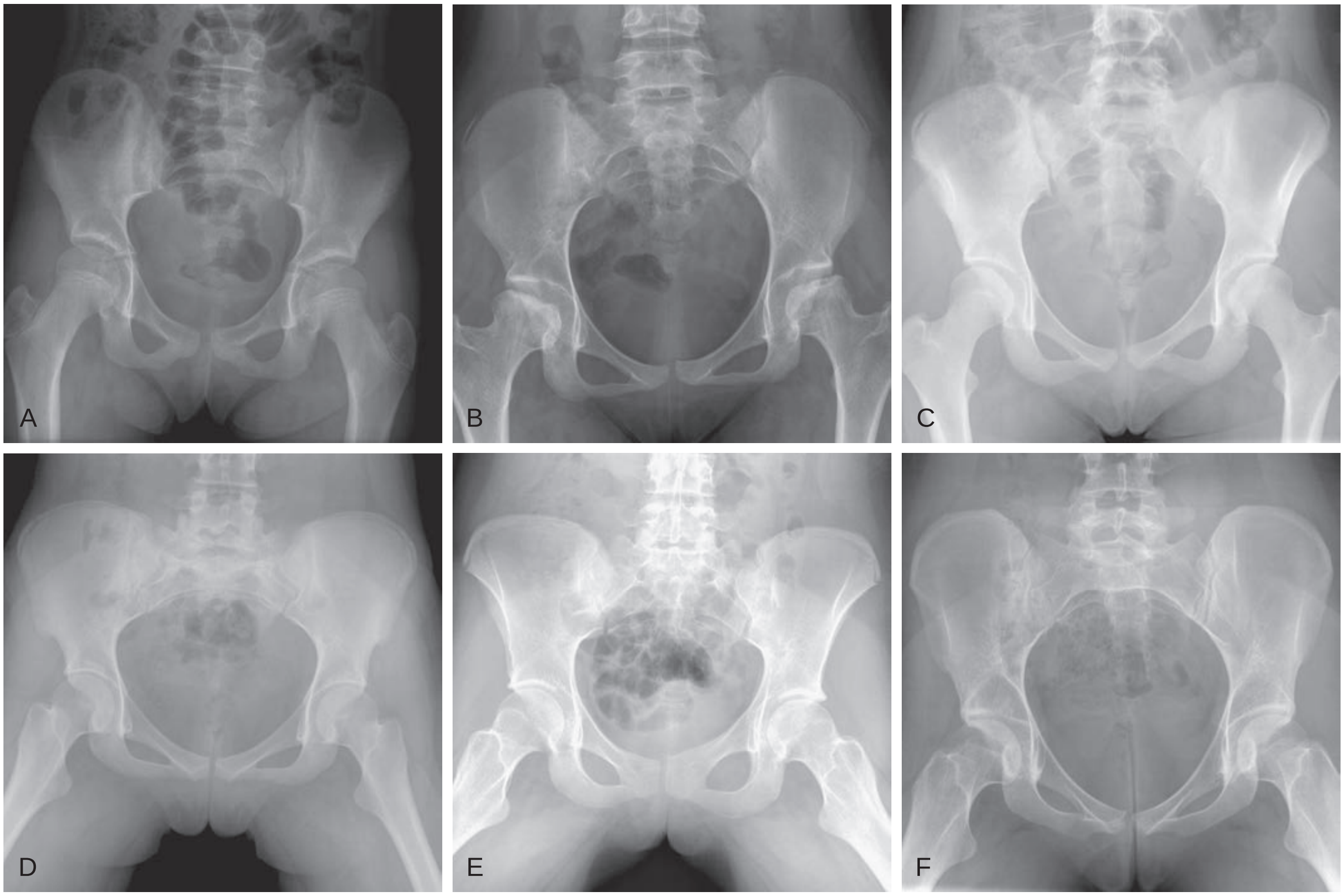

**e-Figure 128.6. Risser stages.** (A) Risser stage 0. (B) Risser stage 1 (with bilateral Perthes). (C) Risser stage 2. (D) Risser stage 3. (E) Risser stage 4. (F) Risser stage 5.

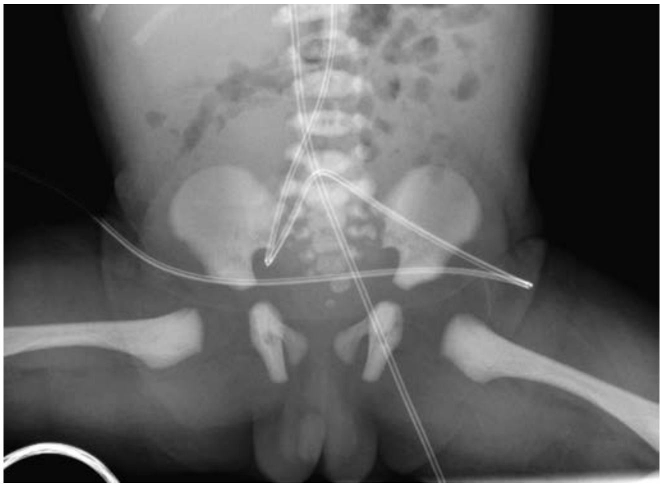

**e-Figure 128.8. Normal osteosclerosis of the newborn.** All of the bones appear dense. The medullary cavities of the pubic bones and proximal femurs are obscured.

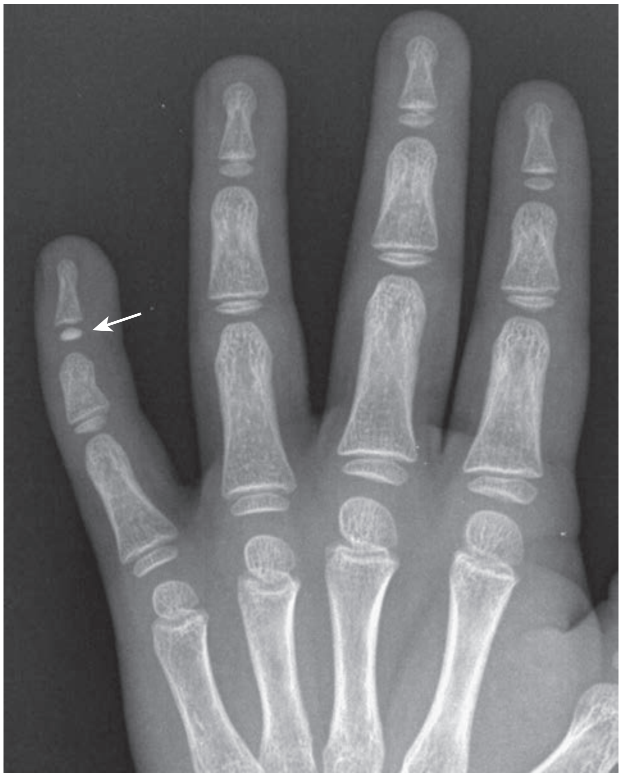

**e-Figure 128.11.** Ivory epiphysis *(arrow)* of the distal phalanx in a 6-year-old boy.

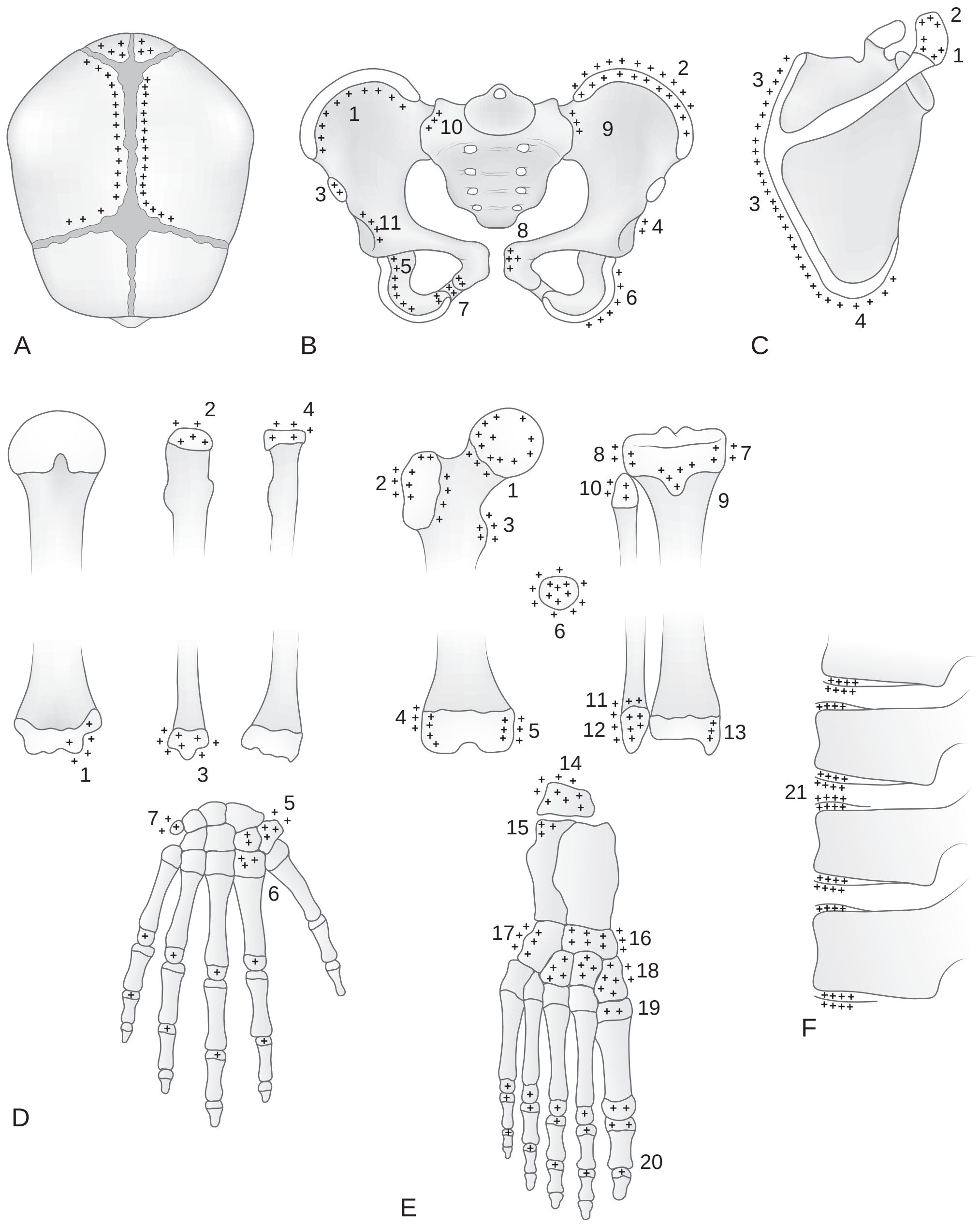

**Figure 128.7. Common sites of normally irregular mineralization in the growing skeleton are marked by crosses.** (A) The cranium. During the first weeks of life and continuing for several months, edges of the bones at the great sutures are commonly irregular, and in many infants deep fissures extend from the sutures into the bodies of the bones. Irregularities also are common on the edges of the temporal suture (not shown). (B) The pelvis: *1,* crest of ilium; *2,* secondary center in iliac crest; *3,* secondary center of anterior superior spine; *4,* os acetabuli marginalis; *5,* body of ischium; *6,* secondary center of ischium; *7,* ischium and pubis at the ischiopubic synchondrosis; *8,* body of pubis; *9,* ilium at sacroiliac joint; *10,* sacrum at sacroiliac joint; *11,* iliac edge and roof of the acetabular cavity. (C) The scapula: *1 and 2,* secondary centers of acromion process; *3,* secondary center of vertebral edge; *4,* secondary center of inferior angle. (D) The upper limb: *1,* secondary center of trochlea, always irregular; *2 and 3,* proximal and distal epiphyseal centers of ulna; *4,* proximal epiphyseal center of radius; *5,* greater and lesser multangulars; *6,* inconstant center of second metacarpal (pseudoepiphysis); *7,* pisiform. (E) The lower limb: *1,* proximal metaphysis of femur; *2 and 3,* secondary center and edges of shaft at greater and lesser trochanters, respectively; *4 and 5,* lateral and medial edges, respectively, of distal epiphyseal center of femur; *6,* patella; *7 and 8,* medial and lateral edges, respectively, of proximal epiphyseal center of tibia; *9,* secondary center in anterior tibial process; *10,* proximal epiphyseal center of fibula; *11 and 12,* distal metaphysis and distal epiphyseal center of fibula, respectively; *13,* internal malleolus of distal epiphyseal center of tibia; *14,* apophysis of calcaneus; *15,* primary center of calcaneus; *16,* navicular; *17,* cuboid; *18,* cuneiforms; *19,* proximal epiphyseal center of first metatarsal; *20,* epiphyseal centers of phalanges. (F) The spine: *21,* marginal centers (end plate ring apophyses).

**Cone-Shaped Epiphyses.** Cone-shaped epiphyses of the phalanges (e-Fig. 128.12) occur singly or in combination and most commonly affect the terminal phalanges. When they occur in isolation, they may be related to trauma with resultant central physeal growth disturbance. When they are multiple, they may be seen in association with dysplastic syndromes such as trichorhinophalangeal syndrome and cartilage hair hypoplasia.[15] Cone-shaped epiphyses are found more frequently in the toes than in the fingers (Fig. 128.13).

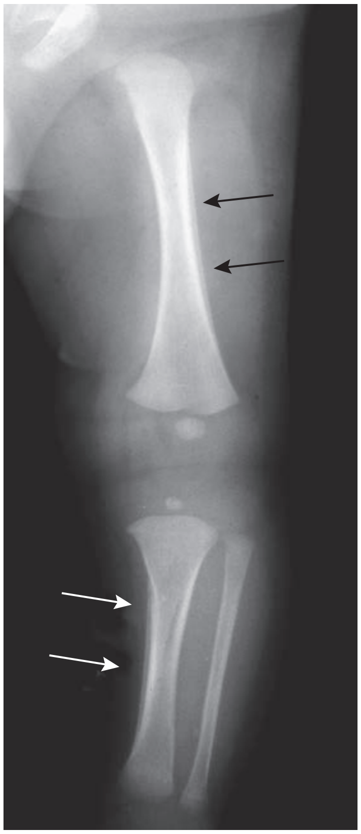

**Figure 128.9. Physiologic periosteal new bone in a 9-week-old boy.** Smooth periosteal new bone is seen on the lateral aspect of the femoral and medial aspect of the tibial diaphyses *(arrows)*.

**Fifth Metatarsal Apophysis.** During puberty, a longitudinally oriented, scalelike secondary ossification center appears within the proximal apophyseal cartilage of the fifth metatarsal (Fig. 128.14). Irregular ossification of the apophysis is common. The normal apophyseal ossification center may appear widely spaced from the underlying fifth metatarsal, simulating fracture.[16] The fifth metatarsal apophysis also may be bifid (e-Fig. 128.15). This presentation should be differentiated from a fifth metatarsal avulsion fracture related to the peroneus brevis insertion, which has a horizontal orientation (e-Fig. 128.16) (see also Chapter 142).

**Pseudoepiphyses.** Pseudoepiphyseal ossification centers may appear in the proximal cartilaginous portion of the growing second through fifth metacarpals and metatarsals and in the distal cartilage of the first metacarpals and metatarsals (Fig. 128.17 and e-Fig. 128.18).[17] They are formed from a thin rod of osteogenic tissue that invades the proximal or distal cartilage from the shaft. The end of the rod enlarges to form a mushroom-shaped mass of bone that appears radiographically as the “pseudoepiphysis.” The site of fusion of the pseudoepiphysis with the shaft often is indicated by a notch. Pseudoepiphyses are well formed by 4 to 5 years of age and fuse with the underlying shaft at the time of skeletal maturation. Sporadic pseudoepiphysis most commonly affects the second metacarpal bone of the hand, occurring in approximately 15% of children.[18,19] Pseudoepiphyses may be seen with higher frequency in children with hypothyroidism, Down syndrome, and cleidocranial dysplasia.

**Sesamoid Bones.** Sesamoid bones are present in the foot and hand. Sesamoids of the great toe reside within the medial and lateral slips of the flexor hallucis brevis tendon overlying the head of the first metatarsal. The medial great toe sesamoid is bipartite in 4% to 33% of patients (e-Fig. 128.19). Sesamoids of the feet may develop a stress reaction or a complete fracture and may be difficult to distinguish from a bipartite sesamoid on radiographs; magnetic resonance imaging (MRI) may be useful in distinguishing a normal bipartite sesamoid and underlying stress injury. For the first metatarsal phalangeal, stress injury tends to affect the medial sesamoid more frequently than the lateral sesamoid.[20] In addition to the sesamoids, numerous other supernumerary ossicles of the foot and ankle exist (Fig. 128.20).

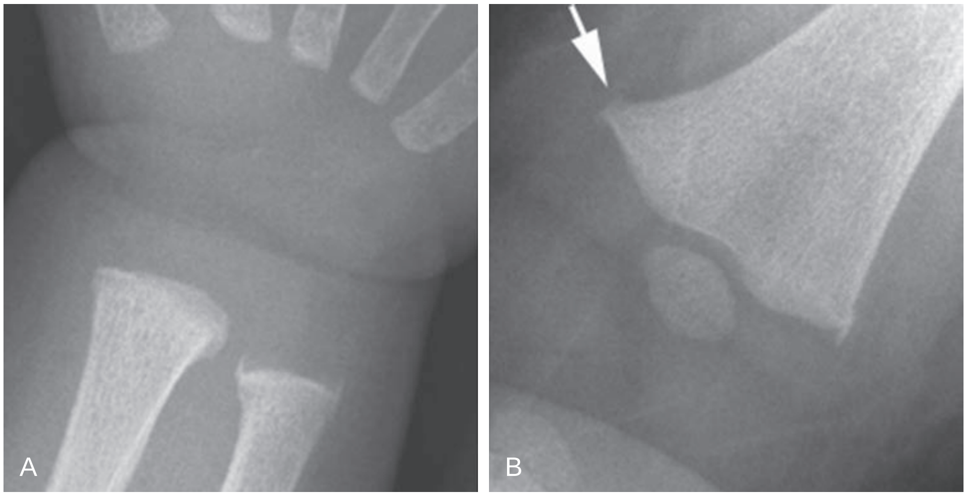

**Figure 128.10. Normal metaphyseal collar.** Small spurs on the distal ulnar (A) and distal femoral (B) metaphyses in a 5-month-old girl due to extension of the subperiosteal bone collar beyond the metaphysis. A normal “step-off” also is noted on the distal femur *(arrow)*.

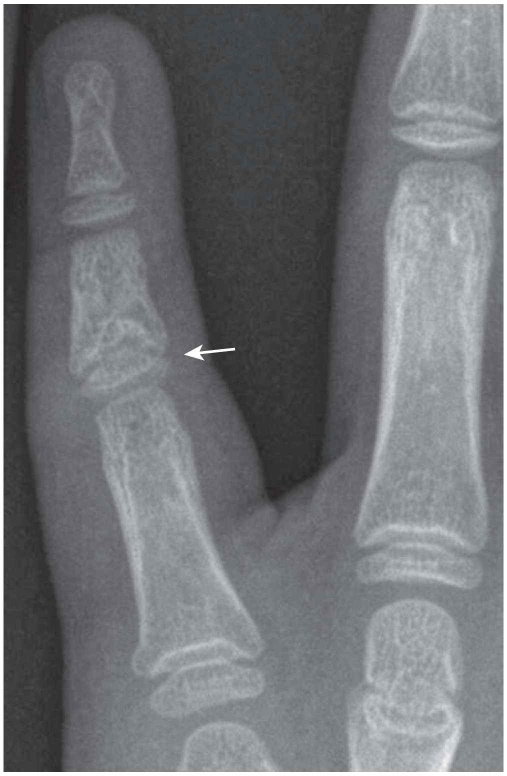

**e-Figure 128.12.** Cone-shaped epiphysis *(arrow)* of the middle phalanx of the fifth digit in a 9-year-old.

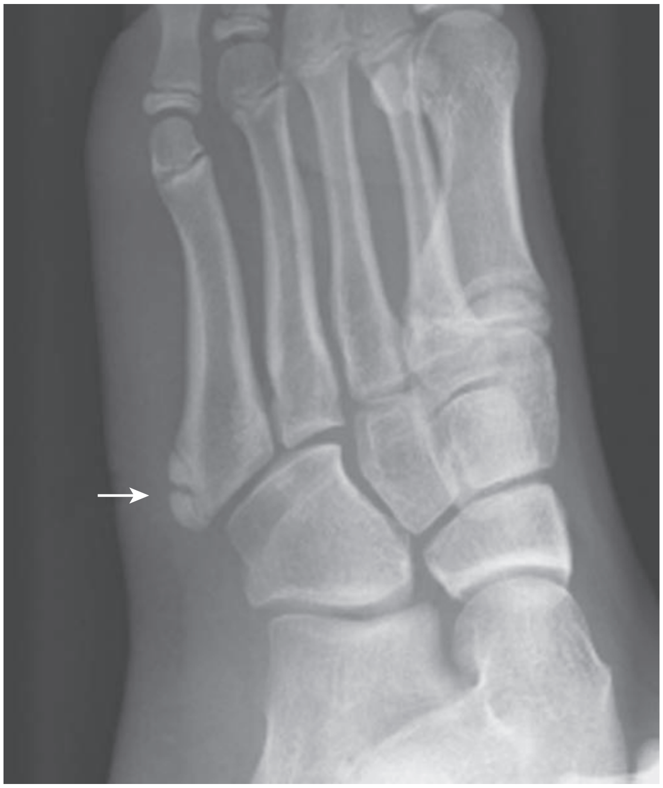

**e-Figure 128.15. Bifid apophysis of the fifth metatarsal in a 13-year-old girl *(arrow)*.** Findings persisted on follow-up examinations without change.

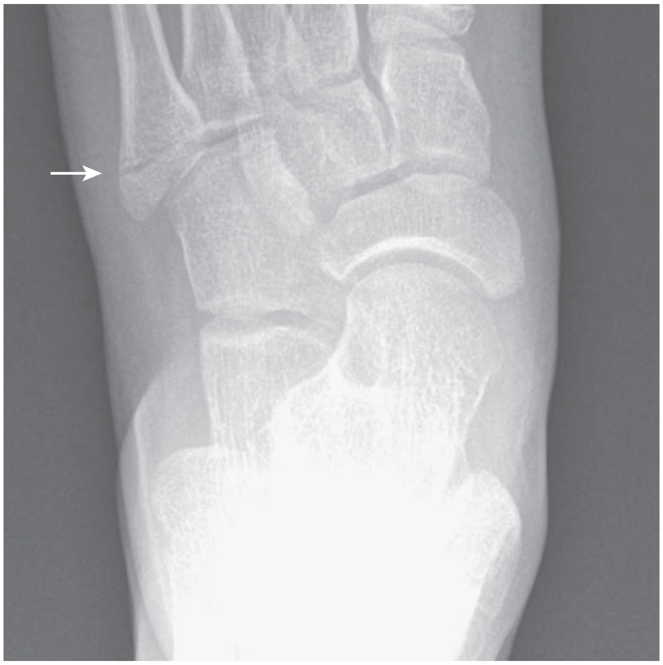

**e-Figure 128.16.** Nondisplaced avulsion fracture *(arrow)* of the base of the fifth metatarsal in a 9-year-old girl.

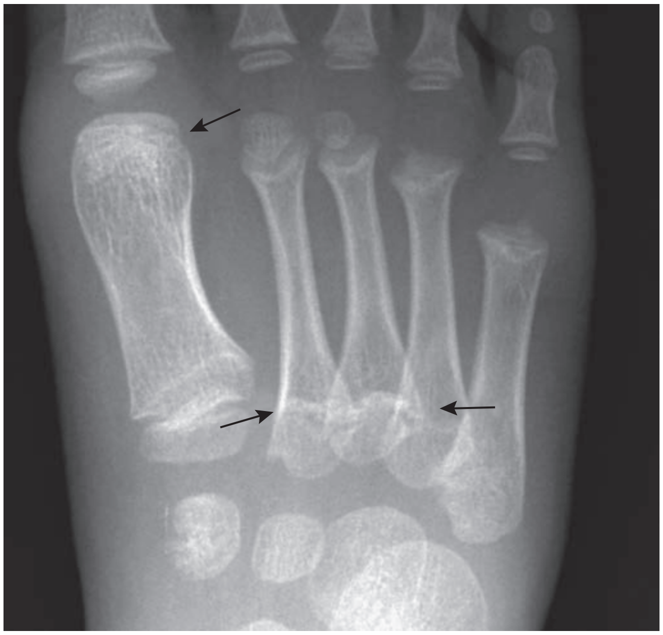

**e-Figure 128.18.** Pseudoepiphyses of the first metatarsal *(distal arrow)* and the second and third metatarsals *(proximal arrows)* in a 6-year-old boy.

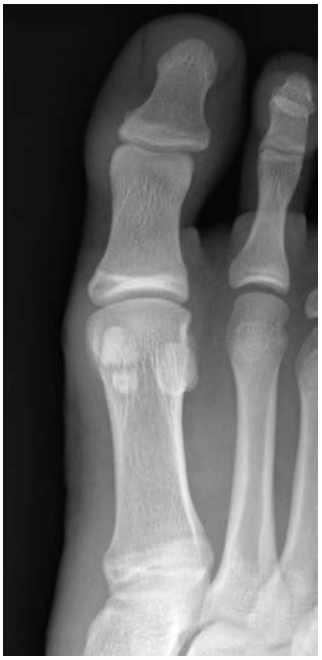

**e-Figure 128.19.** Bipartite medial sesamoid of the great toe in a 15-year-old boy.

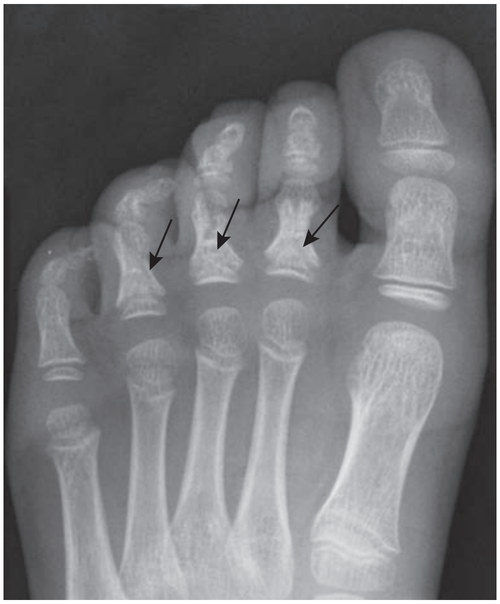

**Figure 128.13. Symmetric conical or bell-shaped epiphyseal ossification centers *(arrows)* in the proximal phalanges of the second, third, and fourth toes of an asymptomatic 5-year-old girl.** The contiguous distal end of each shaft is recessed to receive its elongated ossification center. The epiphyseal ossification centers in the proximal phalanges of the first and fifth toes are the normal, flat, shallow, transverse disks usually present in all of the phalanges.

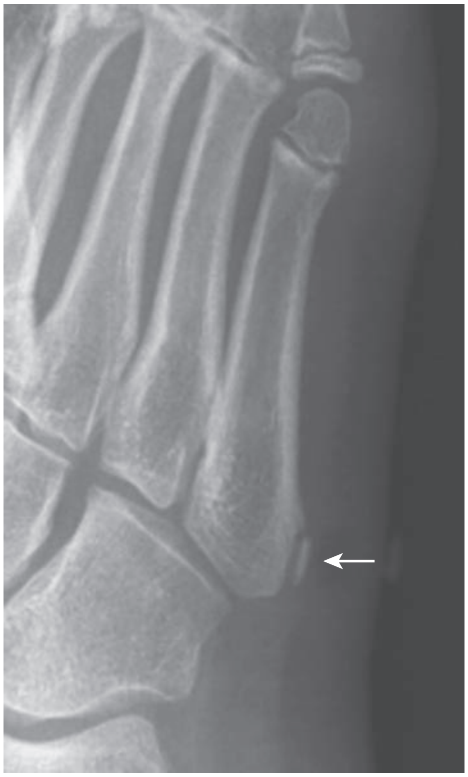

**Figure 128.14. Normal apophysis of the fifth metatarsal in a 10-year-old girl *(arrow)*.** The apophyseal growth plate is longitudinal in orientation, and the apophysis appears "scalelike."

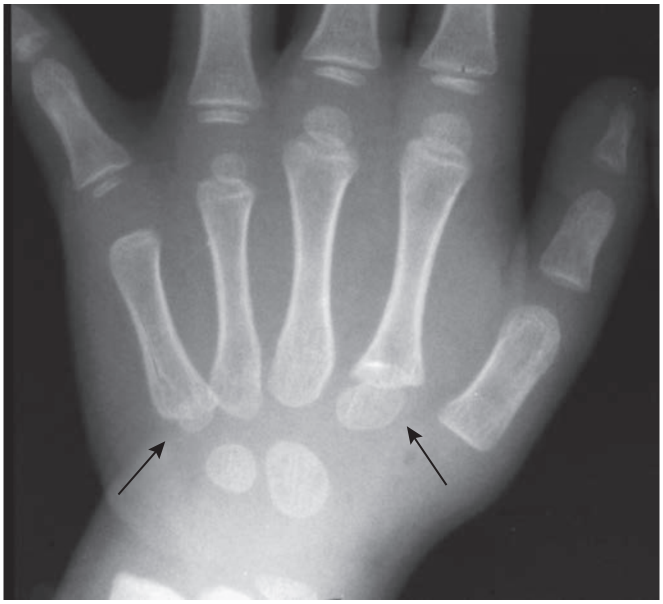

**Figure 128.17.** Pseudoepiphyses *(arrows)* in the proximal second and fifth metacarpals of a 3-year-old boy.

**Irregular Carpal Ossification.** Irregular mineralization often occurs in the developing carpal bones (e-Fig. 128.21). The pisiform is the bone most frequently affected (e-Fig. 128.22). In addition, carpal bones sometimes may have wavy cortical contours most commonly affecting the capitate, which should not be confused with erosions.[21]

**Os Styloideum (Carpal Boss).** The os styloideum is a bony protrusion at the dorsum of the wrist between the trapezoid, capitate, and second and third metacarpals.[22] It may be isolated and mobile or fused to an adjacent bone. The os styloideum is present in 1% to 3% of patients and presents as a palpable mass (Fig. 128.23). The differential diagnosis for a dorsal palpable abnormality along the wrist is an os styloideum versus a ganglion.

**Radial and Ulnar Styloid Processes.** Separate ossification centers may appear in the regions of the ulnar (e-Fig. 128.24) and radial (Fig. 128.25) styloid processes before uniting with the main ossification center. The ulnar accessory ossification center should not be confused with ulnar styloid fracture nonunions.[23]

**Bifid Epiphyses.** Accessory ossification centers may occur in the epiphyses of phalanges and metatarsal bones. Bifid epiphysis is most common in the great toes, where examination before fusion of the centers is complete may simulate fracture (e-Fig. 128.26). The affected epiphysis is relatively sclerotic.[24]

**Absent Epiphyses.** The phalanges, especially the middle group, frequently lack epiphyseal centers in healthy children; this absence may be associated with symphalangism at the affected joints. Forty percent of the population have a biphalangeal (e-Fig. 128.27) fifth toe that may predispose to hammer or claw toe deformities.[25]

**Bifid Calcaneus.** The ossification center for the calcaneus is present at birth. Occasionally the body of the calcaneus may ossify from two or more independent centers (Fig. 128.28). This finding is rare as a normal variant. More often it is associated with an underlying disorder such as Down syndrome, mucolipidosis, or Larsen syndrome.

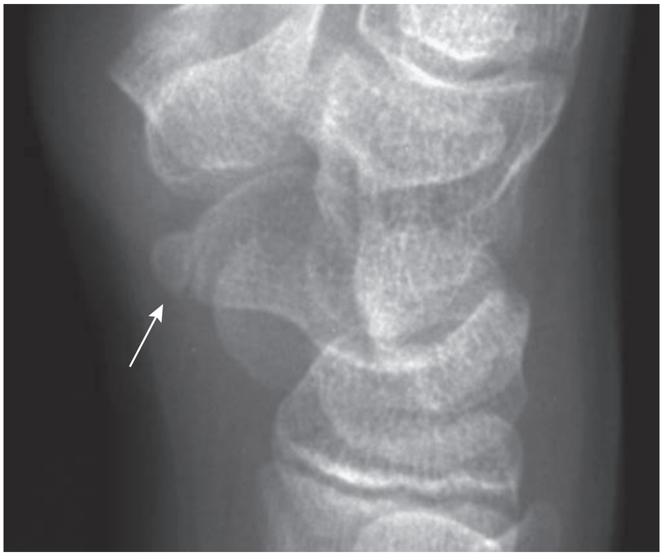

**e-Figure 128.21.** Accessory ossification center of the distal pole of the scaphoid *(arrow)* in an 11-year-old girl.

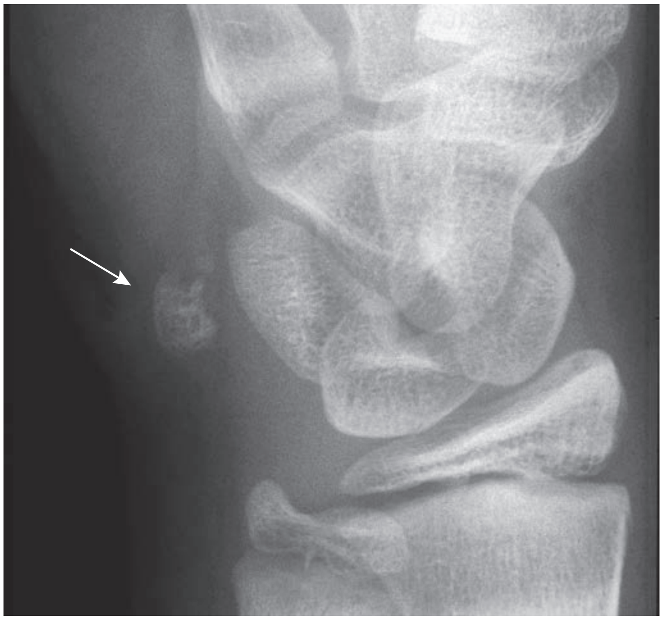

**e-Figure 128.22.** Irregular ossification of the pisiform *(arrow)* in a 12-year-old boy.

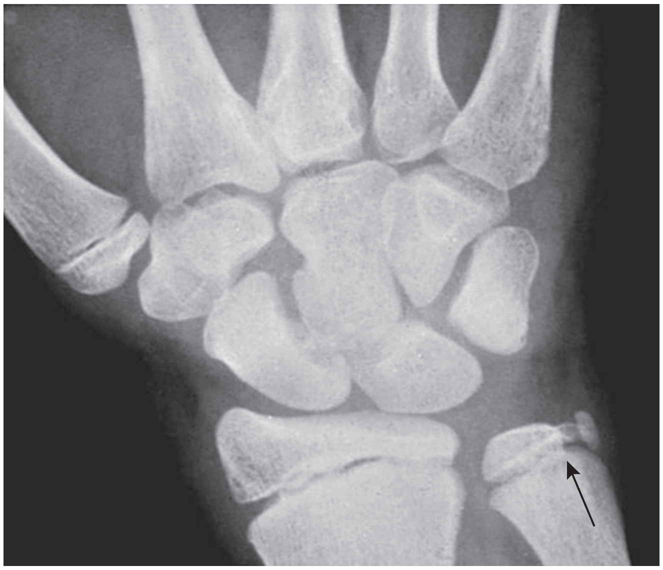

**e-Figure 128.24. Separate secondary epiphyseal ossicles *(arrow)* for the styloid in the distal epiphyseal cartilage of the ulna of an asymptomatic 11-year-old boy.** Ossicles of this type should not be mistaken for fracture fragments in cases of injury.

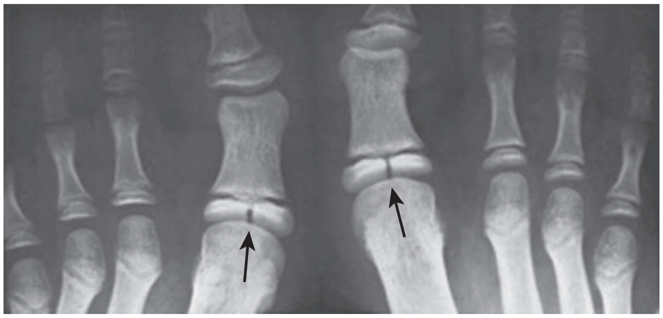

**e-Figure 128.26. Bifid epiphyses.** Symmetric fissures of the secondary ossification centers *(arrows)* in the proximal epiphyses of the proximal phalanges of the great toes of an asymptomatic 11-year-old boy. Radiolucent synchondroses between the segments of each center must not be mistaken for fracture lines.

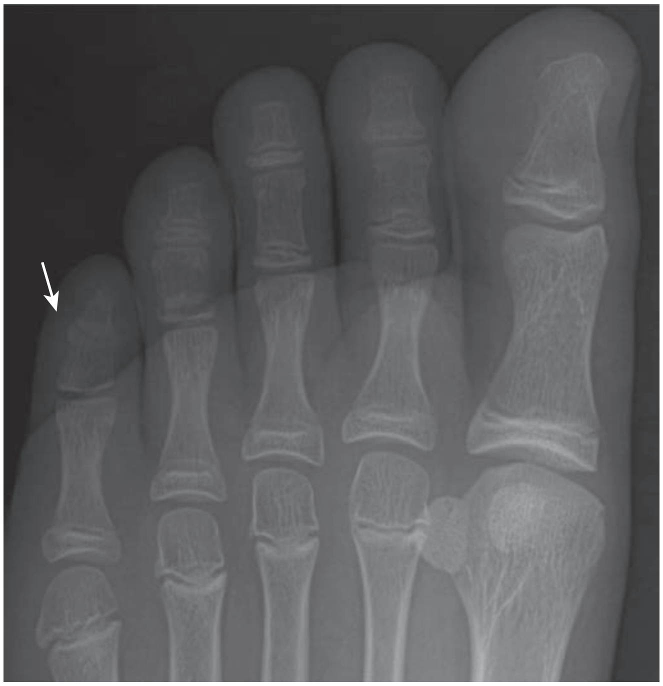

**e-Figure 128.27.** Biphalangeal fifth toe *(arrow)* in a 13-year-old girl.

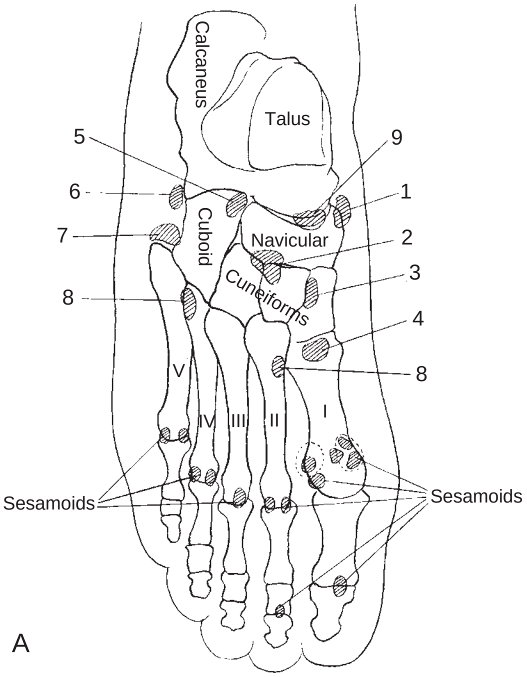

**Figure 128.20.** Normal supernumerary ossicles of the feet in ventrodorsal (A) and lateral (B) projections: *1,* os tibiale externum (accessory navicular); *2,* processus uncinatus; *3,* os intercuneiforme; *4,* pars peronea metatarsalia; *5,* os cuboideum secundarium; *6,* os peroneum; *7,* os vesalianum pedis; *8,* os intermetatarseum; *9,* os supratalare; *10,* talus accessorius; *11,* os sustentaculum; *12,* os trigonum tarsi; *13,* calcaneus secundarius.

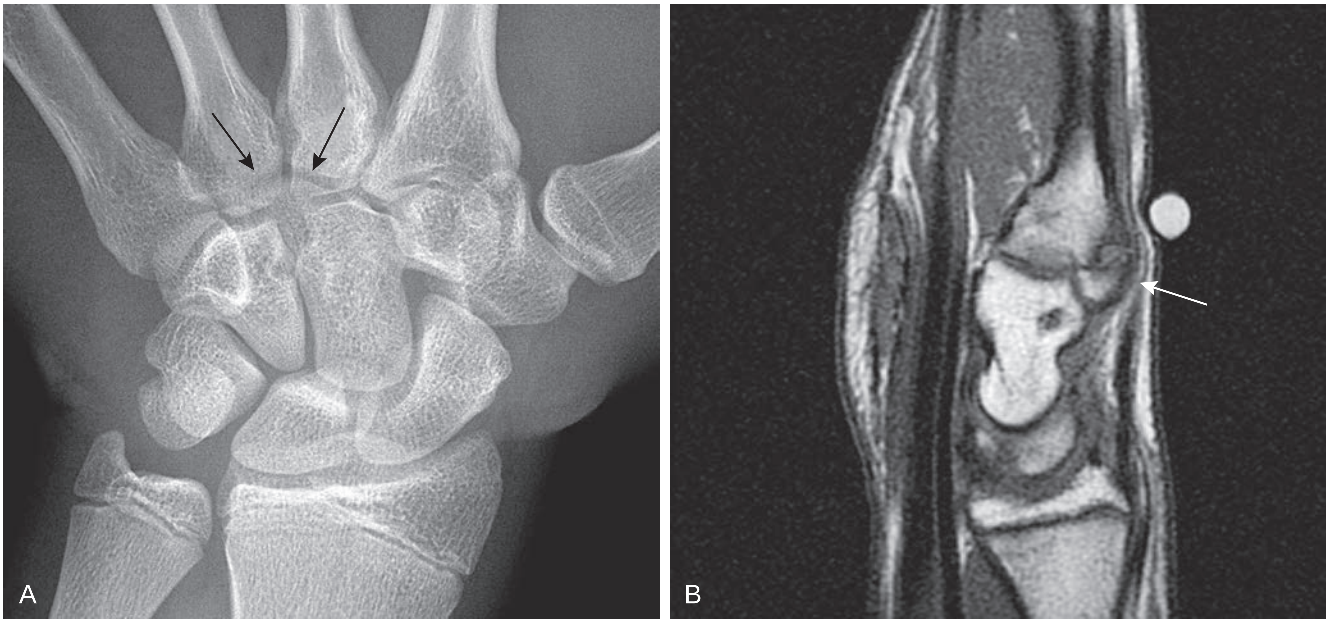

**Figure 128.23. Os styloideum (carpal boss) in a 14-year-old boy.** (A) Anteroposterior radiograph; the accessory bone is barely visible *(arrows)*. (B) Sagittal T1-weighted magnetic resonance (MR) image shows the accessory ossicle *(arrow)* at the dorsum of the carpometacarpal joint. Note that the ossicle causes a bump on the dorsum of the wrist.

**Calcaneal Apophysis.** The calcaneal apophysis appears about the middle of the first decade. It often is fragmented and/or sclerotic well into the second decade until fusion with the body of the calcaneus is complete (e-Fig. 128.29). Calcaneal apophysitis (Sever disease) is a poorly understood cause of heel pain in children, and this diagnosis should not be made on the basis of radiographs alone.[26] MRI findings of apophyseal edema may suggest the diagnosis; however, Sever disease remains a clinical diagnosis.

**Calcaneus Secondarius.** The calcaneus secondarius (e-Fig. 128.30) may simulate an anterior process calcaneal fracture. The ossicle is located in between the anteromedial calcaneus, cuboid, talar

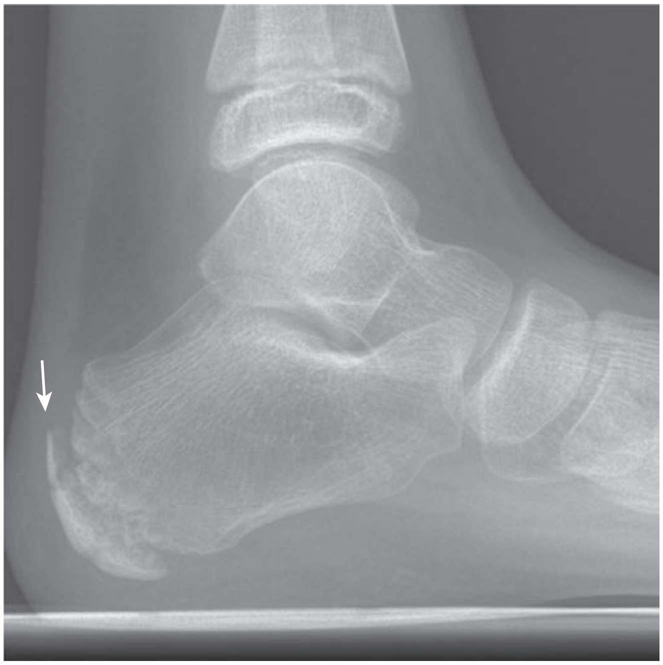

**e-Figure 128.29. Normal calcaneal apophysis.** Lateral radiograph shows a normal, sclerotic, slightly fragmented appearance of the calcaneal apophysis *(arrow)* in a 12-year-old boy.

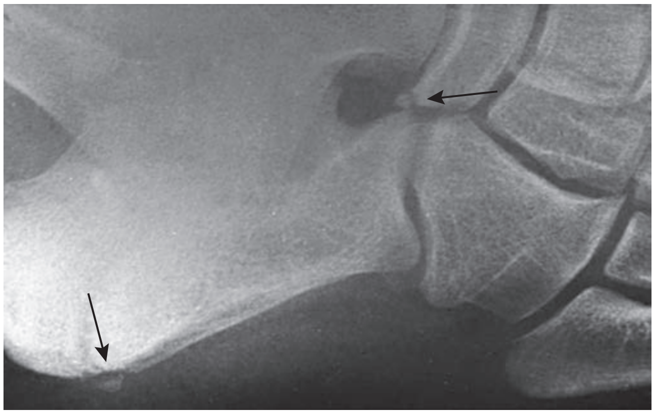

**e-Figure 128.30. Calcaneus secundarius.** Small, round, smooth calcaneus secundarius *(arrow at right)* in the center of the space between the calcaneus, cuboid, navicular, and talus on lateral oblique projection in an asymptomatic 12-year-old boy. The posterior arrow points to a normal fragmentary calcaneal apophysis along the plantar aspect of the calcaneal tuberosity. Similar ossicles were present in the other foot.

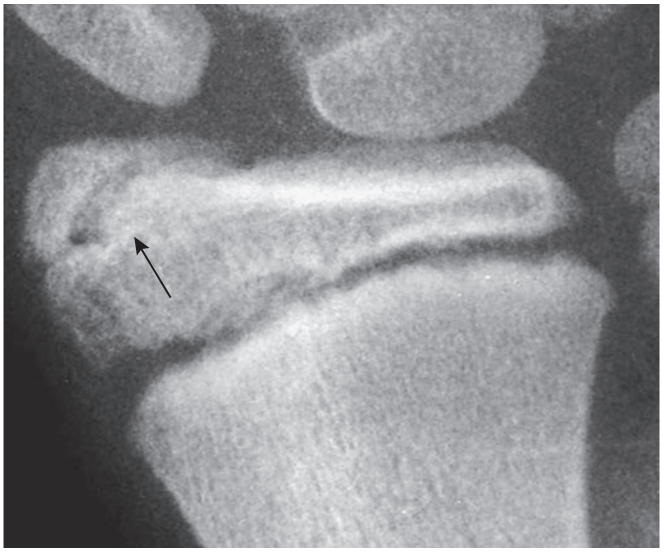

**Figure 128.25. Large accessory ossification center *(arrow)* in the styloid process of the radial epiphyseal ossification center of a healthy 13-year-old boy.** This may simulate a fracture fragment.

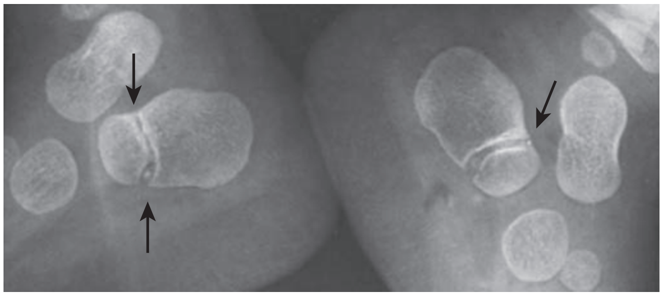

**Figure 128.28. Double ossification centers *(arrows)* in the body of the calcaneus on each side of a 20-month-old infant.** The infant had no known underlying disorder; radiographs were obtained because of an acute injury.

head, and navicular. It is rare and of no clinical significance other than possibly being mistaken for a fracture.

**Calcaneal Pseudocyst.** A pseudocystic triangular area of radiolucency is present in the anterior half of the calcaneal body. At this location, a deficiency of spongy bone is normal. The pseudocyst is of no clinical significance in itself; however, it must be differentiated from true bone cysts or intraosseous lipomas that can develop at this site but tend to have a more round shape. MRI or computed tomography (CT) is helpful for differentiating these lesions when radiographic features are equivocal.

**Os Trigonum.** There is a secondary ossification center within a posterior cartilaginous extension of the talus, which ossifies between 7 to 13 years and typically fuses with the talus within 1 year (Fig. 128.31). If this remains separate from the talus, as it does in approximately 15% of patients, it is referred to as an *os trigonum*.[27] This may mimic a fracture of the posterior process of the talus. Repetitive forced plantar flexion may cause a syndrome of posterior ankle impingement or "os trigonum syndrome." This syndrome occurs most commonly in ballet dancers, soccer players, and basketball players and may cause tendinopathy of the flexor hallucis longus.

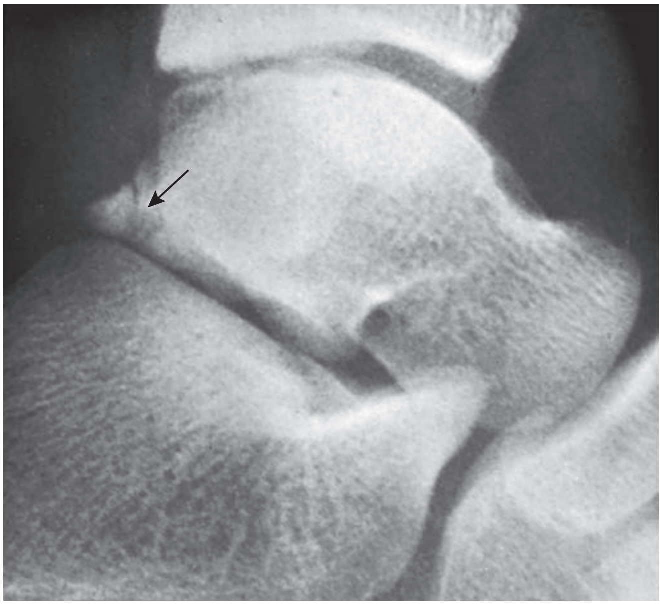

**Figure 128.31. Normal apophyseal ossification center *(arrow)* in the dorsal process of the talus in a healthy 11-year-old boy.** The radiolucent strip between the body of the talus and the ossification center is a normal synchondrosis, not a fracture line. When the synchondrosis persists after the normal age for its fusion with the body of the talus, the persistent ossification center is called the *os trigonum*.

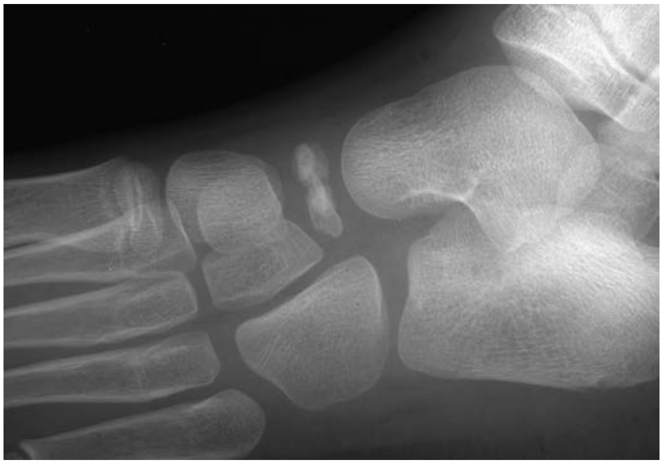

**Figure 128.33.** Irregular ossification of the navicular in a 2-year-old boy.

**Os Supratalare.** The os supratalare on the crest of the head of the talus may simulate injury or be simulated by injury (e-Fig. 128.32).

**Os Supranaviculare.** The ossification center for the navicular bone frequently is irregular and fragmentary up to about 5 years of age (Fig. 128.33). The os supranaviculare (e-Fig. 128.34) is an accessory ossicle along the dorsal navicular that may be seen after 5 years of age. These variants of navicular ossification have well-corticated margins and a characteristic ovoid to circular shape with or without associated sclerosis, which may superficially mimic Kohler disease. These accessory ossification centers must be differentiated from fractures.

**Accessory Navicular.** The accessory navicular is the best known and one of the most important accessory ossification variants in the foot. The accessory navicular is located along the medial aspect

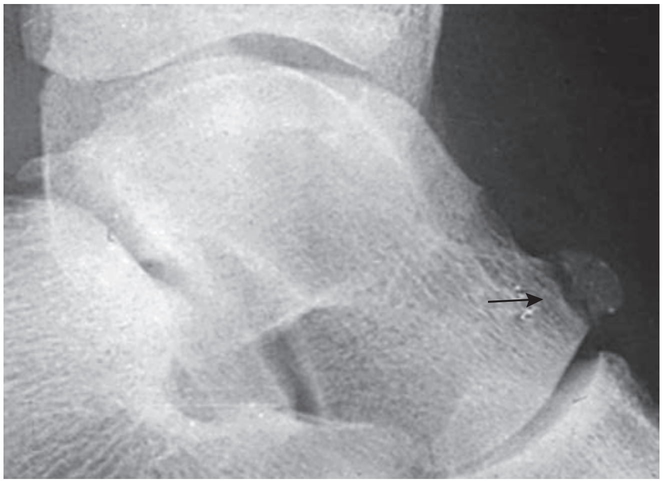

**e-Figure 128.32.** Os supratalare *(arrow)* on the dorsal edge of the talus just proximal to the talonavicular joint in an asymptomatic 18-year-old girl.

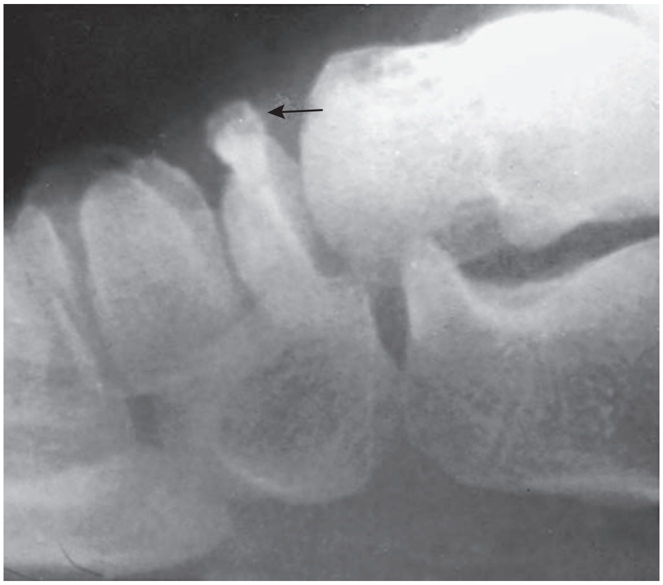

**e-Figure 128.34.** Large supranavicular bone *(arrow)* partially fused with the main mass of the navicular itself and appears to be an accessory ossification center in the periphery of the navicular cartilage; similar changes were present in the other foot. The patient was an asymptomatic 8-year-old boy.

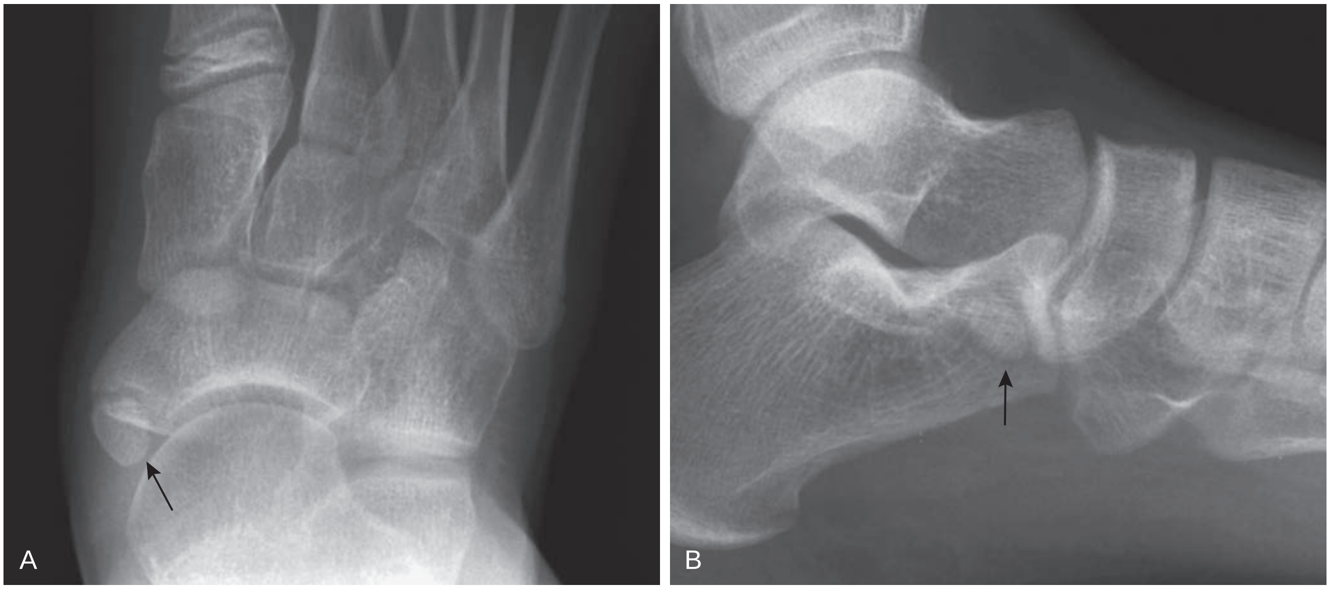

**Figure 128.36.** Type II accessory naviculars *(arrows)*. (A) An 11-year-old girl. (B) A 13-year-old girl.

of the navicular where the tibialis posterior inserts. They are seen in approximately 21% of patients, and 50% to 90% are bilateral.[28] When patients have symptoms related to their accessory navicular, it usually is related to painful flat foot in part as a result of tibialis posterior dysfunction.

The type I variant ("os tibiale externum" or "navicular secundarium") is a true round sesamoid bone measuring 2 to 6 mm that lies within the tibialis posterior tendon and is approximately 3 mm separate from the navicular bone (e-Fig. 128.35). Type I variants account for 10% to 15% of cases in children.

Type II variants ("prehallux" or "bifurcated hallux") are separated from the navicular by a cartilaginous or fibrocartilaginous bridge and represent an accessory ossification center for the tubercle of the navicular (Fig. 128.36). The ossicle is larger (9–12 mm), triangular or heart-shaped, and congruent with and closely apposed to the adjacent navicular. It is connected to the navicular by a synchondrosis. Symptoms generally develop in the second decade.

The type III variant is the cornuate navicular. The cornuate navicular represents medial and plantar elongation of the navicular bone without a separate ossicle, which sometimes may result from fusion of type II accessory navicular with the parent bone.

## Elbow

The six major ossification centers at the elbow ossify in an expected sequence—capitellum, radial head, internal (medial) epicondyle, trochlea, olecranon, and external (lateral) epicondyle. The sequence of ossification can be remembered with the acronym CRITOE (CRMTOL). If this acronym is too cumbersome to remember, a simpler and more relevant acronym to remember for chronologic appearance of elbow ossification centers is IT (Internal [medial] epicondyle followed by Trochlea) (Fig. 128.37). If an osseous density is seen in one area when an earlier-appearing center is lacking, a traumatic fragment is very likely the cause. The medial epicondyle appears earlier than the trochlea as a rule. Therefore if the medial epicondyle is absent but a trochlear ossification is present, a displaced medial epicondylar fracture should be suspected (e-Fig. 128.38; see also Fig. 142.27).

The ossification centers of the elbow can appear quite irregular during initial formation, particularly the trochlea (e-Fig. 128.39), which should not be confused with an osteochondrosis. The olecranon ossification center (Fig. 128.40) varies considerably in size and should be differentiated from an acute olecranon fracture (e-Fig. 128.41) by the shape of the individual ossifications and the nature of the margins. When the margins of the olecranon ossific densities are corticated, they are likely to be normal fragmentary accessory ossification centers, whereas noncorticated and linear ossific densities tend to represent sequelae from acute fracture.

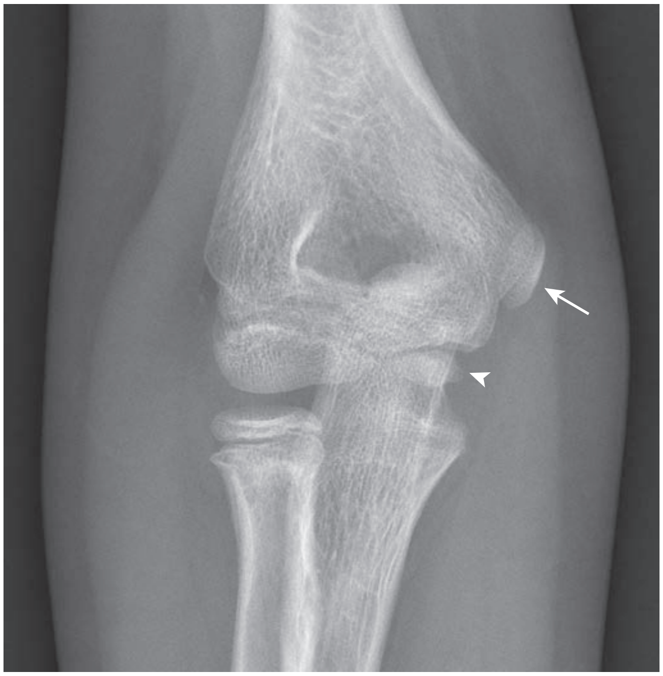

**Figure 128.37. Normal elbow in an 11-year-old boy.** As a rule, the medial (internal) epicondylar ossification center *(arrow)* should appear before the trochlear ossification center *(arrowhead)*. If only the trochlear ossification center is present, a medial epicondylar avulsion fracture should be suspected.

The lateral epicondyle does not fuse directly with the humeral shaft as the medial epicondyle does but fuses first with the adjacent capitellum; their fused mass then joins with the end of the humeral

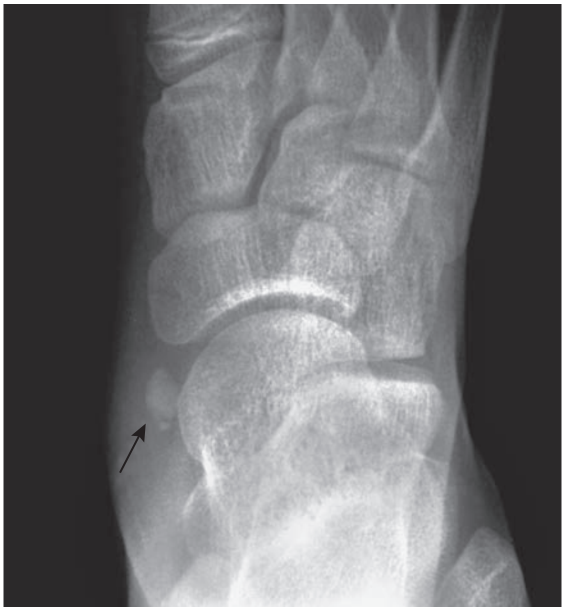

**e-Figure 128.35.** Type I accessory navicular *(arrow)* in a 10-year-old girl.

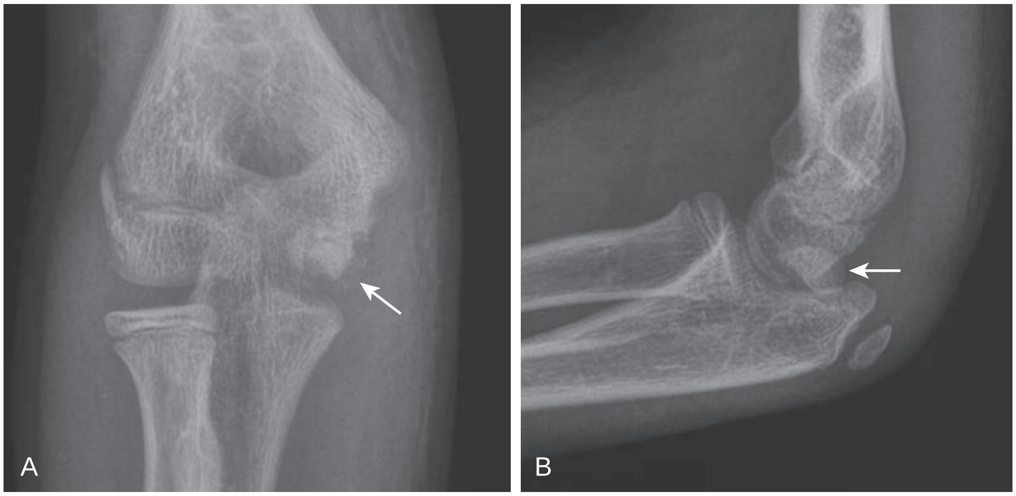

**e-Figure 128.38. Displaced medial epicondylar avulsion fracture.** (A) Frontal and (B) lateral radiographs show a displaced medial epicondylar avulsion fracture *(arrows)* mimicking trochlear ossification center in a 13-year-old boy.

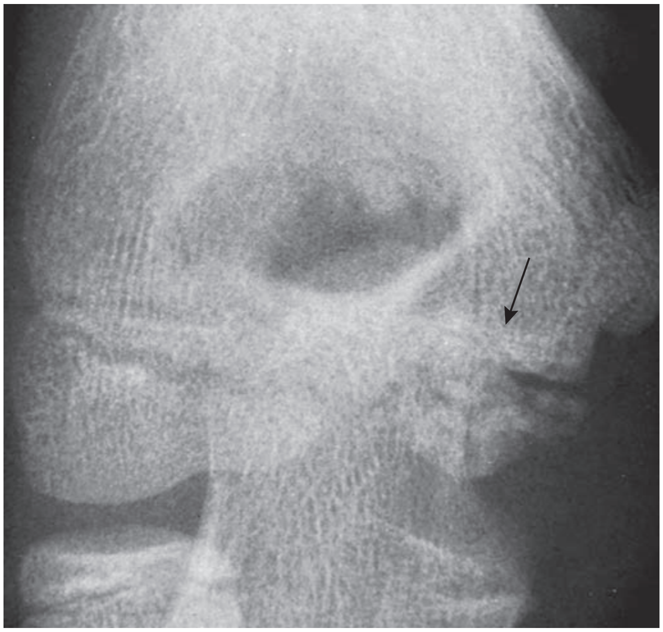

**e-Figure 128.39. Irregular ossification center *(arrow)* of the trochlea of a healthy 13-year-old boy.** This irregular ossification of the trochlea persists throughout the growth period and always should be recognized as a normal variant; actually, it is the norm. The capitellum, in contrast, ossifies uniformly as it expands during the growth period.

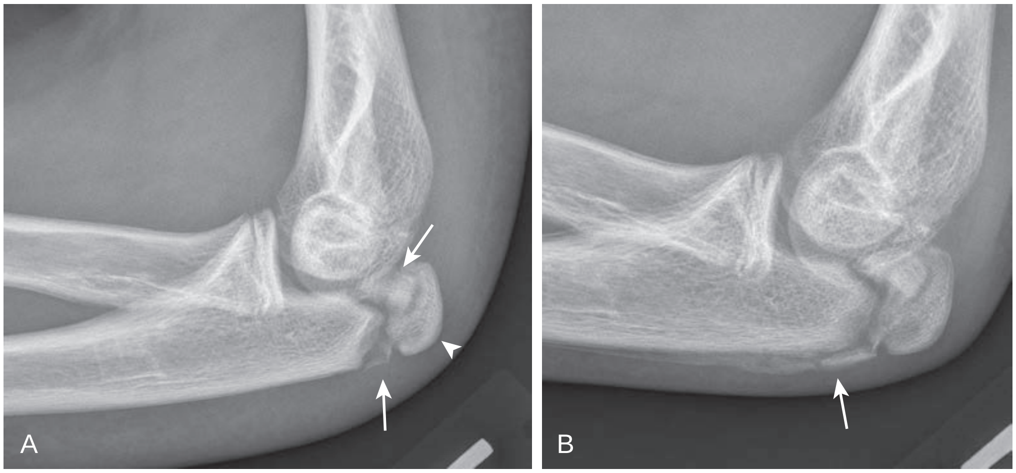

**e-Figure 128.41. Olecranon fracture.** (A) An acute comminuted olecranon fracture involving the metaphyseal equivalent region *(arrows)* separate from the major olecranon ossification center *(arrowhead)* in a 12-year-old boy. (B) A subsequent film 2 weeks later demonstrates callus formation related to the healing fracture *(arrow)*.

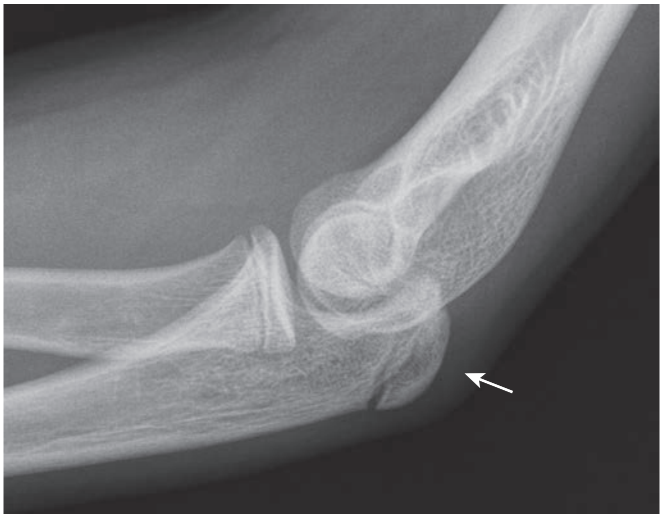

**Figure 128.40.** Normal smooth, corticated olecranon ossification center *(arrow)* in a 12-year-old boy.

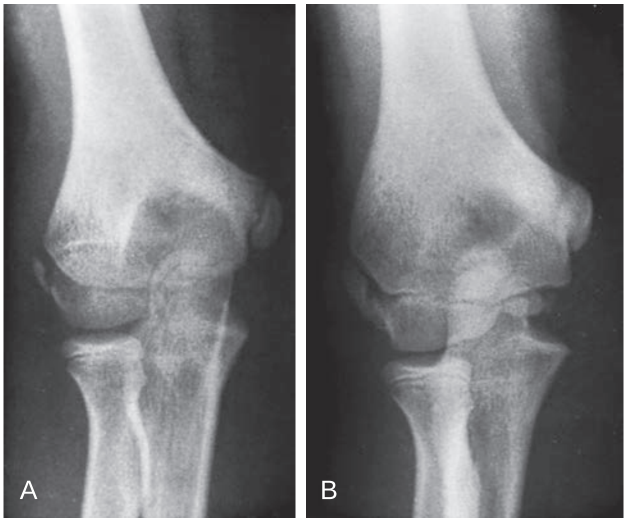

**Figure 128.42. Lateral epicondyle ossification center.** This center is independent of both the capitellum and the shaft at 11 years; (A) it is fusing with the capitellum at 12.5 years, (B) and these combined ossification centers will later fuse with the shaft. The medial epicondyle center is fusing directly with the shaft in (A) and (B). In (B), the trochlea is normally irregular.

shaft (Fig. 128.42). With early ossification, the lateral epicondylar ossification center appears as an irregular flake of bone, which is easily mistaken for an avulsion fragment. The medial epicondyle occasionally has an irregular, fragmentary appearance (Fig. 128.43). This finding must be differentiated from a medial epicondylar chondro-osseous avulsion fracture when widening or irregularity, or both, are present (e-Fig. 128.44).

## Supracondylar Process

The humeral supracondylar process is a vestigial structure that projects from the medial aspect of the anterior surface of the humeral shaft 5 to 7 cm proximal to the medial epicondyle (Figs. 128.45 and 128.46).[29] It occurs in 1% of individuals. The supracondylar process may be connected by the ligament of Struthers to the medial epicondyle. Portions of pronator teres and brachioradialis muscles may attach to the process, to the ligament of Struthers, or to both. Occasionally, median nerve neuralgia occurs as a result of entrapment or compression of the median nerve as it passes through this tunnel created by the supracondylar process, the ligament of Struthers, and associated structures.[30]

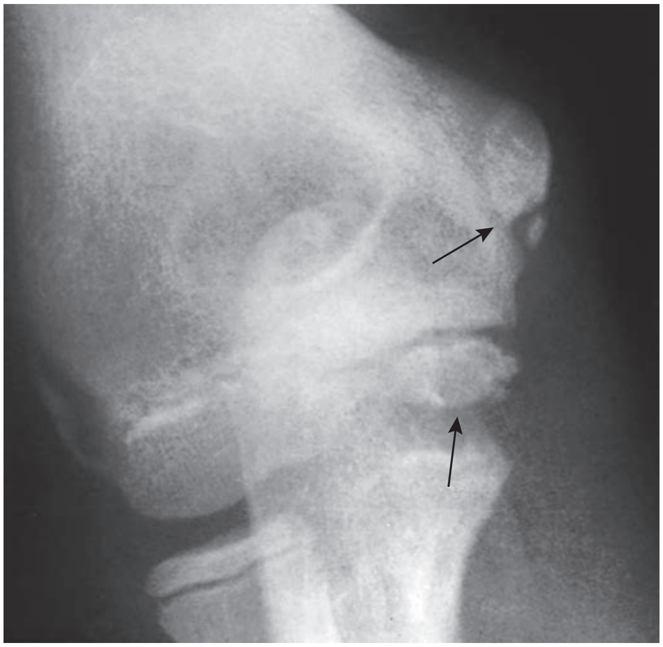

**Figure 128.43. Accessory ossification center *(proximal arrow)* at the lower pole of the medial epicondyle of a healthy 12-year-old boy that simulates a fracture fragment.** The distal arrow points to the normal irregular edges of the trochlear center of the humerus.

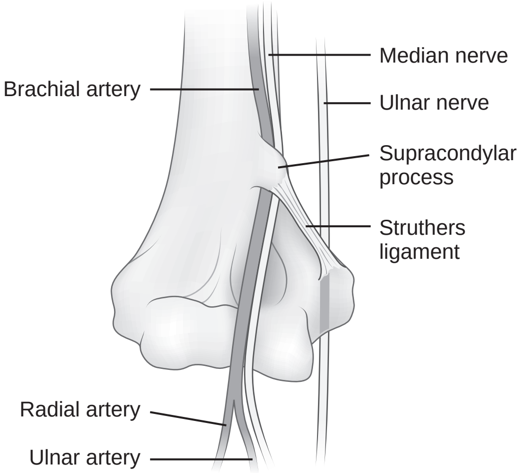

**Figure 128.45. Supracondylar process anatomy.** A drawing of the supracondylar process on the anterior surface of the humerus that shows the relationship of the process to the brachial artery and its branches and to the median nerve. *(From Spinner RJ, Lins RE, Jacobson SR, et al. Fractures of the supracondylar process of the humerus.* J Hand Surg [Am]. *1994;19:1038–1041.)*

## Shoulder

**Proximal Humeral Epiphyseal Ossification.** At the upper end of the humerus, two and occasionally three secondary ossification centers can be observed. The first center (humeral head proper) to appear develops in the medial half of the epiphysis at about 2

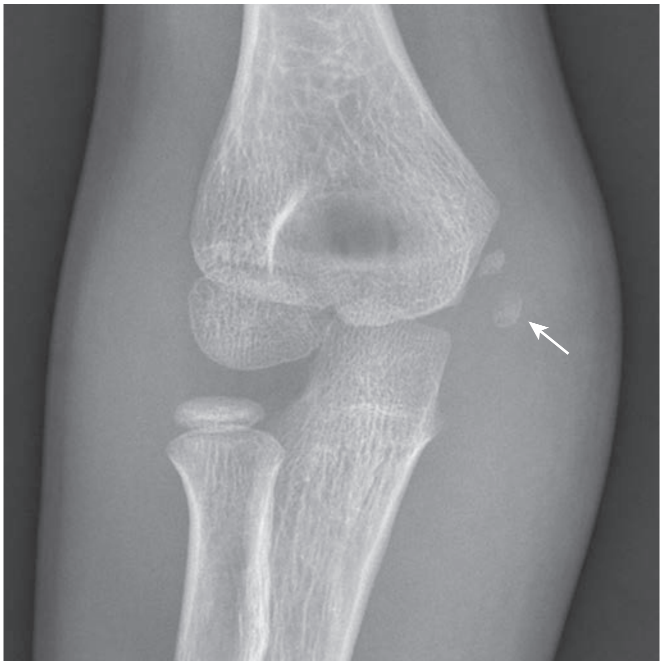

**e-Figure 128.44. Medial epicondylar avulsion fracture.** Frontal radiograph shows a fragmentary medial epicondylar avulsion fracture *(arrow)* in an 8-year-old boy.

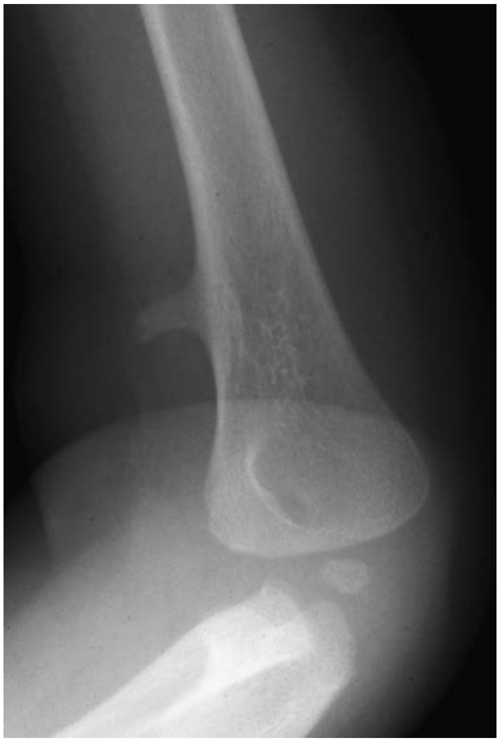

**Figure 128.46.** Supracondylar process of the distal humerus in a 21-month-old girl.

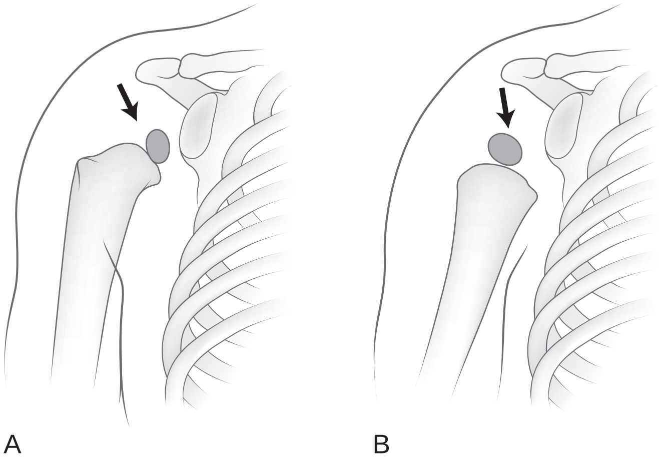

**Figure 128.47. Factitious shift in position *(arrows)* of the normally eccentric proximal ossification center of the humerus caused by rotation of the bone.** (A) In the neutral position the ossification center of the proximal humerus appears to be in the medial segment of the epiphysis. (B) With the humerus in internal rotation, the ossification center appears to be laterally displaced.

weeks of age; because of its eccentric location, it shifts to a factitious lateral position when the arm is internally rotated (Fig. 128.47). The second center appears laterally in the greater tuberosity during the second half of the first year. A rare third center occurs in the lesser tuberosity during the third year and fuses with the humeral head during the sixth to seventh years. This center may be seen in axillary views of the shoulder and may simulate a fracture fragment.

**Proximal Humeral Physis.** The proximal humeral physis is tented, with the apex above the pitched anterior and posterior segments.

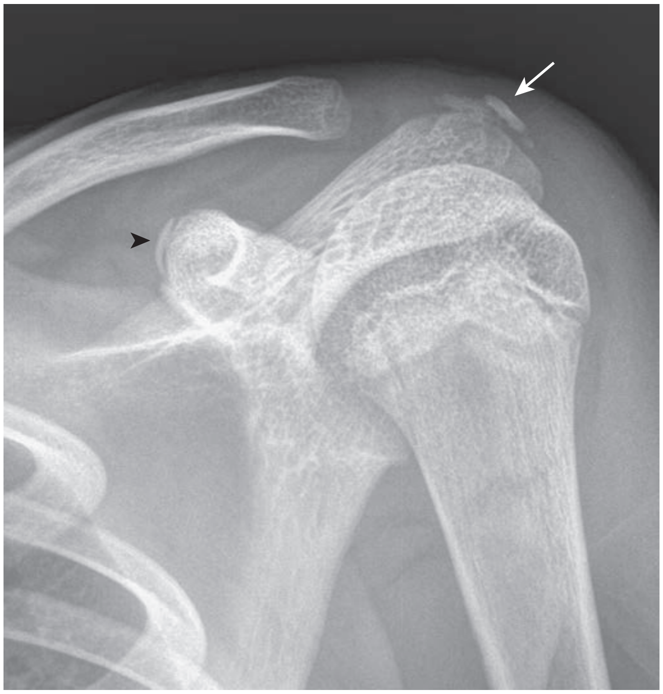

**Figure 128.52.** Normal acromial fragmentation *(arrow)* and coracoid apophysis *(arrowhead)*, which superficially may be mistaken for a fracture in this 12-year-old girl.

In rotated positions of the humerus, these segments are projected at different levels and may simulate fracture (e-Fig. 128.48). Offset of the epiphyseal ossification center relative to the lateral metaphyseal margin may simulate a Salter-Harris fracture.

**Bicipital Groove.** The bicipital groove in the anterior surface of the humerus may simulate local bone destruction or production (e-Fig. 128.49).

**Muscular Insertions.** Local cortical thickening that resembles a periosteal reaction occurs frequently at sites of insertion of major muscles of the upper arm. This finding is most common at the site of the deltoid insertion at the lateral aspect of the humeral diaphysis (e-Fig. 128.50).

**Humeral Head Pseudocyst.** When the humeral head is well ossified, the region of the greater tuberosity appears relatively radiolucent and devoid of trabeculation.[31] This appearance may be mistaken for an underlying osseous lesion (e-Fig. 128.51).

**Acromion and Coracoid Process.** The acromion can have a fragmentary appearance during ossification, and superficially it may resemble an acromion fracture (Fig. 128.52). The acromion usually will fuse with the remainder of the scapula by around age 25 years. When the acromion persists as a separate secondary ossification center beyond 25 years, then it represents an os acromion. Because the acromion in children has a significant cartilaginous component that is radiolucent, the acromioclavicular (AC) joint may appear widened (e-Fig. 128.53). Therefore measurements developed for the AC joint in adult patients as a criterion for determining AC joint injury should not be used in children. The AC joint eventually will narrow as the acromion further ossifies. If AC joint pathology is a concern, comparison with the contralateral asymptomatic side may be helpful.

The coracoid process is the origin of the short head of the biceps tendon and coracobrachialis and is the insertion site of the pectoralis minor muscles. The coracoid process also is the origin

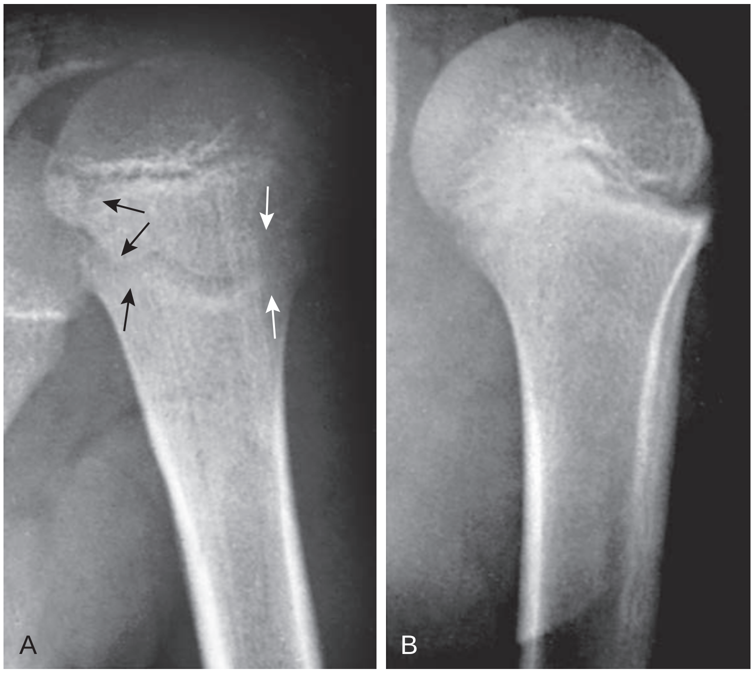

**e-Figure 128.48. Normal humeral neck.** (A) A false fracture *(arrows)* of the humeral neck on internal rotation to 90 degrees. (B) No fracture line is present in the anatomic position. The anterior pitch of the upper end of the humeral shaft is wider and deeper than the posterior, and it is the image of the segment below the posterior end of the shaft that casts the factitious fracture line.

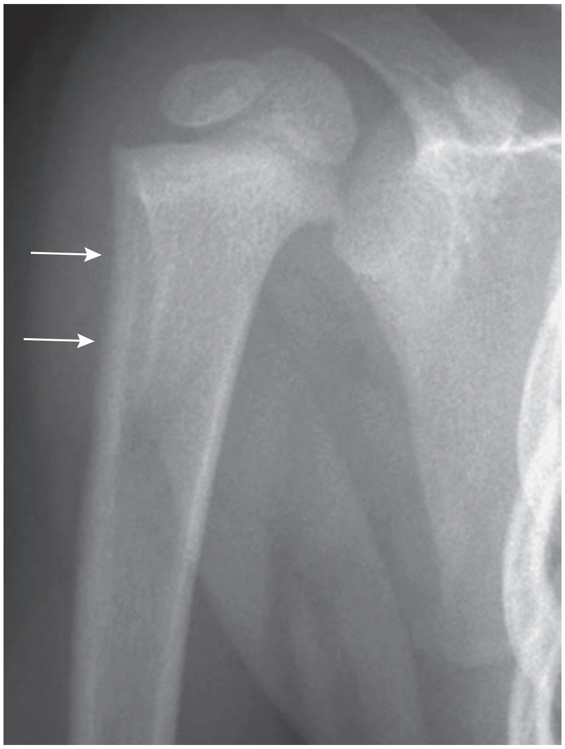

**e-Figure 128.49.** Pseudolesion of the proximal humeral metaphysis *(arrows)* due to a bicipital groove in a 16-month-old girl.

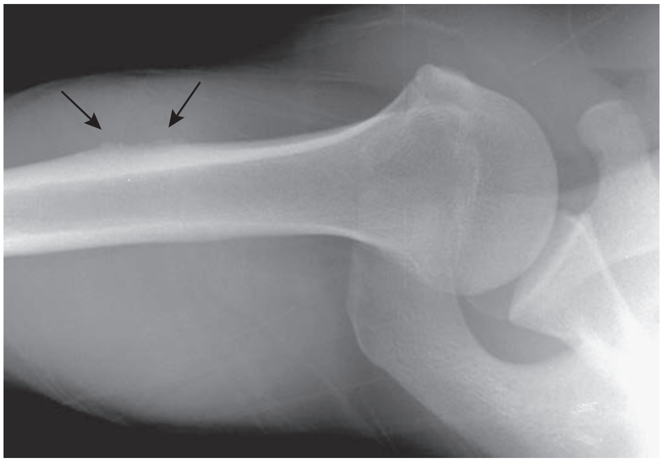

**e-Figure 128.50. Muscle insertion.** Irregularity of the anterior cortex of the proximal humeral diaphysis *(arrows)* due to muscle insertion in a 16-year-old boy. Similar findings were seen on the opposite side.

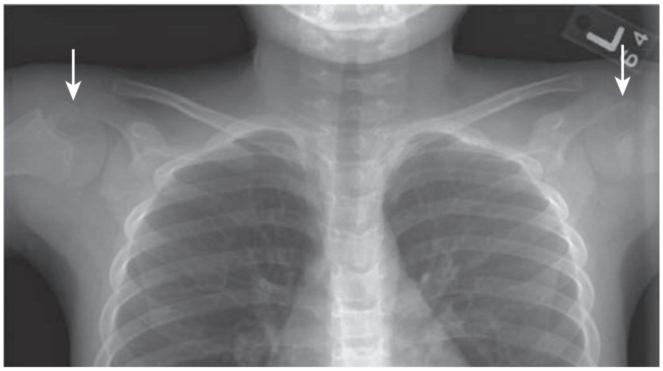

**e-Figure 128.51.** Bilateral humeral head pseudocysts *(arrows)* incidentally seen on the chest radiograph of a 7-year-old boy, with the left more prominent than the right.

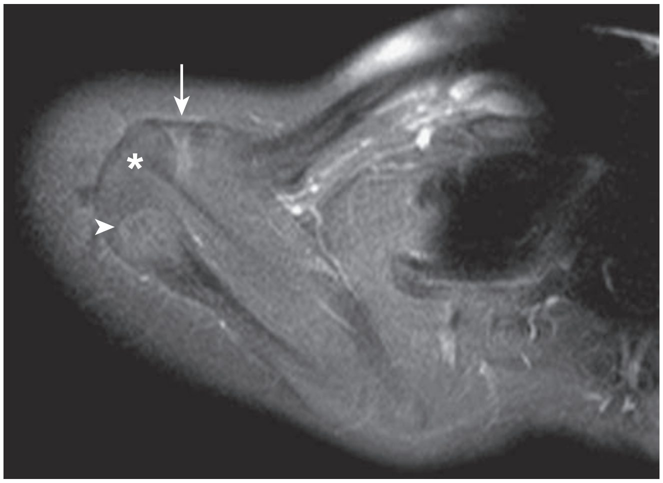

**e-Figure 128.53. Normal acromion and acromioclavicular joint.** Postgadolinium T1 fat-saturated MR image shows that the acromion is mainly cartilaginous *(asterisk)* in this 5-year-old boy, which may cause the AC joint to appear artificially widened on radiography. The *arrow* indicates the AC joint, and the *arrowhead* indicates the metaphyseal equivalent of the bony acromion.

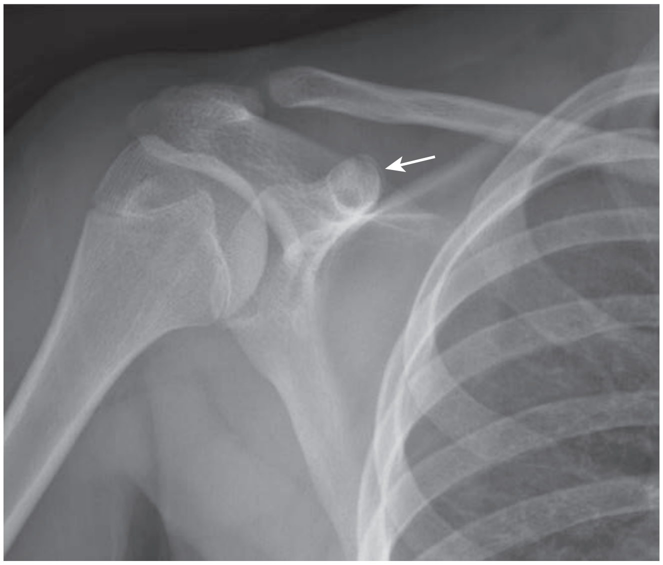

**Figure 128.54. Normal coracoid apophysis.** In this 15-year-old boy, the normal apophysis of the coracoid process *(arrow)* should not be mistaken for an avulsion injury.

and insertion site of various ligaments of the shoulder. The coracoid process apophysis has a complex ossification process with multiple different ossification centers that may develop at various stages and may superficially mimic a fracture (Fig. 128.54). In the beginning of the second decade, a normal lucency is present between the base of the coracoid process and the scapular body that should not be mistaken for a fracture. Later in the teenage years, the tip of the coracoid process may develop a separate ossification center that may superficially resemble an avulsion fracture.

## Pelvis

**Acetabulum.** Irregular ossification of the acetabular roof is a normal phenomenon during growth (e-Fig. 128.55). The regular smooth configuration of the roof develops from a confluence of individual bony foci near the end of the first decade.

**Accessory Ossification Centers.** Accessory centers of ossification may develop in cartilage in the spine of the ischium and also in the rim of the acetabulum (os acetabuli) just below the anterior inferior iliac spine (Fig. 128.56).[32] An os acetabulae should not be confused with an acetabular rim fracture. These acetabular ossification centers usually become visible between the 14th and 18th years, after which they fuse with the parent bone. Rarely, an os acetabuli persists as a separate ossicle. Although a normal variant, os acetabulae are associated with acetabular dysplasia and femoroacetabular impingement.[33] Accessory ossification centers also may form at the pubic symphysis and superior pubic ramus.

**Ischiopubic Synchondrosis.** Asymmetry of the ischiopubic synchondrosis is a very common normal variant and usually is an incidental finding unrelated to patient symptoms. Ossification of the ischiopubic synchondrosis is extremely variable in both velocity and pattern; fusion usually is complete by the teenage years.

The ischiopubic synchondrosis on the opposite side of the dominant leg usually is more prominent compared with the synchondrosis on the dominant leg.[34] Asymmetric ossification of the ischiopubic synchondrosis should be considered a physiologic process and is typically an incidental finding on radiographs. However, the ischiopubic synchondrosis represents fusion of two metaphyseal equivalent sites: (1) the ischial and (2) pubic component. Therefore it is a potential site for pathologies that may affect metaphyseal equivalent sites elsewhere such as osteomyelitis and trauma, typically stress changes (Fig. 128.57).

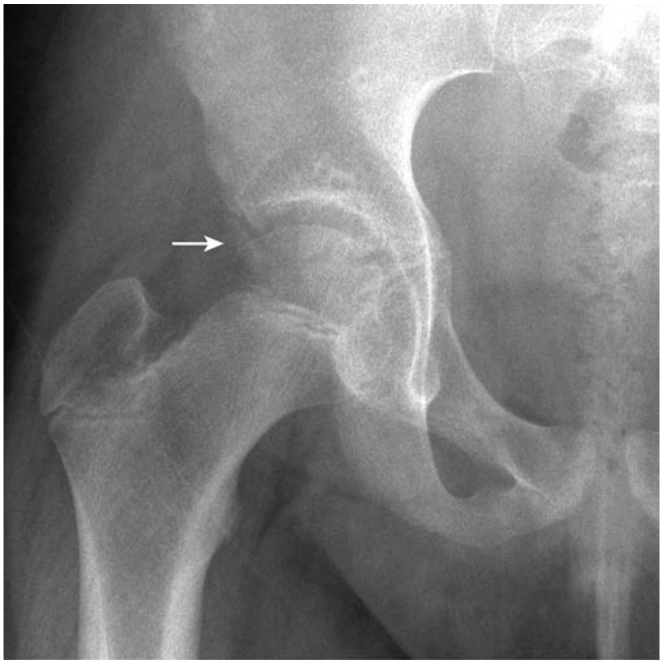

**Figure 128.56.** Os acetabulae *(arrow)* in a 10-year-old girl.

**Ischium.** Apophyseal irregularities along the posterolateral edge of the ischium also may be observed, usually during preadolescence (e-Fig. 128.58). This is the site of origin of the hamstring complex. The two sides may be unequally affected. During growth and before fusion of the body of the ischium, the ischial apophysis is scalelike at the inferior margin of the ischium.

The ischial spine, projecting posteriorly, usually is not visible on frontal radiographs of the pelvis. The lesser sciatic notch lies below it and sometimes appears as an indentation on the lateral margin of the ischium, at the region where the ischial irregularities are most common.

**Pubic Rami.** Delayed and irregular mineralization of the pubic rami may be present at birth, with subsequent mineralization from several ossification centers.[35] Vertical, radiolucent clefts occasionally noted as incidental findings in pelvis radiographs probably represent bars of nonossified cartilage between expanding ossification centers. The medial edges of the bodies of the pubic bones often are irregularly mineralized during the growth period.

## Hip

**Femoral Head Ossification.** A slight disparity in the timing of ossification, the size of the femoral head ossifications centers, or both is normal. In up to 30% of infants 3 to 6 months of age, a disparity of at least 2 mm exists between the two sides.[36] The ossification center for the head of the femur appears at about 4 months of age and enlarges with time. As ossification fills in the hemispheric cartilage of the head, the center may exhibit irregularities of form and density normally (e-Fig. 128.59).[37] Ossification may begin with coarse stippling and may progress, as the size increases, to irregularities along the margin. A bifid or split femoral head is a rare variant (Fig. 128.60) and may simulate Perthes disease. A bifid femoral head diagnosis as a normal variant should only be made after Perthes disease has been definitively excluded. A notch (separate from the fovea capitis) at the vertex of the

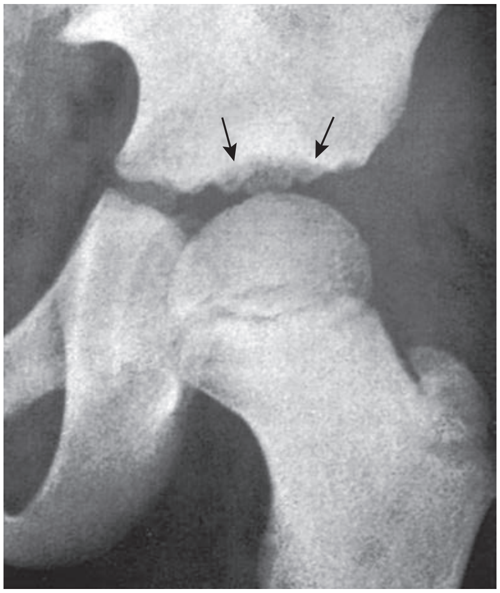

**e-Figure 128.55.** Normal irregular margins of the acetabulum *(arrows)* in a 6-year-old boy.

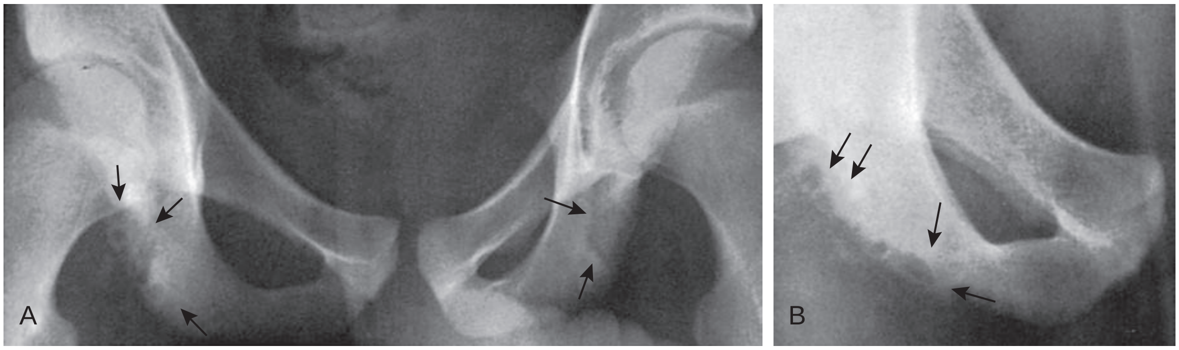

**e-Figure 128.58. Irregularities in both ischia in asymptomatic 12- and 11-year-old boys.** (A) The right ischium is irregularly rarefied at the tuberosity and slightly caudad into the ramus *(arrows)*. The tuberosity of the left ischium is evenly rarefied. (B) Bubbly rarefaction is present in the right tuberosity and caudad into the ramus *(arrows)*.

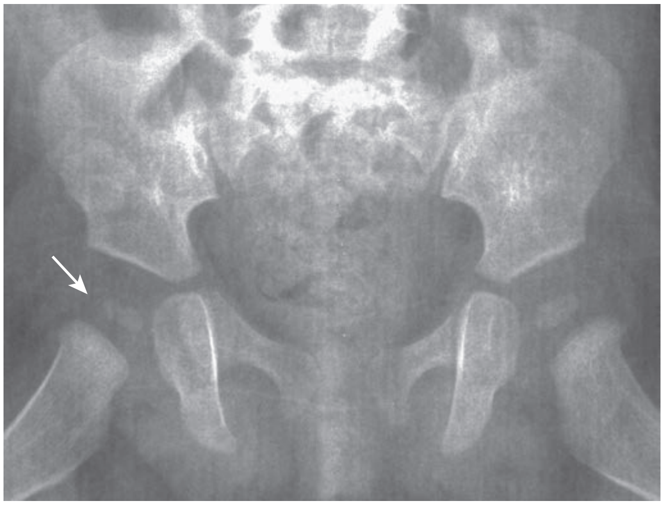

**e-Figure 128.59.** Normal, fragmentary appearance of the capital femoral epiphysis in a 4-month-old girl *(arrow)*.

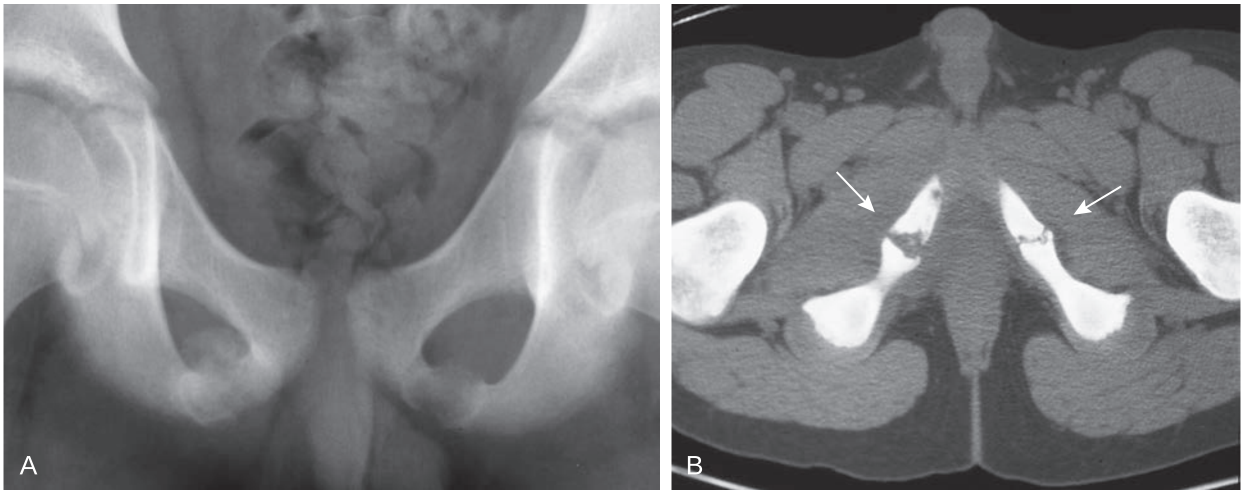

**Figure 128.57. Ischiopubic synchondrosis.** (A) Radiograph showing bilateral prominent ossification and the ischiopubic synchondroses in an 11-year-old male soccer player with right groin pain. Ossification of the ischiopubic synchondrosis is larger on the symptomatic side. (B) Irregularity of the ischiopubic synchondroses is seen on computed tomography *(arrows)*.

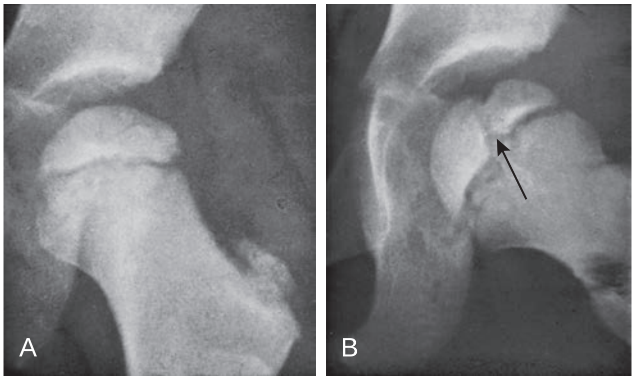

**Figure 128.60. Factitious splitting of the femoral head in an asymptomatic 4-year-old girl.** (A) In the frontal projection, the femoral head image is normal. (B) In the lateral, externally rotated position, the femoral head image is divided longitudinally into two unequal segments by a strip of decreased density *(arrow)* that represents the synchondrosis between the two ossification centers that developed one behind the other ventrodorsally.

femoral head also may be seen (e-Fig. 128.61). Before the ossification center has rounded out fully, some flattening of the contour may be observed where subsequently the fovea capitis can be recognized.

**Positional Coxa Valga.** External rotation of the femur increases the femoral neck-shaft angle and may factitiously suggest coxa valga (e-Fig. 128.62). With true coxa valga (Fig. 128.63), the greater trochanter projects laterally rather than being superimposed on the underlying femur, whereas with external rotation, the greater trochanter is rotated posteriorly and is superimposed along the femoral neck.

**Trochanters.** The centers for the greater and lesser trochanters frequently are irregularly mineralized and this is a normal finding during development (e-Fig. 128.64). Avulsions of the lesser trochanter related to the iliopsoas tendon insertion are uncommon, and thus comparison with the opposite, unaffected side may be helpful.

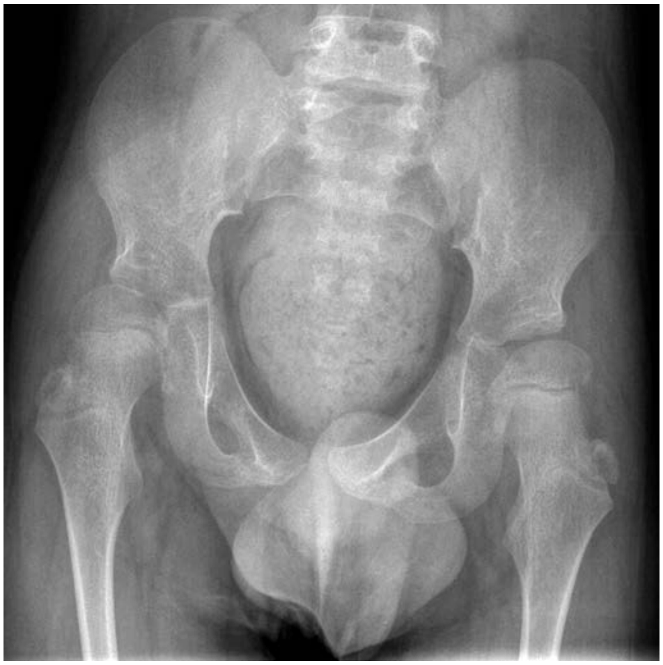

**Figure 128.63. Coxa valga.** An 11-year-old boy with cerebral palsy and coxa valga bilaterally with mild secondary developmental dysplasia of the hips.

## Knee

**Cortical Irregularity of the Distal Femoral Metaphysis (Avulsive Cortical Irregularity).** Irregularity of the cortex of the posteromedial distal femoral metaphysis (Fig. 128.65 and e-Figs. 128.66 and 128.67) is a common finding that easily can be mistaken a healing fracture or even an osteosarcoma.[38] Cystic cortical defects are common at this location, as are proliferative tuglike lesions, which probably are related to either the adductor magnus insertion or the origin of the medial head of the gastrocnemius muscle. When cystic, these lesions also have been termed *cortical desmoids* and may be difficult to differentiate from a nonossifying fibroma. The term "cortical desmoid" should be avoided as these irregularities are normal developmental variants.[39,40]

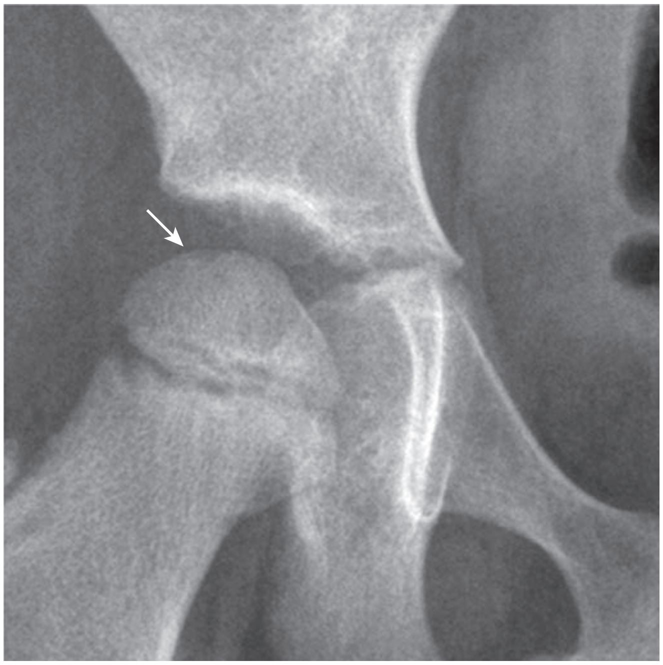

**e-Figure 128.61. Normal subchondral irregularity.** A 6-year-old girl with subchondral irregularity *(arrow)* of the weight-bearing portion of the capital femoral epiphysis, which is a normal finding.

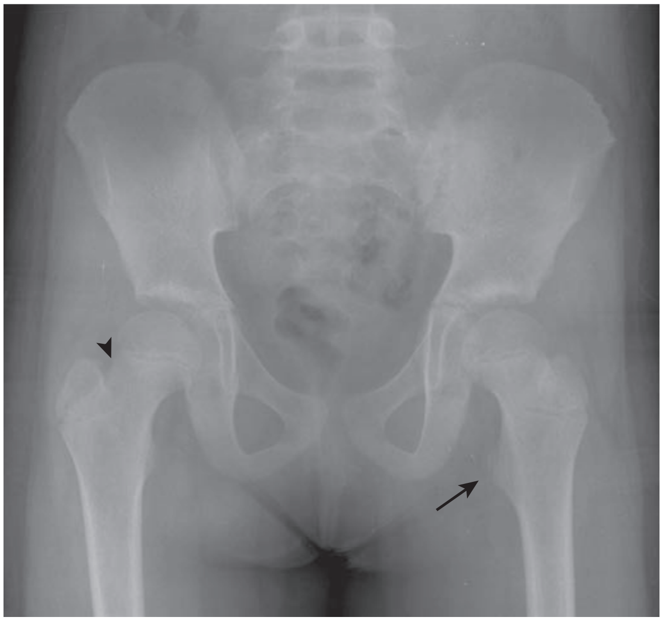

**e-Figure 128.62. Artifactual coxa valga in a 7-year-old girl with artifactual coxa valga.** On the left, external rotation will bring out the lesser trochanter *(arrow)* and cause overlap of the greater trochanter with the neck, which will cause factitious coxa valga. On the right, mild internal rotation causes accentuation of the femoral neck *(arrowhead)*. The more internally rotated the hip is, the more elongated the femoral neck will appear.

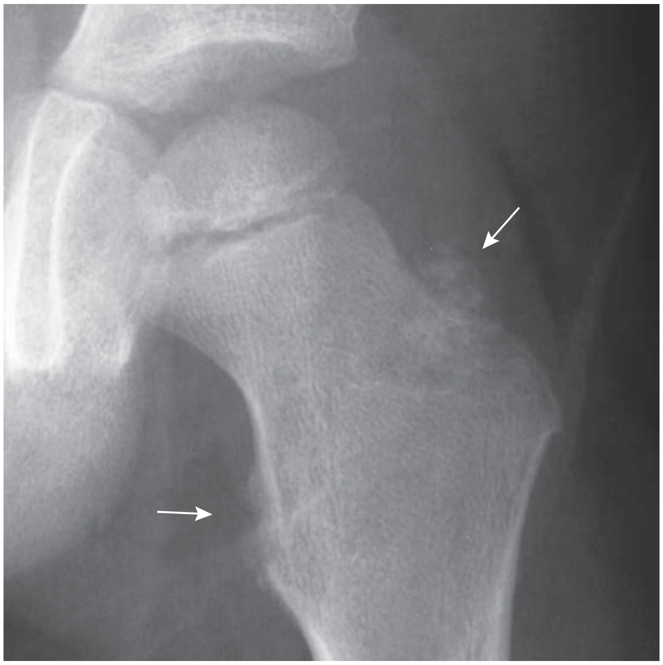

**e-Figure 128.64.** Normal trochanteric ossification irregularities *(arrows)* of the trochanteric ossification centers.

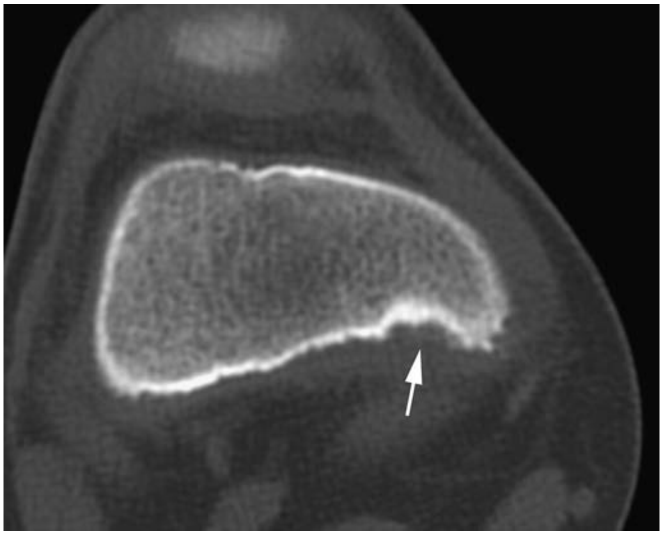

**e-Figure 128.66. Avulsive cortical irregularity.** CT scan shows an avulsive cortical irregularity *(arrow)* in an asymptomatic 6-year-old girl.

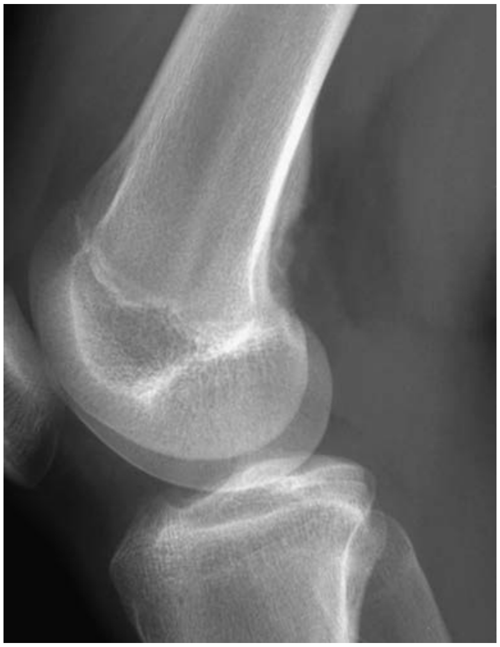

**e-Figure 128.67.** Avulsive cortical irregularity of the posteromedial distal femoral metaphysis in an adolescent.

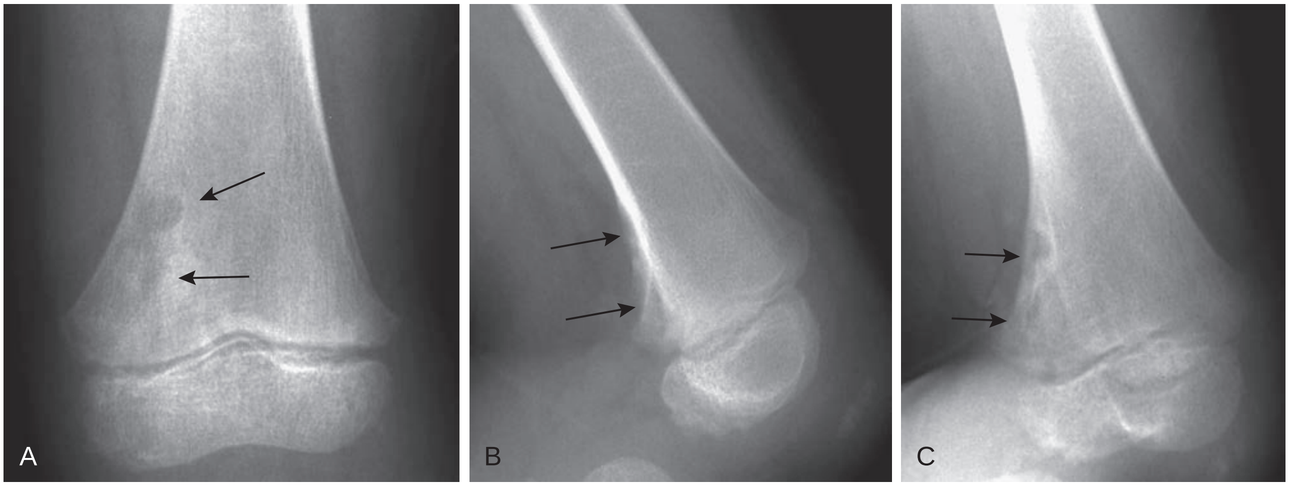

**Figure 128.65. Avulsive cortical irregularity of the distal femoral metaphysis in a 4-year-old girl.** The defect is posteromedial. (A) The anteroposterior view shows an ill-defined lucency *(arrows)*. (B) The lateral view shows irregularity *(arrows)* of the posterior margin of the distal femoral metaphysis. (C) An oblique view shows the cortical lucencies *(arrows)*.

**Irregular Ossification of the Distal Femoral Epiphysis.** The distal femoral epiphyseal ossification center growth in width occurs rapidly between the second and sixth years. As a result, the lateral and medial margins are commonly irregular and ragged (e-Fig. 128.68). In lateral projection, normal distal femoral ossification centers may have a rough, fringelike margin. Accessory ossification centers may persist at the margins of cartilage-bone junctions when ossification is almost complete. In older children, marginal mineralization of the femoral condyles is characteristically uneven and often is associated with independent ossification centers beyond the edge of the main bony mass.

Subchondral, fragmentary ossification of the femoral condyles may simulate osteochondritis dissecans (OCD). Caffey and colleagues found this variant in approximately 30% of healthy children when the knees were examined in tunnel and lateral projections (Fig. 128.69).[41] This variant is more common on the outer aspects of the condyles and tends to involve the non–weightbearing posterior surface, in contradistinction to OCD, which is more commonly located on the inner and weight-bearing aspects of the condyles. In addition, normal femoral condylar irregularities are seen in children younger than the usual age for OCD.

The normal variant is differentiated from OCD on MRI by its position in the outer posterior femoral condyles, intact overlying epiphyseal and articular cartilage, a large residual cartilage model, accessory ossification centers and spiculation, and absence of adjacent bone marrow edema (e-Fig. 128.70).[42] Additionally, the secondary physis of the epiphysis is typically disrupted in OCD but preserved in developmental irregular ossification.[43]

**Patella and Sesamoid Bones.** The patella, lying within the tendon of the quadriceps muscle, is the largest sesamoid bone of the body. Patellar ossification normally develops from several foci. Its edges may be irregular during childhood (e-Fig. 128.71). After fusion of the focal ossification centers, another center may develop in the superolateral portion of the bone and may persist as a distinct ossicle (Fig. 128.72). This common variant, known as *bipartite patella*, occurs in 1% to 6% of the population. Ninety percent of persons affected are male, and 40% have bilateral findings. Stress injury or acute fracture may occur at the synchondrosis between the superolateral ossicle and the patellar body, producing symptoms.[44] Bipartite patella may be related to aberrant traction by the vastus lateralis muscle, which inserts into the patella at its upper and outer quadrant. A bipartite patella is usually an incidental finding but may have an association with patellofemoral tracking abnormalities.[45]

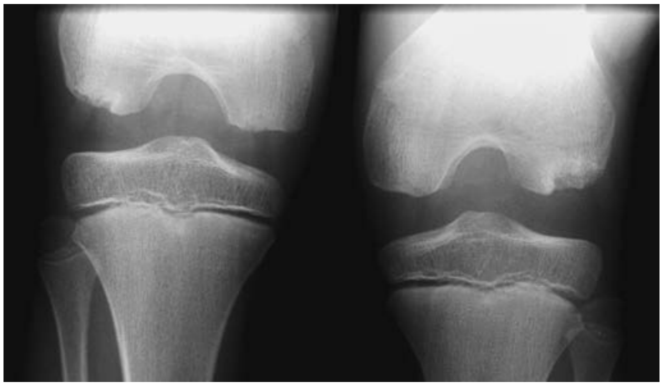

**Figure 128.69. Normal developmental irregularity of the posterior aspect of the femoral condyles seen on a notch view in a 10-year-old boy.** The defects are most prominent in the lateral condyles.

Irregular ossification of the lower pole of the patella is a common finding and may be difficult to differentiate from Sinding-Larsen-Johansson syndrome.[46] Also, it may be impossible to distinguish variation in ossification from an old traumatic avulsion. Acute patellar sleeve injuries will be symptomatic and have a linear nonsclerotic fracture fragment and accompanying soft tissue swelling.

Two other sesamoids of the knee occur as normal variants, the fabella and cyamella. The fabella (more common) forms in the tendon of the lateral head of the gastrocnemius muscle. The cyamella (less common) forms in the tendon of the popliteus muscle. A fabella is best seen on a lateral view (e-Fig. 128.73). The cyamella is found at the edge of the lateral condyle of the femur in the popliteal groove. Fabella syndrome is characterized by intermittent pain at the posterolateral knee accentuated by extension and localized tenderness over the fabella accentuated by compression.[47]

**Dorsal Defect of the Patella.** Dorsal defects of the patella may be seen along its superolateral aspect and usually are asymptomatic (Fig. 128.74). The dorsal defect of the patella is typically an

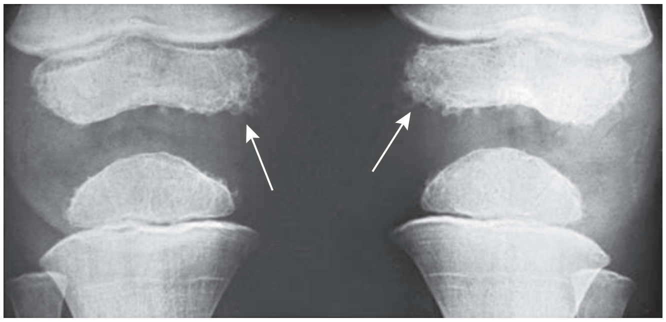

**e-Figure 128.68. Distal femoral epiphyseal irregularities.** Normal irregular mineralization on the margins of the ossification centers *(arrows)* in the distal epiphyses of the femurs of a 3-year-old boy.

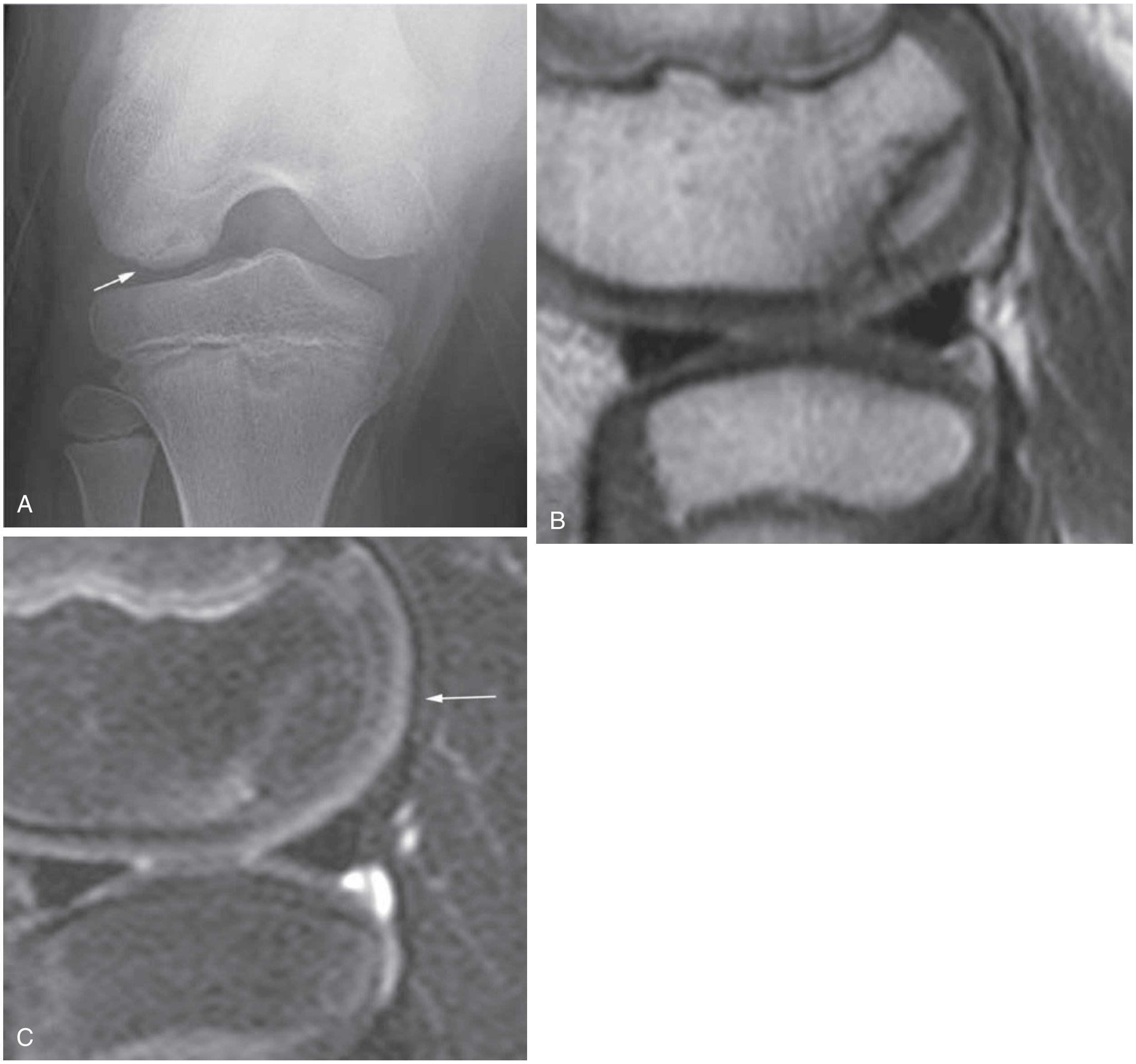

**e-Figure 128.70. Normal lateral femoral condylar irregularities in a 10-year-old boy.** (A) Tunnel view shows subchondral irregularity of the lateral femoral condyle *(arrow)*. Proton density sagittal (B) and T2 fat saturation sagittal (C) MR images demonstrate subchondral irregularity with overlying intact epiphyseal and articular cartilage with absence of edema of the subchondral component of the irregularity *(arrow)*, indicating that this presentation is a normal variation as opposed to a developing osteochondral lesion.

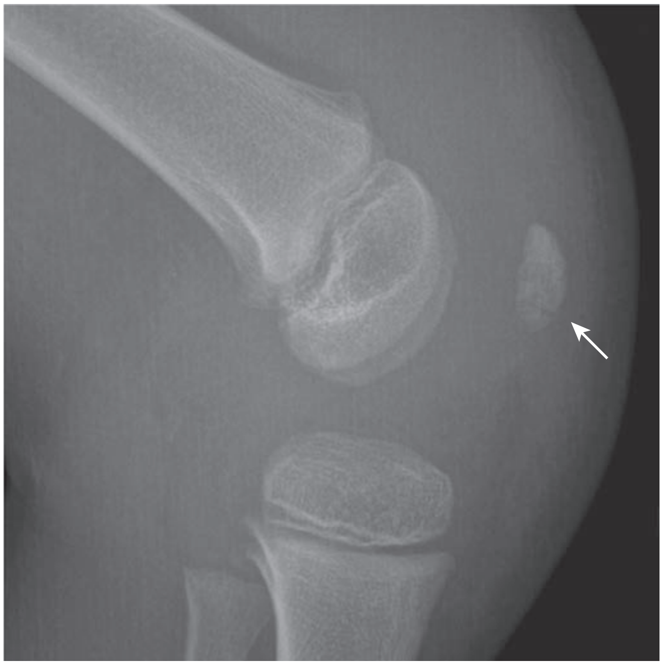

**e-Figure 128.71. Normal patellar irregularity.** Lateral radiograph in a 5-year-old boy with a large knee effusion related to infection shows normal fragmentation and irregularity of the patellar bone *(arrow)* that should not be confused with pathology or fracture.

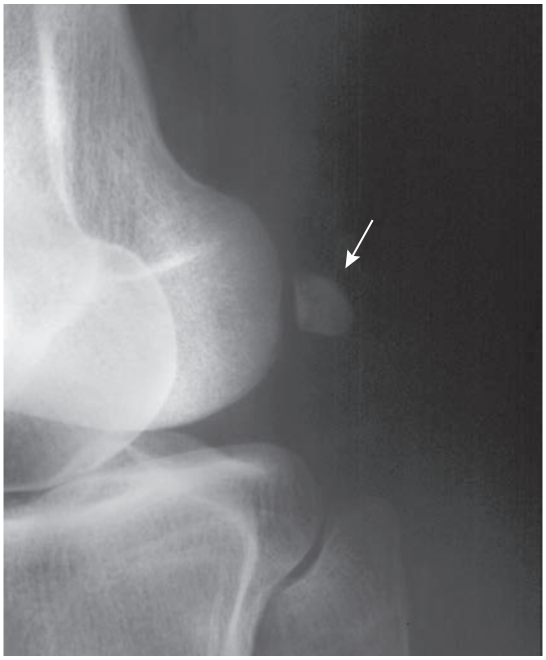

**e-Figure 128.73.** Fabella *(arrow)* in the lateral head of the gastrocnemius in its normal position, well separated from the femur itself.

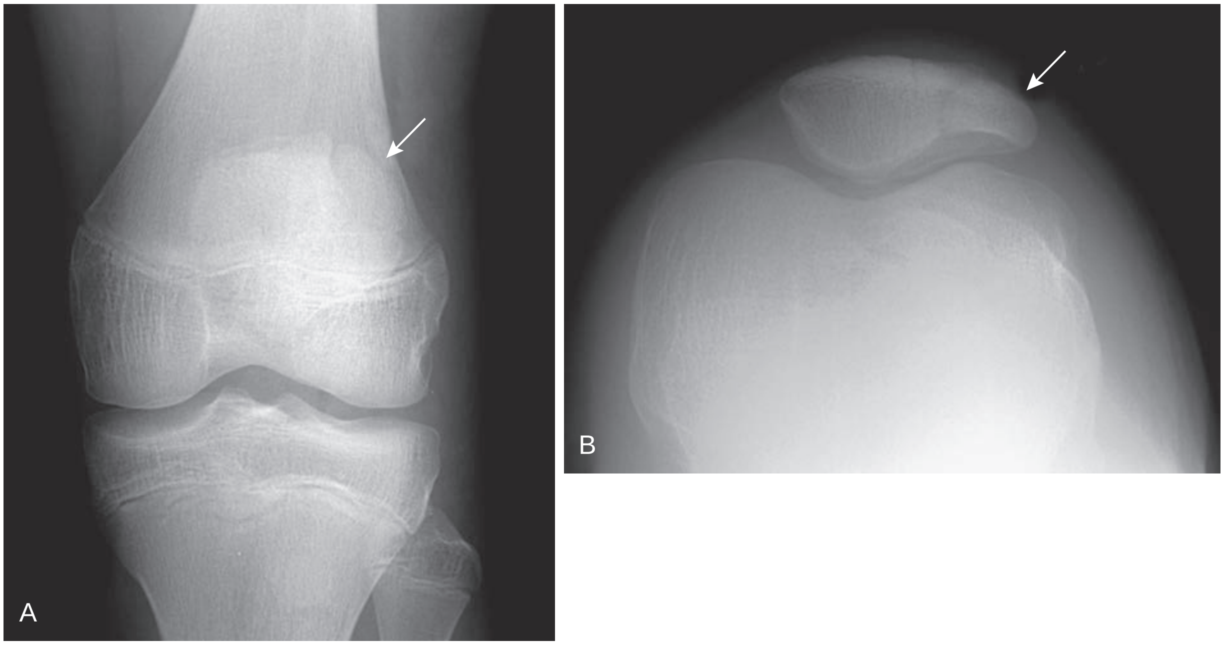

**Figure 128.72. Bipartite patella.** Anteroposterior (A) and axial (B) views of a bipartite patella in a 13-year-old boy. The accessory ossification center is superolateral *(arrows)*.

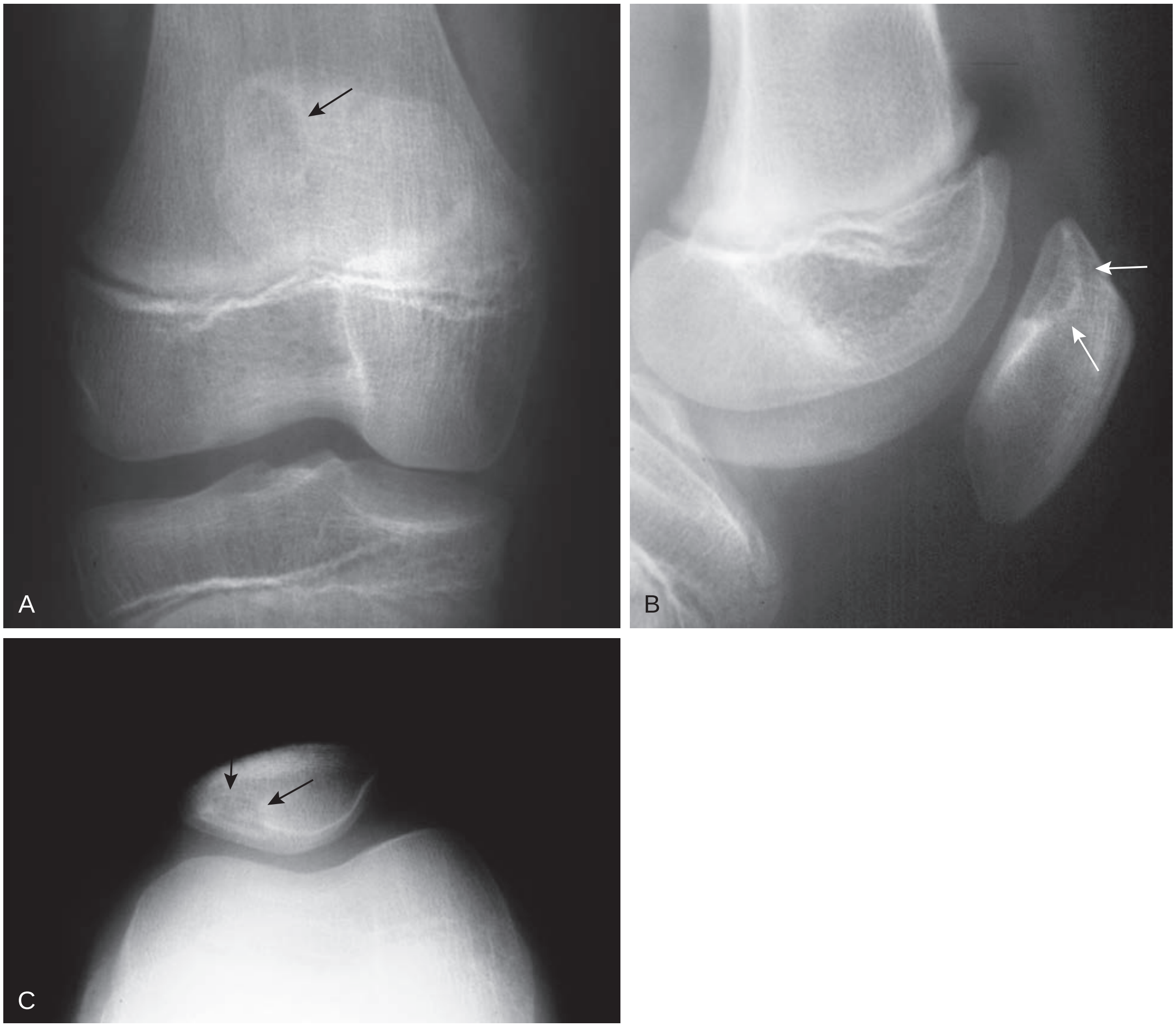

**Figure 128.74. Dorsal defect of the patella.** Anteroposterior (A), lateral (B), and axial (C) views of an 11-year-old girl shows the defect at the posterior aspect of the superolateral portion of the patella *(arrows)*.

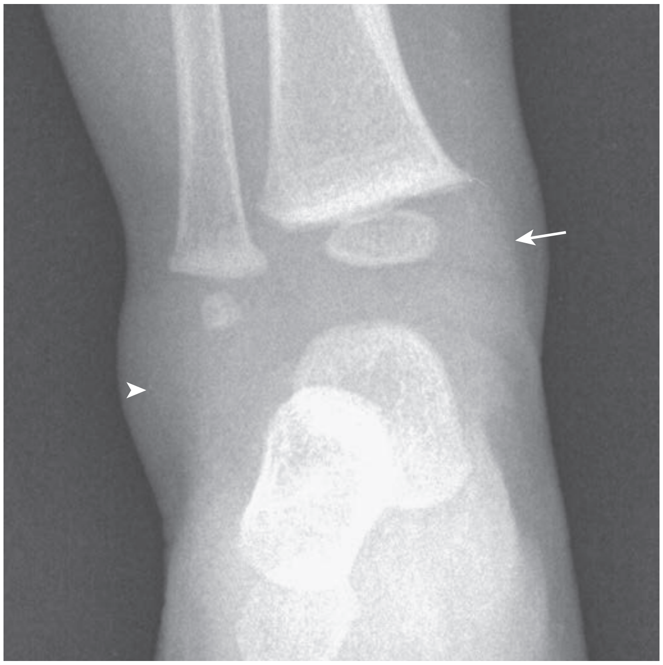

**Figure 128.76. Normal malleoli.** Medial *(arrow)* and lateral *(arrowhead)* cartilaginous epiphyses may superficially mimic ankle soft tissue swelling in this 9-month-old girl.

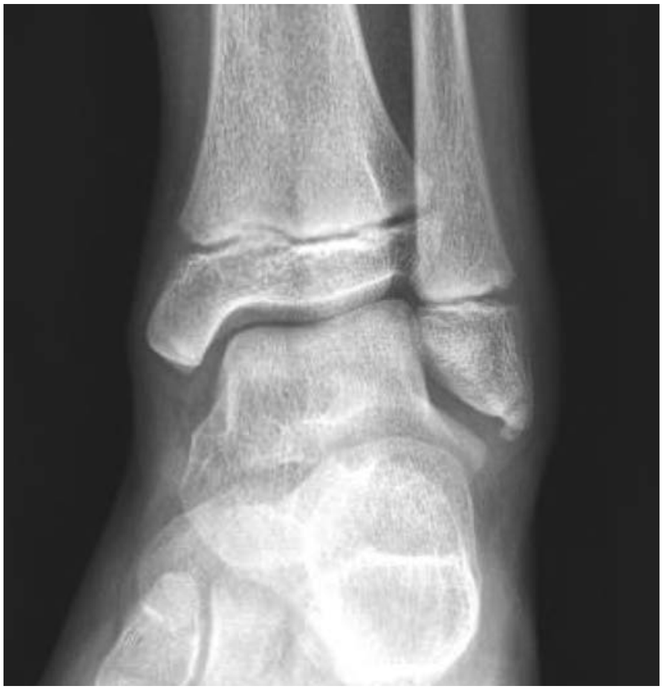

**Figure 128.78. Os subfibulare.** There is a well-corticated os subfibulare at the left lateral malleolus in this 11-year-old boy. This boy was asymptomatic in this ankle, having this radiograph done as a comparison for the contralateral side, which had a similar ossicle (not shown).

incidental finding on radiographs but may cause patellofemoral pain. On MRI, the overlying cartilage is typically intact. A dorsal defect of the patella may be seen concomitantly with a bipartite patella.[48] Dorsal patella defects should be differentiated from OCD of the patella, which usually affects the inferior aspect of the patella.

## Tibia and Fibula

**Tibial Tuberosity.** A steplike notched defect appears in the upper anterior border of the tibia in lateral projection before ossification proceeds in the cartilaginous anterior tibial tuberosity from the main proximal tibial ossification center. The tuberosity also may be ossified from multiple fragmentary accessory centers that, before union, may simulate avulsed fragments of bone. When ossification of the anterior tibial tuberosity is nearly complete, the radiolucent cartilage still separating the process from the shaft may appear as a notch or a horizontal strip (e-Fig. 128.75).

A fragmentary appearance of the tibial tuberosity is a normal finding in children. However, when accompanied by focal tenderness on palpation, edema in adjacent Hoffa's fat pad, and pretibial edema, a diagnosis of Osgood-Schlatter disease should be suggested.

**Irregular Ossification of the Medial and Lateral Malleoli.** The medial and lateral malleolus are initially cartilaginous and may superficially mimic soft tissue swelling (Fig. 128.76). Fragmentary ossification of both the medial and lateral malleoli is a normal finding in the skeletally immature and should not be confused with fracture.[49]

Separate accessory ossification centers are common in the cartilage of the medial malleolus (os subtibiale) and less common in the lateral malleolus (os subfibulare) (e-Fig. 128.77 and Fig. 128.78). At each location, the differential diagnosis is an avulsed fragment. Acute avulsed fragments will have an irregular shape and a sharp, noncorticated margin. A common pitfall is to mistake an acute avulsion fracture of the anterior talofibular ligament with an os subfibulare.

**Fibular Ossicle.** The provisional zone of calcification in the distal fibular metaphysis may be notched upward, and a tiny extra ossicle may develop in the notch. The notching is usually bilateral.

### KEY POINTS

- The spherical growth plate is responsible for epiphyseal ossification, and its physiology is similar to that of the physis.
- The subperiosteal metaphyseal bone collar should not be confused with classic metaphyseal lesions of child abuse.
- The ischiopubic synchondrosis can close asymmetrically and superficially mimic a fracture and a tumor. The irregular side is usually contralateral to the dominant foot.
- Epiphyseal ossification can be quite fragmentary in the femoral condyles and should not be mistaken for fractures.
- The acromion process is mainly cartilaginous, particularly in the first decade, and may cause pseudo-widening of the AC joint, superficially mimicking AC joint diastasis. Imaging the unaffected side may be helpful for comparison.
- Os acetabulae is a normal ossification center along the acetabular rim and should not be confused with acetabular rim fractures or anterior-inferior iliac spine avulsion fractures related to the rectus femoris origin.
- The medial epicondyle of the elbow appears before the trochlear ossification. If only a trochlear ossification is present, a displaced medial epicondylar avulsion fracture should be suspected.

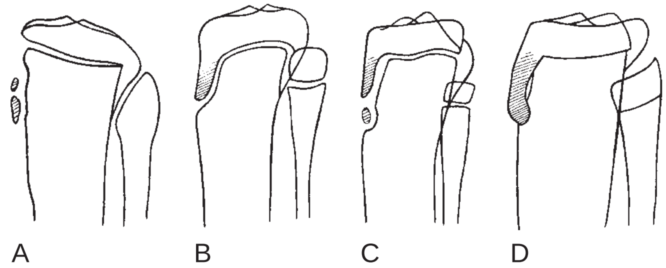

**e-Figure 128.75.** (A–D) Normal variations in the size and configuration of the ossification center(s) of the tibial tubercle. *(Modified from Köhler A, Zimmer EA.* Borderlands of the Normal and Early Pathologic in Skeletal Roentgenology. *4th ed. New York: Grune & Stratton; 1993.)*

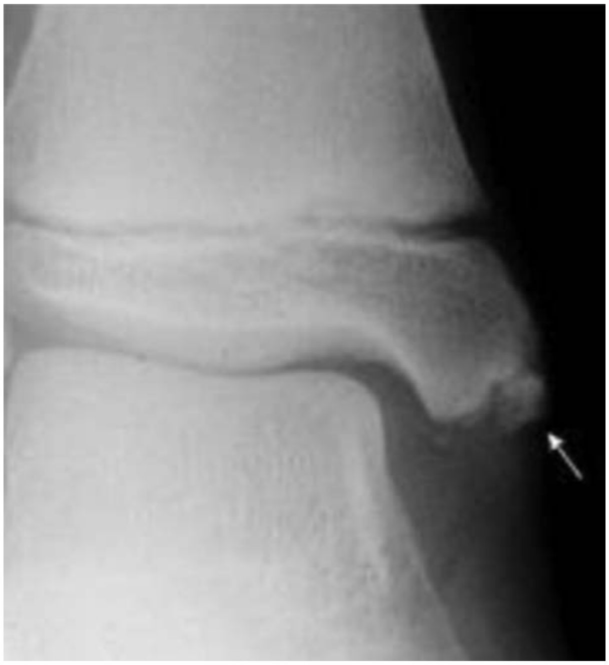

**e-Figure 128.77.** Medial malleolar accessory ossification center *(arrow)* in a 10-year-old girl.

## SUGGESTED READINGS

Berko NS, Kurian J, Taragin BH, et al. Imaging appearances of musculoskeletal developmental variants in the pediatric population. *Curr Probl Diagn Radiol*. 2015;44(1):88–104.

Duncan AW. Normal variants—an approach. In: Carty H, Brunelle F, Stringer D, et al, eds. *Imaging Children*. 2nd ed. Philadelphia: Elsevier; 2005.

Greulich WW, Pyle SI. *Radiographic Atlas of Skeletal Development of the Hand and Wrist*. 2nd ed. Stanford, CA: Stanford University Press; 1959.

Ogden JA. Diagnostic imaging. In: Ogden JA, ed. *Skeletal Injury in the Child*. 3rd ed. New York: Springer; 2000.

Quigley AJ, Stafrace S. Skeletal survey normal variants, artefacts and commonly misinterpreted findings not to be confused with non-accidental injury. *Pediatr Radiol*. 2014;44(1):82–93.

## REFERENCES

Full references for this chapter can be found on www.expertconsult.com.

## REFERENCES

1. Sandler TW. *Langman's Medical Embryology*. 11th ed. Philadelphia: Lippincott Williams & Wilkins; 2009.
2. Boron WF, Boulpaep EL. *Medical Physiology*. 2nd ed. Philadelphia: Saunders; 2009.
3. Kuhns LR, Finnstrom O. New standards of ossification of the newborn. *Radiology*. 1976;119:655–660.
4. Greulich WW, Pyle SI. *Radiographic Atlas of Skeletal Development of the Hand and Wrist*. 2nd ed. Stanford, CA: Stanford University Press; 1959.
5. Ontell FK, Ivanovic M, Ablin DS, et al. Bone age in children of diverse ethnicity. *AJR Am J Roentgenol*. 1996;167(6):1395–1398.
6. Loder RT, Estle DT, Morrison K, et al. Applicability of the Greulich and Pyle skeletal age standards to black and white children of today. *Am J Dis Child*. 1993;147:1329–1333.
7. Pyle SI, Hoerr NL. *A Radiographic Standard of Reference for the Growing Knee*. Springfield, IL: Charles C Thomas; 1969.
8. Hoerr NL, Pyle SI, Francis CC. *Radiographic Atlas of Skeletal Development of the Foot and Ankle*. Springfield, IL: Charles C Thomas; 1962.
9. Risser JC. The iliac apophysis: an invaluable sign in the management of scoliosis. *Clin Orthop*. 1958;1:111–119.
10. Keats TE, Anderson MW. *An Atlas of Normal Roentgen Variants That May Simulate Disease*. 7th ed. St Louis: Mosby; 2001.
11. Freyschmidt J, Brossman J, Wiens J, et al. *Borderlands of Normal and Early Pathological Findings in Skeletal Radiography*. 5th ed. New York: Thieme; 2003.
12. Kwon DS, Spevak MR, Fletcher K, et al. Physiologic subperiosteal new bone formation: prevalence, distribution, and thickness in neonates and infants. *AJR Am J Roentgenol*. 2002;179:985–988.
13. Kleinman PK, Belanger PL, Karellas A, et al. Normal metaphyseal radiologic variants not to be confused with findings of child abuse. *AJR Am J Roentgenol*. 1991;156:781–783.
14. Kuhns LR, Poznanski AK, Harper HA, et al. Ivory epiphyses of the hands. *Radiology*. 1973;109:643–648.
15. Giedeon A. Phalangeal cone-shaped epiphyses of the hand: their natural history, diagnostic sensitivity, and specificity in cartilage hair hypoplasia and the trichorhinophalangeal syndromes I and II. *Pediatr Radiol*. 1998;28:751–758.
16. Dameron TB. Fractures and anatomical variations of the proximal portion of the fifth metatarsal. *J Bone Joint Surg Am*. 1975;57(6):788–792.
17. Ogden JA, Ganey TM, Light TR, et al. Ossification and pseudoepiphysis formation in the "nonepiphyseal" end of bones of the hands and feet. *Skeletal Radiol*. 1994;23:3–13.
18. Laor T, Clarke JP, Yin H. Development of the long bones in the hands and feet of children: radiographic and MR imaging correlation. *Pediatr Radiol*. 2016;46:551–561.
19. Limb D, Loughenbury PR. The prevalence of pseudoepiphyses in the metacarpals of the growing hand. *J Hand Surg Eur Vol*. 2012;37(7):678–681.
20. Sanders TG, Ruthur SK. Imaging of painful conditions of the hallucal sesamoid complex and plantar capsular structures of the first metatarsophalangeal joint. *Radiol Clin North Am*. 2008;46:1079–1092.
21. Wawer R, Budzik JF, Demondion X, et al. Carpal pseudoerosions: a plan x-ray interpretation pitfall. *Skeletal Radiol*. 2014;43(10):1377–1385.
22. Conway WF, Destouet JM, Gilula LA, et al. The carpal boss: an overview of radiographic evaluation. *Radiology*. 1985;156:29–31.
23. Abid A, Accadbled F, Kany J, et al. Ulnar styloid fracture in children: a retrospective study of 46 cases. *J Pediatr Orthop B*. 2008;17(1):15–19.
24. Harrison RB, Keats TE. Epiphyseal clefts. *Skeletal Radiol*. 1980;5:23–27.
25. Dereymaeker G, van der Broek C. Biphalangeal fifth toe. *Foot Ankle Int*. 2006;26(11):948–951.
26. Kose O, Celiktas M, Yigit S, et al. Can we make a diagnosis with radiographic examination alone in calcaneal apophysitis (Sever's disease)? *J Pediatr Orthop B*. 2010;19:396–398.
27. Karasick D, Schweitzer ME. The os trigonum syndrome: imaging features. *AJR Am J Roentgenol*. 1996;166:125–129.
28. Miller TT, Staron RB, Feldman F, et al. The symptomatic accessory tarsal navicular bone: assessment with MR imaging. *Radiology*. 1995;195:849–853.
29. Barnard LB, McCoy SM. The supracondyloid process of the humerus. *J Bone Joint Surg Am*. 1946;28:845–850.
30. Opanova MI, Atkinson RE. Supracondylar process syndrome: case report and literature review. *J Hand Surg Am*. 2014;39:1130–1135.
31. Resnick D, Cone RO III. The nature of humeral pseudocysts. *Radiology*. 1984;150:27–28.
32. Ponseti IV. Growth and development of the acetabulum in the normal child. *J Bone Joint Surg Am*. 1978;60(5):575–585.
33. Martinez AE, Ganz R, Beck M. Os acetabuli in femoro-acetabular impingement: stress fracture or unfused secondary ossification centre of the acetabular rim? *Hip Int*. 2006;16(4):281–286.
34. Herneth AM, Philipp MO, Pretterklieber ML, et al. Asymmetric closure of ischiopubic synchondrosis in pediatric patients: correlation with foot dominance. *AJR Am J Roentgenol*. 2004;182:361–365.
35. Caffey J, Madell SH. Ossification of the pubic bones at birth. *Radiology*. 1956;67:346–350.
36. Lemperg R, Liliequist B, Mattson S. Asymmetry of the epiphyseal nucleus in the femoral head in stable and unstable hip joints. *Pediatr Radiol*. 1973;1:191–195.
37. Harrison MHM, Blakemore ME. A study of the "normal" hip in children with unilateral Perthes' disease. *J Bone Joint Surg Br*. 1980;62(1):31–36.
38. Bufkin WJ. The avulsive cortical irregularity. *Am J Roentgenol Radium Ther Nucl Med*. 1971;112:487–492.
39. Hall FM. Cortical desmoid: A misnomer? *AJR Am J Roentgenol*. 2011;197(4):1022.
40. La Rocca Vieira R, Bencardino JT, Rosenberg ZS, et al. MRI features of cortical desmoid in acute knee trauma. *AJR Am J Roentgenol*. 2011;196:424–428.
41. Caffey J, Madell SH, Royer C, et al. Ossification of the distal femoral epiphysis. *J Bone Joint Surg Am*. 1958;40:647–654.
42. Gebarski K, Hernandez RJ. Stage-I osteochondritis dissecans versus normal variants of ossification in the knee in children. *Pediatr Radiol*. 2005;35:880–886.
43. Laor T, Zbojniewicz AM, Eismann EA, et al. Juvenile osteochondritis dissecans: is it a growth disturbance of the secondary physis of the epiphysis? *AJR Am J Roentgenol*. 2012;199(5):1121–1128. doi:10.2214/AJR.11.8085.
44. Kavanagh EC, Zoga A, Omar I, et al. MRI findings in bipartite patella. *Skeletal Radiol*. 2007;36:209–214.
45. Ishikawa M, Adachi N, Deie M, et al. Unique patellofemoral alignment in a patient with a symptomatic bipartite patella. *Knee*. 2016;23(1):127–132.
46. Kan JH, Vogelius ES, Orth RC, et al. Inferior patellar pole fragmentation in children: just a normal variant? *Pediatr Radiol*. 2015;45(6):882–887.
47. Weiner DS, Macnab I. The "fabella syndrome": an update. *J Pediatr Orthop*. 1982;2:405–408.
48. van Holsbeeck M, Vandamme B, Marchal G, et al. Dorsal defect of the patella: concept of its origin and relationship with bipartite and multipartite patella. *Skeletal Radiol*. 1987;16:304–311.
49. Ogden JA, Lee J. Accessory ossification patterns and injuries of the malleoli. *J Pediatr Orthop*. 1990;10:306–316.

# 129

# Imaging Techniques

Arthur B. Meyers and J. Herman Kan

Pediatric musculoskeletal radiology is a broad field that requires an understanding of normal growth and developmental variations, fracture patterns unique to the immature skeleton, skeletal dysplasias, and knowledge of unique tumor and tumor-like conditions. Advanced imaging has improved our ability to arrive at a precise diagnosis. However, it also has created the need for additional expertise within the field of pediatric imaging to determine how and when to properly use these tools to arrive at a diagnosis. This chapter provides a broad overview of the techniques available to evaluate the spectrum of pediatric musculoskeletal disorders.

## IMAGING TECHNIQUE OVERVIEW

### Radiography

Radiography remains the initial tool for the evaluation of trauma, developmental and congenital disorders, inflammatory arthritis, infection, and suspected bone neoplasms.

In the setting of acute trauma, nonarticular long bones should be imaged with at least two views (frontal and lateral). Osteoarticular regions should be imaged with three views (frontal, lateral, and oblique). Dedicated imaging of the digits is preferred rather than general imaging of an entire hand or foot when a patient has a single symptomatic digit. For alignment disorders, including scoliosis and foot deformities, weight-bearing views should be obtained routinely. In cases of suspected child abuse, a dedicated skeletal survey should be performed.[1]

In the setting of suspected infection, radiography should be performed before advanced imaging to exclude a fracture or bone tumor as the cause of symptoms. However, a normal radiograph should not preclude referral for magnetic resonance imaging (MRI) for suspected acute osteomyelitis.

For bone neoplasms, initial radiographs are typically better at delineating tumor matrix and pattern of bone destruction than MRI. MRI is used to evaluate tumor extent, evaluation of skip lesions, surgical planning, and tumor follow-up.

### Ultrasonography

Sonography is an especially useful tool when imaging children because it can usually be performed without sedation and avoids ionizing radiation. Common indications for musculoskeletal ultrasound in children include evaluation of dysplasias, soft tissue masses, foreign bodies, and pyogenic and nonpyogenic arthritis.[2] Other uses of musculoskeletal sonography are continually expanding for the assessment of muscles, tendons, ligaments, and peripheral nerves. In some cases ultrasound may be an alternative to or complementary to MRI.[3]

Sonographic evaluation of dysplasias includes developmental dysplasia of the hip (DDH), glenohumeral dysplasia related to brachial plexopathy, and selected congenital foot deformities. In DDH and glenohumeral dysplasia, ultrasound allows for detailed assessment of the femoral and humeral heads before their ossification, the shape of the acetabulum and glenoid, and the femoral head/acetabular and humeral head/glenoid relationships. In congenital foot deformities sonography can be used for static and dynamic visualization of unossified tarsal bones.[4]

Sonography is useful in distinguishing solid from cystic soft tissue lesions. Certain soft tissue lesions such as ganglia, synovial cysts, and some vascular anomalies may have a characteristic enough appearance to make a definite diagnosis. However, other lesions (including most solid masses) will have a nonspecific sonographic appearance. Caution is advised against differentiating benign and malignant soft tissue masses with ultrasound, as soft tissue malignancies may be well defined with a nonaggressive appearance.

Identification of the presence or absence of a joint effusion of any region is straightforward with sonography. However, the etiology is predicated on clinical history. It is not possible to differentiate pyogenic, nonpyogenic, and posttraumatic causes based on sonography alone.

### Computed Tomography

Roles for musculoskeletal computed tomography (CT) include the assessment of fractures, orthopedic hardware, lower extremity alignment disorders, and the evaluation of tumor matrix and tumor recurrence in the setting of an existing neoplasm or a resected neoplasm with hardware in place.

A low peak kilovoltage (kVp) technique may be used because of the inherent contrast of bone; however, when hardware is present a higher kVp, along with increased milliampere-second (mAs) and decreased pitch, may help minimize artifacts.[5] These methods need to be employed cautiously because they increase radiation dose. Multiplanar and sometimes volume-rendered reformats are typically performed for musculoskeletal CT applications.

Fracture assessment by CT is performed when there is clinical suspicion for a radiographically occult fracture or when additional characterization of fractures seen on radiographs is needed. CT can better define intraarticular components of fractures (providing precise measurements of fracture diastasis and articular step-off), identify additional fractures, and identify intraarticular bodies not visible on radiographs.

Alignment disorders that can be evaluated by CT include determination of acetabular and femoral version, tibial torsion, glenohumeral dysplasia, and patellofemoral tracking disorders. Patellofemoral tracking disorders usually are dynamic studies in which the knee is placed in varying degrees of flexion to evaluate lateral patellar dislocation.

### Magnetic Resonance Imaging

The volume and varying applications of musculoskeletal MRI in the pediatric population have grown because of the popularity of youth sports and subsequent injuries. In addition to imaging injuries, MRI plays a useful role in imaging congenital/developmental, infectious, inflammatory, metabolic, and oncologic conditions.

Four basic sequence types may be used for musculoskeletal MRI: an anatomy sequence (usually T1, proton density); a fluid-sensitive sequence (proton density with fat saturation, T2 with fat saturation, short-tau inversion recovery, and a fluid-weighted gradient echo sequence); a contrast sequence (postgadolinium T1 typically with fat saturation); and a susceptibility sequence (any gradient echo sequence).

The purpose of the anatomy sequence is to evaluate marrow replacement, trabecular anatomy, and ligamentous abnormality. In general, it is recommended to have a T1-weighted sequence without fat suppression in at least one plane to evaluate bone marrow. Proton density sequences without fat saturation are useful

## Abstract:

Pediatric musculoskeletal radiology requires an understanding of normal growth, developmental variations, fracture patterns unique to the immature skeleton, skeletal dys- plasias, and tumor and tumor-like conditions that arise in children. This chapter provides a broad overview of the techniques available to evaluate the spectrum of pediatric musculoskeletal disorders including: radiographs, ultrasound, computed tomography, magnetic resonance imaging, and nuclear imaging.

## Keywords:

endocrine
hyperparathyroidism
hypoparathyroidism
renal osteodystrophy
hyperthyroidism
gonadal disorders

for evaluating trabecular anatomy and to evaluate ligamentous, labral, and cartilaginous anatomy.

Fluid-sensitive sequences are used to evaluate marrow edema, ligamentous anatomy, and cartilage. Spin echo fluid-sensitive sequences are superior to gradient echo sequences in the evaluation of pediatric cartilage. The primary and secondary physes, epiphyseal cartilage, and articular cartilage can be differentiated on spin echo sequences, whereas all types of cartilage have similar signal intensity on gradient echo sequences.

Gradient echo sequences are useful in the evaluation of entities that cause a susceptibility artifact allowing for detection of blood products, calcification or ossification (including ossified intraarticular bodies), and sites of prior surgery. Thin-slice gradient echo sequences can allow for detailed anatomic evaluation of small structures (e.g., ligamentous evaluation in the wrist). Three-dimensional fat-suppressed gradient echo sequences with dark bone and bright physeal cartilage can be reformatted to provide physeal maps in the setting of bone bars across the physis.

Postcontrast sequences are useful for determining tumor vascularity, detecting abscess in the setting of infection, and evaluating the synovium. Normal synovium will show thin enhancement, which should not be mistaken for pathology.[6] The relative thickness of the synovium as depicted by contrasted sequences is what is important in the setting of a joint effusion if pyogenic or nonpyogenic inflammatory arthritis is suspected. When initial precontrast images are entirely normal, postcontrast images have limited additional value.

Specialized sequences can be added to routine MRI protocols. For instance, a number of advanced sequences are available to assess articular cartilage. Two of the more commonly used are T2 relaxation time mapping and delayed gadolinium-enhanced MRI of cartilage (dGEMRIC).[7] Additionally, ultrashort echo time sequences can be used for qualitative and quantitative evaluation of many musculoskeletal structures, including articular cartilage, tendons, ligaments, and menisci.[8]

Technical innovations have made whole-body MRI possible. Indications for whole-body MRI in children are evolving and include many conditions involving the musculoskeletal system. Indications include fever of unknown origin without localizing symptoms, screening for tumors in children with cancer predisposition syndromes (e.g., Li–Fraumeni syndrome), assessment and follow-up of Langerhans cell histiocytosis, evaluation of benign tumor burden in children with neurofibromatosis type 1, evaluation of generalized vascular malformations, osteonecrosis, chronic recurrent multifocal osteomyelitis, and myopathies.[9]

In general, girls who are older than 6 years and boys who are older than 8 years are able to undergo MRI without the need for sedation. Sedation should be handled by a dedicated and qualified team.

## Nuclear Imaging

Skeletal scintigraphy, typically using technetium-99m methylene-diphosphonate, has a higher sensitivity than skeletal radiography for bone pathology that exhibits osteoblastic activity, including fractures, tumors, and infection. Images obtained after injection of this compound reflect a combination of pathophysiologic functions (blood flow and bone turnover) but are nonspecific and do not provide exceptional anatomic detail. Images therefore should be interpreted in the context of the patient's clinical presentation and relevant radiologic findings. Structures adjacent to open physes are difficult to assess because the high uptake in the physes may mask the activity associated with an adjacent pathologic lesion. Single-photon emission CT helps in localization of such lesions by improving spatial resolution of activity in contiguous and overlapping structures.

Indications for skeletal scintigraphy are varied and include investigation of bone pain, diagnosis of early and chronic osteomyelitis, osteonecrosis, and occult trauma, including nonaccidental trauma and stress fractures. CT and MRI have usurped skeletal scintigraphy in many clinical settings; however, bone scanning remains a very useful imaging tool.[10]

Positron emission tomography (PET) imaging with fluorine-18-deoxyglucose (FDG) offers improved spatial resolution and greater sensitivity for detection of aggressive bone neoplasms. FDG-PET is particularly effective in detecting an active tumor. Because of its high sensitivity, increased signal on PET is nonspecific. The fusion of PET with CT or MRI allows for better spatial localization of lesions and improves the characterization of lesions. PET also is an effective method of determining response of malignant bone tumors to therapy.

### REFERENCES

Full references for this chapter can be found on www.expertconsult.com.

## REFERENCES

1. Offiah A, van Rijn RR, Perez-Rosello JM, et al. Skeletal imaging of child abuse (non-accidental injury). *Pediatr Radiol*. 2009;39: 461–470.
2. Hryhorczuk AL, Restrepo R, Lee EY. Pediatric musculoskeletal ultrasound: practical imaging approach. *AJR Am J Roentgenol*. 2016; 206(5):W62–W72. doi:10.2214/AJR.15.15858.
3. Nazarian LN. The top 10 reasons musculoskeletal sonography is an important complementary or alternative technique to MRI. *AJR Am J Roentgenol*. 2008;190(6):1621–1626. doi:10.2214/AJR.07.3385.
4. Miron MC, Grimard G. Ultrasound evaluation of foot deformities in infants. *Pediatr Radiol*. 2016;46(2):193–209.
5. Fayad LM, Patra A, Fishman EK. Value of 3D CT in defining skeletal complications of orthopedic hardware in the postoperative patient. *AJR Am J Roentgenol*. 2009;193:1155–1163.
6. Ejbjerg B, Narvestad E, Rostrup E, et al. Magnetic resonance imaging of wrist and finger joints in healthy subjects occasionally shows changes resembling erosions and synovitis as seen in rheumatoid arthritis. *Arthritis Rheum*. 2004;50(4):1097–1106.
7. Huang M, Schweitzer ME. The role of Radiology in the evolution of the understanding of articular disease. *Radiology*. 2014;273:S1–S22. doi:10.1148/radiol.14140270.
8. Chang EY, Du J, Chung CB. UTE imaging in the musculoskeletal system. *J Magn Reson Imaging*. 2015;41(4):870–883. doi:10.1002/jmri.24713. [Epub 2014 Jul 16].
9. Chavhan GB, Babyn PS. Whole-body MR imaging in children: principles, technique, current applications, and future directions. *Radiographics*. 2011;31(6):1757–1772.
10. Nadel HR. Pediatric bone scintigraphy update. *Semin Nucl Med*. 2010;40:31–40.

# 130 Prenatal Musculoskeletal Imaging

Christopher I. Cassady

## OVERVIEW

Evaluation of the fetal skeleton is one of the more challenging aspects of prenatal imaging for a variety of reasons. It is such a rapidly changing system in gestation that ossification varies in extent and distribution from week to week; ultrasonography, the primary fetal imaging modality, does not clearly demonstrate the full morphology of a bone because of lack of sound penetration; and many skeletal pathologies that become increasingly obvious with growth are, at best, subtle in the fetus. Still, techniques are available to overcome some of these barriers, and these include evaluation of bone contour abnormalities and proportions by using magnetic resonance imaging (MRI), and rarely, computed tomography (CT) in addition to ultrasound. Musculoskeletal abnormalities in the fetus are diagnosable in the following categories:

1. Generalized skeletal dysplasias
2. Nongeneralized anomalies of segment length, number, or shape
3. Primary anomalies of the spine
4. Neuromuscular disorders, including clubfoot
5. Tumors

## SKELETAL DYSPLASIAS

***Etiology.*** Dysplasias are often the result of genetic mutations that encode for proteins important to development of the growth plate.[1,2] Current clinical application of "skeletal dysplasia testing panels" is, however, very limited. Both the range of included mutations and the sensitivities of their detection are expected to increase with time. Furthermore, the discovery of cell-free fetal DNA in maternal plasma may lead to noninvasive techniques such as capture sequencing for the prenatal diagnosis of some skeletal dysplasias.[3] In utero testing in sporadic cases remains controversial.[4]

***Imaging.*** More than 430 dysplasias have been described in the literature. Only a small percentage is considered diagnosable in utero with imaging.[3–5] Because of the lack of specificity of many of the findings, efforts at ultrasonographic prenatal evaluation have focused on identification of cases in which the neonates are not expected to survive, typically because of an abnormally constricted chest (Box 130.1).[6–9] Most of these criteria correlate limb length with survival, but emphasis is also placed on measures predicting lethal pulmonary hypoplasia.[10–13] Other findings that may be detected in association with lethality and that increase diagnostic certainty are polyhydramnios and nonimmune hydrops fetalis.[7] It is important to avoid making a diagnosis of lethality in borderline cases and to use criteria in combination for the most accurate discrimination. The fetus with intrauterine growth retardation should not be assigned a diagnosis of generalized skeletal dysplasia on the basis of proportionate but short bones. Questionable cases in either category deserve follow-up ultrasonography for interval growth.

Three dysplasias constitute the vast majority of lethal cases: (1) thanatophoric dysplasia, (2) achondrogenesis, and (3) osteogenesis imperfecta type II. A familiarity with their ultrasonographic features is therefore essential (Box 130.2).[14,15]

Certain morphologic findings on ultrasonography suggest particular diagnoses in the setting of a suspected dysplasia. Multiple long bone fractures are very likely from osteogenesis imperfecta or hypophosphatasia, and rib fractures are rarely seen with other diagnoses (Fig. 130.1). Kleeblattschädel, or cloverleaf skull, may be present in several of the acrocephalosyndactyly syndromes (Apert, Carpenter, Crouzon, and Pfeiffer syndromes), campomelic dysplasia, osteocraniostenosis, and thanatophoric dysplasia type II (Fig. 130.2). Hypoplastic scapular bodies are a feature of campomelic dysplasia and Antley-Bixler syndrome.[16] However, many findings (e.g., platyspondyly, short ribs) are not specific and must be considered in relation to other features (abnormal mineralization, solid organ malformations) to arrive at a more narrow differential diagnosis (e-Fig. 130.3 and Fig. 130.4).[17] Three-dimensional ultrasonography can be very helpful when an appropriate volume of fluid is present around the fetus to display the morphology of specific segments, including the face, hands, and feet.[18,19]

Fetal MRI has not been pursued routinely in the evaluation of fetal dysplasia because of the difficulty in imaging the signal-poor ossified skeleton. However, it may have a role in quantification of fetal lung volumes in cases in which ultrasonography has limitations.[20,21] It has also been used successfully to make the diagnosis of dysplasias that primarily involve the epiphyses, taking advantage of the high water content T2-weighted signal characteristics of cartilage (e-Fig. 130.5).[22] Finally, fetal magnetic resonance imaging (MRI) specifically for temporal lobe malformation evaluation has been used when an FGFR3 mutation expression (such as thanatophoric dysplasia) is suspected.[23]

The use of ionizing radiation is generally avoided during pregnancy unless the need to make a diagnosis is critical to patient care, though low-dose CT techniques have been used effectively to reconstruct highly detailed three-dimensional models of the fetal skeleton (Fig. 130.6).[24–27] The features described are compared with an atlas of postmortem radiographs in identified syndromes to aid diagnosis.[28] This strategy can be offered at radiation doses of 3 to 5 millisievert with superb resolution of individual skeletal components.[29]

***Treatment and Follow-up.*** When a lethal skeletal dysplasia is detected using ultrasonography, the parents and fetal care team can make informed decisions about the continuation of the pregnancy and the circumstances of delivery. An opportunity exists for neonatal hospice care coordination, when appropriate. Even though ultrasonography is reliable at separating lethal dysplasias from nonlethal dysplasias, neonatal physical examination and radiographs, appropriate genetic testing, and autopsy, if relevant, are crucial in arriving at a specific diagnosis for accurate family counseling.[30]

## ANOMALIES OF SEGMENT LENGTH, NUMBER, OR SHAPE

***Etiology.*** Limb reductions may be caused by a variety of insults. Some cases of terminal transverse limb defects (TTLD) are from amputation, such as in the amniotic band sequence spectrum. Although the initiating event in this sequence has not been incontrovertibly established, the most commonly supported theory is that a tear is made in the amnion, exposing the fetus to the more adhesive chorion with subsequent loss of tissue or the development of a constrictive band.[31] In other cases of TTLD, primary vascular insults including coagulation abnormalities are blamed. Teratogens (e.g., thalidomide) are highly associated in some instances of phocomelia, in which a proximal segment is

## Abstract:

Evaluation of the fetal skeleton is a challenge in prenatal imaging for a variety of reasons: the fetal skeleton changes rapidly in gestation such that ossification varies in extent and distribution from week to week; ultrasonography, the primary fetal imaging modality, does not demonstrate the full morphology of a bone because of a lack of sound penetration; and many skeletal pathologies that become increasingly obvious with growth are, at best, subtle in the fetus. Techniques are available to overcome some of these barriers, and these include evaluation of bone contour abnormalities and proportions by using magnetic resonance imaging (MRI), and rarely, computed tomography (CT) in addition to ultrasound. This chapter discusses the appropriate imaging evaluation and work up for fetal musculoskeletal abnormalities, with particular emphasis on common dysplasias; abnormalities of the extremities to include limb reductions, overgrowth and malposition; spinal bone malformation; and soft tissue tumors.

## Keywords:

fetal skeleton
fetal skeletal dysplasia
fetal imaging
fetal limb anomaly
fetal spine
fetal teratoma

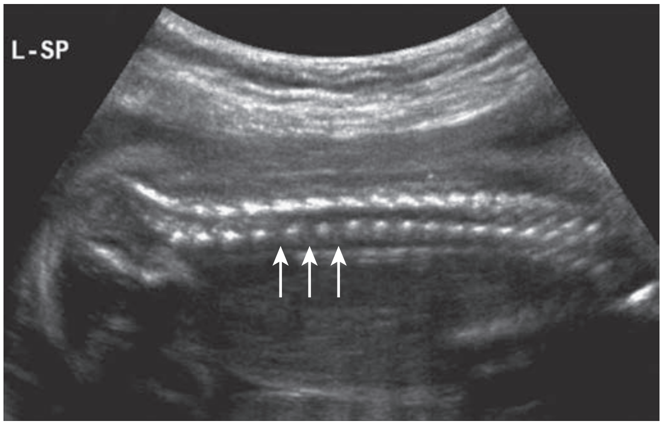

**e-Figure 130.3. Platyspondyly.** Disc spaces *(arrows)* are wider than the ossification centers for the vertebral bodies.

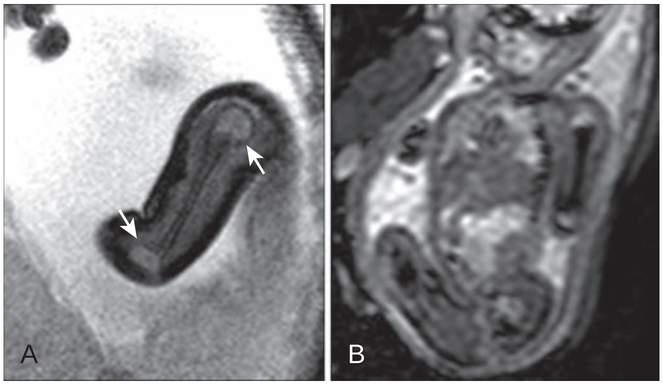

**e-Figure 130.5. MRI evaluation of fetal bones.** (A) Sagittal steady-state free precession gradient-recalled echo image at 33 weeks' gestation. The higher-signal cartilage *(arrows)* is distinct from the ossified diaphysis in the humerus. (B) Coronal gradient-recalled echo-planar imaging at 27 weeks. Echo-planar imaging is more reliable for bone morphology than other sequences at younger gestational ages.

### BOX 130.1 Proposed Ultrasonography Criteria for Lethal Dysplasia

- Micromelias >4 standard deviation behind expected lengths
- Femur length >5 mm below 2 standard deviation in second and third trimesters
- Femur length/abdominal circumference ratio <0.16
- Thoracic/abdominal circumference ratio <0.6
- Thoracic circumference < lower limit of the 95% confidence interval for gestational age
- Chest to trunk ratio <0.32

### BOX 130.2 Imaging Features of the Most Common Lethal Dysplasias*

**THANATOPHORIC DYSPLASIA**

- “Telephone receiver” shaped femurs
- Depressed nasal bridge, macrocephaly
- Platyspondyly
- Short ribs
- Trident hand
- Clover leaf skull in type II
- Oversulcation of the inferomedial temporal lobes

**ACHONDROGENESIS**

- Deficient vertebral ossification, ± calvarial
- Short, flared ribs ± fractures
- Hydrops (25% of cases)
- Micrognathia, midface hypoplasia

**OSTEOGENESIS IMPERFECTA TYPE II**

- Multiple long bone fractures
- Hourglass-shaped thorax (from fractures), normal rib lengths (two-thirds of the way around chest)
- Increased conspicuity of brain anatomy on ultrasound (decreased mineralization)
- Skull deformity with pressure

*All have marked micromelia.

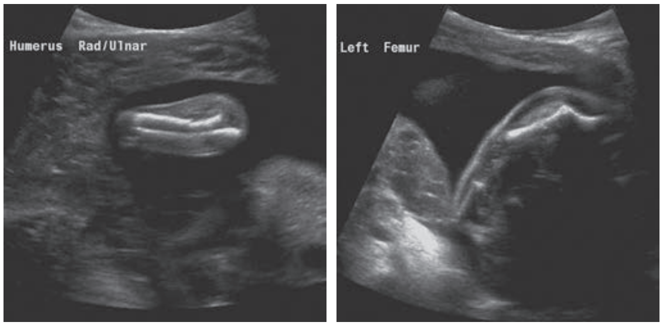

**Figure 130.1. Long bone fractures in a fetus with severe micromelia.** Diagnosis is osteogenesis imperfecta type II.

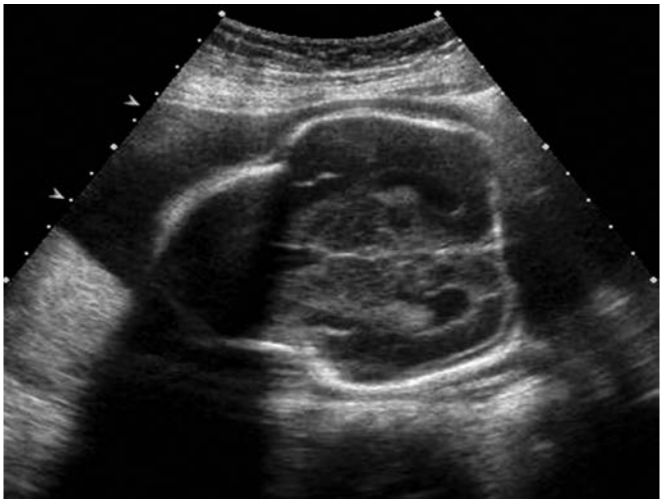

**Figure 130.2. Kleeblattschädel, or cloverleaf skull (pancraniosynostosis).** In the setting of a lethal bone dysplasia, the differential diagnosis includes thanatophoric dysplasia type II, campomelic dysplasia, and osteocraniostenosis.

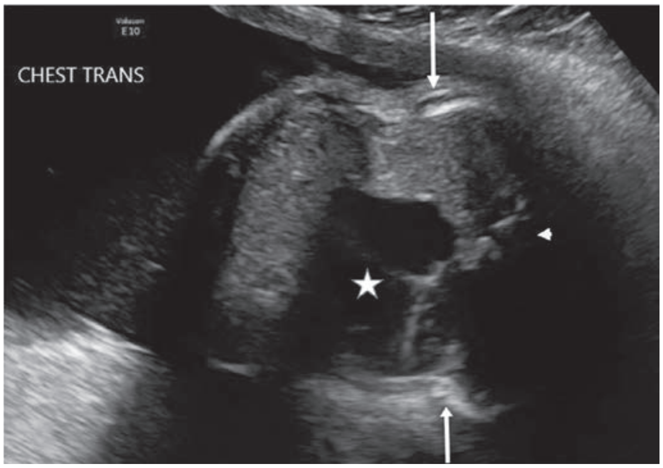

**Figure 130.4. Short ribs.** The ribs *(arrows)* are less than the normal 70% around the chest and are curved inward, with the heart *(star)* bulging outside the bony chest and the liver protuberant ventrally due to the chest:abdomen disproportion. *Arrowhead* indicates the spine on this transverse image.

missing, though phocomelia can be chromosomal or associated with specific syndromes (e.g., thrombocytopenia-absent radius).[32–35] Proximal focal femoral deficiency is a particular, generally isolated form of reduction that affects the femoral head and neck but may include fibular aplasia or hypoplasia. It can be unilateral or bilateral (Fig. 130.7).

Overgrowth is typically syndromic, as with hemihypertrophy in Beckwith-Wiedemann syndrome, or the soft tissue bulk of Proteus, Klippel-Trenaunay-Weber or CLOVES syndromes.[36,37] An increased number of segments over normal typically affects only the fingers or toes, and is often chromosomal though isolated cases can be familial and benign. Bowing of a long bone can affect one bone or several, but in either case genetic associations (dysplasias, neurofibromatosis) should be investigated. Posteromedial bowing of the tibia and fibula is a unique case.[38,39]

***Imaging.*** Limb reduction anomalies may be subtle if isolated or very distal (e.g., fingers/toes). Ultrasonography can often characterize the shape of the affected limb sufficiently well for diagnosis. Associated findings may include edema of the extremity distal to a constricting band (Fig. 130.8 and Video 130.1). Cine ultrasound sequences can capture the abnormal motion that is a consequence of subluxation or dislocation if the affected segment involves a joint. Random isolated or multiple defects are more likely secondary to amniotic band sequence than are symmetric defects, which tend to be related to chromosomal abnormalities or syndromes (Fig. 130.9).[40] As amniotic bands can cause defects

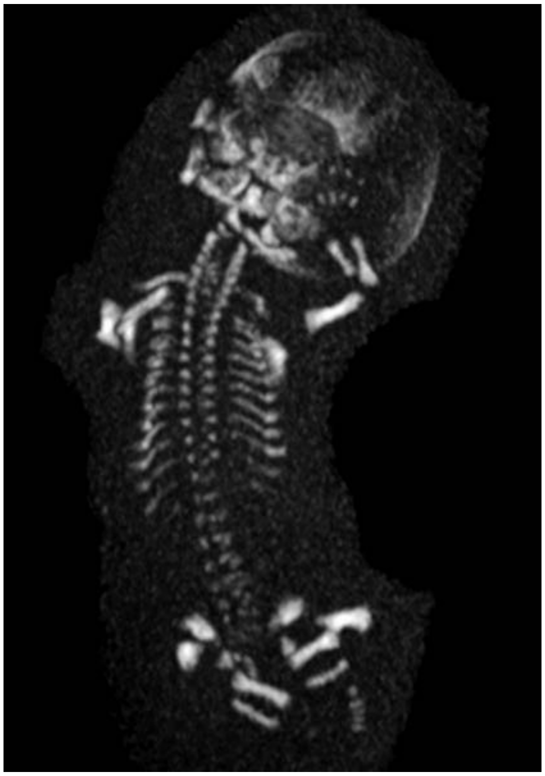

**Figure 130.6. Thanatophoric dysplasia type I.** Three-dimensional volume set acquisitions allow reconstructed CT projections in any plane. Radiation dose to the 21-week fetus was 3.9 millisievert. Gene testing confirmed an *FGFR* mutation. *(Courtesy of Teresa Victoria, MD.)*

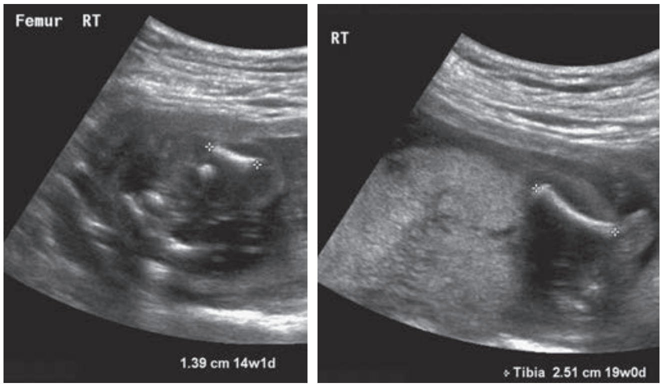

**Figure 130.7. Proximal focal femoral deficiency with fibular aplasia.** Fetus at 20 weeks' gestational age shows a short femur associated with a single long bone in the distal leg.

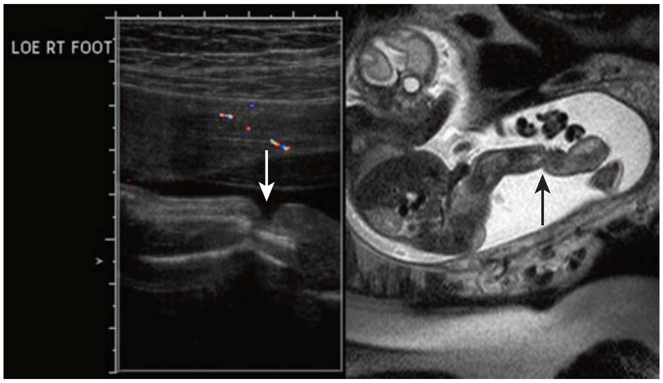

**Figure 130.8. Amniotic band syndrome.** Ultrasound and sagittal T2-weighted single-shot fast spin echo images show focal constriction of both soft tissue and bone *(arrows)* at the distal leg, with edema of the ankle and foot.

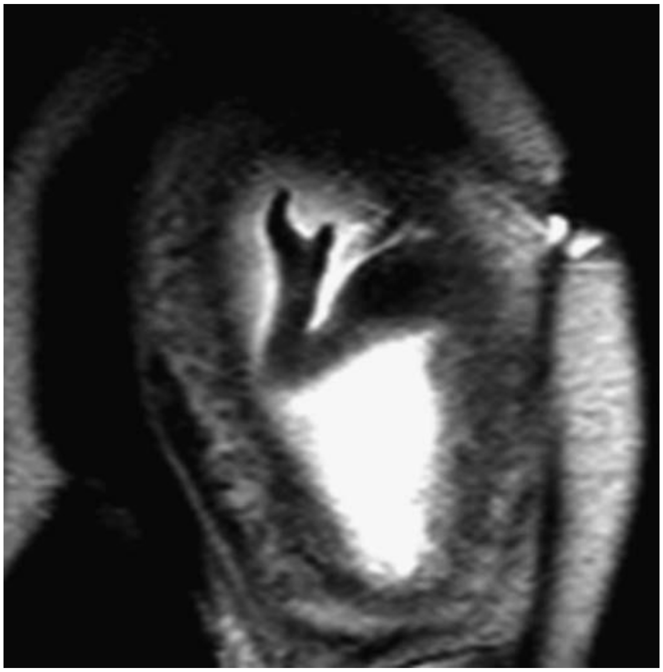

**Figure 130.9. Brachmann-DeLange syndrome.** This 30-week fetus had bilateral ectrodactyly (split hand-foot malformations), with only two digits of the hand. The contralateral hand had a similar appearance *(not shown)*.

in any body part, a thorough evaluation of the entire fetus is indicated. Umbilical cord involvement is often overlooked but has consequences because of the risk of cord occlusion.[41]

Recognition of overgrowth necessitates an evaluation of the types of tissue that are involved, including vascularity and fat, and therefore Doppler interrogation and MR may prove useful.[42] In cases where polydactyly is discovered, a careful search for other fetal anomalies that might give a clue to a genetic association is warranted.[43]

***Treatment and Follow-up.*** Successful cases of fetoscopic lysis of amniotic bands have been reported when it has been thought that release could improve blood flow to and consequent growth of an affected limb segment.[44] Otherwise, plastic surgery consultation is sought for limb salvage after delivery of the fetus.

## PRIMARY ANOMALIES OF THE SPINE

***Etiology.*** Primary anomalies of the spine typically manifest as an unusual curvature. Care must be taken to ensure that this finding is a fixed abnormality and not positional or merely the result of a lack of space (e.g., in anhydramnios). Fixed kypho/scoliosis is abnormal and may be the result of tethering, as with limb–body wall complex (Fig. 130.10), a severe and lethal form of amniotic band sequence; rib fusions, as in Jarcho-Levin syndrome (Fig. 130.11); or fetal akinesia or hypokinesia.[45] Often, the finding is subtle and secondary to segmentation anomalies of the spine (Fig. 130.12). Complex spinal anomalies can be seen with neural

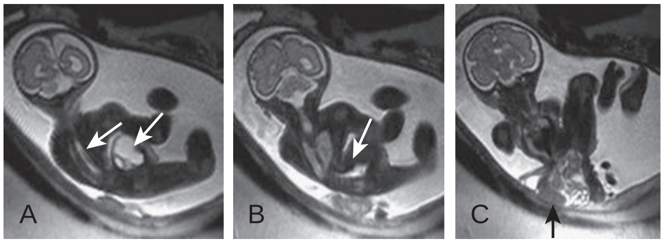

**Figure 130.10. Limb–body wall complex.** (A–C) Contiguous oblique coronal SS-FSE T2-weighted images. Multiple images had shown fixed scoliosis and contortion in a fetus with extrusion of abdominal contents adherent to the amnion *(black arrow)*. *White arrows* indicate the spinal canal in this fetus, who also has a closed neural tube defect.

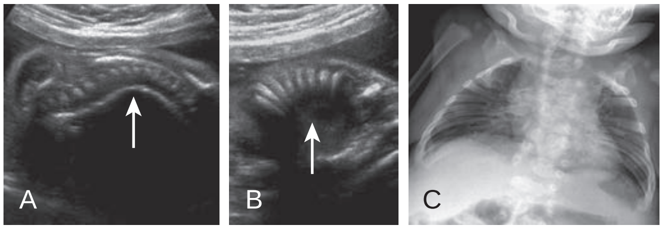

**Figure 130.11. Jarcho-Levin syndrome (spondylocostal dysostosis).** (A and B) Fixed scoliosis associated with thoracic restriction, with ribs fanning out from a central fusion. (C) Typical chest appearance with rib deformities and vertebral segmentation anomalies.

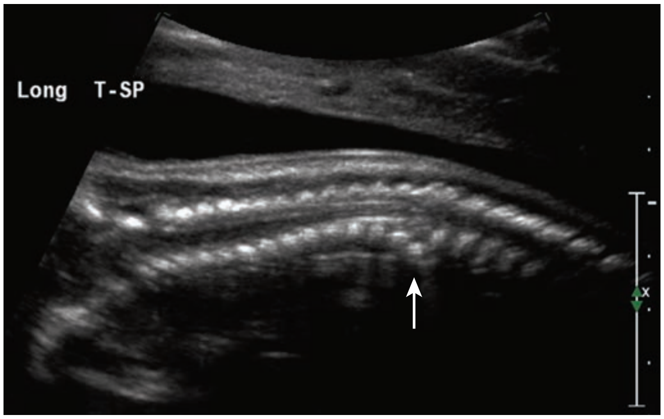

**Figure 130.12. Vertebral segmentation anomaly.** Focal interruption in the continuity of vertebral body ossification centers, signifying a segmentation anomaly (hemivertebra, *arrow*).

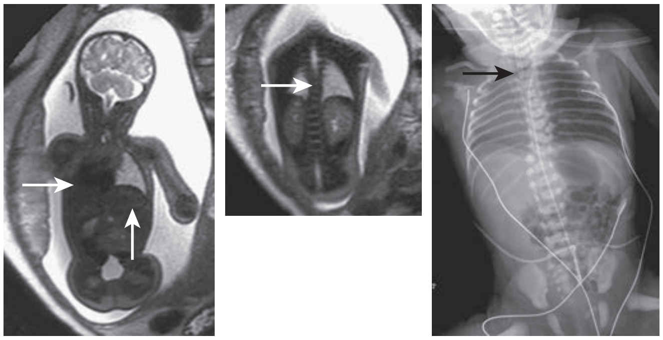

**Figure 130.13. VACTERL association (*v*ertebral anomaly, *a*norectal atresia, *c*ardiac lesion, *t*racheo*e*sophageal fistula, *r*enal anomaly, *l*imb defect).** Coronal T2-weighted single-shot fast spin echo MR images show a right-sided heart *(horizontal arrow on left image),* absence of fluid in the stomach *(vertical arrow on left image),* and thoracic scoliosis from hemivertebrae *(arrow on middle image)*. Subsequent neonatal radiograph also shows the right heart and vertebral segmentation anomalies. Note that the Repogle tube is in the proximal esophageal pouch *(black arrow)* due to esophageal atresia.

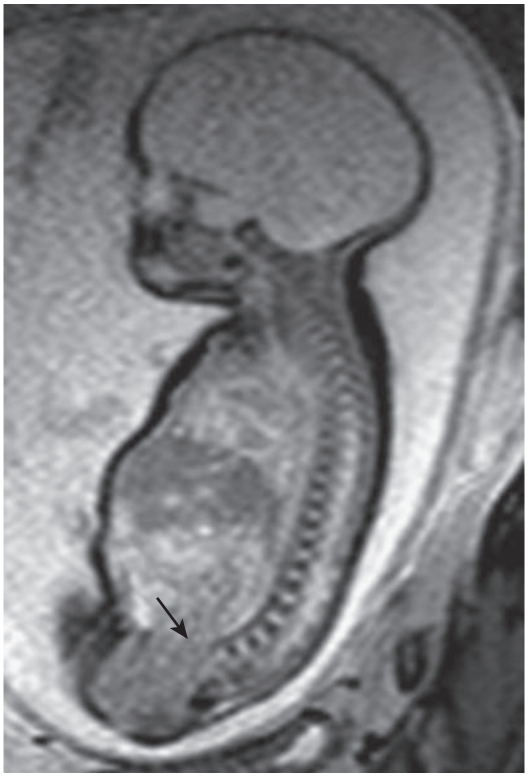

**Figure 130.14. Caudal regression sequence.** Sagittal gradient-recalled echo MR image at 31 weeks' gestation. The spine terminates abruptly *(arrow)* without a sacrum.

tube defects and with the Currarino triad, which is a heritable complex of anomalous sacrum, presacral mass, and anorectal malformation.[46] Absence of the sacrum, with variable involvement of the more proximal spine, occurs in caudal regression syndrome, which is significantly associated with elevated glucose levels in the fetus of a mother with diabetes.[47] The most common spinal anomaly in the fetus involves the dysraphism of posterior elements in a neural tube defect.

***Imaging.*** A spinal anomaly may be an isolated fetal finding, but it does prompt a careful search for associated syndromic abnormalities, including the various components of the VACTERL association (***v***ertebral anomaly, ***a***norectal atresia, ***c***ardiac lesion, ***t***racheo***e***sophageal fistula, ***r***enal anomaly, ***l***imb defect) (Fig. 130.13). The presence of an anal dimple can be confirmed on ultrasonography, where attention is also directed specifically to the size of the stomach and morphology of the radial ray segments. Devoted echocardiography is recommended in suspicious cases. MRI has been used to examine for a transiently distended esophageal pouch proximal to an atresia, using repetitive dynamic T2-weighted sequences in the sagittal midline.[48] The multiplanar capabilities of MRI may be advantageous in sorting out the components of complex spinal anomalies (Fig. 130.14).

***Treatment and Follow-up.*** Correlation with imaging and physical examination after delivery is critical to confirm the suspected anomaly and guide therapy. Because both ultrasonography and MRI have limitations in the evaluation of the spine, prenatal imaging findings may not be straightforward, and it should not be assumed that the most complete diagnosis has been described antenatally.

## NEUROMUSCULAR DISORDERS

***Etiology.*** Several conditions that cause generalized hypotonia in the fetus and neonate are heritable: the most important from the point of view of obstetric management is congenital myotonic dystrophy. This is an autosomal dominant muscular disease in which expansion of abnormal genomic repeats inserted during cell division will be greater in an affected child than in the carrier parent. Milder cases in adults often go undiagnosed, and a carrier mother may not display obvious manifestations of muscular insufficiency until administered respiratory-depressant anesthetics, to which these patients are exquisitely sensitive. Sudden death from cardiac conduction abnormalities during sedation has also been reported.[49] Therefore if myotonic dystrophy is suspected as part of the differential diagnosis in a fetus, maternal genetic testing should be performed and a careful anesthetic strategy planned for the delivery.[50,51]

Most of the time, a specific diagnosis is difficult to establish for a fetus with any combination of limited movement, fixed position of the extremities, or multiple contractures. An unsatisfactory term, *arthrogryposis multiplex congenita*, has been used to describe this combination, with muscular, neurologic, and connective tissue disorders all showing similar manifestations. Differential considerations include multiple pterygium syndrome, in which skin webs tend to tether the limbs at the joints and restrict fetal movement. The major cause of arthrogryposis is fetal akinesia sequence, which has been associated with Pena-Shokeir syndrome (pseudotrisomy 18), nemaline rod myopathy, and maternal myasthenia gravis.[52–54]

"Clubfoot" is a term used generically to describe abnormal foot position relative to the leg; the more accurate term is *talipes*, the most common presentation of which is fixed plantar flexion with internal rotation at the ankle (talipes equinovarus, or clubfoot), though several forms of talipes (combinations of calcaneo- or equino- varus/valgus) are described (see also Chapter 133).[55] If unilateral, it is often an isolated finding with a low likelihood of syndromic association. Bilateral clubfoot, however, is typically secondary to spinal cord abnormalities such as meningomyelocele; anhydramnios or oligohydramnios, as with fetal renal or bladder obstruction; fetal akinesia; or genetic anomalies. Rocker-bottom foot (congenital vertical talus, or rigid flatfoot) is nearly always bilateral and is highly associated with aneuploidy (trisomies 9, 13, or 18), though most cases are related to neurologic disorders such as myelomeningocele (Fig. 130.15).[56]

***Imaging.*** Most fetuses move during ultrasonography, and assessment of fetal posture and movement is an essential part of determining fetal well-being.[57,58] Those that do not move as expected may be sleeping, which can be confirmed by later reimaging. True movement limitation should be determined as generalized versus focal. An effort should be made to look for tethering, constricting bands, or a neural axis lesion, and muscle bulk should be assessed. Polyhydramnios is likely if the fetus is not swallowing; a lack of breathing movements will result in a small chest and pulmonary hypoplasia. Fetal MRI may be indicated to evaluate the neural axis for a cause of generalized hypotonia or contractures and can help measure lung volumes. Alterations on MRI of muscular contour, thickness, and signal have suggested atrophy from neuromuscular disease.[59]

Clubfoot is diagnosed on ultrasonography or MRI when the foot is seen in a coronal long axis orientation on the same image in which the bones of the leg are also seen in coronal plane (Fig. 130.16). Care should be taken to ensure that this is a fixed position over time; spontaneous flexion at the ankle suggests the finding is positional.

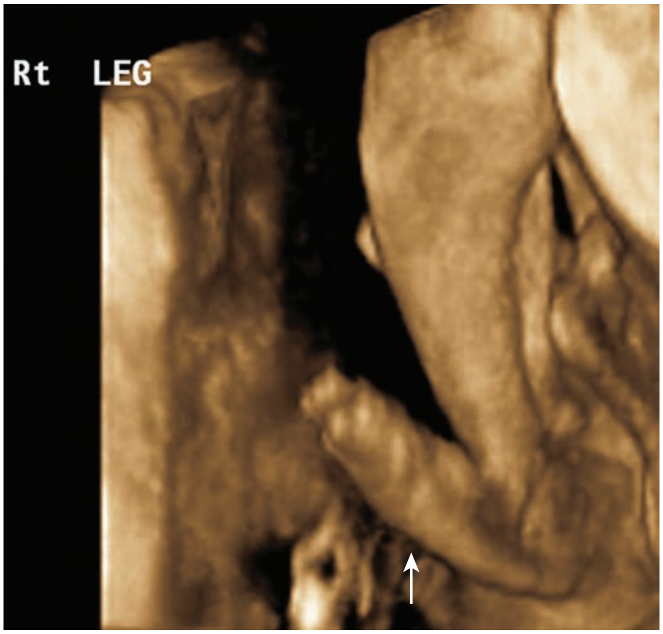

**Figure 130.15. Congenital vertical talus (rocker-bottom foot).** Three-dimensional ultrasound reconstruction using surface rendering shows inferior convexity of the plantar aspect of the foot *(arrow)* and upturned toes.

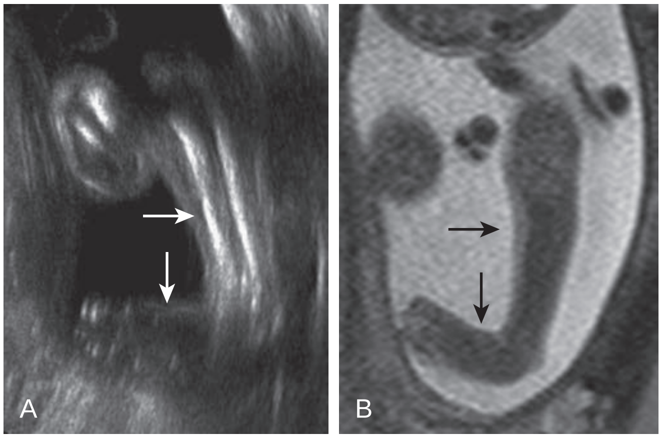

**Figure 130.16. Congenital clubfoot.** Ultrasonography (A) and T2-weighted MR (B) images show the foot in a coronal long axis orientation *(vertical arrows)* on the same image that the tibia and fibula are seen in a coronal orientation *(horizontal arrows)*.

***Treatment and Follow-up.*** Neonatal treatments for hypotonia, arthrogryposis, or both are supportive. No fetal treatments are described, though testing for myotonic dystrophy should be undertaken in appropriate cases to avoid maternal complications. Treatment for clubfoot is generally started in the first days of life, and surgery depends on the success of manipulation and casting.[60]

## TUMORS

***Etiology.*** Tumors of the fetal musculoskeletal system are extraordinarily rare, except for sacrococcygeal teratoma (SCT). Still, this entity is uncommon, with a reported incidence of only 1 per 40,000.[61] SCT is thought to arise from primitive cells associated with the fetal coccyx, which must be removed in entirety at excision

### BOX 130.3 Altman Classification of Sacrococcygeal Teratoma

**Type 1:** Tumor primarily external to the pelvis
**Type 2:** Tumor predominantly external but with a substantial intrapelvic component
**Type 3:** Tumor predominantly within pelvis/abdomen with a smaller external component
**Type 4:** Tumor entirely within pelvis/abdomen without an external component

to prevent recurrence. The Altman classification of SCT applies to the fetus but may change during gestation (Box 130.3).[62]

***Imaging.*** As with teratoma anywhere in the fetal body, tumors are characteristically mixed cystic and solid, with arterial vessels identifiable in the solid components. Ultrasonography is excellent for identifying the abnormal mass at the pelvis and involvement of superficial soft tissue just dorsal to the anus, which is invariably displaced ventrally when an external tumor component is present. Color Doppler interrogation is used to assess the vascularity of the tumor. Because of tumoral vascular shunting, a fetus may develop signs of high cardiac output failure, with subsequent typical findings of hydrops fetalis. Close-interval follow-up with serial ultrasonography for the signs of developing cardiac dysfunction and hydrops is indicated in a fetus with SCT if intervention is to be considered.[63] Because pelvic bones may interfere with clear visualization of the deep structures on ultrasonography, MRI is advantageous for better definition of the extent of a lesion, its relationship to the bladder and rectum, and calculating a tumor–body weight ratio that some institutions use for prognosis (Fig. 130.17).[64] Both single-shot T2- and T1-weighted sequences for meconium–rectal position and hemorrhage are helpful. Fetal MRI can supplant neonatal MRI for preoperative planning in some cases. Although much more rare, neuroblastoma in the low pelvis has been reported to mimic the appearance of SCT.[65]

Rhabdomyoma, rhabdomyosarcoma, fibrosarcoma, or myofibroma (myofibromatosis) are extraordinarily rare in the fetus. These are characteristically solid masses with some internal heterogeneity that grow on serial examination; they are typically found in the fetal neck or pelvis but may be in the extremities, retroperitoneum, or chest wall.[66–72] They may be confused with vascular tumors such as a kaposiform hemangioendothelioma, although the latter are typically more infiltrative. Lymphatic malformation may also be infiltrative and multicompartmental with both solid appearing (microcystic) and cystic (macrocystic) components. The differential diagnosis for solid tumors includes teratoma (which is more common, generally has some cysts, and might be distinguished by a fat component) and potentially neuroblastoma. Either of these tumors can contain calcifications.

***Treatment and Follow-up.*** Before viability, should a fetus develop cardiac failure and hydrops fetalis, in utero surgical resection of SCT has been offered in some centers as an alternative to inevitable demise. The procedure involves a hysterotomy with partial delivery of the fetus, tumor resection, and return of the fetus to the uterus with myometrial closure. A significant complication is preterm labor, and efforts are therefore being directed toward less invasive surgeries.[73,74] This is clearly a rare circumstance but has been successfully managed. After the age of viability, a fetus in distress could be delivered for further ex utero treatment options.

Treatment for SCT in the neonate is complete surgical excision of the tumor; the risk of malignancy is lowest with fetal or neonatal presentation and therapy.[75] Recurrence rates are negligible as long as the coccyx is also removed with the tumor.[76]

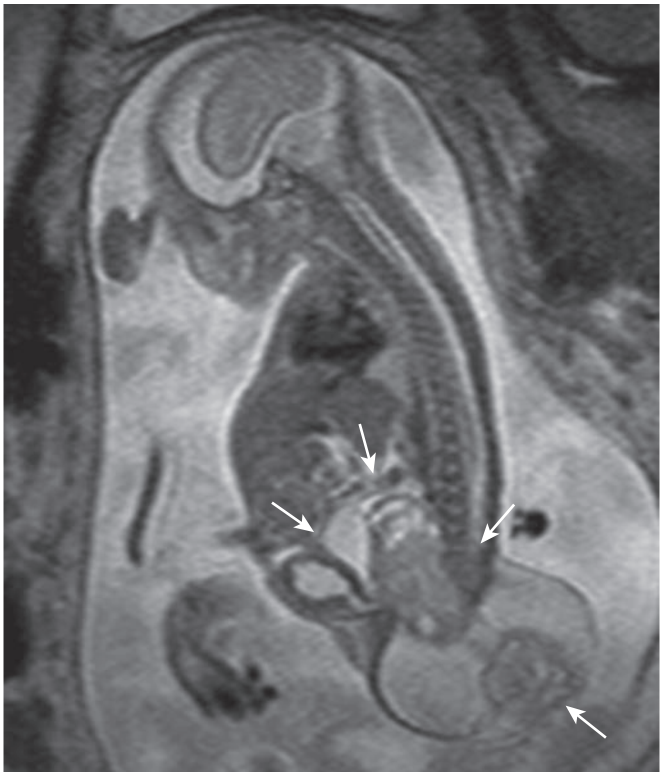

**Figure 130.17. Sacrococcygeal teratoma.** Mixed cystic-solid mass *(arrows)* in the fetal pelvis between the bladder and the spine with internal and external components.

## KEY POINTS

- Marked thoracic restriction portends lethality in cases of skeletal dysplasia.
- The majority of lethal skeletal dysplasias are one of three diagnoses: thanatophoric dysplasia, achondrogenesis, or osteogenesis imperfecta type II.
- Thorough evaluation of the fetus and its environment, including the umbilical cord, is indicated when a limb defect is detected.
- Fetal posture should be assessed for fixed or abnormal positions.
- Fetal musculoskeletal tumors are rare; SCT is the most common and can cause fetal cardiac high-output failure due to arterial shunting.

## SUGGESTED READINGS

Avni FE, Massez A, Cassart M. Tumours of the fetal body: a review. *Pediatr Radiol*. 2009;39:1147–1157.
Cassart M. Suspected fetal skeletal malformations or bone diseases: how to explore. *Pediatr Radiol*. 2010;40:1046–1051.
Dighe M, Fligner C, Cheng E, et al. Fetal skeletal dysplasia: an approach to diagnosis with illustrative cases. *Radiographics*. 2008;28:1061–1077.
Teele R. A guide to the recognition of skeletal disorders in the fetus. *Pediatr Radiol*. 2006;36(6):473–484.

## REFERENCES

Full references for this chapter can be found on www.expertconsult.com.

## REFERENCES

1. Ikegawa S. Genetic analysis of skeletal dysplasia: recent advances and perspectives in the post-genome-sequence era. *J Hum Genet*. 2006;51(7):581–586.
2. Alman BA. Skeletal dysplasias and the growth plate. *Clin Genet*. 2008;73(1):24–30.
3. Dan S, Yuan Y, Wang Y, et al. Non-invasive prenatal diagnosis of lethal skeletal dysplasia by targeted capture sequencing of maternal plasma. *PLoS ONE*. 2016;11(7).
4. Krakow D, Lachman R, Rimoin D. Guidelines for the prenatal diagnosis of fetal skeletal dysplasias. *Genet Med*. 2009;11(2):127–133.
5. Bonafe L, Cormier-Daire V, Hall C, et al. Nosology and classification of genetic skeletal disorders: 2015 revision. *Am J Med Genet A*. 2015;167A(12):2869–2892.
6. Milks KS, Hill LM, Hosseinzadeh K. Evaluating skeletal dysplasias on prenatal ultrasound: an emphasis on predicting lethality. *Pediatr Radiol*. 2016.
7. Nelson DB, Dashe JS, McIntire DD, et al. Fetal skeletal dysplasias: sonographic indices associated with adverse outcomes. *J Ultrasound Med*. 2014;33(6):1085–1090.
8. Kurtz AB, Needleman L, Wapner RJ, et al. Usefulness of a short femur in the in utero detection of skeletal dysplasias. *Radiology*. 1990;177(1):197–200.
9. Parilla BV, Leeth EA, Kambich MP, et al. Antenatal detection of skeletal dysplasias. *J Ultrasound Med*. 2003;22(3):255–258, quiz 259–261.
10. Ishikawa S, Kamata S, Usui N, et al. Ultrasonographic prediction of clinical pulmonary hypoplasia: measurement of the chest/trunk-length ratio in fetuses. *Pediatr Surg Int*. 2003;19(3):172–175.
11. Nimrod C, Nicholson S, Davies D, et al. Pulmonary hypoplasia testing in clinical obstetrics. *Am J Obstet Gynecol*. 1988;158:277–280.
12. Ohlsson A, Fong K, Rose T, et al. Prenatal ultrasonic prediction of autopsy-proven pulmonary hypoplasia. *Am J Perinatol*. 1992;9(5–6):334–337.
13. Barros CA, Rezende Gde C, Araujo Júnior E, et al. Prediction of lethal pulmonary hypoplasia by means fetal lung volume in skeletal dysplasias: a three-dimensional ultrasound assessment. *J Matern Fetal Neonatal Med*. 2016;29(11):1725–1730.
14. Orioli IM, Castilla EE, Barbosa-Neto JG. The birth prevalence rates for the skeletal dysplasias. *J Med Genet*. 1986;23(4):328–332.
15. Camera G, Mastroiacovo P. Birth prevalence of skeletal dysplasias in the Italian Multicentric Monitoring System for Birth Defects. *Prog Clin Biol Res*. 1982;104:441–449.
16. Mortier GR, Rimoin DL, Lachman RS. The scapula as a window to the diagnosis of skeletal dysplasias. *Pediatr Radiol*. 1997;27(5):447–451.
17. Rouse GA, Filly RA, Toomey F, et al. Short-limb skeletal dysplasias: evaluation of the fetal spine with sonography and radiography. *Radiology*. 1990;174(1):177–180.
18. Krakow D, Williams IIIJ, Poehl M, et al. Use of three-dimensional ultrasound in the diagnosis of prenatal onset skeletal dysplasias. *Ultrasound Obstet Gynecol*. 2003;21:467–472.
19. Goncalves LF, Berger JA, Macknis JK, et al. Grebe dysplasia—prenatal diagnosis based on rendered 3-D ultrasound images of fetal limbs. *Pediatr Radiol*. 2016.
20. Tanigaki S, Miyakoshi K, Tanaka M, et al. Pulmonary hypoplasia: prediction with use of ratio of MR imaging-measured fetal lung volume to US-estimated fetal body weight. *Radiology*. 2004;232(3):767–772.
21. Weaver KN, Johnson J, Kline-Fath B, et al. Predictive value of fetal lung volume in prenatally diagnosed skeletal dysplasia. *Prenat Diagn*. 2014;34(13):1326–1331.
22. Yazici Z, Kline-Fath BM, Laor T, et al. Fetal MR imaging of Kniest dysplasia. *Pediatr Radiol*. 2010;40(3):348–352.
23. Pugash D, Lehman AM, Langlois S. Prenatal ultrasound and MRI findings of temporal and occipital lobe dysplasia in a twin with achondroplasia. *Ultrasound Obstet Gynecol*. 2014;44(3):365–368.
24. Ulla M, Aiello H, Cobos MP, et al. Prenatal diagnosis of skeletal dysplasias: contribution of three-dimensional computed tomography. *Fetal Diagn Ther*. 2011;29(3):238–247.
25. Cassart M, Massez A, Cos T, et al. Contribution of three-dimensional computed tomography in the assessment of fetal skeletal dysplasia. *Ultrasound Obstet Gynecol*. 2007;29(5):537–543.
26. Macé G, Sonigo P, Cormier-Daire V, et al. Three-dimensional helical computed tomography in prenatal diagnosis of fetal skeletal dysplasia. *Ultrasound Obstet Gynecol*. 2013;42(2):161–168.
27. Adler-Levy Y, Yagel S, Nadjari M, et al. Use of low dose computed tomography with 3D reconstructions for the prenatal evaluation of suspected skeletal dysplasia. *Isr Med Assoc J*. 2015;17(1):42–46.
28. Spranger JW, Brill PW, Poznanski A. *Bone Dysplasias: An Atlas of Genetic Disorders of Skeletal Development*. 2nd ed. Oxford, UK: Oxford University Press; 2002.
29. Victoria T, Epelman M, Coleman BG, et al. Low-dose fetal CT in the prenatal evaluation of skeletal dysplasias and other severe skeletal abnormalities. *AJR Am J Roentgenol*. 2013;200(5):989–1000.
30. Calder AD, Offiah AC. Foetal radiography for suspected skeletal dysplasia: technique, normal appearances, diagnostic approach. *Pediatr Radiol*. 2015;45(4):536–548.
31. Lockwood C, Ghidini A, Romero R, et al. Amniotic band syndrome: reevaluation of its pathogenesis. *Am J Obstet Gynecol*. 1989;160(5 Pt 1):1030–1033.
32. Gold NB, Westgate MN, Holmes LB. Anatomic and etiological classification of congenital limb deficiencies. *Am J Med Genet A*. 2011;155A(6):1225–1235.
33. McGuirk CK, Westgate MN, Holmes LB. Limb deficiencies in newborn infants. *Pediatrics*. 2001;108(4):E64.
34. Christianson AL, Nelson MM. Four cases of trisomy 18 syndrome with limb reduction malformations. *J Med Genet*. 1984;21(4):293–297.
35. Ermito S, Dinatale A, Carrara S, et al. Prenatal diagnosis of limb abnormalities: role of fetal ultrasonography. *J Prenat Med*. 2009;3(2):18–22.
36. Bornstein E, Bacino CA, Maliszewski K, et al. Isolated fetal macrodactyly: phenotypic and genetic disparities in mosaic overgrowth syndrome. *J Ultrasound Med*. 2014;33(7):1305–1307.
37. Vora N, Bianchi DW. Genetic considerations in the prenatal diagnosis of overgrowth syndromes. *Prenat Diagn*. 2009;29(10):923–929.
38. Zollinger PE, Wessels MW, Wladimiroff JW, et al. Prenatal ultrasonographic diagnosis of posteromedial bowing of the leg: two case reports. *Ultrasound Obstet Gynecol*. 2000;15(2):150–153.
39. De Maio F, Corsi A, Roggini M, et al. Congenital unilateral posteromedial bowing of the tibia and fibula: insights regarding pathogenesis from prenatal pathology. A case report. *J Bone Joint Surg Am*. 2005;87(7):1601–1605.
40. Duckworth HL, Leather AT, Jessop F. Intrauterine death and growth restriction at term, secondary to an umbilical cord amniotic band. *J Obstet Gynaecol*. 2011;31(6):547.
41. Stoll C, Rosano A, Botto LD, et al. On the symmetry of limb deficiencies among children with multiple congenital anomalies. *Ann Genet*. 2001;44(1):19–24.
42. Emrick LT, Murphy L, Shamshirsaz AA, et al. Prenatal diagnosis of CLOVES syndrome confirmed by detection of a mosaic PIK3CA mutation in cultured amniocytes. *Am J Med Genet A*. 2014;164A(10):2633–2637.
43. Rypens F, Dubois J, Garel L, et al. Obstetric US: watch the fetal hands. *Radiographics*. 2006;26(3):811–829.
44. Keswani SG, Johnson MP, Adzick NS, et al. In utero limb salvage: fetoscopic release of amniotic bands for threatened limb amputation. *J Pediatr Surg*. 2003;38(6):848–851.
45. Hunter AG, Seaver LH, Stevenson RE. Limb-body wall defect. Is there a defensible hypothesis and can it explain all the associated anomalies? *Am J Med Genet A*. 2011;155A(9):2045–2059.
46. Emans PJ, Kootstra G, Marcelis CL, et al. The Currarino triad: the variable expression. *J Pediatr Surg*. 2005;40(8):1238–1242.
47. Chan BW, Chan KS, Koide T, et al. Maternal diabetes increases the risk of caudal regression caused by retinoic acid. *Diabetes*. 2002;51(9):2811–2816.
48. Brugger PC. *Methods of Fetal MRI*. Berlin, Germany: Springer-Verlag; 2011:65–80.
49. Barash PG, et al. *Clinical Anesthesia*. 4th ed. Hagerstown, MD: Lippincott, Williams & Wilkins; 1997:32–34, 493–494.
50. Dufour P, Berard J, Vinatier D, et al. Myotonic dystrophy and pregnancy. A report of two cases and a review of the literature. *Eur J Obstet Gynecol Reprod Biol*. 1997;72(2):159–164.
51. Mori K, Mizuno J, Nagaoka T, et al. Combined spinal-epidural anesthesia for cesarean section in a parturient with myotonic dystrophy. *Masui*. 2010;59(8):1000–1003.
52. Brueton LA, Huson SM, Cox PM, et al. Asymptomatic maternal myasthenia as a cause of the Pena-Shokeir phenotype. *Am J Med Genet*. 2000;92(1):1–6.
53. Lammens M, Moerman P, Fryns JP, et al. Fetal akinesia sequence caused by nemaline myopathy. *Neuropediatrics*. 1997;28(2):116–119.

54. Hall JG. Pena-Shokeir phenotype (fetal akinesia deformation sequence) revisited. *Birth Defects Res A Clin Mol Teratol*. 2009;85(8):677–694.
55. Ozonoff MB. *Pediatric Orthopedic Radiology*. Philadelphia, PA: Saunders; 1992.
56. Ogata K, Schoenecker PL, Sheridan J. Congenital vertical talus and its familial occurrence: an analysis of 36 patients. *Clin Orthop Relat Res*. 1979;139:128–132.
57. Alfirevic Z, Neilson JP. Biophysical profile for fetal assessment in high risk pregnancies. *Cochrane Database Syst Rev*. 2000;(2):CD000038.
58. de Vries JI, Fong BF. Changes in fetal motility as a result of congenital disorders: an overview. *Ultrasound Obstet Gynecol*. 2007;29(5):590–599.
59. Nemec SF, Brugger PC, Nemec U, et al. The skeleton and musculature. In: Prayer D, ed. *Fetal MRI*. Berlin, Germany: Springer-Verlag; 2011.
60. Steinman S, Richards BS, Faulks S, et al. A comparison of two nonoperative methods of idiopathic clubfoot correction: the Ponseti method and the French functional (physiotherapy) method. Surgical technique. *J Bone Joint Surg Am*. 2009;91(suppl 2):299–312.
61. Avni FE, Massez A, Cassart M. Tumours of the fetal body: a review. *Pediatr Radiol*. 2009;39(11):1147–1157.
62. Altman RP, Randolph JG, Lilly JR. Sacrococcygeal teratoma: American Academy of Pediatrics Surgical Section Survey—1973. *J Pediatr Surg*. 1974;9(3):389–398.
63. Cass DL, Olutoye OO, Ayres N, et al. Defining hydrops and indications for open fetal surgery for fetuses with lung masses and vascular tumors. *J Ped Surg*. 2012;47(1):40–45.
64. Rodriguez MA, Cass DL, Lazar DA, et al. Tumor volume to fetal weight ratio as an early prognostic classification for fetal sacrococcygeal teratoma. *J Pediatr Surg*. 2011;46(6):1182–1185.
65. Tanaka K, Kanai M, Yosizawa J, et al. A case of neonatal neuroblastoma mimicking Altman type III sacrococcygeal teratoma. *J Pediatr Surg*. 2005;40(3):578–580.
66. Yang HJ, Lee KA, Park CW, et al. Prenatal US and MRI findings of pelvic embryonal rhabdomyosarcoma. *Ultrasound Obstet Gynecol*. 2008;32(3):442.
67. Esfahani SA, Montaser-Kouhsari L, Saeedi P, et al. An antenatally diagnosed rhabdomyosarcoma of the bladder treated without extensive surgery. *Nat Rev Urol*. 2009;6(8):449–453.
68. Gupta SS, Singh O, Sharma SS, et al. Congenital fibrosarcoma of the chest wall: report of a case. *J Cutan Aesthet Surg*. 2010;3(3): 177–180.
69. Valdez TA, Desai U, Volk MS. Recurrent fetal rhabdomyoma of the head and neck. *Int J Pediatr Otorhinolaryngol*. 2006;70(6):1115–1118.
70. Huang SY, Wang CW, Wang CJ, et al. Combined prenatal ultrasound and magnetic resonance imaging in an extensive congenital fibrosarcoma: a case report and review of the literature. *Fetal Diagn Ther*. 2005;20(4):266–271.
71. Govender L, Moodley J. Soft tissue tumour of the fetal thigh. *S Afr Med J*. 2006;96(3):187–188.
72. Wataganara T, Ngerncham S, Kitsommart R, et al. Fetal neck myofibroma. *J Med Assoc Thai*. 2007;90(2):376–380.
73. Hirose S, Farmer DL. Fetal surgery for sacrococcygeal teratoma. *Clin Perinatol*. 2003;30(3):493–506.
74. Peiró JL, Sbragia L, Scorletti F, et al. Management of fetal teratomas. *Pediatr Surg Int*. 2016;32(7):635–647.
75. Holterman AX, Filiatrault D, Lallier M, et al. The natural history of sacrococcygeal teratomas diagnosed through routine obstetric sonogram: a single institution experience. *J Pediatr Surg*. 1998;33(6): 899–903.
76. Tapper D, Sawin R. Teratomas and other germ cell tumours. In: O'Neil JA Jr, Rowe MI, Grosfeld JL, et al, eds. *Pediatric Surgery*. 5th ed. St. Louis, MO: Mosby Yearbook Inc; 1998:447–459.

# 131

# Congenital Anomalies of Bone

J. Herman Kan and Tal Laor

Regardless of origin, abnormal limb development tends to fall into patterns that can be recognized clinically and radiographically (Fig. 131.1). Most classification systems of congenital malformations are based on osseous structures, but it is well recognized that anomalous conditions of surrounding soft tissues are certain to be present. Congenital malformations of the extremity can be generally classified as dysplastic or absent (amelia).

Congenital deficiencies are more common than acquired amputations in children. Frantz and O'Rahilly developed a system of classification that is still commonly used to evaluate congenital anomalies of the extremities.[1] Each malformation is defined by the part that is deficient. For example, the fibula is deficient in fibular hemimelia. The abnormality is considered terminal if the deformity extends to the distal aspect of the extremity; it is intercalary if the limb distal to the deformity is normal. For example, in fibular hemimelia, if the foot is abnormal, the deficiency is terminal, and if the foot is normal, it is intercalary. Likewise, a defect may be classified as longitudinal (paraxial) or transverse. The malformation is paraxial if only the fibular side is affected. If both the tibia and the fibula are affected, the deformity is considered transverse.

The cause of reduction malformations is known in only a small number of cases. A few abnormalities are heritable, but most are sporadic. Environmental factors are implicated infrequently. Medications, such as thalidomide, induced malformations that were reduction deformities, ranging from severe amelias to mild muscular hypoplasia.[2] Most malformations were on the radial or tibial side, and the upper limbs were affected more often than were the lower extremities. Infrequently, excess deformities such as polydactyly were observed.

## EXTREMITY DEFICIENCIES

### Proximal Femoral Focal Deficiency

***Etiology.*** Proximal femoral focal deficiency (PFFD) refers to abnormalities that range from mild shortening and hypoplasia of the femur to severe deficiency of the bone and dysplasia of the acetabulum. The defect is thought to be a result of altered proliferation and maturation of the chondrocytes of the proximal femoral physis in utero, which in turn results in underdevelopment of the ipsilateral acetabulum. A child with PFFD usually presents in infancy with a short extremity and an unstable hip.[3] A well-formed acetabulum implies the presence of a femoral head, which might be cartilaginous and therefore is not apparent radiographically early in life. Most cases are sporadic; however, the combination of bilateral femoral deficiencies and abnormal facies (the femoral hypoplasia–unusual facies syndrome) is thought to be an autosomal-dominant disorder.

PFFD should be distinguished from developmental dysplasia of the hip, infantile coxa vara, and congenitally short femur. In the setting of developmental dysplasia of the hip, proximal femoral neck and head hypoplasia may be present. The subtrochanteric region of the femur is normal and distal congenital anomalies are absent, and the deformities at the level of the acetabulum are more severe than the deformities at the level of the femoral head and neck. Children with infantile coxa vara have varus configuration of the femoral head and neck, with a normal subtrochanteric region and distal bones, and the femur is normal in length. Unlike PFFD, infantile coxa vara is discovered after weight bearing occurs.[4] A congenitally short femur may be unilateral or bilateral and often is associated with reduction defects elsewhere in the same limb. Most cases are sporadic, but several external factors have been implicated in more complex deformities. Known causes include drugs (such as thalidomide), trauma, irradiation, infection, and focal ischemia.[5] Unlike patients with PFFD, patients with a congenitally short femur have a stable hip.

***Imaging.*** The most commonly used classification for PFFD was proposed by Aitken (Fig. 131.2).[6] The least severe type is class A, which refers to an adequate or only mildly dysplastic proximal femur and acetabulum. The femoral head is present but separated from the shortened distal femoral segment. With age, a fibrous connection between the head and the distal femoral segment ossifies—usually, not completely. A subtrochanteric varus deformity invariably is present. Class C deformities have a residual acetabulum present (Fig. 131.3). In the most severe form, class D, most of the femur and the ipsilateral acetabulum are absent. PFFD classification may change over time with osseous maturation.[7]

PFFD is associated with other ipsilateral deformities, including fibular hemimelia (in more than 50% of affected children), shortening of the tibia, equinovalgus deformity of the foot (more often than equinovarus deformity), and deficiency of the lateral rays of the foot. PFFD is bilateral in 15% of affected children.[8]

Sonography can be used to delineate radiographically inapparent structures at an early age. If a cartilaginous femoral head and its connection to the femoral shaft can be shown, the stability of the hip joint is likely greater than is implied from radiographs. Sonography with dynamic stress maneuvers of the affected hip is helpful to determine the presence of coexisting ligamentous laxity and hip subluxation. Similar to sonography, magnetic resonance imaging (MRI) is useful for defining the anatomy of the hip joint and associated deformities of the limb,[9] allowing for appropriate early classification of the deformity. Although the acetabulum might appear developed, even the least severe forms of PFFD are associated with acetabular deficiency. In contrast to the predominantly anterior deficiency of developmental acetabular dysplasia, the acetabulum in PFFD usually has an insufficient posterior wall. Most of the muscles about the affected hip are hypoplastic when compared with a contralateral normal side, with the exception of the sartorius muscle, which often is hypertrophied. This situation results in the characteristic flexion deformity of the hip and knee. MRI also defines the anatomy of soft tissues that can guide surgical exposure and preparation of the limb stump for fitting of a prosthesis.

***Treatment and Follow-up.*** Therapy for children with PFFD is based on the severity of the deficiency and projection of growth and final limb length discrepancy at maturity. Objectives for treatment are to maximize the length of the extremity, to promote stability of the hip, knee, and ankle, and to optimize anatomic alignment. Mild deformities may not require surgery. Stabilization of the upper femoral defect is controversial and usually is indicated if a deformity is progressive. Children with severe deformities

## Abstract:

Objective: To describe common and uncommon congenital deformities of the bone and classification systems when applicable.

Methods: Review of the relevant current literature, and include relevant illustrations and examples.

Results: Congenital deformities of bone are rare. By understanding the underlying embryologic and pathophysiologic basis of these entities and their pertinent classification systems, accurate and succinct description and delineation of these deformities can be achieved.

## Keywords:

radiography
embryology
congenital deformities

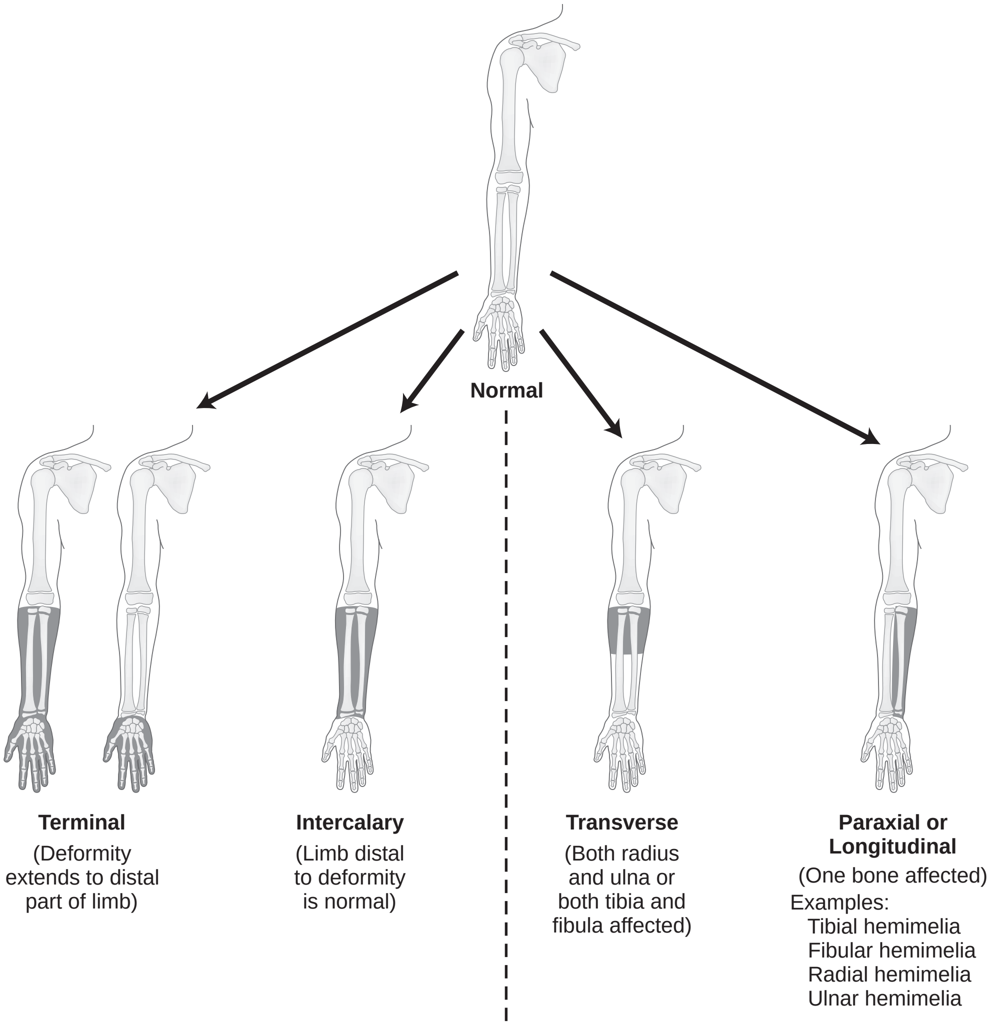

**Figure 131.1. Skeletal deformities of the limbs.** The shaded, blackened areas indicate deficient parts.

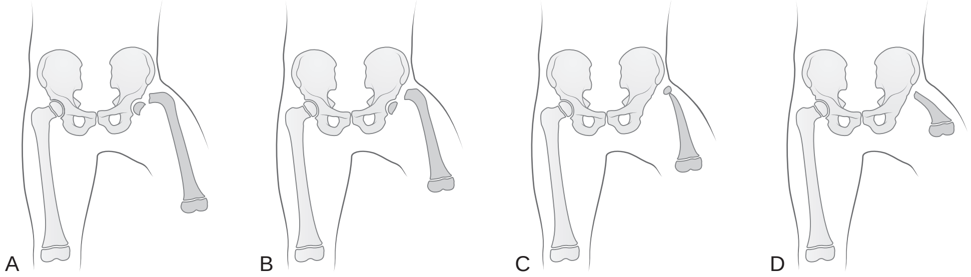

**Figure 131.2. Aitken classification of proximal femoral focal deficiency.** (A) Class A, mildly dysplastic proximal femur with coxa vara and a normal acetabulum. (B) Class B, no osseous connection between the femoral head and shaft, with mild to moderate acetabular dysplasia. (C) Class C, absent or small femoral head with tapered proximal femoral configuration with severely dysplastic acetabulum. (D) Class D, absent proximal femur and absent acetabulum.

benefit from amputation of the foot and fusion of the knee. Van Ness rotationplasty of the tibia, in which the foot is rotated 180 degrees (so that the toes face posteriorly and the ankle now serves as a knee joint), allows the ankle and foot to control a distal prosthesis.[10] Intact sensory feedback from the foot provides proprioceptive control of the knee. Thus it is imperative to assess the morphology of the proximal femur and acetabulum, the cartilaginous epiphyses of the knee, and the supporting soft tissue structures. For example, instability of the knee can result from absence of the anterior cruciate ligament. In the rare case of bilateral PFFD, amputation is contraindicated and therapy is based on extension prostheses that enhance the child's height.

## Fibular Hemimelia

***Etiology.*** Fibular hemimelia is the most common hemimelia and the most common congenital anomaly of the fibula. It also has been referred to as *congenital short tibia with absent fibula syndrome*. Unilateral absence is more frequent than bilateral deformity. A band of strong connective tissue may replace all or most of the

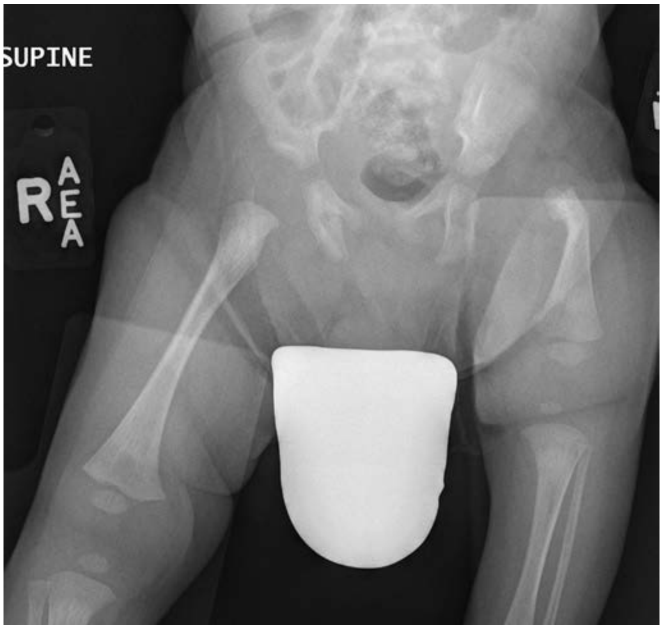

**Figure 131.3. Aitken type C proximal femoral focal deficiency of the left hip in a 4-week-old boy.** The femur is substantially short and the left acetabulum is severely dysplastic. Mild developmental dysplasia of the right acetabulum is present.

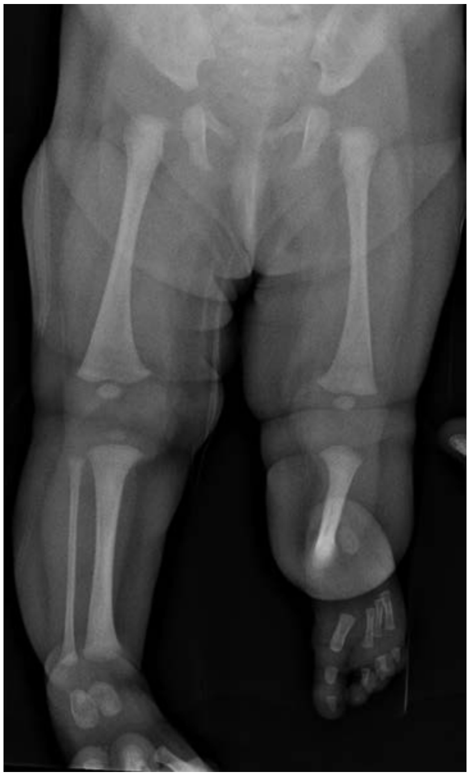

**Figure 131.4. Left fibular hemimelia in a 2-month-old girl.** The left fibula is absent, and the tibia is shortened. The left femur is short, and there are only four digits in the left foot. The left talus is not seen.

fibula.[11] Fibular hemimelia is associated with a short, bowed tibia; absence of lateral rays of the foot; tarsal abnormalities (particularly coalitions); ball and socket ankle deformity; and femoral shortening or deficiency in 15% of patients. Clubfoot or equinovalgus may be seen in up to 39% of patients with fibular hemimelia.[12] Other associations include small, subluxated, or dislocated patellae; hypoplastic femoral condyles; and ligamentous deficiencies of the knee.[11]

***Imaging.*** Fibular hemimelia ranges from mild deficiency of the proximal end of the bone to complete absence accompanied by multiple malformations of neighboring structures (Fig. 131.4). Standing anteroposterior (AP) lower extremity radiographs inclusive of the unaffected side are helpful for evaluation of the degree of fibular deficiency, alignment abnormalities, and presence of additional lower extremity deficiencies. MRI can document associated abnormalities, particularly if surgery is contemplated, including ligamentous deficiencies of the knee.

***Treatment and Follow-up.*** The talipes equinovalgus deformity of the foot and severe shortening of the limb associated with fibular hemimelia result in poor function of the limb. Children with extensive abnormalities involving the fibula, ipsilateral tibia, femur, and foot benefit the most from early amputation of the foot and often the more proximal structures.[13] If the deformity is less severe, lengthening of the affected side, realignment of the tibiotalar articulation, and epiphysiodesis of the contralateral limb often are undertaken. Attempts at lengthening a severely dysplastic limb often are unsatisfactory.

## Tibial Hemimelia

***Etiology.*** Most cases of tibial hemimelia are sporadic, although reported forms (particularly bilateral deformities) display an autosomal-dominant inheritance pattern. There are various classification schemes for tibial hemimelia, all of which describe the various degrees of dysplasia.[14]

***Imaging.*** Radiography of tibial hemimelia (Fig. 131.5) ranges from absence of a portion of the distal tibia to complete absence with multiple malformations of neighboring structures. Complete

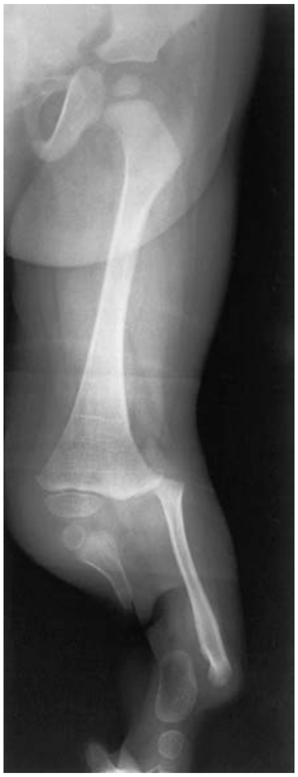

**Figure 131.5. Tibial hemimelia in a 2-year-old girl.** A dysplastic proximal tibial remnant is evident. The fibula is short and subluxed laterally, and multiple tarsal bones are absent.

absence of the tibia may mimic fibular hemimelia, particularly if there is relative overgrowth of the distal portion of the fibula. A differentiating feature between these two entities is that the fibula in the setting of tibial hemimelia always will be laterally located with respect to the knee or ankle joint. Conversely, the tibia in the setting of fibular hemimelia usually will be concentrically located with respect to the knee or ankle joint. With weight bearing, the fibula will usually override the distal femur and talus.[7]

MRI can document associated abnormalities, including associated muscular and ligamentous deficiencies, which is important if surgery is contemplated. MRI may identify a cartilaginous tibial remnant that may not be apparent on radiography and which is necessary for accurate classification.[14]

***Treatment and Follow-up.*** Treatment of tibial hemimelia varies with the severity of the deformity. A knee disarticulation is recommended for complete tibial absence. Brown pioneered centralization of the fibula with a Syme amputation of the foot in children with complete tibial hemimelia.[15] This approach produces adequate results in the rare cases in which the quadriceps muscles are well developed. When the quadriceps mechanism is abnormal, the patella often is absent. MRI can be used to assess deficiencies preoperatively, allowing the clinician to discern who will function better with primary knee disarticulation (most patients) rather than knee reconstruction.

## Radial Longitudinal Deficiency

***Etiology.*** Conditions associated with radial longitudinal deficiency (also referred to as *radial dysplasia* or *radial clubhand*) are listed in Box 131.1.[16] Usually the entire limb is involved to some degree, which often results in joint dysfunction of the shoulder, elbow, wrist, carpus, and small joints of the hand. Muscular deficiencies are proportionate to the degree of skeletal abnormality. Neurovascular abnormalities include an absent radial artery and superficial radial nerve.

**BOX 131.1** Conditions Associated With Radial Longitudinal Deficiency (Dysplasia)

**SYNDROMES ASSOCIATED WITH CONGENITAL HEART DISEASE**

- Holt-Oram syndrome

**SYNDROMES ASSOCIATED WITH BLOOD DYSCRASIAS**

- Fanconi anemia (pancytopenia–dysmelia syndrome)
- Thrombocytopenia—absent radius syndrome

**SYNDROMES ASSOCIATED WITH INTELLECTUAL DISABILITY**

- Brachmann-de Lange (Cornelia de Lange) syndrome
- Seckel syndrome

**SYNDROMES ASSOCIATED WITH CHROMOSOMAL ABNORMALITIES**

- Trisomy 13
- Trisomy 18

**SYNDROMES ASSOCIATED WITH TERATOGENS**

- Thalidomide embryopathy
- Varicella embryopathy

**OTHER**

- VACTERL association

*VACTERL,* Vertebral, anal, cardiac, tracheal, esophageal, renal, limb.
*Modified from Goldberg MJ, Bartoshevsky LE. Congenital hand anomaly: etiology and associated malformations.* Hand Clin. *1985;1:405–415.*

Whether radial deficiency is isolated or is associated with a syndrome, the primary malformation is likely the result of a vascular abnormality occurring before embryonic differentiation of mesenchyme into muscle and bone.[17] Most cases are sporadic, but some autosomal-dominant and autosomal-recessive inheritance patterns are reported. Other cases are likely the result of various environmental insults from viruses, chemicals, radiation, and drugs during limb bud development.

***Imaging.*** Congenital radial longitudinal deficiency ranges from hypoplasia of the thumb to various degrees of radial hypoplasia. Complete radial absence is the most common longitudinal deficiency. This deformity usually is accompanied by radial and volar deviation of the hand, which results in part from unopposed pull by the flexor carpi radialis and brachioradialis muscles.

In most cases of radial aplasia or complete radial longitudinal deficiency, the forearm is bowed with convexity to the radial side and the distal ulna is prominent (Fig. 131.6). The forearm is short (usually approximately two-thirds the length of the normal contralateral side) and remains proportionately so throughout growth. Often, only the capitate, hamate, triquetral bones, and the metacarpals and phalanges of the four ulnar rays are present and normal. The trapezium, scaphoid, and first ray often are deformed or absent. If a remnant of the radius is present proximally, it usually is fused to the ulna, which is curved, shortened, and thickened. Bilateral deficiency occurs in approximately 50% of affected children.[16] The degree of deformity of the hand is related to the severity of deficiency of the forearm.

***Treatment and Follow-up.*** Treatment of a radial longitudinal deficiency begins with serial casting and splinting intended to improve radial deviation by stretching the soft tissues. This is often followed by surgical centralization of the hand over the ulna to improve function and appearance.[18] Thumb reconstruction and pollicization of the index finger often are indicated.

## Ulnar Longitudinal Deficiency

***Etiology.*** Deficiency that occurs along the ulnar or postaxial border of the upper extremity is known as *ulnar longitudinal deficiency* (also referred to as *ulnar dysplasia* or *ulnar clubhand*). It is a relatively uncommon disorder that occurs much less frequently than radial

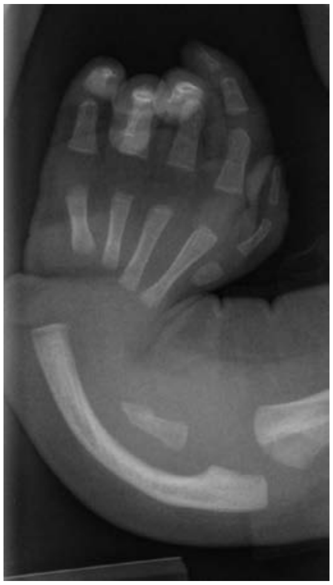

**Figure 131.6. Radial longitudinal deficiency in a 1-month-old boy.** There is a rudimentary proximal radius associated with a short and bowed ulna. The thumb is hypoplastic.

longitudinal deficiency. Approximately 48% of cases have anomalies of the contralateral limb.[19] Most cases are sporadic, but associations with many other syndromes have been reported, most commonly Brachmann-de Lange syndrome.[20]

***Imaging.*** Coexisting abnormalities almost always are present in the carpal, metacarpal, and phalangeal rays (e-Fig. 131.7). The pisiform is always absent, and the hamate frequently is not detected. Syndactyly, carpal fusion, and radiohumeral fusion are frequent. The forearm is shortened and bowed, with a concavity to the ulnar side. The hand is deviated in an ulnar direction, and elbow abnormalities are common. Hypoplasia of the shoulder girdle and the upper arm can coexist with ulnar deficiencies. Anomalies of the contralateral upper limb and the lower limbs (such as PFFD) have been reported.

***Treatment and Follow-up.*** Treatment for ulnar deficiency includes early serial casting to correct ulnar deviation of the hand. Surgical treatment is reserved for cases with significant limitation of function.[21] Forearm instability and associated hand deformities must be addressed.

## GENERALIZED ANOMALIES

### Congenital Constriction Bands

***Etiology.*** Constriction bands are thought to result from intrauterine rupture of the amnion and subsequent mechanical constriction of fetal limbs.[22] Various body parts become entangled in the amnion as it separates from the chorion. In some instances, adjacent structures are pulled together by the bands and ultimately become fused, producing a soft tissue syndactyly. Bony syndactyly is very rare. The earlier the amnion ruptures, the more severe are the malformations. Limb abnormalities range from slight soft tissue grooves to transverse intrauterine amputations. Acrosyndactyly, craniofacial and visceral anomalies, and fetal death are part of the spectrum of congenital constriction band syndrome. Sporadic congenital constriction band syndrome is estimated to occur at an incidence of 1 : 1,200 to 1 : 15,000 births. An alternative explanation is the intrinsic theory, which suggests that an inherent defect leads to bands during limb embryogenesis.[22]

***Imaging.*** Radiography may underestimate the degree of soft tissue compromise, and associated anomalous vascular anatomy may not be recognized. Typical conventional radiographic findings include a tethered appearance of fingers with a characteristic tight distal waist with soft tissue syndactyly (Fig. 131.8). MRI can be used to evaluate the depth of the constriction band, the degree of resultant lymphedema, and the integrity of the involved musculature.

***Treatment and Follow-up.*** Surgical treatment usually is cosmetic, although it may be used to relieve massive edema distal to a constriction band or improve neurovascular function. Intervention for acrosyndactyly may result in partial correction of the deformity and improved longitudinal growth.

### Arthrogryposis

***Etiology.*** Arthrogryposis multiplex congenita is a descriptive term used loosely to refer to conditions that result in congenital contractures involving two or more joints, such as those that limit intrauterine movement.[23] The earlier in gestation that movement is limited and the longer the restriction lasts, the more severe will be the contractures at birth. Normal in utero motion is necessary for normal development of joints.

Arthrogryposis may result from abnormal muscles (such as myopathies), abnormal nerve function or innervation, abnormal connective tissues, or mechanical limitation of movement (such as oligohydramnios or multiple fetuses). Other possible causes include genetic defects, mutagenic agents, mitotic abnormalities, and toxic chemicals or drugs (Box 131.2).

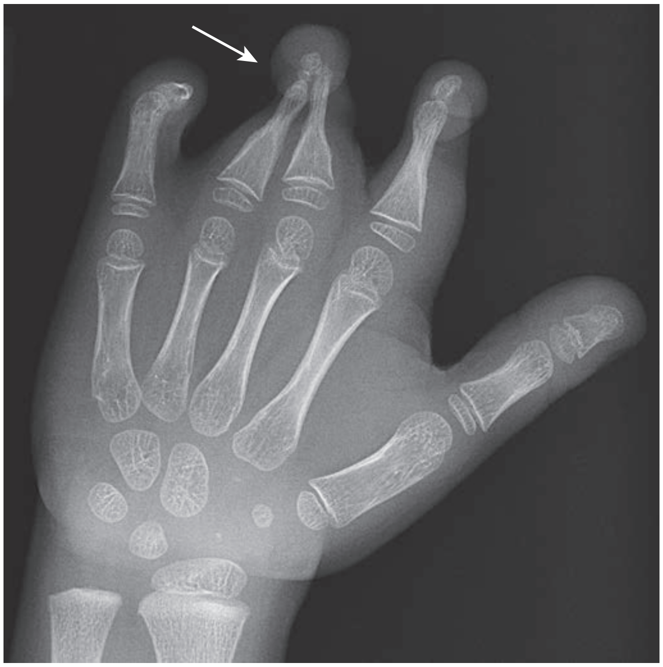

**Figure 131.8. Constriction bands in a 3-year-old girl.** Radiograph of the hand shows a “tight waist” appearance *(arrow)* and multiple distal digital amputations.

**BOX 131.2** Causes of Arthrogryposis: Causes of Limited Fetal Joint Mobility

**NEUROLOGIC**

- Disorders of cerebrum
- Anterior horn cell deficiency
- Abnormalities of nerve function or structure (central or peripheral)

**MUSCULAR**

- Abnormal formation or function
- Congenital muscular dystrophy
- Mitochondrial disorders

**CONNECTIVE TISSUE OR SKELETAL**

- Primary disorders

**VASCULAR COMPROMISE**

- Severe bleeding
- Monozygotic twins
- Amniotic bands

**MECHANICAL COMPRESSION**

- Fetal crowding from multiple births
- Oligohydramnios
- Uterine fibroids/other tumors
- Amniotic bands
- Trauma

**MATERNAL**

- Diabetes mellitus
- Hyperthermia
- Infection
- Drug use and abuse

*Modified from Jones K.* Smith’s Recognizable Patterns of Human Malformation. *5th ed. Philadelphia: WB Saunders; 1997.*

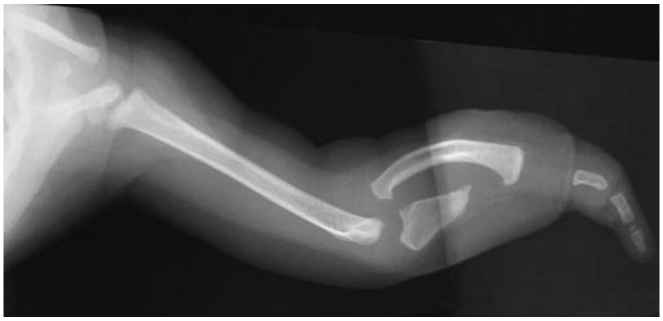

**e-Figure 131.7. Ulnar deficiency.** Partial formation of the proximal ulna is present, with aplasia of the distal portion. The radius is bowed, and only a single digit of the hand is present. The humerus is normal.

***Imaging.*** Contractures that are present at birth often are symmetric, can involve upper and lower extremities, and most commonly affect the distal parts of limbs. Long bone bowing deformities, joint subluxation or dislocation, and clubfoot alignment frequently coexist. Rigid joints and hypotonia contribute to frequent perinatal fractures. Soft tissue dimples may be seen over the affected joints, and muscle mass is decreased in affected limbs (e-Fig. 131.9). Affected muscles are partially or completely replaced by fatty or fibrous tissue. In many children, scoliosis develops. MRI can assess joint integrity when surgery to maximize joint function is planned.

***Treatment and Follow-up.*** The long-term prognosis for most children with arthrogryposis is good. However, children with associated central nervous system abnormalities usually have a limited life span. A neuromuscular workup is recommended for all children with arthrogryposis. Early therapy includes manipulation and possibly surgery to increase range of motion.[24]

## FUSION DEFORMITIES

### Tarsal Coalition

***Etiology.*** Tarsal coalition is a congenital failure of segmentation of the primitive mesenchyme that results in the union of two or more tarsal bones. A preadolescent or adolescent child with pain in the midfoot and hindfoot that is associated with lack of motion in the subtalar region should be suspected of having a tarsal coalition. Prevalence in the US population is approximately 1% or less. At least 50% of patients with coalitions have bilateral findings.[25] An autosomal-dominant inheritance pattern with a high level of penetrance is reported, although the coalition need not involve the same joint. Although it typically presents during the second decade of life, tarsal coalition may not manifest until adulthood.

Tarsal coalition is defined on the basis of anatomic location and completeness of ossification. A complete ossific bar forms a synostosis, a cartilaginous bar forms a synchondrosis, and a fibrous union is termed a *syndesmosis*. The most common fusions are talocalcaneal and calcaneonavicular. The middle facet is the most common location for a talocalcaneal coalition. Talocalcaneal coalitions often may extend posteriorly, with involvement of the junction of the middle and posterior facet. Talonavicular (e-Fig. 131.10), calcaneocuboid, and cubonavicular coalitions are much less common. Synostoses can occur between other bones of the foot but frequently are associated with other limb abnormalities, such as fibular hemimelia or short femur, or disorders such as Apert syndrome.

Symptoms from a tarsal coalition present with advancing ossification. Pain with activity usually is the presenting symptom. The child may have a peroneal spastic flatfoot, which involves pain and rigid valgus deformity of the hindfoot and forefoot, along with peroneal muscle spasm. This condition is not a true spasticity but reflects peroneal shortening to adjust for heel valgus and to maintain a less painful position for the subtalar joint.

***Imaging.*** Weight-bearing views of the foot are recommended to accurately evaluate longitudinal alignment of the foot, as pes planus is associated with tarsal coalitions. A 45-degree lateral oblique radiograph of the foot directly shows a calcaneonavicular coalition. The secondary radiographic features of calcaneonavicular coalitions visible on a lateral radiograph include pes planus, anteater sign (Fig. 131.11), and talar beak sign (e-Fig. 131.12).[26] A reverse anteater sign is seen on the AP view of the foot and is defined as diminished AP height of the lateral portion of the navicular (compared with the medial navicular), with the navicular extending far lateral with respect to the talar head.

Radiographic features of talocalcaneal coalitions include the C sign (Fig. 131.13A), talar beak, an ovoid, enlarged sustentaculum tali (see Fig. 131.13A), and broadened lateral process of the talus.[26]

The talar beak associated with tarsal coalitions is a dorsal extension of the talar head (see e-Fig. 131.12). A talar beak should not be confused with a talar ridge. The talar ridge represents bony proliferation related to the insertion of the anterior tibiotalar capsule and is located along the more proximal dorsal talar neck rather than at the distal talar head.[26]

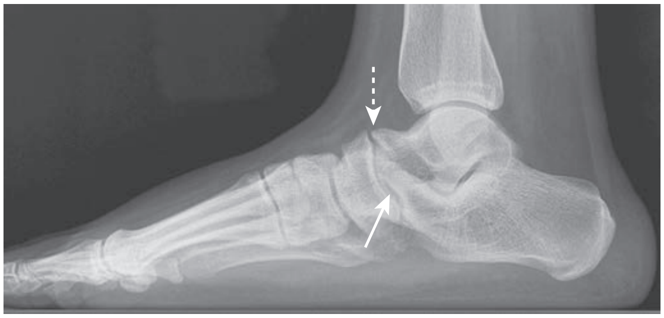

**Figure 131.11. Calcaneonavicular coalition in a child with the anteater sign *(arrow)* and talar beak *(dotted arrow)*.** Elongation of the anterior calcaneus resembling the nose of an anteater is present.

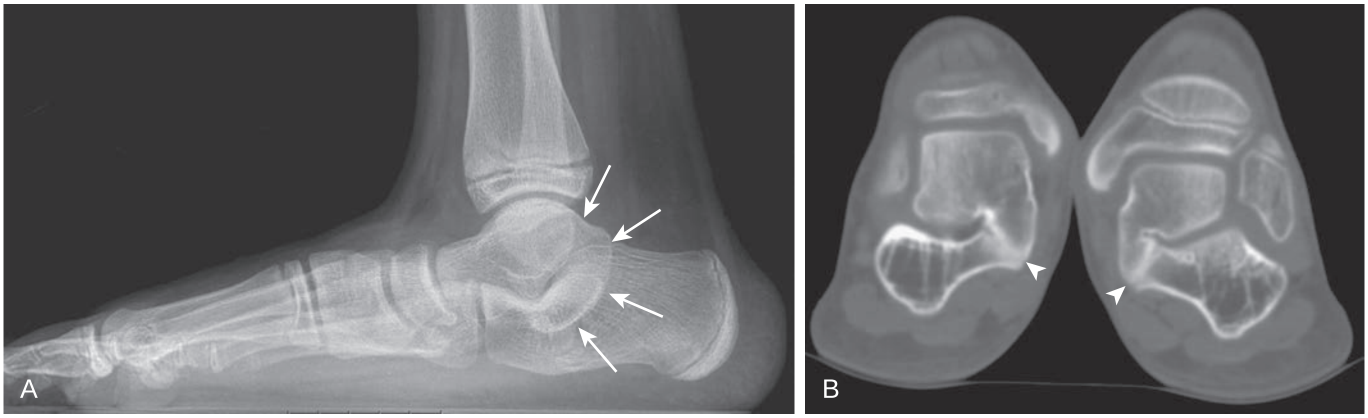

**Figure 131.13. Talocalcaneal coalition.** (A) Lateral radiograph demonstrates the C sign *(arrows)*, ovoid, elongated sustentaculum tali, and pes planus. (B) Coronal reformatted CT image in a different patient demonstrates bilateral middle facet subtalar coalitions *(arrowheads)*.

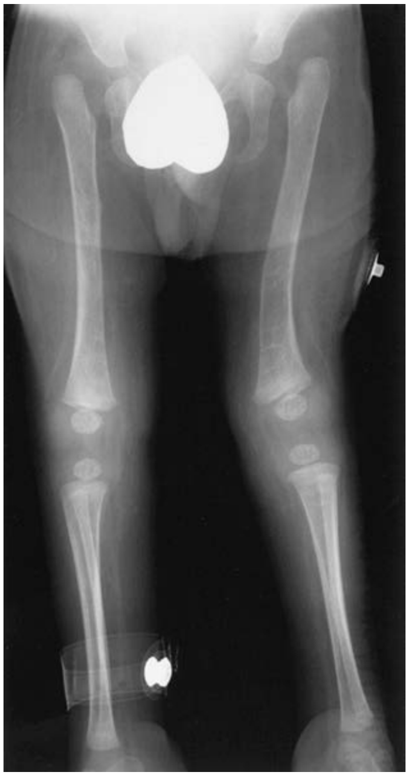

**e-Figure 131.9. Arthrogryposis.** Radiograph of the lower extremities of a child with arthrogryposis shows that the bones are gracile and demineralized, and muscle mass is reduced. The proximal femora are dislocated, and the acetabula are dysplastic. Femoral bowing on the left is the result of previous fractures.

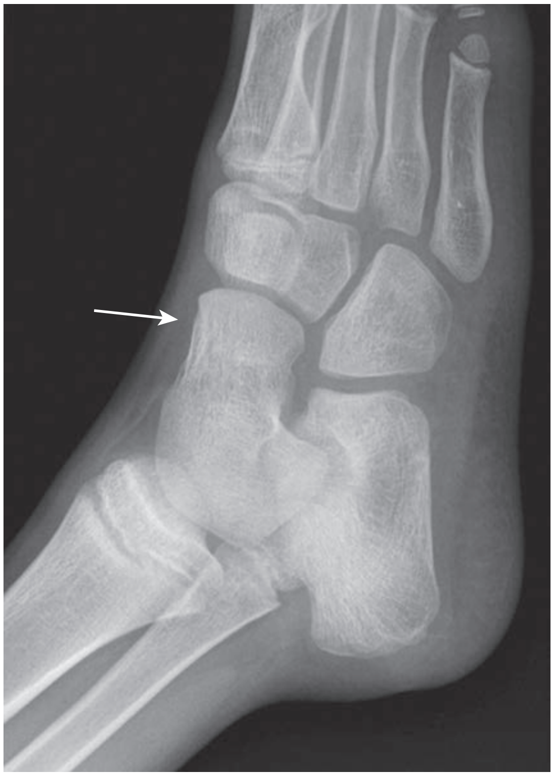

**e-Figure 131.10.** Talonavicular coalition *(arrow)*.

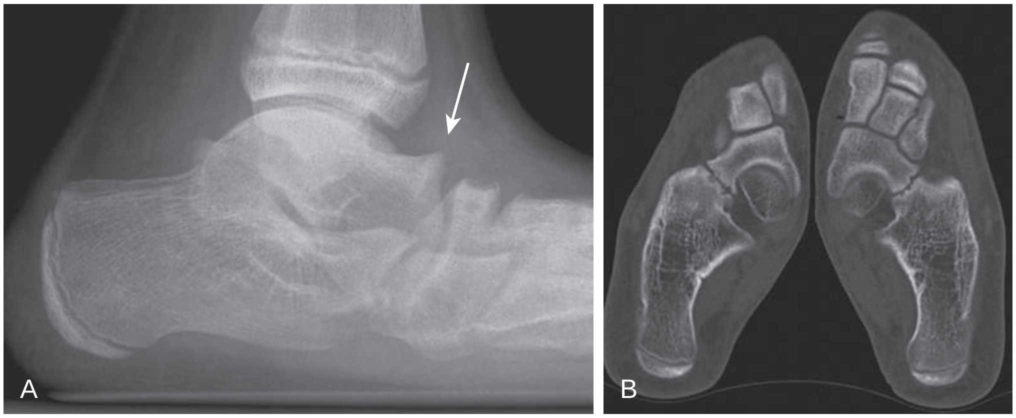

**e-Figure 131.12. Calcaneonavicular coalition.** (A) Lateral radiograph demonstrates a talar beak *(arrow)* at the distal end of a shortened talar neck in a child with a calcaneonavicular coalition. (B) CT reconstructions demonstrate bilateral calcaneonavicular coalitions.

A ball-and-socket articulation of the distal tibia and talus is an uncommon association with tarsal coalition. This configuration at the ankle joint is nonspecific and may be associated with congenital long bone deficiencies, as well as tarsal coalitions.[27]

Computed tomography (CT) and MRI help to define the nature and cross-sectional area of a fusion. CT is more cost-effective if the clinical suspicion for coalition is high (Fig. 131.13B). If other causes of pain and limited hindfoot mobility are considered, then MRI may be indicated. MRI may directly show bony, cartilaginous, and fibrous unions. Bone marrow edema often is noted adjacent to the fused articulation (Fig. 131.14).

***Treatment and Follow-up.*** Casting and nonsteroidal antiinflammatory medications often are the initial treatment for symptomatic children. Steroid injections and physical therapy also may be used. If symptoms are not relieved and no degenerative changes have occurred, then surgical resection of the abnormal tarsal bridging often is attempted.[25] Regrowth of a calcaneonavicular coalition can be halted by interposition of the extensor digitorum brevis tendon. Fat frequently is interposed after resection of a subtalar coalition. Subtalar fusion or triple arthrodesis may be indicated in refractory cases.

## Carpal Fusion

Isolated fusion of the carpal bones is a normal variant that is seen in approximately 0.1% of the white population and approximately 1.6% of the African American population (e-Fig. 131.15).[28] Carpal fusion is seen most frequently between the lunate and triquetrum. Fusion between bones of the proximal and distal carpal rows usually is associated with a syndrome. Fusions also may be acquired, as in juvenile idiopathic arthritis or after trauma.

## Syndactyly

Fusion between adjacent digits resulting from intrauterine failure to separate is termed *syndactyly*. These fusions may involve only soft tissue (simple syndactyly), or they also may involve bone (complex syndactyly). If the entire length of the digit is involved, syndactyly is termed *complete*, and if only a partial length is bridged, it is incomplete. Fusion may be unilateral or bilateral and usually involves the second, third, and fourth digits. Syndactyly may be isolated or may be associated with congenital disorders such as Poland, Apert (Fig. 131.16), and Carpenter syndromes. Poland syndrome includes symbrachydactyly (brachydactyly and syndactyly) and ipsilateral chest wall anomalies, most commonly pectoralis muscle hypoplasia or aplasia. Apert syndrome includes syndactyly, craniosynostosis, and facial bone anomalies. Carpenter syndrome includes polysyndactyly, craniosynostosis, and facial bone anomalies. Syndactyly is thought to have an autosomal-dominant inheritance pattern.[29] Surgery is performed early in life to improve function and appearance when the hand is involved. Surgery is rarely indicated for the foot.

## Symphalangism

Symphalangism is an uncommon autosomal-dominant disorder of fusion of the interphalangeal joints of the hands and feet (Fig. 131.17). Proximal interphalangeal joint fusion is more common than distal interphalangeal joint fusion.[30] The anomaly is usually bilateral, and the little finger and little toe are affected most often. Fusion may not be recognized radiographically until later in childhood. Despite the radiographic appearance of the digits, seldom is disability or loss of function reported. Symphalangism may be associated with other skeletal abnormalities, various digit deformities (e.g., brachydactyly, clinodactyly, and camptodactyly), radioulnar fusion, hip dislocation, tarsal coalition, and spinal anomalies.

## Radioulnar Synostosis

***Etiology.*** Congenital radioulnar synostosis anomaly is due to failure of longitudinal segmentation between the radius and the ulna.[31] In utero, cartilaginous anlagen of the humerus, radius, and ulna are connected. Normal separation progresses from the distal end of the forearm to the proximal end. An insult to segmentation during early in utero development can lead to bony or fibrous synostosis. Radioulnar synostosis is associated with disorders such as Apert and Carpenter syndromes, as well as with other upper

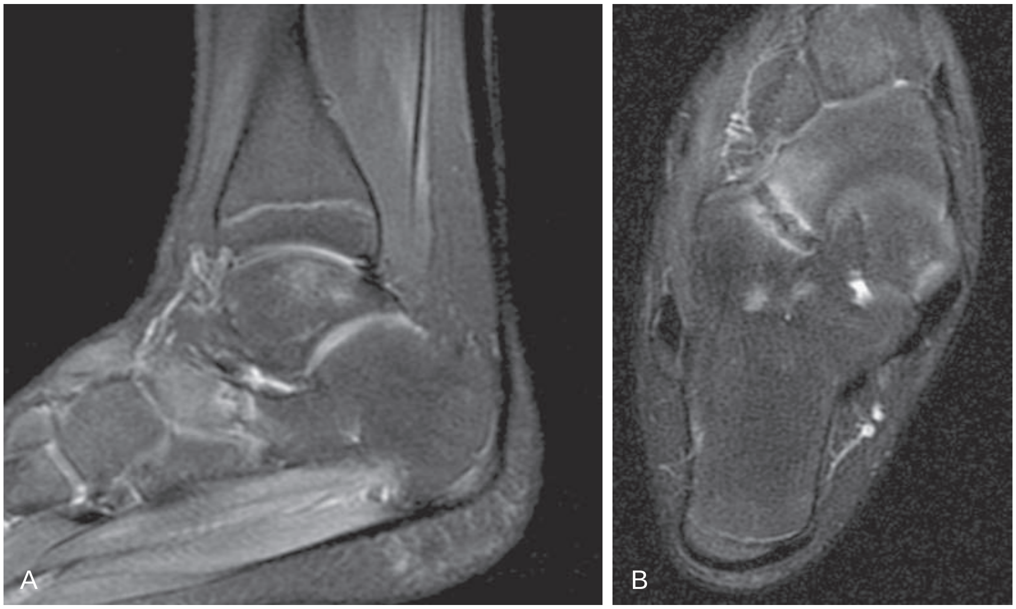

**Figure 131.14. Calcaneonavicular coalition in a 12-year-old girl.** Short Tau inversion recovery sagittal (A) and T2 fat-saturated axial magnetic resonance (MR) (B) images demonstrate marrow edema on both sides of a fibrous coalition.

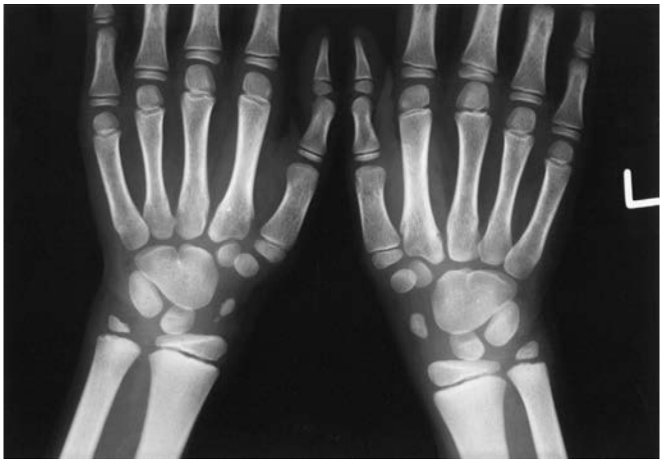

**e-Figure 131.15. Carpal fusion.** There is fusion of the hamate and capitate bones bilaterally.

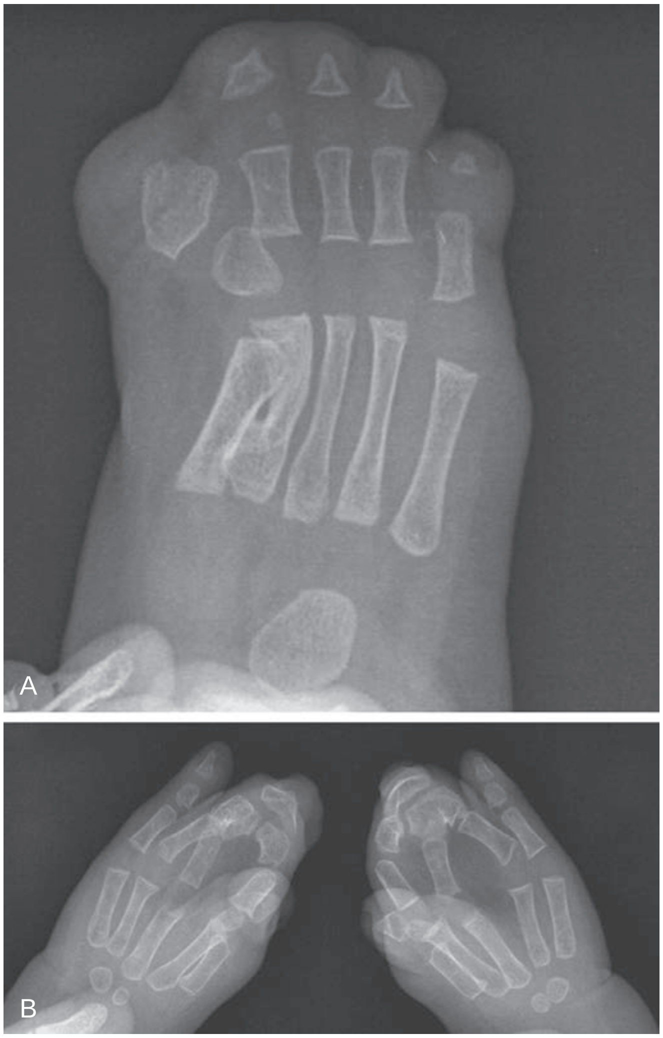

**Figure 131.16. Apert syndrome in a 1-year-old.** (A) Frontal view of the foot shows syndactyly of the digits. Hypoplasia of many bones of the foot is seen with absent middle phalanges. The first and second metatarsals are partially fused. (B) Frontal radiograph of both hands of the same child shows syndactyly, synostosis, and symphalangism bilaterally.

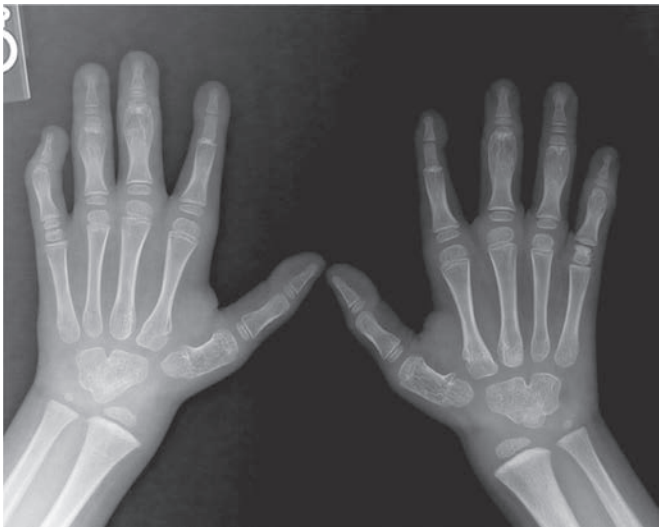

**Figure 131.17.** Bilateral symphalangism involving multiple rays with associated carpal coalitions in a 3-year-old girl.

extremity abnormalities such as polydactyly, syndactyly, and carpal coalition.

On clinical examination, the child may have a fixed degree of pronation and a mild degree of flexion at the elbow. Pain usually occurs during the teen years, when progressive and symptomatic radial head subluxation may be seen.

***Imaging.*** Osseous coalition can be seen on AP and lateral radiographs (Fig. 131.18). Radioulnar synostosis may lead to radial head dorsal dislocation and secondary dysplasia (see Fig. 131.18) due of the lack of articulation with the capitellum, which is needed for normal development.

***Treatment and Follow-up.*** Surgical treatment usually is reserved for patients with a severe pronation deformity or symptomatic radial head subluxation, particularly when it involves the dominant hand. A both bone extra-articular derotational osteotomy of the forearm may improve supination.[32] Resection of the proximal synostosis is complex and may not lead to improved forearm and hand function.

## OTHER CONGENITAL MALFORMATIONS

### Clinodactyly

Clinodactyly is a curvature of the finger in a radial or ulnar direction (in the mediolateral plane) away from the axis of joint flexion and extension. Although it may involve any digit, clinodactyly most often refers to radial curvature of the distal interphalangeal joint of the fifth digit (Fig. 131.19).[33] Clinodactyly is associated with a short middle phalanx and usually is bilateral. It may be seen in the normal population as a sporadic variant but also can be inherited in an autosomal-dominant pattern. It has been described in numerous syndromes (e.g., Down syndrome), in bone dysplasias, after trauma, and in many other conditions. The deformity may occur in the setting of a relatively normal phalanx or related to a longitudinal epiphyseal bracket deformity. Treatment is undertaken for cosmesis or for excessive scissoring of the digits.

### Camptodactyly

Camptodactyly refers to a congenital or acquired flexion contracture of the finger. It usually is located at the proximal interphalangeal joint of the fifth finger but also can involve the second through fourth digits (Fig. 131.20).[33] Occasionally, the distal interphalangeal joints may be affected. The cause remains unknown but may relate to abnormal insertion of the lumbrical muscles or the flexor digitorum superficialis tendon. Similar to clinodactyly, camptodactyly may be sporadic or may show an autosomal-dominant inheritance pattern. Occasionally it is associated with a chromosomal abnormality, a bony dysplasia, or another syndrome. Treatment includes bracing or, infrequently, surgical release.

### Kirner Deformity

Palmar bending of the distal phalanx of the fifth digit is termed *Kirner deformity*.[33] It usually is an isolated abnormality that is bilateral and symmetric. The long axis of the distal phalanx is bent toward the palm, and the epiphysis is normally oriented (Fig. 131.21). The physis is widened. With skeletal maturation, the physis fuses at an angle. The distal phalanx exhibits a permanent palmar curvature. Similar to the other digit deformities, Kirner deformity can be a sporadic or an autosomal-dominant inherited anomaly.

### Brachydactyly

Brachydactyly is a descriptive term that describes shortening of the digits secondary to abnormal development of the phalanges, metacarpals/metatarsals, or both of the hands or feet (e-Fig. 131.22).

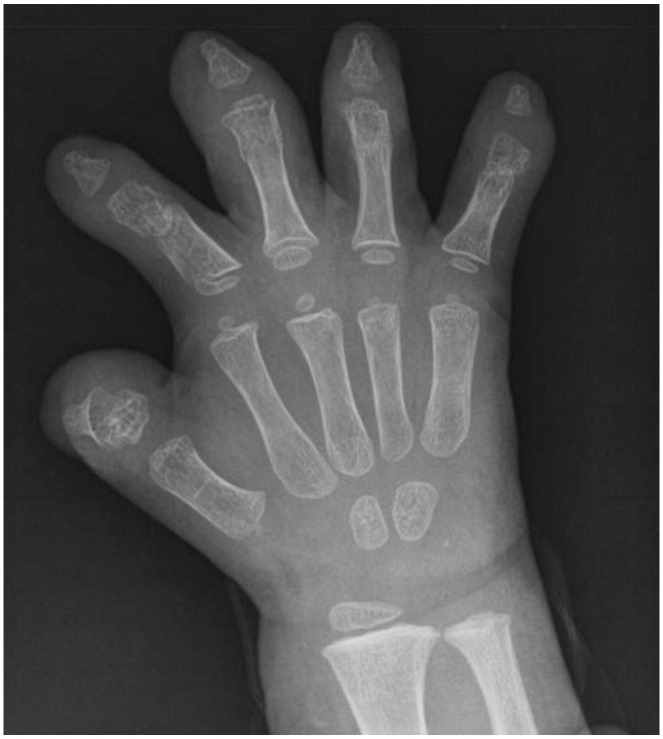

**e-Figure 131.22.** Brachydactyly involving multiple digits and with symphalangism in a 3-month-old boy.

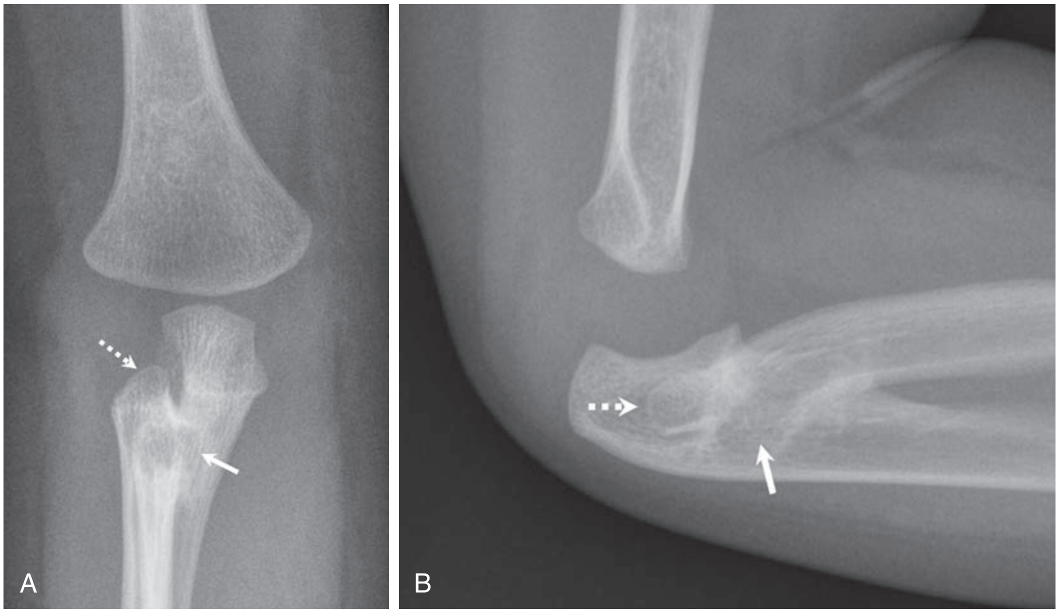

**Figure 131.18. Radioulnar synostosis in a 2-year-old girl.** Anteroposterior (A) and lateral (B) radiographs demonstrate osseous synostosis *(solid arrows)* of the proximal radius and ulna. Also note that the radial head *(dashed arrows)* is abnormally shaped and posteriorly directed with respect to the capitellum.

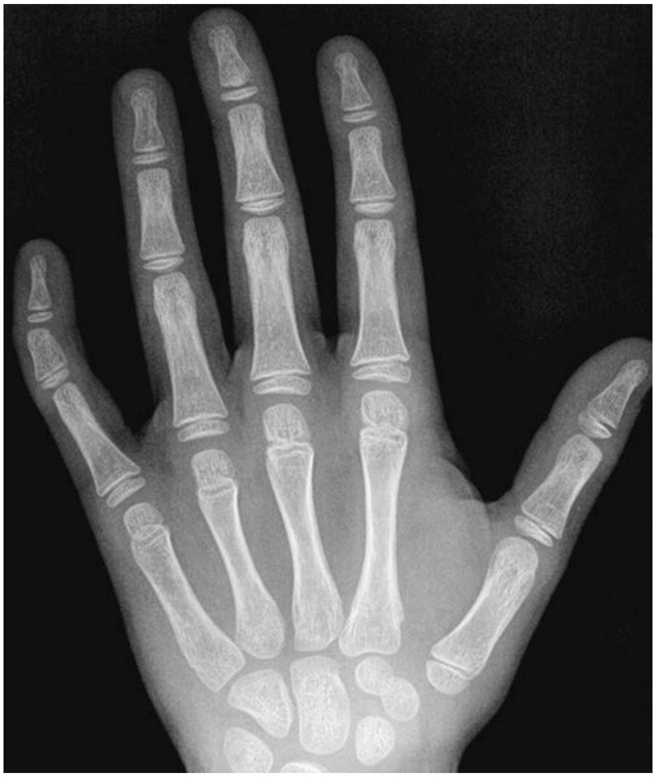

**Figure 131.19. Clinodactyly of the fifth digit in a 7-year-old girl.** Medial bending of the finger and a short middle phalanx are noted.

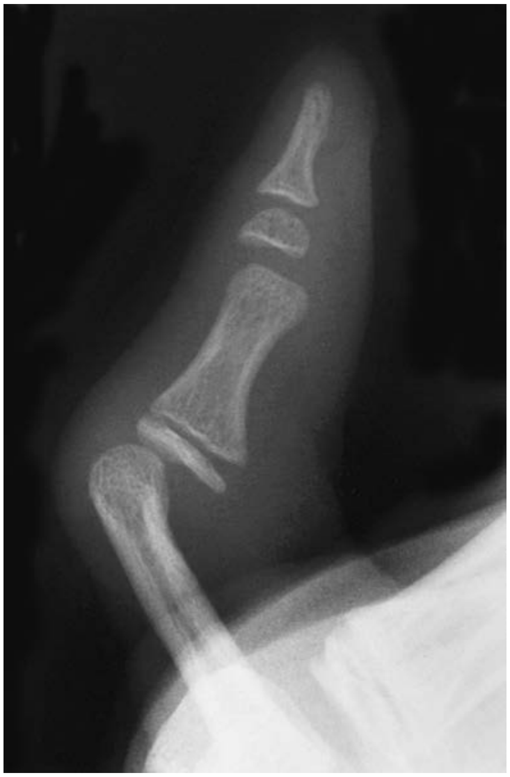

**Figure 131.20. Camptodactyly.** Flexion of the proximal interphalangeal joint is present with palmar subluxation of the middle phalanx of the little digit. The child has no skin crease.

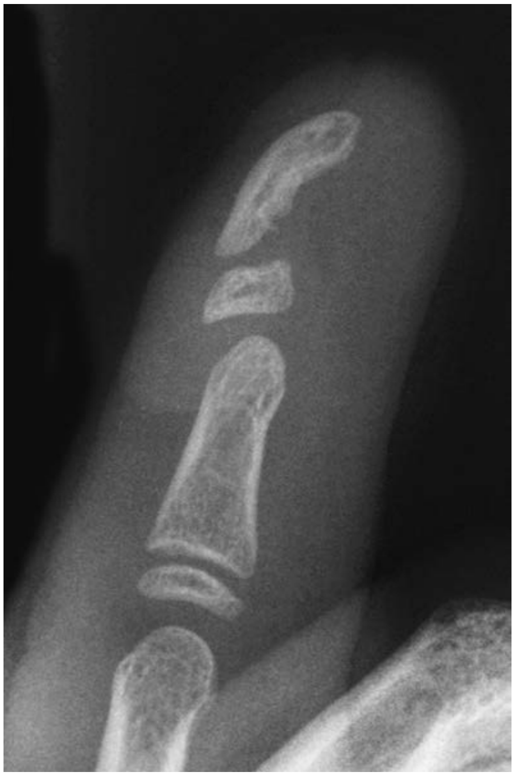

**Figure 131.21. Kirner deformity.** Palmar bending of the distal phalanx of the fifth digit is revealed. The epiphysis is in a normal position. *(From Oestreich AE, Crawford AH.* Atlas of Pediatric Orthopedic Radiology. *New York: Thieme; 1985:166.)*

Morphologically the affected bone may appear normal but just abnormally shortened compared with the other digits. The most commonly affected level is the middle phalanges. Brachydactyly may coexist with other processes such as longitudinal epiphyseal bracket and symphalangism. Brachydactyly may be sporadic or may be inherited in an autosomal-dominant fashion. Brachydactyly also may be seen with syndromes such as Apert and Poland syndromes.

## Longitudinal Epiphyseal Bracket

***Etiology.*** Longitudinal epiphyseal bracket, also referred to as *delta phalanx*, is a congenital deformity that affects the short tubular bones that normally develop a proximal epiphyseal ossification center (e.g., phalanges, first metacarpal, and first metatarsal). The deformity may be sporadic or may occur in association with conditions such as Rubinstein-Taybi syndrome and fibrodysplasia ossificans progressiva. The cause is likely incomplete development of the primary ossification center of the bone during early fetal growth. The growth disturbance relates to the longitudinally oriented cartilaginous bracket, which causes growth to follow a C-shaped curve.[34]

***Imaging.*** The involved bone is trapezoid or triangular in shape (Fig. 131.23). The diaphyseal–metaphyseal osseous unit is bracketed along the longitudinal side by a physis and an epiphysis. The physis is arclike (see Fig. 131.23B), extending from the medial proximal surface along the longitudinal margin of the bone to the distal medial surface, and is similar in configuration to a bracket. Other anomalies of the digits frequently are associated with the longitudinal epiphyseal bracket.

***Treatment and Follow-up.*** Splinting in infancy is not effective. Early surgical intervention, often a wedge osteotomy, is recommended to allow for remodeling and to facilitate longitudinal growth of the bone.[35]

## Split Hand-Foot Malformations

***Etiology.*** Split hand-foot malformation (SHFM) refers to the congenital splitting of the hands or feet into two halves. SHFM is attributed to hypoplasia or aplasia of the phalanges, metacarpals, or metatarsals of one or more fingers or toes. The deformity also is referred to as *ectrodactyly*, cleft hand or cleft foot, or lobster or crab claw deformity.

SHFM may be isolated or associated with congenital constriction band syndrome, or, most commonly, it may occur as a component of the ectrodactyly–ectodermal dysplasia–cleft lip/palate syndrome.[36] More than 75 syndromes have been associated with SHFM. Ectrodactyly–ectodermal dysplasia–cleft lip/palate syndrome usually has an autosomal-dominant inheritance pattern with incomplete penetrance and variable expression, although autosomal-recessive forms have been described. SHFM has been detected on prenatal ultrasonography, which can guide counseling and reconstructive efforts.

***Imaging.*** SHFM is highly variable in presentation. It can range from mild digital changes to the most severe monodactyly with only the fifth digit remaining. Two distinctive clinical forms have been described—typical and atypical forms. The typical form has an autosomal-dominant inheritance pattern and involves the lack of phalanges and metacarpals, resulting in a deep V-shaped cleft with the two halves resembling a lobster claw (Fig. 131.24). The much less frequent atypical form is sporadic and results in a much wider cleft, which forms a U-shaped central defect. The atypical form rarely involves the feet. Vascular disruption has been implicated as the cause. In most forms the digits frequently curve in toward the cleft, and a reduction in the number of digits may occur. Syndactyly or synostosis often is present.

***Treatment and Follow-up.*** Patients affected by SHFM usually have good functional use of their extremities and therefore surgical intervention usually is not indicated.

## Congenital Radial Head Dislocation

***Etiology.*** Congenital radial head dislocation is the most commonly identified congenital abnormality of the elbow. More than half of cases are associated with other conditions, such as anomalies of the lower extremities, scoliosis, and various syndromes (e.g., Klippel-Feil).[37] Whether it is an isolated abnormality or is associated with other conditions, congenital radial head dislocation is believed to have an autosomal-dominant inheritance pattern. The deformity can be unilateral or bilateral.

***Imaging.*** Congenital radial head dislocation is associated with a small, underdeveloped forearm, a flattened and hypoplastic capitellum, and a short ulna. The proximal ulnar diaphysis often may have posterior apex bowing (Fig. 131.25). The radial head is dysplastic with an elongated, thinned, and convex articular surface instead of the normal concave shape. The radial head is most commonly dislocated posteriorly (see Fig. 131.25). The degree of radial head dysplasia is correlated with the severity of dislocation. Radiographs should be carefully evaluated for concomitant radioulnar synostosis (see Fig. 131.18).

***Treatment and Follow-up.*** Asymptomatic dislocations are not treated. If the child has pain, the radial head can be excised. However, excision of the radial head frequently is accompanied by pain from abnormal mechanics at the wrist. Recent work suggests that open reduction of the proximal radius at an early age may be beneficial.

## Tibial Bowing Deformities

***Etiology.*** Posteromedial congenital bowing affects the tibia, fibula, and soft tissues of the lower extremity. The origin and pathogenesis remain uncertain and may be related to abnormal early embryologic development rather than to abnormal fetal

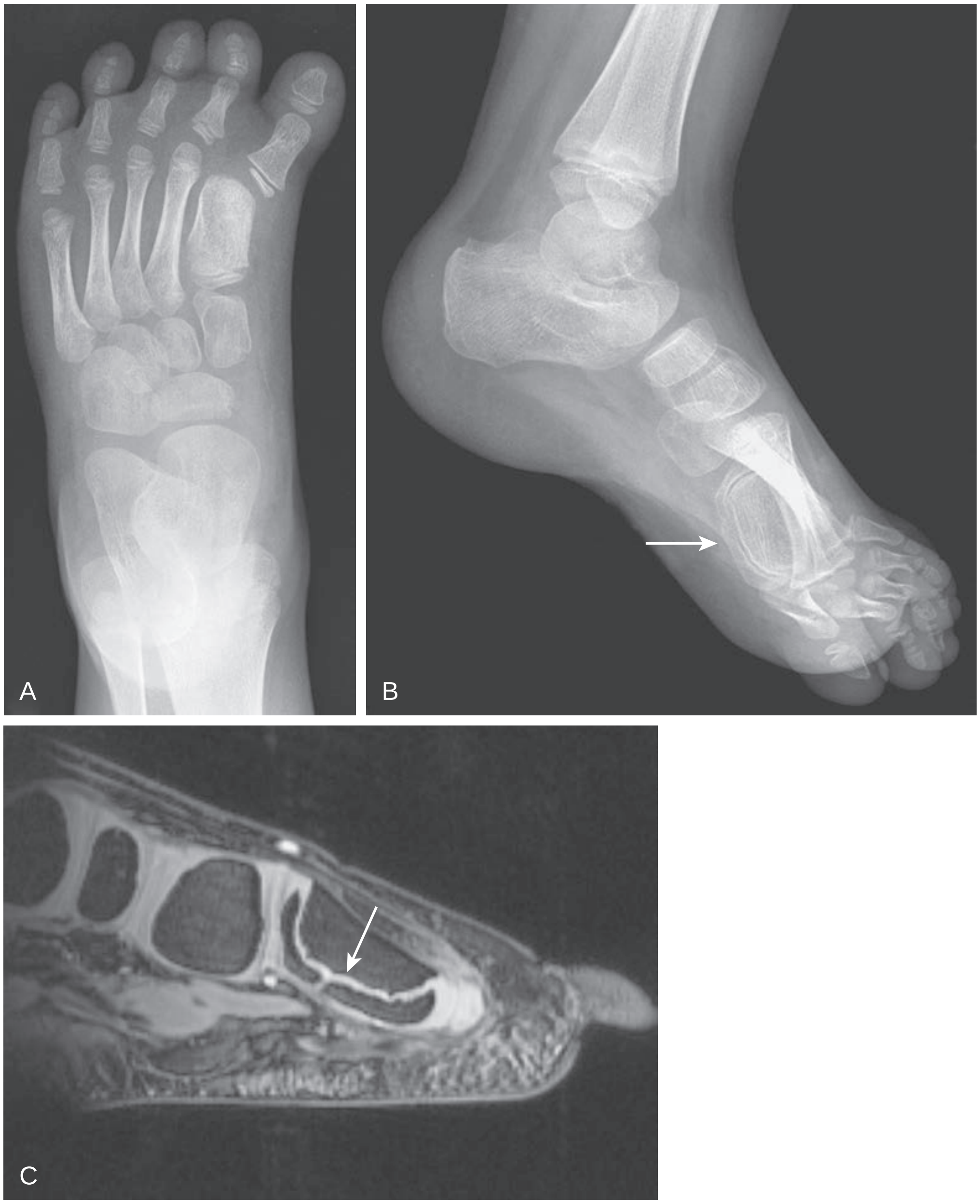

**Figure 131.23. Longitudinal epiphyseal bracket.** (A) Frontal radiograph of the foot of a 4-year-old girl. The first metatarsal is short and widened and has a shorter medial than lateral length, forming a trapezoidal shape. (B) Lateral radiograph of the same child shows the C-shaped epiphysis and physis of the first metatarsal *(arrow)*. (C) Sagittal gradient echo MR image shows a high-signal intensity C-shaped physis *(arrow)* and adjacent epiphysis.

positioning or intrauterine fracture. Fetal vascular insufficiency or compressive events associated with amnion rupture may be responsible.[38] As the child grows, tibial bowing and shortening often partially resolve.

Posteromedial congenital bowing should be differentiated from congenital tibial dysplasia (CTD). Other terms for CTD include anterolateral tibia bowing or congenital pseudoarthrosis of the tibia. It is a rare anomaly but does occur in a small number of patients with neurofibromatosis type 1 (NF1). Approximately 20% to 50% of patients with CTD do not have NF1.[39]

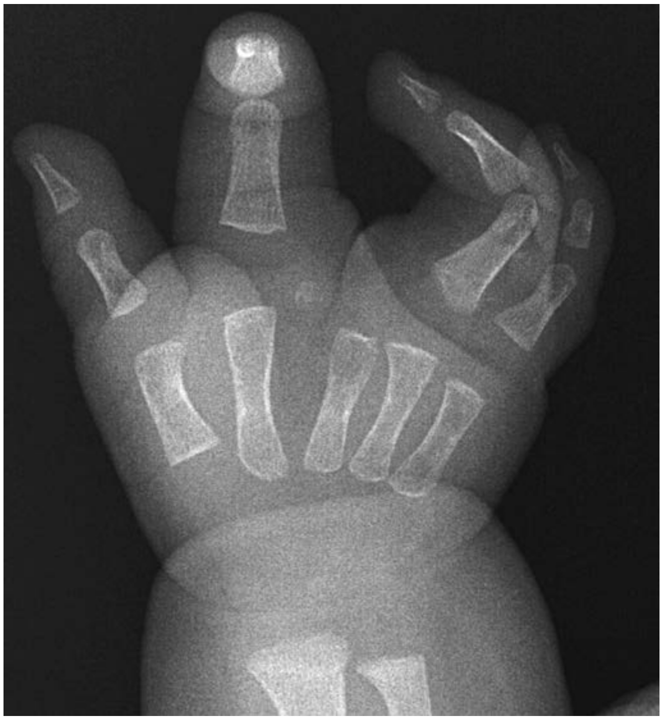

**Figure 131.24. Split hand-foot malformation in a 6-month-old boy.** The child has near complete absence of the long digit.

CTD presents as anterolateral bowing or fracture of the tibia, often before other manifestations of NF1 present. Lack of involvement of the fibula suggests that the bowing will resolve spontaneously. Pathologic studies show abnormal, highly cellular fibrovascular tissue with variable amounts of fibrocartilage and hyaline cartilage within the tibia. Bone growth and repair are abnormal. The pattern of abnormal fibrous tissue results in the dysplastic or cystic changes characteristic of the disorder.

***Imaging.*** With posteromedial congenital bowing, the tibia and the fibula show marked posteromedial bowing at the middle or distal one-third (Fig. 131.26). Rarely is the bowing lateral. At birth, the foot is held in a calcaneovalgus (dorsiflexed) position.

Radiographic changes seen with CTD are variable and include anterolateral bowing of the tibia, fracture, pseudarthrosis, hourglass-like constriction of the midshaft of the tibia, cystic changes usually at the junction of the upper and middle thirds of the tibia, sclerosis that narrows the medullary canal, and, infrequently, involvement of the fibula alone (Fig. 131.27).

***Treatment and Follow-up.*** Treatment for posteromedial congenital bowing of the tibia is conservative; corrective casts or splints may be used to hold the foot and support the leg during growth and remodeling. If a severe persistent deformity continues beyond toddler age, a leg length discrepancy, usually on the order of 3 to 7 cm, may result that requires osteotomies and lengthening procedures. Occasionally, epiphysiodesis of the contralateral side may be needed.

In persons who have anterolateral bowing associated with NF1, fracture and refracture rates are very high. Limb length inequality is frequent and results from disuse atrophy and abnormal growth at the distal tibial physis. Often a valgus deformity is noted at the ankle. Surgical management can be frustrating because nonunion or pseudarthrosis after osteotomy is frequent.

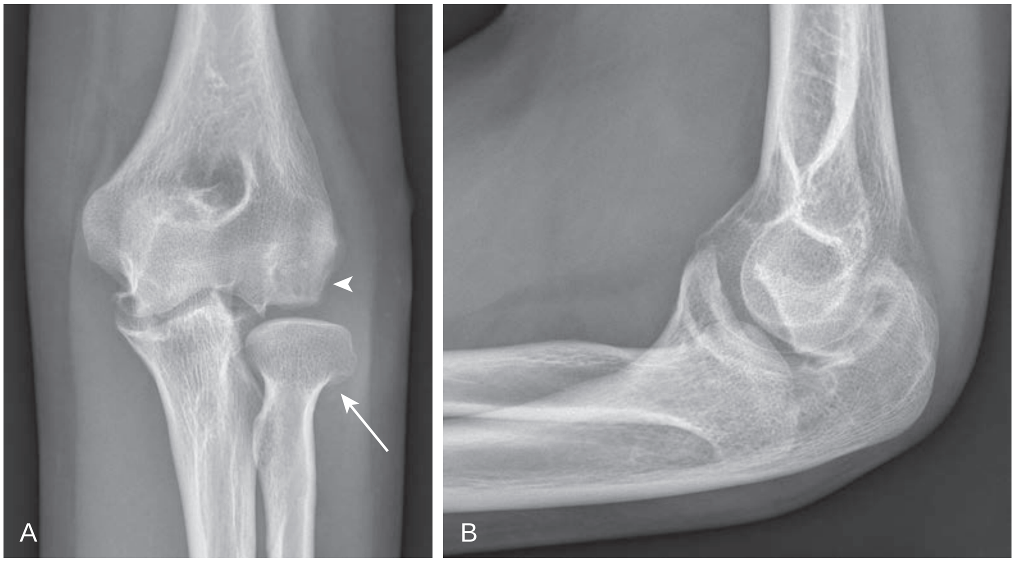

**Figure 131.25. Congenital radial head dislocation in a 12-year-old girl.** Anteroposterior (A) and lateral (B) radiographs show a dysplastic convex-shaped radial head *(arrow)* with posterior dislocation as well as posterior bowing of the proximal ulnar diaphysis. Note the presence of a capitellar osteochondral lesion *(arrowhead)* and medial compartmental osteoarthritis, which likely is related to abnormal elbow biomechanics.

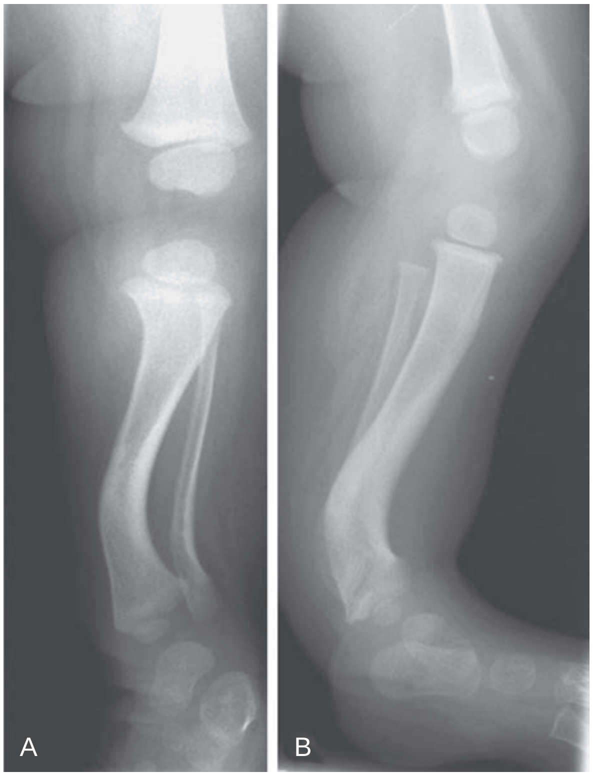

**Figure 131.26. Congenital posteromedial bowing in a 1-year-old girl.** (A) On the frontal radiograph, medial bowing is seen at the junction of the middle and distal one-third of the tibia. The fibula is similarly bowed. (B) The posterior component of the bowing is seen on the lateral radiograph.

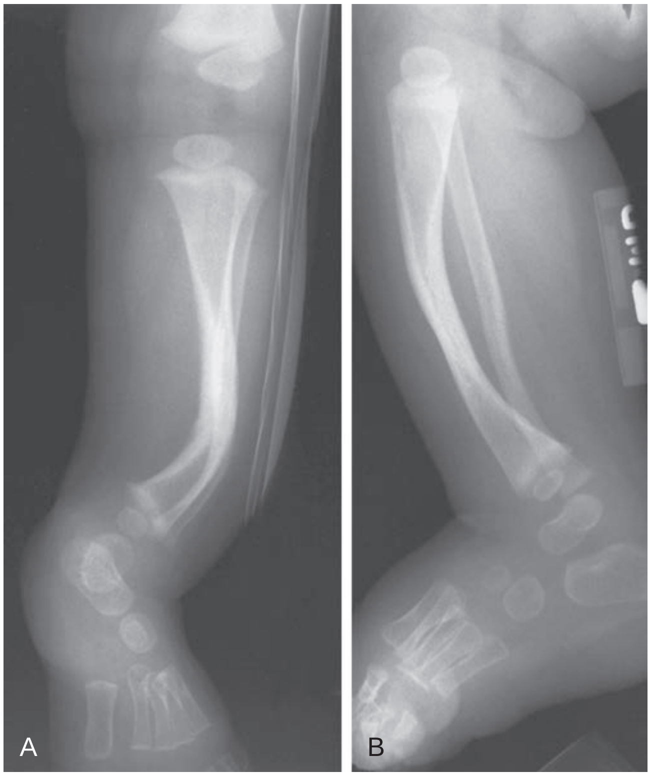

**Figure 131.27. Congenital tibial dysplasia and neurofibromatosis type 1.** Anteroposterior (A) and lateral (B) radiographs show anterolateral tibial bowing. The medullary canal is nearly obliterated, but no fracture is apparent.

## KEY POINTS

- For PFFD, the femoral head and acetabular deformities are related; the more dysmorphic the femoral head, the more severe the acetabular deformity.
- Fibular hemimelia often has coexisting deformities at the level of the knee and foot.
- The most commonly affected facet in subtalar coalitions is the middle facet.
- A complete ossific bar forms a synostosis, a cartilaginous bar forms a synchondrosis, and a fibrous union is termed a *syndesmosis*.
- Congenital radial head dislocation is associated with a convex radial head, whereas traumatic radial head dislocation shows the normal radial articular surface convexity.

## SUGGESTED READING

Bedoya MA, Chauvin NA, Jaramillo D, et al. Common patterns of congenital lower extremity shortening: diagnosis, classification, and follow-up. *Radiographics*. 2015;35(4):1191–1207.

Poznanski A. *The Hand in Radiologic Diagnosis*. 2nd ed. Philadelphia: WB Saunders; 1984.

Winfeld MJ, Otero H. Radiographic assessment of congenital malformations of the upper extremity. *Pediatr Radiol*. 2016;46(10):1454–1470. doi:10.1007/s00247-016-3647-2.

## REFERENCES

Full references for this chapter can be found on www.expertconsult.com.

## REFERENCES

1. Frantz C, O'Rahilly R. Congenital limb deficiencies. *J Bone Joint Surg Am*. 1961;43:1202–1224.
2. Lenz W. Malformations caused by drugs in pregnancy. *Am J Dis Child*. 1966;112:99–106.
3. Schatz SL, Kopts SE. Proximal femoral focal deficiency. *AJR Am J Roentgenol*. 1978;131:289–295.
4. Amstutz HC. Developmental (infantile) coxa vara—a distinct entity: report of two patients with previously normal roentgenograms. *Clin Orthop Relat Res*. 1970;72:242–247.
5. Hamanishi C. Congenital short femur: clinical, genetic and epidemiological comparison of the naturally occurring condition with that caused by thalidomide. *J Bone Joint Surg Br*. 1980;62:307–320.
6. Aitken G, ed. Proximal femoral focal deficiency—definition, classification, and management. In: *Proximal Femoral Focal Deficiency: A Congenital Anomaly*. Washington, DC: National Academy of Sciences; 1969.
7. Bedoya MA, Chauvin NA, Jaramillo D, et al. Common patterns of congenital lower extremity shortening: diagnosis, classification, and follow-up. *Radiographics*. 2015;35(4):1191–1207.
8. Anton CG, Applegate KE, Kuivila TE, et al. Proximal femoral focal deficiency (PFFD): more than an abnormal hip. *Semin Musculoskelet Radiol*. 1999;3:215–226.
9. Biko DM, Davidson R, Pena A, et al. Proximal focal femoral deficiency: evaluation by MR imaging. *Pediatr Radiol*. 2012;42:50–56.
10. VanNes C. Rotation-plasty for congenital defects of the femur: making use of the ankle of the shortened limb to control the knee joint of a prosthesis. *J Bone Joint Surg Br*. 1950;32:12–16.
11. Laor T, Jaramillo D, Hoffer FA, et al. MR imaging in congenital lower limb deformities. *Pediatr Radiol*. 1996;26:381–387.
12. Oberc A, Sulko J. Fibular hemimelia—diagnostic management, principles, and results of treatment. *J Pediatr Orthop B*. 2013;22(5):450–456.
13. McCarthy JJ, Glancy GL, Chang FM, et al. Fibular hemimelia: comparison of outcome measurements after amputation and lengthening. *J Bone Joint Surg Am*. 2000;82-A(12):1732–1735.
14. Weber M. New classification and score for tibial hemimelia. *J Child Orthop*. 2008;2(3):169–175.
15. Simmons ED Jr, Ginsburg GM, Hall JE. Brown's procedure for congenital absence of the tibia revisited. *J Pediatr Orthop*. 1996;16:85–89.
16. Lourie GM, Lins RE. Radial longitudinal deficiency: a review and update. *Hand Clin*. 1998;14:85–99.
17. Van Allen MI, Hoyme HE, Jones KL. Vascular pathogenesis of limb defects. I. Radial artery anatomy in radial aplasia. *J Pediatr*. 1982;101:832–838.
18. Wall LB, Ezaki M, Oishi SN. Management of congenital radial longitudinal deficiency: controversies and current concepts. *Plast Reconstr Surg*. 2013;132(1):122–128.
19. Swanson AB, Tada K, Yonenobu K. Ulnar ray deficiency: its various manifestations. *J Hand Surg Am*. 1984;9:658–664.
20. Bednar MS, James MA, Light TR. Congenital longitudinal deficiency. *J Hand Surg Am*. 2009;34(9):1739–1747.
21. Manske PR, Goldfarb CA. Congenital failure of formation of the upper limb. *Hand Clin*. 2009;25:157–170.
22. Kawamura K, Chung KC. Constriction band syndrome. *Hand Clin*. 2009;25:257–264.
23. Swinyard CA, Bleck EE. The etiology of arthrogryposis (multiple congenital contractures). *Clin Orthop*. 1985;194:15–29.
24. Shapiro F, Specht L. The diagnosis and orthopaedic treatment of childhood spinal muscular atrophy, peripheral neuropathy, Friedreich ataxia, and arthrogryposis. *J Bone Joint Surg Am*. 1993;75:1699–1714.
25. Zaw H, Calder JD. Tarsal coalitions. *Foot Ankle Clin*. 2010;15(2):349–364.
26. Crim J. Imaging of tarsal coalition. *Radiol Clin North Am*. 2008;46:1017–1026.
27. Takakura Y, Tanaka Y, Kumai T, et al. Development of the ball-and-socket ankle as assessed by radiography and arthrography: a long-term follow-up report. *J Bone Joint Surg Br*. 1999;81(6):1001–1004.
28. Poznanski AK, Holt JF. The carpals in congenital malformation syndromes. *AJR Am J Roentgenol*. 1971;112(3):443–459.
29. Tonkin MA. Failure of differentiation part I: syndactyly. *Hand Clin*. 2009;25:171–193.
30. Letts M, Davidson D, Beaule P. Symphalangism in children: case report and review of the literature. *Clin Orthop Relat Res*. 1999;366:178–185.
31. Elliot AM, Kibria L, Reed MH. The developmental spectrum of proximal radioulnar synostosis. *Skeletal Radiol*. 2010;39:49–54.
32. Hung NN. Derotational osteotomy of the proximal radius and the distal ulna for congenital radioulnar synostosis. *J Child Orthop*. 2008;2:481–489.
33. Poznanski AK, Pratt GB, Manson G, et al. Clinodactyly, camptodactyly, Kirner's deformity, and other crooked fingers. *Radiology*. 1969;93:573–582.
34. Mahboub S, Davidson R. MR imaging in longitudinal epiphyseal bracket in children. *Pediatr Radiol*. 1999;29:259–261.
35. Light TR, Ogden JA. The longitudinal epiphyseal bracket: implications for surgical correction. *J Pediatr Orthop*. 1981;1:299–305.
36. Arbues J, Galindo A, Puente JM, et al. Typical isolated ectrodactyly of hands and feet: early antenatal diagnosis. *J Matern Fetal Neonatal Med*. 2005;17:299–301.
37. Sachar K, Mih AD. Congenital radial head dislocations. *Hand Clin*. 1998;14:39–47.
38. De Maio F, Corsi A, Roggini M, et al. Congenital unilateral posteromedial bowing of the tibia and fibula: insights regarding pathogenesis from prenatal pathology: a case report. *J Bone Joint Surg Am*. 2005;87(7):1601–1605.
39. Stevenson DA, Viskochil DH, Schorry EK, et al. The use of anterolateral bowing of the lower leg in the diagnostic criteria for neurofibromatosis type 1. *Genet Med*. 2007;9(7):409–412.

# 132 Skeletal Dysplasias and Selected Chromosomal Disorders

Jerry Dwek and Ralph S. Lachman

As opposed to just a decade ago, the study of congenital syndromes is no longer an exercise in the rote memorization of seemingly disconnected syndromes. Instead, the unveiling of the intricacies of the genetic code has made apparent relationships among many inborn syndromes that had been previously unsuspected. What has emerged is that a relatively few genes are the cause of a multitude of syndromes, and by grouping syndromes and dysplasias into families based on the gene at fault, a taxonomy has emerged and has allowed a framework within which we can understand the relationships among a number of dysplasias and syndromes.

An abridged form of the International Skeletal Dysplasia Society skeletal dysplasia classification serves as the organization of this chapter (Box 132.1).[1] The full nosology text can be found at http://isds.ch/uploads/pdf_files/Nosology2010.pdf (accessed December 12, 2016). The major genetic families are presented with a short description of the salient unifying characteristics of the diseases within each group. When known, the gene and protein involved are considered and the impact of the mechanism of action discussed. The major members of each group are then expanded on to provide a clear picture for the reader.

In this chapter, the terms *syndrome* and *dysplasia* are used somewhat loosely. A syndrome is a set of characteristic findings that occur together and suggest a particular diagnosis, although the cause may not be known. A dysplasia is a set of characteristic findings in which the cause and effect are known. The distinction now has lost its value, as the cause of many "syndromes" are now known, and the term *dysplasia* is used to indicate not just purely a grouping of symptoms but the actual disease entity.

## RADIOLOGIC ASSESSMENT

In the history of the delineation of many of the specific skeletal dysplasias, radiologic assessment plays a major role. By using an orderly approach to the radiographic analysis, the general type of the dysplasia may be elucidated. Many of the skeletal dysplasias and syndromes have distinctive radiographic features that will allow an exact diagnosis when even one of those distinctive features is identified and used as a search criterion in textbooks on skeletal dysplasia. Two such texts are Taybi and Lachman's *Radiology of Syndromes, Metabolic Disorders and Skeletal Dysplasias*, which includes an excellent gamuts section, and *Bone Dysplasias, An Atlas of Genetic Disorders of Skeletal Development* by Spranger and colleagues, in which the images are particularly helpful.[2,3] In the online version of Taybi and Lachman's book, the gamut search may be built iteratively, with the diagnoses becoming more selective as findings are added to the search criteria. Internet searches can also be performed on the Online Mendelian Inheritance in Man database, which is accessed through the US Library of Medicine portal at http://www.ncbi.nlm.nih.gov/pubmed/.

### Step I: Assessment of Disproportion

*Micromelia* is overall shortening of the extremities. *Rhizomelia* is relative shortening of the femurs and humeri. *Mesomelia* is relative shortening of the radii, ulnae, tibiae, and fibulae. *Acromelia* is relative shortening of the bones of hands and feet.

Classification of the shortened appendicular segment is helpful for diagnosis. Rhizomelia may be very helpful to confirm the specific diagnosis of the rhizomelic form of chondrodysplasia punctata. Very significant mesomelia suggests a group of specific disorders loosely classified as the mesomelic dysplasias. Acromelia is found in many disorders; when it occurs by itself, several specific dysplasias are suggested, including acrodysostosis, acromicric dysplasia, or pseudohypoparathyroidism.

The pattern of brachydactyly may facilitate diagnosis. For instance, brachydactyly type E manifests with variable shortening of the metacarpals and distal phalanges, and brachydactyly type A4 manifests with shortening restricted to the second and fifth middle phalanges. Even the absence of acromelia may be helpful. The lack of significant hand and foot shortening is a significant feature of spondyloepiphyseal dysplasia congenita (SEDC), a type 2 collagenopathy.

### Step II: Assessment of Epiphyseal Ossification

If epiphyseal ossification is delayed or if the ossified epiphyses are very small, irregular for age, or both, then an epiphyseal dysplasia of some sort is present. Carpal and tarsal bones are often affected. In diseases that can be considered pure epiphyseal dysplasias such as multiple epiphyseal dysplasia (MED) and pseudoachondroplasia, carpal and the tarsal bones are markedly crenellated and small (Fig. 132.1). Another excellent location for epiphyseal analysis is the ring apophyses of the vertebral bodies, which exhibit delayed and irregular epiphyseal ossification in epiphyseal dysplasia. Central anterior vertebral body protrusions (central tongues or beaking) noted in Morquio syndrome and pseudoachondroplasia are also disorders related to abnormalities of the ring apophyses.

### Step III: Assessment of Metaphyses and Physes

Fraying and irregularity of the physes and abnormal flaring of the metaphyses indicate disturbed endochondral ossification. Marked irregularity of the physes is characteristic of the pure metaphyseal dysplasias such as metaphyseal dysplasia, Jansen or Schmid type. When the metaphyses are merely flared and the physes are fairly normal, endochondral ossification may be slowed, but the actual process of endochondral ossification progresses normally. This occurs in achondroplasia. The metaphyses are flared, whereas the physis and the zone of provisional calcification (ZPC) are sharply defined (Fig. 132.2).

Rickets also disturbs the physis. In rickets, physeal abnormalities lead to the classic appearance of metaphyseal cupping and fraying. Except in healing rickets, the ZPC is inapparent. In metaphyseal chondrodysplasias, the ZPC is present, although it is markedly irregular (Fig. 132.3). Analysis of the sclerotic line of the ZPC is frequently an excellent differentiating feature. Other factors include prominent osteopenia in rickets with blurring of the trabeculae; clinical data are also very helpful.

### Step IV: Assessment of the Diaphyses

Diaphyseal abnormalities primarily include bent bones and thickened sclerotic bones. The classic bent bone dysplasia is

## Abstract:

Contained in this chapter is an updated guide to skeletal dysplasias and select chromosomal disorders. Included are descriptions of some of the more prominent and common syndromes as well as some of the more obscure syndromes. While some of these latter syndromes are indeed rare, the recent advances in molecular genetics makes these rarities important for a deeper understanding of how these syndromes occur and how they manifest themselves. By understanding the interlacing of molecular genetics and radiologic phenotypes, these rare syndromes are no longer isolated in the great mélange of unconnected disease states. Instead they become real and more comprehensible disease states and indeed are made more interesting. In order to run we must first learn to walk and to that end the chapter begins with a stepwise methodology that may be used when a skeletal dysplasia is analyzed. This is probably the most important part of this chapter upon which the rest of the chapter is built. The remainder of the chapter uses an abridged version of the official Nosology and Classification of genetic skeletal disorders as a way to organize the findings and for ease of reading.

## Keywords:

skeletal dysplasia
chromosomal disorder
stepwise methodology
syndromes
nosology

**BOX 132.1** Nosology and Classification of Genetic Skeletal Disorders

**FGFR3 GROUP**

- Thanatophoric dysplasia type 1 and 2
- Homozygous achondroplasia
- Achondroplasia
- Hypochondroplasia

**TYPE 2 COLLAGEN GROUP**

- Achondrogenesis type 2
- Spondyloepiphyseal dysplasia congenital
- Kniest dysplasia

**TYPE 11 COLLAGEN GROUP**

- Stickler syndrome type 2
- Marshall syndrome
- Oto-spondylo-mega-epiphyseal dysplasia

**ABNORMAL SULFATION GROUP**

- Achondrogenesis type 1b
- Diastrophic dysplasia
- Multiple epiphyseal dysplasia: Multilayered patellae/brachydactyly/clubfeet

**FILAMEN GROUP**

- Oto-palato-digital syndrome type 1 and 2
- Larsen syndrome

**TRPV4 GROUP**

- Metatropic dysplasia
- Spondylometaphyseal dysplasia Koslowski type

**SHORT RIB DYSPLASIAS**

- Short rib-polydactyly
- Asphyxiating thoracic dysplasia
- Chrondroectodermal dysplasia

**MULTIPLE EPIPHYSEAL DYSPLASIA AND PSEUDOACHONDROPLASIA GROUP**

- Multiple epiphyseal dysplasia
- Pseudoachondroplasia

**METAPHYSEAL CHONDRODYSPLASIA GROUP**

- Jansen-type metaphyseal chondrodysplasia
- Schmid-type metaphyseal chondrodysplasia
- McKusick-type metaphyseal chondrodysplasia
- Shwachman-Diamond dysplasia

**SPONDYLOMETAPHYSEAL DYSPLASIA GROUP**

- Spondyloenchondromatosis

**ACROMELIC/ACROMESOMELIC DYSPLASIA GROUP**

- Trichorhinophalangeal syndrome types I and II
- Acromesomelic dysplasia of Maroteaux

**MESOMELIC DYSPLASIA GROUP**

- Dyschondrosteosis

**BENT BONE DYSPLASIA GROUP**

- Campomelic dysplasia

**CHONDRODYSPLASIA PUNCTATA GROUP**

- Rhizomelic type

**INCREASED BONE DENSITY GROUP (WITHOUT MODIFICATION OF BONE SHAPE)**

- Osteopetrosis
- Pyknodysostosis
- Osteopoikilosis
- Osteopathia striata
- Melorheostosis

**INCREASED BONE DENSITY GROUP WITH METAPHYSEAL AND/OR DIAPHYSEAL INVOLVEMENT**

- Craniodiaphyseal dysplasia
- Craniometaphyseal dysplasia
- Pyle disease

**OSTEOGENESIS IMPERFECTA AND DECREASED BONE DENSITY GROUP**

- Osteogenesis imperfecta

**ABNORMAL MINERALIZATION GROUP**

- Hypophosphatasia

**LYSOSOMAL STORAGE DISEASES**

- Hunter syndrome or Hurler syndrome
- Morquio syndrome
- Mucolipidosis type II (I-cell disease)

**OSTEOLYSIS GROUP**

- Hajdu-Cheney dysplasia

**OVERGROWTH SYNDROMES WITH SKELETAL INVOLVEMENT**

- Marfan syndrome
- Congenital contractural arachnodactyly
- Proteus syndrome

**CLEIDOCRANIAL DYSPLASIA AND ISOLATED CRANIAL OSSIFICATION DEFECTS GROUP**

- Cleidocranial dysplasia

**DYSOSTOSES WITH PREDOMINANT VERTEBRAL INVOLVEMENT**

- Currarino triad

**BRACHYDACTYLIES**

- Rubinstein-Taybi syndrome
- Poland anomaly

**LIMB HYPOPLASIA REDUCTION DEFECTS GROUP**

- Brachydactyly A-E
- Brachmann-De Lange syndrome
- Holt-Oram syndrome

**MISCELLANEOUS ASSOCIATIONS, SYNDROMES AND CHROMOSOMAL DISORDERS**

- *VATER/VACTERL*
- Klinefelter syndrome
- Trisomy 13
- Trisomy 18
- Trisomy 21
- Turner Syndrome (chromosome X monosomy)

*VACTERL,* Vertebral, anorectal, cardiac, tracheoesophageal, renal, limb.

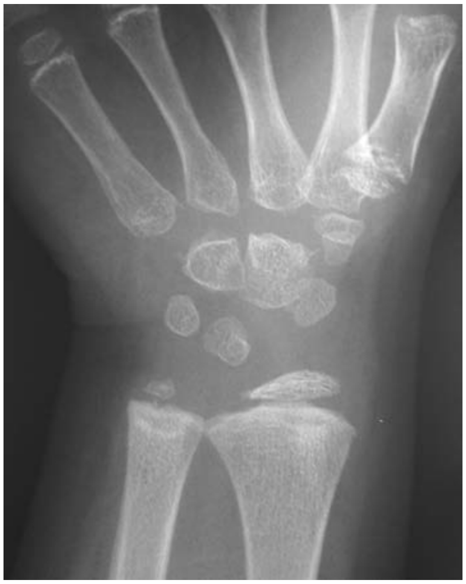

**Figure 132.1. Multiple epiphyseal dysplasia in an 8-year-old boy.** Note the small and crenellated carpal bones.

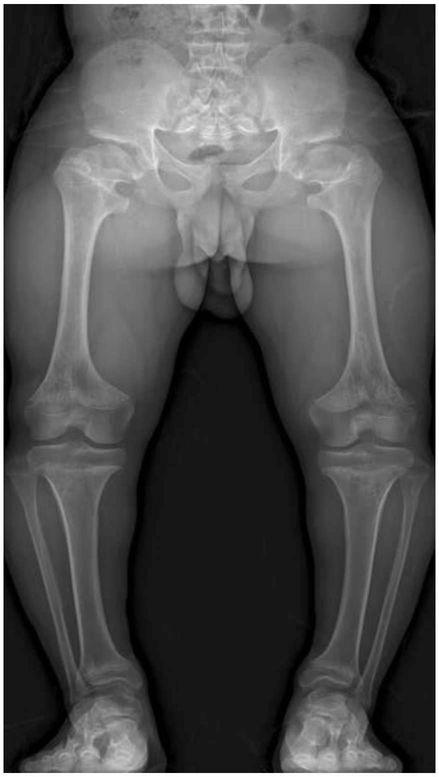

**Figure 132.2. Achondroplasia in a 14-year-old boy.** The long bones are short and thick. Note the normal, sharp-appearing physes.

campomelic dysplasia. Others include hypophosphatasia and kyphomelic dysplasia. Thickened and sclerotic diaphyseal cortices may indicate one of the craniotubular dysplasias.

## Step V: Analysis of the Vertebral Bodies

Decreased height of the vertebral bodies is termed *platyspondyly*. The lumbar vertebral bodies are the best level to analyze compared with the cervical level, especially in infancy. The cervical vertebral bodies tend to appear relatively hypoplastic compared with other levels in the normal infant. This is because ossification occurs later in cervical vertebral bodies compared with vertebral bodies elsewhere. In addition to platyspondyly, other vertebral body changes are important. In the lumbar spine in normal children, the interpediculate distance usually widens on a frontal film moving inferiorly. Inferior narrowing of the interpediculate distance is a feature of fibroblast growth factor receptor 3 (FGFR3) abnormalities such achondroplasia and thanatophoria.

Anisospondyly is when the vertebral body shape varies wildly (e-Fig. 132.4). Multiple ossification centers may also be present. Although rare, this is a specific finding in dyssegmental dysplasia.

## Step VI: Assessment of Bone Mineralization

Bone mineral density should be assessed by not only examining the actual “whiteness” of bones but also by determining the relative thickness of the cortices relative to the medullary cavity and the coarseness of the trabeculae. Osteopenia, especially when severe, indicates defective bone mineralization, as seen in rickets, hypophosphatasia, and osteogenesis imperfecta (OI). Abnormally dense bones may indicate one of the craniotubular disorders such as pyknodysostosis and osteopetrosis. In the neonate, bones are normally sclerotic and the medullary cavity narrowed. Distinguishing abnormally dense bones from normal neonatal sclerosis can be difficult.

## Step VII: Assessment of Joints

Multiple joint dislocations are a salient and persistent feature of some dysplasias. A standard skeletal survey frequently includes only frontal views of the skeleton, which may make it difficult to identify joint dislocations, especially in the infant. The elbow is frequently involved in the setting of dislocations secondary to a dysplasia. Dedicated lateral views are recommended when dislocation is clinically suspected.

## Step VIII: Summation

After all radiologic findings have been established, a gamut search of some or all of these abnormalities, in conjunction with the clinical findings, may lead to the specific diagnosis. If the “group” of dysplasias has been established, then the specific diagnosis can often be made by referring to a differential diagnosis table such as that developed by Taybi and Lachman.[2]

# SELECTED SKELETAL DYSPLASIAS AND SYNDROMES

## Fibroblast Growth Factor Receptor Type 3 Group

***Overview.*** This group includes thanatophoric dwarfism and achondroplasia. The former is probably the most common lethal skeletal dysplasia and the latter the most common skeletal dysplasia. The group includes the milder variant called *hypochondroplasia*, and homozygous achondroplasia, which is similar to thanatophoria.[4]

A common genetic locus *(4p16.3)* is involved. Differing allelic mutations are the cause of the variable severity of expression. The protein encoded is FGFR3, which governs the velocity of endochondral growth. Although long believed that achondroplasia and thanatophoria were caused by loss of function mutations, the mutation in this group actually results in an upmodulation of FGFR3 activity, which is inversely related to the velocity of endochondral growth.[5]

There are common radiologic features in this group. FGFR3 slows endochondral bone growth, so long bones are short. However, it does not affect overall bone thickness because of normal

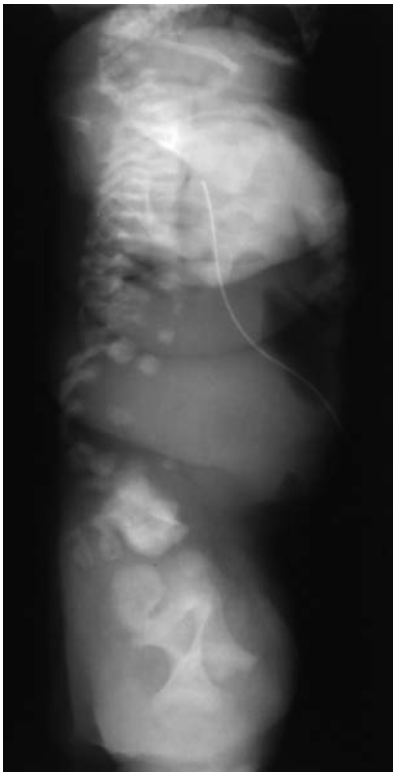

**e-Figure 132.4. Dyssegmental dysplasia in a newborn.** The vertebral bodies vary markedly in size and shape typical of anisospondyly.

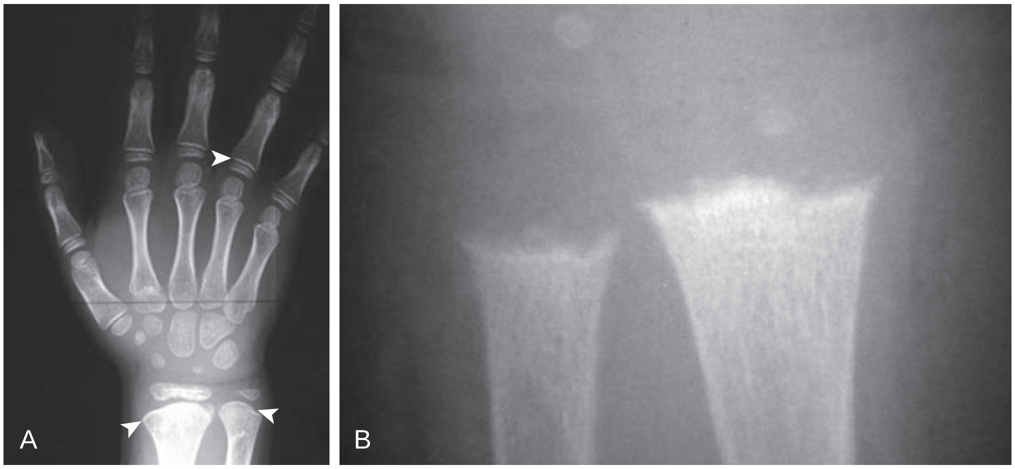

**Figure 132.3. Schmid metaphyseal chondrodysplasia in an 8-year-old boy.** (A) Note the presence of zone of provisional calcification *(arrowheads)*. Normal laboratory values help confirm the diagnosis. (B) Compare this to a 15-month-old girl with rickets. The physes are frayed with mild metaphyseal cupping. The bright white line of the zone of provisional calcification is not evident.

membranous ossification. Therefore long bones are relatively thick. The fibula is usually longer than the tibia. Femoral necks are short and broadened and have a peculiar scooped-out appearance. It is seen as an ovoid lucency of femoral necks, as if an ice cream scoop was radiographed en face. The finding can be seen in all forms of thanatophoria. It is well seen in achondroplasia but not in most forms of hypochondroplasia.

In the normal individual, on a frontal radiograph, the horizontal distance between the pedicles of the vertebral bodies should widen moving inferiorly. FGFR3 group abnormalities exhibit narrowing in the interpediculate distance in the lumber spine. The decrease in the velocity of endochondral ossification also causes platyspondyly. Brachydactyly of all the bones of the hand is present. Because soft tissues are relatively unaffected, fingers are splayed into the "trident configuration."

## Common Features in FGFR3 Group

- Platyspondyly
- Narrow sacrosciatic notch
- Interpediculate narrowing
- Short, thick long bones
- Ovoid lucency at femoral necks (scooped out appearance)
- Frontal bossing
- Trident hands
- Fibula longer than tibia

## Thanatophoric Dwarfism

Given the lethality of this dysplasia, it is aptly named after Thanatos, the Greek god of death (*Thanatophoria*, meaning "death loving").

Type 1 includes "cloverleaf skull," caused by in utero craniosynostosis, and curved long bones. The femurs have a "French telephone receiver" appearance. The type 2 variant has straight long bones and no craniosynostosis.

Platyspondyly is severe. The vertebral bodies are described as U-shaped or H-shaped on an anteroposterior projection.

***Radiographic Findings*** (Fig. 132.5)

1. *Skull:* proportionately large skull in relation to the body, narrow skull base, cloverleaf skull (type 1 only)
2. *Thorax:* long, narrow trunk; very short ribs; handlebar clavicles
3. *Spine:* severely flattened, small vertebral bodies with round anterior ends
4. *Pelvis:* small, flared iliac bones; very narrow sacrosciatic notches; flat, dysplastic acetabula
5. *Extremities:* generalized micromelia; ovoid lucency of femoral necks, round proximal femoral metaphyses with medial spike, curved long bones (type 1 only)

## Achondroplasia

Patients with achondroplasia have normal mentation and a normal or near normal lifespan. As in other members of the FGFR3 family, long bones are short and thick. Interpediculate narrowing is present. In infancy, femoral necks have a scooped out appearance. Since the sacrosciatic notches are narrowed, the pelvic inlet has an appearance of a wide-mouthed champagne glass.

Except for the portions of the occipital bone that form the margin of the foramen magnum, all the bones of the skull are formed by membranous ossification.[6] This results in an enlarged forehead and is termed *frontal bossing*. In contrast, the foramen magnum is narrowed and can cause cervicomedullary compression.

***Radiologic Findings*** (Fig. 132.6 and e-Fig. 132.7)

1. *Skull:* enlarged, with significant midface hypoplasia; hydrocephalus rarely present; small skull base with tight foramen magnum
2. *Thorax:* small; shortened and anteriorly splayed ribs
3. *Spine:* short pedicles with decreased interpediculate distance most marked in the lumbar spine moving downward; posterior vertebral body scalloping, gibbus deformity
4. *Pelvis:* round iliac wings with lack of flaring (elephant ear–shaped), flattened acetabular roofs, narrow sacrosciatic notches with champagne glass shaped pelvic inlet
5. *Extremities:* rhizomelic micromelia
6. *Hands:* brachydactyly with trident hands
7. *Knees:* central deep notch in growth plates (Chevron deformity)
8. *Hips:* proximal femoral ovoid lucency (infancy); hemispheric capital femoral epiphyses, short femoral necks
9. *Legs:* prominent tibial tubercle apophyseal region, fibula overgrowth
10. *Arms:* Cortical hyperostosis at deltoid insertion on anterolateral humerus

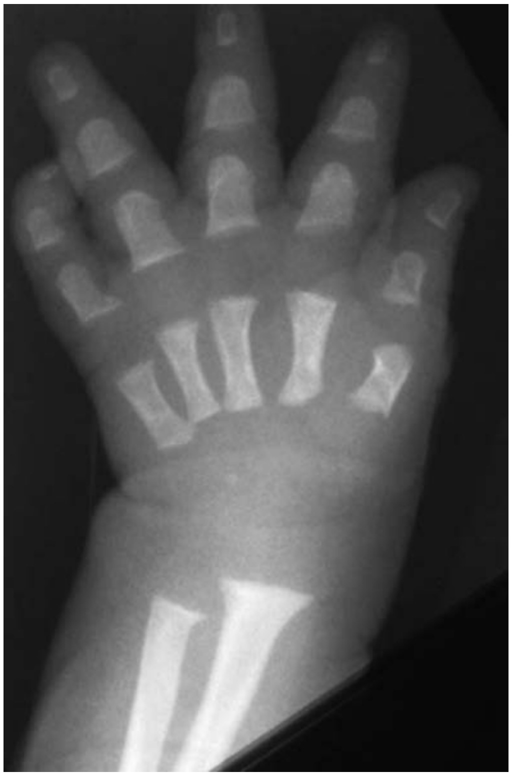

**e-Figure 132.7. Achondroplasia in a 1 year old.** Brachydactyly and trident appearance of the hand is apparent.

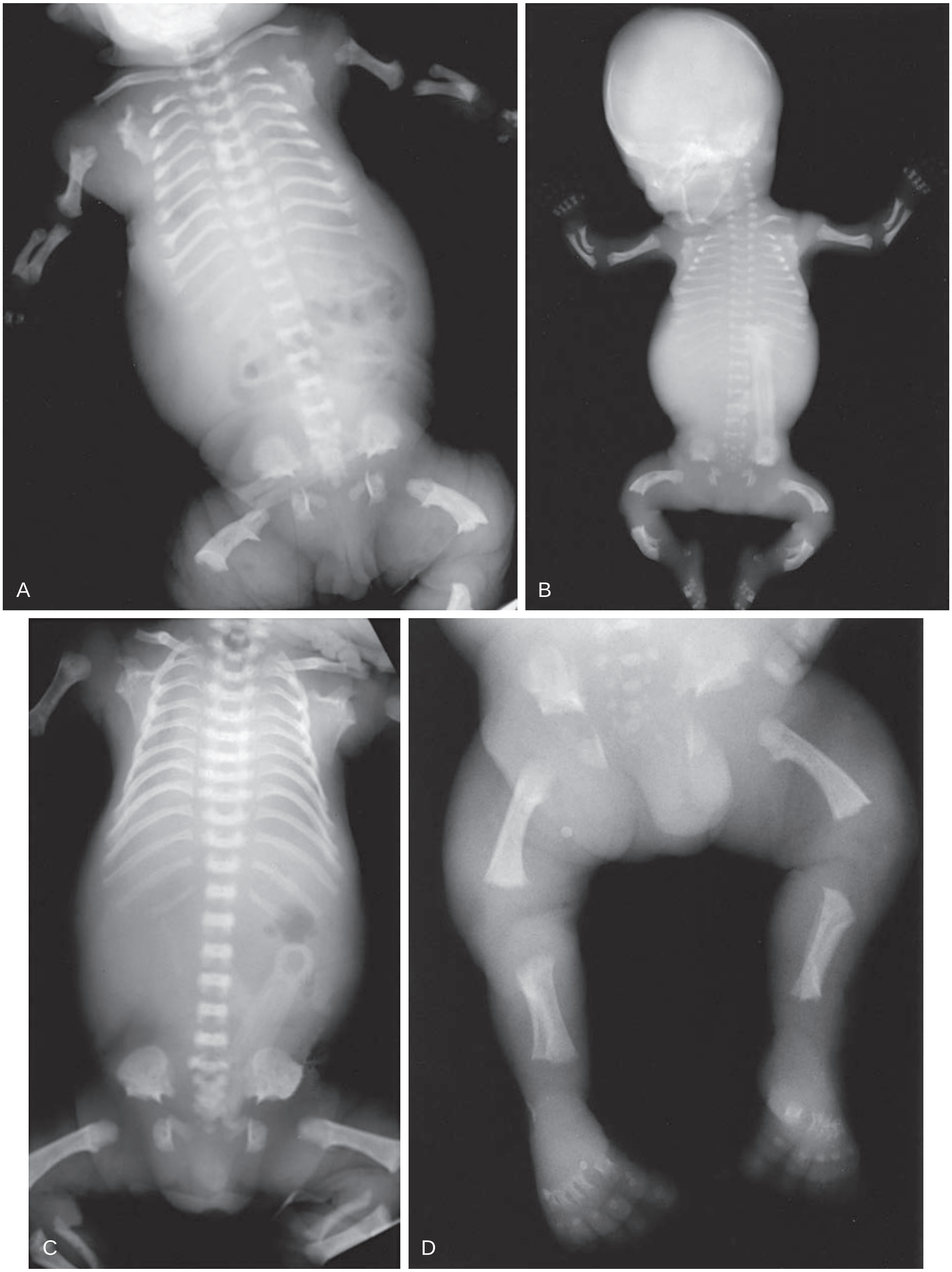

**Figure 132.5. Thanatophoric dysplasia.** (A and B) Radiographic findings in thanatophoric dysplasia type I. In an affected fetus of 30 weeks' gestation (A), a long, narrow trunk; very short ribs; severe platyspondyly are seen. Note the H and U shapes of the vertebral bodies are caused by angle of incidence of the x-ray beam; small, flared iliac wings; narrowed sacrosciatic notches; dysplastic (trident) acetabular roofs; and French telephone receiver–shaped femurs. At 22 weeks' gestation in another affected fetus (B), a proportionally large skull, micromelia, and other findings similar to those in (A) are seen. (C and D) Radiologic findings in thanatophoric dysplasia type II. An affected preterm fetus (C) exhibits findings similar to those in type I except for taller vertebral bodies and straighter femurs. Another affected fetus (D) also shows the same findings as in type I but with straighter femurs.

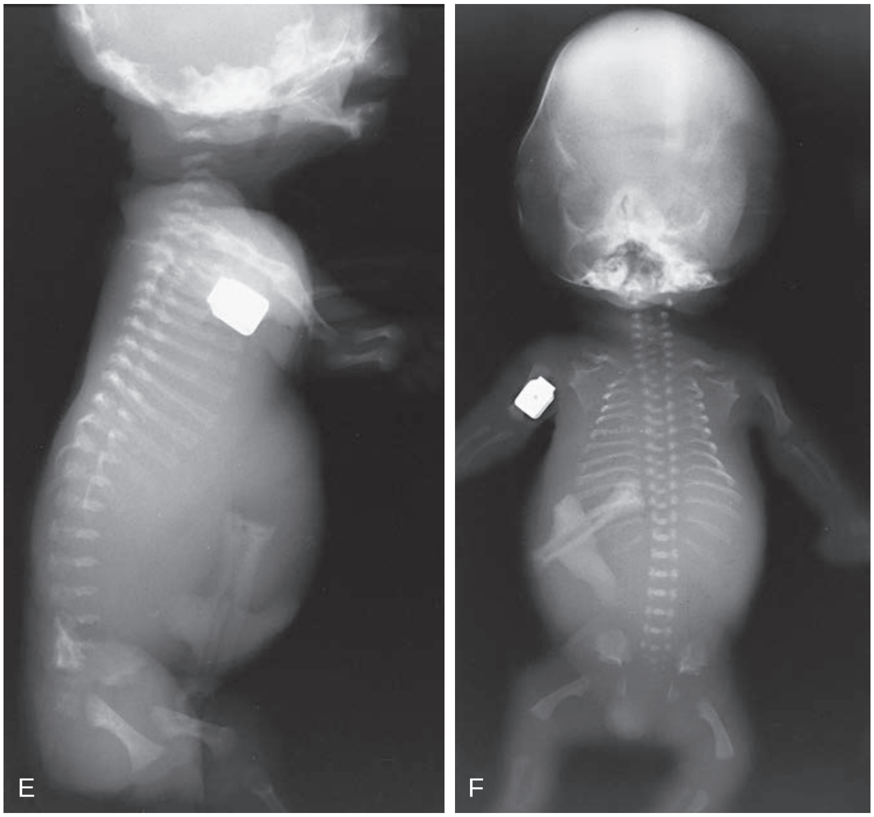

**Figure 132.5, cont'd.** (E) Radiograph of affected infant with severe platyspondyly, anteriorly rounded vertebrae, straight femurs, and severely constricted skull base. (F) Cloverleaf skull and almost straight femurs; otherwise, radiographic findings are similar to those in (C). Note the ovoid lucency at the femoral necks in all cases.

## Hypochondroplasia

In hypochondroplasia, radiographic and clinical findings are less severe compared with achondroplasia, and the diagnosis can be challenging. Stature is slightly shortened but is highly variable and may be normal given the range of normal stature in society. Radiographically, aside from shortening of the long bones, interpediculate narrowing is the most sensitive finding.[7]

## TYPE 2 COLLAGEN GROUP

***Overview.*** Type 2 collagen is present in cartilaginous epiphyses and in the vitreous humor.[8] Therefore abnormalities of collagen 2 manifest with platyspondyly due to lack of normal growth at the vertebral ring apophysis, a general delay in epiphyseal ossification, and myopia. Cleft palate completes the phenotypic picture.

## Common Features in Type 2 Collagenopathy Group

- Platyspondyly
- Delay in epiphyseal ossification most apparent in femoral heads
- Cleft palate
- Myopia
- Short stature
- Occipitoatlantal or atlantodental instability

## Spondyloepiphyseal Dysplasia Congenita

The combination of platyspondyly and short long bones make SEDC a good example of short-limbed, short-trunk dwarfism. It is also a good model for an epiphyseal dysplasia. Ossification in the vertebral bodies begins in the fetus at the lower thoracic spine and progresses superiorly and inferiorly. The cervical spine ossifies last. The normal cervical spine vertebrae at birth are slightly dorsally wedged and are small. In infants with SEDC, the cervical vertebral bodies show little or no ossification. Thoracic and lumbar bodies are, however, small, dorsally wedged, and anteriorly rounded (pear- or oval-shaped), similar in appearance to the cervical spine in the normal infant. In childhood, characteristic central beaks, typical of epiphyseal delay, may be seen. In the adult, vertebral bodies are flattened with irregular end plates.

At birth, no ossification of the talus, calcaneus, or the epiphyses at the knee is present. Normally, the talus and the calcaneus ossify at 20 to 24 weeks' gestation and the epiphyses at about 36 weeks' gestation.

One salient feature is that the hands and feet in patients with SEDC are normal, apart from carpal, midfoot, and hindfoot ossification delay.

***Radiologic Findings*** (Fig. 132.8)

1. *Thorax:* small; short ribs
2. *Spine:* dorsally wedged or oval vertebral bodies (at birth); anteriorly rounded platyspondyly (later)
3. *Pelvis:* absent pubic ossification (at birth and during infancy), vertical ischia with short ilia
4. *Extremities:* normal tubulization with mild micromelia, significant generalized ossification delay (early), and hypoplastic-appearing or dysplastic epiphyses (later), unossified talus or calcaneus in the newborn, normal hands and feet with ossification delay (epiphyses or carpal, tarsal)

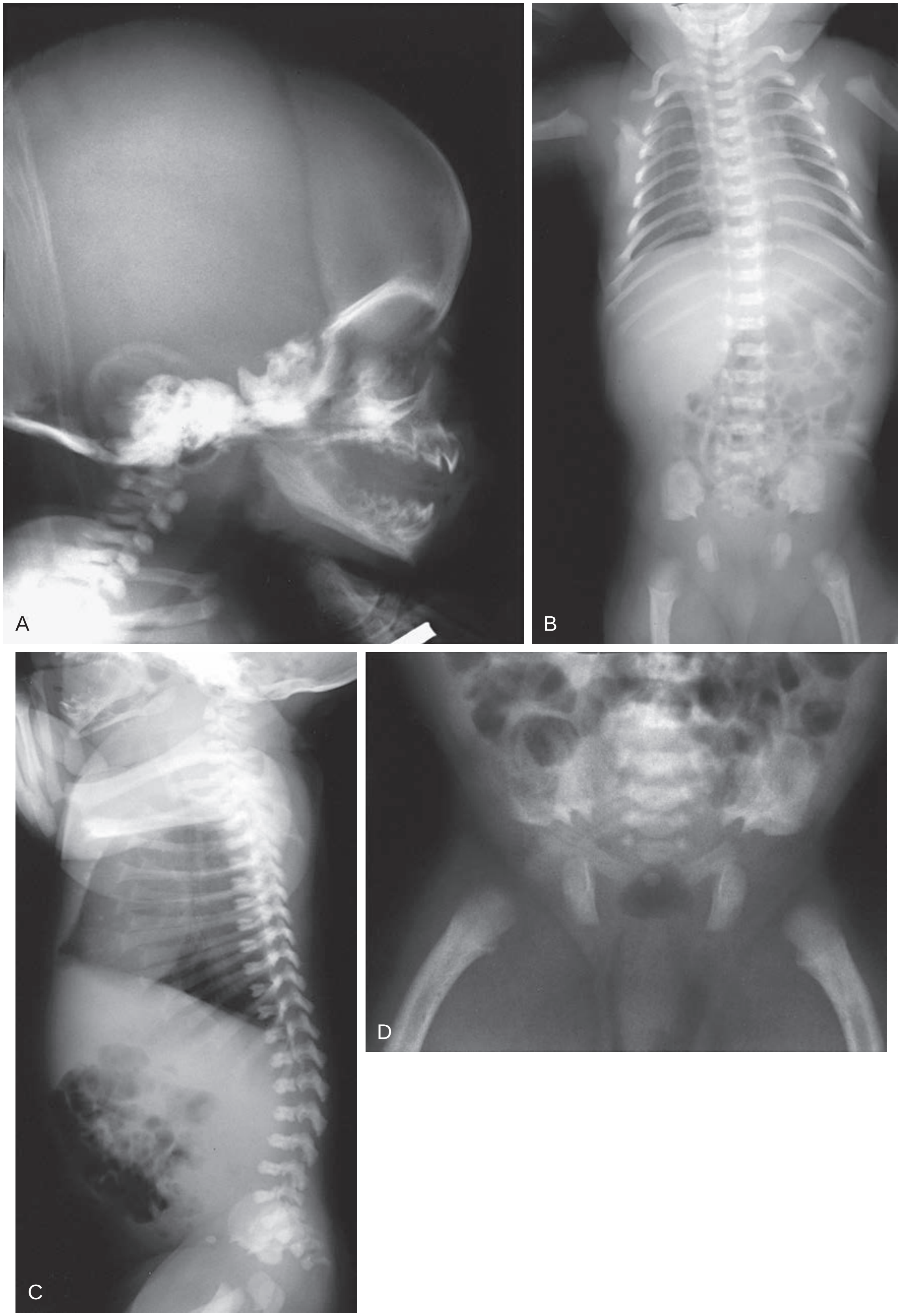

**Figure 132.6. Achondroplasia.** (A–D) Radiographs of an affected newborn. (A) Severe midface hypoplasia. (B) Thorax: small thorax and short ribs. (C) Thorax: short ribs with anterior scalloping and bullet-shaped vertebrae. (D) Pelvis: rounded ilia (elephant ear–shaped) iliac bones, narrow sacrosciatic notches, flat acetabular roof, and proximal femoral ovoid lucency.

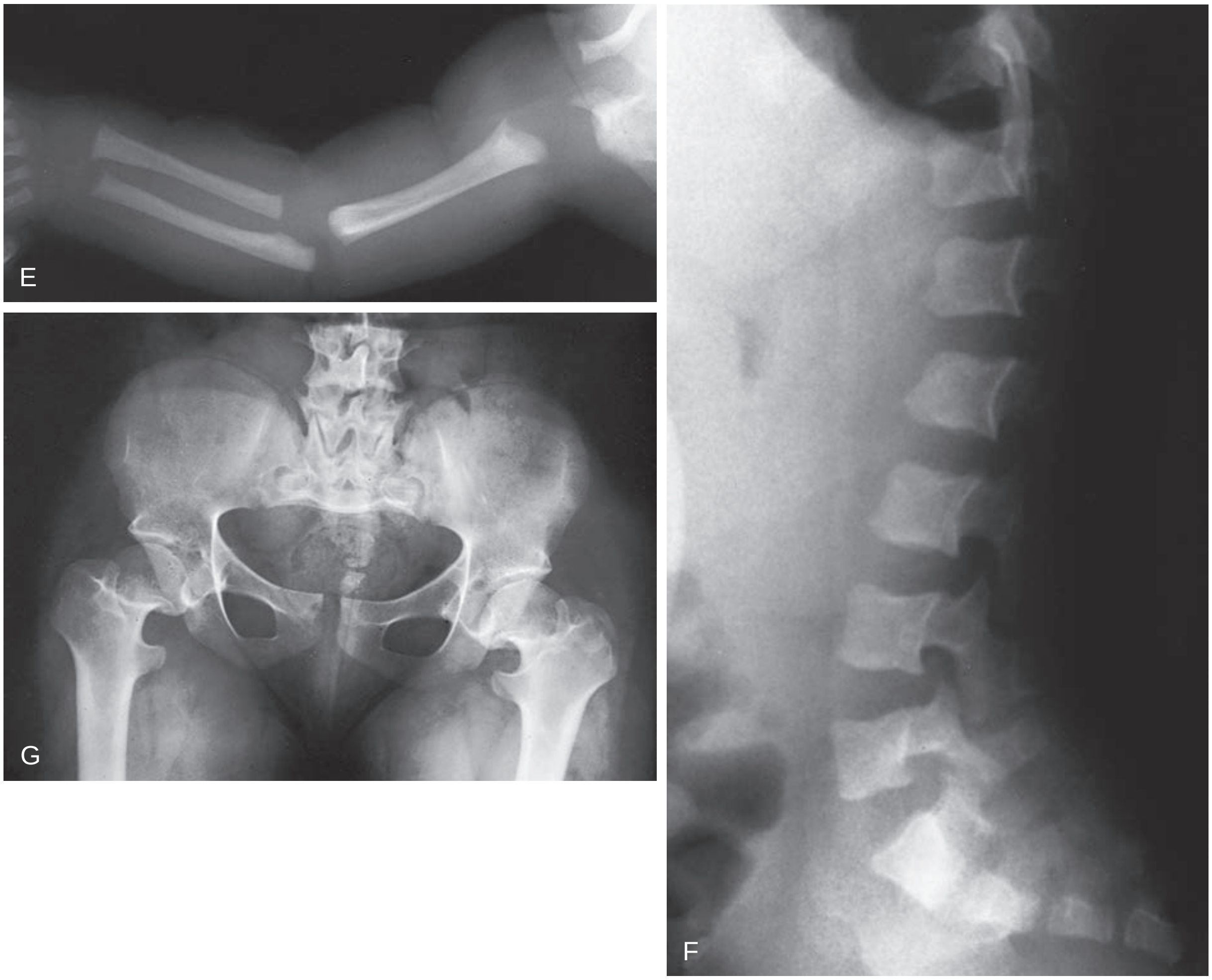

**Figure 132.6, cont'd.** (E) Extremities: rhizomelia and mesomelia. (F) Radiograph in an affected 1½ year old with classic vertebrae with short pedicles, posterior scalloping, and somewhat short vertebral bodies. (G) Radiograph in an affected woman with flat acetabular roofs, elephant ear–shaped iliac wings, and short femoral necks (compare with D). *(G, From Silverman FN. Achondroplasia.* Prog Pediatr Radiol. *1973;4:94–124.)*

## Kniest Dysplasia

The same delay in epiphyseal ossification is seen along with platyspondyly. Cloudlike dystrophic calcification is present in abnormally enlarged epiphyses as the child gets older. On magnetic resonance imaging (MRI), the areas of calcification have prolonged T2 values that are likely related to the degeneration of abnormal collagen matrix.[9]

***Radiologic Findings*** (e-Fig. 132.9)

1. *Thorax:* small to normal
2. *Spine:* coronal clefts (at birth and during infancy), platyspondyly with endplate irregularity (later)
3. *Extremities:* dumbbell femurs; generalized ossification delay, epiphyses becoming hypoplastic or dysplastic and then later even mega-epiphyses, cloudlike irregular calcification in physeal plate regions (in late childhood and early adulthood); hands with bulbous joints (metaphyseal flaring or epiphyseal fragmentation) mimicking rheumatoid arthritis

*Note:* In the newborn, Kniest syndrome is radiographically identical to SEDC except for coronal clefts and dumbbell femurs.

## TYPE 11 COLLAGENOPATHY GROUP

***Overview.*** Members of this group include Stickler syndrome type 2, Marshall syndrome, oto-spondylo-mega-epiphyseal dysplasia (OSMED), autosomal-dominant type (Weisenbach-Zweymuller phenotype and Stickler type 3).[10]

The multiple synonyms and names applied to the different members of the group cause some confusion. Stickler syndrome type 2 is a type 11 collagenopathy and has a similar appearance to Stickler syndrome type 1 (see type 2 collagenopathy previously discussed) with milder ocular changes and more severe auditory changes. It is autosomal recessive. Marshall syndrome is very similar to Stickler syndrome type 2 and may be considered, for all practical purposes, the same entity.

OSMED autosomal-dominant type is a type 11 collagenopathy as well. It is also called *nonocular Stickler syndrome*, *Stickler syndrome type 3*, *or Weisenbach-Zweymuller syndrome*. Osseous changes in OSMED are usually worse with greater shortening of the long bones and platyspondyly.

Adding to the confusion is a very similar form of Stickler syndrome, which is a type 9 collagenopathy. The similarity is not coincidental. Type 11 and type 2 collagens along with type 9 collagen form collagen fibrils so that the phenotypic expression of a type 2, type 11, or type 9 collagenopathy may be similar. This is an important point in the phenotypic expression of genetic abnormalities. Because the tissues of the body are constructed of multiple elements, differing genetic and biochemical abnormalities may have similar outcomes when considering the end results of the tissues produced.

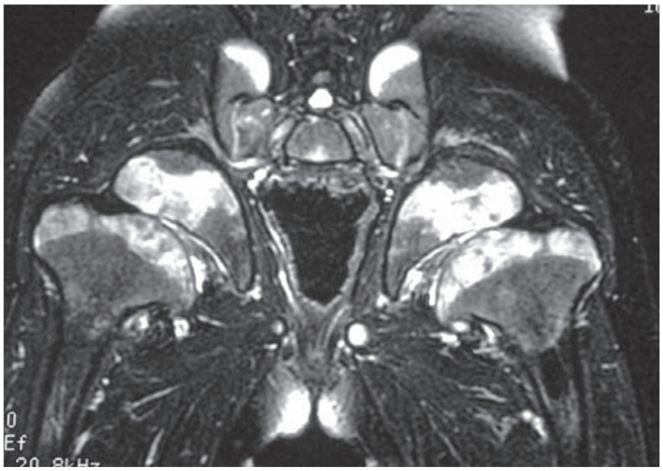

**e-Figure 132.9. Kniest dysplasia in a 5-year-old girl.** Coronal fast-spin echo T2-weighted fat-saturated magnetic resonance (MR) image of the pelvis shows that the unossified epiphyseal cartilage manifests bizarre heterogeneity with lakes of bright signal intensity.

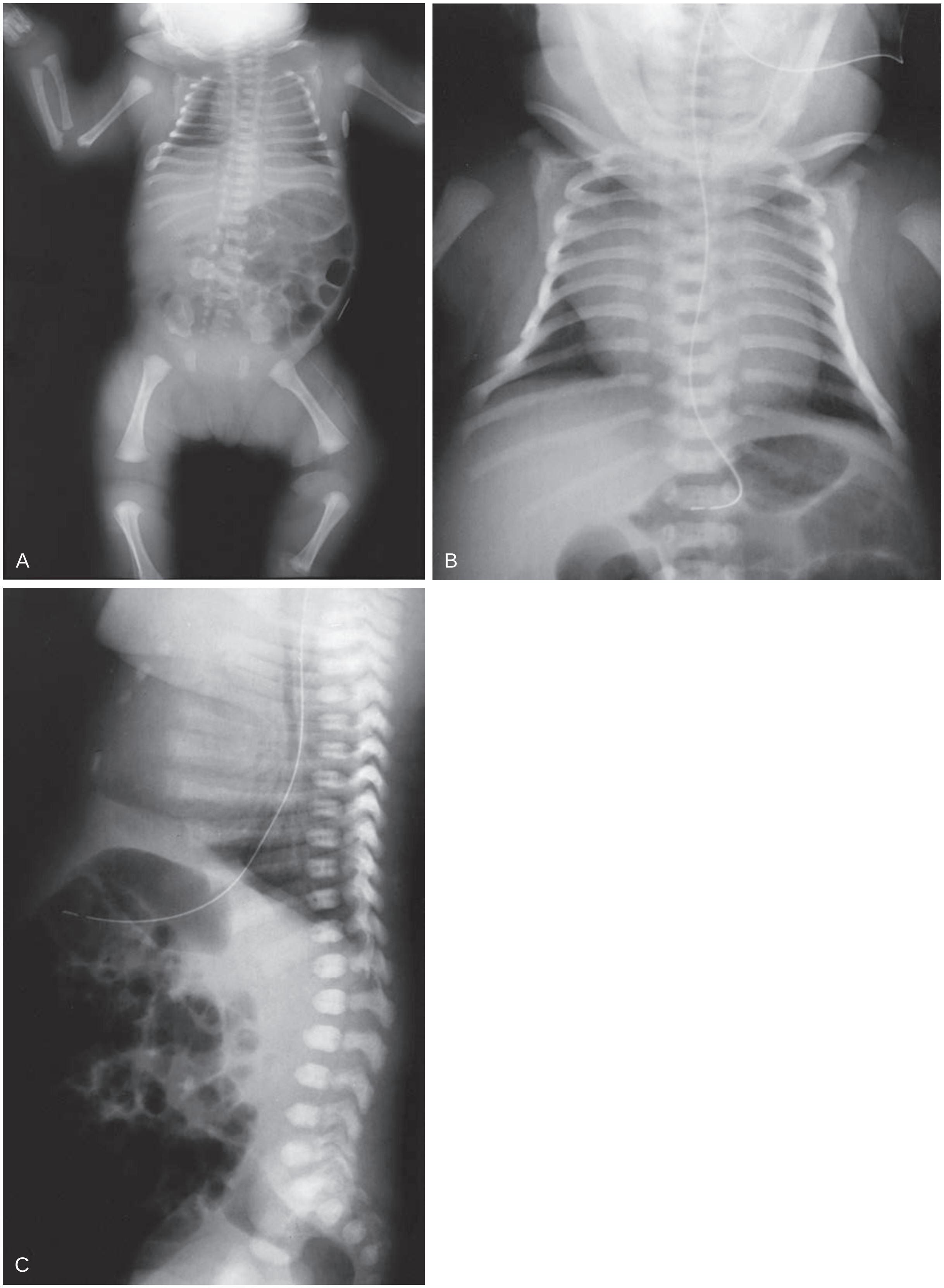

**Figure 132.8. Spondyloepiphyseal dysplasia congenita.** (A) Radiograph in an affected newborn with a small thorax, rounded iliac wings, vertical ischia, absence of pubic ossification, short femurs, and metaphyseal rounding of long bones. (B) Radiograph in an affected newborn with bell-shaped chest, short ribs, and elongated clavicles. (C) Radiograph in an affected newborn with moderately short ribs with mild anterior splaying and anteriorly rounded vertebral bodies with minimal flattening and no coronal clefts.

In practice, when faced with a case with a resemblance to a mild or intermediate severity type 2 or type 11 collagenopathy, both paths should be investigated.

### Common Features in Type 11 Collagenopathy Group

- Similar to type 2 collagenopathy
- Cleft palate
- Sensorineural hearing loss
- Myopia (except for Stickler type 3)
- Epiphyseal dysplasia (may be large or mildly flattened)
- Early arthritis
- Platyspondyly

## ABNORMAL SULFATION GROUP

The abnormal sulfation group is a molecularly defined group of disorders with a defect in the sulfate transporter gene on chromosome 5 coding for the diastrophic dysplasia sulfate transporter (DTDST) protein. This group comprises not only diastrophic dysplasia but also a form of MED as well as achondrogenesis type IB and atelosteogenesis type II.[11] These conditions are all autosomal recessive, and the severity of the phenotype is inversely related to the level of sulfation.[12,13]

### Common Features in Abnormal Sulfation Group

- Platyspondyly
- Scoliosis
- Proximally placed and short first metacarpal ("hitchhiker thumb")
- Clubfoot
- Short, thick long bones

### Diastrophic Dysplasia

Diastrophic dysplasia, like all the other disorders of this group, is an autosomal-recessive condition. It is commonly identifiable at birth and usually nonlethal.

***Radiologic Findings*** (Fig. 132.10)

1. *Head:* ear pinna calcification, cleft or high arched palate
2. *Thorax:* moderately small
3. *Spine:* progressive scoliosis, kyphosis, upper cervical subluxation (odontoid hypoplasia), cervical kyphosis, posterior process clefting (cervical and sacral)
4. *Extremities:* often micromelia; short, thick tubular bones; generalized brachydactyly; short ovoid first metacarpal delta phalanx causing proximal placement of thumb (hitchhiker thumb), twisted metatarsals, accessory and irregular carpal bones; epiphyseal dysplasia with multiple joint contractures
5. *Other sites:* precocious costochondral and laryngeal area cartilage calcification; multiple sternal and patella centers

### Multiple Epiphyseal Dysplasia: Multilayered Patellae/Brachydactyly/Clubfeet

In some cases of MED, *DTDST* gene abnormalities exist. Radiographs reveal MED changes, but patients also exhibit mildly short or normal stature, clubfeet, and additional deformities due to the *DTDST* gene abnormality.

***Radiologic Findings.*** Extremities show the following: epiphyseal dysplasia, especially at the hips; double-layered or multilayered patella (visible on lateral knee radiograph); mild brachydactyly; clubfeet or twisted metatarsals; and mildly shortened long bones, some with mild undertubulation.

## FILAMIN GROUP

The filamin group combines a wide group of dysplasias that have in common an abnormality in the number and configuration of carpal, tarsal, and vertebral bones with joint dislocations. The identification of the group is another triumph in the study of molecular genetics, as it reclassifies correctly a group of disorders described as "syndromes" within a common framework of genetically determined diseases no different from other skeletal dysplasias.[14,15] The group includes oto-palato-digital (OPD) syndrome types 1 and 2, Larsen syndrome, frontometaphyseal dysplasia, Melnick-Needles osteodysplasty, and spondylo-carpal-tarsal synostosis.

### Common Features in the Filamin Group

- Sensorineural hearing loss
- Carpal and digital anomalies
- Joint dislocation
- Skull thickening

### Oto-Palatal-Digital Syndrome

OPD syndrome causes hearing loss, cleft palate, and deformity of the digits, especially the first digit. Hearing loss is caused by malformation of the auditory ossicles. Multiple carpal bone abnormalities, including accessory carpal bones and carpal bone fusion, are present. The capitate may be malformed, with its long axis in the transverse plane. The trapezoid is commonly fused to the base of the second metacarpal, although the finding may not manifest until skeletal ossification nears maturity in late adolescence. The distal phalanx of the thumb is short and wide. The same deformity is present in the foot, where the hallux is short. Prominence of the frontal and occipital bones is present, with a prominent supraorbital ridge. In the more severe type 2 variety, rib shortening is marked. The radial head is usually dislocated.

***Radiographic Findings in OPD*** (e-Fig. 132.11)

1. *Head:* prominent supraorbital ridge
2. *Spine:* small pedicles with wide interpediculate distance
3. *Extremities:* accessory carpal bones, double ossification center of lunate, fusion of carpal bones especially trapezoid and scaphoid, fusion of the second metacarpal to trapezoid in adolescence, similar findings in feet; short first metatarsal and phalanges of great toe, and short and wide distal phalanx of thumb; radial head dislocation

### Larsen Syndrome

In Larsen syndrome, multiple joint dislocations are present. In keeping with the common theme of filamin abnormalities, supernumerary carpal bones are common along with other digital changes. A doubled calcaneal ossification center is a helpful clue to accurate diagnosis. Scoliosis is common.

***Radiographic Findings*** (Fig. 132.12 and e-Fig. 132.13)

1. *Spine:* cervical spine kyphosis
2. *Extremities:* multiple joint dislocations, double or triple calcaneal ossification center, accessory carpal bones, broad irregular metacarpals

## TRPV4 GROUP

TRPV4 (transient receptor potential cation channel, subfamily 5, member 4) is a calcium permeable nonselective cation channel that appears to play an important role in chondrogenesis. This channelopathy is also the cause of several other nonskeletal syndromes such as Charcot Marie-Tooth disease, scapula-peroneal

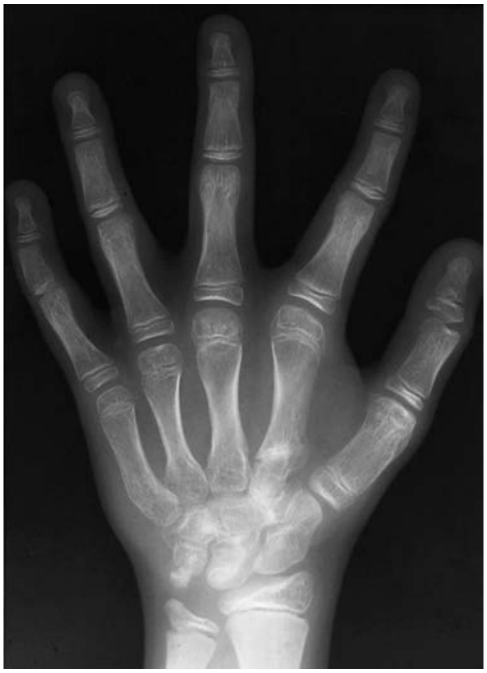

**e-Figure 132.11. Oto-palato-digital syndrome.** Frontal radiograph shows fusion of the second metacarpal with the adjacent deformed carpal bones. Widening and abnormal tubulation of the metacarpals are seen. The distal phalanx of the thumb is short with a coned-shaped epiphysis. Clinodactyly is present.

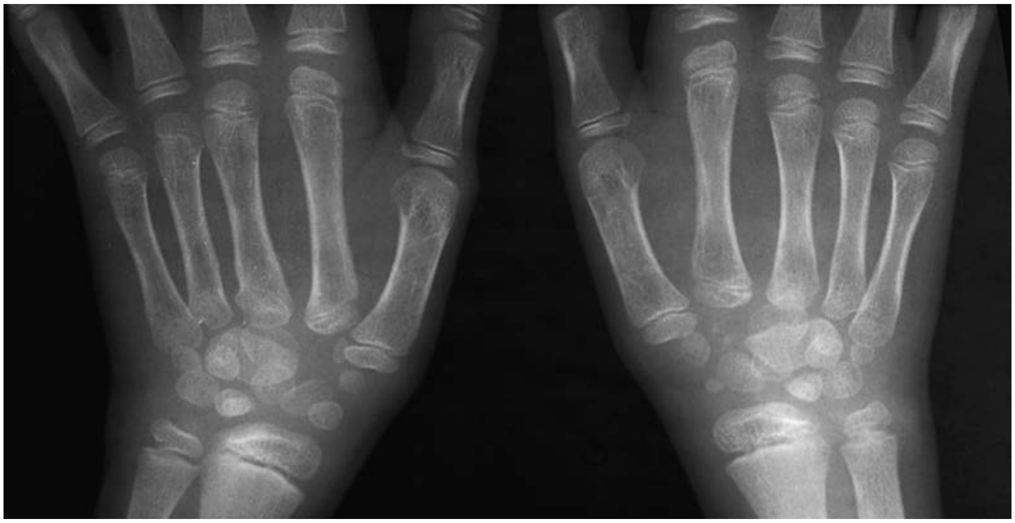

**e-Figure 132.13. Larsen syndrome in an 8-year-old girl.** Posteroanterior radiograph of the wrists shows multiple extra carpal bones with deformity of the second metacarpal heads. An accessory ossification center is seen at the base of the second metacarpal.

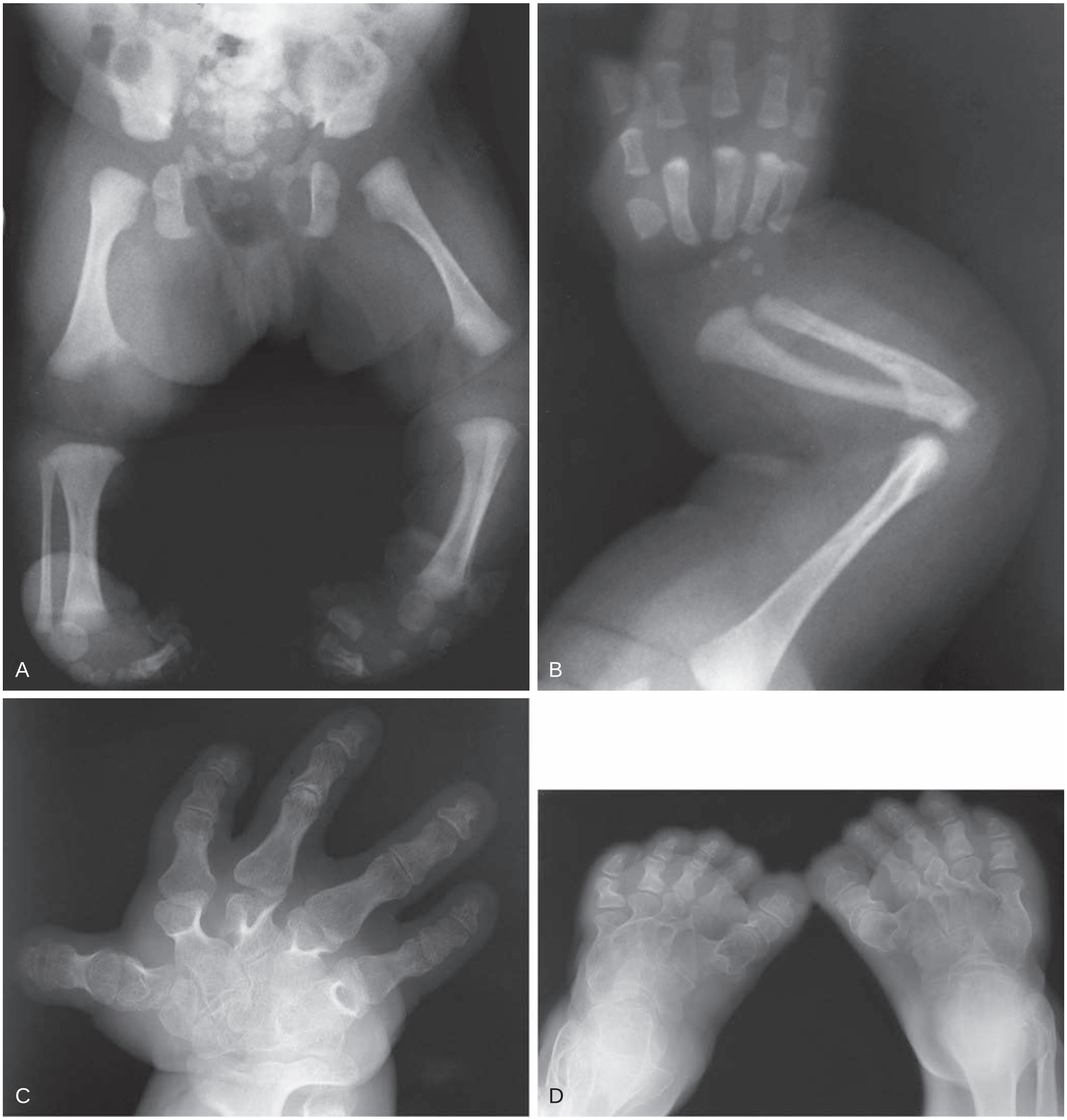

**Figure 132.10. Diastrophic dysplasia.** (A and B) Radiographs from an affected newborn. (A) Lower extremities: rhizomelia and mesomelia and severe clubfeet deformities. (B) Upper extremity: elbow dislocation and short, ovoid first metacarpal. (C and D) Radiographs from an affected 21 year old. (C) Upper extremity: hitchhiker thumb, ovoid first metacarpal, brachydactyly, and irregular and extra carpal bones. (D) Lower extremities: unusual clubfoot and twisted metatarsals.

spinal muscular atrophy, and congenital distal spinal muscular atrophy.[16,17]

The key to this group is the appearance of the vertebral bodies on a frontal view. Because of a relatively wide but flat vertebral body, the pedicles appear "overfaced." This means that the pedicle outline projects completely within the contour of the vertebral body instead of at the margin of the body overlying the superior end plate. The appearance has been also described as an "open staircase." Additionally, the major members of the group—metatropic dysplasia, brachyolmia (autosomal-dominant type), and spondylometaphyseal dysplasia (SMD) Koslowski type—also manifest delay in carpal bone ossification. Although brachyolmia primarily affects the vertebral bodies, subtle metaphyseal changes are seen as they are in metatropic dysplasia and SMD Koslowski type. It may be very difficult to differentiate between metatropic dysplasia and SMD Koslowski type.

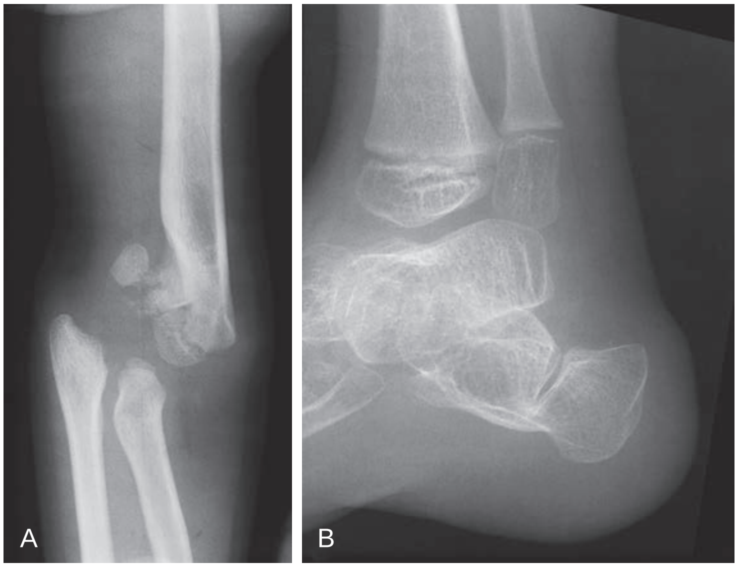

**Figure 132.12. Larsen syndrome in a 5-year-old girl.** (A) Anteroposterior elbow radiograph shows chronic dislocation with epiphyseal deformities. (B) Lateral radiograph of an ankle in a 5-year-old boy shows a bifid calcaneus and deformity of the talus and distal tibial epiphysis.

## Common Features in the TRPV4 Group

- Platyspondyly with overfaced pedicles
- Carpal ossification delay
- Metaphyseal or physeal irregularity

## Metatropic Dysplasia

Metatropic dysplasia, or metatropic dwarfism, is evident in the newborn with a relatively long trunk and markedly shortened limbs. This "changing" dysplasia over time produces a short-trunk or short-limb form of dwarfism. Although heterogeneous, most cases are nonlethal and are autosomal dominant.

***Radiologic Findings*** (Fig. 132.14)

1. *Thorax:* small; short ribs
2. *Spine:* dense wafer vertebral bodies (newborns), reconstituted platyspondyly (children and adults), scoliosis (adults)
3. *Pelvis and hips:* short, squared iliac wings; flat, irregular acetabular roof; narrow sacrosciatic notches; widening of proximal femoral metaphyses with a pronounced medial aspect about lesser trochanter (halberd [hunting ax]–shaped proximal femurs)
4. *Extremities:* flared metaphyses (trumpet shaped), with epiphyseal dysplasia and shortening (dumbbell shape).

## Spondylometaphyseal Dysplasia Koslowski Type

Characteristic radiographic findings (e-Fig. 132.15) include severe platyspondyly with overfaced pedicles. The extremities show sclerosis, flaring, and irregularity at the metaphyses. Carpal bone ossification is delayed and may not be apparent until age 5 to 6 years.

## SHORT RIB DYSPLASIAS

The short rib dysplasias with or without polydactyly (short rib–polydactyly [SRP]) group of disorders is a diverse group, linked only radiologically by extreme rib shortening.

Some members of this group are now known to be ciliopathies. Including several types of SRP and types of asphyxiating thoracic dysplasia (ATD).[18] ATD are caused by mutations in genes encoding for normal dynein heavy chains or other aspects of the ciliogenesis. It is interesting to note that situs abnormalities are a feature of these dysplasias attesting to the important role cilial transport plays in body situs.

## Short Rib–Polydactyly Dysplasia

SRP dysplasia is a subgroup of disorders that are typed largely on radiographic grounds. Types I and III are quite similar, as are types II and IV. The role of the pediatric radiologist is to make the diagnosis of this subgroup as separate from ATD and chondroectodermal dysplasia. To that end, it is important to note the SRP dysplasias have the shortest ribs of any of the skeletal dysplasias.

***Radiologic Findings*** (Fig. 132.16)

1. *Thorax:* small; very short horizontal ribs
2. *Spine:* relatively normally shaped
3. *Pelvis:* small, dysplastic ilia
4. *Extremities:* micromelia; medial and lateral spurs at metaphyses; ovoid or tiny, normal-shaped tibias; severe brachydactyly with hypoplastic middle and distal phalanges; polydactyly commonly present

## Asphyxiating Thoracic Dysplasia (Jeune Syndrome)

ATD is a genetically heterogeneous disorder with a mixed prognosis. Many affected patients die in the perinatal period from respiratory complications related to a small chest. Survivors may die from renal complications (progressive nephropathy) later in life. Sometimes, postaxial polydactyly is present. Definite radiographic (but not clinical) similarities to chondroectodermal dysplasia are evident. Some cases are so alike radiologically that they are best termed *ATD/Ellis–van Creveld syndrome complex*.

***Radiologic Findings*** (Fig. 132.17)

1. *Thorax:* long and barrel-shaped, handlebar clavicles, short horizontal ribs with bulbous anterior ends

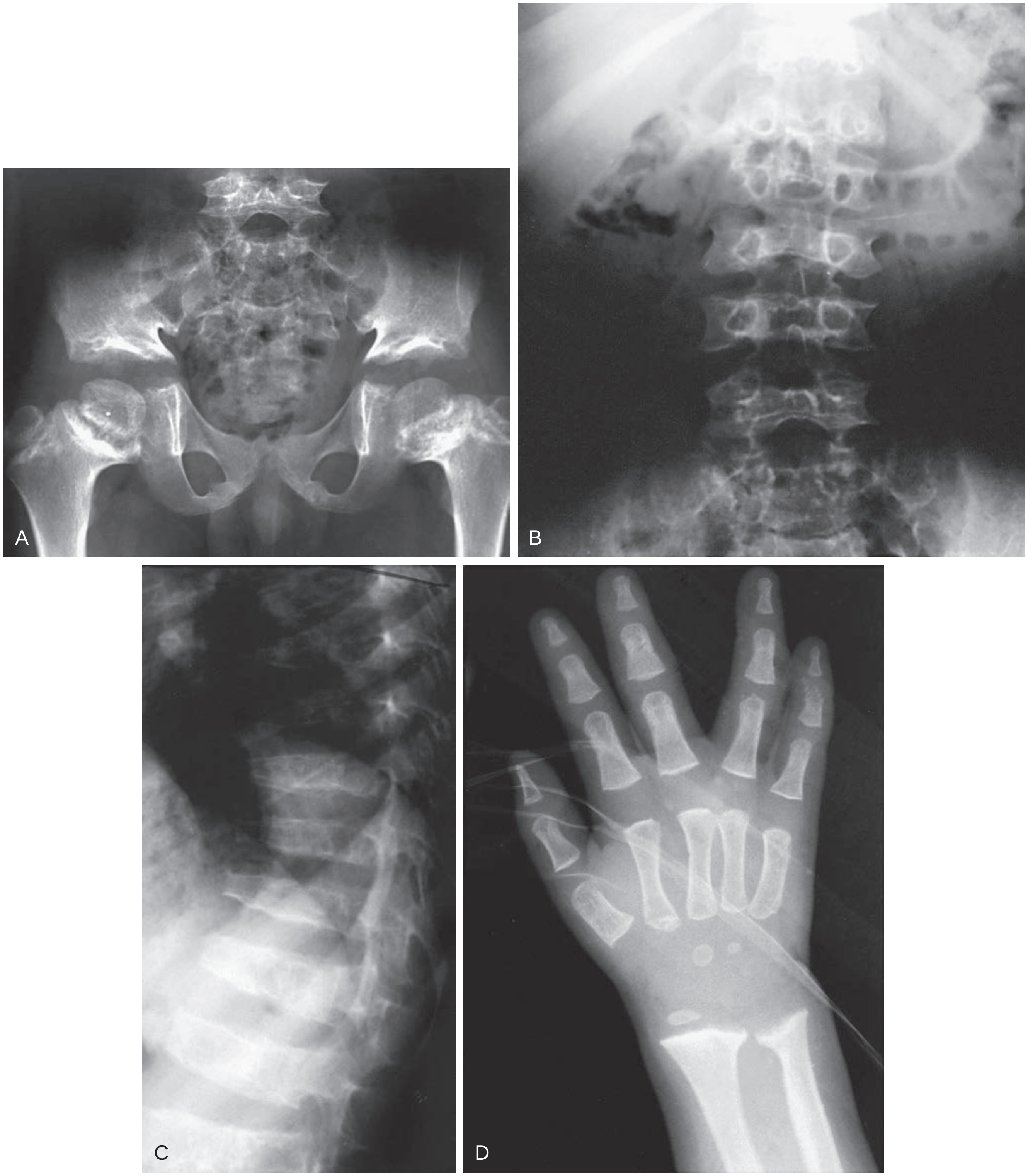

**e-Figure 132.15. Kozlowski-type spondylometaphyseal dysplasia.** (A–C) Radiographs from an affected 8 year old. (A) Pelvis: narrow sacrosciatic notches, ossification defect (acetabular roofs), and widened epiphyseal plates. (B and C) Spine: overfaced vertebral bodies ("open staircase," or closely set pedicles) and flattened, irregular vertebral bodies (platyspondyly). (D) An affected 2 year old with metaphyseal widening and irregularity at the wrist and short tubular bones of the hands, with almost no carpal bone ossification. Note the similarities in proximal femurs to metatropic dysplasia (see Fig. 132.14).

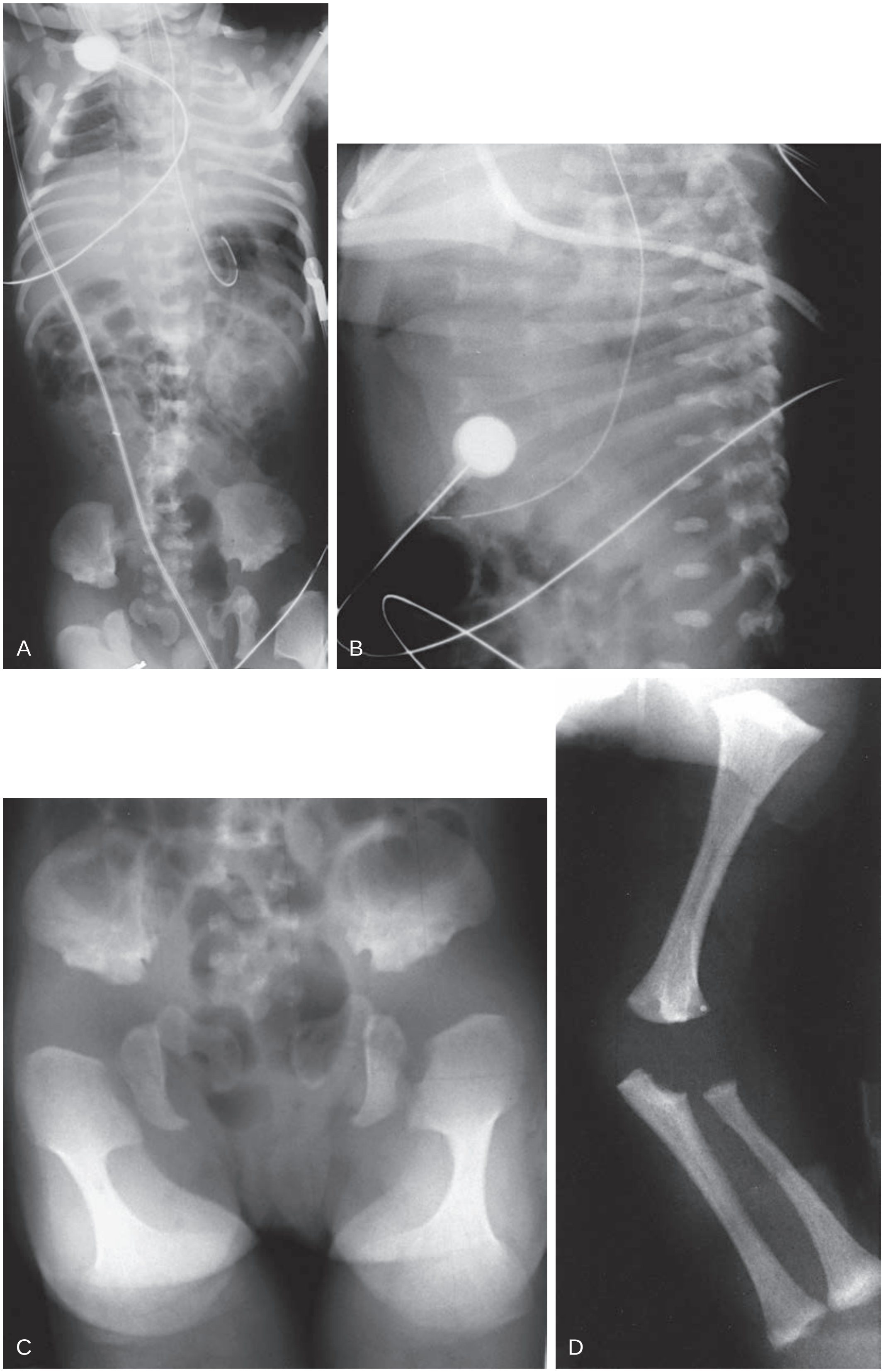

**Figure 132.14. Metatropic dysplasia in a newborn.** (A) Thorax: long trunk and small chest. (B) Spine: dense wafer vertebral bodies and short ribs with anterior splaying. (C) Pelvis: short iliac wings; narrow sciatic notches; irregular acetabular roofs; and rounded, enlarged proximal femoral metaphyses (halberd shaped) with markedly flared distal metaphyses (trumpet-shaped). (D) Upper extremities: flared proximal humeral and distal radial and ulnar metaphyses; shortened long bones.

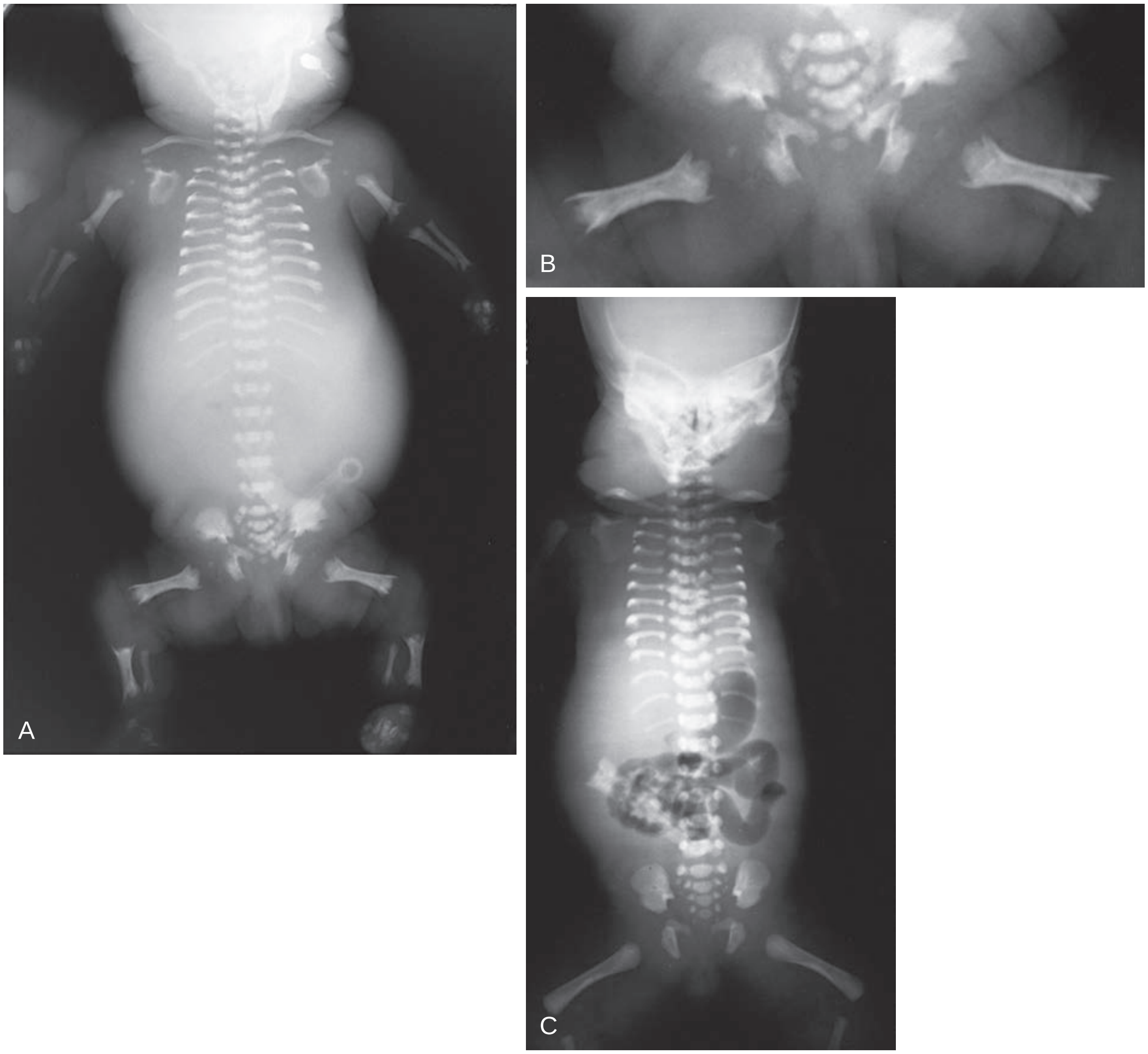

**Figure 132.16. Short rib–polydactyly dysplasia.** (A) Radiograph from a stillborn infant with type I/III form, demonstrating very short ribs and, handlebar clavicles. (B) Magnified, coned view of pelvis shows hypoplastic pelvis with notched acetabula, and metaphyseal-spiked femurs. (C) Radiograph from a stillborn infant with short rib–polydactyly dysplasia type II. Findings are similar to those in type I/III but with round-ended femurs and hypoplastic acetabula.

2. *Spine:* normal
3. *Pelvis:* small; short, flared iliac wings; trident acetabular roof; narrowed sacrosciatic notches
4. *Extremities:* generalized shortening, precocious proximal femoral epiphyseal ossification, cone-shaped epiphyses in hands, metaphyseal flaring with irregularity (more pronounced in childhood)

## Chondroectodermal Dysplasia (Ellis–Van Creveld Syndrome)

Chondroectodermal dysplasia is a nonlethal skeletal dysplasia. The nonskeletal involvement in this disorder is important in defining this condition and distinguishing this lesion from ATD. Signs include hair, nail, and teeth abnormalities, as well as congenital heart disease. Polydactyly is almost invariably present. The radiologic findings are very similar to those of ATD.

***Radiologic Findings*** (e-Fig. 132.18)

1. *Thorax:* small; moderately short ribs
2. *Pelvis:* small; short, flared iliac wings; trident acetabula; narrowed sacrosciatic notches
3. *Spine:* almost normal
4. *Extremities:* generalized shortening with more mesomelia and acromelia; premature ossification of capital femoral epiphyses; delayed ossification of proximal tibial epiphyses; humeral and femoral bowing; exostosis of proximal/medial portion of tibia
5. *Hands:* characteristic postaxial polydactyly, capitate/hamate (and other carpal) fusions, extra carpal bone, cone-shaped epiphyses
6. *Feet:* polydactyly

## MULTIPLE EPIPHYSEAL DYSPLASIA AND PSEUDOACHONDROPLASIA GROUP

Pseudoachondroplasia and some cases of typical MED are cartilage oligomeric protein (COMP) gene defects on chromosome 19 (70%) and share some commonality of radiographic findings.

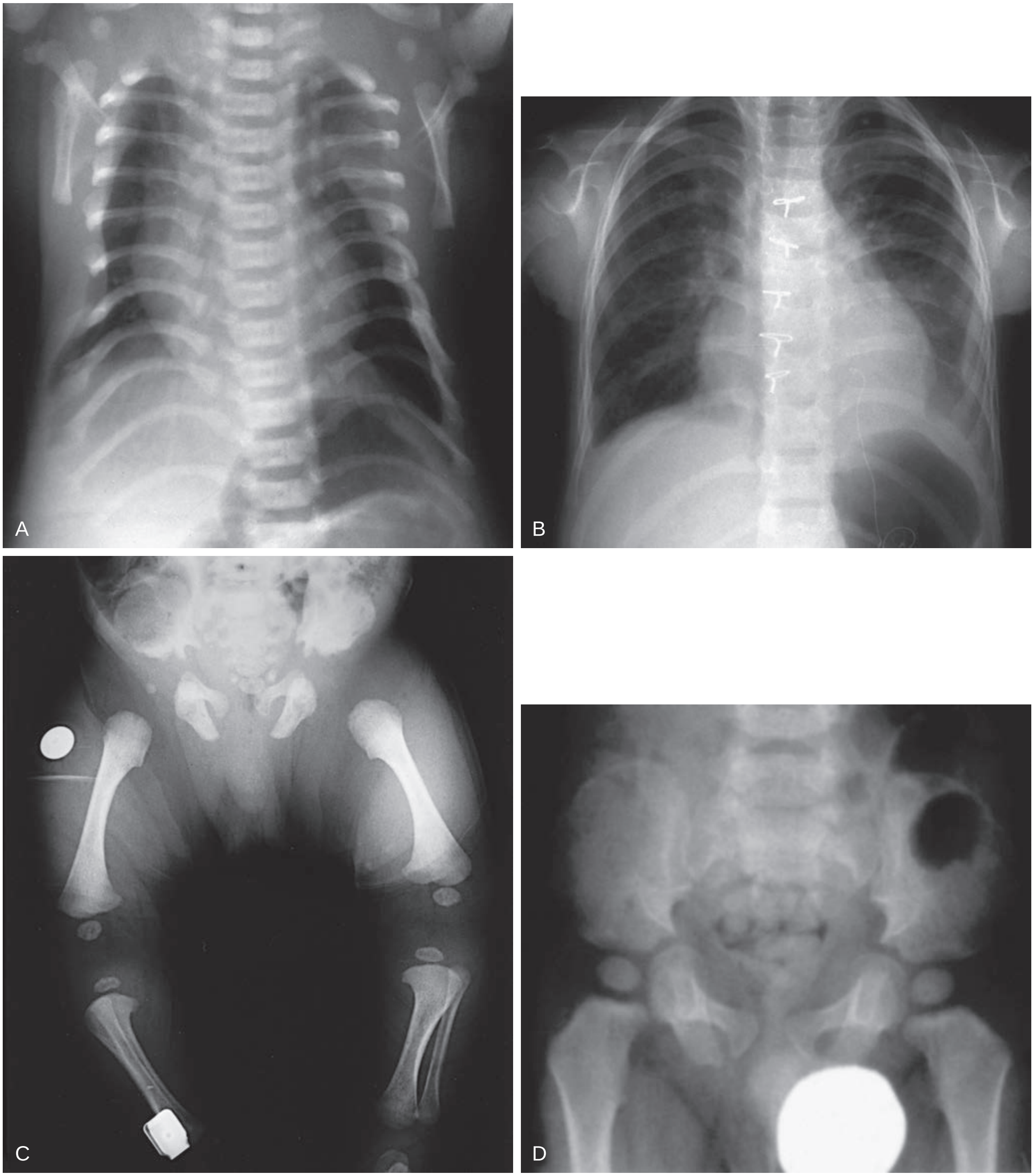

**e-Figure 132.18. Chondroectodermal dysplasia (Ellis–van Creveld syndrome).** (A) Radiograph from an affected 3-month-old infant with a narrow thorax, short ribs, anterior rib flaring, and a normal spine. (B) Radiograph from an affected 5 year old with similar chest configuration; cardiomegaly is present, with sternal sutures from a primum defect repair. (C) Radiograph from an affected 3 month old with short, flared iliac wings; trident acetabula; and mesomelia and rhizomelia. (D and E) Radiographs from an affected child at 2½ (D) and 12 years of age (E), showing near normalization of pelvis. Chondroectodermal dysplasia (Ellis–van Creveld syndrome). (F) Radiograph from an affected 2½ year old with remarkable mesomelia. (G) Radiograph from an affected 2 year old with characteristic hands: polydactyly, middle and distal phalangeal hypoplasia, cone-shaped epiphyses of middle phalanges. (H) Radiograph from the same child as in (G) at 6 years of age. After polydactyly repair, a residual wide fifth metacarpal is seen.

*Continued*

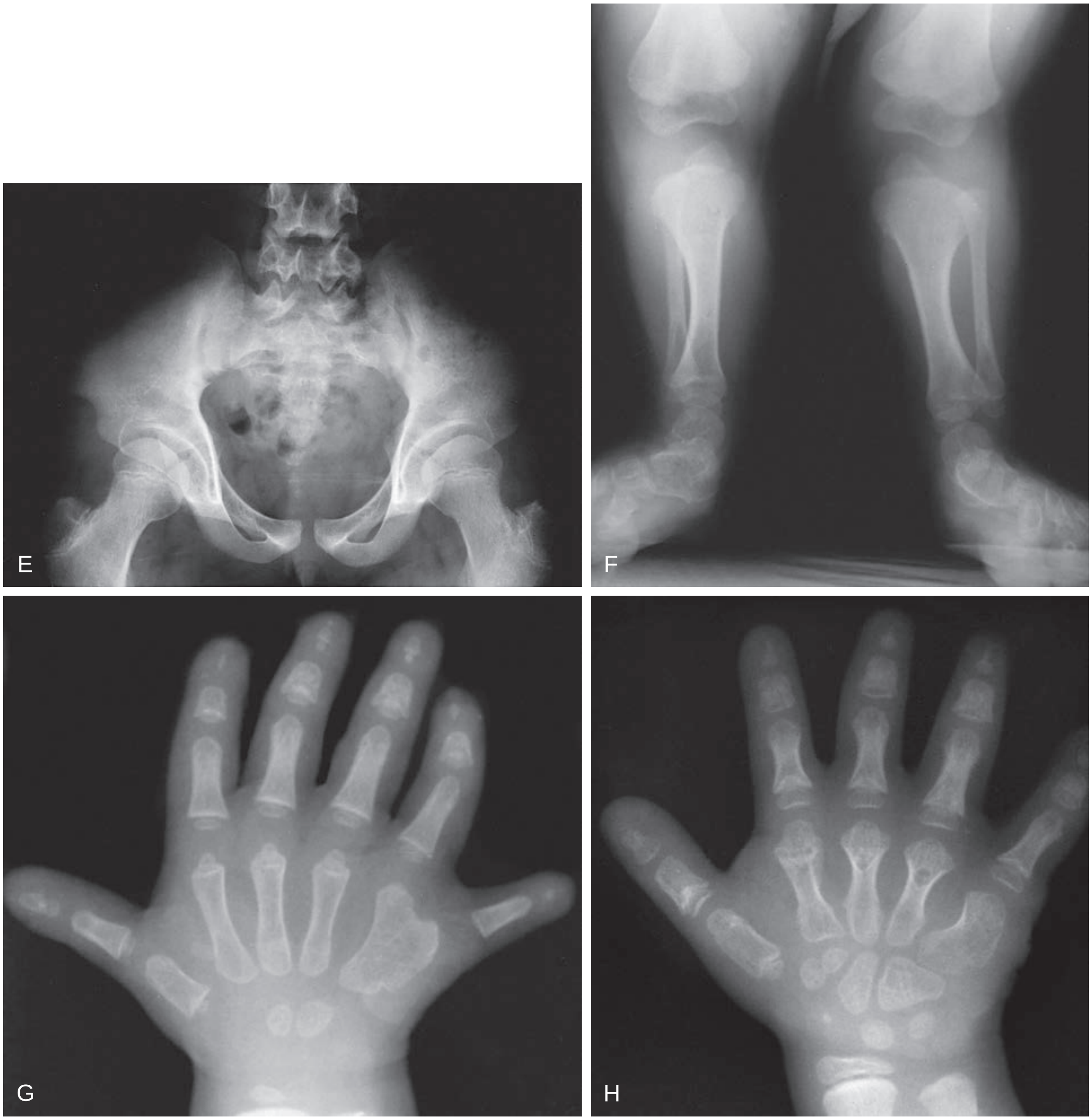

e-Figure 132.18, cont'd.

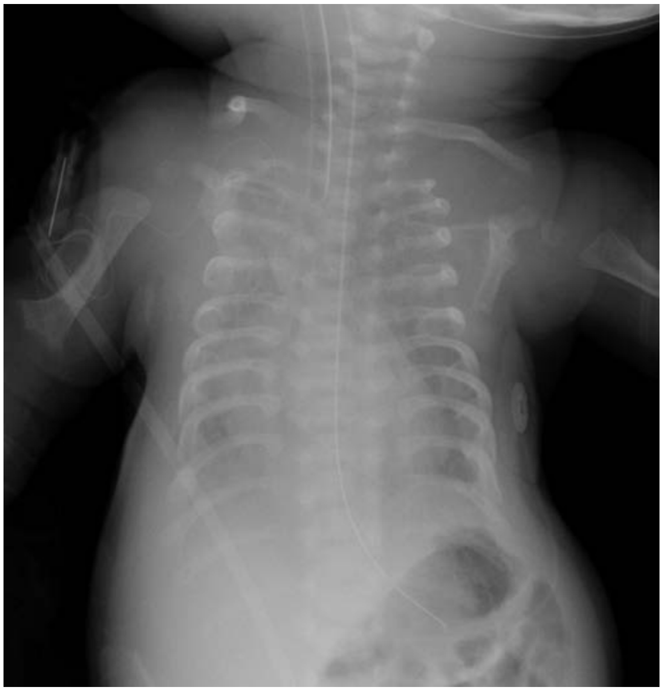

**Figure 132.17. Asphyxiating thoracic dysplasia in a newborn.** Note the short ribs (although not as short as ribs in short rib–polydactyly (see Fig. 132.16) and metaphyseal flaring and irregularity in proximal humeri.

However, many other cases of MED (with the same apparent radiologic abnormalities) represent type IX collagen defects, matrilin 3 defects, or defects on the locus responsible for diastrophic dysplasia (DTDST). The majority of the MED cases belong to either COMP or matrilin abnormalities. The described entities within this group are autosomal-dominant disorders.

### Multiple Epiphyseal Dysplasia

Historically, MED was divided into the milder Ribbing form and the more severe Fairbanks form. Although the classification does not agree with molecular genetics data, the distinction is helpful from a clinical point of view. Ribbing MED may entail only hip involvement and can be confused with bilateral Legg-Calvé-Perthes disease and Meyer dysplasia. Differentiation from these entities is possible because almost all patients with MED have clinically significant short stature. Many patients with MED later go through an asymptomatic phase of avascular necrosis of the capital femoral epiphyses. This makes differentiation of MED from Legg-Calvé-Perthes disease very difficult if old radiographs are not available. The Fairbanks form has involvement of all the long bone epiphyses to some degree. MED manifests after about 2 years of age but is most commonly diagnosed in an adolescent or young adult. Involvement is always bilateral and symmetric. The shortening is quite mild.

It is possible to suggest the molecular defect from the radiologic changes. Those affected by the *COMP* gene locus have tiny capital femoral epiphyses, irregular and poorly formed acetabula, and brachydactyly. On the other hand, vertical striations in the metaphyses point toward an error in matrilin.[19]

***Radiologic Findings*** (Fig. 132.19 and e-Fig. 132.20)

1. *Spine:* in young adults, disk herniations into vertebral end plates (Schmorl nodes)
2. *Extremities:* small, irregular, flattened ossification centers (epiphyses); small, irregular carpal (and tarsal) centers

### Pseudoachondroplasia

This short-limb, short-trunk form of skeletal dysplasia was referred to at first as *achondroplasia with a normal face*.

***Radiologic Findings*** (Fig. 132.21)

1. *Skull:* normal
2. *Thorax:* mild anterior rib widening
3. *Spine:* superiorly and inferiorly rounded vertebral bodies, anterior central tongue (unossified ring epiphyses), normalization of vertebrae (later)
4. *Pelvis:* rounded iliac wings; hypoplastic, poorly formed acetabular roofs
5. *Extremities:* mini-epiphyses in the hips, moderate to severe generalized epiphyseal "dysplasia" (small, irregular, poorly ossified), mushroom-like metaphyseal widening and irregularity in the knees, proximally rounded metacarpals with mini-epiphyses in hands, irregular carpal and tarsal bones

## METAPHYSEAL CHONDRODYSPLASIA GROUP

Metaphyseal chondrodysplasias (MCDs) are also a heterogeneous group of disorders that have common radiologic features. Members of this group include Jansen-type MCD, Schmid-type MCD, McKusick-type MCD, and Shwachman-Diamond dysplasia. Spines are usually normal except in Schmid-type MCD, in which mild platyspondyly may be seen. Immune deficiencies are notable in Shwachman syndrome and McKusick-type MCD (cartilage-hair hypoplasia).

### Jansen-Type Metaphyseal Chondrodysplasia

This is the severest form of MCD. The presentation is in the neonatal period or during late infancy, with marked short stature and a waddling gait. This is a distinct autosomal-dominant disorder with an abnormality in a parathyroid receptor gene *(PTHR)*, leading to hypercalcemia and its complications. However, the radiographic findings in the skeleton are not those of typical hyperparathyroidism or hypoparathyroidism.[20]

***Radiologic Findings*** (Fig. 132.22)

1. *Skull:* brachycephaly, platybasia, underdeveloped mandible
2. *Thorax:* normal size; expanded irregular anterior rib ends
3. *Extremities:* extensive irregularity of markedly expanded metaphyses involving all metaphyseal regions; hands exhibit wide separation of epiphyses from metaphyses

*Note:* As in other parathyroid abnormalities, pathologic fractures (in 45% of affected patients) and subperiosteal bone resorption (in 50%) are common.

### Schmid-Type Metaphyseal Chondrodysplasia

This form of MCD is an autosomal-dominant condition caused by a specific defect in collagen type X, the gene for which is located on chromosome 6. This disorder is the mildest of the MCDs. Presentation is usually at about 2 years of age or later with a waddling gait or bowed legs, or both. Mild short stature is present.

***Radiologic Findings*** (Fig. 132.23)

1. *Thorax:* widened anterior rib ends
2. *Spine:* mild platyspondyly
3. *Extremities:* metaphyseal flaring, cupping and fraying, especially at the knees; rounded capital femoral megaepiphysis with widened growth plate; usually no hand involvement

### McKusick-Type Metaphyseal Chondrodysplasia

*Cartilage-hair hypoplasia*, as this entity is also known, is an autosomal recessive disorder. The genetic defect is at the 9p region (*RMRP*

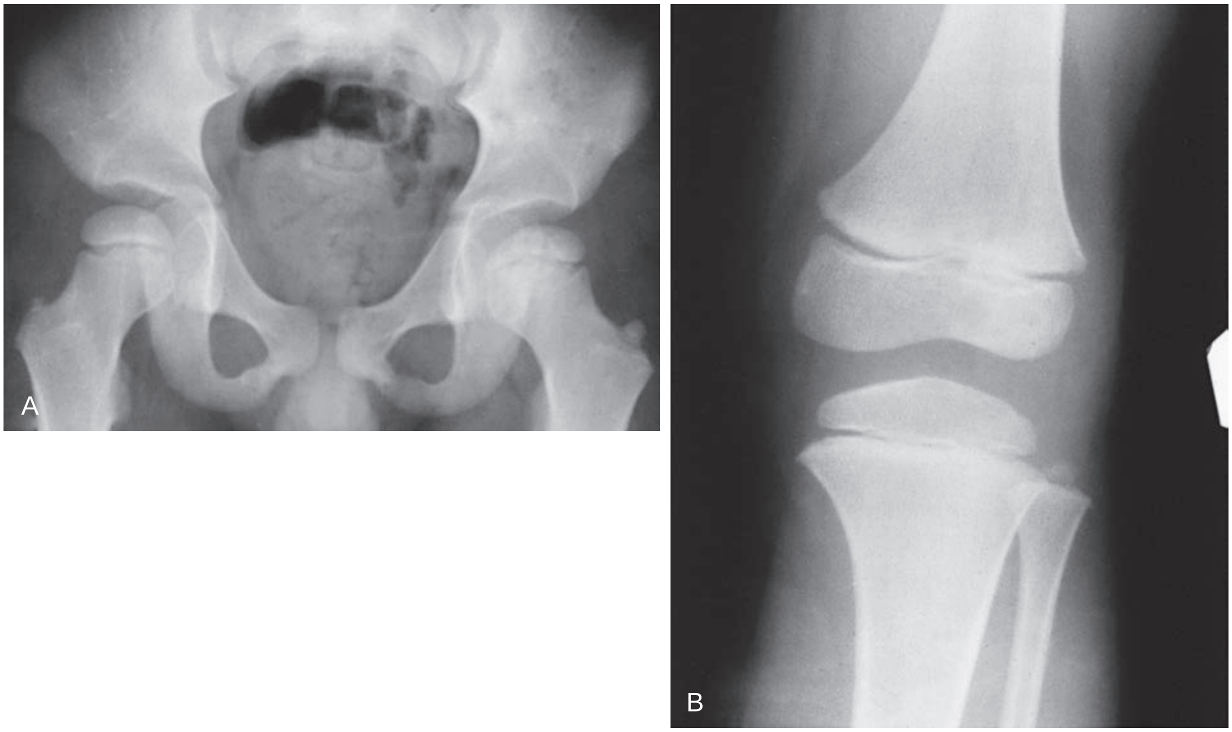

**e-Figure 132.20. Ribbing-type multiple epiphyseal dysplasia in a 7 year old.** Radiographs reveal small-appearing capital femoral epiphyses (A) and relatively normal-sized knee epiphyses (B).

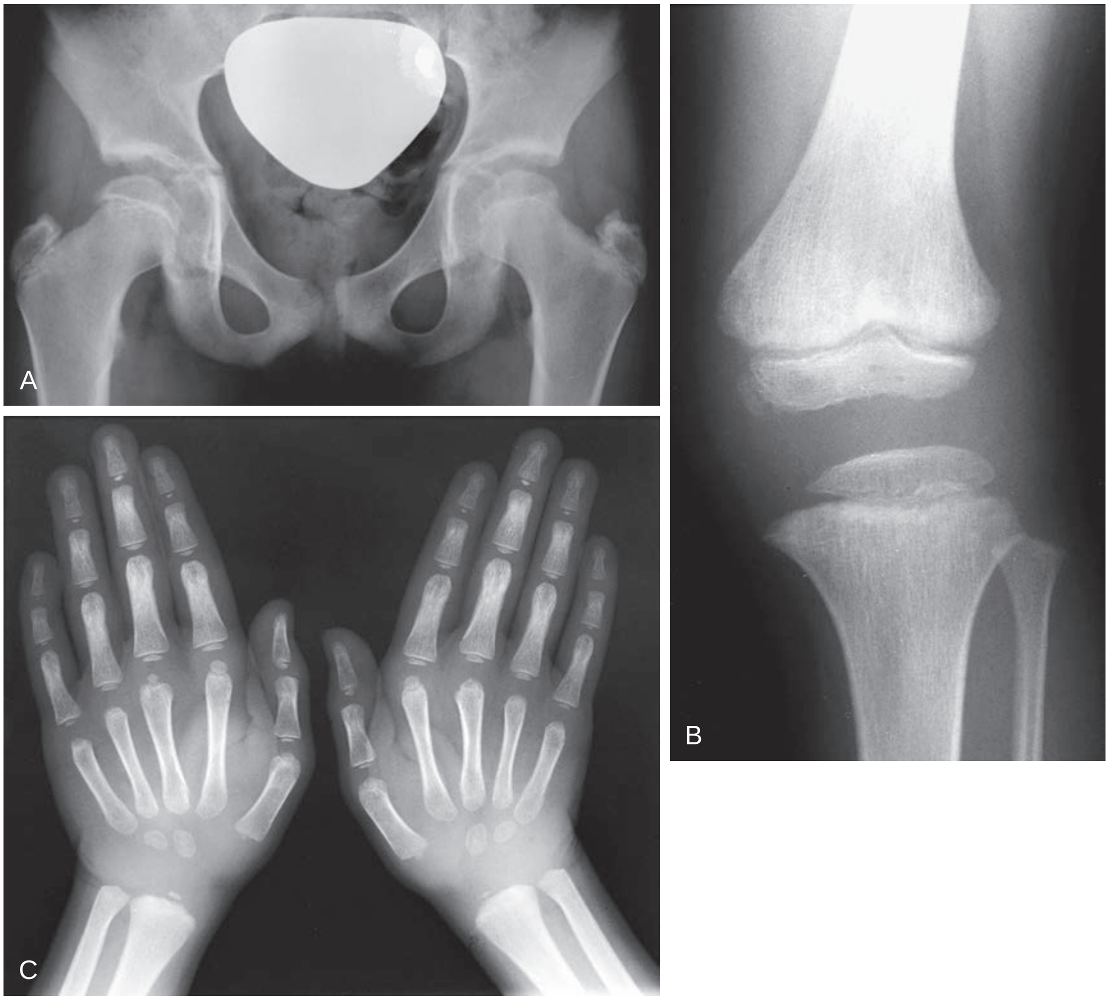

**Figure 132.19. Fairbanks-type multiple epiphyseal dysplasia.** (A) Radiograph from an affected 10 year old with small ossified proximal femoral epiphyses (ossification defect). (B and C) Radiographs from an affected 6 year old. (B) Similar epiphyseal ossification defects in the knee. (C) Small epiphyses of the short tubular bones of the hands and carpal ossification delay (epiphyseal equivalents), but no brachydactyly.

gene), with a high frequency among the Amish and Finnish populations.[21–23] The presentation is of variable short-limbed dwarfism in early childhood. Significant clinical features indicate the diagnosis and are important for medical management: sparse, thin, light-colored hair; Hirschsprung disease; immunologic problems; and increased incidence of malignancy.

***Radiologic Findings*** (e-Fig. 132.24)

1. *Thorax:* anterior rib widening/flaring
2. *Spine:* slightly small square vertebral bodies
3. *Extremities:* flaring, cupping, and fragmentation of metaphyses (especially knees), hips usually spared; brachydactyly with cone shaped epiphysis

### Shwachman-Diamond Dysplasia

This rare autosomal-recessive disorder is also known as *MCD*. Major clinical findings include pancreatic insufficiency and cyclic neutropenia. It manifests in infancy with recurrent infections and failure to thrive. The skeletal radiographic features are quite mild.

***Radiologic Findings*** (e-Fig. 132.25)

1. *Thorax:* anterior rib irregularity or splaying
2. *Extremities:* metaphyseal irregularity and sclerosis, especially at knees and hips
3. *Gastrointestinal:* malabsorption pattern on small bowel examination; lipomatosis of pancreas

## SPONDYLOMETAPHYSEAL DYSPLASIA GROUP

### Spondyloenchondromatosis

This autosomal-recessive disorder is also known as *spondyloenchondrodysplasia*, characterized by low-normal or mild short stature, with kyphosis, lordosis, or both. Prominent joints may be apparent.

***Radiologic Findings*** (e-Fig. 132.26)

1. *Spine:* severe platyspondyly with endplate irregularity
2. *Extremities:* enchondromatosis in long bones, but rarely involving hands and feet

## ACROMELIC/ACROMESOMELIC DYSPLASIA GROUP

The acromelic/acromesomelic dysplasia group consists of a large, heterogeneous collection of disorders. For a number of these dysplasias, the molecular defect has been delineated. Only trichorhinophalangeal syndrome (TRPS) types I and II are described here.

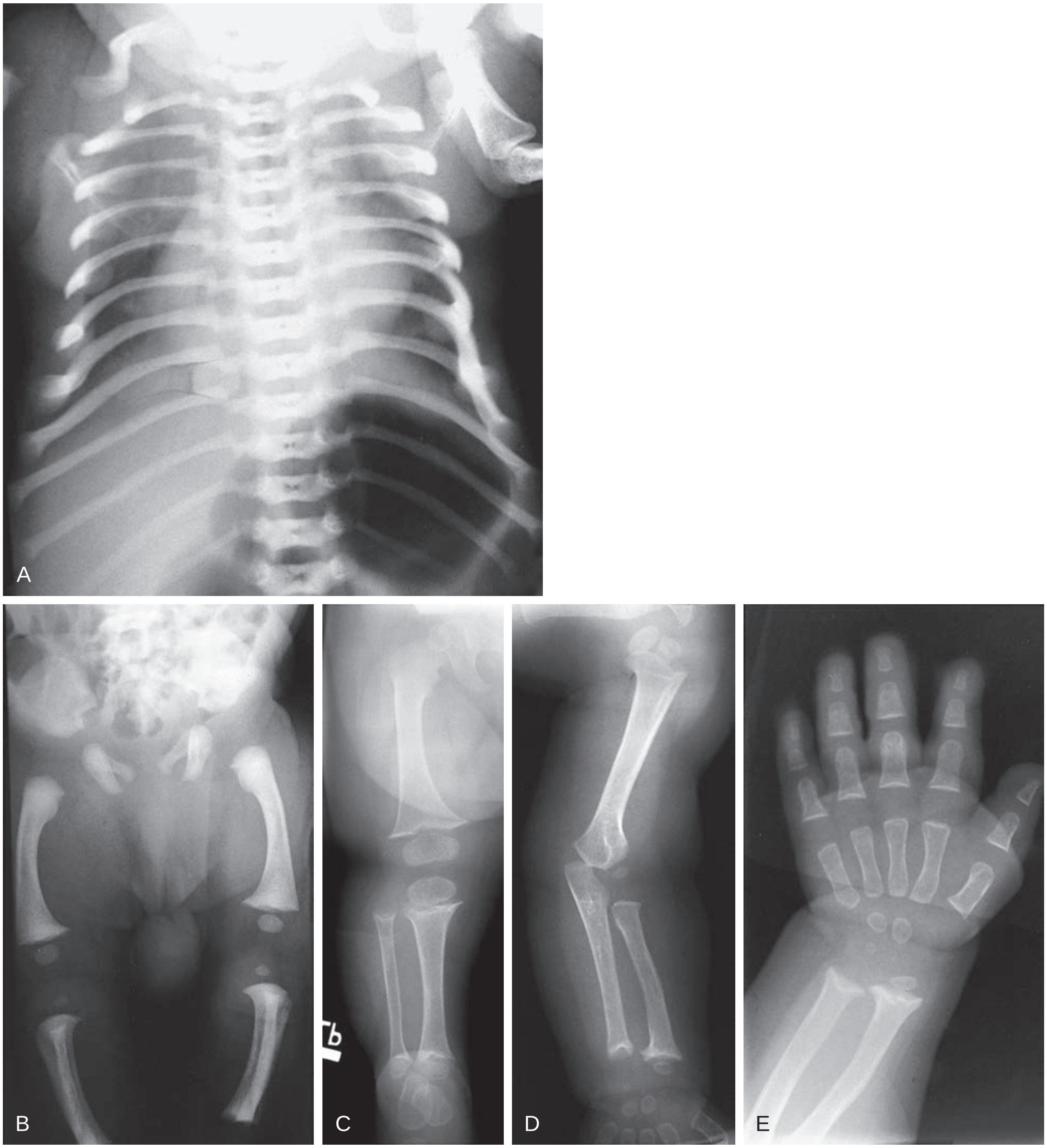

**e-Figure 132.24. McKusick-type metaphyseal chondrodysplasia (cartilage-hair hypoplasia).** (A and B) Radiographs from an affected newborn. (A) Thorax: anterior rib end widening and cupping. (B) Lower extremities: mild femoral bowing with minimal distal femoral flare. (C and D) Radiographic findings in late infancy. (C) Lower extremity: metaphyseal flaring and irregularity at the knees and ankles (but the hips are spared). (D) Upper extremity: similar metaphyseal changes at the wrists (the shoulders are spared). (E) At 6 months of age, metaphyseal widening and cupping of the short tubular bones of the hand, with similar metaphyseal changes in the wrist, are seen.

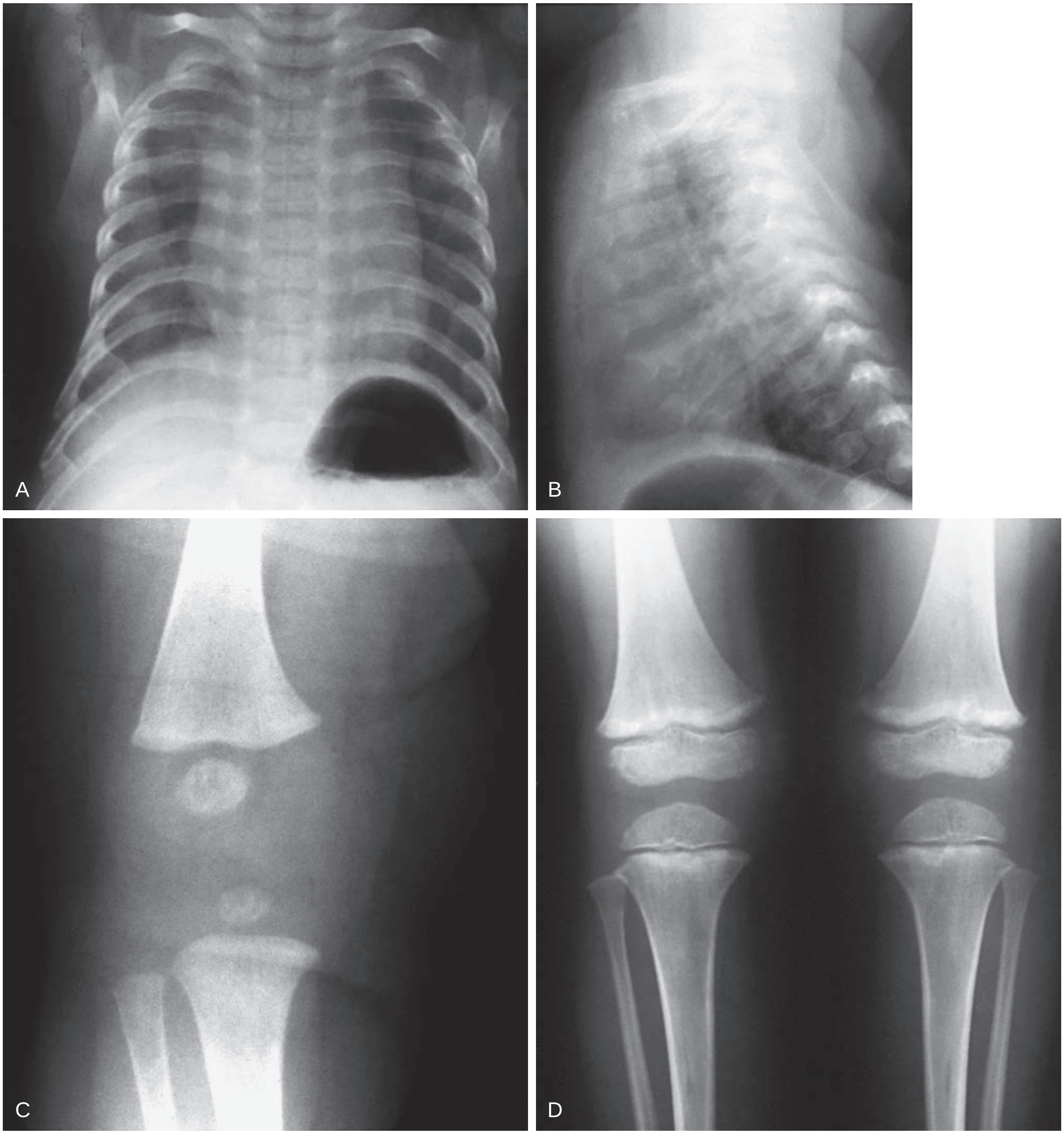

**e-Figure 132.25. Shwachman-Diamond dysplasia.** (A and B) At 2 months, a narrow thorax with anterior rib splaying is seen. (C) At 2 months, the knees are normal. (D) At 4 years, sclerotic, irregular, widened metaphyses in the knees are seen.

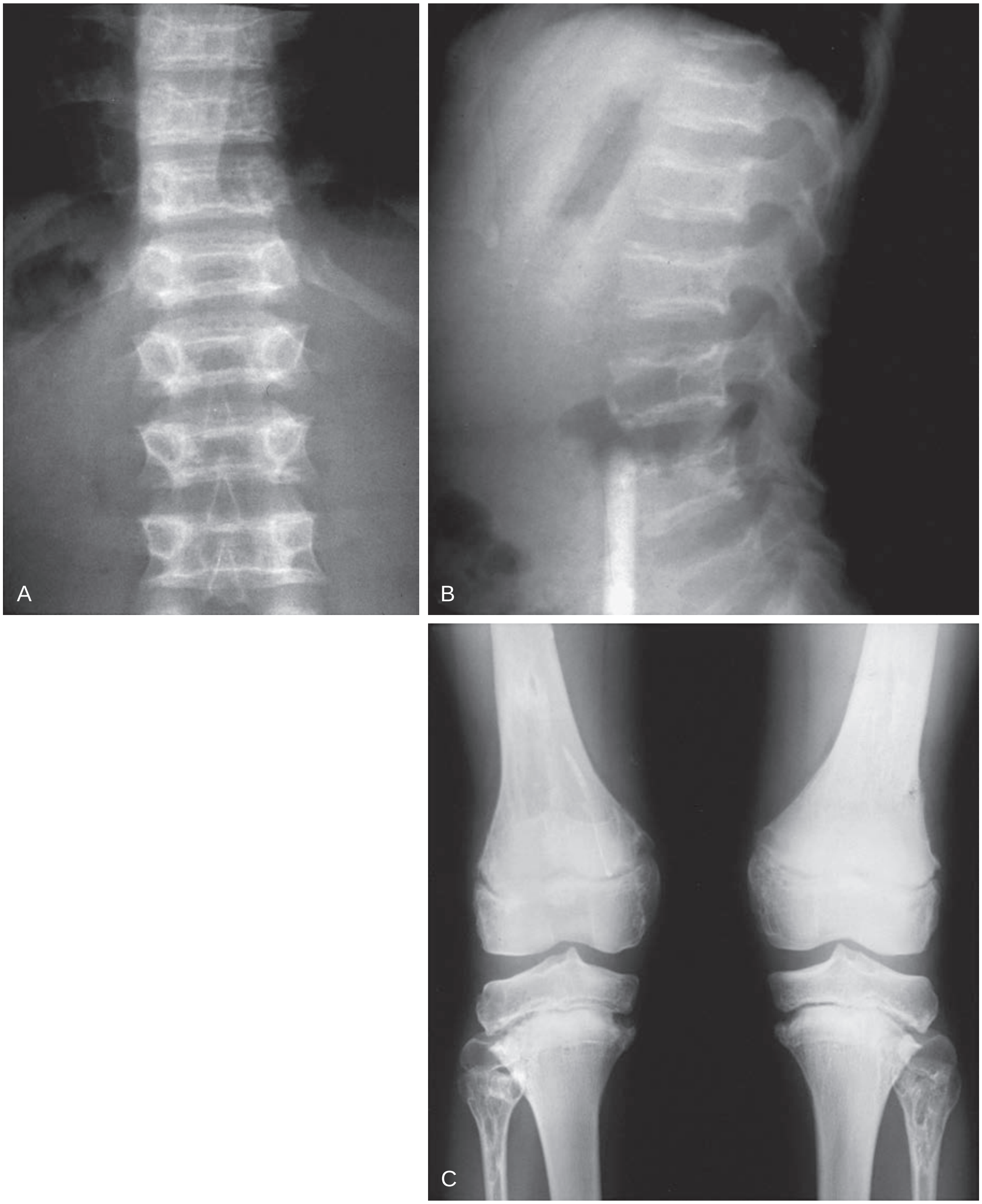

**e-Figure 132.26. Spondyloenchondromatosis in a 14 year old.** (A and B) Platyspondyly with end plate irregularity. (C) Multiple enchondromata in the long bones.

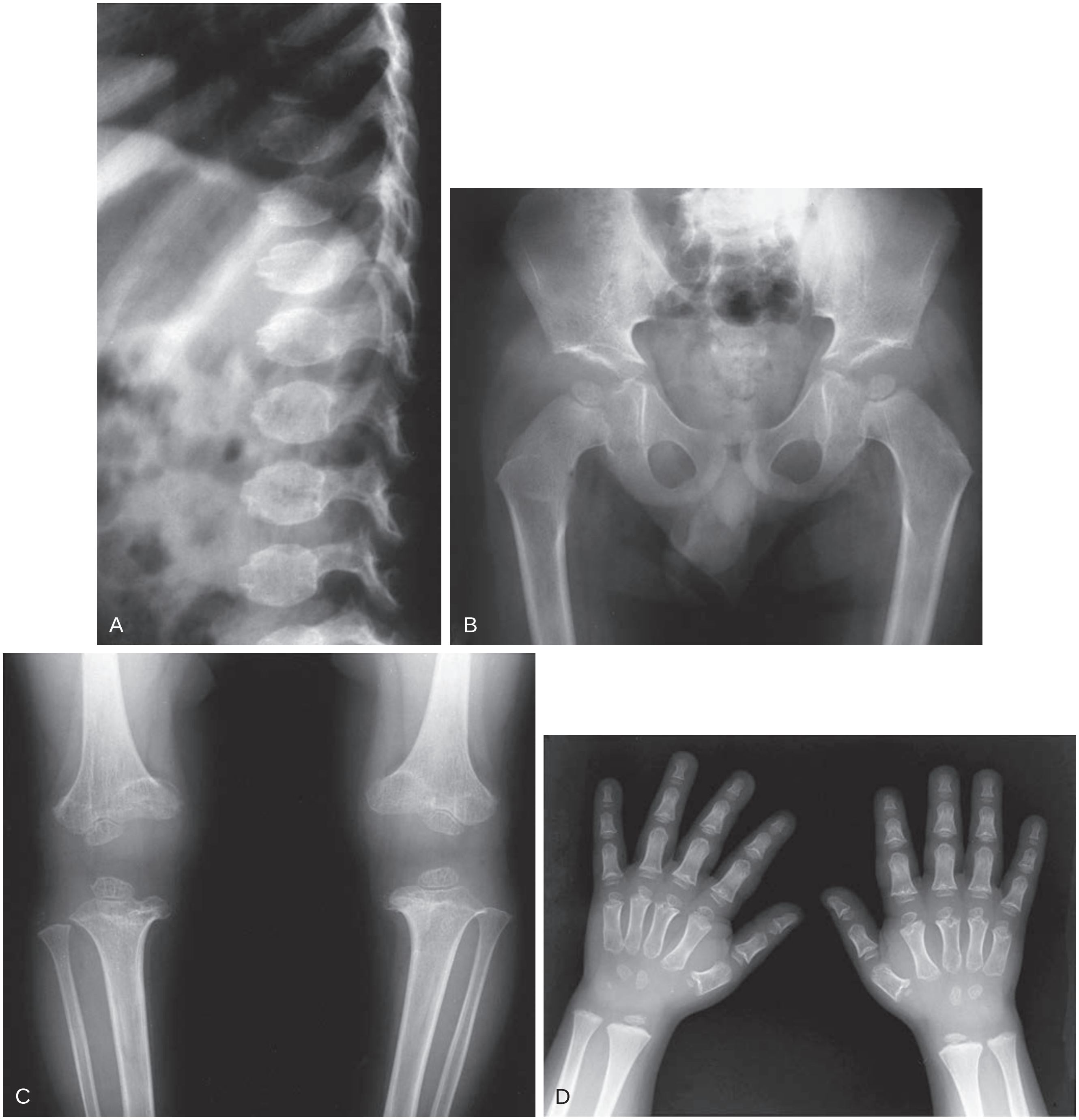

**Figure 132.21. Pseudoachondroplasia.** Radiologic findings at ages 3 years (A and C) and 4 years (B and D). (A) Central anterior tonguing and superior and inferior rounding of vertebral bodies. (B) Acetabular roof hypoplasia and mini-epiphyses. (C) Small knee epiphyses and metaphyseal widening with ossification defects. (D) Proximal metacarpal rounding, small epiphyseal centers, metaphyseal widening and irregularity, and carpal ossification delay.

## Trichorhinophalangeal Syndrome Types I and II

Both of these disorders have been located on the long arm of chromosome 8. The gene implicated in TRPS type I (also known as *Giedion syndrome*) is *TRPS1*. TRPS type II (also known as *Langer-Giedion syndrome*) is slightly more complicated. TRPS type II is the result of a contiguous gene abnormality resulting from the loss of not only *TRPS1* but also *EXT1*, a major cause of multiple hereditary exostoses located distal to *TRPS1*. TRPS type I is autosomal dominant, whereas most cases of TRPS type II are sporadic. The clinical manifestations of both disorders include mild short stature; sparse, slow-growing hair; pear-shaped nose;

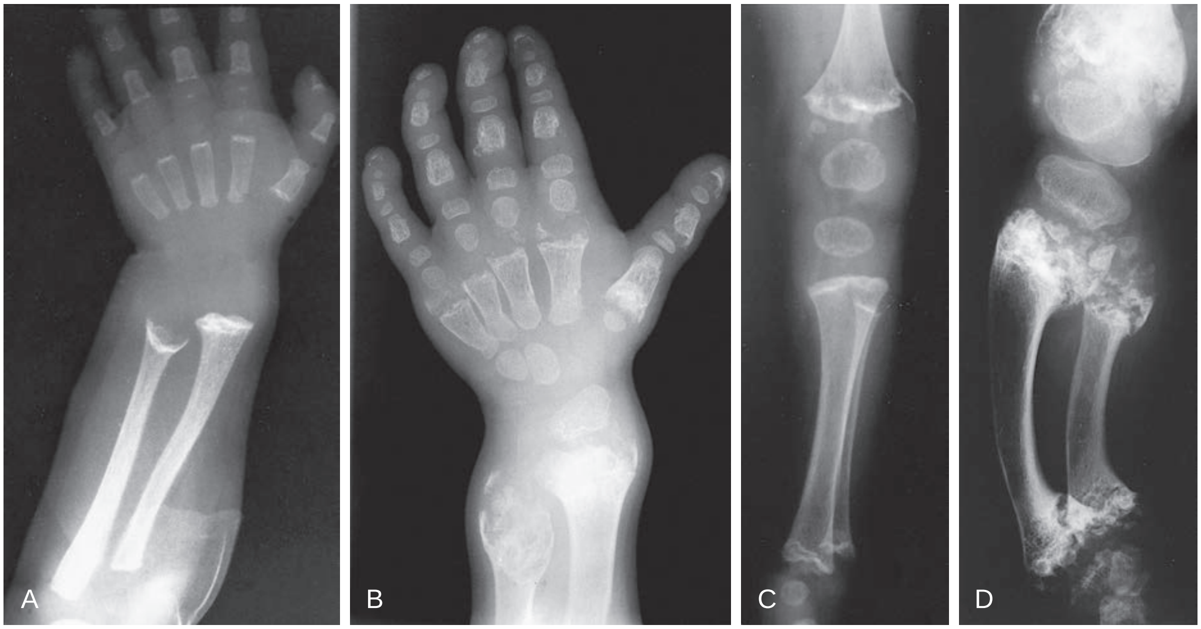

**Figure 132.22. Jansen-type metaphyseal chondrodysplasia.** (A) At 1 year, severe metaphyseal cupping and splaying are present at the wrists and also in the hand bones. (B) At 7 years, increasing metaphyseal change is seen at the wrists with enlarged epiphysis; enlarged epiphyses with wide epiphyseal plates are also present in the hands. (C) At 1 year, severe metaphyseal irregularities at the knees and ankles (femur, tibia, and fibula) and enlarged, rounded epiphyses are present. (D) At 7 years, severely fragmented, sclerotic metaphyses, wide epiphyseal plates, and enlarged epiphyses are present.

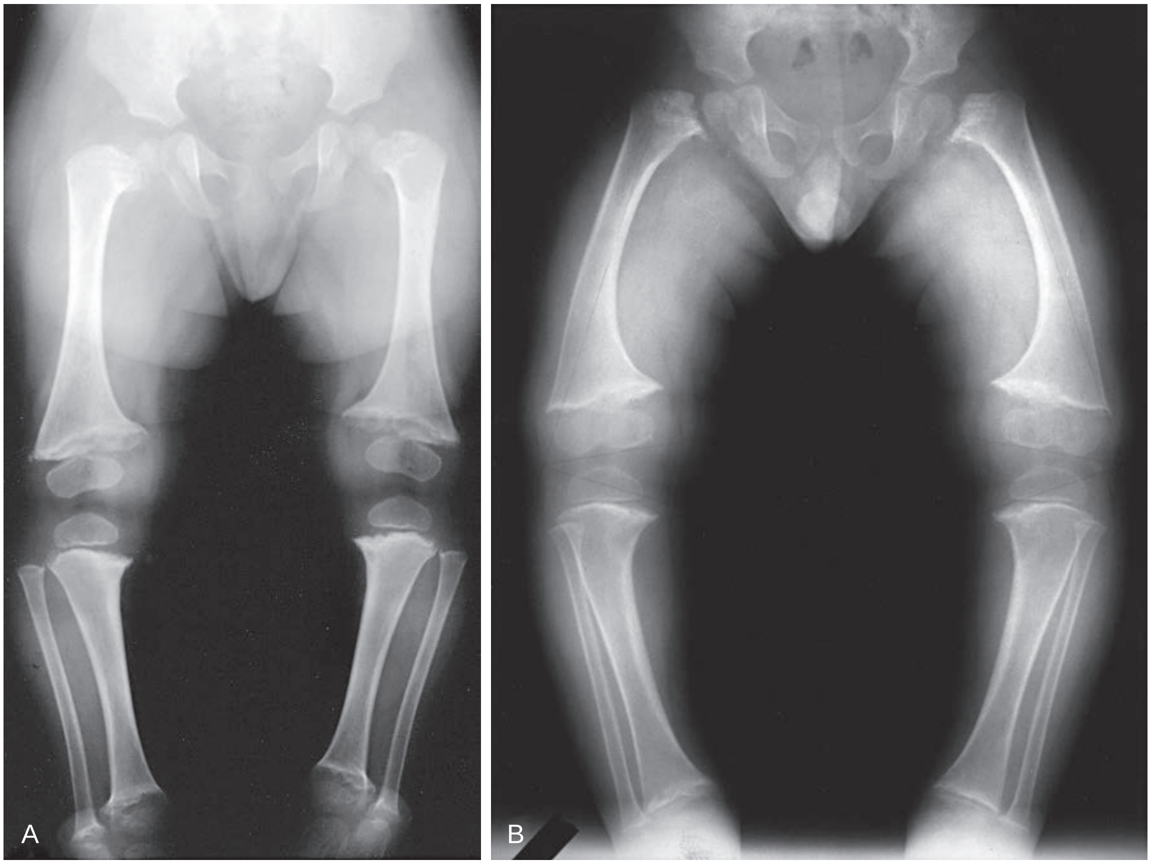

**Figure 132.23. Schmid-type metaphyseal chondrodysplasia.** (A) Radiograph from an affected 19-month-old with severe coxa vara and moderate metaphyseal changes (cupping irregularity, widening) at the knees and ankles. (B) Radiograph from an affected 3 year old with coxa vara, genu varum, and moderate metaphyseal changes at hips and knees (widening, irregularity).

and short, crooked fingers. The contiguous gene abnormality explains the added features in TRPS type II, which include multiple exostoses and mental retardation.[24]

***Radiologic Findings*** (Fig. 132.27)

- *Extremities:* Perthes-like changes at the hips, brachydactyly with multiple cone-shaped epiphyses in the phalanges of both hands. With TRPS type II, multiple exostoses are also present.

## MESOMELIC DYSPLASIA GROUP

The mesomelic dysplasia (mesomelic dwarfism) group consists of a large number of disorders involving shortening of the middle segment bones. Milder shortening of other segments may also be noted. The most common entity in this group is dyschondrosteosis.

### Dyschondrosteosis

This skeletal dysplasia, also known as *Leri-Weill syndrome*, is an autosomal-dominant condition. It consists of a pseudoautosomal homeobox gene (*SHOX* gene) found on the short arm of the X chromosome. Dyschondrosteosis manifests with mild to moderate short stature, usually with both forearm and calf shortening. Madelung deformity is the major marker for this disease. Interestingly, Madelung deformity is also common in Turner syndrome

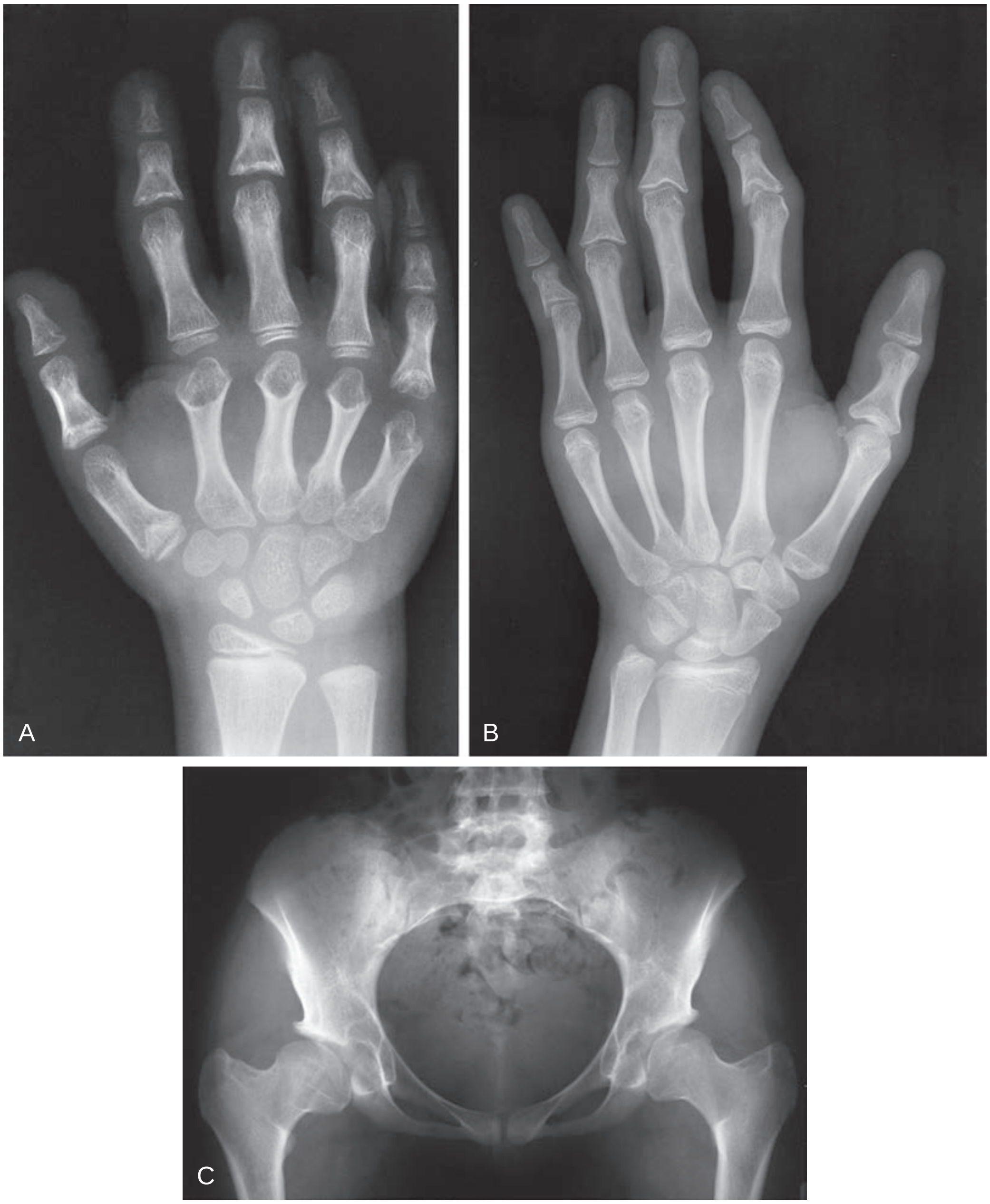

**Figure 132.27. Trichorhinophalangeal syndrome type I.** (A) In an affected 8 year old, cone-shaped epiphyses involving the first metacarpal, the proximal fifth phalanx, and all middle phalanges and metacarpals in the second through fifth digits (early fusion) are present. (B) The radiograph from an affected 18 year old shows similar changes. (C) In an affected young adult, coxa vara and small capital femoral epiphyses are present.

because of the lack of two copies of *SHOX* as only one X chromosome is present (see discussion of Turner syndrome later).

MRI is important here from a therapeutic point of view. A thickened ligament has been described by Vickers and Nielsen, which appears to tether the medial radial physis.[25] It can be found on the volar side of the joint and may be an abnormally thickened volar radiolunotriquetral ligament. Operative lysis of this structure if performed early can ameliorate the Madelung-type deformity. Radiographically, the ligament should be suspected when a triangular lucency is seen at the medial aspect of the distal radial metaphysis. On MRI, the ligament is clearly visible as a thick hypointense band of tissue originating at the medial radial physis.[26]

***Radiologic Findings*** (Fig. 132.28)

- *Extremities:* symmetric bowing and shortening of both radii, shortened ulnas, radiographic Madelung deformity changes, variable tibial and fibular shortening; short stature with abnormal upper to lower segment ratio

## CHONDRODYSPLASIA PUNCTATA GROUP

The chondrodysplasia punctata (stippled epiphyses) group is very diverse, united by the radiographic commonality of epiphyseal stippling. Several but not all of these entities are related to each other. The rhizomelic form of chondrodysplasia punctata is a peroxisomal enzyme abnormality; the Conradi-Hünermann type is associated with a gene on the long arm of the X chromosome (*EBP* gene defect); and the brachytelephalangic type is on the short arm of the X chromosome (a defect in the *ARSE* gene).

### Rhizomelic Chondrodysplasia Punctata

This is a distinct form of chondrodysplasia punctata and has an autosomal-recessive inheritance pattern. It is a symmetric rhizomelic skeletal dysplasia manifesting in the neonatal period. Affected infants usually die in the first year of life. Associated clinical findings include cataracts, skin lesions, alopecia, and joint contractures. Later manifestations are severe psychomotor retardation and spasticity. These infants appear to be in constant pain. Abnormalities in three genes *(PEX7*, *DHPAT*, *AGPS)* have been noted.

***Radiologic Findings*** (Fig. 132.29)

1. *Spine:* coronal clefting, anteriorly rounded vertebral bodies
2. *Extremities:* stippled epiphyseal ossification, symmetric bilateral shortening of femurs (and humeri) with less severe shortening of all the remaining long bones

## BENT-BONE DYSPLASIA GROUP

The bent-bone dysplasia group of disorders is a rather small but diverse group, with campomelic dysplasia (campomelic dwarfism) having been well described molecularly. These dysplasias have been grouped together because of their radiographic expression.

### Campomelic Dysplasia

This unusual entity is an autosomal-dominant disorder diagnosable at birth, manifesting as bent thighs, clubfeet, respiratory distress, and unusual small facies. Sex reversal is often present. All the extremities are moderately short. Neonatal or perinatal death occurs in most cases. The molecular defect is a homeobox gene abnormality called *SOX9*, found on chromosome 17. Radiographically the combination of bent femora with severe hypoplasia of the blade of the scapula makes for an easy diagnosis.

***Radiologic Findings*** (Fig. 132.30)

1. *Skull:* enlarged, narrow with a small face
2. *Thorax:* mildly short ribs, numbering 11; severe hypoplasia of the bodies of the scapulae
3. *Spine:* nonossification of thoracic pedicles, cervical kyphosis, hypoplasia of cervical vertebral bodies
4. *Pelvis:* narrow, tall iliac wings
5. *Extremities:* proportionately long, bowed femurs with shortened bowed tibias; shortened upper extremity long bones

## DISORDERS OF INCREASED BONE DENSITY WITHOUT MODIFICATION OF BONE SHAPE

The disorders of increased bone density without modification of bone shape include several entities of interest. These disorders are grouped by their radiographic expression but have in common either diffuse or focal areas of bone sclerosis.

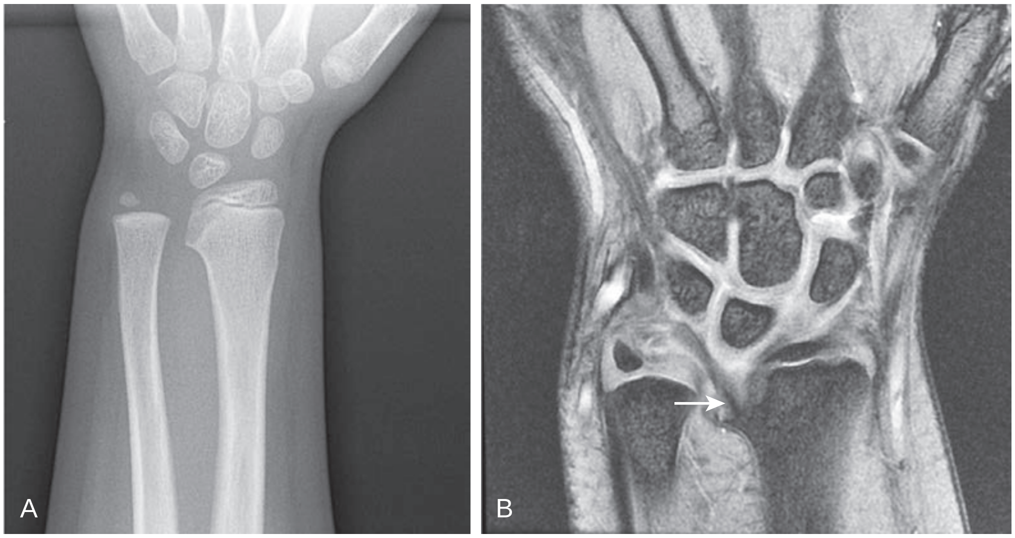

**Figure 132.28. Dyschondrosteosis in a 7-year-old girl.** (A) Frontal radiograph and (B) coronal gradient echo MRI show a Madelung deformity. Note the triangular lucency in the distal radius on the radiograph. The MRI shows Vickers ligament *(arrow)* inserting in this area tethering the physis.

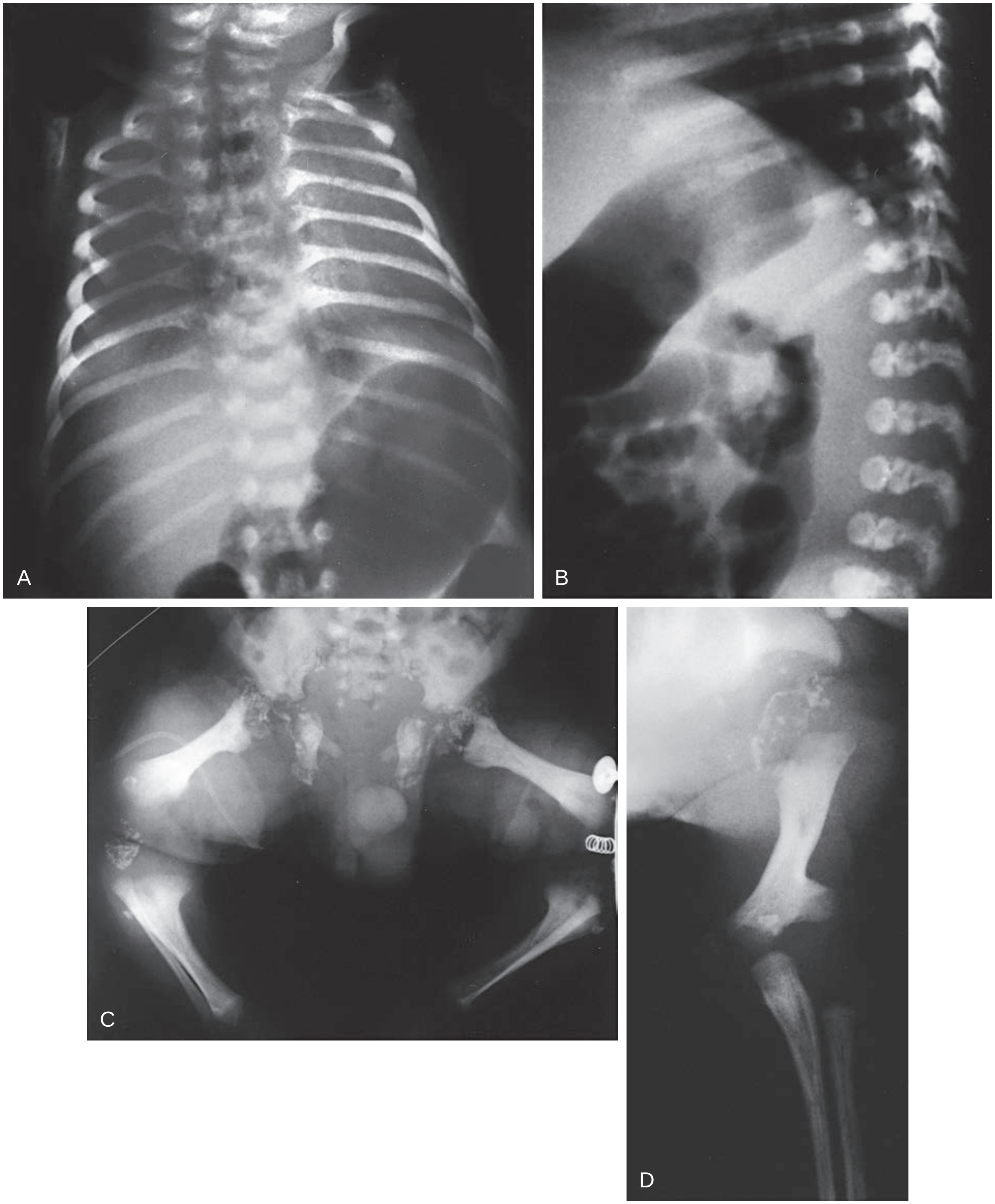

**Figure 132.29. Rhizomelic chondrodysplasia punctate in a newborn.** (A and B) Radiographs reveal a small thorax, punctate vertebral body ossification, and coronal clefting. (C and D) Diffuse stippling in epiphyseal regions and rhizomelia (femurs and humeri).

## Osteopetrosis

Our understanding of osteopetrosis has evolved considerably and no less than 13 general mutation loci have been described. For clinical purposes, the disease can be distinguished by age at onset. The types with onset in infancy are the most severe.

The very severe precocious or malignant type is autosomal recessive. Patients with this type present in infancy with hepatosplenomegaly, pancytopenia, multiple infections (osteomyelitis), and leukemia. Early death is common. The delayed type (late-onset form) is autosomal dominant. Lifespan is normal, and the condition is frequently diagnosed when a radiograph is obtained after minor

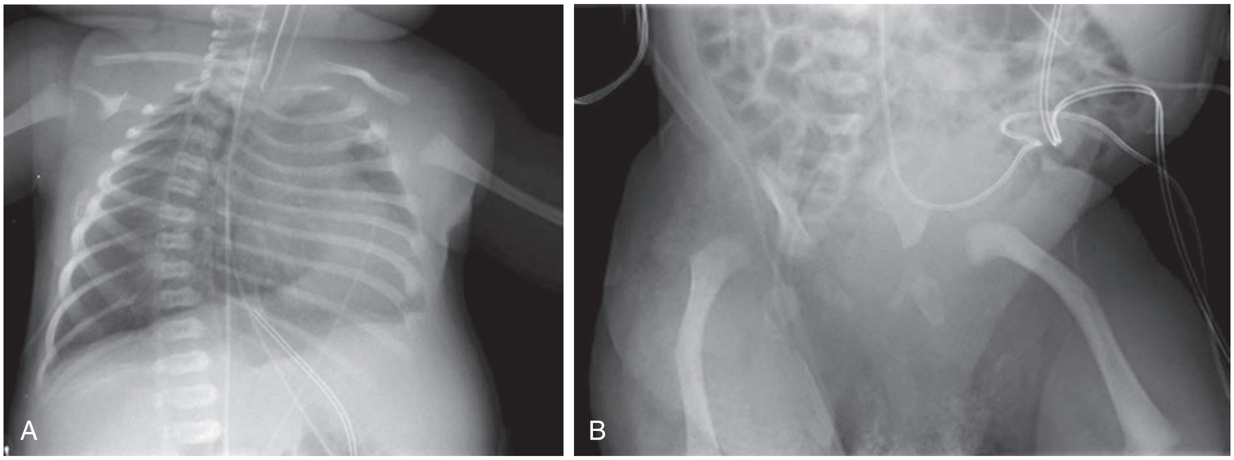

**Figure 132.30. Campomelic dysplasia in a newborn.** (A) Chest radiograph reveals slender ribs and marked scapular hypoplasia. (B) Frontal radiograph of the pelvis and thighs shows classic bent bone appearance of the femurs. Both hips are dislocated and the pelvis is very narrow.

trauma causes a fracture. Individuals with this type sustain multiple fractures and are at increased risk of osteomyelitis, particularly in the mandible.

The condition known as *osteopetrosis with renal tubular acidosis (carbonic anhydrase II deficiency)* is a rare entity localized to chromosomal locus 8q and gene *CA2* (carbonic anhydrase II). Diffuse dense cerebral calcifications suggest the correct diagnosis.

An intermediate form is also recognized with onset within the first decade, and although significant clinical abnormalities are present, including hematologic disease, findings are milder than in the infantile form.

Although multiple genes are involved, the defect ultimately leads to osteoclast dysfunction because of unresponsiveness to parathyroid hormone. Without the remodeling activity of normal osteoclasts, bone becomes sclerotic and brittle. Long bone fractures are common.

Of importance is the seemingly contradictory presentation of osteopetrosis with rickets. This occurs in the severe malignant form. With this combination, dense osteopetrosis changes are seen in conjunction with rickets physeal changes. It can be understood when considering that 99% of the calcium store is bound in highly calcified dense bone. Without osteoclast function, that calcium is unavailable for correct physeal growth and mineralization, and a relative calcium deficiency is present.

Bone marrow transplantation is curative as it repopulates the marrow with normally functioning osteoclasts.

***Radiologic Findings*** (e-Fig. 132.31 and Fig. 132.32)

1. Generalized increased bone density
2. *Skull:* thick and dense, especially at the base
3. *Thorax:* splayed anterior ribs
4. *Spine:* “sandwich” vertebral bodies, “picture frame” vertebral bodies
5. *Extremities:* splayed metaphyses, bone-within-bone configuration, dense metaphyseal bands
6. *Central nervous system*: carbonic anhydrase II deficiency has diffuse dense cerebral calcifications

## Pyknodysostosis

Pyknodysostosis is an autosomal-recessive disorder that often manifests in infancy. Clinical findings include short-limbed dwarfism, micrognathia, fractures, and short fingertips. The impressionist painter Toulouse-Lautrec likely had this condition.[27]

***Radiologic Findings*** (Fig. 132.33)

1. Generalized osteosclerosis
2. *Skull:* marked delay in closure of fontanels and sutures, wormian bones, obtuse or absent mandibular angle, dense skull
3. *Thorax:* resorbed acromial ends of clavicles
4. *Extremities:* resorbed phalangeal tufts mimicking acro-osteolysis

## Osteopoikilosis

This is an autosomal-dominant condition caused by mutations in LEMD3.[28] The gene function and its relationship to this disease are not clear. It is often asymptomatic and identified on routine radiographs. These lesions often show increased uptake on bone scans. When skin lesions of dermatofibrosis are also present, the combination is called *Buschke-Ollendorff syndrome*.

***Radiologic Findings*** (Fig. 132.34)

- Small foci of bone sclerosis (round, oval, lenticular) located primarily in cancellous bone

## Osteopathia Striata

This is an asymptomatic sporadic condition, but when associated with cranial sclerosis, it is an X-linked dominant disorder. It is often identified on routine radiographs as a “normal variant.” It can be seen, however, as a manifestation of other discrete disorders such as the dysplasia of spondylar changes, nasal anomaly, and striated metaphyses (SPONASTRIME).

***Radiologic Findings*** (Fig. 132.35)

1. Vertical, fine, dense, linear striations
2. Most common at the ends of the long tubular bones, skull and clavicles unaffected
3. No uptake on bone scan

## Melorheostosis

This is often sporadic but can be seen as an autosomal dominant entity in families with an *LEMD3* gene mutation, similar to osteopoikilosis. Patients can experience bone pain and joint stiffening, as well as limb asymmetry.

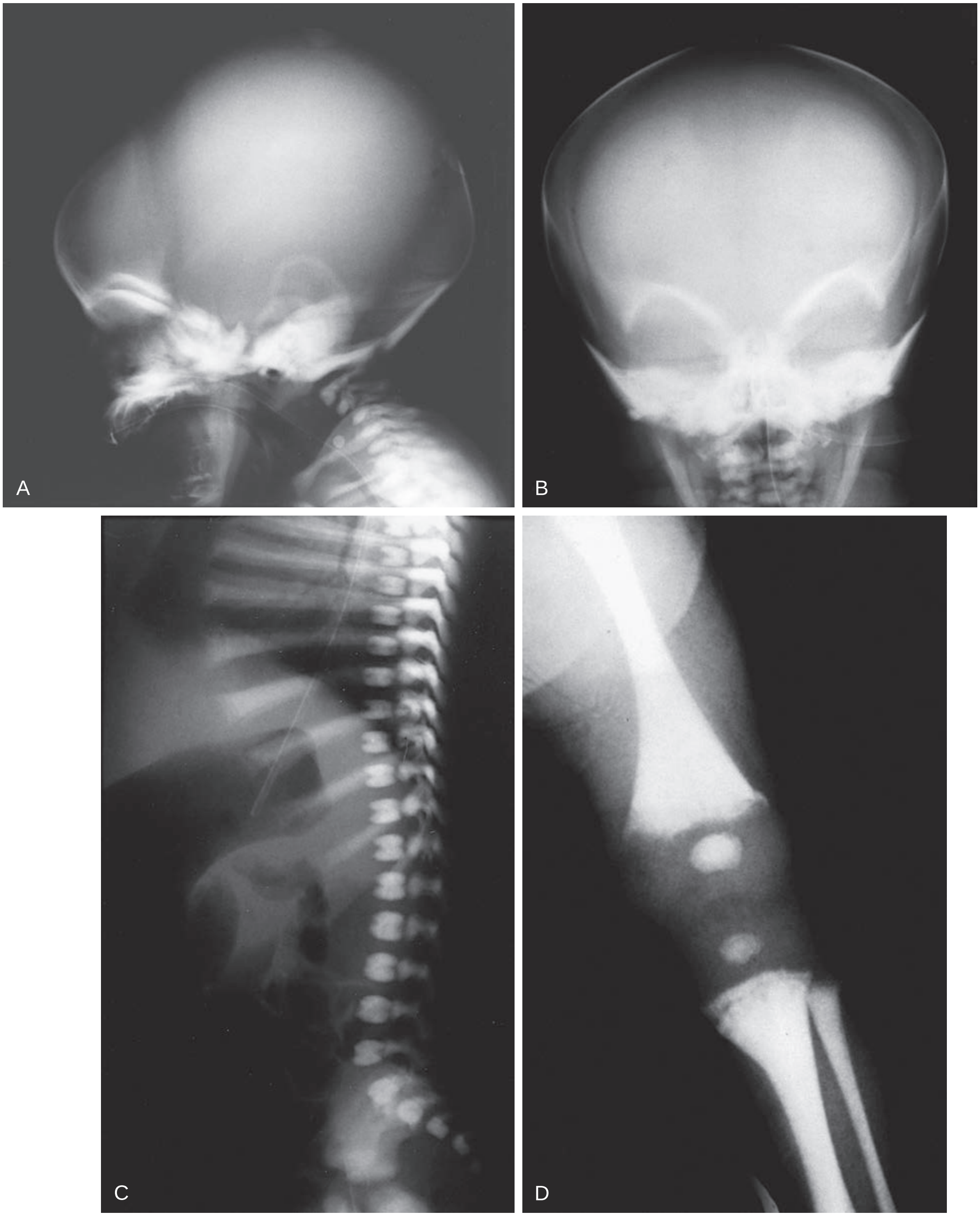

**e-Figure 132.31. Precocious-type osteopetrosis (autosomal recessive).** (A–C) Radiographs from a newborn. (A and B) Dense skull and face, especially skull base. (C) Dense spine and ribs. (D) At 3 months, very dense long bones, medullary obliteration, and frayed metaphyses (rickets) are present. Precocious-type osteopetrosis (autosomal recessive). (E and F) Radiographic findings at 4 years. *Continued*

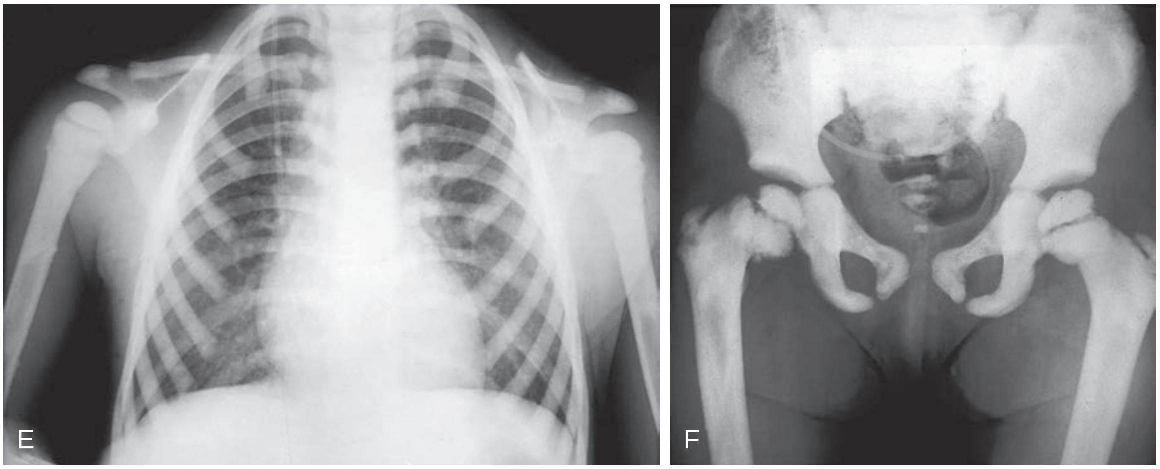

**e-Figure 132.31, cont'd.** (E) Dense thorax (ribs, clavicles, scapulas) and upper extremity long bones (*note:* less medullary obliteration). (F) Dense pelvis and lower extremity long bones (including capital femoral epiphyses), and bilateral pathologic femoral neck fractures.

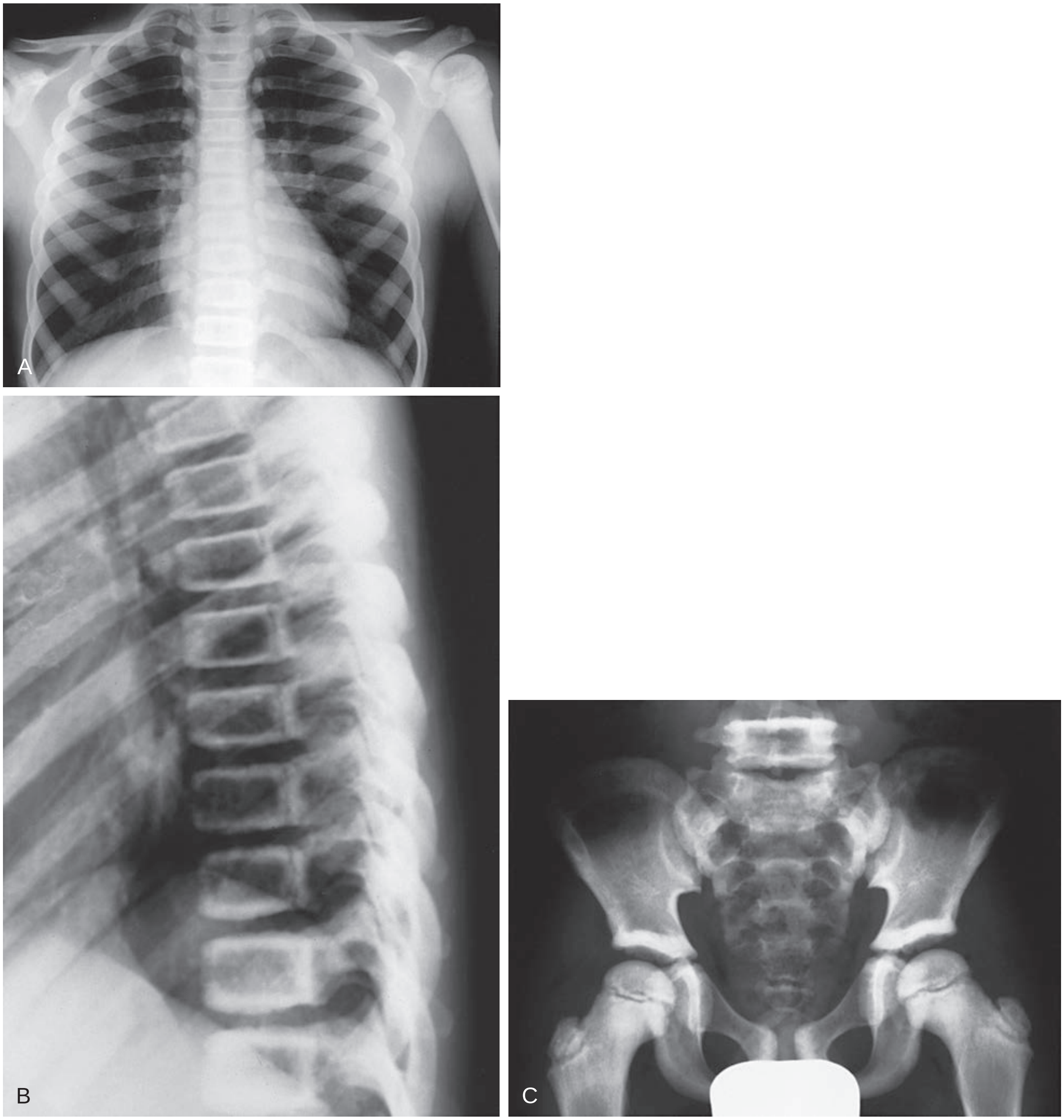

**Figure 132.32. Delayed-type osteopetrosis (autosomal dominant) in an 8 year old.** (A) Radiographs reveal dense thoracic bones without medullary encroachment of left humerus. (B) "Sandwich," almost "picture frame" vertebral bodies (dense outer borders). (C) Increased bone density outlining ileum, including supraacetabular regions, and pubic symphysis region, as well as dense proximal femoral epiphyses and femoral necks with sparing of lower medullary space.

***Radiologic Findings*** (Fig. 132.36)

1. Monostotic or polyostotic usually affecting the same extremity
2. Linear dense cortical hyperostosis following the long axis of bones that resembles melting or dripping candle wax
3. Can be present across joint space
4. Increased uptake on bone scan

## INCREASED BONE DENSITY GROUP WITH METAPHYSEAL AND DIAPHYSEAL INVOLVEMENT

This group includes the craniotubular dysplasias. The hallmark is sclerosis of the long bones with either a diaphyseal or a metaphyseal focus and abnormal calvarial thickening and sclerosis. Craniodiaphyseal dysplasia, craniometaphyseal dysplasia, and Pyle dysplasia are described here.

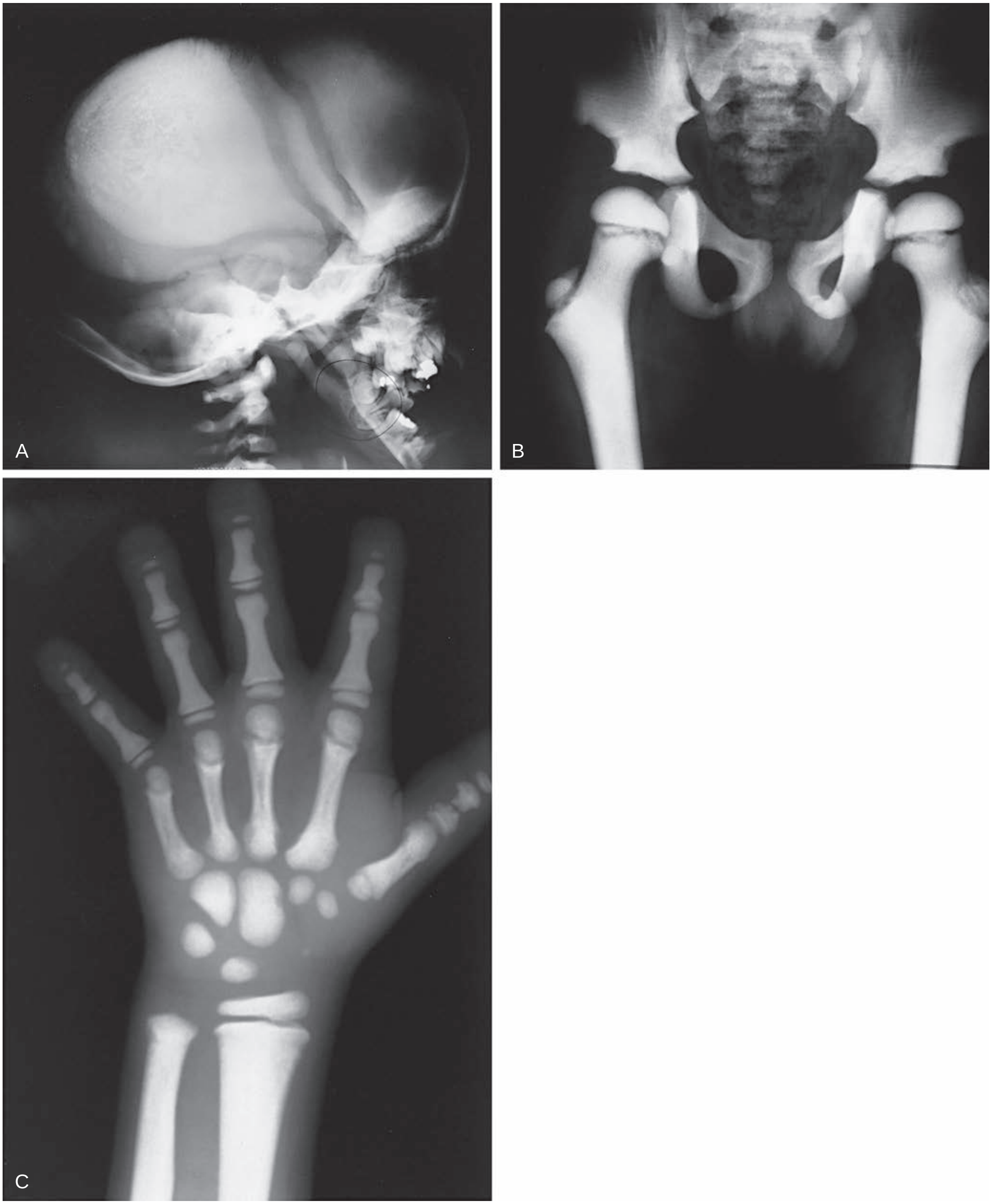

**Figure 132.33. Pyknodysostosis in an 8 year old.** (A) Radiographs reveal dense skull convexity and base, widely separated sutures with open fontanel, and absence of mandibular angle. (B) Hip and pelvis: generalized increased bone density with long, overmodeled (resorbed) femoral necks. (C) Hands: dense bones, overmodeled metacarpals and phalanges, phalangeal tuft resorption.

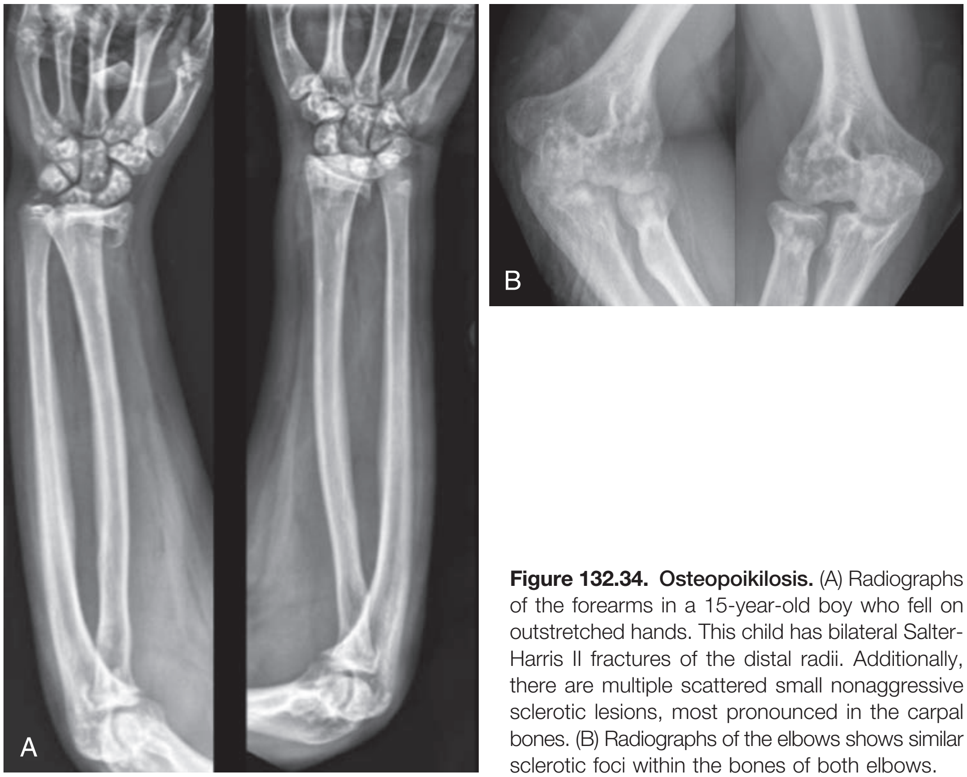

**Figure 132.34. Osteopoikilosis.** (A) Radiographs of the forearms in a 15-year-old boy who fell on outstretched hands. This child has bilateral Salter-Harris II fractures of the distal radii. Additionally, there are multiple scattered small nonaggressive sclerotic lesions, most pronounced in the carpal bones. (B) Radiographs of the elbows shows similar sclerotic foci within the bones of both elbows.

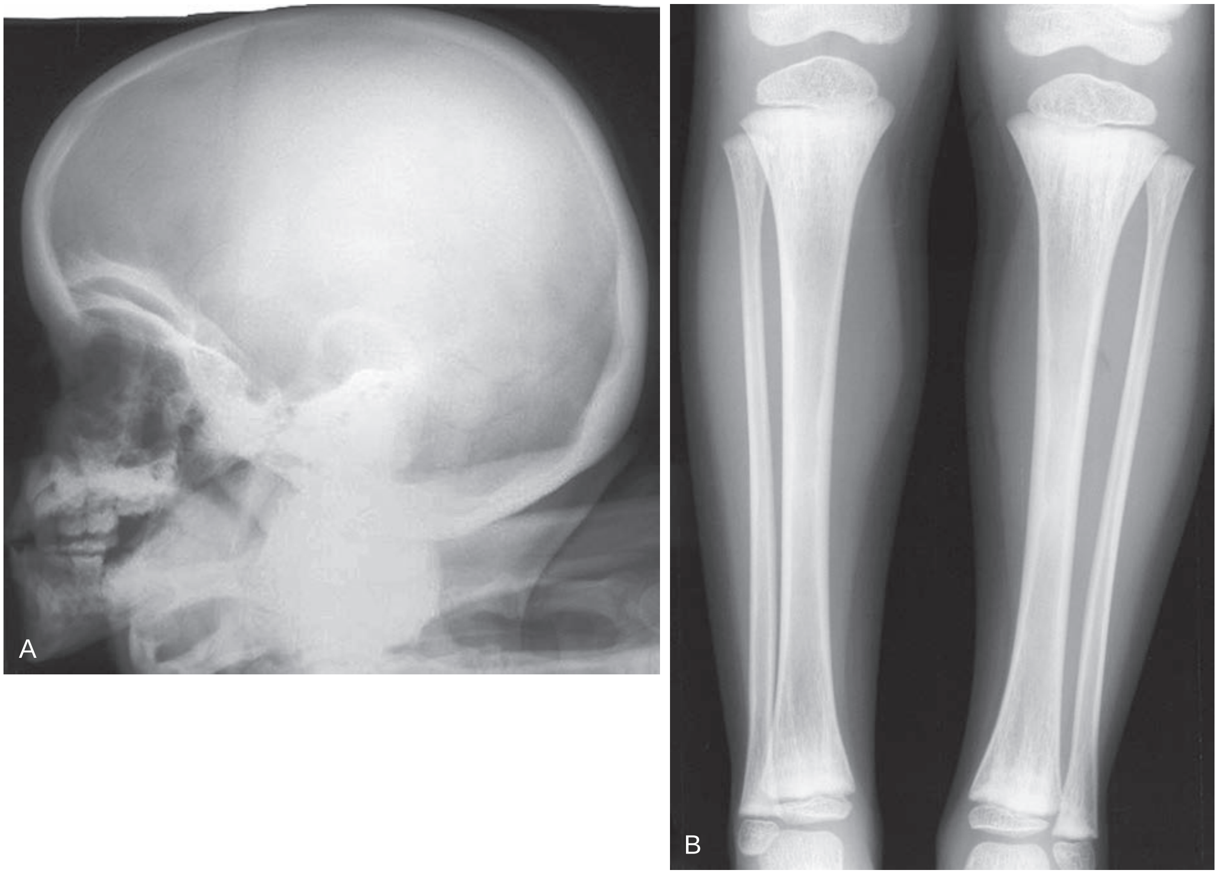

**Figure 132.35. Osteopathia striata with cranial sclerosis.** (A) Lateral skull film revealing dense thickening of the calvaria with increased basilar and orbital sclerosis. (B) An anteroposterior radiograph of the lower extremity reveals linear striations of the metadiaphyseal regions of both ends of the tibias and fibulas.

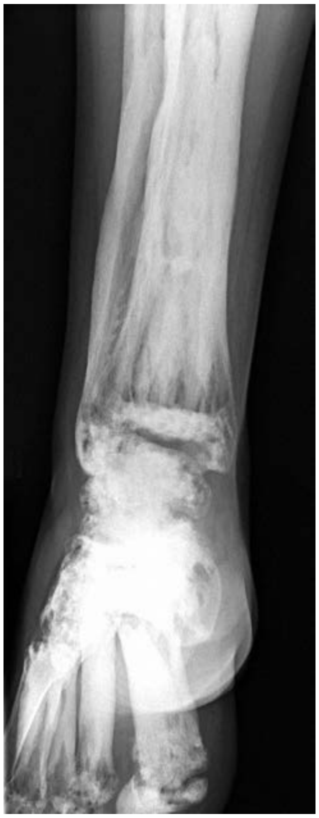

**Figure 132.36. Melorheostosis in a 14-year-old boy.** The image of the tibia and fibula and the ankle shows dense "candle-wax dripping" changes involving both tibia and fibula, extending into the epiphyses and present across the joint into the tarsal–metatarsal bones.

## Craniodiaphyseal Dysplasia

This rare autosomal-recessive condition manifests in early infancy with progressive facial and calvarial thickening. Sudden death, as the result of cranial foraminal narrowing, is frequent.

***Radiologic Findings*** (Fig. 132.37)

1. *Skull:* marked thickening and sclerosis of calvaria and facial bones, obliteration of foramina and sinuses
2. *Thorax:* diffusely widened, sclerotic ribs and clavicles
3. *Extremities:* straightened, undermodeled long bone with diaphyseal widening with metaphyseal sparing; "flame" sclerosis (cortical thickening) of the short-tubular bones (hands)

## Craniometaphyseal Dysplasia

Two forms of this disease are described on two different gene loci. Both are similar but the autosomal-recessive form is more severe and manifests as cranial and facial thickening, often with nasal obstruction. Improvement may occur with age. Cranial encroachment–induced neurologic abnormalities may develop.

***Radiologic Findings*** (e-Fig. 132.38)

1. *Skull:* diffuse hyperostosis of cranial vault base and facial bones, obliterated paranasal sinuses
2. *Extremities:* sclerosis of diaphyses with normal metaphyseal modeling (early), undermodeled flared metaphyses of long bones with normal diaphyses (later)

## Pyle Dysplasia

This autosomal-recessive entity, also known as *familial metaphyseal dysplasia*, is somewhat similar to craniometaphyseal dysplasia but differs in its minimal craniofacial involvement. Patients are often asymptomatic or develop genu valgum (knock knee).

***Radiologic Findings*** (Fig. 132.39)

1. *Skull:* mild skull and facial involvement, minimal base-of-skull sclerosis, prominent supraorbital ridging
2. *Thorax:* mildly thickened clavicles and ribs, mild platyspondyly
3. *Pelvis:* thickened ischium and pubis
4. *Extremities:* marked undertubulation of long bones, especially distal femurs (Erlenmeyer flask deformity); distal flaring of metacarpals and proximal flaring of phalanges

## OSTEOGENESIS IMPERFECTA AND DECREASED BONE DENSITY

The cardinal feature of OI is increased bone fragility. Clinically, a bluish hue to the sclerae may be seen.

OI is classified according to the Sillence classification. Originally including only four types, many types have now been described. The Sillence classification describes a spectrum of disease rather than a strict system based on objective scientific identities such as molecular genetics. In fact, we know now that multiple allelic mutations affect collagen I and cause OI, although other OI types are unrelated to collagen I abnormalities.

***Radiologic Findings, Severe Type*** (Fig. 132.40)

1. *Skull:* very poor to no ossification
2. *Thorax:* small, narrow chest; beaded ribs from healing fractures
3. *Spine:* severe deossification, collapsed vertebral bodies
4. *Extremities:* generalized osteoporosis with or without fractures; shortened, widened long bones with thin cortices; accordion-shaped femurs

***Radiologic Findings, Mild Types*** (e-Fig. 132.41)

1. *Skull:* abnormal number of wormian bones (>8–10), variable decrease in ossification
2. *Spine:* wedged or collapsed vertebrae
3. *Extremities:* at least some osteoporosis, variable number of fractures (especially pathologic fractures)

## ABNORMAL MINERALIZATION GROUP

Among the dysplasias with defective mineralization, one important entity to recognize and discuss is hypophosphatasia.

## Hypophosphatasia

The two distinct genetic forms of hypophosphatasia are (1) the autosomal-recessive perinatal lethal or infantile type and (2) a later-onset autosomal-dominant adult type. Both result from an abnormality of the enzyme alkaline phosphatase. The chromosome loci for both conditions are 1p36.1-34 and involve *TNSALP*. As a consequence of defective alkaline phosphatase, bone formation is impaired because of local increase in phosphate, impaired hydroxyapatite formation, and hypercalcemia with resultant rickets-like changes.

***Radiologic Findings*** (e-Fig. 132.42)

Perinatal lethal/infantile form:

1. *Skull:* decreased ossification with single island-like centers for frontal occipital and parietal bones
2. *Thorax:* poorly ossified ribs; thin, wavy, fractured ribs; clavicles not affected

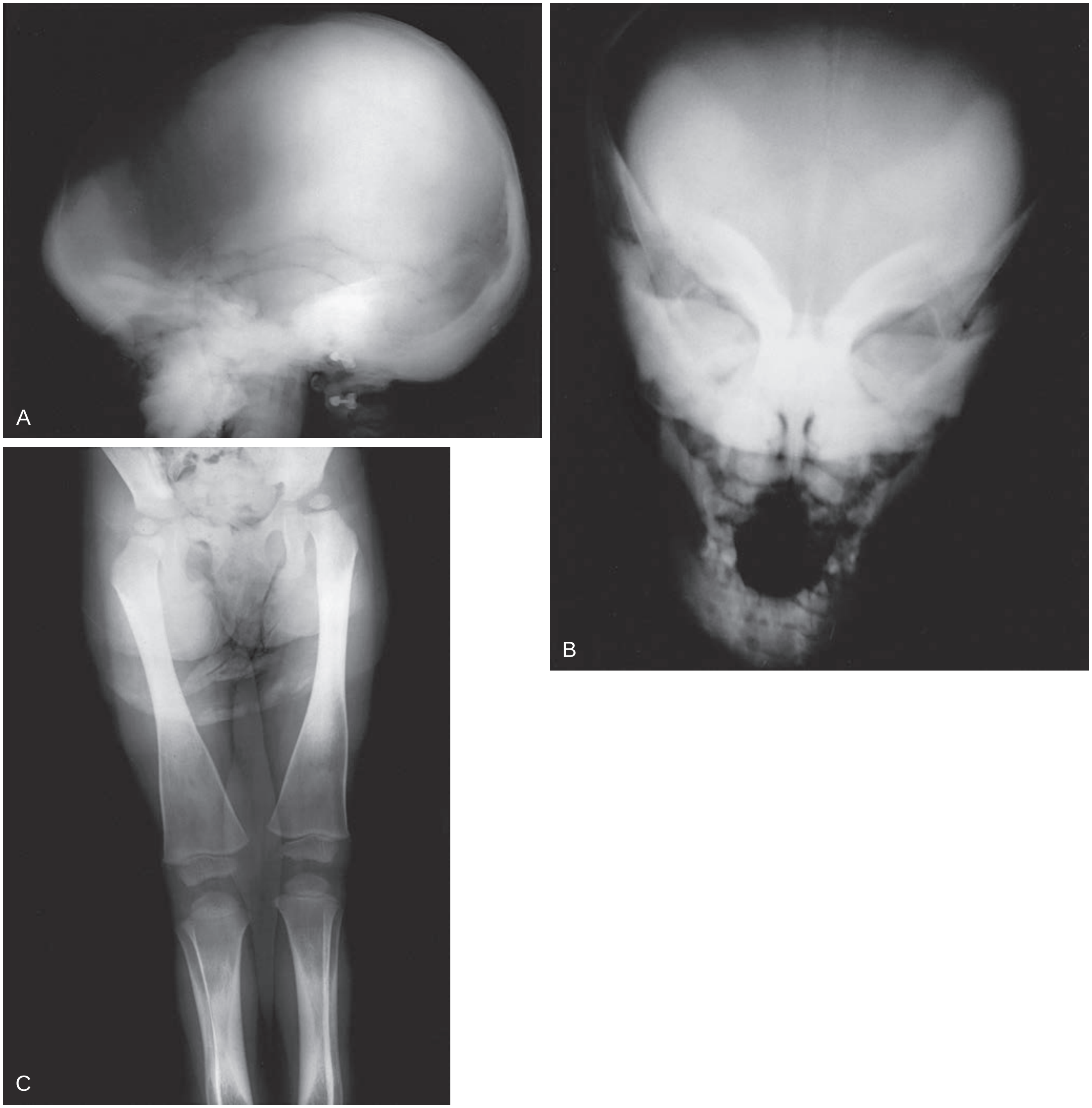

**e-Figure 132.38. Craniometaphyseal dysplasia in a 2 year old.** (A and B) Marked increased bone density of cranial base and vault, and dense facial bones with obliteration of sinuses. (C) Undermodeled flared metaphyses (Erlenmeyer flask deformity) of distal femurs.

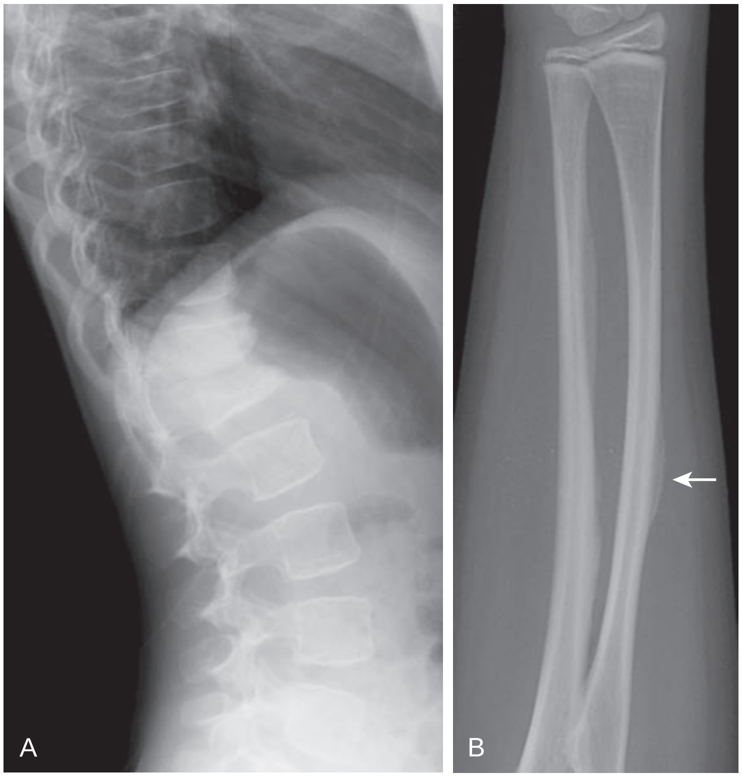

**e-Figure 132.41. Osteogenesis imperfecta type 5 in a 12-year-old girl.** (A) Lateral view of the spine showing multiple vertebral body compression fractures. (B) The anteroposterior view of the forearm shows areas of hyperostosis *(arrow)* and increased density at the zones of provisional calcification at the metaphyses of the distal radius and ulna.

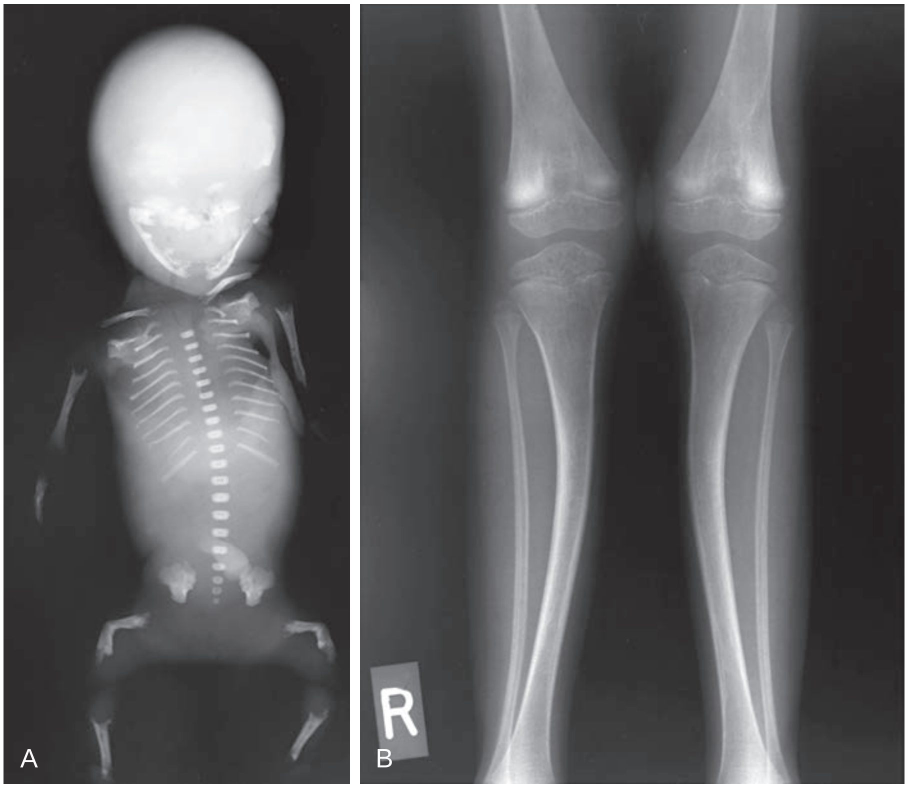

**e-Figure 132.42. Hypophosphatasia.** (A) The radiograph from a fetus with perinatal lethal type demonstrates island-like skull ossification (parietal); thin, wavy ribs; platyspondyly and missing cervical vertebrae ossification; no pedicles; and bent femurs. (B) The radiograph from a 7 year old with adult-type hypophosphatasia demonstrates osteopenia, bent tibias, and punched-out metaphyseal lesions.

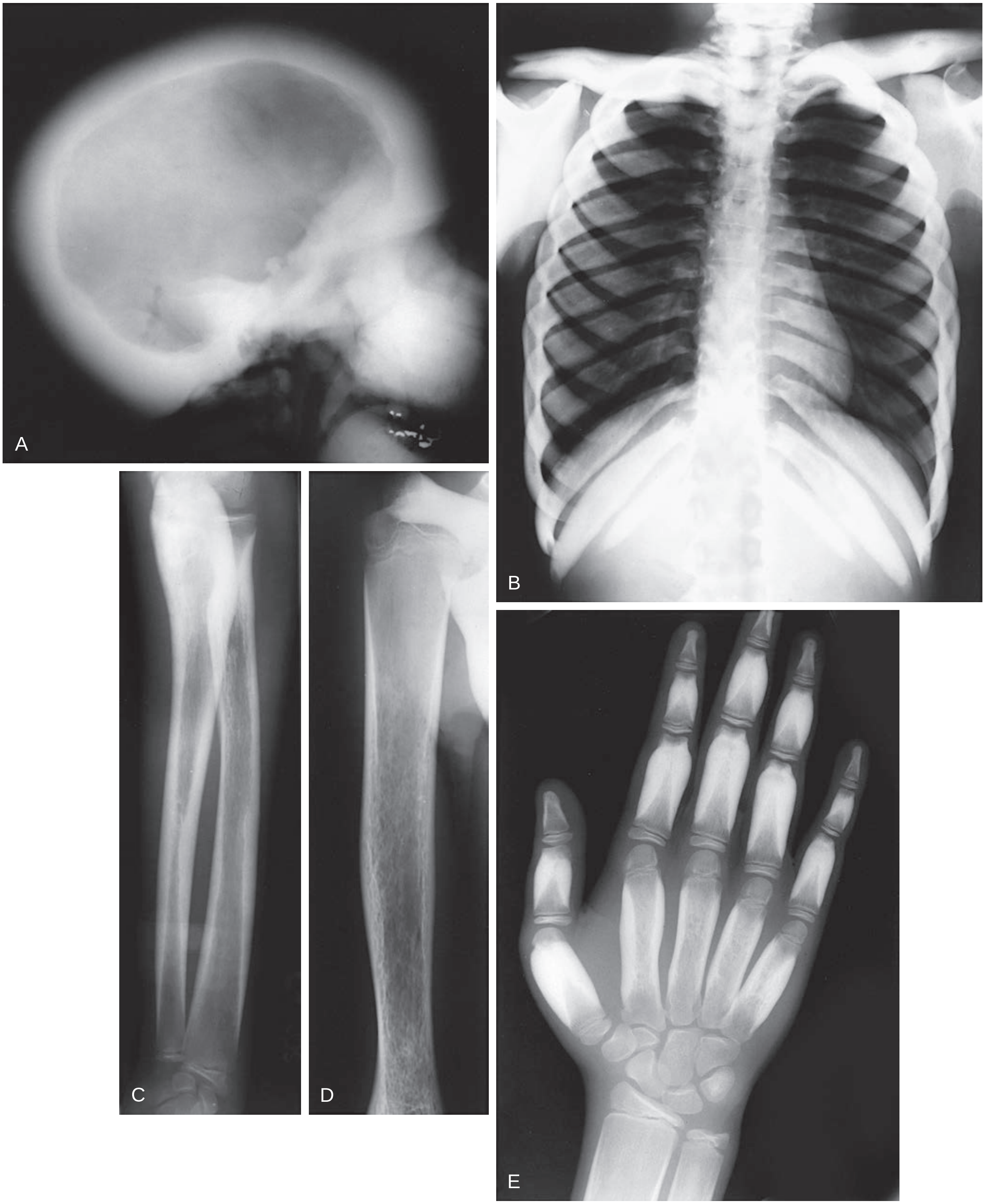

**Figure 132.37. Craniodiaphyseal dysplasia in a 13 year old.** (A) Extremely dense bone filling in the facial region and thickening the diploic space. (B) Diffusely dense, thickened ribs and clavicles. (C and D) Diffuse cortical long bone diaphyseal thickening and diaphyseal undermodeling. (E) “Flame” sclerosis (cortical thickening) of the tubular bones of the hand.

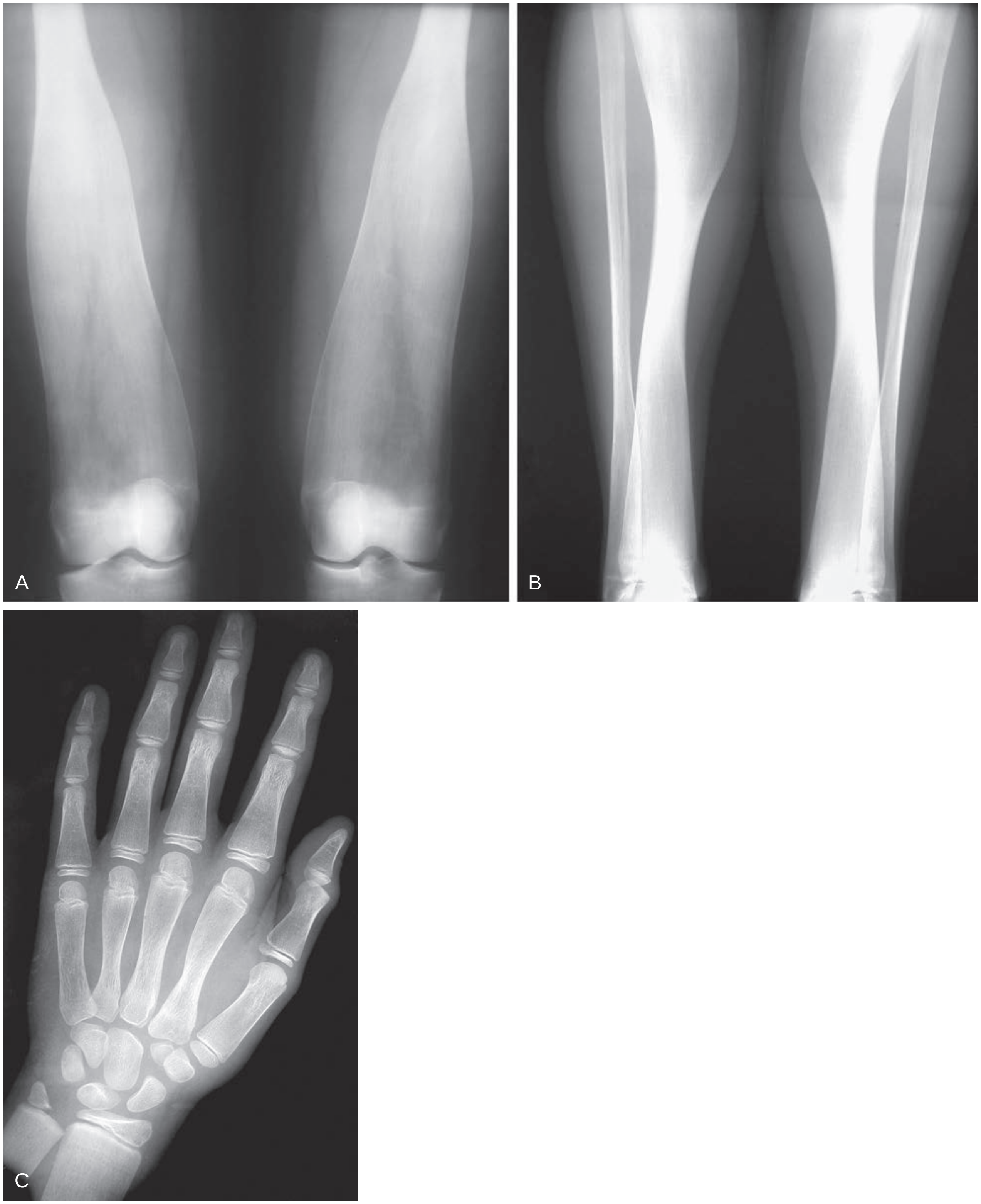

**Figure 132.39. Pyle dysplasia.** (A and B) In an affected 17 year old, markedly broad, undertubulated distal femurs (A) and markedly broad, undertubulated proximal and distal tibias with mild medial bowing proximally (B). (C) In a different patient, distal flaring of metacarpals and proximal flaring of phalanges are seen. The distal radial and ulnar metaphyses are broadened.

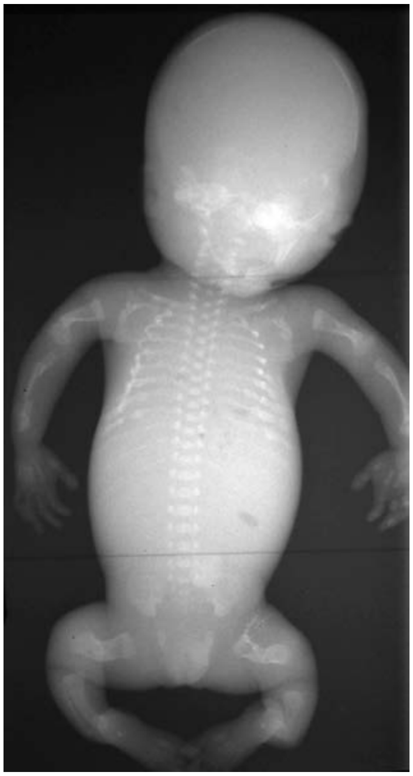

**Figure 132.40. Osteogenesis imperfecta type II in a stillborn full-term fetus.** Findings include generalized osteoporosis, absence of skull ossification, beaded ribs, and crumpled long bones.

3. *Spine:* sporadic unossified vertebral bodies, dense and osteopenic vertebrae, sporadic platyspondyly, butterfly-shaped vertebral bodies, sporadic missing pedicles
4. *Extremities:* generalized decreased ossification, chromosome-shaped femurs, metaphyseal cupping and irregularity, central lucent defect, "campomelic femurs," sporadic "missing" short tubular bones of hands and feet

Adult form:

1. Generalized osteopenia
2. *Extremities:* metaphyseal widening (rickets-like changes), punched-out metaphyseal lesions, pathologic fractures
3. Heterotopic calcifications

## LYSOSOMAL STORAGE DISEASES

The dysostosis multiplex group contains all the mucopolysaccharidoses (MPSs), mucolipidoses, and multiple other storage diseases that produce a skeletal dysplasia. The abnormalities in this entire group consist of well-described enzymatic defects that can be diagnosed by appropriate urine, blood, or fibroblast culture analyses. These diseases act similarly on the skeleton to produce abnormalities of varying severity, termed *dysostosis multiplex*. The real role of the radiologist is to suggest the likelihood of one of these disorders; the geneticist biochemically determines which exact dysplasia is present. Hurler or Hunter syndrome (MPS types IH and II) may be used as stereotypical examples of this group. Morquio syndrome (MPS types IVA and IVB) can often be differentiated from other MPS entities radiographically, as it has very prominent epiphyseal changes. In Hurler or Hunter syndrome, inferior beaking of the vertebral bodies with kyphosis is centered on the thoracolumbar junctions. This is known as *gibbus type abnormality* and is related to hypotonia in affected patients. This is a secondary effect from chronic pressure and stress on the vertebral bodies at the thoracolumbar junction and causes delay in ossification of the inferior portion of the T12 and L1 disc spaces. In Morquio syndrome, the central tongue or beaked appearance is caused by the primary dysplasia from a delay in epiphyseal ossification and causes a delay in ossification at the lower and upper end plates.

### Hurler or Hunter Syndrome (Mucopolysaccharidosis Type IH & II)

The enzyme abnormality is alpha-L-l-iduronidase, located on chromosome 4p. As with all the other members of this group, the inheritance pattern is recessive. Most of the MPS entities manifest clinically in late infancy or early childhood.

***Radiologic Findings (Dysostosis Multiplex)*** (Fig. 132.43)

1. *Skull:* enlarged neurocranium, abnormal J-shaped sella
2. *Thorax:* short, thick clavicles; paddle (oar)–shaped ribs; hypoplastic glenoid
3. *Spine:* gibbus, superior notched (inferior beaked) thoracolumbar vertebral bodies, upper cervical subluxation
4. *Pelvis:* flared, small iliac wings with inferior tapering; steep acetabular roofs
5. *Extremities:* diaphyseal widening of long bones; hands characteristically exhibit brachydactyly, proximal metacarpal "pointing," diaphyseal widening of metacarpals and proximal or middle phalanges, small irregular carpal bones

### Morquio Syndrome (Mucopolysaccharidosis Types IVA and IVB)

The enzyme abnormality is in galactose-6-sulfatase, resulting in the accumulation of excess MPS material in multiple organ systems, including the skeletal system. MPS IVB patients usually have more mild radiographic and clinical findings compared with MPS IVA.

***Radiologic Findings (Differentiating Features From Other Mucopolysaccharidoses)*** (Fig. 132.44)

1. *Skull:* no J-shaped sella
2. *Thorax:* widened, not oar shaped, ribs
3. *Spine:* central vertebral beaking or tongue; odontoid hypoplasia and cervical instability
4. *Pelvis:* no tapering of ileum, steep acetabular roofs
5. *Extremities:* proximal metacarpal rounding, genu valgus; epiphyseal dysplasia especially at carpal bones and femoral heads

### Mucolipidosis Type II (I-Cell Disease)

Mucolipidosis type II is an enzyme abnormality of N-acetylglucosamine phosphotransferase, the gene for which is found on chromosome 4q. It clinically and radiographically manifests in the newborn and can be seen prenatally. Most affected patients die in infancy. Certain radiographic features are quite unique.

***Radiologic Findings*** (e-Fig. 132.45)

1. *Extremities:* severe osteopenia with metaphyseal cupping and fraying, poorly defined cortices, "periosteal cloaking" or reaction seen diffusely with areas of cortical bone destruction; diaphyseal expansion
2. *Pelvis:* wide iliac flare with hypoplastic lower iliac segment, steep acetabular roofs
3. *Spine:* biconvex end plates with anterior concavity of the vertebral bodies
4. The changes of dysostosis multiplex occur later

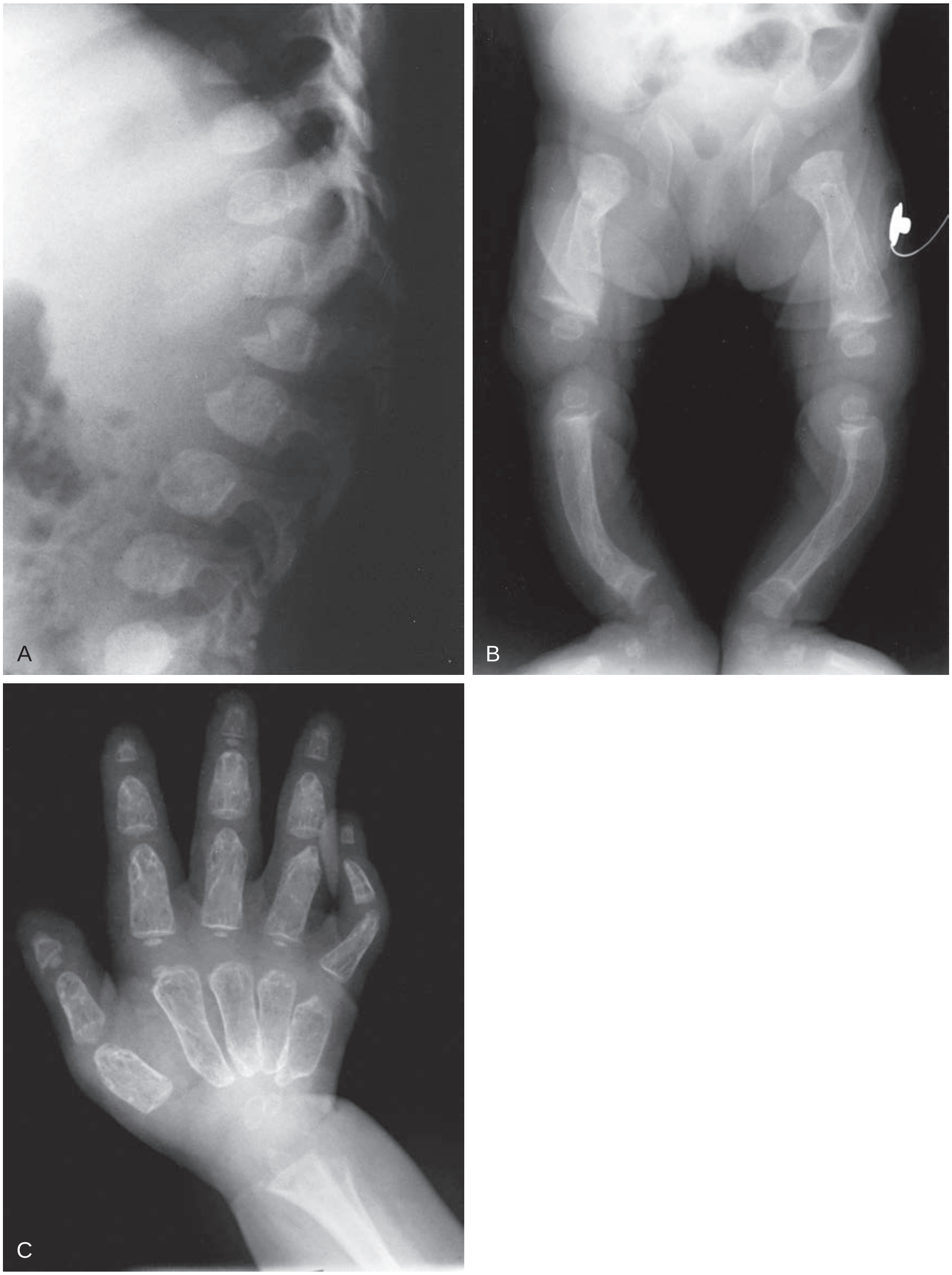

**e-Figure 132.45. Mucolipidosis type II (I-cell disease).** (A) Several hypoplastic superiorly notched vertebral bodies (mucopolysaccharidosis-like). (B) Characteristic periosteal cloaking. (C) Proximal metacarpal pointing and expanded short tubular bones with thin cortices.

## OSTEOLYSIS GROUP

This group includes a range of syndromes all with varying degrees of osteolysis present. The separate syndromes are best classified according to their primary sites of involvement.

1. Multicentric hands and feet
   a. Multicentric carpal or tarsal osteolysis with or without nephropathy
   b. Torg syndrome or Winchester syndrome or nodulosis with arthropathy syndrome
2. Acro-osteolysis
   a. Hajdu-Cheney syndrome (HCS)
   b. Mandubuloacral syndrome
3. Diaphyseal and metaphyseal
   a. Familial expansile osteolysis

## Hajdu-Cheney Syndrome

Distinctive transverse (bandlike) acro-osteolysis is present; skull features, including persistence of the skull sutures, a J-shaped sella, and wormian bones, characterize HCS. More important, however, is the progressive osteoporosis that occurs and can lead to vertebral body fractures. Many patients with confirmed HCS have an elongated and gracile twisting fibula and polycystic kidneys. Serpentine fibula polycystic kidney syndrome had been considered a separate genetic syndrome, but recently, the same genetic defect in the NOTCH2 signaling pathway has been found to cause both syndromes, unifying the picture.[29]

NOTCH2 is interesting for its effects on the skeleton and tumorogenesis. The defect in HCS causes an upmodulation in NOTCH signaling, which inhibits endochondral growth and osteoblastic differentiation resulting in osteopenia.[30] Errors in

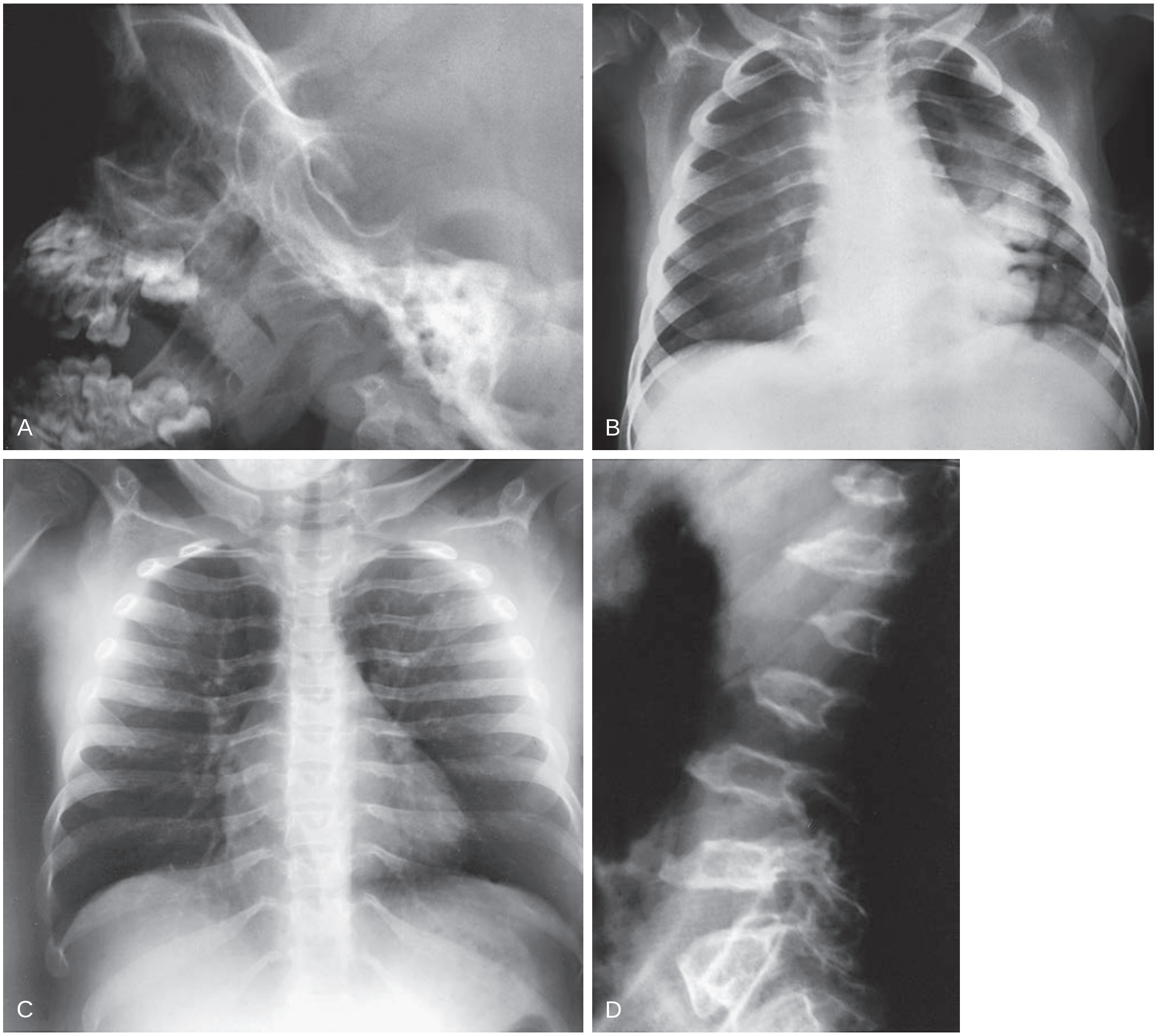

**Figure 132.43. Hurler syndrome (mucopolysaccharidosis type IH).** (A) Skull of an affected 3 year old with abnormal, excavated J-shaped sella turcica. (B) and (C) Thoraces of an affected 3 year old (B) and an affected 8 year old (C) with thick clavicles and paddle-shaped ribs (thin posteriorly and thick anteriorly). (D) Spine of an affected 8 year old with superiorly notched (inferiorly beaked) vertebral bodies. Radiographic findings in Hurler syndrome (mucopolysaccharidosis type IH). *Continued*

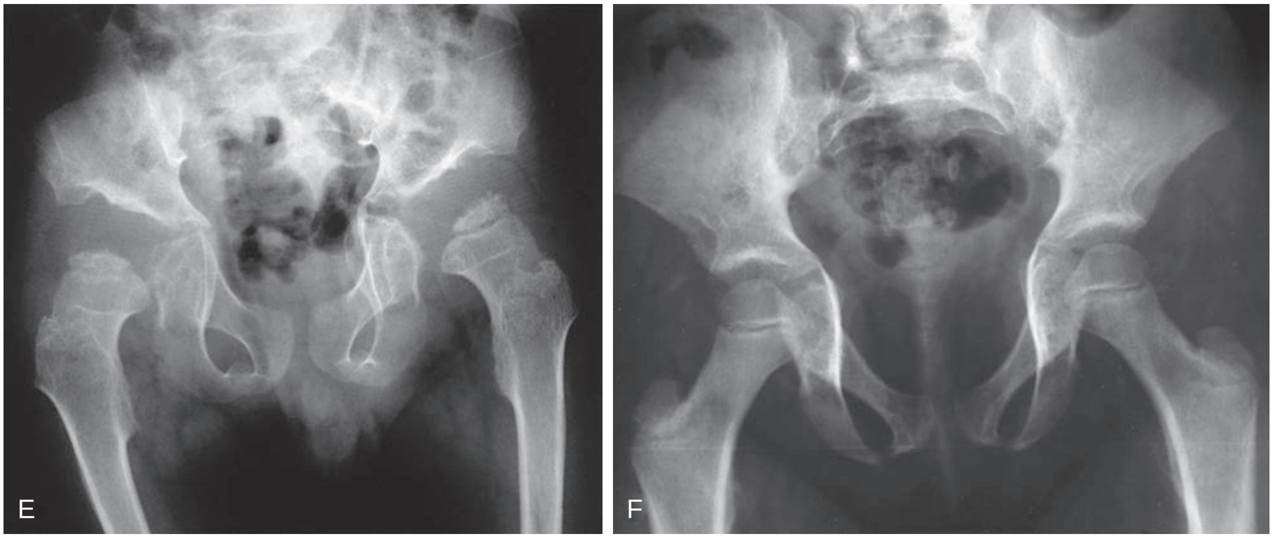

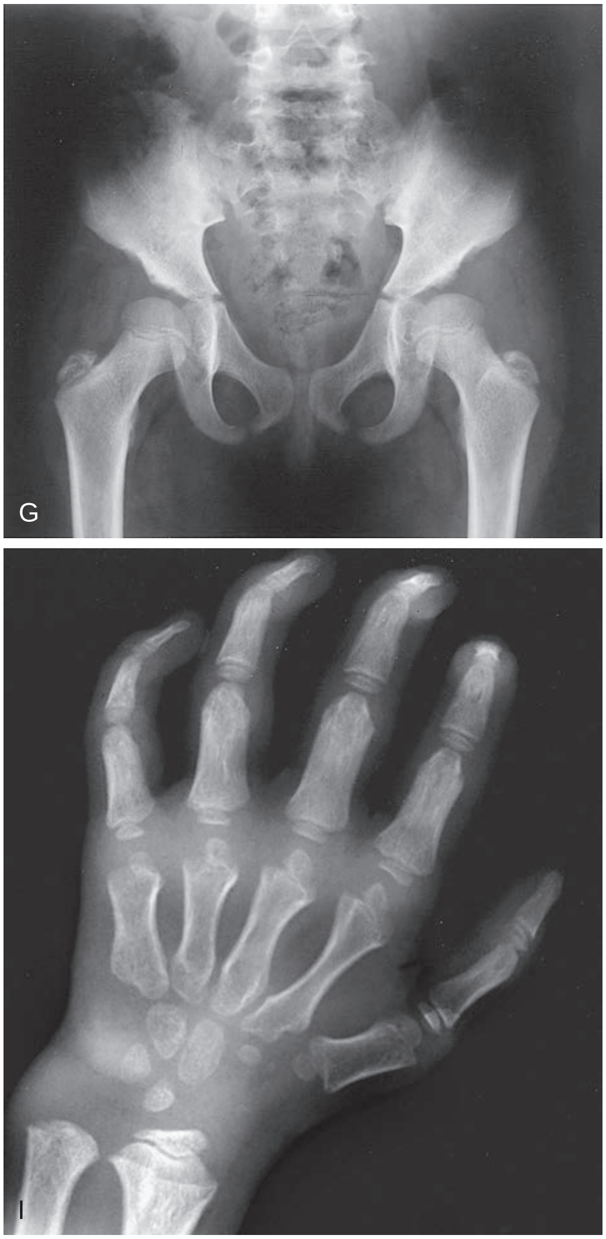

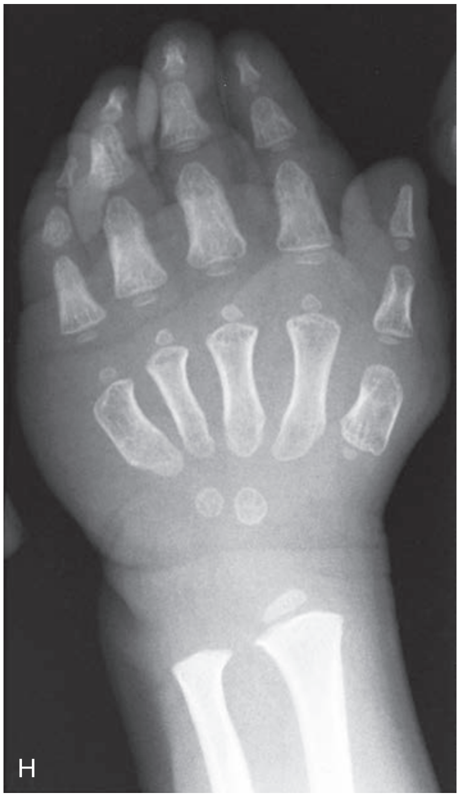

**Figure 132.43, cont'd.** (E–G) Pelvis of an affected 8 year old (E), another affected 8 year old (F), and an affected 12 year old (G) with small iliac wings with inferior tapering, and a slanted, irregular acetabular roof (E and G). (H and I) Hands of an affected 6 year old (H) and an affected 10 year old (I) with proximal metacarpal pointing and epiphyseal ossification delay.

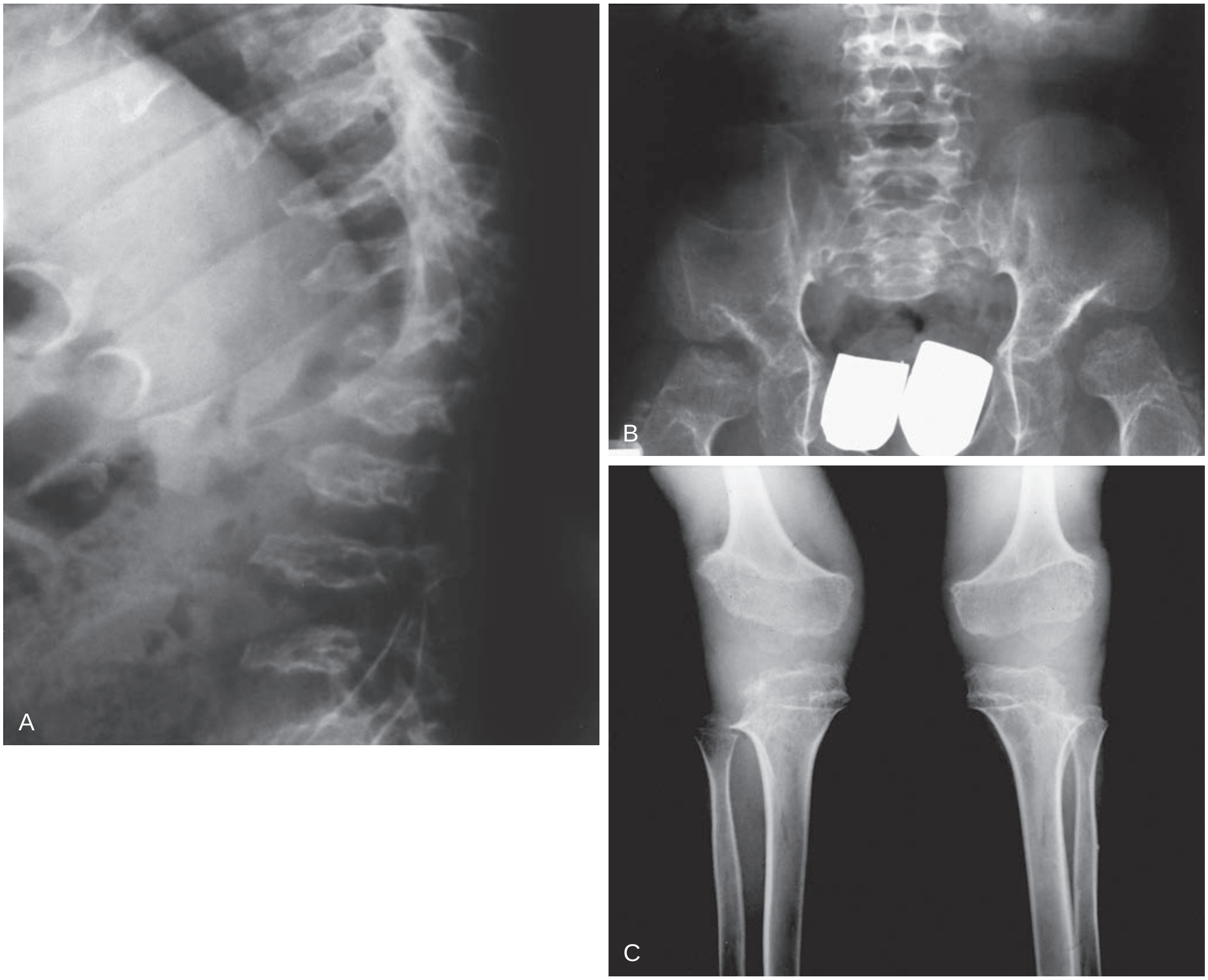

**Figure 132.44. Morquio syndrome (mucopolysaccharidosis types IVA and IVB).** (A) Radiograph from an affected 7 year old with platyspondyly with central beaking (tongue). (B) Radiograph from an affected 18 year old with severe capital femoral epiphyseal and acetabular dysplasia but no inferior iliac tapering. (C) Radiograph from an affected 15 year old with lateral distal femoral and proximal tibial epiphyseal ossification defects with genu varum.

the NOTCH signaling pathway have been associated with T-cell leukemia and lymphoma (NOTCH1).[31] Dysregulated NOTCH signaling is known to occur in multiple myeloma. Recently, enhanced NOTCH2 signaling has been associated with osteosarcoma and is associated with greater tumor invasiveness.[32]

***Radiologic Findings*** (Fig. 132.46)

1. *Skull:* wormian bones; cranial sutures remain open through adult life, hypoplastic sinuses, edentulous mandible
2. *Extremities:* bandlike acro-osteolysis; progressive osteopenia

## OVERGROWTH SYNDROMES WITH SKELETAL INVOLVEMENT

Important members of this group include Marfan syndrome, congenital contractural arachnodactyly (CCA), and Proteus syndrome.

### Marfan Syndrome and Congenital Contractural Arachnodactyly

These two congenital syndromes are caused by errors in fibrillin. Fibrillin is a glycoprotein that functions as a structural scaffold for elastic microfibrils. It can be found in abundance in the connective tissues of the walls of large vessels, lungs, bones, and eyes. The marfanoid body habitus is a constant feature along with long spidery fingers (hence the term *arachnodactyly*) and tall stature. The loss of normal fibrillin may allow liberation of transforming growth factor-β from the connective tissues, thereby allowing greater expressivity as tall stature.[33–35]

Dislocation of the lens of the eye occurs since fibrillin is found in the supportive connective tissues of the lens. The lack of normal fibrillin damages the elastic walls of the large vessels. Aortic root dilatation and rupture are the leading cause of death.

Marfan syndrome is a fibrillin 1 abnormality, whereas CCA is a fibrillin 2 abnormality. The two are phenotypically similar, each

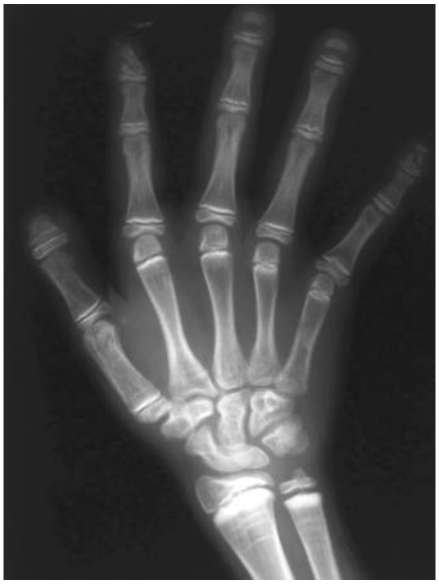

**Figure 132.46. Hajdu-Cheney syndrome in a 14-year-old boy.** Anteroposterior view of the hand shows transverse acro-osteolysis of the distal phalanges. Note the dense sclerosis at metaphyses—the patient takes bisphosphonates to enhance bone mineral density.

manifesting the typical marfanoid body habitus. However, patients with CCA also have joint contractures at the proximal interphalangeal joints, elbows, and knees. Although joint contractures can occur in Marfan syndrome, it is not a hallmark.

***Radiographic Features*** (e-Fig. 132.47)

1. *Skull:* dolicocephaly, arched palate
2. *Thorax:* scoliosis, pectus deformities, dural ectasia
3. *Pelvis:* acetabular protrusion deformity
4. *Extremities:* dolichostenomelia (long thin limbs or bones), arachnodactyly, joint hyperextensibility, osteopenia
5. *Other:* aortic root dilatation, spontaneous pneumothorax

### Proteus Syndrome

Proteus syndrome is named for the Greek god Proteus, who was able to change his shape at will. Proteus syndrome is a congenital hamartomatous disorder, which may be autosomal dominant. Affected patients have overgrowth of the hands and feet, limb asymmetry, gross cranial hyperostosis, and facial asymmetry leading to a frequently grotesque appearance. Patients with Proteus syndrome may also have mixed vascular malformations. Some have suggested that Joseph Merrick, also known as *the elephant man*, may have had Proteus syndrome rather than neurofibromatosis as was originally thought.

The radiographic findings of Proteus syndrome reflect what is seen clinically, namely, overgrowth of limbs and digits from both bone and soft tissues. Several types of tumors are associated with Proteus syndrome, including lipomas that tend to grow aggressively, ovarian cystadenoma, monomorphic parotid adenoma, testicular tumors, and central nervous system tumors (especially meningiomas).

***Radiologic Findings*** (e-Fig. 132.48)

1. *Skull:* macrocrania with cortical hyperostosis, dolichocephaly, and facial asymmetry
2. *Thorax:* scoliosis, kyphosis, large and asymmetric vertebral bodies
3. *Extremities:* asymmetric bone and soft tissue overgrowth
4. *Other:* mixed vascular malformations, hydrocephalus, emphysematous lung disease (12%)

## OTHER DISORDERS

### Cleidocranial Dysplasia

In this autosomal-dominant disorder, the chromosome locus is at 6p21 coding for a gene called *CBFA1* (core binding factor a1), also known as *RUNX2*. This dysplasia is quite common, with marked clinical variability and is often diagnosable at birth. The clinical findings include enlarged skull with large, late-closing fontanels; dental abnormalities; drooping, hypermobile shoulders; mild short stature; and a narrow chest.

***Radiologic Findings*** (Fig. 132.49)

1. *Skull:* large, brachycephalic; wormian bones; wide sutures; persistently open anterior fontanel
2. *Thorax:* absence or hypoplasia of clavicles, mildly shortened ribs with downward slope, 11 ribs
3. *Spine:* significant posterior wedging of thoracic vertebrae
4. *Pelvis:* high narrow iliac wings, absence or hypoplasia of pubic bones
5. *Extremities:* numerous pseudoepiphyses of metacarpals and tapered distal phalanges in the hands

## BRACHYDACTYLY GROUP

### Rubinstein-Taybi Syndrome

Rubinstein-Taybi syndrome is characterized by short stature; distinctive facial features; mental retardation; and broad, short thumbs and great toes. It is caused by sporadic mutations, the majority affecting the CREB-binding protein, which plays an important role in embryonic development. In slightly more than half of the patients, a cytogenetic abnormality can be identified. Radiographically, a delta-phalanx (longitudinal epiphyseal bracket) is seen at the first proximal phalanx (Fig. 132.50). The first distal phalanx is short and broad. At times, it may have a central lucency indicating an attempt at duplication. Other findings include congenital heart defects, agenesis of the corpus callosum, and vertebral and sternal anomalies. Patients have an increased risk of tumors, mainly meningioma, leukemia, and lymphoma.

### Poland Syndrome

Poland syndrome includes a spectrum of abnormalities that includes absence or hypoplasia of the pectoralis major muscle and variable deformities of the ipsilateral upper extremity. In the mildest form, absence or hypoplasia of the pectoralis major muscle is seen. In the most severe presentations in the chest, absence of some ribs, scoliosis, absence of the latissimus dorsi, and mammary hypoplasia are seen. The entire hemithoracic cavity may be shortened with a low-riding clavicular head and high-riding insertion of the rectus abdominus. In the hands, ipsilateral shortening of fingers 2 to 4, with cutaneous syndactyly, is seen.

The cause is thought to be an interruption of the embryonic vascular supply during the sixth week of gestation, at a time when the chest wall musculature and hand are differentiating. Generally, the sternal head of the pectoralis major muscle is affected, as the clavicular head is known to form first and is, therefore, usually present.

***Radiologic Findings*** (Fig. 132.51)

1. Hyperlucent hemithorax and absent axillary fold related to absence of the pectoralis major muscle
2. Syndactyly and polydactyly of ipsilateral upper extremity
3. Brachymesophalangy (brachydactyly of the middle phalanges)

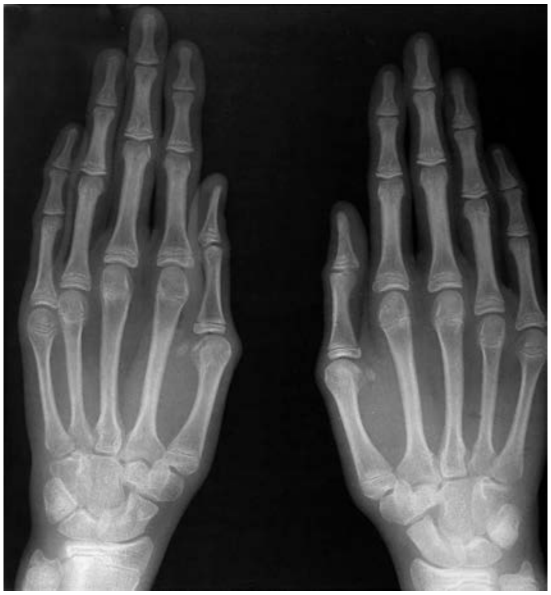

**e-Figure 132.47. Marfan syndrome.** The posteroanterior radiograph of the hand shows arachnodactyly.

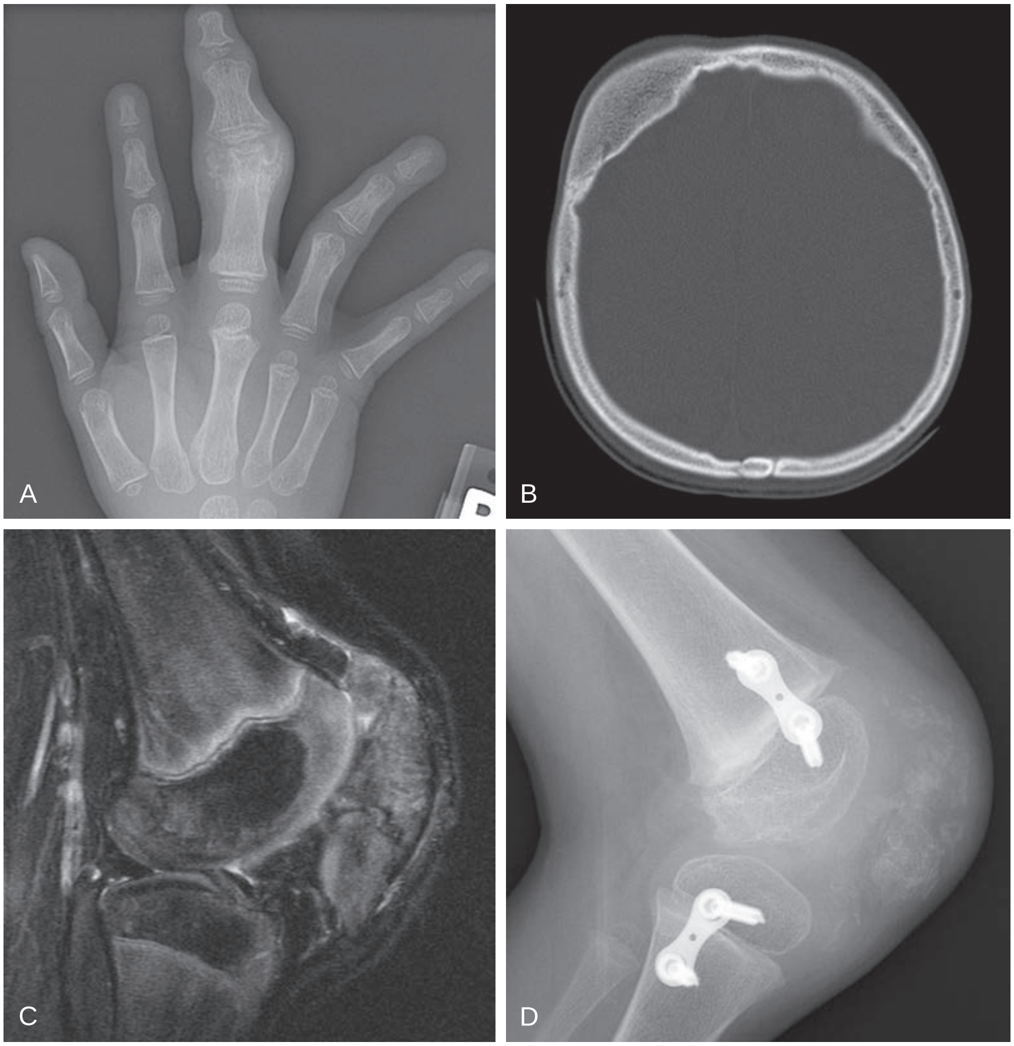

**e-Figure 132.48. Proteus syndrome in a 5-year-old male.** (A) Anteroposterior view of the hand with osseous and soft tissue overgrowth of the third finger. (B) An axial computed tomography scan shows osseous overgrowth of the right frontal bone. (C) Sagittal proton density fat-saturated MRI of the knee shows the cartilaginous patella is enlarged and very irregular. (D) The lateral radiograph of the knee shows irregular ossification and overgrowth of the patella.

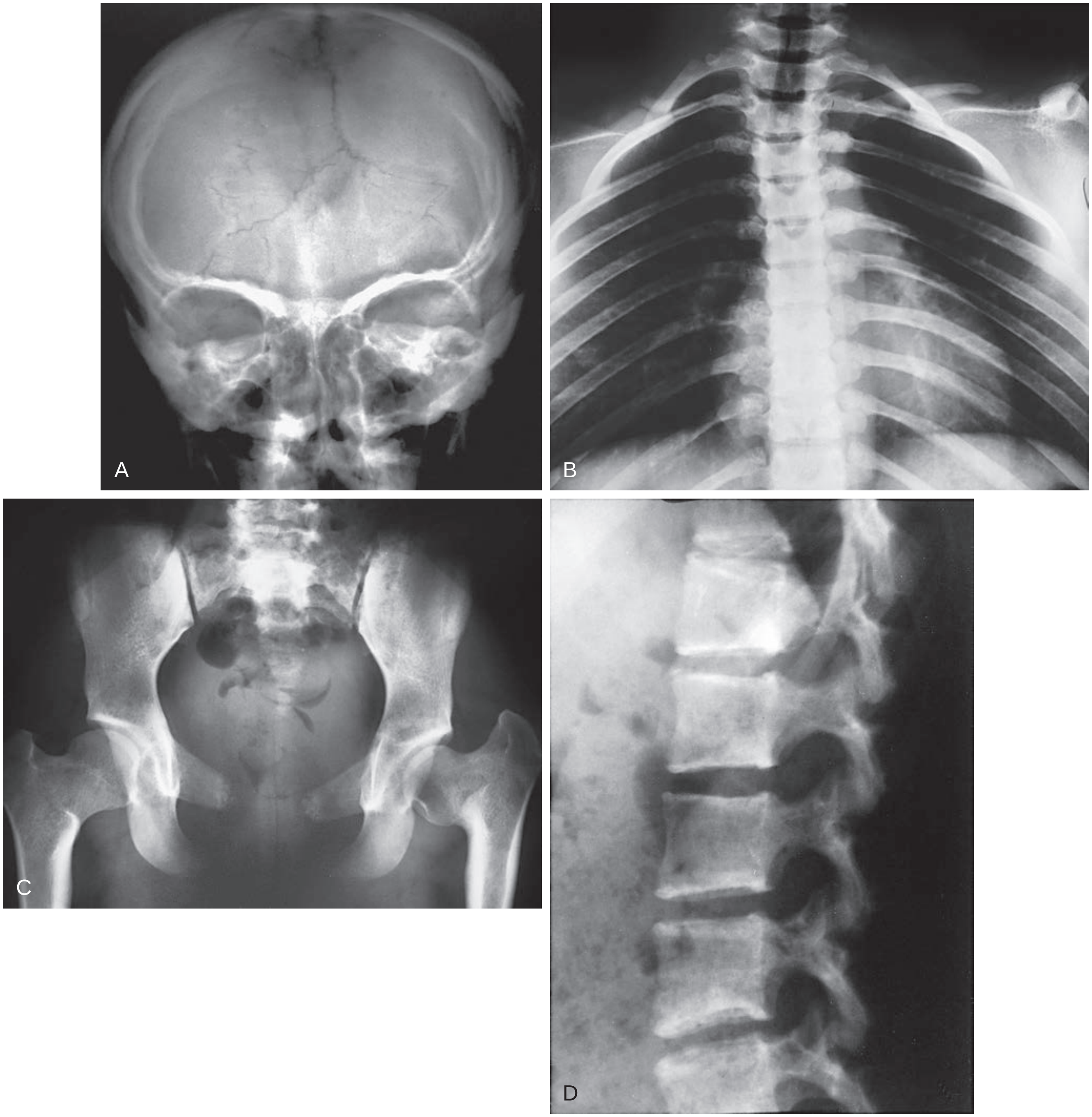

**Figure 132.49. Cleidocranial dysplasia in a 15 year old.** (A) Skull: large open anterior fontanel and multiple wormian bones. (B) Thorax: asymmetric hypoplastic or absent clavicles and downward-sloping ribs. (C) Pelvis: tall, narrow ilia and hypoplastic pubic bones. (D) Spine: posteriorly wedged but otherwise normal vertebral bodies.

## LIMB HYPOPLASIA—REDUCTION DEFECTS GROUP

### Brachydactyly A-E

The brachydactyly classification system most commonly used was described by Bell in 1951 and refined by Temtamy and McKusick in 1978. Since these descriptions, the genetic loci associated with many of the types of isolated brachydactyly have been elucidated. Some of the patterns of shortening of the bones of the hand will be easily recognized by the practicing radiologist. Brachydactyly type A3 in which the fifth middle phalanx is short is especially common. This can be differentiated from (1) Kirner deformity, with palmar/radial bowing of the distal phalanx, and (2) camptodactyly, with a flexion contracture of the interphalangeal joints.

Brachydactylies are usually isolated genetic abnormalities, but some may have associated syndromes or metabolic conditions. Variable shortening of the metacarpals is classified as brachydactyly type E, which most commonly affects the fourth and fifth rays. A short fourth metacarpal is also a well-known feature of many syndromes, including Turner syndrome and pseudohypoparathyroidism or pseudopseudohypoparathroidism (PHP/PPHP). Many

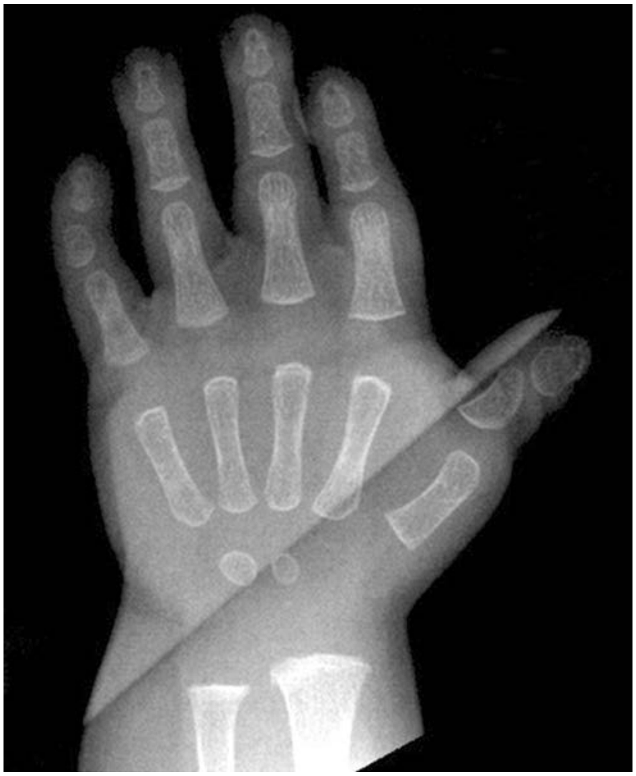

**Figure 132.50. Rubinstein-Taybi syndrome in an 8-month-old boy.** The anteroposterior view of the hand exhibits the classic delta phalanx at the first proximal phalanx.

patients with brachydactyly type E are short and, as such, may be indistinguishable from those with PHP/PPHP.

## Holt-Oram Syndrome

Holt-Oram syndrome, also called *heart–hand syndrome*, is caused by a completely penetrant mutation involving *TBX5* at 12q2. *TBX5* encodes a protein that plays a role in heart development and limb identity and patterning. It is part of the T-box gene family, which encodes transcription factors important in body development.

The disease is familial in 60% to 70% of cases; new mutations account for the remainder. Limb anomalies range from phocomelia with absent or hypoplastic humerus (10% of patients in some series) to triphalangeal thumbs. The most common limb anomalies are radial ray anomalies. These include absence of hypoplasia of the radius, bipartite or hypoplastic scaphoids of abnormalities of the thumb. Because radial ray abnormalities commonly involve the most distal part of the radial ray, the syndrome is well marked for the common occurrence of the triphalangeal thumb. The triphalangeal thumb is an interesting anomaly. In the normal first metacarpal, the epiphysis is proximal in contrast to the metacarpals 2 to 5, in which a distal epiphysis is seen. In the phalanges, however, the epiphyses are always proximal. In the most common form of triphalangeal thumb, in which the so-called "five-fingered hand" is seen, the thumb recapitulates fingers 2 to 5 with a distal metacarpal epiphysis and three phalanges each with basilar epiphyses. In this form, the thumb is frequently not opposable and articulates in the same plane as fingers 2 to 5.

The most common heart defects are septal defects, both atrial (58%) and ventricular (28%). *TBX5* appears to play a significant role specifically in the septation of the heart into four chambers. In addition, it plays a role in determining electrical conductive pathways between the chambers, giving rise to occasional conduction defects (18%).

## MISCELLANEOUS ASSOCIATIONS, SYNDROMES, AND CHROMOSOMAL DISORDERS

### VACTERL Association

VATER association, now expanded to VACTERL association, refers to a specific combination of anomalies in multiple organ systems, which is believed to represent a developmental defect arising during the fifth week of gestation. The acronym indicates the following:

V: vertebral (fusion and segmentation anomalies)
A: anorectal (imperforate anus)
C: cardiac (septal defects, tetralogy of Fallot, transposition of the great vessels)
T: tracheoesophageal (esophageal atresia/tracheoesophageal fistula)
R: renal (agenesis, hypoplasia, horseshoe kidney)
L: limb (especially radial ray anomalies)

VACTERL is referred to as an *association* rather than a syndrome, indicating that the cause is uncertain. The various organ defects occur together and are associated. They are probably caused by a problem in blastogenesis around the fifth week of gestation. It is not associated with facial dysmorphism, learning disability, growth failure, or abnormal head size or shape. If any of these features is present, a genetic condition associated either with esophageal atresia such as Feingold syndrome or CHARGE association or with imperforate anus such as Townes-Brocks syndrome needs to be excluded.

In those patients with imperforate anus, sacral anomalies and posterior spinal fusion defects, including tethered cord and lipomyelomeningocele, are common.

Hydrocephalus associated with the VACTERL association is known to have a high rate of recurrence in subsequent pregnancies. This is referred to as *VACTERL-H association*, with hydrocephalus added to the acronym. VACTERL-H is frequently an X-linked disorder, particularly when aqueductal stenosis is present and the prognosis is poor (e-Fig. 132.52).

### Klinefelter Syndrome

The addition of one or more X chromosomes in the male results in Klinefelter syndrome. Affected patients have greater expression of female characteristics, including gynecomastia, a feminine body fat distribution, small testes, and elevated levels of follicle-stimulating hormone. An increased incidence of male breast cancer, mediastinal germ cell tumor, leukemia, non-Hodgkin lymphoma, and lung cancer is seen, but the risk of prostate cancer is decreased.

Osseous changes are inconstant and include kyphoscoliosis, radioulnar synostosis, and a short fourth metacarpal. Skeletal findings are more apparent when more than two X chromosomes are present.

Other organ systems also may be affected. The risk of lupus, diabetes mellitus, mitral valve prolapse, bronchiectasis and emphysema, and situs inversus is increased.

### Trisomy 13 (Patau Syndrome)

Trisomy 13 occurs as a pure trisomy as well as a mosaic syndrome. Survival beyond the age of 10 years is rare and most die in infancy. Severe intracranial abnormalities, including holoprosencephaly, Dandy-Walker malformation spectrum, agenesis of the corpus callosum, and anencephaly, are often present. Congenital heart disease with various renal anomalies is often present. Additional

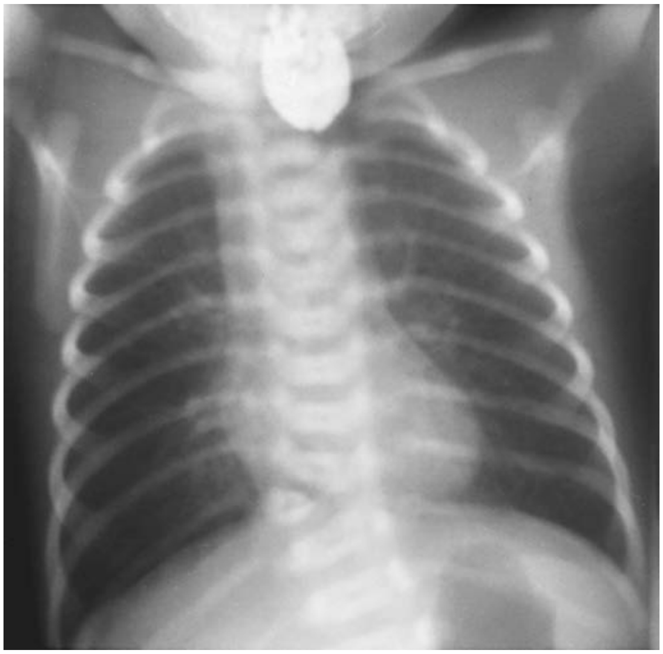

**e-Figure 132.52. VACTERL association (*v*ertebral, *a*norectal, *c*ardiac, *t*racheo*e*sophageal, *r*enal, *l*imb).** The chest radiograph of a newborn with tracheoesophageal fistula and esophageal atresia. Contrast medium is in the proximal esophageal pouch. Air in the stomach indicates the presence of a distal tracheoesophageal fistula. A hemivertebra is noted. The patient also had a pelvic kidney.

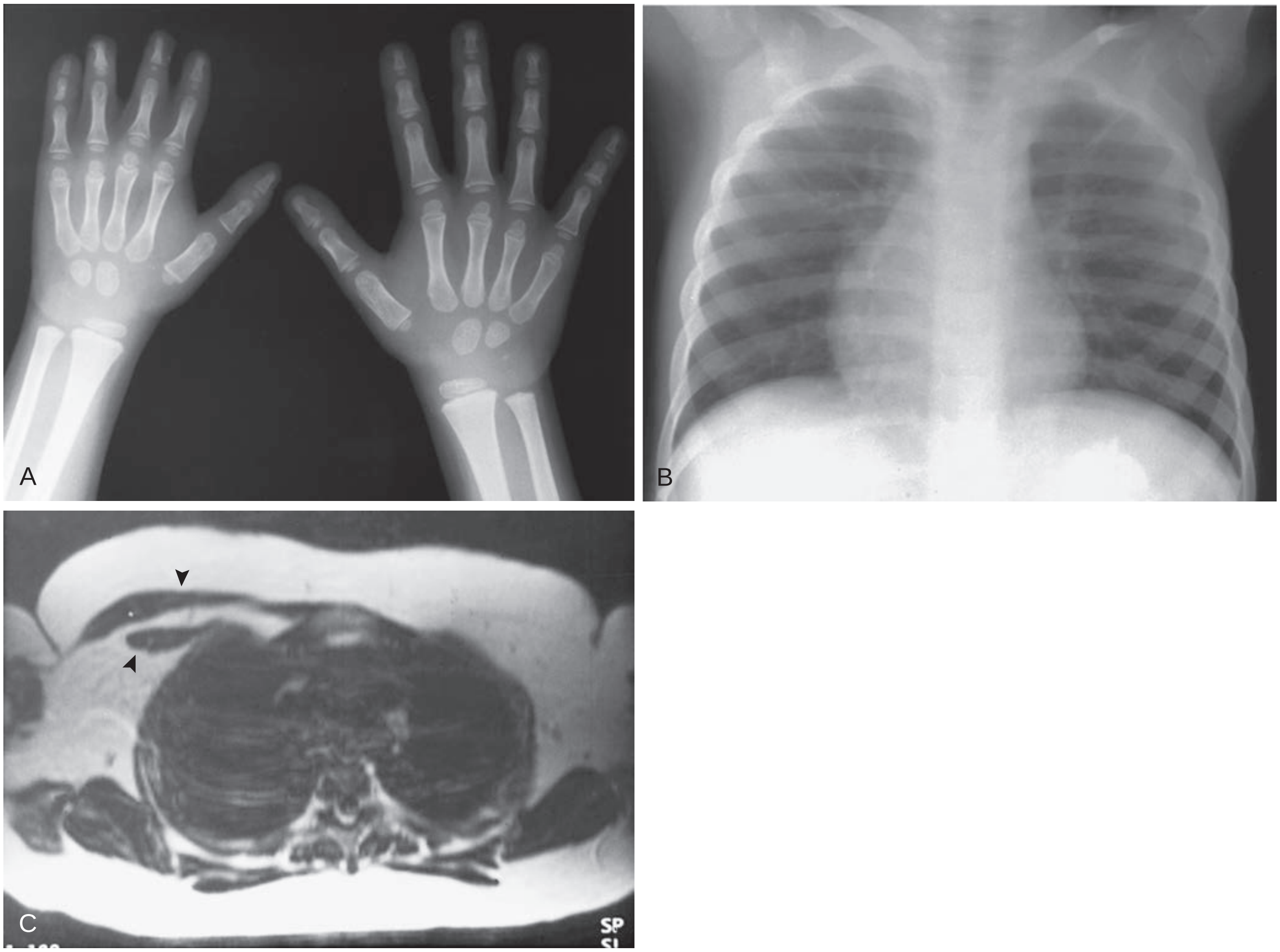

**Figure 132.51. Poland syndrome.** (A) Hand radiograph shows generalized hypoplasia of the left hand, with soft tissue syndactyly affecting the second through fourth digits. (B) The anteroposterior chest radiograph on a different patient shows relative lucency of the left hemithorax with loss of the pectoral shadow. (C) Axial T1-weighted magnetic resonance (MR) image shows absence of the left anterior chest wall musculature (*arrowheads* indicate normal musculature on the right).

components of the syndrome include congenital vertical talus (rocker-bottom foot), digital anomalies, micropthalmia, micrognathia, and cleft palate.

## Trisomy 18 (Edwards Syndrome)

Abnormalities in trisomy 18 include severe central nervous system changes such as holoprosencephaly and nonspecific migrational disorders, congenital heart disease, clubfeet or rocker-bottom feet, and digital anomalies. The hands are clenched in utero, and at birth, the first finger is adducted, and the second finger overlaps the third. Multiple other organ systems, including genitourinary, gastrointestinal, and biliary systems, are also affected. Life expectancy is short. Very few cases survive childhood. Mosaics may be less affected.

## Trisomy 21 (Down Syndrome)

Trisomy 21 is the most common chromosomal syndrome. A host of anomalies involving virtually all organ systems are well described. The most common cause of trisomy 21 is a nondisjunction event during gametogenesis, usually in the mother. At times, a trisomy 21 mosaic situation can occur when the nondisjunction event occurs in an embryo during early cell division. Rarely, trisomy 21 can occur as a result of an unbalanced translocation in one parent when the long arm of chromosome 21 attaches to the long arm of chromosome 14.

Both occipitoatlantal and atlantoaxial instability is found in Down syndrome. Anteroposterior occipitoatlantal instability is defined as more than 2 mm of motion on extension of the occipitoatlantal joints. If present, a neck MRI is recommended to evaluate for signal changes in the cord. An atlantoaxial distance of 4.5 mm or less is considered normal. With a distance from 4.5 to 10 mm and a normal neurologic exam, avoidance of high-risk sports (diving, football) is recommended. If more than 4.5 mm and with a neurologic deficit, activities are restricted and MRI recommended to evaluate for cord changes.[36] However, the poor reproducibility of findings and both intraobserver and interobserver variability may make it difficult to base surgical and clinical treatment protocols for upper cervical spine instability on measurements alone.

The brains of trisomy 21 patients have smaller than normal volumes, but no other consistent changes occur. The level of intellectual performance of affected individuals varies, but many are able to function normally in society with some assistance.

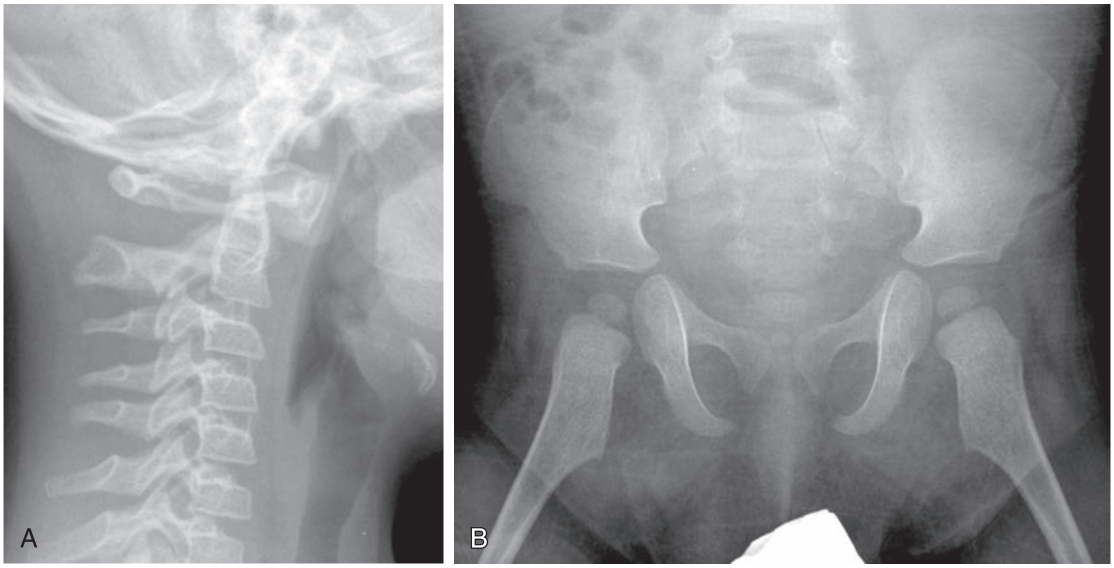

**Figure 132.53. Down syndrome.** (A) Lateral cervical spine radiograph shows abnormal widening between the anterior arch of C1 and the dens. (B) Frontal view of the pelvis in another patient shows flared iliac wings and flat horizontal acetabular roofs.

***Clinical and Imaging Findings*** (Fig. 132.53)

- *Skull:* brachycephaly
- *Spine:* occipitoatlantal and atlantoaxial instability
- *Thorax:* hypersegmented manubrium, 11 rib pairs, small bell-shaped chest with short ribs
- *Pelvis:* flared iliac wings, flat acetabular roofs
- *Gastrointestinal tract:* duodenal atresia, Hirschsprung disease, malrotation, tracheoesophageal fistula, and imperforate anus
- *Cardiac:* endocardial cushion defect most common but other types also occur
- *Other:* increased risk for leukemia (acute lymphoblastic leukemia)

## Turner Syndrome

Turner syndrome is most commonly caused by a 45,XO chromosomal pattern. In 15% of cases, one full X chromosome is present as well as an X isochromosome that contains only the long arms of chromosome X. Although originally it was thought that in the normal 46,XX female, complete inactivation of the second X chromosome occurs, some genes on the short arm of the inactivated X chromosome remain activated and are necessary for proper development, which explains why a patient with an X isochromosome and the classic XO are phenotypically similar.[37] The locus involved on the short arm of the X chromosome is in the pseudoautosomal region at Xp22 at a gene termed the *short stature homeobox gene (SHOX)*. *SHOX* was originally determined to be associated with some patients with idiopathic short stature syndrome who have a significantly short stature (>2 SDS), a persistently low growth rate for age, and no identifiable cause of a specific metabolic growth retarding condition.[38] Subsequently, *SHOX* has been found to be active in Turner syndrome.[39] Later, homozygous loss was found to be the cause of Langer mesomelic dysplasia and heterozygous loss the cause of dyschondrosteosis (Leri-Weill syndrome). In each of these last three conditions, the common thread of short stature, a short fourth metacarpal, and a varying degree of Madelung deformity is present.

Turner syndrome, or monosomy X, was initially described as a triad of infertility, webbing of the neck, and cubitus valgus deformity of the elbow. Since that time, a multitude of associated radiographic findings have been described involving most organ systems:

1. *Skull:* brachycephaly
2. *Spine:* platyspondyly
3. *Thorax:* pectus carinatum, thin lateral clavicles
4. *Pelvis:* sacral hypoplasia
5. *Extremities:* elbow valgus, overtubulation of long bones, flattening of the medial femoral condyle and patellar dislocation, proximal tibial exostosis, phalangeal abnormalities

Hand radiographs demonstrate typical changes with osteopenia, shortening of the fourth and fifth metacarpals (e-Fig. 132.54), delayed maturation, phalangeal predominance, a V-shaped deformity of the distal radiocarpal joint (Madelung deformity), and drumstick-shaped distal phalanges.

The classic cardiovascular finding is postductal coarctation of the aorta, but septal defects, aortic coarctation and dissection, and mitral valve prolapse are also common. Renal anomalies include rotational anomalies, bifid renal pelvis, horseshoe kidney (common), and multicystic dysplastic kidney. Autoimmune conditions, including hypothyroidism, diabetes, and juvenile rheumatoid arthritis, have been associated with Turner syndrome. Genital abnormalities, best evaluated with pelvic ultrasound or MRI, include ovarian and uterine absence or hypoplasia. Vascular abnormalities also include intestinal telangiectasia, lymphedema, and an increased incidence of vascular tumors (hemangioma, lymphatic malformation).

### KEY POINTS

- An ordered segmental approach to the radiographs of a patient with skeletal dysplasia is the key to proper diagnosis.
- Abnormalities should be generally classified as to the area of abnormality. Are the epiphyses or metaphyses involved? Is there vertebral body involvement? Are the findings rhizomelic, mesomelic, or acromelic?
- Following a general classification, a search should be made for any more peculiar or specific changes.
- After appropriate analysis, consultation with any of the excellent referral texts included in this chapter will be very helpful.

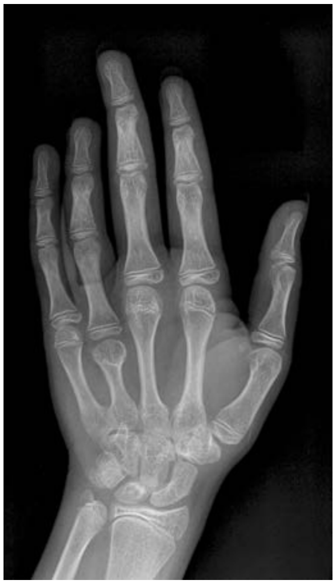

**e-Figure 132.54. Turner syndrome.** Frontal radiograph of the hand shows marked shortening of the fourth metacarpal.

## SUGGESTED READINGS

Alman BA. Skeletal dysplasias and the growth plate. *Clin Genet*. 2008; 73(1):24–30.

Ikegawa S. Genetic analysis of skeletal dysplasia: recent advances and perspectives in the post-genome-sequence era. *J Hum Genet*. 2006; 51(7):581–586.

McAlister WH, Herman TE. Osteochondrodysplasias, dysostoses, chromosomal aberrations, mucopolysaccharidoses, and mucolipidoses. In: Resnick D, ed. *Bone and Joint Disorders*. 4th ed. Philadelphia, PA: Elsevier; 2002.

Rimoin DL, Cohn D, Krakow D, et al. The skeletal dysplasias: clinical-molecular correlations. *Ann N Y Acad Sci*. 2007;1117:302–309.

Superti-Furga A, Bonafe L, Rimoin DL. Molecular-pathogenetic classification of genetic disorders of the skeleton. *Am J Med Genet*. 2001;106(4):282–293.

## REFERENCES

Full references for this chapter can be found on www.expertconsult.com.

## REFERENCES

1. Bonafe L, Cormier-Daire V, Hall C, et al. Nosology and classification of genetic skeletal disorders: 2015 revision. *Am J Med Genet A*. 2015;167A(12):2869–2892.
2. Lachman RS. *Taybi and Lachman's Radiology of Syndromes, Metabolic Disorders and Skeletal Dysplasias*. 5th ed. Philadelphia: Mosby; 2007.
3. Spranger JW, Brill PW, Poznanski A. *Bone Dysplasias: An Atlas of Genetic Disorders of Skeletal Development*. 2nd ed. New York: Oxford University Press; 2002.
4. Bonaventure J, Rousseau F, Legeai-Mallet L, et al. Common mutations in the gene encoding fibroblast growth factor receptor 3 account for achondroplasia, hypochondroplasia and thanatophoric dysplasia. *Acta Paediatr Suppl*. 1996;417:33–38.
5. Ornitz DM, Legeai-Mallet L. Achondroplasia: development, pathogenesis, and therapy. *Dev Dyn*. 2016.
6. Shapiro R, Robinson F. Embryogenesis of the human occipital bone. *AJR Am J Roentgenol*. 1976;126:1063–1068.
7. Matsui Y, Yasui N, Kimura T, et al. Genotype phenotype correlation in achondroplasia and hypochondroplasia. *J Bone Joint Surg Br*. 1998;80:1052–1056.
8. Meredith SP, Richards AJ, Bearcroft P, et al. Significant ocular findings are a feature of heritable bone dysplasias resulting from defects in type II collagen. *Br J Ophthalmol*. 2007;91:1148–1151.
9. Dwek JR. Kniest dysplasia: MR correlation of histologic and radiographic peculiarities. *Pediatr Radiol*. 2005;35:191–193.
10. Spranger J. The type XI collagenopathies. *Pediatr Radiol*. 1998;28:745–750.
11. Hastbacka J, Superti-Furga A, Wilcox WR, et al. Atelosteogenesis type II is caused by mutations in the diastrophic dysplasia sulfate-transporter gene (DTDST): evidence for a phenotypic series involving three chondrodysplasias. *Am J Hum Genet*. 1996;58:255–262.
12. Superti-Furga A, Rossi A, Steinmann B, et al. A chondrodysplasia family produced by mutations in the diastrophic dysplasia sulfate transporter gene: genotype/phenotype correlations. *Am J Med Genet*. 1996;63:144–147.
13. Karniski LP. Mutations in the diastrophic dysplasia sulfate transporter (DTDST) gene: correlation between sulfate transport activity and chondrodysplasia phenotype. *Hum Mol Genet*. 2001;10:1485–1490.
14. Robertson SP. Molecular pathology of filamin A: diverse phenotypes, many functions. *Clin Dysmorphol*. 2004;13:123–131.
15. Robertson SP. Filamin A: phenotypic diversity. *Curr Opin Genet Dev*. 2005;15:301–307.
16. Dai J, Cho TJ, Unger S, et al. TRPV4-pathy, a novel channelopathy affecting diverse systems. *J Hum Genet*. 2010;55:400–402.
17. Dai J, Kim OH, Cho TJ, et al. Novel and recurrent TRPV4 mutations and their association with distinct phenotypes within the TRPV4 dysplasia family. *J Med Genet*. 2010;47:704–709.
18. Hall T, Bush A, Fell J, et al. Ciliopathy spectrum expanded? Jeune syndrome associated with foregut dysmotility and malrotation. *Pediatr Pulmonol*. 2009;44:198–201.
19. Kim OH, Park H, Seong MW, et al. Revisit of multiple epiphyseal dysplasia: ethnic difference in genotypes and comparison of radiographic features linked to the COMP and MATN3 genes. *Am J Med Genet A*. 2011;155A:2669–2680.
20. Bastepe M, Raas-Rothschild A, Silver J, et al. A form of Jansen's metaphyseal chondrodysplasia with limited metabolic and skeletal abnormalities is caused by a novel activating parathyroid hormone (PTH)/PTH-related peptide receptor mutation. *J Clin Endocrinol Metab*. 2004;89:3595–3600.
21. Hermanns P, Bertuch AA, Bertin TK, et al. Consequences of mutations in the non-coding RMRP RNA in cartilage-hair hypoplasia. *Hum Mol Genet*. 2005;14:3723–3740.
22. Hermanns P, Tran A, Munivez E, et al. RMRP mutations in cartilage-hair hypoplasia. *Am J Med Genet A*. 2006;140:2121–2130.
23. Sulisalo T, Francomano CA, Sistonen P, et al. High-resolution genetic mapping of the cartilage-hair hypoplasia (CHH) gene in Amish and Finnish families. *Genomics*. 1994;20:347–353.
24. Bowen P, Biederman B, Hoo JJ. The critical segment for the Langer-Giedion syndrome: 8q24.11—-q24.12. *Ann Genet*. 1985;28:224–227.
25. Vickers D, Nielsen G. Madelung deformity: surgical prophylaxis (physiolysis) during the late growth period by resection of the dyschondrosteosis lesion. *J Hand Surg [Br]*. 1992;17:401–407.
26. Cook PA, Yu JS, Wiand W, et al. Madelung deformity in skeletally immature patients: morphologic assessment using radiography, CT, and MRI. *J Comput Assist Tomogr*. 1996;20:505–511.
27. Bartsocas CS. Pycnodysostosis: Toulouse-Lautrec's and Aesop's disease? *Hormones (Athens)*. 2002;1:260–262.
28. Ben-Asher E, Zelzer E, Lancet D. LEMD3: the gene responsible for bone density disorders (osteopoikilosis). *Isr Med Assoc J*. 2005;7:273–274.
29. Isidor B, Le Merrer M, Exner GU, et al. Serpentine fibula-polycystic kidney syndrome caused by truncating mutations in NOTCH2. *Hum Mutat*. 2011.
30. Zanotti S, Smerdel-Ramoya A, Stadmeyer L, et al. Notch inhibits osteoblast differentiation and causes osteopenia. *Endocrinology*. 2008;149:3890–3899.
31. Zanotti S, Canalis E. Notch and the skeleton. *Mol Cell Biol*. 2010;30:886–896.
32. Zhang P, Yang Y, Zweidler-McKay PA, et al. Critical role of notch signaling in osteosarcoma invasion and metastasis. *Clin Cancer Res*. 2008;14:2962–2969.
33. Ramirez F. Fibrillln mutations in Marfan syndrome and related phenotypes. *Curr Opin Genet Dev*. 1996;6:309–315.
34. Ramirez F, Pereira L, Zhang H, et al. The fibrillin-Marfan syndrome connection. *Bioessays*. 1993;15:589–594.
35. Loeys BL, Mortier G, Dietz HC. Bone lessons from Marfan syndrome and related disorders: fibrillin, TGF-B and BMP at the balance of too long and too short. *Pediatr Endocrinol Rev*. 2013;10(suppl 2):417–423.
36. Pizzutillo PD, Herman MJ. Cervical spine issues in Down syndrome. *J Pediatr Orthop*. 2005;25:253–259.
37. Brown CJ, Willard HF. Localization of a gene that escapes inactivation to the X chromosome proximal short arm: implications for X inactivation. *Am J Hum Genet*. 1990;46:273–279.
38. Hirschfeldova K, Solc R, Baxova A, et al. SHOX gene defects and selected dysmorphic signs in patients of idiopathic short stature and Leri-Weill dyschondrosteosis. *Gene*. 2012;491:123–127.
39. Rao E, Weiss B, Fukami M, et al. Pseudoautosomal deletions encompassing a novel homeobox gene cause growth failure in idiopathic short stature and Turner syndrome. *Nat Genet*. 1997;16:54–63.

# 133 Alignment Disorders

Matthew R. Hammer, Yassine Kanaan, and Peter J. Strouse

## OVERVIEW

Malalignment of extremity bones may be congenital or acquired. Primary bone or secondary soft tissue or neuromuscular disorders can result in abnormal alignment. Malalignment is often seen with congenital deformities characterized by embryologic failure of development, discussed in Chapter 131. One of the most common alignment disorders is developmental dysplasia of the hip, discussed in Chapter 135.

## UPPER EXTREMITIES

### Neonatal Brachial Plexus Palsy/Glenohumeral Dysplasia

***Etiologies, Pathophysiology, and Clinical Presentation.*** Neonatal brachial plexus palsy (also know as *Erb palsy* or *brachial plexopathy*) is caused by injury to the cervicothoracic nerve roots during birth. It is associated with prolonged, difficult delivery (dystocia) and with larger infants. Infants present with decreased motion of the involved extremity. Children with a persistent defect will hold their arms in internal rotation with pronation of the forearm and flexion of the wrist (waiter's tip arm). This is the most common insult leading to secondary glenohumeral dysplasia.

***Imaging.*** At birth, radiographs can exclude fractures of the clavicle and humerus. Ultrasonography (US) and magnetic resonance imaging (MRI) have been used to directly evaluate the brachial plexus; however, the primary goal of advanced imaging is to evaluate orthopedic anatomy to determine function and orthopedic treatment as primary repair of the brachial plexus injury is difficult.[1–3]

Progressive deformity with secondary glenohumeral dysplasia manifests as a small, flattened humeral head, which may sublux, usually in the posterior direction relative to a small, shallow, abnormally retroverted glenoid (Fig. 133.1).[4] In normal shoulders, glenoid version is near neutral, often mildly retroverted by approximately 5 degrees relative to a line perpendicular to the axis of the scapular body.[5] With brachial plexus palsy, glenoid retroversion averages 25 degrees. The scapula is hypoplastic and elevated; the acromion is tapered and inferiorly directed, as is the coracoid; and the clavicle is shortened.

Many of these findings are seen on radiography. Computed tomography (CT) or MRI can be used to quantify the degree of glenoid retroversion, deformity of the glenoid and humeral head, glenoid–humeral head congruence, and relative muscle volume and quality of the affected shoulder.[6–10] Ultrasound is useful, particularly in infants because no sedation is required, to evaluate muscle bulk, degree of glenoid and posterior labral abnormality, and dynamic alignment of the shoulder. The alpha angle can be measured to assess the degree of humeral head subluxation (e-Fig. 133.2).[11–13] The glenoid normally has a concave shape. With glenohumeral dysplasia, the glenoid becomes progressively flat, convex, or biconvex with a pseudoarticulation with the humeral head. MRI is preferred in young children (<5 years old) (e-Fig. 133.3) to evaluate the cartilaginous glenoid; CT is sometimes preferred in older children to evaluate cortical bone.

***Treatment.*** Microsurgery techniques may be attempted to address the underlying traumatic neural injury.[14] Controversy exists as to their role and proper timing. Typical treatment focuses on the reconstructive surgical techniques of the shoulder and distal upper extremity to preserve joint integrity and maximize function.[14,15]

### Madelung Deformity

***Etiologies, Pathophysiology, and Clinical Presentation.*** In Madelung deformity, the radius is short and its distal articular surface tilted toward to ulna.[16] The cause of the deformity is usually unknown. Madelung deformity occurs more often in girls.[17] Patients may have pain; however, treatment is more often sought because of deformity or limited range of motion. Bilateral involvement is more common in the setting of an associated syndrome. Madelung deformity is occasionally seen with Turner syndrome and is a characteristic of Léri-Weill syndrome.[16] Among these cases, 10% to 15% are familial. A Madelung-like deformity may also be seen in patients with hereditary osteochondromatosis or enchondromatosis, also suggesting a defect in normal distal radial maturation. It may also occur as a complication of infection or trauma that results in medial and volar radial physeal growth disturbance.[18]

***Imaging.*** The distal articular surface of the radius is tilted in an ulnar and volar direction.[19,20] The radius is short and bowed dorsally and laterally ("bayonet deformity") (Fig. 133.4). Secondary distortion of the carpus is observed with an abnormally narrow carpal angle and proximal lunate migration.[19,20] The distal ulna is subluxed. The distal radial growth plate may prematurely fuse along its ulnar and volar aspect. CT or MRI may be used to assess the extent of distal radial physeal fusion.[21] MRI can also identify an anomalous radiolunate ligament (Vickers ligament) which is present in true, idiopathic Madelung deformity.[22]

***Treatment.*** Treatment is aimed at relieving pain caused by ulnocarpal impingement and improving wrist mobility.[18] Ulnar shortening and radial wedge osteotomies are common techniques.[18]

### Ulnar Variance

***Etiologies, Pathophysiology, and Clinical Presentation.*** Trauma, infection, inflammatory arthropathy (juvenile idiopathic arthritis), or other causes of premature fusion may lead to shortening of the ulna relative to the radius (negative ulnar variance) or shortening of the radius relative to the ulna (positive ulnar variance) (Fig. 133.5).[23] Most cases are idiopathic. Hyperemia resulting from fracture healing, infection, or vascular anomalies may lead to single bone over growth. Osteochondromas of either the radius or ulna can also lead to shortening of the affected bone.

***Imaging.*** At skeletal maturity, the distal radial and ulnar articular surfaces are nearly at the same level, and the radial styloid projects 9 to 12 mm distal to the ulnar articular surface.[23,24] With negative ulnar variance, the ulna ends more proximally, and with positive ulnar variance, the ulna ends more distally (e-Fig. 133.6).[23,25] Ulnar variance may be exaggerated with forearm pronation and decreased with forearm supination.

## Abstract:

Imaging plays a key role in the evaluation of alignment disorders involving the axial and appendicular skeleton. This chapter explores various imaging modalities and illustrates numerous disorders of alignment in the pediatric population. Abnormal alignment of each joint as well as the tibia and femur can initially be evaluated by radiography. However; advanced cross-sectional imaging techniques can play a key role in the evaluation of potential underlying causes and treatment planning in these patients. This chapter also discusses how imaging plays a role in surveying progression of alignment disorders, including systemic conditions including cerebral palsy and myelomeningocele. Finally, there is guidance to identify treatment outcomes and complications of treatment.

## Keywords:

alignment
cerebral palsy
Madelung
glenohumeral dysplasia
femoral version
tibial torsion
clubfoot

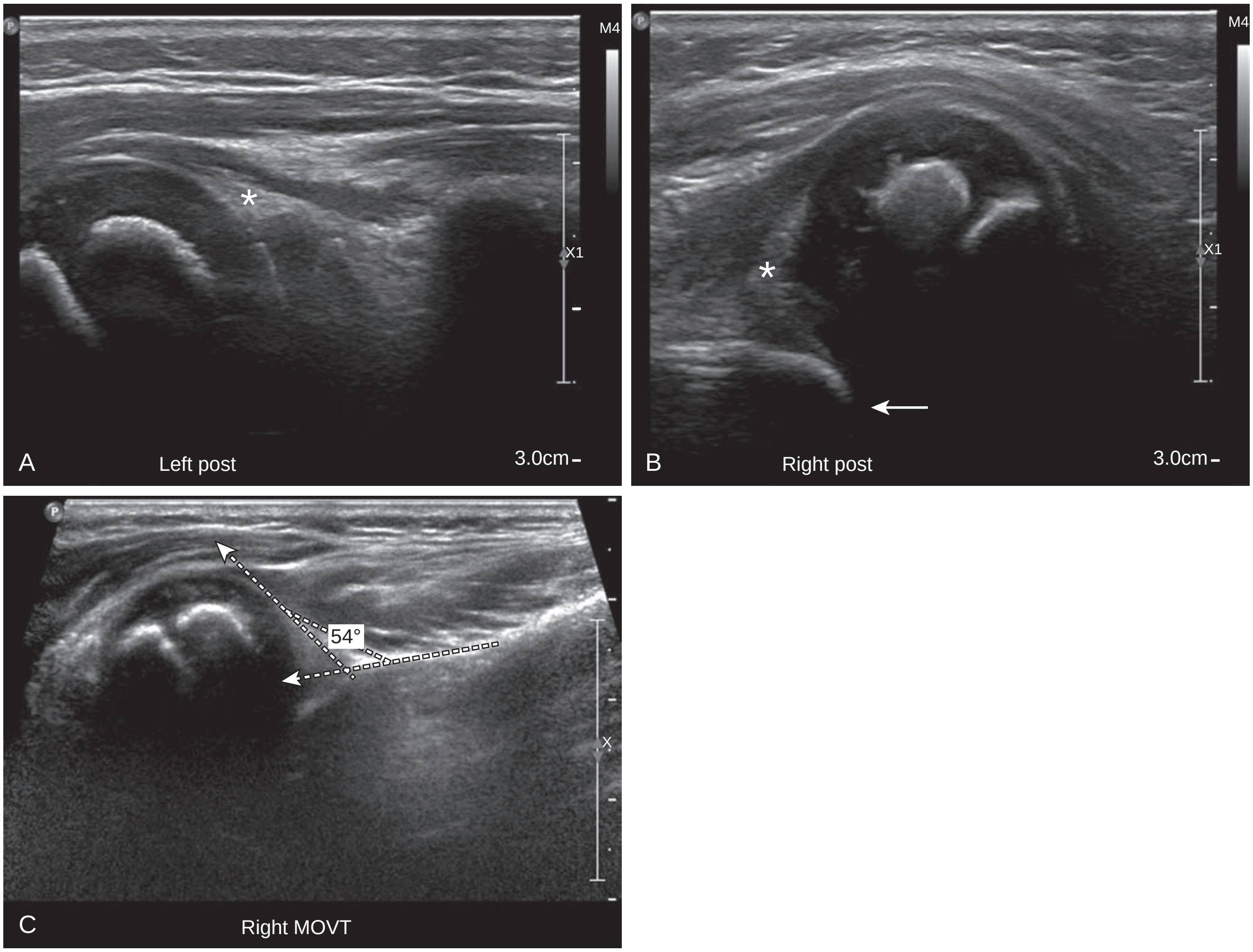

**e-Figure 133.2. Glenohumeral dysplasia and shoulder subluxation in a 10-month-old boy with brachial plexopathy.** (A) Normal shoulder ultrasound imaged posteriorly. Normal small triangular posterior labrum *(asterisk)* and normal articulation and contour of proximal humeral epiphysis with the glenoid. (B) Abnormal contralateral shoulder with dysplasia. The posterior labrum is enlarged and thickened *(asterisk)* and there is posterior subluxation of the humerus with respect to the rounded glenoid *(arrow)*. (C) Posterior subluxation with an alpha angle of 54 degrees. The alpha angle is the angle between the posterior margin of the scapula and a line drawn tangentially to the humeral head and posterior edge of the glenoid. The normal value is 30 degrees or less.

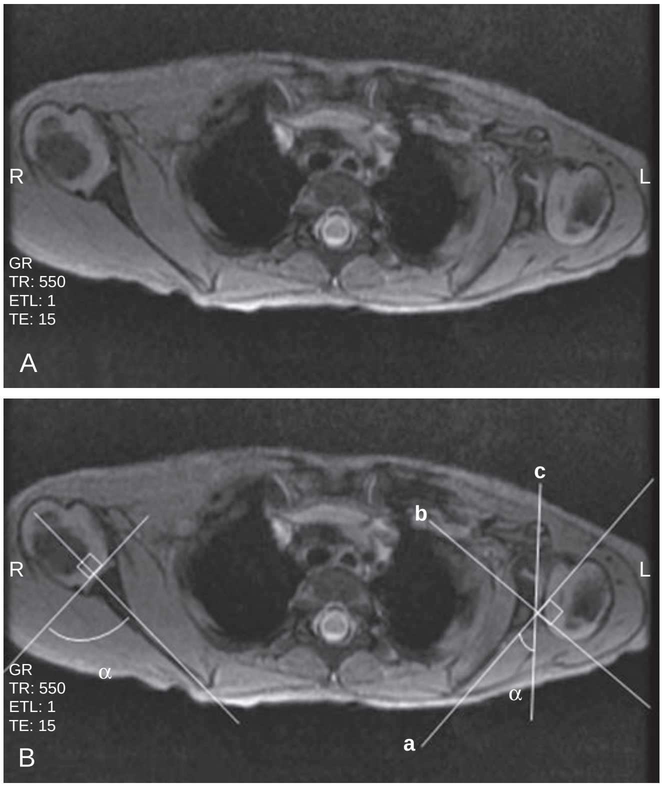

**e-Figure 133.3. Left glenohumeral dysplasia from brachial plexus palsy in a 2-year-old girl.** (A) Gradient recalled echo axial sequence magnetic resonance (MR) image demonstrates severely dysplastic left glenoid that is retroverted, a posteriorly subluxed humeral head and global left shoulder girdle muscle atrophy. (B) Same sequence with glenoid version measurements. Glenoscapular angle is the angle between a line drawn along scapula *(a)* and a line along the articular surface of the glenoid *(c)*. The glenoid version angle is the glenoscapular angle minus 90 degrees. If the glenoid is directed posteriorly with respect to scapula, the glenoid is in retroversion (negative angle). If the glenoid is directed anteriorly, the glenoid is in anteversion.

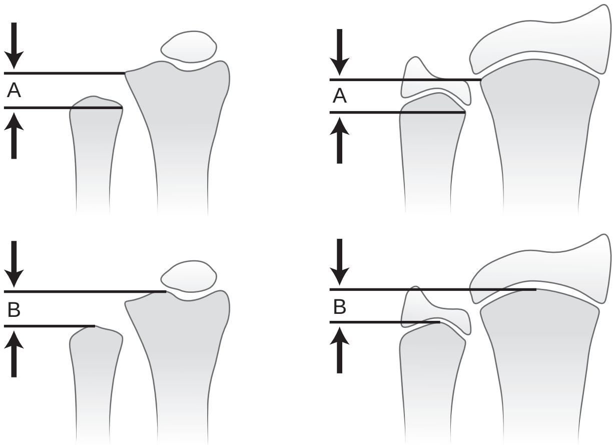

**e-Figure 133.6. Methods of measuring ulnar variance in skeletally immature children.** Method *A* measures the distance from the most proximal point of the ulnar metaphysis to the most proximal point of the radial metaphysis. Method *B* measures the distance from the most distal point of the ulnar metaphysis to the most distal point of the radial metaphysis. *(Modified from Hafner F, Poznanski AK, Donavan JM. Ulnar variance in children—standard measurements for evaluation of ulnar shortening in juvenile rheumatoid arthritis, hereditary multiple exostosis and other bone and joint disorders of childhood.* Skeletal Radiol. *1989;18:513–516.)*

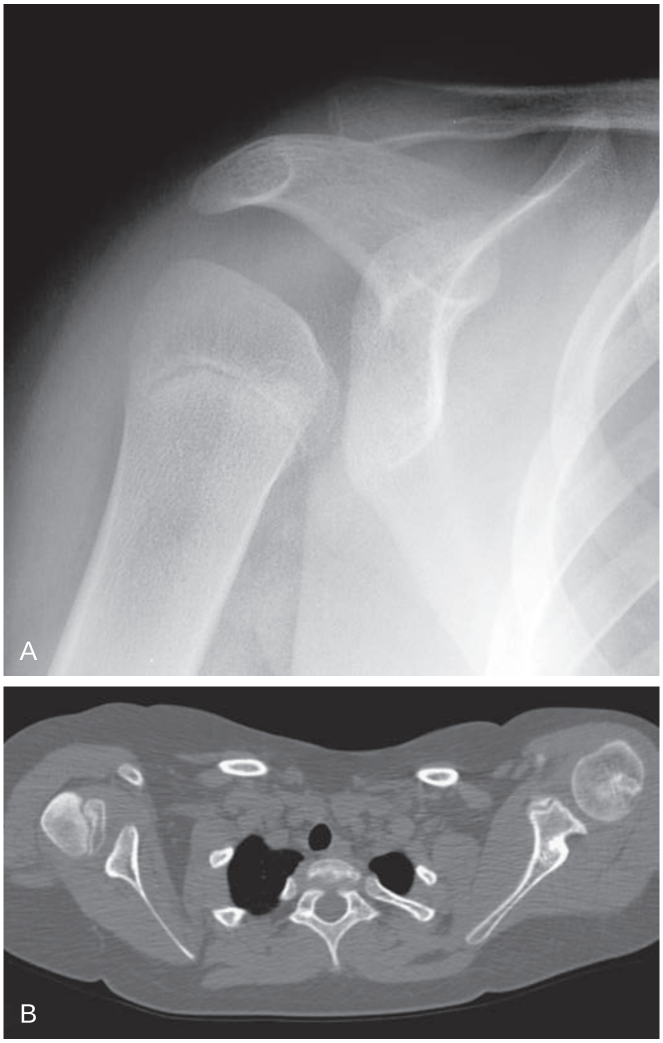

**Figure 133.1. Glenohumeral dysplasia secondary to brachial plexopathy in a 9-year-old girl.** (A) On radiography, the humeral head appears small and abnormally contoured, the glenoid margins are indistinct, and the acromion is curved. (B) Axial CT image shows the right glenoid to be small and retroverted. The right humeral head, which is small and squared in contour, is posteriorly positioned but aligned with the glenoid. Note the asymmetric muscle volume of the right shoulder girdle compared with the left shoulder girdle.

***Treatment.*** Osteotomy with ulnar or radial shortening may be indicated to reduce symptoms and avoid complications. Negative ulnar variance is associated with the development of avascular necrosis of the lunate (Kienböck disease).[26] Positive ulnar variance is associated with ulnolunate impaction syndrome (Fig. 133.7) and triangular fibrocartilage complex degeneration.

## LOWER EXTREMITIES

### Hip/Femur

### Coxa Vara

***Etiologies, Pathophysiology, and Clinical Presentation.*** The normal neck-shaft angle of the proximal femur is approximately 150 degrees at birth and decreases to 120 to 130 degrees in adulthood.[27] External or internal rotation of the hip or femoral anteversion may affect this measurement.[28]

Functional coxa vara occurs with disorders that result in femoral neck shortening, as in trauma, infection, or epiphyseal osteonecrosis.[29] This can result in abnormal growth at the proximal femoral physis that produces abnormal angulation. Coxa vara also occurs as a congenital anomaly that is caused by bone softening (e.g., rickets, osteogenesis imperfecta, fibrous dysplasia) or abnormal growth (e.g., spondyloepiphyseal dysplasia congenita, spondyloepimetaphyseal dysplasia, cleidocranial dysplasia, proximal focal femoral deficiency).[30,31] Children will present with a limp (unilateral deformity) or a waddling gate (bilateral deformities). With infantile or developmental coxa vara, the hip is normal at birth, and deformity is noted when the child begins to walk and can be self-limited.[30,32] Acquired coxa vara is caused by other processes such as trauma.[30]

***Imaging.*** In coxa vara, the femoral neck-shaft angle is decreased from normal. A measurement below 120 degrees is considered coxa vara.[33,34] Fragmentation and sclerosis may be seen at the medial margin of the proximal femoral metaphysis (Fig. 133.8).[32] The Hilgenreiner epiphyseal angle is the angle between the Hilgenreiner line and a line drawn through the proximal femoral physis (e-Fig. 133.9).[30,33] The normal angle is less than 30 degrees. If it is less than 45 degrees, progression is unlikely. If over 60 degrees, progression is likely. If 45 to 60 degrees, prognosis is less predictable.

***Treatment.*** Surgical management may be warranted for progressive disease, especially if asymmetric or associated with pain or leg length discrepancy.[30] Valgus osteotomy is performed, and physeal fixation or tendon transfers may also be performed to deter progression and improve mechanical function.

### Coxa Valga

***Etiologies, Pathophysiology, and Clinical Presentation.*** With coxa valga, the neck-shaft angle of the proximal femur is increased.[35] Coxa valga is most often seen in patients who are nonambulatory and nonerect, such as those with cerebral palsy and other neuromuscular disorders (Fig. 133.10).[28,36]

***Imaging.*** The femoral neck-shaft angle is measured on frontal radiographs. External rotation may mimic coxa valga; with external rotation, the greater trochanter projects through the femur and the lesser trochanter is visualized in profile, whereas with true coxa valga in appropriate position, the appearance of the trochanters are reversed.[28] Increased femoral anteversion may also cause the femoral neck-shaft angle to be overestimated.[35] Acetabular dysplasia and hip subluxation are frequently concomitant findings.

***Treatment.*** Varus osteotomy and iliac osteotomy are often performed together in patients with cerebral palsy to better direct the femoral head into the acetabulum.

### Femoral Anteversion

***Etiologies, Pathophysiology, and Clinical Presentation.*** Femoral version is the angulation of the femoral neck in the transverse plane measured relative to the femoral condyles distally (Fig. 133.11). If the femoral neck is anteriorly angulated with respect to the femoral condyles, the femur is anteverted. If the femoral neck is posterior with respect to the femoral condyles, the femur is retroverted. Normal femoral anteversion is around 35 to 50 degrees at birth, decreasing steadily to around 8 to 15 degrees in adulthood (e-Fig. 133.12).[29]

Increased femoral anteversion may hinder proper localization of the femoral head relative to the acetabulum. Increased femoral anteversion may be idiopathic or seen in hip deformities caused by developmental hip dysplasia, Legg-Calvé-Perthes disease, and cerebral palsy.[35] Increased anteversion is associated with in-toeing of feet.

***Imaging.*** On CT, femoral anteversion is the angle between the axis of the femoral neck and the transcondylar axis at the distal femur (Fig. 133.13).[37–39] Limited low-dose axial images are usually performed; however, axial oblique or three-dimensional

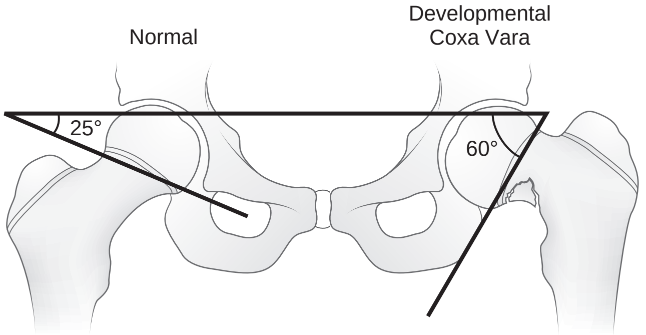

**e-Figure 133.9. Hilgenreiner epiphyseal angle.** This angle is created by a single line through the triradiate cartilage and its intersection with another line through the proximal femoral physis. The normal angle is about 25 degrees. *(From Beals RK. Coxa vara in childhood: evaluation and management.* J Am Acad Orthop Surg. *1998;6:93–99.)*

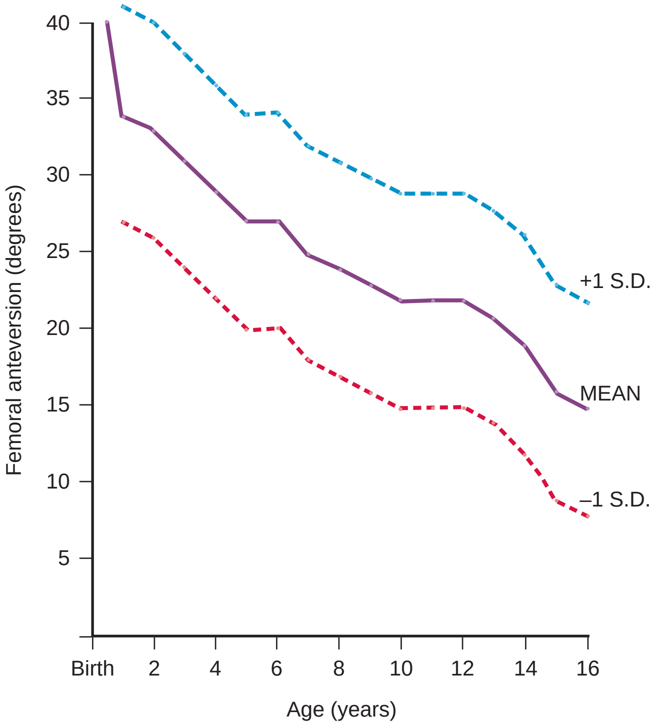

**e-Figure 133.12. Normal femoral anteversion.** The mean value is an average of those reported by Shands and Steele (1958), Crane (1959), and Fabry and associates (1973). Standard deviations are only an approximation and are based on the range of those determined by Fabry and associates. *(From Ozonoff MB:* Pediatric orthopedic radiology, *2nd ed, Philadelphia: WB Saunders; 1992.)*

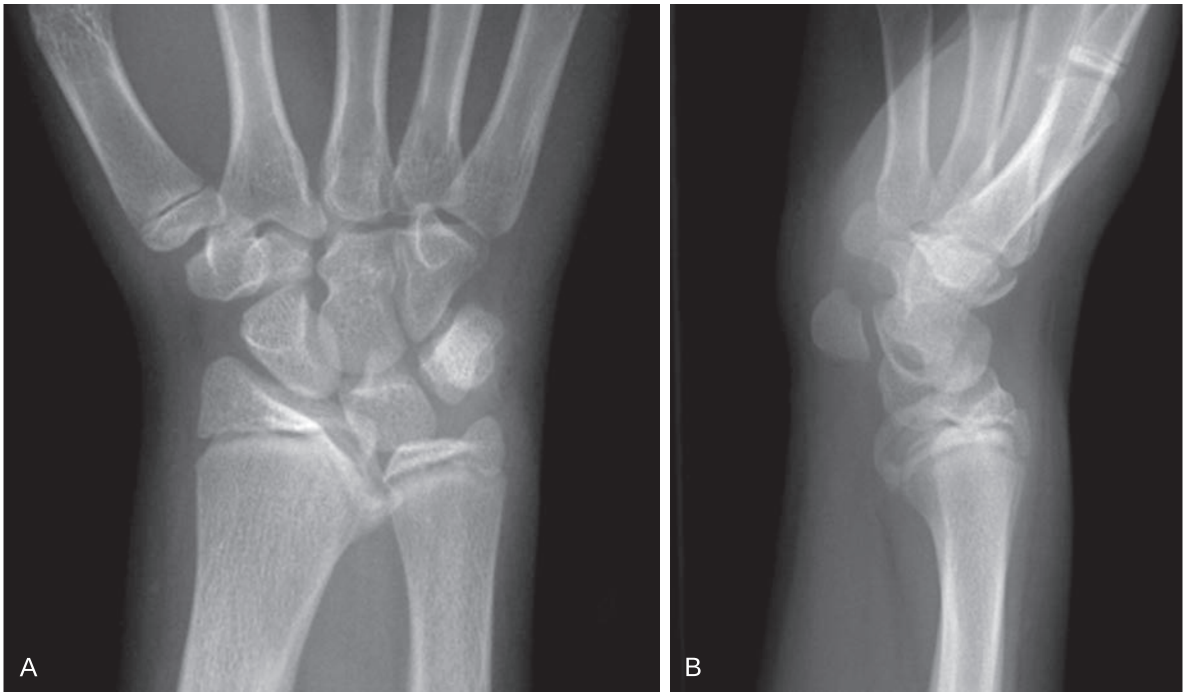

**Figure 133.4. Madelung deformity in a 10-year-old girl who presented with right wrist pain.** (A) Posteroanterior radiograph shows medial tilt of the distal radial articular surface and physis with thinning of the medial aspect of the distal radial epiphysis. Also note the proximal migration of the lunate. (B) Lateral radiograph shows anterior tilt of the distal radial articular surface with mild anterior displacement of the carpus.

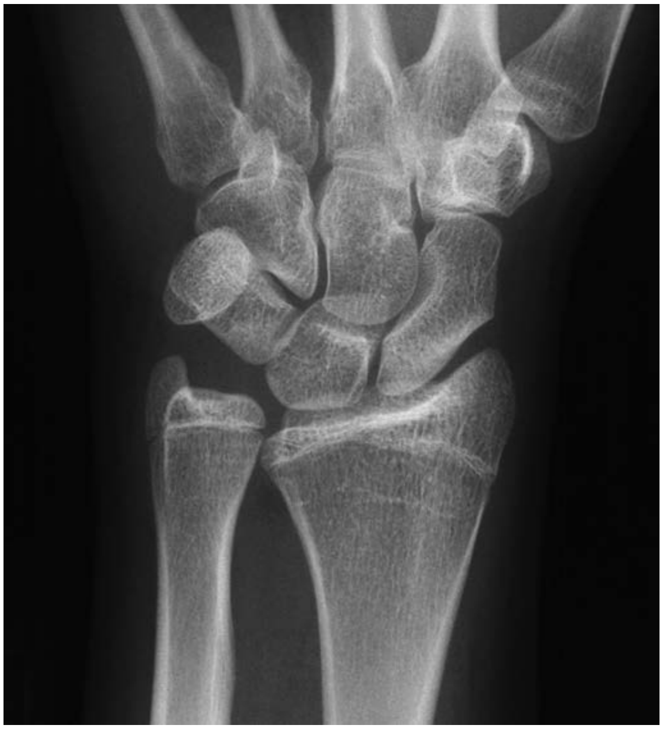

**Figure 133.5. Positive ulnar variance in a 14-year-old girl with a history of prior osteomyelitis of the ulna.** Presumably, resultant overgrowth of the ulna occurred. The patient required ulnar shortening because of clinical evidence of ulnar impaction syndrome.

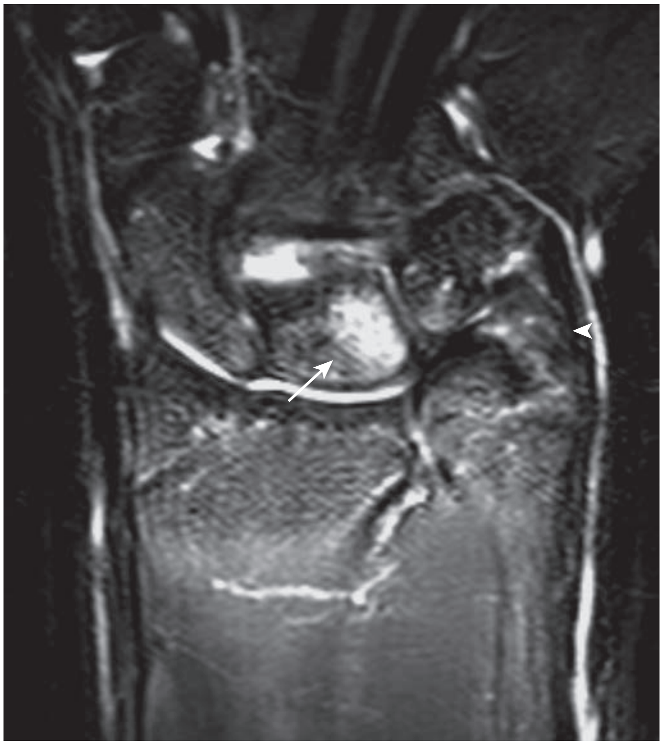

**Figure 133.7. Ulnolunate impaction syndrome in a 14-year-old boy.** Inversion recovery coronal sequence magnetic resonance (MR) image demonstrates a distally located ulna *(arrowhead)* with lunate edema *(arrow)* caused by ulnolunate impaction syndrome.

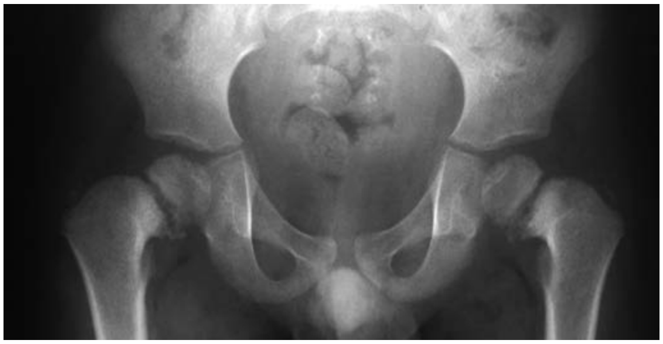

**Figure 133.8. Bilateral congenital coxa vara in a 4-year-old boy.** Proximal femoral growth plates are tilted, medial side down. Slight irregularity is noted adjacent to the medial aspects of each proximal femoral physis.

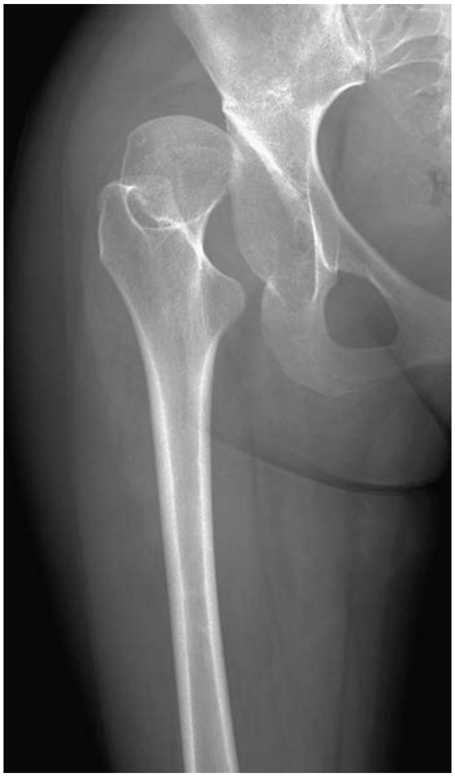

**Figure 133.10. Coxa valga in a 15-year-old girl with cerebral palsy.** The acetabulum is markedly dysplastic. The femoral head is subluxed. Coxa valga is noted.

(3D) images may improve measurement accuracy.[40,41] CT imaging can be obtained concomitantly to evaluate for femoroacetabular impingement and tibial torsion. The biplanar digital slot-scanning radiologic device (EOS Imaging, Paris, France) uses two narrow fan beam sources to acquire concurrent, high-quality, orthogonal radiographic images of the spine or entire lower extremities.[42] Frontal, lateral, and 3D views can be generated from the obtained data. Standard radiographic measurements of the lower extremities can be performed with these images. Also beneficial is lower radiation exposure with this device compared to standard radiographs and CT while maintaining image quality.

***Treatment.*** Most children with increased femoral anteversion are managed conservatively. Surgical indications for treatment include symptomatic in-toeing. Femoral rotational osteotomy may be performed to optimize femoral version.

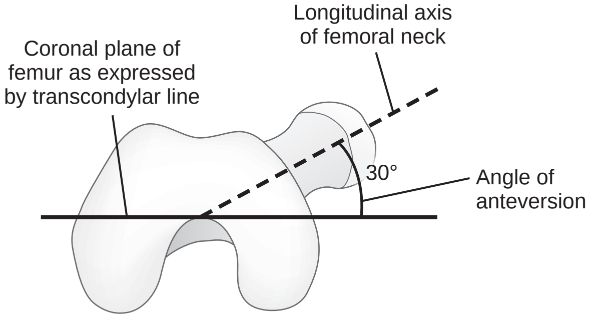

**Figure 133.11. Schematic diagram of the right femur as viewed from below.** The femoral neck is angulated anterior (anteversion) relative to the transcondylar axis of the distal femur. *(Modified from Greenspan A.* Orthopedic imaging: a practical approach*, 4th ed, Philadelphia, PA: Lippincott Williams & Wilkins; 2004.)*

## Leg

### Tibial Torsion

***Etiologies, Pathophysiology, and Clinical Presentation.*** Tibial torsion is the degree of rotation of the distal tibia relative to the upper tibia. Newborns have internal tibial torsion relative to older children and adults. Lack of normal progression leads to in-toeing. Internal tibial torsion is the most common cause of in-toeing in the preschool age group.

***Imaging.*** Assessment of tibial torsion is often performed with assessment of femoral version. Limited axial low-dose CT images are obtained through the proximal and distal tibias.[43,44] Tibial torsion is best measured as the angle between the posterior proximal epiphyseal cortical margin and a bimalleolar line distally. Normal values are neutral to mild (5 degrees) of external torsion in a newborn, which progresses to 18 to 47 degrees of external rotation in an adult.[43,45,46]

***Treatment.*** Surgery is rarely needed as more than 95% of cases resolve spontaneously, usually by 8 years of age. Tibial rotational osteotomy may be performed to improve alignment.

### Bowleg (Genu Varum)

***Etiologies, Pathophysiology, and Clinical Presentation.*** Bowleg deformity manifests as separation of the knees, with the legs in anatomic position. Pathologic causes include rickets, osteogenesis imperfecta, neurofibromatosis, skeletal dysplasias (i.e., campomelic dysplasia, achondroplasia), focal fibrocartilaginous dysplasia, congenital bowing, Blount disease, and growth plate injuries.[47–50] Recently, greater prevalence of bowleg and tibia vara has been noted in some adolescent athletes, most notably soccer players.[51–53] Repetitive stress on the proximal tibial physis may play a role in this.[52] Most lateral bowing in otherwise normal infants and children younger than 2 years of age is normal developmental ("physiologic") bowing and resolves without treatment.[48,54–56] Similar to Blount disease, exaggerated physiologic bowing is seen more commonly in early walkers, African Americans, and heavier children.[48]

***Imaging.*** Imaging characteristics of physiologic bowing include mild lateral and anterior bowing of the femur and tibia, exaggerated tibial torsion, small beaks along the distal femoral and proximal tibial metaphyses (Fig. 133.14), medial femoral and tibial cortical thickening, wedge-shaped and incompletely ossified distal femoral and proximal tibial epiphyses, and lateral tilting of the distal tibial growth plate.[57] Physiologic bowing is usually more marked in the tibias. Occasionally, lateral bowing may almost exclusively be seen in the distal femur (e-Fig. 133.15). A varus angulation is common in normal infants and converts to valgus between 18 and 36 months

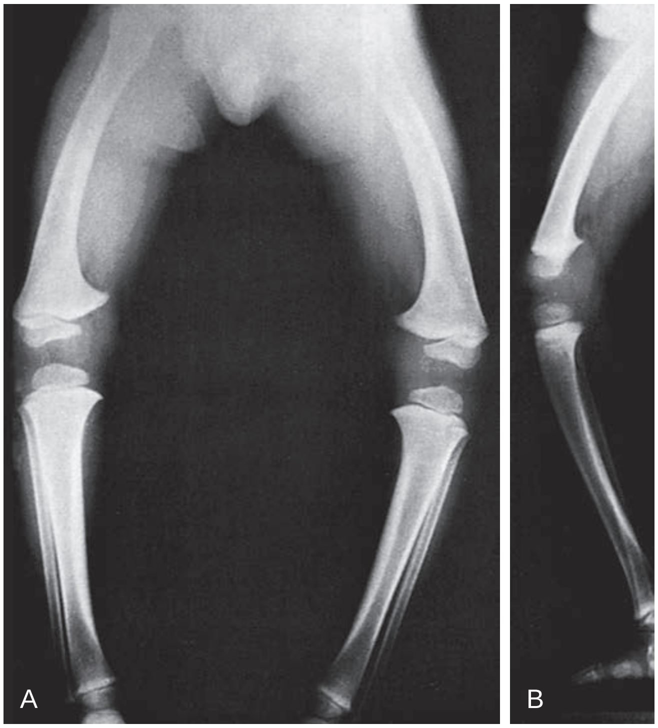

**e-Figure 133.15. Femoral bowed legs (femora vara).** (A) Anteroposterior and (B) lateral projections show marked bowlegs, in which the tibias are straight and both femora are bowed lateral near their distal ends (femora vara). Femoral epiphyseal ossification centers are small and flattened on their medial halves.

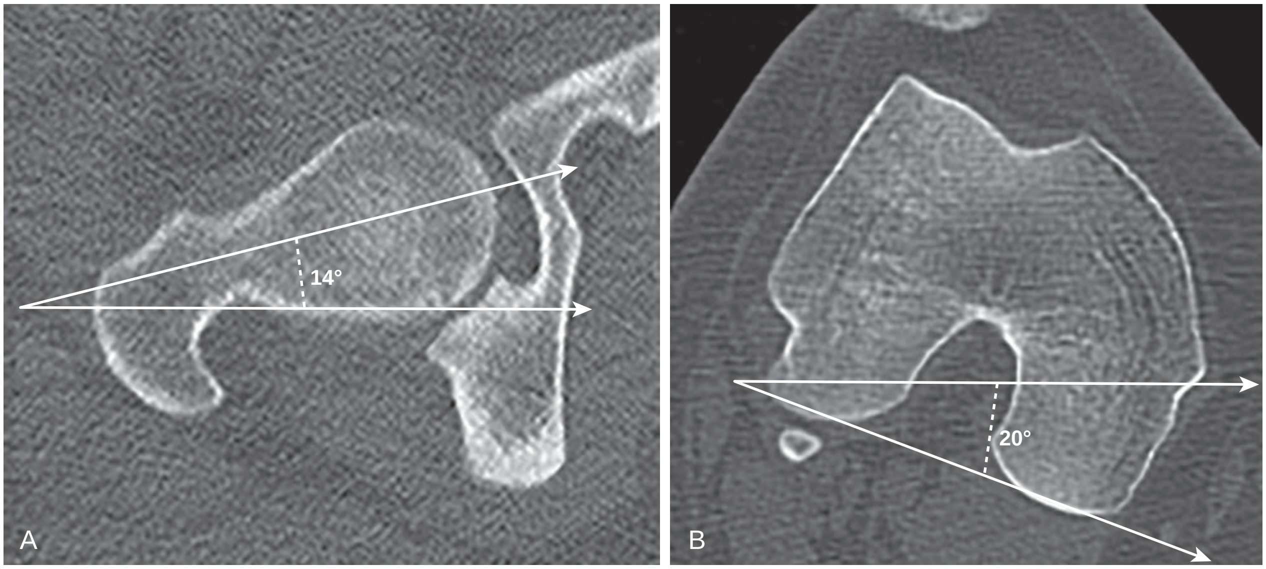

**Figure 133.13. Femoral anteversion in a 16-year-old girl with a history of right femoral fracture.** (A) Axial CT image with line denoting the axis of the femoral neck with respect to the horizontal plane. (B) Axial CT imaging with line denoting the axis of the posterior distal femoral transcondylar axis with respect to the horizontal plane. An angle of 34 degrees of right femoral anteversion was obtained by adding the two angles.

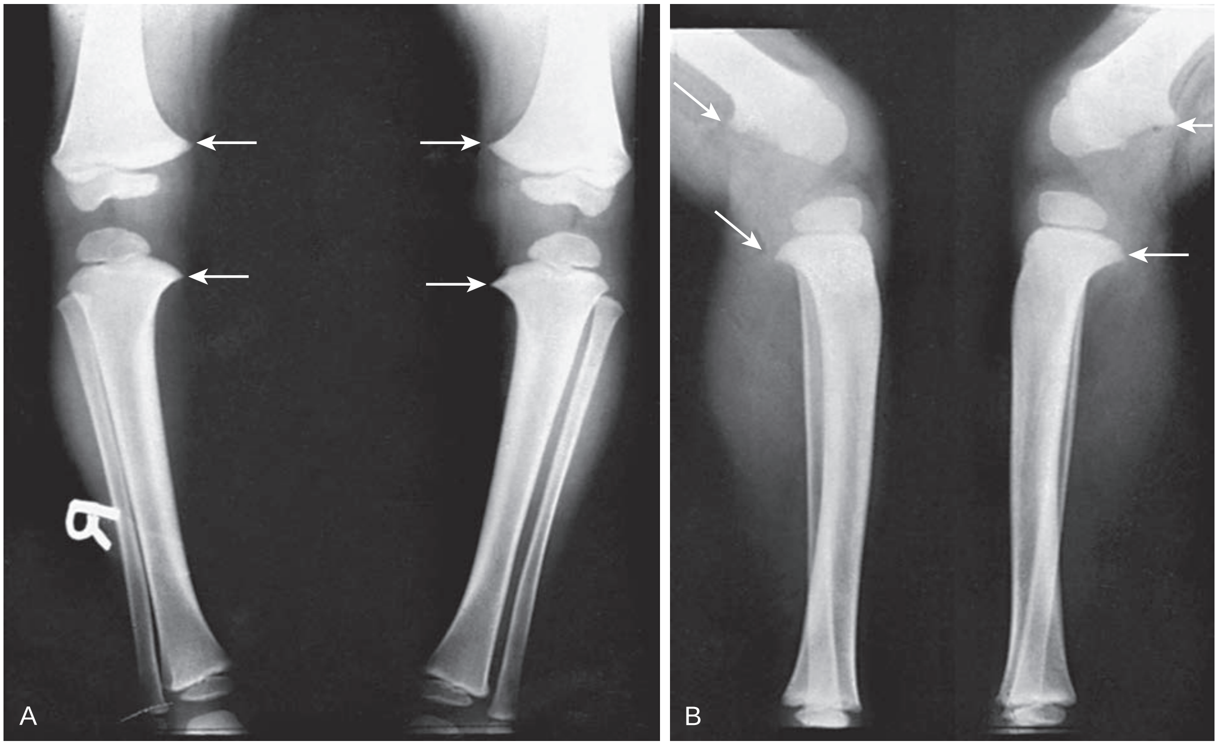

**Figure 133.14. Bilateral idiopathic bowed legs in a 22-month-old boy.** (A) Frontal projection. *Arrows* point to the medial beaking of the femoral and tibial metaphyses at the knees. The increased stress of weight bearing has thickened the medial and dorsal cortical walls of the tibias inward. The medial femoral epiphyseal ossification centers are small, which may reflect the greater stress of weight bearing when the legs are bowed. (B) Lateral projection. *Arrows* point to dorsal beaking of the femoral and tibial metaphyses. After correction of bowed legs, these “stress” phenomena disappear after several months.

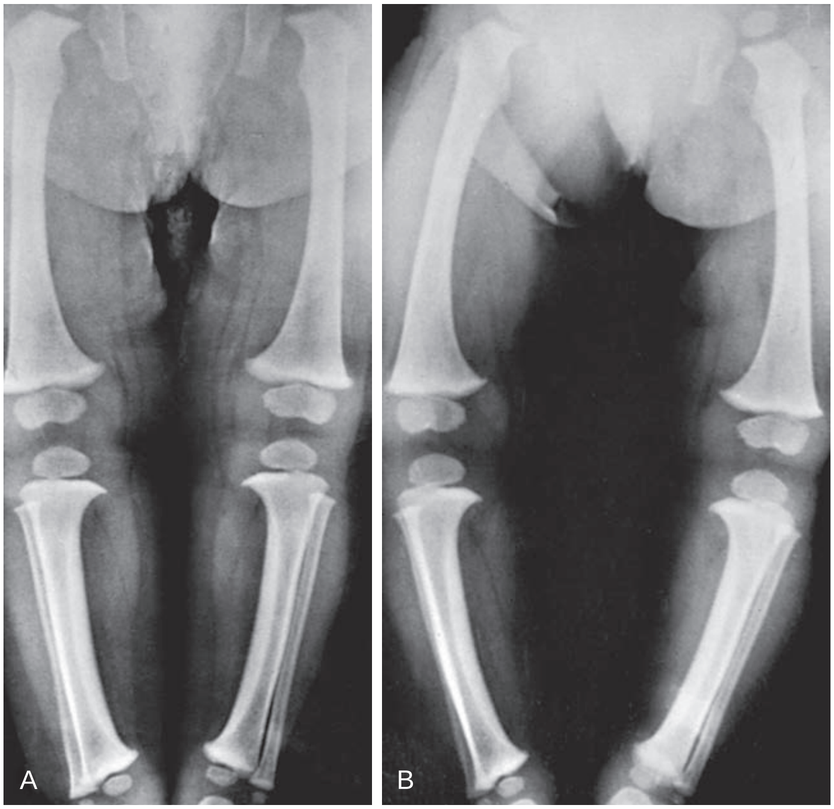

**Figure 133.17. Bowed legs of a 12-month-old girl who started to walk at 8 months.** (A) In recumbent position, the tibias and femora are bowed, but the legs are not bowed because the knees and ankles are in apposition. (B) In the erect position during weight bearing with the ankles in apposition the legs are bowed, with a gap of 12 cm at the knees. The real clinical deformity of bowed legs is shown most accurately when the patient is erect and is bearing weight.

of age. Degree of valgus reduces spontaneously by 6 to 7 years of age to a mild degree that remains throughout life. Approximate normal angles are 17 degrees varus in a newborn, 9 degrees varus at 1 year, 2 degrees valgus at 2 years, 11 degrees valgus at 3 years, and 5 to 6 degrees valgus at 13 years (e-Fig. 133.16).[56,58,59]

Radiographs should be taken with the patient bearing weight as soon as he or she is able to stand (Fig. 133.17). The metaphyseal-diaphyseal angle can help distinguish physiologic bowing from Blount disease (tibia vara), as described in the next section. The radiographs may suggest an underlying disorder such as rickets or a dysplasia.

***Treatment.*** Persistent varus with delayed conversion to valgus may indicate that the varus is not physiologic. In the second year, it may be difficult to distinguish normal physiologic bowing from Blount disease.[60] Exaggerated varus during the second year is likely developmental or physiologic and does not require treatment.[54,55,58] Persistent varus at the knee after 2 years of age should raise concern and prompt monitoring of these children to exclude progression to Blount disease.[59,61] Realignment surgery is rarely needed in isolated bowleg without underlying dysplasia, metabolic bone disease, or Blount disease.

## Blount Disease (Tibia Vara)

***Etiologies, Pathophysiology, and Clinical Presentation.*** Blount disease (tibia vara; osteochondrosis deformans tibiae) is a progressive deformity affecting the proximal tibia (Fig. 133.18).[62–64] It is theorized that stress on the posteromedial proximal tibial physis causes growth suppression.

The infantile form of Blount disease, which develops in children between 1 and 3 years of age, must be differentiated from developmental bowing.[65] Infantile Blount disease may represent normal developmental bowing that fails to correct. The diagnosis is made when progressive clinical bowing is seen in the presence of characteristic radiographic changes in the proximal tibia.[65] The disease is typically bilateral (60%–80%) but often asymmetric and occasionally unilateral (Fig. 133.19). A family history is often reported. The disorder is more common in early walkers, African Americans, and obese children.[48,64,66]

Adolescent or late-onset Blount disease is a separate entity. It occurs in children 8 to 14 years of age; obese African American males of normal height are at particular risk (Fig. 133.20).[47] It is commonly unilateral but may be bilateral. Adolescent Blount disease is slowly progressive and probably results from the repetitive trauma of weight bearing on the medial physis of the proximal tibia.[47] Patients often present with knee pain.

***Imaging.*** The characteristic radiographic feature of infantile Blount disease is deformity of the medial metaphysis of the proximal tibia (Fig. 133.21).[48] Irregularity with a more vertically oriented growth plate creates a beaked appearance. The severity of radiographic changes has been described by the six-stage Langenskiöld classification (e-Fig. 133.22).[67] Higher stage denotes greater abnormality; bone bridging across the physis is seen with stage IV and higher. The medial portion of the epiphyseal ossification center is often smaller than the lateral portion. The tibia may have lateral subluxation.

The metaphyseal–diaphyseal angle (MDA) is measured by drawing a single line through the widest portion of the proximal

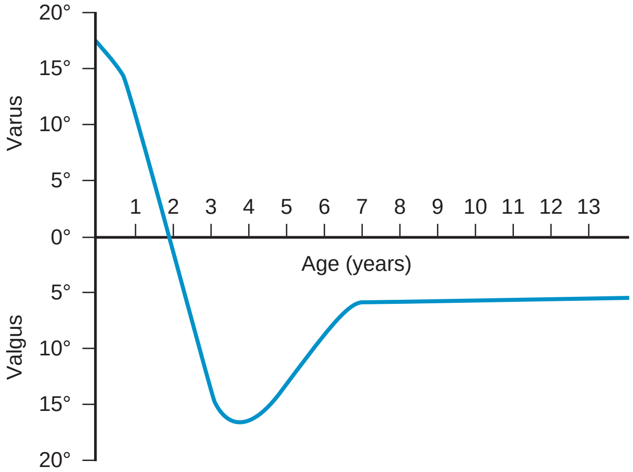

**e-Figure 133.16. Development of the tibiofemoral angle during growth.** This graph shows the normal physiologic progression of varus to valgus and then less pronounced valgus angulation at the knee during childhood. *(From Bruce RW Jr. Torsional and angular deformities.* Pediatr Clin North Am*. 1996;43:867–881.)*

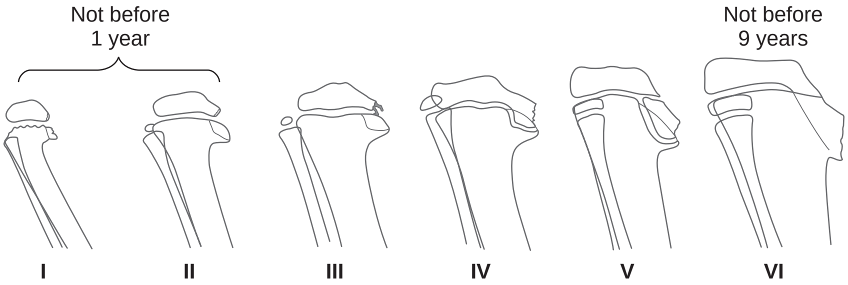

**e-Figure 133.22. Radiographic changes seen in infantile tibia vara with increasing age.** *(From Langenskiöld A, Riska E. Tibia vara [osteochondrosis deformans tibiae].* J Bone Joint Surg Am*. 1964;46:1405–1420.)*

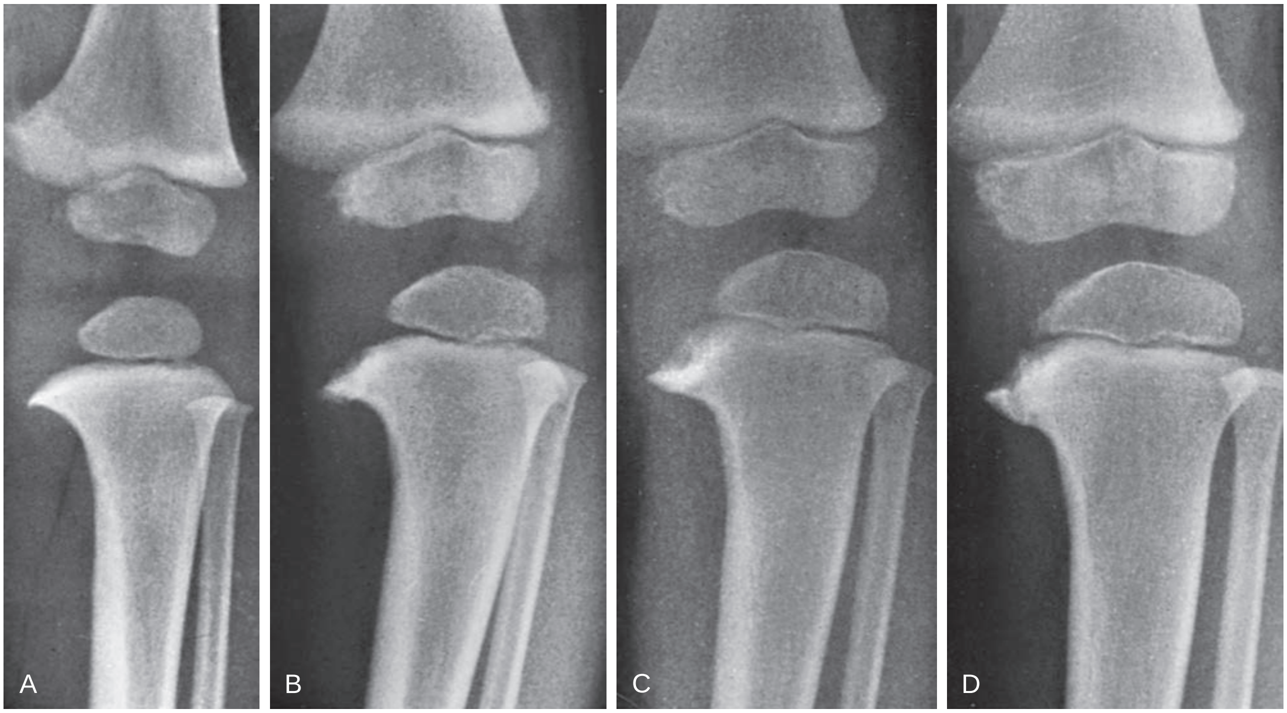

**Figure 133.18. Progressive changes in Blount tibia vara.** (A) At 17 months, the medial segment of the tibial metaphysis is widened and sharpened into a short beak or spur that is bent slightly caudad. (B) At 26 months, the spur is longer, sharper, and more bent; a radiolucent strip on its upper edge represents noncalcified cartilage. (C) At 32 months, the amount of cartilage is increased and the spur thickened. (D) At 38 months, the beak of the spur is displaced caudad, possibly owing to trauma; the medial edge of the epiphyseal ossification center is flattened, and the femur has shifted medial in relation to the tibia.

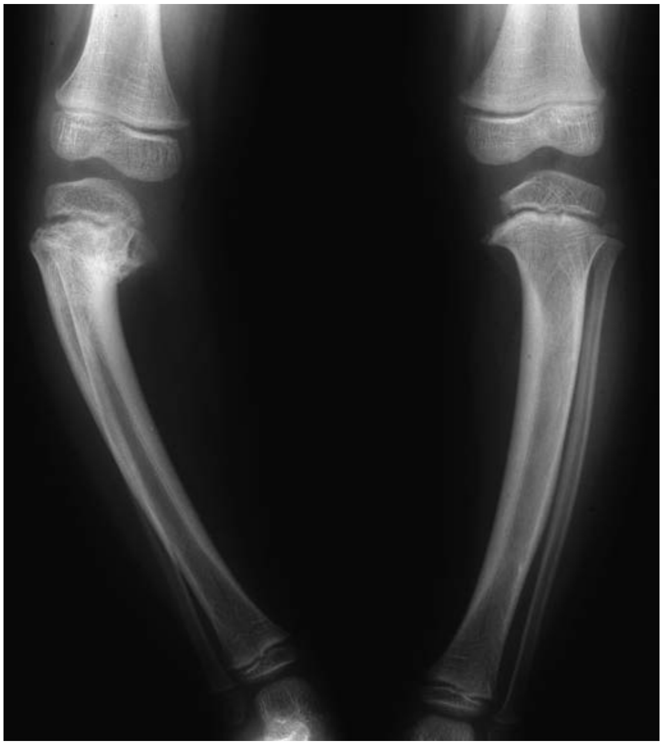

**Figure 133.19. Bilateral Blount disease in a 3-year-old girl.** Abnormality is greater on the right, where more sclerosis and irregularity of the proximal tibial metaphysis are evident.

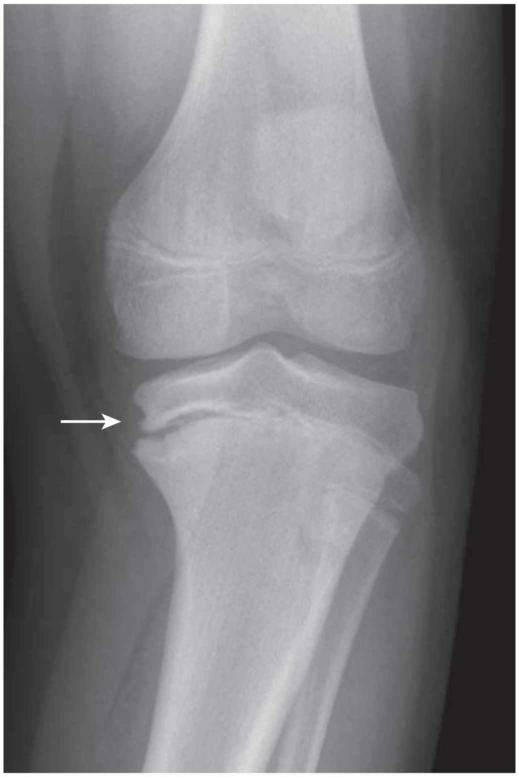

**Figure 133.20. Adolescent Blount disease in a 13-year-old boy.** Note the medial tibial physeal widening, metaphyseal fraying, and diminished medial epiphyseal height *(arrow)*.

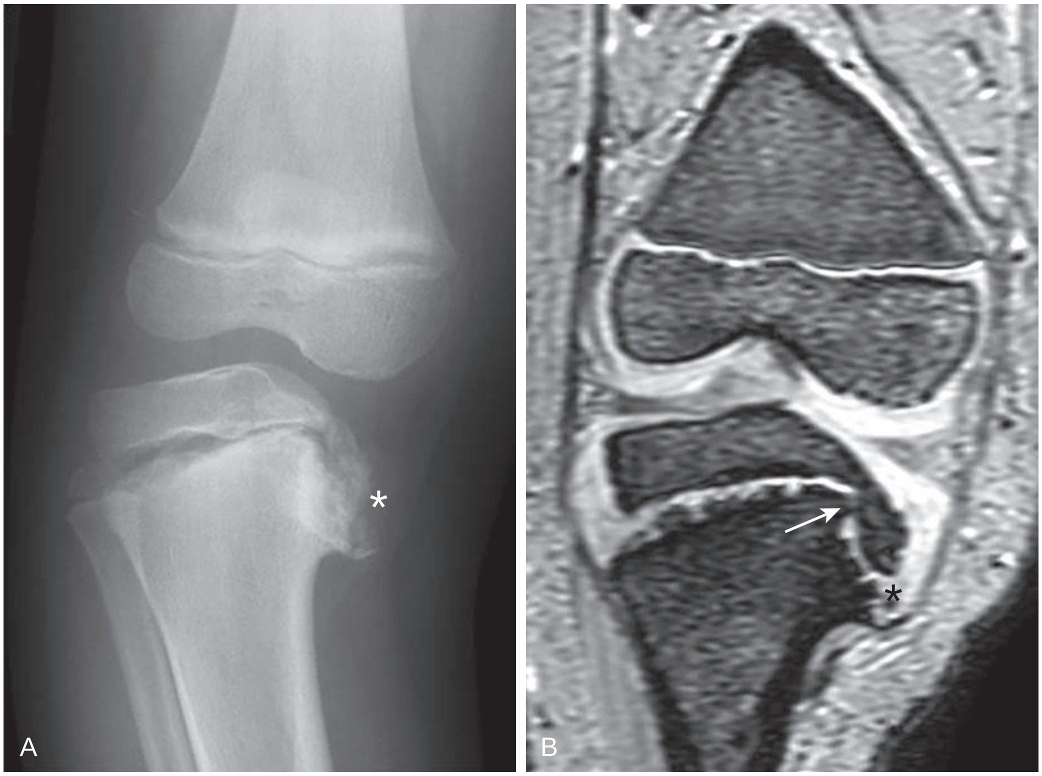

**Figure 133.21. Infantile Blount disease in a 5-year-old girl.** (A) Unlike adolescent Blount disease, sharp metaphyseal angulation *(asterisk)*, beaking, and markedly diminished and near-absent medial epiphyseal ossification of the proximal tibia are seen. (B) MRI cartilage visualization sequence (T1-weighted water selective WATS) in the same patient demonstrates thickened unossified cartilage in the region of metaphyseal irregularity *(asterisk)* and small transphyseal osseous bridge *(arrow)*.

tibial metaphysis (between the medial and lateral beaks) and another line perpendicular to the long axis of the tibial diaphysis.[55] In physiologic bowing, this angle is typically less than 11 degrees (averaging 5 degrees), whereas in Blount disease this angle is typically greater than 11 degrees (averaging 16 degrees) (e-Fig. 133.23). However, there is overlap of the MDAs in these entities in the 8 to 11 degree range, which should be considered borderline and may warrant follow-up.[48–55] Several studies have questioned the validity of the MDA, and measurement may be affected by tibial rotation. Additional angle measurements have been described for the femur and tibia to evaluate deformities in other planes including proximal tibia procurvatum (anterior bowing) and recurvatum (posterior bowing).

Changes related to infantile Blount disease should be distinguished from those of adolescent Blount disease (see Fig. 133.20). The metaphyseal angular deformities, diminished medial epiphyseal height, and degree of tibia vara are typically less severe with adolescent Blount disease.

CT or MRI can assess the degree of proximal tibial growth plate fusion. MRI also allows assessment of associated epiphyseal cartilage abnormalities, stress changes around the knee, meniscal and ligamentous abnormalities (see Fig. 133.21).[68–70]

***Treatment.*** Although spontaneous resolution of infantile Blount disease is reported in some instances, treatment with bracing is begun usually between ages 18 and 24 months and is continued during waking hours for an average of 2 years. If conservative management fails, the patient may undergo a realignment osteotomy, which is most effective when performed before 5 years of age. For adolescent Blount disease, a lateral tibial epiphyseodesis may be performed if sufficient growth potential remains. If the proximal tibial physis is nearly fused, a proximal tibial valgus osteotomy to produce normal alignment may be performed.[64]

## Knock-Knee (Genu Valgum)

***Etiologies, Pathophysiology, and Clinical Presentation.*** Genu valgum is approximation of the knees in standing position. Physiologic genu valgum is a normal developmental phase that lasts from 2 to 12 years of age and is most apparent at 3 to 5 years of age in normal children.[56,58,59,71] Persistent genu valgum can be related to pathologic causes such as trauma, skeletal dysplasia, obesity, metabolic disease, or laxity of muscles and ligaments.

***Imaging.*** In genu valgum, the lower legs deviate laterally when in anatomic position. Wide separation is noted at the ankles (Fig. 133.24). Radiographs may show evidence of an underlying disorder or complicating process.

***Treatment.*** Treatment is conservative, particularly for children with physiologic genu valgum. Bracing is occasionally employed. Rarely, surgical osteotomies are performed for realignment.

## Leg Length Discrepancy

***Overview.*** Some degree of leg length discrepancy (anisomelia) is common and depending upon the source up to 1 to 2 cm of difference is considered within normal limits.[72] The presence of a leg length discrepancy may reflect overgrowth of the long limb or decreased size or growth of the short limb. Leg length discrepancy clinically presents with alteration of gait and pelvic tilt. With significant pelvic tilt, compensatory scoliosis may develop.

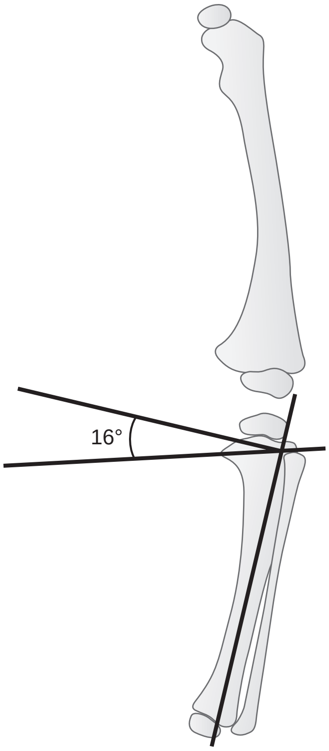

**e-Figure 133.23. Metaphyseal-diaphyseal angle.** This angle is defined as the angle between a line perpendicular to the axis of the tibia and a line through the medial and lateral beaks of the tibial metaphysis. *(From Eggert P, Viemann M. Physiological bowlegs or infantile Blount's disease: some new aspects to an old problem.* Pediatr Radiol*. 1996;26:349–352.)*

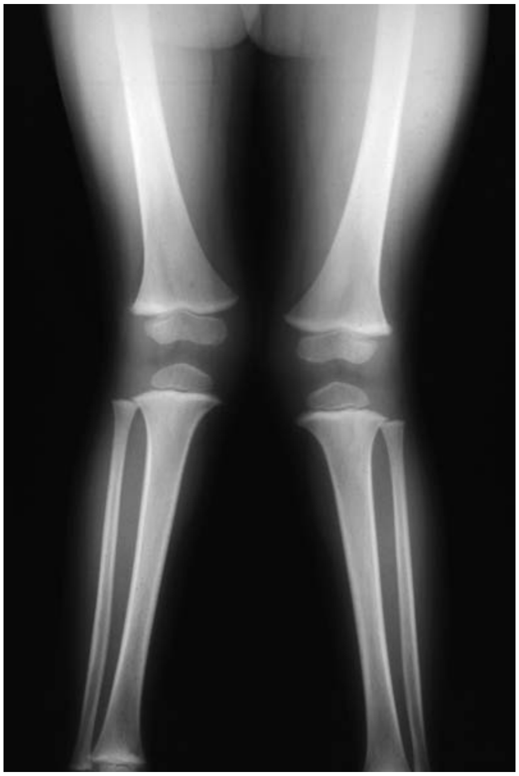

**Figure 133.24. Physiologic knock-knee (genu valgum) in a 3-year-old girl.** In follow-up, the child's legs were seen to have straightened normally, without treatment.

***Etiologies, Pathophysiology, and Clinical Presentation.*** The differential diagnoses for overgrowth and undergrowth is lengthy. Overgrowth is associated with various syndromes and vascular abnormalities. Mild overgrowth may occur as the result of fracture healing. In many cases, the cause is unknown. Undergrowth may be caused by hypoplasia or aplasia of a limb segment. Acquired shortening most often occurs as a consequence of premature growth plate fusion due to trauma, infection, or vascular insufficiency.

***Imaging.*** Radiographic techniques seek to determine bone lengths in a manner that minimizes magnification and other technical factors. Orthoroentgenography ("scanogram") uses three separate exposures collimated to the hip, knee, and ankle with a radiopaque ruler.[73] CT digital scout images may be used to measure bone length.[74,75] However, it is preferable to quantify length and alignment abnormalities with standing radiographs. The EOS 2D/3D system has also been shown to make reliable measurements.[76]

In addition to determining quantitative length and discrepancies in length of the lower extremities, leg length studies should also be evaluated and comments should be made with regard to the alignment of the hips, knees, and ankles. Any underlying cause of the leg length discrepancy such as physeal abnormalities or abnormal bowing deformities should be described.

***Treatment.*** Mild leg length discrepancy does not warrant treatment. The type of treatment varies with age, amount of projected growth remaining, site of abnormality, and degree of leg length discrepancy. Treatment may be aimed at halting growth on the longer side (i.e., epiphyseodesis) or lengthening the shorter side (i.e., lengthening osteotomy procedure).[77] With a lengthening osteotomy procedure, bone on either side of a diaphyseal corticotomy is distracted slowly utilizing an external frame or more recently with expandable intramedullary rods. New bone forms within the gap to add length.

## Feet

***Overview.*** Alignment disorders of the feet may be idiopathic or caused by an underlying disorder. The standard method of radiologic evaluation of the foot involves weight-bearing or simulated weight-bearing anteroposterior (dorsoventral) and lateral views. Diagnosing alignment abnormalities of the feet should be approached with caution when non–weight bearing radiographs are obtained.

The proximally-located talus is considered fixed at the ankle because it has no direct musculotendinous attachments. The calcaneus is linked to the midfoot and forefoot and moves as a unit with these structures relative to the talus. In a normal foot, on the anteroposterior view the axis of the talus extends through the base of the first metatarsal (Fig. 133.25). With hindfoot varus, the more distal calcaneus is angulated inward, and the axis of the talus passes lateral to the base of the first metatarsal. With hindfoot valgus, the more distal calcaneus is angulated outward, and the axis of the talus passes medial to the base of the first metatarsal.[78] The normal lateral talocalcaneal angle is approximately 45 degrees at birth, decreasing to 30 degrees in older children and adults.[78–80] With hindfoot varus, the lateral talocalcaneal angle is decreased (more parallel), whereas with hindfoot valgus, the angle is increased.

Normal elevation of the middle metatarsals relative to the fifth metatarsal reflects the transverse arch of the foot. The anterior calcaneus is slightly inclined upward. Accentuation of this upward inclination is called *calcaneus* position of the os calcis. Equinus position is downward inclination of the distal calcaneus. Normal calcaneal tilt and normal slight downward tilt of the distal metatarsals create slight longitudinal concavity in the osseous contour of the bottom of the foot.

### Clubfoot

***Etiologies, Pathophysiology, and Clinical Presentation.*** Talipes ("talus" = ankle; "pes" = foot) equinovarus, or clubfoot, is a common congenital anomaly that is clinically obvious at birth. The principal components of clubfoot deformity include plantar flexion of the ankle (equinus), inversion of the heel (varus), and adduction of the forefoot (varus) (Fig. 133.26). Abnormal intrauterine pressures contribute to the development of clubfoot.[81] Genetics also appear to play a role.

***Imaging.*** Radiographs are obtained with true or simulated weight bearing, as this is the position of best correction.[81] An anteroposterior radiograph shows superimposition and parallelism of the talus on the calcaneus with the talar axis directed lateral to the first metatarsal (hindfoot varus). Parallelism of the talus and calcaneus is also on the lateral view. The lateral view shows plantar flexion of the calcaneus (equinus) and a step-ladder arrangement of the metatarsals, with the first metatarsal highest and the fifth metatarsal at the weight-bearing surface of the foot. US has been used in select centers to assess the flexibility of clubfoot and to guide therapeutic decision making (e-Fig. 133.27).[82–85]

***Treatment.*** Current treatment approaches to clubfoot have shifted away from aggressive surgeries to manipulation and minimally invasive surgeries. Nonsurgical approaches to treatment include the Ponseti method, which involves serial casting with or without heel cord lengthening, and the French method, which involves physiotherapy, taping, and passive daily motion.[81,86–88] More invasive surgeries are typically reserved for correcting deformities that persist after conservative treatments.[88] Anatomic deformities persist after treatment of clubfoot and should be recognized as children grow. Many treated clubfeet have small, squared tali with flattened heads, decreased talocalcaneal angles, subtalar joint changes, and medial displacement of the navicular. Valgus deformity and flattening of the plantar arch may result from overcorrection.

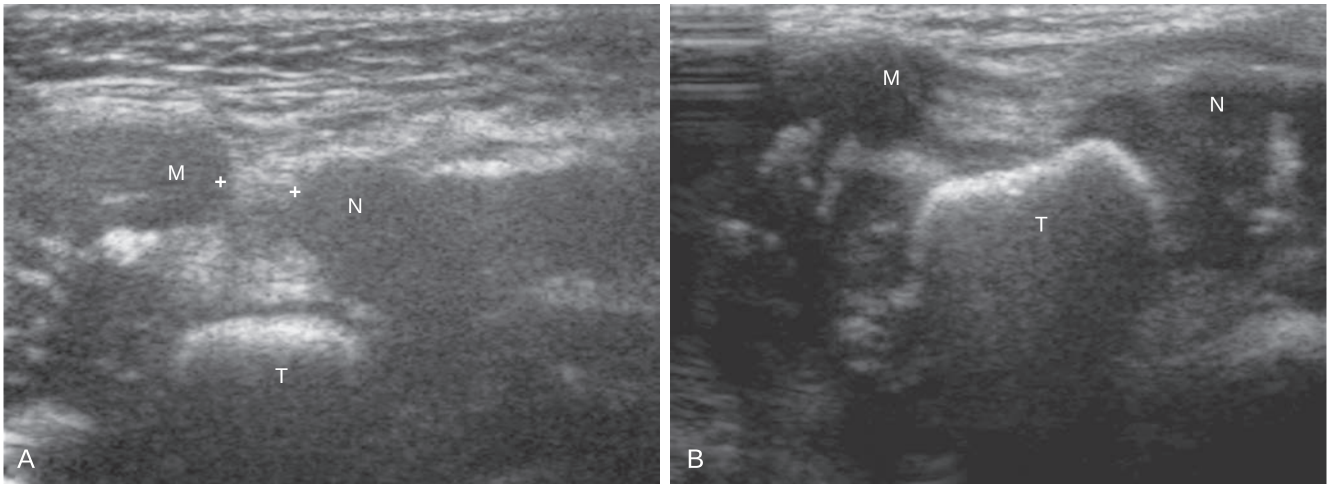

**e-Figure 133.27. Ultrasonography of clubfoot in a 6-month-old girl: longitudinal scans at the medial aspect of the feet.** (A) In clubfoot, the cartilaginous navicular *(N)* and the medial malleolus *(M)* are closely spaced *(cursors)*. These structures overlie the talus *(T)*, which is ossified. (B) In the normal foot, the navicular and the medial malleolus are widely spaced, and the talus is not covered. The distance between the navicular and the medial malleolus is an indicator of the severity of deformity and can be monitored over time. Dynamic assessment can reveal if there is flexibility of the deformed clubfoot. *(Courtesy of Dr. M. A. DiPietro, Ann Arbor, MI.)*

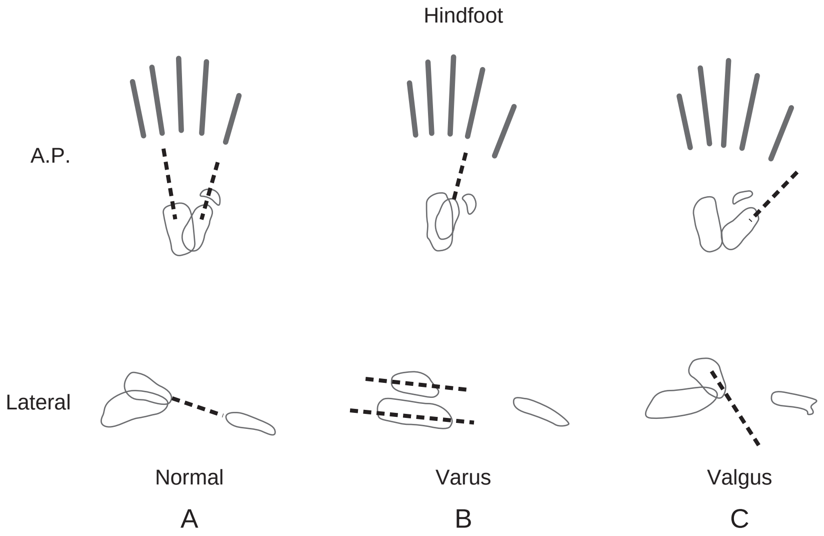

**Figure 133.25. Hindfoot and forefoot relationships in the anteroposterior and lateral projections.** (A) Normal hindfoot. The talar axial line intersects or points slightly medial to the first metatarsal base. The navicular is situated directly distal to the head of the talus. The calcaneus points toward the fourth metatarsal base, forming a definable angle with the talus. On the lateral projection, the anterior portion of the talus is slightly plantarflexed, and the calcaneus is slightly dorsiflexed. The talar axial line points down the shaft of the first metatarsal. (B) Hindfoot varus. The talocalcaneal angle is decreased, with these two bones more parallel to each other and actually superimposed. The navicular is medially displaced, and the axial talar line points lateral to the first metatarsal base. On lateral projection, the calcaneus and the talus are more horizontal and parallel to each other. (C) Hindfoot valgus. The talocalcaneal angle is increased, with the navicular and other midfoot bones displaced lateral to the talus. The talar axial line passes medial to the first metatarsal base. On lateral projection, the talus is more vertical than normal. *(From Ozonoff MB.* Pediatric orthopedic radiology, *2nd ed, Philadelphia: WB Saunders; 1992.)*

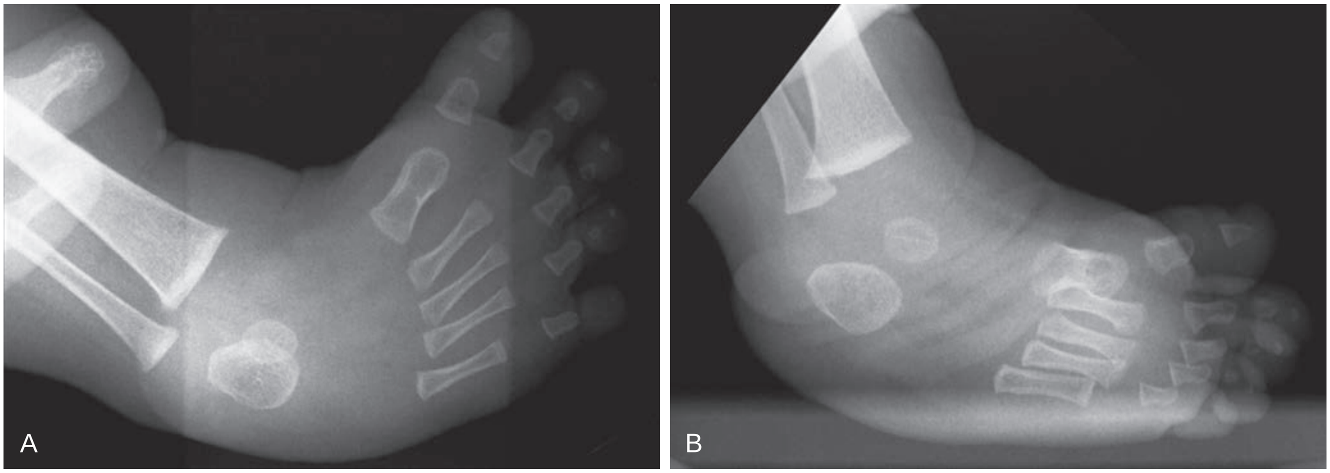

**Figure 133.26. Congenital clubfoot.** Simulated weight-bearing radiographs were obtained for evaluation. (A) Note the ankle inversion and forefoot adduction in the anteroposterior view. (B) Inversion on the lateral view shows “laddering” of the metatarsals. Equinus of the hindfoot and parallelism of the talus and calcaneus are evident.

## Congenital Vertical Talus

***Etiologies, Pathophysiology, and Clinical Presentation.*** Congenital vertical talus (congenital rigid flatfoot) may be an isolated condition or may be seen in association with various syndromes (e.g., trisomies) or other systemic abnormalities (i.e., central nervous system defects, arthrogryposis, and neurofibromatosis).[89,90] The term *oblique talus* refers to a similar abnormality except that it is flexible (reducible) and does not require operative management.

***Imaging.*** The talus is almost completely vertical in this condition (parallel with the longitudinal axis of the tibia), and the calcaneus is fixed in plantar flexion (equinus) (Fig. 133.28). In the anteroposterior projection, the talar axis is medial to the base of the first metatarsal (valgus). The navicular dislocates dorsally, and clinically, a pronated rocker-bottom foot is present. After the navicular ossifies, its abnormal position helps to distinguish congenital vertical talus from severe planovalgus or flatfoot deformity. Prior to ossification, the position of the navicular can

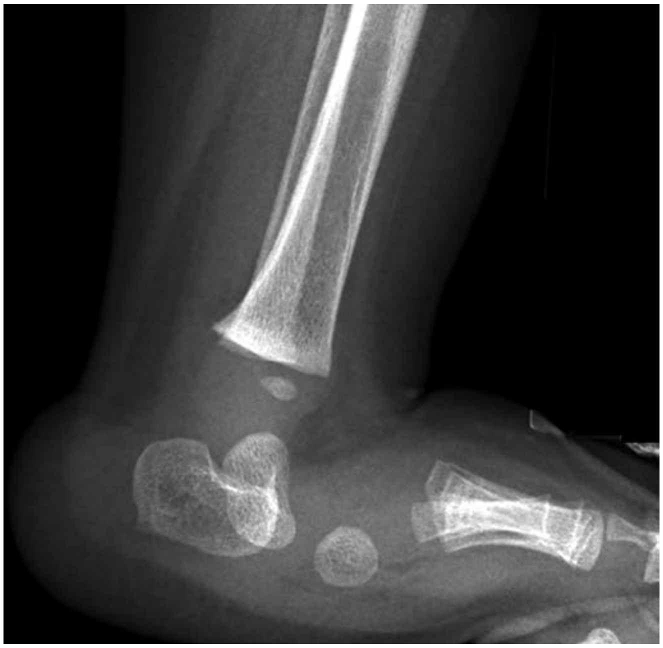

**Figure 133.28. Congenital vertical talus in 5-month-old boy.** Lateral foot radiograph shows hindfoot valgus with the talus nearly vertical in orientation and with the calcaneus plantarflexed.

be determined by US, which can distinguish vertical from oblique talus if this is not evident clinically.[91,92]

***Treatment.*** Congenital vertical talus is initially managed with conservative measures and casting, followed by surgical correction for recalcitrant cases.[90]

## Rocker-Bottom Foot

***Etiologies, Pathophysiology, and Clinical Presentation.*** Rocker-bottom foot is a clinical descriptive term seen with congenital vertical talus, severe cerebral palsy with hindfoot valgus, and as a complication of overcorrected clubfoot.

***Imaging.*** In rocker-bottom foot, the calcaneus is in equinus position and the metatarsals are dorsiflexed, producing a convex surface on the bottom of the foot.

## Metatarsus Adductus (Varus)

***Etiologies, Pathophysiology, and Clinical Presentation.*** Metatarsus adductus, the most common pediatric foot deformity, is a cause of in-toeing that is usually seen in children younger than 5 years of age. Forefoot adduction differs from clubfoot in that midfoot and hindfoot alignment is normal. The foot has a C-shaped contour on examination. Forefoot adduction simulating metatarsus adductus may occur as a result of excessive internal tibial torsion or femoral anteversion.

***Imaging.*** The metatarsals are adducted and hindfoot alignment is normal. There is no stepladder appearance of the metatarsals on the lateral view (e-Fig. 133.29).

***Treatment.*** Metatarsus adductus without other deformity commonly resolves with normal maturation.[93]

## Skewfoot

***Etiologies, Pathophysiology, and Clinical Presentation.*** Skewfoot (Z-foot; serpentine metatarsus adductus) is a rare entity distinct from metatarsus adductus. It develops idiopathically in young children. It can also be seen after treatment of clubfoot or vertical talus, in children with cerebral palsy, and with some dysplasias.[94]

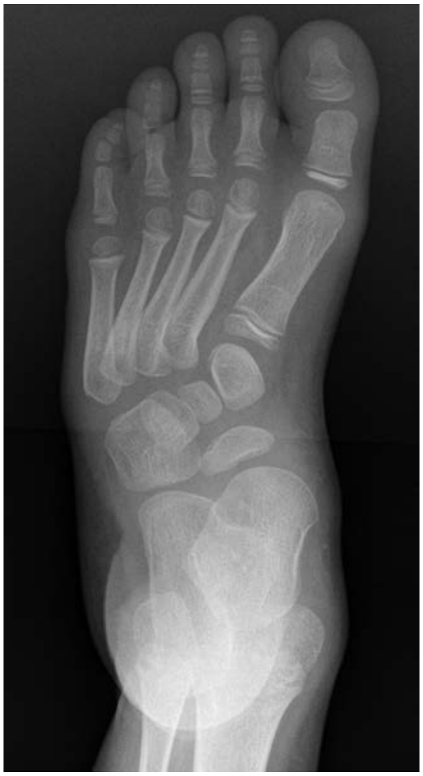

**Figure 133.30. Skewfoot in a 6-year-old girl.** AP radiograph shows the forefoot is adducted, midfoot is abducted with lateral deviation of the navicular, and the hindfoot is in valgus, resulting in a Z-shaped appearance of the feet.

***Imaging.*** In skewfoot, the forefoot is adducted, the midfoot is abducted (navicular shifted lateral to the talar head), and the hindfoot is in valgus, resulting in a “Z”-like distortion of the bones of the foot (Fig. 133.30).[94]

***Treatment.*** Conservative management is applied to most idiopathic cases. A variety of surgical techniques have been applied to reduce deformity in children with fixed or progressive deformity.[93,94]

## Flatfoot (Pes Planus)

***Etiologies, Pathophysiology, and Clinical Presentation.*** Flatfoot (pes planus) is a descriptive term. The differential diagnosis of pes planus includes flexible planovalgus (common flatfoot), peroneal spastic (rigid) flatfoot related to tarsal coalition, congenital vertical talus (rigid flatfoot), and congenital calcaneovalgus (flexible flatfoot, discussed in the next section).[89,95–97] Tarsal coalition is discussed in Chapter 131.

The common flatfoot is a painless, flexible planovalgus foot.[89] Variable degrees of hindfoot valgus, plantar arch flattening, and forefoot pronation occur. Pathology is thought to involve excess ligamentous laxity, which allows the calcaneus to shift into a valgus position under the talus. Abduction and eversion result from loss of calcaneal support. Patients may develop peroneal muscle spasm and pain caused by irritation.

***Imaging.*** With flexible planovalgus foot, the anteroposterior projection shows hindfoot valgus with an increased talocalcaneal angle and the midtalar line passing medial to the first metatarsal. On the lateral projection, hindfoot valgus causes the talus to be more vertical than normal (e-Fig. 133.31). The navicular subluxes dorsally and laterally with respect to the talar head. The calcaneus

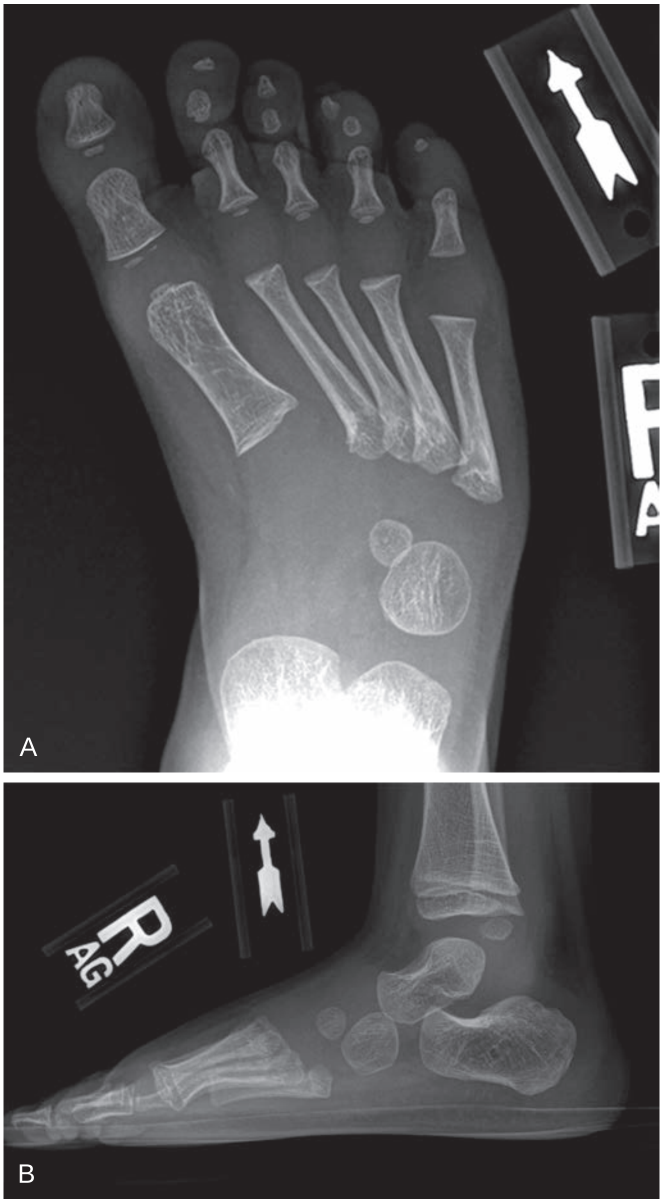

**e-Figure 133.29. Metatarsus Adductus in a 2-year-old boy with pain.** (A) AP weight-bearing radiograph shows adduction of the forefoot and metatarsals. (B) Lateral weight-bearing view shows normal hindfoot alignment and no "laddering" of the metatarsals.

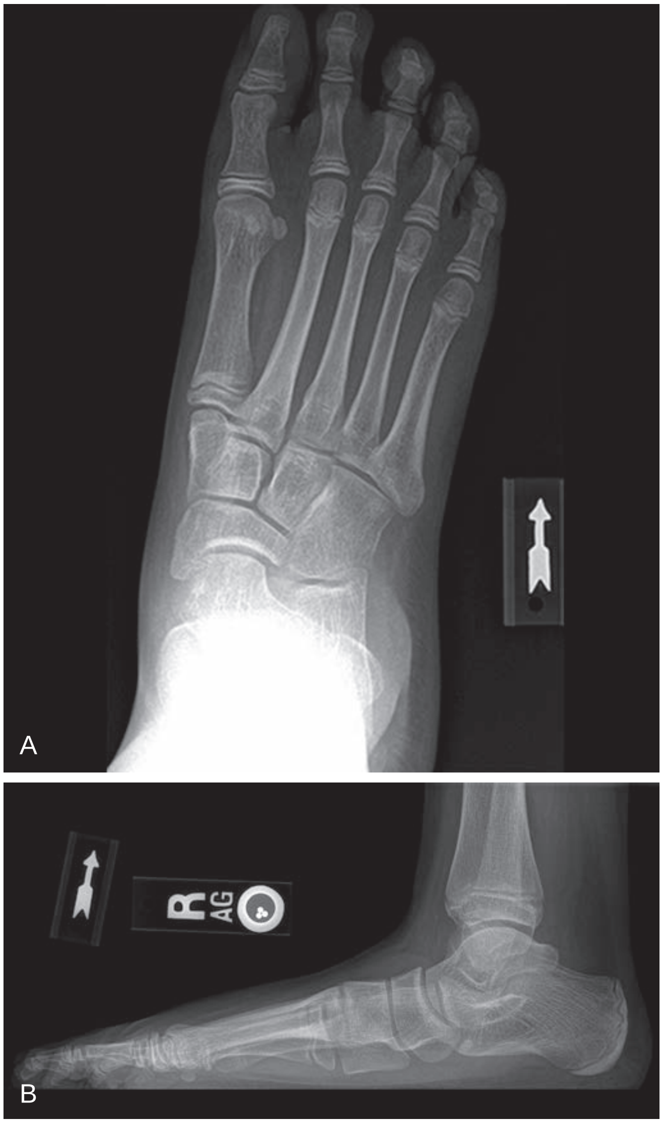

**e-Figure 133.31. Flat foot (planovalgus) in a 10-year-old boy with pain.** (A) Weight-bearing frontal radiograph shows deviation of the talar axis medial to the first metatarsal suggesting hindfoot valgus. (B) Lateral standing view shows flattening of the plantar arch and increased talo-calcaneal angle.

and metatarsals are horizontal longitudinally, and loss of the plantar arch is noted.[89] Similar deformity may occur in children with cerebral palsy (e-Fig. 133.32). With a rigid or painful flatfoot (peroneal spastic flatfoot), CT or MRI may be performed to detect underlying subtalar coalition.

***Treatment.*** Therapy for pes planus depends on the etiology and type of deformity.[95] Flexible planovalgus deformity is managed conservatively.[96] Rigid (spastic) flat foot with tarsal coalition requires surgery.[97]

### Calcaneovalgus

***Etiologies, Pathophysiology, and Clinical Presentation.*** Calcaneovalgus feet are reflective of intrauterine positioning. A total of 30% to 50% of newborns have mild calcaneovalgus deformity.[89] In severe congenital calcaneovalgus, the foot is dorsiflexed with respect to the talus. The defect is flexible and correctable.

***Imaging/Treatment.*** Radiographs are rarely performed but will show a calcaneus deformity and hindfoot valgus. Calcanovalgus foot is treated conservatively with physical therapy.

### Cavus Foot

***Etiologies, Pathophysiology, and Clinical Presentation.*** An idiopathic congenital form of cavus foot exists, but more commonly, the finding is related to neuromuscular abnormalities, including peroneal muscular atrophy (Charcot–Marie–Tooth disease), Friedreich ataxia, myelomeningocele, poliomyelitis, and other paralytic conditions.[98,99] A cavus foot may also result from treated clubfoot deformity.

***Imaging/Treatment.*** In pes cavus, the longitudinal plantar arch is increased. The anterior calcaneus is abnormally dorsiflexed and the metatarsals are plantarflexed (Fig. 133.33). Treatment may involve conservative measures and surgery (soft tissue and plantar fascia release, osteotomy, tendon transfers).[98]

### Hallux Valgus

***Etiologies, Pathophysiology, and Clinical Presentation.*** Hallux valgus deformity begins to develop and may present in childhood.[100] Juvenile hallux valgus affects girls 10 times as frequently as boys and is often bilateral. Patients present with pain and deformity, which may interfere with proper shoe fitting.

***Imaging/Treatment.*** The hallux angle, which is the angle between the long axes of the first metatarsal and first proximal phalanx, is increased in hallux valgus. A hallux angle less than 10 to 15 degrees is normal; in hallux valgus this angle is typically greater than 15 degrees (e-Fig. 133.34). US or MRI can evaluate for inflamed bursa at the metatarsal head in the setting of pain. First metatarsal osteotomy may be performed to correct alignment.[100]

## GENERALIZED DISORDERS

### Cerebral Palsy

***Overview.*** Children with cerebral palsy are afflicted with multiple orthopedic disorders requiring radiographic investigation and surveillance.[35,101,102] Variable manifestations of cerebral palsy are caused by differences in severity and location of the original insult, which can occur during the prenatal or perinatal period as well as a result of injury during early childhood.[101]

***Etiologies, Pathophysiology, and Clinical Presentation.*** The orthopedic disorders of cerebral palsy are caused by imbalanced muscular forces. Although cerebral palsy is a static encephalopathy, the resultant musculoskeletal disease may be progressive, even after skeletal maturity.

***Imaging.*** About 25% of cerebral palsy patients have scoliosis.[35,103] Scoliosis is more prevalent and severe with greater neurologic deficit. As opposed to the S-shaped curves of idiopathic scoliosis, curves in cerebral palsy often have a broad C-shaped contour, and the curves may progress after skeletal maturation.[35,103] Associated findings may include accentuated thoracic kyphosis or lumbar lordosis, spondylolysis or spondylolisthesis, and pelvic obliquity. Nonambulatory patients also show caninization of the vertebral bodies (narrow anteroposterior diameter) caused by lack of weight-bearing forces during development.

Upper extremity defects include radial head dislocation (Fig. 133.35) and contractures at the elbow, wrist, and fingers.[104,105] Kienböck disease and negative ulnar variance are of increased incidence in cerebral palsy.[106] Accelerated degenerative changes in the elbow and wrist are common in older patients.[104]

Abnormalities at the hip include coxa valga caused by lack of weight bearing, increased femoral anteversion, prominence of the lesser trochanter caused by external rotation forces by the iliopsoas tendon, femoral head subluxation or dislocation, acetabular dysplasia, and flattening of the femoral head (see Fig. 133.10).[35,107] Older patients with cerebral palsy show evidence of early degenerative disease at the hips.

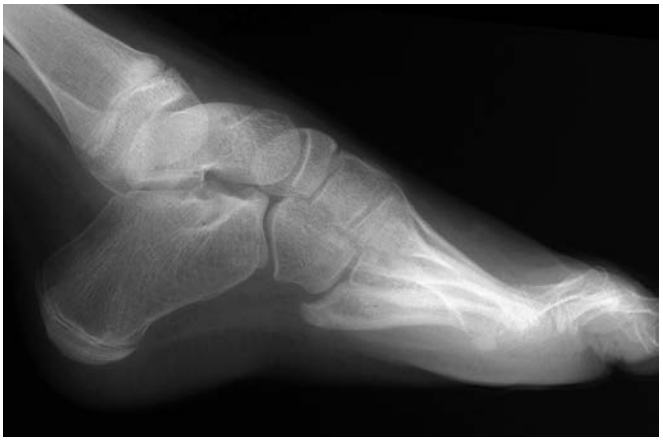

**Figure 133.33. Pes cavus in an 11-year-old girl with Charcot–Marie–Tooth (peroneal muscular atrophy).** Lateral radiograph shows that the talocalcaneal angle is increased, and the longitudinal arch is elevated. The metatarsophalangeal joints are extended, and the interphalangeal joints are flexed (hammertoe deformity).

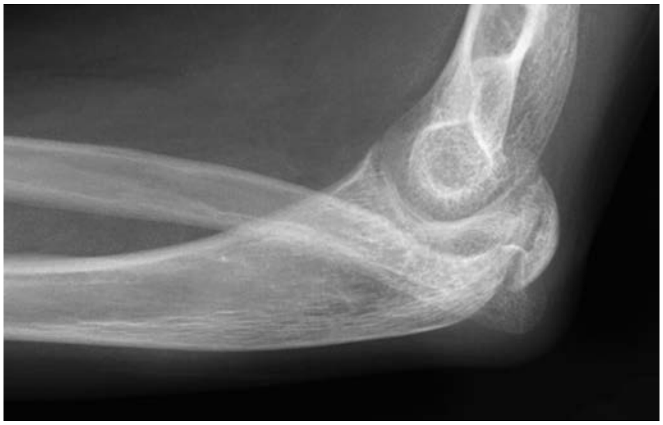

**Figure 133.35. Chronic radial head dislocation in a 14-year-old boy with cerebral palsy.** The radial head is displaced posteriorly and has a rounded contour. The radius is bowed anteriorly. Similar findings were present on the opposite side.

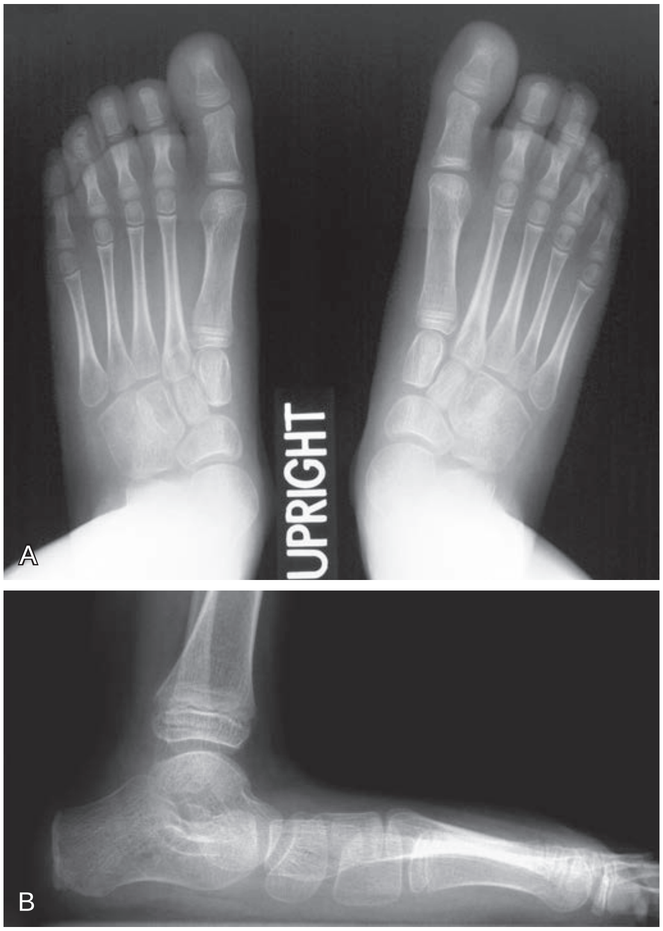

**e-Figure 133.32. Bilateral planovalgus feet in a 9-year-old with cerebral palsy.** (A) In the anteroposterior radiograph, hindfoot valgus is symmetric. (B) Lateral view of the right foot shows pes planus with a mild increase in the lateral talocalcaneal angle, also consistent with hindfoot valgus. The calcaneus is horizontal in orientation.

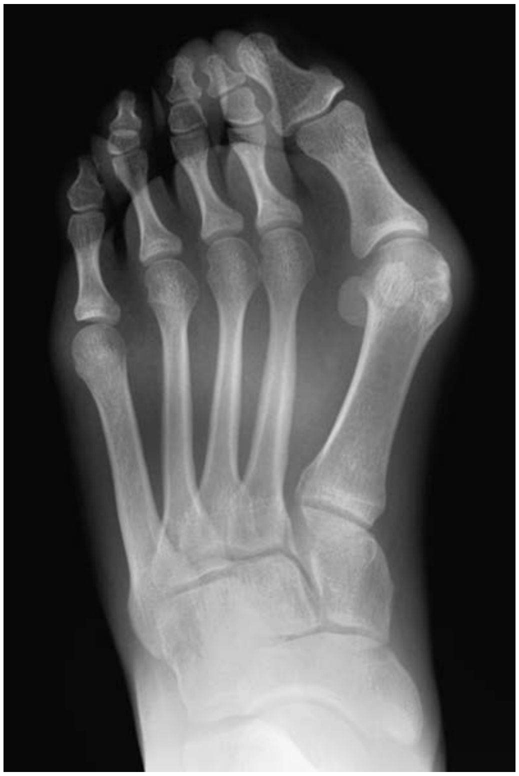

**e-Figure 133.34. Hallux valgus in a 14-year-old girl.** Slight sclerosis is present in the medial aspect of the first metatarsal head.

At the knee, flexion contractures may be present. The patella is often high (patella alta) and elongated.[33,108] Tug lesions are common at the lower pole of the patella, producing a fragmented appearance.[35,109] The tibial tuberosity may appear elevated and irregular. Genu recurvatum may be seen with rectus femoris contracture. Valgus is seen at the ankle, and equinus and hindfoot valgus are common in the foot (see e-Fig. 133.32).[35,110] Osteopenia predisposes patients with cerebral palsy to fracture.[111]

***Treatment.*** Treatment of orthopedic conditions in cerebral palsy is aimed at maximizing function and limiting the progression of deformity.

## Myelomeningocele

***Overview.*** Children with myelomeningocele and related spinal disorders may be afflicted with multiple orthopedic disorders of the spine and lower extremity requiring radiographic investigation and surveillance.[112,113] Variable manifestations of the disease relate to the level of the defect. Children with other spinal pathologies, including those suffering injury to the spinal cord at a young age, may develop orthopedic disorders similar to those with myelomeningocele.

***Etiologies, Pathophysiology, and Clinical Presentation.*** Orthopedic disorders in myelomeningocele patients are caused by lack of normal muscle development and function. This leads to scoliosis and joint malalignments.

***Imaging.*** Scoliosis in patients with myelomeningocele may be congenital or developmental.[113] In 20% of patients, congenital scoliosis is caused by vertebral segmentation anomalies. Congenital kyphosis is most common at L1–L2. Kyphosis may also be acquired.[113] Lumbar lordosis is commonly accentuated.

Up to one-half of patients with myelomeningocele have hip dysplasia. The hips are occasionally dislocated at birth; however, more often, dysplasia develops over time as the result of paralysis of the hip extensors and abductors with unopposed hip flexors and adductors (e-Fig. 133.36).[113] Coxa valga and increased femoral anteversion are common. Excessive tibial torsion may be seen. In all, 80% to 95% of patients have foot deformities. Equinovarus (clubfoot), congenital vertical talus, and other foot deformities are seen.[113]

Infants with myelomeningocele have an increased incidence of fracture of a lower extremity during birth.[114] A higher incidence of fracture is seen with contractures and higher levels of spinal defect. Patients with myelomeningocele may develop neuropathic injuries as the result of osteoporosis and lack of sensation.[113,115,116] Fractures are most commonly metaphyseal or diaphyseal. Periosteal new bone and callous may be exuberant because of delayed diagnosis without immobilization and abundant subperiosteal hemorrhage.[113,115] Such injuries may be mistaken for tumor or infection.

***Treatment.*** Treatment of orthopedic conditions in patients with myelomeningocele is aimed at maximizing function and limiting the progression of deformity.

### KEY POINTS

- Radiography plays a key role in the diagnosis and surveillance of disorders of alignment. Proper positioning of the patient facilitates evaluation.
- Radiography may show findings of an underlying disorder or complications of treatment, either of which might be clinically unsuspected.
- Bowleg and knock-knee may be physiologic, depending on the age of the patient and the degree of abnormality.
- Radiographic assessment of the foot requires a clear understanding of normal anatomic relationships.
- Orthopedic disorders are common in cerebral palsy. Deformity may continue to progress after skeletal maturity because of imbalanced muscular forces.

### SUGGESTED READINGS

Driscoll SW, Skinner J. Musculoskeletal complications of neuromuscular disease in children. *Phys Med Rehabil Clin N Am*. 2008;19:163–194.

Morrell DS, Pearson JM, Sauser DD. Progressive bone and joint abnormalities of the spine and lower extremities in cerebral palsy. *Radiographics*. 2002;22:257–268.

Oestreich AE. *How to Measure Angles From Foot Radiographs: A Primer*. 1st ed. New York: Springer-Verlag; 1990.

Sabharwal S, Zhao C, Edgar M. Lower limb alignment in children: reference values based on a full-length standing radiograph. *J Pediatr Orthop*. 2008;28(7):740–746.

Stein-Wexler R, Wooton-Gorges SL, Ozonoff MB. *Pediatric Orthopedic Imaging*. 1st ed. Berlin-Heidelberg, Germany: Springer; 2015:273–318.

### REFERENCES

Full references for this chapter can be found on www.expertconsult.com.

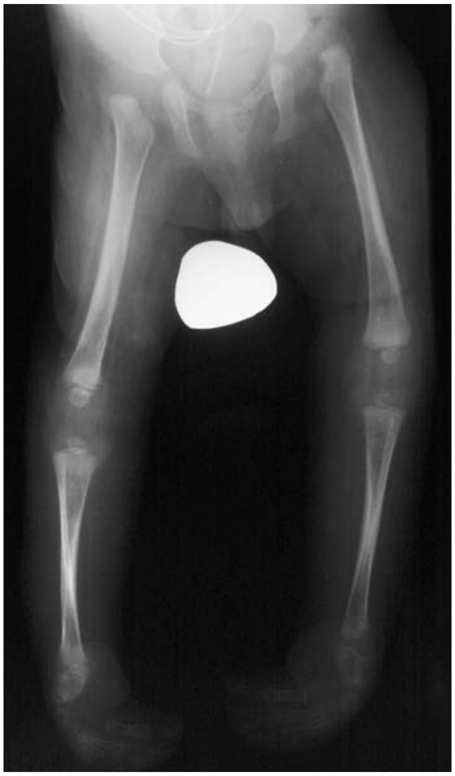

**e-Figure 133.36. A 7-month-old boy with myelomeningocele.** Both hips are dislocated, and clubfeet deformities are present. The musculature is atrophic. A ventriculoperitoneal shunt is present.

## REFERENCES

1. Martinoli C, Bianchi S, Santacroce E, et al. Brachial plexus sonography: a technique for assessing the root level. *AJR Am J Roentgenol*. 2002;179:699–702.
2. Martinoli C, Valle M, Malattia C, et al. Paediatric musculoskeletal US beyond the hip joint. *Pediatr Radiol*. 2011;41:S113–S124.
3. Joseph JR, DiPietro MA, Somashekar D, et al. Ultrasonography for neonatal brachial plexus palsy. *J Neurosurg Pediatr*. 2014;14:527–531.
4. Pollock AN, Reed MH. Shoulder deformities from obstetrical brachial plexus paralysis. *Skeletal Radiol*. 1989;18:295–297.
5. Mintzer CM, Waters PM, Brown DJ. Glenoid version in children. *J Pediatr Orthop*. 1996;16:563–566.
6. Pöyhiä TH, Nietosvaara YA, Remes VM, et al. MRI of rotator cuff muscle atrophy in relation to glenohumeral joint incongruence in brachial plexus birth injury. *Pediatr Radiol*. 2005;35:402–409.
7. Waters PM, Smith GR, Jaramillo D. Glenohumeral deformity secondary to brachial plexus birth palsy. *J Bone Joint Surg Am*. 1998;80:668–677.
8. Hernandez RJ, Dias L. CT evaluation of the shoulder in children with Erb's palsy. *Pediatr Radiol*. 1988;18:333–336.
9. Gudinchet F, Maeder P, Oberson JC, et al. Magnetic resonance imaging of the shoulder in children with brachial plexus birth palsy. *Pediatr Radiol*. 1995;25:S125–S128.
10. Pöyhiä TH, Nietosvaara YA, Remes VM, et al. MRI of rotator cuff muscle atrophy in relation to glenohumeral joint incongruence in brachial plexus birth injury. *Pediatr Radiol*. 2005;35:402–409.
11. Hunter JD, Franklin K, Hughes PM. The ultrasound diagnosis of posterior shoulder dislocation associated with Erb's palsy. *Pediatr Radiol*. 1998;28:510–511.
12. Saifuddin A, Heffernan G, Birch R. Ultrasound diagnosis of shoulder congruity in chronic obstetric brachial plexus palsy. *J Bone Joint Surg Br*. 2002;84:100–103.
13. Pöyhiä TH, Lamminen AE, Peltonen JI, et al. Brachial plexus birth injury: US screening for glenohumeral joint instability. *Radiology*. 2010;254:253–260.
14. Waters PM. Update on management of pediatric brachial plexus palsy. *J Pediatr Orthop*. 2005;25:116–126.
15. Pearl ML. Shoulder problems in children with brachial plexus birth palsy: evaluation and management. *J Am Acad Orthop Surg*. 2009;17:242–254.
16. Zebala LP, Manske PR, Goldfarb CA. Madelung's deformity: a spectrum of presentation. *J Hand Surg Am*. 2007;32:1393–1401.
17. Arora AS, Chung KC, Otto W. Madelung and the recognition of Madelung's deformity. *J Hand Surg Am*. 2006;31:177–182.
18. Schmidt-Rohlfing B, Schwöbel B, Pauschert R, et al. Madelung deformity: clinical features, therapy and results. *J Pediatr Orthop B*. 2001;10:344–348.
19. Tuder D, Frome B, Green DP. Radiographic spectrum of severity in Madelung's deformity. *J Hand Surg Am*. 2008;33:900–904.
20. McCarroll HR Jr, James MA, Newmeyer WL 3rd, et al. Madelung's deformity: quantitative assessment of x-ray deformity. *J Hand Surg Am*. 2005;30:1211–1220.
21. Cook PA, Yu JS, Wiand W, et al. Madelung deformity in skeletally immature patients: morphologic assessment using radiography, CT, and MRI. *J Comput Assist Tomogr*. 1996;20:505–511.
22. Ali S, Kaplan S, Kaufman T, et al. Madelung deformity and Madelung-type deformities: a review of the clinical and radiological characteristics. *Pediatr Radiol*. 2015;45:1856–1863.
23. Hafner R, Poznanski AK, Donovan JM. Ulnar variance in children—standard measurements for evaluation of ulnar shortening in juvenile rheumatoid arthritis, hereditary multiple exostosis and other bone or joint disorders in childhood. *Skeletal Radiol*. 1989;18:513–516.
24. Goldfarb CA, Strauss NL, Wall LB, et al. Defining ulnar variance in the adolescent wrist: measurement technique and interobserver reliability. *J Hand Surg Am*. 2011;36:272–277.
25. Palmer AK, Glisson RR, Werner FW. Ulnar variance determination. *J Hand Surg Am*. 1982;7:376–379.
26. Goeminne S, Degreef I, De Smet L. Negative ulnar variance has prognostic value in progression of Kienböck's disease. *Acta Orthop Bel*. 2010;76:38–41.
27. Zippel H. Normal development of the structural elements of the hip joint in adolescence. *Beitr Orthop Traumatol*. 1971;18:255–270.
28. Robin J, Kerr Graham H, Selber P, et al. Proximal femoral geometry in cerebral palsy: a population-based cross-sectional study. *J Bone Joint Surg Br*. 2008;90:1372–1379.
29. Fabry G, MacEwen GD, Shands AR Jr. Torsion of the femur. A follow-up study in normal and abnormal conditions. *J Bone Joint Surg Am*. 1973;55:1726–1738.
30. Beals RK. Coxa vara in childhood: evaluation and management. *J Am Acad Orthop Surg*. 1998;6:93–99.
31. Aarabi M, Rauch F, Hamdy RC, et al. High prevalence of coxa vara in patients with severe osteogenesis imperfecta. *J Pediatr Orthop*. 2006;26:24–28.
32. Pavlov H, Goldman AB, Freiberger RH. Infantile coxa vara. *Radiology*. 1980;135:631–640.
33. Oh CW, Thacker MM, Mackenzie WG, et al. Coxa vara: a novel measurement technique in skeletal dysplasias. *Clin Orthop Relat Res*. 2006;447:125–134.
34. Grissom LE. The pelvis and hip: congenital and developmental conditions. In: Stein-Wexler R, Wooton-Gorges SL, Ozonoff MB, eds. *Pediatric Orthopedic Imaging*. 1st ed. Berlin-Heidelberg, Germany: Springer; 2015:273–318.
35. Morrell DS, Pearson JM, Sauser DD. Progressive bone and joint abnormalities of the spine and lower extremities in cerebral palsy. *Radiographics*. 2002;22:257–268.
36. Bobroff ED, Chambers HG, Sartoris DJ, et al. Femoral anteversion and neck-shaft angle in children with cerebral palsy. *Clin Orthop Relat Res*. 1999;364:194–204.
37. Gose S, Sakai T, Shibata T, et al. Morphometric analysis of the femur in cerebral palsy: 3-dimensional CT study. *J Pediatr Orthop*. 2010;30:568–574.
38. Davids JR, Marshall AD, Blocker ER, et al. Femoral anteversion in children with cerebral palsy: assessment with two and three-dimensional computed tomography scans. *J Bone Joint Surg Am*. 2003;85:481–488.
39. Hernandez RJ, Tachdjian MO, Poznanski AK, et al. CT determination of femoral torsion. *AJR Am J Roentgenol*. 1981;137:97–101.
40. Jarrett DY, Oliveira AM, Zou KH, et al. Axial oblique CT to assess femoral anteversion. *AJR Am J Roentgenol*. 2010;194:1230–1233.
41. Sugano N, Noble PC, Kamaric E. A comparison of alternative methods of measuring femoral anteversion. *J Comput Assist Tomogr*. 1998;22:610–614.
42. Wybier M, Bossard P. Musculoskeletal imaging in progress: the EOS imaging system. *Joint Bone Spine*. 2013;80:238–243.
43. Staheli LT, Corbett M, Wyss C, et al. Lower-extremity rotational problems in children. Normal values to guide management. *J Bone Joint Surg Am*. 1985;67:39–47.
44. Lee SH, Chung CY, Park MS, et al. Tibial torsion in cerebral palsy: validity and reliability of measurement. *Clin Orthop Relat Res*. 2009;467:2098–2104.
45. Dietz FR. Intoeing—fact, fiction and opinion. *Am Fam Physician*. 1994;50:1249–1259, 1262–1264.
46. Kristiansen LP, Gunderson RB, Steen H, et al. The normal development of tibial torsion. *Skeletal Radiol*. 2001;30(9):519–522.
47. Do TT. Clinical and radiographic evaluation of bowlegs. *Curr Opin Pediatr*. 2001;13:42–46.
48. Cheema JI, Grissom LE, Harcke HT. Radiographic characteristics of lower-extremity bowing in children. *Radiographics*. 2003;23:871–880.
49. Jouve JL, Kohler R, Mubarak SJ, et al. Focal fibrocartilaginous dysplasia ("fibrous periosteal inclusion"): an additional series of eleven cases and literature review. *J Pediatr Orthop*. 2007;27:75–84.
50. Bell SN, Campbell PE, Cole WG, et al. Tibia vara caused by focal fibrocartilaginous dysplasia: three case reports. *J Bone Joint Surg Br*. 1985;67:780–784.
51. Yaniv M, Becker T, Goldwirt M, et al. Prevalence of bowlegs among child and adolescent soccer players. *Clin J Sport Med*. 2006;16:392–396.
52. Laor T, Wall EJ, Vu LP. Physeal widening in the knee due to stress injury in child athletes. *AJR Am J Roentgenol*. 2006;186:1260–1264.
53. Witvrouw E, Danneels L, Thijs Y, et al. Does soccer participation lead to genu varum? *Knee Surg Sports Traumatol Arthrosc*. 2009;17:422–427.
54. Holt JF, Latourette HB, Watson EH. Physiological bowing of the legs in young children. *J Am Med Assoc*. 1954;154:390–394.
55. Levine AM, Drennan JC. Physiological bowing and tibia vara: the metaphyseal-diaphyseal angle in the measurement of bowleg deformities. *J Bone Joint Surg Am*. 1982;64:1158–1163.
56. Salenius P, Vankka E. The development of the tibiofemoral angle in children. *J Bone Joint Surg Am*. 1975;57:259–261.
57. Ozonoff MB. The lower extremity. In: *Pediatric Orthopedic Radiology*. 2nd ed. Philadelphia, PA: WB Saunders; 1992:304–396.

58. Heath CH, Staheli LT. Normal limits of knee angle in white children—genu varum and genu valgum. *J Pediatr Orthop*. 1993;13:259–262.
59. Shopfner CE, Coin CG. Genu varus and valgus in children. *Radiology*. 1969;92:723–732.
60. Eggert P, Viemann M. Physiological bowlegs or infantile Blount's disease. Some new aspects on an old problem. *Pediatr Radiol*. 1996;26:349–352.
61. Davids JR, Blackhurst DW, Allen BL Jr. Radiographic evaluation of bowed legs in children. *J Pediatr Orthop*. 2001;21:257–263.
62. Blount WP. Tibia vara. *J Bone Surg*. 1937;19:1–29.
63. Blount WP. Tibia vara, osteochondrosis deformans tibiae. *Curr Pract Orthop Surg*. 1966;3:141–156.
64. Sabharwal S. Blount disease. *J Bone Joint Surg Am*. 2009;91:1758–1776.
65. Loder RT, Johnston CE 2nd. Infantile tibia vara. *J Pediatr Orthop*. 1987;7:639–646.
66. Gettys FK, Jackson JB, Frick SL. Obesity in pediatric orthopaedics. *Orthop Clin North Am*. 2011;42:95–105.
67. Langenskiöld A. Tibia vara: a critical review. *Clin Orthop Relat Res*. 1989;195–207.
68. Iwasawa T, Inaba Y, Nishimura G, et al. MR findings of bowlegs in toddlers. *Pediatr Radiol*. 1999;29:826–834.
69. Craig JG, van Holsbeeck M, Zaltz I. The utility of MR in assessing Blount disease. *Skeletal Radiol*. 2002;31:208–213.
70. Ho-Fung V, et al. MRI evaluation of the knee in children with infantile Blount disease: tibial and extra-tibial findings. *Pediatr Radiol*. 2013;43(10):1316–1326.
71. Lin C-J, Lin S-C, Huang W, et al. Physiological knock-knee in preschool children: prevalence, correlating factors, gait analysis, and clinical significance. *J Pediatr Orthop*. 1999;19:650–654.
72. Knutson GA. Anatomic and functional leg-length inequality: a review and recommendation for clinical decision-making. Part I, anatomic leg-length inequality: prevalence, magnitude, effects and clinical significance. *Chiropr Osteopat*. 2005;13:11. doi:10.1186/1746-1340-13-11.
73. Green WT, Wyatt GM, Anderson M. Orthoroentgenography as a method of measuring the bones of the lower extremity. *J Bone Joint Surg Am*. 1946;28:60–65.
74. Aaron A, Weinstein D, Thickman D, et al. Comparison of orthoroentgenography and computed tomography in the measurement of limb-length discrepancy. *J Bone Joint Surg Am*. 1992;74:897–902.
75. Poutawera V, Stott NS. The reliability of computed tomography scanograms in the measurement of limb length discrepancy. *J Pediatr Orthop B*. 2010;19:42–46.
76. Escott BG, Ravi B, Weathermon AC, et al. EOS low-dose radiography: a reliable and accurate upright assessment of lower-limb lengths. *J Bone Joint Surg Am*. 2013;95:e1831–e1837.
77. Friend L, Widmann RF. Advances in management of limb length discrepancy and lower limb deformity. *Curr Opin Pediatr*. 2008;20:46–51.
78. Ozonoff MB. The foot. In: *Pediatric Orthopedic Radiology*. 2nd ed. Philadelphia, PA: WB Saunders; 1992:397–460.
79. Vanderwilde R, Staheli LT, Chew DE, et al. Measurements on radiographs of the foot in normal infants and children. *J Bone Joint Surg Am*. 1988;70:407–415.
80. Gentili A, Masih S, Yao L, et al. Pictorial review: foot axes and angles. *Br J Radiol*. 1996;69:9688–9974.
81. Cummings RJ, Davidson RS, Armstrong PF, et al. Congenital clubfoot. *J Bone Joint Surg Am*. 2002;84:290–308.
82. Coley BD, Shiels WE, Kean J, et al. Age-dependent dynamic sonographic measurement of pediatric clubfoot. *Pediatr Radiol*. 2007;37:1125–1129.
83. Shiels WE, Coley BD, Kean J, et al. Focused dynamic sonographic examination of the congenital clubfoot. *Pediatr Radiol*. 2007;37:1118–1124.
84. Aurell Y, Johansson A, Hansson G, et al. Ultrasound anatomy in the normal neonatal and infant foot: an anatomic introduction to ultrasound assessment of foot deformities. *Eur Radiol*. 2002;12:2306–2312.
85. Aurell Y, Johansson A, Hansson G, et al. Ultrasound anatomy in the neonatal clubfoot. *Eur Radiol*. 2002;12:2509–2517.
86. Gore AI, Spencer JP. The newborn foot. *Am Fam Physician*. 2004;69:865–872.
87. Fridman MW, de Almeida Fialho HS. The role of radiographic measurements in the evaluation of congenital clubfoot surgical results. *Skeletal Radiol*. 2007;36:129–138.
88. Horn BD, Davidson RS. Current treatment of clubfoot in infancy and childhood. *Foot Ankle Clin*. 2010;15(2):235–243. doi:10.1016/j.fcl.2010.03.003.
89. Sullivan JA. Pediatric flatfoot: evaluation and management. *J Am Acad Orthop Surg*. 1999;7:44–53.
90. McKie J, Radomisli T. Congenital vertical talus: a review. *Clin Podiatr Med Surg*. 2010;27:145–156.
91. Schlesinger AE, Deeney VF, Caskey PF. Sonography of the nonossified tarsal navicular cartilage in an infant with congenital vertical talus. *Pediatr Radiol*. 1989;20:134–135.
92. Supakul N, Loder RT, Karmazyn B. Dynamic US study in the evaluation of infants with vertical or oblique talus deformities. *Pediatr Radiol*. 2013;43:376–380.
93. Hutchinson B. Pediatric metatarsus adductus and skewfoot deformity. *Clin Podiatr Med Surg*. 2010;27:93–104.
94. Napiontek M. Skewfoot. *J Pediatr Orthop*. 2002;22:130–133.
95. Harris EJ, Vanore JV, Thomas JL, et al. Diagnosis and treatment of pediatric flatfoot. *J Foot Ankle Surg*. 2004;43:341–373.
96. Blitz NM, Stabile RJ, Giorgini RJ, et al. Flexible pediatric and adolescent pes planovalgus: conservative and surgical treatment options. *Clin Podiatr Med Surg*. 2010;27:59–77.
97. Rodriguez N, Choung DJ, Dobbs MB. Rigid pediatric pes planovalgus: conservative and surgical treatment options. *Clin Podiatr Med Surg*. 2010;27:79–92.
98. Schwend RM, Drennan JC. Cavus foot deformity in children. *J Am Acad Orthop Surg*. 2003;11:201–211.
99. Allard P, Sirois JP, Thiry PS, et al. Roentgenographic study of cavus foot deformity in Friedreich ataxia patients: preliminary report. *Can J Neurol Sci*. 1982;9:113–117.
100. Talab YA. Hallux valgus in children: a 5–14-year follow-up study of 30 feet treated with a modified Mitchell osteotomy. *Acta Orthop Scand*. 2002;73:195–198.
101. Kerr Graham H, Selber P. Musculoskeletal aspects of cerebral palsy. *J Bone Joint Surg Br*. 2003;85:157–166.
102. Suh SW, Suh DH, Kim JW, et al. Analysis of sagittal spinopelvic parameters in cerebral palsy. *Spine J*. 2013;13(8):882–888.
103. Imrie MN, Yaszay B. Management of spinal deformity in cerebral palsy. *Orthop Clin North Am*. 2010;41:531–547.
104. Nishioka E, Yoshida K, Yamanaka K, et al. Radiographic studies of the wrist and elbow in cerebral palsy. *J Orthop Sci*. 2000;5:268–274.
105. Abu-Sneineh AK, Gabos PG, Miller F. Radial head dislocation in children with cerebral palsy. *J Pediatr Orthop*. 2003;23:155–158.
106. Leclercq C, Xarchas C. Kienbock's disease in cerebral palsy. *J Hand Surg [Br]*. 1998;23:746–748.
107. Sauser DD, Hewes RC, Root L. Hip changes in spastic cerebral palsy. *AJR Am J Roentgenol*. 1986;146:1219–1222.
108. Topoleski TA, Kurtz CA, Grogan DP. Radiographic abnormalities and clinical symptoms associated with patella alta in ambulatory children with cerebral palsy. *J Pediatr Orthop*. 2000;20:636–639.
109. Kaye JJ, Freiberger RH. Fragmentation of the lower pole of the patella in spastic lower extremities. *Radiology*. 1971;101:97–100.
110. Davids JR. The foot and ankle in cerebral palsy. *Orthop Clin North Am*. 2010;41:579–593.
111. Leet AI, Mesfin A, Pichard C, et al. Fractures in children with cerebral palsy. *J Pediatr Orthop*. 2006;26:624–627.
112. Karol LA. Orthopedic management in myelomeningocele. *Neurosurg Clin N Am*. 1995;6:259–268.
113. Westcott MA, Dynes MC, Remer EM, et al. Congenital and acquired orthopedic abnormalities in patients with myelomeningocele. *Radiographics*. 1992;12:1155–1173.
114. Boytim MJ, Davidson RS, Charney E, et al. Neonatal fractures in myelomeningocele patients. *J Pediatr Orthop*. 1991;11:28–30.
115. Kumar SJ, Cowell HR, Townsend P. Physeal, metaphyseal, and diaphyseal injuries of the lower extremities in children with myelomeningocele. *J Pediatr Orthop*. 1984;4:25–27.
116. Lock TR, Aronson DD. Fractures in patients who have myelomeningocele. *J Bone Joint Surg Am*. 1989;71:1153–1157.

# 134 Scoliosis

Eric P. Eutsler, Arthur B. Meyers, and Sumit Pruthi

*Scoliosis* is defined as a lateral spinal curvature greater than 10 degrees, as measured by the Cobb method.[1] Curves less than 10 degrees are termed *spinal asymmetry*. The lateral curvature is often accompanied by abnormalities in the axial and sagittal planes rendering it a three-dimensional abnormality. Scoliosis is classified into various categories, according to etiology, curve location, age at onset, and curve type. The Scoliosis Research Society has classified scoliosis into the following broad subcategories[2]:

1. Idiopathic (infantile, juvenile, and adolescent)
2. Congenital
3. Neuromuscular (neuropathic and myopathic)
4. Syndromic scoliosis (genetic and nongenetic syndromes)

## BIOMECHANICS AND PATHOGENESIS

Scoliosis is a three-dimensional deformity. The initiation and progression of the scoliotic curve is commonly thought to result from the effect of the Hueter-Volkmann law, which states that, during skeletal immaturity, the ring apophyses in the vertebrae are inhibited by compressive forces and stimulated by tensile forces.[1,3] Due to its physiologic curvature, there are normally increased compressive forces on the ventral aspect and distractive forces on the dorsal aspect of the thoracic spine. Initiation of a scoliotic curvature is believed to start with an abnormal axial rotation of vertebrae leading to abnormal distribution of these forces to the lateral margins of the vertebral bodies. The ventral portion of the spine, which is subjected to compressive forces, undergoes decreased growth and becomes the concave portion of the scoliotic curve. The dorsal portion of the spine, which is subjected to tensile forces, undergoes accelerated growth and becomes the convex portion of the curve.[3] This asymmetric growth is not only the genesis of the curve but may also have significant surgical implications, as the pedicles on the concave side become asymmetrically smaller, complicating pedicle screw placement for spinal fixation.[4]

## TERMINOLOGY

An understanding of the nomenclature and methods of measurement used to describe scoliosis on radiographs is essential for radiologists (Fig. 134.1). Identification of the curve apex, significant vertebrae, and central sacral vertical line (CSVL) is crucial for denoting the curve type, which guides treatment decisions.[5,6]

- *CSVL:* A vertical line (parallel to the edge of the radiograph) drawn on frontal radiographs through the center of the sacrum.[5–7] Also referred to as the *central sacral line (CSL).*
- *Apex:* The vertebra (apical vertebra) or the disk (apical disk) most laterally deviated in the scoliosis curve.
- *End vertebrae:* The vertebrae (cephalad end and caudal end) with the maximum tilt toward the apex of the curve.
- *Stable vertebra:* The most cephalad vertebra below the caudal end vertebra most closely bisected by the CSVL.
- *Neutral vertebrae:* Vertebrae with no axial rotation on a frontal standing radiograph.
- *Cobb method:* Used to measure degree of spinal curvature. The *Cobb angle* is formed between lines drawn along the superior endplate of the cephalad end vertebra and the inferior endplate of the caudal end vertebra. If the endplates cannot be visualized, the lines can be drawn along the borders of the pedicles.
- *Plumb line:* A vertical line drawn on standing frontal and lateral radiographs at the center of the C7 vertebral body. Used to determine coronal and sagittal balance.
- *Coronal balance:* Assessed by measuring the distance between the plumb line and the CSVL on a frontal radiograph. Positive coronal balance is present when the plumb line is greater than 2 cm to the right of the CSVL, and negative coronal balance is present when the plumb line is 2 cm to the left of the CSVL.[5–8]
- *Sagittal balance:* Assessed by measuring the distance between the plumb line and the posterosuperior corner of the S1 vertebral body. Positive sagittal balance is present when the plumb line is greater than 2 cm anterior to this corner, and negative sagittal balance is present when the plumb line is 2 cm posterior to this corner.[5–8]
- *Kyphosis:* Posterior convex angulation of the spine. The primary sagittal curves, which are present since birth, include the thoracic and sacral kyphoses. Thoracic kyphosis is measured on lateral radiographs as the angle between lines drawn along the superior endplate of the superior most thoracic vertebral body identified (usually T2 or T3) and the inferior endplate of T12. Normal thoracic kyphosis measures 20 to 45 degrees.[9–13] Most thoracic idiopathic scoliosis is associated with a decrease in normal thoracic kyphosis. A true kyphotic component may indicate a congenital or neuromuscular origin; however, some idiopathic cases may have a true kyphotic component.[1,6,13]
- *Lordosis:* Anterior convex angulation of the spine. Secondary sagittal curves, which are acquired to assume bipedal stance, include the cervical and lumbar lordoses typically established by age 6 years.[9,10] Lumbar lordosis ranges from 30 to 80 degrees when measured from L1 to L5.[1,11,12,14]
- *Curve location:* This is defined on the basis of the location of the apical vertebra and is classified as *cervical* (apex between C2 and C6), *cervicothoracic* (C7–T1), *thoracic* (T2–T11), *thoracolumbar* (T12–L1), *lumbar* (L2–L4), or *lumbosacral* (L5 and below).[1,6,13]
- *Curve types:* The curve is classified broadly as *primary* (major) or *secondary* (minor) *curves*, or *structural* or *nonstructural curves*.
- *Major (primary) curve:* Curve with the largest Cobb angle on the frontal radiograph.
- *Minor (secondary) curve:* Any curve that does not have the largest Cobb angle on the frontal radiograph. Usually develop after the major curve to stabilize the position of the head and pelvis.[6,13,15,16]
- *Structural curve:* A curve that is >25 degrees and does not correct to <25 degrees on an ipsilateral frontal bending view.[17] Additionally, a minor curve may be considered structural if it has a regional kyphosis of >20 degrees on a lateral radiograph, even if it does not meet the aforementioned criteria.[17]
- *Nonstructural curve:* Curves that do not meet the criteria for *structural curves*. These may be secondary curves or *functional curves* (curves related to posture, secondary to leg length discrepancy, muscle spasm, etc.).[13]
- *Classification of curves:* Various different classification systems exist describing the curve types preoperatively. The importance of classification systems is that they help guide the surgical approach and compare the efficacy of different treatment methods.[6,13] The most widely used classification system is

## Abstract:

Scoliosis is defined as a lateral spinal curvature greater than 10 degrees, as measured by the Cobb method. Curves less than 10 degrees are termed spinal asymmetry. The lateral curvature is often accompanied by abnormalities in the axial and sagittal planes rendering it a three-dimensional abnormality. Scoliosis is classified into various categories, according to etiology, curve location, age at onset, and curve type. This chapter reviews the various measurements and auxiliary findings in patients with scoliosis in order to aid pediatric radiologists in creating value-added reports.

## Keywords:

Scoliosis
Cobb
Idiopathic
Congenital
Neuromuscular
Adolescent

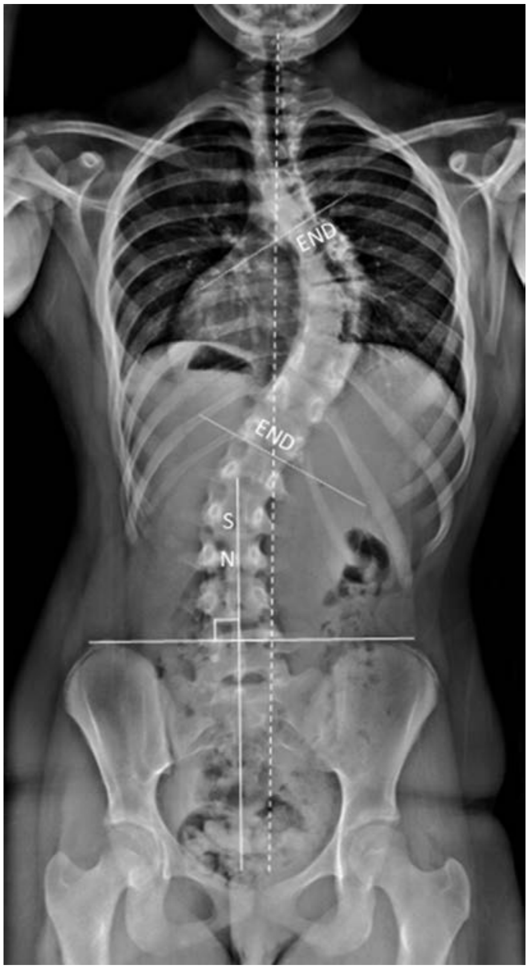

**Figure 134.1. Nomenclature.** Frontal image from a biplanar digital slot-scanning radiologic device (EOS Imaging, Paris, France) from a patient with scoliosis. Note that the image is presented with the patient's left side on the left side of the image, which is the way orthopedic providers typically view these images (similar to how they evaluate scoliosis on physical exam looking at the patient's back from behind). The end vertebrae *(END)* are the vertebra that are most tilted along the curve. The Cobb angle for the thoracic dextrocurvature is the angle between tangents *(thin oblique solid lines)* drawn along the cephalad end plate of superior end vertebra and the inferior end plate of caudal end vertebra. The central sacral vertebral line (CSVL) *(solid vertical line)* is a line that bisects the sacrum and is perpendicular to a tangent across the iliac crests *(solid horizontal line)*. The stable vertebra *(S)* is the most cephalad vertebra below the caudal end vertebra that is most closely bisected by the CSVL. A neutral vertebra *(N)* is one with no axial rotation on a frontal standing radiograph. The plumb line *(vertical thick dashed line)* is a line that is drawn from the center of the C7 vertebral body and is parallel to the edge of the image. If the distance between the CSVL and the plumb line is 2 cm or greater, it indicates coronal imbalance.

the Lenke system.[6,13,17,18] The Lenke system divides curves on the basis of location and type, differentiates structural from nonstructural curves, and includes lumbar and sagittal modifiers.[17,18]

## IDIOPATHIC SCOLIOSIS

Idiopathic scoliosis constitutes 80% of the patients with spinal deformity and is a diagnosis of exclusion.[1]

***Etiologies, Pathophysiology, and Clinical Presentation.*** The reported prevalence of idiopathic scoliosis in children and adolescents ranges from 0.5 to 3 per 100.[1,19,20] In the mild curves (<20 degrees), the female-to-male ratio is 1 : 1, but, when greater and progressive curves are evaluated (>30 degrees), females predominate with a 5 : 1 to 7 : 1 ratio. Only 0.2% of children have severe curves (>30 degrees).[1,20,21]

Idiopathic scoliosis is further divided into the following types based on age at diagnosis: *infantile* (0–3 years); *juvenile* (4–10 years); *adolescent* (11–18 years); and *adult* (≥18 years). Age at onset has significance both in terms of the prevalence of an associated underlying neuraxis abnormality as a cause and the natural history of the curve. The general term *early onset scoliosis* is increasingly being used to classify scoliosis beginning before the ages of 5 to 10 years.[2,22] The rationale behind this distinction is the increased risk of cardiopulmonary compromise in younger children with larger curves.[2,23]

***Imaging.*** The role of imaging is to characterize the curve type and severity, evaluate progression, determine the need for and planning of surgery, monitor treatment-related changes, and identify associated structural and underlying neuraxis abnormalities.[24] Radiography is principally utilized in idiopathic scoliosis to monitor curve progression, with cross-sectional imaging reserved for particular situations, discussed later.[2]

***Screening.*** Upright, standing, posteroanterior radiograph of the entire spine is the standard initial screening examination once the deformity is suspected clinically. The radiograph should include the cervicothoracic junction and pelvis. Standing radiography is preferred because treatment methods are based on standing views, and the magnitude of the curve is greatest in the standing position. However, sitting or supine positioning can be used in nonambulatory children. It is important to be aware of patient position because it is easy to mistake change in curvature as curve progression if an upright radiograph is compared with a prior supine radiograph.[1] The patient should stand with the feet shoulder-width apart, looking straight ahead with the elbows bent and knuckles in the supraclavicular fossa bilaterally, allowing visualization of the upper thoracic region on the lateral radiographs.[25] A lateral radiograph is not required at the time of screening but should be obtained in patients with documented scoliosis to assess sagittal balance. Radiographic techniques should minimize radiation exposure, especially to sensitive organs (e.g., breast, thyroid, and lens of eyes). A posteroanterior technique involves less radiation to the breast compared with an anteroposterior technique. Recently developed, the biplanar digital slot-scanning radiologic device (EOS Imaging, Paris, France) uses two narrow fan beam sources to acquire concurrent, high-quality, orthogonal radiographic images of the spine without the need for a grid, thus reducing radiation exposure.[26] Stereotactic three-dimensional reconstructions can also be created from the images, which is useful for both patient education and surgical planning.[26]

*Curve Magnitude:* The Cobb angle is the accepted standard for assessing the magnitude of the scoliotic curve. Although the Cobb angle provides limited assessment of the deformity and does not take rotation into account, it is still the foundation for diagnosis, follow-up, and treatment.[1] It is important to note that multiple factors, including patient positioning, radiographic techniques, known diurnal variation of 5 degrees, and interobserver and intraobserver variability may all affect the reproducibility of the angle.[27–31] Despite multiple caveats, measurements of the Cobb angle are generally considered reproducible when techniques are kept constant. A progressive curve is usually defined by a Cobb angle increase of 5 degrees or more between consecutive examinations.[1,2,6]

*Assessing Curve Patterns and Progression:* Prognosis and management in scoliosis is highly variable but is usually governed by three important factors: (1) etiology, (2) magnitude and the type of the curve(s) at presentation, and (3) speed of curve progression. The risk of progression is directly related to the spinal growth

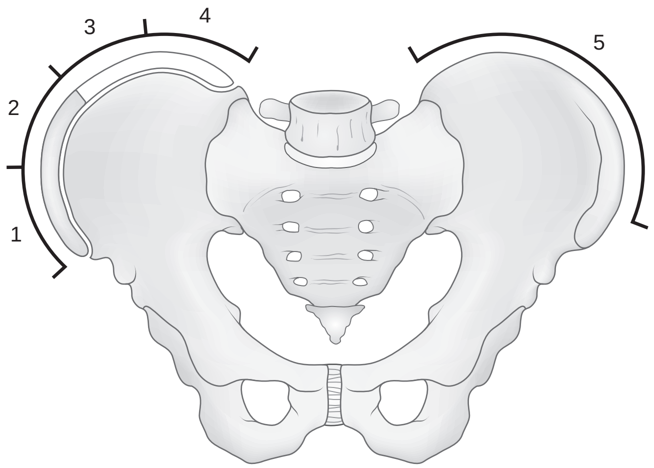

**Figure 134.2. Risser grade.** The Risser grade proceeds from grade 0 (no ossification) to grade 4 (all four quadrants show ossification of the iliac apophysis). When the ossified apophysis fuses completely to the ilium (Risser grade 5), the patient is skeletally mature. *(From Herring JA, ed. Scoliosis. In: Herring JA, ed.* Tachdjian's pediatric orthopedics. *vol 1. 3rd ed. Philadelphia: WB Saunders; 2002:213–321.)*

remaining, the severity of the curve at presentation, and the gender of the patient.[1,10,20,32,33] Various clinical tools to assess residual growth potential include chronologic age, menarche in girls, serial height measurements, and Tanner staging.[10,20,34–38] In general, the onset of the adolescent growth spurt occurs at 13 years in boys and 11 years in girls. In girls, menarche indicates the declining phase of the growing peak and a low risk of progression for idiopathic curves under 30 degrees.[1,10,34,36] Development of the iliac bone apophysis, quantified by Risser, has become a universally accepted sign (Fig. 134.2). Despite the wide use of the Risser grade as a measure of maturity, the appearance of the iliac apophysis generally occurs after the most important period of rapid growth.[1,34,35] As a result, other radiographic parameters are also used to assess bone maturation. Bone age may be assessed from a hand and wrist radiograph; however, use of bone age becomes less accurate in the juvenile age group secondary to the larger standard deviation and interobserver variability.[1,39] Assessment of pelvic triradiate cartilage is considered more accurate than the Risser grade. The triradiate cartilage closes around age 11 years in girls at the time of peak growth velocity.[1,24] More than one imaging parameter is often taken into consideration for accurately assessing skeletal maturation.

With regard to *curve patterns*, curves with an apex above T12 are more likely to progress compared with isolated lumbar curves.[1] With regard to *curve magnitude*, Risser stage 0 or 1 patients with an initial curve of 5 to 19 degrees progressed in 22% of cases, compared with curve progression in 68% of cases with initial curve magnitude of 20 to 29 degrees.[33] The rate of curve progression increased to 90% when the initial curve was 30 to 59 degrees.[1]

Most idiopathic scoliosis cases do not require imaging beyond radiography. Given that the prevalence of central nervous system abnormalities in patients with presumed adolescent idiopathic scoliosis is very low, ranging from 2% to 4%, magnetic resonance imaging (MRI) is typically reserved for patients with an unusual curve pattern or clinical findings that increase the likelihood of an underlying abnormality.[40–42] There is not yet a clear consensus on when to perform MRI in idiopathic scoliosis, but indications include the following: age 10 years or younger; abnormal neurologic examination; painful scoliosis; a left thoracic curve; hyperkyphotic sagittal alignment; rapidly progressing curves; and other radiographic abnormalities (Fig. 134.3).[1,2,6,40,41,43]

***Treatment and Follow-up.*** Treatment of idiopathic scoliosis varies on a case-by-case basis and is surgeon specific. The majority of patients with idiopathic scoliosis present with curves less than 20 degrees with very minimal risk of progression even without treatment. These patients are often monitored with clinical and radiographic follow-up only.[1,6]

*Bracing:* Bracing (e-Fig. 134.4) is generally indicated when a scoliotic curve progresses from 25 to 30 degrees with a documented annual curve progression of at least 5 degrees, with the upper limit of curve magnitude being 45 degrees.[1,44] Bracing modifies spinal growth by applying an external force and is usually effective in patients with substantial spinal growth remaining (Risser 2–3 or less).[1,2,6] Bracing typically limits progression, but it usually does not stop or improve the curve.

*Risser Casting:* In some cases, a molded (Risser) cast is applied as an alternative to bracing to provide increased corrective force (e-Fig. 134.5). The primary indication is in patients who have progressive scoliosis and are too small for rigid instrumentation or in those patients who have severe deformities and are too young to undergo fusion. The idea behind casting is to avoid the repeated surgeries necessary after application of a growing rod instrumentation system.[1] Similar to bracing, Risser casting only limits curve progression.

*Surgery:* The primary goal of surgical treatment is stabilization of curve progression, with secondary goals of improvement in spinal alignment and balance of the body.[1,6] The indications for surgical correction include the degree of curvature, risk for progression, skeletal maturity, and curve pattern. Moreover, the cosmetic perception of the deformity by the patient or the patient's family may also influence the decision for surgery.[1]

Thoracic curves of greater than 40 to 50 degrees in skeletally immature patients are usually surgically corrected; in skeletally mature patients, surgical correction is reserved for curves of 50 degrees or more.[1] Surgical treatment includes corrective instrumentation plus anterior or posterior fusion of the spine, with the aim of correcting both the coronal and sagittal deformities. The surgical goal is to achieve a stable bony fusion mass to maintain the correction over time, with the hardware serving as internal struts while fusion proceeds. Harrington rods were previously used for surgical correction; however, they failed to address the hypokyphotic component occurring in most patients with idiopathic scoliosis, and often resulted in a "flat back deformity."[1] Therefore Harrington rods have been replaced by various hook-and-rod or screw-and-rod systems, which correct the coronal imbalance while maintaining sagittal balance (e-Fig. 134.6).[1,45] Instrumentation without fusion (as with growing rods) is sometimes used in young children with rapidly progressing curves. The vertical expandable prosthetic titanium rib (VEPTR) is one such system, which is more commonly used in the treatment of infantile and juvenile types of idiopathic scoliosis. Traditionally, growing rods required multiple surgeries to lengthen the rods. To eliminate the risks from repeated operations, magnetically controlled growing rods (MCGR) have been developed. These rods can be distracted in small increments in an exam room under ultrasound guidance, eliminating the need for surgery and reducing radiation exposure (Fig. 134.7).

In broad perspective, to improve surgical outcomes, the segment to be fused should be as short as possible but long enough to minimize residual disease. Usually, the stable vertebra defines the lower limit of fusion.[13] Efforts are made to avoid nonstructural curves and to spare as many mobile segments of the lower lumbar spine as possible.[6]

***Follow-up Imaging.*** No standard guidelines are available to monitor patients with idiopathic scoliosis. It is generally recommended that patients with idiopathic scoliosis be monitored every 4 to 12 months, depending on age and growth rate. Those in the rapid phase of growth are seen at more frequent intervals (every 4–6 months).[1,6] After cessation of spinal growth, only curves with

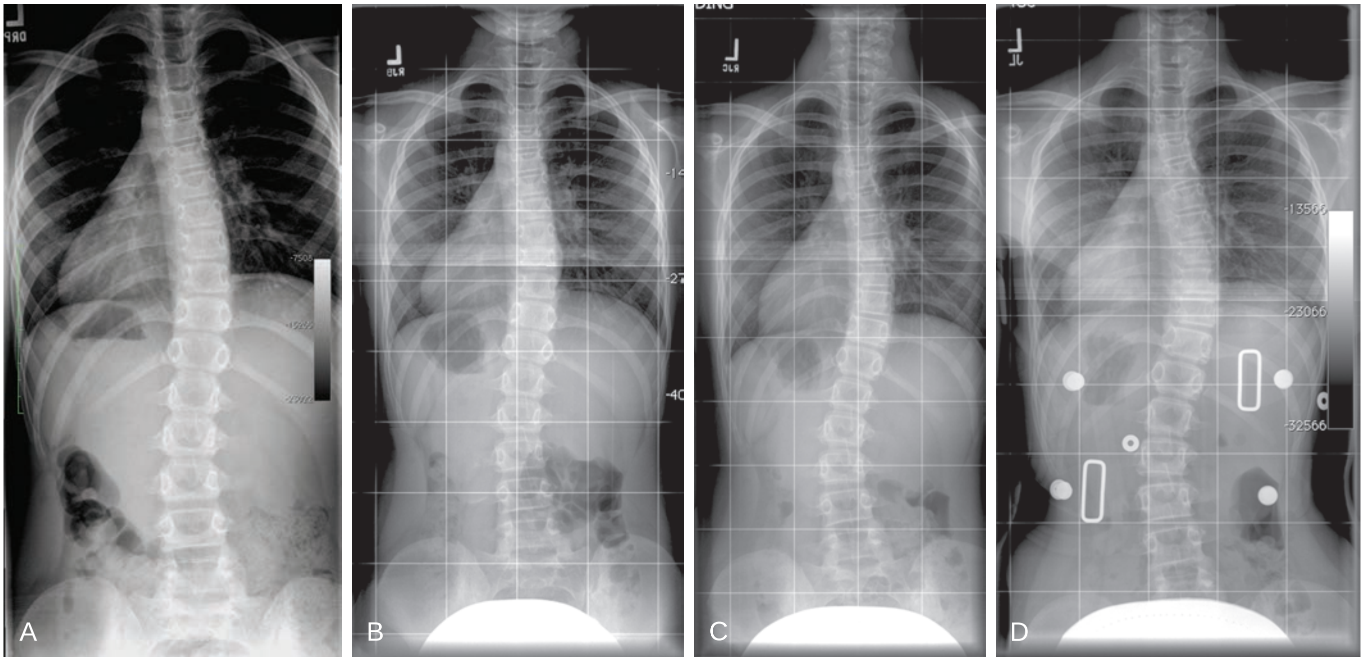

**e-Figure 134.4. Juvenile idiopathic scoliosis.** (A–C) Multiple posteroanterior standing spine radiographs (A, age 9; B, age 10; C, age 11) demonstrates progression of the right thoracic and left lumbar curve in a patient with idiopathic scoliosis (juvenile) with remaining skeletal growth. (D) A brace was finally applied, and it shows reduction of both the curves. In general, bracing is indicated in patients with remaining skeletal growth and curves between 25 degrees and 45 degrees. Usually, a definite progression of 5 degrees is used as a threshold to use a brace in patients with a curve of less than 30 degrees.

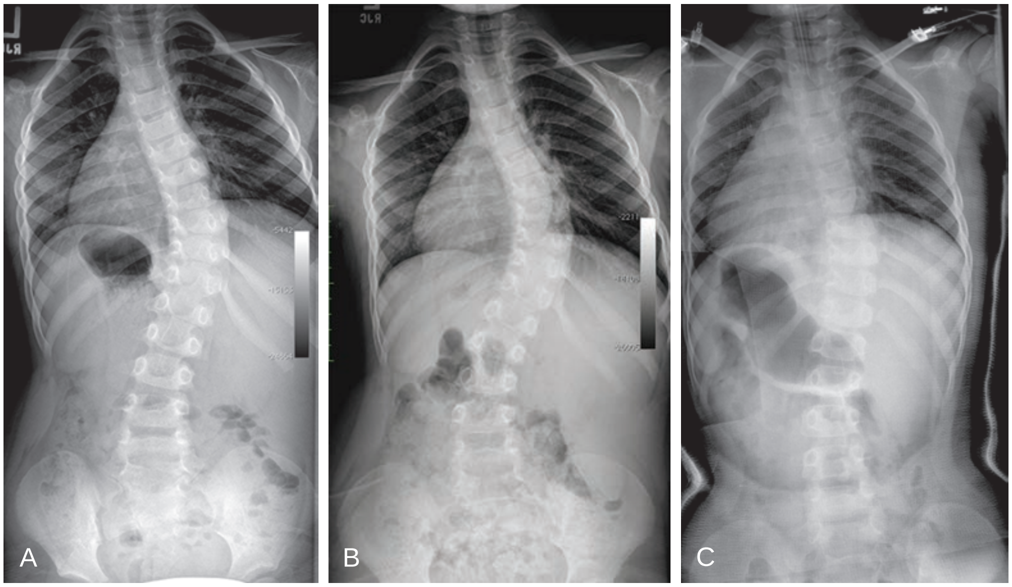

**e-Figure 134.5. Infantile scoliosis.** Posteroanterior spine radiographs at 2 years of age (A) and 4 years of age (B) demonstrate progressive infantile scoliosis. A Risser body cast was finally placed, and it shows decreased thoracic and lumbar curves (C).

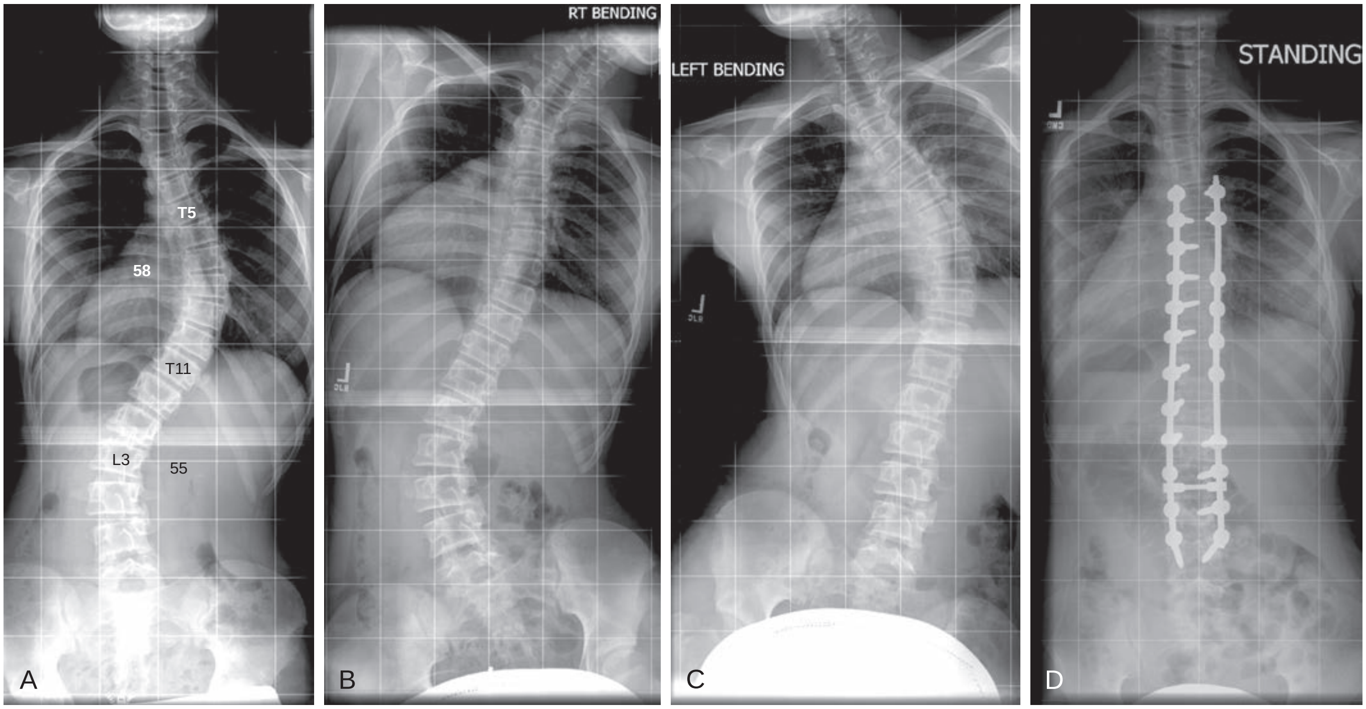

**e-Figure 134.6. Idiopathic scoliosis.** A posteroanterior radiograph (A) shows a right main thoracic curve with the largest Cobb angle of 58 degrees with its apex at the level of the T8-T9 disk and its end vertebrae at T5 and T11. Rightward-bending anteroposterior (AP) radiograph (B) shows some improvement of the main thoracic curve; however, the Cobb angle remains more than 25 degrees, a finding consistent with structural curve based on the Lenke classification. Leftward-bending AP radiograph (C) shows that the Cobb angles of the proximal thoracic and lumbar curves do not exceed 25 degrees, indicating nonstructural curves. A postoperative radiograph (D) shows posterior spinal fusion extending from T5 through L3 level.

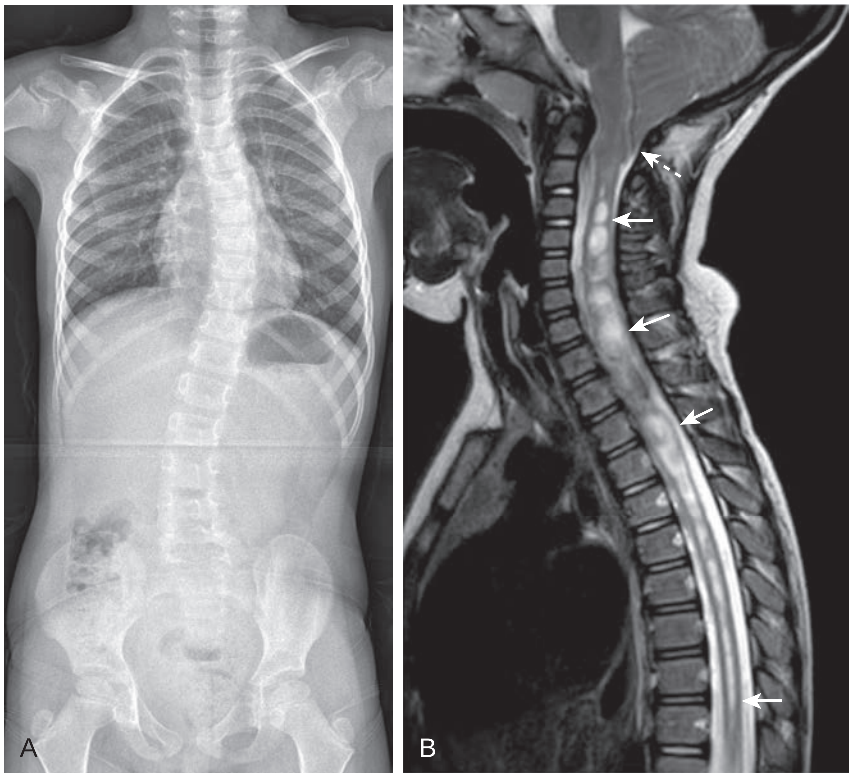

**Figure 134.3. Neuraxis abnormality in juvenile idiopathic scoliosis.** A 6-year-old girl with an atypical levocurvature of the thoracic spine. (A) Frontal radiograph shows levocurvature of the thoracic spine. Idiopathic juvenile scoliosis is typically associated with a thoracic dextrocurvature. (B) Sagittal T2-weighted MRI shows pointed and inferiorly displaced cerebellar tonsils *(dashed arrow)* and hydrosyringomelia expanding the cervical to upper thoracic spinal cord *(solid arrows)*.

Cobb angles greater than 30 degrees should be monitored for progression. Follow-up imaging usually is performed every 5 years, although the follow-up interval depends on the patient's symptoms and the severity of the curvature.[1]

Follow-up usually involves not only monitoring curve progression but also the efficacy of nonsurgical treatment such as bracing. Effective bracing should achieve about 30% correction of the Cobb angle.[46] Subsequent to fixation, patients are usually followed until the fusion has matured to exclude the development of pseudoarthrosis and to exclude recurrence of the deformity.[46]

## CONGENITAL SCOLIOSIS

Congenital scoliosis results from disordered embryologic or intrauterine spine development, presumably during somitogenesis between weeks 5 and 8 of gestation.[47] Vertebral malformations are often associated with coexistent nonspinal malformations. Multiple recognized syndromes are associated with congenital scoliosis. The two most common coexisting conditions are VACTERL (*v*ertebral anomalies, *a*norectal malformation, *c*ardiac lesion, *t*racheo*e*sophageal fistula, *r*enal anomalies, *l*imb anomalies) association and Klippel-Feil syndrome.[47] Scoliosis associated with a skeletal dysplasia is considered separate from congenital scoliosis. Although labeled as congenital, it is important to note that the clinical deformity may not be apparent at birth and usually develops with spinal growth, presenting later in childhood.[47,48]

***Etiologies, Pathophysiology, and Clinical Presentation.*** Congenital scoliosis is caused by failures of vertebral segmentation, formation, or a combination of the two. Classifications by Winter et al. and McMaster (Fig. 134.8) are helpful in describing anomalies and predicting which will be progressive.[48–51] If the failure of formation or of segmentation occurs on the right or left side of the vertebral body, scoliosis results. If the segmentation anomaly occurs along the anterior or posterior vertebral body, then congenital kyphosis or lordosis results, respectively.[47] Most cases involve both coronal and sagittal plane deformities.

The most common underlying spinal abnormality is a hemivertebra, seen in about 40% of cases, usually resulting from unilateral complete failure of formation.[47,52] Hemivertebrae may be further classified as fully segmented, semisegmented, or nonsegmented on the basis of the relationship to the cranial and caudal vertebrae. Wedged vertebrae result from a unilateral partial failure of formation with presence of two pedicles. "Butterfly vertebrae" are presumed to originate from failure of anterior midline fusion between somite pairs. Complete anterior and posterior failure of segmentation creates a block vertebra, whereas unilateral anterior and posterior failure of segmentation causes a unilateral bar.[47]

Natural history and the risk of progression in congenital scoliosis are related to multiple elements: (1) type of anomaly, (2) site, (3) age at presentation, (4) single versus multiple curves, and (5) associated nonspinal abnormalities.[53] Curve progression has been strongly related to the type of vertebral abnormality (Table 134.1), with unilateral unsegmented bars with contralateral hemivertebrae having the poorest prognosis, a less severe progression with hemivertebrae, and the least severe progression with block and wedge vertebrae (e-Fig. 134.9).

***Imaging.*** Fetal imaging, including ultrasonography and MRI, allows for early and more comprehensive detection of fetal spinal anomalies, but the significance of earlier detection and prognosis is debated.[47] The postnatal diagnosis of congenital scoliosis is usually made with radiography. Suggestive findings include absence

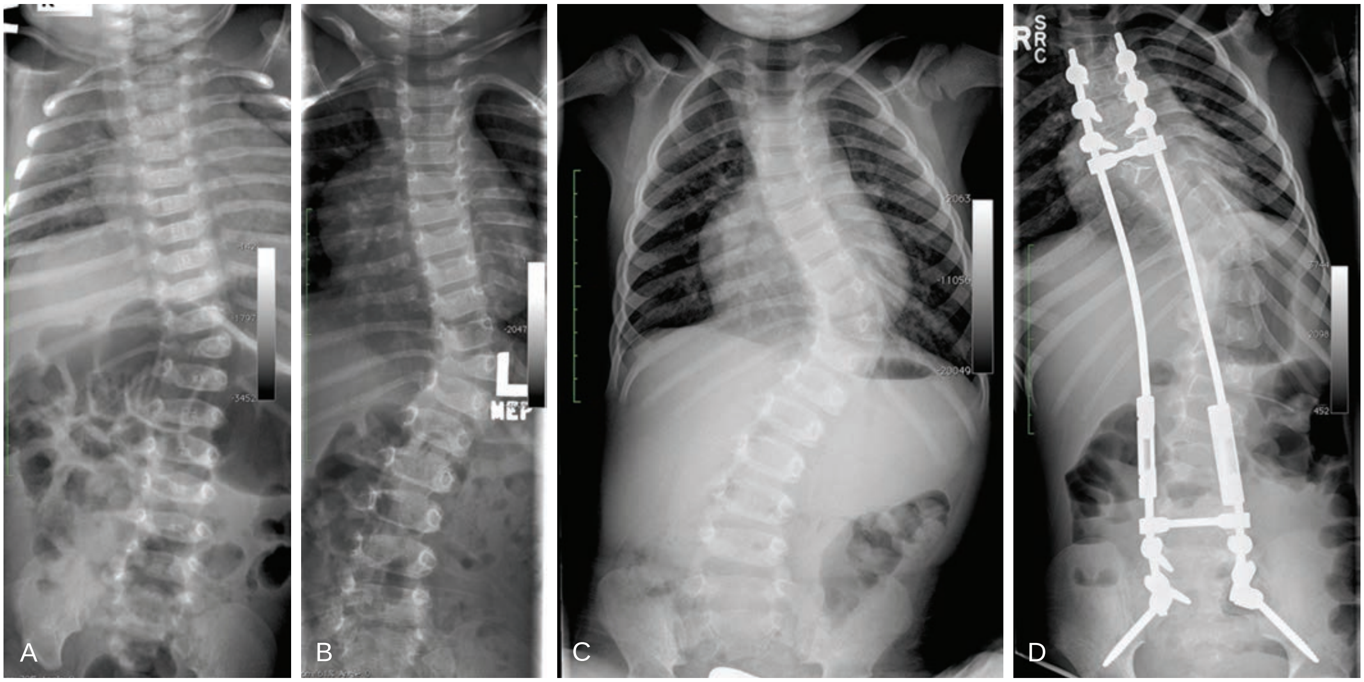

**e-Figure 134.9. Congenital scoliosis.** Rapid progression of curve in a patient with fully segmented hemivertebra from 32 months (A) to 3 years of age (B) to 4 years of age (C). A postoperative radiograph (D) shows placement of expandable posterior spinal fusion hardware, which still allows some continued growth of the abnormal spine with maintaining or controlling the deformity. Curve progression in congenital scoliosis is strongly related to the type of underlying vertebral abnormality, with a poor prognosis associated with unilateral unsegmented bars with contralateral hemivertebrae and fully segmented hemivertebrae, as in this case.

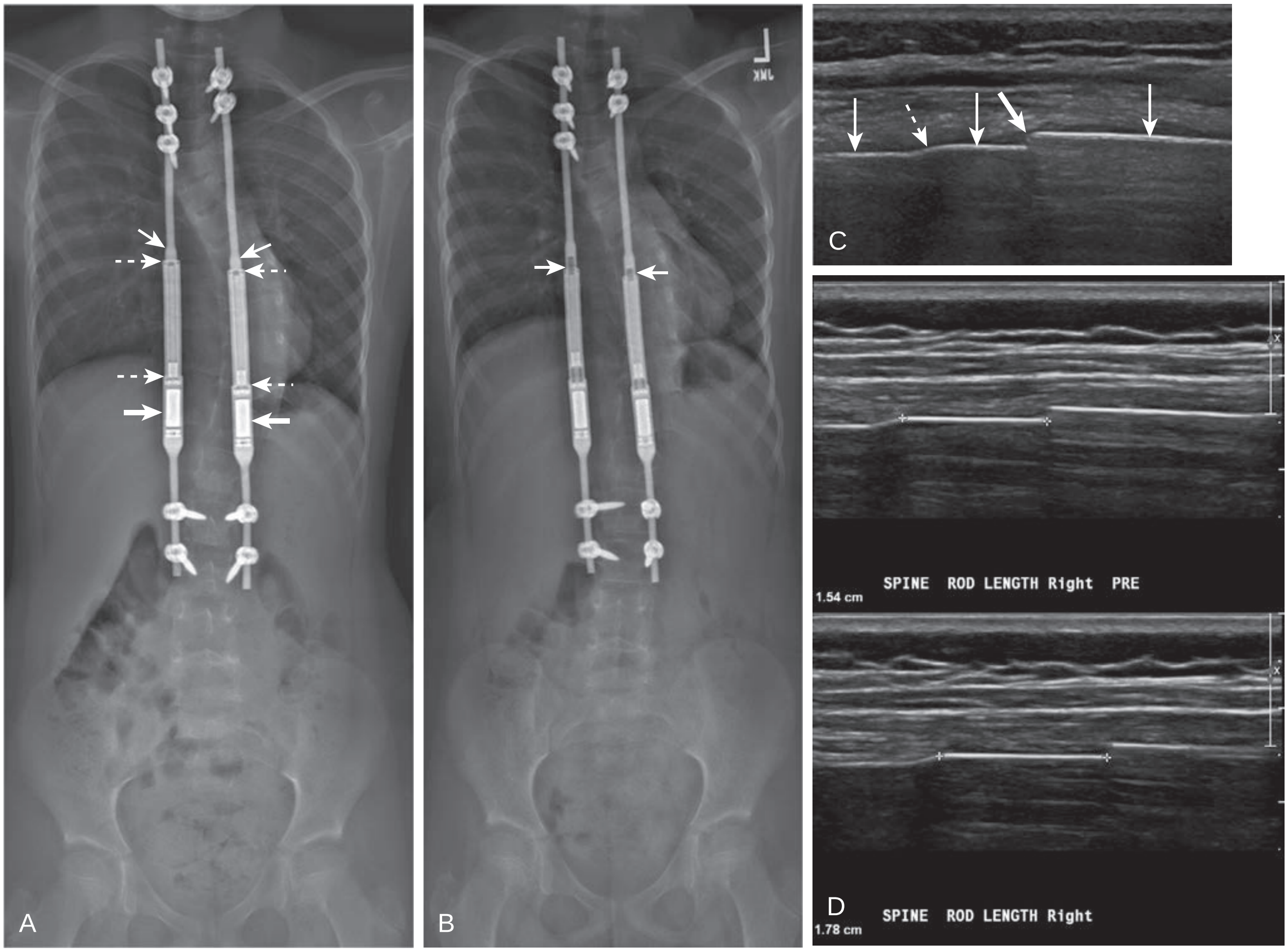

**Figure 134.7. Magnetically controlled growing rods (MCGR).** (A) Bilateral MCGR stabilizing a thoracic curve. *Thick solid arrows* show the motors of the rods. The portions of the rods between the dashed arrows are the housings that contain the expandable portions of the rods. *Thin solid arrows* point to the necks of the rods, where the rods taper. (B) Follow-up radiograph 6-months later after multiple distractions show that the portions of the rods between the necks and the housings *(arrows)* have expanded. (C) Ultrasound evaluation of MCGR rod. Linear bright echogenicity *(solid thin arrows)* along the surface of the MCGR rod is seen deep to the subcutaneous soft tissues. A small step off between the housing and the expandable portion of the rod *(thick solid arrow)* is a normal finding. The neck of the rod *(dashed arrow)* is also noted. (D) Pre- and postspinal rod lengthening ultrasounds show the procedure for measuring MCGRs before and after distraction. Note the calipers are placed at the base of the neck and at the top of the housing to measure the length of the expandable portion of the rod before and after the procedure; this rod was lengthened by 0.24 cm.

**TABLE 134.1** Median Yearly Rate of Deterioration (in Degrees) Without Treatment for Type of Single Congenital Scoliosis in Each Region of the Spine

| | | | **Hemivertebra** | | | |
|---|---|---|---|---|---|---|
| **Site of Curvature** | **Block Vertebra** | **Wedge Vertebra** | **Single** | **Double** | **Unilateral Unsegmented Bar** | **Unilateral Unsegmented Bar and Contralateral Hemivertebrae** |
| Upper thoracic | <1-1† | *-2† | 1-2‡ | 2-2.5§ | 2-4§ | 5-6§ |
| Lower thoracic | <1-1† | 2-2 | 2-2.5‡ | 2-3§ | 5-6.5§ | 5-8§ |
| Thoracolumbar | <1-1† | 1.5-2† | 2-3.5‡ | 5-*§ | 6-9§ | 7-14§ |
| Lumbar | <1-*† | <1-*† | <1-1‡ | * | >5-*§ | * |
| Lumbosacral | * | * | <1-1.5§ | * | * | * |

*, Too few or no curves; †, no treatment required; ‡, may require spinal surgery; §, requires spinal fusion. Ranges represent the degree of deterioration before and after 10 years of age.

*Modified from McMaster MJ, Ohtsuka K. The natural history of congenital scoliosis: A study of 251 patients.* J Bone Joint Surg Am. *1982;66:588–601; McMaster MJ. Congenital scoliosis caused by a unilateral failure of vertebrae segmentation with contralateral hemivertebrae.* Spine. *1998;23:998–1005; McMaster MJ. Congenital scoliosis. In: Weinstein SL, ed.* The pediatric spine. *Philadelphia, PA: Lippincott Williams & Wilkins; 2001: 161–177.*

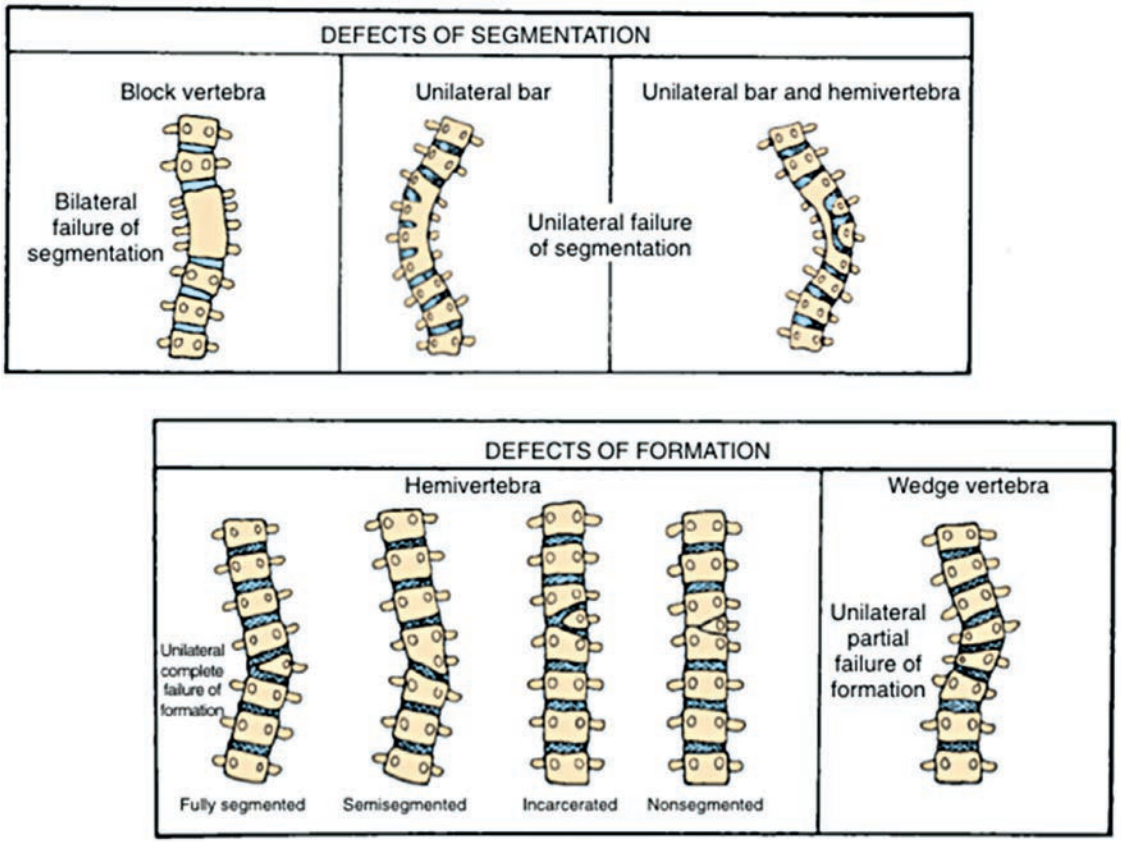
DEFECTS OF SEGMENTATION
Block vertebra
Bilateral failure of segmentation
Unilateral bar
Unilateral failure of segmentation
Unilateral bar and hemivertebra
DEFECTS OF FORMATION
Hemivertebra
Unilateral complete failure of formation
Fully segmented
Semisegmented
Incarcerated
Nonsegmented
Wedge vertebra
Unilateral partial failure of formation

**Figure 134.8. Forms of congenital scoliosis.** Various types of congenital scoliosis based on defects of segmentation versus defects of formation. *(From McMaster MJ. Congenital scoliosis. In: Weinstein SL, ed.* The pediatric spine. *Philadelphia: Lippincott Williams & Wilkins; 2001:161–177.)*

of spinous processes, rib fusions, joined pedicles, or absent or narrowed disk spaces.[47] In the majority of cases, identification of the type of anomaly is possible with radiography. Absolute Cobb angle magnitude is of much less significance than the overall deformity and the change in that deformity over time with growth. Documentation of radiographic change with growth is the mainstay of observation and surgical decision making.[47]

Radiography is very useful if both anterior and posterior structures of anomalous vertebrae correspond to each other. However, it is not uncommon to have differences between the anterior and posterior structures often leading to a complex unclassified pattern of abnormality.[47,52] These characteristics make independent evaluation of the malformation in each vertebra extremely difficult with radiography, which may require three-dimensional computed tomography (CT) in the evaluation of complex malformations, particularly the posterior elements. Radiography has difficulty in accurately identifying the deformities that will be progressive, which has called for a newer three-dimensional classification of congenital scoliosis.[52] CT is currently used as a preoperative evaluation tool to evaluate osseous anomalies not clearly depicted on radiography. Preoperative CT angiography may also be useful for determining coexistent vascular anomalies and to assess the relationship of the aorta and important branches to the spine.

Imaging in congenital scoliosis demands not only detailed evaluation of the spine but also exclusion of extraspinal anomalies, mainly cardiovascular and genitourinary anomalies.[47] Associated intraspinal or neural axis abnormalities with congenital scoliosis may occur in 20% to 37% of patients, mandating screening.[47,54,55] The most common associated abnormalities include syrinx, Chiari I malformation, cord or spinal canal tumors, diastematomyelia, and low conus medullaris.[47] Spinal ultrasonography may be effective for initial screening. The role of MRI as a screening tool in all congenital scoliosis cases is controversial, with some experts believing that MRI should be restricted to presurgical evaluation. If not addressed preoperatively, major associated intraspinal abnormalities, including cord tethering, may lead to progressive deformity and progressive or acute neurologic loss (Fig. 134.10).[47,55]

***Treatment.*** Surgery is the mainstay in the treatment of congenital scoliosis, as nonoperative measures provide no definite efficacy. If an underlying spinal cord abnormality is found, it should be corrected before scoliosis surgery. The various surgical options are complex and beyond the scope of this discussion; however, the traditional approach still includes early fusion to avoid the development of more severe deformities.[47] In some patients, such as those with shortened spines or chest wall anomalies, expansion thoracoplasty with the use of the VEPTR device (e-Fig. 134.11) is performed instead of early fusion.[56] The VEPTR technique allows some continued growth of the abnormal spinal elements while still controlling the deformity. A major disadvantage of this treatment is the need for repetitive lengthening procedures, but it may be an appropriate temporary choice in certain children.[47]

## NEUROMUSCULAR SCOLIOSIS

Neuromuscular scoliosis is caused by a defect in the neural pathways through which the central nervous system controls and coordinates muscle activity.

***Etiologies, Pathophysiology, and Clinical Presentation.*** The Scoliosis Research Society further classifies neuromuscular scoliosis

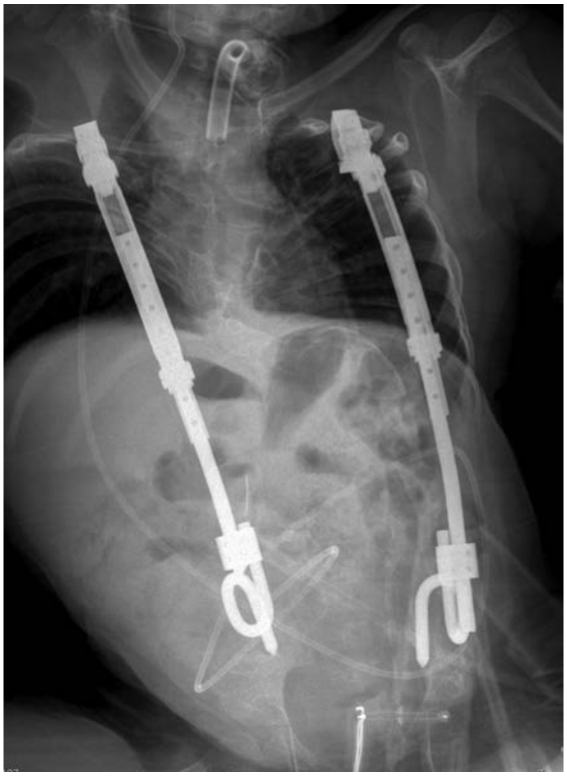

**e-Figure 134.11. Severe thoracolumbar scoliosis due to multiple thoracolumbar segmental fusion anomalies in a 7-year-old girl.** A vertical expandable prosthetic titanium rib (VEPTR), extending from the upper ribs and anchored along the iliac crests, was placed.

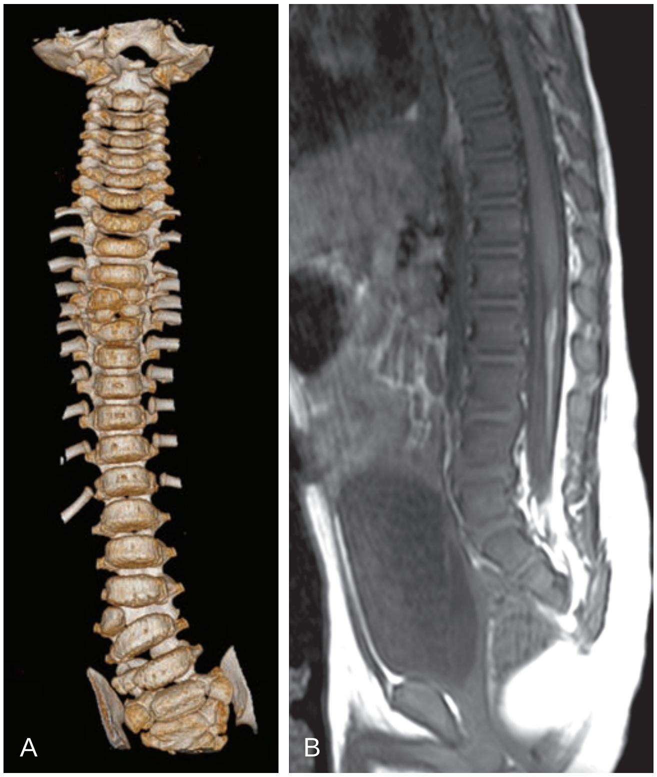

**Figure 134.10. Neural axis abnormality in congenial scoliosis.** A coronal three-dimensional, surface-shaded reformatted image of the spine (A) clearly demonstrates a lumbar hemivertebra with butterfly vertebrae involving the midthoracic spine. A sagittal T1 MRI of the lumbar spine (B) in the same patient shows a low-lying cord with an associated filum lipoma. Intraspinal abnormalities in congenital scoliosis are not uncommon, and magnetic resonance imaging of the neural axis is a routine prerequisite before any treatment is contemplated.

into neuropathic and myopathic scoliosis.[10] The first group includes neurologic disorders such as cerebral palsy or spinomuscular dystrophies, and the second group includes muscular disorders such as the muscular dystrophies.

***Imaging.*** The characteristic curve pattern in neuromuscular scoliosis is an early onset long C-shaped curve (e-Fig. 134.12) with rapid progression, which continues beyond skeletal maturity. Curve patterns similar to adolescent idiopathic scoliosis may also be seen. Affected children also often present with severe kyphosis or lordosis in the sagittal plane, with multiple additional comorbidities related to their primary disease.[10] Because of nonweight-bearing status, the vertebral bodies are often tall and slender. Additional findings include diminished lumbar lordosis with a single, broad-based thoracic kyphosis.

***Treatment.*** Bracing is usually reserved for nonsevere flexible curves, immature children, and ambulatory patients, and usually does not prevent curve progression.[57] Surgical fusion is the mainstay of treatment. The objectives of curve correction in neuromuscular scoliosis are to restore seating balance, to facilitate wheelchair use, to control pain, and to support the trunk so as to reinforce respiratory function.[10] Postoperative complications occur more frequently in patients with neuromuscular scoliosis than in those with idiopathic scoliosis, ranging from 44% to 62%, likely related to the presence of multiple comorbidities.[58]

## SCOLIOSIS AND RADIATION

The radiographic examination of children with scoliosis has historically involved a relatively high radiation dose, particularly to the breast, and may increase the risk of subsequent breast cancer.[59–62] The issues are twofold: (1) Initially, scoliosis radiographs were done in the anteroposterior projection, exposing the adolescent breast to maximum dose; and (2) many patients with scoliosis are adolescent girls with pubertal growth spurt and rapid breast development. Radiography for scoliosis must entail optimization to minimize radiation risk. This includes the use of posteroanterior positioning, high tube voltage, high-speed screen film combinations, contoured filtration, shielding of breasts (if anteroposterior positioning is used), and replacement of antiscatter grids with air gap techniques. The radiation dose may be further reduced by using CT and digital imaging systems.[63,64] As mentioned earlier, utilization of newer biplanar digital slot-scanning devices can dramatically reduce dose, however, the cost of these devices has limited their availability.[26] Finally, early studies have shown that ultrasound can be used to monitor lengthening of MCGRs to limit radiation (see Fig. 134.7).[65,66]

### KEY POINTS

- Curve measurement is usually performed by using the Cobb method. Wide interobserver and intraobserver variations exist with this technique, but measurements are reproducible if the levels measured and patient positioning are kept constant.
- CT imaging with three-dimensional reconstructions is mainly utilized for visualization of and preoperative planning for complex scoliotic deformities and preoperative planning.
- MRI is often utilized in the setting of congenital, infantile, and juvenile idiopathic scoliosis because of higher incidence of associated neural axis abnormality. It is also used in the setting of painful scoliosis, atypical curves, or scoliosis associated with specific neurologic or clinical abnormalities.
- Surgical treatment is usually resorted to in curves greater than 45 degrees in patients with remaining spinal growth.
- Sagittal balance is an important concept in normal spinal stability. All efforts are made to maintain normal thoracic kyphosis and lumbosacral lordosis while treating patients with scoliosis.

## SUGGESTED READINGS

Cassar-Pullicino VN, Eisenstein SM. Imaging in scoliosis: what, why and how? *Clin Radiol*. 2002;57(7):543–562.
Goethem JV, Campenhout AV, Hauwe LVD, et al. Scoliosis. *Neuroimag Clin North Am*. 2007;17:105–115.
Kim H, Kim HS, Moon ES, et al. Scoliosis imaging: what radiologists should know. *Radiographics*. 2010;30:1823–1842.
Lenke LG, Betz RR, Harms J, et al. Adolescent idiopathic scoliosis: a new classification to determine extent of spinal arthrodesis. *J Bone Joint Surg Am*. 2001;83-A(8):1169–1181.
Lenke LG, Edwards IICC, Bridwell KH. The Lenke classification of adolescent idiopathic scoliosis: how it organizes curve patterns as a template to perform selective fusions of the spine. *Spine*. 2003;28(20):S199–S207.

## REFERENCES

Full references for this chapter can be found on www.expertconsult.com.

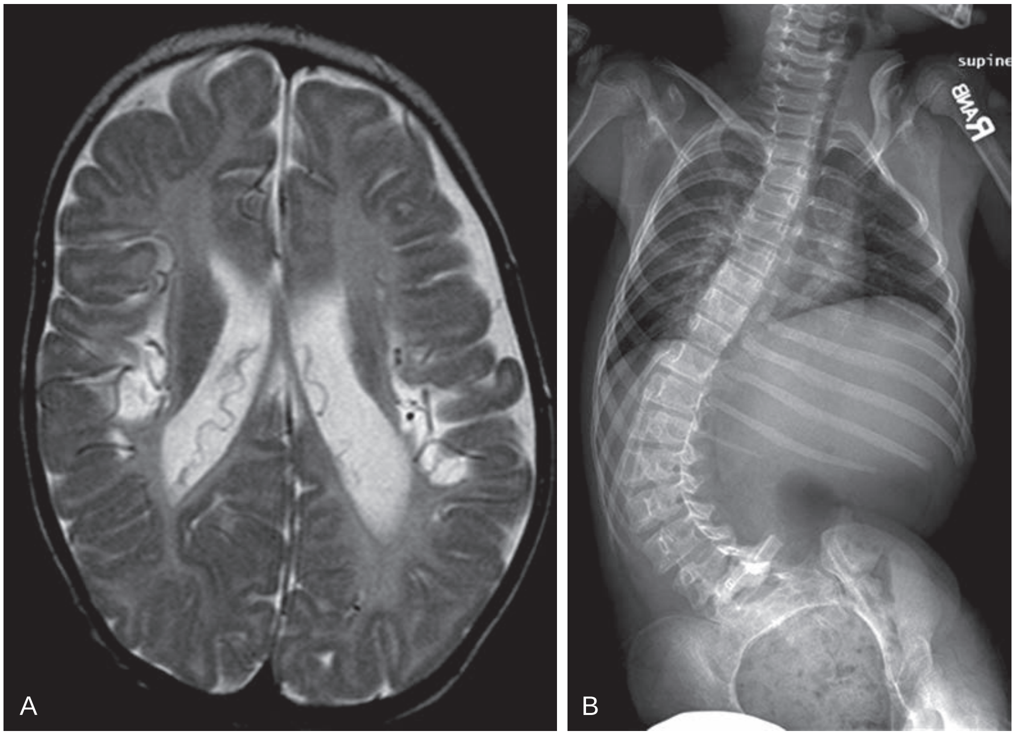

**e-Figure 134.12. Neuromuscular scoliosis.** Axial T2-weighted MRI (A) in a patient with neuromuscular scoliosis shows cystic encephalomalacia and volume loss involving the perirolandic regions bilaterally. A supine radiograph of the spine (B) shows a long C-shaped curve with convexity to the left side and significant pelvic obliquity, a curve pattern often seen in patients with neuromuscular scoliosis.

## REFERENCES

1. Newton P, Wenger D. Idiopathic scoliosis. In: Morrissy R, Weinstein S, eds. *Pediatric orthopaedics*. Philadelphia, PA: Lippincott Williams & Wilkins; 2006:693–762.
2. Cassar-Pullicino VN, Eisenstein SM. Imaging in scoliosis: what, why and how? *Clin Radiol*. 2002;57(7):543–562.
3. Stokes IA. Mechanical effects on skeletal growth. *J Musculoskelet Neuronal Interact*. 2002;2(3):277–280.
4. Parent S, Labelle H, Skalli W, et al. Thoracic pedicle morphometry in vertebrae from scoliotic spines. *Spine*. 2004;29(3):239–248.
5. Potter BK, Rosner MK, Lehman RA Jr, et al. Reliability of end, neutral, and stable vertebrae identification in adolescent idiopathic scoliosis. *Spine*. 2005;30(14):239–248.
6. Kim H, Kim HS, Moon ES, et al. Scoliosis imaging: what radiologists should know. *Radiographics*. 2010;30:1823–1842.
7. King HA, Moe JH, Bradford DS, et al. The selection of fusion levels in thoracic idiopathic scoliosis. *J Bone Joint Surg Am*. 1983;65(9):1302–1313.
8. Malfair D, Flemming AK, Dvorak MF, et al. Radiographic evaluation of scoliosis: review. *AJR Am J Roentgenol*. 2010;194(3 suppl):S8–S22.
9. Bernhardt M. Normal spinal anatomy: normal sagittal plane alignment. In: Bridwell KH, Dewald RL, eds. *The textbook of spinal surgery*. Vol. 1. 2nd ed. Philadelphia, PA: Lippincott-Raven; 1997:185–191.
10. Campos MA, Weinstein SL. Pediatric scoliosis and kyphosis. *Neurosurg Clin N Am*. 2007;18:515–529.
11. Bernhardt M, Bridwell KH. Segmental analysis of the sagittal plane alignment of the normal thoracic and lumbar spines and thoracolumbar junction. *Spine*. 1989;14:717–721.
12. PROPST-Proctor SL, Bleck EE. Radiographic determination of lordosis and kyphosis in normal and scoliotic children. *J Pediatr Orthop*. 1983;3:344–346.
13. Goethem JV, Campenhout AV, Hauwe LVD, et al. Scoliosis. *Neuroimag Clin North Am*. 2007;17:105–115.
14. Been E, Kalichman L. Lumbar lordosis. *Spine J*. 2014;14(1):87–97. doi:10.1016/j.spinee.2013.07.464. [Epub 2013 Oct 2].
15. Glassman SD, Bridwell K, Dimar JR. The impact of positive sagittal balance in adult spinal deformity. *Spine*. 2005;30(18):2024–2029.
16. Malfair D, Flemming AK, Dvorak MF, et al. Radiographic evaluation of scoliosis: review. *AJR Am J Roentgenol*. 2010;194(3 suppl): S8–S22.
17. Lenke LG, Betz RR, Harms J, et al. Adolescent idiopathic scoliosis: a new classification to determine extent of spinal arthrodesis. *J Bone Joint Surg Am*. 2001;83-A(8):1169–1181.
18. Lenke LG, Edwards IICC, Bridwell KH. The Lenke classification of adolescent idiopathic scoliosis: how it organizes curve patterns as a template to perform selective fusions of the spine. *Spine*. 2003; 28(20):S199–S207.
19. Dickson RA. Scoliosis in the community. *Br Med J (Clin Res Ed)*. 1983;286:1745.
20. Miller NH. Cause and natural history of adolescent idiopathic scoliosis. *Orthop Clin North Am*. 1999;30:343–352.
21. Bunnell WP. The natural history of idiopathic scoliosis. *Clin Orthop*. 1988;229:20–25.
22. Dickson RA, Lawton JO, Archer IA, et al. The pathogenesis of idiopathic scoliosis: biplanar spinal asymmetry. *J Bone Joint Surg*. 1984;66B:8.
23. Weinstein SL, Zavala DC, Ponseti IV. Idiopathic scoliosis: long-term follow-up and prognosis in untreated patients. *J Bone Joint Surg Am*. 1981;63(5):702–712.
24. Kotwicki T. Evaluation of scoliosis today: examination, X-rays and beyond. *Disabil Rehabil*. 2008;30(10):742–751.
25. O'Brien MF, Kuklo TR, Blanke KM. *Spinal deformity: radiographic measurement manual*. Memphis, TN: Medtronic Sofamor Danek; 2004.
26. Blumer SL, Dinan D, Grissom LE. Benefits and unexpected artifacts of biplanar digital slot-scanning imaging in children. *Pediatr Radiol*. 2014;44(7):871–882.
27. Pruijs JE, Hageman MA, Keessen W, et al. Variation in Cobb angle measurements in scoliosis. *Skeletal Radiol*. 1994;23(7):517–520.
28. Beauchamp M, Labelle H, Grimard G, et al. Diurnal variation of Cobb angle measurement in adolescent idiopathic scoliosis. *Spine*. 1993;18(12):1581–1583.
29. Carman DL, Browne RH, Birch JG. Measurement of scoliosis and kyphosis radiographs. Intraobserver and interobserver variation. *J Bone Joint Surg Am*. 1990;72:328–333.
30. Morrissy RT, Goldsmith GS, Hall EC, et al. Measurement of the Cobb angle on radiographs of patients who have scoliosis. Evaluation of intrinsic error. *J Bone Joint Surg Am*. 1990;72:320–327.
31. Loder RT, Urquhart A, Steen H, et al. Variability in Cobb angle measurements in children with congenital scoliosis. *J Bone Joint Surg Br*. 1995;77:768–770.
32. Ganey TM, Ogden JA. Development and maturation of the axial skeleton. In: Weinstein SL, ed. *The pediatric spine: principles and practice*. 2nd ed. New York: Lippincott Williams & Wilkins; 2001:3–54.
33. Lonstein JE, Carlson JM. The prediction of curve progression in untreated idiopathic scoliosis during growth. *J Bone Joint Surg Am*. 1984;66(7):1061–1071.
34. Dimeglio A. Growth in pediatric orthopaedics. *J Pediatr Orthop*. 2001;21(4):549–555.
35. Little DG, Song KM, Katz D, et al. Relationship of peak height velocity to other maturity indicators in idiopathic scoliosis in girls. *J Bone Joint Surg Am*. 2000;82(5):685–693.
36. Lonstein JE. Scoliosis: surgical versus nonsurgical treatment. *Clin Orthop Relat Res*. 2006;443:248–259.
37. McCarthy RE. Evaluation of the patient with deformity. In: Weinstein SL, ed. *The pediatric spine: principles and practice*. 2nd ed. New York: Lippincott Williams & Wilkins; 2001:133–157.
38. Song KM, Little DG. Peak height velocity as a maturity indicator for males with idiopathic scoliosis. *J Pediatr Orthop*. 2000;20(3):286–288.
39. Greulich W, Pyle S. *Radiographic atlas of skeletal development of the hand and wrist*. 2nd ed. Stanford, CA: Stanford University Press; 1959.
40. Do T, Fras C, Burke S, et al. Clinical value of routine preoperative magnetic resonance imaging in adolescent idiopathic scoliosis: a prospective study of three hundred and twenty seven patients. *J Bone Joint Surg Am*. 2001;83-A(4):577–579.
41. Davids JR, Chamberlin E, Blackhurst DW. Indications for magnetic resonance imaging in presumed adolescent idiopathic scoliosis. *J Bone Joint Surg Am*. 2004;86-A(10):2187–2195.
42. Jaramillo D, Poussaint TY, Grottkau BE. Scoliosis: evidence-based diagnostic evaluation. *Neuroimag Clin North Am*. 2003;13:335–341.
43. Cheng JC, Guo X, Sher AH, et al. Correlation between curve severity, somatosensory evoked potentials, and magnetic resonance imaging in adolescent idiopathic scoliosis. *Spine*. 1999;24:1679–1684.
44. Nachemson AL, Peterson LE. Effectiveness of treatment with a brace in girls who have adolescent idiopathic scoliosis. A prospective, controlled study based on data from the Brace Study of the Scoliosis Research Society. *J Bone Joint Surg Am*. 1995;77:815–822.
45. Cotrel Y, Dubousset J, Guillaumat M. New universal instrumentation in spinal surgery. *Clin Orthop*. 1988;227:10–23.
46. Thomsen M, Rainer A. Imaging in scoliosis from the orthopedic surgeon's point of view. *Eur J Radiol*. 2008;58:41–47.
47. Emans JB. Congenital scoliosis. In: Morrissy R, Weinstein S, eds. *Pediatric orthopaedics*. Philadelphia, PA: Lippincott Williams & Wilkins; 2006:764–795.
48. McMaster MJ. Spinal growth and congenital deformity of the spine. *Spine*. 2006;31:2284–2287.
49. Winter RB. *Congenital deformities of the spine*. New York: Thieme-Stratton; 1983.
50. Winter RB, Moe JH, Wang JF. Congenital kyphosis—its natural history and treatment as observed in a study of one hundred thirty patients. *J Bone Joint Surg Am*. 1973;55:223–256.
51. Kawakami N, Tsuji T, Imagama S, et al. Classification of congenital scoliosis and kyphosis: a new approach to the three-dimensional classification for progressive vertebral anomalies requiring operative treatment. *Spine*. 2009;34:1756–1765.
52. Shahcheraghi GH, Hobbi MH. Patterns and progression in congenital scoliosis. *J Pediatr Orthop*. 1999;19:766–775.
53. Marks DS, Qaimkhani SA. The natural history of congenital scoliosis and kyphosis. *Spine*. 2009;34:1751–1755.
54. Basu PS, Elsebaie H, Noordeen MH. Congenital spinal deformity: a comprehensive assessment at presentation. *Spine*. 2002;27(20):2255–2259.
55. Prahinski JR, Polly DW Jr, McHale KA, et al. Occult intraspinal anomalies in congenital scoliosis. *J Pediatr Orthop*. 2000;20(1):59–63.
56. Campbell RM Jr, Smith MD, Hell-Vocke AK. Expansion thoracoplasty: the surgical technique of opening-wedge thoracostomy. Surgical technique. *J Bone Joint Surg Am*. 2004;86-A(suppl 1):51–64.
57. Miller A, Temple T, Miller F. Impact of orthoses on the rate of scoliosis progression in children with cerebral palsy. *J Pediatr Orthop*. 1996;16(3):332–335.
58. Murphy NA, Firth S, Jorgensen T, et al. Spinal surgery in children with idiopathic and neuromuscular scoliosis. What's the difference? *J Pediatr Orthop*. 2006;26(2):216–220.

59. Ron E. Ionizing radiation and cancer risks: evidence from epidemiology. *Pediatr Radiol*. 2002;32:232–237.
60. Doody MM, Lonstein JE, Stovall M, et al. Breast cancer mortality after diagnostic radiography: findings from the U.S. Scoliosis Cohort Study. *Spine*. 2000;25:2052–2063.
61. Ronckers CM, Doody MM, Lonstein JE, et al. Multiple diagnostic x-rays for spine deformities and risk of breast cancer. *Cancer Epidemiol Biomarkers Prev*. 2008;17:605–613. doi:10.1158/1055-9965.EPI-07-2628.
62. Ronckers CM, Land CE, Miller JS, et al. Cancer mortality among women frequently exposed to radiographic examinations for spinal disorders. *Radiat Res*. 2010;174:83–90. doi:10.1667/RR2022.1.
63. Geijer H, Verdonck B, Beckman KW, et al. Digital radiography of scoliosis with a scanning method: radiation dose optimization. *Eur Radiol*. 2003;13:543–551.
64. Kluba T, Schafer J, Hahnfeldt T, et al. Prospective randomized comparison of radiation exposure from full spine radiographs obtained in three different techniques. *Eur Spine J*. 2006;15(6):752–756.
65. Yoon WW, Chang AC, Tyler P, et al. The use of ultrasound in comparison to radiography in magnetically controlled growth rod lengthening measurement: a prospective study. *Eur Spine J*. 2015;24:1422–1426. doi:10.1007/s00586-014-3589-z.
66. Stokes OM, O'Donovan EJ, Samartzis D, et al. Reducing radiation exposure in early-onset scoliosis surgery patients: novel use of ultrasonography to measure lengthening in magnetically-controlled growing rods. *Spine J*. 2014;14:2397–2404. doi:10.1016/j.spinee.2014.01.039. doi: 10.1667/RR2022.1.

# 135 Developmental Dysplasia of the Hip

Sabah Servaes

## ETIOLOGY

Developmental dysplasia of the hip (DDH), formerly referred to as *congenital dislocation of the hip*, was first described thousands of years ago. DDH is a spectrum that may vary from a normal congruent hip with normal appearing acetabula with ligamentous laxity, to a structurally abnormal hip with joint incongruity related to primary acetabular dysplasia. Usually, DDH is a result of a combination of both structural and ligamentous laxity leading to an abnormal incongruent hip. Ultimately, the precise underlying etiology of DDH is not known. Purported in utero developmental factors and fetal crowding may result in DDH. Hippocrates is credited with ascribing intrauterine pressure as a possible etiology.[1] During week 7 of gestation, hip joint cleavage occurs.[2] The lower extremity rotates medially during week 12 of gestation and hip muscles develop during week 18. However, it has been suggested that only 2% of cases result from intrauterine factors at this early phase of development and that the remaining 98% of cases are caused by changes to a normal hip during the last 4 weeks of pregnancy or in the immediate postnatal period.[2] Hypothesized postnatal factors include tight swaddling or the use of cradle boards that force the legs into extension and adduction.

Structural causes leading to DDH are related to a primary acetabular dysplasia with secondary changes that may affect the femoral head leading to joint incongruity. Ligamentous laxity is often related to exposure to maternal hormones, particularly in female infants, leading to capsular, ligamentum teres, and transverse ligament laxity and subsequent hip joint incongruity. Proper development of the acetabulum and femoral head requires close approximation of the articular surfaces. Therefore untreated DDH with hip joint incongruity may result in further progression of acetabular dysplasia and secondary femoral head dysplasia, with DDH changes becoming more severe over time.

## EPIDEMIOLOGY

Being the first-born, a breech birth, large for gestational age, and female or having oligohydramnios, skull-molding deformities, and a positive family history is associated with DDH. DDH is more common on the left.[2] The underlying theory of many of these factors relates to constricted in utero space. The uterus of a primiparous woman has less give. The hips are subjected to increased pressure and hyperflexion in breech presentations. With frank breech presentations, the risk is even greater. Decreased amniotic fluid or a large gestation also results in increased constriction. The most common fetal presentation is cephalic, with the fetal spine aligned to the mother's left. This causes the left hip to be wedged against the maternal spine, which limits abduction and leads to a higher incidence of DDH on the left. Females are thought to be more affected because they are more sensitive to the circulating maternal hormone relaxin, resulting in ligamentous laxity.[2]

DDH is associated with myelodysplasia, arthrogryposis, multiple syndromes (e.g., Moebius and Poland syndromes), and chromosomal abnormalities. Other associations include talipes equinovarus or clubfoot, torticollis (fibromatosis colli, with a reported incidence of 5.5%), and congenital knee dislocation.[3,4]

The prevalence of DDH is reported in up to 28.5 per 1000, depending on the population studied.[5] Variation in rates may result from expertise of the examiners and inclusion of children with isolated ligamentous laxity. The incidence of DDH increases with family history: 6% chance with an affected sibling, 12% chance with one affected parent, and 36% chance with both parents affected.[2] During the first 2 weeks of life, physiologic instability exists but resolves with increasing muscle tone and resolving ligamentous laxity as maternal hormones decrease.

## NATURAL HISTORY

If undiagnosed or left untreated, DDH may result in permanent acetabular dysplasia in children of walking age, typically having a shallow acetabular roof with undercoverage of the lateral and/or anterior femoral head. Similarly, the femoral head may become secondarily dysplastic and lose its normal sphericity related to eccentric loads because of an incongruent hip, with resultant spherical growth plate disturbance and remodeling changes.[6] The femoral head must be seated within the acetabulum for normal development to occur. If the femoral head is dislocated, the transverse acetabular ligament and inferior capsular fibers may become interpositioned within the joint, further inhibiting hip congruity. Proliferation of fibrofatty tissue within the joint, termed *pulvinar*, and/or hypertrophy of the ligamentum teres, due to abnormal traction, may interpose between the femoral head and acetabulum, interfering with hip congruity. Compensatory fibrocartilaginous hypertrophy of the labrum, referred to as a *limbus*, can occur and may hinder attempts to reduce a dysplastic hip.[2] Long-term sequelae include incomplete coverage of the femoral head, excessive femoral anteversion, coxa valga, and coxa magna with muscle tightness (with the greatest impact on the adductors) (Fig. 135.1).[7] As a result of these morphologic features, individuals with untreated DDH may develop premature degenerative changes of the hip joint and a permanent limp. Excessive femoral anteversion will lead to in-toeing. Hip degenerative changes are caused by loss of cartilage and labral tears secondary to abnormal eccentric joint contact pressure from chronic incongruent acetabular and femoral head articulation.[8] Degenerative changes caused by hip subluxation typically appear before women reach the age of 40 years and before men reach the age of 55 years; however, symptoms may become apparent during adolescence.[2] Even with completely dislocated hips, many patients may function well even into late adolescence with development of a neoacetabulum that forms along the iliac wing.[2]

## PHYSICAL EXAMINATION

The most commonly used diagnostic physical examination techniques consist of maneuvers described by Ortolani, a pediatrician, and by Barlow, an orthopedic surgeon. In 1937 Ortolani highlighted the importance of clinical testing for the assessment of hip instability.[5] In 1961 Barlow described his technique to demonstrate laxity of the infant hip.[5]

In the Ortolani maneuver, forward pressure is applied to each femoral head with the infant in the supine position and the hips flexed to abduct the hip and to reduce a subluxated or dislocated femoral head. If subluxation or dislocation exists, a "clunk" may occur, which is more often felt than heard, as the femoral head is reduced into the acetabulum. In the Barlow maneuver, the infant is placed in a supine position and the hips are flexed at 90 degrees

## Abstract:

Developmental dysplasia of the hip (DDH) is a spectrum of abnormalities, that may vary from a normal congruent hip with normal appearing acetabula with ligamentous laxity, to a structurally abnormal hip with joint incongruity related to primary acetabular dysplasia. This chapter reviews the etiology, epidemiology, and natural history of DDH. Then primarily focuses on the multimodality diagnostic imaging of DDH and its implications for treatment.

## Keywords:

Developmental dysplasia of the hip
Acetabular dysplasia
MRI
ultrasound
screening

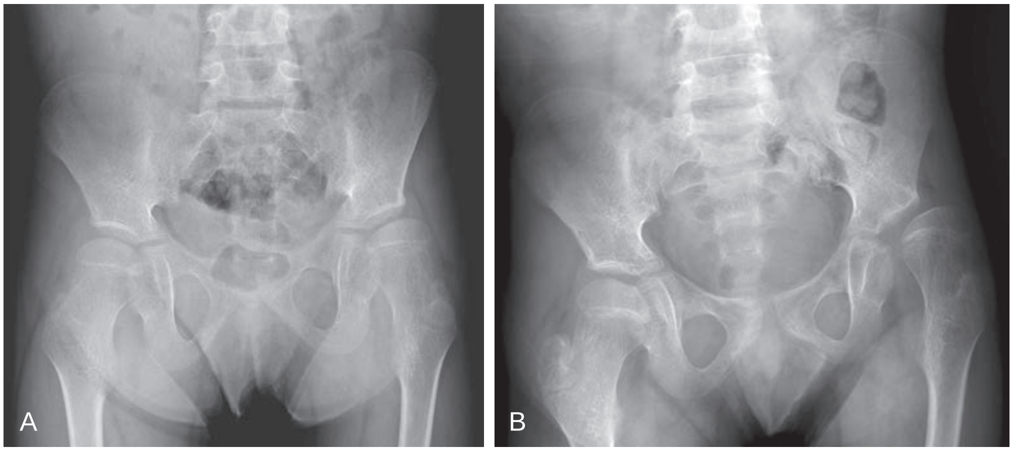

**Figure 135.1. Late presentation and progression of developmental dysplasia of the left hip in an 11-year-old boy.** (A) Frontal radiography at presentation shows a dysplastic left hip with a shallow acetabulum and mild undercoverage of the femoral head. Also the left femoral head is aspherically shaped. (B) Three years later, there is progressive lateral uncovering of the left femoral head, which also shows progressive secondary dysplastic changes.

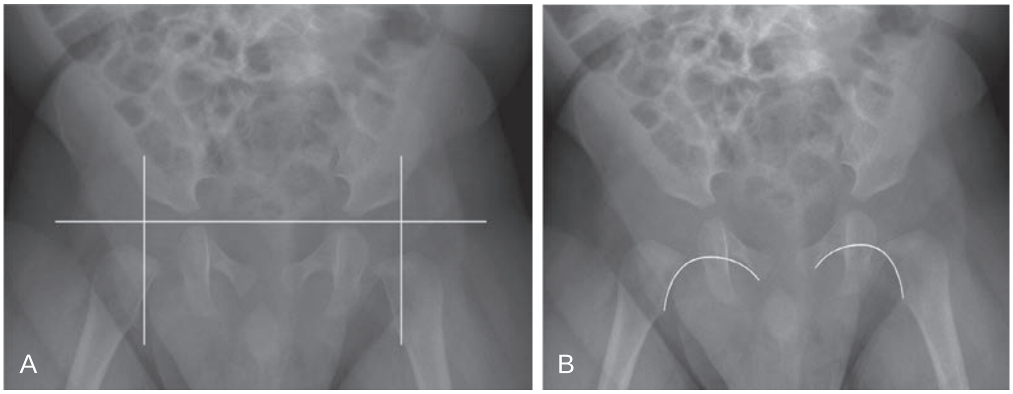

**Figure 135.2.** (A) Frontal radiograph of the pelvis with the horizontal Hilgenreiner and vertical Perkin lines. The expected location of the femoral head is in the medial, inferior quadrant of the intersection of the Hilgenreiner and Perkin lines. (B) The Shenton lines are drawn on this same pelvic radiograph. Disruption of this line will occur if the hip is dysplastic with either a subluxation or a dislocation.

with the knees fully flexed. Then pressure in a posterior/outward direction is applied to the femoral heads; if the hips dislocate, the test is considered positive.[9–11] Both of these maneuvers may fail to diagnose bilateral irreducible hip dislocations.

Asymmetric thigh skin creases, limited abduction, leg length discrepancies, and isolated hip clicks have also been suggested as signs of DDH but are less reliable. The Galeazzi sign may help diagnose DDH in older children. Unequal height of the knees in a supine child with flexed hips and knees is a positive result; however, the result is negative if both hips are abnormal. Older children may have a limp as the only symptom of DDH.

## IMAGING

### Radiography

The infant's lower extremities should be positioned in neutral extension with longitudinal symmetry. For symmetric imaging, the central ray should be directed above the pubic symphysis in the midline. In the presence of abnormality, a frog-leg view may be useful to evaluate reduction of the femoral head and may provide an opportunity for a second look at acetabular morphology.[12] Positioning the thigh in abduction and internal rotation (the von Rosen view) may provide additional information when evaluating DDH.

Several lines may be drawn to assist in the assessment of hips, but attention should be made to the overall configuration rather than to the measured angles, which could have varying rates of interobserver and intraobserver variability. The Hilgenreiner line passes horizontally through the superior aspect of the triradiate cartilages. The Perkin line is the vertical line extending from the lateral margin of the acetabulum. The expected location of the femoral head is in the medial, inferior quadrant of the intersection of the Hilgenreiner and Perkin lines (Fig. 135.2A). The Shenton line curves along the lesser trochanter, femoral neck, and superior margin of the obturator foramen and should be smooth (Fig. 135.2B).

The acetabular index is the angle between a line drawn along the acetabular roof and the Hilgenreiner line on a frontal radiograph. The acetabular index changes with age and normal values are different between girls and boys. Approximate measurements are 28 degrees in newborns, 23.5 degrees at age 6 months, 22 degrees at age 1 year, and 20 degrees at age 2 years. The maximal normal measurement for the acetabular index is 30 degrees up to age 4 months and 25 degrees up to age 2 years. The orientation of the pelvis on the radiograph affects this measurement.[13,14]

Hips should be in slight flexion during radiographic evaluation. Concavity of the acetabulum, which occurs as a result of pressure from the femoral head, should be noted. Typically, in this region of pressure at the acetabular roof normal sclerosis develops, which is called the *sourcil*, and is most prominent in the middle third of the acetabulum. The sourcil should normally have a rounded or arched configuration.

In preschool children and older children, the lateral center edge angle can assess the relative lateral acetabular coverage of the femoral head. The lateral center edge angle is the angle between a vertical line drawn through the center of the femoral head and a line connecting the center of the femoral head and the lateral acetabulum. This measurement is used in children over age 5 years. DDH should be suspected when the center edge angle is less than 19 degrees in children aged 6 to 13 years and less than 25 degrees in those over age 13 years.[13,15]

Radiographs are utilized to screen for DDH after age 4 to 6 months, when ultrasonography becomes more challenging and less reliable because of ossification of the femoral heads. Radiographic findings of DDH include shallow acetabula, with upward slanting sourcils, small capital femoral epiphysis, and superolateral subluxation of the femoral head (Figs. 135.3 and 135.4). Anteroposterior views are sufficient for screening. When abnormal, a frog-leg lateral view or a von Rosen view may be obtained to assess whether the femoral head reduces with hip abduction. When chronic, untreated DDH exists, the ossified portion of the ipsilateral capital femoral epiphysis may be disproportionately smaller (see Fig. 135.4) than a normal contralateral femoral head.

## Ultrasonography

Reinhard Graf, an orthopedist, described the use of ultrasonography in the assessment of the anatomy of the infant hip in 1980.[16] Four years later, Ted Harcke and colleagues, a group of radiologists, described the dynamic technique to assessing infant hips.[17] Advantages of sonography include its lack of ionizing radiation, direct visualization of cartilaginous structures, widespread availability, and the ability to perform a dynamic examination.

The examination is performed with a linear array transducer using the highest frequency that provides adequate penetration (often 12 megahertz [MHz]); however, a lower frequency transducer may be needed in children older than 6 months. The transducer is placed over the lateral aspect of the hip in either the coronal plane, with the hip in neutral or flexed positions, or in the transverse or axial plane, with the hip in adduction or abduction (e-Fig. 135.5). The infant should be placed in the lateral decubitus or supine position. In the coronal plane, the ilium should appear as a horizontal echogenic line, the midportion of the acetabulum visualized to its maximal depth, and the middle of the fibrocartilaginous labrum seen. Without technical accuracy, a normal hip may appear abnormal; the converse is not true. The femoral head should be in close apposition with the acetabulum with at least 50% of the femoral head covered by the acetabulum. Subluxation is present if the femoral head is less than 50% covered but in contact with the acetabulum. In the absence of contact between the femoral head and acetabulum, the hip is dislocated. The hip may reduce with changes in position, typically in abduction and flexion.

The alpha-angle, which is assessed on a coronal ultrasound image, is the angle between a line drawn along the straight edge of the iliac bone and a line along the roof of the bony acetabulum. An alpha-angle greater than or equal to 60 degrees is normal (Fig. 135.6). In infants less than 3 months of age, an alpha-angle between 50 to 60 degrees may represent physiologic immaturity of the hip. The majority of these hips develop normally without treatment, but maturation should be confirmed with a follow-up study. The beta-angle is the angle between a line drawn along the iliac bone and a line drawn along the axis of the fibrocartilaginous labrum on a coronal ultrasound image. This angle, which should be less than 55 degrees, is less commonly used than the alpha-angle.

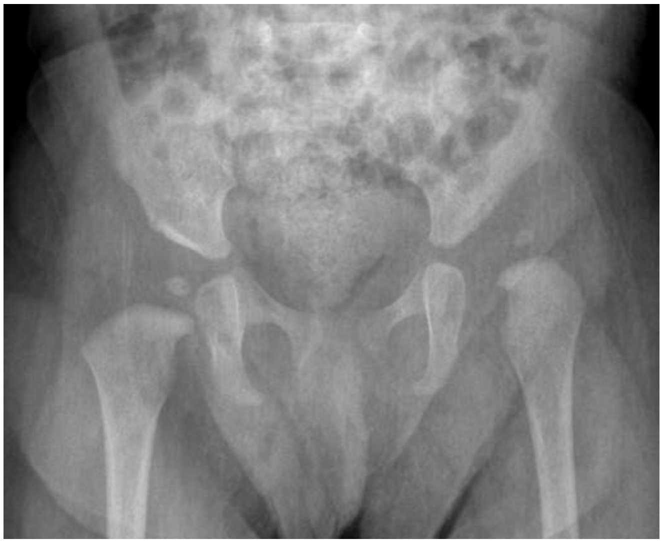

**Figure 135.3. Bilateral developmental dysplasia of the hip, left hip worse than the right hip, in an 8-month-old girl.** Anteroposterior radiograph shows that both acetabula are shallow. The right femoral head is concentrically located within its dysplastic acetabulum. The left femoral head is superolaterally dislocated.

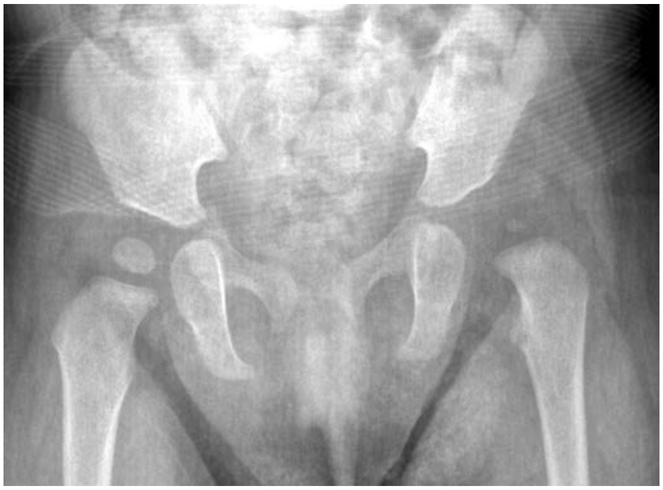

**Figure 135.4. Left-sided developmental dysplasia of the hip in a 1-year-old girl.** Anteroposterior radiograph shows a shallow left acetabulum with an upward slanting sourcil, a superolaterally subluxated femoral head, and delayed ossification of the left capital femoral epiphysis.

In addition to the abnormally lateral and superior positioning of the femoral head and the abnormal angle of the acetabulum seen with DDH, the labrum may become thick and echogenic. The acetabular rim in normal hips has a sharply defined corner at the intersection of the anterior iliac line and lateral acetabulum (see Fig. 135.6). With progressive acetabular dysplasia, this corner becomes rounded and dysplastic (Fig. 135.7A). A deformed labrum that is interposed between the femoral head and acetabulum, pulvinar, and a thickened ligamentum teres may be obstacles to hip joint reduction (see Fig. 135.7).

Dynamic examination includes the use of stress maneuvers, which correspond to the physical tests of Ortolani and Barlow.

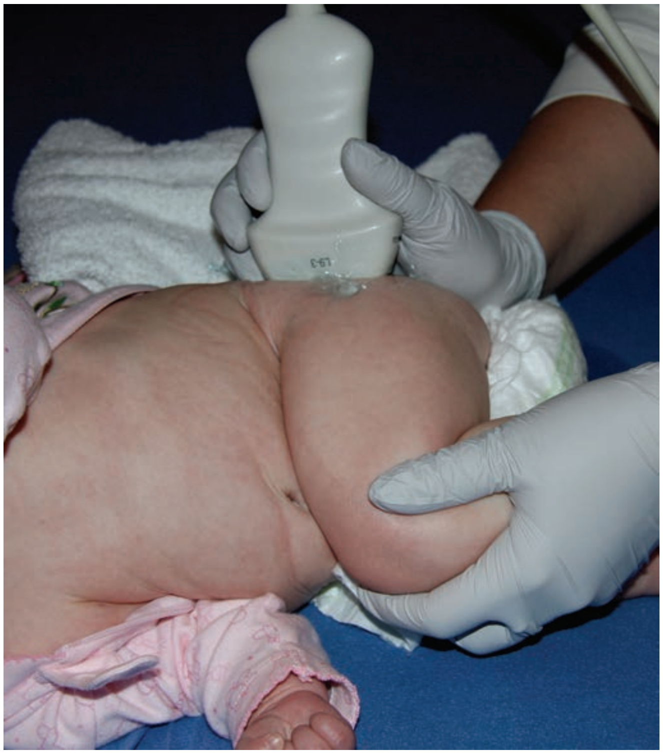

**e-Figure 135.5.** Positioning of the ultrasound transducer on an infant for examination of the left hip in the coronal plane with flexion.

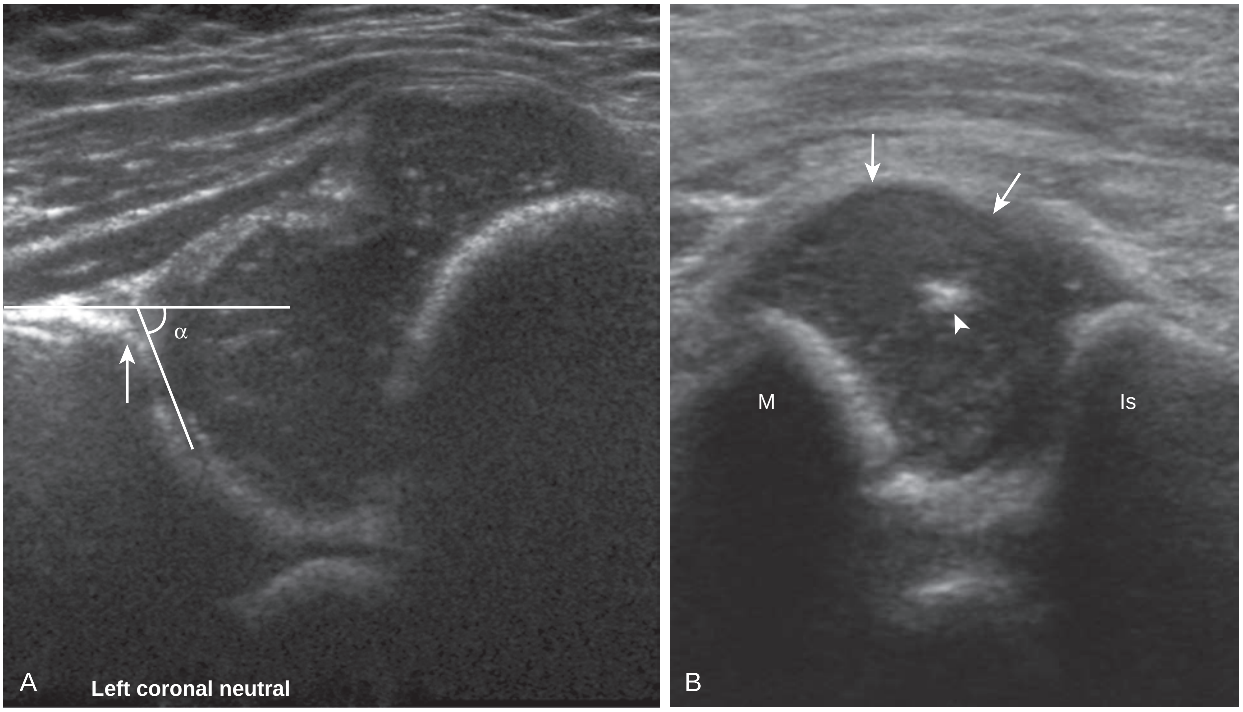

**Figure 135.6. Normal hip.** (A) Coronal sonogram with the hip in neutral position. The alpha-angle is the angle between a line along the straight edge of the iliac bone and the acetabular roof. The alpha-angle is normal, measuring 64 degrees in this example. The acetabular roof is mature, with a sharply angulated acetabular margin *(arrow)*. (B) Transverse sonogram with the hip in a flexed position shows the normal relationship between the femoral head *(arrows)* and ischium *(Is)*. The majority of the femoral head is unossified cartilage but an early ossification center is present *(arrowhead)*. *M*, Proximal femoral metaphysis.

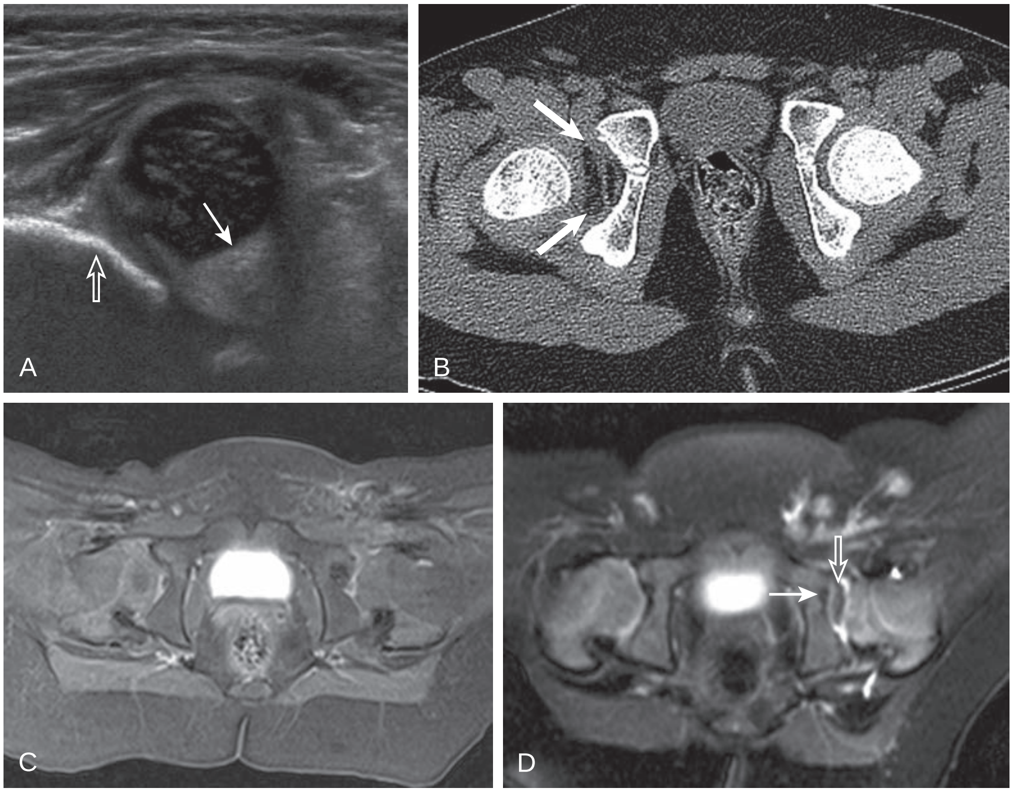

**Figure 135.7. Obstacles to hip reduction.** (A) Coronal sonogram of a dysplastic hip with echogenic pulvinar *(solid arrow)*. Note the dysplastic shallow acetabulum with blunted obtuse margin *(open arrow)*. (B) Low-dose axial CT demonstrating fatty pulvinar *(arrows)* within the right hip joint. (C) An axial T1-weighted MR image in an infant with left hip dysplasia, which was successfully reduced, demonstrates a thickened posterior labrum. (D) An axial T2-weighted MR image shows a thickened ligamentum teres *(open arrow)* between the femoral head and acetabulum *(solid arrow)*.

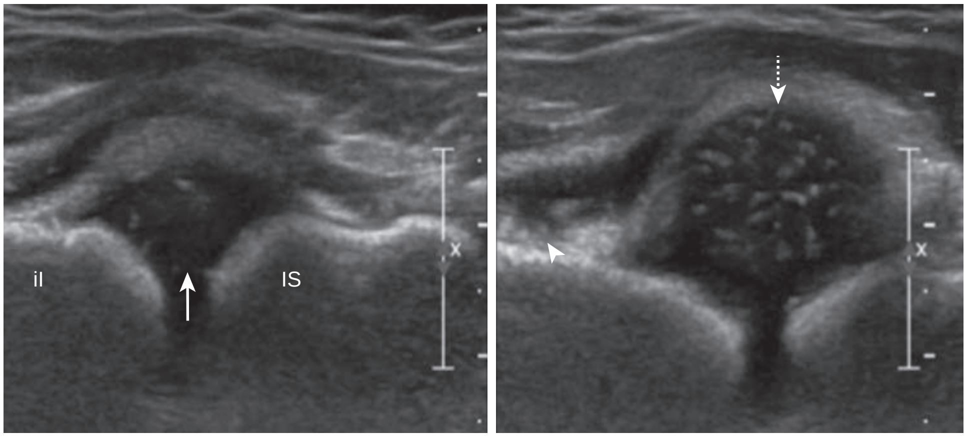

**Figure 135.8. Coronal posterior lip view showing femoral head subluxation with stress.** The left sonogram shows the coronal posterior lip view without stress. The posterior aspect (posterior lip) of the unossified triradiate cartilage *(arrow)* is seen between the iliac bone *(il)* and ischium *(IS)*. The right sonogram shows the coronal posterior lip view with stress. The unossifed femoral head *(dashed arrow)* has subluxed posteriorly over the posterior lip of the acetabulum.

Normally, the femoral head is well seated within the acetabulum at rest and while stress maneuvers are applied. If laxity exists or if the hip is dislocatable, the femoral head moves lateral and posterior when stress is applied. The transverse view and the coronal posterior lip view can be used to evaluate for subluxation or dislocation during stress maneuvers (Fig. 135.8). These maneuvers are typically not performed if the patient is undergoing therapy with a harness.[18]

Because of the physiologic laxity in newborns, hip ultrasound is typically not performed on infants younger than 3 weeks of age unless there are clinical findings of dislocation. Femoral head ossification usually limits hip ultrasound evaluation after 6 months of age unless there is delayed ossification. Therefore, after 6 months of age, pelvic radiographs become the preferred imaging modality.

### Ultrasound Screening

Some advocate for screening of all newborns for DDH, while others recommend screening only those with risk factors or a positive or equivocal clinical examination. Many studies have been published describing the merits of each approach.[19–34] General screening may help prevent delayed diagnosis and the need for surgical intervention but also increases costs and leads to unnecessary treatment. The benefits of screening all newborns are not yet clear, and the current practice in the United Sates is to sonographically screen only patients with an abnormal physical examination or those who have positive risk factors for DDH.[34–36]

## Computed Tomography

Computed tomography (CT) is primarily used for patients who have undergone treatment or will undergo open surgical repair with orthopedic hardware for DDH, rather than as a means of obtaining a diagnosis.[37] CT may be performed immediately after surgical reduction of DDH and is ideally performed using low-dose techniques and a small scan extent (Fig. 135.9). Displacement and subluxation should be described in both the coronal and axial planes. Reconstructions of CT data may assist in demonstrating anatomic relationships.[18,37] CT can also be performed postoperatively to evaluate periacetabular and/or proximal femoral osteotomies and to determine bone graft quality and position.[18,38–40]

CT is particularly useful in children with hardware placement near the joint, which may limit visualization on magnetic resonance imaging (MRI). Identification of any orthopedic hardware failures such as pin extrusion into the joint line, migrated interposition bone grafts, and identification of any intrinsic or extrinsic causes of failed reduction should be made.

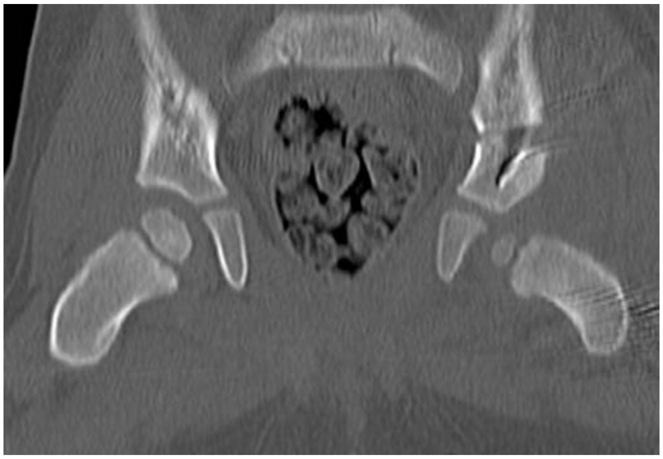

**Figure 135.9. Salter osteotomy for treatment of left-sided developmental dysplasia of the hip in a 2-year-old boy.** On this coronal reformatted CT, note that both femoral heads are concentrically located. The left femoral head is small, an expected finding in the setting of developmental dysplasia of the hip.

As part of surgical planning for older patients (usually in their second decade or older) with DDH, measurement of femoral and acetabular version can be made on a low-dose CT scan of the hips and distal femurs. In addition, preoperative CT is also used to provide additional details of bone quality and joint morphology, which are helpful in planning pelvic and femoral osteotomies.

## Magnetic Resonance Imaging

MRI is increasingly utilized to evaluate hip positioning after reduction and placement of a spica cast. The better visualization of unossifed cartilage and soft tissues and the lack of ionizing radiation are advantages over CT (Fig. 135.10).[41–46] The study can typically be performed without sedation. In addition to providing anatomic information regarding the relationship between the femoral head and the acetabulum, obstacles to reduction are visualized better than with CT (e-Fig. 135.11). Fatty pulvinar,

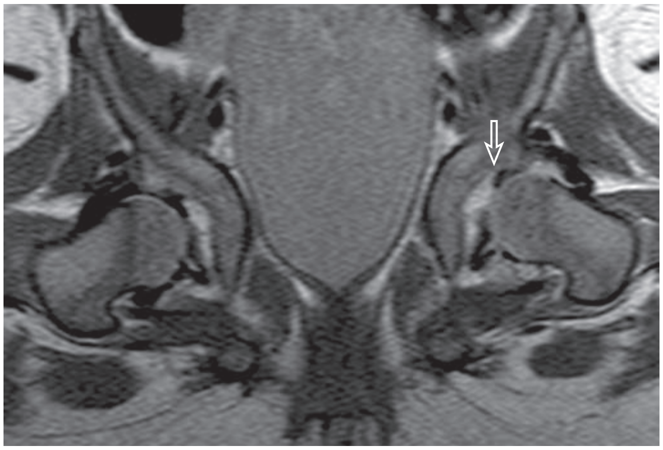

**e-Figure 135.11. Inverted labrum.** Coronal proton density MR image in an 8-month-old girl demonstrates an inverted labrum on the left *(arrow)*. There is susceptibility artifact noted in right hip joint space related to iodinated contrast from intraoperative arthrography performed before MR imaging.

transverse acetabular ligaments, and hypertrophied ligamentum teres (see Fig. 135.7) may be present in the hip joint preventing successful reduction. MRI can also detect hypertrophy and increased signal intensity within the labrum, and if the labrum is inverted, hindering reduction. An abnormal shape of the acetabulum and/or the capital femoral epiphysis may also be contributing factors when reduction is difficult. Extrinsic obstacles to reduction include shortened external rotator and adductor muscles, interpositioning of the iliopsoas muscle, and capsular adhesion to the ilium.[47] The most useful sequences include T1-weighted and proton density–weighted sequences in the axial and coronal planes.[48–50]

Postcontrast magnetic resonance (MR) images can evaluate perfusion of the femoral head. Some studies have shown that globally decreased enhancement of the femoral head on postcontrast MRI is predictive of an increased risk of future avascular necrosis (AVN). Epiphyseal osteonecrosis is the most common serious complication of hip reduction and may occur to some degree in more than 70% of cases. The risk of epiphyseal osteonecrosis is increased with greater hip abduction, which has led to the concept of the "safe zone," which is the amount of abduction that is large enough to prevent redislocation and small enough to prevent avascular necrosis, usually at 55 degrees maximal hip abduction.[46] Abduction greater than this may compromise the blood supply to the femoral head, which arises primarily from the deep medial femoral circumflex vessels. On postcontrast T1-weighted MR images, this is seen as globally decreased enhancement of the vascular channels within the unossifed epiphyseal cartilage and decreased enhancement within the ossification center of the femoral head (Fig. 135.12).[45,46,51] Hips that show decreased global enhancement may be considered for recasting in a less abducted position.[46]

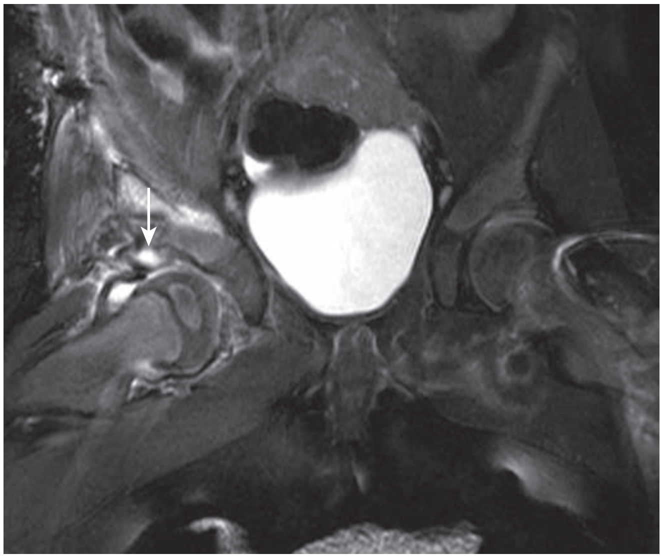

**Figure 135.10. MRI after hip reduction, iliac osteotomy, and spica cast placement.** T2-weighted fat-saturated coronal MR image shows that the femoral heads are concentrically located. Also note the hypertrophy and increased signal within the right superior labrum *(arrow)*. No sedation was used for this study.

## TREATMENT

The objective of DDH treatment is concentric reduction of the femoral head into the acetabulum. The method of achieving this outcome depends on the age of the patient as well as the severity of the presentation. Up to age 6 months, orthoses, often a Pavlik harness, are used to place the hip in flexion and abduction. This treatment aids in developing the acetabulum along the lateral edge. The risk of epiphyseal osteonecrosis increases with greater hip abduction, as discussed above. The harness is often worn for 3 to 6 weeks after successful reduction; both clinical examination and ultrasonography are performed to evaluate the effectiveness of therapy.

Children over 6 months but less than 2 years of age are often treated with a spica cast after closed or open reduction. Intraoperative arthrography is often performed to assess for structures that my impede reduction and to assess the anatomy (e-Fig. 135.13). Positioning of the femoral heads after placement of the cast may be ascertained with CT or MRI, with MRI having the advantages previously discussed. Follow-up radiographs can detect more advanced features of avascular necrosis. Recurrent dislocation may occur in up to 8% of patients and is more common in those with bilateral or right-sided DDH, decreased abduction in the spica cast, and large pelvic width.[52]

DDH that is diagnosed late or that persists despite treatment may require surgical osteotomy. For patients with persistent subluxation and mild to moderate acetabular dysplasia, an innominate or Salter osteotomy, which attempts to better align the acetabulum to cover the femoral head, may be indicated. A horizontal osteotomy is placed in the ilium superior to the acetabulum allowing the acetabulum to be rotated and placement of an iliac bone graft at the osteotomy site (e-Fig. 135.14). There are a number of other surgical procedures that may be used depending upon the clinical scenario and surgeon. These include incomplete iliac osteotomies (e.g., Dega and Pemberton), double and triple innominate osteotomies (e.g., Sutherland and Tonnis), periacetabular osteotomies (e.g., Ganz), as well as salvage procedures (e.g., Chiari and shelf osteotomies) (e-Fig. 135.15). Femoral shortening and derotational osteotomies and adductor tenotomies may also be performed.

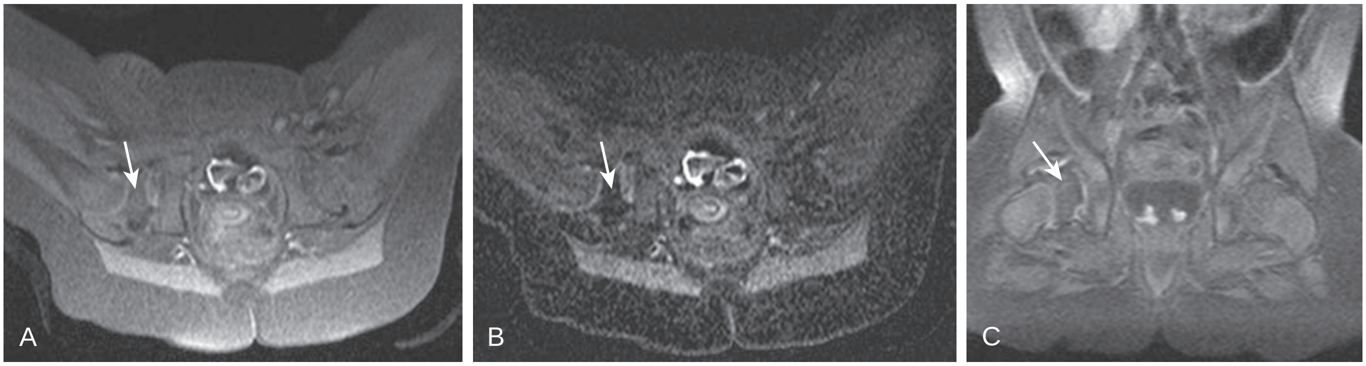

**Figure 135.12. Decreased perfusion of the right femoral head.** (A) Axial T1-weighted, (B) axial subtraction T1-weighted, and (C) coronal T1-weighted fat-suppressed post contrast MR images demonstrate globally decreased perfusion of the right femoral head *(arrows)* best seen on the subtraction images (B).

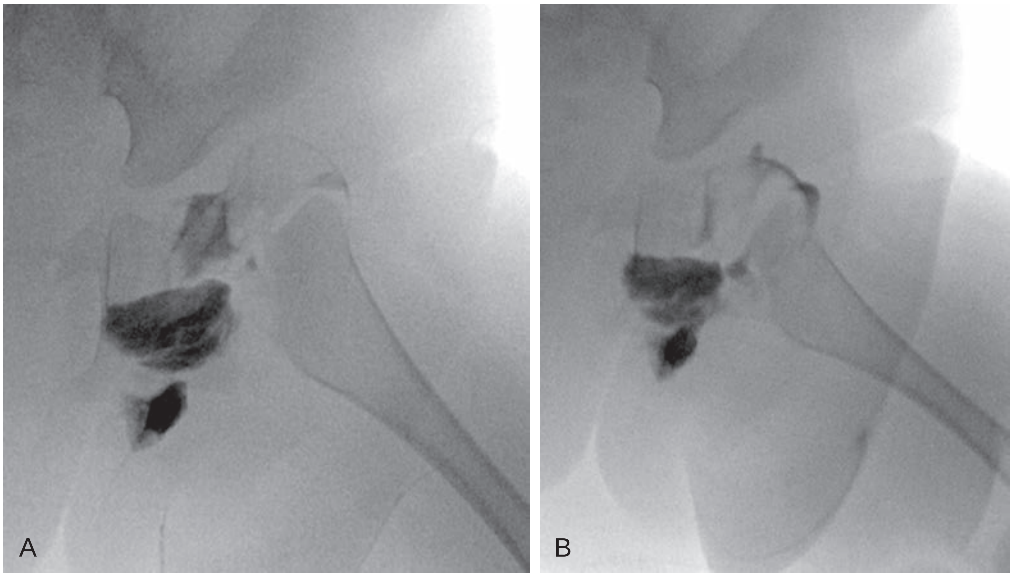

**e-Figure 135.13.** Intraoperative arthrogram obtained before (A) and after (B) reduction of the left hip in this child with Larsen syndrome.

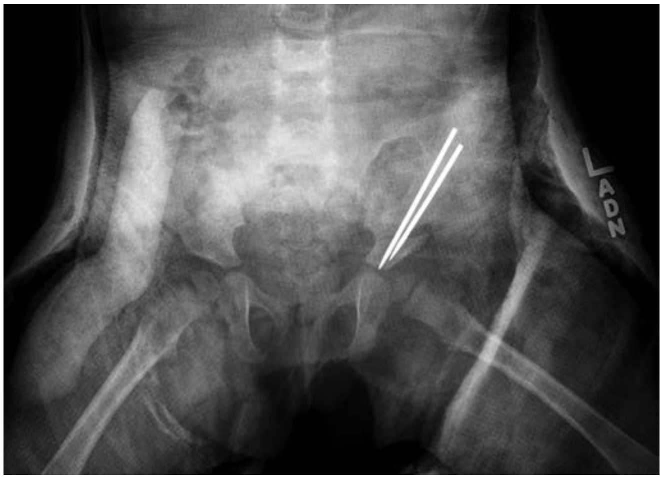

**e-Figure 135.14. Salter osteotomy treatment for left developmental dysplasia of the hip.** A frontal radiograph of patient after left Salter osteotomy while in spica cast shows fixation pins securing the left supraacetabular osteotmy.

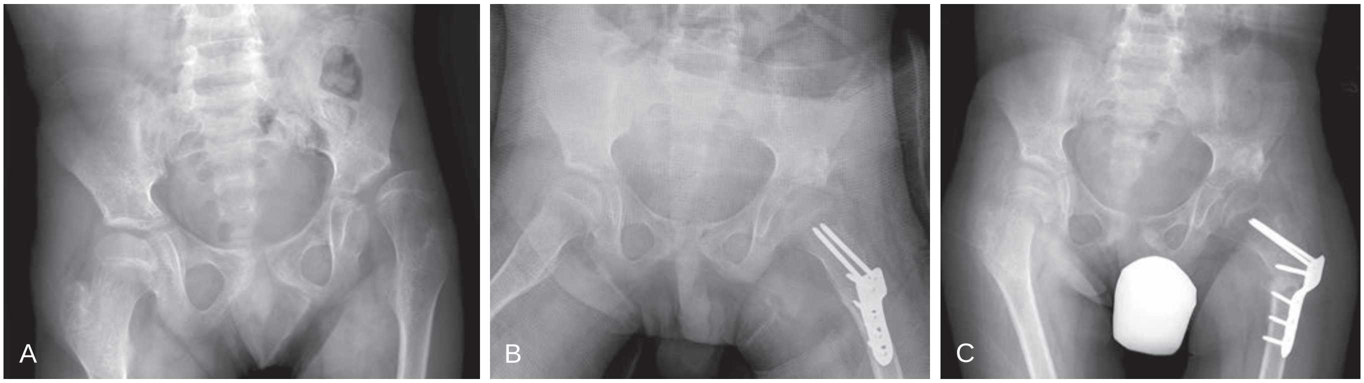

**e-Figure 135.15. Radiographs of a 14-year-old patient who underwent left-sided Dega osteotomy.** (A) Preoperative image demonstrating subluxation of the left hip. (B) After 7 days following surgery. (C) After 1 month following surgery. Note the femoral osteotomy and hardware in place.

## KEY POINTS

- In the United States, screening for DDH is done on the basis of clinical examination findings and patient risk factors.
- Ultrasonography provides a dynamic examination to evaluate the location of the femoral head and the shape of the acetabulum, as well as to identify obstacles to reduction.
- CT may be used for presurgical planning or postoperative evaluation.
- MRI is used to evaluate the success of closed reduction and spica cast placement and may identify obstacles to reduction and, if contrast is administered, decreased femoral head perfusion.

## SUGGESTED READINGS

Dezateux C, Rosendahl K. Developmental dysplasia of the hip. *Lancet*. 2007;369:1541–1552.

Grissom L, Harcke HT, Thacker M. Imaging in the surgical management of developmental dislocation of the hip. *Clin Orthop Relat Res*. 2008;466:791–801.

Karmazyn BK, Gunderman RB, Coley BD, et al. ACR Appropriateness criteria on developmental dysplasia of the hip—child. *J Am Coll Radiol*. 2009;6:551–557.

Shipman SA, Helfand M, Moyer VA, et al. Screening for developmental dysplasia of the hip: a systematic literature review for the US Preventive Services Task Force. *Pediatrics*. 2006;117:e557–e576.

Rosenbaum DG, Servaes S, Bogner EA, et al. MR imaging in postreduction assessment of developmental dysplasia of the hip: goals and obstacles. *Radiographics*. 2016;36(3):840–854.

## REFERENCES

Full references for this chapter can be found on www.expertconsult.com.

## REFERENCES

1. Record RG, Edwards JH. Environmental influences related to the aetiology of congenital dislocation of the hip. *Br J Prev Soc Med*. 1958;12:8.
2. Murray KA, Crim JR. Radiographic imaging for treatment and follow-up of developmental dysplasia of the hip. *Semin Ultrasound CT MR*. 2001;22:306–340.
3. Perry DC, Tawfiq SM, Roche A, et al. The association between clubfoot and developmental dysplasia of the hip. *J Bone Joint Surg Br*. 2010;92:1586–1588.
4. Minihane KP, Grayhack JJ, Simmons TD, et al. Developmental dysplasia of the hip in infants with congenital muscular torticollis. *Am J Orthop*. 2008;37:E155, E158.
5. Dezateux C, Rosendahl K. Developmental dysplasia of the hip. *Lancet*. 2007;369:1541–1552.
6. Sankar WN, Neubuerger CO, Moseley CF. Femoral head sphericity in untreated developmental dislocation of the hip. *J Pediatr Orthop*. 2010;30:558–561.
7. Fujii M, Nakashima Y, Sato T, et al. Pelvic deformity influences acetabular version and coverage in hip dysplasia. *Clin Orthop Relat Res*. 2011;469:1735–1742.
8. Fujii M, Nakashima Y, Jingushi S, et al. Intraarticular findings in symptomatic developmental dysplasia of the hip. *J Pediatr Orthop*. 2009;29:9–13.
9. Barlow TG. Neonatal hip dysplasia—treatment, results and complications. *Proc R Soc Med*. 1975;68:475.
10. Barlow TG. Congenital dislocation of the hip in the newborn. *Proc R Soc Med*. 1966;59:1103–1106.
11. Barlow TG. Early diagnosis and treatment of congenital dislocation of the hip. *Proc R Soc Med*. 1963;56:804–806.
12. Greenspan A. *Orthopedic Radiology: A Practical Approach*. Philadelphia, PA: Lippincott Williams & Wilkins; 2000.
13. Noordin S, Umer M, Hafeez K, et al. Developmental dysplasia of the hip. *Orthop Rev (Pavia)*. 2010;2:e19.
14. van der Bom MJ, Groote ME, Vincken KL, et al. Pelvic rotation and tilt can cause misinterpretation of the acetabular index measured on radiographs. *Clin Orthop Relat Res*. 2011;469:1743–1749.
15. Pedersen DR, Lamb CA, Dolan LA, et al. Radiographic measurements in developmental dysplasia of the hip: reliability and validity of a digitizing program. *J Pediatr Orthop*. 2004;24:156–160.
16. Graf R. The diagnosis of congenital hip-joint dislocation by the ultrasonic compound treatment. *Arch Orthop Trauma Surg*. 1980;97:117–133.
17. Harcke HT, Clarke NM, Lee MS, et al. Examination of the infant hip with real-time ultrasonography. *J Ultrasound Med*. 1984;3:131–137.
18. Grissom L, Harcke HT, Thacker M. Imaging in the surgical management of developmental dislocation of the hip. *Clin Orthop Relat Res*. 2008;466:791–801.
19. Clinical practice guideline: early detection of developmental dysplasia of the hip. Committee on Quality Improvement, Subcommittee on Developmental Dysplasia of the Hip. American Academy of Pediatrics. *Pediatrics*. 2000;105:896–905.
20. Goldberg MJ. Early detection of developmental hip dysplasia: synopsis of the AAP Clinical Practice Guideline. *Pediatr Rev*. 2001;22:131–134.
21. Pashapour N, Golmahammadlou S. Study on the diagnosis time of developmental dysplasia of the hip. *East Mediterr Health J*. 2007;13:465–469.
22. Karmazyn BK, Gunderman RB, Coley BD, et al. ACR Appropriateness Criteria on developmental dysplasia of the hip—child. *J Am Coll Radiol*. 2009;6:551–557.
23. Shipman S, Helfand M, Nygren P, et al. *Screening for developmental dysplasia of the hip*. Agency for Healthcare Research and Quality, 2006. PMID 20722139.
24. Shipman SA, Helfand M, Moyer VA, et al. Screening for developmental dysplasia of the hip: a systematic literature review for the US Preventive Services Task Force. *Pediatrics*. 2006;117:e557–e576.
25. Maxwell SL, Ruiz AL, Lappin KJ, et al. Clinical screening for developmental dysplasia of the hip in Northern Ireland. *BMJ*. 2002;324:1031–1033.
26. Sewell MD, Eastwood DM. Screening and treatment in developmental dysplasia of the hip-where do we go from here? *Int Orthop*. 2011;35:1359–1367.
27. Shorter D, Hong T, Osborn DA. Screening programmes for developmental dysplasia of the hip in newborn infants. *Cochrane Database Syst Rev*. 2011;(9):CD004595.
28. Godward S, Dezateux C. Surgery for congenital dislocation of the hip in the UK as a measure of outcome of screening. MRC Working Party on Congenital Dislocation of the Hip. Medical Research Council. *Lancet*. 1998;351:1149–1152.
29. Holen KJ, Tegnander A, Bredland T, et al. Universal or selective screening of the neonatal hip using ultrasound? A prospective, randomised trial of 15,529 newborn infants. *J Bone Joint Surg Br*. 2002;84:886–890.
30. Eastwood DM. Neonatal hip screening. *Lancet*. 2003;361:595–597.
31. Gray A, Elbourne D, Dezateux C, et al. Economic evaluation of ultrasonography in the diagnosis and management of developmental hip dysplasia in the United Kingdom and Ireland. *J Bone Joint Surg Am*. 2005;87:2472–2479.
32. Elbourne D, Dezateux C, Arthur R, et al. Ultrasonography in the diagnosis and management of developmental hip dysplasia (UK Hip Trial): clinical and economic results of a multicentre randomised controlled trial. *Lancet*. 2002;360:2009–2017.
33. Rosendahl K, Toma P. Ultrasound in the diagnosis of developmental dysplasia of the hip in newborns. The European approach. A review of methods, accuracy and clinical validity. *Eur Radiol*. 2007;17:1960–1967.
34. Woolacott NF, Puhan MA, Steurer J, et al. Ultrasonography in screening for developmental dysplasia of the hip in newborns: systematic review. *BMJ*. 2005;330:1413.
35. Treiber M, Tomazic T, Tekauc-Golob A, et al. Ultrasound screening for developmental dysplasia of the hip in the newborn: a population-based study in the Maribor region, 1997-2005. *Wien Klin Wochenschr*. 2008;120:31–36.
36. von Kries R, Ihme N, Altenhofen L, et al. General ultrasound screening reduces the rate of first operative procedures for developmental dysplasia of the hip: a case-control study. *J Pediatr*. 2012;160(2):271–275.
37. Jia J, Li L, Zhang L, et al. Three dimensional-CT evaluation of femoral neck anteversion, acetabular anteversion and combined anteversion in unilateral DDH in an early walking age group. *Int Orthop*. 2012;36(1):119–124.
38. Eggli KD, King SH, Boal DK, et al. Low-dose CT of developmental dysplasia of the hip after reduction: diagnostic accuracy and dosimetry. *AJR Am J Roentgenol*. 1994;163:1441–1443.
39. Koenig JK, Pring ME, Dwek JR. MR evaluation of femoral neck version and tibial torsion. *Pediatr Radiol*. 2012;41(1):113–115.
40. van Bosse HJ, Lee D, Henderson ER, et al. Pelvic positioning creates error in CT acetabular measurements. *Clin Orthop Relat Res*. 2011;469:1683–1691.
41. Laor T, Roy DR, Mehlman CT. Limited magnetic resonance imaging examination after surgical reduction of developmental dysplasia of the hip. *J Pediatr Orthop*. 2000;20:572–574.
42. McNally EG, Tasker A, Benson MK. MRI after operative reduction for developmental dysplasia of the hip. *J Bone Joint Surg Br*. 1997;79:724–726.
43. Wakabayashi K, Wada I, Horiuchi O, et al. MRI findings in residual hip dysplasia. *J Pediatr Orthop*. 2011;31:381–387.
44. Mitchell PD, Chew NS, Goutos I, et al. The value of MRI undertaken immediately after reduction of the hip as a predictor of long-term acetabular dysplasia. *J Bone Joint Surg Br*. 2007;89:948–952.
45. Westhoff B, Wild A, Seller K, et al. Magnetic resonance imaging after reduction for congenital dislocation of the hip. *Arch Orthop Trauma Surg*. 2003;123:289–292.
46. Tiderius C, Jaramillo D, Connolly S, et al. Post-closed reduction perfusion magnetic resonance imaging as a predictor of avascular necrosis in developmental hip dysplasia: a preliminary report. *J Pediatr Orthop*. 2009;29:14–20.
47. Desai AA, Martus JE, Schoenecker J, et al. Spica MRI after closed reduction for developmental dysplasia of the hip. *Pediatr Radiol*. 2011;41:525–529.
48. Lincoln TL, Vandevenne JE, Rinsky LA, et al. Dynamic magnetic resonance guided treatment of developmental dysplasia of the hip. *J Pediatr Orthop B*. 2002;11:279–283.
49. Chin MS, Shoemaker A, Reinhart DM, et al. Use of 1.5 Tesla and 3 Tesla MRI to evaluate femoral head reduction in hip dysplasia. *J Pediatr Orthop*. 2011;31:633–637.
50. Kim HT, Kim IB, Lee JS. MR-based parameters as a supplement to radiographs in managing developmental hip dysplasia. *Clin Orthop Surg*. 2011;3:202–210.
51. Gornitzky AL, Georgiadis AG, Seeley MA, et al. Does perfusion MRI after closed reduction of developmental dysplasia of the hip reduce the incidence of avascular necrosis? *Clin Orthop Relat Res*. 2016;474(5):1153–1165. doi:10.1007/s11999-015-4387-6.
52. Sankar WN, Young CR, Lin AG, et al. Risk factors for failure after open reduction for DDH: a matched cohort analysis. *J Pediatr Orthop*. 2011;31:232–239.

# 136 Arthritis and Differential Inflammatory Joint Disorders

Arthur B. Meyers, Andrea Schwarz Doria, and Paul Babyn

Rheumatologic conditions in children are myriad in presentation, with overlapping imaging features that may sometimes superficially mimic infection. Rheumatologic conditions in children do not follow the typical course and presentation compared with their counterparts in adults. As a consequence, the International League of Associations for Rheumatology (ILAR) formulated a revised nomenclature to describe the various pediatric rheumatologic conditions (Box 136.1).[1] In this chapter, we discuss imaging of pediatric arthritis from the point of view of noninfectious synovial proliferation using the ILAR classification, including juvenile idiopathic arthritis (JIA) and its differentials: hemophilic arthropathy, lipoma arborescens, synovial chondromatosis, pigmented villonodular synovitis (PVNS), and reactive synovitis (Box 136.2). Subtypes of JIA, enthesitis-related arthritis and psoriatic arthritis, will be discussed in their own subsections because of their unique presentation and imaging findings. Infectious arthritis is discussed in Chapter 137.

## JUVENILE IDIOPATHIC ARTHRITIS

### Clinical Overview

JIA, which occurs worldwide, is the most frequent cause of chronic musculoskeletal pain in youths and the most common chronic musculoskeletal disease of childhood.[2–4] It is a chronic, monoarticular or polyarticular arthropathy of childhood.[2]

The diagnostic criteria for JIA include arthritis in one or more joints for at least 6 weeks before the age of 16 years. The onset type is defined by pattern of disease in the first 6 months of diagnosis (see Box 136.1) and exclusion of other forms of juvenile arthritis.[1] JIA may be associated with systemic manifestations that include fever, erythematous rashes, nodules, leukocytosis, and, less commonly, iridocyclitis, pleuritis, pericarditis, anemia, fatigue, and growth failure.[5] At the time of presentation, other causes of inflammation should be excluded. JIA differs from the adult type of rheumatoid arthritis because of the age of presentation, its preference for large joints, its tendency to generate joint contractures and muscle wasting, and its association with extraarticular clinical manifestations.[6]

A new internationally accepted classification system was established in 1995[1,7] and revised in 2001[1] (see Box 136.1). The previously used terms *juvenile chronic arthritis* and *juvenile rheumatoid arthritis* were incorporated under the term *JIA*.

The early diagnosis of JIA is essential to interrupt or delay the course of the disease, which results in joint deformity, severe functional impairment, and chronic pain if the disease is not treated at its early stage.

The currently available clinical and laboratory tests for assessment of JIA are poor for characterization of early inflammatory, hypoxic, and vascular changes, which are the primary physiologic events involved in the disease.[8–10] Therefore imaging is vitally important for early diagnosis and assessing treatment response during follow-up in persons with this disease.

### Epidemiology

The incidence and prevalence of JIA in Europe varies greatly in published reports, with the incidence and prevalence, respectively, of 1.6 to 42.5 and 3.8 to 400 per 100,000.[11] Twice as many girls as boys have JIA.[12] Although few data are available on geographic or racial groups, studies suggest that, in the United States, proportionately fewer African American than white children have JIA.[13] The onset of JIA before the age of 6 months is distinctly unusual; nevertheless, the age at onset is often quite young, with the highest frequency occurring between 1 and 3 years.[14]

Radiographic changes are seen most frequently in children with JIA who have a polyarticular course.[15,16] Large joints are most commonly affected in persons with this disease. The knee is the most frequently affected joint, followed by the ankle. Changes may also develop in the cervical spine or temporomandibular joint.[17] It has been suggested that patients with JIA who have polyarthritis and wrist disease are at high risk of experiencing radiographic progression.[18] The wrist is the most vulnerable site for early radiographic changes in patients with JIA.[16,19]

### Pathophysiology

Although the etiology of JIA is unknown, some investigators believe that it is multifactorial given the heterogeneity of presentations and course of the disease.[20] JIA is characterized by an acute synovitis that leads to synovial proliferation and formation of a highly cellular pannus.[21] The pannus erodes the adjacent articular cartilage and subchondral bone, leading to centripetal articular destruction; that is, the articular damage starts at the periphery of the joint and progresses toward its center. Inflammatory changes also can involve tendon sheaths and bursa and can give rise to periostitis. With prolonged inflammation, more extensive joint changes, including cartilage destruction, bone erosions, and joint malalignment, often are present.

Despite the fact that JIA is usually transient and self-limited, without active synovitis in adulthood, up to 10% of children become severely disabled in adulthood. Despite therapy, 28% to 54% of children have progressive disease and experience cartilage or bone erosions, with a median onset of radiographic findings between 2.2 to 5.4 years after initial presentation.[22] The disease process may lead to joint instability, subluxation, and ankylosis.[23,24] Disturbance of joint growth can be consequent to the disease itself and/or to the treatment.[17]

### Imaging

Imaging plays a key role in establishing the presence, severity, and extent of joint disease and monitors disease complications, excludes other diagnoses, and assesses treatment response. Advanced imaging allows detailed evaluation of synovitis and osteochondral damage.[25–27]

## Abstract:

Rheumatologic conditions in children have a variety of presentations and imaging is useful in establishing a diagnosis and in the evaluation of treatment response. In this chapter, we discuss the imaging of noninfectious arthritis in children using the International League of Associations for Rheumatology classification of these conditions. Specifically we review juvenile idiopathic arthritis and its differentials: hemophilic arthropathy, lipoma arborescens, synovial chondromatosis, pigmented villonodular synovitis, and reactive synovitis. Subtypes of JIA, enthesitis-related arthritis and psoriatic arthritis, are discussed in their own subsections because of their unique presentation and imaging findings.

## Keywords:

Juvenile idiopathic arthritis
enthesitis-related arthritis
psoriatic arthritis
reactive synovitis
hemophilic arthropathy
synovial chondromatosis
pigmented villonodular synovitis

### BOX 136.1 Classification of Juvenile Idiopathic Arthritis

Onset <16 years
Duration: at least 6 weeks
Other known conditions are excluded

**SUBTYPES**

1. Systemic arthritis
2. Oligoarthritis
    a. Persistent—affecting ≤4 joints throughout the disease course
    b. Extended—affecting a total of >4 joints after the first 6 months of disease
3. Polyarthritis (rheumatoid factor negative)
4. Polyarthritis (rheumatoid factor positive)
5. Psoriatic arthritis
6. Enthesitis-related arthritis
7. Other undifferentiated arthritis
    a. Does not meet any criteria for categories 1–6
    b. Meets criteria for more than one of the categories 1–6

*From Petty RE, Southwood TR, Manners P, et al. International League of Associations for Rheumatology classification of juvenile idiopathic arthritis: second revision, Edmonton, 2001.* J Rheumatol. *2004;31:390–392.*

Radiographs are typically the initial imaging study for the diagnosis of JIA; however, they have low sensitivity (50%) and moderate specificity (85%) for detection of cartilage destruction.[8]

Both magnetic resonance imaging (MRI) and ultrasound can detect synovial hypertrophy, cartilage erosion, and joint effusion in peripheral joints, and clinically meaningful response to treatment in children with JIA. Ultrasound is less sensitive than MRI for assessment of both soft tissue findings (sensitivity, 62%) and superficial cartilage loss (sensitivity, 60%).[8] Overall, MRI is the imaging modality of choice for evaluation of joints in children with JIA. However, ultrasound can be an excellent initial imaging tool for evaluation of young children who otherwise would require sedation for MRI.[8] As expertise and standardization continues to develop, ultrasound will likely prove to be a complementary imaging method along with MRI.[28]

## Radiography

Conventional radiography is not effective in the evaluation of soft tissue abnormalities, which are precursors of cartilage degeneration in persons with JIA.[26] Moreover, available radiographic scoring systems have poor internal consistency and poor criterion and construct validity because they do not take into consideration patients' sex and age.[29] As mentioned earlier, there is low sensitivity (50%) and moderate specificity (85%) in the detection of cartilage

### BOX 136.2 Differential Diagnosis of Juvenile Idiopathic Arthritis

**NONINFECTIOUS DISORDERS**

**Synovial Disorders**

***Pauciarticular***

Acute
- Early rheumatic disease
- Arthritis associated with chromosomal abnormalities—Down, Turner syndromes
- Seronegative spondyloarthropathy
- Acute transient synovitis

Chronic
- Rheumatic diseases
- Arthritis associated with chromosomal abnormalities—Down, Turner syndromes
- Tenosynovial giant cell tumors (pigmented villonodular synovitis)
- Intraarticular venous malformation
- Lipoma arborescens
- Synovial osteochondromatosis

Other
- Foreign body arthritis
- Hemophilic arthropathy
- Sarcoidosis
- Intraarticular osteoid osteoma

***Polyarticular***

Seronegative spondyloarthropathy
Connective tissue disorders
  - Systemic lupus erythematosus
  - Sarcoidosis

Inherited disorders
Familial hypertrophic synovitis
Hemophilic arthropathy
Immunodeficiency

**Nonsynovial Disorders**

***Pauciarticular***

Acute
- Malignancy
- Leukemia
- Neuroblastoma

Chronic
- Noninflammatory disorders
- Avascular necrosis
- Slipped capital femoral epiphysis and dysplasias

Other
- Juvenile osteoporosis
- Multifocal osteolysis

***Polyarticular***

- Metabolic or inherited disorders
- Diabetic arthropathy
- Turner syndrome
- Lysosomal storage disease
- Kniest syndrome
- Winchester syndrome
- Chondrodysplasias
- Frostbite
- Goldbloom disease

**INFECTIOUS DISORDERS**

***Pauciarticular***

Infectious arthritis
Septic arthritis
Reactive arthritis
Tuberculous arthritis
Postinfectious arthritis

***Polyarticular***

Infectious arthritis
Lyme disease
Reactive arthritis

## **BOX 136.3** Radiographic Features of Juvenile Idiopathic Arthritis

### ALIGNMENT ABNORMALITIES

- Atlantoaxial subluxation
- Coxa valga or varus
- Finger deformities including boutonniere or swan neck deformity
- Knee valgus
- Hallux valgus

### BONE DENSITY

- Juxtaarticular osteoporosis
- Diffuse osteoporosis (late)
- Metaphyseal lucent band (rarely)
- Periosteal reaction adjacent to affected small joints

### CARTILAGE AND JOINT SPACES

- Erosions (late), may appear corticated
- Cartilage space narrowing (late)
- Ankylosis (especially spine, wrists)

### DISTRIBUTION

- Monoarticular, oligoarticular, or polyarticular

### GROWTH ABNORMALITIES

- Affected small bones are shorter than normal
- Overgrowth (lengthening) of affected long bones
- Advanced maturation of affected epiphyses
- Large epiphyses
- Micrognathia (may have mandibular notching)
- Protrusio acetabuli
- Small fused cervical vertebrae
- Angular carpal bones
- Square patella
- Intercondylar notch widening (also a feature of hemophilia)

### SOFT TISSUES

- Effusions and joint distension
- Nodules
- Periarticular calcification (probably due to corticosteroid injections)

*From Johnson K, Gardner-Medwin J. Childhood arthritis: classification and radiology.* Clin Radiol. *2002;57:47–58.*

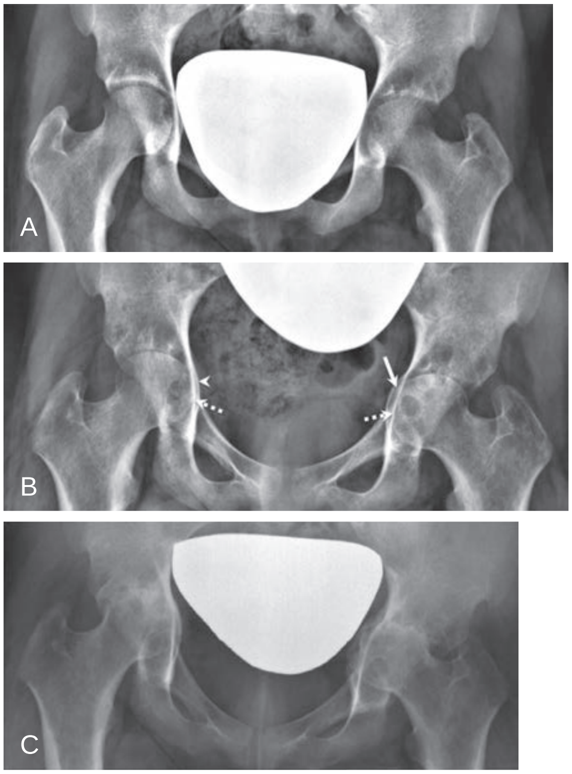

**Figure 136.1. Juvenile idiopathic arthritis in a girl with progressive bilateral hip arthritis.** Frontal radiograph of the pelvis at 16 years of age (A) shows diffuse left hip joint space narrowing and subchondral cystic changes in the left acetabulum. (B) At 18 years of age, despite aggressive treatment, there has been interval progression of disease with marked bilateral joint space loss and progression of subchondral cystic changes in the left acetabulum and left femoral head. Protrusio acetabuli, defined as the femoral head *(solid arrow)* projecting medial to the ilioischial line *(dashed arrow)*, is present on the left. Coxa profunda, defined as the acetabular fossa *(arrowhead)* projecting medial to the ilioischial line *(dashed arrow)*, is present on the right. These findings indicate medial migration of the femoral heads. (C) At 19 years of age, there has been further progression of disease in both hips. At 20 years of age, this patient underwent bilateral hip replacements.

destruction with radiography,[8,29] hence the expanding role for ultrasound and MRI in the evaluation of JIA.[30]

A variety of radiographic features can be encountered with joint disease. Specific joint findings will depend on the underlying abnormality, the chronicity of the disease, and the response to therapy. A systematic approach to the imaging interpretation of any joint is highly recommended. One popular approach is the "ABCDS" of joint disease, featuring assessment of joint *A*lignment, *B*one density and other bone changes, *C*artilage loss, *D*istribution of joint disease (whether monoarticular, oligoarticular, or polyarticular), and *S*oft tissue abnormalities (Box 136.3).

The earliest abnormalities include soft tissue swelling, osteopenia, and effusion. Periosteal reaction occasionally may be seen. Typically, the osteopenia is initially periarticular (Fig. 136.1), becoming more diffuse with time. Osteopenia may be subtle and better recognized by comparison with the contralateral extremity (if it is unaffected). With long-standing disease, uniform bone loss may occur with a thin cortex. Uncommonly, a linear subphyseal demineralization can be observed, but this finding is nonspecific and can also be seen in persons with other conditions such as leukemia.[31]

Joint effusions are encountered commonly and can be seen in inflammatory or noninflammatory joint disease. A sign of knee effusions is fullness in the suprapatellar region, which is best seen on the lateral view. In the elbow, knee, and ankle, adjacent fat lines and fat pads are displaced. Periosteal reaction, when present, is commonly seen in the phalanges, metacarpals, and metatarsals but also can occur in the long bones. Joint space narrowing may be caused by cartilage loss (see Fig. 136.1). In persons with JIA, the joint space narrowing is usually uniform. In some patients with rheumatoid factor positive polyarthritis or systemic arthritis, early erosive disease can occur (Fig. 136.2).

Bone erosions are typically located at joint margins in the bare areas but also may occur at tendinous insertions. Bone erosions also can be seen in persons with septic arthritis or hemophilic arthritis related to the inflammatory reaction caused by intraosseous hemorrhage. Large erosions can also be seen in the camptodactyly arthropathy coxa vara pericarditis syndrome[32] (e-Fig. 136.3). Deformity of the fingers, whether with boutonniere (proximal interphalangeal [PIP] flexion with distal interphalangeal [DIP] extension) or swan neck (PIP extension with DIP flexion) deformity, can be seen in a variety of disorders, including JIA (Fig. 136.4),

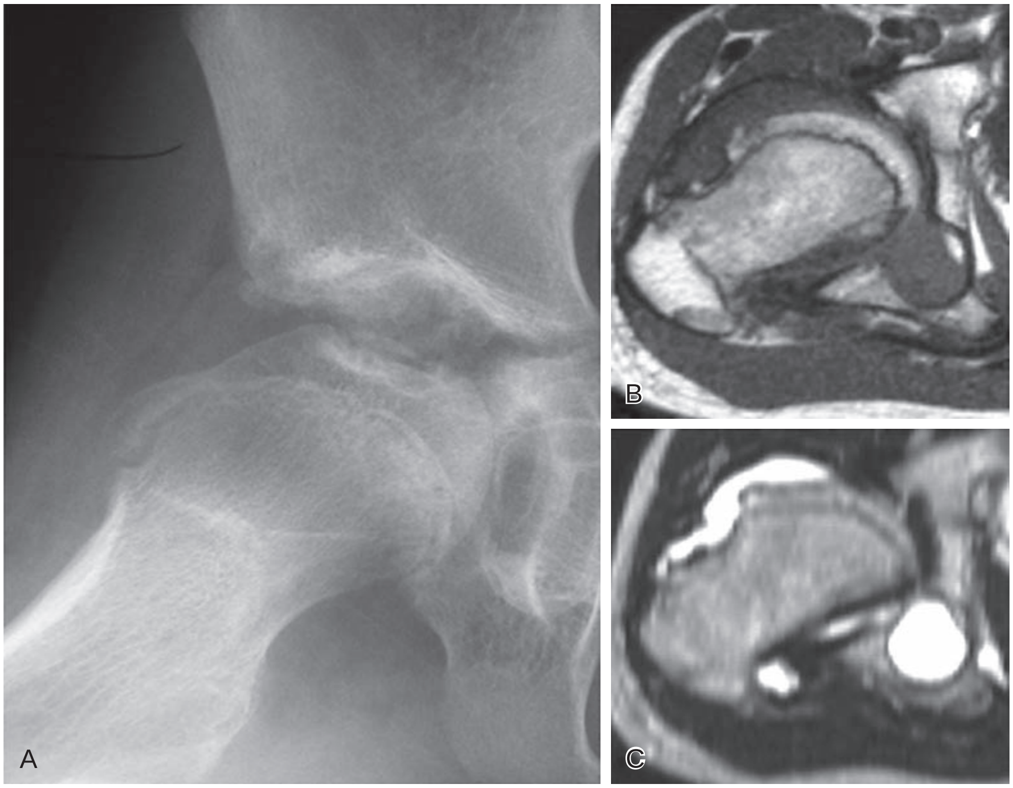

**e-Figure 136.3. Camptodactyly arthropathy coxa vara pericarditis syndrome.** Radiograph (A) axial T1-weighted (B) and axial T2-weighted (C) MR images of the right hip show coxa vara, short broad femoral necks, synovitis/joint effusion, and erosive changes in the right hip.

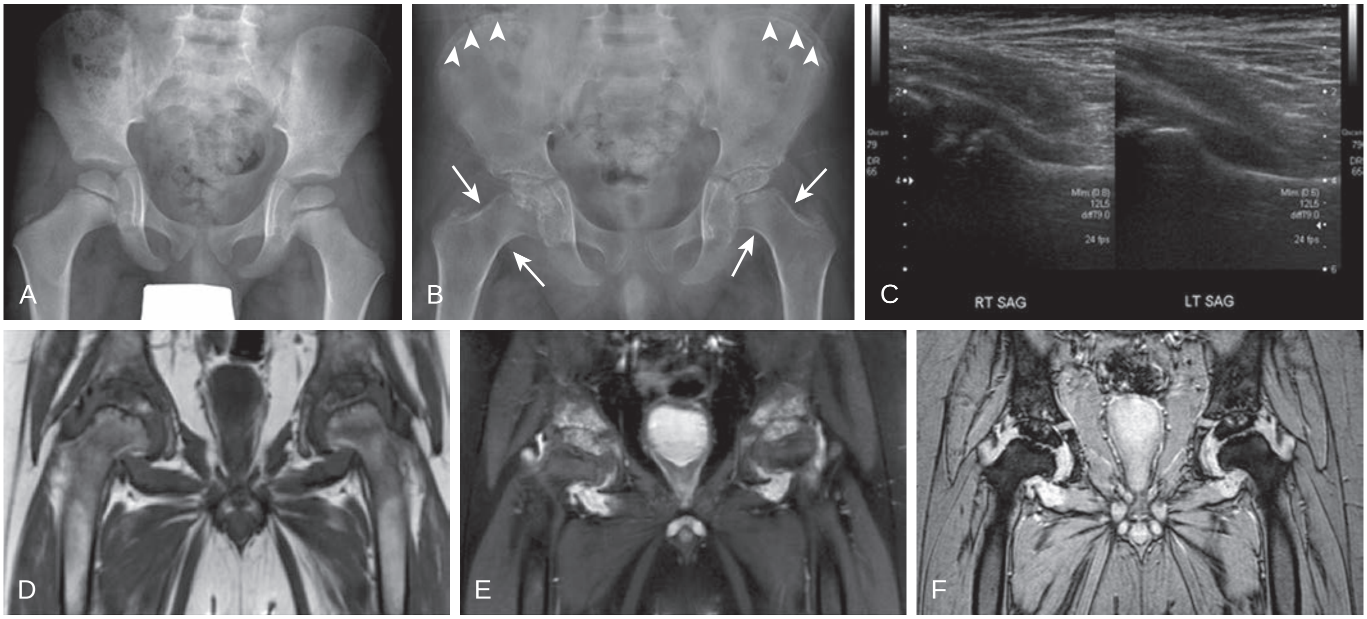

**Figure 136.2. Systemic juvenile idiopathic arthritis in a patient with multiple hip infections.** At the age of 4 years, only slight irregularity of the contour of the proximal femoral epiphyses is noted on a frontal radiograph (A) representing a variation of normal, with preserved joint spaces. At the age of 11 years, extensive erosive changes are seen in the femoral heads and acetabula with further bilateral hip joint space loss, as seen on radiographs (B). Interval increased sclerosis is noted along the acetabular roofs bilaterally. Nonspecific periosteal reaction is seen along the medial aspect of the femoral necks bilaterally *(arrows)*. Sclerotic lines are shown along the iliac wings *(arrowheads)* compatible with previous bisphosphonate therapy. Ultrasound images (C) obtained at 11 years demonstrates a moderate left and mild right hip joint effusion. Coronal noncontrast (D), contrast-enhanced T1-weighted fat-saturated (E), and gradient recalled echo (F) MR images, 1 month after the ultrasound, show markedly thickened, lobulated, heterogeneously enhancing synovium in both hip joints. Enhancing marrow signal abnormality, loss of articular cartilage, and articular surface irregularity is present in the femoral heads and acetabula. The findings are consistent with severe progression of inflammatory arthritis with diffuse pannus formation and secondary avascular necrosis of the femoral heads.

camptodactyly arthropathy coxa vara pericarditis syndrome, or systemic lupus erythematosus. Enlarged or irregular epiphyseal ossification centers can be seen in persons with hemophilia, JIA, and tuberculous arthritis. Atlantoaxial subluxation or cervical vertebrae pseudosubluxation and ankylosis (e-Fig. 136.5) may be noted in persons with JIA, the arthropathy of Down syndrome, dysostosis multiplex, and systemic lupus erythematosus.

In contrast to adult patients with inflammatory arthritis, bone erosions are less commonly seen in children because the epiphyseal ossification center is surrounded not only by articular cartilage but also by epiphyseal cartilage and the spherical growth plate. As a result, significant cartilage loss must occur before osseous erosions are visible with radiography. Therefore the role of MRI is relatively more important in children to detect articular or epiphyseal cartilage erosions before actual bony erosions are visible on radiography.

Changes in bone growth and maturation with changes in the normal size of ossification centers and alteration of normal bone modeling can be seen in persons with JIA, and with infections and hemophilia. Enlargement of ossification centers and epiphyses (see Fig. 136.4), contour irregularity, trabecular changes, and squaring (typically of the patella) can be seen. Tibiotalar slant (ankle valgus) can also be seen.[33]

Late sequelae of JIA include epiphyseal deformity, abnormal angular carpal bones, widening of the intercondylar notch of knees (see Fig. 136.4), and premature fusion of the growth plates. Growth disturbances are more frequent if disease onset is early. Joint space narrowing and osseous erosions are usually late manifestations. At the hip, protrusio acetabuli (see Fig. 136.1), premature degenerative changes, coxa magna, and coxa valga can be seen. Joint space loss can progress to ankylosis, particularly in the apophyseal joints of the cervical spine (see e-Fig. 136.5) and wrist. Rarely, ankylosis also can be seen in larger joints, including the hips. Subluxation of the joints, especially at the wrist, may be evident. Growth disturbance of the temporomandibular joint may lead to micrognathia and temporomandibular disk abnormality.[33]

Although radiography should be used initially in evaluation of joints, cross-sectional imaging techniques have provided a significant improvement in anatomic delineation and diagnosis.

## Magnetic Resonance Imaging

MRI is an optimal tool for evaluation of both soft tissues and osteochondral abnormalities with superb tissue contrast.[34,35] Contrast-enhanced MRI is extremely sensitive for detecting active disease and for early detection of cartilage loss, bone erosions, and synovial hypertrophy in children and adolescents.[35,36] MRI provides multiplanar evaluation with a combination of available imaging sequences, including T1 and fast spin echo T2-weighted sequences, gradient echo sequences, and postcontrast studies all tailored to the specific clinical problem.[37–39] High cost, limited availability, and frequent need for sedation in very young patients are limitations.

Various forms of cartilage can be visualized on MRI, including articular, unossified epiphyseal, and the physeal cartilage.[40] Gadolinium-enhanced MRI can demonstrate normal vessels

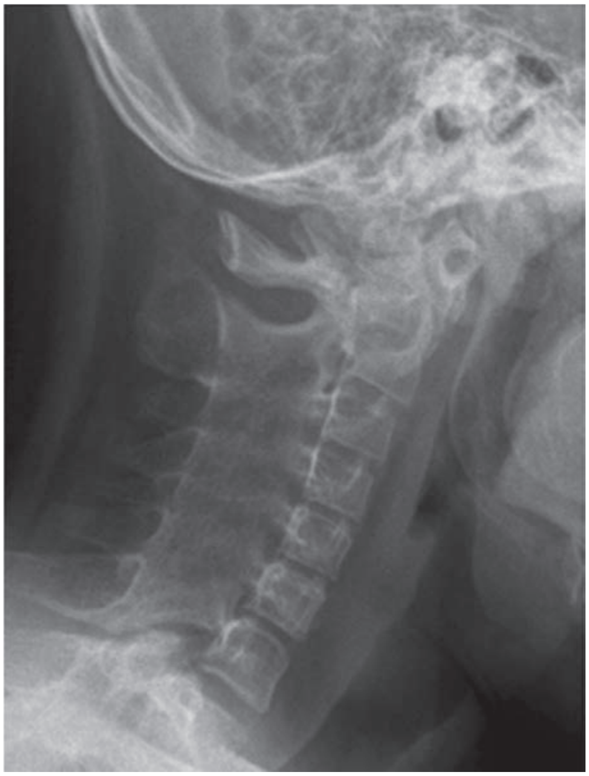

**e-Figure 136.5. Polyarticular juvenile idiopathic arthritis.** Lateral cervical radiograph demonstrates diffuse ankylosis of the posterior elements of C3-T1.

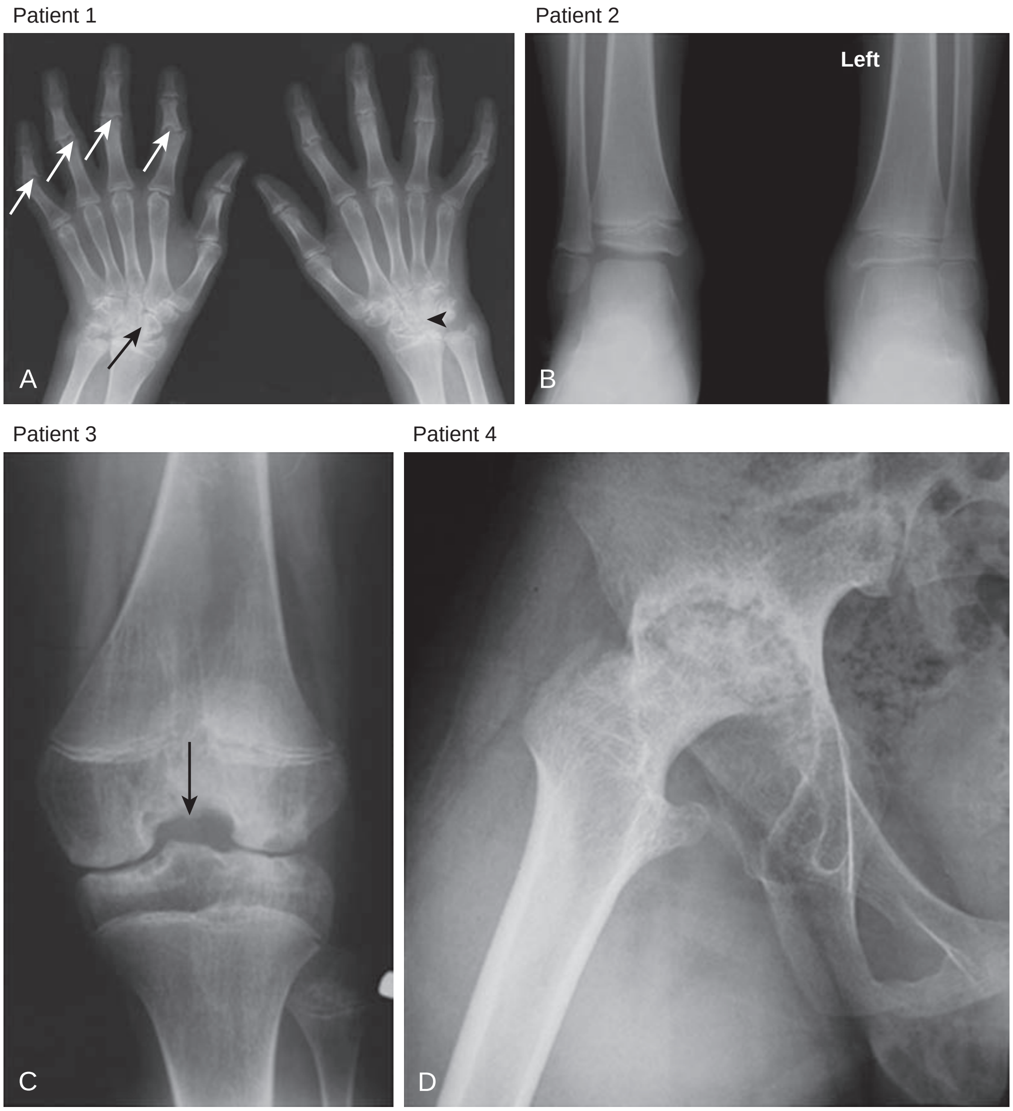

**Figure 136.4. Advanced juvenile idiopathic arthritis in the peripheral skeleton in different patients.** (A) Patient 1: Deformity of the digits as a result of erosive changes is seen at the phalangeal heads and bases *(white arrows)* and metacarpal and carpal bones *(black arrow)*, along with joint space narrowing, carpal ankylosis *(arrowhead)*, and ray subluxation. (B) Patient 2: A radiograph shows joint space narrowing, advanced maturation, and epiphyseal overgrowth (shown in the distal left tibia and fibula in comparison with normal-appearing right counterparts). (C) Patient 3: Widening of intercondylar notch *(arrow)* of the knee. (D) Patient 4: Extensive joint space narrowing of the right hip, articular irregularity, and subchondral cystic changes in the femoral head and acetabulum.

present within the cartilaginous epiphysis.[41] MRI also is helpful in detecting synovial abnormalities[42] and can be used to assess for changes with therapy.[43]

Without contrast material, proliferating synovium on MRI appears as soft tissue thickening, which is typically intermediate signal on T1-weighted and increased signal intensity on T2-weighted images (Fig. 136.6). It may have slightly higher signal intensity than adjacent fluid on unenhanced T1-weighted images. At times, pannus may appear as intermediate to dark signal intensity on T2-weighted images outlined by bright signal joint fluid. Its variable signal intensity reflects the relative amount of fibrous tissue and hemosiderin. Intravenous administration of gadolinium-based contrast agents improves visualization of thickened synovium, especially with use of fat-suppression techniques. Proliferating synovium appears as enhancing linear, villous, or nodular tissue. Images should be obtained immediately after contrast injection because diffusion of contrast material from the synovium into joint fluid occurs over time. Hypervascular inflamed pannus enhances significantly (see Fig. 136.2E), whereas fibrous inactive pannus shows much less enhancement. Subchondral cysts and bone erosions (see Fig. 136.2) appear as low signal areas on T1-weighted sequences,[37] with overlying articular and epiphyseal cartilage loss better delineated on fluid-sensitive sequences. Meniscal hypoplasia can be seen in some cases of JIA (e-Fig. 136.7).[35]

Quantitative techniques have been developed for synovial volume.[44,45] MRI is more sensitive than clinical evaluation in detecting some specific joint involvement, including the temporomandibular joint, which often demonstrates inflammatory change in the absence of clinical symptoms.[46]

With prolonged synovial inflammation, well-defined intraarticular nodules termed “rice bodies” (Fig. 136.8) may be present. Rice bodies likely arise from detached fragments of hypertrophied

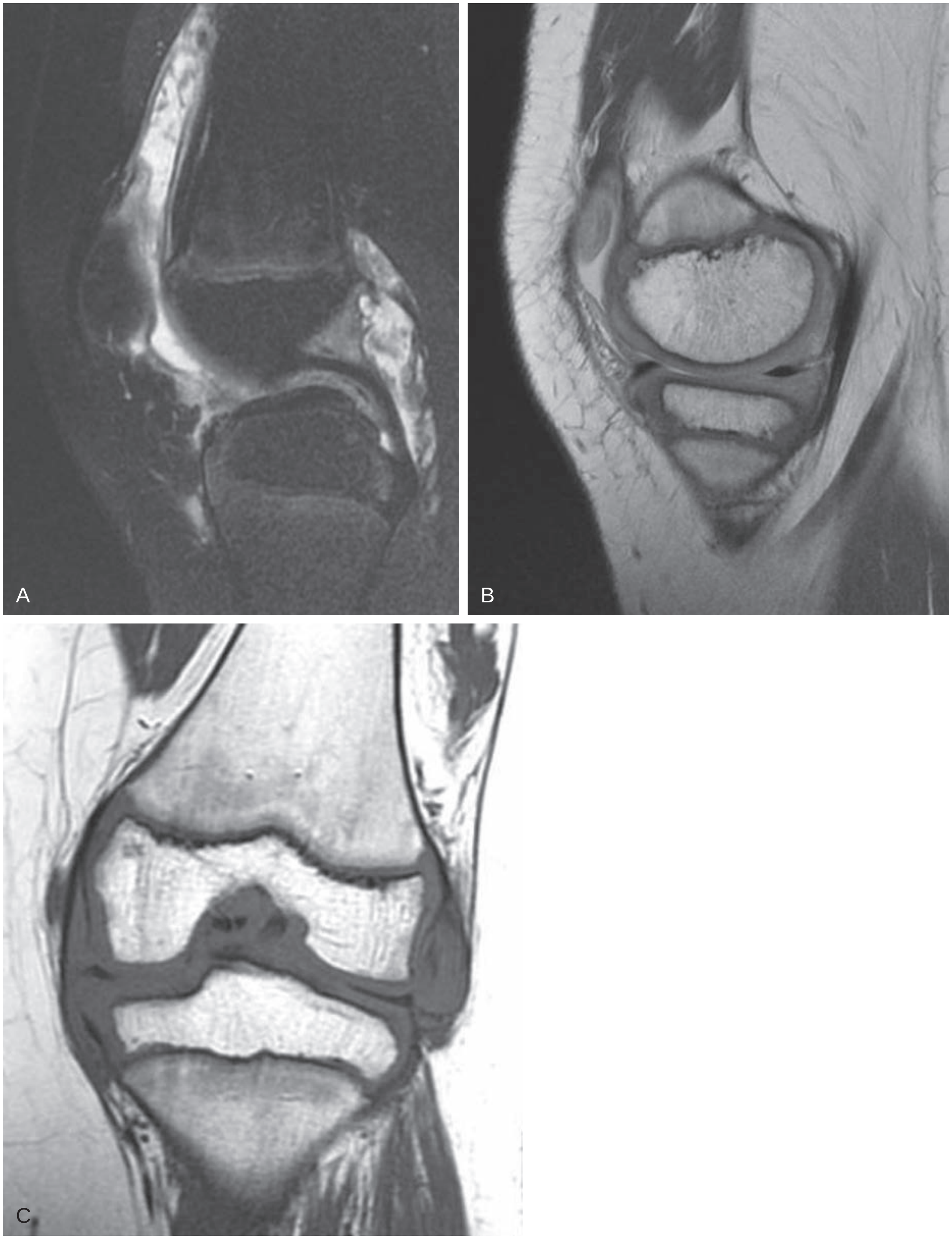

**e-Figure 136.7. Juvenile idiopathic arthritis in a 13-year-old girl.** (A) Sagittal T2-weighted MR image shows diffuse synovitis and a joint effusion. (B) Sagittal proton-density MR image through the medial joint compartment shows hypoplastic anterior and posterior horns of the medial meniscus. (C) Coronal T1-weighted MR image shows hypoplasia of the medial and lateral menisci.

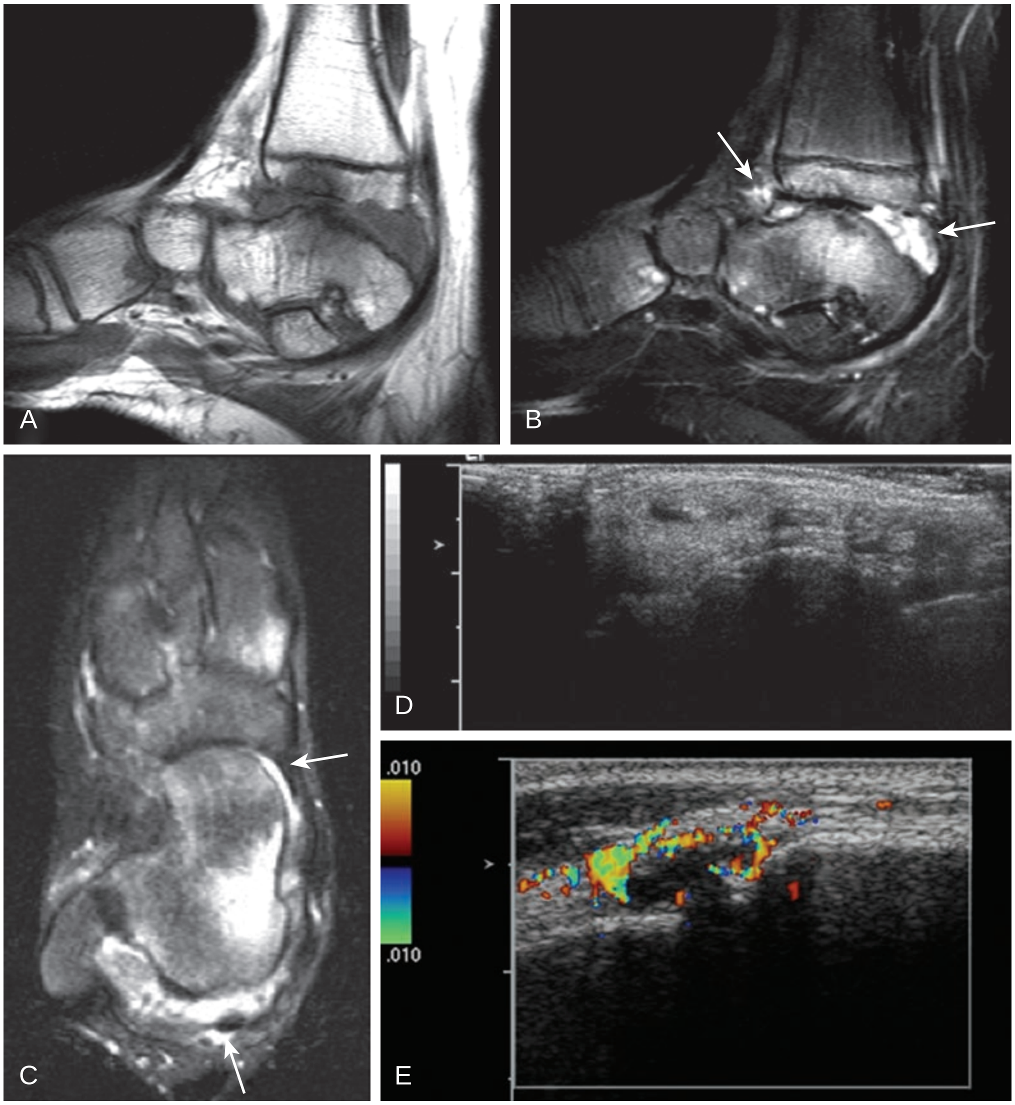

**Figure 136.6. Juvenile idiopathic arthritis and symptomatic tenosynovitis in a 14-year-old girl.** Sagittal T1-weighted (A) and fat-saturated T2-weighted (B) MR images of the right ankle show synovial overgrowth within the tibiotalar *(arrows)* and intertarsal joints. Extensive erosive changes and bone marrow edema are noted at the tibiotalar joint (A and B). Increased signal intensity is seen within the synovial sheaths of the tendons of the medial aspect of the right foot, including the tibialis posterior *(medial arrow)* and flexor hallucis longus *(posterior arrow)* on axial T2-weighted MR images, suggesting tenosynovitis (C). Longitudinal gray-scale (D) and color Doppler (E) ultrasound scans demonstrate a small amount of fluid within the tendon sheaths and synovial proliferation and hyperemia of the tendons of the medial right foot.

synovial villi. On MRI, rice bodies are low signal on T2-weighted images because of their fibrous tissue composition and are associated with joint effusion, synovial hypertrophy, and synovial enhancement after gadolinium administration.[47]

Bone marrow edema is represented by areas of low T1-weighted and high T2-weighted signal intensity (e-Fig. 136.9) and should be differentiated from normal marrow speckling seen on fluid-sensitive sequences, most frequently in the ankle and foot. Studies in adults[48–50] have shown an association between presence of subchondral bone marrow edema in persons with inflammatory arthritis and radiographic erosive progression.

Because cartilage is one of the earliest sites of damage in persons with JIA, it is an important area to be evaluated with MRI. Standard T2-weighted and proton density magnetic resonance (MR) sequences can assess articular cartilage injury, from increased signal intensity within cartilage to articular cartilage thinning, erosions, and areas of full-thickness cartilage loss. Fat-saturated fluid-sensitive sequences will also depict subchondral bone marrow edema. Advanced sequences for cartilage evaluation are discussed later.

Although MRI has been extensively investigated in JIA,[8,51] standardized measures for data acquisition and interpretation are not widely used[52]; hence this technique is underutilized both in clinical practice and in research. Few MRI scales have been designed to specifically assess morphologic changes with JIA.[53,54]

**Novel Magnetic Resonance Imaging Techniques.** A number of novel MRI techniques are under evaluation for improved assessment of synovial, cartilaginous, or osseous abnormalities. These MRI techniques include diffusion-weighted imaging (DWI)

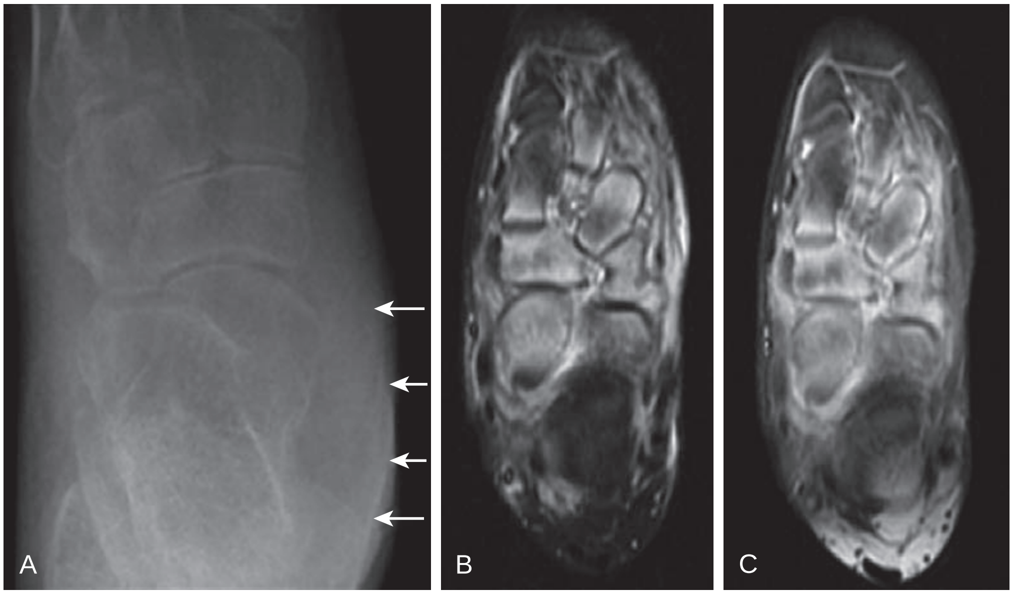

**e-Figure 136.9. Juvenile idiopathic arthritis in an 11-year-old girl with a swollen left ankle and midfoot.** The radiograph (A) and MRI examination (B and C) were obtained 1 week apart. Unenhanced axial inversion-recovery (B) and postcontrast axial T1-weighted spin echo MR images (C) of the left foot obtained with fat saturation are shown. Soft tissue swelling is present along the left ankle (A) *(arrows)*. Marked osteopenia and navicular-cuneiform joint space narrowing (A) are also present. MR images show extensive bone marrow edema predominantly within the anterior aspect of the talus, navicular, and cuneiforms. Increased signal intensity on inversion recovery images (B) and contrast enhancement (C) are also noted in the soft tissues surrounding the involved bones.

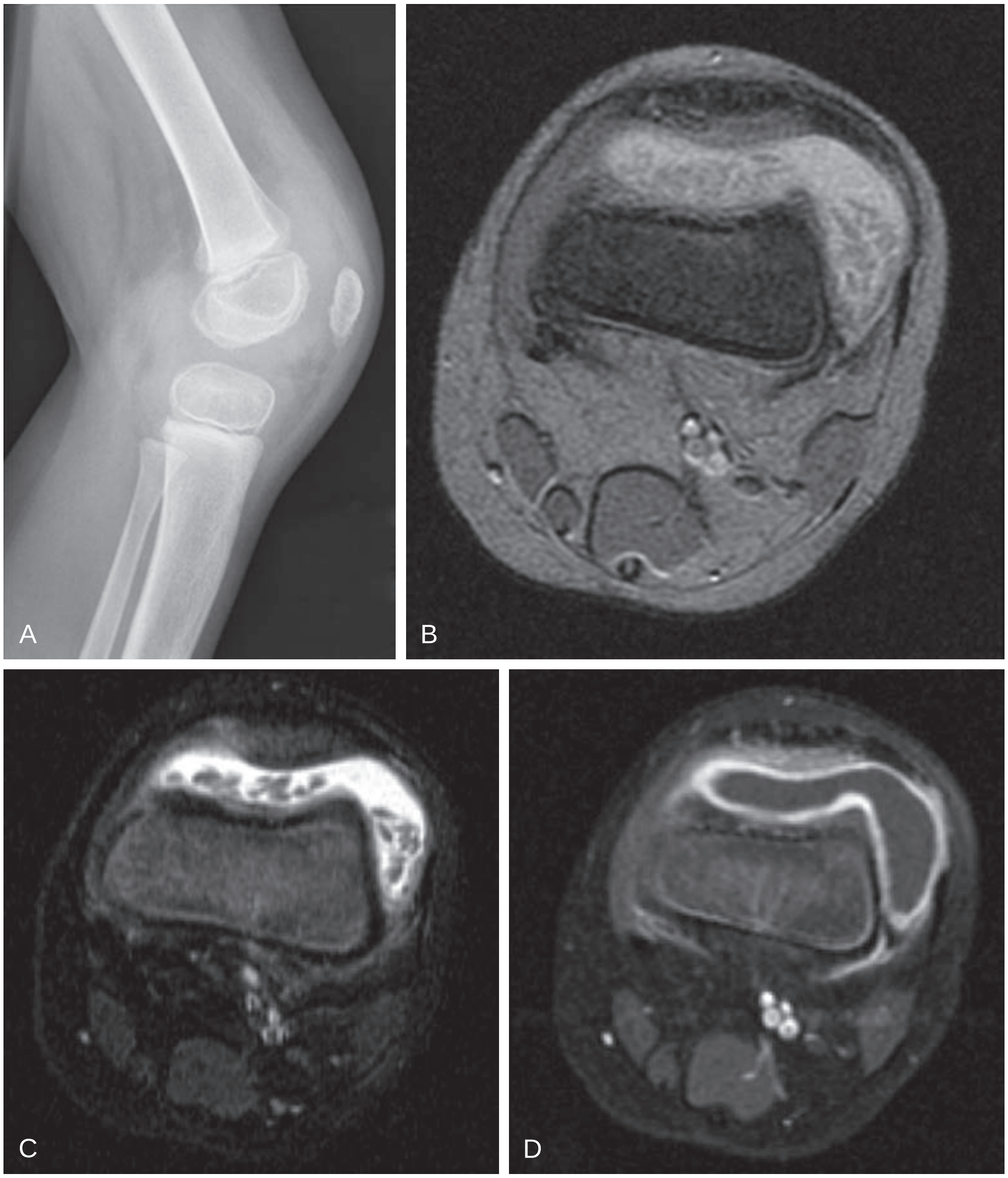

**Figure 136.8. Rice bodies.** A 3-year-old boy had persistent knee pain 1 month after sustaining a trauma. The lateral radiograph view (A) shows moderately large joint effusion distending the suprapatellar bursa. Intraarticular elongated bodies that extend into the recesses of the joint space and layer in dependent portions are seen on axial multiplanar gradient-recalled acquisition (B) and T2-weighted fat-saturated (C) and contrast-enhanced T1-weighted fat-saturated (D) MR images. Marked synovial enhancement also is noted.

and perfusion imaging, delayed gadolinium-enhanced cartilage imaging, T2 quantification, and ultra-short echo time (TE) pulse sequences. DWI evaluates the translational movement (Brownian motion) of water molecules that occurs in all tissues, including synovium and cartilage. Alteration of normal diffusion can occur in diseases including infection, inflammation, and infarction.[55] Diffusion tensor imaging (DTI) is a variant of DWI and has been used to study the structure of ordered biologic tissue, and holds potential to delineate synovial inflammation.[56–58]

Contrast-enhanced perfusion MRI assesses blood flow using intravenously administered paramagnetic contrast agents. Potential uses of this technique include recognition of epiphyseal ischemia and quantification and monitoring of synovial inflammation.[59] The rate of synovial enhancement depends in part on tissue vascularization and capillary permeability, both of which are highly correlated with synovial inflammation.[60,61] Rapid enhancement suggests active synovial inflammation, whereas gradual delayed enhancement suggests subacute/chronic synovial inflammation. Quantitative dynamic contrast-enhanced MRI based on pharmacokinetic modeling has been proposed as an objective measure of therapeutic efficacy in patients with JIA.[62,63]

Delayed gadolinium-enhanced MR cartilage imaging is a sensitive technique for assessing cartilage proteoglycan content using the negative charge of the intravenously administered paramagnetic MR contrast agent.[64] The contrast agent distributes into cartilage inversely to the fixed charge density of negatively charged glycosaminoglycan (GAG). Delayed gadolinium-enhanced MR cartilage imaging may be used to assess early cartilage injury with depletion of GAG before anatomic changes are visible by conventional cartilage sequences.

Cartilage assessment can also be provided by mapping T2 relaxation time measurements. These measurements may help characterize the structural integrity of the cartilaginous tissue and quantitatively assess the degree of cartilaginous hydration and collagen orientation.[65] Typically there is a decrease in T2 relaxation from the cartilage surface to the deeper layers.[66,67] In persons with JIA, increased cartilage T2 relaxation time is thought to be an early marker of disease progression in JIA, because it can identify microstructural changes before damage becomes visible.[68] In a longitudinal study evaluating patients with JIA from 3-month to 2-year follow-up, the clinical assessments improved, whereas T2 maps showed increased T2 values.[69] This increase likely represents progressive microstructural changes, even though clinical symptoms improved with treatment.

Other advanced MRI techniques for cartilage assessment include T1 rho, sodium imaging, and ultrashort TE sequences.[70–79]

## Ultrasonography

Recent advances in ultrasonography, including better transducers and more pediatric musculoskeletal experience, have stimulated increased use of ultrasound in the assessment of pediatric joint disease. Ultrasound is ideal for assessing the pediatric musculoskeletal system because of its ability to visualize intraarticular structures such as cartilage and thickened synovium without the need for radiation. Ultrasound is very sensitive in detecting joint effusion, even in areas where radiographs are insensitive, such as the hip (see Fig. 136.2C) and shoulder.[80] Intraarticular masses may be detected with ultrasound, although their appearance is often nonspecific. Tendons and ligaments also can be assessed with higher-frequency transducers.[81] Fluid within the synovial sheath appears as an anechoic halo surrounding the tendon (Fig. 136.10), whereas synovial thickening appears as a hypoechoic thickening around the tendon. Synovial hyperemia leads to increased signal on Doppler evaluation.[82] Power Doppler has been shown to detect residual disease activity more sensitively than clinical examination and/or MRI both in active disease and when JIA is in remission[83,84] and could be used to predict short-term relapse in patients with JIA who appear to be in remission clinically.[85]

Sonography can also be used to assess other periarticular soft tissue abnormalities, including popliteal cysts (e-Fig. 136.11) or other soft tissue masses, and to guide aspiration or injection of joints.[86]

Disadvantages of ultrasound include lack of standardization of ultrasound techniques for assessment of growing joints and normative data, lack of capability to visualize the central aspect of some joints, and difficulty in assessing some joints such as the temporomandibular joints (Fig. 136.12).[46,87]

Erosions and focal or diffuse thinning of the articular cartilage also can be detected but only peripherally in the joint. Color Doppler ultrasound enables the detection of perisynovial hyperemia. Studies in children[88,89] have demonstrated the ability of color and power Doppler sonography, with or without intravenous injection of contrast agents, to estimate synovial activity in JIA. Resistive indices and fraction of color pixels may be used as quantitative measurements of the blood flow.[90,91] Contrast-enhanced sonography holds potential for detecting active synovial inflammatory disease in persons with subclinical JIA and may help guide early treatment.[88]

Very limited information is available about the diagnostic performance and accuracy of ultrasound compared with MRI or clinical examination (in knees, sensitivity for joint effusion is 62%,[92] ranging between 60% and 90% for clinically active joints and approximately 70% for clinically inactive joints[93–95]; for superficial cartilage destruction, overall sensitivity is 60%).[92] Ultrasound-determined synovial thickness of the knee seems to correlate with clinical and laboratory (sedimentation rate and C-reactive protein levels) disease activity scores and with biomarkers of disease activity.[95] In ankles, however, very poor agreement was observed comparing clinical and ultrasound scores.[96]

## Treatment and Follow-up

A systematic review on evidence-based treatment of JIA[97] showed that nonsteroidal antiinflammatory drugs are effective only for a minority of patients, mainly those with oligoarthritis. Intraarticular corticosteroid injections are very effective for persons with oligoarthritis. Methotrexate is effective for the treatment of persons with extended oligoarthritis and polyarthritis and less effective for persons with systemic arthritis. Sulfasalazine and leflunomide may be alternatives to methotrexate. Antitumor necrosis factor medications are highly effective for polyarticular JIA that is not responsive to methotrexate but are less effective in persons with systemic arthritis. Therefore, despite many treatment advances, evidence is still lacking for treatment of several disease subtypes.

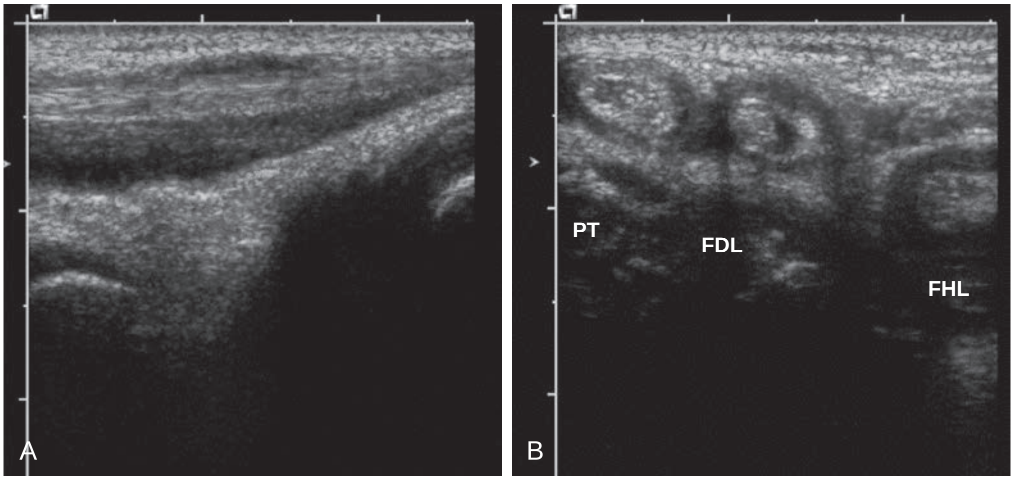

**Figure 136.10. Polyarticular juvenile idiopathic arthritis in a 10-year-old girl.** (A) Longitudinal sonogram along the medial aspect of the patient's left ankle shows an increased amount of fluid within the posterior tibialis tendon. (B) Corresponding transverse sonogram demonstrates tenosynovitis involving the posterior tibialis *(PT)*, flexor digitorum longus *(FDL)*, and flexor hallucis longus *(FHL)* tendons of this ankle.

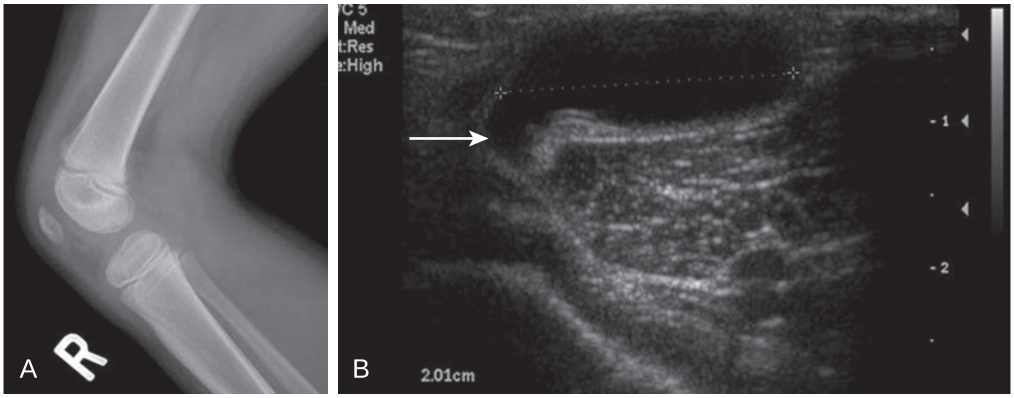

**e-Figure 136.11. Bakers cyst.** A 4-year-old girl with an asymptomatic lump in the popliteal fossa of the right knee. Lateral radiograph (A) shows increased soft tissue density in the popliteal region. Transverse sonogram through the popliteal fossa (B) demonstrates a large cyst with a tail *(arrow)* extending between the medial head of the gastrocnemius and semimembranosus tendons.

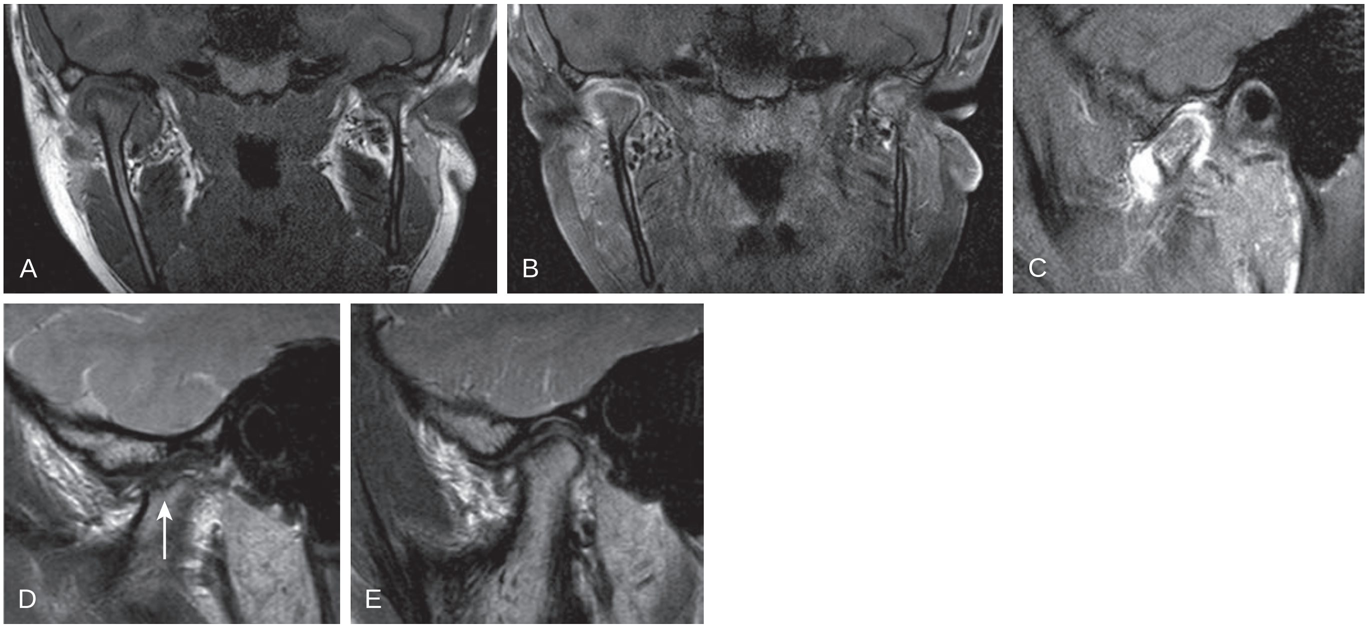

**Figure 136.12. Temporomandibular joint involvement in longstanding juvenile idiopathic arthritis in a symptomatic 12-year-old girl.** Coronal T1 image (A), a contrast-enhanced coronal T1 spectral presaturation inversion recovery (SPIR) image (B), a sagittal contrast-enhanced T1 SPIR image of the right temporomandibular joint (TMJ) (C), sagittal proton density images of the right (D) and left (E) of the TMJs, show moderate right acute TMJ synovitis and mild left acute synovitis. Erosive changes are present *(arrow)*. Note a hypoplastic left mandibular ramus in (A) and (B).

With regard to intraarticular corticosteroids, studies have shown that as many as 70% of patients with oligoarthritis do not have reactivation of disease in the injected joint for at least 1 year, and 40% do not have reactivation for more than 2 years.[98–100] Radiographic and MRI studies have shown a marked decrease in synovial volume after injection without deleterious effects on the cartilage.[101]

## Imaging in the Assessment of Response to Therapy

Once therapy has begun for patients with JIA, imaging can be a helpful adjunct to assess disease activity and response to therapy. To date, several studies have examined radiographic changes before and after initiation of therapy, whereas more recent studies have used CT and/or MRI to describe joint changes and to use more quantitative measures of disease activity.

**Radiography.** Radiography is able to demonstrate epiphyseal overgrowth and osteopenia after the injection of intraarticular triamcinolone hexacetonide.[102] Carpal length, defined as the radiometacarpal length plotted against the length of the second metacarpal bone on a chart with normal growth carpal scores, as described by Poznanski et al.,[103] is another parameter that has been used in follow-up with an interval increase in carpal length (a positive change) indicating improvement.

**Ultrasound.** In a small study of 15 joints, Eich et al.[102] used ultrasound to determine the presence of effusion, pannus, popliteal cysts, and lymphadenopathy before and after intraarticular therapy and concluded that ultrasound was as sensitive as MRI in demonstrating joint effusion and/or pannus but that differentiation between the two was difficult, particularly in the hip joint. Spârchez et al. showed power Doppler ultrasonography correlated with physician global assessment of disease activity on visual analogue scale (PhGA) and to be more sensitive than erythrocyte sedimentation rate (ESR) and C-reactive protein (CRP) levels in assessing disease activity.[104]

**Magnetic Resonance Imaging.** Although CT is able to demonstrate joint space narrowing, erosions, and condylar flattening,[105] MRI is the modality of choice to document changes before and after therapy. MRI can be used to monitor cartilage and bone erosions, effusion, pannus, and synovial volumes.[40] In studies of children with arthritis who received intraarticular steroid injections, MRI has shown a long-lasting beneficial effect, with suppression of synovial inflammation and reversion of pannus formation.[101,102,106]

Quantitative dynamic contrast-enhanced MRI can be used to evaluate disease activity in the knee. A study of pharmacokinetic parameters and synovial volumes showed significant decreases at 12 months after intraarticular steroid therapy; however, improvement in synovial volume appeared to lag behind dynamic parameters, reflecting delay or subclinical synovitis.[63] Of all the imaging modalities, MRI has been shown to be the most sensitive modality in the assessment of temporomandibular joint arthritis in children and has been used as a reference standard measure for comparison of clinical examination and ultrasound in clinical studies.[46] Ultrasound has been shown to be less useful than clinical examination to exclude active temporomandibular joint arthritis in patients with JIA.[46] Standardized and validated assessment systems are still are being developed.

## Complications and Adverse Effects of Joint Injections

It is difficult to determine whether other postinjection changes in JIA patients reflect the underlying severity of the disease or the effects of the local treatment.[107] The most common radiographic finding after injection is intraarticular calcification (e-Fig. 136.13). This calcification can resolve or persist for some time. It typically does not impair joint function. Damage to cartilage during the procedure is a potential complication.[101] Additional complications of intraarticular steroid injections include skin depigmentation, overlying skin atrophy, and iatrogenic infection.

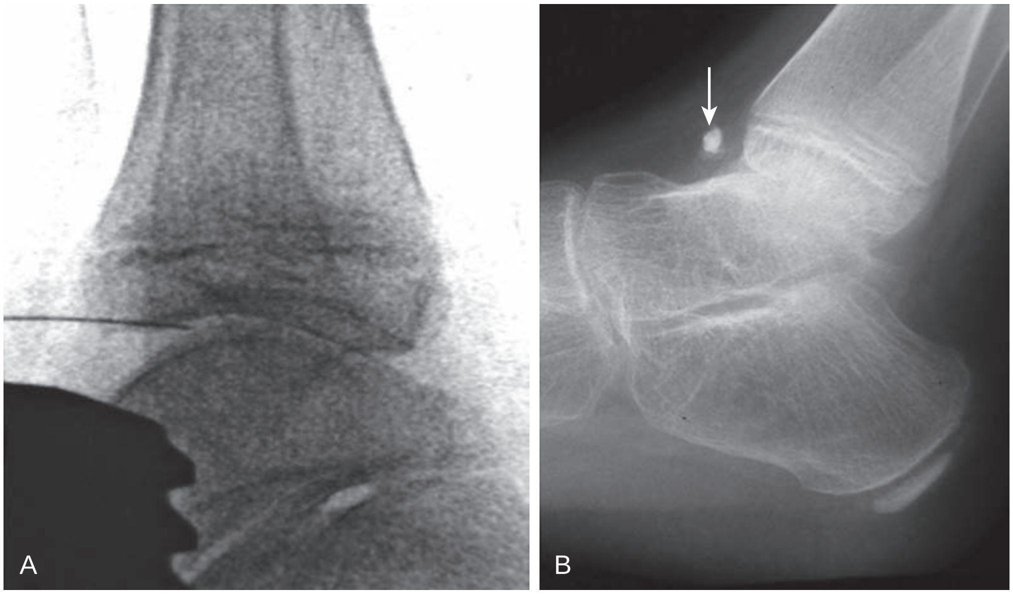

**e-Figure 136.13. Juvenile idiopathic arthritis with symptomatic tenosynovitis.** (A) Steroid injection of the tibiotalar joint under fluoroscopy. On a subsequent radiograph (B), periarticular calcification *(arrow)* is seen within the anterior aspect of the left ankle of this patient.

## ENTHESITIS-RELATED ARTHRITIS

### Etiology, Pathophysiology, and Clinical Presentation

Enthesitis-related arthritis (ERA) affects 1% to 7% of patients with JIA and includes patients with arthritis *and* enthesitis, or with arthritis *or* enthesitis, as well as two of five defined criteria, including a history of sacroiliac joint tenderness and/or lumbosacral pain, the presence of the HLA-B27 antigen, the onset of arthritis in a male patient older than 6 years, uveitis, or a history of ankylosing spondylitis, inflammatory bowel disease, or uveitis in a first-degree relative.[1] The term "ERA" was introduced in lieu of the term "pediatric spondyloarthropathies" to emphasize that (1) axial skeletal involvement in children is rare and large joint appendicular involvement is more common at presentation, and (2) the disease commonly involves tendon/ligamentous insertions and origins in children.

### Imaging

#### Radiography

Radiographic findings of ERA and other spondyloarthropathies are similar to those encountered in other forms of JIA with the exception of sacroiliitis and enthesitis, which are more specific for spondyloarthropathy (Box 136.4).[108,109] In the appendicular skeleton, radiography typically shows asymmetric involvement of the large joints of the lower limb, that is, the hip, ankle, knee, and tarsal joints. The interphalangeal joint of the hallux is also frequently involved. Radiographs may be normal initially or can demonstrate soft tissue swelling, effusion, ossification and epiphyseal overgrowth, erosions (Fig. 136.14), osteopenia, joint space narrowing, or, rarely, fusion. Bone erosions may be associated with irregular bone apposition at joint margins, referred to as "whiskering." With hip involvement, these proliferative changes are noted at the junction of the femoral head and neck. Dactylitis may be seen with soft tissue swelling and periosteal reaction along the shaft of metacarpals, metatarsals, or phalanges.

Enthesitis refers to inflammation at insertion of tendons or ligaments and can present with soft tissue swelling, localized osteopenia, and bone erosion and/or spur formation. Common sites include Achilles tendon insertion, plantar aponeurosis origin, or at the origin/insertion of the patellar tendon. Periostitis also may be seen.

In ERA, changes in the spine and sacroiliac joints generally are not seen until the latter part of the second decade or even adulthood. It is unusual for ERA to present initially with spinal involvement in children. Spinal involvement includes localized osteitis, erosions, and sclerosis, particularly at vertebral margins. Syndesmophytes and atlantoaxial subluxation are rarely seen in children. Radiographs may demonstrate unilateral or bilateral sacroiliitis (see Fig. 136.14) with indistinct articular margins (also known as pseudowidening), erosions, and sclerosis, particularly on the iliac side of the joint. Radiography shows asymmetric sacroiliac joint space widening initially, but eventually the classic bilateral, symmetric joint involvement can be seen, with joint space narrowing and ankylosis. Radiographic evaluation of the sacroiliac joints is especially difficult in teenagers. Diffuse osteopenia of the pelvic bones is a late change.

**BOX 136.4** Radiographic Features of Enthesitis-Related Arthritis and Spondyloarthropathies

**PERIPHERAL JOINTS**

- Asymmetrical involvement of large lower limb joints
- Involvement of interphalangeal joint of the hallux
- New bone at the margins of erosions
- Affected joints show swelling, effusion, epiphyseal overgrowth, erosions, osteopenia, cartilage space narrowing, and rarely fusion
- Dactylitis-swelling and periosteal new bone of fingers or toes
- Periosteal new bone—for example, metatarsals, proximal femur

**ENTHESES**

- Especially tibial tubercle and posterior aspect of calcaneus
- Swelling, erosion, new bone formation

**SACROILIITIS**

- Radiographic changes generally delayed until late teens
- Asymmetrical involvement may occur early, then become symmetrical
- Erosions occur first on the iliac side of the sacroiliac joint
- "Pseudowidening" occurs as a result of erosion
- Sclerosis and finally ankylosis develop

*From Jacobs JC, Berdon WE, Johnston AD. HLA-B27-associated spondyloarthritis and enthesopathy in childhood: clinical, pathologic, and radiographic observations in 58 patients.* J Pediatr. *1982;100:521–528.*

#### Sonography

On sonography, enthesitis may show loss of the normal fibrillar echotexture of the tendon and irregular fusiform thickening.[110] Doppler sonography can be used to assess hyperemia at the cortical bone insertion of entheses and along the adjacent synovium in children before and after treatment.[83,111]

#### Magnetic Resonance Imaging

Bone marrow edema, tenosynovitis, granulation tissue, or cortical erosion at the site of enthesitis in the appendicular skeleton may be seen with MRI.[39] MRI can demonstrate early inflammatory changes in the sacroiliac joints and spine and is especially sensitive for evaluation of subchondral bone marrow edema not shown on other types of imaging.[112]

On MRI during active inflammation, low signal on T1-weighted images, with high signal on T2-weighted and postcontrast sequences, can be seen and often in adjacent soft tissues (Fig. 136.15). The need for postcontrast images in certain joints, the sacroiliac (SI) joints in particular, has been questioned.[113] Chronic sclerosis is low signal on T1- and T2-weighted sequences. MRI also may demonstrate erosions in articular cartilage.[39] Whole-body MRI allows widespread anatomic assessment and is promising for early detection and monitoring of disease activity, which may guide treatment in the future.[114]

#### Computed Tomography

CT can show findings of sclerosis and erosive disease of ERA that are not evident on radiographs. However, MRI is preferable due to the lack of ionizing radiation and the ability to detect edema related to inflammation in the bone marrow and adjacent soft tissues.

### Treatment and Follow-up

Evidence for the optimal treatment of enthesitis-related arthritis is lacking.[97] Conventional treatments frequently offer limited efficacy. Treatment with nonsteroidal antiinflammatory drugs and corticosteroids may provide symptomatic improvement but do not alter disease progression. Sulfasalazine has been shown to be no better than placebo[115] and methotrexate has not been demonstrated to modify disease course.[116] Treatment directed

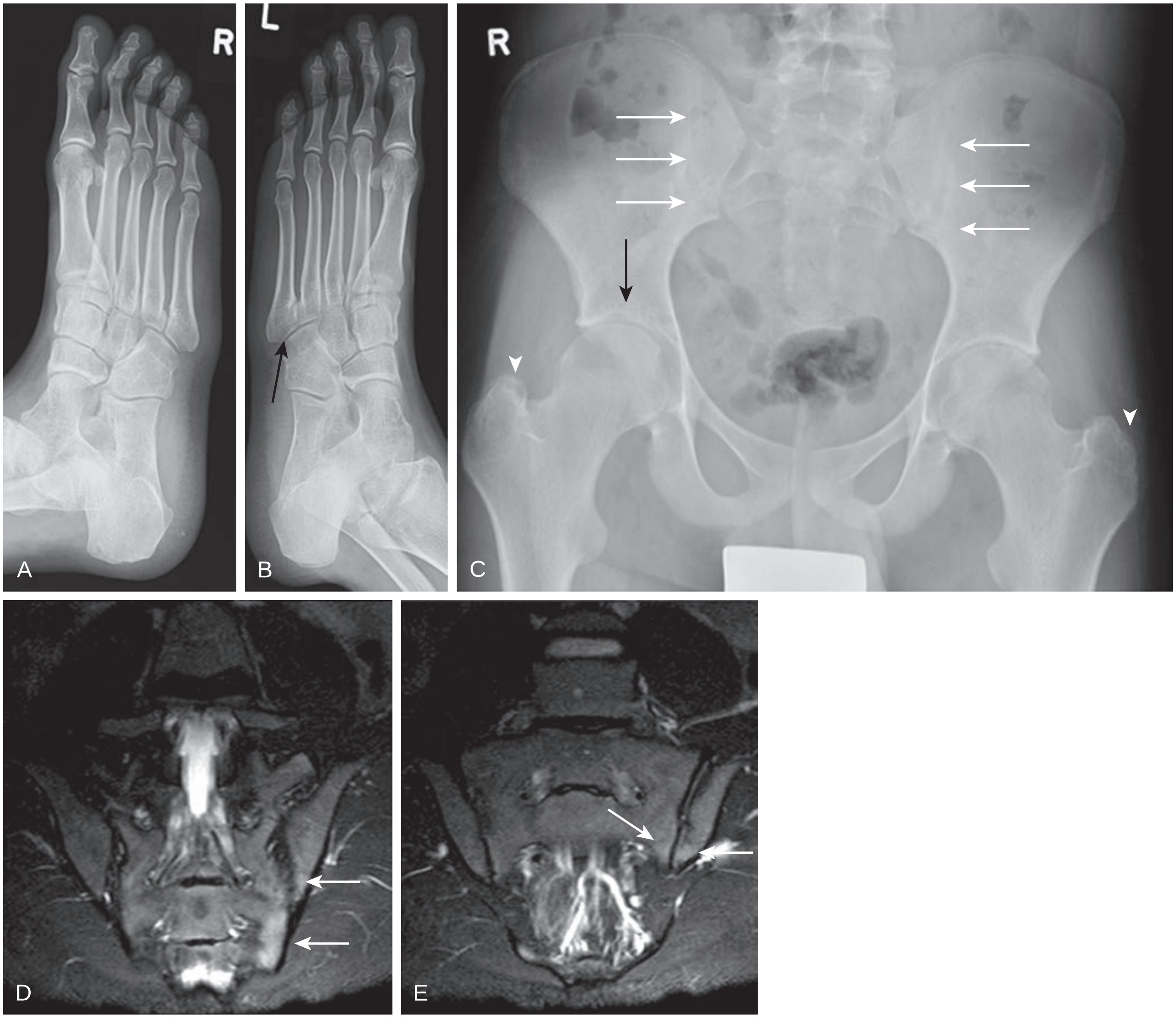

**Figure 136.14. Enthesitis-related B27 negative arthritis in a 16-year-old boy.** (A) Oblique radiographs of the feet show irregularity of the right calcaneal tuberosity at the Achilles tendon insertion consistent with erosive changes, compare to the normal contralateral side in (B). (B) Mild narrowing is noted at the left fifth tarsometatarsal joint *(arrow)*. (C) Frontal radiograph of the pelvis shows slight irregularity and sclerosis along both sacroiliac joints *(white arrows)* suggestive of bilateral sacroiliitis. Uniform narrowing is noted in both hip joints in association with erosions and a subchondral cyst *(black arrow)* along the superior acetabulum and erosive changes at both greater trochanters *(arrowheads)*, representing signs of enthesitis. (D and E) Coronal T2-weighted fat-saturated MR images obtained 2 months after the radiographs show heterogeneous high bone marrow signal involving the iliac and sacral aspect of the left sacroiliac joint *(arrows)* confirming the presence of sacroiliitis.

against tumor necrosis factor-α seems to significantly improve the arthritis and enthesitis.[116,117] Infliximab treatment yielded responses in young adults with peripheral enthesitis inflammatory heel pain.[118]

## PSORIATIC ARTHRITIS

### Etiology, Pathophysiology, and Clinical Presentation

Psoriatic arthritis involves 2% to 15% of patients with JIA and may involve either larger joints such as the knees and ankles or interphalangeal joints of hands and feet, resulting in the characteristic “sausage digits.”[20] Unlike in adults, in children, arthritis actually may precede skin manifestations.

### Imaging

#### Radiography

Radiographs obtained in the initial phase of the disease may be normal or show juxtaarticular osteoporosis. Characteristic radiographic features of psoriatic arthritis include asymmetric involvement, sausage digits (Fig. 136.16), joint erosions, joint space

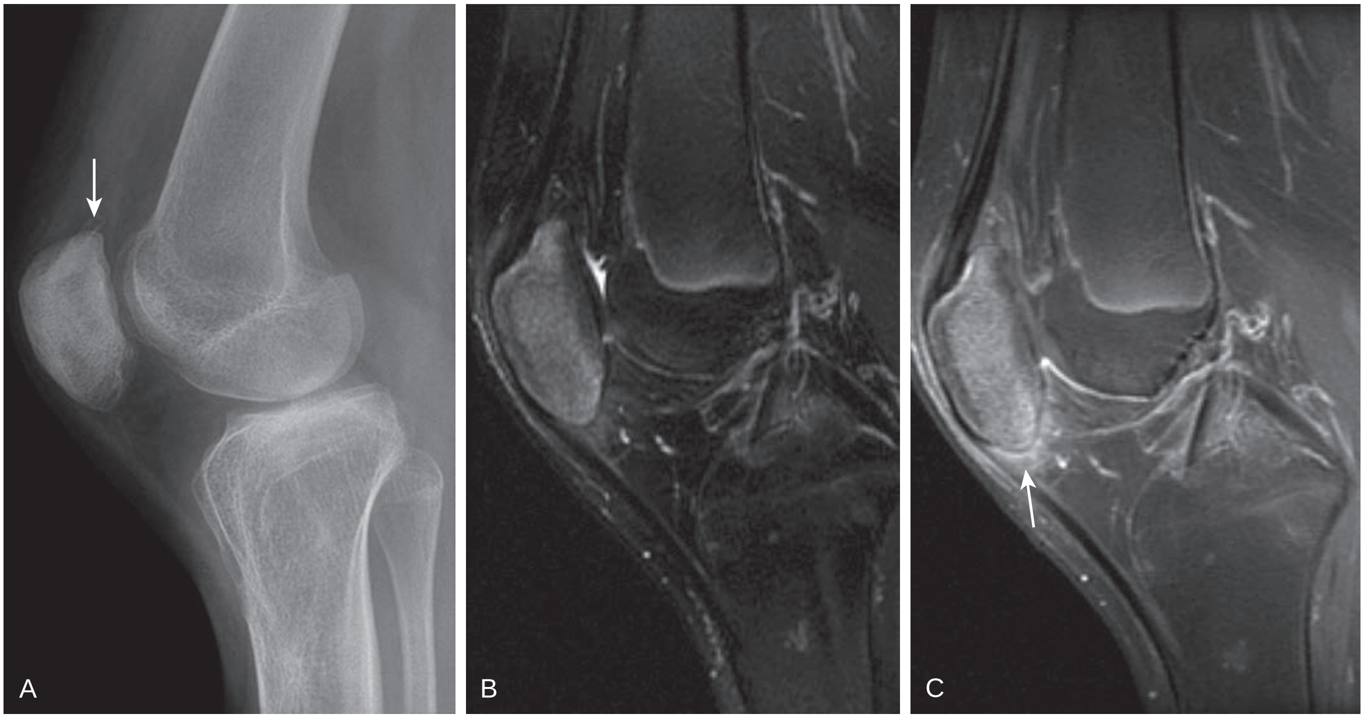

**Figure 136.15. Enthesitis-related arthritis in a 13-year-old boy.** (A) Lateral radiograph shows spurring at the upper aspect of the patella *(arrow)*. Corresponding sagittal T2 fast spin echo fat-saturated (B) and contrast-enhanced sagittal T1-weighted fat-saturated (C) MR images reveal increased signal intensity in the patella and postcontrast enhancement at the origin of the patellar tendon and adjacent Hoffa's fat pad *(arrow)*.

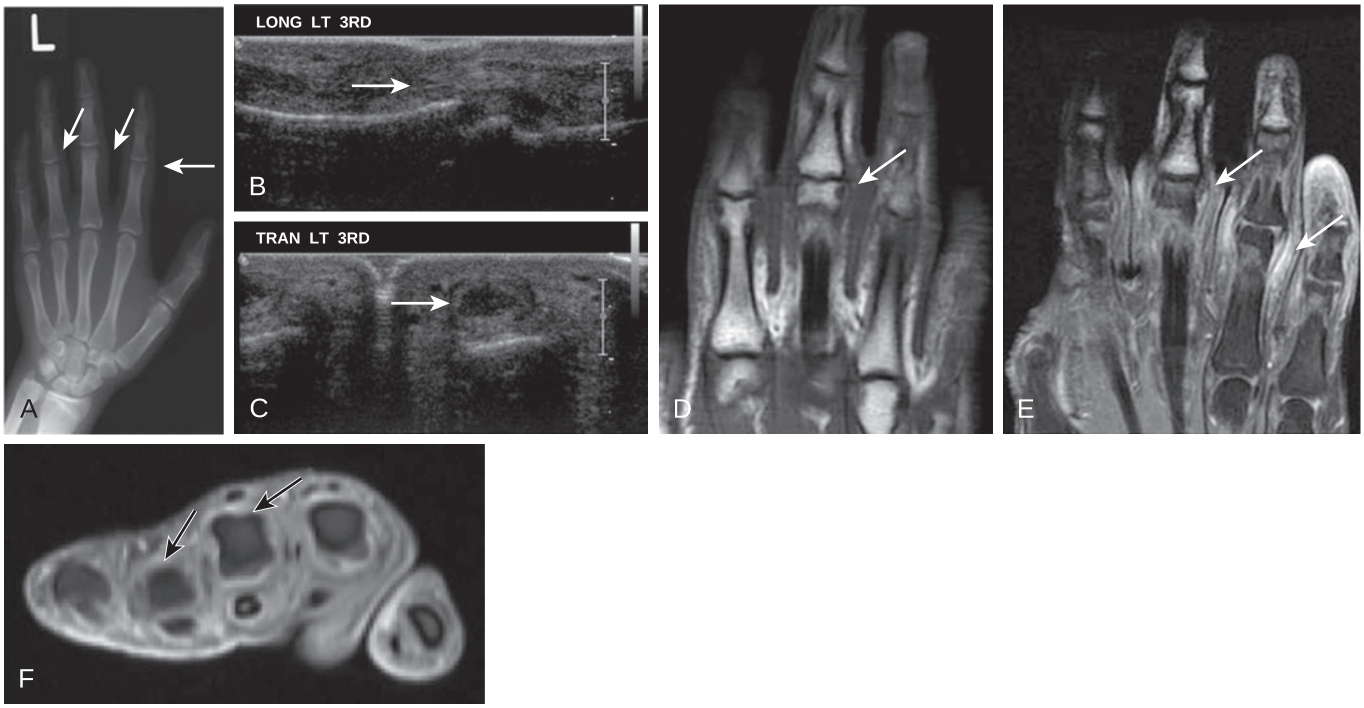

**Figure 136.16. Psoriatic arthritis in a 16-year-old boy.** (A) Frontal radiograph of the left hand shows soft tissue swelling at the proximal interphalangeal joint level at the right second, third, and fourth digits. Corresponding longitudinal (B) and transverse (C) ultrasound images demonstrate fusiform swelling surrounding the proximal interphalangeal joints of the right hand. Localized echogenic thickened tissue compatible with synovial and tenosynovial hypertrophy is seen *(arrows)* within and around the left third interphalangeal joint. Corresponding unenhanced coronal (D) and contrast-enhanced fat-saturated coronal (E) and axial T1-weighted MR images (F) of the left hand show prominent synovial hypertrophy and soft tissue enhancement *(arrows)* of the left third and fourth proximal interphalangeal joints.

narrowing, bony proliferation including periarticular and shaft periostitis, enthesitis, osteolysis including "pencil-in-cup" deformity (e-Fig. 136.17), acro-osteolysis, spur formation, and ankylosis.[36] The bone erosions tend to be larger and more asymmetric than those seen in persons with JIA, but the radiographic features may be indistinguishable from other forms of JIA. The characteristic adult changes seen at the distal interphalangeal joints are uncommon in children.

Sacroiliitis and vertebral involvement typically manifest later with progression of the disease. The sacroiliitis of juvenile psoriasis is usually asymmetric and resembles reactive arthritis. Syndesmophytes, paraspinal calcification, and atlantoaxial subluxation are rare in children.[36]

### Sonography

Sonography with Doppler evaluation is more sensitive than clinical examination to detect abnormalities in the hands and wrists, along with calcaneal enthesitis of adults with psoriatic arthritis. It is a reliable tool for assessing response to therapy with biological agents.

### Magnetic Resonance Imaging

In persons with psoriatic arthritis, MRI demonstrates erosive changes, joint space narrowing, ligament disruption, tenosynovitis, synovitis, and adjacent soft tissue inflammation (e-Fig. 136.18). Sausage digits are seen in patients with psoriatic arthritis and reactive arthritis. These swollen fingers or toes result from tenosynovitis, soft tissue edema, and synovial proliferation.[119] MRI may also be used to evaluate the responsiveness of therapy as noted by a significant reduction in gadolinium uptake after treatment with infliximab.[120]

### Computed Tomography

CT may be useful in assessing spine disease, but it has little role in the assessment of peripheral joints. Previous studies have shown that CT is as accurate as MRI for assessment of erosions in the sacroiliac joints but is not as affective for identifying synovial inflammation.[121] CT can be used to guide sacroiliac joint injection.[120]

# HEMOPHILIC ARTHRITIS

## Etiology, Pathophysiology, and Clinical Presentation

Hemophilia, an X-linked recessive disorder characterized by abnormality of the coagulation mechanism, affects 20 in every 100,000 males in North America.[122] It may be a result of a deficiency in factor VIII as in classic hemophilia (hemophilia A) or result from a deficiency of factor IX in persons with Christmas disease (hemophilia B).[122]

Hemarthrosis occurs in 75% to 90% of patients with hemophilia[123,124] and starts in the first and second decades of life. The most commonly affected joints include the knee, elbow, and ankle. Recurrent joint bleeding leads to secondary inflammation and hypertrophy of the synovium in response to blood products, and the cartilage degeneration and development of erosions and subchondral cysts[125] are similar to a primary inflammatory arthritis. Hemophilic pseudotumors, which are often intramuscular in location, may also develop in these patients.

## Imaging

### Radiography

The radiographic changes may be identical to those in children with JIA, but clinical findings and typical joint involvement help distinguish these entities.[126] Radiodense joint effusions and subchondral cystic changes are more common in persons with hemophilic arthropathy. In the knee, the classic radiographic findings include squaring of the femoral condyles (Fig. 136.19), multiple erosions, a widened intercondylar notch, and squaring of the patella.[25]

### Magnetic Resonance Imaging

MRI can detect acute and subclinical prior hemarthrosis.[123] In a cohort study evaluating ankles, elbows, and knees of 24 boys with severe hemophilia at a median age of 8.8 years (range, 6.2–11.5 years), hemosiderin deposition was detected in 26% of joints (ankles, 63%; elbows, 16%; and knees, 12%) with no history of clinically evident bleeding.[126]

Acute hemarthrosis and chronic joint effusion may be indistinguishable with a low signal on T1-weighted images and a high signal on T2-weighted images.[127] Subacute hemarthrosis usually has a high signal on both T1- and T2-weighted images, which is related to the presence of extracellular methemoglobin.[127] Hemosiderin deposition can occur in persons with JIA but is more frequently seen with other disorders, including hemophilic arthropathy, PVNS, synovial venous malformation, and posttraumatic synovitis.[128–130]

Gradient echo sequences are most sensitive in detecting synovial hemosiderin deposition, with signal loss occurring because of increased magnetic susceptibility (see Fig. 136.19). Synovitis that contains hemosiderin appears very low in signal on all MRI sequences, and this finding is accentuated on gradient echo sequences.[131,132] The synovial thickening often has areas of low signal on T1- and T2-weighted imaging related to fibrosis or hemosiderin deposition (Fig. 136.20).[127] Postcontrast images better delineate the extent of synovial thickening, which shows less enhancement compared with rheumatoid arthritis but adds little in the evaluation of hemophilic arthropathy.[133]

### Sonography

One potential advantage of ultrasound over MRI in the assessment of hemophilic joints is the lack of interference of susceptibility artifacts, which are seen commonly on gradient echo MRI sequences[134] that may obscure the synovium in the joint (e-Fig. 136.21). Recently, systematic protocols for ultrasound imaging of hemophilic joints have been developed,[135–137] which enable systematization of imaging protocols and future comparative clinical trials. Although a prior study found a close relationship between ultrasound and MRI in the assessment of the synovium and a good correlation between ultrasound and radiographs in evaluation of the progression of bone changes,[138] further investigation is required to determine the value of ultrasound for assessment of cartilage changes. Ultrasound has limitations in the assessment of deep cartilage abnormalities that are expected to occur in early stages of hemophilic arthropathy, given the centrifugal progression of cartilage degeneration.[139,140]

## Treatment and Follow-up

Treatments for hemarthrosis include coagulation factor replacement, cryotherapy, arthrocentesis of intraarticular blood, and arterial embolization (in cases of active bleeding).[141] Radioactive injections into joints (radionuclide synovectomy) initially were used in cases of JIA but have been shown to be effective in reducing bleeding and effusion in selected cases of hemophilic arthropathy. Radionuclide synovectomy has low complication rates, but concern remains that the radiation exposure in young children could lead to radiation necrosis or tumor induction.[142]

Prophylaxis is the first therapeutic option in noninhibitor hemophilic patients.[143] This therapy reduces the joint symptoms

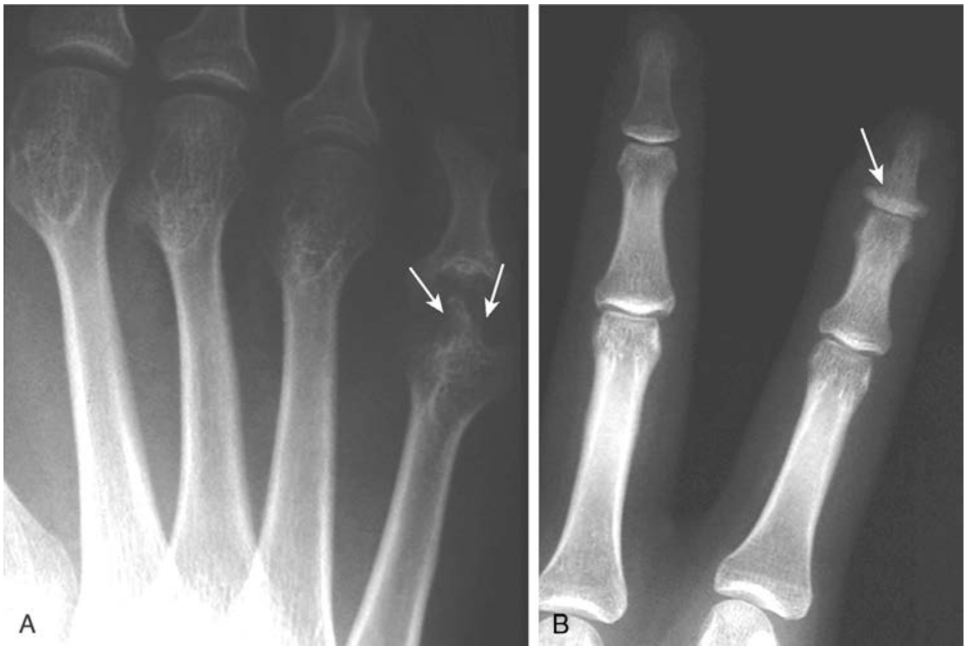

**e-Figure 136.17. Advanced psoriatic arthritis.** Radiograph of the foot (A) shows extensive erosive changes at the distal end of the fifth metatarsal, resulting in a “pencil-in-cup” appearance at the metacarpal-phalangeal joint *(arrows)*. Radiograph of the hand (B) shows bony proliferation at the base of the distal phalanx *(arrow)*.

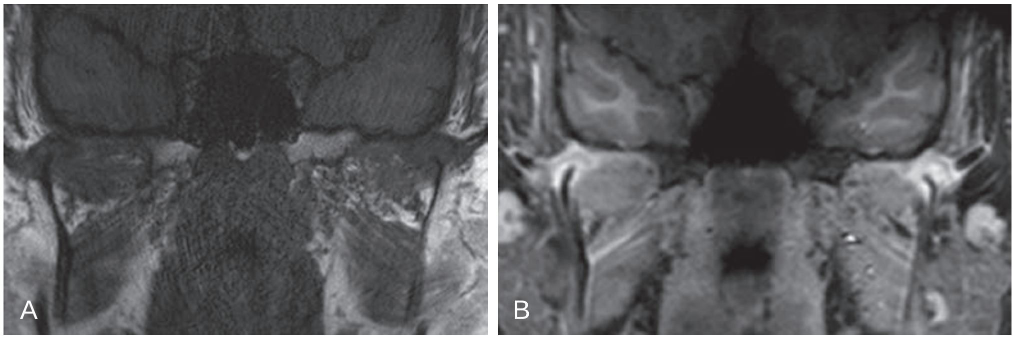

**e-Figure 136.18.** Newly diagnosed psoriatic arthritis in a 15-year-old boy with longstanding symptoms who presented with micrognathia on physical examination. Precontrast and postcontrast coronal T1-weighted MR images demonstrate severely dysplastic mandibular condyles with tapering of the mandibular condyles bilaterally (A). Intense pericondylar synovial enhancement is noted bilaterally after administration of intravenous gadolinium (B).

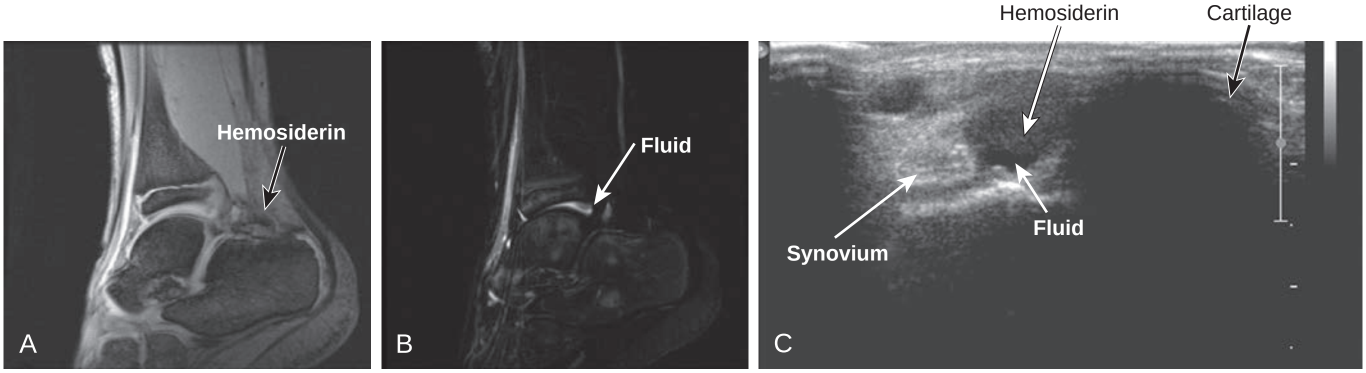

**e-Figure 136.21. Hemophilia.** Sagittal gradient echo (A) and T2-weighted (B) MR images of a hemophilic ankle show a mild amount of hemosiderin deposition and joint effusion. Only minimal “blooming” (susceptibility artifact) is noted within the posterior synovial recess of the ankle; however, the synovium is not promptly identified on the gradient echo images. A corresponding sonogram (C) allows discrimination between synovium (echogenic, “white”), hemosiderin (hypoechoic, “gray”), and fluid (anechoic, “black”).

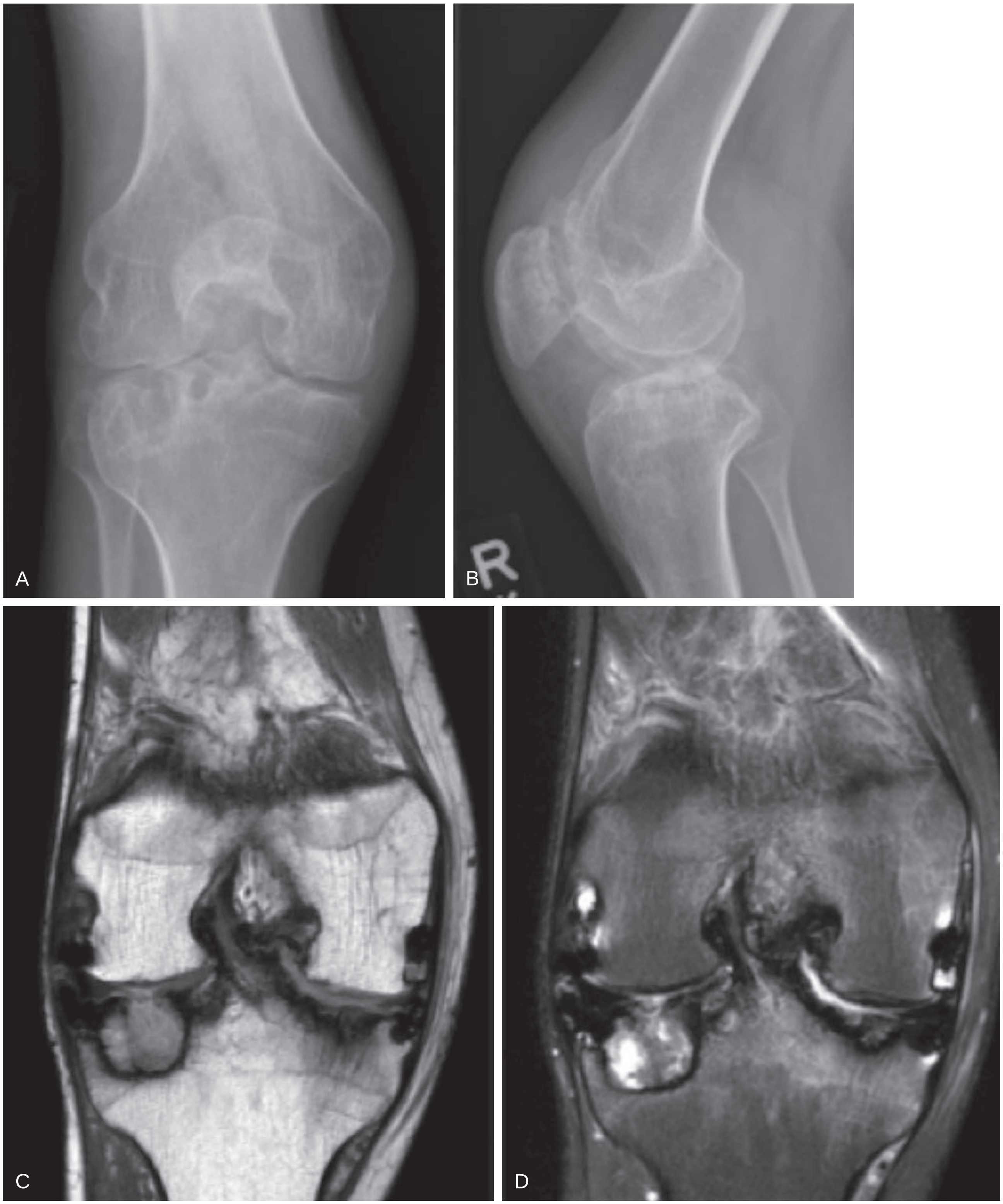

**Figure 136.19. Hemophilic arthritis in a 17-year-old boy.** Frontal (A) and lateral (B) radiographs demonstrate widening of the intercondylar notch, squaring of the femoral condyles, tricompartmental degenerative changes with extensive erosions, and subchondral cystic changes. A joint effusion is also seen on the lateral view (B). Coronal T1-weighted (C) and fat-suppressed T2-weighted (D) MR images show erosive changes of the distal femur and proximal tibia and a large subchondral cyst in the lateral tibial condyle. There is low signal intensity lining the joint on both sequences that "blooms" on the sagittal gradient echo sequence (E).

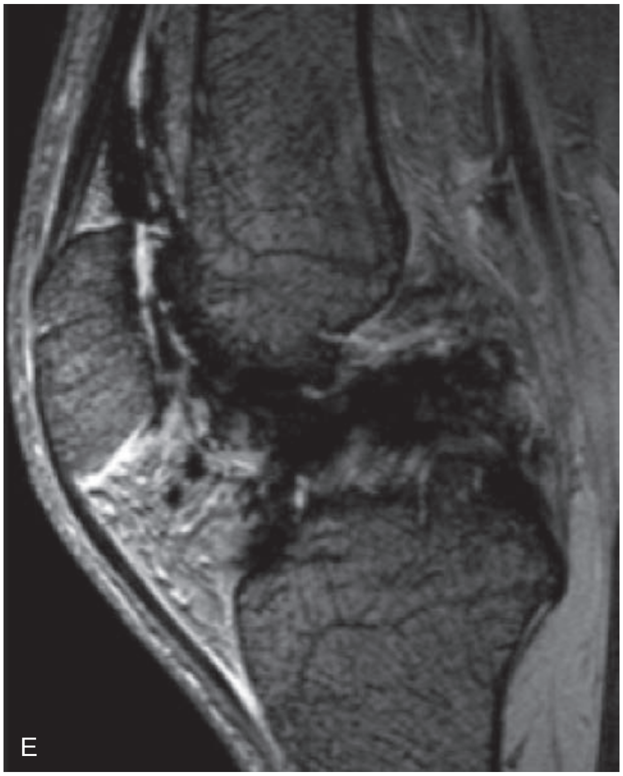

Figure 136.19, cont'd.

and avoids further degeneration of the joints and should be started before the development of cartilage lesions. MRI is used to detect early hemophilic disease and to help direct the appropriate therapy. The role of ultrasound for detecting early cartilage lesions is still under investigation.[144]

## TRANSIENT SYNOVITIS

### Etiology, Pathophysiology, and Clinical Presentation

Transient synovitis is the most common cause of childhood hip pain and can be mimicked by a number of more serious hip disorders, including Legg-Calvé-Perthes disease, slipped capital femoral epiphysis, JIA, septic arthritis, and malignancy.[145] Transient synovitis is an acute, self-limiting disorder of unknown origin.[145]

### Imaging

Imaging is usually performed with conventional radiography or ultrasound. It has been proposed that radiography should not be used in the primary evaluation of most children with hip pain because the results are generally normal or show only subtle findings of joint effusion. Exceptions should be made in infants younger than 1 year of age and in children older than 8 years because of the lower incidence of transient synovitis in these age groups, with the higher risk of child abuse and septic arthritis in infancy, and the occurrence of slipped capital femoral epiphysis in the older age group.[145] Although sonography is a sensitive and noninvasive method of detecting hip joint effusion in persons with transient synovitis (Fig. 136.22),[146] it is unable to distinguish between different types of synovitis. Thus the combination of the patient's age, history of fever, and laboratory studies is useful to distinguish transient synovitis and septic arthritis.[147]

Nevertheless, the major contribution of ultrasound is to confirm the presence of joint effusion.[147] An ultrasound joint space thickness difference greater than 2.0 mm between asymptomatic and symptomatic hips has been considered valid for the presence of effusion.[148] Other modalities such as bone scans, CT, and MRI are not used initially in the evaluation of irritable hips because of their higher cost and limited benefit.[25]

### Treatment and Follow-up

Aspiration is required if infection is a consideration and is readily accomplished with ultrasound guidance.[149] Treatment for hip pain related to transient synovitis can include traction of the hip in 45 degrees of flexion, which may minimize intracapsular pressure. Treatment with ibuprofen may shorten the duration of symptoms.[150]

## MALIGNANCIES

### Etiology, Pathophysiology, and Clinical Presentation

Any of the childhood malignancies, especially the leukemias and neuroblastoma, can mimic rheumatic disease. These malignancies may (Fig. 136.23) or may not involve the joint itself. Leukemic arthritis typically presents with transient arthralgias and joint pain, often involving the knees, shoulders, and ankles.[31] Joint effusion is postulated to occur in relation to either synovial infiltration with leukemic cells and/or an autoimmune response related to the leukemia. However, differentiation of leukemic and septic arthritis is not possible by imaging, and aspiration may be necessary.

### Imaging

Although radiologic findings often are normal, they can include joint effusion, osteopenia, periostitis, lytic or sclerotic bone lesions, and metaphyseal radiolucent bands.[151,152] Diffuse abnormal signal intensity of bone marrow, which is low on T1-weighted sequences and high on T2-weighted sequences, can be seen on MRI (see Fig. 136.23).

## PIGMENTED VILLONODULAR SYNOVITIS (TENOSYNOVIAL GIANT CELL TUMORS)

### Etiology, Pathophysiology, and Clinical Presentation

PVNS is a benign proliferative disorder of uncertain etiology that affects synovial lined joints, bursae, and tendon sheaths. PVNS mostly occurs in the third and fourth decades of life[153] but can affect persons of any age.[154] The latest World Health Organization Classification of Tumors of Bone and Soft Tissues no longer uses the term PVNS but refers to these lesions as tenosynovial giant cell tumors with subclassifications based on whether the lesion is focal or diffuse. By convention, we continue to use PVNS in this chapter.

Gross pathologic features include a thickened synovium with a variable combination of villous and nodular proliferation. PVNS can either be focal or diffuse (i.e., involving nearly the entire synovial lining). On microscopy, PVNS is characterized by the presence of hemosiderin-laden, multinucleated giant cells, along with lipid-laden macrophages, fibroblasts, and other large mononuclear cells. Hemosiderin is found within the surrounding tissues. The ubiquitous presence of hemosiderin lends the tissue a characteristic pigmented appearance. The lesions tend to be hypervascular and demonstrate synovial hyperplasia.[154] PVNS typically invades local tissues and has the potential for extensive local destruction, even though it rarely metastasizes.[155]

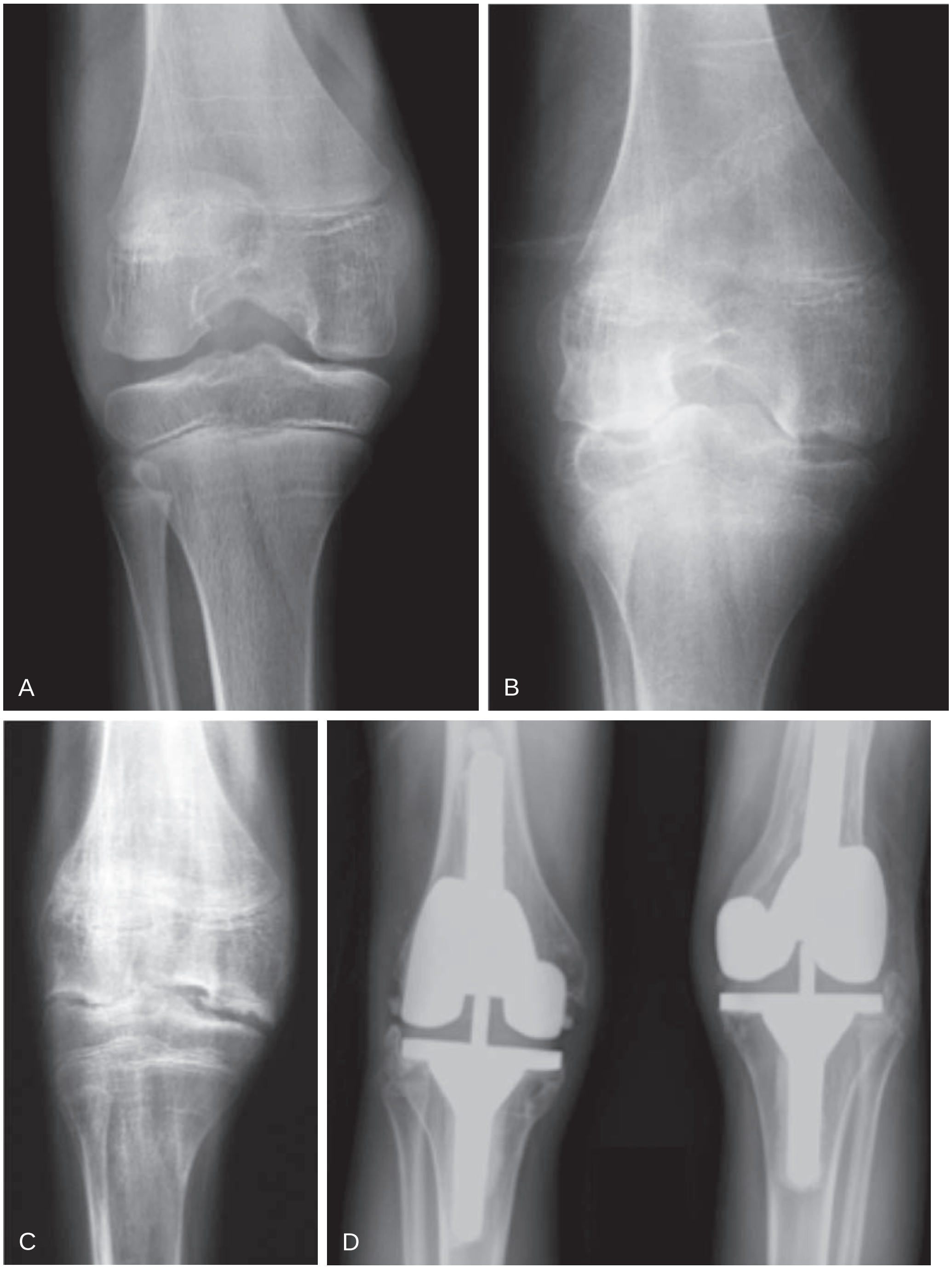

**Figure 136.20. Hemophilia.** Frontal radiograph of the right knee of a boy with hemophilia at 10 years of age (A) shows widening of the intercondylar notch and mild overgrowth and squaring of the femoral condyles. Subsequent radiographs at 12 years (B) and 14 years (C) of age show progressive degenerative changes with joint space narrowing and marked condylar irregularity. Similar findings were present in the left knee, and he subsequently underwent bilateral knee replacements (D). Frontal radiograph of the right shoulder in the same child at 16 years of age (E) shows widening of and soft tissue density within the acromiohumeral interval, suggestive of a joint effusion. Axial T2-weighted (F) and gradient echo (GRE) (G) MR images of the same shoulder show a large joint effusion and synovitis with low signal intensity lining the joint that “blooms” on the GRE sequence *(solid arrows)*. Also note the fluid-fluid level (*dashed arrow* in G) and intraarticular chondral body (*arrowhead* in F). (H) Coronal proton-density fat-saturated MR image shows loss of articular cartilage of the humeral head with subchondral cyst formation *(solid arrow)* and low signal intensity thickened synovium in the axillary recess *(dashed arrow)*. Arthroscopy was performed due to pain and limited mobility. Arthroscopic images (I) show hemosiderin stained synovium *(left image)* and areas of extensive synovial proliferation *(right image)*. (J) Coronal proton-density fat-saturated MR image at 18 years of age shows end-stage degenerative joint disease with full-thickness loss of articular cartilage and subchondral cystic changes in the humeral had and glenoid.

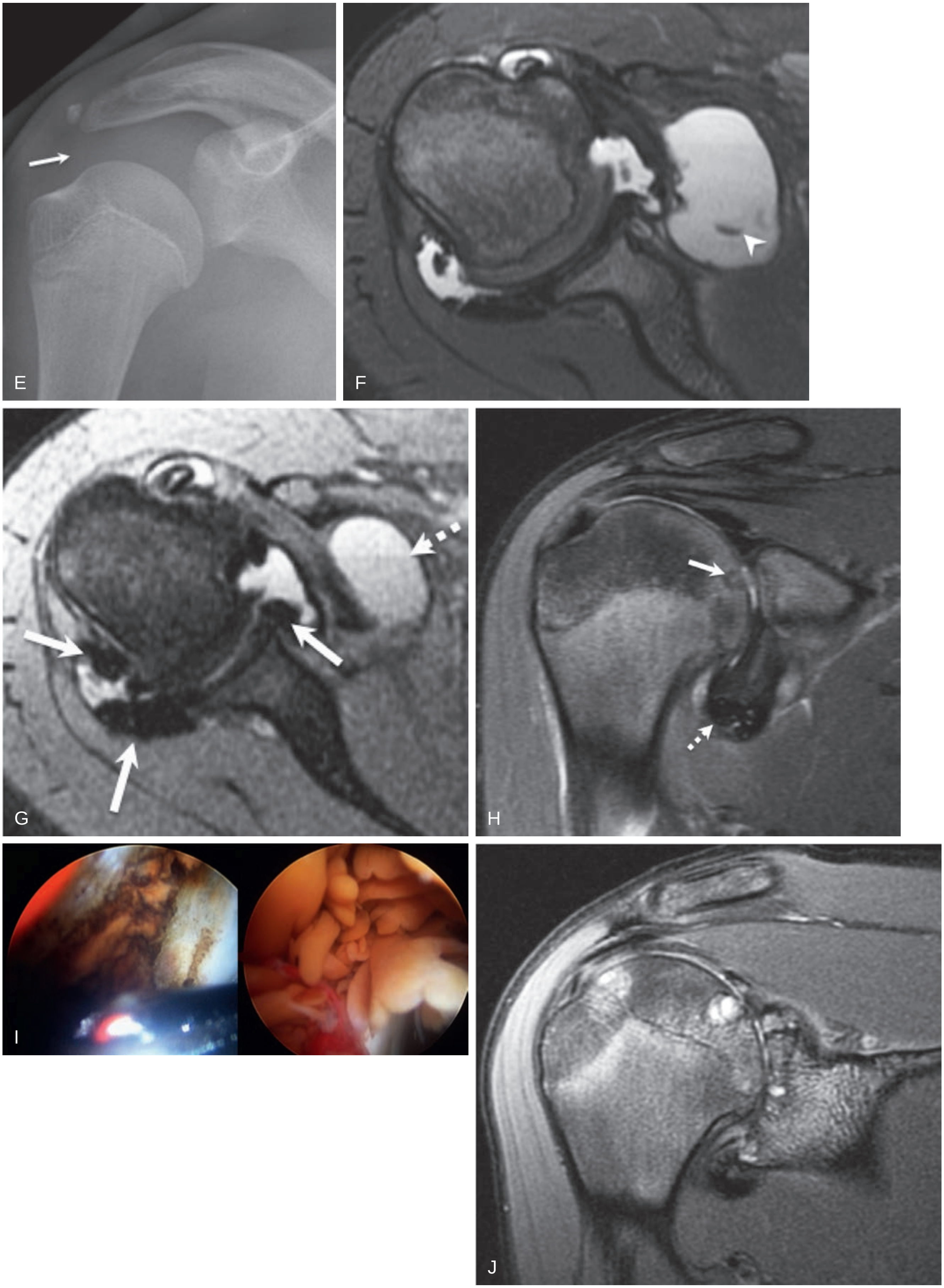

Figure 136.20, cont'd.

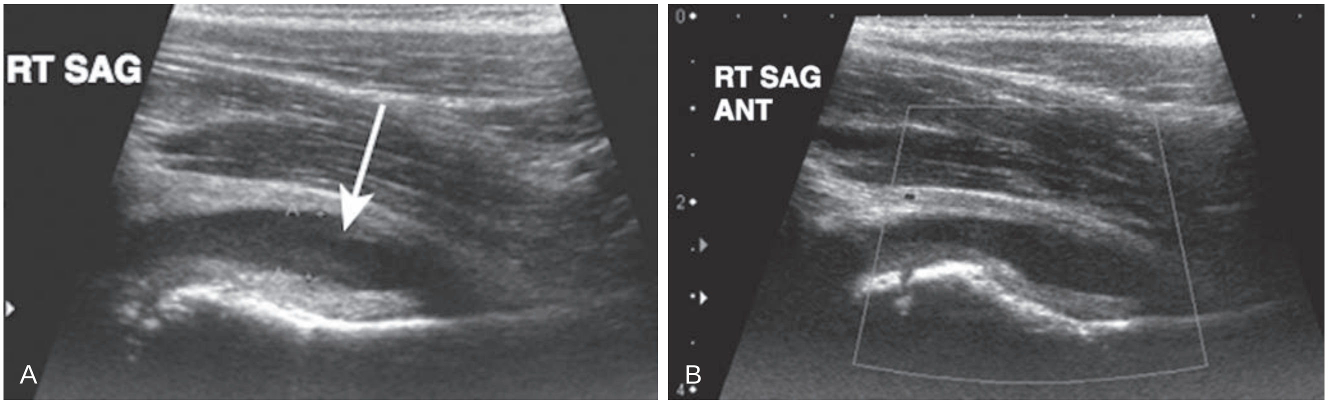

**Figure 136.22. Transient synovitis in a 7-year-old girl.** (A) Longitudinal sonogram of the right hip shows a joint effusion *(arrow)* and synovial hypertrophy. (B) Longitudinal color Doppler sonogram shows no significant synovial hyperemia. *ANT,* Anterior; *RT,* right; *SAG,* sagittal.

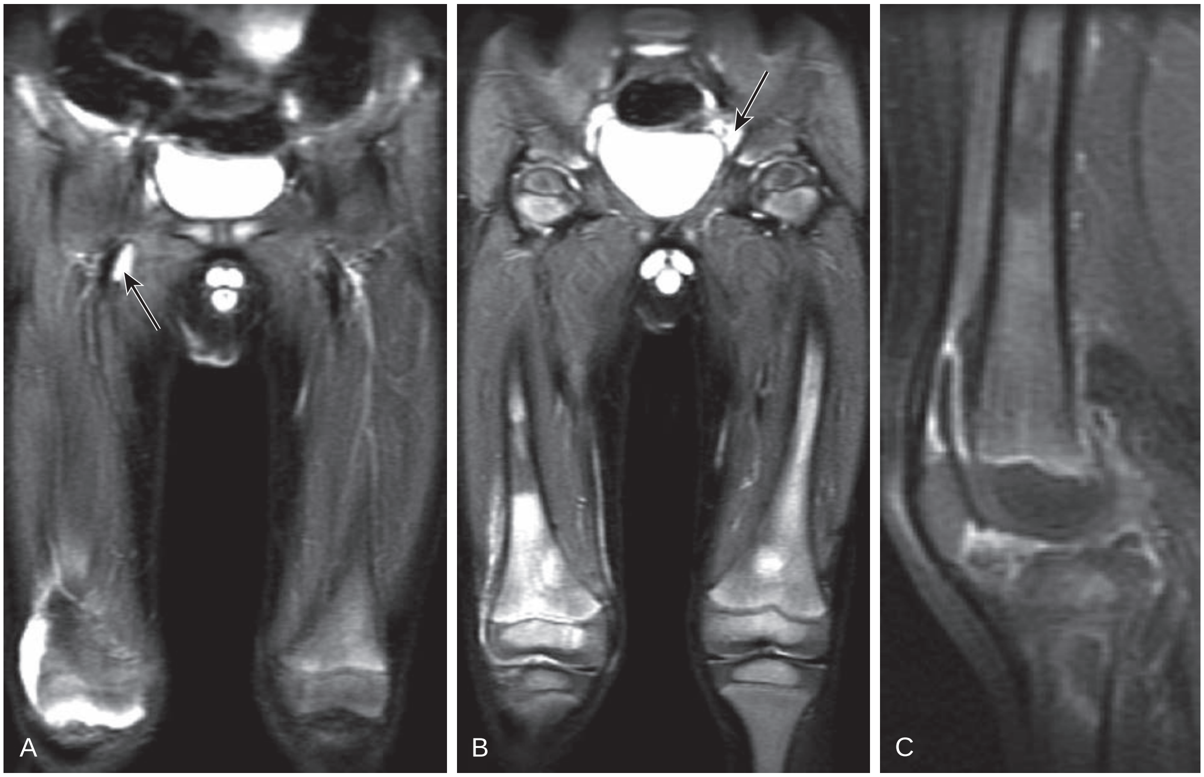

**Figure 136.23. Leukemia.** Coronal inversion-recovery (A and B) and contrast-enhanced sagittal T1-weighted fat-saturated (C) MR images of the lower extremities show a large right joint effusion (A) with synovial enhancement representing synovitis (C). Diffuse heterogeneous signal abnormality is seen within the bone marrow of the femora and proximal tibias, along with generalized adenopathy *(arrows)* (A and B). This patient was diagnosed with acute lymphocytic leukemia.

## Imaging

Radiographs show soft tissue swelling without calcification; in advanced stages, findings are of degenerative arthritis, including bony erosions and subchondral cysts. The invasion of the subchondral bone, with resultant cyst formation, is a characteristic finding.[156] When PVNS involves relatively constricted joint spaces such as the hip, erosions related to intraarticular mass effect may be seen earlier compared with more capacious joints such as the knee.

On MRI, diffuse or nodular synovial thickening is noted, with low to intermediate T1 signal. Thick frondlike synovial excrescences often are identified extending into a joint effusion. Hemosiderin deposition results in low signal on T1- and T2-weighted sequences, particularly at the periphery of the thickened synovium, which shows “blooming” artifact on gradient echo sequences. On postcontrast imaging, there is typically synovial enhancement (Fig. 136.24).[20,157] Focal PVNS usually is a well-defined solitary masslike lesion that superficially may not appear to arise from synovium (Fig. 136.25).

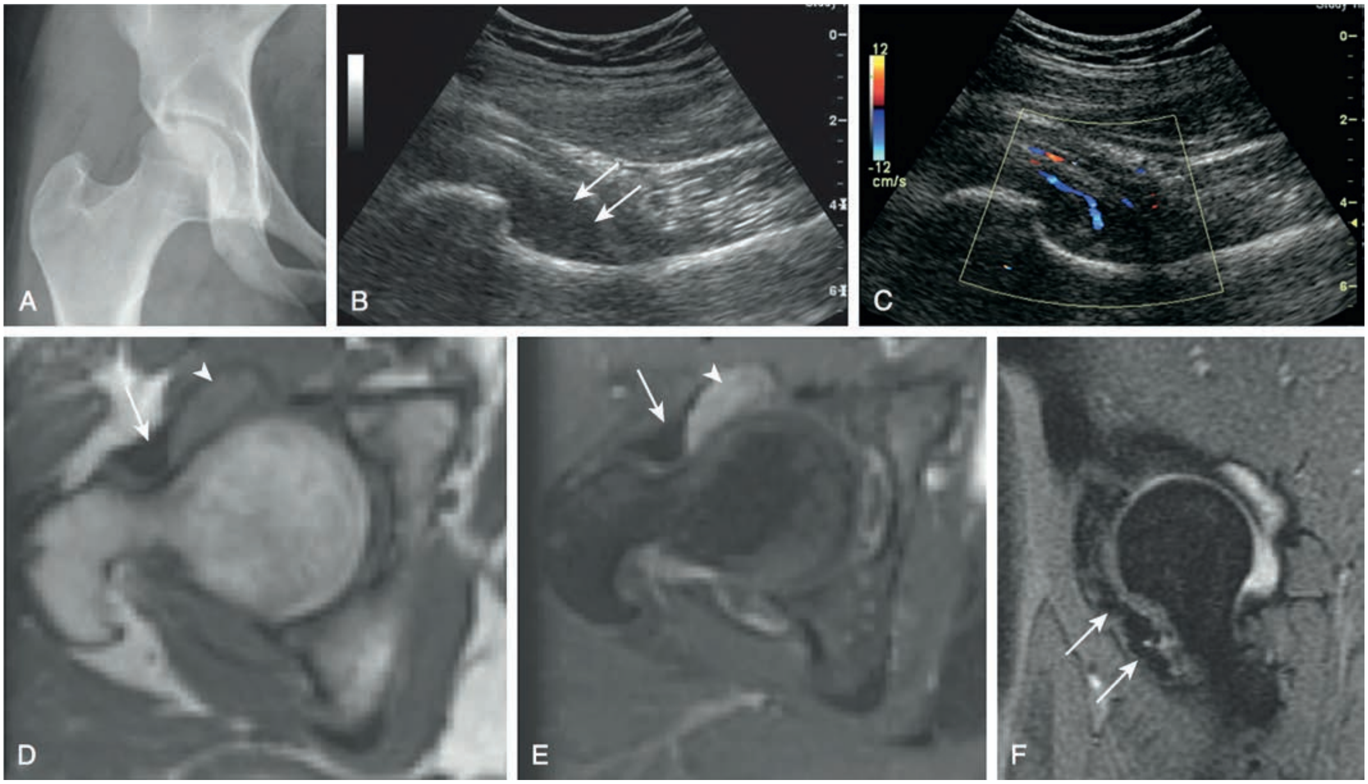

**Figure 136.24. Pigmented villonodular synovitis (PVNS).** A 17-year-old girl with a history of right hip pain for 3 years and a biopsy-proven diagnosis of PVNS. Frontal radiograph of the pelvis (A) shows a slight increase in the right femoroacetabular joint space medially. A subsequent longitudinal ultrasound of the right hip (B and C) demonstrates an area of synovial thickening within the anteroinferior aspect of the right hip with fine internal solid echogenicity (B, *arrows*) and internal vascularity on color Doppler (C). A small right hip effusion was confirmed on the corresponding MR examination. Unenhanced (D) and contrast-enhanced fat-saturated (E) axial T1-weighted MR images of the right hip reveal moderate thickening and enhancement of the synovium *(arrowheads)*. A sagittal multiplanar gradient-recalled acquisition (F) MR image shows synovial and capsular thickening and blooming artifact consistent with hemosiderin deposition *(arrows)*. Also note the mild erosive changes of the anterior femoral neck.

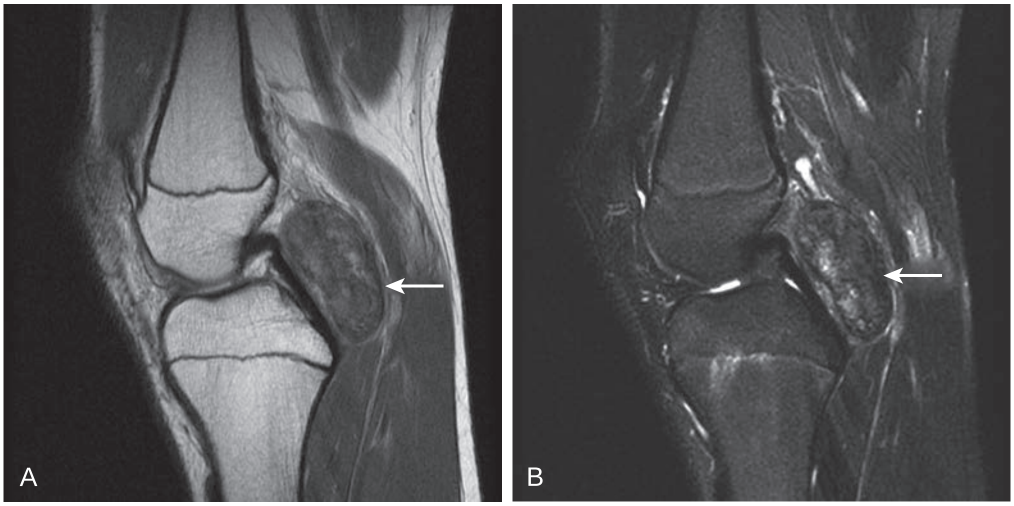

**Figure 136.25. Focal pigmented villonodular synovitis (PVNS) in a 15-year-old girl.** Sagittal proton density (A) and T2-weighted fat-saturated sagittal (B) MR images of the knee demonstrate a well-circumscribed mass in the posterior joint space extending into the popliteal region with heterogeneous signal intensity *(arrow)*.

## Treatment and Follow-up

Definitive treatment requires synovectomy, but there is a high (up to 50%) incidence of local recurrence.[157]

# SYNOVIAL CHONDROMATOSIS/ OSTEOCHONDROMATOSIS

## Etiology, Pathophysiology, and Clinical Presentation

Synovial chondromatosis/osteochondromatosis is a benign condition of unknown etiology characterized by synovial membrane proliferation and metaplasia. This can occur within joints, tendon sheaths, or bursa. It is rare in children[158,159] and mostly occurs in the third to fifth decades of life.[160] The synovium undergoes neoplastic nodular proliferation, and fragments may break off into the joint. There, nourished by synovial fluid, the fragments may grow, remain cartilaginous, or ossify. The fragments may be found free within the joint cavity, or they may be embedded within the proliferating synovium, which may extend into the surrounding soft tissues.[160] The natural history of synovial osteochondromatosis is gradual progression of disease, joint deterioration, and secondary osteoarthritis.

## Imaging

Imaging findings depend on the degree of mineralization of the chondroosseous bodies. Ossification (synovial osteochondromatosis) is seen in 70% of patients.[20] Unlike with adults, children rarely present with radiographically detectable ossified loose bodies. Therefore the initial diagnosis often is suggested from MRI, where these particles may mimic pannus, rice bodies, or PVNS. On MRI, a noncalcified lesion is seen as an isointense T1-weighted and high T2-weighted signal mass. If ossified lesions are large enough, focal areas of yellow marrow signal may be detectable (Fig. 136.26).[20]

When intraarticular particles are relatively uniform in size, the term *primary synovial osteochondromatosis* may be used. When the intraarticular particles are nonuniform and are heterogeneous in size and shape, secondary synovial osteochondromatosis should be considered. Secondary causes include trauma, infection, and nonpyogenic inflammatory arthritis.

## Treatment and Follow-up

Synovial osteochondromatosis is usually treated by surgical resection of the proliferative synovium and removal of the loose bodies, but the local recurrence rate is up to 23%.[160]

# LIPOMA ARBORESCENS

## Etiology, Pathophysiology, and Clinical Presentation

Lipoma arborescens is a rare intraarticular lesion of unknown etiology characterized by replacement of synovial cells by fat cells, producing villous transformation of the synovium. It is not a true neoplasm and most commonly affects the suprapatellar bursa of the knee in patients between the fifth and seventh decades of life.[161,162] Patients present with painless joint swelling and effusions.[161]

Lipoma arborescens associated with degenerative joint disease and chronic inflammatory arthritis (secondary lipoma arborescens) is more common in the adult population, whereas primary lipoma arborescens (without a primary etiology) is seen predominantly in a younger population.[163]

## Imaging

The characteristic MRI appearance is frondlike synovial proliferation with fat signal intensity on all pulse sequences (Fig. 136.27), but it is best seen on T1-weighted and fat-suppressed T2-weighted sequences.[161,162]

## Treatment and Follow-up

Lipoma arborescens is typically treated with synovectomy,[164] but yttrium-90 radiosynovectomy[165] treatments have been described.

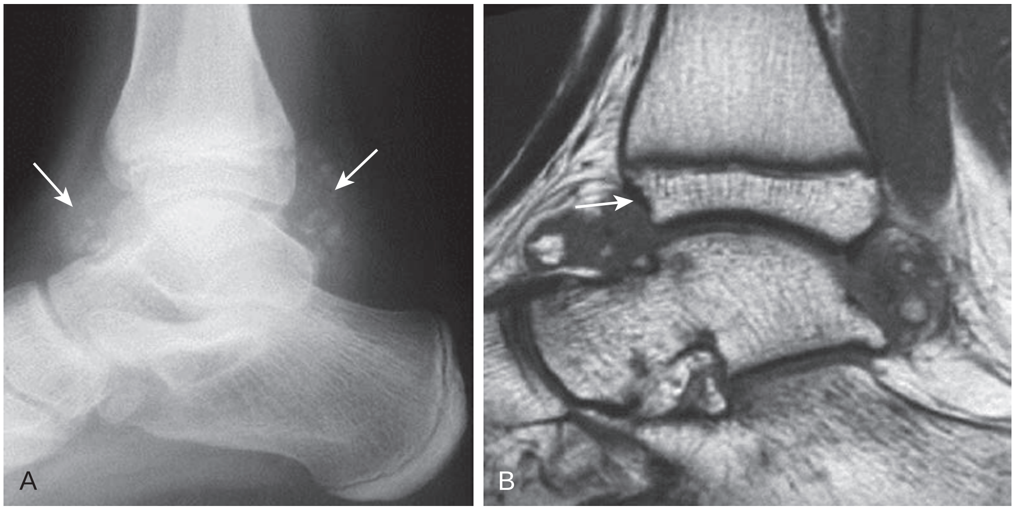

**Figure 136.26. Synovial osteochondromatosis.** An adolescent had a history of pain in the right ankle for years. Lateral radiograph (A) shows soft tissue swelling with multifocal calcific concretions within the anterior and posterior synovial recesses of the ankle *(arrows)*. The corresponding sagittal T1-weighted MR image (B) of this ankle demonstrates large nodular synovial proliferation within the anterior and posterior synovial recesses with ossified fragments, which contain yellow marrow, seen within the synovial tissue. There are associated incipient erosive changes at the anterior distal tibial epiphysis *(arrow)*.

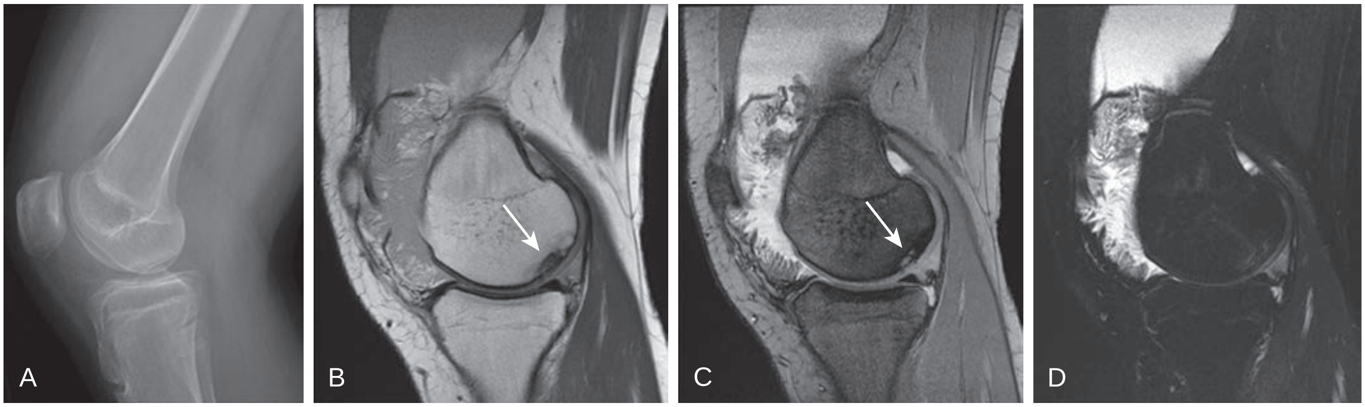

**Figure 136.27. Psoriatic arthritis, lipoma arborescens, and osteochondritis dissecans in a 15-year-old girl.** Lateral radiograph of the right knee (A) shows a large joint effusion and an osteochondral defect in the medial right femoral condyle. Corresponding sagittal proton-density (B), multiplanar gradient-recalled acquisition (C), and T2-weighted fat-saturated fast spin echo (D) MR images demonstrate, in addition to the osteochondral defect *(arrows)*, a large effusion and frondlike synovial proliferation, which follows signal intensity of fat on all sequences, indicating lipoma arborescens.

## VASCULAR MALFORMATIONS

### Etiology, Pathophysiology, and Clinical Presentation

Vascular malformations are benign lesions that usually are diagnosed in childhood or young adulthood. The Mulliken and Glowacki classification for these lesions separates these lesions as high flow (arteriovenous malformations and fistulas) and low flow (venous, lymphatic, capillary) lesions and reserves the term *hemangioma* for vascular tumors that present during infancy.[166] The most frequent vascular malformation that may present with arthropathic changes is a venous malformation with synovial involvement,[167] although these lesions often are erroneously referred to as "synovial hemangiomas."[168] Clinically, they mimic chronic arthritis because of recurrent synovial bleeding, and not uncommonly the diagnosis is delayed. They may have associated cutaneous lesions, recurrent hemarthrosis, and arthropathy. The knee is the most commonly affected joint, but other joints such as the elbow, wrist, and ankle also can be affected, along with tendon sheaths. These lesions often have both a synovial component and a large extrasynovial component.[167]

### Imaging

Radiography can demonstrate phleboliths, a soft tissue mass, joint effusion, osteoporosis, advanced epiphyseal maturation, leg length discrepancy, arthropathy simulating hemophilia, and periosteal reaction.[167]

The MRI appearance varies from slightly lobulated, nonencapsulated masses to infiltrating serpentine vascular masses to a combination of these morphologies. They are usually isointense to hypointense to muscle on T1-weighted images and hyperintense on T2-weighted images, with variable contrast enhancement.[167,168] Venous components tend to enhance but may demonstrate areas of nonenhancment and hematocrit levels within their tubular channels related to sluggish flow and microthrombi. Phleboliths are characteristic of venous malformations and typically present with low signal intensity on all sequences. Intraarticular fluid-fluid levels, synovial blooming artifact on gradient echo images because of the presence of hemosiderin, or bone erosions due to a reactive arthritis as a result of the presence of intraarticular blood may be present (Fig. 136.28).

### Treatment and Follow-up

Intraarticular vascular malformations, particularly venous malformations, have a propensity to bleed. When these lesions bleed, the blood products cause an inflammatory response, and the presentation in a child may be that of inflammatory arthritis. Therefore treatment may be necessary to decrease bleeding incidence, including malformation resection or sclerotherapy, and synovectomy.

## JUVENILE DERMATOMYOSITIS

### Etiology, Pathophysiology, and Clinical Presentation

Juvenile dermatomyositis (JDM) is an autoimmune inflammatory myopathy characterized by diffuse nonsuppurative inflammation of muscle fibers and skin.[169] The inflammatory infiltrates are predominantly perivascular, in the interfascicular septa, or around the fascicles.[170] The incidence of JDM in the United States is 3.2 per million children per year.[171] The ratio of girls to boys is 2.3 : 1.[172] JDM most commonly presents between the ages of 5 and 14 years.[173] Clinical findings include severe proximal muscle weakness, fatigue, heliotrope rash (a pink or purple rash on the face and knuckles), and underlying vasculitic pathology.[173,174]

### Imaging

#### Radiography

In the acute stage, radiologic changes are minimal. However, incipient soft tissue swelling and subcutaneous edema represented by blurring of fat planes can be noted in the proximal appendicular skeleton in some cases. The muscles of the scapular and pelvic girdles are most frequently affected (e-Fig. 136.29 and Fig. 136.30).[175,176] In chronic disease, radiographs demonstrate soft tissue loss and muscle atrophy. Marked osteoporosis of the long bones and vertebral bodies also may be present. The most characteristic finding of chronic disease, however, is the deposition of calcium in the soft tissues (Fig. 136.31), which is identified in 25% to 50% of cases.[177] The calcium deposits may present as subcutaneous plaques, nodules, periarticular calcific foci, and large clumps or sheets of calcium within muscle or subcutaneous tissue.[178]

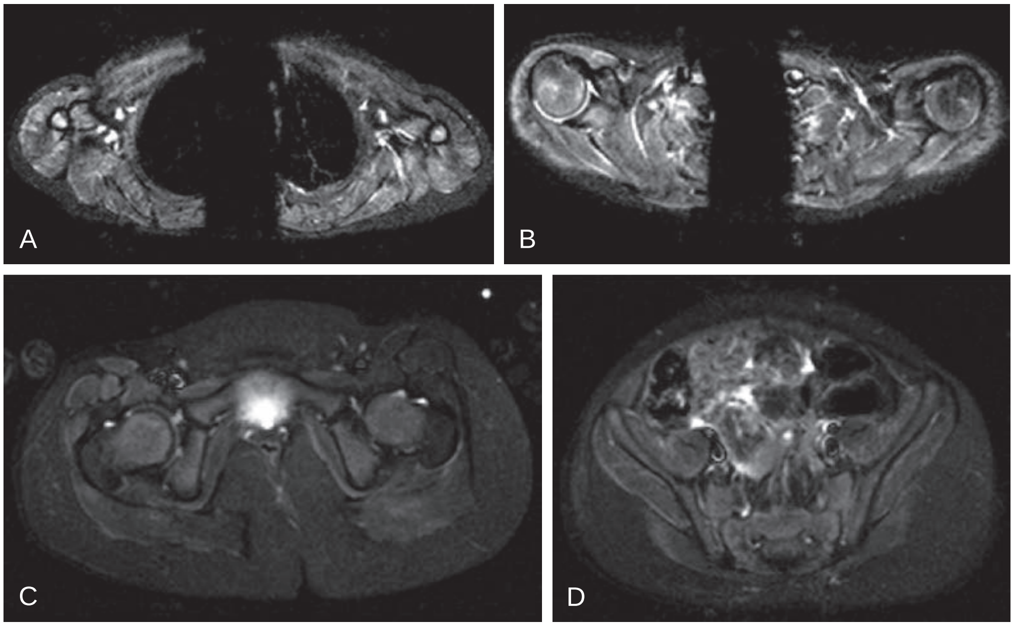

**e-Figure 136.29. Juvenile dermatomyositis in a 3-year-old girl.** Axial inversion-recovery MR images of the shoulder girdle (A and B) demonstrate diffuse bilateral increased signal intensity involving the deltoid, supraspinatus, infraspinatus, and triceps muscles bilaterally. In the pelvic girdle (C and D), faint asymmetric increased signal intensity is noted within the obturator externus, pectineus, rectus femoris, sartorius, vastus lateralis, and gluteus muscles, predominately on the right side.

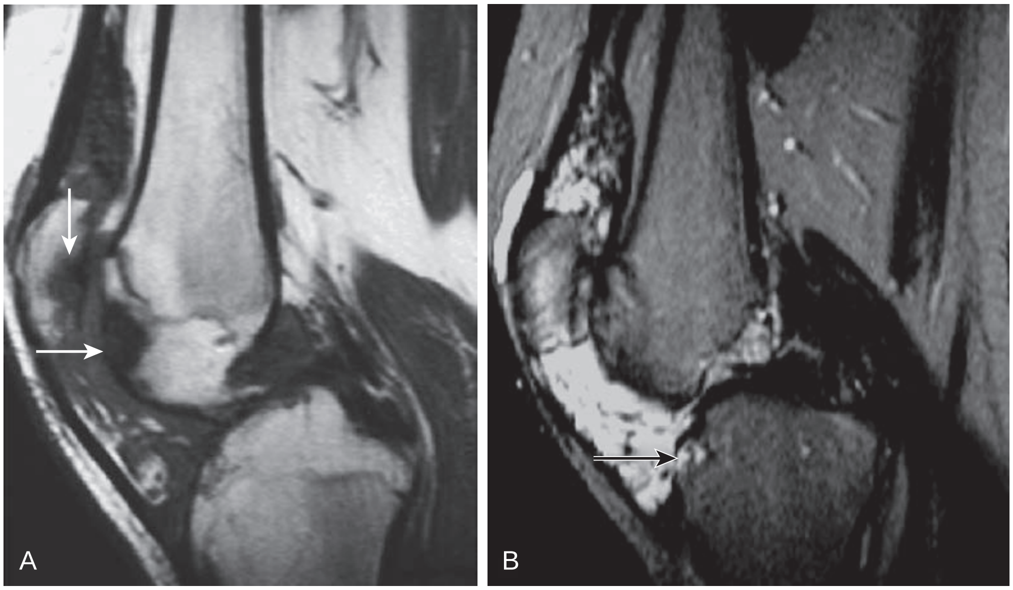

**Figure 136.28. Venous malformation.** An adolescent presented with chronic pain in the left knee. Sagittal T1-weighted (A) and T2-weighted fat-saturated (B) MR images show an extensive soft tissue mass with predominant low signal intensity on a T1-weighted image (A) and high signal intensity on a T2-weighted image (B) involving the suprapatellar bursa and Hoffa's fat pad. Focal areas of low signal intensity suggest the presence of hemosiderin deposition from previous hemarthrosis. There is diffuse articular cartilage loss with subchondral abnormalities *(arrows)* consistent with subchondral sclerosis and cystic changes as a result of inflammatory arthropathy generated by the presence of intraarticular blood products.

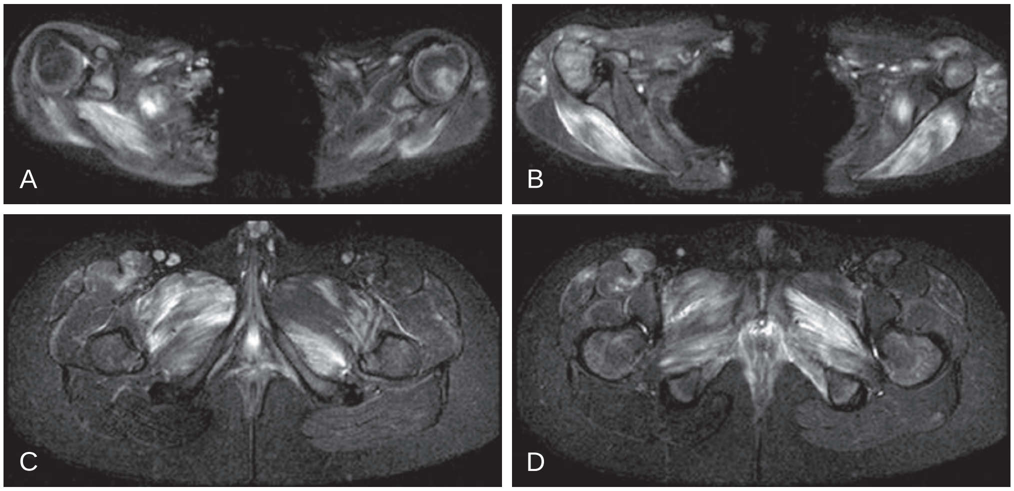

**Figure 136.30. Juvenile dermatomyositis in an 11-year-old boy.** Axial inversion-recovery MR images of the upper extremities (A and B) show patchy asymmetric involvement of bilateral deltoid muscles, pectoralis minor muscle, and supraspinatus, infraspinatus, and subscapularis muscles. Within the lower extremities (C and D), patchy asymmetric signal abnormality is present in the adductor compartment muscles, the internal obturator muscles with less signal abnormality within the quadriceps, tensor fascia lata, and left gluteus maximus muscles.

The arthritis associated with JDM is usually transient and nondeforming in nature.[178]

## Ultrasonography

Ultrasound scanning of the involved musculature shows diffusely increased echogenicity of the soft tissues and acoustic shadowing within the musculature in regions of calcium deposits. Histopathologically, muscle lipomatosis significantly correlates to muscle echogenicity.[170] Other sonographic findings include atrophy and decreased muscular bulk, soft tissue fasciculation, tenosynovitis, and soft tissue nodularities.[179]

## Magnetic Resonance Imaging

Ultrasound and MRI have a similar capacity to demonstrate the features of inflammatory muscle disease, but MRI is more sensitive for the detection of the edema and inflammation in the acute phase of the disease. Both MRI and ultrasound allow guided biopsy and aspiration of muscle abnormalities.[180–183] MRI reveals increased water content (edema) as increased signal intensity on T2-weighted and short-tau inversion recovery MR images (see e-Fig. 136.29 and Fig. 136.30) within infarcted muscles as a result of vasculitis.[184] T2 relaxation time can be used as a quantitative measure of muscle inflammation and correlates well with other

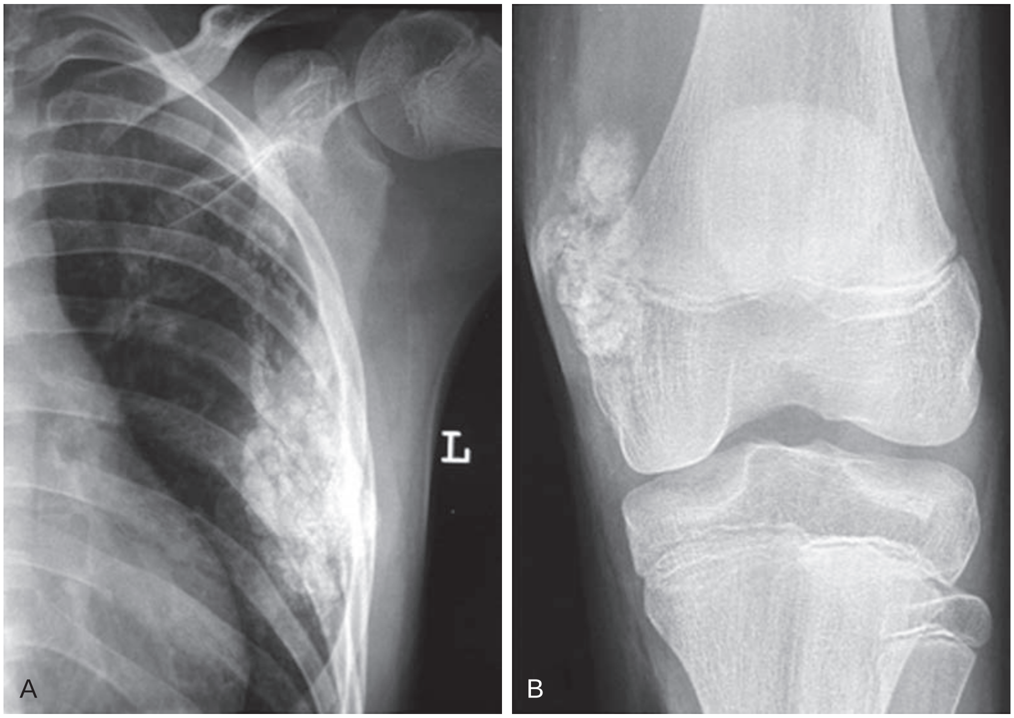

**Figure 136.31. Juvenile dermatomyositis and severe heterotopic calcifications in a 15-year-old boy.** Frontal radiographs of the left lateral chest wall (A) and left knee (B) show extensive soft tissue calcifications.

measures of disease activity.[185] Because physical exercise can induce changes that mimic inflammation of muscle, children with JDM should be at rest for at least 30 minutes before MRI to assess disease activity.[186] At least one study has shown that abnormal subcutaneous fat signal is an insensitive but specific marker of those children with JDM who will progress to a more aggressive chronic disease course.[187]

In chronic disease, focal areas of low signal intensity usually are seen on all MRI sequences, which represent calcific and fibrotic foci. Focal areas of increased signal intensity on T1-weighted images representing fatty replacement of muscles and tenosynovitis-related changes also may be identified.[184]

### Computed Tomography

Although CT does not detect inflammatory changes in muscle tissue, it is the modality of choice for identifying soft tissue calcifications in soft tissues associated with JDM.[188] It also allows quantification of muscle atrophy and fatty replacement in deep muscles.

### Scintigraphy

Whole-body thallium-201 chloride and technetium-99m-methylene diphosphonate ($^{99m}$technetium-MDP) muscle scintigraphy is a potentially useful tool to investigate occult muscle groups affected by dermatomyositis; however, further investigation in the pediatric population is required.[189,190] Furthermore, bone scans with $^{99m}$technetium-MDP can function as auxiliary tools to evaluate calcinosis in patients with JDM.[188–190]

## Treatment and Follow-up

Since the 1970s, standard treatment for JDM has been high-dose daily oral corticosteroids, which is continued until clinical and laboratory improvement are evident and then slowly reduced over at least a 2-year period.[191] Methotrexate is an important ancillary treatment. Early studies suggested that methotrexate improves strength and reduces other signs of disease activity in steroid-resistant patients[192] with acceptable adverse effects.[193,194] Other treatments, including cyclosporine, hydroxychloroquine, tacrolimus, azathioprine, mycophenolate mofetil, and cyclophosphamide for severe disease, have shown some benefit in cases of refractory disease.[195]

Biologic agents, which are used widely in persons with other rheumatic diseases, are being developed for the treatment of childhood myositis. Studies[196,197] of rituximab in persons with JDM suggest a favorable response; however, biologic agents currently are reserved for patients with recalcitrant disease.[198]

Physical disability from muscle weakness or contractures represents a significant problem. Physiotherapy plays an important role in the rehabilitation of patients with JDM.[199] Studies using MRI T2-weighted relaxation time suggest that moderate exercise does not increase muscle inflammation.[200] In another study,[201] aerobic exercise limitation in JDM was shown to correlate best with measures of disease damage.

# CHRONIC RECURRENT MULTIFOCAL OSTEOMYELITIS

## Etiology, Pathophysiology, and Clinical Presentation

Chronic recurrent multifocal osteomyelitis (CRMO) is a skeletal disorder of unknown origin mainly occurring in children and adolescents.[202] It is characterized by multifocal nonpyogenic inflammatory bone lesions, a course of exacerbations and remissions, and an association with other inflammatory disorders.[203] The association of CRMO with dermatologic disorders (such as psoriasis) and inflammatory bowel disease and its response to steroids suggests an autoimmune cause.[204–206] A genetic origin for CRMO has been suggested as a result of observation of disease in siblings and monozygotic twins.[207–209]

SAPHO (synovitis, acne, pustulosis, hyperostosis, osteitis) syndrome is considered by some to be the adult equivalent of CRMO.[210] Whereas CRMO typically manifests in the first decade

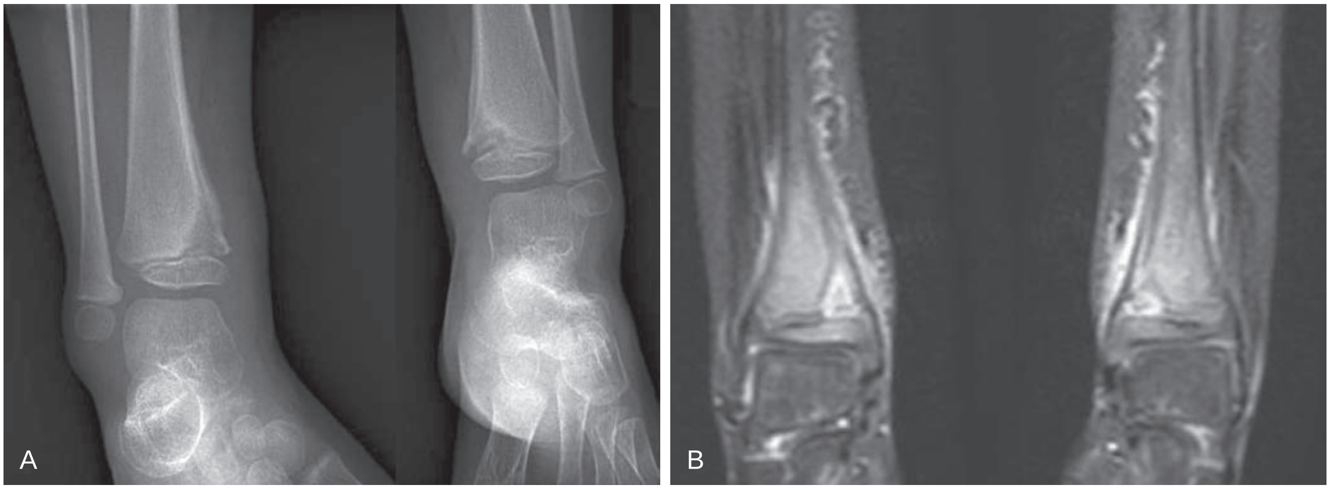

**Figure 136.32. Chronic recurrent osteomyelitis in a 4-year-old girl.** (A) Radiograph of the ankles shows lytic lesions in the bilateral tibial metaphyses with associated periosteal reaction. (B) Coronal STIR MR image of both ankles shows focal high signal intensity lesions in both tibial metaphyses, which involve the adjacent physes, and extensive surrounding bone marrow and periosteal edema.

of life, the mean age of onset for SAPHO syndrome is 28 years.[211] CRMO is a diagnosis of exclusion, distinct from bacterial osteomyelitis, based on the following criteria:

1. Bone lesions with a radiographic picture suggesting subacute or chronic osteomyelitis
2. Frequent multifocality
3. No abscess formation, fistula, or sequestra
4. Lack of a causative organism
5. Nonspecific histopathologic and laboratory findings compatible with subacute or chronic osteomyelitis
6. A characteristic prolonged, fluctuating course with recurrent episodes of pain
7. Occasional accompanying skin disease[202]

## Imaging

The imaging evaluation of CRMO should start with radiographic evaluation of the symptomatic sites. If the radiographs have negative findings in the presence of significant clinical symptoms, further evaluation with MRI should be considered to evaluate for bone marrow edema. Whole-body evaluation traditionally has been performed with $^{99m}$technetium bone scintigraphy,[212] although whole-body MRI is being increasingly used.[213] The diagnosis of CRMO typically is confirmed by means of image-guided bone biopsy.[214]

The three most common sites of disease at initial presentation are the lower extremities (39.7%) (Fig. 136.32 and e-Fig. 136.33), spine (25.9%), and pelvis (20.7%),[210] followed by the clavicle, the spine, the mandible (Fig. 136.34), and pelvic bones.[215,216] In tubular bones, metaphyseal lesions are the most common, accounting for 49% of all long bone lesions.[210]

The differential diagnosis of CRMO includes subacute and chronic infectious osteomyelitis, histiocytosis, hypophosphatasia, and malignancies such as leukemia, lymphoma, and Ewing sarcoma.[217] The imaging features may mimic pyogenic chronic osteomyelitis, and ultimately it may be necessary to perform a biopsy in clinically equivocal cases. Multifocal metaphyseal-based lesions favor a diagnosis of CRMO after pyogenic infection has been excluded.

CRMO of long bones can result in orthopedic complications such as bony overgrowth, angular deformities, and limb-length discrepancy.[218] Because of its tendency to occur near the physes, CRMO can cause premature physeal closure, resulting in growth arrest. The hyperemia caused by chronic inflammation may result in diffuse demineralization, predisposing to fractures.[219]

## Treatment and Follow-up

Suggestion of the diagnosis by a radiologist could help avoid unnecessary diagnostic procedures and antibiotic therapy and initiate an appropriate therapy.[210] Many different treatments have been used in persons with CRMO, including nonsteroidal anti-inflammatory agents, corticosteroids,[220] azithromycin, tumor necrosis factor-blocker (infliximab),[221,222] and interferon.[223] Bisphosphonates have been used in persons with CRMO for pain relief and control of disease progression[224] and when simple therapies fail to control symptoms or disease progression.[224]

### KEY POINTS

- Clinical and laboratory diagnosis of early joint changes in children with JIA is suboptimal. Imaging, particularly with MRI and ultrasound, is important for early detection and for evaluating treatment response in children with JIA.
- Both MRI and ultrasound can detect JIA synovial hypertrophy, erosions, and joint effusions in peripheral joints and monitor clinically meaningful response to treatment.
- Ultrasound is generally less sensitive than MRI.
- Radiographic findings of ERA and other spondyloarthropathies are similar to those encountered in other forms of JIA, with the exception of sacroiliitis and enthesitis.
- Radiographic changes in hemophilic arthropathy may be identical to JIA, but clinical findings distinguish these entities.
- PVNS is a benign proliferative disorder characterized by synovial hyperplasia in joints, bursae, and tendon sheaths. PVNS shows variable villous and nodular synovial proliferation typically with low signal intensity within the joint (from hemosiderin) on MRI.
- In JDM, the muscles of the scapular and pelvic girdles are most frequently affected.
- CRMO is characterized by multifocal nonpyogenic inflammatory bone lesions that may be associated with other inflammatory disorders.

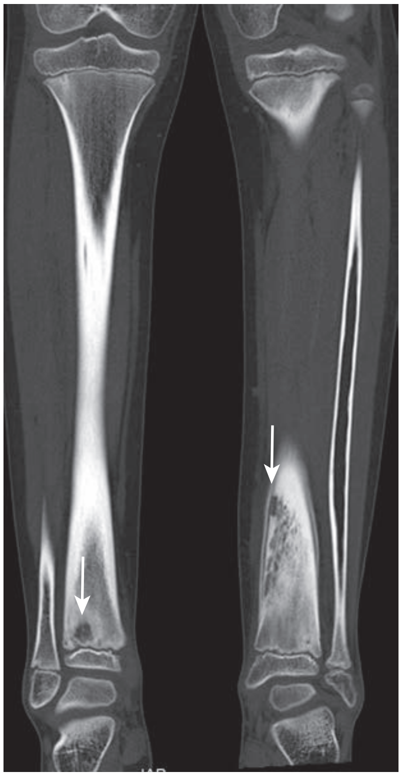

**e-Figure 136.33. Chronic recurrent multifocal osteomyelitis in an 8-year-old girl with bilateral distal tibial lytic lesions.** One lesion is located in the right distal tibial juxtaphyseal metaphysis, and a secondary lytic lesion is located in the left tibia metadiaphysis *(arrows)*. The left tibial metadiaphyseal lesion was biopsied to establish the diagnosis.

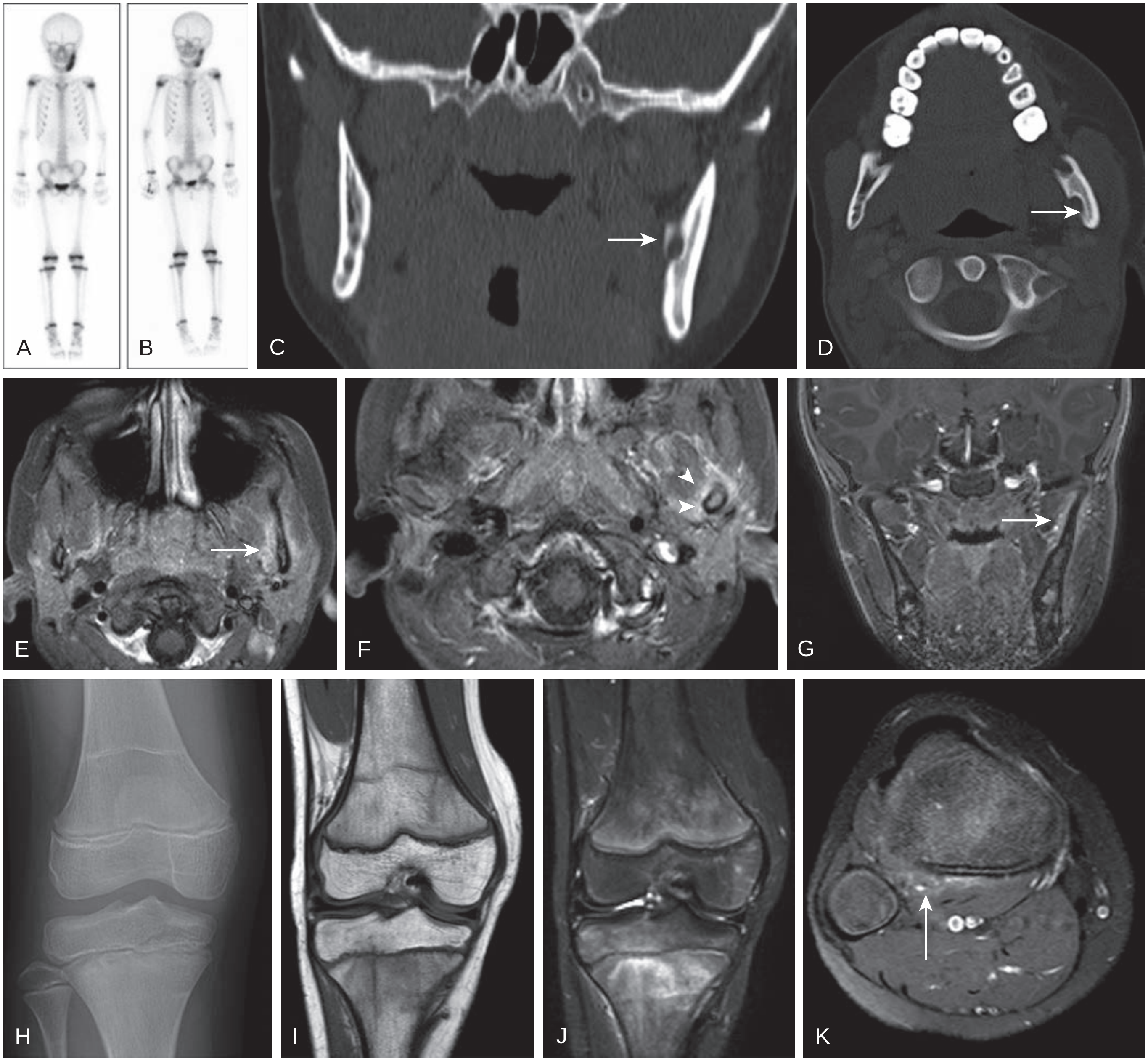

**Figure 136.34. Chronic recurrent multifocal osteomyelitis.** At the age of 6 years, this girl presented with pain in the left mandible. At that time, the bone scan (A) showed a increased uptake in the left mandibular ramus. Eight months later, persistent increased activity was still noted in the left mandible on a bone scan (B); however, it was less intense than in the previous study. Subsequently, the patient started treatment with pamidronate. Three years later, coronal (C) and axial (D) CT images of the mandibles showed a lytic left mandibular lesion posterior to an unerupted molar *(arrows)*. Postcontrast axial T1-weighted turbo spin echo spectral presaturation inversion recovery (SPIR), (E and F) and coronal T1-weighted three-dimensional fast field echo postcontrast (G) MR images performed 2 months after the CT scan shows increased marrow and adjacent soft tissue enhancement in the mid and superior aspects of the left mandibular ramus (*arrows* in E and G) with associated mild reactive synovitis (*arrowheads* in F) of the left TMJ. Three years later, pain started to develop in the right knee. The frontal radiograph (H) and MRI of the right knee coronal T1-weighted, (I) coronal short-tau inversion recovery (STIR), (J) and postcontrast axial T1-weighted SPIR, (K) shows decreased signal on the T1-weighted image and increased signal intensity on the STIR images in the proximal tibial metaphysis with mild adjacent soft tissue inflammation *(arrow)*.

## SUGGESTED READINGS

Khanna G, Sato TS, Ferguson P. Imaging of chronic recurrent multifocal osteomyelitis. *Radiographics*. 2009;29:1159–1177.

Kim HK, Zbojniewicz AM, Merrow AC, et al. MR findings of synovial disease in children and young adults: Part 1. *Pediatr Radiol*. 2011;41(4):495–511, quiz 545-6. doi:10.1007/s00247-011-1971-0.

Kim HK, Zbojniewicz AM, Merrow AC, et al. MR findings of synovial disease in children and young adults: Part 2. *Pediatr Radiol*. 2011;41(4):512–524. doi:10.1007/s00247-011-2007-5.

Meyers AB, Laor T. Magnetic resonance imaging of the temporomandibular joint in children with juvenile idiopathic arthritis. *Pediatr Radiol*. 2013;43(12):1632–1641, quiz 1629-31. doi:10.1007/s00247-013-2769-z.

Sheybani EF, Khanna G, White AJ, et al. Imaging of juvenile idiopathic arthritis: a multimodality approach. *Radiographics*. 2013;33(5):1253–1273. doi:10.1148/rg.335125178.

## REFERENCES

Full references for this chapter can be found on www.expertconsult.com.

## REFERENCES

1. Petty RE, Southwood TR, Manners P, et al. International League of Associations for Rheumatology classification of juvenile idiopathic arthritis: second revision, Edmonton, 2001. *J Rheumatol*. 2004;31:390–392.
2. Cassidy JT. Juvenile rheumatoid arthritis. In: Kelly W, Harris E, Ruddy S, et al, eds. *Textbook of Rheumatology*. Philadelphia: WB Saunders; 2003:1189–1208.
3. Schanberg LE, Sandstrom MJ. Causes of pain in children with arthritis. *Rheum Dis Clin North Am*. 1999;25:31–53, vi.
4. Schanberg LE, Anthony KK, Gil KM, et al. Daily pain and symptoms in children with polyarticular arthritis. *Arthritis Rheum*. 2003;48:1390–1397.
5. Hollister J. Juvenile rheumatoid arthritis. In: Hay W, Levin M, Sondheimer J, et al, eds. *Current Diagnosis & Treatment in Pediatrics*. New York: Lange Medical Books/McGraw-Hill Medical Publishing Division; 2007.
6. Wright D. Juvenile idiopathic arthritis. In: Morrissy R, Weinstein S, eds. *Lovell & Winter's Pediatric Orthopedics*. Philadelphia: Lippincott Williams & Wilkins; 2006:406–410.
7. Fink CW. Proposal for the development of classification criteria for idiopathic arthritides of childhood. *J Rheumatol*. 1995;22:1566–1569.
8. Miller E, Doria AS. Imaging for early assessment of peripheral joints in juvenile idiopathic arthritis. In: Santiago Medina L, Applegate K, Blackmore C, eds. *Evidence-Based Imaging in Pediatrics: Optimizing Imaging in Pediatric Patient Care*. New York: Springer; 2010:219–273.
9. Guzman J, Burgos-Vargas R, Duarte-Salazar C, et al. Reliability of the articular examination in children with juvenile rheumatoid arthritis: interobserver agreement and sources of disagreement. *J Rheumatol*. 1995;22:2331–2336.
10. Forslind K, Larsson EM, Johansson A, et al. Detection of joint pathology by magnetic resonance imaging in patients with early rheumatoid arthritis. *Br J Rheumatol*. 1997;36:683–688.
11. Thierry S, Fautrel B, Lemelle I, et al. Prevalence and incidence of juvenile idiopathic arthritis: a systematic review. *Joint Bone Spine*. 2014;81(2):112–117. doi:10.1016/j.jbspin.2013.09.003.
12. Aaron S, Fraser PA, Jackson JM, et al. Sex ratio and sibship size in juvenile rheumatoid arthritis kindreds. *Arthritis Rheum*. 1985;28:753–758.
13. Hanson V, Kornreich H, Bernstein B. Three subtypes of juvenile rheumatoid arthritis (correlations of age at onset, sex, and serologic factors). *Arthritis Rheum*. 1977;20(suppl):184.
14. Cassidy J, Petty R. Juvenile rheumatoid arthritis. In: *Textbook of Pediatric Rheumatology*. Philadelphia: W.B. Saunders; 1995:133–223.
15. Ravelli A. Toward an understanding of the long-term outcome of juvenile idiopathic arthritis. *Clin Exp Rheumatol*. 2004;22:271–275.
16. Oen K. Long-term outcomes and predictors of outcomes for patients with juvenile idiopathic arthritis. *Best Pract Res Clin Rheumatol*. 2002;16:347–360.
17. Davidson J. Juvenile idiopathic arthritis: a clinical overview. *Eur J Radiol*. 2000;33:128–134.
18. Cassone R, Falcone A, Rossi F, et al. Unilateral destructive wrist synovitis in juvenile idiopathic arthritis. *Clin Exp Rheumatol*. 2004;22:637–642.
19. Lang BA, Schneider R, Reilly BJ, et al. Radiologic features of systemic onset juvenile rheumatoid arthritis. *J Rheumatol*. 1995;22:168–173.
20. Kim HK, Zbojniewicz AM, Merrow AC, et al. MR findings of synovial disease in children and young adults: part 1. *Pediatr Radiol*. 2011;41:495–511.
21. Yulish BS, Lieberman JM, Newman AJ, et al. Juvenile rheumatoid arthritis: assessment with MR imaging. *Radiology*. 1987;165:149–152.
22. Wallace CA, Levinson JE. Juvenile rheumatoid arthritis: outcome and treatment for the 1990s. *Rheum Dis Clin North Am*. 1991;17:891–905.
23. Minden K, Niewerth M, Listing J, et al. Long-term outcome in patients with juvenile idiopathic arthritis. *Arthritis Rheum*. 2002;46:2392–2401.
24. Zak M, Pedersen FK. Juvenile chronic arthritis into adulthood: a long-term follow-up study. *Rheumatology (Oxford)*. 2000;39:198–204.
25. Babyn P, Doria AS. Radiologic investigation of rheumatic diseases. *Pediatr Clin North Am*. 2005;52:373–411, vi.
26. Azouz EM. Juvenile idiopathic arthritis: how can the radiologist help the clinician? *Pediatr Radiol*. 2008;38(suppl 3):S403–S408.
27. Southwood T. Juvenile idiopathic arthritis: clinically relevant imaging in diagnosis and monitoring. *Pediatr Radiol*. 2008;38(suppl 3):S395–S402.
28. Magni-Manzoni S. Ultrasound in juvenile idiopathic arthritis. *Pediatr Rheumatol Online J*. 2016;14(1):33. doi:10.1186/s12969-016-0096-2.
29. Doria AS, Babyn PS, Feldman B. A critical appraisal of radiographic scoring systems for assessment of juvenile idiopathic arthritis. *Pediatr Radiol*. 2006;36:759–772.
30. Lamer S, Sebag GH. MRI and ultrasound in children with juvenile chronic arthritis. *Eur J Radiol*. 2000;33:85–93.
31. Spilberg I, Meyer GJ. The arthritis of leukemia. *Arthritis Rheum*. 1972;15:630–635.
32. Laxer RM, Cameron BJ, Chaisson D, et al. The camptodactyly-arthropathy-pericarditis syndrome: case report and literature review. *Arthritis Rheum*. 1986;29:439–444.
33. Babyn P, Doria AS. Radiologic investigation of rheumatic diseases. *Rheum Dis Clin North Am*. 2007;33:403–440.
34. Backhaus M, Kamradt T, Sandrock D, et al. Arthritis of the finger joints: a comprehensive approach comparing conventional radiography, scintigraphy, ultrasound, and contrast-enhanced magnetic resonance imaging. *Arthritis Rheum*. 1999;42:1232–1245.
35. Gylys-Morin VM, Graham TB, Blebea JS, et al. Knee in early juvenile rheumatoid arthritis: MR imaging findings. *Radiology*. 2001;220:696–706.
36. Babyn P, Doria A. Radiologic investigation of rheumatic diseases. In: Cassidy J, Petty R, Lindsley C, eds. *Textbook of Pediatric Rheumatology*. Philadelphia: Saunders; 2010.
37. Gylys-Morin VM. MR imaging of pediatric musculoskeletal inflammatory and infectious disorders. *Magn Reson Imaging Clin N Am*. 1998;6:537–559.
38. Lamer S, Sebag GH. MRI and ultrasound in children with juvenile chronic arthritis. *Eur J Radiol*. 2000;33:85–93.
39. Daldrup-Link HE, Steinbach L. MR imaging of pediatric arthritis. *Magn Reson Imaging Clin N Am*. 2009;17:451–467, vi.
40. Cakmakci H, Kovanlikaya A, Unsal E. Short-term follow-up of the juvenile rheumatoid knee with fat-saturated 3D MRI. *Pediatr Radiol*. 2001;31:189–195.
41. Laor T, Jaramillo D. MR imaging insights into skeletal maturation: what is normal? *Radiology*. 2009;250:28–38.
42. McQueen FM. The MRI view of synovitis and tenosynovitis in inflammatory arthritis: implications for diagnosis and management. *Ann N Y Acad Sci*. 2009;1154:21–34.
43. Ostergaard M, Stoltenberg M, Henriksen O, et al. Quantitative assessment of synovial inflammation by dynamic gadolinium-enhanced magnetic resonance imaging. A study of the effect of intra-articular methylprednisolone on the rate of early synovial enhancement. *Br J Rheumatol*. 1996;35:50–59.
44. Graham TB, Laor T, Dardzinski BJ. Quantitative magnetic resonance imaging of the hands and wrists of children with juvenile rheumatoid arthritis. *J Rheumatol*. 2005;32:1811–1820.
45. Ostergaard M, Hansen M, Stoltenberg M, et al. Magnetic resonance imaging-determined synovial membrane volume as a marker of disease activity and a predictor of progressive joint destruction in the wrists of patients with rheumatoid arthritis. *Arthritis Rheum*. 1999;42(5):918–929.
46. Muller L, Kellenberger CJ, Cannizzaro E, et al. Early diagnosis of temporomandibular joint involvement in juvenile idiopathic arthritis: a pilot study comparing clinical examination and ultrasound to magnetic resonance imaging. *Rheumatology (Oxford)*. 2009;48:680–685.
47. Chung C, Coley BD, Martin LC. Rice bodies in juvenile rheumatoid arthritis. *AJR Am J Roentgenol*. 1998;170:698–700.
48. Haavardsholm EA, Bøyesen P, Østergaard M, et al. MRI-detected bone marrow edema is a predictor of subsequent radiographic progression in early rheumatoid arthritis. *Ann Rheum Dis*. 2007;66(suppl II):94.
49. McQueen FM. A vital clue to deciphering bone pathology: MRI bone oedema in rheumatoid arthritis and osteoarthritis. *Ann Rheum Dis*. 2007;66:1549–1552.
50. Palosaari K, Vuotila J, Takalo R, et al. Bone oedema predicts erosive progression on wrist MRI in early RA—a 2-yr observational MRI and NC scintigraphy study. *Rheumatology (Oxford)*. 2006;45(12):1542–1548.
51. Miller E, Uleryk E, Doria AS. Evidence-based outcomes of studies addressing diagnostic accuracy of MRI of juvenile idiopathic arthritis. *AJR Am J Roentgenol*. 2009;192:1209–1218.
52. Johnson K. Imaging of juvenile idiopathic arthritis. *Pediatr Radiol*. 2006;36:743–758.
53. Malattia C, Damasio MB, Pistorio A, et al. Development and preliminary validation of a paediatric-targeted MRI scoring system for the assessment of disease activity and damage in juvenile idiopathic arthritis. *Ann Rheum Dis*. 2011;70:440–446.

54. Hemke R, Maas M, van Veenendaal M, et al. MRI findings in the knee of juvenile idiopathic arthritis: experience with a newly developed juvenile arthritis MRI scoring system (JAMRIS). *Ann Rheum Dis*. 2010;69:632.
55. Friedrich KM, Mamisch TC, Plank C, et al. Diffusion-weighted imaging for the follow-up of patients after matrix-associated autologous chondrocyte transplantation. *Eur J Radiol*. 2010;73:622–628.
56. Basser PJ, Pajevic S, Pierpaoli C, et al. In vivo fiber tractography using DT-MRI data. *Magn Reson Med*. 2000;44:625–632.
57. Agarwal V, Kumar M, Singh JK, et al. Diffusion tensor anisotropy magnetic resonance imaging: a new tool to assess synovial inflammation. *Rheumatology (Oxford)*. 2009;48:378–382.
58. Miller KL, Hargreaves BA, Gold GE, et al. Steady-state diffusion-weighted imaging of in vivo knee cartilage. *Magn Reson Med*. 2004;51:394–398.
59. Malattia C, Damasio MB, Basso C, et al. Dynamic contrast-enhanced magnetic resonance imaging in the assessment of disease activity in patients with juvenile idiopathic arthritis. *Rheumatology (Oxford)*. 2010;49:178–185.
60. Konig H, Sieper J, Wolf KJ. Rheumatoid arthritis: evaluation of hypervascular and fibrous pannus with dynamic MR imaging enhanced with Gd-DTPA. *Radiology*. 1990;176:473–477.
61. Yamato M, Tamai K, Yamaguchi T, et al. MRI of the knee in rheumatoid arthritis: Gd-DTPA perfusion dynamics. *J Comput Assist Tomogr*. 1993;17:781–785.
62. Workie DW, Dardzinski BJ. Quantifying dynamic contrast-enhanced MRI of the knee in children with juvenile rheumatoid arthritis using an arterial input function (AIF) extracted from popliteal artery enhancement, and the effect of the choice of the AIF on the kinetic parameters. *Magn Reson Med*. 2005;54:560–568.
63. Workie DW, Graham TB, Laor T, et al. Quantitative MR characterization of disease activity in the knee in children with juvenile idiopathic arthritis: a longitudinal pilot study. *Pediatr Radiol*. 2007;37:535–543.
64. Bashir A, Gray ML, Boutin RD, et al. Glycosaminoglycan in articular cartilage: in vivo assessment with delayed Gd(DTPA)(2-)-enhanced MR imaging. *Radiology*. 1997;205:551–558.
65. Dardzinski BJ, Laor T, Schmithorst VJ, et al. Mapping T2 relaxation time in the pediatric knee: feasibility with a clinical 1.5-T MR imaging system. *Radiology*. 2002;225:233–239.
66. Dardzinski BJ, Mosher TJ, Li S, et al. Spatial variation of T2 in human articular cartilage. *Radiology*. 1997;205:546–550.
67. Mosher TJ, Dardzinski BJ. Cartilage MRI T2 relaxation time mapping: overview and applications. *Semin Musculoskelet Radiol*. 2004;8:355–368.
68. Kight AC, Dardzinski BJ, Laor T, et al. Magnetic resonance imaging evaluation of the effects of juvenile rheumatoid arthritis on distal femoral weight-bearing cartilage. *Arthritis Rheum*. 2004;50:901–905.
69. Kim HK, Laor T, Graham TB, et al. T2 relaxation time changes in distal femoral articular cartilage in children with juvenile idiopathic arthritis: a 3-year longitudinal study. *AJR Am J Roentgenol*. 2010;195:1021–1025.
70. Perman WH, Turski PA, Houston LW, et al. Methodology of in vivo human sodium MR imaging at 1.5 T. *Radiology*. 1986;160:811–820.
71. Shapiro EM, Borthakur A, Gougoutas A, et al. 23Na MRI accurately measures fixed charge density in articular cartilage. *Magn Reson Med*. 2002;47:284–291.
72. Reddy R, Insko EK, Noyszewski EA, et al. Sodium MRI of human articular cartilage in vivo. *Magn Reson Med*. 1998;39:697–701.
73. Madelin G, Jerschow A, Regatte RR. Sodium relaxation times in the knee joint in vivo at 7T. *NMR Biomed*. 2012;25(4):530–537.
74. Schmitt B, Zbyn S, Stelzeneder D, et al. Cartilage quality assessment by using glycosaminoglycan chemical exchange saturation transfer and (23)Na MR imaging at 7 T. *Radiology*. 2011;260:257–264.
75. Wang L, Wu Y, Chang G, et al. Rapid isotropic 3D-sodium MRI of the knee joint in vivo at 7T. *J Magn Reson Imaging*. 2009;30:606–614.
76. Chavhan GB, Babyn PS. Pediatric musculoskeletal imaging at 3 Tesla. *Semin Musculoskelet Radiol*. 2009;13:181–195.
77. Friedrich KM, Chang G, Vieira RL, et al. In vivo 7.0-tesla magnetic resonance imaging of the wrist and hand: technical aspects and applications. *Semin Musculoskelet Radiol*. 2009;13:74–84.
78. Huang M, Schweitzer ME. The role of Radiology in the evolution of the understanding of articular disease. *Radiology*. 2014;273:S1–S22. doi:10.1148/radiol.14140270.
79. Chang EY, Du J, Chung CB. UTE imaging in the musculoskeletal system. *J Magn Reson Imaging*. 2015;41(4):870–883. doi:10.1002/jmri.24713.
80. Backhaus M. Ultrasound and structural changes in inflammatory arthritis: synovitis and tenosynovitis. *Ann N Y Acad Sci*. 2009;1154:139–151.
81. Ruhoy MK, Tucker L, McCauley RG. Hypertrophic bursopathy of the subacromial-subdeltoid bursa in juvenile rheumatoid arthritis: sonographic appearance. *Pediatr Radiol*. 1996;26:353–355.
82. Terslev L, Torp-Pedersen S, Qvistgaard E, et al. Estimation of inflammation by Doppler ultrasound: quantitative changes after intra-articular treatment in rheumatoid arthritis. *Ann Rheum Dis*. 2003;62:1049–1053.
83. Tse SM, Laxer RM, Babyn PS, et al. Radiologic improvement of juvenile idiopathic arthritis-enthesitis-related arthritis following anti-tumor necrosis factor-alpha blockade with etanercept. *J Rheumatol*. 2006;33:1186–1188.
84. Rebollo-Polo M, Koujok K, Weisser C, et al. Ultrasound findings on patients with juvenile idiopathic arthritis in clinical remission. *Arthritis Care Res (Hoboken)*. 2011;63:1013–1019.
85. Scire CA, Montecucco C, Codullo V, et al. Ultrasonographic evaluation of joint involvement in early rheumatoid arthritis in clinical remission: power Doppler signal predicts short-term relapse. *Rheumatology (Oxford)*. 2009;48:1092–1097.
86. Laurell L, Court-Payen M, Nielsen S, et al. Ultrasonography and color Doppler in juvenile idiopathic arthritis: diagnosis and follow-up of ultrasound-guided steroid injection in the ankle region. A descriptive interventional study. *Pediatr Rheumatol Online J*. 2011;9:4.
87. Weiss PF, Arabshahi B, Johnson A, et al. High prevalence of temporomandibular joint arthritis at disease onset in children with juvenile idiopathic arthritis, as detected by magnetic resonance imaging but not by ultrasound. *Arthritis Rheum*. 2008;58:1189–1196.
88. Doria AS, Kiss MH, Lotito AP, et al. Juvenile rheumatoid arthritis of the knee: evaluation with contrast-enhanced color Doppler ultrasound. *Pediatr Radiol*. 2001;31:524–531.
89. Shahin AA, el Mofty SA, el Sheikh EA, et al. Power Doppler sonography in the evaluation and follow-up of knee involvement in patients with juvenile idiopathic arthritis. *Z Rheumatol*. 2001;60:148–155.
90. Klauser A, Frauscher F, Schirmer M, et al. The value of contrast-enhanced color Doppler ultrasound in the detection of vascularization of finger joints in patients with rheumatoid arthritis. *Arthritis Rheum*. 2002;46:647–653.
91. Terslev L, Torp-Pedersen S, Qvistgaard E, et al. Spectral Doppler and resistive index. A promising tool in ultrasonographic evaluation of inflammation in rheumatoid arthritis. *Acta Radiol*. 2003;44:645–652.
92. El Miedany YM, Housny IH, Mansour HM, et al. Ultrasound versus MRI in the evaluation of juvenile idiopathic arthritis of the knee. *Joint Bone Spine*. 2001;68:222–230.
93. Sureda D, Quiroga S, Arnal C, et al. Juvenile rheumatoid arthritis of the knee: evaluation with US. *Radiology*. 1994;190:403–406.
94. Frosch M, Foell D, Ganser G, et al. Arthrosonography of hip and knee joints in the follow up of juvenile rheumatoid arthritis. *Ann Rheum Dis*. 2003;62:242–244.
95. Magni-Manzoni S, Epis O, Ravelli A, et al. Comparison of clinical versus ultrasound-determined synovitis in juvenile idiopathic arthritis. *Arthritis Rheum*. 2009;61:1497–1504.
96. Pascoli L, Wright S, McAllister C, et al. Prospective evaluation of clinical and ultrasound findings in ankle disease in juvenile idiopathic arthritis: importance of ankle ultrasound. *J Rheumatol*. 2010;37:2409–2414.
97. Hashkes PJ, Laxer RM. Medical treatment of juvenile idiopathic arthritis. *JAMA*. 2005;294:1671–1684.
98. Balogh Z, Ruzsonyi E. Triamcinolone hexacetonide versus betamethasone. A double-blind comparative study of the long-term effects of intra-articular steroids in patients with juvenile chronic arthritis. *Scand J Rheumatol Suppl*. 1987;67:80–82.
99. Zulian F, Martini G, Gobber D, et al. Comparison of intra-articular triamcinolone hexacetonide and triamcinolone acetonide in oligoarticular juvenile idiopathic arthritis. *Rheumatology (Oxford)*. 2003;42:1254–1259.
100. Zulian F, Martini G, Gobber D, et al. Triamcinolone acetonide and hexacetonide intra-articular treatment of symmetrical joints in juvenile idiopathic arthritis: a double-blind trial. *Rheumatology (Oxford)*. 2004;43:1288–1291.
101. Huppertz HI, Tschammler A, Horwitz AE, et al. Intraarticular corticosteroids for chronic arthritis in children: efficacy and effects on cartilage and growth. *J Pediatr*. 1995;127:317–321.
102. Eich GF, Halle F, Hodler J, et al. Juvenile chronic arthritis: imaging of the knees and hips before and after intraarticular steroid injection. *Pediatr Radiol*. 1994;24:558–563.

103. Poznanski AK, Hernandez RJ, Guire KE, et al. Carpal length in children—a useful measurement in the diagnosis of rheumatoid arthritis and some congenital malformation syndromes. *Radiology*. 1978;129:661–668.
104. Spârchez M, Fodor D, Miu N. The role of Power Doppler ultrasonography in comparison with biological markers in evaluation of disease activity in Juvenile Idiopathic Arthritis. *Med Ultrason*. 2010;12:97–103.
105. Ringold S, Torgerson TR, Egbert MA, et al. Intraarticular corticosteroid injections of the temporomandibular joint in juvenile idiopathic arthritis. *J Rheumatol*. 2008;35:1157–1164.
106. Neidel J, Boehnke M, Kuster RM. The efficacy and safety of intraarticular corticosteroid therapy for coxitis in juvenile rheumatoid arthritis. *Arthritis Rheum*. 2002;46:1620–1628.
107. Sparling M, Malleson P, Wood B, et al. Radiographic follow-up of joints injected with triamcinolone hexacetonide for the management of childhood arthritis. *Arthritis Rheum*. 1990;33:821–826.
108. Jacobs JC, Berdon WE, Johnston AD. HLA-B27-associated spondylarthritis and enthesopathy in childhood: clinical, pathologic, and radiographic observations in 58 patients. *J Pediatr*. 1982;100:521–528.
109. Prieur AM. Spondyloarthropathies in childhood. *Baillieres Clin Rheumatol*. 1998;12:287–307.
110. Balint PV, Kane D, Wilson H, et al. Ultrasonography of entheseal insertions in the lower limb in spondyloarthropathy. *Ann Rheum Dis*. 2002;61:905–910.
111. Kamel M, Eid H, Mansour R. Ultrasound detection of heel enthesitis: a comparison with magnetic resonance imaging. *J Rheumatol*. 2003;30:774–778.
112. Bollow M, Braun J, Biedermann T, et al. Use of contrast-enhanced MR imaging to detect sacroiliitis in children. *Skeletal Radiol*. 1998;27:606–616.
113. Weiss PF, Xiao R, Biko DM, et al. Detection of inflammatory sacroiliitis in children with magnetic resonance imaging: is gadolinium contrast enhancement necessary? *Arthritis Rheumatol*. 2015;67(8):2250–2256. doi:10.1002/art.39159.
114. Aquino MR, Tse SM, Gupta S, et al. Whole-body MRI of juvenile spondyloarthritis: protocols and pictorial review of characteristic patterns. *Pediatr Radiol*. 2015;45(5):754–762. doi:10.1007/s00247-015-3319-7. [Epub 2015 Apr 21].
115. Burgos-Vargas R, Vazquez-Mellado J, Pacheco-Tena C, et al. A 26 week randomised, double blind, placebo controlled exploratory study of sulfasalazine in juvenile onset spondyloarthropathies. *Ann Rheum Dis*. 2002;61:941–942.
116. Tse SM, Burgos-Vargas R, Laxer RM. Anti-tumor necrosis factor alpha blockade in the treatment of juvenile spondylarthropathy. *Arthritis Rheum*. 2005;52:2103–2108.
117. Henrickson M, Reiff A. Prolonged efficacy of etanercept in refractory enthesitis-related arthritis. *J Rheumatol*. 2004;31:2055–2061.
118. D'Agostino MA, Said-Nahal R, Hacquard-Bouder C, et al. Assessment of peripheral enthesitis in the spondylarthropathies by ultrasonography combined with power Doppler: a cross-sectional study. *Arthritis Rheum*. 2003;48:523–533.
119. Lee EY, Sundel RP, Kim S, et al. MRI findings of juvenile psoriatic arthritis. *Skeletal Radiol*. 2008;37:987–996.
120. Ory PA, Gladman DD, Mease PJ. Psoriatic arthritis and imaging. *Ann Rheum Dis*. 2005;64(suppl 2):ii55–ii57.
121. Puhakka KB, Jurik AG, Egund N, et al. Imaging of sacroiliitis in early seronegative spondylarthropathy. Assessment of abnormalities by MR in comparison with radiography and CT. *Acta Radiol*. 2003;44:218–229.
122. Venkateswaran L, Wilimas JA, Jones DJ, et al. Mild hemophilia in children: prevalence, complications, and treatment. *J Pediatr Hematol Oncol*. 1998;20:32–35.
123. Rand T, Trattnig S, Male C, et al. Magnetic resonance imaging in hemophilic children: value of gradient echo and contrast-enhanced imaging. *Magn Reson Imaging*. 1999;17:199–205.
124. Resnick D. *Diagnosis of Bone and Joint Disorders*. 4th ed. Philadelphia: Saunders; 2002.
125. Kerr R. Imaging of musculoskeletal complications of hemophilia. *Semin Musculoskelet Radiol*. 2003;7:127–136.
126. Kraft J, Blanchette V, Babyn P, et al. Magnetic resonance imaging and joint outcomes in boys with severe hemophilia A treated with tailored primary prophylaxis in Canada. *J Thromb Haemost*. 2012;10:2494–2502.
127. Baunin C, Railhac JJ, Younes I, et al. MR imaging in hemophilic arthropathy. *Eur J Pediatr Surg*. 1991;1:358–363.
128. Cotten A, Flipo RM, Herbaux B, et al. Synovial haemangioma of the knee: a frequently misdiagnosed lesion. *Skeletal Radiol*. 1995;24:257–261.
129. Hughes TH, Sartoris DJ, Schweitzer ME, et al. Pigmented villonodular synovitis: MRI characteristics. *Skeletal Radiol*. 1995;24:7–12.
130. Bravo SM, Winalski CS, Weissman BN. Pigmented villonodular synovitis. *Radiol Clin North Am*. 1996;34:311–326, x-xi.
131. Kilcoyne RF, Nuss R. Radiological assessment of haemophilic arthropathy with emphasis on MRI findings. *Haemophilia*. 2003;9(suppl 1):57–63.
132. Kilcoyne RF, Lundin B, Pettersson H. Evolution of the imaging tests in hemophilia with emphasis on radiography and magnetic resonance imaging. *Acta Radiol*. 2006;47:287–296.
133. Lundin B, Berntorp E, Pettersson H, et al. Gadolinium contrast agent is of limited value for magnetic resonance imaging assessment of synovial hypertrophy in hemophiliacs. *Acta Radiol*. 2007;48:520–530.
134. Doria A, Lundin B. Imaging modalities for assessment of hemophilic arthropathy. In: Lee C, Berntorp E, Hoots K, eds. *Textbook of Hemophilia*. West Sussex, UK: Wiley-Blackwell.; 2009:191–199.
135. Merchan EC, De Orbe A, Gago J. Ultrasound in the diagnosis of the early stages of hemophilic arthropathy of the knee. *Acta Orthop Belg*. 1992;58:122–125.
136. Zukotynski K, Jarrin J, Babyn PS, et al. Sonography for assessment of haemophilic arthropathy in children: a systematic protocol. *Haemophilia*. 2007;13:293–304.
137. Muca-Perja M, Riva S, Grochowska B, et al. Ultrasonography of haemophilic arthropathy. *Haemophilia*. 2012;18(3):364–368.
138. Klukowska A, Czyrny Z, Laguna P, et al. Correlation between clinical, radiological and ultrasonographical image of knee joints in children with haemophilia. *Haemophilia*. 2001;7:286–292.
139. Roosendaal G, van Rinsum AC, Vianen ME, et al. Haemophilic arthropathy resembles degenerative rather than inflammatory joint disease. *Histopathology*. 1999;34:144–153.
140. Speer DP. Early pathogenesis of hemophilic arthropathy. Evolution of the subchondral cyst. *Clin Orthop Relat Res*. 1984;185:250–265.
141. Rodriguez-Merchan EC, Jimenez-Yuste V, Aznar JA, et al. Joint protection in haemophilia. *Haemophilia*. 2011;17(suppl 2):1–23.
142. Kilcoyne RF *Imaging in musculoskeletal complications of hemophilia*, *WebMD* (website): http://emedicine.medscape.com/article/401842-overview. Accessed January 8, 2013.
143. Manco-Johnson MJ, Abshire TC, Shapiro AD, et al. Prophylaxis versus episodic treatment to prevent joint disease in boys with severe hemophilia. *N Engl J Med*. 2007;357:535–544.
144. Doria AS, Keshava S, Mohanta A, et al. *Reliability of blinded and unblinded acquisition and interpretation of ultrasound for assessment of hemophilic knees and ankles*; 2010. Buenos Aires, Argentina: Presented at the XXIX International Congress of the World Federation of Hemophilia.
145. Murray JRD, Holmes EJ, Misra RR. Irritable hip/transient synovitis. In: Murray JRD, Holmes EJ, Misra RR, eds. *A-Z of Musculoskeletal and Trauma Radiology*. Cambridge, UK: Cambridge University Press; 2008:74–75.
146. Martinoli C, Garello I, Marchetti A, et al. Hip ultrasound. *Eur J Radiol*. 2012;81(12):3824–3831.
147. Merino R, de Inocencio J, Garcia-Consuegra J. Differentiation between transient synovitis and septic arthritis of the hip with clinical and ultrasound criteria. *An Pediatr (Barc)*. 2010;73:189–193.
148. Yabunaka K, Ohue M, Morimoto N, et al. Sonographic measurement of transient synovitis in children: diagnostic value of joint effusion. *Radiol Phys Technol*. 2012;5(1):15–19.
149. Marchal GJ, Van Holsbeeck MT, Raes M, et al. Transient synovitis of the hip in children: role of US. *Radiology*. 1987;162:825–828.
150. Kermond S, Fink M, Graham K, et al. A randomized clinical trial: should the child with transient synovitis of the hip be treated with nonsteroidal anti-inflammatory drugs? *Ann Emerg Med*. 2002;40(3):294–299.
151. Evans TI, Nercessian BM, Sanders KM. Leukemic arthritis. *Semin Arthritis Rheum*. 1994;24:48–56.
152. Gallagher D, Heinrich SD, Craver R, et al. Skeletal manifestations of acute leukemia in childhood. *Orthopedics*. 1991;14:485–492.
153. Neubauer P, Weber AK, Miller NH, et al. Pigmented villonodular synovitis in children: a report of six cases and review of the literature. *Iowa Orthop J*. 2007;27:90–94.
154. Goldman AB, DiCarlo EF. Pigmented villonodular synovitis. Diagnosis and differential diagnosis. *Radiol Clin North Am*. 1988;26:1327–1347.

155. Layfield LJ, Meloni-Ehrig A, Liu K, et al. Malignant giant cell tumor of synovium (malignant pigmented villonodular synovitis). *Arch Pathol Lab Med*. 2000;124:1636–1641.
156. Dorwart RH, Genant HK, Johnston WH, et al. Pigmented villonodular synovitis of the shoulder: radiologic-pathologic assessment. *AJR Am J Roentgenol*. 1984;143:886–888.
157. Llauger J, Palmer J, Roson N, et al. Pigmented villonodular synovitis and giant cell tumors of the tendon sheath: radiologic and pathologic features. *AJR Am J Roentgenol*. 1999;172:1087–1091.
158. Kistler W. Synovial chondromatosis of the knee joint: a rarity during childhood. *Eur J Pediatr Surg*. 1991;1:237–239.
159. Carey RP. Synovial chondromatosis of the knee in childhood. A report of two cases. *J Bone Joint Surg Br*. 1983;65:444–447.
160. Murphey MD, Vidal JA, Fanburg-Smith JC, et al. Imaging of synovial chondromatosis with radiologic-pathologic correlation. *Radiographics*. 2007;27:1465–1488.
161. Donnelly LF, Bisset GS III, Passo MH. MRI findings of lipoma arborescens of the knee in a child: case report. *Pediatr Radiol*. 1994;24:258–259.
162. Martin S, Hernandez L, Romero J, et al. Diagnostic imaging of lipoma arborescens. *Skeletal Radiol*. 1998;27:325–329.
163. Vilanova JC, Barcelo J, Villalon M, et al. MR imaging of lipoma arborescens and the associated lesions. *Skeletal Radiol*. 2003;32:504–509.
164. Sola JB, Wright RW. Arthroscopic treatment for lipoma arborescens of the knee: a case report. *J Bone Joint Surg Am*. 1998;80:99–103.
165. Erselcan T, Bulut O, Bulut S, et al. Lipoma arborescens; successfully treated by yttrium-90 radiosynovectomy. *Ann Nucl Med*. 2003;17:593–596.
166. Mulliken JB, Glowacki J. Hemangiomas and vascular malformations in infants and children: a classification based on endothelial characteristics. *Plast Reconstr Surg*. 1982;69:412–422.
167. Jans L, Ditchfield M, Jaremko JL, et al. MRI demonstrates the extension of juxta-articular venous malformation of the knee and correlates with joint changes. *Euro Radiol*. 2010;20:1792–1798.
168. Sasho T, Nakagawa K, Matsuki K, et al. Two cases of synovial haemangioma of the knee joint: Gd-enhanced image features on MRI and arthroscopic excision. *Knee*. 2011;18:509–511.
169. Pachman LM. Juvenile dermatomyositis. Pathophysiology and disease expression. *Pediatr Clin North Am*. 1995;42:1071–1098.
170. Reimers CD, Fleckenstein JL, Witt TN, et al. Muscular ultrasound in idiopathic inflammatory myopathies of adults. *J Neurol Sci*. 1993;116:82–92.
171. Mendez EP, Lipton R, Ramsey-Goldman R, et al. US incidence of juvenile dermatomyositis, 1995-1998: results from the National Institute of Arthritis and Musculoskeletal and Skin Diseases Registry. *Arthritis Rheum*. 2003;49:300–305.
172. Pachman LM, Lipton R, Ramsey-Goldman R, et al. History of infection before the onset of juvenile dermatomyositis: results from the National Institute of Arthritis and Musculoskeletal and Skin Diseases Research Registry. *Arthritis Rheum*. 2005;53:166–172.
173. Park JH, Niermann KJ, Ryder NM, et al. Muscle abnormalities in juvenile dermatomyositis patients: P-31 magnetic resonance spectroscopy studies. *Arthritis Rheum*. 2000;43:2359–2367.
174. Chan WP, Liu GC. MR imaging of primary skeletal muscle diseases in children. *AJR Am J Roentgenol*. 2002;179:989–997.
175. Ozonoff MB, Flynn FJ Jr. Roentgenologic features of dermatomyositis of childhood. *Am J Roentgenol Radium Ther Nucl Med*. 1973;118:206–212.
176. Steiner RM, Glassman L, Schwartz MW, et al. The radiological findings in dermatomyositis of childhood. *Radiology*. 1974;111:385–393.
177. Sullivan DB, Cassidy JT, Petty RE. Dermatomyositis in the pediatric patient. *Arthritis Rheum*. 1977;20:327–331.
178. Cassidy JT, Petty RC. Juvenile dermatomyositis. In: *Textbook of Paediatric Rheumatology*. Philadelphia: Saunders; 1995:323–364.
179. Rose AL. Childhood polymyositis. A follow-up study with special reference to treatment with corticosteroids. *Am J Dis Child*. 1974;127:518–522.
180. Bureau NJ, Cardinal E, Chhem RK. Ultrasound of soft tissue masses. *Semin Musculoskelet Radiol*. 1998;2:283–298.
181. Reimers CD, Finkenstaedt M. Muscle imaging in inflammatory myopathies. *Curr Opin Rheumatol*. 1997;9:475–485.
182. Fornage BD. The case for ultrasound of muscles and tendons. *Semin Musculoskelet Radiol*. 2000;4:375–391.
183. Yosipovitch G, Beniaminov O, Rousso I, et al. STIR magnetic resonance imaging: a noninvasive method for detection and follow-up of dermatomyositis. *Arch Dermatol*. 1999;135:721–723.
184. Hernandez RJ, Keim DR, Sullivan DB, et al. Magnetic resonance imaging appearance of the muscles in childhood dermatomyositis. *J Pediatr*. 1990;117:546–550.
185. Maillard SM, Jones R, Owens C, et al. Quantitative assessment of MRI T2 relaxation time of thigh muscles in juvenile dermatomyositis. *Rheumatology (Oxford)*. 2004;43:603–608.
186. Summers RM, Brune AM, Choyke PL, et al. Juvenile idiopathic inflammatory myopathy: exercise-induced changes in muscle at short inversion time inversion-recovery MR imaging. *Radiology*. 1998;209:191–196.
187. Ladd PE, Emery KH, Salisbury SR, et al. Juvenile dermatomyositis: correlation of MRI at presentation with clinical outcome. *Am J Roentgenol*. 2011;197(1):W153–W158. doi:10.2214/AJR.10.5337.
188. Agarwal V, Sachdev A, Dabra AK. Case 104: calcinosis in juvenile dermatomyositis. *Radiology*. 2007;242:307–311.
189. Wu Y, Seto H, Shimizu M, et al. Extensive soft-tissue involvement of dermatomyositis detected by whole-body scintigraphy with 99mTc-MDP and 201TL-chloride. *Ann Nucl Med*. 1996;10:127–130.
190. Bar-Sever Z, Mukamel M, Harel L, et al. Scintigraphic evaluation of calcinosis in juvenile dermatomyositis with Tc-99m MDP. *Clin Nucl Med*. 2000;25:1013–1016.
191. Bowyer SL, Blane CE, Sullivan DB, et al. Childhood dermatomyositis: factors predicting functional outcome and development of dystrophic calcification. *J Pediatr*. 1983;103:882–888.
192. Fischer TJ, Rachelefsky GS, Klein RB, et al. Childhood dermatomyositis and polymyositis. Treatment with methotrexate and prednisone. *Am J Dis Child*. 1979;133:386–389.
193. Miller LC, Sisson BA, Tucker LB, et al. Methotrexate treatment of recalcitrant childhood dermatomyositis. *Arthritis Rheum*. 1992;35:1143–1149.
194. Al Mayouf S, Al Mazyed A, Bahabri S. Efficacy of early treatment of severe juvenile dermatomyositis with intravenous methylprednisolone and methotrexate. *Clin Rheumatol*. 2000;19:138–141.
195. Feldman BM, Rider LG, Reed AM, et al. Juvenile dermatomyositis and other idiopathic inflammatory myopathies of childhood. *Lancet*. 2008;371:2201–2212.
196. Miles L, Bove KE, Lovell D, et al. Predictability of the clinical course of juvenile dermatomyositis based on initial muscle biopsy: a retrospective study of 72 patients. *Arthritis Rheum*. 2007;57:1183–1191.
197. Tezak Z, Hoffman EP, Lutz JL, et al. Gene expression profiling in DQA1*0501+ children with untreated dermatomyositis: a novel model of pathogenesis. *J Immunol*. 2002;168:4154–4163.
198. Bader-Meunier B, Decaluwe H, Barnerias C, et al. Safety and efficacy of rituximab in severe juvenile dermatomyositis: results from 9 patients from the French Autoimmunity and Rituximab registry. *J Rheumatol*. 2011;38:1436–1440.
199. Stringer E, Feldman BM. Advances in the treatment of juvenile dermatomyositis. *Curr Opin Rheumatol*. 2006;18:503–506.
200. Maillard SM, Jones R, Owens CM, et al. Quantitative assessments of the effects of a single exercise session on muscles in juvenile dermatomyositis. *Arthritis Rheum*. 2005;53:558–564.
201. Hicks JE, Drinkard B, Summers RM, et al. Decreased aerobic capacity in children with juvenile dermatomyositis. *Arthritis Rheum*. 2002;47:118–123.
202. Jurik AG. Chronic recurrent multifocal osteomyelitis. *Semin Musculoskelet Radiol*. 2004;8:243–253.
203. Ferguson PJ, El Shanti HI. Autoinflammatory bone disorders. *Curr Opin Rheumatol*. 2007;19:492–498.
204. Laxer RM, Shore AD, Manson D, et al. Chronic recurrent multifocal osteomyelitis and psoriasis—a report of a new association and review of related disorders. *Semin Arthritis Rheum*. 1988;17:260–270.
205. Dagan O, Barak Y, Metzker A. Pyoderma gangrenosum and sterile multifocal osteomyelitis preceding the appearance of Takayasu arteritis. *Pediatr Dermatol*. 1995;12:39–42.
206. Bousvaros A, Marcon M, Treem W, et al. Chronic recurrent multifocal osteomyelitis associated with chronic inflammatory bowel disease in children. *Dig Dis Sci*. 1999;44:2500–2507.
207. El Shanti HI, Ferguson PJ. Chronic recurrent multifocal osteomyelitis: a concise review and genetic update. *Clin Orthop Relat Res*. 2007;462:11–19.

208. Grosse J, Chitu V, Marquardt A, et al. Mutation of mouse Mayp/Pstpip2 causes a macrophage autoinflammatory disease. *Blood*. 2006;107:3350–3358.
209. Jansson A, Renner ED, Ramser J, et al. Classification of non-bacterial osteitis: retrospective study of clinical, immunological and genetic aspects in 89 patients. *Rheumatology (Oxford)*. 2007;46:154–160.
210. Khanna G, Sato TS, Ferguson P. Imaging of chronic recurrent multifocal osteomyelitis. *Radiographics*. 2009;29:1159–1177.
211. Hayem G, Bouchaud-Chabot A, Benali K, et al. SAPHO syndrome: a long-term follow-up study of 120 cases. *Semin Arthritis Rheum*. 1999;29:159–171.
212. Mandell GA, Contreras SJ, Conard K, et al. Bone scintigraphy in the detection of chronic recurrent multifocal osteomyelitis. *J Nucl Med*. 1998;39:1778–1783.
213. Fritz J, Tzaribatchev N, Claussen CD, et al. Chronic recurrent multifocal osteomyelitis: comparison of whole-body MR imaging with radiography and correlation with clinical and laboratory data. *Radiology*. 2009;252:842–851.
214. Fritz J, Tzaribachev N, Thomas C, et al. Magnetic resonance imaging-guided osseous biopsy in children with chronic recurrent multifocal osteomyelitis. *Cardiovasc Intervent Radiol*. 2012;35:146–153.
215. Huber AM, Lam PY, Duffy CM, et al. Chronic recurrent multifocal osteomyelitis: clinical outcomes after more than five years of follow-up. *J Pediatr*. 2002;141:198–203.
216. Job-Deslandre C, Krebs S, Kahan A. Chronic recurrent multifocal osteomyelitis: five-year outcomes in 14 pediatric cases. *Joint Bone Spine*. 2001;68:245–251.
217. Girschick HJ, Mornet E, Beer M, et al. Chronic multifocal non-bacterial osteomyelitis in hypophosphatasia mimicking malignancy. *BMC Pediatr*. 2007;7:3.
218. Duffy CM, Lam PY, Ditchfield M, et al. Chronic recurrent multifocal osteomyelitis: review of orthopaedic complications at maturity. *J Pediatr Orthop*. 2002;22:501–505.
219. Prose NS, Fahrner LJ, Miller CR, et al. Pustular psoriasis with chronic recurrent multifocal osteomyelitis and spontaneous fractures. *J Am Acad Dermatol*. 1994;31:376–379.
220. Holden W, David J. Chronic recurrent multifocal osteomyelitis: two cases of sacral disease responsive to corticosteroids. *Clin Infect Dis*. 2005;40:616–619.
221. Carpenter E, Jackson MA, Friesen CA, et al. Crohn's-associated chronic recurrent multifocal osteomyelitis responsive to infliximab. *J Pediatr*. 2004;144:541–544.
222. Deutschmann A, Mache CJ, Bodo K, et al. Successful treatment of chronic recurrent multifocal osteomyelitis with tumor necrosis factor-alpha blockage. *Pediatrics*. 2005;116:1231–1233.
223. Gallagher KT, Roberts RL, MacFarlane JA, et al. Treatment of chronic recurrent multifocal osteomyelitis with interferon gamma. *J Pediatr*. 1997;131:470–472.
224. Simm PJ, Allen RC, Zacharin MR. Bisphosphonate treatment in chronic recurrent multifocal osteomyelitis. *J Pediatr*. 2008;152:571–575.

# 137 Musculoskeletal Infections

J. Herman Kan, Arthur B. Meyers, and E. Michel Azouz

## OVERVIEW OF MUSCULOSKELETAL INFECTIONS

Musculoskeletal infections remain a diagnostic and therapeutic challenge. Historically, the workup and treatment of such infections has been based on clinical grounds supplemented by diagnostic aspiration and subsequent surgical incision and drainage. Today, imaging plays a critical role in the diagnosis and management of musculoskeletal infections.

This chapter will review the clinical presentation, pathophysiology, imaging, and treatment spectrum of osteomyelitis, septic arthritis, and soft tissue infections of the appendicular skeleton.

### Acute Pyogenic Osteomyelitis

***Etiology, Pathophysiology, and Clinical Presentation.*** Osteomyelitis may occur from direct or hematogenous inoculation; it may be iatrogenic, related to orthopedic implants; or it may be from secondary extension from primary septic arthritis or pyomyositis. Hematogenous osteomyelitis is a common disease in children; however, infantile and even neonatal cases are not uncommon. Bacteria are the most common inflammatory agents, but growing bones may also be invaded by other pathogens, including viruses, spirochetes, and fungi.

The incidence of pediatric osteomyelitis in the United States is 1 in 5150 and has increased 2.8-fold in 20 years.[1] This increased incidence is confounded, however, because of differences in access to health care and advances in imaging diagnosis. *Staphylococcus aureus* remains the most common causative organism of acute osteomyelitis in children. Unfortunately, community-acquired methicillin-resistant *S. aureus* (MRSA) strains are increasing in prevalence.[2,3] *Haemophilus influenzae* osteomyelitis and septic arthritis have become less common since the availability of effective vaccination (*H. influenzae* type B vaccine).[4]

In sickle cell disease, bone complications include osteonecrosis and osteomyelitis. Osteonecrosis is approximately 50 times more frequent than osteomyelitis.[5] The proposed mechanism of osteomyelitis is hematogenous, with bacteria gaining entrance to blood vessels through ischemic bowel and finding suitable culture material in foci of infarcted bone marrow. Both *S. aureus* and *Salmonella* commonly occur in sickle cell patients.[2]

In chronic granulomatous disease of childhood, an X-linked recessive disorder of leukocyte function, repeated infections occur in solid organs, skin, and bone. Approximately one-third of patients develop osteomyelitis. Phagocytes are unable to kill catalase-positive organisms such as *Staphylococcus* and fungi.[6–8]

Hematogenous osteomyelitis usually involves the highly vascularized metaphysis of the fastest growing bones, such as the distal femur and radius and the proximal tibia and humerus. The most common location for hematogenous osteomyelitis is about the knee (distal femur, proximal tibia).[2] Pain, localized signs, fever, reduced range of motion, and reduced weight bearing are the most common initial clinical features. A history of trauma is seen in approximately 30% of cases,[2] and the male-to-female ratio is approximately 1 : 8.

Organisms lodge most frequently in the terminal capillary sinusoids of the metaphyses (Fig. 137.1).[7] Rarely, they may locate initially in the epiphyses related to the terminal capillary sinusoids of the metaphyseal equivalent region immediately next to the spherical growth plate. A small abscess forms in the marrow of the metaphysis, followed by local decalcification and destruction of the adjacent bone. When focal abscesses are generated, multiple small foci of bone destruction develop and later coalesce. Inflammatory swelling increases the intraosseous pressure because of the rigid bony walls of the marrow cavity; this can force extension of the infected exudate into several sites, as indicated in Fig. 137.2. The most common route is via the haversian canals of the cortex to the subperiosteal space, where a subperiosteal abscess is formed. Simultaneously, spread also occurs farther within the medullary cavity. Rupture of the periosteal abscess is responsible for extension of infection into the adjacent soft tissues. Inflammation and rapidly increased intraosseous pressure may cause thrombosis of the vascular channels.

The most common location for direct inoculation osteomyelitis is the foot. Plantar puncture wounds secondary to walking on broken glass, metal (nail), or vegetable matter (thorn, toothpick) may result in infectious cellulitis, plantar fasciitis, and osteomyelitis, whether the foreign body is removed or retained. The calcaneus is often involved, and *Pseudomonas aeruginosa* is often found related to direct inoculation, usually with a history of a puncture through a shoe.[7]

***Imaging.*** Imaging guidelines for the evaluation of suspected osteomyelitis include radiographs first to exclude alternative etiologies, such as a fracture or neoplasm, as an explanation for symptoms. If radiographs are normal and symptoms are localized to an osteoarticular region, ultrasound (US) may be performed to evaluate for suspected septic arthritis. Targeted magnetic resonance imaging (MRI) of the affected region should be performed to identify underlying osteomyelitis and to guide surgical treatment.[9,10] Both MRI and US can also identify subperiosteal and soft tissue abscesses. When symptoms are not localizable a whole body MRI can be performed.[11] Three-phase bone scintigraphy is recommended when symptoms are nonlocalizable and there are relative contraindications to MRI such as the need for sedation.[12]

***Radiography.*** With acute osteomyelitis, the earliest change on radiographs is soft tissue swelling; osseous changes are seldom present until the second week of disease (Fig. 137.3).[13] The earliest bone changes seen on conventional images are one or more small radiolucencies, usually in the metaphyseal region, where necrosis and destruction of bone has occurred (Fig. 137.4). On serial examinations, these areas of bone destruction enlarge and become confluent.

With continuing appropriate antibiotic therapy, periostitis is visible when the periosteum begins to produce new bone on its undersurface after the second or third week (Fig. 137.5). Osteogenic function by the periosteum suggests that infection has been at least partly locally controlled. Subsequent healing may involve remodeling of the cortical new bone and reconstitution of the underlying bone or, if damage has been extensive, it may involve an increase in the amount of periosteal reaction to form an

## Abstract:

Musculoskeletal infections children are a diagnostic and therapeutic challenge. Imaging plays a critical role in the initial diagnosis and follow up of musculoskeletal infections. This chapter reviews the clinical presentation, pathophysiology, imaging, and treatment spectrum of osteomyelitis, septic arthritis, and soft tissue infections of the appendicular skeleton.

## Keywords:

Pediatric
osteomyelitis
septic arthritis
pyomyositis
cellulitis
fasciitis
imaging

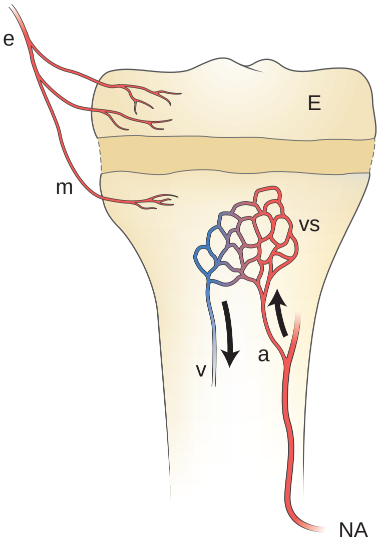

**Figure 137.1. Blood supply to the metaphysis and epiphysis of a child and the arterial channels through which invading organisms enter the growing bone.** An epiphyseal artery *(e)* supplies the epiphysis *(E)* and may branch to give minor metaphyseal vessels *(m)*. The major blood supply of the metaphysis comes from the nutrient artery. *a*, Arteriole; *NA*, nutrient artery; *v*, venule; *vs*, venous sinuses in the metaphysis.

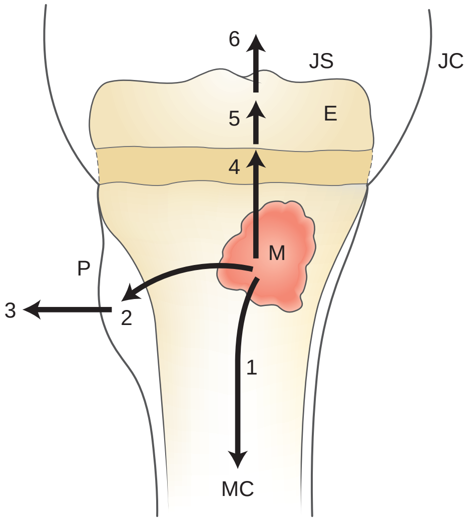

**Figure 137.2. Pathways of infection after hematogenous implantation in the metaphysis and formation of a metaphyseal focus *(M)* of bone infection (bone abscess).** (1) Spread to the medullary canal *(MC)*; (2) formation of a subperiosteal abscess; (3) penetration of the periosteum *(P)* and spread to the adjacent soft tissues; (4) through (6) spread across the growth plate to the epiphysis *(E)*, and eventually to the joint space *(JS)*. *JC*, Joint capsule.

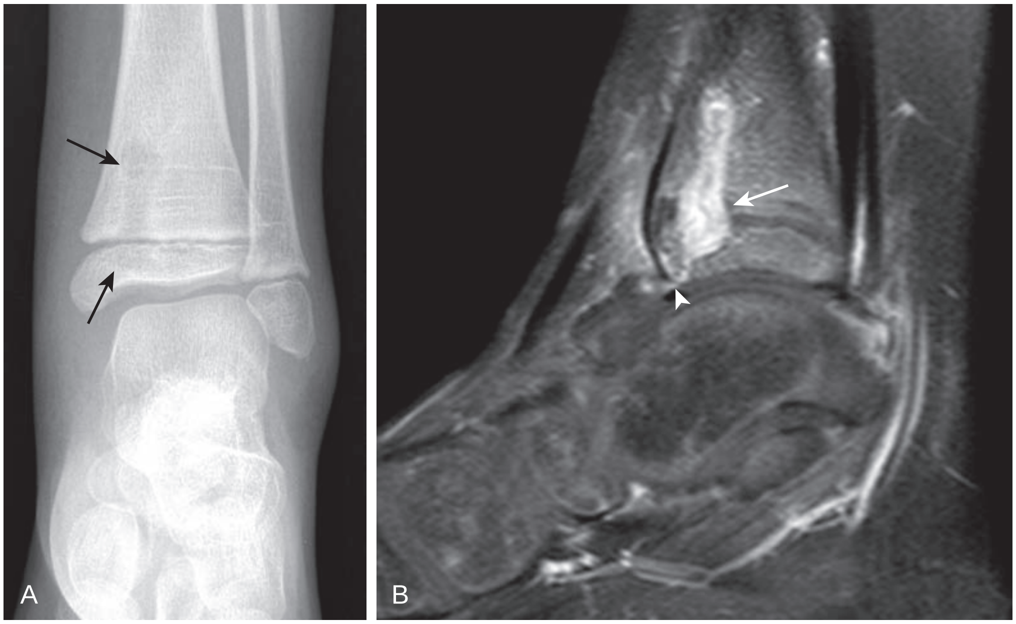

**Figure 137.3. Osteomyelitis in a 6-year-old girl.** (A) Frontal radiograph demonstrates a lytic lesion in the distal tibia metaphysis extending into the epiphysis *(arrows)*. (B) T1-weighted, fat-saturated, postgadolinium sagittal view demonstrates a thick, rim-enhancing lesion with a small amount of nonenhancing fluid consistent with early abscess formation with epiphyseal extension *(arrow)* and a small cloaca *(arrowhead)* extending to the tibiotalar joint.

involucrum (Fig. 137.6), a living bone sheath around the fragments of the old devitalized bone (sequestrum).

***Scintigraphy.*** Bone scans are particularly helpful in the evaluation of suspected osteomyelitis when symptoms are not localizable due to its ability to scan the entire skeleton. Early bone scans may demonstrate a “cold” metaphyseal lesion as a result of compression or occlusion of the metaphyseal vessels. In these cases, increased activity is observed toward the diaphysis, beyond the cold metaphyseal area, which subsequently becomes “hot” and merges with the adjacent increased activity (Fig. 137.7). The multiphase bone scan is very sensitive and is usually positive 24 to 48 hours after the onset of symptoms.[12] It can detect extension of metaphyseal osteomyelitis into the epiphysis through the growth plate (see Fig. 137.7).

Another application of nuclear medicine imaging of musculoskeletal infections is to evaluate for infection in the setting of orthopedic hardware. In this situation, MRI may be of limited value due to susceptibility artifact. A normal bone scan can rule out infection. However, increased activity on a bone scan in this situation may be due to infection or hardware loosening. If this occurs, then a radiolabeled leukocyte scintigraphy scan (white blood cell scan) can be performed in conjunction with a Tc-99m sulfur colloid scan. Areas of increased radiotracer uptake on the leukocyte scan that are normal on the sulfur colloid scan are consistent with infection.

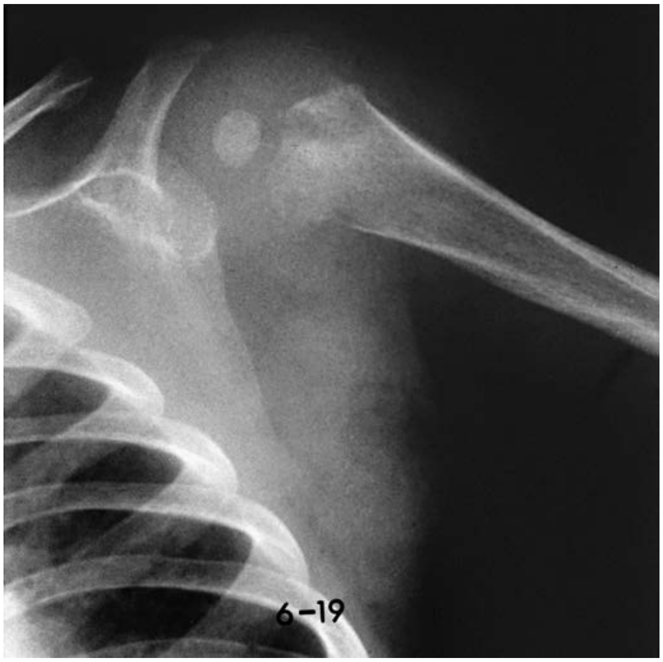

**Figure 137.4. Early radiographic changes of osteomyelitis in the proximal left humeral metaphysis.** This 9-month-old boy had fever and local signs and symptoms for 12 days. Metaphyseal areas of bone destruction are visualized as irregular, ill-defined lucencies.

***Computed Tomography.*** Computed tomography (CT) is of limited clinical value in acute osteomyelitis.[14] It is more useful in advanced or chronic disease to help determine the quality of bone stock, including determinations of cortical destruction, involucrum, and sequestra (see Fig. 137.6).

***Magnetic Resonance Imaging.*** MRI is the optimal study to evaluate for infection and alternative etiologies for symptoms, particularly when radiographs are normal. When precontrast MRI examinations are entirely normal and show no evidence to suggest osteomyelitis, routine postgadolinium images may not be necessary.[15,16] When abnormal, MRI can reveal marrow alterations and extent of disease in bone, soft tissues, or adjacent joints (Fig. 137.8).[17] Early MRI findings of osteomyelitis may have a tumefactive appearance and may be paradoxically hypointense on fluid-sensitive sequences (e-Fig. 137.9). Over time, the lesion may remain masslike and demonstrates the expected, more homogeneous hyperintense signal on fluid-sensitive sequences, indicative of its inflammatory nature (Fig. 137.10). Eventually, periostitis and adjacent soft tissue involvement may be seen in the early phase of osteomyelitis (e-Fig. 137.11). Subperiosteal abscess formation may be seen by sonography (Fig. 137.12) or MRI (Fig. 137.13), preceding radiographic bony changes. A salt-and-pepper appearance to the marrow may be seen in the late acute phase of osteomyelitis and is presumed to represent small areas of noncoalescent microabscess formation and early bone destruction (Fig. 137.14). It is difficult to distinguish acute osteonecrosis from osteomyelitis in the setting of sickle cell disease on MRI (Fig. 137.15).

Musculoskeletal infections typically have localizable symptoms to the area of involvement allowing performance of a focal MRI. However, these infections may present as fever without a source

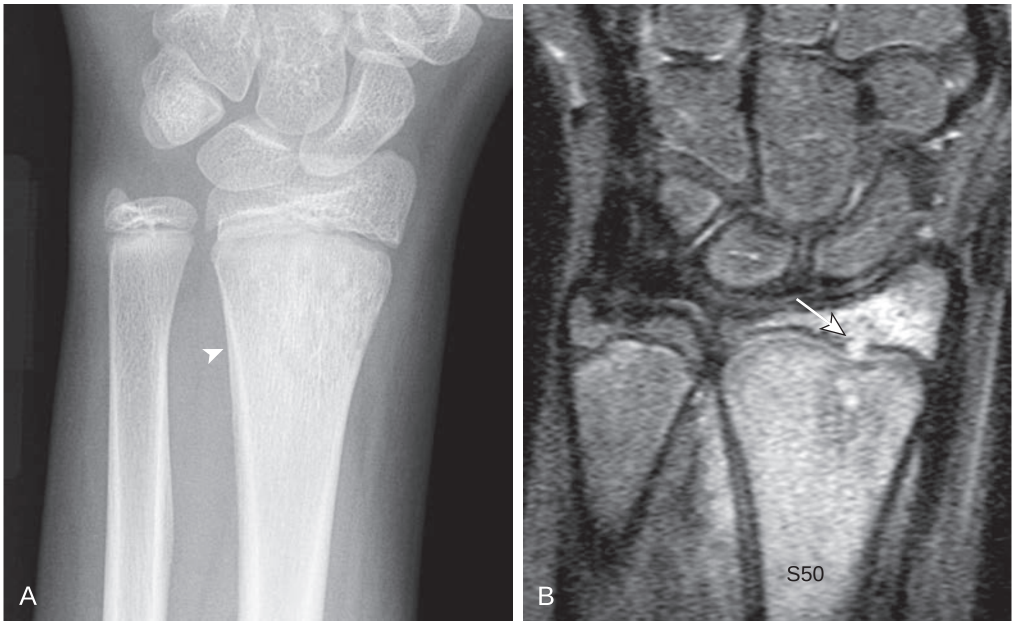

**Figure 137.5. Osteomyelitis in a 12-year-old boy.** (A) Frontal radiograph demonstrates distal radial moth-eaten bone destruction with periostitis *(arrowhead)*. (B) Coronal STIR magnetic resonance (MR) image demonstrates diffuse marrow edema with transphyseal extension *(arrow)* into the epiphysis.

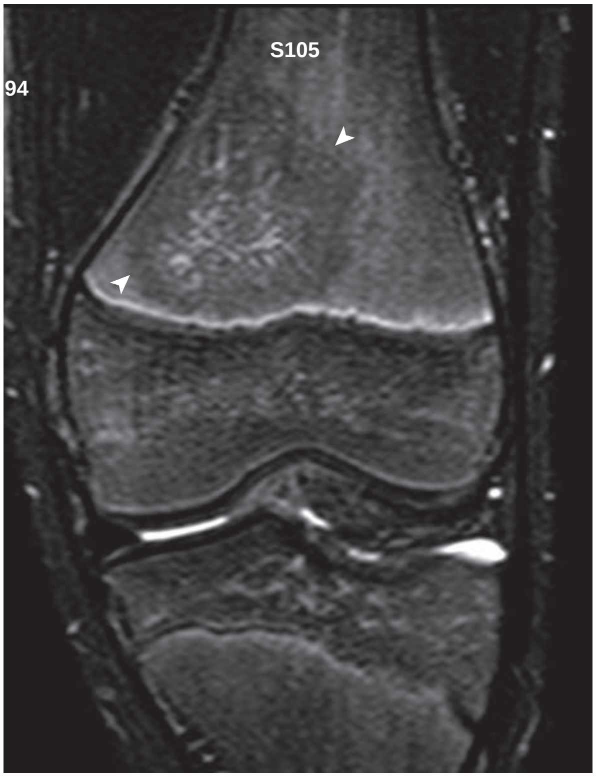

**e-Figure 137.9. Biopsy-confirmed osteomyelitis in a 13-year-old boy.** Coronal MR image demonstrates round masslike hypointensity in the distal femur metadiaphysis *(arrowheads)*.

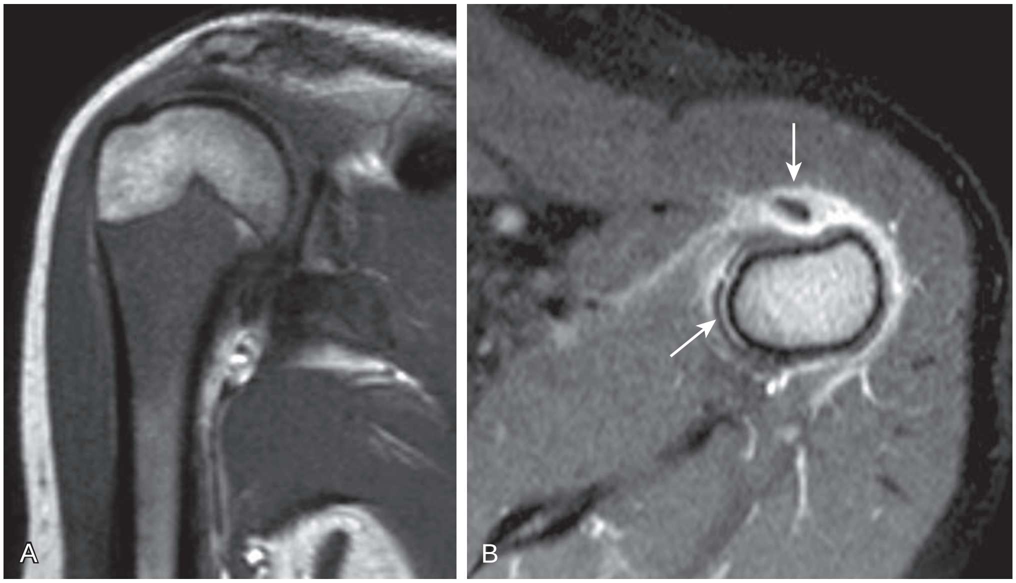

**e-Figure 137.11. Proximal humeral osteomyelitis in a 12-year-old girl.** (A) Coronal T1-weighted MR image demonstrates diffusely decreased marrow signal in the proximal humerus. (B) Axial T1-weighted, fat-saturated, postgadolinium MR image demonstrates hyperenhancement in the periosteal and juxtacortical soft tissues and around the long head of the biceps tendon *(arrows)*.

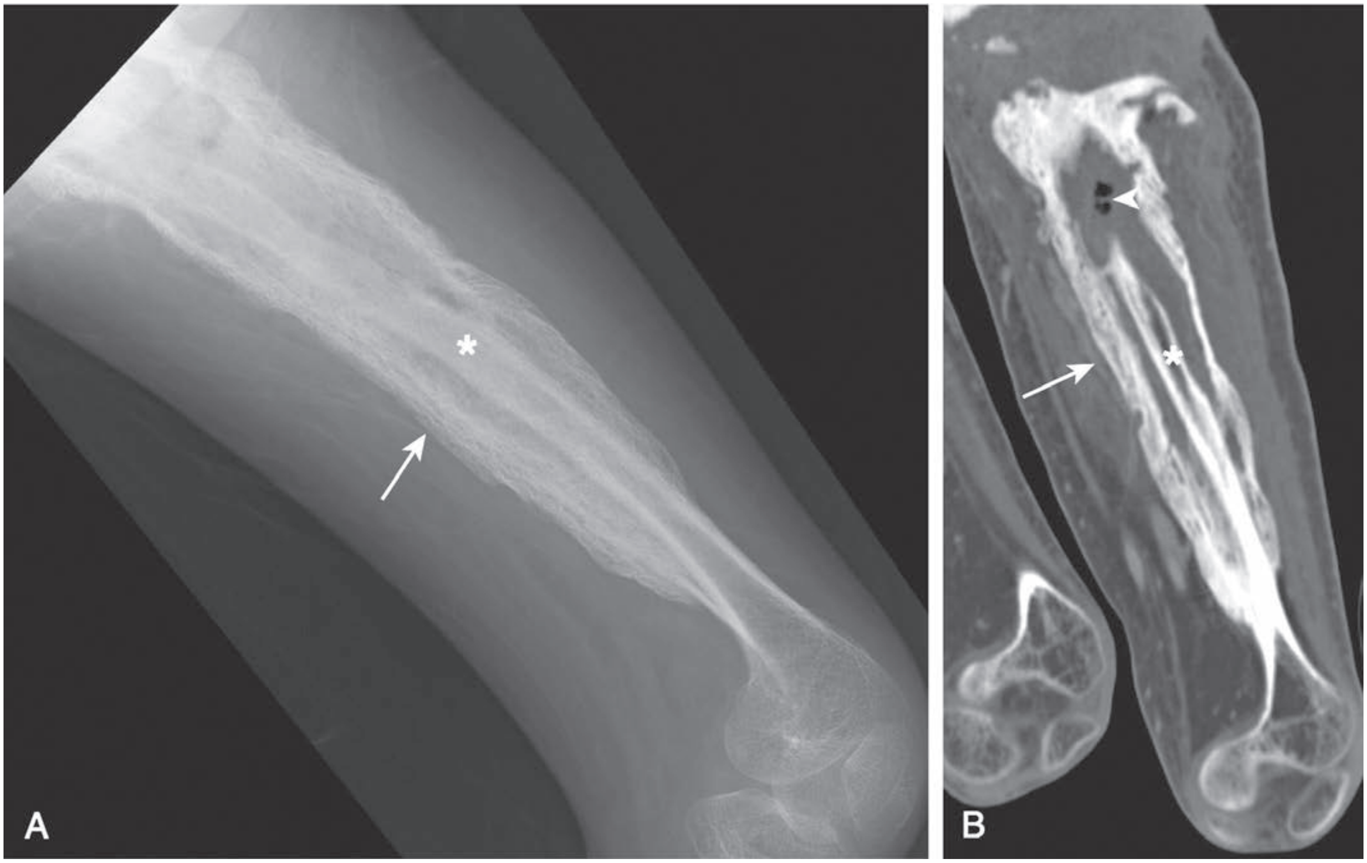

**Figure 137.6. Chronic osteomyelitis of the left femur in a 17-year-old boy.** Radiograph (A) and CT scan (B) demonstrate involucrum *(arrow)* that surrounds a sequestrum *(asterisk)*. Note air *(arrowhead)* within the proximal femoral diaphysis related to abscess formation.

or fever of unknown origin, particularly in very young children or developmentally disabled children who are not able to verbalize symptoms. One of the applications of whole body MRI is to evaluate for a nonlocalizable infection. Large field of view fluid-sensitive sequences, typically a short-tau inversion recovery (STIR) sequence, are typical of whole body protocols with the use of T1-weighted and diffusion sequences being used at some institutions. These allow for detection and localization of osteomyelitis (Fig. 137.16) and other musculoskeletal infections (e.g., septic arthritis, infectious myositis, cellulitis, and periosteal and soft tissue abscesses).[11]

## Subacute and Chronic Osteomyelitis

Subacute or chronic osteomyelitis may develop as a result of partial host response to contain the infection. Distinguishing between subacute and chronic osteomyelitis is arbitrary.[18] The initial purulent exudate is replaced by granulation tissue, and the clinical manifestations are mild and consist mainly of local pain. A Brodie abscess may then develop, typically in the metaphysis and less commonly in the epiphysis, because the growth plate is only a partial barrier against the spread of infection. A Brodie abscess is characterized radiographically by a central or eccentric round or oval radiolucency.[19] The cavity may contain a small, dense sequestrum. On MRI, lesions have a characteristic layered appearance with a high-signal periphery as a result of edema (penumbra sign)[20] and a double-line sign (rim sign), which on fluid-sensitive sequences is delineated as a low-signal outer rim because of sclerosis; an inner rim of intermediate signal because of granulation tissue; and a central, hyperintense region related to abscess formation (Fig. 137.17).[21] With contrast-enhanced imaging, the inner granulation layer will show enhancement around the nonenhancing central abscess.

Adjacent soft tissue swelling and edema and periosteal new bone formation may be present. In spite of occasional growth plate involvement, the incidence of premature growth plate fusion after subacute osteomyelitis is rare.[22]

Cortical and trabecular bone sclerosis, cavities, involucra, and sequestra are characteristic of advanced osteomyelitis.[23] The affected bone is thickened, and its outline may be wavy, with or without periosteal cloaking of new bone. An involucrum of reactive, viable bone may cloak an area of infection (Fig. 137.18). The involucrum may be perforated by a cloaca, which is a tract or communication between bone and the surrounding soft tissues (e-Fig. 137.19). If the cloaca extends to the skin surface, it is termed a *sinus tract* (see Fig. 137.18).[24] The necrotic, devitalized bone of a sequestrum is surrounded by inflammatory granulation tissue and may be located within a bone abscess cavity. The dead bone of a sequestrum is relatively sclerotic. Sequestra may be demonstrated on radiography, CT, or MRI, but it is best seen with CT (see Figs. 137.6 and 137.18). Sequestration is now relatively rare owing to earlier diagnosis, largely because of advances in imaging and more effective antibiotic therapies.

Radiographs will suggest the diagnosis of subacute or chronic osteomyelitis and may be used to follow up for gross changes.

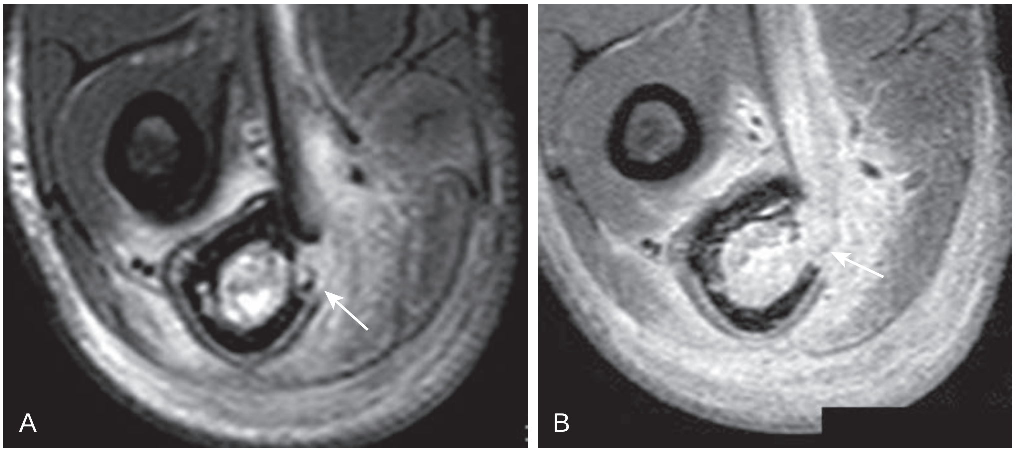

**e-Figure 137.19. Chronic osteomyelitis and cloaca in a 17-year-old boy.** Axial T2-weighted fat-saturated axial (A) and postgadolinium, T1-weighted, fat-saturated (B) MR images demonstrate cortical destruction with communication (*arrow* in A) between marrow and adjacent soft tissues (cloaca).

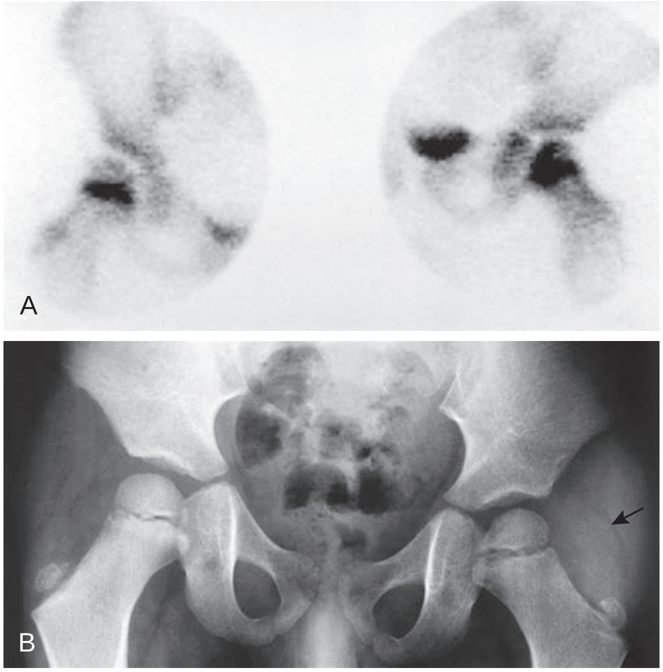

**Figure 137.7. Osteomyelitis in a 4-year-old boy with fever and inability to walk or move the left lower extremity for 6 days.** (A) Bone scan shows increased uptake in the femoral neck and head on the left side, likely resulting from extension of an initial metaphyseal focus of infection into the epiphysis. The right hip shows normal increased uptake in the region of the growth plate. (B) Radiograph of the hips 2 weeks after the beginning of symptoms shows osteopenia on the left side, and ill-defined medial metaphyseal and epiphyseal bone lucencies on each side of the growth plate. Also the lateral fat plane is displaced laterally *(arrow)*, which is indirect evidence of a joint effusion. Adjacent deep soft tissues also appear swollen and edematous compared with the normal right side.

Although CT is of limited clinical value in acute osteomyelitis, it is very useful in imaging chronic disease to evaluate bone stock quality and to detect cortical metaphyseal tracts and channels, sequestra, and bone destruction. Serial MRI after an established diagnosis of osteomyelitis has been made, and after medical or surgical treatment, has limited utility but can be useful in patients who do not respond to therapy or who have a persistently elevated C-reactive protein level.[25]

Not all marrow edema and granulation tissue identified on MRI represents a diagnosis of osteomyelitis; therefore a combination of imaging features and clinical history should be used in concert to arrive at such a diagnosis. Stress reaction may superficially mimic early osteomyelitis, and Ewing sarcoma may superficially mimic subacute or chronic osteomyelitis, with the mass related to Ewing sarcoma mimicking granulation tissue.

***Treatment.*** Although the mortality and morbidity of bone infection have decreased significantly, permanent sequelae do occur, largely as a result of delay in diagnosis or inadequate treatment with complications related to generalized bacterial sepsis.[26] Complications of bone infection include pathologic fracture through regions of bone destruction,[27] venous thrombosis,[28] premature physeal closure, and adjacent infectious arthritis and destruction of joints (Fig. 137.20).

Identification of a bacterial pathogen for underlying osteomyelitis ranges from 9% to 22% by blood culture and 40% to 50% by bone or joint aspiration.[26] MRI is useful for confirming or excluding the diagnosis of osteomyelitis, identifying fluid for culture, and preoperative planning for incision and drainage of potential intraosseous and extraosseous abscesses.[9]

To decrease the chance of complications, empiric antibiotic therapy is often initiated even before bacterial culture is isolated.[29] Treatment includes parenteral antibiotics followed by a long course of oral antibiotics, provided the child is not immunocompromised.[30]

Surgical drainage is recommended if the child has not responded to antibiotics after 48 to 72 hours or if a substantial abscess is

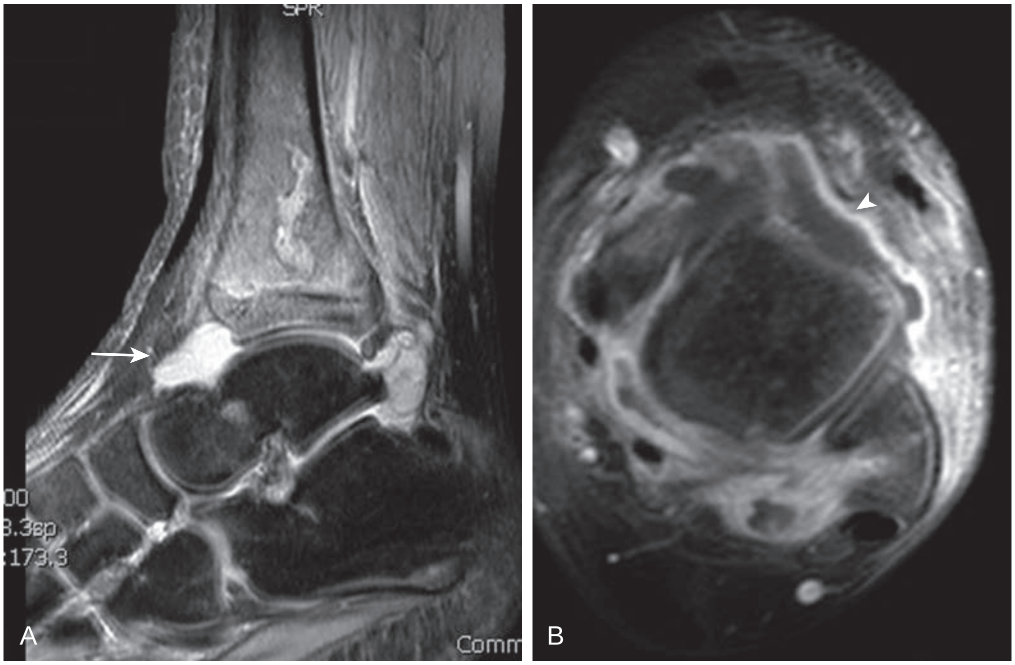

**Figure 137.8. Distal tibial osteomyelitis and tibiotalar septic arthritis in an 11-year-old boy.** (A) T2-weighted fat-saturated sagittal MR image demonstrates diffuse marrow edema that includes transphyseal extension to the epiphysis and juxtacortical soft tissue edema. A large joint effusion is present *(arrow)* with T1-weighted, fat-saturated, postgadolinium axial images (B) that demonstrate thick synovial enhancement *(arrowhead)*.

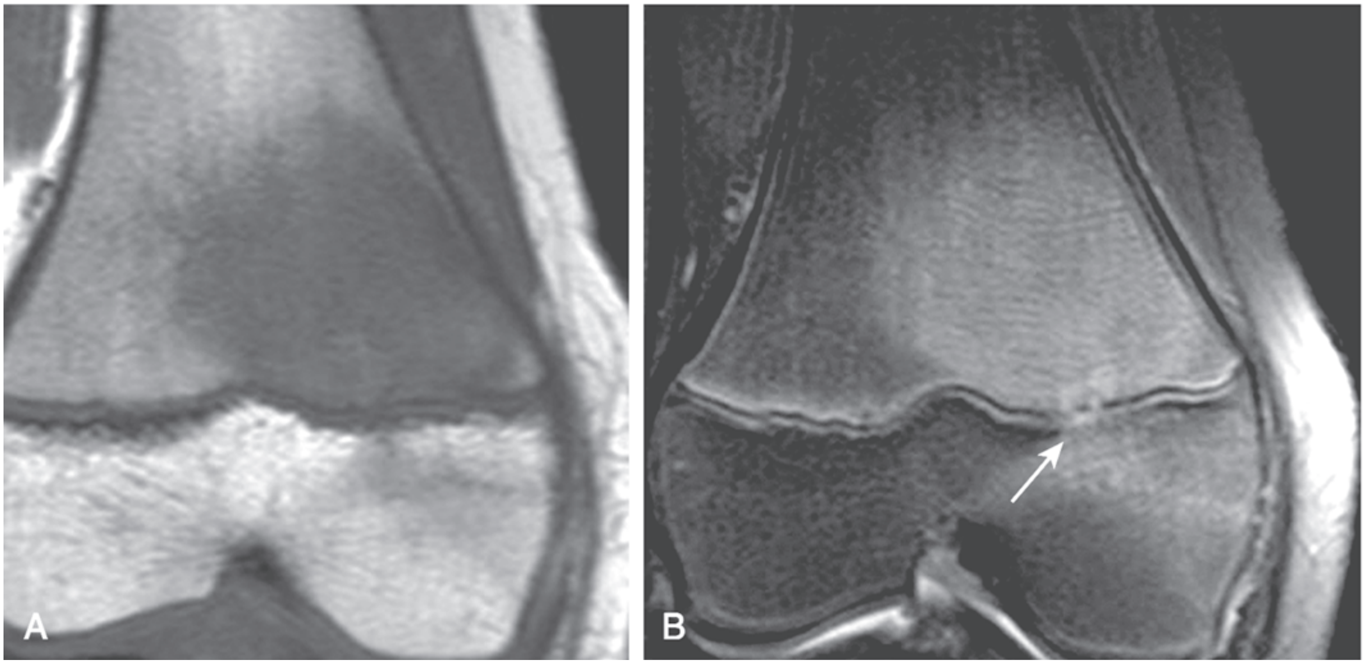

**Figure 137.10. Biopsy-confirmed osteomyelitis of the distal femur.** (A) Coronal T1-weighted MR image demonstrates tumefactive marrow replacement in the distal femur. (B) Coronal STIR MRI demonstrates diffuse homogeneous hyperintensity in the same distribution with early physeal extension of infection *(arrow)*.

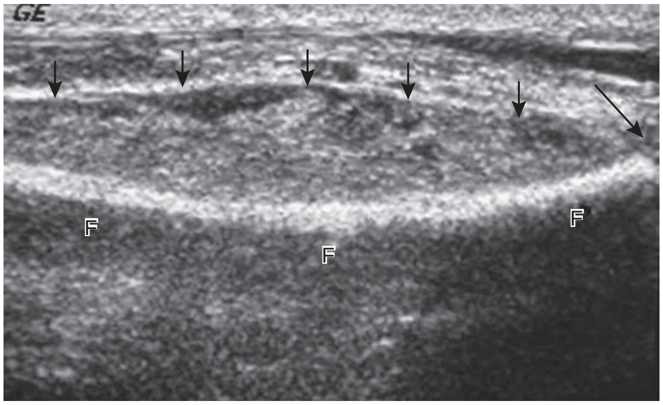

**Figure 137.12. Acute osteomyelitis of the distal fibula in a 12-year-old boy.** Ultrasound shows a large subperiosteal abscess *(short arrows)* extending up to the distal fibular growth plate *(long arrow)*. *F*, Fibula.

identified by MRI.[26] If adjacent septic arthritis is present, the joint will need to be debrided as well.[5]

## Neonatal Osteomyelitis

In the young infants, the incidence of epiphyseal and joint involvement is higher (Fig. 137.21), and multifocal disease may be seen.[31] This is because of the persistence of metaphyseal vessels that cross the physis and extend into the intraarticularly located epiphysis. The most common causative organism is *S. aureus*. Other isolated organisms include *Escherichia coli*, group B streptococci, gram-negative rods, and *Candida albicans*.[31] The hip is frequently involved,[32] and neonatal calcaneal osteomyelitis may develop after heel pad puncture for blood drawing.[33]

## Epiphyseal Osteomyelitis

***Etiology, Pathophysiology, and Clinical Presentation.*** In tubular bones, the early changes of pyogenic hematogenous osteomyelitis are usually localized to the metaphysis, where capillary vascularization is very rich and blood flow is slow on the venous side of the sinusoidal loops. Infection may spread from the metaphysis through the growth plate to the epiphysis (see Fig. 137.2).[14] Epiphyseal osteomyelitis and septic arthritis occur more commonly in infants younger than 15 months of age, because metaphyseal vessels penetrate the growth plate and enter the epiphysis.[34]

***Imaging.*** Radiography usually demonstrates a focus of epiphyseal bone destruction (Fig. 137.22A). In subacute and chronic cases, a small round or oval epiphyseal abscess cavity with well-defined borders is seen. CT is useful for imaging of the bone cavity and detection of a sequestrum. MRI reveals the epiphyseal focus of infection as low signal on T1-weighted images and high signal on T2-weighted images (Fig. 137.22B). Imaging after gadolinium injection may show rim enhancement outlining the abscess cavity of the epiphyseal ossification center. Browne et al. showed epiphyseal cartilage involvement was seen in 52% of cases of *S. aureus* infections in children under 18 months of age.[35] Enhancement defects in the epiphyseal cartilage are commonly seen in the setting of osteomyelitis, but only one-fifth to one-third represent true epiphyseal cartilage abscesses (see Fig. 137.21).[34]

The differential diagnosis of an epiphyseal (or apophyseal) lucent lesion in a child includes infection, chondroblastoma, and Langerhans cell histiocytosis.

***Treatment.*** Epiphyseal osteomyelitis may lead to growth disturbance of the epiphyseal ossification center and physis.[35] Early osteoarthritis may also occur with epiphyseal and articular cartilage destruction. Because the epiphysis is an intraarticular structure, coexisting septic arthritis may be present. Surgically, these children will require exploration and debridement of both the epiphyseal bone and joint space, when those are involved, based on preoperative MRI. Care should be made to differentiate epiphyseal cartilage enhancement defects from true epiphyseal abscesses.[34]

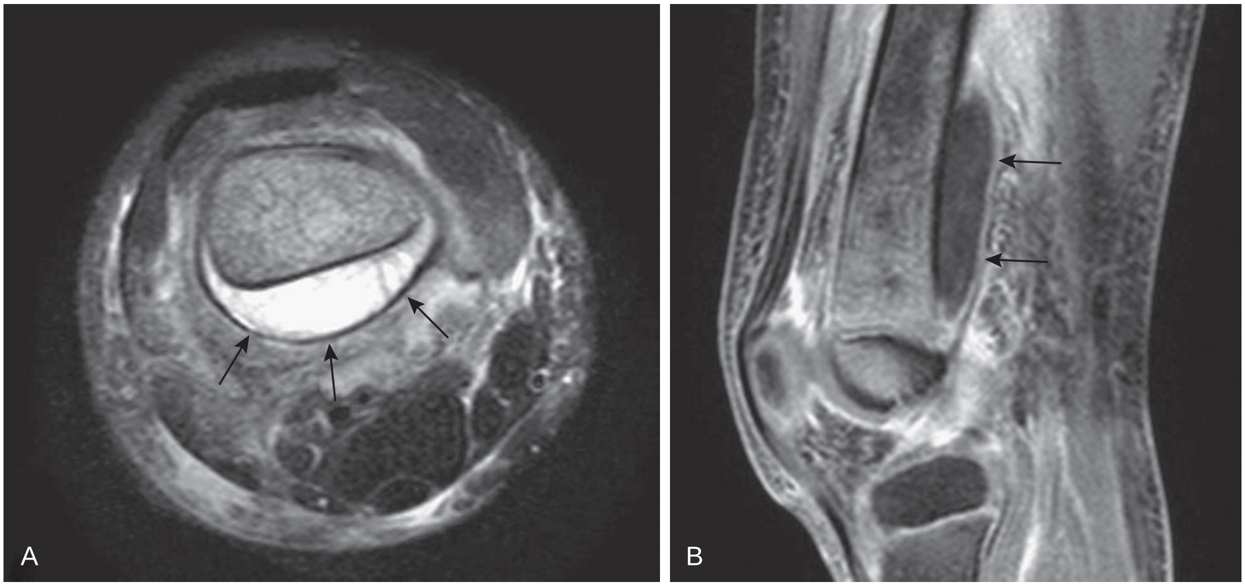

**Figure 137.13. Acute osteomyelitis of the distal femur in a 5-year-old boy.** (A) Axial T2-weighted fat-saturated MR image shows a large subperiosteal abscess *(arrows)* at the posterior aspect of the femur. Increased signal is seen within the bone, and there is adjacent soft tissue edema. (B) Sagittal T1-weighted, fat-saturated, post-gadolinium MR image shows the longitudinal extent of the subperiosteal abscess with peripheral enhancement *(arrows)*.

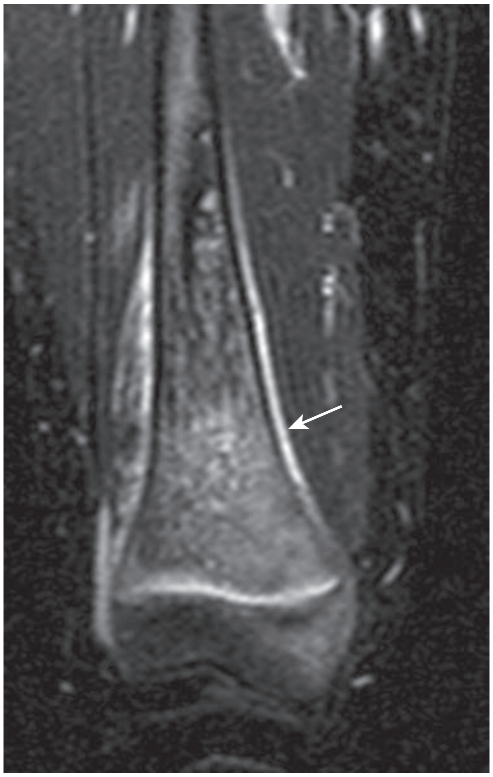

**Figure 137.14. Femoral osteomyelitis in a 13-year-old girl.** Coronal STIR MR image demonstrates a salt-and-pepper appearance of marrow edema and periosteal reaction *(arrow)*.

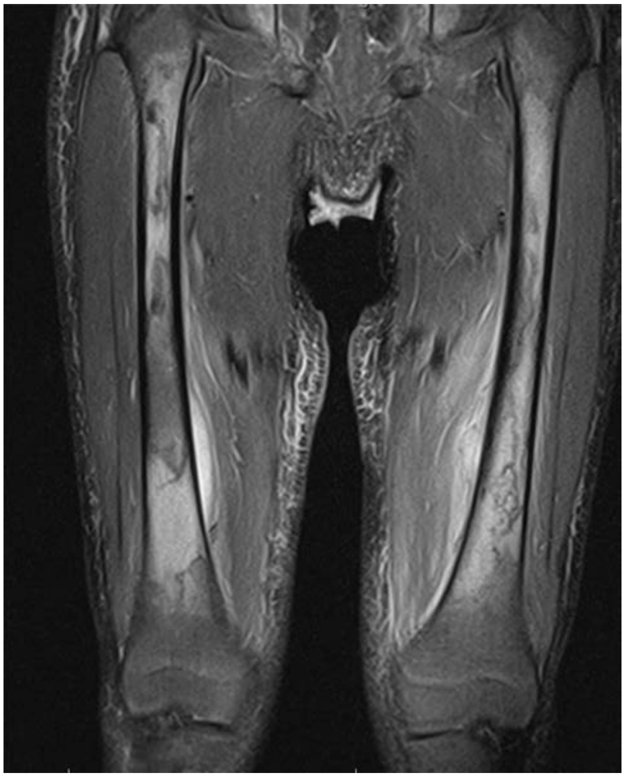

**Figure 137.15. Bilateral acute femoral osteonecrosis in a 5-year-old boy with sickle cell disease.** Coronal STIR MR image demonstrates heterogeneous marrow and juxta-cortical soft tissue edema. Juxta-cortical fluid collections along the medial aspects of both femurs are seen, which showed rim enhancement on postcontrast images *(not shown)*. Surgical biopsy demonstrated changes of osteonecrosis.

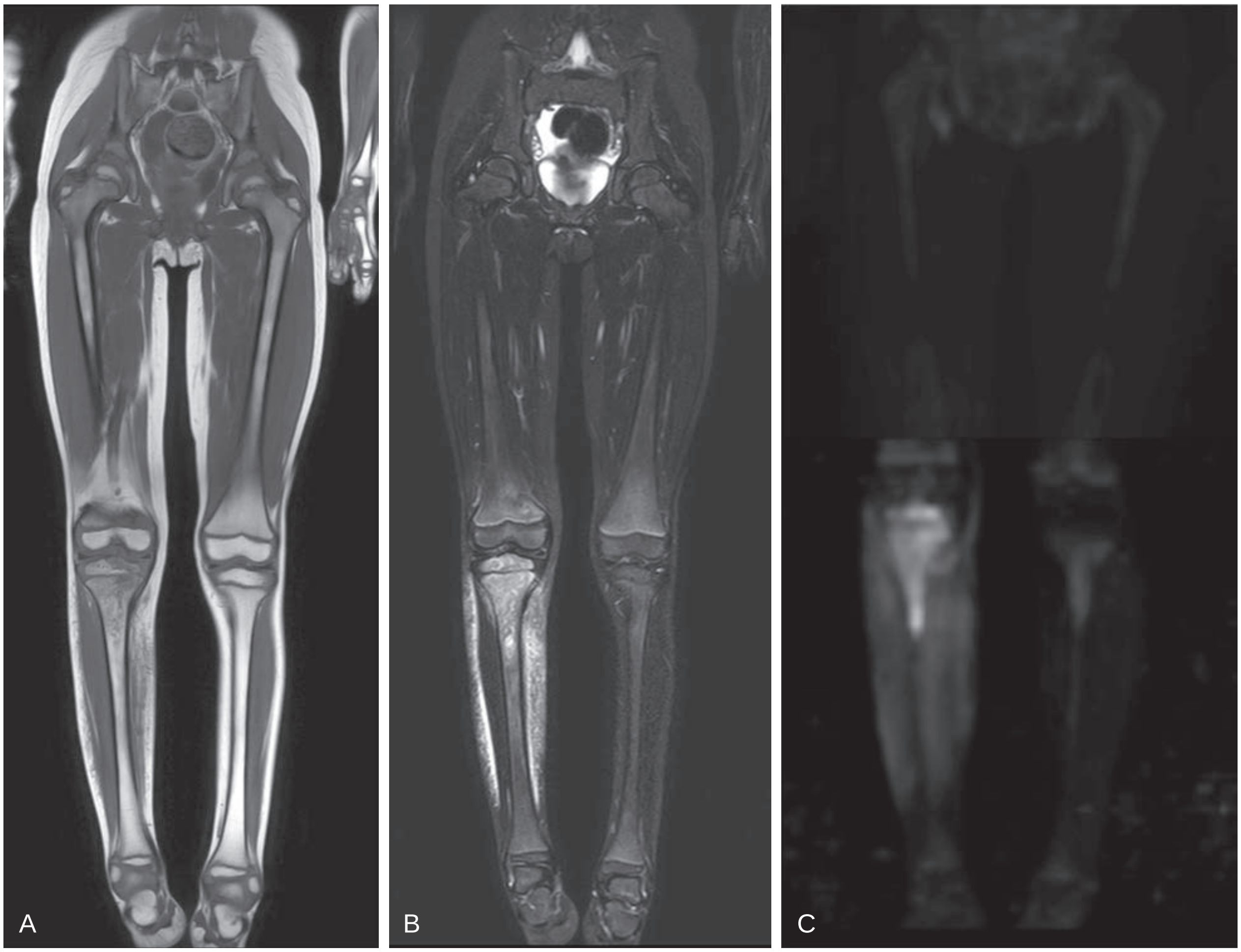

**Figure 137.16. Osteomyelitis in a 5-year-old girl with fever of unknown origin.** Lower extremity portion of a whole body MRI protocol including coronal T1-weighted (A), STIR (B), and diffusion-weighted whole-body imaging with background body signal suppression (DWIBS) (C) images show decreased signal intensity on T1-weighted images and increased signal intensity the STIR and DWIBS sequences within the right proximal tibial metaphysis, diaphysis, and epiphysis, and adjacent soft tissue edema. Biopsy confirmed osteomyelitis.

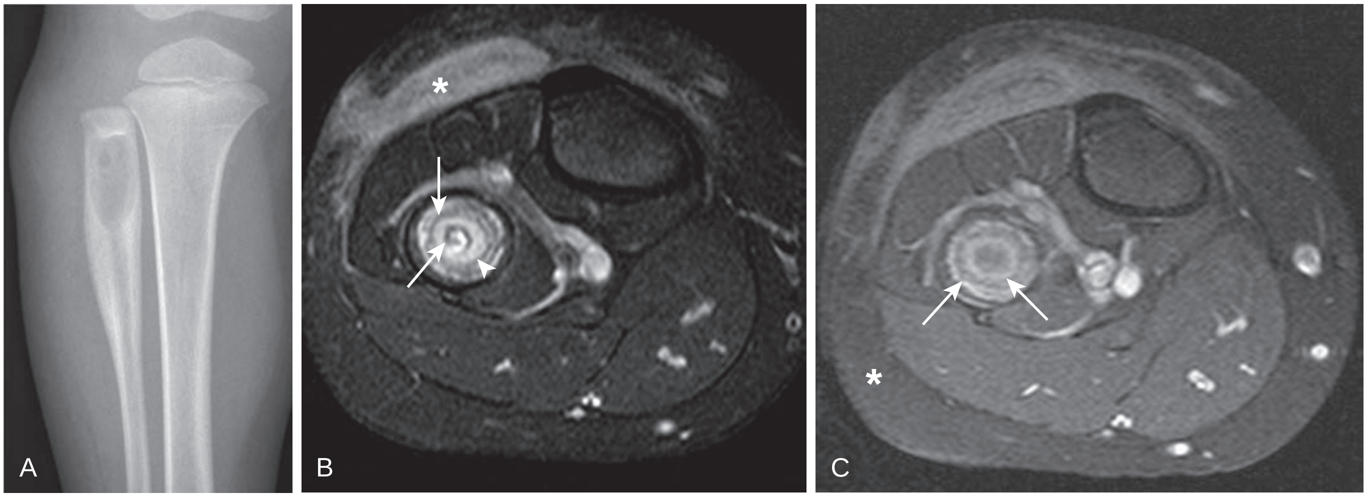

**Figure 137.17. Brodie abscess in a 3-year-old boy.** (A) Radiograph demonstrates a lytic lesion in the proximal fibula with laminated thick periostitis. Axial T2-weighted fat-saturated MR image (B) shows a layered appearance with intermediate signal *(arrowhead)* between inner and outer rims of lower signal intensity *(arrows)* and a more central hyperintense region. Also note the soft tissue phlegmon/early abscess formation *(asterisk)*. On an axial T1-weighted, fat-saturated, postgadolinium MR image (C) a rim of low signal sclerosis *(outer arrow)* surrounds an inner rim of enhancing granulation tissue *(inner arrow)*, which surrounds the nonenhancing abscess.

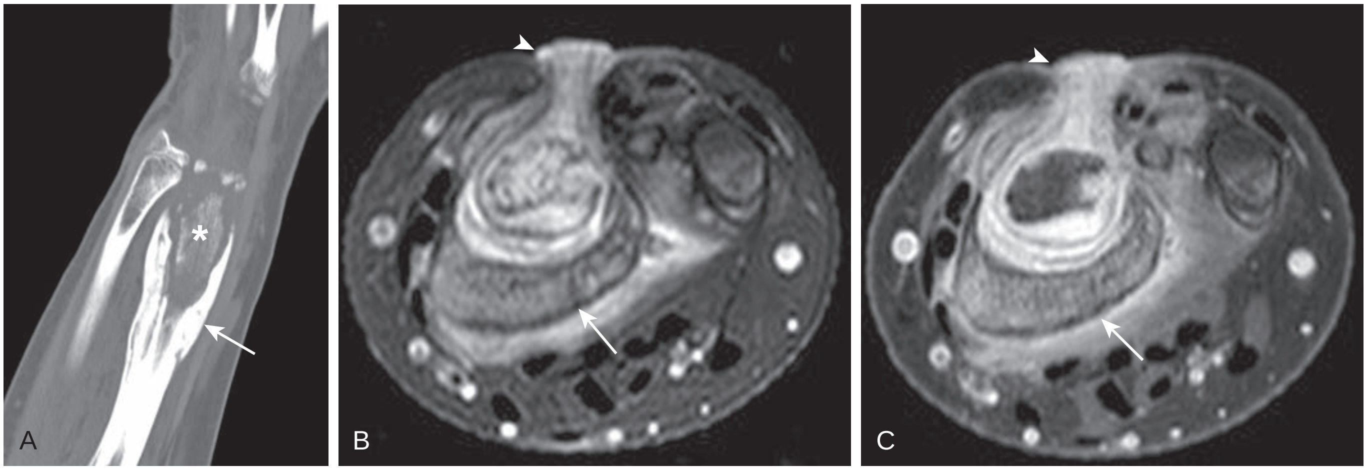

**Figure 137.18. Chronic osteomyelitis of the distal radius in a 13-year-old girl.** (A) Coronal reformat CT image shows involucrum *(arrow)* surrounding sequestrum *(asterisk)*. Axial T2-weighted fat-saturated (B) and T1-weighted fat-saturated (C) postgadolinium MR images show involucrum *(arrow)* that surrounds the nonenhancing sequestrum. Note granulation along the sinus tract that extends from the radial metaphysis sequestrum and abscess to the skin surface *(arrowhead)*.

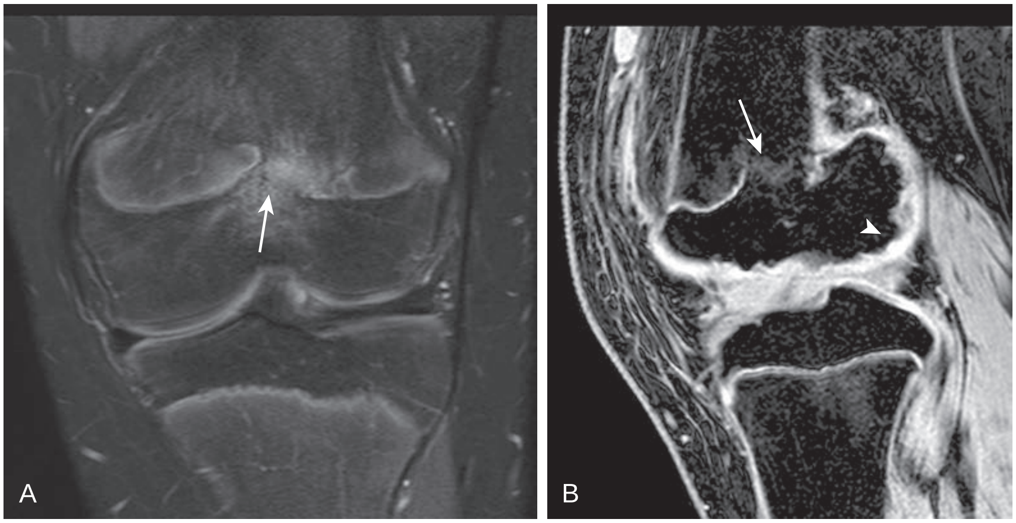

**Figure 137.20. Remote history of distal femoral osteomyelitis and septic arthritis in a 14-year-old boy.** Physeal bar *(arrows)* and femoral condylar epiphyseal irregularity *(arrowhead)* are seen on coronal T2-weighted fat-saturated (A) and gradient recalled echo sagittal (B) MR images.

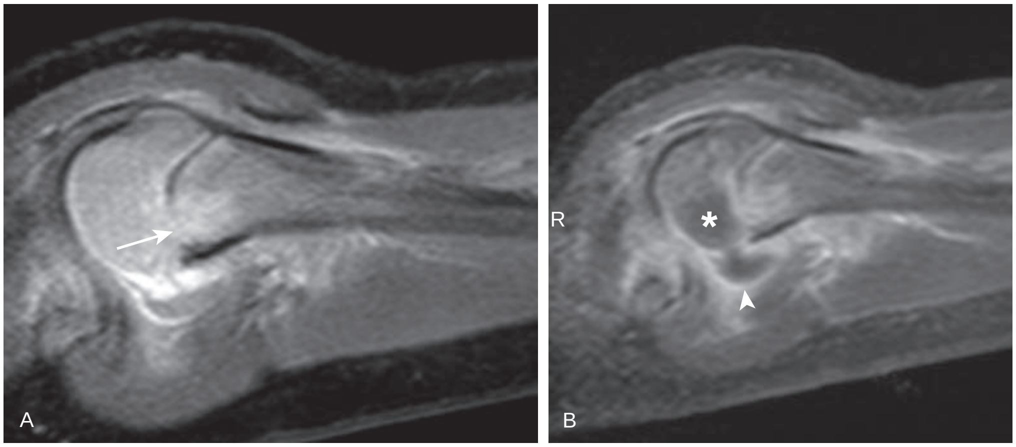

**Figure 137.21. Acute proximal humeral osteomyelitis and septic arthritis in a 3-month-old boy.** (A) Sagittal STIR MR image demonstrates proximal metaphyseal edema with physeal involvement *(arrow)*. (B) Sagittal T1-weighted postgadolinium MR image demonstrates glenohumeral effusion with synovial enhancement *(arrowhead)* and nonenhancing humeral epiphyseal cartilage, consistent with chondral involvement *(asterisk)*.

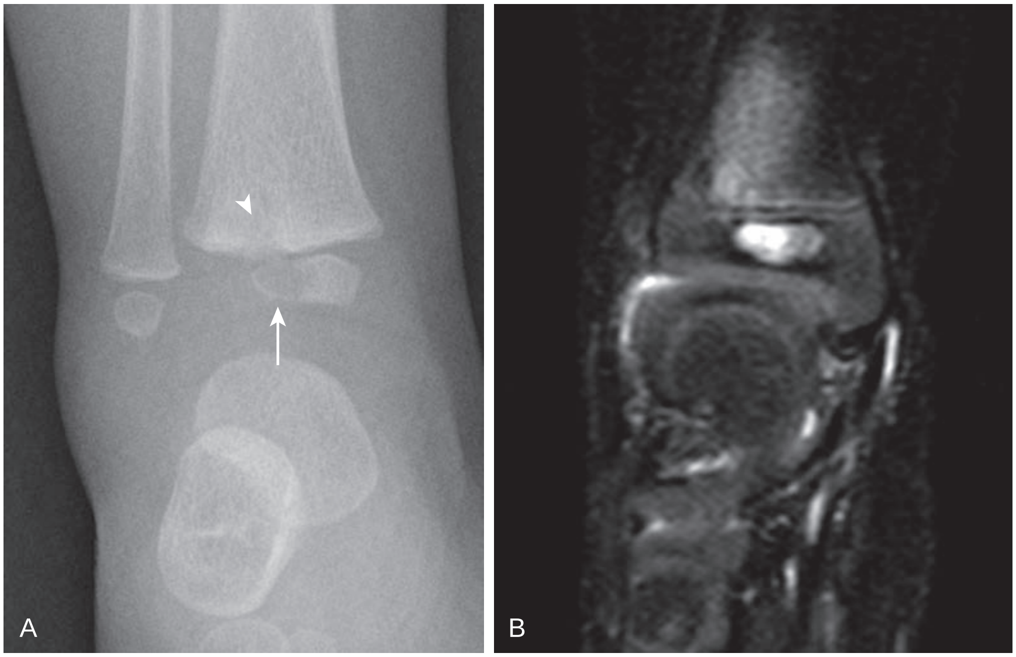

**Figure 137.22. Epiphyseal osteomyelitis in a 1-year-old girl.** (A) Radiograph demonstrates lucency within the epiphysis *(arrow)* and metaphysis *(arrowhead)*. (B) Coronal STIR MR image demonstrates epiphyseal bone abscess and metaphyseal edema.

## Fungal Osteomyelitis

Fungal infections of bone are becoming more common as the immunosuppressed population increases. *Aspergillus*, *Candida*, *Histoplasma*, *Blastomyces*, and other pathogens have been implicated. The radiographic changes are similar to those of chronic pyogenic osteomyelitis or tuberculosis (TB): destruction of bone and periosteal reaction with areas of cortical thickening and trabecular sclerosis. Fungal osteomyelitis may be multicentric, masslike, and may superficially mimic osteonecrosis.[32,36,37]

## Tuberculous Osteomyelitis

***Etiology, Pathophysiology, and Clinical Presentation.*** Although osseous TB is a relatively rare condition today, cases are still encountered that are not diagnosed until an extensive workup has been completed. Hematogenous metastases of tubercle bacilli to the skeleton may take place early during the active phase of the primary complex in the thorax or later from postprimary tuberculous foci. Musculoskeletal involvement of TB is seen in approximately 10% to 15% of all TB cases.[38] After implantation in the bone, an immediate active inflammatory reaction may develop, or the bacilli may be dormant for years until activated by local factors, such as trauma to the bone or joint. The synovial surface may be infected before the bones are involved; the infection may then spread from the joint into the contiguous epiphysis and metaphysis. In a large South African experience, the distribution of childhood skeletal TB is 60% to 70% vertebral, 20% to 25% large joints, and 10% to 15% tubular and flat bones.[39]

***Imaging.*** TB produces a chronic inflammatory reaction in the bones similar in its macroscopic aspects to chronic pyogenic osteomyelitis. Local necrosis of the intraosseous tissues develops at the site of implantation and is then followed by regional decalcification and bone destruction. Spread of infection takes place through the same pathways as those described in the pathogenesis of pyogenic osteomyelitis. During infancy and early childhood, when the epiphyseal cartilages are relatively thick, direct transfer of the infection from the joint to the bone, or infection across joints, is uncommon. The articular cartilages are preserved longer in tuberculous osteomyelitis and arthritis than in pyogenic arthritis because of the lack of a destructive proteolytic enzyme in tuberculous exudates.[40] Sinus formation and cold abscesses are common; involucrum formation and sequestration are rare.

The radiographic findings also are similar to those of chronic pyogenic osteomyelitis, so TB should be added regularly to the differential diagnosis of focal bone disease. Unlike pyogenic osteomyelitis, radiographs are usually abnormal at the initial clinical presentation of tuberculous osteomyelitis.[38]

Certain imaging features can suggest the diagnosis of TB. In the metaphyses and epiphyses, destruction of bone is more prominent than production of bone (Fig. 137.23).[40] The joint space is characteristically preserved in the early phases of tuberculous arthritis. The epiphysis is a site of predilection in primary skeletal TB. In the diaphyses of tubular bones, long segments may exhibit destructive and productive changes, whereas metaphyseal regions are unaffected (e-Fig. 137.24). Sometimes, sharply defined rarefactions are present that gave rise to the term *cystic TB* of bone. In the short bones of the hands and feet, tuberculous lesions may cause bone expansion, so-called spina ventosa (Fig. 137.25). Skeletal TB may affect multiple sites, and a bone scan is recommended to detect the presence of quiescent lesions. MRI is useful in certain cases and clearly demonstrates the full extent of the bone marrow, subperiosteal, and soft tissue involvement as well as any extension into the adjacent joint. TB joint and tenosynovial involvement can mimic juvenile idiopathic arthritis because of its chronic nature and because it can produce rice bodies.[41]

When multifocal at presentation, TB (osteitis cystica tuberculosa multiplex) and fungal infections may superficially mimic metastatic disease.

***Treatment.*** The standard treatment for TB is multidrug therapy inclusive of isoniazid, rifampin, pyrazinamide, and ethambutol for a minimum of 6 to 9 months.[38] Extrapulmonary TB treatment is

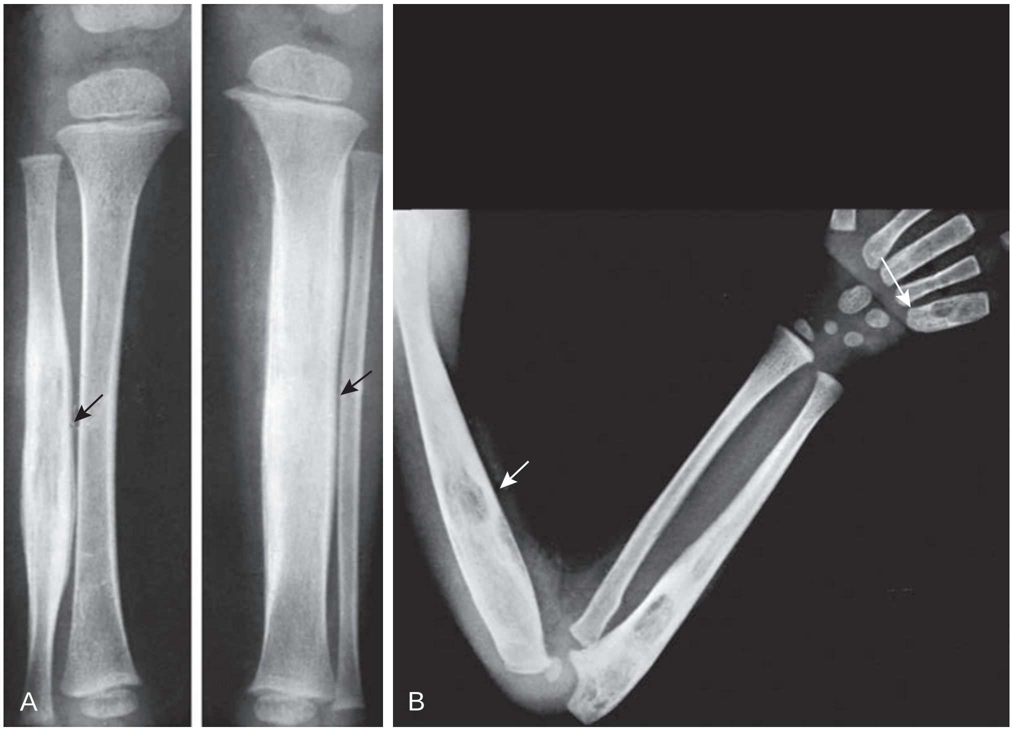

**e-Figure 137.24. Multiple sites of tuberculous diaphysitis with cold abscesses on the dorsal surfaces of the hands in an 18-month-old boy.** (A) Lower extremities. The left tibia and right fibula are enlarged; the medullary canals are expanded, and the overlying cortex is thickened *(arrows)*. (B) Left upper extremity. The distal half of the humerus is enlarged into a sausage-shaped contour, and the cortex is thickened; the medullary canal is expanded and exhibits cystic rarefaction *(short arrow)*. The proximal half of the ulna is enlarged and irregularly cystic; its cortex is thickened. The fifth left metacarpal is expanded and irregularly lytic and osteoporotic *(long arrow)*. All of these lesions healed slowly but completely. On images made 2 years later, the skeleton appeared to be normal.

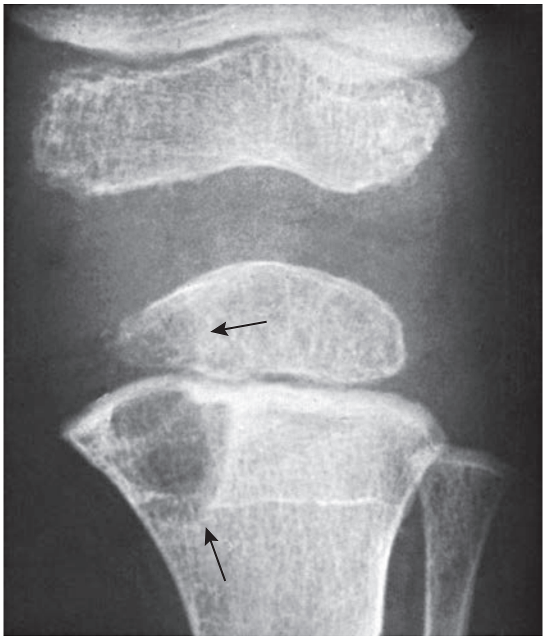

**Figure 137.23. Tuberculous metaphysitis and epiphysitis of the tibia and arthritis of the knee in a 3-year-old boy.** Large areas of destruction are present in the medial aspects of the metaphysis and the epiphyseal ossification center *(arrows)*.

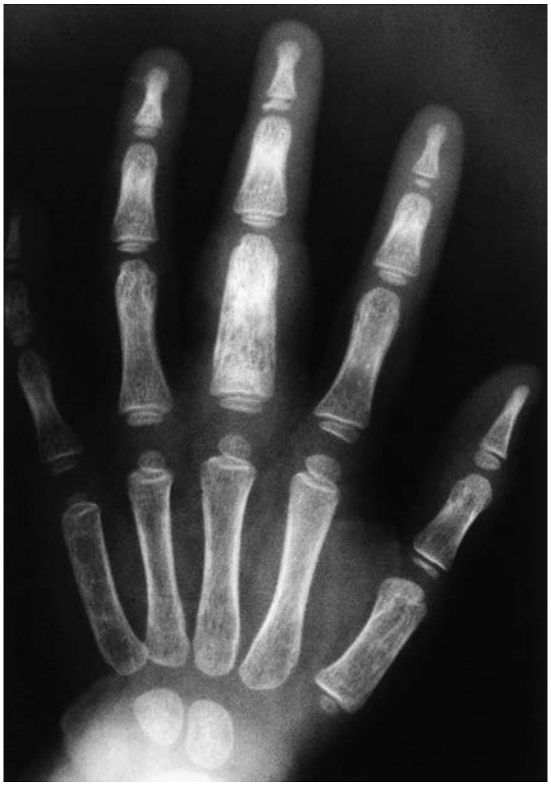

**Figure 137.25. Tuberculous dactylitis (spina ventosa) in the proximal phalanx of the third finger in a 2-year-old girl.** The whole diaphysis is involved, but the epiphysis is spared. Expansion of the rest of the phalanx shows mixed areas of bone destruction and sclerosis.

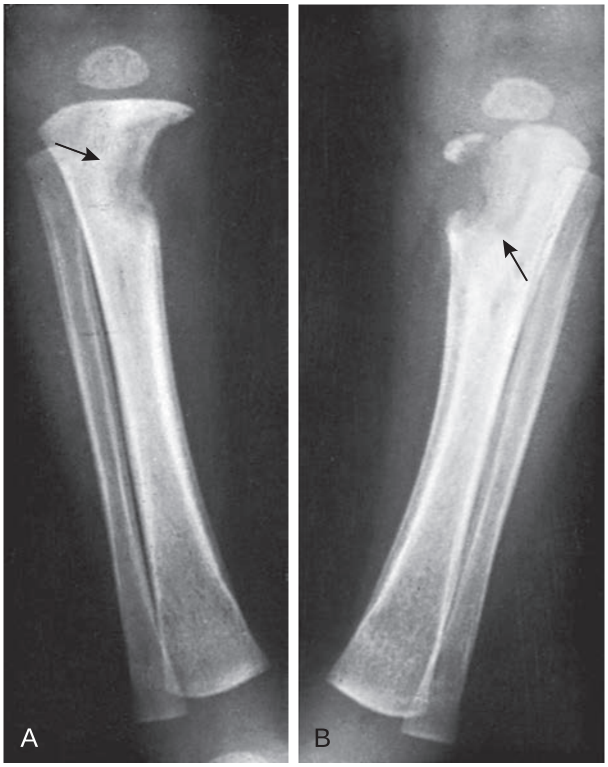

**Figure 137.28. Syphilitic metaphysitis of the proximal ends of the tibias (Wimberger sign) in a 2-month-old infant.** Frontal radiographs of the right (A) and left (B) legs show bilateral, symmetric, large areas of destruction of the spongiosa and overlying cortex are seen at the medial aspects of the tibias *(arrows)*. In the left tibia, the medial segment of the epiphyseal plate is partially destroyed. Note also diffuse periosteal thickening of the diaphyses.

longer (12–18 months) because of relatively poor osseous and fibrous tissue penetration.

## Congenital Syphilis

***Etiology, Pathophysiology, and Clinical Presentation.*** Congenital syphilis (*Treponema pallidum*) causes hepatosplenomegaly, lymphadenopathy, skin rash, and anemia.[42] Bones are often involved, but this may not clinically or radiologically manifest in the first weeks of life. Bone pain in one or more extremities may be severe and result in lack of movement of those extremities, a condition termed *Parrot pseudoparalysis.* Syphilis of bone can be suggested on the basis of radiologic signs, when it has not been considered on clinical grounds. The diagnosis, however, still rests on appropriate serologic tests. Two main forms are observed, infantile and juvenile, and their radiographic features are different.

***Imaging.*** The unique imaging characteristic of *infantile syphilis* is multiple bone involvement with almost selective localization in the metaphyses. Broad bands of metaphyseal radiolucency were considered evidence of "metaphysitis" but are now known to be nonspecific responses to the stress of disseminated infection.[43] Syphilitic granulation tissue can, however, occur in these regions (e-Fig. 137.26). Radiographically, the two causes cannot be distinguished, but when associated with metaphyseal serration, the so-called sawtooth metaphysis (e-Fig. 137.27), the diagnosis of congenital syphilis is practically ensured. Similar diagnostic "specificity" is provided by the Wimberger sign after the newborn period, when destructive foci are found in the metaphyseal regions of tubular bones, particularly the medial tibial metaphyses at the knee (Fig. 137.28). Metaphyseal destructive lytic lesions may

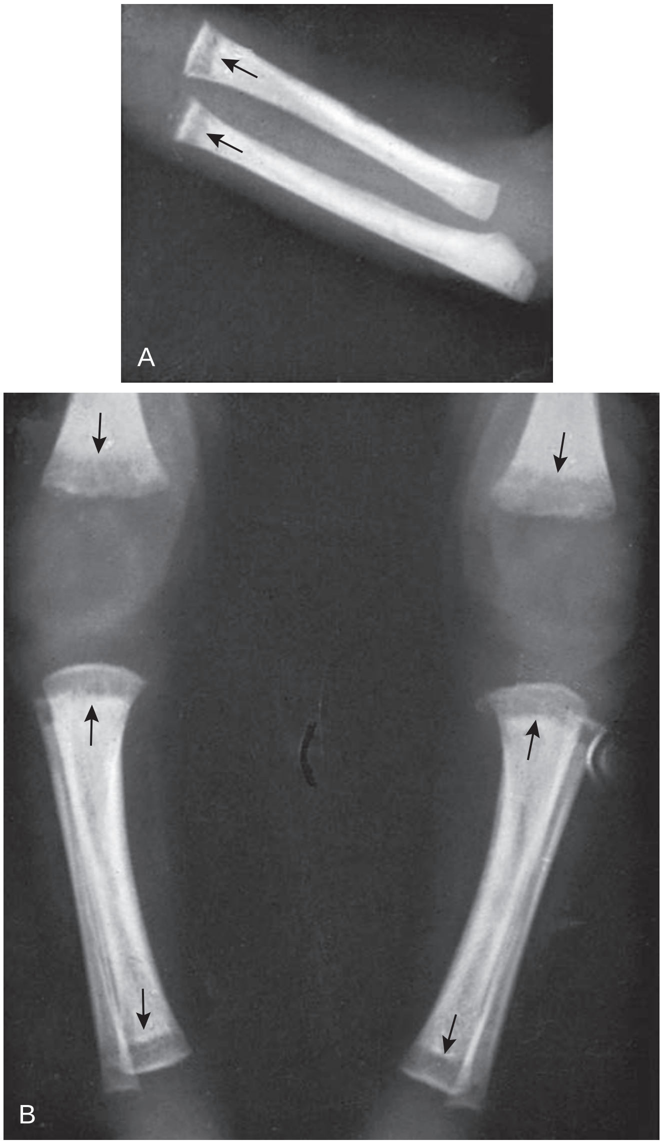

**e-Figure 137.26. Syphilitic metaphysitis in a 1-month-old former premature infant.** Radiographs show deep segments of diminished density *(arrows)*. The spongiosa in these segments has been replaced by radiolucent syphilitic granulation tissue. (A) Upper limb. (B) Lower limbs.

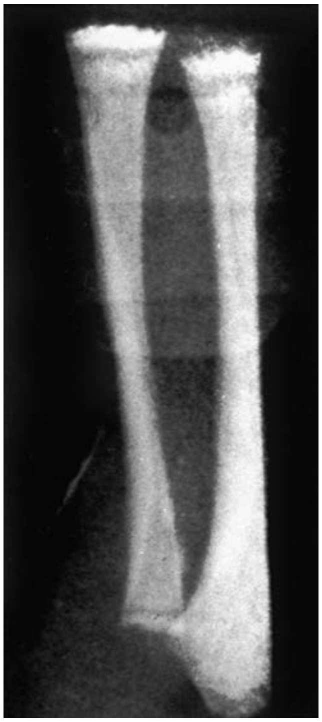

**e-Figure 137.27. Newborn infant with congenital syphilis and sawtooth metaphysis.** This patient had a rash and mucocutaneous lesions characteristic of the disease.

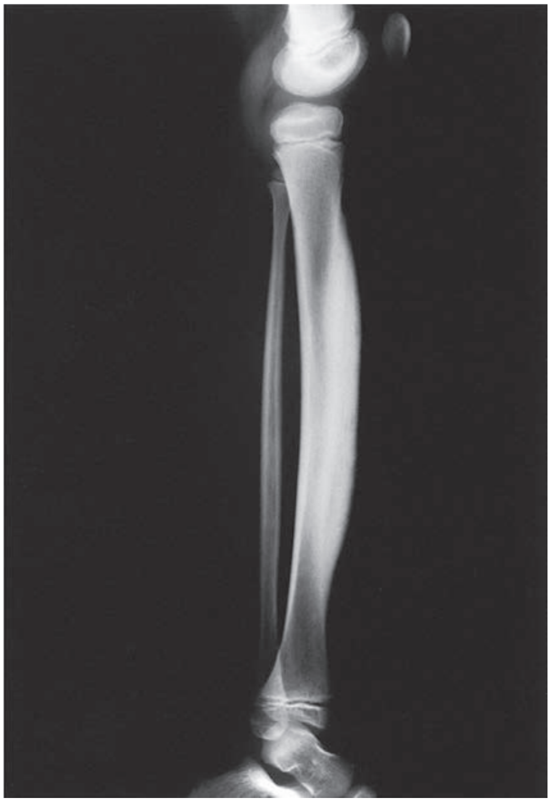

**Figure 137.30. Saber shin as a result of congenital syphilis in an 8-year-old boy.** Lateral view of the leg shows extensive anterior cortical and periosteal thickening of the tibial diaphysis.

lead to pathologic fractures, and child abuse is in the differential diagnosis.[44] Although metaphyseal lesions are characteristic of congenital syphilis, they are not pathognomonic and may be seen with ordinary osteomyelitis, hyperparathyroidism, skeletal infantile myofibromatosis, and metastases. Diaphyseal involvement, especially with periosteal new bone formation, also tends to occur after the first month and may be associated with destructive foci and even scattered focal cortical destruction and expansion of the medullary cavity (e-Fig. 137.29). The epiphyses are generally spared. Healing of the bone lesions in the infantile form of the disease occurs with or without therapy, usually without deformity.

Juvenile syphilis is observed radiographically in childhood and is manifested by diffuse or localized subperiosteal thickening of the cortex (Fig. 137.30). Associated focal destructive lesions, resembling cystic TB, occasionally are present. Thickening of the anterior cortex of the tibia is responsible for the "saber shin" deformity of congenital syphilis that appears in late childhood.[45]

## Septic Arthritis

***Etiology, Pathophysiology, and Clinical Presentation.*** The annual per capita incidence of septic arthritis in the United States is approximately 1 in 93,500.[1] *S. aureus* is the most commonly isolated organism, the majority of which are MRSA. The knee is most commonly affected joint (41.4%) followed by the hip (22.6%) and ankle (13.6%).

Bacterial entry into the joint can occur by two mechanisms: direct inoculation from a penetrating injury and hematogenous inoculation. The vascular synovium may be hematogenously inoculated.[14] Alternatively, inoculation may occur secondarily by way of osteomyelitis. This may occur with higher frequency in infants when transphyseal vessels extend from the metaphysis to the intraarticular epiphysis.[46]

Septic arthritis causes rapid cartilage loss and joint destruction and therefore is a medical and surgical emergency. Diagnosis is based on clinical grounds and laboratory data. A history of fever, nonweight bearing, an erythrocyte sedimentation rate above 40 mm/hour, and a white blood cell count greater than 12,000 cells/mm$^3$ are four consistent variables that occur frequently in the setting of septic arthritis as extensively studied in the hip.[47] When present in isolation, each of these individual variables has low accuracy for the diagnosis of septic arthritis, but when three or more of these variables are present at the same time, the chance of a positive diagnosis of septic arthritis of the hip is greater than 93%.[47]

Many nonbacterial entities may mimic septic arthritis; these include transient synovitis, juvenile idiopathic arthritis (JIA), Lyme arthritis, reactive joint effusions, posttraumatic arthritis, and epiphyseal osteonecrosis.

***Imaging.*** Radiography is the first line of imaging in the setting of suspected septic arthritis to rule out an obvious alternative cause for symptoms. The initial findings may be nonspecific soft tissue swelling about a joint. In certain joints—such as the elbow, knee, and ankle—a joint effusion may be seen and is best delineated on a lateral radiograph.

The role of US is to identify the presence or absence of an underlying joint effusion or to determine whether pathology is intraarticular or extraarticular, such as adjacent tenosynovitis.[48,49] When a joint effusion is present, no sonographic features are evident that predict the presence or absence of septic arthritis.[50–52] Capsular distension with anechoic or hypoechoic fluid is usually seen. Debris and septations within the joint, as well as hyperemic flow in the synovium, can be seen on power Doppler; but this can also be seen in JIA, transient synovitis (e-Fig. 137.31),[52] and posttraumatic arthritis.

The MRI findings of isolated septic arthritis are also nonspecific.[53,54] Synovial thickening, enhancement, effusions, and juxtasynovial soft tissue edema may be seen, but this is indistinguishable from transient synovitis and JIA. The role of MRI is not to diagnose septic arthritis but to identify the presence or absence of coexisting osteomyelitis (see Fig. 137.8), epiphyseal cartilage involvement (e-Fig. 137.32), and juxtasynovial muscle inflammation (Fig. 137.33) or abscesses, because this will affect medical and surgical management. Coexisting septic arthritis and osteomyelitis is frequent in children, particularly in children under 2 years of age.[55] When a joint effusion is present in the setting of metaphyseal osteomyelitis, the reported incidence of coexisting septic arthritis is approximately 75%.[56]

***Treatment.*** US may be used to both identify the presence or absence of a joint effusion and to provide needle guidance for diagnostic joint aspiration.[49] Emergent arthrotomy and washout is recommended to prevent complications of septic arthritis. If septic arthritis is a complicating feature of osteomyelitis, the underlying bone should also be debrided. Complications of septic arthritis include sepsis, chondrolysis, and osteonecrosis.[57] Antibiotic treatment is similar to the treatment of osteomyelitis at all ages: a total of 4 to 6 weeks of therapy.[58]

## Pyomyositis

***Etiology, Pathophysiology, and Clinical Presentation.*** Pyomyositis is a localized primary infection of muscle characterized by progression to abscess formation that can mimic tumor, trauma (hematoma), osteomyelitis, septic arthritis, cellulitis, or thrombophlebitis. This disorder is endemic in Africa, South America, southeastern Asia, and the South Pacific; it is increasingly reported in temperate climates, including the northern United States. Pyomyositis occurs in otherwise healthy children and in those predisposed to infection by debilitating diseases,

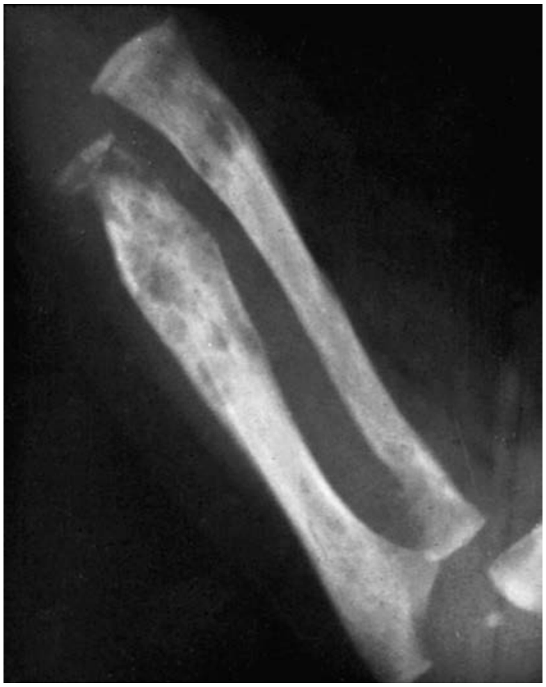

e-Figure 137.29. Congenital syphilis with expansion and destructive metaphyseal and diaphyseal changes in a 3-month-old infant.

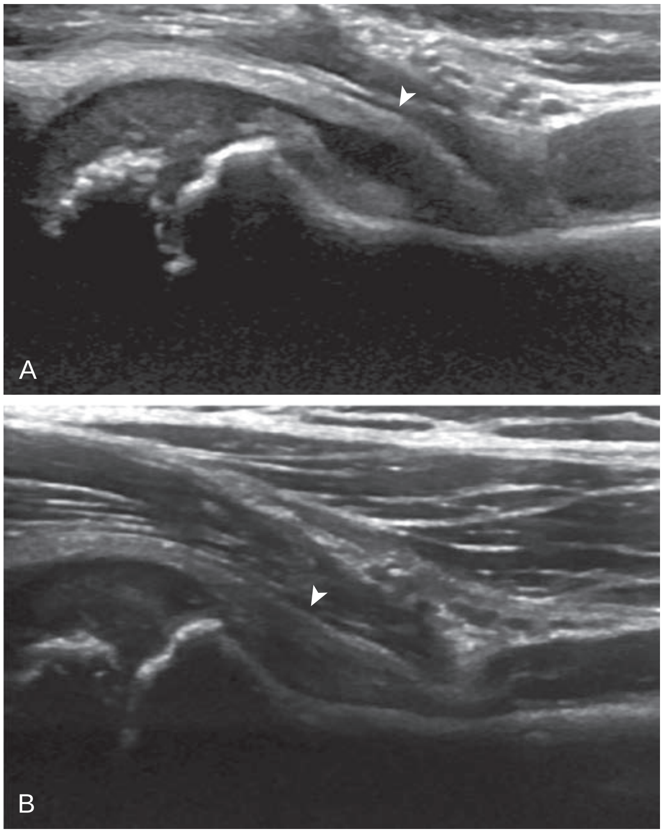

**e-Figure 137.31.** **Transient synovitis of the hip in a 1-year-old girl.** (A) Longitudinal sonogram of the symptomatic right hip shows capsular distension *(arrowhead)* because of a large effusion. (B) Sonogram of the asymptomatic left hip shows a normal appearance of the hip joint capsule *(arrowhead)* with only small amount of physiologic fluid.

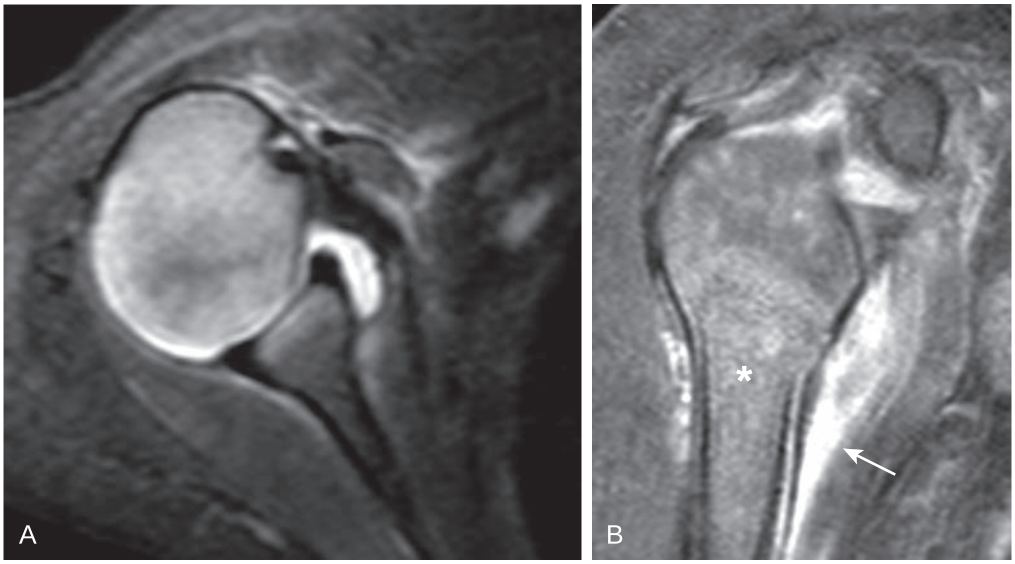

**e-Figure 137.32.** **Glenohumeral septic arthritis related to humeral osteomyelitis in a 4-month-old boy.** (A) Axial T2-weighted fat-saturated MR image demonstrates a nonspecific glenohumeral joint effusion. B, Coronal T1-weighted, fat-saturated, postgadolinium MR image shows abnormal patchy enhancement of the proximal humeral epiphyseal cartilage, abnormal heterogeneous marrow enhancement *(asterisk)*, and periostitis with juxtacortical edema *(arrow)*.

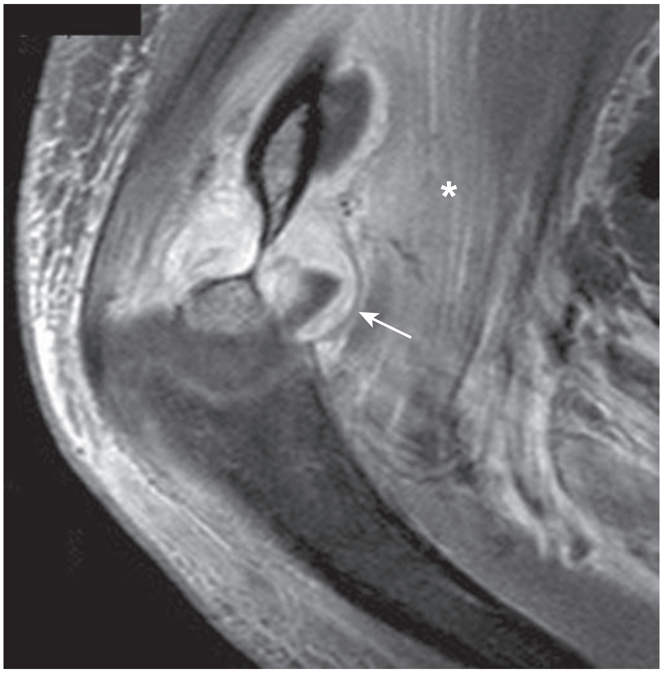

**Figure 137.33. Elbow septic arthritis and distal humeral osteomyelitis in an 11-year-old boy.** Sagittal T1-weighted, fat-saturated, postgadolinium MR image demonstrates thick synovial enhancement *(arrow)* and juxtasynovial myositis *(asterisk)*. Marrow hyperenhancement is also seen in the distal humerus.

including those with human immunodeficiency virus infection. *S. aureus* is the most commonly identified organism; it is isolated in 45% of cases in a U.S.-based study, followed by group A β-hemolytic streptococci (GABHS; 10%).[1] GABHS infections may occur in the setting of *Varicella* infection,[59] and multifocal pyomyositis may be seen as a complication of bacterial endocarditis. Secondary pyomyositis may also occur as the result of extension from adjacent osteomyelitis, particularly in the pelvis. Damaged muscle with some degree of underlying immune suppression and a source of bacteremia are the key predisposing elements.

Clinically, the gluteal muscles, thighs, and calves are more commonly affected than the upper extremities, trunk, and chest wall.[60] Approximately 25% of patients have a history of antecedent trauma. Usually, only a single muscle is involved. Early in the course of illness, patients experience low-grade fevers, general malaise, and dull, cramping pain.[61] The involved area lacks the cutaneous erythema usually evident with cellulitis, and it has a "woody" nonfluctuant feel. Fever usually occurs as infection advances. Infections of the pelvic musculature may clinically mimic osteomyelitis or septic arthritis by producing hip or groin pain. Infection of the piriformis muscle may irritate the adjacent sciatic nerve and produce pain that extends into the ipsilateral lower extremity.[62] Pyomyositis is usually accompanied by elevations in white blood cell count, erythrocyte sedimentation rate, and C-reactive protein level.

***Imaging.*** Early in the development of pyomyositis, the affected muscle is enlarged and edematous without a frank abscess. Without treatment, the process progresses to form an intramuscular abscess. US may be helpful in localizing relatively superficial sites of pyomyositis (Fig. 137.34).[63] Infections at deeper sites and infections that have not yet formed an intramuscular abscess are less readily detected with US.

MRI is the preferred modality for imaging of suspected pyomyositis, and it is particularly valuable in cases of pelvic involvement.[64,65] On MRI, the involved muscle appears enlarged and edematous with increased signal on T2-weighted and inversion recovery sequences. On T2-weighted images, the abscess is seen as high signal with a hypointense rim and less well-defined hyperintensity of the adjacent muscle (Fig. 137.35). Postgadolinium T1-weighted images best reveal the abscess, and the abscess wall densely enhances (see Fig. 137.34). Changes may result from associated cellulitis and include skin thickening, stranding of subcutaneous fat, and swelling of fascial planes; these findings are best seen on fat-saturated T2-weighted and inversion recovery images. A sympathetic effusion may be present if infection is near a joint.

***Treatment.*** Appropriate antibiotic therapy is usually curative for pyomyositis. More aggressive abscesses may require abscess drainage and debridement of muscle.[66]

## Necrotizing Fasciitis/Cellulitis

***Etiology, Pathophysiology, and Clinical Presentation.*** Necrotizing fasciitis is a rapidly progressive, sometimes fatal soft tissue infection that characteristically involves the deep fascia of the extremities and trunk.[61] The disease tends to affect the elderly and those with impaired immunity, but it can occur in immune-competent patients of any age. Underlying skin infection related to lesions such as furuncles, insect bites, and even minor trauma or surgery has been associated. Necrotizing fasciitis is most commonly a polymicrobial infection with both aerobic and anaerobic organisms. In children with chicken pox, secondary infection of vesicular skin lesions with *S. aureus* or GABHS has been linked to development of cellulitis and, less frequently, necrotizing fasciitis.[67]

The early clinical presentation of necrotizing fasciitis is nonspecific and may be accompanied by vague complaints of fever and malaise with rapid progression to sepsis and acute renal failure. Initial soft tissue findings are those of warmth and induration. A high index of suspicion is paramount for early diagnosis.

***Imaging.*** Pathologic changes and extent of necrotizing fasciitis and cellulitis are detected most sensitively on MRI with fat-suppressed, T2-weighted, STIR sequences, and postgadolinium, fat-suppressed, T1-weighted imaging (Fig. 137.36). Cellulitis is characterized by high T2 signal thickening and gadolinium enhancement with or without fluid collections in the subcutaneous tissue and superficial fascia (e-Fig. 137.37). Necrotizing fasciitis should be considered when these changes extend to the deep fascia. Patients with necrotizing fasciitis may have thick (>3 mm) fascial signal intensity or low signal intensity in the deep fascia on T2-weighted images, along with focal or diffuse nonenhancing portions of deep fascia and involvement of three or more compartments in one extremity.[68] Soft tissue gas appears as areas of signal absence with susceptibility artifact. To help guide therapy, it is important to distinguish by MRI whether necrotizing fasciitis is related to underlying osteomyelitis and/or septic arthritis versus infection confined to the muscles and fascia.

Edema of fascia and muscles is nonspecific on MRI and overlaps with that of other pathologic conditions, including dermatomyositis, pyomyositis, and lymphedema. Additionally, in the very early stages of necrotizing fasciitis, deep fascial involvement may be minimal or lacking. Although absence of deep fascial involvement on MRI is fairly reliable for exclusion of necrotizing fasciitis, ultimate patient management relies on a combination of imaging and clinical findings.

***Treatment.*** Cellulitis is amenable to medical therapy with intravenous antibiotics; necrotizing fasciitis is a life-threatening emergency that requires additional urgent surgical debridement of necrotic tissue.[69] Therefore distinction between these two entities is critical for patient management.

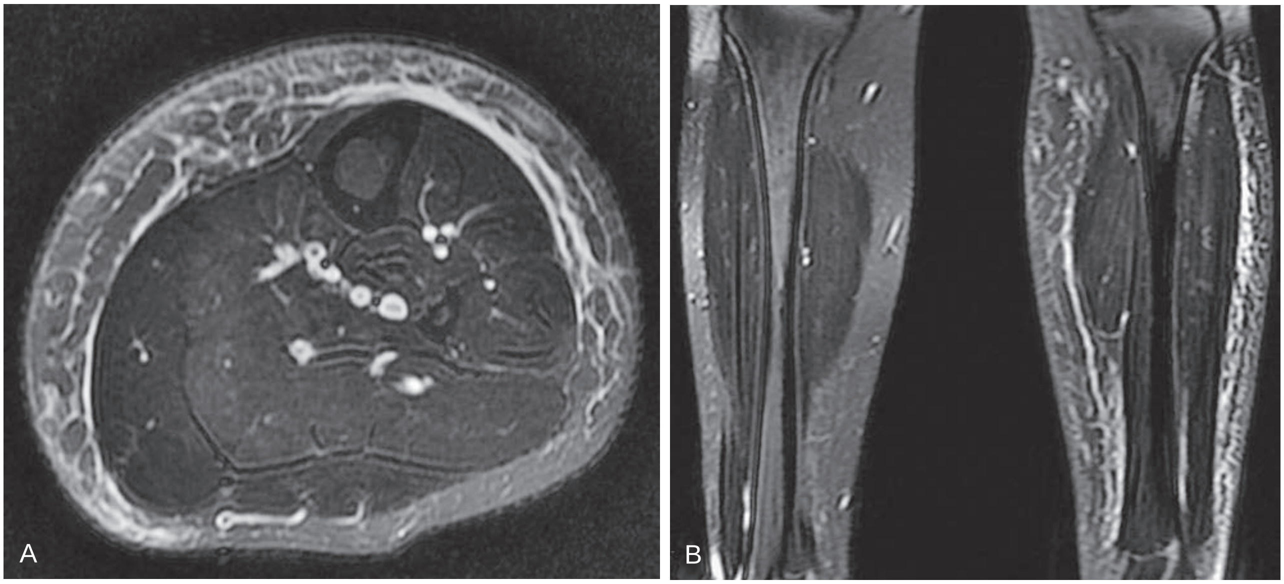

**e-Figure 137.37. Cellulitis.** This 16-year-old girl presented with left leg swelling, fever, and rash. Axial (A) and coronal (B) T2-weighted MR images show reticulated high signal in the subcutaneous fat and superficial fascia without deep involvement.

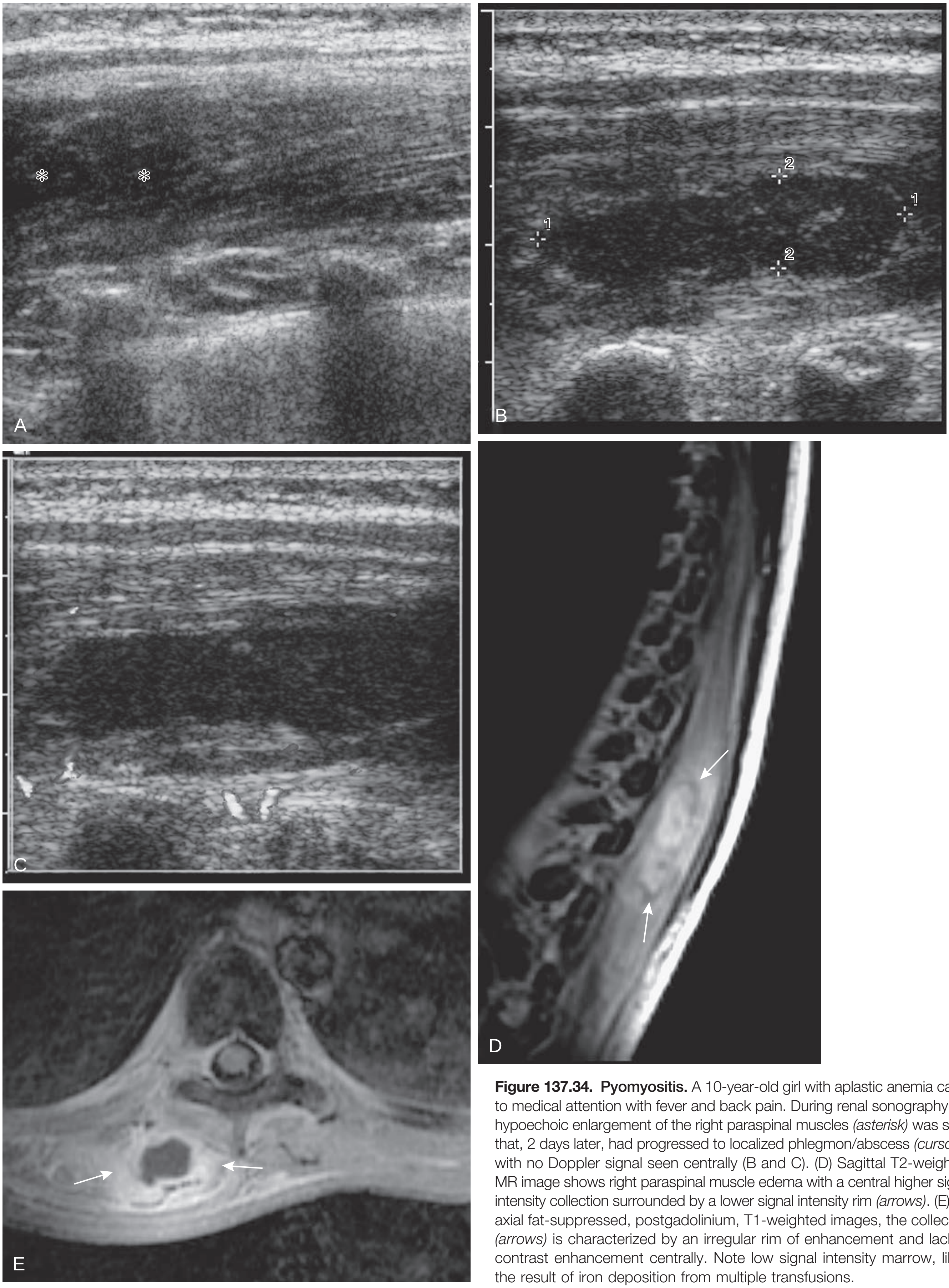

**Figure 137.34. Pyomyositis.** A 10-year-old girl with aplastic anemia came to medical attention with fever and back pain. During renal sonography (A), hypoechoic enlargement of the right paraspinal muscles *(asterisk)* was seen that, 2 days later, had progressed to localized phlegmon/abscess *(cursors)*, with no Doppler signal seen centrally (B and C). (D) Sagittal T2-weighted MR image shows right paraspinal muscle edema with a central higher signal intensity collection surrounded by a lower signal intensity rim *(arrows)*. (E) On axial fat-suppressed, postgadolinium, T1-weighted images, the collection *(arrows)* is characterized by an irregular rim of enhancement and lack of contrast enhancement centrally. Note low signal intensity marrow, likely the result of iron deposition from multiple transfusions.

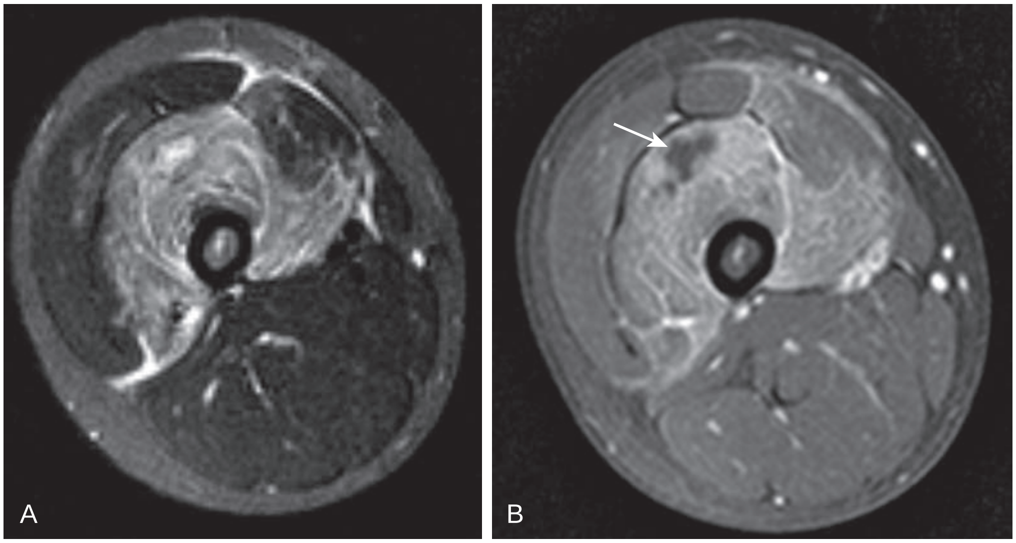

**Figure 137.35.** Pyomyositis and abscess in a 6-year-old girl. Pyomyositis and early abscess formation *(arrow)* in the quadriceps mechanism seen on axial STIR (A) and postgadolinium T1 fat-saturated (B) MR images.

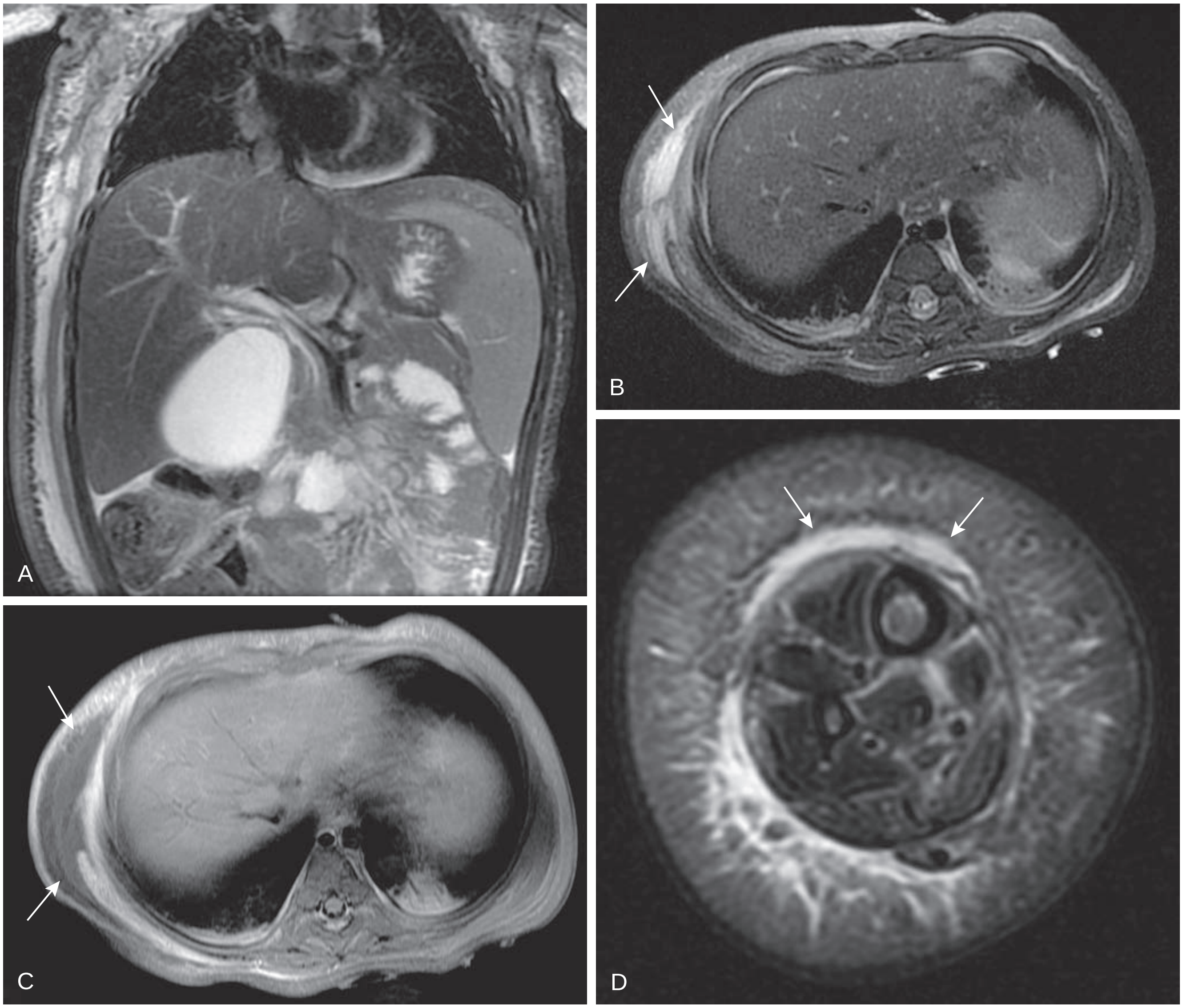

**Figure 137.36. Necrotizing fasciitis.** A 1-year-old girl with a 2-week history of progressive fever, leukocytosis, and swelling of the right side of the chest wall and right calf. Coronal (A) and axial (B) T2-weighted MR images show asymmetric high signal in the muscle and superficial and deep fascial layers of the right chest and abdominal wall *(arrows)*. Axial fat-suppressed T1-weighted image (C) after intravenous gadolinium administration shows enhancement of these areas with more superficial nonenhancing fluid lacking rim enhancement *(arrows)*. Similar changes *(arrows)* are seen in the right lower leg on axial T2-weighted (D) and postcontrast fat-suppressed T1-weighted images (E). Biopsy of both sites showed acute inflammation with coagulative necrosis. Cultures were negative, but dramatic clinical improvement was noted with intravenous antibiotic therapy.

*Continued*

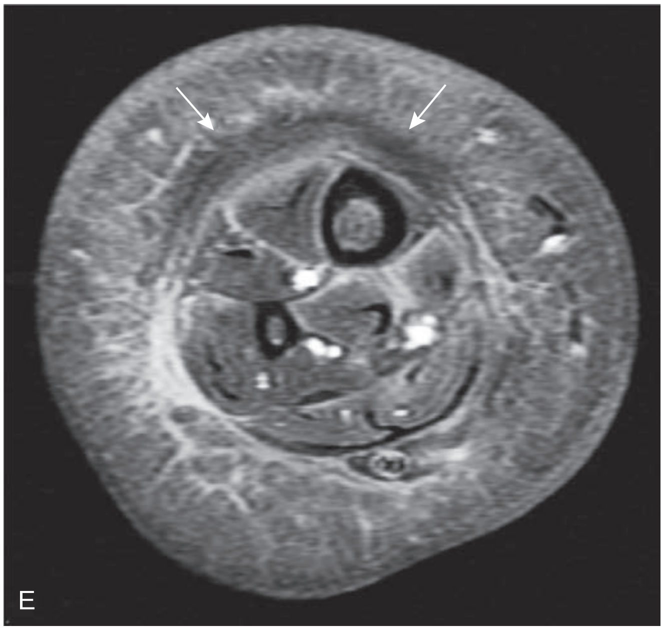

**Figure 137.36, cont'd.**

## KEY POINTS

- Radiographs should always be obtained before advanced imaging to rule out obvious alternative causes for symptoms, such as a fracture.
- When infection is a concern and symptoms are nonlocalizing, whole body MRI or bone scan can be performed. If symptoms are localizing, a focused MRI is recommended.
- When osteomyelitis is present, identify and measure all abscesses, their location, and whether there is secondary involvement of a nearby joint.
- US and MRI are not able to distinguish pyogenic and nonpyogenic joint effusions.

## Acknowledgment

This chapter includes material from Chapter 159, "The Soft Tissues," in a previous edition of this text, originally written by Kathleen H. Emery, MD.

## SUGGESTED READINGS

Jaramillo D. Infection: musculoskeletal. *Pediatr Radiol*. 2011;41(suppl 1):S127–S134.

Tureck MB, Taljanovic MS, Stubbs AY, et al. Imaging of musculoskeletal soft tissue infections. *Skeletal Radiol*. 2010;39(10):957–971.

## REFERENCES

Full references for this chapter can be found on www.expertconsult.com.

## REFERENCES

1. Gafar OA, Copley LAB, Hollmig ST, et al. The impact of the current epidemiology of pediatric musculoskeletal infection on evaluation and treatment guidelines. *J Pediatr Orthop*. 2008;28(7):777–785.
2. Dartnell J, Ramachandran M, Katchburian M. Hematogeneous acute and subacute paediatric osteomyelitis. *J Bone Joint Surg Br*. 2012;94-B:584–595.
3. Sarkissian EJ, Gans I, Gunderson MA, et al. Community-acquired methicillin-resistant Staphylococcus aureus musculoskeletal infections: emerging trends over the past decade. *J Pediatr Orthop*. 2016;36(3):323–327.
4. Howard AW, Viskontas D, Sabbagh C. Reduction in osteomyelitis and septic arthritis related to Haemophilus influenza type B vaccination. *J Pediatr Orthop*. 1999;19(6):705–709.
5. Lonergan GJ, Cline DB, Abbondanzo SL. Sickle cell anemia. *Radiographics*. 2001;21(4):971–994.
6. Falcone EL, Holland SM. Invasive fungal infection in chronic granulomatous disease: insights into pathogenesis and management. *Curr Opin Infect Dis*. 2012;25(6):658–669.
7. Puffinbarger WR, Gruel CR, Herndon WA, et al. Osteomyelitis of the calcaneus in children. *J Pediatr Orthop*. 1996;16(2):224–230.
8. Blickman JG, van Die CE, de Rooy JWJ. Current imaging concepts in pediatric osteomyelitis. *Eur Radiol*. 2004;14:L55–L64.
9. Kan JH, Hilmes MA, Martus JE, et al. Value of MRI after recent diagnostic or surgical intervention in children with suspected osteomyelitis. *AJR*. 2008;191(5):1595–1600.
10. Metwalli ZA, Kan JH, Munjal KA, et al. MR imaging of suspected lower extremity musculoskeletal infection in the pediatric patient: how useful is bilateral imaging? *AJR*. 2012.
11. Dasmasio MB, Magnaguagno F, Stagnaro G. Whole-body MRI: non-oncological applications in paediatrics. *Radiol Med*. 2016;121(5):454–461. doi:10.1007/s11547-015-0619-9. Epub 2016 Feb 19.
12. DiPoce J, Jbara ME, Brenner AI. Pediatric osteomyelitis: a scintigraphic case based review. *Radiographics*. 2012;32:865–878.
13. Saigal G, Azouz EM, Abdenour G. Imaging of osteomyelitis with special reference to children. *Semin Musculoskelet Radiol*. 2004;8(3):255–265.
14. Jaramillo D. Infection: musculoskeletal. *Pediatr Radiol*. 2011;41(suppl 1):S127–S134.
15. Kan JH, Young RS, Yu C, et al. Clinical impact of gadolinium in the MRI diagnosis of musculoskeletal infections in children. *Pediatr Radiol*. 2010;40(7):1197–1205.
16. Averill LW, Hernandez A, Gonzalez L, et al. Diagnosis of osteomyelitis in children: utility of fat-suppressed contrast enhanced MRI. *AJR*. 2009;192:1232–1238.
17. Connolly SA, Connolly LP, Drubach LA, et al. MRI for detection of abscess in acute osteomyelitis of the pelvis in children. *AJR*. 2007;189:867–872.
18. Bohndorf K. Infection of the appendicular skeleton. *Eur Radiol*. 2004;14:E53–E63.
19. McWilliams CA. Central bone abscess: Brodie's abscess; chronic suppurative osteomyelitis. *Ann Surg*. 1921;74(5):568–578.
20. Grey AC, Davies AM, Mangham DC, et al. The "penumbra sign" on T1-weighted MR imaging in subacute osteomyelitis: frequency, cause, and significance. *Clin Radiol*. 1998;53(8):587–592.
21. Erdman WA, Tamburro F, Jayson HT, et al. Osteomyelitis: characteristics and pitfalls of diagnosis with MRI. *Radiology*. 1991;180:533–539.
22. Rasool MN. Primary subacute haematogenous osteomyelitis in children. *J Bone Joint Surg Br*. 2001;83-B:93–98.
23. Jones HW, Harrison JW, Bates J, et al. Radiologic classification of chronic hematogenous osteomyelitis in children. *J Pediatr Orthop*. 2009;29(7):822–827.
24. Pineda C, Espinosa R, Pena A. Radiographic imaging in osteomyelitis: the role of plain radiography, computed tomography, ultrsonography, magnetic resonance imaging, and scintigraphy. *Semin Plast Surg*. 2009;23:80–89.
25. Courtney PM, Flynn JM, Jaramillo D, et al. Clinical indications for repeat MRI in children with acute hematogenous osteomyelitis. *J Pediatr Orthop*. 2010;30(8):883–887.
26. Fause SN, Clark J, Pallett A, et al. Managing bone and joint infection in children. *Arch Dis Child*. 2012;97:545–553.
27. Taylor MN, Chaudhuri R, Davis J, et al. Childhood osteomyelitis presenting as a pathological fracture. *Clin Radiol*. 2008;63:348–351.
28. Mantadakis E, Plessa E, Vouloumanou EK, et al. Deep venous thrombosis in children with musculoskeletal infections: the clinical evidence. *Int J Infect Dis*. 2012;16(4):e236–e243.
29. Lew DP, Waldvogel FA. Osteomyelitis. *Lancet*. 2004;364:369–379.
30. Hatzenbuehler J, Pulling TJ. Diagnosis and management of osteomyelitis. *Am Fam Physician*. 2011;84(9):1027–1033.
31. Offiah AC. Acute osteomyelitis, septic arthritis, and discitis: differences between neonates and older children. *Eur J Radiol*. 2006;60:221–232.
32. Winterstein AR, Bohndorf K, Vollert K, et al. Invasive aspergillosis osteomyelitis in children-a case report and review of the literature. *Skeletal Radiol*. 2010;39:827–831.
33. Canale ST, Manugian AH. Neonatal osteomyelitis of the os calcis: a complication of repeated heel punctures. *Clin Orthop Relat Res*. 1981;156:178–182.
34. Johnson DP, Hernanz-Schulman M, Martus JE, et al. Significance of epiphyseal enhancement defects in pediatric osteomyelitis identified by MRI with surgical correlation. *Pediatr Radiol*. 2011;41(3):355–361.
35. Browne LP, Guillerman RP, Orth RC, et al. Community-acquired staphylococcal musculoskeletal infection in infants and young children: necessity of contrast-enhanced MRI for the diagnosis of growth cartilage involvement. *AJR*. 2012;198:194–199.
36. Gamaletsou MN, Kontoyiannis DP, Sipsas NV, et al. Candida osteomyelitis: analysis of 207 pediatric and adult cases (1970-2011). *Clin Infect Dis*. 2012;55(10):1338–1351.
37. Moore RM, Green NE. Blastomycosis of bone. A report of six cases. *J Bone Joint Surg Am*. 1982;64(7):1097–1101.
38. Shikhare SN, Singh DR, Shimpi TR, et al. Tuberculous osteomyelitis and spondylodiscitis. *Semin in Musculoskeletal Radiology*. 2011;15(5):446–458.
39. Cremin BJ. Tuberculosis: the resurgence of our most lethal infectious disease: a review. *Pediatr Radiol*. 1995;25:620–625.
40. Teo HEL, Peh WCG. Skeletal tuberculosis in children. *Pediatr Radiol*. 2004;34:853–860.
41. Woon CY, Phoon ES, Lee JY, et al. Rice bodies, millet seeds, and melon seeds in tuberculous tenosynovitis of the hand and wrist. *Ann Plast Surg*. 2011;66(6):610–617. doi:10.1097/SAP.0b013e3181e35ca5.
42. Woods CR. Congenital syphilis-persisting pestilence. *Pediatr Infect Dis J*. 2009;28(6):536–537.
43. Coblentz DR, Cimini R, Mikity VG, et al. Roentgenographic diagnosis of congenital syphilis in the newborn. *JAMA*. 1970;212(6):1061–1064.
44. Fiser RH, Kaplan J, Holder JC. Congenital syphilis mimicking the battered child syndrome. How does one tell them apart? *Clin Pediatr*. 1972;11(5):305–307.
45. Fiumara NJ. Manifestations of late congenital syphilis: an analysis of 271 patients. *Arch Derm*. 1970;102:78–83.
46. Daldrup-Link HE, Steinbach L. MR imaging of pediatric arthritis. *Magn Reson Imaging Clin N Am*. 2009;17:451–467.
47. Kocher MS, Zurakowski D, Kasser JR. Differentiating between septic arthritis and transient synovitis of the hip in children: an evidence-based clinical prediction algorithm. *J Bone Joint Surg*. 1999;81-A(12):1662–1670.
48. Lim-Dunham JE, Ben-Ami TE, Yousefzadeh DK. Septic arthritis of the elbow in children: the role of sonography. *Pediatr Radiol*. 1995;25(7):556–559.
49. Zawin JK, Hoffer FA, Rand FF, et al. Joint effusion in children with an irritable hip: US diagnosis and aspiration. *Radiology*. 1993;187(2):459–463.
50. Zamzam MM. The role of ultrasound in differentiating septic arthritis from transient synovitis of the hip in children. *J Pediatr Orthop B*. 2006;15(6):418–422.
51. Chau CL, Griffith JF. Musculoskeletal infections: ultrasound appearances. *Clin Radiol*. 2005;60(2):149–159.
52. Strouse PJ, DiPietro MA, Adler RS. Pediatric hip effusions: evaluation with power Doppler sonography. *Radiology*. 1998;206(3):731–735.
53. Lee SK, Suh KJ, Kim YW, et al. Septic arthritis versus transient synovitis at MR imaging: preliminary assessment with signal intensity alterations in bone marrow. *Radiology*. 1999;211:459–465.
54. Graif M, Schweitzer ME, Deely D, et al. The septic versus nonseptic inflamed joint: MRI characteristics. *Skeletal Radiol*. 1999;28:616–620.
55. Monsalve J, Kan JH, Schallert EK, et al. Septic arthritis in children: frequency of coexisting unsuspected osteomyelitis and implications on imaging work-up and management. *AJR*. 2015;204(6):1289–1295.
56. Schallert EK, Kan JH, Monsalve J, et al. Metaphyseal osteomyelitis in children: how often does MRI-documented joint effusion or epiphyseal extension of edema indicate coexisting septic arthritis? *Pediatr Radiol*. 2015;45(8):1174–1181.
57. Nunn TR, Cheung WY, Rollinson PD. A prospective study of pyogenic sepsis of the hip in childhood. *J Bone Joint Surg*. 2007;89-B:100–106.

58. Faust SN, Clark J, Pallett A, et al. Managing bone and joint infection in children. *Arch Dis Child*. 2012;97:545–553.
59. Cowan MR, Primm PA, Scott SM, et al. Serious group A beta-hemolytic streptococcal infections complicating varicella. *Ann Emerg Med*. 1994;23(4):818–822.
60. Chiedozi LC. Pyomyositis: Review of 205 cases in 112 patients. *Am J Surg*. 1979;137(2):255–259.
61. Frank G, Mahoney HM, Eppes SC. Musculoskeletal infections in children. *Pediatr Clin N Am*. 2005;52:1083–1106.
62. Burton DJ, Enion D, Shaw DL. Pyomyositis of the piriformis muscle in a juvenile. *Ann R Coll Surg Engl*. 2005;87(1):W9–W12.
63. Tureck MB, Taljanovic MS, Stubbs AY, et al. Imaging of musculoskeletal soft tissue infections. *Skeletal Radiol*. 2010;39(10):957–971.
64. Gordon BA, Martinez S, Collins AJ. Pyomyositis: characteristics at CT and MR imaging. *Radiology*. 1995;197(1):279–286.
65. Karmazyn B, Loder RT, Kleiman MB, et al. The role of pelvic magnetic resonance in evaluating nonhip sources of infection in children with acute nontraumatic hip pain. *J Pediatr Orthop*. 2007;27(2):158–164.
66. Mitsionis GI, Manoudis GN, Lykissas MG, et al. Pyomyositis in children: early diagnosis and treatment. *J Pediatr Surg*. 2009;44(11):2173–2178.
67. Shirley R, Mackey S, Meagher P. Necrotising fasciitis: a sequelae of varicella zoster infection. *J Plast Reconstr Aesthet Surg*. 2011;64(1):123–127.
68. Kim KT, Kim YJ, Won Lee J, et al. Can necrotizing infectious fasciitis be differentiated from nonnecrotizing infectious fasciitis with MR imaging? *Radiology*. 2011;259(3):816–824.
69. Endorf FW, Garrison MM, Klein MB, et al. Characteristics, therapies, and outcome of children with necrotizing soft tissue infections. *Pediatr Infect Dis J*. 2012;31(3):221–223.

# 138 Soft Tissue and Bone Tumors

*Mahesh M. Thapa, Sue Creviston Kaste, and James S. Meyer*

## SOFT TISSUE TUMORS

### Overview

In general, clinical presentation and findings guide diagnostic imaging in the assessment of soft tissue neoplasms. In children with subtle masses, the primary objective of imaging is to confirm or exclude the presence of a mass. In children with obvious masses, imaging is performed to assess the local extent of the tumor, to provide a differential diagnosis, and to guide potential biopsy.

Most soft tissue tumors in children are benign.[1] When the mass is hard and fixed, conventional radiographs are often performed to determine whether an underlying bone lesion is present that is simulating, or is associated with, a soft tissue mass. Conventional radiographs may show secondary changes in the configuration of adjacent bones and may also reveal the presence of cortical bone erosion, periosteal reaction, and soft tissue calcifications. Occasionally, radiolucency indicates the presence of a fat-containing tumor.[1]

Superficial masses are often assessed by ultrasonography (US), a modality that is easily accessible, lacks ionizing radiation, and rarely requires sedation.[2] Color and spectral Doppler analysis can assess and characterize vascularity.

Nuclear medicine also plays a significant role in the assessment of soft tissue tumors. Many soft tissue sarcomas (STS) are detected by gallium-67 and thallium-201 scintigraphy.[3,4] Technetium-99m–methylene diphosphonate (99mTc-MDP) bone scintigraphy may be performed to identify local bone involvement and distant skeletal metastases. In addition, positron emission tomography (PET) and PET computed tomography (CT) are playing an increasing role in initial tumor assessment and evaluation of tumor response and recurrence.

With continuing advances in magnetic resonance imaging (MRI), the role of CT has become limited. CT offers similar but more detailed information than that provided by conventional radiographs. Two areas in which CT has a clear advantage over MRI are in the detection of calcification, such as in myositis ossificans, and when lesions are present along the anterior abdominal wall or chest, where artifact may significantly degrade MRI quality.[1] Also, CT of the lungs is usually performed to assess for metastatic disease.

MRI is the imaging study of choice for assessment of most soft tissue tumors. The superb soft tissue contrast and multiplanar images provide details on the tumor's extent and relationship to underlying anatomic structures.

Although MRI technology continues to evolve, the basic tenets of the MRI examination of a soft tissue tumor remain constant. First, quality images should cover the entire tumor, including its margins and important adjacent structures, and they should include any needle biopsy tracts that may have to be excised at the time of surgical resection. The area that contains the tumor should be imaged in at least two orthogonal planes. T1- and T2-weighted images should be obtained. Fat saturation is often added to confirm the presence of fat in a lesion and/or to highlight the presence of enhancement after intravenous gadolinium administration. Short-tau inversion recovery (STIR) sequences are also useful, because they inherently suppress signal from fat and do not require a homogeneous magnetic field. Gadolinium-enhanced T1-weighted images add information about tumor vascularity and are helpful in guiding percutaneous biopsy by differentiating viable tumor from areas of necrosis.[5] Cystic lesions may be identified by their lack of central enhancement.[6] MR angiography (MRA) is useful for characterizing tumor vascularity and for planning the optimal surgical approach when large vessels may be involved. Most soft tissue tumors have prolonged T1 and T2 signal characteristics.[7] The MRI signal characteristics of most soft tissue tumors are nonspecific and usually cannot predict histology nor can they differentiate between benign and malignant neoplasms. Biopsy is necessary for histologic diagnosis.

### Benign Soft Tissue Tumors

#### Desmoid Tumors

***Overview.*** Desmoid tumors, representing deep or aggressive fibromatosis, are rare mesenchymal neoplasms with a fibrotic texture.[8,9] Although distant metastases do not occur, these tumors are locally aggressive and can lead to significant morbidity and mortality. Desmoid tumors are slightly more common in females, with an incidence of 2 to 4 cases per million per year. The peak incidence is in the third and fourth decades of life.[10] When these tumors occur in younger patients, they tend to be more aggressive, with recurrence rates up to 87%.[11]

***Etiology.*** Desmoid tumors are classified into superficial and deep groups. Superficial tumors are usually small and slow growing, and deep lesions may occur in the abdomen or extraabdominally. In children, extraabdominal desmoid tumors are more common than the abdominal type. Most desmoid tumors in patients with Gardner syndrome are found in the abdomen. Extraabdominal desmoid tumors, also referred to as *aggressive fibromatosis*, are usually solitary and arise from the fascial sheaths and aponeuroses of striated muscle. In one series, head and neck, trunk, and extremity involvement was seen with approximately equal frequency.[12] Histologically, desmoid tumors consist of benign fibrous tissues that contain spindle cells and abundant collagen. Although they do not metastasize, desmoid tumors can infiltrate contiguous structures, including bone.

***Imaging.*** Desmoid tumors are variably echogenic on US, and their borders may be smooth or irregular. On contrast-enhanced CT, most appear more attenuated than striated muscle (Fig. 138.1). On MRI, these tumors may be nodular with infiltrative or well-defined margins. Tumors may be homogeneous or heterogeneous with varying signal characteristics. Some lesions are low signal on T1- and T2-weighted images, but more often tumors are heterogeneous and contain areas that are hyperintense to "fat" on T2-weighted images. On T1-weighted images, these masses contain areas that are hypointense, isointense, or slightly hyperintense when compared with muscle. This variability in signal reflects differences in the relative proportions of collagen, spindle cells, and mucopolysaccharides within the lesion (e-Fig. 138.2). On T2-weighted images, low signal generally reflects collagen, and high signal reflects a greater quantity of cellular tissue.[13] Tumors with high signal on T1-weighted images have been found to contain fat or myxoid material. Contrast enhancement may be

## Abstract:

There are a variety of musculoskeletal tumors, which occur in children. These include primary tumors of the bones and soft tissues and metastases. Imaging is essential in the detection these lesions, which may have characteristic features that allow for a definitive diagnosis without biopsy. Even when a definitive diagnosis cannot be made based upon imaging findings alone; imaging is essential to the workup and treatment planning of pediatric musculoskeletal tumors. This chapter reviews the radiographic, CT and MRI features of these tumors.

## Keywords:

Bone tumor
soft tissue tumor
osteosarcoma
Ewing sarcoma
rhabdomyosarcoma
synovial cell sarcoma
pediatric

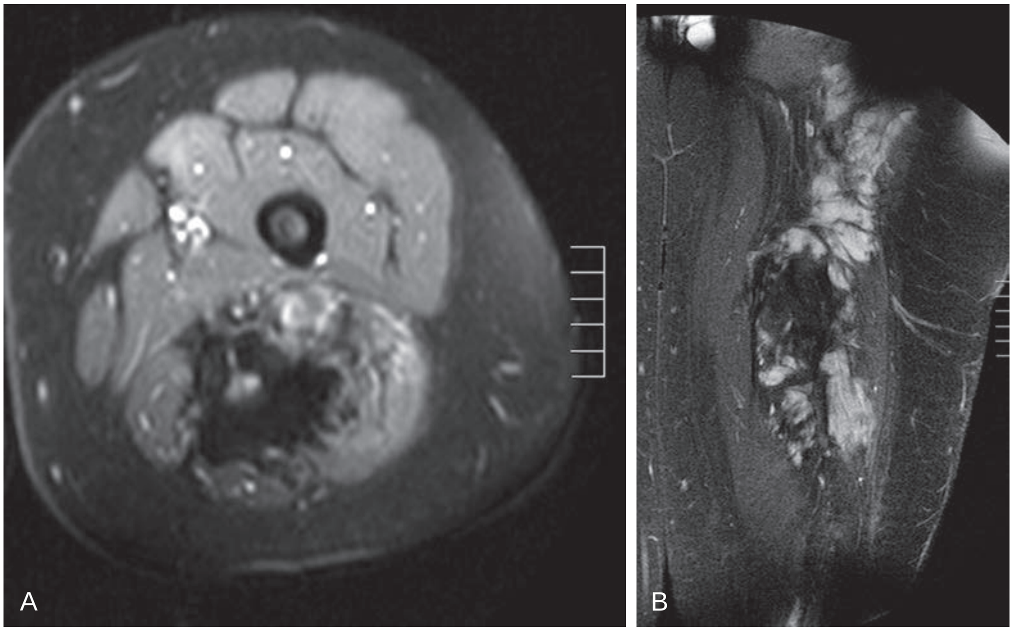

**e-Figure 138.2. Desmoid tumor in a 17-year-old boy.** (A) T2-weighted fat-saturated axial MR image demonstrates hyperintense and hypointense components of the mass in the posterior thigh. Hyperintense areas likely represent cellular-dominant components of the mass, whereas hypointense areas likely represent colloid components. (B) T1-weighted postgadolinium coronal image demonstrates heterogeneous enhancement of the mass.

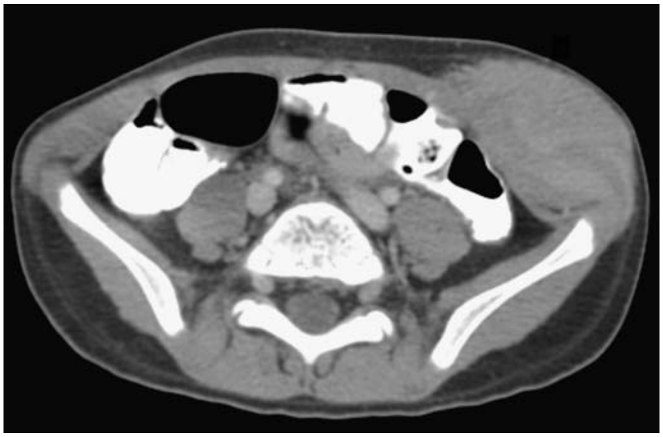

**Figure 138.1. Extraabdominal desmoid tumor (Gardner fibroma) in a 5-year-old girl.** Axial contrast-enhanced CT image shows a large lenticular-shaped mass originating in the anterior abdominal wall musculature.

homogeneous, heterogeneous, or absent and does not correlate with clinical outcome.[14]

A desmoid tumor may be prospectively suggested by the presence of areas of T2 hypointensity suggestive of collagen stroma within the mass, but biopsy is ultimately required for definitive diagnosis.

***Treatment.*** Stable asymptomatic desmoid tumors are often treated conservatively and observed for changes.[15] Symptomatic desmoids must be treated, and therapy often depends on anatomic location. If possible, surgical resection with wide margins is the treatment of choice.[10] However, recurrence is common (19%–77%) and is more frequent with extraabdominal desmoids (30%–50%) than with intraabdominal desmoids (15%–30%).[8,9,16] If surgery is not possible, systemic therapy should be considered. This is often the case when desmoids are associated with familial adenomatous polyposis or Gardner syndrome. These conditions increase the likelihood of postoperative complications such as hemorrhage, short-bowel syndrome, intestinal ischemia, obstruction, or fistula formation.[9,15] Nonsurgical treatment options include radiation and systemic therapy. Patients treated with chemotherapy have a lower incidence of tumor recurrence compared with those treated with radiation.[13]

## Infantile Myofibromatosis

Infantile myofibromatosis is the most common fibrous tumor of infancy. Tumors may involve skin, muscle, bone, or viscera and may be solitary (myofibroma) or multiple (myofibromatosis). Myofibromatosis occurs in children younger than 2 years of age. The prognosis of musculoskeletal lesions is excellent and spontaneous resolution usually occurs, although visceral involvement may portend a poorer prognosis. Lesions have a variable appearance on US and range from solid to anechoic centrally with a thick wall. On CT, myofibromas enhance to a lesser degree or similarly to muscle and often exhibit a peripheral rim of enhancement. On MRI, lesions are low signal on T1 weighting and usually high signal on T2 weighting. Some masses show decreased central signal on T2 weighting, likely due to collagen components. Enhancement of the fibrous and cellular components is seen with gadolinium administration (Fig. 138.3).[12,17–21] Osseous lesions tend to occur in the metaphysis and have a lytic appearance (Fig. 138.4).[20]

## Benign Peripheral Nerve Sheath Tumors

***Overview.*** Benign peripheral nerve sheath tumors are divided into schwannomas, also known as *neurinomas* and *neurilemomas*, and neurofibromas. Benign neurofibromas and, less commonly, schwannomas are frequently multiple and are associated with neurofibromatosis type 1 (NF1). However, both tumors may be solitary and may occur sporadically.

***Etiologies and Clinical Presentation.*** Schwannomas account for approximately 5% of all benign soft tissue neoplasms, and they are usually found as a solitary lesion in individuals between 20 and 50 years of age. Although they may occur virtually anywhere in the body, the head and neck, flexor surfaces of extremities (notably the ulnar and peroneal nerves), mediastinum, and retroperitoneum are the most commonly involved sites.[22] If the lesion is large, pain and neurologic symptoms may be clinical manifestations; otherwise, patients are usually asymptomatic.[23,24]

Neurofibromas may be localized, plexiform, or diffuse. The localized form accounts for 90% of cases and less often is associated with NF1, unlike the diffuse and plexiform subtypes.[22] *Localized neurofibromas* account for approximately 5% of all benign soft tissue tumors and are typically seen in younger patients between 20 and 30 years of age.[22] They often come to medical attention as a painless, slowly growing mass.[23]

Schwannomas and localized neurofibromas are similar histologically and are composed primarily of Schwann cells; therefore they exhibit similar imaging characteristics. Microscopic examination reveals a dense central core of Schwann cells surrounded by a peripheral zone of myxoid tissue. Peripheral nerve sheath tumors have a low incidence of malignant degeneration.[22]

***Imaging.*** A tumor can be suspected to have a neurogenic origin if it is located along the distribution of a peripheral nerve. Calcification in degenerating ("ancient") schwannomas may be visible radiographically; on bone scintigrams, these tumors have been observed to take up 99mTc-MDP.[25] Peripheral nerve sheath tumors may be accompanied by subtle atrophy of surrounding or distally innervated muscle. Most of these tumors are well-defined spherical or fusiform masses. On CT images, they tend to be hypoattenuated, possibly because of lipids in their Schwann cells, adipocytes, and perineural tissues.[26] On MRI, the bulk of the tumor shows low intensity on T1-weighted sequences and high intensity on T2-weighted sequences. Typically, the central zone consists of collagen and neurofibroma cells and is hypointense on T2-weighted images, lending a "target" appearance to the lesion that can also be seen on contrast-enhanced T1-weighted images; it is more easily appreciated when wide window settings are used to view the images. The presence of a target sign helps distinguish these benign tumors from their less well-organized malignant counterparts (Fig. 138.5).[27–30]

On MRI, differentiating a schwannoma from a neurofibroma can be difficult; however, schwannomas may contain more prominent areas of hemorrhage, cystic change, and necrosis with resultant heterogeneous signal intensities. In addition, neurofibromas intimately involve and are inseparable from the normal nerve. Schwannomas are eccentric to the nerve, which may be apparent on MRI in tumors that involve larger nerves. In smaller nerves, schwannomas may obliterate the nerve of origin and be indistinguishable from neurofibromas.[31]

*Plexiform neurofibromas* arise from the axis of a primary nerve and form tortuous, cordlike tumors along its axis. They are regarded as indicators of neurofibromatosis, even when they are the sole manifestation of the disease. Tumors tend to appear as lobulated, amorphous masses. Similar to solitary neurofibromas, these tumors are usually hyperintense on T2-weighted imaging and often have well-defined, central, tubular, hypointense structures, or they may form large masses that resemble a "bag of worms" on transverse images.[32]

*Diffuse neurofibromas* are uncommon and are often associated with NF1.[33] These lesions occur primarily in children and young adults and most commonly involve the head and neck regions. These ill-defined, infiltrative lesions tend to be located in the skin and subcutaneous tissues. They appear as linear or reticular strands

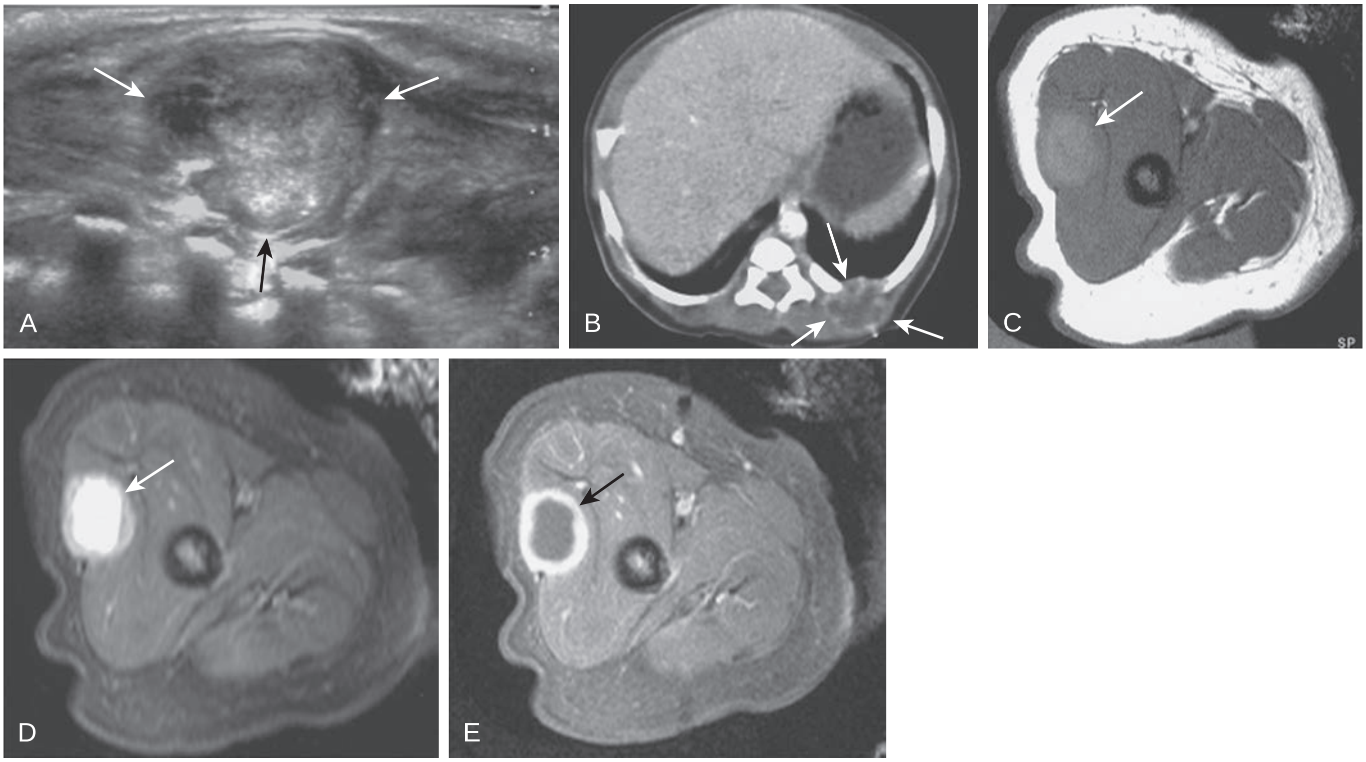

**Figure 138.3. Infantile myofibromatosis in a neonate.** (A) Ultrasound shows a solid, intramuscular subscapular mass *(arrows)*. (B) Axial contrast-enhanced CT image shows peripheral enhancement within the mass *(arrows)*. (C) Thigh lesion in the same patient shows hyperintense signal on T1-weighted MR imaging. (D) T2-weighted fat-saturated image demonstrates central increased signal intensity with a thick, irregular rind of soft tissue. (E) Postgadolinium T1-weighted fat-saturated images demonstrate enhancement of the rind of soft tissue and central areas of nonenhancement.

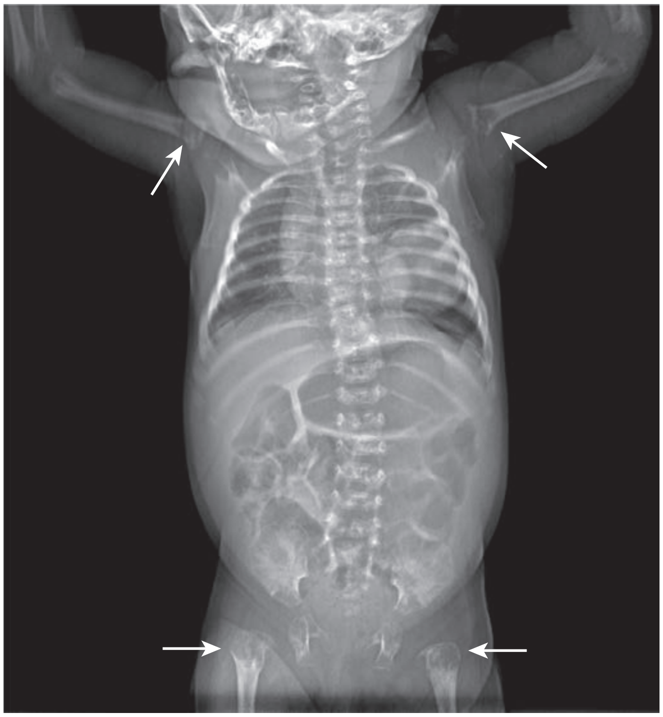

**Figure 138.4. Myofibromatosis.** Newborn girl with multifocal myofibromatosis with preferential involvement of metaphyses *(arrows)*.

of intermediate signal on T1-weighted and high signal intensity on T2-weighted images, with linear areas of enhancement after gadolinium administration.

## Benign Fatty Tumors

***Overview.*** The 2002 World Health Organization (WHO) Soft Tissue Tumor Classification includes nine types of benign fatty tumor: lipoma, lipomatosis, lipomatosis of nerve, lipoblastoma/lipoblastomatosis, angiolipoma, myolipoma of soft tissue, chondroid lipoma, spindle cell/pleomorphic lipoma, and hibernoma. Except for lipoblastoma, all of these tumors are more common in adults than in children.[24]

Lipoblastoma and lipoblastomatosis are benign mesenchymal tumors of immature fat that occur primarily in infants and young children, most often in boys younger than 8 years of age. The average age of patients at the time of presentation is 3.6 years.[34] Lipoblastomas are usually painless superficial tumors most commonly located in the extremities and the head and neck region, but they may also involve the trunk and deeper structures, such as the mediastinum, mesentery, and retroperitoneum. The tumor consists of lobules of immature adipose tissue with a variable amount of myxoid stroma separated by richly vascularized septa composed of connective tissue. The discrete form, *lipoblastoma*, is a well-circumscribed lesion that occurs in approximately 70% of cases and involves the superficial soft tissues. Lipoblastomas eventually evolve into mature lipomas. The term *lipoblastomatosis* refers to the diffuse type that often infiltrates adjacent deeper tissues, such as muscle, and has a tendency to recur locally[35]; spontaneous resolution has also been reported.[36,37]

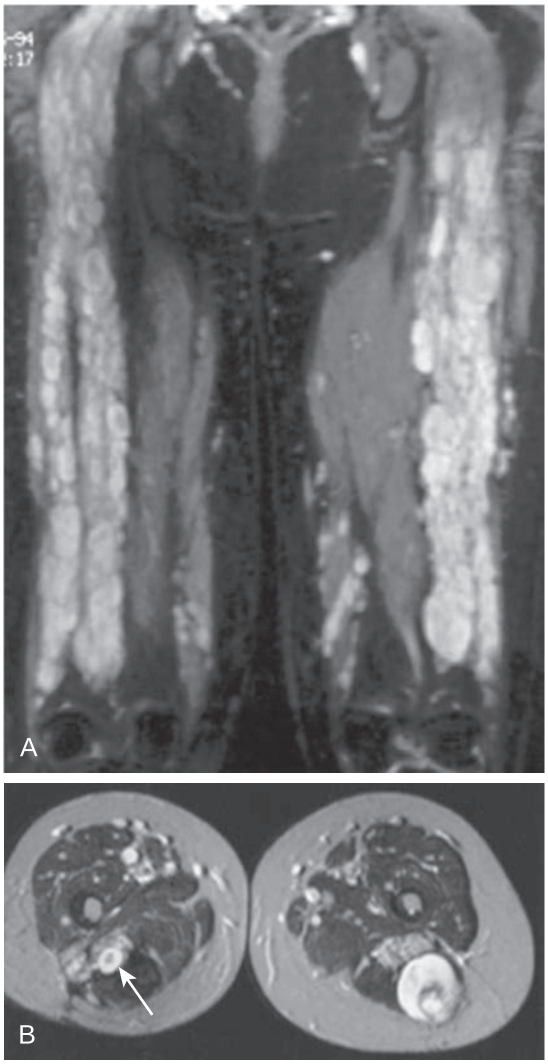

**Figure 138.5. Multiple neurofibromas and a malignant peripheral nerve sheath tumor in a young woman with NF-1.** (A) Coronal short-tau inversion recovery MR image of the thighs shows multiple plexiform neurofibromas distributed along the sciatic nerves. (B) Axial T2-weighted images show multiple, discrete, high-intensity neurofibromas. A characteristic target sign is evident *(arrow)*. The larger lesion in the posterior left thigh, which had shown recent growth, was a low-grade malignant peripheral nerve sheath tumor.

***Imaging.*** Imaging features reflect the amount of fatty tissue present. On US, hyperechoic fat can be clearly delineated from the myxoid component, and CT shows a similar combination of hypoattenuated fat and denser myxoid tissue. On MRI, the signal is often heterogeneous (e-Fig. 138.6) with lipomatous elements appearing hyperintense to muscle on T1-weighted images and isointense to subcutaneous fat on T2-weighted images; nonfatty tissues produce lower signal intensity than fat on T1-weighted images and are more intense than fat on T2-weighted images. In addition to low-signal myxoid components on T1 imaging, the fatty mass may contain low-signal fibrous septa that show contrast enhancement.[38–40]

The differential diagnosis includes lipoma; hibernoma, a rare tumor analogous to brown fat; and myxoid liposarcoma. However, liposarcoma is very rare in children younger than 10 years of age.[41] Thus a fat-containing tumor in a young child is much more likely to be a lipoblastoma.

***Treatment.*** The majority of fat-containing masses in children are benign. Although complete surgical resection is the treatment of choice for focal lesions,[34] subtotal resection may be considered, particularly when surgical resection may involve critical neurovascular structures, or when it may lead to significant cosmetic deformity.

## Malignant Soft Tissue Tumors

### Rhabdomyosarcoma

***Overview.*** The head and neck and genitourinary tract are the most frequent locations of rhabdomyosarcoma (RMS). About 20% of these tumors occur in the extremities. Most extremity RMS is of the alveolar or undifferentiated histologic types. The embryonal or botryoid types are found more often in the face, neck, and genitourinary system.[42] Prognosis is less favorable for patients with RMS of the extremities.[43] In the extremities, tumors tend to be deep and tend to spread along fascial planes and may cause erosion of adjacent bone.

***Etiologies, Pathophysiology, and Clinical Presentation.*** RMS contains a mixture of rhabdomyoblasts, which are recognized by their typical cross striations, and undifferentiated cells. These tumors are thought to arise from progenitor cells for striated muscle and can occur anywhere in the body, even in areas with no striated muscle. RMS accounts for more than 60% of STS in children younger than 5 years of age but only 25% of STS in those aged 15 to 19 years.[44]

***Imaging.*** Imaging is usually nonspecific but is essential for staging and surgical management. MRI has superseded CT and US in this clinical setting, because it can define the anatomic location of the tumor (unicompartmental vs. multicompartmental), indicate its relationship to important nerves and blood vessels, and reveal local involvement of bone or lymph nodes. MRI characteristics are nonspecific, and most tumors are predominantly low signal on T1-weighted images, high signal on T2-weighted images, and demonstrate central tumoral enhancement (Fig. 138.7). Only 15% to 20% of patients have clinically detectable metastases at presentation. The lungs, bone marrow, and bone are the most common sites of distant metastases. Lymph nodes may also be involved. Bone metastases resemble those that occur with neuroblastoma; they have been reported even in the absence of detectable primary tumor.

***Treatment.*** Even if not clinically detectable, all patients are considered to have micrometastatic disease; this has resulted in the universal use of chemotherapy. The 5-year survival rate for children with RMS has improved from 55% in the 1970s to more than 70% currently.[45]

### Peripheral Primitive Neuroectodermal Tumor and Extraosseous Ewing Sarcoma

***Overview.*** Peripheral primitive neuroectodermal tumor (PPNET) and extraosseous Ewing sarcoma (EOES) are small round cell neoplasms that belong to the Ewing sarcoma family of tumors; they can arise in both soft tissue and bone. These neoplasms are related histogenetically and share a common cytogenetic characteristic, the translocation of bands 24 and 12 of the short arms of chromosomes 11 and 22. They are often indistinguishable histologically. Also known as *peripheral neuroepithelioma*, PPNETs have a higher degree of neural differentiation than is seen with Ewing sarcoma; thus these two tumors can be distinguished on the basis of immunohistochemical markers. This distinction is important, because disease-free survival is poorer for patients with PPNET than for those with EOES.[46,47]

***Etiologies, Pathophysiology, and Clinical Presentation.*** Both tumors occur most commonly in truncal and paravertebral soft tissues (50%–60% of cases) and in the extremities (25% of cases).

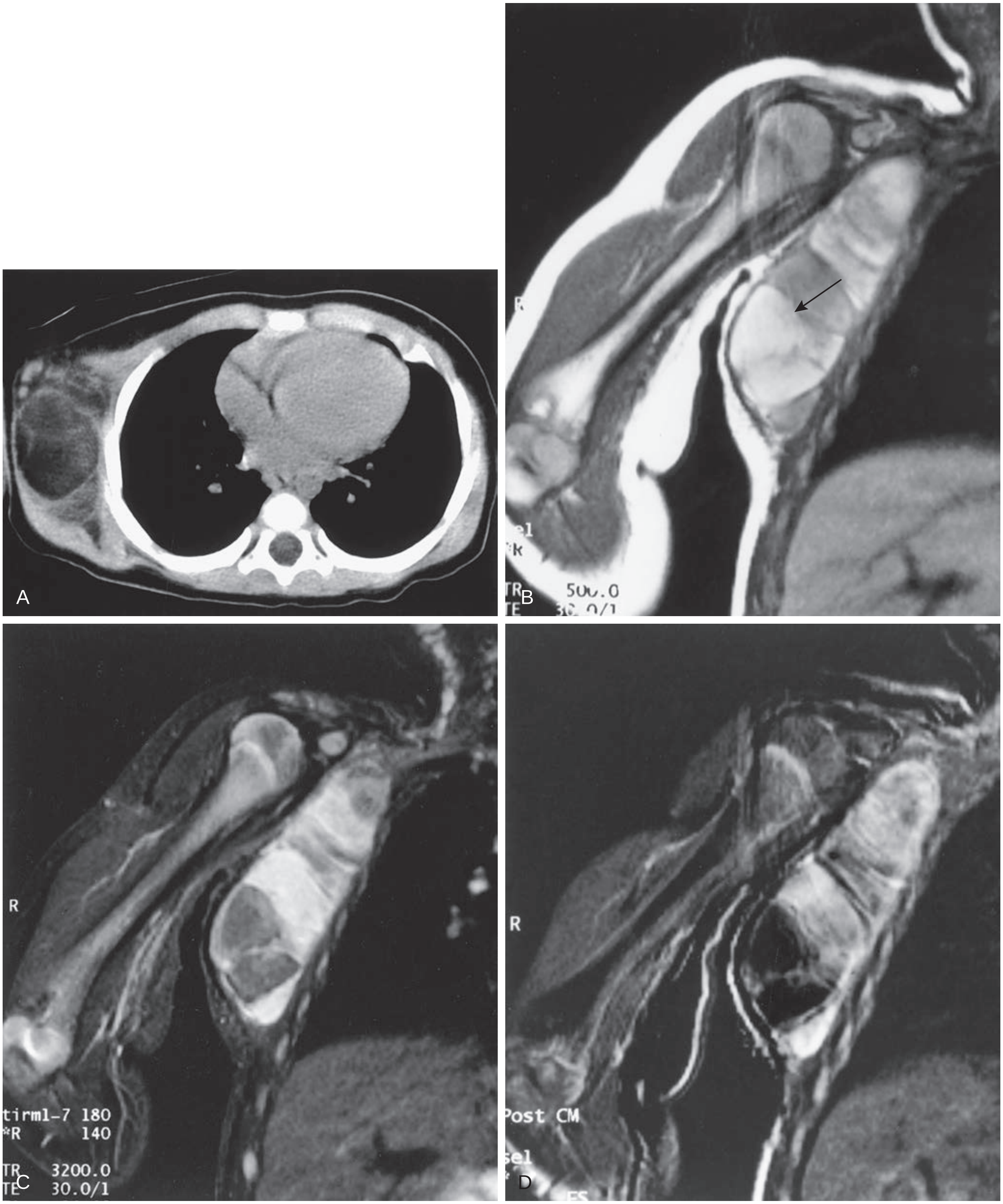

**e-Figure 138.6. Lipoblastoma in a 5-month-old.** (A) CT image of the chest of shows a low-attenuation mass in the right axilla. (B) Coronal T1-weighted MR image shows the inferior portion of the mass *(arrow)* is markedly hyperintense as a result of adipose tissue. The low signal in this portion of the mass shown in short-tau inversion recovery (C) and fat-suppressed contrast-enhanced T1-weighted (D) images is also characteristic of fat. Note exuberant enhancement of the superior half of the solid mass (D).

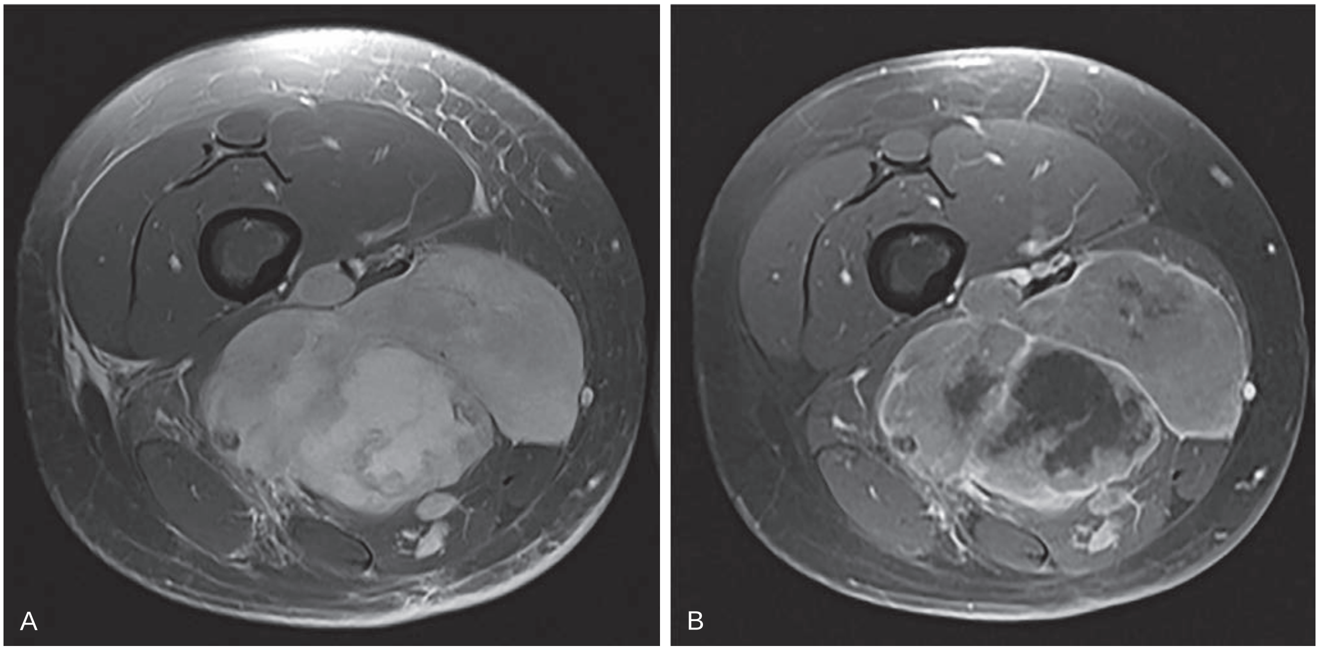

**Figure 138.7. Alveolar rhabdomyosarcoma of the thigh in an 16-year-old girl.** (A) T2-weighted fat-suppressed axial MR image demonstrates a multilobulated, hyperintense intramuscular mass. (B) Postgadolinium T1-weighted fat-suppressed axial MR image demonstrates predominantly diffuse tumoral enhancement of the mass with areas of necrosis.

PPNET occurs less commonly in the extremities than does EOES, and patients with EOES are generally younger. Askin tumors are thoracic PPNETs that involve the chest wall.[48] These tumors can be very large at the time of presentation and tend to be poorly circumscribed. They typically do not calcify but may erode adjacent bone.

***Imaging.*** On MRI, these tumors have a nonspecific imaging appearance. PPNET and EOES are typically isointense to muscle on T1-weighted images and inhomogeneously hyperintense on T2-weighted and STIR images; they show variable contrast enhancement. When these lesions outgrow their blood supply or, alternatively, when masses hemorrhage spontaneously or after minor trauma, cystic components may be seen; these lesions may superficially mimic a hematoma (Fig. 138.8). Postcontrast imaging is helpful in these circumstances to help identify solid soft tissue components and guide biopsy of viable tumor cells. Distant spread occurs to bone, lung, liver, and brain.[49,50]

***Treatment.*** Treatment is dictated by location and extent of disease and may involve surgery for localized disease with or without adjuvant/neoadjuvant chemoradiotherapy.[51]

## Synovial Sarcoma

***Overview, Etiologies, Pathophysiology, and Clinical Presentation.*** Synovial sarcomas predominantly occur in adults younger than 50 years of age, but they account for about 10% of pediatric STS. These tumors arise from undifferentiated mesenchymal cells, not from true synovial cells. A monophasic variety comprises spindle cells, and a biphasic variety consists of spindle cells and epithelial elements. Although synovial sarcomas often occur close to joints, tendons, and bursae, they are rarely intraarticular.[52] About 80% of synovial sarcomas occur in the extremities, and considerably more lower than upper extremity involvement has been noted. Synovial sarcomas may spread to regional lymph nodes, and the lungs are the most common sites of distant metastasis.[53]

***Imaging.*** Radiographically visible calcifications are present in 30% of cases. On MRI, synovial sarcomas are often lobulated, well-defined, deep-seated lesions, although they may be infiltrative and can encase major blood vessels. Femoral vein invasion has been described, and erosion of the cortex of adjacent bones is present in up to 20% of patients.

MRI signal characteristics are nonspecific. Synovial sarcomas are usually isointense to muscle on T1-weighted images. Foci of high T1-weighted signal may be present, and fluid-fluid levels are caused by hemorrhage; tumors generally have heterogeneous signal with areas of high intensity on T2-weighted images (Fig. 138.9). In one large series, 35% of tumors showed a triple-signal pattern on T2-weighted images; these findings are consistent with high (fluid)-signal intensity, intermediate-signal intensity similar to that of fat, and low-signal intensity resembling that of fibrous tissue (Fig. 138.9B).[54] A multilocular appearance with fluid-fluid levels may be seen in 18% to 25% of these tumors. Some synovial sarcomas may appear predominately cystic (e-Fig. 138.10), particularly on T2-weighted images, which could be confused with a ganglion. Postcontrast images can help identify solid components. As a rule of thumb, a diagnosis of ganglion should only be considered when a fluid-filled neck can be seen extending from the lesion to a joint or tendon sheath, and no solid components lie within the lesion. Otherwise, a diagnosis of neoplasm should be favored, with biopsy recommended.[54–57]

***Treatment.*** The treatment of choice is surgery with or without adjuvant and neoadjuvant chemotherapy. A recent multicenter study of patients under 20 years of age with a minimum of 10 years of follow-up found that wide surgical resection is the most efficacious method of treatment. Presence of tumor in the trunk and high histologic grade were negative factors for recurrence-free and metastasis-free survival.[58]

## Malignant Peripheral Nerve Sheath Tumor

***Overview.*** *Malignant peripheral nerve sheath tumor* (MPNST) is the accepted name for a spindle cell sarcoma that arises from a nerve or a neurofibroma. In contrast to other STS of mesenchymal cell origin, MPNSTs are of neuroectodermal origin. The MPNST

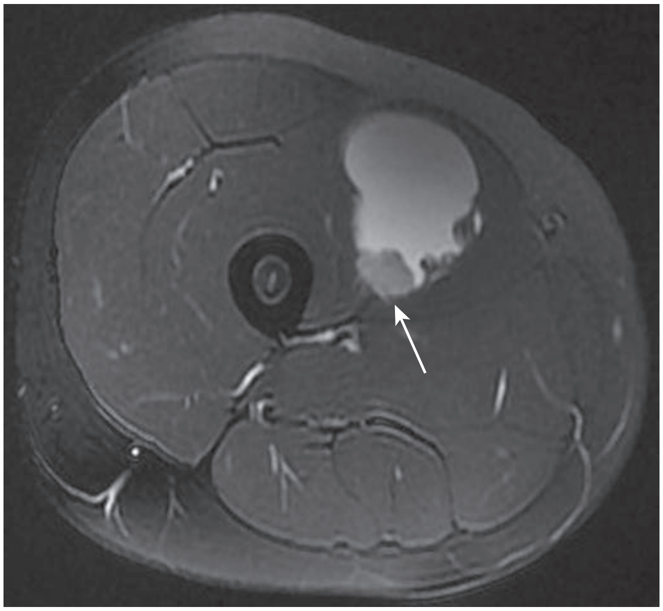

**e-Figure 138.10. Synovial sarcoma in a 17-year-old girl.** T2-weighted fat-saturated axial MR image demonstrates a cystic mass with solid soft tissue elements posteriorly *(arrow)*.

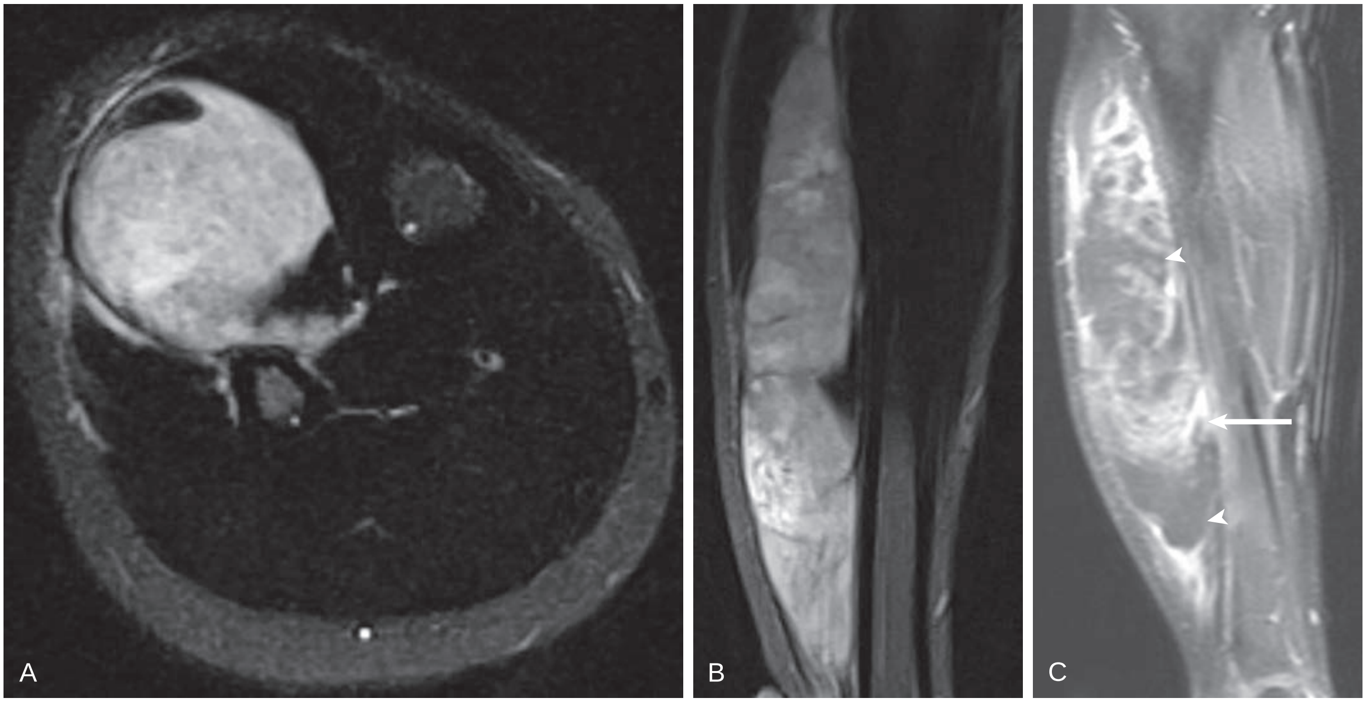

**Figure 138.8. Primitive neuroectodermal tumor in a 12-year-old boy.** Short-tau inversion recovery axial (A) and coronal (B) MR images demonstrate an extraosseous mass in the anterior leg with peritumoral edema. (C) Postgadolinium T1-weighted fat-saturated coronal MR image demonstrates cystic nonenhancing components of the tumor *(arrowheads)* and solid enhancing components *(arrow)*.

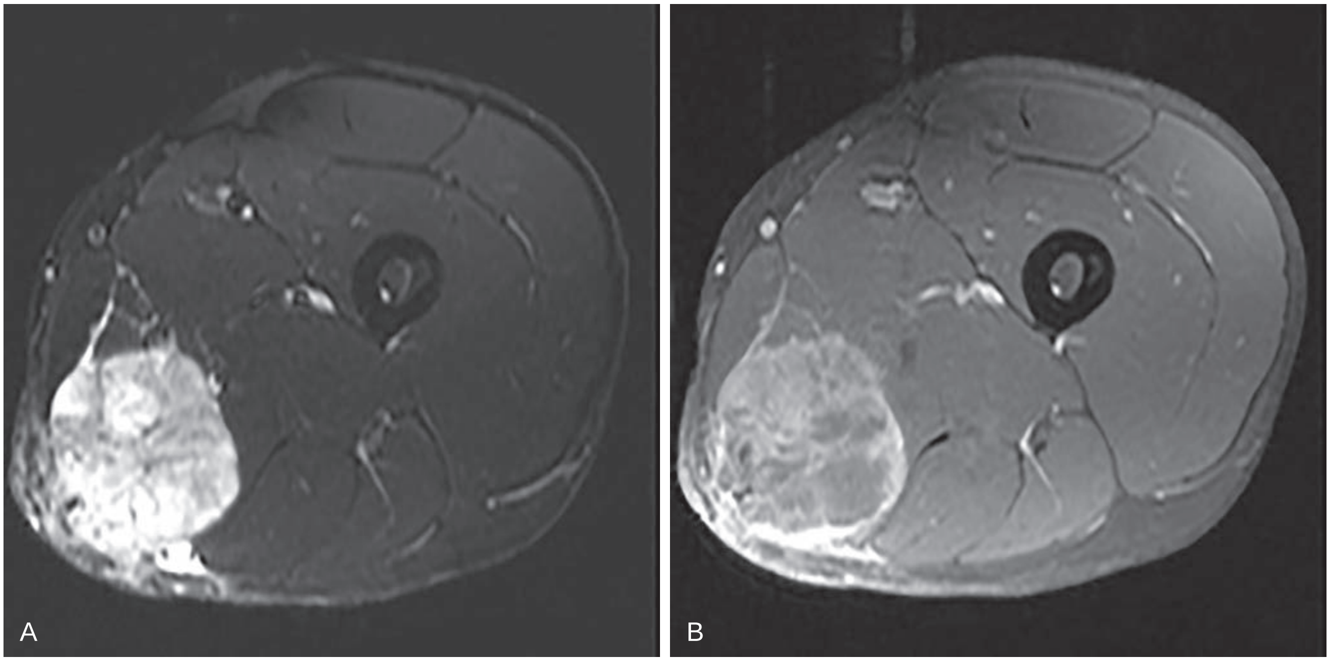

**Figure 138.9. Synovial sarcoma in a 16-year-old boy.** (A) Transverse STIR MR image shows a mixed intermediate and high signal intensity mass in the posterior thigh musculature and adjacent subcutaneous tissues. (B) A transverse T1-weighted fat-saturated MR image at the same level shows heterogeneous enhancement.

designation has replaced many formerly used terms, including *malignant schwannoma*, *neurofibrosarcoma*, *neurogenic sarcoma*, and *malignant neural neoplasm*. A variant of MPNST is the so-called triton tumor (named after a salamander) that contains neural and rhabdomyosarcomatous elements.[22]

***Etiologies, Pathophysiology, and Clinical Presentation.*** MPNST accounts for about 4% to 10% of STS and is the most common malignancy associated with NF1. Half of these tumors occur in patients with NF1; conversely, 2% to 29% of patients with NF1 develop MPNSTs—a much higher incidence than is seen in the general population. MPNST patients with NF1 are usually younger than those without associated NF1. Furthermore, in patients with NF1, MPNSTs tend to arise in preexisting benign neurofibromas; they are high-grade tumors that have a tendency to recur locally and metastasize. MPNSTs may also arise at previously irradiated sites.[31]

***Imaging.*** Similar to benign neurofibromas, MPNSTs are deep soft tissue lesions that are often associated with primary nerves, especially those of the thigh and lower extremities. CT and MRI appearance is nonspecific. Tumors may be well or poorly defined, homogeneous or inhomogeneous, and they occasionally erode bone. Malignant transformation of benign neurofibromas should be considered in patients in whom the mass is painful or enlarging, or when the typical target appearance of a benign neurofibroma is absent (see Fig. 138.5). Fluorodeoxyglucose (FDG) PET/CT may be helpful in detecting transformation of a neurofibroma to MPNST. A lesion with an SUVmax greater than or equal to 3.5, while nonspecific, raises concern for malignant transformation.[59]

***Treatment.*** Surgical resection with or without adjuvant and neoadjuvant chemoradiotherapy is used for treatment, depending on the tumor's location.

### Infantile Fibrosarcoma

***Overview, Etiologies, Pathophysiology, and Clinical Presentation.*** Infantile fibrosarcoma is an uncommon tumor that contains fibroblasts and myoblasts and occurs in young children, especially in the first 3 months of life.[60] This tumor is now considered a low-grade malignancy, in distinction from an adult-type fibrosarcoma that occurs in older children (10–15 years of age) and is more aggressive. Clinically, infantile fibrosarcomas present as enlarging, sometimes painful masses. Tumors often occur in the distal ends of the extremities and occasionally in the head, neck, and trunk. Because of their high degree of vascularization, they may be confused with hemangiomas on physical and imaging examinations.[61] These tumors may erode adjacent bone, and angiographic studies may reveal tumor vasculature.[62,63]

***Imaging.*** Because these masses are often present during fetal life, extensive remodeling of adjacent bones may occur (e-Fig. 138.11). MRI characteristics are nonspecific. Fibrosarcomas are usually isointense to muscle on T1-weighted images and are hyperintense on T2-weighted images. They may contain hypointense foci, which correlate with fibrosis.[64]

***Treatment.*** These tumors recur in up to 30% of cases, and metastases occur in about 5%.[65,66] Infantile fibrosarcoma has an excellent prognosis, with 5-year survival up to 84%.[67]

### Dermatofibrosarcoma Protuberans

***Overview, Etiologies, Pathophysiology, and Clinical Presentation.*** *Dermatofibrosarcoma protuberans* is an intermediate-grade malignancy that involves the dermis. This tumor is most often seen in adults; it occurs rarely in children but may be seen at birth. It most commonly appears as a red-blue or pink plaque that grows slowly and may become nodular. A less common atrophic variant occurs as a depressed plaque. Lesions are typically fixed to the dermis but may extend into the underlying tissues. Lesions frequently recur locally, and metastasis occurs in 1% to 6% of patients; 75% of metastases occur in the lungs.[68,69]

***Imaging.*** MRI is useful for determining the extent of disease, especially with deep tumor invasion. MRI characteristics are nonspecific. On T1-weighted images, lesions are hypointense to fat and may be isointense, hyperintense, or slightly hypointense to muscle. On T2-weighted images, lesions are isointense or hyperintense to fat. Lesions can enhance after gadolinium administration. On MRI, these tumors may be confused with subcutaneous granuloma annulare, a benign localized inflammatory dermatosis that occurs in children.[70]

***Therapy.*** Treatment involves surgical resection with or without adjuvant and neoadjuvant chemoradiotherapy. One review found that the presence of metastasis had an overall decreased patient survival rate, and those with fibrosarcomatous change or acral location had a decreased disease-free interval despite wide local resection.[71]

### Malignant Fibrous Histiocytoma

The 2002 WHO Soft Tissue Tumor Classification has changed the designation of *malignant fibrous histiocytoma* (MFH). As a result, many lesions that had been regarded as MFH will be classified as other entities. MFH rarely occurs in children.[72-74]

## Disseminated Disease of Soft Tissues

### Lymphoma

***Overview, Etiologies, Pathophysiology, and Clinical Presentation.*** Muscle involvement by non-Hodgkin lymphoma (NHL) is usually due to metastatic spread via lymphatic and hematogenous routes; however, it may be the result of direct extension from primary bone lymphoma. Much less commonly, muscle lymphoma occurs as a primary extranodal tumor. The disease can cross compartmental boundaries, or it may invade subcutaneous tissues. Involvement of adjacent bone and bone marrow may occur. Primary T-cell lymphoma of the skin is referred to as *mycosis fungoides*. Typical findings include focal thickening caused by dermal and epidural infiltrates and lymphadenopathy in advanced-stage disease.[75]

***Imaging.*** Muscle involvement results in solitary or multiple masses detectable on CT, MRI, and FDG-PET. On CT, affected muscles appear diffusely enlarged with or without obliteration of normal fat planes. The tumor may be poorly defined, and its attenuation is equal to or slightly less than that of normal muscle on contrast-enhanced and noncontrast CT images. On MRI, masses are isointense or slightly hypointense to normal muscle on T1-weighted images; they are hyperintense on T2-weighted and STIR images, and enhance inhomogeneously (e-Fig. 138.12). Increased activity on FDG-PET scans correlates well with MRI findings.[76-78]

### Granulocytic Sarcoma

***Overview, Etiologies, Pathophysiology, and Clinical Presentation.*** *Granulocytic sarcoma* is a rare solid tumor of primitive precursors of white blood cells and is also known as *chloroma* and *extramedullary myeloblastoma*. It occurs in patients with acute and chronic myelogenous leukemia and other myeloproliferative diseases. Children are more often affected than adults, and 60% of these tumors occur in children younger than 15 years of age.[79]

***Imaging.*** Chloromas may be solitary or multiple, and they can involve any part of the body, including the brain and muscles. Orbits and subcutaneous tissues, however, are the most common sites (see Chapter 7). These tumors are typically isoattenuating to slightly hyperattenuating to muscle on noncontrast CT and hyperattenuating to muscle on contrast CT. On MRI, lesions are typically isointense to muscle on T1-weighted images and hyperintense to muscle on T2-weighted images. Tumors usually enhance after gadolinium administration.[80–82]

### Metastases

Subcutaneous tissues and muscles may be involved in metastatic lesions. Neuroblastoma, in particular, may metastasize to the skin, subcutaneous tissue, or muscle (Fig. 138.13). Despite its large volume, muscle is not a frequent site for metastatic disease. On

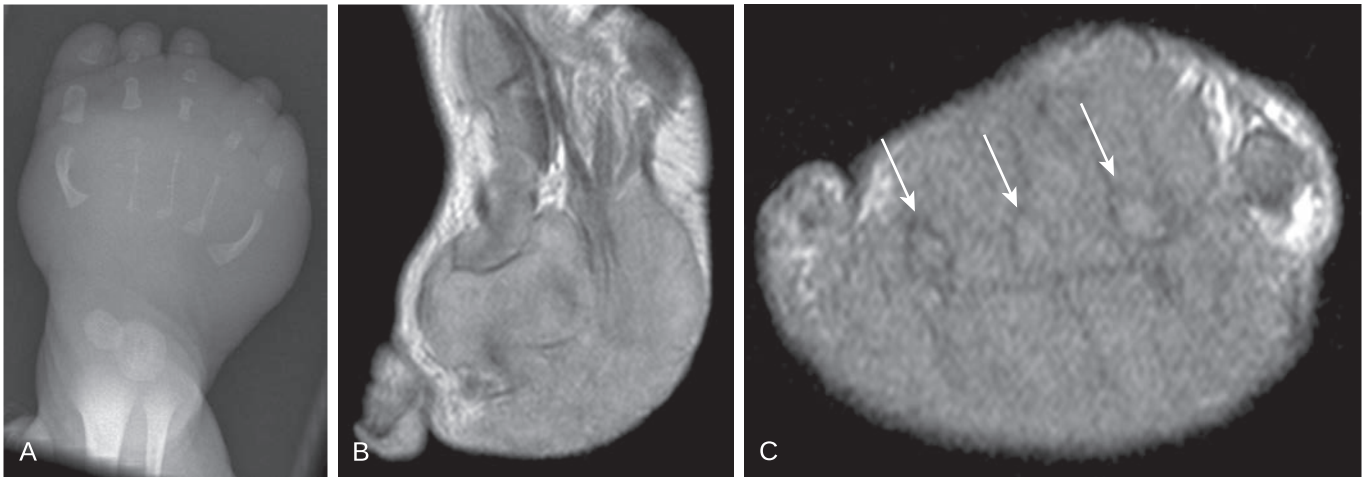

**e-Figure 138.11. Infantile fibrosarcoma with rhabdoid elements in a 1-week-old boy.** (A) Anteroposterior radiograph of the foot demonstrates gracile metatarsal bones and a large soft tissue density mass. T1 sagittal (B) and T1 short-axis (C) MR images demonstrate a large multicompartment soft tissue mass enveloping metatarsal bones *(arrows)*.

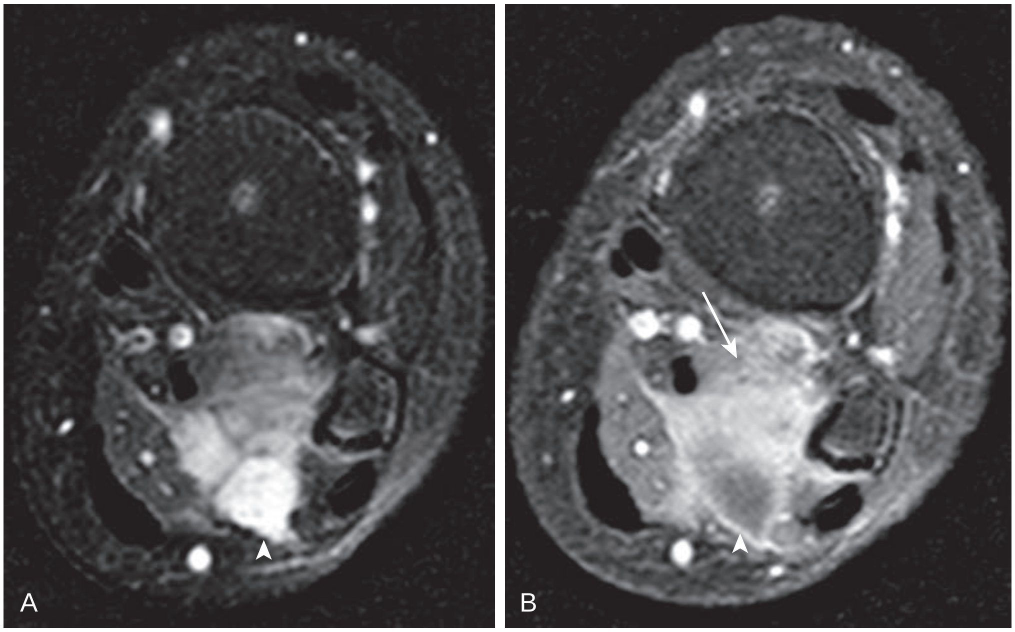

**e-Figure 138.12. Extranodal non-Hodgkin lymphoma of calf muscle in a child.** (A) T2-weighted fat-saturated axial MR image shows multicompartment involvement of the soleus and popliteus muscle. (B) Posterior cystic components *(arrowhead)* do not enhance after contrast. Solid enhancing components are noted in the anterior aspect of the mass *(arrow)*.

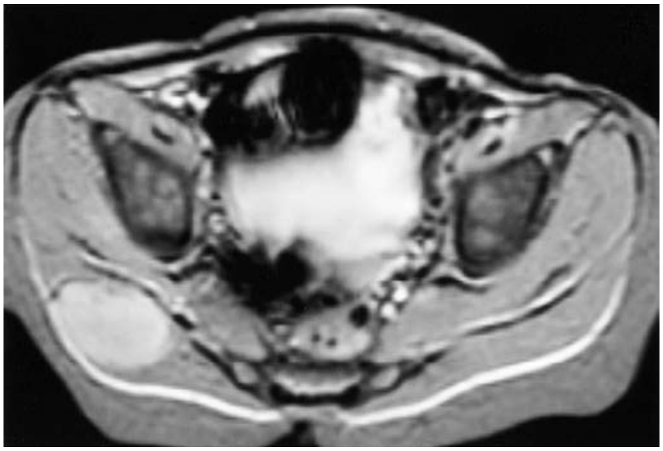

**Figure 138.13. Neuroblastoma metastasis.** Axial T2-weighted MR image of the pelvis of a 2-year-old girl with stage IV neuroblastoma shows a large metastasis in the right gluteal muscle.

CT, muscle metastases produce low-attenuation masses with loss of normal muscle planes. On MRI, metastases are similar in intensity to muscle on T1-weighted images and are hyperintense on T2-weighted images. Postcontrast images typically show enhancement with or without areas of necrosis.[83,84]

## BONE TUMORS

### Radiographic Evaluation of Bone Tumors

The initial mode of imaging of bone tumors is radiography. Radiographs serve to confirm the presence and site of a tumor, assist in the formulation of differential diagnoses, characterize the tumor, and guide in the selection of further imaging.[85,86] The decision to obtain radiographs is a clinical one, based on presentation, history, physical examination, and occasionally on laboratory tests. The differential diagnosis of a pediatric bone tumor can be narrowed down by asking a few simple questions.

#### How Old Is the Child?

Most bone tumors have a proclivity to occur within a certain age range. The differential diagnosis of a bone tumor in a 1-year-old infant is much different than that of a 16-year-old teenager or a 5-year-old child. Box 138.1 lists common pediatric bone tumors in accordance with the peak age at which they most commonly occur.[87–89]

#### What Is the Location of the Lesion? What Bone? What Part of the Bone?

Many bone tumors have a proclivity to affect certain bones within the skeleton or to occur at certain locations within a bone. Box 138.2 lists common pediatric bone tumors according to their preferred location in growing long bones. Lesions also vary in their centricity relative to the involved bone. Some tumors, such as a simple bone cyst, are central, whereas others are eccentric within bone (nonossifying fibroma) or juxtacortical (osteochondroma, periosteal osteosarcoma).[87,88,90]

#### Is the Lesion Unifocal or Multifocal?

Some lesions are always solitary, and others are usually multifocal. Some may be solitary or multifocal, although multifocal disease often implies a systemic disease or an underlying syndrome predisposing the patient to the development of a particular type of bone tumor. Box 138.3 lists common pediatric bone tumors that are multifocal.

**BOX 138.1** Pediatric Bone Tumors: Peak Age of Occurrence

**INFANT AND TODDLER (≤5 YEARS)**

Infantile myofibromatosis
Leukemia
Langerhans cell histiocytosis (multifocal)
Metastatic neuroblastoma
Osteofibrous dysplasia

**CHILD (5–10 YEARS)**

Ewing sarcoma of long bone
Langerhans cell histiocytosis (unifocal)

**ADOLESCENT (10–20 YEARS)**

Aneurysmal bone cyst
Chondroblastoma
Chondromyxoid fibroma
Ewing sarcoma of axial skeleton
Fibrous dysplasia
Osteochondroma
Leukemia (second peak)
Nonossifying fibroma/fibrous cortical defect
Osteoblastoma
Osteoid osteoma
Osteosarcoma
Periosteal chondroma
Primary lymphoma of bone
Simple bone cyst

**ADULT**

Adamantinoma
Enchondroma
Giant cell tumor (rare until physes fuse)
Parosteal osteosarcoma
Periosteal osteosarcoma

#### Is the Lesion Aggressive or Nonaggressive in Appearance?

In general, unlike malignant lesions, benign lesions have a nonaggressive radiographic appearance. However, exceptions are common, and some lesions may have both aggressive and nonaggressive features. Box 138.4 lists lesions covered in this chapter by their characteristic radiographic appearance—aggressive, nonaggressive, or indeterminate.

Radiographic features of a nonaggressive bone tumor are well-defined margins with a narrow zone of transition, particularly with sclerosis; expansion of bone contour from slow growth; smooth, single-layered periosteal new bone; and absence of an associated soft tissue mass. Radiographic features of an aggressive bone tumor are poorly defined margins with a wide zone of transition, permeative or "moth-eaten" bone destruction, frank destruction of bone without remodeling, aggressive forms of periosteal new bone, interrupted periosteal new bone, and the presence of an associated soft tissue mass. Aggressive forms of periosteal reaction include layering, or "onionskin," and "hair-on-end" periosteal new bone. Interrupted periosteal new bone may take the form of a Codman triangle, a sign of an aggressive process.[91]

By answering the aforementioned four questions, the radiologist can often narrow the differential and sometimes arrive at a single diagnosis. Most significant is the distinction between an aggressive and nonaggressive lesion; this is of major importance in guiding further imaging and initial therapy.

### BOX 138.2 Pediatric Bone Tumors: Location in Long Bones

**EPIPHYSIS**

- Chondroblastoma
- Giant cell tumor (after physeal fusion)
- Langerhans cell histiocytosis

**METAPHYSIS**

- Aneurysmal bone cyst
- Chondromyxoid fibroma
- Enchondroma
- Leukemia
- Metastases
- Nonossifying fibroma/fibrous cortical defect*
- Osteochondroma*
- Osteoid osteoma
- Osteosarcoma
- Parosteal osteosarcoma
- Simple bone cyst*

**DIAPHYSIS**

- Adamantinoma
- Ewing sarcoma/primitive neuroectodermal tumor
- Fibrous dysplasia
- Nonossifying fibroma/fibrous cortical defect (in older patients)*
- Osteochondroma (in older patients)*
- Osteofibrous dysplasia
- Osteoid osteoma
- Periosteal osteosarcoma
- Simple bone cyst (in older patients)*

*Osteochondromas, nonossifying fibromas/fibrous cortical defects, and simple bone cysts begin in the metaphyses. With maturation, these lesions may "migrate" into metadiaphysis and diaphysis.

### BOX 138.3 Pediatric Bone Tumors: Multifocal Lesions

- Brown tumors (hyperparathyroidism)
- Cystic angiomatosis/lymphangiomatosis
- Enchondroma (Ollier disease, Maffucci syndrome)
- Fibrous dysplasia (McCune–Albright syndrome)
- Infantile myofibromatosis
- Langerhans cell histiocytosis
- Leukemia
- Metastases (i.e., from neuroblastoma)
- Multifocal osteosarcoma
- Nonossifying fibromas/fibrous cortical defects
- Osteochondroma (oteochondromatosis)

### BOX 138.4 Pediatric Bone Tumors: Aggressive Versus Nonaggressive Radiographic Appearance*

**NONAGGRESSIVE**

- Aneurysmal bone cyst
- Chondroblastoma
- Chondromyxoid fibroma
- Enchondroma
- Fibrous dysplasia
- Nonossifying fibroma/fibrous cortical defect
- Osteoblastoma
- Osteoid osteoma
- Osteochondroma
- Simple bone cyst

**INDETERMINATE**

- Adamantinoma
- Desmoplastic fibroma
- Giant cell tumor
- Langerhans cell histiocytosis
- Osteofibrous dysplasia

**AGGRESSIVE**

- Ewing sarcoma/primitive neuroectodermal tumor
- Leukemia
- Lymphoma
- Metastases
- Osteoblastoma (aggressive form)
- Osteosarcoma

*Lesions are listed based on their most common radiographic presentations. With some lesions, variation from the norm is common.

Some benign bone tumors are adequately defined by radiography and do not require any further imaging for diagnosis or treatment. Most bone tumors, however, do require additional imaging; this may take the form of CT, MRI, scintigraphy, PET scanning, and rarely even US. The choice of imaging for a given tumor depends on the differential diagnostic considerations, possible treatment options, and whether the lesion is aggressive or nonaggressive. MRI is usually the preferred modality in the delineation of aggressive and suspected malignant lesions, and radiographs followed by MRI adequately define most bone lesions. As opposed to radiography, on MRI an aggressive lesion may have a well-defined margin, particularly with T1 weighting. Although MR is also very good at delineating nonaggressive and likely benign lesions, CT is better able to delineate ossified bone and thus occasionally may better define the characteristics and anatomy of some lesions. Image-guided biopsy has become a viable option to determine or confirm the diagnosis of many bone lesions. CT, US, fluoroscopy, and even MRI may be used for guidance.[92–96]

## Benign Bone Tumors

The vast majority of pediatric bone tumors are benign. It is important that radiologists recognize the typical benign tumors to avoid unnecessary diagnostic procedures. The differentiation of a nonaggressive lesion from an aggressive lesion will significantly affect the course of subsequent imaging evaluations, the approach to biopsy, and the preliminary choice of definitive treatment.

### Cartilaginous Tumors

#### Osteochondroma (Exostosis)

***Overview, Etiologies, Pathophysiology, and Clinical Presentation.*** Rather than a true tumor, osteochondromas are thought to be a developmental defect of growing bone in which an injury to the perichondrium causes bone growth in an aberrant direction. It is theorized that islets of cartilage from the physis are displaced along the metaphyseal surface and then grow. Osteochondromas occur in approximately 1% of the general population. Solitary osteochondroma is slightly more common in boys than girls. Growth ceases at skeletal maturity, and lesions are usually detected in the second decade of life as they grow. Most osteochondromas are asymptomatic and are discovered incidentally. However, a host of complications can occur (Box 138.5). When one of a pair of adjacent bones is affected, the osteochondroma can cause pressure deformity of the other bone. Symptomatic presentations of osteochondroma are usually due to irritation of adjacent muscles,

### BOX 138.5 Complications of Osteochondroma

**MUSCULOSKELETAL COMPLICATIONS**

Cosmetic and functional deformity
Pseudo-Madelung deformity
Radial head subluxation/dislocation
Coxa valga
Genu valga
Tibiotalar tilt
Leg-length discrepancy
Decreased range of motion
Impingement syndrome
Muscle/tendon irritation
Tenosynovitis
Snapping tendon
Tendon dislocation
Bursa formation
Synovial (osteo)chondromatosis
Synostosis
Pseudarthrosis
Short stature
Fracture

**VASCULAR COMPLICATIONS**

Displacement
Stenosis/occlusion
Claudication
Pseudoaneurysm
Venous compression/deep venous thrombosis/pulmonary embolism

**NEUROLOGIC COMPLICATIONS**

Peripheral nerve compression/entrapment
Cranial neuropathy
Spinal stenosis

**THORACIC COMPLICATIONS**

Hemothorax
Pneumothorax
Ruptured pericardium
Thoracic outlet syndrome
Dysphagia
Malignant transformation

tendons, nerves, or rarely blood vessels.[97,98] Pseudoaneurysm is a rare complication. A bursa may develop over an osteochondroma as a result of inflammation, and a pedunculated osteochondroma may fracture. Presentation with pain as a result of malignant transformation of a solitary osteochondroma in a child is extraordinarily rare.[99,100]

Osteochondromas develop in 6% to 12% of patients who received radiation at a young age. Latent periods vary from 3 to 16 years. Osteochondromas can occur even after low doses of radiation therapy and often occur in bones that were in the periphery of the radiation field. Multiple osteochondromas have been found in patients who received total-body irradiation as preparation for bone marrow transplantation at a young age. Sarcomatous degeneration of radiation-induced osteochondroma is very rare and of no greater incidence than with other osteochondromas.[101]

Patients with hereditary osteochondromatosis (hereditary multiple exostoses, diaphyseal aclasis) develop multiple osteochondromas throughout the skeleton. The disorder is autosomal dominant, and 10% of cases arise spontaneously. Patients have a mutation of the *EXT1* gene family that results in an error in regulation of normal chondrocyte proliferation and maturation.[102,103] In most patients, the disorder becomes manifest by 10 years of age. The multiplicity of lesions in these patients may lead to substantial deformity. Axial osteochondromas are frequently seen and may cause complications. Small lesions are common on the tubular bones of the hand. A pseudo-Madelung deformity of the wrist may occur because of forearm exostoses that cause ulnar shortening and angular deformity of the distal radius. Multiple metaphyseal lesions may interfere with normal modeling of the metaphyses.[104]

Malignant transformation of solitary osteochondromas, even those that are radiation induced, is exceedingly rare and probably occurs in fewer than 1% of patients.[101,105] However, the reported incidence of transformation to chondrosarcoma in patients with hereditary osteochondromatosis is 0.5% to 25%. Wide variation reflects patient selection biases; the actual incidence is probably less than 5%. Malignant transformation does not occur until well after skeletal maturity. Clinical and imaging findings suggestive of malignant transformation include an osteochondroma that grows or begins to produce symptoms after physeal closure, a cartilaginous cap greater than 1.5 to 2 cm thick in a skeletally mature patient, indistinct lesion margins, new lucency within an osteochondroma, and an associated soft tissue mass. Chondrosarcomas tend to arise at the periphery of an osteochondroma and are usually of low histologic grade.[106,107]

*Dysplasia epiphysealis hemimelica* (DEH), also known as *Trevor disease*, may be a manifestation of epiphyseal osteochondroma. Patients come to medical attention before 15 years of age, and 75% of patients are boys. Patients are seen initially with deformity, swelling, and pain. These patients form osteochondroma-like protuberances from the epiphyses. The lesions are usually confined to one side of the joint (medial more than lateral) and may occasionally involve contiguous joints in one extremity. The lower extremity (femur, tibia, talus) is usually affected, and the most commonly affected region is the ankle and hindfoot.[108]

*Subungual exostosis* is a broad-based irregular osteochondroma of the tuft of the finger under the nail bed. The lesion is most common in males in the second decade of life and most commonly affects the great toe. Unlike conventional osteochondroma, there is no medullary continuity of the exostosis with the underlying bone.[109,110]

***Imaging.*** On radiography, CT, and MRI, a hallmark of osteochondroma is continuity of the cortex and medullary space from the underlying bone into the lesion. On radiography, osteochondromas are most often found on the long-bone metaphyses, and 35% occur at the knee. Lesions in younger patients tend to be closer to the growth plates. Osteochondromas may also form on the pelvis, ribs, and scapulae; spinal lesions are rare. Underlying metaphyses are broadened as a result of disturbance of normal modeling. The shape of osteochondromas varies from sessile, plaquelike lesions (Fig. 138.14) to pedunculated lesions (Fig. 138.15) with a long stalk. The stalk of a pedunculated lesion is directed away from the adjacent joint. En face, osteochondromas may be mistaken for sclerotic intramedullary lesions.

CT nicely demonstrates the morphology of the lesions and usually confirms the diagnosis; however, MRI much better demonstrates the cartilaginous cap characteristic of the lesion (Fig. 138.16). On T2-weighted images and with other cartilage-sensitive sequences, the cartilaginous cap is seen as a well-defined, high-signal crescent that caps the osteochondroma. The role of MRI is not to define the presence or absence of malignancy but to identify pathologic fractures or overlying soft tissue impingement. Pedunculated osteochondromas tend to fracture and cause soft tissue impingement, whereas sessile osteochondromas tend to only cause soft tissue impingement.[111]

In DEH, radiographs show deformity with irregular enlargement of one side of the epiphysis (Fig. 138.17). MRI is necessary to define the abnormality in younger children, because the lesions may be predominantly cartilaginous.

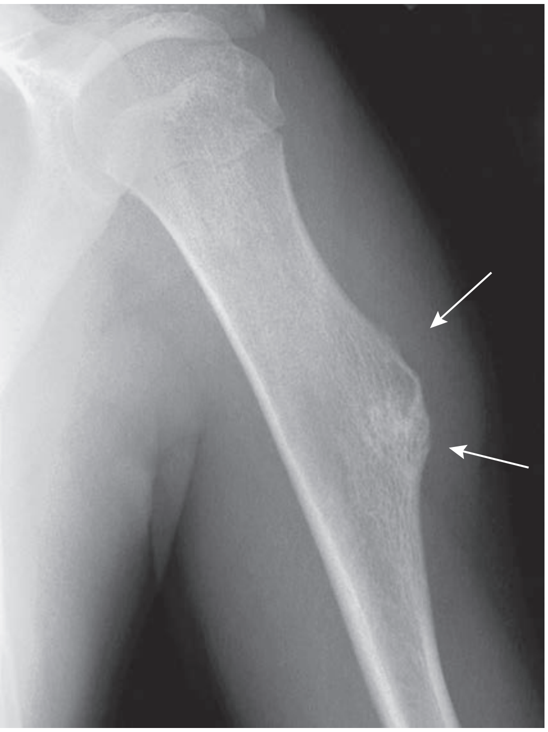

**Figure 138.14.** Sessile osteochondroma *(arrows)* of the proximal humeral diaphysis in a 16-year-old girl.

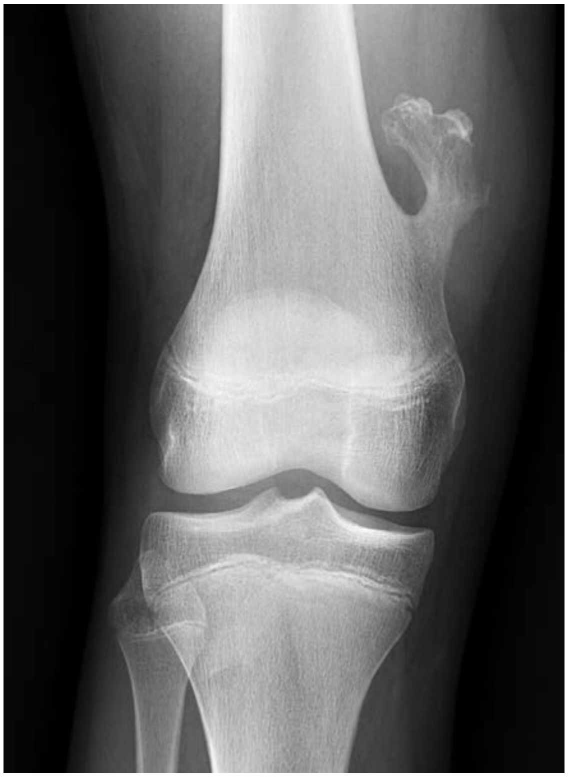

**Figure 138.15.** Pedunculated osteochondroma of the right distal femoral metaphysis in a 16-year-old boy.

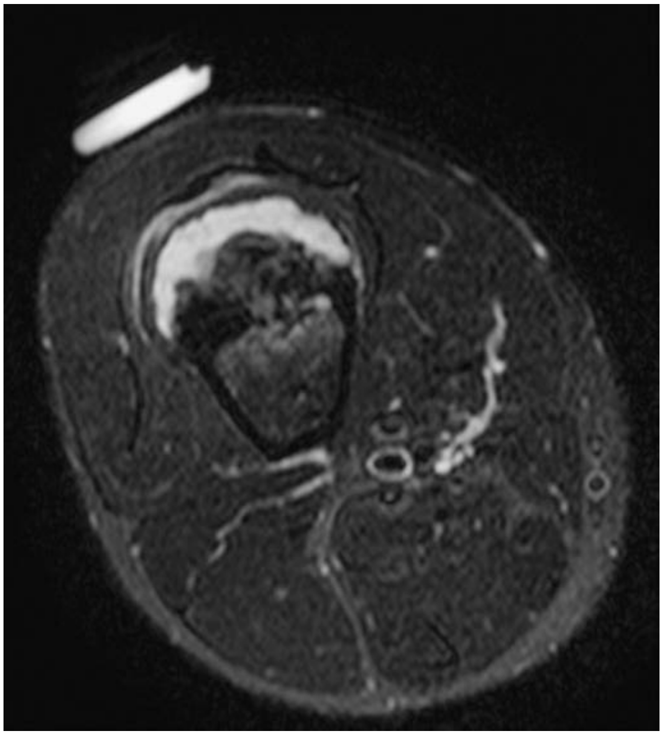

**Figure 138.16. Sessile osteochondroma in a 14-year-old boy.** T2-weighted MR image with fat saturation shows a broad, high-signal cartilaginous cap that covers the osteochondroma. Note the developing, overlying bursa. The anterior cortex under the cartilaginous cap is thickened. An external vitamin E marker was placed anteriorly over the palpable abnormality for localization.

***Treatment.*** Osteochondromas are treated nonoperatively, unless soft tissue impingement is significant, or the lesion causes biomechanical alignment disorders. Treatment of epiphyseal osteochondromas are problematic, but nonarticular components may be resected. The articular components of epiphyseal osteochondromas usually are smooth, and the affected joint typically adapts over time.[112]

### Enchondroma

***Overview, Etiologies, Pathophysiology, and Clinical Presentation.*** Enchondromas form owing to a failure of normal endochondral ossification adjacent to a physis. Tumors are composed of cartilage cells derived from the neighboring physis. Enchondromas are most frequently located in the small tubular bones of the hands and feet and in the metaphyses and metadiaphyses of the long bones. Enchondromas represent 80% of primary hand tumors in children and can form in any bone that forms in cartilage. Rib and vertebral lesions are uncommon. Enchondromas become more common with age, with a peak age for diagnosis in the third decade.

Enchondroma protuberans is an enchondroma variant that can resemble either a periosteal chondroma or a sessile osteochondroma (e-Fig. 138.18).[113] It has been described as an exophytic, exaggerated, eccentric from of enchondroma. This tumor arises in the medulla and expands eccentrically through the cortex so that the tumor eventually protrudes beyond it.[114] Rather than a cartilaginous cap, the tumor is covered by a thin layer of cortex and periosteum. This enchondroma variant most commonly occurs in the proximal humerus and in the hand.[115]

Ollier disease (enchondromatosis) is a nonheritable disorder of cartilage proliferation in which enchondromas involve multiple

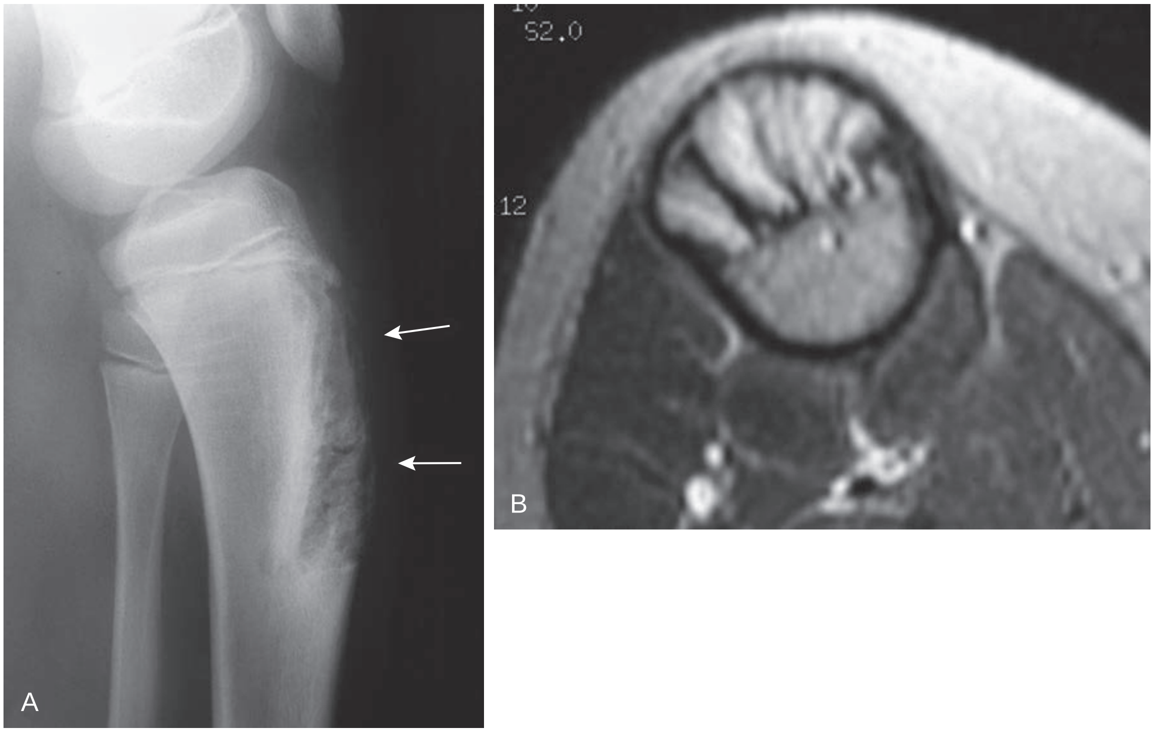

**e-Figure 138.18. Enchondroma protuberans in an 11-year-old boy.** (A) Radiograph shows an ill-defined lucent lesion in the anterior cortex of the proximal tibia *(arrows)* abutting the physeal equivalent region of the tibial tuberosity. (B) Axial T2-weighted MR image shows a well-defined, high-signal lesion in the anterior tibial cortex and intramedullary space.

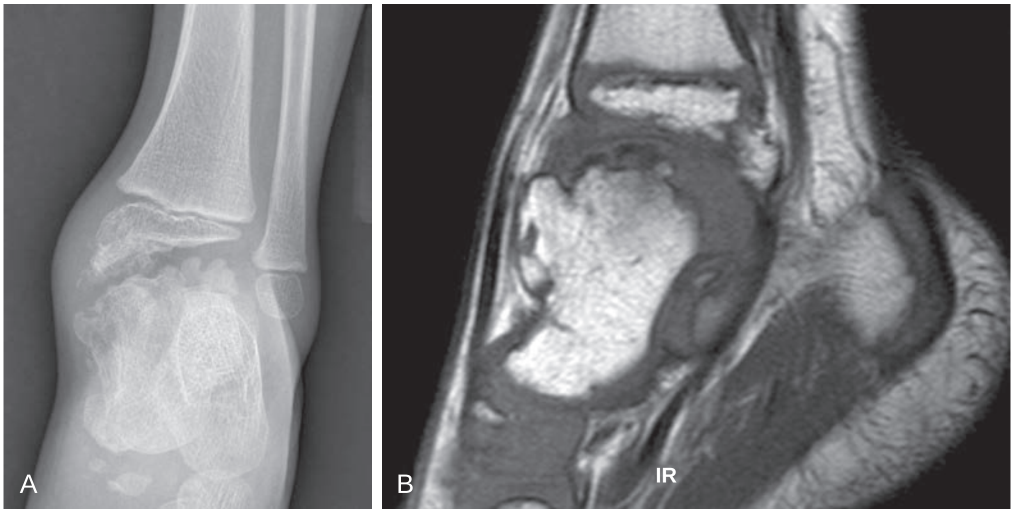

**Figure 138.17. Trevor disease (dysplasia epiphysealis hemimelica) in a 3-year-old boy.** (A) Radiography demonstrates “kissing” epiphyseal/epiphyseal equivalent osteochondromas at the level of the tibiotalar joint. (B) T1-weighted sagittal MR image shows marrow continuity with the osteochondromas.

bones. It is a mesodermal dysplasia and broader dyschondrogenesis that can affect any part of endochondrally formed bones, and it is more common in boys. Enchondromas form in any bone with a physis, although the hands may be disparately affected and may be grotesquely deformed. Enchondromas are bilateral but usually asymmetric in severity. Onset during infancy or early childhood may result in severe skeletal deformity. Enchondromas may interfere with growth plate function and may lead to limb shortening. The lesions of Ollier disease are expansile and lucent or trabeculated, usually with a shell of thin cortex. In the long bones, longitudinal lucent columns or streaks are characteristic.

Enchondromatosis accompanied by vascular malformations is known as *Maffucci syndrome*, which is also nonhereditary and a form of mesodermal dysplasia. The vascular malformations are predominantly venous but may be capillary and occasionally lymphatic. Calcified phleboliths may be demonstrated in the vascular soft tissue masses.

Malignant transformation is extremely rare with a solitary enchondroma, particularly in childhood. There is increased risk of malignant transformation in enchondromatosis, and Maffucci syndrome also carries an increased risk for extraskelatal malignancies.

*Metachondromatosis* is a very rare disorder that is a combination of enchondromatosis and osteochondromatosis.[116]

***Imaging.*** On radiography, as with other cartilaginous tumors, enchondromas exhibit a lobulated growth pattern that results in asymmetric expansion of the medullary cavity and endosteal scalloping (e-Fig. 138.19). The lesions may have characteristic channel-like lucencies that are perpendicular to the physis. Lesions are oval, well-circumscribed, and lucent with thin eggshell-like margins (Fig. 138.20). Focal, punctate calcifications may be evident on radiographs but are better appreciated with CT. The cartilaginous “ring and arc” pattern may be seen on CT. Margins of the lesion are sclerotic. The lesion may scallop the endosteum, erode cortex, and expand or distort the bone. Periosteal reaction is absent. The tumor is isointense with muscle on T1-weighted MRI and exhibits a heterogeneous, predominantly high T2-weighted signal. Signal intensity of the lesion parallels cartilage on all sequences. Enhancement with gadolinium varies; some lesions enhance peripherally, whereas others enhance more homogeneously. Adjacent bone marrow edema and enhancement are typically absent, but bone scans typically show increased activity.[117]

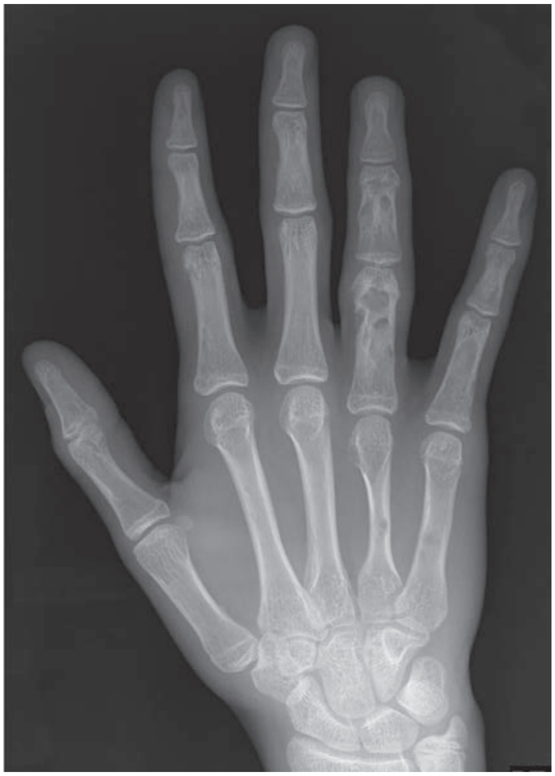

**Figure 138.20. Enchondromatosis in a 14-year-old boy.** Multiple, well-defined, lucent, expansile lesions are present in the metacarpals and phalanges of the ring and little fingers.

***Treatment.*** Enchondromas are managed nonoperatively and do not need to be longitudinally followed by imaging, unless new symptoms of pain or a pathologic fracture occur. These lesions do not have to be biopsied to confirm diagnosis.

### Periosteal (Juxtacortical) Chondroma

***Overview, Etiologies, Pathophysiology, and Clinical Presentation.*** This rare tumor is a surface variant of an enchondroma that arises from the periosteal surface of the cortex of the large and

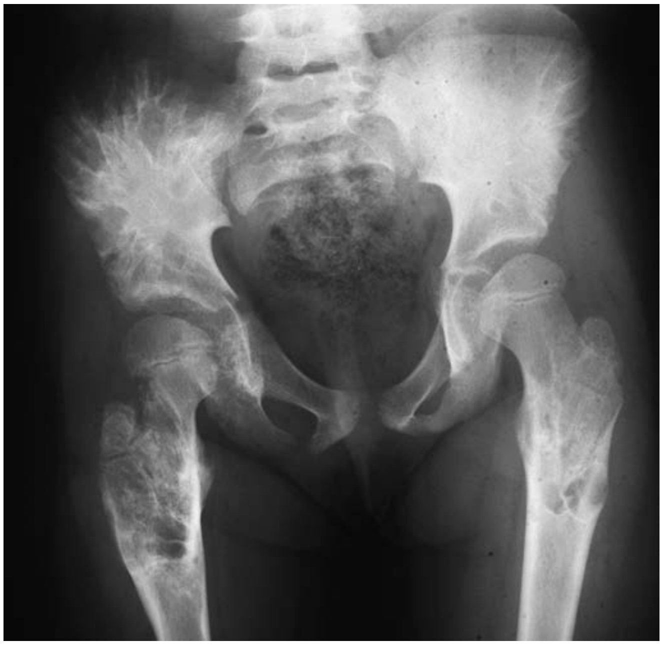

**e-Figure 138.19. Enchondromatosis in an 8-year-old girl.** Multiple lesions are present within the proximal femurs and the iliac bones. The iliac lesions on the right are confluent and produce a radial pattern of tubular lytic channels. The proximal femoral diaphyses are mildly expanded with rim sclerosis, and speckled cartilaginous calcifications are present in some of the lesions.

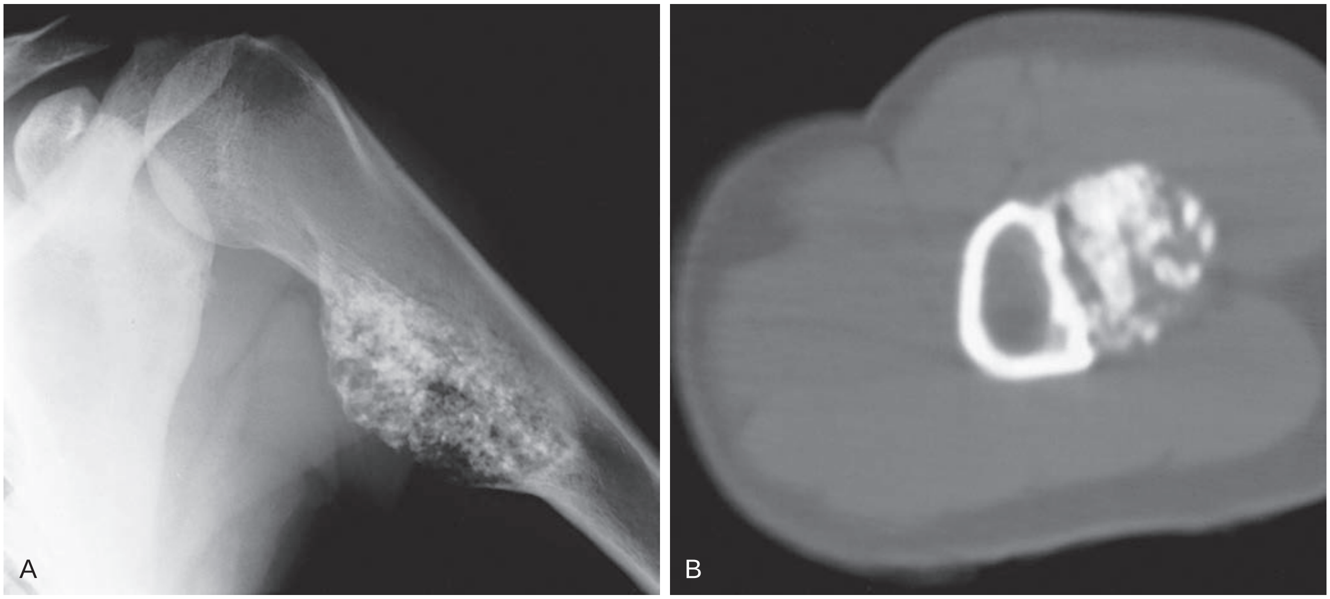

**Figure 138.22. Periosteal chondroma in a 19-year-old girl.** (A) Anteroposterior view of the humerus shows a broad-based tumor with a lobular mineralized matrix. (B) CT shows the superficial nature of the lesion, which is separated from the medullary cavity by cortical bone.

small tubular bones. One theory holds that the tumor is post-traumatic in origin, located under the periosteum and external to the cortex. Some tumors, such as within the femoral neck, are not covered with periosteum and are better labeled "juxtacortical." Periosteal chondroma most commonly occurs in the proximal humerus metaphysis, phalanges of the hands and feet, femur, and tibia. Patients are usually 10 to 30 years of age, and peak incidence is in the second decade of life; most come to medical attention with mild pain and swelling.[118] The lesion is more frequent in boys, and periosteal chondromas may be seen in patients with Ollier disease.

Periosteal chondroma does not have malignant potential, but biopsy may be advisable to distinguish it from periosteal osteosarcoma.

***Imaging.*** Radiographically, although periosteal chondroma may bear superficial similarity to a sessile osteochondroma, it is associated with sclerosis and external cortical scalloping, forming a periosteal shelf (e-Fig. 138.21). Focal calcifications of matrix within the lesion may be seen. Cross-sectional imaging delineates the underlying cortex and clearly distinguishes the lesion from a sessile osteochondroma. CT may show chondroid calcification (Fig. 138.22). MRI shows chondroid composition of the lesion, and peripheral enhancement is usually seen with gadolinium.[119] The tumor is usually 1 to 3 cm in size. A shell of reactive bone may be seen around the lesion, adjacent cortex is eroded or saucerized, and reactive bone sclerosis and buttressing is typically seen.

***Treatment.*** These benign lesions require biopsy to distinguish them from periosteal osteosarcomas. Lesions do not have to be followed by imaging after histologic diagnosis.

### Chondroblastoma

***Overview, Etiologies, Pathophysiology, and Clinical Presentation.*** Chondroblastoma, an uncommon tumor composed of primitive cartilage cells, usually occurs in the second decade of life. Roughly half occur before the physes close. The most specific feature of chondroblastoma is its location in the epiphysis of a long bone, most often the proximal humerus, distal femur, or proximal tibia. Chondroblastoma may also occur in epiphyseal equivalent regions such as apophyses, the patella, and carpal and tarsal bones. Larger lesions often may extend into an adjacent metaphysis, particularly in skeletally mature patients.[120] Up to 15% of chondroblastomas have a component of aneurysmal bone cyst (ABC). The tumor evokes a striking inflammatory response, which may help to distinguish it from other lesions.[121,122]

Included in the differential diagnoses for a lucent epiphyseal lesion in a child are chondroblastoma, osteomyelitis, and, after physeal closure, giant cell tumor (GCT).

***Imaging.*** Radiographically, a chondroblastoma is seen as an eccentric, lucent, well-defined smooth or lobulated lesion with sclerotic borders within an epiphysis or epiphyseal equivalent (Fig. 138.23). The lesion may expand the bone, but the cortex is usually intact. Periosteal reaction distant from the lesion is another common feature suggestive of an accompanying inflammatory process.[123] Periosteal reaction on an adjacent metaphysis is seen in 30% to 50% of cases. Approximately one-third of chondroblastomas have a calcified chondroid matrix (see Fig. 138.23). This is better demonstrated by CT, which may also show cortical destruction. On MRI, chondroblastoma typically parallels cartilage signal intensity on all sequences. Signal intensity varies with the degree of calcification in the lesion. The rim of the tumor may have a lower intensity, and some foci give no signal because of calcification. Adjacent inflammatory changes consist of bone marrow and soft tissue edema and joint effusion and are usually prominent (see Fig. 138.23).[124,125]

Chondroblastomas superficially may mimic an epiphyseal Brodie abscess. MRI is useful in this circumstance. Both chondroblastomas and epiphyseal Brodie abscesses may demonstrate exuberant adjacent marrow and soft tissue edema, effusions, and reactive bone proliferation. However, on postcontrast imaging, chondroblastomas will demonstrate central enhancement, whereas Brodie abscesses will not.[126]

***Treatment.*** Chondroblastomas are treated with curettage and bone grafting. Approximately 20% of lesions recur. Otherwise, the prognosis is good. There are rare reports of metastatic chondroblastoma.

### Chondromyxoid Fibroma

***Overview, Etiologies, Pathophysiology, and Clinical Presentation.*** Chondromyxoid fibroma (CMF) is a benign rare tumor that predominantly affects males in the second or third decade of life.

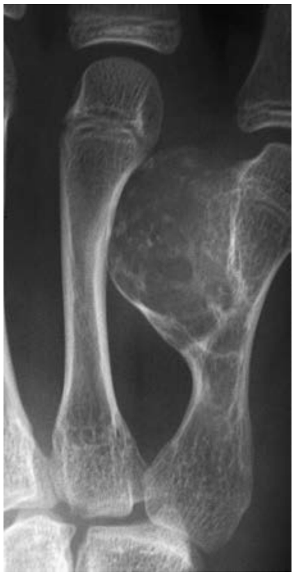

**e-Figure 138.21. Periosteal chondroma in a 13-year-old girl.** An expansile lesion originates at the surface of the metacarpal. Chondroid matrix is seen within the lesion, and the underlying cortex is externally scalloped.

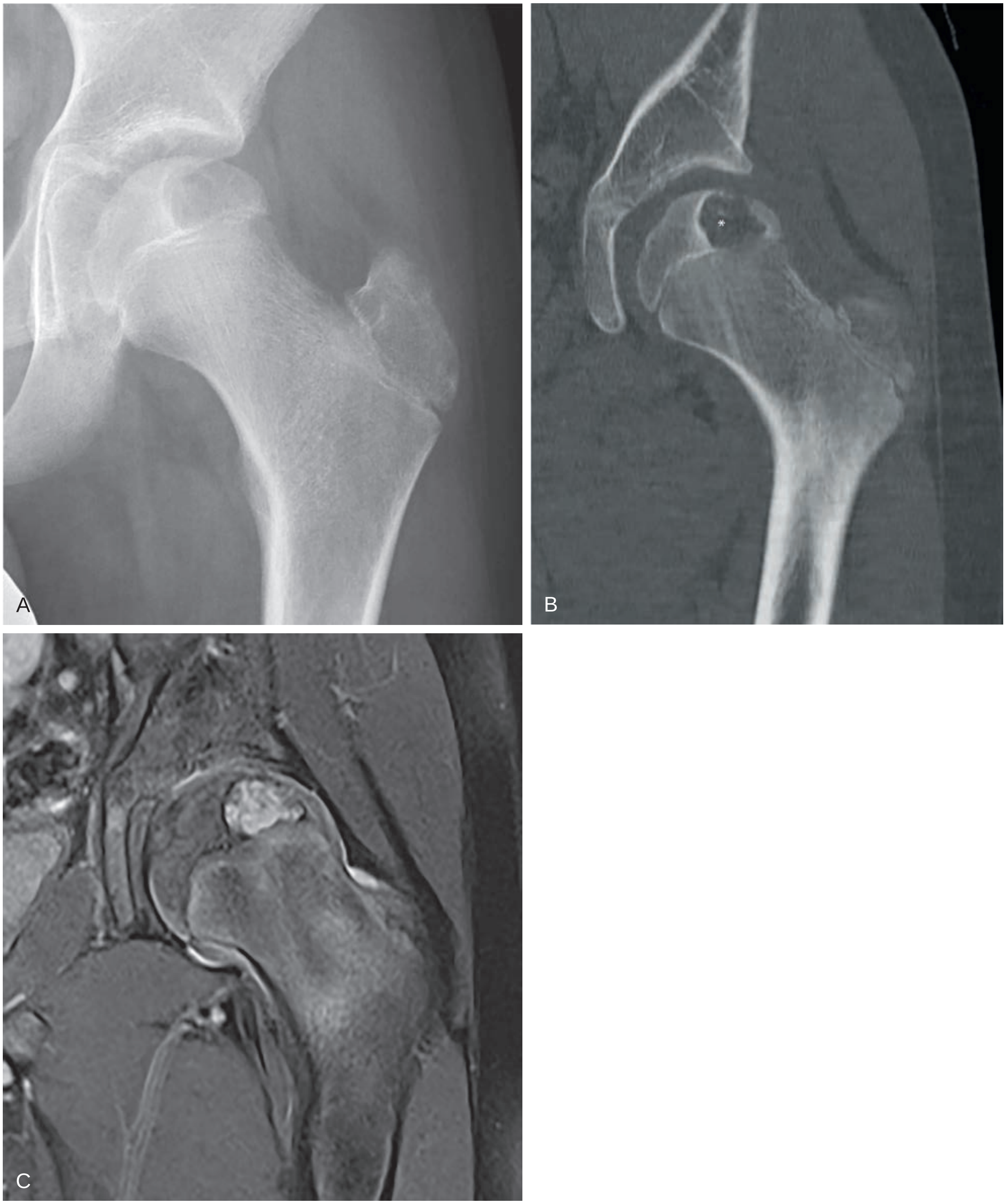

**Figure 138.23. Chondroblastoma in a 12-year-old boy.** (A) Radiograph shows a lucent lesion within the capital femoral epiphysis. (B) Coronal reformatted CT image shows a well-defined lesion with some calcified cartilaginous matrix *(asterisk)*. (C) Coronal STIR MR image shows the lesion to be of high signal intensity with regions of low signal representing chondroid matrix. Also note the adjacent marrow edema within the epiphysis and metaphysis.

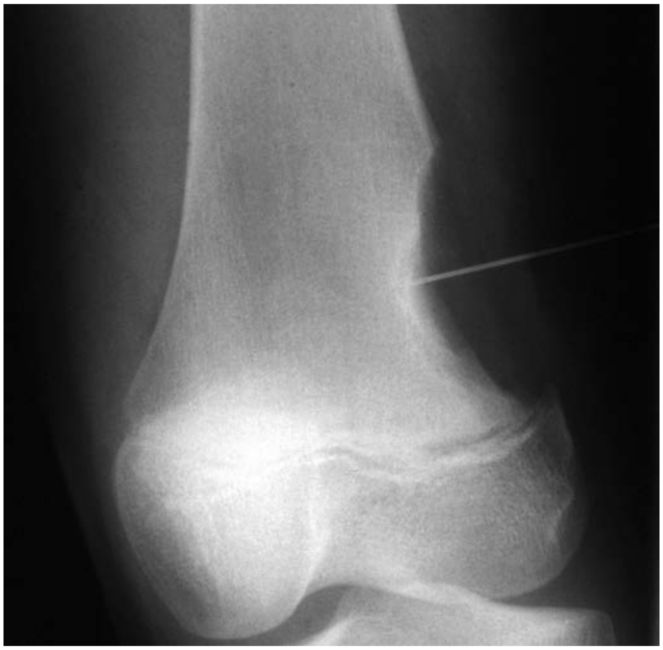

**Figure 138.24. Chondromyxoid fibroma in a 14-year-old boy.** The lesion has produced a well-defined scalloped defect in the distal femoral metaphysis. A biopsy needle is shown.

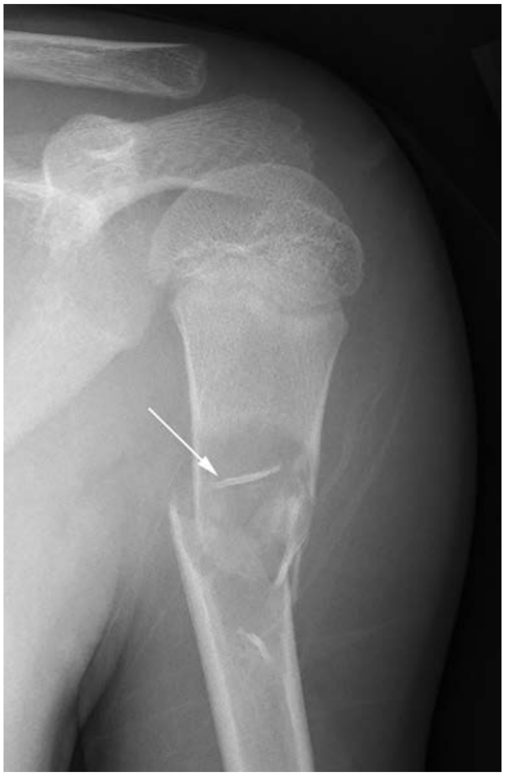

**Figure 138.25. Simple bone cyst with pathologic fracture in a 11-year-old boy.** The cyst has thinned and scalloped the overlying cortex. A fallen fragment is noted *(arrow)*.

Patients come to medical attention with pain. The lesion is a rubbery mix of fibrous, myxoid, and chondroid tissue. The most common site is the proximal tibia, but CMF may also arise within the ilium, other long bones at the knee, and tubular bones of the foot. The tumor is metaphyseal and often extends into metadiaphysis, but very rarely does it extend past a physis.[127,128]

***Imaging.*** On radiography, CMF has a characteristic but nonspecific appearance of a solitary, eccentric, lucent, well-defined lesion with sclerotic margins, which may show septations. In the short bones of the hands and feet, the lesion appears more central. The underlying cortex may be expanded, thinned, and occasionally absent. The lesion may appear bubbly, similar to an ABC.[129] Most lesions are elongated and oriented parallel to the long axis of the involved bone (Fig. 138.24). Matrix calcification and periosteal new bone formation usually do not occur. On MRI, CMF produces variable and often heterogeneous signal intensity depending on the composition of the lesion. In general, the lesion is of low signal on T1- and intermediate to high signal on T2-weighted imaging.[127]

***Treatment.*** Treatment of CMF is excision, and 25% of lesions recur. Multiple recurrences are common.

## Cysts

### Simple Bone Cyst

***Overview, Etiologies, Pathophysiology, and Clinical Presentation.*** A simple bone cyst is also referred to as a *solitary cyst* or *unicameral bone cyst* (UBC), although the latter term is a misnomer, because these cysts are often septated. One theory holds that bone cysts arise because of a defect in endochondral bone formation or altered hemodynamics with venous occlusion that elevates intraosseous pressure and leads to cyst formation. Bone cysts have a membrane of loose vascular connective tissue and contain osteoclast-like giant cells and accumulations of fibrinoid material. The cyst space is usually filled with yellow, sometimes bloody fluid.

Cysts are more common in boys than girls by threefold, and 75% are seen in patients younger than 25 years of age; 25% are found incidentally. Bone cysts typically occur centrally in the metaphyses of the long bones and most commonly involve the proximal humerus (50%) and proximal femur (20%). Cysts have an "active phase," during which they increase in size and remain in close proximity to the physis. "Latent phase" cysts are found farther from the physis and usually do not continue to grow. Cysts may appear to "migrate" into the diaphysis, but actually it is the growth plate that migrates away from the cyst. In older patients, pelvic and calcaneal bone cysts become more common.[130]

Bone cysts are occasionally found in the calcanei of pediatric patients.[131] Often, these cysts are painless and are first detected by radiography of acute injuries to the feet. Calcaneal bone cysts are nearly always located near the base of the neck of the calcaneus. The thin, overlying lateral cortical wall of the calcaneus forms a well-defined bony border that allows differentiation from the "physiologic" pseudocystic radiolucent areas observed in the same region of normal bones.

Bone cysts are asymptomatic unless complicated by fracture; however, 75% of patients present with a pathologic fracture. Bone cysts are the most common cause of pathologic fracture in children.

***Imaging.*** On radiography, bone cysts have a central, medullary location within the metaphysis. Most cysts are less than 3 cm in diameter but may be much larger in the long axis. The cyst wall is well defined and sclerotic; the overlying cortex is thinned, and the lesion may be mildly expansile.[132] With fracture, a fragment of bone may be seen dependently within the cyst. This "fallen fragment" sign is considered pathognomonic for a simple bone cyst (Fig. 138.25). CT delineates the cyst and confirms a fallen fragment but is rarely necessary. In atypical cases, MRI may be performed to confirm the cystic nature of the lesion. The fluid contents are low signal on T1- and high signal on T2-weighted imaging. With contrast, the cyst lining enhances, but the contents do not (e-Fig. 138.26).[133] Increased areas of enhancement may be seen after pathologic fractures.

Occasionally, with preceding intralesional hemorrhage from fracture, fluid-fluid levels may be seen that represent settled, degraded blood products. When bone cysts heal after pathologic fracture, they may have multiple septations and fluid-fluid levels within them, and they may superficially mimic an ABC. As a general rule, if the lesion diameter is smaller than the thickest diameter of the affected bone, the lesion should be considered a complicated solitary bone cyst. If the lesion diameter is greater than the thickest diameter of the affected bone, an ABC should be considered.

***Treatment.*** Fractured cysts tend to heal spontaneously; however, larger cysts with or without fracture are usually treated with curettage and bone grafting. The prognosis is excellent, although 35% to 50% of bone cysts recur, in some cases multiple times. Treated cysts often have a complex appearance with mixed sclerosis and lucency, septations, and mild expansion and deformity of the involved bone. Premature growth plate closure may occur as a complication of treatment or pathologic fracture but not as a result of the cyst itself. Cyst aspiration with corticosteroid injection or sclerotherapy has also been used for treatment.

### Aneurysmal Bone Cyst

***Overview, Etiologies, Pathophysiology, and Clinical Presentation.*** Histologically an ABC is composed of anastomosing channels that contain blood and are variably lined with fibrous walls that contain red blood cells, hemosiderin granules, foreign body giant cells, and spicules of reactive bone. The etiology of an ABC is poorly understood and may be primary or secondary and/or reactive. A wide variety of lesions may act as the nidus for ABC development, and underlying lesions are pathologically identified in one third of cases. A large ABC may obscure the underlying lesion, or it may represent only a small component of a larger tumor. In lesions without an underlying tumor, the role of antecedent trauma and intraosseous or subperiosteal hemorrhage acting as a nidus has been proposed. ABC is slightly more common in girls. Whether primary or secondary, the lesion is most common in the first three decades of life, and it is rare in patients younger than 5 years. Patients usually come to medical attention with nonspecific pain and swelling, and 10% present with pathologic fracture.[134] ABC is most common in the metaphyses of long bones, the craniofacial bones, and the posterior elements of the spine. Long-bone lesions can be subclassified as either *intramedullary* or *juxtacortical* (cortical or subperiosteal). A subperiosteal ABC is rare and mimics other subperiosteal tumors and pathologies.[135–137]

An unusual solid variant of ABC has radiographic features similar to those of the typical ABC.[138,139] The solid variant lacks cavernous, blood-containing spaces and is characterized histologically by the solid elements—proliferating fibrous tissue, benign giant cells, and newly formed osteoid matrix. A third of these tumors are not "aneurysmal." The solid variant of ABCs is histologically indistinguishable from extragnathic giant cell (reparative) granuloma. It is most common in the second and third decade. The lesion favors the axial skeleton over appendicular locations, and the most common locations are in the craniofacial bones, small tubular bones of the hands and feet, and the femur.

***Imaging.*** On radiography, ABC appears as a lucent, expansile, "blowout" or "soap-bubble" lesion with thin, smooth, bony walls (e-Fig. 138.27 and Fig. 138.28). As previously mentioned, if the lesion diameter is greater than the widest part of the affected normal bone, an ABC should be considered (see e-Fig. 138.27). ABCs are multiloculated, and the cortex is usually intact but may be markedly thinned to the point of being undetectable on imaging, and periosteal new bone may be present. Both CT and MRI demonstrate fluid-fluid levels, which are characteristic of the lesion.[140,141] This finding is due to sedimentation of degraded blood products, especially methemoglobin, which has a much shorter T1 relaxation time than that of hemoglobin. Fluid-fluid levels may be single or multiple and may be seen as varying horizontal levels within separate loculations (see e-Fig. 138.27 and Fig. 138.28). If the loculations are very small, fluid-fluid levels may be less

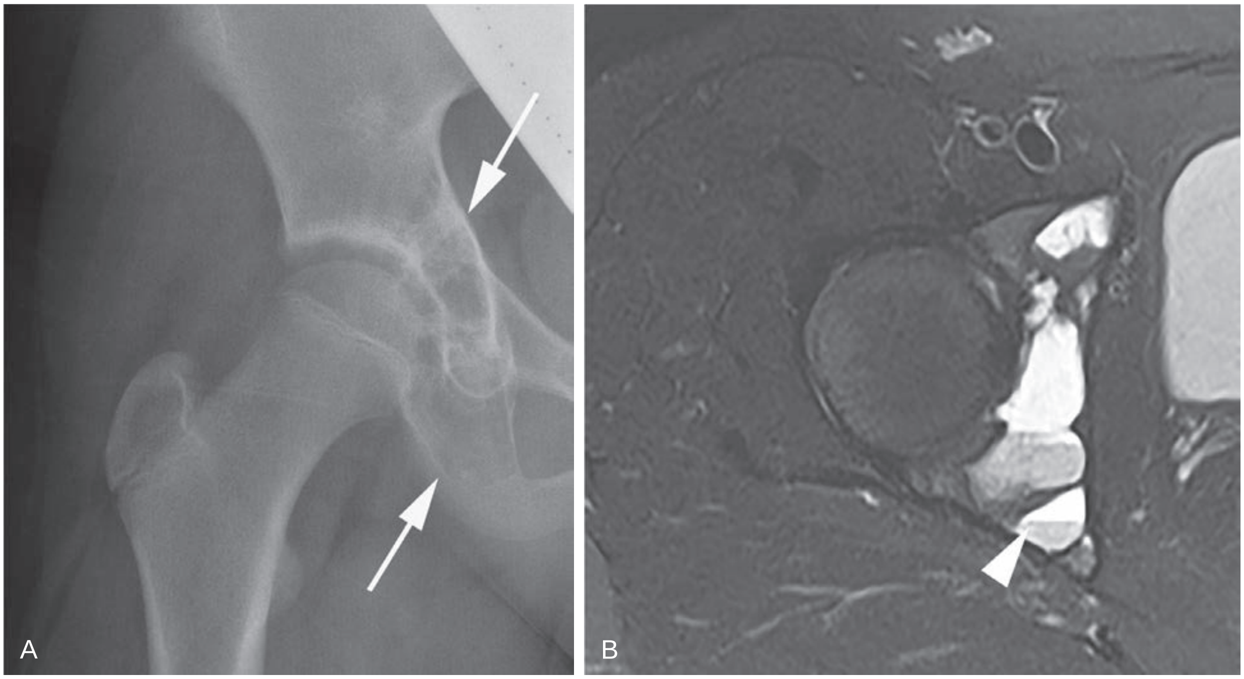

**Figure 138.28. Aneurysmal bone cyst in a 10-year-old girl.** (A) Radiograph of the hip shows an expansile, lucent lesion with a thin, bony shell *(arrows)*. (B) Axial STIR MR image shows several fluid-fluid levels *(arrowhead)* within the lesion.

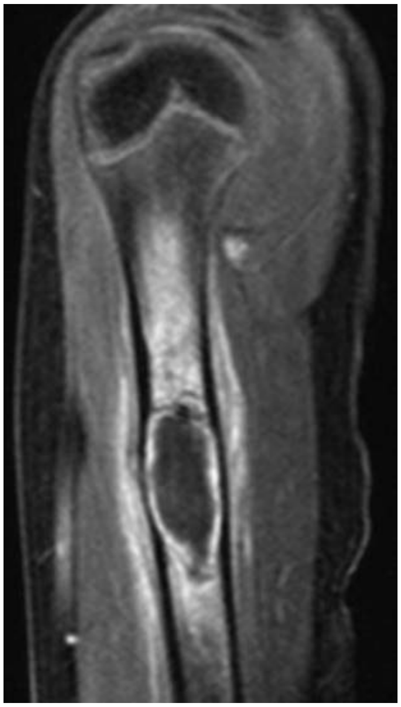

**e-Figure 138.26. Simple bone cyst in an 8-year-old boy.** Sagittal contrast-enhanced fat-saturated T1-weighted MR image shows a lesion that contains fluid with an enhancing rim. Enhancement is also seen in the adjacent marrow and soft tissues. The degree of enhancement is increased in this patient owing to a healing pathologic fracture through the lesion.

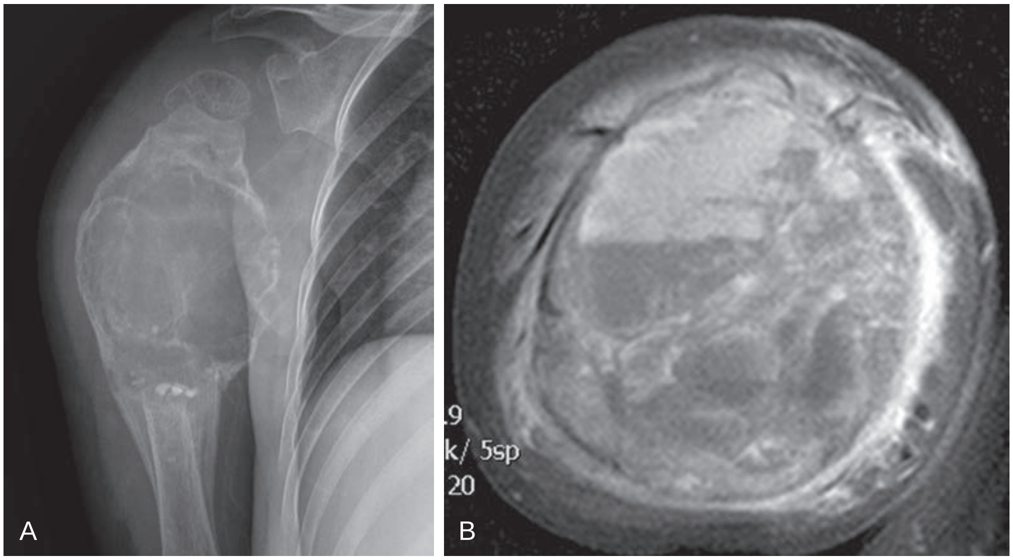

**e-Figure 138.27. Recurrent aneurysmal bone cyst (ABC) in a 4-year-old boy.** (A) Radiograph of the humerus shows a “blowout” lesion, whose width is wider than the widest part of normal bone. Note the bone graft material in the dependent components of this treated ABC. (B) T2-weighted fat-saturated axial MR image demonstrates multiple fluid-fluid levels.

apparent. The signal characteristics of the cyst contents are variable and are probably dependent on the relative age and concentration of the blood components. Abundant hemosiderin may produce foci of low signal, which may be diffuse throughout the lesion. Septal enhancement is seen on postcontrast images.

It may not be possible to differentiate primary and secondary ABCs. Secondary ABCs can occur with numerous benign and malignant bone lesions, including fibrous dysplasia, chondroblastoma, GCT, nonossifying fibroma, simple bone cyst, and osteosarcoma, particularly the telangiectatic variant.[142,143] Any solid component suggests an underlying tumor. Lesions composed of a greater percentage composition of fluid-fluid levels are more likely benign. Solid enhancing soft tissue components on MRI should raise suspicion for primary bone tumor causing a secondary ABC or a telangiectatic osteosarcoma. In such cases, MRI can direct biopsy to the solid components.

On MRI, solid ABCs demonstrate low signal on both T1 and T2 images because of fibrosis. The lesion enhances with gadolinium. The solid variant of ABC may occasionally produce osteoid that may be evident on radiographs or CT.

***Treatment.*** ABC is treated with curettage and bone grafting, although 20% of ABCs recur after grafting. Vascular embolization and percutaneous sclerotherapy have also been used.

### Giant Cell Tumor

***Overview, Etiologies, Pathophysiology, and Clinical Presentation.*** GCT, also known as *osteoclastoma*, is an uncommon neoplasm that rarely occurs before skeletal maturity. Approximately 5% of cases are reported before skeletal maturity,[144] most in the second decade and rarely in the first decade of life.[145] The lesion is most common in the long bones, particularly the distal femur and proximal tibia; it is less common in the short bones of the hands and feet, and in children, it rarely occurs elsewhere.[146] In skeletally mature individuals, the lesion originates in the metaphysis and extends into the epiphysis, typically extending to the subarticular region. In skeletally immature patients, the lesion is almost uniformly metaphyseal and usually abuts the physis. Epiphyseal involvement is very rare before physeal closure, and multifocal GCT is very rare in children. Patients with GCT come to medical attention with pain and tenderness, swelling, and limited range of motion of the adjacent joint.[147]

***Imaging.*** On radiographs, GCT appears as a geographic, lytic lesion (Fig. 138.29). Margins vary from sclerotic to ill defined. Frequently, a relatively sharp but nonsclerotic margin is apparent. Periosteal new bone, expansion of bone, and pathologic fracture are common. The metaphyseal end of the lesion tends to be less well defined. No calcified or ossified matrix is seen.

MRI findings vary. In one large series, 56% of tumors were solid or solid with cystic change, and 44% were cystic.[144] Solid areas tend to have intermediate T1 and T2 signal. Hemosiderin from intratumoral hemorrhage may produce foci of low signal. Occasionally, a GCT may have a more aggressive appearance, with cortical penetration and soft tissue extension. Approximately 15% of GCTs have an associated component of ABC and appear more expansile.[148] The prognosis of GCT is excellent, although up to 25% of tumors recur locally. Malignant GCT and metastasizing GCT have rarely been reported in children. The pulmonary “implants” from GCT usually have self-limiting growth potential, but recurrence and disease progression is possible.[149]

***Treatment.*** For resectable GCTs, en bloc excision has a lower recurrence rate, approximately 20%, compared with intralesional curettage, which has an approximately 50% recurrence rate.[150]

## Fibrous Tumors

### Fibrous Cortical Defect and Nonossifying Fibroma (Fibroxanthoma)

***Overview, Etiologies, Pathophysiology, and Clinical Presentation.*** Fibrous cortical defect (FCD) and nonossifying fibroma (NOF) are extremely common tumors that occur in the metaphyses of the long bones of children. FCDs are essentially a normal variant and are found in up to 40% of children during development. FCD and NOF are histologically identical and are composed of highly cellular stroma with spindle-shaped fibroblasts, osteoclast-like multinucleated giant cells, and foam or xanthoma cells. Arbitrarily, lesions smaller than 2 cm are considered an FCD, and those larger than 2 cm are called NOFs. Lesions probably represent a developmental defect in the periosteum of cortical bone and are seen in the latter

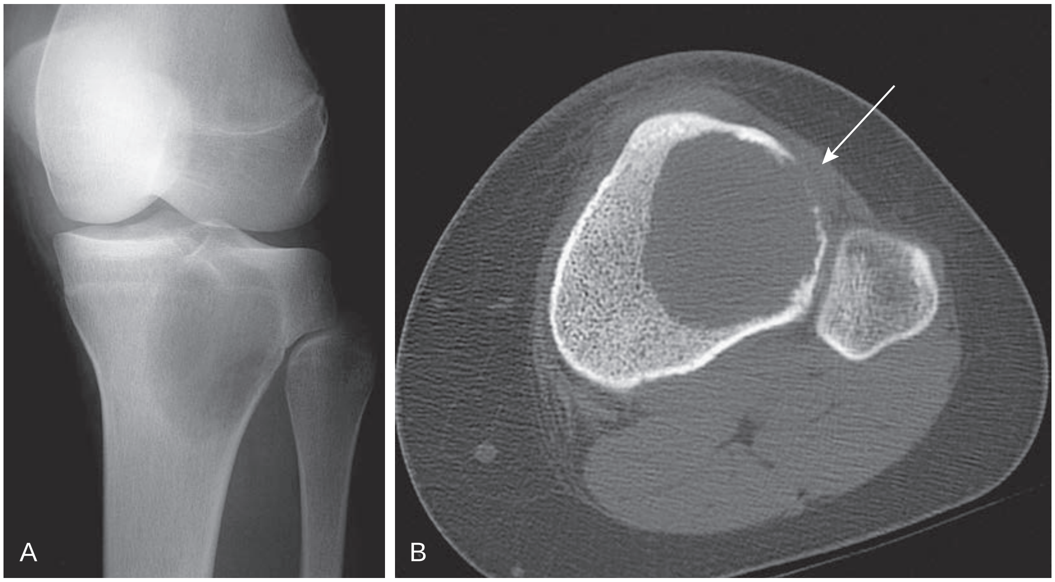

**Figure 138.29. Giant cell tumor in a 14-year-old girl.** (A) Radiograph shows a relatively well-defined lucent lesion in the proximal tibial metaphysis and epiphysis. The lesion does not have sclerotic margins and is near the articular surface but does not abut it. (B) Axial CT shows a large lucent lesion of the tibia. The lesion margins are well-defined but not sclerotic. The anterolateral cortex is destroyed *(arrow)*.

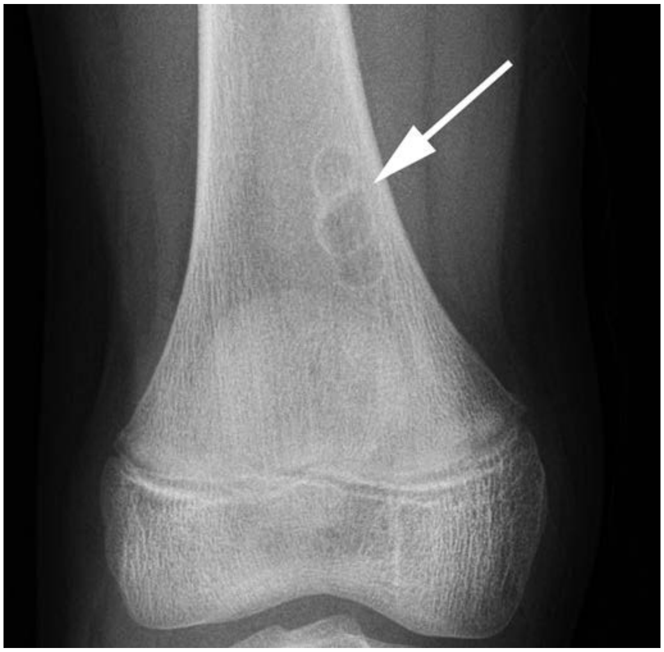

**Figure 138.30. Nonossifying fibroma in a 12-year-old boy.** The lesion is well-defined, with a “soap bubble” appearance and sclerotic margins *(arrow)*.

part of the first decade until shortly after skeletal maturation. The average time from diagnosis to spontaneous regression is 29 to 52 months; lesions become inactive after skeletal maturity, although rarely, an NOF may persist into adulthood.[151,152]

FCD and NOF are usually detected incidentally. The lesions are asymptomatic, with the exception of very large lesions, which may cause dull pain. Uncommonly, an NOF may be large enough to cause a pathologic fracture or lead to a stress fracture. FCD and NOF are most common in the metaphyses of the long bones of the lower extremity, especially at the knee. FCDs and the distal medial femoral avulsive irregularity are histologically similar.[153]

Multiple NOFs may be seen with neurofibromatosis. In Jaffe–Campanacci syndrome, disseminated NOFs are associated with cystic lesions of the jaw, café-au-lait skin lesions, and other anomalies but without neurofibromas. Some believe Jaffe–Campanacci syndrome is a *forme fruste* of neurofibromatosis.[154–157]

***Imaging.*** On radiography, FCDs are seen as small, well-defined, ovoid, cortically based lesions. NOFs are similar but larger (Fig. 138.30), more lobular, and multilocular with a characteristic “soap bubble” appearance. Usually, the lesions extend inward; however, the outer cortex may be thinned and bulging. In thinner bones, such as the fibula, the lesion may occupy the entire width of the bone. FCDs and NOFs originate in metaphysis near the growth plate and migrate into metadiaphysis and diaphysis with maturation. Their radiographic appearance is sufficiently specific that neither additional imaging nor biopsy is indicated.

The radiographic features of FCD and NOF are similar on CT. On MRI, lesions are well defined, lobular, and cortically based. Low signal is seen on T1, and T2 signal and enhancement with gadolinium varies with the stage of lesion development. Active, early lesions are high signal on T2-weighted imaging, and they enhance. Involuting lesions are low signal on T2 and do not enhance, and no peritumoral edema is seen.[158] Active, early lesions may also show uptake on bone scans and PET scans.[159]

***Treatment.*** The natural history is for involution to occur with progressive sclerosis of the lesion.

## Fibrous Dysplasia

***Overview, Etiologies, Pathophysiology, and Clinical Presentation.*** Although it is not a true neoplasm, fibrous dysplasia that involves a long bone may mimic a bone tumor or cyst, especially when it causes localized expansion of the bone and is monostotic.[160] Pathologically, fibro-osseous tissue replaces the normal medullary space. Fibrous dysplasia can be monostotic (70%–80% of cases) or polyostotic, and monomelic or polymelic. Fibrous dysplasia is more common in girls than in boys. Most patients with focal disease are adolescents or young adults, but patients are occasionally seen in the first decade of life. Any bone may be affected. The most common presentation is monostotic disease that affects craniofacial bones, especially the skull base; a long bone, most commonly the femur; or a rib. Lesions may involve metaphysis and diaphysis but spare the epiphysis before physeal fusion. Patients with solitary lesions come to medical attention with pain, edema, deformity, or pathologic or fatigue fracture. Patients with polyostotic disease are seen with similar signs and symptoms, but often at a younger age (i.e., first decade). Polyostotic disease predominates on one side, is often syndrome related, and may be suspected based on other clinical findings.[161,162]

In 2% to 3% of patients, fibrous dysplasia is associated with endocrine disorders, mostly of hypothalamic dysfunction. In McCune–Albright syndrome, female patients are seen with precocious puberty, cutaneous café-au-lait spots, and unilateral polyostotic fibrous dysplasia. Mazabraud syndrome, characterized by polyostotic fibrous dysplasia and intramuscular myxoma, is rare in children.[163]

***Imaging.*** Fibrous dysplasia in the long bones causes expansion of the medullary cavity, endosteal scalloping, coarse trabeculation, and sclerotic margins that form a “rind.” Bowing of the affected bone may occur. In the femur, the resulting deformity is called a *shepherd’s crook* (Fig. 138.31). Lesions may be central or eccentric. Because the radiographic opacity of a fibrous dysplasia lesion depends on the relative amount of dysplastic bone and fibrous material within the lesion, the appearance varies, from having the look of ground glass to appearing radiolucent. The ground-glass appearance is due to a matrix that contains a fine meshlike pattern of delicate bone spicules (Fig. 138.32). It is relatively specific for fibrous dysplasia but may be simulated by other lesions that replace the medullary trabeculae. Lucent lesions usually have a sclerotic margin, and small cartilaginous foci within the lesion may develop chondroid calcification (osteocartilaginous fibrous dysplasia). In addition, a single lesion or involved bone may demonstrate varying appearances within different areas. Active, early lesions tend to be radiolucent, whereas older lesions may be more sclerotic. No periosteal reaction is present unless there is a fracture. Similar findings are visible with CT.

On MRI, lesions are similar in signal intensity to muscle on T1-weighted imaging. On T2-weighted imaging, lesion signal intensity varies depending on the composition of the lesion; pure fibrous tissue is hypointense on T2. However, lesions of fibrous dysplasia are often hyperintense[164] because of the inhomogeneous nature of the lesion, which consists of spindle cells, trabeculae of immature woven bone with osteoid seams, and small cysts. Fluid-fluid levels have been reported,[165] but soft tissue extension is rare. Central or, less frequently, peripheral enhancement may occur with gadolinium, and lesion uptake on bone scans is variable and may even be normal.

***Treatment.*** Imaging findings often are diagnostic, biopsy is rarely necessary, and treatment is supportive. Surgical treatment is predicated on the presence or absence of pathologic fracture or impending biomechanical failure. Orthopedic implants are used to reinforce and stabilize affected bones.

## Osteofibrous Dysplasia

***Overview, Etiologies, Pathophysiology, and Clinical Presentation.*** Osteofibrous dysplasia (OFD), also known as *extragnathic*

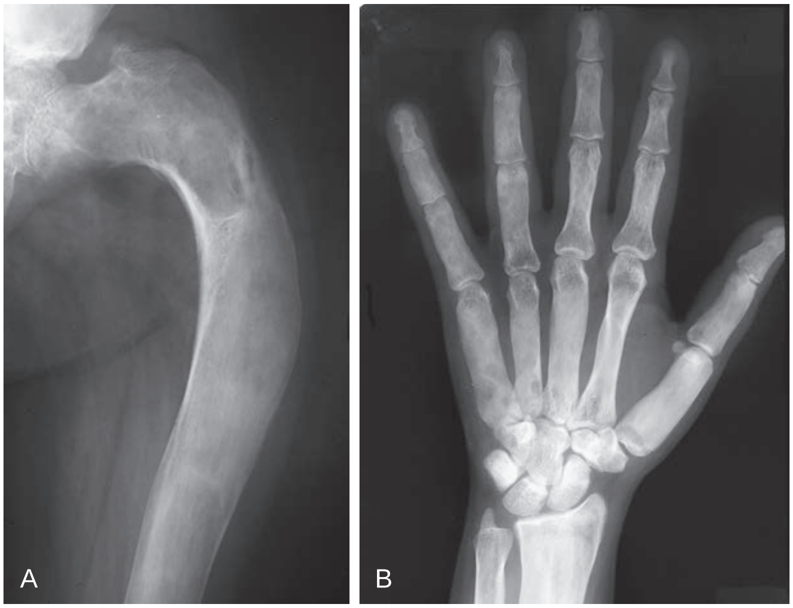

**Figure 138.31. Polyostotic fibrous dysplasia in a 22-year-old woman.** (A) The femur is expanded and bowed with a "shepherd's crook" deformity. The femoral trabeculae are replaced by "ground-glass" matrix. (B) Diffuse sclerosis is seen in the hand and wrist with mild expansion and indistinct transition from cortex to medullary space.

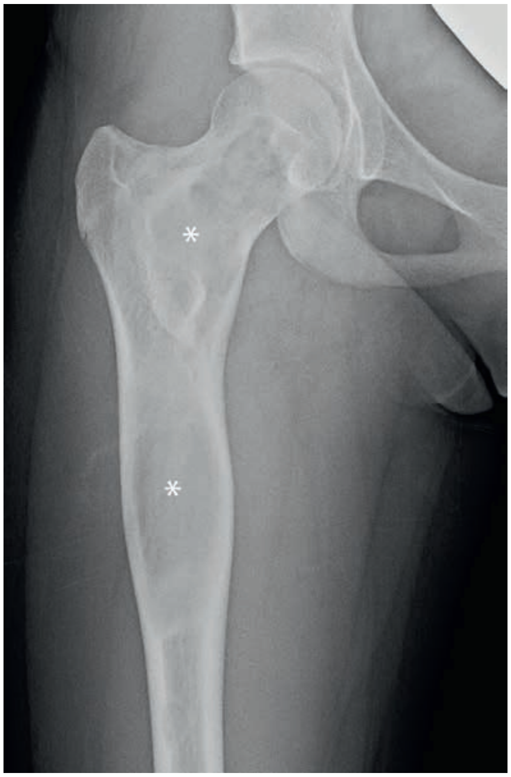

**Figure 138.32. Focal fibrous dysplasia in an 13-year-old girl.** The lesion has well-defined, sclerotic margins and a ground-glass matrix *(asterisks)*.

*ossifying fibroma* or *intracortical fibrous dysplasia*, is a proliferation of fibro-osseous tissue. OFD is usually sporadic, although autosomal-dominant inheritance has been reported.[166] Most cases occur during the first decade of life, and some tumors have been found in newborns.[167,168] OFD is a rare lesion that is usually confined to the diaphysis and metadiaphysis of the tibia but can also involve the fibula, sometimes synchronously in the same patient. Rarely, lesions may be multiple and bilateral. OFD is usually painless and characterized by deformity that can progress until physeal fusion occurs. Patients may come to medical attention with anterior bowing, and fracture or pseudoarthrosis may occur.

OFD is histologically similar to fibrous dysplasia in that it contains well-differentiated fibroblasts, collagen, and bony trabeculae. The main differentiating feature is the presence of active osteoblasts in OFD. Differentiated adamantinoma and adamantinoma are closely related to OFD, because they share similar histochemical properties.[169] Especially in the second decade, radiologic and even pathologic distinction between OFD, differentiated adamantinoma, and adamantinoma is difficult, although OFD tends to occur at a younger age than adamantinoma. This differentiation is discussed later in this chapter.

***Imaging.*** By radiography, OFD is an eccentric, lucent, solitary, or multiloculated lesion that involves the anterior cortex of the tibia (Fig. 138.33). The lesion may be rounded in appearance or ovoid and may be longitudinally oriented with the tibial shaft; it may be purely intraosseous, or it may have a minor extraosseous component. Involvement of the tibia is more commonly proximal, but distal lesions occur and may be complicated by pseudarthrosis. The cortex is expanded, and larger lesions will expand posteriorly and may replace the medullary cavity. Lesions appear lucent or ground glass and are associated with cortical thickening and anterior bowing of the bone. Cross-sectional imaging is very helpful in determining the lesion's intracortical location, an important feature in distinguishing OFD from fibrous dysplasia, which is intramedullary.

### Long-Bone Adamantinoma

***Overview, Etiologies, Pathophysiology, and Clinical Presentation.*** Long-bone adamantinomas are rare tumors in children, and patients are often seen initially with pain and anterior tibial bowing.[170] As opposed to OFD, adamantinoma is a low-grade malignancy. Up to 15% of affected patients die of metastatic disease. On the basis of clinical, radiologic, histologic, and histochemical characteristics, long-bone adamantinomas (unrelated to the jaw

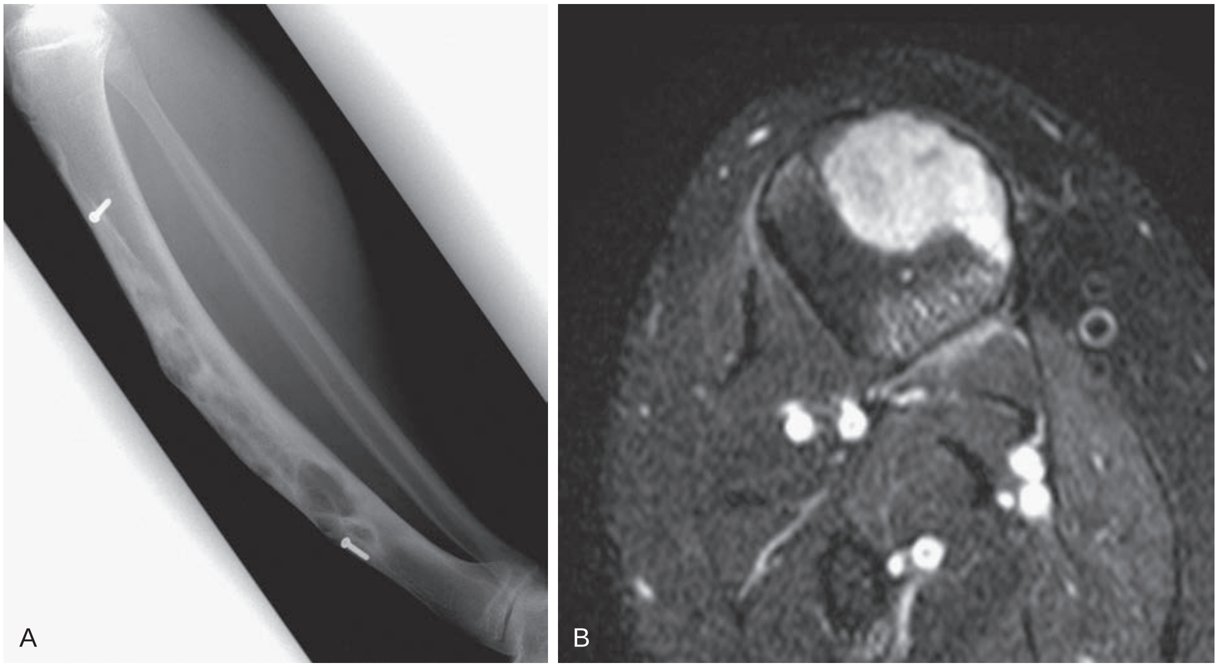

**Figure 138.33. Osteofibrous dysplasia in a 15-year-old boy.** Biopsies obtained several years prior had led to a diagnosis of adamantinoma, for which surgical excision with grafting had been performed (screws are related to the prior graft). Symptoms recurred. (A) Lateral radiograph shows anterior tibial bowing with mixed sclerosis and cystic lucencies centered anteriorly within the tibia. (B) Axial T2-weighted MR image with fat saturation shows homogeneous, high-signal soft tissue within the lesion. Percutaneous and excisional biopsies both showed osteofibrous dysplasia.

lesion previously referred to as an adamantinoma) have recently been divided into two groups: *classic* and *differentiated* (OFD-like). Both types involve the tibia, the fibula, or both bones. The classic form occurs almost exclusively in adults and is found in either the cortex or the medulla, but it can expand through the cortex and periosteum. The differentiated form is seen in children and young adults up to 20 years of age and has been reported in newborn infants. The tumor is limited to the bony cortex and has a radiographic appearance identical to that of OFD. Adamantinoma and OFD do have some pathologic distinctions. Epithelial and mesenchymal cells, which express immunoreactive cytokeratin and vimentin, are present in adamantinomas. Epithelial elements are absent in classic OFD and are minimal in differentiated adamantinoma.[171]

Clinical, radiologic, and pathologic distinction of adamantinoma from OFD is challenging. The concept of a differentiated form implies a continuum between OFD and adamantinoma and suggests that OFD may be a regressive phase of adamantinoma. Some well-documented cases in the literature support this contention. Czerniak and colleagues[172,173] suggested that patients with the differentiated type have a more favorable prognosis than those with classic adamantinoma—no differentiated tumors have been known to metastasize—and that long-bone adamantinoma could be included among the few neoplasms capable of spontaneous regression.

***Imaging.*** Radiographic findings of long-bone adamantinoma are similar to those of OFD. Variable features that might raise suspicion for adamantinoma are periosteal reaction, moth-eaten destruction, and soft tissue extension. MRI of adamantinoma is nonspecific. The T1- and T2-weighted signal characteristics are similar to those of other tumors. Soft tissue extension may also be evident.[169,174,175]

***Treatment.*** Treatment of adamantinoma is usually en bloc resection. Treatment for OFD and differentiated adamantinoma is much more conservative. If surgery is to be performed for OFD or differentiated adamantinoma, it should be performed after the child reaches puberty, and only if the disease is extensive and has caused deformity.[169]

### Langerhans Cell Histiocytosis

***Overview, Etiologies, Pathophysiology, and Clinical Presentation.*** The cause of Langerhans cell histiocytosis (LCH) is unknown. Recent evidence of clonal proliferation of Langerhans cells suggests a neoplastic etiology. The unifying pathologic feature of LCH is in an inappropriate proliferation of Langerhans cells. Like the cells of monocyte-macrophage lineage, the Langerhans cell originates from CD34+ stem cells of the bone marrow. Immunohistochemical staining for S100 protein and CD1a antigen are used in making the diagnosis.[176,177]

Focal LCH is a relatively common pediatric bone tumor and represents a continuum of disease that ranges from a single, indolent, self-limiting osseous lesion to a fulminant disseminated disorder that involves multiple organs systems. Approximately 80% of patients with LCH have osseous involvement. In the past, patients with LCH pathology were divided into three diagnoses: *eosinophilic granuloma* referred to localized skeletal disease, usually a single lesion, and approximately 70% of patients fall into this category; children with *Hand–Schüller–Christian disease* had the triad of geographic bone lesions, proptosis, and diabetes insipidus—a triad rarely seen in an individual patient; and *Letterer–Siwe disease* referred to the fulminant, disseminated, often fatal multisystem form. Fewer than 10% of patients fall into this last category. It is now recognized that LCH is a spectrum of disease rather than these three distinct entities.[178,179]

LCH is more common in whites, is twice as common in boys, and is seen from the neonatal period into adulthood. Most patients are younger than 15 years at presentation, with a peak incidence from 1 to 5 years of age. Focal lesions tend to be found in children

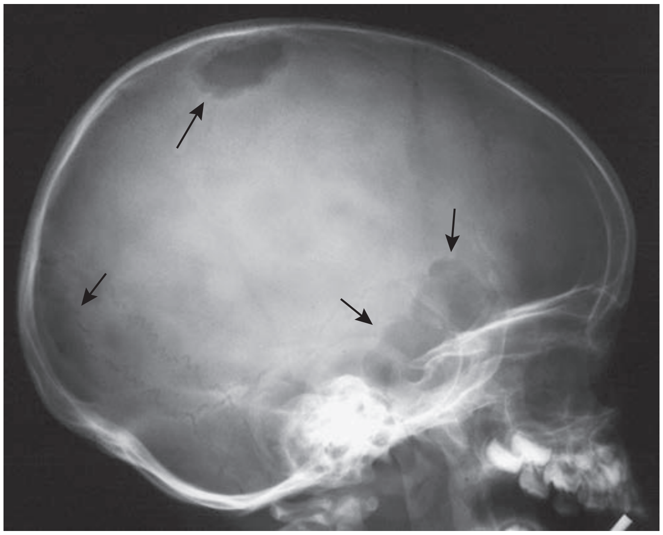

**Figure 138.34. Langerhans cell histiocytosis in a 2-year-old girl.** Lateral skull radiograph shows three lytic lesions in the skull. The lesion at the vertex has beveled edges.

who are slightly older, with an average age of 10 to 12 years. Multifocal and systemic disease is most common in infants and younger children. Fulminant life-threatening LCH is usually seen in the first two decades of life and is rare beyond 3 years of age. Disseminated disease may cause lymphadenopathy, hepatosplenomegaly, skin lesions (purpuric rash), diabetes insipidus, exophthalmos, thrombocytopenia, and anemia. Pulmonary involvement of LCH in children is seen almost always in the setting of disseminated disease, in which osseous lesions vary from relatively few to diffuse, confluent involvement.[180,181]

Solitary LCH lesions usually come to attention with local pain, tenderness, and an occasional palpable mass. Symptoms also relate to the involved bone; mastoid lesions may manifest as ear disease, and spinal lesions may show up as painful scoliosis or kyphosis. In addition, patients may have a low-grade fever, and elevated erythrocyte sedimentation rates and C-reactive protein levels.

The skull is the most frequent site of LCH, followed by the femur, mandible, pelvis, ribs, and spine; in addition, 70% of lesions occur in flat bones, and 30% occur in tubular bones (long bones, clavicle, hands, and feet). Lesions are usually located in the medulla. Primary lesions of the cortex are rare; however, the cortex is often secondarily affected by expansion of an intramedullary lesion. Long-bone lesions occur in the diaphysis or metaphysis, with rare involvement of the epiphysis. Rarely, lesions may cross an open growth plate. Multiple bone lesions occur in approximately 25% of patients.[182,183]

***Imaging.*** In the extremities, most LCH lesions are purely osteolytic with well-defined, minimally sclerotic borders. Many lesions are mildly expansile. Endosteal scalloping may be prominent and may progress to cortical disruption. Some lesions are permeative, and periosteal new bone formation may occur, giving them an aggressive appearance. Periosteal new bone may be in single or multiple layers. Although it is often said that LCH can have any radiographic appearance, lesions often have both aggressive and nonaggressive features. When such an indeterminate lesion is identified, LCH is high on the list of differential diagnoses.

Radiographically, LCH of the calvaria typically appears as a lytic bone lesion with a well-defined "punched out" appearance. Skull lesions appear geographic with beveled borders as a result of differential destruction of the inner and outer tables (Fig. 138.34). A so-called button sequestrum may be seen, and lesions of the maxilla and mandible produce "floating teeth" (e-Fig. 138.35). Vertebral lesions produce compression deformities, most commonly in the thoracic spine, followed by the lumbar and cervical regions. LCH often produces vertebra plana with marked loss of height of a single vertebral body (Fig. 138.36). With vertebral involvement, soft tissue extension into the spinal canal may be apparent and is best assessed by MRI. The height of affected vertebral segments tends to reconstitute after therapy. Involvement of the posterior elements may occur but is less common than vertebral body involvement.[184–186]

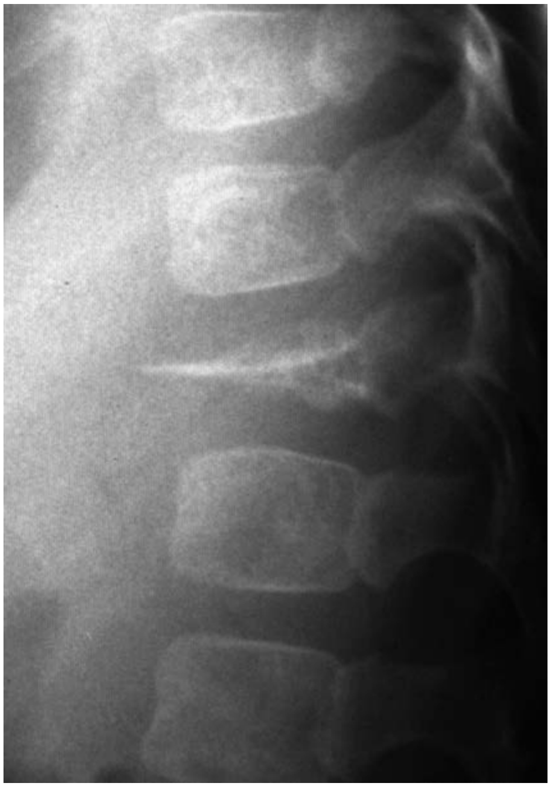

**Figure 138.36. Vertebra plana.** Lateral spine radiograph shows vertebra plana of a single vertebral body as a sequela of Langerhans cell histiocytosis in a 20-month-old girl.

The imaging appearance of LCH depends on the stage and activity of the lesions. The natural history is for spontaneous involution of some lesions to occur. Even at the time of diagnosis, some lesions may be present that are already in a state of involution or quiescence. Involuting lesions will be less well defined and will show sclerosis. Both CT and MRI can be used for further delineation of osseous lesions. On CT, active lesions usually have a well-defined, nonsclerotic margin. A cortical break and soft tissue mass may be seen. MRI is preferred to CT, owing to the lack of ionizing radiation and superior tissue contrast. On MRI, active lesions are composed of soft tissue, which is low signal on T1- and high signal on T2-weighted imaging, which enhances relatively homogeneously (see e-Fig. 138.35). About half of the lesions will be hyperintense to muscle on T1-weighted images, and extensive bone marrow and soft tissue edema produces high signal on T2-weighted images and enhances (Fig. 138.37). LCH lesions that disrupt the cortex may produce a sizable soft tissue mass (seen in 30% of cases on MRI). Older, involuted, or involuting lesions appear as low signal on T1- and T2-weighted images. Also, a multiplicity of lesions is very suggestive of LCH, as opposed to many other entities that are usually unifocal. If LCH is a consideration, a radiographic skeletal survey may be beneficial in identifying other lesions. Often, the presenting lesion is not at the best site for biopsy, and other

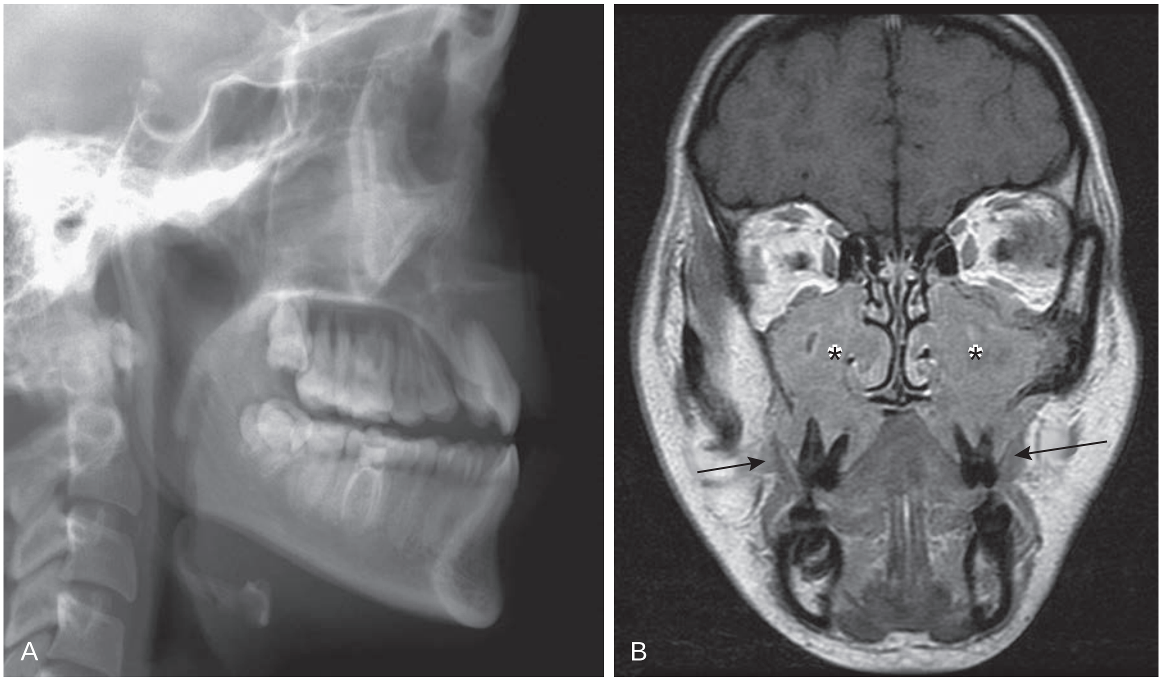

**e-Figure 138.35. Langerhans cell histiocytosis in a 16-year-old girl.** Lateral radiograph (A) and coronal T1-weighted MR image with gadolinium show “floating” maxillary teeth with loss of the normal lamina dura (*arrows* in B). Enhancing soft tissue (*asterisks* in B) fills the maxillary sinuses and replaces the maxilla.

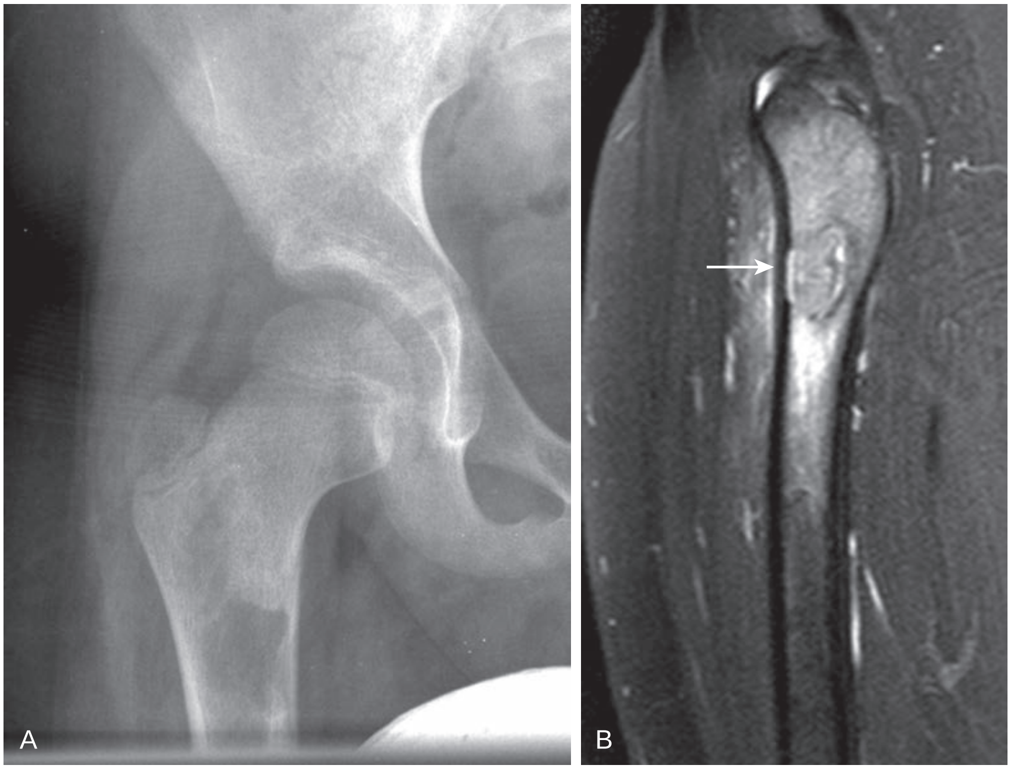

**Figure 138.37. Langerhans cell histiocytosis in an 8-year-old boy.** (A) Radiograph demonstrates a lytic lesion in the right subtrochanteric femur. (B) Short-tau inversion recovery sagittal MR image of the right femur demonstrates the primary mass *(arrow)* with extensive adjacent bone and soft tissue edema.

unsuspected sites may prove more suitable for tissue diagnosis. Because multiple skeletal lesions may coexist, skeletal imaging is necessary at the time of diagnosis and for purposes of follow-up. Some controversy exists about the relative accuracy of radiographic skeletal surveys and radionuclide bone scintigraphy, because up to 35% of lesions may be missed by bone scans.

Whole-body MRI may become an alternative method for identifying and following multifocal disease. PET scans have also shown utility in identifying sites of active disease and for following response to therapy.[187–189]

***Treatment.*** LCH localized to the skeleton carries a favorable prognosis. Recurrences are not uncommon. Solitary lesions are watched and usually involute spontaneously. More aggressive therapy may be occasionally warranted, depending on symptoms and lesion characteristics. Curettage and ablative techniques have been used, and children with multiple lesions and/or associated systemic disease are treated more aggressively with steroids and chemotherapy.[190] The disease is thus treated in a manner similar to that for a malignant process. The morbidity in children with systemic disease varies depending on the organs involved and the histologic pattern of disease. Children in whom organ function is unaffected and who respond well to initial therapy show a better long-term prognosis. Mortality of disseminated disease is approximately 10%.

## Osseous Tumors

### Osteoid Osteoma

***Overview, Etiologies, Pathophysiology, and Clinical Presentation.*** Osteoid osteoma is a common, benign tumor of bone that has a characteristic presentation and radiologic appearance. These tumors occur predominantly in boys, usually those in the second decade of life; however, it is not uncommon in both sexes from the first decade until the mid fourth decade, with a strong prevalence in whites. Pathologically, osteoid osteoma consists of a nidus that is usually surrounded by dense sclerotic bone. The nidus contains interlacing trabeculae at various stages of ossification within a stroma of loose, vascular connective tissue. Three types of osteoid osteoma are recognized: cortical (most common), cancellous or medullary, and subperiosteal (least common). The latter two types produce less sclerotic bone than cortical lesions, making radiologic diagnosis difficult. Osteoid osteomas can also be subdivided into *extraarticular* and *intraarticular* types. The incidence of medullary and subperiosteal types is higher at juxtaarticular and intraarticular locations.

Osteoid osteomas may develop in any bone. The single most common location of osteoid osteoma is the femur, and specifically, the femoral neck. The tibia is the next most frequent site. Osteoid osteomas occur less frequently in the upper extremities than in the lower extremities but frequently affect the tubular bones of the hands and feet. Osteoid osteomas most commonly affect the metaphysis or metadiaphysis, less commonly the diaphysis, and rarely the epiphysis. They are less common in flat bones and the spine, where they tend to affect the vertebral posterior arches. In such cases, patients usually are seen initially with painful scoliosis.[191] The classic presentation of osteoid osteoma is localized pain that is worse at night and relieved by nonsteroidal anti-inflammatory drugs (NSAIDs). Lesions near a joint may mimic arthritis.

***Imaging.*** Radiographically, the nidus may be purely radiolucent or may contain a dense center. The lucent nidus ranges from a few millimeters to 15 mm in diameter. With cortical osteoid osteomas, the nidus is encased by a broad zone of dense bone (Fig. 138.38).[192] Intraarticular osteoid osteomas tend to have little reactive bone or periosteal new bone formation. This type most frequently affects the hip, where it causes osteopenia and joint effusion.[193] Regardless of location, the nidus of an osteoma may be difficult to see on radiography.

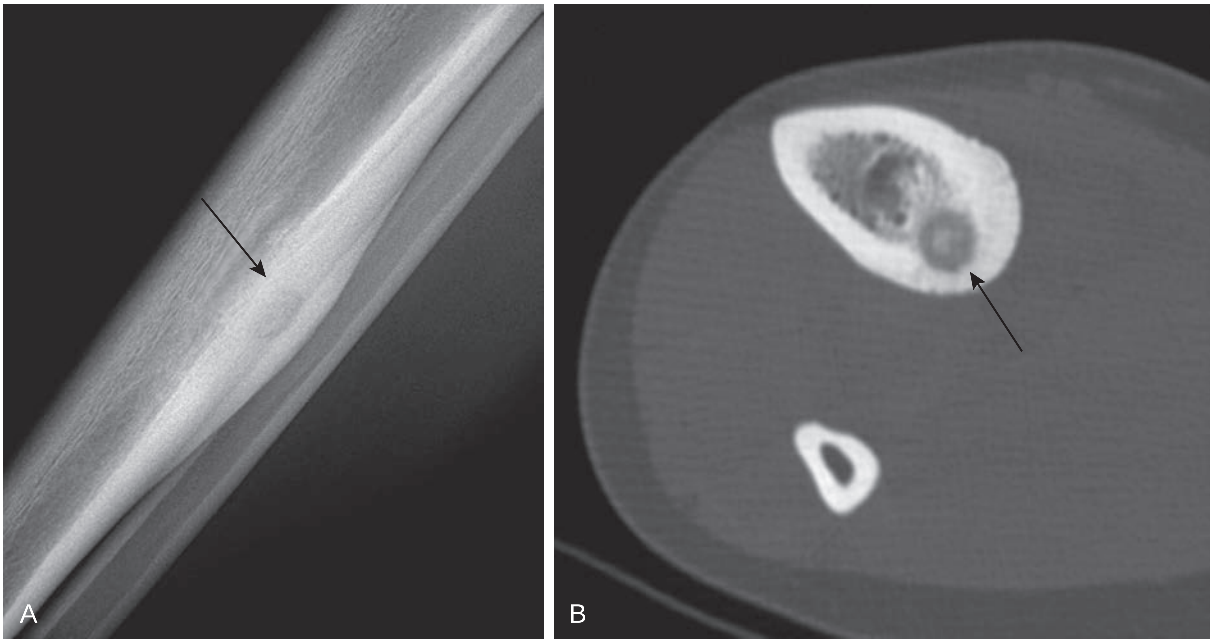

**Figure 138.38. Osteoid osteoma of the tibia in a 15-year-old girl.** (A) Radiograph shows cortical thickening posteriorly. The lucent nidus is faintly seen *(arrow)*. (B) CT better shows the nidus *(arrow)*. A small radiopaque sequestrum is present within the nidus.

CT is valuable in showing the lesion, confirming the diagnosis, and determining the anatomic location of the lesion before percutaneous therapy or surgical excision. The CT appearance of a lucent nidus with central sequestrum opacity and surrounding sclerosis is usually diagnostic of osteoid osteoma, particularly if the clinical presentation is classic (see Fig. 138.38). Intramedullary and subperiosteal lesions show less sclerosis. Subperiosteal osteoid osteomas lie on top of and may erode the cortex.[194] Also they may or may not have ossification within the nidus. Without the ossification, findings are less specific.

On MRI, low intensity may be seen on both T1 and T2 images, depending on the relative amount of ossification and fibrovascular tissue. Although there is no signal from the sclerotic bone, the inherent contrast resolution of MRI provides precise definition of potentially extensive reactive changes in the bone marrow and adjacent soft tissues. Osteoid osteoma may produce an intense inflammatory response within adjacent bone, joint, and soft tissues. If the nidus is not identified, a more aggressive process can be suggested.[195] Both the nidus and the adjacent inflamed tissues enhance with gadolinium.[196] However, if dynamic postcontrast images are obtained, the nidus will show peak enhancement in the early arterial phase with subsequent partial washout, while the reactive changes in the adjacent marrow will show slower, progressive enhancement.[197] The use of dynamic enhancement on MRI is even more important in atypical subperiosteal, juxtaarticular, and intraarticular locations.[198] Juxta- and intraarticular osteoid osteomas may produce reactive joint effusions and synovitis seen on MRI.

The chief imaging-based differential diagnoses for osteoid osteoma are stress fracture and osteomyelitis. Usually, clinical presentation and laboratory results point toward the correct diagnosis. Imaging findings of osteoid osteoma tend to be specific.

***Treatment.*** The traditional treatment for osteoid osteoma has been surgical excision, however, localization of the lesion and confirmation of excision may be challenging in the operating room. Therefore percutaneous methods of treatment have been developed, including excision with a large-bore needle or drill, cryoablation, and percutaneous radiofrequency ablation, which is now the preferred method of treatment.[199,200] Complex lesions or lesions located where percutaneous methods are contraindicated may still require surgical excision. Surgical or percutaneous methods are successful in approximately 90% of patients on the initial attempt.

### Osteoblastoma

***Overview, Etiologies, Pathophysiology, and Clinical Presentation.*** Osteoblastomas are closely related to osteoid osteomas and have in the past been considered a larger version of that tumor (giant osteoid osteoma). The two lesions are nearly identical histologically.[201] Osteoblastomas consists of numerous osteoblast-lined trabeculae that contain osteoid, however, these trabeculae are less organized than those in osteoid osteomas.[202] These tumors are often distinguished by size: tumors less than 1.5 cm in diameter are considered to be osteoid osteomas, whereas tumors larger than 1.5 cm are usually osteoblastomas.[203] The two types of tumors can also be distinguished by differences in clinical presentation, anatomic location, and imaging features. Osteoblastoma most commonly occurs in patients in the second and third decades of life,[204] and it is more common in boys. Osteoblastomas are not associated with a typical pattern of pain, and if painful, they do not typically respond to NSAIDs. Many osteoblastomas are found in the posterior elements of the vertebrae, where they can cause scoliosis and neurologic deficits. Nearly half of these tumors occur in the appendicular skeleton, primarily in the proximal femoral diaphysis and metaphysis. Tibial lesions are next most common. Long-bone lesions may be cortical or medullary in location. Another characteristic location for osteoblastoma is the neck of the talus, usually at its dorsal margin.

***Imaging.*** Osteoblastoma appears as three distinct radiologic variants: (1) an osteoid osteoma–like appearance, but larger; (2) an ABC-like appearance, most commonly in the spine; and (3) an aggressive appearance that mimics a malignancy, which is uncommon.[205] Osteoblastomas vary from 1.5 to 10 cm in size. Most are lytic with a well-defined sclerotic margin, but the tumor usually lacks the wide, dense rim of sclerosis typical of osteoid osteoma. Lesions in the spine are often expansile (Fig. 138.39). Adjacent sclerosis with spinal lesions may be minimal or absent. In the long bones, osteoblastomas appear radiologically as round or oval lucent, eccentric tumors within the medulla or cortex. Some sclerosis is

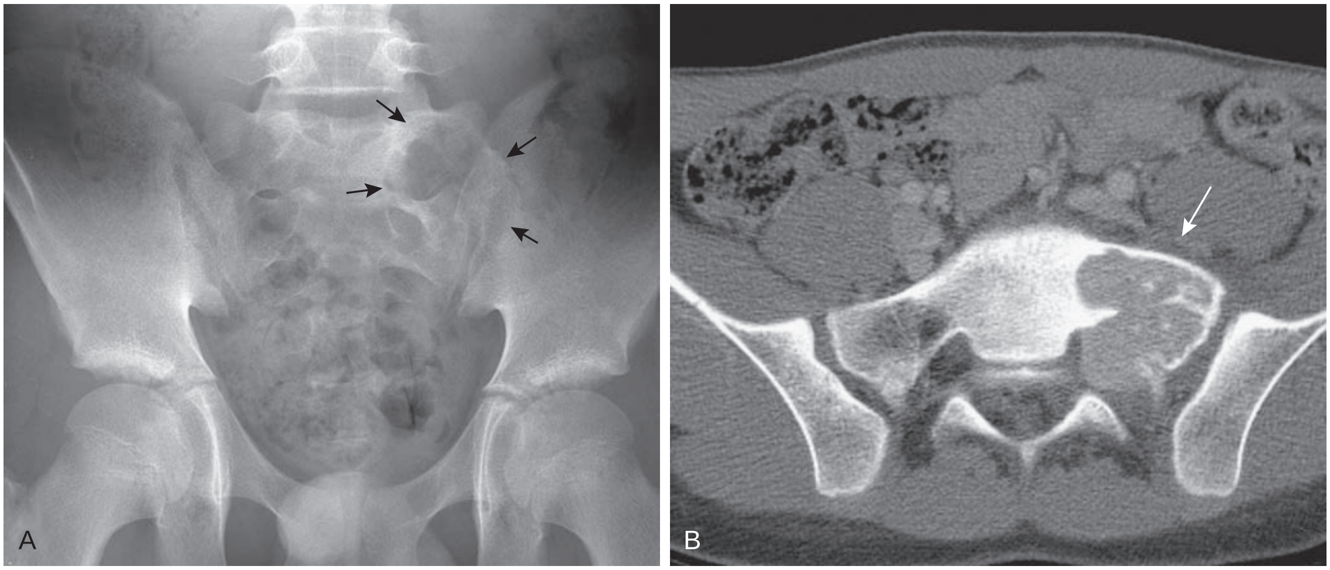

**Figure 138.39. Osteoblastoma of the sacrum in a 12-year-old boy.** A well-defined, lucent, expansile lesion *(arrows)* is seen within the left sacrum on radiography (A) and CT (B).

**TABLE 138.1** Differentiating Features of Osteosarcoma and Ewing Sarcoma

| Feature | Osteosarcoma | Ewing Sarcoma |
|---|---|---|
| Age range | 15-25 years | 0-25 years |
| Incidence | More common | Less common<br>Rare in nonwhites |
| Location | Metaphyses of long bones | Metadiaphysis of long bones<br>Axial, flat-bone involvement more common than osteosarcoma |
| Matrix | Usually “cloudlike” mineralization | Not mineralized or sclerotic |
| Periosteal reaction | “Sunburst”<br>Codman triangles | “Onionskin” |
| Metastases | Lung (80%)<br>Bone (20%) | Lung, rarely bone, marrow, lymph nodes |
| Other | Occasional multifocal disease<br>Association with retinoblastoma | 11 : 22 translocation<br>Radiation sensitive |

seen adjacent to the lesion, and mineralization of the matrix is frequently present. Periosteal reaction is common and is solid or layered. Talar lesions may expand into the soft tissues, and osteoporosis of the talus and other bones of the foot may be an associated finding. The calcified or ossified matrix of an osteoblastoma and the thin, bony outer shell are especially well visualized on CT images. Edema in the soft tissues or marrow may give high signal on T2-weighted MRI, but signal characteristics are not specific; osteoid within the lesion may cause areas of decreased signal, and bone scans may help in determining the location of a lesion. In addition, osteoblastomas are relatively vascular; hence angiography may reveal a dense capillary blush.

***Treatment.*** Treatment is by surgical excision or curettage. There is a moderate recurrence rate.

## Malignant Bone Tumors

Approximately 50% of all bone tumors in the pediatric age group are malignant; nearly two-thirds of these are osteosarcomas. Ewing sarcomas of bone comprise most of the remainder. Other types of osseous malignancies, such as chondrosarcoma, are extremely rare in children, although NHL occasionally occurs as a primary bone neoplasm. Osteosarcoma and Ewing sarcoma differ sufficiently, both in their clinical and imaging presentation, such that they can usually be distinguished from one another. Their characteristic features, discussed in this chapter, are summarized in Table 138.1.

### Osteosarcoma

***Overview, Etiologies, Pathophysiology, and Clinical Presentation.*** Osteosarcoma is the most common malignant primary bone tumor in the pediatric population. The peak incidence of osteosarcoma is in patients 15 to 25 years of age, but it has been described in a 19-month-old girl.[206] The tumors are slightly more common in males, and the long bones are affected in approximately 70% of cases. Most occur around the knee. The femur is the most common bone affected, followed by the tibia and then the humerus. The face, mandible, cranium, and axial skeleton are among the less commonly affected sites (Fig. 138.40). Most osteosarcomas are single, primary neoplasms that arise from the medullary cavity of the metaphyses of the long bones. The diaphyses alone are less commonly involved, which occurs in 2% to 11% of cases; an epiphyseal origin of osteosarcoma is extremely rare. Osteosarcomas can involve multiple skeletal sites synchronously, a condition known as *osteosarcomatosis.*[207,208] Extremely rare in children, extraskeletal osteosarcomas are found in various organs or in the soft tissues of the extremities of adults.[209,210]

Often referred to as *conventional osteosarcomas*, most are considered to be high grade because of their degree of cellular atypia and anaplasia. Other much less common categories of this tumor include well-differentiated medullary osteosarcoma, telangiectatic osteosarcoma, and surface osteosarcomas, including intracortical osteosarcoma and parosteal, periosteal, and high-grade surface

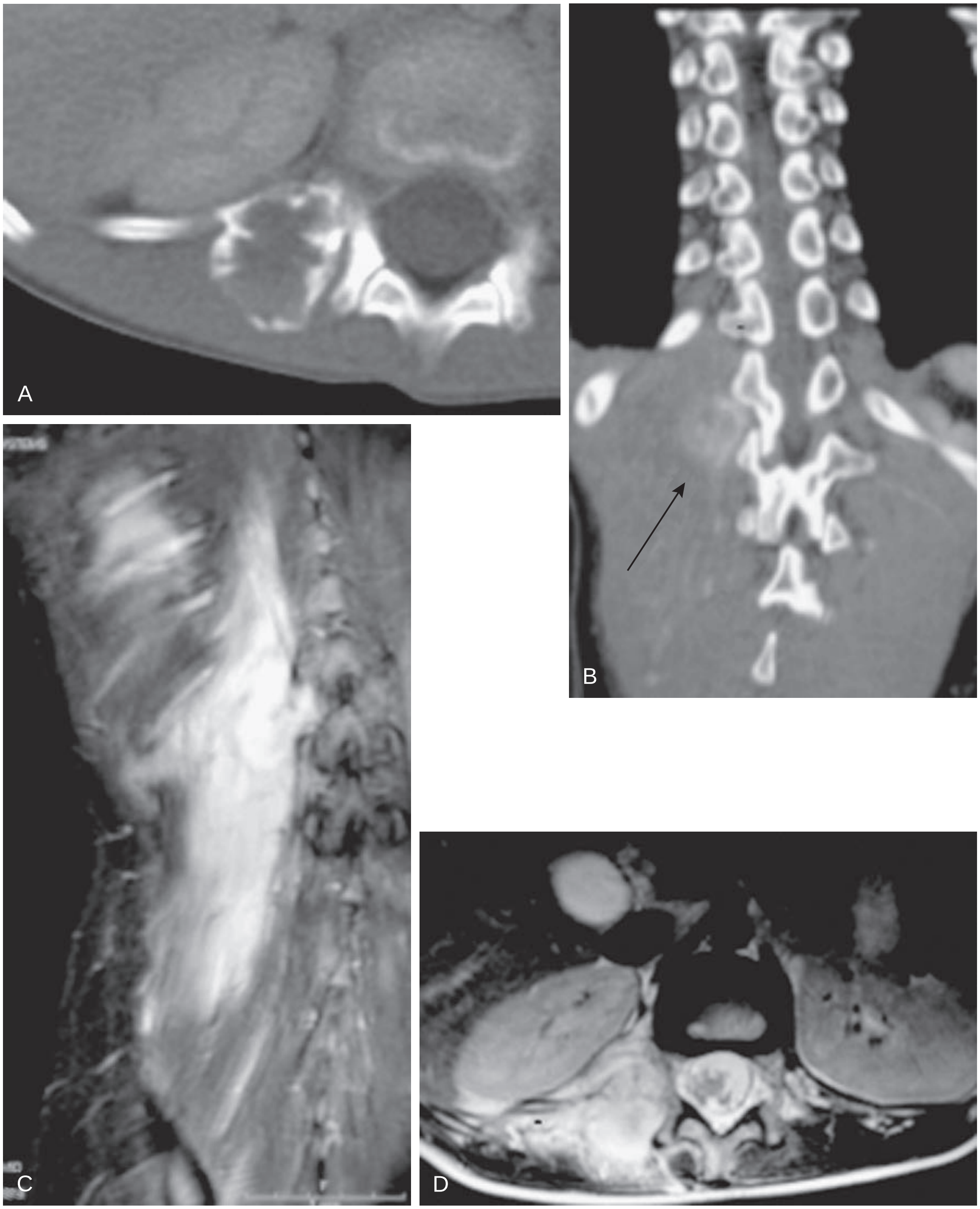

**Figure 138.40. Osteosarcoma of the spine in an 8-year-old girl.** (A) Axial contrast-enhanced CT through T12 after 10 weeks of chemotherapy shows a peripherally sclerotic expansile mass arising from the right costovertebral junction. Note disruption of the cortex posteriorly. (B) Coronal reconstruction shows the relationship of the mass *(arrow)* to the apex of the scoliosis. (C) Coronal short-tau inversion recovery MR image demonstrates massive edema in the paraspinal muscles in response to the osteosarcoma. (D) Axial contrast-enhanced fat saturated T1-weighted MR image demonstrates intense tumor enhancement and moderate enhancement of the surrounding paraspinous musculature.

osteosarcomas. Secondary osteosarcomas, which are rare in children, are usually associated with previous radiation therapy. Osteosarcoma can also arise in patients with inherited (usually bilateral) retinoblastoma who have a defect in a specific gene, or it can arise in patients who have undergone a spontaneous mutation of that gene. Although radiation therapy increases the incidence of osteosarcoma in these patients, secondary osteosarcoma may develop in sites remote from radiation fields. Osteosarcoma unassociated with other malignancies is occasionally familial and has been identified in siblings.

## Intramedullary Osteosarcoma

### Conventional Osteosarcoma

***Overview, Etiologies, Pathophysiology, and Clinical Presentation.*** Approximately 75% of osteosarcomas are the high-grade variant, and 75% of cases occur in patients between the ages of 15 and 25 years. The histologic hallmark of osteosarcoma is the presence of an osteoid matrix produced by sarcoma cells. In most cases, there is extensive immature bone formation. However, other tissues may predominate in the tumor matrix. The three main types of osteosarcoma, based on matrix type, are *osteoblastic*, *chondroblastic*, and *fibroblastic*. These tumors have differing mineral content.[210]

***Imaging.*** Radiography remains the primary method of diagnosis for conventional osteosarcoma. Other imaging methods are used mainly for staging purposes and to assist with surgical planning. Osteosarcoma typically manifests as a large, mixed sclerotic–lytic mass with a cloudlike matrix that involves the long-bone metaphyses. The tumors cause cortical erosion and destruction rather than expansion. Resultant periosteal new bone formation, often of the spiculated "sunburst" variety (Fig. 138.41), and periosteal elevation are often observed, frequently with Codman triangles (Fig. 138.42). However, conventional osteosarcomas are occasionally purely lytic and exhibit no periosteal reaction. Osteosarcomas with chondroblastic elements tend to be more lytic on radiography (see Fig. 138.42), and osteoblastic dominant osteosarcomas will demonstrate increased osteoid matrix (see Fig. 138.41).

CT is superior to radiographs for delineating osteoid matrix. Like radiographs, CT often underestimates the true extent of bone involvement (Fig. 138.43).

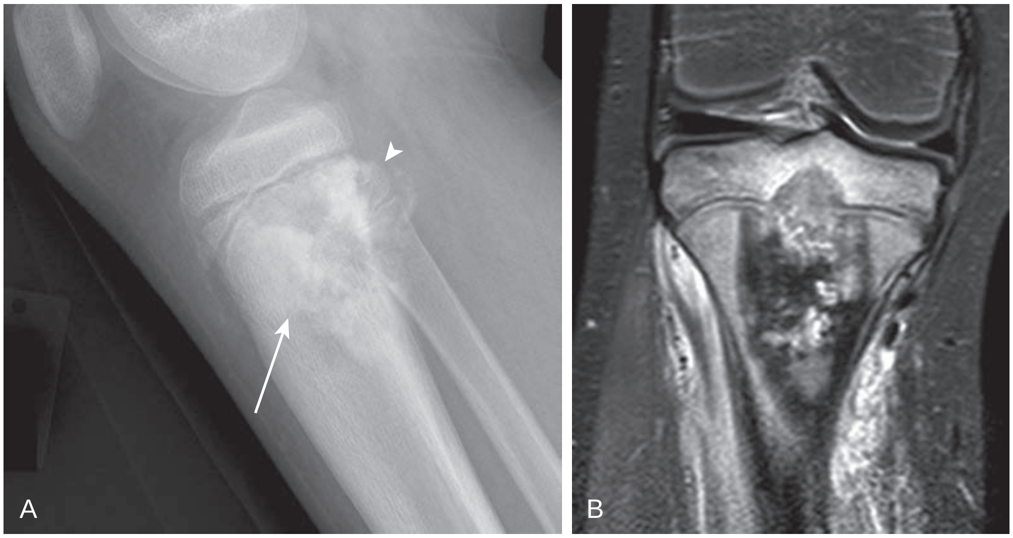

**Figure 138.41. Proximal tibial osteosarcoma in an 11-year-old boy.** (A) Radiograph demonstrates osteoblastic osteosarcoma with osteoid matrix *(arrow)* and "sunburst" periostitis *(arrowhead)*. (B) Corresponding short-tau inversion recovery coronal MR image shows low signal intensity throughout the majority of the mass, indicative of osteoid matrix. Note also the presence of transphyseal extension through the central physis.

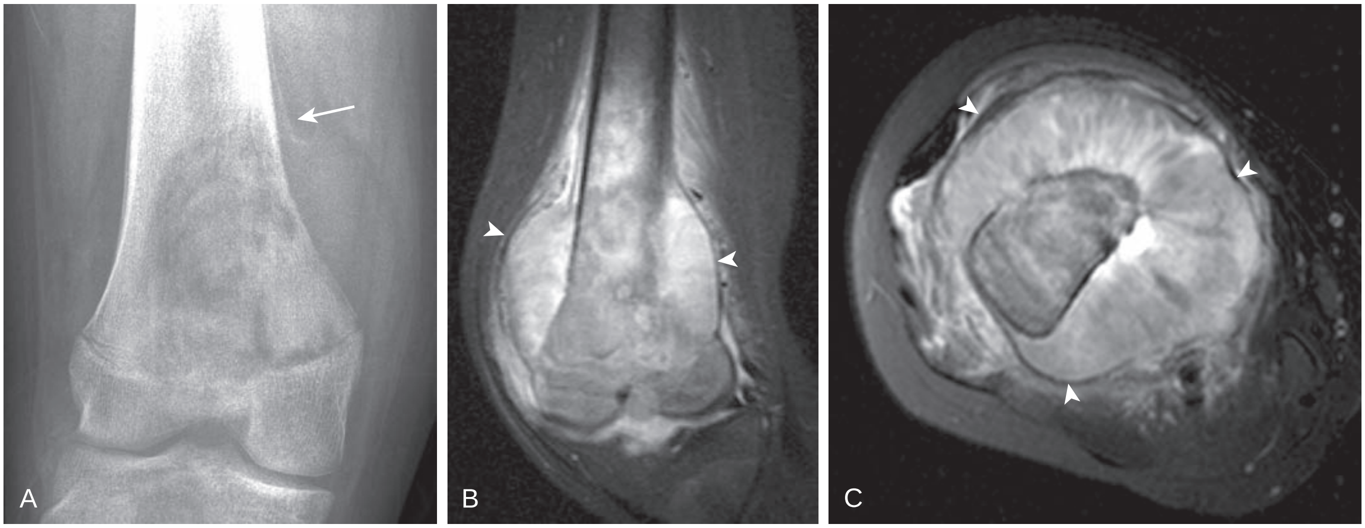

**Figure 138.42. Osteosarcoma in a 13-year-old girl.** (A) Radiograph demonstrates permeative lytic destruction in the distal femur metaphysis with aggressive periosteal reaction with a Codman triangle *(arrow)*. Short-tau inversion recovery coronal (B) and axial (C) MR image demonstrates distal femoral metaphyseal mass with transphyseal transgression into the epiphysis with a large extraosseous tumor component. Note the displaced periosteal envelope *(arrowheads)*.

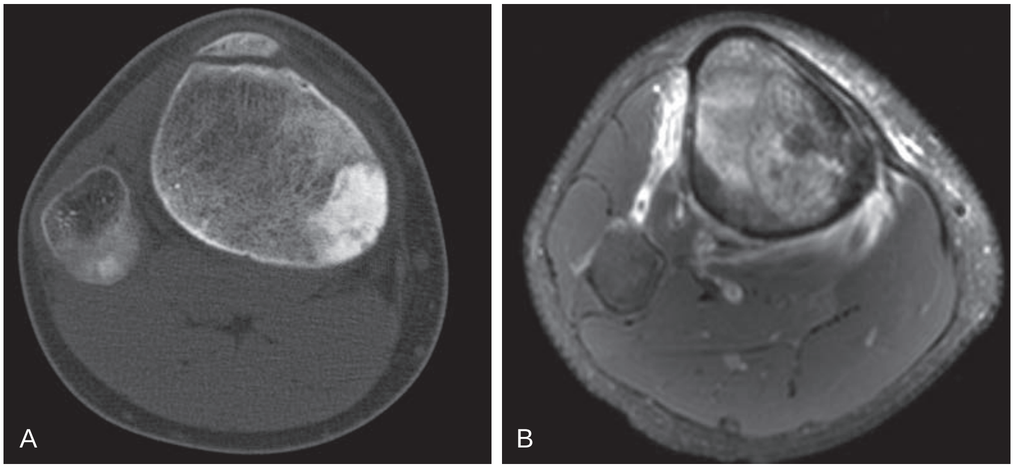

**Figure 138.43. Tibial osteosarcoma in a 14-year-old boy.** (A) Axial CT demonstrates intraosseous osteoblastic matrix replacing a portion of the medullary cavity. (B) Short-tau inversion recovery axial MR image through the same level demonstrates more extensive intramedullary involvement.

MRI is used to evaluate osteosarcoma. The longitudinal extent of marrow involvement, an important determinant of surgical therapy, is accurately shown as well-defined hypointense signal within hyperintense fatty marrow on T1-weighted images obtained in either coronal or sagittal planes. It is important to obtain a longitudinal T1-weighted image of the entire bone to measure intramedullary tumor length, to assess possible epiphyseal involvement (seen in as many as 80% of metaphyseal tumors), and to detect skip metastases that occur in a small percentage of cases. On T2-weighted images, the tumor-containing marrow can be either hyperintense or, if there is sufficient bone formation, hypointense to normal fat (see Fig. 138.41). The soft tissue component is usually of heterogeneous, mainly high-intensity signal that contrasts greatly with surrounding structures. STIR images are very sensitive to the water content of tumors and adjacent bone marrow edema, thus the intramedullary length of tumor extension may be overestimated on STIR sequences.[211] Contrast-enhanced T1-weighted images, preferably obtained with fat saturation, provide similar contrast and better signal-to-noise ratios than T2-weighted images. Furthermore, contrast-enhanced T1-weighted images are especially useful in determining the relationship between the tumor and the major blood vessels, in detecting joint involvement in the presence of effusion,[212] and in estimating the amount of necrosis within the tumor. Osteosarcoma is frequently accompanied by edema of the adjacent soft tissues that is hyperintense to muscle on T2-weighted STIR images and contrast-enhanced T1-weighted images. This edema can be localized to the tumor periphery, or it can involve whole muscle groups, as in the case of larger tumors. The latter finding has been associated with a poor prognosis.[213]

Between 10% and 20% of patients with osteosarcoma have metastases at the time of diagnosis, mainly to the lungs; therefore chest CT is essential in the search for pulmonary lesions at presentation. Like the primary tumor, these metastases can be calcified and therefore difficult to distinguish from calcified granulomas. Pleural-based lung metastases can also produce pneumothorax, hemothorax, or malignant pleural effusion. Such findings may be the first sign of pulmonary metastases at the time of diagnosis or at follow-up. Bone metastases are much less frequent, but radionuclide bone scans are justified to detect these lesions and to assess the extent of the primary tumor.

### Telangiectatic Osteosarcoma

***Overview, Etiologies, Pathophysiology, and Clinical Presentation.*** Telangiectatic osteosarcoma comprises about 2% of all osteosarcomas. Like conventional osteosarcomas, telangiectatic osteosarcoma tends to occur in the long bones adjacent to the knee and is seen more frequently in boys than in girls. These tumors contain little osteoid and do not form bone but rather are composed of single or multiple cavities that contain blood or necrotic tumor with septa of anaplastic cells.[214,215] Telangiectatic osteosarcomas by definition are composed of approximately 90% cystic components before treatment.[216]

***Imaging.*** Radiographically, telangiectatic osteosarcomas tend to be lytic and expand rather than destroy the cortex; they may also be associated with a soft tissue mass. Except for the presence of malignant cells that are often at the periphery of the cavity, the pathologic appearance of telangiectatic osteosarcoma mimics that of an ABC. Indeed, on MRI, the appearance of telangiectatic osteosarcoma and ABC may be identical; both may have single or multiple fluid-fluid levels produced by blood products of differing ages that are best demonstrated on T2-weighted images.[217] Telangiectatic osteosarcomas are characterized by enhancing soft tissue in the periphery and septations of the tumor, features absent in ABCs.[218] Biopsy of the soft tissue component is necessary to differentiate telangiectatic osteosarcoma from an ABC. The prognosis of patients with telangiectatic osteosarcoma is similar to those with conventional osteosarcoma.

### Surface Osteosarcomas

***Overview, Etiologies, Pathophysiology, and Clinical Presentation.*** Surface osteosarcomas are classified by histologic grade as low-, intermediate-, and high-grade lesions.[219] *Parosteal osteosarcoma* is more common in girls than in boys, tends to occur after skeletal maturity has been achieved, and is of low histologic grade. *Periosteal osteosarcoma* probably arises from the deep layers of periosteum or the outer cortex and is classified as an intermediate-grade osteosarcoma; most periosteal osteosarcomas are chondroblastic,[220] and they may be mistaken for a chondrosarcoma by pathologists unfamiliar with pediatric orthopedic oncology. *High-grade surface osteosarcomas* comprise dedifferentiated parosteal osteosarcoma and high-grade surface osteosarcoma. The origin of high-grade surface osteosarcoma is controversial; histologically, it is difficult to differentiate from the much more common, conventional, intramedullary high-grade osteosarcomas.

Patients with parosteal osteosarcoma generally have an excellent prognosis, although this may be affected adversely by ingrowth into the medullary cavity. Parosteal osteosarcomas are composed of extensive osteoid tissue with a fibrous stroma and form a lobulated, ossified, juxtacortical mass. Patients with periosteal and high-grade surface osteosarcomas have similar prognoses

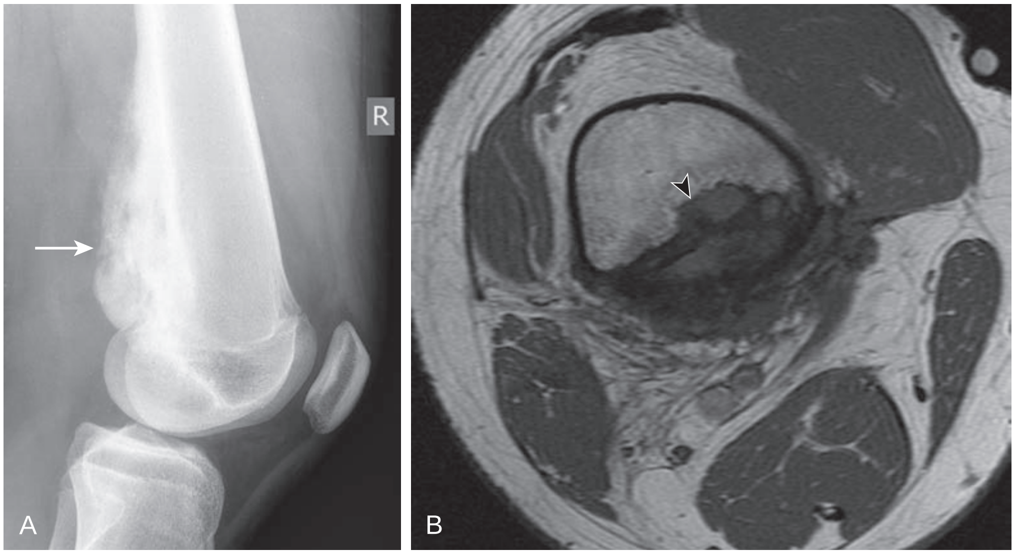

**Figure 138.44. Parosteal osteosarcoma in a 14-year-old boy.** (A) Lateral radiograph demonstrates a surface-based osteoblastic mass in the distal femur *(arrow)*. (B) T1-weighted axial MR image through the distal femur demonstrates the surface-based mass with intramedullary extension *(arrowhead)*.

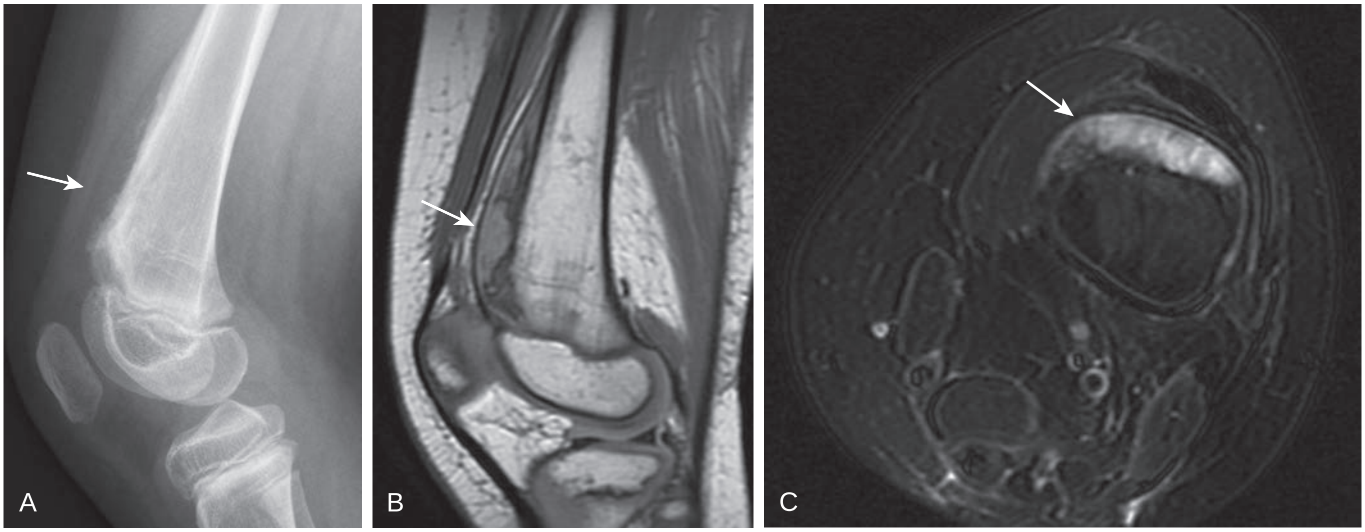

**Figure 138.45. Periosteal osteosarcoma in an 11-year-old boy.** (A) Lateral radiograph demonstrates aggressive, perpendicularly oriented periosteal reaction with little to no matrix *(arrow)*. (B) Sagittal proton-density MR image demonstrates an intermediate signal lesion. (C) On T2-weighted fat-saturated axial MRI, it is hyperintense and surface based, indicative of its chondroblastic composition *(arrow)*.

compared with those with conventional, intramedullary high-grade osteosarcomas.

***Imaging.*** Parosteal osteosarcomas are very osteoblastic and are slow growing. They demonstrate mature periosteal ossification and most commonly occur in the posterior aspect of the distal femur (Fig. 138.44). Early lesions may have a radiologic cleavage plane between the cortex and the tumor. Superficially, parosteal osteosarcoma may mimic a sessile osteochondroma. MRI is used to define the degree of intramedullary extension, if present, and adjacent neurovascular and muscle involvement.

Periosteal osteosarcomas also arise from the surface and may have adjacent intramedullary marrow edema, but true invasion is rare.[220] Because these lesions are invariably chondroblastic, they often have little to no matrix on radiography and are hyperintense on fluid-sensitive sequences (Fig. 138.45). Superficially, these lesions may mimic a juxtacortical chondroma.

***Treatment.*** Osteosarcomas are not radiosensitive. Thus treatment consists of preoperative chemotherapy; extirpation of resectable lesions, usually by limb-sparing surgery; and postoperative chemotherapy. MRI serves as a surgical road map to define the presence or absence of neurovascular involvement, physeal and epiphyseal extension, and joint involvement. If the physis is spared, physeal-sparing surgery can be attempted with an intercalary graft. When the epiphysis is involved, morbidity is higher, and a joint prosthesis is necessary.

Prognosis is influenced by response to initial chemotherapy, which is evaluated postoperatively by histologic estimation of necrosis within the treated tumor. Little change in tumor size is expected, even in tumors that respond well to chemotherapy. Imaging methods of assessing the effects of therapy include thallium-201 scintigraphy and dynamic contrast-enhanced MRI. Although PET and PET-CT appear to be useful in both staging and monitoring response, experience is currently limited in its use for osteosarcoma and other bone tumors. Long-term follow-up of osteosarcoma and other malignant bone tumors in children is essential.[221,222]

Bone scintigraphy and chest CT should be performed periodically after treatment, especially within the 2 years after therapy: 80% of relapses occur in the lung only, and 20% occur in the skeleton. Local or distant lymph node involvement is extremely rare.

### Ewing Sarcoma

***Overview, Etiologies, Pathophysiology, and Clinical Presentation.*** In 1921 James Ewing described a radium-sensitive bone tumor, which he called an *endothelioma*, that consisted of sheets of small polyhedral cells of probable endothelial origin.[223] Although the origin of this undifferentiated tumor has been debated since its initial description, what we now know as *Ewing sarcoma* has proved to be a distinct entity with characteristic histologic, radiologic, and cytogenetic features. The Ewing family of tumors includes Ewing sarcoma of bone, EOES, and primitive neuroectodermal tumor (PNET), also known as *peripheral neuroepithelioma*. PNETs exhibit neural differentiation and may arise from either bone or soft tissues. The Ewing family of tumors shares a distinctive cytogenetic feature: reciprocal translocation of chromosome bands q24 and q12 of chromosomes 11 and 22. This same translocation is also found in Askin tumor of the thorax.[224-226]

In younger patients, Ewing sarcoma of bone occurs less frequently than osteosarcoma, with 2.9 cases per million diagnosed in patients younger than 20 years of age. Most cases are detected in patients between 10 and 25 years of age (median 15 years). Like osteosarcoma, Ewing sarcoma occurs slightly more often in boys and is much more common in whites. Fever, leukocytosis, and elevation of the erythrocyte sedimentation rate may accompany these neoplasms. More than 50% of Ewing sarcomas involve a single long bone. Flat bones are more commonly involved than osteosarcoma, particularly the pelvis, but also other flat bones such as the ribs, clavicle, and scapula. Within long bones, the metaphysis and diaphysis are the usual locations. Ewing sarcoma involving the bones of the hands and feet, often initially misdiagnosed as an infection, is rare. Most Ewing sarcomas appear to arise from the medullary cavity. Multifocal osseous involvement at the time of diagnosis is rare.[226-228]

***Imaging.*** The typical radiographic appearance of Ewing sarcoma in the long bones is that of a permeative lesion with a lamellar "onionskin" periosteal reaction (Fig. 138.46). However, nearly 40% of these tumors display diffuse sclerosis, sometimes with a mixed lytic–sclerotic pattern. The sclerosis correlates histologically with the presence of dead bone.[229] Because Ewing sarcomas do not ossify, soft tissue extension is often poorly detected by radiographs but is almost always apparent on CT or MRI (Fig. 138.47). Indeed, the soft tissue masses tend to be disproportionately large in comparison to the amount of bone destruction, and they are especially extensive in Ewing sarcoma of the pelvis (Fig. 138.48). Cortical permeation and destruction may be visible on CT or MRI. However, these tumors can permeate Haversian canals and can grow into the soft tissues without causing large areas of cortical loss. Extensive marrow involvement is particularly well shown as nonspecific low signal, isointense to muscle on T1-weighted images. Ewing sarcomas found in the medullary cavity display intermediate to high signal intensity on T2-weighted images. Rarely, Ewing sarcoma can arise from the surface of the bone rather than from the medullary cavity. In this periosteal or subperiosteal location, Ewing sarcoma resembles other surface malignancies, such as periosteal osteosarcoma with periosteal elevation and Codman triangles.[230] The affected cortex is typically excavated or saucerized,[231] and cross-sectional imaging is required to exclude medullary involvement. Patients with this form of Ewing sarcoma are thought to have a relatively favorable prognosis.

***Treatment.*** With appropriate multimodal therapy, the long-term survival rate of patients with nonmetastatic medullary Ewing sarcoma approaches that of patients with osteosarcoma (about 65%). In some series, tumor volume has been shown to influence prognosis. Survival of patients with pelvic tumors may be somewhat shortened and is much reduced in patients with metastatic disease. As many as 25% of patients with Ewing sarcoma have detectable metastases at the time of diagnosis; most of these are found in the lung, therefore chest CT is necessary for disease staging. Local and regional lymph node involvement may rarely occur, and metastases in bone or bone marrow are less frequent, although skip metastases have been reported.[232]

In addition to MRI of the primary tumor, bone scintigraphy, thoracic CT scanning, and bone marrow examination should be performed to detect possible disseminated disease. Early experience indicates that PET and PET-CT are useful for detection of metastatic sites of disease and for monitoring therapeutic response. Most Ewing sarcomas respond well to initial chemotherapy; increased bony sclerosis develops, and the soft tissue mass disappears.

Percentage change in size of the soft tissue mass appears to be an important prognostic indicator.[233] T2-weighted MRI may show an increase in intensity of the treated medullary component because of serous atrophy, with increased interstitial fluid of the yellow marrow and replacement of cytoplasmic lipid with serous material.

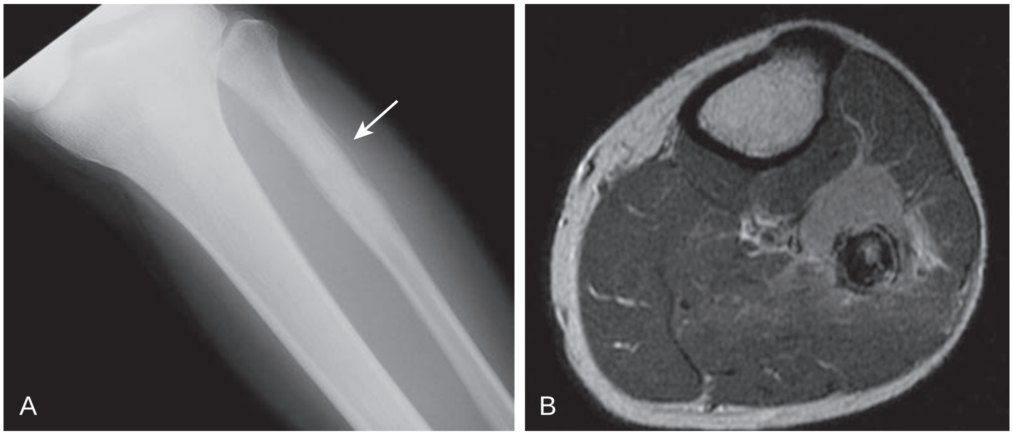

**Figure 138.46. Ewing sarcoma of the fibula in a 17-year-old.** (A) Anteroposterior radiograph of the leg demonstrates aggressive "onionskin" periostitis of the proximal fibula *(arrow)*. (B) T1-weighted axial postcontrast MR image demonstrates a large extraosseous mass that arises from the fibula with cortical destruction.

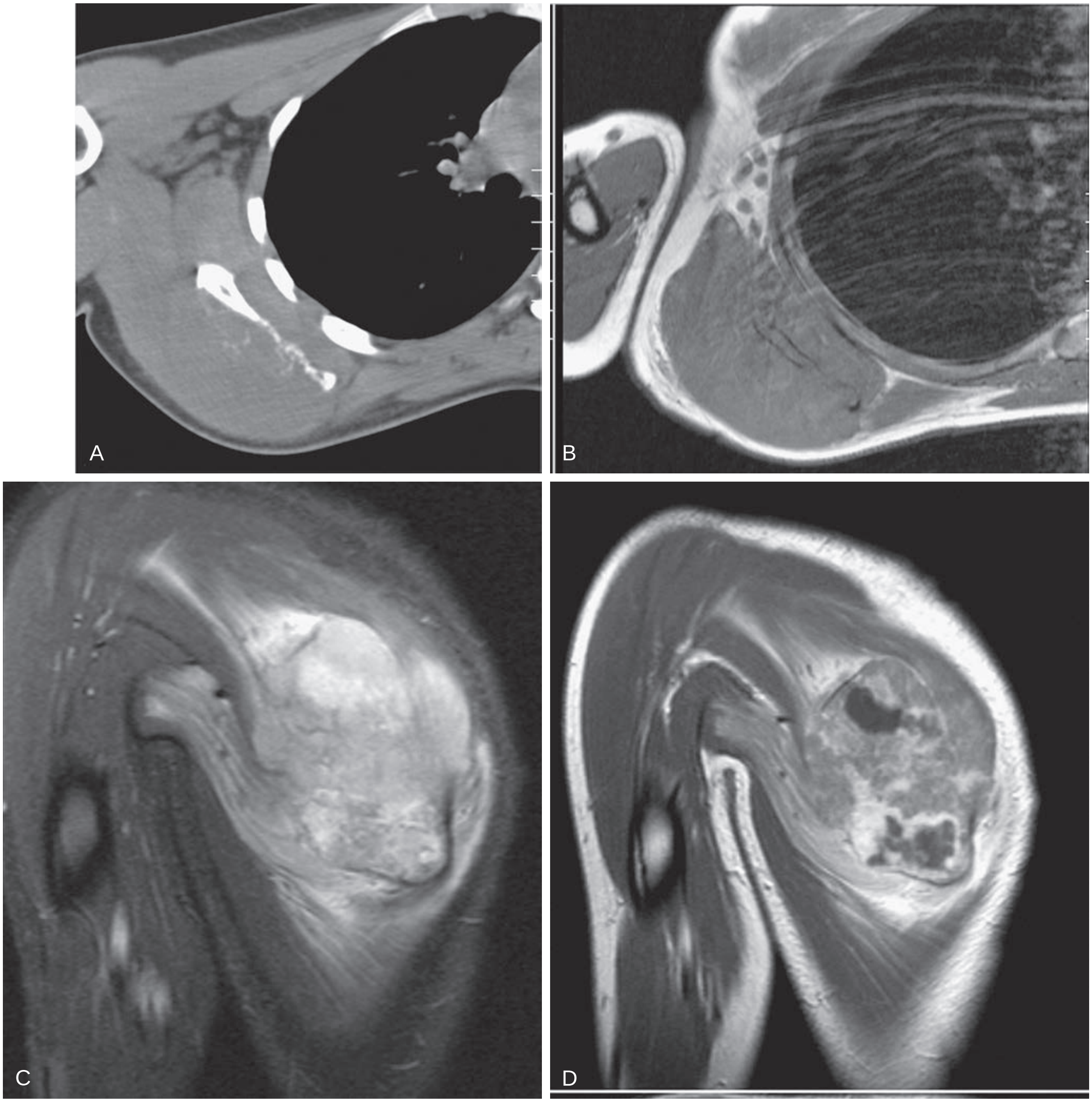

**Figure 138.47. Ewing sarcoma of the right scapula in a 16-year-old girl.** (A) Axial CT image shows a permeative pattern to the scapula with subtle dystrophic calcifications within the soft tissue mass. (B) T1 axial MR image shows marrow replacement and cortical destruction by the mass. (C) Short-tau inversion recovery sagittal MR image demonstrates a large heterogeneous mass with cortical destruction and intramuscular invasion. (D) T1 postcontrast MR image demonstrates heterogeneous central tumoral enhancement with areas of nonenhancement consistent with tumoral necrosis.

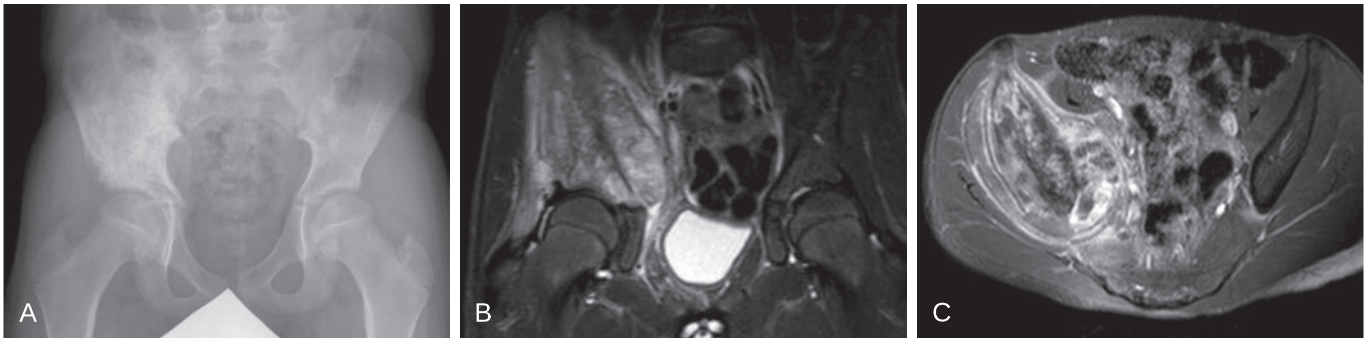

**Figure 138.48. Ewing sarcoma of the right iliac bone in an 11-year-old girl.** (A) Frontal radiograph of the pelvis demonstrates a mixed lytic and sclerotic lesion of the right iliac bone. (B) Short-tau inversion recovery coronal MR image demonstrates a right iliac mass with extraosseous extension. (C) Postcontrast T1-weighted axial MR image demonstrates heterogeneous enhancement of the mass, as it better delineates both extraperitoneal extension and posterior extension into the pelvic abductor muscles.

High T2-weighted signal intensity caused by radiation-induced inflammatory reactions may also be observed in those patients treated with radiation therapy.[234–237]

The surgical approach to resection of Ewing sarcoma is similar to osteosarcoma.

### KEY POINTS

- MRI features highly suggestive of soft tissue malignancy are neurovascular encasement, adjacent bone or joint involvement, and marrow abnormality.
- Fat-containing soft tissue masses in a child younger than 3 years of age is likely benign.
- In general, osteosarcoma has a predilection for the metaphysis, and Ewing sarcoma, for the diaphysis and flat bones.
- ABCs may be primary or secondary to another benign or malignant lesion.

## SUGGESTED READINGS

Laor T. MR imaging of soft tissue tumors and tumor-like lesions. *Pediatr Radiol*. 2004;34(1):24–37.

Levine SM, Lambiase RE, Petchprapa CN. Cortical lesions of the tibia: characteristic appearances at conventional radiography. *Radiographics*. 2003;23:157–177.

Murphey MD, Robbin MR, McRae GA, et al. The many faces of osteosarcoma. *Radiographics*. 1997;17:1205–1231.

Navarro OM, Laffan EE, Ngan B-Y. Pediatric soft-tissue tumors and pseudo-tumors: MR imaging features with pathologic correlation: part 1. Imaging approach, pseudotumors, vascular lesions, and adipocytic tumors. *Radiographics*. 2009;29(3):887–906.

## REFERENCES

Full references for this chapter can be found on www.expertconsult.com.

## REFERENCES

1. Brisse H, Orbach D, Klijanienko J, et al. Imaging and diagnostic strategy of soft tissue tumors in children. *Eur Radiol*. 2006;16(5):1147–1164.
2. Finlay K, Probyn L. Ultrasonography of lumps and bumps. *Can Assoc Radiol J*. 2002;53(1):39–49.
3. Bitran JD, Bekerman C, Golomb HM, et al. Scintigraphic evaluation of sarcomata in children and adults by Ga67 citrate. *Cancer*. 1978;42(4):1760–1765.
4. Howman-Giles R, Uren RF, Shaw PJ. Thallium-201 scintigraphy in pediatric soft-tissue tumors. *J Nucl Med*. 1995;36(8):1372–1376.
5. Navarro OM, Laffan EE, Ngan B-Y. Pediatric soft-tissue tumors and pseudo-tumors: MR imaging features with pathologic correlation: part 1. Imaging approach, pseudotumors, vascular lesions, and adipocytic tumors. *Radiographics*. 2009;29(3):887–906.
6. van Rijswijk CSP, Geirnaerdt MJA, Hogendoorn PCW, et al. Soft-tissue tumors: Value of static and dynamic gadopentetate dimeglumine-enhanced MR imaging in prediction of malignancy. *Radiology*. 2004;233(2):493–502.
7. Laor T. MR imaging of soft tissue tumors and tumor-like lesions. *Pediatr Radiol*. 2004;34(1):24–37.
8. Dinauer PA, Brixey CJ, Moncur JT, et al. Pathologic and MR imaging features of benign fibrous soft-tissue tumors in adults. *Radiographics*. 2007;27(1):173–187.
9. Shinagare AB, Ramaiya NH, Jagannathan JP, et al. A to Z of desmoid tumors. *AJR Am J Roentgenol*. 2011;197(6):W1008–W1014.
10. Shields CJ, Winter DC, Kirwan WO, et al. Desmoid tumours. *Eur J Surg Oncol*. 2001;27(8):701–706.
11. Romero JA, Kim EE, Kim CG, et al. 11 Different biologic features of desmoid tumors in adult and juvenile patients: MR demonstration. *J Comput Assist Tomogr*. 2006;19(5):782–787.
12. Rao BN, Horowitz ME, Parham DM, et al. Challenges in the treatment of childhood fibromatosis. *Arch Surg*. 1987;122(11):1296–1298.
13. McCarville MB, Hoffer FA, Adelman CS, et al. MRI and biologic behavior of desmoid tumors in children. *AJR*. 2007;189:633–640.
14. Casillas J, Sais GJ, Greve JL, et al. Imaging of intra- and extraabdominal desmoid tumors. *Radiographics*. 1991;11(6):959–968.
15. Sturt NJH, Clark SK. Current ideas in desmoid tumours. *Fam Cancer*. 2006;5(3):275–285, discussion 287-288.
16. Murphey MD, Ruble CM, Tyszko SM, et al. From the archives of the AFIP: musculoskeletal fibromatoses: radiologic-pathologic correlation. *Radiographics*. 2009;29(7):2143–2173.
17. Koujok K, Ruiz RE, Hernandez RJ. Myofibromatosis: imaging characteristics. *Pediatr Radiol*. 2004;35(4):374–380.
18. Kransdorf MJ, Jelinek JS, Moser RP, et al. Magnetic resonance appearance of fibromatosis. A report of 14 cases and review of the literature. *Skeletal Radiol*. 1990;19(7):495–499.
19. Patrick LE, O'Shea P, Simoneaux SF, et al. Fibromatoses of childhood: the spectrum of radiographic findings. *AJR Am J Roentgenol*. 1996;166(1):163–169.
20. Robbin MR, Murphey MD, Temple HT, et al. Imaging of musculoskeletal fibromatosis. *Radiographics*. 2001;21(3):585–600.
21. Soper J, De Silva M. Infantile myofibromatosis: a radiological review. *Pediatr Radiol*. Springer. 1993;23(3):189–194.
22. Woertler K. Tumors and tumor-like lesions of peripheral nerves. *Semin Musculoskelet Radiol*. 2010;14(5):547–558.
23. Murphey MD, Smith WS, Smith SE, et al. From the archives of the AFIP. Imaging of musculoskeletal neurogenic tumors: radiologic-pathologic correlation. *Radiographics*. 1999;19(5):1253–1280.
24. Vilanova JC, Woertler K, Narváez JA, et al. Soft-tissue tumors update: MR imaging features according to the WHO classification. *Eur Radiol*. 2006;17(1):125–138.
25. Mandell GA, Herrick WC, Harcke HT, et al. Neurofibromas: location by scanning with Tc-99m DTPA. Work in progress. *Radiology*. 1985;157(3):803–806.
26. Kumar AJ, Kuhajda FP, Martinez CR, et al. Computed tomography of extracranial nerve sheath tumors with pathological correlation. *J Comput Assist Tomogr*. 1983;7(5):857–865.
27. Huang G-S, Huang C-W, Lee H-S, et al. On the AJR viewbox. Diffuse neurofibroma of the arm: MR characteristics. *AJR Am J Roentgenol*. 2005;184(5):1711–1712.
28. Levine E, Huntrakoon M, Wetzel LH. Malignant nerve-sheath neoplasms in neurofibromatosis: distinction from benign tumors by using imaging techniques. *AJR Am J Roentgenol*. 1987;149(5):1059–1064.
29. Lin J, Martel W. Cross-sectional imaging of peripheral nerve sheath tumors: characteristic signs on CT, MR imaging, and sonography. *AJR Am J Roentgenol*. 2001;176(1):75–82.
30. Stull MA, Moser RP, Kransdorf MJ, et al. Magnetic resonance appearance of peripheral nerve sheath tumors. *Skeletal Radiol*. 1991;20(1):9–14.
31. Suh JS, Abenoza P, Galloway HR, et al. Peripheral (extracranial) nerve tumors: correlation of MR imaging and histologic findings. *Radiology*. 1992;183(2):341–346.
32. Ros PR, Eshaghi N. Plexiform neurofibroma of the pelvis: CT and MRI findings. *Magn Reson Imaging*. 1991;9(3):463–465.
33. Hassell DS, Bancroft LW, Kransdorf MJ, et al. Imaging appearance of diffuse neurofibroma. *AJR Am J Roentgenol*. 2008;190(3):582–588.
34. Collins MH, Chatten J. Lipoblastoma/lipoblastomatosis: a clinicopathologic study of 25 tumors. *Am J Surg Pathol*. 1997;21(10):1131–1137.
35. Moholkar S, Sebire NJ, Roebuck DJ. Radiological-pathological correlation in lipoblastoma and lipoblastomatosis. *Pediatr Radiol*. 2006;36(8):851–856.
36. Chung EB, Enzinger FM. Benign lipoblastomatosis. An analysis of 35 cases. *Cancer*. 1973;32(2):482–492.
37. Cowling MG, Holmes SJ, Adam EJ. Benign chest wall lipoblastoma of infancy producing underlying bone enlargement. *Pediatr Radiol*. 1995;25(1):54–55.
38. Fisher MF, Fletcher BD, Dahms BB, et al. Abdominal lipoblastomatosis: radiographic, echographic, and computed tomographic findings. *Radiology*. 1981;138(3):593–596.
39. Katz DS, Merchant N, Beaulieu CF, et al. Clinical image. Lipoblastoma of the thigh: MR appearance. *J Comput Assist Tomogr*. 1996;20(6):1002–1003.
40. Murphey MD, Carroll JF, Flemming DJ, et al. From the archives of the AFIP: Benign musculoskeletal lipomatous lesions. *Radiographics*. 2004;24(5):1433–1466.
41. Shmookler BM, Enzinger FM. Liposarcoma occurring in children. An analysis of 17 cases and review of the literature. *Cancer*. 1983;52(3):567–574.
42. Arndt CAS, Crist WM. Common musculoskeletal tumors of childhood and adolescence. *N Engl J Med*. 1999;341:342–352.
43. Gehan EA, Glover FN, Maurer HM. Prognostic factors in children with rhabdomyosarcoma. *Natl Cancer Inst Monogr*. 1981;56:83–92.
44. Maurer HM. The intergroup rhabdomyosarcoma study: update, November 1978. *Natl Cancer Inst Monogr*. 1981;56:61–68.
45. Shapeero LG, Couanet D, Vanel D, et al. Bone metastases as the presenting manifestation of rhabdomyosarcoma in childhood. *Skeletal Radiol*. 1993;22:433–438.
46. Dehner LP. Primitive neuroectodermal tumor and Ewing's sarcoma. *Am J Surg Pathol*. 1993;17:1–13.
47. Ibarburen C, Haberman JJ, Zerhouni EA. Peripheral primitive neuroectodermal tumors: CT and MRI evaluation. *Eur J Radiol*. 1996;21:225–232.
48. Askin FB, Rosai J, Sibley RK, et al. Malignant small cell tumor of the thoracopulmonary region in childhood: a distinctive clinicopathologic entity of uncertain histogenesis. *Cancer*. 1979;43:2438–2451.
49. Kushner BH, Hajdu SI, Gulati SC, et al. Extracranial primitive neuroectodermal tumors: the Memorial Sloan-Kettering Cancer Center experience. *Cancer*. 1991;67:1825–1829.
50. Schmidt D, Herrmann C, Jürgens H, et al. Malignant peripheral neuroectodermal tumor and its necessary distinction from Ewing's sarcoma. *Cancer*. 1991;68:2251–2259.
51. Orr WS, Denbo JW, Billups CA, et al. Analysis of prognostic factors in extraosseous Ewing sarcoma family of tumors: review of St. Jude Children's Research Hospital experience. *Ann Surg Oncol*. 2012;19:3816–3822.
52. Kan JH, Hernanz-Schulman M, Damon BM, et al. MRI features of three paediatric intra-articular synovial lesions: a comparative study. *Clin Radiol*. 2008;63(7):805–812.
53. Cadman NL, Soule EH, Kelly PJ. Synovial sarcoma: an analysis of 134 tumors. *Cancer*. 1965;18:613–627.
54. Jones BC, Sundaram S, Kransdorf MJ. Synovial sarcoma: MR imaging findings in 34 patients. *AJR Am J Roentgenol*. 1993;161:827–830.
55. Blacksin MF, Siegel JR, Benevenia J, et al. Synovial sarcoma: frequency of non-aggressive MR characteristics. *J Comput Assist Tomogr*. 1997;21:785–789.
56. Mahajan H, Lorigan JG, Shirkhoda A. Synovial sarcoma: MR imaging. *Magn Rason Imaging N Am*. 1989;7:211–216.
57. Morton MJ, Berquist TH, McLeod RA, et al. MR imaging of synovial sarcoma. *AJR Am J Roentgenol*. 1991;156:337–340.
58. Speth BM, Krieg AH, Kaelin A, et al. Synovial Sarcoma in patients under 20 years of age: a multicenter study with a minimum follow-up of 10 years. *J Child Orthop*. 2011;5:335–342.

59. Warbey VS, Ferner RE, Dunn JT, et al. [18F] FDG PET/CT in the diagnosis of malignant peripheral nerve sheath tumours in neurofibromatosis type-1. *Eur J Nucl Med Mol Imaging*. 2009;36(5):751–757. doi:10.1007/s00259-008-1038-0. [Epub 2009 Jan 14].
60. Dahlin DC. Case report 189: infantile fibrosarcoma (congenital fibrosarcoma-like fibromatosis). *Skeletal Radiol*. 1982;8:77–78.
61. Boon LM, Fishman SJ, Lund DP, et al. Congenital fibrosarcoma masquerading as congenital hemangioma: report of two cases. *J Pediatr Surg*. 1995;30:1378–1381.
62. Exelby PR, Knapper WH, Huvos AG, et al. Soft-tissue fibrosarcoma in children. *J Pediatr Surg*. 1973;8:415–420.
63. Lilleng PK, Monge OR, Walløe A, et al. Fibrosarcoma in children. *Acta Oncol*. 1997;36:438–440.
64. Lee MJ, Cairns RA, Munk PL, et al. Musculoskeletal radiology: congenital-infantile fibrosarcoma: magnetic resonance imaging findings. *Can Assoc Radiol J*. 1996;47:121–125.
65. Ninane J, Gosseye S, Panteon E, et al. Congenital fibrosarcoma: preoperative chemotherapy and conservative surgery. *Cancer*. 1986;58:1400–1406.
66. Soule EH, Pritchard DJ. Fibrosarcoma in infants and children: a review of 110 cases. *Cancer*. 1977;40:1711–1721.
67. McCarville MB, Kaste SC, Pappo AS. Soft tissue malignancies in infancy. *AJR*. 1999;173:973–977.
68. Mendenhall WM, Zlotecki RA, Scarborough MT. Dermatofibrosarcoma protuberans. *Cancer*. 2004;101:2503–2508.
69. Weinstein JM, Drolet BA, Esterly NB, et al. Congenital dermatofibrosarcoma protuberans. *Arch Dermatol*. 2003;139:207–211.
70. Chung S, Frush DP, Prose NS, et al. Subcutaneous granuloma annulare: MR imaging features in six children and literature review. *Radiology*. 1999;210:845–849.
71. Clarke LE. Fibrous and fibrohistiocytic neoplasms: an update. *Dermatol Clin*. 2012;30:643–656.
72. Munk PL, Sallomi DF, Janzen DL, et al. Malignant fibrous histiocytoma of soft tissue imaging with emphasis on MRI. *J Comput Assist Tomogr*. 1998;22:819–826.
73. Raney RB Jr, Allen A, O'Neill J, et al. Malignant fibrous histiocytoma of soft tissue in childhood. *Cancer*. 1986;57:2198–2201.
74. Ros PR, Viamonte M Jr, Rywlin AM. Malignant fibrous histiocytoma: mesenchymal tumor of ubiquitous origin. *AJR Am J Roentgenol*. 1984;142:753–759.
75. Lee VS, Martinez S, Coleman RE. Primary muscle lymphoma: clinical and imaging findings. *Radiology*. 1997;203:237–244.
76. Eustace S, Winalski CS, McGowen A, et al. Skeletal muscle lymphoma: observations at MR imaging. *Skeletal Radiol*. 1996;23:425–430.
77. Malloy PC, Fishman EK, Magid D. Lymphoma of bone, muscle, and skin: CT findings. *AJR Am J Roentgenol*. 1992;159:805–809.
78. Metzler JP, Fleckenstein JL, Vuitch F, et al. Skeletal muscle lymphoma: MRI evaluation. *Magn Reson Imaging*. 1992;10:491–494.
79. Willemze R, Jaffe ES, Burg G, et al. WHO-EORTC classification for cutaneous lymphomas. *Blood*. 2005;105:3768–3785.
80. Gomez N, Ocon E, Friera A, et al. Magnetic resonance imaging features of chloroma of the shoulder. *Skeletal Radiol*. 1997;26:70–72.
81. Guermazi A, Feger C, Rousselot P, et al. Granulocytic sarcoma (chloroma) imaging findings in adults and children. *AJR Am J Roentgenol*. 2002;178:319–325.
82. Pui MH, Fletcher BD, Langston JW. Granulocytic sarcoma in childhood leukemia: imaging features. *Radiology*. 1992;190:698–702.
83. Schultz SR, Bree RL, Schwab RE, et al. CT detection of skeletal muscle metastases. *J Comput Assist Tomogr*. 1986;10:81–83.
84. Williams JB, Youngberg RA, Bui-Mansfield LT, et al. MR imaging of skeletal muscle metastases. *AJR Am J Roentgenol*. 1997;168:555–557.
85. Dorfman HD, Czerniak B. *Bone Tumors*. St. Louis: Mosby; 1998.
86. Mirra JM, Picci P, Gold RH. *Bone Tumors: Clinical, Radiologic, and Pathologic Correlations*. Philadelphia: Lea & Febiger; 1989.
87. Levine SM, Lambiase RE, Petchprapa CN. Cortical lesions of the tibia: characteristic appearances at conventional radiography. *Radiographics*. 2003;23:157–177.
88. Lodwick GS. A probabilistic approach to the diagnosis of bone tumors. *Radiol Clin North Am*. 1965;3:487–497.
89. Senac MO Jr, Isaacs H, Gwinn JL. Primary lesions of bone in the 1st decade of life: retrospective survey of biopsy results. *Radiology*. 1986;160:491–495.
90. Seeger LL, Yao L, Eckardt JJ. Surface lesions of bone. *Radiology*. 1998;206:17–33.
91. Hayes CW, Conway WF, Sundaram M. Misleading aggressive MR imaging appearance of some benign musculoskeletal lesions. *Radiographics*. 1992;12:1119–1134.
92. Aoki J, Watanabe H, Shinozaki T, et al. FDG PET of primary benign and malignant bone tumors: standardized uptake value in 52 lesions. *Radiology*. 2001;219:774–777.
93. Daldrup-Link HE, Franzius C, Link TM, et al. Whole-body MR imaging for detection of bone metastases in children with skeletal scintigraphy and FDG PET. *AJR Am J Roentgenol*. 2001;177:229–236.
94. Franzius C, Schober O. Assessment of therapy response by FDG PET in pediatric patients. *Q J Nucl Med*. 2003;47:41–45.
95. Gyorke TA, Zajic TB, Lange AB, et al. Impact of FDG PET for staging of Ewing sarcomas and primitive neuroectodermal tumours. *Nucl Med Commun*. 2006;27:17–24.
96. Hawkins DS, Rajendran JG, Conrad EU III, et al. Evaluation of chemotherapy response in pediatric bone sarcomas by [F-18]-fluorodeoxy-d-glucose positron emission tomography. *Cancer*. 2002;94:3277–3284.
97. Karasick D, Schweitzer ME, Eschelman DJ. Symptomatic osteochondromas: imaging features. *AJR Am J Roentgenol*. 1997;168:1507–1512.
98. Vasseur M-A, Fabre O. Vascular complications of osteochondromas. *J Vasc Surg*. 2000;31:532–538.
99. Brien EW, Mirra JM, Kerr R. Benign and malignant cartilage tumors of bone and joint: their anatomic and theoretical basis with an emphasis on radiology, pathology and clinical biology. I. The intramedullary cartilage tumors. *Skeletal Radiol*. 1997;26:325–353.
100. Brien EW, Mirra JM, Luck JV Jr. Benign and malignant cartilage tumors of bone and joint: their anatomic and theoretical basis with an emphasis on radiology, pathology and clinical biology. II. Juxtacortical cartilage tumors. *Skeletal Radiol*. 1999;28:1–20.
101. Jaffe N, Ried HL, Cohen M, et al. Radiation induced osteochondroma in long-term survivors of childhood cancer. *Int J Radiat Oncol Biol Phys*. 1983;9:665–670.
102. Pierz KA, Womer RB, Dormans JP. Pediatric bone tumors: osteosarcoma, Ewing's sarcoma, and chondrosarcoma associated with multiple hereditary osteochondromatosis. *J Pediatr Orthop*. 2001;21:412–418.
103. Vanhoenacker FM, Van Hul W, Wuyts W, et al. Hereditary multiple exostoses: from genetics to clinical syndrome and complications. *Eur J Radiol*. 2001;40:208–217.
104. Stieber JR, Dormans JP. Manifestations of hereditary multiple exostoses. *J Am Acad Orthop Surg*. 2005;13:110–120.
105. Libshitz HI, Cohen MA. Radiation-induced osteochondromas. *Radiology*. 1982;142:643–647.
106. Mahboubi S, Dormans JP, D'Angio G. Malignant degeneration of radiation-induced osteochondroma. *Skeletal Radiol*. 1997;26:195–198.
107. Marcovici PA, Berdon WE, Liebling MS. Osteochondromas and growth retardation secondary to externally or internally administered radiation in childhood. *Pediatr Radiol*. 2007;37:301–304.
108. Azouz EM, Slomic AM, Marton D, et al. The variable manifestations of dysplasia epiphysealis hemimelica. *Pediatr Radiol*. 1985;15:44–49.
109. Richardson RR. Variants of exostosis of the bone in children. *Semin Roentgenol*. 2005;40:380–390.
110. Vázquez-Flores H, Domínguez-Cherit J, Vega-Memije ME, et al. Subungual osteochondroma: clinical and radiologic features and treatment. *Dermatol Surg*. 2004;30:1031–1034.
111. Murphey MD, Choi JJ, Kransdorf MJ, et al. Imaging of osteochondroma: variants and complications with radiologic-pathologic correlation. *Radiographics*. 2000;20:1407–1434.
112. Saglik Y, Altay M, Unal VS, et al. Manifestations and management of osteochondromas: a retrospective analysis of 382 patients. *Acta Orthop Belg*. 2006;72:748–755.
113. Caballes RL. Enchondroma protuberans masquerading as osteochondroma. *Hum Pathol*. 1982;13:734–739.
114. Keating RB, Wright PW, Staple TW. Enchondroma protuberans of the rib. *Skeletal Radiol*. 1985;13:55–58.
115. Crim JR, Mirra JM. Enchondroma protuberans: report of a case and its distinction from chondrosarcoma and osteochondroma adjacent to an enchondroma. *Skeletal Radiol*. 1990;19:431–434.
116. Hunter AG, Kozlowski K, Hochberger O. Metachondromatosis. *Can Assoc Radiol J*. 1995;46:202–208.
117. Woertler K, Lindner N, Gosheger G, et al. Osteochondroma: MR imaging of tumor-related complications. *Eur Radiol*. 2000;10:832–840.
118. Lewis MM, Kenan S, Yabut SM, et al. Periosteal chondroma: a report of ten cases and review of the literature. *Clin Orthop*. 1990;256:185–192.
119. Woertler K, Blasius S, Brinkschmidt C, et al. Periosteal chondroma: MR characteristics. *J Comput Assist Tomogr*. 2001;25:425–430.

120. Bloem JL, Mulder JD. Chondroblastoma: a clinical and radiological study of 104 cases. *Skeletal Radiol*. 1985;14:1–9.
121. Bloem JL, Mulder JD. Chondroblastoma: a clinical and radiological study of 104 cases. *Skeletal Radiol*. 1985;14:1–9.
122. Ramappa AJ, Lee FYI, Tang P, et al. Chondroblastoma of bone. *J Bone Joint Surg Am*. 2000;82:1140–1145.
123. Brower AC, Moser RP, Kransdorf MJ. The frequency and diagnostic significance of periostitis in chondroblastoma. *AJR Am J Roentgenol*. 1990;154:309–314.
124. Oxtoby JW, Davies AM. MRI characteristics of chondroblastoma. *Clin Radiol*. 1996;51:22–26.
125. Weatherall PT, Maale GE, Mendelsohn DB, et al. Chondroblastoma: classic and confusing appearance at MR imaging. *Radiology*. 1994;190:467–474.
126. Yamamura S, Sato K, Sugiura H, et al. Inflammatory reaction in chondroblastoma. *Skeletal Radiol*. 1996;25:371–376.
127. Marin C, Gallego C, Manjón P, et al. Juxtacortical chondromyxoid fibroma: imaging findings in three cases and a review of the literature. *Skeletal Radiol*. 1997;26:642–649.
128. Wu CT, Inwards CY, O'Laughlin S, et al. Chondromyxoid fibroma of bone: a clinicopathologic review of 278 cases. *Hum Pathol*. 1998;29:438–446.
129. Wilson AJ, Kyriakos M, Ackerman LV. Chondromyxoid fibroma: radiographic appearance in 38 cases and in a review of the literature. *Radiology*. 1991;179:513–518.
130. Baker DM. Benign unicameral bone cyst: a study of forty-five cases with long-term follow up. *Clin Orthop Relat Res*. 1970;71:140–151.
131. Van Linthoudt D, Lagier R. Calcaneal cysts: a radiological and anatomico-pathological study. *Acta Orthop Scand*. 1978;49:310–316.
132. Jaffe HL, Lichtenstein L. Solitary unicameral bone cyst: with emphasis on the roentgen picture, the pathologic appearance and the pathogenesis. *Arch Surg*. 1942;44:1004–1025.
133. Margau R, Babyn P, Cole W, et al. MR imaging of simple bone cysts in children: not so simple. *Pediatr Radiol*. 2000;30:551–557.
134. Kransdorf MJ, Sweet DE. Aneurysmal bone cyst: concept, controversy, clinical presentation, and imaging. *AJR Am J Roentgenol*. 1995;164:573–580.
135. Campanacci M, Capanna R, Picci P. Unicameral and aneurysmal bone cysts. *Clin Orthop Relat Res*. 1986;204:25–26.
136. Mankin HJ, Hornicek FJ, Ortiz-Cruz E, et al. Aneurysmal bone cyst: a review of 150 patients. *J Clin Oncol*. 2005;23:6756–6762.
137. Woertler K, Brinkschmidt C. Imaging features of subperiosteal aneurysmal bone cyst. *Acta Radiol*. 2002;43:336–339.
138. Bertoni F, Bacchini P, Capanna R, et al. Solid variant of aneurysmal bone cyst. *Cancer*. 1993;71:729–734.
139. Ilaslan H, Sundaram M, Unni KK. Solid variant of aneurysmal bone cysts in long tubular bones: giant cell reparative granuloma. *AJR Am J Roentgenol*. 2003;180:1681–1687.
140. Hudson TM. Fluid levels in aneurysmal bone cysts: a CT feature. *AJR Am J Roentgenol*. 1984;142:1001–1004.
141. Munk PL, Helms CA, Holt RG, et al. MR imaging of aneurysmal bone cysts. *AJR Am J Roentgenol*. 1989;153:99–101.
142. O'Donnell P, Saifuddin A. The prevalence and diagnostic significance of fluid-fluid levels in focal lesions of bone. *Skeletal Radiol*. 2004;33:330–336.
143. Tsai JC, Dalinka MK, Fallon MD, et al. Fluid-fluid level: a nonspecific finding in tumors of bone and soft tissue. *Radiology*. 1990;175:779–782.
144. Kransdorf MJ, Sweet DE, Buetow PC, et al. Giant cell tumor in skeletally immature patients. *Radiology*. 1992;184:233–237.
145. Stratil PG, Stacy GS. Multifocal metachronous giant cell tumor in a 15-year-old boy. *Pediatr Radiol*. 2005;35:444–448.
146. Krajca-Radcliffe JB, Thomas JR, Nicholas RW. Giant-cell tumor of bone: a rare entity in the hands of children. *J Pediatr Orthop*. 1994;14:776–780.
147. Schütte HE, Taconis WK. Giant cell tumor in children and adolescents. *Skeletal Radiol*. 1993;22:173–176.
148. Schajowicz F, Granato DB, McDonald DJ, et al. Clinical and radiological features of atypical giant cell tumours of bone. *Br J Radiol*. 1991;64:877–889.
149. Murphey MD, Nomikos GC, Flemming DJ, et al. Imaging of giant cell tumor and giant cell reparative granuloma of bone: radiologic-pathologic correlation. *Radiographics*. 2001;21:1283–1309.
150. Thomas DM, Skubitz KM. Giant cell tumour of bone. *Curr Opin Oncol*. 2009;21:338–344.
151. Betsy M, Kupersmith LM, Springfield DS. Metaphyseal fibrous defects. *J Am Acad Orthop Surg*. 2004;12:89–95.
152. Moser RP Jr, Sweet DE, Haseman DB, et al. Multiple skeletal fibroxanthomas: radiologic-pathologic correlation of 72 cases. *Skeletal Radiol*. 1987;16:353–359.
153. Parekh SG, Donthineni-Rao R, Ricchetti E, et al. Fibrous dysplasia. *J Am Acad Orthop Surg*. 2004;12:305–313.
154. Caffey J. On fibrous defects in cortical walls of growing tubular bones: their radiologic appearance, structure, prevalence, natural course, and diagnostic significance. *Adv Pediatr*. 1955;7:13–51.
155. Campanacci M, Laus M. Osteofibrous dysplasia of the tibia and fibula. *J Bone Joint Surg Am*. 1981;63:367–375.
156. Colby RS, Saul RA. Is Jaffe-Campanacci syndrome just a manifestation of neurofibromatosis type 1? *Am J Med Genet A*. 2003;123:60–63.
157. Mirra JM, Gold RH, Rand F. Disseminated nonossifying fibromas in association with cafe-au-lait spots (Jaffe-Campanacci syndrome). *Clin Orthop Relat Res*. 1982;192–205.
158. Jee WH, Choe BY, Kang HS, et al. Nonossifying fibroma: characteristics at MR imaging with pathologic correlation. *Radiology*. 1998;209:197–202.
159. Goodin GS, Shulkin BS, Kaufman RA, et al. PET/CT characterization of fibroosseous defects in children: 18F-FDG uptake can mimic metastatic disease. *AJR Am J Roentgenol*. 2006;187:1124–1128.
160. Bloem JL, van der Heul RO, Schuttevaer HM, et al. Fibrous dysplasia vs adamantinoma of the tibia: differentiation based on discriminant analysis of clinical and plain film findings. *AJR Am J Roentgenol*. 1991;156:1017–1023.
161. DiCaprio MR, Enneking WF. Fibrous dysplasia. Pathophysiology, evaluation, and treatment. *J Bone Joint Surg Am*. 2005;87:1848–1864.
162. Fitzpatrick KA, Taljanovic MS, Speer DP, et al. Imaging findings of fibrous dysplasia with histopathologic and intraoperative correlation. *AJR Am J Roentgenol*. 2004;182:1389–1398.
163. Cabral CEL, Guedes P, Fonseca T, et al. Polyostotic fibrous dysplasia associated with intramuscular myxomas: Mazabraud's syndrome. *Skeletal Radiol*. 1998;27:278–282.
164. Utz JA, Kransdorf MJ, Jelinek JS, et al. MR appearance of fibrous dysplasia. *J Comput Assist Tomogr*. 1989;13:845–851.
165. Fisher AJ, Totty WG, Kyriakos M. MR appearance of cystic fibrous dysplasia. *J Comput Assist Tomogr*. 1994;18:315–318.
166. Karol LA, Brown DS, Wise CA, et al. Familial osteofibrous dysplasia: a case series. *J Bone Joint Surg Am*. 2005;87:2297–2307.
167. Hindman BW, Bell S, Russo T, et al. Neonatal osteofibrous dysplasia: report of two cases. *Pediatr Radiol*. 1996;26:303–306.
168. Komiya S, Inoue A. Aggressive bone tumorous lesion in infancy: osteofibrous dysplasia of the tibia and fibula. *J Pediatr Orthop*. 1993;13:577–581.
169. Kahn LB. Adamantinoma, osteofibrous dysplasia and differentiated adamantinoma. *Skeletal Radiol*. 2003;32:245–258.
170. Hazelbag HM, Taminiau AH, Fleuren GJ, et al. Adamantinoma of the long bones. A clinicopathological study of thirty-two patients with emphasis on histological subtype, precursor lesion, and biological behavior. *J Bone Joint Surg Am*. 1994;76:1482–1499.
171. Ishida T, Iijima T, Kikuchi F, et al. A clinicopathological and immunohistochemical study of osteofibrous dysplasia, differentiated adamantinoma, and adamantinoma of long bones. *Skeletal Radiol*. 1992;21:493–502.
172. Czerniak B, Rojas-Corona RR, Dorfman HD. Morphologic diversity of long bone adamantinoma. The concept of differentiated (regressing) adamantinoma and its relationship to osteofibrous dysplasia. *Cancer*. 1989;64:2319–2334.
173. Van Rijn R, Bras J, Schaap G, et al. Adamantinoma in childhood: report of six cases and review of the literature. *Pediatr Radiol*. 2006;36:1068–1074.
174. Van der Woude HJ, Hazelbag HM, Bloem JL, et al. MRI of adamantinoma of long bones in correlation with histopathology. *AJR Am J Roentgenol*. 2004;183:1737–1744.
175. Yao L, Eckardt JJ, Seeger LL. Fibrous dysplasia associated with cortical bony destruction: CT and MR findings. *J Comput Assist Tomogr*. 1994;18:91–94.
176. Egeler RM, D'Angio GJ. Langerhans cell histiocytosis. *J Pediatr*. 1995;127:1–11.
177. Kransdorf MJ, Smith SE. Lesions of unknown histiogenesis: Langerhans cell histiocytosis and Ewing sarcoma. *Semin Musculoskel Radiol*. 2000;4:113–125.
178. Azouz EM, Saigal G, Rodriguez MM, et al. Langerhans' cell histiocytosis: pathology, imaging and treatment of skeletal involvement. *Pediatr Radiol*. 2005;35:103–115.

179. Kilpatrick SE, Wenger DE, Gilchrist GS, et al. Langerhans' cell histiocytosis (histiocytosis X) of bone: a clinicopathologic analysis of 263 pediatric and adult cases. *Cancer*. 1995;76:2471–2484.
180. Kilborn TN, Teh J, Goodman TR. Paediatric manifestations of Langerhans cell histiocytosis: a review of the clinical and radiological findings. *Clin Radiol*. 2003;58:269–278.
181. Schmidt S, Eich G, Hanquinet S, et al. Extra-osseous involvement of Langerhans' cell histiocytosis in children. *Pediatr Radiol*. 2004;34:313–321.
182. Meyer JS, Harty MP, Mahboubi S, et al. Langerhans cell histiocytosis: presentation and evolution of radiologic findings with clinical correlation. *Radiographics*. 1995;15:1135–1146.
183. Stull MA, Kransdorf MJ, Devaney KO. Langerhans cell histiocytosis of bone. *Radiographics*. 1992;12:801–823.
184. David R, Oria RA, Kumar R, et al. Radiologic features of eosinophilic granuloma of bone. *AJR Am J Roentgenol*. 1989;153:1021–1026.
185. Hindman BW, Thomas RD, Young LW, et al. Langerhans cell histiocytosis: unusual skeletal manifestations observed in thirty-four cases. *Skeletal Radiol*. 1998;27:177–181.
186. Van Nieuwenhuyse JP, Clapuyt P, Malghem J, et al. Radiographic skeletal survey and radionuclide bone scan in Langerhans cell histiocytosis of bone. *Pediatr Radiol*. 1996;26:734–738.
187. Beltran J, Aparisi F, Bonmati LM, et al. Eosinophilic granuloma: MRI manifestations. *Skeletal Radiol*. 1993;22:157–161.
188. Goo HW, Yang DH, Ra YS, et al. Whole-body MRI of Langerhans cell histiocytosis: comparison with radiography and bone scintigraphy. *Pediatr Radiol*. 2006;36:1019–1031.
189. Kaste SC, Rodriguez-Galindo C, McCarville ME, et al. PET-CT in Langerhans cell histiocytosis. *Pediatr Radiol*. 2007;37:615–622.
190. Windebank K, Nanduri V. Langerhans cell histiocytosis. *Arch Dis Child*. 2009;94:904–908.
191. Azouz EM, Kozlowski K, Marton D, et al. Osteoid osteoma and osteoblastoma of the spine in children: report of 22 cases with brief literature review. *Pediatr Radiol*. 1986;16:25–31.
192. Kransdorf MJ, Stull MA, Gilkey FW, et al. Osteoid osteoma. *Radiographics*. 1991;11:671–696.
193. Allen SD, Saifuddin A. Imaging of intra-articular osteoid osteoma. *Clin Radiol*. 2003;58:845–852.
194. Shankman S, Desai P, Beltran J. Subperiosteal osteoid osteoma: radiographic and pathologic manifestations. *Skeletal Radiol*. 1997;26:457–462.
195. Assoun J, Richardi G, Railhac J-J, et al. Osteoid osteoma: MR imaging versus CT. *Radiology*. 1994;191:217–223.
196. Yamamura S, Sato K, Sugiura H, et al. Magnetic resonance imaging of inflammatory reaction in osteoid osteoma. *Arch Orthop Trauma Surg*. 1994;114:8–13.
197. Liu PT, Chivers FS, Roberts CC, et al. Imaging of osteoid osteoma with dynamic gadolinium-enhanced MR imaging. *Radiology*. 2003; 227(3):691–700.
198. Zampa V, Bargellini I, Ortori S, et al. Osteoid osteoma in atypical locations: the added value of dynamic gadolinium-enhanced MR imaging. *Eur J Radiol*. 2009;71(3):527–535. doi:10.1016/j.ejrad.2008.05.010. [Epub 2008 Jul 2].
199. Torriani M, Rosenthal DI. Percutaneous radiofrequency treatment of osteoid osteoma. *Pediatr Radiol*. 2002;32:615–618.
200. Ghanem I. The management of osteoid osteoma: updates and controversies. *Curr Opin Pediatr*. 2006;18:36–41.
201. Jambhekar NA, Desai S, Khapake D. Osteoblastoma: a study of 12 cases. *Indian J Pathol Microbiol*. 2006;49:487–490.
202. Lucas DR, Unni KK, McLeod RA, et al. Osteoblastoma: clinicopathologic study of 306 cases. *Hum Pathol*. 1994;25:117–134.
203. Greenspan A. Benign bone-forming lesions: osteoma, osteoid osteoma, and osteoblastoma: clinical, imaging, pathologic, and differential considerations. *Skeletal Radiol*. 1993;22:485–500.
204. Kroon HM, Schurmans J. Osteoblastoma: clinical and radiologic findings in 98 new cases. *Radiology*. 1990;175:783–790.
205. McLeod RA, Dahlin DC, Beabout JW. The spectrum of osteoblastoma. *AJR Am J Roentgenol*. 1976;126:321–325.
206. Graham NJ, Cairns RA, Anderson RA. Osteosarcoma in a 19-month-old-girl. *Can Assoc Radiol J*. 1996;47:33–35.
207. Hopper KD, Moser RP, Haseman DB, et al. Osteosarcomatosis. *Radiology*. 1990;175:233–239.
208. Olson PN, Prewitt L, Griffiths HJ, et al. Case report 703: multifocal osteosarcoma. *Skeletal Radiol*. 1991;20:624–627.
209. Doud TM, Moser RP Jr, Giudici MAI, et al. Case report 704: extraskeletal osteosarcoma of the thigh with several suspected skeletal metastases and extensive metastases to the chest. *Skeletal Radiol*. 1991;20:628–632.
210. Goorin AM, Abelson HT, Frei E III. Osteosarcoma: fifteen years later. *N Engl J Med*. 1985;313:1637–1643.
211. Onikul E, Fletcher BD, Parham DM, et al. Accuracy of MR imaging for estimating intraosseous extent of osteosarcoma. *AJR Am J Roentgenol*. 1996;167:1211–1215.
212. Schima W, Amann G, Stiglbauer R, et al. Preoperative staging of osteosarcoma: efficacy of MR imaging in detecting joint involvement. *AJR Am J Roentgenol*. 1994;163:1171–1175.
213. Hanna SL, Fletcher BD, Parham DM, et al. Muscle edema in musculoskeletal tumors: MR imaging characteristics and clinical significance. *J Magn Reson Imaging*. 1991;1:441–449.
214. Gomes H, Menanteau B, Gaillard D, et al. Telangiectatic osteosarcoma. *Pediatr Radiol*. 1986;16:140–143.
215. Weiss A, Khoury JD, Hoffer FA, et al. Telangiectatic osteosarcoma: the St. Jude Children's Research Hospital's experience. *Cancer*. 2007;109:1627–1637.
216. Huvos AG, Rosen G, Bretsky SS, et al. Telangiectatic osteogenic sarcoma: a clinico-pathologic study of 124 patients. *Cancer*. 1982; 49:1679–1689.
217. Kaufman RA, Towbin RB. Telangiectatic osteosarcoma simulating the appearance of an aneurysmal bone cyst. *Pediatr Radiol*. 1981;11:102–104.
218. Murphey MD, Robbin MR, McRae GA, et al. The many faces of osteosarcoma. *Radiographics*. 1997;17:1205–1231.
219. Klein MJ, Siegal GP. Osteosarcoma: anatomic and histologic variants. *Am J Clin Pathol*. 2006;125:555–581.
220. Murphey MD, Jelinek JS, Temple HT, et al. Imaging of periosteal osteosarcoma: radiologic-pathologic comparison. *Radiology*. 2004; 233:129–138.
221. Bloem JL, Taminiau AHM, Eulderink F, et al. Radiologic staging of primary bone sarcoma: MR imaging, scintigraphy, angiography, and CT correlated with pathologic examination. *Radiology*. 1988;169:805–810.
222. Brown ML. The role of radionuclides in the patient with osteogenic sarcoma. *Semin Roentgenol*. 1989;24:185–192.
223. Ewing J. Diffuse endothelioma of bone. *Proc N Y Pathol Soc*. 1921;21:17. reprinted in Clin Orthop 1984;185:2-5.
224. Hameed M. Small round cell tumors of bone. *Arch Pathol Lab Med*. 2007;13:192–204.
225. Jaffe R, Santamaria M, Yunis EJ, et al. The neuroectodermal tumor of bone. *Am J Surg Pathol*. 1984;8:885–898.
226. Kretschmar CS. Ewing's sarcoma and the "peanut" tumors. *N Engl J Med*. 1994;331:325–327.
227. Coombs RJ, Zeiss J, McCann K, et al. Case report 360: multifocal Ewing tumor of the skeletal system. *Skeletal Radiol*. 1986;15:254–257.
228. Coombs RJ, Zeiss J, Paley KJ, et al. Case report 802: Ewing's tumor of the proximal phalanx of third finger with radiographic progression documented over a 6-year-period. *Skeletal Radiol*. 1993;22:460–463.
229. Shirley SK, Gilula LA, Siegal GP, et al. Roentgenographic-pathologic correlation of diffuse sclerosis in Ewing sarcoma of bone. *Skeletal Radiol*. 1984;12:69–78.
230. Shapeero LG, Vanel D, Sundaram M, et al. Periosteal Ewing sarcoma. *Radiology*. 1994;191:825–831.
231. Mueller DL, Grant RM, Riding MD, et al. Cortical saucerization: an unusual imaging finding of Ewing sarcoma. *AJR Am J Roentgenol*. 1994;163:401–403.
232. Davies AM, Makwana NK, Grimer RJ, et al. Skip metastases in Ewing's sarcoma: a report of three cases. *Skeletal Radiol*. 1997;26:379–384.
233. Reinus WR, Gilula LA, Donaldson S, et al. Prognostic features of Ewing sarcoma on plain radiograph and computed tomography scan after initial treatment: Pediatric Oncology Group Study (8346). *Cancer*. 1993;72:2503–2510.
234. Daugaard S, Sunda LM, Kamby C, et al. Ewing's sarcoma: a retrospective study of prognostic factors and treatment results. *Acta Oncol*. 1987;26:281–287.
235. Jürgens H, Exner U, Gadner H, et al. Multidisciplinary treatment of primary Ewing's sarcoma of bone: a 6-year experience of a European cooperative trial. *Cancer*. 1988;61:23–32.
236. Lemmi MA, Fletcher BD, Marina NM, et al. Use of MR imaging to assess results of chemotherapy for Ewing sarcoma. *AJR Am J Roentgenol*. 1990;155:343–346.
237. Taber DS, Libshitz HI, Cohen MA. Treated Ewing sarcoma: radiographic appearance in response, recurrence, and new primaries. *AJR Am J Roentgenol*. 1983;140:753–758.

# 139 Metabolic Bone Disease

Lauren W. Averill and Richard M. Shore

Skeletal ossification and mineralization are influenced by many metabolic factors, with sometimes arbitrary distinctions between metabolic bone disorders, endocrine bone disorders, and inherited skeletal dysplasias. Accurate diagnosis is essential because many of these disorders require specific therapy for both their skeletal and extraskeletal effects.

## ABNORMALITIES OF MINERALIZATION

### Bone Mineral Physiology

In the process of bone formation, osteoblasts produce organic bone matrix (osteoid), which then must be mineralized with deposition of hydroxyapatite crystals.[1–4] Mineralization of cartilage and osteoid requires sufficient levels of circulating calcium and phosphate as reflected in an adequate calcium x phosphate product. Mineralization also requires alkaline phosphatase to hydrolyze pyrophosphate, which otherwise would inhibit crystal formation.[5] Hence deficient mineralization of cartilage and osteoid may be due to either an insufficient calcium x phosphate product as in rickets and osteomalacia, or alkaline phosphatase deficiency as in hypophosphatasia.

Rickets is a complex disorder of the growth plate that involves not only deficient mineralization of cartilage and osteoid but also disruption of endochondral ossification, leading to the accumulation of excessive cartilage. This phenomenon results from failure of hypertrophic chondrocytes to undergo normal apoptosis, which is now believed to be caused by hypophosphatemia as the common metabolic pathway of all forms of rickets.[6] Osteomalacia is a pure disorder of insufficient mineralization of osteoid at sites other than the physes, hence at either sites of bone turnover or intramembranous bone formation.

Forms of rickets due to insufficient calcium (calcipenic rickets) mostly result from abnormalities of vitamin D, whose major function is maintenance of a sufficient calcium x phosphate product. Vitamin D may be synthesized in the skin from 7-dehydrocholesterol upon exposure to sunlight containing ultraviolet B radiation (290–315 nm), or it may be provided in the diet, although natural dietary sources of vitamin D are quite limited. Vitamin D then undergoes 25-hydroxylation in the liver followed by 1-α-hydroxylation in the kidney to produce 1,25$(OH)_2$-vitamin D, which is the active form of vitamin D (calcitriol). The most important biologic function of calcitriol is facilitation of gastrointestinal absorption of calcium by inducing transcription of the gene for calcium-binding protein. Calcitriol synthesis by 1-α-hydroxylase is promoted by parathyroid hormone (PTH) in response to hypocalcemia.

Rickets also may result from a variety of disorders that cause renal tubular phosphate wasting (phosphopenic rickets). Renal tubular phosphate handling is regulated by PTH and by a variety of other factors, most of which are produced in bone by osteocytes.[7–12] The most important of these is fibroblast growth factor 23 (FGF23), which causes renal tubular phosphate wasting by downregulating the sodium-phosphate cotransporter that facilitates phosphate reabsorption. Additionally, FGF23 downregulates 1-α-hydroxylase, leading to diminished calcitriol.

### Nutritional (Vitamin D–Deficiency) Rickets

***Etiology.*** Both inadequate exposure to sunlight and insufficient dietary intake of vitamin D must be present for rickets to occur.[1–3,13,14] The first and most severe epidemic of rickets occurred during the industrial revolution as a result of urbanization and diminished exposure to sunlight from smog and the practice of staying indoors. This epidemic largely ended with food fortification after the discovery of vitamin D synthesis. However, rickets then became more prevalent in the United States during the mid-1990s with increased breast-feeding in the African American and Hispanic populations, because breast milk provides relatively little vitamin D. Less commonly, nutritional rickets may result from insufficient calcium intake.[15]

Because 25(OH)D readily crosses the placenta, infants born to vitamin D–replete mothers have sufficient stores, and thus nutritional rickets usually is not apparent before 3 to 6 months of age. Only if the mother is extremely deficient in vitamin D will nutritional rickets be seen in the newborn period.[15a]

Clinical manifestations of rickets include failure to thrive, short stature, bowing deformities, and predisposition to fractures. However, fractures do not occur in the absence of classic radiographic findings of rickets. Furthermore, the fractures that do occur in cases of severe rickets do not resemble those of child abuse.[15b] In addition, prominence of anterior rib ends causing a “rachitic rosary” and craniotabes (a softening of the skull bones) may be seen. Weakness is a clinical feature of rickets, correlating with the presence of vitamin D receptors in skeletal muscle.[16]

***Imaging.*** The features of rickets are most pronounced in regions of greatest bone growth, particularly the distal radius and ulna, distal femur, proximal tibia, proximal humerus, and anterior rib ends. An insufficient calcium x phosphate product causes decreased mineralization of the zone of provisional calcification and lack of normal chondrocytic terminal differentiation. As a result, the initial radiographic finding is rarefaction of the normally sharply defined zone of provisional calcification on the metaphyseal side of the growth plate so that metaphyseal bone fades gradually into the lucent physeal and epiphyseal cartilage (Fig. 139.1 and e-Fig. 139.2). There is loss of definition of the Laval-Jeantet collar, a short cylindric segment of the metaphysis adjacent to the growth plate that is an indicator of the most recently formed bone in young infants.[17] Deficient chondrocyte terminal differentiation and apoptosis causes accumulation of disorganized cartilage in the metaphysis in addition to nonmineralized osteoid, leading to widening of the distance between the epiphysis and metaphysis, metaphyseal fraying, and metaphyseal concavity (cupping). Metaphyseal concavity varies by site, being most pronounced in the distal radius and ulna (see Fig. 139.1). However, distal ulnar metaphyseal concavity with no other abnormality may be a normal finding. Metaphyseal findings that may be recognized on chest radiographs include involvement of the proximal humeral metaphyses and rib ends, producing the rachitic rosary (Fig. 139.3) of bulbous rib ends felt on physical examination.

Long bone shaft findings lag behind those in the metaphysis. In rickets due to vitamin D abnormality, PTH rises in an attempt

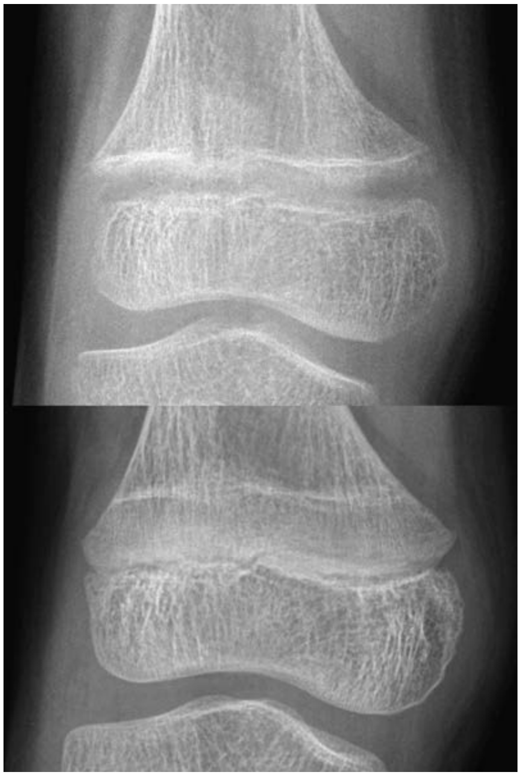

**e-Figure 139.2. Vitamin D deficiency rickets.** A less severe case than shown in Fig. 139.1. At 9½ years of age *(top),* distal femoral physeal widening and metaphyseal fraying is noted that resolved several months later after treatment *(bottom)*.

to restore a normal serum calcium concentration, producing secondary hyperparathyroidism (HPTH) with subperiosteal bone resorption, intracortical tunneling, and overall demineralization (Fig. 139.4). With ongoing bone remodeling, as nonmineralized osteoid replaces mineralized bone (osteomalacia), cortical demineralization and coarsening of the trabecular pattern in the shafts occurs, predisposing a person to insufficiency fractures. Paradoxically, periosteal new bone formation also may be seen in rickets even before healing, which likely is an anabolic effect of PTH (see Fig. 139.1).

Bowing in rickets is most pronounced in the tibias and is due to loss of normal bone rigidity in the metaphyses and shafts. The large zone of nonmineralized cartilage and osteoid in the rachitic metaphyses is particularly deformable and subject to bending.

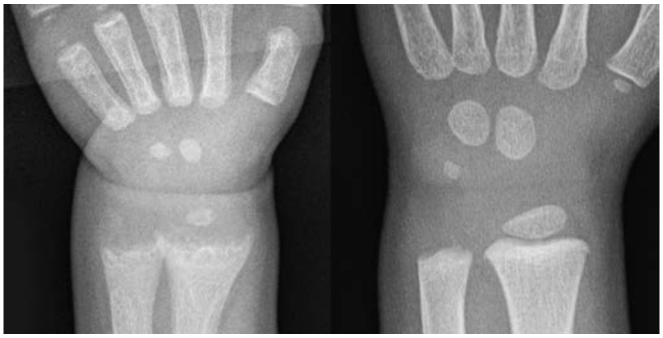

**Figure 139.1. Vitamin D deficiency rickets.** A 14-month-old child with growth failure and severe rickets who responded well to vitamin D therapy. The initial image *(left)* shows loss of definition of the zones of provisional calcification for the distal radial and ulnar metaphyses along with metaphyseal fraying and concavity ("cupping") and physeal widening with an increased distance between the epiphysis and visualized portion of the metaphysis. Periosteal new bone also is present that is seen best along the metacarpals but also is present along the distal radius. With healing *(right),* the zone of provisional calcification is well mineralized and the other findings have resolved.

With healing (see Fig. 139.1, e-Fig. 139.2, and Fig. 139.4), mineral deposition in the zone of provisional calcification and restoration of chondrocyte terminal differentiation occur. The initial radiographic finding of healing is reidentification of the zone of provisional calcification as a thin opaque line separated from the identifiable shaft by the intervening lucent nonmineralized cartilage and osteoid. With further healing, this metaphyseal region calcifies, which may give the false impression of rapid bone growth. Less often, newly mineralized osteoid also may be seen in the metaphyseal equivalent region of the epiphysis (e-Fig. 139.5). With healing of cortical bone, the subperiosteal osteoid becomes calcified, producing either a uniform or lamellated layer.

Additional imaging features of rickets include chest wall (Harrison) grooves, which are deformities of softened ribs at the diaphragmatic insertions. Scoliosis and kyphosis also may be seen.

***Treatment and Follow-up.*** Prevention of vitamin D deficiency is a controversial issue because of lack of consensus regarding the level of vitamin D that is considered sufficient. The 2011 Institute of Medicine report[18] concluded that a serum level of 25-hydroxy-vitamin D of at least 20 ng/mL is normal, although many experts in vitamin D research argue that higher levels are needed. Accordingly, the Institute of Medicine recommends 400 IU of vitamin D daily during the first year of life and 600 IU daily thereafter.

Treatment guidelines for vitamin D deficiency are those of the Lawson Wilkins Pediatric Endocrine Society.[19] Treatment is recommended for clinical manifestations of vitamin D deficiency or 25-hydroxy-vitamin D levels less than 15 ng/mL, beginning with higher doses than those used for prevention. With treatment, if radiographic evidence of healing is seen by 3 months, vitamin D dosage can be reduced to preventive levels.

## Other Forms of Rickets

Many other conditions may result in an insufficient calcium x phosphate product, causing rickets. The radiographic manifestations

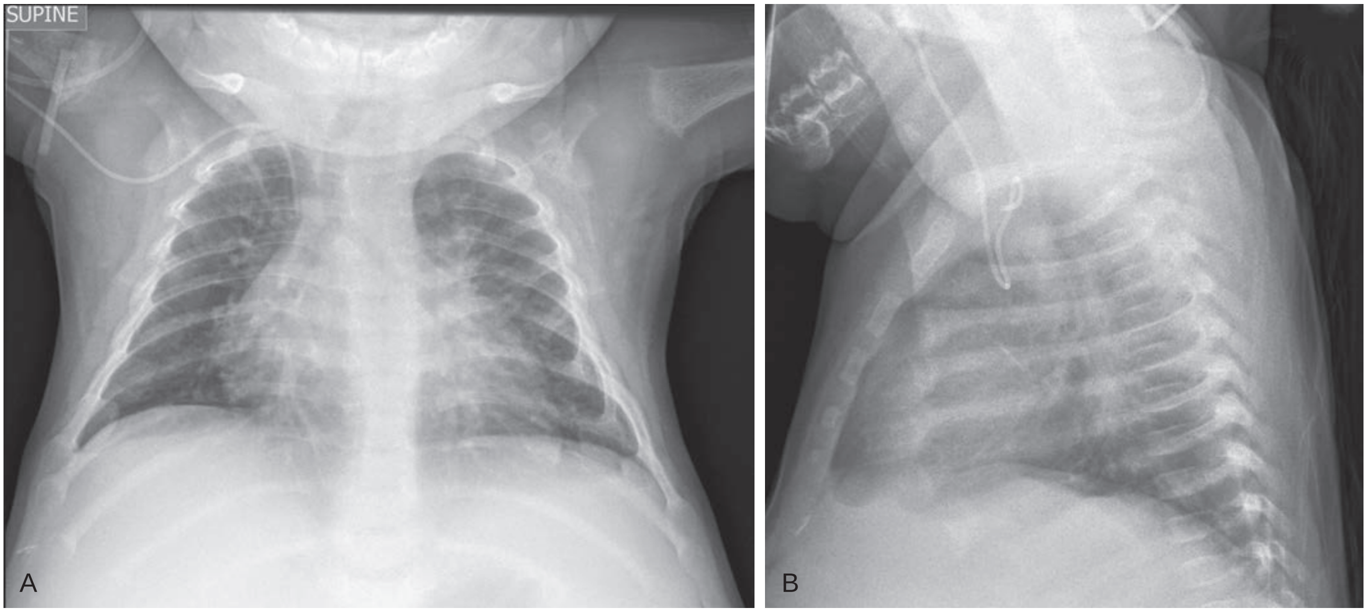

**Figure 139.3. Rickets secondary to biliary atresia in a 5-month-old child.** Anteroposterior (A) and lateral (B) chest radiographs show rachitic changes in the proximal humeral metaphyses and anterior rib ends. The rib findings are best seen on the lateral view.

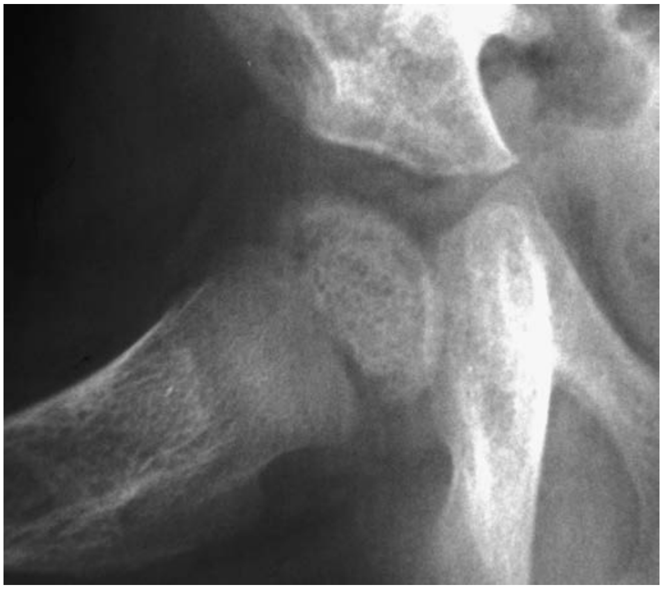

**e-Figure 139.5. Healing rickets with mineralization of previously lucent osteoid.** Newly mineralized bone is seen in the proximal femoral metaphysis, as well as the equivalent portion of the epiphysis.

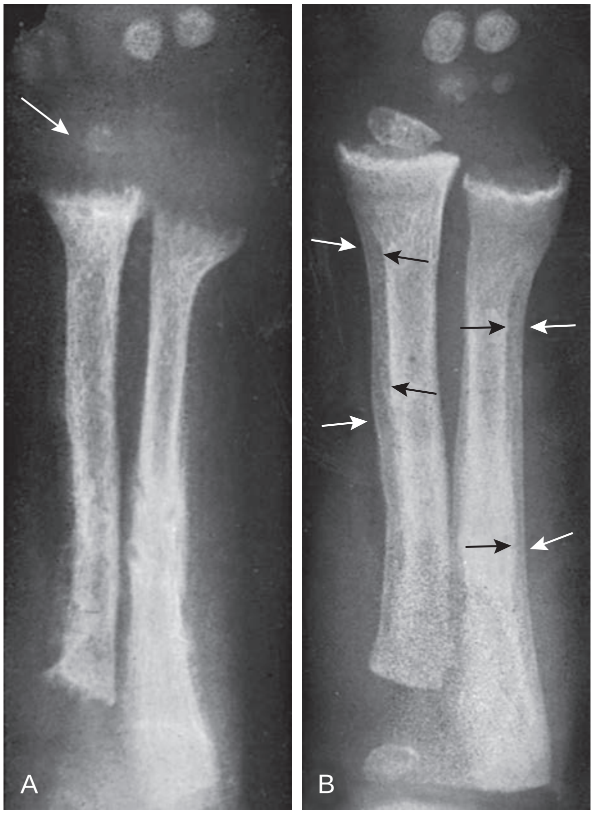

**Figure 139.4. Diaphyseal findings in a patient with severe vitamin D deficiency rickets.** Radiographs of the forearm during the active phase (A) show coarse demineralization and subperiosteal bone resorption, which are indicative of hyperparathyroidism as a result of rickets. Also note the severe rachitic findings in the metaphysis and poor mineralization of the distal radial epiphysis *(arrow)* with loss of the zones of provisional calcification. With healing 3 months later (B), extensive periosteal new bone is seen *(white arrows)* with calcification of previously nonmineralized osteoid *(black arrows)* produced by periosteal osteoblasts.

described for vitamin D insufficiency rickets are etiologically nonspecific and are similar in the other forms of rickets unless otherwise indicated.

**Malabsorption and Hepatobiliary Disease.** Vitamin D malabsorption may cause rickets in disorders such as celiac disease and cystic fibrosis. Rickets with hepatobiliary disease (see Fig. 139.3) is mostly a result of decreased intake and intestinal absorption of fat-soluble vitamins (A, D, E, and K); decreased hepatic 25-hydroxylation of vitamin D usually is not significant. Associated vitamin K deficiency in hepatobiliary disease may lead to recurrent hemarthrosis, most frequently involving the knee.

**Vitamin D–Dependent Rickets, Types I and II.** In autosomal-recessive vitamin D–dependent rickets (VDDR) type I, a defect in the renal 1-α-hydroxylase leads to undetectable or very low calcitriol levels.[20,21] Rickets in VDDR I is severe, presents in the first few months of life, and has more secondary HPTH than do other forms of rickets. VDDR I responds to physiologic doses of calcitriol. Rickets also can result from a defect in the receptor for calcitriol, causing vitamin D nonresponsiveness.[21,22] The designation of VDDR type II for this disorder is inappropriate because it is resistant to all forms of vitamin D, and hence the term "calcitriol-resistant rickets" is preferred. In addition to severe rickets, approximately half of the patients have manifestations of ectodermal dysplasia.

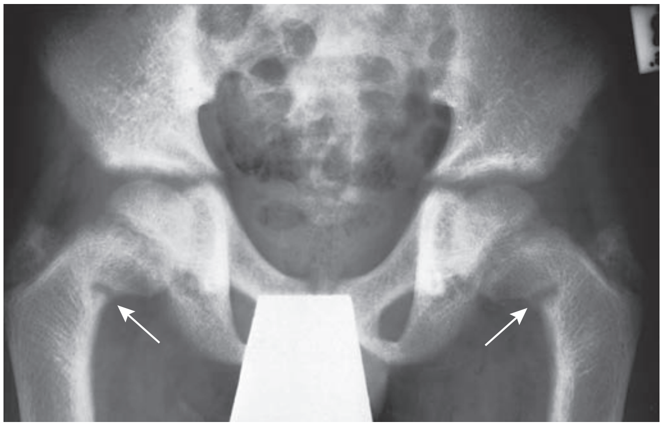

**Figure 139.7. Looser zones in a child with X-linked hypophosphatemia.** Pelvic radiograph shows symmetric transverse lucent areas in the medial aspect of the femoral necks *(arrows)* that are a manifestation of osteomalacia. Also note the patchy increased density, coarse trabeculations, and rachitic irregularity of the metaphyses.

**Phosphopenic Rickets.** Phosphopenic forms of rickets are seen in hereditary hypophosphatemia, tumor-induced rickets and osteomalacia, and intrinsic renal tubular disease. Additionally, a major component of rickets of prematurity (i.e., metabolic bone disease of prematurity) is likely phosphate deficiency.

### Hereditary Hypophosphatemic Disorders

***Etiology.*** X-linked hypophosphatemia (XLH), also known as familial vitamin D–resistant rickets, is the most common hereditary cause of hypophosphatemia, with rare autosomal-dominant and recessive variants.[7,9,11] The discovery that the autosomal-dominant variant was due to a gain of function for FGF23 led to the recognition of FGF23 as a major phosphaturic factor. The relationship of FGF23 and mutations of the *PHEX* gene, the causative defect in XLH, is under investigation.[23]

XLH is characterized clinically by short stature and prominent bowing deformities of the lower extremities. Although X-linked dominant, it often is less severe in female heterozygotes than in male hemizygotes. Biochemically, serum phosphate is low and phosphate excretion is elevated. Calcium and PTH are normal and calcitriol is either low or inappropriately normal.

***Imaging.*** Lower extremity bowing usually is quite prominent in XLH (e-Fig. 139.6), whereas the rachitic findings of XLH are often (but not always) relatively mild. Because no hypocalcemia is present, secondary HPTH is not seen in hypophosphatemic rickets. Looser zones (a feature of osteomalacia) are present more often in XLH than in nutritional rickets, likely because of the chronicity of the mineralization disorder. Looser zones, or pseudofractures, are radiolucent lines oriented perpendicular to the cortex as a result of poor mineralization of osteoid at sites of stress, which lead to increased bone remodeling. Characteristic sites include the medial aspect of the femoral neck (Fig. 139.7), the extensor surface of the ulna, the axillary border of the scapula, and the pubic ramus, with these findings often being bilateral. In infants, craniosynostosis may complicate XLH.[24,25] In older patients, XLH may be associated with enthesopathy and paravertebral ossification, similar to diffuse idiopathic skeletal hyperostosis.

***Treatment and Follow-up.*** Treatment of XLH includes oral phosphate replacement and calcitriol because phosphate replacement alone often leads to secondary HPTH. However, excessive calcitriol may lead to hypercalcemia, nephrocalcinosis, and nephrolithiasis; renal ultrasonography often is used to screen for this complication.[26]

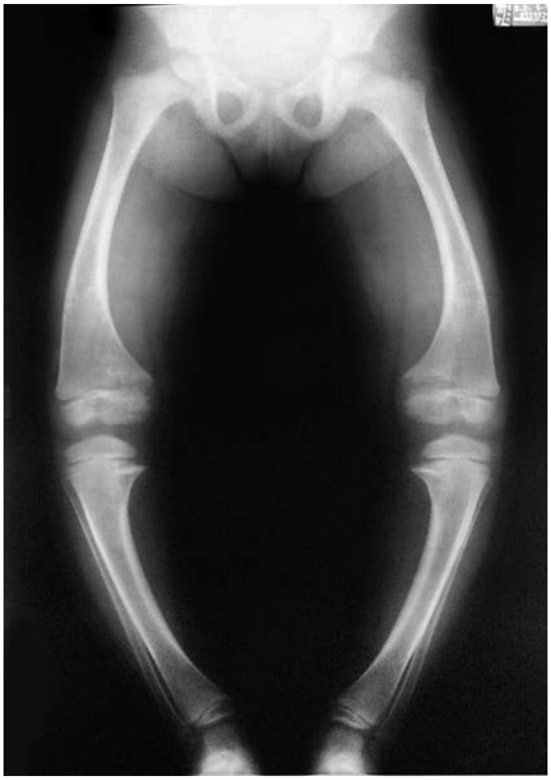

**e-Figure 139.6. X-linked hypophosphatemia in a 3½-year-old girl.** Prominent convex lateral bowing of the femurs and tibias is present, along with rachitic findings in the metaphyses.

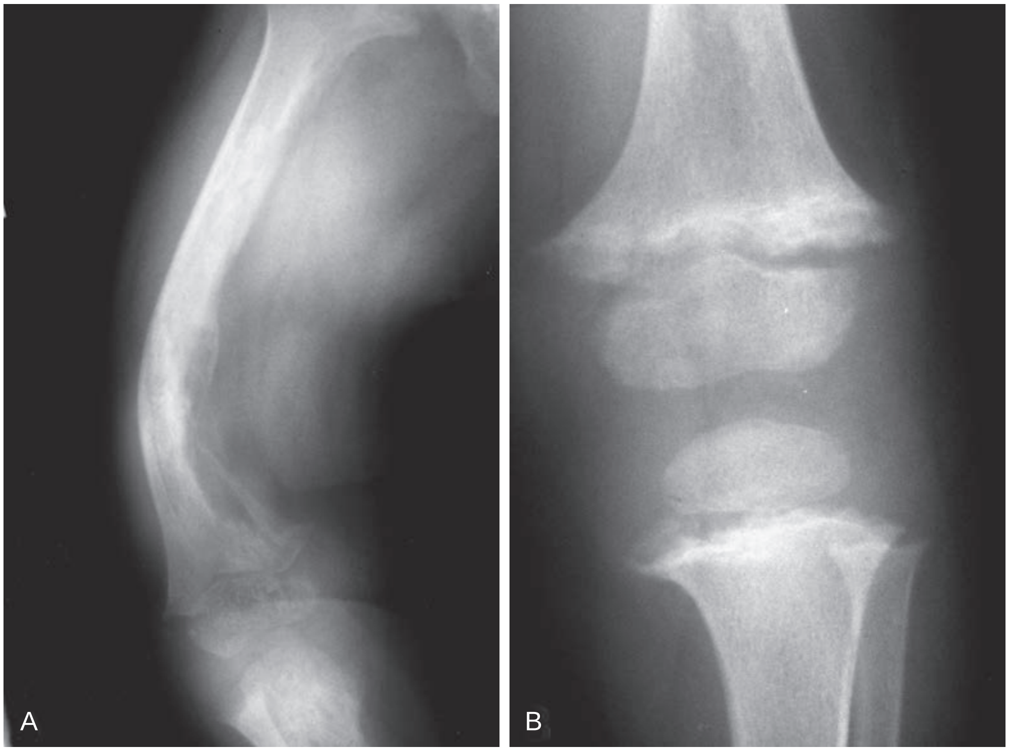

**Figure 139.8. Hypophosphatemic rickets in a girl aged 2 years and 4 months with Gorham massive osteolysis syndrome.** Radiograph of the right femur (A) shows extensive osteolysis. The left hemiskeleton was unaffected by osteolysis, but the left knee (B) shows typical features of rickets.

### Tumor-Induced Rickets and Osteomalacia (Oncologic Osteomalacia)

***Etiology.*** Hypophosphatemic rickets and osteomalacia may be caused by certain tumors and tumor-like conditions that are capable of producing FGF23, with healing of rickets after removal of the tumor.[27,28] Tumor-induced rickets and osteomalacia (TIRO) may occur at any age but is quite uncommon in children. Although a large variety of benign and malignant mesenchymal neoplasms initially were described, many of these neoplasms more recently have been recategorized pathologically as “phosphaturic mesenchymal tumor, mixed connective tissue variant.”[29] Other conditions causing rickets that are considered to be within the spectrum of TIRO include neurofibromatosis, polyostotic fibrous dysplasia (with or without other features of McCune–Albright syndrome), epidermal nevus syndrome, and Gorham massive osteolysis syndrome (Fig. 139.8).

Patients with TIRO may present with chronic vague symptoms, including generalized pain and muscle weakness. TIRO should be suspected in cases of hypophosphatemic rickets with no family history or evidence of renal tubular disease.

***Imaging.*** The radiographic findings of TIRO are similar to those of other forms of chronic rickets such as XLH. Imaging also plays a role in the search for the causative tumor, which usually is small and grows slowly. Because phosphaturic mesenchymal tumors often express somatostatin receptors, In-111 octreotide scintigraphy has been used.[30] Reports also indicate that fluorine-18-deoxyglucose positron emission tomography/computed tomography or whole-body MRI may be helpful.[31,32]

***Renal Tubular Disease.*** Many disorders including cystinosis, tyrosinemia, galactosemia, Lowe syndrome, Wilson disease, and toxins may cause global renal tubular dysfunction, hyperphosphaturia, renal tubular acidosis, and wasting of other substances.

### Rickets of Prematurity

***Etiology.*** Rickets of prematurity, also known as metabolic bone disease of prematurity, is most common in infants with a birth weight below 1 kg or gestational age younger than 28 weeks.[33,34] Normally, 80% of gestational bone mineral accretion occurs during the third trimester,[34] and thus infants born prematurely must accumulate minerals at a high rate to make up for this deficit. Although dietary mineral deficiency is rare in term infants and older children, inadequate intake of calcium and especially phosphorus is a major cause of metabolic bone disease of prematurity. Breast milk and infant formulas do not supply sufficient calcium and phosphorus for premature infants, and this deficiency becomes most pronounced during the period of “catch-up” growth, often near the time of hospital discharge.

***Imaging.*** Radiographic features include generalized osteopenia, fractures, and rachitic changes in the metaphyses (Fig. 139.9). However, the rachitic findings may be masked when the infant is not growing. The fractures often are not recognized acutely and, if first discovered after discharge, may be confused with nonaccidental trauma. Extremity fractures are common and usually do not lead to long-term morbidity because ample opportunity exists for remodeling.

## Hypophosphatasia

***Etiology.*** Hypophosphatasia is a rare inherited condition in which deficient mineralization of cartilage and osteoid are attributed to alkaline phosphatase deficiency rather than an insufficient calcium x phosphate product (which characterizes rickets).[5,35,36] In hypophosphatasia, a defect in the gene encoding alkaline phosphatase results in accumulation of pyrophosphate, which interferes with the formation of hydroxyapatite crystals.

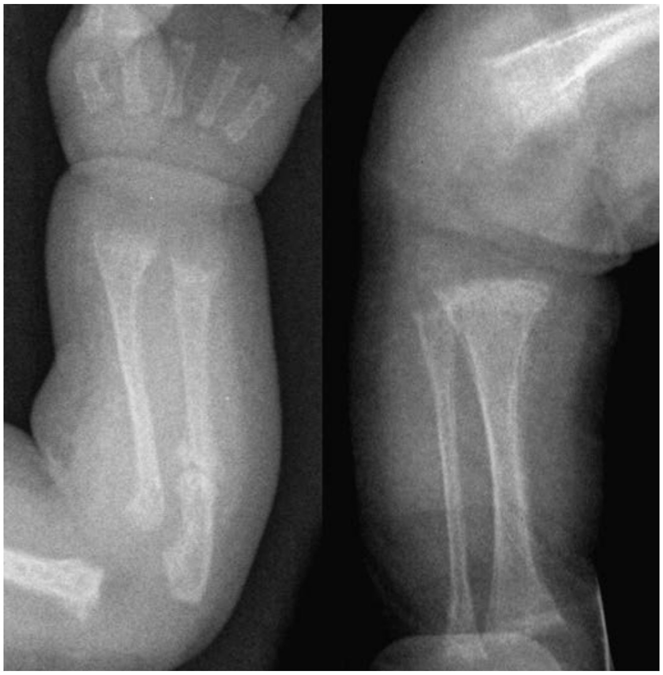

**Figure 139.9. Metabolic bone disease of prematurity in a former premature infant who is now 3 months of age.** Radiographic findings include severe diffuse demineralization, rachitic findings in major long bone metaphyses, and healing fractures of the ulnar diaphysis and distal femur.

Hypophosphatasia is divided clinically into perinatal, infantile, childhood, and adult forms, with decreasing severity as the age of presentation increases. Two other variants have also been described; ondontohypophosphatasia involving only dentition, and benign prenatal hypophosphatasia characterized by spontaneous improvement of prenatal long bone bowing.[37] The perinatal form features severe lack of mineralization of the skeleton and short and deformed limbs. Absence of structural support for the thorax leads to respiratory insufficiency, predisposition to pneumonia, and early death. The infantile form has a less severe mineralization defect. Patients present before 6 months of age with lethargy, leading to poor feeding and failure to thrive. Rachitic-appearing ribs and multiple rib fractures may be seen. Craniosynostosis often is present and may be associated with increased intracranial pressure despite a wide appearance of the sutures radiographically. The childhood and adult forms are milder with extremity pain, gait disturbance, weakness, and premature loss of deciduous teeth. The skeletal manifestations of childhood hypophosphatasia improve during adolescence, but symptoms of the "adult" form recur later in life simulating osteomalacia.

***Imaging.*** The perinatal form (Fig. 139.10) is characterized by severe failure of mineralization of much of the skeleton. Although the skull base usually is mineralized, the calvarium may be nearly completely nonmineralized. The remainder of the axial skeleton has varying mineralization. In infantile and childhood hypophosphatasia, the diaphyses appear normal and the metaphyses are poorly mineralized, suggesting a process similar to rickets. However, the "rachitic" changes of hypophosphatasia are not as uniformly distributed across the growth plate. Rather, it involves a more localized portion of the growth plate with deficient mineralization extending into the metaphysis, creating a "chewed out" appearance of the metaphyses (Fig. 139.11). Because of poor calvarial mineralization, the sutures may appear widened despite actual premature closure. Whole-body MRI of childhood hypophosphatasia shows metaphyseal bone marrow signal T2 hyperintensity predominantly in the lower extremities.[38] The adult form simulates osteomalacia with a coarse trabecular pattern, Looser zones, and metatarsal fractures.

***Treatment and Follow-up.*** Initial attempts to treat severe forms of hypophosphatasia with alkaline phosphatase infusion were ineffective, although more recent work with a bone-targeted human recombinant enzyme is encouraging.[39] Bone marrow transplantation also has been used in the treatment of infantile hypophosphatasia.[40] The milder forms are treated symptomatically.

### Hyperphosphatemic Disorders

***Etiology.*** The major conditions causing hyperphosphatemia include renal insufficiency, tumoral calcinosis (TC), and hyperostosis hyperphosphatemia syndrome (HHS). TC and HHS are now considered to be different manifestations of the same disorder, with some patients showing features of each.[41] TC is an autosomal-recessive disorder characterized by prominent calcific deposits and hyperphosphatemia. It usually is seen in adolescents and young adults but may present earlier. In the United States, TC is most common in African Americans. HHS is most common in the Middle East and usually presents in childhood with extremity pain and swelling along with imaging findings that mimic osteomyelitis. Hyperphosphatemia and elevated or inappropriately normal calcitriol levels are secondary to decreased FGF23 signaling, which in turn is caused by mutations affecting either FGF23, an enzyme that stabilizes it, or its receptor.[42–45]

TC should be distinguished from secondary causes of heterotopic bone formation, such as is seen in chronic renal insufficiency and posttraumatic myositis ossificans.

***Imaging.*** The major finding in TC is the deposition of large calcific masses in the paraarticular soft tissues (Fig. 139.12A).[46–48] In descending order, the hips, elbows, shoulders, and feet are most frequently involved. These masses often are cystic and may show layering of chalky fluid on cross-sectional imaging or horizontal beam radiography. Some patients with TC may also have manifestations of HHS, including medullary sclerosis, extensive periosteal new bone, abnormalities on skeletal scintigraphy, and edema-like signal in the marrow on MRI (Figs. 139.12B and C). These features are related to bone marrow involvement and may mimic osteomyelitis or other infiltrative disorders.

***Treatment and Follow-up.*** The calcified masses of TC are amenable to surgical excision if they become painful or cause deformity or functional impairment. Many forms of therapy have been used to diminish or prevent these deposits, although they all have limited supporting data. Most often used is dietary phosphate restriction, which often is combined with aluminum-based phosphate binders. No forms of therapy have been found to be useful in patients with HHS, a disorder that usually shows spontaneous subsidence, often followed by recurrence.

## ABNORMALITIES OF BONE MATRIX FORMATION

Bone matrix (osteoid) is the organic framework upon which mineral, in the form of hydroxyapatite, is deposited. The prototypical cause of insufficient matrix formation is osteogenesis imperfecta with defects in the genes encoding type I collagen. Normal collagen synthesis also depends on ascorbic acid (vitamin C) and ascorbic acid oxidase, a copper-dependent enzyme. Hence matrix synthesis is impaired in vitamin C deficiency (scurvy), copper deficiency, and some abnormalities of copper metabolism.

### Scurvy

***Etiology.*** Scurvy is caused by dietary deficiency of vitamin C.[49–51] Children with developmental and behavioral disorders such

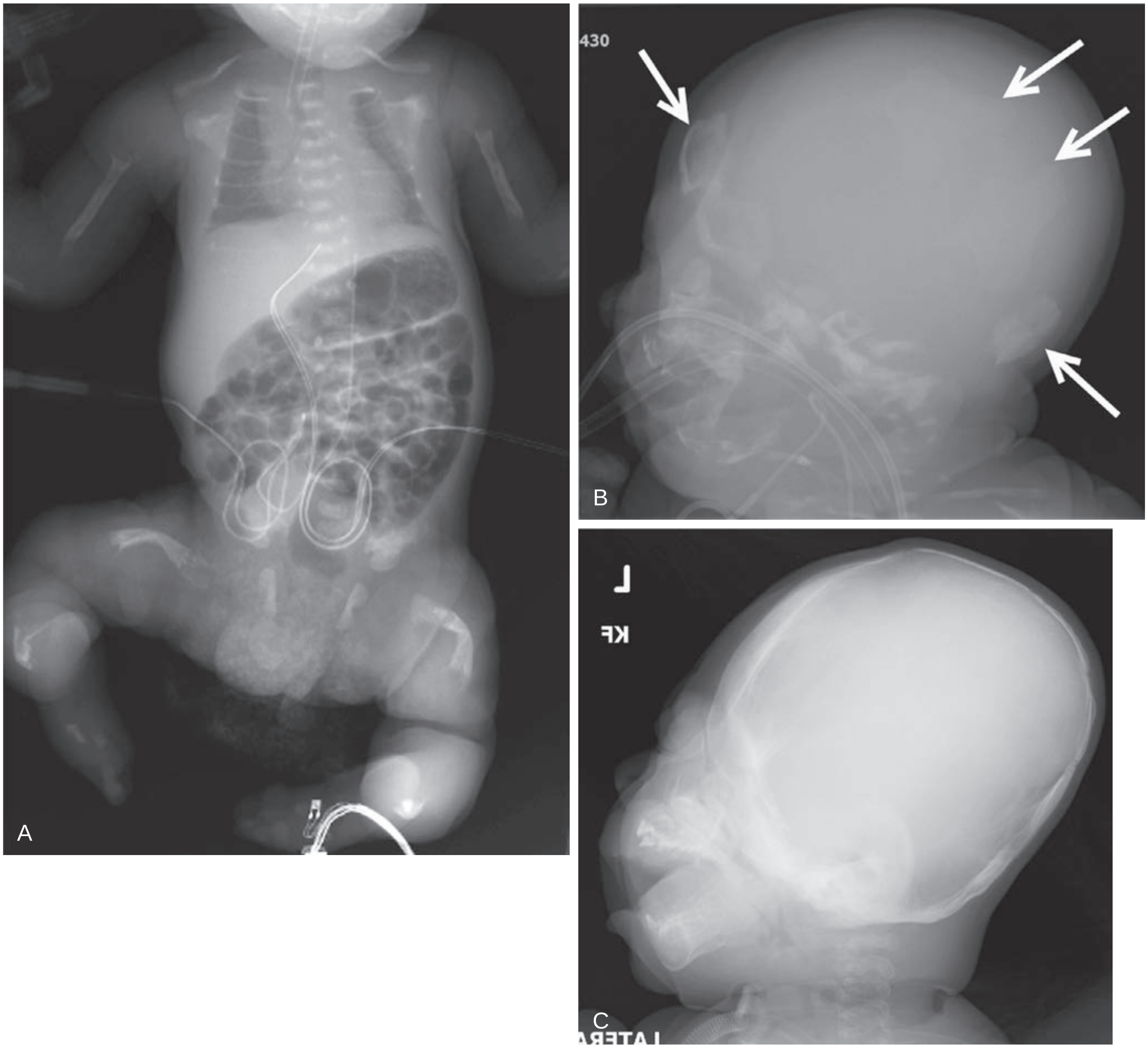

**Figure 139.10. Perinatal hypophosphatasia.** (A) Babygram shows severely gracile ribs with pulmonary hypoplasia. The vertabrae are wafer-like. There is irregular ossification and hypoplasia of the long bones with bowing of the extremities. (B) The skull is nonmineralized except for part of the skull base and small islands of the frontal, parietal, and occipital bones *(arrows)*. (C) With experimental therapy, there has been increased ossification of the skull at 6 months of age, but development of craniosynostosis. The child died 1 month later.

as autism may present with limping due to scurvy caused by a highly restrictive diet.[52] Children with transfusion-related iron overload are also at risk for scurvy due to accelerated ascorbic acid catabolism by high iron stores, exacerbated in the setting of poor diet.[53]

***Imaging.*** Decreased osteoid formation in scurvy causes an imbalance between bone production and resorption, leading to generalized atrophy of the cortex and spongiosa. However, chondrocyte terminal differentiation and cartilage calcification are normal, forming a well-mineralized zone of provisional calcification. On the diaphyseal side of the physis, resorption of calcified cartilage is diminished, leading to a thickened zone of provisional calcification. Radiographically, this thickened zone is seen as a prominent opaque line (Fig. 139.13), designated as the white line of scurvy (white line of Fränkel). Despite its thickness, this zone is brittle and may fracture. The bone just beneath the thickened provisional zone is demineralized and also brittle with a sparse trabecular pattern, producing a lucent zone adjacent to the zone of provisional calcification known as the scurvy zone (the Trümmerfeld zone). Later, transverse fractures may develop through the brittle zone of provisional calcification and the demineralized metaphyseal scurvy zone. If this fracture is limited to a peripheral portion of the scurvy zone, a subphyseal lucent cleft will be seen (Fig. 139.14). With transverse displacement of the epiphysis and zone of provisional calcification from the rest of the shaft, the heavily mineralized zone of provisional calcification projects

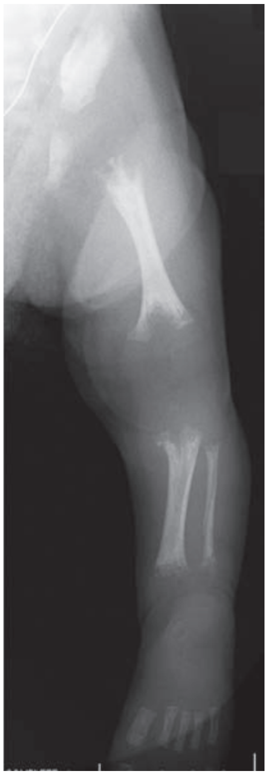

**Figure 139.11. Infantile hypophosphatasia.** Lower extremity radiograph at 1 month of age shows irregular "chewed out" appearance of the metaphyses. There is poor ossification of the epiphyses of the knee as well as the talus and calcaneus.

peripherally, forming a metaphyseal spur (Pelkan spur), another characteristic radiographic feature of scurvy. These changes should not be confused with metaphyseal fractures of child abuse. Similar changes in the epiphyses lead to a thickened peripheral shell of calcified cartilage surrounding rarefied trabecular bone within the epiphysis, producing the Wimberger ring (see Fig. 139.13), one of the most characteristic findings of scurvy. In the diaphyses, the findings are those of generalized osteopenia with cortical thinning, although diaphyseal fractures are uncommon. Subperiosteal hemorrhage due to capillary fragility is a frequent manifestation of scurvy and is most common in the larger tubular bones such as the femur, tibia, and humerus. Initially, subperiosteal hemorrhage is seen as increased soft tissue opacity on radiographs, or as heterogeneous subperiosteal collections on ultrasound or MRI.[54,55] Subsequently, the periosteum produces a cloak of new bone surrounding the shaft, which eventually will become the new cortex (Fig. 139.15).

***Treatment and Follow-up.*** The diagnosis of scurvy usually is based on a combination of the clinical and radiographic findings. An appropriate dietary history and laboratory testing may also be helpful. The clinical response to ascorbic acid is usually rapid, confirming the diagnosis.

## Copper Deficiency and Menkes Disease

Ascorbic acid oxidase is a copper-dependent enzyme, and hence copper deficiency results in deficient matrix formation and osteopenia. Menkes disease, an X-linked neurodegenerative and connective tissue disorder, is caused by deficiency of a cation-transporting enzyme needed for transport of copper.[36,51] This deficiency results in abnormal collagen and elastin, leading to osteopenia and increased bone fragility. Fractures in Menkes disease may follow minor trauma, and metaphyseal fractures with spurring may appear similar to the metaphyseal fractures of nonaccidental trauma[57] (e-Fig. 139.16). C2 posterior arch defects simulating Hangman's fracture have also been described.[58]

## HYPERVITAMINOSIS A

***Etiology.*** Vitamin A is a fat-soluble vitamin needed for vision and many other essential processes. In addition to its role in light reception, it is essential for normal epithelial differentiation of mucous membranes, and hence vitamin A deficiency causes xerophthalmia (dry ulcerating eye), the leading cause of blindness worldwide. Historically, fish liver oil and other preparations used for prevention and treatment xerophthalmia had been the major cause of vitamin A toxicity in young children, with cases often blamed on overly diligent caregivers. Infantile hypervitaminosis A is now quite rare, but vitamin A toxicity can still be seen with excessive supplementation, especially in children with cystic fibrosis and chronic renal failure.[59,60]

Chronic vitamin A toxicity usually presents at least 6 months after the beginning of excessive vitamin A intake. Initial symptoms are nonspecific, with anorexia and irritability. Dry, pruritic skin with desquamation, lip fissuring, and hepatomegaly may be present. The extremities demonstrate focal regions of swelling and pain that overlie the skeletal findings. Acute vitamin A poisoning is rare and usually presents with central nervous system signs and symptoms from increased intracranial pressure.

***Imaging.*** The skeletal manifestation of hypervitaminosis A may be extremely helpful in establishing this diagnosis in a child with a confusing clinical picture.[61,62] Long bone hyperostosis is the most frequent and most well-recognized finding, with periosteal new bone formation leading to undulating diaphyseal cortical thickening, most frequently involving the ulnae (e-Fig. 139.17) and metatarsals. Radiographically, these findings have been confused with infantile cortical hyperostosis (Caffey disease). However, age and distribution usually differentiate these, with presentation after 11 months and metatarsal involvement suggesting hypervitaminosis A, whereas presentation before 5 months and mandibular involvement suggests infantile cortical hyperostosis.[61] Premature central growth plate closure also may be seen in hypervitaminosis A,[63,64,65] leading to cone-shaped epiphyses that are invaginated into the metaphyses, mimicking the appearance of prior meningococcemia (Fig. 139.18). Retinoids (e.g., isotretinoin), which are chemically related to vitamin A, are used for treatment of dermatologic disorders as well as in chemotherapeutic regimens for certain malignancies (e.g., neuroblastoma) can also cause skeletal deformities and growth disturbances.[66]

## HYPERVITAMINOSIS D

***Etiology.*** Production of calcitriol, the most active vitamin D metabolite, is a highly regulated process that provides inherent protection against vitamin D toxicity, but acute or chronic intoxication can occur with excessive doses of vitamin $D_2$ or $D_3$ supplements.[67] Most symptoms and signs are associated with manifestations of hypercalcemia. Massive overdosage (4–18 million U/day) may cause severe illness or even death. Manifestations may include vomiting, dehydration, fever, coma, convulsions, abdominal cramps, and "bone pain." In cases of chronic poisoning, the common early symptoms are lethargy, thirst, anorexia, vomiting, diarrhea, and abdominal discomfort. Excessive calcium excretion leads to renal damage.

***Imaging.*** Skeletal findings include cortical thickening, osteoporosis, and alternating bands of increased and decreased opacity (e-Fig. 139.19). Metastatic calcifications also may be present in blood vessels, the falx cerebri, and many organs, including the kidneys, stomach, lungs, bronchi, and adrenal gland.[49]

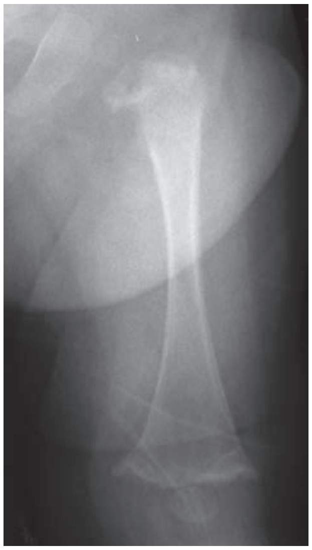

**e-Figure 139.16. Menkes disease.** Radiograph of the left femur shows diffuse demineralization and a proximal femoral metaphyseal fracture. Healing rib fractures also were present. The infant presented with subdural hygromas related to the associated central nervous system disease and initially was suspected to be a victim of child abuse.

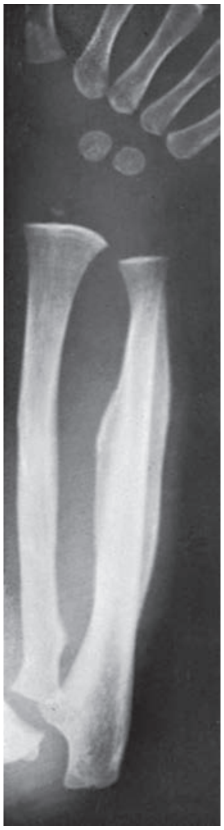

**e-Figure 139.17. Vitamin A toxicity.** Radiograph of the forearm shows mature periosteal new bone producing cortical hyperostosis in the right ulna from. The finding was symmetrical with an identical appearance of the left ulna (not shown).

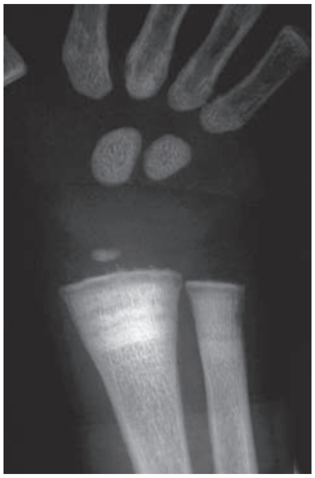

**e-Figure 139.19. Iatrogenic vitamin D intoxication in a child with physiologic bowlegs who mistakenly was thought to have X-linked hypophosphatemia.** Multiple opaque bands are present in the distal radial metaphysis.

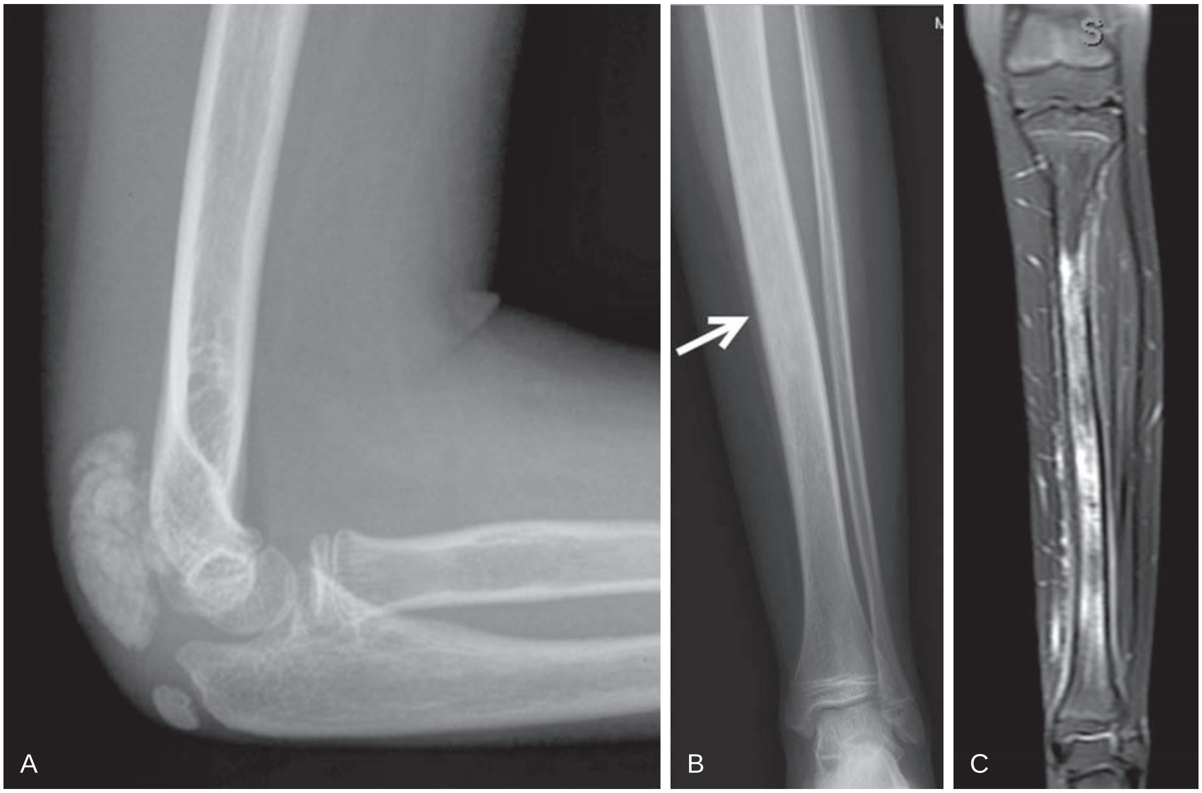

**Figure 139.12. Tumoral calcinosis/hyperostosis hyperphosphatemia syndrome.** (A) Left elbow radiograph in an 8-year-old girl shows a multilobulated calcified mass posterior to the left elbow. The mass was excised with confirmation of tumoral calcinosis. At age 9 years, evaluation for left leg pain included a frontal radiograph (B) showing diaphyseal sclerosis and mild periosteal reaction of the tibia *(arrow),* and a corresponding coronal T2-weighted fat suppresssed MRI (C) demonstrating extensive marrow hyperintensity and periostitis. A nuclear medicine bone scan also showed increased radiotracer activity (not shown). This appearance of "diaphysitis" seen with tumoral calcinosis/hyperostosis syndrome can be confused with osteomyelitis. One year later, she presented with pain and similar findings in the contralateral tibia.

## HEAVY METAL POISONING

***Etiology.*** Lead poisoning is the most common form of heavy metal poisoning. In children, lead poisoning usually occurs as a result of the ingestion of paint chips or dust containing lead in older housing; in the United States, the sale of house paint containing lead was discontinued in 1978. Although the incidence of lead poisoning has declined with public health and education efforts, it remains a significant problem, with growing concern about drinking water contamination from corroded lead pipes. Lead bullets result in toxicity only if they are within a serous space such as a synovium-lined joint, where lead will cause both systemic toxicity and synovitis, resulting in lead arthropathy.

Lead poisoning is characterized by abdominal pain, encephalopathy, peripheral neuropathy, and anemia with basophilic stippling.

***Imaging.*** Chronic lead toxicity causes bands of increased opacity (lead lines) in the metaphyses. The amount of lead in these regions is far below the amount that would be needed to produce opaque bands. Rather, lead toxicity causes defective resorption of calcified cartilage in the primary spongiosa, which builds up, producing the opaque bands. Usually, the more opaque the metaphyseal band, the more likely it is to be pathologic. However, lead lines can be clearly distinguished from normal opaque metaphyseal bands once interval bone growth separates the abnormally sclerotic bone from the zone of provisional calcification. Normal opaque metaphyseal bands are always contiguous with the zone of provisional calcification (Fig. 139.20). Abdominal radiographs may detect ingested radiopaque lead chips within the gastrointestinal tract.

***Treatment and Follow-up.*** Steps to prevent further exposure to lead are mandatory. Removal of radiographically identified lead chips from the stomach by gastric lavage has been performed but is controversial because the lead chips usually are poorly absorbed. In addition, no evidence exists to support the use of charcoal as a gastrointestinal binder to prevent absorption. For patients with particularly high lead levels, chelation therapy is indicated.

### KEY POINTS

- The initial radiographic finding in rickets is loss of mineralization of the zone of provisional calcification.
- Isolated distal ulnar metaphyseal cupping is a normal variant in an infant and should not be confused with rickets.
- In scurvy, maintenance of the zone of provisional calcification with subjacent demineralization occurs and gives an opposite appearance to rickets in both the metaphyses and epiphyses.
- Metaphyseal skeletal changes with scurvy may superficially mimic classic metaphyseal fractures of child abuse.

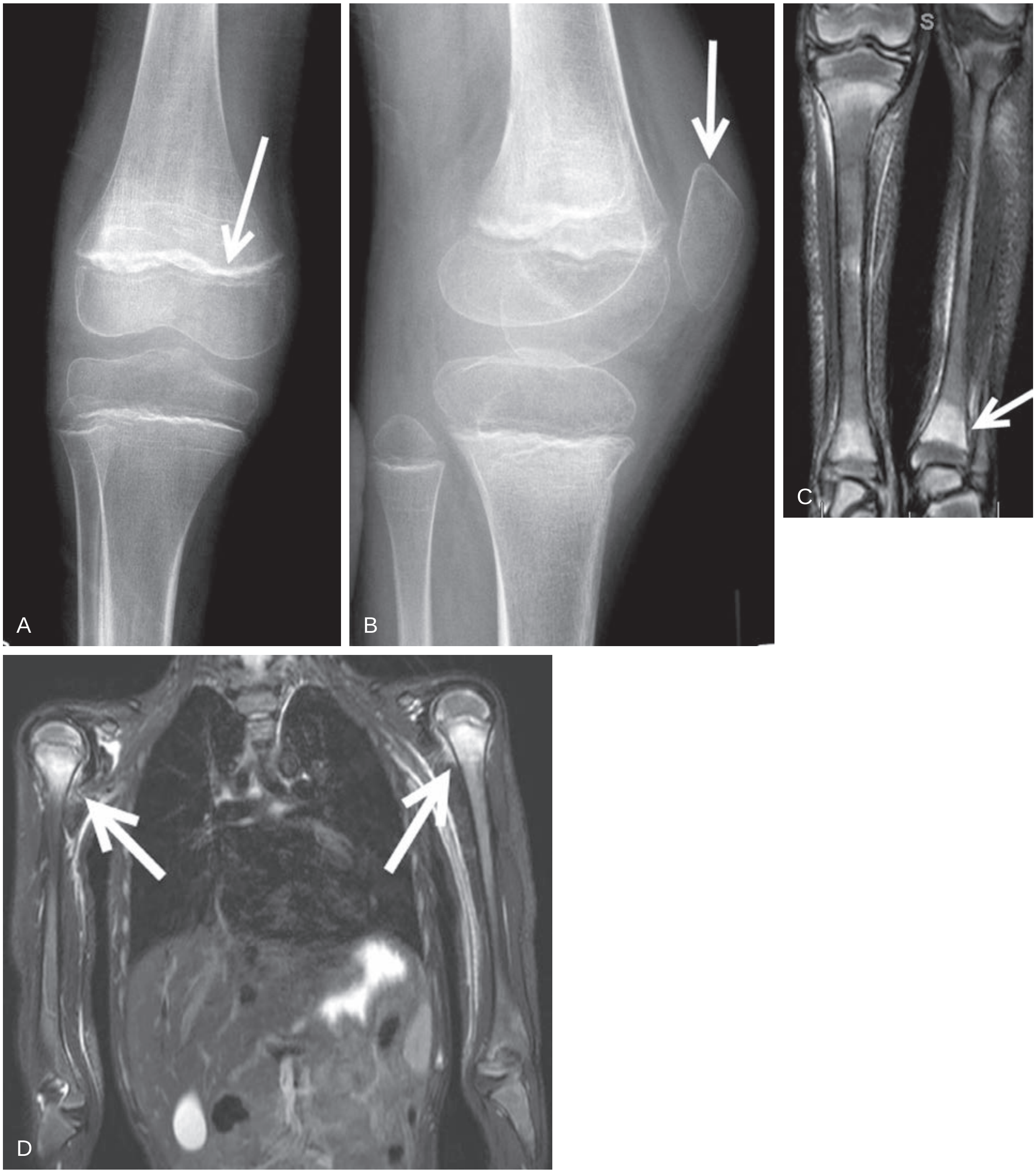

**Figure 139.13. Scurvy.** Eight-year-old boy with behavioral problems, parental neglect, and a severely restrictive diet who presented with lower extremity pain, refusal to bear weight and bleeding gums. (A) Frontal view of the right knee shows prominent zones of provisional calcification, forming the white line of scurvy *(arrow)*. (B) Lateral view of the knee shows the epiphyseal zone of provisional calcification, forming the Wimberger ring surrounding the centrally lucent epiphyses and patella *(arrow)*. (C) A coronal short-tau inversion recovery (STIR) image of the legs from whole-body MRI shows hyperintense bone marrow signal in the metaphyses of the tibiae and fibulae *(arrow),* as well as adjacent periosteal hyperintensity. (D) A coronal STIR image of the chest shows similar hyperintensity in the humeral metaphyses *(arrows)*.

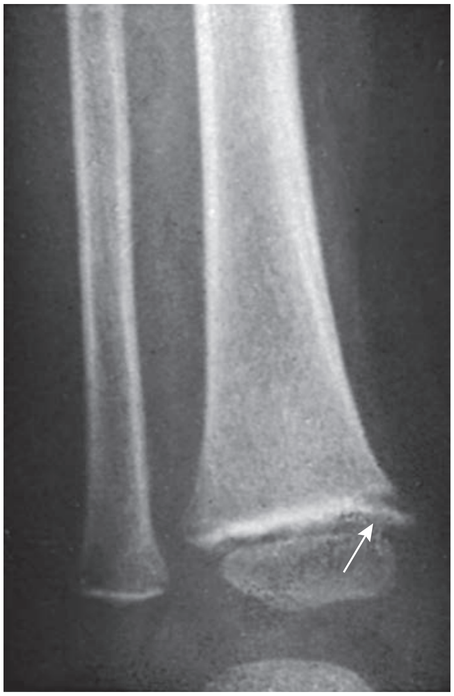

**Figure 139.14. Peripheral metaphyseal cleft in a 14-month-old child with scurvy.** An eccentric lucent cortical and trabecular defect produces a cleft *(arrow)* just beneath the zone of provisional calcification, with the peripheral aspect of the zone of provisional calcification separated from the shaft and tilted off the shaft toward the epiphysis.

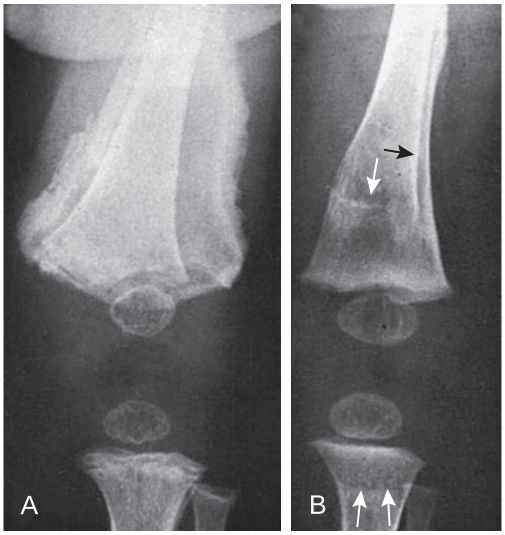

**Figure 139.15. Scurvy with displaced fracture and a subperiosteal hematoma.** (A) The left distal femoral epiphysis is displaced laterally relative to the metaphysis with a fracture through the brittle zone of provisional calcification. A large subperiosteal hematoma is present with periosteal calcification. Also note Wimberger rings of the distal femur and proximal tibia. (B) Four months later, the periosteal new bone is producing a new cortex with remodeling and eventual anatomic alignment of the prior epiphyseal displacement. *Arrows* indicate the initial cortex and zone of provisional calcification.

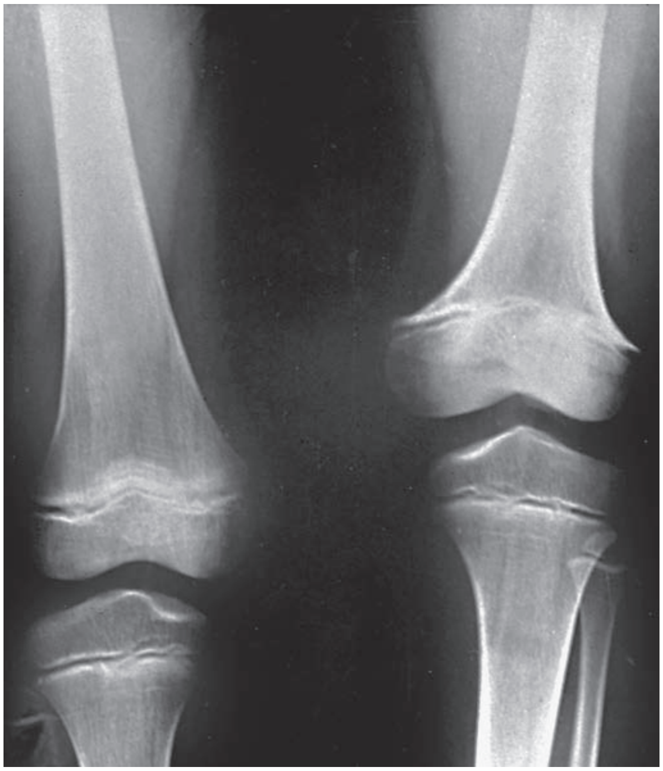

**Figure 139.18. Premature central growth plate closure from vitamin A.** Frontal radiograph shows premature closure of the central portion of the left distal femoral physis causing a left femoral longitudinal growth disturbance. In other cases involvement may be more generalized. *(Courtesy Charles N. Pease, Chicago, IL.)*

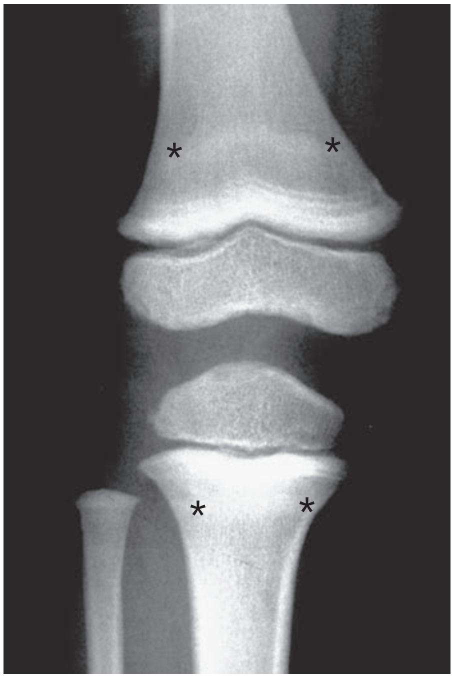

**Figure 139.20. Lead toxicity.** In addition to the opaque bands at the zones of provisional calcification, faint opaque bands also are present (between *asterisks*) that have “migrated away,” clearly establishing that they are abnormal rather than normal-variant opaque metaphyseal bands, which are always in continuity with the zone of provisional calcification.

## SUGGESTED READINGS

Alizadeh Naderi AS, Reilly RF. Hereditary disorders of renal phosphate wasting. *Nat Rev Nephrol*. 2010;6:657–665.
Chang CY, Rosenthal DI, Mitchell DM, et al. Imaging findings of metabolic bone disease. *Radiographics*. 2016;36:1871–1887.
Servaes A, Brown SD, Choudhary AK, et al. The etiology and significance of fractures in infants and young children: a critical multidisciplinary review. *Pediatr Radiol*. 2016;46(5):591–600.
Shore RM, Chesney RW. Rickets: Part I. *Pediatr Radiol*. 2013;43:140–151.
Whyte MP. Hypophosphatasia – aetiology, nosology, pathogenesis, diagnosis and treatment. *Nat Rev Endocrinol*. 2016;12(4):233–246.

## REFERENCES

Full references for this chapter can be found on www.expertconsult.com.

## REFERENCES

1. Bikle D, Adams J, Christakos S, et al. production, metabolism, mechanism of action, and clinical requirements. In: Rosen CJ, ed. *Primer on the Metabolic Bone Diseases and Disorders of Mineral Metabolism*. 7th ed. Washington, DC: American Society for Bone and Mineral Research; 2008.
2. DeLuca HF. Overview of general physiological features and functions of vitamin D. *Am J Clin Nutr*. 2004;80:1689S–1696S.
3. Lips P, van Schoor NM, Bravenboer N, et al. related disorders. In: Rosen CJ, ed. *Primer on the Metabolic Bone Diseases and Disorders of Mineral Metabolism*. 7th ed. Washington, DC: American Society for Bone and Mineral Research; 2008.
4. Resnick D, Manolagas SC, Niwayama G, et al. Histogenesis, anatomy, and physiology of bone. In: Resnick D, ed. *Diagnosis of Bone and Joint Disorders*. 4th ed. Philadelphia: Saunders; 2002.
5. Whyte MP. Hypophosphatasia: nature's window on alkaline phosphatase function in man. In: Bilezikian JP, Raisz LG, Rodan GA, eds. *Principles of Bone Biology*. 2nd ed. San Diego: Academic Press; 2002.
6. Tiosano D, Hochberg Z. Hypophosphatemia: the common denominator of all rickets. *J Bone Miner Metab*. 2009;27:392–401.
7. Bastepe M, Jüppner H. Inherited hypophosphatemic disorders in children and the evolving mechanisms of phosphate regulation. *Rev Endocr Metab Disord*. 2008;9(2):171–180.
8. Farrow EG, White KE. Recent advances in renal phosphate handling. *Nat Rev Nephrol*. 2010;6(4):207–217.
9. Glorieux FH. Hypophosphatemic vitamin-D resistant rickets. In: Favis MJ, ed. *Primer on the Metabolic Bone Diseases and Disorders of Mineral Metabolism*. 5th ed. Washington, DC: American Society for Bone and Mineral Research; 2003.
10. Levine BS, Kleeman CR, Felsenfeld AJ. The journey from vitamin D-resistant rickets to the regulation of renal phosphate transport. *Clin J Am Soc Nephrol*. 2009;4(11):1866–1877.
11. Liu S, Quarles LD. How fibroblast growth factor 23 works. *J Am Soc Nephrol*. 2007;18:1637–1647.
12. Ruppe MD, Jan de Beur SM. Disorders of phosphate homeostasis. In: Rosen CJ, ed. *Primer on the Metabolic Bone Diseases and Disorders of Mineral Metabolism*. 7th ed. Washington, DC: American Society for Bone and Mineral Research; 2008.
13. Chesney RW. Rickets: an old form for a new century. *Pediatr Int*. 2003;45:509–511.
14. Parfitt AM, Vitamin D. and the pathogenesis of rickets and osteomalacia. In: Feldman D, Pike JW, Glorieux FH, eds. *Vitamin D*. 2nd ed. San Diego: Elsevier Academic Press; 2005.
15. Pettifor JM. Nutritional rickets: deficiency of vitamin D, calcium, or both? *Am J Clin Nutr*. 2004;80(suppl 6):1725S–1729S.

15a. Kovacs CS. Maternal vitamin D deficiency: Fetal and neonatal implications. *Semin Fetal Neonatal Med*. 2013;18:129–135.

15b. Chapman T, Sugar N, Done S, et al. Fractures in infants and toddlers with rickets. *Pediatr Radiol*. 2010;40(7):1184–1189.

16. Simpson RU, Thomas GA, Arnold AJ. Identification of 1,25-dihydroxyvitamin D3 receptors and activities in muscle. *J Biol Chem*. 1985;260:8882–8891.
17. Oestreich AE. The Acrophysis: a unifying concept for understanding enchondral bone growth and its disorders. II. Abnormal growth. *Skeletal Radiol*. 2004;33:119–128.
18. Institute of Medicine. *Dietary Reference Intakes for Calcium and Vitamin D*. Washington, DC: National Academies Press; 2011.
19. Misra M, Pacaud D, Petryk A, et al; Drug and Therapeutics Committee of the Lawson Wilkins Pediatric Endocrine Society. Vitamin D deficiency in children and its management: review of current knowledge and recommendations. *Pediatrics*. 2008;122:398–417.
20. Fraser D, Kooh SW, Kind HP, et al. Pathogenesis of hereditary vitamin-D-dependent rickets. An inborn error of vitamin D metabolism involving defective conversion of 25-hydroxyvitamin D to 1-alpha, 25-dihydroxyvitamin D. *N Engl J Med*. 1973;289:817–822.
21. Malloy PJ, Feldman D. Genetic disorders and defects in vitamin D action. *Endocrinol Metab Clin North Am*. 2010;39:333–346.
22. Brooks MH, Bell NH, Love L, et al. Vitamin-D-dependent rickets type II. Resistance of target organs to 1,25-dihydroxyvitamin D. *N Engl J Med*. 1978;298:996–999.
23. Li SS, Gu JM, Yu WJ, et al. Seven nove land six de novo PHEX gene mutations in patients with hypophosphatemic rickets. *Int J Mol Med*. 2016;38:1703–1714.
24. Currarino G. Sagittal synostosis in X-linked hypophosphatemic rickets and related diseases. *Pediatr Radiol*. 2007;37:805–812.
25. Murthy AS. X-linked hypophosphatemic rickets and craniosynostosis. *J Craniofac Surg*. 2009;20:439–442.
26. Carpenter TO, Imel EA, Holm IA, et al. A clinician's guide to X-linked hypophosphatemia. *J Bone Miner Res*. 2011;26:1381–1388.
27. Drezner MK. Tumor-induced osteomalacia. *Rev Endocr Metab Disord*. 2001;2:175–186.
28. Farrow EG, White KE. Tumor-induced osteomalacia. *Expert Rev Endocrinol Metab*. 2009;4:435–442.
29. Folpe AL, Fanburg-Smith JC, Billings SD, et al. Most osteomalacia-associated mesenchymal tumors are a single histopathologic entity: an analysis of 32 cases and a comprehensive review of the literature. *Am J Surg Pathol*. 2004;28:1–30.
30. Duet M, Kerkeni S, Sfar R, et al. Clinical impact of somatostatin receptor scintigraphy in the management of tumor-induced osteomalacia. *Clin Nucl Med*. 2008;33:752–756.
31. Roarke MC, Nguyen BD. PET/CT localization of phosphaturic mesenchymal neoplasm causing tumor-induced osteomalacia. *Clin Nucl Med*. 2007;32:300–301.
32. Nakanishi K, Sakai M, Tanaka H, et al. Whole-body MR imaging in detecting phophaturic mesenchymal tumor (PMT) in tumor-induced hypophosphotemic osteomalacia. *Magn Reson Med Sci*. 2013;12(1):47–52.
33. Figueras-Aloy J, Alvarez-Dominguez E, Perez-Fernandez JM, et al. Metabolic bone disease and bone mineral density in very preterm infants. *J Pediatr*. 2014;164:499–504.
34. Sharp M. Bone disease of prematurity. *Early Hum Dev*. 2007;83:653–658.
35. Whyte MP. Hypophosphatasia. In: Favis MJ, ed. *Primer on the Metabolic Bone Diseases and Disorders of Mineral Metabolism*. 5th ed. Washington, DC: American Society for Bone and Mineral Research; 2003.
36. Whyte MP. Enzyme defects and the skeleton. In: Rosen CJ, ed. *Primer on the Metabolic Bone Diseases and Disorders of Mineral Metabolism*. 7th ed. Washington, DC: American Society for Bone and Mineral Research; 2008.
37. Matsushita M, Kitoh H, Michigami T, et al. Benign prenatal hypophosphatasia: a treatable disease not to be missed. *Pediatr Radiol*. 2014;44:340–343.
38. Beck C, Morbacj H, Wirth C, et al. Whole-body MRI in the childhood form of hypophosphatasia. *Rheumatol Int*. 2011;31:1315–1320.
39. Whyte M, Greenberg CR, Wenkert D, et al. Hypophosphatasia: enzyme replacement therapy for children using bone-targeted, tissue-nonspecific alkaline phosphatase. *J Bone Miner Res*. 2010;25(suppl 1):Available at: http://www.asbmr.org/Meetings/AnnualMeeting/AbstractDetail.aspx?aid=bb726d8a-643b-4fb9-9282-0ddfc214bfce. Accessed January 13, 2011.
40. Whyte MP, Kurtzberg J, McAlister WH, et al. Marrow cell transplantation for infantile hypophosphatasia. *J Bone Miner Res*. 2003;18:624–636.
41. Narchi H. Hyperostosis with hyperphosphatemia: evidence of familial occurrence and association with tumoral calcinosis. *Pediatrics*. 1997;99:745–748.
42. Chefetz I, Sprecher E. Familial tumoral calcinosis and the role of O-glycosylation in the maintenance of phosphate homeostasis. *Biochim Biophys Acta*. 2009;1792:847–852.
43. Gok F, Chefetz I, Indelman M, et al. Newly discovered mutations in the GALNT3 gene causing autosomal recessive hyperostosis-hyperphosphatemia syndrome. *Acta Orthop*. 2009;80:131–134.
44. Ichikawa S, Imel EA, Kreiter ML, et al. A homozygous missense mutation in human KLOTHO causes severe tumoral calcinosis. *J Clin Invest*. 2007;117:2684–2691.
45. Ichikawa S, Baujat G, Seyahi A, et al. Clinical variability of familial tumoral calcinosis caused by novel GALNT3 mutations. *Am J Med Genet A*. 2010;152A:896–903.
46. Clarke E, Swischuk LE, Hayden CK Jr. Tumoral calcinosis, diaphysitis, and hyperphosphatemia. *Radiology*. 1984;151:643–646.
47. Martinez S, Vogler JB 3rd, Harrelson JM, et al. Imaging of tumoral calcinosis: new observations. *Radiology*. 1990;174:215–222.
48. Olsen KM, Chew FS. Tumoral calcinosis: pearls, polemics, and alternative possibilities. *Radiographics*. 2006;26:871–885.
49. Grewar O. Infantile scurvy. *Clin Pediatr*. 1965;4:82–89.
50. Park EA, Guild HG, Jackson D. Recognition of scurvy with especial reference to early x-ray changes. *Arch Dis Child*. 1935;10:265–294.
51. Resnick D. Hypervitaminosis and hypovitaminosis. In: Resnick D, ed. *Diagnosis of Bone and Joint Disorders*. 4th ed. Philadelphia: Saunders; 2002.
52. Ma NS, Thompson C, Weston S. Brief report: Scurvy as a manifestation of food selectivity in children with autism. *J Autism Dev Disord*. 2016;46:1464–1470.

53. Golriz F, Donnelly LF, Devaraj S, et al. Modern American scurvy – experience with vitamin C deficiency at a large children's hospital. *Pediatr Radiol*. 2016; epub ahead of print.
54. Polat AV, Bekci T, Say F, et al. Osteoskeletal manifestations of scurvy: MRI and ultrasound findings. *Skeletal Radiol*. 2015;44:1161–1164.
55. Gulko E, Collins LK, Murphy RC, et al. MRI findings in pediatric patients with scurvy. *Skeletal Radiol*. 2015;44:291–297.
56. [deleted in review]
57. Brill PW, Winchester P. Differential diagnosis of child abuse. In: Kleinman PK, ed. *Diagnostic Imaging of Child Abuse*. Baltimore: Williams and Wilkins; 1987.
58. Hill SC, Dwyer AJ, Kaler SG. Cervical spine anomalies in Menkes disease: a radiologic finding potentially confused with child abuse. *Pediatr Radiol*. 2012;42:1301–1304.
59. Safi KH, Filbrun AG, Nasr SZ. Hypervitaminosis A causing hypercalcemia in cystic fibrosis. *Ann Am Thorac Soc*. 2014;11(8):1244–1247.
60. Manickavasagar B, McArdle AJ, Yadav P, et al. Hypervitaminosis A is prevalent in children with CKD and contributes to hypercalcemia. *Pediatr Nephrol*. 2015;30:317–325.
61. Caffey J. Chronic poisoning due to excess of vitamin A. *Am J Roentgenol Radium Ther*. 1951;65:12–26.
62. Resnick D. Disorders due to medications and other chemical agents. In: Resnick D, ed. *Diagnosis of Bone and Joint Disorders*. 4th ed. Philadelphia: Saunders; 2002.
63. Pease CN. Focal retardation and arrestment of growth of bones due to vitamin A intoxication. *JAMA*. 1962;182:980–985.
64. Woodard JC, Donovan GA, Fisher LW. Pathogenesis of vitamin (A and D)-induced premature growth-plate closure in calves. *Bone*. 1997;21:171–182.
65. Wang W, Xu J, Kirsch T. Annexin-mediated Ca2+ influx regulates growth plate chondrocyte maturation and apoptosis. *J Biol Chem*. 2003;278:3762–3769.
66. DiGiovanna JJ. Isotretinoin effects on bone. *J Am Acad Dermatol*. 2001;45:S176–S182.
67. Vogiatzi MG, Jacobson-Dickman E, deBoer MD. Vitamin D supplementation and risk of toxicity in pediatrics: A review of current literature. *J Clin Endocrinol Metab*. 2014;99(4):1132–1141.

# 140 Endocrine Disorders

Eric P. Eutsler and Richard M. Shore

Several endocrine glands have significant effects on skeletal growth, maturation, and modeling, and understanding these effects facilitates correct radiographic interpretation.[1,2] Renal osteodystrophy is also included in this chapter because of the importance of hyperparathyroidism (HPTH) in its pathophysiology, as are other related conditions causing disorders of bone physiology.

## HYPERPARATHYROIDISM AND RENAL OSTEODYSTROPHY

***Etiology.*** The parathyroid glands help maintain a normal circulating calcium concentration by releasing parathyroid hormone (PTH) in response to hypocalcemia. PTH then has many effects that increase the serum calcium concentration, such as promoting bone resorption to mobilize calcium. In the kidney, PTH upregulates renal 1-α-hydroxylase to produce calcitriol (1,25[OH]$_2$-vitamin D), which then acts on the gut to absorb calcium. PTH also decreases renal calcium excretion and increases phosphate excretion.

Bone resorption is mediated by multinucleated osteoclasts. Their development is stimulated by osteoclast differentiation factor, which is produced by osteoblasts. Osteoclast differentiation factor (RANKL) binds to a cell surface receptor called *RANK* on osteoclast precursor cells. PTH has a major role in stimulating osteoclastic bone resorption, likely through stimulation of *RANK*. Calcitriol also stimulates osteoclastic differentiation and function through *RANK*, whereas calcitonin transiently inhibits osteoclastic resorption. Activated osteoclasts then form a sealed-off compartment along the resorption surface, where bone is dissolved by highly concentrated enzymes in acidified extracellular fluid.

Primary HPTH may be caused by parathyroid hyperplasia or a parathyroid adenoma. Parathyroid adenomas are infrequent in children and are usually associated with multiple endocrine neoplasia (MEN) I. Parathyroid hyperplasia may be seen with MEN II and MEN III.

In secondary HPTH, PTH secretion is increased in response to hypocalcemia. Secondary HPTH is more frequent than primary HPTH in children and is most often caused by chronic kidney disease. Rickets and some other disorders of calcium metabolism may also cause secondary HPTH.

### Renal Osteodystrophy

Renal osteodystrophy[3–5] comprises a variety of skeletal manifestations of chronic kidney disease, the most important of which is secondary HPTH. In chronic kidney disease, phosphate retention and the resulting slight decrease in the ionized calcium concentration stimulate PTH, which then acts to promote phosphaturia and increase calcium. Although this initially normalizes calcium and phosphate concentrations, it does so at the expense of elevating PTH and mobilizing calcium and phosphate from bone. With advancing renal failure, decreased renal mass also reduces calcitriol synthesis, leading to rickets and osteomalacia. However, this effect on the skeleton is less pronounced than is HPTH, and many of the manifestations of "renal rickets" are actually those of HPTH.

***Imaging.*** PTH stimulation of osteoclasts leads to bone resorption at multiple sites.[3–6] The most specific radiographic manifestation of HPTH is subperiosteal resorption, initially seen along the radial aspects of the index and the middle finger middle phalanges (Fig. 140.1). The distal phalangeal tufts are also involved relatively early (see Fig. 140.1). With progression, subperiosteal resorption occurs at the ulnar aspects of the phalanges and other bones, including the medial aspects of the humeral and femoral necks, and the medial aspects of the proximal tibial metaphyses. Although less specific than subperiosteal resorption, HPTH may lead to intracortical resorption, or "tunneling," causing a striated appearance of the cortex, as well as endosteal, subchondral, and subligamentous resorption (Fig. 140.2). Subphyseal resorption at the zone of provisional calcification on the metaphyseal side of the physis may simulate the appearance of rickets (Fig. 140.3).

Slipped epiphyses (e-Fig. 140.4) are an important complication of renal osteodystrophy in children and are seen most frequently in the proximal femur. Although subphyseal resorption can mimic the radiographic appearance of rickets, the radiolucent material beneath the growth plate is fibrous tissue (osteitis fibrosa cystica), which is weaker than the nonmineralized osteoid in true rickets, accounting for slipped epiphyses occurring in renal osteodystrophy, but not in true rickets. The risk of epiphyseal slippage is particularly high when growth hormone (GH) is used to treat short stature, a major clinical problem in children with chronic kidney disease.

Additional findings of HPTH include resorption of the lamina dura surrounding the tooth roots (e-Fig. 140.5), cystic-appearing "brown tumors" (osteoclastomas), and bone sclerosis. Although brown tumors are more characteristic of primary HPTH, in children they are more commonly seen in secondary HPTH because of its higher prevalence in children. Osteosclerosis, most often seen with renal osteodystrophy, may be generalized or most pronounced subjacent to the vertebral end plates, resulting in a "rugger jersey" appearance (Fig. 140.6).

In patients with chronic kidney disease, true rickets and osteomalacia may also be seen from decreased production of calcitriol. It is often not possible to distinguish true rickets from the rachitic appearance of osteitis fibrosa cystica. Looser zones, if present, indicate true rickets. Renal osteodystrophy usually manifests a "high turnover" state from HPTH. Less often, an adynamic "low turnover" state may also be seen. Previously, adynamic bone disease was often due to aluminum toxicity, which occurred as a complication of aluminum-based phosphate binders. Presently, causes of adynamic bone disease include calcitriol therapy (which suppresses PTH), malnutrition, immobilization, corticosteroid therapy, and prior parathyroidectomy. Fractures may occur in renal osteodystrophy, with HPTH predisposing to metaphyseal fractures (e-Fig. 140.7).

***Treatment and Follow-up.*** Treatment of secondary HPTH in children with chronic kidney disease is directed toward normalization of mineral metabolism to improve growth, decreasing skeletal deformity and fragility, and preventing extraskeletal calcification, most importantly vascular calcification.[4,7] Treatment is often initiated at stage 3 chronic kidney disease (GFR <60 mL/min/1.73 m$^2$) when positive phosphate balance and calcitriol deficiency appear. Dietary phosphate restriction is often difficult to achieve while maintaining adequate protein intake. Hence, intestinal phosphate binders are used. Aluminum-containing phosphate binders may cause aluminum bone disease and should be avoided. Sevelamer is a phosphate binder that does not contain calcium and has been shown to lower phosphate and control the skeletal lesions of HPTH without many of the adverse effects seen with other types of binders.

Vitamin D analogs are also important in control of secondary HPTH, as many patients are deficient. Additionally, active vitamin

## Abstract:

Many endocrine glands affect skeletal growth and maturation. An understanding of the effects of the various endocrine glands on bone development aids in correct radiographic interpretation. This chapter outlines their effects on the appearance of the skeleton in children. Emphasis is given to hyperparathyroidism (HPTH) and renal osteodystrophy.

## Keywords:

endocrine
hyperparathyroidism
hypoparathyroidism
renal osteodystrophy
hyperthyroidism
gonadal disorders

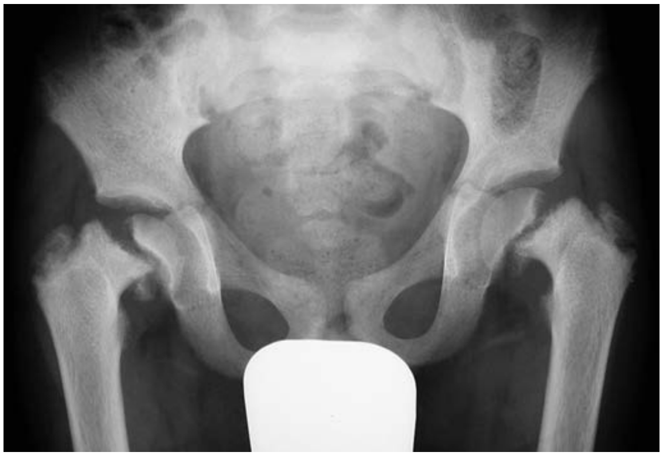

**e-Figure 140.4. Bilateral slipped capital femoral epiphyses in 11-year-old with renal osteodystrophy.** This finding was made at the time of presentation with previously undiagnosed end-stage renal failure.

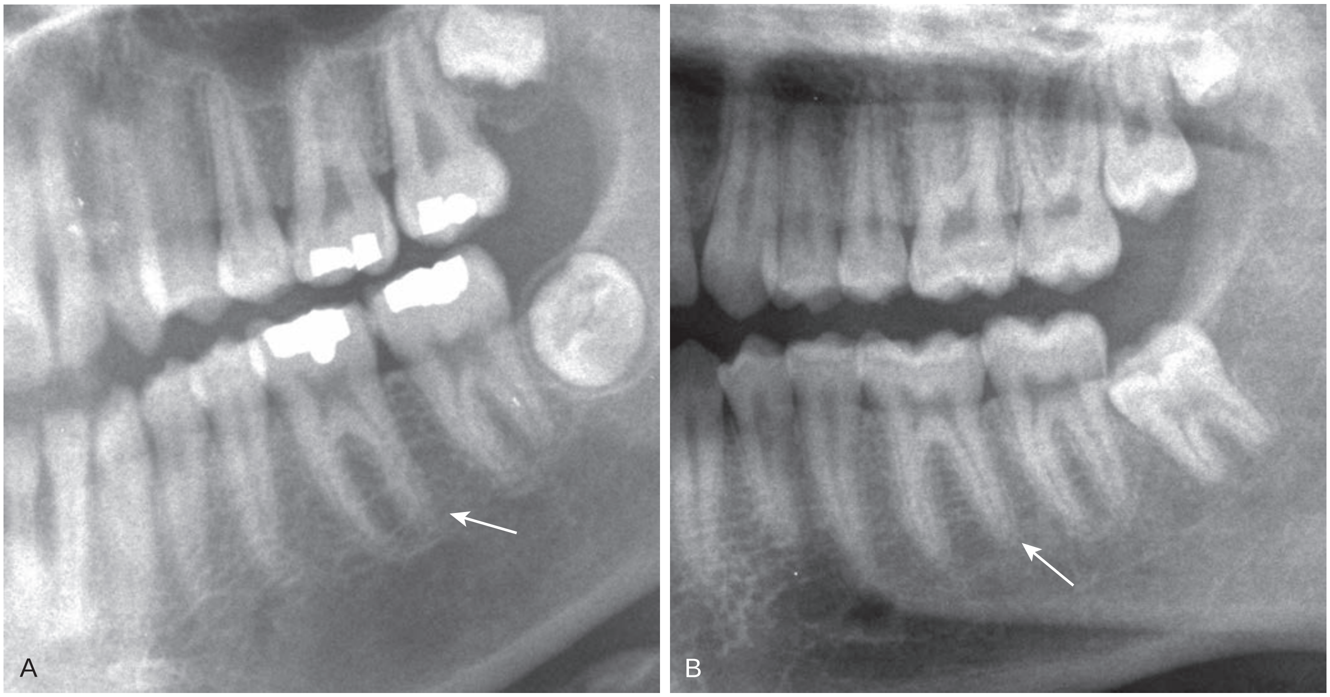

**e-Figure 140.5. Loss of normal lamina dura in hyperparathyroidism.** (A) A 16-year-old girl with loss of normal lamina dura *(arrow)* and a history of hyperparathyroidism caused by chronic renal failure. (B) 16-year-old boy with an intact lamina dura *(arrow)* for comparison.

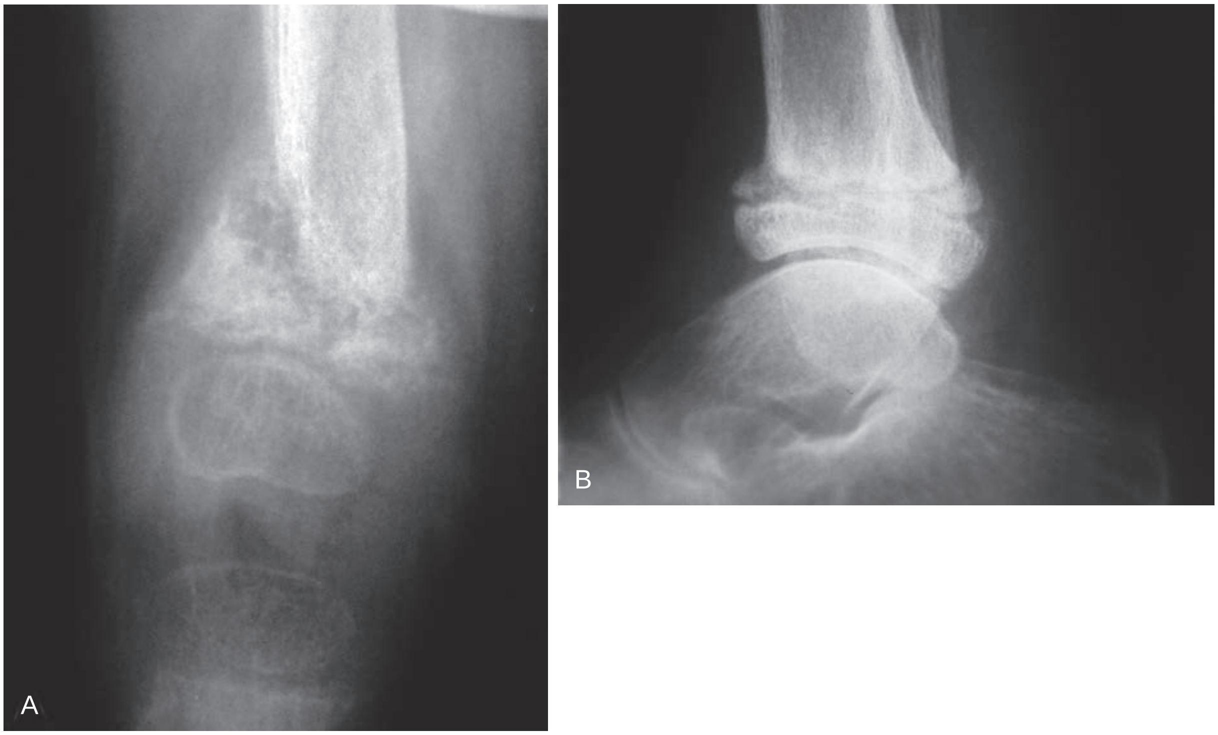

**e-Figure 140.7. Metaphyseal fractures in renal osteodystrophy.** (A) Distal femur in a 2.6-year-old child. (B) Distal tibial fracture in an 18-year-old.

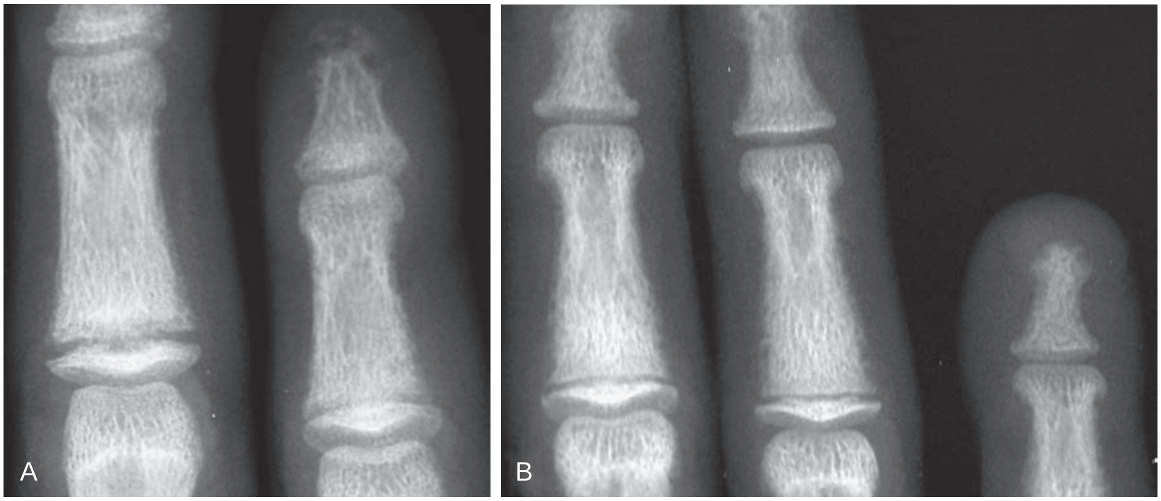

**Figure 140.1. Osseous findings of hyperparathyroidism in renal osteodystrophy.** Magnified frontal radiographs of the (A) left second and third digits and (B) right third to fifth digits show subperiosteal bone resorption involving the radial aspects of the middle phalanges. Areas of reabsorption of the distal tufts of the left second and right fifth fingers are also present.

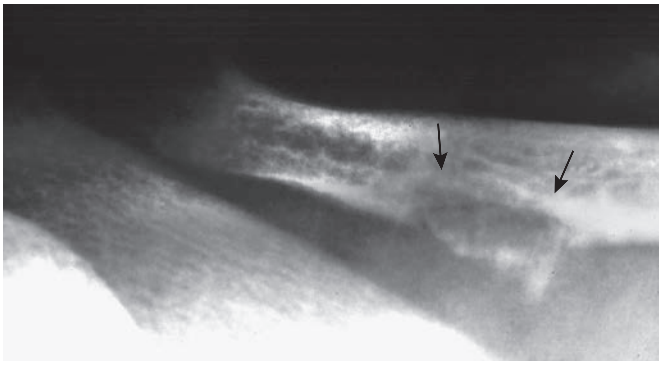

**Figure 140.2. Subligamentous resorption in secondary hyperparathyroidism.** Radiograph of the clavicle shows subligamentous resorption at the coracoclavicular ligament *(arrows)* in this child with secondary hyperparathyroidism of renal osteodystrophy.

D metabolites, most often calcitriol, act to lower PTH both indirectly by increasing intestinal calcium absorption and directly by inhibiting transcription for the gene encoding PTH. The use of calcitriol requires monitoring for hypercalcemia. Calcimimetics increase the sensitivity of the parathyroid calcium sensing receptor to calcium. This effectively lowers the level at which the circulating calcium concentration suppresses PTH synthesis and secretion, thereby lowering both calcium and PTH.

Despite medical therapy, parathyroidectomy may still be needed in some patients with renal osteodystrophy and severe HPTH. Postoperative hypocalcemia should be expected and managed accordingly.

## OTHER DISORDERS OF HYPERPARATHYROIDISM AND CAUSES OF BONE RESORPTION

### Neonatal Hyperparathyroidism

Primary HPTH in neonates is quite rare and is usually caused by hyperplasia rather than parathyroid adenoma.[8] Some cases of neonatal HPTH may result from homozygosity of the gene for familial hypocalciuric hypercalcemia, which usually causes asymptomatic hypercalcemia in adults.[9] Additional causes of HPTH in neonates include Jansen metaphyseal chondrodysplasia and I-cell disease. Although Williams syndrome may also cause neonatal hypercalcemia, PTH is not elevated.

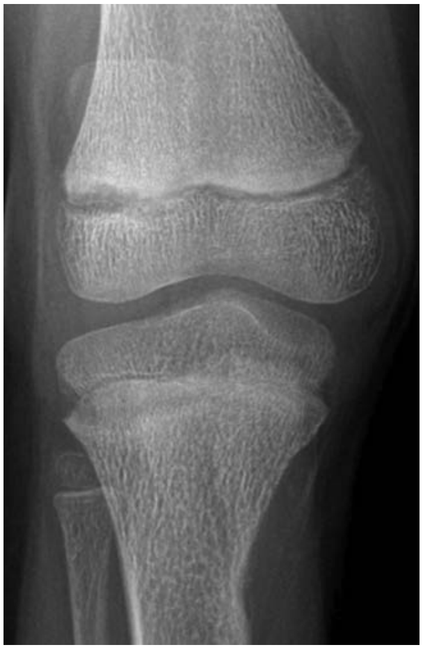

**Figure 140.3. Renal osteodystrophy in a 10-year-old boy.** Frontal radiograph of the knee shows irregularity and widening of the distal femoral and proximal tibial physes. When more diffuse, this appearance can mimic rickets. Also note subperiosteal resorption at the medial aspect of the proximal tibial metaphysis.

### Jansen Metaphyseal Chondrodysplasia

Jansen metaphyseal chondrodysplasia is an autosomal dominant condition with hypercalcemia and other findings suggestive of

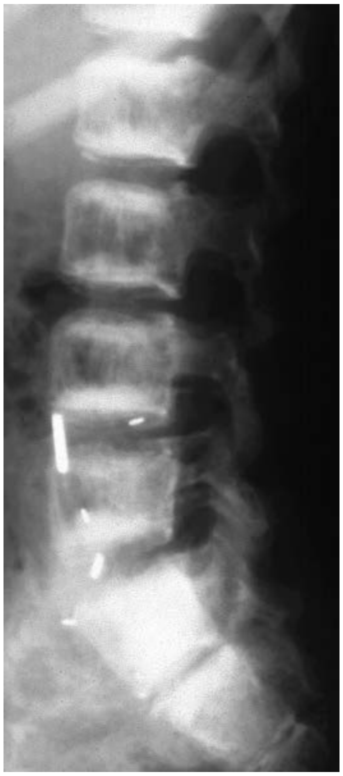

**Figure 140.6. Rugger jersey spine.** Lateral radiograph of the lumbar spine shows vertebral end plate sclerosis producing rugger jersey appearance.

severe HPTH during the neonatal period and short-limbed dwarfism later in life. It is caused by a mutation of the receptor for PTH and PTH-related peptide (PTHrP) that causes the receptor to be constantly activated.[10,11] Hence, even though no PTH nor PTHrP is detectable, PTH signaling is increased, producing effective HPTH with hypercalcemia and bone resorption, which are most prominent early in life (Fig. 140.8). Similarly, constitutive activation of the PTH/PTHrP receptor also leads to excessive PTHrP signaling, which inhibits endochondral ossification by preventing proliferating chondrocytes from entering hypertrophic differentiation.[12] This causes an ossification defect leading to buildup of a large amount nonossified cartilage and creating a lucent gap between the epiphysis and the ossified portion of the shaft (see Fig. 140.8). Subsequently, bizarre chondroid calcifications develop within these regions, which become widened and dysplastic. Eventually, the skeleton becomes fully ossified with residual shortening and deformity.

## Mucolipidosis II

Mucolipidosis II (I-cell disease) is an autosomal recessive storage disorder with radiographic features of dysostosis multiplex, similar to those of the mucopolysaccharidoses. Several additional radiographic findings have recently been shown to strongly suggest this diagnosis, including periosteal cloaking, talocalcaneal stippling, and sacrococcygeal or generalized vertebral body sclerosis and rounding.[13] In addition, some infants have skeletal features of HPTH, including generalized demineralization and subperiosteal bone resorption.[14] Although PTH is elevated, calcium is not, indicating that this is a form of secondary HPTH. It is speculated that placental involvement by this storage disorder impairs calcium transport leading to fetal and neonatal calcium deficiency causing secondary HPTH.

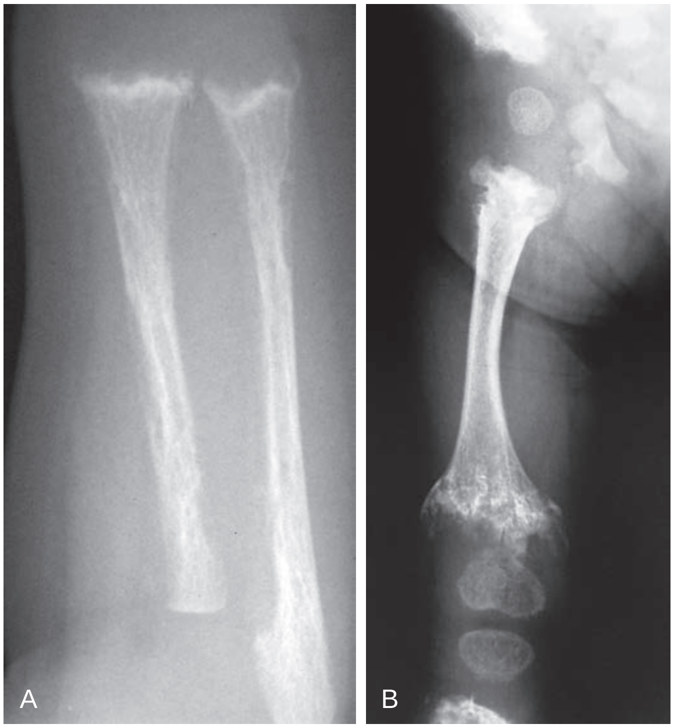

**Figure 140.8. Jansen metaphyseal chondrodysplasia, with manifestations of parathyroid hormone/parathyroid hormone–related peptide (PTH/PTHrP) receptor activation.** (A) At 5 days of age, forearm radiograph shows severe demineralization and subperiosteal resorption indicative of a hyperparathyroid state from increased PTH signaling. Also prominent are rachitic findings in the metaphyses. (B) Impaired endochondral ossification from excessive PTHrP signaling is demonstrated in the right femur at 15 months with a large lucent zone between the shaft and epiphyses, comprising nonossified cartilage. These lucent zones are beginning to fill in with disorganized chondroid calcifications, which are most apparent distally. This disorganized ossification leads to the marked metaphyseal dysplasia of this condition.

## Other Disorders of Bone Resorption

Abnormal bone resorption may also be seen in conditions other than HTPH. Decreased resorption, usually caused by a defect in osteoclastic acidification, leads to osteopetrosis. Increased resorption is seen in hyperphosphatasia and some endocrine disorders such as glucocorticoid excess. Hyperphosphatasia, also known as *juvenile Paget disease*, is a rare autosomal recessive condition with increased bone turnover caused by deficiency of osteoprotegerin, which normally suppresses bone turnover.[15,16] Hyperphosphatasia often presents at 2 to 3 years of age with short stature, bone fragility, and deformity, including long bone bowing, kyphoscoliosis, and pectus carinatum. Unlike adult Paget disease, which most often involves the axial skeleton, hyperphosphatasia is generalized. The radiographic features may be striking, with overall demineralization, coarse trabecular pattern, cortical thickening, widened cylindric long bones with decreased tubulation, and markedly variable bone texture with osteosclerosis intermixed with regions of cystic-appearing lucency (Fig. 140.9). Bowing and pathologic fractures are common. The skull shows thickening and regions of lucency combined with “cottonwool” sclerosis, similar to adult Paget disease. Familial expansile osteolysis is a related condition with deafness, loss of teeth, expansion of bones, painful phalanges, and episodic hypercalcemia caused by duplication of the gene for the osteoclast membrane-bound receptor that is activated by RANKL.[17]

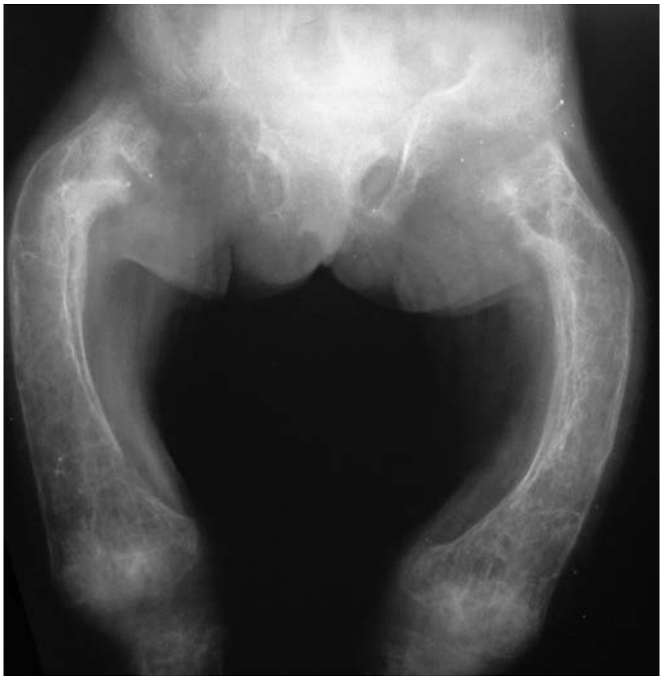

**Figure 140.9. Hyperphosphatasia.** Frontal radiograph shows that the diaphyses of both femurs are expanded and bowed. Demineralization is marked and has a highly heterogeneous pattern. The findings are symmetric and bilateral, unlike adult Paget disease, which is more commonly unilateral in the appendicular skeleton.

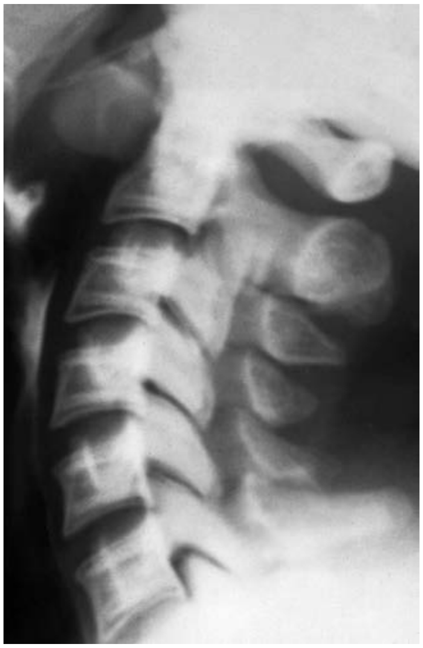

**Figure 140.10. Idiopathic hypoparathyroidism.** Lateral cervical spine radiograph shows bone-within-bone appearance and patchy osteosclerosis of cervical vertebrae.

## Hypoparathyroidism

***Etiology.*** Idiopathic hypoparathyroidism in children is most commonly part of polyglandular autoimmune disease type I.[18] This autosomal recessive condition targets multiple endocrine glands, most frequently the parathyroids and adrenals. Other causes of hypoparathyroidism in children include congenital absence of the parathyroids, which may accompany thymic absence in DiGeorge syndrome, surgical removal during thyroidectomy, and transient suppression of fetal parathyroids by maternal HPTH.[19]

***Imaging.*** Skeletal manifestations of hypoparathyroidism include osteosclerosis, dense metaphyseal bands, cranial vault thickening, intracranial calcifications, and dental abnormalities. Vertebral findings include marginal sclerosis, "bone within bone" appearance (Fig. 140.10), and paravertebral ossification.

## Pseudohypoparathyroidism

***Etiology.*** Pseudohypoparathyroidism is characterized by variable resistance to PTH and, less often, other hormones, as well as typical somatic features known as *Albright hereditary osteodystrophy (AHO)*.[18,20] The hormone resistance results from an inactivating mutation of the *GNAS1* gene. In pseudopseudohypoparathyroidism, the somatic features of AHO are seen without hormone resistance.

***Imaging.*** The somatic features of AHO include short stature, obesity, a round face, variable degrees of subnormal intelligence, subcutaneous calcification and ossification, small exostoses, and brachydactyly of the hands and feet (Fig. 140.11). The brachydactyly is often associated with premature growth plate closure that results from impaired PTHrP signaling leading to accelerated endochondral ossification. Brachydactyly E, Turner syndrome, and acrodysostosis are differential considerations. Resistance to PTH leads to manifestations of hypoparathyroidism including hypocalcemia and soft tissue and basal ganglia calcifications despite elevated PTH levels. Although hormone resistance often involves both kidney and bone, skeletal resistance is variable. With skeletal responsiveness to PTH, manifestations of HPTH such as subperiosteal bone resorption and brown tumors (Fig. 140.12) may be seen.[21,22]

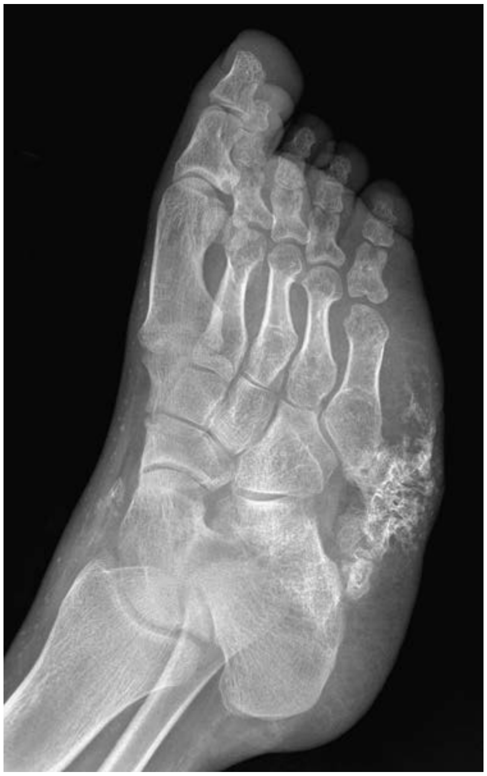

**Figure 140.11. Pseudohypoparathyroidism.** Foot radiograph in a 14-year-old shows extensive heterotopic ossification along the lateral aspect of foot. Also note brachydactyly involving some of the metatarsals.

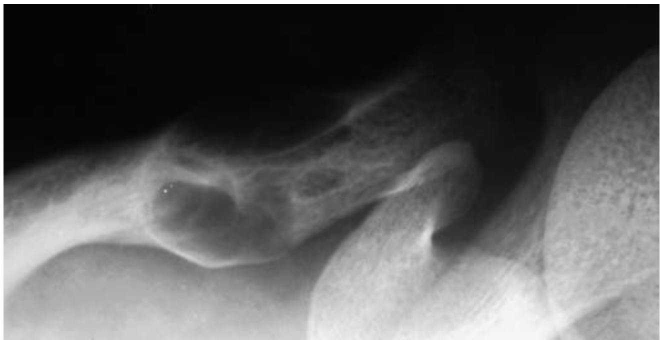

**Figure 140.12. Pseudohypoparathyroidism with skeletal responsiveness to parathyroid hormone leading to a brown tumor in the distal clavicle.** Other manifestations of hyperparathyroidism in this patient included subperiosteal bone resorption and bilateral slipped capital femoral epiphyses (not shown).

## NONPARATHYROID ENDOCRINE DISORDERS

Several other endocrine disorders have important skeletal effects. These primarily influence skeletal growth and maturation often by their effects on endochondral bone formation at the growth plates.

### Growth Hormone Disorders

***Etiology.*** GH is an important positive regulator of postnatal longitudinal growth, acting directly as well as indirectly through insulin-like growth factor (IGF) to stimulate proliferation of physeal chondrocytes.[23–25] Prenatal growth depends mostly on IGF, accounting for the relative preservation of prenatal growth in GH deficiency. In GH deficiency, skeletal growth and maturation are retarded to a similar degree, resulting in similar delays in height and bone age. The effects of GH excess are different in children than in adults. Before skeletal maturity, GH excess causes gigantism, while after skeletal maturity, it leads to acromegaly. The former is typically caused by an isolated pituitary adenoma, while the later may be caused by either a pituitary adenoma or hyperplasia. Approximately 20% of cases of GH excess are associated with McCune–Albright.

***Imaging.*** In GH deficiency, radiographs may show delayed bone age. Maturation of the carpal bones is often more delayed compared with the phalanges. Slipped capital femoral epiphysis (SCFE) may be seen with GH deficiency either before or after GH therapy. The retarded growth and maturation of GH deficiency may be mimicked by deprivational dwarfism ("psychosocial dwarfism"), although the presence of multiple growth restart lines favors deprivational dwarfism (e-Fig. 140.13).[26]

Gigantism, caused by GH excess before skeletal maturity, leads to increased linear skeletal growth. Radiographs in patients with GH excess after skeletal maturity can show increased periosteal bone formation, reactivation of endochondral bone formation at chondro-osseous junctions, and cartilage and soft tissue hypertrophy. These are the processes that lead to acromegaly, which is predominantly an adult disorder. Brain MRI is essential in these patients to evaluate for pituitary lesions.

### Hypothyroidism

***Etiology.*** Thyroid hormone (TH) is essential for normal brain development during the first 3 years of life, as well as for normal skeletal growth and maturation.[23,24,27–29] Although TH does not directly affect chondrocyte proliferation, the positive effects of GH and IGF on proliferation require the presence of TH. Additionally, TH has a major effect on skeletal maturation by inhibiting PTHrP signaling, which ordinarily regulates endochondral ossification. Hence increased PTHrP signaling in hypothyroidism causes abnormalities in endochondral ossification.

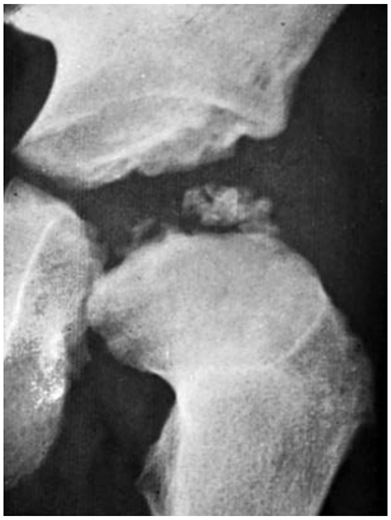

**Figure 140.14. Hypothyroidism and epiphyseal dysgenesis in a 9-year-old girl.** She had started treatment 1 year earlier. Frontal radiograph show a small and flattened femoral head that contains multiple small fragmented ossification centers. At the beginning of treatment 1 year earlier, no ossification of the femoral heads was seen. On follow-up, these ossification centers coalesced, but the femoral heads remained flattened. Similar finding were also present in several major epiphyses.

***Imaging.*** Skeletal maturation is delayed to a greater degree than linear growth. Impaired ossification not only delays the appearance of epiphyses but also leads to an abnormal pattern with multiple fragmented ossification centers, which is known as *epiphyseal dysgenesis*, which is particularly common in the hips. Although the fragments eventually coalesce, the epiphysis often has uneven density and irregular margins (Fig. 140.14). With treatment, the findings of epiphyseal dysgenesis resolve. SCFE may be a presenting manifestation of hypothyroidism, often bilateral and occurring at a younger age than idiopathic SCFE (see also Chapter 142).[30,31] In the skull, hypothyroidism may cause multiple wormian bones, enlargement of the sella turcica from pituitary hyperplasia, and brachycephaly from decreased growth at the spheno-occipital synchondrosis. Radiographs of hands may show small projections of bone extending from the distal phalangeal metaphyses into the growth plates (Fig. 140.15).[32]

### Hyperthyroidism

***Etiology.*** As discussed for hypothyroidism, TH inhibits PTHrP and hence promotes hypertrophic differentiation of proliferating chondrocytes leading to accelerated skeletal maturation. Hyperthyroidism in the pediatric age range is most frequent in adolescent girls. Hyperthyroidism may also occur as a manifestation of McCune–Albright syndrome, although precocious puberty is most common.

***Imaging.*** Skeletal maturation in hyperthyroidism may be normal or mildly advanced. Accelerated maturation may be seen in infants born to mothers with uncontrolled hyperthyroidism during the last trimester of pregnancy. Although hyperthyroidism is uncommon in infancy, acceleration of skeletal maturation is greatest in this group and may produce premature craniosynostosis.[33] Other skeletal manifestations of hyperthyroidism include calcification of costal cartilage and tracheal rings, diffuse osteopenia, and cortical striations, which are indicative of increased bone turnover. Due to osteoid overproduction, hyperthyroidism may mimic osteomalacia, including the presence of Looser transformation zones.

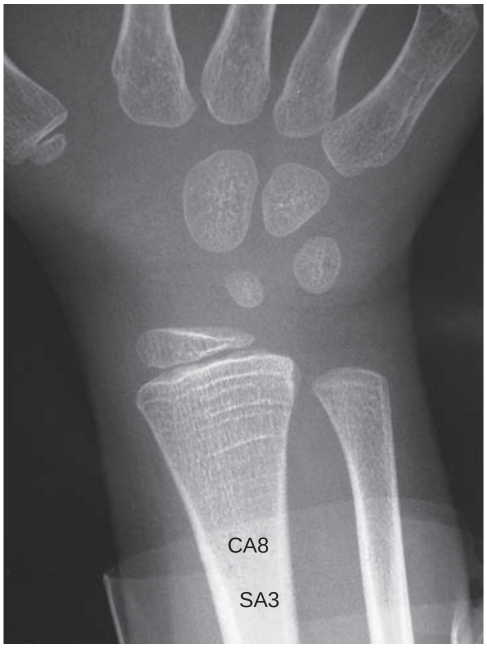

**e-Figure 140.13. Deprivational dwarfism.** Delayed skeletal maturation with a skeletal age of 3 years and chronologic age of 8 years. There are multiple growth restart lines in the distal radial metaphysis. Similar findings were also present in the distal femur (not shown). *(Courtesy Andrew K. Poznanski, MD, Chicago, IL.)*

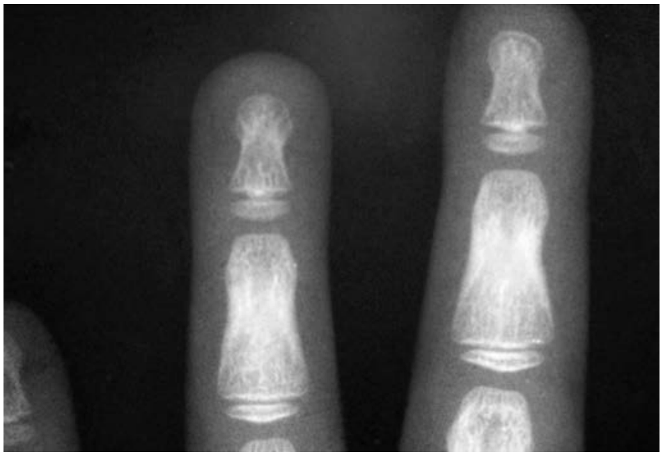

**Figure 140.15. Hypothyroidism in an 11-year-old boy.** Frontal radiograph of the fingers shows small spikelike projections of bone extend into the growth plates from the distal phalangeal metaphyses.

## Glucocorticoid Excess

***Etiology.*** Cushing syndrome refers to the systemic effects of glucocorticoid excess. Most cases of Cushing syndrome in children are iatrogenic and result from pharmacologic dosages of glucocorticoids used for treatment of chronic inflammatory or autoimmune disorders. Endogenous Cushing syndrome in children is uncommon and usually caused by primary adrenal lesions in those below 5 years of age and pituitary lesions in those above 5 years. Glucocorticoids decrease linear growth and maturation, acting at multiple levels to negatively regulate physeal chondrogenesis by decreasing GH secretion and downregulating GH and IGF receptors in physeal chondrocytes.[24]

Glucocorticoids also impair skeletal mineralization by negating the positive influence of sex steroids on mineralization, decreasing calcium absorption in the gut, and by acting directly to decrease bone formation and to increase osteoclastic resorption by increasing RANKL and decreasing osteoprotegerin expression.[34,35] Osteonecrosis is an additional complication of endogenous or exogenous glucocorticoid excess.

***Imaging.*** The skeletal findings of endogenous or exogenous corticosteroid excess are nonspecific and include generalized osteopenia with cortical thinning, trabecular rarefaction, and vertebral compression fractures. In addition, more specific findings include vertebral end plate sclerosis, abundant callus formation at fracture sites, and osteonecrosis. Excessive callus formation associated with compression fractures of vertebral bodies probably accounts for end plate sclerosis, which may be a clue in the diagnosis of Cushing syndrome in a patient with osteopenia (Fig. 140.16). Glucocorticoid induced osteonecrosis most frequently involves the femoral head, with the humeral head and femoral condyles next in frequency. Radiographic findings include subcortical fracture, bone collapse, fragmentation, and patchy osteosclerosis (see also Chapter 141).

## Adrenal Androgen Excess

***Etiology.*** Adrenogenital syndrome, the most frequent cause of excessive adrenal androgens excess, results from a biosynthetic defect in the production of cortisol with a compensatory increase in adrenocorticotropic hormone driving excessive production of adrenal androgens.[35] Excessive amounts of adrenal androgens may also be secreted by adrenal cortical neoplasms. Although they are weaker than testosterone, adrenal androgens promote virilization and accelerate skeletal maturation.

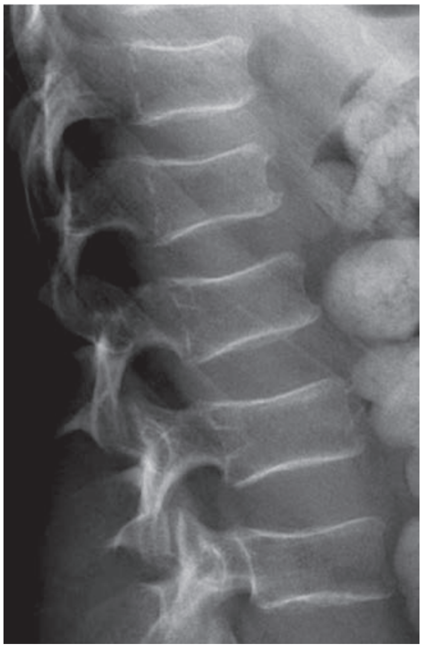

**Figure 140.16. Cushing disease in an 11-year-old boy with a pituitary adenoma and back pain.** Lateral radiograph shows generalized osteopenia with multiple age-indeterminate vertebral body compression fractures and end plate sclerosis, likely a combination of trabecular compression and callus.

***Imaging.*** Although growth is initially accelerated, this effect is less pronounced than is advancement of maturation. Hence, physeal closure occurs prematurely, and final height is decreased rather than increased. Advancement of skeletal maturation caused by excessive androgens is more pronounced than that caused by hyperthyroidism.

## Gonadal Disorders

***Etiology.*** The effects of sex steroids on physeal fusion and bone mineralization are currently believed to be caused by estrogen, with these processes mediated in males by estrogens formed from peripheral conversion of androgens.[36–38]

***Imaging.*** Increased production of androgens and estrogens by gonadal tumors may accelerate skeletal maturation, whereas gonadal insufficiency delays maturation.[24]

### KEY POINTS

- The most common cause of HPTH in children is chronic kidney disease, and the major manifestations of renal osteodystrophy are those of HPTH.
- In renal osteodystrophy, the lucent material adjacent to the growth plates is fibrous tissue of osteitis fibrosa cystica. This simulates the appearance of rickets but is weaker than osteoid, leading to slipped epiphyses.
- In GH deficiency, skeletal growth and maturation are proportionally decreased.
- TH promotes hypertrophic differentiation. Hence, in hypothyroidism, skeletal maturation is impaired to a greater degree than is growth.
- Cushing syndrome is suggested by the combination of osteopenia, vertebral body compression fractures, and vertebral end plate sclerosis.

## SUGGESTED READINGS

Bakkaloglu SA, Wesseling-Perry K, Pereira RC, et al. Value of new bone classification system in renal osteodystrophy. *Clin J Am Soc Nephr*. 2010;5(10):1860–1866.

Bastepe M. The GNAS locus and pseudohypoparathyroidism. *Adv Exp Med Biol*. 2008;626:27–40.

Dabbagh S. Renal osteodystrophy. *Curr Opin Pediatr*. 1998;10:190–196.

Lacroix A, Feelders RA, Stratakis CA, et al. Cushing's syndrome. *The Lancet*. 2015;386(9996):913–927.

Witbreuk M, van Kemenade FJ, van der Sluijs JA, et al. Slipped capital femoral epiphysis and its association with endocrine, metabolic and chronic diseases: a systematic review of the literature. *J Child Orthop*. 2013;7(3):213–223.

## REFERENCES

Full references for this chapter can be found on www.expertconsult.com.

## REFERENCES

1. Nissenson RA, Jüppner H. Parathyroid hormone. In: Rosen CJ, ed. *Primer on the Metabolic Bone Diseases and Disorders of Mineral Metabolism*. 7th ed. Washington, DC: American Society for Bone and Mineral Research; 2008:123–127.
2. Ross FP. Osteoclast biology and bone resorption. In: Rosen CJ, ed. *Primer on the Metabolic Bone Diseases and Disorders of Mineral Metabolism*. 7th ed. Washington, DC: American Society for Bone and Mineral Research; 2008:16–22.
3. Goodman WG, Coburn JW, Slatopolsky E, et al. Renal osteodystrophy in children and adults. In: Favis MJ, ed. *Primer on the Metabolic Bone Diseases and Disorders of Mineral Metabolism*. 5th ed. Washington, DC: American Society for Bone and Mineral Research; 2003:430–447.
4. Hruska KA, Mathew S. Chronic kidney disease mineral bone disorder (CKD-MBD). In: Rosen CJ, ed. *Primer on the Metabolic Bone Diseases and Disorders of Mineral Metabolism*. 7th ed. Washington, DC: American Society for Bone and Mineral Research; 2008:343–348.
5. Resnick D. Parathyroid disorders and renal osteodystrophy. In: Resnick D, ed. *Diagnosis of bone and joint disorders*. 4th ed. Philadelphia, PA: WB Saunders; 2002:2043–2111.
6. Pugh DG. Subperiosteal resorption of bone: roentgenologic manifestation of primary hyperparathyroidism and renal osteodystrophy. *Am J Roentgenol Radium Ther Nucl Med*. 1951;66:577–586.
7. Wesseling K, Bakkaloglu S, Salusky I. Chronic kidney disease mineral and bone disorder in children. *Pediatr Nephrol*. 2008;23:195–207.
8. Langman CB. Hypercalcemic syndromes in infants and children. In: Favis MJ, ed. *Primer on the Metabolic Bone Diseases and Disorders of Mineral Metabolism*. 5th ed. Washington, DC: American Society for Bone and Mineral Research; 2003:267–270.
9. Arnold A, Marx SJ. Familial hyperparathyroidism (including MEN, FHH, and HPT-JT). In: Rosen CJ, ed. *Primer on the Metabolic Bone Diseases and Disorders of Mineral Metabolism*. 7th ed. Washington, DC: American Society for Bone and Mineral Research; 2008:361–366.
10. Schipani E, Langman CB, Parfitt AM, et al. Constitutively activated receptors for parathyroid hormone and parathyroid hormone-related peptide in Jansen's metaphyseal chondrodysplasia. *N Engl J Med*. 1996;335:708–714.
11. Schipani E, Provot S. PTHrP, PTH, and the PTH/PTHrP receptor in endochondral bone development. *Birth Defects Res C Embryo Today*. 2003;69:352–362.
12. Kronenberg HM. PTHrP and skeletal development. *Ann N Y Acad Sci*. 2006;1068:1–13.
13. Lai LM, Lachman RS. Early characteristic radiographic changes in mucolipidosis II. *Pediatr Radiol*. 2016;46(12):1713–1720.
14. Unger S, Paul DA, Nino MC, et al. Mucolipidosis II presenting as severe neonatal hyperparathyroidism. *Eur J Pediatr*. 2005;164:236–243.
15. Eroglu M, Taneli NN. Congenital hyperphosphatasia (juvenile Paget's disease): eleven years follow-up of three sisters. *Ann Radiol (Paris)*. 1977;20:145–150.
16. Whyte MP, Obrecht SE, Finnegan PM, et al. Osteoprotegerin deficiency and juvenile Paget's disease. *N Engl J Med*. 2002;347:175–184.
17. Whyte MP, Mills BG, Reinus WR, et al. Expansile skeletal hyperphosphatasia: a new familial metabolic bone disease. *J Bone Miner Res*. 2000;15:2330–2344.
18. Rubin MR, Levine MA. Hypoparathyroidism and pseudohypoparathyroidism. In: Rosen CJ, ed. *Primer on the Metabolic Bone Diseases and Disorders of Mineral Metabolism*. 7th ed. Washington, DC: American Society for Bone and Mineral Research; 2008:354–361.
19. DiGeorge AM. Congenital absence of the thymus and its immunologic consequences: concurrence with congenital hypoparathyroidism. *Birth Defects*. 1968;4:116–123.
20. Levine MA. Parathyroid hormone resistance syndromes. In: Favis MJ, ed. *Primer on the Metabolic Bone Diseases and Disorders of Mineral Metabolism*. 5th ed. Washington, DC: American Society for Bone and Mineral Research; 2003:278–285.
21. Frame B, Hanson CA, Frost HM, et al. Renal resistance to parathyroid hormone with osteitis fibrosa: pseudohypohyperparathyroidism. *Am J Med*. 1972;52:311–321.
22. Burnstein MI, Kottamasu SR, Peffifor JM, et al. Metabolic bone disease in pseudohypoparathyroidism: radiologic features. *Radiology*. 1985;155:351–356.
23. Siebler T, Robson H, Shalet SM, et al. Glucocorticoids, thyroid hormone and growth hormone interactions: implications for the growth plate. *Horm Res*. 2001;56(suppl 1):7–12.
24. Nilsson O, Marino R, De Luca F, et al. Endocrine regulation of the growth plate. *Horm Res*. 2005;64:157–165.
25. Resnick D. Pituitary disorders. In: Resnick D, ed. *Diagnosis of bone and joint disorders*. 4th ed. Philadelphia, PA: WB Saunders; 2002:2003–2025.
26. Hernandez RJ, Poznanski AK, Hopwood NJ, et al. Incidence of growth lines in psychosocial dwarfs and idiopathic hypopituitarism. *AJR Am J Roentgenol*. 1978;131:477–479.
27. Robson H, Siebler T, Stevens DA, et al. Thyroid hormone acts directly on growth plate chondrocytes to promote hypertrophic differentiation and inhibit clonal expansion and cell proliferation. *Endocrinology*. 2000;141:3887–3897.
28. Stevens DA, Hasserjian RP, Robson H, et al. Thyroid hormones regulate hypertrophic chondrocyte differentiation and expression of parathyroid hormone-related peptide and its receptor during endochondral bone formation. *J Bone Miner Res*. 2000;15:2431–2442.
29. Resnick D. Thyroid disorders. In: Resnick D, ed. *Diagnosis of Bone and Joint Disorders*. 4th ed. Philadelphia, PA: WB Saunders; 2002:2026–2042.
30. Heyerman W, Weiner D. Slipped epiphysis associated with hypothyroidism. *J Pediatr Orthop*. 1984;4:569–573.
31. Loder RT, Wittenberg B, DeSilva G. Slipped capital femoral epiphysis associated with endocrine disorders. *J Pediatr Orthop*. 1995;15:349–356.
32. Hernandez RJ, Poznanski AK. Distinctive appearance of the distal phalanges in children with primary hypothyroidism. *Radiology*. 1979; 132:83–84.
33. Riggs W Jr, Wilroy RS Jr, Etteldorf JN. Neonatal hyperthyroidism with accelerated skeletal maturation, craniostenosis and brachydactyly. *Radiology*. 1972;105:621–625.
34. Weinstein RS. Glucocorticoid induced osteoporosis. In: Rosen CJ, ed. *Primer on the Metabolic Bone Diseases and Disorders of Mineral Metabolism*. 7th ed. Washington, DC: American Society for Bone and Mineral Research; 2008:267–272.
35. Resnick D. Disorders of other endocrine glands and of pregnancy. In: Resnick D, ed. *Diagnosis of Bone and Joint Disorders*. 4th ed. Philadelphia, PA: WB Saunders; 2002:2112–2143.
36. Morishima A, Grumbach MM, Simpson ER, et al. Aromatase deficiency in male and female siblings caused by a novel mutation and the physiological role of estrogens. *J Clin Endocrinol Metab*. 1995;80:3689–3698.
37. Frenkel B, Hong A, Baniwal SK, et al. Regulation of adult bone turnover by sex steroids. *J Cell Physiol*. 2010;224(2):305–310.
38. Weise M, De-Levi S, Barnes KM, et al. Effects of estrogen on growth plate senescence and epiphyseal fusion. *Proc Natl Acad Sci USA*. 2001;98:6871–6876.

# 141

# Skeletal Manifestations of Systemic Disease

Robert C. Orth and R. Paul Guillerman

## NORMAL BONE MARROW

### Overview

Bone marrow is one of the largest and most dynamic tissues in the body. Its functions include the production of red blood cells, white blood cells, and platelets for tissue oxygenation, cellular immunity, and blood coagulation, respectively. Bone marrow occupies approximately 85% of the medullary cavity and is supported by a network of trabecular bone.[1] In addition to hematopoietic elements, it contains stromal cells, collagen, nerves, and a variable amount of fat.

### Function and Composition

***Physiology.*** On gross examination, bone marrow may be red because of hemoglobin in the erythrocytes and their precursors, indicating active hematopoietic marrow, or it may be yellow due to the presence of carotenoid derivatives dissolved in fat droplets within adipocytes.[1] Hematopoietic marrow is rich in vascular sinusoids, whereas fatty marrow is considerably less vascular. During periods of decreased hematopoiesis, the fat cells increase in size and number. During periods of increased hematopoiesis, the fat cells atrophy.

The cellularity of bone marrow diminishes most rapidly in the first two decades of life. The cellularity of hematopoietic marrow is near 100% at birth and decreases to between 50% and 75% by 15 years of age. By adulthood, hematopoietic marrow is composed of approximately 40% fat, 40% water, and 20% protein, with 60% of cells being hematopoietic and 40% being adipocytes.[1] In contrast, fatty marrow is composed of 80% fat, 15% water, and 5% protein, with 95% of cells being adipocytes (e-Fig. 141.1).[1,2]

***Imaging.*** Conventional radiography, computed tomography, and ultrasonography are of limited value in the assessment of bone marrow.[3] Since the first reports of magnetic resonance imaging (MRI) of the marrow in children were published in 1984, MRI has emerged as the primary imaging modality to evaluate the bone marrow. It provides a noninvasive method for visualizing the gross anatomic structure of a large sample of the bone marrow and for inferring alterations in its chemical and cellular composition related to a variety of physiologic and pathologic processes. Furthermore, MRI can provide valuable information about regions of the bone marrow that may be inaccessible or difficult to biopsy.

The constituents of bone marrow that contribute to the signal characteristics on MRI are fat, water, and, to a lesser extent, mineralized matrix.[3] Fat is the dominant contributor to both hematopoietic and fatty marrow signal intensity patterns. Most fat protons are in hydrophobic methylene ($-CH_2-$) groups of relatively heavy molecular complexes, conferring very efficient spin-lattice relaxation; this results in a short T1 relaxation time, which results in high signal intensity on T1-weighted sequences.[1] The T2 relaxation time of fat is much shorter than that of free water protons, and water contributes much more to the signal intensity of hematopoietic marrow than fatty marrow.[1] The mineralized matrix of bone has a low density of hydrogen protons that lack mobility within the crystalline structure of bone, accounting for very long T1 and short T2 relaxation times and low signal intensity of mineralized matrix on T1- and T2-weighted sequences. In addition, local field gradients at the trabecular surface are generated by the fixed dipole from the immobile protons and cause magnetic field inhomogeneity. This magnetic susceptibility effect, as well as that resulting from iron deposition, can play a large role in the signal characteristics of hematopoietic and fatty marrow on gradient echo (GRE) images.[1]

The normal intervertebral disks, skeletal muscle, and subcutaneous fat have little interindividual and intraindividual signal intensity variation on T1-weighted sequences during childhood and consequently serve as convenient internal reference standards for comparison with bone marrow.[1,4] Fatty marrow has high signal intensity on conventional spin echo T1-weighted sequences. The relative amounts of fat, water, and protein contribute in a complex fashion to produce a longer T1 relaxation time in hematopoietic marrow, with signal intensity that ranges from intermediate to low (less than that of muscle or intervertebral disks) in fat-poor hematopoietic marrow to intermediate-high (greater than that of muscle or the intervertebral disks but less than that of subcutaneous fat) in hematopoietic marrow with larger proportions of fat.[1,5] In neonates, hematopoietic marrow contains minimal fat and has low signal intensity on T1-weighted sequences. With aging, hematopoietic marrow signal intensity progressively increases on T1-weighted sequences, reflecting a progressive increase in fat content. After the neonatal period, hematopoietic marrow has signal intensity equal to or slightly greater than muscle and the intervertebral disks but much less than subcutaneous fat on T1-weighted sequences, whereas fatty marrow approaches the signal intensity of subcutaneous fat on T1-weighted sequences.[5] Because of the similar proton densities of hematopoietic and fatty marrow, proton density sequences without fat suppression are less useful than T1-weighted sequences.[6]

On fat-suppressed fast spin echo (FSE) T2-weighted and short-tau inversion recovery (STIR) sequences, normal hematopoietic marrow in childhood shows higher signal intensity than fatty marrow and higher signal intensity than muscle; the signal intensity of hematopoietic marrow decreases with age and approaches that of muscle by adolescence.

The degree of contrast enhancement of normal marrow varies with the contrast dose, timing of image acquisition following contrast administration, age of the patient, and composition of the marrow. Marrow enhancement peaks within a minute of contrast administration and then slowly declines.[7] Enhancement is greater in children than in adults, greater in the metaphyses than in the epiphyses, and greater in hematopoietic marrow than in fatty marrow. Enhancement can be imperceptible by visual inspection in the marrow of adults and in the marrow of the epiphyses in patients aged more than 2 years. The variation between individuals in the degree of enhancement is also substantial.[7] If gadolinium-enhanced T1-weighted sequences are acquired without fat suppression, contrast between hematopoietic and fatty marrow is decreased, which potentially obscures marrow lesions or age-related marrow conversion changes.[8] Image-subtraction and fat-suppression techniques facilitate the detection of abnormal marrow enhancement on postcontrast T1-weighted sequences.[6]

## Abstract:

In this chapter, normal attributes of bone marrow are discussed including function, composition, distribution, and conversion. Subsequently, skeletal manifestations of systemic diseases are reviewed with specific attention to those processes affecting marrow reconversion, hyperplasia, and infiltration. The etiology, pathophysiology, and clinical presentation of several forms of osteonecrosis are presented. Finally, the effects of several systematic and localized therapies on the pediatric skeleton are considered.

## Keywords:

bone marrow
thalassemia
sickle cell disease
leukemia
lymphoma
osteonecrosis

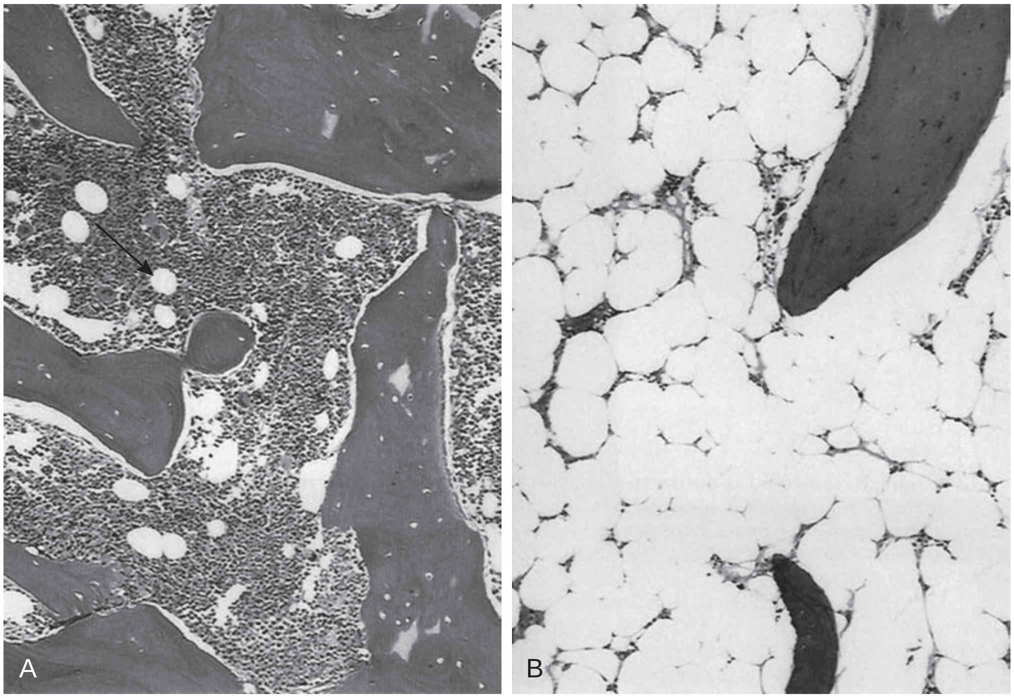

**e-Figure 141.1. Histologic sections of normal bone marrow (hematoxylin-eosin, ×75).** (A) Hematopoietic elements and bony trabeculae of hematopoietic marrow with few adipocytes *(arrow)*. (B) Fatty marrow contains numerous adipocytes. *(From Babyn PS, Ranson M, McCarville ME. Normal bone marrow: signal characteristics and fatty conversion.* Magn Reson Imaging Clin N Am. *1998;6:474.)*

A combination of T1-weighted and fat-suppressed FSE T2-weighted or STIR sequences is sufficient for the detection and characterization of most marrow lesions.[9] Contrast-enhanced T1-weighted sequences increase the cost and duration of the MRI examination while providing only modest incremental added sensitivity; because of this, they should be reserved for cases with unclear findings on the precontrast sequences. GRE sequences are valuable for the assessment of the iron content of the marrow, and chemical-shift techniques are useful to detect subtle changes in the fat and water fractions of the marrow.[10]

Practical time constraints initially limited MRI scanning of the marrow to only sections of the skeleton. This disadvantage has been mitigated by the development of fast, whole-body MRI scanning techniques that include FSE and single-shot sequences, parallel imaging, rolling table platforms with a large field of view, and global matrix coil concepts.[11–13] Obscuration of lesions by motion artifact may be overcome to some extent by the use of respiratory triggering or other motion-suppression techniques. The lower signal-to-noise ratios in smaller children on whole-body MRI exams can be ameliorated by using magnetic resonance (MR) systems with a higher field strength.[14]

Diffusion-weighted whole-body MRI holds particular promise as a technique to globally assess bone marrow for hematologic disorders and tumor metastases.[15–18] A positive correlation exists between the degree of marrow cellularity and the marrow apparent diffusion coefficient (ADC). Hematopoietic marrow or marrow infiltrated by neoplastic cells has more abundant microvasculature and more intracellular and interstitial free water than fatty marrow, and it exhibits higher ADC values.[19]

Motion and susceptibility artifacts are especially problematic in diffusion-weighting imaging (DWI) of the marrow, which is contained by bone and in proximity to physiologic motions, such as cerebrospinal fluid pulsations in the case of the spine.[17] Recent advances have largely overcome these technological challenges, and diffusion-weighted whole-body MRI is being used to evaluate an increasing number of benign and malignant conditions that include chronic recurrent multifocal osteomyelitis, Langerhans cell histiocytosis, and bony metastases.[20–22]

## Distribution and Conversion

***Physiology.*** Hematopoiesis occurs in the yolk sac in the early stages of fetal development; later in gestation it shifts to the liver and to a lesser extent the spleen. Bone marrow begins hematopoiesis in the fourth intrauterine month, overtakes the liver in this function by the sixth month, and is entirely responsible for hematopoietic cell production by birth.[23] Shortly before birth, conversion from hematopoietic to fatty marrow begins in the distal phalanges of the hands and feet and proceeds in a centripetal fashion from the distal to the more proximal portions of the appendicular skeleton.[4] Within the long bones, conversion from hematopoietic to fatty marrow proceeds from the mid diaphyses to the distal metaphyses and then to the proximal metaphyses. Conversion also progresses from the central medullary canal to the endosteum. Fatty transformation in the epiphyses and apophyses begins almost as soon as they begin to ossify. In infants, the skull and limbs contain about half of the total amount of hematopoietic marrow.[1,4] By early adulthood, hematopoietic marrow becomes confined to the vertebrae, sternum, ribs, pelvis, skull, proximal humeri, and proximal femurs. Approximately half of the bone marrow volume is fatty marrow in early adulthood and is located in the appendicular skeleton. The involution of hematopoietic marrow continues throughout adult life, although at a slower pace than during childhood.[1,4,24] Unlike skeletal maturation, there are generally no gender differences in the rate of marrow conversion during childhood.[2] Knowledge of the normal age-related changes in the distribution of hematopoietic and fatty marrow is necessary for the recognition of abnormal conversion and reconversion patterns and for the detection of marrow infiltration by other pathologic processes.

***Imaging.*** Conversion from hematopoietic to fatty marrow is readily detected by MRI because of the high sensitivity of T1-weighted spin echo sequences to fat (e-Table 141.1).[1] In fact, marrow conversion is observed earlier by MRI than by gross pathologic inspection because of the capability of MRI to detect microscopic fat present in marrow.[2,4,5,25] Numerous publications detail the temporal and spatial sequence of marrow conversion revealed by MRI. Although there are discrepancies among these publications in the precise ages of transformation, the sequence of conversion is consistent along the long axes of individual bones and in the skeleton as a whole. Conversion occurs at a faster pace in the appendicular skeleton (extremities, shoulders, and pelvic girdle) than in the axial skeleton (skull, spine, ribs, and sternum).[1,4]

### Appendicular Skeleton

Marrow conversion follows a similar pattern in both the upper and lower limbs. Within the long bones, conversion initially begins within the diaphysis before spreading to the metaphysis.[25] In general, low signal intensity on T1-weighted images marrow within the long-bone diaphyses is unusual after 10 years of age.[1,5] Long-bone metaphyseal marrow demonstrates high signal intensity on T1-weighted images by 15 to 25 years of age, except for low to intermediate signal intensity hematopoietic marrow that may persist through adulthood in the proximal femoral metaphyses, the metaphyses around the knee, and the proximal humerus, particularly in populations with increased hematopoiesis, such as smokers, endurance athletes, and obese women.[1,4,26]

Under normal circumstances, the epiphyseal ossification centers do not participate in hematopoiesis to any appreciable degree. Soon after the onset of epiphyseal ossification, the low signal intensity bony trabeculae and hematopoietic marrow begin to be replaced by high signal intensity fatty marrow, with near complete conversion within 6 to 8 months from the onset of ossification.[27] Fatty marrow appears earlier in the proximal humeral epiphysis, compared with the femur, because of the earlier onset of proximal humeral epiphyseal ossification.[1,28] The apophyses and sesamoid bones follow patterns similar to the epiphyses.

Fatty marrow conversion first occurs within the phalanges and is completed in the fingers and toes by 1 year of age.[4] Conversion in the femurs begins in infancy. Fatty marrow is seen in the femoral diaphyses as early as 3 months of age and is commonly observed by 12 months of age.[25] At 1 to 5 years of age, the diaphyseal fat signal becomes homogeneous, and the hematopoietic marrow in the distal femoral metaphyses becomes replaced by fatty marrow at 6 to 15 years of age (Fig. 141.2).[25] However, a mottled pattern of relatively low to intermediate signal intensity in the proximal femoral metaphyses may remain, related to persistent hematopoietic marrow and bony trabeculae extending from the inferolateral aspect of the femoral neck to the superomedial aspect of the femoral head.

Bone marrow conversion in the humerus follows a similar predictable pattern. Conversion to fatty marrow is complete in the proximal humeral epiphyses by 1 year of age, nearly complete in the diaphyses by 5 years of age, and nearly complete in the distal metaphyses by 10 years of age.[28] Conversion occurs less rapidly in the proximal humeral metaphyses but is nearly complete by 15 years of age. However, low to intermediate signal intensity hematopoietic marrow is retained in the proximal humeral metaphyses and subchondral medial aspects of the humeral heads into adulthood, particularly in women.[2,29] The acromion behaves like an epiphysis in regard to marrow distribution and conversion rate.[2]

Conversion of marrow in the forearm and leg bones may lag slightly behind the proximal arms and thighs. Conversion to fatty marrow begins in the diaphyses between 1 and 5 years of age and is complete in all portions of the forearm and leg bones by 10 to 15 years of age.[4] Marrow conversion ensues in the tarsal and carpal

**e-TABLE 141.1** T1-Weighted Signal Intensities Associated with Bone Marrow Conversion

| | Signal Intensity | | | | |
|---|---|---|---|---|---|
| **Marrow Site*** | **0-1 yr** | **1-5 yr** | **6-10 yr** | **11-15 yr** | **15+ yr** |
| **FEMUR** | | | | | |
| Diaphysis | L-H | M-H | H | H | H |
| PM | L | L | M | M | M |
| DM | L | M | M | H | H |
| Epiphyses | L-H | H | H | H | H |
| **Sternum** | L | L | M | M | M |
| **Clavicle** | L | L | M | M | M |
| **HUMERUS** | | | | | |
| PE | L-H | H | H | H | H |
| PM | L | M | M | M | M |
| Diaphysis | M | H | H | H | H |
| DM | L | M | M | H | H |
| **Pelvis** | L | M | M | M | M |
| **Vertebrae** | L-I | I-H | H | H | H |
| **SKULL** | | | | | |
| Clivus | L | L-M | M-H | H | H |
| Calvarium | L | L-M | M-H | H | H |

*DM,* Distal metaphysis; *H,* hyperintense; *I,* isointense; *L,* hypointense; *M,* intermediate and/or heterogeneous signal intensity; *PE,* proximal epiphysis; *PM,* proximal metaphysis.

*Intensity of vertebral bodies compared with intervertebral disks. All other marrow sites compared with muscle (hypointense) and fat (hyperintense).

bones at 2 to 6 months of age and is complete by 6 years of age, with the possible exception of small foci of residual hematopoietic marrow that persists in the tarsal bones up to 15 years of age.[30]

In the first year after birth, hematopoietic marrow is present in the pelvis. Conversion to fatty marrow initially occurs in the anterior ilium and acetabulum, beginning as early as 2 years of age (Fig. 141.3). In the second decade of life, the remainder of the pelvic marrow increases to intermediate signal intensity. Except in infancy, heterogeneous signal intensity of the pelvic marrow is a normal finding and is most prominent in adolescents and adults in the acetabulum and anterior ilium because of macroscopic foci of both hematopoietic and fatty marrow.[31]

## Axial Skeleton

During the first month after birth, the vertebral marrow lacks fat and exhibits uniformly lower signal than the adjacent cartilaginous disks on T1-weighted sequences. Later in infancy, as the vertebral ossification center increases in size and the cartilaginous end plates decrease in prominence, the vertebral body marrow increases in signal intensity on T1-weighted sequences, particularly adjacent to the cartilaginous end plates.[4] Compared with the intervertebral disks and cartilaginous end plates, vertebral body marrow is usually hypointense on T1-weighted images up to the age of 1 year.[32] Vertebral body marrow is commonly isointense or hyperintense on T1-weighted images compared with the intervertebral disks from 1 to 5 years of age. After the age of 5 years, vertebral body marrow signal on T1-weighted images is typically greater than that of the intervertebral disks, and a band of fatty marrow may be conspicuous in the vertebral body centrally or along the basivertebral venous plexus (Fig. 141.4).[4,32] The spine continues as a site of hematopoietic marrow throughout life, although the proportion of fatty marrow gradually rises approximately 7% per decade.

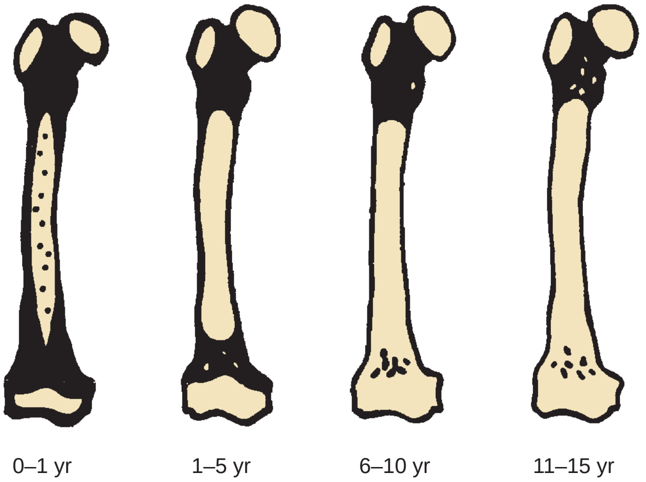

**Figure 141.2. Diagrammatic representation of changes in magnetic resonance imaging appearance of the femoral marrow with increasing age.** *Black areas* represent hematopoietic marrow, *yellow areas* represent fatty marrow, and *stippled areas* indicate heterogeneous hematopoietic and fatty marrow. *(From Waitches G, Zawin JK, Poznanski AK. Sequence and rate of bone marrow conversion in the femora of children as seen on MR imaging: are accepted standards accurate?* AJR Am J Roentgenol. *1994;162:1401.)*

The skull is where the bone marrow is most frequently imaged by MRI in childhood, typically incidentally in studies obtained to evaluate the brain.[33] The skull contains 25% of the active hematopoietic marrow at birth, and conversion to fatty marrow begins by 2 years of age within the facial bones and skull base before proceeding to the calvarium.[4] Marrow at the site of the future paranasal sinuses becomes fatty before pneumatization.[33] By 3 to 4 years of age, foci of high signal intensity on T1-weighted sequences are seen in the clivus, and complete conversion is typical by 15 years of age. In the calvarium, conversion begins earlier in the frontal and occipital bones than in the parietal bones.[24] Conversion in the calvarium should be obvious by 7 years of age, and it is complete in the great majority by 15 years of age.[4] The conversion to fatty marrow in the calvarium may occur more slowly in females, an exception to the rule of no gender differences.[3]

Marrow conversion in the sternum precedes that in the ribs. Development of foci of intermediate to high signal intensity on T1-weighted sequences occurs in the sternum after 5 years of age and in the ribs by 10 years of age.[4] The sternum and, to a lesser extent, the ribs remain hematopoietic into adulthood.

Detection of primary or systemic pathology that affects the marrow is usually easier in fatty marrow than in hematopoietic marrow.[34] This includes processes associated with hematopoietic hypercellularity (hemolytic anemia, hematopoietic growth factor treatment, leukemoid reaction, glycogen storage disease type 1b [GSD1b], myelodysplastic syndrome, leukemia), marrow infiltration (metastatic tumor cells, inflammatory cells, Gaucher cells), iron overload, and myelofibrosis.[7] Some of these processes are also associated with an increase in free water in the marrow and manifest as signal intensity higher than that of normal hematopoietic or fatty marrow on fat-suppressed FSE T2-weighted or STIR sequences.

Features that favor normal hematopoietic marrow include signal intensity equal to or only slightly higher than that of muscle on

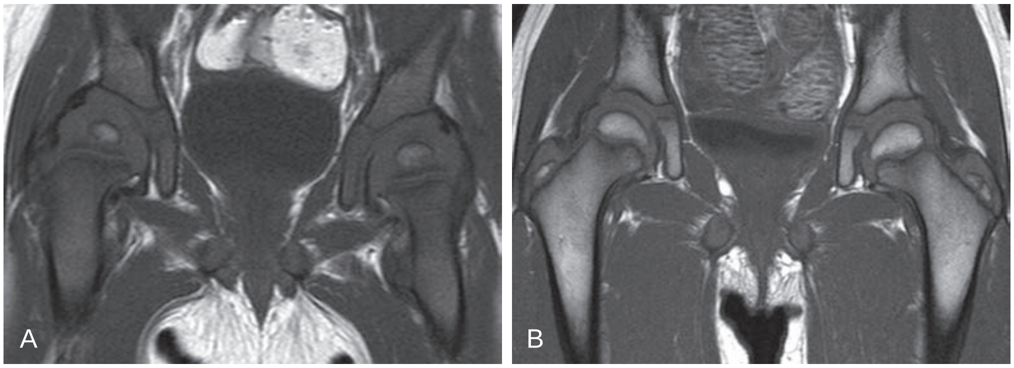

**Figure 141.3. Normal marrow changes.** (A) Coronal T1-weighted magnetic resonance (MR) image of the pelvis in an 11-month-old boy shows normal low signal intensity hematopoietic marrow is present in the pelvis and proximal femurs. (B) In a 3-year-old girl, normal conversion to fatty marrow has occurred by this age, manifested by increased signal intensity throughout the pelvis and proximal femurs.

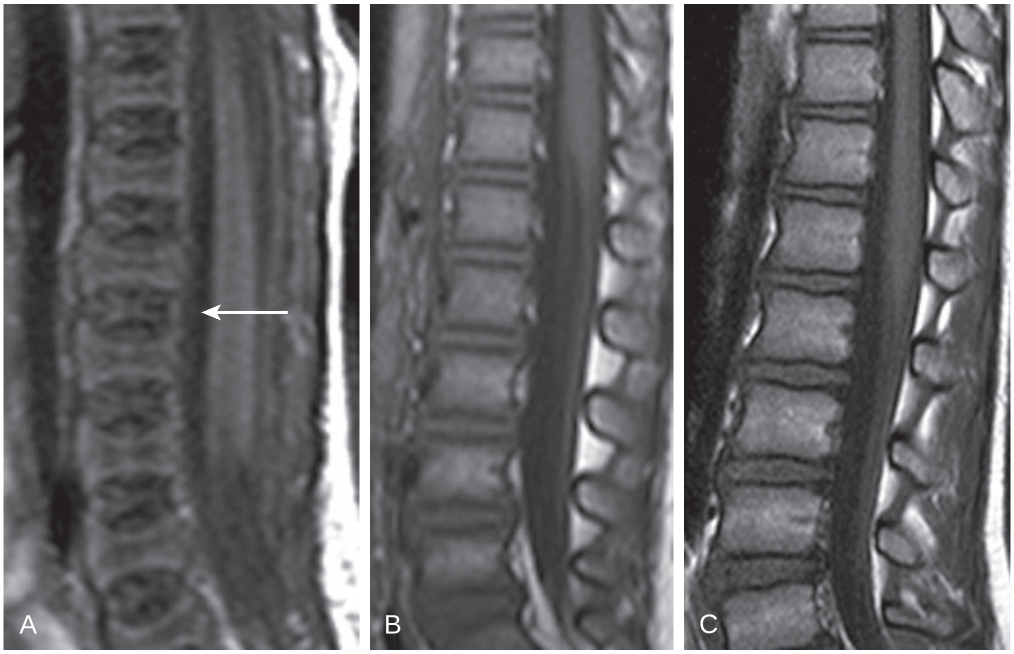

**Figure 141.4. Changes in signal intensity of vertebral body marrow with age.** Sagittal T1-weighted magnetic resonance images of the lumbar spine show (A) in a 2-day-old infant girl, the paucity of marrow fat accounts for the low signal intensity of the marrow of the vertebral body *(arrow)* relative to the that of the adjacent intervertebral disks. (B) In a 2-year-old girl, vertebral body marrow is hyperintense compared with that of the intervertebral disks. (C) In a 7-year-old girl, marrow signal intensity is greater than the signal intensity of the intervertebral disks, and there is a central band of more fatty, higher signal intensity marrow in the vertebral bodies.

fat-suppressed FSE T2-weighted or STIR sequences, dropout of signal intensity on opposed-phase GRE sequences, a "flame" or "paintbrush" shape (Fig. 141.5), no underlying trabecular disruption, symmetry with the contralateral side, and no associated abnormalities of the cortical bone or extraosseous soft tissues. Residual red marrow may sometimes have a globular appearance on T1-weighted sequences, and this is a normal finding (Fig. 141.6). However, a low-grade infiltrative or edematous process of the marrow can be difficult or impossible to distinguish from hematopoietic marrow on MRI, particularly when the hematopoietic marrow is relatively hypercellular, such as in very young children and in states of marrow reconversion in patients on granulocyte colony-stimulating factor (G-CSF) therapy (Fig. 141.7). Normal red marrow should never have a round, well-circumscribed configuration, which typically indicates a neoplastic process (Fig. 141.8).[35]

Processes in which the proportion of fat is increased relative to other components of the bone marrow appear as a focal or diffuse increase in the bone marrow signal intensity on T1-weighted sequences. This occurs physiologically during aging with the conversion from active hematopoietic marrow to hematopoietically quiescent fatty marrow. A pathologic example is the hematopoietic cell depletion associated with aplastic anemia. Some processes are associated with varying degrees of marrow cellularity and fat content, and their MRI appearances vary correspondingly. These include the myelodysplastic syndromes and the responses of marrow to chemotherapy, radiation therapy, and hematopoietic cell transplantation.

## MARROW HYPERPLASIA AND RECONVERSION

***Overview.*** Reconversion is a process by which established fatty marrow is replaced by hyperplastic hematopoietic marrow in response to conditions that create a demand for increased hematopoiesis. In children, reconversion is commonly encountered in patients with chronic anemia—such as from sickle cell disease, thalassemia, and spherocytosis—and in those administered hematopoietic growth factors, such as G-CSF, granulocyte-macrophage colony-stimulating factor (GM-CSF), and erythropoietin.

***Etiology, Pathophysiology, and Clinical Presentation.*** The stimulus for increased oxygen-carrying capacity of the blood in cyanotic congenital heart disease patients, endurance athletes, heavy smokers, and high-altitude dwellers also induces hematopoietic marrow hyperplasia and reconversion. Because marrow conversion is a process that occurs throughout childhood, some of what is construed as reconversion in children actually represents an arrest or delay in conversion from hematopoietic to fatty marrow and is attributable to increased hematopoietic demands (e-Fig. 141.9).[4]

Reconversion occurs in the reverse order of normal marrow conversion, beginning in the axial skeleton and proceeding sequentially to the proximal metaphyses, distal metaphyses, and diaphyses of the long bones of the appendicular skeleton.[4,6] The more distal long bones are the last to undergo this process. The epiphyses are usually spared but can undergo reconversion in response to very high hematopoietic demands.

***Imaging.*** On MRI, reconverted marrow follows the signal intensity of hematopoietic marrow and tends to involve the appendicular skeleton in a symmetric fashion.[1,4] The reconverted hematopoietic marrow may be distributed in either a homogeneous or patchy pattern and may have an appearance overlapping with that of pathologic processes, such as leukemia and storage disorders. Although MRI is very sensitive to changes in marrow fat content, disease specificity is low. Also, some of the conditions that exhibit marrow reconversion have additional superimposed marrow processes that complicate MRI interpretation, such as transfusion hemosiderosis in thalassemia and marrow infarction and fibrosis in sickle cell disease. Positron-emission tomography (PET) with 18-fluorodeoxyglucose (FDG) is also sensitive to marrow conversion and may reveal increased FDG uptake in areas of marrow hyperplasia because of the metabolic demands of increased hematopoiesis.[36]

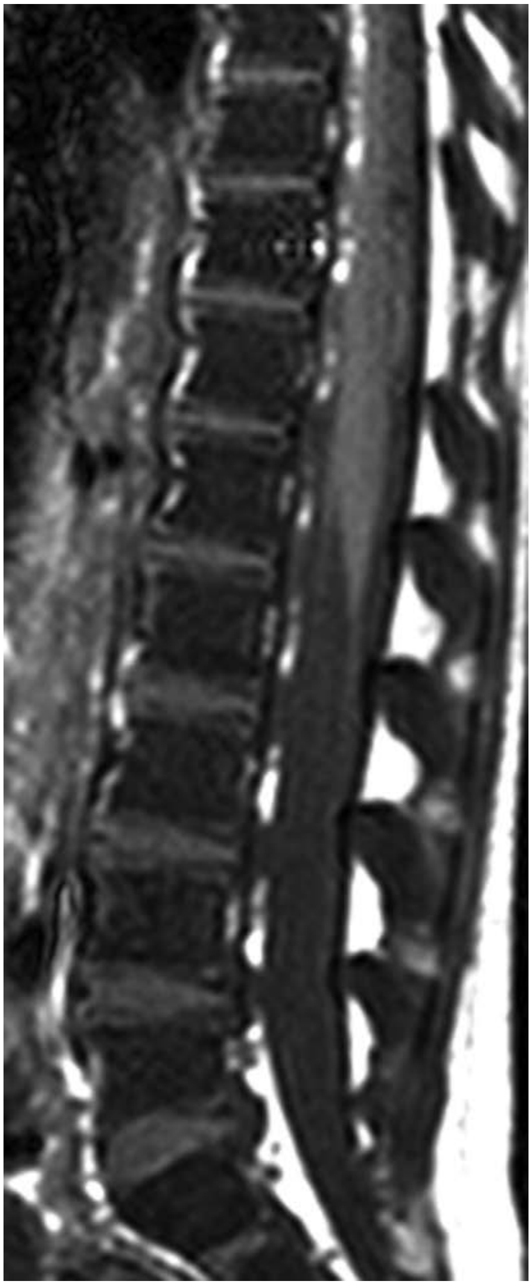

**e-Figure 141.9. Homozygous sickle cell disease in a 5-year-old girl.** Sagittal T1-weighted magnetic resonance image of the lumbar spine shows that the marrow signal intensity is lower than the adjacent intervertebral disks because of the hematopoietic marrow hyperplasia associated with chronic hemolytic anemia.

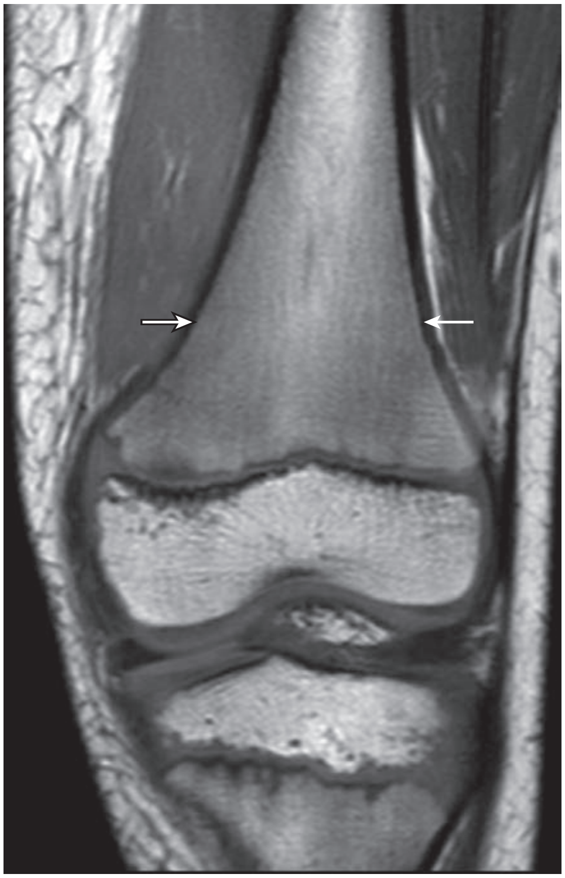

**Figure 141.5. Normal marrow in an 8-year-old boy.** T1-weighted coronal MR image demonstrates paintbrush-like pattern of hypointensity *(arrows)* in the femoral metaphysis without underlying trabecular disruption, consistent with normal residual red marrow.

## Thalassemia

***Etiology, Pathophysiology, and Clinical Presentation.*** Thalassemia is an inherited hemoglobinopathy characterized by ineffective erythropoiesis, intramedullary hemolysis, and anemia. With effective transfusion therapy, hematopoietic to fatty marrow conversion may proceed in the extremities by puberty. However, hematopoietic marrow hyperplasia in the skull, spine, and pelvis can remain pronounced. The paranasal sinuses often fail to develop, in part as a result of abrogation of the normal fatty conversion of marrow that precedes sinus pneumatization.[33]

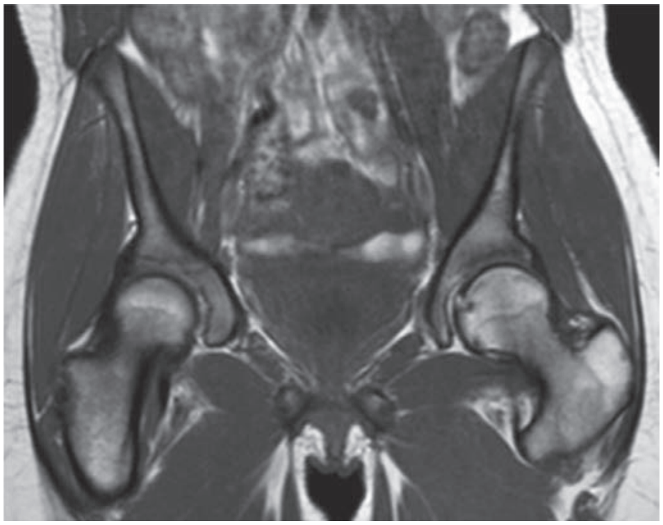

**Figure 141.6. Normal marrow in a 15-year-old girl.** T1-weighted coronal MR image demonstrates globular areas of decreased signal throughout the proximal femurs and pelvic bones, consistent with normal, residual hematopoietic marrow.

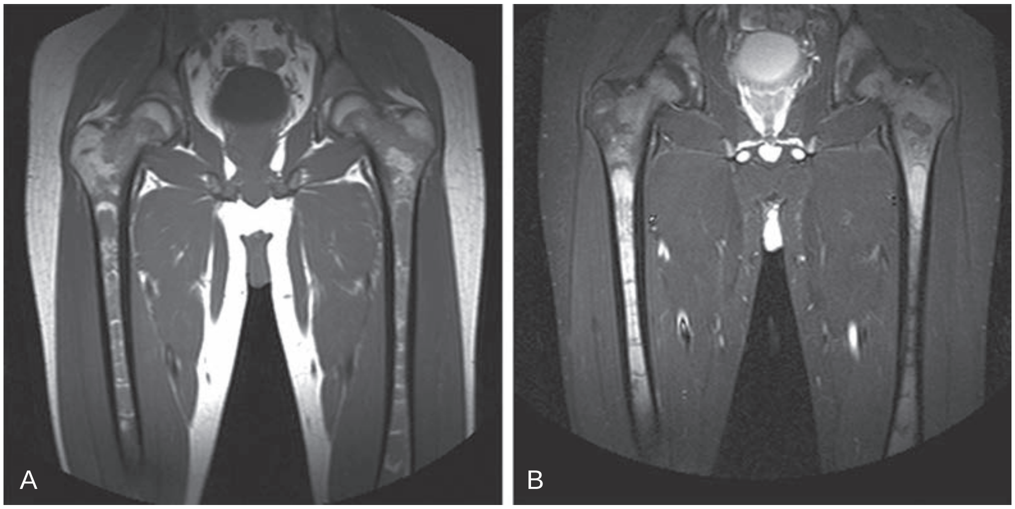

**Figure 141.7. A 17-year-old boy on granulocyte colony-stimulating factor (G-CSF) therapy for myelosuppression related to chemotherapy for Hodgkin disease.** Coronal T1-weighted MR image (A) and coronal short-tau inversion recovery (STIR) MR image of the thighs (B) show masslike, patchy, bilateral foci of marrow replacement with low signal intensity on T1-weighted images and high signal intensity on STIR images representing regenerating granulopoietic marrow in response to G-CSF stimulation. Clinical correlation with the timing of therapy is necessary to distinguish these findings from neoplastic involvement of the marrow.

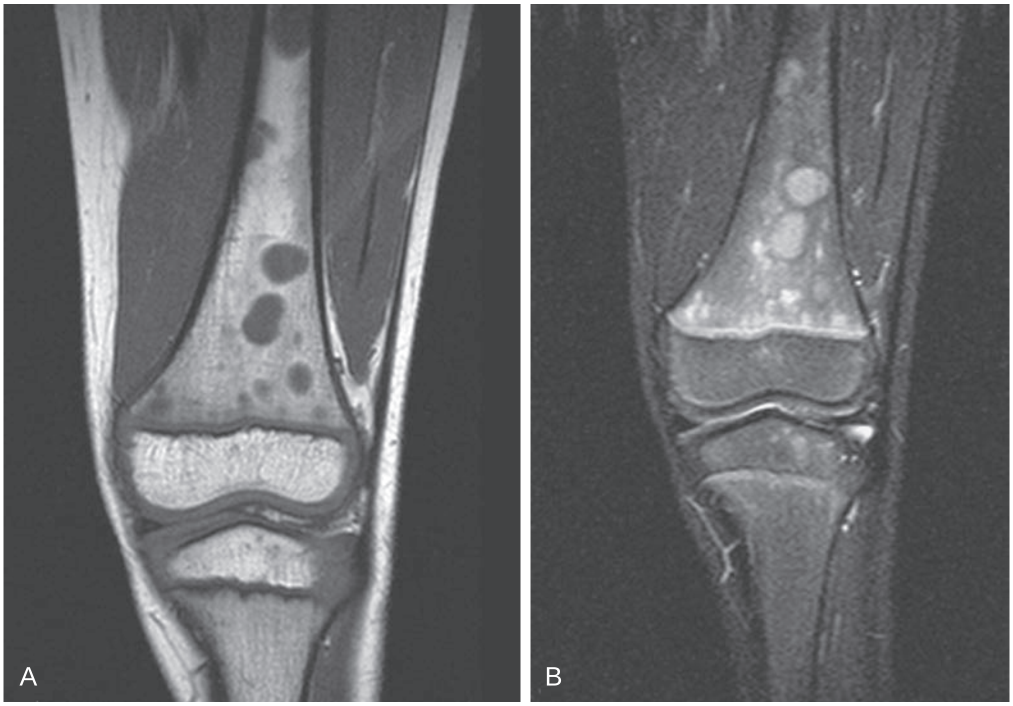

**Figure 141.8. Burkitt lymphoma and knee pain in a 6-year-old boy.** (A) Coronal T1-weighted and (B) short-tau inversion recovery (STIR) MR images of the left knee. Multiple round, sharply defined hypointense masses identified on the T1-weighted image are hyperintense on the STIR image because of marrow involvement by Burkitt lymphoma.

Thalassemia patients are at increased risk of pathologic fractures from osteopenia, arthralgias that are believed to result from iron overload or the use of chelation therapy, and back pain from scoliosis and early intervertebral disk degeneration.[37]

***Imaging.*** The radiographic changes of thalassemia are due to chronic hematopoietic marrow hyperplasia. These include diffuse osteopenia, undertubulization of bone, premature physeal fusion, "hair-on-end" appearance of the calvarium with widening of the diploic space (Fig. 141.10), decreased pneumatization of the paranasal sinuses, coarse trabeculation of appendicular bones, expansion of costochondral junctions, scoliosis, and soft tissue masses related to extramedullary hematopoiesis.[38]

The appearance of the bone marrow on MRI is a reflection of the diffuse erythroid marrow hyperplasia, chronic transfusions, and iron chelation therapy.[4] Iron deposition in the marrow results in lowered signal intensity on T1-, T2-, and especially T2*-weighted sequences because of T2 relaxation-time shortening and magnetic susceptibility effects.[39] Excess iron deposition can even be identified by MRI in some patients whose chelation is thought to be clinically adequate on the basis of serum ferritin levels, and the degree of iron deposition in bone marrow and other organs can be quantified by R2 relaxometry with MRI.[40] In severe cases of thalassemia, bone marrow transplantation may be pursued as a potentially curative treatment, and MRI can reveal the consequent degree of marrow conversion. FDG-PET in patients with thalassemia shows diffuse increased marrow uptake.[41]

***Treatment.*** Transfusion therapy suppresses the marrow hyperplasia of thalassemia but at the cost of iron overload. The iron deposition occurs preferentially in areas of hematopoietic marrow and is reduced by chelation therapy.[39]

## Sickle Cell Disease

***Etiology, Pathophysiology, and Clinical Presentation.*** Sickle cell disease is an inherited hemoglobinopathy characterized by deformation of red blood cells and resultant hemolytic anemia and intravascular sludging of blood. The bone marrow imaging manifestations of sickle cell disease are primarily related to hematopoietic marrow hyperplasia, osteonecrosis, and perivascular fibrosis.[42] Because the circulation normally passes centrifugally from the medullary cavity to the cortex, sludging of blood flow in the nutrient artery branches places increased demands on the radially arranged periosteal-cortical system of anastomosing blood

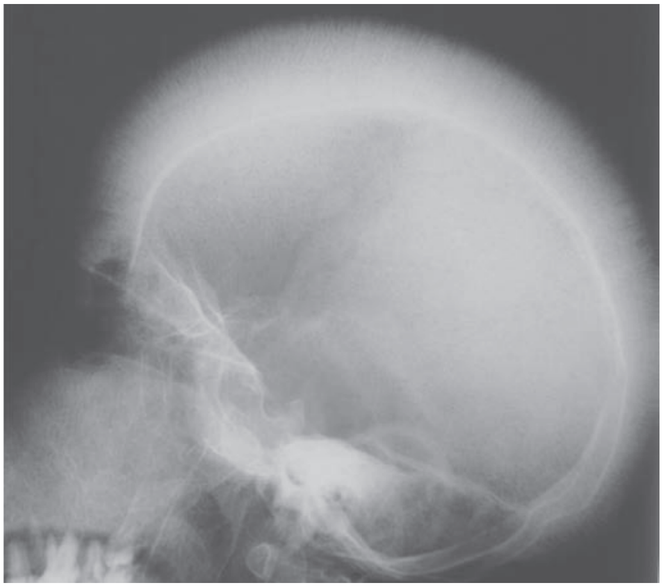

**Figure 141.10. Thalassemia.** Lateral radiograph of the skull shows diffuse "hair-on-end" appearance of the calvarium. *(Courtesy Edward Singleton, MD.)*

vessels to supply the marrow, particularly in the peripheral subcortical medullary cavity.[42,43] This, coupled with the increased oxygen needs from increased hematopoietic activity, accounts for the vulnerability of the bone marrow to osteonecrosis.

***Imaging.*** Osseous abnormalities in sickle cell disease are secondary to osteonecrosis and, less often, osteomyelitis. Radiographic findings are similar to osteonecrosis from other causes, with geographic and patchy areas of sclerosis (Fig. 141.11) that most commonly involve the femoral heads. Other common radiographic abnormalities include dactylitis (e-Fig. 141.12), H-shaped or "Lincoln log" vertebral bodies from central growth plate osteonecrosis (Fig. 141.13), diffuse osteosclerosis, and widespread periostitis.[44]

Findings on MRI include bone marrow changes that reflect red marrow reconversion secondary to chronic anemia, with decreased signal intensity on T1-weighted sequences and increased signal intensity on fat-suppressed T2-weighted and STIR sequences. Marrow changes secondary to osteonecrosis are more complex and often reflect a combination of acute and chronic processes. Foci of low, serpentine signal intensity on T1-weighted sequences and abnormal high signal intensity on fat-saturated T2-weighted or STIR sequences are classic imaging features of osteonecrosis. Chronic osteonecrosis may be suggested when these findings are confined to the marrow itself with absent joint effusions or juxtacortical soft tissue edema (Fig. 141.14). Acute osteonecrosis may be suggested when there is also infiltrative marrow edema, periostitis, and/or juxtacortical soft tissue edema (Fig. 141.15).

Acute osteomyelitis may be difficult to differentiate by MRI from the more common acute osteonecrosis and vasoocclusive crisis (see Fig. 141.15). Ultimately, aspiration and biopsy may be necessary to distinguish these entities, because both can manifest with marrow signal intensity abnormalities, periosteal reaction, and intraosseous, subperiosteal, or extraosseous soft tissue fluid collections. Gadolinium-enhanced MRI can distinguish vascularized inflammatory tissue from fluid collections and can guide fluid aspiration.[45] Some evidence suggests the ability of unenhanced T1-weighted fat-saturated images to differentiate acute osteonecrosis from acute osteomyelitis based on the T1 shortening effects of sequestered red blood cell aggregates in the marrow. However, adequately powered studies have not been undertaken and published studies to date present conflicting results.[46,47]

***Treatment.*** The two most common acute musculoskeletal manifestations of sickle cell disease are vasoocclusive crisis followed by infection. Osteonecrosis is the most frequent presentation of vasoocclusive crisis and is treated with supportive care and pain management.[48] Infections include osteomyelitis, with or without associated subperiosteal abscesses, and less commonly septic arthritis. Unlike the general pediatric population with musculoskeletal infections, *Salmonella* is most commonly identified by culture, followed by *Staphylococcus aureus*.[44]

## Glycogen Storage Disease Type 1b

***Etiology, Pathophysiology, and Clinical Presentation.*** The musculoskeletal manifestations of GSD1b are related to a defect in myeloid maturation that leads to bone marrow hypercellularity

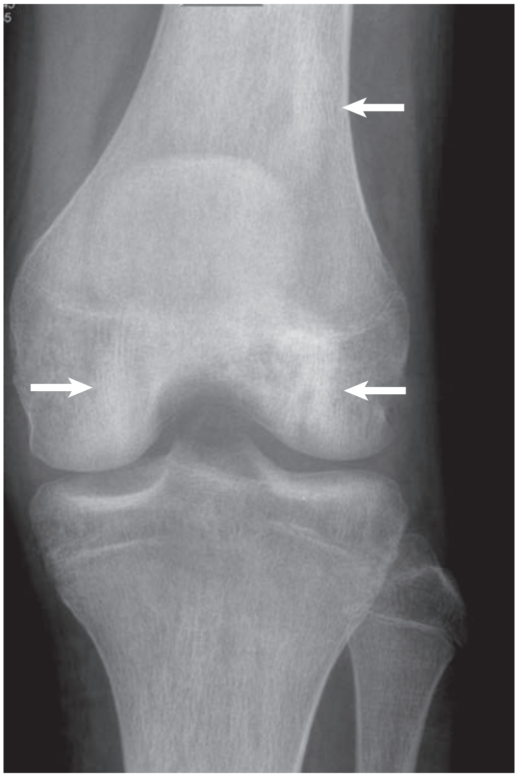

**Figure 141.11. Sickle cell disease in a 17-year-old boy.** Anteroposterior radiograph of the knee demonstrates multiple areas of sclerosis in the condyles and femoral shaft consistent with areas of osteonecrosis *(arrows)*.

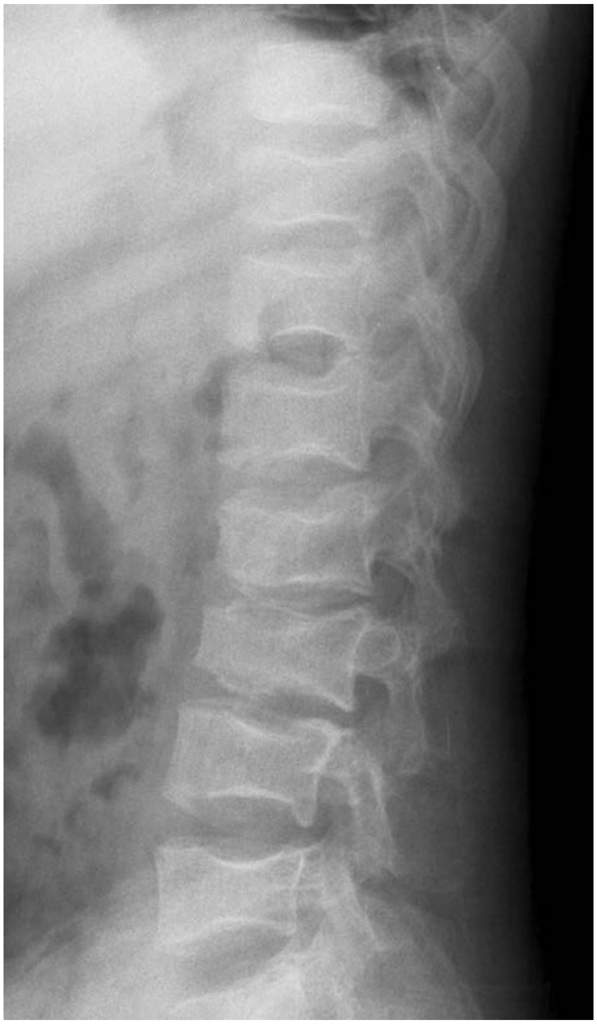

**Figure 141.13. Sickle cell disease in an 18-year-old man.** Numerous angulated end plate depressions ("H-shaped" or "Lincoln log" vertebrae) are consistent with central growth plate osteonecrosis.

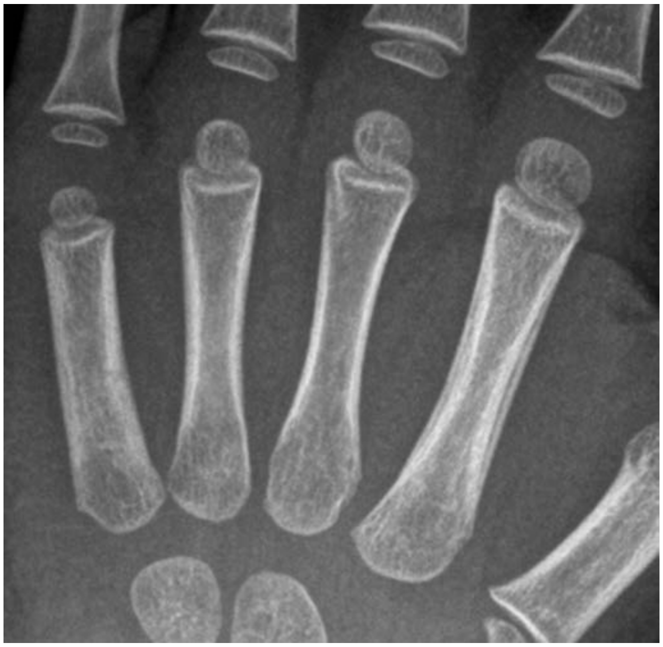

**e-Figure 141.12. Sickle cell dactylitis in a 2-year-old girl with left hand swelling.** Radiograph of the left hand shows smooth periosteal new bone formation along the second metacarpal.

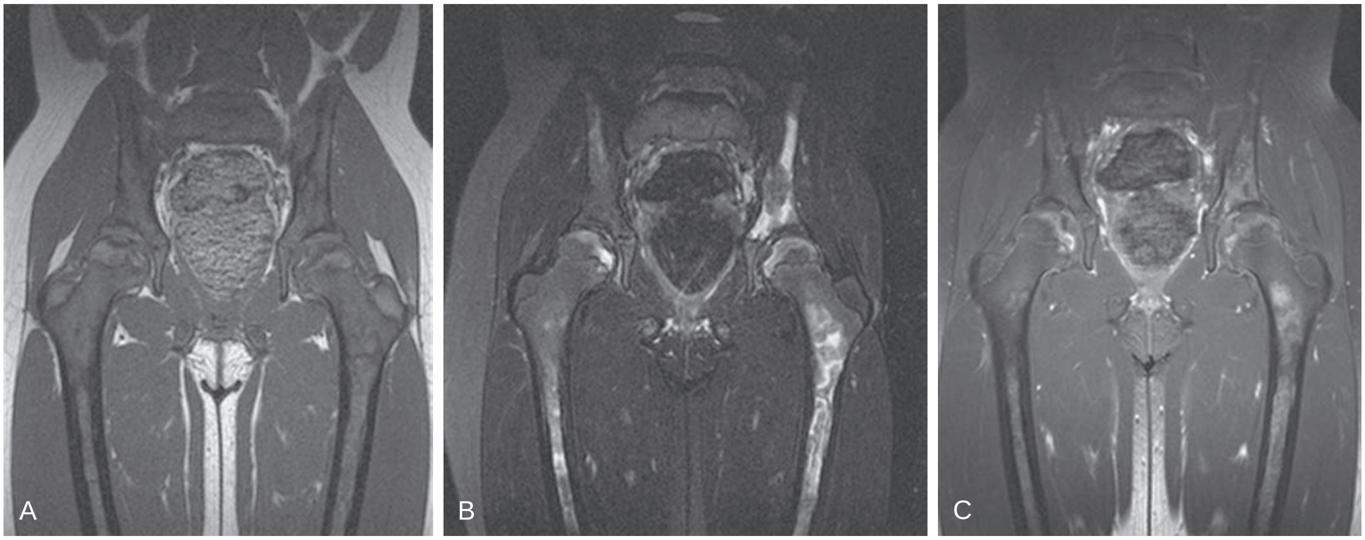

**Figure 141.14. Homozygous sickle cell disease in a 10-year-old girl with diffuse changes of osteonecrosis of the pelvic bones and femurs.** Coronal T1-weighted (A), T2-weighted fat-saturated (B), and postgadolinium T1-weighted fat-saturated (C) MR images of the pelvis. Note absence of juxtacortical soft tissue edema or hip joint effusions, suggesting that the process is subacute or chronic in nature.

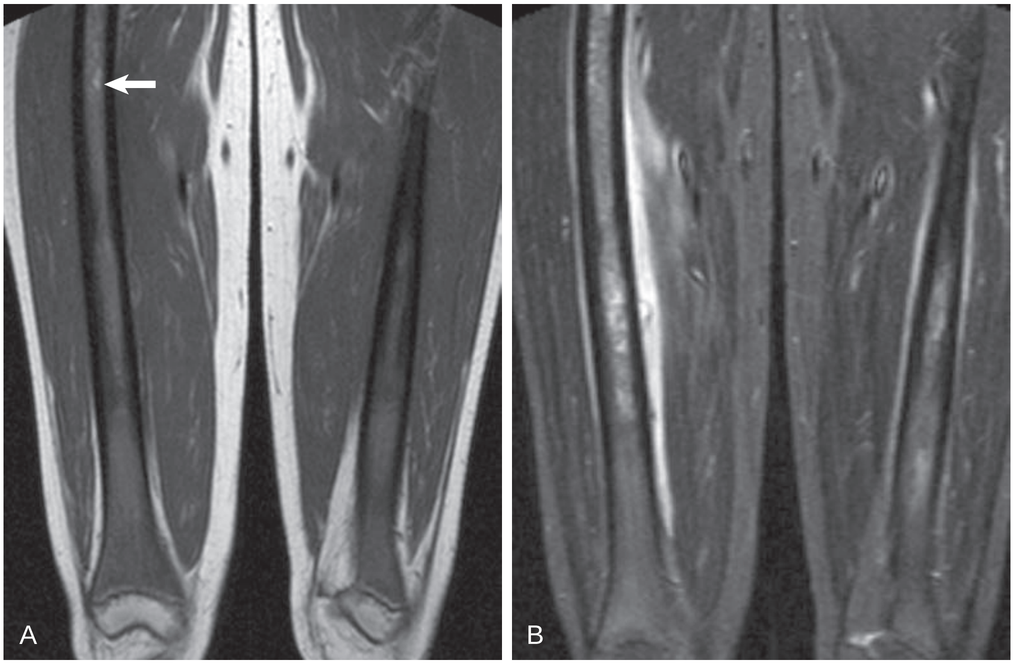

**Figure 141.15. Sickle cell disease acute vasoocclusive crisis in a 16-year-old girl.** (A) T1-weighted coronal MR image demonstrates diffuse hematopoietic marrow hyperplasia with variegated sclerosis throughout the femoral shafts consistent with prior episodes of osteonecrosis. Note hyperintense T1 focus *(arrow)*, which may represent sequestered blood. (B) Short-tau inversion recovery coronal sequence reveals diffuse marrow edema bilaterally, as well as exuberant periostitis bilaterally, and exuberant juxtacortical soft tissue edema on the right.

with hyperplasia of the myelopoietic cells and a propensity to develop bacterial infections related to chronic neutropenia.[49]

***Imaging.*** The most common radiographic changes in GSD1b during childhood are osteoporosis, undertubulization of appendicular bones, marked growth retardation, and delayed physeal closure.[50,51] Epiphyseal ossification is often delayed and irregular, and open physes may persist into early adulthood.

On MRI, the signal intensity of the bone marrow varies and is dependent upon whether G-CSF has been administered for treatment. Without such treatment, patchy areas of low signal intensity on T1-weighted sequences and high signal intensity on T2-weighted FSE and STIR sequences reflect myeloid hyperplasia throughout the axial and appendicular skeleton. MRI features of glycogen storage disease may be indistinguishable from marrow hyperplasia related to profound anemia or leukemia. With G-CSF treatment, marrow hyperplasia becomes even more profound, and replacement of yellow marrow at the epiphyses may occur. In addition, G-CSF therapy often creates transverse bands of increased signal intensity on T2-weighted FSE and STIR sequences at the level of the juxtaphyseal metaphysis, likely related to hematopoietic recruitment.[26,49]

***Treatment.*** Medical nutrition therapy is the primary treatment. Additional therapies include allopurinol to prevent gout, lipid-lowering agents, citrate supplementation to help prevent urinary calculi, angiotensin-converting enzyme inhibitors to treat microalbuminuria, surgery for hepatic adenomas, human G-CSF for recurrent infections, and organ transplantation for end-stage kidney and liver disease.[52]

## MARROW INFILTRATION

### Storage Disorders

#### Gaucher Disease Type 1

***Etiology, Pathophysiology, and Clinical Presentation.*** Gaucher disease is the most prevalent heritable lysosome storage disorder. Mutations that confer a deficient level of β-glucocerebrosidase activity lead to accumulation of the lipid glucocerebroside in the lysosomes of macrophage-like Gaucher cells.[53] The symptoms and pathology of the type 1 form of Gaucher disease result from the accumulation of Gaucher cells in various organ systems, including the skeletal system. Those with Gaucher disease are subject to recurrent painful bone crises, like those with sickle cell disease.

***Imaging.*** Skeletal imaging manifestations relate to marrow infiltration by Gaucher cells, leading to osteonecrosis, osteosclerosis, osteomyelitis, and predisposition to fractures.[53,54] The most common radiographic abnormality in untreated Gaucher disease is undertubulation of the distal femoral metaphysis as a result of marrow infiltration, termed the *Erlenmeyer flask deformity* (Fig. 141.16). This undertubulation is not specific to Gaucher disease (e-Fig. 141.17) and is much less commonly identified in treated patients.

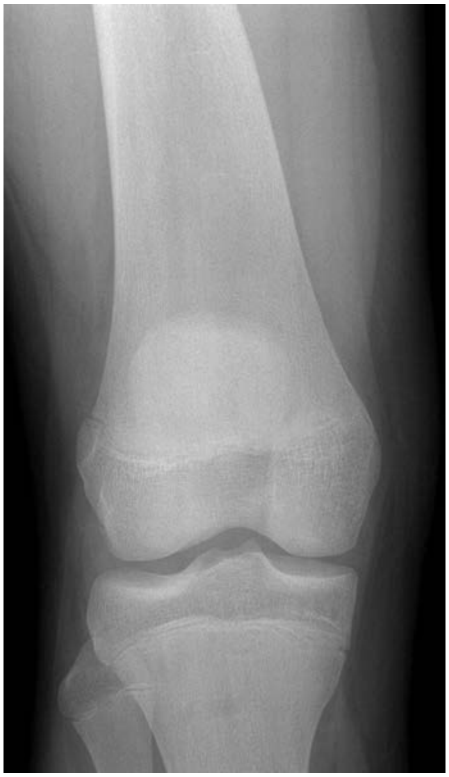

**Figure 141.16. Gaucher disease with undertubulation in a 16-year-old boy.** Frontal radiograph of the distal right femur shows mild to moderate Erlenmeyer deformity of the distal right femur.

On MRI, replacement of fatty marrow by Gaucher cells results in low signal intensity on T1- and T2-weighted sequences. Initially, marrow replacement is often diffuse and homogeneous and mimics a number of systemic metabolic disorders.[55] Marrow replacement is usually confined to the metaphysis and diaphysis, and epiphyseal involvement is unusual except in severe cases.[56] With time and treatment, marrow changes become patchy. Islands of Gaucher cells are separated by intervening fatty marrow throughout the skeleton with relative preservation of the epiphyseal fatty marrow (Fig. 141.18). The intramedullary presence of Gaucher cells is thought to hinder blood flow within the marrow, thereby predisposing these patients to osteonecrosis (e-Fig. 141.19).

***Treatment.*** Enzyme-replacement therapy results in degradation of Gaucher cell deposits and reconversion to normal fatty marrow.[56] MRI has been advocated to monitor the bone marrow fat fraction as an indicator of therapy response. Several MRI-based methods of quantifying the bone marrow infiltration and the effects of treatment on patients with Gaucher disease are under investigation, including Dixon chemical-shift imaging, T1 relaxation-time calculation, and MR spectroscopy.[51,57,58]

### Neoplasms

#### Leukemia

***Etiology, Pathophysiology, and Clinical Presentation.*** Leukemia is the most common childhood malignancy, accounting for up to one-third of childhood cancer.[59] Leukemia is classified by the morphology, immunophenotype, and cytogenetics of the leukemic cells. Acute lymphoblastic leukemia (ALL) and acute myeloid leukemia (AML) account for three-quarters and one-fifth of childhood leukemia cases, respectively. The peak incidence of childhood ALL is 2 to 3 years of age, and there is evidence that ALL can initiate in utero.[60] AML rates are highest in the first 2 years of life, decline to a nadir at 6 years of age, and slowly increase during the adolescent years.[61] An increased risk of leukemia is associated with certain genetic disorders, including trisomy 21, monosomy 7, neurofibromatosis type 1, and DNA repair disorders such as ataxia-telangiectasia.[59] Of particular interest to the radiologist is the reported increased risk of leukemia from prenatal or postnatal radiation exposure.[62,63]

***Imaging.*** Radiography of the appendicular and axial skeleton is most often normal when the patient is brought to medical attention. When radiographs are abnormal, the most common finding is osteopenia. *Leukemic lines* refer to juxtaphyseal radiolucent metaphyseal bands (Fig. 141.20), which have been attributed to various causes, including disruption of the zone of hypertrophy related to leukemic infiltration and insufficiency fractures of the metaphysis just above the physis. Leukemic lines have even been proposed to be a visual artifact related to profound osteopenia. Periostitis at initial presentation may be due to the disease process itself or to insufficiency fractures resulting from osteopenia (e-Fig. 141.21).

On MRI, leukemic infiltration causes diffusely decreased signal intensity on T1-weighted sequences[64,65] and increased signal intensity on fat-suppressed T2-weighted and STIR sequences. The epiphysis is often involved (Fig. 141.22). Marrow involvement may also have a well-defined nodular appearance, especially in the setting of leukemic relapse.[35] The findings are less conspicuous in hematopoietic marrow than in fatty marrow, and consequently are more difficult to appreciate in younger children, in whom marrow conversion has not yet occurred.[34] The MRI appearance of diffuse cellular infiltration of the marrow in children is not specific for acute leukemia and can also be seen in conditions associated with hematopoietic marrow hyperplasia, in myelodysplastic and myeloproliferative syndromes, and in lymphoma and

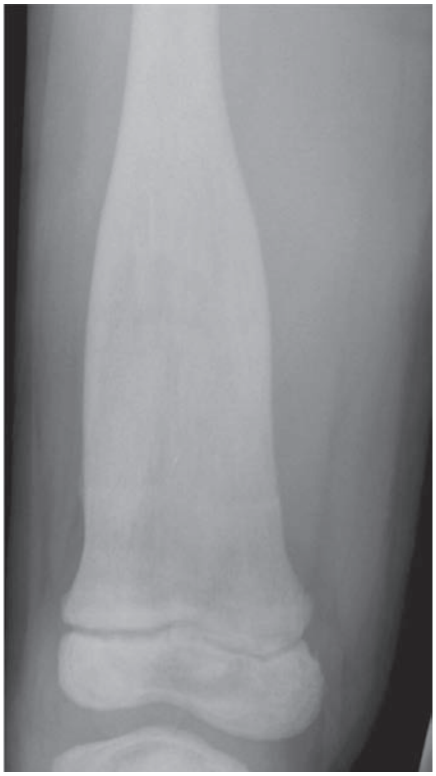

**e-Figure 141.17. Osteopetrosis and undertubulation in a 12-year-old.** Frontal radiograph of the distal right femur shows Erlenmeyer deformity resulting from moderate to severe diaphyseal undertubulation.

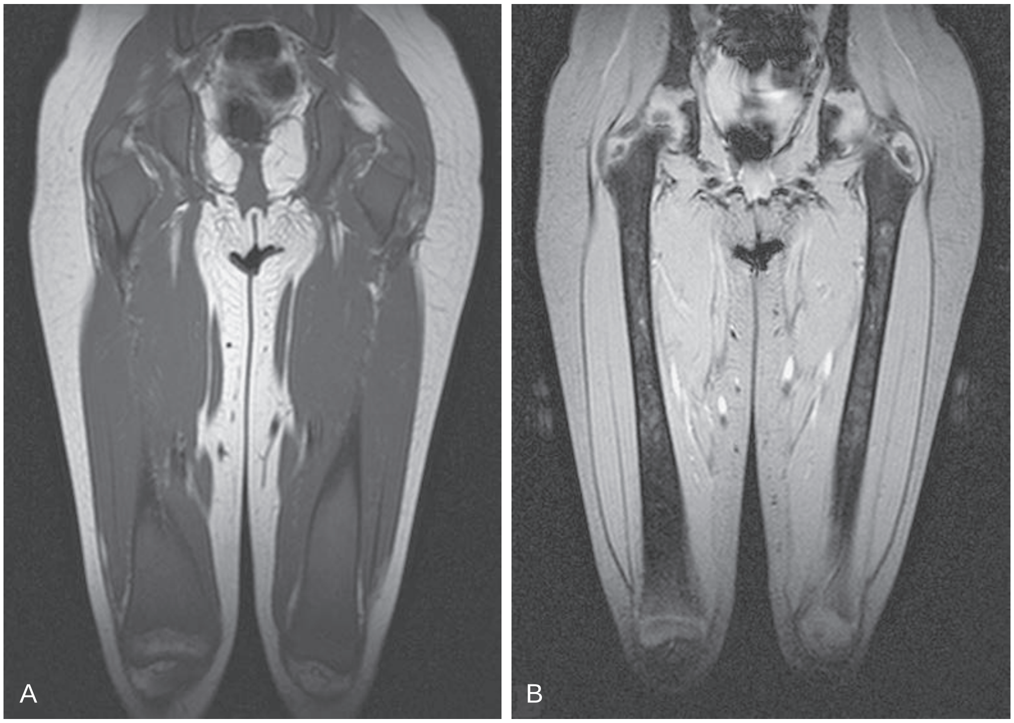

**e-Figure 141.19. Type 1 Gaucher disease in a 5-year-old girl with diffuse Gaucher cell infiltration and osteonecrosis.** Diffuse metadiaphyseal low signal intensity of the marrow is noted on the coronal T1-weighted MR image, (A) and corresponding patchy high signal intensity with intervening serpentine margins related to osteonecrosis is evident on the coronal fast field echo T2*-weighted MR image (B).

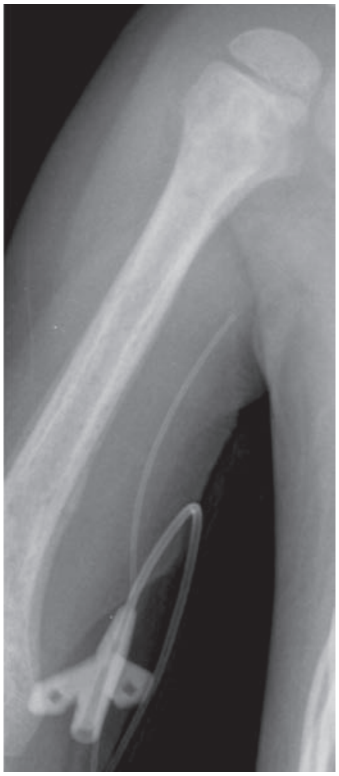

**e-Figure 141.21. Three-year-old boy with trisomy 21 and anemia.** Coned-down image of the right humerus from a chest radiograph shows an aggressive, permeative lesion with a poorly defined zone of transition and periosteal reaction that affects the mid and distal humerus. Bone marrow biopsy revealed acute myeloid leukemia.

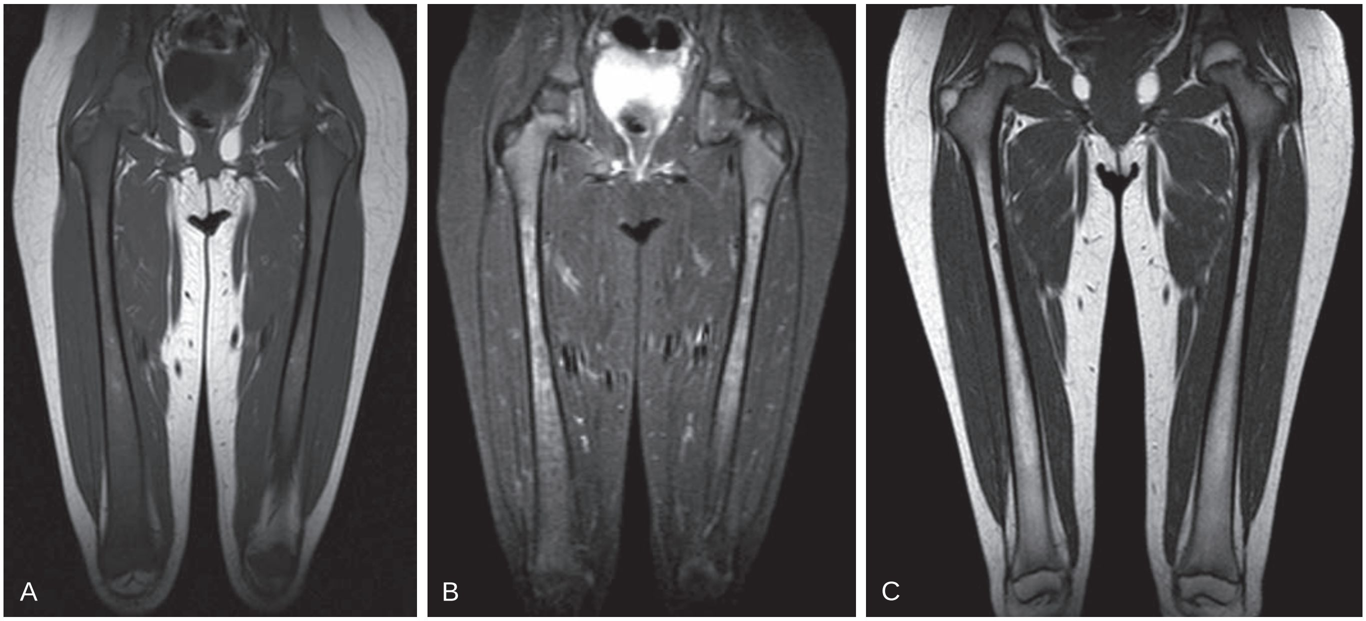

**Figure 141.18. Gaucher disease in a 4-year-old girl.** (A) T1-weighted coronal MR image shows diffuse fatty marrow replacement with small diaphyseal islands of fatty marrow. (B) Short-tau inversion recovery coronal image shows lobulated marrow replacement with increased signal with respect to muscle. (C) T1-weighted coronal image after treatment 7 years later shows fatty marrow conversion.

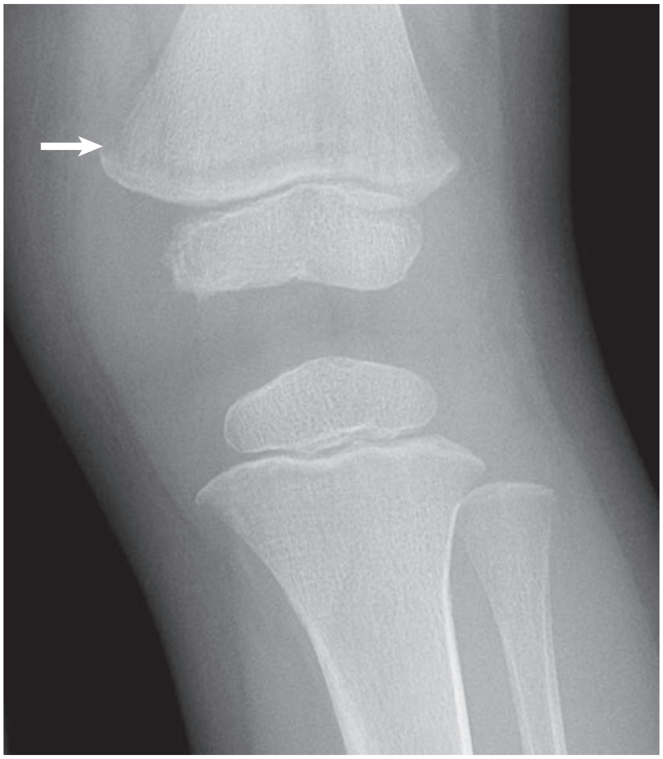

**Figure 141.20. Newly diagnosed acute lymphoblastic leukemia in a 1-year-old boy.** Leukemic lines manifesting as juxtaphyseal metaphyseal lucency are most pronounced in the distal femur *(arrow)*.

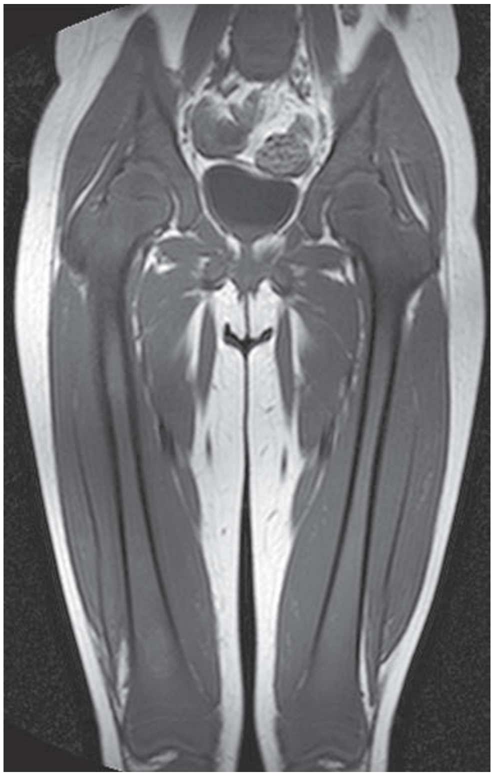

**Figure 141.22. Newly diagnosed acute lymphoblastic leukemia in a 6-year-old girl.** Coronal T1-weighted MR image of the pelvis and thighs demonstrates diffuse low signal intensity of the bone marrow consistent with leukemic replacement.

solid tumor metastases. The findings of periostitis, geographic replacement of fatty marrow by hematopoietic marrow throughout the entirety of the long bones and axial skeleton, and juxtacortical soft tissue edema favor a diagnosis of leukemia over hematopoietic marrow hyperplasia. During chemotherapy for leukemia, the bone marrow becomes hypocellular and edematous. Following chemotherapy, there is progressive regeneration of normal hematopoietic cells and fat (e-Fig. 141.23).[66] In children with ALL who enter remission, marrow T1 relaxation time normalizes, whereas it remains prolonged in those who do not enter remission.[65,67]

***Treatment and Follow-up.*** No standard guidelines exist for routine imaging follow-up in children with leukemia. PET imaging, bone densitometry, and whole-body MRI at presentation, treatment, or follow-up may be components of clinical trials or other research investigations but are not part of routine clinical practice.

Musculoskeletal complaints are common in children treated for leukemia at presentation and during follow-up.[68] The most common complications amenable to imaging diagnosis are osteonecrosis and insufficiency fractures. Up to 70% of children with leukemia screened by MRI are diagnosed with osteonecrosis, and 15% to 20% have symptoms.[69] The reported incidence of fractures in leukemic patients is 18.5% with low lumbar spine bone mineral density and age greater than 10 years as independent predictors of fracture risk.[70]

The most common site of ALL relapse is the marrow, followed by the central nervous system and testes.[61] MRI may be used to evaluate for relapse; however, its specificity is limited by difficulty in differentiating relapse from the effects of therapy.[71–73] Because of this limitation, MRI has not replaced marrow aspirate or biopsy for assessment of therapeutic response in leukemia.[74]

## Lymphoma

***Etiology, Pathophysiology, and Clinical Presentation.*** Marrow involvement by lymphoma in children usually occurs with Burkitt lymphoma, lymphoblastic lymphoma, and with lymphocyte-depleted Hodgkin disease. The pattern of involvement is usually multifocal, and there is a predilection for sites of predominantly hematopoietic marrow. When involvement is diffuse, an arbitrary threshold of neoplastic lymphoid cells constituting 25% or greater of the marrow cellularity differentiates the diagnosis of lymphoblastic leukemia from lymphoma.[75]

Primary lymphoma of bone should be distinguished from Hodgkin and non-Hodgkin lymphoma with bone involvement. When isolated disease is confined to the bone marrow without disease elsewhere for at least 6 months, a diagnosis of primary bone lymphoma can be made.[76]

***Imaging.*** Disseminated lymphoma with marrow involvement may be indistinguishable from leukemia by imaging. However, primary lymphoma of bone initially present as isolated focal bone involvement that may mimic other primary bone neoplasms. The most common radiographic pattern is lytic-destructive (Fig. 141.24).[77] The lytic pattern may be permeative, consisting of many uniform small lucencies or “moth-eaten” areas made of larger, poorly marginated lucencies.[76] Primary bone lymphoma often involves the flat bones of the pelvis and shoulder girdle as well as the diaphyses of long bones, similar to Ewing sarcoma.

Unlike leukemia, primary bone lymphoma often presents as a well-defined intramedullary mass with variable cortical destruction and soft tissue extension. The involved sites typically show low signal intensity on T1-weighted sequences and high signal intensity on fat-suppressed T2-weighted and STIR sequences (see Fig. 141.8). When primary bone lymphoma is unifocal on MRI with masslike features, it cannot be distinguished from other aggressive lesions, such as Ewing sarcoma and Langerhans cell histiocytosis. When diffuse, involvement is often patchy, and up to one-third of lymphoma patients with negative bone marrow biopsies have lymphoma involvement visible by MRI distant from the standard iliac crest biopsy sites.[73,78]

Although MRI is a sensitive modality for detecting marrow infiltration, it is not routinely used for the staging of lymphoma. FDG-PET detects lymphoma on the basis of increased metabolic activity and may be used as a complement to bone marrow biopsy for initial staging as it can guide the biopsy location to areas of active marrow involvement.[79]

***Treatment and Follow-up.*** Marrow involvement in patients with systemic lymphoma portends a worse prognosis and is considered stage IV disease.[59] Imaging follow-up is based on nonosseous

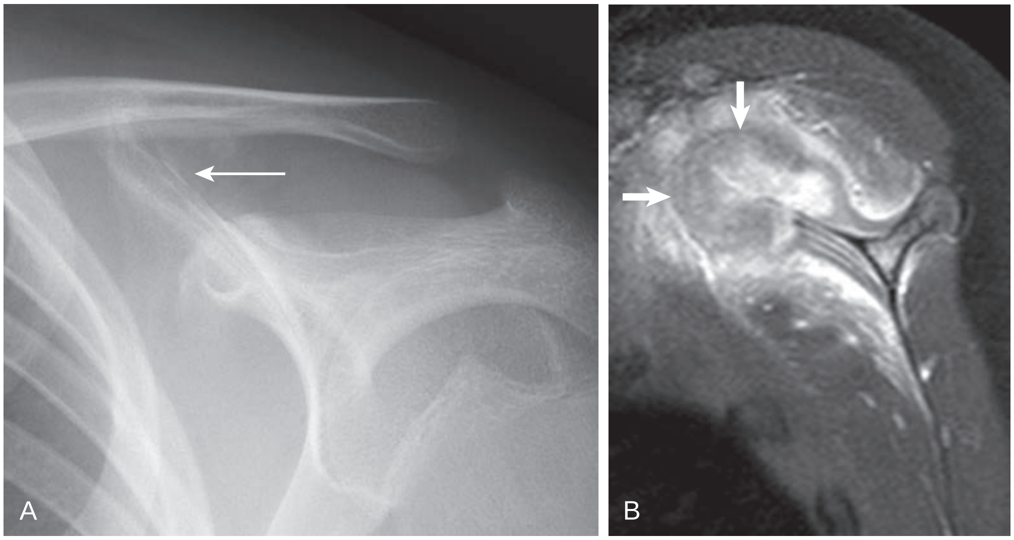

**Figure 141.24. Primary bone lymphoma in a 14-year-old boy with left shoulder pain.** (A) Frontal radiograph of the left scapula at initial presentation shows periosteal reaction and irregularity *(arrow)* at the superomedial scapula. (B) T1-weighted MR image with fat saturation shows cortical destruction, bone marrow edema, and a large heterogeneously enhancing soft tissue mass arising from the superior scapula *(arrows)* with adjacent soft tissue edema. Open surgical biopsy revealed large cell anaplastic lymphoma.

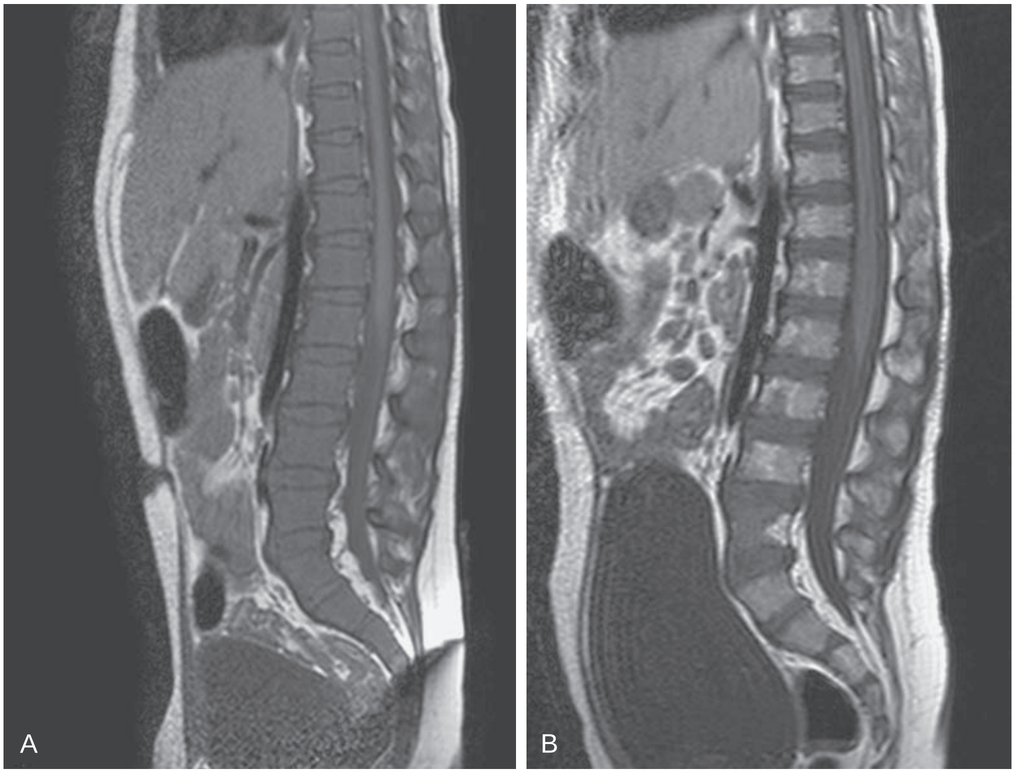

**e-Figure 141.23. Down syndrome and acute lymphoblastic leukemia in a 5-year-old boy.** Sagittal T1-weighted MR image of the lower spine at the time of leukemia diagnosis shows that the marrow is hypercellular owing to diffuse infiltration of the marrow by lymphoblasts and resultant diffuse abnormal low signal intensity of the marrow (A). The increase in marrow signal intensity after chemotherapy is consistent with an increase in the fat content and a reduction in the cellularity of the marrow (B).

disease, including nodal involvement. Patients with primary bone lymphoma have an excellent prognosis, and treatment is usually tailored to the site of involvement.[80]

## OSTEONECROSIS

***Etiology, Pathophysiology, and Clinical Presentation.*** Although often asymptomatic and rarely extensive enough to impair hematopoietic function, osteonecrosis can cause pain and disability. It can be separated into *epiphyseal* and *nonepiphyseal* osteonecrosis. The terms *aseptic* and *avascular necrosis* are alternative terms for *epiphyseal osteonecrosis*, and *bone infarction* is an alternative term for *nonepiphyseal osteonecrosis*.

Epiphyseal osteonecrosis portends a worse prognosis compared with nonepiphyseal osteonecrosis. This is because epiphyseal osteonecrosis and its complications—including cartilage injury, subchondral collapse, and subsequent early osteoarthritis—may compromise joint function.

Conditions associated with an increased risk of osteonecrosis include repetitive trauma, sickle cell disease, Gaucher disease, chronic renal failure, bone marrow transplantation, steroid therapy, pancreatitis, and highly active antiretroviral therapy for HIV infection.[81] Putative pathophysiologic mechanisms related to nontraumatic spontaneous osteonecrosis include vascular occlusion, elevated medullary cavity pressure, coagulopathy, and altered lipid metabolism. Osteonecrosis most commonly occurs in regions of fatty marrow and is unusual in hematopoietic marrow, except in patients with hemoglobinopathies.[81]

*Legg-Calvé-Perthes (LCP) disease*, also called *idiopathic osteonecrosis of the capital femoral epiphysis*, is one of the most common forms of epiphyseal osteonecrosis. LCP is a classic illustrative example of the clinical course and prognosis related to epiphyseal osteonecrosis at the femoral head and elsewhere. LCP affects boys between 2 and 14 years of age with peak incidence around 5 to 6 years (male/female ratio, 5 : 1). Involvement is bilateral in 10% to 15% of cases, although it is almost always asynchronous.[82] Forms of idiopathic osteonecrosis that affect other bones include but are not limited to Kienböck disease (lunate) (Fig. 141.25), Köhler disease (navicular; Fig. 141.26), and Freiberg infraction (second or third metatarsal head; Fig. 141.27).

For LCP, deformity of the femoral head, neck, and acetabulum is a common cause of degenerative disease of the hip, particularly in men. Children who come to medical attention before 6 years of age generally have a benign course, whereas those who seek care after 8 years of age fare less well and often require surgery.[83]

Children with LCP are typically seen after having had several weeks or months of limping, often without pain. Physical findings include spasm, limitation of abduction and internal rotation, and atrophy of the thigh and buttocks in an otherwise normal child.

***Imaging.*** In acute osteonecrosis, radiographs are usually normal. With subacute and chronic osteonecrosis, radiographs will show geographic and patchy areas of sclerosis (see Fig. 141.11).

During the acute phase of osteonecrosis, MRI findings of marrow hemorrhage, edema, and liquefactive necrosis may be difficult to distinguish from infection and/or superimposed stress reaction. Acute-on-chronic osteonecrosis may occur, and the

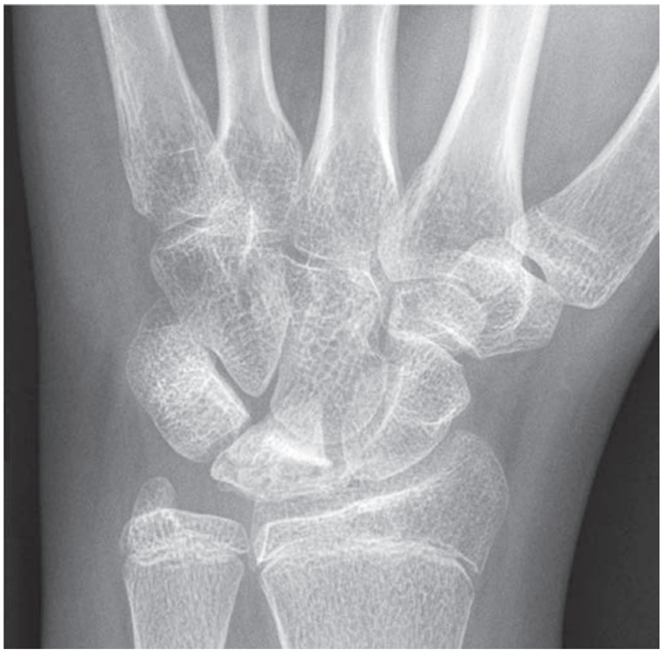

**Figure 141.25.** Fourteen-year-old girl with Keinböck disease with flattening and sclerosis of the lunate bone.

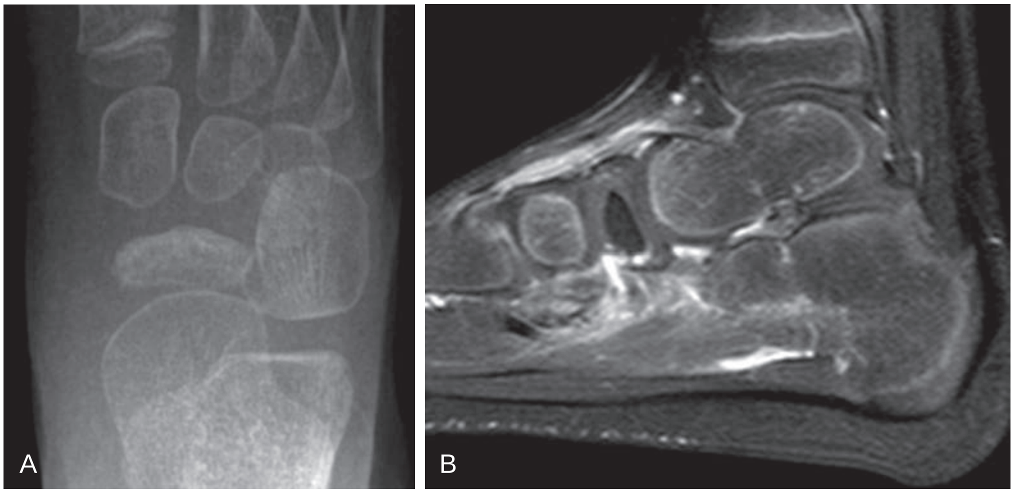

**Figure 141.26. Köhler disease in a 15-year-old girl.** (A) Anteroposterior view of the foot shows sclerosis and mild flattening of the navicular bone. (B) Postcontrast T1-weighted fat-saturated sagittal MR image shows nonenhancement of the navicular bone and soft tissue edema about the dorsal and plantar surface of the midfoot.

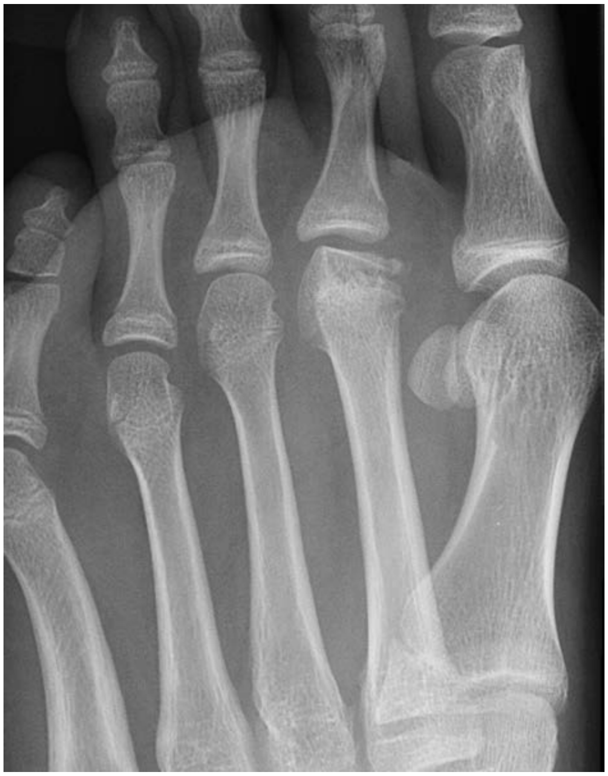

**Figure 141.27. Freiberg infraction in an 11-year-old girl.** Oblique view of the forefoot shows flattening and collapse of the second metatarsal head.

presence of edema and periostitis are helpful clues to identify the acute component (Fig. 141.28). Rarely, this may superficially mimic a neoplastic process. Unfortunately, early infection and superimposed stress reaction may be indistinguishable. During the reparative phase, central fatty marrow replacement usually occurs (Fig. 141.29). Osteonecrosis often has a geographic shape with a serpentine margin of low signal intensity on T1-weighted sequences that often does not respect epiphyseal, metaphyseal, and diaphyseal boundaries of the long bones (see Fig. 141.29). T2-weighted sequences may demonstrate a characteristic “double-line sign” consisting of an outer rim of low signal intensity corresponding to sclerotic bone and an inner rim of high signal intensity corresponding to vascularized granulation tissue (Fig. 141.30). Areas of low signal intensity on both T1- and T2-weighted sequences related to osteonecrosis represent fibrosis or calcification. Fatty marrow infiltration manifested by increased signal intensity on T1-weighted sequences within the area of osteonecrosis is believed to indicate central revascularization (see Fig. 141.29). Intense contrast enhancement is common at the periphery of evolving areas of osteonecrosis, and dynamic contrast-enhanced MRI has been advocated for early diagnosis but probably is not necessary in children with established osteonecrosis. The diagnosis can usually confidently be made on conventional MRI sequences without intravenous contrast.[81]

Imaging findings of epiphyseal osteonecrosis related to other causes are indistinguishable from those of LCP, which progresses through four main stages: (1) avascularity, (2) revascularization, (3) healing, and (4) residual deformity (Fig. 141.31). Early radiographic diagnosis is based on the detection of periarticular osteoporosis, medial joint space widening, lateral displacement of the femoral head, and eventually a relatively smaller and denser appearance of the femoral head.[84,85]

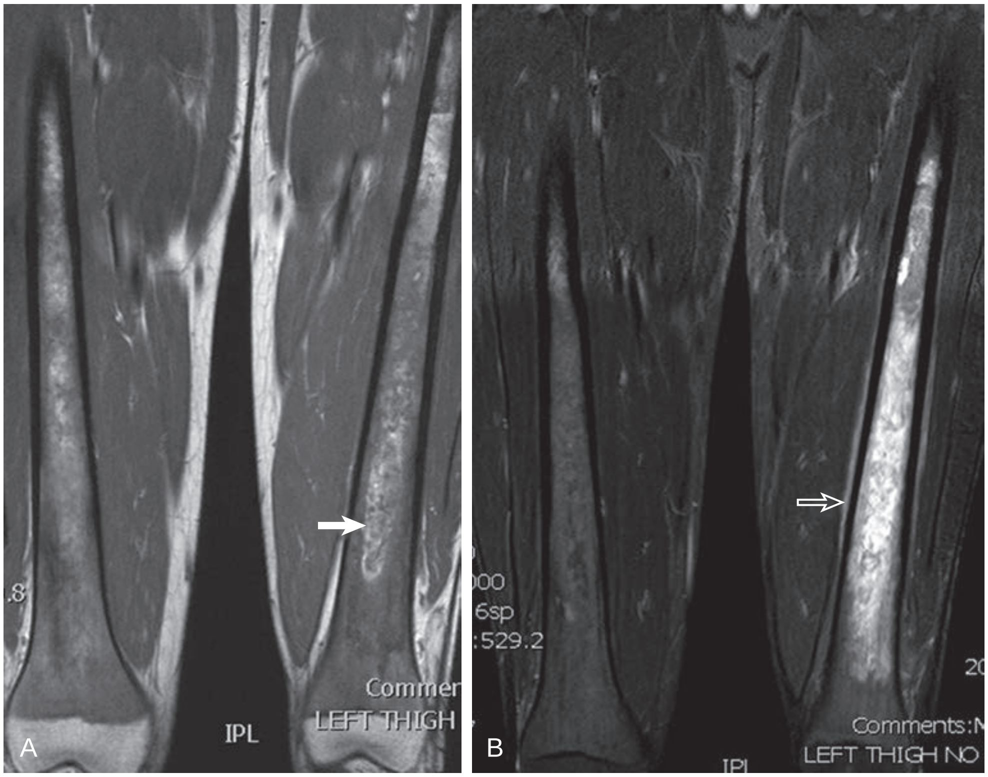

**Figure 141.28. Sickle cell disease with acute bone infarction in a 20-year-old man.** (A) T1-weighted coronal MR image shows diffuse red marrow of the metaphyses and diaphyses. Hyperintense foci are apparent within the medullary cavity *(arrow)*, presumably representing sequestered blood. (B) Short-tau inversion recovery coronal image shows diffuse marrow edema and periostitis *(open arrow)*, consistent with acute bone infarction.

During the revascularization stage, which lasts from 1 to 4 years, surrounding tissues react to the dead bone. In this stage, the child experiences pain, and the most dramatic radiographic changes occur.[86] The ossific nucleus appears even denser because of new bone formation that occurs within the dead trabeculae; it is easily flattened and deformed. A pathologic subchondral fracture in the anterosuperior ossific nucleus creates the radiographic "crescent sign." The epiphyseal ossification center undergoes varying degrees of fragmentation, primarily in its central portion (Fig. 141.32). The adjacent metaphysis sometimes develops cystic changes and broadens. Disturbed endochondral ossification from ischemia probably results in residual cartilage in the metaphysis.[87]

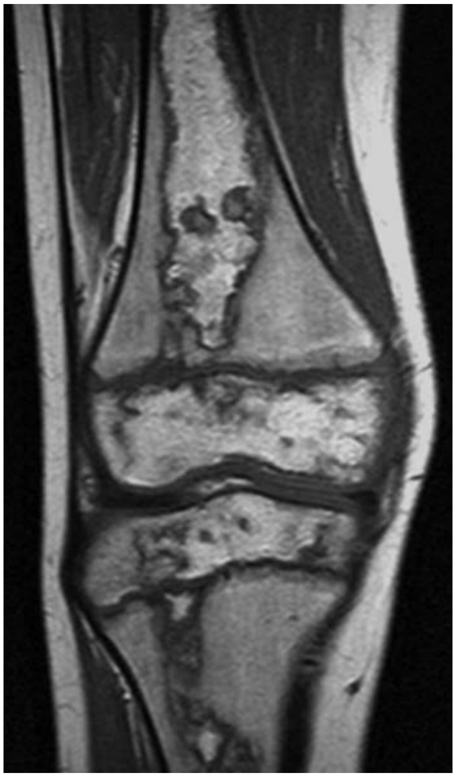

**Figure 141.29. Diffuse osteonecrosis in an 11-year-old boy.** T1-weighted coronal MR image shows diaphyseal, metaphyseal, and epiphyseal involvement of osteonecrosis. Note the central areas of increased signal intensity within the areas of osteonecrosis, consistent with fatty marrow conversion.

During the healing phase, new bone slowly replaces granulation tissue in the ossific nucleus, and the epiphysis regains its height. The better the femoral head is contained by the acetabulum, the more spherically the femoral head will remodel. On MRI performed during the healing phase, the physeal cartilage may exhibit irregularity or bridging. Epiphyseal deformity is more pronounced anteriorly; hence sagittal images are an essential part of the evaluation.

Residual deformity persists after healing, although the articular cartilage is reasonably preserved. As a result, joint function may be satisfactory for several years. Abnormal shape of the healed epiphysis is characterized by *coxa magna*, a residual enlargement of the femoral head and neck, and *coxa breva*, a short femoral neck as a result of premature physeal arrest. Subsequent varus or valgus hip deformity may occur, depending on the location of the physeal fusion. A deformed femoral head, especially with a large anterolateral segment that is uncovered, can impinge on the lateral acetabular lip and cause clinical symptoms of decreased range of motion, pain, and a "clunking" sensation. This joint incongruity leads to labral pathology and degenerative joint disease later in life.

***Treatment.*** Treatment for osteonecrosis is aimed at managing the underlying condition or modifying administration of the causative agent, such as decreasing corticosteroid dosage. Resting the affected joint may help slow disease progression and may prevent complications, including pathologic fractures. Children with osteonecrosis are predisposed to pathologic fractures, and subchondral collapse occurs with epiphyseal osteonecrosis and pathologic long-bone fractures with nonepiphyseal involvement. For epiphyseal osteonecrosis, the most important predictors of patient outcome, aside from age of onset, are joint congruency and motion.

Treatment of LCP is individualized on the basis of clinical and radiographic findings, including age of onset, range of motion in the hip joint, extent of femoral head involvement, presence or absence of femoral deformity, and lateral subluxation of the femoral

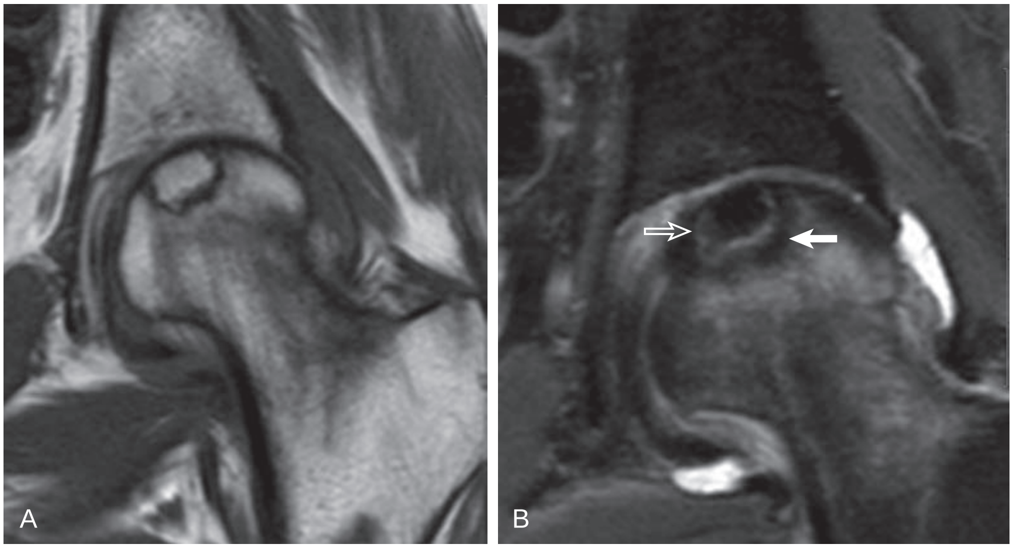

**Figure 141.30. Epiphyseal osteonecrosis of the femoral head in an 18-year-old woman.** T1-weighted (A) and short-tau inversion recovery coronal MR images (B) demonstrate a "double-line sign" with inner white line *(open arrow)* and outer dark line *(solid arrow)*. Note central area of increased T1 signal consistent with fatty marrow replacement.

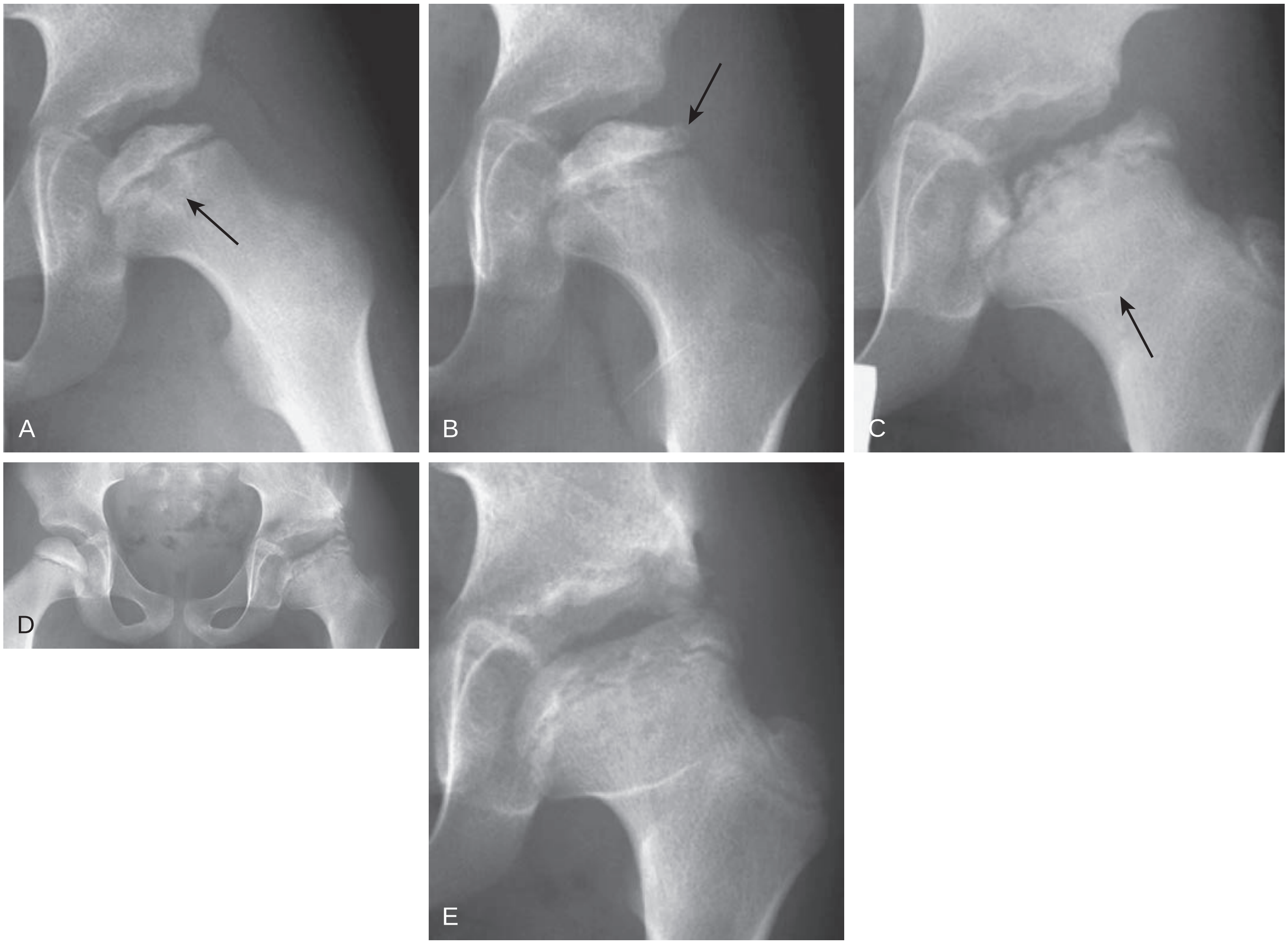

**Figure 141.31. Osteonecrosis of the left proximal femoral epiphysis in a 7-year-old boy with a limp.** (A) Radiograph of the left hip reveals a small, sclerotic proximal femoral epiphysis with an irregular articular surface. The metaphysis of the proximal femur also shows cystic changes *(arrow)*, which indicates a poor prognosis. (B) Radiograph performed 2 months later shows continued sclerosis and flattening. Very early fragmentation of the epiphysis is noted in the lateral pillar *(arrow)*. (C) At 18 months after presentation, a radiograph of the left hip reveals further fragmentation with lateral extrusion of the epiphysis. The acetabulum is beginning to impinge on the portion of the lateral column that is uncovered, and incongruence of the hip joint is apparent. The "sagging rope sign" *(arrow)* is produced by the outline of an abnormally oriented physis, which indicates growth arrest, and widening of the femoral neck (coxa magna) is seen. (D) At 25 months after diagnosis, a left iliac osteotomy is evident, attempting to cover the widened, flattened, left capital femoral epiphysis that is starting to coalesce. Early sclerosis of the right proximal femoral epiphysis indicates early avascular necrosis in the contralateral hip. (E) At 3 years after presentation, the left hip radiograph shows healed Legg-Calvé-Perthes disease with residual flattening, coxa magna, and an irregular acetabulum.

head. For many patients, a combination of traction treatment with an abduction cast, nonsteroidal antiinflammatory agents, and gentle range-of-motion exercises are used to enhance molding of the femoral head by the acetabulum. Surgery is indicated in children younger than 8 years who have femoral head deformity and in those older than 8 years even in the absence of deformity. Because LCP often affects the proximal femoral physeal vertex while preserving normal medial physeal physiology, a relative coxa valga may develop related to vertex physeal growth disturbance. As a consequence, surgical reduction to contain the femoral head is often indicated, including subtrochanteric varus osteotomies with or without congruent periacetabular shelf osteotomies, particularly in older patients (second decade). The main goals of surgical therapy are to preserve joint congruity during the active phase of the disease and to contain the femoral head within the acetabulum, preventing extrusion and subluxation. A femoral head that is contained by the acetabulum tends to heal more spherically than one that is partially subluxed. In severe cases, a vicious cycle ensues in which decreased containment leads to increased deformity that in turn leads to further subluxation. Surgery can prevent this progression and can be used to maintain a full range of motion at the hip joint.[88]

## EFFECTS OF THERAPY

### Hematopoietic Growth Factors

***Etiology, Pathophysiology, and Clinical Presentation.*** Hematopoietic growth factors such as G-CSF, granulocyte macrophage colony-stimulating factor (GM-CSF), and erythropoietin are

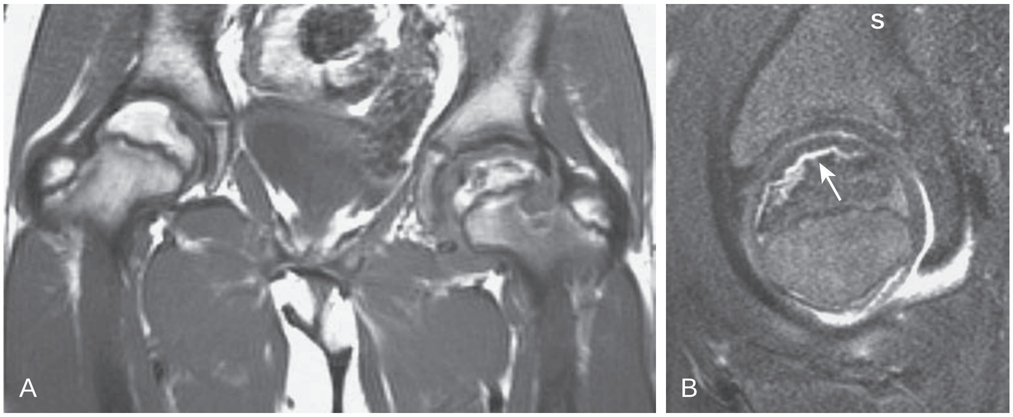

**Figure 141.32. Legg-Calvé-Perthes disease in a 10-year-old boy.** (A) Coronal T1-weighted MR image reveals crescentic low signal in the left proximal femoral epiphysis with irregularity of the articular surface. Epiphyseal height is also decreased. Some normal high signal is present, indicating preserved fat in the epiphysis. The lateral left femoral metaphysis reveals a rounded area of lower signal, indicating cystic changes. Additionally, cartilaginous hypertrophy is evident within the left hip joint that often accounts for apparent radiographic joint space widening. (B) Sagittal T2-weighted fat-saturated MR image shows a hyperintense crescentic fracture *(white arrow)* along the anterior portion of the left femoral epiphysis with an associated joint effusion.

cytokines that regulate the proliferation and differentiation of hematopoietic progenitor cells in the bone marrow.[89,90] Recombinant human hematopoietic growth factors are commonly used to hasten the recovery of hematopoietic marrow from myelosuppressive chemotherapy or bone marrow failure syndromes.

***Imaging.*** In those treated with G-CSF or GM-CSF, MRI will show signal intensity changes associated with reconversion of fatty marrow to hypercellular hematopoietic marrow that coincide temporally with increases in the absolute neutrophil count. These changes may be observed incidentally on routine imaging studies or on imaging studies prompted by bone pain accompanying G-CSF administration.[26] As in other instances of marrow hyperplasia, the imaging changes follow signal intensity similar to that of red marrow. GRE out-of-phase sequences designed to detect altered proportions of fat and water may be the most sensitive for the effects of G-CSF therapy. The peak of hematopoietic marrow hyperplasia observed by MRI occurs about 2 weeks after discontinuation of G-CSF administration, and the bone marrow alterations normalize in most patients within 6 weeks after treatment. The marrow changes may be diffuse, patchy, or have a masslike appearance, and they can be asymmetric and simulate bone marrow involvement by leukemia, metastatic disease, or other infiltrative process.[72] The masslike appearance of red marrow on T1-weighted images may have well-defined margins rather than the wisplike, feathery appearance of residual red marrow (see Fig. 141.5). Marrow changes as a result of G-CSF may not follow the typical red marrow pattern of reconversion seen in patients who are anemic. For instance, diaphyseal red marrow islands may appear before metaphyseal red marrow changes. The changes can also obscure underlying marrow lesions.[91] Masslike marrow replacement owing to G-CSF is usually not associated with juxtacortical soft tissue edema at the same level of the lesion, which is more likely with metastatic marrow replacement. Consideration of the timing of the therapy and imaging is necessary to avoid misinterpretation of the marrow changes (see Fig. 141.7).

Similarly, FDG-PET, $^{99}$mTc sulfur colloid scintigraphy, gallium-67 scintigraphy, and thallium-201 scintigraphy can show elevated radiopharmaceutical uptake by the stimulated hematopoietic marrow (Fig. 141.33). Large interindividual variability is seen in marrow FDG uptake induced by hematopoietic growth factors. FDG marrow uptake returns to normal within 1 month after the discontinuation of G-CSF treatment in most individuals.[91]

The anemia of end-stage renal disease can be treated with recombinant human erythropoietin, which induces an increase in the erythropoietic marrow that manifests as decreased signal intensity on T1-weighted sequences. Erythropoietin also increases the bone marrow uptake of FDG.

## Radiation Therapy

***Etiology, Pathophysiology, and Clinical Presentation.*** In the acute phase, radiation therapy causes depression of the marrow cellularity and vascular sinusoid injury with edema and hemorrhage.[92] In the chronic phase, the vascular sinusoids are obliterated, and hematopoietic marrow is replaced by fat and fibrosis.[93]

The process of fatty marrow replacement is largely irreversible for doses higher than 30 to 40 Gy, because destruction of the vascular sinusoids prevents migration of hematopoietic cells into the irradiated marrow.[6] For doses less than 30 to 40 Gy, the fatty marrow replacement is less complete, and regeneration of the hematopoietic marrow may occur. This regeneration of hematopoietic marrow manifests as a mottled or band pattern in the vertebrae of children between 11 and 30 months after spinal irradiation of doses no greater than 40 Gy, and similar findings have been observed in the marrow of the long bones after irradiation. Marrow regeneration is more likely to occur with larger volumes of irradiated marrow, suggesting that partial spinal irradiation may not provide enough stimulation to induce regeneration, because the nonirradiated marrow is sufficient to meet hematopoietic demands.

***Imaging.*** STIR sequences are the most sensitive conventional MRI technique for depicting early postradiation changes in the marrow, and they can detect the effects of radiation therapy within a few days after initiation of treatment.[6] Areas of increased signal intensity in the marrow on STIR sequences peak 9 days after therapy and reflect edema, hemorrhage, and early influx of nonirradiated cells.[4,26,91] T1-weighted sequences in the acute phase show a corresponding decrease in the signal intensity of the bone marrow and a corresponding increased signal intensity on STIR sequences indicative of marrow edema. From 2 to 6 weeks after irradiation, the signal intensity of the bone marrow begins to increase on T1-weighted sequences and decrease on STIR sequences (Fig. 141.34).[91] After 6 weeks, the marrow pattern either becomes more homogeneous, with high signal intensity on T1-weighted sequences

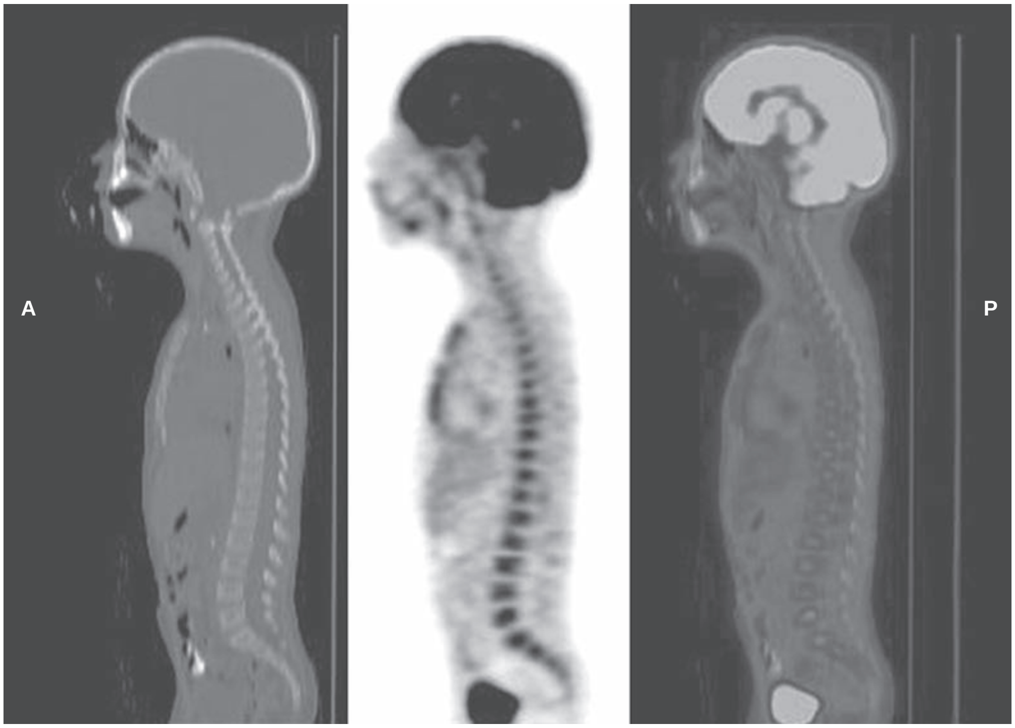

**Figure 141.33. Fluorodeoxyglucose positron-emission tomography (FDG-PET) and computed tomographic images of a 4-year-old boy on granulocyte-colony stimulating factor therapy to mitigate the myelosuppressive effects of Wilms tumor treatment.** Diffuse increased uptake of FDG by the bone marrow of the spine and sternum reflects the increased metabolic demand from stimulation of granulopoiesis in the marrow. *(Courtesy Dr. Barry Shulkin, St. Jude Children's Research Hospital, Memphis, TN.)*

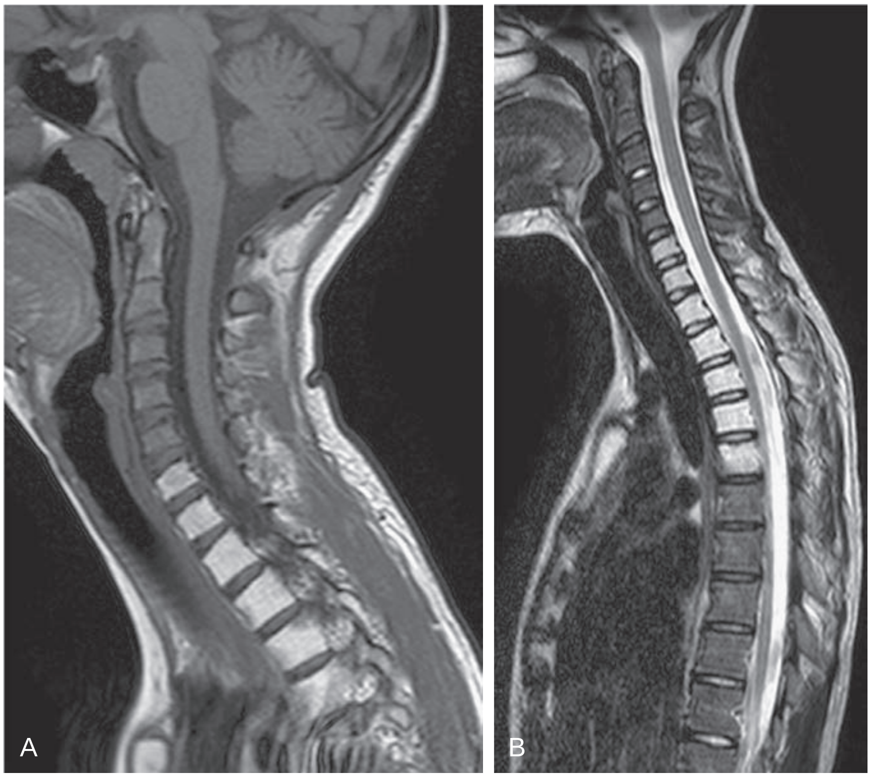

**Figure 141.34. Fifteen-year-old girl with a history of local radiation therapy for an extraosseous Ewing sarcoma in the left supraclavicular region.** Sagittal T1-weighted (A) and turbo spin echo T2-weighted (B) MR imaging of the upper spine reveals sharply demarcated, homogeneous high signal intensity of the marrow of the lower cervical spine, upper thoracic spine, and upper sternum that corresponds to fatty transformation of the marrow within the irradiated field.

and low signal intensity on STIR sequences, or it develops a band pattern of peripheral intermediate signal intensity surrounding central high signal intensity on T1-weighted sequences and produces reciprocal changes on STIR sequences.[91] In the chronic phase, the marrow also shows a marked decrease in contrast enhancement, reflecting vascular obliteration.[26,92] Additional late changes after radiation therapy include osteonecrosis and radiation-induced osteochondromas.[26]

## Bone Marrow Transplantation

***Etiology, Pathophysiology, and Clinical Presentation.*** Bone marrow transplantation is used in the treatment of numerous pediatric malignancies, as well as severe aplastic anemia, hereditary hemoglobinopathies, inborn errors of metabolism, and certain immunodeficiency and autoimmune syndromes. In preparation for bone marrow transplantation, the host marrow is ablated and conditioned by chemotherapy and possibly also by fractionated total-body irradiation to induce immune suppression and eliminate residual malignant cells, if applicable. Stem cells are then infused intravenously and engraft in the marrow within 2 to 4 weeks. Typical fatty and hematopoietic bone marrow is usually seen within 90 days after transplantation.[4]

***Imaging.*** In the interval after bone marrow transplantation, until the recovery of hematopoiesis, hematopoietic growth factors and multiple blood transfusions may be given, and the appearance of the marrow on MRI during this time will reflect the combined effects of marrow necrosis, early hematopoietic reconstitution, and possibly iron overload.[94,95]

Within 40 to 90 days after transplantation, a band pattern in the vertebral bodies may develop, consisting of a peripheral zone of intermediate signal intensity and a central zone of high signal intensity on T1-weighted sequences with reciprocal signal intensities on STIR sequences.[94] This pattern corresponds to regenerating hematopoietic marrow peripherally and fatty marrow centrally. The band pattern may gradually evolve into a more homogeneous appearance.[6] However, the hematopoietic marrow recovery after bone marrow transplantation may not achieve full reconstitution, corroborated by the observation that the fat fraction in the vertebral and pelvic marrow determined by chemical-shift MRI is higher in transplanted patients for several years after transplantation.[26]

### KEY POINTS

- MRI is the primary imaging modality for evaluating bone marrow. A combination of T1-weighted and fat-saturated T2-weighted or STIR sequences are sufficient for the detection and characterization of most marrow lesions. Contrast-enhanced MRI is reserved for when findings are unclear on precontrast images.
- Conversion from hematopoietic to fatty marrow in the axial skeleton occurs in a distal-to-proximal direction and from diaphyses to metaphyses in the long bones. Fatty conversion in the epiphyses and apophyses begins soon after ossification, and marrow reconversion occurs in the reverse order of marrow conversion.
- The MRI appearance of marrow in thalassemia and sickle cell disease reflects the combined effects of red marrow hyperplasia, iron deposition, iron chelation therapy, and in the case of sickle cell disease, medullary infarcts. Acute medullary infarcts are often indistinguishable from acute osteomyelitis on MRI.
- Treatment-related marrow changes, particularly with hematopoietic growth factors, cause bone marrow changes that can simulate involvement by leukemia, metastatic disease, and other infiltrative processes. Knowledge of the timing of therapy and imaging is necessary for accurate image interpretation.

### SUGGESTED READING

Burdiles A, Babyn PS. Pediatric bone marrow MR imaging. *Magn Reson Imaging Clin N Am*. 2009;17(3):391–409.
Fletcher BD. Effects of pediatric cancer therapy on the musculoskeletal system. *Pediatr Radiol*. 1997;27(8):623–636.
Foster K, Chapman S, Johnson K. MRI of the marrow in the paediatric skeleton. *Clin Radiol*. 2004;59(8):651–673.
Jaramillo D, Kasser JR, Villegas-Medina OL, et al. Cartilaginous abnormalities and growth disturbances in Legg-Calvé-Perthes disease: evaluation with MR imaging. *Radiology*. 1995;197(3):767–773.
Saini A, Saifuddin A. MRI of osteonecrosis. *Clin Radiol*. 2004;59(12):1079–1093.

### REFERENCES

Full references for this chapter can be found on www.expertconsult.com.

## REFERENCES

1. Vande Berg BC, Malghem J, Lecouvet FE, et al. Magnetic resonance imaging of normal bone marrow. *Eur Radiol*. 1998;8(8):1327–1334.
2. Richardson ML, Patten RM. Age-related changes in marrow distribution in the shoulder: MR imaging findings. *Radiology*. 1994;192(1):209–215.
3. Okada Y, Aoki S, Barkovich AJ, et al. Cranial bone marrow in children: assessment of normal development with MR imaging. *Radiology*. 1989;171(1):161–164.
4. Foster K, Chapman S, Johnson K. MRI of the marrow in the paediatric skeleton. *Clin Radiol*. 2004;59(8):651–673.
5. Moore SG, Dawson KL. Red and yellow marrow in the femur: age-related changes in appearance at MR imaging. *Radiology*. 1990;175(1):219–223.
6. Moulopoulos LA, Dimopoulos MA. Magnetic resonance imaging of the bone marrow in hematologic malignancies. *Blood*. 1997;90(6):2127–2147.
7. Baur A, Stabler A, Bartl R, et al. MRI gadolinium enhancement of bone marrow: age-related changes in normals and in diffuse neoplastic infiltration. *Skeletal Radiol*. 1997;26(7):414–418.
8. Dwek JR, Shapiro F, Laor T, et al. Normal gadolinium-enhanced MR images of the developing appendicular skeleton: part 2. Epiphyseal and metaphyseal marrow. *AJR Am J Roentgenol*. 1997;169(1):191–196.
9. Mirowitz SA, Apicella P, Reinus WR, et al. MR imaging of bone marrow lesions: relative conspicuousness on T1-weighted, fat-suppressed T2-weighted, and STIR images. *AJR Am J Roentgenol*. 1994;162(1):215–221.
10. Winfeld M, Ahlawat S, Safdar N. Utilization of chemical shift MRI in the diagnosis of disorders affecting pediatric bone marrow. *Skeletal Radiol*. 2016;45:1205–1212.
11. Ghanem N, Uhl M, Brink I, et al. Diagnostic value of MRI in comparison to scintigraphy, PET, MS-CT and PET/CT for the detection of metastases of bone. *Eur J Radiol*. 2005;55(1):41–55.
12. Schmidt GP, Schoenberg SO, Reiser MF, et al. Whole-body MR imaging of bone marrow. *Eur J Radiol*. 2005;55(1):33–40.
13. Schmidt GP, Reiser MF, Baur-Melnyk A. Whole-body imaging of bone marrow. *Semin Musculoskelet Radiol*. 2009;13(2):120–133.
14. Goo HW, Choi SH, Ghim T, et al. Whole-body MRI of paediatric malignant tumours: comparison with conventional oncological imaging methods. *Pediatr Radiol*. 2005;35(8):766–773.
15. Jaramillo D. Whole-body MR imaging, bone diffusion imaging: How and why? *Pediatr Radiol*. 2010;40(6):978–984.
16. Kwee TC, Takahara T, Vermoolen MA, et al. Whole-body diffusion-weighted imaging for staging malignant lymphoma in children. *Pediatr Radiol*. 2010;40(10):1592–1602, quiz 1720-1591.
17. Raya JG, Dietrich O, Reiser MF, et al. Techniques for diffusion-weighted imaging of bone marrow. *Eur J Radiol*. 2005;55(1):64–73.
18. Nonomura Y, Yasumoto M, Yoshimura R, et al. Relationship between bone marrow cellularity and apparent diffusion coefficient. *J Magn Reson Imaging*. 2001;13(5):757–760.
19. Herneth AM, Friedrich K, Weidekamm C, et al. Diffusion weighted imaging of bone marrow pathologies. *Eur J Radiol*. 2005;55(1):74–83.
20. Daldrup-Link HE, Franzius C, Link TM, et al. Whole-body MR imaging for detection of bone metastases in children and young adults: comparison with skeletal scintigraphy and FDG PET. *AJR Am J Roentgenol*. 2001;177(1):229–236.
21. Fritz J, Tzaribatchev N, Claussen CD, et al. Chronic recurrent multifocal osteomyelitis: comparison of whole-body MR imaging with radiography and correlation with clinical and laboratory data. *Radiology*. 2009;252(3):842–851.
22. Goo HW, Yang DH, Ra YS, et al. Whole-body MRI of Langerhans cell histiocytosis: comparison with radiography and bone scintigraphy. *Pediatr Radiol*. 2006;36(10):1019–1031.
23. Mayani H, Alvarado-Moreno JA, Flores-Guzman PF. Biology of human hematopoietic stem and progenitor cells present in circulation. *Arch Med Res*. 2003;34:476–488.
24. Ricci C, Cova M, Kang YS, et al. Normal age-related patterns of cellular and fatty bone marrow distribution in the axial skeleton: MR imaging study. *Radiology*. 1990;177(1):83–88.
25. Waitches G, Zawin JK, Poznanski AK. Sequence and rate of bone marrow conversion in the femora of children as seen on MR imaging: Are accepted standards accurate? *AJR Am J Roentgenol*. 1994;162(6):1399–1406.
26. Fletcher BD. Effects of pediatric cancer therapy on the musculoskeletal system. *Pediatr Radiol*. 1997;27(8):623–636.
27. Jaramillo D, Laor T, Hoffer FA, et al. Epiphyseal marrow in infancy: MR imaging. *Radiology*. 1991;180(3):809–812.
28. Zawin JK, Jaramillo D. Conversion of bone marrow in the humerus, sternum, and clavicle: changes with age on MR images. *Radiology*. 1993;188(1):159–164.
29. Mirowitz SA. Hematopoietic bone marrow within the proximal humeral epiphysis in normal adults: investigation with MR imaging. *Radiology*. 1993;188(3):689–693.
30. Shabshin N, Schweitzer ME, Morrison WB, et al. High-signal T2 changes of the bone marrow of the foot and ankle in children: red marrow or traumatic changes? *Pediatr Radiol*. 2006;36(7):670–676.
31. Dawson KL, Moore SG, Rowland JM. Age-related marrow changes in the pelvis: MR and anatomic findings. *Radiology*. 1992;183(1):47–51.
32. Sebag GH, Dubois J, Tabet M, et al. Pediatric spinal bone marrow: assessment of normal age-related changes in the MRI appearance. *Pediatr Radiol*. 1993;23(7):515–518.
33. Simonson TM, Kao SC. Normal childhood developmental patterns in skull bone marrow by MR imaging. *Pediatr Radiol*. 1992;22(8):556–559.
34. Nobauer I, Uffmann M. Differential diagnosis of focal and diffuse neoplastic diseases of bone marrow in MRI. *Eur J Radiol*. 2005;55(1):2–32.
35. Kan JH, Hernanz-Schulman M, Frangoul HA, et al. MRI diagnosis of bone marrow relapse in children with ALL. *Pediatr Radiol*. 2008;38:76–81.
36. Elstrom RL, Tsai DE, Vergilio JA, et al. Enhanced marrow [18F] fluorodeoxyglucose uptake related to myeloid hyperplasia in Hodgkin's lymphoma can simulate lymphoma involvement in marrow. *Clin Lymphoma*. 2004;5:62–64.
37. Haidar R, Musallam KM, Taher AT. Bone disease and skeletal complications in patients with beta thalassemia major. *Bone*. 2011;48:425–432.
38. Tyler PA, Madani G, Chaudhuri R, et al. The radiological appearances of thalassaemia. *Clin Radiol*. 2006;61:40–52.
39. Levin TL, Sheth SS, Ruzal-Shapiro C, et al. MRI marrow observations in thalassemia: the effects of the primary disease, transfusional therapy, and chelation. *Pediatr Radiol*. 1995;25(8):607–613.
40. Papakonstantinou O, Alexopoulou E, Economopoulos N, et al. Assessment of iron distribution between liver, spleen, pancreas, bone marrow, and myocardium by means of R2 relaxometry with MRI in patients with beta-thalassemia major. *J Magn Reson Imaging*. 2009;29: 853–859.
41. Aflalo-Hazan V, Gutman F, Kerrou K, et al. Increased FDG uptake by bone marrow in major beta-thalassemia. *Clin Nucl Med*. 2005;30(11):754–755.
42. Manci EA, Culberson DE, Gardner JM, et al. Perivascular fibrosis in the bone marrow in sickle cell disease. *Arch Pathol Lab Med*. 2004;128(6):634–639.
43. Mankad VN, Williams JP, Harpen MD, et al. Magnetic resonance imaging of bone marrow in sickle cell disease: clinical, hematologic, and pathologic correlations. *Blood*. 1990;75(1):274–283.
44. Ejindu VC, Hine AL, Mashayekhi M, et al. Musculoskeletal manifestations of sickle cell disease. *Radiographics*. 2007;27:1005–1021.
45. Bonnerot V, Sebag G, de Montalembert M, et al. Gadolinium-DOTA enhanced MRI of painful osseous crises in children with sickle cell anemia. *Pediatr Radiol*. 1994;24(2):92–95.
46. Jain R, Sawhney S, Rizvi SG. Acute bone crises in sickle cell disease: the T1 fat-saturated sequence in differentiation of acute bone infarcts from acute osteomyelitis. *Clin Radiol*. 2008;63(1):59–70.
47. Delgado J, Bedoya MA, Green AM, et al. Utility of unenhanced fat-suppressed T1-weighted MRI in children with sickle cell disease – can it differentiate bone infarcts from acute osteomyelitis? *Pediatr Radiol*. 2015;45:1981–1987.
48. Field JJ, Knight-Perry JE, Debaun MR. Acute pain in children and adults with sickle cell disease: management in the absence of evidence-based guidelines. *Curr Opin Hematol*. 2009;16:173–178.
49. Scherer A, Engelbrecht V, Neises G, et al. MR imaging of bone marrow in glycogen storage disease type IB in children and young adults. *AJR Am J Roentgenol*. 2001;177(2):421–425.
50. Preger L, Sanders GW, Gold RH, et al. Roentgenographic skeletal changes in the glycogen storage diseases. *Am J Roentgenol Radium Ther Nucl Med*. 1969;107(4):840–847.
51. Miller JH, Stanley P, Gates GF. Radiography of glycogen storage diseases. *AJR Am J Roentgenol*. 1979;132(3):379–387.
52. Bali DS, Chen YT, Goldstein JL. Glycogen storage disease type I. *GeneReviews*. 2006.
53. Wenstrup RJ, Roca-Espiau M, Weinreb NJ, et al. Skeletal aspects of Gaucher disease: a review. *Br J Radiol*. 2002;75(suppl 1):A2–A12.
54. Katz R, Booth T, Hargunani R, et al. Radiological aspects of Gaucher disease. *Skeletal Radiol*. 2011;40(12):1505–1513.

55. Maas M, Poll LW, Terk MR. Imaging and quantifying skeletal involvement in Gaucher disease. *Br J Radiol*. 2002;75(suppl 1):A13–A24.
56. Allison JW, James CA, Arnold GL, et al. Reconversion of bone marrow in Gaucher disease treated with enzyme therapy documented by MR. *Pediatr Radiol*. 1998;28(4):237–240.
57. Jaramillo D, Bedoya MA, Wang DJ, et al. Quantification of bone marrow involvement in treated gaucher disease with proton MR spectroscopy: correlation with bone marrow mri scores and clinical status. *AJR Am J Roentgenol*. 2015;204:1296–1302.
58. Fedida B, Touraine S, Stirnemann J, et al. Bone marrow involvement in Gaucher disease at MRI: What long-term evolution can we expect under enzyme replacement therapy? *Eur Radiol*. 2015;25:2969–2975.
59. Guillerman RP, Voss SD, Parker BR. Leukemia and lymphoma. *Radiol Clin North Am*. 2011;49(4):767–797, vii.
60. Greaves M. In utero origins of childhood leukaemia. *Early Hum Dev*. 2005;81(1):123–129.
61. Altekruse SF, Kosary CL, Krapcho M. *SEER cancer statistics review, 1975–2007*, National Cancer Institute. Bethesda (MD), based on November 2009 SEER data submission, posted to the SEER Web site, 2010. Available at: http://seer.cancer.gov/csr/1975_2007/. Accessed September 7, 2010.
62. Dainiak N. Hematologic consequences of exposure to ionizing radiation. *Exp Hematol*. 2002;30(6):513–528.
63. Pearce MS, Salotti JA, Little MP, et al. Radiation exposure from CT scans in childhood and subsequent risk of leukaemia and brain tumours: a retrospective cohort study. *Lancet*. 2012;380:499–505.
64. Moore SG, Gooding CA, Brasch RC, et al. Bone marrow in children with acute lymphocytic leukemia: MR relaxation times. *Radiology*. 1986;160(1):237–240.
65. Jensen KE, Thomsen C, Henriksen O, et al. Changes in T1 relaxation processes in the bone marrow following treatment in children with acute lymphoblastic leukemia. A magnetic resonance imaging study. *Pediatr Radiol*. 1990;20(6):464–468.
66. Vande Berg BC, Michaux L, Scheiff JM, et al. Sequential quantitative MR analysis of bone marrow: differences during treatment of lymphoid versus myeloid leukemia. *Radiology*. 1996;201(2):519–523.
67. Takagi S, Tanaka O, Miura Y. Magnetic resonance imaging of femoral marrow in patients with myelodysplastic syndromes or leukemia. *Blood*. 1995;86(1):316–322.
68. Sinigaglia R, Gigante C, Bisinella G, et al. Musculoskeletal manifestations in pediatric acute leukemia. *J Pediatr Orthop*. 2008;28:20–28.
69. Vora A. Management of osteonecrosis in children and young adults with acute lymphoblastic leukaemia. *Br J Haematol*. 2011;155(5):549–560.
70. Rayar MS, Nayiager T, Webber CE, et al. Predictors of bony morbidity in children with acute lymphoblastic leukemia. *Pediatr Blood Cancer*. 2012;59(1):77–82.
71. Kan JH, Hernanz-Schulman M, Frangoul HA, et al. MRI diagnosis of bone marrow relapse in children with ALL. *Pediatr Radiol*. 2008;38(1):76–81.
72. Fletcher BD, Wall JE, Hanna SL. Effect of hematopoietic growth factors on MR images of bone marrow in children undergoing chemotherapy. *Radiology*. 1993;189(3):745–751.
73. Vande Berg BC, Lecouvet FE, Michaux L, et al. Magnetic resonance imaging of the bone marrow in hematological malignancies. *Eur Radiol*. 1998;8(8):1335–1344.
74. Benz-Bohm G, Gross-Fengels W, Bohndorf K, et al. MRI of the knee region in leukemic children. Part II. Follow up: responder, non-responder, relapse. *Pediatr Radiol*. 1990;20(4):272–276.
75. Miles RR, Arnold S, Cairo MS. Risk factors and treatment of childhood and adolescent Burkitt lymphoma/leukaemia. *Br J Haematol*. 2012;156(6):730–743.
76. Krishnan A, Shirkhoda A, Tehranzadeh J, et al. Primary bone lymphoma: radiographic-MR imaging correlation. *Radiographics*. 2003;23(6):1371–1383, 1384-1377.
77. Mulligan ME, McRae GA, Murphey MD. Imaging features of primary lymphoma of bone. *AJR Am J Roentgenol*. 1999;173(6):1691–1697.
78. Even-Sapir E. Imaging of malignant bone involvement by morphologic, scintigraphic, and hybrid modalities. *J Nucl Med*. 2005;46(8):1356–1367.
79. Cortés-Romera M, Sabaté-Llobera A, Mercadal-Vilchez S, et al. Bone marrow evaluation in initial staging of lymphoma: 18F-FDG PET/CT versus bone marrow biopsy. *Clin Nucl Med*. 2014;39:e46–e52.
80. Beal K, Allen L, Yahalom J. Primary bone lymphoma: treatment results and prognostic factors with long-term follow-up of 82 patients. *Cancer*. 2006;106(12):2652–2656.
81. Saini A, Saifuddin A. MRI of osteonecrosis. *Clin Radiol*. 2004;59(12):1079–1093.
82. Barker DJ, Hall AJ. The epidemiology of Perthes' disease. *Clin Orthop Relat Res*. 1986;209:89–94.
83. Wiig O, Terjesen T, Svenningsen S, et al. The epidemiology and aetiology of Perthes' disease in Norway. A nationwide study of 425 patients. *J Bone Joint Surg Br*. 2006;88(9):1217–1223.
84. Caffey J. The early roentgenographic changes in essential coxa plana: their significance in pathogenesis. *Am J Roentgenol Radium Ther Nucl Med*. 1968;103(3):620–634.
85. Jaramillo D, Galen TA, Winalski CS, et al. Legg-Calve-Perthes disease: MR imaging evaluation during manual positioning of the hip—comparison with conventional arthrography. *Radiology*. 1999;212(2):519–525.
86. Frick SL. Evaluation of the child who has hip pain. *Orthop Clin North Am*. 2006;37(2):133–140, v.
87. Jaramillo D, Kasser JR, Villegas-Medina OL, et al. Cartilaginous abnormalities and growth disturbances in Legg-Calve-Perthes disease: evaluation with MR imaging. *Radiology*. 1995;197(3):767–773.
88. Herring JA, Kim HT, Browne R. Legg-Calve-Perthes disease. Part II: prospective multicenter study of the effect of treatment on outcome. *J Bone Joint Surg Am*. 2004;86-A(10):2121–2134.
89. van de Laar L, Coffer PJ, Woltman AM. Regulation of dendritic cell development by GM-CSF: molecular control and implications for immune homeostasis and therapy. *Blood*. 2012;119:3383–3393.
90. Held TK, Gundert-Remy U. Pharmacodynamic effects of haematopoietic cytokines: the view of a clinical oncologist. *Basic Clin Pharmacol Toxicol*. 2010;106:210–214.
91. Kazama T, Swanston N, Podoloff DA, et al. Effect of colony-stimulating factor and conventional- or high-dose chemotherapy on FDG uptake in bone marrow. *Eur J Nucl Med Mol Imaging*. 2005;32(12):1406–1411.
92. Otake S, Mayr NA, Ueda T, et al. Radiation-induced changes in MR signal intensity and contrast enhancement of lumbosacral vertebrae: Do changes occur only inside the radiation therapy field? *Radiology*. 2002;222(1):179–183.
93. Stevens SK, Moore SG, Kaplan ID. Early and late bone-marrow changes after irradiation: MR evaluation. *AJR Am J Roentgenol*. 1990;154(4):745–750.
94. Stevens SK, Moore SG, Amylon MD. Repopulation of marrow after transplantation: MR imaging with pathologic correlation. *Radiology*. 1990;175(1):213–218.
95. Kornreich L, Horev G, Yaniv I, et al. Iron overload following bone marrow transplantation in children: MR findings. *Pediatr Radiol*. 1997;27(11):869–872.

# 142

# Skeletal Trauma

Deepa R. Pai and Peter J. Strouse

## GENERAL OVERVIEW

The dictum "Children are not small adults" is especially true regarding skeletal trauma. Fracture patterns, fracture healing, and fracture complications differ between children and adults.[1,2] Fortunately, fracture complications are relatively uncommon. In healthy children, the process of fracture healing and remodeling is rapid, particularly in the vascularized metaphysis.[3] Most posttraumatic deformities readily correct with healing and remodeling.[1,2] The composition of a child's bones and the presence of the growth process both predispose children to types and complications of fractures that are different from those seen in adults.[1,2,4]

## GENERAL ETIOLOGIES, PATHOPHYSIOLOGY, AND CLINICAL PRESENTATION (MECHANISM, HEALING, COMPLICATIONS)

***Mechanism.*** Falls, injuries at play, and motor vehicle accidents account for a majority of childhood fractures.[5] Unfortunately, children may suffer fractures as a consequence of nonaccidental trauma (child abuse). These injuries may have characteristic patterns and are covered in Chapter 143. Children are increasingly involved in athletics and competitive sports. Certain types of injuries, including stress injuries, are often associated with sporting activities (see Chapter 144). Pathologic fractures may be seen with underlying bone tumors, and insufficiency fractures may be seen with metabolic bone disease (see Chapters 138 and 139).

***Fracture Description and Nomenclature.*** Understanding basic fracture nomenclature is important for effective communication. Fractures are subdivided into two basic categories: (1) incomplete (plastic) and (2) complete. Incomplete fractures include *greenstick* and *buckle* fractures. Complete fractures should be described based on orientation: *transverse*, *oblique*, *longitudinal*, and *spiral*. Spiral fractures are defined by an approximately 180-degree or greater twist in the fracture plane. For any fracture, angulation, displacement, diastasis, comminution, and impaction must be described. On follow-up radiographs, any change, in addition to the presence or absence of fracture healing, should be described. Involvement of an open physis and articular surface also should be described. For physeal fractures, it is acceptable to describe the fracture using the Salter-Harris classification.

***Fracture Healing.*** Fracture healing in children has been described in three phases: (1) inflammatory, (2) reparative, and (3) remodeling (e-Fig. 142.1).[6] At the time of fracture, bone and periosteum are disrupted. An inflammatory response is initiated (inflammatory phase), and the organization of a hematoma begins. Bone resorption occurs at areas of necrosis.[7] This peaks 2 to 3 weeks after injury and appears as a poorly defined fracture line.[8] Initial callus is formed during the reparative phase.[6] Callus forming within the hematoma envelops the fracture fragments, joining and stabilizing them. Endosteal callus also forms within the fracture fragments and is seen as increased density on radiographs. Devitalized portions of bone at the margin of the fracture fragments may undergo resorption and appear demineralized on radiographs. An injury that is less than 5 to 7 days old will not show any of these described radiographic features.[7] In time, the woven bone of callus is replaced by organized lamellar bone during the remodeling phase. Remodeling lasts months and occasionally years.[6,7] The healing process is more rapid and complete in children than in adults. Most childhood fractures heal completely and without residual deformity.

***Complications.*** Complications may occur at the time of fracture, during treatment, or as a failure of normal, complete fracture healing. Box 142.1 lists potential complications of pediatric fractures. The incidence of a particular complication varies, depending on many factors, including the site and severity of the fracture, complicating factors (i.e., open fracture), the age and overall health of the patient, associated injuries, and the adequacy of therapy.[9]

In *nonunion*, healing stops before osseous continuity of the fracture fragments occurs. The fracture fragments may form a pseudoarthrosis. Pseudoarthrosis is most common in the clavicle, humerus, and tibia. Nonunion and pseudoarthroses are uncommon in normal children but may be seen with underlying abnormalities such as neurofibromatosis or congenital insensitivity to pain.[10,11] Nonunion is suggested when there is lack of progression to union greater than 6 months after injury when there are corresponding clinical signs and symptoms. The incidence of nonunion is increased with greater injury, comminution, and distraction, and with open fractures complicated by substantial soft tissue injury, infection, or both.[11] Mild degrees of malalignment are well tolerated and usually result in no permanent deformity and resolve over time because of remodeling. Surgical interruption of the healing process to correct residual malalignment is occasionally necessary. Posttraumatic synostoses are most common in the paired bones of the forearm and leg. Infection may occur due to an open fracture or as a complication of surgery or percutaneous pinning.[11]

Fracture at certain sites may result in neurovascular injury; however, such injuries are rare and usually only seen with substantial displacement and deformity, as may occur with supracondylar fractures of the distal humerus.[9] Compartment syndrome is an uncommon complication of extremity fractures, most commonly in the leg or with supracondylar elbow fractures, and may lead to Volkmann contracture caused by ischemia.[9]

Premature fusion occurs in approximately 15% of physeal fractures.[12] A bony "bridge" or "bar" forms across the physis.[13] Prognosis depends on the involved bone, the extent and location of the physeal bar (central versus eccentric), and the amount of remaining growth.[11,12] Morbidity is greater when the remaining growth potential is higher. The phalanges and distal radius are the most common sites of physeal fracture; however, growth arrest is rare in these locations.[12] The distal femur and proximal tibia have a high incidence of posttraumatic physeal fusion but are less common sites for physeal fracture.[12] Premature fusion in the distal femur and tibia is also of greater clinical importance because of possible resultant leg length discrepancy or angular deformity.[12] Indirect physeal insult such as burns, frostbite, and electrical injury, which are discussed later in this chapter, and other processes such as infection, ischemic insult, metabolic bone disease, and iatrogenic causes can also lead to premature physeal fusion (Box 142.2).

Central fusions cause longitudinal growth disturbances. Central fusions can result in a cupped appearance of the physis, with the epiphysis and physis invaginating into the center of the metaphysis

## Abstract:

Fracture patterns, fracture healing, and fracture complications differ between children and adults. Fracture complications are relatively uncommon in healthy children, in whom traumatic deformities typically heal and remodel rapidly. However, the presence of growth processes both predisposes children to types and complications of fractures that are seen in adults. This chapter reviews the imaging of skeletal trauma in children.

## Keywords:

pediatric
skeletal trauma
fractures
physeal bar
growth disturbance
malunion
nonunion

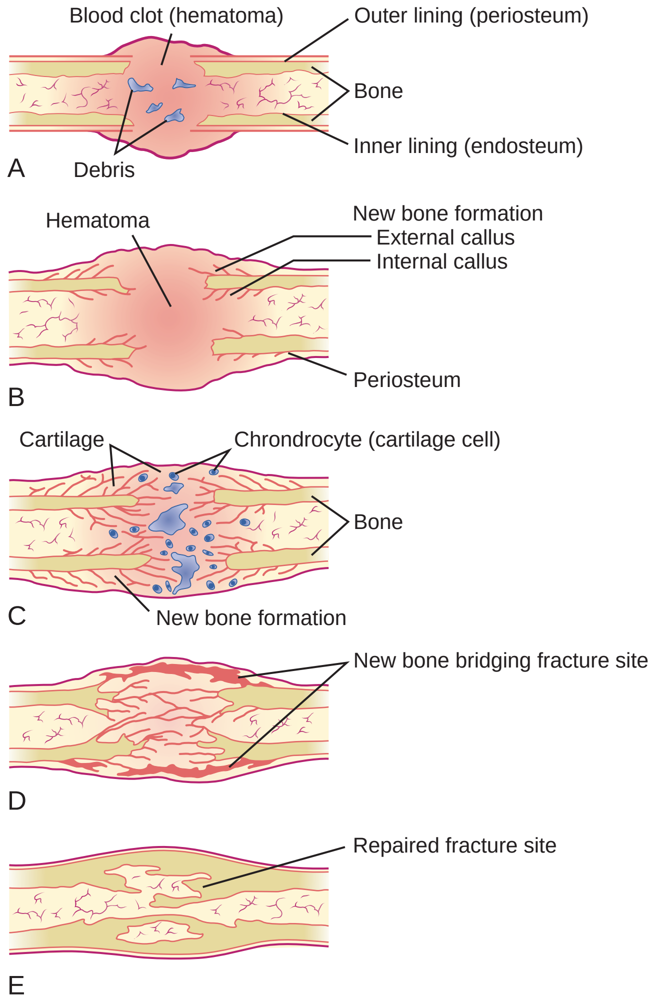

**e-Figure 142.1. Stages of fracture healing.** (A) Hematoma under the periosteum surrounding the fracture, communicating through the fracture with blood clot within the medullary cavity. (B) Subperiosteal and endosteal cellular proliferation encroaching on the hematoma. Islands of cartilage may be present. Bone at the margins of the fracture has been devitalized. (C) Fibroblasts, chondroblasts, and osteoblasts are all present at different stages replacing the hematoma with their characteristic extracellular matrix. Callus formation continues from osteoblastic cells in the proliferating cellular masses. The intracellular substance becomes calcified to form woven bone. The dead bone at the margins of the fracture undergoes resorption. (D) Replacement of woven bone by lamellar bone with bone continuity across the fractured area. (E) Remodeling. Cortical bone is organized to conform to the cortex. Resorption of excess bone results in recanalization of the medullary cavity. *(From Bleck EE, Nagel DA.* Physically Handicapped Children*. New York: Grune & Stratton; 1982.)*

### **BOX 142.1** Complications of Fracture

**ACUTE**

- Neurovascular injury
- Hemorrhage
- Fat embolism
- Compartment syndrome

**SUBACUTE OR CHRONIC**

- Premature growth plate fusion
- Delayed union
- Nonunion or pseudoarthrosis
- Malunion or deformity
- Synostosis (cross-union)
- Heterotopic ossification or myositis ossificans
- Overgrowth
- Refracture
- Premature degenerative joint disease (osteoarthritis)
- Osteomyelitis or septic arthritis
- Posttraumatic osteolysis
- Avascular necrosis
- Posttraumatic cyst
- Osteochondroma
- Fibrous cortical defect
- Aneurysmal bone cyst
- Reflex sympathetic dystrophy syndrome (Complex regional pain syndrome)

**IATROGENIC**

- Soft tissue infection
- Hardware misplacement, migration, or infection
- Casting complications
- Hypocalcemia of immobilization
- Superior mesenteric artery syndrome (cast syndrome)
- Deep venous thrombosis or pulmonary embolism

### **BOX 142.2** Causes of Physeal Arrest

- Injuries
    - Fractures involving the physis (Salter-Harris I–IV)
    - Physeal crush injuries (Salter-Harris V)
    - Overuse injuries
    - Electrical injuries
- Burns
- Frostbite
- Infection
- Ischemia and osteochondroses
- Neuropathic (i.e., myelodysplasia)
- Tumor
- Congenital/developmental deformities
- Metabolic bone diseases
- Iatrogenic causes
- Radiation therapy
- Medications (vitamin A analogues)
- Surgical epiphysiodesis

due to tethering.[11,12] Peripheral fusions result in angular deformities.[11,12] Premature physeal fusion usually occurs approximately 3 months after injury.[12] Radiographs may show obliteration of the physeal clear space. Comparison views are often helpful, particularly when evaluating an older child in whom the time of normal physeal closure is near. A secondary sign of premature physeal fusion is tethering of growth lines.[12] Growth lines normally form during the healing process. Normal growth lines parallel the physis, whereas with premature fusion, growth lines are angled toward a bony bar.[12]

Both computed tomography (CT) and magnetic resonance imaging (MRI) have been used to diagnose premature fusion. A limited CT scan with narrow collimation obtained through the physis can depict physeal bridges, which are best seen on sagittal and coronal reformatted images. Small bars may be seen as a sclerotic band across the physis, whereas with larger areas of fusion, continuity of the marrow space across the fusion is seen.[11,12,14] MRI can accurately depict physeal bridges on multiple sequences. The small bridges may appear as low-signal intensity on all sequences, however, if there are stress changes, edema-like signal may be present on T2-weighted sequences. Larger bridges often show signal following fatty marrow on all sequences. A thin-slice sequence with bright physeal cartilage and dark bone (e.g., three-dimensional [3D] spoiled gradient recalled echo with fat saturation) should be performed when evaluating bridges on MRI (Fig. 142.2). Reformatting this sequence into a maximum intensity projection (MIP) image of the physis can be used to create a "physeal map". On this reformatted image, the physeal cartilage is bright while a bridge across the physis is low-signal intensity.[12,15] This allows the radiologist to obtain the area of the bridge and the total area of the physis to obtain the percentage of the physis occupied by the bridge (area of bridge total area of physis = percent of physis occupied by bridge). This percentage is important to the orthopedic surgeon considering bar resection, as discussed later. MRI can also detect the potential fracture complication of trapped periosteum within the physis.[16]

Bar resection is considered when a deformity is present or developing from a physeal bridge, which occupies *less than* 50% of the area of the physis, *and* the child has at least 2 cm or 2 years of expected remaining growth.[11,17] Direct and indirect (metaphyseal) resection approaches can be used and an interposition material is placed in the resection site.[17] Bridges occupying greater than 50% of the physis are not resected because of poor outcomes, and very small bridges may resolve with physiologic growth. Depending on the deformity and growth potential of the patient, other orthopedic techniques may be utilized to minimize morbidity from the premature fusion, including osteotomies, lengthening and realignment procedures, and contralateral epiphysiodesis.[11]

***Imaging.*** Radiographs are the mainstay of imaging of traumatic injuries to the pediatric skeleton. As a general rule, two orthogonal views are obtained to assess for fracture at nonosteoarticular locations and an additional oblique view is added at osteoarticular locations. At some locations, normal anatomy limits the value of orthogonal projections (i.e., the pelvis). At other locations, unique projections are helpful for delineation of anatomy (i.e., an axillary view of the shoulder). When imaging a long bone, both the proximal and distal joints must be included.

Contralateral comparison views are not routinely obtained but frequently aid in differentiating normal developmental variation from pathology.[18] Comparison views are most helpful in areas of complex anatomy such as the elbow. Normal variants are common and may mimic fracture.

At certain sites and with complex patterns of injury, CT is very helpful in diagnosing fractures and delineating the anatomy of fracture planes, resultant deformity, and the extent and type of articular involvement. Occasionally, MRI or ultrasonography can be used to diagnose fractures in children; however, these modalities excel in delineating associated soft tissue injury rather than osseous injury. Ultrasonography, however, may be particularly helpful in infants whose epiphyses are not yet ossified. The cartilaginous epiphysis is well seen with ultrasound and its relationship and continuity with an adjacent metaphysis can be readily assessed. It also can be used to detect lipohemarthrosis as an indirect sign of fracture or to aid in diagnosis of an occult fracture.[19]

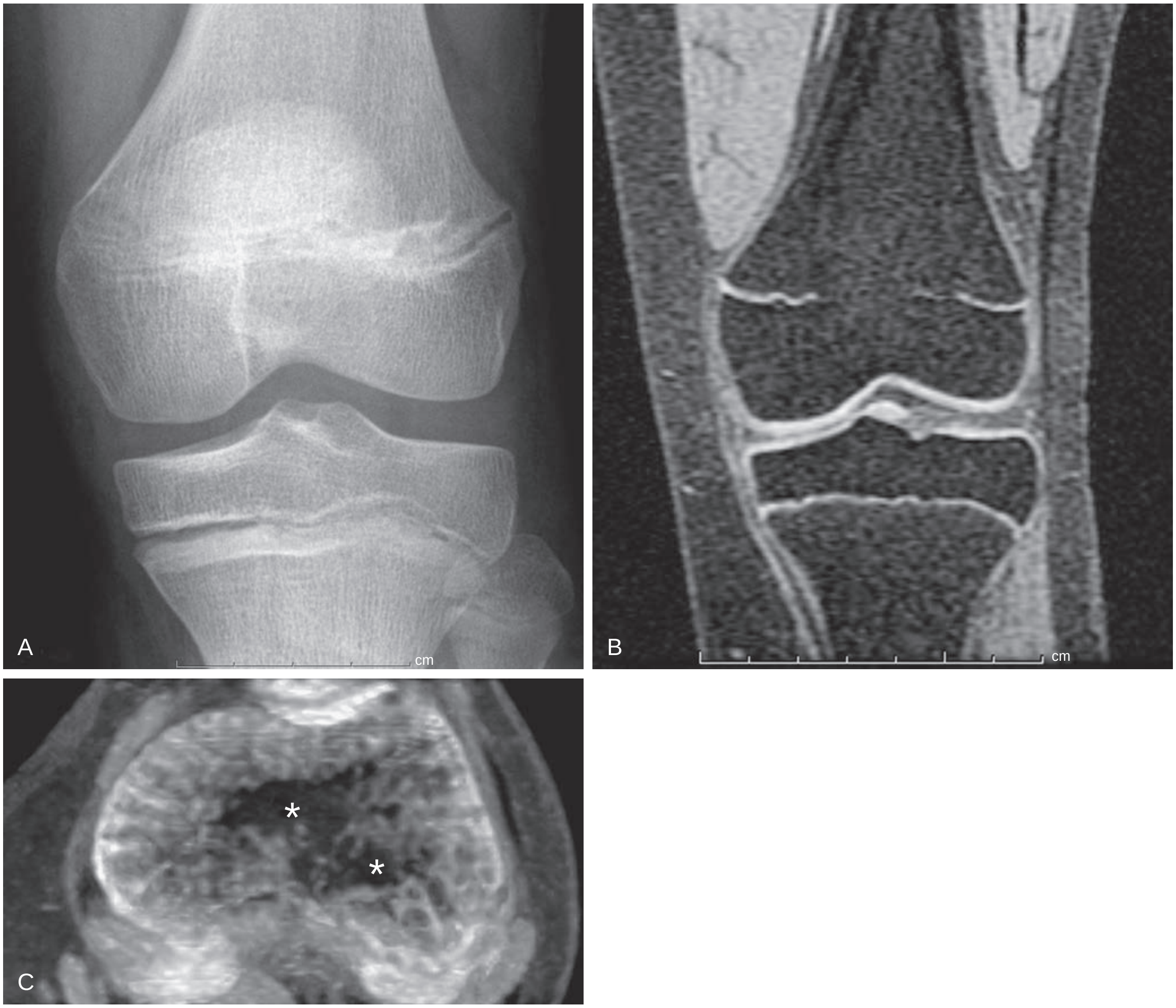

**Figure 142.2. Premature growth plate fusion.** (A) On radiography, the central portion of the distal femoral growth plate is poorly defined; however, the extent of fusion is poorly delineated. (B) Coronal spoiled gradient recalled echo magnetic resonance (MR) image with fat saturation. There is a central physeal bridge, seen as low signal extending across the bright physeal cartilage. (C) Axial maximum intensity projection (MIP) image constructed from the stack of coronal spoiled gradient recalled echo with fat saturation images. The area of the bridge *(asterisks)* and the total area of the physis can be obtained on this MIP image. *(Courtesy of Dr. K. Ecklund, Boston, MA.)*

## PLASTIC FRACTURES

***Etiology, Pathophysiology, and Clinical Presentation.*** The composition of bones in a child is different from that of the bones in an adult.[20] The most apparent anatomic differences in the pediatric skeleton are the presence of the physis and a thick periosteum.[21] The plasticity of a child's bones allows for substantial deformity before fracture (e-Fig. 142.3).[2] Bone may give way and may become permanently deformed before a complete break. The result is an "incomplete fracture" or a "plastic fracture."

A *greenstick fracture* occurs when a cortical fracture occurs on the tension side of bone with intact cortex on the loading side of bone. A torus or buckle fracture is a cortical fracture occurring on the loading side of bone with intact cortex on the tension side. A bowing deformity does not have a radiographically identifiable fracture line on either the tension or loading side of bone.

Greenstick fractures most commonly occur in long bones, particularly the radius and ulna.[2] These fractures are most common in the first decade of life, are uncommon in the second decade of life, and are not seen in normally developed and mineralized bones of adults.[2] *Buckle fractures* most commonly affect the distal radius and ulna, tibia, and proximal first metatarsal bone.

***Imaging.*** Radiographs are the standard method of evaluation and advanced imaging is usually not indicated. Subtypes of incomplete fractures are buckle or torus fractures (Fig. 142.4), lead pipe fractures (part transverse fracture or part buckle fracture), greenstick fractures (Fig. 142.5), and bowing deformities (e-Fig. 142.6). With incomplete fractures, the periosteum is intact wherever the cortex is intact.[2]

***Treatment.*** Cast and splinting is usually performed for pain control because most of these fractures are stable. Plastic fractures usually heal completely and have a good prognosis. Rarely, it may

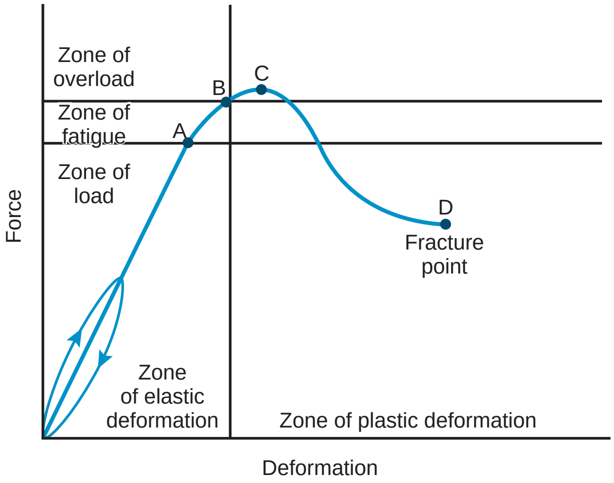

**e-Figure 142.3. Graphic relation of bony deformation (bowing) and force (longitudinal compression).** The limit of an elastic response is not a fracture but plastic deformation. If the force continues, a fracture results. (A) Reversible bowing with stress. (B) Microfractures occur. (C) Point of maximal strength, between (C) and (D) bowing fractures. (D) Linear fracture occurs. *(Modified from Borden S IV. Roentgen recognition of acute plastic bowing of the forearm in children.* Am J Roentgenol Radium Ther Nucl Med. *1975;125:524–530.)*

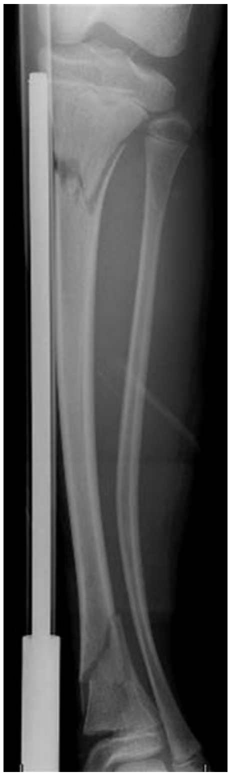

**e-Figure 142.6. Bowing fracture of the fibula in a 12-year-old boy.** The fibula is bowed, without a fracture line or cortical buckle. Complete fractures of the proximal and distal tibia are present.

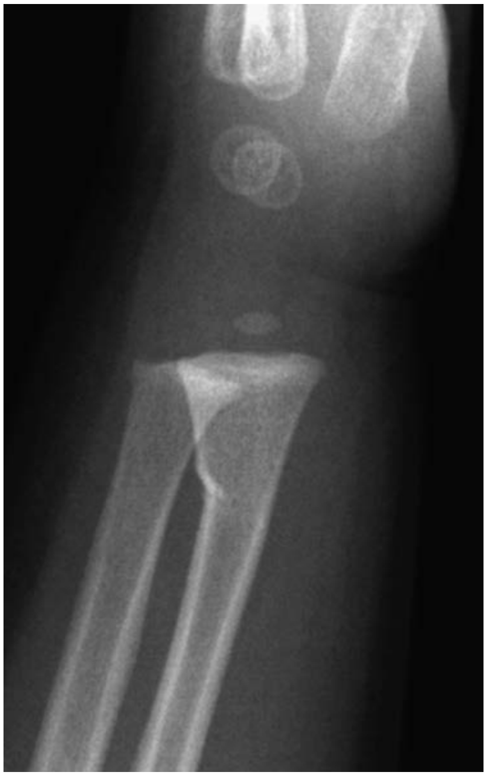

**Figure 142.4. Buckle fracture of the distal radius in a 19-month-old boy.** The dorsal aspect of the distal radius is slightly angulated.

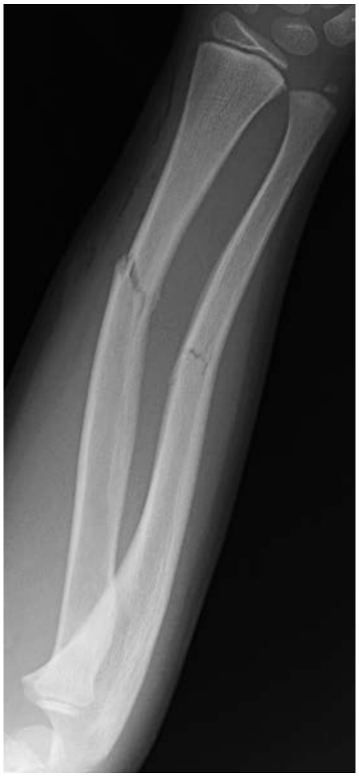

**Figure 142.5. Greenstick fractures of the radial and ulnar diaphyses in an 8-year-old boy.** The fracture lines only extend through part of the cortex.

be necessary to operatively "complete" the fracture for reduction of severe angular deformity. Mild angular deformities (<15 degrees) usually do not need to be reduced and will remodel nicely without permanent sequelae.

## PHYSEAL (SALTER-HARRIS) FRACTURES

***Etiology, Pathophysiology, and Clinical Presentation.*** For the musculoskeletal unit of the child, the physis and physeal equivalent regions are points of relative weakness and are thus predisposed to mechanical failure leading to fractures.[22] The physis usually fails before ligamentous or tendinous soft tissue structures fail after biomechanical stress. Once the physis fuses, ligamentous and tendon soft tissue injuries become more frequent, as do metadiaphyseal fractures. Fracture patterns in skeletally mature adolescents are similar to fracture patterns seen in adults.

Approximately 18% of pediatric fractures involve the physes.[23] Physeal fractures are classified by the system of Salter and Harris (Fig. 142.7). This well-accepted classification scheme for describing physeal fractures facilitates efficient communication between clinicians and radiologists.

***Imaging.*** Most physeal fractures are adequately delineated by radiography. The Salter-Harris classification, the degree of displacement and angulation, and intraarticular involvement should be described.

Fractures may pass solely through the physis (Salter-Harris I; e-Fig. 142.8), involve the physis and metaphysis (Salter-Harris II; Fig. 142.9), involve the physis and epiphysis (Salter-Harris III; e-Fig. 142.10), or cross the physis involving both epiphysis and metaphysis (Salter-Harris IV; e-Fig. 142.11). Crush injury of the physis (Salter-Harris V) is rare as an isolated injury to the bone and are typically diagnosed retrospectively.

The Salter-Harris classification serves to assign prognosis. Higher grade Salter-Harris fractures have a higher incidence of premature physeal fusion. Most physeal fractures, however, are either Salter-Harris I (approximately 10%) or Salter-Harris II (approximately 75%). Thus although premature physeal fusion is more likely to occur with a higher grade Salter-Harris fracture, this complication is probably more commonly the result of the more common lower grade Salter-Harris fractures. Lesser grades of Salter-Harris fractures that proceed to premature physeal fusion may have a component of crush (Salter-Harris V) injury.

At certain locations, CT or MRI may be used to confirm or further delineate fractures, especially for defining exact measurements of fracture diastasis and whether involvement of an articular surface exists. On MRI, physeal fractures are diagnosed by widening and increased T2-weighted signal within the physis, adjacent bone marrow edema, associated metaphyseal (Salter-Harris II or IV) or epiphyseal (Salter-Harris III or IV) fracture lines, and periosteal disruption.[24] The most significant complication of physeal injuries is growth arrest (see Fig. 142.2), which can lead to deformity and longitudinal growth arrest, potentially with limb length discrepancies.[25] A rare complication of physeal fracture diagnosed by MRI is entrapment of periosteum within the fracture (Fig. 142.12). The entrapped periosteum will prevent complete reduction of the fracture.

***Treatment.*** Salter-Harris I and II fractures are usually treated by closed manipulation followed by casting. Salter-Harris type III and IV fractures usually require open reduction and internal fixation, as these types of fractures often are displaced and extend to the joint. To prevent posttraumatic osteoarthritis, it is important to create a smooth articular surface; therefore Salter-Harris fractures with epiphyseal involvement and greater than 2 mm of diastasis or significant angulation usually require surgical fixation.

## TRAUMATIC INJURIES OF THE HUMERUS

***Etiology, Pathophysiology, and Clinical Presentation.*** Infants and toddlers are likely to have a Salter-Harris I fracture of the proximal

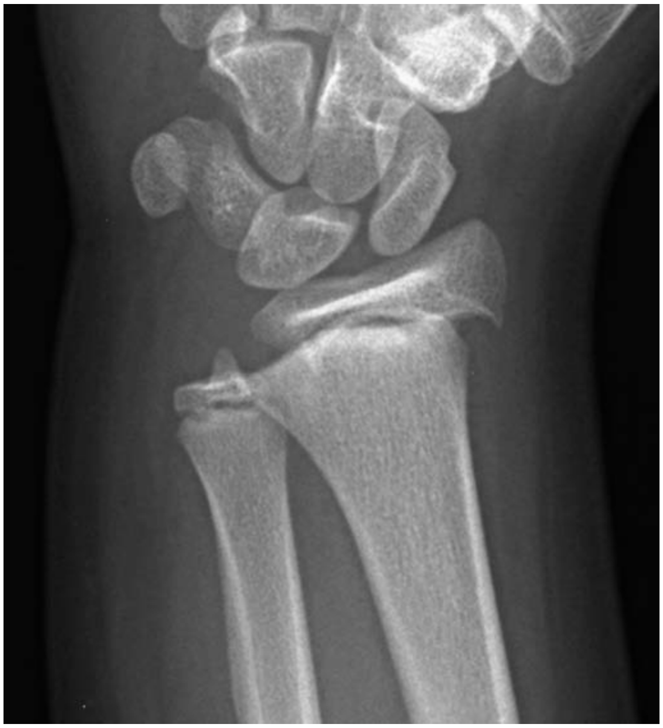

**e-Figure 142.8. Apparent Salter-Harris I fracture of the distal radius in an 11-year-old girl.** The distal radial epiphysis is displaced laterally. No metaphyseal component was seen on this anteroposterior view or on the lateral view *(not shown)*. However, this may represent a Salter-Harris II fracture with a small metaphyseal component, which is radiographically occult, which is much more common in this location.

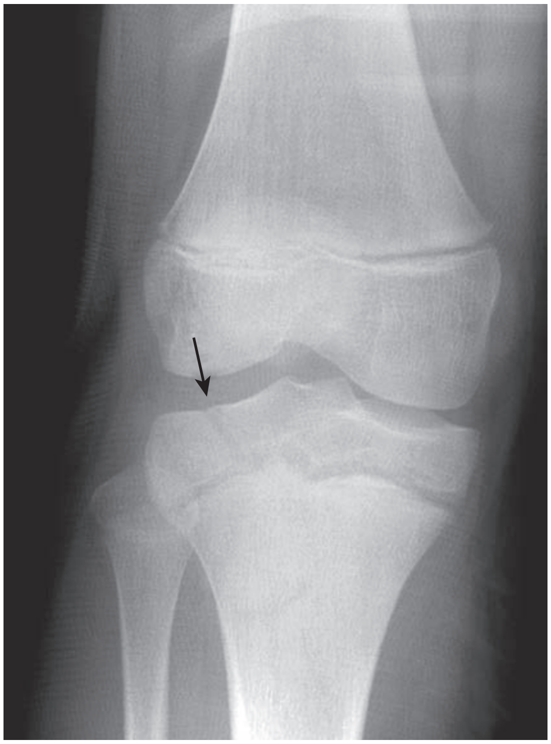

**e-Figure 142.10. Salter-Harris III fracture of the proximal tibia in a 10-year-old girl.** The proximal tibial physis is wide. The *arrow* shows the vertical epiphyseal fracture line.

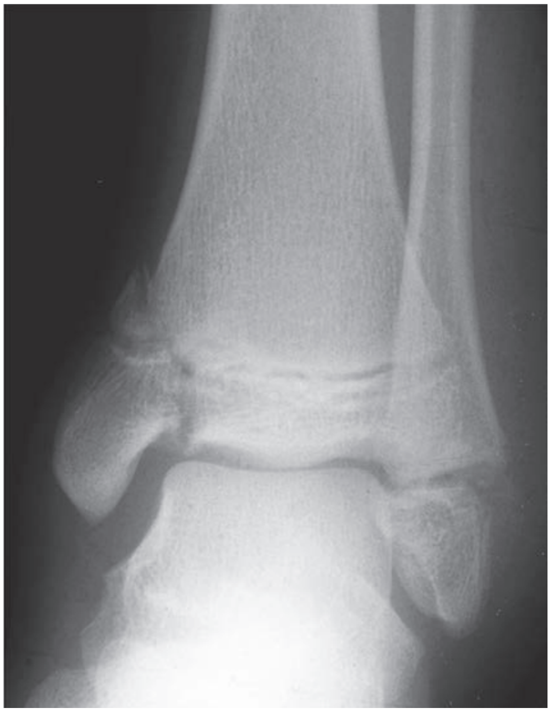

**e-Figure 142.11. Salter-Harris IV fracture of the distal tibia in a 13-year-old boy who fell from a tree.** A Salter-Harris I fracture of the distal fibula with overlying soft tissue swelling is also present.

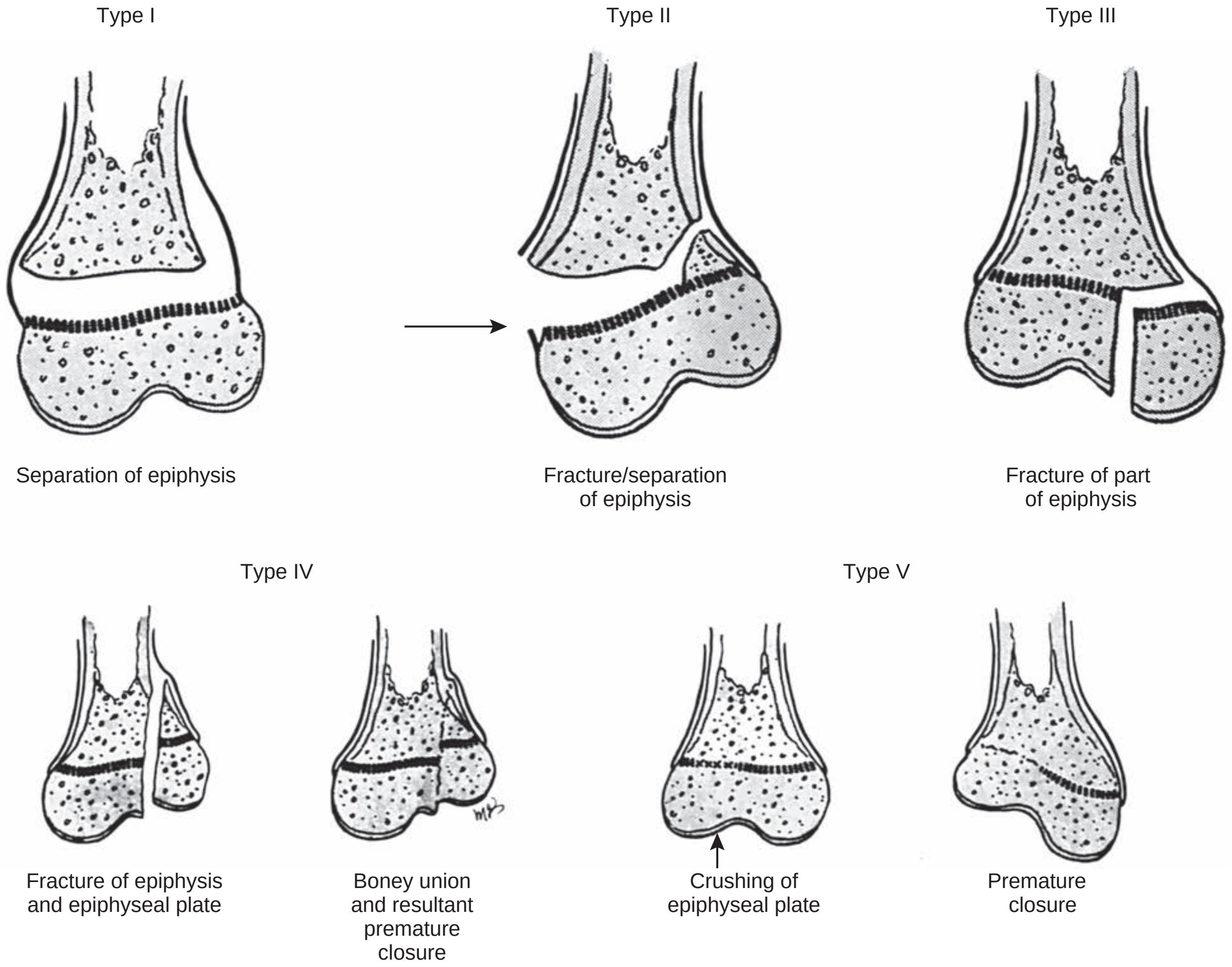
Type I
Type II
Type III
Separation of epiphysis
Fracture/separation of epiphysis
Fracture of part of epiphysis
Type IV
Type V
Fracture of epiphysis and epiphyseal plate
Boney union and resultant premature closure
Crushing of epiphyseal plate
Premature closure

**Figure 142.7. Injuries to the cartilage plate classified according to Salter and Harris.** *Type I,* Fracture involving only the physis. The fracture does not involve the ossified portions of the bone. *Type II,* Fracture involves the physis and metaphysis with a triangular fragment of metaphysis attached to the displaced epiphysis. The prognosis is good. *Type III,* Partial transverse fracture of the physis with a longitudinal or oblique component extending through the epiphyseal ossification center to the articular surface. The prognosis is poor if the epiphyseal fracture is not reduced with smooth joint surfaces. *Type IV,* Oblique longitudinal fracture extending from the articular cartilage through the epiphyseal ossification center, across the physis, and through a segment of the metaphysis. These fractures frequently require open reduction for proper alignment. *Type V,* Compression (crush) injury of the physis, often followed by premature physeal closure and growth arrest. *(From Salter RE, Harris WR. Injuries involving the epiphyseal plate.* J Bone Joint Surg Am. *1963;45:587–622.)*

humeral physis. From 5 to 10 years of age, buckle fractures of the proximal humeral metaphysis are most prevalent (e-Fig. 142.13). In older children, Salter-Harris II fractures predominate (e-Fig. 142.14). Fractures of the humeral diaphysis are also common.[26]

The proximal humeral physis can be a site of birth trauma (e-Fig. 142.15).[27] Similar injuries can also be seen with child abuse.

***Imaging.*** Anteroposterior and lateral radiographs of the humerus should be obtained to initially evaluate a fracture. If the fracture is near or involves the glenohumeral joint, an additional axillary view is recommended. If a Salter-Harris type I fracture is suspected in the neonate, evaluation with ultrasonography is preferable, as the proximal humeral epiphysis is cartilaginous readily seen. For older patients or those with complex proximal humeral fractures, CT or MRI may be useful to evaluate for intraarticular extension and for involvement of the greater and lesser tuberosities.

Radiographically, because the humeral head is usually not ossified or only slightly ossified at birth, fracture through the physis mimics dislocation of the shoulder (see e-Fig. 142.15). The humeral metaphysis may appear to align inferior to the glenoid. In the newborn, Salter-Harris I fracture of the proximal humerus is much more common than glenohumeral dislocation.[28] Ultrasound may be used to diagnose the fracture by showing malalignment of the cartilaginous humeral head with the proximal humeral metaphysis and showing motion at the physis (e-Fig. 142.16).[28,29]

Salter-Harris fractures of the proximal humerus in older children are usually Salter-Harris II fractures, although the metaphyseal fragment is often very small. Occasionally, no metaphyseal fragment exists. Such Salter-Harris I fractures are sometimes called *slipped capital humeral epiphysis*. Typically, with a Salter-Harris I or II fracture of the proximal humerus, the epiphyseal fragment rotates medially because of unopposed pull by the rotator cuff.[27] Salter-Harris III and IV fractures of the proximal humerus are extraordinarily rare. Avulsion of the greater tuberosity is a Salter-Harris III fracture. Avulsions of the lesser tuberosity caused by hyperextension with avulsion of the subscapularis tendon are rare, often delayed in diagnosis, and are best delineated by an axillary view.[30,31]

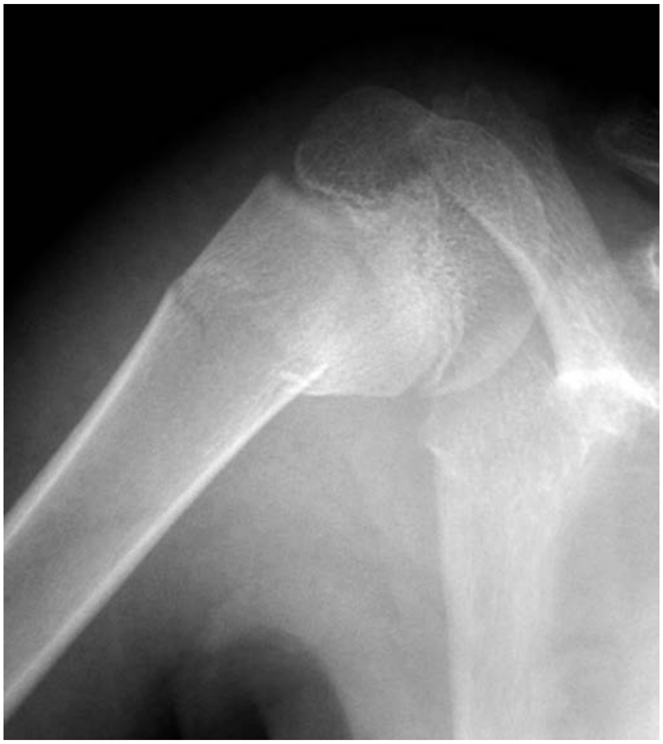

**e-Figure 142.13.** **Incomplete fracture of the proximal humeral metaphysis in a 9-year-old girl.**

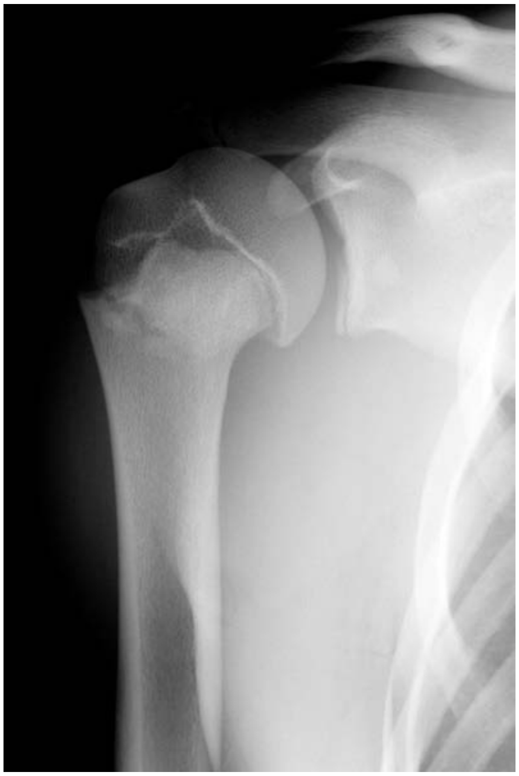

**e-Figure 142.14.** **Salter-Harris II fracture of the proximal humerus in an adolescent.** The fracture involves the proximal humeral physis with a small metaphyseal fragment. There is slight medial rotation of the humeral head due to pull of the rotator cuff tendons on the greater tuberosity.

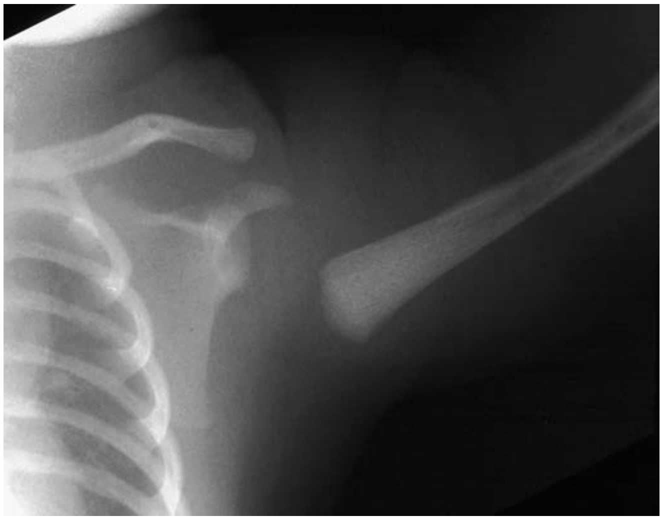

**e-Figure 142.15.** **Proximal humeral Salter-Harris I fracture in a newborn caused by birth trauma.** The proximal humeral metaphysis appears malaligned with the glenoid. The humeral head is not ossified. In an infant, this finding is more likely from epiphyseal fracture and separation than dislocation.

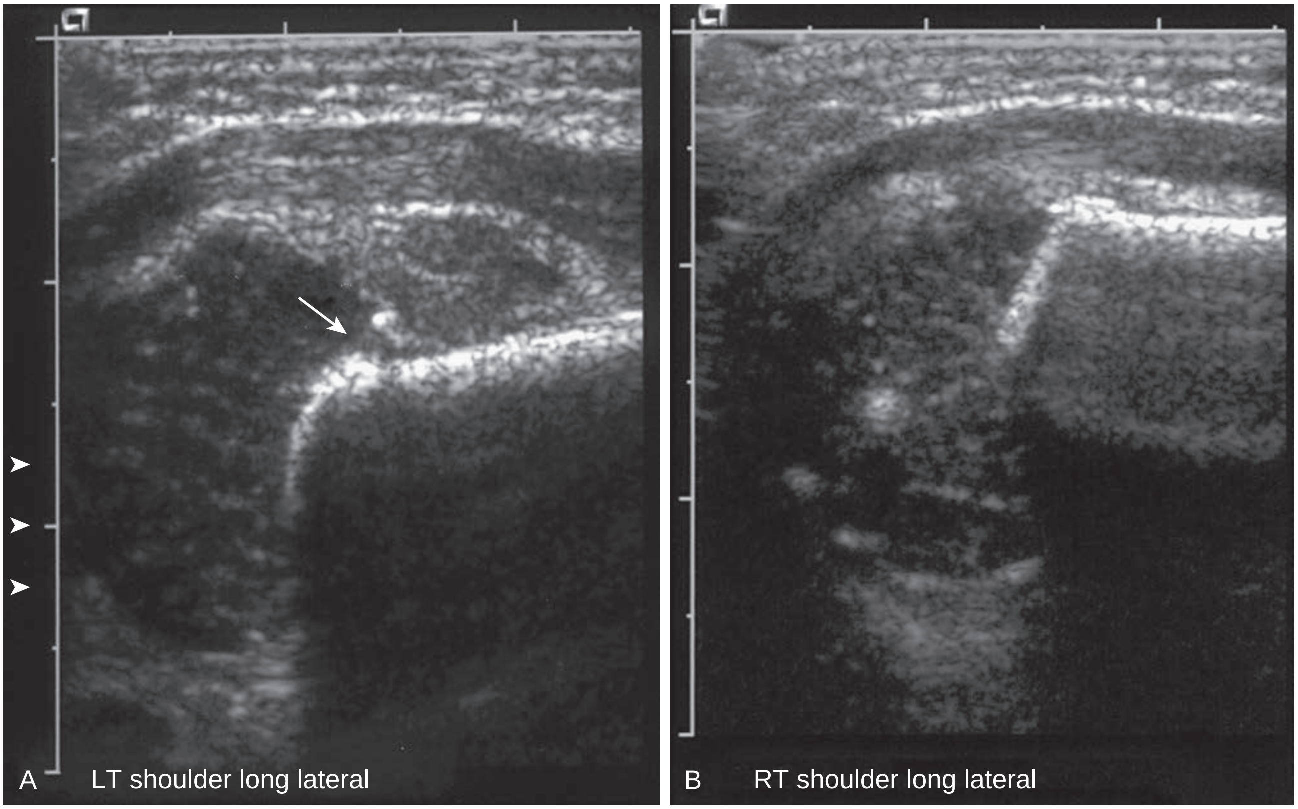

**e-Figure 142.16. Proximal left humeral fracture in a 16-day-old girl with decreased arm movement and normal radiograph.** Sonographic images of the shoulders were obtained in the coronal plane with lateral transducer positioning. (A) In the left shoulder, the cartilaginous epiphysis is displaced laterally from the metaphysis *(arrow)*. There is soft tissue swelling adjacent to the fracture site. (B) Normal right shoulder for comparison.

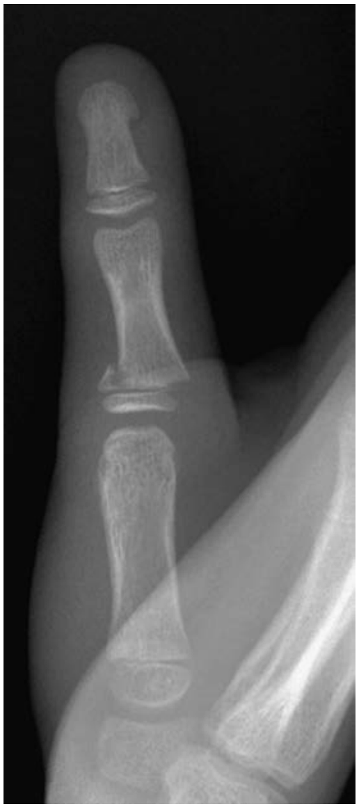

**Figure 142.9. Salter-Harris II fracture of the proximal phalanx of the thumb in a 10-year-old boy.** There is mild ulnar displacement of the distal fragment.

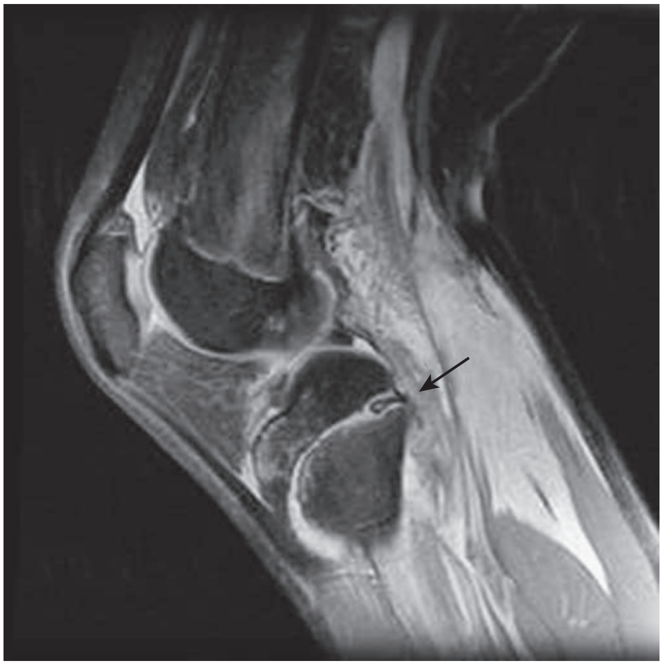

**Figure 142.12. Salter-Harris I fracture of the proximal tibia with trapped periosteum in an adolescent.** Proton density weighted sagittal MR image with fat saturation shows disrupted periosteum is trapped within the physeal fracture *(arrow)*. Abundant soft tissue edema is seen posteriorly. *(Courtesy of Dr. D. Grattan-Smith, Atlanta, GA.)*

In very young children, fractures of the humeral diaphysis may be incomplete fractures; however, beyond the toddler years, most fractures of the humeral diaphysis are complete fractures. The humerus is one of the more common sites for a pathologic fracture because of its propensity to develop solitary bone cysts.[32] The positioning and alignment of the fragments of a humeral fracture are dependent on the site of fracture and its relationship to the deltoid and pectoral muscular insertions.

***Management.*** Proximal humeral fractures are usually treated nonsurgically, including those with significant angulation and displacement. Fractures will heal and remodel without long-term orthopedic sequelae. However, some advocate operative management in certain situations.[33,34] Reduction may be necessary in patients near skeletal maturity if the fracture has more than 50 to 70 degrees of angulation in the coronal or sagittal plane.[35] Operative intervention also is indicated in those patients with associated neurovascular injury or who have intraarticular or open fractures.

## TRAUMATIC INJURIES OF THE ELBOW

### Overview

The complex anatomy of the elbow joint and the immaturity of the pediatric skeleton make this joint particularly susceptible to injury.[36] Complications, although uncommon, include neurovascular injury, malunion, and compartment syndrome.[37]

### Ossification Centers

The normal, orderly progression of the appearance of the ossification of the six major ossifications centers of the elbow (Fig. 142.17) is as follows: capitellum (~1–2 years), radial head (~2–4 years), medial (internal) epicondyle (~4–6 years), trochlea (~9–10 years), olecranon (~9–11 years), and lateral (external) epicondyle (~9.5–11.5 years).[38] This can be remembered by the mnemonics CRMTOL or CRITOE. With very rare exceptions, the medial epicondyle ossifies before the trochlea. If the trochlea is ossified, so should be the medial epicondyle. Fusion of the elbow ossification centers is less orderly, occurring after puberty.

### Joint Effusion

Patients with acute fractures at the elbow that extend into the synovial cavity will usually have an elbow joint effusion.[39,40] The effusion causes displacement of the anterior and posterior fat pads of the elbow (Fig. 142.18). Although the anterior fat pad is seen normally, it may appear elevated by an effusion ("sail sign"). The posterior fat pad normally resides within the olecranon fossa and is not seen on radiographs unless a joint effusion is present causing posterior displacement. The presence of an elbow joint effusion is strong evidence for the presence of a fracture.[41,42] Usually, the fracture is obvious. In younger children, a subtle buckle or greenstick fracture of the supracondylar distal humerus may occur. In older children, a subtle fracture of the radial head or radial neck may occur. The presence of an effusion is not unequivocal evidence for a fracture.[43] However, as fractures are often subtle or occult, the presence of an effusion without an identifiable fracture usually prompts splinting of the arm with follow-up radiographs to assess for healing of an occult fracture.

### Alignment Lines

On a properly positioned lateral view, the anterior humeral cortical line is drawn along the anterior cortex of the humerus. This line should pass through the middle third of the capitellum. Disruption of this relationship aids in the detection of supracondylar fractures, which are usually posteriorly angulated and displaced. The

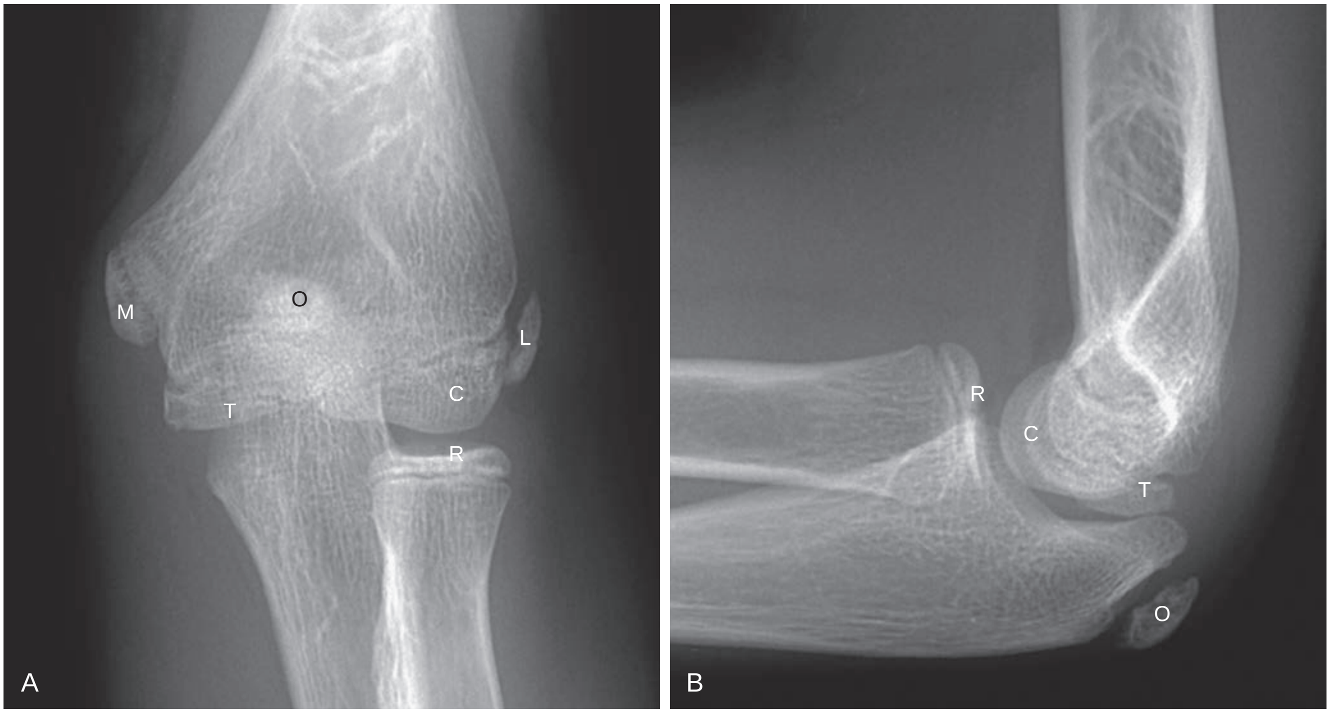

**Figure 142.17. Normal elbow in a 14-year-old boy.** Anteroposterior (A) and lateral (B) radiographs. *C,* Capitellum; *L*, lateral epicondyle; *M*, medial epicondyle; *O*, olecranon; *R*, radial head; *T*, trochlea.

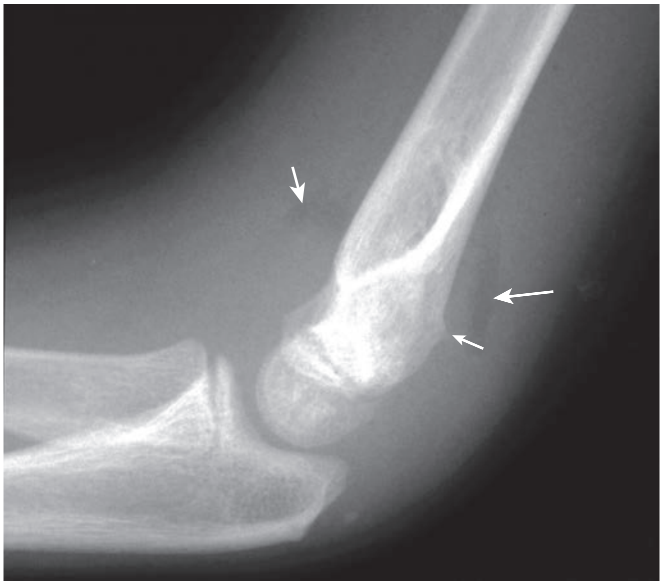

**Figure 142.18. Buckle-type supracondylar fracture *(small arrow)* in a 6-year-old boy.** The anterior and posterior fat pads *(large arrows)* are displaced by an elbow joint effusion. Note that the anterior humeral cortical line passes along the anterior margin of the capitellum, indicating posterior angulation of the distal fragment.

radiocapitellar line is drawn along the axis of the radius. Regardless of patient positioning or projection, this line should pass through the capitellum (Fig. 142.19). Disruption of this relationship aids in detection of radiocapitellar dislocation.[44] Other reasons for radiocapitellar line disruption include lateral condylar, radial neck, and Monteggia fractures.[45]

## SUPRACONDYLAR FRACTURES

***Etiology, Pathophysiology, and Clinical Presentation.*** Supracondylar fractures of the distal humerus account for 60% of pediatric elbow fractures.[46] The usual mechanism of injury is hyperextension with impingement of the olecranon on the posterior distal humerus.[47]

***Imaging.*** The distal fragment of a supracondylar fracture is often displaced or angulated posteriorly. As a result, the anterior humeral cortical line will not bisect the capitellum. If this line passes through the anterior third of the capitellar ossification center or anterior to it, then a supracondylar fracture is likely present.[45]

The modified Gartland classification system of supracondylar fractures is the most commonly used to succinctly describe the fracture and for treatment planning.[48] Type I supracondylar fractures are nondisplaced or minimally displaced less than 2 mm and have an intact anterior humeral line (see Fig. 142.18). Type II fractures are displaced greater than 2 mm with angulation and disruption of the anterior humeral line, but with an intact posterior cortex. Type III fractures are displaced with no cortical continuity (e-Fig. 142.20). Most type II and all type III fractures are treated surgically.[47] The risk of developing trochlear epiphyseal osteonecrosis increases with delayed reduction.[49] Neurovascular injury may occur with displaced supracondylar fractures.

Inadequately reduced supracondylar fractures may cause clinically significant limitations in elbow flexion.[50] After reduction, supracondylar fractures often demonstrate a mild degree of posterior displacement or angulation. This will not adversely affect functional outcome; however, fusion with loss of normal cubitus valgus will potentially inhibit the range of motion of the elbow. Normally, slight lateral angulation of the radius exists relative to the humerus (cubitus valgus) and is greater in females. The Baumann angle is created by the intersection of the humeral axis with a line tangent to the physis of the capitellum (e-Fig. 142.21). This angle can be used to reliably predict the final carrying angle of the elbow after

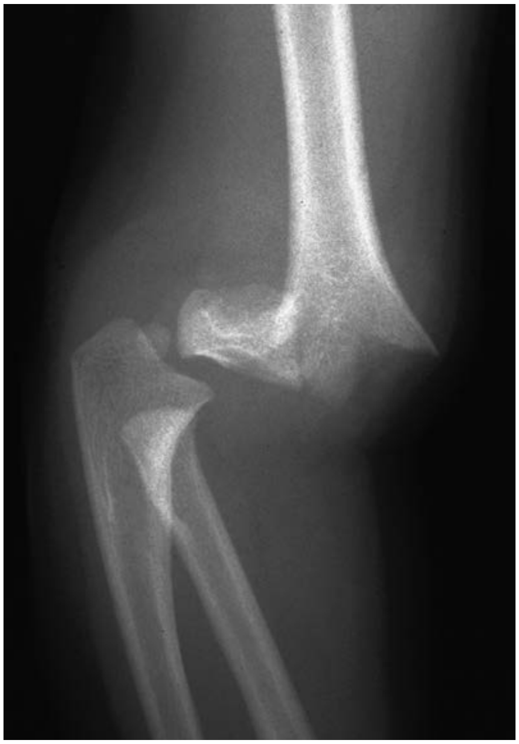

**e-Figure 142.20. Supracondylar fracture in a 2-year-old boy.** The distal fragment is displaced and angulated posteriorly.

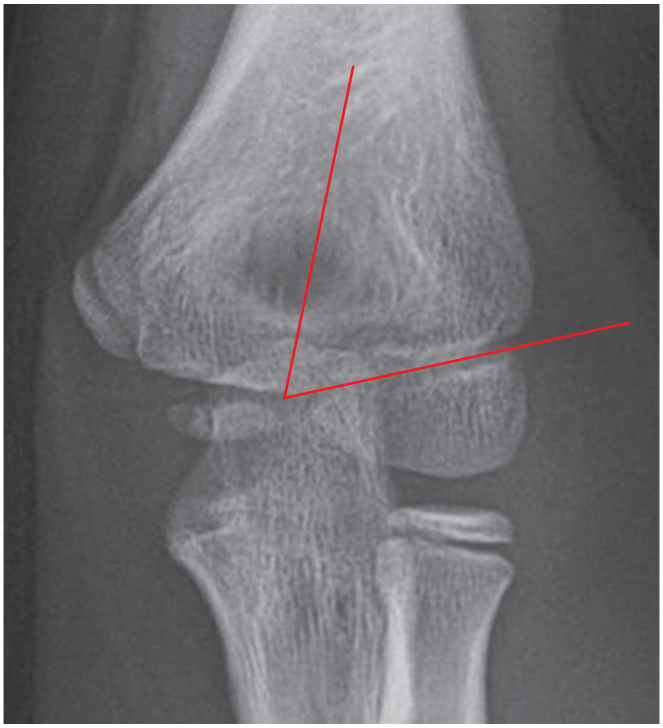

**e-Figure 142.21. Normal elbow of a 10-year-old boy demonstrating a normal Bauman's angle.** On the frontal radiograph the Baumann angle is created by the intersection of the humeral axis with a line tangent to the physis of the capitellum. The normal range is 64 to 81 degrees, but increase in the angle compared with the contralateral side is more predictive of abnormality.

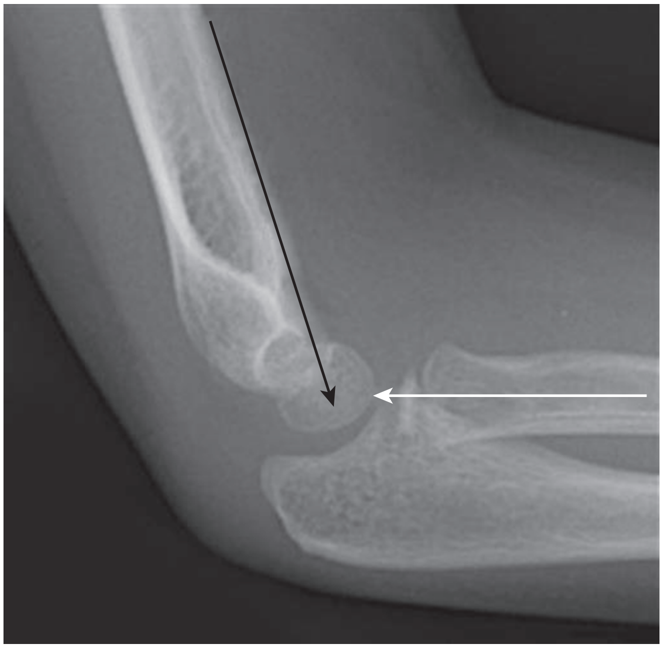

**Figure 142.19. Normal elbow alignment on a lateral radiograph.** The anterior humeral line *(black arrow)* is drawn along the anterior cortex of the humerus and should intersect the middle third of the capitellum. The radiocapitellar line *(white arrow)* is drawn along the axis of the radius. Regardless of patient positioning or projection, this line should pass through the capitellum.

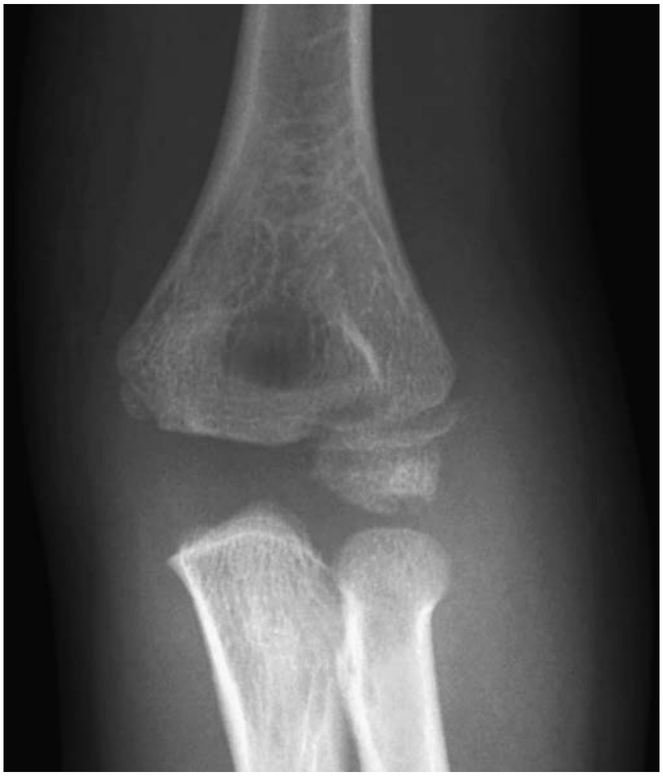

**Figure 142.23. Nondisplaced lateral condylar fracture in a 6-year-old boy.**

supracondylar fractures. The normal angle ranges from 64 to 81 degrees. With posttraumatic cubitus varus, the Baumann angle is increased.[51,52] An increase in the Bauman angle compared with the contralateral, unaffected elbow is more reliable than using an exact number to predict cubitus varus.

***Treatment.*** Conservative versus operative management depends on the degree of displacement, age of the patient, location and stability of the fracture, and associated injuries. Most type I or nondisplaced supracondylar fractures can be treated conservatively in a long arm cast. Most type II and III supracondylar fractures are treated operatively with closed reduction and percutaneous pinning.[53,54]

## LATERAL CONDYLAR FRACTURES

***Etiology, Pathophysiology, and Clinical Presentation.*** Lateral condylar fractures are the second most common type of fracture of the pediatric elbow, accounting for 12% to 20% of pediatric elbow fractures.[55] The mechanism is hyperextension with varus stress.[46] Lateral condylar fractures which extend through the distal humeral epiphysis are Salter-Harris IV fractures.

***Imaging.*** An internal oblique view may better delineate the lateral condylar fracture.[56] The fracture may or may not extend through the unossified portion of the distal humeral epiphysis (e-Fig. 142.22). “Stable” lateral condylar fractures (type I) do not traverse the cartilaginous epiphysis and are incomplete and thus nondisplaced or minimally displaced (Fig. 142.23). Type II lateral condylar fractures are complete and thus “unstable” but with little or no displacement. The lateral condylar fracture line may be quite subtle, often paralleling the adjacent metaphyseal margin. Both MRI and ultrasonography have proven capable of demonstrating the fracture through epiphyseal cartilage indicating a Salter-Harris IV fracture.[57] Type III fractures are complete and “unstable”, and the lateral condylar fragment is displaced and rotated; e-Fig. 142.24.

***Treatment.*** Lateral condylar fractures that are nondisplaced (stable) or are displaced 2 mm or less are managed with cast immobilization. Those that are displaced greater than 2 mm (unstable) are treated with surgical fixation with lateral entry pins.[55] Physeal growth arrest and posttraumatic osteoarthritis are more common complications of lateral condylar fractures compared with supracondylar fractures. The most common long-term deformity is relative lateral overgrowth with subsequent cubitus varus.[58]

## MEDIAL EPICONDYLE AVULSION

***Etiology, Pathophysiology, and Clinical Presentation.*** The medial epicondyle ossifies by around age 7 years and fuses by around age 16 years.[59] The medial epicondyle is the origin of the forearm flexor mechanism and ulnar collateral ligament. Avulsions thus occur within this age range, although rare avulsions of the unossified medial epicondyle have been reported.[60] Medial epicondyle avulsions may occur secondary to a single acute injury, including elbow dislocations, or from chronic repetitive stress, as is seen in skeletally immature throwing atheletes.[59,61,62] The avulsion occurs because of hyperextension, with valgus stress producing traction on the apophysis by the flexor tendons and pronators. In the setting of an acute avulsion, the child will experience sudden-onset medial elbow pain and have point tenderness over the medial epicondyle.[62] Rarely, the avulsed medial epicondyle may displace into the joint mimicking a trochlear ossification center. This occurs because the valgus stress temporarily widens the joint.

***Imaging.*** Initial assessment should include anteroposterior, oblique, and lateral radiographs of the elbow (Fig. 142.25). With elbow dislocation in the skeletally immature patient, the medial epicondyle is often avulsed from its normal location. When assessing

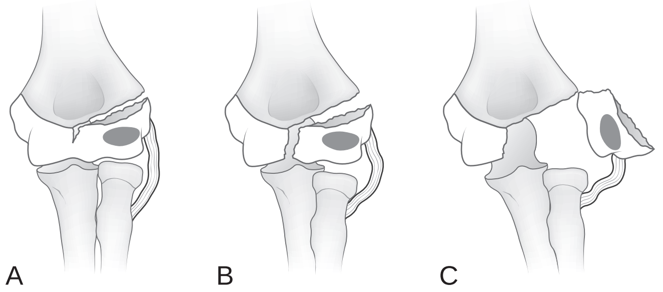

**e-Figure 142.22. Classification of lateral condylar fractures according to the amount of displacement.** (A) Type I (incomplete) fracture. Note that the fracture line enters the cartilaginous surface of the distal humerus between the capitellum and trochlea. However, the fracture is not complete and does not extend to the articular surface. And it is therefore nondisplaced. (B) Type II (complete) fracture. The fracture extends completely through the cartilaginous distal humerus to the articular surface but has little to no displacement. (C) Type III (complete, displaced) fracture. The fracture extends completely through the cartilaginous distal humerus to the articular surface and is displaced. *(From Green NE, Swinotowski MF.* Skeletal Trauma in Children*, 3rd ed. Philadelphia, PA: Saunders; 2003.)*

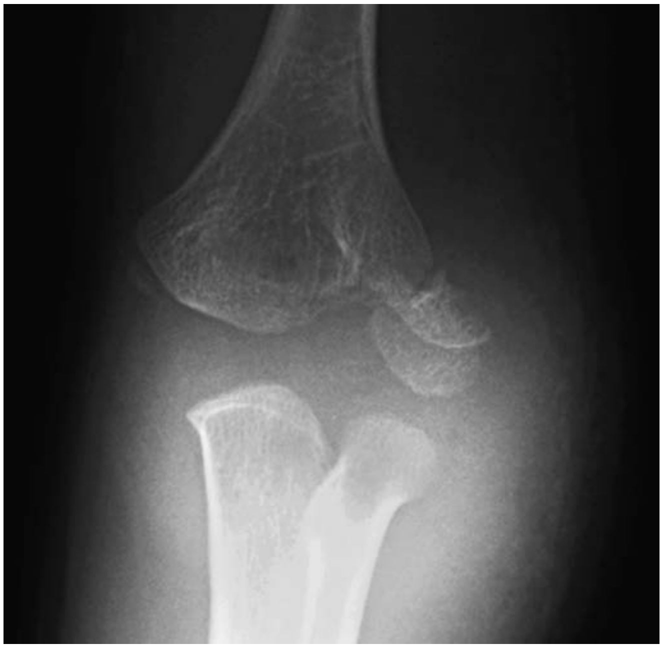

**e-Figure 142.24. Displaced lateral condylar fracture in a 6-year-old boy.** Marked soft tissue swelling is present.

the images of a dislocated elbow, the status of the medial epicondyle should be specifically addressed (e-Fig. 142.26).

Some cases of medial epicondyle avulsion fracture occur with a transient, unrecognized dislocation. When an elbow dislocation is reduced, the medial epicondyle may be trapped in the elbow joint (Fig. 142.27). A trapped medial epicondyle may superficially mimic a trochlear ossification center in the first decade of life. However, absence of the medial epicondyle at its normal location should prompt a search for it within the joint. If the trochlea is ossified, the medial epicondyle should be as well. This illustrates the importance of the mnemonics CRMTOL or CRITOE for remembering that the medial (internal) epicondyle typically ossifies before the trochlea.

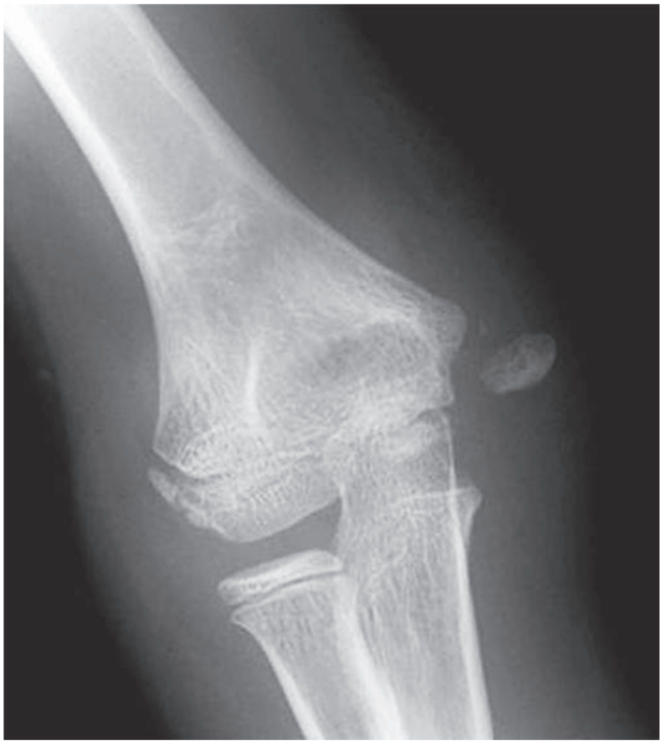

**Figure 142.25. Avulsed medial epicondyle in an adolescent boy.**

Comparison views may be helpful in confirming mildly displaced medial epicondylar avulsion injuries at the level of the medial epicondyle physeal equivalent region; however, they are usually not necessary. Avulsion of the medial epicondyle before its ossification is distinctly rare but has been reported. Ultrasonography, CT, or MRI can be used for fracture delineation.[63]

***Treatment.*** Medial epicondyle avulsion fractures can be treated conservatively if the avulsed fragment is not intraarticular, if the child is less than 5 years of age or the degree of displacement is less than 4 mm. Generally, the need for intervention increases with the age of the child, degree of dislocation, and athletic activity.[64]

## DISTAL HUMERAL SALTER-HARRIS I FRACTURE (TRANSCONDYLAR)

***Etiology, Pathophysiology, and Clinical Presentation.*** Distal humeral Salter-Harris I fracture is an uncommon fracture that occurs from birth to approximately age 7 years, peaking at age 2.5 years. It is typically an injury of infants and young toddlers, and is caused by child abuse in half of the cases or by a rare birth injury.[46,65,66]

***Imaging.*** Radiographically, the fracture may be mistaken for a dislocation of the elbow, as the bones do not appear to align. However, the radial axis will be normally aligned with the capitellum, but the capitellum itself will be abnormally related to the distal humeral metaphysis (e-Figs. 142.28–142.30). The radius, ulna, and humeral epiphysis will be medially displaced. Fractures may occur before capitellar ossification.[67]

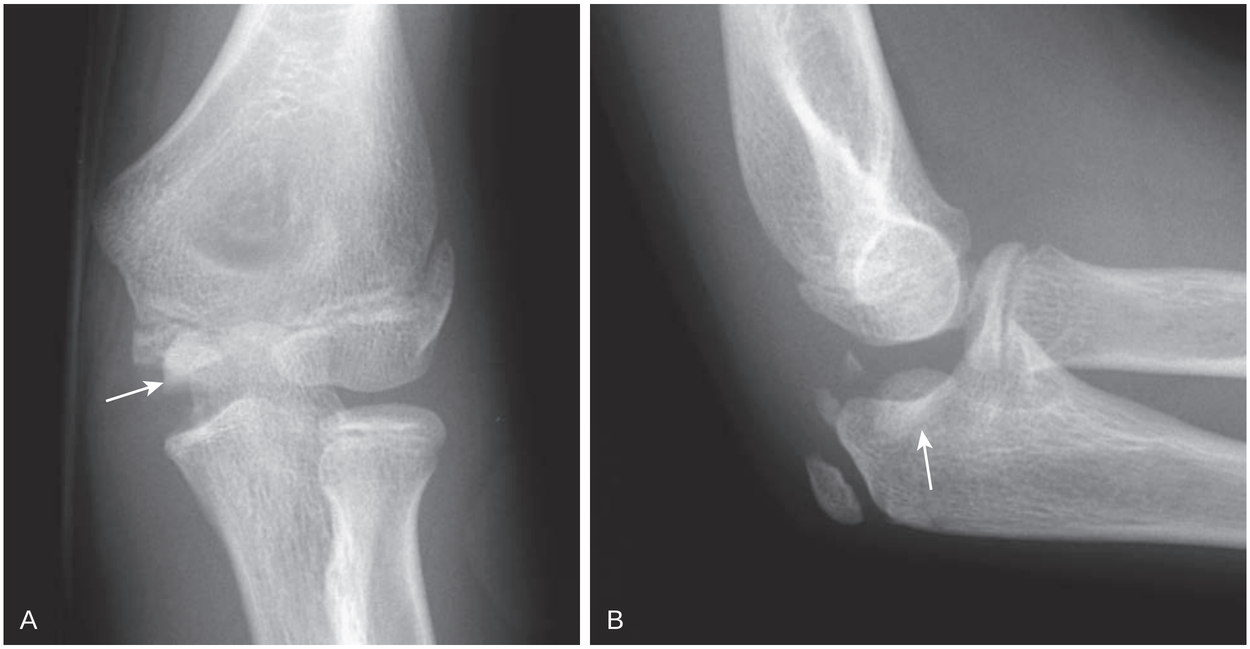

**Figure 142.27. Avulsed medial epicondylar entrapment.** Anteroposterior (A) and lateral (B) radiographs after reduction of a dislocated elbow in a 10-year-old girl show an avulsed medial epicondyle *(arrows)* trapped in the elbow joint.

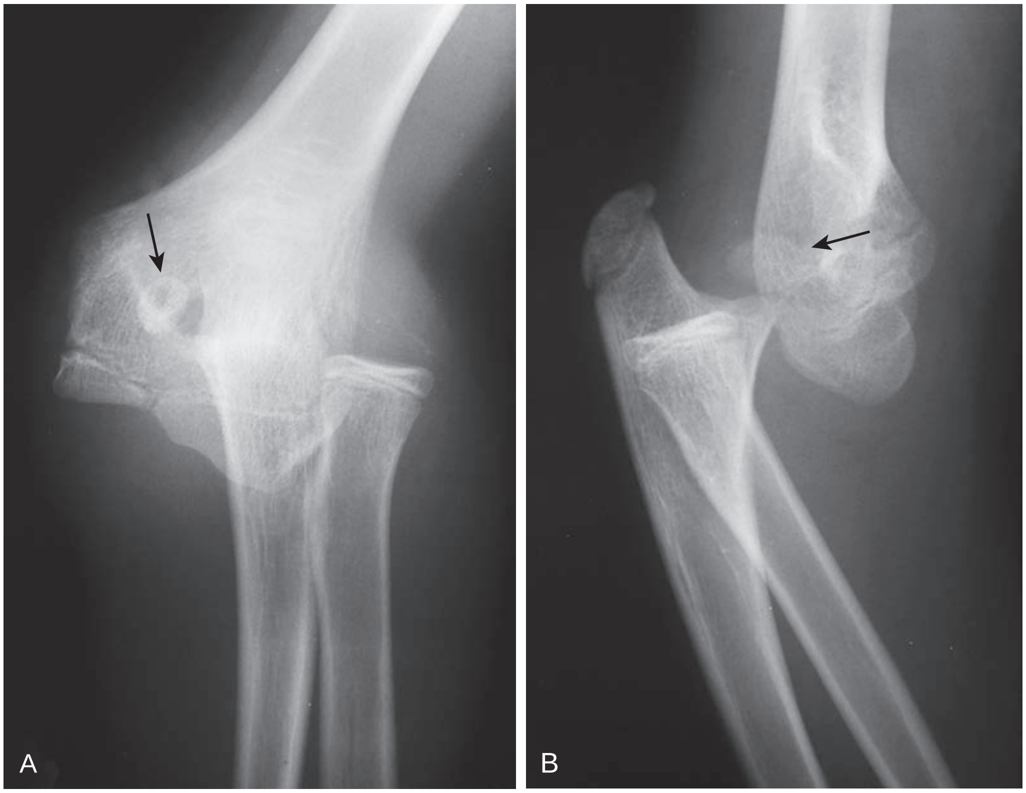

**e-Figure 142.26. Elbow dislocation in a 12-year-old boy.** Anteroposterior (A) and lateral (B) radiographs show an avulsed medial epicondyle *(arrows)* displaced into the joint space.

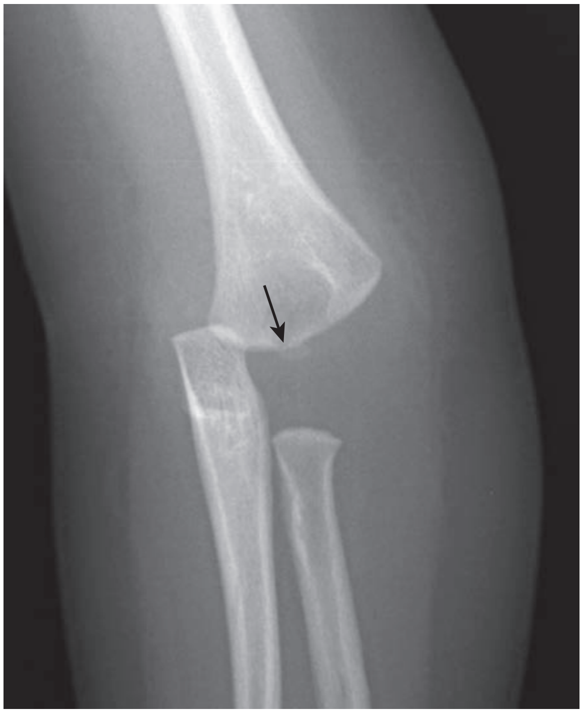

**e-Figure 142.28. Salter-Harris I fracture (transcondylar fracture) of the distal humerus in a 16-month-old boy.** The capitellum *(arrow)* is not properly aligned with the distal humeral metaphysis, and the whole forearm is shifted medially relative to the humerus. Note that the radial head ossification center is normally aligned with the capitellum.

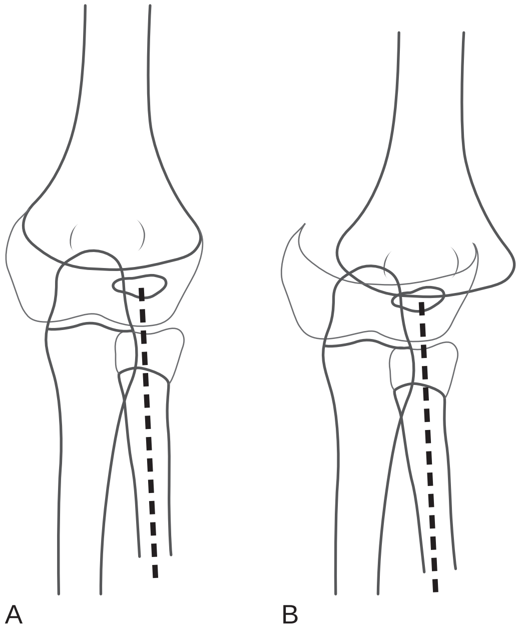

**e-Figure 142.29. Separation of the entire distal humeral epiphysis.** (A) Normal elbow of a 2-year-old child. Heavy lines represent cortex, and fine lines represent the margin of the cartilaginous epiphysis of the humerus and radius. The radiocapitellar line *(dashed line)* defines the normal relationship of the radius and the capitellum. (B) Salter-Harris type I separation of the entire distal humeral epiphysis. Note the medial displacement of the radius, ulna, and humeral epiphysis. The normal relationship of the radius and capitellum is maintained. *(From Rogers LF.* Radiology of Skeletal Trauma*, 3rd ed. New York: Churchill Livingstone; 2002.)*

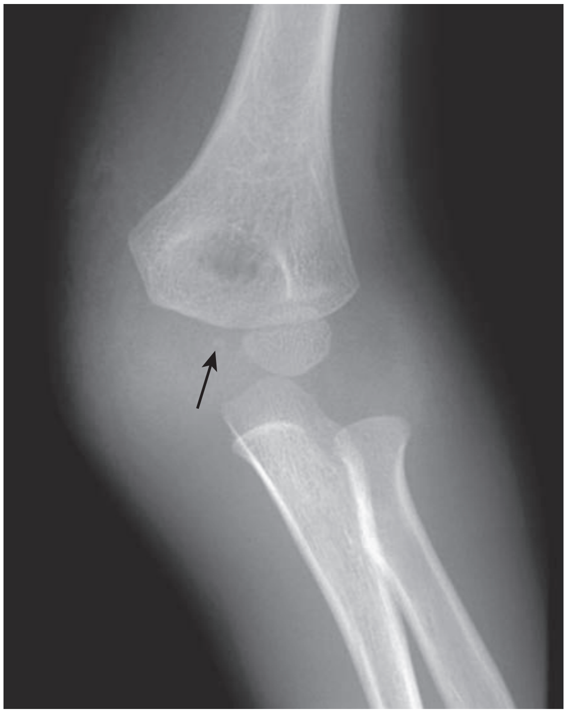

**e-Figure 142.30. Elbow dislocation in a 5-year-old boy.** The capitellum is normally aligned with the distal humerus; however, the radius is not properly aligned with the capitellum. Marked soft tissue swelling is seen medially. The medial epicondyle is undoubtedly avulsed and may be represented by a small ossific density *(arrow)*.

***Treatment.*** Nondisplaced fractures will be treated with splinting or percutaneous pinning. Displaced fractures usually are treated with open reduction and internal fixation.

## RADIAL HEAD AND NECK FRACTURES

***Etiology, Pathophysiology, and Clinical Presentation.*** Fractures of the radial head and neck account for 5% of pediatric elbow fractures.[46] Mechanism of injury is falling on an outstretched hand. Fractures in children often occur at or just distal to the physis; this is unlike the adult population where fractures typically involve the radial head.[46] Associated injuries include fracture of the olecranon, avulsion of the medial epicondyle, or medial collateral ligament injury.[46]

***Imaging.*** Radiographs are usually sufficient for diagnosis and follow-up. External oblique views best delineate the radial head and neck morphology. Radial neck fractures are usually buckle fractures or Salter-Harris II fractures. Isolated radial neck fractures as well as fractures with extension to the radial head are unusual. The radiocapitellar joint is often preserved even when radial neck fractures are displaced and angulated.

***Treatment.*** Most pediatric radial head and neck fractures can be treated nonoperatively with closed reduction and immobilization. If there is greater than 30 degrees of residual angulation, greater than 3 to 4 mm of displacement at the fracture site or less than 45 degrees of pronation or supination, then operative intervention is suggested.[68]

## OLECRANON FRACTURES

***Etiology, Pathophysiology, and Clinical Presentation.*** Olecranon fractures are relatively uncommon accounting for approximately 4% to 6% of elbow fractures in children.[46] Common mechanisms include falling on an outstretched hand, twisting injury, or direct trauma.[46] The olecranon is the insertion site of the triceps muscle and prone to avulsion fractures. Olecranon fractures commonly have associated injuries, including radial neck fractures, medial epicondylar fractures, coronoid fractures, and osteochondral injuries.[46]

***Imaging.*** Radiography is usually sufficient for defining olecranon fractures. Olecranon fractures may be transverse, oblique, or longitudinal. Buckle, bowing, or greenstick fractures are common in younger patients.

The olecranon physis and apophyseal ossification centers vary considerably in size, location, and degree of fragmentation.[69] The juxtaphyseal fragmentary appearance of the olecranon ossification center may be mistaken for fracture, and vice versa. Comparison views may be helpful. Olecranon ossifications are well corticated and appear oval or round. Olecranon fractures have a thin, sliver-like appearance, are usually not corticated, and are located near and parallel the olecranon metaphyseal equivalent zone (e-Fig. 142.31). Other olecranon injuries include stress fractures and sleeve fractures. An olecranon sleeve fracture is an avulsion of the triceps tendon from the olecranon process (e-Fig. 142.32). Stress fractures of the olecranon physis occur in adolescent baseball pitchers.[70] Nondisplaced stress fractures of the olecranon most commonly occur in adolescence and may require MRI for diagnosis.

***Treatment.*** Nondisplaced or minimally displaced olecranon fractures are treated conservatively with immobilization and splinting.[69] Displaced fractures are treated with tension wiring across the apophysis rather than screw fixation.[68]

## NURSEMAID'S ELBOW

***Etiology, Pathophysiology, and Clinical Presentation.*** *Nursemaid's elbow* occurs due to an upward pull on an extended elbow in pronation. The annular ligament of the proximal radius is disrupted or displaced, allowing the radial head to sublux or dislocate anteriorly relative to the capitellum (e-Fig. 142.33).[71] This injury most commonly occurs in the toddler years, up to age 5 years.[72]

***Imaging.*** An astute pediatrician will make the diagnosis clinically and reduce the radius without imaging. Often, when imaging is requested, the dislocation is reduced in the course of properly positioning the hand in supination for the anteroposterior view of the elbow. Ultrasonography may also play a role in detecting dislocation of the radial head with respect to the annular ligament.[73] The utility of radiography is not to make the diagnosis of nursemaid's elbow, but to exclude an underlying fracture. After nursemaid's elbow is successfully reduced, the only radiographic sequelae may be a joint effusion without underlying fracture.

When radiographs demonstrate a persistent anterior dislocation despite attempts at reduction, a congenital radial head dislocation should be considered, which has characteristic findings including a convex radial head, small capitellum, and concave shaped posterior margin of the olecranon.

MRI may be indicated when radiographs show persistent radial head dislocation despite attempted reduction to look for obstacles to reduction such as an entrapped annular ligament.

***Treatment.*** Supinating the child's forearm with the elbow in flexion will usually reduce the dislocation. Often, the dislocation is reduced at the time of imaging as previously described. A small percentage of children may have recurrent dislocations, with a higher risk the younger the first dislocation occurs.

## TRAUMATIC INJURIES OF THE FOREARM

***Etiology, Pathophysiology, and Clinical Presentation.*** Fractures of the distal radius and ulna are very common. The distal radius is the most common site of buckle fractures in children and usually occurs after a fall on an outstretched arm. Salter-Harris fractures of the distal radius (usually Salter-Harris II) and transverse fractures of the distal radial metadiaphysis are also common.[74] Stress injury to the distal radial physis is frequently seen in gymnasts. Fractures of the radial and ulnar shafts usually occur together. Often, the fracture in one bone is complete, whereas the other bone may be incomplete fracture.

Forearm fractures may also be associated with dislocations. *Monteggia injury* is defined as a fracture of the proximal third of the ulna with dislocation of the radiocapitellar joint.

*Galeazzi injury* is a fracture of the distal radial shaft with a dislocation of the distal radioulnar joint. These injuries are rarely diagnosed in children, as distal radioulnar joint disruption is uncommon, perhaps because of underrecognition. The distal ulna is most commonly subluxed or dislocated in the direction opposite that of distal radial displacement.

***Imaging.*** In radial buckle fractures, the cortex tends to buckle dorsally. A fracture line may be present volarly. It is important to look at all views for a subtle disruption of the normal smooth flared curve of the metadiaphyseal margin. Any extra angulation or "bump" is likely a fracture (see Fig. 142.4). An associated distal ulnar fracture may or may not be present. With a subtle distal radial fracture, the accompanying distal ulnar buckle fracture may be occult, often not identified until signs of healing are seen on follow-up radiographs. Distal radial buckle fractures may also be associated with triangular fibrocartilage injuries and fractures of the ulnar styloid process. Associated carpal injuries are uncommon.[75]

As with buckle fractures, Salter-Harris fractures of the distal radius and transverse fractures of the distal radial metadiaphysis often occur from falling on an outstretched arm. The distal fragment is usually dorsally displaced or angulated, or both.

Several subtypes of Monteggia fractures are determined on the basis of the anatomy of the ulnar fracture and the direction of radial head dislocation.[76–78] The most common direction of radial head dislocation is anterior with respect to the capitellum (Fig. 142.34).

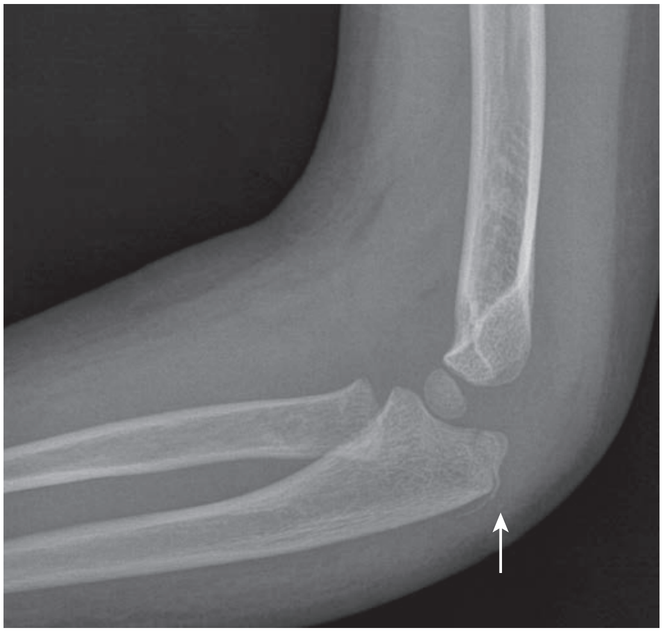

**e-Figure 142.31. Olecranon fracture involving the metaphyseal equivalent region *(arrow)* in a 4-year-old boy.** The olecranon epiphyseal equivalent is cartilaginous in a 4 year old.

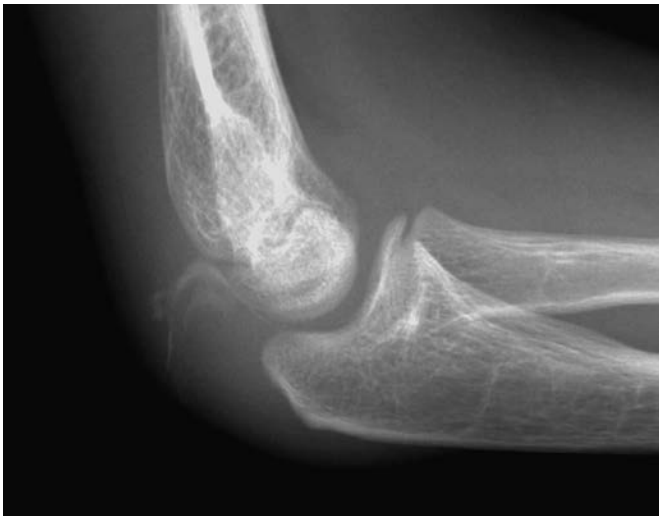

**e-Figure 142.32. Olecranon sleeve fracture in an 11-year-old boy.** A shell of bone is avulsed from the olecranon process and displaced proximally related to the triceps muscle insertion.

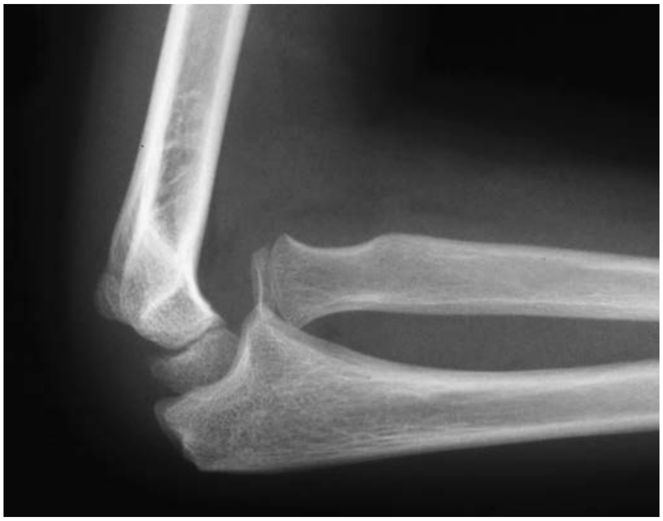

**e-Figure 142.33.** Radial head dislocation in a 9-year-old girl.

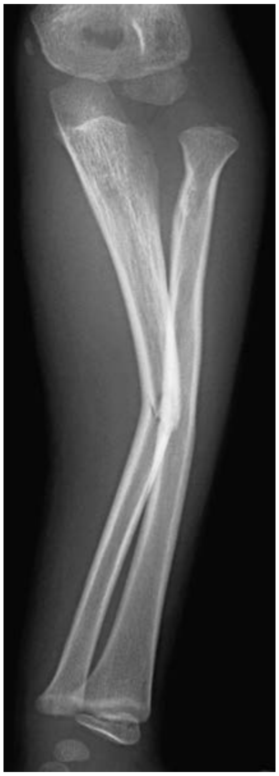

**Figure 142.34. Monteggia fracture–dislocation in a 6-year-old boy.** A greenstick fracture of the ulna is present with medial angulation of the distal ulna. The radial head is anteriorly dislocated.

***Treatment.*** Buckle fractures, including those with mild angulation, are usually treated with a splint. Nondisplaced, complete, nonphyseal fractures are casted. Fractures that involve the distal radial physis usually require closed reduction if displaced. The amount of accepted displacement depends on the type and location of the fracture, age of the child, and direction of angular deformity. In children older than age 10 years, fractures involving the proximal one-third of the radius and those with angulation appear to be at higher risk for failure when treated nonoperatively.[79] Surgical reduction is performed with pin fixation across the fracture. With Monteggia fractures, it is the nature of the ulnar fracture rather than the direction of radial head dislocation that is useful in determining optimal treatment for these injuries. Stable anatomic reduction of the ulnar fractures results in stable anatomic reduction of the radial head.[80] Nonsurgical management of Galeazzi fractures with anatomic reduction and immobilization in a long-arm cast has been successful in children.[81]

## TRAUMATIC INJURIES OF THE WRIST

***Etiology, Pathophysiology, and Clinical Presentation.*** Carpal bone fractures and intercarpal ligament injuries usually occur during the second decade, when children are near skeletal maturity, and follow an adult pattern of injury. Carpal fractures in the first decade are exceedingly rare because of two reasons: (1) the carpal bones have significant epiphyseal equivalent cartilage cushioning the primary carpal ossification centers from injury; and (2) the point of maximal weakness of the forearm and wrist is at the level of the radial and ulnar physes, leading to Salter-Harris fractures, as well as the level of metadiaphyseal cortex where buckle fractures occur. Therefore in the first decade, Salter-Harris fractures and buckle fractures are far more common than carpal bone fractures and ligamentous injuries.

The scaphoid is the most frequently fractured carpal bone. Scaphoid fractures most commonly are transverse and extend through the scaphoid waist. Fractures of the triquetrum are the next most reported carpal bone fracture, followed by the trapezium.[2]

***Imaging.*** Scaphoid views with ulnar deviation will better profile the scaphoid and can be added as a supplement to the standard three view wrist series. CT or MRI (e-Fig. 142.35) can be used to confirm the diagnosis and assess for alternative etiologies for wrist pain.[82] Alternatively, if clinical suspicion persists because of mechanism or physical examination findings (snuffbox tenderness), then splints may be applied, with follow-up radiographs obtained after 10 to 14 days or MRI to reassess for fracture.

The scaphoid artery enters from the distal pole and extends proximally to supply the proximal pole. As a result, proximal pole osteonecrosis may occur after midpole scaphoid fractures. Osteonecrosis is less frequent in the pediatric population compared with the adult population.[2] The affected proximal pole of the scaphoid will appear dense relative to the other bones of the wrist (Fig. 142.36). Nonunion of the scaphoid can occur with or without osteonecrosis. The incidence of nonunion is increased with delay in diagnosis.[83,84] Other complications of scaphoid fractures include humpback deformity, when there is abnormal angulation between the proximal and distal poles, and carpal instability.

Fractures of the triquetrum (e-Fig. 142.37) are seen as a small bony fragment projecting dorsally. Fractures of the hook of the hamate may occur in athletes. Carpal dislocations are rare in children. As in adults, these dislocations may involve a fracture of the scaphoid. Carpal instability rarely manifests in childhood.[83]

***Treatment.*** Scaphoid fractures usually heal with closed treatment and immobilization. Displaced fractures may require either open or closed reduction with internal fixation to minimize the risk of nonunion.[83] Triquetral fractures are usually treated nonoperatively.

## TRAUMATIC INJURIES OF THE HANDS

***Etiology, Pathophysiology, and Clinical Presentation.*** Fractures of the hand are common in children. The incidence peak is bimodal, the first peak being at age 1 to 2 years and the second at age 12 years. At age 1 to 2 years, the most common hand injury is a distal phalanx fracture with soft tissue laceration. At age 12 years, the most common hand injury is fracture of the proximal phalanx of the little finger, followed by metacarpal fractures.[85] In general, phalangeal fractures and interphalangeal dislocations are relatively common injuries. Fractures of the hand often involve the physis,[86] and Salter-Harris fractures are common. Growth disturbances in this region are relatively uncommon.[2]

***Imaging.*** Radiography with at least anteroposterior, oblique, and lateral views should be obtained tailored to the specific injured digit rather than imaging the entirety of the hand.

Avulsion injuries usually occur from hyperextension, hyperflexion, or “jamming” of the finger into an object. “Mallet finger” is the result of forced flexion of a distal interphalangeal joint leading to Salter-Harris III fracture–avulsion of the dorsal aspect of the terminal phalanx (e-Fig. 142.38).[86] Volar plate Salter-Harris III avulsion fractures occur along the volar side and may occur at either the terminal phalanx or middle phalanx insertion of the flexor digitorum tendons (e-Fig. 142.39).

Salter-Harris II fractures are common and frequently involve the proximal phalanx of the thumb.[86] Displacement is variable. The fractures may be very subtle with minimal physeal widening or a tiny metaphyseal fragment (e-Fig. 142.40). It may be difficult to distinguish between a Salter-Harris III fracture of the proximal phalanx and a bifid epiphysis, an uncommon normal variant. Salter-Harris I and III fractures occur occasionally in the digits.

Fracture of the fifth metacarpal (“boxer’s fracture”) is the most common metacarpal fracture in adolescents.[85] The fracture plane is transverse or oblique through the metaphysis at the distal aspect

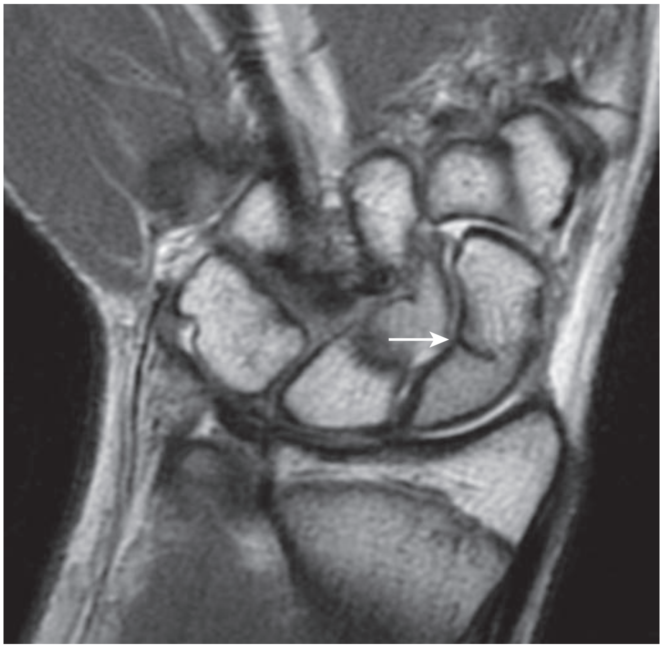

**e-Figure 142.35. Scaphoid fracture.** A 15-year-old boy with T1-weighted coronal MR image demonstrating a nondisplaced incomplete scaphoid waist fracture *(arrow)*.

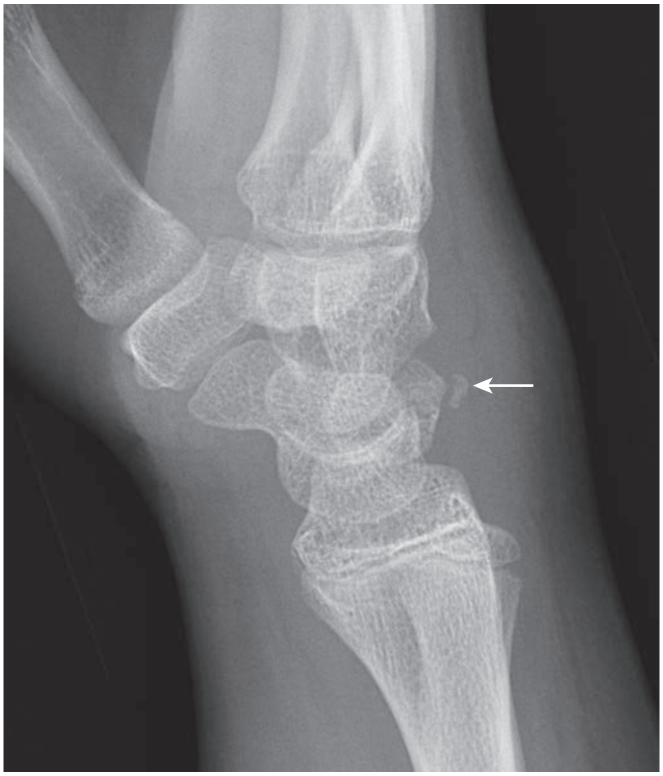

**e-Figure 142.37. Triquetral fracture.** An 11-year-old girl with minimally displaced triquetral fracture seen on lateral view *(arrow)*.

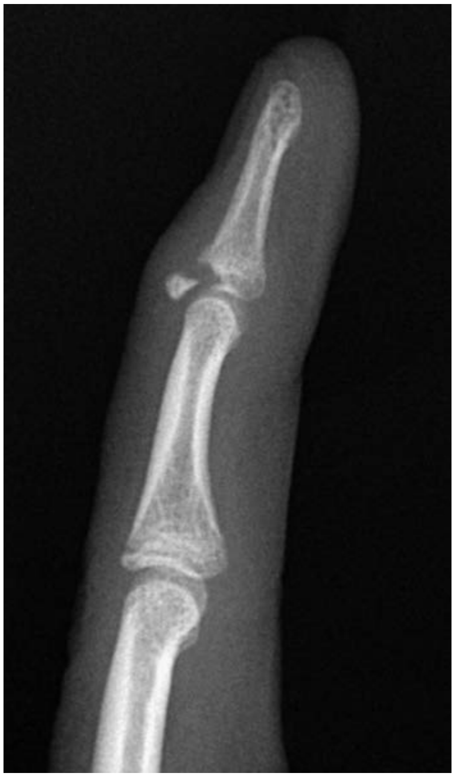

**e-Figure 142.38.** Mallet finger in a 13-year-old boy.

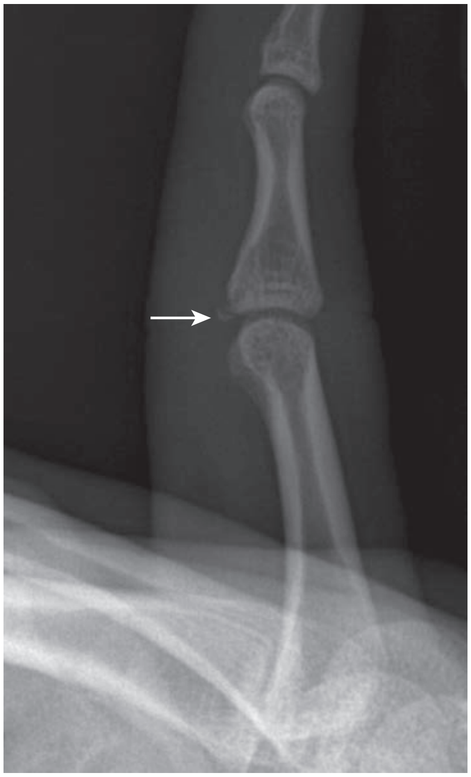

**e-Figure 142.39.** Phalangeal volar plate fracture *(arrow)* in a 15-year-old boy.

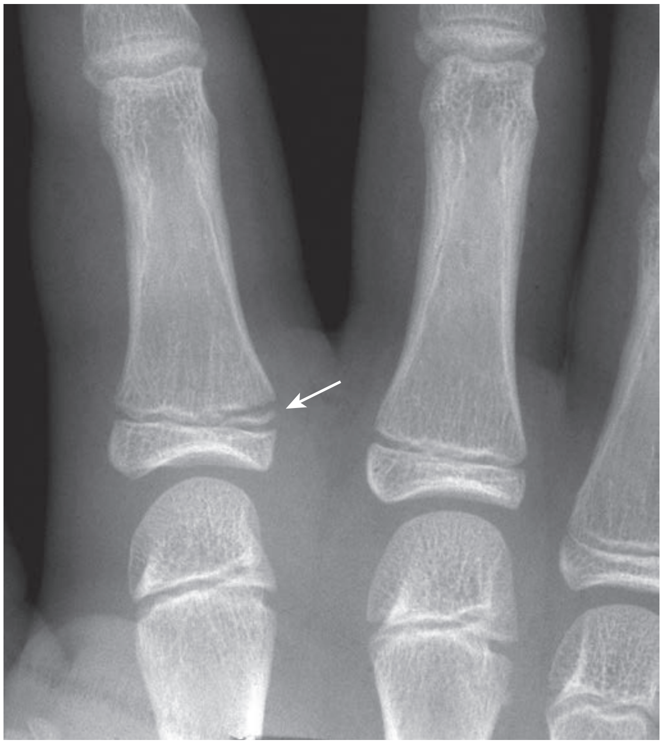

**e-Figure 142.40. Salter-Harris II fracture of the proximal phalanx of the index finger *(arrow)* of a 9-year-old girl.** The child was hit with a ball with the finger extended.

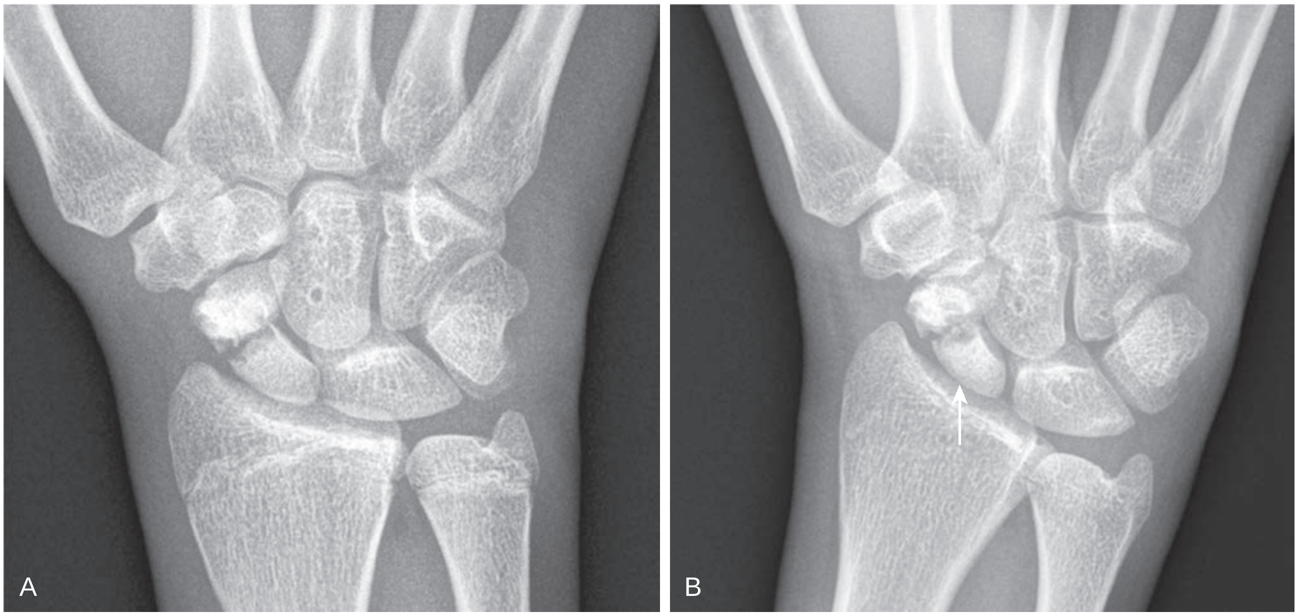

**Figure 142.36. Scaphoid waist fracture in a 16-year-old boy.** (A) Radiograph at presentation demonstrates a mildly displaced scaphoid waist fracture. (B) Repeat radiograph 6 months later shows lack of healing at the fracture site, and subtle increased proximal pole radiodensity *(arrow)* without collapse, suggestive of nonunion and early osteonecrosis.

of the fifth metacarpal. The distal fragment is angulated toward the palm (e-Fig. 142.41).

Salter-Harris III fractures of the first metacarpal bone are analogous to a Bennett fracture occurring after skeletal maturity (e-Fig. 142.42). A Bennett fracture is an intraarticular fracture at the base of the first metacarpal with first carpometacarpal subluxation. A Rolando fracture is a comminuted version of the Bennett fracture. These injuries are rare in children.

"Gamekeeper's thumb" (e-Fig. 142.43) is a traumatic avulsion fracture at the first proximal phalangeal insertion of the ulnar collateral ligament. This injury can be seen in children from a ski pole injury.[87] An avulsion may be seen at the ulnar volar base of the proximal phalanx of the thumb or a Salter-Harris III fracture if the physis is not yet fused. Radial subluxation of the proximal phalanx may be evident, but stress views may be required to show instability in the absence of fracture. Ulnar collateral ligament avulsion may also cause a Stener lesion with the adductor aponeurosis interposed between the torn ulnar collateral ligament and its insertion, preventing approximation, which can be diagnosed on MRI.

***Treatment.*** Nearly all metacarpal and phalangeal fractures are treated nonsurgically with 3 to 4 weeks of immobilization.[2] Surgical pinning is required for intraarticular fractures, particularly those involving the interphalangeal and metacarpophalangeal joints. Nondisplaced avulsion fractures are typically treated by brace taping or buddy taping the injured digit to its neighbor. Stener lesions are managed operatively.[86]

## TRAUMATIC INJURIES OF THE PELVIS AND HIP

### Pelvic Fractures

***Overview.*** Pelvic fractures are not common in children.[88] Pedestrian–motor vehicle collisions account for the majority of cases, followed by falls. The majority of victims are boys.[88,89] A pelvic injury in a child is a marker of severe injury and should alert the clinician to search for additional injury.[89,90] Apophyseal avulsion injuries of the pelvis are covered in Chapter 144.

***Etiology, Pathophysiology, and Clinical Presentation.*** Once a patient has reached skeletal maturity, pelvic ring fracture patterns follow the adult fracture pattern and classification.[91] Several classifications schemes have been applied to pediatric pelvic fractures such as the classification scheme of Torode and Zieg (e-Fig. 142.44).[92] Disruption of the sacroiliac joints or pubic symphysis may accompany pelvic fractures. Plastic or incomplete fractures may be seen in children. Usually, if a break in the obturator ring or pelvic ring is present, another break is also present. Younger children, however, may not follow this rule because of the plasticity of their bones.[93,94]

Fractures involving the acetabulum of young children are fortunately rare. Acetabular fractures become more common in the later teen years because of motor vehicle accidents[93] and follow patterns similar to those in adults. Most occur in association with hip dislocations.[94]

***Imaging.*** CT is the preferred modality for delineation of unstable pelvic fractures. Although most fractures are seen on radiography, CT better delineates the full extent of fracture.[95] Radiography is not necessary if CT will be performed to evaluate for other injuries.[96]

Asymmetric widening of the triradiate cartilage may be noted in acetabular fractures (e-Figs. 142.45 and 142.46). In younger children, fractures involving the triradiate cartilage are prone to complications, particularly when displaced fragments are present. Premature fusion of the triradiate cartilage may lead to a shallow acetabulum and progressive hip instability.[93] This complication is more common in children under age 10 years at the time of fracture.

***Treatment.*** The majority of pelvic fractures can be treated nonsurgically.[89,97,98] Surgical intervention is needed for unstable fractures or fracture-dislocations.

### Hip Dislocation

***Overview.*** Traumatic hip dislocations are more common in adolescence. The hip usually dislocates posteriorly. Compared with adults, these injuries are less commonly associated with acetabular fractures.[94]

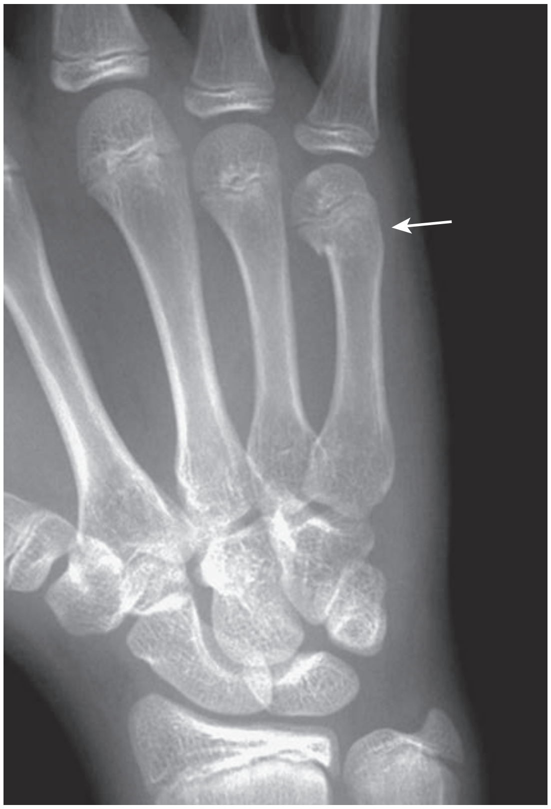

**e-Figure 142.41. Boxer's fracture of the fifth metacarpal *(arrow)* in a 17-year-old boy who punched a wall.** Slight palmar angulation of the distal fracture fragment is seen distally.

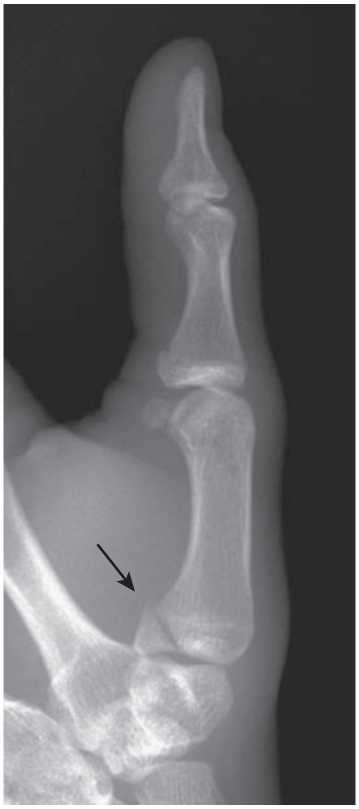

**e-Figure 142.42. Salter-Harris III fracture of the base of the thumb metacarpal *(arrow)* in a 16-year-old boy.** The injury occurred when the boy's thumb caught on another player's equipment while playing football.

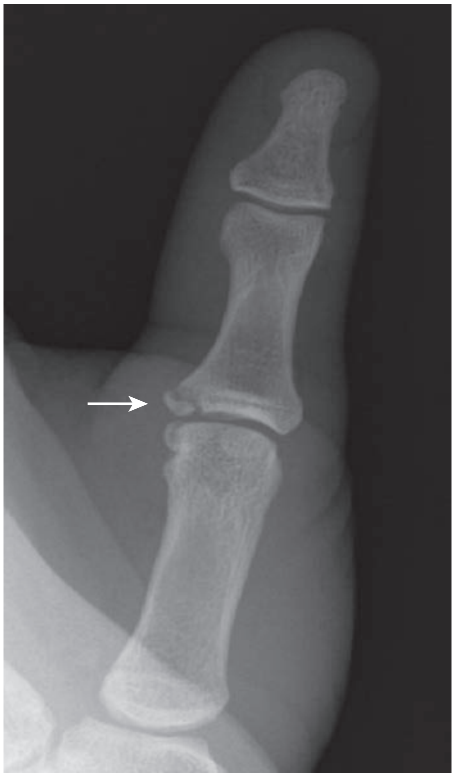

**e-Figure 142.43. Gamekeeper's thumb fracture *(arrow)* in a 14-year-old boy.**

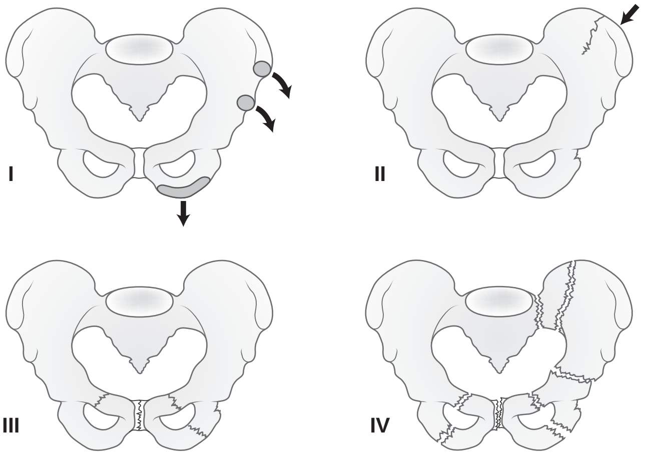

**e-Figure 142.44. Pelvic fractures in children—Torode and Zieg classification.** *Type I,* Avulsion fracture. *Type II,* Iliac wing fracture. *Type III,* Simple ring fracture. *Type IV*, Ring disruption fracture. *(Modified from Beaty JH, Kasser JR.* Rockwood and Wilkins' Fractures in Children*, 6th ed. Philadelphia, PA: Lippincott Williams & Wilkins; 2006.)*

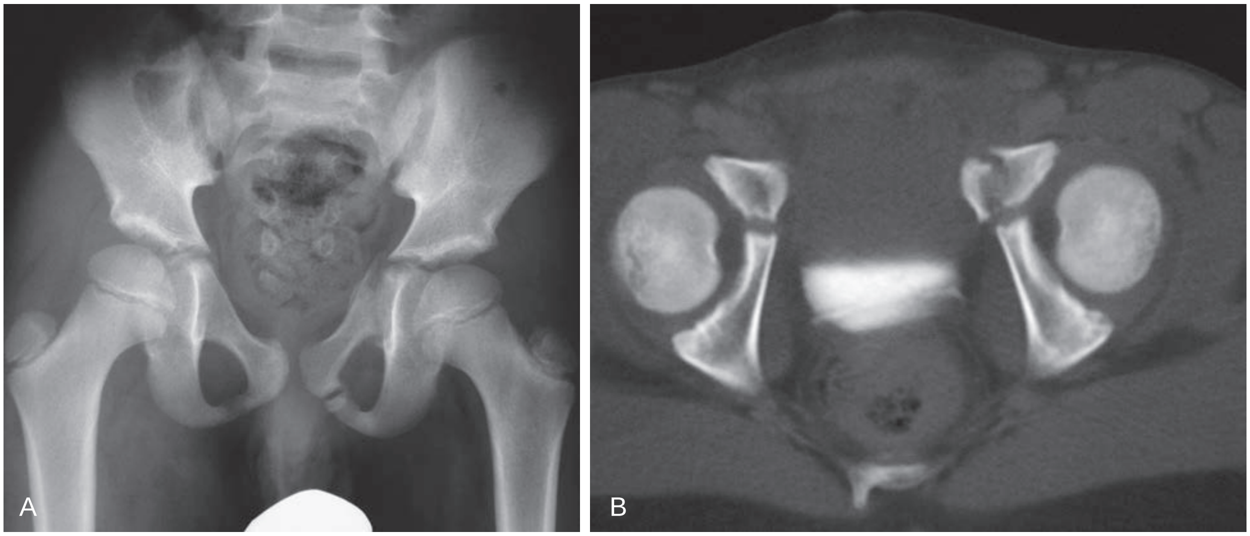

**e-Figure 142.45. Pelvic fracture involving the triradiate cartilage.** Radiographs from an 8-year-old boy who was struck by an automobile. (A) Anteroposterior radiograph of the pelvis shows left pubic fractures and widening of the left triradiate cartilage. (B) Axial CT image shows the superior pubic ramus fracture to extend to involve the triradiate cartilage.

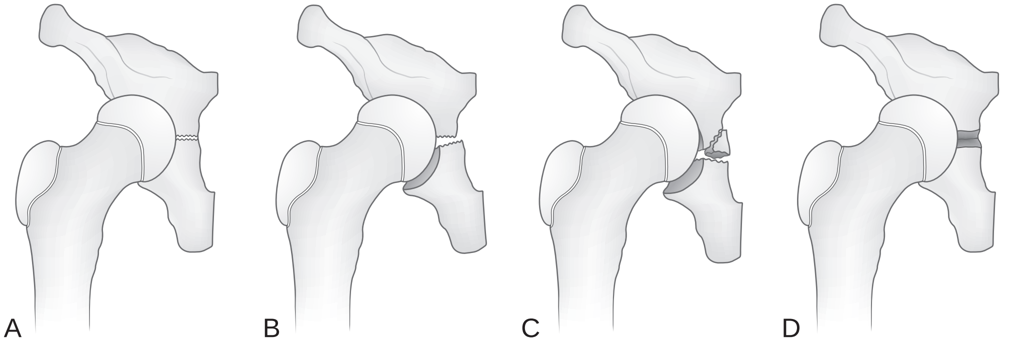

**e-Figure 142.46. Types of triradiate cartilage fractures.** (A) Normal triradiate cartilage. (B) Salter-Harris I fracture. (C) Salter-Harris II fracture. (D) Salter-Harris V (compression) fracture. *(From Scuderi G, Bronson MJ. Triradiate cartilage injury: report of two cases and review of the literature.* Clin Orthop Relat Res*. 1987;217:179–189.)*

***Etiology, Pathophysiology, and Clinical Presentation.*** In adolescents, hip dislocation is usually the sequela of significant trauma such as that sustained in motor vehicle accidents, whereas younger children may dislocate their hips with relatively minor trauma, usually falls.[99] Fractures of the acetabulum and femoral head can occur at the same time. When dislocations occur with minimal trauma, ligamentous laxity should be considered as a possible underlying condition such as that seen with Ehlers-Danlos syndrome, Larsen syndrome, and Down syndrome.

***Imaging.*** Initial imaging evaluation should be radiographs (Fig. 142.47). If asymmetry of the hip joint persists on radiography after reduction, then further evaluation with either CT or MRI (e-Fig. 142.48) should be considered to evaluate for labral entrapment or interposed osteochondral fragments. If a fracture of the acetabular wall or femoral head is suspected, CT or MRI should be obtained, as it could alter patient management.

***Treatment.*** Most hip dislocations in children are reducible with gentle manipulation; however, closed reduction of the hip in the adolescent population carries a risk of epiphyseal osteonecrosis. Open reduction is necessary when closed reduction fails or when interposition of soft tissue or bone exists. Additional complications of hip dislocations include premature osteoarthritis and sciatic nerve injury. If the delay in reduction is greater than 6 hours, the risk of osteonecrosis is significantly increased.[100,101]

## Slipped Capital Femoral Epiphysis

***Etiology, Pathophysiology, and Clinical Presentation.*** Slipped capital femoral epiphysis (SCFE) is the most common hip disorder affecting the adolescent population.[102] SCFE is essentially a Salter-Harris I fracture of the proximal femoral physis. SCFE occurs more frequently in boys than in girls, tends to occur earlier in age in girls compared with boys, and occurs more commonly in African Americans. SCFE is usually idiopathic with a higher incidence in children who are clinically obese.[102,103] Risk factors for SCFE include hypothyroidism, pituitary dysfunction, hypogonadism, and renal osteodystrophy.[104,105] Hips previously exposed to a radiation treatment field are at increased risk. When a child presents with bilateral symmetric SCFE or outside of the typical age range, an underlying disorder should be suspected.[106]

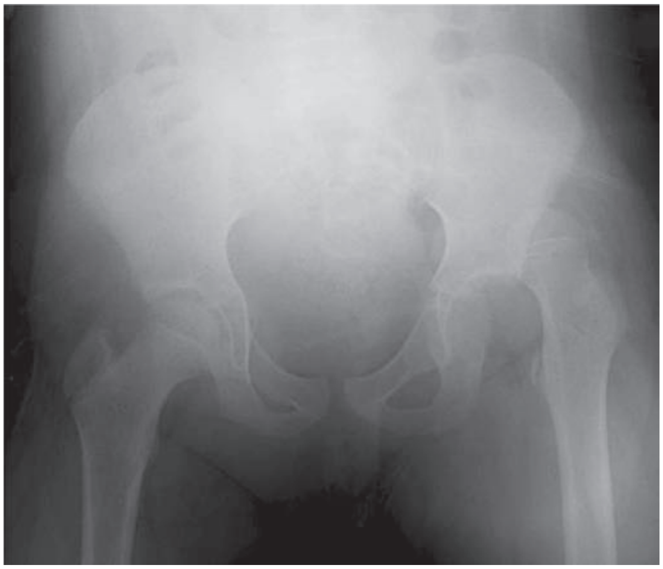

**Figure 142.47. Hip dislocation.** A single anteroposterior radiograph of the pelvis in a 9-year-old girl demonstrates superolateral position of the left femoral head compatible with a posterior hip dislocation.

Approximately 25% of patients will have bilateral SCFEs,[104,105] and approximately half of these present synchronously. Risk for contralateral SCFE is greatest in the first 2 years after initial diagnosis.[104]

Children with SCFE usually present with hip, groin, or thigh pain. Symptoms may first occur after minor trauma. Up to one-quarter of patients present with referred knee pain.[106] Hip radiographs are therefore recommended in the adolescent with unexplained knee pain. SCFE can be categorized as acute or chronic and stable or unstable.[107–110] By definition, patients with stable SCFE are able to bear weight.

***Imaging.*** Radiography for suspected SCFE should include a pelvic anteroposterior and "frogleg" lateral view. Both hips should be included. Epiphyseal slips may occur in the medial direction, posterior direction, or both. The frogleg lateral view is helpful, as most epiphyseal slips occur in the posterior direction, which can be subtle on the anteroposterior view (Fig. 142.49). The anteroposterior view best assesses the degree of medial displacement, which is often subtle. Klein's line is drawn parallel to the lateral margin of the femoral neck on the anteroposterior view. Normally, a small portion of the femoral head extends lateral to Klein's line. When the femoral head does not extend lateral to Klein's line, medial displacement should be suspected (see Fig. 142.49).[111] Theoretically, Klein's line can potentially be preserved if the SCFE is directly posterior without a medial component. The smaller the capital femoral epiphysis appears on the anteroposterior view, the greater is the degree of posterior slip.

With chronic slips, sclerosis may be seen in the medial femoral neck with bone remodeling ("buttressing") in response to altered mechanics (e-Fig. 142.50).

CT and MRI may also be used to make the diagnosis of SCFE; however, radiographs usually suffice. MRI can be used to detect a "pre-slip" state, as evidenced by physeal widening with adjacent bone marrow edema.[112] MRI may also be used in follow up to evaluate cartilage and labral abnormalities that can result as chronic sequelae of SCFE, the latter due to femoral acetabular impingement secondary to CAM-type deformities, which may form at the femoral head-neck junction.

***Treatment.*** In situ fixation with transphyseal screw is the treatment for SCFE. Prophylactic pinning of the contralateral hip may be performed in high-risk individuals. Timing of treatment is predicated on symptoms. Stable SCFEs can be electively pinned. Unstable SCFEs usually require urgent or emergent pinning, as they are at higher risk for epiphyseal osteonecrosis. Reduction of the capital femoral epiphysis is performed with extreme caution, because even minimal manipulation may disrupt the epiphyseal blood supply.

Complications after SCFE treatment include epiphyseal osteonecrosis (Fig. 142.51) and chondrolysis (e-Fig. 142.52). Epiphyseal osteonecrosis is more frequent after treatment of unstable SCFE. Chondrolysis used to complicate 5% to 10% of patients with SCFE, but the incidence has substantially lessened with newer fixation techniques.[113] Chondrolysis is now rarely seen without accompanying epiphyseal osteonecrosis. An additional complication of SCFE is cam-type femoroacetabular impingement related to abnormal offset of the femoral head and neck junction (see Chapter 144).

## TRAUMATIC INJURIES OF THE KNEE

***Overview.*** Before physeal fusion, the physes are the usual site of traumatic injury at the knee.[114] Once the physes fuses, cruciate ligament injury becomes much more common.[115] Hemarthrosis of the knee joint may be the consequence of soft tissue injury and/or fracture.

## DISTAL FEMUR

***Etiology, Pathophysiology, and Clinical Presentation.*** Two types of distal femoral fractures have been described. Juvenile type injuries

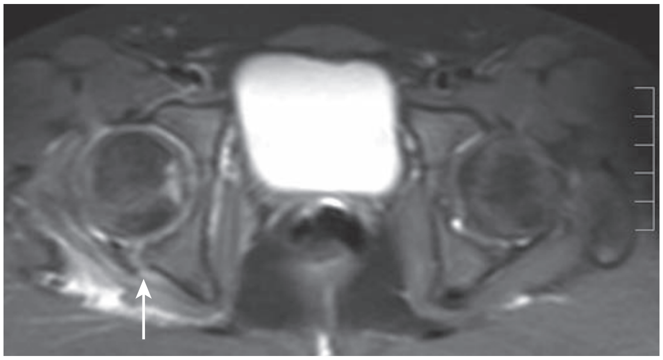

**e-Figure 142.48. Acetabular fracture.** A 10-year-old boy with posterior osteolabral acetabular wall fracture *(arrow)* on short tau inversion recovery axial magnetic resonance imaging after dashboard injury related to motor vehicle accident.

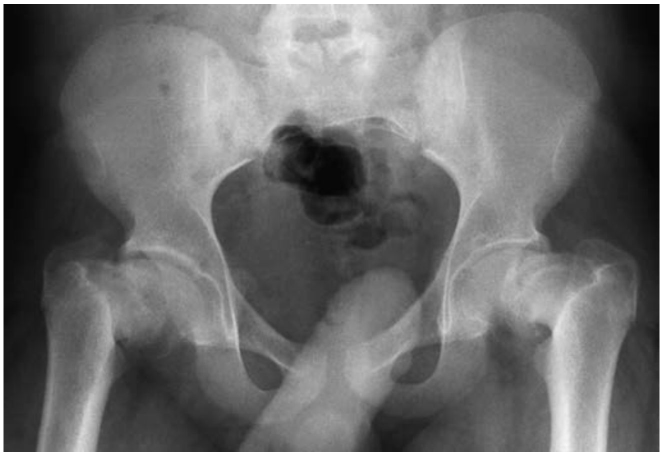

**e-Figure 142.50. Advanced, chronic bilateral slipped capital femoral epiphyses at presentation in a 16-year-old boy.** The femoral heads are rotated medially with varus deformity. The femoral necks are sclerotic with buttressing medially.

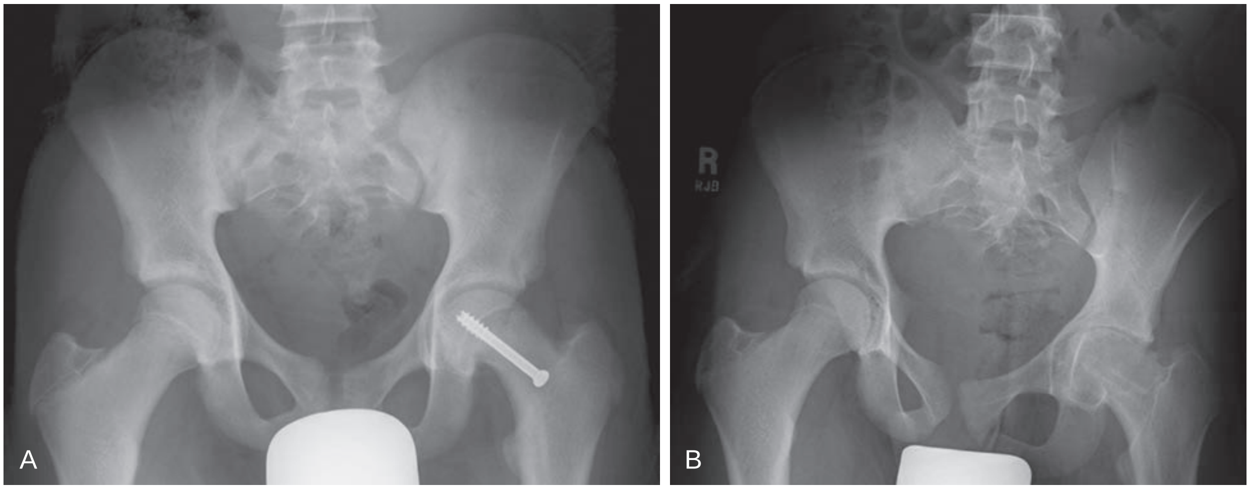

**e-Figure 142.52. Chondrolysis after treatment of slipped capital femoral epiphysis in a 15-year-old boy.** (A) Postoperative radiograph demonstrates pin fixation of left-sided SCFE with normal hip joint space. (B) One year later, uniform joint space narrowing of the left hip consistent with chondrolysis is seen.

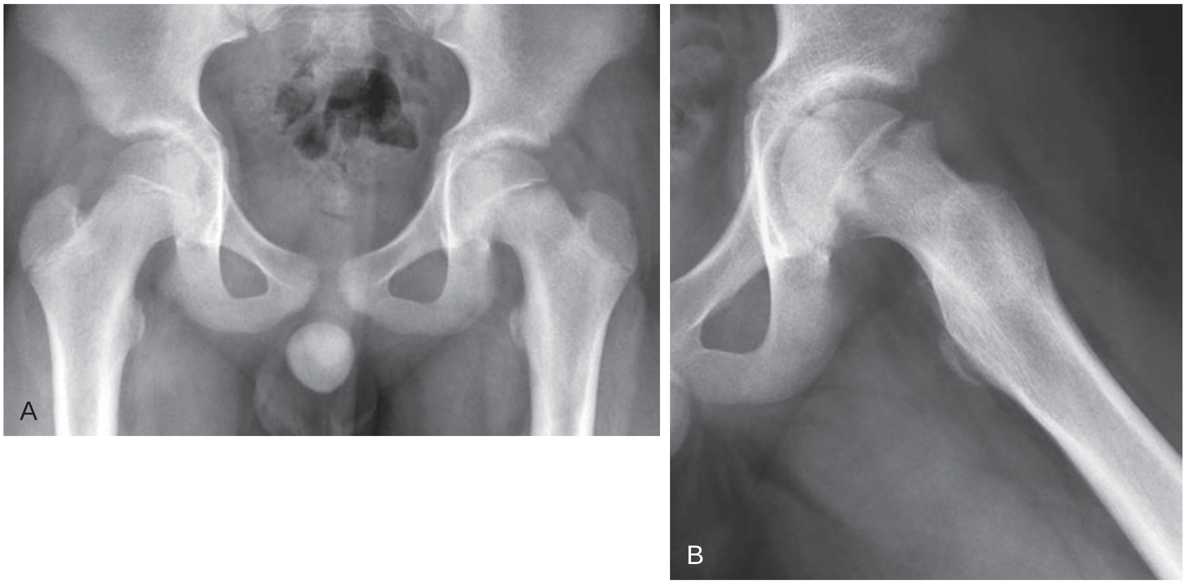

**Figure 142.49. Slipped capital femoral epiphysis in an 11-year-old boy with left hip pain.** (A) On the anteroposterior view, the growth plate of the left proximal femur is wide and indistinct. The left femoral epiphysis is slightly medially positioned on the metaphysis with no portion of the left femoral head projecting lateral to Klein's line. The right proximal femur is normal. (B) On the lateral view, malalignment of the femoral epiphysis is better seen. The femoral epiphysis is displaced posteromedially relative to the femoral metaphysis but is still in continuity.

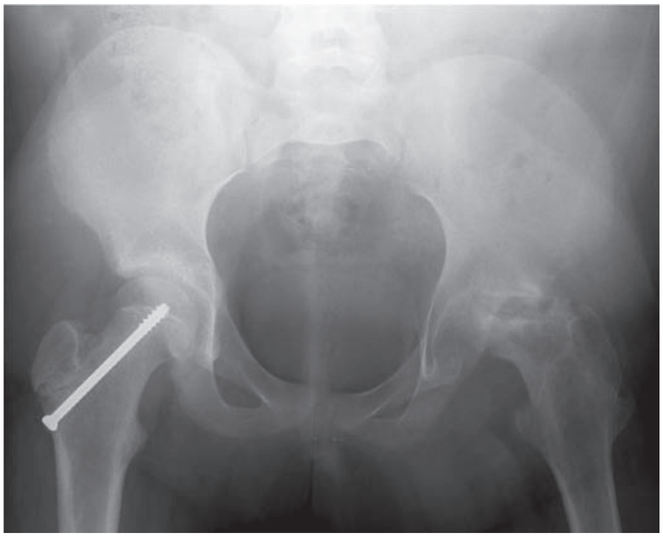

**Figure 142.51. Complication of slipped capital femoral epiphysis.** Single anteroposterior radiograph of the pelvis in a 14-year-old girl demonstrates left femoral head fragmentation and collapse consistent with osteonecrosis. There are postsurgical changes of the right femur.

(age 2–10 years) are most common secondary to high-energy trauma such as a motor vehicle accident, whereas adolescent type injuries are typically sports-related.[116] Salter-Harris type II fractures are the most common injury with usual displacement in the coronal plane, medial physeal separation, and associated medial collateral ligament sprain.[116] Salter-Harris type fractures are more common in the distal femur compared with ligamentous injuries of the knee, particularly during periods of rapid growth.

***Imaging.*** Initial evaluation begins typically with anteroposterior, lateral, and axial (e.g., merchant, sunrise) views of the knee. Axial views are usually not helpful in children under age 5 years, because the patella is undermineralized and patellar fractures are unusual in the first decade. Depending on the mechanism of injury, MRI or CT may be used in certain situations. MRI review must include specific attention to the unfused physes as part of the search pattern.[115] MRI is particularly useful in evaluating tendon and ligamentous injuries and bone contusions. With intraarticular fracture, lipohemarthrosis may be seen on cross-table lateral radiographs, MRI, or CT.[117] This indicates breech of the bone marrow due to fracture.

Most displaced Salter-Harris fractures of the distal femoral metaphysis are obvious on clinical examination and on radiographs; however, subtle distal femoral Salter-Harris injuries may be occult on radiography and not diagnosed until MRI is performed (e-Fig. 142.53). On follow-up imaging, close assessment of the physis should be performed due to the high incidence of physeal bridges that occur after distal femoral fractures involving the growth plate.

***Treatment.*** Distal femoral physeal fractures are treated conservatively with immobilization if nondisplaced and stable. Unstable, intraarticular, or displaced fractures are treated operatively with fixation.

## PATELLA

***Etiology, Pathophysiology, and Clinical Presentation.*** Fractures of the patella in skeletally immature patients are rare.[118] Osteochondral fractures and avulsions related to patellar dislocation and patellar sleeve avulsion fractures are discussed in Chapter 144.[119,120] Direct impaction injury is the most common cause of patellar fractures that are not related to sleeve avulsions of dislocations. Like the scaphoid, the patella has a recurrent blood supply. Avascular necrosis of the proximal fragment is a rare complication of transverse patellar fractures.

***Imaging.*** Initial evaluation begins with anteroposterior, lateral and axial (e.g., merchant, sunrise) radiographs of the knee.

Patellar fractures may be simple (e-Fig. 142.54) or comminuted. Intraarticular involvement is important to define for

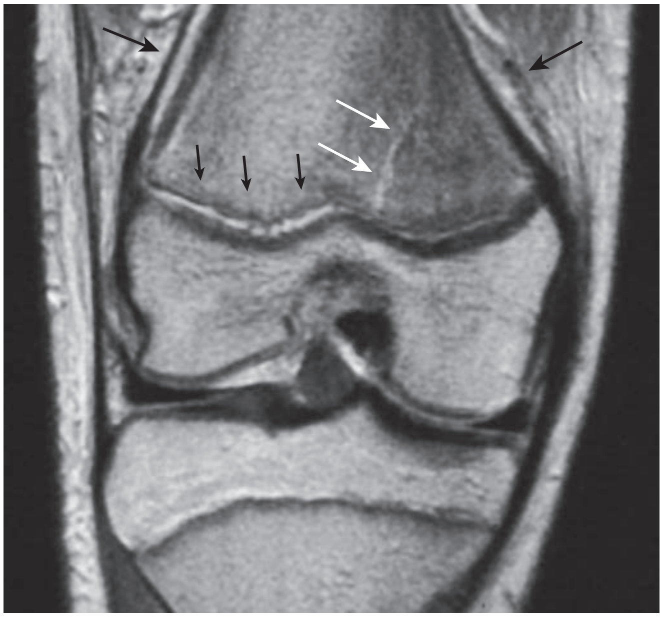

**e-Figure 142.53. Salter-Harris II fracture of the distal femur in a 12-year-old girl.** Proton density MR image shows widening of the distal femoral growth plate *(small black arrows)* and bone marrow edema. A metaphyseal fracture line is also seen *(white arrows)*. Periosteum is elevated *(large black arrows)*.

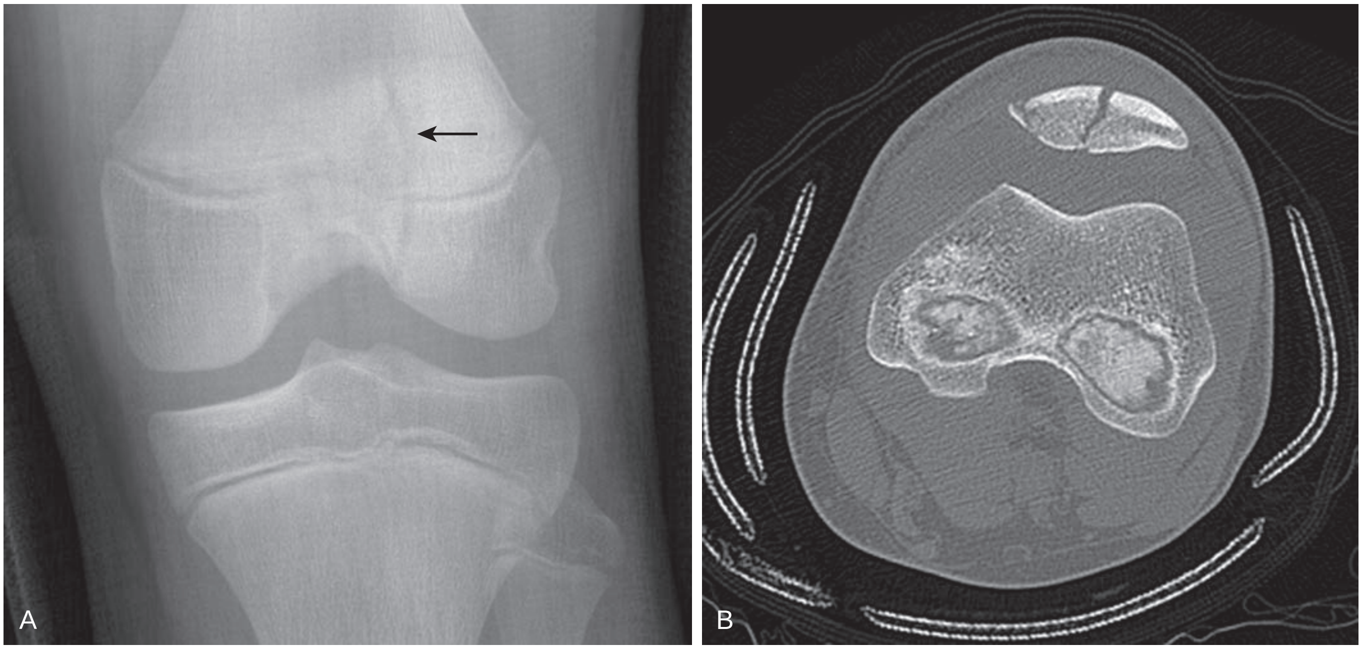

**e-Figure 142.54. Intraarticular nondisplaced patellar fracture in a 13-year-old boy.** The fracture line is seen on the (A) anteroposterior radiograph *(arrow)* and (B) axial CT. CT also demonstrates a medial patellar fracture.

surgical planning, and CT and MRI may be obtained for further evaluation. These fractures should be differentiated from a bipartite patella, which may fracture at the synchondrosis between the patellar body and the smaller superolateral ossification center.

***Treatment.*** Patellar fractures are treated surgically, depending on several factors, including integrity of the extensor mechanism, degree of displacement, and articular extension. Patellar fractures are particularly difficult to treat conservatively because of issues with nonunion (from chronic traction related to the extensor mechanism), and premature osteoarthritis, when the articular surface is involved.

## TIBIAL TUBEROSITY AND PROXIMAL TIBIA

***Etiology, Pathophysiology, and Clinical Presentation.*** Tibial tuberosity acute and chronic avulsion injuries, physeal equivalent Salter-Harris injuries of the tibial tuberosity, and tibial eminence anterior cruciate ligament avulsion fractures are covered in detail in Chapter 144.

The proximal tibia has an upside-down L–shaped physis and epiphysis. Both the tibial epiphysis and tuberosity are a single entity that fuses to the underlying tibia at approximately age 15 years in girls and age 17 years in boys.[121,122] Therefore any proximal tibial fracture extending to the tibial physis or tibial tuberosity physeal equivalent region should be considered a Salter-Harris type fracture.

Tibial hyperextension toddler fractures (also referred to as *trampoline fractures*) occur in the upper tibial metadiaphysis. These occur secondary to anterior forces being applied to knee during hyperextension.[123,124]

Unlike in adult patients, tibial plateau fractures in children are less likely to be depressed because the epiphyseal cartilage is more resilient and acts as a cushion for the tibial epiphyseal bone.

***Imaging.*** Initial evaluation begins with anteroposterior and lateral radiographs of the knee. Transverse fractures of the proximal tibia may appear innocuous but are technically Salter-Harris II fractures if they extend to the tibial tuberosity physeal equivalent zone. Avulsion fractures that violate the tibial epiphysis or tibial tuberosity are Salter-Harris III fractures (e-Fig. 142.55).

CT and MRI are useful to determine the 3D orientation of the fracture and its involvement of the physis, with MRI allowing a more detailed assessment of potential injury to the extensor mechanism. Tibial plateau fractures are best evaluated with MRI to assess the articular cartilage injury as well as coexisting meniscal and ligamentous injury.

Hyperextension fractures can be subtle; typically a buckle deformity of the anterior cortex of the proximal tibial metaphysis can be seen (Fig. 142.56).

***Treatment.*** Salter-Harris fractures involving the proximal tibia weight-bearing zone (tibial plateau) and Salter-Harris fractures involving the physeal equivalent region of the tibial tuberosity have different biomechanical challenges related to management. The tibial tuberosity is the insertion of the knee extensor mechanism, and therefore tibial epiphyseal equivalent fractures in this region may be unstable with knee motion. Tibial plateau fractures are also unstable, but because these are loadbearing surfaces, when the overlying cartilage is violated, it should cause concern for posttraumatic osteoarthritis and coexisting internal derangement and meniscal tears of the knee. For these reasons, a low threshold exists for surgical fixation and immobilization for both tibial tuberosity and tibial epiphyseal Salter-Harris fractures in children.

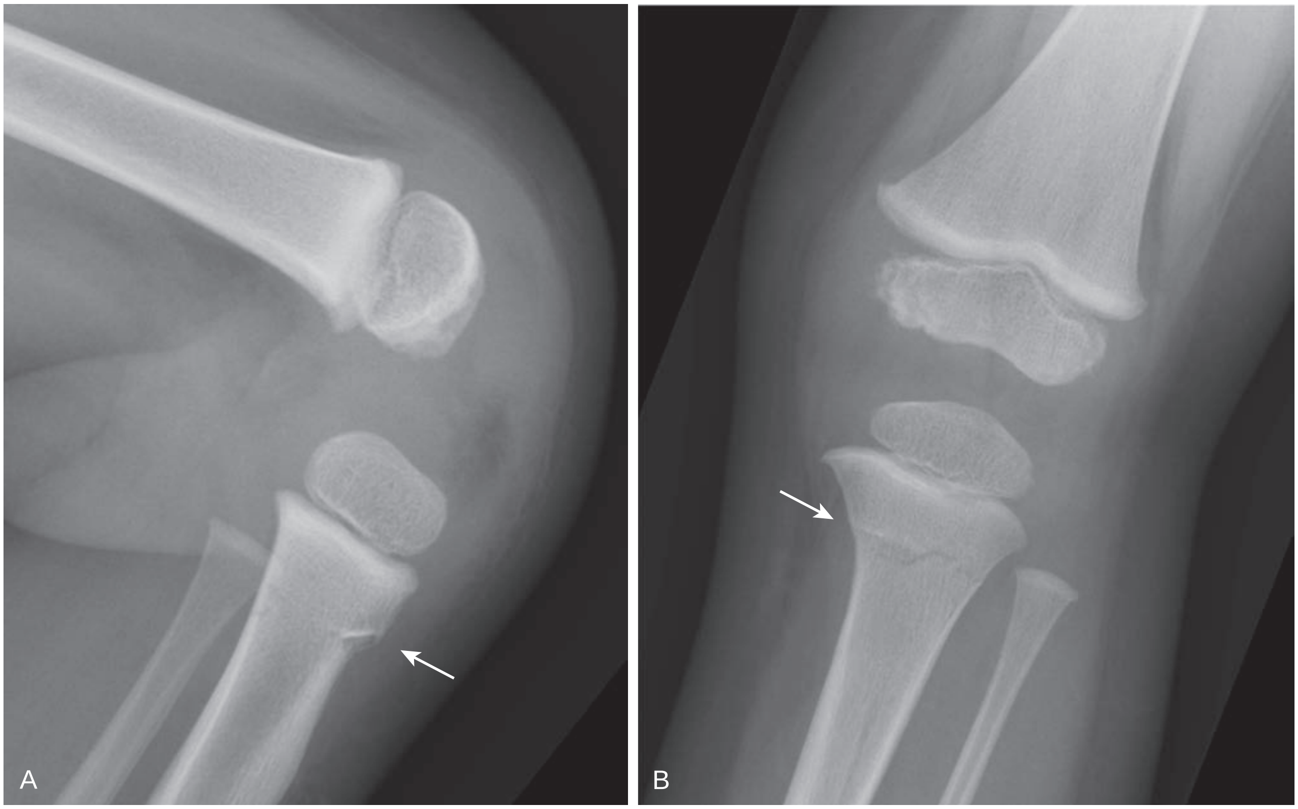

**Figure 142.56. Toddler's hyperextension fracture in a 23-month-old girl while jumping on a trampoline with an adult.** (A) Lateral radiograph shows a buckle fracture *(arrow)* of the anterior cortex of the proximal tibial metadiaphysis. Normally, the anterior proximal tibial cortex has a smooth appearance, which may be concave due to the unossified tibial tubercle. (B) Anteroposterior radiograph shows a faint transverse fracture line *(arrow)*.

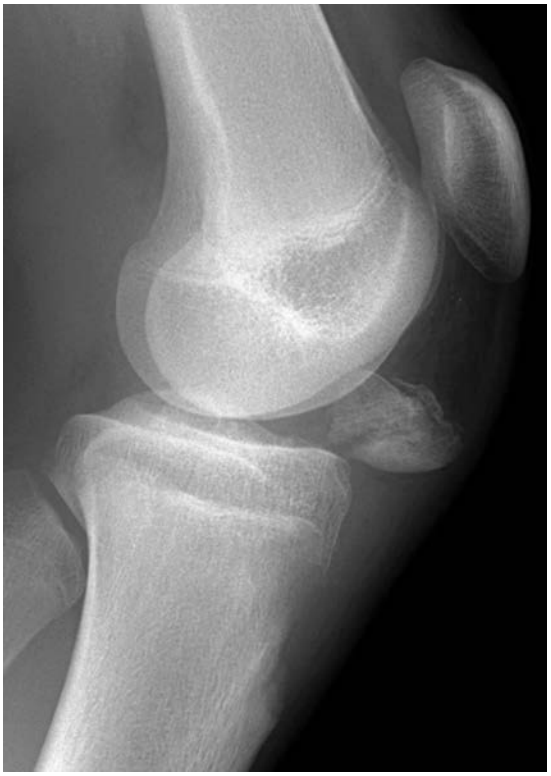

**e-Figure 142.55. Tibial tuberosity avulsion in a 16 year old after a bicycle accident.** The avulsed fragment is distracted proximally and rotated.

## TODDLER FRACTURES

***Etiology, Pathophysiology, and Clinical Presentation.*** Toddler fractures are typically seen between ages 9 months and 3 years. The term “toddler fracture” is used to describe any fracture of the leg or foot in the toddler. The tibia diaphysis is the most commonly fractured, followed by the fibula, femur, and cuboid bone.[125]

In the classic clinical toddler fracture history, the child’s leg is caught on an object, the leg twists, and the child falls. Other children present with pain and refusal to bear weight without a specific precipitating incident. On physical examination, the child will be point tender over the fracture.[126] Toddler fractures are common once children begin to cruise and walk.

***Imaging.*** Toddler fractures may occur anywhere within the proximal metadiaphysis, diaphysis, or distal metadiaphysis of the tibia. The fracture line is oblique or spiral usually with little to no distraction or displacement (Fig. 142.57). Acutely, the fracture line may be very subtle. In some patients, follow-up radiographs are necessary to confirm the fracture (e-Fig. 142.58). Similarly, acute toddler fractures of the fibula, femur, and cuboid (e-Fig. 142.59) may be subtle. The healing process, with sclerosis at the margins of the fracture line and development of periosteal new bone, may increase the conspicuity of the fracture.

Because the fracture line is oblique or spiral and because a particular event may not have led to the fracture, toddler fractures may erroneously be ascribed to child abuse. In the absence of other injury, however, the typical radiographic appearance of a toddler fracture in a child of appropriate age should not in itself raise suspicion.

***Treatment.*** Treatment is conservative, consisting of immobilization and casting, as well as avoidance of weight bearing.

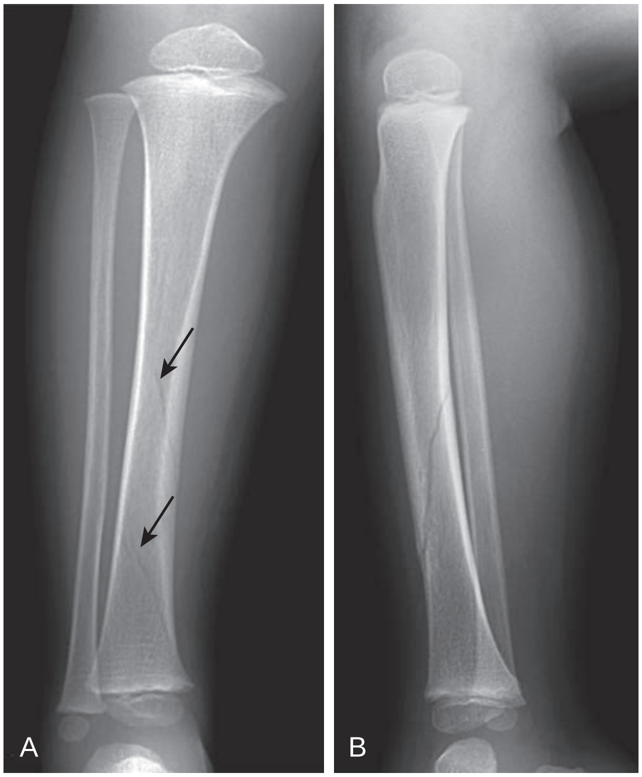

**Figure 142.57. Toddler fracture of the tibia in a 2-year-old girl.** Anteroposterior (A) and lateral (B) views of the tibia shows a spiral fracture line as shown by two apparent fracture lines on the anteroposterior view *(arrows)* and the intervening single fracture line on the lateral view. Slight soft tissue swelling is seen anterior to the fracture on the lateral view.

## OTHER TIBIAL AND FIBULAR FRACTURES

***Etiology, Pathophysiology, and Clinical Presentation.*** Most tibial fractures occur in the distal metadiaphysis,[127] which is a common site for buckle fractures in young children. Salter-Harris fractures are also very common at the distal tibia and are covered in detail in the section on ankle fractures (see later). In older children, fractures of the tibial shaft are usually complete with a transverse or oblique fracture plane. The fibula is commonly fractured when a complete fracture of the tibial diaphysis occurs.[128]

Maisonneuve fractures of the proximal fibula may occur with medial ligamentous injury or medial malleolar fracture at the ankle. The mechanism for Maisonneuve fractures is forced ankle valgus injury. These fractures may also occur with juvenile Tillaux or triplane fractures of the distal tibia. With a disruption of medial support at the ankle, the injury force may traverse the interosseous membrane up the leg and pass obliquely through the proximal fibular diaphysis. The presence of a Maisonneuve fracture thus indicates disruption of the interosseous membrane and potential instability if the ligamentous injury is not surgically addressed.

***Imaging.*** Nonphyseal and extra-articular fractures of the leg can be assessed with anteroposterior and lateral views. Once the physis of either end of the leg are involved, dedicated osteoarticular imaging is necessary to comprehensively characterize physeal and intraarticular involvement, if present.

Whenever a medially located fracture or ligamentous disruption of the ankle occurs, radiographs of the remainder of the leg should be obtained to rule out a Maisonneuve fracture (e-Fig. 142.60).[129]

Distal tibial Salter-Harris III fractures may be seen medially or laterally (juvenile Tillaux fracture; see later). The distal tibia is one of the more common locations of Salter-Harris IV fractures (see e-Fig. 142.11 and e-Fig. 142.61).

***Treatment.*** Treatment of tibial fractures depends on the age of the child, type and location of the fracture, and degree of fracture displacement and angulation. Most tibial fractures can be managed nonoperatively provided that they are purely extra-articular and do not involve a physis. Fibular fractures, including those that have physeal involvement, invariably are treated nonsurgically, because the fibula is a relatively non–load-bearing bone.

Maisonneuve fractures can be managed nonsurgically if the fracture is stable. With unstable fractures, the syndesmosis needs to be approximated and medial malleolus fixated. The associated proximal fibular fracture is treated conservatively, and the deltoid ligament need not be directly repaired.[130]

## TRAUMATIC INJURIES OF THE ANKLE

### Transitional Ankle Fractures (Juvenile Tillaux and Triplane)

***Etiology, Pathophysiology, and Clinical Presentation.*** “Transitional” fractures occur in the early teen years when the distal tibial physis is nearing the time of fusion or is already partially fused. The distal tibial physis begins to fuse in the medial central physis. Fusion then proceeds medially and posteriorly (e-Fig. 142.62). The anterolateral portion of the physis is the last portion of the physis to close and thus is the plane of least resistance to fracture.[131,132] The unique pattern of physeal fusion of the distal tibia leads to characteristic fracture patterns in the distal tibia.

Juvenile Tillaux fracture is a Salter-Harris III fracture of the distal tibial physis and epiphysis. Juvenile Tillaux fractures probably represent an anterolateral avulsion of the distal tibial epiphysis pulled by the anterior tibiofibular ligament and anterior syndesmosis caused by forced external rotation.[133] Triplane fractures are closely related to juvenile Tillaux fractures; however, there is an additional fracture plane of the distal tibial metaphysis, usually coronal in orientation (Fig. 142.63). The three planes of a triplane fracture are thus: (1) a sagittal fracture through the epiphysis, (2) a transverse

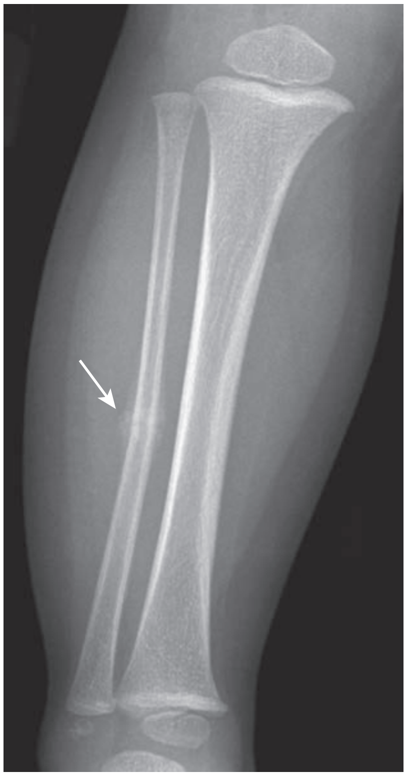

**e-Figure 142.58. Fibular toddler fracture in a 19-month-old boy.** Callus is present *(arrow)* with a faint transverse fracture line.

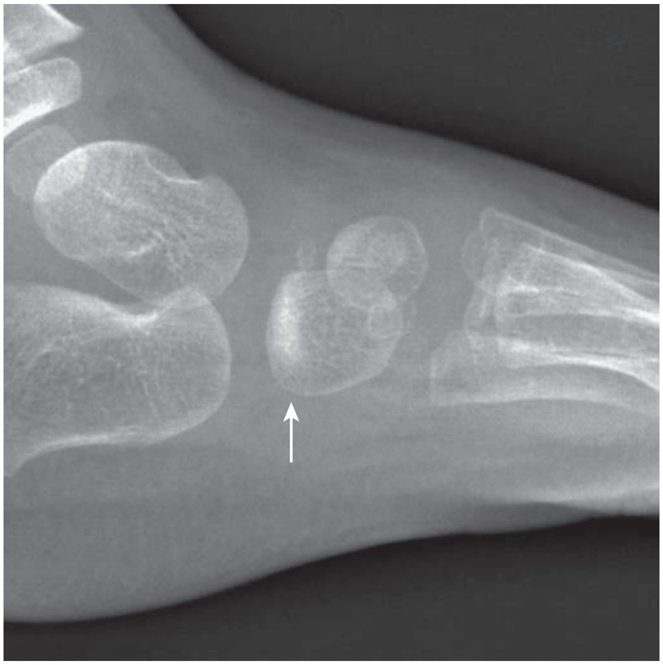

**e-Figure 142.59. Healing toddler fracture of the cuboid in a 19-month-old boy.** A band of sclerosis is seen within the proximal aspect of the cuboid *(arrow)*.

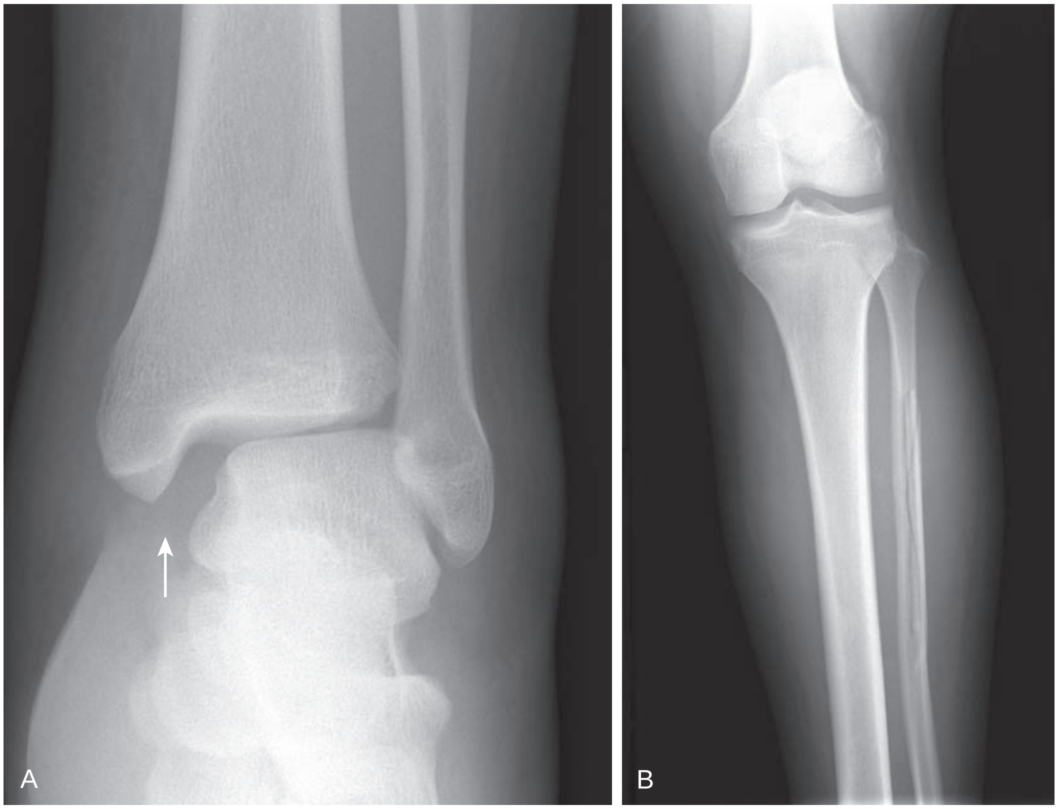

**e-Figure 142.60. Maisonneuve fracture in a 14-year-old boy.** (A) Anteroposterior radiograph of the ankle demonstrates medial tibiotalar widening consistent with deltoid ligament injury *(arrow)*. (B) Anteroposterior radiograph of the leg demonstrates a proximal fibular fracture.

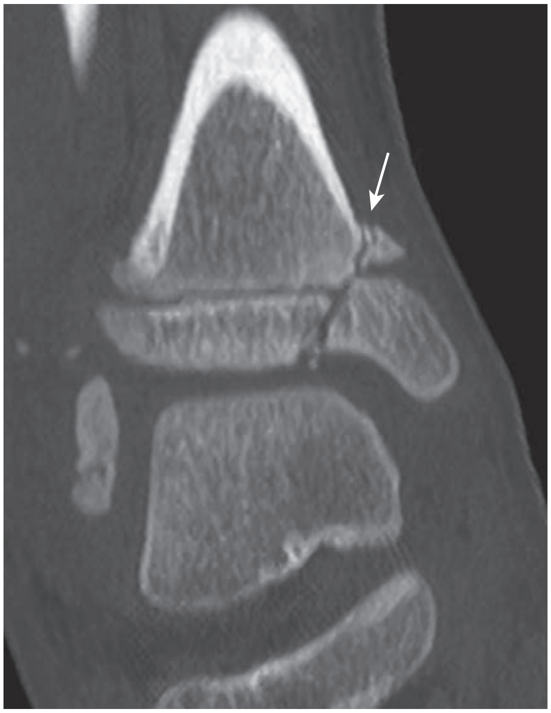

**e-Figure 142.61. Salter-Harris IV fracture of the distal tibia in an 8-year-old boy.** Coronal CT reconstruction shows the course of the fracture *(arrow)*. Note the apposition of metaphysis and epiphysis across the fracture.

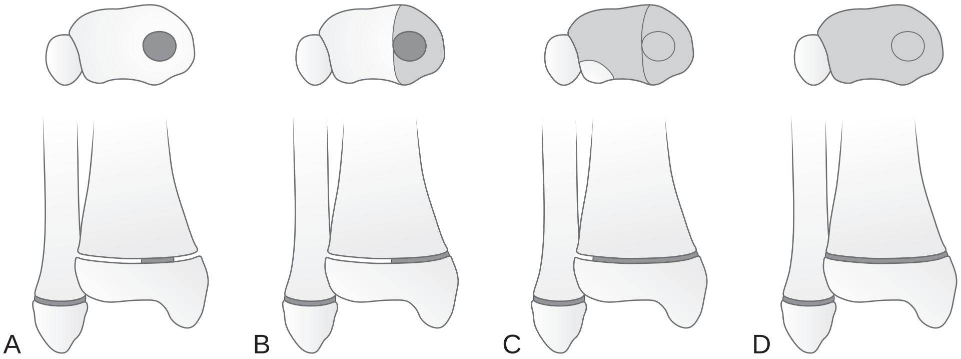

**e-Figure 142.62. Diagram of the path of distal tibial physeal closure.** Closure begins centrally (A) and proceeds medially (B) and then laterally (C) before fusion is complete (D). *(Modified from Beaty JH, Kasser JR.* Rockwood and Wilkins' Fractures in Children*, 6th ed. Philadelphia: Lippincott Williams & Wilkins; 2006.)*

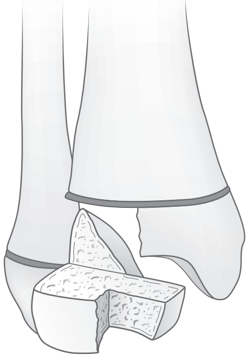

**Figure 142.63. Triplane fracture.** In a two-part triplane fracture, typically sagittal epiphyseal, transverse physeal, and coronal metaphyseal fracture lines are present. *(Modified from Beaty JH, Kasser JR.* Rockwood and Wilkins' Fractures in Children*, 6th ed. Philadelphia, PA: Lippincott Williams & Wilkins; 2006.)*

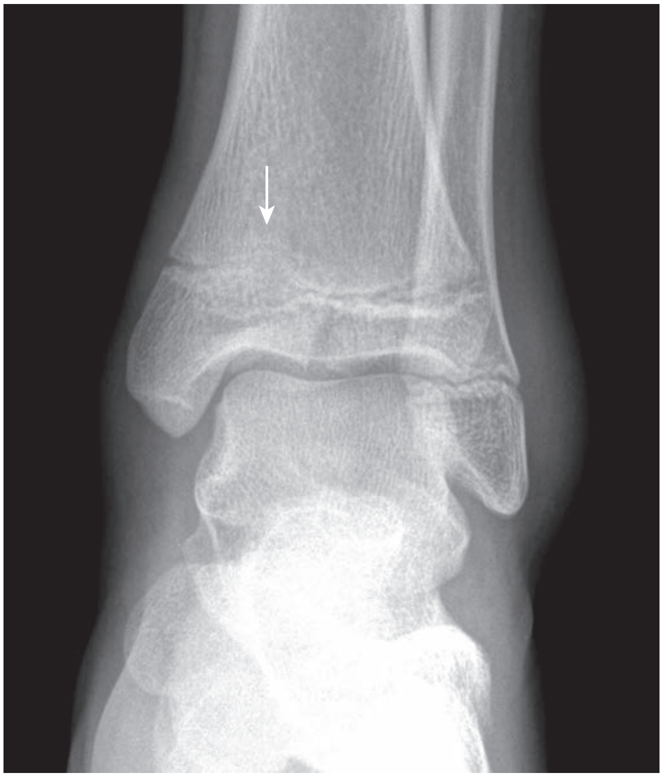

**Figure 142.64. Juvenile Tillaux fracture in a 15-year-old boy.** Note the Salter-Harris III vertical fracture line is lateral to Kump's bump *(arrow)*, the site of initial distal tibia physeal closure.

fracture through the physis, and (3) a coronal fracture through the metaphysis.[134,135]

***Imaging.*** The vertical fracture line in juvenile Tillaux fractures is invariably located lateral with respect to anteromedial tibial physeal fusion, which is called *Kump's bump* (Fig. 142.64). This should be distinguished from epiphyseal fractures that are medially located (see e-Fig. 142.61). The concern with juvenile Tillaux fracture of the distal tibia is not possible premature fusion of the physis, because the physis is already fusing, but rather involvement of the articular surface. A significant gap or incongruity of the fracture fragments at the articular surface may portend an early progression to degenerative disease in the ankle.

For triplane fractures, the epiphyseal and metaphyseal fracture planes may vary somewhat from true orthogonal orientation. A classic triplane fracture has two parts; however, three-part and four-part variants occasionally occur (Fig. 142.65).[136] Triplane fractures are complex fractures that some authors classify as Salter-Harris IV fractures and others as a combination of Salter-Harris type II and type III fractures; however, classification systems specific to triplane fractures (such as those developed by Von Laer, van Laarhoven, and Rapariz) provide a more useful classification.[137]

Superficially, triplane fractures on anteroposterior view may mimic juvenile Tillaux fracture (see Fig. 142.65A). If a Salter-Harris II fracture component is not visualized on the lateral view, CT may be helpful to distinguish these two fractures, as this will alter management.

Radiography is usually sufficient for detecting both juvenile Tillaux and triplane fractures. CT is often used in preoperative planning to measure displacement at the articular surface and to map the anatomy of the fracture planes (e-Fig. 142.66), and has been shown to impact the classification and treatment planning of triplane fractures.[137–142]

***Treatment.*** If the fracture line is wider than 2 mm, a transitional fracture will undergo operative fixation.[133] Widening of the medial joint space may be a sign of fracture displacement.[143] Nondisplaced fractures can be treated with immobilization.[144] Juvenile Tillaux fractures are surgically fixed at the level of the epiphysis. Displaced triplane fractures will require surgical fixation of both the epiphyseal and metaphyseal fracture components.

## TRAUMATIC INJURIES OF THE FOOT

***General Overview.*** Foot fractures account for approximately 5% to 8% of pediatric fractures.[145] These fractures are generally uncommon in infants and toddlers given the significant cartilaginous composition of the foot during this age; the incidence of fractures increases with age as the foot becomes more ossified.[145] The majority of pediatric foot fractures are isolated injuries.[145]

## Hindfoot Fractures

### Talar Fractures

***Etiology, Pathophysiology, and Clinical Presentation.*** Fractures of the talus are uncommon, compromising approximately 2% of pediatric foot fractures.[145] Avulsion fractures are the most common, followed by osteochondral fractures, talar neck, then talar body fractures.[146]

The majority of talar neck and body fractures occur with high-energy trauma, usually from a fall or a motor vehicle accident.[145] Complete fractures of the talar neck are seen in older children but are rare.

Younger children may have buckle fractures of the talar neck. The buckle is evident along the dorsal surface of the bone and may be very subtle.[147] The talus is one location of the so-called *tarsal toddler fracture*. These fractures occur from compression of the talar neck against the anterior margin of the tibia with forced dorsiflexion.[148]

***Imaging.*** Anteroposterior, oblique, and lateral radiographs of the ankle are initially obtained. Given the complexity of some talar fractures, CT can be used to delineate fracture anatomy and articular involvement (e-Fig. 142.67). Because of the recurrent blood supply of the body of the talus, fractures may be complicated by osteonecrosis of the proximal pole. The presence of a subchondral lucency in the talar dome (Hawkins sign) seen approximately 2 months after injury indicates that the talar dome has an adequate blood supply, and therefore the risk of developing osteonecrosis is low; loss of this sign is abnormal indicating osteonecrosis.[145] Other significant complications include post-traumatic arthritis caused by malalignment.[148]

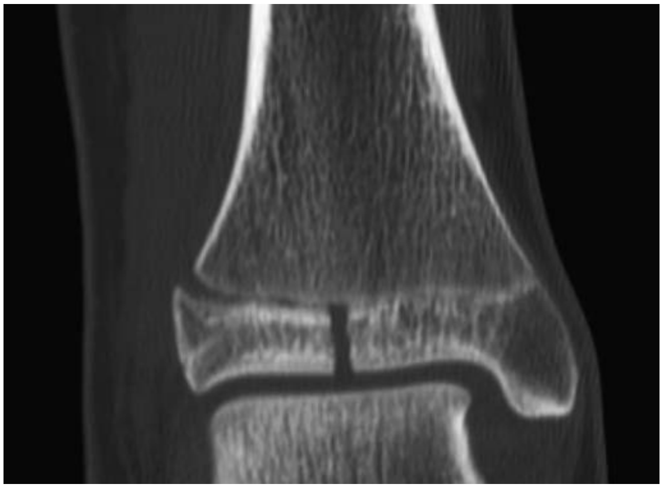

**e-Figure 142.66. Juvenile Tillaux fracture in a 14-year-old boy.** Coronal CT reconstruction shows the Salter-Harris III fracture of the anterolateral distal tibial epiphysis.

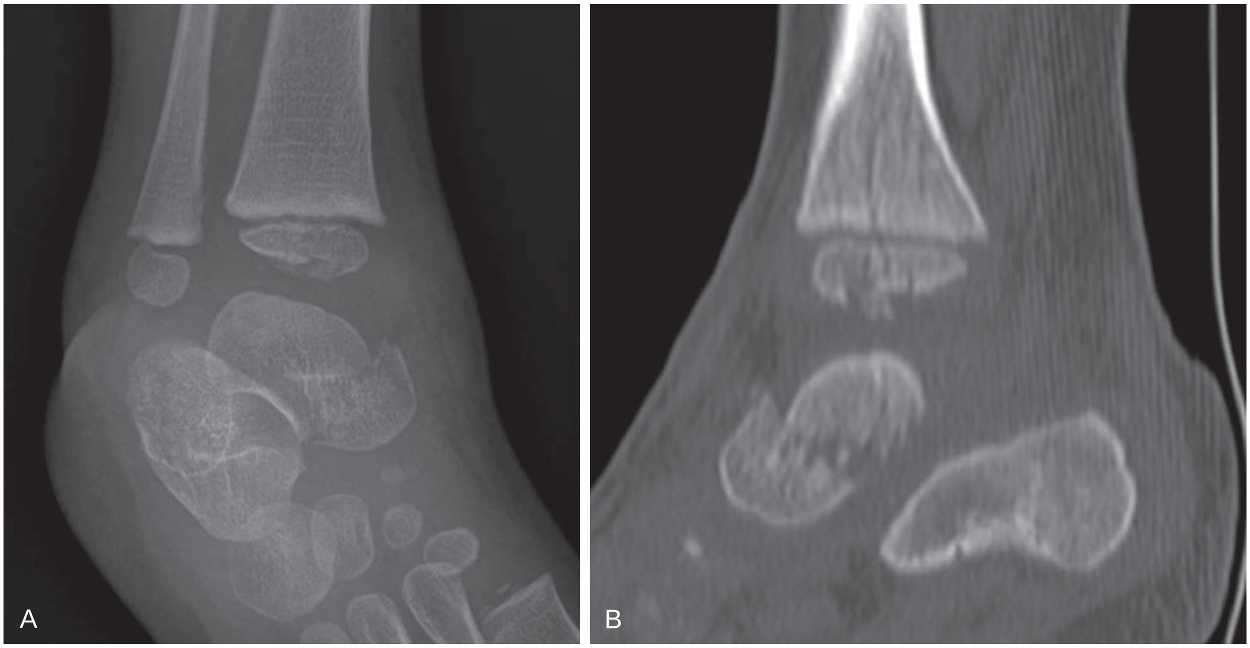

**e-Figure 142.67. Talar neck fracture and a complex distal tibia Salter-Harris fracture in a 2-year-old girl.** (A) Radiographs show talar and distal tibial fractures that are better depicted on CT (B).

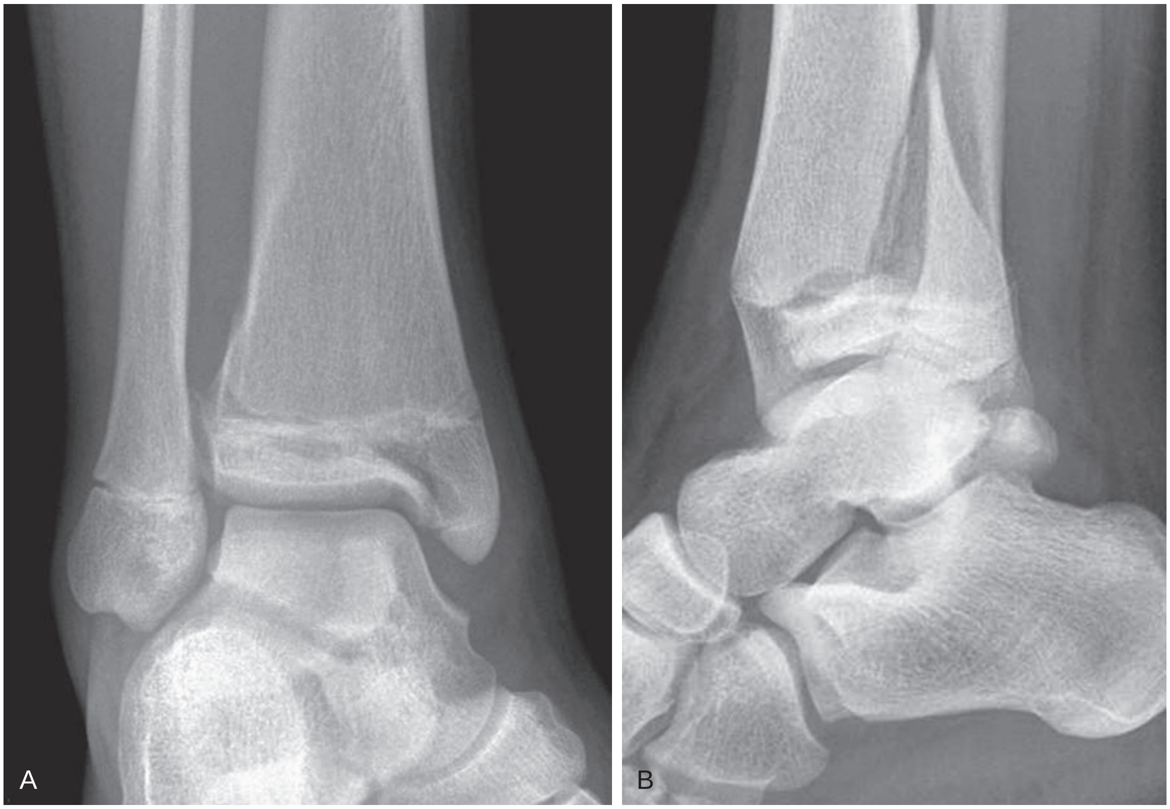

**Figure 142.65. Triplane fracture.** Anteroposterior (A) and lateral (B) radiographs of a triplane fracture in an adolescent. *(Courtesy of Dr. Brent H. Adler, Columbus, OH.)*

***Treatment.*** Treatment of nondisplaced talar fractures includes immobilization and casting, while either closed or open reduction is performed for displaced fractures.

### Calcaneal Fractures

***Overview.*** Calcaneal fractures are uncommon, comprising only 2% of all pediatric foot fractures. Associated injuries are common.[145] Toddler fractures of the calcaneus, which have been described in the literature, are uncommon.[149]

***Etiology, Pathophysiology, and Clinical Presentation.*** Calcaneal fractures most commonly occur with jumps or falls from a large height and from motor vehicle accidents.[145] The mechanism of injury is usually an axial loading force.[150] Prior to apophyseal fusion, the posterior calcaneus may experience fractures involving the apophyseal physis and apophysis that can be classified by the Salter-Harris system.[151]

***Imaging.*** Calcaneal fractures may have a variable degree of comminution and of depression of the superior margin of the calcaneus. The Böhler angle can be used to assess for calcaneal depression caused by the fracture. This angle is the posterior angle between two lines, one drawn tangent to the anterior process of the calcaneus and the highest point of the posterior facet, and the other drawn from the latter point to the superior margin of the posterior calcaneus. Normally, the Böhler angle measures around 25 to 40 degrees in adults but is less in children.[152] With depressed calcaneal fractures, the Böhler angle is decreased. Although the Essex-Lopresti classification system is widely used, it is important to differentiate between intraarticular and extra-articular fractures with reference to involvement of the subtalar joint (Fig. 142.68).[145]

CT is utilized for full delineation of calcaneal fracture anatomy. Subtle compression fractures of the calcaneal body are not infrequent in younger children. These injuries may be virtually impossible to diagnose acutely from radiographs unless a buckle of the margin of the bone exists. Follow-up radiographs will show an oblique band of sclerosis within the midcalcaneal body (e-Fig. 142.69).

***Treatment.*** Displaced, intraarticular fractures of the calcaneus are typically treated surgically with open reduction and internal fixation.[153,154] Most patients have a good clinical outcome with few complications.[152]

## Midfoot Injury

***Overview.*** Isolated fractures of the cuneiform bones are rare. “Bunk bed” fractures of the cuboid have been reported (see later). Lisfranc injuries may occur throughout childhood but become more common in older children.

***Etiology, Pathophysiology, and Clinical Presentation.*** The mechanism may be direct, from a falling object, or indirect, from forced plantar flexion, abduction, or both.[145] Falls from a height account for the largest number of Lisfranc injuries in children.[145] The Lisfranc joint, which courses between the distal tarsals and the metatarsals, is disrupted. Fractures may be seen within the bases of the metatarsals or within the cuneiforms. Fracture at the base of the second metatarsal is a consistent finding. Multiple metatarsal fractures and midtarsal bone injuries are more likely in children.[2] These fractures may be chondro-osseous separations seen only as small slivers of bone but are often occult with radiographs. Lisfranc injuries can be classified as homolateral, with the first metatarsal displaced in the same direction as the other four metatarsals, or divergent, with the first metatarsal displaced medially and the other metatarsals displaced laterally (e-Figs. 142.70 and 142.71). A fracture of the cuboid with a fracture of the second metatarsal base is compatible with significant tarsometatarsal joint injury.

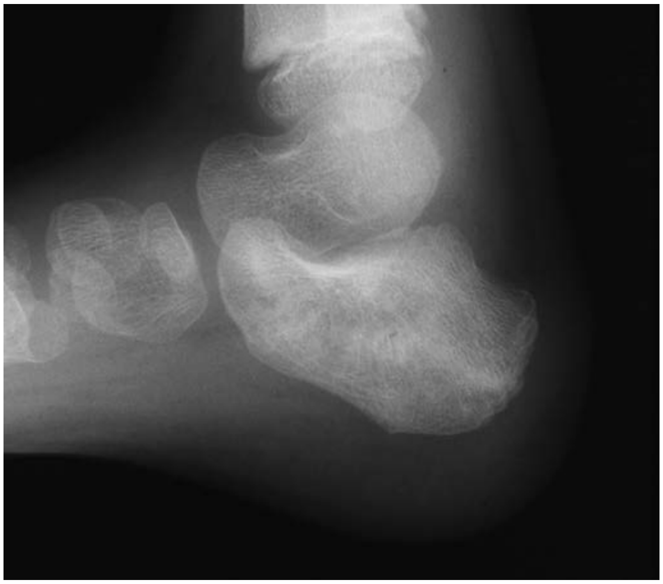

**e-Figure 142.69. Healing calcaneal fracture in a 6-year-old boy.** A horizontal band of sclerosis is seen within the body of the calcaneus.

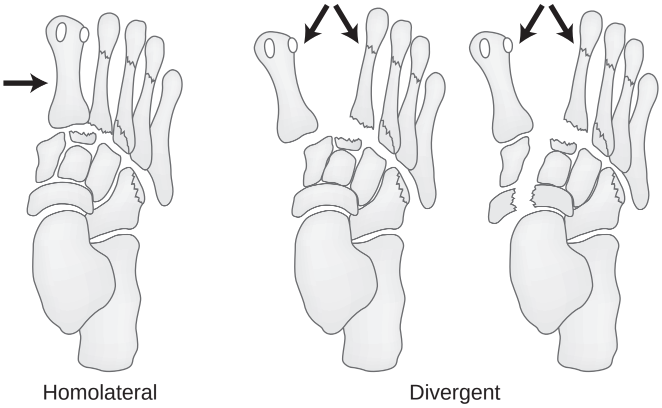

**e-Figure 142.70. Lisfranc tarsometatarsal fracture–dislocations.** The two basic types are homolateral and divergent. A fracture is consistently seen at the base of the second metatarsal. Jagged lines represent additional potential sites of fracture. *(From Rogers LF.* Radiology of Skeletal Trauma*, 3rd ed. New York: Churchill Livingstone; 2002.)*

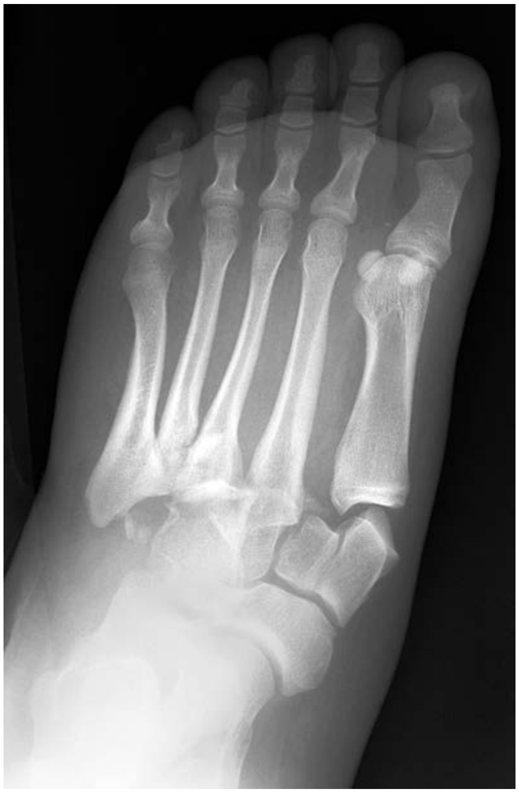

**e-Figure 142.71. Lisfranc fracture-dislocation in a 15-year-old morbidly obese boy from a motor vehicle accident.** The injury is homolateral. The space between the first and second metatarsals is widened. The tarsal-metatarsal joint is completely disrupted. A fracture is present at the base of the second metatarsal as well as other metatarsals.

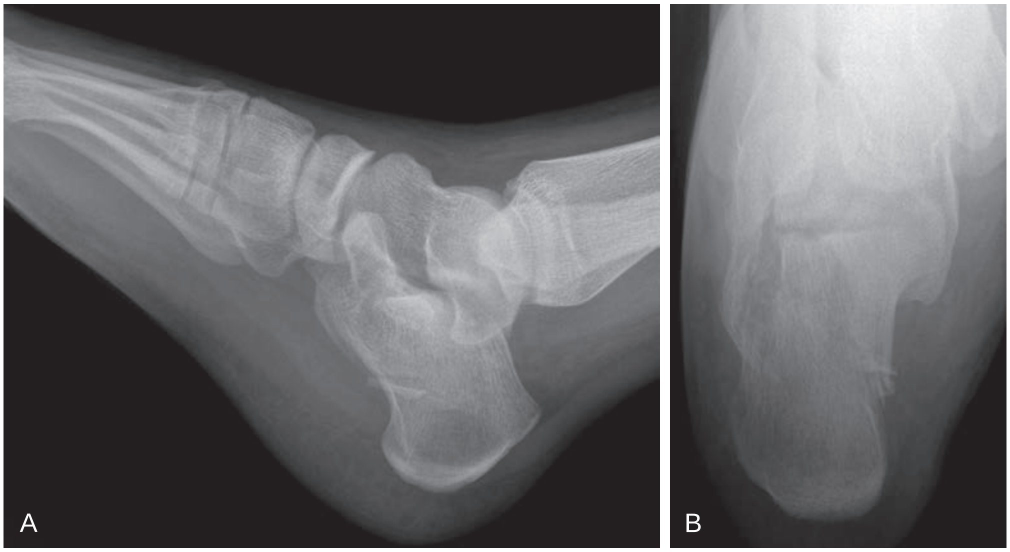

**Figure 142.68. Comminuted intra-articular fracture of the calcaneus in a 15-year-old boy.** (A) Lateral radiograph. (B) The subtalar involvement is best seen on the Harris view.

***Imaging.*** Radiographic abnormalities may be subtle. Weight-bearing views of the foot are necessary to accurately evaluate alignment of the forefoot and midfoot. Weight bearing will stress the tarsometatarsal joints and may bring out subtle Lisfranc injuries. Any malalignment between the bases of the metatarsals or with their corresponding tarsal bones on any view should be regarded with suspicion. The midfoot should be closely evaluated for possibility of avulsion fractures. CT is used for confirmation of diagnosis and delineation of comorbid anatomy. MRI and less commonly ultrasound are used to evaluate the Lisfranc ligament.[155]

***Treatment.*** Nondisplaced or minimally displaced tarsometatarsal dislocations may be treated conservatively. Patients with Lisfranc fracture–dislocations with more than minimal displacement are treated surgically.[145] If closed reduction is not successful, percutaneous pin fixation may be employed for stabilization. Stabilizing the fracture of the proximal second metatarsal is important.[2]

## Forefoot Fractures

***Overview.*** Metatarsal fractures are one of the most common pediatric foot fractures. Most are nondisplaced or minimally displaced.[156] If the fractures involve the base of the metatarsal, injury to the tarsometatarsal joint must be considered. Buckle fractures of the phalanges and metatarsals are common in younger children. The most commonly injured metatarsal in younger children is the first metatarsal and in older children the fifth.[156]

***Etiology, Pathophysiology, and Clinical Presentation.*** Phalangeal fractures usually occur from objects falling directly on the foot, particularly on the great toe.[150] Salter-Harris fractures may affect the physes of these bones. Salter-Harris III fractures at the base of the proximal phalanx of the great toe may be mistaken for a bifid epiphysis and vice versa. Buckle fractures of the phalanges and metatarsals are common in younger children. Often, adjacent bones are fractured together. Oblique or transverse fractures of the metatarsal shafts may be caused by dropped objects, falls, or twisting injuries. In severe twisting injuries in which the foot is caught, multiple adjacent metatarsals may be fractured.

***Imaging.*** Dedicated radiographs in three planes of the injured phalanx is preferred rather than imaging the foot in its entirety. True lateral radiographs of the isolated symptomatic toe are challenging to obtain because of overlap of adjacent toes but are nevertheless important to obtain for complete assessment and for identifying toe dislocations that may be missed on only anteroposterior and oblique views.

***Treatment.*** Displaced fractures need reduction and occasionally K-wire fixation.[150] Phalangeal fractures heal quickly and usually only buddy taping is required.[150]

## STUBBED GREAT TOE FRACTURE

***Overview.*** Stubbed great toe fractures are considered Salter-Harris I or II fractures of the base of the proximal or distal phalanx of the great toe until proven otherwise.[157] Fractures of the distal phalanx of the great toe are unique given the relationship of the nail bed to the physis, which increases the risk for osteomyelitis.

***Etiology, Pathophysiology, and Clinical Presentation.*** The nail bed of the great toe is closely apposed to the physis of the distal phalanx, with the skin directly attached to the juxtaphyseal periosteum. After an injury, this relationship is thought to allow contamination of the underlying bone and physis.[158] Therefore any nail bed injury with associated physeal fracture should be considered an open fracture.[159]

***Imaging.*** Physeal widening of the terminal phalanx is the most common finding seen with stubbed toe fractures (Fig. 142.72). Rarefaction and physeal widening can be related to the primary injury, related to superimposed osteomyelitis, or both and usually cannot be distinguished on the basis of radiography alone. If a high clinical concern for superimposed infection exists, MRI is necessary.

***Treatment.*** Prophylactic antibiotic therapy is recommended, as these are considered open fractures. The fracture is treated nonsurgically unless complicated by osteomyelitis with abscess formation.

## BUNK BED FRACTURE

***Etiologies, Pathophysiology, and Clinical Presentation.*** A bunk bed fracture is a buckle fracture of the first metatarsal. This is most commonly seen in children 3 to 6 years of age.[125,147]

These fractures occur with a fall or a jump from a height onto a hard surface, with the prototypical injury occurring with a jump from the top bunk of a bunk bed onto a hardwood floor,

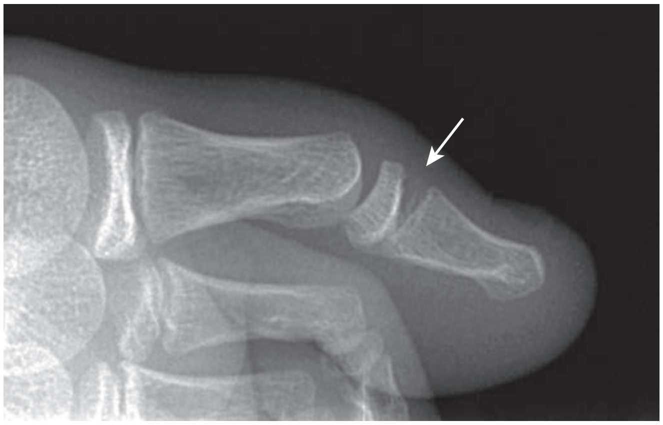

**Figure 142.72. Stubbed great toe fracture in a 12-year-old boy *(arrow)*.** A tiny metaphyseal fragment is present. The patient was prophylactically placed on antibiotics.

landing in a tiptoe position.[160] The child's entire weight is placed on the first metatarsal (axial loading injury), leading to a buckle fracture. The bunk bed fracture is associated with ligamentous injury at the tarsometatarsal junction and is considered a Lisfranc variant.

***Imaging.*** Radiography is the primary modality to evaluate these fractures (e-Fig. 142.73). Occasionally, the normal undulation of the physis of the first metatarsal may mimic a bunk bed fracture. This should not cause interruption or buckling of the metaphyseal cortex, however, as is seen with a fracture.

***Management.*** Bunk bed fractures are treated conservatively with immobilization; surgical intervention is rarely indicated unless significant displacement or articular involvement has occurred.

## FRACTURES OF THE FIFTH METATARSAL

***Overview.*** Fractures at the base of the fifth metatarsal are common.[161] The types of fifth metatarsal fractures described in children include apophyseal avulsions, intraarticular, proximal metadiaphyseal, diaphyseal, and neck fractures.

***Etiologies, Pathophysiology, and Clinical Presentation.*** The Jones fracture is a fracture of the proximal fifth metatarsal caused by repetitive inversion.[145] The fracture is transversely oriented and approximately 1.5 cm distal to the tip of the fifth metatarsal tuberosity and extends into the adjacent intermetatarsal facet (e-Fig. 142.74). This should be differentiated from fifth metatarsal stress fractures, which are located greater than 2 cm distal with respect to the fifth metatarsal tuberosity.

Jones and stress fractures of the fifth metatarsal should be differentiated from fifth metatarsal tuberosity avulsion fractures, which are tarsometatarsal fractures related to forced flexion and inversion, often due to an unexpected step or falling when on stairs. Tuberosity avulsion fractures were previously thought to be caused by avulsion at the insertion of the peroneus brevis but now appear to be an avulsion from the origin of the abductor digiti minimi.[145] In children, avulsions of the tuberosity are more common than true Jones fractures.

***Imaging.*** Initial evaluation should include anteroposterior, lateral, and oblique views. A comparison view of the opposite side obtained in the same position will be confirmatory particularly when apophyseal avulsions are a consideration. The physis of the avulsed apophysis will appear widened. The key is to differentiate base of the fifth metatarsal fractures from the normal fifth metatarsal apophysis. The fifth metatarsal apophysis is longitudinally oriented (e-Fig. 142.75) whereas metatarsal stress and avulsion fractures are horizontally oriented. To add to the confusion of the growing appendicular skeleton, the apophysis of the fifth metatarsal may rarely avulse (Fig. 142.76).

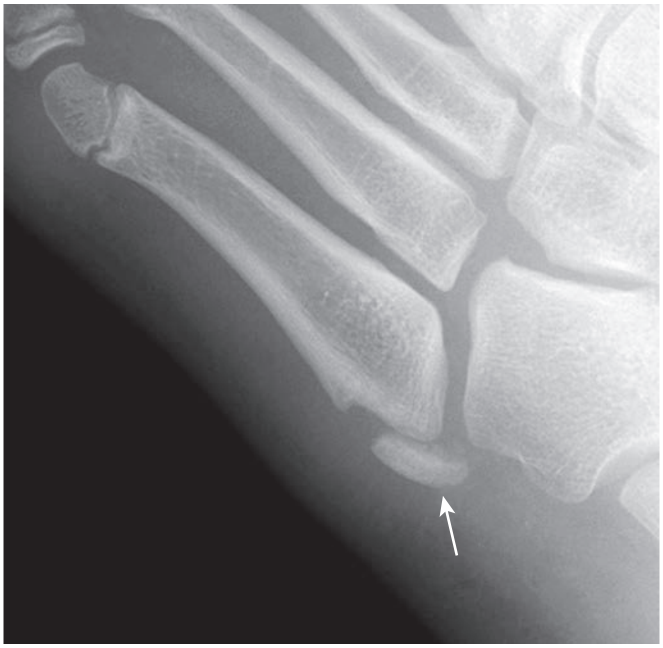

**Figure 142.76. Avulsion of the fifth metatarsal apophysis *(arrow)* in a 13-year-old boy.** The apophysis is displaced from the underlying bone and retracted proximally.

The transverse fracture line of a tuberosity avulsion may extend through the apophysis and its physis (e-Fig. 142.77). Injuries to the base of the metatarsal can extend into the fifth metatarsal–cuboid joint or into the region between the fourth and fifth metatarsal bases. These fractures should be differentiated from more distally located Jones or stress fractures (e-Fig. 142.78) of the fifth metatarsal shaft.

***Treatment.*** Apophyseal avulsions are treated conservatively with immobilization. Jones fractures have a higher rate of delayed union or nonunion and may need to be treated with longer immobilization or surgically management. The tenuous blood supply at the fracture site in Jones fractures has been implicated as a cause of delayed healing.[162]

## NEUROPATHIC INJURY

***Etiologies, Pathophysiology, and Clinical Presentation.*** Causes of neuropathic injury in children include myelomeningocele, syrinx, congenital insensitivity to pain, and familial dysautonomia (Riley-Day syndrome).[163–166] Superimposed infection is common.[163] Neuropathic fractures and joints ("Charcot joints") are much less common in pediatric patients than in adults.

***Imaging.*** Neuropathic injury is characterized by the four Ds: (1) dislocation, (2) debris, (3) disorganization (deformity), and (4) density (sclerosis). Injuries fail to heal. Physeal fractures may occur and are often associated with subperiosteal hematoma and exuberant periosteal new bone. Findings may mimic tumor or infection. Repetitive trauma may lead to chronic physeal injury that may lead to premature fusion. Other sequelae include acro-osteolysis, joint deformity, joint dislocation, and epiphyseal osteonecrosis.[163] Neuropathic fractures are most common in the lower extremities in the diaphysis or metaphysis (e-Fig. 142.79). Injury to the fingertips is caused by crush, thermal damage, and chewing (e-Fig. 142.80).

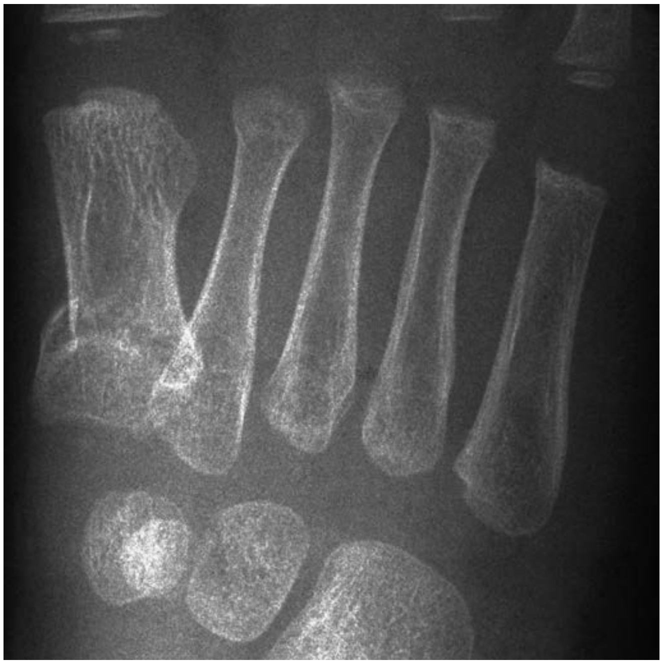

**e-Figure 142.73. Bunk bed first metatarsal fracture in a 3-year-old boy.** The cortex is buckled proximally.

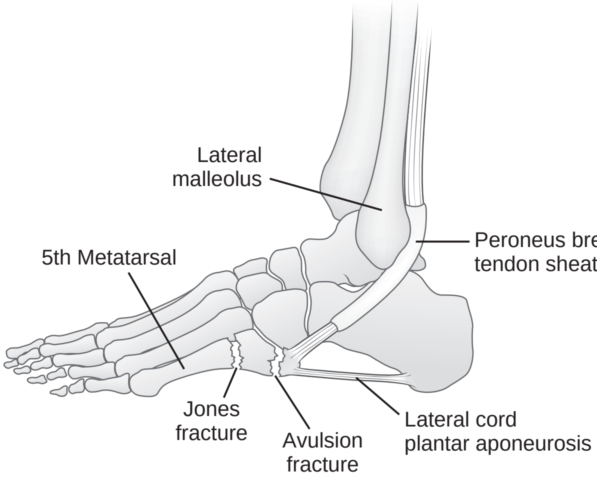

**e-Figure 142.74. Fractures at the base of the fifth metatarsal.** These fractures result from inversion of the foot, which places tension on the peroneus brevis tendon and the lateral cord of the plantar aponeurosis. An avulsion fracture of the proximal bulbous tip of the metatarsal is to be distinguished from the classic Jones fracture, a transverse fracture at the base of the metatarsal located 1.5 to 2 cm distal to the tip of the metatarsal. *(From Rogers LF.* Radiology of Skeletal Trauma*, 3rd ed. New York: Churchill Livingstone; 2002.)*

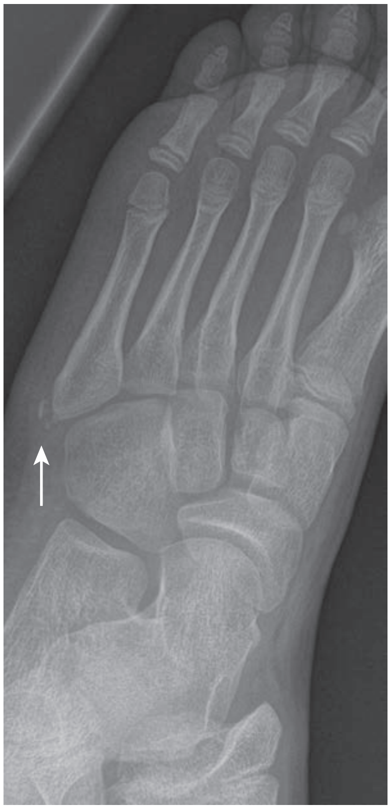

**e-Figure 142.75. Normal longitudinally oriented fifth metatarsal apophysis in a 9-year-old girl *(arrow)*.**

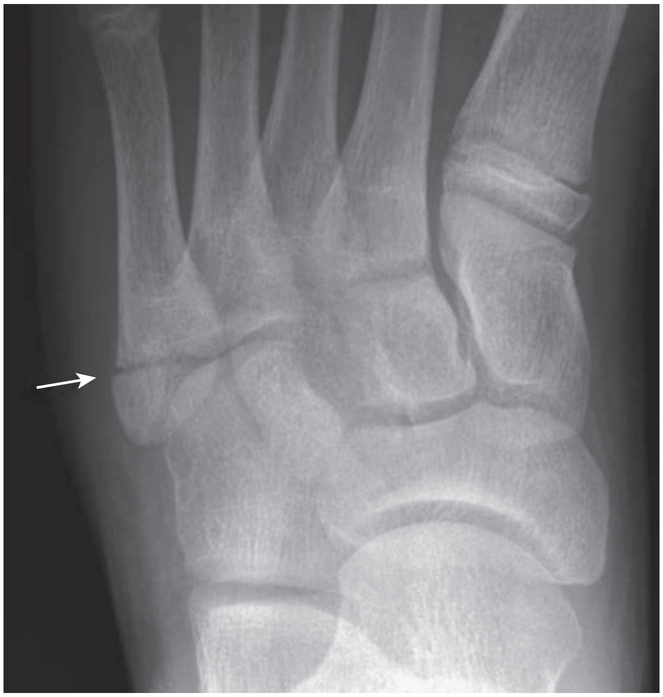

**e-Figure 142.77. Transverse fracture of the tuberosity of the fifth metatarsal *(arrow)* in a 12-year-old boy.**

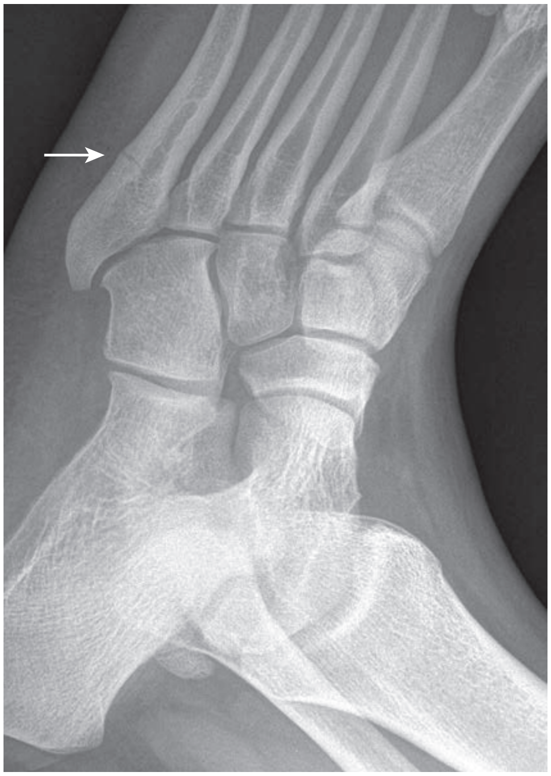

**e-Figure 142.78. Fifth metatarsal stress fracture in a 17-year-old boy.** The fracture *(arrow)* is located approximately 3 cm distal to the fifth metatarsal tuberosity.

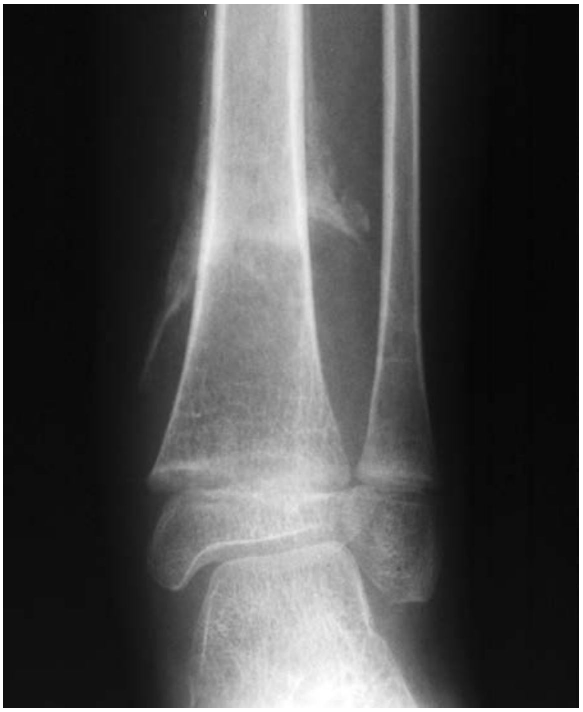

**e-Figure 142.79. Neuropathic fracture of the distal tibial growth plate in an 11-year-old girl with myelomeningocele.** The patient presented with swelling. The distal tibial growth plate is widened. Periosteal new bone is elevated and interrupted because of subperiosteal hemorrhage, which was caused by delayed diagnosis and lack of immobilization.

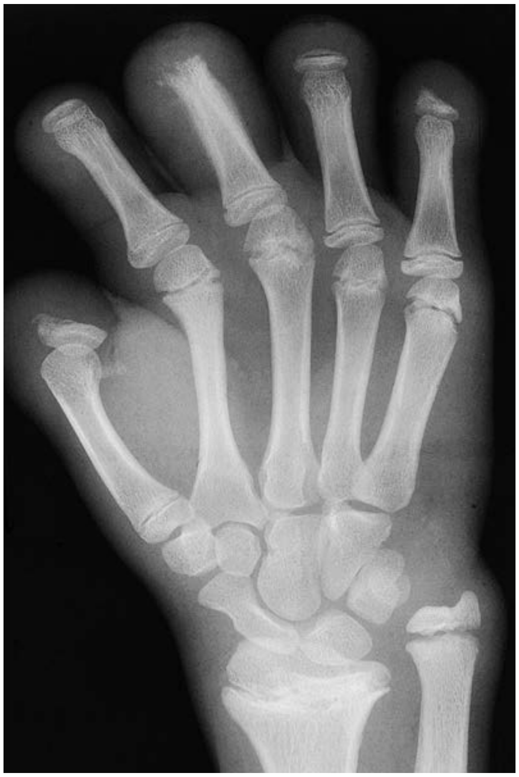

**e-Figure 142.80. Sequelae of congenital insensitivity to pain in a 16-year-old boy.** All of the fingers are amputated because of chronic injury. Premature fusion of the distal radial growth plate is noted with resultant shortening of the radius. The ulna is dislocated.

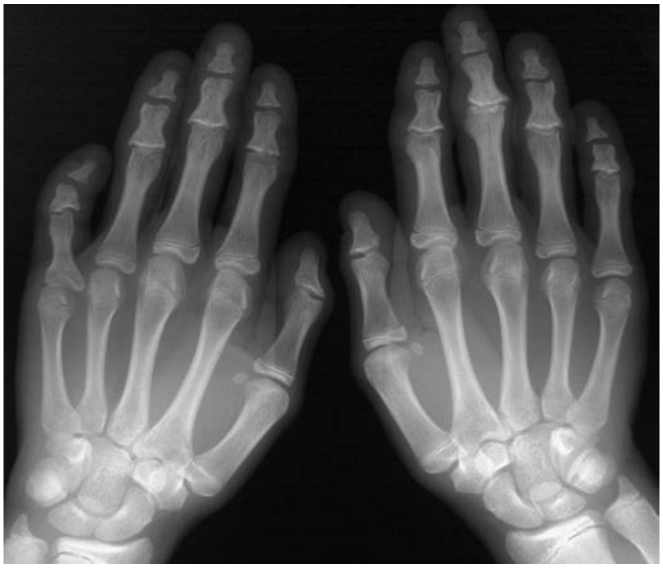

**Figure 142.81. Sequelae of frostbite in a 15-year-old girl.** Brachydactyly of the distal and middle phalanges was caused by premature growth plate closure. In this patient, the thumbs were not spared. The proximal phalanx of the right fifth finger is also shortened.

***Treatment.*** Treatment is variable and tailored to the underlying problem. Both nonsurgical management and surgical management are used for treating Charcot arthropathy. Nonsurgical treatment includes immobilization and reduction of stress. Examples of surgical management include removal of bony prominences, arthrodesis, plate and screw fixation, bone grafting, and reconstructive surgery.

## PHYSICAL AGENTS

### Frostbite

***Etiologies, Pathophysiology, and Clinical Presentation.*** Frostbite injury is most common in children ages 5 to 10 years. The pathophysiologic mechanism of frostbite is not well defined, but a direct injury to chondrocytes may occur within the physis.[167] The sequelae in children are premature fusion of the physis and shortening of the involved digits. Bone fragmentation may be caused by ischemic damage.[167] Secondary degenerative changes develop from direct articular injury and malapposition of joint surfaces in the affected digits.[168]

***Imaging.*** Immediate radiographic findings occurring 1 week after exposure include soft tissue swelling and soft tissue gas, which is a poor prognostic sign.[167] Radiographically identifiable osseous changes manifest weeks to months after injury. Characteristically, the thumb is spared as it is clenched at the time of exposure and covered by the other digits. Findings are most pronounced in the distal phalanges, occasionally affect the middle phalanges, and rarely involve the proximal phalanges or metacarpals (Fig. 142.81).[168]

***Treatment.*** Treatment is variable and depends on the degree of injury. Rewarming the extremity, surgical debridement of nonviable tissue and thrombolytics are potential treatments. Antibiotics are commonly used to prevent or treat superimposed infection.

## THERMAL AND ELECTRICAL INJURY

***Etiologies, Pathophysiology, and Clinical Presentation.*** Thermal injuries are a significant cause of morbidity and mortality in children, most commonly affecting children under age 6 years.[169] The hand is most commonly injured, followed by the face.[169,170]

***Imaging.*** Injury from thermal burns is usually to the soft tissues, leading to contractures and ankylosis. Heterotopic bone contributes to ankylosis, as does direct thermal injury of a joint.[171] Direct thermal injury to the physis may lead to premature fusion or growth disturbance (e-Fig. 142.82).[171,172] Electrical injury may lead similar sequelae because of tissue heating. Osteolysis may also occur.

***Treatment.*** Wound infection and sepsis are common, and surgical intervention may be necessary in some cases.[173,174]

## RADIATION

***Etiologies, Pathophysiology, and Clinical Presentation.*** Irradiation of tissues may cause immediate or delayed injury to tissues.[175] Radiation affects the immature skeleton by interfering with chondrogenesis and causing resorption of bone and cartilage at the physis, therefore affecting younger children with greater growth potential to the greatest degree.[175] Therapeutic radiation doses may be sufficient to cause permanent injury to bone. Microscopic changes are seen with as little as 300 centigrays (cGy) and growth retardation with as low as 400 cGy.[175] Histologic recovery occurs with doses up to 1200 cGy; however, beyond this level, almost uniformly permanent cell damage and premature physeal fusion occur.[175] Radiation-induced sarcomas are uncommon and occur years after therapy.[175]

***Imaging.*** Radiation injury includes growth retardation with hypoplasia (e-Fig. 142.83), premature physeal fusion, SCFE, osteonecrosis, osteochondroma formation, and radiation-induced sarcoma.[175–177]

Metaphyseal sclerosis, fraying, and widening can be seen 1 to 2 months after long bone irradiation, resembling rickets.[175] The affected bone may return to normal after 6 months. A dense metaphyseal band may also be seen shortly after therapy.[175] SCFE can occur anywhere from 1 to 8 years after therapy, and long-term radiographic follow-up is warranted.[175] Horizontal sclerotic lines parallel to the vertebral body endplates may be seen (bone in bone appearance) 9 to 12 months after irradiation to the spine. With higher doses of radiation (2000–3000 cGy), vertebral body scalloping, loss of vertebral body height, and scoliosis from asymmetric vertebral body growth have been reported.[175]

### KEY POINTS

- The composition of a child's bones and the presence of the growth process predispose the child to different types of fractures and complications than are seen in adults.
- Higher grade Salter-Harris fractures have a higher incidence of premature physeal fusion.
- The medial epicondyle ossifies before the trochlea. In an injured elbow, visualization of an ossified trochlea without an ossified medial epicondyle in its normal location should raise suspicion for an avulsed medial epicondyle.
- When a child presents with bilateral symmetric SCFE or outside of the typical age range, an underlying metabolic disorder should be suspected.
- Classic toddler fracture of the tibia is one cause of pain and refusal to bear weight. Toddlers may also incur fractures of the fibula and tarsal bones (talus and cuboid) and present similarly.
- Because of the proximity of the nail bed, Salter-Harris fractures of the distal phalanx of the great toe are considered open fractures. Children should receive prophylactic antibiotics to prevent osteomyelitis.

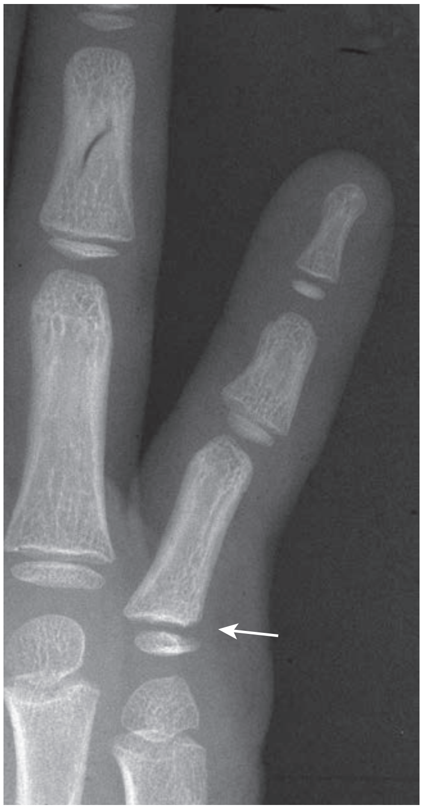

**e-Figure 142.82. Sequelae of thermal injury.** The child was burned 7 years ago. Although the growth plate of the proximal phalanx appears patent *(arrow)*, growth disturbance has resulted in medial deviation of the phalanx.

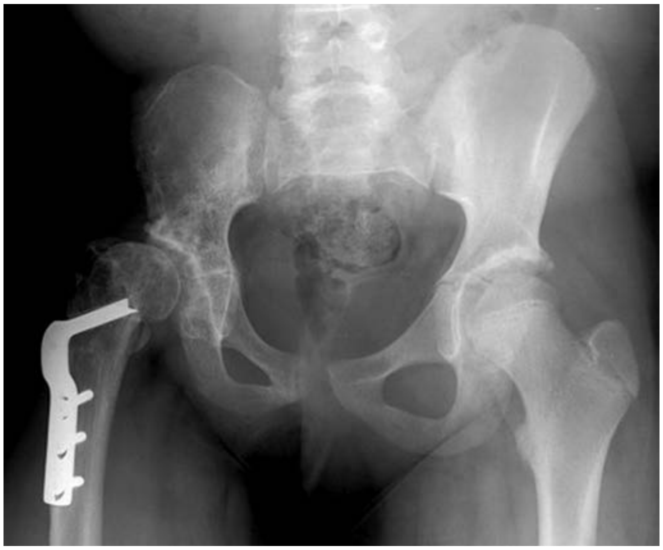

**e-Figure 142.83. Sequelae of radiation therapy in an 11-year-old girl.** The patient underwent radiation therapy for Ewing sarcoma of the right ileum at age 3 years. Bones of the right hemipelvis are small. Premature fusion of the right proximal femoral growth plate and triradiate cartilage has occurred. A varus osteotomy of the proximal femur was performed to better center the right femoral head within the diminutive right acetabulum.

## SUGGESTED READINGS

Ogden JA. *Skeletal Injury in the Child*. 3rd ed. New York: Springer; 2000.

Rogers LF, Poznanski AK. Imaging of epiphyseal injuries. *Radiology*. 1994;191:297–308.

Stein-Wexler R, Wootton-Gorges SL, Ozonoff MB. *Pediatric orthopedic imaging*. Springer Berlin Heidelberg; 2014.

Swischuk L, Hernandez JA. Frequently missed fractures in children (value of comparative views). *Emerg Radiol*. 2004;11:22–28.

Wilkins KE. Principles of fracture remodeling in children. *Injury*. 2005;36(suppl 1):A3–A11.

## REFERENCES

Full references for this chapter can be found on www.expertconsult.com.

## REFERENCES

1. Rogers LF. *Radiology of Skeletal Trauma*. 3rd ed. New York, NY: Churchill Livingstone; 2002.
2. Ogden JA. *Skeletal Injury in the Child*. 3rd ed. New York, NY: Springer; 2000.
3. Jacobsen FS. Periosteum: its relation to pediatric fractures. *J Pediatr Orthop*. 1997;6:84–90.
4. Stein-Wexler R, Wootton-Gorges SL, Ozonoff MB. *Pediatric orthopedic imaging*. Springer Berlin Heidelburg; 2014.
5. Beaty JH, Kasser JR. *Rockwood and Wilkins' Fractures in Children*. 6th ed. Philadelphia, PA: Lippincott Williams and Wilkins; 2006.
6. Wilkins KE. Principles of fracture remodeling in children. *Injury*. 2005;36(suppl 1):A3–A11.
7. Islam O, Soboleski D, Symons S, et al. Development and duration of radiographic signs of bone healing in children. *AJR Am J Roentgenol*. 2000;175:75–78.
8. O'Conner JF, Cohen J. Dating fractures. In: Kleinman PK, ed. *Diagnostic Imaging in Child Abuse*. Baltimore, MD: Williams & Wilkins; 1987:168–177.
9. Boles CA, Hendrix RW. Complications of fracture. In: Rogers LF, ed. *Radiology of Skeletal Trauma*. 3rd ed. Philadelphia, PA: Churchill Livingstone; 2002:231–271.
10. Lewallen RP, Peterson HA. Nonunion of long bone fractures in children: a review of 30 cases. *J Pediatr Orthop*. 1985;5:135–142.
11. Hensinger RN. Complications of fractures in children. In: Ogden JA, ed. *Skeletal Injury in the Child*. 3rd ed. New York, NY: Springer; 2000:124–151.
12. Ecklund K, Jaramillo D. Patterns of premature physeal arrest: MR imaging of 111 children. *AJR Am J Roentgenol*. 2002;178:967–972.
13. Peterson HA. Partial growth plate arrest and its treatment. *J Pediatr Orthop*. 1984;4:246–258.
14. Loder RT, Swinford AE, Kuhns LR. The use of helical computed tomographic scan to assess bony physeal bridges. *J Pediatr Orthop*. 1997;17:356–359.
15. Sailhan F, Chotel F, Guibal A, et al. Three-dimensional MR imaging in the assessment of physeal growth arrest. *Eur Radiol*. 2004;14:1600–1608.
16. Whan A, Breidahl W, Janes G. MRI of trapped periosteum in a proximal tibial physeal injury of a pediatric patient. *AJR Am J Roentgenol*. 2003;181(5):191.
17. Khoshhal K, Kiefer G. Physeal bridge resection. *J Am Acad Orthop Surg*. 2005;13:47–58.
18. Swischuk L, Hernandez JA. Frequently missed fractures in children (value of comparative views). *Emerg Radiol*. 2004;11:22–28.
19. Alison M, Axoulay R, Tilea B, et al. Imaging strategies in paediatric musculoskeletal trauma. *Pediatr Radiol*. 2009;29:S414–S421.
20. Hussain H, Barnes C. Pediatric skeletal trauma—plain film to MRI. *Appl Radiol*. 2007;36:24–33.
21. Rodriguez-Merchan EC. Pediatric skeletal trauma. *Clin Orthop Relat Res*. 2005;432:8–13.
22. Salter RB, Harris WR. Injuries involving the epiphyseal plate. *J Bone Joint Surg Am*. 1963;45:587–632.
23. Mizuta T, Benson WM, Foster BK, et al. Statistical analysis of the incidence of physeal injuries. *J Pediatr Orthop*. 1987;7:518–523.
24. Close BJ, Strouse PJ. MRI of physeal fractures of the adolescent knee. *Pediatr Radiol*. 2000;30:756–762.
25. Jaramillo D, Shapiro F, Hoffer F, et al. Posttraumatic growth-plate abnormalities: MR imaging of bony-bridge formation in rabbits. *Radiology*. 1990;175:767–773.
26. Bishop JY. Pediatric shoulder trauma. *Clin Orthop*. 2005;432:41–48.
27. Caviglia H, Garrido CP, Palazzi FF, et al. Pediatric fractures of the humerus. *Clin Orthop Rel Res*. 2005;432:49–56.
28. Grissom LE, Harcke HT. Infant shoulder sonography: technique, anatomy and pathology. *Pediatr Radiol*. 2001;31:863–868.
29. Sherr-Lurie N, Bialik GM, Ganel A, et al. Fractures of the humerus in the neonatal period. *Isr Med Assoc J*. 2011;13:363–365.
30. Levine B, Pereira D, Rosen J. Avulsion fractures of the lesser tuberosity of the humerus in adolescents: review of the literature and case report. *J Orthop Trauma*. 2005;19:349–352.
31. Shibuya S, Ogawa K. Isolated avulsion fracture of the lesser tuberosity of the humerus. *Clin Orthop Relat Res*. 1986;211:215–218.
32. Shaw BA, Murphy KM, Shaw A, et al. Humerus shaft fractures in young children: accident or abuse? *J Pediatr Orthop*. 1997;17:293–297.
33. Binder H, Schurz M, Aldrian S, et al. Physeal injuries of the proximal humerus: long-term results in seventy two patients. *Int Orthop*. 2011;35:1497–1502.
34. Pahlavan S, Baldwin KD, Pandya NK, et al. Proximal humerus fractures in the pediatric population: a systematic review. *J Child Orthop*. 2011;5:187–194.
35. Rab GT, Grottkau BG. Operative treatment of children's fractures and injuries of the physis. In: Chapman MW, ed. *Orthopedic Surgery*. 3rd ed. Philadelphia, PA: Lippincott Williams & Wilkins; 2001:4175–4194.
36. John SD, Wherry K, Swischuk LE, et al. Improving detection of pediatric elbow fractures by understanding their mechanics. *Radiographics*. 1996;16:1443–1460.
37. Brubacher JW, Dodds SD. Pediatric supracondylar fractures of the distal humerus. *Curr Rev Musculoskelet Med*. 2008;1:190–196.
38. Girdany BR, Golden R. Centers of ossification of the skeleton. *Am J Roentgenol Radium Ther Nucl Med*. 1952;68:922–924.
39. Norell HG. Reontgenologic visualization of extracapsular fat: its importance in diagnosis of traumatic injuries to elbow. *Acta Radiol (Diagn)*. 1954;42:205.
40. Bledsoe RC, Izenstark JL. Displacement of fat pads in diseases and injury of the elbow: a new radiographic sign. *Radiology*. 1959;73:717–724.
41. Major N, Crawford S. Elbow effusions in trauma in adult and children: is there an occult fracture? *AJR Am J Roentgenol*. 2002;178:413–418.
42. Skaggs DL, Mirzayan R. The posterior fat pad sign in association with occult fractures of the elbow in children. *J Bone Joint Surg Am*. 1999;81:1429–1433.
43. Donnelly LF, Klostermeier TT, Klosterman LA. Traumatic elbow effusions in pediatric patients: are occult fractures the rule? *AJR Am J Roentgenol*. 1998;171:243–245.
44. Miles KA, Finlay DB. Disruption of the radiocapitellar line in the normal elbow. *Injury*. 1989;20:365–367.
45. Skaggs DL. Elbow fractures in children: diagnosis and management. *J Am Acad Orthop Surg*. 1997;5:303–312.
46. Lins RE, Simovitch RW, Waters PM. Pediatric elbow trauma. *Orthop Clin North Am*. 1999;30:119–132.
47. Omid R, Choi PD, Skaggs DL. Supracondylar humeral fractures in children. *J Bone Joint Surg Am*. 2008;90:1121–1132.
48. Gartland JJ. Management of supracondylar fractures of the humerus in children. *Surg Gynecol Obstet*. 1959;109:145–154.
49. Silva M, Wong TC, Bernthal NM. Outcomes of reduction more than 7 days after injury in supracondylar humeral fractures in children. *J Pediatr Orthop*. 2011;31:751–756.
50. Simanovsky N, Lamdan R, Mosheiff R, et al. Underreduced supracondylar fracture of the humerus in children: clinical significance at skeletal maturity. *J Pediatr Orthop*. 2007;27:739–742.
51. Keenan WN, Clegg J. Variation of Baumann's angle with age, sex, and side: implications for its use in radiological monitoring of supracondylar fracture of the humerus in children. *J Pediatr Orthop*. 1996;16:97–98.
52. Labelle H, Bunnell WP, Duhaime M, et al. Cubitus varus deformity following supracondylar fractures of the distal humerus in children. *J Pediatr Orthop*. 1982;2:539–546.
53. Lawson C, Midbrandt T. Common elbow injuries in children: evaluation, treatment and clinical outcomes. *Curr Opin Orthopaed*. 2004;14:286–294.
54. Abzug JM, Herman MJ. Management of supracondylar fractures in children: current concepts. *J Am Acad Orthop Surg*. 2012;20: 69–77.
55. Tejwani N, Phillips D, Goldstein RY. Management of lateral humeral condylar fracture in children. *J Am Acad Orthop Surg*. 2011;19:350–358.
56. Song KS, Kang CH, Min BW, et al. Internal oblique radiographs for diagnosis of nondisplaced or minimally displaced lateral condylar fractures of the humerus in children. *J Bone Joint Surg Am*. 2007;89:58–63.
57. Kamegaya M, Shinohara Y, Kurokawa M, et al. Assessment of stability in children's minimally displaced lateral humeral condyle fracture by magnetic resonance imaging. *J Pediatr Orthop*. 1999;19:570–572.
58. Koh KH, Seo SW, Kim KM, et al. Clinical and radiographic results of lateral condylar fracture of distal humerus in children. *J Pediatr Orthop*. 2010;30:425–429.
59. Klingele KE, Kocher MS. Little league elbow: valgus overload injury in the paediatric athlete. *Sports Med*. 2002;32:1005–1015.
60. Harrison RB, Keats TE, Frankel CJ, et al. Radiographic clues to fractures of the unossified medial humeral condyle in young children. *Skeletal Radiol*. 1984;11:209–212.
61. Chambers HG, Wilkens KE. Fractures involving the medial epicondylar apophysis. In: Rockwood CA Jr, Wildens KE, Beaty JH,

eds. *Fractures in Children*. 4th ed. Philadelphia, PA: JB Lippincott; 1998:801–819.

62. Osbahr DC, Chalmers PN, Frank JS, et al. Acute, avulsion fractures of the medial epicondyle while throwing in youth baseball players: a variant of Little League elbow. *J Shoulder Elbow Surg*. 2010;19: 951–957.
63. May DA, Disler DG, Jones EA, et al. Using sonography to diagnose an unossified medial epicondyle avulsion in a child. *AJR Am J Roentgenol*. 2000;174:1115–1117.
64. Haxhija EQ, Mayr JM, Grechenig W, et al. Treatment of medial epicondyle apophyseal avulsion injury in children. *Oper Orthop Traumatol*. 2006;18:120–134.
65. Stricker SJ, Thomson JD, Kelly RA. Coronal-plane transcondylar fracture of the humerus in a child. *Clin Orthop Related Res*. 1993;294:308–311.
66. Jacobsen S, Hansson G, Nathorst-Westfelt J. Traumatic separation of the distal epiphysis of the humerus sustained at birth. *J Bone Joint Surg*. 2009;91-B:797–802.
67. Rogers LF, Rockwood CA Jr. Separation of the entire distal humeral epiphysis. *Radiology*. 1973;106:393–400.
68. Dormans JP, Rang M. Fractures of the olecranon and radial neck in children. *Orthop Clin North Am*. 1990;21(2):257–268.
69. Evans MC, Graham MK, Kerr H. Olecranon fractures in children: Part 1: a clinical review: Part 2: a new classification system and management algorithm. *J Pediatr Orthop*. 1999;19:559–569.
70. Retting AC, Wurth TR, Mieling P. Nonunion of olecranon stress fractures in adolescent baseball pitchers. *Am J Sports Med*. 2006;34:653–656.
71. Salter RB, Zaltz C. Anatomic investigations of the mechanism of injury and pathologic anatomy of "pulled elbow" in young children. *Clin Orthop Relat Res*. 1971;77:134–143.
72. Bretland PM. Pulled elbow in childhood. *Br Radiol*. 1994;67:1176–1185.
73. Kim MC, Eckhardt BP, Craig C, et al. Ultrasonography of the annular ligament partial tear and recurrent pulled elbow. *Pediatr Radiol*. 2004;34:999–1004.
74. Rodriguez-Merchan EC. Pediatric skeletal trauma: a review and historical perspective. *Clin Orthop Relat Res*. 2005;432:8–13.
75. Pretell-Mazzini J, Carrigan RB. Simultaneous distal radial fractures and carpal bone injuries in children: a review article. *J Pediatr Orthop Bull*. 2011;20:330–333.
76. Kay RM, Skaggs DL. The pediatric Monteggia fracture. *Am J Orthop*. 1998;27:606–609.
77. Wiley JJ, Galey JP. Monteggia injuries in children. *J Bone Joint Surg Br*. 1985;67:728–731.
78. Reckling FW, Cordell LD. Unstable fracture-dislocations of the forearm: the Monteggia and Galeazzi lesions. *Arch Surg*. 1968;96:999–1007.
79. Bowman EN, Mehlman CT, Lindsell CJ, et al. Nonoperative treatment of both bone forearm shaft fractures in children: predictors of early radiographic failure. *J Pediatr Orthop*. 2011;31:23–32.
80. Ring D, Jupiter JB, Waters PM. Monteggia fractures in children and adults. *J Am Acad Orthop Surg*. 1998;6:215–224.
81. Atesok KL, Jupiter JB, Weiss AP. Galeazzi fracture. *J Am Acad Orthop Surg*. 2011;19:622–633.
82. Johnson KL, Haigh SF, Symonds KE. MRI in the management of scaphoid fractures in skeletally immature patients. *Pediatr Radiol*. 2000;30:685–688.
83. Goddard N. Carpal fractures in children. *Clin Orthop Relat Res*. 2005;432:73–76.
84. Huckstadt T, Klitscher D, Weltzien A, et al. Pediatric fractures of the carpal scaphoid: a retrospective clinical and radiological study. *J Pediatr Orthop*. 2007;27:447–450.
85. Valencia J, Leyva F, Gomez-Bajo GJ. Pediatric hand trauma. *Clin Orthop Relat Res*. 2005;432:77–86.
86. Nofsinger CC, Wolfe SF. Common pediatric hand fractures. *Curr Opin Pediatr*. 2002;14:42–45.
87. Deibert MC, Aronsson DD, Johnson RJ, et al. Skiing injuries in children, adolescents and adults. *J Bone Joint Surg Am*. 1998;80: 25–32.
88. Momiy JP, Clayton JL, Villalba H, et al. Pelvic fractures in children. *Am Surg*. 2006;72:962–965.
89. Chia JP, Holland AJ, Little D, et al. Pelvic fractures and associated injuries in children. *J Trauma*. 2004;56:83–88.
90. Leonard M, Ibrahim M, McKenna P, et al. Paediatric pelvic ring fractures and associated injuries. *Injury*. 2011;42:1027–1030.
91. Silber JS, Flynn JM. Changing patterns of pediatric pelvic fractures with skeletal maturation: implications for classification and management. *J Pediatr Orthop*. 2002;22:22–26.
92. Silber JS, Flynn JM, Koffler KM, et al. Analysis of the cause, classification, and associated injuries of 166 consecutive pediatric pelvic fractures. *J Pediatr Orthop*. 2001;21:446–450.
93. Schlickwei W, Keck T. Pelvic and acetabular fractures in childhood. *Injury*. 2005;36:A57–A63.
94. Quick TJ, Eastwood DM. Pediatric fractures and dislocations of the hip and pelvis. *Clin Orthop Relat Res*. 2005;432:87–96.
95. Guillamondegui OD, Mahboubi S, Stafford PW, et al. The utility of the pelvic radiograph in the assessment of pediatric pelvic fractures. *J Trauma*. 2003;55:236–239.
96. Stewart BG, Rhea JT, Sheridan RL, et al. Is the screening portable pelvis film clinically useful in multiple trauma patients who will be examined by abdominopelvic CT? Experience with 397 patients. *Emerg Radiol*. 2002;9:266–271.
97. Schneidmueller D, Wutzler S, Kelm A, et al. Pelvis injuries in childhood and adolescence: retrospective analysis of 5 year data from a national trauma centre. *Unfallchirurg*. 2011;116:510–516.
98. Holden CP, Holman J, Herman MJ. Pediatric pelvic fractures. *J Am Acad Orthop Surg*. 2007;15:172–177.
99. Schlonsky J, Miller P. Traumatic hip dislocations in children. *J Bone Joint Surg Am*. 1973;55:1057–1063.
100. Herrera-Soto J, Price CT. Traumatic hip dislocations in children and adolescents: pitfalls and complications. *J Am Acad Orthop Surg*. 2009;17:15–21.
101. Mehlman CT, Hubbard GW, Crawford AH, et al. Traumatic hip dislocations in children: long-term follow-up of 42 patients. *Clin Orthop*. 2000;376:68–79.
102. Restrepo R, Reed MH. Impact of obesity in the diagnosis of SCFE and knee problems in obese children. *Pediatr Radiol*. 2009;39:S220–S225.
103. Brenkel IJ, Dias JJ, Davies TG, et al. Hormone status in patients with slipped capital femoral epiphysis. *J Bone Joint Surg Br*. 1989;71:33–38.
104. Loder RT, Aronson DD, Greenfield ML. The epidemiology of bilateral slipped capital femoral epiphysis: a study of children in Michigan. *J Bone Joint Surg Am*. 1993;75:1141–1147.
105. Loder RT, Wittenberg B, DeSilva G. Slipped capital femoral epiphysis associated with endocrine disorders. *J Pediatr Orthop*. 1995;15:349–356.
106. Boles CA, El-Khoury GY. Slipped capital femoral epiphysis. *Radiographics*. 1997;17:809–823.
107. Mannoff EM, Banffy MB, Winnell JJ. Relationship between body mass index and slipped capital femoral epiphysis. *J Pediatr Orthop*. 2005;25:744–746.
108. Loder RT, Aronson D, Dobbs MB, et al. Slipped capital femoral epiphysis. *J Bone Joint Surg Am*. 2000;82:1170–1188.
109. Tins B, Cassar-Pullicino V, McAll I. The role of pretreatment MRI in established cases of slipped capital femoral epiphysis. *Eur J Radiol*. 2009;70:570–578.
110. Loder RT. Unstable slipped capital femoral epiphysis. *J Pediatr Orthop*. 2001;21:694–699.
111. Klein A, Joplin RJ, Reidy JA, et al. Roentgenographic features of slipped capital femoral epiphysis. *AJR Am J Roentgenol*. 1951;66:361–374.
112. Miese FR, Zilkens C, Holstein A, et al. Assessment of early cartilage degeneration after slipped capital femoral epiphysis using T2 and T2* mapping. *Acta Radiol*. 2011;52:106–110.
113. Vrettos BC, Hoffman EB. Chondrolysis in slipped upper femoral epiphysis: long-term study of the aetiology and natural history. *J Bone Joint Surg Br*. 1993;75:956–961.
114. Strouse PJ. MRI of the knee: key points in the pediatric population. *Pediatr Radiol*. 2010;40:447–452.
115. Pai DR, Strouse PJ. MRI of the pediatric knee. *AJR Am J Roentgenol*. 2011;196:1019–1027.
116. Edwards PH Jr, Grana WA. Physeal fractures about the knee. *J Am Acad Orthop Surg*. 1995;3:63–69.
117. Lee JH, Weissman BN, Nikpoor N, et al. Lipohemarthrosis of the knee: a review of recent experiences. *Radiology*. 1989;173:189–191.
118. Khanna G, El-Khoury GY. Sleeve fracture at the superior pole of the patella. *Pediatr Radiol*. 2007;37:720–723.
119. Ray JM, Hendrix J. Incidence, mechanism of injury, and treatment of fractures of the patella in children. *J Trauma*. 1992;32:464–467.
120. Dai LY, Zhang WM. Fractures of the patella in children. *Knee Surg Sports Traumatol Arthosc*. 1999;7:243–245.
121. McKoy BE, Stanitski CL. Acute tibial tubercle avulsion fractures. *Orthop Clin North Am*. 2003;34:397–403.

122. Dupuis CS, Westra SJ, Makris J, et al. Injuries and conditions of the extensor mechanism of the pediatric knee. *Radiographics*. 2009;29:877–886.
123. Swischuk LE, John SD, Tschoepe EJ. Upper tibial hyperextension fractures in infants: another occult toddler's fracture. *Pediatr Radiol*. 1999;29:6–9.
124. Bruyeer E, Geusens E, Catry F, et al. 'Trampoline fracture' of the proximal tibia in children: report of 3 cases and review of literature. *JBR-BTR*. 2012;95:10–12.
125. Blumberg K, Patterson RJ. The toddler's cuboid fracture. *Radiology*. 1991;179:93–94.
126. Dunbar JS, Owen HF, Nogrady MB, et al. Obscure tibial fracture of infants—the toddler's fracture. *J Can Assoc Radiol*. 1964;15:136–144.
127. Heinrick S. Fractures of the shaft of the tibia and fibula. In: Beaty JH, Kasser JR, eds. *Rockwood and Wilkins' Fractures in Children*. Philadelphia: Lippincott Williams & Wilkins; 2011:1077–1118.
128. Hart ES, Luther B, Grottkau BE. Broken bones: common pediatric lower extremity fractures—part III. *Orthop Nurs*. 2006;25:390–407.
129. Kalyani BS, Roberts CS, Giannoudis PV. The Masionneuve injury: a comprehensive review. *Orthopedics*. 2010;33:196–197.
130. Stufkens SA, van den Bekrom MP, Doornberg JN, et al. Evidence-based treatment of Maisonneuve fractures. *J Foot Ankle Surg*. 2011;50:62–67.
131. Kleiger B, Mankin HJ. Fracture of the lateral portion of the distal tibial epiphysis. *J Bone Joint Surg*. 1964;46:25–32.
132. Stefanich RJ, Lozman J. The juvenile Tillaux fracture. *Clin Orthop Relat Res*. 1986;210:219–227.
133. Kay RM, Matthys GA. Pediatric ankle fractures: evaluation and treatment. *J Am Acad Orthop Surg*. 2001;9:268–278.
134. Benson M, Fixsen J, Macnicol M, et al, eds. *Children's Orthopedics and Fractures*. 3rd ed. London, UK: Springer-Verlag; 2010.
135. Ho-Fung V, Pollock A. Triplane fracture. *Pediatr Emerg Care*. 2011;27:70–72.
136. Spiegel PG, Mast JW, Cooperman DR, et al. Triplane fractures of the distal tibial epiphysis. *Clin Orthop Relat Res*. 1984;188:74–89.
137. Eismann EA, Stephan ZA, Mehlman CT, et al. Pediatric triplane ankle fractures: impact of radiographs and computed tomography on fracture classification and treatment planning. *J Bone Joint Surg Am*. 2015;97(12):995–1002. doi:10.2106/JBJS.N.01208.
138. Horn BD, Crisci K, Krug M, et al. Radiologic evaluation of juvenile Tillaux fractures of the distal tibia. *J Pediatr Orthop*. 2001;21:162–164.
139. Cutler L, Molloy A, Dhukuram V, et al. Do CT scans aid assessment of distal tibial physeal fractures? *J Bone Joint Surg Br*. 2004;86:239–243.
140. Brown SD, Kasser JR, Zurkowski D, et al. Analysis of 50 tibial triplane fractures using CT with multiplanar reconstruction. *AJR Am J Roentgenol*. 2004;183:1489–1495.
141. Kim JR, Song KH, Song KJ, et al. Treatment outcomes of triplane and Tillaux fractures of the ankle in adolescence. *Clin Orthop Surg*. 2010;2:34–38.
142. Happamaki W, Kiuru MJ, Koskinen SK. Ankle and foot injuries: analysis of MDCT findings. *AJR Am J Roentgenol*. 2004;183:615–622.
143. Gourineni P, Gupta A. Medial joint space widening of the ankle in displaced Tillaux and triplane fractures in children. *J Orthop Trauma*. 2011;25:608–611.
144. Schnetzler KA, Hoerschemeyer D. The pediatric triplane ankle fracture. *J Am Acad Orthop Surg*. 2007;15:738–747.
145. Kay RM, Tang CW. Pediatric foot fractures: evaluation and treatment. *J Am Acad Orthop Surg*. 2001;9:308–319.
146. Jensen I, Wester JU, Rasmussen F, et al. Prognosis of fracture of the talus in children. 20 (7-34)-year follow-up of 14 cases. *Acta Orthop Scand*. 1994;65:398–400.
147. John SD, Moorthy CS, Swischuk LE. Expanding the concepts of the toddler's fracture. *Radiographics*. 1997;17:367–376.
148. Eberl R, Singer G, Schalamon J, et al. Fractures of the talus—differences between children and adolescents. *J Trauma*. 2010;68:126–130.
149. Laliotis N, Pennie BH, Carty H, et al. Toddler's fracture of the calcaneum. *Injury*. 1993;24:169–170.
150. Ribbans WJ, Natarajan R, Alavala S. Pediatric foot fractures. *Clin Orthop Relat Res*. 2005;432:107–115.
151. Walling AK, Grogan DP, Carty CT, et al. Fractures of the calcaneal apophysis. *J Orthop Trauma*. 1990;4:349–355.
152. Gross RH. Fractures and dislocations of the foot. In: Rockwood CA Jr, Wilkins KE, Beaty JH, eds. *Fractures in Children*. 4th ed. Philadelphia: Lippincott-Raven; 1996:1429–1497.
153. Summers H, Kramer AP, Benirschke SK. Pediatric calcaneal fractures. *Orthop Rev (Pavia)*. 2009;30:e9.
154. Petit CJ, Lee BM, Kasser JR, et al. Operative treatment of intraarticular calcaneal fractures in the pediatric population. *J Pediatr Orthop*. 2007;27:856–882.
155. Woodward S, Jacobson JA, Femino JE, et al. Sonographic evaluation of Lisfranc ligament injuries. *J Ultrasound Med*. 2009;28:351–357.
156. Singer G, Cichocki M, Schalamon J, et al. A study of metatarsal fractures in children. *J Bone Joint Surg Am*. 2008;90:772–776.
157. Swischuk LE. Musculoskeletal: what is different in children? Tripped and jammed my toe. *Emerg Radiol*. 2010;17:1–2.
158. Pinckney LE, Currarino G, Kennedy LA. The stubbed great toe: a cause of occult compound fracture and infection. *Radiology*. 1981;138:375–377.
159. Kensinger DR, Guille JT, Horn BD, et al. The stubbed great toe: importance of early recognition and treatment of open fractures of the distal phalanx. *J Pediatr Orthop*. 2001;21:31–34.
160. Swischuk LE. Musculoskeletal: what is different in children? Jumped off bed; foot pain. *Emerg Radiol*. 2009;16:171–174.
161. Arsal, Swiontkowski MF, eds. *Skeletal Trauma in Children*. Philadelphia, PA: WB Saunders; 1994:449–516.
162. Herrera-Soto JA, Scherb M, Duffy MF, et al. Fractures of the fifth metatarsal in children and adolescents. *J Pediatr Orthop*. 2007;27:427–431.
163. Schulman H, Tsodikow V, Einhorn M, et al. Congenital insensitivity to pain with anhidrosis (CIPA): the spectrum of radiological findings. *Pediatr Radiol*. 2001;31:701–705.
164. Laplaza FJ, Turajane T, Axelrod FB, et al. Nonspinal orthopaedic problems in familial dysautonomia (Riley-Day Syndrome). *J Pediatr Orthop*. 2001;21:229–232.
165. Zimmerman A, Law C, Blount J, et al. Neuropathic arthropathy of the elbow in a paediatric patient with myelomeningocele. *Dev Neurorehabil*. 2007;10:261–264.
166. Mobini M, Javadzadeh A, Forghanizadeh J. Neuropathic osteoarthropathy in a patient with congenital insensitivity to pain. *Arch Iran Med*. 2009;12:599–602.
167. Crouch C, Smith WL. Long term sequelae of frostbite. *Pediatr Radiol*. 1990;20:365–366.
168. Carrera GF, Kozin F, Flaherty L, et al. Radiographic changes in the hands following childhood frostbite injury. *Skeletal Radiol*. 1981;6:33–37.
169. D'Souza AL, Nelson NG, McKenzie LB. Pediatric burn injuries treated in US emergency departments between 1990 and 2006. *Pediatrics*. 2009;124:1424–1430.
170. Choi M, Armstrong MB, Panthaki ZJ. Pediatric hand burns: thermal, electrical, chemical. *J Craniofac Surg*. 2009;20:1045–1048.
171. Balen PF, Helms CA. Bony ankylosis following thermal and electrical injury. *Skeletal Radiol*. 2001;30:393–397.
172. Kumar D, Papini R, Tillman RM. Partial growth plate fusion caused by burn. *Burns*. 2001;27:664–667.
173. Cox SG, Rode H, Darani AN, et al. Thermal injury within the first 4 months of life. *Burns*. 2011;37:828–834.
174. Bingham H. Electrical burns. *Clin Plast Surg*. 1986;13:75–85.
175. Williams HJ, Davies AM. The effect of x-rays on bone: a pictorial review. *Eur Radiol*. 2006;16:619–633.
176. Jaffe N, Ried HL, Cohen M, et al. Radiation induced osteochondroma in long-term survivors of childhood cancer. *Int J Radiat Oncol Biol Phys*. 1983;9:665–670.
177. Fletcher BD, Crom DB, Krance RA, et al. Radiation-induced bone abnormalities after bone marrow transplantation for childhood leukemia. *Radiology*. 1994;191:231–235.

# 143 Child Abuse

Peter J. Strouse

## OVERVIEW

Radiology played a major role in defining child abuse as a medical entity, most notably with the landmark publications by Caffey (1946) and Silverman (1953).[1,2] Silverman also contributed to Kempe's 1962 paper, "The Battered Child," which demonstrated the prevalence of severe injury and death from child abuse and brought widespread public awareness to the diagnosis.[3] In the ensuing years, an enormous experience base and wealth of literature have defined and refined our knowledge of the radiologic appearance of child abuse and its differential diagnosis. In spite of this, child abuse remains a difficult and emotionally charged topic. Today, the diagnosis is increasingly challenged in the legal system, and radiologists are more frequently called upon to participate in legal proceedings. It behooves any radiologist interpreting pediatric imaging to be very familiar with the findings of child abuse and its differential diagnoses.

***Etiology, Pathophysiology, and Clinical Presentation.*** According to the most recent survey from the US Department of Health and Human Services, in the year 2014, 43.7 of every 1000 children (or approximately 3,248,006 children) in the United States were evaluated by child protective services for suspected abuse or neglect, and 9.3 of every 1000 children were confirmed as abused or neglected (24.4 of 1000 for those <1 year of age).[4] In 2014, 75.0% were victims of neglect, 17.0% of physical abuse, 8.3% of sexual abuse, 6.0% of psychological maltreatment, 2.2% of medical neglect, and 6.8% of other forms of maltreatment.[4] This totals 115.4%, as many children are victims of multiple forms of abuse or neglect.[4] Young children are at greatest risk for fatality; 70.7% of fatalities from child abuse are in children less than 3 years of age and 44.2% are in children less than 1 year of age.[4] An estimated 1580 children died from abuse or neglect in 2014.[4]

Clinical presentations of child abuse are myriad. Abuse may be suspected early in the clinical course; however, presentation is often cryptic until traumatic findings are made clinically or by imaging.[5,6] Children often present with bruising, burns, or evidence of neglect. Children may present with symptoms related to neuroaxis, thoracoabdominal, or extremity trauma. Manifestations of abuse may be found incidentally on imaging performed to evaluate a nontraumatic process.

***Imaging.*** Initial imaging of the abused child is directed by the clinical presentation.[6–10] Imaging is performed to evaluate for processes that need immediate management or may further threaten the child's well-being if not diagnosed and treated. Once the child's acute medical issues are addressed and their condition is stable, further imaging in the form of a radiographic skeletal survey is performed. The role of such imaging is to (1) catalog and document injuries; (2) identify occult injuries, especially those requiring treatment; (3) confirm or disprove abuse; and importantly, (4) make alternative diagnoses when present.[10]

Computed tomography (CT) and magnetic resonance imaging (MRI) are used to evaluate suspected head trauma.[10] There are no firm indications for CT of the chest in suspected physical abuse or infants with blunt traumatic injury. CT of the abdomen and pelvis is indicated only in children with physical examination and/or laboratory findings suggesting traumatic intraabdominal injury.[11–13]

In children less than 2 years of age who are possible victims of abuse, a skeletal survey is mandatory (Box 143.1).[8–10,14] A "babygram" consisting of single or few images of the entire infant is unsatisfactory. Ideally, a radiologist should review the images before the child leaves the radiography suite. Poorly positioned and otherwise suboptimal images should be repeated. Additional views may be obtained to further define positive or suspected abnormalities. Commonly acquired additional views include lateral views of the extremities, coned views centered at the joints (wrist, ankle, knee), and Townes view of the skull.

Follow-up skeletal survey performed 2 weeks later may provide additional information (e-Fig. 143.1).[15,16] As noted by Kleinman, the follow-up survey aids by (1) detecting additional fractures; (2) differentiating fractures from normal developmental variants; and (3) assisting in dating injuries.[15] Follow-up surveys may be limited or tailored to areas of interest.[17]

Beyond 2 years of age, the yield of radiographic skeletal survey is low as fractures are less common, fractures are less commonly occult, and the fracture patterns highly specific for abuse are no longer seen.[18] A skeletal survey may still be warranted if there is a high clinical suspicion for abusive trauma, particularly in children who are mentally incapacitated.

Radiographic skeletal surveys should be performed in all cases of fatal suspected abuse and unexplained infant death, following the same protocol as used in living infants.[19–22] Postmortem whole body CT may aid in delineation of some fractures.[23,24]

***Imaging Findings.*** No single radiographic finding is pathognomonic of child abuse. Individual findings vary from high to low specificity (Box 143.2).[9,25,26] High-specificity lesions are seen with abusive trauma but rarely with other forms of trauma. Low-specificity lesions are commonly seen with abusive trauma but are also common with other forms trauma.

Every patient is considered individually with respect to the presenting clinical history and the possibility of underlying abnormality or disease, which would predispose to fracture.[9] The plausibility of the injury having occurred from accidental nonabusive trauma must also be considered. Is the explanation offered for the injury plausible? Is the developmental level of the child consistent with that history? Answering these questions requires input of the radiologist to a multidisciplinary child protection team.

Nonambulatory infants do not normally incur fractures. The appropriateness of the provided history in relation to the mechanism of injury and age of the child is thus often an important clue to the diagnosis of abusive injuries. Inappropriate delay in seeking treatment is also concerning.

The constellation of radiographic findings within the context of the clinical presentation usually carries greater specificity than any single finding. Multiple fractures in different stages of healing are highly specific for child abuse, unless there is underlying bone dysplasia or metabolic disease.

## RIB FRACTURES

Rib fractures are found in approximately 50% of fatally abused infants.[27] In a surviving infant, the physician may palpate callus or, rarely, crepitus, but typically rib fractures are clinically occult. Most acute rib fractures are nondisplaced or minimally displaced buckle or greenstick fractures, which are subtle or not evident on radiography until callus formation (see e-Fig. 143.1).[28] Fractures may occur at any point along the arc of the rib including the rib head, costovertebral, posterior, lateral, anterior, or costochondral

## Abstract:

Radiology played a major role in defining child abuse as a medical entity in the 1940s and 1950s. Since then an enormous experience base and wealth of literature have defined and redefined our knowledge of the imaging appearance of child abuse and its differential diagnosis. Still child abuse remains a difficult and emotionally charged topic. Today, the diagnosis is increasing challenged in the legal system and radiologists are more frequently called upon to participate in legal proceedings. This chapter reviews the imaging evaluation of abuse in the skeleton of children.

## Keywords:

Bones
Children
Child abuse
Fractures
Infants
Non-accidental trauma
Radiography

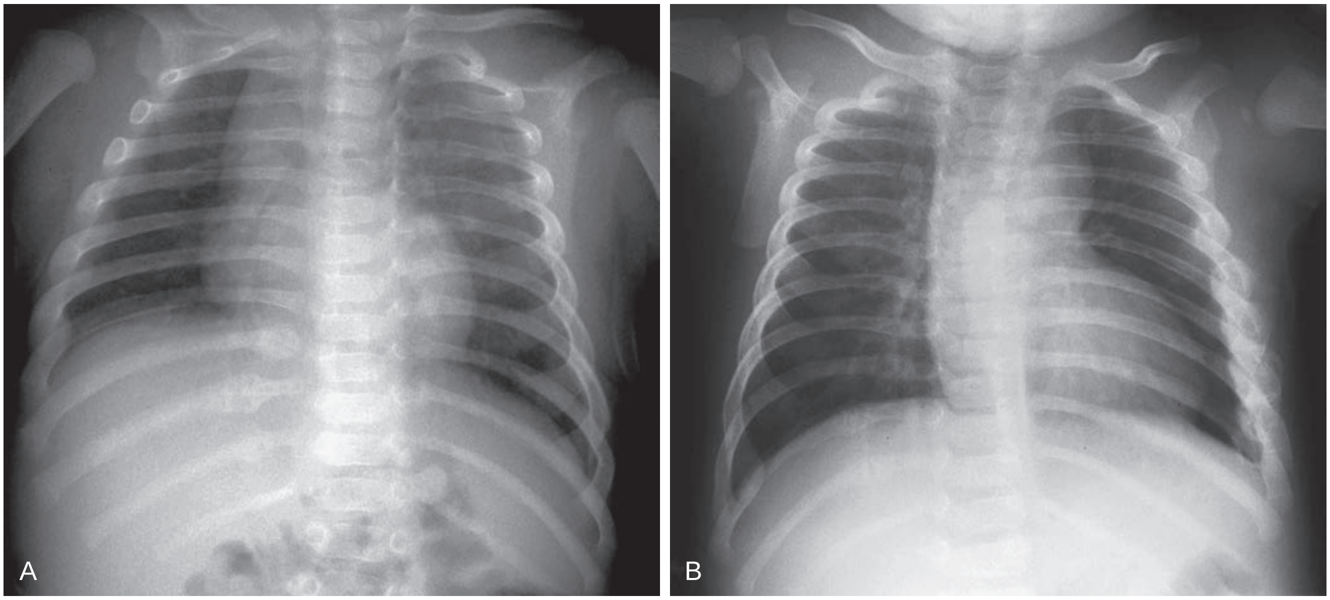

**e-Figure 143.1. A 6-week-old male infant sent for an upper gastrointestinal series for evaluation of colicky pain.** (A) Initial chest radiograph identified healing fractures at the right 9th, 10th, and 11th ribs. (B) Follow-up chest radiograph 2 weeks later showed additional fractures, now healing, at the lateral aspect of the left 3rd through 9th ribs. The father admitted to shaking the infant.

**BOX 143.1** Skeletal Survey*

- Anteroposterior (AP) and lateral of skull (Townes view optional; add if any fracture seen)
- Lateral spine (C-spine may be included on skull radiographs; AP spine is included on AP chest and AP pelvis to include entire lumbar spine)
- AP, right posterior oblique, left posterior oblique of chest—rib technique
- AP pelvis
- AP of each femur
- AP of each leg
- AP of each humerus
- AP of each forearm
- Posteroanterior of each hand
- AP (dorsoventral) of each foot

*Images are reviewed by a radiologist before the child leaves. Poorly positioned or otherwise suboptimal images should be repeated. Lateral views are added for positive or equivocal findings in the extremities. Coned views of positive or equivocal findings (i.e., at the ends of the long bones, ribs) may be obtained.

**BOX 143.2** Skeletal Injuries From Child Abuse

**HIGH SPECIFICITY FINDINGS**

- Classic metaphyseal lesions
- Posterior rib fracture
- Scapular fracture
- Sternal fracture
- Spinous process fracture
- First rib fracture

**MODERATE SPECIFICITY FINDINGS**

- Multiple fractures
- Fractures of differing age
- Spine fracture
- Complex skull fracture
- Physeal fractures of the long bones
- Digital fractures

**LOW SPECIFICITY FINDINGS**

- Diaphyseal fractures of the long bones
- Simple skull fractures
- Clavicle fracture
- Subperiosteal new bone formation

*Modified from Kleinman PK.* Diagnostic Imaging of Child Abuse. *2nd ed. St Louis, MO: Mosby; 1998.*

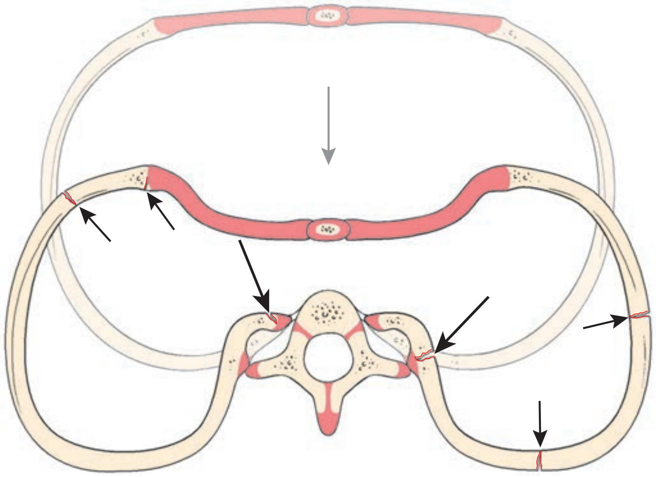

**Figure 143.2. Mechanism of rib injury.** With anteroposterior compression *(gray arrow)* of the chest, excessive leverage of the posterior ribs occurs over the fulcrum of the transverse processes. This places tension along the inner aspects of the rib head and neck regions, resulting in fractures at these sites *(long black arrows)*. This mechanism is consistent with morphologic patterns of injury occurring at other sites along the rib arcs and at the costochondral junctions *(short black arrows)*. *(From Kleinman PK.* Diagnostic Imaging of Child Abuse. *2nd ed. St Louis, MO: Mosby; 1998.)*

portions.[27,29] Posterior rib fractures at the costovertebral junction have a high specificity for abuse.[30–32] Boal et al reviewed 1463 rib fractures in 141 abused infants and noted that, when individual sites along the rib arc were compared, costovertebral junction fractures outnumbered all other individual sites but represented only 33% of the total number of rib fractures.[30] Fractures at the costochondral junction and rib heads appear radiographically similar to classic metaphyseal lesions of the long bones. Costochondral junction fractures have a high association with visceral trauma.[33] First rib fractures bear high specificity for child abuse.[34]

Squeezing injury results in leveraging of the posteromedial rib over the spinal transverse process. Excessive compression and distraction forces are also placed on the lateral and anterior rib arc and at the metaphyseal equivalent regions of the costovertebral junctions and rib heads (Fig. 143.2).[28,35] Multiple fractures may involve a single rib. Oblique views of the ribs increase the sensitivity for rib fractures and aid in their characterization (Fig. 143.3).[36,37] Follow-up radiographs (see e-Fig. 143.1 and Fig. 143.3) and CT also provide increased sensitivity.[38,39] CT is more sensitive for rib fractures than radiography, but the greater radiation dose of CT limits its use.[38] Nevertheless, focused CT may be helpful in problematic cases. If CT is performed for evaluation of visceral trauma, reconstruction of images with narrow slice thickness, bone detail algorithm, and multiplanar reformats facilitate identification and delineation of rib fractures (Fig. 143.4). Postmortem CT with increased tube current (mAs) exquisitely delineates rib fractures.

Rib fractures due to cardiopulmonary resuscitation (CPR) are rare in infants but may occur particularly with newer methods of infant CPR.[40–43] Infant rib fractures from CPR are predominantly anterolateral, middle ribs (4th–7th) and usually radiographically occult.[40,41,44] Rib fractures caused by birth trauma are extremely rare (except for in infants with osteogenesis imperfecta congenita).[45] Rib fractures are frequently found in infants with acquired metabolic bone disease and have been reported after thoracotomy, chest tube placement, chest physiotherapy, and blunt accidental trauma.[34,46–48] However, rib fractures in infants younger than age 12 months without a predisposing condition or instrumentation are strongly suspicious for abuse.[34,49,50]

## LONG BONE FRACTURES

### Metaphyseal Fractures

The classic metaphyseal lesion, commonly referred to as a *corner* or *bucket-handle* fracture, was reexamined by Kleinman in 1986 with correlation of histopathology and radiography.[51] Klienman showed that the lesions represent a shearing or planar fracture that extends through the primary spongiosa of the metaphysis and not an avulsion injury.[51,52] Depending on size and displacement of the metaphyseal fragment, positioning of the child and radiographic projection, the fracture may have the appearance of a “corner” or a “bucket-handle” (Figs. 143.5 and 143.6). These

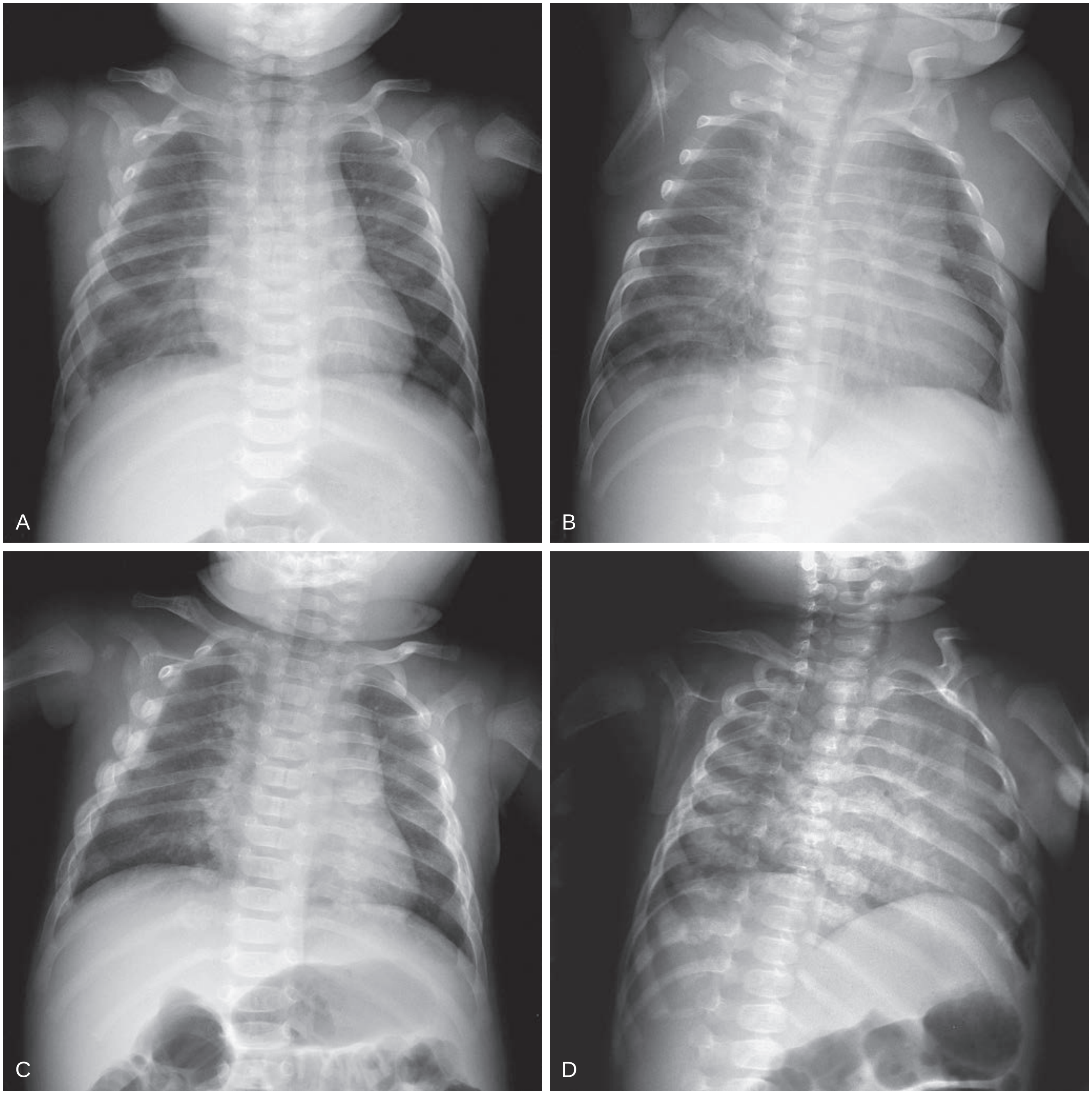

**Figure 143.3. A 2-month-old male infant with right pleural effusion.** (A) Anteroposterior radiograph shows healing right clavicular fracture and nine fractures of the right ribs and four fractures of the left ribs on initial survey. Adjacent pleural effusion is seen. (B) Some fractures are better depicted on the left posterior oblique view. (C and D) Two weeks later, anteroposterior and left posterior oblique radiographs of the chest clearly show 18 right rib fractures and 11 left rib fractures with multiple individual ribs fractured in multiple locations. This illustrates the value of a follow-up skeletal survey. The pleural effusion has also resolved on the follow-up radiographs.

fractures are thought to occur from violent forces as the infant is held by the trunk (Fig. 143.7, e-Fig. 143.8, and Fig. 143.9). Torsional forces directly on a limb probably cause some fractures. Typically, no bruising is evident with a classic metaphyseal lesion. Classic metaphyseal lesions are most commonly seen distal femur, proximal and distal tibia, distal fibula, proximal humerus, and distal radius.[53–56]

Some classic metaphyseal lesions may become more conspicuous on short-term follow-up radiography.[52] With healing, classic metaphyseal lesions typically become indistinct and sclerotic (Fig. 143.10). Kleinman demonstrated subtle extension of physeal cartilage into the metaphysis as a sign of healing.[57] Subperiosteal new bone is not seen unless there is an associated periosteal injury.

Transverse, greenstick, and buckle fractures of the metaphysis may also be caused by child abuse but do not carry the same specificity as classic metaphyseal lesions. Such fractures are considered to be of low specificity. A small step off, beak, or spur

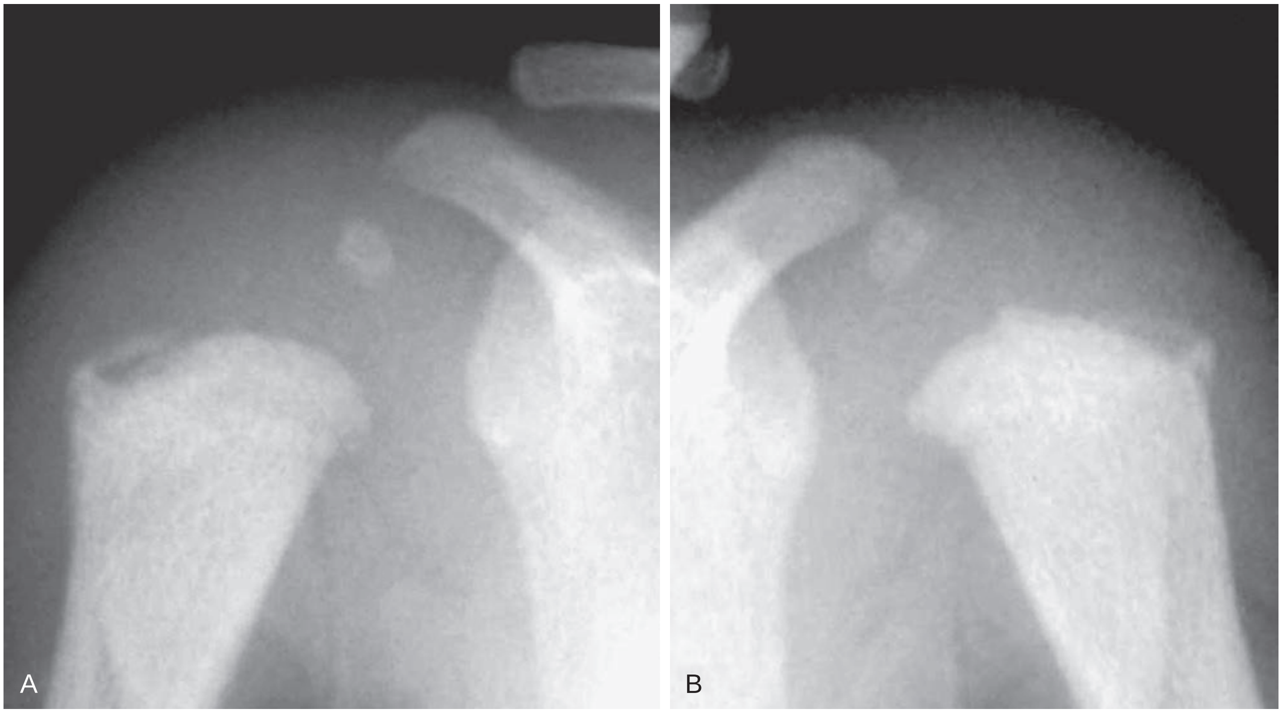

**e-Figure 143.8. Anteroposterior right (A) and left (B) shoulders of a 5-month-old female infant, deceased, cause of death unknown.** Eight fractures were identified at postmortem skeletal survey, including bilateral proximal humeral classic metaphyseal lesions.

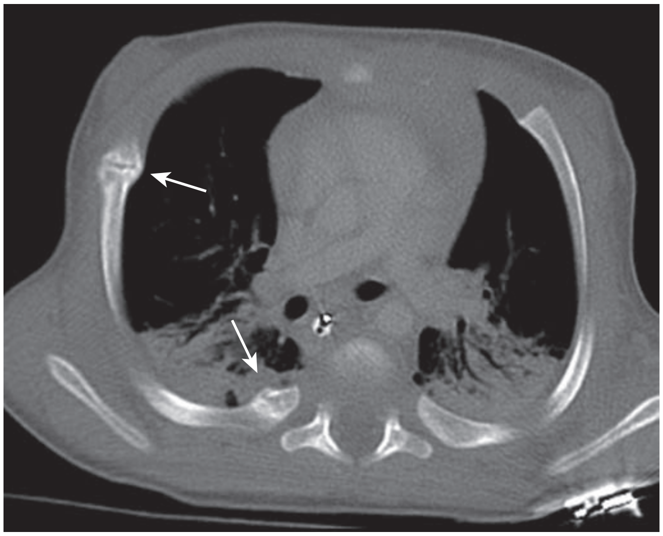

**Figure 143.4. A 3-month-old male with multiple rib fractures, multiple metaphyseal fractures (classic metaphyseal lesions), a small subdural hematoma, and disruption of the posterior wall of the hypopharynx.** This computed tomography scan was performed for concern of extension of infection into the chest. Images were also reconstructed with bone algorithm. *Arrows* indicate healing posterior and anterolateral rib fractures. The fracture lines are indistinct. Callus is present. Note the normal appearance of the costochondral junction of an anterior left rib.

related to the perichondrial ring at the margin of the metaphysis may mimic abusive injury.[58] Slight fragmentation of metaphyseal margins with physiologic bowing may also mimic abuse.[59] Iatrogenic classic metaphyseal-like lesions have been reported with birth trauma and as a complication of treatment of clubfeet.[60,61] Such reports are rare, and it is likely that the reported fractures occurred with a similar torsional mechanism as occurs in child abuse.

### Physeal Fractures

Physeal fractures are uncommon in child abuse. Fractures may be occult or subtle at presentation and some are not recognized until healing occurs.[62] Ultrasonography or MRI may be helpful to image the unossified epiphyses and assess the integrity of the physis.[63] Common sites of physeal fracture are the proximal and distal humerus and the proximal femur (Fig. 143.11).[62–64] As opposed to classic metaphyseal lesions, which heal without sequelae because the fracture does not traverse the growth plate, physeal fractures may be complicated by premature physeal fusion.

### Diaphyseal Fractures

Transverse, oblique, and spiral diaphyseal fractures of the long bones in the nonambulatory young infant should raise suspicion for abuse.[65–68] Once ambulatory, accidental fractures become common.[69] Factors that increase the likelihood of an abuse-related injury include association with another fracture (particularly if fractures are in different stages of healing) and other clinical features that produce a high level of suspicion for abuse, inappropriate clinical history, failure to seek medical attention, and discovery of the fracture in a healing state (see Figs. 143.7 and 143.12).[68,70,71]

## FRACTURES OF THE SCAPULA AND STERNUM

Although uncommon, fractures of the scapula are highly specific for abuse (e-Fig. 143.13).[72] Acromial fractures probably result from direct or indirect forces applied during shaking. It is usually accompanied by other bony thoracic trauma. Variants in ossification of the acromion may appear similar to a fracture.[73,74]

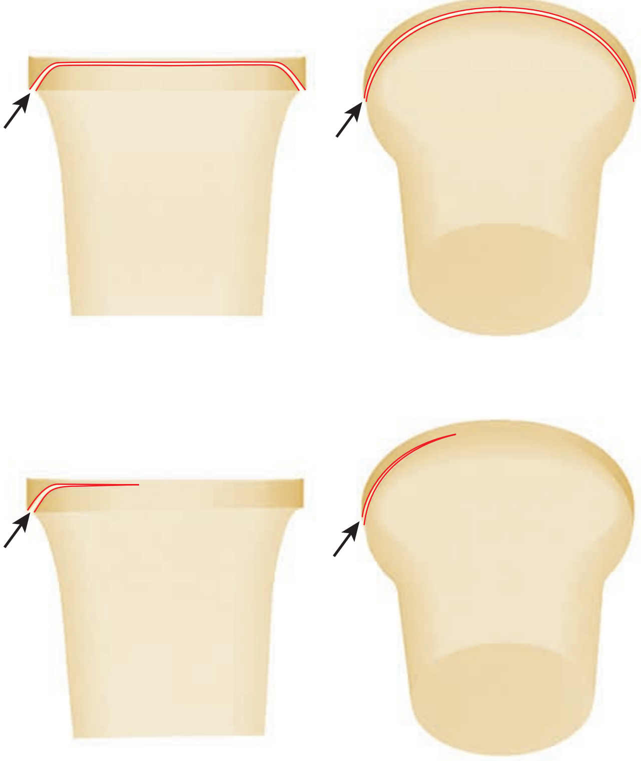

**Figure 143.5. Corner and bucket-handle fracture patterns of the classic metaphyseal lesion.** Fractures *(arrows)* extend adjacent to the chondro-osseous junction and then veer toward the diaphysis to undercut the larger peripheral segment that encompasses the subperiosteal bone collar. When the physis is viewed tangentially, the classic metaphyseal lesion appears as a corner fracture *(left images)*. When a view is obtained through beam angulation, a bucket-handle pattern results *(right images)*. *Top images,* Diffuse injury; *bottom images,* localized injury. *(From Kleinman PK.* Diagnostic Imaging of Child Abuse. *2nd ed. St Louis: Mosby; 1998. Originally modified from Kleinman PK, Marks SC, Jr. Relationship of the subperiosteal bone collar to metaphyseal lesions in abused infants.* J Bone Joint Surg Am. *1995;77:1471–1476.)*

Fractures of the sternum are very uncommon in infants, including those who are abused.[72,75] Although Kleinman classifies sternal fractures as highly specific for child abuse, a recent series found these fractures less specific.[75]

## CLAVICLE FRACTURES

Fractures of the clavicle (Fig. 143.14) are common in child abuse but are also common from accidental and birth trauma and are therefore considered to be of low specificity for child abuse. Clavicle fractures occur in 0.5% of newborns.[76] Usually, a history of dystocia exists. It is not uncommon for clavicle fractures to escape detection on the newborn physical examination.[77] Clavicle fractures from birth exhibit callus by 10 to 14 days after birth.[77] A fracture that appears acute without visible callus in a child older than 10 to 14 days therefore becomes suspicious for having been incurred after birth.

## SPINAL FRACTURES

Although rare, spinal fractures in infants and young children are strongly associated with abuse.[9,72,78–80] The mechanism is usually

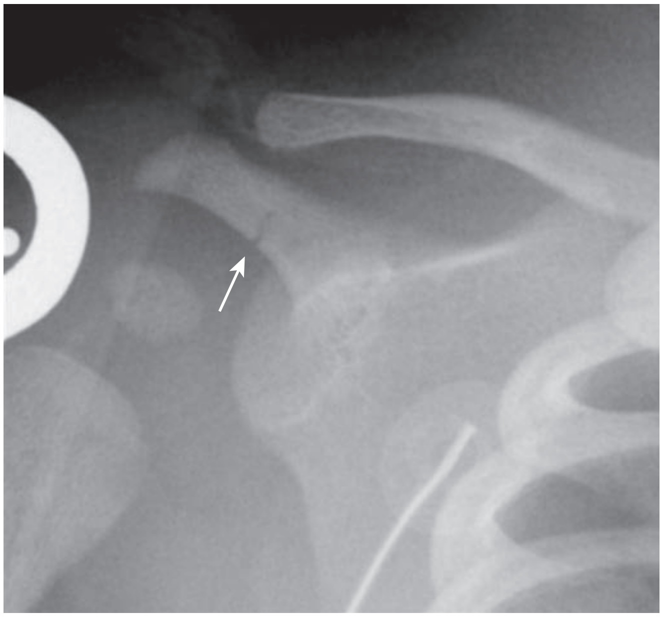

**e-Figure 143.13. A 10-week-old girl with fatal abusive head injury.** An acromial fracture *(arrow)* was the only fracture found by a postmortem skeletal survey.

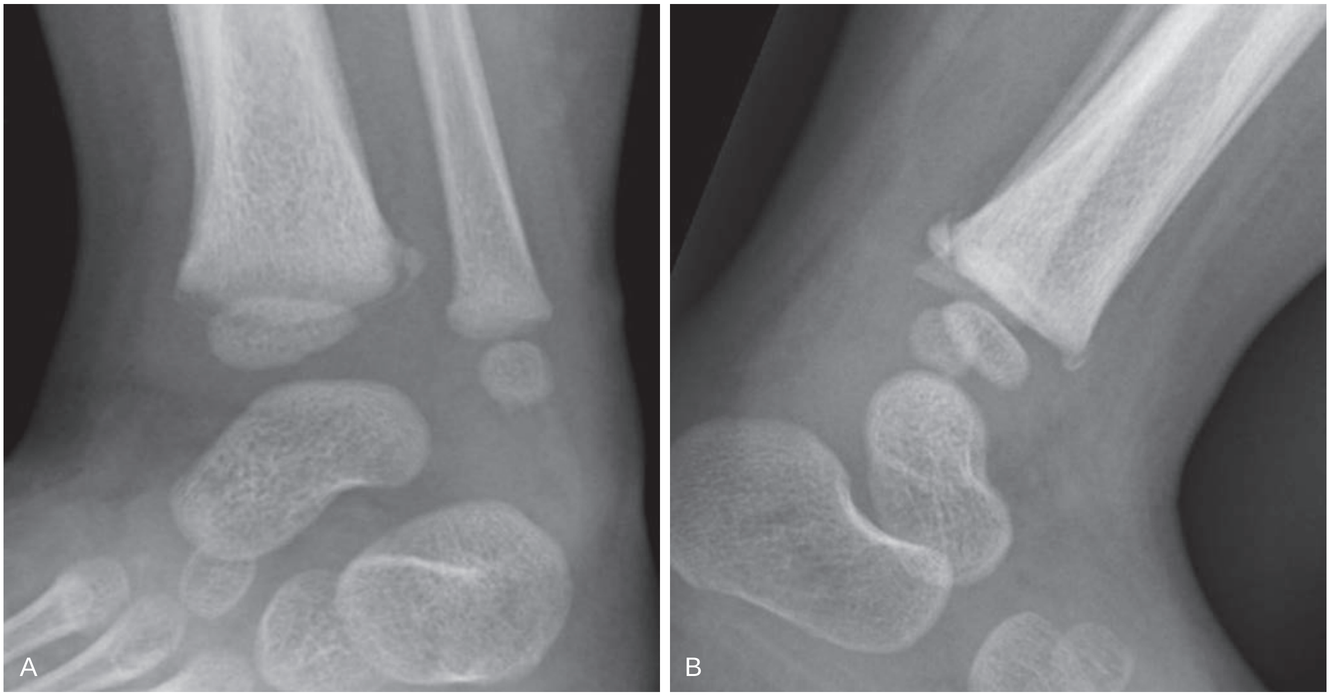

**Figure 143.6. Acute classic metaphyseal lesion fracture of the distal tibial metaphysis in a 9-month-old boy.** The fracture is seen as a “bucket handle fracture” on the anteroposterior view (A) and as a “corner fracture” on the lateral view (B).

due to hyperflexion and/or axial loading. On radiographs, injuries manifest as compression deformities of the vertebral bodies, often with associated end plate defects and avulsive injuries of the spinous processes.[79] Fractures may result in listhesis.[80,81] Injuries often involve multiple adjacent vertebral bodies and are most common near the thoracolumbar junction (Fig. 143.15).[78,80]

Cervical spine fractures are fortunately uncommon in child abuse but may be devastating.[80] Severe fracture-dislocations have been described, including classic hangman’s fracture of the C2 vertebra (e-Fig. 143.16).[82] Spinal cord injury is uncommon but can occur.[83,84]

Isolated spinous process fractures are considered highly specific for child abuse.[85] Avulsions may be caused by hyperflexion with axial loading or shaking.

## SKULL FRACTURES

Skull fractures are frequent in abuse and indicative of an impact injury. Skull fractures also commonly result from accidental injury. Multiple fractures, bilateral fractures, diastasis of fractures and sutures, fractures that cross suture lines, and occipital fractures are associated with abuse (e-Fig. 143.17).[86–88] However, no particular pattern of skull fracture is diagnostic of abuse.[89] Simple linear fractures are commonly seen in abuse and in accidental trauma are thus considered to be of low specificity for abuse.[25] Such fractures are common in short-distance falls onto a hard surface. Complex skull fractures are not expected from short-distance falls in the home environment and are thus considered to be of moderate specificity for abuse.[25] Soft tissue swelling is seen with acute fractures; lack of soft tissue swelling suggests that a fracture is not acute.[90] Diastatic fractures or widened skull sutures indicate a space-occupying process within the cranium such as diffuse swelling or large subdural hematoma (Fig. 143.18).

Anteroposterior and lateral skull radiographs are part of the radiographic skeletal survey in suspected abuse. A Townes view

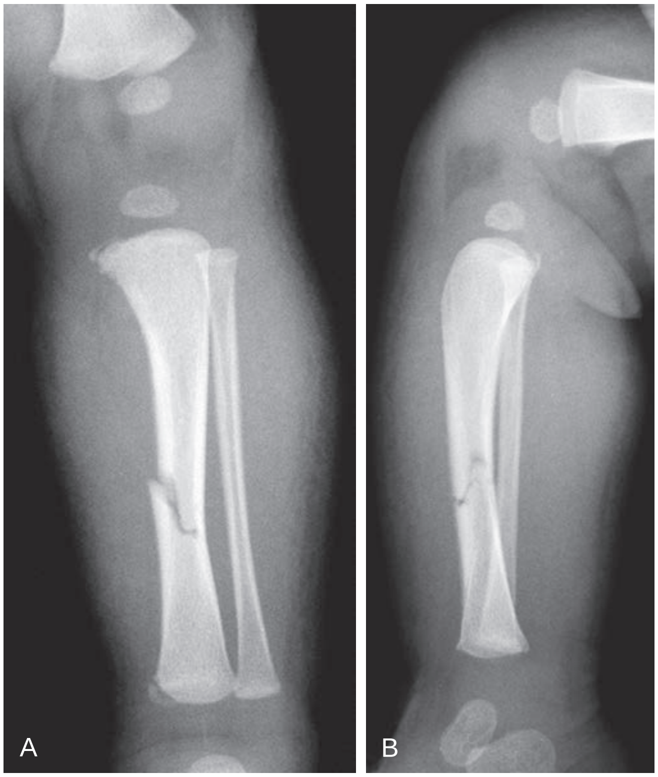

**Figure 143.7. A 1-month-old female infant was brought to the emergency department for swelling of the leg without history of trauma.** (A) Anteroposterior and (B) lateral radiographs of the left leg shows classic metaphyseal lesions at the proximal and distal tibia, as well as a short oblique mid-diaphyseal fracture. Multiple rib fractures and classic metaphyseal lesions of the right tibia were also discovered.

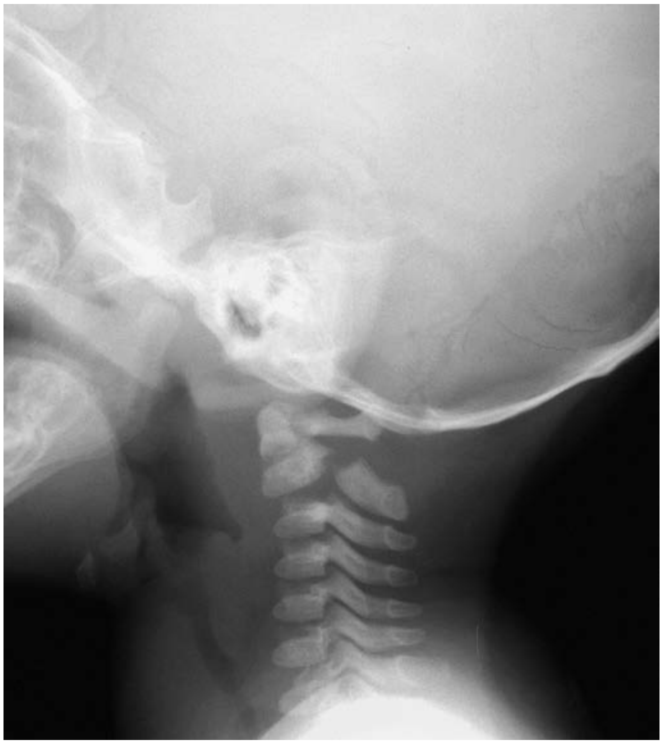

**e-Figure 143.16. Lateral cervical spine radiograph of a 6-month-old infant who presented with bruising over the left neck.** Although the infant was neurologically intact, 14 fractures, including hangman's fracture of C2, were identified.

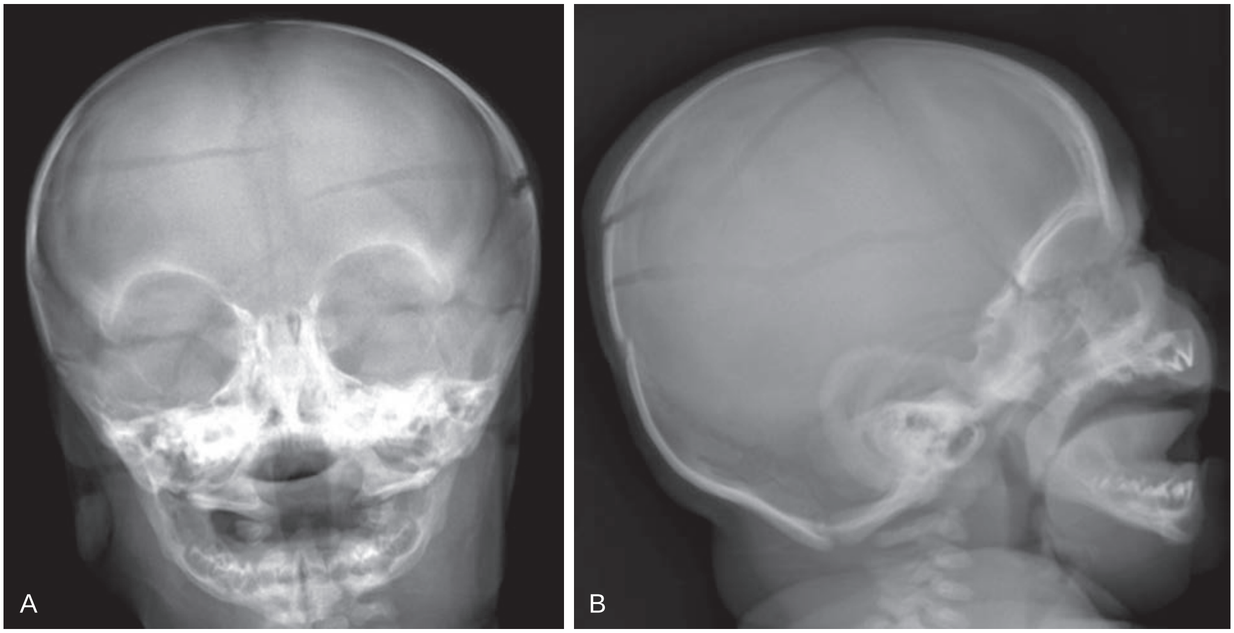

**e-Figure 143.17.** A 2-month-old boy with bilateral parietal bone fractures. Anteroposterior (A) and lateral views (B) show bilateral parietal fractures. The two fractures lines are offset (not continuous) across the sagittal suture posteriorly. Mild extracranial soft tissue swelling is seen posteriorly and laterally over the fractures. The child presented to the emergency room with facial bruising and lip swelling. Small bilateral subdural hematomas were found on computed tomography. Multiple healing rib fractures and metaphyseal fractures (classic metaphyseal lesions) were found on skeletal survey.

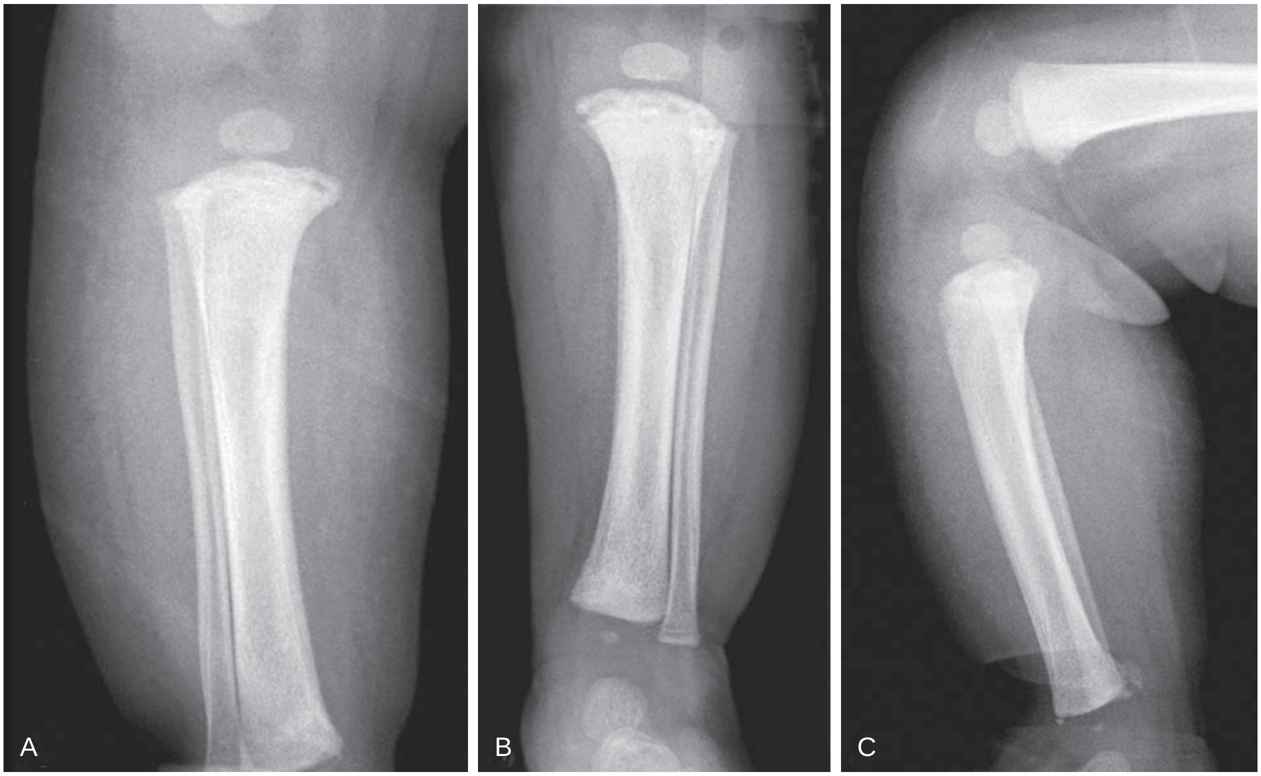

**Figure 143.9. Anteroposterior right (A) and left (B) leg, and lateral right (C) leg of 3-month-old male infant with an acute occipital skull fracture and 23 rib fractures.** Classic metaphyseal lesions are seen in both proximal tibias and the distal right tibia.

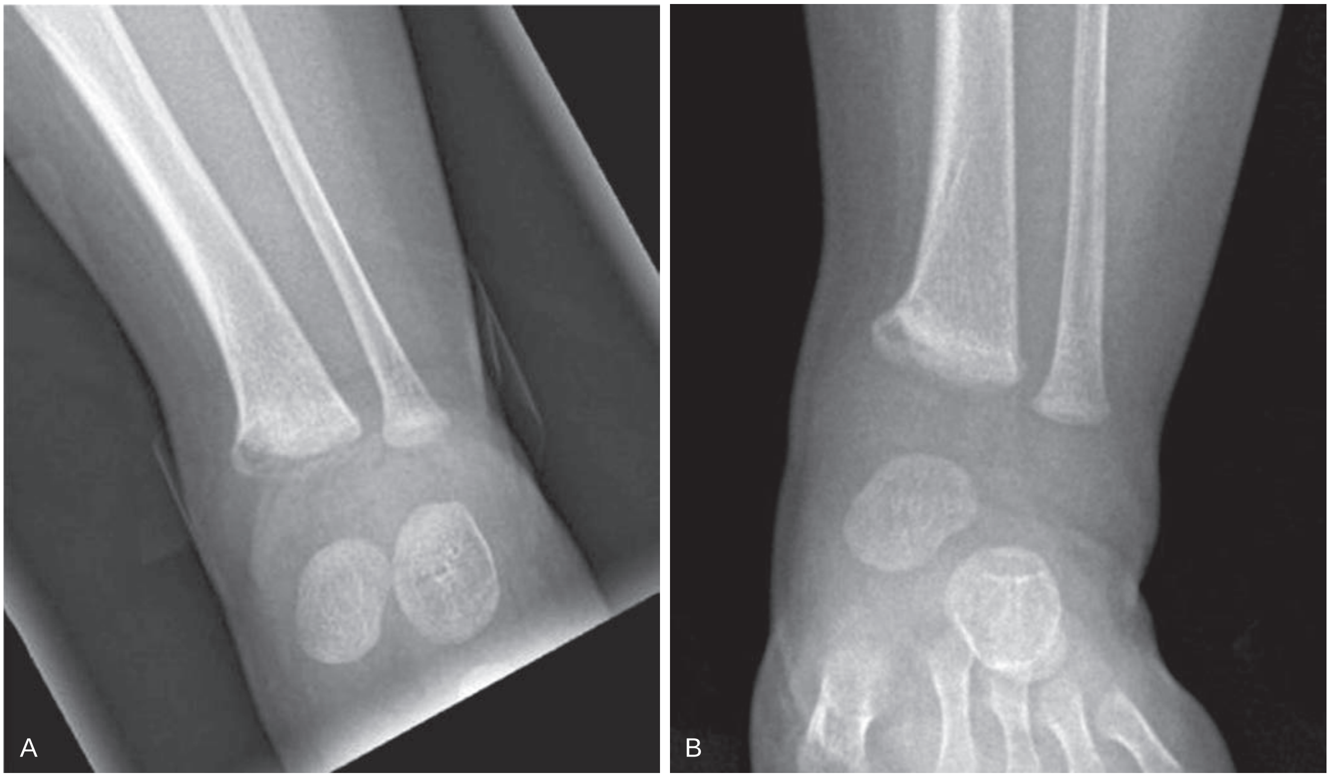

**Figure 143.10. Healing classic metaphyseal lesion of the distal tibia in a 4-month-old boy.** (A) The initial anteroposterior (AP) radiograph shows a well-defined metaphyseal corner fracture, consistent with an acute or subacute fracture. (B) On a follow-up AP radiograph 2 weeks later, the fracture is more ill-defined with sclerosis, consistent with interval healing.

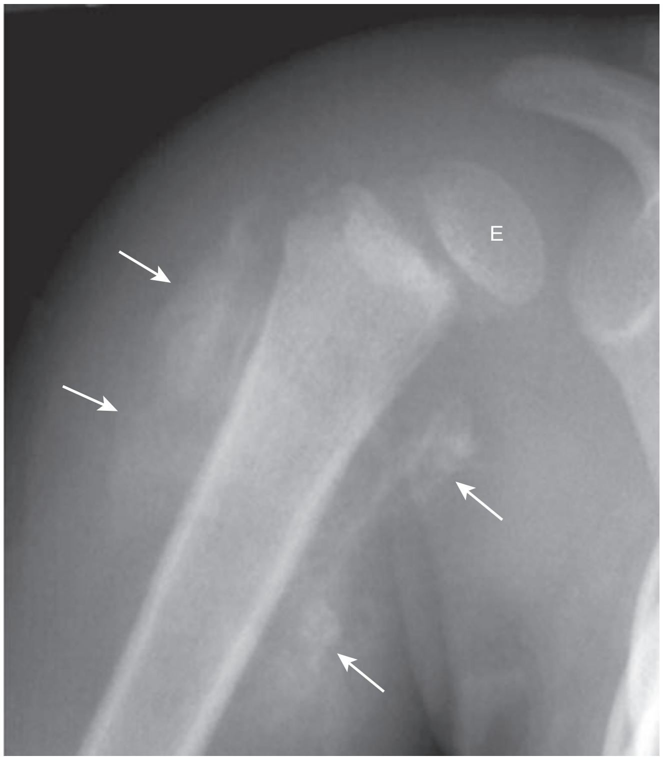

**Figure 143.11.** **A 2-year-old girl with delayed diagnosis of a Salter I fracture of the proximal right humerus.** The epiphysis *(E)* is displaced medial relative to the proximal humeral metaphysis. A cloak of early callus and subperiosteal new bone is seen around the proximal humerus *(arrows)*. The child presented with mental status changes caused by a head injury. This fracture and a subtler fracture of the left proximal humerus were noted on chest radiography after intubation. No other fractures were found on a skeletal survey. Follow-up radiographs demonstrated premature fusion of the right proximal humeral physis with marked shortening of humerus noted at age 6 years.

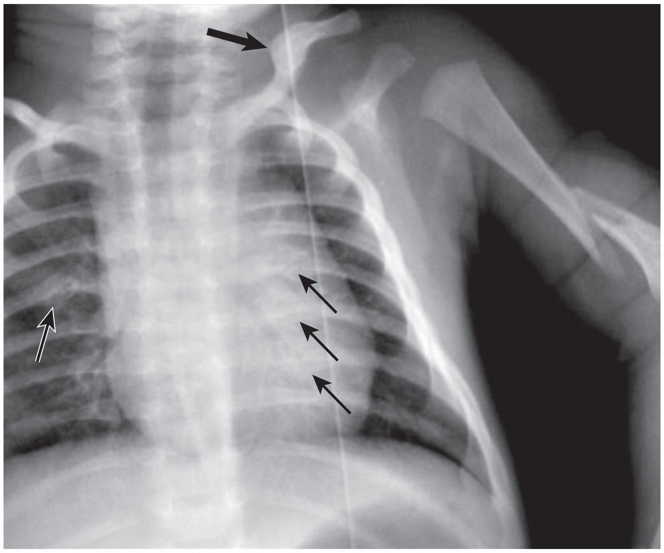

**Figure 143.12.** **A 7-week-old boy with an acute left humeral fracture.** The mechanism provided by history was suspect. Additional imaging demonstrated healing clavicular *(large arrow)* and posterior rib fractures *(small arrows)*. While it is possible that the healing clavicle fracture is due to unrecognized birth trauma, the healing posterior rib fractures are not compatible with birth injury.

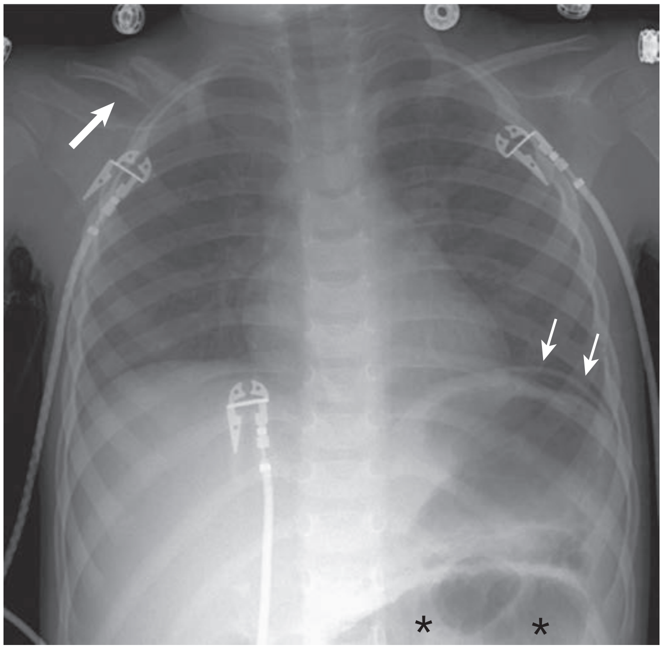

**Figure 143.14.** **A 2-year-old boy with clavicle fracture.** The child presented with fever and vomiting. Multiple bruises were noted. This chest radiograph demonstrated a healing, displaced right clavicle fracture with callus *(large arrow)*, free air underneath the left hemidiaphragm *(small arrows)*, and dilated small bowel in the left abdomen *(asterisks)*. At surgery, multiple small bowel perforations were found.

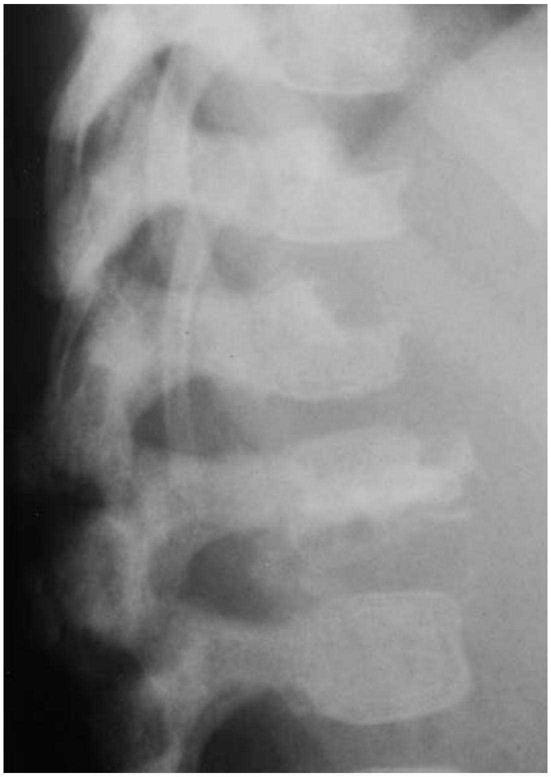

**Figure 143.15.** **A 10-month-old girl with compression fractures of the T12, L1, and L2 vertebral bodies.** She presented with paralysis of the lower extremities, and no history of trauma was initially provided. Unfortunately, the child did not recover lower extremity function.

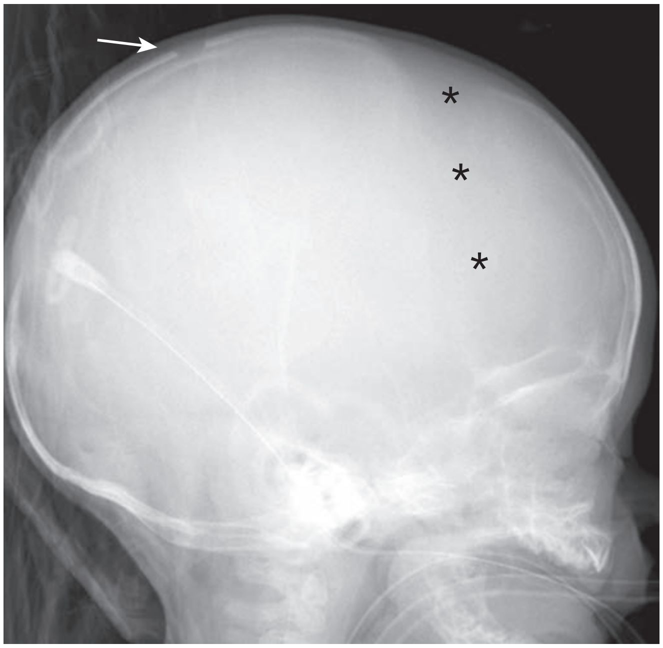

**Figure 143.18.** **A 3-month-old boy with a mildly diastatic parietal skull fracture *(arrow)* and splayed coronal sutures *(asterisks)*.** Computed tomography showed large bilateral subdural hematomas.

is helpful to evaluate the occipital bone and look for wormian bones in the sutures. Wormian bones are accessory intrasutural bones associated with metabolic bone disease, most notably osteogenesis imperfecta and Menkes syndrome.[91] Modern CT scan technique with orthogonal reformat images and three-deminsional volume rendered reconstructions may obviate the need for skull radiographs.[92,93]

Accessory sutures of the skull may mimic fractures on both radiography and CT.[94] Findings suggesting a fracture are a sharp linear lucency with nonsclerotic edges, widening of the lucency approaching a suture, crossing of a suture, unilaterality or asymmetry, and associated soft tissue swelling.[95] Findings suggesting an accessory suture are a zigzag pattern with sclerotic borders merging with an adjacent suture, bilaterality and symmetry, and lack of associated soft tissue swelling.[95] Accessory sutures tend to occur at characteristic locations.

## FRACTURES OF THE PELVIS

Fractures of the pelvic bones are uncommon in child abuse (e-Fig. 143.19).[96] Fractures of the pubic rami may occur from blunt trauma particularly in cases of sexual abuse.[97] Variants in pubic ossification may mimic fracture.[98]

## FRACTURES OF HANDS AND FEET

Nonaccidental fractures of the hands and feet occur in abused infants and toddlers (Fig. 143.20).[99,100] These fractures are often subtle torus fractures and may be better appreciated on oblique views or follow-up radiographs.[99] Fractures of the tubular bones of the hands and feet are probably caused by squeezing of the child's hands by the abuser.

## DATING OF FRACTURES

Dating of fractures is dependent on many variables, including the age of the child, the state of nutrition, immobilization or lack thereof, repetitive injury, and fracture location.[101,102] Fractures of the skull and spine cannot be satisfactorily dated, and the classic metaphyseal lesion is difficult to date with any degree of precision.

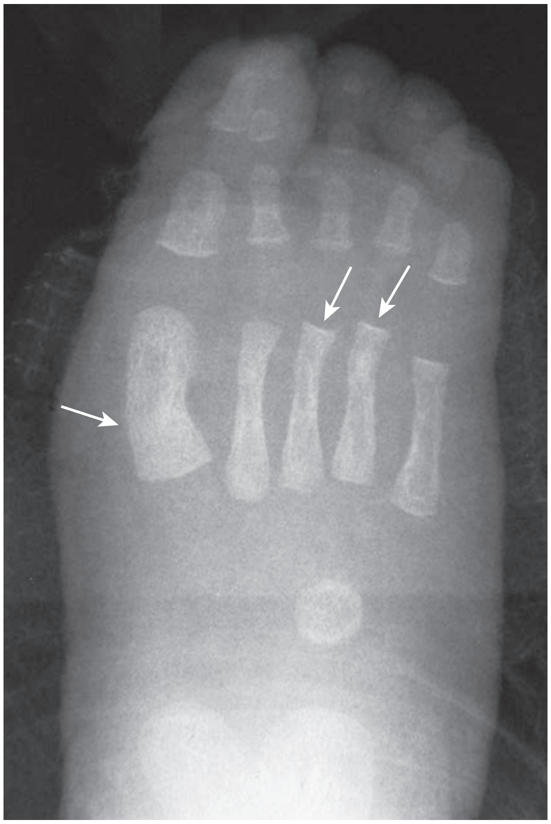

**Figure 143.20.** **A 3-month-old girl with healing fractures of the first, third, and fourth metatarsals *(arrows)*.** Her twin sister also had metatarsal fractures. Both twins had rib fractures, classic metaphyseal lesions, and skull fractures.

Infants develop subperiosteal new bone earlier and form callus more quickly but usually not until 10 to 14 days after injury.[102] Soft tissue swelling resolves during this same period with subsequent loss of fracture line definition. Although it is often possible to identify separate fractures as acute or subacute and others as healing, it is very difficult is ascribe different ages to fractures that are healing. Precise dating of fractures is not possible, and speculation of fracture age is merely an estimate.[103,104] Some general guidelines are provided in Table 143.1 (Fig. 143.21).[101,102,104]

## DIFFERENTIAL DIAGNOSIS

The differential diagnosis for child abuse is broad and varies considerably, depending on both the clinical presentation and the radiologic findings (Box 143.3).[105,106] Accidental injury is not the only consideration. Unrecognized obstetric trauma may not be noted until days or weeks after birth. Normal processes including metaphyseal variants, physiologic new bone formation, accessory ossification centers, and accessory skull sutures may mimic fracture.[107–109]

Metabolic bone disease of prematurity may result in multiple rib fractures, diaphyseal fractures, and metaphyseal fractures.[48,110–112] Such fractures are typically buckle or transverse fractures, not classic metaphyseal lesions. Other disease processes including inherited bone dysplasias, copper deficiency, Menkes syndrome, congenital syphilis, Caffey disease, neurologic disorders, and osteogenesis imperfecta may have radiographic features that overlap with those of abuse (see Box 143.3).[105,106,113–120] Metaphyseal abnormalities

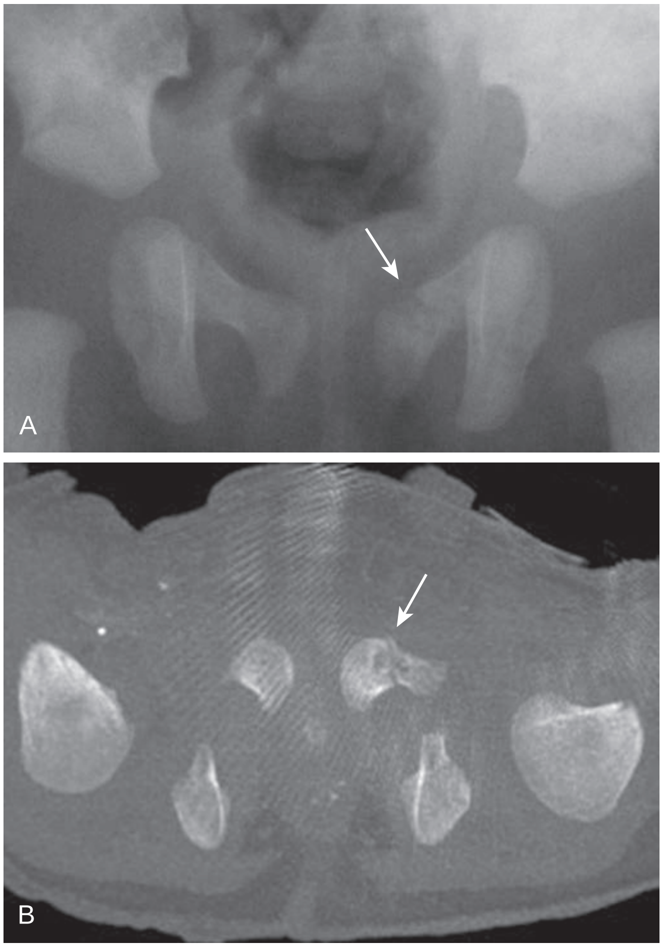

**e-Figure 143.19. A 1-month-old boy presented with failure to thrive and fever.** A fracture of the left superior pubic symphysis *(arrows)* is seen on radiography (A) and axial bone algorithm computed tomography (CT) image (B), reformatted from a CT scan of the abdomen and pelvis to evaluate for suspected visceral injury. He was also found to have subdural hematomas and healing rib fractures.

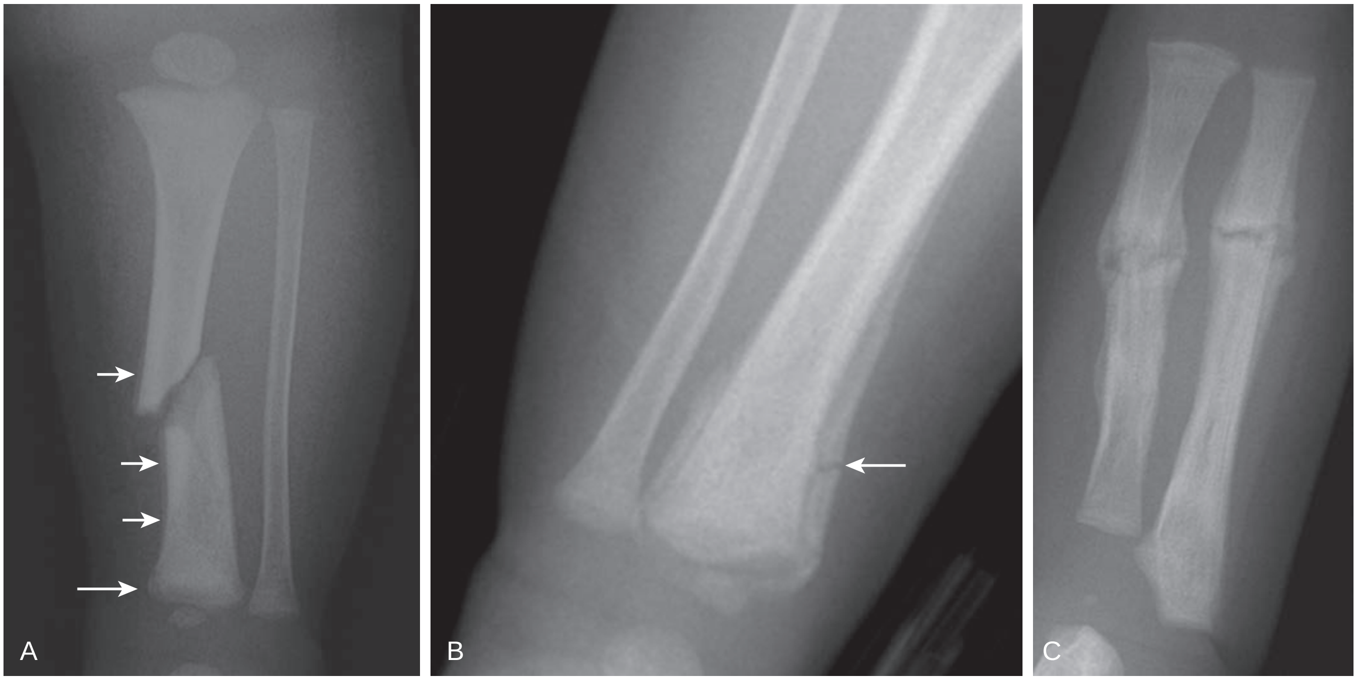

**Figure 143.21. A 3-month-old boy with multiple fractures of differing age.** The child presented with left leg swelling. (A) Radiograph of the left leg shows an acute or subacute oblique fracture of the left tibia. No ossified callus is seen; however, subperiosteal new bone *(short arrows)* is present along the medial margin of the distal tibia, possibly unrelated to the oblique fracture. Irregularity of the distal metaphysis *(long arrow)* is suggestive of a preceding classic metaphyseal lesion, but not definitive. Soft tissue swelling is noted. (B) Radiograph of the distal right leg shows a healing bucket handle fracture with associated distal tibial subperiosteal new bone indicative of an injury at least 10 to 14 days old. A fracture through the subperiosteal new bone *(arrow)* indicates injuries of different age. (C) Transverse fractures of the left radius and ulna show a more advanced state of healing with abundant callus and indistinct, partially obliterated fracture lines. These fractures are clearly older than the oblique left tibial fracture. Images of the ribs showed multiple healing lateral and posterior rib fractures with mature callus.

**TABLE 143.1** Approximate Timetable of Radiographic Healing of Children's Fractures*

| Finding | Early | Peak | Late |
|---|---|---|---|
| Resolution of soft tissue swelling | 2-5 days | 4-10 days | 10-21 days |
| Subperiosteal new bone formation | 4-10 days | 10-14 days | 14-21 days |
| Loss of fracture line definition | 10-14 days | 14-21 days | |
| Soft callus | 10-14 days | 14-21 days | |
| Hard callus | 14-21 days | 21-42 days | 42-90 days |
| Remodeling | 3 months | 1 year | 2 years to physeal closure |

*Assessment of fracture dates is an estimate. Healing is affected by repetitive injury, immobilization or lack thereof, and the general health and metabolic state of the patient.

*From Kleinman PK.* Diagnostic Imaging of Child Abuse. *2nd ed. St Louis: Mosby; 1998.*

similar to child abuse are seen with some rare skeletal dysplasias, notably spondylometaphyseal dysplasia (Sutcliffe "corner fracture" type) and metaphyseal dysplasia (Schmid type).[121,122] Clues as to the presence of a dysplasia include family history, short stature, and lack of change of the findings on follow-up radiographs.

Kleinman's seminal text *Diagnostic Imaging of Child Abuse* presents an excellent overview of the differential diagnosis and a review of diseases that may simulate abuse.[25] It should be remembered that the presence of an underlying bone disease or dysplasia does not exclude the possibility of physical abuse or neglect.

With regard to the differential diagnosis of the radiographic findings of child abuse, two topics of generated controversy warrant brief mention—temporary brittle bone disease (TBBD) and vitamin D deficiency/rickets.

TBBD was proposed as a variant of osteogenesis imperfecta by Paterson et al, who identified a group of young infants who were thought to have diminished bone strength, possibly because of temporary deficiency of a metalloenzyme related to copper deficiency.[123] Evidence provided to support the existence of TBBD included denial by caregivers of wrongdoing, absence of episodes of trauma that may explain fractures, lack of bruising, absence of systemic injury, radiographs revealing normal bones, and normal laboratory studies.[123] The purported evidence and the particular diagnosis of TBBD has been refuted by others, including the authors of a critical review of TBBD prepared by the Committee on Child Abuse of the Society for Pediatric Radiology.[117,124,125] To date, no scientific proof definitively supports the existence of TBBD.

More recently, fractures consistent with abuse have been ascribed to vitamin D deficiency and rickets by some authors.[126,127] While literature supports a high prevalence of infants with low vitamin D levels, no evidence exists in the literature to support low levels of vitamin D predisposing children to the high-specificity lesions characteristic of child abuse.[6,128–131] In fact, fractures in children with overt rickets are uncommon, not seen until ambulatory or mobile, and have low specificity patterns, and are only seen with florid radiographic changes of rickets.[132]

**BOX 143.3** Radiographic Differential Diagnostic Considerations for Child Abuse

**TRAUMA**
- Accidental trauma
- Birth trauma
- Iatrogenic trauma

**VARIANTS OF OSSIFICATION AND MATURATION**
- Accessory acromial ossification center(s)
- Normal metaphyseal variants of development
- Accessory skull sutures
- Physiologic subperiosteal new bone
- Sternal ossification center (mimicking posterior rib fracture)

**METABOLIC BONE DISEASE**
- Metabolic bone disease of prematurity
- Copper deficiency (Menkes syndrome)
- Rickets
- Scurvy
- Vitamin A toxicity

**DYSPLASIA**
- Osteogenesis imperfecta
- Metaphyseal and spondylometaphyseal dysplasia

**DRUG INDUCED**
- Prostaglandin $E_1$ therapy

**NEUROGENIC**
- Spina bifida
- Congenital insensitivity to pain

**MISCELLANEOUS**
- Caffey disease
- Congenital syphilis
- Neoplastic-metastatic round cell tumors
- Leukemia
- Osteomyelitis

## TREATMENT

Treatment of the individual patient with abuse-related injuries is dictated by the injuries that are present. Injuries to the brain, spinal cord, and viscera may be life-threatening. Brain and spinal cord injuries may cause substantial lifelong morbidity. Fortunately, most skeletal injuries heal without permanent sequelae, with fractures of the growth plate being an occasional exception.

Intracranial trauma is the leading cause of death and permanent morbidity in abused infants. Debate is ongoing about whether or not shaking alone is sufficient to result in brain injury or whether an impact injury must accompany the shaking event.[133] Apnea and cerebral hypoxia also play a prominent role.

Infants with shaken baby syndrome commonly have subdural hematomas, retinal hemorrhages, and characteristic skeletal injuries (posterior rib fractures and classic metaphyseal lesions). The presence of characteristic osseous lesions is therefore indication for brain imaging and ophthalmologic evaluation.

Reporting of suspected child abuse is mandated by law. Failure to report suspected child abuse may result in fines, censure, and even prosecution. Radiologists should be aware of the legal requirements and mechanisms for reporting in their state. Responsible treating clinicians or child protection team personnel will take ownership of this task. Nevertheless, the radiologist bears responsibility for reporting if he or she suspects child abuse and no one else reports it.

Imaging findings are just one piece of the clinical, social, and legal investigation of possible child abuse. The radiologist must function as part of the child protection team by providing timely and accurate interpretations that are properly communicated, by providing expertise on the significance of the radiologic findings, and by providing guidance as the utility of additional imaging studies. Radiology reports should be complete, precise, and must appropriately consider the specificity of the findings and the possibility of differential diagnoses. Verbal communications of the report should be properly documented. Proper wording and careful editing of reports avoids embarrassment or confusion in court.

Radiologists are frequently called upon to testify in civil and criminal court proceedings related to cases of suspected child abuse. If called to testify, it is the duty of the radiologist to do so in a professional manner, providing only honest opinions based on personal experience and scientific evidence.

### KEY POINTS

- The radiologist is occasionally the first to suggest the diagnosis of child abuse.
- No single radiographic finding is pathognomonic for child abuse.
- Individual radiographic findings may be of low, moderate, or high specificity for child abuse.
- The constellation of radiographic findings may bear greater specificity than any one finding.
- Accidental trauma, normal processes, and diseases may mimic child abuse radiographically.

### SUGGESTED READINGS

Dwek JR. The radiographic approach to child abuse. *Clin Orthop Relat Res*. 2011;469:776–789.

Kleinman PK. *Diagnostic Imaging of Child Abuse*. 3rd ed. Cambridge: Cambridge University Press; 2015.

Lonergan GJ, Baker AM, Morey MK, et al. From the archives of the AFIP. Child abuse: radiologic-pathologic correlation. *Radiographics*. 2003;23:811–845.

Offiah A, van Rijn RR, Perez-Rossello JM, et al. Skeletal imaging of child abuse (non-accidental injury). *Pediatr Radiol*. 2009;39:461–470.

Van Rijn RR, Sieswerda-Hoogendoorn T. Educational paper: imaging child abuse: the bare bones. *Eur J Pediatr*. 2012;171:215–224.

### REFERENCES

Full references for this chapter can be found on www.expertconsult.com.

## REFERENCES

1. Caffey J. Multiple fractures in the long bones of infants suffering from chronic subdural hematoma. *Am J Roentgenol Radium Ther*. 1946;56:163–173.
2. Silverman FN. The roentgen manifestations of unrecognized skeletal trauma in infants. *Am J Roentgenol Radium Ther Nucl Med*. 1953;69:413–427.
3. Kempe CH, Silverman FN, Steele BF, et al. The battered child syndrome. *JAMA*. 1962;181:17–24.
4. U.S. Department of Health and Human Services, Administration for Children and Families, Administration on Children, Youth and Families, Children's Bureau. *Child Maltreatment 2014*; 2016. http://www.acf.hhs.gov/programs/cb/research-data-technology/statistics-research/child-maltreatment.
5. Ravichandiran N, Schuh S, Bejuk M, et al. Delayed identification of pediatric abuse-related fractures. *Pediatrics*. 2010;125:60–66.
6. Servaes S, Brown SD, Choudhary AK, et al. The etiology and significance of fractures in infants and young children: a critical multidisciplinary review. *Pediatr Radiol*. 2016;46:591–600.
7. Van Rijn RR, Sieswerda-Hoogendoorn T. Educational paper: imaging child abuse: the bare bones. *Eur J Pediatr*. 2012;171:215–224.
8. Section on Radiology, American Academy of Pediatrics. Diagnostic imaging of child abuse. *Pediatrics*. 2009;123:1430–1435.
9. Flaherty EG, Perez-Rossello JM, Levine MA, et al. Evaluating children with fractures for child physical abuse. *Pediatrics*. 2014;133:e477–e489.
10. Meyer JS, Gunderman R, Coley BD, et al. ACR appropriateness criteria on suspected physical abuse – child. *J Am Coll Radiol*. 2011;8:87–94.
11. Trout AT, Strouse PJ, Mohr BA, et al. Abdominal and pelvic CT in cases of suspected abuse: can clinical and laboratory findings guide its use? *Pediatr Radiol*. 2011;41:92–98.
12. Lindberg D, Makoroff K, Harper N, et al. Utility of hepatic transaminases to recognize abuse in children. *Pediatrics*. 2009;124:509–516.
13. Hilmes MA, Hernanz-Schulman M, Greeley CS, et al. CT identification of abdominal injuries in abused pre-school children. *Pediatr Radiol*. 2011;41:643–651.
14. American College of Radiology. *ACR-SPR practice parameter for the performance and interpretation of skeletal surveys in children*; 2016. http://www.acr.org. Accessed December 15, 2016.
15. Kleinman PK, Nimkin K, Spevak MR, et al. Follow-up skeletal surveys in suspected child abuse. *AJR Am J Roentgenol*. 1996;167:893–896.
16. Zimmerman S, Makoroff K, Care M, et al. Utility of follow-up skeletal surveys in suspected child physical abuse evaluations. *Child Abuse Negl*. 2005;29:1075–1083.
17. Harlan SR, Nixon GW, Campbell KA, et al. Follow-up skeletal surveys for nonaccidental trauma: can a more limited survey be performed? *Pediatr Radiol*. 2009;39:962–968.
18. Lindberg DM, Berger RP, Reynolds MS, et al Yield of skeletal survey by age in children referred to abuse specialists. *J Pediatr*. 2014;164:1268-1273.
19. McGraw EP, Pless JE, Pennington DJ, et al. Postmortem radiography after unexpected death in neonates, infants, and children: should imaging be routine? *AJR Am J Roentgenol*. 2002;178:1517–1521.
20. The Society for Pediatric Radiology—National Association of Medical Examiners. Post-mortem radiography in the evaluation of unexpected death in children less than 2 years of age whose death is suspicious for fatal abuse. *Pediatr Radiol*. 2004;34:675–677.
21. McGraw EP, Pless JE, Pennington DJ, et al. Postmortem radiography after unexpected death in neonates, infants and children: should imaging be routine? *AJR Am J Roentgenol*. 2002;178:1517–1521.
22. Kleinman PK, Blackbourne BD, Marks SC, et al. Radiologic contributions to the investigation and prosecution of cases of fatal infant abuse. *N Engl J Med*. 1989;321:1045–1046.
23. Hong TS, Reyes JA, Moineddin R, et al. Value of postmortem thoracic CT over radiography in imaging of pediatric rib fractures. *Pediatr Radiol*. 2011;41:736–748.
24. Proisy M, Marchand AJ, Loget P, et al. Whole-body post-mortem computed tomography compared with autopsy in the investigation of unexpected death in infants and children. *Eur Radiol*. 2013;23:1711–1719.
25. Kleinman PK. *Diagnostic Imaging of Child Abuse*. 3rd ed. Cambridge: Cambridge University Press; 2015.
26. Kleinman PK. Diagnostic imaging in infant abuse. *AJR Am J Roentgenol*. 1990;155:703–712.
27. Kleinman PK, Marks SC, Nimkin K, et al. Rib fractures in 31 abused infants: postmortem radiologic-histopathologic study. *Radiology*. 1996;200:807–810.
28. Kleinman PK, Marks SC, Adams VI, et al. Factors affecting visualization of posterior rib fractures in abused infants. *AJR Am J Roentgenol*. 1988;150:635–638.
29. Worn MJ, Jones MD. Rib fractures in infancy: establishing the mechanisms of cause from the injuries—a literature review. *Med Sci Law*. 2007;47:200–212.
30. Boal DK, Felman AH, Krugman RD. Controversial aspects of child abuse: a roundtable discussion. 43rd annual meeting, Society for Pediatric Radiology. *Pediatr Radiol*. 2001;31:760–774.
31. Merten DF, Radkowski MA, Leonidas JC. The abused child: a radiological reappraisal. *Radiology*. 1983;46:377–381.
32. Thomas PS. Rib fractures in infancy. *Ann Radiol (Paris)*. 1977;20:115–122.
33. Ng CS, Hall CM. Costochondral junction fractures and intra-abdominal trauma in non-accidental injury (child abuse). *Pediatr Radiol*. 1998;28:671–676.
34. Strouse PJ, Owings CL. Fractures of the first rib in child abuse. *Radiology*. 1995;197:763–765.
35. Kleinman PK, Schlesinger AE. Mechanical factors associated with posterior rib fractures: laboratory and case studies. *Pediatr Radiol*. 1997;27:87–91.
36. Ingram J, Connell J, Hay T, et al. Oblique radiographs of the chest in nonaccidental trauma. *Emerg Radiol*. 2000;7:42–46.
37. Marine MB, Corea D, Steenburg SD, et al. Is the new ACR-SPR practice guideline for additional of oblique views of the ribs to the skeletal survey for child abuse justified? *AJR Am J Roentgenol*. 2014;202:868–871.
38. Wootton-Gorges SL, Stein-Wexler R, Walton JW, et al. Comparison of computed tomography and chest radiography in the detection of rib fractures in abused infants. *Child Abuse Negl*. 2008;32:659–663.
39. Anilkumar A, Fender LJ, Broderick NJ, et al. The role of the follow-up chest radiograph in suspected non-accidental injury. *Pediatr Radiol*. 2006;36:216–218.
40. Maguire S, Mann M, John N, et al. Does cardiopulmonary resuscitation cause rib fractures in children? A systematic review. *Child Abuse Negl*. 2006;30:739–751.
41. Betz P, Liebhardt E. Rib fractures in children—resuscitation or child abuse? *Int J Legal Med*. 1994;106:215–218.
42. Feldman KW, Brewer KD. Child abuse, cardiopulmonary resuscitation, and rib fractures. *Pediatrics*. 1984;73:339–342.
43. Spevak MR, Kleinman PK, Belanger PL, et al. Cardiopulmonary resuscitation and rib fractures in infants. A postmortem radiologic-pathologic study. *JAMA*. 1994;272:617–618.
44. Matshes EW, Lew EO. Two-handed cardiopulmonary resuscitation can cause rib fractures in infants. *Am J Forensic Med Pathol*. 2010;31:303–307.
45. van Rijn RR, Bilo RA, Robben SG. Birth-related mid-posterior rib fractures in neonates: a report of three cases (and a possible fourth case) and a review of the literature. *Pediatr Radiol*. 2009;39:30–34.
46. Bixby SD, Abo A, Kleinman PK. High-impact trauma causing multiple posteromedial rib fractures in a child. *Pediatr Emerg Care*. 2011;27:218–219.
47. Chalumeau M, Foix-l'Helias L, Scheinmann P, et al. Rib fractures after chest physiotherapy for bronchiolitis or pneumonia in infants. *Pediatr Radiol*. 2002;32:644–647.
48. Lucas-Herald A, Butler S, Mactier H, et al. Prevalence and characteristics of rib fractures in ex-preterm infants. *Pediatrics*. 2012;130:1116–1119.
49. Cadzow SP, Armstrong KL. Rib fractures in infants: red alert! The clinical features, investigations and child protection outcomes. *J Paediatr Child Health*. 2000;36:322–326.
50. Barsness KA, Cha ES, Bensard DD, et al. The positive predictive value of rib fractures as an indicator of nonaccidental trauma in children. *J Trauma*. 2003;54:1107–1110.
51. Kleinman PK, Marks SC, Blackbourne B. The metaphyseal lesion in abused infants: a radiologic-histopathologic study. *AJR Am J Roentgenol*. 1986;146:895–905.
52. Kleinman PK, Marks SC Jr. Relationship of the subperiosteal bone collar to metaphyseal lesions in abused infants. *J Bone Joint Surg Am*. 1995;77:1471–1476.

53. Kleinman PK, Marks SC Jr. A regional approach to the classic metaphyseal lesion in abused infants: the proximal humerus. *AJR Am J Roentgenol*. 1996;167:1399–1403.
54. Kleinman PK, Marks SC Jr. A regional approach to the classic metaphyseal lesion in abused infants: the distal femur. *AJR Am J Roentgenol*. 1998;170:43–47.
55. Kleinman PK, Marks SC Jr. A regional approach to the classic metaphyseal lesion in abused infants: the proximal tibia. *AJR Am J Roentgenol*. 1996;166:421–426.
56. Kleinman PK, Marks SC Jr. A regional approach to classic metaphyseal lesions in abused infants: the distal tibia. *AJR Am J Roentgenol*. 1996;166:1207–1212.
57. Kleinman PK, Marks SC Jr, Spevak MR, et al. Extension of growth-plate cartilage into the metaphysis: a sign of healing fracture in abused infants. *AJR Am J Roentgenol*. 1991;156:775–779.
58. Kleinman PK, Belanger PL, Karellas A, et al. Normal metaphyseal radiologic variants not to be confused with findings of infant abuse. *AJR Am J Roentgenol*. 1991;156:781–783.
59. Kleinman PK, Sarwar ZU, Newton AW, et al. Metaphyseal fragmentation with physiologic bowing: a finding not to be confused with the classic metaphyseal lesion. *AJR Am J Roentgenol*. 2009;192:1266–1268.
60. O'Connell A, Donoghue VB. Can classic metaphyseal lesions follow uncomplicated caesarean section? *Pediatr Radiol*. 2007;37:488–491.
61. Grayev AM, Boal DK, Wallach DM, et al. Metaphyseal fractures mimicking abuse during treatment for clubfoot. *Pediatr Radiol*. 2001;31:559–563.
62. Merten DF, Kirks DR, Ruderman RJ. Occult humeral epiphyseal fracture in battered infants. *Pediatr Radiol*. 1981;10:151–154.
63. Nimkin K, Kleinman PK, Teeger S, et al. Distal humeral physeal injuries in child abuse: MR imaging and ultrasonography findings. *Pediatr Radiol*. 1995;25:562–565.
64. Jones JC, Feldman KW, Bruckner JD. Child abuse in infants with proximal physeal injuries of the femur. *Pediatr Emerg Care*. 2004;20:157–161.
65. Strait RT, Siegel RM, Shapiro RA. Humeral fractures without obvious etiologies in children less than 3 years of age: when is it abuse? *Pediatrics*. 1995;96:667–671.
66. Anderson WA. The significance of femoral fractures in children. *Ann Emerg Med*. 1982;11:174–177.
67. Scherl SA, Miller L, Lively N, et al. Accidental and nonaccidental femur fractures in children. *Clin Orthop Relat Res*. 2000;96–105.
68. Pandya NK, Baldwin KD, Wolfgruber H, et al. Humerus fractures in the pediatric population: an algorithm to identify abuse. *J Pediatr Orthop B*. 2010;19:535–541.
69. Schwend RM, Werth C, Johnston A. Femur shaft fractures in toddlers and young children: rarely from child abuse. *J Pediatr Orthop*. 2000;20:475–481.
70. Pierce MC, Bertocci GE, Vogeley E, et al. Evaluating long bone fractures in children: a biomechanical approach with illustrative cases. *Child Abuse Negl*. 2004;28:505–524.
71. Baldwin K, Pandya NK, Wolfgruber H, et al. Femur fractures in the pediatric population: abuse or accidental trauma? *Clin Orthop Relat Res*. 2011;469:798–804.
72. Kogutt MS, Swischuk LE, Fagan CJ. Patterns of injury and significance of uncommon fractures in the battered child syndrome. *Am J Roentgenol Radium Ther Nucl Med*. 1974;121:143–149.
73. Currarino G, Prescott P. Fractures of the acromion in young children and a description of a variant in acromial ossification which may mimic a fracture. *Pediatr Radiol*. 1994;24:251–255.
74. Kleinman PK, Spevak MR. Variations in acromial ossification simulating infant abuse in victims of sudden infant death syndrome. *Radiology*. 1991;180:185–187.
75. Hechter S, Huyer D, Manson D. Sternal fractures as a manifestation of abusive injury in children. *Pediatr Radiol*. 2002;32:902–906.
76. McBride MT, Hennrikus WL, Mologne TS. Newborn clavicle fractures. *Orthopedics*. 1998;21:317–319.
77. Cumming WA. Neonatal skeletal fractures. Birth trauma or child abuse? *J Can Assoc Radiol*. 1979;30:30–33.
78. Swischuk LE. Spine and spinal cord trauma in the battered child syndrome. *Radiology*. 1969;92:733–738.
79. Kleinman PK, Marks SC. Vertebral body fractures in child abuse. Radiologic-histopathologic correlates. *Invest Radiol*. 1992;27:715–722.
80. Kemp AM, Joshi AH, Mann M, et al. What are the clinical and radiological characteristics of spinal injuries from physical abuse: a systematic review. *Arch Dis Child*. 2010;95:355–360.
81. Levin TL, Berdon WE, Cassell I, et al. Thoracolumbar fracture with listhesis—an uncommon manifestation of child abuse. *Pediatr Radiol*. 2003;33:305–310.
82. Kleinman PK, Shelton YA. Hangman's fracture in an abused infant: imaging features. *Pediatr Radiol*. 1997;27:776–777.
83. Brown RL, Brunn MA, Garcia VF. Cervical spine injuries in children: a review of 103 patients treated consecutively at a level 1 pediatric trauma center. *J Pediatr Surg*. 2001;36:1107–1114.
84. Feldman KW, Avellino AM, Sugar NF, et al. Cervical spinal cord injury in abused children. *Pediatr Emerg Care*. 2008;24:222–227.
85. Kleinman PK, Zito JL. Avulsion of the spinous processes caused by infant abuse. *Radiology*. 1984;151:389–391.
86. Fernando S, Obaldo RE, Walsh IR, et al. Neuroimaging of nonaccidental head trauma: pitfalls and controversies. *Pediatr Radiol*. 2008;38:827–838.
87. Meservy CJ, Towbin R, McLaurin RL, et al. Radiographic characteristics of skull fractures resulting from child abuse. *AJR Am J Roentgenol*. 1987;149:173–175.
88. Hobbs CJ. Skull fracture and the diagnosis of abuse. *Arch Dis Child*. 1984;59:246–252.
89. Kemp AM, Dunstan F, Harrison S, et al. Patterns of skeletal fractures in child abuse: systematic review. *Br Med J*. 2008;337:a1518. doi:10.1136/bmj.a1518.
90. Kleinman PK, Spevak MR. Soft tissue swelling and acute skull fractures. *J Pediatr*. 1992;121:737–739.
91. Cremin B, Goodman H, Spranger J, et al. Wormian bones in osteogenesis imperfecta and other disorders. *Skeletal Radiol*. 1982;8:35–38.
92. Culotta PA, Crowe JE, Tran QA, et al. Performance of computed tomography of the head to evaluate for skull fractures in infants with suspected non-accidental trauma. *Pediatr Radiol*. 2016; doi:10.1007/s00247-016-3707-7. [Epub ahead of print].
93. Parisi MT, Wiester RT, Done SL, et al. Three-dimensional computed tomography skull reconstructions as an aid to child abuse evaluations. *Pediatr Emerg Care*. 2015;31:779–786.
94. Idriz S, Patel JH, Ameli Renani S, et al. CT of normal developmental and variant anatomy of the pediatric skull: distinguishing trauma from normality. *Radiographics*. 2015;35:1585–1601.
95. Sanchez T, Stewart D, Walvick M, et al. Skull fracture vs. accessory sutures: how can we tell the difference? *Emerg Radiol*. 2010;17:413–418.
96. Ablin DS, Greenspan A, Reinhart MA. Pelvic injuries in child abuse. *Pediatr Radiol*. 1992;22:454–457.
97. Johnson K, Chapman S, Hall CM. Skeletal injuries associated with sexual abuse. *Pediatr Radiol*. 2004;34:620–623.
98. Perez-Rossello JM, Connolly SA, Newton AW, et al. Pubic ramus radiolucencies in infants: the good, the bad and the indeterminate. *AJR Am J Roentgenol*. 2008;190:1481–1486.
99. Nimkin K, Spevak MR, Kleinman PK. Fractures of the hands and feet in child abuse: imaging and pathologic features. *Radiology*. 1997;203:233–236.
100. Kleinman PK, Morris NB, Makris J, et al. Yield of radiographic skeletal surveys for detection of hand, food, and spine fractures in suspected child abuse. *AJR Am J Roentgenol*. 2013;200:641–644.
101. Prosser I, Maguire S, Harrison SK, et al. How old is this fracture? Radiologic dating of fractures in children: a systematic review. *AJR Am J Roentgenol*. 2005;184:1282–1286.
102. O'Connor J, Cohen J. Dating fractures. In: Kleinman PK, ed. *Diagnostic Imaging of Child Abuse*. St. Louis, MO: Mosby; 1998:168–177.
103. Halliday KE, Broderick NJ, Somers JM, et al. Dating fractures in infants. *Clin Radiol*. 2011;66:1049–1054.
104. Prosser I, Lawson Z, Evans A, et al. A timetable for the radiologic features of fracture healing in young infants. *AJR Am J Roentgenol*. 2012;198:1014–1020.
105. Swischuk L. Not everything is child abuse. *Emerg Radiol*. 2000;7:218–224.
106. Radkowski MA. The battered child syndrome: pitfalls in radiological diagnosis. *Pediatr Ann*. 1983;12:894–903.
107. Shopfner CE. Periosteal bone growth in normal infants. A preliminary report. *Am J Roentgenol Radium Ther Nucl Med*. 1966;97:154–163.
108. Kwon DS, Spevak MR, Fletcher K, et al. Physiologic subperiosteal new bone formation: prevalence, distribution, and thickness in neonates and infants. *AJR Am J Roentgenol*. 2002;179:985–988.
109. Quigley AJ, Starface S. Skeletal survey normal variants, artefacts and commonly misinterpreted findings not to be confused with non-accidental injury. *Pediatr Radiol*. 2014;44:82-93.

110. Dabezies EJ, Warren PD. Fractures in very low birth weight infants with rickets. *Clin Orthop Relat Res*. 1997;335:233–239.
111. Amir J, Katz K, Grunebaum M, et al. Fractures in premature infants. *J Pediatr Orthop*. 1988;8:41–44.
112. Carroll DM, Doria AS, Babyn PS. Clinical-radiological features of fractures in premature infants—a review. *J Perinat Med*. 2007;35:366–375.
113. Lim HK, Smith WL, Sato Y, et al. Congenital syphilis mimicking child abuse. *Pediatr Radiol*. 1995;25:560–561.
114. Bacopoulou F, Henderson L, Philip SG. Menkes disease mimicking non-accidental injury. *Arch Dis Child*. 2006;91:919.
115. Kleinman PK. Problems in the diagnosis of metaphyseal fractures. *Pediatr Radiol*. 2008;38(suppl 3):S388–S394.
116. Ablin DS, Greenspan A, Reinhart M, et al. Differentiation of child abuse from osteogenesis imperfecta. *AJR Am J Roentgenol*. 1990;154:1035–1046.
117. Chapman S, Hall CM. Non-accidental injury or brittle bones. *Pediatr Radiol*. 1997;27:106–110.
118. Singh Kocher M, Dichtel L. Osteogenesis imperfecta misdiagnosed as child abuse. *J Pediatr Orthop B*. 2011;20:440–443.
119. Marquardt ML, Done SL, Sandrock M, et al. Copper deficiency presenting as metabolic bone disease in extremely low birth weight, short-gut infants. *Pediatrics*. 2010;130:e695–e698.
120. Renaud A, Aucourt J, Weill J, et al. Radiographic features of osteogenesis imperfecta. *Insights Imaging*. 2013;4:417–429.
121. Kleinman PK. Schmid-like metaphyseal chondrodysplasia simulating child abuse. *AJR Am J Roentgenol*. 1991;156:576–578.
122. Kozlowski K, Robben S, Bellemore M, et al. Spondylo-metaphyseal dysplasia corner fracture type a cautionary tale. *Radiol Med*. 1993; 85:7–11.
123. Paterson CR, Burns J, McAllion SJ. Osteogenesis imperfecta: the distinction from child abuse and the recognition of a variant form. *Am J Med Genet*. 1993;45:187–192.
124. Mendelson KL. Critical review of temporary brittle bone disease. *Pediatr Radiol*. 2005;35:1036–1040.
125. Ablin DS, Sane SM. Non-accidental injury: confusion with temporary brittle bone disease and mild osteogenesis imperfecta. *Pediatr Radiol*. 1997;27:111–113.
126. Keller KA, Barnes PD. Rickets vs. abuse: a national and international epidemic. *Pediatr Radiol*. 2008;38:1210–1216.
127. Ayoub DM, Hyman C, Cohen M, et al. A critical review of the classic metaphyseal lesion: traumatic or metabolic? *AJR Am J Roentgenol*. 2014;202:185–196.
128. Slovis TL, Chapman S. Evaluating the data concerning vitamin D insufficiency/deficiency and child abuse. *Pediatr Radiol*. 2008;38:1221–1224.
129. Schilling S, Wood JN, Levine MA, et al. Vitamin D status in abused and nonabused children younger than 2 years old with fractures. *Pediatrics*. 2011;127:835–841.
130. Strouse PJ. ‘Keller & Barnes’ after 5 years – still inadmissible as evidence. *Pediatr Radiol*. 2013;43:1424.
131. Brown SD, Servaes S, Hayes LL. Society for Pediatric Radiology Child Abuse Committee. SPR Child Abuse Committee response regarding classic metaphyseal lesion. *AJR Am J Roentgenol*. 2014;203:W232.
132. Chapman T, Sugar N, Done S, et al. Fractures in infants and toddlers with rickets. *Pediatr Radiol*. 2010;40:1184–1189.
133. Cory CZ, Jones BM. Can shaking alone cause fatal brain injury? A biomechanical assessment of the Duhaime shaken baby syndrome model. *Med Sci Law*. 2003;43:317–333.

# 144 Sports Medicine

J. Herman Kan and Erica K. Schallert

In the United States, more than than 30 million (approximately one-third) of school-aged children participate in organized sports.[1] Sports-related injuries occur more frequently in the lower extremities compared with the upper extremities. This section will review acute and chronic sports injury patterns with an emphasis on entities that are unique in children as well as cover multimodality imaging with an emphasis on important magnetic resonance imaging (MRI) features. Skeletal trauma, including acute fractures and dislocations, is covered in Chapter 142.

## AVULSION INJURIES AND MUSCLE INJURIES

***Etiology.*** Avulsion injuries or fractures may occur at musculotendinous or ligamentous attachments to an apophysis. Avulsion injuries may occur at either the physeal equivalent or chondro-osseous junction of an apophysis.

The musculoskeletal unit of the child is composed of the apophysis, tendon, myotendinous junction, and muscle belly. In the skeletally mature patient, the weakest component of the musculoskeletal unit is the myotendinous junction, whereas in the skeletally immature patient, particularly during periods of rapid growth, the cartilaginous physeal equivalent region of the apophysis is the weakest link in the musculoskeletal unit.[2] As a consequence, apophyseal avulsion injuries (Fig. 144.1), rather than myotendinous tears, may occur when the musculoskeletal unit is stressed.

Apophyseal and ligamentous avulsion injuries are more frequent in the lower extremity than in the upper extremity. In particular in the lower extremity, the pelvis and knee are the most common sites for apophyseal avulsion injuries.[3]

After the apophysis, the next weakest component of the musculoskeletal unit is the myotendinous junction, which is therefore the most common site of muscular injury. Myotendinous tears are an acute event during a physical activity in which a child can pinpoint the time (within seconds) in which the injury occurred. This should be differentiated clinically from delayed onset muscle soreness (DOMS), which is not related to a single event but rather an activity with repetitive eccentric and concentric muscle contractions with no acute pain at the time of the activity. Instead, symptoms and pain usually are felt in the days after the activity.[4]

***Imaging.*** In the acute setting, the displaced avulsion fracture fragment is present without proliferative callus formation (see Fig. 144.1). During healing, proliferative callus will form, suggesting its subacute or chronic nature.

When radiographs are negative and no displaced fragment exists, an MRI scan may be obtained. MRI may demonstrate subtle edema of the apophysis and metaphyseal equivalent bone, physeal equivalent edema and widening, and adjacent soft tissue edema (e-Fig. 144.2). The term *fracture* should be used only when a linear displaced or nondisplaced fracture is present. When edema alone is present within the apophysis and adjacent soft tissues, the term *avulsion injury* can be used.

MRI may also demonstrate avulsion injuries and fractures at the level of the chondro-osseous junction (Fig. 144.3).

MRI is preferred for delineating the remainder of the musculoskeletal unit. When muscle edema is present related to trauma, three possible etiologies exist: (1) DOMS (Fig. 144.4), (2) direct muscle contusion (e-Fig. 144.5), and (3) myotendinous muscle tear (Fig. 144.6). With DOMS, MRI shows diffuse edema on fluid sensitive sequences without discrete fiber disruption. Direct muscle contusions show similar changes to DOMS but are more focal in nature when the injury is mild, with discrete fiber disruption and hematoma formation when the injury is more severe. In the setting of muscle hematomas, these may mimic an intramuscular abscess. Gadolinium-enhanced, T1-weighted, fat-saturated magnetic resonance (MR) imaging may demonstrate rim enhancement for both hematomas and intramuscular abscess. T1-weighted imaging without gadolinium may demonstrate T1-weighted hyperintense foci related to blood products and may suggest muscle hematoma and, less likely, intramuscular abscess with proteinaceous content. Evidence of myotendinous muscle injury can range from edema to complete disruption with muscle fiber and aponeurosis retraction.

***Treatment and Follow-up.*** Treatment varies, depending on the location of the apophyseal avulsion injury. In the pelvis, the majority of apophyseal avulsion injuries are treated conservatively with rest. Surgical reduction and fixation may be necessary when the avulsed fracture fragment is greater than 2 cm.[3] During the healing phase, radiographs may be helpful to monitor callus formation and alignment. Apophyseal avulsion fractures elsewhere are usually treated conservatively, and surgical reduction is based on degree of apophyseal displacement. For instance, medial epicondylar avulsion fractures are typically treated surgically when the displaced fragment is greater than 5 mm.[5]

Myotendinous tears are treated conservatively with 2 to 3 weeks of rest before returning to sport activities.[4] DOMS is also treated conservatively, and symptoms usually resolve within a week.

## ANTERIOR COMPARTMENT INJURIES OF THE KNEE

***Etiology.*** The anterior compartment of the knee is composed of the quadriceps tendon, patellar bone, patellar tendon, and tibial tuberosity. The patella is a sesamoid equivalent for the quadriceps mechanism. Acute forceful concentric or eccentric contraction of the quadriceps muscle may lead to acute avulsion injuries of the inferior patellar pole (chondro-osseous avulsion injury, patellar sleeve fractures) and tibial tuberosity (apophyseal avulsion injury); whereas repetitive motion is the culprit for tendinopathy and chronic avulsive injuries affecting the inferior patellar pole in *Sinding-Larsen-Johansson disease* and the tibial tuberosity in *Osgood-Schlatter disease*.[1] When pathology is isolated to only the proximal patellar tendon, it is called *jumper's knee* and tends to occur in patients who are skeletally mature. Sinding-Larsen-Johansson and Osgood-Schlatter diseases usually occur during adolescence and often affect both knees. Both bone and tendon injuries often coexist in the same knee.

***Imaging.*** Although imaging is helpful for the diagnosis of Sinding-Larsen-Johansson and Osgood-Schlatter diseases, the diagnosis for these chronic conditions is made clinically with radiographic confirmation of findings, not by imaging alone. Advanced imaging confirms the diagnosis and excludes alternative etiologies. MRI should not be performed routinely on these patients if radiography and clinical diagnosis confirm the disease.

Patellar sleeve fractures represent an acute avulsion fracture of the inferior pole of the patella. This occurs at the chondro-osseous junction of the patella tendon origin. On radiography and MRI, a small linear or curvilinear fragment of bone may be identified (Fig. 144.7). On MRI, edema within the patella, the superior aspect of Hoffa's fat pad and in the peripatellar soft tissues are present in the acute setting. This should be differentiated

## Abstract:

With increasing participation in organized sports and emphasis on high level performance, sports-related injuries are a high volume component of pediatric musculoskeletal imaging. Due to the nature of their developing musculoskeletal system, they are prone to a wide spectrum of both acute and chronic injury patterns. This section will review these injury patterns, emphasizing those unique to children as well as cover multimodality imaging with an emphasis on important magnetic resonance imaging(MRI) features. Topics covered include acute and chronic avulsion injuries, anterior compartment injuries, osteochondral injuries and internal derangement of the hip.

## Keywords:

pediatric sports related injuries
acute sports injuries
chronic sports injuries
transient patellar dislocation
osteochondral injuries
throwing injuries

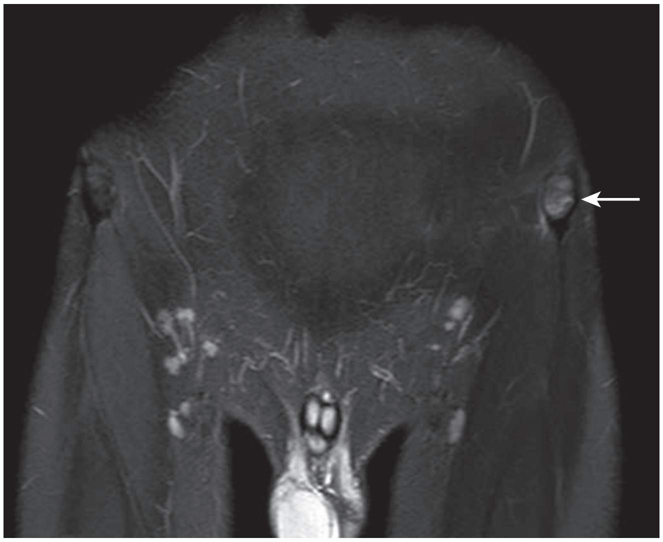

**e-Figure 144.2. Nondisplaced left anterosuperior iliac spine avulsion fracture in a 16-year-old boy.** Coronal short-tau inversion recovery coronal MR image shows abnormal increased signal at the avulsion *(arrow)* related to the sartorius muscle origin.

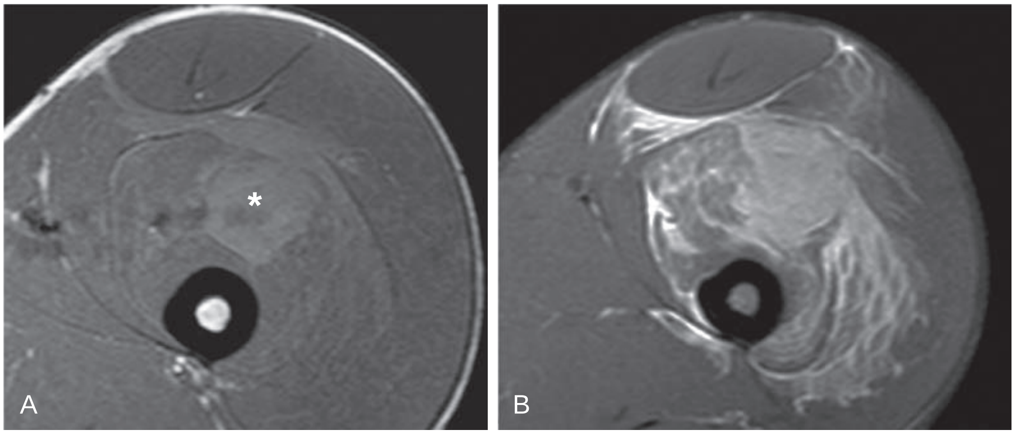

**e-Figure 144.5. Vastus intermedius direct muscle contusion in a 17-year-old boy.** (A) T1-weighted axial MR image demonstrates hyperintense material, consistent with blood products, located in the vastus intermedius muscle belly *(asterisk)*. (B) T2-weighted fat-suppressed axial MR image demonstrates muscle fiber disruption of the vastus intermedius and associated muscular and fascial edema-like signal.

from chronic repetitive avulsive injuries to the inferior patellar pole occurring in Sinding-Larsen-Johansson disease in which the inferior patellar bone has had time to remodel. Therefore on radiography and MRI, well-corticated variable size ossicles are typically seen (Fig. 144.8) with adjacent soft tissue swelling and edema. As previously noted, this is typically a clinical diagnosis and, if well-corticated ossific fragments are present without adjacent edema, this finding may be related to an accessory ossicle(s).

Acute tibial tuberosity avulsion fractures result from forceful contraction of the patella tendon leading to a tibial tuberosity–sided linear or curvilinear avulsion fracture fragment at the level of the chondro-osseous junction (Fig. 144.9) or to uplifting of the entirety of the tibial tuberosity, with resultant Salter-Harris-type injury with physeal equivalent widening (Fig. 144.10). On MRI, edema is seen within the tibial tuberosity, and this may extend posteriorly to involve the remainder of the tibial epiphysis. Inferior Hoffa's fat pad and pretibial edema are often present. These changes should be differentiated from chronic repetitive avulsive injury affecting the tibial tuberosity and leading to Osgood-Schlatter disease. With Osgood-Schlatter disease, rather than linear avulsion fracture fragments, the tibial tuberosity and tibial tuberosity avulsion fragments have had time to remodel. Therefore on radiography and MRI, well-formed, variable-size, well-corticated ossicles may be seen (e-Fig. 144.11). On MRI, edema within the avulsed separate ossicles and tibial tuberosity are present and are related to the acute on chronic nature of the injury. In addition, edema within Hoffa's fat pad and pretibial edema are often present as well.

Patella tendinopathy and patellar tears (e-Figs. 144.12 and 144.13) may be evaluated by ultrasonography or MRI. Thickening of the tendon with longitudinally or transversely oriented tears may be seen as well as edema within the prepatellar soft tissues and Hoffa's fat pad. Marked tendinous hyperemia on color sonography denotes neovascularity and has been associated with a higher degree of pain.[6] MRI diagnosis of jumper's knee should ideally be made on longer echo time sequences to avoid "magic angle artifact."

***Treatment and Follow-up.*** Sinding-Larsen-Johansson disease, Osgood-Schlatter disease, and jumper's knee are all treated conservatively with rest. When displaced, acute avulsion fractures of the inferior patellar pole or tibial tuberosity may be treated by open reduction with patellar tendon reconstruction, particularly if patella alta is also present.[7] For avulsion fractures, care should be made to determine if the fracture is complete, incomplete, displaced, or nondisplaced. If the avulsion fracture is incomplete (see Fig. 144.9), affected children may benefit from conservative nonsurgical treatment.

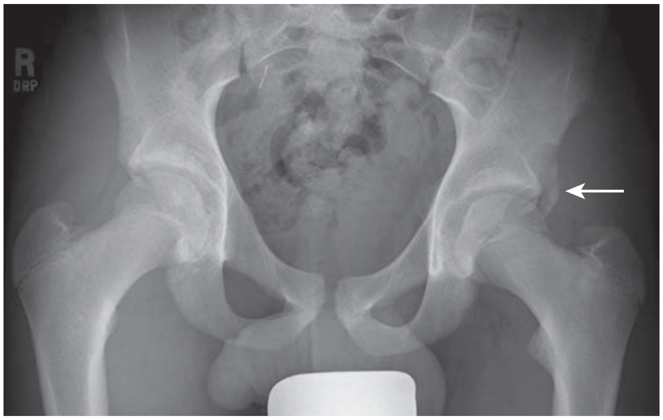

**Figure 144.1.** A 15-year-old boy with left anteroinferior iliac spine avulsion fracture *(arrow)* related to the rectus femoris origin.

## PATELLAR DISLOCATION AND PATELLOFEMORAL DYSPLASIA

***Etiology.*** The patella is a sesamoid bone in the extensor mechanism that lies within the concave-shaped femoral trochlear fossa. It has two primary facets: medial and lateral. The lateral facet is usually the dominant and larger facet, and articulates with the lateral aspect of the trochlear fossa. With knee flexion, the patella will concentrically locate within the trochlear fossa. With knee extension, the patella preferentially subluxes laterally in patients with or without underlying patellofemoral dysplasia because the lateral patellofemoral articulation is shallow compared with the medial articulation, and the vastus lateralis activates when the knee is extended.

Multiple variables may predispose a patient to patellar dislocation. This includes a large Q-angle, muscle imbalance with dominant vastus lateralis musculature, patella alta, rotational abnormalities of the tibia and femur, and overall ligamentous laxity.[8] Larger Q-angles direct the quadriceps muscle vector force on the

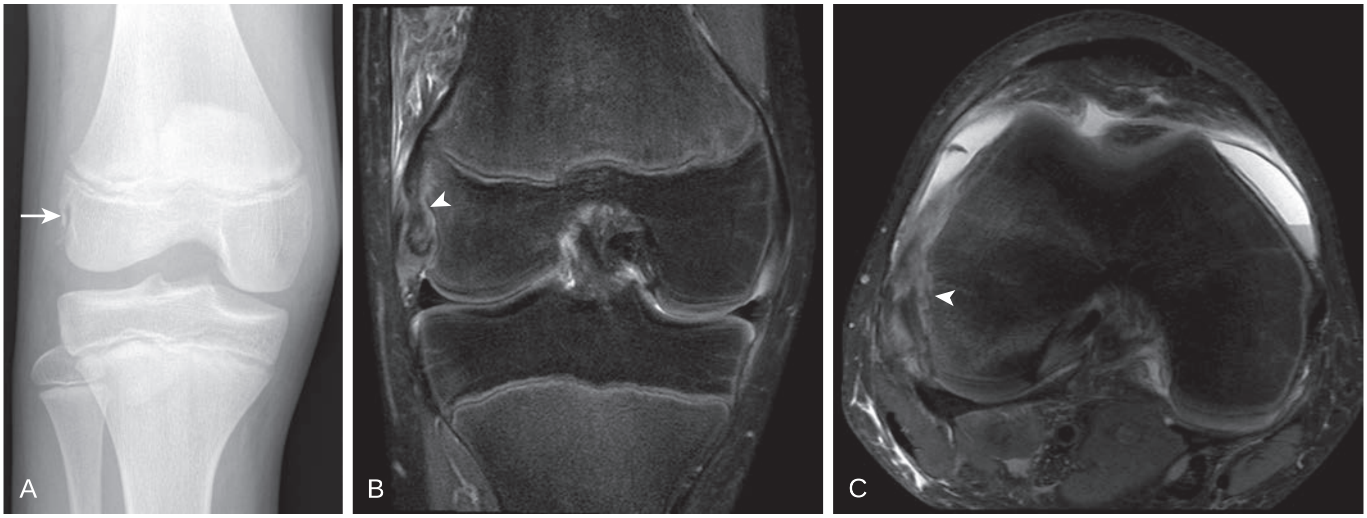

**Figure 144.3. Popliteus origin chondro-osseous avulsion fracture in a 13-year-old boy.** (A) An anteroposterior knee radiograph Popliteus origin chondro-osseous avulsion fracture at *(arrow)*. (B) Proton density fat-saturated coronal MR image. (C) Proton density fat suppression axial MR image demonstrates chondro-osseous fracture line *(arrowhead)*.

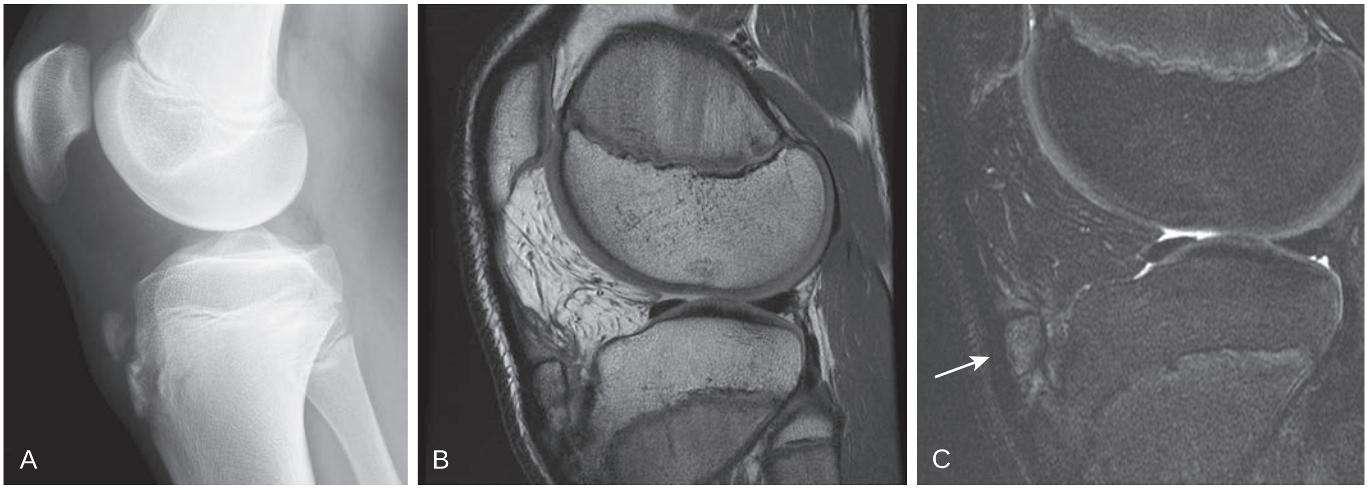

**e-Figure 144.11. Osgood-Schlatter disease in a 15-year-old.** (A) Lateral radiograph and (B) proton density sagittal MR image of the knee demonstrates chronic appearing tibial tuberosity fragmentation. (C) T2-weighted fat-suppressed sagittal MR image demonstrates edema of the tibial fragmentation *(arrow)* and adjacent Hoffa's fat pad.

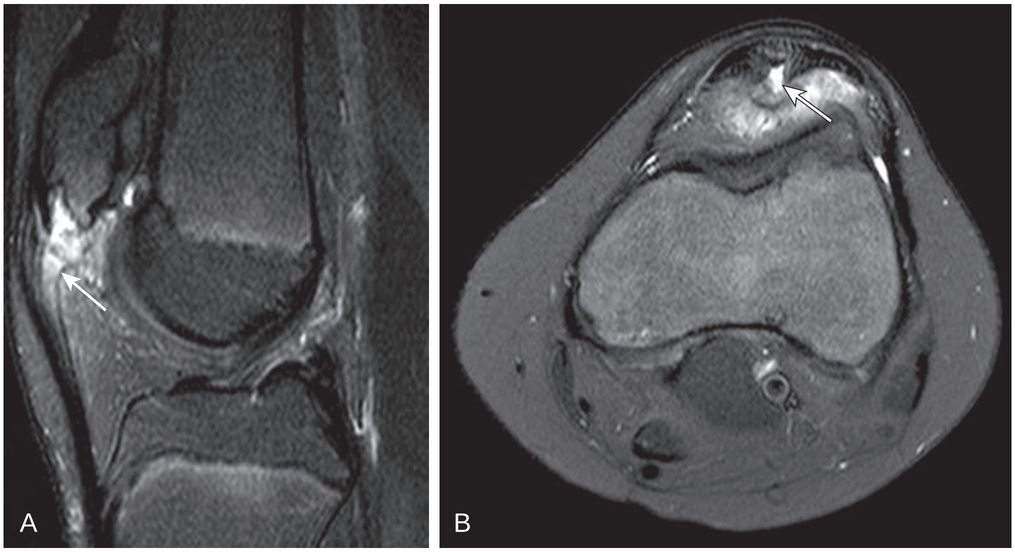

**e-Figure 144.12. Partial patellar tendon tear.** (A) T2-weighted fat-suppressed sagittal and (B) proton density fat-suppressed axial MR images demonstrate a partial tear of the patellar tendon at its patellar bone origin *(arrow)*.

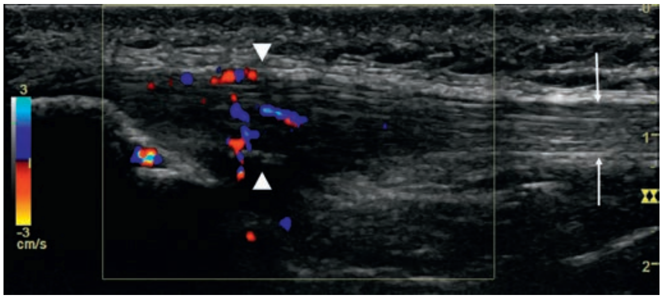

**e-Figure 144.13. Proximal patellar tendinopathy (jumper's knee) in a 17-year-old male.** Longitudinal color Doppler sonogram demonstrates a thickened and hypoechoic proximal patellar tendon *(arrowheads)* with superimposed more well-defined hypoechoic areas and a few anechoic clefts representing superimposed interstitial tearing. There is associated hyperemia and mild edema in the anterior superior aspect of Hoffa's fat pad. Note normal width and hyperechoic fibrillar architecture of the normal mid to distal tendon.

patella laterally. Because the patellar bone captures within the trochlear groove with knee flexion, in the setting of patella alta, it takes relatively more knee flexion for the patellar bone to capture. Both excessive external tibial torsion and increased femoral anteversion can predispose a child to patellar dislocation.[8,9] The normal degree of external tibial torsion is approximately 28 degrees at age 4 years and increases to approximately 38 degrees at skeletal maturity.[10] The normal degree of femoral anteversion is approximately 40 degrees at birth and approximately 15 degrees at skeletal maturity.

The earlier age at the first time patellar dislocation occurs, the higher the incidence of recurrent patellar dislocation and the higher the propensity to develop more severe secondary patellofemoral dysplasia. This may be related to laxity of the injured medial retinaculum and remodeling at the level of the patellofemoral joint after initial injury. Secondary patellofemoral dysplasia results from poor articulation at the level of the patellofemoral joint and can be exacerbated by muscle imbalance and traumatic patellar dislocation. Therefore patients with secondary patellofemoral dysplasia may have had a normally appearing patellofemoral joint at birth, but over time, the joint becomes dysplastic. Patellofemoral dysplasia can also occur as a primary congenital anomaly.

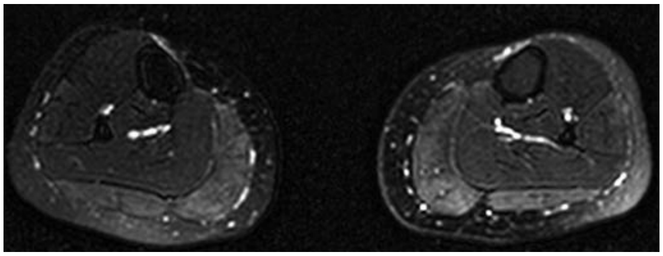

**Figure 144.4. Delayed onset muscle soreness in an adolescent.** A short-tau inversion recovery axial MR image of both legs shows edema-like signal within the gastrocnemius muscles.

***Imaging.*** Radiographs can identify risk factors for patellar dislocations, such as patella alta and patellofemoral dysplasia, as well as injuries related to a dislocation/relocation event, such as joint effusions, osteochondral fractures, and osseous avulsions. An axial view of the patella (i.e., merchant or sunrise view) is helpful to evaluate for avulsion fractures, which occur along the medial pole and are a result of avulsion injury at the insertion of the medial patellofemoral ligament in both the acute setting (Fig. 144.14) and for old injuries (e-Fig. 144.15). Acute patellar avulsion fractures are sliver-like, whereas old injuries are round and corticated.

The axial view should also be assessed for osteoarthritic changes of the patellofemoral joint, lateral patellar tilt, and patellar subluxation/dislocation. With regard to patellar location, the axial view may be misleading if not obtained with the knee in 30 degrees flexion. Knee flexion facilitates patella reduction, whereas knee extension may exaggerate patellar tilt and lateral patellar subluxation. When the knee axial view is obtained with less knee flexion, the trochlear fossa may appear shallow and should not be mistaken for patellofemoral dysplasia. Because of positioning variability, a true lateral view of the knee is a great resource that displays the entire trochlear floor and can support a diagnosis of trochlear dysplasia.[11] A positive crossing sign indicates that the lateral side of the trochlea is flat or in plane with the lateral condyle.[12] This can be correlated with a properly flexed axial view to confirm a flat or even convex-appearing trochlear fossa. On the axial view, a lateral dominant patellar facet can be a feature suggestive of patellofemoral dysplasia. With progressive patellofemoral dysplasia, the trochlear fossa becomes more convex in appearance, and the patellar bone loses its normal angular appearance.

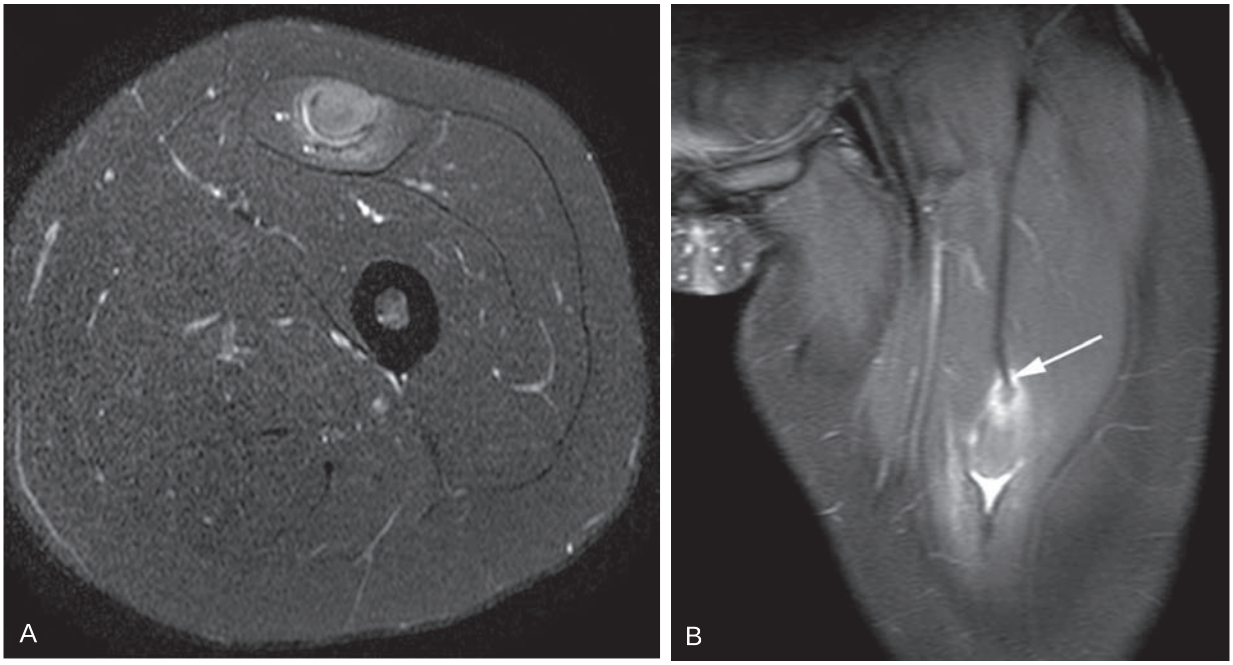

**Figure 144.6. Intramuscular degloving type injury of the rectus femoris musculotendinous junction in a 17-year-old female.** (A) T2-weighted fat suppression axial MR image demonstrates edema-like signal within the central portion of the rectus femoris with fluid signal replacing the normal low signal intensity of the central tendon *(indirect head)* of the rectus femoris. (B) Short-tau inversion recovery coronal MR image demonstrates proximal retraction of the torn central tendon *(indirect head)* of the rectus femoris *(arrow)* with a small amount of fluid separating it from the outer muscle at the myotendinous junction.

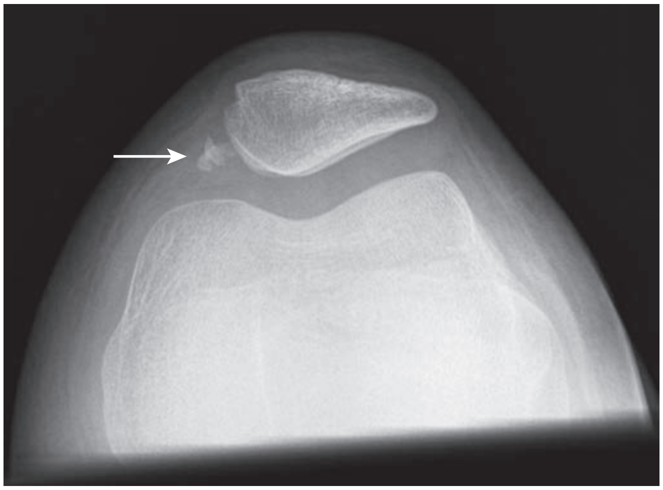

**e-Figure 144.15. Old avulsion fracture fragments caused by prior patellar dislocation in an 11-year-old girl.** These fracture fragments *(arrow)* are corticated (indicative that they are old) in contrast to acute fracture fragments that would not be corticated (see Fig. 144.14).

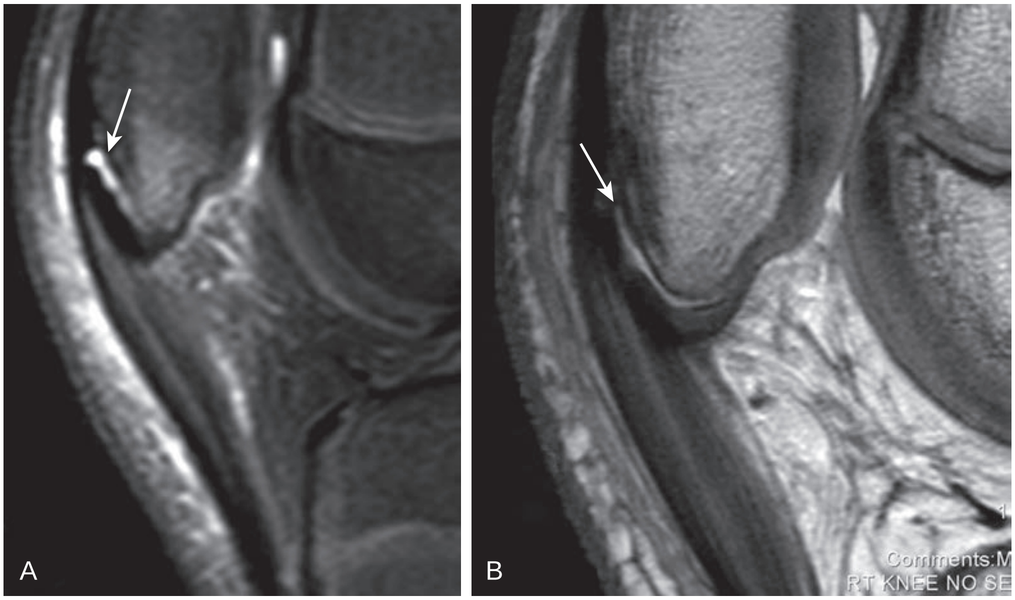

**Figure 144.7. Patellar sleeve avulsion in a 12-year-old boy.** (A) T2-weighted fat suppression sagittal MR image and (B) proton density sagittal MR image show a nondisplaced acute, inferior pole patellar sleeve fracture *(arrows)*.

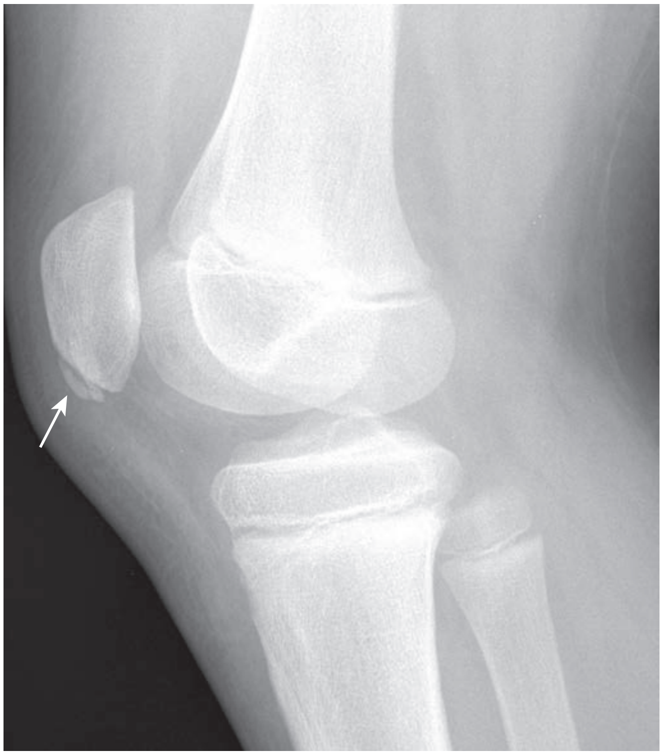

**Figure 144.8. Sinding-Larsen-Johansson.** Lateral radiograph of the knee demonstrates variable-sized, well-corticated ossicles *(arrow)* and adjacent soft tissue swelling.

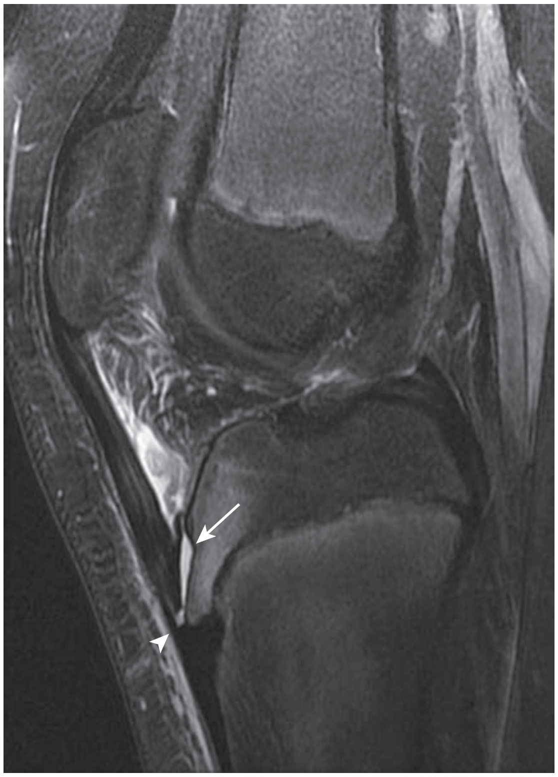

**Figure 144.9. Acute minimally displaced partial tibial tuberosity avulsion fracture *(arrow)* on a sagittal T2-weighted fat suppression MR image from a 13-year-old boy.** Note that some patella tendon fibers are not attached to the fracture fragment *(arrowhead)*.

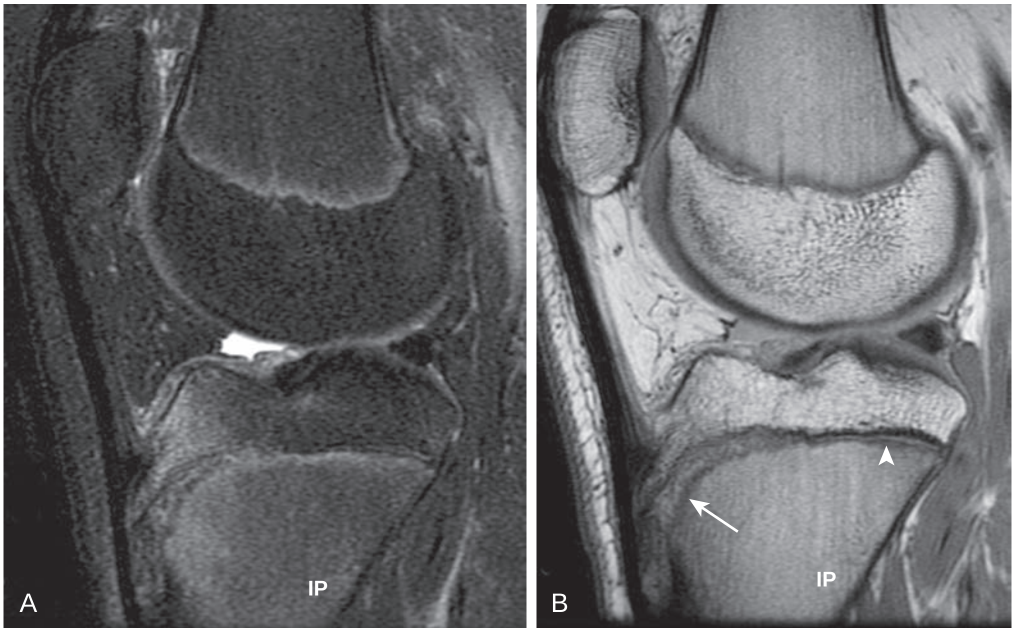

**Figure 144.10. Tibial tuberosity avulsive injury in a 14-year-old girl.** (A) T2-weighted fat-suppressed sagittal MR image demonstrates diffuse edema of the tibial tuberosity, physis, and deep metaphyseal equivalent region of the tibia. (B) Proton density sagittal image delineates physeal equivalent widening of the tibial tuberosity *(arrow)*. Compare this with the normal posteriorly located tibial physis *(arrowhead)*.

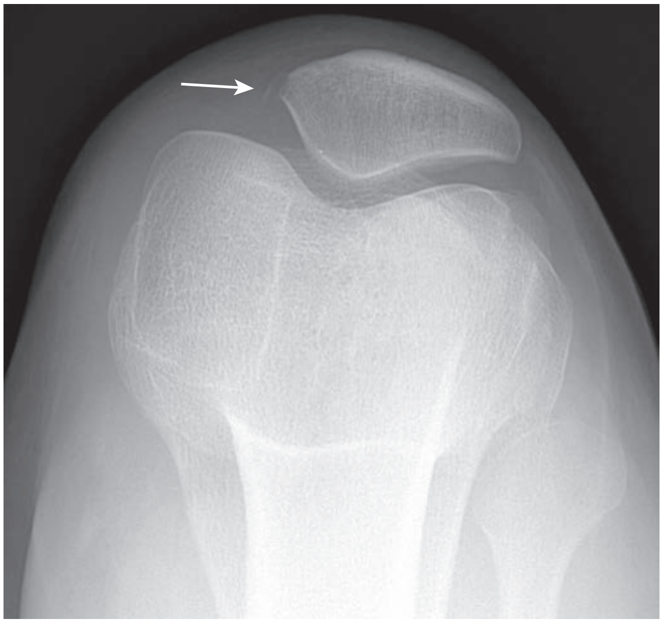

**Figure 144.14. Acute patellar dislocation/relocation in an 18-year-old.** There is an acute avulsion fracture *(arrow)* from the medial patella.

Computed tomography (CT) may be obtained in the workup of patellofemoral dysplasia to evaluate for rotational abnormalities (namely excessive external tibial torsion and femoral anteversion) and for a dynamic evaluation (e-Fig. 144.16). Three separate CT acquisitions are obtained at different degrees of knee flexion (e.g., 45, 30, and 15 degrees). If the patella dislocates at 15 degrees but is located at 45 and 30 degrees, it is considered a mild degree of patellar dislocation. However, if the patella dislocates at 30 or 45 degrees of knee flexion, it is a more severe degree of patellar dislocation. CT for patellar dislocation can also be used to evaluate the degree of patellofemoral dysplasia and secondary patellofemoral osteoarthritis, with changes similar to what may be seen on axial-view radiographs. The degree of lateralization of the tibial tuberosity should also be determined. This represents the distance between the midpoint of the tibial tuberosity and the deepest component of the trochlear groove on axial slices, the tibial tuberosity-trochlear groove (TT-TG) distance. If the tibial tuberosity is greater than 2 cm lateral with respect to the trochlear groove, a higher incidence of patellar instability exists (e-Fig. 144.17).[13]

MRI complements radiography and CT findings and can also evaluate rotational abnormalities.[14] Sometimes, children are referred for knee pain, and the diagnosis of patellar dislocation and patellofemoral dysplasia may be first suspected on MRI. On MRI for acute patellar dislocation, characteristic bone contusions may be seen along the medial patellar pole and anterolateral femoral condyle (Fig. 144.18). The bone contusions occur from compressive forces during relocation of the patella after the dislocation. Other findings that may be seen include patellar avulsion fractures, medial retinacular and patellofemoral ligament tears, cartilage injuries, and intraarticular bodies. Patellofemoral dysplasia (Fig. 144.19) and secondary degenerative changes should also be assessed by MRI.

***Treatment and Follow-up.*** Treatment for patellar dislocation should be approached from two perspectives: (1) treat biomechanical instability, which can be addressed by physical therapy and operative repair, and (2) treat mechanical symptoms related to sequelae from acute dislocation usually from intraarticular bodies or chondral injuries.

Patients with first-time patellar dislocation and those with recurrent patellar dislocation may be treated conservatively with physical therapy and bracing. The goal of treatment is to improve gluteal and vastus medialis muscle activity, which facilitates medial location of the patella.[13] Should physical therapy not improve symptoms, surgical repair is considered, although no single effective surgical technique has been advocated in the literature. Surgical approaches include lateral retinacular release, patellofemoral ligament repair and reconstruction, trochleoplasty (to deepen the

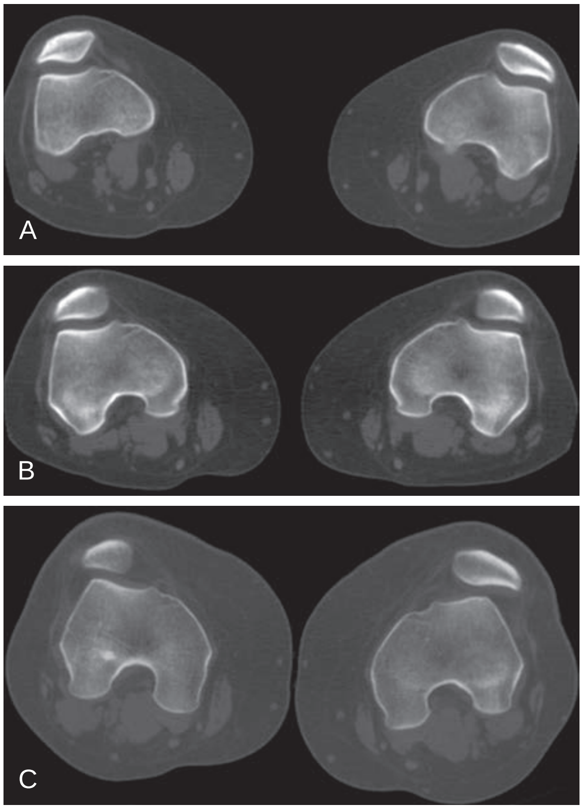

**e-Figure 144.16. Patellofemoral dysplasia.** A dynamic CT scan of bilateral patellofemoral joints at 45 degrees (A), 30 degrees (B), and 15 degrees (C) of knee flexion shows that, with progressive knee extension, the patella subluxes and tilts laterally, left greater than right.

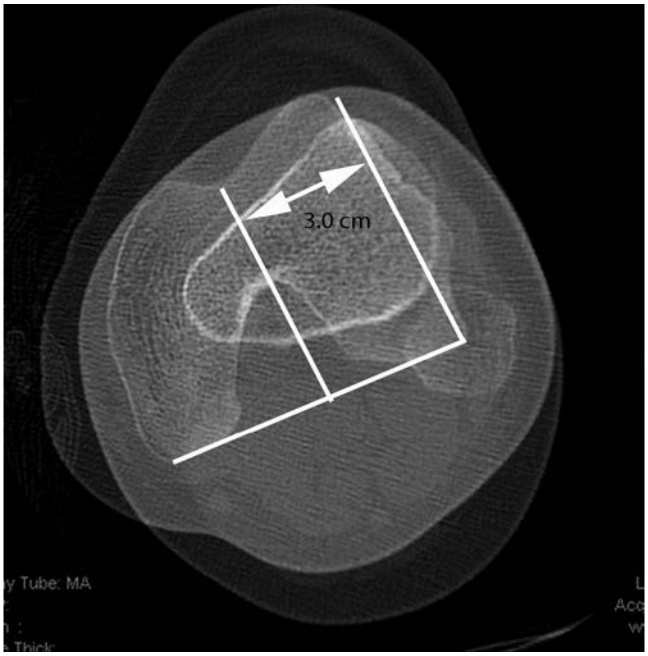

**e-Figure 144.17. Tibial tubercle-trochlear groove (TT-TG) distance.** A 15-year-old with chronic lateral patellar dislocation with a TT-TG distance of 3 cm. CT axial images with the trochlear groove and tibial tuberosity are overlayed. The distance is calculated between the deepest portion of the trochlear groove and midpoint of the tibial tuberosity at the patella insertion. The measurement should be made parallel to the posterior margins of the femoral condyles.

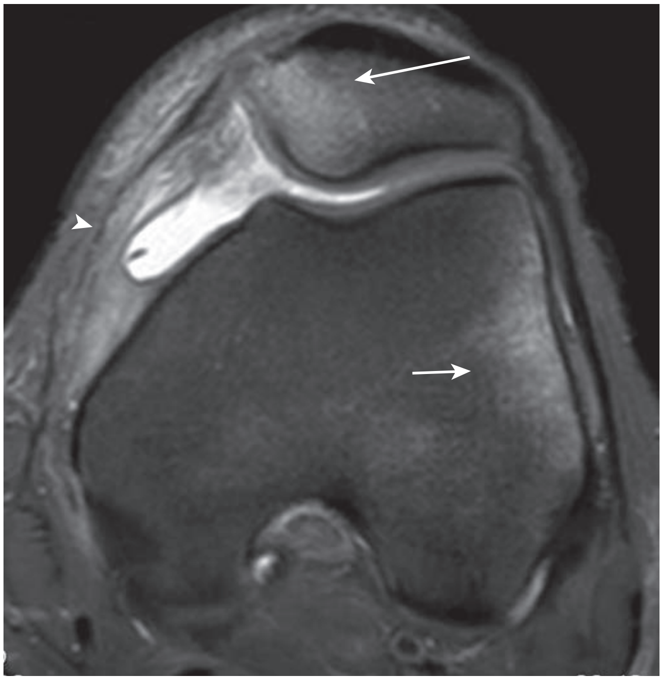

**Figure 144.18. Lateral patellar dislocation with characteristic kissing contusions in a 19-year-old.** Axial proton density fat-suppressed MR image shows increased signal *(arrows)*. Note partial tearing of the medial patellofemoral ligament *(arrowhead)* as well.

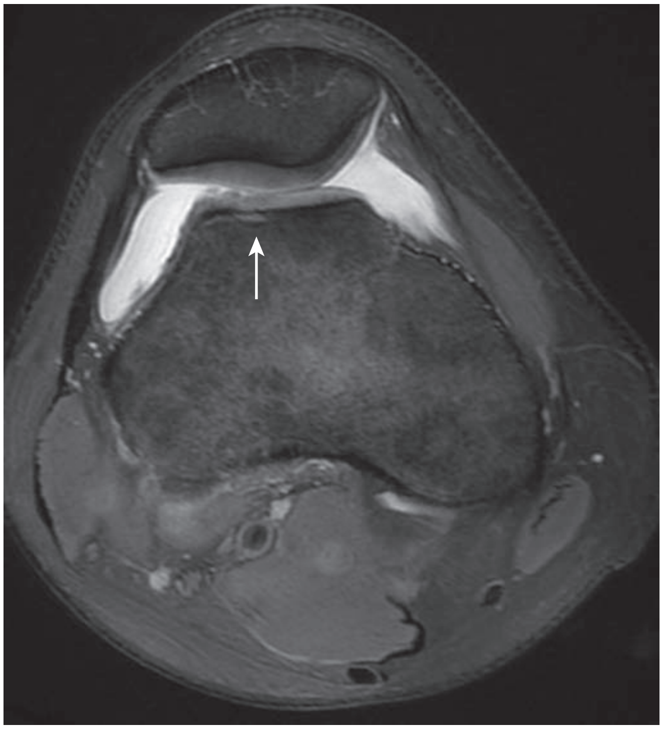

**Figure 144.19. Patellofemoral dysplasia in a 16-year-old boy.** Axial proton density fat-suppressed MR image shows a flat *(arrow)* dysplastic trochlear fossa. The normal trochlear fossa has a concave shape.

sulcus), and tibial tubercle transfers (medialization of the tibial tubercle), as well as rotational osteotomies to treat excessive tibial torsion and femoral version. The surgical goal is to facilitate patellar bone capture by the trochlear fossa and medialization of patellar biomechanical vector forces.

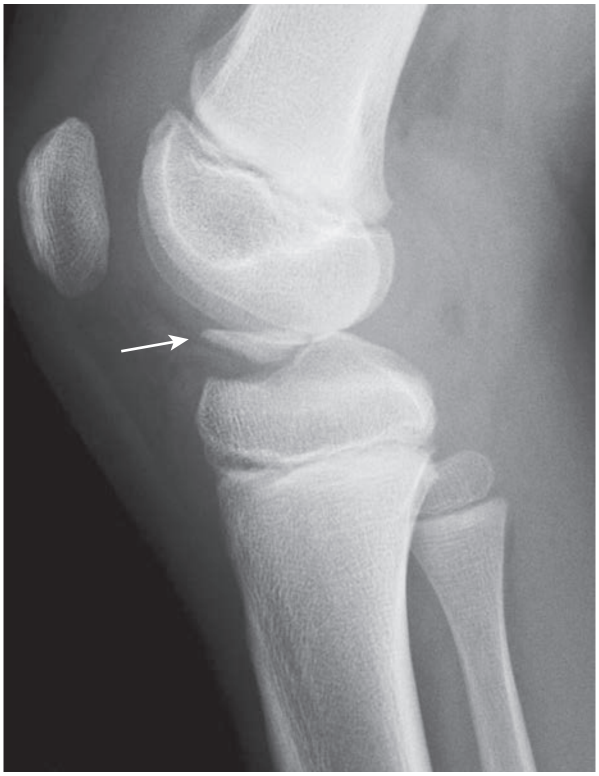

**Figure 144.21. Posteriorly hinged tibial eminence avulsion fracture in a 9-year-old boy *(arrow)*.**

When intraarticular bodies or cartilage injury is identified and the child has mechanical symptoms such as locking, arthroscopy may be performed to remove the bodies and perform cartilage debridement or more advanced cartilage restoration techniques.[13]

## ANTERIOR CRUCIATE LIGAMENT COMPLEX INJURIES

***Etiology.*** The anterior cruciate ligament (ACL) complex is composed of the ACL, its femoral origin, and its tibial insertion. The femoral and tibial chondro-osseous attachments of the ACL complex are relatively weak in the skeletally immature and are predisposed to chondro-osseous avulsion fractures.[15] Chondro-osseous avulsion fractures occur far more commonly at the tibial eminence insertion compared with the femoral origin. The ACL is composed of two fiber bundles: the anteromedial and posterolateral bundles, which extend from the medial aspect of the lateral femoral condyle to the level of the tibial eminence.[16] Coexisting full-thickness ACL tear and complete tibial eminence fractures are unusual as the force of injury usually is dissipated by either the ACL tear or the avulsion fracture. However, arthroscopic evidence of partial ACL tears is often present in the setting of a complete tibial eminence avulsion fracture. ACL tears are often seen in children with a narrow intercondylar notch, and ACL tibial eminence avulsion fractures tend to occur in children with a wider intercondylar notch.[17,18]

Multiple mechanisms of injury have been attributed as causes for ACL complex injuries in children, including varus or valgus stress, and twisting injuries of the knee. Risk factors include female gender, noncontact indirect injuries, and contact direct injuries (e.g., forceful blow to the lateral knee).[18]

***Imaging.*** Radiographic findings that may indicate an ACL complex injury include Segond (e-Fig. 144.20) and tibial eminence avulsion fractures (Fig. 144.21). A Segond fracture represents an

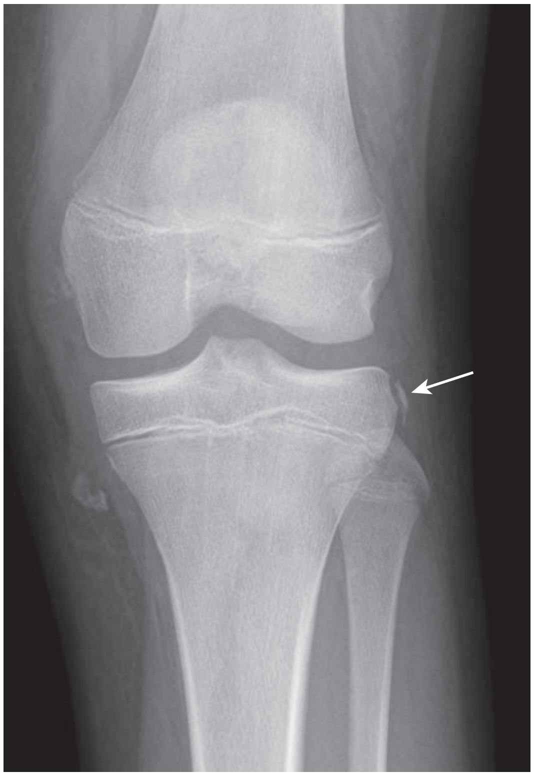

**e-Figure 144.20. Segond fracture.** Frontal radiograph in an 11-year-old girl shows a Segond fracture *(arrow)*, as well as osteochondral fragments in the medial aspect of the joint.

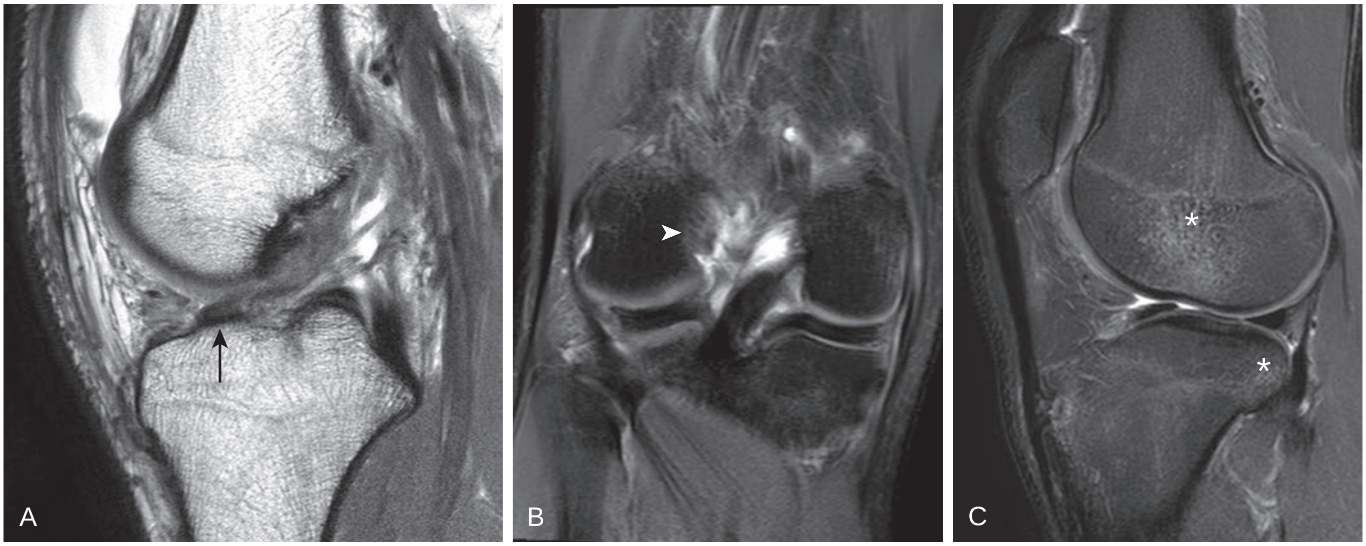

**Figure 144.22. Full-thickness anterior cruciate ligament (ACL) tear in a 16-year-old boy.** (A) Proton density sagittal MR image demonstrates full-thickness intrasubstance tear of the ACL near its femoral origin. Distal to the tear, ACL fibers are intact at the tibial insertion *(arrow)*. (B) Proton density fat-suppressed coronal MR image demonstrates full-thickness tear with residual femoral origin ACL fibers *(arrowhead)*. (C) T2-weighted fat-suppressed sagittal MR image demonstrates characteristic kissing contusion pattern related to ACL mechanism injury *(asterisks)*.

anteromedial capsular avulsion fracture at the chondro-osseous junction of the lateral tibial plateau. Tibial eminence avulsion fractures should be categorized as nondisplaced, minimally displaced with intact posterior hinge, or completely displaced with comment on comminution as this determines nonoperative versus operative management.[19] Because of ligamentous instability related to an ACL deficient knee, anterior translation of the tibia may be present on the lateral view.

On MRI, identification of complete disruption of the ACL should be confirmed on all three orthogonal planes (Fig. 144.22). ACL tears should be subcategorized as partial versus full-thickness tears. Some of the additional features to suggest ACL complex injuries are bone contusions related to anterior translation and twisting of the tibia, including anteromedial or anterolateral femoral condylar bone contusions, with kissing posteromedial or posterolateral tibial plateau contusions (see Fig. 144.22). When bone contusions are evident, a T1-weighted or proton-density sequence is useful for determining the presence of an underlying subchondral fracture. When subchondral bone contusions are present, the presence or absence of overlying articular cartilage injury should be identified. MRI also demonstrates tibial eminence avulsion fractures.

Additional findings on MRI include medial collateral ligament tears (e-Fig. 144.23) and meniscal tears. Medial collateral ligament injuries are subclassified as involving superficial or deep (meniscofemoral or meniscotibial) fibers. Tear location (femoral or tibial-sided) must be identified and whether the tear is partial or full thickness. Meniscal tears can be seen in up to 69% of ACL injuries in children.[20] The most common location for meniscal tears is the posterior horn of the lateral meniscus (e-Fig. 144.24).

Classification of meniscal tears includes vertical (see e-Figs. 144.24 and 144.25), horizontal, displaced (Fig. 144.26), and location (red or white zone) types. Vertical tears extend from the superior to inferior articular surface. They are subclassified into radial, longitudinal, or parrot-beak tears. Horizontal tears usually extend to only one articular surface and are usually degenerative in nature. Displaced tears include bucket handle tears (see Fig. 144.26) and displaced free fragment tears. Bucket handle tears result from large vertical longitudinal tears.

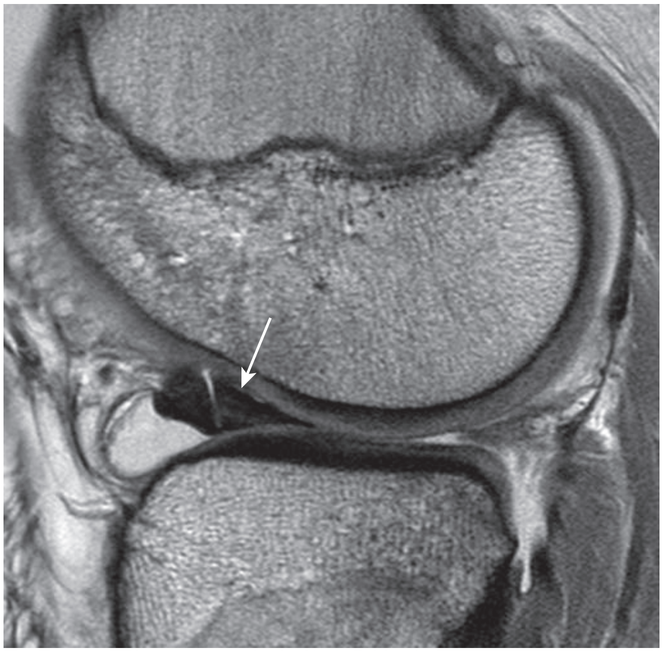

**Figure 144.26. Lateral meniscus bucket handle tear in a 14-year-old girl.** Proton density sagittal MR image shows that the posterior horn of the lateral meniscus has flipped anteriorly *(arrow)*, leading to a double anterior horn sign.

***Treatment and Follow-up.*** Treatment for full-thickness ACL tears is surgical. The natural evolution of ACL-deficient knees includes early osteoarthritis with cartilage injury and meniscal tears.[21] Diagnosing high-grade partial ACL tears should be approached with extreme caution, as partial ACL tears may heal nonsurgically with appropriate physical therapy and rest. High-grade partial ACL tears are surgically significant if clinical examination suggests an ACL deficient knee or progressive instability of the knee

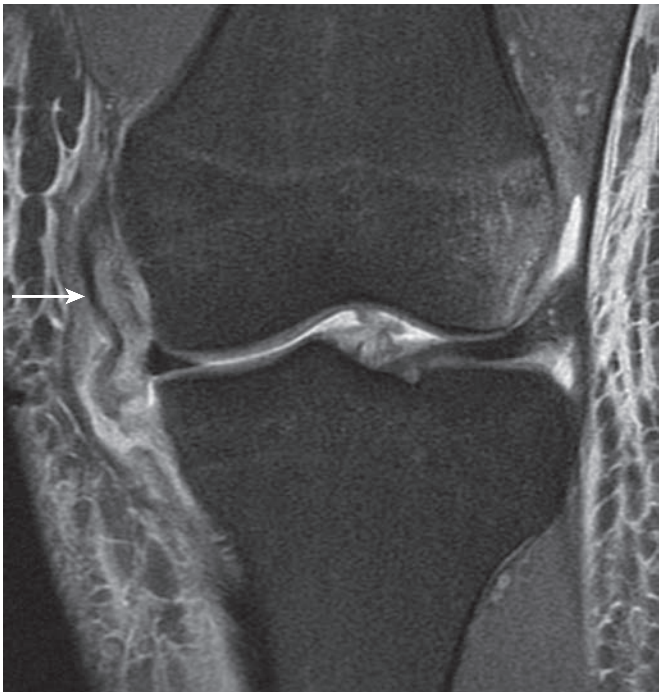

**e-Figure 144.23. Medial collateral ligament tear in a 16-year-old boy.** Coronal inversion recovery MR image shows a full thickness medial collateral ligament tear *(arrow)* with retraction from the tibial insertion. Note disruption of meniscotibial and meniscofemoral ligaments as well.

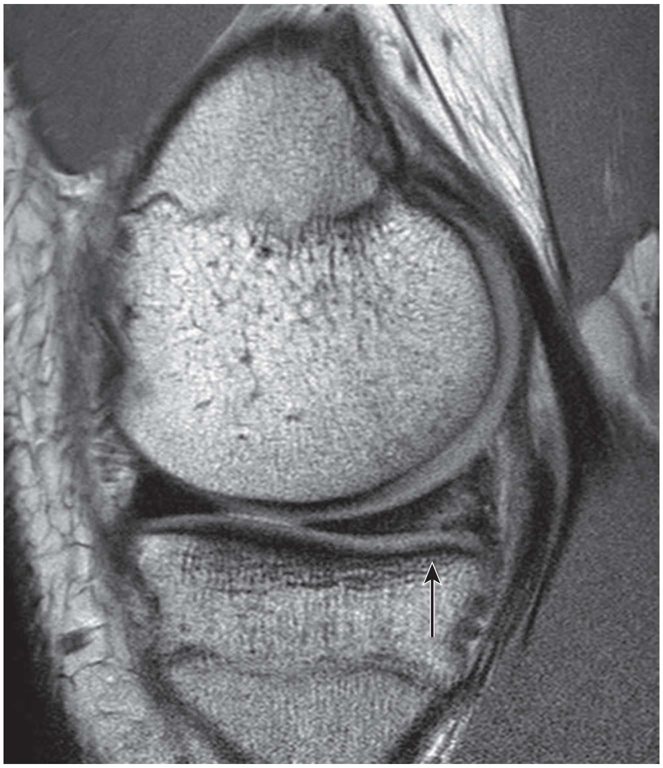

**e-Figure 144.25. Vertical tear of the posterior horn of the medial meniscus in a 16-year-old boy *(arrow)*.**

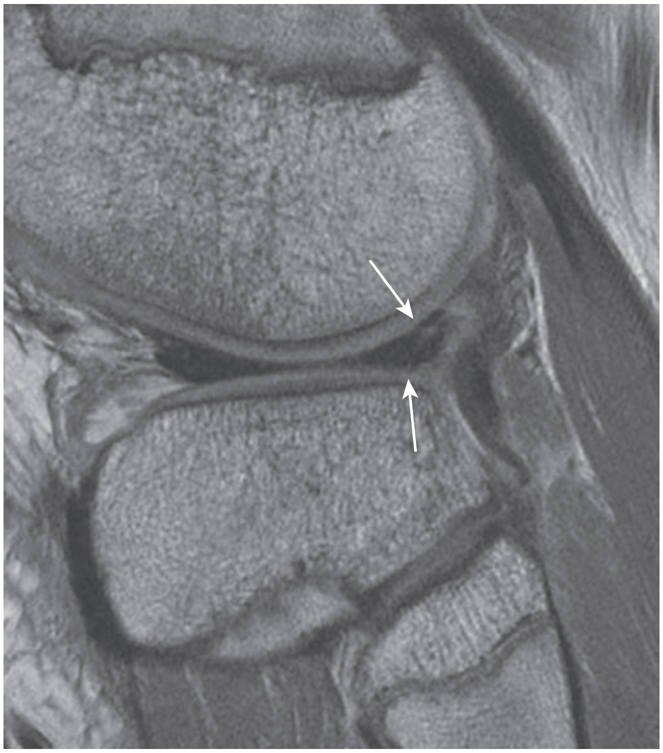

**e-Figure 144.24. Peripheral vertical tear of the posterior horn of the lateral meniscus in a 14-year-old boy *(arrows)*.** This should be distinguished from the meniscofemoral ligament that can simulate a tear because of its superior sulcus. Meniscofemoral sulci should only involve the peripheral aspect of the superior articular surface of the posterior horn of the lateral meniscus.

occurs after initial injury. Surgical treatment for complete ACL tears includes tibial eminence repairs and various types of ACL reconstruction surgeries including physeal sparing, transepiphyseal, and transphyseal approaches. Boys over age 16 years, girls age 14 years or older, or those at Tanner stage 5 with closed or near closed physes may be treated with conventional adult methods for ACL reconstruction.[21] MRI is important presurgically to identify not only the ACL injury but also additional meniscal and cartilage injuries so that these areas can be repaired or débrided during ACL reconstruction.

## DISCOID LATERAL MENISCUS

***Etiology.*** Discoid menisci most frequently affect the lateral meniscus. This represents a congenital enlargement of the lateral meniscus with respect to the lateral tibiofemoral joint compartment. The relative disproportionate size of the lateral meniscus alters the biomechanics of the lateral tibiofemoral compartment, and the meniscus is predisposed to tears and degeneration. The utilization of approximate coverage of the lateral joint space is preferred compared with reference measurement of meniscal size in children. Using the adult reference of 12 mm width for normal meniscal size may be inaccurate in children, particularly in preschoolers who present with suspected discoid lateral menisci.[22]

The Watanabe arthroscopic classification of discoid lateral menisci includes (1) complete, (2) incomplete, and (3) Wrisberg variant.[23] The Wrisberg variant is a discoid meniscus with absence of normal posterior meniscocapsular fascicles and coronary ligaments, with the meniscofemoral ligament being the only attachment.[24] Type 1 and 2 discoid lateral menisci are usually stable, and type 3 is unstable because of its lack of posterolateral meniscocapsular attachment.

***Imaging.*** Radiographs may show relative widening of the lateral tibiofemoral joint space in the setting of a discoid lateral meniscus. However, radiographs are not adequate to suggest or exclude the diagnosis, as the lateral joint space may be artifactually widened by patient positioning or weight-bearing status.

MRI is the optimal method for diagnosing a discoid lateral meniscus. All three orthogonal planes should be used to determine size of the lateral meniscus and degree of coverage of the lateral tibiofemoral joint compartment. When a discoid lateral meniscus is present, it can be partial (e-Fig. 144.27), complete (Fig. 144.28), or a Wrisberg variant. Counting sagittal slices to determine meniscal size is not useful, as no meniscal size references are available for children. The Wrisberg variant may be suggested when normal posterior meniscocapsular fascicles and coronary ligaments are absent, independent of the size and shape of the lateral meniscus.

It is important to describe the discoid lateral meniscus morphology, including presence or absence of tears or degeneration, and the nature of the discoid morphology. Discoid lateral meniscus may be uniformly enlarged or may be asymmetrically enlarged with a dominant posterior, midbody, or anterior horn.[24]

***Treatment and Follow-up.*** Asymptomatic discoid lateral meniscus may be observed; however, the Wrisberg type may be treated preemptively due to its inherent instability. Treatment of symptomatic discoid lateral meniscus is surgical. Discoid lateral menisci are usually trimmed and saucerized to conform to the expected normal size and shape of the lateral meniscus and any tears are repaired. Tears are débrided and trimmed until a stable margin is created. Wrisberg-type discoid menisci may be treated with reduction and posterior fixation.

## OSTEOCHONDRAL INJURIES

***Etiology.*** Osteochondral lesions represent a broad spectrum of acute or chronic injuries with variable involvement of the articular and epiphyseal cartilage, spherical growth plate, and epiphyseal ossification center. Osteochondral lesions are separated into two basic lesions: (1) acute osteochondral fractures and (2) osteochondritis dissecans (OCD). OCD results from chronic repetitive injury.

OCD has juvenile and adult types.[25] Juvenile OCD tends to involve epiphyseal and spherical growth plates with either growth disturbance or injury to the epiphyseal ossification center. These have a greater tendency for spontaneously healing than adult types. Adult OCD affects articular cartilage and the epiphyseal bone. These lesions occur when the epiphyseal ossification is mature and usually only articular cartilage remains; they less commonly heal spontaneously and are more likely to be unstable compared with the juvenile variant.

Osteochondritis dissecans most commonly affects the knee but also can occur in the ankle and elbow (Table 144.1). These locations often have different prognostic significance, symptoms, and underlying etiology. For instance, OCDs of the talus tends to be asymptomatic and incidentally noted when the medial talar dome is involved, whereas lateral talar dome lesions tend to be symptomatic. At the elbow, capitellar OCDs are often seen in

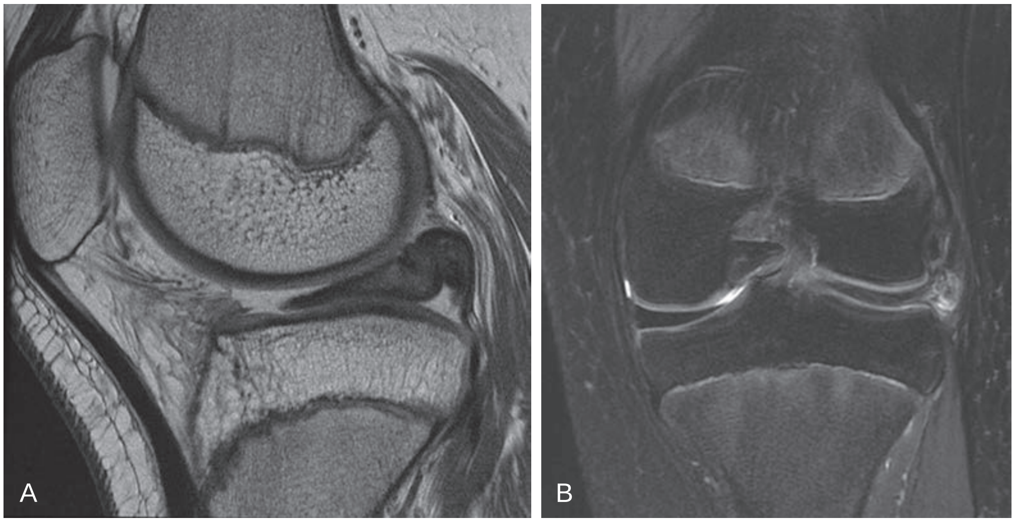

**Figure 144.28. Complete discoid lateral meniscus in a 14-year-old boy.** (A) Proton density sagittal and (B) proton density fat-saturated coronal MR images show a discoid lateral meniscus with a capsular tear and posterior subluxation.

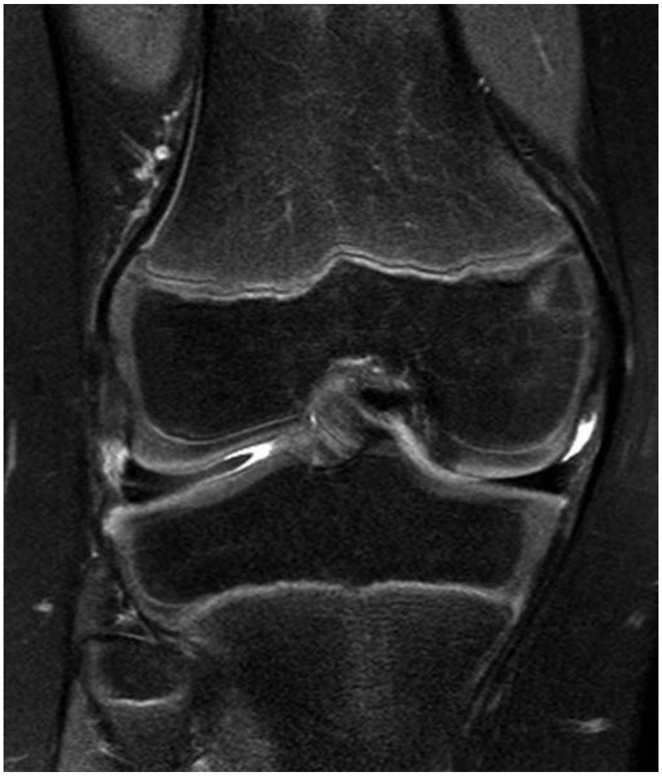

**e-Figure 144.27. Partial discoid lateral meniscus in a 6-year-old boy.** Notice how the free edge of the meniscus tapers toward the intercondylar notch, making this a partial discoid meniscus.

throwing athletes. Because of repetitive valgus loading of the elbow, capitellar OCDs occur related to repetitive compressive forces of the radial head abutting the capitellum in the lateral elbow compartment.

Osteochondral lesions may also occur as a secondary process when the underlying epiphyseal bone is abnormal, as can be seen in the setting of Perthes disease (e-Fig. 144.29).

***Imaging.*** Radiography is typically the first line of imaging for osteochondral lesions. However, MRI is more sensitive and provides a more detailed evaluation. In OCD, subchondral fragmentation may be seen (Fig. 144.30). Tunnel views are important in the evaluation of OCDs of the knee, but these can be misleading, as they delineate the posterior femoral condylar area in which normal femoral condylar irregularities are often seen (Fig. 144.31).

MRI is the optimal method for imaging osteochondral injuries. Noncontrast images are usually sufficient, and intraarticularly administered contrast agent is not necessary in most cases when MRI studies are performed using dedicated coils and on a high field magnet.

Acute chondral or osteochondral fractures are classified as partial (Fig. 144.32), full-thickness (Fig. 144.33), or delamination injuries (Fig. 144.34). When only cartilage is involved, these should technically be referred to as *acute chondral fractures* (see Fig. 144.32). The presence or absence of a chondral or osteochondral intraarticular bodies should be documented when reporting an osteochondral injury.

**TABLE 144.1** Common Locations for Osteochondritis Dissecans

| Location | Most Common | Less Common |
|---|---|---|
| Elbow | Capitellum | Radial head |
| Knee | Lateral aspect of the medial femoral condyle | Lateral femoral condyle, trochlear fossa, patella |
| Ankle | Medial talar dome | Lateral talar dome, midtalar dome |

Osteochondritis dissecans are classified as unstable (Fig. 144.35) or stable (Fig. 144.36). Criteria for instability are different when assessing juvenile (those seen in skeletally immature children with open physes) and adult types of OCDs. MRI findings with high specificity for instability of juvenile OCDs include: fluid signal

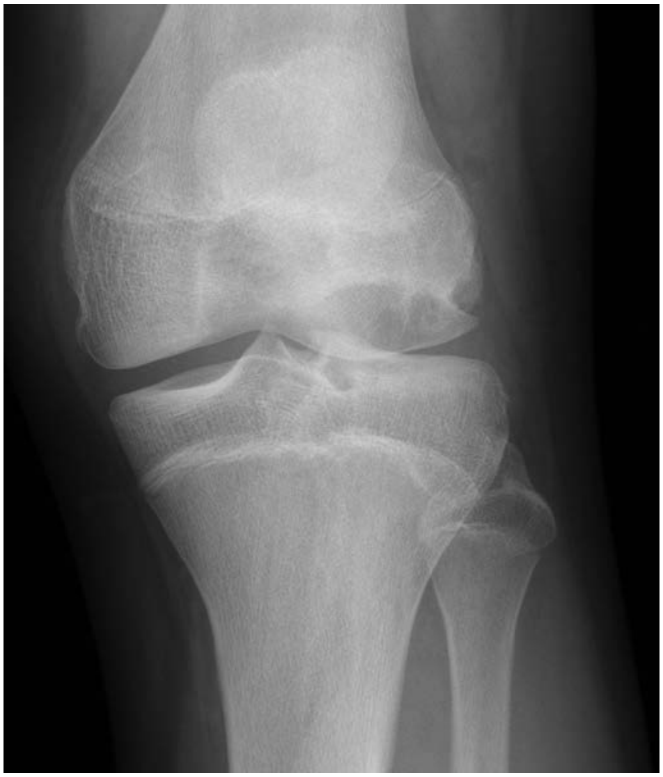

**Figure 144.30. Osteochondritis dissecans (OCD) of the lateral femoral condyle.** Anteroposterior radiograph of the knee in a 16-year-old shows a large OCD lesion.

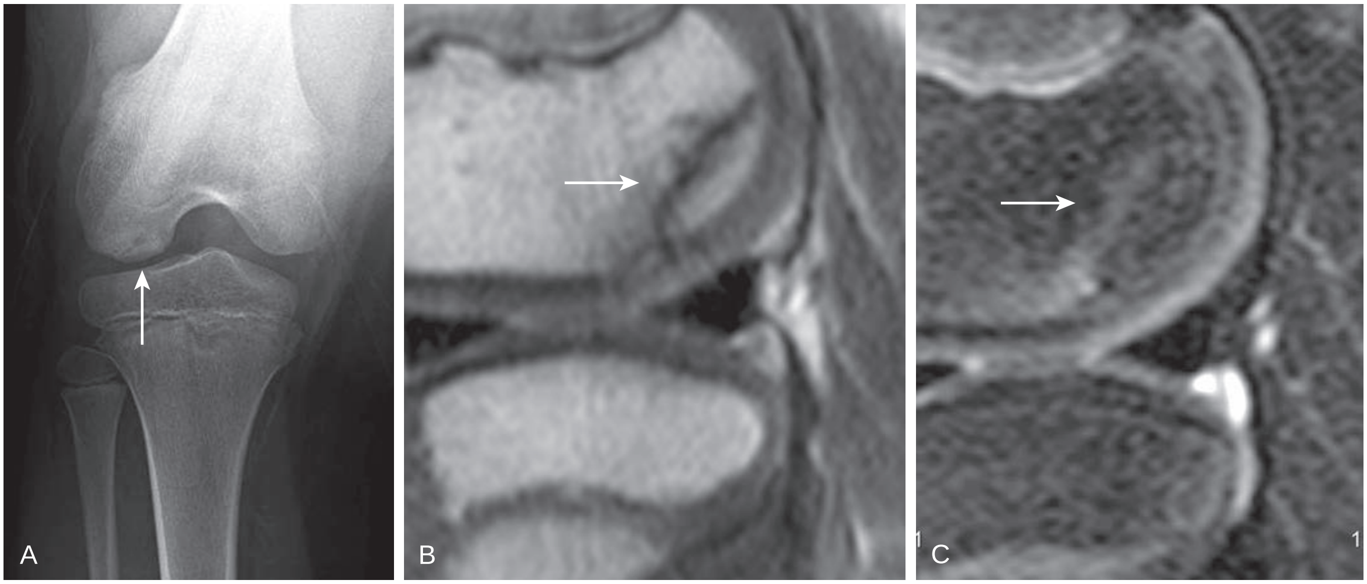

**Figure 144.31. Normal femoral condylar irregularity in a 10-year-old boy.** (A) Tunnel view radiograph demonstrates lateral femoral condylar irregularities *(arrow)*. (B) Proton density sagittal MR image and (C) T2-weighted fat-suppressed sagittal MR image demonstrates subchondral semilunar sharp demarcation between the condylar irregularity and epiphyseal parent bone *(arrow)*. Because substantial edema of the subchondral irregularity is not present and because the overlying articular cartilage and spherical growth plate are intact, this is considered a normal finding, not osteochondritis dissecans.

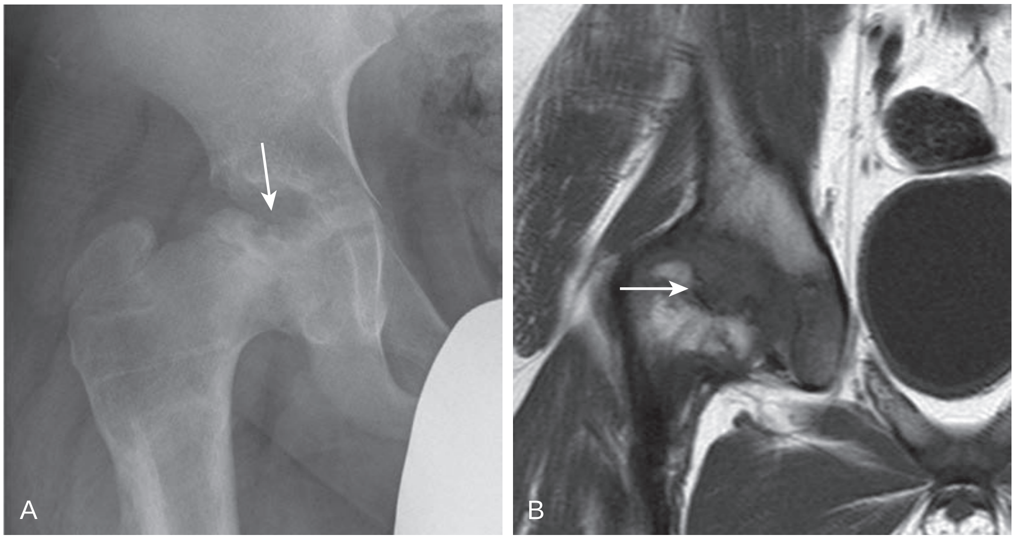

**e-Figure 144.29. Perthes disease in a 9-year-old girl.** (A) Anteroposterior hip radiograph and (B) T1-weighted coronal MR image demonstrates a large central osteochondral lesion *(arrows)* along the weight-bearing portion of the capital femoral epiphysis related to Perthes disease.

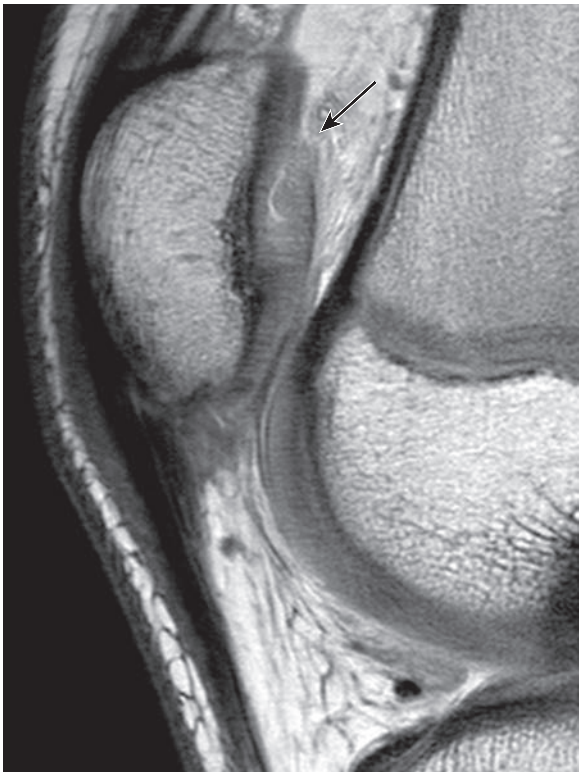

**Figure 144.32.** Acute partial thickness cartilage injury *(arrow)* of the patella on a proton density sagittal MR image.

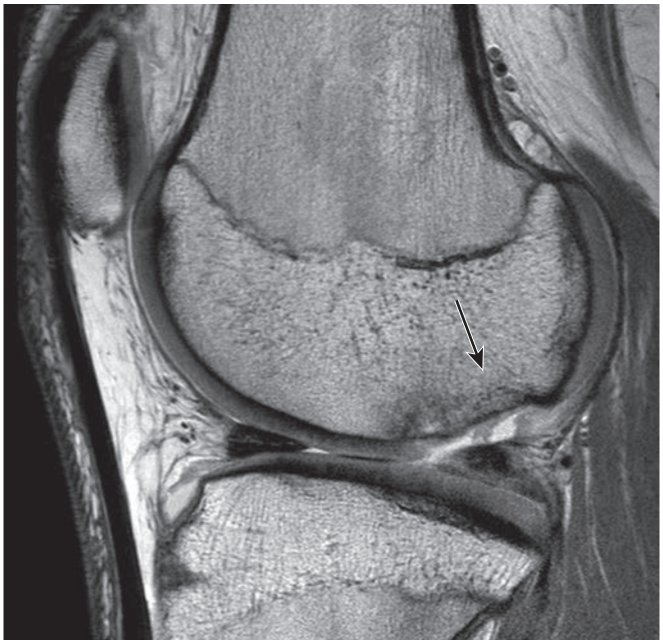

**Figure 144.33.** Full thickness cartilage injury *(arrow)* of the lateral femoral condyle with subchondral bone involvement on a proton density sagittal MR image.

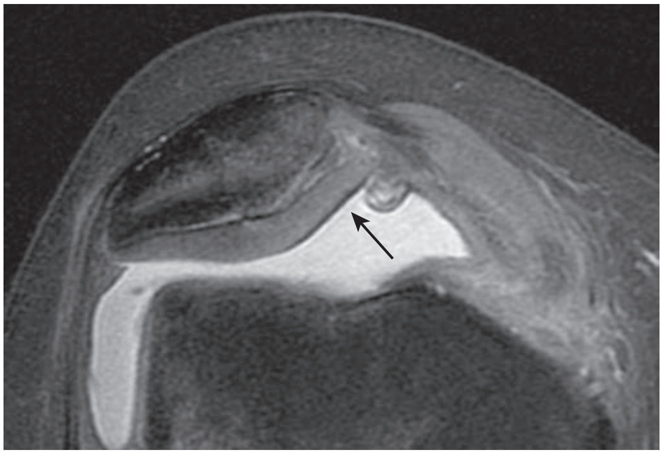

**Figure 144.34.** Delamination injury of the medial patella facet *(arrow)* secondary to a prior lateral patellar dislocation on a proton density fat-suppressed axial MR image.

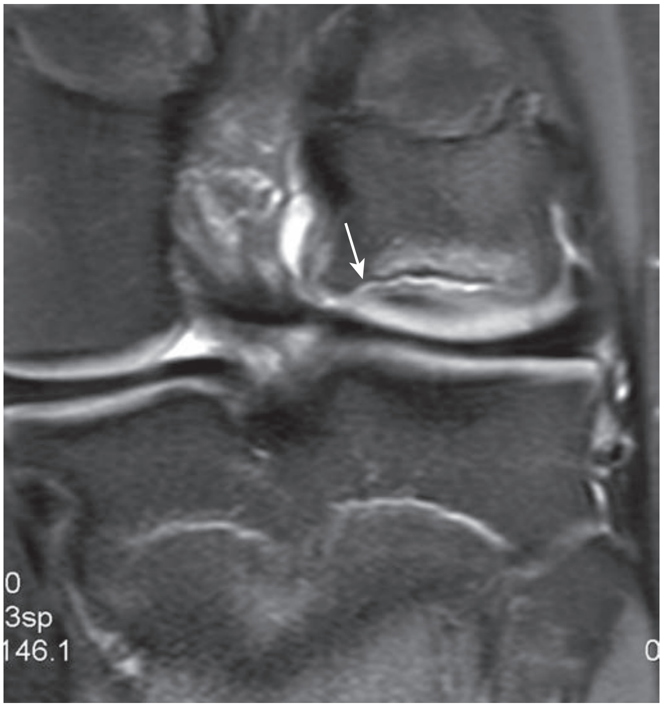

**Figure 144.35. Unstable lateral femoral condylar osteochondritis dissecans in a 14-year-old boy.** Proton density fat-suppressed coronal MR image demonstrates fluid signal insinuating between the parent bone and osteochondral fragment *(arrow)*.

deep to the lesion (Fig. 144.35), a junctional cyst >5 mm or multiple cysts, multiple breaks in the subchondral bone plate on T2-weighted images, articular cartilage fracture lines on T2-weighted images, a rim of low T2 signal intensity deep to a hyperintense rim, a fluid-filled osteochondral cavity, and intraarticular bodies.[26] Unlike adult type OCDs, single cysts smaller than 5 mm and increased signal on T2-weighted images that is not isointense to fluid alone are not specific for instability in juvenile OCDs. This difference is likely due to the greater ability of juvenile OCD lesions to heal with conservative measures, which in turn is likely because the spherical growth plate remains open in these skeletally immature children. Fat-suppressed T1-weighted gradient echo sequences can be helpful in differentiating marrow edema (hypointense signal intensity) from fibrovascular tissue (hyperintense signal intensity), which may have prognostic and treatment implications.[27]

Osteochondritis dissecans should be differentiated from normal condylar fragmentation, which is usually identified along the far

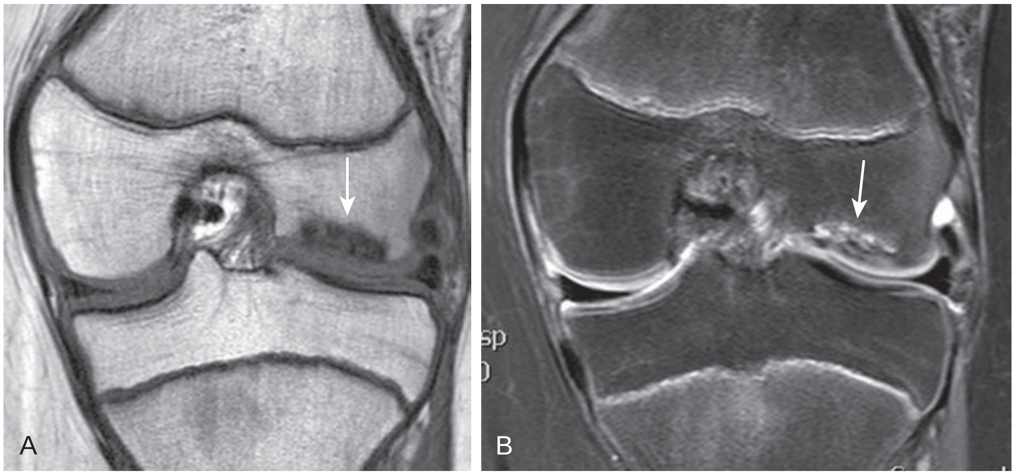

**Figure 144.36. Stable lateral femoral condylar osteochondritis dissecans in a 13-year-old boy.** (A) T1-weighted coronal and (B) proton density fat-suppressed coronal MR image demonstrates a well-demarcated osteochondritis dissecans with edema-like signal deep to the lesion *(arrow)*, but no fluid intensity signal was present deep to the lesion and no other MRI findings of instability were present.

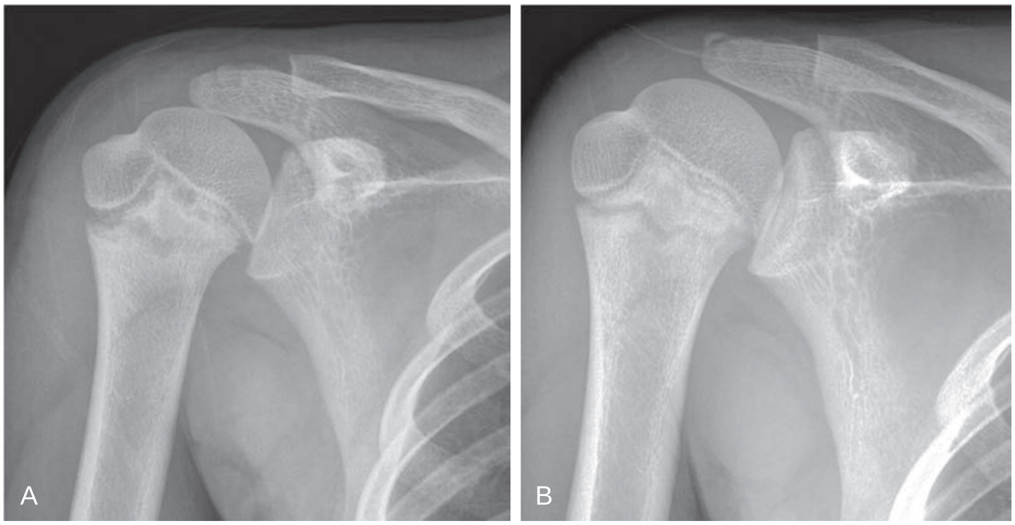

**Figure 144.37. "Little League" shoulder in a 12-year-old.** (A) Anteroposterior radiograph at presentation demonstrates proximal humeral physeal widening and metaphyseal fraying. (B) Anteroposterior radiograph 3 months later shows resolution with rest.

posterior, nonweight-bearing portion of the femoral condyles (see Fig. 144.31).

***Treatment.*** Nonsurgical therapy is recommended when imaging features suggest stability. OCDs in patients with an open physis are more likely to heal spontaneously, compared with osteochondritis dissecans in older children with closing or closed physis.[25] Surgical management of unstable OCDs includes arthroscopic drilling or microfracture methods to improve blood supply and healing, removal of any potential loose bodies, autologous osteochondral plugs, and autologous chondrocyte implantation.[25]

## THROWING INJURIES

***Etiology.*** "Little league shoulder" is an overuse injury that may occur with throwing activities, leading to a chronic Salter-Harris I injury of the proximal humerus.[28] This physeal injury occurs related to rotational torque created during throwing.

Little league elbow represents a constellation of medial and lateral compartment soft tissue, cartilage, and bone injuries related to throwing. With overhead throwing, repetitive elbow valgus stress occurs and causes tensile forces along the medial joint line and compressive forces along the lateral joint line. Along the medial joint line, this results in medial epicondylar apophysitis and medial epicondylar avulsion fractures in younger children, and anterior band ulnar collateral ligament injuries in adolescents who are skeletally mature.[29] Along the lateral joint line, repetitive compressive forces lead to osteochondral lesions of the capitellum, and less frequently osteochondral lesions of the radial head. In younger children, Panner disease of the capitellum may result, rather than discrete osteochondral lesions.

***Imaging.*** Radiographs of little league shoulder manifests with proximal physeal widening, juxtaphyseal metaphyseal fraying (Fig. 144.37), or proximal humeral metaphyseal periostitis. Imaging the contralateral asymptomatic shoulder may be necessary when the only finding present is physeal widening. This should be differentiated from physiologic proximal humeral physeal widening related to growth spurts. Physiologic proximal humeral physeal widening should be bilateral and symmetric.

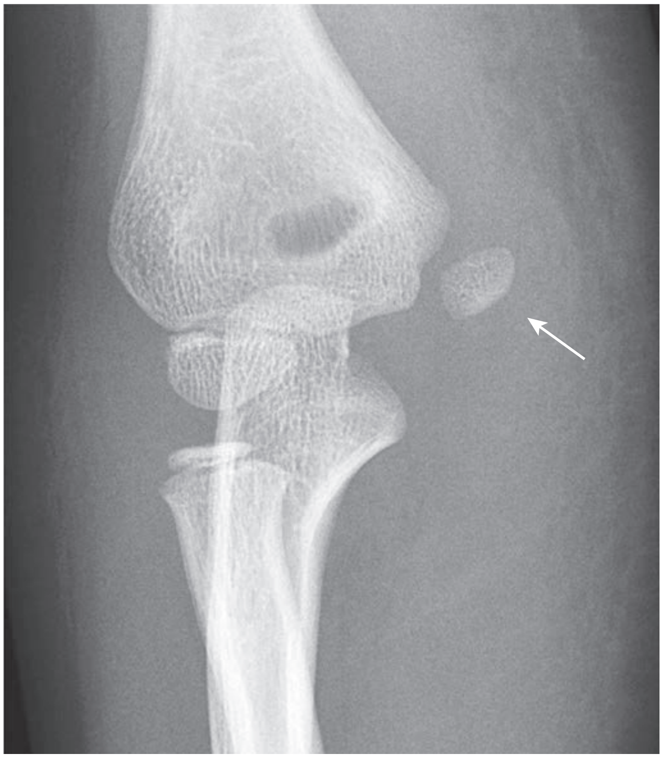

Figure 144.38. Medial epicondylar avulsion fracture in a 5-year-old girl *(arrow)*.

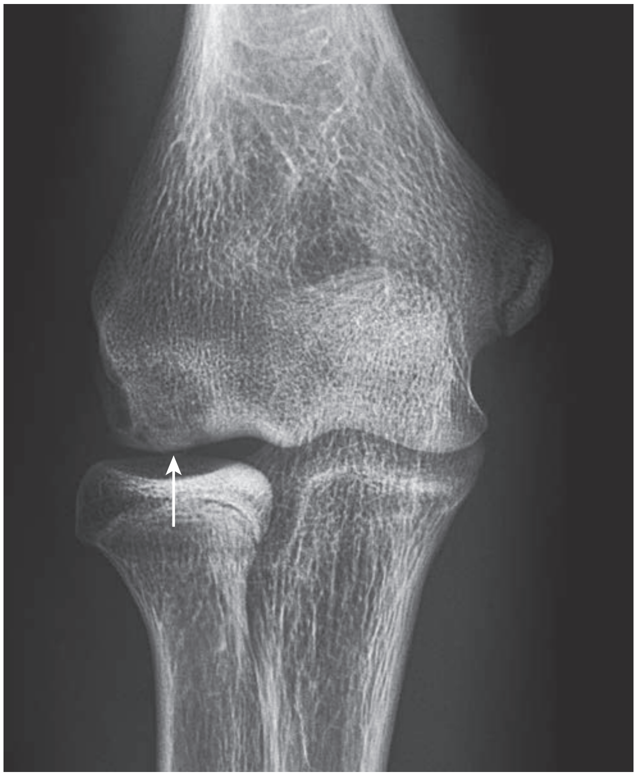

**Figure 144.40. Capitellar osteochondritis dissecans in a 14-year-old boy.** Frontal radiograph shows subchondral lucency and irregularity *(arrow)*.

Radiographic findings related to throwing injuries of the elbow include medial epicondylar avulsion fractures (Fig. 144.38). The avulsion injury may alternatively occur at the level of the chondro-osseous junction of the medial epicondyle with an intact medial epicondylar physeal equivalent region (e-Fig. 144.39). Radiographic features of capitellar osteochondritis dissecans include subchondral lucency (Fig. 144.40), fragmentation, and intraarticular loose bodies.

When radiographs are negative for medial epicondylar avulsion fractures, MRI may be helpful for evaluation of medial epicondylar pain. On MRI, marrow edema may be seen in the medial epicondyle and adjacent soft tissue. In adolescents who are skeletally mature, common flexor tendon tears and ulnar collateral ligament tears are more commonly seen. The most common ligament that is torn is the anterior band of the ulnar collateral ligament (e-Fig. 144.41), which is best evaluated by magnetic resonance arthrography. The most common location of anterior band ulnar collateral ligament tears is at its insertion on the sublime tubercle of the ulna.

Panner disease is seen in younger children compared with patients with osteochondritis dissecans and presents with diffuse sclerosis and fragmentation of the capitellum, with diffuse marrow edema seen on MRI.

***Treatment.*** Little league shoulder is treated nonsurgically with rest and activity modification.[28] Elbow medial epicondylitis and Panner disease are also treated conservatively. Medial epicondylar avulsion fractures are surgically reduced if greater than 5 mm displacement exists. Anterior band ulnar collateral ligament tears are treated conservatively in most instances. In high-level athletes, reconstruction with tendon autograft may be performed.[29] Osteochondritis dissecans of the capitellum are surgically treated if MRI features of instability are present.

## INTERNAL DERANGEMENT OF THE HIP

***Etiology.*** *Femoroacetabular impingement* describes a constellation of femoral head or acetabular anatomic deformities causing hip joint incongruity that may lead to early osteoarthritis and labral tears. Femoral-sided deformities are classified as *cam-type impingement*, and acetabular-sided deformities are classified as *pincer-type impingement*. Both cam- and pincer-type impingements coexist in patients 86% of the time.[30]

The diagnosis of femoroacetabular impingement is controversial, as many patients may have the anatomic deformity present and yet be asymptomatic.[31,32] The diagnosis may be suggested when positive clinical symptoms such as pain with hip flexion and hip internal rotation, as well as imaging findings of femoroacetabular impingement are present.

Common etiologies for cam-type femoroacetabular impingement in children include Perthes disease and slipped capital femoral epiphysis (SCFE).[33] Perthes disease may lead to a primary cam-type femoroacetabular impingement because the femoral head becomes aspherical. A secondary pincer-type femoroacetabular impingement may occur because the acetabulum is relatively too large compared with the aspherical small femoral head. SCFE may also lead to an abnormal femoral head–neck offset with a cam-type femoroacetabular bump, which may impinge on the labral acetabular rim, leading to labral tears and acetabular chondral injuries. In more severe cases, a “pistol grip” deformity (loss of the normal concavity of the lateral femoral neck) may occur.

Etiologies that may cause a pincer-type impingement include acetabular retroversion, sequelae of inflammatory arthritis, and acetabular protrusio deformity. *Acetabular version* describes the orientation of the acetabular cup, which is normally mildly anteverted. *Acetabular retroversion* describes a posteriorly oriented acetabular cup and can cause a pincer-type impingement due to anterosuperior overcoverage of the femoral head. Acetabular retroversion may be congenital or secondary as a developmental alteration caused by femoral head deformities (a congruent normal femoral head is necessary to develop a normal acetabulum, and

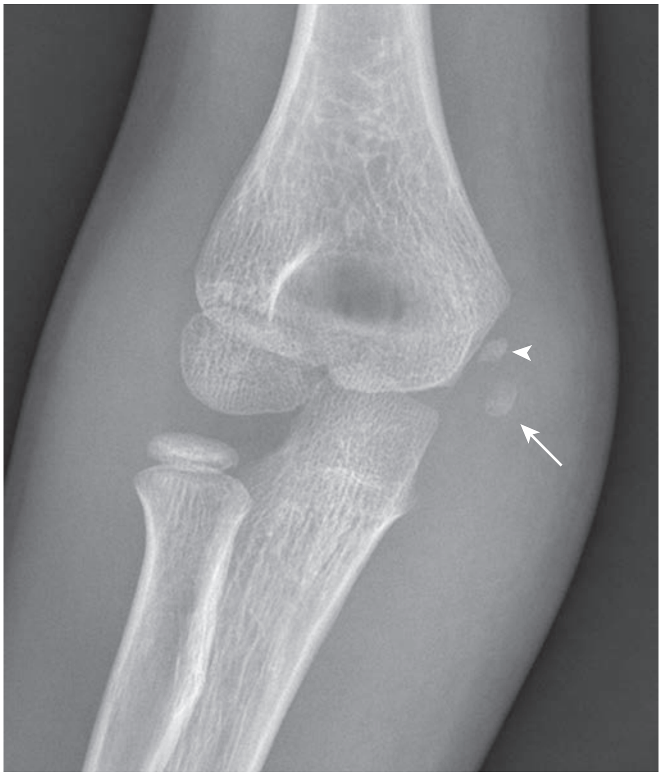

**e-Figure 144.39. Medial epicondylar chondro-osseous avulsion fracture in an 8-year-old boy.** Frontal radiograph shows that when the medial epicondylar ossification center is disrupted, both an *in situ* portion of the epicondyle *(arrowhead)* and an avulsed fragment *(arrow)* are seen.

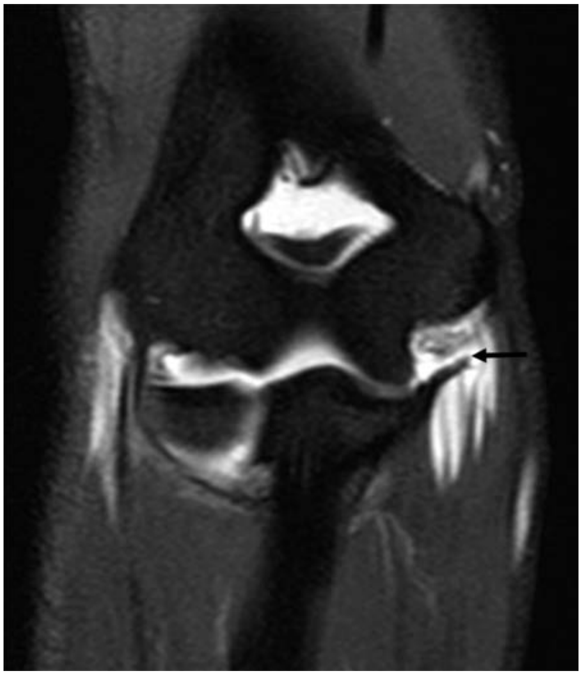

**e-Figure 144.41. Complete tear of the anterior band of the ulnar collateral ligament in a 16-year-old wrestler.** MR arthrogram demonstrates full thickness disruption of the midportion of the anterior band fibers *(arrow)*.

vice versa). Inflammatory arthritis may cause concentric narrowing of the joint, which leads to a pincer-type deformity from relative overcoverage of the femoral head. In the setting of inflammatory arthritis with uniform decreased joint space, less space is available for the femoral head to clear during hip motion. Acetabular protrusio deformity, which may also result from inflammatory arthritis, similarly leads to overcoverage of the femoral head, which causes a pincer-type deformity.

Developmental dysplasia of the hip (DDH) may cause a pincer-type impingement, cam-type impingement, or a combination of both. Cam-type femoroacetabular impingement results from a size mismatch between a small dysplastic acetabular cup and relatively large femoral head (Fig. 144.42). Subtrochanter varus osteotomy to relocate the hip may further exacerbate a cam-type impingement. Alternatively, periacetabular osteotomies such as a Salter osteotomy may increase the acetabular coverage, resulting in a pincer-type deformity.

***Imaging.*** Radiographic findings suggesting cam-type femoroacetabular impingement include insufficient offset at the femoral head–neck junction (Fig. 144.43), coxa vara, and femoral retroversion. On MRI, anterosuperior labral tears are most frequently related to cam-type femoroacetabular deformities (Fig. 144.44). More obvious deformities leading to cam-type femoroacetabular impingement include Perthes disease (e-Fig. 144.45) and DDH (see Fig. 144.42). Labral tears are best assessed with magnetic resonance arthrography.

On MRI or CT, an alpha-angle may be used to calculate the degree of femoral head deformity related to a cam-type deformity. The normal alpha-angle is less than 55 degrees. The alpha-angle is calculated by doing the following:

1. Drawing a best-fit circle around the femoral head outlining the cortical margin.
2. Drawing a line from the center of the circle parallel to the femoral neck.

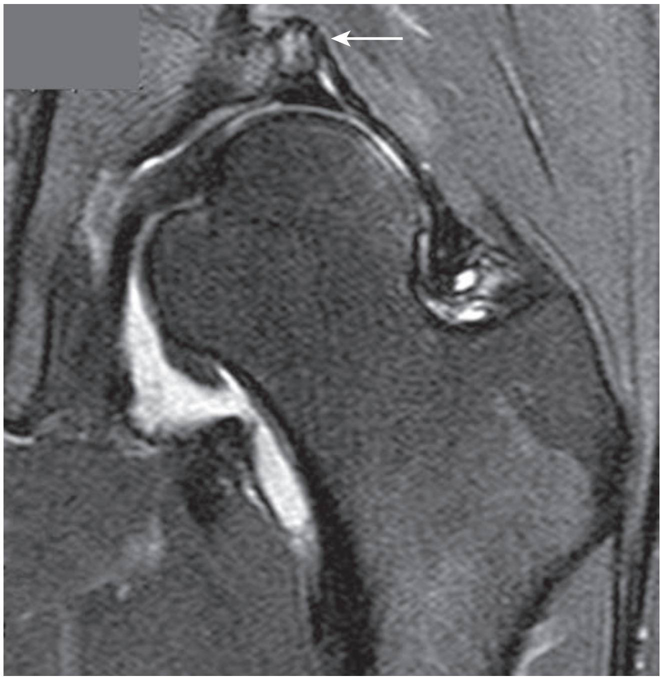

**Figure 144.42. Untreated developmental dysplasia of the left hip in a 19-year-old girl.** T2-weighted fat-suppressed coronal MR image demonstrates size mismatch of relatively large femoral head and small acetabular fossa leading to cam-type impingement with resultant early labral degeneration and a chronic acetabular rim fragment *(arrow)*.

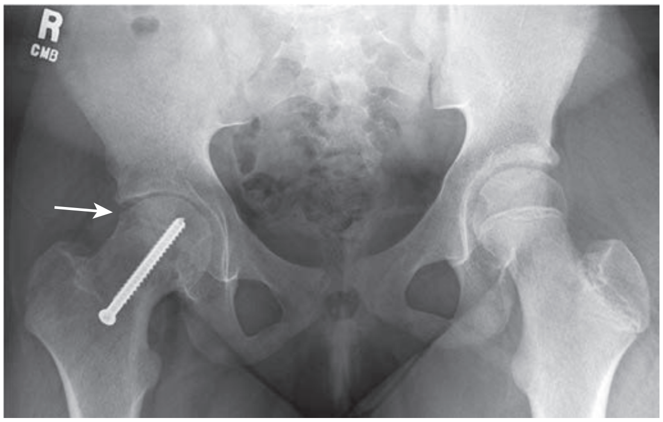

**Figure 144.43. Femoroacetabular impingement after slipped capital femoral epiphysis in a 10-year-old girl.** Frontal radiograph shows a right-sided healed slipped capital femoral epiphysis with idiopathic chondrolysis and development of a junctional osteophyte *(arrow)*, with resultant mixed cam-type and pincer-type femoroacetabular impingement.

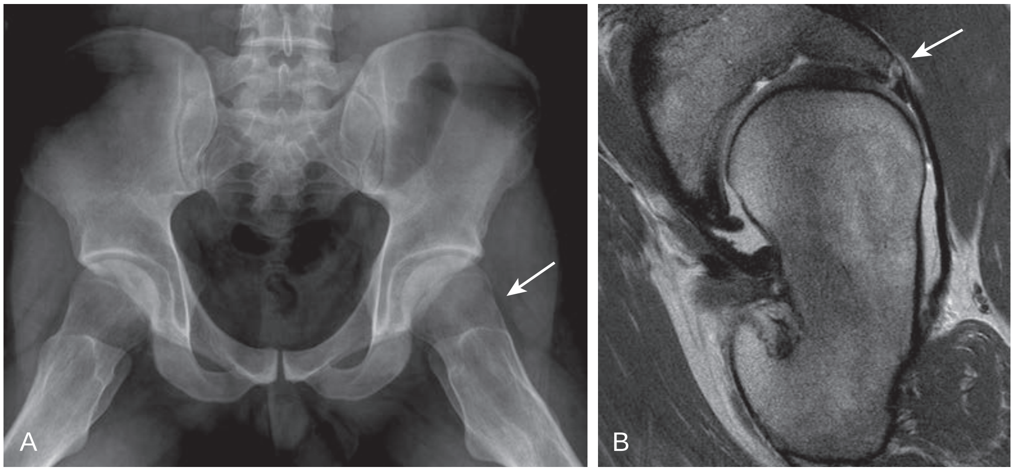

**Figure 144.44. Femoroacetabular impingement.** (A) Frog-leg lateral radiograph shows cam-type femoroacetabular impingement with pistol-grip deformity and loss of normal femoral head–neck offset *(arrow)*. (B) Proton density radial MR image again shows loss of femoral head-neck offset and a anterosuperior labral tear *(arrow)*.

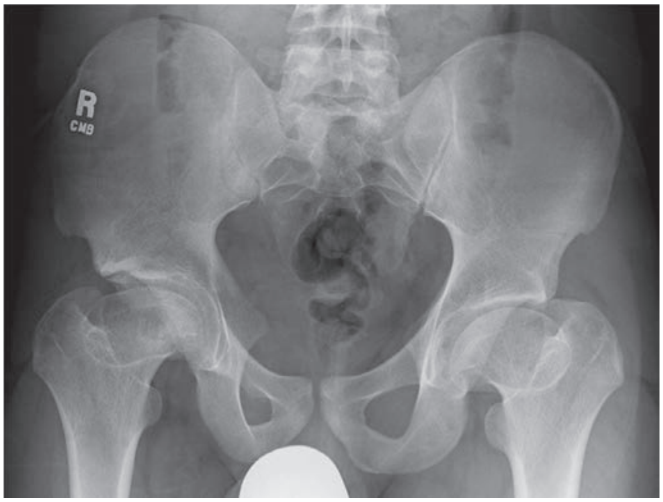

**e-Figure 144.45. Sequela of bilateral Perthes disease in an 18-year-old male.** Frontal pelvis radiograph shows bilateral cam-type femoroacetabular impingement caused by flattened, aspherical femoral heads, loss of the normal femoral head–neck offset, and lateral femoral neck concavity bilaterally.

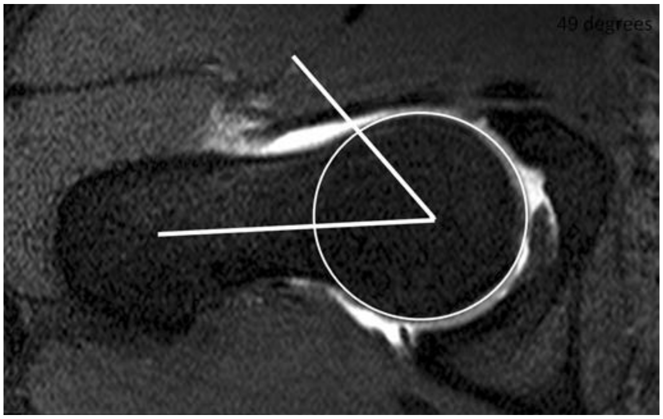

**Figure 144.46. Alpha-angle calculation.** Oblique axial T1-weighted fat-suppressed MR arthrogram image demonstrating lines for calculating the alpha-angle.

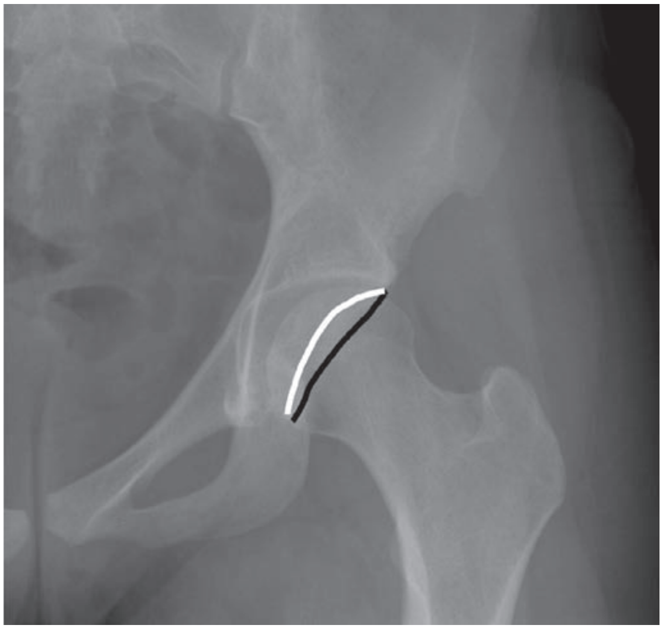

**Figure 144.47. Normal hip showing the no cross-over sign.** Anteroposterior radiograph of the hip: the *white line* represents the anterior acetabular wall, the *black line* represents the posterior acetabular wall.

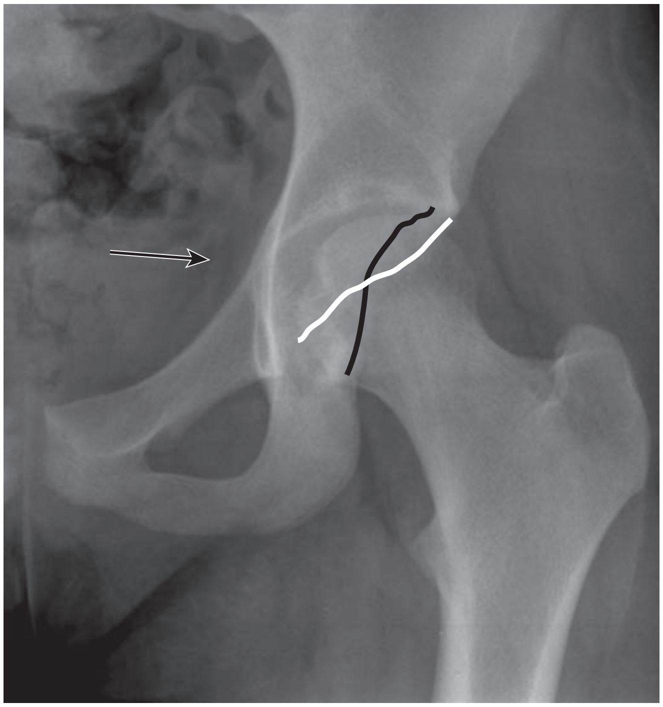

**Figure 144.48. Acetabular retroversion and cross-over sign.** Anteroposterior radiograph of the hip: the white line represents the anterior acetabular wall, the black line represents the posterior acetabular wall. Note the ischial spine sign is present as well *(arrow)*, an additional indicator of a pincer deformity.

3. Drawing a line from the center of the circle to where the femoral head or neck protrudes from the circle.
4. Calculating an angle between lines created from items 2 and 3 (Fig. 144.46).

Radiographic findings associated with pincer-type femoroacetabular impingement include the cross-over sign (Figs. 144.47 and 144.48), a lateral center edge angle greater than 29 degrees (e-Fig. 144.49), prominent posterior wall, coxa profunda, protrusio acetabuli, and ischial spine sign.[30,34] On frontal radiographs of the pelvis, the anterior acetabular wall is normally more medial with respect to the posterior acetabular wall (see Fig. 144.47) and they should meet at the superolateral margin of the sourcil. The cross-over sign occurs when the anterior and posterior acetabular wall lines intersect, indicative of acetabular retroversion (see Fig. 144.48). This should be evaluated for an appropriately positioned frontal view of the pelvis, as obliquity and pelvic tilt may cause an artifactual cross-over sign. The normal acetabulum is usually in 19 degrees of anteversion in adult patients.[35] With acetabular retroversion, anterior overcoverage of the femoral head occurs. There is little consensus on where in the acetabulum to measure version, therefore it is best to confer with local referring orthopedic surgeons.

***Treatment.*** Treatment is predicated on symptoms, not on the degree of imaging deformity. When surgery is indicated, treatment focuses on removal of the anatomic cause of the impingement to improve acetabular and femoral head congruity so that the acetabulum and the femoral head–neck junction do not abnormally abut during normal range of motion.[36] This includes removing cam-type deformities at the femoral head–neck junction as well as reshaping the femoral head to conform to a spherical shape and addressing any associated labral tears and chondral injuries. For pincer-type femoroacetabular deformity related to acetabular retroversion, a periacetabular rotational osteotomy or acetabuloplasty may be performed to decrease the amount of anterior overcoverage.

## STRESS INJURIES OF BONE

***Etiology.*** A fatigue fracture occurs when supraphysiologic repetitive stress is applied to normal bone. Insufficiency fractures occur when normal stress is applied to abnormal bone.[37] Stress injuries to bone can occur on either the compressive side or the tensile side of bone, leading to trabecular injury. Before fracture, stress changes to bone can include periosteal edema, marrow edema, cortical edema, and microfractures (occult fractures not visible on imaging). With proper training, bone and muscle physiologic adaptation to repetitive stress is protective and may prevent stress reaction and stress fractures to bone.

Risk factors for stress injuries to bone include inadequate or improper athletic training, postpubertal females (female athlete triad: [1] menstrual irregularity, [2] disordered eating, and [3] osteoporosis), and abnormal biophysical geometry of the child such as leg length discrepancies, varus alignment, abnormal femoral version, and pes cavus.[38]

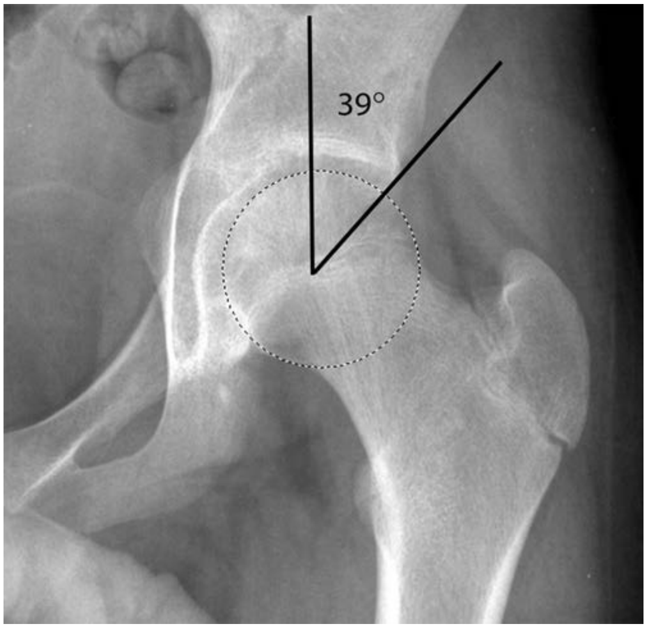

**e-Figure 144.49. Acetabula protrusio in a 12-year-old boy.** Frontal radiograph shows mild protrusio deformity with a lateral center-edge angle measuring approximately 39 degrees. Center-edge angle is the angle between a vertical line drawn through the center of the femoral head and line from the center of the femoral head to the lateral edge of the sourcil.

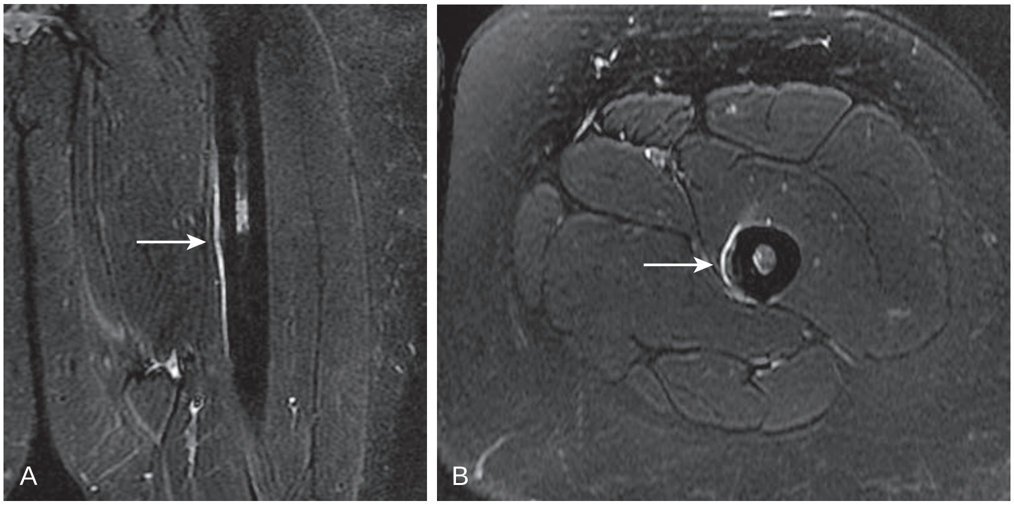

**Figure 144.50. Stress reaction of the femur without discrete fracture in a 16-year-old boy.** Short-tau inversion recovery axial (A) and coronal (B) MR images show periosteal reaction *(arrows)* and endosteal edema.

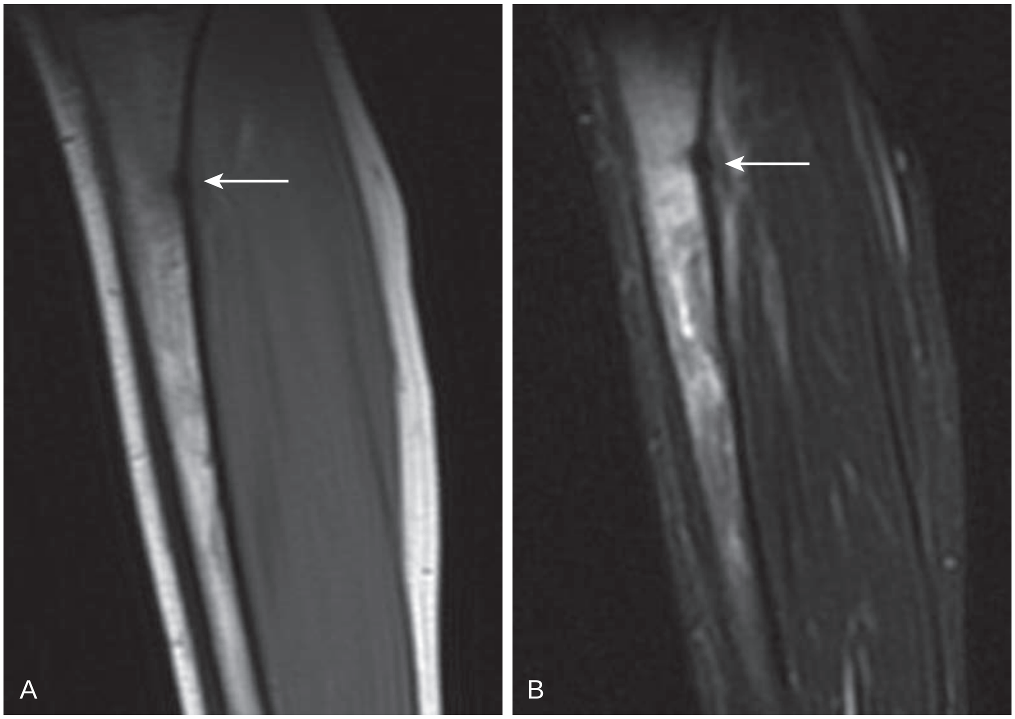

**Figure 144.51. Nondisplaced proximal tibial stress fracture in an 8-year-old boy.** T1-weighted sagittal (A) and short-tau inversion recovery sagittal (B) MR images show abnormal signal *(arrows)*.

Symptoms related to stress fractures are not present at rest but occur with physical activity.[38] *Shin splints*, or *medial tibial stress syndrome*, is a vague term to describe pain that most often occurs over the posteromedial aspect of the distal third of the tibia.[39] Proposed etiologies include muscle attachment inflammation, fascial edema, posterior compartment syndrome, and tibial stress fractures. Because of its nonspecific broad definition, shin splints should be reserved as a clinical diagnosis, not a radiologic diagnosis.

***Imaging.*** With radiography, the spectrum of stress reaction to bone includes normal (most common), periostitis, and discrete fracture. Radiographs are the first line of imaging when suspected fracture is present. MRI is a complementary tool when radiographs are normal.

MRI is indicated when symptoms do not resolve with conservative management or failed physical rehabilitation in the setting of normal radiographs. When radiographs are abnormal, demonstrating a discrete nondisplaced stress fracture, MRI does not add additional value with regard to treatment in most cases. MRI will add value if the fracture has an intraarticular component, may involve the physis, or the fracture is pathologic because of an underlying primary neoplasm of bone.

MRI grading for bone stress injuries includes the spectrum from isolated periosteal edema (Fig. 144.50) to a true fracture (Fig. 144.51) (Table 144.2).[38] MRI may also suggest alternative soft tissue etiologies for symptoms such as muscle tears or DOMS.

**TABLE 144.2** Magnetic Resonance Grading of Stress Injuries to Bone

| Grade | T2 | T1 |
|---|---|---|
| 0 | Normal | Normal |
| 1 | Periosteal edema, no marrow edema | Normal |
| 2 | Periosteal edema, marrow edema | Normal |
| 3 | Periosteal edema, marrow edema | Periosteal edema, marrow edema |
| 4 | Fracture line present | Fracture line present |

*Adapted from Fredericson M, Jennings F, Beaulieu C, et al. Stress fractures in athletes.* Top Magn Reson Imaging. *2006;17(5):309–325.*

***Treatment.*** Treatment will vary, depending on location of fractures and symptoms. For nondisplaced stress fractures, treatment includes local pain control, including physical therapy and nonsteroidal antiinflammatory drugs. Weight-bearing for normal activities is allowed. Eventually, return to athletic activity may begin if the child is pain free for 10 to 14 days.[38]

## KEY POINTS

- Pelvic avulsion fractures are usually treated conservatively unless fracture displacement is greater than 2 cm.
- In the setting of lateral patellar dislocation, the presence or absence of underlying patellofemoral dysplasia should always be noted.
- Identification of loose bodies in acute patellar dislocation has more impact on surgical management than identifying bone contusions and medial retinacular injuries.
- The Wrisberg variant of discoid lateral meniscus may occur in the setting of a meniscus of normal size and shape.
- Among throwing athletes, skeletally immature children tend to develop medial epicondylitis and medial epicondylar avulsion fractures, whereas skeletally mature children tend to suffer flexor tendon and ulnar collateral ligament tears.
- Femoroacetabular impingement treatment is predicated on both symptoms and imaging findings. Therefore the imaging diagnosis without supportive clinical symptoms may generate unnecessary orthopedic referrals.

## SUGGESTED READINGS

Braithwaite KA, Marshall KW. The skeletally immature and newly mature throwing athlete. *Radiol Clin North Am*. 2016;54(5):841–855. doi:10.1016/j.rcl.2016.04.006.

Delgado J, Jaramillo D, Chauvin NA. Imaging the injured pediatric athlete: upper extremity. *Radiographics*. 2016;36(6):1672–1687.

O'Dell MC, Jaramillo D, Bancroft L, et al. Imaging of sports-related injuries of the lower extremity in pediatric patients. *Radiographics*. 2016;36(6):1807–1827.

## REFERENCES

Full references for this chapter can be found on www.expertconsult.com.

## REFERENCES

1. Davis KW. Imaging sports injuries: lower extremities. *Radiol Clin North Am*. 2010;48:1213–1235.
2. Ecklund K. Magnetic resonance imaging of pediatric musculoskeletal trauma. *Top Magn Reson Imaging*. 2002;13(4):203–218.
3. Sanders TG, Zlatkin MB. Avulsion injuries of the pelvis. *Semin Musculoskelet Radiol*. 2008;12:42–53.
4. Boutin RD, Fritz RC, Steinbach LS. Imaging of sports-related muscle injuries. *Radiol Clin North Am*. 2002;40:333–362.
5. Cain EL, Dugas JR, Wolf RS, et al. Elbow injuries in throwing athletes: a current concepts review. *Am J Sports Med*. 2003;31(4):621–635.
6. Hoksrud A, Ohberg L, Alfredson H, et al. Color Doppler ultrasound findings in patellar tendinopathy (jumper's knee). *Am J Sports Med*. 2008;36:1813–1820.
7. Gottsegen CJ, Eyer BA, White EA, et al. Avulsion fractures of the knee: imaging findings and clinical significance. *Radiographics*. 2008;28(6):1755–1770.
8. Boden BP, Pearsall AW, Garrett WE, et al. Patellofemoral instability: evaluation and management. *J Am Acad Orthop Surg*. 1997;5(1):47–57.
9. Cameron JC, Saha S. External tibial torsion: an underrecognized cause of recurrent patellar dislocation. *Clin Orthop Relat Res*. 1996;328:177–184.
10. Kristiansen LP, Gunderson RB, Steen H, et al. The normal development of tibial torsion. *Skeletal Radiol*. 2001;30(9):519–522.
11. Malgehm J, Maldague B. Depth insufficiency of the proximal trochlear groove on lateral radiographs of the knee: relation to patellar dislocation. *Radiology*. 1989;170(2):507–510.
12. Dejour H, Walch G, Nove-Josserand L, et al. Factors of patellar instability: an anatomic radiographic study. *Knee Surg Sports Traumatol Arthrosc*. 1994;2(1):19–26.
13. Colvin AC, West RV. Patellar instability. *J Bone Joint Surg Am*. 2008; 90:2751–2762.
14. Koenig JK, Pring ME, Dwek JR. MR evaluation of femoral neck version and tibial torsion. *Pediatr Radiol*. 2012;42:113–115.
15. Prince JS, Laor T, Bean JA. MRI of anterior cruciate ligament injuries and associated findings in the pediatric knee: changes with skeletal maturation. *AJR Am J Roentgenol*. 2005;185:756–762.
16. Milewski MM, Sanders TG, Miller MD. MRI-arthroscopy correlation: the knee. *J Bone Joint Surg Am*. 2011;93(A):1735–1745.
17. Kocher MS, Mandiga R, Klingele K, et al. Anterior cruciate ligament injury versus tibial spine fracture in the skeletally immature knee. *J Pediatr Orthop*. 2004;24(2):185–188.
18. Domzalski M, Grzelak P, Gabos P. Risk factors for anterior cruciate ligament injury in skeletally immature patients: analysis of intercondylar notch width using magnetic resonance imaging. *Int Orthop*. 2010;34:703–707.
19. Coyle C, Jagernauth S, Ramachandran M. Tibial eminence fractures in the paediatric population: a systematic review. *J Child Orthop*. 2014;8(2):149–159.
20. Samora WP, Palmer R, Klingele KE. Meniscal pathology associated with acute anterior cruciate ligament tears in patients with open physes. *J Pediatr Orthop*. 2011;31(3):272–276.
21. Schub D, Saluan P. Anterior cruciate ligament injuries in the young athlete: evaluation and treatment. *Sports Med Arthrosc*. 2011;19(1):34–43.
22. Kelly BT, Green DW. Discoid lateral meniscus in children. *Curr Opin Pediatr*. 2002;14:54–61.
23. Watanabe M, Takada S, Ikeuchi H. *Atlas of arthroscopy*. Tokyo: Igaku-Shoin; 1969.
24. Singh K, Helms CA, Jacobs MT, et al. MRI appearance of Wrisberg variant of discoid lateral meniscus. *AJR Am J Roentgenol*. 2006;187:384–387.
25. Kocher MS, Tucker R, Ganley TJ, et al. Management of osteochondritis dissecans of the knee: current concepts review. *Am J Sports Med*. 2006;34(7):1181–1191.
26. Kijowski R, Blankenbaker DG, Shinki K, et al. Juvenile versus adult osteochondritis dissecans of the knee: appropriate MR imaging criteria for instability. *Radiology*. 2008;248(2):571–578. doi:10.1148/radiol.2482071234. [Epub 2008 Jun 13].
27. Zbojniewicz AM, Stringer KF, Laor T, et al. Juvenile osteochondritis dissecans: correlation between histopathology and MRI. *AJR Am J Roentgenol*. 2015;205:W114–W123.
28. Osbahr DC, Kim HJ, Dugas JR. Little league shoulder. *Curr Opin Pediatr*. 2010;22:35–40.
29. Kijowski R, Tuite MJ. Pediatric throwing injuries of the elbow. *Semin Musculoskelet Radiol*. 2010;14:419–429.
30. Tannast M, Siebenrock KA, Anderson SE. Femoroacetabular impingement: radiographic diagnosis—what the radiologist should know. *AJR Am J Roentgenol*. 2007;188:1540–1552.
31. Jung KA, Restrpo C, Hellman M, et al. The prevalence of cam-type femoroacetabular deformity in asymptomatic adults. *J Bone Joint Surg Br*. 2011;93-B:1303–1307.
32. Laborie LB, Lehmann TG, Engesaeter IO, et al. Prevalence of radiographic findings thought to be associated with femoroacetabular impingement in a population-based cohort of 2081 healthy young adults. *Radiology*. 2011;260:494–502.
33. Kassarjian A, Belzile E. Femoroacetabular impingement: presentation, diagnosis, and management. *Semin Musculoskelet Radiol*. 2008;12(2):136–145.
34. Kalberer F, Sierra RJ, Madan SS, et al. Ischial spine projection into the pelvis: a new sign for acetabular retroversion. *Clin Orthop Relat Res*. 2008;466:677–683.
35. Dandachli W, Ul Islam S, Tippet R, et al. Analysis of acetabular version in the native hip: comparison between 2D axial CT and 3D CT measurements. *Skeletal Radiol*. 2011;40:877–883.
36. Ganz R, Parvizi J, Beck M, et al. Femoroacetabular impingement: a cause for osteoarthritis of the hip. *Clin Orthop Relat Res*. 2003;417:112–120.
37. Navas A, Kassarjian A. Bone marrow changes in stress injuries. *Semin Musculoskelet Radiol*. 2011;15(3):183–197.
38. Fredericson M, Jennings F, Beaulieu C, et al. Stress fractures in athletes. *Top Magn Reson Imaging*. 2006;17(5):309–325.
39. Wilder RP, Sethi S. Overuse injuries: tendinopathies, stress fractures, compartment syndrome, and shin splints. *Clin Sports Med*. 2004;23: 55–81.